Invited review

Recombinant bispecific antibodies for cancer therapy

Roland E KONTERMANN[1]

Institute of Cell Biology and Immunology, University of Stuttgart, Allmandring 31, 70569 Stuttgart, Germany

Key words

antibody engineering; bispecific antibody; diabodies; single-chain diabodies; tandem scFv; targeting; effector cells; cancer therapy

[1] Correspondence to Prof. Roland E KONTERMANN. Phn 49-711-685-6989. Fax 49-711-685-7484.
E-mail Roland.Kontermann@izi.uni-stuttgart.de

Received 2004-11-02
Accepted 2004-11-12

doi: 10.1111/j.1745-7254.2005.00008.x

Abstract

Bispecific antibodies can serve as mediators to retarget effector mechanisms to disease-associated sites. Studies over the past two decades have revealed the potentials but also the limitations of conventional bispecific antibodies. The development of recombinant antibody formats has opened up the possibility of generating bispecific molecules with improved properties. This review summarizes recent developments in the field of recombinant bispecific antibodies and discusses further requirements for clinical development.

Introduction

The concept of using bispecific molecules in therapy is based on the selective recruitment of an effector mechanism to a defined disease-related target structure. Thus, bispecific molecules serve as mediators (adaptors) between an effector and a target. A plethora of effector mechanisms can be envisaged for therapeutic applications and a large number have already been evaluated. These include the recruitment of effector molecules (e.g. toxins, drugs, prodrugs, cytokines, radionuclides), the retargeting of effector cells (e.g. cytotoxic T lymphocytes, NK cells, macrophages, granulocytes) and the retargeting of carrier systems (e.g. viral vectors for gene therapy)[1].

Antibodies are ideally suited as starting material for the construction of bispecific molecules as they normally bind specifically and with high affinity to antigens. Using different technologies, for instance hybridoma or phage display technology, antibodies can be generated against virtually any given antigen. Smaller portions of an antibody retaining antigen-binding activity can be produced by proteolytic cleavage or in recombinant form. Several methods have been developed for the generation of bispecific antibodies. Besides chemical cross-linking of two IgG molecules or two Fab or Fab' fragments, bispecific antibodies can also be produced by fusion of two hybridomas. This hybrid-hybridoma technology results in cell lines (quadroma) that produce bispecific IgG molecules. However, the production and random association of two different heavy chains and two different light chains within one cell leads to the assembly of a substantial proportion of non-functional molecules. Thus, the hybrid-hybridoma technology and also chemical methods produce poorly defined products and require elaborate purification steps to obtain defined and clinically useful material. Nevertheless, several clinical studies have been performed to analyze the therapeutic potentials of bispecific antibodies. Most of these studies were focused on the retargeting of effector cells (cytotoxic T lymphocytes, NK cells) of the immune system to tumor cells. Mostly disappointing findings were obtained from these studies[1,2]. The main reasons were the induction of neutralizing antibodies against the murine bispecific antibodies and Fc-mediated side effects, including cytokine-release syndrome, thrombocytopenia and leukopenia, which limited the maximal applicable dose. Further studies indicate that the induction of inflammation within the tumor, for example, the co-application of inflammatory cytokines, is essential to achieve an effective treatment. It was concluded that besides strong and selective binding to a disease-related antigen clinically useful bispecific antibodies should fulfill several requirements[2]: They should be non-immunogenic to avoid a neutralizing immune response. They should have a defined struc-

ture and should bind monovalently to the effector cells to induce activation of the effector cells only after binding to the target cells. They should not contain an Fc-region to avoid Fc-mediated side effects. They should have a size which allows penetration into the tumor tissue but should circulate sufficiently long to induce therapeutic effects.

Recombinant bispecific antibodies

Recombinant bispecific antibodies offer several advantages over conventional bispecific antibodies made by chemical cross-linking or fusion of two hybridoma clones and can be designed to meet the requirements described above. By using only the variable domains as building blocks, recombinant antibodies lack the Fc-region of an antibody, and thus do not induce Fc-mediated effects. Recombinant antibodies are constructed by genetic means allowing for the generation of human molecules in order to reduce or even avoid the induction of a neutralizing antibody response. Human antibody molecules used as starting blocks can be isolated, for instance, from human antibody libraries by means of phage display[3] or by using transgenic mice expressing human antibodies[4]. Recent studies have shown, however, that even fully human antibodies can be immunogenic leading to the generation of human anti-human antibodies (HAHA)[5]. By identification and removal of the responsible T cell epitopes ("deimmunization") the immunogenicity risk associated with human antibodies can be further reduced[6]. These developments in the generation of recombinant antibody molecules have led to a revival in the use of bispecific antibodies for therapeutic applications[7].

A wide variety of different recombinant bispecific antibody formats have been developed over the past years[8]. Amongst them tandem single-chain Fv molecules and diabodies and various derivatives there of are the most widely used formats for the construction of recombinant bispecific antibodies (Figure 1). Routinely, construction of these molecules starts from two single-chain Fv (scFv) fragments that recognize different antigens[9].

Tandem scFv molecules (taFv) represent a straightforward format simply connecting the two scFv molecules with an additional peptide linker (Figure 1). The two scFv fragments present in these tandem scFv molecules form separate folding entities. Thus various linkers can be used to connect the two scFv fragments and linkers with a length of up to 63 residues have been reported[10]. Although the pa-

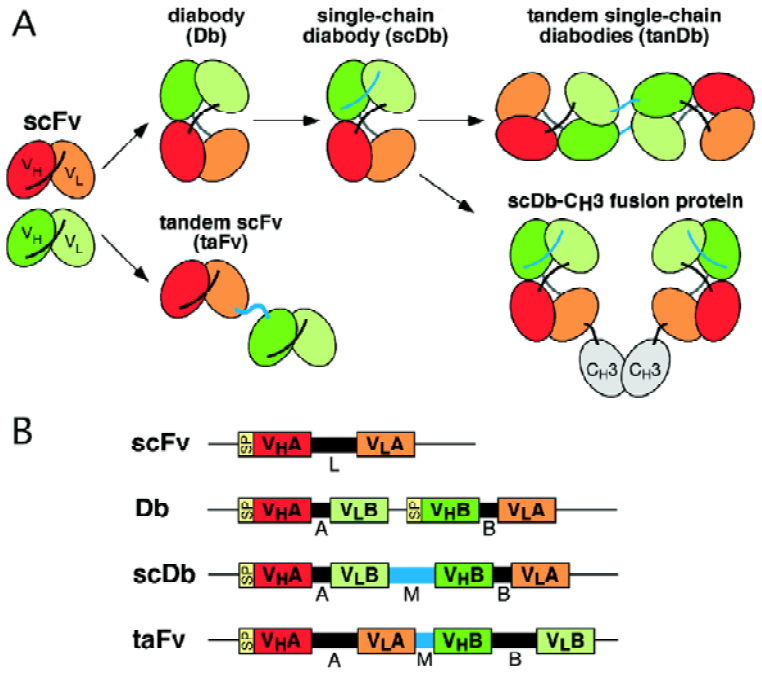

Figure 1. A) Structures of various recombinant bispecific antibody formats derived from single-chain Fv (scFv) fragments. B) Domain and linker arrangements in single-chain Fv fragments (scFv), diabodies (Db), single-chain diabodies (scDb), and tandem scFv molecules (taFv). Linker L in scFv consists of approximately 15 amino acid residues. In Db and scDb linkers A and B have a length of approximately 5 amino acids. Linker M in scDb is approximately 15 amino acids long. In taFv linkers A and B have a length of approximately 15 amino acids and linker M can be of varying length (e.g. from 0 to >25 amino acids). SP=signal peptide.

rental scFv fragments can normally be expressed in soluble form in bacteria, it is, however, often observed that tandem scFv molecules form insoluble aggregates in bacteria. Hence, refolding protocols or the use of mammalian expression systems are routinely applied to produce soluble tandem scFv molecules. In a recent study, *in vivo* expression by transgenic rabbits and cattle of a tandem scFv directed against CD28 and a melanoma-assocated proteoglycan was reported[11]. In this construct the two scFv molecules were connected by a C_H1 linker and serum concentrations of up to 100 mg/L of the bispecific antibody were found. Various strategies including variations of the domain order or using middle linkers with varying length or flexibility were employed to allow soluble expression in bacteria. A few studies have now reported expression of soluble tandem scFv molecules in bacteria[12–14] using either a very short Ala_3 linker or long glycine/serine-rich linkers. In a recent study, we employed phage display of a tandem scFv repertoire containing randomized middle linkers with a length of 3 or 6 residues to enrich for those molecules which are produced in soluble and active form in bacteria. This approach resulted in the isolation of a preferred tandem scFv molecule with a 6 amino acid residue linker[15]. At present it is unclear if this linker sequence represents a general solution to the soluble expression of tandem scFv molecules. Nevertheless, this study demonstrate that phage display of tandem scFv molecules in combination with directed mutagenesis is a powerful tool to enrich for those molecules which can be expressed in bacteria in active form.

Bispecific diabodies (Db) utilize the diabody format for expression. Diabodies are produced from scFv fragments by reducing the length of the linker connecting the V_H and V_L domain to approximately 5 residues[16]. This reduction forces dimerization of two polypeptide chains by crossover pairing of the V_H and V_L domains (Figure 1). Bispecific diabodies are produced by expressing two polypeptide chains with either the structure V_HA-V_LB and V_HB-V_LA (V_H-V_L configuration) or V_LA-V_HB and V_LB-V_HA (V_L-V_H configuration) within the same cell. A large variety of different bispecific diabodies have been produced in the past and most of them could be expressed in soluble form in bacteria (Table 1). A recent comparative study demonstrate, however, that the orientation of the variable domains can influence expression and formation of active binding sites[17]. Nevertheless, the soluble expression in bacteria represents an important advantage over tandem scFv molecules. However, since two different polypeptide chains are expressed within a single cell inactive homodimers can be produced together with active heterodimers. This puts some obstacles towards the use as therapeutic molecules as it necessitates the implementation of additional purification steps in order to obtain homogenous preparations of bispecific diabodies.

One approach to force the generation of bispecific diabodies is the production of knob-into-hole diabodies[18]. This was demonstrated for a bispecific diabody directed against HER2 and CD3. A large knob was introduced in the V_H domain by exchanging Val_{37} with Phe and Leu_{45} with Trp and a complementary hole was produced in the V_L domain by mutating Phe_{98} to Met and Tyr_{87} to Ala, either in the anti-HER2 or the anti-CD3 variable domains. By using this approach the production of bispecific diabodies could be increased from 72% by the parental diabody to over 90% by the knob-into-hole diabody. Importantly, production yields did only slightly decrease by these mutations. However, a reduction in antigen-binding activity was observed for several analyzed constructs. Thus, this rather elaborate approach requires the analysis of various constructs in order to identify those mutations which produce heterodimeric molecule with unaltered binding activity.

Single-chain diabodies (scDb) represent an alternative strategy to improve the formation of bispecific diabody-like molecules[19,20]. Bispecific single-chain diabodies are produced by connecting the two diabody-forming polypeptide chains with an additional middle linker with a length of approximately 15 amino acid residues (Figure 1). Consequently, all molecules with a molecular weight corresponding to monomeric single-chain diabodies (50-60 kDa) are bispecific. Several studies have demonstrated that bispecific single-chain diabodies are expressed in bacteria in soluble and active form (Table 1) with the majority of purified molecules present as monomers[19–22]. Thus, single-chain diabodies combine the advantages of tandem scFvs (all monomers are bispecific) and diabodies (soluble expression in bacteria).

Stability improvements

Stability of the recombinant bispecific antibodies under storage conditions as well as after *in vivo* application is a critical parameter with strong impact for clinical application. The antibody has to be sufficiently stable to allow the molecules to induce a therapeutic benefit before being degraded[23]. Unfortunately, several studies showed that tandem scFv molecules as well as diabodies were inactivated under physiological conditions, with varying half-lives depending on the antibody construct tested[15,20].

One approach to improve the stability of antibody molecules is the generation of disulfide-stabilized molecules

Table 1. Applications of recombinant bispecific antibodies for cancer therapy.

Format	Antibody	Target	Effector	Expression	Reference
taFv	CD19 x CD3	CD19	CTL	mammalian cells	[45,47,48,51,52]
	CD19 x CD3	CD19	CTL	*E.* coli	[53]
	EpCAM x CD3	EpCAM	CTL	mammalian cells	[10,54-56]
	HER2 x CD3	ErbB2	CTL	mammalian cells	[55]
	LeY x CD3	Lewis Y	CTL	mammalian cells	[55]
	BCL-1 x CD3	IgG idiotpye	CTL	mammalian cells	[43]
	FAP x CD3	FAP	CTL	mammalian cells	[41]
	OKT9 x CD3	TR	CTL	mammalian cells	[57]
			E. coli (refolding)		
	L6 x CD3	tumor Ag	CTL	mammalian cells	[58]
	Wue x CD3	Wue	CTL	mammalian cells	[59]
	M x CD28	melanoma proteoglycan	CTL	rabbits, cattle	[11]
	HLA-II x CD16	MHC complex	NK cells	mammalian cells	[60]
	HER2 x CD16	ErbB2	NK cells	*E. coli*	[12,61]
	EGFR x Ad	EGFR	adenovirus	mammalian cells	[62-67]
	EpCAM x Ad	EpCAM	adenovirus	mammalian cells	[67]
	CD40 x Ad	CD40	adenovirus	*E. coli*	[13]
	CEA x Ad	CEA	adenovirus	*E. coli*	[15]
	3E10 x p53	cell penetration	apoptosis	mammalian cells	[38]
Db	BCL-1 x CD3	IgG idiotype	CTL	*E. coli*	[68]
	CEA x CD3	CEA	CTL	*E. coli*, *Pichia*	[24,46]
	HER2 x CD3	ErbB2	CTL	*E. coli*	[69]
	EpCAM x CD3	EpCAM	CTL	*E. coli*	[70]
	IL-6 x CD3	IL-6	CTL	*E. coli*	[71]
	CD19 x CD3	CD19	CTL	*E. coli*	[44,49]
	CD20 x CD3	CD20	CTL	*E. coli*	[72]
	EGFR x CD3	EGFR	CTL	*E. coli* (refolding)	[73]
	MUC-1 x CD3	MUC-1	CTL	*E. coli* (refolding)	[74]
	Pgp x CD3	P glycoprotein	CTL	*E. coli*	[75]
	CD19 x CD16	CD19	NK cells	*E. coli*	[50]
	CD30 x CD16	CD30	NK cells	*E. coli*	[76]
	Lys x C1q	lysozyme	complement	*E. coli*	[77]
	Lym-1 x DOTA	HLA-DR	^{90}Y	E coli	[78,79]
scDb	CEA x CD3	CEA	CTL	*E. coli*	unpublished
	CD19 x CD3	CD19	CTL	*E. coli*	[14]
	EDG x CD3	endoglin	CTL	*E. coli*	[22]
	EDG x Ad	endoglin	adenovirus	*E. coli*	[40]
	HMW-MAA x Ad	HMW-MAA	adenovirus	*E. coli*	[80]
	CEA x Ad	CEA	adenovirus	*E. coli*	[15]
	CEA x b-Gal	CEA	prodrug	*E. coli*	[19]
tanDb	CD19 x CD3	CD19	CTL	*E. coli*	[20,81]
scFv-C_H3	HER2 x CD16	ErbB2	CTL	mammalian cells	[29]

Abbreviations: Ad, adenovirus knob domain; β-Gal, β-galactosidase; CEA, carcinoembryonic antigen; CTL, cytotoxic T lymphocytes; Db, diabody; DOTA, 1,4,7,10-tetraazacyclododecane-*N*,*N*′,*N*″,*N*‴-tetraacetic acid; EGFR, epidermal growth factor receptor; EpCAM, epithelial cell adhesion molecule; FAP, fibroblast activation protein; HMW-MAA, high molecular weight melanoma-associated antigen; NK cells, natural killer cells; scDb, single-chain diabody; taFv, tandem scFv; tanDb, tandem diabody; TR, transferrin receptor.

introducing cysteine bridges between the V_H-V_L interfaces to inhibit dissociation of the V_H and V_L domains. That this results in an increased thermal stability has been shown for a bivalent anti-CEA diabody[24]. A subsequent study with a disulfide-stabilized bispecific diabody demonstrated that this approach also resulted in an increase in the formation of heterodimers similar to the knob-into-hole approach[18]. However, a marked reduction in production yield was reported for this disulfide-stabilized bispecific diabody in *E coli*. Principally, this approach to improve stability by introducing disulfide-bonds between the V_H and V_L domains is applicable for any recombinant bispecific format including tandem scFv molecules.

Several comparative studies have revealed that single-chain diabodies are more stable than diabodies and tandem scFv molecules[14,15,19,20]. This is probably a result of the physical linkage of the four variable domains, similar to the improved stability of single-chain Fv fragments compared to Fv fragments[25]. A recent study demonstrated that the length and composition of the three linkers present in a single-chain diabody molecule and its dimeric tandem form had a strong influence on stability and functional activity[26]. In this study tandem diabodies composed of 10 residue long flanking linkers and a long middle linker (27 residues) showed highest stability and activity. These results emphasize the fact that modest variations in the composition of recombinant bispecific antibodies have strong impacts on their biological properties.

Improvement of pharmacokinetics

One of the drawbacks of small recombinant bispecific antibodies for therapeutic applications is the short circulation time in the body. Diabodies, single-chain diabodies and tandem-scFv molecules have a molecular weight of 50-60 kDa. This causes rapid clearance from circulation by extravasation and renal elimination with an initial half-life ($t_{1/2\alpha}$) below 30 min[20]. This is much shorter than the half-life of whole antibody molecules, which can be in the range of several weeks, due to its larger size and Fn receptor mediated recycling.

Several approaches have been undertaken to improve the pharmacokinetics of recombinant antibodies. One approach is to increase the size of these molecules. For example, this was achieved by fusion of a bispecific single-chain diabody to the IgG C_H3 or Fc region via an IgG hinge[27]. A similar approach was also applied for bispecific diabodies fusing one of the two diabody chains to a C_H3 domain (di-diabody)[28]. These fusions result in the formation of dimeric molecules with molecular weights of 150-180 kDa containing four functional antigen-binding sites, two for each antigen. The advantage of using single-chain diabodies for this approach is that a single polypeptide chain is expressed resulting in the assembly of defined molecules with identical size and binding activity. In contrast, the usage of two different polypeptide chains for the expression of di-diabody may cause formation of a mixture of non-functional diabody molecules produced by homodimeric assembly of two identical polypeptide chains and functional diabody-C_H3 fusion proteins. Interestingly, Lu and co-workers[28] could not detect such non-functional diabody molecules in their preparations indicating that heterodimeric assembly of the two polypeptide chains is favored, at least for the described construct. Heterodimer-forming C_H3 domains containing knob-into-hole structures were also used to generate bispecific antibodies by fusion of two different scFv fragments directed against HER2 and CD16 to these domains[29]. Although not tested *in vivo* this bispecific minibody was stable in mouse and human serum at 37 °C for several days and biologically active.

Dimeric single-chain diabody molecules with a molecular weight of 100-115 kDa can also be generated by varying the length of the linkers connecting the variable domain. Reducing the middle linker of a single-chain diabody to less than 13 amino acid residues results in the formation of dimeric single-chain diabody (tandem diabodies, tanDb) most likely with a linear arrangement of the two polypeptide chains (Figure 1)[20,21]. Similarly, reduction of the flanking linkers to 0-1 amino acid residue results also in dimeric molecules, presumably in a tetrabody-like arrangement[21]. For tandem diabodies it has been shown that this dimerization results in a four- to eight fold increase in circulation time compared to diabodies and an improved therapeutic efficacy[20,30].

The covalent attachment of polyethylene glycol (PEG) chains may represent another possibility to improve the pharmacokinetics of recombinant bispecific antibodies. Several PEGylated protein therapeutics which exhibit increased half-lives and improved therapeutic efficacy compared to their non-PEGylated forms have been clinically approved[31]. Although as yet not applied for recombinant bispecific antibodies, it was shown for single-chain Fv fragments that PEGylation could prolong serum half-life up to 200-fold[32]. In this study single reactive cysteine residues were introduced into the scFv molecules at defined positions, e.g. at the C-terminus or in the linker region. This additional cysteine residue allowed for a site-specific coupling of a single PE.G. chain without impairing binding activity of the scFv fragment.

A rather new approach is the combination of recombinant bispecific antibodies with gene-therapeutic protocols aiming at a direct *in vivo* expression of the antibody molecules[33]. This should result in high and constant levels of antibody molecules over an extended period of time. Furthermore, this approach obviates the need for extensive purification and characterization of the therapeutic proteins. However, one has to keep in mind that for therapeutic applications it is essential that expression is tightly controlled in order to stall expression in the event of severe side effects. In 1999 we postulated that this approach should be applicable for the *in vivo* production of recombinant bispecific antibody molecules[19]. In this study we show that bispecific single-chain diabodies are secreted in an active form from mammalian producer cells *in vitro* and are able to selectively recruit a prodrug-converting enzyme to tumor cells. Subsequently, we developed an adenoviral system containing the gene for an anti-CD3 x anti-CEA bispecific single-chain diabody. Injection of these recombinant adenoviruses into mice resulted in high-level expression of the antibody molecule over a period of several weeks[34]. The therapeutic effects of *in vivo* produced proteins were recently demonstrated with an anti-CEA x anti-CD3 bispecific diabody in combination with a B7-anti-CEA scFv fusion protein[35]. *In vivo* expression was achieved by implanting near the tumor site 293 producer cells stably transfected with the DNA encoding these proteins. After injection of human T cells, antitumor effects were observed in a colon carcinoma tumor model demonstrating the feasibility of this approach. Further studies are, however, needed to establish the most effective and safe protocol, including an evaluation of *in vivo* and *ex vivo* gene transfer, a comparison of local versus systemic production, identification of suitable transcriptional control elements and safe gene transfer vehicles.

Therapeutic applications

Recombinant bispecific antibodies have already been developed for a variety of different applications with potential use in cancer therapy. These applications include the retargeting of effector molecules (prodrug-converting enzymes, radio-isotopes, complement components), effector cells (CTLs, NK cells) and adenoviral vectors (Table 1), covering various therapeutic strategies, e.g. radiotherapy, chemotherapy, immunotherapy and gene therapy. In addition, recent work explored their use as intracellular bispecific antibodies (intrabodies)[36]. In one study an intracellularly expressed diabody was used to induce a functional knockout of two cell surface receptors[37]. In another study a bispecific tandem scFv with cell-penetrating abilities was applied to restore p53 wild-type function by intracellular binding to p53[38].

Most applications of recombinant bispecific antibodies for cancer therapy focus on the retargeting of effector cells of the immune system to tumor cells (Table 1). Extensive work has been done on the retargeting of cytotoxic T lymphocytes (CTLs) through binding to the T cell co-receptor molecule CD3. In addition, natural killer cells (NK) were retargeted with recombinant bispecific antibodies directed against Fcγ receptor III (CD16). A large variety of different target antigens have been evaluated. Most of them represent tumor-associated antigens (TAA) over-expressed by tumor cells, including CD19, CD20, epithelial cell adhesion molecule (EpCAM), epidermal growth factor receptor (EGFR), HER2, MUC-1, and carcinoembryonic antigen (CEA) (Table 1). In addition, recent focus has switched to tumor vasculature as a target structure. Targeting tumor vasculature of solid tumors has several advantages compared to direct targeting of tumor cells[39]. Tumor endothelial cells are directly accessible for circulating agents, ie extravasation of effector molecules and cells is not necessary. All solid tumors depend on neovascularization to grow beyond a few millimeters in diameter. Thus, this approach is broadly applicable. Endothelial cells are genetically stable and do not become resistant to therapy. A few studies have demonstrated that recombinant bispecific antibodies can be employed to retarget effector cells (CTLs) or adenoviral vectors to endothelial cells *in vitro*. These studies used endoglin (CD105) or fibroblast activation protein (FAP) as vascular targeting structures[22,40,41]. Other suitable antigens are described, e.g. vascular endothelial growth factor (VEGF) receptor, α_v-integrins and the ED-B domain of a tumor-associated fibronectin splice variant[42], which allows these studies to be extended to other targets but also to other effector mechanisms.

Several animal studies have been performed with recombinant bispecific antibodies and curative effects have been demonstrated[10,30,35,43-45]. Most studies with anti-CD3 bispecific antibody molecules have shown that T cells need a second stimulus to efficiently lyse target cells. This second stimulus can be provided by pre-activation of isolated T lymphocytes, e g with IL-2 and anti-CD28 antibodies. Several studies developed approaches to provide this co-stimulus *in vivo* by co-administering anti-CD28 antibodies or B7-scFv fusion proteins[30,46]. Interestingly, one anti-CD3 antibody used for the construction of bispecific tandem scFv molecules was shown to induce a co-stimulation independent T cell response[47,48].

Other studies evaluated various combinations of recom-

binant bispecific antibodies with other compounds to further improve anti-tumor responses. These approaches include the co-application of anti-CD19 x anti-CD3 diabodies, anti-CD28 antibodies and anti-CD19 x anti-CD16 bispecific diabodies targeting and activating two different effector cell types and the co-application of an anti-CD19 x anti-CD16 bispecific diabody together with thalidomide as chemotherapeutic drug[49,50]. Interestingly, these studies described synergistic effects between the different compounds indicating that further dramatic improvements of the systems are possible.

Currently there is one bispecific tandem scFv molecule (MT103) directed against CD19 and CD3 in a clinical phase I safety trial for the treatment of Non-Hodgkin's Lymphoma (NHL). This antibody was shown to be very potent in destroying CD19-expressing tumor cells *in vitro* and *in vivo* in a T cell costimulation-independent way[48]. A final report of the outcome is currently not available.

Conclusions

The past decade has led to enormous improvements in the generation and application of recombinant bispecific antibodies. These molecules combine the potentials of bispecific molecules for therapeutic applications with the advantages provided by antibody engineering technologies. Although further improvements are necessary, recent studies have shown that recombinant bispecific antibodies can find their way into the clinic.

References

1 van Spriel AB, van Ojik HH, van de Winkel JGJ. Immunotherapeutic perspectives for bispecific antibodies. Immunol Today 2000; 21: 391–6.

2 Segal DM, Weiner GJ, Weiner LM. Bispecific antibodies in cancer therapy. Curr Opin Immunol 1999; 11: 558–62.

3 Hoogenboom HR, Chames P. Natural and designer binding sites made by phage display technology. Immunol Today 2000; 21: 371–8.

4 Brüggemann M, Taussig MJ. Production of human antibody repertoires in transgenic mice. Curr Opin Biotechnol 1997; 8: 455–8.

5 Ritter G, Cohen LS, Williams C, Richards EC, Old LJ, Welt S. Serological analysis of human anti-human antibody responses in colon cancer patients treated with repeated doses of humanized monoclonal antibody A33. Cancer Res 2001; 61: 685–9.

6 Hellendoorn K, Jones T, Watkins J, Baker M, Hamilton A, Carr F. Limiting the risk of immunogenicity by identification and removal of T-cell epitopes (DeImmunisation™). Cancer Cell Int 2004; 4: S20.

7 Kufer P, Lutterbüse R, Baeuerle PA. A revival of bispecific antibodies. Trends Biotechnol 2004; 22: 238–44.

8 Kriangkum J, Xu B, Nagata LP, Fulton RE, Suresh MR. Bispecific and bifunctional single chain recombinant antibodies. Biomol Eng 2001; 18: 31–40.

9 Kontermann RE, Völkel T, Korn T. Production of recombinant bispecific antibodies. In: Antibody Engineering Protocols, 2nd edition-Methods in Molecular Biology Vol 51. Lo BKC (Ed). Totowa: Humana Press; 2003. p 227–42.

10 Ren-Heidenreich L, Davol PA, Douttab NM, Elfenbein GJ, Lum LG. Redirected T-cell cytotoxicity to epithelial cell adhesion molecule-overepressing adenocarcinomas by a novel recombinant antibody, E3Bi, *in vitro* and in an animal model. Cancer 2004; 100: 1095–103.

11 Grosse-Hovest L, Müller S, Minoia R, Wolf E, Zakhartchenko V, Wenigerkind H, *et al*. Cloned transgenic farm animals produce a bispecific antibody for T cell-mediated tumor cell killing. Proc Natl Acad Sci USA 2004; 101: 6858–63.

12 McCall AM, Adams GP, Amoroso AR, Nielsen UB, Zhang L, Horak E, *et al*. Isolation and characterization of an anti-CD16 single-chain Fv fragment and construction of an anti-HER2/neu/anti-CD16 bispecific scFv that triggers CD16-dependent tumor cytolysis. Mol Immunol 1999; 36: 433–45.

13 Brandaõ JG, Scheper RJ, Lougheed SM, Curiel DT, Tillman BW, Gerritsen WR, *et al*. CD40-targeted adenoviral gene transfer to dendritic cells through the use of a novel bispecific single-chain Fv antibody enhances cytotoxic T cell activation. Vaccine 2003; 21: 2268–72.

14 Kipriyanov SM, Moldenhauer G, Braunagel M, Reusch U, Cochlovius B, Le Gall F, *et al*. Effect of domain order on the activity of bacterially produced bispecific single-chain Fv antibodies. J Mol Biol 2003; 330: 99–111.

15 Korn T, Nettelbeck DM, Völkel T, Müller R, Kontermann RE. Recombinant bispecific antibodies for the targeting of adenoviruses to CEA-expressing tumour cells: a comparative analysis of bacterially expressed single-chain diabody and tandem scFv. J Gene Med 2004; 6: 642–51.

16 Holliger P, Prospero T, Winter G. "Diabodies": small bivalent and bispecific antibody fragments. Proc Natl Acad Sci USA 1993; 90: 6444–8.

17 Lu D, Jimenez X, Witte L, Zhu Z. The effect of variable domain orientation and arrangement on the antigen-binding activity of a recombinant bispecific diabody. Biochem Biophys Res Commun 2004; 318: 507–13.

18 Zhu Z, Presta LG, Zapata G, Carter P. Remodeling domain interfaces to enhance heterodimer formation. Protein Sci 1997; 6: 781–8.

19 Brüsselbach S, Korn T, Völkel T, Müller R, Kontermann RE. Enzyme recruitment and tumor cell killing *in vitro* by a secreted bispecific single-chain diabody. Tumor Targeting 1999; 4: 115–23.

20 Kipriyanov SM, Moldenhauer G, Schuhmacher J, Cochlovius B, Von der Lieth CW, Matys ER, *et al*. Bispecific tandem diabody for tumor therapy with improved antigen binding and pharmacokinetics. J Mol Biol 1999; 293: 41–56.

21 Völkel T, Korn T, Bach M, Müller R, Kontermann R. Optimized linker sequences for the expression of monomeric and dimeric bispecific single-chain diabodies. Protein Eng 2001; 14: 815–23.

22 Korn T, Müller R, Kontermann RE. Bispecific single-chain diabody-mediated killing of endoglin-expressing endothelial cells by cytotoxic T lymphocytes. J Immunother 2004; 27: 99–106.

23 Willuda J, Honegger A, Waibel R, Schubiger PA, Stahel R,

Zangemeister-Wittke U, *et al*. High thermal stability is essential for tumor targeting of antibody fragments: engineering of a humanized anti-epithelial glycoprotein-2 (epithelial cell adhesion molecule) single-chain Fv fragment. Cancer Res 1999; 59: 5758–67.

24 FitzGerald K, Holliger P, Winter G. Improved tumour targeting by disulphide stabilized diabodies expressed in Pichia pastoris. Protein Eng 1997; 10: 1221–5.

25 Glockshuber R, Malia M, Pfitzinger I, Plückthun A. A comparison of strategies to stabilize immunoglobulin Fv-fragments. Biochemistry 1990; 29: 1362–7.

26 Le Gall F, Reusch U, Little M, Kipriyanov SM. Effect of linker sequences between the antibody variable domains on the formation, stability and biological activity of a bispecific tandem diabody. Protein Eng Des Sel 2004; 17: 357–66.

27 Alt M, Müller R, Kontermann R. Novel tetravalent and bispecific IgG-like antibody molecules combining single-chain diabodies with the immunoglobulin g1 Fc or CH3 region. FEBS Lett 1999; 454: 90–4.

28 Lu D, Jimenez X, Zhang H, Atkins A, Brennan L, Balderes P, *et al*. Di-diabody: a novel tetravalent bispecific antibody molecule by design. J Immunol Meth 2003; 279: 219–32.

29 Shahied LS, Tang Y, Alpaugh RK, SomerR, Greenspon D, Weiner LM. Bispecific minibodies targeting HER2/neu and CD16 exhibit improved tumor lysis when placed in a divalent tumor antigen-binding format. J Biol Chem 2004 Oct 7; [Epub ahead of print).

30 Cochlovius B, Kipriyanov SM, Stassar MKKG, Schuhmacher J, Benner A, Moldenhauer G, *et al*. Cure of Burkitt's lymphoma in severe combined immunodeficiency mice by T cells, tetravalent CD3 x CD19 tandem diabody, and CD28 costimulation. Cancer Res 2000; 60: 4336–41.

31 Harris JM, Chess RB. Effect of pegylation on pharmaceuticals. Nat Rev Drug Discov 2003; 2: 214–21.

32 Yang K, Basu A, Wang M, Chintala R, Hsieh MC, Liu S, *et al*. Tailoring structure-function and pharmacokinetic properties of single-chain Fv proteins by site-specific PEGylation. Protein Eng 2003; 16: 761–70.

33 Bakker JM, Bleeker WK, Parren PWHI. Therapeutic antibody gene transfer: An active approach to passive immunity. Mol Ther 2004; 10: 411–6.

34 Kontermann RE, Korn T, Jérôme V. Recombinant adenoviruses for *in vivo* expression of antibody fragments. In: Recombinant antibody technology for cancer therapy: reviews and protocols. Welschof M, Krauss J (Eds). Methods in Molecular Medicine. Totowa: Humana Press; 2002. p 421–33.

35 Blanco B, Holliger P, Vile RG, Álvarez-Vallina L. Induction of human T lymphocyte cytotoxicity and inhibition of tumor growth by tumor-specific diabody-based molecules secreted from gene-modified bystander cells. J Immunol 2003; 171: 1070–7.

36 Kontermann RE, Müller R. Intracellular and cell surface displayed single-chain diabodies. J Immunol Meth 1999; 226: 179–88.

37 Jendreyko N, Popkov M, Beerli RR, Chung J, McGavern DB, Rader C, *et al*. Intradiabodies, bispecific, tetravalent antibodies for the simultaneous functional knockout of two cell surface receptors. J Biol Chem 2003; 278: 47812–9.

38 Weisbart RH, Wakelin R, Chan G, Miller CW, Koeffler PH. Construction and expression of a bispecific single-chain antibody that penetrates mutant p53 colon cancer cells and binds p53. Int J Oncol 2004; 25: 1113–8.

39 Augustin HG. Antiangiogenic tumour therapy: will it work? Trends Pharmacol Sci 1998; 19: 216–22.

40 Nettelbeck DM, Miller DW, Jerome V, Zuzarte M, Watkins SJ, Hawkins RE, *et al*. Targeting of adenovirus to endothelial cells by a bispecific single-chain diabody directed against the adenovirus fiber knob domain and human endoglin (CD105). Mol Ther 2001; 3: 882–91.

41 Wüst T, Moosmayer D, Pfizenmaier K. Construction of a bispecific single chain antibody for recruitment of cytotoxic T cells to the tumour stroma associated antigen fibroblast activation protein. J Biotechnol 2001; 92: 159–68.

42 Thorpe PE. Vascular targeting agents as cancer therapeutics. Clin Cancer Res 2004; 10: 415–27.

43 De Jonge J, Heirman C, de Veerman M, Van Meirvenne S, Moser M, Leo O, *et al*. *In vivo* retargeting of T cell effector function by recombinant bispecific single-chain Fv (anti-CD3 x anti-idiotype) induces long-term survival in the murine BCL1 lymphoma model. J Immunol 1998; 161: 1454–61.

44 Cochlovius B., Kipriyanov SM, Stassar MKKG, Christ O, Schuhmacher J, Strauß G, *et al*. Treatment of huma B cell lymphoma xenografts with a CD3 x CD19 diabody and T cells. J Immunol 2000; 165: 888–95.

45 Dreier T, Baeuerle PA, Fichtner I, Grun M, Schlereth B, Lorenczewski G, *et al*. T cell costimulus-independent and very efficacious inhibition of tumor growth in mice bearing subcutaneous or leukemic human B cell lymphoma xenografts by a CD19-/CD3- bispecific single-chain antibody construct. J Immunol 2003;170: 4397–402.

46 Holliger P, Manzke O, Span M, Hawkins R, Fleischmann B, Qianghua L, *et al*. Carcinoembryonic antigen (CEA)-specific T-cell activation in colon carcinoma induced by anti-CD3 x anti-CEA bispecific diabodies and B7 x anti-CEA bispecific fusion proteins. Cancer Res 1999; 59: 2909–16.

47 Löffler A, Kufer P, Lutterbüse R, Zettl F, Daniel PT, Schwenkenbecher JM, *et al*. A recombinant bispecific single-chain antibody, CD19 x CD3, induces rapid and high lymphoma-directed cytotoxicity by unstimulated T lymphocytes. Blood 2000; 15: 2098–103.

48 Dreier T, Lorenczewski G, Brandl C, Hoffmann P, Syring U, Hanakam F, *et al*. Extremely potent, rapid and costimulation-independent cytotoxic T-cell response against lymphoma cells catalyzed by a single-chain bispecific antibody. Int J Cancer 2002; 100: 690–7.

49 Kipriyanov SM, Cochlovius, B, Schäfer HJ, Moldenhauer G, Bähre A, Le Gall F, *et al*. Synergistic antitumor effects of bispecific CD19 x CD3 and CD19 x CD16 diabodies in a preclinical model of Non-Hodgkin's lymphoma. J Immunol 2002; 169: 137–44.

50 Schlenzka J, Moehler TM, Kipriyanov SM, Kornacker M, Benner A, Bähre A, *et al*. Combined effect of recombinant CC19 x CD16 diabody and thalidomide in a preclinical model of human B cell lymphoma. Anticancer Drug 2004; 15: 915–9.

51 Löffler A, Gruen M, Wuchter C, Schriever F, Kufer P, Dreier T, *et al*. Leukemia 2003; 17: 900–9.

52 Gruen M, Bommert K, Bargou RC. T-cell-mediated lysis of B cells induced by a CD19xCD3 bispecific single-chain antibody is perforin dependent and death receptor independent. Cancer Immunol Immunother 2004; 53: 625–32.

53 Kipriyanov SM, Moldenhauer G, Strauss G, Little M. Bispecific CD3 x CD19 diabody for T cell-mediated lysis of malignant

human B cells. Int J Cancer 1998; 77: 763–72.
54 Mack M, Gruber R, Schmidt S, Riethmüller G, Kufer P. Biological properties of a bispecific single-chain antibody directed against 17-1A (EpCAM) and CD3. J Immunol 1997; 158: 3965–70.
55 Maletz K, Kufer P, Mack M, Raum T, Pantel K, Riethmüller G, *et al*. Bispecific single-chain antibodies as effective tools for eliminating epithelial cancer cells from human stem cell preparations by redirected cell cytotoxicity. Int J Cancer 2001; 93: 409–16.
56 Wimberger P, XiangW, Mayr D, Diebold J, Dreier T, Baeuerle PA, *et al*. Efficient tumor cell lysis by autologous, tumor-resident T lymphocytes in primary ovarian cancer samples by an EP-CAM-/CD3-bispecific antibody. Int J Cancer 2003; 105: 241–8.
57 Jost CR, Titus JA, Kurucz I, Segal DM. A single-chain bispecific Fv_2 molecule produced in mammalian cells redirects lysis by activated CTL. Mol Immunol 1996; 33: 211–9.
58 Hayden MS, Linsley PS, Gayle MA, Bajorath J, Brady WA, Norris NA, *et al*. Single-chain mono- and bispecific antibody derivatives with novel biological properties and antitumour activity from a COS cell transient expression system. Ther Immunol 1994; 1: 3–15.
59 Honemann D, Kufer P, Rimpler MM, Chatterjee M, Friedl S, Riecher F, *et al*. A novel recombinant bispecific single-chain antibody, bscWue-1 x CD3, induces T-cell-mediated cytotoxicity towards human multiple myeloma cells. Leukemia 2004; 18: 636–44.
60 Bruenke J, Fischer B, Barbin K, Schreiter K, Wachter Y, Mahr K, *et al*. A recombinant bispecific single-chain Fv antibody against HLA class II and FcgammaRIII (CD16) triggers effective lysis of lymphoma cells. Br J Haematol 2004; 125: 167–79.
61 McCall AM, Shahied L, Amoroso AR, Horak EM, Simmons HH, Nielsen U, *et al*. Increasing the affinity for tumor antigen enhances bispecific antibody cytotoxicity. J Immunol 2001; 166: 6112–7.
62 Haisma HJ, Grill J, Curiel DT, Hoogeland S, van Beusechem VW, Pinedo HM, *et al*. Targeting of adenoviral vectors through a bispecific single-chain antibody. Cancer Gene Ther 2000; 7: 901–4.
63 Grill J, van Beusechem VW, van der Valk P, Dirven CMF, Leonhart A, Pherai DS, *et al*. Combined targeting of adenoviruses to integrins and epidermal growth factor receptors increased gene transfer into primary glioma cells and spheroids. Clin Cancer Res 2001; 7: 641–50.
64 Witlox MA, van Beusechem VW, Grill J, Haisma HJ, Schaap G, Bras J, *et al*. Epidermal growth factor receptor targeting enhances adenoviral vector based suicide gene therapy of osteosarcoma. J Gene Med 2002; 4: 510–6.
65 Dirven CMF, Grill J, Lamfers MLM, van der Valk P, Leonhart AM, van Beusechem VW, *et al*. Gene therapy for meningioma: improved gene delivery with targeted adenoviruses. J Neurosurg 2002; 97: 441–9.
66 van Beusechem VW, Grill J, Mastenbroek DCJ, Wickham TJ, Roelvink PW, Haisma HJ, *et al*. Efficient and selective gene transfer into primary human brain tumors by using single-chain antibody-targeted adenovrial vectors with native tropism abolished. J Virol 2002; 76: 2753–62.
67 Heideman DA, van Beusechem VW, Offerhaus GJ, Wickham TJ, Roelvink PW, Craanen ME, *et al*. Selective gene transfer into primary human gastric tumors using epithelial cell adhesion molecule-targeted adenoviral vectors with ablated native tropism. Hum Gene Ther 2002; 13: 1677–85.
68 Holliger P, Brissinck J, Williams RL, Thielemans K, Winter G. Specific killing of lymphoma cells by cytotoxic T-cells mediated by a bispecific diabody. Protein Eng 1996; 9: 299–305.
69 Zhu Z, Zapata G, Shalaby R, Snedecor B, Chen H, Carter P. High level secretion of a humanized bispecific diabody from *Escherichia coli*. Biotechnology 1996; 14: 192–6.
70 Helfrich W, Kroesen BJ, Roovers RC, Westers L, Molema G, Hoogenboom HR, *et al*. Construction and characterization of a bispecific diabody for retargeting T cells to human carcinomas. Int J Cancer 1998; 76: 232–9.
71 Krebs B, Griffin H, Winter G, Rose-John S. Recombinant human single chain Fv antibodies recognizing human interleukin-6. Specific targeting of cytokine-secreting cells. J Biol Chem 1998; 273: 2858–65.
72 Xiong D, Xu Y, Liu H, Peng H, Shao X, Lai Z, *et al*. Efficient inhibition of human B-cell lymphoma xenografts with an anti-CD20 x anti-CD3 bispecific diabody. Cancer Lett 2002; 177: 29–39.
73 Hayashi H, Asano R, Tsumoto K, katayose Y, Suzuki M, Unno M, *et al*. A highly effective and stable bispecific diabody for cancer immunotherapy: cure of xenografted tumors by bispecific diabody and T-LAK cells. Cancer Immunol Immunother 2004; 53: 497–509.
74 Takemura S, Kudo T, Asano R, Suzuki M, Tsumoto K, Sakurai N, *et al*. A mutated superantigen SEA D227A fusion diabody specific to MUC1 and CD3 in targeted cancer immunotherapy for bile duct carcinoma. Cancer Immunol Immunother 2002; 51: 33–44.
75 Gao Y, Xiong D, Yang M, Liu H, Peng H, Shao X, *et al*. Efficient inhibition of multidrug-resistant human tumors with a recombinant bispecific anti-P-glycoprotein x anti-CD3 diabody. Leukemia 2004; 18: 513–20.
76 Arndt MA, Krauss J, Kipriyanov SM, Pfreundschuh M, Little M. A bispecific diabody that mediates natural killer cell cytotoxicity against xenotransplantated human Hodgkin's tumors. Blood 1999; 94: 2562–8.
77 Kontermann RE, Wing MG, Winter G. Complement recruitment using bispecific diabodies. Nat Biotechnol 1997; 15: 629–31.
78 DeNardo SJ, DeNardo GL, DeNardo DG, Xiong CY, Shi XB, Winthrop MD, *et al*. Antibody phage libraries for the next generation of tumor targeting radioimmunotherapeutics. Clin Cancer Res 1999; 5: 3213s–3218s.
79 DeNardo DG, Xiong CY, Shi XB, DeNardo GL, DeNardo SJ. Anti-HLA-DR/anti-DOTA diabody construction in a modular gene design platform: bispecific antibodies for pretargeted radioimmunotherapy. Cancer Biother Radiopharm 2001; 16: 525–35.
80 Nettelbeck DM, Rivera AA, Kupsch J, Dieckmann D, Douglas JT, Kontermann RE, *et al*. Retargeting of adenoviral infection to melanoma: combining genetic ablation of native tropism with a recombinant bispecific single-chain diabody (scDb) adapter that binds to fiber knob and HMWMAA. Int J Cancer 2004; 108: 136–45.
81 Reusch U, Le Gall F, Hensel M, Moldenhauer G, Ho AD, Little M, *et al*. Effect of tetravalent bispecific CD19xCD3 recombinant antibody construct and CD28 costimulation on lysis of malignant B cells from patients with chronic lymphocytic leukemia by autologous T cells. Int J Cancer 2004; 112: 509.

Full-length article

Tonic activation of presynaptic $GABA_B$ receptors on rat pallidosubthalamic terminals[1]

Lei CHEN[2,3], Wing-ho YUNG[2,4]

[2]Department of Physiology, The Chinese University of Hong Kong, Hong Kong, China; [3]Department of Physiology, Qingdao University, Qingdao 266021, China

Key words

GABA-B receptor; baclofen; CGP55845; presynaptic inhibition; subthalamic nucleus; globus pallidus

[1] Project supported by the Research Grants Council of Hong Kong (No CUHK 4080/00M).
[4] Correspondence to Prof Wing-ho YUNG.
Phn 852-2609-6880. Fax 852-2603-5022.
E-mail whyung@cuhk.edu.hk

Received 2004-02-11
Accepted 2004-10-10

doi: 10.1111/j.1745-7254.2005.00012.x

Abstract

Aim: The subthalamic nucleus plays a critical role in the regulation of movement, and abnormal activity of its neurons is associated with some basal ganglia motor symptoms. We examined the presence of functional presynaptic $GABA_B$ receptors on pallidosubthalamic terminals and tested whether they were tonically active in the *in vitro* subthalamic slices. **Methods:** Whole-cell patch-clamp recordings were applied to acutely prepared rat subthalamic nucleus slices. The effects of specific $GABA_B$ agonist and antagonist on action potential-independent inhibitory postsynaptic currents (IPSCs), as well as holding current, were examined. **Results:** Superfusion of baclofen, a $GABA_B$ receptor agonist, significantly reduced the frequency of $GABA_A$ receptor-mediated miniature IPSCs (mIPSCs), in a Cd^{2+}-sensitive manner, with no effect on the amplitude, indicating presynaptic inhibition on GABA release. In addition, baclofen induced a weak outward current only in a minority of subthalamic neurons. Both the pre- and post-synaptic effects of baclofen were prevented by the specific $GABA_B$ receptor antagonist, CGP55845. Furthermore, CGP55845 alone increased the frequency of mIPSCs, but had no effect on the holding current. **Conclusion:** These findings suggest the functional dominance of presynaptic $GABA_B$ receptors on the pallidosubthalamic terminals over the postsynaptic $GABA_B$ receptors on subthalamic neurons. Furthermore, the presynaptic, but not the postsynaptic, $GABA_B$ receptors are tonically active, suggesting that the presynaptic $GABA_B$ receptors in the subthalamic nucleus are potential therapeutic target for the treatment of Parkinson disease.

Introduction

Being the only nucleus in the basal ganglia containing glutamatergic neurons, the subthalamic nucleus occupies a critical position in the 'indirect' pathway by providing an excitatory drive to the output nuclei of this motor circuit. Anatomical studies have shown that the subthalamic nucleus receives GABAergic innervation from the globus pallidus and glutamatergic innervation from the cortex as well as the thalamus. The subthalamic nucleus then sends glutamatergic projection back to the globus pallidus, and to the substantia nigra pars reticulata and entopeduncular nucleus[1-7].

By influencing the output of the basal ganglia, the subthalamic nucleus plays a significant role in mediating movement in health and in diseased state. It has been demonstrated that the modification of the activity of subthalamic nucleus neurons constitutes the central origin of parkinsonian symptoms. For example, in Parkinson disease and its animal models, it is widely believed that depletion of dopamine in the basal ganglia leads to overactivity of the subthalamic nucleus. The resulting increased glutamatergic output of the subthalamic nucleus contributes to excessive inhibition of basal ganglia targets leading to akinesia and hypokinetic symptoms[8]. Recent studies on the firing properties of neurons from organotypic culture of the globus pallidus-subthalamic nucleus network[9], and from the *in vivo* brain[10,11] suggest that the reciprocally connected glutamatergic subthalamic and GABAergic pallidal neurons

are involved in the generation of low-frequency oscillatory activity in Parkinson disease, which is associated with tremor in parkinsonian subjects[12]. Indeed, disruption of the activity of the subthalamic nucleus could alleviate both the pathological neuronal activity and motor symptoms observed in Parkinson disease[13-15]. Thus, deep brain stimulation of the subthalamic nucleus has been introduced as a surgical procedure for the treatment of Parkinson disease[16].

GABAergic innervation from the globus pallidus is the major inhibitory factor affecting the activity of the subthalamic nucleus. GABAergic input from the globus pallidus affects the oscillation frequency of burst firing cells in the subthalamic nucleus[17]. There are two types of GABA receptors in the central nervous system: the ionotropic, bicuculline-sensitive $GABA_A$ receptors and the metabotropic, G-protein coupled $GABA_B$ receptors which are activated by baclofen. By inhibiting calcium influx and facilitating potassium conductance, activation of $GABA_B$ receptors produces pre- and postsynaptic inhibitory effects, respectively. A previous report [18] showed the presence of presynaptic $GABA_B$ receptors in the subthalamic nucleus based on the changes of the paired-pulse ratio of evoked IPSCs. In the current study, the presence of presynaptic $GABA_B$ receptors is studied by examining the direct effect of a $GABA_B$ agonist on the constitutive release of GABA from the presynaptic terminals, with the aid of a more specific $GABA_B$ antagonist. Because the differential activation of pre- and postsynaptic $GABA_B$ receptors is a potential therapeutic strategy in the treatment of basal ganglia motor disorders, we also compared the degree of activation of the pre- and postsynaptic $GABA_B$ receptors and tested whether they were tonically active.

Materials and methods

Brain slice preparation Sprague-Dawley rats aged 13–15 d were used for the preparation of acutely prepared brain slices. The animals were killed by decapitation. The brains were then immediately removed and placed in ice-cold artificial cerebrospinal fluid (ACSF) of the following composition (in mmol/L): NaCl 125, KCl 2.0, $MgSO_4$ 1.2, $CaCl_2$ 2.5, KH_2PO_4 1.2, glucose 11, and $NaHCO_3$ 26, which was continuously bubbled with 95% O_2 and 5% CO_2. Thin hemicoronal slices (250 μm) containing the subthalamic nucleus were sectioned using a vibrating microtome (Camden Instrument). After equilibration in a holding chamber for at least 30 min, the slices were transferred to a small volume chamber mounted on an upright microscope (Zeiss Axioskop), and superfused with ACSF at a rate of 1.5–2.0 mL/min maintained at a temperature of 34±1 ºC. Neuronal soma and proximal dendrities of neurons were directly visualized by a combination of differential interference contrast (DIC) optics and contrast-enhanced infrared (IR) video microscopy.

Whole-cell patch-clamp recordings Whole-cell patch-clamp recordings from the subthalamic nucleus neurons were obtained using a patch-clamp amplifier (LM/PCA, List Medical). Whole-cell pipettes had a resistance of 3-4 MΩ, when filled with an internal solution of the following composition (in mmol/L): KCl 140, HEPES 10, EGTA 1, $MgCl_2$ 2, Na_2ATP 2, and Tris GTP 0.4. The inclusion of 140 mmol/L of KCl in the recording pipettes reversed the polarity of the inhibitory postsynaptic currents (IPSCs) from outward to inward and enhanced their detection. Capturing of data and subsequent analysis followed the procedure of our previous report[19]. Monitoring through a television connected to the camera, a pipette was placed on the soma of a subthalamic nucleus neuron and conventional whole-cell recording was made. Normally no series resistance compensation was applied but the cell was rejected if the series resistance increased significantly (>20%) during recording. The voltage and current signals were filtered at 3 kHz and were taped using a DAT recorder (Sony) modified for recording AC and DC signals at a sampling rate of 32 kHz. On- or off-line digitization (10 kHz) was made via the Digidata-pClamp system (Axon Instruments). Synaptic currents were analyzed by a program developed in our laboratory[19]. Once a synaptic current is detected, information on the time of occurrence, peak amplitude and kinetics are generated automatically. The program also performed statistical comparison of two cumulative probabilities using the Kolmogorov-Smirnov test.

Drugs and statistics (±)-Baclofen used in the present study will be referred to as baclofen and was obtained from RBI. CGP55845 was purchased from Tocris. (±)-2-Amino-5-phosphonopentanoic acid (AP5), 6-cyano-7-nitroquinoxaline-2,3-dione (CNQX), bicuculline and tetrodotoxin (TTX) were also obtained from RBI.

The data were expressed as mean±SEM. Paired Student's *t*-test was used. The level of significance was presented by using a P value of 0.05.

Results

Pre- and postsynaptic $GABA_B$ receptors activated by baclofen The $GABA_A$ receptor-mediated miniature IPSCs (mIPSCs) were isolated by the addition of AP5 50 μmol/L and CNQX 20 μmol/L to eliminate glutamate receptor-

mediated synaptic currents and TTX 0.5 μmol/L to block action potential-dependent transmitter release. These currents were sensitive to 10 μmol/L $GABA_A$ receptor antagonist bicuculline, confirming their GABAergic nature. Spontaneous synaptic currents were found in most subthalamic nucleus neurons. Superfusion of baclofen, a specific $GABA_B$ receptor agonist, at 30 μmol/L significantly reduced the frequency of mIPSCs. This effect was reversible when baclofen was removed (Figure 1A, 1B). The inhibitory effect of baclofen was selective to the frequency (control: 1.69±0.27 Hz; baclofen: 0.64±0.09 Hz; wash: 1.08±0.16 Hz, n=12, P< 0.01) but not the amplitude of the mIPSCs (control: 31.4± 1.9 pA; baclofen: 32.5±2.3 pA, n=12, P>0.05), indicating that the effect was presynaptic (Figure 1C). Furthermore, in five cells, application of 200 μmol/L of $CdCl_2$ reduced the mIPSC frequency (control: 1.58±0.22 Hz; Cd^{2+}: 0.86±0.38 Hz; P<0.01). In this case, the effect of balcofen was largely abolished (0.82±0.38 Hz; P>0.05 *vs* Cd^{2+} alone).

To study whether baclofen directly inhibits the subthalamic nucleus neurons through activation of postsynaptic $GABA_B$ receptors, we also quantified the effect of baclofen in inducing an outward current in subthalamic nucleus neurons in the brain slice. In contrast to its presynaptic effect, which was observed in all neurons tested, baclofen at 30 μmol/L induced a weak outward current in only six out of 23 neurons (21.7 %), with a mean of 20.1±3.1 pA.

Receptor specificity and tonic activity revealed by CGP55845 To confirm that baclofen acts on $GABA_B$ receptors and to test whether the receptors are tonically active in the subthalamic nucleus, the effects of a recently introduced potent and specific $GABA_B$ receptor antagonist, CGP55845, were studied. When CGP55845 2 μmol/L was applied into the superfusion solution, there was no changes in the holding current in all six cells tested. In contrast, CGP55845 caused a clear increase in the frequency of the mIPSC, from 1.22±0.29 Hz to 2.14±0.56 Hz (n=6, P<0.05). These data suggest that the pre- but not the postsynaptic $GABA_B$ receptors are tonically active (The results from a typical cell were shown in Figure 2A, 2B). Consistent with a presynaptic site of action, the increase in the mIPSC frequency induced by CGP55845 was not accompanied by a change in the amplitudes (control: 38.3±3.7 pA; CGP55845: 39.2±3.7 pA; CGP55845+baclofen: 36.7±3.5 pA, n=6, P> 0.05). Furthermore, in the presence of CGP55845, baclofen did not decrease the frequency of mIPSCs in these neurons (CGP55845+baclofen: 2.26±0.48 Hz, P>0.05 *vs* CGP55845 alone, Figure 2). These data indicate that the presynaptic inhibitory effect observed when baclofen was applied alone was mediated by $GABA_B$ receptors (Figure 2).

In the presence of CGP55845, baclofen did not activate any outward current (n=6), suggesting that CGP55845 prevented the activation of postsynaptic $GABA_B$ receptors. The receptor specificity of the postsynaptic effect of baclofen was also tested in those neurons that responded to baclofen. Addition of CGP55845 in the presence of baclofen completely reversed the effect of baclofen (n=3). A typical result was shown in Figure 3.

Discussion

In the present study, we provide evidence for the existence of functional presynaptic $GABA_B$ receptors in the pallidosubthalamic pathway. This conclusion is based on the effect of balcofen on mIPSCs recorded from subthalamic neurons. This effect of balcofen is sensitive to specific $GABA_B$ receptors antagonist CGP55845, and also the broad-spectrum calcium channel blocker Cd^{2+}, which presumably blocks the influx of calcium into nerve terminals necessary for the release of GABA. Thus, Ca^{2+}-influx is likely to be involved in the presynaptic effect of baclofen.

The pallidosubthalamic GABAergic pathway is the major inhibitory pathway controlling the activity of the subthalamic nucleus neurons. The present study revealed that activation of $GABA_B$ receptors in this pathway could, in principle, exert two opposite effects on subthalamic nucleus neurons. On the one hand, by activating presynaptic $GABA_B$ receptor, baclofen reduces the release of GABA from pallidosubthalamic GABAergic terminals and then disinhibits the subthalamic nucleus neurons. On the other hand, by activating postsynaptic $GABA_B$ receptors, baclofen directly inhibits the subthalamic neurons. These electrophysiological results corresponded with anatomical observations in primates, which revealed the existence of pre- and postsynaptic $GABA_B$ receptor type 1 subunits in the subthalamic nucleus[20]. Since only a minority of subthalamic neurons responded to baclofen by exhibiting an outward current, which were nevertheless small in the amplitude, this implies that either there is a smaller number, or a less efficient coupling and signaling mechanism, of the postsynaptic $GABA_B$ receptors compared with their presynaptic counterpart. However, subcellular immunolabelling under an electron microscope showed a dense postsynaptic $GABA_B$ receptor labeling in the monkey subthalamic nucleus[20]. Also, our recent pre-embedding immunolabelling in the adult rat globus pallidus showed a similar level of $GABA_{B1}$ and $GABA_{B2}$ subunits at pre- and postsynaptic sites of GABAergic synapses[21] although the pharmacological data in young rats revealed a stronger presynaptic effects in this nucleus[22,23].

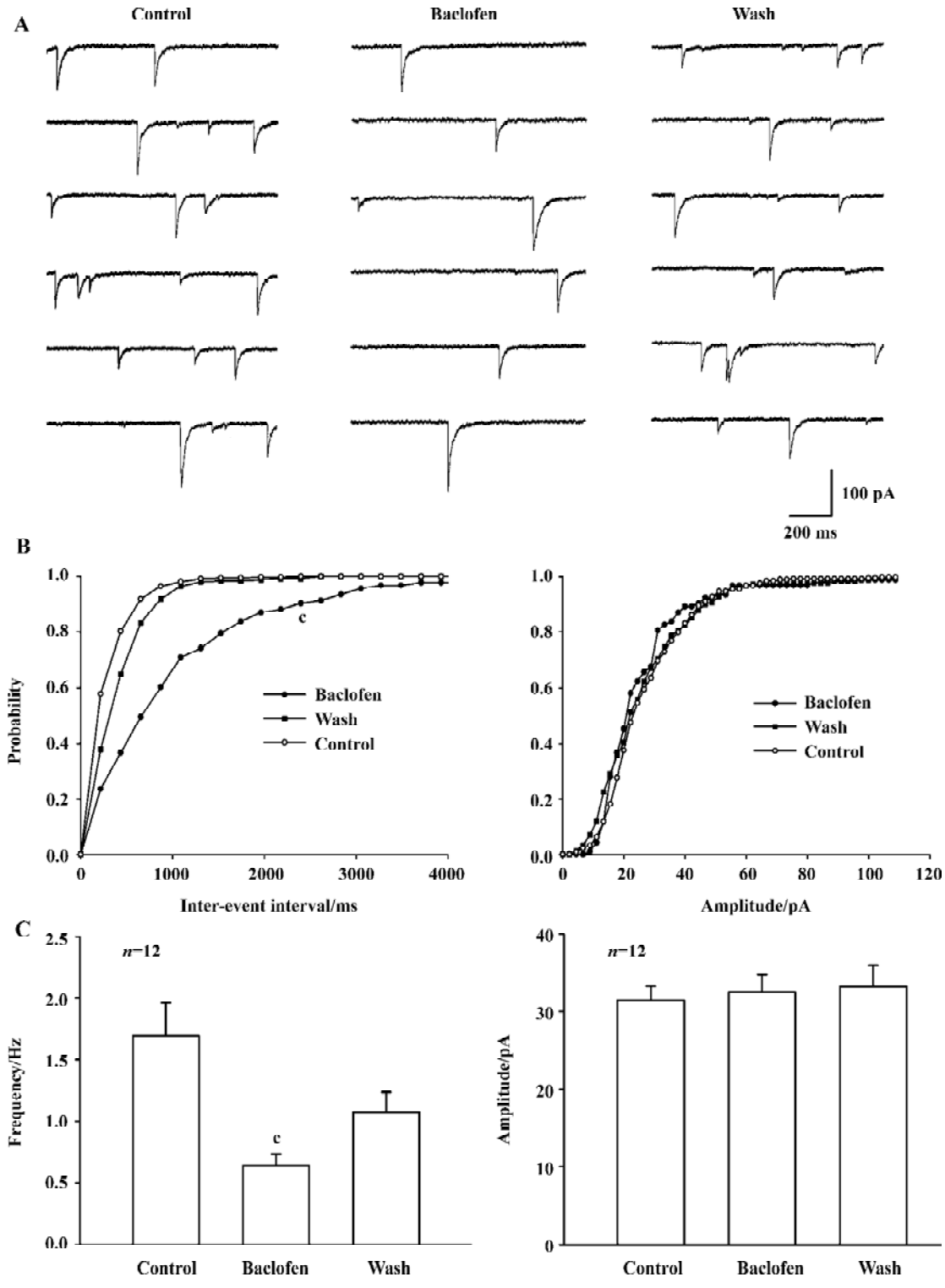

Figure 1. Presynaptic inhibition of GABA release by baclofen. (A) Typical traces showing that 30 μmol/L baclofen significantly and reversibly reduced the frequency of bicuculline-sensitive mIPSCs in the rat subthalamic nucleus neurons. (B) Cumulative probability distributions of the inter-event intervals and amplitudes of the mIPSCs from the experiment shown in panel A. Significant reduction was found in the distribution of the inter-event intervals. (C) Means values obtained from 12 neurons showing that the inhibitory effect of baclofen was selective to the frequency but not the amplitude. Mean±SEM. $^{c}P<0.01$ *vs* control.

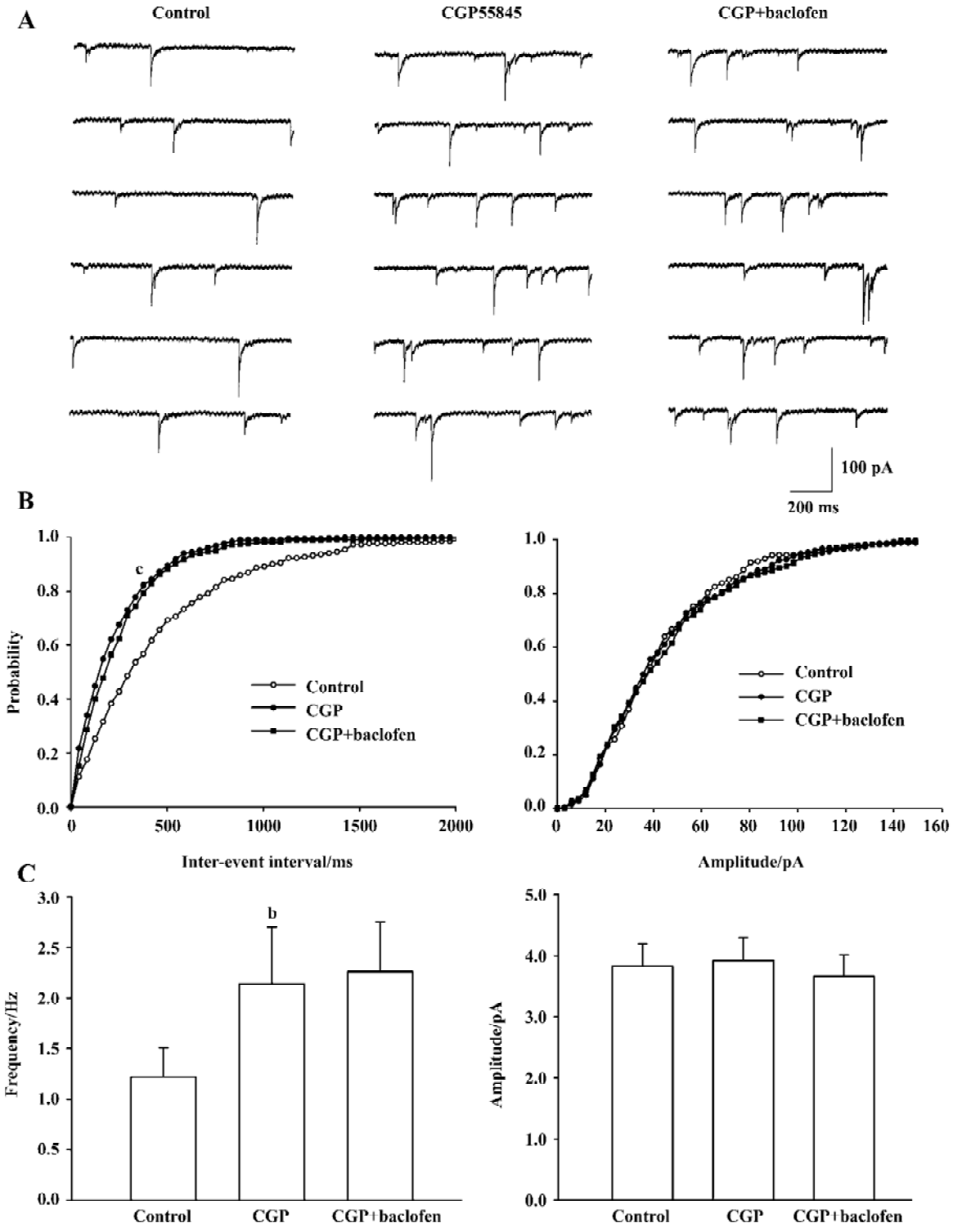

Figure 2. Presynaptic effect of baclofen was sensitive to CGP55845. (A) Typical traces showing that CGP55845 2 μmol/L increased the frequency and prevented the inhibitory effect of baclofen on the mIPSCs. (B) Cumulative probability distribution of the inter-event intervals and amplitudes of the mIPSCs from panel A. $^{c}P<0.01$ *vs* control. (C) Pooled data obtained from 6 cells showing that CGP55845 significantly increased the frequency of mIPSCs and blocked the presynaptic inhibition of baclofen. Mean±SEM. $^{b}P<0.05$ compared with control.

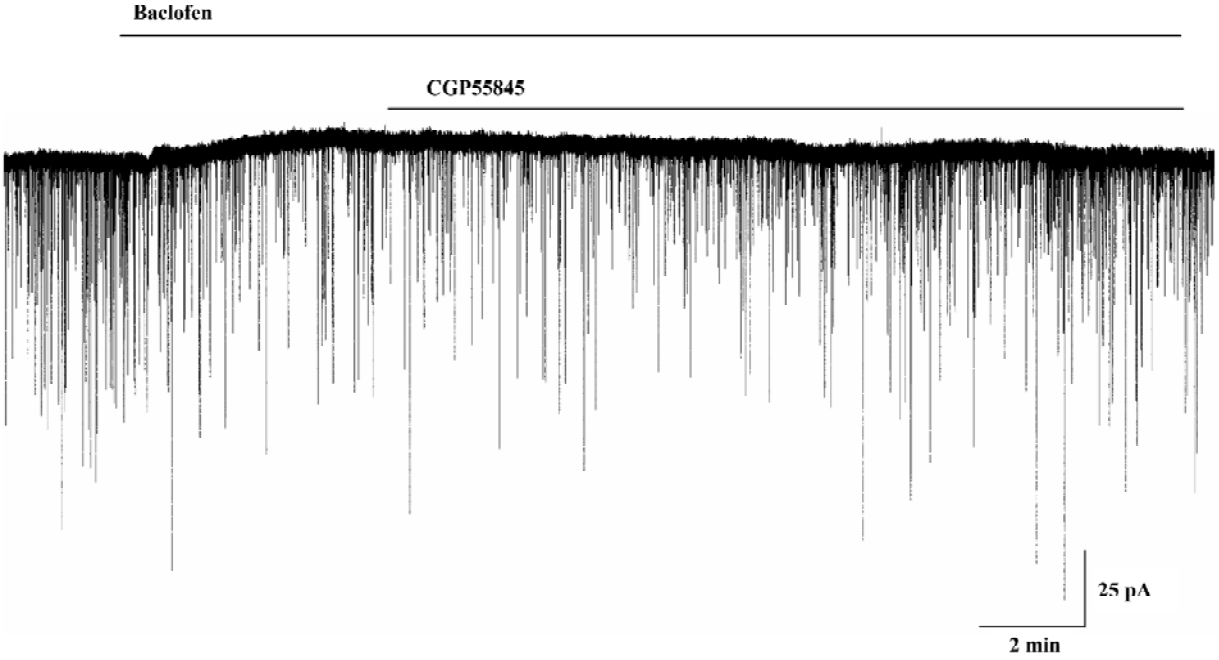

Figure 3. Postsynaptic effect of $GABA_B$ receptor activation. Typical trace showing the outward current induced by 30 μmol/L baclofen which was reversed by CGP55845 2 μmol/L.

Therefore, other factors like species variation and age might affect the outcome of the electrophysiological studies.

The presence of presynaptic $GABA_B$ receptors in the rat subthalamic nucleus has been reported by Shen and Johnson[18], based on a study of evoked IPSCs and their paired-pulse ratio. Our present study confirmed their work by showing that baclofen directly decreased the probability of action potential-independent release of GABA from presynaptic terminals. The conclusion was also enhanced by the use of a more specific and potent $GABA_B$ receptor antagonist, CGP55845. One surprising and intriguing finding of the present study is that CGP55845 increased the frequency of the mIPSCs but had no effect on the holding current, indicating that there is tonic activation of the pre- but not postsynaptic $GABA_B$ receptors. These data therefore suggest that the tonic release of GABA from pallidosubthalamic terminals, either from tonic firing of pallidal neurons, or from action potential-independent activities, may play a significant role in controlling the activity of subthalamic neurons. This finding has interesting implications in the therapeutic management of Parkinson disease. It is known that, in parkinsonian subjects, decreased activity of the GABAergic projection from the globus pallidus disinhibits the activity of subthalamic nucleus neurons, which results in enhanced inhibition on the basal ganglia targets. Since the tonic activity of presynaptic $GABA_B$ receptor on GABA release is expected to maintain the excitability of subthalamic nucleus, selective blockade of this tonic inhibition would help suppressing the subthalamic nucleus hyperactivity and therefore beneficial to parkinsonian subjects. This reasoning is supported by recent morphological evidence that parkinsonism is associated with an increased $GABA_B$ receptor immuno-reactivity, especially in the neurophil, of the subthalamic nucleus, reflecting an upregulation of presynaptic $GABA_B$ receptors[24].

In addition to the involvement in Parkinson's disease, the subthalamic nucleus has been reported to be involved in the genesis of epilepsy. Focal inhibition of the activity of the subthalamic nucleus by $GABA_A$ receptor agonist or high frequency deep brain stimulation exerted anticonvulsant effect in animal model and epilepsy patients[25-28]. Therefore, the results of the present study also provide a rationale for exploring the role of subthalamic $GABA_B$ receptor systems in the etiology and the treatment of epilepsy.

References

1 Bolam JP, Hanley JJ, Booth PAC, Bevan MD. Synaptic organisation of the basal ganglia. J Anat 2000; 196: 527–42.
2 Chesselet MF, Delfs JM. Basal ganglia and movement disorders: an update. Trends Neurosci 1996; 19: 417–22.
3 Smith Y, Parent A. Neurons of the subthalamic nucleus in primates

display glutamate but not GABA immunoreactivity. Brain Res 1988; 453: 353–6.
4 Smith Y, Bolam JP, Von Krosigk M. Topographical and synaptic organization of the GABA-containing pallidosubthalamic projection in the rat. Eur J Neurosci 1990; 2: 500–11.
5 Smith Y, Hazrati LN, Parent A. Efferent projections of the subthalamic nucleus in the squirrel monkey as studied by the PHA-L anterograde tracing method. J Comp Neurol 1990; 294: 306–23.
6 Smith Y, Wichmann T, DeLong MR. Synaptic innervation of neurones in the internal pallidal segment by the subthalamic nucleus and the external pallidum in monkeys. J Comp Neurol 1994; 343: 297–318.
7 Smith Y, Bevan MD, Shink E, Bolam JP. Microcircuity of the direct and indirect pathways of the basal ganglia. Neuroscience 1998; 86: 353–87.
8 DeLong MR. Primate models of movement disorders of basal ganglia origin. Trends Neurosci 1990; 13: 281–5.
9 Plenz D, Kitai ST. A basal ganglia pacemaker formed by the subthalamic nucleus and external globus pallidus. Nature 1999; 400: 677–82.
10 Magill PJ, Bolam JP, Bevan MD. Relationship of activity in the subthalamic nucleus-globus pallidus network to cortical electroencephalogram. J Neurosci 2000; 20: 820–33.
11 Magill PJ, Bolam JP, Bevan MD. Dopamine regulates the impact of the cerebral cortex on the subthalamic nucleus globus pallidus network. Neuroscience 2001; 106: 313–30.
12 Bevan MD, Magill PJ, Terman D, Bolam JP, Wilson CJ. Move to the rhythm: oscillations in the subthalamic nucleus-external globus pallidus network. Trends Neurosci 2002; 25: 525–31.
13 Bergman H, Wichmann T, DeLong MR. Reversal of experimental parkinsonism by lesions of the subthalamic nucleus. Science 1990; 249: 1436–8.
14 Krack P, Benazzouz A, Pollak P, Limousin P, Piallat B, Hoffmann D, *et al*. Treatment of tremor in Parkinson's disease by subthalamic nucleus stimulation. Mov Disord 1998; 13: 907–14.
15 Limousin P, Pollak P, Benazzouz A, Hoffmann D, Le Bas JF, Broussolle E, *et al*. Effect of parkinsonian signs and symptoms of bilateral subthalamic nucleus stimulation. Lancet 1995; 345: 91–5.
16 Olanow CW, Brin MF, Obeso JA. The role of deep brain stimulation as a surgical treatment for Parkinson's disease. Neurology 2000; 55: S60–6.
17 Wilson CL, Puntis M, Lacey MG. Overwhelmingly asynchronous firing of rat subthalamic nucleus neurones in brain slices provides little evidence for intrinsic interconnectivity. Neuroscience 2004; 123: 187–200.
18 Shen KZ, Johnson SW. Presynaptic GABA(B) receptors inhibit synaptic inputs to rat subthalamic neurons. Neuroscience 2001; 108: 431–6.
19 Chan PK, Yung WH. Inhibitory postsynaptic currents of rat substantia nigra pars reticulate neurons: role of GABA receptors and GABA uptake. Brain Res 1999; 838: 18–26.
20 Charara A, Heilman TC, Levey AI, Smith Y. Pre- and postsynaptic localization of $GABA_B$ receptors in the basal ganglia in monkeys. Neuroscience 2000; 95: 127–40.
21 Chen L, Boyes J, Yung WH, Bolam JP. Subcellular localization of $GABA_B$ receptor subunits in rat globus pallidus. J Comp Neurol 2004; 474: 340–52.
22 Chan SC, Yung KK, Yung WH. Pre-and postsynaptic distribution of $GABA_B$ receptors in rat globus pallidus revealed by immunocytochemistry and electrophysiology. Soc Neurosci Abstr 2000; 26: 622.17.
23 Chen L, Chan SC, Yung WH. Rotational behavior and electrophysiological effects induced by $GABA_B$ receptor activation in rat globus pallidus. Neuroscience 2002; 114: 417–25.
24 Ng TK, Yung KK. Increase in expression of $GABA_B$ receptor immunoreactivity in the subthalamic nucleus and the substantia nigra of 6-hydroxydopamine-lesioned rats. Soc Neurosci Abstr 2002; 28: 63. 12.
25 Dybdal D, Gale K. Postural and anticonvulsant effects of inhibition of the rat subthalamic nucleus. J Neurosci 2000; 20: 6728–33.
26 Lado FA, Velisek L, Moshe SL. The effect of electrical stimulation of the subthalamic nucleus on seizures is frequency dependent. Epilepsia 2003; 44: 157–64.
27 Vercueil L, Benazzouz A, Deransart C, Bressand K, Marescaux C, Depaulis A, *et al*. High-frequency stimulation of the subthalamic nucleus suppresses absence seizures in the rat: comparison with neurotoxic lesions. Epilepsy Res 1998; 31: 39–46.
28 Benabid AL, Minotti L, Koudsie A, de Saint Martin A, Hirsch E. Antiepileptic effect of high-frequency stimulation of the subthalamic nucleus (corpus luysi) in a case of medically intractable epilepsy caused by focal dysplasia: a 30-month follow-up: technical case report. Neurosurgery 2002; 50: 1385–92.

Full-length article

Intracellular dopamine oxidation mediates rotenone-induced apoptosis in PC12 cells[1]

Hua-qing LIU[2], Xing-zu ZHU[2,3], En-qi WENG[4]

[2] *Department of Pharmacology, Institute of Materia Medica, Shanghai Institutes for Biological Sciences, Chinese Academy of Sciences, Shanghai 201203, China;* [4] *Department of Environmental Science and Technology, East China Normal University, Shanghai 200062, China*

Key words

Parkinson disease; rotenone; reserpine; deprenyl; reactive oxygen species; neurotoxicity

[1] Work supported by a grant from the Chinese Academy of Science and Grant G (1998) 051108 from the Ministry of Sciences and Technology of China.
[3] Correspondence to Xing-zu ZHU, PhD.
Phn 86-21-5080-6096. Fax 86-21-5080-7088.
E-mail xzzhu@mail.shcnc.ac.cn

Received 2004-03-15
Accepted 2004-10-10

doi: 10.1111/j.1745-7254.2005.00003.x

Abstract

Aim: To study the role of dopamine (DA) in rotenone-induced neurotoxicity in PC12 cells. **Methods:** Cell viability was assessed by detecting the leakage of lactate dehydrogenase (LDH) into the medium. Apoptosis rate was measured by flow cytometry. Caspase-3-like activity was measured by fluorescence assay using the probe Ac-DEVD-AMC. The level of intracellular hydrogen peroxide and other peroxides in PC12 cells were quantified by loading cells with 2'-7'-Dichlorodihydrofluorescein diacetate (DCFH-DA) in fluorescence assay. Lactic acid was measured spectrophotometrically. The DA levels in PC12 cells were determined by HPLC-ECD. **Results:** A 48-h incubation of PC12 cells with rotenone caused an apoptotic cell death and elevated intracellular reactive oxygen species (ROS) and lactic acid accumulation. Intracellular DA depletion with reserpine significantly attenuated rotenone-induced ROS accumulation and apoptotic cell death. No change was found in rotenone-induced ROS accumulation when cells were co-treated with deprenyl. Brief treatment with reserpine at the end of rotenone treatment had no effect on rotenone-induced neurotoxicity. However, when cells were first incubated with deprenyl, a monoamine oxidase-B inhibitor for 30 min then co-incubated with rotenone plus deprenyl, a brief treatment with reserpine enhanced cell injury. **Conclusion:** Rotenone-induced apoptosis in PC12 cells was mediated by intracellular dopamine oxidation.

Introduction

Parkinson disease (PD) is a chronic neurodegenerative disorder characterized by the loss of dopamine (DA) neurons in the substantia nigra, decreased striatal DA levels, and consequent extrapyramidal motor dysfunction. Although the genes responsible for a few rare familial cases of PD have been discovered[1-3], the causes of more prevalent idiopathic PD are still unknown. Substances that are toxic to dopaminergic cells have been proposed as contributors to this neurological disease[4,5]. MPTP (1-Methyl-4-phenyl-1, 2,3,6-tetrahydropyridine) is one of the best described neurotoxins. Evidence has shown that the neurotoxicity of MPTP depends on its active metabolite, 1-methyl-4-phenyl-pyridinium (MPP^+), which inhibits mitochondrial complex I and depletes cellular ATP levels, resulting in cell death[6]. Thus, one hypothesis has focused on mitochondrial dysfunction[7].

Rotenone, a naturally occurring, lipophilic compound from the roots of certain plants (*Derris* species), is a specific inhibitor of mitochondrial complex I and is used as the main component of many insecticides. Based on the mitochondrial dysfunction hypothesis of PD, a number of studies have evaluated the effects of rotenone on dopaminergic neurons both *in vitro* and *in vivo*[8-15]. Treatment of mesencephalic cultures and striatal synaptosomes with rotenone caused neurotoxicity which was measured by a decreased uptake of neurotransmitters[8,9]. Studies *in vivo* have shown that rotenone was capable of causing degeneration of dopaminergic neurons and induction of parkinsonian symptoms in animals[10-15]. An important morphological finding in rotenone-treated rats was that the nigrostriatal DA neurons had accumulated fibrillar cytoplasmic inclusions containing

ubiquitin and alpha-synuclein, similar to Lewy bodies in idiopathic PD[13,16]. This finding is interesting, because recent discoveries of the two causative gene products of familial PD, Parkin[1,17,18] and alpha-synuclein[3] indicate that failure of the ubiquitin-proteasome system might be common in both familial PD and idiopathic PD[19]. Another reason is that rotenone is widely used as insecticide, and therefore is a real threat as an environmental substance to cause PD. Thus, elucidation of its mode of action is of high importance in understanding and potentially treating this disorder. The present study was designed to assess the neurotoxicity of rotenone on DA-producing PC12 cells and explore the possible mechanism.

Materials and methods

Reagents Dulbecco's modified Eagle's medium (DMEM) was purchased from GibcoBRL (Gaithersburg, MD, USA). Horse serum and fetal calf serum were obtained from Hyclone (Logan, UT, USA). Rotenone, reserpine, deprenyl, *N*-acetyl-*L*-cysteine (NAC), propidium iodide (PI), dihydroxybenzylamine (DHBA) and 2′,7′-dichlorofluorescein-diacetate (DCFH-DA) were purchased from Sigma (St Louis, MO, USA). Caspase-3 substrate AC-*L*-aspartic-*L*-glutamic-*L*-alyl-*L*-aspartic acid-7-amino-4-methylcoumarin (Ac-DEVD-AMC) was obtained from Calbiochem (La Jolla, CA, USA).

Cell culture The rat pheochromocytoma cell line PC12 cells (American Type Culture Collection, Rockville, MD, USA) were propagated in DMEM, supplemented with heat-inactivated horse serum (10%, v/v) and fetal calf serum (5%, v/v), 100 g/L streptomycin and 100 kU/L penicillin. The cultures were maintained in an incubator at 37 ºC in a high humidity atmosphere of 5% CO_2. The medium was changed every 2 d and cells were passaged once a week. Twenty-four hours before addition of various reagents, the cells were seeded on 60-mm-dishes (Falcon), covered with collagen (Sigma), at a density of $1\times10^5/cm^2$ in normal medium. Rotenone and reserpine were first dissolved in dimethyl sulfoxide (Me_2SO) and then diluted in medium to a final concentration of Me_2SO less than 0.1%. Controls for each drug condition consisted of sister cultures treated with the vehicle used to dissolve that drug. Stock solutions of deprenyl and NAC were prepared in Hanks' balanced salt solution containing 2 mmol/L HEPES.

Assessment of cell viability Cell viability was assessed by detecting the leakage of lactate dehydrogenase (LDH) into the medium. Cells were treated with rotenone or other reagents, then an aliquot of medium was taken and centrifuged at 250×*g* for 5 min. Supernatant (10 mL) was added into phosphate buffer 0.1 mol/L (pH 7.0) containing sodium pyruvate 2.3 mmol/L and NADH 5 mmol/L to a total volume of 200 mL. The decrease in absorbance over time at 340 nm was monitored at 25 ºC. Then the activity of LDH in medium was calculated. Cell total LDH was obtained after exposure of culture to 0.2% TritonX-100 at 37 ºC for 30 min. LDH leakage was expressed as percentage of LDH in medium to total LDH.

Analysis of apoptosis by flow cytometry Apoptosis rate was measured by flow cytometry as reported previously[19]. Briefly, PC12 cells were washed with PBS (pH 7.4), fixed in cold 70% (v/v) ethanol, and incubated under -20 ºC for at least 2 h. The fixed cells were harvested by centrifugation at 250×*g* for 5 min. The cell pellets were resuspended in 1 mL PBS at room temperature for 10 min. After another centrifugation, the cell pellets were resuspended in 500 mL PBS containing 0.2 g/L RNase A and incubated at 37 ºC for 30 min. After incubation, the cells were stained with 20 g/L PI at 4 ºC for 30 min. The fluorescence of cells was measured with FACSCalibur flow cytometer (BD Immunocytometry Systems, San Jose, CA, USA). The relative content of DNA indicated the distribution of a population of cells throughout the cell cycle. Apoptotic cells caused the appearance of a sub-diploid peak in the cell-cycle profile. The percentage of apoptotic cells was determined by using BD CellQuest software.

Assay for caspase-3 activity Caspase-3-like activity was measured as described in a previous study with modification[20]. In brief, the PC12 cells were collected and washed with PBS (pH 7.4). After centrifugation at 250×*g* for 5 min, cell pellets were lysed with NP-40 (0.5%)/HEPES (10 mmol/L) (pH 7.4), containing EDTA 2 mmol/L, PMSF 0.5 mmol/L and leupeptin 5 mg/L. The lysates were centrifuged at 7500×*g* for 10 min. The protein concentration in the supernatant was determined with Lowry method. Then 50 μg of protein was incubated with caspase-3 substrate Ac-DEVD-AMC 50 μmol/L. The increase of fluorescence was measured every 1 min in a 30 min period using a PolarStar plate reader (BMG labtechnologies, Australia) with an excitation wavelength of 380 nm and an emission wavelength of 450 nm. The enzyme activity was expressed as fluorescent units per min per mg protein.

Measurement of reactive oxygen species production The level of intracellular hydrogen peroxide and other peroxides in PC12 cells were quantified by loading cells with 2′-7′-dichlorodihydrofluorescein diacetate (DCFH-DA) as described previously[19]. In brief, the PC12 cells were washed with PBS (pH 7.4), resuspended in Krebs-Ringer buffer

(HEPES 20 mmol/L, dextrose 10 mmol/L, NaCl 127 mmol/L, $CaCl_2$ 1 mmol/L, KCl 5.5 mmol/L, $MgSO_4$ 2 mmol/L, pH 7.4), and then loaded with DCFH-DA 5 mmol/L for 60 min. The cells were again washed with Krebs-Ringer buffer to remove the extracellular dye and lysed in Tris-HCl 10 mmol/L (pH 7.4) containing 0.5% Triton X-100. The fluorescence in lysates was detected using a PolarStar plate reader (BMG labtechnologies, Australia) with an excitation wavelength of 485 nm and an emission wavelength of 520 nm. The fluorescence intensity was normalized based on the protein concentration of individual extract. The ROS production was expressed as percentage compared with cells without treatment.

Determination of lactic acid accumulation Lactic acid accumulation was measured as described previously[21]. In brief, PC12 cells were homogenized with sodium phosphate 50 mmol/L (pH 6.5) and boiled for 15 min. Lactic acid content was measured spectrophotometrically at 340 nm in a buffer containing LDH and hydrazine (0.4 mol/L)/glycine (0.5 mol/L) (pH 9.0). Lactic acid accumulation was normalized based on the protein concentration of individual extract, and expressed as percentage compared with cells without treatment. Protein concentration was detected by the Lowry method.

Measurement of dopamine in PC12 cells The DA levels in PC12 cells were determined by a modification of the methods described previously[22-24]. In brief, cells were lysed in 1% metaphosphoric acid containing EDTA 1 mmol/L. Each sample added with 20 mL of DHBA was regarded as an internal standard. After centrifugation (17 500×*g* for 10 min at 4 ºC), the supernatant was filtered, and a 20 mL aliquot was immediately injected into the HPLC system for DHBA and DA determination. The assay was done with a BAS PM80 pump, a Waters Nova-Pak C18 column, and an electrochemical detector (BAS LC-4C). The mobile phase was citric acid 0.1 mol/L, K_2HPO_4 0.1 mol/L, EDTA 0.1 mmol/L, 5% methanol, and sodium octylsulfate 70 mg/L (pH 3.0); the flow rate was 1.0 mL/min. The potential of the electrode was set at +0.7 V. DA level in each sample was quantified by comparing DA and DHBA peak areas with those of standard solutions containing DA and DHBA, and then normalized based on the protein concentration of each individual sample. The DA level was expressed as percentage compared with control cells without reserpine treatment.

Statistics Data for cell viability, caspase-3 activity, ROS production and lactic acid accumulation were presented as mean±SD of four independent experiments. Data for dopamine levels in cells are means±SD of three experiments performed in triplicate. Statistical analysis was performed by applying the Student's *t*-test and one-way ANOVA.

Results

Oxidative stress is involved in rotenone-induced neurotoxicity When PC12 cells were treated with 12.5 and 25 nmol/L rotenone for 48 h, LDH leakage increased from 7.8%±1.1% to 19.7%±1.1% and 30.1%±3.6% ($P<0.01$ *vs* control), respectively (Figure 1A). The rotenone-induced cell injury was associated with caspase-3 activation (Figure 1B), supporting the notion that an apoptotic cell death mechanism was involved in rotenone-induced neurotoxicity. Rotenone treatment induced a concentration-dependent increase of ROS levels within PC12 cells (Figure 1C). Rotenone treatment also induced an increase in lactic acid accumulation in PC12 cells (Figure 1D), suggesting that both oxidative stress and mitochondrial dysfunction were responsible for cell injury. The effects of rotenone were attenuated by 2.5 and 5 mmol/L NAC co-treatment (Figure 2A-2C), further supporting the notion that oxidative stress was involved in rotenone neurotoxicity. In addition, 2.5 and 5 mmol/L NAC also attenuated rotenone-induced increase in lactic acid accumulation (Figure 2D).

Rotenone-induced ROS accumulation is mediated by DA oxidation To test whether manipulation of DA levels would attenuate rotenone-induced cell death, PC12 cells were first depleted of intracellular DA using reserpine and then treated with rotenone. Reserpine (1 and 5 μmol/L) treatment for 3 h induced 66% and 87% depletions of DA respectively as compared with the control (Figure 3). The rotenone-induced elevation of LDH leakage and caspase-3 activation were attenuated in reserpine-pretreated PC12 cells (Figure 4A–4B), suggesting that DA played an important role in rotenone-induced cell injury. The rotenone-induced intracellular accumulation of ROS was also attenuated by this manipulation (Figure 4C). The results suggest that DA oxidation is involved in the production of ROS. In addition, lactic acid accumulation assay indicated that the rotenone-induced energy crisis was partially alleviated if PC12 cells were pretreated with reserpine (Figure 4D).

Analyzed quantitatively by flow cytometry, the apoptotic rates increased significantly in PC12 cells treated with rotenone (12.5 and 25 nmol/L) for 48 h (Figure 5A). The co-treatment with NAC 2.5 and 5 mmol/L or pre-treatment with reserpine 1 and 5 mmol/L for 3 h also decreased the rotenone-induced apoptotic rate (Figure 5B and 5C).

DA auto-oxidation is responsible for rotenone-induced neurotoxicity To test whether DA deamination or auto-oxidation was more responsible for rotenone-induced neuro-

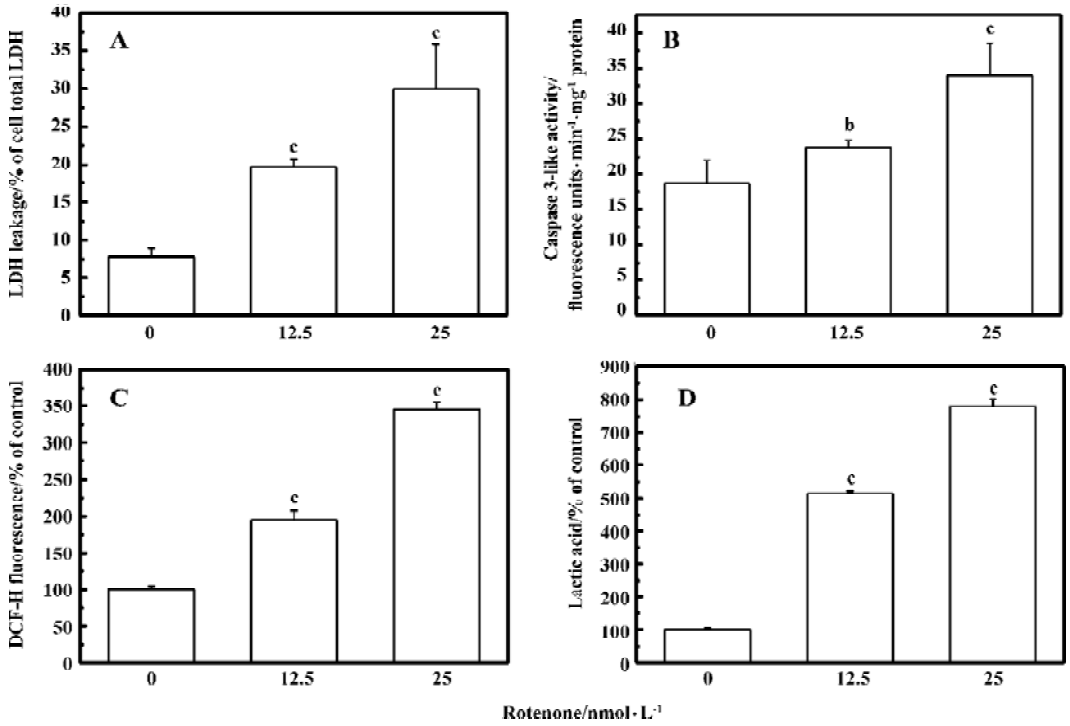

Figure 1. Effects of rotenone on PC12 cells. The leakage of LDH was expressed as percentage of LDH in medium to total LDH (A). Caspase-3-like activity was expressed as fluorescence units per min per mg protein (B). ROS production was expressed as percentage compared with control group (C). Lactic acid content expressed as percentage compared with control group (D). n=4. Mean±SD. $^{b}P<0.05$, $^{c}P<0.01$ *vs* control.

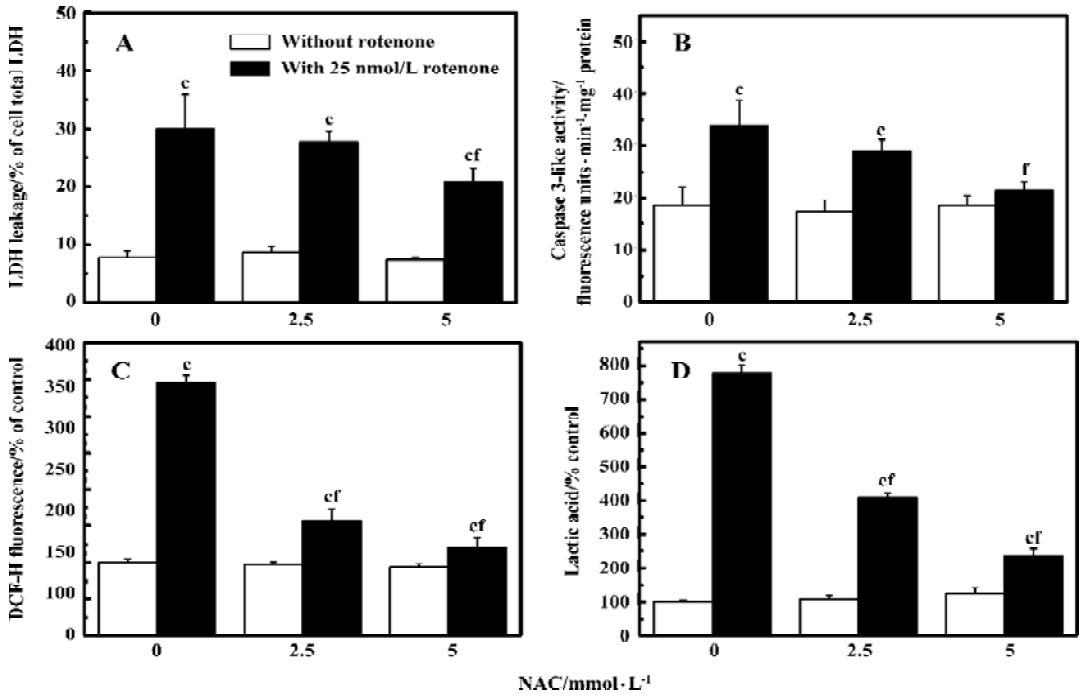

Figure 2. Effect of *N*-acetyl-*L*-cysteine on rotenone-induced PC12 cell injury. Cell viability (A), caspase-3-like activity (B), ROS production (C), and lactic acid accumulation (D) were assessed respectively as described in Figure 1. n=4. Mean±SD. $^{c}P<0.01$ *vs* control. $^{f}P<0.01$ *vs* 25 nmol/L rotenone treatment in the absence of NAC.

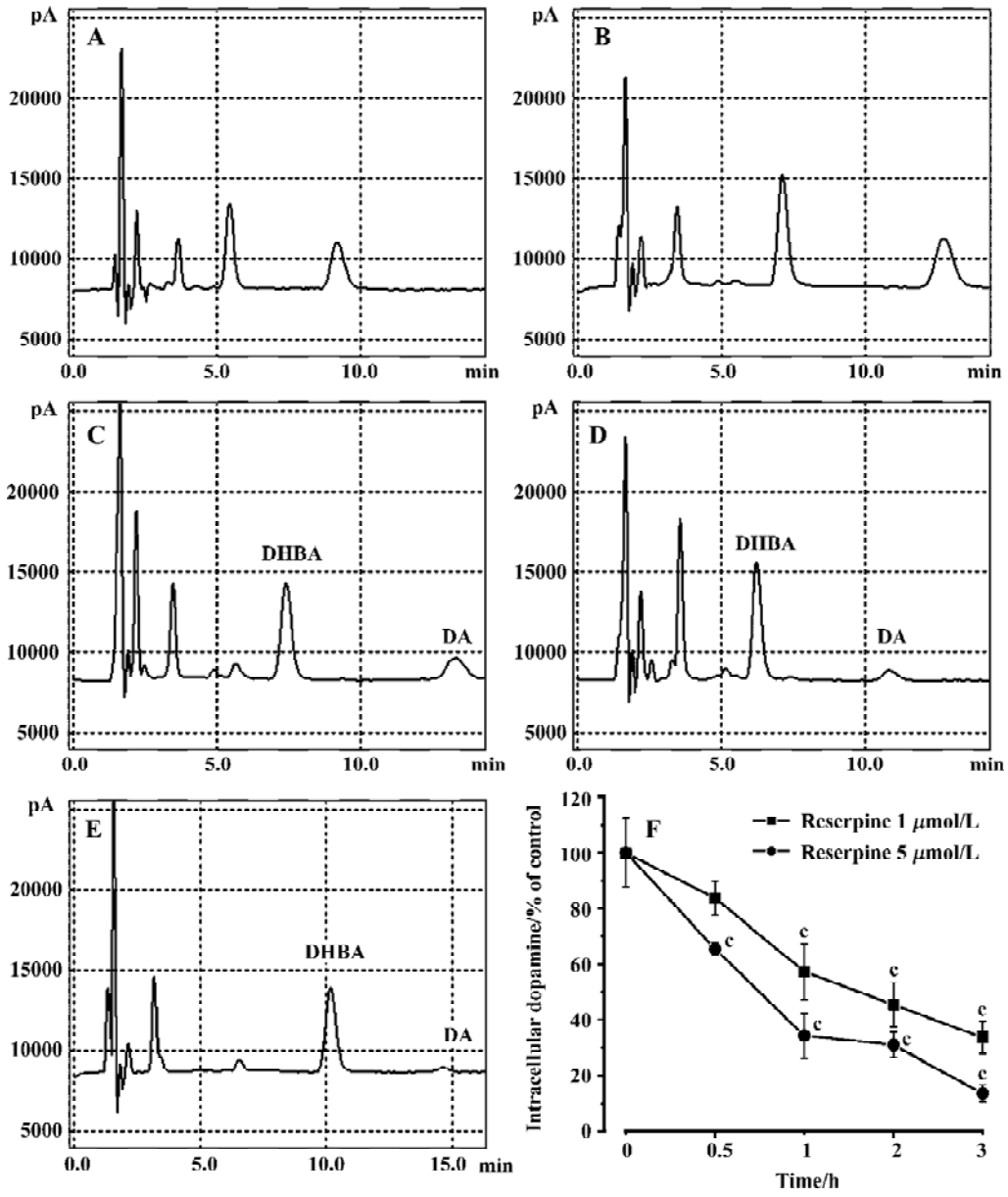

Figure 3. Reserpine-induced intracellular dopamine depeletion in PC12 cells. Representative of HPLC-EC of lysate from control cells (A) and cells treated with reserpine 5 mmol/L for 30 min (B), 1 h (C), 2 h (D), and 3 h (E). (F): Mean±SD of three experiments performed in triplicate. $^{c}P<0.01$ *vs* control.

toxicity in PC12 cells, deprenyl, a monoamine oxidase-B (MAO-B) inhibitor, was used. The treatment with deprenyl at concentration between 25 to 200 μmol/L for 48 h had no significant effects on the LDH leakage in PC12 cells (Figure 6). When PC12 cells were first treated with 100 μmol/L deprenyl for 30 min and then co-treated with deprenyl 100 μmol/L plus rotenone 25 nmol/L for 48 h, no significant difference was found in the LDH leakage, caspase-3 activation or ROS production if compared with PC12 cells treated with rotenone 25 nmol/L alone (Table 1). The results suggest that the oxidative deamination of DA catalyzed by MAO-B was not a major source of ROS in the present studies.

Vesicular monoamine transporter is crucial for cell survival when there is mitochondrial dysfunction plus enchanced DA auto-oxidation To examine whether vesicular monoamine transporter (VMAT) was involved in roten-

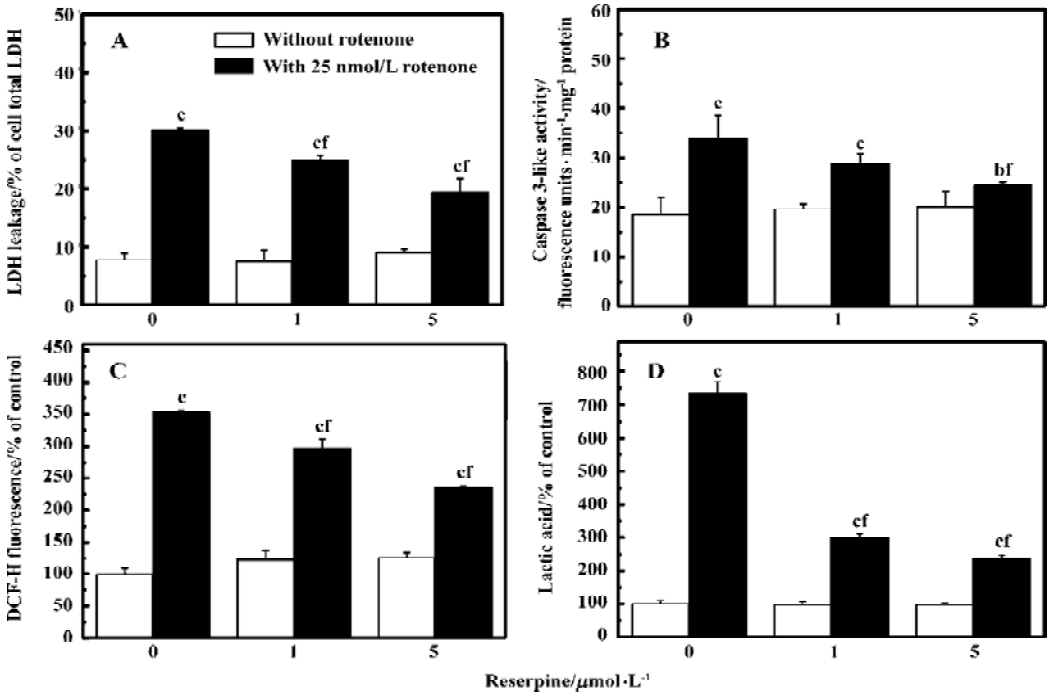

Figure 4. Effect of reserpine on rotenone-induced PC12 cell injury. LDH leakage (A), caspase-3-like activity (B), ROS production (C), and lactic acid accumulation (D) were measured respectively as described in Figure 1. n=4. Mean±SD. $^{b}P<0.05$, $^{c}P<0.01$ *vs* control. $^{f}P<0.01$ *vs* 25 nmol/L rotenone treatment in the absence of reserpine.

Table 1. Effects of brief reserpine treatment before the completion of 48 h deprenyl plus rotenone treatment on LDH leakage, caspase-3-like activity, and ROS production. Mean±SD from four independent experiments. $^{c}P<0.01$ *vs* control. $^{f}P<0.01$ *vs* 100 μmol/L deprenyl plus 25 nmol/L rotenone treatment.

	LDH leakage/ % of cell total LDH	Caspase-3-like activity/ fluorescence unit ·min^{-1}·mg^{-1} protein	DCF-H fluorescence/ % of control
Control	7.83±1.10	18.60±3.41	100.00±5.09
Rotenone (25 nmol/L)[1]	30.12±0.34^{c}	33.87±4.70^{c}	351.77±4.27^{c}
Reserpine (1 mmol/L)[2]	7.54±2.01	19.56±1.08	122.78±13.98
Reserpine (5 mmol/L)[3]	9.08±0.59	20.12±3.10	125.92±8.54
Rotenone (25 nmol/L)+Reserpine (1 mmol/L)[4]	32.47±2.01^{c}	34.46±2.31^{c}	360.23±5.87^{c}
Rotenone (25 nmol/L)+Reserpine (5 mmol/L)[5]	33.01±1.79^{c}	34.89±0.79^{c}	369.49±7.81^{c}
Deprenyl (100 μmol/L)+Rotenone (25 nmol/L)[6]	31.27±2.22^{c}	34.02±1.14^{c}	357.39±7.83^{c}
Deprenyl (100 μmol/L)+Rotenone (25 nmol/L)+Reserine (1 mmol/L)[7]	44.68±3.49^{f}	38.78±2.02^{f}	378.45±2.08^{f}
Deprenyl (100 μmol/L)+Rotenone (25 nmol/L)+Reserpine (5 mmol/L)[8]	51.37±2.62^{f}	42.54±1.84^{f}	435.72±5.47^{f}

[1] PC12 cells were treated with 25 nmol/L rotenone for 48 h.
[2] PC12 cells were treated with 1 mmol/L reserpine for 30 min.
[3] PC12 cells were treated with 5 mmol/L reserpine for 30 min.
[4] PC12 cells were treated with 25 nmol/L rotenone for 48 h and then with 1 mmol/L reserpine before the end of 48 h rotenone treatment.
[5] PC12 cells were treated with 25 nmol/L rotenone for 48 h and then with 5 mmol/L reserpine before the end of 48 h rotenone treatment.
[6] PC12 cells were pretreated with 100 μmol/L deprenyl for 30 min and then with 100 μmol/L deprenyl plus 25 nmol/L rotenone for 48 h.
[7] PC12 cells were pretreated with 100 μmol/L deprenyl for 30 min and then with 100 μmol/L deprenyl plus 25 nmol/L rotenone for 48 h. Reserpine (1 mmol/L) was added 30 min before the end of 48 h deprenyl plus rotenone treatment.
[8] PC12 cells were pretreated with 100 μmol/L deprenyl for 30 min and then with 100 μmol/L deprenyl plus 25 nmol/L rotenone for 48 h. Reserpine (5 mmol/L) was added 30 min before the end of 48 h deprenyl plus rotenone treatment.

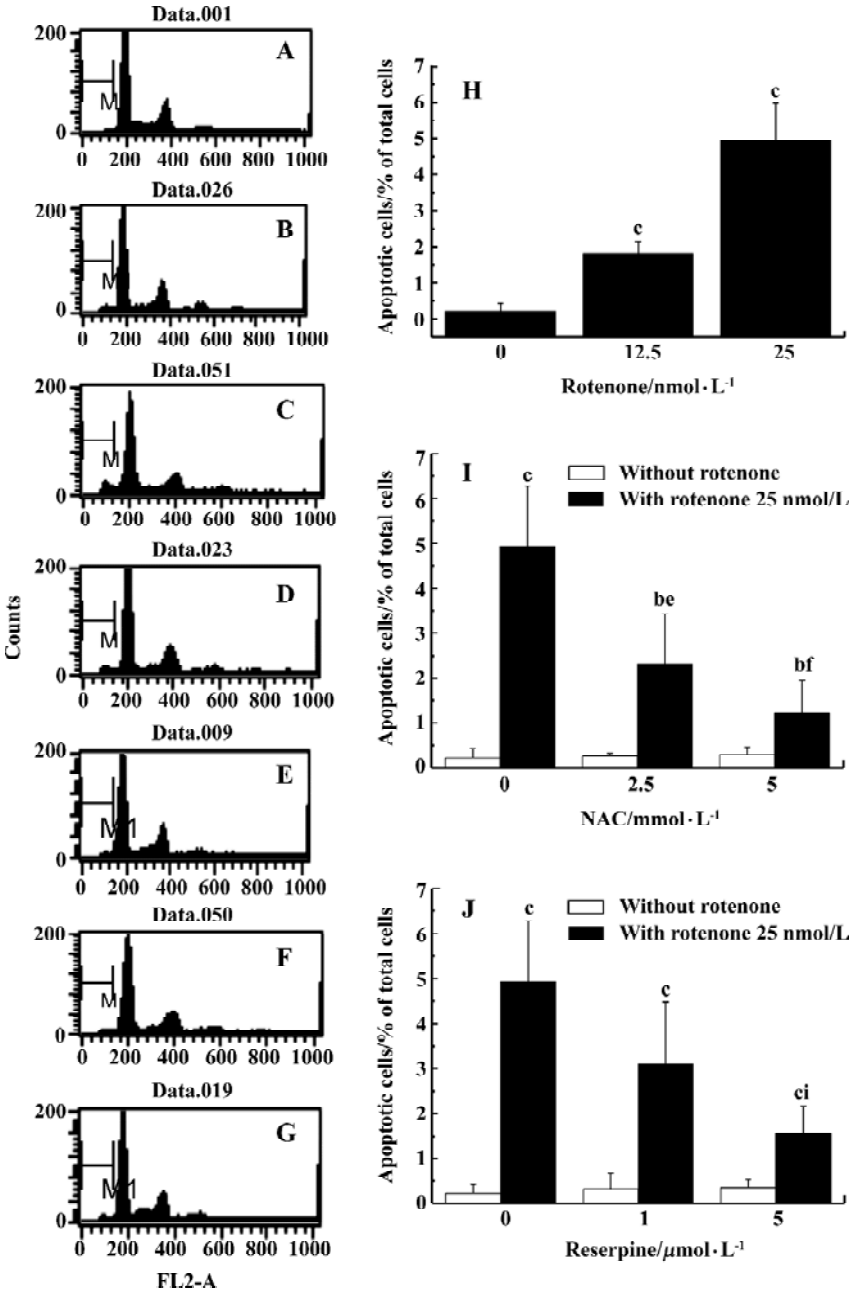

Figure 5. Rotenone-induced increased apoptotic rate in PC12 cells. Representative of flow cytometry of control cells (A), and cells treated with 12.5 nmol/L rotenone (B) or 25 nmol/L rotenone for 48 h (C). (D): Representative of flow cytometry of PC12 cells were incubated with 25 nmol/L rotenone plus 2.5 mmol/L NAC, or 25 nmol/L rotenone plus 5 mmol/L NAC (E); cells were treated with 1 mmol/L reserpine for 3 h and then with 25 nmol/L rotenone for 48 h (F), or 5 mmol/L reserpine for 3 h and then with 25 nmol/L rotenone for 48 h (G). Mean±SD of four independent experiments for each treatment group. $^{b}P<0.05$, $^{c}P<0.01$ *vs* control. $^{e}P<0.05$, $^{f}P<0.01$ *vs* 25 nmol/L rotenone treatment in the absence of NAC. $^{i}P<0.01$ *vs* 25 nmol/L rotenone treatment in the absence of reserpine.

one-induced neurotoxicity in PC12 cells, 1 or 5 μmol/L reserpine was added 30 min before the end of 48 h-rotenone treatment. No change was found in rotenone-induced neurotoxicity with the brief reserpine treatment. However, when PC12 cells were pretreated with deprenyl 100 μmol/L for 30 min and then with deprenyl 100 μmol/L plus rotenone 25 nmol/L for 48 h, the 30-min incubation with reserpine 1 or 5 μmol/L before the end of 48-h treatment with deprenyl plus rotenone induced significant increases in LDH leakage, caspase-3 activation, and ROS (Table 1).

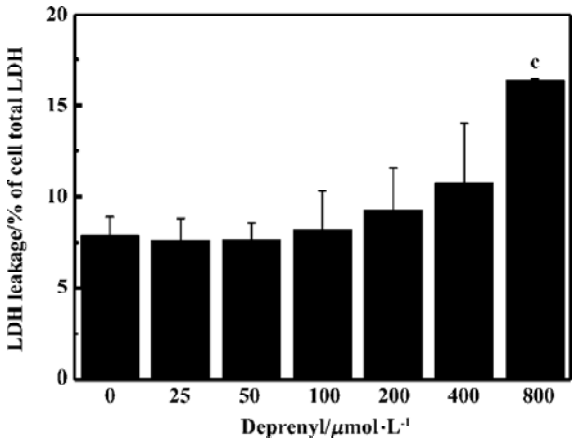

Figure 6. Effects of deprenyl on PC12 cells. Mean±SD values of four independent experiments for each treatment group. $^{c}P<0.01$ *vs* control.

Discussion

In the present study, the mechanisms of rotenone-induced neurotoxicity in DA-producing PC12 cells was invesigated. We found that rotenone induced an apoptotic type of cell death. This result is similar to the results reported by Bal-Price and Brown[25]. They found that a 24-h incubation of PC12 cells with nitric oxide donors or rotenone, in the presence of glucose, induced apoptosis of PC12 cells as determined by nuclear morphology and caspase-3 activation. We found that rotenone induced apoptosis in PC12 cells accompanied with an elevated ROS production. Given that mitochondria is a major cellular source of ROS[26] and that rotenone is a kind of complex I inhibitor, it could be hypothesized that rotenone-induced ROS might be originated from mitochondria. Indeed, high concentrations of rotenone have been reported to induce superoxide production *in vitro* and *in vivo*[27-30]. In isolated nerve terminals, Sipos *et al*[31] found that inactivation of complex I to a small extent (16%) resulted in a significant increase in ROS formation. However, other studies have suggested converse results[32-34]. Lotharius and O'Malley[35] found that low doses (5-50 nmol/L) of rotenone killed dopaminergic neurons with a similar time course and morphology to MPP^+. However, no increase was found in intracellular superoxide levels after the dopaminergic neurons were treated with rotenone for 0.5, 1, 3, and 6 h. Because the classic complex I inhibitor rotenone did not induce ROS, they concluded that MPP^+-induced superoxide did not arise from blockade of electron transport. In the present study, however, we found a significant increase of ROS production from PC12 cells after rotenone treatment for 48 h. While DCFH-DA was used as a probe to measure the redox state of a cell, the resluts were validated carefully. We found that the rotenone-induced ROS accumulation and cell death were attenuated by an antioxidant, NAC. This result supports the notion that an oxidative stress mechanism is involved in rotenone-induced neurotoxicity in PC12 cells.

If toxic agents were involved in the pathogenesis of PD, this should likely reflects a multifactorial etiology in which the effects of environmental insults are compounded by predisposing genetic traits, age-related changes and interactions with endogenous elements (i.e. factors inherent to the nigrostriatal tissue). The presence of dopamine within nigrostriatal neurons may itself constitute a risk factor that enhances their vulnerability to toxic events, such as increased production of oxidizing species. To test whether manipulation of DA levels would attenuate rotenone-induced cell death, cells were depleted of intracellular DA using reserpine prior to rotenone treatment. In the present studies, we demonstrated that reserpine induced a concentration- and time-dependent DA depletion in PC12 cells. When PC12 cells were treated with 1 and 5 mmol/L reserpine for 3 h, 66% and 87% decreases in DA levels were found respectively, as compared with the control (Figure 3). Our results were similar to those reported by Brautigam *et al*[36] who reported more that 50% depletion of intracellular DA in PC12 cells after reserpine incubation. Our finding that DA depletion significantly attenuated rotenone-induced ROS production and cell death suggests that DA plays an important role in rotenone-induced ROS production and cell death. Since DA in the cytoplasm can be readily autoxidized[37] or deaminated[38] by MAO-B to produce ROS[39], deprenyl, a MAO-B inhibitor, was used to test whether MAO-B inhibition could protect PC12 cells from rotenone-induced ROS accumulation and cell death. Although it has been shown that MAO-B inhibition by pretreatment with deprenyl significantly reduces cellular DOPAC formation in PC12 cells[40], it had no effect on the rotenone-induced ROS accumulation and cell death in our studies, suggesting that the oxidative deamination of DA catalyzed by MAO-B was not the main source of ROS in rotenone-treated PC12 cells and that DA auto-oxidation is responsible for rotenone-induced oxidative stress.

The presence of dopamine within nigrostriatal neurons can itself constitute a risk factor that enhances their vulnerability to toxic agents. For example, rotenone-induced dendrite loss was severe in the substantia nigra, whereas noncatecholamine neurons, such as those in the perifornical nucleus, were more resistant[41]. Other factors might also play roles in the vulnerability to toxic agents since some dopamine neurons in hypothalamic A11 and the ventral tegmental area were spared when treated with rotenone. By *in*

situ hybridization, a weaker expression of VMAT was found in the rat substantia nigra than in the ventral tegmental area[42]. If VMAT effectively protects the cell against oxidative stress induced by dopamine, the weak expression of VMAT in substantia nigra might account for its particular vulnerability to toxic agents.

No change was found in the rotenone-induced neurotoxicity. However, when PC12 cells were pretreated with deprenyl and then with deprenyl plus rotenone for 48 h, significant increases in LDH leakage, caspase-3 activation, and ROS production were found. The results suggest that VMAT activity might be important for cell survival if there is mitochondrial dysfunction. In other words, disruption in dopamine disposition and/or metabolism could underlie the progressive degeneration of dopaminergic neurons in PD.

As a specific inhibitor of mitochondrial complex I, the metabolic consequence of mitochondrial electron flow blockage induced by rotenone would be the incomplete oxidation of glucose and consequent lactic acid accumulation. Indeed, we showed that rotenone treatment also induced an increase in lactic-acid accumulation. The results support the notion that mitochondrial dysfunction is responsible for rotenone-induced cell death in PC12 cells. Mitochondria in PC12 cells can become more vulnerable to hydrogen peroxide-induced oxidative stress when complex I is inhibited.

Taken together, our results demonstrated that both oxidative stress and mitochondrial dysfunction were responsible for rotenone-induced apoptotic cell death in PC12 cells, and that rotenone-induced ROS accumulation was mainly DA auto-oxidation mediated.

Acknowledgment

The authors wish to thank Dr Ren-gang WANG and Ms Li-zhen WANG for their technical suggestions.

References

1 Kitada T, Asakawa S, Hattori N, Matsumine H, Yamamura Y, Minoshima S, *et al.* Mutations in the parkin gene cause autosomal recessive juvenile parkinsonism. Nature 1998; 392: 605–8.

2 Leroy E, Boyer R, Auburger G, Leube B, Ulm G, Mezey E, *et al.* The ubiquitin pathway in Parkinson's disease. Nature 1998; 395: 451–2.

3 Polymeropoulos MH, Lavedan C, Leroy E, Ide SE, Dehejia A, Dutra A, *et al.* Mutation in the alpha-synuclein gene identified in families with Parkinson's disease. Science 1997; 276: 2045–7.

4 Jenner P. Parkinson's disease, pesticides and mitochondrial dysfunction. Trends Neurosci 2001; 24: 245–7.

5 Sherer TB, Betarbet R, Greenamyre JT. Environment, mitochondria, and Parkinson's disease. Neuroscientist 2002; 8: 192–7.

6. Tipton KF, Singer TP. Advances in our understanding of the mechanisms of the neurotoxicity of MPTP and related compounds. J Neurochem 1993; 61: 1191–206.

7 Schapira AH. Mitochondrial function and neurotoxicity. Curr Opin Neurol 1994; 7: 531–6.

8 Marey-Semper I, Gelman M, Levi-Strauss M. A selective toxicity toward cultured mesencephalic dopaminergic neurons is induced by the synergistic effects of energetic metabolism impairment and NMDA receptor activation. J Neurosci 1995; 15: 5912–8.

9 Mizuno Y, Ohta S, Tanaka M, Takamiya S, Suzuki K, Sato T, *et al.* Deficiencies in complex 1 subunits of the respiratory chain in Parkinson's disease. Biochem Biophys Res Commun 1989; 163: 1450–5.

10 Heikkila RE, Nicklas WJ, Vyas I, Duvoisin RC. Dopaminergic toxicity of rotenone and the 1-methyl-4-phenylpyridinium ion after their stereotaxic administration to rats: implication for the mechanism of 1-methyl-4-phenyl-1,2,3,6-tetrahydropyridine toxicity. Neurosci Lett 1985; 62: 389–94.

11 Ferrante RJ, Schulz JB, Kowall NW, Beal MF. Systemic administration of rotenone produces selective damage in the striatum and globus pallidus, but not in the substantia nigra. Brain Res 1997; 753: 157–62.

12 Thiffault C, Langston JW, Di Monte DA. Increased striatal dopamine turnover following acute administration of rotenone to mice. Brain Res 2000; 885: 283–8.

13 Betarbet R, Sherer TB, MacKenzie G, Garcia-Osuna M, Panov AV, Greenamyre JT. Chronic systemic pesticide exposure reproduces features of Parkinson's disease. Nat Neurosci 2000; 3: 1301–6.

14 Alam M, Schmidt WJ. Rotenone destroys dopaminergic neurons and induces parkinsonian symptoms in rats. Behav Brain Res 2002; 136: 317–24.

15 Sherer TB, Kim JH, Betarbet R, Greenamyre JT. Subcutaneous rotenone exposure causes highly selective dopaminergic degeneration and alpha-synuclein aggregation. Exp Neurol 2003; 179: 9–16.

16 Shimura H, Hattori N, Kubo S, Mizuno Y, Asakawa A, Minoshima S, *et al.* Familial Parkinson disease gene product, parkin, is a ubiquitin-protein ligase. Nat Genet 2000; 25: 302–5.

17 Shimura H, Schlossmacher MG, Hattori N, Frosch MP, Trockenbacher A, Schneider R, *et al.* Ubiquitination of a new form of α-synuclein by Parkin from human brain: implications for Parkinson's disease. Science 2001; 293: 263–9.

18 McNaught KSP, Olanow CW, Halliwell B, Isacson O, Jenner P. Failure of the ubiquitin-proteasome system in Parkinson's disease. Nat Rev Neurosci 2001; 2: 589–94.

19 Wang RG, Zhu XZ. Subtoxic concentration of manganese synergistically potentiates 1-14 methyl-4-phenylpyridinium-induced neurotoxicity in PC12 cells. Brain Res 2003; 961: 131–8.

20 Zhou LJ, Zhu XZ. Reactive oxygen species-induced apoptosis in PC12 cells and protective effect of Bilobalide. J Pharmacol Exp Ther 2000; 293: 982–5.

21 Hirata Y, Adachi K, Kiuchi K. Activation of JNK pathway and induction of apoptosis by manganese in PC12 cells. J Neurochem 1998; 71: 1607–15.

22 Mefford IN, Giberg M, Barchas JD. Simultaneous determination of catecholamines and unconjugated 3,4-dihydroxyphenylacetic acid (DOPAC) by ion-pairing reverse phase high performance liquid chromatography with electrochemical detection. Anal Biochem 1980; 104: 469–72.

23 Zhu XZ, Luo LG. Effect of nitroprusside (nitric oxide) on endogenous dopamine release from rat striatal slices. J Neurochem 1992;

59: 932–5.

24 Wu WR, Zhu XZ, Guan HJ, Wang RG, Ji XQ. Neuroprotective rather than neurorescue or neurorestorative effect of selegiline against MPTP-induced dopaminergic toxicity. Acta Pharmacol Sin 1999; 20: 146–50.

25 Bal-Price A, Brown GC. Nitric-oxide-induced necrosis and apoptosis in PC12 cells mediated by mitochondria. J Neurochem 2000; 75: 1455–64.

26 Richter C, Gogvadze V, Laffranchi R, Schlapbach R, Schweizer M, Suter M, *et al.* Oxidants in mitochondria: from physiology to disease. Biochim Biophys Acta 1995; 1271: 67–74.

27 Takeshige K, Minakami S. NADH- and NADPH-dependent formation of superoxide anions by bovine heart submitochondrial particles and NADH-ubiquinone reductase preparation. Biochem J 1979; 180: 129–35.

28 Turrens JF, Boveris A. Generation of superoxide anion by the NADH dehydrogenase of bovine heart mitochondria. Biochem J 1980; 191: 421–7.

29 Hasegawa E, Takeshige K, Oishi T, Murai Y, Minakami S. 1-Methyl-4-phenylpyridinium (MPP^+) induces NADH-dependent superoxide formation and enhances NADH-dependent lipid peroxidation in bovine heart submitochondrial particles. Biochem Biophys Res Commun 1990; 170: 1049–55.

30 Packer MA, Miesel R, Murphy MP. Exposure to the parkinsonian neurotoxin 1-methyl-4-phenylpyridinium (MPP^+) and nitric oxide simultaneously causes cyclosporin A-sensitive mitochondrial calcium efflux and depolarisation. Biochem Pharmacol 1996; 51: 267–73.

31 Sipos I, Tretter L, Adam-Vizi V. Quantitative relationship between inhibition of respiratory complexes and formation of reactive oxygen species in isolated nerve terminals. J Neurochem 2003; 84: 112–8.

32 Budd SL, Nicholls DG. Mitochondria, calcium regulation, and acute glutamate excitotoxicity in cultured cerebellar granule cells. J Neurochem 1996; 67: 2282–91.

33 Rottenberg H, Wu S. Quantitative assay by flow cytometry of the mitochondrial membrane potential in intact cells. Biochim Biophys Acta 1998; 1404: 393–404.

34 Chinopoulos C, Tretter L, Adam-Vizi V. Depolarization of *in situ* mitochondria due to hydrogen peroxide-induced oxidative stress in nerve terminals: inhibition of alpha-ketoglutarate dehydrogenase. J Neurochem 1999; 73: 220–8.

35 Lotharius J, O'Malley KL. The parkinsonism-inducing drug 1-methyl-4-phenylpyridinium triggers intracellular dopamine oxidation. A novel mechanism of toxicity. J Biol Chem 2000; 275: 38581–8.

36 Brautigam M, Laschinski G, Kittner B, Herken H. Effect of apomorphine, alpha-methylparatyrosine, haloperidol and reserpine on DOPA production in clonal cell lines (PC-12 and N1E-115). Biochem Pharmacol 1985; 34: 941–7.

37 Fornstedt B. Role of catechol autooxidation in the degeneration of dopamine neurons. Acta Neurol Scand Suppl 1990; 129: 12–4.

38 Maker HS, Weiss C, Silides DJ, Cohen G. Coupling of dopamine oxidation (monoamine oxidase activity) to glutathione oxidation via the generation of hydrogen peroxide in rat brain homogenates. J Neurochem 1981; 36: 589–93.

39 Graham DG. Oxidative pathways for catecholamines in the genesis of neuromelanin and cytotoxic quinones. Mol Pharmacol 1978; 14: 633–43.

40 Kitazawa M, Wagner JR, Kirby ML, Anantharam V, Kanthasamy AG. Oxidative stress and mitochondrial-mediated apoptosis in dopaminergic cells exposed to methylcyclo-pentadienyl manganese tricarbonyl. J Pharmacol Exp Ther 2002; 302: 26–35.

41 Bywood PT, Johnson SM. Mitochondrial complex inhibitors preferentially damage substantia nigra dopamine neurons in rat brain slices. Exp Neurol 2003; 179: 47–59.

42 Liu Y, Peter D, Roghani A, Schuldiner S, Prive GG, Eisenberg D, *et al.* A cDNA that suppresses MPP^+ toxicity encodes a vesicular amine transporter. Cell 1992; 70: 539–51.

Full-length article

Cloning, expression, and functional analysis of human dopamine D1 receptors[1]

Wan-chun SUN[2], Lei JIN[2], Yan CAO[2], Li-zhen WANG[2], Fan MENG[3], Xing-zu ZHU[2,4]

[2]Department of Pharmacology, Institute of Materia Medica, Shanghai Institutes for Biological Sciences, Chinese Academy of Sciences, Shanghai 201203, China; [3]Department of Psychiatry, University of Michigan, The Psychiatry/MHRI Microarray Laboratory, 205 Zina Pitcher Place, Ann Arbor, MI 48109-0720, USA

Key words

cAMP response element-binding protein; alkaline phosphatase; reporter genes; G-protein-coupled receptors; dopamine D1 receptor; radioligand assay; calcium; fluorescence; screening

[1] Project supported by the National Natural Science Foundation of China (No 30128004) and Shanghai Metropolitan Fund for Research and Development (No 04DZ14005).
[3] Correspondence to Xing-zu ZHU, PhD.
Phn 86-21-5080-6096. Fax 86-21-5080-6096.
E-mail xzzhu@mail.shcnc.ac.cn

Received 2004-06-15
Accepted 2004-09-28

doi: 10.1111/j.1745-7254.2005.00017.x

Abstract

Aim: To construct an HEK293 cell line stably expressing human dopamine D_1 receptor (D_1R). **Methods:** cDNA was amplified by RT-PCR using total RNA from human embryo brain tissue as the template. The PCR products were subcloned into the plasmid pcDNA3 and cloned into the plasmid pcDNA3.1. The cloned D_1R cDNA was sequenced and stably expressed in HEK293 cells. Expression of D_1R in HEK293 cells was monitored by the [^{3}H]SCH23390 binding assay. The function of D_1R was studied by the cAMP accumulation assay, CRE-SEAP reporter gene activity assay, and intracellular calcium assay. **Results:** An HEK293 cell line stably expressing human D_1R was obtained. A saturation radioligand binding experiment with [^{3}H]SCH23390 demonstrated that the K_d and B_{max} values were 1.5±0.2 nmol/L and 2.94±0.15 nmol/g of protein, respectively. In the [^{3}H]SCH23390 competition assay, D_1R agonist SKF38393 displaced [^{3}H]SCH23390 with an IC_{50} value of 2.0 (1.5–2.8) μmol/L. SKF38393 increased the intracellular cAMP level and CRE-SEAP activity through D_1R expressed in HEK293 cells in a concentration-dependent manner with an EC_{50} value of 0.25 (0.12–0.53) μmol/L and 0.39 (0.27–0.57) μmol/L at 6 h/0.59 (0.22–1.58) μmol/L at 12 h, respectively. SKF38393 also increased the intracellular calcium level in a concentration-dependent manner with EC_{50} value of 27 (8.6–70) nmol/L. **Conclusion:** An HEK293 cell line stably expressing human D_1R was obtained successfuly. The study also demonstrated that the CRE-SEAP activity assay could be substituted for the cAMP accumulation assay for measuring increase in cAMP levels. Thus, both intracellular calcium measurements and the CRE-SEAP activity assay are suitable for high-throughput screening in drug research.

Introduction

The neurotransmitter dopamine (DA) plays a prominent role in a variety of vital brain functions including motor control, short-term memory, attention and reward[1–3]. In the CNS, DA modulates neuronal excitability by regulating ligand- and voltage-gated ion channels[4]. The actions of DA are mediated by a family of seven-transmembrane G protein-coupled receptors (GPCRs), i.e., D_1, D_2, D_3, D_4, and D_5, encoded by five distinct genes[5]. These five subtypes have been grouped into two different classes based on pharmacology and biochemistry: the D_1-like and D_2-like receptors. The D_1-like receptors, D_1 and D_5, mediate dopamine stimulation of adenylyl cyclase, whereas D_2-like receptors, D_2, D_3 and D_4, mediate dopamine inhibition of adenylyl cyclase[5,6].

Assays capable of detecting and quantifying GPCR-ligand interactions are valuable tools for both fundamental studies of cell siganaling and drug development. Drug screening has mainly relied upon binding assays on membrane preparations using radioligands or assays measuring second messengers or enzymes modulated by these receptors. The abil-

ity to conduct high-throughput screening based upon functional activity of a given GPCR in a cell-based assay offers a more direct way of identifying lead agonists or antagonists[7–9].

In the present study, by using HEK293 cell lines stably expressing human D_1R, we developed a series of method check character for analyzing GPCR activities in cell lines including CRE-SEAP activity assay and the intracellular calcium assay.

Materials and methods

Materials High glucose Dulbecco's modified Eagle's medium (DMEM), fetal calf serum, G418, penicillin and streptomycin were obtained from Gibco. Restricted enzyme (*Hind*II*, Eco*RI*, Xho*I*, Bam*HI), T4 DNA ligase, reverse transcriptase and buffer were purchased from Promega (USA). Pyrobest DNA polymerase and buffer for PCR were obtained from TaKaRa (Dalian, China). (±)-SKF-38393 hydrochloride (SKF38393) and (+)-Butaclamol hydrochloride (Butaclamol) were obtained from RBI (Natick, MA, USA). Forskolin, Fluo-3/AM, p-(dipropylsulfamoyl)benzoic acid, 3-isobutyl-1-methyl-2,6(1*H*,3*H*)-purine-dione (IBMX), pluronic F-127, 4-methyl-umbelliferyl phosphate (4-MUP), HEPES, Triton X-100 , bovine serum albumin leupeptin, pepstatin A, aprotinin and PMSF were purchased from Sigma (USA). [^{3}H]SCH23390 was purchased from Amersham (USA). Plasmids pcDNA3, pcDNA3.1(+) and Lipofectamine^{2000} were purchased from Invitrogen (USA), and pCRE-SEAP was from BD Biosciences Clontech (USA). cAMP assay kit was purchased from Shanghai Second Medical University (Shanghai, China). Human embryo brain tissue was donated by Huashan Hospital (Shanghai, China). PCR primers were synthesized by Shenyou (Shanghai, China).

Cloning of the human dopamine D_1R cDNA Human brain total RNA was obtained from human embryo brain tissue. The total RNA was reverse-transcribed using oligo-dT18 as a primer. With the cDNA, PCR was carried out using the primers D_1R-1SE and D_1R-1AS (Table 1). Gel-purified PCR product was treated with *Bam*HI/*Xho*I and subcloned into the *Bam*HI/*Xho*I site of the mammalian expression vector pcDNA3. With the subcloned D_1R-pcDNA3 plasmid as a template, PCR was carried out using the primers D_1R-2SE and D_1R-2AS (Table 1), which resulted in full length codon sequence of cDNA. Gel-purified PCR product was treated with *Bam*HI/*Eco*RI and cloned into the *Bam*HI/*Eco*RI site of the mammalian expression vector pcDNA3.1(+).

Production of HEK293 cell lines stably expressing human dopamine D_1R HEK293 Cells were transfected with the D_1R-pcDNA3.1(+) expression vector, using the Lipofectamine reagent. Cells were treated with selection medium containing G418 (1 g/L) for 3 weeks to select stably transfected cells displaying neomycin resistance. Between 2 and 3 weeks into the selection process, resistant cells began to appear. They were separated out by serial dilution and allowed to grow from single cells. Receptor expression of single cell-derived colonies was tested by the radioligand binding assay.

Cell culture Human embryonic kidney (HEK293) cell lines were cultured in DMEM containing streptomycin (100 μg/mL), penicillin G (1000 kU/L) and fetal bovine serum (10%). Cells were incubated at 37 ºC in 5% CO_2. Stably transfected HEK293 cell lines were cultured in DMEM high glucose medium containing streptomycin (100 mg/L), benzylpenicillin (1000 kU/L), G-418 (200 mg/L) and fetal bovine serum (10%). Cells were incubated at 37 ºC in 5% CO_2. For passaging, the cells were detached from the cell culture flask by washing with phosphate-buffered saline (PBS) and brief incubation with trypsine (0.5 g/L)/EDTA (0.2 g/L). The cells were passaged every 3 d.

Membrane preparation The D_1 cells were lifted from Petri dishes with a cell scraper. Harvested cells were washed twice with ice-cold PBS and centrifuged at 420×*g* for 5 min at 4 ºC. The cell pellet was resuspended with hypotonic buffer (5 mmol/L Tris-Cl, 2 mmol/L EDTA, pH7.4, leupeptin 1 mg/L, pepstatin A 1 mg/L, aprotinin 1 mg/L, PMSF 1 mmol/L) and sonicated (18 s) three times on ice. The homogenate was centrifuged at 960×*g* for 10 min at 4 ºC. The precipitated nucleic fraction was discarded and the supernatant was centrifuged at 40 000×*g* for 30 min at 4 ºC. The pellet was washed with 50 mmol/L Tris-Cl buffer (pH 7.4) and centrifuged again with the same conditions. Finally, the pellet was resuspended in the same buffer, and protein concentration was determined by the BCA Kit (Pierce) as described previously[10].

[^{3}H]SCH23390 binding assay Membranes (30–50 μg protein) from D_1 cells were resuspended in 50 mmol/L Tris-Cl (pH 7.4, 120 mmol/L NaCl, 5 mmol/L KCl, 2 mmol/L $CaCl_2$ and 1 mmol/L $MgCl_2$). Saturation assays were performed at different concentrations of [^{3}H]SCH23390 (0.05–6 nmol/L), using butaclamol (10 μmol/ L) to obtain nonspecific binding. Competition curves were obtained by using 0.5 nmol/L [^{3}H]SCH23390 and different concentrations of dopamine D_1R agonist SKF38393. The incubation was carried out at 37 ºC for 30 min.

Binding assays were stopped by rapid filtration through Whatman GF/B filters, which were immediately washed three times with ice-cold buffer. Filters were then transferred to

Eppendoff tubes, and scintillation liquid was added to measure the radioactivity.

cAMP accumulation experiment After scraping the cells off the culture plates, they were washed twice with PBS and resuspended in PBS at a concentration of 0.5×10^6–1.0×10^6 cells/mL. Aliquots of 0.2 mL were transferred to test tubes along with the phsophodiesterase inhibitor IBMX (100 μmol/L) and different concentrations of dopamine D_1R agonist SKF38393 added to a final volume of 0.3 mL. The reaction was terminated with 1 mol/L perchloric acid to a final concentration of 0.5 mol/L after a 15 min incubation at 37 ºC. Samples were neutralized with 75 μL 2 mol/L KOH, and the cAMP content in the supernatants were determined with a protein binding assay[11]. cAMP concentrations were calculated using a standard curve according to the protocol of the assaykit.

CRE-SEAP activity assay Using the secreted form of human placental alkaline phosphatase (SEAP) as the reporter enzyme transcriptionally regulated by cAMP response elements (CREs)[12,15], CRE-SEAP activity was measured. The pCRE-SEAP plasmid was transfected into D_1 cells using the calcium phosphate precipitation method (Promega). Cells were seeded in 100 m^2 plates, and transfection was performed when cells were 50% confluent. DNA 25 μg and 60 μL $CaCl_2$ 2 mol/L were mixed in H_2O in a total volume of 500 μL and then slowly mixed with HEPES buffered saline (HBS). The reaction mixture was incubated at room temperature for 30 min and then evenly added to the cell culture dish containing 10 mL of fresh media. After 12 h, the transfection media was replaced with fresh media, and the transfected D_1 cells were seeded into 24-well plates (1.5×10^5 cells per well) and cultured overnight before experiment[12]. The medium was then replaced with 500 μL of free serum DMEM containing 100 μmol/ L IBMX and the different concentrations of SKF38393 then cells were incubated for 6 h and 12 h, respectively. The SEAP assay was subsequently performed (see below).

Following the incubation period of transiently transfected cells, the culture medium was inactivated for 30 min at 65 ºC and centrifuged at 15 000×*g* at 4 ºC. The supernatant (80 μL), was transferred to a new 96-well plate and mixed with 100 μL SEAP assay buffer (50 mmol/L Tris/0.1% BSA buffer, pH 8.0) containing 36 μmol/L 4-methylumbelliferyl phosphate (4-MUP). The mixture was incubated for 1 h at 37 ºC, and the fluorescence intensity was measured at 460 nm using FLUOstar plate reader. Excitation wavelength was 355 nm.

Intracellular Ca^{2+} concentration ($[Ca^{2+}]_i$) measurement Ca^{2+} fluorescence measurements were performed using a NOVOstar plate reader with a pipettor system (BMG Labtechnologies, Offenburg, Germany). D_1 cells were harvested with 0.05% trypsin/0.02% EDTA and rinsed with high glucose DMEM containing 10% fetal bovine serum, 100 mg/ L streptomycin, 1000 U/mL penicillin G. Pelleted cells were resuspended in fresh medium and kept under 5% CO_2 at 37 ºC for 1h and vortexed every 15 min. After twice washes with Krebs-HEPES buffer, cells were loaded with 5 μmol/ L Fluo-3/AM containing 1% pluronic F-127 and 2.5 mmol/L p-(Dipropylsulfamoyl)benzoic acid for 30 min. Then cells were rinsed three times with Krebs-HEPES buffer containing 0.5% bovine serum albumin, diluted, and evenly plated into 96-well plates at a density of 1×10^4 cells/well. Microplates were kept at 37 ºC for 15 min[13]. Buffer alone or different concentrations of SKF38393 were then injected sequentially into separate wells, and fluorescence intensity was measured at 520 nm for 50 s at 0.2 s intervals. The excitation wavelength was 485 nm.

$[Ca^{2+}]_i$ was calculated as follows: $[Ca^{2+}]_i=K_d\,(F-F_{min})/(F_{max}-F)$. F_{max} refers to the fluorescence intensity measured after permeabilization of the cells with 1% Triton X-100. Ten mmol/L EDTA was added to chelate Ca^{2+} and minimum fluorescence intensity was obtained (F_{min}). A K_d value of 324 nmol/L was used for Fluo-3.

Data analysis Experiments were performed in triplicate. All data were expressed as mean±SD and analyzed with the GraphPad Prism 4.0 program (GraphPad Software, San Diego, CA, USA). Student's *t*-test was used for statistical analysis.

Results

Cloning of the human dopamine D_1RcDNA To obtain the cDNA with full length codon sequence of D_1R, a reverse transcription reaction was carried out using the total RNA extracted from embryo brain tissue. Using cDNA with the full length codon sequence of D_1R, a PCR product (1707 bp) was obtained using primers described previously. The PCR product was subcloned into pcDNA3 plasmid and a cDNA (1341 bp) containing the full D_1R codon sequence was obtained using this subcloned vector as a template. The cDNA was then cloned into the mammalian expression vector pcDNA3.1. Sequence analysis demonstrated that the sequence of the constructed D_1-pcDNA3.1 expression vector was identical to that of human D_1R cDNA in the gene bank.

Selection of cell clones Colonies of the selected stable integrants were initially analyzed for human D_1R expression by receptor binding assay using [^{3}H]SCH23390. From the transfected HEK293 cell clones, one cell line was obtained with specific [^{3}H]SCH23390 binding.

Binding assays with the D_1R antagonist [^{3}H]SCH-23390 Scatchard analysis revealed a K_d value of 1.5±0.2 nmol/L) and B_{max} value of 2.95±1.53 nmol/g of protein (Figure 1). Figure 2 shows a competition of a D_1R agonist SKF38393 for [^{3}H]SCH23390 with an IC_{50} value of 2.0 (1.5–2.8) μmol/L (means, 95% confidence intervals, n=3).

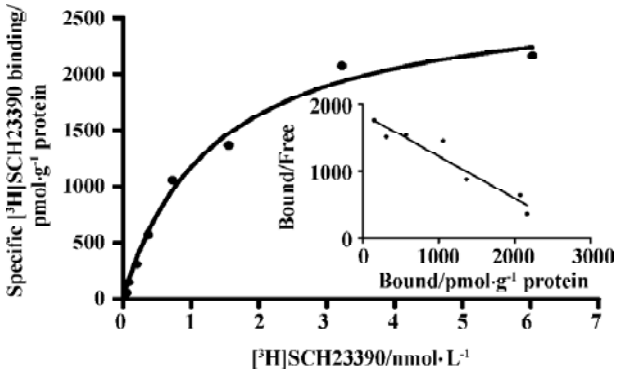

Figure 1. Saturation curve of [^{3}H]SCH23390 binding to dopamine D_1 receptors in plasma membrane isolated from D_1 cells. Inset: Scatchard plot of the data and analysis gave the K_d and B_{max} values indicated in RESULTS. Mean±SD from three independent experiments performed in triplicate.

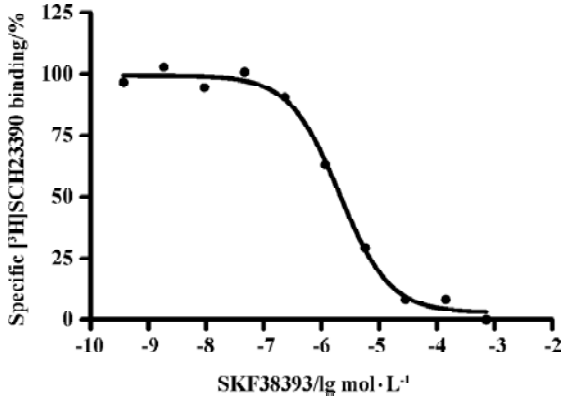

Figure 2. Representative competitive inhibition curve of the dopamine D_1 receptor agonist SKF38393 versus the D_1 receptor antagonist [^{3}H]SCH23390 in membrane preparations from D_1 cells. IC_{50} values were expressed as means (95% confidence intervals) obtained from three independent experiments performed in triplicate.

D_1R agonist SKF38393 induced accumulation of cAMP D_1R agonist SKF38393 induced a concentration-dependent accumulation of cAMP with a EC_{50} value of 0.25 μmol/L (0.12–0.53) (means, 95% confidence intervals, n=3, Figure 3).

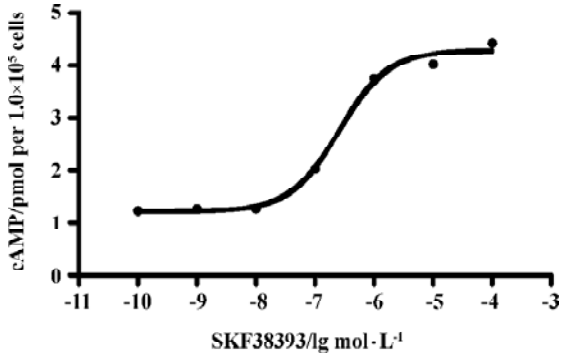

Figure 3. The cAMP accumulation induced by the D_1 receptor agonist SKF38393 in D_1 cells. The EC_{50} value was expressed as a mean (95% confidence intervals) obtained from three independent experiments performed in triplicate.

D_1R agonist SKF38393 induced CRE-SEAP activity In D_1 cells transiently transfected with pCRE-SEAP reporter vector, SKF38393 induced a concentration-dependent increase in the CRE-SAEP activity. EC_{50} values at 6 h and 12 h were 0.39 (0.27–0.57) and 0.59 (0.22–1.58) μmol/L (means, 95% confidence intervals, n=3), respectively. No significant difference was found between these two values (Figure 4).

D_1R agonist SKF38393 induced elevated intracellular calcium level D_1R agonist SKF38393 induced a concentration-dependent increase in the intracellular calcium level. The EC_{50} value was 27 (8.5–70) nmol/L (means, 95% confidence intervals, n=3). The SKF38393-induced increase of the intracellular calcium level was completely blocked by butaclamol (100 μmol/ L), a DA receptor antagonist (Figure 5).

Discussion

In the present study, a HEK293 cell line stably expressing human D_1R was constructed. Functional analysis with cAMP accumulation assay, the CRE-SEAP activity assay, and intracellular calcium assay demonstrated that their EC_{50} values were 0.25 (0.12–0.53) μmol/L, 0.39 (0.27–0.57) μmol/L for 6 h and 0.59 (0.22–1.58) μmol/L for 12 h and 27 (8.6–70) nmol/ L, respectively. No significant difference in the EC_{50} values was found between SKF38393-induced cAMP accumulation and CRE-SEAP activation.

D_1R can activate adenylyl cyclase, which then results in cAMP production. At present, radioimmunoassay is one of the most widely used methods for the measurement of cAMP accumulation[14]. Cell based assays relying on transcriptionally controlled reporter gene have been developed and are suited to monitoring the cellular responses induced by

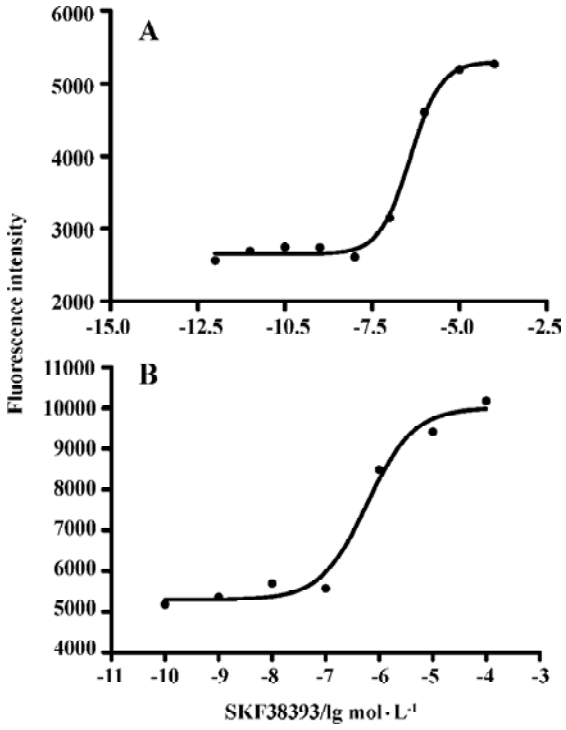

Figure 4. CRE-SEAP activity induced by dopamine D_1 receptor agonist SKF38393. (A) incubation with SKF38393 for 6 h; (B) incubation with SKF38393 for 12 h. EC_{50} values were expressed as mean (95% confidence intervals) obtained from three independent experiments performed in triplicate.

GPCRs. Since CRE is a pivotal target in GPCR signaling pathways, it has become one of the most widely used response elements in reporter gene assays. The cAMP response element binding protein (CREB), a transcription factor, is the major regulator of CREs. It can be activated (phosphoryl-ated) by protein kinase A (PKA) and members of calcium/calmodulin kinase (CaMK) family *in vitro*. Both $G_{\alpha s}$- and $G_{\alpha q}$-coupled receptors are signaled through CREs [12,15,16]. Since the transcription of CRE-SEAP reporter genes is controlled by CRE-containing promoters, CRE-SEAP activity can be used to monitor the activation of receptors. In the present study, the EC_{50} value obtained using CRE-SEAP activity assay is similar to that obtained from cAMP accumulation assay. These results suggest that CRE-SEAP activity assay can be used to estimate the $G_{\alpha s}$-coupled receptor function.

$G_{\alpha s}$-coupled receptors activate adenylyl cyclase, leading to an increase in cAMP level. cAMP activates PKA, which subsequently phosphorylates different targets. This pathway can lead to an increase in intracellular [Ca^{2+}] either from intracellular Ca^{2+} stores or from the extracellular matrix[13,17].

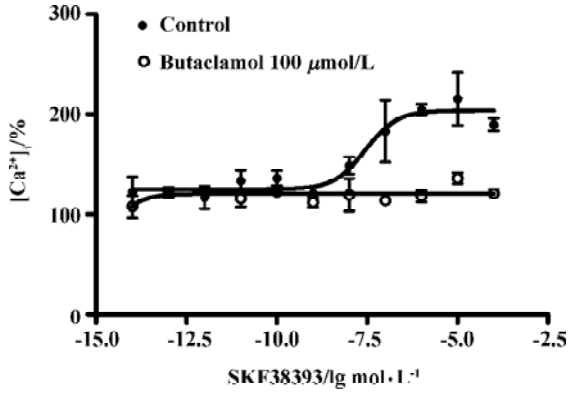

Figure 5. Concentration-response curves for the effect of SKF38393 on intracellular $[Ca^{2+}]_i$ in D_1 cells. n=3. Mean±SD. EC_{50} value was mean (95% confidence intervals) obtained from three independent experiments performed in triplicate.

Direct activation of Ca^{2+} ion channels by $G_{\alpha s}$ is also possible[13,18]. We found that a significant difference was observed in the EC_{50} value of the intracellular calcium assay and cAMP accumulation assay. While the EC_{50} value to induce the cAMP accumulation was 0.25 (0.12–0.53) μmol/L, the EC_{50} value to induce an increase in the intracellular calcium was 27 (8.6–70) nmol/L. This is likely to reflect the difference in signaling between intracellular calcium increase and cAMP accumulation. Intracellular calcium signals may be directly transduced, bypassing the adenylyl cyclase pathway and representing transient binding with ligand. Therefore, combination CRE-SEAP activity assay or a cAMP accumulation assay with an intracellular calcium assay will obtain more information on the effect of ligands. Our study demonstrates that the CRE-SEAP activity assay and intracellular calcium assay are suitable for high-throughput screening in drug research.

References

1 Goldman-Rakic PS. The cortical dopamine system: role in memory and cognition. Adv Pharmacol 1998; 42: 707–11.
2 Schultz W. Getting formal with dopamine and reward. Neuron 2002; 36: 241–63.
3 Yelnik J. Functional anatomy of the basal ganglia. Mov Disord 2002; 17: Suppl 3: S15–S21.
4 Nicola SM, Surmeier J, Malenka RC. Dopaminergic modulation of neuronal excitability in the striatum and nucleus accumbens. Annu Rev Neurosci 2000; 23: 185–215.
5 Missale C, Nash SR, Robinson SW, Jaber M, Caron MG. Dopamine receptors: from structure to function. Physiol Rev 1998; 78: 189–225.
6 Zhou QY, Grandy DK, Thambi L, Kushner JA, Van Tol HH, Cone R, *et al*. Cloning and expression of human and rat D1 dopamine receptors.

Nature 1990; 347: 76–80.
7 Knight PJ, Pfeifer TA, Grigliatti TA. A functional assay for G-protein-coupled receptors using stably transformed insect tissue culture cell lines. Anal Biochem 2003; 320: 88–103.
8 Okun I, Veerapandian P. New methods to mimic nature in high-throughput screening. Nat Biotechnol 1997; 15: 287–8.
9 Dove A. Drug screening — beyond the bottleneck. Nat Biotechnol 1999; 7: 859–63.
10 Sorensen K, Brodbeck U. Assessment of coating-efficiency in ELISA plates by direct protein determination. J Immunol Methods 1986; 95: 291–3.
11 Nordstedt C, Fredholm BB. A modification of a protein-binding method for rapid quantification of cAMP in cell-culture supernatants and body fluid. Anal Biochem 1990; 189: 231–4.
12 Durocher Y, Perret S, Thibaudeau E, Gaumond MH, Kamen A, Stocco R, *et al*. A reporter gene assay for high-throughput screening of G-protein-coupled receptors stably or transiently expressed in HEK293 EBNA cells grown in suspension culture. Anal Biochem 2000; 284: 316–26.
13 Kassack MU, Hofgen B, Lehmann J, Eckstein N, Quillan JM, Sadee W. Functional screening of G protein-coupled receptors by measuring intracellular calcium with a fluorescence microplate reader . J Biomol Screen 2002;7: 233–46.
14 Johnson RA, Salomon Y. Assay of adenylyl cyclase catalytic activity. Methods Enzymol 1991;195: 3–21.
15 Chen W, Shields TS, Stork PJ, Cone RD. A colorimetric assay for measuring activation of Gs- and Gq-coupled signaling pathways. Anal Biochem 1995; 226: 349–54.
16 Stratowa C, Himmler A, Czernilofsky AP. Use of a luciferase reporter system for characterizing G-protein-linked receptors. Curr Opin Biotechnol 1995, 6: 574–81.
17 Pieroni JP, Jacobowitz O, Chen JQ, Lyengar R. Signal recognition and integration by G_S-stimulated adenylyl cyclases. Curr Opin Neurobiol 1993; 3: 345–51
18 Hescheler J, Schultz G. G-proteins involved in the calcium channel signalling system. Curr Opin Neurobiol 1993; 3: 360–7.

Full-length article

Antiapoptotic effect both *in vivo* and *in vitro* of A20 gene when transfected into rat hippocampal neurons[1]

Hong-sheng MIAO[2,3], Lu-yang YU[4], Guo-zhen HUI[2], Li-he GUO[2,5]

[2] *Institute of Biochemistry and Cell Biology, Shanghai Institutes for Biological Sciences, Chinese Academy of Sciences, Shanghai 200031, China;*
[3] *Department of Neurosurgery, First Hospital of Soochow University, Suzhou 215007, China*

Key words

A20 protein; tumor necrosis factor; primary hippocampal neurons; middle cerebral artery infarction; apoptosis

[1] Project supported by Major State Basic Research Development Program of China (No G1999053905).
[2,4] These two authors contribute equally to this work.
[5] Correspondence to Prof. Li-he GUO.
E-mail lhguo@sibs.ac.cn
Phn/Fax 86-21-5492-1391

Received 2004-05-26
Accepted 2004-09-17

doi: 10.1111/j.1745-7254.2005.00002.x

Abstract

Aim: To evaluate the antiapoptotic effect of the A20 gene in primary hippocampal neurons both *in vivo* and *in vitro*. **Methods:** Primary hippocampal neurons in embryonic day 18 (E18) rats were transfected with the A20 gene by using the new Nucleofector electroporation transfection method. We then examined, whether A20 -neurons possessed anti-apoptotic abilities after TNF-α stimulation *in vitro*. A20-neurons and pcDNA3 -neurons were transplanted into the penumbra of the brains of rats that had been subjected to 90-min of ischemia induced by left middle cerebral artery occlusion (MCAO). **Results:** A20-neurons resisted TNF-α induced apoptosis *in vitro*. The apoptosis rate of neurons overexpressing A20 (28.46%±3.87%) was lower than that in neurons transfected with pcDNA3 (53.06%±5.36%). More A20-neurons survived in the penumbra both 3-d and 7-d after transplantation than did sham pcDNA3 neurons. **Conclusion:** The novel function of A20 may make it a potential targets for the gene therapy for neurological diseases.

Introduction

Uncontrolled gene expression and apoptosis result in the development of various diseases. Excessive apoptosis plays a role in the pathogenesis of AIDS and neurological diseases such as Alzheimer disease and stroke[1].

The zinc finger protein A20 is a novel protein type in that it seems to have a dual activity, both as an inhibitor of NF-κB activation and as an antiapoptotic molecule in some cell systems, but not in the case of human cervix carcinoma HeLa cells, lung epithelial A549 cell, or human hepatoma HepG2 cells[2–6]. The reason why some cell lines are protected by A20 and others not are still unclear.

Little research work has been done on the functions of A20 in primary cultured neurons, although cell apoptosis is involved in many neurological diseases. The poor transfection efficiency resulting from the extreme resistance of cultured neurons to chemical transfection vectors has limited further research[7].

In this study, we overexpressed A20 by means of electroporation gene transfer into neurons to investigate whether A20 can inhibit TNF-induced apoptosis in primary cultured neurons both *in vivo* and *in vitro*.

Materials and methods

Cloning of the A20 gene Human umbilical vein endothelial cells were treated with TNF-α 1000 kU/L and cycloheximide 10 μg/L for 4 h. Poly(A)$^+$-mRNA was extracted with Trizol Reagents (Gibco) and identified by electrophoresis on a 1.2% agarose gel. cDNA was obtained by using reverse transcription-polymerase chain reaction (PCR). The PCR was performed with a sense primer (5′-AAC GAGCG-GTTCCGATGCC-CTGAG-3') and an anti-sense primer (5′-TGTCGCCTTCACCGTTC-CAGTT-3′) using 30 cycles of 95 ºC for 1 min, 62 ºC for 1.5 min, 72 ºC for 2.5 min. The pcDNA3 expression vector containing the CMV immediate early promoter was used for this study.

Analysis of A20 mRNA contents Isolation of total mRNA from the transfected neurons cultured *in vitro* or in the penumbra tissue was performed using Trizol reagent (Promega, Charbonnieres, France), followed by RT-PCR

using the following primers: forward 5′-CGGTACCGCACA-ATGGCTGAACAAGTCCTTCCT-3′ and reverse 5′-CGTC-TAGAGTTAGCCATACATC-TGCTTGAACTG-3′. The PCR was run at 95 ºC for 5 min, followed by 30 cycles of 95 ºC for 1 min, 62 ºC for 1.5 min, and 72 ºC for 2.5 min, with a 10 min final extension period at 72 ºC. The house-keeping gene β-actin was used as a control.

Western blotting Protein was isolated from the transfected neurons and the penumbra of the MCAO rats using RIPA reagent 10 d after transfection. The samples were then resolved on a 15% SDS-PAGE gel and electrophoretically transferred onto poly-vinylidene difluoride membranes. The membranes were probed overnight at 4 ºC with mouse monoclonal anti-human A20 antibody (1/2000, Oncogene). After being incubated with goat anti-mouse-HRP (1/5000) for 1 h at room temperature, antigens were revealed by enhanced chemilumincescence reaction buffer.

Cell culture Hippocampal neurons from embryonic day 18 were freshly prepared by hippocampal dissection. The C-shaped hippocampus was cut off and trypsinized for 20 min at 37 ºC in a 5% CO_2 incubator. The cells were broken apart by pipetting with complete media and were then plated with a density of 3×10^8 cells/L in neurobasal medium supplemented with B27 (all materials from Gibco Invitrogen, Grand Island, NY).

Rat neuron Nucleofector transfection Transfection was accomplished using a Rat Neuron Nucleofector kit and the device from Amaxa. For each example, the prepared neurons were resuspended in Rat Neuron Nucleofector Solution to a final concentration of 1×10^6–6×10^6 cells/L. Then, 100 μL of cell suspension was mixed with 1–3 μg DNA (in 1–5 μL H_2O or TE). Each nucleofection sample was transferred into an Amaxa certified cuvette. Insert the cuvette into the cuvette holder (Amaxa, Germany) and rotate the turning wheel clockwise to the final position. And tranfection program G-13 was initiated. The transfections efficiencies were evaluated and cell transplantation was carried out 3 d later.

Immunocytochemistry Three days after transfection, the wells were fixed with 4% paraformaldehyde for 15 min. Then the wells were incubated for 12 h at 4 ºC with mouse anti-rat NF antibody (1:100, DAKO) and mouse anti-human A20 antibody (1:200, Oncogene), diluted in blocking buffer. The wells were incubated with rhodamine-labeled secondary antibodies (1/500, Kirkegaard Perry Laboratories, MD, USA) and FITC-labeled secondary antibodies (1/200, DAKO) in blocking buffer for 60 min at room temperature. Fluorescence staining was evaluated using a Leica fluorescent microscope.

Cell counting Neurons stained positively for A20 were counted on coded slides using an Olympus CAST Grid system (Denmark). The area of each culture well was delineated and a counting frame was randomly placed to mark the first area to be sampled. The frame was then systematically moved through the delineated area. The total number of neurons and A20-immunoreactive neurons was extrapolated from the data, and the transfection efficiency was evaluated.

For the experiments *in vivo*, 3 d and 7 d after transplantation, rats were anesthetized and perfused intracardially with phosphate buffered saline (PBS, pH 7.4) followed by 4% paraformaldehyde dissolved in PBS (pH 7.4). Then, serial coronal brain cryostat sections were cut at 20 μm thickness and every third section was used to count the surviving cells. To assess the survival of grafted Hoechst-stained neurons, a similar method was employed[8].

Neurons cultured with TNF-α Three days after transfection, TNF-α was added to A20-neurons and pcDNA3-neurons to a final concentration of 2000 kU/L, and the cells were incubated at 37 ºC in 5% CO_2 for 8 h. Then, the apoptosis rates were accessed by flow cytometry using a FACStar (Becton Dickinson) with excitation wavelength set at 585 nm.

Labeling of neurons for transplantation Seventy-two hours after transfection, Hoechst 33258 (Sigma) was added to each well to achieve a final concentration of 10 mg/L. One hour later, cells were rinsed 3 times with PBS to completely flush out excess fluorescence and the cells were then collected for transplantation.

Surgical procedure All animal experimental procedures were approved by the local animal protection authority. Twenty-four male Sprague-Dawley rats (250–300 g) were randomly allocated to four groups of equal size (group A-D). Rats in groups C and D were anesthetized with 10% chloralhydrate, a midline neck incision was made and a 30-mm long piece of 4–0 monofilament nylon suture was advanced from the external carotid artery (ECA) through the common carotid artery (CCA) and into the lumen of the internal carotid artery (ICA) until it blocked the origin of the middle cerebral artery (MCA). One and a half hours after the occlusion, the filament was withdrawn[9]. The rats were allowed to recover and were monitored daily for behavioral and neurological deficits (motor weakness of extremities). The rats that did not show neurological deficits were excluded[10].

Transplantation surgery Immediately after MCAO, the rats' heads were immobilized in a stereotaxic frame. Either A20 or pcDNA3 neurons (3×10^5 cells) 2 μL were injected

into the penumbra at the following coordinates: 1.00 mm rostral to bregma, 3.0 mm right of the midline, and 1.2 mm ventral from the dural surface, with the incisor bar set at zero. Another 12 normal rats serving as controls received identical grafts[11]. Rats were divided into 4 groups: normal rats with A20-neurons (group A), normal rats with pcDNA3-neurons (group b), MCAO rats with A20-neurons (group C), MCAO rats with pcDNA3-neurons (group D).

Statistical analysis Data are expressed as mean±SD. Statistical analysis was performed by one-way ANOVA and the *t*-test, using statistical software package SPSS 10.0. Statistical significance was set at a level of $P<0.05$.

Results

Identification of primary cultured cells and evaluation of transfection efficiency The fact that most cells were immunoreactive for NF indicates that most cells were neurons (Figure 1). Seventy-two hours after gene delivery, neurons immunoreactive for A20 were counted as described above for quantitative determination of transfection efficiency (Figure 2). The percentage of neurons successfully transfected with A20 was 52.46%±5.26%.

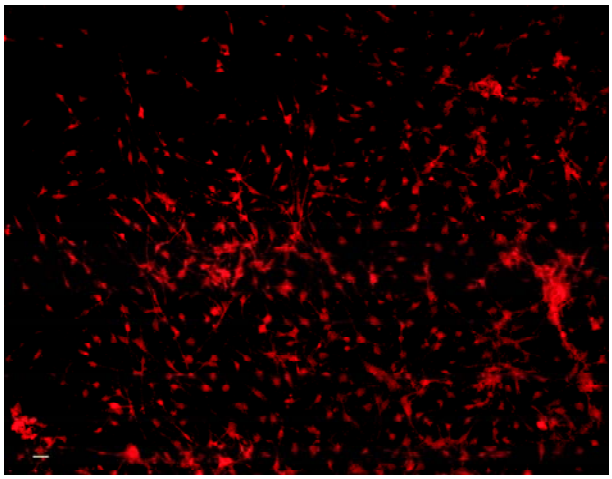

Figure 1. E18 hippocampal neurons tagged with anti-NF antibody on day 3 after plating (×100).

Expression of A20 in neurons *in vitro* and after transplantion into MCAO brains Activation of A20 was detected 10 d after transfection by both RT-PCR (Figure 3A) and Western blot analysis (Figure 3B).

Induction of apoptosis by TNF-α *in vitro* The results of FACS analysis showed that after the proapoptotic insult with TNF-α, the apoptosis rate of neurons overexpressing A20 (28.46%±3.87%) was lower than that in neurons transfected with pcDNA3 (53.06%±5.36%) ($P<0.05$, Figure 4A, 4B).

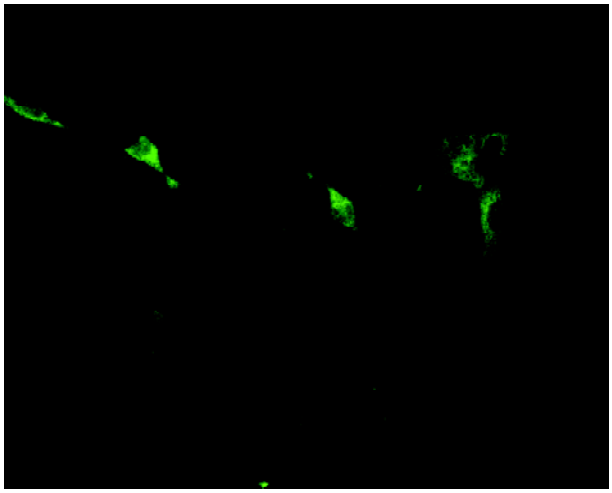

Figure 2. The immunocytochemical staining for protein A20 of the rat E18 primary hippocampal neurons 3 d after transfection (×100).

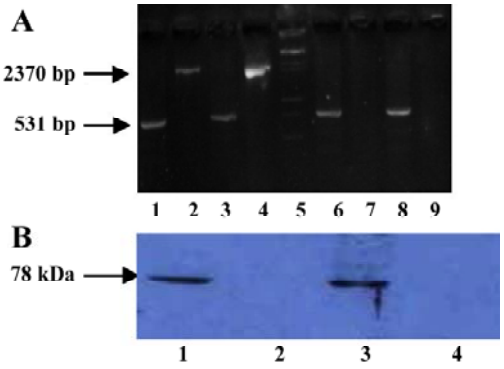

Figure 3. A) RT-PCR showed the expression of A20 in neurons 10 d after transfection both *in vivo* (lane 2) and *in vitro* (lane 4). Neurons transfected with pcDNA3 were chosen as the negative control both *in vivo* (lane 7) and *in vitro* (lane 9). The β-actin was selected as intrinsic standard (lanes 1, 3, 6, 8). B) Western blot analysis showed the expression of protein A20 in neurons 10 d after transfection both *in vivo* (lane 1) and *in vitro* (lane 3). Neurons transfeced with pcDNA3 were chosen as the negative control both *in vivo* (lane 2) and *in vitro* (lane 4).

A20 protected the transplanted neurons from apoptosis in the penumbra of the MCAO brain Cells derived from the hippocampus of E18 Sprague-Dawley rats were transfected with A20 or pcDNA3 and grafted into the apoptotic zone (penumbra) of MCAO rats, and at an identical position in normal rats. Grafts were identified *in vivo* 3 d and 7 d after transplantation by staining using the Hoechst 33258 stain. A large number of cells implanted into the nor-

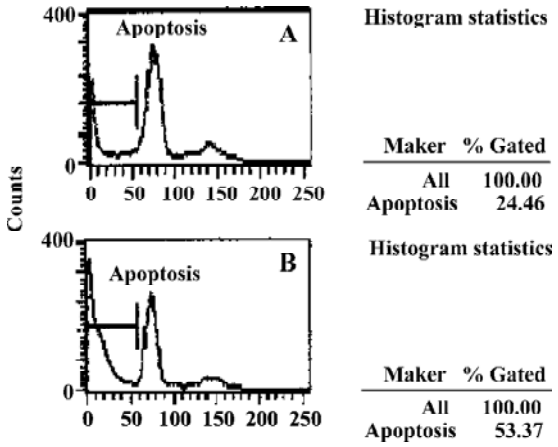

Figure 4. The apoptosis rate of the cultured neurons at 3 d after transfected with A20 under TNF-α stimulus (B). The neurons transfected with native pcDNA3 was as the control group (A).

mal rat brain survived, with no significant difference in the cell survival rate between the A20 group and the pcDNA3 group on d 3 or d 7 (P>0.05). On the other hand, a great deal of grafted cells died when transplanted into the apoptotic zone of the ischemic brain. In this case, neurons with A20 that were grafted into MCAO rats had a greater survival rate compared to pcDNA3 cells both on d 3 and d 7 (P<0.05, Figure 5A-5H, 6).

Discussion

A20 is encoded by a primary response gene which was originally identified as a TNF-inducible gene in human umbilical vein endothelial cells[12]. It seems to have a dual activities, serving not only as an inhibitor of NF-κB activation, but also as an antiapoptotic gene in some cell systems. Primary cells that are taken directly from the body are morphologically and physiologically similar to the parent tissue. Gene transfer using primary cells is a much better way to mimic the *in vivo* situation. This method permits much more precise medical and scientific conclusions than when genes are transferred into degenerated cell lines[14].

In our research, we used rat primary hippocampal neurons, which form an important *in vitro* model for the research of many central nervous system diseases (such as brain ischemia and Parkinson disease) and for studying routine events in most parts of the brain. And a newly developed electroporation method known as Nucleofector technology was employed in the study of the rat primary hippocampal neurons. It is a physical method that is suitable for the transfection of nonphagocytic and nonproliferating cells, such as peripheral leukocytes and stem cells, which are usually refractory to chemical transfection vectors. In addition, it is free of biocontaminants and does not induce immune reactions[15]. The results of immunocytochemical analysis indicated that Nucleofector technology obtained a 52.46%± 5.26% transfection efficiency for the A20 gene, which is the highest transfection efficiency reported so far involving nonviral gene transfer of primary cell cultures. This high rate of efficiency is important for advanced functional experiments. RT-PCR and Western bloting analysis further proved the continuous expression of A20 proteins both *in vitro* and i*n vivo* 10 d after transfection.

FACS analysis demonstrated that the A20 could protect the primary culture neurons from TNF-induced apoptosis *in vitro*. The mechanism of action has not yet been completely clarified. Some researchers speculate that A20 might interfere with TNF-R-associated death domain (TRADD) binding to TNF-R1 and might, thus, negatively regulate TNF induced cytotoxicity[6].

Most of the evidence supporting the role of apoptosis in neuronal cell death comes from studies using animal models of global or focal cerebral ischemia. In the focal ischemia models, which create a condition emulating human strokes, transient ischemia followed by reperfusion is often associated with massive induction of apoptosis-like cell death[16]. After reversible middle cerebral artery occlusion in adult rats, both TNF and TRAIL proteins are expressed in the apoptotic areas of the post-ischemic brain (the penumbra), thus providing conditions for inducing apoptosis. TRAIL mRNA levels increase in response to ischemia and reperfusion, reaching a maximum after 3 d. In contrast to TRAIL, TNF-α mRNA is not consistently upregulated in the ischemic hemisphere. TNF-α mRNA exhibits a first peak after 24 h, followed by a decline after 3 d, and a second rise after 5 d[17]. Furthermore, in focal cerebral ischemia, NF-κB is activated and promotes cell death[17,18]. So when cultured neurons are injected into this zone, apoptosis is expected to occur. Cell counting of surviving neurons in the present study confirmed this speculation. Higher levels of cell death were observed in the case of both A20-neurons and pcDNA3-neurons when grafted into MCAO rats than when grafted into normal rats. This result proves that apoptosis-inducing circumstances definitely exist in the penumbra following transient cerebral ischemia. On the other hand, among the two groups of MCAO rats, more A20-neurons survived than the sham group pcDNA3-neurons. This result indicates that A20 protein can protect the neurons from the cytotoxicity associated with the ischemic zone. Some further points should be made. First, the transfection efficiency was approximately 50%, and neu-

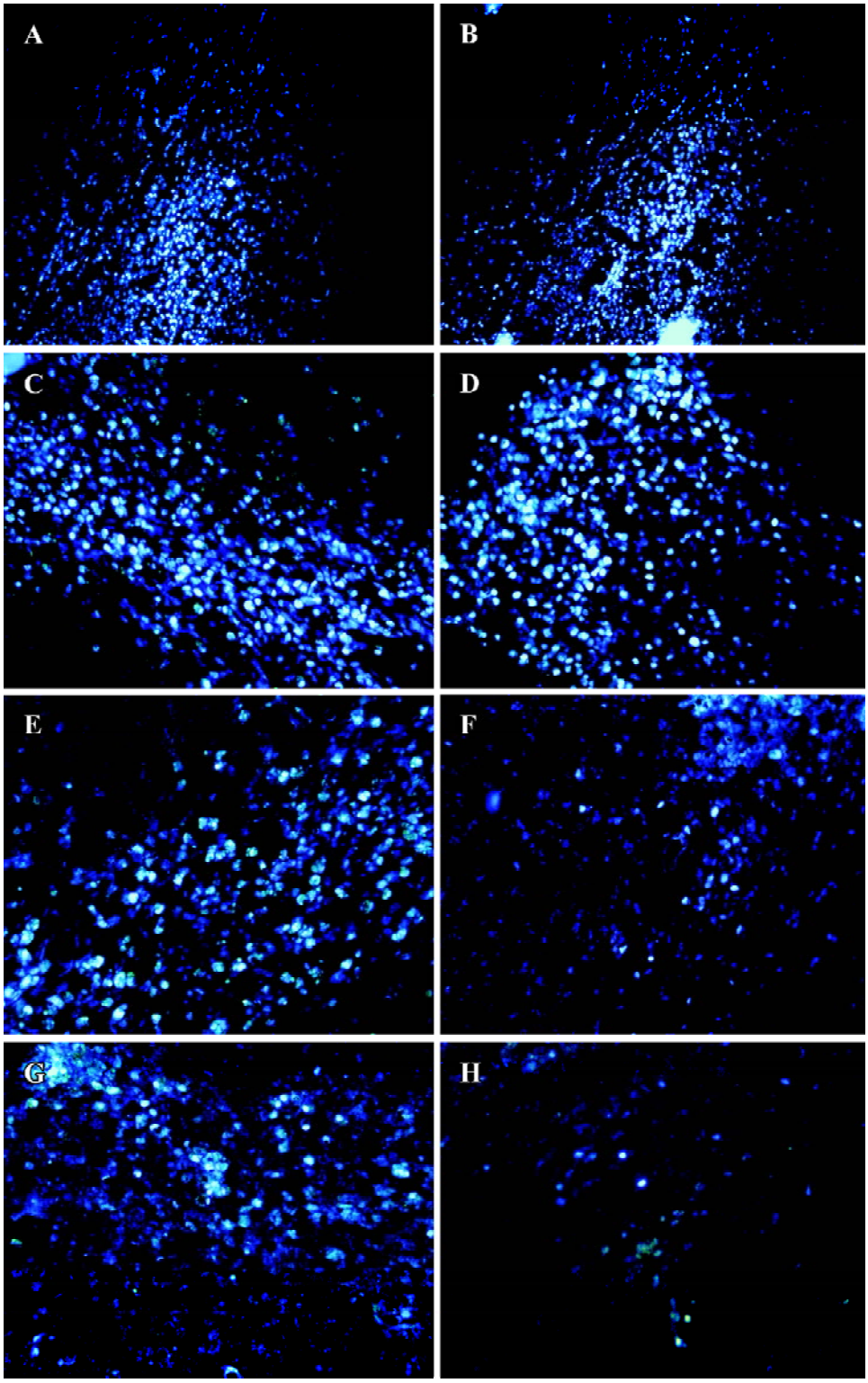

Figure 5. Immunostained 20-μm cryosections of surviving neurons from Sprague-Dawley rats subjected to MCAO and subsequently reperfused for different lengths of time (×200). Hoechst reactive neurons which had been transfected with A20 and pCDNA3 were seen scattered throughout the penumbra at 3 d after A20-neurons (E) and pcDNA3-neurons (F) transplanted to the penumbra of MCAO rats, and 7 d after A20-neurons (G) and pcDNA3-neurons (H) transplanted to the penumbra of MCAO rats. There were corresponding controls to normal rats at 3 d after A20-neurons (5A) and pcDNA3-neurons (B) transplanted to the normal rats, and 7 d after A20-neurons (C) and pcDNA3-neurons (D) transplanted to the normal rats.

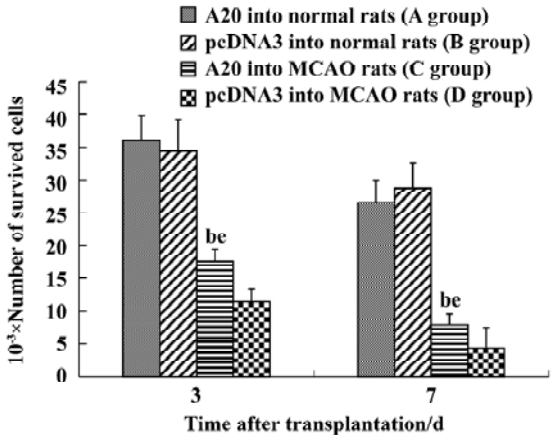

Figure 6. Number of the surviving cells at 3 d and 7 d after transfected neurons were transplanted into the brains of MCAO rats and normal rats. n=3. Mean±SD. $^{b}P<0.05$ *vs* A group. $^{e}P<0.05$ *vs* D group.

rons that did not express the A20 protein would likely be induced to undergo apoptosis. Second, the transplanted neurons were influenced not only by TNF and TRAIL, but also by multiple other toxic factors, such as the CD95-ligand, starvation, etc. Thus 7 d after transplantation into the ischemic zone, the fact that large number of A20-neurons nevertheless died indicates that the function of A20 protein can only partly and not completely protect the neurons *in vivo*.

In conclusion, our study showed that the zinc finger protein A20 was an effective neuroprotective agent that improved the survival of both cultured and grafted embryonic hippocampal neurons, which suggests that the A20 may have therapeutic potential in gene therapy for diseases of the central nervous system.

Acknowledgment

We would like to thank Mr Zhi-hua JIANG, and Miss Sheng LI for their technical and material assistance.

References

1 Thompson CB. Apoptosis in the pathogenesis and treatment of disease. Science 1995, 267: 1456–62.

2 Opipari AW Jr, Hu HM, Yabkowitz R, Dixit VM. The A20 zinc finger protein protects cells from tumor necrosis factor cytotoxicity. J Biol Chem 1992; 267: 12424–7.

3 Yu LY, Lin B, Zhang ZL, Guo LH. Direct transfer of A20 gene into pancreas protected mice from streptozotocin-induced diabetes. Acta Pharmacol Sin 2004; 25: 721–6.

4 Song HY, Rothe M, Goeddel DV. The tumor necrosis factor-inducible zinc finger protein A20 interacts with TRAF1/TRAF2 and inhibits NF-kappaB activation. Proc Natl Acad Sci USA 1996; 93: 6721–5.

5 Ferran C, Stroka DM, Badrichani AZ, Cooper JT. A20 inhibits NF-kappaB activation in endothelial cells without sensitizing to tumor necrosis factor-mediated apoptosis. Blood 1998; 91: 2249–58.

6 Beyaert R, Heyninck K, Van Huffel S. A20 and A20-binding proteins as cellular inhibitors of nuclear factor-kappa B-dependent gene expression and apoptosis. Biochem Pharmacol 2000; 60: 1143–51.

7 Costantini LC, Bakowska JC, Breakefield XO, Isacson O. Gene therapy in the CNS. Gene Therapy 2000; 7: 93–109.

8 West MJ, Slomianka L, Gundersen HJ. Unbiased stereological estimation of the total number of neurons in the subdivisions of the rat hippocampus using the optical fractionator. Anat Rec 1991; 231: 482–97.

9 Stephenson D, Yin T, Smalstig EB, Hsu MA, Clemens J. Transcription factor nuclear factor-kappa B is activated in neurons after focal cerebral ischemia. J Cereb Blood Flow Metab 2000; 20: 592–603.

10 Markgraf CG, Green EJ, Hurwitz BE, Morikawa E, Schneiderman N, *et al*. Sensorimotor and cognitive consequences of middle cerebral artery occlusion in rats. Brain Res 1992; 575: 238–46.

11 Yao H, Takasawa R, Fukuda K, Shiokawa D, Sadanaga-Akiyoshi F, Ibayashi S, *et al*. DNA fragmentation in ischemic core and penumbra in focal cerebral ischemia in rats. Brain Res Mol Brain Res 2001; 91: 112–8.

12 Dixit VM, Green S, Sarma V, Holzman LB, Wolf FW, O'Rourke K, *et al*. Tumor necrosis factor-alpha induction of novel gene products in human endothelial cells including a macrophage-specific chemotaxin. J Biol Chem 1990; 265: 2973–8.

13 Grossmann M, Nakamura Y, Grumont R, Gerondakis S. New insights into the roles of ReL/NF-κB transcription factors in immune function, hemopoiesis and human disease. Int J Biochem Cell Biol 1999; 31: 1209–19.

14 Nussbaum RL, Ellis CE. Alzheimer's disease and Parkinson's disease. N Engl J Med 2003; 348: 1356–64.

15 Neumann E, Schaefer-Ridder M, Wang Y, Hofschneider PH. Gene transfer into mouse lyoma cells by electroporation in high electric fields. The EMBO J 1982; 1: 841–5.

16 Snider BJ, Gottron FJ, Choi DW. Apoptosis and necrosis in cerebrovascular disease. Ann N Y Acad Sci 1999; 893: 243–53.

17 Martin-Villalba A, Herr I, Jeremias I, Hahne M, Debatin KM, *et al*. CD95 ligand (Fas-L/APO-1L) and tumor necrosis factor-related apoptosis-inducing ligand mediate ischemia-induced apoptosis in neurons. J Neurosci 1999; 19: 3809–17.

18 Schneider A, Martin-Villalba A, Weih F, Vogel J, Wirth T, Schwaninger M. NF-kappaB is activated and promotes cell death in focal cerebral ischemia. Nat Med 1999; 5: 554–9.

Full-length article

Validation of a simple automated movement detection system for formalin test in rats[1]

Yu-feng XIE, Jing WANG, Fu-quan HUO, Hong JIA, Jing-shi TANG[2]

Department of Physiology, School of Medicine, Xi'an Jiaotong University, Key Laboratory of Environment and Genes Related to Diseases, Ministry of Education, Xi'an 710061, China

Key Words

pain measurement; automated movement detection system; formalin test; analgesia; lidocaine; rats

[1] Project supported by the National Natural Science Foundation of China (No 30270453).
[2] Correspondence to Dr Jing-shi TANG.
Phn 86-29-8265-5172. Fax 86-29-8265-6364.
E-mail jstang@mail.xjtu.edu.cn

Received 2004-04-12
Accepted 2004-07-21

doi: 10.1111/j.1745-7254.2005.00001.x

Abstract

Aim: To investigate the validity and sensitivity of an automatic movement detection system developed by our laboratory for the formalin test in rats. **Methods:** The effects of systemic morphine and local anesthetic lidocaine on the nociceptive behaviors induced by formalin subcutaneously injected into the hindpaw were examined by using an automated movement detection system and manual measuring methods. **Results:** Formalin subcutaneously injected into the hindpaw produced typical biphasic nociceptive behaviors (agitation). The mean agitation event rate during a 60-min observation period increased linearly following increases in the formalin concentration (0.0%, 0.5%, 1.5%, 2.5%, and 5%, 50 μL). Systemic application of morphine of different doses (1, 2, and 5 mg/kg) 10-min prior to formalin injection depressed the agitation responses induced by formalin injection in a dose-dependent manner, and the antinociceptive effect induced by the largest dose (5 mg/kg) of morphine was significantly antagonized by systemic application of the opioid receptor antagonist naloxone (1.25 mg/kg). Local anesthetic lidocaine (20 mg/kg) injected into the ipsilateral ankle subskin 5-min prior to formalin completely blocked the agitation response to formalin injection. These results were comparable to those obtained from manual measure of the incidence of flinching or the duration time of licking/biting of the injected paw. **Conclusion:** These data suggest that this automated movement detection system for formalin test is a simple, validated measure with good pharmacological sensitivity suitable for discovering novel analgesics or investigating central pain mechanisms.

Introduction

The formalin test, first established by Dubuisson and Dennis[1], is a model of acute and tonic pain that is commonly used in studies of nociception in rodents and in the discovery of novel analgesics. The test has been characterized most extensively in rats, cats, and mice[1–3]. The injection of diluted formalin into the hindpaw of rats elicits a biphasic nociceptive behavioral response. This response is complex and includes such behavior as rearing, turning, jumping, crossings, flinching, shaking, elevating, clutching, and licking the affected paw and dysphoria. These responses have been most frequently monitored either by assessing a single, presumably representative, behavior (eg, the incidence of flinching, the duration of licking/biting)[4–7], or by using a weighted-scored measure[1] to evaluate the global response. However, these measurements, based on a subjective interpretation of the behaviors, are labor-intensive, time-consuming, tedious, and dependent on human judgement. The need to automate behavioral pain tests is obvious not only to facilitate their use but also to allow researchers from academic institutes and pharmaceutical companies to easily use more sophisticated and perhaps more predictive tests than the usual acute pain test. Therefore, different automated detection systems have been established for nociceptive behavior in the formalin test[8–10]. However, the computer-

driven, dynamic-force automatic system[8] or the automated method of pain scoring[9–11] were difficult to purchase. Recently, a simple automated movement detection system has been described primarily by our laboratory to quantify the agitation responses elicited by subcutaneous (sc) formalin injection into the rats' hindpaw[12]. The purpose of the present study was to further investigate the pharmacological sensitivity and validity of this system. The agitation responses elicited by different concentrations of formalin (50 μL) sc injected into the rat hindpaw were determined with this automated system, and then the effects of systemic morphine of different doses and local anesthetic lidocaine on the agtitation responses induced by the largest concentration of formalin (5%) were examined in the rat. As comparable control, manual measurement of the duration of licking/biting and the incidence of flinching of the injected paw were also simultaneously monitored in each test.

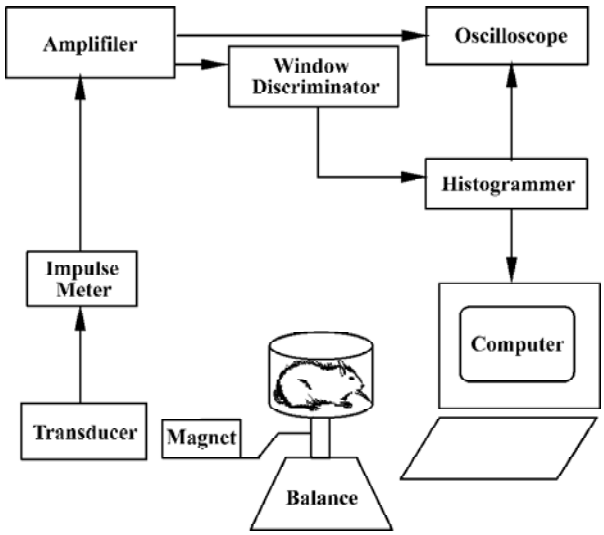

Figure 1. Schematic diagram of the automated movement detection system for recording the agitation response induced by formalin.

Materials and methods

Subjects Sixty adult male Sprague-Dawley rats weighing 260–280 g were provided by the Experimental Medical Animal Center of Shaanxi Province, China. Animals were housed in cages in groups of six with food and water available *ad libitum* on a 12 h light/dark schedule (lights on at 8: 00 AM). The experiment was performed according to the Guidelines of the International Association for the Study of Pain[13] and approved by the Institutional Animal Care Committee of Xi'an Jiaotong University.

Formalin test

Automated movement detection system The transformed part of the automated movement detection system consisted only of a spring balance (0–2.0 kg) and an electromagnetic transducer, a permanent magnet (1.5 cm×1.5 cm× 1.0 cm) with an intensity of 0.5 T connected to the plane of the balance, which placed both the N and S poles of the magnet in a horizontal plane. One thousand five-hundred turns were wound on an E6 electric core and then installed in the magnetic field. Such an electromagnetic transducer was able to pick up and transform the mechanical movement of the spring balance plane into the induced current in the winding in the magnetic field, as shown in Figure 1. On the day of testing, each rat was moved to the laboratory and placed in a hexagonal polycarbonate chamber (L:16 cm; H: 8 cm) for about 15–20 min to acclimate it to the experimental environment. The criterion for adequate acclimation was that rats did not freeze or defecate in the test chamber[14] and rarely exhibited spontaneous activities. Then, the rat was talen from this chamber and formalin (50 μL) was administered sc into the hindpaw pad. The rat was immediately replaced in the chamber, which was placed on the spring balance with the electromagnetic transducer. Nociceptive behavior (agitation) elicited by the formalin injection such as flinching shaking, elevating, clutching, and favoring the affected paw, and dysphoria activities-induced movements of the balance, which was picked up and transformed into electrical signals via the electromagnetic transducer. The electrical signals were amplified, filtered (100 Hz), and displayed on an oscilloscope, and fed into a window discriminator to minimize the non-specific signals induced by spontaneous movement of the animal. A computer system that allowed quantitative recording of the number of agitation events and construction of time histograms over a 60-min observation period. To examine the different concentrations of formalin-induced agitation responses, rats were restrained lightly and received a single sc injection of saline (50 μL) or formalin (0.5, 1.5, 2.5, 5.0%, 50 μL, respectively) into the plantar surface of right hindpaw. Each rat was used only once and was killed by a lethal dose of pentobarbital at the end of the experiment.

Manual detection method To evaluate the validity of the automated movement detection system for formalin test, the classical manual detection methods were also used synchronously. A mirror was positioned below the chamber at a 45º angle for unobstructed observation of the rats' paws. The response to formalin injection was monitored by measuring the total duration(s) of licking/biting and the incidence (times) of flinching of the injected hindpaw over 5-min in the 60-min observation period, respectively, by two

experimenters, as reported previously[4–6].

Pharmacological experiment To determine the pharmacological validity of the automated movement detection system, the effects of sc injection of morphine hydrochloride of different doses (1, 2, and 5 mg/kg, dissolved in 0.9% saline) 10 min before formalin injection on the formalin-induced agitation responses were observed. In the subsequent experiments, the blocking effects of opioid receptor antagonist naloxone on morphine-induced inhibition of the agitation responses were further examined, ie, after administertion of the largest dose (5.0 mg/kg) morphine, which produced a maximal antinociceptive effect, naloxone hydrochloride (1.25 mg/kg, dissolved in 0.9% saline, Sigma, MO, USA) was administered sc just before formalin injection. The doses of morphine and naloxone were selected according to previous studies by using the weighted-scores method for behavioral measurement of nociception in the formalin test[8,15]. In another experimental group rats received an injection of lidocaine (2%, 20 mg/kg) into the ipsilateral ankle subskin of the rat 5 min prior to formalin (5%, 50 μL) injection to observe the effects of the local anesthetic on the formalin-induced agitation responses. The same volume of saline was injected before formalin injection in the control experiment. In all these experiments, after formalin injection, the nociceptive agitation responses were monitored for 60-min by using both the automated movement detection system and the manual detection method.

Data analysis Data were expressed as the agitation event rate (Hz), the duration(s) of licking/biting and the incidence (times) of flinching of the injected paw per 5-min observation period. The correlation coefficient between the concentration or dose of drug and effect on nociceptive behavior was calculated with linear regression. Differences in drugs effects among groups were tested statistically by two-way repeated measures of analysis of variance (two-way RM ANOVA) with a *post hoc* multiple comparison (Bonferroni *t*-test) for analysis of the differences over the entire observation time or at each time point among different groups. $P<0.05$ was considered to indicate statistical significance.

Results

Nociceptive behavior induced by formalin injection to the hindpaw Injection of formalin into the rat hindpaws elicited a characteristic biphasic nociceptive agitation response when the response was monitored with the automatic system. The first phase (early phase) began immediately after formalin injection and lasted for approximately 5-6 min. After the first phase, there was one 6–10 min interphase, during which the rat was relative quiet in the chamber and rarely exhibited nociceptive agitation activities. The second phase (late phase) began approximately 10–15 min after formalin injection and lasted for approximately 40-50 min. In the second phase, the response peak appeared at about 35 min after formalin injection. The time histograms of the mean agitation events induced by formalin of different concentration (saline, 0.5, 1.5, 2.5, and 5.0%, 50 μL, $n=6$ for each treated group) was shown in Figure 2A–2E. The agitation event rate induced by 5.0% formalin during a 60-min observation period was significant larger than that of the saline, 0.5% or 1.5% formalin group ($P<0.01$, $n=6$) and that induced by 2.5% formalin was significantly larger than that of the saline group ($P<0.05$). Although there was no significant difference between the 5.0% and 2.5% formalin groups in overall effects, there were significant differences at three of 12 time points ($P<0.05$, Figure 2E). Linear regression analyses indicated that the nociceptive agitation response to formalin increased following the formalin concentration increase with a correlation coefficient (r) of 0.781 ($P<0.01$).

Similarly, the formalin-elicited biphasic response measured manually was comparable to that obtained with the automatic detection system (Figure 2G, 2H). These results were similar to previous reports using either automatic or manual methods[8,10,15].

Effect of morphine on formalin-elicited nociceptive behavior Injection of morphine (0, 1, 2, and 5 mg/kg) depressed the nociceptive agitation response to the largest dose (5%, 50 μL) of formalin injection in a dose-dependent manner with a correlation coefficient (r) of 0.876 as monitored by the automatic detection system (Figure 3A–3D). The inhibitory effect induced in both the 2 and 5 mg/kg morphine group during the 60-min observation period was significantly larger than that of the saline group ($P<0.01$, $n=6$). Although there was no significant difference between the 1.0 mg/kg morphine and saline groups ($P>0.05$, $n=6$) in the overall effect, the differences were significant at two of 12 time points ($P<0.05$). The inhibitory effect of the 1 mg/kg morphine group was significantly smaller than that of 2 mg/kg and 5 mg/kg morphine groups ($P<0.05$) at the 35 min time point after formalin injection (Figure 3E).

The inhibitory effect of morphine to the formalin-evoked nociceptive behavior was also measured manually. The decreases in the licking/biting duration induced in the 2 and 5 mg/kg morphine groups were significantly different from that of the saline group ($P<0.05$, $P<0.01$, $n=6$) during the 60-min observation period. At two time points the effect in 1 mg/kg morphine group was different from saline group

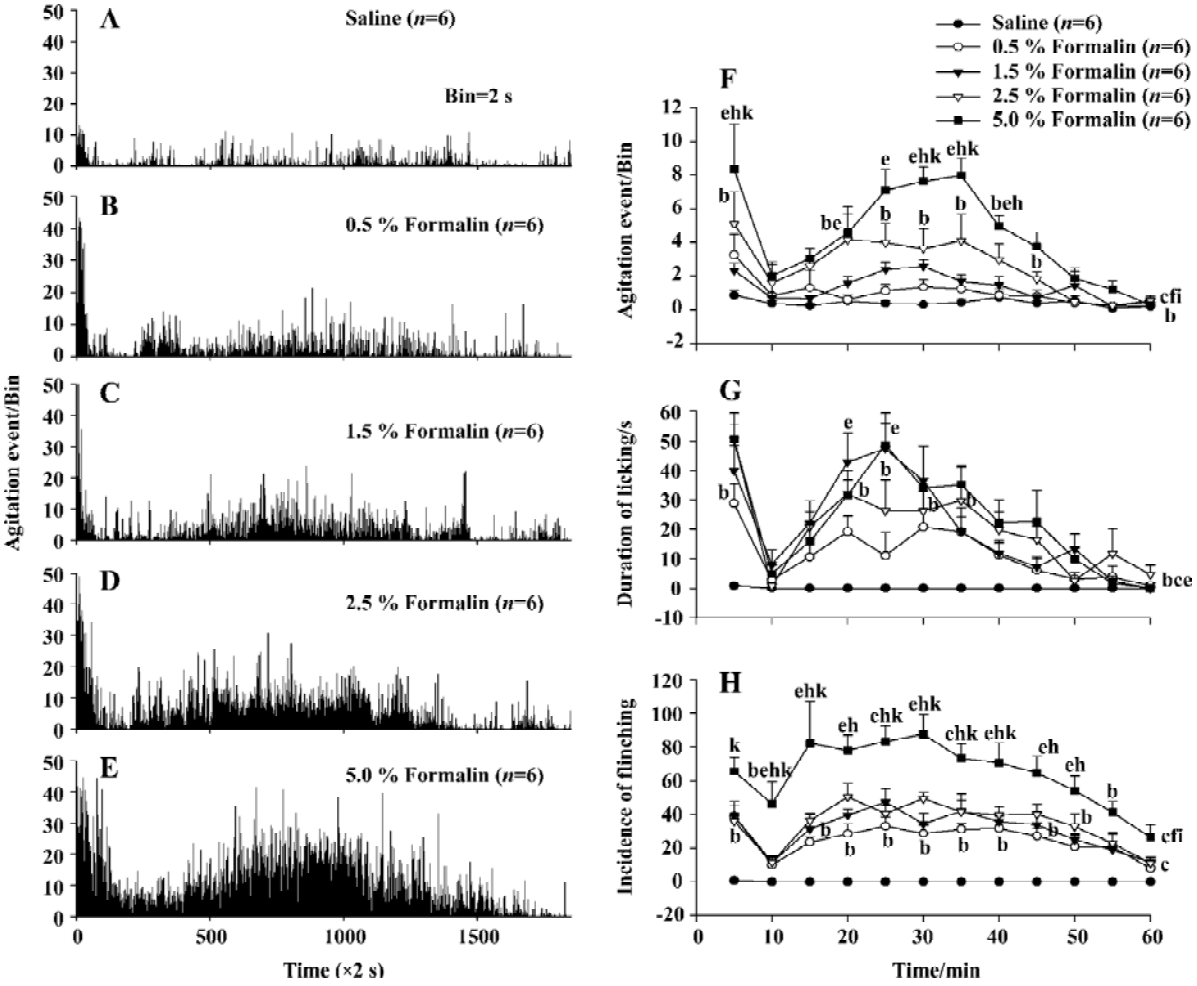

Figure 2. Left side (A-E): Mean time histograms showing the nociceptive agitation responses induced by different concentrations of formalin injected into the hindpaw detected using the automatic detection system. Bin=2 s. Right side: Time course curves showing the nociceptive behavior induced by different concentrations of formalin injected into rat hindpaw per 5-min observation period. (F) Agitation event rate (Hz) recorded using automated system; (G) duration time (s) of licking/biting the injected paw; (H) incidence (times) of flinching the injected paw. Mean±SEM. n=6. ^{b}P<0.05, ^{c}P<0.01 *vs* saline. ^{e}P<0.05, ^{f}P<0.01 *vs* 0.5 % formalin. ^{h}P<0.05, ^{i}P<0.01 *vs* 1.5 % formalin. ^{k}P<0.05 *vs* 2.5 % formalin.

(P<0.05). The inhibitory effect of 5 mg/kg morphine was significantly different from those of the 1 and 2 mg/kg morphine in overall effects (P<0.01, n=6). Similarly, the decreases in the flinching incidence in the 1, 2, or 5 mg/kg morphine group were all different from the saline group (P<0.01, n=6). However, no-significant differences were found among the three morphine groups either in the entire effects or at any time point, as shown in Figure 3F, 3G.

Effect of naloxone on morphine-induced inhibition of nociceptive behavior in the formalin test Injection of the opioid receptor antagonist naloxone 1.25 mg/kg after morphine (5.0 mg/kg) application completely antagonized the morphine-evoked inhibition of agitation responses induced by formalin injection (Figure 4A–4C). There was statistically significant difference (P<0.01, n=6) between the effects induced by naloxone plus morphine and those by morphine alone, but no significant difference (P>0.05) was detected between effects in the naloxone plus morphine group and the saline group (Figure 4E).

When manual detection methods were used, naloxone significantly blocked the decrease in the licking/biting duration (P<0.01) and flinching incidence (P<0.01) elicited by morphine (Figure 4F, 4G).

Effect of lidocaine on the nociceptive behavior induced by formalin Injection of lidocaine 20 mg/kg into the ipsilateral ankle subskin completely blocked the agitation response to formalin injection as measured by the automatic system. There was a statistically significant difference

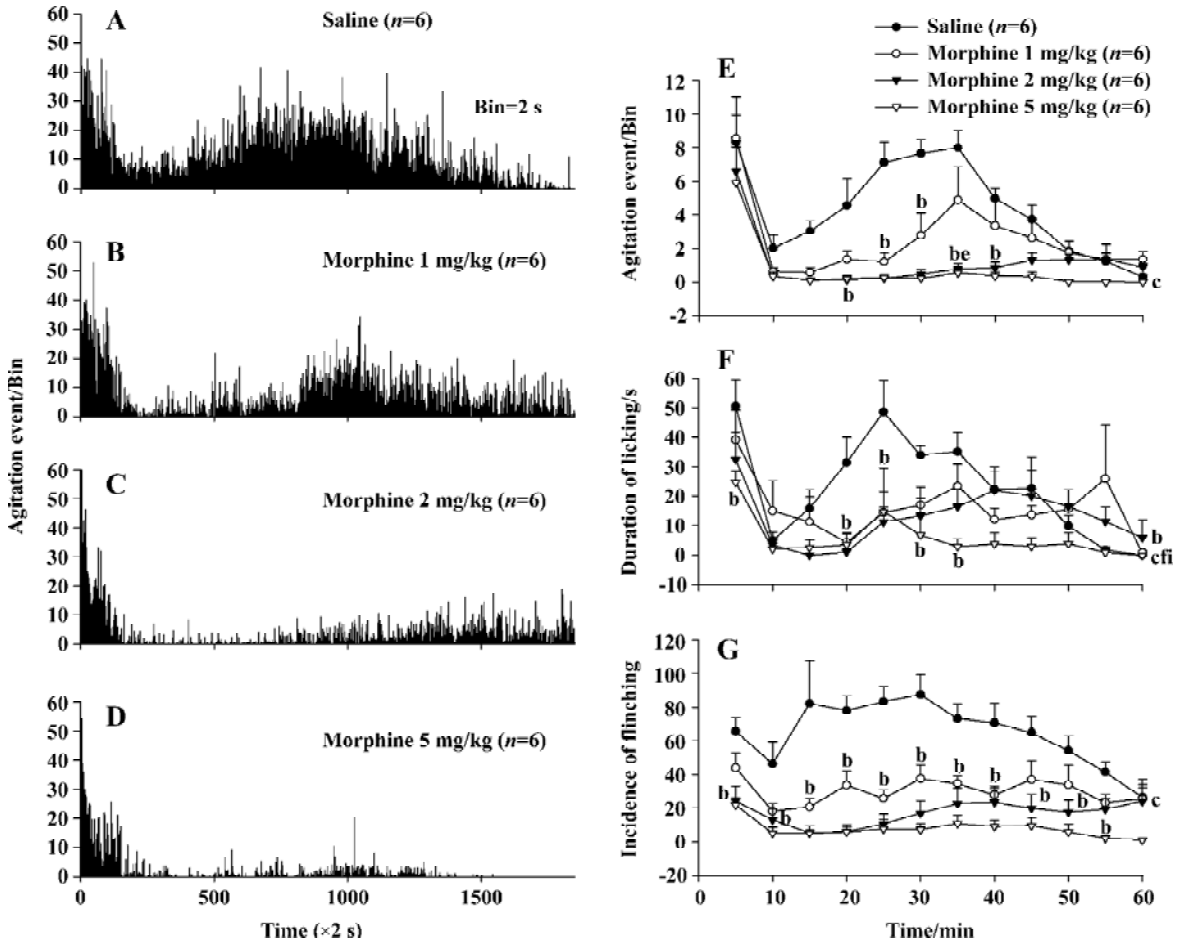

Figure 3. Lift side (A-D): Mean time histograms showing the inhibitory effects of different doses of morphine on the agitation responses induced by 5.0 % formalin injection using the automatic detection system. Bin=2 s. Right side: Time course curves showing the effects of different doses of morphine (0, 1, 2, 5 mg/kg) on 5.0 % formalin-evoked nociceptive behavior per 5 min observation period. (E) Agitation event rate (Hz), (F) duration time (s) of licking/biting the injected paw, (G) incidence (times) of flinching the injected paw. Mean±SEM. $^{b}P<0.05$, $^{c}P<0.01$ *vs* saline. $^{e}P<0.05$, $^{f}P<0.01$ *vs* 1.0 mg/kg morphine. $^{i}P<0.01$ *vs* 2.0 mg/kg morphine.

($P<0.01$) between the effects in saline group and the lidocaine group (Figure 4A, 4D).

When manual detection methods were used, there were also significant differences in the duration of licking/biting ($P<0.01$) and flinching incidence ($P<0.01$) between the saline and the lidocaine groups (Figure 4F, 4G).

Discussion

The present study found that a typical biphasic nociceptive behavior (agitation) induced by formalin injection into the rat hindpaw could be detected by the automated movement detection system developed by our laboratory[12], and that this response was proportional to those obtained from manual scoring method both in the time course and the magnitude of change. It is identical to previously reports about the formalin test in rats[1,9,10], either using a weighted-scores measurement or a single nociceptive behavior measurement such as licking/biting or flinching the injected paw. This indicates that the simple automated movement detection system for quantifying the nociceptive behavior elicited in the formalin test is a validated measure and produces results that are comparable to those found using a computer-driven, dynamic-force automatic detection system[7] or a new automated method of pain scoring[9,11].

The first phase of response elicited in the formalin test was believed to be a result of direct activation of peripheral nociceptors, whereas the second was mediated by a combination of low ongoing activity in primary afferents and increased sensitivity of spinal cord neurons (inflammatory

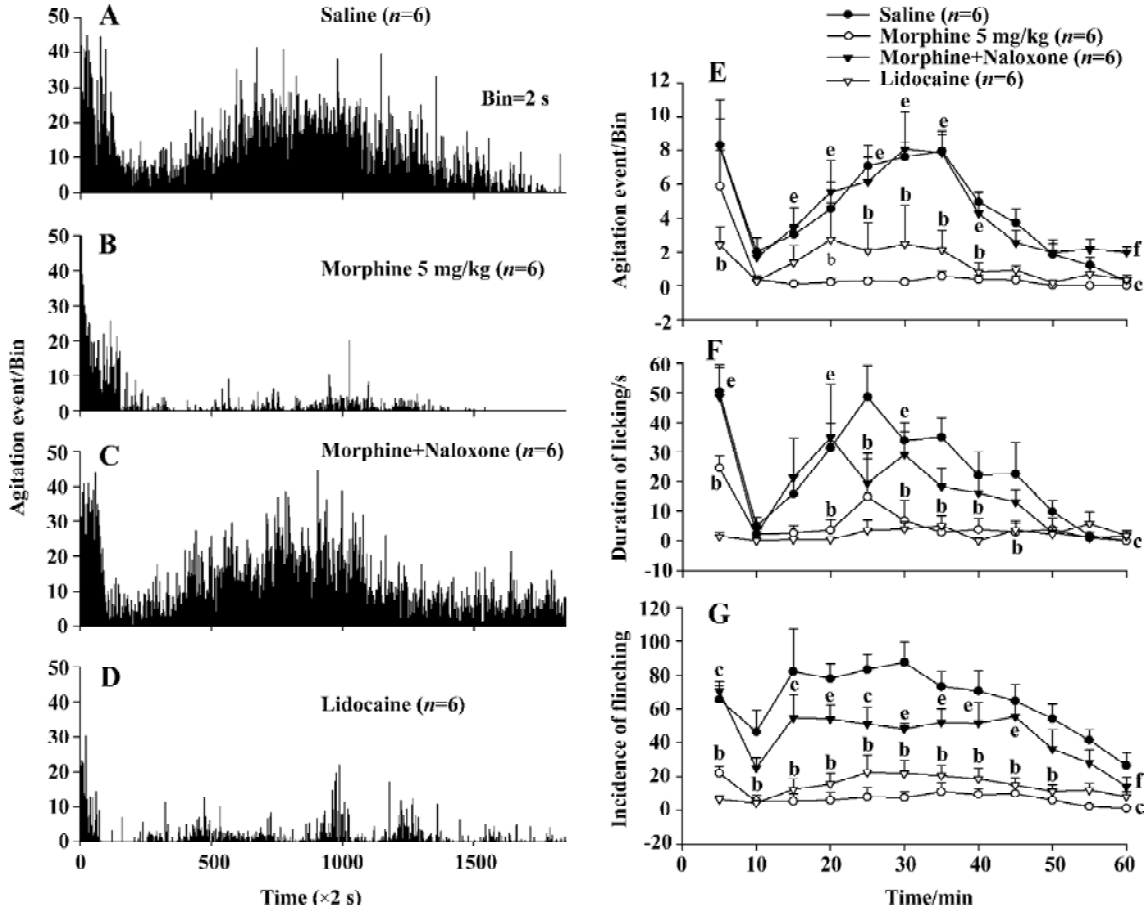

Figure 4. Left side (A–D): Mean time histograms showing the blocking effects of naloxone on 5 mg/kg morphine-evoked inhibition of agitation responses and of lidocaine on agitation responses induced by 5% formalin applied to rat hindpaw using the automatic detection system. Bin=2 s. Right side: Time course curves indicating the blocking effects of naloxone on morphine-evoked inhibition of nociceptive behavior and of lidocaine on nociceptive behavior induced by 5% formalin applied to rat hindpaws per 5-min observation period. (E) Agitation event rate (Hz) recorded by using the automatic detection system; (F) duration time (s) of licking/biting the injected paw; (G) incidence (times) of flinching the injected paw. Mean±SEM. $^{b}P<0.05$, $^{c}P<0.01$ *vs* saline. $^{e}P<0.05$, $^{f}P<0.01$ *vs* morphine.

hyperalgesia)[16,17]. Therefore, the intensity of the agitation response to formalin recorded by using the automatic system should be of a stimulation-response relationship. The results of this study demonstrated that the nociceptive agitation response increased linearly following the increase of stimulation intensity with a greater correlation coefficient which is similar to the results that obtained from manual detection methods. These results were also consistent with those obtained by using a weighted-scores method of behavioral pain rating[4] and using a computer-driven, dynamic-force automatic detection system[7]. Therefore, the results reinforced the validity of the new automatic detection system for monitoring the nociceptive response to formalin injection.

The validity of the automatic system was further confirmed by the results obtained from systemic morphine-evoked analgesia. The nociceptive agitation response to formalin as monitored by the automatic detection system was inhibited by sc injection of morphine in a dose-dependent manner which was similar to that described in other studies[8,9,15]. The antinociceptive effect of the largest dose (5.0 mg/kg) of morphine could be effectively antagonized by opioid receptor antagonist naloxone. These results were also comparable to those obtained using manual methods suggesting that the automatic system has a good sensitivity to analgesics and therefore provides a good measurement to evaluate the effect of analgesics.

In the present study, the data obtained with both the automatic detection system and manual methods indicated that the nociceptive response could be completely blocked by

pre-administration of the local anesthetic lidocaine. The results are identical to those reported previously[18,19]. It has been demonstrated that intraperitoneal injection of lidocaine (10–30 mg/kg) induced significant antinociceptive effect in both phases of the formalin test using the paw-licking measurement[18]. A pre-injection of lidocaine (sc) into the ankle before formalin could markedly decrease the formalin-evoked Fos-immunoreactivity in the dorsal horn neurons[19]. These studies showed that the automated movement detection system provided a good pain measurement and a pharmacological validation for the system. The results correlate well with the licking duration and incidence of flinching measures for invention and detection of new analgesic drugs.

In summary, the data from the present study show the validity of an automatic detection system with following advantages: (1) it is an objective measure; (2) global analysis of pain-induced behaviors superior to the recording of a single parameter such as licking duration or flinching incidence; (3) the system is less time consuming spent by the experimenter; (4) that the new automatic detection system could be used in pharmacological studies in inflammatory pain; and (5) the transducer equipment in the automatic system is very simple and cheap. In a general electrophysiological laboratory, this system can be easily made and used in studies of nociception and antinociception. Although the automatic system cannot clearly distinguish the agitation response and the spontaneous activities, the latter can be reduced to smallest if the animal adequately habituated to the experimental arena and were kept quiet in the chamber before formalin administration.

References

1 Dubuisson D, Dennis SG. The formalin test: a quantitative study of the analgesic effects of morphine, meperidine, and brainstem stimulation in rats and cats. Pain 1977; 4: 161–74.

2 Murrary CW, Porreca F, Cowan A. Methodological refinements to the mouse paw formalin test: an animal model of tonic pain. J Pharmacol Methods 1988; 20: 175–86.

3. Yang Q, Lu JT, Zhou AW, Wang B, He GW, Chen MZ. Antinociceptive effect of astragalosides and its mechanism of action. Acta Pharmacol Sin 2001; 22: 809–12.

4 Manning BH. A lateralized deficit in morphine antinociception after unilateral inactivation of the central amygdala. J Neurosci 1998; 18: 9453–70.

5 Noble F, Blommaert A, Fournie-Zaluski MC, Roques BP. A selective CCK_B receptor antagonist potentiates μ-, but not δ-opioid receptor-mediated antinociception in the formalin test. Eur J Pharmacol 1995; 273: 145–51.

6 Przewlocka B, Mika J, Labuz D, Toth G, Przewlocki R. Spinal analgesic action of endomorphines in acute, inflammatory and neuropathic pain in rats. Eur J Pharmacol 1999; 367:189–96.

7 Wheeler AH, Cowan A. Standardization of the rat paw formalin test for the evaluation of analgesics. Psychopharmacology 1991; 104: 35–44.

8 Jett MF, Michelson S. The formalin test in rats: validation of an automated system. Pain 1996; 64: 19–25.

9 Jourdan D, Ardid D, Bardin L, Bardin M, Neuzere D, Lanphouthacoul L, *et al*. A new automated method of pain scoring in the formalin test in rats. Pain 1997; 71: 265–70.

10 Yaksh TL, Ozaki G, McCumber D, Rathbun M, Svensson C, Malkmus S, *et al*. An automated flinch detecting system for use in the formalin nociceptive bioassay. J Appl Physiol 2001; 90: 2386–402.

11 Jourdan D, Alloui A, Eschalier A. Pharmacological validation of an automated method of pain scoring in the formalin test in rats. J Pharmacol Toxicol Methods 1999; 42: 163–70.

12 Li Y, Yuan B, Tang JS, Xiang RK. A simple automated detecting system for formalin test in rats. Chin J Neurosci 2001; 17: 145–8.

13 Zimmermann M. Ethical guideline for investigations of experimental pain in conscious animals. Pain 1983; 16: 109–10.

14 Abbott, FV, Franklin KBJ, Westbrook RF. The formalin test: scoring properties of the first and second phases of the pain response in rats. Pain 1995; 60: 91–102.

15 Coderre TJ, Fundytus ME, McKenna JE, Dalal S, Melzack R. The formalin test: a validation of the weighted-scores method of behavioural pain rating. Pain 1993; 54: 43–50.

16 Dickenson AH, Sullivan AF. Subcutaneous formalin-induced activity of dorsal horn neurons in the rat: differential response to an intrathecal opiate administered pre or post formalin. Pain 1987; 30: 349–60.

17 Malmberg AB, Yaksh TL. Antinociceptive actions of spinal nonsteroidal anti-inflammatory agents on the formalin test in the rat. J Pharmacol Exp Ther 1992; 263: 136–46.

18 Bittencourt AL, Takahashi RN. Mazindol and lidocaine are antinociceptive in the mouse formalin model: involvement of dopamine receptor. Eur J Pharmacol 1997; 330: 109–13.

19 Tokunaga A, Doi M, Senba E. Effects of local anaesthesia on formalin-induced Fos expression in the rat dorsal horn. Neuroreport 1995; 6: 2301–4.

Full-length article

Intrathecal administration of roscovitine inhibits Cdk5 activity and attenuates formalin-induced nociceptive response in rats[1]

Cheng-haung WANG[2,3], Wen-ying CHOU[2], Kung-sheng HUNG[4], Bruno JAWAN[2], Cheng-nann LU[5], Jong-kang LIU[3], Yi-ping HUNG[2], Tsung-hsing LEE[2]

[2]Department of Anesthesiology, Kaohsiung Chang-Gung Memorial Hospital; [3]Department of Biological Sciences, "National" Sun Yat-sen University, Kaoshiung 804; [4]Department of Trauma and Neurosurgery, Kaohsiung Chang-Gung Memorial Hospital; [5]Department of Chinese Medicine, Kaohsiung Chang-Gung Memorial Hospital, Kaoshiung 833 Taiwan, China

Key words

roscovitine; cyclin-dependent kinase-5; DARPP-32

[1] This work was supported by research grants from the Chang Gung Memorial Hospital (CMRPG- 83027, 83030, and 83033).
[5] Correspondence to Tsung-hsing LEE, MD, PhD. Phn 886-7-731-7123, ext 5046.
Fax 886-7-711-2776.
E-mail thleemd@adm.cgmh.org.tw

Received 2004-03-26
Accepted 2004-07-28

doi: 10.1111/j.1745-7254.2005.00007.x

Abstract

Aim: To investigate effects of the cyclin-dependent kinase5 (Cdk5) inhibitor roscovitine on formalin-induced nociceptive responses in rats. **Methods:** The flinch response as a methood of pain threshold measurement and intrathecal injection techniques were used. Cdk5 and phosphorylation of its downstream target, DARPP-32 (dopamine- and cAMP-regulated phosphoprotein of M_r 32 kDa), were investigated by Western blot analysis. **Results:** Rats demonstrated a typical flinch response after formalin injection. Intrathecal roscovitine injections significantly suppressed the flinch response in a dose-dependent manner. Western blot analysis showed that phosphorylated DARPP-32 at Thr75 increased in concentration after formalin hyperalgesia, with this effect reduced by roscovitine administration. This antinociception was partially attenuated by administration of naloxone before the formalin test. **Conclusion:** DARPP-32 phosphorylation is involved in acute inflammatory pain response. Intrathecal roscovitine administration attenuates formalin-induced nociceptive responses and there is potential for further application.

Introduction

Tissue injury is associated with sensitization of nociceptors and subsequent changes in the excitability of central neurons, known as central sensitization. Nociceptor sensitization and central sensitization are believed to underlie the development of primary and secondary hyperalgesia[1]. Glutamate, acting at the spinal *N*-methyl-*D*-asparate (NMDA) receptor, has been implicated in the development of secondary hyperalgesia[2,3]. Downstream of NMDA receptor activation, spinal nitric oxide (NO), protein kinase C, and other mediators have been implicated in maintaining such hyperalgesia[4]. Among these mediators, cyclin-dependent kinase-5 (Cdk5) has been found to be involved in modulation of the NMDA and metabotropic glutamate receptors[5].

DARPP-32 (dopamine- and cAMP-regulated phosphoprotein of M_r 32 kDa) is a cytosolic protein that is selectively enriched in medium spiny neurons in the neostriatum[6]. When DARPP-32 is phosphorylated by cAMP-dependent protein kinase (PKA) on Thr34, it is converted into a potent inhibitor of protein phosphatase-1 (PP-1)[7]. This leads to an increase in the phosphorylation of downstream PP-1 substrates, including various neurotransmitter receptors and voltage-gated ion channels[6]. If DARPP-32 is phosphorylated at Thr75 by Cdk5, it inhibits PKA activity and thereby reduces the efficacy of dopamine signaling[8]. Thus, DARPP-32 is a bi-functional signal transduction molecule that controls the activity of PP-1 and PKA by phosphorylation at different sites.

Roscovitine is a potent selective inhibitor of Cdk5, and competes for the ATP-binding site of the kinase (ED_{50}=0.16 μmol/L)[9]. Injection of roscovitine inhibits Cdk5 activity in the hippocampus and reduce the NMDA-evoked currents[10]. Recently, we demonstrated roscovitine mediated antinociception and attenuated morphine tolerance in rats[11]. Therefore, in the present study, the effect of roscovitine on the nocice-

ptive flinch response, evoked by subcutaneous formalin injection, and its possible molecular mechanism, was investigated.

Materials and methods

Drug Roscovitine was obtained from LC Laboratories (Woburn, MA, US) and Me_2SO was purchased from Sigma-Aldrich (St Louis, MO, USA).

Animal care and intrathecal catherterization Male Sprague-Dawley rats (250–300 g) were provided by the "National" Science Council, Taiwan, China. The rats were housed in a room with a 12:12 h dark-light cycle, and a temperature of 22±0.5 ℃, with food and water *ad libitum*. The ethical guidelines specified by the Chang-Gung Memorial Hospital Animal Ethics Committee were followed throughout the study. Chronic intrathecal catheters were implanted under isoflurane anesthesia. Through an incision in the atlanto-occipital membrane, a polyethylene (PE-5) catheter, filled with 0.9% saline, was advanced 8.5 cm caudally to position its tips at the level of the lumbar enlargement. The rostral tip of the catheter was passed subcutaneously, externalized on top of the skull, and sealed with a stainless-steel plug. Rats showing neurological deficits after implantation were excluded from the study. Rats were used for experimentation three days after implantation.

Behavioral testing and animal grouping For formalin injection, 50 μL of a 5 % formalin solution was injected subcutaneously into the dorsal surface of the right hind paw using a 27-gauge needle. Animals were then placed in a clear Plexiglas cylinder (30 cm×30 cm) for observation. A mirror was placed below the floor (Plexiglas) at a 45º angle, to enable unencumbered observation during the test. Within 1 min of the injection, the rats displayed the typical behavior of this model, holding the paw just off the floor. During this period, spontaneous flinching of the injected paw was also observed. Flinching was readily discriminated, and was characterized as a rapid and brief withdrawing or flexing of the injected paw. Pain-related behavior was quantified by counting the number of flinches over 1 min intervals during the first 5 min, and then at 5 min intervals 10–60 min after formalin injection. Two phases of spontaneous flinching responses were observed. An initial acute pain response (phase I, during the first 1–5 min after formalin injection) was followed by a relatively short quiescent period and then by a prolonged tonic phase (phase II, beginning approximately 10–60 min after formalin injection). Criteria for exclusion from the study included incomplete formalin injection, or excessive bleeding from the injection site. Time-response data was presented as the mean±SD per minute for the period of 1–9 min, and then at 5 min intervals up to 60 min. For the dose-response analysis, data from phase I and phase II observations were considered separately. In each case, the observation interval was calculated for each rat. The cumulative flinching response was calculated for each animal, and the dose-response curve represents the mean±SD. To determine the dose dependency and time course of the antinociceptive action of an intrathecal injection of roscovitine, animals were randomly assigned to five groups receiving different doses of roscovitine: 0, 10, 50, 100, 200 μg (n=6 in each group), injected intrathecally 30 min before formalin administration. For exploring possible μ-opioid involvement in the effect of intrathecal roscovitine, naloxone (1 mg/kg) was given intraperitoneally 1 h before the formalin test in the 200 μg roscovitine group (n=6). Roscovitine was dissolved in dimethyl sulfoxide (Me_2SO) and delivered with a microsyringe in a total volume of 10 μL, followed immediately by 5 μL of Me_2SO to flush out the catheter.

Western blot analysis One hour after formalin injection, the rats were killed under deep isoflurane anesthesia, then decollated and spinal cord was removed. The lumbar spinal cords were homogenized in a lysis buffer (20 mmol/L Tris pH 7.6, 150 mmol/L NaCl, 1 mmol/L EGTA, 5 mmol/L NaF and 1 mmol/L dTT, supplemented with protease inhibitor cocktail tablets (Roche, Mannheim, Germany) and complete phosphatase inhibitors. For analysis of Cdk5 and DARPP-32 protein expression after the formalin test, 25 μg protein extracts were electrophoresed on a 12% acrylamide SDS polyacrylamide gel electrophoresis and immunoblotted onto polyvinylidene fluoride membranes. The membranes were blocked for 1 h at room temperature and incubated overnight with Cdk5 (C-8) (1:1000) (Santa Cruz Biotechnology, Santa Cruz, CA, USA), DARPP-32 (1:1000) (Cell Signaling Technology, Beverly, MA, USA), phospho-DARPP-32 (Thr-75) antibody (1:500) (Cell Signaling Technology), and α-tubulin antibody (1:1000) (Santa Cruz Biotechnology) was used as an internal control. Antibody binding was detected using a goat anti-rabbit horseradish peroxidase-linked IgG. The bands were visualized by an ECL detection system (Amersham-Pharmacia Biotech, Little Chalfont, England). Band intensities were quantified by using an image analyzer (Densitograph AE-6900M, Atto, Tokyo, Japan).

Statistical analysis All the data in this study are presented as means±SD and analyzed by one-way ANOVA followed by Dunnett's test for *post-hoc* analysis. P<0.05 was considered significant.

Results

Roscovitine attenuated the formalin-induced flinch response Formalin (5%, 50 μL) injected into the dorsal surface of a rat hind paw produced characteristic behaviors. The intrathecal administration of 0, 10, 50, 100, and 200 μg roscovitine produced a dose-dependent decrease in the flinch response to formalin (Figure 1). The cumulative phase I flinch counts were 79±6, 81±4, 60±7, 60±6, and 23±2, respectively. There was a statistically significant difference between the 200 μg group and the 0 μg group (P<0.01). The cumulative phase II flinch counts were 117±6, 112±7, 65±25, 46±11, and 16±2. The 50, 100, and 200 μg groups all showed significant inhibition of the phase II flinch response compared to the 0 μg group (P<0.01).

Naloxone reversed the roscovitine mediated antinociception Another six rats were given naloxone (1 mg/kg) 1 h before the formalin test in the 200 μg roscovitine group. The cumulative phase I flinch count was 48±5 and the phase II flinch counting was 92±10. The difference in phases I and II were statistically significant compared to the 200 μg group (P<0.01) (Figure 1).

Roscovitine attenuated the phosphorylated DARPP-32 upregulation after formalin hyperalgesia Western blot analysis showed that the Cdk5 expression did not change significantly in any groups, and neither did the total DARPP-32, the downstream target of Cdk5 (Figure 2). However, the phosphorylated-DARPP-32 at Thr-75 was upregulated significantly after formalin hyperalgesia compared to the sham group, which did not receive formalin injection on the paw. Intrathecal roscovitine attenuated the increase in the proportion of phosphorylated DARPP-32 proportion significantly as compared to the 0 μg group [25±6, 10±5, 15±6, 20±7, and 10±4 (arbitrary percentage calculated by phosphorylated-DARPP-32 Thr-75/DARPP-32) in 10 μg , 50 μg, 100 μg, 200 μg, and sham groups respectively after three separate experiments, P<0.01] (Figure 3).

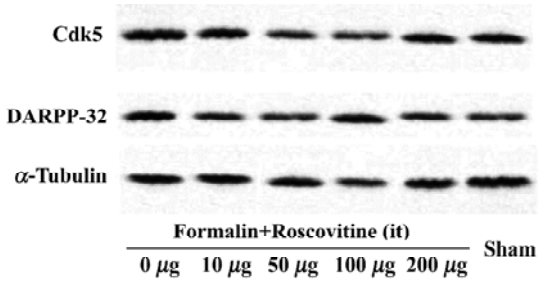

Figure 2. Western blot analysis of the effect of intrathecal roscovitine administration on Cdk5, total DARPP-32, and α-tubulin after the formalin test. α-Tubulin was used as an internal control. There was no significant change in Cdk5 and total DARPP-32 between groups.

Discussion

The formalin test is a model that is believed to underlie abnormal pain perception in humans following injury[12,13]. Following subcutaneous injection of formalin into the hind paw of a rat, the animal displays spontaneous pain behavior,

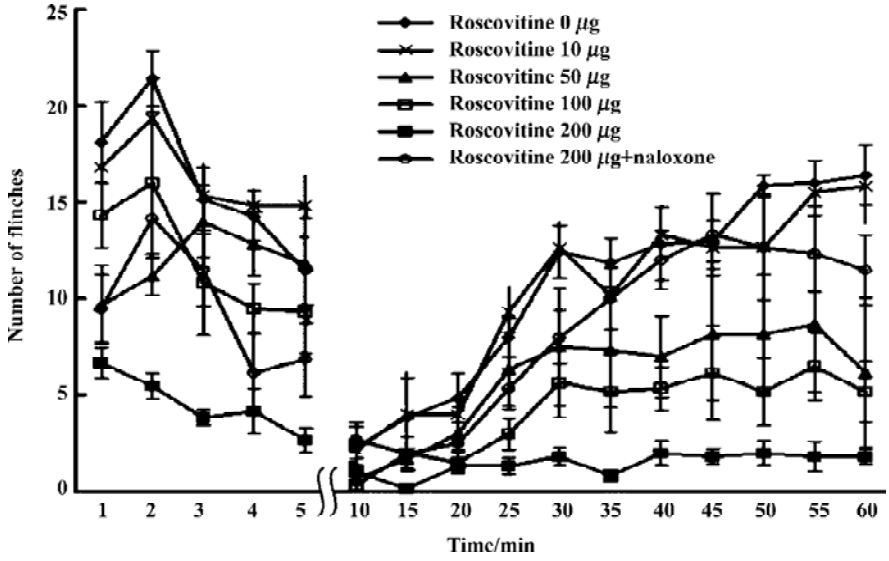

Figure 1. Number of flinches per minute in the formalin test over time, assessed after intrathecal administration of the Cdk5 inhibitor roscovitine. Mean±SEM. n=6.

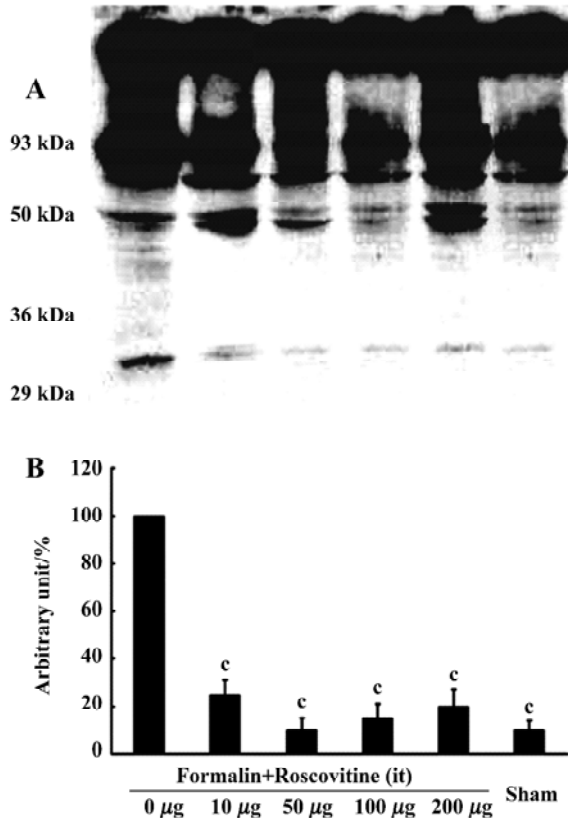

Figure 3. A) Immunobloting of phosphorylated DARPP-32 at Thr-75. B) Quantitative analysis of the proportion of phosphorylated DARPP-32 at Thr-75 after formalin hyperalgesia. Intrathecal roscovitine attenuated the increase of phosphorylated form with statistical significances as compared to the 0 μg group ($P<0.01$ *vs* 0 μg group. Three separate experiments). Arbitrary unit (100 %) was defined as percentage of phosphorylated DARPP-32 in the formalin+roscovitine 0 μg group.

that is, increased hind paw flinching and licking[14]. Two distinct phases were observed, an early acute phase (phase I) followed by a later tonic phase (phase II). The response to formalin during the acute phase is attributed to the pain intensity itself. The response during tonic phase is believed to be mediated through increased spontaneous activity of the spinal cord dorsal horn neurons[15].

Cdk5 is a member of the Cdk family of serine/threonine kinases. Recently, both NMDA and metabotropic glutamate receptors have been shown to be modulated by Cdk5[5]. Previous experiments have shown that inhibition of Cdk5 activity in hippocampal CA1 neurons by roscovitine injection results in a reduction of long-term potentiation and NMDA-evoked currents[10]. Cdk5 may be one of the most important kinases in the regulation of neurotransmitter release. The induction of neurotransmitter release by Cdk5 inhibitors is caused by the regulation of P/Q-type voltage-dependent calcium channel activity[16]. Therefore, Cdk5 might play an important role in nociception by controlling neurotransmitter release.

In this study, intrathecal roscovitine reduced the flinch response after formalin hyperalgesia in a dose-dependen manner. Western blot analysis revealed that the levels of phosphorylated DARPP-32 at Thr-75 were increased after formalin hyperalgesia, and this upregulation was blocked by intrathecal roscovitine administration. Hence, Cdk5 may affect this inflammatory pain model through the DARPP-32 pathway.

Interestingly, naloxone markedly decreased intrathecal roscovitine-induced antinociception, suggesting the involvement of μ-opioid receptors. It is noteworthy that naloxone did not completely block roscovitine-induced antinociception. The exact underlying mechanism is not clear. However, it might suggest that the μ-opioid receptor and Cdk5 are integrated in the DARPP-32 pathway as reported by Greengard[6].

This is the first study exploring the antinociceptive effect of intrathecal roscovitine on formalin-induced pain. Our findings suggest an induction of phosphorylated-DARPP-32 at Thr-75 after formalin hyperalgesia. Intrathecal roscovitine administration attenuated these flinch responses, at least in part, through inhibition of Cdk5 activity. Taken together, these data suggest that spinal Cdk5 activity might play an important role in nociception, and that its inhibitor, roscovitine, could be applied in the management of acute inflammatory pain.

References

1 Yaksh TL, Hua XY, Kalcheva I, Nozaki-Taguchi N, Marsala M. The spinal biology in humans and animals of pain states generated by persistent small afferent input. Proc Natl Acad Sci USA 1999; 96: 7680–6.

2 Urban MO, Gebhart GF. Supraspinal contributions to hyperalgesia. Proc Natl Acad Sci USA 1999; 96: 7687–92.

3 Afrah AW, Stiller CO, Olgart L, Brodin E, Gustafsson H. Involvement of spinal *N*-methyl-*D*-aspartate receptors in capsaicin-induced *in vivo* release of substance P in the rat dorsal horn. Neurosci Lett 2001; 316: 83–6.

4 Dolan S, Nolan AM. *N*-methyl-*D*-aspartate induced mechanical allodynia is blocked by nitric oxide synthase and cyclooxygenase-2 inhibitors. Neuroreport 1999; 10: 449–52.

5 Nishi A, Bibb JA, Matsuyama S, Hamada M, Higashi H, Nairn AC, *et al*. Regulation of DARPP-32 dephosphorylation at PKA- and Cdk5-sites by NMDA and AMPA receptors: distinct roles of calcineurin and protein phosphatase-2A. J Neurochem 2002: 81: 832–41.

6 Greengard P. The neurobiology of slow synaptic transmission. Science 2001; 294: 1024–30.

7 Hemmings HC, Nairn AC, Greengard P. DARPP-32, a dopamine-

and adenosine 3':5'-monophosphate-regulated neuronal phosphoprotein. II. Comparison of the kinetics of phosphorylation of DARPP-32 and phosphatase inhibitor 1. J Biol Chem 1984; 259: 14491–7.
8 Bibb JA, Snyder GL, Nishi A, Yan Z, Meijer L, Fienberg AA, *et al*. Phosphorylation of DARPP-32 by Cdk5 modulates dopamine signalling in neurons. Nature 1999; 402: 669–71.
9 Meijer L, Borgne A, Mulner O, Chong JP, Blow JJ, Inagaki N, *et al*. Biochemical and cellular effects of roscovitine, a potent and selective inhibitor of the cyclin-dependent kinases cdc2, cdk2 and cdk5. Eur J Biochem 1997: 243: 527–36.
10 Li BS, Sun MK, Zhang L, Takahashi S, Ma W, Vinade L, *et al*. Regulation of NMDA receptors by cyclin-dependent kinase-5. Proc Natl Acad Sci USA 2001; 98: 12742–7.
11 Wang CH, Lee TH, Tsai YJ, Liu JK, Chen YJ, Yang LC, *et al*. Intrathecal cdk5 inhibitor, roscovitine, attenuates morphine antinociceptive tolerance in rats. Acta Pharmacol Sin 2004; 25: 1027–30.
12 Malmberg AB, Yaksh TL. Antinociceptive actions of spinal nonsteroidal anti-inflammatory agents on the formalin test in the rat. J Pharmacol Exp Ther 1992; 263: 136–46.
13 Coderre TJ, Vaccarino AL, Melzack R. Central nervous system plasticity in the tonic pain response to subcutaneous formalin injection. Brain Res 1990: 535: 155–8.
14 Tjolsen A, Berge OG, Hunskaar S, Rosland JH, Hole K. The formalin test: an evaluation of the method. Pain 1992; 51: 5–17.
15 Dickenson AH, Sullivan AF. Subcutaneous formalin-induced activity of dorsal horn neurons in the rat: differential response to an intrathecal opiate administered pre or post formalin. Pain 1987; 30: 349–60.
16 Tomizawa K, Ohta J, Matsushita M, Moriwaki A, Li ST, Takei K, *et al*. Cdk5/p35 regulates neurotransmitter release through phosphorylation and downregulation of P/Q-type voltage-dependent calcium channel activity. J Neurosci 2002; 22: 2590–7.

Full-length article

Construction of phospholamban antisense RNA recombinant adeno-associated virus vector and its effects in rat cardiomyocytes[1]

Jiang LI, Shen-jiang HU[2], Jian SUN, Zhao-hui ZHU, Xia ZHENG, Guo-zhong WANG, Yu-mei YAO, Nai-yun CHEN, Xiao-yan ZHAO

Department of Cardiology, First Affiliated Hospital, Medical College of Zhejiang University, Hangzhou 310003, China

Key words

phospholamban; dependovirus; antisense RNA; sarcoplasmic reticulum calcium ATPase; calcium

[1] Project supported by the Scientific and Technological Agency of Zhejiang Province (No 021107817).
[2] Correspondence to Prof. Shen-jiang HU, MD, PhD. Phn 86-571-8723-6794.
E-mail s0hu0001@hotmail.com

Received 2004-04-12
Accepted 2004-08-31

doi: 10.1111/j.1745-7254.2005.00006.x

Abstract

Aim: To construct a recombinant adeno-associated virus (rAAV) vector containing gene encoding phospholamban antisense RNA (asPLB), and analyse its effect on expression of PLB, expression and activity of sarco-endoplasmic reticulum Ca^{2+}-ATPase (SERCA), and the change of intracellular free Ca^{2+} concentration ($[Ca^{2+}]_i$) in rat cardiomyocytes. **Methods:** The target gene encoding PLB antisense RNA was inserted inversely into the adeno-associated virus plasmid pAAV-MCS digested by corresponding restricted endonuclease enzyme. The recombinant plasmid and pAAV-RC and pHelper were co-transfected into 293 cell. At the same time, a viral production positive control (rAAV-LacZ) and negative control were performed. The recombinant viruses were used to transfect the cultured rat cardiomyocytes. Site β-Galactosidase staining were performed to observe the transfer efficiency. Reverse transcription-PCR and Western blot were used to determine the mRNA and protein expression of PLB and SERCA. The activity of SERCA and the $[Ca^{2+}]_i$ were measured. **Results:** The rAAV vectors were constructed successfully and were transfected into rat cardiomyocytes effectively. The PLB mRNA and protein expression were reduced in rat cardiomyocytes transfected by rAAV-asPLB compared with controls. The activity of SERCA was increased. In rest state, the level of $[Ca^{2+}]_i$ in the rAAV-asPLB transfected group decreased. The level of $[Ca^{2+}]_i$ increased when induced by isoproterenol. **Conclusion:** AAV-asPLB vector was constructed successfully, which disrupted the expression of PLB, enhanced the activity of SERCA, reduced the resting $[Ca^{2+}]_i$, and improved the cardiac function.

Introduction

Alterations in intracellular calcium signaling has played a key role in the pathophysiology of heart failure, and gene therapy has been identified as an important tool to help understand the relative contribution of specific calcium-handing proteins in heart failure[1].

Phospholamban (PLB) was a critical regulator of the Ca^{2+} affinity of the cardiac sarcoplasmic reticulum Ca^{2+} ATPase (SERCA2a) and of cardiac contractility[2]. Studies on PLB-knockout and PLB-over expression mice have indicated that the expression ratio of PLB to SERCA2a was a potential target for improvement of diastolic function of the failing heart[3]. The ablation of PLB in mice resulted in stimulated SR Ca^{2+} uptake and enhanced contractile performance, whereas PLB over expression resulted in opposite effects[4,5]. Thus, PLB is an attractive target for treatment of cardiovascular diseases, and decreasing the level of PLB through the use of PLB antisense RNA (asPLB) would be a novel strategy for gene therapy of heart failure[6,7].

The ideal vector for myocardial gene delivery would allow the efficient and stable transduction of cardiomyocytes. The method of injection of plasmid DNA vectors directly into the left ventricular myocardium has been limited by the lower efficiency of cardiomyocyte transduction, while, the adenovirus-mediated gene transfer had been limited by

immue responses to viral and foreign transgene protein. In the present study, adeno-associated viruses (AAV) were chosen as the gene transfer vector because AAV featured versatility in the host rang, long-term gene transfer potential, and minimum immune response. Recombinant adeno-associated viruses (rAAV) of rAAV-asPLB and rAAV-LacZ were constructed by AAV Helper-Free system, and the effect on expression of PLB in cultured rat cardiomyocytes was analyzed. This was to make arrangements for future PLB gene therapy in animal models.

Materials and methods

Plasmids and reagents The AAV Helper-Free System was obtained from Stratagene. The system includes: pAAV-MCS containing inverted terminal repeat (ITR) of adeno-associated virus, multiple clone site (MCS), and cytomegalovirus enhance/promotor and SV 40 poly-adenylation; pAAV-RC containing AAV replication and capsid genes; pHelper contains adenovirus-derived genes (i.e. E2A, E4, and VA RNA gene); pAAV-LacZ containing ITR and report gene *lac*Z. AAV-293 cells and XL10-Gold ultracompetent *E coli* cells, were also obtained from Stratagene, too. Restriction enzymes were obtained from Promega. Mouse monoclonal antibody and IgG were from ABR. Fluo 3-AM was from Molecular Probes, Eugene, OR, USA.

Cloning of rat PLB cDNA and construction of PLB antisense RNA plasmid vector (pAAV-asPLB) Rat PLB cDNA fragment (695 bp) was synthesized by reverse transcription-polymerase chain reaction (RT-PCR) from total RNA isolated from the heart of Wistar rats. The primers used for PCR contained a *Bam*H I (5′) and *Eco*R I (3′) linker (in lower-case letters): 5′-cgggatccCGCAGCTGAGCTGAGCTCCAGACTTCA-3′, and 5′-cggaattcTTTAAATTTCATTTATTCCCCAA-3′. PCR was carried out as follows: 94 ºC for 5 min followed by 30 cycles at 94 ºC for 30 s, 55 ºC for 60 s, and 72 ºC for 60 s, followed by the final step at 72 ºC for 10 min.

The synthesized PLB cDNA was subsequently digested by *Bam*H I and *Eco*R I simultaneously, while the adeno-associated virus plasmid pAAV-MCS digested by corresponding restricted endonuclease enzyme. The ligation reaction was conducted with DNA ligase at 4 ºC for 16 h. The pAAV-asPLB was generated by cloning the PLB cDNA into *Eco*R I/*Bam*H I sites of pAAV-MCS reversed orientation relative to the promoter. Identification of the gene was confirmed by restriction enzymes digestion and sequencing.

Construction of recombinant adeno-associated virus To construct the rAAV, AAV-293 cells were co-transfected with three AAV Helper-Free System plasmids: an ITR-containing plasmid (pAAV-asPLB or pAAV-LacZ), pAAV-RC, and pHelper. AAV-293 cells maintained in DMEM medium supplemented with 10% fetal calf serum, in a 37 ºC incubator at 5% CO_2. When 293 cells reached 70%–80% confluence in 100-mm culture plate, the concentration of each plasmid was adjusted to 1 g/L in TE buffer, pH 7.5. The three plasmids (10 μL of each) and $CaCl_2$/HBS were mixed gently, and the mixture were co-transfected into 293 cells immediately. After 6 h, the medium was replaced with 10 mL of fresh DMEM medium, and 293 cells were cultured for an additional 66–72 h.

To monitor the progress of AAV particle production, 293 cells were divided into four groups according to the difference of mixture: (1) AAV-asPLB group: pAAV-asPLB, pAAV-RC, pHelper, and $CaCl_2$/HBS; (2)AAV- LacZ group: pAAV-LacZ, pAAV-RC, pHelper, and $CaCl_2$/HBS, which served as a positive control; (3) pAAV-RC, pHelper, and $CaCl_2$/HBS ,which served as a negative control; (4) only $CaCl_2$/HBS served as a blank control.

The 293 transfected cells were subject to four rounds of freeze/thaw and centrifugation at 10 000×*g* for 10 min. The supernatant (primary rAAV) was purified by CsCl gradient centrifugation. rAAV was verified by PCR. The genome titer and infectious titer of rAAV were measured by PCR and in site β-galactosidase staining according to instruction [8,9].

Rat cardiomyocytes culture and infection Rat neonatal cardiomyocytes were isolated, cultured conventionally, and infected with the rAAV at a multiplicity of infection (MOI) of 100 for 48 h[10]. Cardiomyocytes were divided into three groups: (1) infected with rAAV-asPLB; (2) infected with rAAV- LacZ; (3) normal control.

X-gal staining to detect the infection efficiency Cardiomyocytes were fixed with glutaraldehyde-formaldehyde solution for 10 min at room temperature, stained overnight with staining solution that contains X-gal. In infected cells, β-galactosidase cleaves X-gal to produce a blue stain. The infection efficiency was the percentage of stained cells in the total population.

Semi-quantitative RT-PCR analysis of PLB and SERCA gene expression Total cellular RNA was isolated from cells using TRIzol. Semiquantitative RT-PCR was performed to analyse PLB and SERCA gene expression. β-actin (332 bp) served as endogenous control. The primers of β-actin used for PCR were: 5′-GAGACCTTCAACACCCCAGCC-3′, and 5′-GGCCATCTCTTGCTCGAAGTC-3′. The primers of PLB gene were described in previous text. The primers of SERCA (134 bp) gene were: 5′-AAGCAGT-

TCATCCGCTACCT-3′, and 5′-AGACCATCCGTCACCA-GATT-3′. PCR products were resolved on a 2% agarose gel and the bands could be seen using ethidium bromide staining. Each band was analyzed on Kodak Digital Science Image Analysis System. The gene expression level was determined semi-quantitatively by calculating the ratio of density metric value from the PLB gene in relation to internal standards.

Western blot analysis of PLB and SERCA protein expression Cells were lysed in lysis solution at 4 ºC. The concentration of the protein in each lysate was determined with Coomassie Brilliant Blue G-250. Protein was fractionated on sodium dodecyl sulfate-polyacrylamide gel electrophoresis (SDS-PAGE) and transferred onto nitrocellulose membranes. The membrane was incubated with monoclonal antibody (1:1000) and IgG (1:500). The immune complexes were visualized by the ECL chemiluminescence method. Each protein band was analyzed on Kodak Digital Science Image Analysis System. The protein expression level was determined by calculating the ratio of density metric value from rAAV infected group in relation to normal control.

SERCA activity The activity of SERCA was determined following the methods of Larsen[11]. Assays for complete quantification of Ca^{2+}-ATPase in homogenates of rat ventricular myocardium by determination of Ca^{2+}-dependent *p*-nitrophenyl phosphatase (pNPPase) activities were evaluated and optimized.

Measurement of $[Ca^{2+}]_i$[12] After Fluo 3-AM (5 μmol/L) loading, the coverslip was mounted in the cell chamber with 200 μL Hanks' solution. The fluorescence intensity (FI) was detected by confocal microscope (Leica, Mannheim, Germany) and inverted microscope with 40×objective and 488 nm blue laser for excitation and 530 nm for emission at room temperature. Stimulating agent (isoproterenol, 50 μmol/L) 10 μL was added to the preparation and the data were stored in disk. The fluorescence signals were normalized as $\Delta F/F_0$ (%), where F_0 was the resting fluorescence and ΔF was Ca^{2+} change relatively the resting fluorescence.

Statistical analysis Data were expressed as mean±SD and statistically compared by one-way ANOVA with Dunnett's test. $P<0.05$ was taken as statistically significant.

Results

Construction and infection efficiency of recombinant adeno-associated virus The results of pAAV-asPLB restriction enzymes digestion and sequencing demonstrated that the sequence and direction of PLB cDNA fragment (695 bp) were precise (Figure 1). The rAAV-asPLB and rAAV-LacZ were harvested in rAAV-asPLB group and rAAV-LacZ group,

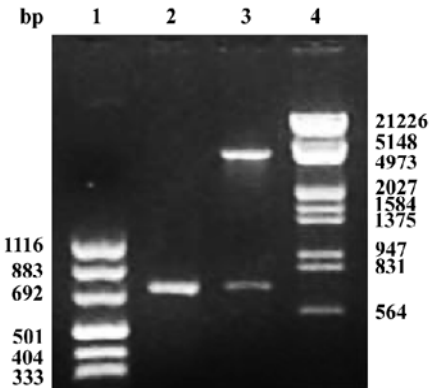

Figure 1. Identification of the pAAV-asPLB by restriction enzymes digestion. Lane 1: pUC Mix Marker; Lane 2: PCR production of PLB cDNA fragment (695 bp); Lane 3: pAAV-asPLB digested by *Eco*R I and *Bam*H I; Lane 4: λDNA/*Eco*R I+*Hind*III Marker.

respectively. However, the negative control and blank control showed nothing. The genome titer and infectious titer of rAAV were 1×10^{15} particles/L and 3×10^{13} infectious units/L, respectively. Cardiomyocytes were infected with rAAV-LacZ and stained with X-gal, the percentage of blue stained cells is approximately 80% (Figure 2).

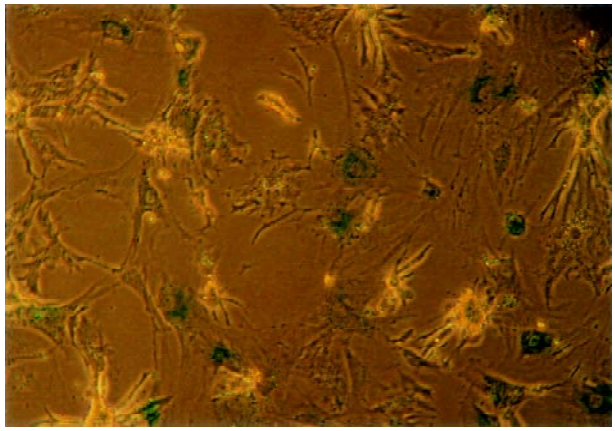

Figure 2. Infection efficiency of rAAV were detected by X-Gal staining (×200). A blue stain was produced in infected cardiomyocytes.

PLB mRNA expression in infected cardiomyocytes Total RNA was extracted from rAAV-asPLB infected cardiomyocytes, rAAV-LacZ infected cardiomyocytes, and normal control cardiomyocytes, respectively. The result of RT-PCR showed that the level of PLB mRNA expression was decreased in rAAV-asPLB infected cardiomyocytes compared with rAAV-LacZ infected cardiomyocytes and normal

control cardiomyocytes (P<0.05, Figure 3).

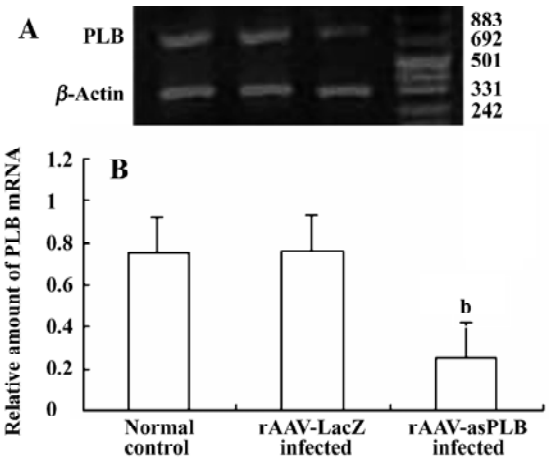

Figure 3. PLB mRNA expression in normal control, rAAV-LacZ infected, and rAAV-asPLB infected cardiomyocytes. β-Actin (332 bp) served as an endogenous control. Data from three independent experiments were expressed as % *vs* endogenous control. ^{b}P<0.05 *vs* normal control.

PLB protein expression in infected cardiomyocytes The level of PLB protein expression was decreased in rAAV-asPLB infected cardiomyocytes compared with rAAV-LacZ infected cardiomyocytes and normal control cardiomyocytes (P<0.05, Figure 4).

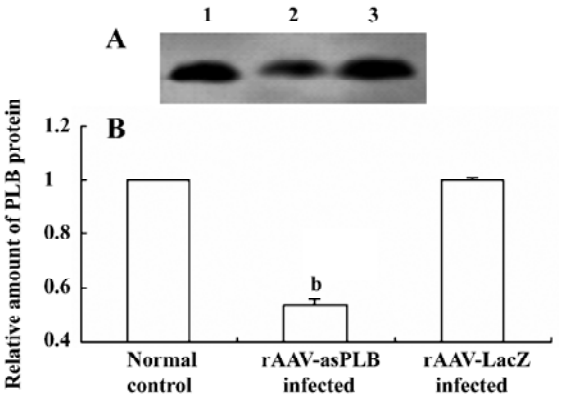

Figure 4. Analysis of PLB protein expression in normal control, rAAV-LacZ infected, and rAAV-asPLB, infected cardiomyocytes. Data were expressed as % of control. n=3. Mean±SD. ^{b}P<0.05 *vs* control.

SERCA mRNA and protein expression and activity The level of SERCA mRNA and protein expression was not changed in rAAV-asPLB infected cardiomyocytes. However, the PLB/SERCA ratio was decreased because of a decrease of PLB expression. While the activity of SERCA was higher in rAAV-asPLB group than that in rAAV-LacZ group (2.04±0.09 *vs* 1.83±0.22 μmol·g^{-1} protein·min^{-1}) and normal control (2.04±0.09 *vs* 1.84±0.03 μmol·g^{-1} protein·min^{-1}) (P<0.05).

Effect of rAAV-asPLB on $[Ca^{2+}]_i$ Resting state, fluorescent intensity of $[Ca^{2+}]_i$ in rAAV-asPLB group (9.13±0.80) was lower than that in rAAV-LacZ group (13.82±0.80) and normal control (14.98±1.08) (P<0.05). Isoproterenol induced $[Ca^{2+}]_i$ increase in cultured cardiomyocytes. The $\Delta F/F_0$ of $[Ca^{2+}]_i$ in rAAV-LacZ group and normal control was 354% and 324%, respectively. However, the level of $\Delta F/F_0$ in rAAV-asPLB group was 459%.

Discussion

Heart failure represents an enormous clinical challenge in need of effective therapeutic approaches. The possibility of gene therapy for heart failure merits considerations at this time because of improvements in vector technology, cardiac gene delivery, and most importantly, our understanding of the molecular pathogenesis of heart failure. PLB is an endogenous muscle-specific inhibitor of SERCA2, cardiac-specific disruption of PLB in mice results in a marked increase in myocardial contractility[13]. In this study, PLB cDNA fragment was cloned and inserted inversely into pAAV-MCS, which constructed the plasmid vector of pAAV-asPLB.

Previous gene transfer approaches that used direct injection of plasmid DNA or replication-defective adenovirus vectors have been limited by low transduction frequencies and transient transgene expression due to immune response, respectively[14]. In this study, adeno-associated virus (AAV) was chosen as the gene transfer vector. In traditional AAV recombinant systems, the requirement for wild-type adenovirus co-infection, the contamination of adenovirus and the regeneration of wild-type AAV are major problems. However, the AAV Helper-Free system allows the production of infective recombinant AAV-2 virus without the use of a helper virus. Most of the adenovirus gene products required for the production of infective AAV particles are supplied on the plasmid pHelper that is co-transfected into 293 cells.

We constructed the rAAV vectors containing target gene (*PLB*) and reporter gene (*lacZ*) with AAV Helper-Free system. The rAAV vectors were identified and measured by PCR and in site β-galactosidase staining. Cardiomyocytes was infected with rAV-LacZ and stained with X-gal. The result shows that the rAAV is able to infect the cardiomyocytes effectively.

The antisense RNA can bind to its target RNA (sense RNA) thereby controlling expression of the target gene. In comparison to the ribozyme technique, antisense RNA technique has the advantages of simple designing, strong specialty, easy operating, and being economic and time saving[15]. In the present study , rat neonatal cardiomyocytes were cultured and infected by rAAV vectors. RT-PCR and Western blot results showed that the expression of PLB was decreased as compared with normal group and the rAAV-*LacZ* infected group. This indicated that the as *PLB* had partly blocked the transcription of PLB mRNA and inhibited the translation of PLB protein.

The PLB/SERCA ratio was decreased in rAAV-asPLB infected cardiomyocytes because the SERCA mRNA and protein expression had no change. While, the activity of SERCA was enhanced. Our results demonstrated that reducing *PLB* inhibition to SERCA enhanced the SERCA activity. Further study on $[Ca^{2+}]_i$ showed the concentration of resting $[Ca^{2+}]_i$ was decreased in rAAV-asPLB-infected cardiomyocytes. The $[Ca^{2+}]_i$ was elevated after isoproterenol was induced. However, a higher $[Ca^{2+}]_i$ was observed in rAAV-asPLB infected cardiomyocytes. These data suggested that asPLB enhanced the affinity of SERCA for Ca^{2+} and therefore improved diastolic/contractile function in rAAV-asPLB-infected cardiomyocytes.

References

1 Bernecker OY, del Monte F, Hajjar RJ. Gene therapy for the treatment of heart failure-calcium signaling. Semin Thorac Cardiovasc Surg 2003; 15: 268–76.

2 Zhai J, Schmidt AG, Hoit BD, Kimura Y, MacLennan DH, Kranias EG. Cardiac-specific overexpression of a superinhibitory pentameric phospholamban mutant enhances inhibition of cardiac function *in vivo*. J Biol Chem 2000; 275(14): 10538–44.

3 Koss KL, Grupp IL, Kranias EG. The relative phospholamban and SERCA2 ratio: a critical determinant of myocardial contractility. Basic Res Cardiol 1997; 92 (Suppl 1): 17–24.

4 Luo W, Grupp IL, Harrer J, Ponniah S, Grupp G, Duffy JJ, *et al*. Targeted ablation of the phospholamban gene is associated with markedly enhanced myocardial contractility and loss of β-agonist stimulation. Circ Res 1994; 75: 401–9.

5 Kadambi VJ, Ponniah S, Harrer JM, Hoit BD, Dorn GW, Walsh RA, *et al*. Cardiac-specific overexpression of phospholamban alters calcium kinetics and resultant cardiomyocytes mechanics in transgenic mice. J Clin Invest 1996; 97: 533–9.

6 He H, Meyer M, Martin JL, McDonough PM, Ho P, Lou X, *et al*. Effects of mutant and antisense RNA of phospholamban on SR Ca^{2+}-ATPase activity and cardiac myocyte contractility. Circulation 1999; 100: 974–80.

7 Monte F, Harding SE, Dec GW, Gwathmey JK, Hajjar RJ. Targeting phospholamban by gene transfer in human heart failure. Circulation 2002; 105: 904–7.

8 Clark KP, Voulgaropoulou F, Johnson P R. A stable cell line carrying adenovirus-inducible rep and cap genes allow for infectivity titration of adeno-associated virus vectors. Gene Ther 1996; 3: 1124–32.

9 Zhang YB, Leng XS, Peng JR, He XJ, LU JF, Weng SG, *et al*. Construction, packaging, and titration of recombinant adeno-association virus vectors contaning antitumor genes. Natl Med J China 2002; 82: 564–7.

10 Svensson EC, Marshall DJ, Woodard K, Lin H, Jing F, Chu L, *et al*. Efficient and stable transduction of cardiomyocytes after intramyocardiol injection or intracoronary perfusion with recombinant adeno-associated virus vectors. Circulation 1999; 99: 201–5.

11 Larsen JS, Kjeldsen K. Quantification in crude homogenates of rat myocardial Na^+, K^+- and Ca^{2+}-ATPase by K^+ and Ca^{2+}-dependent pNPPase age-dependent changes. Basic Res Cardiol 1995; 90: 323–31.

12 Qiao GF, Zhou H, Li BY. Antagonistic effects of berbamine on $[Ca^{2+}]_i$ mobilization by KCl, norepinephrine, and caffeine in newborn rat cardiomyocytes. Acta Pharmacol Sin 1999; 20: 292–6.

13 Brittsan AG, Kranias EG. Phospholamban and cardiac contractile function. J Mol Cell Cardiol 2000; 32: 2131–9.

14 Teramoto S, Ishii T, Matsuse T, Fukuchi Y. Recombinant adeno-associated virus vectors efficiently transduce foreign gene into bovine aortic endothelial cell: comparison with adenovirus vectors. Jpn J Pharmacol 2000; 84: 206–12.

15 Wang L, Zhang GM, Feng ZH. Down-regulation of *survivin* expression reversed multidrug resistance in adriamycin-resistant HL-60/ADR cell line. Acta Pharmacol Sin 2003; 24: 1235–40.

Full-length article

Ginsenoside Rg1 reduces MPTP-induced substantia nigra neuron loss by suppressing oxidative stress[1]

Xiao-chun CHEN[2], Yi-can ZHOU, Ying CHEN, Yuan-gui ZHU, Fang FANG, Li-min CHEN

Fujian Institute of Geriatrics, Union Hospital, Fujian Medical University, Fuzhou 350001, China

Key words

ginsenoside Rg1; *N*-acetylcystein; apoptosis; JNK mitogen-activated protein kinases; inbred C57BL mice

[1] Project supported by Major Funding from the Fujian Department of Education (JA02219) and Key Grant from the Fujian Science and Technology Bureau (2001Z037).

[2] Correspondence to Prof. Xiao-chun CHEN.
Phn 86-591-337-7664.
Fax 86-591-337-0393.
E-mail chenxc998@sohu.com

Received 2004-05-25
Accepted 2004-08-31

doi: 10.1111/j.1745-7254.2005.00019.x

Abstract

Aim: To investigate the effect of ginsenoside Rg1, an effective ingredient from ginsenoside, on 1-methyl-4-phenyl-1,2,3,6-tetrahydropyridine (MPTP)-induced substantia nigra neuron lesion. **Methods:** C57-BL mice were given MPTP to prepare Parkinson disease mice model. Different doses of Rg1 (5, 10, and 20 $mg \cdot kg^{-1} \cdot d^{-1}$) or *N*-acetylcystein (NAC) (300 $mg \cdot kg^{-1} \cdot d^{-1}$) were given 3 d prior to MPTP in the pretreatment groups. Glutathione (GSH) level and total superoxide dismutase (T-SOD) activity in substantia nigra were determined by spectrophotometry. Nissl staining, tyrosine hydroxylase immunostaining, and TUNEL labeling were used to observe the damage and apoptosis of nigral neurons. Western blot analysis was used to detect the phospho-JNK and phospho-c-Jun levels in midbrain homogenates. **Results:** Pretreatments of C57-BL mice with different doses of Rg1 or NAC were found to protect against MPTP-induced substantia nigra neurons loss. Rg1 or NAC prevented GSH reduction and T-SOD activation in substantia nigra, and attenuated the phosphorylations of JNK and c-Jun following MPTP treatment. **Conclusion:** The antioxidant property of Rg1 along with the blocking of JNK signaling cascade might contribute to the neuroprotective effect of ginsenoside Rg1 against MPTP.

Introduction

The pathological hallmark of Parkinson disease (PD) is the loss of dopaminergic neurons in the substantia nigra (SN), which leads to the major clinical and pharmacological abnormalities that characterize the disease. Although the exact cause of neuronal loss is still unknown, current evidence points to the presence of ongoing oxidative stress and the generation of radical oxygen species (ROS) selectively in the pars compacta of substantia nigra (SNPC) of parkinsonian brains[1, 2]. Human postmortem studies also suggested that oxidative damage to lipids, proteins, and DNA occurred in the SNPC of PD patients[3–5]. The neurotoxin 1-methyl-4-phenyl-1,2,3,6-tetrahydropyridine (MPTP) is metabolized in the brain by monoamine oxidase-B to its toxic metabolite, 1-methyl-4-phenylpyridinium ion (MPP^+), which is then selectively taken up into the dopaminergic neurons. MPP^+ exerts its toxic effect in the dopaminergic neurons by inhibiting mitochondrial NADH dehydrogenase (NADH-DH)[6]. MPTP could induce PD-like symptoms in humans and primates and causes degeneration of dopaminergic neurons in several animal species. The MPTP animal model is the ideal PD model for studying the pathogenesis of the disease.

The c-Jun NH_2-terminal kinase (JNK) signaling cascade has been implicated as a mediator of MPTP-induced apoptotic neuronal death[7,8]. Oxidative stress is an important activator of the JNK signaling cascade. In differentiated PC12 cells and cultured sympathetic neurons, increases in oxidative stress induced by antisense inactivation of superoxide dismutase led to increased JNK activity[9].

Current treatments of PD are symptomatic and lack neuroprotective effect. Antioxidants have been focused on as candidates for the future treatment of PD. Ginsenoside Rg1, one of the active ingredients of ginseng, has potential neurotrophic and neuroprotective effects[10]. In our previous study, we found Rg1 could protect substantia nigra neu-

rons against MPTP-induced apoptosis[11], and in a *in vitro* study we revealed that Rg1 could suppress intracellular oxidative stress to prevent PC12 cells from dopamine-induced apoptosis[12]. The aim of the current study is to further investigate whether Rg1 could suppress oxidative stress and block the activation of the JNK signaling cascade, and therefore protects dopaminergic neurons from apoptosis in an MPTP animal model. One antioxidant *N*-acetylcystein, which has been proved to protect against MPTP-induced substantia nigra neurons loss[13], was used as a positive contrast in this study.

Materials and methods

Animals and treatment Male C57-BL mice weighing 18-22 g were divided into six groups (n=8). MPTP (Sigma, St Louis, MO, USA) was dissolved in saline at concentrations of 4 g/L. Ginsenoside Rg1 (purity >98 %), obtained from the Department of Organic Chemistry of Norman Bethune Medical University (Changchun, Jilin, China), was also dissolved in saline at concentrations of 1 g/L. Model animals were injected subcutaneously with saline for 3 d, followed by injection (subcutaneously) of MPTP (30 $mg \cdot kg^{-1} \cdot d^{-1}$) for 5 consecutive days. Three preventive groups were injected (ip) with Rg1 (5 $mg \cdot kg^{-1} \cdot d^{-1}$, 10 $mg \cdot kg^{-1} \cdot d^{-1}$, 20 $mg \cdot kg^{-1} \cdot d^{-1}$). Positive contrast group was injected (sc) with NAC (Jingke, Beijing, China, 300.0 $mg \cdot kg^{-1} \cdot d^{-1}$) for 8 days, and from the fourth day both Rg1 preventive groups and the positive contrast group were received injection (sc) of MPTP (30 $mg \cdot kg^{-1} \cdot d^{-1}$, 2 h after Rg1 or NAC injection) for 5 consecutive days. The control group received saline only. The animals were killed 24 h after the last injection. The mice were anaesthetized with euthanal and perfused transcardially with ice-cold saline prior to decapitation. The midbrain containing the substantia nigra was dissected, and quickly frozen at -80 ºC until ready for later analysis. For immunohistochemistry analysis, the midbrain was fixated in 4 % formal-dehydum polymerisatum-PB and imbedded in paraffin. Serial 5-μm-thick sections were cut transversely from the middle of the midbrain.

Spectrophotometry Substantia nigra were homogenized with 0.01 mol/L Tris-HCl (pH 7.4) consisting of 0.01 mol/L sucrose and 0.1 mmol/L EDTA, followed by centrifugation at 4000×g for 15 min. The supernatant was saved and analyzed. The dithio-binitrobenzoic acid method and xanthine/xanthine oxidase method were used to test glutathione (GSH) level and total superoxide dismutase (T-SOD) activity. Reaction product was determined by spectrophotometry. Test Kits were purchased from Jian Cheng Bioengineering Institute (Nanjing, China).

TUNEL Deparaffinized and hydrated sections were incubated with proteinase K (20 mg/L in 10 mmol/L Tris/HCl, pH=7.4-8.0) for 30 min at 37 ºC, then incubated with TdT reaction mixture and AP-conjugated anti-fluorescein antibody (TUNEL detection kit, BM, Germany) for 1 h at 37 ºC. Finally sections were visualized with NBT-BCIP. The nuclei of positive cells were stained blue-black.

Nissl staining Paraffin sections were deparaffinized and hydrated, stained with methylene blue buffer for 10 min and then immersed into acetic acid buffer for 2 min.

Immunohistochemistry Paraffin sections were deparaffinized and hydrated, then incubated with a goat anti-mouse TH polyclonal antibody (1:40 dilution in 0.01 mmol/L phosphate buffer saline, pH 7.4) at 4 ºC overnight. Slides were then incubated with a biotinylated rabbit anti-goat IgG and SABC-reagent (SABC kit, BOSTER, Wuhan, Hubei, China), respectively for 30 min at 37 ºC. At last, sections were stained with diaminobenzidine (DAB). Hemotoxylin was used to counterstain nuclei for one minute.

Western blot analysis Substantia nigra was homogenized (50 g/L) in lysis buffer (10 mmol/L Tris, 50 mmol/L NaCl, 0.03 μmol/L sodium pyrophosphate, 50 mmol/L sodium fluoride, and 1% Triton X-100) containing 1 mmol/L phenylmethylsulfonyl fluoride, 20 mg/L aprotinin, and 1 mmol/L sodium vanadate[14]. After homogenization, samples were centrifuged at 15 000×g for 15 min. The supernatants were taken for further analysis. Protein concentration was determined by the Bradford method[15]. Approxiamately 10 μg of total protein was separated by 12% sodium dodecyl sulfate-polyacrylamide gel electrophoresis (SDS-PAGE) and transferred to nitrocellulose membranes. The membranes were probed with polyclonal anti-p-JNK1/2 or anti-p-c-Jun rabbit antibody (Cell Signaling, Beverly, MA, USA). Immunoreactive bands were visualized by the addition of horseradish peroxidase-conjugated antibodies against rabbit Fab and chemiluminescent substrates (Pierce, Rockford, IL, USA), according to the manufacturer's instruction.

Image analysis The numbers of Nissl, TH, TUNEL-positive neurons in full microscopic fields of SN were counted with a digital medical image analysis system (Motic, Beijing, China). Three tissue sections per animal were counted for each index.

Data analysis Data were expressed as means±SEM. TUNEL-positive cells were calculated as: [TUNEL-positive cells/(TUNEL-positive cells+Nissl staining cells)]×100%. For statistical evaluation one-way analysis of variance (ANOVA) was employed. Student Newman Keuls test was performed when variance was equal, and Games-Howell test

was performed when variance was not equal. *Pearson* correlation analysis was also carried out to some indices. Statistical difference was considered to be significant only if $P<0.05$.

Results

Effect of ginsenoside Rg1 on MPTP-induced apoptosis of substantia nigra neurons MPTP clearly had a detrimental effect on dopaminergic neurons. Treatment with MPTP decreased the numbers of TH-positive and Nissl-positive neurons and increased the percent of TUNEL-positive neurons in SN. Pretreatment with ginsenoside Rg1 or NAC significantly ameliorated the neuronal loss and apoptosis induced by MPTP ($P<0.01$) (Figure 1–3). Rg1 at 10 mg/kg showed the best protective effect among all the doses but made no significant difference ($P>0.05$) at 5 mg/kg and 20 mg/kg, which suggested that the effect of ginsenoside Rg1 might have an optimal dose range. There was no significant difference between NAC and Rg1 (10 mg/kg) treatment group.

Effect of ginsenoside Rg1 on GSH level and T-SOD activity in SN Decreased GSH level and increased T-SOD activity were detected in the substantia nigra of MPTP-treated mice. Both changes were attenuated by pre-administration with ginsenoside Rg1 or NAC (Table 1, $P<0.01$). Better preventive effects were observed at doses of 10 and 20 mg/kg than at 5 mg/kg among Rg1 treated groups, but there was no significant difference among 10 mg/kg, 20 mg/kg of Rg1, and NAC (300.0 mg/kg). Correlation analysis showed a positive correlation between the positive neuron ratio of TH and the GSH level ($r=0.885$, $P<0.01$), and negative correlation between the positive neuron ratio of TH and the T-SOD activity ($r=-0.882$, $P<0.01$). These results indicate that enhanced oxidative stress was involved in the neurotoxicity of MPTP; and suitable doses of Rg1 could attenuate the oxidative stress induced by MPTP, while overdoses of Rg1 did not show better preventive effect.

Table 1. Effect of ginsenoside Rg1 on GSH level and T-SOD activity. Mean±SEM. $n=8$. $^{c}P<0.01$ *vs* control group. $^{f}P<0.01$ *vs* MPTP group. $^{i}P<0.01$ *vs* MPTP+Rg1 5 mg/kg group.

Group	GSH level/ mg·mg^{-1} protein	SOD activity/ NU·mg^{-1} protein
MPTP	35.30±0.81^{c}	142.42±1.0^{c}
Control	56.96±0.41	116.53±1.03
MPTP+NAC(300 mg/kg)	56.18±0.74^{fc}	118.38±0.85^{fi}
MPTP+Rg1(5 mg/kg)	40.36±0.53^{f}	131.85±0.79^{f}
MPTP+Rg1(10 mg/kg)	50.09±0.48^{fi}	120.90±0.89^{fi}
MPTP+Rg1 (20 mg/kg)	50.44±0.36^{fi}	122.84±0.73^{fi}

Influence of MPTP-induced JNK and c-Jun phosphorylation by ginsenoside Rg1 MPTP treatment increased the levels of p46 and p54 phospho-JNK protein, as compared with the control. Preadministration of Rg1 or NAC partially attenuated the MPTP-mediated elevation in phospho-JNK and phospho-c-Jun levels in midbrain homogenates. A 10 mg/kg dose of Rg1 showed the greatest inhibition as did NAC, but the weak inhibition was observed at the dose of 20 mg/kg. These results suggested that Rg1 attenuated MPTP-induced phosphorylation of JNK and c-Jun, but a higher dosage was detrimental.

Discussion

Ginseng has been used in traditional Chinese medicine to enhance stamina and capacity to deal with fatigue and physical stress for thousands of years. Ginsenoside Rg1 is one of the active ingredients of ginseng. Previous *in vitro* studies showed that Rg1 could save cell from oxidative stress induced-apoptosis[16]. In the current study, we observed that TH-positive neurons loss in SN caused by MPTP could be attenuated by Rg1 or NAC pretreatment; the result showed the neuronal protective effect of ginsenoside Rg1 against MPTP. Our study also revealed the neuroprotective mechanisms of Rg1 in preventing MPTP-induced loss of dopaminergic neurons in SN. The neurotoxin of MPTP is dependent on the inhibition of Complex I in the mitochondrial respiratory chain by MPP^{+}, subsequently followed by ATP depletion and increased production of ROS[17], eventually leads to the cell death. As one of the most important antioxidant molecule, GSH could clear H_2O_2 and prevent its reaction with iron to form the highly reactive $OH^{\cdot}$ radical in the Fenton reaction. Following MPTP treatment, GSH was consumed and its level dropped[18,19]. We also observed the activity of T-SOD (including Cu/Zn-SOD and Mn-SOD), another important radical scavenger, was elevated in SN of MPTP treated mice; this change corresponded with those observed in PD patients[20–22]. NAC is a free radical oxygen scavenger. Furthermore, it can be converted into cysteine after entering cells, and is an important substrate for GSH production. In our current study, pretreatment with NAC could attenuate the loss of GSH and the increased activity of T-SOD following MPTP treatment, same changes were observed among Rg1 pretreatment groups. We found that the antioxidative effect of Rg1 had an optimal dose of 10 mg/kg, this dosage

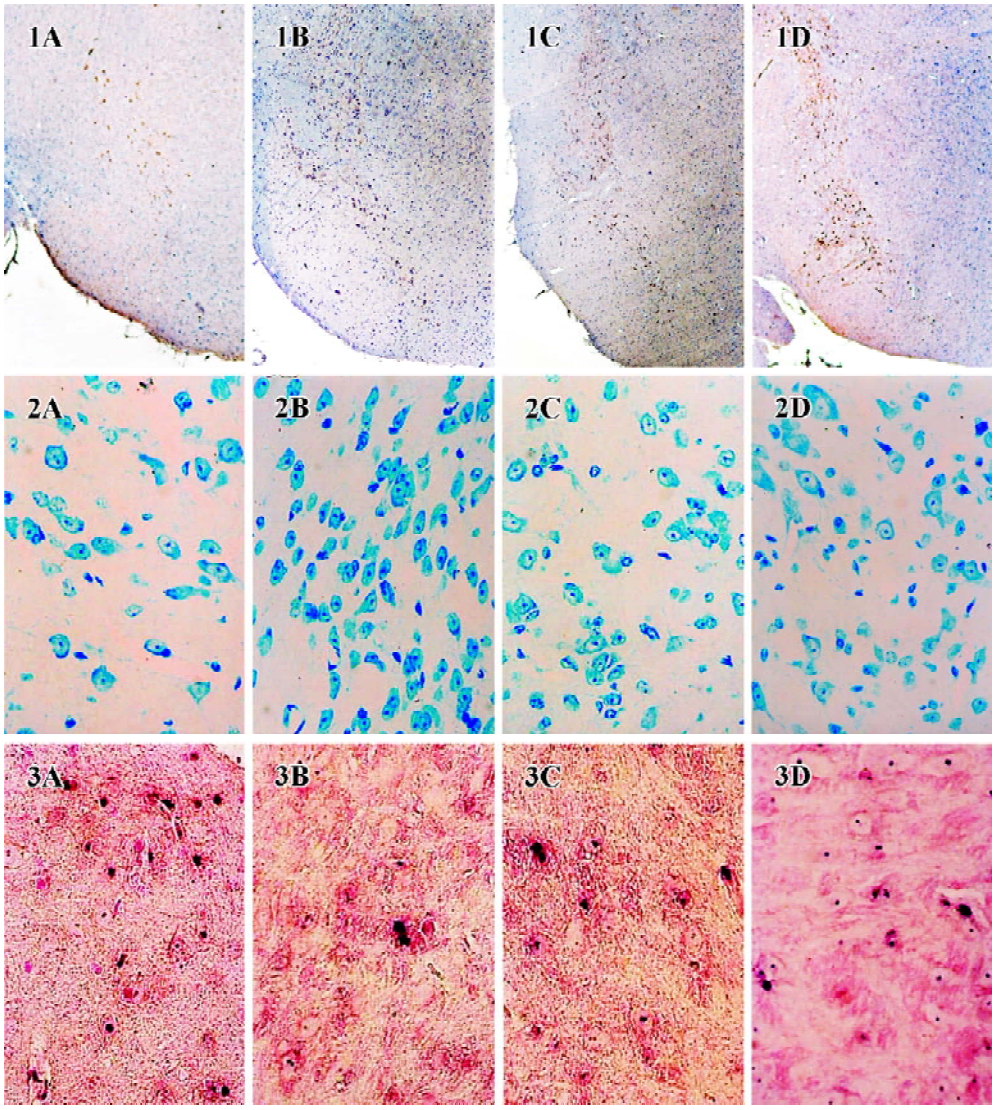

Figure 1. TH immunostaining (1), Nissl staining (2), and TUNEL staining (3) of mouse substantia nigra neurons. A: model group; B: control group; C: pretreatment with NAC group at 300.0 mg/kg; D: pretreatment with Rg1 group at 10.0 mg/kg; 1: ×40. 2, 3: ×400.

of Rg1 showed the similar effect as NAC, but there was no improvement beyond this dose. The results demonstrated that Rg1 possessed the same antioxidant property as NAC.

There has been no direct evidence indicating that Rg1 could scavenge radical by itself, therefore we tried to investigate whether Rg1 act as an antioxidant through mediator. In our previous study, we found the protective effect of Rg1 against MPTP-induced nigral neurons apoptosis was related to enhancing Bcl-2 expression and reducing iNOS expression[11]. Bcl-2 is an anti-apoptotic protein located in the outer mitochondrial membrane, nuclear membrane and endoplasmic reticulum membrane. Bcl-2 participates in the regulation of cell death through multiple mechanisms, one of which regulates the steady state of cellular ROS levels. This can be achieved either by modulating their production, usually by the mitochondria, or by affecting the antioxidant capacity of the cells. *In vitro* and *in vivo* studies provided evidences that Bcl-2 could attenuate cell injuries caused by oxidative stress. Bcl-2 could protect against the increased level of ROS caused by dopamine metabolism in PC12 cells[23]. Transfection with Bcl-2 provided the PC12 cells with marked protection against dopamine-induced apoptosis and inhibited dopamine oxidation to dopamine-melanin[24]. Further studies demonstrated enhanced oxidative stress and susceptibility to oxidants in the brains of Bcl-2-deficient mice[25]. Our previous study showed that Rg1 could prevent

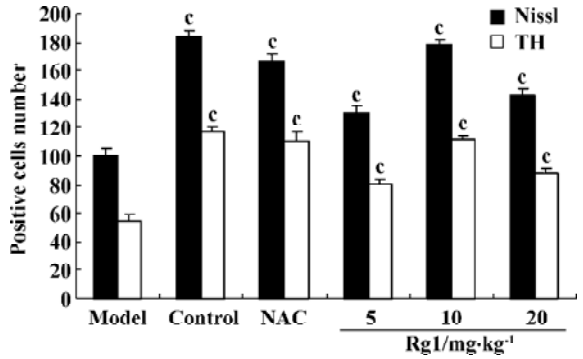

Figure 2. Number of Nissl (black) and TH (white) staining-positive neurons in SN. Pretreatment with Rg1 significantly increased the number of survival neurons and TH-positive neurons, as determined by one-way ANOVA. A 10 mg/kg dose of Rg1 showed the best protective effect among all the doses, and showed no significant difference with NAC. n=8. Mean±SEM. ^cP<0.01 *vs* the model group.

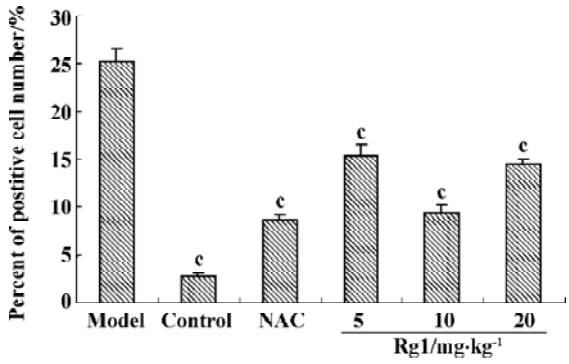

Figure 3. Percentage of TUNEL-positive neuron numbers in SN. The percentage of TUNEL-positive neurons in the model group increased significantly compared with other groups. Pretreatment with Rg1 significantly decreased the percentage of TUNEL-positive neurons. A 10 mg/kg dose of Rg1 showed the best preventive effect of all the doses, and showed no significant difference with NAC. n=8. Mean±SEM. ^cP<0.01 *vs* the model group.

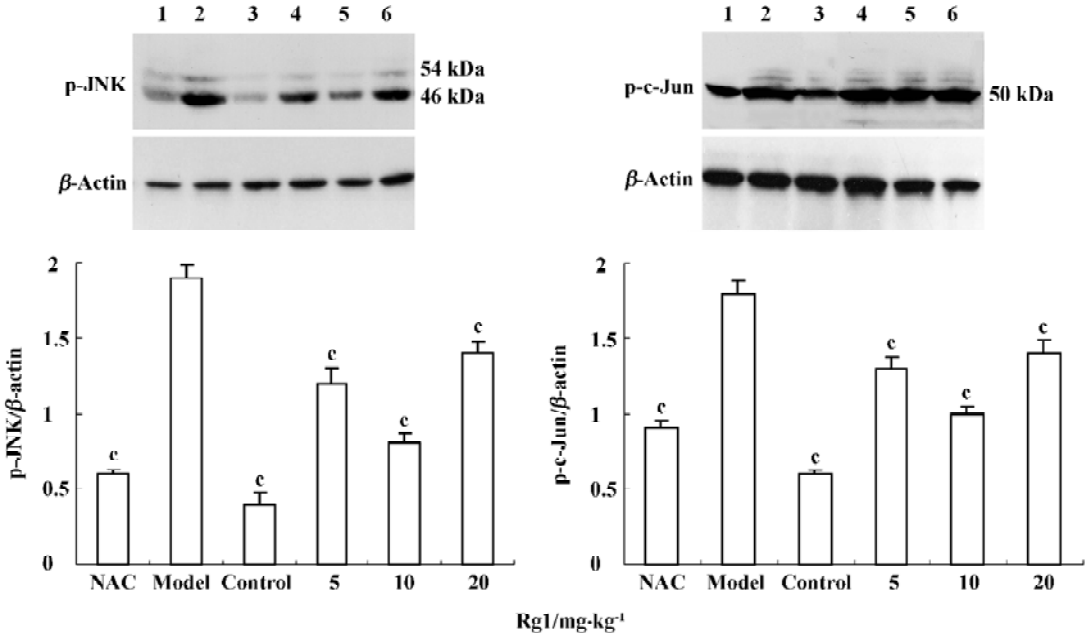

Figure 4. Western blot detection of phospho-JNK and phospho-c-Jun levels respectively. The histogram showed the comparisons of *OD* odds among different groups. 1: NAC; 2: model; 3: control; 4: 5 mg/kg Rg1+MPTP; 5: 10 mg/kg Rg1+MPTP; 6: 20 mg/kg Rg1+MPTP. n=3. Mean±SEM. ^cP<0.01 *vs* the MPTP group.

the decrease of Bcl-2-positive cell numbers following MPTP treatment, so this might contribute to the antioxidant property of Rg1.

Another important protein involved in oxidative stress is nitric oxide synthase (NOS), of which three isoforms have been described: neuronal NOS (nNOS) and endothelial NOS are calcium-calmodulin-dependent enzymes, while inducible NOS (iNOS) activity is independent of intracellular calcium levels. Nitric oxide (NO), an important free radical generated by NOS, can react with superoxide radicals to form the oxidizing agents peroxynitrite ($ONOO^-$) and OH^- [26], and eventually induce DNA strand breakage and apoptosis[27].

Numerous experimental studies have shown that iNOS play an important role in MPTP-induced dopaminergic neuron injury or in PD patients[28,29], it is in agreement with our previous observation that MPTP increased the numbers of iNOS-positive cells. Therefore, changes of Bcl-2 and iNOS expressions could play important roles in the antioxidative effect of Rg1, this could explain the antioxidant property of Rg1. However, the exact pathway leading to the changes of Bcl-2 and iNOS expression in SN is still unclear.

The JNK signaling cascade is a main pathway that mediates the neurotoxicity of MPTP[14], CEP-1347/KT-7515, an inhibitor of JNK activation, can attenuate MPTP-induced nigrostriatal dopaminergic degeneration[7]. Transgenic mice expressing the JNK binding domain (JBD) of JNK interacting protein 1 could resist the neurotoxicity of MPTP[8]. Oxidative stress is an important activator of the JNK signaling cascade. In differentiated PC12 cells and cultured sympathetic neurons, oxidative stress induced by antisence inactivation of superoxide dismutase increased JNK activity[9]. In our previous study, we observed that JNK pathway was activated after the exposure of SHSY5Y cells to the mitochondrial complex I inhibitor MPP^+, Rg1 could attenuate the elevation of ROS and reduce the JNK activation after MPP^+ treatment[30]. In the present *in vivo* study, we also found that pretreatment with Rg1 or NAC could attenuate the elevated phosphorylation of JNK and c-Jun induced by MPTP in SN. The dose of 10 mg/kg of Rg1 showed better effect than dose of 5 mg/kg and 20 mg/kg. There was no significant difference between NAC and 10 mg/kg Rg1, but it is a puzzle why 20 mg/kg Rg1 had weaker inhibition than 10 mg/kg Rg1. The toxicity of higher doses of Rg1 could compromise its ability as a radical scavenger. However, this change is associated with the loss of dopaminergic neurons at different Rg1 doses. This results confirms previous studies that JNK signaling cascade play an important role in dopaminergic neuron apoptosis induced by MPTP, and appropriate dose of Rg1 could attenuate the MTPT induced activation of JNK signaling cascade. It requires further study to find out whether Rg1 influences JNK pathway through mechanisms other than antioxidation.

In conclusion, the present study indicates that pretreatment with certain doses of Rg1 could reduce the loss of dopaminergic neurons caused by MPTP in SN. The neuroprotective effects of Rg1 are potentially due to its antioxidant property that involves Bcl-2 and iNOS, and its inhibitory effect on JNK signaling cascade activation. Further studies will be carried out to evaluate whether ginsenoside Rg1, an important ingredient of ginsenoside, could benefit as a future preventive and therapeutic drug of PD.

References

1 Gerlach M, Ben-Shachar D, Riederer P, Youdim MB. Altered brain metabolism of iron as a cause of neurodegenerative diseases? J Neurochem 1994; 63: 793–806.

2 Jenner P, Olanow CW. Pathological evidence for oxidative stress in Parkinson's disease and related degenerative disorders. In: Olanow CW, Jenner P, Youdim MBH, editors. Neurodegeneration and neuroprotection in Parkinson's disease. London: Academic Press; 1996. p 24–45.

3 Alam ZI, Jenner A, Daniel SE, Lees AJ, Cairns N, Marsden CD, *et al*. Oxidative DNA damage in the parkinsonian brain: an apparent selective increase in 8-hydroxyguanine levels in substantia nigra. J Neurochem 1997; 69: 1195–203.

4 Dexter DT, Holley AE, Flitter WD, Slater TF, Wells FR, Daniel SE, *et al*. Increased levels of lipid hydroperoxides in the parkinsonian substantia nigra: an HPLC and ESR study. Mov Disord 1994; 9: 92–7.

5 Zhang J, Perry G, Smith MA, Robertson D, Olson SJ, Graham DG, *et al*. Parkinson's disease is associated with oxidative damage to cytoplasmic DNA and RNA in substantia nigra neurons. Am J Pathol 1999; 154: 1423–9.

6 Ramsay RR, Salach JI, Dadgar J, Singer TP. Inhibition of mitochondrial NADH dehydrogenase by pyridine derivatives and its possible relation to experimental and idiopathic parkinsonism. Biochem Biophys Res Commun 1986; 135: 269–75.

7 Saporito MS, Brown EM, Miller MS, Carswell S. CEP-1347/KT-7515, an inhibitor of c-jun N-terminal kinase activation, attenuates the 1-methyl-4-phenyl-tetrahydro-pyridine-mediated loss of nigrostriatal dopaminergic neurons *in vivo*. J Pharmacol Exp Ther 1999; 288: 421–7.

8 Xia XG, Harding T, Weller M, Bieneman A, Uney JB, Schulz JB. Gene transfer of the JNK interacting protein-1 protects dopaminergic neurons in the MPTP model of Parkinson's disease. Proc Natl Acad Sci USA 2001; 98: 10433–8.

9 Maroney AC, Finn JP, Bozyczko-Coyne D, O'Kane TM, Neff NT, Tolkovsky AM, *et al*. CEP-1347 (KT-7515), an inhibitor of JNK activation, rescues sympathetic neurons and neuronally differentiated PC12 cells from death evoked by three distinct insults. J Neurochem 1999; 73: 1901–12.

10 Rudakewich M, Ba F, Benishin CG. Neurotrophic and neuroprotective actions of ginsenoside Rb(1) and Rg(1). Planta Med 2001; 67: 533–7.

11 Chen XC, Chen Y, Zhu YG, Fang F, Chen LM. Protective effect of ginsenoside Rg1 on MPTP-induced apoptosis in mouse substantia nigra neurons and its mechanisms. Acta Pharmacol Sin 2002; 23: 829–34.

12 Chen XC, Zhu YG, Zhu LA, Huang C, Chen Y, Chen LM, *et al*. Ginsenoside Rg1 attenuates dopamine-induced apoptosis in PC12 cells by suppressing oxidative stress. Eur J Pharmacol 2003; 473: 1–7.

13 Perry TL, Yong VW, Clavier RM, Jones K, Wright JM, Foulks JG, *et al*. Partial protection from the dopaminergic neurotoxin *N*-methyl-4-phenyl-1,2,3,6 tetrahydropyridine by four different antioxidants in the mouse. Neurosci Lett 1985; 60: 109–14.

14 Saporito MS, Thomas BA, Scott RW. MPTP activates c-Jun NH_2-terminal kinase (JNK) and its upstream regulatory kinase MKK4 in nigrostriatal neurons *in vivo*. J Neurochem 2000; 75: 1200–8.

15 Bradford MM. A rapid and sensitive for the quantitation of microgram quantitites of protein utilizing the principle of protein-dye binding. Anal Biochem 1976; 72: 248–54.

16 Liao B, Newmark H, Zhou R. Neuroprotective effects of ginseng total saponins and ginsenosides Rb1 and Rg1 on spinal cord neurons *in vitro*. Exp Neurol 2002; 173: 224–34.
17 Ali SF, David SN, Newport GD, Cadet JL, Slikker W Jr. MPTP-induced oxidative stress and neurotoxicity are age-dependent: evidence from measures of reactive oxygen species and striatal dopamine levels. Synapse 1994; 18: 27–34.
18 Grunblatt E, Mandel S, Maor G, Youdim MBH. Effect of *R*- and *S*-apomorphine on MPTP-induced nigro-striatal dopamine neuronal loss. J Neurochem 2001; 77: 146–56.
19 Sriram K, Pai KS, Boyd MR, Ravindranath V. Evidence for generation of oxidative stress in brain by MPTP: *in vitro* and *in vivo* studies in mice. Brain Res 1997; 749: 44–52.
20 Marttila RJ, Lorentz H, Rinne UK. Oxygen toxicity protecting enzymes in Parkinson's disease. Increase of superoxide dismutase-like activity in the substantia nigra and basal nucleus. J Neurol Sci 1988; 86: 321–31.
21 Saggu H, Cooksey J, Dexter D, Wells FR, Lees A, Jenner P, *et al*. A selective increase in particulate superoxide dismutase activity in Parkinsonian substantia nigra. J Neurochem 1989; 53: 692–7.
22 Yoritaka A, Hattori N, Mori H, Kato K, Mizuno Y. An immunohistochemical study on manganese superoxide dismutase in Parkinson's disease. J Neurol Sci 1997; 148: 181–6.
23 Ziv I, Offen D, Barzilai A, Haviv R, Stein R, Zilkha-Falb R, *et al*. Modulation of control mechanism of dopamine-induced apoptosis-a future approach to the treatment of Parkinson's disease? J Neural Transm Suppl 1997; 49: 195.
24 Offen D, Ziv I, Panet H, Wasserman L, Stein R, Melamed E, *et al*. Dopamine-induced apoptosis is inhibited in PC12 cells expressing Bcl-2. Mol Cell Neurol 1997; 17: 289–304.
25 Hochman A, Sternin H, Gorodin S, Korsmeyer S, Ziv I, Melamed E, *et al*. Enhanced oxidative stress and altered antioxidants in brains of Bcl-2-deficient mice. J Neurochem 1998; 71: 741–8.
26 Beckman JS, Beckman TW, Chen J, Marshall PA, Freeman BA. Apparent hydroxyl radical production by peroxynitrite: implications for endothelial injury from nitrite oxide and superoxide. Proc Natl Acad Sci USA 1990; 87: 1620–4.
27 Lin KT, Xue JY, Nomen M, Spur B, Wong PY. Peroxynitrite-induced apoptosis in HL-60 cells. J Biol Chem 1995; 270: 16487–90.
28 Dehmer T, Lindenau J, Haid S, Dichgans J, Schulz JB. Deficiency of inducible nitric oxide synthase protects against MPTP toxicity *in vivo*. J Neurochem 2000; 74: 2213–6.
29 Hunot S, Boissiere F, Faucheux B, Brugg B, Mouatt-Prigent A, Agid Y, *et al*. Nitrite oxide synthase and neuronal vulnerability in Parkinson's disease. Neuroscience 1996; 72: 355–63.
30 Chen XC, Fang F, Zhu YG, Chen LM, Zhou YC, Chen Y. Protective effect of ginsenoside Rg1 on MPP^+-induced apoptosis in SHSY5Y cells. J Neural Transm 2003; 110: 835–45.

Full-length article

Neuropeptide Y expression in mouse hippocampus and its role in neuronal excitotoxicity[1]

Yong-fei WU, Sheng-bin LI[2]

State Key Laboratory of Forensic Sciences, State Key Laboratory of Environment and Disease Related Genes, Xi'an Jiaotong University College of Medicine, Xi'an 710061, China

Key words

neuropeptide Y; hippocampus; kainic acid; excitotoxicity; apoptosis; epilepsy

[1] Project supported by a grant from the National Natural Science Foundation of China (No 30200241).
[2] Correspondence to Prof. Sheng-bin LI.
Phn 86-29-8265-5474. Fax 86-29-8265-5113.
E-mail shbinlee@mail.xjtu.edu.cn

Received 2004-07-21
Accepted 2004-10-11

doi: 10.1111/j.1745-7254.2005.00011.x

Abstract

Aim: To investigate neuropeptide Y (NPY) expression in mouse hippocampus within early stages of kainic acid (KA) treatment and to understand its role in neuronal excitotoxicity. **Methods:** NPY expression in the hippocampus within early stages of KA intraperitoneal (ip) treatment was detected by immunohistochemistry (IHC) and *in situ* hybridization (ISH) methods. The role of NPY and Y5, Y2 receptors in excitotoxicity was analyzed by terminal deoxynucleotidyl transferase-mediated UTP nick end-labeling (TUNEL) assay. **Results:** Using IHC assay, in granule cell layer of the dentate gyrus (DG), NPY positive signals appeared 4 h after KA injection, reached the peak at 8 h and leveled off at 16 and 24 h. In CA3, no positive signal was found within the first 4 h after KA injection, but strong signal appeared at 16 and 24 h. No noticeable signal was detected in CA1 at all time points after KA injection. Using the ISH method, positive signals were detected at 4, 8, and 16 h in CA3, CA1, and hilus. In DG, much stronger ISH signals were detected at 4 h, but leveled off at 8 and 16 h. TUNEL analysis showed that intracerebroventricularly (icv) infusion of NPY and Y5, Y2 receptor agonists within 8 h after KA insult with proper dose could remarkably rescue pyramidal neurons in CA3 and CA1 from apoptosis. **Conclusion:** NPY is an important anti-epileptic agent. The preceding elevated expression of NPY in granule cell layer of DG after KA injection might partially explain its different excitotoxicity-induced apoptotic responses in comparison with the pyramidal neurons from CA3 and CA1 regions. NPY can not only reduce neuronal excitability but also prevent excitotoxicity-induced neuronal apoptosis in a time- and dose-related way by activation of Y5 and Y2 receptors.

Introduction

Excitotoxicity is a process by which glutamate or other excitatory amino acids induce neuronal cell death in the central nervous system[1,2]. It is thought that excitotoxicity might contribute to the pathogenesis of human neuronal cell loss by sustained epilepsy, trauma, ischemia, and hypoglycemia, and might also underlie certain neurodegenerative diseases[3–5]. Excessive stimulation of the three types of ionotropic glutamate receptors, including the *N*-methyl-*D*-aspartate (NMDA), α-amino-3-hydroxy-5-methyl-4-isoxazole propionic acid (AMPA), and KA receptors, produces neuronal cell death by increasing intracellular Ca^{2+} and Na^{+}, and therefore drastically changing normal cellular physiology[1,2].

KA is an analog for glutamate and is also an excitotoxin in the hippocampus[6–8] that induces ongoing convulsions by directly stimulating KA receptors and indirectly increasing the release of excitatory amino acids from nerve terminals, degeneration of *cornu ammonis* (CA) pyramidal neurons in the hippocampus, and hyper-excitability of surviving CA neurons[9–11]. Thus, KA-induced seizures have been widely used as an epilepsy model for studying mechanisms underlying both seizure susceptibility and neuronal cell loss[12–14].

Increasing evidence suggests that NPY is a powerful endogenous anticonvulsant in the hippocampus[12,15–17]. NPY knockout mice exhibit uncontrollable seizures and enhanced

fatality in response to KA administration[12]. Moreover, intracerebroventricular infusion of NPY reduces epileptiform after discharges and inhibits KA-induced seizures[18]. The possible mechanism for the anticonvulsant properties of NPY is the inhibition of calcium influx and glutamate release[12,15,17]. However, the exact role of NPY *in vivo* in excitotoxicity is unknown. Although excitotoxicity induced an ongoing neuronal apoptosis, it was mainly determined at early stages after excitatory amino acids treatment[7,8,14]. Thus, to investigate the sequential and spatial expression of NPY in the hippocampus within early stage of KA injection, and to understand its role in excitotoxicity, could be of unique importance.

Materials and methods

Animals and drugs Mice of 8 to 9 weeks age were used for analysis. All mice were housed with food and water *ad libitum* in a 12-h light cycle room. Our protocol was approved by the Institutional Animal Care and Use Committee of Xi'an Jiaotong University, and we strictly followed NIH guidelines for the care and use of laboratory animals. All efforts were taken to minimize both animal suffering and the number of mice used. KA (Sigma Chemical, St Louis, MO, USA) was dissolved in ddH_2O, neutralized by NaOH and injected (ip) in a dose of 20 mg/kg of body weight to the mice. Human NPY, NPY13-36 (Y2 agonist), or human pancreatic polypeptide (hPP) (Y5 agonist) were purchased from Bachem (Torrance, CA, USA).

IHC analysis of NPY expression At 0 (normal control treated with saline), 2, 4, 8, 16, or 24 h (8 each group) after KA injection, surviving mice were deeply anesthetized with sodium pentobarbital (60 mg/kg of body weight, ip), and then transcardially perfused with phosphate buffered saline (PBS), pH 7.4, and 4% paraformaldehyde in PBS for 15 min. After perfusion, their brains were removed, postfixed overnight with 4% paraformaldehyde in PBS at 4 ºC, submerged in 20% sucrose at 4 ºC for 48 h, and then sections were cut coronally at 40 μm to encompass the entire hippocampus using a freezing microtome. Every eighth of serial coronary brain sections through the rostral-caudal extent of the hippocampus in 40-μm thickness were selected for immunohistochemistry (IHC) detection of NPY expression in the hippocampus using rabbit anti-NPY antibody (1:1,000, Chemicon, CA, USA) as previously described[14,19].

Probe preparation for *in situ* hybridization (ISH) analysis The plasmid construct pT7T3D-Pac, containing 561 bp mouse NPY gene, was from the University of Cincinnati Microarray Center. The construct was first linearized by *Eco*R I or *Hin*d III respectively. The *Eco*R I linearized template containing T3 promoter was used for anti-sense probe transcription. The *Hin*d III linearized template containing T7 promoter was used for sense probe transcription (negative control). Transcription reaction mixture 20 μL in a RNase free eppendorf tube [4 μL 5×transcription buffer (Promega, USA), 1 μL linearized DNA (1 μg), 2 μL NTP mix (Dig-UTP) (Roche, Germany), 2 μL 0.1 mol/L DTT, 9 μL H_2O, 1 μL RNase inhibitor (Invitrogen, USA), 1 μL RNA polymerase (T3 or T7) (Promega, USA)] was incubated at 37 ºC for 2 h, then 2U DNase I (RNase free) (Promega) was added, incubated at 37 ºC for 15 min to digest DNA template. Reaction was stopped with 2 μL of 0.2 mol/L EDTA, pH 8.0. Then 2.5 μL LiCl 4 mol/L and 75 μL prechilled (-20 ºC) 100% EtOH was added and mixed well. It was placed at -20 ºC for 2 h and centrifuged at 2–8 ºC, 44 500×*g*, for 15 min. The supernatant was discarded carefully. Samples were dried under a vacuum and then dissolved for 30 min at 37 ºC in 100 μL diethyl-pyrocarbonate (DEPC) H_2O. RNA probe was quantified by spectrophotometric analysis (OD_{260}/OD_{280}) and stored at -80 ºC, or stored in aliquots at -20 ºC.

ISH detection of NPY expression For ISH analysis, 0 (normal control), 4, 8, or 16 h (8 each group) after KA injection, mice were killed by cervical dislocation, brains were removed quickly and kept in dry ice powder for 5 min and then stored at -80 ºC for at least 48 h before sectioning. Brain sections of 12 μm, containing hippocampal formation, were cut and placed on Superfrost Plus slides (pretreated with 0.1% DEPC H_2O for 2 h at 37 ºC) and air dried at room temperature for 30 min and then stored at -80 ºC before use. Every fifteenth of serial coronary brain sections through the rostral-caudal extent of the hippocampus were analyzed by ISH as described previously[20].

Cannula implantation and infusion of NPY and its agonists Mice were anesthetized with an injection of Equithesin (34 mg/kg of body weight, ip) and atropine (0.35 mg/kg of bodyweight, ip). Animals were placed in a stereotactic device (Kopf Instruments), and cannulas were implanted into the lateral ventricle (0.6 mm posterior; 1.9 mm lateral; and 2.0 mm ventral to bregma). Mice were allowed to recover from surgery for 2 d. First, to determine the timing of NPY infusion after KA injection, icv injection of human NPY (5.0 μg in 1 μL of neutral buffered solution) or saline was performed 2, 8, or 24 h after KA injection (8 to 10 each group) using an infusion pump (KD Scientific) at a constant rate of 1 μL/min as described[12]. Then, to determine the dose of NPY infusion, 8 h after KA injection, the effect of icv infusion of NPY at a dose of 2.5, 5.0, and 10.0 μg was compared. Finally, to investigate the receptors that mediate its role in excitotoxicity, icv infusion of 3.0 μg

NPY13-36 or 5.0 μg hPP was carried out 8 h after KA injection. The dose of NPY and its agonists were based on previous studies[12,16]. Cannula placement was verified *post-hoc* in all animals by injection of 1% cresyl violet solution before brain dissection. Three days after KA injection, brain sections were made as IHC assay above for TUNEL staining.

TUNEL assays Every eighth of serial coronary brain sections through the rostral-caudal extent of the hippocampus in 40-μm thickness were used for TUNEL staining using the *in situ* Cell Death Detection Kit (TUNEL POD) (Roche Applied Science, Germany) as described[14].

Statistical analysis IHC and ISH signal is in every of sub-region of each section was obtained with densitometric scanning, and data were analyzed by one–way ANOVA. All TUNEL positive cells in every sub-region of each section were counted regardless of sizes and shapes. The mean number of cells per section was used for comparison. Data were analyzed by one-way ANOVA and *post-hoc* Student-Newman-Keuls (SNK) test. Statistical significance was set as $P<0.05$.

Results

NPY expression in the hippocampus by IHC method In the granule cell layer of DG, no NPY positive cell was detected at basal condition (0 h) and 2 h after KA injection (Figure 1A, 1B). NPY positive cells appeared at 4 h (Figure 1C), reached the peak at 8 h (Figure 1D), and were reduced remarkably at 16 and 24 h (Figure 1E, 1F). In the CA3 sub-region, no positive signal was found within the first 4 h after KA injection (Figure 1A,1C), NPY positive signals appeared at 8 h (Figure 1D), strong signals appeared at 16 and 24 h (Figure 1E, 1F). No noticeable signal was detected in the CA1 sub-region at all time points within the first 24 h after KA injection. In the hilus, NPY positive signals were noticeably intensified at 8 h (Figure 1D), and reached the peak at 16 and 24 h (Figure 1E, 1F). One-way ANOVA results showed a significant time-dependent effect ($P<0.05$) in both DG and CA3 regions (Figure 2).

NPY expression in the hippocampus by ISH analysis Under physiological condition, NPY expression in the granule cell layer of DG, CA3, and CA1 was less noticeable (Figure 3A). Positive ISH signals were detected in DG, CA3, and CA1 sub-regions at each time point after KA treatment (Figure 3B–3D). Four hours after KA injection, ISH signals in the DG sub-region were stronger than those in CA3 and CA1 (Figure 3B). Eight and sixteen hours after KA injection, ISH signals were significantly reduced in DG sub-region but remarkably elevated in CA3, CA1, and hilus sub-regions (Figure 3C, 3D, $P<0.05$). One-way ANOVA result showed a significant time-dependent effect ($P<0.05$) in all regions (Figure 4).

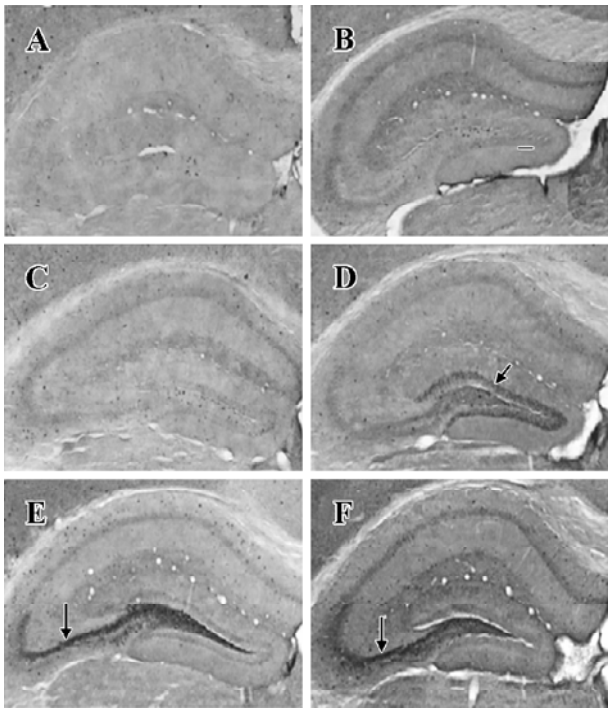

Figure 1. Expression of NPY in the hippocampus by IHC method. In the granule cell layer of DG region, no positive signals were detected at 0 (control) and 2 h (A, B), positive signals appeared at 4 h (C), reached the peak at 8 h (D), were remarkably reduced at 16 and 24 h (E, F). In CA3 regions, no positive signals were detected at 0, 2, and 4 h (A–C), positive signal appeared at 8 h (D), reached the maximum at 16 h (E), and became less stronger at 24 h (F). No obvious signal was detected at all time points in CA1. *Arrow* denotes positive signal. Scale bar: 100 μm. ×40.

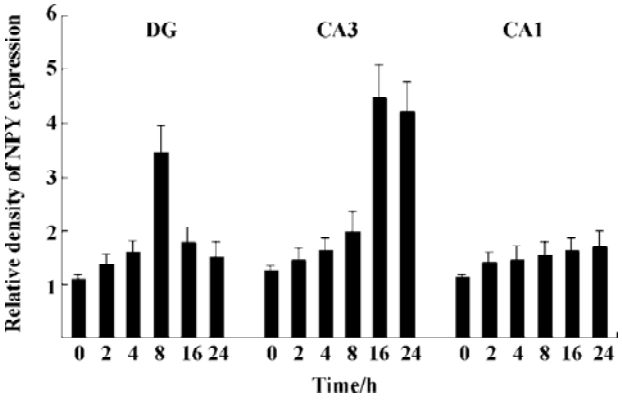

Figure 2. Quantitative analysis of NPY expression from IHC results. NPY expression in the hippocampus was detected by IHC and followed by analysis with densitometric scanning. Data represent the ratio of mean signal density relative to background±SEM. NPY expression was in a time-dependent manner in DG and CA3 regions ($P<0.05$).

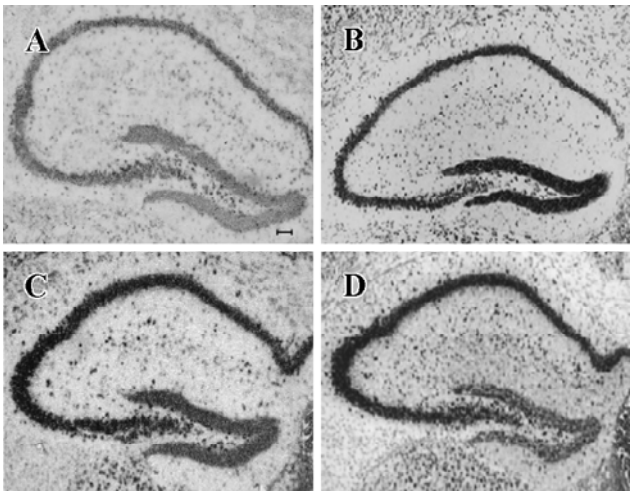

Figure 3. ISH analysis of NPY expression in the hippocampus. Weak signal was detected under physiological condition (A). Positive signals were elevated in DG, CA3, and CA1 4 h after KA injection (B), but signals in DG were much stronger than that in other regions. At 8 and 16 h (C, D), NPY positive signals in DG were remarkably leveled off, but in CA3 and CA1, signals were more intensified in comparison with the 4 h-group. Scale bar: 100 μm. ×40.

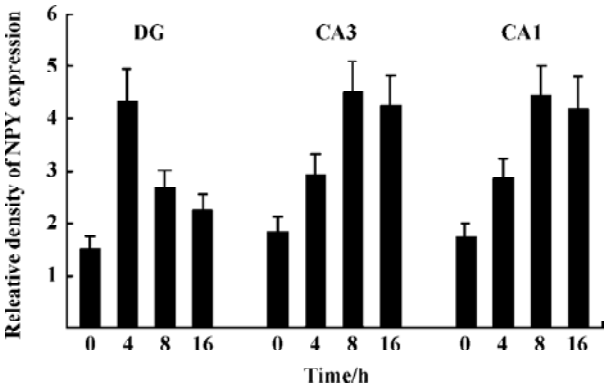

Figure 4. Quantitative analysis of NPY expression from ISH results. NPY expression in the hippocampus was detected by ISH and followed by analysis with densitometric scanning. Data represent the ratio of mean signal density relative to background±SEM. NPY expression was time-dependent in DG, CA3, and CA1 regions (P<0.05).

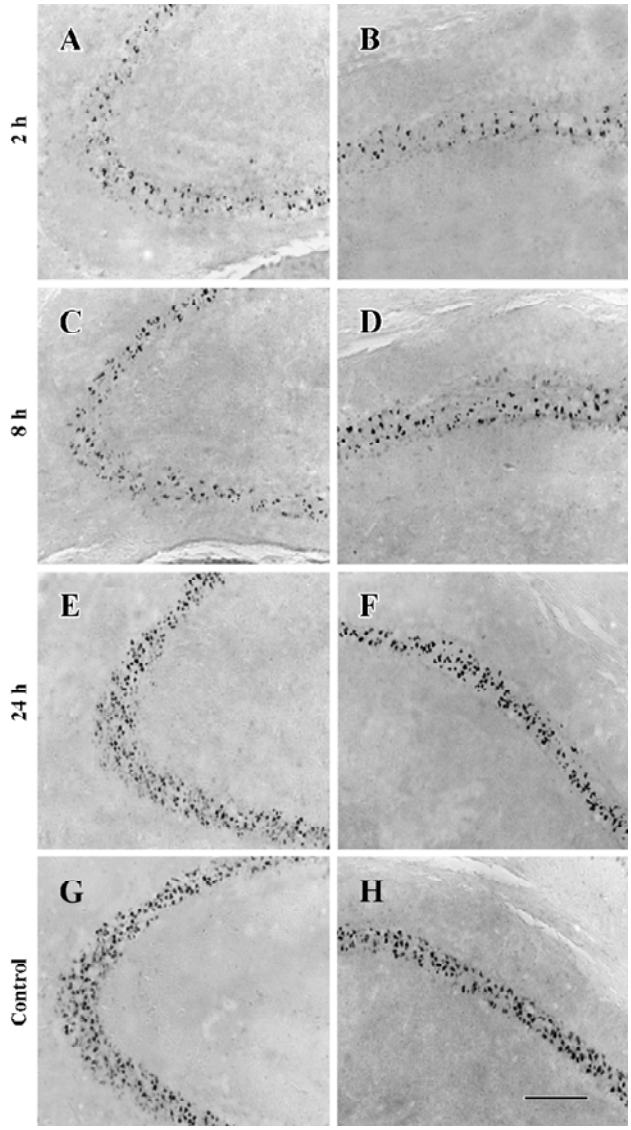

Figure 5. NPY prevents neuronal cells from excitotoxic-induced apoptosis in a time related manner. In CA3 and CA1, less massive apoptotic pyramidal cells were detected in NPY treated mice at 2 and 8 h after KA injection (A, C, and B, D) than in control mice (G, H). But NPY infusion at 24 h after KA treatment (E, F) had no noticeable effect in comparison with control mice (G, H). Scale bar: 100 μm. ×200.

NPY prevents neuronal cells from apoptosis in a time- and dose-related manner In CA3 and CA1, less massive apoptotic pyramidal cells were detected in mice with NPY infusion at 2 and 8 h after KA treatment (Figure 5A-5D) compared with control mice (Figure 5G, H). Similar TUNEL signals were detected in CA3 and CA1 between mice infused with NPY at 24 h after KA injection and control mice (Figure 5E-H). One-way ANOVA showed significant time-dependent effects in both CA3 and CA1 (P<0.05, Figure 6A). *Post hoc* SNK test showed a more noticeable effect at 2 h than that at 8 h of NPY infusion (P<0.05) though they both significantly reduced apoptosis in comparison with control mice (P<0.05) (Figure 6A). Figure 6B shows the quantitative results of TUNEL staining in CA3 and CA1 sub-regions 3 d after KA treatment with icv infusions of 2.5, 5.0, or 10.0 μg human NPY or saline (8 to 10 mice each group) at 8 h after KA injection. One-way ANOVA showed significant dose-dependent effect in both CA3 and CA1 among

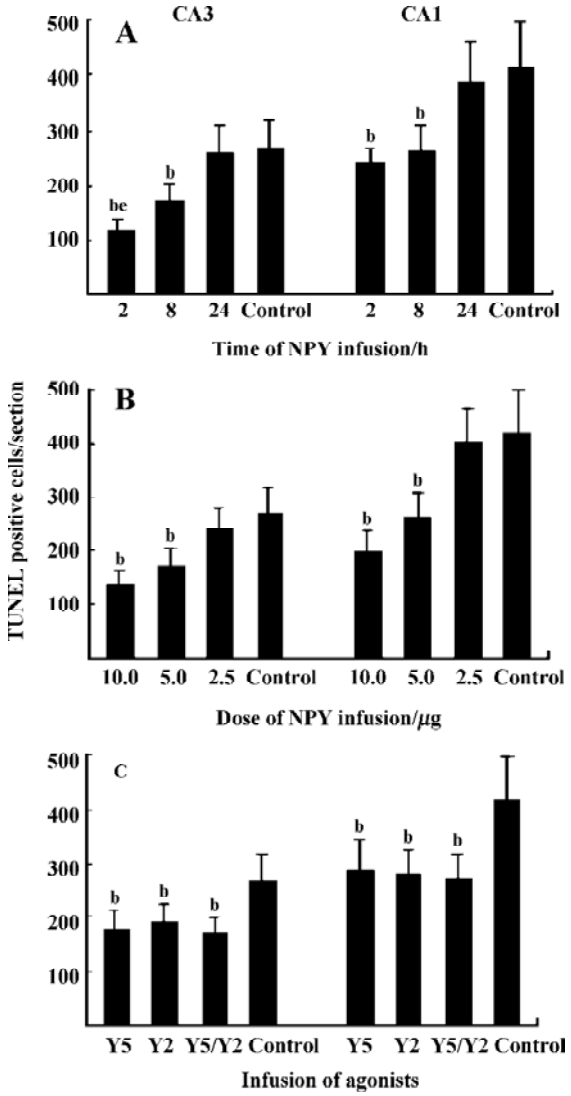

Figure 6. Quantitative analysis of neuronal apoptosis from TUNEL results. (A) The time-related effect of NPY on neuronal apoptosis. (B) The dose-related effect of NPY on neuronal apoptosis. A significant anti-apoptotic effect with infusion of 10.0 and 5.0 μg NPY at 8 h after KA injection was shown (P<0.05). (C) Neuronal protective role of Y5 and Y2 receptors. Y5 and Y2 agonists could both prevent neuronal cells from death in comparison with control (P<0.05), but there was no additive effect between them (P>0.05). Data represent means±SEM/each section. ^{b}P<0.05 *vs* control. ^{e}P<0.05 *vs* 8 h.

four groups (P<0.05). *Post hoc* SNK test showed a significant effect with infusion of 10.0 and 5.0 μg NPY at 8 h in comparison with control (P<0.05).

NPY prevents neuronal cells from apoptosis by activating both Y5 and Y2 receptors Y5 and Y2 agonists icv could both prevent neuronal cells from death 8 h after KA injection, but there was no additive effect between them. One-way ANOVA showed significant effects in both CA3 and CA1 (P<0.05). *Post hoc* SNK test showed no significant difference among Y5, Y2, and Y5/Y2 agonists treated three groups, but significant difference was detected between these three groups and control mice, respectively (Figure 6C, P<0.05).

Discussion

Increasing evidence suggests that NPY is a powerful endogenous anticonvulsant in the hippocampus[12,15–17]. Its expression can be elevated by experimentally induced seizures initiated by electrical kindling, kainic acid, and pentylenetetrazol[21-25]. Excitotoxicity induced an ongoing neuronal apoptosis, which was mainly determined at early stage after excitatory amino acid treatment[7,8,14]. According to these findings, we for the first time focused on NPY expression pattern in the hippocampus within early stages after KA injection using both IHC and ISH methods, and tried to understand its implication in excitotoxicity. From our IHC and ISH results (Figure 1–4), we concluded that NPY expression in the granule cell layer of DG sub-region was prior to CA3 and CA1 after KA-treatment, seizure-induced increase of NPY in the hippocampus was the result of transcriptional activation, and might be a compensatory mechanism to reduce excitatory neurotransmission. ICV infusion of NPY and its Y5, Y2 receptor agonists at 2 and 8 h after KA insult could rescue pyramidal neurons in CA3 and CA1 regions from apoptosis (Figure 3-6). It is also well established that the pyramidal cells in CA3 and CA1 are more susceptible to KA-induced apoptosis than the granule cells in DG[7,8,14]. Taken together, we presume that the preceded elevation of NPY expression in the granule cell layer of DG after KA injection might partially explain its different excitotoxicity-induced apoptotic responses in comparison with the pyramidal neurons from CA3 and CA1 regions.

Activation of NPY receptors is neuroprotective against excitotoxicity in rat hippocampal slice cultures[26]. For dentate granule cells and CA3 pyramidal cells, selective activation of Y1, Y2, or Y5 receptors, respectively had a neuroprotective effect against AMPA and KA, whereas only the activation of Y2 receptors was effective for CA1 pyramidal cells in the rat. Some physiological and pharmacological work showed intracerebroventricular administration of NPY reduced epileptiform afterdischarges and inhibited KA-induced seizures in rats; and Y5 and/or Y2 receptors were responsible for modulation of seizure activity in mouse hippocampal slices[18,27]. But, to date, whether NPY can pre-

vent neuronal cells from excitotoxicity-induced apoptosis *in vivo*, what receptors are responsible for this function, what is the effective time and dose of NPY and its agonists infusion, are not known. We found icv infusion of NPY and its Y5, Y2 agonists within 8 h of a proper dose, after excitatory amino acid injection, could rescue neuronal cells from apoptosis in mice (Figure 5, 6). These data are quite useful for the potential clinical application of NPY in anti-epilepsy. The protective signal transduction pathway of its different receptors should be included in our future research.

With IHC detection, NPY positive or negative signal does not mean that NPY is synthesized or is not synthesized. As a neurotransmitter[28], NPY can be released from one cell where it is synthesized and be taken up by other cells through synaptic formation. Comparing the IHC result (Figure 1) with the ISH result (Figure 3), we found although NPY mRNA transcripts were synthesized in all regions of the hippocampus at 4, 8, and 16 h after KA treatment, no noticeable signals were detected in the CA1 region by IHC assay at any point. Probably, NPY in this region was transmitted to other places as a neurotransmitter after translation. Or the sensitivity of IHC is not high enough to detect NPY expression in this region.

In conclusion, the preceding elevated expression of NPY in granule cell layer of DG after KA injection may explain partially its different excitotoxicity-induced apoptotic responses in comparison with the pyramidal neurons from CA3 and CA1 regions. NPY can not only reduce neuronal excitability but also prevent excitotoxicity-induced neuronal apoptosis by activation of Y5 and Y2 receptors.

References

1 Choi DW. Glutamate neurotoxicity and diseases of the nervous system. Neuron 1988; 1: 623–34.
2 Choi DW. Excitotoxic cell death. J Neurobiol 1992; 23: 1261–76.
3 Lee JM, Zipfel GJ, Choi DW. The changing landscape of ischaemic brain injury mechanisms. Nature 1999; 399: A7–14.
4 Coyle JT, Puttfarcken P. Oxidative stress, glutamate, and neurodegenerative disorders. Science 1993; 262: 689–95.
5 McNamara JO. Emerging insights into the genesis of epilepsy. Nature 1999; 399: A14–22.
6 Campocdhiaro P, Coyle J. Ontogenetic development of kainite neurotoxicity: correlates with glutamatergic innervation. Proc Natl Acad Sci USA 1978; 75: 2025–9.
7 Cook T, Crutcher K. Intrahippocampal injection of kainic acid produces significant pyramidal cell loss in neonatal rats. Neuroscience 1986; 18: 79–92.
8 Nadler J, Perry B, Cotman C. Intraventricular kainic acid preferentially destroys hippocampal pyramidal cells. Nature 1978; 271: 676–7.
9 Ben-Ari Y. Limbic seizure and brain damage produced by kainic acid: mechanisms and relevance to human temporal lobe epilepsy. Neuroscience 1985; 14: 375–403.
10 Dudek F, Obenaus A, Schweitzer J, Wuarin J. Functional significance of hippocampal plasticity in epileptic brain: electrophysiological changes of the dentate granule cells associated with mossy fiber sprouting. Hippocampus 1994; 4: 259–65.
11 Nadler J. Kainic acid as a tool for the study of temporal lobe epilepsy. Life Sci 1981; 29: 2031–42.
12 Baraban SC, Hollopeter G, Erickson JC, Schwartzkroin PA, Palmiter RD. Knock-out mice reveal a critical antiepileptic role for neuropeptide Y. J Neurosci 1997; 17: 8927–36.
13 Zhao WJ, Ma YH, Fei J, Mei ZT, Guo LH. Increase in drug-induced seizure susceptibility of transgenic mice overexpressing GABA transporter-1. Acta Pharmacol Sin 2003; 24: 991–5.
14 Dong H, Csernansky CA, Goico B, Csernansky JG. Hippocampal neruogenesis follows kainic acid-induced apoptosis in neonatal rats. J Neurosci 2003; 23: 1742–9.
15 Colmers WF, Bleakman D. Effects of neuropeptide Y on the electrical properties of neurons. Trend Neurosci 1994; 17: 373–9.
16 Marsh DJ, Baraban SC, Hollopeter G, Palmiter RD. Role of the Y5 neuropeptide Y receptor in limbic seizures. Proc Natl Acad Sci USA 1999; 96: 13518–23.
17 Vezzani A, Sperk G, Colmers W. Neuropeptide Y. Emerging evidence for a functional role in seizure modulation. Trends Neurosci 1999; 22: 25–33.
18 Woldbye D, Madsen TM, Larsen PJ, Mikkelsen JD, Bolwig TG. Neuropeptide Y inhibits hippocampal seizures and wet dog shakes. Brain Res 1996; 737: 162–8.
19 Wu Y, Zhang D, Lou D, Fan Y, Aronow D, Xu M, *et al*. c-fos regulates neuropeptide Y expression in mouse dentate gyrus. Neurosci Lett 2004; 363: 6–10.
20 Braissant O, Wahli W. A simplified *in situ* hybridization protocol using non-radioactively labeled probes to detect abundant and rare mRNAs on tissue sections. Biochemica 1998; 1: 10–6.
21 Marksteiner J, Sperk G, Maas D. Differential increases in brain levels of neuropeptide Y and vasoactive intestinal polypeptide after kainic acid-induced seizures in the rat. Naunyn Schmiedebergs Arch Pharmacol 1989; 339: 173–7.
22 Pitkänen A, Beal MF, Sirviö J, Swartz KJ, Männistö PT, Riekkinen PJ. Somatostatin, neuropeptide Y, GABA and cholinergic enzymes in brain of pentylenetetrazol-kindled rats. Neuropeptides 1989; 14: 197–207.
23 Tønder N, Kragh J, Finsen BR, Bolwig TG, Zimmer J. Kindling induces transient changes in neuronal expression of somatostatin, neuropeptide Y, and calbindin in adult rat hippocampus and fascia dentata. Epilepsia 1994; 35: 1299–308.
24 Gruber B, Greber S, Rupp E, Sperk G. Differential NPY mRNA expression in granule cells and interneurons of the rat dentate gyrus after kainic acid injection. Hippocampus 1994; 4: 474–82.
25 Kragh J, Tønder N, Finsen BR, Zimmer J, Bolwig TG. Repeated electroconvulsive shocks cause transient changes in rat hippocampal somatostatin and neuropeptide Y immunoreactivity and mRNA *in situ* hybridization signals. Exp Brain Res 1994; 98: 305–13.
26 Silva AP, Pinheiro PS, Carvalho AP, Carvalho CM, Jakobsen B, Zimmer J, *et al*. Activation of neuropeptide Y receptors is neuroprotective against excitotoxicity in organotypic hippocampal slice cultures. FASEB J 2003; 10: 122–31.
27 Guo H, Castro PA, Palmiter RD, Baraban SC. Y5 receptors mediate neuropeptide Y actions at excitatory synapses in area CA3 of the mouse hippocampus. J Neurophysiol 2002; 87: 558–66.
28 Wahlestedt C, Reis DJ. Neuropeptide Y-related peptides and their receptors-are the receptors potential therapeutic drug targets? Annu Rev Pharmacol Toxicol 1993; 32: 309–52.

Full-length article

Alteration of binding sites for [^{3}H]P1075 and [^{3}H]glibenclamide in reno-vascular hypertensive rat aorta[1]

Hua-mei HE[2,3,5], Chao-liang LONG[2,5], Le-zhi ZHANG[3,5], Ai-ling FU[3], Hai WANG[4]

[2]Institute of Pharmacology and Toxicology, Academy of Military Medical Sciences, Beijing 100850, China; [3]Department of Pharmacology, Third Military Medical University, Chongqing 400038, China

Key words

potassium channels; glibenclamide; P1075; pinacidil; hypertension; aorta; radioligand binding

[1] Project supported by the Key State 863 Project (No 2002AA2Z3137).
[4] Correspondence to Prof. Hai WANG.
Phn 86-10-6693-2651. Fax 86-10-6821-1656.
E-mail wh@nic.bmi.ac.cn
[5] The first three authors contributed equally to this paper.

Received 2004-06-03
Accepted 2004-07-14

doi: 10.1111/j.1745-7254.2005.00016.x.

Abstract

Aim: The alterations of the binding sites for ATP-sensitive K^+ channel (K_{ATP}) openers and blockers in aortic strips were investigated in hypertensive rats. **Methods:** Radioligand binding techniques were used to compare the specific binding properties of [^{3}H]P1075 and [^{3}H]glibenclamide (Gli) in normotensive (NWR) and reno-vascular hypertensive rat (RVHR) aortic strips. **Results:** The K_D values of [^{3}H]P1075 binding were increased by 1.5-fold, while the B_{max} values were unchanged in RVHR. The IC_{50} values of P1075 and pinacidil (Pin) for displacing the [^{3}H]P1075 binding in RVHR were increased by 1.8- and 1.7-fold, respectively. The kinetic processes of association and dissociation of [^{3}H]P1075 binding were slower in RVHR. Glibenclamide pretreatment slowed down the kinetic processes of the association and dissociation of [^{3}H]P1075 binding in NWR, but failed to alter the kinetic processes of [^{3}H]P1075 binding in RVHR. The IC_{50} values of Gli for displacing the [^{3}H]Gli binding at high-affinity sites were increased by 3-fold, while those at low-affinity sites remained to be unchanged in RVHR. The kinetic processes of association of [^{3}H]Gli binding were decreased and those of the dissociation were accelerated in RVHR. The treatment with Pin slowed down the association kinetic processes but accelerated the process of the dissociation of [^{3}H]Gli binding in NWR, but did not alter the kinetics of [^{3}H]Gli binding in RVHR. **Conclusion:** The affinity of binding sites for [^{3}H]P1075 and of high-affinity binding sites for [^{3}H]Gli are decreased, and the negative allosteric interactions between the two binding sites are impaired in RVHR aorta.

Introduction

ATP-sensitive K^+ channels(K_{ATP}) have been identified in multiple cells[1,2]. In vascular smooth muscles, K_{ATP} can regulate vascular tone[3]. The functions of vascular K_{ATP} can be modulated by nucleotides, potassium channel blockers, sulfonylureas, such as glibenclamide (Gli), and K_{ATP} openers, such as pinacidil (Pin)[4]. Recent molecular biological and electrophysiological studies on recombinant K_{ATP} have identified that K_{ATP} is a hetero-octameric complex composed of an inwardly rectifying K^+ channel ($Kir_{6.x}$) serving as a pore-forming subunit and regulatory sulfonylurea receptors (SURs) belonging to the ATP-binding cassette protein superfamily[5]. The binding sites for nucleotides, sulfonylureas, and potassium channel openers are localized in the SURs, which explains the complex sensitivity to these drugs[6]. Furthermore, it has been found that binding experiments have been carried out in vascular smooth muscles, using [^{3}H]Gli and [^{3}H]P1075, that the binding sites of K_{ATP} openers are different from those of blockers, and negatively allosteric interaction exists between these two binding sites[7,8]. The functional alterations of K_{ATP} in vascular smooth muscles from hypertensive animals have been investigated by using patch-clamp techniques; the dose-response curves of the K_{ATP} openers pinacidil and aprikalim, for inducing relaxation of isolated aorta and basilar arteries, were shifted rightward[9], and the effects of levcromakalim on K_{ATP} currents in mesen-

teric arteries were decreased in SHR[10]. But the mechanisms underlying the hypertensive changes of K_{ATP} remain to be investigated.

In the present study, the characteristics of [^{3}H]P1075 and [^{3}H]Gli binding in aortic strips, derived from normotensive and hypertensive rats, were compared for investigation of the hypertensive changes of K_{ATP} in vascular smooth muscles.

Materials and methods

Drugs [^{3}H]Gli (specific activity 1850 GBq/mmol=50 Ci/mmol) was purchased from Dupont/ New England Nuclear (Boston, MA, USA). [^{3}H]P1075 (specific activity 121 Ci/mmol) from Amersham International (Buckinghamshire, United Kingdom). The radiolabels were stored in ethanol at -20 ºC. Gli, Pin, and Tris from Sigma Chemical Co (St Louis, MO, USA). HEPES from Boehringer Mannheim (Baden-Wurttemberg, Germany). Dimehylsulphoxide (Me_2SO) from Merck Company (West point, USA). P1075 was kindly donated by Leo Pharmaceuticals (Ballerup. Denmark). All other chemicals and reagents were of analytical grade. Both P1075 and Pin were dissolved in Me_2SO (25 g/L) and were diluted as appropriate so that the final concentration of Me_2SO was less than 0.1%.

Animals Wistar rats (NWR, male, weighing 235±21 g, n=106), were provided by the Laboratory Animal Center of Institute of Pharmacology and Toxicology, Academy of Military Medical Sciences, Beijing, China.

Reno-vascular hypertension Reno-vascular hypertension was produced by coarctation of the abdominal aorta between the origin of the renal arteries, under ether anesthesia, as described by Liu *et al*[11]. The rats were used 30 d after the surgery. One day before the experiment, a polyethylene catheter was inserted into the carotid artery for blood pressure measurements with a two-channel physiological recorder (LMS-LB). Mean arterial pressure was 202±25 mmHg in RVHR and 140±11 mmHg in NWR. All animals were kept in a temperature-controlled room on a 14 h/10 h light/dark cycle and had free access to a standard rat chow diet and tap water.

Aorta strips All rats (NWR, n=55; RVHR, n=51) were decapitated and exsanguinated. Aorta strips were prepared as described in a previous study[12]. The preparations were then weighed and assigned into tissue holders and immersed in ice-cold HEPES-buffered physiological salt solution (PSS) containing (in mmol/L): NaCl 139, KCl 5, $CaCl_2$ 25, $MgCl_2$ 1.2, glucose 11, HEPES 5, gassed with 95% O_2/5% CO_2 and titrated to pH 7.40 with NaOH at 37 ºC.

Equilibrium binding experiments

Saturation assay Binding assays of [^{3}H]P1075 or [^{3}H]Gli were routinely performed in duplicate in 0.50 mL PSS containing 3–5 mg wet weight of aorta strips at 25 ºC or 37 ºC. Nonspecific binding, determined in the presence of 50 μmol/L unlabeled P1075 or 30 μmol/L Gli, accounted for 48.6%±6.4% or 44%±6% of total bound ligand under the conditions employed. Specific binding was obtained by subtracting the nonspecific binding from the total binding.

For saturation experiments, aorta strips were incubated with different concentrations of label (0.25-30 nmol/L) for 90 min. They were then washed by adding 9 mL of ice-cold quench solution (NaCl 154 mmol/L, Tris 50 mmol/L, pH 7.40) for 1 min, blotted, and dissolved hermetically over 2 h in 50 μL of 60% perchloric acid and 100 μL of 30% H_2O_2 at 80 ºC. The samples were supplemented with 2.5 mL of ethylene glycol ethyl ether and 5 mL of dimethylbenzene containing 1% 2-(4-tert-butylphenyl)-5-(4-biphenylyl)-1,3,4-oxadiazole for 8 h. Radioactivity was determined with liquid scintillation spectrometry (at an efficiency of 42%-55%). The equilibrium dissociation (K_D) and the maximum number of binding sites (B_{max}) of label were determined by Scatchard analysis, and Hill coefficient (n_H) was calculated from Hill equation.

Displacement assay Aorta strips were incubated with 5 nmol/L [^{3}H]P1075 or 3 nmol/L [^{3}H]Gli and unlabeled inhibitors of interest, then washed and determined as described above. Specific binding of [^{3}H]P1075 or [^{3}H]Gli in the presence of unlabeled drugs was normalized to percentage of specific binding in the absence of these drugs. The concentration of drug inhibiting 50% of specific labeled-ligand binding (IC_{50}) was analyzed using the weighted non-linear least-squares regression program. This program fits data assuming the presence of one or more binding sites and allows comparison of the relative goodness-of-fit using F-test. A two-site fit was accepted as superior to one-site fit only if significance exceeded P<0.05.

Kinetic assay To determine the association kinetics, the aorta strips were incubated with 3 nmol/L [^{3}H]Gli or 5 nmol/L [^{3}H]P1075 and aliquots were withdrawn at various time points for separation of bound and free ligand as described above. To measure the dissociation kinetics, the labels were equilibrated with aorta strips for 90 min. Dissociation was initiated by addition of a large excess of unlabeled ligands (Gli 30 μmol/L, P1075 50 μmol/L) and bound-label was determined at various time intervals ranging from 1 to 90 min. The constants of association and dissociation were calculated according to equations (1) $LN[B_{eq}\cdot(B\cdot B)^{-1}]=K_{app}\cdot t$, (2) $K_{app}=K_1\cdot[L]+K_2$, and (3) $LN(B\cdot B_{eq}^{-1})=-K_2\cdot t$ where B represents the amount of specific [^{3}H]Gli or [^{3}H]P1075 binding at dif-

ferent time points, B_{eq} denotes the amount of the receptor-label complex at equilibrium and K_{app} the apparent rate constant of association, which depends on the rate constants of the association and dissociation (K_1, K_2), and on the concentration of labeled ligand employed ([L]).

Statistical analysis Results are expressed as mean±SD. Statistical significance of differences between groups of means was assessed by ANOVA followed by Dunnet's test using the Instat Programme (Graphpad SAS Software, San Diego, USA) and was accepted at the $P<0.05$ level.

Results

[^{3}H]P1075 bindings [^{3}H]P1075 bound in a saturated manner to aorta preparations in NWR and RVHR within the concentration range employed. Scatchard analysis of the data suggested that in NWR aorta strips [^{3}H]P1075 bound to a single class of sites with a K_D value of 7.7±2.0 nmol/L, and B_{max} value of 26±8 pmol/g wet weight. In RVHR, [^{3}H]P1075 also bound to a single class of sites. The K_D value, however, increased ~1.5-fold and the B_{max} value showed no change compared with those in NWR (Figure 1, Table 1).

K_{ATP} opener P1075 and Pin, as well as blocker Gli, concentration-dependently inhibited specific [^{3}H]P1075 binding. However, only K_{ATP} opener P1075 and Pin were able to inhibit the specific [^{3}H]P1075 binding completely, whereas inhibition at saturation by Gli was incomplete only by up to 72% of maximal specific binding in NWR and RVHR

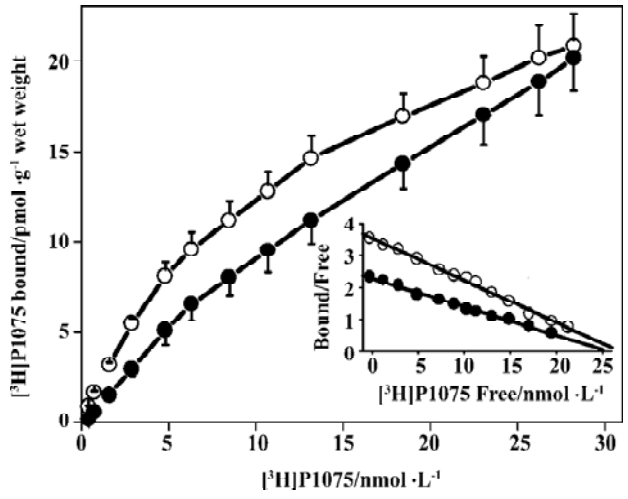

Figure 1. Equilibrium binding of [^{3}H]P1075 to aorta strips in normotensive Wistar rats (NWR, open circle) and reno-vascular hypertensive rats (RVHR, solid circle). Strips were incubated with varying concentrations (0.01–25.00 nmol/L) of [^{3}H]P1075 in a 0.50 mL assay volume at pH 7.40 and 37 ºC. Inset: Scatchard analysis of the specific binding data. The data are summarized in Table 1.

Table 1. Scatchard analysis of [^{3}H]P1075 binding in normotensive Wistar rats (NWR) and reno-vascular hypertensive rats (RVHR). Mean±SD. $^bP<0.05$ *vs* NWR.

Animals	*n*	K_D/ nmol·L^{-1}	B_{max}/ pmol·g^{-1} wet weight	n_H
NWR	5	7.7±2.0	26±8	1.2±0.4
RVHR	4	11.2±4.0^b	25±4	1.1±0.2

aorta preparations. Compared with those in NWR, inhibition curves of [^{3}H]P1075 binding to aorta strips in RVHR by these modulators were shifted to the right along the concentration axis (Figure 2). Statistical analysis with the *F*-test showed that the fit of inhibition curves by P1075 and Pin to the one-site model was significantly superior to two-site model, which corresponded to their n_H being close to unity. IC_{50} for the inhibition of [^{3}H]P1075 binding to RVHR aorta preparations by P1075 and Pin were increased by approximately 1.8- and 1.7-fold, respectively, compared with those in NWR. The change in IC_{50} value for inhibition of [^{3}H]P1075 binding by P1075 in RVHR aorta strips was in fair agreement with that in the K_D value obtained in the saturation equilibrium experiments in Figure 1.

Inhibition of [^{3}H]P1075 binding by Gli exhibited a biphasic plot (Figure 2) with n_H significantly different from unity (Table 3). In addition, statistical analysis with the *F*-test showed the fit of inhibition curve by Gli to the two-site

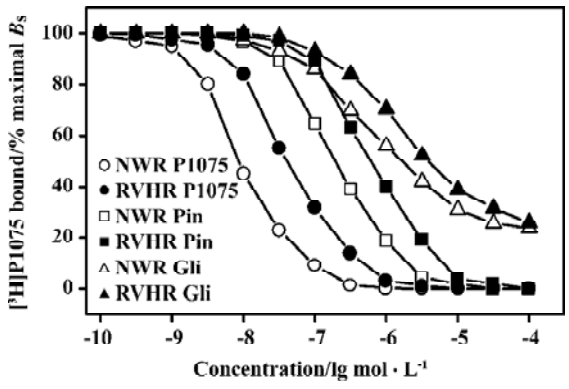

Figure 2. Inhibition of [^{3}H]P1075 binding to aorta strips by P1075, Pin, or Gli in NWR and RVHR. Aorta strips were incubated with 5 nmol/L [^{3}H]P1075 and increasing concentrations of these compounds for 90 min at 37 ºC. Specific binding (B_s) was 10.5±1.5 fmol·mg^{-1} wet weight, corresponding to 51.4%±6.4% of total binding. Data (as B_s) were fitted with one-site and two-site model; the fitting parameters were listed in Table 2. Depicted were representative plots of 4–5 separate experiments performed in duplicate.

Table 2. Analysis of inhibition curves in Fig 2 of [^{3}H]P1075 binding to aorta strips by K_{ATP} channel modulators. For experiment details see Figure 2. n=4-5 experiments. Mean±SD. ^cP<0.01 *vs* NWR.

Groups	Modulators	One-site fit		Two-site fit		F-test for hypothesis: one-site model is correct	
		IC_{50}/nmol·L^{-1}	n_H	$IC_{50,H}$/nmol·L^{-1}	$IC_{50,L}$/μmol·L^{-1}	F value	P[1)]
NWR	P1075	9.1±1.3	1.14±0.10	8.2±0.9	0.03±0.007	0.42	0.6651
	Pinacidil	200±44	1.16±0.14	181±42	1.0±0.2	0.76	0.4798
	Glibenclamide	589±46	0.79±0.08	204±22	3.0±0.5	164	<0.0001
RVHR	P1075	16.5±0.8^c	1.13±0.11	15.7±1.1	2.1±0.3	0.85	0.4429
	Pinacidil	337±36^c	1.10±0.13	258±34	1.4±0.2	1.65	0.2165
	Glibenclamide	1478±81^c	0.74±0.10	443±109^c	3.4±0.7	46.6	<0.0001

[1)] If P>0.05, the hypothesis will be accepted; If P<0.05, the hypothesis is rejected, and the fit of the two-site model is significantly superior, statistically, to the one-site model.

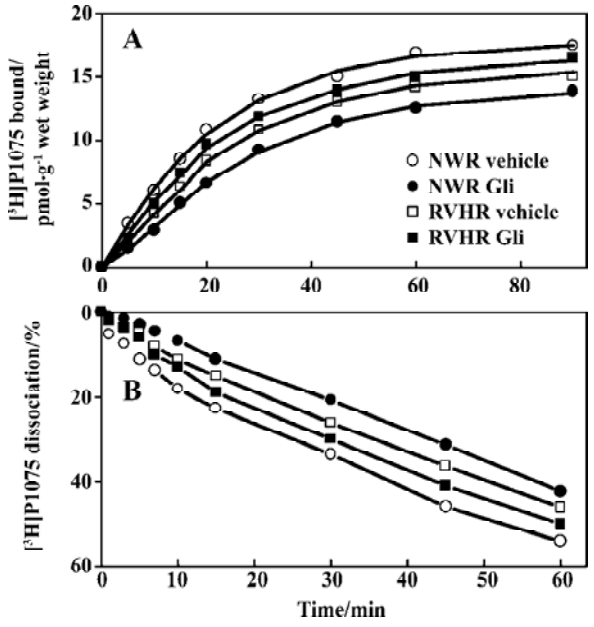

Figure 3. Modulation of association (A) and dissociation (B) kinetics of [^{3}H]P1075 (5 nmol/L) with aorta strips in NWR and RVHR by vehicle or Gli 100 μmol/L preincubated for 10 min. Data fitted equation 1 and 3, respectively. The traces were representative of 4-7 experiments.

model was significantly superior to one-site model (Table 2). These results suggested that two binding sites for Gli were present. The IC_{50} values for the high- and low-affinity binding sites of Gli were shown in Table 2. Their respective n_H values were found to be close to unity (not shown). IC_{50} value for inhibition of [^{3}H]P1075 binding in RVHR aorta strips by Gli at high affinity site increased by more than 2-fold compared with that in NWR aorta preparation, but there was no significant difference between IC_{50} values at the low affinity site in RVHR and in NWR (Table 2).

The kinetics of association and dissociation of [^{3}H] P1075, measured at large excess of label over binding sites, are illustrated in Figure 3. In NWR, association kinetics of [^{3}H]P1075 at 5 nmol/L followed a pseudo first-order kinetics, and the fit of this kinetics to equation 1 yielded a K_{app} value of 0.044±0.004 min^{-1}. After equilibrium was reached, dissociation of the receptor-label complex was initiated by addition of 50 μmol/L unlabeled P1075. The dissociation also followed a pseudo first-order kinetics with a K_2 value of 0.029±0.005 min^{-1}. Using equation 2, these values of K_{app} and K_2 allowed calculation of the second order rate constant of association, K_1 to 0.009±0.001 nmol·L^{-1}·min^{-1}. From these rate constants, K_D value of 3.3±1.0 nmol/L, where the large error in this value is explained by the propagation of errors, was calculated.

After NWR aorta strips were pretreated with Gli 100 μmol/L for 10 min, association and dissociation kinetics of [^{3}H]P1075 still followed the pseudo first-order kinetics. However, association and dissociation were slowed down with the reduced K_{app} and K_2 value, but with increased K_D value compared to those in vehicle (Table 3).

In RVHR, the association and dissociation of [^{3}H] P1075 with aorta strips were also fitted the pseudo first-order kinetics, but slower association and dissociation kinetics were observed with increased K_D value compared to those in NWR. Gli at 100 μmol/L preincubated with aorta strips for 10 min, did not alter the association and dissociation of [^{3}H]P1075 with RVHR aorta strips (Figure 3, Table 3).

[^{3}H]Gli binding experiments The competitive inhibition curve of 3 nmol/L [^{3}H]Gli binding to aorta strips in NWR and RVHR by unlabeled Gli exhibited biphasic plots with

Table 3. Modulation by vehicle or Gli 100 μmol/L, preincubated for 10 min, of the association and dissociation kinetics of [^{3}H]P1075 with aorta strips in NWR and RVHR. n=4–7 separate determinations performed in duplicate. Mean±SD. $^bP<0.05$, $^cP<0.01$ *vs* NWR, $^eP<0.05$, $^fP<0.01$ *vs* vehicle. For experiment details see Figure 3.

Animal groups	Pretreated factors	Association kinetics		Dissociation kinetics	
		K_{app}/min^{-1}	K_1/nmol·L^{-1}·min^{-1}	K_2/min^{-1}	K_D/nmol·L^{-1}
NWR	Vehicle	0.044±0.004	0.009±0.001	0.029±0.005	3.3±1.0
	Glibenclamide	0.031±0.002^f	0.002±0.001^f	0.020±0.005^e	8.3±2.1^f
RVHR	Vehicle	0.034±0.004^b	0.003±0.001^b	0.021±0.003^b	8.1±1.0^e
	Glibenclamide	0.035±0.004	0.003±0.001	0.022±0.004	8.5±1.2

n_H significantly different from unity (Figure 4, Table 4). Inhibition curves were fitted with the one-site and two-site model, respectively. Statistical analysis with the *F*-test showed that the fit of curves of the two-site model was significantly superior to the one-site model (Table 4). Thus, two distinct binding sites for [^{3}H]Gli were present in NWR and RVHR aorta preparations. In NWR aorta strips, the IC_{50} value for the inhibition of [^{3}H]Gli binding at the high- and low-affinity sites by unlabeled Gli was 18±2 nmol/L and 21±4 μmol/L, respectively. The fit of one-site model gave n_H equal to 0.80±0.09; a value in favor of heterogeneous class of binding sites with a negative cooperativity. In RVHR aorta strips, the IC_{50} value for inhibition of [^{3}H]Gli binding at low-affinity sites by unlabeled Gli showed no difference from that in NWR aorta preparations, but IC_{50} at high-affinity sites increased approximately 4 fold. Pin, at concentrations up to 500 μmol/L neither inhibited the [^{3}H]Gli binding to aorta strips in NWR nor in RVHR (Figure 4).

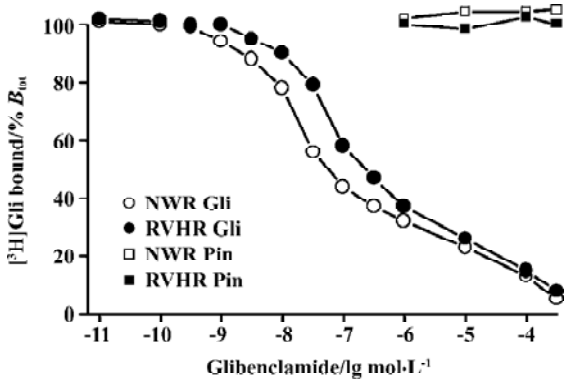

Figure 4. Inhibition of [^{3}H]glibenclamide (Gli) binding to aorta strips in NWR and RVHR by unlabeled Gli and Pin. Aorta strips were incubated with [^{3}H]Gli 3 nmol/L in the presence of various concentrations of unlabeled Gli or pinacidil for 90 min at 25 ºC. Depicted are representative plots. B_{tot} was 30.5±2.5 pmol·g^{-1} wet weight. The Data are summarized in Table 4.

[^{3}H]Gli binding to NWR aorta strips was rapid and approached equilibrium after a 40-50 min incubation period at 25 ºC (data not shown). After equilibrium was reached, the dissociation of [^{3}H]Gli-receptor complex was initiated by the addition of 30 μmol/L unlabeled Gli. Association and dissociation of [^{3}H]Gli followed pseudo first-order kinetics. The fit of the association and dissociation to equation 1 and 3 yielded K_{app} and K_2 of 0.046±0.004 and 0.007±0.001 min^{-1}, respectively. After NWR aorta strips were pretreated with Pin (100 μmol/L) for 10 min, association and dissociation

Table 4. Displacement of [^{3}H]Gli binding to aorta strips in NWR and RVHR by unlabeled Gli. For experiment details see Fig 4. Analysis with one-site model showed n_H was significantly different from unity. n=4-5 experiments performed in duplicate. Mean±SD. $^bP<0.05$, $^cP<0.01$ *vs* NWR.

Group	One-site fit		Two-site fit		*F*-test for hypothesis: one-site model is correct	
	IC_{50}/nmol·L^{-1}	n_H	$IC_{50,H}$/nmol·L^{-1}	$IC_{50,L}$/μmol·L^{-1}	*F* value	$P^{1)}$
NWR	35±7	0.80±0.09	18±2	21±4	171	<0.0001
SHR	54±9^b	0.82±0.12	59±4^c	22±6	142	<0.0001

[1)] If $P>0.05$, the hypothesis will be accepted; If $P<0.05$, the hypothesis is rejected, and the fit of the two-site model is significantly superior, statistically, to the one-site model.

of [^{3}H]Gli still followed pseudo first-order kinetics. However, when the association was retarded, K_{app} was reduced by 45.6%, but when the dissociation was accelerated, K_2 was increased approximately 2 fold (Table 5).

In RVHR aorta strips, association and dissociation of [^{3}H]Gli were also fitted pseudo first-order kinetics, but when association became slower, K_{app} was reduced by 39%, but when dissociation was faster, K_2 was increased 1.5-fold. From these kinetics, the K_D value calculated was increased 3.3-fold compared with those in NWR aorta strips. After RVHR aorta strips were pretreated with Pin 100 μmol/L for 10 min, the association and dissociation of [^{3}H]Gli were not altered. From these kinetics, the K_D value calculated was also unchanged (Table 5).

Discussion

Comparison of [^{3}H]P1075 binding in NWR with that in RVHR In the present study, saturation experiments in NWR showed that aorta strips [^{3}H]P1075 bound to a single class of sites with high affinity (K_D=7.7±2.0 nmol/L) and relatively low density (B_{max}=26±4 nmol·g^{-1} wet weight). These results are similar to those reported by Quast *et al*[13]. The K_D value determined here corresponded well to the potency of P1075 as a vasorelaxant agent[14]. The K_{ATP} opener P1075 and Pin, as well as blocker Gli, inhibited [^{3}H]P1075 binding according to the Law of Mass Action. The IC_{50} value (9.1±1.3 nmol/L) for inhibition of [^{3}H]P1075 binding by P1075 was in fair agreement with the K_D value obtained in the saturation experiments. The association and dissociation of [^{3}H]P1075 with NWR aorta strips were time-dependent and monoexponential, these kinetic experiments allow a calculation of K_D value of 3.3±1.0 nmol/L in reasonable agreement with the result of the saturation experiments (Table 1) and of competitive inhibition experiments (Table 2).

In the present study, [^{3}H]P1075 binding in RVHR aorta strips was reported. The binding data showed that [^{3}H]P1075 binding sites in RVHR aorta strips had similar qualities to those in NWR aorta preparations. However, some differences in [^{3}H]P1075 binding in RVHR aorta strips were found: (1) K_D value of [^{3}H]P1075 binding increased approximately 1.5-fold; (2) IC_{50} value for the inhibition of [^{3}H]P1075 binding by P1075 and Pin increased by 1.8- and 1.7-fold, respectively; (3) association and dissociation became slower. These results suggest that the affinity of [^{3}H]P1075 binding sites to K_{ATP} openers is reduced in RVHR aorta strips. Therefore, we suggest that chronic hypertension might reduce the affinity of binding sites for K_{ATP} openers in aorta. Furthermore, the B_{max} value of [^{3}H]P1075 binding to aorta strips and the maximum inhibition of [^{3}H]P1075 binding by P1075 and Pin showed no difference between RVHR and NWR. It is suggested that the number of [^{3}H]P1075 binding sites is not altered in RVHR aorta strips. The present findings might explain why the dilatation of isolated aorta precontracted with norepinephrine or KCl in response to activation of K_{ATP} channels by Pin was impaired in SHR, why dilatation of the basilar artery by aprikalim was impaired in stroke-prone SHR *in vivo*[9]; and why the action of levcromakalim on K_{ATP} channels in mesenteric artery muscle cells of SHR was decreased compared to normotensive rat cells[10]. The present findings also exclude the possibility that differences in response to Pin, aprikalim and levcromakalim are related to genetic differences between normotensive rats and SHR that are unrelated to hypertension.

Comparison of [^{3}H]Gli binding in NWR with RVHR In the present study, the binding of [^{3}H]Gli in NWR aorta strips was specific and reversible. Using a wide range of concentrations for Gli, we obtained evidence for the presence of both high and low affinity Gli-binding sites in aorta preparations: the former ranging from 1×10^{-11} to 1×10^{-7} mol/L

Table 5. Modulation by Pin(100 μmol/L) preincubated for 10 min, of the association and dissociation kinetics of [^{3}H]Gli binding to aorta strips in NWR and RVHR. n=4–7 separate determinations performed in duplicate. Mean±SD. ^bP<0.05, ^cP<0.01 *vs* NWR; ^eP<0.05, ^fP<0.01 *vs* Vehicle. For experiment details see Figure 3.

Animal groups	Pretreated factors	Association kinetics		Dissociation kinetics	
		K_{app}/min^{-1}	K_1/nmol·L^{-1}·min^{-1}	K_2/min^{-1}	K_D/nmol·L^{-1}
NWR	Vehicle	0.046±0.004	0.013±0.001	0.007±0.001	0.55±0.14
	Pinacidil	0.025±0.007^e	0.004±0.002^f	0.014±0.003^e	3.50±0.87^f
SHR	Vehicle	0.028±0.009^c	0.006±0.003^c	0.011±0.002^b	1.83±0.67^c
	Pinacidil	0.026±0.005	0.005±0.002^f	0.012±0.004	2.00±0.42

K_{app} denote apparent rate constant of association, K_1: rate constant of association, K_2: rate constant of dissociation.

with nanomolar affinity constant, and the latter from 1×10^{-7} to $1\times10^{-3.5}$ mol/L with micromolar affinity constant. Our results are consistent with those reported previously in retarding vascular smooth muscle[12].

[^{3}H]Gli binding in these preparations had similar qualities to those in NWR. However, [^{3}H]Gli exhibited slower association and faster dissociation with an increased K_D value in RVHR than in NWR (Table 5). The IC_{50} value for the inhibition of [^{3}H]Gli binding by Gli at the high affinity component was increased, but was unchanged at the low affinity component. This indicates that the affinity of high affinity sulfonylurea sites is decreased in RVHR aorta strips.

Interaction of binding sites for K_{ATP} openers and blockers in NWR In the present study, [^{3}H]P1075 bound to a single site in NWR aorta strips, whereas [^{3}H]Gli bound to both high and low affinity sites in NWR aorta strips. [^{3}H]P1075 binding can be inhibited by opener P1075 and Pin, but not completely by blocker Gli, whereas [^{3}H]Gli binding could be inhibited by Gli, but not by Pin. Furthermore, [^{3}H]P1075 and [^{3}H]Gli binding present a similar association rate (0.044 and 0.046 nmol·L^{-1}·min^{-1}) but different dissociation rate(0.029 and 0.007 nmol·L^{-1}·min^{-1}, respectively). The most plausible explanation for these results is that K_{ATP} openers and blockers bind to different binding sites. In addition, Pin, preincubated with NWR aorta strips, slowed down the association of [^{3}H]Gli and sped up the dissociation of [^{3}H]Gli-receptor complex. It is suggested that the binding sites for K_{ATP} channel opener Pin negatively allosterically couple to the binding sites for K_{ATP} channel blocker Gli. The plausible mechanism is that the binding of Pin to its sites in SURs brings about configuration alteration in the Gli-sites, which hinders the binding of [^{3}H]Gli to its sites and facilitates faster release of the radiolabel from receptor-label complex. Likewise, Gli, preincubated with NWR aorta strips, also slowed down the association of [^{3}H]P1075 and sped up the dissociation of [^{3}H]P1075-receptor complex. It was indicated that the sites for K_{ATP} channel blocker Gli also negatively allosterically coupled to the sites for K_{ATP} channel opener P1075. Alternatively, Gli down-regulates the affinity of the P1075 binding sites through inducing its configuration alteration. The evidence for a negative allosteric coupling between the sites for P1075 and Gli has been previously obtained for the rat aorta[8]. In the experiments, however, rat aorta preparations were only labeled with [^{3}H]P1075, and the dissociation of [^{3}H]P1075-receptor complex was initiated by addition of an excess of Gli rather than P1075 after [^{3}H]P1075 binding reached equilibrium. In the present study, aorta strips were pretreated with Gli, and dissociation was initiated by addition of an excess of P1075 rather than Gli. A negative allosterism between the sites for openers and blockers was identified in a different experimental protocol in this study.

Interaction of binding sites for K_{ATP} openers and blockers in RVHR In the present paper, we studied the interaction between the binding sites for K_{ATP} openers and blockers in RVHR aorta strips. The evidence that K_{ATP} openers and blockers bound to different binding sites was also obtained in RVHR. In contrast to NWR, pretreatment with Gli failed to alter the association and dissociation kinetics of [^{3}H]P1075 with aorta strips in RVHR. It is suggested that the negative allosteric action of sulfonylurea Gli on the binding sites for the opener P1075 was damaged in RVHR aorta strips. Similarly, pretreatment of Pin did not alter the association and dissociation kinetics of [^{3}H]Gli with RVHR aorta strips. It is indicated that the negative allosteric action of opener Pin on the binding sites for sulfonylurea Gli is also damaged in SHR aorta strips.

In conclusion, the affinity of P1075 binding sites and high-affinity sulfonylurea binding sites are reduced, and the negative allosteric interactions between the two binding sites are impaired in RVHR aorta strips.

References

1 Ashcroft SJ, Ashcroft FM. Properties and functions of ATP-sensitive K-channels. Cell Signal 1990; 2: 197–214.

2 Nichols CG, Lederer WJ. Adenosine triphosphate-sensitive potassium channels in the cardiovascular system. Am J Physiol 1991; 261: H1675–86.

3 Jackson WF. Arteriolar tone is determined by activity of ATP-sensitive potassium channels. Am J Physiol 1993; 265: H1797–803.

4 Davies NW, Standen NB, Stanfield PR. ATP-dependent K^+ channels of muscle cells: their properties, regulation, and possible functions. J Bioenerg Biomembr 1991; 23: 509–35.

5 Inagaki N, Gonoi T, Clement JP 4th, Namba N, Inazawa J, Gonzalez G, *et al*. Reconstitution of $I_{K_{ATP}}$: an inward rectifier subunit plus the sulfonylurea receptor. Science 1995; 270: 1166–70.

6 Inagaki N, Gonoi T, Clement JP 4th, Wang CZ, Aguilar BL, Bryan J, *et al*. A family of sulfonylurea receptors determines the pharmacological properties of ATP-sensitive potassium channels. Neuron 1996; 16: 1011–7.

7 Löffler C, Quast U. Pharmacological characterization of the sulphonylurea receptor in rat isolated aorta. Br J Pharmacol 1997; 120: 476–80.

8 Bray KM, Quast U. Specific binding site for K^+ channel openers in rat aorta. J Biol Chem 1992; 267: 11689–92.

9 Kitazono T, Heistad DD, Faraci FM. ATP-sensitive potassium channels in the basilar artery during chronic hypertension. Hypertension 1993; 22: 677–81.

10 Ohya Y, Setoguchi M, Fujii K, Nagao T, Abe I, Fujishima M. Impaired action of levcromakalim on ATP-sensitive K^+ channels in mesenteric artery cells from spontaneously hypertensive rats. Hyperten-

sion 1996; 27: 1234–9.

11 Liu J, He ZY, Xu SM, Liu FY, Wang PY. Inositol 1,4,5-triphosphate receptor (IP3Rs) in myocardial nuclei involved in pressure overload-induced hypertrophy of rat heart. Acta Physiol Sin 2001; 53: 281–5.

12 Zhu QL, He HM, Xiao WB, Wang H. Modulation by nucleotides of binding sites for [^{3}H]glibenclamide in rat aorta and cardiac ventricular membranes. J Cardiovasc Pharmacol 2001; 37: 522–31.

13 Quast U, Bray KM, Andres H, Manley PW, Baumlin Y, Dosogne J. Binding of the K^+ channel opener [^{3}H]P1075 in rat isolated aorta: relationship to functional effects of openers and blockers. Mol Pharmacol 1993; 43: 474–81.

14 Higdon NR, Khan SA, Buchanan LV, Meisheri KD. Tissue and species variation in the vascular receptor binding of ^{3}H-P1075, a potent K_{ATP} opener vasodilator. J Pharmacol Exp Ther 1997; 280: 255–60.

Full-length article

Ca^{2+} participates in α_{1B}-adrenoceptor-mediated cAMP response in HEK293 cells[1]

Yao SONG, Yun-fang LI, Er-dan DONG, Qi-de HAN, You-yi ZHANG[2]

Institute of Vascular Medicine, Peking University Third Hospital, Key Laboratory of Molecular Cardiovascular Sciences, Ministry of Education, Beijing 100083, China

Key words

alpha-1 adrenergic receptors; HEK293 cells; cyclic AMP; signal transduction; phospholipase C; protein kinase C; protein-tyrosine kinase; calcium

[1] Project supported by the National Natural Science Foundation of China (No 30171083) and the Major State Basic Research Development Program of the People's Republic of China (No G2000056906).
[2] Correspondence to You-yi ZHANG, MD, PhD. Phn 86-10-8280-2306. Fax 86-10-8280-2306. E-mail zhangyy@bjmu.edu.cn

Received 2004-05-31
Accepted 2004-09-29

doi: 10.1111/j.1745-7254.2005.00018.x

Abstract

Aim: To investigate the α_{1B}-adrenoceptor (α_{1B}-AR)-mediated cAMP response and underlying mechanisms in HEK293 cells. **Methods:** Full-length cDNA encoding α_{1B}-AR was transfected into HEK293 cells using the calcium phosphate precipitation method, and α_{1B}-AR expression and cAMP accumulation were determined by using the saturation radioligand binding assay and ion-exchange chromatography, respectively. **Results:** Under agonist stimulation, α_{1B}-AR mediated cAMP synthesis in HEK293 cells, and blockade by PLC-PKC or tyrosine kinase did not reduce cAMP accumulation induced by NE. Pretreatment with pertussis toxin (PTX) had little effect on basal cAMP accumulation as well as norepinephrine (NE)-stimulated cAMP accumulation. In addition, pretreatment with cholera toxin (CTX) neither mimicked nor blocked the effect induced by NE. The extracellular Ca^{2+} chelator egtazic acid (EGTA), nonselective Ca^{2+} channel blocker $CdCl_2$ and calmodulin (CaM) inhibitor W-7 significantly reduced NE-induced cAMP accumulation from 1.59%±0.47% to 1.00%±0.31%, 0.78%±0.23%, and 0.90%±0.40%, respectively. **Conclusion:** By coupling with a PTX-insensitive G protein, α_{1B}-AR promotes Ca^{2+} influx via receptor-dependent Ca^{2+} channels, then Ca^{2+} is linked to CaM to form a Ca^{2+}-CaM complex, which stimulates adenylyl cyclase (AC), thereby increasing the cAMP production in HEK293 cell lines.

Introduction

It is well known that the classic signaling pathway of α_1-adrenoceptor (AR) is to couple with the $G_{q/11}$ protein and then stimulate phosphatidylinositol turnover[1,2]. However, it has been recently discovered that α_1-AR can also stimulate adenosine 3':5'-cyclic monophosphate (cAMP) accumulation in several cell lines, tissues and organs[3–12]. Our previous study showed that each of the three α_1-AR subtypes was able to mediate cAMP generation in human embryonic kidney 293 (HEK293) cells. As for the signal transduction pathway by which α_1-AR mediates cAMP production, several studies have shown that cAMP production is secondary to the α_1-AR-induced phospholipase C (PLC)-phosphokinase C (PKC) stimulation[10–12], which cross-talked with AC[13]. Horie *et al*[14] found that in a Chinese hamster ovary (CHO) cell line transfected with α_{1B}-AR, none of the PKC inhibitor, the Ca^{2+} ionophore, or the pertussis toxin (PTX) was able to inhibit NE-induced cAMP accumulation, whereas anti-$G_{s\alpha}$ antiserum inhibited the response, which suggests that α_{1B}-AR activates AC and increases intracellular cAMP by directly coupling with $G_{s\alpha}$. In fact the signal transduction pathway involved in α_{1B}-AR-mediated cAMP generation remains unclear. Therefore, we transfected HEK293 cells (human embryonic kidney 293 cell line, which does not express any other adrenoceptors except native β_2-AR) with full-length cDNA encoding α_{1B}-AR and selected for subcloning cell lines stably expressing α_{1B}-AR. This was a good model to investigate the regulating effects of the PLC-PKC pathway, the tyrosine kinase pathway, the Ca^{2+} signal system, and G proteins on cAMP production.

Materials and methods

Norepinephrine (NE), phenylephrine (PE), methoxamine (ME), prazosin (PRZ), propranolol (Prop), Triton X-100,

cAMP, 3-isobutyl-1-methyl-xanthine (IBMX), pyruvic acid, hygromycin B, cyclopiazonic acid (CPA), phorbol 12-myristate 13-acetate (PMA), genistein, tyrphostin A25, egtazic acid (EGTA), nifedipine (Nif), $CdCl_2$, PTX, and cholera toxin (CTX) were from Sigma Chemical Co (St Louis, USA); BAPTA/AM, Ro-31-8220, calphostin C, and W-7 were products of Calbiochem-Novabiochem International (San Diego, USA). BE2254 {[2-β(4-hydroxyphenyl)-ethylaminomethyl]-tetralone} was from Beiersdorf Co (Hamburg, Germany); [^{3}H]adenine was from Amersham Biosciences (Piscataway, United States); 2,5-diphenyl-oxazole (PPO) was bought from Farco-Pharma (Koln, Germany); fetal bovine serum (FBS) and Dulbecco's Modified Eagle's Medium (DMEM) were from Hyclone China (Beijing, China); HEK293 (human embryonic kidney 293) cells and full-length cDNA of hamster α_{1B}-AR (pREP4) were kindly provided by Prof Kenneth P MINNEMAN (Emory University, USA).

Transfection of HEK293 cells with cDNA encoding α_{1B}-AR using the calcium phosphate precipitation method HEK293 cells were cultured in DMEM containing 10% FBS at 5% CO_2 at 37 ºC. The cells were transfected with pREP4/α_{1B}-AR by calcium phosphate precipitation at 70% confluence and selected with hygromycin B (0.05 g/L). Three days later the cells were diluted and planted in a 96-well dish, with 0-5 cells in each well. After 2 to 3 cloning sessions, a cell line stably expressing α_{1B}-AR was obtained. The cells were continuously cultured and kept in DMEM containing selective antibiotics.

Determination of α_{1B}-AR expression by a saturation radioligand binding assay The cells were grown in 75-mL flasks and harvested in PBS. After centrifugation at 3000×*g*, 4ºC for 10 min then at 21 000×*g*, 4ºC, for 20 min, the pellet was resuspended with 30 mL PBS and kept on ice. The ligand-binding properties of the receptors were determined in a series of radioligand binding studies using the α_1-AR antagonist radioligand [^{125}I]BE2254, which was radioiodinated to theoretical specific activity as described by Engel and Hoyer[19]. Saturation reactions (total volume 250 μL) containing 100 μL or 50 μL PBS with 1% bovine serum albumin (BSA), 50 μL of [^{125}I] BE2254 at different concentrations (15 000-500 000), and 100 μL cell membranes. Nonspecific binding was determined in the presence of 50 μmol/L phentolamine. Reactions were allowed to proceed for 20 min at 37 ºC. Reactions were terminated by adding 7 mL ice-cold Tris-HCl buffer (pH 7.4) and the mixture was filtered onto glass fiber filters. Filters were washed twice with 7 mL ice-cold Tris-HCl buffer and then dried. Bound radioactivity was measured using an auto-gamma counter. Binding data were analyzed by using nonlinear regression and Scatchard analysis (GraphPad Prizm Software) on a computer and thus the dissociation constant (K_D) between the receptor and antagonist and maximal bound capacity (B_{max}) could be obtained. Protein content was determined by using the Coomassie protein quantitation method.

cAMP determination in intact cells using ion-exchange chromatography HEK293 cells expressing α_{1B}-AR were cultured in 24-well dishes at 37 ºC, 5% CO_2, with 2.5×10^5 cells per mL medium. When the cells were fully confluent, the medium was changed, and [^{3}H]adenine 18.5 MBq (0.5 mCi) was added into each well. After incorporation for 4 h at 37 ºC in 5% CO_2 , the medium was discarded and the cells were washed twice with pre-warmed Krebs' solution. After addition of antagonists in 1 mL Krebs' solution containing 200 μmol/L IBMX and incubation for 30 min, the cells were incubated for a further 20 min with different concentrations of agonists. The reaction was terminated by adding 100 μL of 77% trichloracetic acid, followed by a centrifugation at 3000×*g*, 4 ºC, for 20 min. Then 50 μL supernatant was transferred into 3 mL scintillation liquid to measure radioactivity as total activity (cpm). The remaining supernatant was applied to Dowex columns and aluminal columns. After being washed with distilled water, the aluminal columns were eluted with 2 mL Tris-HCl (pH 8.0), and the radioactivities of the eluates were measured as newly-produced cAMP. cAMP accumulation is equal to proportion of total radioactivity represented by newly-produced cAMP as a percentage. The formula is as follows:

$$\text{cAMP accumulation} = \frac{\text{Radioactivity of newly-produced cAMP (cpm)} \times 100\ \%}{\text{Total radioactivity (cpm)} \times 22}$$

Twenty-two is the volume constant.

Statistical analysis Results are expressed as mean±SD. To compare mean values between two groups, Student's *t*-test was used; ANOVA was used for comparison among three or more groups. $P<0.05$ was considered statistically significant.

Results

Density of α_{1B}-AR HEK293 cells transfected with α_{1B}-AR were cultured under selective pressure from hygromycin B for several passages, thus we obtained a cell line stably expressing α_{1B}-AR. The density of α_{1B}-AR was 2004±138 pmol/g as determined by a radioligand binding assay (n=5, data not shown).

cAMP accumulation induced by stimulation of α_{1B}-AR In blank HEK293 cells , NE (100 nmol/L–30 μmol/L),

PE (100 nmol/L–300 μmol/L), or ME (1 μmol/L–1 mmol/L) did not cause cAMP accumulation in the presence of propranolol, an antagonist of β-AR (data not shown).

However, NE, PE, and ME all increased cAMP accumulation in HEK293 cells transfected with α_{1B}-AR in a dose-dependent manner, with R_{max}/pD_2 of (3.32%± 0.34%)/(6.15±0.33) (n=7), (2.43%±0.46%)/(5.37±0.55) (n=8), and (0.66%±0.17%)/(3.79±0.39) (n=6), respectively (Figure 1), all of which were antagonized by prazosin (100 nmol/L) (Data not shown).

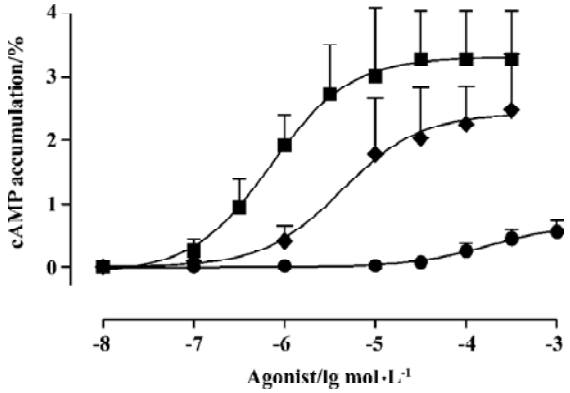

Figure 1. NE (■, n=7), PE (◆, n=8) and ME (●, n=6) induced cAMP synthesis in a dose-dependent manner in the presence of propranolol (1 μmol/L) in HEK293 cells transfected with α_{1B}-AR.

PLC-PKC pathway In the presence of propranolol (10 μmol/L) to block β_2-AR in HEK293 cells, NE (10 μmol/L) increased cAMP accumulation from a basal level of 0.28%± 0.07% to 4.93%±1.13% (n=11, P<0.01). The PLC inhibitor, U73122, had no effect on the NE-induced cAMP accumulation at 1 μmol/L (4.91%±1.43%, n=11) or 10 μmol/L (4.97%±1.15%, n=11, Fig 2A) for 1 h incubation. Neither U73122 itself (0.26%±0.09%, n=5) nor the vehicle alone (Me_2SO, 0.1% v/v final, 0.26%±0.05%, n=3) affected the basal level of cAMP (0.28%±0.07%, n=11). Similarly, when PKC inhibitors were added, neither Ro31-8220 (5.37%± 1.33%) and (4.99%±1.56%, n=8) nor calphostin C (5.14%± 1.09%) and 4.70%±1.28%, n=8) at 10 nmol/L and 100 nmol/L affected NE-induced cAMP production (4.93%± 1.13%, n=11, Figure 2B). The two inhibitors had no effect on the basal cAMP level (0.24%±0.07%, n=5, and 0.22%± 0.09%, n=5, respectively, *vs* 0.28%±0.07%, n=11). To further clarify the role of PKC in this response, we examined whether PKC activator had any effect on cAMP synthesis. Without any AR agonist or antagonist, pretreatment with 1, 10, and 100 nmol/L PMA did not increase cAMP synthesis,

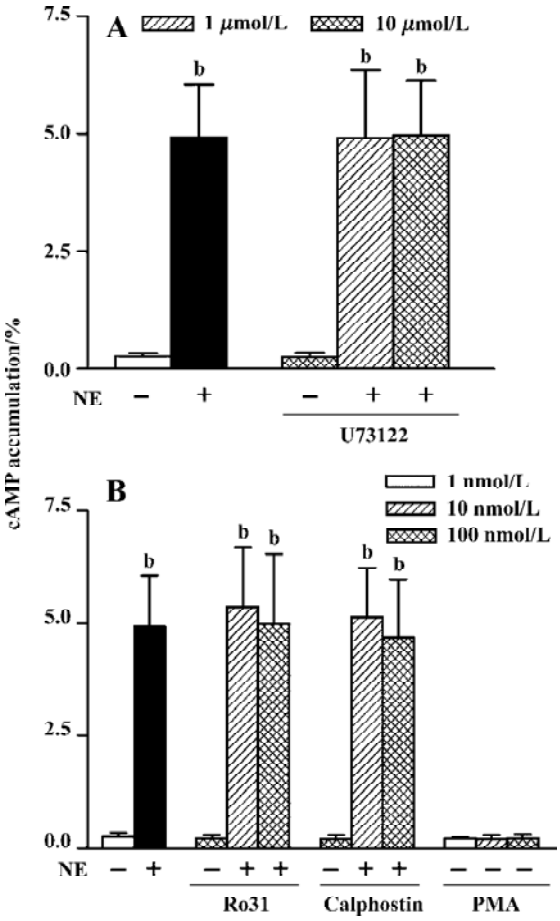

Figure 2. (A) NE-induced cAMP accumulation and the effect of U73122 (n=11) in the presence of 10 μmol/L propranolol in HEK293 cells expressing α_{1B}-AR. (B) NE-induced cAMP accumulation and the effects of Ro31 and calphostin C (n=8) in the presence of 10 μmol/L propranolol and cAMP accumulation in the presence of PMA at 1–100 nmol/L (n=7), respectively. Mean±SD. ^bP<0.05 *vs* basal accumulation.

the levels of which were (0.23%±0.03%, n=7), (0.22%± 0.08%, n=7), and (0.24%±0.08%, n=7), respectively, showing no significant difference compared with the basal level (0.28%±0.07%, n=11).

Tyrosine kinase signaling pathway The effects of two kinds of tyrosine kinase inhibitors, tyrphostin A25 and genistein, on NE-induced cAMP synthesis were examined. Tyrphostin A25 and genistein (0.30%±0.07% and 0.30%± 0.04%, n=5, respectively) or the vehicle alone (Me_2SO, 0.1% v/v final, 0.26%±0.03%, n=3) had no effect on the basal cAMP level (0.28%± 0.07%, n=11). After pretreating cells with tyrphostin A25 or genistein at 1 μmol/L and 10 μmol/L for 1 h, neither tyrphostin A25 (4.98%±1.33% and 4.75%± 1.07% at the two concentrations, respectively, n=7) nor genistein (4.97%±1.30% and 4.69%±0.62%, respectively,

n=7) influenced NE-induced cAMP synthesis (4.93%± 1.13%, *n*=11 in the presence of propranolol 10 μmol/L) (Figure 3).

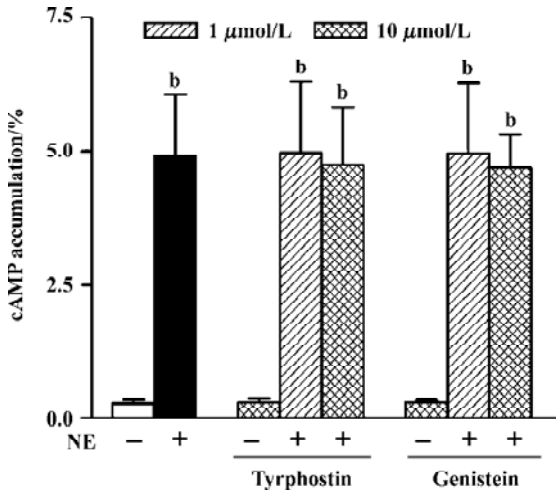

Figure 3. The effects of tyrphostin A25 and genistein (*n*=7) on NE-induced cAMP accumulation in the presence of 10 μmol/L propranolol in HEK293 cells transfected with α_{1B}-AR. Mean±SD. $^{b}P<0.05$ *vs* basal accumulation.

Regulation of cAMP response by G proteins After incubating cells with PTX 500 μg/L for 16 h, the effects of PTX on basal or NE-induced cAMP accumulation were examined. The results showed that PTX neither had any effect on basal cAMP (0.31%±0.07% *vs* 0.23%±0.07%, *n*=8) nor affected the NE-induced cAMP response (1.76%±0.50% *vs* 1.52%±0.44%, *n*=8, Figure 4). In order to examine whether α_1-AR mediates cAMP response by directly coupling with the G_s protein, we compared cAMP accumulation upon stimulation of the G_s protein after incubation with 500 μg/L CTX for 3 h with NE-induced cAMP accumulation. The results showed that cAMP accumulation induced by CTX alone was significantly higher than that induced by 10 μmol/L NE (2.50%±0.60% *vs* 1.52%±0.44%, *n*=8, *P*<0.05), and when CTX and NE were used simultaneously, cAMP accumulation (5.24%±1.37%, *n*=8) was significantly higher than their combined effect when used alone (*P*<0.05, Figure 4).

Regulating effects of Ca^{2+} signaling system Because α_1-AR can induce the release of the IP_3-sensitive Ca^{2+} store, CPA, a Ca^{2+}-ATPase inhibitor, was used to block Ca^{2+} being taken in sarcoplasmic reticulum again so as to increase $[Ca^{2+}]_i$ and deplete the Ca^{2+} store. The results showed that CPA 10 μmol/L alone did not increase cAMP accumulation (0.20%±0.03% *vs* 0.22%±0.12%, *n*=8), neither did it have any effect on NE-induced cAMP production (1.63%±0.56%, *n*=8 *vs* 1.59%±0.47%, *n*=9, Figure 5A).

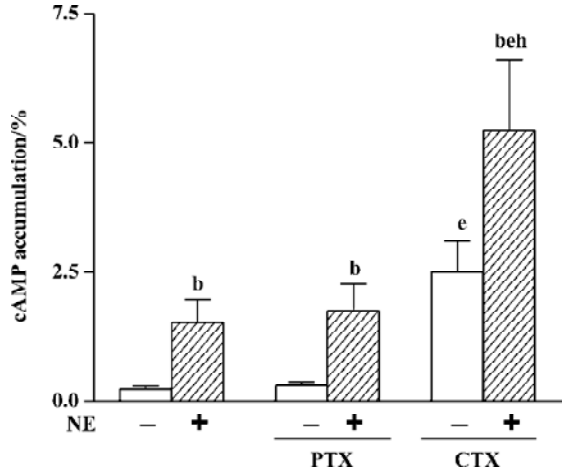

Figure 4. The effects of PTX 500 μg/L and CTX on basal and NE-induced cAMP accumulation (*n*=8) in the presence of propranolol 10 μmol/L in HEK293 cells transfected with α_{1B}-AR. Mean±SD. $^{b}P<0.05$ *vs* basal accumulation. $^{e}P<0.05$ *vs* NE-induced cAMP accumulation. $^{h}P<0.05$ *vs* CTX-induced cAMP accumulation.

In addition, the influence of the Ca^{2+} influx on cAMP synthesis was studied. It was found that NE-induced cAMP accumulation under Ca^{2+}-free condition was equal to that when Ca^{2+} was present (1.63%± 0.40% *vs* 1.59%±0.47%, *n*=9). However, when an extracellular Ca^{2+} chelator, EGTA (50 μmol/L), was added in Ca^{2+}-free Krebs buffer to pretreat the cells for 1 h, the NE-induced cAMP synthesis was obviously reduced (1.00%±0.31%, *n*=9, *P*<0.05, Figure 5B), whereas 10 μmol/L intracellular Ca^{2+} chelator, BAPTA/AM, had no effect on the NE-induced cAMP response under Ca^{2+}-free conditions (1.62%±0.58% *vs* 1.59±0.47%, *n*=9). There was no further inhibition on cAMP synthesis when BAPTA was used in combination with EGTA (1.03%±0.28% *vs* 1.00%±0.31%, *n*=9, Figure 5B).

To find out what type of Ca^{2+} channel admitted Ca^{2+}, we examined the effects of two kinds of Ca^{2+} channel blockers on cAMP response and found that nifedipine 10 μmol/L (L-type Ca^{2+} channel blocker) did not affect the NE-induced cAMP synthesis (1.47%±0.38% *vs* 1.59%±0.47%,*n*=9), whereas $CdCl_2$ 1 mmol/L (nonselective Ca^{2+} channel blocker) obviously reduced NE-induced cAMP accumulation (from 1.59%±0.47% to 0.78%±0.23%, *n*=9, *P*<0.05, Figure 5C). Moreover, when pretreating cells with W-7, a calmodulin (CaM) inhibitor, NE-induced cAMP synthesis decreased markedly (0.90%± 0.40%, *n*=8, *P*<0.05, Figure 5C), and the extent of decrease was similar to that induced by EGTA or $CdCl_2$ (*P*>0.05), while neither of them had any effect on the basal cAMP level.

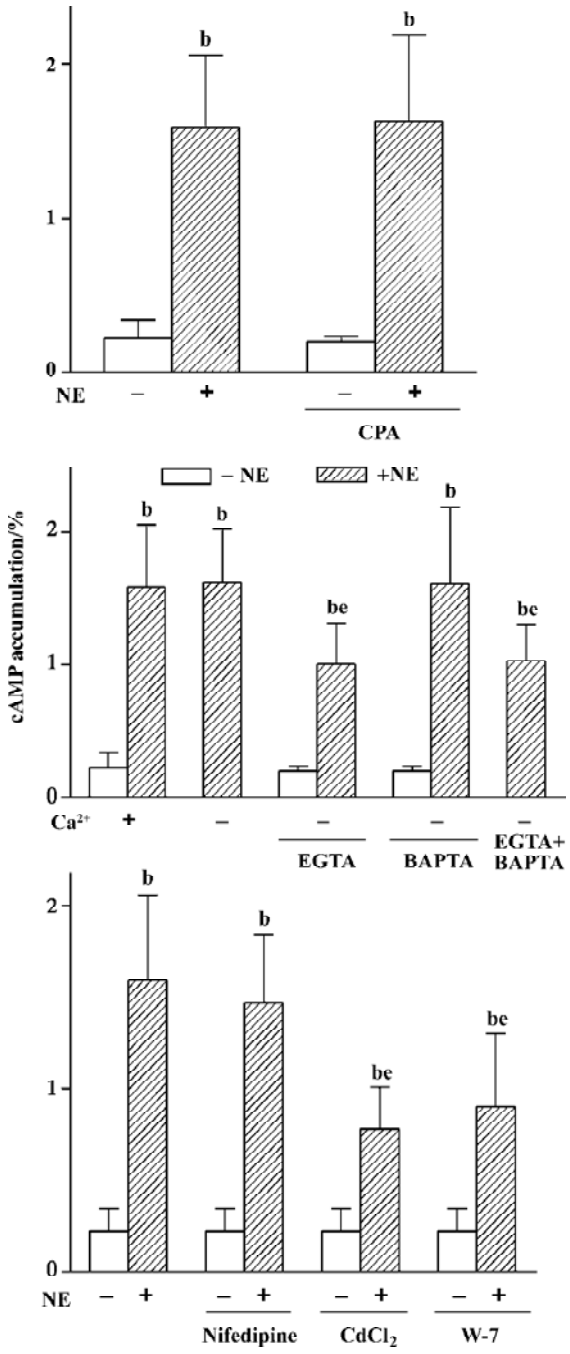

Figure 5. (A) NE-induced cAMP accumulation (n=9) and the effect of CPA 10 μmol/L (n=8) in the presence of propranolol 10 μmol/L in HEK293 cells transfected with α_{1B}-AR. (B) NE-induced cAMP response in Krebs' buffer and in Ca^{2+}-free Krebs' buffer, and the effects of EGTA 50 μmol/L, BAPTA 10 μmol/L , and EGTA plus BAPTA (n=9) on NE-induced cAMP response under Ca^{2+}-free conditions in the presence of propranolol 10 μmol/L. (C) NE-induced cAMP response and the effects of nifedipine 10 μmol/L (n=9), $CdCl_2$ 1 mmol/L (n=9), and W-7 500 μmol/L (n=8) in the presence of propranolol 10 μmol/L in HEK293 cells transfected with α_{1B}-AR. Mean±SD. $^bP<0.05$ *vs* basal accumulation. $^eP<0.05$ *vs* NE-induced cAMP accumulation.

Discussion

Several studies have demonstrated that α_{1B}-AR mediates the cAMP response in HEK293 cells. However, the signaling pathway through which α_1-AR mediates the cAMP response is unknown. Many studies have indicated that besides its classical signaling pathway, α_1-AR can stimulate many other signal transduction pathways as well, such as the tyrosine kinase pathway[15-18], the phospholipase A_2-arachidonic acid (PLA_2-AA) signaling system[20], etc. Moreover, α_1-AR also associates with other signaling pathways through its classical signal transduction pathway and consequently produces cross-talk. cAMP is a second messenger, a product of ATP catalyzed by adenylyl cyclase (AC), and a substrate of phosphodiesterase (PDE). There are at least 10 isozymes of AC. Besides the G_s and G_i proteins, many factors have been found to regulate their activities[21,22]. In the present study, we investigated the underlying mechanism involved in α_1-AR-mediated cAMP synthesis using HEK293 cells transfected with α_{1B}-AR.

PLC-PKC pathway α_1-AR preferentially activates its classical signaling pathway. It stimulates PLC by coupling with the $G_{q/11}$ protein, then PLC hydrolyzes PIP_2 to produce IP_3 and DAG, which induces Ca^{2+} release and stimulates PKC, thereby producing biological effects. It has been reported that in some cell lines transfected with α_1-AR subtypes, α_1-AR first stimulates PI turnover to activate PKC, and then stimulates AC. This means that α_1-AR-mediated cAMP response is secondary to the PLC-PKC pathway[10-12]. However, our results indicated that neither the PLC antagonist, U73122, nor the PKC antagonists, Ro31 and calphostin C, inhibited α_1-AR-mediated cAMP synthesis, and the PKC activator, PMA, did not increase cAMP accumulation. Furthermore, there was no influence on cAMP synthesis when using the Ca^{2+}-ATPase inhibitor, CPA, to block Ca^{2+} restoration and thus deplete the Ca^{2+} pool. All of the above suggests the taches lying in downstream of PLC in the classical pathway are not connected with α_1-AR-mediated cAMP response.

Tyrosine kinase signal transduction pathway The tyrosine kinase signal transduction pathway relates closely to the classical signaling pathway of α_1-AR. Some studies have shown that tyrosine kinase probably participates in α_1-AR-mediated biological effects[15-18]. In our previous study, we found that the major functional α_1-AR subtype of the vascular bed in rat hind legs was α_{1A}-AR, and that tyrosine kinase antagonists could dose-dependently reduce the vascular contractive response to NE. Moreover, tyrosine kinase antagonists can inhibit α_1-AR-mediated increase in intracellular Ca^{2+} in HEK293 cells[23], showing that α_1-AR can

activate tyrosine kinase. It is also known that tyrosine kinase can indirectly stimulate AC through the PLC-γ-IP_3/DAG pathway, which results in intracellular Ca^{2+} mobilization and stimulation of PKC[22]. Since we have confirmed that α_1-AR does not mediate cAMP synthesis through the PLC-PKC pathway in HEK293 cells, the possibility mentioned above can be excluded. Although it is known that tyrosine kinase can indirectly stimulate AC through the PLC-γ-IP_3/DAG pathway[21], this would not happen in HEK293 cells because our study indicated that the PLC-PKC pathway was not involved in α_1-AR-mediated cAMP accumulation. However, whether tyorsine kinase plays a role through other pathways or taches is unclear. In our present study, two kinds of tyrosine kinase inhibitors, different in structure and mechanism, exerted no influence on NE-induced cAMP synthesis, suggesting that tyrosine kinase is not involved in α_{1B}-AR-mediated cAMP response in HEK293 cells.

Regulation of cAMP response by G proteins α_1-AR is a typical G protein coupled receptor, whose classical signaling pathway is to couple with the $G_{q/11}$ protein. But it has been found that α_1-AR also couples with G_s and G_i proteins[14,24]. Overexpressed α_1-AR in the heart of transgenic mice can couple with the G_i protein and inhibit AC[24]. Horie *et al*[14] found that stimulation of transfected α_1-AR directly activated G_s and increased cAMP accumulation. These phenomena occur when the density of α_1-AR is much higher than normal. Some researchers[14,25] consider that receptor-G promiscuity happens when receptors are overexpressed, ie, receptors not only couple with their traditional G proteins, but also couple with irrelevant G proteins under normal conditions, and then produce new biological effects. This phenomenon is called receptor-G protein promiscuity, which would occur when receptors are overexpressed[14,25]. Since our experiments were performed under similar conditions, this leads to the following question: did promiscuity occur between α_1-AR and other G proteins? Firstly, the results showed α_{1B}-AR-mediated cAMP response was not affected by PTX, thereby excluding the possibility that G_i protein or $G_{\beta\gamma}$, which is sensitive to PTX[27] and activates ACII and IV[21,22,28], which is involved in the response. Secondly, cAMP accumulation induced by CTX alone was markedly higher than that induced by NE, and when CTX and NE worked together cAMP accumulation was far higher than the sum of cAMP accumulation when each of them worked alone. The response induced by NE 10 μmol/L almost reached a maximum, and since there is no receptor reserve in cloned HEK293 cells[25], if α_{1B}-AR directly coupled with the G_s protein while the number of G_s were relatively insufficient or equally by the number of α_{1B}-AR, cAMP accumulation induced by NE should equal that induced by CTX, and should not increase further when NE was added together with CTX. However, it did not occur. Thus there are two possibilities, one is that α_{1B}-AR directly couples with the G_s protein but that the amount of G_s protein far exceeds what α_{1B}-AR requires; another is that α_{1B}-AR itself does not couple with the G_s protein, which is more likely, because in our study, stimulation of α_{1B}-AR and the G_s protein at the same time induced a synergistic effect. In addition, the G_α, $G_{\beta\gamma}$ subunit should not be ignored, because it has been shown to activate ACII and IV[21,22,28]. However, because $G_{\beta\gamma}$ is PTX-sensitive[27], and PTX did not inhibit NE-induced cAMP sythesis in our study, we conclude that $G_{\beta\gamma}$ does not participate in the response.

Regulating effects of Ca^{2+} signaling system α_1-AR can induce the mobilization of intracellular Ca^{2+} as well as the influx of extracellular Ca^{2+}. As the most ubiquitous and most active second messenger in cells, Ca^{2+} not only mediates many physiological effects directly, but also regulates many signaling pathways and molecules. It has been shown that the Ca^{2+}-CaM complex can stimulate ACI, III, and VIII[21,22]. For this reason the effect of Ca^{2+} on α_{1B}-AR-mediated cAMP response was investigated. Our results showed that the Ca^{2+}-ATPase inhibitor, CPA, had no effect on NE-induced cAMP accumulation, indicating that mobilization of intracellular Ca^{2+} was not involved in the response. NE-induced cAMP accumulation was not reduced under Ca^{2+}-free condition, but reduced after addition of the extracellular Ca^{2+} chelator, EGTA. We speculate that it is because even under Ca^{2+}-free conditions, there inevitably existed a little Ca^{2+} in the buffer, which is enough to meet with the needs of the α_{1B}-AR-mediated cAMP response. When extracellular Ca^{2+} is chelated by EGTA, Ca^{2+} cannot flow into cells, thereby reducing cAMP production. So cAMP production was reduced. All of the above shows that extracellular Ca^{2+} influx plays a role in the α_{1B}-AR-mediated cAMP response. It is well known that extracellular Ca^{2+} enters cells mainly via voltage-dependent Ca^{2+} channels (VDCC) or voltage-independent Ca^{2+} channels, which includes Ca^{2+} store depletion-dependent Ca^{2+} channels (SDDCC), receptor-dependent Ca^{2+} channels, and so on. Then arises the new question of what kind of channel is involved in this response. It has been proving that there is no VDCC in HEK293 cells[29], and in our study, the L-type Ca^{2+} channel inhibitor nifedipine did not affect NE-induced cAMP sythesis. The nonselective Ca^{2+} channel inhibitor $CdCl_2$ obviously reduced NE-induced cAMP accumulation, and the extent of reduction was the same as that with EGTA. If these facts are taken together with the fact that CPA-induced Ca^{2+} store depletion did not increase cAMP

accumulation, it seems that it was via receptor-dependent Ca^{2+} channels that extracellular Ca^{2+} entered the cells. CaM inhibitor W-7 significantly reduced NE-induced cAMP accumulation, with the extent of reduction almost equal to that induced by EGTA and $CdCl_2$, which indicates that it is Ca^{2+}-CaM that activates AC. Intracellular Ca^{2+} chelator BAPTA can chelate Ca^{2+} released from the Ca^{2+} store as well as Ca^{2+} entering cells from the outside, so theoretically it should have an effect similar to EGTA. In fact, it neither inhibited NE-induced cAMP synthesis nor enhanced the inhibitory effect of EGTA. As for the reason why intracellular Ca^{2+} chelator BAPTA could not inhibit NE-induced cAMP synthesis, we suppose either that the penetrability of BAPTA/AM into HEK293 cells was rather weak, or that the activity of esterase in HEK293 cells is so low that BAPTA/AM cannot be degraded to active BAPTA. Furthermore, our previous study showed that $[Ca^{2+}]_i$ increased to 4-5 times the basal level 8 s after activation of α_1-AR. Active BAPTA was perhaps not enough to chelate all intracellular Ca^{2+} completely and rapidly, so BAPTA/AM had little effect. However, the exact mechanism by which the system functions remains to be studied. In summary, the results suggest that stimulation of α_{1B}-AR triggers the receptor-dependent Ca^{2+} channel via an unknown pathway and lets extracellular Ca^{2+} in, then Ca^{2+} links CaM into a Ca^{2+}-CaM complex, which activates AC to increase cAMP synthesis. However none of EGTA, $CdCl_2$, and W-7 are able to completely inhibit NE-induced cAMP accumulation, suggesting that the Ca^{2+} influx is only partly involved in the response.

In conclusion, by coupling with a PTX-insensitive G protein, α_{1B}-AR promotes Ca^{2+} influx via receptor-dependent Ca^{2+} channels, then Ca^{2+} links to CaM to form a Ca^{2+}-CaM complex, which stimulates adenylyl cyclase (AC) and thereby increases the cAMP production in HEK293 cell lines. But Ca^{2+} only partly contributes to α_{1B}-AR-mediated cAMP accumulation. The other mechanisms remain to be investigated.

References

1 Williams S, Meij JT, Panagia V. Membrane phospholipids and adrenergic receptor function. Mol Cell Biochem 1995; 149/150: 217–21.

2 Bylund DB, Eikenberg DC, Hieble JP, Langer SZ, Lefkowitz RJ, Minneman KP, *et al*. International union of pharmacology nomenclature. Pharmacol Rev 1994; 46: 121–36.

3 Morgan NG, Blackmore PF, Exton JH. Age-related changes in the control of hepatic cyclic AMP levels by α_1- and β_2-adrenergic receptors in male rats. J Biol Chem 1983; 258: 5103–9.

4 Morgan NG, Waynick LE, Exton JH. Characterization of the α_1-adrenergic control of hepatic cAMP in male rats. Eur J Pharmacol 1983; 96: 1–10.

5 Chan TM, Exton JH. α_1-Adrenergic-mediated accumulation of adenosine 3′:5′-monophosphate in calcium depleted hepatocytes. J Biol Chem 1977; 252: 8645–51.

6 Blair JB, James ME, Foster JL. Adrenergic control of glucose output and adenosine 3′:5′ monophosphate levels in hepatocytes from juvenile and adult rats. J Biol Chem 1979; 254: 7579–84.

7 Johnson RD, Minneman KP. Differentiation of α_1-adrenergic receptors linked to phosphatidylinositol turnover and cyclic AMP accumulation in rat brain. Mol Pharmacol 1986; 31: 239–46.

8 Perkins JP, Moore MM. Characterization of the adrenergic receptors mediating a rise in cyclic 3′,5′-adenosine monophosphate in rat cerebral cortex. J Pharmacol Exp Ther 1973; 185: 371–8.

9 Robinson JP, Kendall DA. *Niguldipine* discriminates between α_1-adrenoceptor-mediated second messenger responses in rat cerebral cortex slices. Br J Pharmacol 1990; 100: 3–4.

10 Schwinn DA, Page SO, Middleton JP, Lorenz W, Liggett SB, Yamamoto K, *et al*. The α_{1C}-adrenergic receptor: characterization of signal transduction pathways and mammalian tissue heterogeneity. Mol Pharmacol 1991; 40: 619–26.

11 Perez DM, DeYoung MB, Graham RM. Coupling of expressed α_{1B}- and α_{1D}-adrenergic receptors to multiple signaling pathways is both G protein and cell type specific. Mol Pharmacol 1993; 44: 784–95.

12 Cotecchia S, Kobilka BK, Daniel KW, Nolan RD, Lapetina EY, Caron MG, *et al*. Multiple second messenger pathways of α_1-adrenergic receptor subtypes expressed in eukaryotic cells. J Biol Chem 1990; 265: 63–9.

13 Yoshimasa T, Sibley DR, Bouvier M, Lefkowitz JR, Caron MG. Cross-talk between cellular signalling pathways suggested by phorbol-ester-induced adenylate cyclase phosphorylation. Nature (Lond) 1987; 327: 67-70.

14 Horie K, Itoh H, Tsujimoto G. Hamster α_{1B}-adrenergic receptor directly activates G_s in the transfected Chinese hamster ovary cells. Mol Pharmacol 1995; 48: 394–400.

15 Filipeanu CM, Brailoiu E, Huhurez G, Slatineanu S, Baltatu O, Branisteanu DD. Multiple effects of tyrosine kinase inhibitors on vascular smooth muscle contraction. Eur J Pharmacol 1995; 281: 29–35.

16 Abebe W, Edwards JD, Agrawal DK. G-proteins in rat blood vessels-II: assessment of functional involvement. Gen Pharmacol 1995; 26: 75–83.

17 Thorburn J, Thorburn A. The tyrosine kinase inhibitor, genistein, prevents α-adrenergic-induced cardiac muscle cell hypertrophy by inhibiting activation of the Ras-MAP kinase signaling pathway. Biochem Biophys Res Commun 1994; 202: 1586–91.

18 Slupsky JR. Raf-dependent signaling pathways in cell growth and differentiation. Cell Growth Oncogenes 1998; 75–95.

19 Engel G, Hoyer D. ^{125}I-BE2254, a new high affinity radioligand for alpha1-adrenoceptors. Eur J Pharmacol 1981; 73: 221–4.

20 Weiss BL, Insel PA. Intracellular Ca^{++} and protein kinase C interact to regulate alpha-1-adrenergic and bradykinin receptor stimulated phospholipase A_2 activation in Madin-Darby carby canine kidney cell. J Biol Chem 1991; 266: 2126–33.

21 Sunahara RK, Dessauer CW, Gilman AG. Complexity and diversity of mammalian adenylyl cyclases. Annu Rev Pharmacol Toxicol 1996; 36: 461–80.

22 Dolphin AC. G-proteins. Textbook of receptor pharmacology. Boca Raton (USA): CRC Press, Inc; 1996. page 194–5.

23 Zhu WZ, Gao BB, Li HW, Zhang YY, Han QD. Differential activation of adenylyl cyclase by protein kinase C isoenzymes. Acta Pharmacol Sin 1999; 20: 1025–30.
24 Shahab A. Transgenic mice with cardiac overexpression of α_{1B}-adrenergic receptors. J Biol Chem 1997; 272: 21253–9.
25 Zhu X, Gilbert S, Birnbaumer M, Birnbaumer L. Dual signaling potential is common among G_s-coupled receptors and dependent on receptor density. Mol Pharmacol 1994; 46: 460–9.
26 Minneman KP, Theroux TL, Hollinger S, Han C, Esbenshade TA. Selectivity of agonists for cloned α_1-adrenergic receptor subtypes. Mol Pharmacol 1994; 46: 929–36.
27 Exton JH. Phosphoinositide phospholipase and G proteins in hormone action. Annu Rev Physiol 1994; 56: 349–69.
28 Taussig R, Tang WJ, Hepler JR, Gilman AG. Distinct patterns of bidirectional regulation of mammalian adenylyl cyclases. J Biol Chem 1994; 269: 6093–100.
29 Tao L, Guan YY, He H, Han C, Zhang YY, Sun JJ. Comparison of the Ca^{2+} movement by activation of alpha 1-adrenoceptor subtypes in HEK293 cells. Life Sci 1997; 61: 2127–36.

Full-length article

Signal pathways underlying homocysteine-induced production of MCP-1 and IL-8 in cultured human whole blood[1]

Xiao-kun ZENG[2], You-fei GUAN[3], Daniel G REMICK[5], Xian WANG[3,4,6]

[2]Institute of Vascular Medicine, Peking University Third Hospital; [3]Department of Physiology, Basic Medical College; [4]Key Laboratory of Molecular Cardiovascular Science of Education Ministry; Peking University, Beijing 100083, China; [5]Department of Pathology, University of Michigan Medical School, Ann Arbor, MI 48109, USA

Key words

homocysteine; monocyte chemoattractant protein-1; interleukin-8; protein kinase C; protein-tyrosine kinase; NF-κB; mitogen-activated protein kinases; calmodulin

[1] Project supported by the Major National Basic Research Program of China (No G2000056908) and a grant from the National Natural Science Foundation of China (No 30330250) awarded to Prof. Xian WANG as well as a grant from NIH (No GM 50401) awarded to Prof. Daniel G REMICK.
[6] Correspondence to Prof. Xian WANG.
Phn 86-10-8280-1443. Fax 86-10-8280-1443.
E-mail xwang@bjmu.edu.cn

Received 2004-05-31
Accepted 2004-10-15

doi: 10.1111/j.1745-7254.2005.00005.x

Abstract

Aim: To elucidate the mechanisms underlying homocysteine (Hcy)-induced chemokine production. **Methods**: Human whole blood was pretreated with inhibitors of calmodulin (CaM), protein kinase C (PKC), protein tyrosine kinase (PTK), mitogen-activated protein kinase (MAPK), and NF-κB and activators of PPARγ for 60 min followed by incubation with Hcy 100 μmol/L for 32 h. The levels of mitogen chemokine protein (MCP)-1 and interleukin-8 (IL-8) were determined by enzyme-linked immunosorbant assay (ELISA). **Results**: Inhibitors of PKC (calphostin C, 50-500 nmol/L and RO-31-8220, 10–100 nmol/L), CaM (W7, 28–280 μmol/L), ERK1/2 MAPK (PD 98059, 2–20 μmol/L), p38 MAPK (SB 203580, 0.6–6 μmol/L), JNK MAPK (curcumin, 2–10 μmol/L), and NF-κB (PDTC, 10-100 nmol/L) markedly reduced Hcy 100 μmol/L-induced production of MCP-1 and IL-8 in human cultured whole blood, but the inhibitors of PTK (genistein, 2.6–26 μmol/L and tyrphostin, 0.5-5 μmol/L) had no obvious effect on MCP-1 and IL-8 production. PPARγ activators (ciglitazone 30 μmol/L and troglitazone 10 μmol/L) depressed the Hcy-induced MCP-1 production but not IL-8 production in the cultured whole blood. **Conclusion**: Hcy-induced MCP-1 and IL-8 production is mediated by activated signaling pathways such as PKC, CaM, MAPK, and NF-κB. Our results not only provide clues for the signal transduction pathways mediating Hcy-induced chemokine production, but also offer a plausible explanation for a pathogenic role of hyperhomocysteinemia in these diseases.

Introduction

Hyperhomocysteinemia is an independent risk factor for atherosclerosis and venous thrombosis. We have found that an increased homocysteine (Hcy) levels in cultured whole blood can promote the production of monocyte chemoattractant protein-1 (MCP-1) and interleukin-8 (IL-8)[1]. As potent proatherosclerotic factors, MCP-1 and IL-8 are considered to be vital contributing factors in the pathogenesis of atherosclerosis and venous thrombosis[2–6]. Therefore, increased MCP-1 and IL-8 levels in plasma may be an important mechanism by which hyperhomocysteinemia promotes the progression of atherosclerosis.

In addition, the relationship between hyperhomocysteinemia and the cardiovascular disease and thrombosis has been well established. Recent clinical investigations have found that hyperhomocysteinemia is also associated with many different diseases such as inflammation, autoimmune diseases, and cognitive diseases[7–13]. These new findings imply that Hcy may also mediate the development of these medical conditions by presently-unknown mechanism(s).

Previous studies have found that the signaling pathways involving protein kinase C (PKC), protein tyrosine kinase (PTK), or mitogen-activated protein kinase (MAPK) play a vital role in the mediation of MCP-1 and IL-8 production in response to other stimuli[14–18]. Thus, these signaling pathways are examined in the present study to explore which

signaling pathways are involved in the Hcy-induced production of MCP-1 and IL-8. Our results presented here demonstrate that inhibitors of PKC, CaM, MAPK and NF-κB inhibit Hcy-induced MCP-1 and IL-8 production in cultured whole blood. Our results suggest that activation of these signaling pathways is involved in Hcy-induced chemokine production. Considering the fact that abnormally activated PKC, CaM, MAPK, and NF-κB play important roles in the initiation and progression of autoimmune and cognitive diseases[19-22], our study provides useful clues as to why Hcy may be involved in these diseases.

Materials and methods

Human whole blood culture The investigation conforms to the principles outlined in the Declaration of Helsinki. The human whole blood cultures were slightly modified from our previous studies[23,24]. Briefly, blood from healthy donors was drawn into heparinized syringes. Whole blood was then placed on a rotator and incubated at 37 ºC in an atmosphere containing 5% CO_2. Cell viability was evaluated by Trypan blue exclusion. Only cell preparations with a 95% or greater viability were used.

Measurement of MCP-1 and IL-8 protein secretion Human whole blood was treated with Hcy for indicated times and/or preincubated for 60 min with genistein, tyrphostin, calphostin C, RO-31-8220, W7, SB 203580, PD 98059, and curcumin or other pharmacological reagents. The plasma was harvested and transferred to other polypropylene tubes and stored at -30 ºC for not more than 1 week before measurement of chemokines MCP-1 and IL-8 protein concentrations in the plasma, which were determined by ELISA (R&D Systems Inc, Minneapolis, MN).

Chemicals *L*-homocysteine *(L*–Hcy), *L*-cysteine, *L*-methione, genistein, tyrphostin, and pyrrolidine dithiocarbamate (PDTC) were purchased from Sigma Co (St Louis, MO). Calphostin C, RO-31-8220, W7, SB 203580, PD 98059, and curcumin were purchased from Calbiochem Co (La Jolla, CA). 2′-7′-DCFH-DA was obtained from Molecular Probes (Eugene, OR). RPMI-1640 was purchased from Gibco Laboratories (Grand Island, NY). Other chemicals were purchased from the Chinese Chemical Co (Beijing, China).

Statistical analysis Results are expressed as mean±SEM. The number of samples used for each group is presented in the figure legends. The data were analyzed using one-way ANOVA and further analyzed using the Student-Newmen-Keuls test for multiple comparisons within treatment groups or the *t*-test (unpaired test with Welch's correction) for comparison between two groups with non-normal distribution. $P<0.05$ was considered a significant difference between treatment groups.

Results

Effect of *L*-methionine and *L*-cysteine on MCP-1 and IL-8 production from human whole blood To understand the role of thiol residues in Hcy-induced chemokine production, human whole blood was treated with sulfur-containing amino acids, *L*-methionine and *L*-cysteine 100 μmol/L for 32 h. Neither *L*-methionine nor *L*-cysteine elevated the production of MCP-1 and IL-8 in cultured human whole blood (Figure 1A, 1B). These data suggest that the thiol residues do not play an important role in the Hcy mechanisms.

PKC, PTK, and CaM in Hcy-induced secretion of MCP-1 and IL-8 A substantial body of evidence indicates that activation of PKC, CaM, PTK, MAPK, and NF-κB may

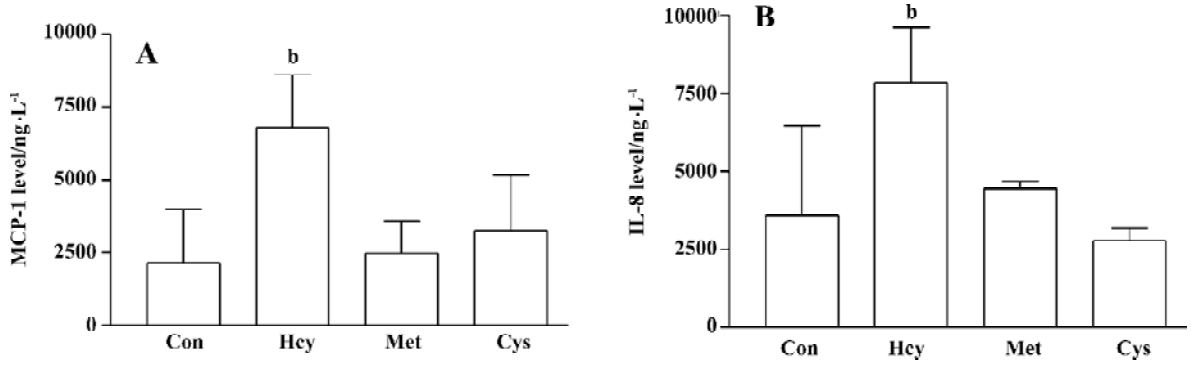

Figure 1. Effects of *L*-methionine (Met) and *L*-cysteine (Cys) on the secretion of MCP-1 and IL-8 in cultured human whole blood. The levels of MCP-1 (A) and IL-8 (B) in cultured human whole blood were measured by ELISA assays after incubation with Met or Cys 100 μmol/L for 32 h. $n=6$. Mean±SEM. $^bP<0.05$ *vs* corresponding untreated control (con) group.

be involved in chemokine production. Therefore, we hypothesize that such signaling pathways might contribute to Hcy-induced chemokine expression and secretion in cultured whole blood. Human whole blood was pretreated with inhibitors of CaM (W7, 28–280 μmol/L), PKC (calphostin C, 50–500 nmol/L and RO-31-8220, 10–100 nmol/L), PTK (genistein, 2.6-26 μmol/L and tyrphostin, 0.5-5 μmol/L). CaM and PKC inhibitors significantly inhibited Hcy-induced MCP-1 and IL-8 production in cultured human whole blood (Figure 2). However, the inhibitors of PTK had no obvious effect on chemokine production (Figure 3). These data show that the activated signaling pathways of PKC and CaM are involved in the Hcy-induced production of MCP-1 and IL-8 in cultured whole blood.

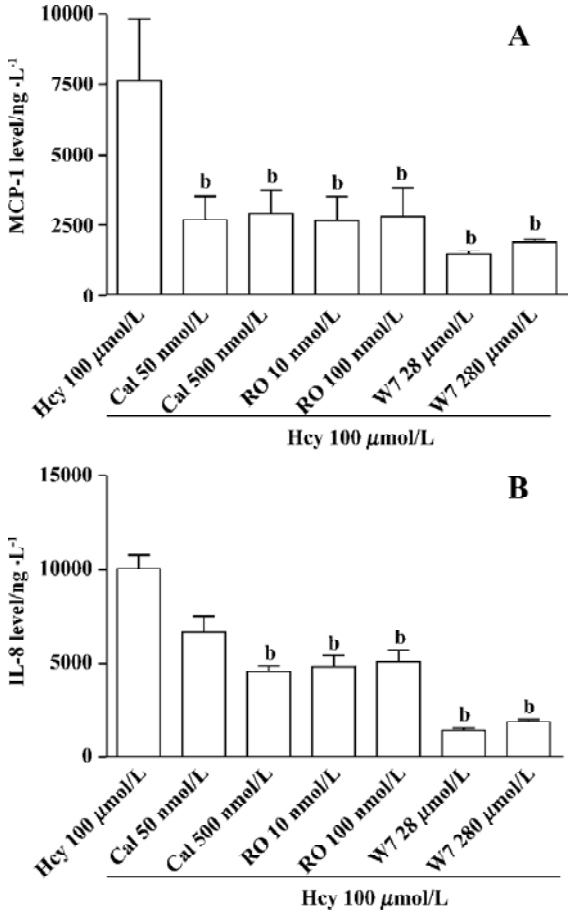

Figure 2. Effects of CaM and PKC inhibitors on Hcy-induced MCP-1 (A) and IL-8 (B) production in cultured human whole blood. Cultured whole blood was pretreated with the CaM inhibitor W7 or the PKC inhibitors calphostin C (Cal) and RO 31-8220 (RO) for 60 min and then stimulated by Hcy 100 μmol/L for 32 h. n=4. Mean±SEM. $^bP<0.05$ *vs* the Hcy only group.

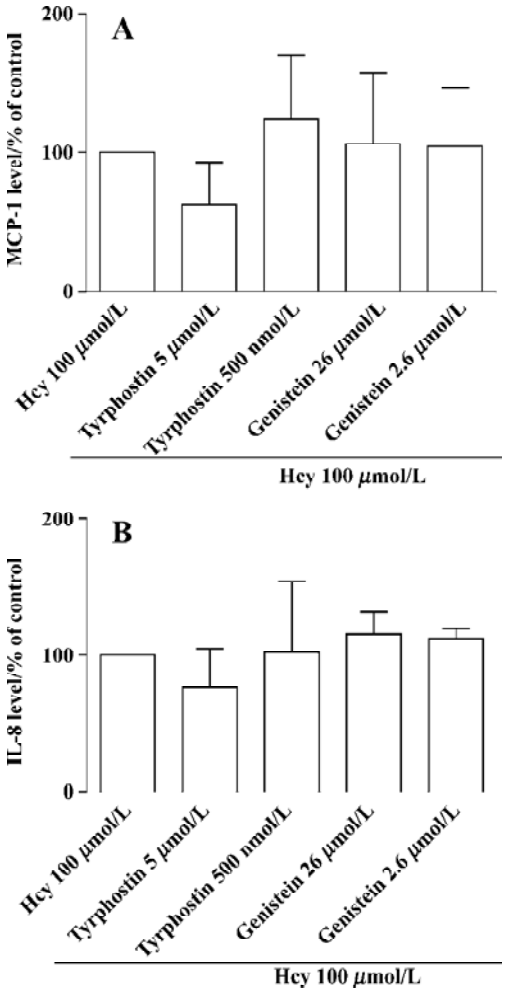

Figure 3. Effects of PTK blockers on Hcy-induced MCP-1 (A) and IL-8 (B) in cultured human whole blood. Cultured whole blood was pretreated with the the PKC inhibitors tyrphostin and genistein for 60 min and then stimulated by Hcy 100 μmol/L for 32 h. n=4. Mean±SEM. $^bP<0.05$ *vs* the Hcy-treated only group.

MAPK and NF-κB in Hcy-induced MCP-1 and IL-8 production To further study the role of the downstream signaling molecules of PKC and CaM, such as MAPK and NF-κB, in the Hcy-induced MCP-1 and IL-8 production, the inhibitors of ERK1/2 MAPK (PD 98059, 2–20 μmol/L), p38 MAPK (SB 203580, 0.6-6 μmol/L), JNK MAPK (curcumin, 2–10 μmol/L), and NF-κB (PDTC, 10–100 nmol/L) were added to cultured whole blood for 60 min, respectively. This was followed by stimulation with Hcy 100 μmol/L for 32 h. As shown in Figure 4, MAPK (p38, ERK1/2, and JNK) inhibitors significantly inhibited Hcy-induced MCP-1 and IL-8 production in cultured human whole blood. In addition, the NF-κB inhibitor PDTC also prevented Hcy-induced

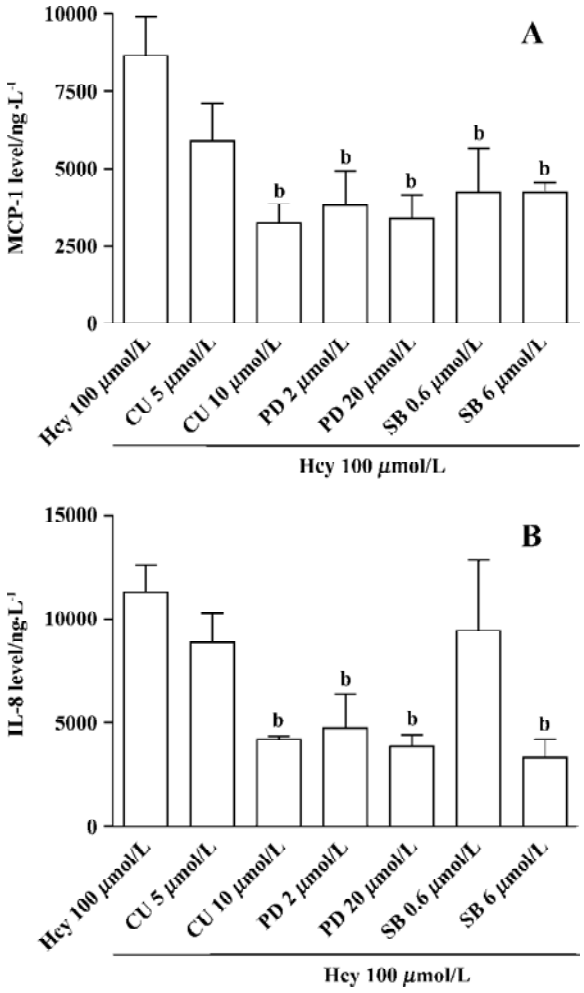

Figure 4. Effects of MAPK blockers on Hcy-induced MCP-1 (A) and IL-8 (B) in cultured human whole blood. Cultured whole blood was pretreated with the p38 MAPK inhibitor SB 203580 (SB), or the ERK1/2 inhibitor PD 98059 (PD) or the JNK inhibitor curcumin (CU) for 60 min and then stimulated by Hcy 100 μmol/L for 32 h. n=3. Mean±SEM. $^bP<0.05$ *vs* the Hcy-treated only group.

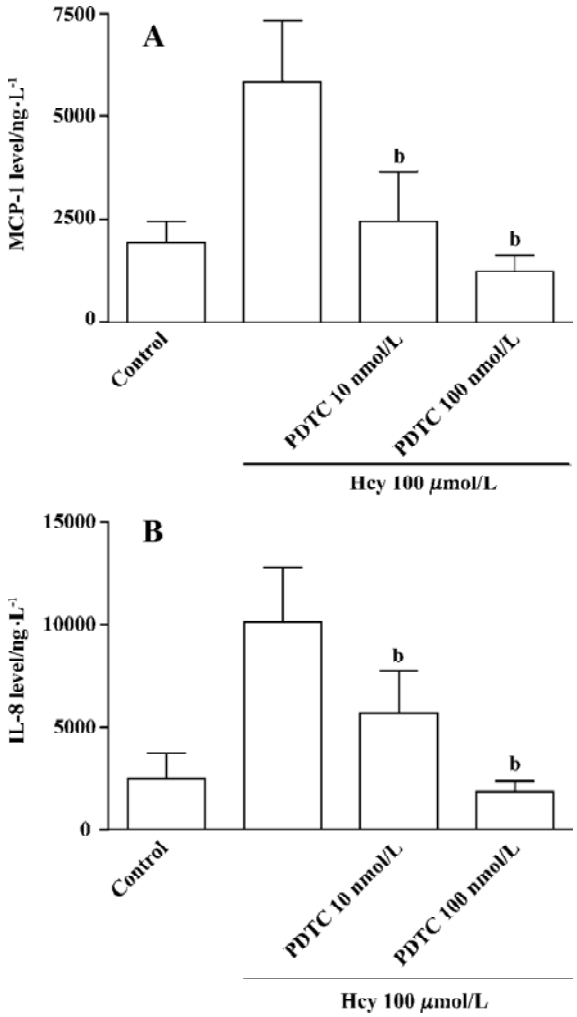

Figure 5. Effects of NF-κB on Hcy-induced MCP-1 (A) and IL-8 (B) in cultured human whole blood. Cultured whole blood was pretreated with the NF-κB inhibitor, PDTC (10–100 nmol/L) for 60 min and then stimulated with Hcy 100 μmol/L for 32 h. n=3 independent experiments. Mean± SEM. $^bP<0.05$ *vs* the Hcy-treated only group.

MCP-1 and IL-8 production in the cultured whole blood (Figure 5A, 5B). These data show that the activation pathways of MAPK and NF-κB are involved in the regulation of the Hcy-induced secretion of MCP-1 and IL-8. In the range of inhibitors examined, Hcy (10–1000 μmol/L) did not significantly increase LDH release as compared with the control (data not shown), indicating that Hcy plus the inhibitors did not have an obvious toxic effect on human whole blood.

Influence of PPARγ activators on Hcy-induced MCP-1 and IL-8 production Cultured whole blood was pretreated with the activators of PPARγ (ciglitazone 30 μmol/L and troglitazone 10 μmol/L) for 60 min, respectively. It is followed by stimulation with Hcy 100 μmol/L for 32 h. The data showed that PPARγ activators depressed the Hcy-induced MCP-1 production but not IL-8 production in the cultured whole blood (Figure 6A, 6B).

Discussion

Our previous work showed that an increased Hcy level promoted the production of MCP-1 and IL-8 in cultured whole blood. This suggests that hyperhomocysteinemia may upregulate MCP-1 and IL-8 levels in plasma and consequently promote the initiation and progression of atherosclerosis and venous thrombosis. Our present study demonstrated that activated signaling pathways such as PKC, CaM,

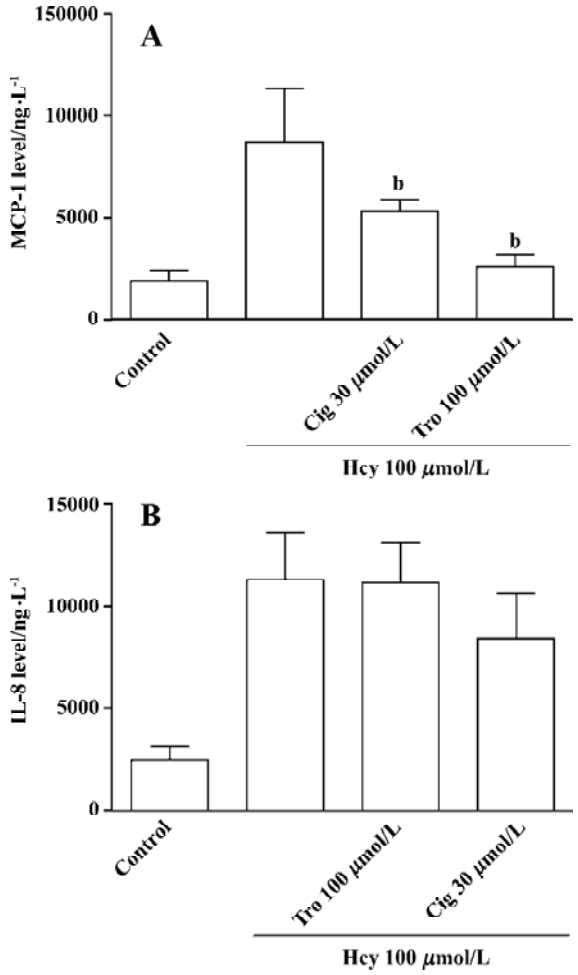

Figure 6. Effects of PPARγ agonists on Hcy-induced MCP-1 (A) and IL-8 (B) in cultured human whole blood. Cultured whole blood was pretreated with PPARγ activators, ciglitazone (30 μmol/L) and troglitazone (10 μmol/L) for 60 min and then stimulated by Hcy 100 μmol/L for 32 h, respectively. n=3 independent experiments. Mean±SEM. $^bP<0.05$ *vs* the Hcy-treated only group.

MAPK, and NF-κB were involved in the mediation of Hcy-induced MCP-1 and IL-8 production. These data indicate that Hcy promotes MCP-1 and IL-8 production in cultured whole blood by activating these signaling pathways. It further suggested that abnormally activated signaling pathways, which were caused by Hcy, might play roles as vital mechanisms underlying Hcy-mediated inflammatory, autoimmune, and cognitive diseases.

PKC is thought to play an important role in Hcy-induced MCP-1 production in cultured vascular smooth muscle cell lines, but not in endothelial lines[25,26]. Our present results shows that the activation of PKC is necessary for both IL-8 and MCP-1 production induced by Hcy, since calphostin C and RO31-8220, inhibitors of PKC, significantly reduced MCP-1 and IL-8 synthesis. No inhibitory effect was observed with the PTK inhibitors, genistein and tyrphostin, which indicates that protein tyrosine kinase might not be involved in Hcy-mediated MCP-1 and IL-8 synthesis. Previous studies have also shown that calcium/CaM plays an important role in the mediation of IL-8 production in several other cell systems[27,28]. To test whether calcium/CaM is involved in the Hcy-induced chemokine synthesis, we used W7, a potent inhibitor of CaM, to study its influence on Hcy-induced chemokine synthesis in cultured whole blood. Our data demonstrated that W7 significantly decreased both MCP-1 and IL-8 production. Taken together, these results reveal that both activated PKC and CaM are involved in Hcy-induced MCP-1 and IL-8 production in cultured whole blood. PTK, however, had no significant effect on Hcy action.

MAPKs represent a family of eukaryotic protein kinases involved in various cellular processes. Three parallel cascades are now commonly described, each of which is named after its end-moiety: p38, the extracellular signal regulated protein kinases (ERK), and stress activated protein kinase/c-Jun N-terminal kinases (JNK)[29]. As the upstream signaling molecules of MAPK, the activated PKC and CaM may mediate the activation of MAPK, such as MEK, p38MAPK, and JNK. For example, as the intermediate signaling pathway molecules, MAPK is indispensable in the PKC-mediated signaling transduction system[30,31]. Thus, we investigated specific downstream signaling molecules that could be potentially important as the targets of activated PKC and CaM. We demonstrated that PD98059, SB 203580, and curcumin, the selective inhibitors of MEK1, p38 MAPK, and JNK respectively, significantly decreased IL-8 and MCP-1 production. This data is consistent with other reports that MAPK is required for IL-8 and MCP-1 production in several other cell systems in response to various stimuli[30].

NF-κB is an important transcription factor in the initiation of cell growth and secretion. Consistent with its role as a primer in synthesis, NF-κB binds to the IκB site of various gene promoter regions[32]. Our data demonstrate that Hcy-induced chemokine production is almost competently blocked by PDTC, a specific inhibitor of NF-κB. These results agree with those obtained in other studies[33], suggesting that NF-κB has a role in the regulation of IL-8 and MCP-1 production.

Another interesting finding is that PPAR-γ activation can lead to a decrease in Hcy-induced MCP-1 production in cultured whole blood. PPAR-γ is a ligand-activated transcription factor belonging to the nuclear receptor family. PPAR-γ is expressed in differentiated human mono/macrophages and functions as a regulator of cellular proliferation, differen-

tiation, and apoptosis[34]. Although PPAR-γ seems to be absent from isolated monocytes, PPAR-γ can regulate mono/macrophage physiology[34,35]. Furthermore, Jiang *et al*[36] reported that incubation of human monocytes with the natural PPAR-γ ligand, or with synthetic agonists, inhibited the production of proinflammtory cytokines. Other studies showed that PPAR-γ inhibited the transcriptional activity of genes by interfering with transcription factors such as NF-κB[37]. Our data showed that Hcy-mediated MCP-1 and IL-8 production was NF-κB-dependent, thereby the influence of activated PPAR-γ in the Hcy-induced chemokine production was detected. The activators of PPAR-γ significantly depressed the production of MCP-1 but not IL-8. It suggests that this is an important pathway for attenuating the damage of Hcy or other inflammatory mediators. The different inhibitory effects on MCP-1 and IL-8 production imply that the regulation of Hcy-induced MCP-1 and IL-8 production is slightly different, at least in the cultured whole blood system.

Our previous studies and other work showed that Hcy potentiated lymphocyte proliferation. Also the thiol-containing compounds, such as cysteine had similar effects on lymphocyte proliferation[17,18]. The other compounds without thiol have no such effect. This suggests that thiol residue plays a key role in Hcy-induced lymphocyte proliferation. Our current studies found that thiol-containing compounds, such as cysteine and methionine, failed to promote MCP-1 and IL-8 production in the cultured whole blood. These results are consistent with previous work[38], suggesting that thiol may play a less important role in Hcy-induced chemokine production. Thus, there is the possibility that different sites of Hcy are responsible for different Hcy action.

Our current research has three implications; first, Hcy-induced MCP-1 and IL-8 production is mediated by activated signaling pathways such as PKC, CaM, MAPK, and NF-κB. Second, although the exact mechanism is unclear, current studies suggest that Hcy is able to activate the PKC, CaM, MAPK, and NF-κB signaling pathways. When we take the consideration that these activated signaling pathways are involved in many pathological and physiological functions, especially, in the initiation and progression of many immune and cognitive diseases, our findings shed light on a possible answer to why hyperhomocysteinemia has been found to be linked with not only cardiovascular diseases, but also so many inflammatory, autoimmune and cognitive diseases. Finally, activated PPAR-γ inhibited Hcy-induced MCP-1 production. This study provides a novel approach to partly attenuate the proatherogenic effect of hyperhomocysteinemia.

References

1 Zeng X, Remick DG, Wang X. Homocysteine induces production of monocyte chemoattractant protein-1 and interleukin-8 in cultured human whole blood. Acta Pharmacol Sin 2004; 25; 1419–25.

2 Reape TJ, Groot P. Chemokines and atherosclerosis. Atherosclerosis 1999; 147: 213–5.

3 de Lemos JA, Morrow DA, Sabatine MS, Murphy SA, Gibson CM, Antman EM, *et al*. Association between plasma levels of monocyte chemoattractant protein-1 and long-term clinical outcomes in patients with acute coronary syndromes. Circulation 2003; 107: 690–5.

4 Romuk E, Skrzep-Poloczek B, Wojciechowska C, Tomasik A, Birkner E, Wodniecki J, *et al*. Selectin-P and interleukin-8 plasma levels in coronary heart disease patients. Eur J Clin Invest 2002; 32: 657–61.

5 Van Aken BE, den Heijer M, Bos GM, van Deventer SJ, Reitsma PH. Recurrent venous thrombosis and markers of inflammation. Thromb Haemost 2000; 83: 536–9.

6 Van Aken BE, Reitsma PH, Rosendaal FR. Interleukin 8 and venous thrombosis: evidence for a role of inflammation in thrombosis. Br J Haematol 2002; 116: 173–7.

7 Morgenstern I, Raijmakers MT, Peters WH, Hoensch H, Kirch W. Homocysteine, cysteine, and glutathione in human colonic mucosa: elevated levels of homocysteine in patients with inflammatory bowel disease**.** Dig Dis Sci 2003; 48: 2083–90.

8 Yxfeldt A, Wallberg-Jonsson S, Hultdin J, Rantapaa-Dahlqvist S. Homocysteine in patients with rheumatoid arthritis in relation to inflammation and B-vitamin treatment. Scand J Rheumatol 2003; 32: 205–10.

9 Vrethem M, Mattsson E, Hebelka H, Leerbeck K, Osterberg A, Landtblom AM, *et al*. Increased plasma homocysteine levels without signs of vitamin B12 deficiency in patients with multiple sclerosis assessed by blood and cerebrospinal fluid homocysteine and methylmalonic acid. Mult Scler 2003; 9: 239–45.

10 Lazzerini PE, Capecchi PL, Bisogno S, Galeazzi M, Marcolongo R, Pasini FL. Reduction in plasma homocysteine level in patients with rheumatoid arthritis given pulsed glucocorticoid treatment. Ann Rheum Dis 2003; 62: 694–5.

11 Martinez-Taboada VM, Bartolome MJ, Fernandez-Gonzalez MD, Blanco R, Rodriguez-Valverde V, Lopez-Hoyos M. Homocysteine levels in polymyalgia rheumatica and giant cell arteritis: influence of corticosteroid therapy. Rheumatology (Oxford) 2003; 42: 1055–61.

12 Miller AL. The methionine-homocysteine cycle and its effects on cognitive diseases. Altern Med Rev 2003; 8: 7–19.

13 Herrmann W, Knapp JP. Hyperhomocysteinemia: a new risk factor for degenerative diseases. Clin Lab 2002; 48: 471–81.

14 Rovin BH, Tan LC. Role of protein kinase pathways in IL-1-induced chemoattractant expression by human mesangial cells. Kidney Int 1994; 46: 1059–68.

15 Roebuck KA. Oxidant stress regulation of IL-8 and ICAM-1 gene expression: differential activation and binding of the transcription factors AP-1 and NF-kappaB (Review). Int J Mol Med 1999; 4: 223–30.

16 Steube KG, Meyer C, Schupp P, Proksch P, Drexler HG. Differential effects of staurosporine and its analogues on chemokine release by promyelocytic leukemia cell line NB-4. Leuk Res 2003; 27: 957–63.

17 Zhang Q, Zeng X, Guo J, Wang X. Effect of homocysteine on murine splenic B lymphocyte proliferation and its signal transduction mechanism. Cardiovasc Res 2001; 52: 328–36.

18 Zhang Q, Zeng X, Guo J, Wang X. Oxidant stress mechanism of homocysteine potentiating ConA-induced proliferation in murine T lymphocytes. Cardiovasc Res 2002; 53:1035–42.
19 Buchs AE, Rapoport MJ. T cell signaling and autoimmune diabetes. T cell signaling and autoimmune diabetes. J Pediatr Endocrinol Metab 2000; 13: 1549–54.
20 Marchetti C. Molecular targets of lead in brain neurotoxicity. Neurotox Res 2003; 5: 221–36.
21 Kumar S, Blake SM, Emery JG. Intracellular signaling pathways as a target for the treatment of rheumatoid arthritis. Curr Opin Pharmacol 2001; 1: 307–13.
22 Drosos AA. Newer immunosuppressive drugs: their potential role in rheumatoid arthritis therapy. Drugs 2002; 62: 891–907.
23 DeForge LE, Kenney JS, Jones ML, Warren JS, Remick DG. Biphasic production of IL-8 in lipopolysaccharide (LPS)-stimulated human whole blood. Separation of LPS- and cytokine-stimulated components using anti-tumor necrosis factor and anti-IL-1 antibodies. J Immunol 1992; 148: 2133–41.
24 DeForge LE, Fantone JC, Kenney JS, Remick DG. Oxygen radical scavengers selectively inhibit interleukin 8 production in human whole blood. J Clin Invest 1992; 90: 2123–9.
25 Sung FL, Slow YL, Wang G, Lynn EG, O K. Homocysteine stimulates the expression of monocyte chemoattractant protein-1 in endothelial cells leading to enhanced monocyte chemotaxis. Mol Cell Biochem 2001; 216: 121–8.
26 Wang G, Siow YL, O K. Homocysteine stimulates nuclear factor kappaB activity and monocyte chemoattractant protein-1 expression in vascular smooth-muscle cells: a possible role for protein kinase C. Biochem J 2000; 352: 817–26.
27 Miura I, Miyamoto K, Nakamura K, Watanabe Y. Hydrogen peroxide induced chemokine production in the glia-rich cultured cerebellar granule cells under acidosis. Life Sci 2002; 70: 821–31.
28 Yu Y, De Waele C, Chadee K. Calcium-dependent interleukin-8 gene expression in T84 human colonic epithelial cells. Inflamm Res 50: 220–6.
29 Kim RD, Stein GS, Chari RS. Impact of cell swelling on proliferative signal transduction in the liver. J Cell Biochem 2001; 83: 56–69.
30 Bian ZM, Elner VM, Yoshida A, Kunkel SL, Elner SG. Signaling pathways for glycated human serum albumin-induced IL-8 and MCP-1 secretion in human RPE cells. Invest Ophthalmol Vis Sci 2001; 42: 1660–8.
31 Cobb MH, Goldsmith EJ. How MAP kinases are regulated. J Biol Chem 1995; 270: 14843–6.
32 Chen F, Castranova V, Shi X. New insights into the role of nuclear factor-kappaB in cell growth regulation. Am J Pathol 2001; 159: 387–97.
33 Zoja C, Angioletti S, Donadelli R, Zanchi C, Tomasoni S, Binda E, *et al*. Shiga toxin-2 triggers endothelial leukocyte adhesion and transmigration via NF-kappaB dependent up-regulation of IL-8 and MCP-1. Kidney Int 2002; 62: 846–56.
34 Chinetti G, Griglio S, Antonucci M, Torra IP, Delerive P, Majd Z, *et al*. Activation of proliferator-activated receptors alpha and gamma induces apoptosis of human monocyte-derived macrophages. J Biol Chem 1998; 273: 25573–80.
35 Ricote M, Li AC, Willson TM, Kelly CJ, Glass CK. The peroxisome proliferator-activated receptor-gamma is a negative regulator of macrophage activation. Nature 1998; 391: 79–82.
36 Jiang C, Ting AT, Seed B. PPAR-gamma agonists inhibit production of monocyte inflammatory cytokines. Nature 1998; 391: 82–6.
37 Su CG, Wen X, Bailey ST, Jiang W, Rangwala SM, Keilbaugh SA, *et al*. A novel therapy for colitis utilizing PPAR-gamma ligands to inhibit the epithelial inflammatory response. J Clin Invest 1999; 104: 383–9.
38 Poddar R, Sivasubramanian N, DiBello PM, Robinson K, Jacobsen DW. Homocysteine induces expression and secretion of monocyte chemoattractant protein-1 and interleukin-8 in human aortic endothelial cells. Circulation 2001; 103: 2717–30.

Full-length article

Effect of pravastatin on impaired endothelium-dependent relaxation induced by lysophosphatidylcholine in rat aorta[1]

Hua-fei DENG, Yan XIONG[2]

Department of Pharmacology, School of Pharmaceutical Sciences, Central South University, Changsha 410078, China

Key words

pravastatin; lysophosphatidylcholine; vascular endothelium; vasodilation; superoxide dismutase; *L*-arginine; nitric oxide; thoracic aorta; rats

[1] Project supported by grants from the National Natural Science Foundation of China (No 39970848 & 30271507).
[2] Correspondence to Prof. Yan XIONG.
Phn 86-731-2355-080.
E-mail xiongyan2001@yahoo.com

Received 2004-06-21
Accepted 2004-09-10

doi: 10.1111/j.1745-7254.2005.00013.x

Abstract

Aim: To investigate the effects of pravastatin, a potent 3-hydroxy-3-methylglutaryl coenzyme A (HMG-CoA) reductase inhibitor, on impaired endothelium-dependent relaxation induced by lysophosphatidylcholine (LPC), the major component of oxidized low-density lipoprotein, in rat thoracic aorta. **Methods:** Both the endothelium-dependent relaxation response to acetylcholine and the endothelium-independent relaxation response to sodium nitroprusside of aortic rings were measured by recording isometric tension after the rings were exposed to LPC in the absence or presence of pravastatin to estimate the injury effect of LPC and the protective effect of pravastatin on the aortic endothelium, respectively. **Results:** Exposure of aortic rings to LPC (1–10 μmol/L) for 30 min induced a significant concentration-dependent inhibition of endothelium-dependent relaxation to acetylcholine, but did not affect endothelium-independent relaxation in response to sodium nitroprusside. Pre-incubation of aortic rings with pravastatin (0.3-3 mmol/L) for 15 min and then co-incubation of the rings with LPC (3 μmol/L) for another 30 min significantly attenuated the inhibition of endothelium-dependent relaxation induced by LPC. This protective effect of pravastatin (1 mmol/L) was abolished by N^G-nitro-*L*-arginine methyl ester (30 μmol/L), an inhibitor of nitric oxide synthase, but not by indomethacin (10 μmol/L), an inhibitor of cyclo-oxygenase. Moreover, protein kinase C inhibitor chelerythrine (1 μmol/L) the superoxide anion scavenger superoxide dismutase (200 kU/L), and the nitric oxide precursor *L*-arginine (3 mmol/L) also improved the impaired endothelium-dependent relaxation induced by LPC, similar to the effects of pravastatin. **Conclusion:** Pravastatin can protect the endothelium against functional injury induced by LPC in rat aorta, a fact which is related to increasing nitric oxide bioavailability.

Introduction

Endothelial dysfunction is an early step in the pathogenesis of atherosclerosis and is characterized by an impaired endothelium function associated with a decreased production of nitric oxide (NO), reduced vasodilatation or abnormal vasoconstriction in response to acetylcholine. Oxidized low-density lipoprotein (ox-LDL) is an oxidative product of native LDL *in vivo*. It has been well established that ox-LDL plays an important role in the development of atherosclerosis[1]. Lysophosphatidylcholine (LPC) is the major component of ox-LDL[2–3]. LPC has been shown to increase the production of superoxide anions by activation of protein kinase C (PKC)[4] and has been implicated in impaired endothelium-dependent relaxation[2,3]. Exposure of normal blood vessels to LPC *in vitro* also mimicked the inhibitory effects of ox-LDL on endothelium-dependent relaxation[2,3]. Therefore, preventing the deleterious effects of LPC on endothelium is an effective approach for preventing the development of atherosclerosis.

Statins, 3-hydroxy-3-methylglutaryl coenzyme A (HMG-

CoA) reductase inhibitors, are cholesterol-lowering drugs and widely used in the treatment of hypercholesterolemia to prevent the development of atherosclerosis[5,6]. However, many studies have shown that statins have some beneficial effects on the cardiovascular system-independent of their cholesterol-lowering effect, such as restoring the endothelium-dependent relaxation function[7,8], preventing the adhesion of monocytes to endothelial cells[8], inhibiting the aggregation of platelets[9], suppressing the proliferation of vascular smooth muscle cells[10], and regulating angiogenesis[11] and blood pressure[12], which may be related to the up-regulation of nitric oxide synthase (NOS) expression. In addition, statins have been demonstrated to have anti-oxidative properties, as shown by their ability to reduce LDL oxidation[13] and scavenge oxygen-derived free radicals[14]. Pravastatin is a potent inhibitor of HMG-CoA reductase. Recently, a number of studies have demonstrated that pravastatin significantly inhibits the production of superoxide anions stimulated by phorbol ester in vascular endothelial cells[14], suppresses the increase in oxidative stress induced by LPC in vascular smooth muscle cells[15], and improves the impairment of endothelium-dependent relaxation in humans and animals with atherosclerosis and diabetes[16–18]. Therefore, it is important to determine whether pravastatin protects the vascular endothelium against damage due to LPC. In the present study, we sought to investigate the effects of pravastatin and its mechanisms on impaired endothelium-dependent relaxation induced by LPC in isolated rat aortic rings.

Materials and methods

Chemicals All chemicals were of the highest purity available. LPC, phenylephrine, acetylcholine, sodium nitroprusside, *L*-arginine, N^G-nitro-*L*-arginine methyl ester (*L*-NAME), indomethacin, and chelerythrine were purchased from Sigma Chemical Co (St Louis, MO, USA). Superoxide dismutase (SOD) was the product of Changsha Biological Pharmaceutical Factory (Hu-nan, China). Pravastatin was kindly presented by Blue Treasure Pharmaceutical Factory (Guangdong, China). They were dissolved in distilled water and diluted with Krebs' buffer before use.

Organ chamber experiments The study protocol was approved by the Animal Care and Use Committee of Central South University. Male Sprague-Dawley rats weighing 200-220 g were used. Rats were anaesthetized by intraperitoneal injection of sodium pentobarbital (30 mg/kg). The thoracic aorta was immediately isolated and placed in 4 ºC Krebs' bicarbonate buffer of the following composition (in mmol/L): 118.3 NaCl, 4.7 KCl, 2.5 $CaCl_2$, 1.2 $MgSO_4$, 1.2 KH_2PO_4, 25.0 $NaHCO_3$, 11.0 glucose. The thoracic aorta was then dissected free of adherent connective tissue. The aortic segment was cut into rings of 3–4 mm in length, taking special care to avoid stretching or touching the luminal surface of the rings. The rings were suspended horizontally between two stirrups in organ chambers filled with 5 mL Krebs' solution at 37 ºC and aerated continuously with 95 % O_2 and 5 % CO_2. One stirrup was connected to an anchor and the other was connected to a force transducer for recording isometric tension. The solution in the chambers was changed every 15-20 min. Rings were equilibrated for 60 min under 2 g resting tension and then challenged with 60 mmol/L KCl at least three times until a reproducible maximal contractile response was obtained. After repeated washing and a further equilibration period of 30 min, rings were contracted with a submaximal concentration of phenylephrine (1 μmol/L) and relaxed with cumulative concentrations of acetylcholine (0.03–3 μmol/L) at the plateau phase of the phenylephrine contraction to assess the integrity of the endothelium. The rings with the maximal relaxation (E_{max}) to 3 μmol/L acetylcholine of more than 80 % were considered to be endothelium-intact and used in the study.

Experimental protocol After each ring was serially washed and re-equilibrated, the rings of the control group were incubated for 45 min with Krebs' buffer. The rings of LPC group were incubated with Krebs' buffer for 15 min and then exposed to LPC (1–10 μmol/L) for 30 min. In the pravastatin group, the rings were pre-incubated with various concentrations of pravastatin (0.3–3 mmol/L) for 15 min before exposure to 3 μmol/L LPC for 30 min, respectively. To determine whether increasing prostacyclin or NO production is involved in the protective effect of pravastatin on impaired endothelium-dependent relaxation induced by LPC, aortic rings were pretreated with indomethacin 10 μmol/L, an inhibitor of cyclooxygenase or *L*-NAME 30 μmol/L, an inhibitor of NOS in the presence of pravastatin (1 mmol/L) for 15 min and then exposed to 3 μmol/L LPC for 30 min.

To determine whether the activation of PKC, increased production of superoxide anions, and decreased NO synthesis contribute to the detrimental effects of LPC, rings were pre-incubated with chelerythrine (1 μmol/L), an inhibitor of PKC, SOD (200 kU/L), a scavenger of superoxide anions, or *L*-arginine (3 μmol/L), a precursor of NO for 15 min and then exposed to LPC (3 μmol/L) for another 30 min.

After the above incubations, all rings were re-contracted with 1 μmol/L phenylephrine and concentration responses to acetylcholine (0.03–3 μmol/L) were repeated. Before finishing the experiment, the relaxation response to sodium ni-

troprusside (10 μmol/L) at the plateau phase of the phenylephrine contraction was also tested in isolated aortic rings.

Statistical analysis Results are expressed as Mean±SEM. Relaxation and the maximal relaxation (E_{max}) produced by acetylcholine was calculated and expressed as the percentage of contraction elicited by phenylephrine. The half-maximal relaxation (EC_{50}) response to acetylcholine was estimated by linear regression from log concentration-effect curves. Differences between groups were tested for statistical significance by analysis of variance followed by the Newman-Keuls test. $P<0.05$ was considered significant.

Results

Effects of LPC on endothelium-dependent relaxation There was no difference in the relaxation response to acetylcholine in rat aortic rings during the initial examination between groups (data not shown). After incubation with Krebs' solution for 45 min, acetylcholine (0.03–3 μmol/L) still evoked a significant concentration-dependent relaxation in aortic rings in the control group during the later repeat examination (Figure 1), in which the E_{max} value reached 90.4%±4.3%, and the EC_{50} value was 74.9±9.6 nmol/L (Table 1). Exposure of aortic rings to LPC (1–10 μmol/L) for 30 min significantly inhibited the endothelium-dependent relaxation response to acetylcholine in a dose-dependent manner; there were lower E_{max} and higher EC_{50} values in aortic rings of the LPC groups compared with the control rings (Figure 1, Table 1). These results indicated that LPC impaired the endothelium-dependent relaxation response to acetylcholine in rat aortic rings.

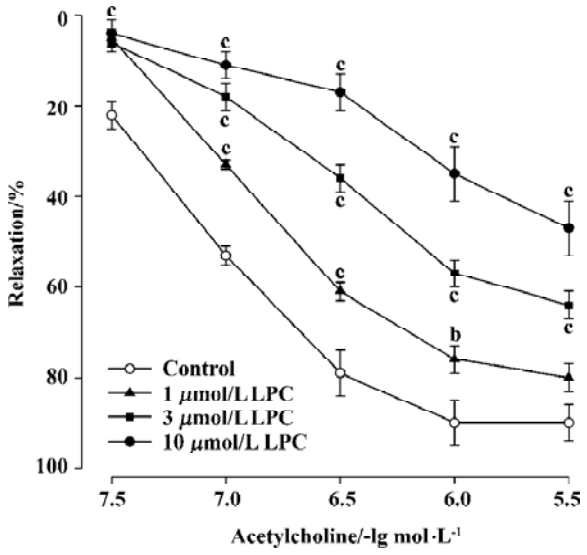

Figure 1. Effect of lysophosphatidylcholine on the endothelium-dependent relaxation in isolated rat aortas. n=5. Mean±SEM. $^bP<0.05$, $^cP<0.01$ *vs* control group.

Table 1. Effects of drugs on the E_{max} and EC_{50} values for acetylcholine-induced relaxation of rat aortic rings. n=5. Mean±SEM. $^cP<0.01$ *vs* control group. $^eP<0.05$, $^fP<0.01$ *vs* LPC 3 μmol/L group. $^iP<0.01$ *vs* PT 1 mmol/L+LPC 3 μmol/L group (Newman-Keuls test).

Treatment	ACh E_{max}/%	ACh EC_{50}/ nmol·L^{-1}
Control	90.4±4.3	74.9±9.6
LPC 1 μmol/L	80.2±3.0	160.9±13.7
LPC 3 μmol/L	63.8±3.1^c	268.8±31.1^c
LPC 10 μmol/L	46.8±6.0^c	273.6±49.7^c
PT 0.3 mmol/L+LPC 3 μmol/L	87.4±2.2^f	159.0±23.0^e
PT 1 mmol/L+LPC 3 μmol/L	86.2±3.4^f	99.2±19.1^f
PT 3 mmol/L+LPC 3 μmol/L	86.4±4.0^f	75.9±11.1^f
Indo 10 μmol/L+PT 1 mmol/L +LPC 3 μmol/L	86.0±3.2	93.0±9.1
L-NAME 30 μmol/L +PT 1 mol/L+LPC 3 μmol/L	63.0±5.0^i	203.1±36.7^i
Che 1 μmol/L+LPC 3 μmol/L	87.0±6.0^f	151.3±9.4^e
L-Arg 3 mmol/L+LPC 3 μmol/L	94.2±2.9^f	87.0±10.1^f
SOD 200 kU/L+LPC 3 μmol/L	91.8±3.5^f	87.6±13.3^f

The maximal relaxation (E_{max}) response to acetylcholine (ACh) 3 μmol/L of rat aortic rings was expressed as percentage of contraction elicited by phenylephrine 1 μmol/L. The half-maximum effective concentration (EC_{50}) response to ACh was calculated by linear regression from lg concentration-effect curves of ACh. Pravastatin: PT; lysophosphatidylcholine: LPC; indomethacin: Indo; chelerythrine: Che; *L*-arginine: *L*-Arg.

Effects of pravastatin on the inhibition by LPC Preincubation of rat aortic rings with pravastatin (0.3-3 mmol/L) for 15 min and then co-incubation of rat aortic rings with LPC 3 μmol/L for 30 min attenuated the inhibitory effect of LPC on endothelium-dependent relaxation. The E_{max} value increased and the EC_{50} value was reduced in aortic rings of pravastatin groups compared with the LPC 3 μmol/L group (Figure 2, Table 1).

Incubation of aortic rings with *L*-NAME (30 μmol/L) in the presence of pravastatin (1 mmol/L) for 15 min abolished the protective effect of pravastatin on the impairment of endothelium-dependent relaxation induced by LPC, whereas indomethacin did not change the beneficial effects of pravastatin. Significant differences were obtained when the E_{max} and EC_{50} values of the *L*-NAME group, but not of the indomethacin group were compared with those of pravastatin group (Figure 3, Table 1). In addition, pravastatin per se did not affect the endothelium-dependent relaxation of aortic

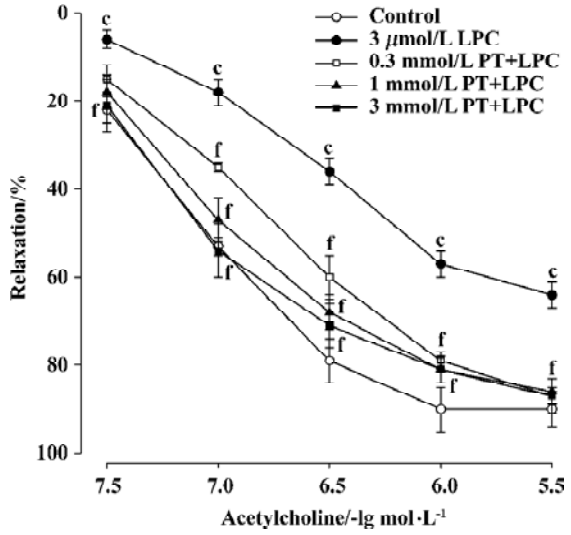

Figure 2. Effect of pravastatin (PT) on the impaired endothelium-dependent relaxation of rat aortas induced by lysophosphatidylcholine (LPC). n=5. Mean±SEM. ^cP<0.01 *vs* control group. ^fP<0.01 *vs* LPC 3 μmol/L group.

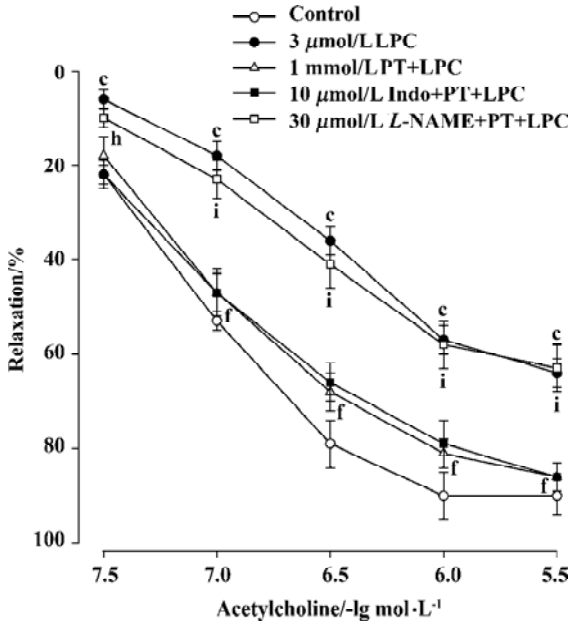

Figure 3. Effects of *L*-NAME and indomethacin (Indo))on the protection by pravastatin (PT) against impairment of endothelium-dependent relaxation induced by lysophosphatidylcholine (LPC). n=5. Mean±SEM. ^cP<0.01 *vs* control group. ^fP<0.01 *vs* LPC 3 μmol/L group.

rings in the absence of LPC or endothelium-independent relaxation of aortic rings in the presence of LPC (data not shown).

Effects of chelerythrine, *L*-arginine, and SOD on the inhibition by LPC In an analogous manner, pre-incubation of aortic rings with chelerythrine (1 μmol/L), *L*-arginine (3 mmol/L), or SOD (200 kU/L) also decreased the inhibition of endothelium-depedent relaxation by LPC. Significant differences were observed when the E_{max} and EC_{50} values of chelerythrine, *L*-arginine, or SOD group were compared with those of LPC group (Figure 4, Table 1).

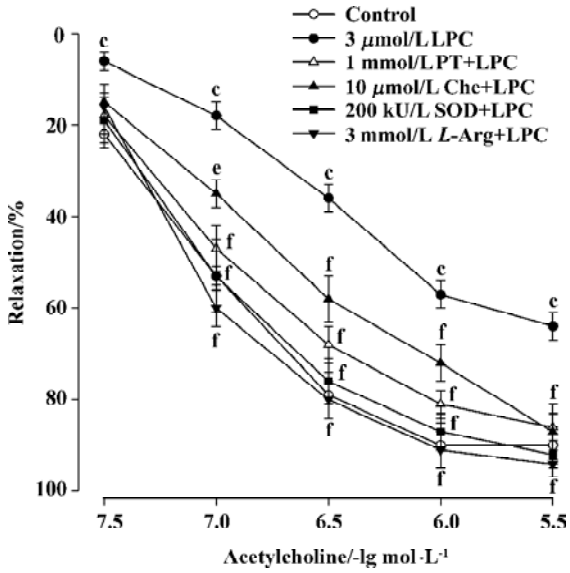

Figure 4. Effects of chelerythrine (Che), superoxide dismutase (SOD), and *L*-arginine (*L*-Arg) on the impaired endothelium-dependent relaxation of rat aortas induced by lysophosphatidylcholine (LPC). n=5. Mean±SEM. ^cP<0.01 *vs* control group. ^eP<0.05, ^fP<0.01 *vs* LPC 3 μmol/L group.

Discussion

The present study confirmed previous reports that LPC inhibited endothelium-dependent relaxation of isolated rat aortas in a concentration-dependent manner[2], and demonstrated that pravastatin, an inhibitor of HMG-CoA reductase, reduced the inhibition by LPC on endothelium-dependent relaxation. The protective effect of pravastatin on the impairment of endothelium-dependent relaxation induced by LPC is very similar to that of chelerythrine, SOD, and *L*-arginine. These results suggest that pravastatin protects endothelium against injury from LPC and this may be related to enhancing the bioavailability of NO through increasing NO synthesis and decreasing NO oxidative inactivation in endothelial cells.

NO-mediated and endothelium-dependent relaxation is inhibited early in the atherosclerotic process, even before histological evidence of plaque formation is evident. Ox-LDL, an oxidative product of native LDL in endothelial

cells and/or macrophages which presents in atherosclerotic lesions, is primarily responsible for this inhibition[1–3]. The inhibitory action of ox-LDL has generally been attributed to LPC, which is abundant in oxidized LDL and also accumulates in atherosclerotic lesions[1–3]. Removal of LPC from ox-LDL with phospholipase B[3] or albumin[19] has been shown to render ox-LDL inactive, and conversely, direct treatment of arterial rings with LPC can mimic the inhibitory effects of ox-LDL on endothelium-dependent relaxation[2,3]. In the present study, we also confirmed that exposure of rat aortic rings to LPC (1–10 μmol/L) did inhibit the endothelium-dependent relaxation response to acetylcholine, but did not affect the endothelium-independent relaxation response to sodium nitroprusside. These results are consistent with other studies[2,3], and suggest that the concentrations of LPC used in the current study had endothelium-specific effects that were not due to its cytotoxicity.

Although the precise mechanisms responsible for the inhibition of endothelium-dependent relaxation induced by LPC have not been elucidated, increasing oxidative degradation of NO and decreasing production of NO in endothelial cells could be implicated in this inhibition. A number of studies[4,20] have suggested that LPC stimulates superoxide anion production by activating PKC in vascular cells, which can inactivate NO by oxidation. In addition, LPC has been shown to inhibit the high-affinity arginine transporter in endothelial cells, decrease the availability of arginine, and subsequently reduce the synthesis of NO; supplementation with exogenous *L*-arginine reversed the inhibition by LPC[21]. In the present study, we found that chelerythrine, an inhibitor of PKC, improved the impairment of endothelium-dependent relaxation by LPC. Furthermore, the current study also demonstrated that the inhibition of endothelium-dependent relaxation induced by LPC was completely reversed by SOD, a scavenger of superoxide anions and by *L*-arginine, a precursor of NO. Taken together, these findings strongly support the proposal that LPC-induced inhibition of endothelium-dependent relaxation may be due to decreasing the bioavailability of NO via increasing the oxidative degradation of NO and reducing the synthesis of NO.

Evidence has accumulated that ox-LDL plays a critical role in atherogenesis, and LPC, the major lipid constituent of ox-LDL, has been recognized as an important factor that triggers disturbed endothelium-dependent vasodilatation of atherosclerosis. Therefore, finding effective drugs to reverse endothelial dysfunction induced by LPC may prevent the development of atherosclerosis. Pravastatin, like the other statins, is a competitive inhibitor of HMG-CoA reductase, which markedly reduces hepatic cholesterol *in vivo* by inhibiting the rate-limiting step in cholesterol synthesis catalyzed by HMG-CoA reductase[5]. A number of studies have demonstrated that pravastatin can reduce adverse cardiovascular events in patients suffering from coronary artery disease with or without hypercholesterolemia[5,22]. Recently, some authors have reported that pravastatin improved the defective endothelium-dependent vasodilatation of atherosclerotic vessels before the reduction of plasma cholesterol levels in humans and animals[16–18]. However, it is still unknown that whether pravastatin acts directly against the adverse effect of LPC on endothelium-dependent relaxation in addition to its cholesterol-lowering action. This study provides the first evidence that pravastatin protects endothelium against injury induced by LPC in isolated rat aortas. Although experiments *in vitro* can not completely mimic the conditions *in vivo* and are not good for studying the chronic effects of drugs, they are useful because they can exclude the effects of many factors *in vivo* and directly investigate the effects of drugs in some (pathological) conditions. Therefore, the endothelium-dependent relaxation of isolated aortic rings is extensively used to measure the function of endothelium in physiological conditions and some pathological conditions, such as atherosclerosis, or mimic intervention with ox-LDL or LPC.

The mechanisms by which pravastatin improves endothelial function are not completely understood. Results from the present study indicate that the protective effect of pravastatin on vascular endothelium is related to increasing the synthesis of endothelial NO. We found that the protective effect of pravastatin on the inhibition of endothelium-dependent relaxation induced by LPC was similar to that of *L*-arginine. Furthermore, the beneficial effect of pravastatin was reversed by *L*-NAME, but not by indomethacin. Another study has reported that pravastatin can up-regulate the expression of NOS and enhance the production of NO in endothelial cells[23]. Treatment with statins including pravastatin of patients and rabbits with atherosclerosis results in up-regulated eNOS expression, increased NO synthesis, and simultaneously improved endothelium-dependent relaxation, which was reversed by N^{ω}-nitro-*L*-arginine[24,25]. These findings suggested that pravastatin enhanced the production and release of NO from endothelium to improve endothelial function. However, Parker *et al*[26] reported that treatment of normal rats with simvastatin, but not with pravastatin, impaired the endothelium-dependent relaxation of their isolated aortic rings although it was able to enhance eNOS expression in endothelial cells. Chen *et al*[27] reported that pravastatin did not influence IL-1β-induced NO synthesis in vascular smooth muscle cells. The discrepan-

cies between our findings and theirs could be attributed to the different functional states of vascular endothelium, in different cells and under treatment with different stimulated factors or different drugs. In fact, many studies have shown that pravastatin did increase NO production and restore endothelium-dependent relaxation in atherosclerotic animals and humans[16–18,25]. Another potential mechanism by which pravastatin improved endothelial function is by reducing the oxidative inactivation of NO. Recent investigations have demonstrated that statins can decrease lipid peroxidation production[7], suppress NADPH oxidase activity[28], and increase the activity of catalase[29], and superoxide dismutase[7], which decreases the generation of oxygen free radicals resulting in reduction of NO activation. Moreover, a number of studies have shown that pravastatin can also reduce superoxide anion production by suppressing PKC activity in vascular cells[14,15]. In the present study, we demonstrated that chelerythrine, an inhibitor of PKC and SOD, a scavenger of superoxide anions, reversed the inhibition of endothelium-dependent relaxation induced by LPC, which was similar to effects of pravastatin. These results indirectly suggest that the protective effect of pravastatin against the damage to endothelium induced by LPC is related to decreasing NO oxidative inactivation via suppressing PKC activity and reducing superoxide anion production.

In conclusion, the present study demonstrates for the first time that pravastatin has a protective effect on endothelium against injury elicited by LPC, and that this protective effect is related to enhancing the bioavailability of NO through increasing NO synthesis and decreasing NO oxidative inactivation in endothelial cells.

References

1 Yla-Herttuala S, Palinski W, Rosenfeld ME, Parthasarathy S, Carew TE, Butler S, *et al*. Evidence for the presence of oxidatively modified low density lipoprotein in atherosclerotic lesions of rabbit and man. J Clin Invest 1989; 84: 1086–95.

2 Kugiyama K, Kerns SA, Morrisett JD, Roberts R, Henry PD. Impairment of endothelium-dependent arterial relaxation by lysolecithin in modified low-density lipoproteins. Nature 1990; 344: 160–2.

3 Mangin EL Jr, Kugiyama K, Nguy JH, Kerns SA, Henry PD. Effects of lysolipids and oxidatively modified low density lipoprotein on relaxation of rabbit aorta. Circ Res 1993; 72: 161–6.

4 Ohara Y, Peterson TE, Zheng B, Kuo JF, Harrison DG. Lysophosphatidylcholine increases vascular superoxide anion production via protein kinase C activation. Arterioscler Thromb 1994; 14: 1007–13.

5 Koizumi J, Shimizu M, Miyamoto S, Origasa H, Mabuchi H. Effect of pravastatin-induced LDL-cholesterol reduction on coronary heart disease and cerebrovascular disease in Japanese: Hokuriku lipid coronary heart disease study-pravastatin atherosclerosis trial (HolicosPAT). J Atheroscler Thromb 2002; 9: 251–9.

6 Corti R, Fuster V, Fayad ZA, Worthley SG, Helft G, Smith D**,** *et al*. Lipid lowering by simvastatin induces regression of human atherosclerotic lesions: two years' follow-up by high-resolution noninvasive magnetic resonance imaging. Circulation 2002; 106: 2884–7.

7 Ma FX, Liu LY, Xiong XM. Protective effects of lovastatin on vascular endothelium injured by low density lipoprotein. Acta Pharmacol Sin 2003; 24: 1027–32.

8 Jiang JL, Jiang DJ, Tang YH, Li NS, Deng HW, Li YJ. Effect of simvastatin on endothelium-dependent vasorelaxation and endogenous nitric oxide synthase inhibitor. Acta Pharmacol Sin 2004; 25: 893–901.

9 Laufs U, Gertz K, Huang P, Nickenig G, Bohm M, Dirnagl U, *et al*. Atorvastatin upregulates type III nitric oxide synthase in thrombocytes, decreases platelet activation, and protects from cerebral ischemia in normocholesterolemic mice. Stroke 2000; 31: 2442–9.

10 Sindermann JR, Fan L, Weigel KA, Troyer D, Muller JG, Schmidt A, *et al*. Differences in the effects of HMG-CoA reductase inhibitors on proliferation and viability of smooth muscle cells in culture. Atherosclerosis 2000; 150: 331–41.

11 Weis M, Heeschen C, Glassford AJ, Cooke JP. Statins have biphasic effects on angiogenesis. Circulation 2002; 105: 739–45.

12 Kishi T, Hirooka Y, Mukai Y, Shimokawa H, Takeshita A. Atorvastatin causes depressor and sympatho-inhibitory effects with upregulation of nitric oxide synthases in stroke-prone spontaneously hypertensive rats. J Hypertens 2003; 21: 379–86.

13 Kagota S, Yamaguchi Y, Nakamura K, Kunitomo M. Functional evidence for anti-oxidant action of fluvastatin on low-density lipoprotein using isolated macrophages and aorta. Clin Exp Pharmacol Physiol 2000; 27: 401–5.

14 Wagner AH, Kohler T, Ruckschloss U, Just L, Hecker M. Improvement of nitric oxide-dependent vasodilatation by HMG-CoA reductase inhibitors through attenuation of endothelial superoxide anion formation. Arterioscler Thromb Vasc Biol 2000; 20: 61–9.

15 Yasunari K, Maeda K, Minami M, Yoshikawa J. HMG-CoA reductase inhibitors prevent migration of human coronary smooth muscle cells through suppression of increase in oxidative stress. Arterioscler Thromb Vasc Biol 2001; 21: 937–42.

16 Wassman S, Faul A, Hennen B, Scheller B, Bohm M, Nickenig G. Rapid effect of 3-hydroxy-3-methylglutaryl coenzyme a reductase inhibition on coronary endothelial function. Circ Res 2003; 93: 98–103.

17 Silva EP, Fonseca FA, Ihara SS, Izar MC, Lopes IL, Pinto LE, *et al*. Early benefits of pravastatin to experimentally induced atherosclerosis. J Cardiovasc Pharmacol 2002; 39: 389–95.

18 Kobayashi T, Matsumoto T, Kamata K. Mechanisms underlying the chronic pravastatin treatment-induced improvement in the impaired endothelium-dependent aortic relaxation seen in streptozotocin-induced diabetic rats. Br J Pharmacol 2000; 131; 231–8.

19 Vuong TD, Kimpe SD, Roos RD, Rabelink TJ, Koomans HA, Joles JA. Albumin restores lysophosphatidylcholine-induced inhibition of vasodilation in rat aorta. Kidney Int 2001; 60: 1088–96.

20 Murohara T, Kugiyama K, Ota Y, Doi H, Ogata N, Ohgushi M, *et al*. Effects of atrial and brain natriuretic peptides on lysophosphatidylcholine-mediated endothelial dysfunction. J Cardiovasc Pharmacol 1999; 34: 870–8.

21 Kikuta K, Sawamura T, Miwa S, Hashimoto N, Masaki T. High-affinity arginine transport of bovine aortic endothelial cells is impaired by lysophosphatidylcholine. Circ Res 1998; 83: 1088–96.

22 Hague W, Forder P, Simes J, Hunt D, Tonkin A: LIPID Investigators. Effect of pravastatin on cardiovascular events and mortality in 1516 women with coronary heart disease: results from the Long-Term Intervention with Pravastatin in Ischemic Disease (LIPID) study. Am Heart J 2003; 145: 643-51.
23 Kaesemeyer WH, Caldwell RB, Huang J, Caldwell RW. Pravastatin sodium activates endothelial nitric oxide synthase independent of its cholesterol-lowering actions. J Am Coll Cardiol 1999; 33: 234-41.
24 Thakur NK, Hayashi T, Sumi D, Kano H, Tsunekawa T, Iguchi A. HMG-CoA reductase inhibitor stabilizes rabbit atheroma by increasing basal NO and decreasing superoxide. Am J Physiol Heart Circ Physiol 2001; 281: H75-83.
25 Masumoto A, Hirooka Y, Hironaga K, Eshima K, Setoguchi S, Egashira K, *et al*. Effect of pravastatin on endothelial function in patients with coronary artery disease (cholesterol-independent effect of pravastatin). Am J Cardiol 2001; 88: 1291-4.
26 Parker RA, Huang Q, Tesfamariam B. Influence of 3-hydroxy-3-methylglutaryl-CoA (HMG-CoA) reductase inhibitors on endothelial nitric oxide synthase and the formation of oxidants in the vasculature. Atherosclerosis 2003; 169: 19-29.
27 Chen H, Xing Y, Liu RH. Lovastatin increases nitric oxide synthesis in IL-1β- stimulated smooth muscle cells. Chin Med J 2001; 114: 1123-7.
28 Bandoh T, Sato EF, Mitani H, Nakashima A, Hoshi K, Inoue M. Antioxidative potential of fluvastatin via the inhibition of nicotinamide adenine dinucleotide phosphate (NADPH) oxidase activity. Biol Pharm Bull 2003; 26: 818-22.
29 Wassmann S, Laufs U, Muller K, Konkol C, Ahlbory K, Baumer AT, *et al*. Cellular antioxidant effects of atorvastatin *in vitro* and *in vivo*. Arterioscler Thromb Vasc Biol 2002; 22: 300-5.

4th National Congress of Chinese Society of Toxicology

2005 Sep 18-21 Shenyang, China

Please contact
Director Tian-en WANG
Chinese Toxicology Society
27 Taipin Road
Beijing 100850, China
Phn 86-10-6693-2387
Fax 86-10-6818-3899

Director Yu-hong SONG
National Shenyang Center for Safety Evaluation of New Drugs
8 Liaodong Road
Shenyang 110021, China
Phn 86-24-2581-2684
Fax 86-24-8935-3490

Full-length article

Enzymatic activity characterization of SARS coronavirus 3C-like protease by fluorescence resonance energy transfer technique[1]

Shuai CHEN[2], Li-li CHEN[2], Hai-bin LUO, Tao SUN, Jing CHEN, Fei YE, Jian-hua CAI, Jing-kang SHEN, Xu SHEN[3], Hua-liang JIANG[3]

Drug Discovery and Design Center, State Key Laboratory of Drug Research, Shanghai Institute of Materia Medica, Shanghai Institutes for Biological Sciences, Chinese Academy of Sciences, Graduate School of the Chinese Academy of Sciences, Shanghai 201203, China

Key words

severe acute respiratory coronavirus; 3C-like protease; fluorescence resonance energy transfer; fluorogenic substrate; enzyme activity; site-directed mutagenesis

[1] Project supported by the State Key Program of Basic Research of China (grants 2003-CB514125, 2003CB514124, 2002CB512807, 2002CB512802, 2002AA233011), Sino-European Project on SARS Diagnostics and Antivirals (Proposal/Contract No 003831), and the special programs of oppugning SARS from the Ministry of Science and Technology, Chinese Academy of Sciences, National Natural Science Foundation of China and Shanghai Science and Technology Commission.
[2] Authors contributed equally to this work.
[3] Correspondence to Prof. Xu SHEN, Prof Hua-liang JIANG.
Phn 86-21-5080-6600. Fax 86-21-5080-7088.
E-mail xshen@mail.shcnc.ac.cn, hljiang@mail.shcnc.ac.cn

Received 2004-05-31
Accepted 2004-09-01

doi: 10.1111/j.1745-7254.2005.00010.x

Abstract

Aim: To characterize enzymatic activity of severe acute respiratory syndrome (SARS) coronavirus (CoV) 3C-like protease ($3CL^{pro}$) and its four site-directed mutants. **Methods:** Based on the fluorescence resonance energy transfer (FRET) principle using 5-[(2′-aminoethyl)-amino] naphthelenesulfonic acid (EDANS) and 4-[[4-(dimethylamino) phenyl] azo] benzoic acid (Dabcyl) as the energy transfer pair, one fluorogenic substrate was designed for the evaluation of SARS-CoV $3CL^{pro}$ proteolytic activity. **Results:** The kinetic parameters of the fluorogenic substrate have been determined as K_m=404 μmol·L^{-1}, k_{cat}=1.08 min^{-1}, and k_{cat}/K_m=2.7 mmol^{-1}·L·min^{-1}. SARS-CoV $3CL^{pro}$ showed substantial pH and temperature-triggered activity switches, and site-directed mutagenesis analysis of SARS-CoV $3CL^{pro}$ revealed that substitutions of His^{41}, Cys^{145}, and His^{163} resulted in complete loss of enzymatic activity, while replacement of Met^{162} with Ala caused strongly increased activity. **Conclusion:** This present work has provided valuable information for understanding the catalytic mechanism of SARS-CoV $3CL^{pro}$. This FRET-based assay might supply an ideal approach for the exploration SARS-CoV $3CL^{pro}$ putative inhibitors.

Introduction

Between the end of 2002 and June 2003, a severe epidemic disease called severe acute respiratory syndrome (SARS) broke out in China and quickly spread to more than 30 other countries. A novel coronavirus, SARS-CoV, was identified as the etiological agent of SARS infection by using biophysical and biochemical techniques[1–3]. Coronavirus (CoV) is a positive-stranded RNA virus and involves the largest viral RNA genome known to date. Phylogenetic studies have shown that SARS-CoV is a previously unknown coronavirus, which is neither a member nor a mutant of any known coronavirus group, and is believed to be a novel human coronavirus, possibly originating from a non-human host[4].

Proteolytic processing of viral polyproteins is a vital step in the replication cycle of many positive-strand RNA viruses and such processing is commonly performed by virus-genome encoded protease[5,6]. The open reading frame (ORF) of the coronavirus replicase gene for encoding the proteins which is required for virus replication and transcription, encompasses more than 20 000 nucleotides[7,8] and encodes two overlapping polyproteins, pp1a (replicase1a, around 450 kDa) and pp1ab (replicase1ab, approximately 750 kDa). It is known that the replicase gene features the sequence motifs of both papain-like protease and 3-chymotrypsin like pro-

tease ($3CL^{pro}$)[9,10]. $3CL^{pro}$, which is also called main protease, functions as a key protease to control the activities of coronavirus replication complexes.

It has been concluded from previous research data that $3CL^{pro}$-mediated processing pathways are conserved in coronaviruses. Coronavirus main proteases employ cysteine and histidine residues as the catalytic dyad in the catalytic site but lack a corresponding third catalytic site[5,11–13], which is an acidic residue in chymotrypsin. Previous research has also confirmed that substrate specificities for the coronavirus main proteases are well defined, with the known proteolytic sites involving bulky hydrophobic residues (mainly leucine/ isoleucine) at the P2 position, conserved glutamine at the P1 position, and small aliphatic residues at the P1' position[14,15]. In addition, secondary structural studies for substrates of SARS-CoV $3CL^{pro}$ have revealed that substrates with more beta-sheet like structures tend to be cleaved quickly[16]. The determination of the crystal structures for human coronavirus (strain 229E) $3CL^{pro}$ and the inhibitor complex of porcine coronavirus (transmissible gastroenteritis virus, TGEV) $3CL^{pro}$ also confirmed a remarkable degree of conservation of the substrate binding sites for coronavirus $3CL^{pro}$ [17]. The recently reported crystal structures of SARS-CoV $3CL^{pro}$ and its complex with an inhibitor revealed substantial pH-dependant conformational changes that correlate well with the varying activity of $3CL^{pro}$ at different pH levels, and an unexpected model of inhibitor binding[18]. In fact, it has already been shown that $3CL^{pro}$ is an ideal target for screening anti-virus agents[15,19,20]. Like other $3CL^{pro}$, SARS-CoV $3CL^{pro}$ might become an attractive target in discovering new agents for the treatment of SARS[17].

In our previous work, we reported a 3D model of SARS-CoV $3CL^{pro}$ with its inhibitors, designed by virtual screening[21], and the molecular cloning, expression and purification of SARS-CoV $3CL^{pro}$, with a preliminary study on its mass spectral characterization[22].

To date, the proteolytic activity of SARS-CoV $3CL^{pro}$ has been almost determined by substrate-analog peptide cleavage assays using conventional RP-HPLC techniques[16]. In fact, the fluorescence-based assay is another method for quantitative protease activity assay, eg fluorescence resonance energy transfer (FRET) has been successfully used to develop spectrophotometric assays for many proteases[23–25]. The FRET-based method is more sensitive and less time-consuming compared with the RP-HPLC technique. Recently, a fluorogenic 14-amino acid peptide has been reported to measure SARS-CoV $3CL^{pro}$ enzymatic activity[26]. In the present report, we describe how this methodology can be used to design a 12-amino acid fluorogenic peptide with EDANS/ Dabcyl as the fluorescence quenching pair. This fluorogenic substrate has been successfully used to characterize the proteolytic activities of wild type SARS-CoV $3CL^{pro}$ at different pH levels and temperatures, and its four site-directed mutants including two catalytic residues and two substrate-binding sites as well. To our knowledge, such a fluorescence-based assay is the first to be used for site-directed mutation analysis of SARS-CoV $3CL^{pro}$. We hope that this present FRET-based assay will supply an ideal platform for the exploration of SARS-CoV $3CL^{pro}$ putative inhibitors.

Materials and methods

Materials All chemicals were of HPLC grade and purchased from Sigma (St Louis, MO). The Ni-NTA chelating affinity column, protease for tag-cleavage and low molecular weight marker for SDS-PAGE were from Amersham Pharmacia Biotech (Uppsala, Sweden).

Cloning, expression and purification of SARS-CoV $3CL^{pro}$ SARS-CoV $3CL^{pro}$ was cloned, expressed, and purified, as described by Sun *et al*[22]. The purified His-tagged SARS-CoV $3CL^{pro}$ was analyzed by SDS-PAGE, concentrated by centriprep (Milipore), and stored in sodium phosphate 20 mmol·L^{-1} pH 7.5/NaCl 100 mmol·L^{-1}/dithiothreitol (DTT) 5 mmol·L^{-1}/ethylene diaminetetraacetic acid (EDTA) 1 mmol·L^{-1} at 4 ºC. The structural integrity was analyzed by circular dichroism (CD).

Site-directed mutagenesis of SARS-CoV $3CL^{pro}$ Site-directed mutagenesis was effected by using a modified recombinant PCR method. Four mutant SARS-CoV $3CL^{pro}$ (SARS-CoV $3CL^{pro}$ $His^{41}Ala$, Cys^{145} Ala, $His^{163}Ala$, and $Met^{162}Ala$) were prepared with the QuickChange site-directed mutagenesis kit (Stratagene) using pQE30-SARS-CoV $3CL^{pro}$ as a template. The nucleotide sequences of the primers used for site-directed mutagenesis were given in Table 1. The pQE30-SARS-CoV $3CL^{pro}$ plasmids encoding mutant forms of SARS-CoV $3CL^{pro}$ were verified by sequencing and then transformed into *E coli* M15 cells, and the mutant proteins were expressed and purified in a similar procedure to that for the wild type protease. The purity and structural integrity of the mutant proteins were analyzed by SDS-PAGE. The circular dichroism (CD) spectra of four site-directed mutants were compared with those of wild type SARS-CoV $3CL^{pro}$ to exclude the possibility of structural misfolding caused by site-directed mutation (data not shown).

Synthesis of fluorogenic substrate The 12-amino acid fluorogenic substrate EDANS-Val-Asn-Ser-Thr-Leu-Gln-Ser-Gly-Leu-Arg-Lys(Dabcyl)-Met was synthesized and

characterized using a modified procedure described by Garcia-Echeverria and Rich[27]. N^{α}-tert-butyloxycarbonyl (Boc)-protected amino acids were used in all coupling steps. The base liable-protecting group, 9-fluorenylmethyloxycarbonyl (Fmoc), was used for the protection of the side chain of lysine, while the benzyl (Bzl) group was employed for the protection of C-terminal carboxyl group of the peptide. The Boc protecting group was removed before coupling by using HCl 4 mol/L in dioxane. Peptide couplings were achieved by overnight reaction with 1,3-dicyclohexylcarbodiimide (DCC) or 1-(3-dimethylaminopropyl)-3-ethylcarbodiimide hydrochloride and 1-hydroxybenzotriazole (HOBt) in *N*,*N*-dimethylformamide (DMF). After completion of synthesis, the benzyl group was removed by hydrogenolysis in methanol. The commercially available 5-[(2′-aminoethyl)-amino] naphthelenesulfonic acid (EDANS) and 4-[[4-(dimethylamino) phenyl] azo] benzoic acid (Dabcyl) groups were attached to the peptides with conventional condensation reactions[28], and the Fmoc group was removed from the lysine ε-amine group by treatment with piperidine-*N*,*N*-dimethylformamide (1:1 v/v) to give the final fluorogenic substrate. The crude products were purified by means of HPLC on a Kromasil 7-μm C_8 column (25 mm×250 mm). The purity of the final products was evaluated by reversed-phase HPLC on a Kromasil 5-μm C_8 column (4.6 mm×250 mm). The integrity of the purified peptides was determined by LCQ-DECA mass spectrometry (Thermofinnigan, San Jose, CA), and the observed molecular mass was found to agree with the calculated value.

Enzymatic activity assay Stock solution for the fluorogenic substrate was prepared in Me_2SO and stored at 4 ºC. Subsequent dilutions were performed using the assay buffer (sodium phosphate 20 mmol/L, pH 7.5, NaCl 100 mmol/L, DTT 5 mmol/L, EDTA 1 mmol/L) with the final concentration of Me_2SO less than 1 % (v/v).

Initial fluorimetric assays were performed in a 1 mL quartz cuvette with a 1 cm path length at 25 ºC. During the assay, SARS-CoV $3CL^{pro}$ (final concentration 1 μmol/L) was preincubated at 25 ºC for 30 min in the cuvette containing the assay buffer, followed by the addition of the fluorogenic substrate stock solutions to a final concentration of 10 μmol/L. The increase in emission fluorescence intensity was recorded at 10 min intervals on a Hitachi F-2500 fluorescence spectrophotometer connected to a thermostat. When fluorescence was being measured, the instrument was first set to zero with the fluorogenic substrate itself in the assay buffer. Cleavage of the peptide as a function of time was followed by monitoring the emission fluorescence intensity at a wavelength of 490 nm upon excitation at 340 nm (slit width 10 nm), and the initial reaction velocity (v_0) was determined from the linear portion of the progress curve. The final emission fluorescence intensity of the totally hydrolyzed substrate was determined by adding excess SARS-CoV $3CL^{pro}$ until no emission fluorescence intensity change at a wavelength of 490 nm was recorded.

Kinetic parameters (K_m and k_{cat}) of SARS-CoV $3CL^{pro}$ for the fluorogenic substrate were determined by incubation of the substrate at different concentrations ranging from 1 mmol/L to 5 μmol/L with SARS-CoV $3CL^{pro}$ 1 μmol/L at 25 ºC in the assay buffer. The reaction velocity (v_0) for each substrate concentration was averaged from three assay results. K_m and k_{cat} values were calculated by using a Lineweaver-Burk plot.

The relative enzymatic activity at varying pH levels was investigated at 25 ºC in citric acid/phosphate buffer (pH =5, 6, 7, and 8) and glycine/NaOH buffer (pH=9, 10) containing

Table 1. Nucleotide sequences of the primers used for site-directed mutagenesis of SARS-CoV $3CL^{pro}$*.

Oligonucleotide sequence (5′→3′)	Polarity	Mutation introduced
CAGTATACTGTCCAAGA**GCT**GTCATTTGCACAGCAG	Forward	SARS-CoV $3CL^{pro}$ $His^{41}Ala$
CTGCTGTGCAAATGAC**AGC**TCTTGGACAGTATACTG	Reverse	SARS-CoV $3CL^{pro}$ $His^{41}Ala$
GGTTCTTTCCTTAATGGATCA**GCT**GGTAGTGTTGGTTTTAAC	Forward	SARS-CoV $3CL^{pro}$ $Cys^{145}Ala$
GTTAAAACCAACACTACC**AGC**TGATCCATTAAGGAAAGAACC	Reverse	SARS-CoV $3CL^{pro}$ $Cys^{145}Ala$
GTGTCTTTCTGCTATATG**GCT**CATATGGAGCTTCCAACAGG	Forward	SARS-CoV $3CL^{pro}$$His^{163}Ala$
CCTGTTGGAAGCTCCATATG**AGC**CATATAGCAGAAAGACAC	Reverse	SARS-CoV $3CL^{pro}$ $His^{163}Ala$
GCGTGTCTTTCTGCTAT**GCG**CATCATATGGAGCTTCC	Forward	SARS-CoV $3CL^{pro}$$Met^{162}Ala$
GGAAGCTCCATATGATG**CGC**ATAGCAGAAAGACACGC	Reverse	SARS-CoV $3CL^{pro}$$Met^{162}Ala$

* The mutant codons in the oligonucleotide sequences are highlighted in boldface. SARS-CoV $3CL^{pro}$ amino acids are numbered continuously from the N-terminal residue, Ser^{1}, to the C-terminal residue, Gln^{303}.

DTT 5 mmol/L, EDTA 1 mmol/L, SARS-CoV 3CL^{pro} 1 μmol/L and fluorogenic substrate 10 μmol/L. The reaction velocity (v_0) at each pH value was measured in triplicate and averaged.

The enzymatic activity at different temperatures (10, 20, 30, 40, and 50 ºC) was measured in an assay buffer containing SARS-CoV 3CL^{pro} 1 μmol·L^{-1}and substrate 10 μmol/L. The enzyme was equilibrated at the same temperature as that for the assay buffer and substrate solution before mixing. During the assay, the cuvette temperature was stabilized by a thermostat connected to a Hitachi F-2500 fluorescence spectrophotometer. The reaction velocity (v_0) at each temperature was the average of the three parallel assays and the reaction velocity at 40 ºC was taken as 1.0.

The enzymatic activity of four site-directed mutants of SARS-CoV 3CL^{pro} (SARS-CoV 3CL^{pro} His^{41}Ala, Cys^{145} Ala, His^{163}Ala, and Met^{162}Ala) was the average of three parallel assays performed in an identical way as described above for wild type SARS-CoV 3CL^{pro}.

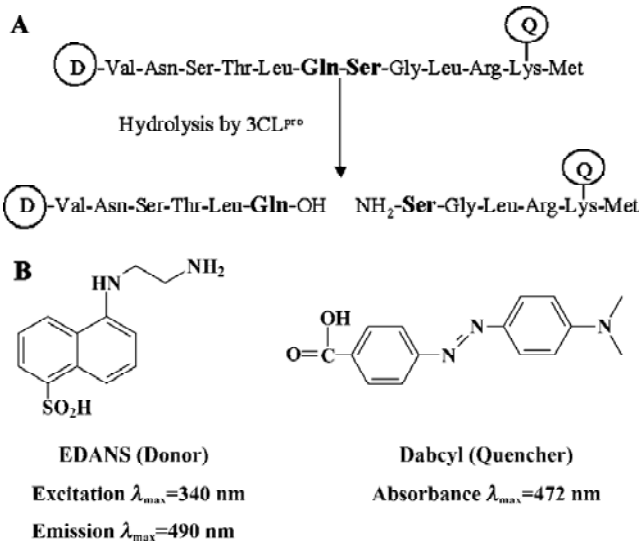

Figure 1. (A) Proposed design of fluorogenic substrate. Cleavage site is highlighted in boldface; D, the fluorescent donor chromophore; Q, quencher. (B) Structures and fluorescent properties of the donor/quencher pair EDANS/Dabcyl.

Results and discussion

Fluorogenic substrate design and initial fluorimetric assay It is well estabished that the specificities of CoV 3CL^{pro} for the substrate involves bulky hydrophobic residues (mainly leucine/isoleucine) at the P2 position, conserved glutamine at the P1 position, and small aliphatic residues at the P1' position. A 12-amino acid peptide representing the NH_2-terminal autoprocessing site of TGEV 3CL^{pro} with the sequence of substrate-analog chloromethyl ketone inhibitor Cbz-Val-Asn-Ser-Thr-Leu-Gln-CMK was devised to separate the quencher from the fluorescent donor chromophore for designing the fluorogenic substrate in this study (Figure 1A), considering that a published cleavage experiment found that a 15-amino acid substrate involving these sequences could be efficiently cleaved by SARS-CoV 3CL^{pro}[17]. To ensure efficient internal quenching, a commercially available donor/quencher pair was chosen for this study: 5-[(2′-aminoethyl)-amino] naphthelenesulfonic acid (EDANS) and 4-[[4-(dimethylamino) phenyl] azo] benzoic acid (Dabcyl) (Figure 1B). These dyes had already been used in FRET-based procedures[25,29,30]. Most importantly, the EDANS/Dabcyl pair possessed adequate spectral overlap which allowed almost complete quenching of EDANS's fluorescence. The detailed experimental procedure for characterzing the enzymatic activity of SARS-CoV 3CL^{pro} was illustrated in Figure 2.

To evaluate the availability of the synthesized peptide as a potential substrate of SARS-CoV 3CL^{pro}, an initial fluorimetric assay was performed. Comparison of the fluorescence emission spectrum of only the fluorogenic substrate (data not shown) with those spectra incubated with SARS-CoV 3CL^{pro} (Figure 3A) clearly showed that the Dabcyl group almost exclusively quenched the donor emission of the EDANS fluorophore in the fluorogenic substrate and the fluorogenic substrate was efficiently hydrolyzed by SARS-CoV 3CL^{pro}. The obvious emission fluorescence intensity enhancement over time implies that the fluorogenic substrate is ideal for subsequent enzymatic activity assays against SARS-CoV 3CL^{pro}.

Enzymatic activity assays Considering the data obtained from the initial fluorimetric assay, SARS-CoV 3CL^{pro} proteolysis against the fluorogenic substrate resulted in an appreciable increase in emission fluorescence intensity at a wavelength of 490 nm as a function of time, and a typical fluorescence profile following hydrolysis of the substrate is shown in Figure 3B. As a control, incubation of the substrate in assay buffer in the absence of SARS-CoV 3CL^{pro} showed no fluorescence intensity change over time (data not shown).

Measurement of the kinetic parameters (K_m and k_{cat}) was accomplished by conducting hydrolysis of the fluorogenic substrate at various concentrations. A typical Lineweaver-Burk plot is shown in Figure 4, which plots the reciprocal of the initial velocity (v_0) versus the reciprocal of the substrate concentration. The data for each concentration were ob-

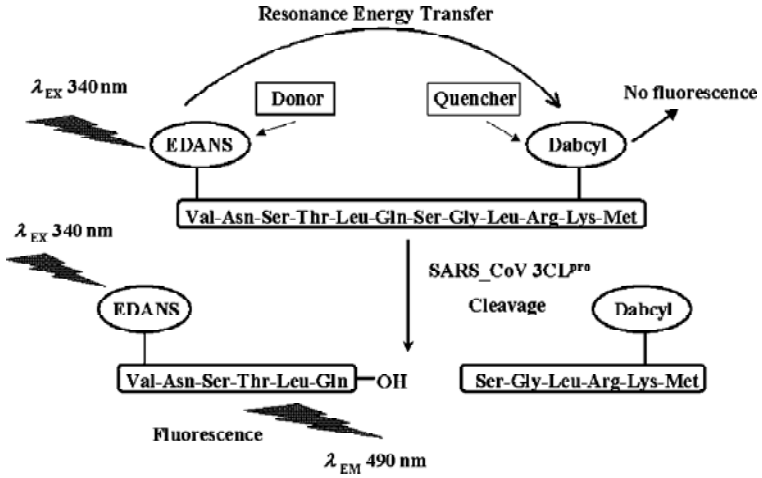

Figure 2. The experimental procedure of enzymatic activity characterization of SARS-CoV 3CL^{pro} using the fluorogenic substrate.

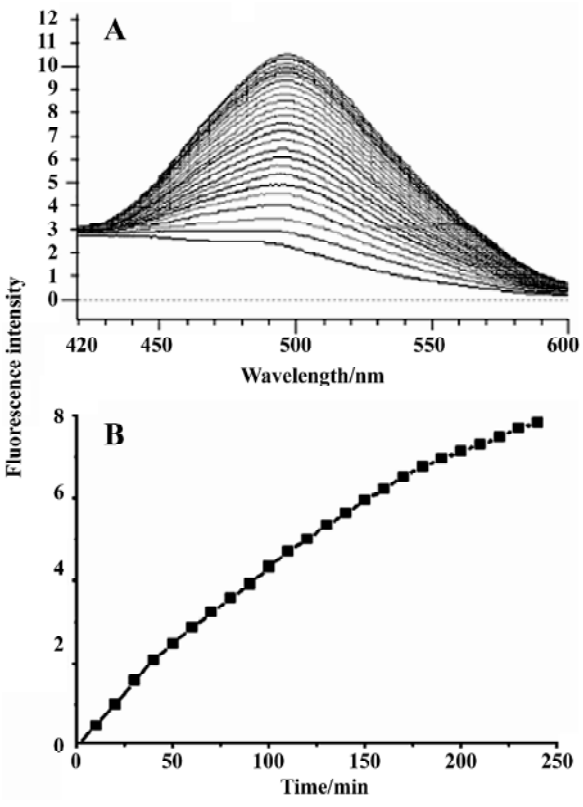

Figure 3. Initial fluorimetric assay and representative fluorescence profile of hydrolysis of the substrate by SARS-CoV 3CL^{pro}. (A) Emission spectra of the synthesized substrate incubated with SARS-CoV 3CL^{pro} recorded at 10 min intervals; λ_{EX}= 340 nm; $\lambda_{peak\ EM}$=490 nm. (B) The initial reaction velocity (v_0) was determined from the linear portion of the progress curve, which corresponded to between 2% and 10% hydrolysis of the substrate.

tained in triplicate. The calculated K_m and k_{cat} values were

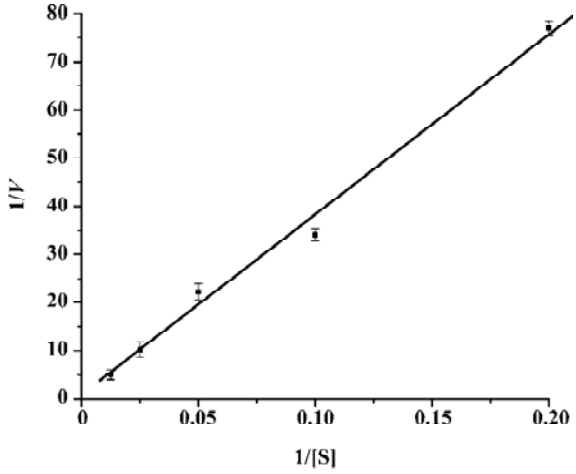

Figure 4. Determination of the kinetic parameters (K_m and k_{cat}) by Lineweaver-Burk plot. Enzymatic activity at different substrate concentrations varying from 1 mmol/L to 5 μmol/L was measured. The K_m and k_{cat} values were calculated by linear fitting method using ORIGIN 7.0. V: μmol·L^{-1}·min^{-1}; S: μmol·L^{-1}.

404±9 μmol/L and 1.08±0.14 min^{-1}, respectively. Obviously, the relatively small k_{cat}/K_m value (2.7±0.3 mmol^{-1}·L·min^{-1}) indicated that the *in vitro* activity of SARS-CoV 3CL^{pro} was low, in common with other reported coronavirus 3CL^{pro}[5]. Such a low activity for SARS-CoV 3CL^{pro} may be due to the fact that only the dimer of 3CL^{pro} was the active form, and efficient active dimeric form was often at relatively low concentrations during the enzyme assay[16,26].

Figure 5 showed the results concerning the relative enzymatic activity at various pH values for SARS-CoV 3CL^{pro}. The protease exhibited a stable proteolytic activity at pH 7.0–x9.0, and displayed only 50% activity at pH 6.0 and 10.0.

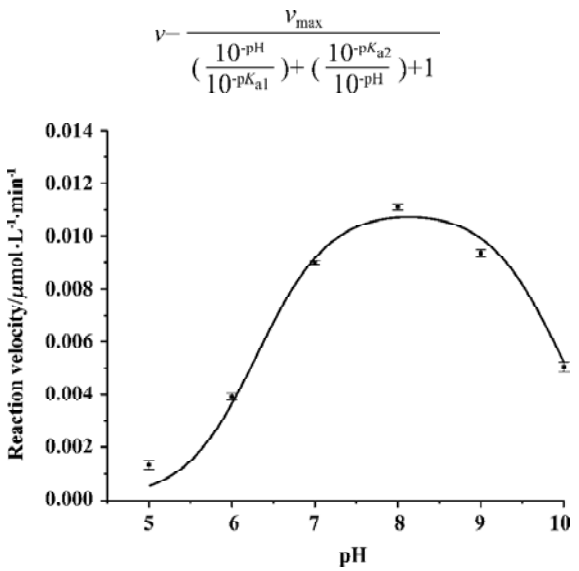

Figure 5. Enzymatic activity of SARS-CoV 3CL^{pro} at different pH. The reaction velocity (v_0) was determined in citric acid/phosphate buffer (pH=5, 6, 7, 8) or glycine/NaOH buffer (pH=9, 10). The curve was fitted by an equation described by Copeland[32] using ORIGIN 7.0.

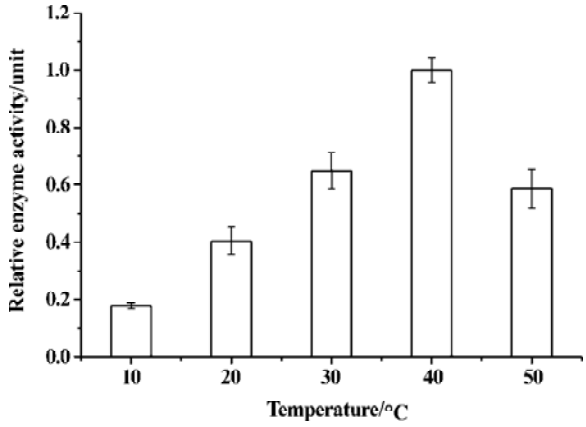

Figure 6. Enzymatic activity of SARS-CoV 3CL^{pro} at varying temperatures. The reaction velocity (v_0) was determined at 10, 20, 30, 40 and 50 ºC respectively. The reaction velocity (v_0) at 40 ºC was taken as 1.0.

However, when pH decreased to 5.0, it almost lost its activity completely. These results were strongly supported by a recent study, which discussed the pH dependence and the catalytic mechanism of SARS-CoV 3CL^{pro} [31]. The pH profile shown in Figure 5 can be fitted by the following equation[32]:

Where v is the measured reaction velocity that is plotted on the y axis, v_{max} is the observed maximum value of the reaction velocity, and pK_{a1} and pK_{a2} refer to the pK_a values for the two relevant acid-base catalytic groups being titrated. A fit of the curve in Fig 5 to the equation yielded values of pK_{a1} and pK_{a2} of 6.31±0.12 and 9.95±0.11, respectivexxxand Cys^{145} formed a catalytic dyad in the active site of SARS-CoV 3CL^{pro}, and ionization of sulfhydryl group of Cys^{145} and imidazole group of His^{41} played an important role in catalytic processing of substrate hydrolysis[18].

The relative enzymatic activity of SARS-CoV 3CL^{pro} at different temperatures was depicted in Figure 6; the activity of SARS-CoV 3CL^{pro} nearly doubled with every 10 ºC increase from 10 to 40 ºC, and such a result accorded well with the thermodynamics of a typical chemical reaction. Like all proteins, SARS-CoV 3CL^{pro} undergoes thermal denaturation at elevated temperatures, hence the increases in the catalytic efficiency of the protease with increasing temperature might be compromised by the competing effects of the enzyme denaturation at high temperature. As indicated in Figure 6, the enzymatic activity diminished significantly at 50 ºC which was consistent with thermal denaturation of SARS-CoV 3CL^{pro} as monitored by circular dichroism[16].

Mutation analysis of the catalytic dyad and two substrate-binding residues Based on the sequence alignments, previous mutagenesis studies with other CoV 3CL^{pro} [7,9,33,34] and the recently reported crystal structure of SARS-CoV 3CL^{pro} [18], the two residues His^{41} and Cys^{145} are fully conserved and considered to be the principal catalytic residues of CoV 3CL^{pro}. Therefore, to confirm these two residues' functions in the enzymatic activity of SARS-CoV 3CL^{pro}, both residues were mutated into Ala. As indicated in Table 2, the proteolytic activity in SARS-CoV 3CL^{pro} His^{41}Ala and Cys^{145} Ala mutants were below the detection limit of the enzyme assay, which suggested a complete loss of enzymatic activities for these two mutants. Furthermore, these data strongly supported an indispensable catalytic function for His^{41} and Cys^{145}, and were fully consistent with the mutagenesis data analysis published previously on the HCoV, IBV, MHV, and FIPV 3CL^{pro} [5,11,35,36].

Additionally, it has been proposed that coronavirus 3CL^{pro} might employ the characteristic sequence signature Tyr^{161}-Met^{162}-His^{163} for substrate binding[33]. However, to date, this theoretical functional character has not been tested experimentally for SARS-CoV 3CL^{pro}. The need for experimental data becomes more evident considering the relatively low sequence identity between SARS-CoV 3CL^{pro} and 3CL^{pro} of other coronavirus groups. With these facts in mind, we focused on the Met^{162} and His^{163} residues of SARS-CoV 3CL^{pro} by site-directed mutagenesis analysis.

First of all, we exchanged Ala for the conserved His^{163}.

Table 2. Enzymatic activities of wild type and site-directed mutants of SARS-CoV $3CL^{pro}$*.

Protein	Proteolytic activity/%
SARS-CoV $3CL^{pro}$	100 %
SARS-CoV $3CL^{pro}$ $His^{41}Ala$	<1 %
SARS-CoV $3CL^{pro}$ $Cys^{145}Ala$	<1 %
SARS-CoV $3CL^{pro}$ $His^{163}Ala$	<1 %
SARS-CoV $3CL^{pro}$ $Met^{162}Ala$	182 %

* Enzymatic activities were averages determined in three parallel experiments. The activity of wild type SARS-CoV $3CL^{pro}$ was taken as 100 %.

As shown in Table 2, the proteolytic activity of this mutant dropped below the detection limit of the enzyme assay. Such an obvious indispensability of His^{163} for proteolytic activity supported the conclusion that His^{163} remained uncharged at physiological pH to facilitate optimal interaction with the Gln-P1 of the substrate in substrate-binding subsite S1 as determined by the recently reported crystal structure of SARS-CoV $3CL^{pro}$ [18]. This was also consistent with the mutagenesis data obtained previously for the same His residue in other CoV $3CL^{pro}$[36]. Secondly, when Met^{162} residue was substituted with Ala, it was found that such a mutation did not decrease the proteolytic activity. On the contrary, it exhibited strongly increased activity: almost double compared with the wild type SARS-CoV $3CL^{pro}$. This result was consistent with the corresponding research for FIBV $3CL^{pro}$ [36], and indicated that Met^{162} was not indispensable for proteolytic activity even though it was conserved among CoV $3CL^{pro}$. It was tentatively suggested that such an increase of proteolytic activity for SARS-CoV $3CL^{pro}$ caused by Met^{162} mutation might be due to the fact that the substitution changed the spatial properties of the substrate-binding subsite S1 and facilitated substrate binding.

In summary, in this report, based on FRET theory, a fluorogenic substrate for detection of proteolytic activity of SARS-CoV $3CL^{pro}$ was successfully synthesized and evaluated. The kinetic parameters showed that the *in vitro* activity of SARS $3CL^{pro}$ was relatively low, perhaps due to the low concentration of the active dimeric form under the enzyme assay conditions. The pH profile of enzymatic activity yielded pK_{a1} and pK_{a2} values of 6.2 and 10.0, respectively, which correlated well with the finding that ionization of the catalytic dyad of His^{41} and Cys^{145} was perhaps vital during the catalytic processing of substrate hydrolysis. In addition, SARS-CoV $3CL^{pro}$ displayed nearly a twofold increase in activity with every 10 ºC increase at 10–40 ºC, and diminished its activity significantly at 50 ºC owing to thermal denaturation. Mutation analysis revealed that substitution of either His^{41} and Cys^{145} residues resulted in complete loss of proteolytic activity, which was also observed for the residue His^{163} in the substrate-binding subsite S1. Replacement of Met^{162} with Ala caused increased activity, although the detailed mechanism was still unknown. The present FRET-based assay might supply an ideal platform for the exploration of SARS-CoV and other CoV $3CL^{pro}$ putative inhibitors, given the conserved substrate specificities of CoV $3CL^{pro}$.

References

1 Holmes KV. SARS coronavirus: a new challenge for prevention and therapy. J Clin Invest 2003; 111: 1605–9.

2 Peiris JS, Lai ST, Poon LL, Guan Y, Yam LY, Lim W, *et al*. Coronavirus as a possible cause of severe acute respiratory syndrome. Lancet 2003; 361: 1319–25.

3 Fouchier RA, Kuiken T, Schutten M, Van Amerongen G, Van Doornum GJ, Van Den Hoogen BG, *et al*. Aetiology: Koch's postulates fulfilled for SARS virus. Nature 2003; 423: 240–7.

4 Holmes KV. SARS-associated coronavirus. N Engl J Med 2003; 348: 1948–51.

5 Ziebuhr J, Heusipp G, Siddell SG. Biosynthesis, purification, and characterization of the human coronavirus 229E 3C-like proteinase. J Virol 1997; 71: 3992–7.

6 Dougherty WG, Semler BL. Expression of virus-encoded proteinases: functional and structural similarities with cellular enzymes. Microbiol Rev 1993; 57: 781–822.

7 Eleouet JF, Rasschaert D, Lambert P, Levy L, Vende P, Laude H. Complete sequence (20 kilobases) of the polyprotein-encoding gene 1 of transmissible gastroenteritis virus. Virology 1995; 206: 817–22.

8 Thiel V, Herold J, Schelle B, Siddell SG. Viral replicase gene products suffice for coronavirus discontinuous transcription. J Virol 2001; 75: 6676–81.

9 Herold J, Raabe T, Schelle-Prinz B, Siddell SG. Nucleotide sequence of the human coronavirus 229E RNA polymerase locus. Virology 1993; 195: 680–91.

10 Lee HJ, Shieh CK, Gorbalenya AE, Koonin EV, Monica N, Tuler J, *et al*. The complete sequence (22 kilobases) of murine coronavirus gene 1 encoding the putative proteases and RNA polymerase. Virology 1991; 180: 567–82.

11 Liu DX, Brown TD. Characterization and mutational analysis of an ORF 1a-encoding proteinase domain responsible for proteolytic processing of the infectious bronchitis virus 1a/1b polyprotein. Virology 1995; 209: 420–7.

12 Ziebuhr J, Snijder EJ, Gorbalenya AE. Virus-encoded proteinases and proteolytic processing in Nidovirales. J Gen Virol 2000; 81: 853–79.

13 Hegyi A, Ziebuhr J. Conservation of substrate specificities among coronavirus main proteases. J Gen Virol 2002; 83: 595–9.

14 Ziebuhr J, Herold J, Siddell SG. Characterization of a human coronavirus (strain 229E) 3C-like proteinase activity. J Virol 1995;

69: 4331–8.
15 Anand K, Plam GJ, Mesters JR, Siddell SG, Ziebuhr J, Higenfeld R. Structure of coronavirus main proteinase reveals combination of a chymotrypsin fold with an extra alpha-helical domain. EMBO J 2002; 21: 3213–24.
16 Fan KQ, Wei P, Feng Q, Chen SD, Huang CK, Ma L, *et al*. Biosynthesis, purification, and substrate specificity of severe acute respiratory syndrome coronavirus 3C-like proteinase. J Biol Chem 2004; 279: 1637–42.
17 Anand K, Ziebuhr J, Wadhwani P, Mesters JR, Hilgenfeld R. Coronavirus main proteinase ($3CL^{pro}$) structure: basis for design of anti-SARS drugs. Science 2003; 300: 1763–7.
18 Yang HT, Yang MJ, Ding Y, Liu YW, Lou ZY, Zhou Z, *et al*. The crystal structures of severe acute respiratory syndrome virus main protease and its complex with an inhibitor. Proc Natl Acad Sci USA 2003; 100: 13190–5.
19 Kim JC, Spence RA, Currier PF, Liu X, Denison MR. Coronavirus protein processing and RNA synthesis is inhibited by the cysteine protease inhibitor E43d. Virology 1995; 208: 1–8.
20 Someya Y, Takeda N, Miyamura T. Identification of active-site amino acid residues in the Chiba virus 3C-like protease. J Virol 2002; 76: 5949–58.
21 Xiong B, Gui CS, Xu XY, Luo C, Chen J, Luo HB, *et al.* A 3D model of SARS-CoV 3CL proteinase and its inhibitors design by virtual screening. Acta Pharmacol Sin 2003; 24: 497–504.
22 Sun HF, Luo HB, Yu CY, Sun T, Chen J, Peng SY, *et al*. Molecular cloning, expression, purification, and mass spectrometric characterization of 3C-like protease of SARS coronavirus. Protein Exp Purif 2003; 32: 302–8.
23 Knight CG, Willenbrock F, Murphy G. A novel coumarin-labelled peptide for sensitive continuous assays of the matrix metalloproteinases. FEBS Lett 1992; 296: 263–6.
24 Angliker H, Neumann U, Molloy SS, Thomas G. Internally quenched fluorogenic substrate for furin. Anal Biochem 1995; 224: 409–12.
25 Mittoo S, Sundstrom LE, Bradley M. Synthesis and evaluation of fluorescent probes for the detection of calpain activity. Anal Biochem 2003; 319: 234–8.
26 Kuo CJ, Chi YH, Hsu JT, Liang PH. Characterization of SARS main protease and inhibitor assay using a fluorogenic substrate. Biochem Biophys Res Commun 2004; 318: 862–7.
27 Garcia-Echeverria C, Rich DH. New intramolecularly quenched fluorogenic peptide substrates for the study of the kinetic specificity of papain. FEBS Lett 1992; 297: 100–2.
28 Wang GT, Matayoshi E, Jan Huffaker H, Krafft GA. Design and synthesis of new fluorogenic HIV protease substrates based on resonance energy transfer. Tetrahedron Lett 1990; 31: 6493–6.
29 Matayoshi ED, Wang GT, Krafft GA, Erickson J. Novel fluorogenic substrates for assaying retroviral proteases by resonance energy transfer. Science 1990; 247: 954–8.
30 Maggiora LL, Smith CW, Zhang ZY. A general method for the preparation of internally quenched fluorogenic protease substrates using solid-phase peptide synthesis. J Med Chem 1992; 35: 3727–30.
31 Huang CK, Wei P, Fan KQ, Liu Y, Lai LL. 3C-like proteinase from SARS coronavirus catalyzes substrate hydrolysis by a general base mechanism. Biochemistry 2004; 43: 4568–74.
32 Copeland RA. Enzymes: A Practical Introduction to Structure, Mechanism, and Data Analysis. 2nd ed. New York: Wiley-VCH Inc; 2000.
33 Gorbalenya AE, Koonin EV, Donchenko AP, Blinov VM. Coronavirus genome: prediction of putative functional domains in the non-structural polyprotein by comparative amino acid sequence analysis. Nucleic Acids Res 1989; 17: 4847–61.
34 Marra MA, Jones SJM, Astell CR, Holt RA, Wilson AB, Butterfield YSN, *et al*. The genome sequence of the SARS-associated coronavirus. Science 2003; 300: 1399–403.
35 Lu Y, Denison MR. Determinants of mouse hepatitis virus 3C-like proteinase activity. Virology 1997; 230: 335–42.
36 Hegyi A, Friebe A, Gorbalenya AE, Ziebuhr J. Mutational analysis of the active centre of coronavirus 3C-like proteases. J Gen Virol 2002; 83: 581–93.

Full-length article

Using support vector classification for SAR of fentanyl derivatives[1]

Ning DONG, Wen-cong LU[2], Nian-yi CHEN, You-cheng ZHU[3], Kai-xian CHEN[3]

[2]Laboratory of Chemical Data Mining, Department of Chemistry, School of Science, Shanghai University, Shanghai 200436, China; [3]Shanghai Institute of Materia Medica, Chinese Academy of Sciences, Shanghai 201203, China

Key words

structure-activity relationship; support vector machine; fentanyl derivatives; support vector classification

[1] Project supported by the National Natural Science Foundation of China (No 20373040).
[2] Correspondence to Prof. Wen-cong LU.
Phn 86-21-6613-3513. Fax 86-21-6613-4275.
E-mail wclu@mail.shu.edu.cn

Received 2004-06-15
Accepted 2004-09-10

doi: 10.1111/j.1745-7254.2005.00014.x

Abstract

Aim: To discriminate between fentanyl derivatives with high and low activities. **Methods:** The support vector classification (SVC) method, a novel approach, was employed to investigate structure-activity relationship (SAR) of fentanyl derivatives based on the molecular descriptors, which were quantum parameters including ΔE [energy difference between highest occupied molecular orbital energy (HOMO) and lowest empty molecular orbital energy (LUMO)], MR (molecular refractivity) and M_r (molecular weight). **Results:** By using leave-one-out cross-validation test, the accuracies of prediction for activities of fentanyl derivatives in SVC, principal component analysis (PCA), artificial neural network (ANN) and K-nearest neighbor (KNN) models were 93%, 86%, 57%, and 71%, respectively. The results indicated that the performance of the SVC model was better than those of PCA, ANN, and KNN models for this data. **Conclusion:** SVC can be used to investigate SAR of fentanyl derivatives and could be a promising tool in the field of SAR research.

Introduction

Fentanyl, a synthetic opioid commonly used during anesthesia, is also used to relieve pain in terminally ill patients[1]. Fentanyl is lipophilic and has high potency as an analgesic or anesthetic, which can rapidly penetrate the central nervous system once taken by patients[2].

Support vector classification (SVC) is a machine learning method based on the support vector machine (SVM) proposed by Vladimir N Vapnik[3]. It has been recently proposed as a very effective method for pattern recognition. It has also been successfully used in such research fields as vowel recognition[4], drug design[5], combinatorial chemistry[6], prediction of beta-turn and alpha-turn types of proteins etc[7,8]. In the present work, the qualitative model was built based on SVC, with structural descriptors calculated by using the software Hyperchem, to explore the structure-activity relationship of fentanyl derivatives. The outstanding performance of the SVC model proved the significance of this method.

Methodology

Computational theory The SVC method was used in this work. The geometrical interpretation of SVC is that it chooses the optimal separating surface, ie the hyperplane equidistant from two classes. This optimal separating hyperplane has many nice statistical properties, which are detailed by Vapnik[3,9].

Consider the problem of separating the set of training vectors belonging to two separate classes, $(y_1, \mathbf{x}_1)$, ..., $(y_n, \mathbf{x}_n)$, $\mathbf{x}\in R^m$, $y\in$-1, +1, with a hyperplane

$$\mathbf{w}^T\mathbf{x}+b=0$$

If the training data are linearly separable, then there exists a pair $(\mathbf{w}, b)$ such that:

$$y_i(\mathbf{w}^T\mathbf{x}_i+b)-1\geq 0,\ i=1, 2, ..., l$$
$$\mathbf{w}^T\mathbf{x}+b\geq+1, \text{ for all } \mathbf{x}\in\boldsymbol{T};$$
$$\mathbf{w}^T\mathbf{x}+b\geq-1, \text{ for all } \mathbf{x}\in\boldsymbol{F};$$

The decision rule is:

$$f_{\mathbf{w},b}(\mathbf{x})=\text{sgn}(\mathbf{w}^T\mathbf{x}+b)$$

where $\mathbf{w}$ is termed the weight vector and b the bias. Without loss of generality the pair $(\mathbf{w}, b)$ can be rescaled such that:

$$\min_{i=1,2,\ldots,l} | \mathbf{w}^T\mathbf{x}_i+b | =1$$

The learning problem is hence reformulated as: minimize $\|\mathbf{w}\|^2$ subject to the constraints of linear separability. This is equivalent to maximizing the distance, normal to the hyperplane, between the convex hulls of two classes. The optimization is now a quadratic programming (QP) problem:

$$\underset{\mathbf{w},b}{Minimize}\ \phi(\mathbf{w})=\frac{1}{2}\|\mathbf{w}\|^2$$

subject to $y_i(\mathbf{w}^T\mathbf{x}_i+b)\geq 1$, $i=1, 2, \ldots, l$.

This problem has a global optimum. The Lagrangian for this problem is:

$$L(\mathbf{w}, b, \Lambda)=\frac{1}{2}\|\mathbf{w}\|^2-\sum_{i=1}^{l}\lambda_i[y_i(\mathbf{w}^T\mathbf{x}_i+b)-1]$$

where $\Lambda=\{\lambda_1,\mathrm{K},\ldots,\lambda_l\}$ are the Lagrange multipliers, one for each data point.

Hence we can write:

$$F(\Lambda)=\sum_{i=1}^{l}\lambda_i-\frac{1}{2}\|\mathbf{w}\|^2=\sum_{i}^{l}\lambda_i-\frac{1}{2}\sum_{i=1}^{l}\sum_{j=1}^{l}\lambda_i\lambda_j y_i y_j \mathbf{x}_i^T\mathbf{x}_j$$

note that the Lagrange multipliers are only non-zero when $y_i(\mathbf{w}^T\mathbf{x}_i+\mathrm{b})=1$, vectors for these cases are called support vectors since they lie closest to the separating hyperplane. Then the optimal separating hyperplane is given by:

$$\mathbf{w}^*=\sum_{i=1}^{l}\lambda_i^*\mathbf{x}_i y_i$$

and the bias is given by:

$$b^*=-\frac{1}{2}(\mathbf{w}^*)^T(\mathbf{x}_s+\mathbf{x}_r)$$

where $\mathbf{x}_r$ and $\mathbf{x}_s$ are any support vector from each class satisfying

$$y_r=1, y_s=-1$$

The hard classifier is then,

$$f(\mathbf{x})=\mathrm{sgn}[(\mathbf{w}^*)^T\mathbf{x}+b^*]$$

In the case where a linear boundary is inappropriate the SVC can map the input vector, $\mathbf{x}$, into a high dimensional feature space, F. By choosing a non-linear mapping Φ, the SVC constructs an optimal separating hyperplane in this higher dimensional space. Among the acceptable mappings are polynomials, radial basis functions and certain sigmoid functions. Then the optimization problem becomes,

$$W(\alpha)=\sum_{i=1}^{l}\alpha_i-\frac{1}{2}\sum_{i=1}^{l}\sum_{j=1}^{l}y_i y_j\alpha_i\alpha_j<\Phi(\mathbf{x}_i)\cdot\Phi(\mathbf{x}_j)>$$

In this case, the decision function in SVC is as follows:

$$g(\mathbf{x})=\mathrm{sgn}(f(\mathbf{x}))=\mathrm{sgn}\{\sum_{i\in SV}\alpha_i y_i<\Phi(\mathbf{x})\cdot\Phi(\mathbf{x}_i)>+b\}$$

$$=\mathrm{sgn}\{\sum_{i\in SV}\alpha_i y_i K(\mathbf{x},\mathbf{x}_i)]+b\}$$

where $\mathbf{x}_i$ is the support vectors and $K(\mathbf{x}, \mathbf{x}_i)$ is called kernel function.

Implementation of SVC The SVM software package including SVC was programmed according to the literature[3]. The software was tested in some applications in chemistry and chemical engineering[9,10]. All computations were carried out on a Pentium IV computer with a 1.3G Hz processor.

Results

Data set The data set consists of 14 fentanyl derivatives available[11]. The molecular formula investigated in this work is shown in Figure 1. The substituents of the compounds include R_1, R_2, and R_3. The data set can be divided into two classes according to the analgesic bioactivities ED_{50} (hot plate method in mice)[11] of samples. Here Class 1 contains the compounds with high activities, ie the molecules with ED_{50} $<1.0\times10^{-6}$ (mol/kg). Class 2 contains the compounds with low activities, ie the molecules with $ED_{50}>1.0\times10^{-6}$ (mol/kg).

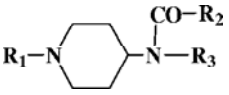

Figure 1. Structure of fentanyl derivatives.

Computation of descriptors The three-dimensional structures of the molecules were drawn, and optimized with the software Hyperchem3 (Release 7.0 for Windows Molecular Modeling System, Hypercube Inc. 2002), which was utilized for the computation of MM+ and PM3 later. Prior to the semi-empirical computation of quantum chemistry, all structures of the compounds were submitted to MM+ computation of molecular mechanics for energy optimization. The computations were carried out at a restricted Hartree-Fock level with no configuration interaction. The molecular structures were optimized using the Polak-Ribiere algorithm until the root-mean-square gradient was 0.001. Only the most stable conformation of molecule has been used to obtain the structural descriptors via the computational results of semi-empirical method PM3. Using the software Hyperchem3, the descriptors obtained were as follows: HOMO (highest occupied molecular orbital energy), LUMO (lowest empty molecular orbital energy), ΔE (energy difference between HOMO and LUMO), TE (total energy), HF (heat of formation), EE (electronic energy), SA (surface area), MV (molecular volume), lgP (partition coefficient), MR (molecular refractivity), MP (molecular polarizability), M_r (molecular weight), N1 (charge density of the atom N connecting with R_1), C2 (charge density of the atom C connecting with R_2), N3 (charge density of the atom N connecting

with R_3).

Selection of descriptors The selection of descriptors is a relatively tough job due to the redundancy of some parameters. The result used to depend on the experience of the researcher. Recently, some of promising results have been reported on the problem of feature selection[12,13]. In this work, the entropy method was applied to the selection of descriptors[14]. Through the computation of entropy for the data set available, the three descriptors (ΔE, MR, M_r) are determined to be more important than the others. Table 1 lists the samples with bioactivity ED_{50} and selected descriptors, including ΔE, MR, and M_r. It should be mentioned that there possibly exist other combinations of descriptors useful for the classification of data set used here, but the three descriptors above are enough to be used as the determining factors for the prediction of activities of the compounds (refer to the good results described in the following sections).

Selection of the kernel function and the capacity of parameter *C* used in the SVC model Similar to other multivariate statistical models, the performance of SVC is related to dependent and independent variables as well as the

Table 1. The descriptors of structures and bioactivities of the samples.

No	R_1	R_2	R_3	ED_{50}/mol·kg^{-1}	ΔE/eV	MR	M_r
1	$PhCH_2CH_2$–	Et–	Ph–	1.70×10^{-10}	8.767	103.5	336.5
2	PhCH(OH)-CH(CH_3)-	Et–	Ph–	1.40×10^{7}	8.947	109.1	366.5
3	$PhCH_2CH_2$–	CH_2=CH–	Ph–	2.20×10^{-7}	9.136	103.5	334.5
4	$PhCH_2CH_2$–	FCH_2CH_2–	Ph–	3.30×10^{7}	9.186	103.6	354.5
5	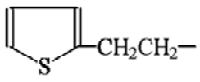	Et–	Ph–	5.70×10^{-7}	8.752	105.0	342.5
6	PhCH(OH)CH_2—	Et–	Ph–	8.40×10^{-7}	8.797	104.7	352.5
7	$PhCH_2CH_2$–	Et–	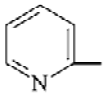	8.80×10^{-7}	8.523	104.2	337.5
8	$PhCH_2CH_2$–	Et–	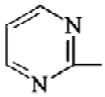	8.90×10^{-7}	8.856	101.3	338.5
9	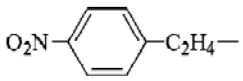	Et–	Ph–	1.10×10^{-5}	8.057	110.8	381.5
10	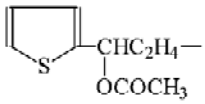	Et–	Ph–	1.60×10^{-5}	8.811	120.1	414.6
11	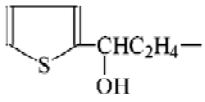	Et–	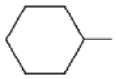	2.40×10^{-5}	8.502	112.2	378.6
12	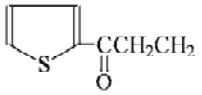	Et–	Ph–	3.70×10^{-5}	8.235	110.1	370.5
13	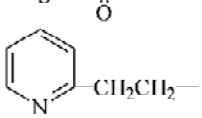	Et–	Ph–	3.80×10^{-5}	8.911	105.4	337.5
14	CH_2=$CHCH_2$–	Et–	Ph–	4.60×10^{-5}	9.238	83.28	272.4

combination of parameters used in a model. In the computation of SVC, we have to deal with the capacity parameter *C* (also called the regularization parameter) and the kernel type used in modeling.

In this work, the cross validation test, using the leaving-one-out (LOO) method was undertaken to find a suitable capacity parameter *C* and the appropriate kernel function for the SVC model. Suppose that P_w is the number of samples misclassified using the LOO method; it can then be employed as a criterion to obtain the appropriate kernel function and the optimal capacity parameter *C*. Figure 2 illustrated P_w (concerned with different kernel functions including linear, radial, polynomial and sigmoid functions) versus the capacity parameter *C* from 0.1 to 250. It was found that the SVC model with the best performance could be ascertained by using the radial kernel function with capacity parameter *C* from 50 to 100.

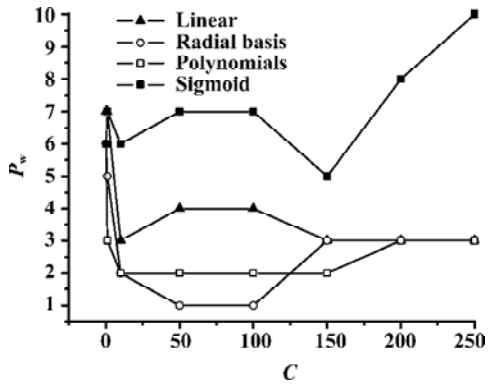

Figure 2. P_w (the number of samples misclassified using LOO method) versus the *C* (capacity parameter) using LOO method with different kernel functions.

Modeling of SVC According to the results we abtained, the optimal model of SVC for discriminating between high and low activities of compounds could be built as follows, using the radial kernel function with capacity parameter *C*=100:

$$g(\mathbf{x})=\mathrm{sgn}\left(\sum_{i\in SV}\alpha_i y_i \exp\{-\frac{\|\mathbf{x}-\mathbf{x}_i\|^2}{\sigma^2}\}+b\right)$$

where σ=1, *b*=0.68, α_i=36.1 (*i*=2), 21.8 (*i*=3), 55.1 (*i*=5), 19.3 (*i*=7), 0 (*i*=10), 30.5 (*i*=11), 100 (*i*=13), 1.84 (*i*=14), correspond to the Lagrange multipliers of support vectors, while all the others. α_i=*0*. y_i=1 for the samples of class 1; y_i=-1 for the samples of class 2. $\mathbf{x}_i$ is a vector (pattern of sample) with unknown activity to be discriminated, $\mathbf{x}_i$ is one of the support vectors. Based on this SVC model, the samples were discriminated as those of high bioactivities (ED_{50}< 1.0×10^{-6} mol/kg), if $g(\mathbf{x})\geq0$. Using SVC model for the classification of activities of fentanyl derivatives, the accuracy of classification was 93% by using radial basis kernel functions with the capacity parameter *C*=100. Table 2 lists the trained results from SVC model obtained above. Figure 3 illustrated the effect of classification with trained SVC model. It was found that only one sample (compound No 13) was misclassified.

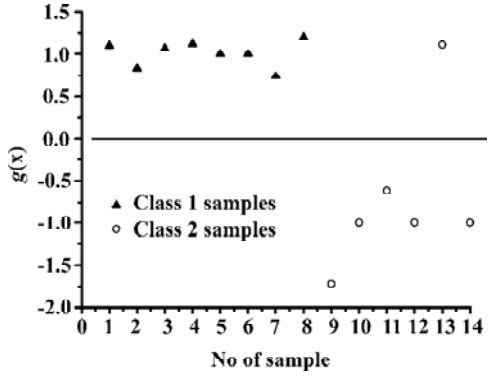

Figure 3. Effect of classification with trained SVC model.

Results of cross validation tests Figure 4 illustrated the effect of the cross validation test using LOO method of SVC. It is obvious that the quality of prediction results (Figure 4) is as good as that of trained results (Figure 3), also with only one sample (compound No 13) discriminated wrong. Table 2 lists the predicted results obtained by using LOO method of SVC model.

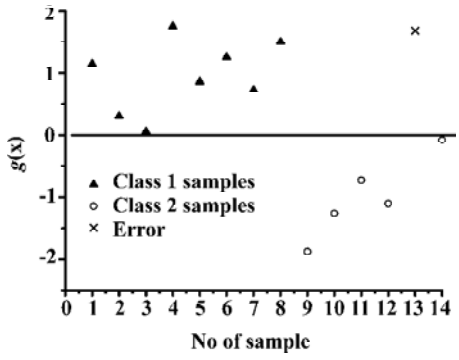

Figure 4. Predicted effect of classification with LOO (leaving-one-out) test of SVC.

For comparisons with other data mining methods, three commonly used chemometric methods including principal

Table 2. Data set available and results of computation using the LOO test.

Sample No	1	2	3	4	5	6	7	8	9	10	11	12	13	14
Actual Class	1	1	1	1	1	1	1	1	2	2	2	2	2	2
TSVC[a] Class	1	1	1	1	1	1	1	1	2	2	2	2	1	2
PSVC[b] Class	1	1	1	1	1	1	1	1	2	2	2	2	1	2
TPCA[c] Class	1	1	1	1	1	1	1	1	2	2	2	2	1	2
PPCA[d] Class	1	1	2	1	1	1	1	1	2	2	2	2	1	2
TANN[e] Class	2	1	2	1	2	1	1	1	2	2	2	2	2	2
PANN[f] Class	1	2	2	1	1	1	2	1	2	2	1	2	1	1
PKNN[g] Class	1	1	1	1	1	1	1	1	1	2	1	1	1	2

a: TSVC Class means trained class by using SVC method; b: PSVC Class means predicted class by using leaving-one-out (LOO) test of SVC method; c: TPCA Class means trained class by using PCA method; d: PPCA Class means predicted class by using leaving-one-out (LOO) test of PCA method; e: TANN Class means trained Class by using ANN method; f: PANN Class means predicted class by using leaving-one-out (LOO) test of ANN method; g: PKNN Class means predicted class by using K-nearest neighbor (KNN) method.

Table 3. The number of samples predicted wrongly using the LOO test of different models.

Algorithm	SVC	PCA	ANN	KNN
N_w (No in Table 2)	1 (13)	2 (3,13)	6 (2,3,7,11,13,14)	4 (9,11,12,13)

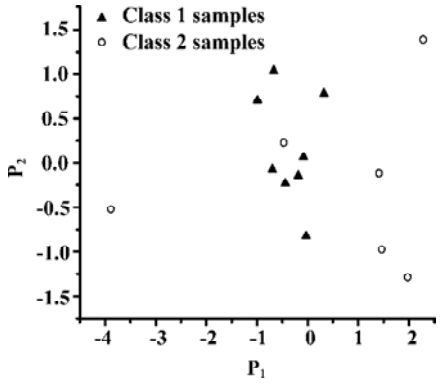

Figure 5. Classification diagram using PCA method.

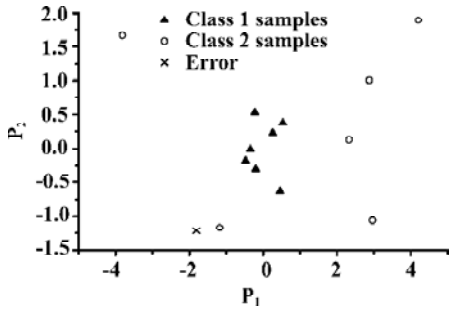

Figure 6. Location of No 3 sample predicted using PCA

component analysis (PCA), K-nearest neighbor (KNN) and artificial neural network (ANN) were utilized to investigate SAR of fentanyl derivatives, with special consideration of their predictive ability (generalization ability) from cross validation tests using LOO method.

Figure 5 illustrated the trained results of classification for the same data set using PCA method. It could be seen from Figure 5 that the quality of classification results was as good as thoses from the SVC model, with only one sample misclassified. However, there were two samples predicted wrong from the results of cross validation test using LOO method of PCA. Figure 6 and Figure 7 illustrated the locations of samples marked No 3 and No 13, whose predicted classes did not agree with the actual ones determined using the LOO test of PCA method.

KNN method, as a helpful pattern recognition tool, was utilized to discriminate between high and low activities of compounds for the same data set, with the accuracy of prediction being 71% (K=5). Obviously, the predictive ability of KNN model was poor compared to that of SVC model in this situation.

So far as BP ANN model is concerned, ANN with three

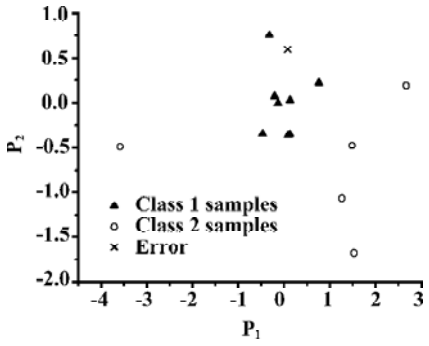

Figure 7. Location of No 13 sample predicted using PCA method.

layers was used to build the relationship between the features and activities of compounds. The number of hidden nodes was three; the transformation function used was Sigmoid; the number of training steps was 250 000. Table 2 lists both trained results and predicted results using LOO method, based on the ANN model built. It was found from Table 2 that the trained results of classification were not as good as the predicted ones. There were only three (No 1, No 3, and No 5) samples misclassified for the trained set, with the accuracy of classification being 79%. However, there were six samples that were wrongly classified from the results of the cross validation test using LOO method of ANN model. Table 3 lists *N*w (the number of samples to be predicted wrong) using LOO test of different models. It could be concluded that the predictive ability of SVC model was superior to that of PCA, KNN, and ANN models for the data set available.

Discussion

The SVC has been introduced as a robust and highly accurate intelligent classification technique, likely to be a useful chemometrics tool. On a simple but real chemometric problem the predictive ability of SVC for the data set available here outperforms that of PCA, KNN and ANN methods, which are the most frequently used chemometric techniques. The SVC exhibits better overall performance because it embodies the structural risk minimization principle. It has an advantage over the other techniques because it converges to the global optimum, and not to a local optimum that depends on the initialization and parameters affecting the rate of convergence. It can be concluded that (1) the selected descriptors can account for the features of the fentanyl derivatives; (2) the SVC is a very promising tool for the approximation of qualitative classification and (3) the SVC is especially suitable for finding the regularities of the small data set, ie, data set with fewer samples, giving modeling results with good generalization ability.

Training and optimization using SVC are easier and faster compared with other machine learning techniques, because there are fewer free parameters and only support vectors (only a fraction of all data) are used in the generalization process. The results show that the SVC is a good approach for predicting the classes of fentanyl derivatives. At the same time, the models proposed could identify and provide some insight into what features are related to the classification of these compounds and afford some instruction for further recognizing new fentanyl derivatives. It should be noted that no single method or paradigm is uniformly superior, although the preliminary evidence presented in this work suggests that the SVC is a data-mining tool with great potential in chemometric application.

References

1 Maddocks I. Subcutaneous administration of fluid and drugs in palliative care. Aust J Hosp Pharm 1992; 22: 181–4.
2 Gerak LR, Moerschbaecher JM, Bagley JR, Brockunier LL, France CP. Effects of a novel fentanyl derivative on drug discrimination and learning in rhesus monkeys. Pharmacol Biochem Behav 1999; 64: 367–71.
3 Vapnik VN. Statistical learning theory. New York: John Wiley and Sons; USA; 1998.
4 Wan V, Campbell WM. Support vector machines for speaker verification and identification. Neural networks for signal processing X, Proceedings of the 2000 IEEE Signal Processing Workshop. IEEE 2000; 2: 775–84.
5 Burbidge R, Trotter M, Buxton B, Holden S. Drug design by machine learning support vector machines for pharmaceutical data analysis. Comput Chem 2001; 26: 5–14.
6 Trotter M, Buxton B, Holden S. Support vector machines in combinatorial chemistry. Meas Control 2001; 34: 235–9.
7 Cai YD, Liu XJ, Li YX, Xu XB, Chou KC. Prediction of beta-turns with learning machines. Peptides 2003; 24: 665–9.
8 Cai YD, Feng KY, Li YX, Chou KC. Support vector machine for predicting alpha-turn types. Peptides 2003; 24: 629–30.
9 Lu WC, Chen NY, Ye CZ, Li GZ. Introduction to the algorithm of support vector machine and the software ChemSVM. Comput Appl Chem 2002; 19: 697–702.
10 Chen NY, Lu WC. Support vector machine applied to chemistry and chemical technology. Comput Appl Chem 2002; 19: 673–6.
11 Zhu YC, Fang SN, Ge BL, Li QZ, Dai QY, Huang ZM, *et al*. Studies on potent analgesics 2. Synthesis and analgesic activity of the derivatives. Acta Pharm Sin 1981; 16: 97–104. [in Chinese]
12 Li GZ, Wang ZX, Yang J, Yao LX, Chen NY. A SVM-based feature selection method and its applications. Comput Appl Chem 2002; 19: 703–5.
13 Dash M, Liu H. Feature selection for classification. Intell Data Anal 1997; 1: 131–56.
14 Chen NY, Qin P, Chen RL, Lu WC. Pattern recognition applied to chemistry and chemistral industry. Beijing: Science Press; 2000.

Full-length article

Evaluation of drug-muscarinic receptor affinities using cell membrane chromatography and radioligand binding assay in guinea pig jejunum membrane

Bing-xiang YUAN[1], Jin HOU, Lang-chong HE[2], Guang-de YANG[2]

Department of Pharmacology; [1]Pharmacy College, Xi-an Jiaotong University, Xi-an 710061, China

Key words

chromatography; cell membrane; muscarinic receptors; radioligand assay; jejunum

[1] Corresponding to Prof. Bing-xiang YUAN.
Phn 86-29-8265-5165.
E-mail ybx@mail.xjtu.edu.cn

Received 2004-02-03
Accepted 2004-06-22

doi: 10.1111/j.1745-7254.2005.00015.x

Abstract

Aim: To study if cell membrane chromatography (CMC) could reflect drug-receptor interaction and evaluate the affinity and competitive binding to muscarinic acetylcholine receptor (mAChR). **Methods:** The cell membrane stationary phase (CMSP) was prepared by immobilizing guinea pig jejunum cell membrane on the surface of a silica carrier, and was used for the rapid on-line chromatographic evaluation of ligand binding affinities to mAChR. The affinity to mAChR was also evaluated from radioligand binding assays (RBA) using the same jejunum membrane preparation. **Results:** The capacity factor (*k'*) profiles in guinea pig jejunum CMSP were: (-)QNB (15.4)>(+)QNB (11.5)>atropine (5.35)>pirenzepine (5.26)>4-DAMP (4.45)>AF-DX116 (4.18)>pilocarpine (3.93)>acetylcholine (1.31). These results compared with the affinity rank orders obtained from radioligand binding assays indicated that there was a positive correlation (r^2= 0.*8525, P*<0.0001) between both data sets. **Conclusion:** The CMC method can be used to evaluate drug-receptor affinities for drug candidates.

Introduction

Radioligand binding assay (RBA) is a traditional method in studying drug-receptor interactions. Although radioligand binding assay has some advantages, such as high sensitivity, it results in radioactive pollution and needs special separation methods. Cell membrane chromatography (CMC), a new bio-affinity chromatography technique originated by Dr He in 1999[1], can be used to observe the binding of a drug and target (including receptor), simply and conveniently.

Previous experiments have indicated that the receptors immobilizing on the cell membrane stationary phase (CMSP) remain bio-active[2,3]. However, it is necessary to study whether this approach can be adopted to evaluate drug-receptor interaction and reflect affinity and competitive binding, although CMC has previously been used to screen for drug and herb candidates[4,5].

Materials and methods

Animals and drugs Adult guinea pigs (350–400 g) of either sex were provided by the Experimental Animal Center of Xi-an Jiaotong University, China. Atropine, pirenzepine, nicotine, pilocarpine, 4-diphenylacetoxy-*N*-methylpiperidine (4-DAMP), 11-2{[2-[(diethylamino) methyl]-1-piperidinyl]acetyl}-5,11-dihydro-6*H*-pyrido-(2,3-b) (1,4) benzodiazepine-6-one (AF-DX116) were purchased from Sigma Co. Acetylcholine (ACh) was purchased from Shanghai Medical Co. (-)QNB and (+)QNB was provided by RBI Co. Tritiated quinuclidinyl benzilate ([^{3}H]QNB) was purchased from Amersham Radio-Chemical Center with a radioactivity of 1813 TBq/mol.

Membrane preparation of jejunum vertical muscle Guinea pigs were killed and the jejunum was removed immediately. The intestine was washed thoroughly in normal saline and the canal was rubbed vertically using a tampon; then the vertical muscle was cut into small pieces and added to ice-cold PBS buffer. The tissue suspension was homogenized under a cradle at 4 ºC (twice, for 1 min each). The crude homogenate was centrifuged at 600×*g* for 10 min to remove cellular debris. The supernatant was filtered through cheesecloth and then centrifuged for 40 min at 20 000×*g*. The buff-colored layer around the pellet was gen-

tly resuspended in the above buffer and centrifuged as previously explained[6,7].

Radioligand-receptor binding assay [^{3}H]QNB with a radioactivity of 37 PBq/L, was used as a ligand to label muscarinic binding sites in membrane prepared from guinea pig jejunum. Aliquots (200 μL) of the membrane suspensions were incubated with 0.5 nmol/L [^{3}H]QNB in 50 mmol/L PBS buffer for 40 min at 37 ºC. Non-specific binding was estimated from the duplicate tube containing 0.01 mmol/L atropine. The drug-receptor affinities were estimated by pK_D.

$$pK_D = - \lg K_D$$

Chromatography experiment With a known concentration-competitive ligand added in the mobile phase, the combination between ligand and receptor protein was saturated on the CMSP. At the key time, the solute eluted from CMSP was increased drastically, thus forming a characteristic curve breakage. Conceptually, there are mean breakage sites in the curve, which only relate to the equilibrium dissociation constant or relationship between drug concentration and the number of receptors on the CMSP column. Moreover, in the solute disassociation process, the result can be analyzed by Scatchard-Plot method:

$$\frac{1}{M_{Lapp}} = \frac{1}{K_a M_L [D]} + \frac{1}{M_L}$$

where M_{Lapp} is the mole number of drug at mean breakage site, [D] is drug concentration, K_a is association constant of the drug, and M_L is the total number of combination site of receptor protein on the column. If non-specific combination can not be neglected, the following formula is obtained: where V is the retention volume of drug, [P] is the concentration of receptor combination site, V_{min} is retention volume

$$\frac{1}{V_{max}-V_i} = \frac{1+[D]K_a}{V_{min}[P]K_{aX}} + \frac{(1+[D]K_a)^2}{V_{min}[P]K_{aX}} \cdot \frac{1}{[X]}$$

of drug when the specific interaction is completely inhibited, and V_{max} is obtained from the formula. [X] is the concentration of additive, which completes the same site of D. V_{max} is the retention volume of [D] at low concentration ([D]<<1/K_a, V=V_{max}) and V_x is the retention volume of D when competitive interaction exists. The value of V_{min} can be determined by regressing 1/(V_{max}-V)versus 1/[D] extrapolating to infinite (V_I=V_{min}).

$$\frac{1}{V-V_{min}} = \frac{1}{V_{min}[P]K_a} + \frac{1}{V_{min}[P]} \cdot [D]$$

In the chromatographic system, the capacity factor (k') can reflect the mole fraction ratio of stationary and mobile phase at equilibrium. The silica surface is completely coated by the cell membrane in CMSP, so k' is characteristic of the action between the drug and the cell membrane, which means, the larger k' showes a stronger affinity for the same chromatographic condition.

CMSP was prepared by immobilizing above guinea pig jejunum cell membrane on the surface of a silica carrier, provided by the Pharmacy Center of Xi'an Jiaotong University[4], China. CMSP was packed in the chromatography column (50 mm×2 mm, id, 7 μm) and equilibrated with at least 15 mL PBS buffer 50 mmol/L before runing different ligands. The mobile phase was pumped through the column at a flow rate of 0.5 mL/min at 37 ºC. Before different ligands were injected, the column was equilibrated with at least 15 mL PBS mobile phase 50 mmol/L. When 0.01 mmol/L atropine was added to the PBS buffer, the column was equilibrated again with this mobile phase before injection. Capacity factors were calculated from:

$$k' = (t_R - t_0)/t_0$$

where t_R is retention time of ligands, and t_0 is retention time of solvent. Ligand retention time was detected by ultraviolet on-line in 190-230 nm wavelength.

Statistical analysis Values were presented as mean±SD. Correlation between both data sets were analyzed by linear regression using GraphPad Prism 2.01.

Results

Radioligand-receptor binding experiment Competition for [^{3}H]QNB binding by unlabelled ligands showed different affinity in guinea pig jejunum membrane. None of the Hill coefficient was significantly different from unity. The rank orders of potency (pK_d) were (-)QNB>(+)QNB> atropine>4-DAMP>AF-DX116>pirenzepine>pilocarpine> ACh. Nicotine had little affinity with muscarinic receptor (Table 1).

Cell membrane chromatography experiment In the CMC experiment, capacity factors (k') were used to describe the ligand-CMSP affinity. The bigger the capacity factor, the stronger the affinity will be. The sequence of the relative affinities of selected ligands were (-)QNB >(+)QNB> atropine>pirenzepine>4-DAMP>AF-DX116>pilocarpine> ACh, which were consistent with results calculated from radioligand binding assays, except for pirenzepine. Yet and nicotine had some capacity factor. When atropine was added in the mobile phase the capacity factor of (-)QNB, (+)QNB, atropine, pirenzepine, 4-DAM, AF-DX116, pilocarpine and ACh could be reduced, while the capacity factor of nicotine could not be reduced (Table 2).

Table 1. Binding parameters of different ligands in muscarinic receptor of guinea pig jejunum membrane detected by using [^{3}H]QNB displacement experiment.

Ligand	pK_D			
	x_1	x_2	x_3	Mean±SD
(-)QNB	8.72	8.66	8.84	8.74±0.09
(+)QNB	7.23	7.12	7.21	7.19±0.06
Atropine	7.05	6.60	6.75	6.80±0.23
4-DAMP	6.38	6.18	6.30	6.29±0.10
AF-DX116	6.21	6.40	6.23	6.28±0.10
Pirenzepine	5.67	6.05	6.03	5.92±0.21
Pilocarpine	5.33	5.28	5.40	5.34±0.06
Ach	5.07	4.70	4.86	5.25±0.17
Nicotine	2.97	3.05	3.04	3.02±0.04

QNB: quinuclidinyl benzilate; 4-DAMP: 4-diphenylacetoxy-*N*-methylpiperidine; AF-DX116: 11-2{[2-[(diethylamino)methyl]-1-piperidinyl] acetyl}-5,11–dihydro-6*H*-pyrido-(2,3-b)(1,4) benzodiazepine-6-one; ACh: acetylcholine. The guinea pig jejunum homogenates were incubated with 0.5 nmol/L [^{3}H]QNB for 40 min at 37 ºC in the presence of tested ligands.

Discussion

The results of the present study demonstrated that membrane preparation including mACh receptor could be immobilized on the stationary phase with retention of their binding activities. Different ligands had different capacity factors and the rank orders were consistent with results from radioligand binding assay except for pirenzepine. During the experiment, when atropine was added to the mobile phase the capacity factor of (-)QNB, (+)QNB, atropine, pirenzepine, 4-DAMP, AF-DX116, pilocarpine, and ACh decreased. This indicated that those ligands could bind to mACh receptor on CMSP and the affinity could be inhibited in competitive displacement by atropine. The capacity factor of nicotine could not be decreased in competitive displace-ment, so the ligands have no competitive site with atropine. Therefore, we can infer that capacity factor can evaluate the affinity of ligand-mACh receptor and reflect the selectivity and specificity of drug-receptor interaction. While at present the equilibrium dissociation constant can not be calculated by CMC method directly, linear regression analysis showed that both the data sets correlated with r^2=0.8525 (n=24), P<0.0001 in PBS mobile phase, or with r^2=0.8461 (n=24), P<0.0001 in PBS mobile phase with 0.01 mmol/L atropine (Figure 1).

It was demonstrated that the CMC model could be used to observe binding of the drug and receptor on a dynamic condition, and the characters of drug-receptor interactions can be shown by chromatographic parameters of drugs on the CMC model. However, we noticed that affinity rank orders from different methods were not entirely consistent. In the CMC model, affinity of pirenzepine according to the k' value was relatively higher than the corresponding affinity determined using radioligand binding assay. Similar results about pirenzepine were observed in other study[8]. When atropine was added in the mobile phase, the affinity discrepancy was not eliminated. The source of the different affinity orders is not readily elucidatory. It would be likely to blame low sensitivity of the CMC model for the ligands, because most ligands of mACh receptor are at the margin of ultraviolet on-line in 190–230 nm wavelength, or outward of the range. It is necessary for us to improve the sensitivity of the

Table 2. Capacity factor (k') of different ligands measured using cell membrane stationary phase in mobile phase of PBS and PBS with 0.01 mmol/L atropine.

Ligand	k'							
	PBS				PBS with 0.01 mmol/L atropine			
	x_1	x_2	x_3	Mean±SD	x_1	x_2	x_3	Mean±SD
(-)QNB	14.9	15.6	15.7	15.4±0.44	11.7	12.2	10.7	11.5±0.76
(+)QNB	11.6	12.0	10.9	11.5±0.56	8.24	8.89	8.11	8.41±0.42
Atropine	5.19	5.93	4.94	5.35±0.51	4.03	4.47	4.13	4.21±0.23
Pirenzepine	5.12	5.40	5.25	5.25±0.14	4.38	4.86	4.67	4.64±0.24
4-DAMP	4.12	4.94	4.29	4.45±0.43	3.85	3.29	3.36	3.50±0.31
AF-DX116	4.44	3.97	4.12	4.18±0.24	2.99	3.31	3.11	3.14±0.16
Pilocarpine	3.54	4.13	4.13	3.93±0.34	3.02	3.30	3.08	3.13±0.15
ACh	1.14	1.43	1.37	1.31±0.15	1.13	0.97	0.97	1.02±0.09
Nicotine	1.14	0.99	1.08	1.07±0.08	1.03	1.20	1.08	1.10±0.09

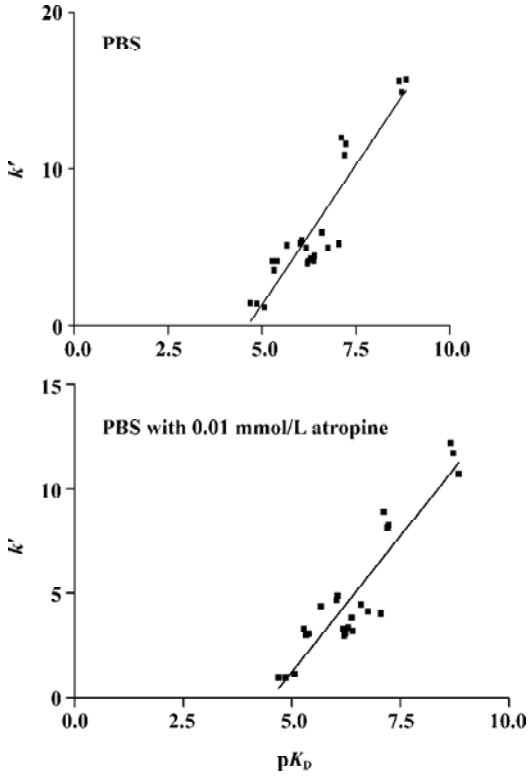

Figure 1. Relationship between capacity factor (k') and negative logarithm of equilibrium dissociation constant (pK_D). PBS: Y=3.754X-16.55, r^2=0.8525, n=24, P <0.0001; PBS with 0.01 mmol/L atropine: Y=2.607X-11.81, r^2=0.8461, P<0.0001.

CMC model by using other detectors, like a fluorescence detector or laser detector. Before further study, CMC can be used to screen for drug candidates and accuracy can be validated by traditional radioligand binding assay. The development of CMC could offer a number of unique advantages. The receptors can be placed in a stabilized format and could therefore be reused over a long period of time. Thus, it might be possible to perform multiple experiments with hard-to-obtain receptors using an immobilized format.

References

1 He LC, Yang GD, Geng XD. Enzymatic activity and chromatographic characteristics of the cell membrane immobilized on silica surface. Chin Sci Bull 1999; 44: 826–31.

2 He LC, Wang SC, Geng XD. Coating and fusing cell membranes onto a silica surface and their chromatographic characteristics. Chromatographia 2001; 54: 71–6.

3 He LC, Geng XD. Cell membrane chromatography-a new technique in studying drug-receptor interaction. In: Zhou TH , Liu GQ, editors. Biomedical Chromatography Progress. Beijing: Chemical Industry Publishing House; 1996. p 8–10.

4 He LC, Yang GD, Wang SC. Evaluation of drug-calcium channels reaction using cell membrane chromatography. Chin J Pharmacol Toxicol 1998; 14: 959–61.

5 Zhao HR, Yang GD, He LC, Yang YJ. Screening effective components of angelica using cell membrane chromatography. Chin Pharm J 2000; 35: 13–5.

6 Michael ID, Robert PS. Ligand interactions with membrane-bound porcine atrial muscarinic receptors. Biochemistry 1980; 19: 3407–13.

7 Nedoma J, Slavikova J, Tucek S. Muscarinic acetylcholine receptors in the heart of rats before and after birth. Pflugers Arch 1986; 406: 45–50.

8 Hou J, Yuan BX, He LC, Yang GD, Mi M. Evaluation of drug-muscarinic receptor affinities by using cell membrane chromatography. Chin J Pharmacol Toxicol 2003; 17: 70–3.

Full-length article

Melatonin attenuates 1-methyl-4-phenylpyridinium-induced PC12 cell death

Jin-feng BAO[1], Ren-gang WU[2], Xiao-ping ZHANG, Yan SONG, Chang-ling LI

Department of Pharmacology, School of Pharmaceutical Sciences,[2]Department of Medical Psychology, Beijing University Health Science Center, Beijing 100083, China

Key words

PC12 cells; melatonin; 1-methyl-4-phenylpyridinium; glucose

[1] Correspondence to Dr Jin-feng BAO.
Phn 86-10-6305-1366.
E-mail srgltlsn93@hotmail.com
Now in *Beijing Institute for Neuroscience, Capital University of Medical Sciences, Beijing 100054, China*.

Received 2004-06-11
Accepted 2004-08-13

doi: 10.1111/j.1745-7254.2005.00004.x

Abstract

Aim: To explore the effect of melatonin on PC12 cell death induced by 1-methyl-4-phenylpyridinium (MPP^+). **Methods:** MTT assay, lactate dehydrogenase (LDH) efflux assay, and immunohistochemistry methods were used to measure neurotoxicity of PC12 cells treated acutely with MPP^+ in low glucose and high glucose conditions, and to assess the neuroprotective effect of melatonin on PC12 cell death induced by MPP^+. **Results:** In a low glucose condition, MPP^+ significantly induced PC12 cell death, which showed time and concentration dependence. In a serum-free low glucose condition, the percentages of viability of cells treated with MPP^+ for 12, 24, 48, 72, and 96 h were 85.1%, 75.4%, 64.9%, 28.15%, and 9%, respectively. The level of LDH in the culture medium increased and tyrosine hydroxylase positive (TH^+) cell count decreased. However, in a serum-free high glucose condition, MPP^+ did not significantly induce PC12 cell death compared with control at various concentrations and time regimens. When the cells were preincubated with melatonin 250 μmol/L for 48, 72, and 96 h in a serum-free low glucose condition, cell survival rate significantly increased to 78.1%, 58.8%, and 31.6%, respectively. Melatonin abolished the LDH leakage of cells treated with MPP^+ and increased TH^+ cells count. **Conclusion:** MPP^+ caused concentration-dependent PC12 cell death. The level of glucose was an important factor to MPP^+ induced dopaminergic PC12 cell death. Low glucose level could potentiate MPP^+ toxicity, while high glucose level could reduce the toxicity. In addition, melatonin attenuated PC12 cell death induced by MPP^+.

Introduction

1-Methyl-4-phenyl-1,2,3,6-tetrahydropyridine (MPTP)-mediated selective damage to dopaminergic neurons of the nigrostriatal pathway has been widely used as a model of Parkinson's disease (PD)[1–3]. MPTP is a lipophilic molecule that is able to cross the blood-brain barrier. This cytotoxin has provided important information on the potential mechanisms of PD. It induces toxicity through its conversion of astrocytes to 1-methyl-4-phenylpyridinium (MPP^+) in the reaction catalyzed by monoamine oxidase type B (MAO-B)[4]. MPP^+ is selectively transported into the dopaminergic neurons through a high-affinity dopamine (DA) transporter and accumulates in the neuronal mitochondria, where it disrupts cellular respiration inhibiting complex I of the electron transport chain, depletes adenosine triphosphate (ATP) in the mitochondria[5,6], increases sensitivity to oxidative attack, and eventually causes apoptotic or necrotic neuronal cell death. It is reported that the deleterious effects of MPTP are results of the generation of oxygen free radicals either during oxidation of MPTP to MPP^+, or during electron transport chain disruption by MPP^+. In addition, MPP^+ might induce the release of DA, which in turn could generate free radicals from auto-oxidation[7,8]. Although it has been found that the accumulation of MPP^+ in dopaminergic neurons is a critical step for DA neurotoxicity, the exact molecular mechanisms underlying MPP^+-induced neuronal death have not been clear. Thus, elucidating the molecular basis of the cell death trig-

gered by MPP^+ could provide valuable insight into the pathogenesis of PD.

Melatonin is an indole hormone produced primarily in the pineal gland and the retina. It is classically known to be involved in the regulation of circadian and seasonal rhythms and sleep-inducing properties. In 1993, it was first reported by Tan *et al* as an efficient endogenous antioxidant[9]. Since then, evidence is shown that this molecule is one of the best physiological antioxidants. Different from other potent antioxidants, melatonin is soluble in both lipids and water, allowing itself to easily enter cells or pass the blood-brain barrier. So melatonin is available to all nerve cell compartments and shows high levels, especially in the nucleus and mitochondria. Recently, it has been proposed that the most important function of this hormone is scavenging harmful free radicals, especially hydroxyl radicals. Tan *et al*[9] made the unexpected observation that melatonin was much more efficient than the important intracellular antioxidant glutathione (GSH) in scavenging ·OH. Mayo *et al*[10] also reported that melatonin regulated the mRNA of antioxidant enzymes in dopaminergic cells after addition of the neurotoxin 6-OHDA, which might indicate a neuroprotective mechanism. However, intracellular effects of melatonin are largely unknown at present, in contrast to well-studied antioxidant activity.

PC12 cell is a clonal cell line of rat pheochromocytoma cells that respond to nerve growth factor by extending neuritis and acquiring the appearance of neurons. Cells with and without nerve growth factor treatment synthesize, store, secrete, and take up dopamine by similar processes to those of dopaminergic neurons[11], and express DA transporter[12]. Although they are not true brain DA neurons, PC12 cells have been used extensively as an experimental system for the study of various aspects of dopaminergic neurons and neurotoxins[13–15]. In this study, we used PC12 cells as a model cell line of DA-containing neurons and investigated the effects of melatonin on MPP^+-induced cell death.

Materials and methods

Materials Dulbecco's modified Eagle's medium (DMEM), fetal calf-serum and benzylpenicillin/streptomycin were pruchased from GIBCO (Langley, OK, USA). Poly-*L*-lysine, trypsin, dimethylsulfoxide (Me_2SO), diaminobenzidine (DAB), 3-(4,5-Dimethylthiazol-2-yl)-2,5-diphenyltetrazolium bromide (MTT) were purchased from Sigma (St Louis, MO, USA). MPP^+-iodine was purchased from Sigma-Aldrich. Rabbit polyclonal anti-tyrosine hydroxylase (TH) antiserum was purchased from Chemicon (Tenecula, CA, USA). Biotinylated goat anti-rabbit IgG, horseradish peroxidase-conjugated secondary antibodies, ABC kit were purchased from Santa Cruz Biotechnology (Santa Cruz, CA, USA). Melatonin was purchased from Sigma and dissolved in absolute ethanol before being diluted with saline. All other chemicals were of analytical grade and commercially available.

PC12 cells culture and treatment PC12 cells were obtained from the Shanghai Cell Research Institute and cultured at a density of 1×10^4 cells/cm^2 on poly-*L*-lysine-coated plates. Cells were cultured in high-glucose DMEM supplemented with heat-inactivated 10% fetal bovine serum, 5% horse serum, benzylpenicillin 100 kU/L, and streptomycin 100 mg/L. They were grown at 37 ºC in a humidified atmosphere containing 5% CO_2 and subcultured every 2–3 d at approximately 70%–80% confluence. Cells were subsequently switched to 5% fetal calf serum low glucose, serum-free high glucose, and serum-free low glucose DMEM medium, containing various experimental reagents, and further incubated for the indicated intervals. Drugs and other agents were dissolved in Me_2SO, which was added at a maximum ratio of 1:1000 to the culture media. Cultures were used for no more than 20 passages. Cell viability experiments were performed in 96-well plates, 8 times, using 2–3 replicates per treatment. In dose-response studies, cells were treated with MPP^+ (0–500 μmol/L) for 48 h with or without melatonin (0.1–1000 μmol/L). In time course studies, cells were exposed to MPP^+ (200 μmol/L) for 0, 24, 48, 72, and 96 h with or without melatonin 250 μmol/L. The cells were preincubated with melatonin for 1 h before treatment with MPP^+. The final concentration of ethanol per well did not exceed 0.01% for all melatonin concentrations used. The vehicle-treated control cultures received an equal amount of ethanol (0.01%). For cytotoxicity, cells were seeded on plates previously coated with poly-*L*-lysine. Untreated cells were used as control. For TH immunocytochemistry, the cells were subcultured for 48 h before use of 22-mm coverslips (Fisher Scientific, Pittsburgh, PA, USA), coated with poly-*L*-lysine in 35-mm culture dishes (Fisher Scientific).

MTT assay Cell viability was measured by MTT assay[16], which was based on the conversion of MTT to formazan crystals by mitochondrial dehydrogenase. Cells were plated at a density of 2×10^4 cells in 96-well dishes in 10% serum high-glucose DMEM medium for 2 d, and switched to 5% fetal calf serum low glucose, serum-free high glucose, and serum-free low glucose DMEM medium containing the experimental reagents. Four hours before the desired end point, MTT (5 g/L in PBS, final concentration 0.5 g/L) was added at 1/10 culture volume and cells were returned to the

incubator. After the end point, culture medium was removed, and 100 μL of Me_2SO was added to each well to dissolve formazan. Absorbance (OD value) was measured at 570 nm in a microplate reader (Bio-Rad model 550). Cell viability was expressed by OD value.

LDH release assay[15] Cytotoxicity of MPP^+ was evaluated by colorimetric assay based on the measurement of LDH activity. Briefly, after cells were treated with MPP^+, an aliquot of medium was taken and centrifuged at 250×*g* for 5 min. Supernatant (10 μL) was added to the LDH buffer [lactic acid 50 mmol/L/Tris (pH 8.9) 0.1 mol/L and NAD^+ (the oxidized form of nicotinamide-adenine dinucleotide) 4.6 g/L] to a total volume of 200 μL. Intracellular LDH content was determined by lysing the cells with Triton X-100 detergent. Spectrophotometric analysis was performed at room temperature (20–24 ºC) using a Bio-Rad microplate reader measuring optical density at 340 nm in both the medium and lysis buffer. LDH release values were calculated by subtracting the background reading (media only) from the observed reading. LDH leakage was expressed as a percentage of the total LDH release (extracellular LDH extracellular+ intracellular LDH).

Tyrosine hydroxylase (TH) immunocytochemistry TH activity was identified using the streptavidin-biotin-peroxidase complex**.** Cultured in poly-*L*-lysine coated coverslips, PC12 cells (2×10^4) were treated with MPP^+ 200 μmol/L with or without melatonin in serum-free low glucose medium. Melatonin was added 1 h before MPP^+ treatment. Cultures were incubated at 37 ºC, 5% CO_2 for a further 48 h, PC12 cells were washed with phosphate-buffered saline 0.1 mol/L (PBS, pH 7.4) and then fixed in 4% paraformaldehyde (pH 7.4) in PBS for at least 1 h. PC12 cells were incubated with 1% H_2O_2 and 30% methanol in 0.3 mol/L PBS to block endogenous peroxidases. The sections were rinsed three times in PBS and incubated successively with 1) normal sheep serum (20% in PBS) to reduce nonspecific binding for 30 min in a moisture -saturated chamber at 37 ºC; 2) antityrosine hydroxylase rabbit antiserum at 1/300 overnight in a moisture-saturated chamber at 4 ºC for 48 h; 3) biotinylated anti-rabbit IgG at 1:200 for 30 min in a moisture saturated-chamber at room temperature (20–24 ºC); and 4) streptavidin-peroxidase complex at 1:100 for 30 min in a moisture-saturated chamber at room temperature (20–24 ºC). Sections were rinsed with PBS after each step (3×5 min). In step 2, control sections were incubated with an equal volume of PBS, rather than antiserum, as negative controls. The streptavidin-biotin-peroxidase activity was revealed using 3,3′-diaminobenzidine tetrachloride (DAB, 0.5 g/L), in the presence of 0.03% H_2O_2 in PBS for 5 min. Coverslips were washed with PBS and dehydrated through ethanol. Finally, sections were mounted on gelatin-coated slides, air-dried, dehydrated, and coverslipped with permount. Immunocytochemical staining was analyzed at 400×magnification on an Olympus inverted phase-contrast microscope. Micrographs were taken with a camera mounted on the phototube using a Kodak film.

Statistical analysis Statistical analysis was performed using *t*-test for paired data. Data were expressed as the mean±SD. $P<0.05$ was considered to be statistically significant.

Results

Effect of MPP^+ on PC12 cells viability The reduction was markedly decreased after PC12 cultures were exposed to MPP^+ (200 μmol/L) in low glucose condition. MTT reduction was significantly decreased after MPP^+ treatment in serum low glucose condition. The percentage of cell viability was approximately 50%, 44%, and 30% at 48, 72, and 96 h, respectively. In serum-free low glucose condition, the percentages of cell viability were 85.1%, 75.4%, 64.9%, 28.1%, and 9% at 12, 24, 48, 72, and 96 h after MPP^+ treatment, respectively. However, when cells were exposed to MPP^+ 200 μmol/L in high glucose condition, no significant cell death appeared compared to control. MPP^+ induced a slight decrease in cell viability at 25 and 50 μmol/L, and more significantly at 100 μmol/L in the serum-free low glucose condition. In the 5% serum low glucose condition, the cell viabilities after MPP^+ (25, 50, and 100 μmol/L) treatment had no obvious changes compared with control, and significant cell death was observed at MPP^+ 200 μmol/L. Therefore, MPP^+ induced dose-dependent cell death in the low glucose condition. However, in the high glucose condition, no cell death was seen for all concentrations of MPP^+. We found that supplementing glucose increased the number of surviving cells for all concentrations of MPP^+.

Melatonin promotes PC12 survial after MPP^+ treatment The percentage of viable cells in serum-free low glucose condition with low dose melatonin (0.1, 1, and 10 μmol/L) did not change after treatment with MPP^+. However, when the cells were preincubated with melatonin (100, 250, 500, 1000 μmol/L), MPP^+-induced cell toxicity was significantly attenuated. Surviving PC12 cells were significantly increased from 53% in MPP^+ to 80% when melatonin was added. Melatonin was protective against MPP^+ toxicity in PC12 cells. Melatonin at 500 and 1000 μmol/L showed similar protection as 250 μmol/L melatonin, although a tendency to increase effects with higher doses was observed, indicating that the dose of 250 μmol/L might be close to the maxi-

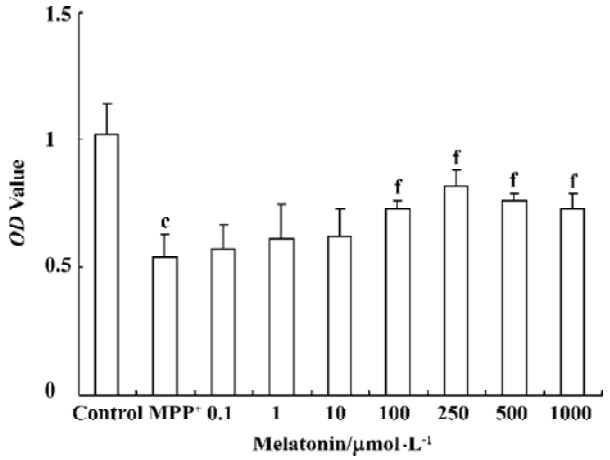

Figure 1. Melatonin protected PC12 from MPP^+-induced cytotoxicity. Cell viability monitored by MTT assay following 48-h exposure to various concentrations of melatonin in MPP^+ (200 μmol/L) in serum-free low glucose condition. Cell viability was expressed by optical density (OD) value and represented by mean±SD. n=8. ^cP<0.01 *vs* control. ^fP<0.01 *vs* MPP^+-treated cells.

mal effect (Figure 1).

The cultures were preincubated with melatonin (250 μmol/L) for 1 h and then exposed to MPP^+ (200 μmol/L) for 0, 12, 24, 48, 72, and 96 h in serum or serum-free low glucose condition. At the end of each time period, cell viability was assessed by MTT reduction. In serum-free low glucose condition, cell viability was decreased at 24, 48, 72, and 96 h to 75.4%, 64.9%, 28.1%, and 9% respectively, after MPP^+ treatment (200 μmol/L). Melatonin (250 μmol/L) significantly increased survival of cells exposed to MPP^+ (200 μmol/L), cell viability was 78.1%, 58.8%, and 31.6% at 48, 72, and 96 h, respectively. In 5% serum low glucose condition, melatonin also significantly enhanced survival of cells exposed to MPP^+ (P<0.05) (Figure 2).

LDH release MPP^+ caused membrane damage, which was determined by the release of the 24 kDa cytosolic enzyme LDH into the culture medium. The level of LDH into the culture medium was found to be 2-fold lower after MPP^+ treatment in 5% serum condition than after treatment with MPP^+ in serum-free medium for 48 h (16.3%±1.3%, and 29.4%±1.4%, respectively). MPP^+ treatment for 12 h at 200 μmol/L did not affect cell viability as revealed by lactate LDH (data not shown). However, after PC12 cells were incubated for 48 h with MPP^+, in either serum or serum-free condition, there was a significant increase in LDH leakage into the medium. LDH levels were further increased after MPP^+ treatment for 72 and 96 h. Melatonin 250 μmol/L significantly abolished the increment in LDH leakage produced by MPP^+ (Figure 3).

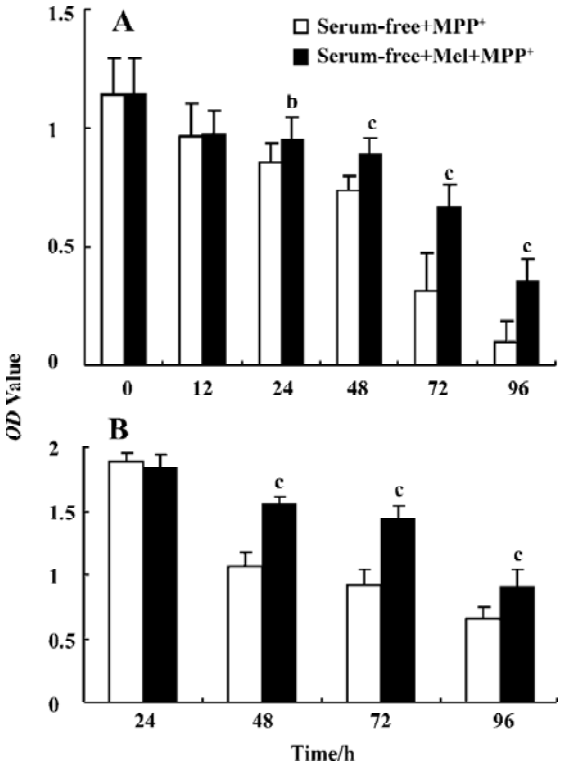

Figure 2. Melatonin protected PC12 from MPP^+-induced cytotoxicity. Cell viability was monitored by the MTT reduction assay and expressed as OD value. n=8. Mean±SD. ^bP<0.05, ^cP<0.01 *vs* cells treated with MPP^+ 200 μmol/L. (A) serum-free low glucose condition. (B) 5% serum low glucose condition.

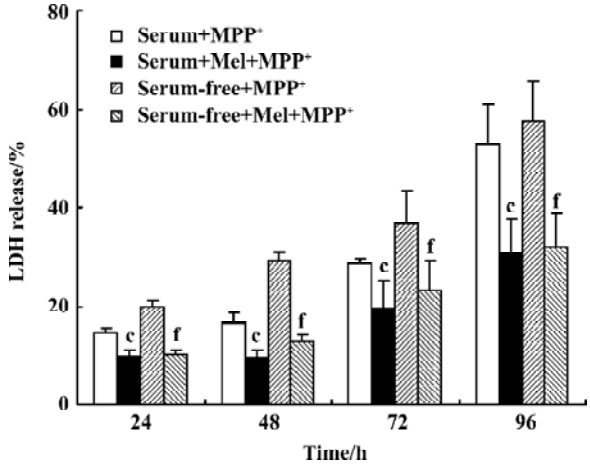

Figure 3. Effect of melatonin on MPP^+-induced LDH release in PC12 cells. Efflux of LDH from the cells was expressed as a percentage of total LDH (extracellular plus intracellular). The bars are mean±SD of eight experiments. ^cP<0.01 *vs* serum+MPP^+. ^fP<0.01 *vs* serum free+MPP^+.

TH immunocytochemistry Tyrosine hydroxylase immunocytochemistry studies showed loss of the TH immunoreactivity in the PC12 cells after MPP^+ treatment. Addition of melatonin 250 μmol/L significantly increased the survival of TH^+ cells. The number of TH-immunoreactive cells after melatonin treatment was greater than that in MPP^+-treated only cells, but less than that in control cells (Figure 4).

Discussion

An increasing body of evidence suggests that the cell energy path is an important target in the pathogenesis of neurodegenerative diseases. MPTP induces direct inhibition of complex I of the mitochondrial respiratory chain, which produces a large number of free radicals and energy crisis in the mitochondria. An excess of free radicals leads to mitochondrial damage, causing a failure of cellular energy metabolism followed by a secondary excitotoxicity. During our research, on the effect of melatonin on PC12 cell death induced by MPP^+, we noticed that melatonin at low glucose condition had a neuroprotective effect. The neurotoxicity of MPP^+ is widely acknowledged. In addition, we discovered that this neurotoxicity was dependent on the glucose level. MPP^+ had obvious toxicity in low glucose condition but not in high glucose condition. Our results suggested that PC12 cells might be vulnerable to MPP^+ in a low glucose condition but resistant to the injury induced by MPP^+ in a high glucose condition. Basma *et al*[17] demonstrated that the toxicity of an MPTP derivative to PC12 cells was exacerbated by inhibiting glycolysis. This was consistent with our results. Indeed, increasing the concentration of glucose reduced MPP^+-induced cytotoxicity at all MPP^+ concentrations accordingly. Depletion of glucose in the medium limited the ability of the cells to drive energy from glycolysis and, furthermore, rapid depletion of limited ATP supply through inhibition of mitochondrial function by MPP^+ resulted in cell death. At lower glucose concentrations, the depletion would occur more rapidly, which resulted in higher toxicities. At higher glucose concentrations, glycolysis was able to compensate longer for loss of ATP as a result of the MPP^+-induced inhibition of mitochondrial respiration and hence attenuated cell death. Kutty *et al*[18] reported similar findings using the neuroblastomax glioma hybrid NG 108-15 neuronal cell culture system. Using leakage of LDH and release of adenine as indices of toxicity, they found that the death of cells exposed to MPTP, MPP^+, or 2'Et-MPP^+, and the depletion of ATP caused by the neurotoxins, was markedly reduced owing to high glucose concentration (25 μmol/L) in the medium. The enhanced susceptibility of the cells grown in low glucose medium to the toxic effects of the neurotoxins was, most likely, caused by the action of the toxins on the glucose-depleted cells rather than directly because of the depletion of glucose.

The conversion of dye MTT to formazan crystals in cells

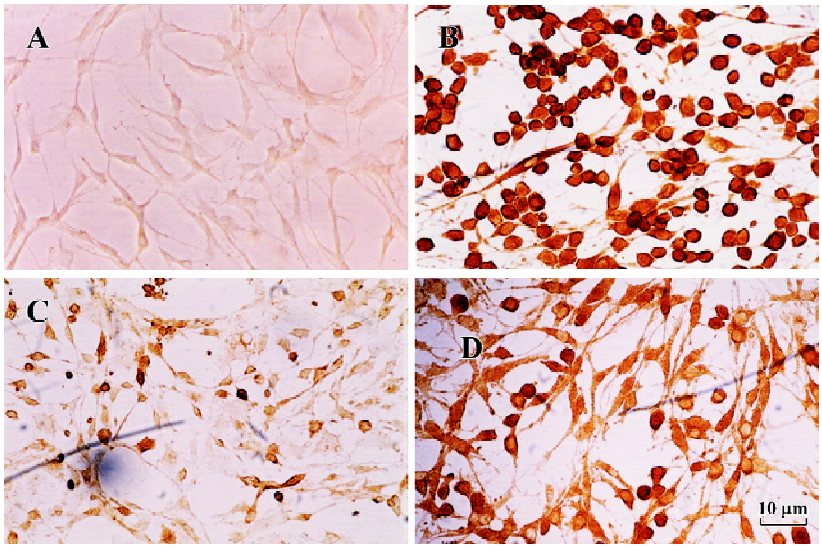

Figure 4. The effect of melatonin on TH immunoreaction on PC12 cells. Representative photomicrographs of TH-immunostained PC12 cells following MPP^+ and/or melatonin treatments (×400). Cells were cultured for 2 d and then treated for 48 h with A: Negative control; B: vehicle; C: MPP^+ 200 μmol/L; D: MPP^+ and melatonin 250 μmol/L.

has been shown to be related to mitochondrial redox state and respiratory chain activity[19]. In the present study, the result of MTT reduction could indicate a great role for mitochondrial dysfunction and cellular energy in these models of cell death. The reason seems to be that energy compromise plays a large role in the progression of PD. It is well known that the brain consumes large quantities of oxygen relative to total body mass. MPP^+ could induce PC12 cell death by depleting cellular levels of ATP through inhibition of complex I. Low glucose levels or the inhibition of glycolysis potentiates MPP^+ toxicity, while supplementation with fructose reduces the toxicity[17,20]. The data in this study provided additional support for the hypothesis that MPP^+ kill cells by inhibiting mitochondrial respiration, and that cell energy status was an important factor for MPP^+ induced cell death. These observations could prove useful in both the formulation of an accurate cell culture model of PD-like neuro-degeneration and the elucidation of the molecular basis of MPP^+ toxicity.

In the present study on the efficacy of melatonin to MPP^+-treated PC12 cells in low glucose culture, melatonin increased cell viability according to the MTT and LDH release assay. Single dose treatment of PC12 cells with melatonin (250 μmol/L) induced a significant decrease in LDH release after 48 h compared with vehicle-treated cultures. TH immunocytochemistry was used to visualize catecholaminergic neurons and monitor MPP^+-induced changes at the cellular level. As shown here, melatonin also protected PC12 cells against MPP^+-induced morphological changes. These results indicate that melatonin possesses the remarkable ability to rescue PC12 cells from cell death in our experimental paradigms associated with MPP^+. The present findings indicate that the protective effects of melatonin against MPP^+ toxicity may be a result of, at least partially, its antioxidant ability and mitochondria protection. Therefore, supplemental melatonin could ameliorate the severity of neurodegenerative changes caused by free radicals and mitochondrial dysfunction. However, this remains to be confirmed with further investigation.

Our study also showed indications for susceptible neuronal populations. As nerve cells exclusively use glucose as an energy source, increasing glucose concentration in susceptible neuronal populations might be an alternative approach to treat patients with neurodegenerative diseases. Further studies of the actions of melatonin on neurons might also provide a basis for the development of new therapeutic approach to overcome neurodegenerative diseases, such as PD.

References

1 Heikkila RE, Hess A, Duvoisin RC. Dopaminergic neurotoxicity of 1-methyl-4-phenyl-1,2,5,6-tetrahydropyridine in mice. Science 1984; 224: 1451–3.

2 Langston JW, Ballard P, Tetrud JW, Irwin I. Chronic parkinsonism in human due to a product of meperidine-analog synthesis. Science 1983; 219: 979–80.

3 Yang SF, Wu Q, Sun AS, Huang XN, Shi JS. Protective effect and mechanism on *Ginkgo biloba* leaf extracts for Parkinson disease induced by 1-methyl-4-phenyl-1,2,3,6-tetrahydro-pyridine. Acta Pharmacol Sin 2001; 22: 1089–93.

4 Singer TP, Castagnoli N Jr, Ramsay RR, Trevor AJ. Biochemical events in the development of parkinsonism induced by 1-methyl-4-phenyl-1,2,3,6-tetrahydropyridine. J Neurochem 1987; 49: 1–8.

5 Nicklas WJ, Vyas I, Heikkila RE. Inhibition of NADH-linked oxidation in brain mitochondria by 1-methyl-pyridine-1,2,3,6-tetrahydropyridine. Life Sci 1985; 36: 2503–8.

6 Mizuno Y, Suzuki K, Sone N, Saitoh T. Inhibition of mitochondrial respiration by 1-methyl-4-phenyl-1,2,3,6-tetrahydropyridine (MPTP) in mouse brain *in vivo*. Neurosci Lett 1988; 91: 349–53.

7 Hasegawa E, Takeshige K, Oishi T, Murai Y, Minakami S. 1-methyl-4-phenylpyridinium (MPP^+) induced NADH-dependent superoxide formation and enhances NADH-dependent lipid peroxidation in bovine heart submitochondrial particles. Biochem Biophys Res Commun 1990; 170: 1049–55.

8 Rossetti ZL, Sotgiu A, Sharp DE, Hadjiconstantinou M, Zeff NH. 1-methyl-4-phenyl-1,2,3,6-tetrahydropyridine (MPTP) and free radicals *in vitro*. Biochem Pharmacol 1988; 37: 4573–84.

9 Tan DX, Chen LD, Poeggeler B, Manchester LC, Reiter RJ. Melatonin: a potent endogenous hydroxyl radical scavenger. Endocrine J 1993; 1: 57–60.

10 Mayo JC, Sainz RM, Uría H, Antolín I, Esteban MM, Rodríguez C, Melatonin prevents apoptosis induced by 6-hydroxydopamine in neuronal cells: implications for Parkinson's disease. J Pineal Res 1998; 24: 179–92.

11 Greene LA, Rein G. Release, storage and uptake of catecholamines by clonal cell line of nerve growth factor (NGF) responsive pheochromocytoma cells. Brain Res 1977; 129: 247–63.

12 Kadota T, Yamaai T, Saito Y, Akita Y, Kawashima S, Moroi K. Expression of dopamine transporter at the tips of growing neuritis of PC12 cells. J Histochem Cytochem 1996; 44: 989–96.

13 Desole MS, Sciola L, Delogu MR, Sircana S, Miqnel R, Miek E. Role of oxidative stress in the manganese and 1-methyl-4-(2´-ethylphenyl)-1,2,3,5-tetrahydropyridine-induced apoptosis in PC12 cells. Neurochem Int 1996; 31: 169–76

14 Hartley A, Stone JM, Heron C, Cooper JM, Schspira AHV. Complex I inhibitors induce dose-dependent apoptosis in PC12 cells. J Neurochem 1994; 63: 1987–90.

15 Song W, Guan HJ, Zhu XZ, Chen ZL, Yin ML, Cheng XF. Protective effect of bilobalide against nitric oxide-induced neurotoxicity in PC12 cells. Acta Pharmacol Sin 2000; 21: 415–23.

16 Mosmann T. Rapid colorimetric assay for cellular growth and survival: application to proliferation and cytotoxicity assays. J Immunol Methods 1983; 65: 55–63.

17 Basma AN, Heikkila RE, Saporito MS, Philbert M, Geller HM, Nicklas WJ. 1-Methyl-4-(2´-ethylphenyl)-1,2,3,6-tetrahydropyridine-induced

toxicity in PC12 cells is enhanced by preventing glycolysis. J Neurochem 1992; 58: 1052–9.
18 Kutty RK, Santostasi G, Horng J, Krishna G. MPTP induced ATP depletion and cell death in neuroblastoma×glioma hybrid NG 108-15 cells: protection by glucose and sensitization by tetraphenylborate. Toxicol Appl Pharmacol 1991; 107: 377–88.
19 Cohen G, Kesler N. Monoamine oxidase and mitochondrial respiration. J Neurochem 1999; 73: 2310–5.
20 Chan P, Langston JW, Irwin I, DeLanney LE, Di Monte DA. J Neurochem 1993; 61: 610–6.

Full-length article

Pharmacokinetics of His-tag recombinant human endostatin in Rhesus monkeys[1]

Hai-feng SONG[2], Xiu-wen LIU, Hai-ning ZHANG, Bao-zhen ZHU, Shou-jun YUAN, Shang-yi LIU, Zhong-ming TANG

Department of Pharmacology and Toxicology, Beijing Institute of Radiation Medicine, Beijing 100850, China

Key words

endostatin; pharmacokinetics; *Macaca mulatta*; immunoenzyme techniques

[1] Project supported by the National Natural Science Foundation of China, No 39930180.
[2] Correspondence to Assoc Prof Hai-feng SONG.
Phn 86-10-6693-1230. Fax 86-10-6693-1230.
Email songhf@nic.bmi.ac.cn

Received 2004-05-12
Accepted 2004-08-03

doi: 10.1111/j.1745-7254.2005.00009.x

Abstract

Aim: To study the pharmacokinetics and accumulation of an *Escherichia coli*-expressed His-tag fused recombinant human endostatin (rh-endostatin) in Rhesus monkeys. **Methods:** Rh-endostatin was iv or sc injected in Rhesus monkeys, and the rh-endostatin concentration in serum samples was determined by an enzyme immunoassay (EIA) method. The serum drug concentration-time data were analyzed by compartmental analysis using the practical pharmacokinetic program 3p97. **Results:** Following iv administration at a dose rate of 1.5, 4.5, and 13.5 mg/kg in rhesus monkeys, the concentration-time curves of rh-endostatin were best fitted to a three-compartment open model. $AUC_{(0-\infty)}$ linearly increased with dose, while Cl_s exhibited no significant difference among different dose groups. The terminal half-lives (λ_3) were 8±8, 3.1±1.4, and 20±14 h, respectively. After sc administration at a dose rate of 1.5 mg/kg, the concentration-time curve was best fitted to a two-compartment open model, with a terminal half-life ($T_{1/2\beta}$) of 8±3 h. Bioavailability following sc injection was approximately 70%±3%. After consecutive iv injection of rh-endostatin at a dose rate of 1.5 $mg \cdot kg^{-1} \cdot d^{-1}$ for 7 d, the $AUC_{(0\text{-}24\ h)}$ substantially increased from 22±13 $mg \cdot h \cdot L^{-1}$ (d 1) to 50±29 $mg \cdot h \cdot L^{-1}$ (d 7), with an accumulation factor of 2.3±0.6 ($P<0.05$). **Conclusion:** The pharmacokinetic behavior of rh-endostatin in Rhesus monkeys complies with linear kinetics within the examined dose range. It tends to be accumulated in bodies after repeated administration at a dose level of 1.5 $mg \cdot kg^{-1} \cdot d^{-1}$ for more than 7 consecutive days.

Introduction

Endostatin, which contains 178 amino acid residues, is a 20 kDa COOH-terminal fragment of collagen XVIII[1]. It was firstly identified as an angiogenesis inhibitor in 1997. Endostatin specifically inhibits endothelial proliferation and potently inhibits angiogenesis and tumor growth[2]. Subsequently, *Escherichia coli*-derived recombinant endostatin was shown to induce regression and prevent growth of experimental tumors in mice when administered in daily doses as high as 20 mg/kg[2,3]. A novel *Escherichia coli* derived rh-endostatin was developed by MedGen Ltd (Yantai City, China). Compared with the rh-endostatin reported in the literature, an additional nine-amino acid-sequence (MGGSHHHHH) was added at the N-terminal of the protein, which resulted in the formation of a six-histidine tag (His-tag). The His-tag can be chelated with metal ions such as Ni^{2+} with a relatively high affinity, so it was utilized to simplify purification and to improve stability of the protein. The present study attempted to reveal the pharmacokinetics and the possibility of accumulation after single or multiple doses of this novel rh-endostatin in Rhesus monkeys.

Materials and methods

Drugs and reagents The rh-endostatin used in this study was provided by MedGen (lot YH0502, purity >98%). The drug was dissolved in 5 mmol/L Tris·HCl (pH 7.2) and stored at 4 ºC before use.

The ACCUCYTE® Human Endostatin™ enzyme immunoassay (EIA) kit was purchased from CytImmune Sciences Inc (lot 5AE002-SA, Maryland, USA). All other reagents were purchased from commercial sources and were of analytical grade.

Animals Rhesus monkeys (weighing 5.3 kg±0.8 kg, Grade I, Certificate BDW95002) were provided by the Animal Raising Center of the Academy of Military Medical Sciences, China. The animals were individually housed in stainless-steel cages and fed with a standard monkey diet. Fresh fruit was provided twice per day and water was available *ad libitum*.

Experimental design Three iv groups (at a dose rate of 1.5, 4.5, and 13.5 mg/kg body weight, respectively) were assigned to a 3×3 crossover design to perform an auto-control experiment, in which each animal received the three doses mentioned above, with an interval of 7 d between doses (washing out period). Three animals in the sc group were administered rh-endostatin at the dose rate of 1.5 mg/kg. Finally, a multiple-dose group comprising three animals was also designed, in which the monkeys received seven consecutive iv injections of rh-endostatin at the dose rate of 1.5 mg/kg, once per day.

Sample collection and assay Whole blood samples were drawn from the femoral veins of the animals using a puncture needle immediately before administration and at 2, 10 min in the iv group and 20, 40 min, 1, 1.5 h in the sc group, then at 2, 4, 8, 12, 24, 36, 48, and 72 h in all groups after a single dose and the 1st and the 7th dose in the multiple-dose group. In the multiple-dose group, samples were also collected at 2 min and 24 h after the 4th dose. The blood was kept undisturbed at room temperature, then centrifuged at 3000×*g* for 10 min. The serum was separated and stored at -20 ℃ untill the assay.

The EIA kit was utilized to determine the rh-endostatin levels in the serum samples. The assay was performed according to the guidance of the procedure specified by the manufacturer. A series of calibration standards provided by Medgen was set up in each microplate. The rh-endostatin levels in the unknown samples were obtained by being calculated from the Medgen calibration standard curves on the same microplate.

Data analysis The concentration-absorbance curves were drawn with the MicroCal Origin software (ver 5.0), and then the experimental data were fitted by Logistic function according to the following formula:

$$Y=\frac{(E_{max}-E_{min})}{(1+(X/EC_{50})^{Slope})}+E_{min}$$

In which, "*X*" represents rh-endostatin concentration in samples, "*Y*" represents the absorbance at 492 nm. The E_{max} and E_{min} were the maximal and the minimal absorbance, respectively.

The pharmacokinetic parameters were obtained by the computer program 3p97. Statistical inference was obtained by means of Student's *t* test or Chi-square test.

Results

Validity of the method for determination of rh-endostatin in monkey serum The ACCUCYTE® Human Endostatin™ kit has been developed using rh-endostatin as the antigen for polyclonal antibody production, and is used in the kit as the assay standard. Studies have demonstrated that it has no cross-reactivity against a variety of cytokines and growth factors, including heat inactivated rh-endostatin and mouse endostatin.

Within the concentration range of 7.8–8000 μg/L, the concentration-absorbance behavior of the rh-endostatin standard provided by Medgen is presented as an inhibitory sigmoid curve that could be described by 4 parameter logistic fitting. Maximal coefficients of variation (CV%) of intra-assay and inter-assay were 13.7% and 20.8%, respectively. The limit of quantitation (LOQ) was 125 μg/L (with CV% of 6.1%). The average endogenous endostatin level observed in the rhesus monkey was 375±175 μg/L (n=12).

The results of the blank serum samples fortified with 2000, 500, and 125 μg/L tested rh-endostatin showed that the recovery rates were 87%±5% (81%–91%), 93%±18% (79%–114%), and 94%±4% (90%–99%), respectively (n=5 parallel experiments). The CV% of the intra-assay was less than 11.5%, and the CV% of the inter-assay was higher (as high as 19.7%), so it is important to calculate the rh-endostatin concentration in samples by the parameters obtained from the standard curve of the same microplate.

The validity studies demonstrated that the ACCUCYTE® Human Endostatin™ kit was reliable for the determination of serum endostatin levels. The specificity, sensitivity, accuracy, and precision all met the requirements for pharmacokinetics (PK) study.

Concentration-time curves and PK following single dose of rh-endostatin Serum concentration-time profiles of rh-endostatin following iv bolus injections at doses of 1.5, 4.5, and 13.5 mg/kg were best fitted to a three-compartment open model (Figure 1). Rh-endostatin concentration in serum dramatically decreased after iv injection, with the initial half lives (λ_1) of 0.027±0.016 h, 0.04±0.03 h, and 0.10±0.04 h (P<0.05 *vs* the other two groups) following iv

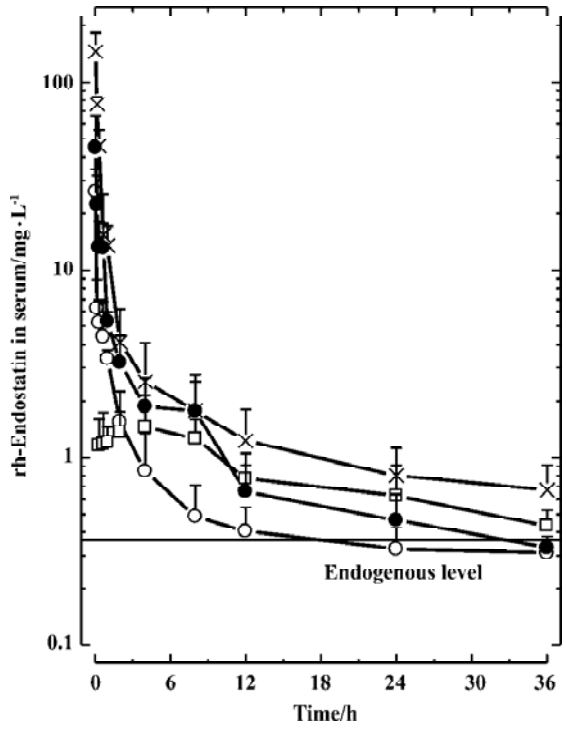

Figure 1. Concentration-time curves of rh-endostatin after a single iv and sc injection in rhesus monkeys. ○, iv 1.5 mg/kg; ●, iv 4.5 mg/kg; ×, iv 13.5 mg/kg; □, sc 1.5 mg/kg. The endogenous endostatin level set at 375±175 μg/L.

injection of 1.5, 4.5, and 13.5 mg/kg, respectively. The half-lives of the terminal elimination phase (λ_3) were 8±8 h, 3.1±1.4 h, and 20±14 h, respectively. At a high dose rate of 13.5 mg/kg, the value of λ_3 was obviously prolonged but without any statistically significant differences. Increased with dose, the mean areas under the serum concentration-time curve [$AUC_{(0-\infty)}$] of the three iv groups were 15±5 mg·h·L^{-1}, 33±7 mg·h·L^{-1} and 93±25 mg·h·L^{-1}, respectively. With a dose ratio of 1:3:9, the ratio of $AUC_{(0-\infty)}$ in the groups was 1:2.2:6.1.

Despite the increase in $AUC_{(0-\infty)}$, the systemic clearances (Cl_s) among the iv groups were not significantly different (Table 1), indicating that the pharmacokinetic behavior of endostatin within the examined dose range is of linear profile.

The concentration-time profiles following sc administration at a dose rate of 1.5 mg/kg can be described approximately by a two-compartment model (Figure 1). After injection, rh-endostatin was absorbed rapidly, with the time to peak (T_{max}) of 1.1±0.8 h. The mean peak serum concentration (C_{max}) and $AUC_{(0-\infty)}$ were 1.3±0.4 mg/L and 11±4 mg·h·L^{-1}, respectively. The terminal half-life ($T_{1/2\beta}$) was 8±3 h. Compared with the iv group at the same dose, rh-endostatin had a relatively high bioavailability (F) of 70% after sc administration (Table 1).

PK after multiple dosing Following repeated iv administration of rh-endostatin for a 7-d period (once daily) at a dose rate of 1.5 mg/kg, most of the rh-endostatin concentrations at the same time points following injection at d 1 and d 7 were with statistically significant difference (Figure 2). The trough level increased from 388±61 μg/L (d 1) to 623±261 μg/L (d 4) and 1008±892 μg/L (d 7), and the $AUC_{(0\text{-}24\,h)}$ also increased from 22±13 mg·h·L^{-1} (d 1) to 50±29 mg·h·L^{-1} (d 7), but the difference was not significant (P= 0.053). The calculated accumulation factor ($AUC_{d\,7}/AUC_{d\,1}$)

Table 1. Pharmacokinetic parameters of the rh-endostatin after iv and sc injection in rhesus monkeys. n=3. Mean±SD. $^bP<0.05$, $^fP<0.001$ *vs* the iv 1.5 mg/kg group.

Parameters	iv			sc
	1.5 mg/kg	4.5 mg/kg	13.5 mg/kg	1.5 mg/kg
V_C/L·kg^{-1}	0.030±0.019	0.08±0.04	0.078±0.019^f	1.3±0.4^f
$T_{1/2\,ka}$/h	-	-	-	0.34±0.14
$T_{1/2\,\lambda1}$/h	0.027±0.016	0.04±0.03	0.10±0.04^b	-
$T_{1/2\,\lambda2}$/h	0.80±0.28	0.5±0.4	0.8±0.5	1.9±2.0
$T_{1/2\,\lambda3}$/h	8±8	3.1±1.4	20±14	8±3
T_{max}/h	-	-	-	1.1±0.8
C_{max}/mg·L^{-1}	-	-	-	1.3±0.4
$AUC_{0-\infty}$/mg·h·L^{-1}	15±5	33±7^b	93±25^b	11±4
$MRT_{0-\infty}$/h	3.6±0.9	2.7±1.5	9.2±2.3^b	9.3±1.7
CL_S/L·h^{-1}·kg^{-1}	0.11±0.03	0.046±0.010	0.017±0.004	0.15±0.05
V_{SS}/L·kg^{-1}	0.39±0.22	0.12±0.04	0.148±0.013	1.4±0.6
F %	-	-	-	70±3

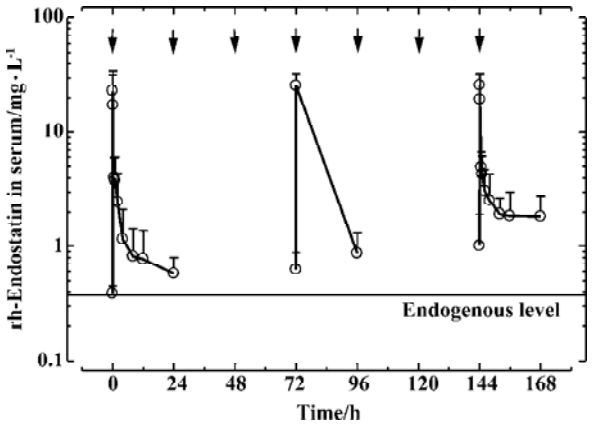

Figure 2. Concentration-time data of rh-endostatin after consecutive iv injection (q.d.×7) at a dose of 1.5 mg/kg in Rhesus monkeys. The endogenous endostatin levels set at 375±175 μg/L.

was 2.3±0.6 (P=0.012), indicating that the rh-endostatin had a tendency to accumulate in the body after successive iv administrations over 7 d with an interval of 24 h between doses.

Discussion

Folkman *et al* firstly descrbied the angiogenesis inhibitor endostatin in January 1997[2]. Although the molecular mechanisms behind the inhibition of angiogenesis have not yet been elucidated, endostatin seemed to inhibit endothelial cell migration *in vitro* and appeared to be highly effective in murine *in vivo* studies[4]. Endostatin thought to be an ideal anticancer weapon, was quickly pushed into clinical trials[5-8]. Thus far, however, recombinant endostatin prepared from *Escherichia coli* is insoluble after purification and therefore inappropriate for clinical settings. A soluble form of endostatin is available from a yeast system that has a relatively low yield and high cost, which has made it difficult to produce endostatin in quantities sufficient for extensive clinical evaluation[9].

Researches attempted to solve the problems mentioned above, including using the His-tag technique[10–12]. The rh-endostatin used in this study was His-tagged , containing a six-histidine residue sequence and an affinity tag at its N-terminal, so it could be effectively extracted by affinity chromatography based on immobilized metal ions such as Ni^{2+}. In this capture step, we were able to purify 100% of the recombinant protein with more than 99% purity just as reported previously[13]. The *in vivo* antiangiogenic and anticancer activities of this His-tag recombinant endostatin are as potent as those of the previously reported soluble form. Further, His-tag endostatin is also more convenient for analysis. In our study, we utilized a rapid and sensitive approach, Matrix-Assisted Laser Desorption Ionization-Time of Flight-Mass Spectrometry (MALDI-TOF-MS), to analyze the proteins, which provided highly accurate the molecular weight information about the protein (data not shown).

There was a relatively high basic endostatin level in monkeys (375±175 μg/L), and it was consistent with endostatin being an endogenous protein. Moreover, to obtain an effect on tumors, the dose of endostatin in precilinical experiments and the recommended dose used in clinical trials are much higher than the dose required of most other therapeutical proteins, which reached the level of mg/kg (or mg/m^2). Our PK studies showed that, although statistically not significant, λ_3 of the high dose group was obviously prolonged, suggesting that an exorbitant dose might affect the clearance of endostatin in the body. The results of the multiple dose study for 7 d continuously at the dose level of 1.5 mg/kg also suggested that rh-endostatin tended to accumulate in the body with a statistically significant accumulation factor of 2.3. Some clinical trials have shown that endostatin may cause side effects in the cardiovascular system, especially a dose-dependent toxicity in the heart. So it is best to avoid over accumulation of endostatin in the body by regulating the intervals between each administration. Furthermore, the PK study shows that differences between individuals are great, so individual monitoring during the course of treatment is also recommended in clinical trials.

Acknowledgment

The study was financially supported partly by MedGen Ltd (Yantai City, Shandong Province, China).

References

1 Sasaki T, Fukai N, Mann K, Gohring W, Olsen BR, Timpl R. Structure, function and tissue forms of the C-terminal globular domain of collagen XVIII containing the angiogenesis inhibitor endostatin. EMBO J 1998; 17: 4249–56.

2 O'Reilly MS, Boehm T, Shing Y, Fukai N, Vasios G, Lane WS, *et al*. Endostatin: an endogenous inhibitor of angiogenesis and tumor growth. Cell 1997; 88: 277–85.

3 Beohm T, Folkman J, Browder T, O'Reilly MS. Antiangiogenic therapy of experimental cancer does not induce acquired drug resistance. Nature 1997; 390: 404–7.

4 Zatterstrom UK, Felbor U, Fukai N, Olsen BR. Collagen XVIII/endostatin structure and functional role in angiogenesis. Cell Struct Funct 2000; 25: 97–101.

5 Iughetti P, Suzuki O, Godoi PH, Alves VA, Sertie AL, Zorick T, *et al*. A polymorphism in endostatin, an angiogenesis inhibitor, predisposes for the development of prostatic adenocarcinoma. Cancer Res 2001; 61: 7375–8.

6 Maio M, Altomonte M, Calabro L, Fonsatti E. Bioimmunotherapeutic

targets on angiogenetic blood vessels in solid malignangies. Front Biosci 2001; 6: D776–84.
7 Ryan CJ, Wilding G. Angiogenesis inhibitors. New agents in cancer therapy. Drugs Aging 2000; 17: 249–55.
8 Mundhenke C, Thomas JP, Wilding G, Lee FT, Kelzc F, Chappell R, *et al*. Tissue examination to monitor antiangiogenic therapy: a phase I clinical trial with endostatin. Clin Cancer Res 2001; 7: 3366–74.
9 Huang X, Wong MK, Zhao Q, Zhu Z, Wang KZ, Huang N, *et al*. Soluble recombinant endostatin purified from *Escherichia coli*: antiangiogenic activity and antitumor effect. Cancer Res 2001; 61: 478–81.
10 Hengen P. Purification of His-Tag fusion proteins from *Escherichia coli*. Trends Biochem Sci 1995; 20: 285–6.
11 Tallet B, Astier-Gin T, Castroviejo M, Santarelli X. One-step chromatographic purification procedure of a His-tag recombinant carboxyl half part of the HTLV-I surface envelope glycoprotein overexpressed in *Escherichia coli* as a secreted form. J Chromatogr B Biomed Sci Appl 2001; 753: 17–22.
12 Gibert S, Bakalara N, Santarelli X. Three-step chromatographic purification procedure for the production of a his-tag recombinant kinesin overexpressed in *E. coli*. J Chromatogr B Biomed Sci Appl 2000; 737: 143–50.
13 Huang YW, Lu ML, Qi H, Lin SX. Membrane-bound human 3beta-hydroxysteroid dehydrogenase: overexpression with His-tag using a baculovirus system and single-step purification. Protein Expr Purif 2000; 18: 169–74.

Invited review

Development of novel therapies for Huntington's disease: hope and challenge[1]

Zheng-hong QIN[2,3,5], Jin WANG[4], Zhen-lun GU[2]

[2]Department of Pharmacology, Soochow University School of Medicine, Suzhou 215007, China; [3]Laboratory of Cellular Neurobiology, Massachusetts General Hospital and Harvard Medical School, Charlestown, MA 02129, USA; [4]Molecular Neurogenetics Unit, Center for Human Genetics Research, Massachusetts General Hospital and Harvard Medical School, Charlestown, MA 02129, USA

Key words

Huntington disease; huntingtin; aggregates; caspases; nerve growth factors; cell transplantation; coenzyme Q10

[1] Supported by the National Natural Science Foundation of China (No 30370506).
[5] Correspondence to Zheng-hong QIN, PhD.
Phn 86-512-6512-2087.
Fax 86-512-6519-0599.
E-mail zhqin5@hotmail.com

Received 2004-11-04
Accepted 2004-12-07

doi: 10.1111/j.1745-7254.2005.00020.x

Abstract

Huntington's disease (HD) is an autosomal dominant neurological disease. It is a fatal neurological disorder affecting 5–10 out of 10 000 people. While there are intensive research efforts focusing on uncovering molecular mechanisms of the pathogenesis of HD, a number of studies have begun to look for effective therapies for HD. There is a large body of encouraging news on novel therapeutic developments. The present paper reviews drugs used for symptomatic treatment of HD and experimental therapies targeting HD molecular pathology.

Introduction

Huntington's disease (HD) is a devastating neurological disorder without effective treatment. It is characterized by involuntary movement, cognition impairment, and psychological disturbance. The disease affects 5–10 out of 10 000 people in western countries. HD is a fatal neurological disorder and death usually occurs approximately 20 years after the onset of symptoms. Therefore, there is an urgent need for developing effective therapies for HD. The genetic cause of HD was uncovered in 1993[1]. The disease is linked to an expansion of polyglutamine in the novel protein, huntingtin. Since 1993, extensive research efforts have been made to understand pathogenic mechanisms of mutant huntingtin. Multiple molecular mechanisms seem to be involved in HD pathogenesis[2]. Researchers are actively investigating possible effective therapies based on our current understanding of the molecular pathology of HD. One approach that has been explored is high-throughput screening for small molecules affecting specific molecular targets. Potential targets for high-throughput chemical screenings include molecular chaperones, caspases, the ubiquitin/proteasome proteases, transcription factors, and the offending polyglutamine-containing proteins themselves. Much attention has been focused on screening for drugs that prevent aggregation of huntingtin with expanded polyglutamine tract. *In vivo* screenings are also being planned or are under-way using transgenic HD mice and Drosophila[3]. The other approach is to use recent advances in molecular biology of neurotrophic factors, neuronal tissue transplantation and cell engineering in HD therapeutic developments with the aim of retarding or reversing HD pathology, but without complete understanding of the molecular pathogenic mechanisms. Both approaches are moving at a fast pace and we expect new therapies will be available clinically soon. This paper reviews current treatments for clinical symptoms of HD and the development of novel therapies targeted at the molecular pathogenic mechanisms of mutant huntingtin.

Developing novel therapies aimed at mutant huntingtin

The expansion of the polyglutamine tract in huntingtin causes the "gain-of-function" mutation. Gained functions include misfolding and aggregation, abnormal protein interactions, and dysregulation of transcription conferred

on mutant huntingtin. The ideal therapy should correct these acquired properties in mutant huntingtin.

Compounds inhibit mutant huntingtin aggregation The *in vitro* aggregation of huntingtin involves a conformational change of the polyglutamine segment from a random coil to an amyloid structure, and is in some ways paralleled in cell culture by the formation of cytoplasmic aggregates and nuclear inclusions[4–6]. Neuronal inclusions containing amino-terminal fragments have also been detected in HD brains and have become a hallmark of HD pathology. The role of huntingtin aggregates and inclusions in pathogenesis is still being debated, as they may or may not correlate to cell death[7]. Whether the formation of huntingtin aggregates in the brain is the cause or merely the consequence of the disease is unclear. However, aggregation of mutant huntingtin has been shown to be related to HD progress. Keeping mutant huntingtin from aggregation would provide a way to prevent the progression of the disease.

Several laboratories have screened the NIH (National Institutes of Health) Small Compounds Library with *in vitro* aggregation assay using purified bacterial-expressed N-terminal huntingtin fragments or *in vivo* cell-based aggregation assay. Table 1 shows some published small compounds that directly inhibit aggregation of mutant huntingtin.

These direct aggregation inhibitors have been tested in various HD models such as cell culture, HD Drosophila and transgenic HD mice. Congo Red showed protective effects on survival, weight loss, and motor function even after the onset of symptoms of HD in R6/2 transgenic mice. The underlying mechanisms of Congo red include keeping mutant huntingtin fragments from aggregating and increasing the accessibility of huntingtin by proteasome[14]. Y-27632, an inhibitor of the Rho-associated kinase p160ROCK, prevents polyglutamine protein aggregation in cultured cells and reduces neurodegeneration in an HD Drosophila model[9]. Among benzothiazoles, the strongest inhibitors of mutant huntingtin aggregation, with IC_{50} ranging from 1.2–11.0 μmol/L in the *in vitro* assay, are very toxic to the cells. But two weak inhibitors with lower IC_{50} are nontoxic and effective in reducing the aggregation of mutant huntingtin fragments in a cell-based assay. Riluzole, a glutamate release inhibitor, showed neuroprotective effects in R6/2 transgenic HD mice by prolonging their survival and delaying progressive weight loss, but had no effect on motor coordination, locomotor activity, and the formation of neuronal intranuclear inclusions (NII)[11]. Trehalose, a disaccharide, reduced aggregation of mutant huntingtin fragments in cells and NII in R6/2 HD transgenic mice. It was proposed that trehalose binds to expanded polyglutamines to prevent aggregation. R6/2 HD mice treated with trehalose showed improved motor function and extended lifespan[12]. Celastrol, a natural bioactive compound, was effective in reversing the abnormal cellular localization of full-length mutant huntingtin observed in striatal cells derived from $Hdh^{Q111/Q111}$ knock in mice[13].

Compounds identified by cell-free aggregation assay are usually either non-effective in the cell-based aggregation assay or toxic to cells. For example, many active benzothiazoles[10], compounds identified by cell-based assay usually reduce aggregation of mutant huntingtin fragments by indirect mechanisms, such as Y-27632[9]. Combining both cell-free and cell-based assays would make a more reliable prediction of potential small molecules for further drug development. Most experiments used for screening and testing compounds, including *in vitro* aggregation assays, cell-based aggregation assays, HD Drosophila and HD transgenic mice, are based on small N-terminal huntingtin fragments with an expanded ploy glutamine tract. Still uncertain is the effectiveness of these compounds in transgenic HD mice, particularly when full-length mutant huntingtin is expressed. As more and more laboratories are conducting screening and developing aggregation inhibitors, it is expected that more and more effective compounds will be identified.

In addition to direct aggregation inhibitors, inhibitors of cell toxicity caused by over-expression of N-terminal fragments with expanded ploy glutamine tract were also screened from bioactive compounds[15]. Caspase inhibitors and cannabinoids showed protective effects with EC_{50} of 10 μmol/L and 30 μmol/L, respectively. Induction of expression of heat

Table 1. Some published small compounds inhibiting aggregation of mutant huntingtin.

Compounds	IC_{50} (μmol/L)	Assay system	Reference
Congo Red	0.3	*In vitro*, exon 1 fragment with 51Q	[8]
Y-27632	~5	Cell based FRET	[9]
Benzothiazoles derivatives, including riluzole	1.2–100	*In vitro*, exon 1 fragment with 51Q	[10,11]
Trehalose	Not determined	*In vitro*, a mutant myoglobin with 35Q	[12]
Celastrol and its derivatives	3.6	*In vitro*, N-terminal first 171aa with 58Q	[13]

shock proteins with geldanamycin also inhibited huntingtin aggregation and huntingtin induced cellular toxicity[16].

Transglutaminase inhibitor It has been shown *in vitro* that transglutaminase (TGase) can use huntingtin as a substrate to cross-link huntingtin molecules[17], and gives preference to huntingtin with polyglutamine more than 36 repeat[18]. TGase activity was found to have increased in HD postmortem brains, and aggregated huntingtin catalyzed by TGase were found in NII[18]. TGase provides an additional mechanism for the formation of aggregation of mutant huntingtin. This suggests that TGase might play a role in HD pathogenesis and, therefore, is a potential therapeutic target. Cystamine is an inhibtor of TGase[19]. Treatment of R6/2 transgenic HD mice with cystamine showed a small but significant neuroprotective effect with improvement of motor function, survival and loss of bodyweight**.** However, whether it can reduce mutant huntingtin aggregates is not clear as contradictory results were reported[20]. The underlying mechanism(s) is complicated as cystamine is also an antioxidant and increases transcription of certain neuroprotective chaperones, HDJ1/Hsp40[21].

Protease inhibitors Recent findings showed that huntingtin can be cleaved by proteases, including caspases[22,23], calpain[24,25], and aspartyl protease[26]. N-terminal huntingtin fragments were found in postmortem HD patients' brains[27], and YAC transgenic mice that expressed full-length human huntingtin with expanded polyglutamine tract[28]. Because caspase and calpain-mediated partial cleavage of mutant huntingtin promotes huntingtin aggregation and cellular toxicity, inhibitors of huntingtin partial cleavage might have therapeutic values.

The potential capases cleavage sites are located within amino acids 513–586 and only capases 2, 3, and 6 were found to be effective[23]. Calpain cleaves huntingtin at amino acids 469 and 536[25]. Aspartic endopeptidases release two distinct mHtt fragments, cp-A and cp-B, by cleaving huntingtin between amino acids 104–114. Cp-A is the major fragment that aggregates in the nucleus[26]. In the cell based assays, caspase-resistant and calpain-resistant htts with expanded polyglutamine tract were reported to decrease aggregate formation and reduce cytotoxicity[23,25]. Caspase inhibitors, z-VAD-fmk and z-DEVD-fmk, can prevent cleavage of huntingtin by caspases and reduce cytotoxicity caused by expanded polyglutamine tract[23,29]. As N-terminal huntingtin fragments produced by caspase and calpain mediated cleavage are localized in the nucleus and prone to aggregate, this might contribute to HD pathogenesis. Protease inhibitors could reduce N-htt fragments and, in turn, prevent or delay disease progression. A few studies demonstrate that the caspase inhibitor minocycline was able to inhibit huntingtin aggregation, retard disease progress and prolong the lifespan of HD mice[30,31]. So far, there is no good inhibitor for calpain and aspartic endopeptidases that have been developed and tested against mutant huntingtin.

Apoptosis or programmed cell death is implicated in HD pathogenesis by the observations of the elevation of cytochrome c in the cytoplasm[32] and activation of caspases 1, 3, 8, and 9[32–34]. Thus, the apoptosis pathway is a reasonable target for HD therapy. In one study, intracerebroventricular administration of z-VAD-fmk, as an inhibitor of apoptosis, for 4 weeks starting at the age of 7 weeks improved survival of R6/2 mice by 24.8%[34]. However, in another study, administration of other apoptosis inhibitors, YVAD-fmk and DEVD-fmk individually, showed no effects at all, though they can extend the lifespan of R6/2 mice by 17.2%[30,31]. As therapeutic agents, caspase inhibitors might act on two targets: mutant huntingtin to prevent the release of toxic N-terminal fragments and apoptosis to prevent neurons from death caused by mutant huntingtin.

Histon deacetylase (HDAC) inhibitors Huntingtin interacts with several important transcription factors, including cAMP-response element binding protein (CBP), TATA box binding protein (TBP), specificity protein-1 (SP1), nuclear factor-κB (NF-κB)[35–37]. Some of these are reportedly found in huntingtin aggregates. Altered gene expression was found in the R6/2 transgenic HD mice at the ages of 6 and 12 months[38], and in full-length huntingtin transgenic mice[39]. Abnormal transcription might be caused by direct interactions between mutant full-length huntingtin or its fragments and transcription factors, which in turn change the normal transcription mediated by these transcription factors. Mutant huntingtin can affect transcription by altered binding to transcription factors not recruiting them into aggregates. This means that altered transcription is an early event in HD pathogenesis caused by soluble mutant huntingtin, either full-length or fragmented before forming aggregates. This notion is supported by several lines of evidence: (1) no CBP, TBP, or SP1 could be found in huntingtin inclusions in several HD mouse models and they maintained normal cellular levels in these mice[40]; (2) less SP1 was found to bind to DNA in the presence of mutant huntingtin *in vitro*[36] and *in vivo*[41].

Reversal of the altered transcription might be a way to retard HD progression. Inhibitors of histone deacetylase (HDAC) can increase gene transcription and have been examined as a potential therapy in both HD Drosophila and transgenic R6/2 HD mice. Suberoylanilide hydroxamic acid (SAHA), a selective HDAC inhibitor, reduced neurodegener-

ation in HD Drosophila[42]. In R6/2 mice, SAHA increased histone acetylation and ameliorated motor deficits. However, it did not affect the aggregation and loss of brain weight[43]. Another HDAC inhibitor, sodium butyrate, improved survival of R6/2 mice in a dose-dependent manner by up to 21.7% when administered intraperitoneally at a dose of 200–10 000 $mg \cdot kg^{-1} \cdot d^{-1}$. This treatment increased acetylation of histon 3, histon 4, and SP1, improved motor performance and bodyweight loss, and decreased atrophy of the brain and striatum. But sodium butyrate had no effect on the formation of immunoreactive huntingtin aggregates[44].

Gene therapy Gene therapy is another potential therapeutic method for HD in addition to the small compounds described above. Intracellular antibodies (intrabodies) and RNA interference (RNAi) are 2 potential methods that could be used for gene therapy of HD. Intrabodies are a powerful tool to study protein functions *in vivo* and also a potential therapeutic approach delivered by gene therapy[45]. This is achieved by expressing single-chain variable region fragments (svFv or sFv) of the antibody intracellularly to bind an intracellular target[46]. One intrabody selected from a human sFv phage display library, which is specific for the first 17 amino acids of human huntingtin, dramatically reduced the aggregates formation when cotransfected with huntingtin, with expanded polyglutamine tract and a GFP tag[47]. A recent study reported that an intrabody consisting of only a single light chain variable domain selected from a non-immune human antibody library against the first 20 N-terminal amino acids of human huntingtin and affinity matured with yeast surface display method, inhibited mutant huntingtin aggregation in both cell-free and cell-based assays[48]. The small size of this single-domain intrabody enables it to diffuse into the nucleus readily. Given its small size and human origin, it should be a more practical approach in gene therapy. The recognition site of the intrabody determines whether the intrabody has beneficial effects. In addition to intrabodies recognizing the first 17 or 20 amino acids of huntingtin, the intrabody recognizes the polyproline domains of huntingtin inhibited aggregation and reduces the cell death caused by mutant huntingtin. However, an intrabody recognizing polyglutamine region actually promoted aggregation and apoptosis[49].

Recently developed RNAi technology provides a powerful way to reduce target gene expression in cell cultures and in brains[50]. To explore its potential therapeutic effects in polyglutamine diseases, double-stranded RNA (dsRNA), which induces RNA interference, was used to test against polyglutamine induced cell toxicity[51]. dsRNA can cause sequence-specific, not allele-specific inhibition of huntingtin translation. In mammalian cells, dsRNA reduced the toxicity and caspase-3 activation caused by expression of expanded polyglutamine tract. The outcome of a recent breakthrough in studying spinocerebella ataxia 1 (SCA1) demonstrated a bright future in using RNAi in HD[52]. Both SCA1 and HD belong to a group of severe neurodegenerative diseases caused by expansion of the polyglutamine tract in proteins. In the study, after recombinant adeno-associate virus (AAV) vectors expressing short-hairpin RNA (shRNA) were injected into the cerebellar region of the brain of transgenic SCA1 mice expressing transgenic human disease allele (ataxin-1-Q82), the cerelellar morphology was significantly improved and ataxin-1 inclusions were reduced in Purkinje cells, while there was no effect of the RNAi vectors in wild-type mice[52]. RNAi targets both the mutant and wild-type allele, however, it does not completely eliminate the mRNA and protein synthesis. Huntingtin plays a critical role during development as shown by the fact that huntingtin knock-out mice are embryonic lethal. However, reducing huntingtin after birth and before the onset of the disease could have minor effects on its normal function. Also, reduction of mutant huntingtin should delay the onset of disease or disease progression. Taken together, RNAi is a potential therapy for HD and will be tested in transgenic mice soon. RNAi targeting mutant huntingtin allele is also currently under development.

Neuron protection and replacement therapy

The goal of neuroprotective therapy is to preserve vulnerable neurons, restore neuronal function or replace lost neurons. These therapies do not require a full understanding of the molecular mechanisms of HD. Thus, they could be useful strategies for the present treatment of HD.

Neurotrophic factors Neurotrophic factors interact with three types of membrane receptors, named TrKA, TrKB, and TrKC. These receptors have tyrosine kinase activity. Nerve growth factor (NGF) binds to TrKA receptors, and brain derived neurotrophic factor (BDNF) and neurotrophin-4/5 (NT-4/5) bind to TrkB, whereas neurotrophin-3 (NT-3) binds preferentially to TrkC[53]. Neurotrophic factors play critical roles in neurodevelopment and support neuronal survival and plasticity of mature neurons. In a variety of neuronal injury models, neurotrophic factors have been shown to protect neurons from death and to promote functional recovery. Thus, neurotrophic factors have long been suggested as therapeutic candidates for neurodegenerative disorders including Parkinson disease and HD.

Beneficial effects of neurotrophic factors in HD have been

demonstrated in animal models of HD. Excitotoxins and mitochondrial toxins have been used for producing animal models of HD because they induce degeneration of striatal neurons mimicking pathological features of HD. In these HD animal models, administration of neurotrophic factors reduced neuronal damage and behavioral deficits. Neurotrophins are introduced into brains by direct injection, implantation of engineered cells producing neurotrophins, or using viral expression vectors. Direct injection of neurotrophins into brains would not be clinically practical, but transplantation of neurotrophin producing cells into brains is feasible to achieve long lasting delivery of neurotrophins[54]. To minimize immunoresponse to implanted cells, different methods of encapsulation of cells have been developed. These technologies have greatly reduced host immune response and prolonged survival of implanted cells. In a reported study, polymer-encapsulated cells secreting human NGF survived as long as one year after transplantation into rat ventricles[55].

Instriatal administration of quinolinic acid (QA), a selective NMDA receptor agonist, causes apoptotic death of striatal projection neurons, but striatal interneurons are mostly spared[56]. This pathology is similar to that found in HD brains. In QA-induced rodent models of HD, intrastriatal injection of adenovirus encoding BDNF protected neurons from QA-induced striatal lesions as revealed by histological examinations. Immunocytochemistry revealed that viral expression of BDNF increased survival of striatal GABAergic projection neurons[57]. In another study, cell lines expressing BDNF, NT-3, or NT-4/5 were grafted in the adult rat striatum before QA injection. Seven days after QA injection, immunohistological examination confirmed protection of striatal projection neurons by neurotrophins. QA injection alone or in combination with the control cell line induced a selective loss of striatal projection neurons. Grafting of a BDNF-secreting cell line prevented the loss of all types of striatal projection neurons analyzed[58]. Neuroprotective effects of transplantation of CTNF producing cells were also demonstrated in non-human primate HD models. Emerich *et al* gave Cynomolgus monkeys intrastriatal implants of polymer-encapsulated kidney fibroblasts from baby hamsters that had been genetically modified to secrete human CNTF[59]. Human CNTF was found to exert a neuroprotective effect on striatal neurons, including GABAergic, cholinergic and diaphorase-positive neurons. Human CNTF also prevented the retrograde atrophy of layer V neurons in the motor cortex and exerted a significant protective effect on the GABAergic innervation of the two important target fields of the striatum[59].

Another useful method for delivery of neurotrophins is to use a viral expression vector. Introduction of viral vector into brains can achieve local production of exogenous neurotrophic factors. In 3-nitropropionic acid (3-NP)-induced rodent HD model, Jodi *et al* investigated the neuroprotective effects of glial-derived neurotrophic factor (GDNF) delivered by an AAV. Lewis rats received bilateral injections of either AAV-GDNF or AAV-green fluorescence protein into the striatum followed by chronic subcutaneous infusions of the mitochondrial toxin, 3-NP (38 mg/kg). All rats underwent 4 weeks of behavioral testing and were then killed. Following 3-NP, the motor performance of AAV-GFP-treated rats on a raised platform deteriorated, while the performance by AAV-GDNF-treated rats was near normal. Histological analysis found that 3-NP-treated rats receiving AAV-GDNF displayed 70% more NeuN-immunoreactive neurons compared to 3-NP-treated rats receiving AAV-GFP[60]. Other studies on QA-induced rodent HD models also found that enhanced expression of BDNF or GDNF, achieved by AAV vector-mediated gene delivery, protected striatal neurons. Both AAV-BDNF and AAV-GDNF significantly reduced the loss of NeuN and calbindin-immunopositive striatal neurons 2 weeks after lesion compared to controls[61].

Neurotrophins not only reduced neuronal loss in chemical models of HD, but also improved behavioral deficits. In rats, bilateral infusion of QA produced a significant loss of bodyweight and mortality, which was prevented by prior implantation of hCNTF-secreting cells. QA produced impairments in motor function and cognitive function. The behavioral deficits induced by QA were abolished by implantation of hCNTF-secreting cells prior to QA infusion. Consistent with behavioral improvements after implantation of hCTNF secreting cells, neurochemical examination revealed that CNTF-treated animals did not exhibit any decrease in ChAT levels and only a 10% decrease in GAD levels in the striatum, whereas in control animals QA decreased striatal ChAT levels by 35% and striatal GAD levels by 45%[59]. Further studies in primates also showed that intracerebral delivery of low doses of CNTF at the onset of HD symptoms not only protects neurons from degeneration but also restores neostriatal functions[62]. These results support the hypothesis that CNTF infusion into the striatum of HD patients could not only block the degeneration of neurons but also alleviate motor and cognitive symptoms associated with persistent neuronal dysfunction.

The elucidation of the genetic defect in patients with HD has allowed for the detection of individuals at risk for HD prior to the onset of symptoms. Thus "neuroprotection strategies" aimed at preventing the neuropathological and behavioral sequelae of this disease might be powerful therapeu-

tically, as they could be introduced to healthy patients before the initiation of a massive degenerative cascade principally localized to the striatum. After some issues, such as immunoresponse and long-term survival of transplanted cells, are resolved this type of therapeutic strategy could be ready for clinical testing in HD patients.

Neural cell transplantation For many years investigators have proposed the replacement of lost neurons and the restoration of functions by grafting new cells into specific brain regions. HD pathology affects multiple brain regions, but the striatum is most affected in the early stages. Now many studies have been conducted in animal models and HD patients, giving HD patients new hope for a potential novel therapy.

In early studies on a rodent HD model, intrastriatal injection of striatal neurons obtained from 14 to 15-day-old rat fetuses re-established a new striatum-like structure at the site of the ibotenic acid-induced lesions. This reduced striatal atrophy on average to approximately 50%–70% of normal control in the rats with lesions and to approximately 30%–40% in the animals with grafts. In the rats with grafts, there was a significant recovery of striatal neuronal markers after excitotoxic lesions[63]. Both cell suspensions and tissue chunks can be implanted into the striatum. But grafts derived from cell suspensions triturated in the presence of trypsin contained larger quantities of striatal tissue within the graft and more DARPP-32-positive medium spiny neurons than grafts implanted as fragments of tissue. Afferent and efferent connectivity was also better in the trypsinized suspension graft group[64].

The rationale for neuronal replacement as a possible therapy for HD is strengthened by showing functional recovery after cell transplantation in a primate HD model. A complete and persistent recovery was demonstrated in a frontal-type cognitive task 2 to 5 months after intrastriatal allografting. The striatal allografts also reduced the occurrence of dystonia, a major abnormal movement associated with HD[65]. These results further support the use of neural transplantation as a potential therapy for HD. Grafted cells must establish connection with target neurons to have their functions. The establishment of a neuronal network was revealed in the experiments with transplantation of neural precursor cells into a rat model of HD. Neural precursors survived transplantation and large numbers differentiated to express neuronal markers, including DARPP-32, indicating a mature striatal phenotype had been adopted. Neuronal fibers from the grafts projected diffusely throughout the host brain, although there was no evidence that outgrowth was specifically target directed[66]. The thalamostriatal projections to rat neostriatal grafts were studied using the Phaseolus vulgaris-leucoagglutinin (PHA-L) axonal tracing technique. Two to six months after implantation of striatal primordia into adult neostriata, PHA-L was injected into two different portions of the intralaminar nuclear complex of the thalamus and examined with an electron microscope. Some of the labeled fibers in the grafts formed dense, focal arborizations. However, the synaptic connections in grafts were different from the normal striatum. The shift of postsynaptic elements in the grafts suggests a loss of pathway specificity in the induction of dendritic spines on neostriatal neurons in grafts [67]. In a QA-induced experimental HD model, DA-mediated electrophysiological depression was studied after fetal striatal tissue transplants were grafted. QA lesioning reduced responses to DA in the striatal neurons. The dose of DA required to inhibit striatal neuron activity in the lesioned rats was significantly increased compared to that in the non-lesioned rats. Transplantation of the fetal striatal tissue restored electrophysiological sensitivity to DA in the lesioned striatum. Tyrosine hydroxylase-positive terminals were found innervating the striatal grafts[68]. The survival of grafts and the effects of the grafts on the development of neurological deficits in HD transgenic mice have also been examined. Hemizygote transgenic and wild-type littermate female mice received striatal grafts at the 10 weeks of age and were allowed to survive for 6 weeks. Normal healthy grafts were seen to survive and differentiate within the striatum of transgenic mice in a manner comparable to that seen in control mice. The transgenic mice exhibited a progressive decline in bodyweight from 9 weeks of age and a progressive hypoactivity in an open field test of general locomotor behavior. Although striatal grafts exerted a statistically significant influence on several indices of this impairment, all behavioral effects were small and did not exert any clinically relevant effect on the profound neurological deficiency of the transgenic mice[69]. This could be a result of the rapid development of neurological deficits in this HD model.

The safety and therapeutic effects of neural transplantation have been tested in HD patients. The first clinical trial in HD patients was reported in 1995 by Madrazo *et al*[70]. In their trial, homotopic fetal striatal homotransplantations were performed on two HD patients. Each patient was implanted in the ventricular wall of the right caudate nucleus with striata from a 13 week-old and a 12 week-old human fetus. After surgery both patients were kept on cyclosporine A for immunosuppression. The two patients were observed for 16–33 months post-transplantation for neurological progression of their disease. The results showed that the disease in both patients had progressed slower in relation to their pre-

operative state. The effects of fetal tissue transplantation on HD symptoms were carefully evaluated in three patients who had received surgery. Four to six months after surgery, all patients demonstrated increased scores on some measures of cognitive functions. These findings suggest that fetal striatal transplantation could improve some of the cognitive symptoms associated with HD[71].

In a safety evaluation of three HD patients who received fetal striatal tissue transplantation for one year, MRI revealed that the grafts survived and grew within the striatum without displacing the surrounding tissue. No patients demonstrated adverse effects from the surgery or the associated cyclosporin immunosuppression, nor did any patient exhibit deterioration following the procedure[72]. In a post-mortem examination of an HD patient, who died from cardiovascular disease 18 months after transplantation, histological analysis demonstrated surviving transplanted cells with typical morphology of the developing striatum. Selective markers of both striatal projection and interneurons showed positive transplant regions clearly innervated by host tyrosine hydroxylase fibers. Neuronal protein aggregates of mutant htt, a biohallmark of HD neuropathology, were not found within the transplanted fetal tissue[73]. These results suggest that grafts derived from human fetal striatal tissue can survive for a relatively long time after transplantation into a patient with HD[73]. Functional improvements were demonstrated in the Gaura *et al* report with three HD patients[74]. They showed that the clinical changes in these three patients were associated with a reduction of the striatal and cortical hypometabolism, demonstrating that grafts were able to restore the function of striato-cortical loops. Conversely, in the two patients not improved by the grafts, striatal and cortical hypometabolism progressed over the 2-year follow-up. Finally, detailed anatomical/functional analysis of the grafted striata, enabled by the 3D fusion of MRI and metabolic images, revealed considerable heterogeneity in the anatomic and metabolic profiles of grafted tissue, both within and between HD patients.

The safety of fetal striatal tissue transplantation was demonstrated in a few clinical trials[75–78]. All these studies reported that surgical procedures were safe and patients tolerated grafts well. The major adverse events related to the procedure were associated with immunotherapy. However, a report from Hauser *et al* raised big concerns on the safety of fetal tissue transplantation[79]. In their clinical trial of 7 patients undergoing bilateral engraftment, there were 4 subdural haematomas (in 3 subjects), 2 requiring neurosurgical drainage. One subject died 18 months after surgery from probable cardiac arrhythmia secondary to severe atherosclerotic cardiac disease. Autopsy demonstrated clearly demarcated grafts of typical developing striatal morphology, with host-derived dopaminergic fibers extending into the grafts and no evidence of immune rejection. These latter subjects might have had more advanced HD with a greater degree of brain atrophy, and this could be a contraindication to engraftment.

Other neuroprotective approaches Mitochondria dysfunction has been implicated in HD pathogenesis. The supporting evidence includes deficiency in mitochondria complex I, II and IV in HD brains and HD transgenic mice. Toxins inhibiting mitochondria complex produce striatal HD pathology. Therefore, compounds enhancing energy metabolism have been evaluated for treatment of HD. In HD patients, lactate was increased in cerebrospinal fluid and cerebral cortex. Treatment with coenzyme Q10 (CoQ10), an essential cofactor of the electron transport chain and an important antioxidant, resulted in significant decreases in cortical lactate concentrations in 18 patients. These findings provide evidence for a generalized energy defect in HD, and suggest a possible therapy[54]. Thus, its neuroprotective effects have been investigated in a variety of animal models. These studies have demonstrated that CoQ10 can protect against striatal lesions produced by the mitochondrial toxins malonate and 3-nitropropionic acid. Oral administration of CoQ10 significantly decreased elevated lactate levels in patients with HD[80]. CoQ10 in combination with the NMDA antagonist remacemide was examined to determine the efficacy in ameliorating the motor dysfunction and premature death of HD transgenic mice. Motor performance was specifically but transiently improved beginning 3 weeks after drug administration. Survival, however, was not prolonged[81]. In another study in HD transgenic mice with CoQ10 and remacemide, Ferrante *et al* found that oral administration of either CoQ10 or remacemide significantly extended survival and delayed the development of motor deficits, weight loss, cerebral atrophy, and neuronal intranuclear inclusions in the R6/2 transgenic mouse model of HD. The combined treatment, using CoQ10 and remacemide, was more efficacious than either compound alone, resulting in a 32% and 17% increase in survival in the R6/2 and N171-82Q mice, respectively[82].

Huntington *et al* completed a multicenter, parallel group, double-blind, 2×2 factorial, randomized clinical trial with CoQ10 in 2001[83]. Research participants with early HD (n=347) were randomized to receive CoQ10 300 mg bid, remacemide hydrochloride 200 mg three times daily, both, or neither treatment, and were evaluated every 4 to 5 months for a total of 30 months on assigned treatment. The prespecified primary measure of efficacy was the change in total

functional capacity (TFC) between baseline and 30 months. This study, however, yielded limited beneficial results. Neither intervention significantly altered the decline in TFC. Patients treated with CoQ10 showed a trend toward slowing in TFC decline (13%) over 30 months as well as beneficial trends in some secondary measures. There were increased frequency of nausea, vomiting, and dizziness with remacemide, and an increased frequency of stomach upset with CoQ10.

Another compound having an effect on bioenergy metabolism is creatine. In HD-transgeneic mice, dietary supplementation of 2% creatine significantly improved survival, slowed the development of motor symptoms, and delayed the onset of weight loss. Creatine lessened brain atrophy and the formation of intranuclear inclusions[84]. Later studies suggested that creatine treatment started after onset of clinical symptoms in HD mice was able to significantly extend survival and improve motor performance. There was reduced brain levels in both creatine and ATP in R6/2 mice, consistent with a bioenergetic defect. Oral creatine supplementation significantly increased brain concentrations of creatine and ATP to wild-type control levels [85]. These studies suggest that creatine might be useful in the treatment of HD. A preliminary clinical trial with creatine has been performed in 41 patients for 1 year. Creatine 5 g/d was administered. At baseline and after 6 and 12 months, the functional, neuromuscular, and cognitive status of the patients was assessed by a test battery that consisted of: (1) the Unified Huntington's Disease Rating Scale (UHDRS); (2) an exercise test on an isokinetic dynamometer to assess strength of the elbow flexor muscles; (3) a maximal exercise test on a bicycle ergometer to evaluate cardiorespiratory fitness; and (4) a test to assess bimanual coordination ability. One year of creatine intake, at a rate that can improve muscle functional capacity in healthy subjects and patients with neuromuscular disease (5 g/d), did not improve functional, neuromuscular, and cognitive status in patients with stage I to III HD[86].

It has been suggested that excitotoxicity contributes to the pathogenesis of HD. Riluzole is a substance with glutamate antagonistic properties that is used for neuroprotective treatment in amyotrophic lateral sclerosis, and which is currently being tested in clinical trials for treatment of HD. R6/2 transgenic mice were treated with riluzole orally beginning at a presymptomatic stage until death to investigate its potential neuroprotective effects in the mouse model and it was found that survival time in the riluzole group was significantly increased in comparison to placebo-treated transgenic controls. Additionally, the progressive weight loss was delayed and significantly reduced by riluzole treatment; behavioral testing of motor coordination and spontaneous locomotor activity, however, showed no statistically significant differences. These data suggest that riluzole is a promising candidate for neuroprotective treatment in human HD[11].

Recently a few studies have produced interesting results on the beneficial effects of environment enrichment on HD. van Dellen *et al* housed HD mice in large standard cages that contained cardboard, paper and plastic objects, which were changed every two days, from the age of 4 weeks[87]. They showed that exposure of these mice to a stimulating, enriched environment from an early age helps to prevent the loss of cerebral volume and delays the onset of motor disorders. In the brains of humans diagnosed with HD cannabinoid CB1 receptors are selectively lost from the basal ganglia output nuclei prior to the development of other identifiable neuropathology. In animal studies, they further showed that HD mice housed in a normal environment show a loss of cannabinoid CB1 and dopamine D1 and D2 receptors in the striatum and the corresponding output nuclei of the basal ganglia. HD mice exposed to an enriched environment showed equivalent loss of D1 and D2 receptors as their "non-enriched" counterparts; in contrast, the "enriched" mice show significantly less depletion of CB1 receptors. These results therefore show that an enhanced environment slows the rate of loss of one of the first identifiable neurochemical deficits of HD[88]. Environment enrichment slowed a decline in RotaRod performance in R6/2 mice. Enrichment also delayed the loss of peristriatal cerebral volume in R6/2 brains[89]. Improvement of motor functions and prevention of loss of bodyweight in HD mice were found. HD patients and transgenic mice expressing mutant human huntingtin exhibit reduced levels of BDNF, hyperglycemia, and tissue wasting. Enrichment entirely corrected these changes. BDNF levels are unaltered in HD in the anterior cortex, suggesting that enrichment might prevent HD-induced impairment of anterograde transport of this neurotrophin to the striatum[90].

It has been shown that dietary restriction (DR) slows down the aging process and increases life expectancy. Further, the progression of neuropathological (formation of huntingtin inclusions and apoptotic protease activation), behavioral (motor dysfunction), and metabolic (glucose intolerance and tissue wasting) abnormalities in HD mice were shown to be retarded when the mice were maintained on a DR feeding regimen, which resulted in an extension of their lifespan. DR increases levels of brain-derived neurotrophic factor and the protein chaperone heat-shock protein-70 in the striatum and cortex, which are depleted in HD mice fed a

normal diet. These results suggest a dietary intervention that could suppress the disease process and increase the lifespan of humans that carry the mutant huntingtin gene[91]. These results could provide a molecular basis for ameliorating the effects of HD by some simple yet effective approaches.

Symptomatic treatment

Movement disorder is a prominent feature of HD. The motor component of HD consists of involuntary choreiform movements and increasing difficulties with voluntary movement. Behavioral and psychological problems are the first manifested symptoms in nearly 50% of HD patients. The most common symptoms are loss of energy and initiative, poor perseverance and quality of work, impaired judgment, poor self-care, and emotional blunting. Affective symptoms such as depression, anxiety, irritability, dementia, and schizophrenia-like psychosis occur with a relatively high frequency in HD [92,93]. At present, in the absence of a cure for HD, it is desirable to treat HD symptoms aimed at enhancing the quality of life of patients and improving overall functioning. These types of treatments should include medication, social service, and physical/occupational therapy.

Management of motor dysfunction In general, treatment of chorea is not recommended unless symptoms are disabling. Degeneration of striatal GABAergic neurons can cause hyperactivity of dopaminergic systems. Reducing dopaminergic activity might help restore the balance of neurotransmitter functions. Neuroleptics are dopamine receptor antagonists used for the treatment of psychosis. These drugs have been tried for treatment of choreiform movement in HD patients. Haloperidol is a protoform neuroleptic for the treatment of schizophrenia. Haloperidol is a dopamine D2 receptor antagonist. This drug has been tested in HD for reducing abnormal movements. Eighteen patients with Huntington's chorea were examined before and after treatment with haloperidol, pimozide and tiapride to study the effect of such treatment on hyperkinesia and motor performance. Pimozide and haloperidol improved hyperkinesia; none of the drugs significantly affected motor performance[94]. The relationship between serum haloperidol concentration and improvement in abnormal movements was investigated in 20 adult HD patients. Serum samples and assessments of the severity of chorea were simultaneously obtained from each patient. Results showed that significant improvement of abnormal movements, greater than 30% from baseline, occurred at serum concentrations between 2 and 5 μg/L, which corresponded to doses of 1.5 to 10 mg/d[95]. The main adverse effect of haloperidol is the high frequency of dyskinesia. Clinically the most problematic of these are sedation, cognitive slowing, increased mobility problems, and hypotension. The inability of traditional dopamine antagonists to improve functional capacity, despite ameliorating chorea, is possibly a result of the suppression of voluntary motor activity. The antipsychotic drug risperidone was reported to be effective in the treatment of chorea and psychosis in HD patients. After initiating the treatment, the patient experienced improvement in maintaining gait and increased hand skills. It was noticed that the patient had decreased choreiform movements in the second week of the treatment[96].

Chorea in HD and in the levodopa-induced dyskinesias of PD can be clinically indistinguishable. In PD, hyperphosphorylation of NMDA receptors expressed on striatal medium spiny neurons contributes to peak-dose dyskinesias, and drugs that block these receptors can diminish chorea severity. Because these spiny neurons are the primary target of the neurodegenerative process in HD, sensitization of NMDA receptors on residual striatal neurons might also participate in the generation of motor dysfunction in HD. Movement disorder is also treated with the NMDA receptor antagonists riluzole and amantadine. In a 6-week open-label trial of riluzole (50 mg twice a day) in eight subjects with HD, subjects were evaluated before riluzole treatment, on treatment, and off treatment, with the chorea, dystonia, and total functional capacity (TFC) scores from the Unified Huntington's Disease Rating Scale, and magnetic resonance spectroscopy measurements of occipital cortex and basal ganglia lactate levels. The chorea rating score improved by 35% on treatment and worsened after discontinuation of treatment. There was no significant effect on the dystonia or TFC score[97]. In another open label study, riluzole was given (50 mg twice a day) to nine HD patients (clinical stages 1–3; mean age 46.4 years; mean disease duration 8 years). Patients were evaluated at baseline and after 3 and 12 months of riluzole therapy. Results demonstrated that riluzole was well tolerated. At 3 months, mean total motor scale (TMS), mean TMS chorea subscore, and mean total functional capacity scale were significantly improved compared with predrug baseline. At 12 months, however, this beneficial effect on motor status and overall function was not sustained. In contrast, severity and frequency of behavioral dysfunction as well as psychomotor speed assessed by the symbol digit modalities test were improved compared with baseline. These data suggest that there are transient antichoreatic effects and more sustained effects of riluzole on psychomotor speed and behavior in patients with HD[98]. In a case report pre-

sented by Bonelli *et al*, two HD patients with severe motor dysfunction were initially treated with olanzapine (20 mg daily)[99]. Improvement of motor performance was obtained with olanzapine in both patients. After 2 weeks of treatment with olanzapine, riluzole (50 mg twice a day) was added. A further slight improvement of motor function (especially in the fine motor tasks) was seen in the next 2 weeks without additional side-effects.

Another NMDA receptor antagonist tested for use in HD patients is amantadine. In a clinical study conducted by Verhagen *et al*, 24 patients with HD entered a double-blind placebo-controlled crossover study of amantadine with two 2-week arms[100]. Chorea scores were lower with amantadine (usually 400 mg/d) than placebo, with a median reduction in extremity chorea at rest of 36% for all 22 patients evaluated and of 56% in the 10 individuals with the highest plasma drug levels. Improvement correlated with plasma amantadine concentrations but not CAG repeat length. The acute antidyskinetic effects of IV amantadine in HD were evaluated. A 2-h IV infusion of amantadine or placebo was given to 9 patients with HD on two different days in a double-blind, randomized crossover fashion. All patients subsequently received oral amantadine unblinded for a 1-year period. A reduction of dyskinesia scores was reported during both IV and oral amantadine treatment ($P<0.05$)[101].

Management of psychological disturbance There are not many studies on the treatment of the psychopathology of HD although psychological disturbance is common in HD patients. Episodic aggressive behavior in HD that responded poorly to neuroleptics was reduced by a carefully titrated dose of propranolol in 3 patients with advanced HD. The optimal doses were 180 and 30 mg/d, respectively[102]. Lithium is a mood stabilizer used for bipolar disorder. It has been reported that 6 patients with a family history of HD chorea participated in a double blind crossover trial involving four treatments: lithium carbonate, haloperidol, lithium carbonate and haloperidol, and placebo. None of the treatments significantly affected chorea measurements. With regard to the psychological variables, the levels of irritability, the frequency of angry outbursts and depression did appear to be affected by the treatment in some patients. Three patients improved on a combination of lithium carbonate and haloperidol while the remaining three did not. It is suggested that lithium carbonate and haloperidol together should be seriously considered in the treatment of HD when patients are excessively irritable and impulsive[103].

Atypical antipsychotic drugs have recently been found to be useful in the treatment of HD symptoms including motor dysfunction. Risperidone is a novel antipsychotic drug with a balanced serotonin 5-HT2 and dopamine D2 receptor antagonism. In a case report, risperidone was introduced in combination with clozapine therapy. Risperidone was started at 0.5 mg/d and gradually increased to 6 mg/d over a 6-week period. This coincided with marked improvement in abnormal involuntary movements (AIMS score of 7) and further improvement in psychosis (BPRS score of 7). Choreiform movements of the limbs ceased almost completely, gait improved significantly, and dysarthria and facial grimacing decreased[104]. Olanzapine is a new atypical antipsychotic drug. It is a thienodibenzodiazepine and is structurally very similar to clozapine. Olanzapine has been shown to have a high affinity for a large number of receptors including D1, D2, D4, 5HT2A, 5HT2C, 5HT3, α1-adrenergic, histamine H1, and five muscarinic receptors. Unlike clozapine it is not associated with the potentially serious side effect of agranulocytosis and therefore frequent blood monitoring is not necessary. Dipple reported the first case of using olanzapine in HD[105]. An HD patient who had shown no improvement after using other typical anti-psychotic drugs showed a positive response in improving motor function with olanzapine. As a result, more HD patients were treated with olazapine. In a clinical study with 11 HD patients, 9 patients were treated with olanzapine for 9.8±5.9 months. Assessment of the drug's effects was carried out using the Clinical Global Impression of Change Scale (CGIC) and the United Huntington's Disease Rating Scale behavioral (UHDRS-b) and motor (UHDRS-m) at 6-month intervals. The Mean CGIC was 2.1±0.8. UHDRS-b improved significantly and UHDRS-m did not change. It was concluded that olanzapine is a good alternative treatment in HD, mainly for psychiatric symptoms and is moderately effective for motor symptoms, possibly because of its effect on chorea[106].

Symptomatic treatment of HD like symptoms with Chinese medicine HD diagnosis is difficult in China as autopsy and genetic testing are usually not performed. However, there are many reports describing successful treatment of choreiform movement disorders (named chorea minor) with Chinese medicine. Among these reported cases, most involve HD-like symptoms caused by other diseases. But these treatments might also be effective in relief of HD symptoms. Recent studies reported that a natural product derived from six herbs, including Ginsheng and Shouwu, protected 3-nitropropionic acid induced striatal lesions and reduced behavioral deficits. This herbal product increased expression of BDNF and GDNF in the brain[107–109].

Summary and conclusion

The therapeutic benefits of current symptomatic treat-

ments remain to be determined. The effectiveness of drug treatment usually has been evaluated only in a small number of patients, and varies in patients with different stages of HD. In order to confirm the value of these treatments in the management of symptoms of HD, more clinical trials involving a larger number of patients and better design are needed. It should be noted that improvement of chorea by typical neuroleptics might be at the expense of worsening voluntary movement. Extensive studies have greatly advanced our understanding of the molecular mechanisms of HD pathogenesis. The main challenge in finding a cure for HD is the selection of molecular targets. Multiple parallel and sequential signaling pathways are involved in cultivating ultimate neuronal dysfunction and death induced by mutant huntingtin. Identifying upstream and core molecular events could be crucial for therapeutic development. Thus far, these key issues have not been resolved. Another big challenge is an effective read-out for the assay of therapeutic effects. Many novel therapies targeting molecular pathogenesis are awaiting safe and clinical studies. With regards to fetal tissue transplantation, the resources are limited and there is still debate on the ethical issues of using this technology. The safety and rationale of tissue transplantation have also now been questioned[110]. Compounds improving energy production are safe but their effectiveness needs to be further evaluated. At present, NMDA receptor antagonists, riluzole and amantadine, and energy production boosters, CoQ10 and creatine, might be worth testing. The use of Chinese medicine for HD treatment also needs further investigation. We have made great progress, but we still have long way to go in developing a cure for HD.

References

1 The Huntington's Disease Collaborative Research Group. A novel gene containing a trinucleotide repeat that is expanded and unstable on Huntington's disease chromosomes. Cell 1993; 72: 971–83.

2 Qin ZH, Gu ZL. Huntingtin processing in pathogenesis of Huntington disease. Acta Pharmacol Sin 2004; 25: 1243–9.

3 Hughes RE, Olson JM. Therapeutic opportunities in polyglutamine disease. Nature Med 2001; 7: 419–23.

4 Scherzinger E, Lurz R, Turmaine M, Mangiarini L, Hollenbach B, Hasenbank R, *et al*. Huntingtin-encoded polyglutamine expansions form amyloid-like protein aggregates *in vitro* and *in vivo*. Cell 1997; 90: 549–58.

5 Huang CC, Faber PW, Persichetti F, Mittal V, Vonsattel JP, MacDonald ME, *et al*. Amyloid, formation by mutant huntingtin: threshold, progressivity and recruitment of normal polyglutamine proteins. Somatic Cell Mol Gen 1998; 24: 217–33.

6 Scherzinger E, Sittler A, Schweiger K, Heiser V, Lurz R, Hasenbank R, *et al*. Self-assembly of polyglutamine-containing huntingtin fragments into amyloid-like fibrils: implications for Huntington's disease pathology. Proc Natl Acad Sci USA 1999; 96: 4604–9.

7 Davies SW, Turmaine M, Cozens BA, DiFiglia M, Sharp AH, Ross CA, *et al*. Formation of neuronal intranuclear inclusions underlies the neurological dysfunction in mice transgenic for the HD mutation. Cell 1997; 90: 537–48.

8 Heiser V, Scherzinger E, Boeddrich A, Nordhoff E, Lurz R, Schugardt N, *et al*. Inhibition of huntingtin fibrillogenesis by specific antibodies and small molecules: implications for Huntington's disease therapy. Proc Natl Acad Sci USA 2000; 97: 6739–44.

9 Pollitt SK, Pallos J, Shao J, Desai UA, Ma AA, Thompson LM, *et al*. A rapid cellular FRET assay of polyglutamine aggregation identifies a novel inhibitor. Neuron 2003; 40: 685–94.

10 Heiser V, Engemann S, Brocker W, Dunkel I, Boeddrich A, Waelter S, *et al*. Identification of benzothiazoles as potential polyglutamine aggregation inhibitors of Huntington's disease by using an automated filter retardation assay. Proc Natl Acad Sci USA 2002; 99: 16400–6.

11 Schiefer J, Landwehrmeyer GB, Luesse HG, Sprunken A, Puls C, Milkereit A, *et al*. Riluzole prolongs survival time and alters nuclear inclusion formation in a transgenic mouse model of Huntington's disease. Mov Disord 2002; 17: 4: 748–57.

12 Tanaka M, Machida Y, Niu S, Ikeda T, Jana NR, Doi H, *et al*. Trehalose alleviates polyglutamine-mediated pathology in a mouse model of Huntington disease. Nat Med 2004; 10: 148–54.

13 Wang J, MacDonald ME, Gusella JF. Reversal of a full-length mutant huntingtin neuronal cell phenotype by chemical inhibitors of polyglutamine-mediated aggregation. BMC Neurosci 2005; in press.

14 Sanchez I, Mahlke C, Yuan J. Pivotal role of oligomerization in expanded polyglutamine neurodegenerative disorders. Nature 2003; 421: 373–9.

15 Aiken CT, Tobin AJ, Schweitzer ES. A cell-based screen for drugs to treat Huntington's disease. Neurobiol Dis 2004; 16: 546–55.

16 Sittler A, Lurz R, Lueder G, Priller J, Lehrach H, Hayer-Hartl MK, *et al*. Geldanamycin activates a heat shock response and inhibits huntingtin aggregation in a cell culture model of Huntington's disease. Human Mol Genet 2001; 10: 1307–15.

17 Kahlem P, Green H, Djian P. Transglutaminase action imitates Huntington's disease: selective polymerization of Huntingtin containing expanded polyglutamine. Mol Cell 1998; 1: 595–601.

18 Karpuj MV, Garren H, Slunt H, Price DL, Gusella J, Becher MW, *et al*. Transglutaminase aggregates huntingtin into nonamyloidogenic polymers, and its enzymatic activity increases in Huntington's disease brain nuclei. Proc Natl Acad Sci USA 1999; 96: 7388–93.

19 Lorand L, Parameswaran KN, Stenberg P, Tong YS, Velasco PT, Jonsson NA, *et al*. Specificity of guinea pig liver transglutaminase for amine substrates. Biochemistry 1979; 18: 1756–65.

20 Dedeoglu A, Kubilus JK, Jeitner TM, Matson SA, Bogdanov M, Kowall NW, *et al*. Therapeutic effects of cystamine in a murine model of Huntington's disease. J Neurosci 2002; 22: 8942–50.

21 Karpuj MV, Becher MW, Springer JE, Chabas D, Youssef S, Pedotti R, *et al*. Prolonged survival and decreased abnormal movements in transgenic model of Huntington disease, with administration of the transglutaminase inhibitor cystamine. Nat Med 2002; 8: 143–9.

22 Goldberg YP, Nicholson DW, Rasper DM, Kalchman MA, Koide HB, Graham RK, *et al*. Cleavage of huntingtin by apopain, a proapoptotic cysteine protease, is modulated by the polyglutamine tract. Nat Gen 1996; 13: 442–9.
23 Wellington CL, Singaraja R, Ellerby L, Savill J, Roy S, Leavitt B, *et al*. Inhibiting caspase cleavage of huntingtin reduces toxicity and aggregate formation in neuronal and nonneuronal cells. J Biol Chem 2000; 275: 19831–8.
24 Kim YJ, Yi Y, Sapp E, Wang Y, Cuiffo B, Kegel KB, *et al*. Caspase 3-cleaved N-terminal fragments of wild-type and mutant huntingtin are present in normal and Huntington's disease brains, associate with membranes, and undergo calpaindependent proteolysis. Proc Natl Acad Sci USA 2001; 98: 12784–9.
25 Gafni J, Hermel E, Young JE, Wellington CL, Hayden MR, Ellerby LM. Inhibition of calpain cleavage of huntingtin reduces toxicity: accumulation of calpain/caspase fragments in the nucleus. J Biol Chem 2004; 279: 20211–20.
26 Lunkes A, Lindenberg KS, Ben-Haiem L, Weber C, Devys D, Landwehrmeyer GB, *et al*. Proteases acting on mutant huntingtin generate cleaved products that differentially build up cytoplasmic and nuclear inclusions. Mol Cell 2002; 10: 259–69.
27 DiFiglia M, Sapp E, Chase KO, Davies SW, Bates GP, Vonsattel JP, *et al*. Aggregation of huntingtin in neuronal intranuclear inclusions and dystrophic neurites in brain. Science 1997; 277: 1990–3.
28 Hodgson JG, Agopyan N, Gutekunst CA, Leavitt BR, LePiane F, Singaraja R, *et al*. A YAC mouse model for Huntington's disease with full-length mutant huntingtin, cytoplasmic toxicity, and selective striatal neurodegeneration. Neuron 1999; 23: 181–92.
29 Kim M, Lee HS, LaForet G, McIntyre C, Martin EJ, Chang P, *et al*. Mutant huntingtin expression in clonal striatal cells: dissociation of inclusion formation and neuronal survival by caspase inhibition. J Neurosci 1999; 19: 964–73.
30 Chen M, Ona VO, Li M, Ferrante RJ, Fink KB, Zhu S, *et al*. Minocycline inhibits caspase-1 and caspase-3 expression and delays mortality in a transgenic mouse model of Huntington disease. Nat Med 2000; 6: 797–801.
31 Wang X, Zhu S, Drozda M, Zhang W, Stavrovskaya IG, Cattaneo E, *et al*. Minocycline inhibits caspase-independent and -dependent mitochondrial cell death pathways in models of Huntington's disease. Proc Natl Acad Sci USA 2003; 100: 10483–7.
32 Kiechle T, Dedeoglu A, Kubilus J, Kowall NW, Beal MF, Friedlander RM, *et al*. Cytochrome C and caspase-9 expression in Huntington's disease. Neuromolecular Med 2002; 1: 183–95.
33 Ona VO, Li M, Vonsattel JP, Andrews LJ, Khan SQ, Chung WM, *et al*. Inhibition of caspase-1 slows disease progression in a mouse model of Huntington's disease. Nature 1999; 399: 263–7.
34 Sanchez I, Xu CJ, Juo P, Kakizaka A, Blenis J, Yuan J. Caspase-8 is required for cell death induced by expanded polyglutamine repeats. Neuron 1999; 22: 623–33.
35 Zuccato C, Ciammola A, Rigamonti D, Leavitt BR, Goffredo D, Conti L, *et al*. Loss of huntingtin-mediated BDNF gene transcription in Huntington's disease. Science 2001; 293: 493–8.
36 Li SH, Cheng AL, Zhou H, Lam S, Rao M, Li H, *et al*. Interaction of Huntington disease protein with transcriptional activator Sp1. Mol Cell Biol 2002; 22: 1277–87.
37 Li SH, Li XJ. Huntingtin-protein interactions and the pathogenesis of Huntington's disease. Trends Gen 2004; 20: 146–54.
38 Luthi-Carter R, Strand A, Peters NL, Solano SM, Hollingsworth ZR, Menon AS, *et al*. Decreased expression of striatal signaling genes in a mouse model of Huntington's disease. Human Mol Gen 2000; 9: 1259–71.
39 Chan EY, Luthi-Carter R, Strand A, Solano SM, Hanson SA, DeJohn MM, *et al*. Increased huntingtin protein length reduces the number of polyglutamine-induced gene expression changes in mouse models of Huntington's disease. Human Mol Gen 2002; 11: 1939–51.
40 Yu ZX, Li SH, Nguyen HP, Li XJ. Huntingtin inclusions do not deplete polyglutamine-containing transcription factors in HD mice. Human Mol Gen 2002; 11: 905–14.
41 Dunah AW, Jeong H, Griffin A, Kim YM, Standaert DG, Hersch SM, *et al*. Sp1 and TAFII130 transcriptional activity disrupted in early Huntington's disease. Science 2002; 296: 2238–43.
42 Steffan JS, Bodai L, Pallos J, Poelman M, McCampbell A, Apostol BL, *et al*. Histone deacetylase inhibitors arrest polyglutamine-dependent neurodegeneration in Drosophila. Nature 2001; 413: 739–43.
43 Hockly E, Richon VM, Woodman B, Smith DL, Zhou X, Rosa E, *et al*. Suberoylanilide hydroxamic acid, a histone deacetylase inhibitor, ameliorates motor deficits in a mouse model of Huntington's disease. Proc Natl Acad Sci USA 2003; 100: 2041–6.
44 Minamiyama M, Katsuno M, Adachi H, Waza M, Sang C, Kobayashi Y, *et al*. Sodium butyrate ameliorates phenotypic expression in a transgenic mouse model of spinal and bulbar muscular atrophy. Hum Mol Genet 2004; 13: 1183–92.
45 Alvarez RD, Barnes MN, Gomez-Navarro J, Wang M, Strong TV, Arafat W, *et al*. A cancer gene therapy approach utilizing an anti-erbB-2 single-chain antibody-encoding adenovirus (AD21): a phase I trial. Clin Cancer Res 2000; 6: 3081–7.
46 Marasco WA, Haseltine WA, Chen SY. Design, intracellular expression, and activity of a human anti-human immunodeficiency virus type 1 gp120 single-chain antibody. Proc Natl Acad Sci USA 1993;90: 7889–93.
47 Lecerf JM, Shirley TL, Zhu Q, Kazantsev A, Amersdorfer P, Housman DE, *et al*. Human single-chain Fv intrabodies counteract *in situ* huntingtin aggregation in cellular models of Huntington's disease. Proc Natl Acad Sci USA 2001; 98: 4764–9.
48 Colby DW, Garg P, Holden T, Chao G, Webster JM, Messer A, *et al*. Development of a human light chain variable domain (V(L)) intracellular antibody specific for the amino terminus of huntingtin via yeast surface display. J Mol Biol 2004; 342: 901–12.
49 Khoshnan A, Ko J, Patterson PH. Effects of intracellular expression of anti-huntingtin antibodies of various specificities on mutant huntingtin aggregation and toxicity. Proc Natl Acad Sci USA 2002; 99: 1002–7.
50 Xia H, Mao Q, Paulson HL, Davidson BL. siRNA-mediated gene silencing *in vitro* and *in vivo*. Nat Biotechnol 2002; 20: 1006–10.
51 Caplen NJ, Taylor JP, Statham VS, Tanaka F, Fire A, Morgan RA. Rescue of polyglutamine-mediated cytotoxicity by double-stranded RNA-mediated RNA interference. Hum Mol Gen 2002; 11: 175–84.
52 Xia H, Mao Q, Eliason SL, Harper SQ, Martins IH, Orr HT, *et al*. RNAi suppresses polyglutamine-induced neurodegeneration in a model of spinocerebellar ataxia. Nat Med 2004; 10: 816–20.
53 Barbacid M. The Trk family of neurotrophin receptors. J Neurobiol 1994; 25: 1386–403.

54 Koroshetz WJ, Jenkins BG, Rosen BR, Beal MF. Energy metabolism defects in Huntington's disease and effects of coenzyme Q10. Ann Neurol 1997; 41:160–5.
55 Winn SR, Lindner MD, Lee A, Haggett G, Francis JM, Emerich DF. Polymer-encapsulated genetically modified cells continue to secrete human nerve growth factor for over one year in rat ventricles: behavioral and anatomical consequences. Exp Neurol 1996; 40: 126–38.
56 Qin ZH, Wang Y, Chase TN. Stimulation of NMDA receptors induces apoptosis in rat brain. Brain Res 1996; 725: 166–76.
57 Bemelmans AP, Horellou P, Pradier L, Brunet I, Colin P, Mallet J. Brain-derived neurotrophic factor-mediated protection of striatal neurons in an excitotoxic rat model of Huntington's disease, as demonstrated by adenoviral gene transfer. Hum Gene Ther 1999; 10: 2987–97.
58 Pérez-Navarro F, Canudas AM, Åkerud P, Alberch J, Arenas E. Brain-derived neurotrophic factor, neurotrophin-3, and neurotrophin-4/5 prevent the death of striatal projection neurons in a rodent model of Huntington's disease. J Neurochem 2000; 75: 2190–9.
59 Emerich DF, Winn SR, Hantraye PM, Peschanski M, Chen EY, Chu Y, *et al*. Protective effect of encapsulated cells producing neurotrophic factor CNTF in a monkey model of Huntington's disease. Nature 1997; 386: 395–9.
60 McBride JL, During MJ, Wuu J, Chen EY, Leurgans SE, Kordowera JH. Structural and functional neuroprotection in a rat model of Huntington's disease by viral gene transfer of GDNF. Exp Neurol 2003; 181: 213–23.
61 Kells AP, Fong DM, Dragunow M, During MJ, Young D, Connor B, AAV-mediated gene delivery of BDNF or GDNF is neuroprotective in a model of Huntington disease. Mol Therapy 2004; 9: 682–8.
62 Mittoux V, Joseph JM, Conde F, Palfi S, Dautry C, Poyot T, *et al*. Restoration of cognitive and motor functions by ciliary neurotrophic factor in a primate model of Huntington's disease. Hum Gene Ther 2000; 20; 11: 1177–87.
63 Isacson O, Brundin P, Gage FH, Bjorklund A. Neural grafting in a rat model of Huntington's disease: progressive neurochemical changes after neostriatal ibotenate lesions and striatal tissue grafting. Neuroscience 1985; 16: 799–817.
64 Watts C, Brasted PJ, Dunnett SB. The morphology, integration, and functional efficacy of striatal grafts differ between cell suspensions and tissue pieces. Cell Transplant 2000; 9: 395–407.
65 Palfi S, Conde F, Riche D, Brouillet E, Dautry C, Mittoux V, *et al*. Fetal striatal allografts reverse cognitive deficits in a primate model of Huntington disease. Nat Med 1998; 4: 963–6.
66 Armstrong RJ, Watts C, Svendsen CN, Dunnett SB, Rosser AE. Survival, neuronal differentiation, and fiber outgrowth of propagated human neural precursor grafts in an animal model of Huntington's disease. Cell Transplant 2000; 9: 55–64.
67 Xu ZC, Wilson CJ, Emson PC. Restoration of thalamostriatal projections in rat neostriatal grafts: an electron microscopic analysis. J Comp Neurol 1991; 303: 22–34.
68 Chena GJ, Jengb CH, Lina SZ, Tsaic SH, Wangd Y, Chianga YH. Fetal striatal transplants restore electrophysiological sensitivity to dopamine in the lesioned striatum of rats with experimental Huntington's disease. J Biomed Sci 2002; 9: 303–10.
69 Dunnett SB, Carter RJ, Watts C, Torres EM, Mahal A, Mangiarini L, *et al*. Striatal transplantation in a transgenic mouse model of Huntington's disease. Exp Neurol 1998; 154: 31–40.
70 Madrazo I, Franco-Bour RE, Castrejon H, Cuevas C, Ostrosky-Solis F. Fetal striatal homotransplantation for Huntington's disease: first two case reports. Neurol Res 1995; 17: 312–5.
71 Philpott LM, Kopyov OV, Lee AJ, Jacques S, Duma CM, Caine S, *et al*. Neuropsychological functioning following fetal striatal transplantation in Huntington's chorea: three case presentations. Cell Transplant 1997; 6: 203–12.
72 Kopyov OV, Jacques S, Lieberman A, Duma CM, Eagle KS. Safety of intrastriatal neurotransplantation for Huntington's disease patients. Exp Neurol 1998; 49: 97–108.
73 Freemana TB, Cicchettid F, Hauserb RA, Deaconf TW, Li XJ, Herschi SM, *et al*. Transplanted fetal striatum in Huntington's disease: phenotypic development and lack of pathology. Proc Natl Acad Sci USA 2000; 97: 13877–82.
74 Gaura VR, Bachoud-Levi AC, Ribeiro MJ, Nguyen JP, Frouin V, Baudic S, *et al*. Striatal neural grafting improves cortical metabolism in Huntington's disease patients. Brain 2004; 127: 65–72.
75 Bachoud-Lévi AC, Nguyen JP, Brugières P, Lefaucheur JP, Cesaro P, P Rémy P, *et al*. Motor and cognitive improvements in patients with Huntington's disease after neural transplantation. Lancet 2000; 356: 1975–9.
76 Bachoud-Lévi AC, Bourdet C, Brugiéres P, Nguyen JP, Grandmougin T, Haddad B, *et al*. Safety and tolerability assessment of intrastriatal neural allografts in five patients with Huntington's disease. Exp Neurol 2000; 161: 194–202.
77 Fink JS, Schumacher JM, Ellias SL, Palmer EP, Saint-Hilaire M, Shannon K, *et al*. Porcine xenografts in Parkinson's disease and Huntington's disease patients: preliminary results. Cell Transplant 2000; 9: 273-8.
78 Rosser AE, Barker RA, Harrower T, Watts C, Farrington M, Ho AK, *et al*. Unilateral transplantation of human primary fetal tissue in four patients with Huntington's disease: NEST-UK safety report. J Neurol Neurosurg Psychiatry 2002; 73: 678–85.
79 Hauser RA, Furtado S, Cimino CR, Delgado H, Eichler S, Schwartz S, *et al*. Bilateral human fetal striatal transplantation in Huntington's disease. Neurology 2002; 58: 687–95.
80 Beal MF. Coenzyme Q10 administration and its potential for treatment of neurodegenerative diseases. BioFactors 1999; 9: 261–6.
81 Schillinga G, Coonfielda ML, Rossb CA, Borchelta DR. Coenzyme Q10 and remacemide hydrochloride ameliorate motor deficits in a Huntington's disease transgenic mouse model. Neurosci Lett 2001; 315: 149–53.
82 Ferrante RJ, Andreassen OA, Dedeoglu A, Ferrante AL, Jenkins BG, Hersch SM, *et al*. Therapeutic effects of coenzyme Q10 and remacemide in transgenic mouse models of Huntington's disease. J Neurosci 2002; 22: 1592–9.
83 Huntington Study Group. A randomized, placebo-controlled trial of coenzyme Q10 and remacemide in Huntington's disease. Neurology 2001; 57: 397–404.
84 Andreassen OA, Dedeoglu A, Ferrante RJ, Jenkins BG, Ferrante KL, Homas M, *et al*. Creatine increases survival and delays motor symptoms in a transgenic animal model of Huntington's disease. Neurobiol Disease 2001; 8: 479–91.
85 Dedeoglu A, Kubilus JK, Yang L, Ferrante KL, Hersch SM, Beal MF, *et al*. Creatine therapy provides neuroprotection after on-

set of clinical symptoms in Huntington's disease transgenic mice. J Neurochem 2003; 85: 1359–67.
86 Verbessem P, Lemiere J, Eijnde BO, Swinnen S, Vanhees L, van Leemputte M, *et al*. Creatine supplementation in Huntington's disease: a placebo-controlled pilot trial. Neurology 2003; 61: 925–30.
87 van Dellen A, Blakemore C, Deacon R, York D, Hannan AJ. Delaying the onset of Huntington's in mice. Nature 2000; 404: 721–2.
88 Glass M, van Dellen A, Blakemore CC, Hannand CAJ, Faullb RLM. Delayed onset of Huntington's disease in mice in an enriched environment correlates with delayed loss of cannabinoid CB1 receptors. Neuroscience 2004; 123: 207–12.
89 Hockly E, Cordery PM, Woodman B, Mahal A, van Dellen A, Blakemore C, *et al*. Environmental enrichment slows disease progression in R6/2 Huntington's disease mice. Ann Neurol 2002; 51: 235–42.
90 Spires TL, Grote HE, Varshney NK, Cordery PM, van Dellen A, Blakemore C, *et al*. Environmental enrichment rescues protein deficits in a mouse model of Huntington's disease, indicating a possible disease mechanism. J Neurosci 2004; 24: 2270–6.
91 Duan W, Guo Z, Jiang H, Ware M, Li X-J, Mattson MP. Dietary restriction normalizes glucose metabolism and BDNF levels, slows disease progression, and increases survival in huntingtin mutant mice. Proc Natl Acad Sci USA 2003; 100: 2911–6.
92 Leroi I, Michalon M. Treatment of the psychiatric manifestations of Huntington's disease: a review of the literature. Can J Psychiatry 1998; 43: 933–40.
93 Craufurd D, Thompson JC, Snowden JS. Behavioral changes in Huntington disease. Neuropsychiatry Neuropsychol Behav Neurol 2001; 14: 219–26.
94 Girotti F, Carella F, Scigliano G, Grassi MP, Soliveri P, Giovannini P, *et al*. Effect of neuroleptic treatment on involuntary movements and motor performances in Huntington's disease. J Neurol Neurosurg Psychiatry 1984; 47: 848–52.
95 Barr AN, Fischer JH, Koller WC, Spunt AL, Singhal A. Serum haloperidol concentration and choreiform movements in Huntington's disease. Neurology 1988; 38: 84–8.
96 Erdemoglua AK, Boratavb C. Risperidone in chorea and psychosis of Huntington's disease. Eur J Neurol 2001; 9: 177–85.
97 Rosas HD, Koroshetz WJ, Jenkins BG, Chen YI, Hayden DL, Beal MF, *et al*. Riluzole therapy in Huntington's disease (HD). Mov Disorders 1999; 14: 326–30.
98 Seppi K, Mueller J, Bodner T, Brandauer E, Benke T, Weirich-Schwaiger H, *et al*. Riluzole in Huntington's disease (HD): an open label study with one year follow up. J Neurol 2001; 248: 866–9.
99 Bonelli RM, Niederwieser G, Diez J, Tringer PK. Riluzole and olanzapine in Huntington's disease. Eur J Neurol 2001; 9: 177–85.
100 Verhagen Metman L, Morris MJ, Farmer C, Gillespie M, Mosby K, Wuu J, *et al*. Huntington's disease: a randomized, controlled trial using the NMDA-antagonist amantadine. Neurology 2002; 59: 694–9.
101 Lucetti C, Del Dotto P, Gambaccini G, Dell' Agnello G, Bernardini S, Rossi G, *et al*. IV amantadine improves chorea in Huntington's disease: an acute randomized, controlled study. Neurology 2003; 60: 1995–7.
102 Stewart JT, Mounts ML, Clark RL Jr. Aggressive behavior in Huntington's disease: treatment with propranolol. J Clin Psychiatry 1987; 48: 106–8.
103 Leonard DP, Kidson MA, Brown JG, Shannon PJ, Taryan S. A double blind trial of lithium carbonate and haloperidol in Huntington's chorea. Aust N Z J Psychiatry 1975; 9: 115–8.
104 Parsa, MA, Szigethy E, Voci JM, Meltzer HY. Risperidone in treatment of choreoathetosis of Huntington's disease. J Clin Psychopharmacol 1997; 17: 134–5.
105 Dipple HC. The use of olanzapine for movement disorder in Huntington's disease: a first case report. J Neurol Neurosurg Psychiatry 1999; 67: 123–4.
106 Paleacu D, Anca M, Giladi N. Olanzapine in Huntington's disease. Acta Neurol Scand 2002; 105: 441–4.
107 Zhang L, Zhang RY, Li L, Wang H, Xia J. Effect of Chinese compound 962 on behavior deficit in Huntington's disease model rats. Chin J Behav Med Sci 2002; 3: 243–6. Chinese.
108 Zhang RY, Zhang L, Wang H, Yei CF. Effects of Shen-wu capsule on motor function andcontent of dopamine in striatum in Huntington model rats. Chin J Rehabil 2002; 9: 513–5. Chinese.
109 Zhang RY, Li L, Zhang L, Wang H, Yei CF. Effects of Shenwu capsule on the behavior and neurotrophic factors in the rats with mimic Huntington's disease. J Beijing University TCM 2003; 26: 34–8.
110 Albin RL. Fetal striatal transplantation in Huntington's disease: time for a pause. [editorial commentaries: huntington's disease]. J Neurol Neurosurg Psychiatry 2002; 73: 612.

Invited review

Anti-amnestic and anti-aging effects of ginsenoside Rg1 and Rb1 and its mechanism of action

Yong CHENG, Li-hong SHEN, Jun-tian ZHANG[1]

Institute of Materia Medica, Peking Union Medical College and Chinese Academy of Medical Sciences, Beijing 100050, China

Key words

ginseng; ginsenoside-Rg1; ginsenoside-Rb1; learning memory; neural progenitor cells; apoptosis; immunity; synaptic plasticity; muscarinic cholinergic receptor; long-term potentiation

[1] Correspondence to Prof Jun-tian ZHANG.
Phn 86-10-6316-5179.
Fax 86-10-6316-5211.
E-mail zhangjt@imm.ac.cn

Received 2004-08-30
Accepted 2004-10-27

doi: 1.111/j.1745-7254.2005.00034.x

Abstract

In the present paper, we overview the discovery of new biological activities induced by ginsenoside Rg1 and Rb1 and discuss possible mechanisms of action. Both compounds could increase neural plasticity in efficacy and structure; especially Rg1, as one small molecular drug, can increase proliferation and differentiation of neural progenitor cells in dentate gyrus of hippocampus of normal adult mice and global ischemia model in gerbils. This finding has great value for treatment of Alzheimer's disease and other neurodegenerative disorders which is characterized by neurons loss. Increase of expression of brain derived neurotrophic factor, Bcl-2 and antioxidant enzyme, enhanced new synapse formation, inhibition of apoptosis and calcium overload are also important neuron protective factors. Rg1 and Rb1 have common effects, but there are some differences in pharmacology and mechanism. These differences may attribute to their different chemical structure. Rg1 is panaxtriol with two sugars, while Rb1 is panaxtriol with four sugars.

Introduction

Ginseng, the root and rhizome of *Panax ginseng* C A Meyer, has been used as a tonic remedy in Chinese traditional medicine for over 2000 years. The word panax is derived from panacea, which means cure-all and longevity. In 200 AD when this herb was described in the oldest Chinese materia medica book: Shen Nong Ben Cao Jing, the author depicted many pharmacological functions of ginseng, including both nootropic and anti-aging effects. Since then, ginseng has been widely used as a supplemental medicine. However, it is neither a tonic nor a remedy for a certain disease.

With the development of modern technology, more and more active principles have been isolated and purified from this herb, and the field of ginseng research has drawn intense attention in Asia, Europe, and the United States. Every year, there are hundreds of papers published and new uses for ginseng discoveried. More than 40 ginsenosides have been isolated from several species of ginseng. Among all the active ingredients isolated from ginseng, we selected Rg1 and Rb1 for study because Rg1 and Rb1 are the representative constituents of panax ginseng and American ginseng, respectively. Rg1 and Rb1 have different chemical structure: Rg1 is panaxtriol with 2 sugars, while Rb1 is panaxtriol with 4 sugars. The chemical structure of Rg1 and Rb1 are shown in Figure 1 and 2. Many researchers believe that they share many beneficial effects of ginseng, including alleviating learning and memory impairment, reversing pathological and physiological changes induced by stress and aging, *etc*. In the review, we take an overview of the proven anti-amnestic and anti-aging effects of both compounds and discuss their possible mechanisms in detail.

Anti-amnestic effects

Various memory-impairment models have been used to evaluate how ginseng and its active ingredients affect learning and memory. In a passive avoidance test, ginsenoside Rg1, (25–100 mg/kg) improved learning and memory's acquisition, consolidation and retrieval, which were impaired by anisodine, cycloheximide, and alcohol respectively, indicating that Rg1 can improve all stages of memory. To study the effect of Rg1 on the learning and memory induced by β-

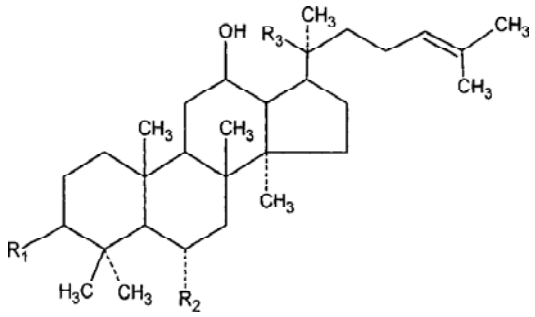

Figure 1. The structure of ginsenoside Rg1. R_1=OH; R_2=OGlc; R_3=OGlc

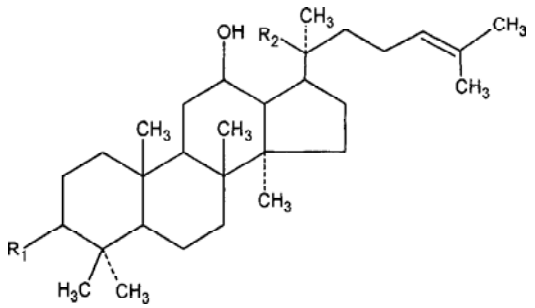

Figure 2. The structure of ginsenoside Rb1. R_1=OGlc(2-1)Glc; R_2=OGlc(6-1)Glc

amyloid (25–35), passive avoidance and performance in Morris water maze were assayed after final treatment, and we found that Rg1 at 5–10 mg/kg significantly decreased latency and swimming distance, and improved corresponding changes in search strategies in the Morris water maze and increased step-through latency also. Rg1 significantly improved memory deficits in aged rats, ovariectomizde rats, and cerebral ischemia-reperfesion rats. Results of the present study showed that ginseng extract and ginsenoside Rg1, Rb1 (25–100 mg/kg) facilitated acquisition and retrieval of memory. Moreover, they also antagonized memory loss and cognitive deficit under various pathological conditions such as cerebral ischemia and dementia. However, the nootropic effect of Rg1 was generally stronger than that of Rb1. All the beneficial effects of ginsenosides observed in the memory-impairment models have been repeated many times in different labs[1–7].

Long-term potentiation (LTP) was first observed in 1973. Since then, it has been thoroughly investigated. Many scientists believe that LTP in the hippocampus is the key form of long-lasting synaptic plasticity and it connects the behavior of learning and memory with the plasticity of neurons. Therefore, LTP has been considered as an important index of cognitive activities in cellular and synaptic levels. In Zhang's lab[8,9], both total ginsenosides (25–100 mg/kg, ip) and ginsenoside Rg1 (10 and 100 nmol/L, icv) were found to improve the basic synaptic transmission and increased the amplitude of LTP induced by high-frequency-stimulation (HFS) in anesthetized rats. In contrast, although ginsenoside Rb1 (10 and 100 nmol/L, icv) administered 30 min after tetanic stimulation was found to increase population spike (PS) amplitude[10], it exerted an inhibitory effect on LTP induced by HFS when given at the same time of stimulation and showed no influence on basic synaptic transmission. Further research suggests that nitric oxide (NO) synthesized by nitric oxide synthase (NOS), especially by nNOS, was involved in synaptic transmission improving the effect of Rg1[11]. In order to eliminate the influence of anesthetics on synaptic transmission, rats were chronically implanted with a stimulation electrode in the perforated path and a recording electrode in the granule cell of dentate gyrus. After Rg1 was administrated (10 and 30 mg/kg, ip) for 12 d, an extracellular recording technique was used to record PS. The results demonstrated that Rg1 significantly increased the sensitivity of evoking PS and the amplitude of PS in freely moving rats[11].

Mechanisms underlying the nootropic effect of ginseng

First, ginsenoside might potentiate the cholinergic system in the central nervous system (CNS). Acetylcholine (ACh) is a very important neurotransmitter in the brain and its scarcity often leads to learning and memory impairment. In Zhang's lab, Rg1 and Rb1 were found to enhance cholinergic system's function through two different pathways: first, both ginsenosides showed the ability to increase the density of central M-cholinergic receptors, although they showed no specific binding to the receptors. Second, Rg1 and Rb1 increased the level of ACh in the CNS, which might be the result of ginsenoside-induced enhancement on choline acetyltransferase activity and inhibition on acetylcholine esterase activity[2,12]. Meanwhile, Banishin *et al* reported that both ginsenosides facilitated cholinergic neurotransmission by increasing cholinergic metabolism in the CNS[13].

It is very interesting to point out that according to existing theory, receptor density is directly dependent on transmitter activity in the brain. For instance, muscarinic receptor level falls in response to the administration of its agonists, while there is a rise in response to chronic administration of muscarinic antagonists. However, findings in Zhang's lab show simultaneous increases in M receptor density and Ach level, which is not in line with previous observations[14]. So, maybe a new theory should be provided to elucidate the effects of ginseng on the cholinergic system.

First, both Rg1 and Rb1 were found to increase protein biosynthesis in the mouse brain[12]. This finding could also explain ginseng's function on memory consolidation. In addition, the increment of M-receptor density could be one of the secondary effects of the enhancement of protein synthesis.

Second, ginsenoside may interfere with immediate early genes. The c-fos proto-oncogene is the prototype of the early-response class of genes and its expression can be considered as a marker of neuronal activity. Rg1 was found to significantly increase the expression of *c-fos* gene in both young and old rats[15]. Furthermore, it had the ability to increase cyclic adenosine monophosphophate (cAMP) level in rat hippocampus. This might provide another explanation for the nootropic effect of Rg1.

Third, apoptosis or programmed cell death is a process by which a cell actively commits suicide under tightly controlled circumstances. Apoptosis is required for maintenance of the homeostasis and is essential in physiological processes such as development, differentiation and aging. However, defective regulation of apoptosis might play a role in the etiology of cancer, acquired immunodeficiency syndrome, autoimmune diseases and neural degenerative disorders. Therefore, pharmacological manipulation of this process may offer new possibilities for the prevention and treatment of many illnesses. In 1997, Zhang's lab reported firstly that Rg1 at concentration of 1 μmol/L and 10 μmol/L inhibited apoptosis induced by withdrawing serum from the culture system of primary cortical neurons[16]. *In vivo* study, an anti-apoptotic effect of Rg1 was seen in aged rats (24–27 month). Further study showed that mechanisms underlying Rg1's effect on apoptosis involved decreasing NO content and NOS activity, reducing intracellular calcium concentration and enhancing superoxide dismutase (SOD) activity. Researchers from the same lab also found that both NOS expression and the activity of NOS enhanced significantly in aged rats (27 months old), which leads to the increment of NO concentration in rat's cortex. This change was reversed by Rg1 administration (20 and 40 mg/kg daily for 5 d)[17]. Taken together with previous *in vitro* results, they confirmed that NO played a role in the acceleration of senescence and that the inhibitory effect of Rg1 on NOS activity might provide an explanation for its anti-aging function.

Recently, the anti-apoptotic effect of Rg1 on neurons was further proved by both *in vivo* and *in vitro* experiments done in other labs[18,19]. The authors of these studies suggested that this effect of Rg1 might attribute to enhancing the ratio of Bcl-2 to Bax protein and inhibiting activation of caspase-3.

Fourth, ginsenoside may modulate synaptic plasticity. Synapses are the essential structure in the CNS through which signals are transmitted, processed and integrated among neurons. The plasticity of synaptic function is also regarded as one of the most important mechanisms underlying the process of learning and memory. Interestingly, in weaning mice administered with Rg1 and Rb1 for 14 d, the thickness of cortex and density of synapses in the hippocampal CA3 region were significantly increased (Table 1)[20]. Meanwhile, Rg1 was found to induce the sprouting of mossy fiber and the expression of the growth-associate protein (GAP-43) dose-dependently in hippocampus in adult rats (Figure 3)[9]. Furthermore, both Rg1 and Rb1 were found to increase hippocampal synaptic density[21]. These experiment proofs provided morphological and physiological evidence to support nootropic effect of ginseng.

Table 1. Effects of ginsenoside Rb1 and Rg1 on the number of synapses in the hippocampus CA3 region in mice. n=5. Mean±SD. ^cP<0.01 *vs* control group [Ref 20].

Group	Dose/mg·kg^{-1}	Number/μm^2
Control	–	0.1718±0.07128
Rb1	28.6	0.2557±0.1382^c
Rb1	56.1	0.2134±0.07327^c
Rg1	27.4	0.2023±0.08330^c
Rg1	53.9	0.2340±0.07447^c

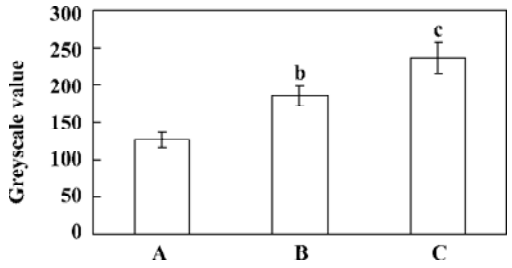

Figure 3. Effect of ginsenoside Rg1 on the mossy fiber sprouting in CA3 field of hippocampus. A: Control group. B: Rg1 10 mg/kg. C: Rg1 30 mg/kg. n=6. Mean±SD. ^bP<0.05, ^cP< 0.01 *vs* control [Ref 9].

Finally, ginsenoside, especially Rg1 might regulate the proliferation and/or surviving ability of neural progenitor cells. A neural progenitor cell (NPC) or Neural stem cell (NSC) is a special kind of neural cell. Previous studies have shown that NPC existed in certain areas in the adult brain as well as in developing brain[22]. Recently, several rodent stud-

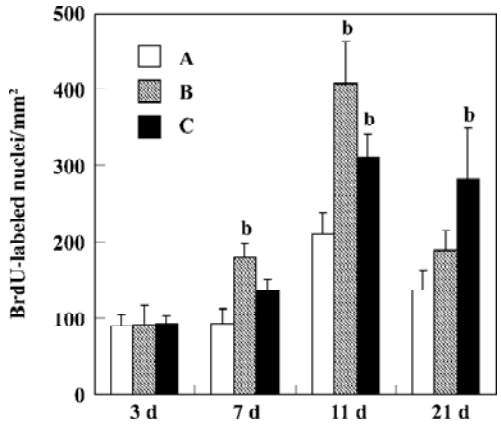

Figure 4. Increase of ischemia-induced proliferation of cells by ginsenoside Rg1 in the dentate gyrus of adult gerbils. The number of bromodeoxyuridine-positive nuclei in the subgranular zone (SGZ) of animals killed 3 d (n=4), 7 d (n=4), 11 d (n=6), and 21 d (n=4) after 6 min of global ischemia. Bromodeoxyuridine (BrdU) was injected every 4 h for 12 h on the day prior to sacrifice. A: Ischemia; B: Ischemia+Rg1 (5 mg/kg); C: Ischemia+Rg1 (10 mg/kg). Each bar shows mean±SEM. $^bP<0.05$ *vs* ischemic group[27].

ies have suggested that the proliferation ability of NPC was reduced in association with age or diseases related cognitive decline[23–25]. Hence, many scientists hypothesize that damage of neurogenesis may be one of the elementary reasons for function-declines in aging and neurodegenerative diseases. Recently, Shen *et al*[26] reported that Rg1 enhanced proliferation ability of rodent hippocampal progenitor cells both *in vitro* and *in vivo*. Incubation of neural progenitor cells with Rg1 resulted in significant increase in absorbency value, [^{3}H]thymidine incorporation and the number of proliferating progenitor cell spheres. In addition, Rg1 administrated for 2 weeks (ip) led to marked enhancement of the number of dividing cells in hippocampus of adult mice. Meanwhile, the same authors found that Rg1 systemically administered not only promoted cell proliferation, but also enhanced the surviving rate of newborn cells in the dentate gyrus of adult gerbils suffered from transient global ischemia (Figure 4)[27]. The authors suggested that influencing the NPC function might serve as one of the elementary mechanisms underlying pharmacological effects of Rg1 and ginseng on the CNS.

To summarize, the nootropic effect of ginseng and ginsenosides has been proved in both behavioral and electrophysiological studies, which is unique among existing nootropic drugs.

Anti-aging effects

Anti-stress effects Various kinds of stress, especially chronic stress, cause many diseases and accelerate aging, so anti-stress drugs are in high demand. Ginseng has long been considered to act as an adaptogen, but the mechanisms underlying its effect are still unclear. Recently, acute, chronic, and repeated stress models were used to observe the effects of ginsenosides on stress.

Repeated hanging stress was used to observe the effect of stress on the reproduction-endocrine system. The results indicated that repeated stress reduced sexual behavior (licking, mounting, and mating), decreased plasma androgen or estrogen levels and increased corticorsterone level in male and female mice. Treatment with ginsenoside Rb1 at dosage of 2.5, 5, and 10 mg/kg prior to stress prevented the decrease of sexual behavior and the increase of corticorsterone. Rb1 brought the concentration of plasma sexual hormones back to normal level [28]. Further study proved that Rb1 (2.5, 5 and 10 mg/kg, ip for 14 d) significantly improved sexual function in mice. The mechanism underlying its "zhuang yang" effects might be the activation of NO/cyclic guanosine monophosphophate (cGMP) pathway in mice corpus cavernosum[29].

Dysfunction of reproductive-endocrine system is often accompanied by the degeneration of cognitive processes in middle and late age. Therefore, the influence of chronic stress on cognitive abilities in mice was observed. The result showed that 60 consecutive days of stress caused a neuronal damage as well as cognitive impairment. Further study suggested that chronic stress decreased brain-derived neurotrophic factor and neurotrophin-3 (NT-3) protein expression throughout the brain area especially in the hippocampus. In addition, stress also induced the release of noradrenaline in the homogenates of the hippocampus and the hypothalamus. Similarly, ginsenoside Rb1 showed the ability to reverse all the pathological changes induced by stress[30]. However, ginsenoside Rg1 had no effect on both repeated and chronic stress-related changes. Instead, it accelerated stress-induced pathological changes in mice, showing another difference between Rg1 and Rb1. Based on these results, Rb1 is believed to be the main anti-stress principle in ginseng and it might be a promising candidate for prevention and treatment of stress-related diseases.

Immunoregulatory effects It has been well documented that aging leads to a substantial decline of T cell function. The possible reasons for the decline include the inability of lymphocytes to proliferation in response to mitogenic stimulation and the decrease of interleukin-2 (IL-2) production. Rg1 given at the concentration of 20 mg/kg *in vivo* and 10 μmol/L *in vitro* enhanced the proliferation of lymphocytes and the production of IL-2 in aged rats[31]. However, it had

no influence on the immune function in young and adult rats. Thus, it is reasonable to consider Rg1 as an "immunoregulator" rather than an "immunopotentiating agent". Further investigation suggested that the mechanism underlying Rg1's effect on immune function in aged rats might be involved in increasing cAMP and cGMP levels in lymphocytes[32].

In contrast, Rb1 had no effect on the decline of immune function in aged rats, which was the third difference found between Rg1 and Rb1.

Other effects In the previous paragraphs, we summarized the pharmacological effects of ginseng, especially ginsenoside Rg1 and Rb1, and the possible mechanisms of these actions. Recent studies have shown that ginseng saponins are a diverse group of steroidal saponins that demonstrates the ability to target a myriad of tissues and produce an array of pharmacological responses, such as anti-osteoporosis, anti-platelet aggregation, anti-arrhythmia, and anti-cancer[7,33–39]. Furthermore, besides ginsenosides, there are also other constituents existing in ginseng, including glucoside, protein, poly-peptides, amino acids, vitamins, *etc*. Their pharmacological functions have been investigated too[40,41].

Senescence is a physiological process and cannot be reversed. Many factors act together in this process (Figure 5). As discussed above, ginseng, especially ginsenoside Rg1 and Rb1, have the ability to interfere almost all of the pathways that accelerate aging process. Besides the effects we mentioned above, some researchers also found that both ginsenosides to some extent inhibited lipid peroxidation induced by VitC-reduced nicotinamide adenine dinucleotide phosphate and Fe^{2+}-cysteine in rat liver and brain microsome; reduced the concentration of intercelluar calcium; and prevented hippocampal neurons from the damage induced by excitatory amino acids[42–46]. All those findings may prove the anti-aging and nootropic effects of this ancient herb.

Concluding remarks

Rg1 and Rb1 are believed to be the main active principles in ginseng. As we discussed above, both Rg1 and Rb1 showed similar effects in improving learning and memory, increasing B_{max} of M-cholinergic receptors, and accelerating cerebral protein and ACh biosynthesis. However, they do behave differently in some areas. For example, Rg1, but not Rb1, enhanced basic synaptic transmission and magnitude of LTP induced by HFS, and showed immunoregulatory action in aged rats as well as an anti-osteoporosis effect in ovariectomized rats. However, Rb1 showed anti-stress effect in acute, chronic, and repeated stress models, whereas Rg1 aggravated stress-induced damage; in addition, Rb1 protected mice against low temperature damage, and Rg1 showed no such effect at the same dose. For the reason of the function differences between the two ginsenosides, some researchers hypothesize it may be due to the difference between their chemical structures (Rb1 has two more glucose as compared to Rg1).

With the application of modern scientific technology, the research of ginseng has made big progress. Ginseng is believed to be the most unique traditional medical herb because it contains the maximum numbers of active constituents, has the most extensive pharmacological effects and specific mechanism of actions in Chinese materia medica.

Chemists have already acquired nearly 40 kinds of ginsenosides from various parts of this plant and new structures continue to identified[47–52]. Becuase ginsenosides and other constituents of ginseng produce different effects and a single ginsenoside initiates multiple actions in the same tissue, the overall pharmacology of ginseng is complicated. Therefore, we must investigate the effects of individual sa-

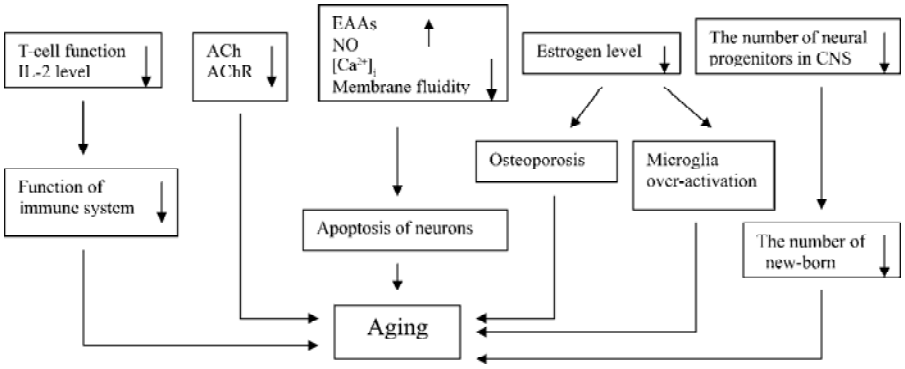

Figure 5. Sketch map of the pathophysiology of aging.

ponin and its mechanisms of actions one by one. But we still cannot synthesize any ginsenosides because of the complexity of their structures. Currently, the only way to prepare active principles from ginseng is to separate and purify them from various parts of the plant. But with the application of modern technology, the yield of some ginsenosides such as Rb1, Rg1, Rg3, and Re has reached up to 1 kg in a number of Chinese corporations. Hence, we can predict that the preparation of active constituents in ginseng has reached the level of industrial production, which makes it possible to further investigate this mysterious herb.

Ginseng and ginsenoside can increase immune function, enhance central cholinergic system function, inhibit free radical and NO generation, and promote proliferation of rodent progenitor cells *in vitro* and *in vivo* (Figure 5). These effects benefit aged people and aging-ralated diseases.

References

1 Chang SY, Kuang PG, Zhang JT, Chen YY, Yu CM. Memory facilitation induced by gynostemma, pentaphyllum and gypensode III (ginsenoside b1) in mice. Chin Pharmacol Bull 1988; 4: 358–61.

2 Zhang JT, Qu ZW, Liu Y, Deng HL. Preliminary study on antiamnestic mechanism of ginsenoside Rg1 and Rb1. Chin Med J 1990; 103: 932–8.

3 Qiu Y, Du GH, Qu ZW, Zhang JT. Protective effects of ginsenoside on the learning and memory impairment induced by transient cerebral ischemia-reperfusion in mice. Chin Pharmacol Bull 1995; 11: 299–302.

4 Zhang DS, Zhang JT. Effects of total ginsenoside on learning and memory impairment induced by beta-amyloid peptide (25-35). Chin Pharmacol Bull 2000; 16: 422–5.

5 Wang XY, Zhang JT. Effects of ginenoside Rg1 on learning and memory impairment induced by β-amyloid peptide (25-35) and its mechanism of action. Acta Pharm Sin 2001; 36: 1–4.

6 Mook-Jung I, Hong HS, Boo JH, Lee KH, Yun SH, Cheong MY, *et al*. Ginsenoside Rb1 and Rg1 improve spatial learning and increase hippocampal synaptophysin level in mice. J Neurosci Res 2001; 63: 509–15.

7 Chen J, Gong YS, Zhang JT. Effects of 17 estradiol and total ginsenoside on the spatial learning and memory impairment of ovariectomy rats. Chin Pharm J 2001; 36: 522–6.

8 Zhang DS, Zhang JT. Effect of total ginsenoside on synaptic transmission in dentate gyrus in rats. Acta Pharm Sin 2000; 35: 185–8.

9 Wang XY, Zhang JT. NO mediates ginsenoside Rg1-induced long-term potentiation in anesthetized rats. Acta Pharmacol Sin 2001; 22: 657–62.

10 Wang XY, Zhang JT. Effect of ginsenoside Rb1 on long-term potentiation in the dentate gyrus of anaesthetized rats. J Asian Nat Prod Res 2003; 5: 1–4.

11 Wang XY, Zhang JT. Effects of ginsenoside Rg1 on synaptic plasticity of freely moving rats and its mechanism of action. Acta Pharmacol Sin 2001; 22: 1099–102.

12 Zhang JT, Liu Y, Qu ZhW, Zhang XL, Xiao HL. Influence of ginsenoside Rb1 and Rg1 on some central neurotransmitter receptors and protein biosynthesis in mouse brain. Acta Pharm Sin 1988; 23: 12–6.

13 Banishin CG, Liu HJ, Wang LCH, Pang PKT. Ginsenosides Rb1 and Rg1 increase central nervous system cholinergic metabolism. In: Shojishibata *et al,* editors. Recent advances in ginseng studies. Tokyo: Hirokawa Publishing Company 1989; 139–43.

14 Burgen ASV. Regulation of acetylcholine receptors. In: Yoshida H, *et al*, eds. Advances in pharmacology and therapeutics: II. Neurotransmitters receptors. Tokyo: Pergamon press 1981; 51–2.

15 Liu M, Zhang JT. Influence of ginsenoside Rb1 and Rg1 on some central neurotransmitter receptors and protein biosynthesis in mouse brain. Acta Pharmacol Sin 1996; 17: 171–4.

16 Li JQ, Zhang XG, Zhang JT. Inhibition of apoptosis by ginsenoside Rg1 in cultured cortical neurons. Acta Pharm Sin 1997; 32: 406-10.

17 Li JQ, Li ZK, Duan H, Zhang JT. Effect of age and ginsenoside Rg1 on nitric oxide content and nitric oxide synthase activity of cerebral cortex on rats. Acta Pharm Sin 1997; 32: 251–4.

18 Chen XC, Chen Y, Zhu YG, Fang F, Chen LM. Protecive effect of ginsenoside Rg1 against MPTP-induced apoptosis in mouse substantia nigra neurons. Acta Pharmacol Sin 2002; 23: 829–34.

19 Chen XC, Zhu YG, Wang XZ, Zhu LA, Huang C. Protective effect of ginsenoside Rg1 on dopamine-induced apoptosis in PC12 cells. Acta Pharmacol Sin 2001; 22: 673–8.

20 Yang Y, Zhang JT, Shi CZ, Qu ZW, Liu Y. Study on the nootropic mechanism of ginsenoside Rb1 and Rg1 influence on mouse brain development. Acta Pharm Sin 1994; 29: 241–5.

21 Mook-Jung I, Hong HS, Boo JH, Lee KH, Yun SH, Cheong MY, *et al*. Ginsenoside Rb1 and Rg1 improve spatial learning and increase hippocampal synaptophysin level in mice. J Neurosci Res 2001; 63: 509–15

22 Gage FH. Mammalian neural stem cells. Science 2000; 287: 1433–8.

23 Kuhn HG, Dickinson-Anson H, Gage FH. Neurogenesis in the dentate gyrus of the adult rat: age-related decrease of neuronal progenitor proliferation. J Neurosci 1996; 16: 2027–33.

24 Shors TJ, Miesegaes G, Beylin A, Zhao M, Rydel T, Gould E. Neurogenesis in the adult is involved in the formation of trace memories. Nature 2001; 410: 372–6.

25 Haughey NJ, Liu D, Nath A, Borchard AC, Mattson MP. Disruption of neurogenesis in the subventricular zone of adult mice, and in human cortical neuronal precursor cells in culture, by amyloid beta-peptide: implications for the pathogenesis of Alzheimer's disease. Neuromolecular Med 2002; 1: 125–35.

26 Shen LH, Zhang JT. Ginsenoside Rg1 promotes proliferation of hippocampal progenitor cells. Neurol Res 2004; 26: 422–8.

27 Shen LH, Zhang JT. Ginsenoside Rg1 increases ischemia-induced cell proliferation and survival in the dentate gyrus of adult gerbils. Neurosci Lett 2003; 344: 1–4.

28 Lian XY, Zhang JT. Effect of ginsenoside Rb1 on repeated stress-induced sexual deficiencies in male mice. Acta Pharm Sin 1998; 33: 184–7.

29 Wang XY, Zhang JT. Effect of ginsenoside Rb1 on mouse sexual function and its mechanism. Acta Pharm Sin 2002; 35: 492–5.

30 Lian XY, Zhang JT. Chronic stress and gonadectomy decrease the levels of neurotrophin-3 and brain-derived neurotrophic factor in adult mouse brain. Chin J Pharmacol Toxicol 2001; 15: 245–50.
31 Liu M, Zhang JT. The immunoregulatory effects of ginsenoside Rg1 in aged rats. Acta Pharm Sin 1995; 30: 818–23.
32 Liu M, Zhang JT. Studies on the mechanisms of immunoregulatory effects of ginsenoside Rg1 in aged rats. Acta Pharm Sin 1996; 31: 95–100.
33 Chan RY, Chen WF, Dong A, Guo D, Wong MS. Estrogen-like activity of ginsenoside Rg1 derived from *Panax notoginseng*. J Clin Endocrinol Metab 2002; 87: 3691–5.
34 Teng CM, Kuo SC, Ko FN, Lee JC, Lee LG, Chen SC, *et al*. Antiplatelet actions of panaxynol and ginsenosides isolated from ginseng. Biochim Biophys Acta 1989; 990: 315–20.
35 Kimura Y, Okuda H, Arichi S. Effects of various ginseng saponins on 5-hydroxytryptamine release and aggregation in human platelets. J Pharm Pharmacol 1988; 40: 838–43.
36 Wu W, Zhang XM, Liu PM, Li JM, Wang JF. Effects of *Panax notoginseng* saponin Rg1 on cardiac electrophysiological properties and ventricular fibrillation threshold in dogs. Acta Pharmacol Sin 1995; 16: 459–63.
37 Park KH, Shin HJ, Song YB, Hyun HC, Cho HJ, Ham HS, *et al*. Possible role of ginsenoside Rb1 on regulation of rat liver triglycerides. Biol Pharm Bull 2002; 25: 457–60.
38 Ota T, Maeda M, Odashima S, Ninomiya-Tsuji J, Tatsuka M. G1 phase-specific suppression of the Cdk2 activity by ginsenoside Rh2 in cultured murine cells. Life Sci 1997; 60: PL39–44.
39 Han R. Highlight on the studies of anticancer drugs derived from plants in China. Stem Cells 2002; 12: 53–63.
40 Zhang JT. The retrospection and prospect of ginseng research. Acta Pharm Sin 1995; 30: 321–5.
41 Dou DQ, Jin L, Chen YJ. Advances and prospects of the study on chmical constituents and pharmacological activities of Panax ginseng. J Shenyang Pharm Univ 1999; 16: 151–6.
42 Huang YS, Liu Y, Qu ZW, Zhang JT. Effect of ginsenoside Rb1 and Rg1 on lipid peroxidation of rat *in vitro*. Acta Acad Med Sin 1989; 11: 460–2.
43 Deng HL, Zhang JT. Anti-lipid peroxydative effect of ginsenoside Rb1 and Rg1. Chin Med J 1991;104: 395–8.
44 Liu M, Zhang JT. Effects of ginsenoside Rb1 and Rg1 on synaptosomal free calcium level, ATPase and calmudulin in rat hippocampus. Chin Med J 1995; 108: 544–7.
45 Jiang XY, Zhang JT, Shi CZ. Mechanism of action of ginsenoside Rb1 in decreasing intracellular Ca^{2+}. Acta Pharm Sin 1996; 31: 321–6.
46 Liu M, Zhang JT. Protective effects of ginsenoside Rb1 and Rg1 in cultured hippocampal neurons. Acta Pharm Sin 1995; 30: 674–8.
47 Wang JH, Li W, Sha Y, Tezuka Y, Kadota S, Li X. Triterpenoid saponins from leaves and stems of *Panax quinquefolium* L. J Asian Nat Prod Res 2001; 3: 293–7.
48 Yang XW, Li LY, Tian JM, Zhang ZW, Ye JM, Gu WF. Ginsenoside-Rg6, a novel triterpenoid saponin from the stem-leaves of *Panax ginseng* CAMey. Chin Chem Lett 2000; 11: 909–12.
49 Le TO, Quan LT, Adnyana IK, Tezuka Yasuhiro, Nagaoka T, Qui KT, *et al*. Triterpene saponins from *Vietnamese Ginseng* (*Panax vietnamensis*) and their hepatocytoprotective activities. J Nat Prod 2001; 64: 456–61.
50 Dou DQ, Chen YJ, Liang LH, Pang FG, Shimizu N, Takeda T. Six new dammarane-type triterpene saponins from the leaves of *Panax ginseng*. Chem Pharm Bull 2001; 49: 442–6.
51 Park JD, Lee YH, Kim SI. Ginsenoside Rf2, a new dammarane glycoside from Korean red ginseng (*Panax ginseng*). Arch Pharm Res 1998; 21: 615–7.
52 Qiu F, Ma ZZ, Pei YP, Xu SX, Yao XS, Chen YT, *et al*. A new dammarane glycoside from the flower-buds of *Panax ginsen*g CA Meyer. Chin Chem Lett 1998; 9: 643–5.

Full-length article

Caspase-1 inhibitor Ac-YVAD-CHO attenuates quinolinic acid-induced increases in p53 and apoptosis in rat striatum[1]

Yi CAO, Zhen-lun GU, Fang LIN, Rong HAN, Zheng-hong QIN[2]

Department of Pharmacology, Soochow University School of Medicine, Suzhou 215007, China

Key words

caspase 1; Ac-YVAD-CHO; Huntington disease; protein p53; NF-kappaB inhibitor alpha; apoptosis; NF-kappaB

[1] Project supported by the National Natural Science Foundation of China (No 30370506).
[2] Correspondence to Zheng-hong QIN, PhD.
Phn 86-512-6512-2087.
Fax 86-512-6519-0599.
Email zhqin5@hotmail.com

Received 2004-07-21
Accepted 2004-10-25

doi: 10.111/j.1745-7254.2005.00025.x

Abstract

Aim: To study the effects of the caspase-1 inhibitor Ac-YVAD-CHO on quinolinic acid (QA)-induced apoptosis. **Methods:** Rats were pre-treated with intrastriatal infusion of Ac-YVAD-CHO (2-8 μg) before intrastriatal injection of QA (60 nmol). Striatal total proteins, genomic DNA, and nuclear proteins were isolated. The effects of Ac-YVAD-CHO on QA-induced caspase-1 activity, internucleosomal DNA fragmentation, IκB-α degradation, NF-κB, and AP-1 activation, and increases in p53 protein levels were measured with enzyme assays, agarose gel electrophoresis, electrophoresis mobility shift assays, and Western blot analysis. **Results:** Pre-treatment with Ac-YVAD-CHO inhibited QA-induced internucleosomal DNA fragmentation. Ac-YVAD-CHO inhibited QA-induced increases in caspase-1 activity and p53 protein levels, but had no effect on QA-induced IκB-α degradation, NF-κB or AP-1 activation. **Conclusion:** Caspase-1 is involved in QA-induced p53 upregulation but not IκB-α degradation. Inhibition of caspase-1 attenuates QA-induced apoptosis in rat striatum.

Introduction

Excitotoxin-induced degeneration of striatal neurons in amimals has been used as an animal model of Huntington's disease (HD). Recent studies in transgenic animal models of HD demonstrated increased response of striatal neurons to excitotoxin, supporting a role of glutamate receptors in HD[1]. Excitotoxins acting on *N*-methyl-*D*-aspartate (NMDA) and kainic acid (KA) receptors will induce destruction of striatal GABAergic neurons by apoptotic mechanisms[2–4]. Caspases and tumor suppresser p53 play essential roles in apoptosis in a variety of cells including neurons[5–8]. Previous studies have reported that excitotoxin induces the activation of caspases and induces p53 expression[9–11]. Excitotoxin also reportedly activates nuclear factor-kappaB (NF-κB), but the mechanism by which this occurs remains unknown[12,13].

Recent studies have demonstrated that quinolinic acid (QA) induced significant increases in NF-κB binding activity in the nucleus[14]. NF-κB nuclear translocation mediates the upregulation of p53 and c-Myc in striatal neurons exposed to excitotoxic injury[15–17]. NMDA receptors activate NF-κB by selective degradation of an inhibitor protein, IκB-α. Excitotoxin-induced degradation of IκB-α involves a caspase-3-dependent mechanism in rat striatum and can be blunted by a caspase-3 inhibitor and a free radical scavenger[18,19]. In the present study we evaluated the role of caspase-1 inhibitor Ac-YVAD-CHO in QA-induced NF-κB activation, p53 induction, and apoptosis.

Materials and methods

Stereotaxic drug administration Sprague-Dawley rats (300–350 g) were obtained from the Experimental Animal Center of Soochow University (Certificate No 20020008, Grade II). Rats were anesthetized with pentobarbital sodium (50 mg/kg). Stereotaxic drug administration was performed using a Kopf stereotaxic apparatus as described by Qin *et al*[3]. To study the effects of a caspase-1 inhibitor on QA-induced internucleosomal DNA fragmentation, rats were either pre-treated with an intrastriatal infusion of Ac-YVAD-CHO (2–8 μg) or Me_2SO (2 μL) 10 min before instrastriatal injection of QA (60 nmol) and then killed 24 h after QA administration, or pre-treated with intrastriatal infusion of Ac-YVAD-CHO (4 μg) 10 min before instrastriatal injection of QA (60 nmol) and

killed 12, 24, or 48 h after QA administration. Striatal genomic DNA was isolated and electrophoresed on a 2% agarose gel. To study the effect of a caspase-1 inhibitor on QA-induced increases in caspase-1 activity, rats were pre-treated with an intrastriatal infusion of Ac-YVAD-CHO (4 μg) or Me_2SO (2 μL) 10 min before intrastriatal injection of QA (60 nmol) and then killed 12 h after QA treatment. Striatal homogenates were used for assay of caspase-1 activity. To study the effect of a caspase-1 inhibitor on QA-induced increases in p53 proteins and NF-κB and AP-1 binding activities, rats were pre-treated with intrastriatal infusion of Ac-YVAD-CHO (4 μg) or Me_2SO (2 μL) 10 min before intrastriatal injection of QA (60 nmol) and then killed 24 h after QA treatment. Total striatal proteins were extracted for Western blot analysis. Other animals were killed 12 h after QA treatment and nuclear proteins were isolated from the striatum for an electrophoresis mobility shift assay.

Isolation of genomic DNA and electrophoresis Striatal genomic DNA was prepared as described by Qin *et al*[3]. Briefly, striatal tissues were homogenized in a buffer containing NaCl 100 mmol/L, edetic acid 25 mmol/L, Tris-HCl 10 mmol/L (pH 8.0), 0.5% SDS, and RNase A 0.5 mg/L. Homogenates were incubated at 55 ºC for 2 h. Incubation was continued overnight after 0.6 mg protease K was added to the hoogenates. DNA was extracted with phenol: chlorform:isoamyl alcohol (24:25:1). DNA fragments were separated on 2% agarose gel and detected with a UV trasmilluminator after being stained with ethidium bromide.

Caspase-1 activity assay The caspase-1 activity assay was performed with an enzyme activity assay kit (Caspase-I/ ICE Colorimetric Assay Kit, BioVision) according to the manufacturer's instructions. Each striatal tissue was homogenized in 500 μL cell lysis buffer and centrifuged for 10 min at 10 000×*g*. The supernatant was transferred to a fresh tube and kept on ice. Protein concentration was determined using BCA kit (Pierce, Rockford, IL). For each 100 mg protein was diluted to 50 μL with cell lysis buffer and 50 μL 2×reaction buffer (containing DTT 10 mmol/L) was added, then 5 μL of the 4 μmol/L YVAD-pNA substrate (200 μmol/L) and the mixture was inculated at 37 ºC for 1 h. Read samples at 405 nm in a spectrophotometer (Bio-Rad Smart Spec 3000).

Western blot analysis Western blot analysis was performed as described previously[16]. Striatal tissues were homogenized in a buffer containing Tris-HCl 10 mmol/L (pH 7.4), NaCl 150 mmol/L, 1% Triton X-100, 1% sodium deoxycholate, 0.1% SDS, edetic acid 5 mmol/L, PMSF 1 mmol/L, aprotinin 0.28 kU/L, leupeptin 50 mg/L, benzamidine 1 mmol/L, pepstain A 7 mg/L. Protein concentration was determined using the BCA kit. Thirty micrograms of protein from each sample was subjected to electrophoresis on a 12% SDS-PAGE gel using a constant current. Proteins were transferred to nitrocellulose membranes and incubated with anti-p53 antibody (p53, p240, Santa Cruz, CA) in Tris buffered saline containing 0.2% Tween-20 (TBST) and 3% nonfat dry milk for 3 h. Membranes were washed and incubated with horseradish peroxidase-conjugated second antibody in TBST containing 3% nonfat dry milk for 1 h. Immunoreactivity was measured with enhanced chemoluminescent autoradiography (ECL kit, Amersham, Arlington Heights, IL) according to the manufacturer's instructions.

Electrophoresis mobility shift assay Striatal nuclear proteins were prepared as described by Qin *et al*[14]. Protein concentration was determined with the BCA kit (Pierce, Rockford, IL). Synthetic double-stranded NF-κB and AP-1 oligonucleotidyl probes were purchased from Promega (Madison, WI) and labeled with [^{32}P]ATP using T4 polynucleotide kinase (Promega). Nuclear proteins (6–14 μg) were incubated with [^{32}P]labeled probes (40 000 c/min) for 15 min at room temperature in the binding buffer (Promega). Reaction mixtures were electrophoresed on a 4.5% non-denaturing polyacrymide gel, then dried and exposed to x-ray film at –80 ºC with intensifying screens for 24 to 48 h. The results were quantitatively analyzed using an image analyzer (SigmaPlot Pro 4).

Results

Effects of Ac-YVAD-CHO on QA-induced inter-nucleosomal DNA fragmentation To evaluate the consequences of caspase-1 inhibition on apoptosis, we studied the effect of Ac-YVAD-CHO on QA-induced internucleosomal DNA fragmentation. The results showed that QA (60 nmol) induced intense internucleo-somal DNA fragmentation 24 h after drug administration. The DNA fragments were generally multimers of 180–200 base pairs, indicating internucleosomal DNA digestion by an endonuclease. QA-induced DNA fragmentation was strongly attenuated by Ac-YVAD-CHO in a dose-dependent manner (Figure 1A). The results also showed that Ac-YVAD-CHO (4 μg) inhibited QA-induced DNA fragmentation at all time points examined (12, 24, and 48 h after QA administration; Figure 1B).

Effects of Ac-YVAD-CHO on a QA-induced increase in caspase-1 activity QA injection significantly activated caspase-1 activity in comparison with saline injected animals ($P<0.05$, $n=6$). The increase in caspase-1 activity induced by QA was significantly inhibited by Ac-YVAD-CHO ($P<0.05$, $n=6$); however, pre-treatment with Me_2SO had no effect on the QA-induced activation of caspase-1 (Figure 2).

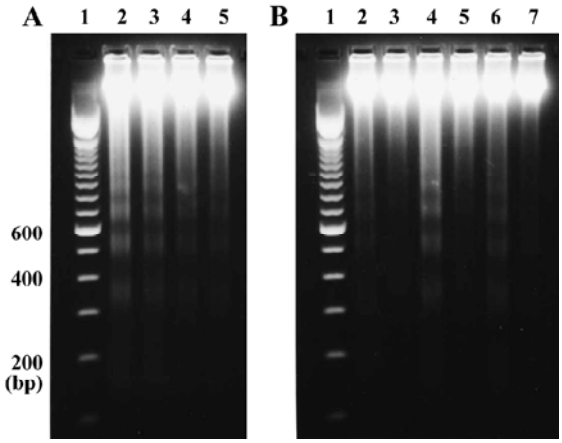

Figure 1. Effects of Ac-YVAD-CHO on QA-induced internucleosomal DNA fragmentation. (A): Rats were pre-treated with intrastriatal injection of Ac-YVAD-CHO (2–8 μg) or Me_2SO (2 μL) 10 min before intrastriatal injection of QA (60 nmol) and then killed 24 h after QA treatment. Genomic DNA from the injected striatum was isolated and electrophoresed on a 2% agarose gel. Lane 1:100-base pair DNA ladder; 2: QA+Vehicle; 3: QA+Ac-YVAD-CHO (2 μg); 4: QA+Ac-YVAD-CHO (4 μg); 5: QA+Ac-YVAD-CHO (8 μg). (B): Rats were pre-treated with Ac-YVAD-CHO (4 μg) and QA (60 nmol) as described above. Lane 1: 100-base pair DNA ladder; 2: QA+Vehicle, 12 h; 3: QA+Ac-YVAD-CHO, 12 h; 4: QA+Vehicle, 24 h; 5: QA+Ac-YVAD-CHO, 24 h; 6: QA+Vehicle, 48 h; 7: QA+Ac-YVAD-CHO, 48 h.

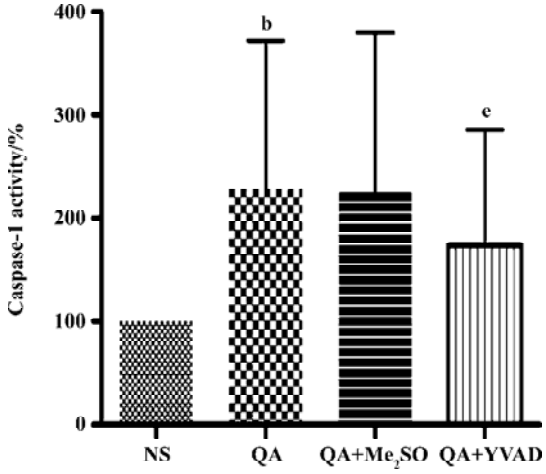

Figure 2. Effects of Ac-YVAD-CHO on the QA-induced increase in caspase-1 activity. The results were expressed as a percentage of control (saline injection) after using statistical analysis. Statistical analysis was carried out with Student's *t*-test. n=6. Mean±SD. $^bP<0.05$ *vs* NS; $^eP<0.05$ *vs* QA-treated group.

Effect of Ac-YVAD-CHO on QA-induced p53 induction QA induced significant increases in p53 protein levels by approximately 100%, which was significantly inhibited by Ac-YVAD-CHO ($P<0.05$, n=6, Figure 3).

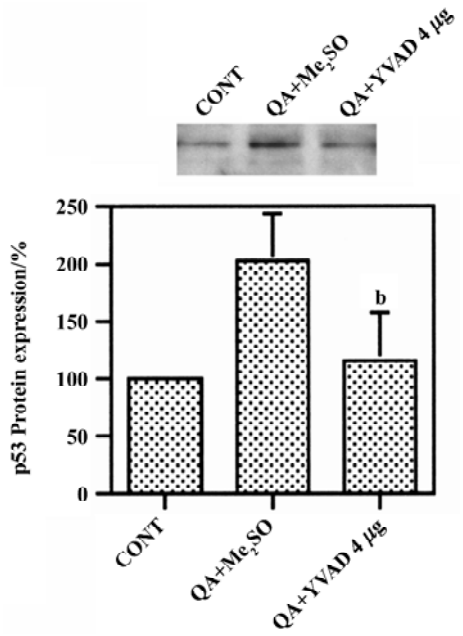

Figure 3. Effects of Ac-YVAD-CHO on QA-induced increase in p53 proteins expression. The results from 4 animals in each group were analyzed with an image analyzer and were expressed as percent of control (untreated animals). Statistical comparisons were carried out with ANOVA followed by Dunnett *t*-test. n=4. Mean±SD. $^bP<0.05$ *vs* QA+Me_2SO group.

Effects of Ac-YVAD-CHO on QA-induced degradation of IκB-α QA treatment significantly reduced protein levels of IκB-α, indicating that IκB-α was degraded after QA treatment. Pre-treatment with various doses of Ac-YVAD-CHO (2–8 mg) had no significant effect on QA-induced degradation of IκB-α (Figure 4).

Effect of Ac-YVAD-CHO on the QA-induced activation of NF-κB and AP-1 Changes in NF-κB and AP-1 binding in nuclear extracts were measured by using an electrophoresis mobility shift assay. QA induced dramatic increases in NF-κB binding activity in nuclei. However, Ac-YVAD-CHO (4 mg) had no significant effect on QA-induced NF-κB activation (Figure 5A). Similarly, AP-1 binding activity was increased markedly after QA administration and Ac-YVAD-CHO failed to inhibit the QA-induced activation of AP-1 (Figure 5B).

Discussion

Apoptotic mechanisms are involved in the degeneration of strial neurons induced by the glutamate receptor agonist QA. In the present study, the role of caspase-1 in QA-induced p53 upregulation and NF-κB activation was investigated using the selective cell-permeable caspase-1 inhibitor

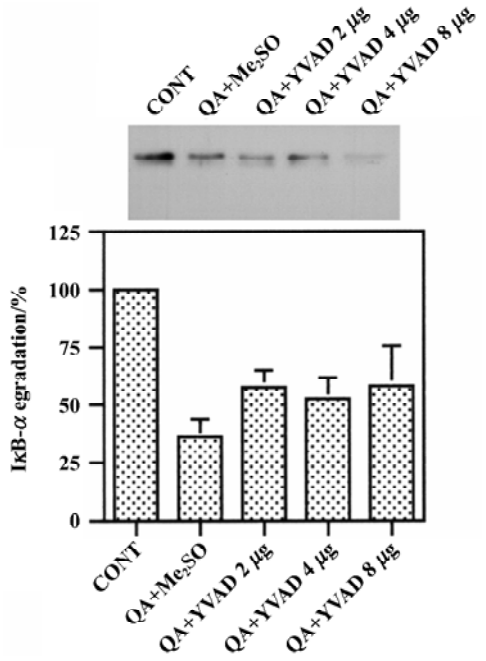

Figure 4. Effect of Ac-YVAD-CHO on the QA-induced degradation of IκB-α. The results from 5-6 animals in each group were analyzed with an image analyzer and expressed as percentage of control (untreated animals). Statistical comparisons were carried out using ANOVA analysis. Mean±SD.

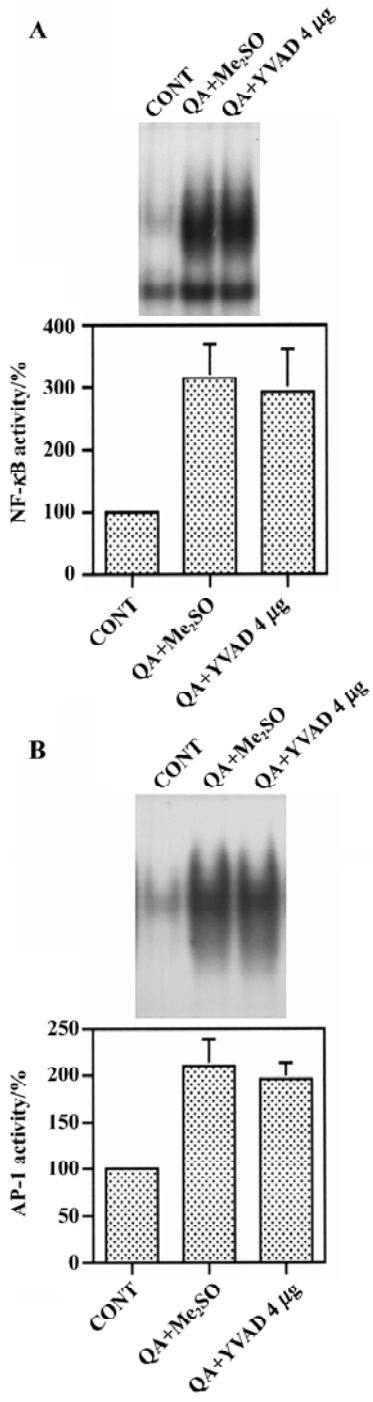

Figure 5. Effect of Ac-YVAD-CHO on QA-induced NF-κB activation. Vertical bars represent mean±SD. n=6. Statistical comparisons were carried out with ANOVA analysis. A: Effect of Ac-YVAD-CHO on the QA-induced NF-κB activation. B: Effect of Ac-YVAD-CHO on AP-1 activation.

Ac-YVAD-CHO. The results of the study showed that pretreatment with Ac-YVAD-CHO dose-dependently inhibited QA-induced internucleosomal DNA fragmentation. Ac-YVAD-CHO had no significant effect on the QA-induced IκB-α degradation and NF-κB activation. However, Ac-YVAD-CHO partially inhibited QA-induced increase in p53 protein levels. These results suggest that caspase-1 plays a role in QA-induced p53 upregulation but not QA-induced IκB-α degradation.

It has been reported that glutamate receptor agonists activate NF-κB via the degradation of IκB-α[15,16]. Previous studies have further suggested that caspase-3 , like protease, is involved in NMDA receptor-stimulated degradation of IκB-α[18,19]. Activation of NF-κB upregulates c-Myc and p53, indicating that NF-κB contributes to excitotoxin-induced apoptosis via the induction of cell cycle regulators[16,17,20]. p53 plays a critical role in cell death and survival. Its level is usually regulated by the rate of its degradation[21]. Now studies show that the levels of p53 can be regulated by NF-κB[16,17,22]. In the present study, caspase-1 inhibitor Ac-YVAD-CHO had no effect on either QA-induced IkB-α degradation or NF-κB activation. In contrast, Ac-YVAD-CHO significantly attenuated QA-induced increases in p53 protein levels and apoptosis. This study indicated that both NF-κB dependent and independent mechanisms are involved

in the QA-induced upregulation of p53 and apoptosis.

In conclusion, we found that the caspase-1 inhibitor Ac-YVAD-CHO inhibited the QA-induced increase in p53 protein levels and internucleosomal DNA fragmentation, but had no effect on QA-induced IκB-α degradation and NF-κB activation. These results suggest that caspase-1 plays an important role in QA-induced p53 induction and apoptosis, but caspase-1 does not contribute to the QA-induced degradation of IκB-α or NF-κB activation.

References

1 Zeron MM, Hansson O, Chen N, Wellington CL, Leavitt BR, Brundin P, *et al*. Increased sensitivity to *N*-methyl-*D*-aspartate receptor-mediated excitotoxicity in a mouse model of Huntington's disease. Neuron 2002; 33: 849–60.

2 Bonfoco E, Krainc D, Ankarcrona M, Nicotera P, Lipton SA. Apoptosis and necrosis events induced, respectively, by mild and intense insults with *N*-methyl-*D*-aspartate or nitric oxide/superoxide in cortical cell culture. Proc Natl Acad Sci USA 1995; 92: 7162–6.

3 Qin ZH, Wang Y, Chase TN. Stimulation of NMDA receptors induces apoptosis in rat brain. Brain Res 1996; 725: 166–76.

4 Simonia NA, Getz RL, Leveque JC, Konradi C, Coyle JT. Kainate induces apoptosis in neurons. Neuroscience 1996; 74: 675–83.

5 Slack RS, Belliveau DJ, Rosenberg M, Atwal J, Lochmuller H, Aloyz R, *et al*. Adenovirus-mediated gene transfer of the tumor suppressor, p53, induces apoptosis in postmitotic neurons. J Cell Biol 1996; 135: 1085–96.

6 Armstrong RC, Aja TJ, Hoang KD, Gaur S, Bai X, Alnemri ES, *et al*. Activation of the CED3/ICE-related protease CPP32 in cerebellar granule neurons undergoing apoptosis but not necrosis. J Neurosci 1997; 17: 553–62.

7 Eldadah BA, Yakovlev A, Faden AI. The role of CED-3-related cysteine proteases in apoptosis of cerebellar granule cells. J Neurosci 1997; 17: 6105–13.

8 Jordan J, Galino MF, Prehn JHM, Weichselbaum RR, Beckett M, Ghadge GD, *et al*. p53 expression induces apoptosis in hippocampal pyramidal neurons cultures. J Neurosci 1997; 17: 1397–405.

9 Sakhi S, Bruce A, Sun N, Tocco G, Baudry M, Schreiber SS. p53 induction is associated with neuronal damage in the central nervous system. Proc Natl Acad Sci USA 1994; 91: 7525–9.

10 Hughes PE, Alexi T, Yoshida T, Schreiber SS, Knusel B. Excitotoxic lesion of rat brain with quinolinic acid induces expression of p53 messenger RNA and protein and p53-inducible genes Bax and GADD-45 in brain areas showing DNA fragmentation. Neuroscience 1997; 74: 1143–60.

11 Du Y, Bales KR, Dodel RC, Hamilton-Byrd E, Horn JW, Czilli DL, *et al*. Activation of a caspase 3-related cysteine protease is required for glutamate-mediated apoptosis of cultured cerebellar granule neurons. Proc Natl Acad Sci USA 1997; 94: 11657–62.

12 Guerrini L, Blasi F, Denis-Donini S. Synaptic activation of NF-κB by glutamate in cerebellar granule neurons *in vitro*. Proc Natl Acad Sci USA 1995; 92: 9077–81.

13 Kaltschmidt C, Kaltschmidt B, Baeuerle PA. Stimulation of ionotropic glutamate receptors activate transcription factor NF-κB in primary neurons. Proc Natl Acad Sci USA 1995; 92: 9618–22.

14 Qin ZH, Wang Y, Nakai M, Chase TN. Nuclear factor-κB contributes to excitotoxin-induced apoptosis. Mol Pharmacol 1998; 53: 33–42.

15 Nakai M, Qin ZH, Chen JF, Wang Y, Chase TN. Kanic acid-induced apoptosis is associated with NF-κB activation. J Neurochem 1999; 74: 647–58.

16 Qin ZH, Chen RW, Wang Y, Nakai M, Chuang DM, Chase TN. NF-κB nuclear translocation up-regulates c-Myc and p53 during *N*-methyl-*D*-aspartate receptor-mediated apoptosis. J Neurosci 1999; 19: 4023–33.

17 Aleyasin H, Cregan SP, Iyirhiaro G, O'Hare MJ, Callaghan SM, Slack RS, *et al.* Nuclear factor-κB modulates the p53 response in neurons exposed to DNA damage. J Neurosci 2004; 24: 2963–73.

18 Nakai M, Qin Z-H, Wang Y, Chase TN. NMDA and non-NMDA receptor-stimulated IκB-α degradation: differential effects of the caspase-3 inhibitor DEVD.CHO, free radical scanvenger OPC-14117 and ethanol. Brain Res 2000; 859: 207–16.

19 Qin ZH, Wang Y, Chase TN. A caspase-3-like protease is involved in NF-κB activation induced by stimulation of *N*-methyl-*D*-aspartate receptors in rat striatum. Mol Brain Res 2000; 80: 111–22.

20 Grilli M, Memo M. Possible role of NF-κB and p53 in the glutamate-induced pro-apoptotic neuronal pathway. Cell Death Differ 1999; 6: 22–7.

21 Levine AJ. p53, the cellular gatekeeper for growth and division. Cell 1997; 88: 323–31.

22 Wu H, Lozano G. NF-κB activation of p53: a potential mechanism for supressing cell growth in response to stress. J Biol Chem 1994; 269: 20067–74.

Full-length article

Orexin A promotes histamine, but not norepinephrine or serotonin, release in frontal cortex of mice[1]

Zong-yuan HONG[2,3], Zhi-li HUANG[3,4,5], Wei-min QU[3], Naomi EGUCHI[3]

[2]School of Life Science, University of Science and Technology of China, Hefei 230027, China; [3]Department of Molecular Behavioral Biology, Osaka Bioscience Institute, Furuedai, Suita, Osaka 565-0874, Japan; [4]Department of Pharmacology, Shanghai Medical College of Fudan University, Shanghai 200032, China

Key words

orexin A; histamine; noradrenaline; serotonin; microdialysis; frontal cortex

[1] Project supported in part by a grant-in-aid for scientific research from the Japan Society for the Promotion of Science (ZLH) and Osaka City.
[5] Correspondence to Zhi-li HUANG, MD, PhD.
Phn 81-6-6872-4851.
Fax 81-6-6872-2841.
E-mail huangzl@obi.or.jp

Received 2004-09-13
Accepted 2004-10-28

doi: 10.1111/j.1745-7254.2005.0023.x

Abstract

Aim: To investigate the effects of orexin A on release of histamine, norepinephrine, and serotonin in the frontal cortex of mice. **Methods:** Samples for measuring histamine, norepinephrine, and serotonin contents were collected by *in vivo* microdialysis of the frontal cortex of anesthetized mice. The histamine, noradrenaline, and serotonin content in dialysates were measured by HPLC techniques. **Results:** Intracrebroventricular injection of orexin A at doses of 12.5, 50, and 200 pmol per mouse promoted histamine release from the frontal cortex in a dose-dependent manner. At the highest dose given, 200 pmol, orexin A significantly induced histamine release, with the maximal magnitude being 230% over the mean basal release. The enhanced histamine release was sustained for 140 min, and then gradually returned to the basal level. However, no change in norepinephrine or serotonin release was observed under application of the same dose of orexin A. **Conclusion:** These results suggest that the arousal effect of orexin A is mainly mediated by histamine, not by norepinephrine or serotonin.

Introduction

The neuropeptides orexin A and B (also called hypocretins 1 and 2) have recently been isolated from rat hypothalamic extracts, and have been reported to be involved in sleep-wake regulation[1–3]. Intracerebroventricular (icv) application of orexin A strongly enhances arousal in rats and mice[4–6]. Furthermore, c-fos expression in orexin neurons and prepro-orexin mRNA levels show a diurnal variation, with the strongest expression being observed during waking[7,8]. Mice lacking either the orexin gene (*preproorexin* knock-out mice) or orexin neurons (*orexin/ataxin*-3 transgenic mice) have phenotypes remarkably similar to the human sleep disorder narcolepsy[9–11], a disabling neurological disorder characterized by symptoms including excessive daytime sleepiness, sleep attacks, sleep fragmentation, cataplexy, and sleep-onset periods of rapid eye movement[12]. Lesions of the lateral hypothalamus by orexin-2-saporin produce narcoleptic-like sleep behavior in rats[13]. Consistent with these findings, recent reports suggest that human narcolepsy is accompanied by a loss of orexin neuropeptide production and specific destruction of orexin neurons[14–17]. These results suggest that the orexinergic system is involved in sleep-wake regulation and mainly contributes to arousal.

Orexin neurons are located specifically in the lateral hypothalamic area and project to almost all parts of the brain except the cerebellum[2,10,18]. Particularly dense projections of these neurons are observed in monoaminergic nuclei, such as the noradrenergic locus ceruleus (LC), serotonergic raphe nuclei (DRN), and histaminergic tuberomammillary nucleus (TMN). These monoaminergic nuclei expressing orexin receptors (OX1R and/or OX2R)[19] play important roles in the promotion of wakefulness. Electro-physiological studies have revealed that orexins had mainly excitatory effects on all monoaminergic neurons *in vitro*[20–24], suggesting that the arousal effect of orexins is mediated by these monoaminergic systems. However, which type(s) of these monoaminergic systems is involved in orexin-induced arousal remains to be elucidated.

In the present study, we investigated the effects of orexin A on the release of the monoaminergic neurotransmitters histamine, norepinephrine (NE), and serotonin (5-HT) in the frontal cortex (FrCx) of mice by using *in vivo* microdialysis to further clarify the mechanism underlying the arousal effects of orexin A.

Materials and methods

Animals Male C57BL/6 mice (Shizuoka Laboratory Animal Center, Shizuoka, Japan) weighing 24–28 g (11–13 weeks old) were housed at a constant temperature (24±0.5 ℃) and relative humidity (60%±2%), an automatically controlled 12:12 h light/dark cycle (light on at 8 AM), and *ad libitum* access to food and water. All animal experiments used in this study were approved by the Animal Care Committee of Osaka Bioscience Institute.

Microdialysis procedure The microdialysis was performed as previously described[5]. As shown in Figure 1, under urethane anesthesia (1.8 g/kg, ip), a micro-dialysis probe (CUP7, membrane length of 2-mm; Carnegie Medicin, Stockholm, Sweden) was inserted in the FrCx of mice at a position 1.8 mm anterior and 0.8 mm lateral to the bregma and 2.3 mm depth from the dura. One stainless steel cannula (outer diameter, 0.2 mm) was stereotaxically placed at the site of 2.0 mm lateral to the bregma and inserted to a depth of 2.2 mm from the surface of the cortex at an angle of 25° from the midsagittal plane according to the atlas of Franklin and Paxinos[25]. The microdialysis probe was perfused with Ringer's solution (NaCl 147 mmol/L, KCl 4.0 mmol/L , and $CaCl_2$ 2.3 mmol/L; pH 7.3) at a flow rate of 2 μL/min to stabilize the release of histamine, NE, and 5-HT. Two hours after insertion of the microdialysis probe, dialysates were continuously collected from the FrCx at 20-min interval (40 μL each) for 1 h as the basal value before the orexin A injection, and until 4 h after administration of the peptide.

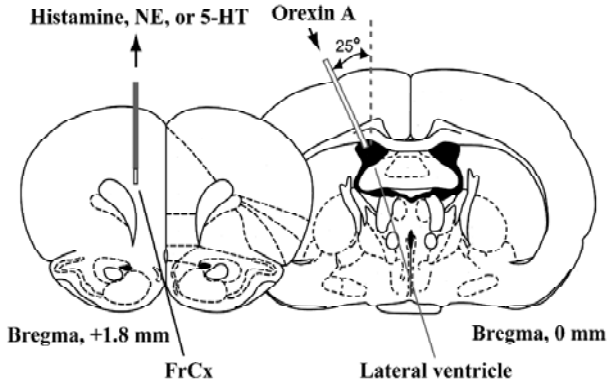

Figure 1. Schematic representation of the implantation sites for the microdialysis probe in the FrCx and the stainless steel cannula in the lateral ventricle of mice. Orexin A was infused into the lateral ventricle through the stainless steel cannula; and dialysate samples for monitoring histamine, NE, or 5-HT levels were collected from the microdialysis probe. FrCx, frontal cortex.

Determination of histamine, NE, and 5-HT levels by HPLC The histamine levels in the dialysates were measured by using a fluorometric HPLC system[26], and NE and 5-HT levels were determined by using HPLC with electrochemical detection[27]. Since the absolute basal release of histamine, NE, and 5-HT varied between subjects, the mean of the first 3 fractions before administration of orexin A was defined as the mean basal release, and subsequent fractions were expressed as a percentage of the mean basal release.

Drugs Orexin A (Peptide Institute, Osaka, Japan) was diluted in saline to the concentrations needed and was injected into the lateral ventricle of mice from the cannula at doses of 200, 50, or 12.5 pmol per mouse in 2 μL of saline at a speed of 2 μL/min. Fluoxetine (Sigma-Aldrich, St Louis, MO, USA), a 5-HT reuptake inhibitor which has been reported to also increase NE release through activation of postsynaptic 5-HT_{1A} receptors by increased 5-HT[28,29], was dissolved in saline and injected ip (20 mg/kg).

Statistical analysis Data were expressed as mean±SD. Differences between groups were analyzed by analysis of variance (ANOVA) followed by the *post-hoc* Newman-Keuls test. The significant level of difference was set at $P<0.05$.

Results

Effect of orexin A on histamine release The mean basal release of histamine was 0.06±0.01 pmol per 20 min. Compared with the control, orexin A at doses of 12.5 and 50 pmol produced a rapid and significant elevation of histamine release, with the maximal magnitude being 150% and 175% over the mean basal release, respectively; and these higher levels maintained for approximately 1 and 2 h (Figure 2A), respectively. At the highest dose (200 pmol) tested, orexin A markedly promoted histamine release, and the release reached its maximal level of 230% over the mean basal level. The significant increase lasted 140 min.

For comparison of the differences between different dosage groups, we calculated the total amount of histamine released over a 3-h period after the administration of orexin A. The total amounts of histamine released were 0.55±0.08, 0.74±0.09, and 0.79±0.11 pmol per 3 h in the groups treated with orexin A at doses of 12.5, 50, and 200 pmol, respectively. In the latter 2 groups the release was significantly higher than that of the control (0.43±0.05 pmol per 3 h, $P<0.05$) (Figure

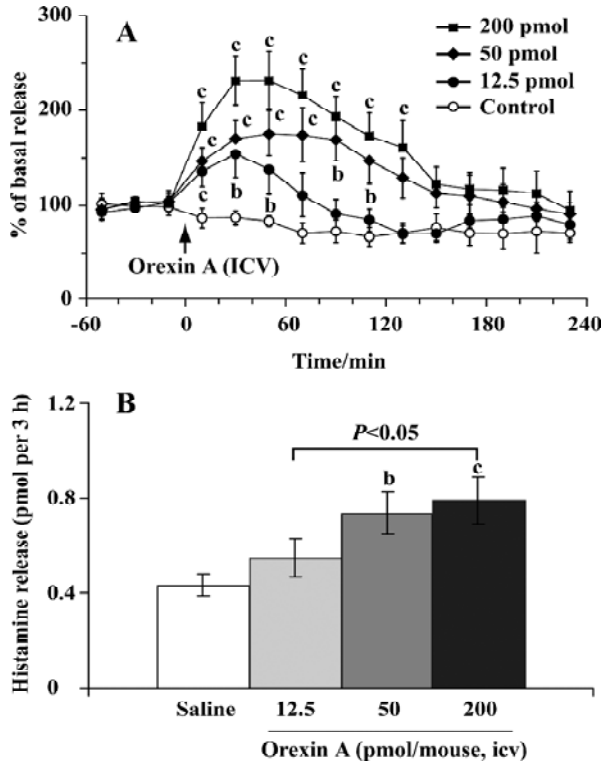

Figure 2. Effect of orexin A on histamine release in the FrCx of anesthetized mice. Time-courses of histamine release (A) and the total amounts of histamine released over 3 h after the administration of orexin A (B) in the FrCx are shown. n=5–6 mice. Mean±SD. $^bP<0.05$, $^cP<0.01$ *vs* the control.

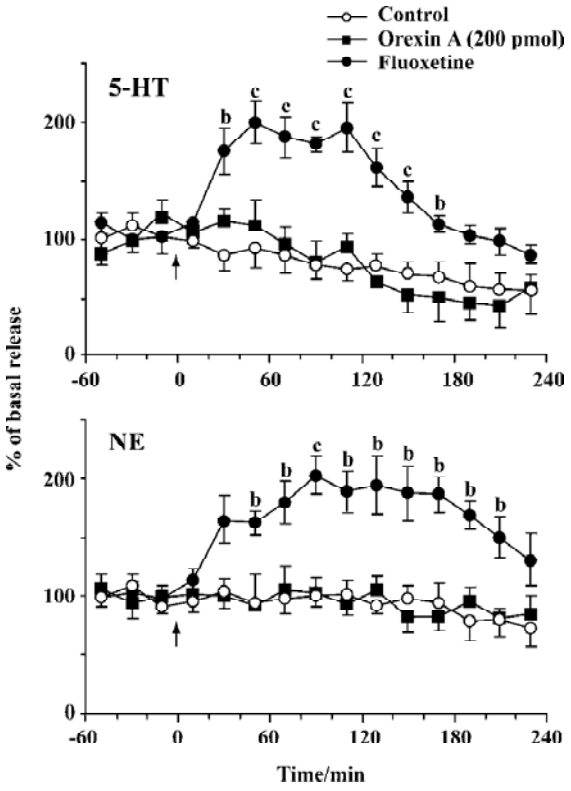

Figure 3. Effects of orexin A on 5-HT and NE release in the FxCr of anesthetized mice. Time-courses of 5-HT and NE release in the FrCx are shown. The arrow stands for the time point of administration. n=5–6 mice. Mean±SD. $^bP<0.05$, $^cP<0.01$ *vs* the control.

2B). These results indicated that orexin A induced histamine release in a dose-dependent manner.

Effects of orexin A on NE and 5-HT release The mean basal release of NE and 5-HT was 1.75±0.21 and 16.9±2.33 pg per 20 min, respectively. No difference was observed in NE or 5-HT release between the group treated with orexin A (200 pmol) and the control. As the positive control, fluoxetine, significantly elevated the extracellular levels of NE and 5-HT, with the maximal magnitude being approximately 200% over the mean basal release at approximately 1.5 h and 1 h after administration (20 mg/kg, ip), respectively. Compared with the control, the increase in NE and 5-HT lasted about 180 and 160 min, respectively (Figure 3).

Discussion

In the present study we found that orexin A activated a histaminergic system in mice. An increasing body of evidence indicates the interaction between the orexinergic and histaminergic systems. For example, with respect to neuroanatomy, orexin cells densely innervate the histaminergic TMN[18,30], a nucleus enriched in orexin 2 receptors[19]. Most human narcolepsy is caused by a loss of orexin neurons[16] and a consequent reduction in orexin levels[15,31]. Gliosis accompanies this loss of orexin neurons and is most intense in the posterior hypothalamus where the histaminergic TMN is located[16,17], suggesting that the orexinergic terminals are lost in this region and that the consequent loss of orexinergic innervation of histaminergic cells is an important component of the pathology of narcolepsy. Based on neurochemical studies, Nishino *et al*[31] reported that the histamine content was markedly decreased in the cortex of orexin-2 receptor-mutated narcoleptic Dobermans and that the decrease was due to a lack of excitatory input of orexin neurons caused by a loss of function of orexin-2 receptors in histaminergic TMN cell groups. Furthermore, Lin *et al*[32] found that orexin A and B contents were significantly lower in histamine H_1 receptor knockout mice. These results indicate that there exist functional connections between histaminergic and orexinergic systems.

The FrCx is a brain region that has higher EEG frequency during waking[33], and which receives projections of monoaminergic neurons such as the noradrenergic, serotonergic, and histaminergic neurons that originate from the LC, DRN, and TMN, respectively. Microdialysis studies have revealed that extracellular levels of histamine and 5-HT in the FrCx showed typical changes across the sleep-wake cycle, with their highest levels during the waking period[34–37]. Thus, orexin-activated release of these neurotransmitters in the FrCx reflects their contributions to the arousal effect of orexin. In the present study, we found that orexin A significantly promoted histamine release in the FrCx in a dose-dependent manner, but not release of NE or 5-HT, although orexin A excites noradrenergic and serotonergic neurons *in vitro*[20–22]. We previously reported that a prostaglandin E_2 receptor subtype EP_4 agonist enhanced histaminergic neuron activity with an increase in histamine release in the FrCx to produce arousal[38]. Together with our previous observations that orexin induced wakefulness in wild-type mice but not all in histamine H_1 receptor knockout mice[5], these findings suggest that the arousal effect of orexin is largely mediated by histaminergic systems and activation of H_1 receptors. In contrast to the histaminergic activity linked to the maintenance of wakefulness, John *et al*[39] found that noradrenergic and serotonergic neurons were more tightly coupled to the maintenance of muscle tone during wakefulness and its loss during rapid eye movement sleep and cataplexy.

Taken these findings together, we conclude that the arousal effect of orexin A is mainly mediated by the activation of histaminergic systems.

Acknowledgment

We sincerely thank Dr Yoshihiro URADE and Dr Larry FYRE for their critical readings of the manuscript and valuable comments.

References

1 Gautvik KM, de Lecea L, Gautvik VT, Danielson PE, Tranque P, Dopazo A, *et al*. Overview of the most prevalent hypothalamus-specific mRNAs, as identified by directional tag PCR subtraction. Proc Natl Acad Sci USA 1996; 93: 8733–8.

2 Sakurai T, Amemiya A, Ishii M, Matsuzaki I, Chemelli RM, Tanaka H, *et al*. Orexins and orexin receptors: a family of hypothalamic neuropeptides and G protein-coupled receptors that regulate feeding behavior. Cell 1998; 92: 573–85.

3 Hayaishi O, Huang ZL. Role of orexin and prostaglandin E_2 in activating histaminergic neurotransmission. Drug News Perspect 2004; 17: 1–5.

4 Piper DC, Upton N, Smith MI, Hunter AJ. The novel brain neuropeptide, orexin-A, modulates the sleep-wake cycle of rats. Eur J Neurosci 2000; 12: 726–30.

5 Huang ZL, Qu WM, Li WD, Mochizuki T, Eguchi N, Watanabe T, *et al*. Arousal effect of orexin A depends on activation of the histaminergic system. Proc Natl Acad Sci USA 2001; 98: 9965–70.

6 Mieda M, Willie JT, Hara J, Sinton CM, Sakurai T, Yanagisawa M. Orexin peptides prevent cataplexy and improve wakefulness in an orexin neuron-ablated model of narcolepsy in mice. Proc Natl Acad Sci USA 2004; 101: 4649–54.

7 Taheri S, Sunter D, Dakin C, Moyes S, Seal L, Gardiner J, *et al*. Diurnal variation in orexin A immunoreactivity and prepro-orexin mRNA in the rat central nervous system. Neurosci Lett 2000; 279: 109–12.

8 Estabrooke IV, McCarthy MT, Ko E, Chou TC, Chemelli RM, Yanagisawa M, *et al*. Fos expression in orexin neurons varies with behavioral state. J Neurosci 2001; 21: 1656–62.

9 Hara J, Beuckmann CT, Nambu T, Willie JT, Chemelli RM, Sinton CM, *et al*. Genetic ablation of orexin neurons in mice results in narcolepsy, hypophagia, and obesity. Neuron 2001; 30: 345–54.

10 Chemelli RM, Willie JT, Sinton CM, Elmquist JK, Scammell T, Lee C, *et al*. Narcolepsy in orexin knockout mice: molecular genetics of sleep regulation. Cell 1999; 98: 437–51.

11 Mochizuki T, Crocker A, McCormack S, Yanagisawa M, Sakurai T, Scammell TE. Behavioral state instability in orexin knock-out mice. J Neurosci 2004; 24: 6291–300.

12 Aldrich MS. Narcolepsy. N Engl J Med 1990; 323: 389–94.

13 Gerashchenko D, Kohls MD, Greco M, Waleh NS, Salin-Pascual R, Kilduff TS, *et al*. Hypocretin-2-saporin lesions of the lateral hypothalamus produce narcoleptic-like sleep behavior in the rat. J Neurosci 2001; 21: 7273–83.

14 Nishino S, Ripley B, Overeem S, Lammers GJ, Mignot E. Hypocretin (orexin) deficiency in human narcolepsy. Lancet 2000; 355: 39–40.

15 Peyron C, Faraco J, Rogers W, Ripley B, Overeem S, Charnay Y, *et al*. A mutation in a case of early onset narcolepsy and a generalized absence of hypocretin peptides in human narcoleptic brains. Nat Med 2000; 6: 991–7.

16 Thannickal TC, Moore RY, Nienhuis R, Ramanathan L, Gulyani S, Aldrich M, *et al*. Reduced number of hypocretin neurons in human narcolepsy. Neuron 2000; 27: 469–74.

17 Thannickal TC, Siegel JM, Nienhuis R, Moore RY. Pattern of hypocretin (orexin) soma and axon loss, and gliosis, in human narcolepsy. Brain Pathol 2003; 13: 340–51.

18 Peyron C, Tighe DK, van den Pol AN, de Lecea L, Heller HC, Sutcliffe JG, *et al*. Neurons containing hypocretin (orexin) project to multiple neuronal systems. J Neurosci 1998; 18: 9996–10015.

19 Marcus JN, Aschkenasi CJ, Lee CE, Chemelli RM, Saper CB, Yanagisawa M, *et al*. Differential expression of orexin receptors 1 and 2 in the rat brain. J Comp Neurol 2001; 435: 6–25.

20 Brown RE, Sergeeva OA, Eriksson KS, Haas HL. Convergent excitation of dorsal raphe serotonin neurons by multiple arousal systems (orexin/hypocretin, histamine and noradrenaline). J Neurosci 2002; 22: 8850–9.

21 Hagan JJ, Leslie RA, Patel S, Evans ML, Wattam TA, Holmes S, *et al*. Orexin A activates locus coeruleus cell firing and increases arousal in the rat. Proc Natl Acad Sci USA 1999; 96: 10911–6.

22 Liu RJ, van den Pol AN, Aghajanian GK. Hypocretins (orexins) regulate serotonin neurons in the dorsal raphe nucleus by excitatory direct and inhibitory indirect actions. J Neurosci 2002; 22:

9453–64.
23 Yamanaka A, Tsujino N, Funahashi H, Honda K, Guan JL, Wang QP, *et al*. Orexins activate histaminergic neurons via the orexin 2 receptor. Biochem Biophys Res Commun 2002; 290: 1237–45.
24 Nakamura T, Uramura K, Nambu T, Yada T, Goto K, Yanagisawa M, *et al*. Orexin-induced hyperlocomotion and stereotypy are mediated by the dopaminergic system. Brain Res 2000; 873: 181–7.
25 Franklin KBJ, Paxinos G. The mouse brain in stereotaxic Coordinates. San Diego (CA): Academic Press; 1997.
26 Yamatodani A, Fukuda H, Wada H, Iwaeda T, Watanabe T. High-performance liquid chromatographic determination of plasma and brain histamine without previous purification of biological samples: cation-exchange chromatography coupled with post-column derivatization fluorometry. J Chromatogr 1985; 344: 115–23.
27 Ago Y, Sakaue M, Baba A, Matsuda T. Selective reduction by isolation rearing of 5-HT_{1A} receptor-mediated dopamine release *in vivo* in the frontal cortex of mice. J Neurochem 2002; 83: 353–9.
28 Suzuki M, Matsuda T, Asano S, Somboonthum P, Takuma K, Baba A. Increase of noradrenaline release in the hypothalamus of freely moving rat by postsynaptic 5-hydroxytryptamine1A receptor activation. Br J Pharmacol 1995; 115: 703–11.
29 Gobert A, Rivet JM, Cistarelli L, Melon C, Millan MJ. Buspirone modulates basal and fluoxetine-stimulated dialysate levels of dopamine, noradrenaline and serotonin in the frontal cortex of freely moving rats: activation of serotonin1A receptors and blockade of alpha2-adrenergic receptors underlie its actions. Neuroscience 1999; 93: 1251–62.
30 Eriksson KS, Sergeeva O, Brown RE, Haas HL. Orexin/hypocretin excites the histaminergic neurons of the tuberomammillary nucleus. J Neurosci 2001; 21: 9273–9.
31 Nishino S, Fujiki N, Ripley B, Sakurai E, Kato M, Watanabe T, *et al*. Decreased brain histamine content in hypocretin/orexin receptor-2 mutated narcoleptic dogs. Neurosci Lett 2001; 313: 125–8.
32 Lin L, Wisor J, Shiba T, Taheri S, Yanai K, Wurts S, *et al*. Measurement of hypocretin/orexin content in the mouse brain using an enzyme immunoassay: the effect of circadian time, age and genetic background. Peptides 2002; 23: 2203–11.
33 Buchsbaum MS, Mendelson WB, Duncan WC, Coppola R, Kelsoe J, Gillin JC. Topographic cortical mapping of EEG sleep stages during daytime naps in normal subjects. Sleep 1982; 5: 248–55.
34 Chu M, Huang ZL, Qu WM, Eguchi N, Yao MH, Urade Y. Extracellular histamine level in the frontal cortex is positively correlated with the amount of wakefulness in rats. Neurosci Res 2004; 49: 417–20.
35 Cespuglio R, Sarda N, Gharib A, Chastrette N, Houdouin F, Rampin C, *et al*. Voltammetric detection of the release of 5-hydroxyindole compounds throughout the sleep-waking cycle of the rat. Exp Brain Res 1990; 80: 121–8.
36 Portas CM, Bjorvatn B, Fagerland S, Gronli J, Mundal V, Sorensen E, *et al*. On-line detection of extracellular levels of serotonin in dorsal raphe nucleus and frontal cortex over the sleep/wake cycle in the freely moving rat. Neuroscience 1998; 83: 807–14.
37 de Saint Hilaire Z, Orosco M, Rouch C, Python A, Nicolaidis S. Neuromodulation of the prefrontal cortex during sleep: a microdialysis study in rats. Neuroreport 2000; 11: 1619–24.
38 Huang ZL, Sato Y, Mochizuki T, Okada T, Qu WM, Yamatodani A, *et al*. Prostaglandin E2 activates the histaminergic system via the EP4 receptor to induce wakefulness in rats. J Neurosci 2003; 23: 5975–83.
39 John J, Wu MF, Boehmer LN, Siegel JM. Cataplexy-active neurons in the hypothalamus: implications for the role of histamine in sleep and waking behavior. Neuron 2004; 42: 619–34.

Full-length article

Modulating effect of adenosine deaminase on function of adenosine A_1 receptors[1]

Wan-chun SUN, Yan CAO, Lei JIN, Li-zhen WANG, Fan MENG[2], Xing-zu ZHU[3]

Department of Pharmacology, Shanghai Institute of Materia Medica, Shanghai Institutes for Biological Sciences, Chinese Academy of Sciences, Shanghai 201203, China; [2]Department of Psychiatry, University of Michigan, The Psychiatry/MHRI Microarray Laboratory, 205 Zina Pitcher Place, Ann Arbor, MI 48109-0720, USA

Key words

adenosine deaminase; adenosine A_1 receptor; radioligand assay; calcium; fluorescence; diagnosis

[1] Project supported by the National Natural Science Foundation of China (No 30128004) and Shanghai Metropolitan Fund for Research and Development (No 04DZ14005).
[3] Correspondence to Xing-zu ZHU, PhD.
Phn/Fax 86-21-5080-6096.
E-mail xzzhu@mail.shcnc.ac.cn

Received 2004-09-13
Accepted 2004-11-15

doi: 10.1111/j.1745-7254.2005.00024.x

Abstract

Aim: To study the modulating effect of adenosine deaminase (ADA) on yhe adenosine A_1 receptor (A_1R) in HEK293 cells stably expressing the human A_1R. **Methods:** cDNA was amplified by RT-PCR using total RNA from human embryo brain tissue as the template. The PCR products were subcloned into the plasmid pcDNA3 and cloned into the plasmid pcDNA3.1. The cloned A_1R cDNA was sequenced and stably expressed in HEK293 cells. The modulating effect of adenosine deaminase on A_1R was studied by using [^{3}H]DPCPX binding assay and an intracellular calcium assay. **Results:** HEK293 cells stably expressing human A_1R were obtained. Saturation studies showed that the K_D value and B_{max} value of [^{3}H]DPCPX were 1.6±0.2 nmol/L and 1.819±0.215 nmol/g of protein respectively, in the absence of ecto-ADA respectively, and 1.3±0.2 nmol/L and 1.992±0.130 nmol/g of protein in the presence of ecto-ADA respectively, suggesting that the K_D value and B_{max} value of [^{3}H]DPCPX were unaffected by ecto-ADA. In the case of [^{3}H]DPCPX competition curves obtained from intact cells or membranes, A_1R agonist CCPA/[^{3}H]DPCPX competition curve could be fitted well to a one-site model in the absence of ecto-ADA and a two-site model in the presence of ecto-ADA with a K_H value of 0.74 (0.11–4.8) nmol/L (intact cells) or 1.8 (0.25–10) nmol/L (membrane) and a K_L value of 0.94 (0.62–1.41) μmol/L (intact cells) or 0.77 (0.29–0.99) μmol/L (membrane). The K_L value is not significantly different from the IC_{50} value of 0.84(0.57–1.23) μmol/L (intact cells) or 0.84 (0.63–1.12) μmol/L (membrane) obtained in the absence of ecto-ADA. Similar results were obtained from the CPA/[^{3}H]DPCPX competition curve in the absence or presence of ecto-ADA on intact cells or membranes. Intracellular calcium assay demonstrated that the EC_{50} value of CPA were 10 (5–29) nmol/L and 94 (38–229) nmol/L in the presence or absence of ecto-ADA, respectively. **Conclusion:** A_1R stably expressed in the HEK293 cells display a low affinity for agonists in the absence of ADA and high and low affinities for agonists in the presence of ADA. The presence of ADA may promote the signaling through the adenosine A_1 receptor in HEK293 cells.

Introduction

Adenosine is a ubiquitous physiological regulator and neuromodulator capable of ultiple physiological actions in various systems[1]. Adenosine receptors are members of the G-protein-coupled receptor superfamily, and comprise A_1, A_{2a}, A_{2b}, and A_3 adenosine receptors, identified by convergent data from molecular, biochemical, and pharmacological studies[2]. A_1R is widely expressed in the brain, adipose tissue, the testis, and the spinal cord[3]. Via A_1R, adenosine reduces heart rate[4], glomerular filtration rate, and renin release in the kidney[5], induces bronchoconstriction[6,7] and inhibits

lipolysis. A_1R can be coupled to different pertussis toxin-sensitive G proteins[8–10], which mediate the inhibition of adenylyl cyclase[11] and regulate Ca^{2+} and K^+ channels and inositol phosphate metabolism[12]. A_1R present two different affinities for agonists, which have classically been attributed to a different coupling to heterotrimeric G proteins[13], coupled receptor-G protein complexes display high affinity for A_1R agonists, whereas uncoupled receptors display low affinity[13,14].

Adenosine deaminase (ADA, E.C.3.5.4.4) is an enzyme which catalyzes the hydrolytic deamination of adenosine to inosine. ADA is located both in the cytosol and on the cell membrane. Recent evidence suggest that ecto-ADA had extra-enzymatic and co-stimulatory functional roles. ADA modulates ligand binding and signaling through A_1R on DDT_1MF-2 cells, a smooth muscle cell line[15]. ADA seems to be necessary for the high affinity binding of agonists to A_1R[16,17]. In the present study, the effect of ADA on the ligand-mediated regulation of A_1R in HEK293 cells stably expressing human A_1R has been studied.

Materials and methods

Materials High glucose Dulbecco's modified Eagle's medium (DMEM), fetal calf serum, G418, benzylpenicillin and streptomycin were obtained from Gibco. Restricted enzyme (*Hind*III, *EcoR*I, *Xho*I), T4 DNA ligase, reverse transcriptase enzyme and buffer were purchased from Promega (USA). Pyrobest DNA polymerase and PCR buffer were obtained from TaKaRa (Dalian, China). N^6-cyclopentyladenosine (CPA), 8-cyclopentyl-1,3-dipropylxanthine (DPCPX), and 2-Chloro-N^6-cyclopentyladenosine (CCPA) were obtained from RBI (Natick, MA, USA). Adenosine deaminase was obtained from Roche Biochemicals (Mannheim, Germany). Fluo-3/AM, *p*-(dipropylsulfamoyl)benzoic acid, pluronic F-127, HEPES, Triton X-100, bovine serum albumin, leupeptin, pepstatin A, aprotinin and PMSF were purchased from Sigma (USA). [^{3}H]DPCPX was purchased from Amersham (USA). Plasmids pcDNA3, pcDNA3.1(+), and Lipofectamine^{2000} were purchased from Invitrogen (USA). Human embryo brain tissue was donated by Huashan Hospital (Shanghai, China). PCR primers were synthesized by Shenyou (Shanghai, China).

Table 1. Human A_1 receptor PCR primers.

A_1R-1SE	GCGCGAATTCTTGGTGACCTTGGGTGCTTG
A_1R-1AS	GCGCCTCGAGGCTCAGAACACTGTTGCCTCTA
A_1R-2SE	GCGCAAGCTTGCCGCCACCATGGCCCCGCCCT-CCATCTCAGCTTTCC
A_1R-2AS	GCGCGAATTCCTAGTCATCAGGCCTCTCTTCTGGG

Cloning of the human A_1R cDNA Human brain total RNA was obtained from human embryo brain tissue. The total RNA was reverse-transcribed using oligo-dT18 as a primer. With the cDNA, PCR was carried out using the primers A_1R-1SE and A_1R-1AS (Table 1). Gel-purified PCR product was treated with *EcoR*I/*Xho*I and subcloned into the *EcoR*I/*Xho*I site of the mammalian expression vector pcDNA3. With the subcloned A_1R-pcDNA3 plasmid as template, PCR was carried out using the primers A_1R-2SE and A_1R-2AS (Table 2), which resulted in full length codon sequence cDNA. Gel-purified PCR product was treated with *Hind*III/*EcoR*I and cloned into the *Hind*III/*EcoR*I site of the mammalian expression vector pcDNA3.1(+).

Production of HEK293 cell lines stably expressing human A_1R HEK293 Cells were transfected with the A_1R-pcDNA3.1(+) expression vector, using the Lipofectamine2000 reagent. Cells were treated with selection medium containing G418 (1 g/L) for 3 weeks to select stably transfected cells displaying neomycin resistance. Between 2 and 3 weeks in the selection process, resistant cells began to appear. They were sought out by serial dilutions and allowed to grow from single cells. Receptor expression of single cell-derived colonies was tested by radioligand binding assay.

Table 2. Representative competition inhibition experiments of CCPA and CPA versus the A_1R antagonist [^{3}H]DPCPX in intact cells and membrane preparations from A_1R cells. R_H is expressed as a mean. K_H, and K_L/IC_{50} are expressed as a mean with 95% confidence intervals.

		ADA	R_H (%)	K_H (nmol/L)	K_L/IC_{50} (μmol/L)
CCPA	Intact cells	–	0		0.84 (0.57–1.23)
		+	18 (3)	0.74 (0.11–4.8)	0.94 (0.62–1.41)
	Membranes	–	0		0.84 (0.63–1.12)
		+	25 (5.0)	1.8 (0.25–10)	0.77 (0.29–0.99)
CPA	Intact cells	–	0		1.3 (0.9–1.7)
		+	18 (3)	0.62 (0.1–4.9)	2.1 (1.3–3.3)
	Membranes	–	0		2.0 (1.5–2.5)
		+	32 (3)	0.47 (0.16–1.3)	2.7 (1.6–4.6)

Cell culture Human embryonic kidney (HEK293) cells were cultured in DMEM containing streptomycin (100 mg/L), benzylpenicillin (1000 kU/L) and fetal bovine serum (10%). Cells were incubated at 37 °C in 5% CO_2. Stably transfected HEK293 cell lines were cultured in DMEM high glucose medium containing streptomycin (100 mg/L), benzylpenicillin (1000 kU/L), G-418 (200 mg/L), and fetal bovine serum (10%). Cells were incubated at 37 °C in 5% CO_2. For passaging, the cells were detached from the cell culture flask by washing with phosphate-buffered saline (PBS) and brief incubation with trypsin (0.5 g/L)/EDTA (0.2 g/L). The cells were passaged every 3 d.

Membrane preparation The A_1R cells (HEK293 cells stably expressing human A_1R) were lifted from Petri dishes with a cell scraper. Harvested cells were washed twice with ice-cold PBS and centrifuged at 420×*g* for 5 min at 4 °C. The cell pellet was resuspended with hyponic buffer (Tris-HCl 5 mmol/L, EDTA 2 mmol/L, pH 7.4, leupeptin 1 mg/ L, pepstatin A 1 mg/L, aprotinin 1 mg/L, PMSF 1 mmol/ L) and sonicated (18 s) three times on ice. The homogenate was centrifuged at 960×*g* for 10 min at 4 °C. The precipitated nucleic fraction was discarded and the supernatant was centrifuged at 40 000×*g* for 30 min at 4 °C. The pellet was washed with 50 mmol/L Tris-HCl buffer (pH 7.4) and centrifuged again under the same conditions. Finally, the pellet was resuspended in the same buffer, and protein concentration was determined by using the BCA Kit (Pierce) as described previously[18].

[^{3}H]DPCPX binding assays in intact cells and membranes Binding assays in intact cells were performed in a reaction tube at a density of 2.0×10^5 cells per tube, using [^{3}H]DPCPX as a radioligand. Cells were resuspended in 50 mmol/L Tris-HCl (pH 7.4) and treated with ADA 65 nmol/L at 4 °C for 30 min[17]. After this treatment, cells were incubated for 1 h at 37 °C with [^{3}H]DPCPX 0.5 nmol/L for competition assays. Different concentrations of the A_1R agonist CCPA or CPA were used in the competition curves.

Membranes (30–50 μg proteins) from A_1R cells were resuspended in Tris-Cl 50 mmol/L (pH 7.4) and treated with ADA 65 nmol/L at 4 °C for 30 min. Saturation assays were performed at different concentrations of [^{3}H]DPCPX (0.05–10 nmol/L) using unlabeled DPCPX (20 μmol/L) to obtain nonspecific binding. Competition curves were carried out by using [^{3}H]DPCPX 0.5 nmol/L and different concentrations of A_1R agonists CCPA or CPA.

After incubation for 1 h, the binding assays were stopped by rapid filtration through Whatman GF/B filters, and the filters were immediately washed three times with ice-cold buffer. Filters were then transferred to Eppendoff tubes, and scintillation liquid was added to measure the radioactivity.

Intracellular Ca^{2+} measurements Ca^{2+} fluorescence measurements were performed using a NOVOstar plate reader with a pipettor system (BMG labtechnologies, Offenburg, Germany). A_1 cells were harvested with 0.05% trypsin/0.02% EDTA and rinsed with high glucose DMEM containing 10% fetal bovine serum, streptomycin 100 mg/L, and benzylpenicillin 1000 kU/L. Pelleted cells were resuspended in fresh medium and kept under 5% CO_2 at 37 °C for 1 h and vortexed every 15 min. After two washes with Krebs-HEPES buffer, cells were loaded with Fluo-3/AM 5 μmol/L for 30 min containing 1% pluronic F-127 and *p*-(dipropylsulfamoyl)benzoic acid 2.5 mmol/L. Then cells were rinsed 3 times with Krebs-HEPES buffer containing 0.5% bovine serum albumin, the diluted, and evenly plated into 96-well plates at a density of 1×10^4 cells/well. Microplates were kept at 37 °C for 15 min[19, 20]. Buffer alone or different concentrations of CPA were then injected sequentially into separate wells, and fluorescence intensity was measured at 520 nm for 50 s at 0.2 s intervals. The excitation wavelength was 485nm.

$[Ca^{2+}]_i$ was calculated as follows: $[Ca^{2+}]_i=K_d(F-F_{min})/(F_{max}-F)$. F_{max} refers to fluorescence intensity measured after permeabilization of the cells with 1% Triton X-100. Ten mmol/L EDTA was added to chelate Ca^{2+} and minimum fluorescence intensity was obtained (F_{min}). A K_d value of 324 nmol/L was used for Fluo-3.

Data analysis Experiments were performed in triplicate. All data were expressed as mean±SD and data were analyzed with the GraphPad Prism 4.0 program (GraphPad Software, San Diego, CA, USA). Student's *t*-test was used for statistical analysis.

Results

Cloning of the human adenosine A_1R cDNA To obtain the cDNA with the full length codon sequence of human A_1R, a reverse transcription reaction was carried out using the total RNA extracted from human embryo brain tissue. Using cDNA with full length codon sequence of A_1R, a PCR product (1332 bp) was obtained using primers described previously. The PCR product subcloned into a pcDNA3 plasmid and cDNA (981 bp) containing the full A_1R codon sequence was obtained using this subcloned vector as a template. The cDNA was then cloned into the mammalian expression vector pcDNA3.1. Sequence analysis demonstrated that the sequence of the constructed A_1R-pcDNA3.1 expression vector was identical to that of human A_1R cDNA in the gene bank.

Selection of cell clones Colonies of the selected stable

integrants were initially analyzed for human A_1R expression by using a receptor binding assay using [^{3}H]DPCPX. From the transfected HEK293 cell clones, one cell line was obtained with specific [^{3}H]DPCPX binding.

Saturation experiments with the adenosine A_1 receptor antagonist [^{3}H]DPCPX As Figure 1 shown, no significant difference was found between the A_1R cells in the absence and presence of ADA with respect to the B_{max} and K_D values for the A_1R binding sites labeled with [^{3}H]DPCPX. The B_{max} values for the A_1R cells were 1.819±0.215 and 1.992±0.130 nmol/g of protein (n=3) in the absence and presence of ADA, respectively. The K_D values for the A_1R cells were 1.6±0.2 and 1.3±0.2 nmol/L (n=3) in the absence and presence of ADA, respectively. The non-specific binding was <5% of the total binding.

Competition experiments of A_1R agonist CCPA or CPA versus the A_1R antagonist [^{3}H]DPCPX Competition experiments with CCPA versus the A_1R antagonist [^{3}H]DPCPX in intact A_1R cells or membrane preparations from A_1R cells incubated previously with ADA showed a significantly better fit with the 2 binding sites model than that with the 1 binding site model (F test, P<0.05). Similar K_H and K_L values were obtained in intact cells or membrane preparations from A_1R cells incubated previously with ADA, and the proportions of the A_1R in the high affinity state (R_H values) were 18%±3% and 20%±5% , respectively (Figure 2 and Table 2). In intact A_1R cells or membrane preparations from A_1R cells in the absence of ADA, a significant better fit for one binding site (R_H=0) was obtained, with the IC_{50} values very similar to the K_L value obtained in intact cells or membrane preparations previously treated with ADA. Similar results were obtained from competition experiments with CPA versus the adenosine A_1R antagonist [^{3}H]DPCPX in intact A_1R cells or membrane preparations from A_1 cells in the absence of ADA (Figure 3, Table 2).

Effects of A_1R agonist CPA on intracellular calcium level in the presence or absence of ADA An increase in intracellular Ca^{2+} appears to be a universal second messenger signal for a majority of recombinant GPCRs[20]. A_1R agonists evoked a concentration-dependent and reproducible Ca^{2+} signal at A_1R[22]. To assess the effect of the presence of ADA on A_1R signal transduction, we performed an intracellular calcium assay. A significant difference was found between the A_1R cells in the absence and presence of ADA with respect to the EC_{50} values of A_1R agonist CPA. A_1R agonist CPA induced an intracellular [Ca^{2+}] increase. The EC_{50} values for the A_1R cells in the absence and presence of ADA were 94 (38–229) and 10 (5–29) nmol/L, respectively. CPA appears more potent at the A_1 cells in the presence of ADA compared with the A_1R cells in the absence of ADA (Figure 4).

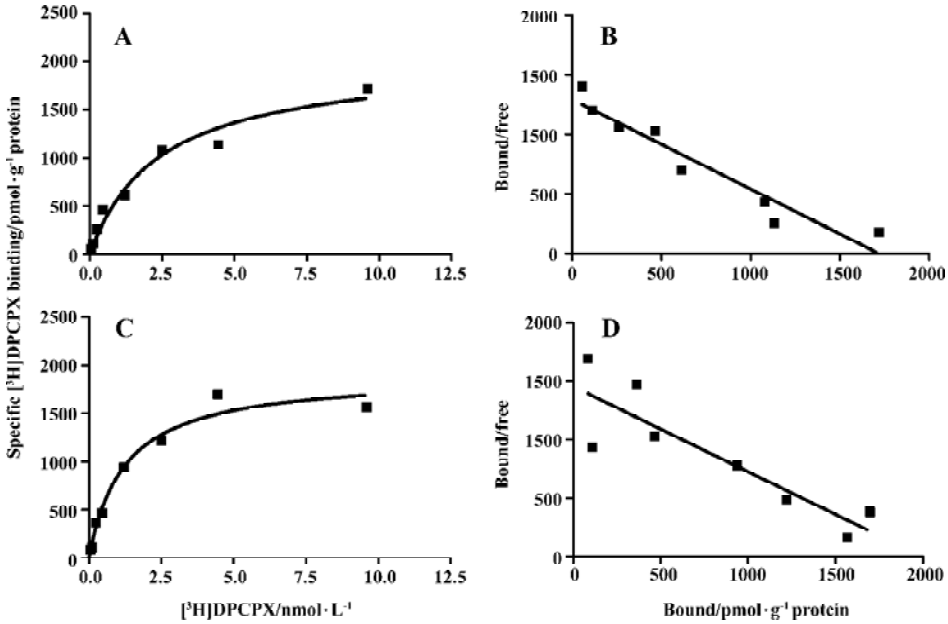

Figure 1. Saturation curve of [^{3}H]DPCPX binding to adenosine A_1R in plasma membrane isolated from A_1R cells untreated (A, B) and treated (C, D) with ADA. Binding assays were performed as described in Methods, using A_1R antagonist [^{3}H]DPCPX as radioligand in a concentration range from 0.05 to 10 nmol/L. A and C: Saturation curve of [^{3}H]DPCPX binding to adenosine A_1 receptors. B and D: Scatchard plot of these data and analysis gave the K_D and B_{max} values indicated in Results. Data are mean±SD and were obtained from three independent experiments performed in triplicate.

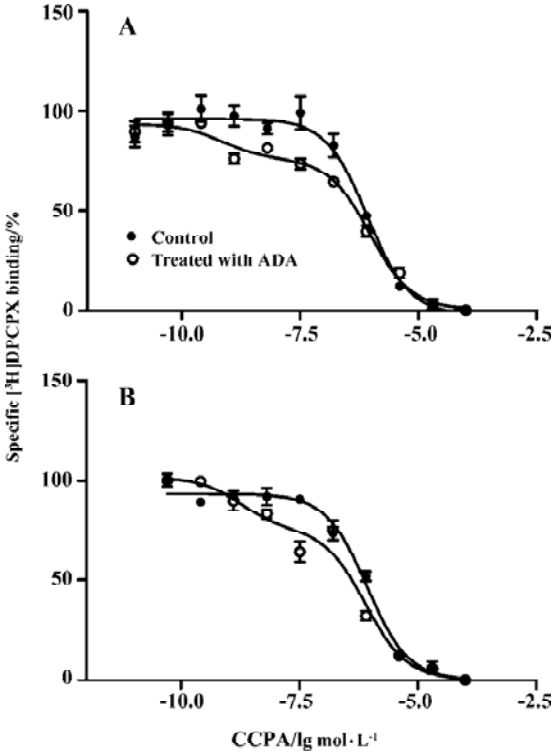

Figure 2. Representative competitive inhibition curve of A_1R agonist CCPA versus the A_1R antagonist [^{3}H]DPCPX in intact cells (A) and membrane preparations (B) from A_1R cells untreated and treated with ADA. Competition assays were done at 0.5 nmol/L [^{3}H]DPCPX and increasing concentrations of CCPA. IC_{50} values are means (95% confidence intervals) obtained from three independent experiments performed in triplicate.

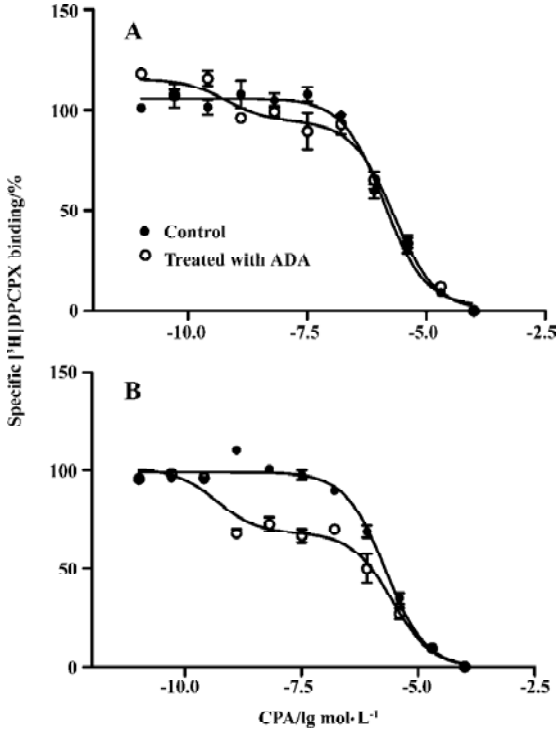

Figure 3. Representative competitive inhibition curve of A_1R agonist CPA versus the A_1R antagonist [^{3}H]DPCPX in intact cells (A) and membrane preparations (B) from A_1R cells untreated and treated with ADA. Competition assays were done at 0.5 nmol/L [^{3}H]DPCPX and increasing concentrations of CPA. IC_{50} values are means (95% confidence intervals) obtained from three independent experiments performed in triplicate.

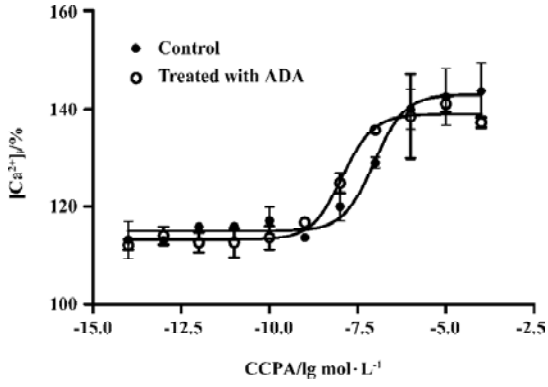

Figure 4. Concentration-response curves for the effect of A_1R agonist CPA on intracellular [Ca^{2+}] in A_1R cells untreated and treated with ADA. Mean±SD. n=3. EC_{50} values is mean (95% confidence intervals) obtained from three independent experiments performed in triplicate.

Discussion

Recently, several evidences demonstrated that cell-surface ADA interacted with A_1 receptors in brain cortex and DDT_1MF-2 cells and that the enzyme was able to modulate ligand binding and signaling through A_1R[16,21–23]. By immunoprecipitation and affinity chromatography, it was found that ADA and A_1R interacted in pig brain cortical membranes. By means of this interaction ADA led to the appearance of the high-affinity site of the receptor. Thus, it seems that ADA is necessary for coupling A_1R to heterotrimeric G proteins[16]. In Chinese hamster ovary (CHO) cells, stably transfected with the human adenosine A_1R, it was found that in the presence of ADA, the [^{3}H]DPCPX/cyclohexyladenoine competition curve could be analysed by a two-site model with 93% of the sites having high affinity and the remainder having low affinity. In the absence of ADA, the [^{3}H]DPCPX/cyclohexyladenosine competition curve was well described by a two-site model. Under these conditions, 70% of the binding of [^{3}H]DPCPX was associated with a high-affinity site with the remaining sites having low affinity. Thus there is a clear difference in the potency of cyclohexyladenosine

at the high-affinity state[24]. In the present study, human adenosine A_1R were cloned and stably expressed in the HEK293 cells and the effects of ecto-ADA on adenosine A_1R were studied. By using competitive inhibition assay of adenosine A_1R agonists CCPA or CPA against [^{3}H]DPCPX, we found that A_1R displayed two different affinities for agonists in the presence of ADA. However, A_1R only displayed a low affinity for agonists in the absence of ADA, suggesting that most of the binding of [^{3}H]DPCPX was associated with the low-affinity site under these conditions and that the interaction of ADA with A_1 adenosine receptors led to the appearance of the high-affinity site of the receptor.

To further demonstrate possible interaction between A_1R and ADA, intracellular calcium assay was carried out in the present studies. The results demonstrated that the EC_{50} value of CPA for inducing increase of intracellular calcium level was lower in the presence of ADA than that in the absence of ADA, suggesting that the presence of ADA may promote signaling through A_1 receptors in the stably transfected HEK293 cells. Our results further support the notion that ADA may promote the signaling through A_1 receptors.

References

1 Wlliams M. Purine receptors in mammalian tissues:pharmacology and functional significance. Annu Rev Pharmacol Toxicol 1987; 27:315–45.

2 Ralevic V, Burnstock G. Receptors for purines and pyrimidines. Pharmacol Review 1998; 50: 413–92.

3 Ren H, Stiles G L. Characterization of the human A1 adenosine receptor gene: evidence for alternative splicing. J Biol Chem 1994; 269: 3104–10.

4 Amoah-Apraku B, Xu J, Lu JY, Pelleg A, Bruns RF, Belardinelli L. Selective potentiation by an A1 adenosine receptor enhancer of the negative dromotropic action of adenosine in the guinea pig heart. J Pharmacol Exp Ther 1993; 266: 611–7.

5 Spielman WS, Arend LJ. Adenosine receptors and signaling in the kidney. Hypertension 1991; 17: 117–30.

6 el-Hashim AD, Agostino B, Matera MG, Page C. Characterization of adenosine receptors involved in adenosine-induced bronchoconstriction in allergic rabbits. Br J Pharmacol 1996; 119: 1262–8.

7 Nyce JW, Metzger WJ. DNA antisense therapy for asthma in an animal model. Nature 1997; 385: 721–5.

8 Munshi R, Pang IH, Sternweis PC, Linden J. A1 adenosine receptors of bovine brain couple to guanine nucleotide-binding proteins Gi1, Gi2 and Go. J Biol Chem 1991; 266: 22285–9.

9 Jockers R, Linder ME, Hohenegger M, Nanoff C, Bertin B, Strosberg AD, *et al*. Species difference in the G protein selectivity of the human and bovine A1-adenosine receptor. J Biol Chem 1994; 269: 32077–84.

10 Figler RA, Graber SG, Lindorfer MA, Yasuda H, Linden J, Garrison JC. Reconstitution of recombinant bovine A1 adenosine receptors in Sf9 cell membranes with recombinant G proteins of defined composition. Mol Pharmacol 1996; 50: 1587–95.

11 Londos C, Cooper DM, Wolff J. Subclasses of external adenosine receptors. Proc Natl Acad Sci USA 1980; 77: 2551–4.

12 Palmer TM, Stiles GL. Adenosine receptors. Neuropharmacology 1995; 34: 683–94.

13 Lohse MJ, Lenschow V, Schwabe U. Two affinity states of Ri adenosine receptors in brain membranes. Analysis of guanine nucleotide and temperature effects on radioligand binding. Mol Pharmacol 1984; 26: 1-9.

14 Casado V, Canti C, Mallol J, Canela EI, Lluis C, Franco R. Solubilization of A1 adenosine receptor from pig brain: characterization and evidence of the role of the cell membrane on the coexistence of high- and low-affinity states. J Neurosci Res 1990; 26: 461–73.

15 Ciruela F, Casado V, Mallol J, Canela EI, Lluis C, Franco R. Immunological identification of A1 adenosine receptors in brain cortex. J Neurosci Res 1995; 42: 818–28.

16 Saura C, Ciruela F, Casado V, Canela EI, Mallol J, Lluis C, *et al*. Adenosine deaminase interacts with A1 adenosine receptors in pig brain cortical membranes. J Neurochem 1996; 66: 1675–82.

17 Saura CA, Mallol J, Canela EI, Lluis C, Franco R. Adenosine deaminase and A1 adenosine receptors internalize together following agonist-induced receptor desensitization. J Biol Chem 1998; 273: 17610–7.

18 Sorensen K, Brodbeck U. Assessment of coating-efficiency in ELISA plates by direct protein determination. J Immunol Methods 1986; 95: 291–3.

19 Sun WC, Jin L, Cao Y, Wang LZ, Meng F, Zhu XZ. Cloning, expression, and functional analysis of human dopamine d1 receptors. Acta Pharmacol Sin 2005; 26: 27-32.

20 Kassack MU, Hofgen B, Lehmann J, Eckstein N, Quillan JM, Sadee W. Functional screening of G protein-coupled receptors by measuring intracellular calcium with a fluorescence microplate reader. J Biomol Screen 2002; 7: 233–46.

21 Franco R, Casado V, Ciruela F, Saura C, Mallol J, Canela EI, *et al*. Cell surface adenosine deaminase: much more than an ectoenzyme. Prog Neurobiol 1997; 52: 283–94.

22 Ciruela F, Saura C, Canela EI, Mallol J, Lluis C, Franco R. Adenosine deaminase affects ligand-induced signalling by interacting with cell surface adenosine receptors. FEBS Lett 1996; 380: 219–23.

23 Escriche M, Burgueno J, Ciruela F, Canela EI, Mallol J, Enrich C, *et al*. Ligand-induced caveolae-mediated internalization of A1 adenosine receptors: morphological evidence of endosomal sorting and receptor recycling. Exp Cell Res 2003; 285: 72–90.

24 Cohen FR, Lazareno S, Birdsall NJ. The affinity of adenosine for the high- and low-affinity states of the human adenosine A1 receptor. Eur J Pharmacol 1996; 309: 111–4.

Full-length article

Modulation of P-glycoprotein function by amlodipine derivatives in brain microvessel endothelial cells of rats[1]

Bian-sheng JI, Ling HE, Guo-qing LIU[2]

Department of Pharmacology, China Pharmaceutical University, Nanjing 210009,China

Key words

amlodipine derivatives; CJX1; CJX2; verapamil; P-glycoprotein; blood brain barrier; vascular endothelium

[1] Project supported by Natural Science Foundation of Jiangsu Province (No BK2004110).
[2] Correspondence to Prof Guo-qing LIU.
Phn 86-25-8335-2126.
E-mail Liugq@vip.163.com

Received 2004-06-11
Accepted 2004-11-08

doi: 10.1111/j.1745-7254.2005.00028.x

Abstract

Aim: To investigate whether the amlodipine derivatives, CJX1 and CJX2, have a modulative effect on P-glycoprotein (P-gp) function in rat brain microvessel endothelial cells (RBMEC). **Methods:** Isolated RBMEC were cultured in DMEM/F12 (1:1) medium. The amount of intracellular rhodamine (Rh123) was determined, using a fluorescence spectrophotometer, to evaluate the function of P-gp. **Results:** The accumulation of Rh123 in RBMEC was potentiated in a concentration-dependent manner after incubation with CJX1 and CJX2 at 1, 2.5, 5, and 10 μmol/L ($P<0.01$), but no accumulation of Rh123 was observed in human umbilical vein endothelial cells after incubation with CJX1 and CJX2 10 μmol/L ($P>0.05$). Accumulation of intracellular Rh123 was increased and efflux of intracellular Rh123 was decreased in a time-dependent manner from 0–100 min after CJX1 and CXJ2 at 10 μmol/L treatment. The inhibitory effect of CJX1 and CJX2 on P-gp function was reversible and remained even at 120 min after removal of CJX1 and CJX2 at 2.5 μmol/L from the medium. **Conclusion:** CJX1 and CJX2 exhibited a potent effect in the inhibition of P-gp function *in vitro*.

Introduction

The treatment of cancer with chemotherapeutic drugs is frequently impaired or ineffective as a result of acquired resistance of tumor cells. This phenomenon is termed as multidrug resistance (MDR) and characterized by the over-expression of P-glycoprotein (P-gp) at the surface of cancer cells. As a 170 kDa protein, P-gp is encoded by MDR gene and belongs to a membrane transporter of the ABC superfamily. It acts as an energy-dependent drug efflux pump preventing adequate intracellular accumulation of a broad range of cytotoxic drugs including anthracyclines, *Vinca* alkaloids, epipodophyllotoxins, and taxanes[1–3]. P-gp is also expressed in normal tissues such as the endothelial cells of the blood brain barrier (BBB) capillaries[4]. The capillary endothelial cells protect the brain against many exogenous toxin injuries and sudden fluctuation in the levels of systemic substances. The hydrophobic agents, such as vinblastine and doxorubicin and lipid-soluble compounds, such as cyclosporin A, cannot accumulate in the brain[5-7]. P-gp expression in the BBB capillaries is responsible for the extrusion of these compounds from the endothelial cells, and thereby attenuates the accumulation of the drugs in the brain leading to the failure of therapy for the brain disease. There are a variety of agents, such as verapamil (Ver) and cyclosporine A for overcoming MDR[8,9]. However, vera-pamil and cyclosporine A, are used as anti-arrhythmic agents and immunosuppressants, respectively. Therefore, they will cause side effects when used as MDR-reversing agents. In light of these findings, the development of compounds specially inhibiting P-gp function in cancer cells or BBB may contribute to the treatment of cancers and central nervous system diseases. Amlodipine, a calcium channel antagonist, belongs to dihydropyridines family and is currently applied in the treatment of hypertension[10]. A previous report has revealed that amlodipine has an inhibitory effect on P-gp-mediated transport of dauxorubicin and digoxin[11]. CJX1 and CJX2, the amlodipine derivatives, were synthesized by substituting the hydrogen of the amino group on amlodipine with 4,5-dihydro-imidazole and 4,5-dihydro-thiazole, respectively. The aim of this study was to investigate the

effects of CJX1 and CJX2 on the P-gp function in rat brain microvessel endothelial cells (RBMEC).

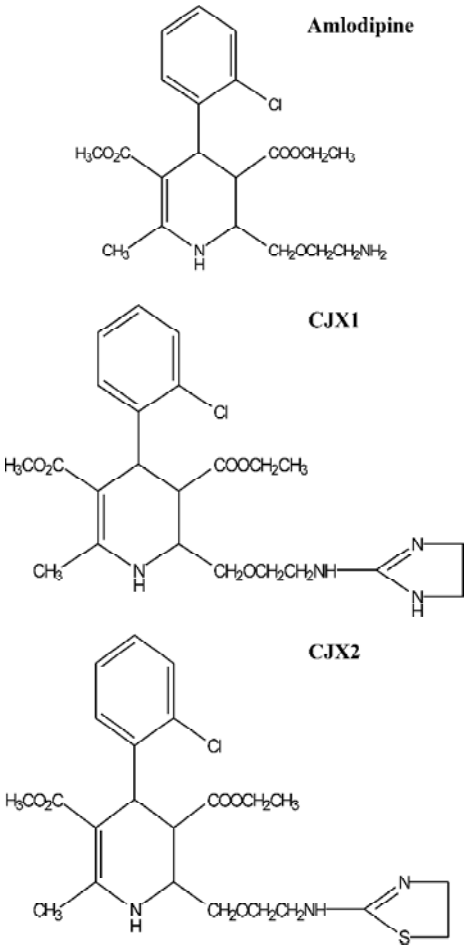

Figure 1. The chemical structure of amlodipine, CJX1, and CJX2.

Materials and methods

Materials The cell line of human umbilical vein endothelial cells (HUVEC) was a gift from Prof Zhuang ZHANG (Beijing University of Chinese Medicine); CJX1 (M_r 471) and CJX2 (M_r 488) were obtained from Dr Yun-gen XU (Novel Drug Research Centre, China Pharmaceutical University). Rhodamine123 (Rh123) and verapamil were purchased from Sigma Co (St Louis, USA). Fetal calf serum and DMEM/F12 (1:1) medium were purchased from GIBCO (USA). All other chemicals used in the experiments were commercial products of reagent grade.

Culture of RBMEC RBMEC were isolated according to the method of Abbott *et al*[12] with minor modification. Isolated cortex from ten rats was placed in ice-cold phosphate-buffered saline (PBS). After removal of surface vessels and meninges, cortex gray matter was minced and incubated at 37 ºC for 25 min in D-Hanks' solution containing 0.05% trypsin. The samples were filtered through a 150-μm nylon mesh. After centrifugation at 800×*g* for 5 min, the pellet was re-suspended in PBS containing 20% bovine serum albumin (BSA) and centrifuged at 2000×*g* at 37 ºC for 5 min. After removal of fat, cell debris, and myelin floating on BSA, the pellet containing microvessels was resuspended and incubated in PBS containing 0.1% collagenase II at 37 ºC for 30 min. The microvessels were finally collected by centrifugation at 800×*g* for 5 min, then the pellet was washed twice with PBS and cultured in DMEM/F12 (1:1) medium supplemented with 20% fetal bovine serum at 37 ºC in a 5% CO_2 humidified atmosphere.

Intracellular Rh123 accumulation assay RBMEC were seeded at a density of 5×10^7/L in 24-well plates. After reaching confluence, cell monolayers were exposed to Rh123 5 μmol/L in serum-free DMEM/F12 medium containing CJX1 and CJX2 at 1, 2.5, 5, and 10 μmol/L at 37 ºC for 90 min, respectively. Verapamil was used as a positive control for an P-gp inhibitor. After incubation, the medium was removed, and all monolayers were washed three times with ice-cold PBS and then dissolved in 1% Triton X-100. Fluorescence of Rh123 was measured using fluorescence spectrophotometer and concentration of Rh123 was calculated from the fluorescence value on the Rh123 standard curve. The amount of Rh123 in cell samples was normalized with the amount of protein in each sample as described previously[13,14].

Rh123 uptake assay RBMEC were seeded at a density of 5×10^7/L in 24-well plates, and then incubated in DMEM/F12 (1:1) medium containing Rh123 at 5 μmol/L in the presence or absence of CJX1 or CJX2 10 μmol/L at 37 ºC in a humidified atmosphere of 5% CO_2 for 10, 25, 45, 60, and 90 min, respectively. After removal of the medium, the cell monolayers were washed three times in ice-cold PBS and dissolved in 1% Triton X-100. The amount of Rh123 was determined as described in the accumulation assay. The uptake constant (k_{up}) was obtained by fitting the data to $F_t=F_{ss}(1\text{-}e^{-kt})$, where F_t is the amount of Rh123 at time t, F_{ss} is the amount of Rh123 at 90 min. The amount of intracellular Rh123 was plotted against time.

Rh123 efflux assay The RBMEC were incubated in the medium containing Rh123 5 μmol/L at 37 ºC in a humidified atmosphere of 5% CO_2 for 90 min. After washing three times in ice-cold PBS, RBMEC were incubated in the presence or absence of CJX1 and CJX2 1-10 μmol/L or verapamil 10 μmol/L at 37 ºC for 5, 10, 25, 30, 60, and 90 min, respectively. The amount of intracellular Rh123 was determined

as described in the accumulation assay. The efflux constant (k_e) of CJX1 and CJX2 10 μmol/L was obtained by fitting the data to $F_t=F_o\ e^{-kt}$, where F_t is the amount of Rh123 at time t. The amount of intracellular Rh123 was plotted against time.

Persistence of CJX1 and CJX2 activity The RBMEC were incubated in the medium containing Rh123 5 μmol/L in the presence or absence of CJX1 and CJX2 2.5 μmol/L or verapamil 2.5 μmol/L in the humidified atmosphere of 5% CO_2 for 90 min at 37 ºC, respectively. After washing three times in rhodamine-free and drug-free medium, the amount of intracellular Rh123 was measured after 10, 30, 60, 90, and 120 min, respectively. The amount of Rh123 in cell samples at different time points was determined as described in the accumulation assay. T_0 represents the amount of Rh123 which was monitored immediately after incubation with CJX1, CJX2 or verapamil.

Data analysis All data were expressed as mean±SD and analyzed by *t*-test.

Results

Effect of CJX1 and CJX2 on intracellular accumulation of Rh123 After RBMEC were incubated with Rh123 for 90 min in the presence of CJX1 and CJX2 1-10 μmol/L, the amount of intracellular Rh123 was greatly increased in a concentration-dependent manner compared with the control group ($P<0.01$). Accumulation of Rh123 was not increased in HUVEC. The amount of intracellular Rh123 in CJX1 10 μmol/L-treated group was comparable to that of the verapamil 10 μmol/L-treated group (Table 1).

Effect of CJX1 and CJX2 on uptake of Rh123 After the RBMEC were incubated in the presence of CJX1 and CJX2 10 μmol/L, Rh123 was accumulated in a time-dependent manner from 0-100 min. The rate constants (k_{up}) of the uptake in CJX1 and CJX2-treated group was 0.0508 and 0.0495 respectively, and higher than those of control group (0.0264) and verepamil-treated group (0.044) (Figure 2).

Effect of CJX1 and CJX2 on Rh123 efflux CJX1 and CJX2 1-10 μmol/L inhibited the efflux of Rh123 from RBMEC from 0 to 100 min (Figure 3). The inhibitory effects remained even at 120 min after removal of CJX1 or CJX2 2.5 μmol/L from the medium (Figure 4). This amount suggested that the inhibitory effects of CJX1 and CJX2 on P-gp function was reversible and that the inhibitory effects of CJX1 on P-gp persisted longer compared with verapamil. The efflux constants in CJX1 and CJX2 10 μmol/L-treated groups was 0.0097 and 0.0127, respectively, and was lower than those in control group (0.0312) and verapamil-treated group (0.0131).

Table 1. Effect of CJX1 and CJX2 on the accumulation of Rh123 in rat brain microvessel endothelial cells (RBMEC) and human umbilical vein endothelial cells (HUVEC). n=3 experiments (each 4 wells). Mean±SD. $^cP<0.01$ *vs* control group. $^eP<0.05$ *vs* verapamil group.

Group/μmol·L^{-1}		Rh123/nmol·g^{-1} protein		
		RBMEC	HUVEC	Increasing rate/%
Control		68±10	315±39	
CJX1	1	91±6^c		34.1
	2.5	197±30^c		191.4
	5	282±44^c		316.5
	10	323±11^{ce}	310±28	377.1
CJX2	1	85±12^c		25.9
	2.5	161±31^c		137.8
	5	220±28^c		224.9
	10	282±44^c	320±19	317.2
Ver	10	269±50^c	320±53	297.3

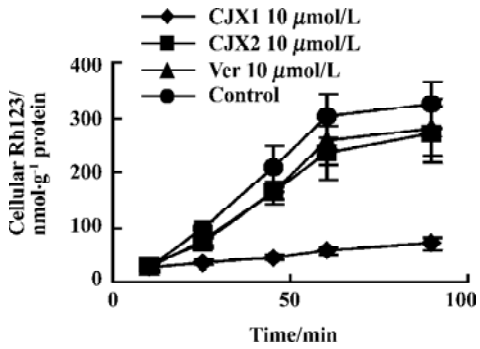

Figure 2. Effect of CJX1 and CJX2 on the uptake of Rh123 in rat brain microvessel endothelial cells. n=3 experiments (each 4 wells). Mean±SD.

Discussion

Beaulieu *et al* showed that P-gp was localized in the luminal membranes of RBMEC[15]. RBMEC was a valuable tool for the study of BBB permeability *in vitro*[13]; however, HUVEC was often used as a negative control and had no detectable P-gp expressions[16,17]. The efflux of fluorescent dye Rh123 was known to be P-gp-dependent and consequently was used extensively to determine the efflux rate from the cells expressing P-gp and to screen novel effective P-gp reversal agents[18].

The present study showed that before the RBMEC and HUVEC were exposed to Rh123, the amount of intracellular Rh123 in RBMEC was lower than that in HUVEC. After CJX1 and CJX2 treatment, intracellular accumulation of Rh123 was elevated greatly in RBMEC in a concentration-

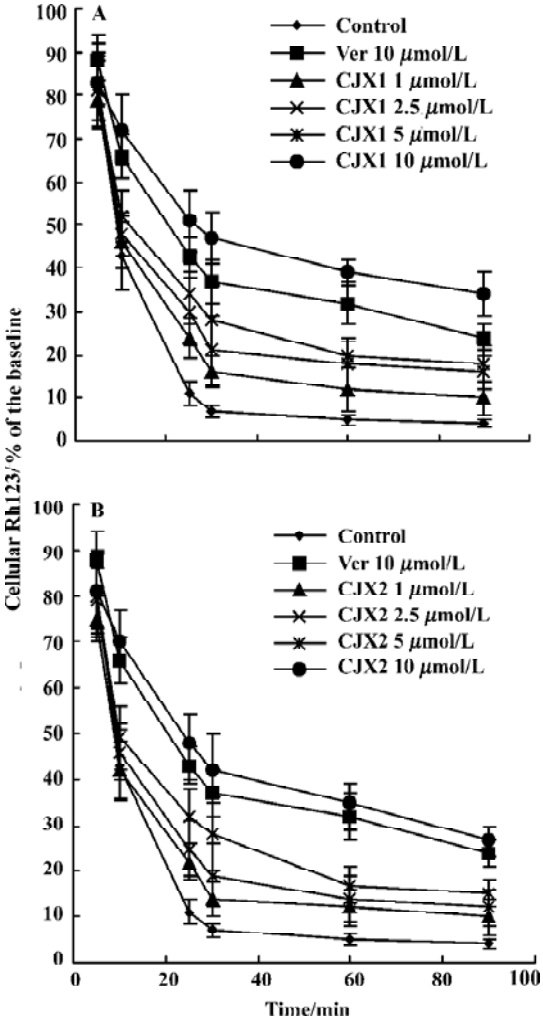

Figure 3. Effect of CJX1 (A) and CJX2 (B) on the efflux of Rh123 in rat brain microvessel endothelial cells. *n*=3 experiments (each 4 wells). Mean±SD.

dependent manner. But no increase was observed in HUVEC. The intracellular amounts of Rh123 in the CJX1 10 μmol/L-treated group were higher than those in the verapamil 10 μmol/L-treated group. CJX1 and CJX2 significantly enhanced the uptake of Rh123 over the uptake phase. The uptake of Rh123 by RBMEC was more rapid in the CJX1- and CJX2-treated group compared with verapamil-treated group. In contrast, CJX1 and CJX2 significantly reduced the efflux of Rh123. The efflux of Rh123 were slower in the CJX1- and CJX2-treated groups than in the verapamil-treated group. All the results indicated that CJX1 had more potent effect in inhibiting the P-gp-mediated transport of Rh123.

The amount of Rh123 was decreased and returned to the control level after washout of CJX1 and CJX2 at different

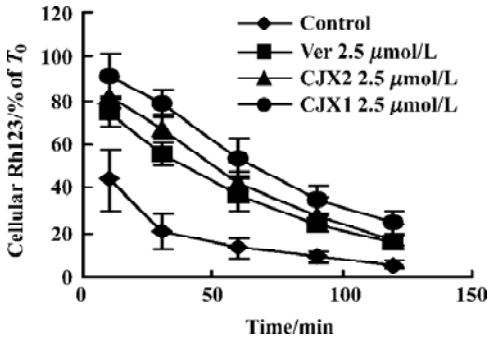

Figure 4. Persistence of activity of CJX1 and CJX2. *n*=3 experiments (each 4 wells). Mean±SD.

time points. This suggested that P-gp function recovered and the inhibitory effect of CJX1 and CJX2 on P-gp was reversible. The amount of Rh123 was less than 40% of basement at 60 min after washout of verapamil and CJX2. But in the CJX1-treated group, there was about 40% Rh123 in RBMEC at 90 min after washout of CJX1. This result showed that the inhibitory effect of CJX1 persisted longer than that of verapamil.

The inhibitory effect of CJX1 and CJX2 on P-gp function in RBMEC indicated that the two compounds may be able to reverse MDR mediated by P-gp. This study has been performed on doxorubicin-resistant human myelogenous leukemia (K562/DOX) cells in our laboratory and the results will be published. The effect of CJX1 and CJX2 on P-gp function *in vivo* will be observed in our laboratory in the near future.

In conclusion, CJX1 and CJX2 exhibited a potent effect on the inhibition of P-gp function *in vitro*. They may become candidates of the effective P-gp reversal agents.

References

1 Germann UA. P-glycoprotein-a mediator of multidrug resistance in tumour cells. Eur J Cancer 1996; 32A: 927–44.

2 Gottesman MM, Pastan I. Biochemistry of multidrug resistance mediated by the multidrug transporter. Annu Rev Biochem 1993; 62: 385–427.

3 Childs S, Ling V. The MDR superfamily of genes and its biological implications. Important Adv Oncol 1994; 21–36.

4 Elsinga PH, Hendrikse NH, Bart J, Vaalburg W, van Waarde A. PET studies on P-glycoprotein function in the blood-brain barrier: how it affects uptake and binding of drugs within the CNS. Curr Pharm Des 2004; 10: 1493–503.

5 Cisternino S, Rousselle C, Debray M, Scherrmann JM. *In vivo* saturation of the transport of vinblastine and colchicine by P-glycoprotein at the rat blood-brain barrier. Pharm Res 2003; 20: 1607–11.

6 Zhao YL, Du J, Kanazawa H, Sugawara A, Takagi K, Kitaichi K, *et al*. Effect of endotoxin on doxorubicin transport across blood-brain

barrier and P-glycoprotein function in mice. Eur J Pharmacol 2002; 445: 115–23.
7 Sakata A, Tamai I, Kawazu K, Deguchi Y, Ohnishi T, Saheki A, *et al*. *In vivo* evidence for ATP-dependent and P-glycoprotein-mediated transport of cyclosporin A at the blood-brain barrier. Biochem Pharmacol 1994; 48: 1989–92.
8 Twentyman PR. Modification of cytotoxic drug resistance by non-immuno-suppressive cyclosporins. Br J Cancer 1988; 57: 254–8.
9 Aszalos A, Thompson K, Yin JJ, Ross DD. Combinations of P-glycoprotein blockers, verapamil, PSC833, and cremophor act differently on the multidrug resistance associated protein (MRP) and on P-glycoprotein (Pgp). Anticancer Res 1999; 19: 1053–64.
10 Ohbayashi Y, Tsutamoto T, Sakaguchi T, Tanaka T, Kanamori T, Yokohama H, *et al*. Effect of an angiotensin II type 1 receptor blocker, valsartan, on neurohumoral factors in patients with hypertension: comparison with a long-acting calcium channel antagonist, amlodipine. J Cardiovasc Pharmacol 2003; 42 Suppl 1: S71–4.
11 Katoh M, Nakajima, M, Yamazaki H, Yokoi T. Inhibitory potencies of 1,4-dihydropyridine calcium antagonists to P-glycoprotein-mediated transport: comparison with the effects on CYP3A4. Pharm Res 2000; 17: 1189–97.
12 Abbott NJ, Hughes CC, Revest PA, Greenwood J. Development and characterization of a rat brain capillary endothelial culture: towards an *in vitro* blood-brain barrier. J Cell Sci 1992; 103: 23–37.
13 Fontaine M, Elmquist WF, Miller DW. Use of rhodamine 123 to examine the functional activity of P-glycoprotein in primary cultured brain microvessel endothelial cell monolayers. Life Sci 1996; 59: 1521–31.
14 Sarver JG, Klis WA, Byers JP, Erhardt PW. Microplate screening of the differential effects of test agents on Hoechst 33342, rhodamine 123, and rhodamine 6G accumulation in breast cancer cells that overexpress P-glycoprotein. J Biomol Screen 2002; 7: 29–34.
15 Beaulieu E, Demeule M, Ghitescu L, Beliveau R. P-glycoprotein is strongly expressed in the luminal membranes of the endothelium of blood vessels in the brain. Biochem J 1997; 326 (Pt 2): 539–44.
16 Zhu HJ, Liu GQ. Effect of E6, a novel calmodulin inhibitor, on activity of P-glycoprotein in purified primary cultured rat brain microvessel endothelial cells. Acta Pharmacol Sin 2003; 24: 1143–9.
17 He L, Liu GQ. Effects of various principles from Chinese herbal medicine on rhodamine123 accumulation in brain capillary endothelial cells. Acta Pharmacol Sin 2002; 23: 591–6.
18 Green LJ, Marder P, Slapak CA. Modulation by LY335979 of P-glycoprotein function in multidrug-resistant cell lines and human natural killer cells. Biochem Pharmacol 2001; 61: 1393–9.

Full-length article

Estrogen stimulates release of secreted amyloid precursor protein from primary rat cortical neurons via protein kinase C pathway[1]

Sun ZHANG[2], Ying HUANG[2], Yi-chun ZHU[2], Tai YAO[2,3,4]

[2]Department of Physiology and Pathophysiology; [3]State Key Laboratory for Medical Neurobiology, Shanghai Medical College of Fudan University, Shanghai 200032, China

Key words

Alzheimer disease; estrogen; amyloid precursor protein; estrogen receptors; protein kinase C

[1] Project supported by the National Natural Science Foundation of China (No 39970241).
[4] Correspondence to Prof Tai YAO.
Phn 86-21-6417-1179.
Fax 86-21-6417-1179 or 86-21-5423-7098.
E-mail tyao@shmu.edu.cn

Received 2004-09-24
Accepted 2004-11-19

doi: 10.1111/j.1745-7254.2005.00038.x

Abstract

Aim: To investigate the mechanism of the action of estrogen, which stimulates the release of secreted amyloid precursor protein α (sAPPα) and decreases the generation of amyloid-β protein (Aβ), a dominant component in senile plaques in the brains of Alzheimer's disease patients. **Methods:** Experiments were carried out in primary rat cortical neurons, and Western blot was used to detect sAPPα in a culture medium and the total amount of cellular amyloid precursor protein (APP) in neurons. **Results:** 17β-Estradiol (but not 17α-estradiol) and β-estradiol 6-(*O*-carboxymethyl) oxime: BSA increased the secretion of sAPPα and this effect was blocked by protein kinase C (PKC) inhibitor calphostin C, but not by the classical estrogen receptor antagonist ICI 182,780. Meanwhile, 17β-estradiol did not alter the synthesis of cellular APP. **Conclusion:** The effect of 17β-estradiol on sAPPα secretion is likely mediated through the membrane binding sites, and needs molecular configuration specificity of the ligand. Furthermore, the action of the PKC-dependent pathway might be involved in estrogen-induced sAPPα secretion.

Introduction

Alzheimer's disease (AD) is characterized by two major pathological lesions in the brain: intracellular neurofibrillary tangles and extracellular deposition of senile plaques composed mainly of amyloid-β protein (Aβ)[1]. Efforts have been made to explore the relative contribution of plaques and tangles to the pathogenesis of AD. In recent years, the amyloid hypothesis has been accepted by many researchers, who regard accumulation of Aβ in the brain as the primary factor driving AD pathogenesis[2,3]. Aβ is derived from a larger ubiquitous transmembrane protein, amyloid precursor protein (APP). APP is cleaved through at least two different pathways: α-secretase pathway and β-secretase pathway. Through the β-secretase pathway, which involves β-secretase and γ-secretase, APP is cleaved into two fragments: sAPPβ and Aβ. Alternatively, through the α-secretase pathway, which involves α-secretase and γ-secretase, APP is cleaved within the domain of amyloidogenic Aβ, thus precluding the generation of Aβ and producing non-amyloidogenic secreted APP (sAPPα) and p3 (Aβ 17-40/42). Several studies demonstrated that the increased activity of the α-secretase pathway led to a decrease in the activity of the β-secretase pathway[4].

Estrogen is considered as a neurotropic and neuro-protective agent[5]. Estrogen replacement therapy (ERT) in post-menopausal women is related with a reduced risk and delayed onset of AD[6]. It is therefore worthwhile investigating whether estrogen produces its neuroprotective effect through the regulation of APP processing[7].

There are several lines of evidence supporting this hypothesis. In cell culture, the addition of estrogen resulted in increase in the production of sAPPα and a decrease in Aβ[8,9]. In animal models, estrogen treatment prevented the accumulation of Aβ in the brain of guinea pigs and transgenic mutant APP/PS1-expressing mice[10,11]. It was suggested that the increased release of sAPPα by estrogen was mediated through the phosphorylation of extracellular-regulated kinase 1 and 2 (ERK1/2)[12]. However, the precise mechanism of the neuroprotective effects of estrogen remains to be fur-

ther investigated. The purposes of the present study are to explore: (1) whether the effect of estrogen on sAPPα release is mediated through the membrane sites or the nuclear receptors; (2) whether the effect of estrogen depends on its molecular configuration specificity; (3) whether protein kinase C (PKC) is involved in the regulation of APP processing; and (4) whether classical estrogen receptor antagonist ICI 182 780 blocks the sAPPα secretion induced by estrogen.

Materials and methods

Cells and cell culture procedures Cortical neurons from 1-d postnatal Sprague-Dawley female or male rats were prepared as described previously[13]. Cells were plated in DMEM (Life Technologies, Gaithersburg, Germany) containing 10% fetal bovine serum (GIBCO) in poly-*L*-lysine-coated (0.1 g/L; Sigma, St Louis, USA) 100-mm dishes (approximately 1.8×10^7 cells per dish) under standard conditions (37 ºC, 5% CO_2). On the following day, the medium was replaced with phenol red-free Neurobasal Medium (GIBCO), supplemented with B27 (GIBCO), which produced cultures with >99% neuronal composition[14]. The medium was replaced every 3 d. On the ninth day, the medium was replaced with phenol red-free Neurobasal Medium, supplemented with N_2 (10% volume as described in guideline, GIBCO, Rockville, USA). Estrogen and/or other chemicals were added to the dishes. The chemicals used were 17β-estradiol (Sigma) dissolved in dimethyl sulfoxide (Me_2SO), 17β-estradiol (Sigma) dissolved in Me_2SO; β-estradiol 6-(*O*-carboxymethyl) oxime: BSA (Sigma) dissolved in PBS, β-estradiol 17-hemisuccinate: BSA (Sigma, St Louis, USA) dissolved in PBS, ICI 182, 780 (TOCRIS) dissolved in Me_2SO, and PKC inhibitor calphostin C (Calbiochem, La Jolla, USA) dissolved in Me_2SO. After a 12-h incubation, the medium was collected for measurement of sAPPα. The medium was then centrifuged at 4000×*g* for 10 min to remove the cellular debris. The cleared supernatant was concentrated with 30 kDa pore size Amicon Ultra (Millipore Co, Billerica,USA) for analysis. Cell monolayers were washed three times with ice-cold PBS and lysed in 1×SDS loading buffer with protease inhibitors for 10 min on ice. The cell lysates were boiled for 5 min and then centrifuged for 10 min at 14 000×*g*. The proteins were stored at -20 ºC.

Western blot analysis The protein concentrations were determined by BCA protein quantitative analysis kit (Shenergy Biocolor BioScience & Technology Company). An equal amount of protein from the medium was subjected to 7%–10% gradient SDS-poly-acrylamide gel electrophoresis (PAGE) (Amresco). After electrophoretic separation, proteins were transferred onto a PVDF membrane and the polyclonal antibody Rat A Beta (1:1000, Signet), which is specific for Ab 3-16, was used to detect sAPPα. The efficiency of transfer was confirmed by staining the membrane with Ponceau S. The Ponceau S stain was then removed from the membrane by washing in PBST. Cellular APP was detected using monoclonal antibody 22C11 (1:200, Roche), which is specific for the amino terminus of APP. The amount of β-actin on the same membrane, which was determined by polyclonal antibody β-actin (1:1000, Santa Cruz), was taken as control. Antibody binding was detected by counter-staining with horseradish peroxidase-conjugated antibodies (1:1000, Calbiochem) and visualized using an ECL-detection kit (Pierce). The relative intensity of immunoreactive bands on the exposed film was quantified by a computer-assisted densitometry program (Smart view, Life Science Research Products and System Engineering).

Statistics Data from sAPPα measurement were analyzed by one-way ANOVA followed by Tukey *post hoc* test (SPSS software). Student's *t*-test was used to analyze the data of cellular APP content. $P<0.05$ was considered to be statistically significant. Each experiment was repeated three to four times to verify the reproducibility of the results.

Results

Effect of 17β-estradiol on sAPPα secretion and cellular APP content Primary cortical neurons were treated with 10, 100, and 1000 nmol/L 17β-estradiol. Figure 1 shows that a 12-h treatment with increasing concentrations of 17β-estradiol

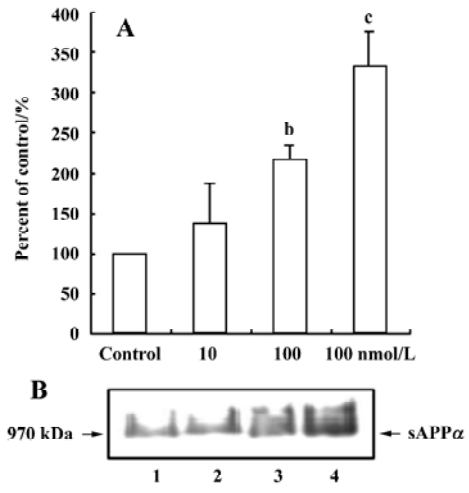

Figure 1. Effect of 17β-estradiol on sAPPα secretion from the rat cortical neurons. (A) Effect of 17β-estradiol of various concentrations. n=3. Mean±SD. $^bP<0.05$, $^cP<0.01$ *vs* control. (B) Electrophoresis results from a representative experiment. (1) Control; (2) 10 nmol/L 17β-estradiol; (3) 100 nmol/L 17β-estradiol; (4) 1000 nmol/L 17β-estradiol.

resulted in a significant dose-dependent increase in sAPPα release into the medium as compared with the sAPPα level in the control. 17β-Estradiol (100 nmol/L) did not alter the total cellular APP content in cultured cortical neurons (Figure 2).

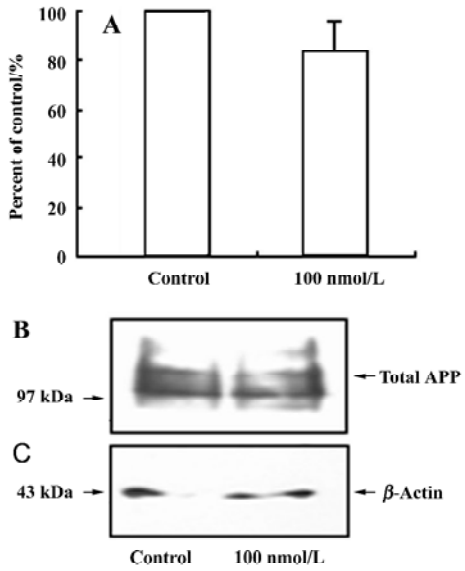

Figure 2. Effect of 17β-estradiol on total cellular APP content in the cultured rat cortical neurons. (A) Cellular APP content with or without 17β-estradiol administration. n=3. Mean±SD. (B) Results from a representative experiment for total cellular APP. (C) β-actin on the same film as (B).

Effect of β-estradiol 6-(*O*-carboxymethyl) oxime: BSA on the release of sAPPα To investigate whether the membrane-impermeable estradiol-BSA conjugates, β-estradiol 6-(*O*-carboxymethyl) oxime: BSA and β-estradiol 17-hemisuccinate: BSA, exerted similar actions on sAPPα secretion as 17β-estradiol, neurons were incubated with these two agents. After a 12-h incubation, the supernatant was collected for measurement of sAPPα. β-Estradiol 6-(*O*-carboxymethyl) oxime:BSA (1000 nmol/L) increased sAPPα secretion, although the magnitude of the effect was smaller than that of 1000 nmol/L 17β-estradiol. Estradiol 17-hemisuccinate: BSA (1000 nmol/L) also stimulated sAPPα secretion, but the difference was not statistically significant (Figure 3).

Effect of 17α-estradiol on the release of sAPPα In order to investigate whether estradiol stimulates sAPPα secretion depending on its configuration specificity, we treated the neurons with 100 nmol/L, 1000 nmol/L 17α-estradiol and 100 nmol/L 17β-estradiol. Twelve hours later, the supernatant was collected and concentrated for Western blot analysis.

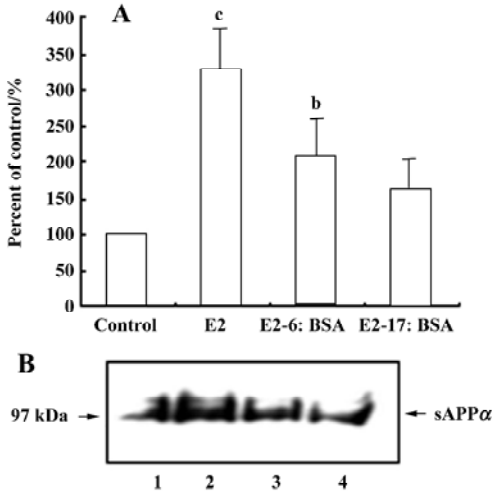

Figure 3. (A) Effects of 17β-estradiol(E2), β-estradiol 6-(*O*-carboxymethyl) oxime:BSA(E2-6:BSA), and β-estradiol 17-hemisuccinate:BSA (E2-17:BSA), respectively, on the release of sAPPα. n=4. Mean±SD. $^bP<0.05$, $^cP<0.01$ *vs* control. (B) Electrophoresis results from a representative experiment. (1) Control; (2) 17β-estradiol; (3) β-estradiol 6-(*O*-carboxymethyl) oxime:BSA; (4) β-estradiol 17-hemisuccinate:BSA.

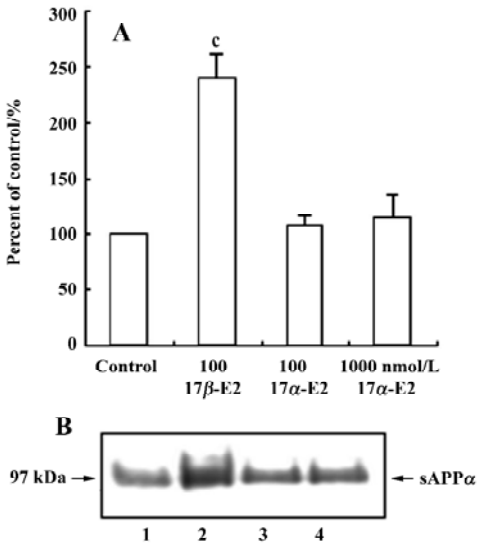

Figure 4. Effect of 17α-estradiol on sAPPα release from rat cortical neurons. (A) Effects of 100, 1000 nmol/L 17α-estradiol and 100 nmol/L 17β-estradiol on the release of sAPPα. n=3. Mean±SD. $^bP<0.05$, $^cP<0.01$ *vs* control.

The results showed that, in contrast to 17β-estradiol, 17α-estradiol did not alter sAPPα secretion (Figure 4).

Effect of PKC inhibitor on 17β-estradiol-induced sAPPα secretion Calphostin C, a PKC inhibitor, was used to investigate the role of PKC on 17β-estradiol-induced secretion of

sAPPα. Incubation with calphostin C (250 nmol/L) alone for 12 h did not change the sAPPα secretion. However, when the neurons were co-treated with calphostin C (250 nmol/L) and 17β-estradiol (100 nmol/L) for 12 h, the stimulatory

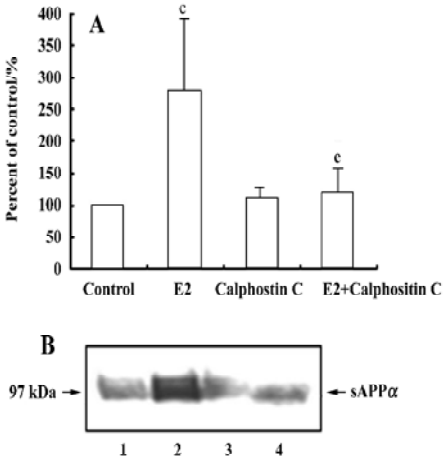

Figure 5. Involvement of PKC in 17β-estradiol effect on sAPPα secretion. (A) Effects of 17β-estradiol, calphostin C, and 17β-estradiol+calphostin C on the release of sAPPα, respectively. n=3. Mean±SD. ^cP<0.01 *vs* control. ^eP<0.05 *vs* E2. (B) Results from a representative experiment. (1) control; (2) 17β-estradiol; (3) calphostin C; (4) 17β-estradiol+calphostin C.

effect of 17β-estradiol on sAPPα secretion disappeared (Figure 5).

Effect of estrogen receptor antagonist on the 17β-estradiol-induced sAPPα secretion To explore whether activation of the classical estrogen receptors is involved in 17β-estradiol stimulating sAPPα secretion, rat cortical neurons were treated with 17β-estradiol (100 nmol/L), estrogen receptor antagonist ICI 182 780 (1 μmol/L) alone, and 17β-estradiol (100 nmol/L) together with ICI 182 780 (1 μmol/L). The results showed that ICI 182 780 alone produced no alteration in sAPPa secretion, while simultaneous administration of ICI 182 780 and 17β-estradiol resulted in a significant increase in sAPPα secretion, similar to the effect of 17β-estradiol (Figure 6).

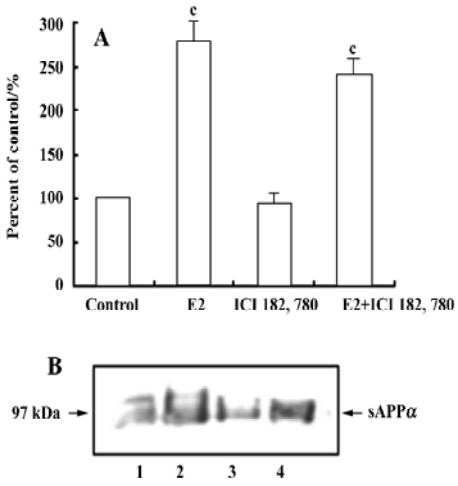

Figure 6. No antagonism by ICI 182 780 against the 17β-estradiol-induced sAPPα secretion. (A) Effects of 100 nmol/L 17β-estradiol, 1 μmol/L ICI 182 780 alone, and 100 nmol/L 17β-estradiol+1 μmol/L ICI 182 780 on the release of sAPPα. n=3. Mean±SD. ^cP<0.01 compared with the control. (B) Results from a representative experiment. (1) control; (2) 17β-estradiol; (3) ICI 182 780; (4) 17β-estradiol+ICI 182 780.

Discussion

It appears that ERT prevents the onset of AD, but is not an effective treatment for AD[6]. However, recent clinical studies revealed that ERT brought beneficial as well as adverse effects[15]. Therefore, it is important to elucidate the mechanisms of the neuronal action of estrogen and to develop new drugs that retain the beneficial effects, but do not have the side effects of estrogen[16]. It is generally accepted that the effect of estrogen in preventing AD is mediated through regulating APP processing[2,7]. Our study provides evidence that estrogen increases sAPPα release without changing the total cellular APP content in cultured rat cortical neurons. Because the up-regulation of the α-secretase pathway mediating sAPPα production occurs within the same time course as down-regulation of the β-secretase pathway[4], it is reasonable to suggest that estrogen could reduce the generation of Aβ secondary to increases in sAPPα secretion and, in turn, exert its neuroprotective functions.

In addition to classical intracellular estrogen receptor, estrogen binding sites are also present on the cell membrane[5]. The actions of estrogen on its target tissues include a long-term "genomic" action mediated by intracellular estrogen receptors, and a rapid action through membrane binding sites that modulate a diversity of intracellular signal transduction pathways[17]. Therefore, it is interesting to know whether the estradiol-induced release of sAPPα is brought about through the mediation of nuclear or membrane binding sites. Our data clearly demonstrated that β-estradiol 6-(*O*-carboxymethyl) oxime: BSA, a membrane-impermeable estradiol conjugate[18,19], produced a similar effect like estrogen to increase the release of sAPPα, suggesting the involvement of the membrane binding sites. Furthermore, the estrogen receptor antagonist ICI 182 780 did not affect the effect of estrogen, suggesting that the classical estrogen receptors ERα or ERβ

were not involved in the above-mentioned estradiol effect. The role of classical estrogen receptors in the neuronal effect of estrogen is controversial. Some studies showed that the estrogen-induced rapid intracellular signal transduction cascades were unaffected by the classical estrogen receptor antagonists[18,20,21], such as tamoxifen and ICI 182 780, in cell lines that did or did not express estrogen receptors ERα and ERβ; while other studies showed that the rapid intracellular signal transduction was blocked by the classical estrogen receptor antagonists[13,22–24]. The reason for the difference in these studies is unknown, but it is probably a result of the different cells the researchers used and different parameters chosen for study, which appear through different membrane binding sites. The results of the present study suggest that the structure of the membrane binding sites responsible for the estradiol-induced sAPPα secretion is probably different from that of the classical estrogen receptors.

In present study, 17β-estradiol and its two BSA conjugates produced effects with different potencies. One of the possible explanations is that the combination of BSA alters the dimensional configuration of estradiol and thus changes its affinity for the membrane binding sites. In β-estradiol 6-(*O*-carboxymethyl) oxime: BSA, BSA attaches to estradiol at position 6, that is, on the "bottom" of the structure of estradiol, making the "top" (the C and D rings) of estradiol accessible. In contrast, in β-estradiol 17-hemisuccinate: BSA, BSA attaches to position 17 on the "top" of estradiol, making the "bottom" (the A and B rings) of the estradiol accessible. The difference in the configuration between the two conjugates can change the binding ability to the membrane sites and therefore change the effect in regulating sAPPα secretion. It is possible that a small amount of estradiol might dissociate from the conjugates, however, some studies reported that a very small amount of estradiol that dissociated from the conjugates did not exert effects on estrogen receptors[25].

Behl *et al* indicated that both 17β-estradiol and its isomer 17α-estradiol exhibited neuroprotective actions against oxidative stress[26]. 17α-estradiol does not bind to the nuclear ER, but 17α-estradiol was reported to stimulate phosphorylation of ERK1/2 in immature rat neurons[27]. Our present study showed that 17α-estradiol was unable to regulate the APP processing. Therefore, the mechanism for anti-oxidation effects of estrogens might be different from those of regulating APP metabolism.

Estrogen stimulates a rapid Ca^{2+} release from the intracellular calcium stores[28]. Yeon *et al* indicated that PKCε played an important role in modulating APP and that overexpression of the PKCεV1 region, which specifically binds to the receptor for activated C-kinase (RACK), blocked the phorbol ester-induced enhancement of sAPPα secretion[29]. Recently, Beyer *et al* reported that estrogen activated G-protein-coupled phospholipase C, leading to the release of Ca^{2+} from intracellular stores and the activation of PKC[30]. In the present study, we demonstrated that calphostin C prevented the increase of sAPPα secretion induced by 17β-estradiol, indicating the involvement of PKC.

In summary, our data indicate that, in cultured rat cortical neurons, estrogen stimulates sAPPα secretion through mechanisms involving membrane binding sites and the activation of PKC. The effects of estradiol are not mediated by classical ER. The details of the estrogen membrane binding sites and the related signaling pathways remain to be further studied.

Acknowledgement

We would like to express our sincere gratitude to Dr Xiliang ZHA, Prof Yu HUANG, and Prof Li-min LU for their helpful suggestions and critical advices; and to Mr Zhen XU, Ms Bei FAN, and Yan-xia WANG for their assistance in Western blot performance.

References

1 Hardy J. Amyloid, the presenilins and Alzheimer's disease. Trends Neurosci 1997; 4: 154–9.
2 Hardy J, Selkoe DJ. The amyloid hypothesis of Alzheimer's disease: progress and problems on the road to therapeutics. Science 2002; 297: 353–6.
3 Hardy JA, Higgins GA. Alzheimer's disease: the amyloid cascade hypothesis. Science 1992; 256: 184–5.
4 Evin G, Weidemann A. Biogenesis and metabolism of Alzheimer's disease Aβ amyloid peptides. Peptides 2002; 23: 1285–97.
5 Garcia-Segura LM, Azcoitia I, DonCarlos LL. Neuroprotection by estradiol. Prog Neurobiol 2001; 63: 29–60.
6 Owens CT. Estrogen replacement therapy for Alzheimer disease in postmenopausal women. Ann Pharmacother 2002; 36: 1273–6.
7 Gandy S, Duff K. Post-menopausal estrogen deprivation and Alzheimer's disease. Exp Gerontol 2000; 35: 503–11.
8 Jaffe AB, Toran-Allerand CD, Greengard P, Gandy SE. Estrogen regulates metabolism of Alzheimer amyloid beta precursor protein. J Biol Chem 1994; 269: 13065–8.
9 Xu H, Gouras GK, Greenfield JP, Vincent B, Naslund J, Mazzarelli L, *et al*. Estrogen reduces neuronal generation of Alzheimer beta-amyloid peptides. Nat Med 1998; 4: 447–51.
10 Petanceska SS, Nagy V, Frail D, Gandy S. Ovariectomy and 17β-estradiol modulate the levels of Alzheimer's amyloid β peptides in brain. Neurology 2000; 54: 2212–7.
11 Zheng H, Xu H, Uljon SN, Gross R, Hardy K, Gaynor J, *et al*. Modulation of A (beta) peptides by estrogen in mouse models. J Neurochem 2002; 80: 191–6.
12 Manthey D, Heck S, Engert S, Behl C. Estrogen induces a rapid secretion of amyloid precursor protein via the mitogen-acti-

vated protein kinase pathway. Eur J Biochem 2001; 268: 4285–91.
13 Singer CA, Figueroa-Masot XA, Batchelor RH, Dorsa DM. The mitogen-activated protein kinase pathway mediates estrogen neuroprotection after glutamate toxicity in primary cortical neurons. J Neurosci 1999; 19: 2455–63.
14 Brewer GJ, Torricelli JR, Evege EK, Price PJ. Optimized survival of hippocampal neurons in B27-supplemented neurobasal, a new serum-free medium combination. J Neurosci Res 1993; 35: 567–76.
15 Couzin J. Estrogen research. The great estrogen conundrum. Science 2003; 302: 1136–8.
16 Wickelgren I. Estrogen research. Brain researchers try to salvage estrogen treatments. Science 2003; 302: 1138–9.
17 Belcher SM, Zsarnovszky A. Estrogenic actions in the brain: estrogen, phytoestrogens, and rapid intracellular signaling mechanisms. J Pharmacol Exp Ther 2001; 299: 408–14.
18 Beyer C, Karolczak M. Estrogenic stimulation of neurite growth in midbrain dopaminergic neurons depends on cAMP/protein kinase A signaling. J Neurosci Res 2000; 59: 107–16.
19 Moats RK, Ramirez VD. Electron microscopic visualization of membrane-mediated uptake and translocation of estrogen-BSA: colloidal gold by hep G2 cells. J Endocrinol 2000; 166: 631–47.
20 Morales A, Diaz M, Ropero AB, Nadal A, Alonso R. Estradiol modulates acetylcholine-induced Ca^{2+} signals in LHRH-releasing GT1-7 cells through a membrane binding site. Eur J Neurosci 2003; 18: 2505–14.
21 Singh M, Setalo GJR, Guan X, Frail DE, Toran-Allerand CD. Estrogen-induced activation of the mitogen-activated protein kinase cascade in the cerebral cortex of estrogen receptor-alpha knock-out mice. J Neurosci 2000; 20: 1694–700.
22 Mabuchi S, Ohmichi M, Kimura A, Nishio Y, Arimoto-Ishida E, Yada-Hashimoto N, *et al*. Estrogen inhibits paclitaxel-induced apoptosis via the phosphorylation of apoptosis signal-regulating kinase 1 in human ovarian cancer cell lines. Endocrinology 2004; 145: 49–58.
23 Sato K, Matsuki N, Ohno Y, Nakazawa K. Estrogens inhibit l-glutamate uptake activity of astrocytes via membrane estrogen receptor alpha. J Neurochem 2003; 86: 1498–505.
24 Guerra B, Diaz M, Alonso R, Marin R. Plasma membrane oestrogen receptor mediates neuroprotection against beta-amyloid toxicity through activation of Raf-1/MEK/ERK cascade in septal-derived cholinergic SN56 cells. J Neurochem 2004; 91: 99–109.
25 Stevis PE, Deecher DC, Suhadolnik L, Mallis LM, Frail DE. Differential effects of estradiol and estradiol-BSA conjugates. Endocrinology 1999; 140: 5455–8.
26 Behl C, Skutella T, Lezoualc'h F, Post A, Widmann M, Newton CJ, *et al*. Neuroprotection against oxidative stress by estrogens: structure-activity relationship. Mol Pharmacol 1997; 51: 535–41.
27 Wong JK, Le HH, Zsarnovszky A, Belcher SM. Estrogens and ICI182, 780 (Faslodex) modulate mitosis and cell death in immature cerebellar neurons via rapid activation of p44/p42 mitogen-activated protein kinase. J Neurosci 2003; 23: 4984–95.
28 Beyer C, Raab H. Nongenomic effects of oestrogen: embryonic mouse midbrain neurones respond with a rapid release of calcium from intracellular stores. Eur J Neurosci 1998; 10: 255–62.
29 Yeon SW, Jung MW, Ha MJ, Kim SU, Huh K, Savage MJ, *et al*. Blockade of PKC epsilon activation attenuates phorbol ester-induced increase of alpha-secretase-derived secreted form of amyloid precursor protein. Biochem Biophys Res Commun 2001; 280: 782–7.
30 Beyer C, Ivanova T, Karolczak M, Küppers E. Cell type-specificity of nonclassical estrogen signaling in the developing midbrain. J Steroid Biochem Mol Biol 2002; 81: 319–25.

Full-length article

Visual recognition memory is related to basic expression level of NMDA receptor NR1/NR2B subtype in hippocampus and striatum of rats[1]

Shu-jun XU, Zhong CHEN, Li-jun ZHU, Hai-qing SHEN, Jian-hong LUO[2]

Department of Neurobiology, Zhejiang University School of Medicine, Hangzhou 310031, China

Key words

N-methyl-*D*-aspartate receptors; NR1 subunit; NR2B subunit; Western blotting; visual recognition memory

[1] Project supported by Key National Basic Research Program of China (No G2002CB-713808), and Outstanding Cross-Century Faculty Grant of the Ministry of Education of China, the National Natural Science Foundation of China (No 30270436 and 30371638).

[2] Correspondence to Prof Jian-hong LUO.
Phn 86-571-8721-7268.
Fax 86-571-8721-7044.
E-mail luojianhong@zju.edu.cn

Received 2004-08-11
Accepted 2004-11-15

doi: 10.1111/j.1745-7254.2005.00032.x

Abstract

Aim: To examine the basic expression levels of *N*-methyl-*D*-aspartate (NMDA) receptor NR1 and NR2B subunits in six brain regions of Sprague-Dawley (SD) rats with different visual recognition memory. **Methods:** Rats were tested by a novel-object-recognition model and grouped into the high and the low visual recognition memory groups. The expression levels of NR1 and NR2B subunits in the cortex, hippocampus, striatum, amygdala, diencephalon, and olfactory bulb were measured by semiquantitative immunoblotting. **Results:** The NR1 and NR2B subunit protein levels in the hippocampus of the high visual recognition memory group were 35.9% ($P<0.01$) and 53.4% ($P<0.05$) higher respectively than those in the low group. In addition, the NR2B level in the striatum in the high visual recognition memory group was 25.0% ($P<0.05$) higher than that in the low one. However, no significant difference was found in the levels of the subunits between the two groups in other brain regions. **Conclusion:** The visual recognition memory in rats is related to the basic expression level of NMDA receptor NR1/NR2B subtype in the hippocampus and striatum.

Introduction

N-Methyl-*D*-aspartate (NMDA) receptors, the major ionotropic glutamate receptors in the central nervous system, play key roles in excitatory synaptic transmission and plasticity, and are involved in many physiological and pathological processes[1,2]. NMDA receptors are mainly composed of NR1 subunit and NR2A, NR2B, NR2C, or NR2D subunit, respectively, and the different subunit combinations form different NMDA receptor subtypes with distinct functional properties[3,4].

It has been demonstrated that NMDA receptors are involved in long-term synaptic plasticity and certain forms of learning and memory[5–8]. For example, numerous data indicate that NMDA receptor activity and NMDA receptor-dependent synaptic plasticity in the hippocampus are crucial for spatial recognition memory[7,8]. However, there have been a few reports about the role of NMDA receptors in visual recognition memory[9–12], and there are some discrepant or even contradictory results in the visual recognition memory with regard to different doses of NMDA receptors antagonist, and animal species. Furthermore, most of those findings were mainly obtained from animals with specific brain region injuries, pharmacological manipulated animals or transgenic mice with one of NMDA receptor subunits abnormally expressed. Little is known whether the basic expression levels of NMDA receptors is related to different visual recognition memory in normal adult rats.

Therefore, the objective of our studies was to examine the relationship between the basic expression levels of NR1 and NR2B subunits in six specific regions (cortex, hippocampus, striatum, amygdala, diencephalons, and olfactory bulb) and visual recognition memory in rats.

Materials and methods

Animals All experiments were carried out in accordance with the National Institutes of Health Guide for the Care and Use of Laboratory Animal. The animals used in this study were 6-week old male Sprague-Dawley (SD) rats, weighing 175–190 g (Grade II, Certificate No 22-9601018, Experimental Animal Center, Zhejiang University, China), maintained in

an air-conditioned room with controlled temperature (22–26 ºC) and humidity (40%–70%), housed in cages with a 12-h light/dark cycle (lights on from 8:00 AM–20:00 PM) with food and water available. Experiments were carried out each day between 10:00 AM–17:00 PM.

Novel object recognition task Rat was individually habituated to an open-field box (50 cm×50 cm×30 cm high) for 3 d. During training sessions, two novel objects were placed into the open field and the animal was allowed to explore for 5 min. The time spent for exploring each object was recorded. During retention tests, the animal was placed back into the same box after a 24-h delay, in which one of the objects used during training was replaced by a novel object, and allowed to explore freely for 5 min. Behaviour was considered exploratory when an animal was touching or directed towards the object at a distance ≤2 cm with its nose; while behaviour was not considered exploratory when an animal was turning around or sitting on the object. To avoid interference effect of the olfactory cue due to scent traces left, after each experiment, both the objects and the arena were scraped by 10% ethanol. The preference index, a ratio of the amount of time spent exploring any one of the two objects (training session) or the novel one (retention session) over the total time spent exploring both objects, was used to measure recognition memory. All 40 male SD rats were ranked by the preference index. From these, eight superior and eight inferior rats were used as high visual recognition memory group and low visual recognition memory group, respectively, in the present study.

Preparation of tissue The rats were killed by decapitation and the brains were quickly removed. The brains were dissected on ice into six specific regions (cortex,hippocampus, striatum, amygdala, diencephalon, and olfactory bulb), and homogenized twice in 100 volumes (100×wet weight) of ice-cold 10 mmol/L Tris-HCl (pH 7.4) containing 320 mmol/L sucrose with a Tissuemizer (Heidolth DIA×900) at speed 5 for 10 s with a 20 s interval between bursts. The tissue homogenate was centrifuged at 700×*g* for 10 min at 4 ºC. The supernatant was collected and centrifuged at 37 000×*g* for 40 min at 4 ºC. This high-speed pellet was resuspended in 10 mmol/L Tris-HCl (pH 7.4). Protein concentrations were determined using Folin phenol reagent with bovine serum albumin as a standard.

Semiquantitative Western blot Sodium dodecyl sulfate-polyacrylamide gel electrophoresis (SDS-PAGE) and transfer of proteins to nitrocellulose membranes were performed according to conventional methods. The denatured membrane proteins were separated on 7.5% polyacrylamide gels and transferred to nitrocellulose membranes in transfer buffer (Tris 25 mmol/L, glycine 192 mmol/L, 20% methanol and 0.05 % SDS, pH 8.3). The membranes were incubated with a blocking buffer of 5% non-fat dry milk in TBST (Tris-HCl 20 mmol/L, NaCl 140 mmol/L, 0.1% Tween-20, pH 7.4) at room temperature for 1 h. The membranes were then incubated with anti-NR1, and anti-NR2B antibodies (1 g/L) in blocking buffer overnight at 4 ºC. After several washes with TBST, the membranes were incubated with horseradish peroxidase-conjugated secondary antibody in blocking buffer for 1 h at room temperature. Following washes for 20 min with four intermediate changes with TBST, proteins were visualized with enhanced chemiluminescence. The resulting film was scanned and analyzed using a laser densitometer and GelScan XL software (Pharmacia LKB). In order to make different gel samples evaluable, every gel was run with three lanes of the same cortex proteins as a standard[13,14].

Statistical analysis All results were expressed as mean± SD. Differences were analyzed by group comparisons *t*-test with Mann-Whitney Test by SPSS 11.0 software. $P<0.05$ was considered statistically significant.

Results

Novel object recognition task The preference indexes for the high visual recognition memory group and the low visual recognition memory group were summarized in Figure 1. During the training sessions, no significant difference was found in the exploratory preference between the two groups (0.43±0.12 *vs* 0.49±0.11, $P>0.05$). During the retention sessions, the exploratory preference of the high visual recognition memory group was significantly higher than that of the low one ($P<0.01$).

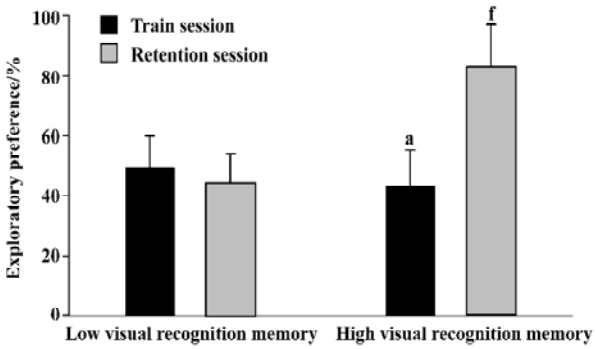

Figure 1. Exploratory preference of rats with different visual recognition memory during the training session and the retention session in the novel-object-recognition task. $n=8$. Mean±SD. $^{a}P>0.05$ *vs* the training session of the group with low visual recognition memory. $^{f}P<0.01$ *vs* the retention session of the group with low visual recognition memory.

Relationship between the basic expression level of NR1 subunit and visual recognition memory in rats The protein level of NR1 subunit in the hippocampus in the high visual recognition memory group was 35.9% higher than that in the low group (1.89±0.18 *vs* 1.39±0.39, $P<0.01$). However, no significant difference was found in the protein levels of NR1 subunit in the cortex, striatum, amygdala, diencephalon and olfactory bulb of rats between the two groups (Figure 2).

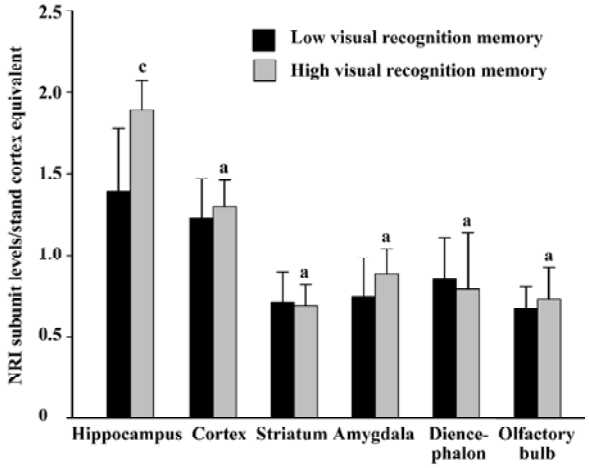

Figure 2. Relative expression levels of NR1 subunits in six brain regions in rats with different visual recognition memory. $n=8$. Mean±SD. $^aP>0.05$, $^cP<0.01$ *vs* the group with low visual recognition memory.

Relationship between basic expression level of NR2B subunit and visual recognition memory in rats As shown in Figure 3, the protein level of NR2B subunit in the hippocampus in the high visual recognition memory group was 53.3% higher than that in the low group (2.04±0.22 *vs* 1.33±0.57, $P<0.05$). In addition, the NR2B level in the high one was 25.0% higher than that in the low group in the striatum ($P<0.05$). While, no significant difference was found in the protein levels of NR2B subunit in other brain regions between the two groups ($P>0.05$).

Discussion

In the present study, we observed that both NR1 and NR2B subunits in the hippocampus in the high visual recognition memory group were remarkably higher than those in the low group. So the NMDA receptor NR1/NR2B subtype is higher in the high visual recognition memory group, although it is unclear whether there is any difference in the basic expression levels of the other subtypes of NMDA

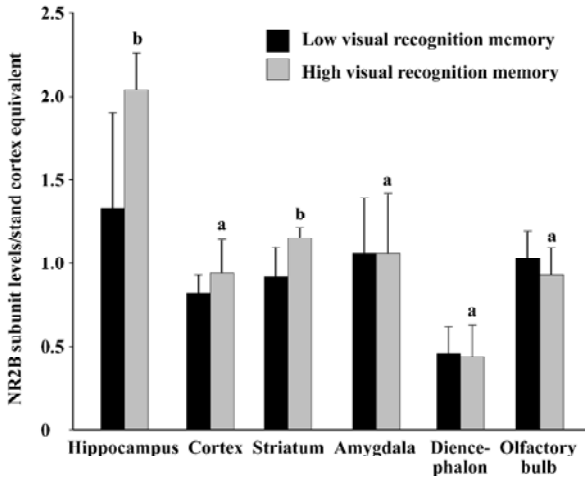

Figure 3. Relative expression levels of NR2B subunits in six brain regions in rats with different visual recognition memory. $n=8$. Mean±SD. $^aP>0.05$, $^bP<0.05$ *vs* the group with low visual recognition memory.

receptors. The result is consistent with the previous studies, which found that the transgenic mice overexpressing NR2B subunit in the forebrains exhibited an enhancement of novel -object-recognition memory[10], and the CA1-specific NR1 subunit knockout mice exhibited impairment in object recognition[15]. Therefore, our data provided more evidence *in vivo* to support the concept that NMDA receptors in the hippocampus are involved in visual recognition memory.

Previous studies showed that lesions to the perirhinal, postrhinal cortex and associated structures induced deficits in the ability to recognize single objects[16,17], and that NMDA receptor blockade in the perirhinal cortex impaired object discrimination in rats[18]. It seems that NMDA receptors in the cortex are related to visual recognition memory. However, in our study, no change in the basic expression levels of NR1 and NR2B subunits in the cortex was found between the groups with different visual recognition memory. Quinlan *et al* also reported that the NR2B subunit level in the visual cortex remained unchanged by visual experience[19]. The explanation for these converse results might be that the cortical coding of object recognition decays quickly and is not sufficient for maintaining information about objects across longer retention intervals (eg 24 h)[20]. It is also possible that the NMDA receptor NR2B subunit in some sub-regions of the cortex is related to visual memory. So our results at least suggest that the basic expression levels of NR1 and NR2B subunits in the cortex correlated less with visual recognition memory when a 24 h retention interval was imposed.

The striatum is a brain region involved in procedural

memory and diverse forms of implicit memory[21,22]. It is well known that glutamatergic input from the cortex to the striatum is critical for striatal learning[23] and NR2B subunit in the striatum is correlated with water maze performance in the inferior group of the aged rats[24]. Our results here provided more evidences that the basic expression level of NR2B subunit in the striatum was also correlated with visual recognition memory.

The novel-object-recognition task was used in this study, which is based on the spontaneous preference that animals display for novel objects. This task is considered to need only "familiarity judgment" as to whether the objects presented in the choice phase are novel or familiar to the animals[25]. The advantage of this method is that performance does not depend on the retention of a rule, and it is not influenced by changes in response to reward, which can provide a relatively pure measure of "working memory"[26].

In conclusion, the main finding of the present study is that the basic expression level of the NMDA receptor NR1/NR2B subtype in the hippocampus and striatum is related to visual recognition memory.

References

1 Constantine-Paton M, Cline HT, Debski E. Patterned activity, synaptic convergence, and the NMDA receptor in developing visual pathways. Annu Rev Neurosci 1990; 13: 129–54.

2 Mori H, Mishina M. Structure and function of the NMDA receptor channel. Neuropharmacology 1995; 34: 1219–37.

3 Nakanishi S. Molecular diversity of glutamate receptors and implications for brain function. Science 1992; 258: 597–603.

4 Monyer H, Burnashev N, Laurie DJ, Sakmann B, Seeburg PH. Developmental and regional expression in the rat brain and functional properties of four NMDA receptors. Neuron 1994; 12: 529–40.

5 Bliss TV, Collingridge GL. A synaptic model of memory: long-term potentiation in the hippocampus. Nature 1993; 361: 31–9.

6 Bear MF, Malenka RC. Synaptic plasticity: LTP and LTD. Curr Opin Neurobiol 1994; 4: 389–99.

7 Tsien JZ, Huerta PT, Tonegawa S. The essential role of hippocampal CA1 NMDA receptor-dependent synaptic plasticity in spatial memory. Cell 1996; 87: 1327–38.

8 Nakazawa K, McHugh TJ, Wilson MA, Tonegawa S. NMDA receptors, place cells and hippocampal spatial memory. Nat Rev Neurosci 2004; 5: 361–72.

9 Baker KB, Kim JJ. Effects of stress and hippocampal NMDA receptor antagonism on recognition memory in rats. Learn Mem 2002; 9: 58–65.

10 Tang YP, Shimizu E, Dube GR, Rampon C, Kerchner GA, Zhuo M, *et al*. Genetic enhancement of learning and memory in mice. Nature 1999; 401: 63–9.

11 Paule MG, Fogle CM, Allen R, Hammond TG, Popke EJ. Chronic exposure to NMDA receptor and sodium channel blockers during development in monkeys and rats: long-term effects on cognitive function. Ann N Y Acad Sci 2003; 993: 116–22.

12 Puma C, Bizot JC. Intraseptal infusions of a low dose of AP5, a NMDA receptor antagonist, improves memory in an object recognition task in rats. Neurosci Lett 1998; 248: 183–6.

13 Zhu LJ, Chen Z, Zhang LS, Xu SJ, Xu AJ, Luo JH. Spatiotemporal changes of the *N*-methyl-*D*-aspartate receptor subunit levels in rats with pentylenetetrazole-induced seizures. Neurosci Lett 2004; 356: 53–6.

14 Luo J, Wang Y, Yasuda RP, Dunah AW, Wolfe BB. The majority of *N*-methyl-*D*-aspartatereceptor complexes in adult rat cerebral cortex contain at least three different subunits (NR1/NR2A/NR2B). Mol Pharmacol 1997; 51: 79–86.

15 Rampon C, Tang YP, Goodhouse J, Shimizu E, Kyin M, Tsien JZ. Enrichment induces structural changes and recovery from nonspatial memory deficits in CA1 NMDAR1 knockout mice. Nat Neurosci 2000; 3: 238–44.

16 Bussey TJ, Muir JL, Aggleton JP. Functionally dissociating aspects of event memory: the effects of combined perirhinal and postrhinal cortex lesions on object and place memory in the rat. J Neurosci 1999; 19: 495–502.

17 Murray EA, Mishkin M. Object recognition and location memory in monkeys with excitotoxic lesions of the amygdala and hippocampus. J Neurosci 1998; 18: 6568–82.

18 Abe H, Iwasaki T. NMDA and muscarinic blockade in the perirhinal cortex impairs object discrimination in rats. Neuroreport 2001; 12: 3375–9.

19 Quinlan EM, Philpot BD, Huganir RL, Bear MF. Rapid, experience-dependent expression of synaptic NMDA receptors in visual cortex *in vivo*. Nat Neurosci 1999; 2: 352–7.

20 Hammond RS, Tull LE, Stackman RW. On the delay-dependent involvement of the hippocampus in object recognition memory. Neurobiol Learn Mem 2004; 82: 26–34.

21 Kelley AE, Andrzejewski ME, Baldwin AE, Hernandez PJ, Pratt WE. Glutamate-mediated plasticity in corticostriatal networks: role in adaptive motor learning. Ann N Y Acad Sci 2003; 1003: 159–68.

22 Sgambato V, Minassian R, Nairn AC, Hyman SE. Regulation of ania-6 splice variants by distinct signaling pathways in striatal neurons. J Neurochem 2003; 86: 153–64.

23 Da Cunha C, Angelucci ME, Canteras NS, Wonnacott S, Takahashi RN. The lesion of the rat substantia nigra pars compacta dopaminergic neurons as a model for Parkinson's disease memory disabilities. Cell Mol Neurobiol 2002; 22: 227–37.

24 Schulz D, Sergeeva OA, Ianovskii E, Luhmann HJ, Haas HL, Huston JP. Behavioural parameters in aged rats are related to LTP and gene expression of ChAT and NMDA-NR2 subunits in the striatum. Eur J Neurosci 2004; 19: 1373–83.

25 Ennaceur A, Delacour J. A new one-trial test for neurobiological studies of memory in rats. 1: behavioral data. Behav Brain Res 1988; 31: 47–59.

26 Ennaceur A, Neave N, Aggleton JP. Spontaneous object recognition and object location memory in rats: the effects of lesions in the cingulate cortices, the medial prefrontal cortex, the cingulum bundle and the fornix. Exp Brain Res 1997; 113: 509–19.

Full-length article

Effects of adenosine agonist R-phenylisopropyl-adenosine on halothane anesthesia and antinociception in rats[1]

Hai-chun MA[2,4], Yan-fen WANG[3], Chun-sheng FENG[2], Hua ZHAO[4,5], Shuji DOHI[6]

[2]Department of Anesthesiology, the First Hospital of Jilin University, Changchun 130021, China; [3]Department of Digestive Disease, the Second Hospital of Jilin University, Changchun 130041, China; [4]Department of Physiology, Basic Medical School, Jilin University, Changchun 130021, China; [6]Department of Anesthesiology, School of Medicine, Gifu University, Gifu 5008705, Japan

Key words

adenosine; inhalation anesthesia; analgesia; potassium channels; subarachnoid space; cerebral ventricles

[1] Project supported by Young Teacher Research Grants from Jilin University and by Sciences and Technology Commission of Changchun (No 0317009).
[5] Correspondence to Prof Hua ZHAO.
Phn 86-431-561-9472.
Fax 86-431-563-9362.
E-mail hzhao57@excite.com

Received 2004-05-06
Accepted 2004-10-19

doi: 10.111/j.1745-7254.2005.00021.x

Abstract

Aim: To investigate the antinociceptive effect of adenosine agonist R-phenylisopropyl-adenosine (R-PIA) given to conscious rats by intracerebroventricular (ICV) and intrathecal (IT), and identify the effect of R-PIA on minimum alveolar concentration (MAC) of halothane with pretreatment of A_1 receptor antagonist 8-cyclopentyl-1,3-dipropylxanthine (DPCPX) or K^+ channel blocker 4-aminopyridine (4-AP). **Methods:** Sprague-Dawley rats were implanted with 24-gauge stainless steel guide cannula using stereotaxic apparatus and ICV method, and an IT catheter (PE-10, 8.5 cm) was inserted into the lumbar subarachnoid space, while the rats were under pentobarbital anesthesia. After one week of recovery from surgery, rats were randomly assigned to one of the following protocols: MAC of halothane, or tail-flick latency. All measurements were performed after R-PIA (0.8–2.0 μg) microinjection into ICV and IT with or without pretreatment of DPCPX or 4-AP. **Results:** Microinjection of adenosine agonist R-PIA in doses of 0.8–2.0 μg into ICV and IT produced a significant dose- and time-dependent antinociceptive action as reflected by increasing latency times and ICV administration of adenosine agonist R-PIA (0.8 μg) reducing halothane anesthetic requirements (by 29%). The antinociception and reducing halothane requirements effected by adenosine agonist R-PIA was abolished by DPCPX and 4-AP. **Conclusion:** ICV and IT administration of adenosine agonist R-PIA produced an antinociceptive effect in a dose-dependent manner and decreased halothane MAC with painful stimulation through activation of A_1 receptor subtype, and the underlying mechanism involves K^+ channel activation.

Introduction

Adenosine, a purine nucleotide, is present in the brain in concentrations sufficient to be important in the regulation of central nervous system (CNS) function[1]. The compound adenosine has various modulatory effects in the peripheral and central nervous system, mediated through specific cell-surface associated receptors[2]. For example, in addition to the antinociceptive action of adenosine in animal models[3], adenosine is used to treat the symptoms of paroxysmal supraventricular tachycardias, and to produce controlled hypotension during some surgical procedures, and in the diagnosis of coronary artery disease[4]. The current view is that adenosine receptors of the A_1 subtype are associated with a modulatory effect on pain transmission at brain and spinal cord level. Animal studies have repeatedly demonstrated that adenosine-mediated inhibitory influences presumed nociceptive reflex responses[5]. These examinations on rodents have tested acute pain models involving tactile, pressure and heat stimulations. More recently, animal lesion models, presumably reflecting chronic pain, have shown that adenosine analogue can suppress nociceptive behavior both by systemic and intrathecal administration[6]. Consequently, there are substantial evidence that adenosine can modulate

nociceptive input. The general thinking about the mechanism of analgesic-anesthetic action of adenosine is that adenosine interacts with G-protein-coupled adenosine receptor and activates K^+ channel in CNS. However the roles of K^+ channel activation by adenosine in the antinociceptive action of adenosine in CNS and spinal cord has not been well demonstrated. Thus, in the present study we investigated whether adenosine agonist R-phenylisopropyl-adenosine (R-PIA) administered through intracerebroventricular (ICV) or intrathecal (IT) methods will produce an antinociceptive effect and enhance the halothane-anesthetized state.

Materials and methods

Animal preparation With approval of the Animal Care and Use Committee of our institution, studies were performed on 70 male Sprague-Dawley rats weighing 300±20 g (9 weeks old). Rats were housed individually in a temperature-controlled (21±1 ºC) room with a 12-h light/dark cycle, and they were given free access to water and food. All experimental measurements were performed between 10:00 AM and 5:00 PM. Each rat was assigned to only one of the following protocols: minimum alveolar concentration (MAC) of halothane (n=30), or tail-flick latency (IT injection, n=20; ICV injection, n=20). Each animal was studied two to four times in an experimental series with an interval of at least 5 d.

Surgical preparation For the ICV cannular placement, as previously described by Ma *et al*[7], animals were anesthetized with pentobarbital (50 mg/kg), and positioned in a stereotaxic apparatus (Narishige, Tokyo, Japan). A 24-gauge stainless steel guide cannula was unilaterally implanted 1 mm above the lateral ventricle using the following stereotaxic coordinates: 1.5 mm lateral to the midline, 1.0 mm posterior to bregma, 2.5 mm ventral to dura. The guide cannula was then fixed to the skull with two steel screws and dental cement. The IT catheter was implanted as previously described by Zeng *et al*[8], and animals were placed in a stereotaxic head holder with the head fixed forward. At the site of occipital a midline incision was made till the escape of cerebrospinal fluid. Intrathecal catheter was inserted at a length of 8.5 cm to the lumbar intrathecal level. The catheter's external arm was tunneled subcutaneously to emerge at the neck. After the surgery the rats were allowed to recover for one week before the experiments began. Only animals exhibiting no motor deficits as a result of surgery were used.

Minimum alveolar concentration measurement Anesthesia was induced through inhalation of halothane in a transparent container. The rat's trachea was intubated with a 16-gauge cannula, and the lungs were mechanically ventilated with 1.0% halothane in oxygen and air (F_IO_2 0.3–0.5). End-tidal carbon dioxide pressure was maintained at 35 to 40 mmHg. Rectal temperature was continuously monitored and maintained at 37.5 ºC with a heating pad. Fifteen minutes after the initiation of halothane anesthesia, saline or 4-aminopyridine (4-AP) 2 mg/kg was injected intraperitoneally, then a 30-gauge stainless steel internal cannula connected to polyethylene tubing was inserted into the guide cannula and positioned 1.0 mm beyond the tip. R-PIA at the dose of 0.8 μg, 1.0 μg, and 2.0 μg, or combined with A_1 antagonist 8-cyclopentyl-1,3-dipropylxanthine (DPCPX) 5.0 μg was injected into the lateral cerebral ventricle at a volume of 5.0 μL over 90 s using a microinjection pump. Five minutes after the drug or vehicle injection, MAC was determined using the up and down technique[9]. Briefly, the administration of halothane was adjusted in steps of 0.1%, and a stable end-tidal concentration for 15 min was obtained before stimulation. Noxious stimulation was applied with a 6-inch hemostat to the middle third of the tail for 60 s at the first ratchet position. The criteria for positive movements included purposeful movements of either the head or the four extremities. When animal had a positive response, the halothane concentration was increased; when there was no response, the concentration was decreased until movement was observed. When the interval was bracketed by positive and negative responses, the midpoint of the interval was then the MAC of halothane. End-tidal gas samples were obtained with an airtight glass syringe through a 26-gauge needle inserted to a tracheal tube during 15 expirations. Halothane concentrations were analyzed using an infrared analyzer (M1025B; Hewlett Packard). Calibration with the standard gas was performed before study. All chemicals were purchased from Sigma Chemical (St Louis, MO, USA).

Measurements of antinociception The antinociceptive effect was measured by the tail-flick (TF) latency response. A high-intensity light was focused on the dorsal surface of the rat tail; the time for the rat to move its tail out of the light beam was automatically recorded (Thermal Analgesimeter KN-205E, Natume, Tokyo, Japan). A different patch of the middle one-third portion of the tail was exposed to the light beam on each trial to minimize the risk of tissue damage during the experiment. A cut-off time of 10 s was predetermined, at which time the trial was terminated if no response occurred. TF latency was determined 5, 10, 15, 20, 30, 40, 50, and 60 min after ICV or IT administration of R-PIA (0.8 μg, 1.0 μg, and 2.0 μg), with or without pretreatment of DPCPX 5.0 μg or 4-AP 2 mg/kg. Each TF latency data point consisted of a mean of three trials on an individual animal.

Histology examination At the end of the experiments, bromophenol blue (5.0 μL) was microinjected to label the site of ICV injection. The rat was then killed with an overdose of pentobarbital. The brain was removed and fixed in 10% neutral buffered formalin. Dye spots were localized from 0.3–0.5 mm serial coronal sections and identified on diagrams from the atlas of Paxinos and Watson[10]. Bromophenol blue (10 μL) was used to confirm the position of the intrathecal catheter and likely spread of the injectate.

Statistical analysis All data were presented as mean± SEM. In MAC measurements statistical testing were performed with a Student's *t*-test. Because a cut-off value was used in the TF latency test, data were converted to the percentages of the maximum possible effect (% MPE). Where % MPE=(postdrug TF latency-baseline TF latency)/(cut-off time-baseline TF latency)×100. The cut-off time was defined as a stimulus time of 10 s. For the effect of drugs on TF latency, statistical differences were analyzed using a two-way analysis of variance (ANOVA), followed by Fisher's test for *post hoc* analysis of means. $P<0.05$ was considered to be statistically significant.

Results

Effect of ICV R-PIA injection on the MAC of halothane with pretreatment 4-AP or DPCPX The MAC of halothane was significantly reduced by direct application of adenosine agonist R-PIA in doses of 0.8 μg, 1.0 μg, and 2.0 μg. The MAC of halothane in the control group (saline injection) was 0.95%±0.05% (Figure 1), which corresponds with our previously reported MAC values[9]. R-PIA 0.8 μg decreased MAC of halothane by 29%. Pretreatment of 4-AP 2 mg/kg intraperitoneal injection or ICV injection DPCPX 5 μg inhibited the effect of R-PIA 0.8 μg, whereas the dose of 4-AP or DPCPX itself did not affect the MAC of halothane (Figure 2).

ICV and IT administration of R-PIA on antinocicep-tion Time courses were determined for adenosine agonists R-PIA in the TF latency test. IT administration of R-PIA in doses of 0.8–2.0 μg induced antinociception as reflected by the increase in latency times compared with the control animals. The antinociceptive action reached maximal effect within 10 min and lasted over 60 min, and showed a dose-dependent manner (Figure 3). The ICV administration of adenosine agonist R-PIA (0.8–2.0 μg) produced the antinociceptive effect as reflected by increasing the TF latency (Figure 4). The peak effect of antinociception of R-PIA was within 5 min and showed a dose-dependent manner. The intraperitoneal injection of 4-AP or ICV injection of DPCPX had no effect on the baseline of TF latency, but its pretreatment produced a significant reverse effect elicited by the ICV or IT administration of R-PIA (Figure 3, 4). The experiment dose of R-PIA did not show any detectable effect on motor function or general behavior during the observation period (60 min).

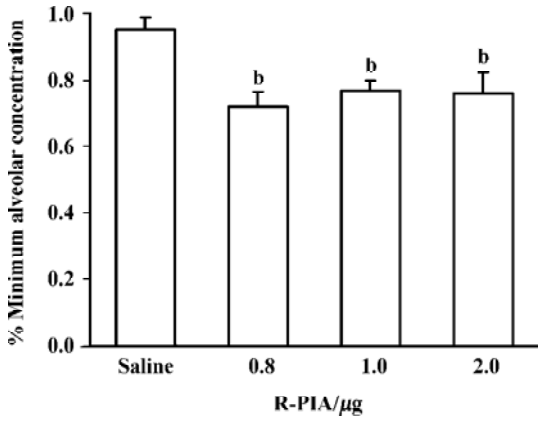

Figure 1. Effect of adenosine analogue R-PIA 0.8 μg, 1.0 μg, and 2.0 μg administrated by ICV methods on MAC of halothane. $^bP<0.05$ *vs* saline.

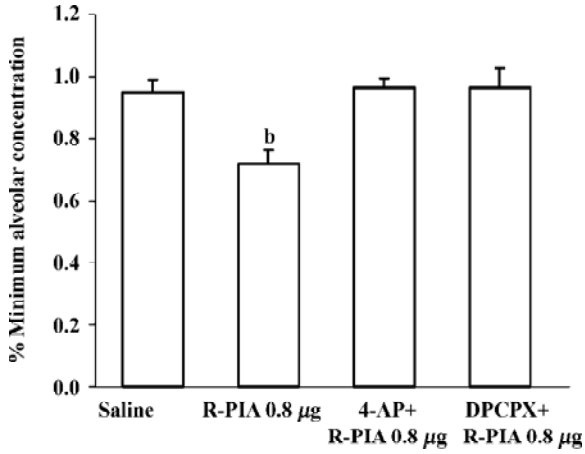

Figure 2. Effect of adenosine analogue R-PIA 0.8 μg administrated by ICV methods with pretreatment of K^+ channel antagonist 4-AP or A_1 receptor blocker DPCPX on MAC of halothane. Mean±SEM from 5 or 7 rats. $^bP<0.05$ *vs* saline.

Discussion

The present data demonstrated that adenosine agonist R-PIA injection by ICV and IT, produced antinociceptive effect in a dose-related manner and enhanced halothane anesthesia. Because such effects of R-PIA were attenuated with pretreatment of DPCPX, an A_1 receptor antagonist, and 4-AP, a voltage-gated K^+ channel blocker, the action of R-PIA is mediated via A_1 receptor subtype activation and its

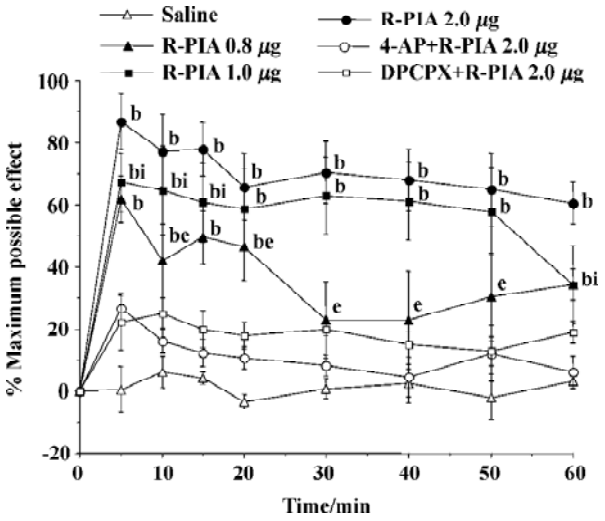

Figure 3. Time course of the antinociceptive effect (%MPE) of adenosine analogue R-PIA via IT method with or without pretreatment of A_1 receptor antagonist DPCPX and K^+ channel blocker 4-AP in tail flick tests. Mean±SEM. $^bP<0.05$ *vs* saline. $^eP<0.05$ *vs* R-PIA (1.0 μg). $^iP<0.05$ *vs* R-PIA 2.0 (μg).

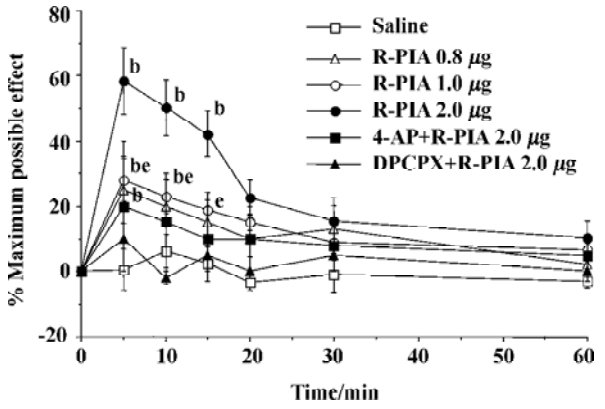

Figure 4. Time course of the antinociceptive effect (%MPE) of adenosine analogue R-PIA 0.8-2.0 μg via ICV, of rats with or without pretreatment of A_1 receptor antagonist DPCPX and K^+ channel blocker 4-AP in tail flick tests. n=5–8. Mean±SEM. $^bP<0.05$ *vs* saline. $^eP<0.05$ *vs* R-PIA 2.0 μg.

mechanisms are likely to be involved in, at least in part, K^+ channel activation.

Adenosine and its analogues were shown to produce antinociception in the tail flick and hot plate tests following both IT and central administration[5,6]. Such antinociception has been diminished by methylxanthines, such as caffeine and theophylline, suggesting the involvement of specific adenosine receptor[11]. In the present study, we administered R-PIA through IT method to induce dose-dependent antinociception. Pretreatment A_1 antagonist DPCPX reversed this effect. The results indicate that R-PIA inhibits nociceptive responses by acting on A_1 receptors. By using selective adenosine agonist on the evoked potential record of the rat spinal cord, the adenosine A_1 receptor agonist obviously inhibited the slow ventral root potential, which is the C-fiber-evoked excitatory response associated with nociceptive information[2]. In the present study, ICV administration of R-PIA produced a very short period (15 min) of antinocicep-tion. Systemically administered adenosine analogue R-PIA did not affect synaptic neurotransmission in the hippo-campus, which are enriched in A_1-type adenosine receptors, because they failed to reach the appropriate receptors[11]. Thus, it is likely with the tail flick test that the site of action of R-PIA is probably at the spinal cord, because ICV injection of R-PIA only produced fewer responsesin the tail flick test, although it has previously been reported that activity in the hot-plate test was observed [12]. In the hot-plate test, the potential for an additional supraspinal action would need to be considered.

Adenosine modulation of anesthesia has been extensively studied in the past[13]. The standard for determining anesthetic requirements is the MAC of an inhaled agent that prevents gross purposeful movement in response to a supramaximal painful stimulus. Because of its simplicity and reproducibility, the MAC concept has remained an important tool for studying anesthetic action. Previous studies have shown that on a halothane anesthetized rat the effect of adenosine in decreasing the halothane MAC was probably related to an adenosine-induced decrease in CNS noradrenergic transmission because noradrenergic neurotransmission was decreased following R-PIA administration in all brain regions[13]. The present results provided evidence that into R-PIA injection significantly reduced MAC of halothane by 29%, and this reduction in MAC of halothane was inhibited with pretreatment of A_1 antagonist DPCPX suggests that R-PIA increased the effects of anesthetic suppression was directly mediated A_1 receptor. However, ICV injection of R-PIA also exhibited antinociceptive action, and the relationships between neurotransmitter and adenosine decrease MAC of halothane are not very clear. It is important that the behavioral responses consist of nociception, motor responses and central processing were measured with MAC. We are still unable to dissect which element(s) are affected by the central action of R-PIA.

Agonists of adenosine A_1 receptors (including R-PIA) have activation action on K^+ channels in neurons of the CNS. ATP-sensitive K^+ channel blocker could inhibit the antinociception of adenosine in mice[14]. Other responses

induced by adenosine A_1 receptor agonist also appear to be linked to the opening of K^+ channels. Adenosine A_1 receptors in cardiac and vascular muscle cells are coupled to ATP-sensitive K^+ channels[4]. In the present study, the effect of R-PIA on reducing the MAC of halothane and antinociception were antagonized by pretreatment with voltage-gated K^+ channel blocker 4-AP. The apparent involvement of voltage-gated K^+ channels in R-PIA-induced effect, as our results suggest, was not unexpected because 4-AP, as a potent voltage-gated K^+ channel blocker, blocks outward conducting potassium channels, thereby lowering the threshold for initiation of action potentials as well as prolonging action potential duration in excitable membrane. In addition, the antinociceptive effect of $GABA_B$ receptor agonist baclofen and [*D*-ala^2]-deltorphin II was also antagonized by 4-AP[15]. K^+ channel opener could potentiate the analgesic effect of morphine[16], and the spinal antinociceptive action of morphine was caused by the release of adenosine and subsequent activation of adenosine receptors within the spinal cord[6]. Taken together, it is possible that adenosine affected the A_1 receptor, resulted in increased K^+ conductance preventing pain signal transmission to produce spinal antinociception and ICV methods reducing the requirement of halothane. Thus voltage-gated K^+ channels play a key role in the R-PIA-induced effect both by IT and ICV administration.

In summary, the results provide implications for the use of adenosine analog in anesthetic settings and pain management. As evidenced from our data, the use of an adenosine analog during painful stimuli and halothane anesthesia profoundly decreased the response to nociception and increased the anesthetic depression through the A_1 receptor subtype, and its mechanisms involves K^+ channel activation. This observation pertains during other forms of volatile anesthesia and other types of pain treatment although definitive conclusions require further investigation.

References

1 Zetterstrom T, Vernet L, Ungerstedt U. Purine levels in the intact rat brain: studies with an implanted prefused hollow fiber. Neurosci Lett 1982; 29: 111–5.

2 Nakamura I, Ohta Y, Kemmotsu O. Characterization of adenosine receptors mediating spinal sensory transmission related to nociceptive information in the rat. Anesthesiology 1997; 87: 577–84.

3 Sollevi A. Adenosine for pain control. Acta Anaesthesiol Scand 1997; 59: 135–6.

4 Lerman BB, Belardinelli L. Antiadrenergic effects of adenosine on His-Purkinje automaticity: evidence for accentuated antagonism. Circulation 1991; 83: 1499–509.

5 Huang QJ, Hao XL, Minor TR. Brain adenosine mediates interleukin-1β-induced behavioral depression in rats. Acta Pharm Sin 2002; 34: 421–5.

6 Kekesi G, Dobos I, Benedek G. The antinociceptive potencies and interactions of endogenous ligands during continuous intrathecal administration: adenosine, agmatine, and endomorphin-1. Anesth Analg 2004; 98: 420–6.

7 Ma HC, Dohi S, Wang YF. Antinociceptive and Sedative effects induced by carbachol and oxycodone into brainstem pontine reticular formation in rats. Anesth Analg 2001; 92: 1307–15.

8 Zeng W, Dohi S, Shimonaka H. Spinal antinociceptive action of Na^+-K^+ pump inhibitor ouabain and its interaction with morphine and lidocaine in rats. Anesthesiology 1999; 90: 500–8.

9 Ishizawa Y, Ma HC, Dohi S. Effects of cholinomimetic injection into the brain stem reticular formation on halothane anesthesia and antinociception in rats. J Pharmacol Exp Ther 2000; 293: 845–51.

10 Paxinos G, Watson C. The rat brain in stereotaxic coordinates. San Diego: Academic Press; 1998. p 21–3.

11 Bantel C, Tobin G, Li X. Intrathecal adenosine following spinal nerve ligation in rat: short residence time in cerebrospinal fluid and no change in A_1 receptor binding. Anesthesiology 2002; 96: 103–8.

12 Huang QJ, Jiang H, Hao XL, Minor TR. Brain IL-1β was involved in reserpine-induced behavioral depression in rats. Acta Pharmacol Sin 2004; 25: 293–6.

13 Birch BD, Louie GL, Vickery RS. *L*-Phenylisopropyladeno-sine diminishes halothane requirements and decreases noradrenergic neurotransmission in rats. Life Sci 1988; 42: 1355–60.

14 Maria O, Jose MB. Role of ATP-sensitive K^+ channels in antinociception induced by R-PIA, an adenosine A_1 receptor agonist. Nauyn-Schmiedeberg's Arch Pharmacol 1994; 350: 57–62.

15 Ong J, Kerr DI. Recent advances in GABAB receptors: from pharmacology to molecular biology. Acta Pharmacol Sin 2000; 21: 111–23.

16 Asano T, Dohi S, Iida H. Antinociceptive action of epidural K^+ (ATP) channel openers via interaction with morphine and α_2-adrenergic agonist in rats. Anesth Analg 2000; 90: 1146–51.

Full-length article

Effects of intrathecal 6-hydroxydopamine, α_1 and α_2 adrenergic receptor antagonists on antinociception of propofol in mice

Zhi-jun GE[1,2], Yin-ming ZENG[1], Yong-fei TAN[2]

[1]Jiangsu Province Key Laboratory of Anesthesiology, Xuzhou Medical College, Xuzhou 221002, China; [2]Jiangsu Province People's Hospital of Yixing, Yixing 214200, China

Key words

propofol; spinal cord; antinociception; prazosin; yohimbine; norepinephrine

[1] Correspondence to Prof Yin-ming ZENG.
Phn 86-516-580-2018.
Fax 86-516-5708, ext 135.
E-mail zym_xzmc@163.com

Received 2004-07-21
Accepted 2004-10-19

doi: 10.1111/j.1745-7254.2005.00033.x

Abstract

Aim: To investigate the relationship between spinal cord norepinephrine, α_1 and α_2 adrenergic receptors and antinociception of propofol in mice. **Methods:** Kunming mice were used. Antinociceptive tests were investigated with the tail-immersion test and the acetic acid-induced writhing test. The effects of subcutaneous (sc), intrathecal (ith) and intracerebroventricular (icv) injection propofol on pain threshold were observed. The influences of pretreatment with ith 6-hydroxydopamine, α_1R antagonist prazosin, or α_2R antagonist yohimbine on the antinociception of propofol were studied. **Results:** Significant antinociception was produced by propofol (25, 50 mg/kg, sc) and propofol (20, 40 μg, ith) in tail-immersion test and acetic the acid-induced writhing test ($P<0.05$ or $P<0.01$). Icv propofol (10, 20, and 40 μg) did not produce any effect on pain threshold in mice ($P>0.05$). The 6-hydroxydopamine (5 and 10 μg), prazosin (5 and 10 μg), or yohimbine (5 and 10 μg) ith alone did not affect basal tai-flick latency (TFL) in conscious mice, but significantly reduced the TFL as measured by tail-immersion test in propofol (50 mg/kg, sc)-treated mice, compared with basal TFL and vehicle groups ($P<0.05$ or $P<0.01$). **Conclusion:** The spinal cord is a target of propofol antinociception. In mice propofol antinociception is partly mediated by spinal norepinephrine, α_1R and α_2R.

Introduction

Propofol (2,6-diisopropylphenol, Diprivan) is widely used in the clinical setting as an iv anesthetic. Its antinociceptive effect results from an excitation of spinal $GABA_A$ receptors[1] and an inhibition of spinal NMDA, AMPA receptors[2], *etc*. A study by Antognini *et al* also suggested that propofol has a direct depressant effect on dorsal horn neuronal responses to noxious stimulation[3]. Therefore, these studies suggested a spinal mediation of propofol-induced antinociception. However there was also a study that concluded that propofol could control pain and this action might be centrally modulated through the opioid system rather than at the level of the spinal cord[4]. Therefore the contribution of supraspinal sites versus spinal sites to the antinociception of propofol is still unclear.

The mechanism whereby stimulation of opiate receptors in supraspinal regions produced analgesia has been extensively investigated and appeared, in part, to involve a descending noradrenergic pathway[5,6]. Norepinephrine (NE) is a major neurotransmitter in the descending inhibition of nociceptive transmission. Available evidence suggests that at the level of the spinal cord, there appear to be at least two neuronal systems that are involved. The first is the direct presynaptic inhibition of the nociception of the primary afferent neurons or postsynaptic inhibition of the second order neurons through activation of α_2 adrenergic receptor (α_2Rs)[7,8]. The second is the indirect activation of the inhibitory interneurons through α_1Rs located on these neurons[8,9].

Based on these observations, in the present study, we injected propofol systemically, intrathecally, or intracerebroventricularly to further examine the role of spinal and supraspinal sites in mediating the antinociception of propofol.

We sought evidences of the involvement of spinal NE, α_1R, and α_2R in the antinociception induced by sc propofol in mice.

Materials and methods

Animals With the approve of the Committee of Animal Research of Xuzhou Medical College, we conducted experiments on Kunming mice (22±3 g, Grade II, Certificate No SCXK-SU-2002-0022) of both sexes, obtained from the Laboratory Animal Center of Xuzhou Medical College, housed individually in a temperature-controlled 22±2 ºC room with a 12-h light-dark cycle and given free access to food and water. Each animal was used in only one experiment.

Chemicals Propofol and vehicle (10% intralipid) were supplied by the AstraZeneca Company. Prazosin, yohimbine and 6-hydroxydopamine (6-OHDA) were purchased from Sigma-Alexis (USA). Ice acetic acid was produced by Beijing Chemical Factory. All drugs were all freshly prepared. Prazosin was first dissolved in 50% dimethyl sulfoxide (Me_2SO) in normal saline (NS) and the solution was diluted with NS. Yohimbine was dissolved in NS. 6-OHDA was dissolved in a saline vehicle (0.02% ascorbic acid in 0.9% saline). Systemic drug administration was sc performed in a single volume of 0.01 L/kg.

Intracerebroventricular injection in conscious mice[10] A 25-gauge needle was inserted in the left lateral ventricle of the brain with the following coordinates: left 2 mm of sagittal suture on the linking line of ears, and 2 mm down the skull surface. Volume of icv injections was 5 μL. The proper position of the icv localization was verified at the end of each protocol by injection of methylene blue staining with the same coordinates.

Intrathecal injection in conscious mice[2] A 25-gauge needle was inserted at L_5–L_6 intrathecal space. Ith placement was confirmed by a sudden lateral movement of the tail. All mice were injected with a 5-μL volume of drugs or vehicles and, after allowing 5 s for the injectant to disperse, the needle was slowly withdrawn. While developing this technique we injected 5 μL of 2% lidocaine ith in 10 mice, which consistently caused a transient hind-paw paralysis.

Tail-immersion test[11] The caudal 1/3 of tails of mice were immersed in 48±0.5 ºC water. The time for the mice to remove their tails from the water was expressed as the tail-flick latency (TFL). All mice were tested twice at a 5-min interval and the mean value was considered as the basal pain threshold. A cut-off time of 60 s was used to minimize damage to the skin of the tail. The influences of sc propofol (12.5, 25, and 50 mg/kg, n=10) alone on the TFL and the effects of pretreatment with ith prazosin and yohimbine 10 min before propofol (50 mg/kg, sc, n=10) injection on the TFL were investigated, respectively. To demonstrate the sc propofol-induced prolongation of TFL was not caused by its hypnotic effect, the time courses for the development of propofol-induced hypnosis were established. The loss of righting reflex was assessed by placing the mice on their backs and determining if the animals could right themselves within 30 s.

In a separate study, groups of mice were pretreated intrathecally with 6-OHDA (5, 10, and 20 μg) for 3 d (one injection in all). The dosing scheme of 6-OHDA was chosen according to the study by Hung *et al*[12] with minor modification. The tail-immersion test was performed on d 4 and the effect of propofol (50 mg/kg, sc, n=10) on TFL was observed.

Acetic acid-induced writhing test[2] Mice were administered NS, intralipid or propofol 30 min before ip injection of 0.9% ice acetic acid in a volume of 10 mL/kg. The number, latency and times of writhing mice were recorded within 15 min after the last injection.

Statistical analysis All data were present as mean±SD. Statistical comparisons in each group were performed by one-way analysis of variance (ANOVA) followed by t-test. Difference was considered to be significant at $P<0.05$.

Results

Hypnotic and antinociceptive effects of propofol were temporarily uncoupled Propofol 12.5, 25 mg/kg sc had no appreciable effect on the general behavior in mice. After 2–5 min treatment of propofol (50 mg/kg, sc), mice showed slight sedation. The sedative effect reached maximum after 5 min of propofol injection, and 20% mice (2/10) developed a loss of righting reflex; however, after this time there was no significant increase in TFL. In contrast, sc propofol resulted in a significant increase in TFL 10–30 min after its injection with the peak effect at 10 min ($P<0.01$, Table 1), but after 30 min, all mice remained righting reflex and there was no appreciable effect on general behavior. Neither propofol ith nor icv resulted in any appreciable abnormal behavior.

Effects of propofol on pain threshold in tail-immersion test and acetic acid-induced writhing test in mice There was no significant change of TFL before and after sc, ith, or icv injection of 10% intralipid compared with the NS (sc, ith, or icv) group, respectively in tail-immersion test ($P>0.05$, Table 1). Propofol (12.5 mg/kg, sc) and propofol (5 μg, ith) showed no effect on TFL. However, propofol (25 and 50 mg/kg, sc) and propofol (10, 20 μg, ith) increased

Table 1. Effect of propofol on the tail-flick latency (TFL) in tail-immersion test on mice. n=10. Mean±SD. $^{b}P<0.05$, $^{c}P<0.01$ *vs* baseline. $^{e}P<0.05$, $^{f}P<0.01$ *vs* NS (sc). $^{h}P<0.05$, $^{i}P<0.01$ *vs* NS (ith).

Groups	TFL/s					
	Before treated	After treated				
		5 min	10 min	20 min	30 min	40 min
Normal saline(sc)	11.3±1.3	10.2±1.7	12.5±2.3	10.9±1.9	13±3	12.2±2.7
Intralipid (sc)	11.5±0.8	10.8±1.3	10.8±1.5	11±3	11.5±2.5	10.9±2.2
Propofol (12.5 mg/kg,sc)	10.4±2.1	13±4	12±3	12.2±2.5	12±3	12±3
Propofol (25 mg/kg, sc)	10.7±1.0	12±3	28±5^{be}	24±5^{be}	16±4^{be}	10.8±1.3
Propofol (50 mg/kg, sc)	12±3	14±4	35±8^{cf}	30±9^{cf}	20±4^{be}	14±3
Normal saline (ith)	11.2±2.0	11.2±2.6	10.8±1.5	12.2±2.7	12±3	12±3
Intralipid (ith)	10.2±1.3	12.1±2.3	12±3	10.8±1.5	11.8±2.3	10.8±1.3
Propofol (5 μg, ith)	10.9±2.3	10±3	13±4	11.1±2.2	12.4±1.8	11±3
Propofol (10 μg, ith)	11.6±1.7	10.8±2.9	27±5^{ci}	20±4^{bi}	16±5^{bh}	12±4
Propofol (20 μg, ith)	10.8±1.3	13±3	32±6^{ci}	28±6^{ci}	18±4^{bh}	14±3
Normal saline (icv)	11.9±1.5	10.5±2.2	10.8±2.2	10.8±2.3	10.6±2.0	11±3
Intralipid (icv)	10.8±1.3	11.7±2.3	10.9±1.9	13±4	12.1±2.3	10.8±1.2
Propofol (5 μg, icv)	11.4±1.6	11±3	10.8±1.5	11±3	11.4±1.6	11.5±1.3
Propofol (10 μg, icv)	10.1±2.1	10.5±2.2	10.5±2.2	10.5±2.2	10.1±2.1	10.5±2.2
Propofol (20 μg, icv)	11.5±1.8	10.9±1.3	13±3	11.8±1.3	11.5±1.8	11±1.3

the TFL in a dose- and time-dependent manner 10–30 min after its injection($P<0.05$ or $P<0.01$ *vs* NS, Table 1).

No significant difference existed in the number of writhing mice, writhing latency writhing times before and after sc, ith, or icv injection of 10% intralipid. Propofol (12.5 mg/kg, sc) and propofol (5 μg, ith) showed no anti-nociceptive effect in acetic acid-induced writhing test. But propofol (25 and 50 mg/kg, sc) and propofol (10 and 20 μg, ith) significant reduced the writhing times in a dose-dependent way (sc or ith) group ($P<0.05$ or $P<0.01$ *vs* NS, Table 2). Icv propofol (10, 20, and 40 μg) did not produce any antinociceptive effects in the tail-immersion test and acetic acid-induced writhing test ($P>0.05$, Table 1, 2).

Effects of intrathecal prazosin and yohimbine on TFL in conscious mice in tail-immersion test No significant difference existed in the TFL between NS group and Me_2SO group ($P>0.05$, Table 3). Ith prazosin (5 and 10 μg) or yohimbine (5 and 10 μg) alone had no effect on the general behavior and TFL. However, mice in prazosin (20 μg) and yohimbine (20 μg) groups exhibited less movement and the muscle strength of hindlimbs decreased at least for 1 h followed by a full recovery. The TFL in prazosin 20 μg and yohimbine 20 μg groups was significantly shortened, compared with its own baseline and NS group ($P<0.05$, Table 3). Therefore, prazosin (5 and 10 μg) and yohimbine (5 and 10 μg) were used in the subsequent antinociceptive studies of propofol.

Table 2. Effect of propofol on acetic acid-induced writhing in mice. n=12. Mean±SD. $^{b}P<0.05$, $^{c}P<0.01$ *vs* NS (sc). $^{e}P<0.05$, $^{f}P<0.01$ *vs* NS (ith).

Groups	Writhing latency/min	Writhing times	Number of Writhing mice
Normal Saline (sc)	3.8±0.9	44±10	12/12
Intralipid (sc)	3.2±0.7	43±11	12/12
Propofol (12.5 mg/kg, sc)	3.2±0.5	34±11	12/12
Propofol (25 mg/kg, sc)	3.8±0.9	28±9^{b}	11/12
Propofol (50 mg/kg, sc)	3.9±1.0	15±4^{c}	10/12
Normal Saline (ith)	3.5±1.0	43±10	12/12
Intralipid (ith)	4.0±0.9	45±11	12/12
Propofol (5 μg, ith)	3.8±0.9	38±12	12/12
Propofol (10 μg, ith)	4.1±1.0	27±9^{e}	11/12
Propofol (20 μg, ith)	3.8±0.6	16±5^{f}	10/12
Normal Saline (icv)	3.7±0.5	44±12	12/12
Intralipid (icv)	4.0±0.9	43±11	12/12
Propofol (5 μg, icv)	3.6±0.9	38±10	12/12
Propofol (10 μg, icv)	3.1±0.6	42±12	12/12
Propofol (20 μg, icv)	3.9±0.5	40±13	12/12

Effects of pretreatment with intrathecal prazosin and yohimbine on TFL in propofol (50 mg/kg, sc)-treated mice in tail-immersion test The mice were injected intrathecally

Table 3. Changes of tail-flick latency (TFL) after intrathecal prazosin or yohimbine in tail-immersion test in conscious mice. n=10. Mean±SD. $^bP<0.05$ *vs* baseline. $^eP<0.05$ *vs* NS.

Groups	TFL/s					
	Before treated	After treated				
	Baseline	5 min	10 min	20 min	30 min	40 min
NS	11.9±1.6	12±3	11.8±1.5	11.3±1.4	11.4±2.1	11.8±1.7
Me_2SO	11.1±2.3	11.5±2.2	10.7±1.2	10.9±2.1	11.1±1.1	12±3
Prazosin 5 μg	12±3	10.4±1.2	10.8±1.5	11.1±2.1	11.3±1.1	10.7±1.3
Prazosin 10 μg	10.9±1.5	10.5±1.3	11±3	10.8±1.7	10.5±1.6	10.4±2.0
Prazosin 20 μg	10.8±1.7	7.9±1.2^{be}	6.8±1.3^{be}	7.8±0.5^{be}	8.3±1.4^{bc}	9.5±1.0
Yohimbine 5 μg	11.1±2.3	11.5±2.4	10.7±1.2	10.9±2.1	11.1±1.1	10.9±2.0
Yohimbine 10 μg	10.7±1.6	10.9±1.5	12±3	11.7±1.7	11.3±1.6	11.4±1.3
Yohimbine 20 μg	10.9±1.5	7.2±0.9^{be}	8.3±1.3^{be}	8.6±0.7^{be}	7.6±0.7^{bc}	9.8±0.8

with NS, Me_2SO, prazosin, or yohimbine at different doses 10 min before sc propofol. No significant differences existed in the TFL between NS group and Me_2SO group. Pretreatment with ith prazosin (5, 10 μg) and yohimbine (5, 10 μg) significantly decreased the TFL 10-30 min after propofol injection with the doses of prazosin and yohimbine increasing ($P<0.05$ *vs* NS, Table 5).

Effects of pretreatment with 6-OHDA on TFL in conscious mice and propofol (50 mg/kg, sc)-treated mice in tail-immersion test Mice in the 6-OHDA (20 μg) alone group exhibited biting and scratching behavior and the TFL significantly decreased in comparison with its own baseline and the NS group ($P<0.05$, Table 4). No change in behavior and TFL was observed after treatment with ith NS, vehicle or 6-OHDA (5, 10 μg) in conscious mice. However, pretreatment with ith 6-OHDA (5, 10 μg) significantly decreased the TFL 10–30 min after propofol treatment with the dose of 6-OHDA increasing ($P<0.05$ *vs* NS, Figure 1).

Discussion

In attempting to eluciate the mechanisms for the antinociceptive effect of propofol, it is important to obviate sedation that can exert on the antinociceptive assay. In the present study, we found that the hypnotic and antinociceptive effects of propofol were temporarily uncoupled. In addition, the anesthetic on awareness was clearly supraspinal. Ith 6-OHDA, prazosin, or yohimbine significantly inhibited the antinociception of propofol but not consciousness of animals. Furthermore, we used the heat tail-flick assay, which measures the latency of a spinal withdraw reflex to noxious heat, which is independent of hypnotic-induced decrement in purposeful movement. These results indicated that propofol-induced prolongation of TFL observed in the present study was a result of antinociception but not sedation.

Propofol (50 mg/kg, sc) produced a motor block 2–5 min after injection, but there was no significant increase in TFL. Furthermore, Kerz T *et al* have suggested that immobility

Table 4. Changes of tail-flick latency (TFL) after intrathecal 6- hydroxydopamine (6-OHDA) in tail-immersion test in conscious mice. n=10. Mean±SD. $^bP<0.05$ *vs* baseline. $^eP<0.05$ *vs* vehicle.

Groups	TFL/s					
	Before treated	After treated				
	Baseline	5 min	10 min	20 min	30 min	40 min
NS	11.6±1.4	10.2±1.9	12±3	10.9±1.9	11.8±2.3	11.2±1.7
Vehicle	10.8±2.1	11.2±1.8	10.6±1.4	10.7±2.1	11.4±2.5	10.5±1.9
6-OHDA 5 μg	10.5±1.8	11.8±2.3	10.9±1.5	12±3	11.7±2.5	10.9±1.2
6-OHDA 10 μg	11.7±1.8	11.2±1.9	10.8±1.3	10.9±1.7	10.8±2.3	10.6±1.6
6-OHDA 20 μg	10.5±1.4	7.5±0.9^{be}	6.8±1.4^{be}	6.9±1.1^{be}	7.2±1.2^{be}	6.8±1.0^{be}

Table 5. Effect of pretreatment with intrathecal prazosin or yohimbine on the antinociception of propofol (50 mg/kg, sc) in tail-immersion test on mice. n=10. Mean±SD. $^{b}P<0.05$, $^{c}P<0.01$ *vs* baseline. $^{e}P<0.05$, $^{f}P<0.01$ *vs* NS.

Groups	TFL/s				
	Before treated	After treated			
	Baseline	5 min	10 min	20 min	30 min
NS	10.8±1.3	12±3	31±7^{c}	27±4^{c}	22±5^{b}
Me_2SO	11.2±2.3	11±3	29±7^{c}	26±4^{c}	21±4^{b}
Prazosin 5 μg	11.1±2.3	11.5±1.8	23±4^{be}	19±4^{be}	19±3^{be}
Prazosin 10 μg	10.5±2.4	13±4	17±4^{bf}	16±3^{bf}	15±3^{be}
Yohimbine 5 μg	10.5±1.6	14.3±1.6	23±4^{be}	18.9±1.5^{be}	17.7±2.7^{be}
Yohimbine 10 μg	10.9±1.5	12.6±1.9	18±5^{bf}	16.2±1.2^{bf}	14.5±2.1^{bf}

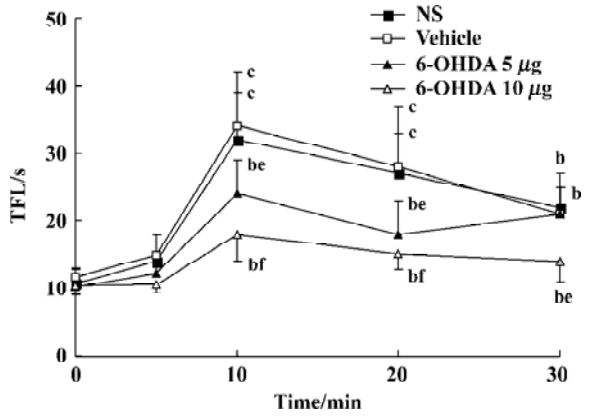

Figure 1. Effect of pretreatment with intrathecal 6-hydroxydopamine (6-OHDA) on the antinociception of propofol (50 mg/kg, sc) in tail-immersion test on mice. n=10. Mean±SD. $^{b}P<0.05$, $^{c}P<0.01$ *vs* baseline (0 min). $^{e}P<0.05$, $^{f}P<0.01$ *vs* NS.

during propofol anesthesia was not caused by a depression of spinal motoneuron circuit excitability[13]. In addition, pretreatment with ith 6-OHDA, prazosin, or yohimbine inhibited the antinociception of propofol but not propofol-induced motor impairment. Therefore, it is not probable that motor nerve conduction block affects TFL nonspecifically.

In the present study, propofol (25 and 50 mg/kg, sc) caused no noticeable sedation 30 min after its injection, but dose-dependently decreased the writhing times in the acetic-acid writhing test on mice. Therefore, these results suggested that systemic propofol also inhibited the chemical stimulation. The same results were shown in a previous study [2]. However, propofol had no effect on the writhing latency, which suggested that the antinociceptive effect of propofol at subanesthesia doses on inflammatory pain might be not very strong.

In the present study, systemic propofol (25 and 50 mg/kg, sc) and propofol (10 and 20 μg, ith) displayed a dose- and time-dependent antinociceptive effect. However, icv propofol did not produce any antinociceptive effects. Taken together, these results suggest that propofol produced antinociception at the spinal level but not at the supraspinal sites.

Ith 6-OHDA (20 μg) treatment for 3 d, which markedly depleted NE contents by more than 90% but not serotonin in the spinal cord study[12], significantly shortened the basal TFL in conscious mice in our study. Additionally, α_1R antagonist prazosin (20 μg, ith) or α_2R antagonist yohimbine (20 μg, ith) alone significantly shortened the basal TFL. These results supported the previous finding that noradrenergic synaptic transmission was important in pain sensory processing in the spinal dorsal horn. The effect of ith high dose of yohimbine on tail response was consistent with the conclusion that NE mediated the inhibition of nociception by α_2Rs in the spinal cord. The reduction of TFL after ith higher dose of prazosin suggested that spinal α_1Rs also contributed to the pain sensory modulation, which agrees with the purpose that NE mediated the inhibition of nociception by activation of α_1Rs located on inhibitory interneurons[8,9]. This possibility is supported by several studies which demonstrated that ith α_1R agonist activated dorsal horn to produce antinociception. For example ith selective α_1R agonists, such as methoxamine[14,15] and phenylephrine[16] produced antinociception that could be reduced by pretreatment with ith α_1R antagonist prazosin[14,15].

Pretreatment with ith 6-OHDA (5 and 10 μg), which markedly depleted NE contents in the spinal cord, significantly attenuated the antinociception of propofol. Furthermore, pretreatment with ith α_1R antagonist prazosin or α_2R antagonist yohimbine significantly inhibited the

antinociception of sc propofol in tail-immersion test. Therefore, these results strongly indicated that spinal noradrenergic system had a significant modulatory role in propofol antinociception. However, ith 6-OHDA, prazosin and yohimbine did not completely reverse the antinociception of propofol. This suggested that other mechanisms, such as an excitation of spinal $GABA_A$ receptors[1] and an inhibition of spinal NMDA, AMPA receptors[2], contributed to antinociception of propofol. In the present study, we used only α_1R and α_2R antagonists; therefore it was unclear whether propofol could bind directly with α_1Rs or α_2Rs in the spinal cord.

Taken together, our data suggest that systemic propofol activates the central noradrenergic system to produce antinociception, which increases the spinal release of NE and results in an antinociceptive effect via α_1Rs and α_2Rs in the spinal cord. To further prove this speculation, a direct measurement of the spinal release of NE induced by propofol will be necessary in the near future.

References

1 Nadeson R, Goodchid CS. Antinociceptive properties of propofol: involvement of spinal cord gamma-aminobutyric acid (A) receptors. J Pharmacol Exp Ther 1997; 282: 1181–6.

2 Xu AJ, Duan SM, Zeng YM. Effects of intrathecal NMDA and AMPA receptors agonists or antagonists on antinociception of propofol. Acta Pharmacol Sin 2004; 25: 9–14.

3 Antognini JF, Wang XW, Piercy M, Carstens E. Propofol directly depresses lumbar dorsal horn neuronal responses to noxious stimulation in goats. Can J Anaesth 2000; 47: 273–9.

4 Anwar MM, Abdel-Rahman MS. Effect of propofol on perception of pain in mice: mechanisms of action. Comp Biochem Physiol A Mol Integr Physiol 1998; 120: 249–53.

5 Fang F, Proudfit HK. Antinociception produced by microinjection of morphine in the rat periaqueductal gray is enhanced in the foot, but not the tail, by intrathecal injection of alpha1-adrenoceptor antagonists. Brain Res 1998; 790: 14–24.

6 Feng CY, McAdoo DJ, Willis WD. Periaqueductal gray stimulation-induced inhibition of nociceptive dorsal horn neurons in rats is associated with the release of norepinephrine, serotonin, and amino acids. J Pharmacol Exp Ther 1999; 289: 868–76.

7 Pan YZ, Li DP, Pan HL. Inhibition of glutamatergic synaptic input to spinal Lamina II_o neurons by presynaptic α_2-adrenergic receptors. J Neurophysiol 2002; 87: 1938–47.

8 Baba H, Shimoji K, Yoshimura M. Norepinephrine facilitates inhibitory transmission in substantia gelatinosa of adult rat spinal cord (part 1): effects on axon terminals of GABAergic and glycinergic neurons. Anesthesiology 2000; 92: 473–84.

9 Baba H, Goldstein PA, Okamoto M, Kohno T, Ataka T, Yoshimura M, *et al*. Norepinephrine facilitates inhibitory transmission in substantia gelatinosa of adult rat spinal cord (part 2): effects on somatodendritic sites of GABAergic neurons. Anesthesiology 2000; 92: 485–92.

10 Zhang CY, Zhu TJ, Hu GX, Chen XY, Liu DX, Chen ZK. Effect of sodium dimercaptopropanesulfonate on antagonism of tetramethylenedisulphotetramine to GABA receptor. Acta Pharmacol Sin 2001; 22: 435–9.

11 Xu SY, Bian RL, Chen X. Methodology of pharmacological experiments. 3 rd ed. Beijing: People's Medical Publishing House; 2002. p 882–7.

12 Hung KC, Wu HE, Mizoguchi H, Leitermann R, Tseng LF. Intrathecal treatment with 6-hydroxydopamine or 5,7-dihydroxytryptamine blocks the antinociception induced by endomorphin-1 and endomorphin-2 given intracerebroventricularly in the mouse. J Pharmacol Sci 2003; 93: 299–306.

13 Kerz T, Hennes HJ, Feve A, Decq P, Filipetti P, Duvaldestin P. Effects of propofol on H-reflex in humans. Anesthesiology 2001; 94: 32–7.

14 Loomis CW, Arunachalam KD. Intrathecal St-587: effects on nociceptive reflexes and blood pressure in the rat. J Pharmacol Exp Ther 1992; 263: 428–35.

15 Howe JR, Wang JY, Yaksh TL. Selective antagonism of the antinociceptive effect of intrathecally applied alpha adrenergic agonists by intrathecal prazosin and intrathecal yohimbine. J Pharmacol Exp Ther 1983; 224: 552–8.

16 Aran S, Proudfit HK. Antinociceptive interactions between intrathecally administered alpha noradrenergic agonists and 5'-*N*-ethylcarboxamide adenosine. Brain Res 1990; 519: 287–93.

Full-length article

Effects of complete Freund's adjuvant on immunohistochemical distribution of IL-1β and IL-1R I in neurons and glia cells of dorsal root ganglion[1]

Man LI, Jing SHI[2], Jun-rui TANG[3], Di CHEN[3], Bo AI[3], Jun CHEN[3], Li-na WANG, Fu-yuan CAO, Ling-li LI, Chuan-you LIN, Xin-min GUAN

Department of Neurobiology, Tongji Medical College of Huazhong University of Science and Technology, Wuhan 430030, China

Key words

experimental arthritis; interleukin-1; interleukin-1 receptors; spinal ganglia

[1] Project supported by the grant of Major Research Plan of National Natural Science Foundation of China (No 90209009) and the grant of Natural Science Foundation of Hubei Province (No 2002AB124).
[2] Correspondence to Dr Jing SHI.
Phn 86-27-8369-2630.
Fax 86-27-8369-2608.
E-mail jingshitj@hotmail.com
[3] Seven year system students of 2000, Tongji Medical College of Huazhong University of Science and Technology

Received 2004-04-22
Accepted 2004-11-17

doi: 10.1111/j.1745-7254.2005.00022.x

Abstract

Aim: To investigate the effects of complete Freund's adjuvant (CFA) on inflammatory hyperalgesia and morphological change of the coexsistence of interleukin-1 beta (IL-1β) and type I IL-1 receptor (IL-1RI) in neurons and glia cells of rat dorsal root ganglion (DRG). **Methods:** The pain-related parameters and the expression of IL-1RI and IL-1β positive neurons and glia cells of DRG in normal saline (NS) and adjuvant-induced arthritic (AA) group were examined with pain behavior assessment methods and immunohistochemical assay, respectively. **Results:** Five hours, 1 d, and 2 d after intra-articular injection of 50 μL CFA, tactile hyperalgesia induced by CFA was observed in the foot flexion and extension scores of the ipsilateral hindpaw of AA group. Three days after injection, the distribution of IL-1RI/IL-1β double-stained coexisted neurons and glia cells were observed in ipsilateral DRG of both groups. The number of IL-1β positive neurons, IL-1RI positive neurons, IL-1β/IL-1RI double-stained neurons, and IL-1RI positive glia cells in ipsilateral DRG of the AA group were higher than that of NS group ($P<0.05$ or $P<0.01$). **Conclusion:** The coexsistence of IL-1β and IL-1RI in neurons and nonneuronal cells suggests an as yet unknown autocrine and/or paracrine function of IL-1β in the DRG. The function was enhanced in articular arthritis induced by CFA and could play an important role in hyperalgesia under inflammatory conditions.

Introduction

Interleukin-1 beta (IL-1β) is a bioactive polypeptide cytokine that is produced by a large variety of cells, including macrophages, fibroblasts, keratinocytes, synovicytes, mast cells, glial cells, and neurons; and has various immune roles responding to antigens, malignant cells, inflammatory stimuli, and tissue injury[1]. IL-1β also has proinflammatory cytokine activity and induces hyperalgesia after subcutaneous injection into the rat paw[2] or after intrathecal administration in rats and mice[3,4]. This means administration of exogenous IL-1β can produce hyperalgesia. However, inflammation can also induce the release of endogenous IL-1β which was responsible for hyperalgesia as well. A previous study showed that intraplantar injection of complete Freund's adjuvant (CFA) in adult rats resulted in a significant elevation in IL-1β and nerve growth factor (NGF) levels in the inflamed tissue[5–6]. IL-1β exerts its effects through high-affinity receptors on target cells, of which two types have been identified: IL-1RI and IL-1RII[7]. IL-1 receptor antagonist (IL-1Ra), has been shown conclusively to block the effects of IL-1β[8]. Targeted deletion of the IL-1 receptor type I or the IL-1 receptor accessory protein, and transgenic over-expression of IL-1Rα within the brain and spinal cord significantly lowered thermal and mechanical pain sensitivity in mice[9].

The major cellular source of IL-1β production in the central nervous system are from glial cells, predominantly microglia. However, several studies have provided evidence for the neuronal expression of IL-1β in the peripheral ner-

vous system: sensory neurons in the dorsal root ganglia (DRG) as well as sympathetic neurons[10]. Moreover, cytokines released in the periphery by sensory and by sympathetic neurons have an established role in regulating immune cell activation, connective tissue and vascular responses, and nociception in peripheral inflammatory processes. Among the cytokines produced and released by both sensory and sympathetic neurons are transforming growth factor-β (TGF-β), tumor necrosis factor-alpha (TNF-α), and interferon-gama (IFN-γ)[11,12]. Sympathetic neurons have also been demonstrated to express IL-1β[13,14]. IL-1β appears to be an important mediator in nocicepsis and has been shown to induce the release of substance P from nociceptive sensory neurons[15]. The expression of IL-1β as well as the type I IL-1 receptor in sensory neurons in rat DRG has been investigated using nonradioactive *in situ* hybridization and immunohistochemistry[16]. However, there is no morphological evidence for the coexistence of IL-1β and IL-1RI of neurons and glia cells in DRG and the effects of articular injection of CFA.

In the present study, we investigated the effects of CFA on inflammatory hyperalgesia and the morphological changes of IL-1β and IL-1RI coexistence in neurons and glia cells of rat DRG.

Materials and methods

Animals Experiments were carried out on male adult Sprague-Dawley rats (180–200 g), purchased from the Experimental Animals Center of Tongji Medical College of Huazhong University of Science and Technology (Grade II, Certificate No 19-053). The rats were housed individually in cages with a 12-h light/dark cycle, and had free access to food and water for a week before experiments began. They were randomly divided into two groups: (1) normal saline (NS) group (n=7), the rats were pretreated with an intra-articular injection of 50 μL normal saline into the left (ipsilateral) tibio-tarsal joint under light anesthesia with 10% chlorohydrate (300 mg/kg, ip) injection; (2) adjuvant-induced arthritic (AA) group (n=7), the rats were pretreated with an intra-articular injection of 50 μL complete Freund's adjuvant (CFA, Sigma) into the left tibio-tarsal joint under the same light anesthesia[17,18].

Preclinical tests The following parameters were measured: (1) weight; (2) mobility score[19] (0=the rat only lies down; 1=the rat only crawls; 2=the rat walks with difficulty; 3=the rat walks and runs with difficulty; 4=the rat walks and runs normally); (3) diameter of the tibiotarsal joint, detected with vernier caliper.

Pain behavioral parameters The following pain parameters were measured using teo tests in the following sequence[20]: (1) flexion scores: mean scores of rats was evaluated by flexion of one hind paw. Under these conditions a squeak or leg-withdrawal could be elicited. Five such stimuli were repeated at 5-s intervals, and a rating of 1 or 0 was respectively given depending on whether the animal emitted a squeak or leg-withdrawal. Thus for each animal the total scores of squeak and leg-withdrawal ranged from 0 to 10; (2) extension scores: mean scores of rats as evaluated by extension of one hind paw (identical rating used as for flexion score).

Each group animals were tested before injection to obtain baseline value and continued to be detected in 5 h, 1 d, and 2 d post-injection.

Tissue preparation On d 3 post-injection, all animals were deeply anesthetized with 20% urethane (1 g/kg) by abdominal injection, cleared with 200 mL of saline solution and perfused with 300 mL of 4% phosphate-buffered paraformaldehyde (pH 7.4) through left ventricle. After perfusion, the L4-L5 ipsilateral DRG was removed and post-fixed for 8-10 h. They were then soaked in 20% sucrose phosphate-buffered solution at 4 ºC overnight prior to freezing and subsequent cryosectioning. Sections (10 μm) were cut on a cryostat.

The sections were put in 0.01 mol/L PBS buffered solution. Sections were selected randomly to do experiments with double immunofluorescence staining of IL-1RI/IL-1β, or IL-1RI immunohistochemistry single staining procedure.

Double immunofluorescence staining procedure We used the following steps: (1) sections were incubated with 0.25% Triton X-100 for 30 min at 37 ºC; (2) after being rinsed by 0.01 mol/L PBS, sections were incubated with 15% normal goat serum for 30 min at 37 ºC; (3) sections were then incubated for 48 h at 4 ºC in a mixture of the two primary antibodies (rabbit anti-rat IL-1RI, 1:100, Santa Cruz; mouse anti-rat IL-1β, 1:100, Serotec); (4) after being rinsed in PBS, sections were incubated for 3 h at room temperature in a mixture of the two secondary antibodies, Cy3-conjugated anti-rabbit IgG (Sigma, 1:200) and FITC-conjugated anti-mouse IgG (Sigma, 1:200); (5) the sections were picked and mounted on slides with glycerin-PBS buffered solution (1:9).

Omission of the primary antibody and incubation in IL-1β or IL-1RI pre-absorbed antibody served as negative controls. Laser scanning confocal microscope (Lesia, German) was used to take photos and fluorescent microscope (Olympus, Japan) was used to capture images and count positive cells.

IL-1RI immunohistochemistry procedure We used fol-

lowing steps: steps (1) and (2) were the same as above double immunofluorescence stain procedure; (3) sections were then incubated for 48 h at 4 ℃ in the primary antibodies (rabbit anti-rat IL-1RI , Santa Cruz,1:200). (4) after being rinsed in PBS, sections were incubated for 30 min at room temperature of the secondary antibodies, biotinylated goat anti-rabbit IgG (Santa Cruz, 1:200); (5) after being thoroughly washed in PBS, the sections were incubated in a streptavidine-peroxidase conjugate (Santa Cruz, 1:200) for 30 min at room temperature; (6) after being rinsed with 0.05 mol/L Tris-buffered saline, the immunoreaction product was revealed by a freshly prepared solution containing 0.04% 3,3-diamino-benzidine and 0.01% H_2O_2. The sections were picked up and mounted on slides with glutin. They were dehydrated with graded alcohol and transparentized with xylene, then covered with neutral gum. Each experiment had set up blank antitheses as described before.

Statistic analysis Seven rats per group were used for analysis. Digital images were captured in four sections per animal and 10 squares (38.4 mm^2 each) per section of immunofluorescence or immunohistochemistry respectively, using an Olympus microscope (objective×20; eyepiece×10) and a 3CC immunohistochemistry-D color video camera (Sony). The number of immunofluorescence-stained IL-1RI/IL-1β positive neurons or immunohistochemistry-stained IL-1RI positive glia cells in each image were counted by a blinded experimenter with a computer-assisted image analyzer (Image Pro-plus Kodak, USA). The number of positive DRG large-, medium-, and small-sized neurons were calculated. As reported previously, the primary sensory neurons in the DRG have been classified into large type A neurons (diameter over 30 μm), medium diameter neurons type B, and small type C neurons (diameter under 20 μm)[21]. For large neurons were regarded as medium sized ones when they were not cut through their nucleus. In our study we calculated the total of medium and large neurons of immunofluorescence-stained IL-1RI/IL-1β positive neurons. The SPSS software (SPSS 11.0) was used for data analysis. The data was expressed as mean±SD, and analysis of variance (ANOVA) was used to compare the difference among different groups.

Results

Preclinical and behavioral studies After 5 h, 1 d, and 2 d of intra-articular injection of 50 μL CFA, the weight of the rats was unchanged (P>0.05, data not shown). The rats of the AA group developed inflammation which was confined to the inoculated articular characterized by edema of ipsilateral tibiotarsal joint (Table 1). There was a dramatic decrease observed in the mobility scores of rats of the AA group compared with the NS group (P<0.05, P<0.01, Table 2). In other words, the inoculated rats are impaired in their ambulatory activities.

Table 1. Diameter of the ipsilateral tibiotarsal joint of rats in NS group and AA group. n=7. Mean±SD. ^bP<0.05, ^cP<0.01 *vs* NS group.

Group	Diameter of the ipsilateral tibiotarsal joint/mm			
	Before injection	5 h after injection	1 d after injection	2 d after injection
NS	4.32±0.02	5.33±0.11	5.46±0.40	4.86±0.08
AA	4.52±0.07	6.34±0.15^c	6.37±0.24^b	5.86±0.40^b

Table 2. Mobility score of rats in NS group and AA group. n=7. Mean±SD. ^bP<0.05, ^cP<0.01 *vs* NS group.

Group	Mobility score of rats in NS group and AA			
	Before injection	5 h after injection	1 d after injection	2 d after injection
NS	4	3.71±0.18	3.43±0.20	3.71±0.18
AA	4	2.57±0.20^c	2.71±0.29^b	2.86±0.14^c

Effects of CFA on the pain behavioral parameters of rats Five hours, 1d, and 2 d after intra-articular injection of 50 μL CFA, tactile hyperalgesia induced by CFA was observed in the foot flexion and extension scores of ipsilateral hindpaw of AA group (Table 3, 4), while the pain scores of the contralateral hindpaw of both groups were close to 0 and had no significant difference (P>0.05, data not shown).

Table 3. Ipsilateral flexion score of rats in NS group and AA group. n=7. Mean±SD. ^bP<0.05, ^cP<0.01 *vs* NS group.

Group	Ipsilateral flexion score			
	Before injection	5 h after injection	1 d after injection	2 d after injection
NS	0	3.86±1.50	3.43±1.70	2.86±1.10
AA	0.43±0.30	7.43±1.34^b	7.71±1.41^b	7.57±1.32^c

Effects of CFA on double immunofluorescence staining of IL-1β and IL-1RI of ipsilateral DRG Three days after

Table 4. Ipsilateral extention score of rats in NS group and AA group. n=7. Mean±SD. $^bP<0.05$, $^cP<0.01$ *vs* NS group.

Group	Ipsilateral extention score			
	Before injection	5 h after injection	1 d after injection	2 d after injection
NS	0.29±0.18	1.14±0.26	2.57±0.75	2.29±0.97
AA	0.29±0.18	7.57±1.23^c	6.14±1.55^b	5.86±0.91^b

injection, IL-1β and IL-1RI positive products were detected in the same neurons as well as in some glial-like cell types. IL-1β/IL-1RI immunoreactivity positive products were mainly located in the cytoplasma and nucleus of the positive neurons of NS group (Figure 1), while immunoreactivity positive products were distributed in the membrane and nucleus of the positive neurons of the AA group (Figure 2). There were still a few neurons presented no IL-1β or IL-1RI immunoreactivity in the DRG of the NS group, but most neurons in the DRG of AA group presented IL-1β or IL-1RI immunoreactivity (Figure 1C, 2C).

With statistic analysis, it was found that the number of IL-1RI single stained neurons, IL-1β/IL-1RI double-stained neurons, and the percentages of the number of double-stained neurons to the number of IL-1β positive neurons of small neurons in DRG of AA group were higher than that of NS group ($P<0.05$ or $P<0.01$, Table 5). The number of IL-1RI single stained neurons, IL-1β/IL-1RI double-stained neurons of large and medium neurons in DRG of AA group were higher than that of NS group ($P<0.05$, Table 6). The percentage of double-stained neurons to IL-1β or IL-1RI positive neurons of large and medium neurons in DRG presented no significant difference between the two groups ($P>0.05$, Table 6).

Effects of CFA on single immunohistochemistry staining of IL-1RI of ipsilateral DRG Three days after injection, the IL-1RI in DRG was expressed in glial-like cell types as well as in sensory neurons using a microscope under normal light. Some of the glial-like cells were satellite cells ensheathing the large sensory cell bodies, some sparsely distributed in the connective tissues between neurons of DRG. The IL-1RI immunoreactivity positive products were stained as brown and mainly located in the membrane and cytoplasma of glia cells. The stained color of glia cells in DRG of AA group was deeper than that of the NS group (Figure 3, 4). The number of glia cells of DRG of AA group was 13.45± 2.35/38.4 mm^2, which was higher than that of NS group (5.31±1.58/38.4mm^2)($P<0.01$).

Table 5. The percentage of IL-1β/IL-1RI double-stained small neurons to IL-1β or IL-1RI single-stained small neurons of DRG. n=7. Mean±SD. $^bP<0.05$, $^cP<0.01$ *vs* NS group.

	Double-stained neurons Number/38.4mm^2	IL-1β positive neurons Number/38.4mm^2	IL-1RI positive neurons Number/38.4mm^2	%[1)]	%[2)]
NS group	21.5±2.1	33.8±3.7	29.1±3.2	58.8±6.0	68.2±6.8
AA group	35.9±2.6^b	45.1±4.2	45.0±3.1^b	82.4±4.0^b	81.4±4.3

[1)] The percentages of the number of double-stained neurons to the total number of the IL-1β positive neurons; [2)] The percentages of the number of double-stained neurons to the total number of the IL-1RI positive neurons.

Table 6. The percentage of IL-1β/IL-1RI double-stained large, medium neurons to IL-1β or IL-1RI single-stained Large, medium neurons of DRG. n=7. Mean±SD. $^bP<0.05$ *vs* NS group.

	Double-stained neurons Number/38.4mm^2	IL-1β positive neurons Number/38.4mm^2	IL-1RI positive neurons Number/38.4mm^2	%[1)]	%[2)]
NS group	17.9±1.8	25.9±2.7	21.3±2.3	63.6±6.6	76.1±7.0
AA group	26.2±2.3^b	34.8±3.2	30.0±2.4^b	76.8±4.8	87.5±2.8

[1)] The percentages of the number of double-stained neurons to the total number of the IL-1β positive neurons; [2)]The percentages of the number of double-stained neurons to the total number of the IL-1RI positive neurons.

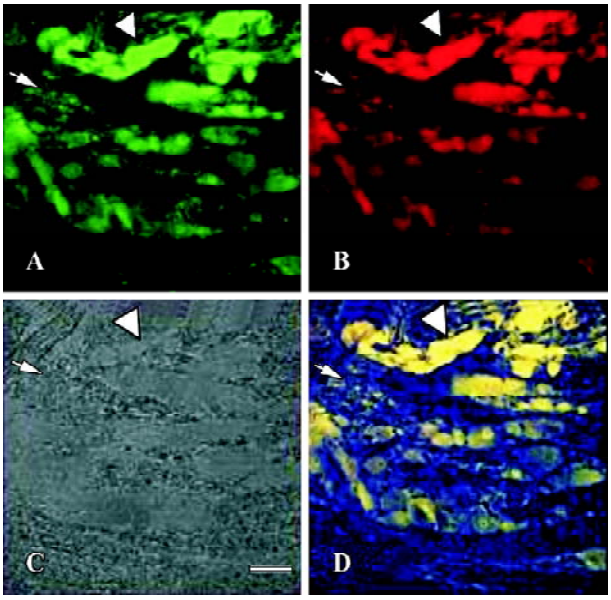

Figure 1. The FITC labeled IL-1β immunoreactivity positive cells (A), Cy3 labeled IL-1RI immunoreactivity positive cells (B), cells under normal light (C), and IL-1β/IL-1RI double-stained immunoreactivity positive cells (D) in DRG of NS group. Arrowhead pointed to double-stained neurons, while arrow pointed to double-stained glia cells. The immunoreactivity positive products were mainly located in the cytoplasma and nucleus. Scale bar=100 μm.

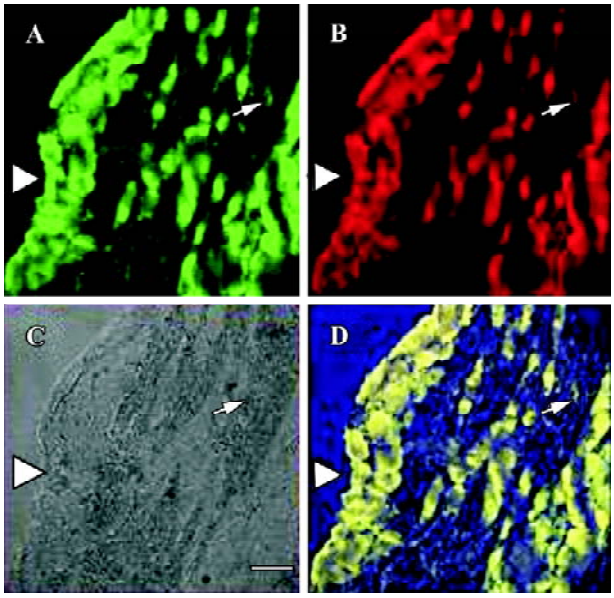

Figure 2. The FITC labeled IL-1β immunoreactivity positive cells (A), Cy3 labeled IL-1RI immunoreactivity positive cells (B), and cells under normal light (C), and IL-1β/IL-1RI double-stained immunoreactivity positive cells (D) in DRG of AA group. Arrowhead pointed to double-stained neurons, while arrow pointed to double-stained glia cells. The immunoreactivity positive products were mainly located in the membrane and nucleus. Scale bar=100 μm.

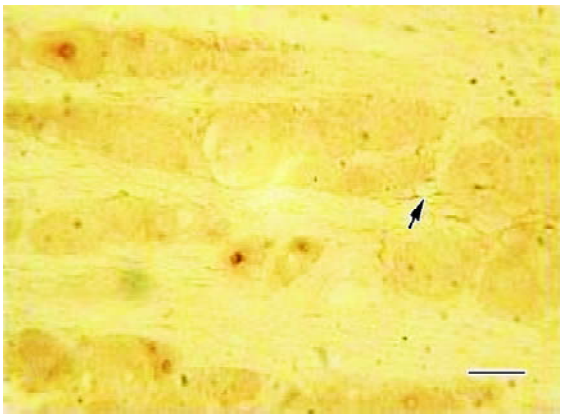

Figure 3. The IL-1RI positive glia cells sparsely distributed in the connective tissues between neurons of DRG of NS group, whose cytoplasm was stained as light brown (arrow). Scale bar=25 μm.

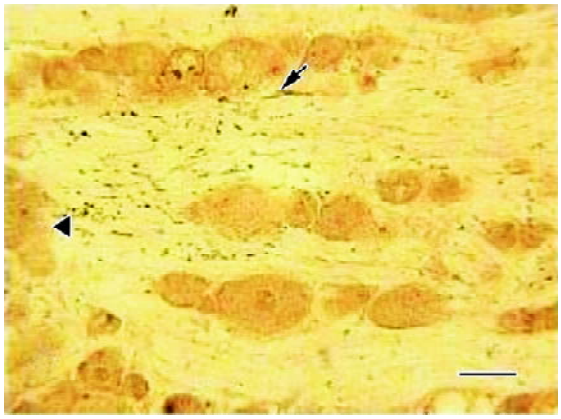

Figure 4. The IL-1RI positive glia cells sparsely distributed in the connective tissues between neurons of DRG (arrowhead) or ensheathened the large sensory cell bodies (arrow) of AA group, whose cytoplasm was stained as deep brown. Scale bar=25 μm

Discussion

IL-1β is one of the cytokines synthesized and released from immunocytes and considered to be an important mediator during inflammation and hyperalgesia. Indeed, the injection of IL-1β into animals has been shown to produce hyperalgesia in response to mechanical and thermal stimuli [2–4,22]. There are several lines of evidence indicating that IL-1β alters primary afferent neural activity or sensitivity in mice and rats[10,23–25]. Nociceptive primary afferent neurons contain neuropeptides such as SP, neurokinin A, and calcitonin gene-related peptide that are released on stimulation of these afferent fibers. A previous study of cellular culture experiment demonstrated that IL-1β can induce SP to release from cultured DRG by activating the COX-2 system. IL-1R antago-

nist can block this access, which suggests an IL-1β exerted effect by combine with IL-1R on DRG[15]. Using RT-PCR with *in situ* hybridization, it was found that type I IL-1R, not type II, expressed on the DRG of normal rats[26]. However, there is no study on the coexistence of IL-1RI and IL-1β in neurons and glia cells of DRG and the influence of adjuvant-induced arthritic on it.

In the present study, we demonstrated that both IL-1RI and IL-1β coexsisted in the sensory neurons and glia cells of normal saline injected rats. The combined expression of IL-1β and the type I IL-1 receptor suggests autocrine or paracrine IL-1β signaling in sensory neurons.

Meanwhile a significant increase in the IL-1RI and IL-1β double stained neurons in ipsilateral DRG were observed in the AA group than in the NS group, and IL-1RI mainly distributed in the membrane of the AA group than in the cytoplasma of NS group. This morphological change also paralleled to the pain behaviour scores. It indicated that the inflammation resulted in the up-regulation of the expression of IL-1RI on the membrane of neurons in ipsilateral DRG, and the increase of IL-1β sythesis as well.

It has been found that intraplantar injection of CFA increased the concentration of IL-1β and NGF accompanied by elevation of the level of substance P and calcitonin gene-related peptide (CGRP) in the L4 dorsal root ganglion 48 h post CFA injection[5]. The author demonstrated that IL-1β could alter neuropeptide expression in primary sensory neurons secondary to an increase of NGF levels as NGF has well known actions on the regulation of both SP and CGRP in adult rat DRG neurons[6]. It has been recently proved that IL-1β increases SP synthesis by enhancing the expression of preprotachykinin mRNA encoding for SP and other tachykinins in the DRG[27]. Our results showed that IL-1β could be synthesized in neurons of DRG, as wells as in the inflamed tissue from previous study, it indicated that more IL-1β was able to release by neurons of DRG and excite more IL-1RI, which presumably brought about more SP synthesis and release in the central and peripheral terminals of neurons in the DRG, which in turn led to hyperalgesia.

We also found that the number of glia cells in ipsilateral DRG, which express IL-1RI, increased after CFA injection. The expression of type I IL-1 receptor in non-neuronal cells in the DRG might mediate another possible function of IL-1β synthesized by the sensory neurons. It has been reported that IL-1β enhances neurite outgrowth in DRG[28], which would contribute to tactile hypersensitivity of articular arthritis. This effect of IL-1β seems to be indirect and presumably involves an IL-1β-induced increased in release of neurotrophins from nonneuronal cells[29]. It could be that, under inflammatory condition sensory neurons regulate their own maintenance by releasing more IL-1β and thus stimulating their environment to release neurotrophins to induce hyperalgesia.

Our study showed that IL-1β/IL-1RI doubled stained immunoreactivity positive products were located in the nucleus as well as the cytoplasma or membrane of positive neurons in ipsilateral DRG of both groups. This is consistent with the results of immunoelectron microscopy, which found that GSSP-intensified IL-1β immunoreaction products were found dispersed in small aggregates throughout the cytoplasm and a few small immuno-aggregates of IL-1β were also found in the nucleus of neurons in DRG. The functional significance of intranuclear IL-1β/IL-1RI is as yet unclear, but might suggest involvement in transcriptional regulation[16].

In conclusion, we found coexistence of IL-1β and IL-1RI in sensory neurons and glia cells of DRG. The presence of the type I IL-1 receptor in neurons and non-neuronal cells suggests an as yet unknown autocrine and/or paracrine function of IL-1β in the DRG. The function was enhanced in the articular arthritis induced by CFA and might play an important role in hyperalgisia under the inflammatory condition.

References

1 Cunha FQ, Ferreira SH. Peripheral hyperalgesic cytokines. Adv Exp Med Biol 2003; 521: 22–39.

2 Sachs D, Cunha FQ, Poole S, Ferreira SH. Tumour necrosis factor-alpha, interleukin-1beta and interleukin-8 induce persistent mechanical nociceptor hypersensitivity. Pain 2002; 96: 89–97.

3 Sung CS, Wen ZH, Chang WK, Ho ST, Tsai SK, Chang YC, *et al.* Intrathecal interleukin-1beta administration induces thermal hyperalgesia by activating inducible nitric oxide synthase expression in the rat spinal cord. Brain Res 2004; 1015: 145–53.

4 Tadano T, Namioka M, Nakagawasai O, Tan-No K, Matsushima K, Endo Y, *et al.* Induction of nociceptive responses by intrathecal injection of interleukin-1 in mice. Life Sci 1999; 65: 255–61.

5 Safieh-Garabedian B, Poole S, Allchorne A, Winter J, Woolf CJ. Contribution of interleukin-1 beta to the inflammation-induced increase in nerve growth factor levels and inflammatory hyperalgesia. Br J Pharmacol 1995; 115: 1265–75.

6 Woolf CJ, Safieh-Garabedian B, Ma QP, Crilly P, Winter J. Nerve growth factor contributes to the generation of inflammatory sensory hypersensitivity. Neuroscience 1994; 62: 327–31.

7 Cunningham ET, De Souza EB. Interleukin-1 receptors in the brain and endocrine tissues. Immunol Today 1993; 14: 171–6.

8 Cutolo M. IL-1Rα: its role in rheumatoid arthritis. Reumatismo 2004; 56: 41–5.

9 Wolf G, Yirmiya R, Goshen I, Iverfeldt K, Holmlund L, Takeda K, *et al.* Impairment of interleukin-1 (IL-1) signaling reduces basal pain sensitivity in mice: genetic, pharmacological and de-

velopmental aspects. Pain 2003; 104: 471–80.
10 Watkins LR, Maier SF, Goehler LE. Immune activation: the role of pro-inflammatory cytokines in inflammation, illness responses and pathological pain states. Pain 1995; 63: 289–302.
11 Kiefer R, Kreutzberg GW. Gamma interferon-like immunoreactivity in the rat nervous system. Neuroscience 1990; 37: 725–34.
12 Xian CJ, Zhou XF. Neuronal-glial differential expression of TGF-alpha and its receptor in the dorsal root ganglia in response to sciatic nerve lesion. Exp Neurol 1999; 157: 317–26.
13 Freidin M, Bennett MV, Kessler JA. Cultured sympathetic neurons synthesize and release the cytokine interleukin 1 beta. Proc Natl Acad Sci USA 1992; 89: 10440–3.
14 Kreicbergs A, Ahmed M, Ehrnberg A, Schultzberg M, Svenson SB, Bjurholm A. Interleukin-1 immunoreactive nerves in heterotopic bone induced by DBM. Bone 1995; 17: 341–5.
15 Morioka N, Takeda K, Kumagai K, Hanada T, Ikoma K, Hide I, *et al*. Interleukin-1beta-induced substance P release from rat cultured primary afferent neurons driven by two phospholipase A2 enzymes: secretory type IIA and cytosolic type IV. J Neurochem 2002; 80: 989–97.
16 Copray JCVM, Mantingh I, Brouwer N, Biber K, Kust BM, Liem RSB, *et al*. Expression of interleukin-1 beta in rat dorsal root ganglia. J Neuroimmunology 2001; 118: 203–11.
17 Butler SH, Godefroy F, Besson JM, Weil-Fugazza J. A limited arthritic model for chronic pain studies in the rat. Pain 1992; 48: 73–81.
18 Liu HX, Xu W, Luo F, Wang JS, Han JS. A limited arthritic model for the chronic pain in rats. Chin J Pain Med 1996; 2: 223–8.
19 Butler SH, Weil-Fugazza J, Godefroy F, Besson JM. Reduction of arthritis and pain behaviour following chronic administration of amitryptiline or impipramine in rats with adjuvant-induced arthritis. Pain 1985; 23: 159–75
20 Liu HX, Xiong L, Luo F, Han JS. Improved scoring method for arthritic flexion pain test in Freund's adjuvant monoarthiritic model in the rat. Chin J Pain Med 1998; 4: 173–8.
21 Kai-Kai MA. Cytochemistry of the trigeminal and dorsal root ganglia and spinal cord of the rat. Comp Biochem Physiol 1989; 93A: 183–93.
22 Oka T, Oka K, Hosoi M, Hori T. Inhibition of peripheral interleukin-1β-induced hyperalgesia by the intracerebroventricular administration of diclofenac and α-melanocyte-stimulating hormone. Brain Res 1996; 736: 237–42.
23 Perretti M, Ahluwalia A, Flower RJ, Manzini S. Endogenous tachykinins play a role in IL-1-induced neutrophil accumulation: involvement of NK-1 receptors. Immunology 1993; 80: 73–7.
24 Fukuoka H, Kawatani M, Hisamitsu T, Takeshige C. Cutaneous hyperalgesia induced by peripheral injection of interleukin-1β in the rat. Brain Res 1994; 657: 133–40.
25 Malcangio M, Bowery NG, Flower RJ, Perretti M. Effect of interleukin-1β on the release of substance P from rat isolated spinal cord. Eur J Pharmacol 1996; 299: 113–8.
26 Obreja O, Rathee PK, Lips KS, Distler C, Kress M. IL-1β potentiates heat-activated currents in rat sensory neurons: involvement of IL-1RI, tyrosine kinase, and protein kinase C. FASEB J 2002; 16: 1497–503.
27 Igwe OJ. c-Src kinase activation regulates preprotachykinin gene expression and substance P secretion in rat sensory ganglia. Eur J Neurosci 2003; 18: 1719–30.
28 Horie H, Sakai I, Akahori Y, Kadoya T. IL-1 beta enhances neurite regeneration from transected-nerve terminals of adult rat DRG. Neuroreport 1997; 8: 1955–9.
29 Zhou XF, Deng YS, Chie E, Xue Q, Zhong JH, McLachlan EM, *et al*. Satellite-cell-derived nerve growth factor and neurotrophin-3 are involved in noradrenergic sprouting in the dorsal root ganglia following peripheral nerve injury in the rat. Eur J Neurosci 1999; 11: 1711–22.

Full-length article

Inhibition of ATP-induced calcium influx in HT4 cells by glucocorticoids: involvement of protein kinase A[1]

Jian-zhong HAN, Wen LIN[2], Yi-zhang CHEN[3]

Neuroscience Research Institute and Department of Neurobiology, [2]Department of Pharmacology, College of Pharmacy, Second Military Medical University, Shanghai 200433, China

Key words

calcium; glucocorticoids; adenosine triphosphate; protein kinase C; protein kinase A

[1] Project supported by the National Basic Research Program of China (No G1999054003) and the National Natural Science Foundation of China (No 39330100 and 39840019).
[3] Correspondence to Prof Yi-zhang CHEN. Phn/Fax 86-21-6534-3087. E-mail yzchen@public.sta.net.cn

Received 2004-05-25
Accepted 2004-11-19

doi: 10.1111/j.1745-7254.2005.00039.x

Abstract

Aim: In our previous observations, adenosine triphosphate (ATP) was found to evoke immediate elevations in intracellular free calcium concentration ($[Ca^{2+}]_i$) in HT4 neuroblastoma cells of mice. We tried to see if a brief pretreatment of glucocorticoids could inhibit the Ca^{2+} response and reveal the underlying signaling mechanism. **Methods:** Measurement of $[Ca^{2+}]_i$ was carried out using the dual-wavelength fluorescence method with Fura-2 as the indicator. **Results:** Preincubation of HT4 cells for 5 min with corticosterone (B) or bovine serum albumin conjugated corticosterone (B-BSA) inhibited the peak $[Ca^{2+}]_i$ increments in a concentration-dependent manner. Cortisol and dexamethasone had a similar action, while deoxycorticosterone and cholesterol were ineffective. Both extracellular Ca^{2+} influx and internal Ca^{2+} release contributed to ATP-induced $[Ca^{2+}]_i$ elevation. The brief treatment with only B attenuated Ca^{2+} influx. Furthermore, the $[Ca^{2+}]_i$ elevation induced by the P2X receptor agonist adenosine 5'-(β,γ-methylene) triphosphate (β,γ-meATP) was also suppressed. The rapid inhibitory effect of B can be reproduced by forskolin 1 mmol/L and blocked by H89 20 mmol/L. Neither nuclear glucocorticoid receptor antagonist mifepristone nor protein kinase C inhibitors influenced the rapid action of B. **Conclusion:** Our results suggest that glucocorticoids modulate P2X receptor-medicated Ca^{2+} influx through a membrane-initiated, non-genomic and PKA-dependent pathway in HT4 cells.

Introduction

Glucocorticoids (GC) play an important role in the developmental organization and ongoing activities of the nervous system[1]. At cellular level, they work in a diverse manner. A genomic mechanism where the complex of GC and their receptors acts as nuclear transcription factor has been well elucidated over the past 30 years, and accounts for the long-latency effects of most GC. However, some of their actions take place so rapidly (onset in seconds or minutes) that they do not fit into the paradigm of the genomic mechanism[2,3]. There are many examples in which GC act through the rapid, non-genomic way in the nervous system, ranging from the regulation of neuronal excitability to the modulation of neurotransmitter secretion and uptake[1,2].

The HT4 neuroblastoma cell line was derived from the hippocampal neurons of mice[4]. In our previous observations, we found an ATP-induced transient in $[Ca^{2+}]_i$ within the cells[5]. The Ca^{2+} response was decreased by the activation of protein kinase A (PKA) or protein kinase C (PKC) (unpublished data). As it is already known that some of the rapid actions of GC are mediated by protein kinases[6,7], we wonder whether there is a similar signaling pathway for GC in HT4 cells, which may result in fast modification of the ATP-induced Ca^{2+} response. We provide evidence showing that ATP-induced Ca^{2+} response can be rapidly modified by GC through a membrane-initiated, nongenomic pathway that is PKA dependent.

Materials and methods

Materials ATP, β, γ-meATP, bovine serum albumin con-

jugated corticosterone (B-BSA), cholesterol, corticosterone (B), cortisol, deoxycorticosterone, dexametha-sone, egtazic acid, *N*-[2-hydroxyethyl] piperazine-*N'*-[2-ethanesulfonic acid] (HEPES), ionomycin, pluronic F-127, phorbol 12-myristate 13-acetate (PMA), and thapsigargin (TG) were obtained from Sigma (St Louis, MO, USA). Forskolin, H-89, GF-109203X, and Ro31-8220 were obtained from Calbiochem-Novabiochem (San Diego, CA). DMEM and *L*-glutamine used for cell culture from Life Technologies (Gaithersburg, MD, Germany). Trypsin from Amresco Inc (Solon, OH, USA). Fura-2 acetoxymethyl (AM) ester from Molecular Probes (Eugene, OR, USA). Newborn calf serum was from Sijiqing Co (Hangzhou, China). All other chemicals used were of analytical grade.

Cell culture HT4 cells, a kind gift from Dr B AMES (University of California at Berkeley), were maintained in DMEM containing 10% newborn calf serum and 4 mmol/L *L*-glutamine in a humidified atmosphere of 95% air and 5% CO_2 at 37 ºC. No antibiotic was added to the media. For $[Ca^{2+}]_i$ measurements, cells were seeded on glass coverslips and used with in 3–4 d.

Fura-2 loading In the present study, fluorescent dye Fura-2 was used to indicate the $[Ca^{2+}]_i$. The cells on the coverslips were loaded *in situ* at 37 ºC for 30–60 min in HEPES-buffered saline (in mmol/L: NaCl 140, KCl 5, $MgCl_2$ 1, $CaCl_2$ 2.5, glucose 11.5, HEPES 10, pH 7.2–7.4) containing Fura-2 AM 2 μmol/L and 0.04% pluronic F-127. The Fura-2-loaded cells were then rinsed three times with saline and mounted in a perfusion chamber for immediate $[Ca^{2+}]_i$ measurements. Alternatively, they were kept in dark conditions at room temperature for up to 2 h. Fura-2 loading was uniform over the cytoplasm, and compartmentalization of the dye was seldom observed.

$[Ca^{2+}]_i$ measurements Measurement of $[Ca^{2+}]_i$ was carried out by the dual-wavelength fluorescence method as described previously[8] with some modifications. Fura-2-loaded cells were mounted in a perfusion chamber and placed under an inverted microscope (IX70, Olympus). Light emitted from a 75-Wxenon arc lamp (AH2-RX, Olympus) passed through an excitation filter set (Chroma) to generate ultraviolet monochromatic waves of 340 and 380 nm. With the aid of a computerized filter wheel (Lambda 10-2, Sutter Instruments), the cells in the chamber were alternately exposed to the two waves through an Olympus objective (UApo/340, 40× /0.90). The resulting fluorescent emission from the Ca^{2+}-sensitive dye was collected through a 510 nm-long pass filter (Chroma) with a cooled charge-coupled device camera (MicroMax 5 MHz system, Princeton Instruments). All image acquisition was computer-controlled by MetaFluor Imaging program (v.4.01, Universal Imaging Corporation). Images were acquired at 3-s intervals to reduce photobleaching. All measurements were made at 22–25 ºC.

Images acquired were corrected for background fluorescence and shading across the field of view. Conversion of the ratio to $[Ca^{2+}]_i$ was carried out using the equation: $[Ca^{2+}]_i = K_d \times [(R-R_{min})/(R_{max}-R)] \times (F^{380}{}_{min}/F^{380}{}_{max})$[8], where R_{max} and R_{min} are the maximum and minimum ratio obtained by the addition of ionomycin (10 μmol/L) and egtazic acid (10 mmol/L) respectively, $F^{380}{}_{min}/F^{380}{}_{max}$ is the ratio of Ca^{2+}-free and Ca^{2+}-saturated fluorescence signals at the excitation wavelength of 380 nm, and K_d is the dissociation constant of the Fura-2/Ca^{2+} complex (224 nmol/L). R is the acquired ratio value at each time point.

Perfusion chamber and drug applications The custom-built chamber, with a coverglass at the bottom, was continuously perfused with HEPES-buffered saline during measurements. The perfusion rate was set at 2 mL/min to aid drug removal. All drugs were diluted in saline from their stock solutions immediately before the experiments and applied directly to the cells using a computer/manual operated 7-barrel local superfusion system for desired lengths of time. The tip (100 μm inside diameter) of the outlet was placed approximately 200 μm away from the cells, and the gravity force was adjusted to achieve rapid drug application while avoiding any mechanical disturbance of the cells. The time delay for arrival of drugs at the cells was less than 100 ms (data not shown).

Data analysis $[Ca^{2+}]_i$ values were expressed as means± SD. Statistical analysis was performed using *t*-test or analysis of variance (ANOVA) depending on data types. $P<0.05$ was considered to be significant.

Results

Inhibition of ATP-induced $[Ca^{2+}]_i$ increase by GCs In HT 4 cells, the basal level of $[Ca^{2+}]_i$ was 54±8 nmol/L[5]. ATP 100 μmol/L induced an immediate rise in $[Ca^{2+}]_i$, which was significantly attenuated by pre-incubation with B (1 μmol/L) for 5 min (Figure 1A). The original Ca^{2+} response recovered 5–10 min after B was washed out (data not shown). The inhibitory effect was concentration-dependent (0.1–100 μmol/L). B-BSA was also effective in suppressing the Ca^{2+} response with a similar potency compared to B (Figure 1B), while BSA had no effect on either basal or stimulated $[Ca^{2+}]_i$ levels (data not shown). To further elucidate the rapid action of B, we studied the effect of mifepristone (a GR antagonist) on the response. Pretreatment with mifepristone (1 μmol/L) for 30 min did not influence the inhibitory effect

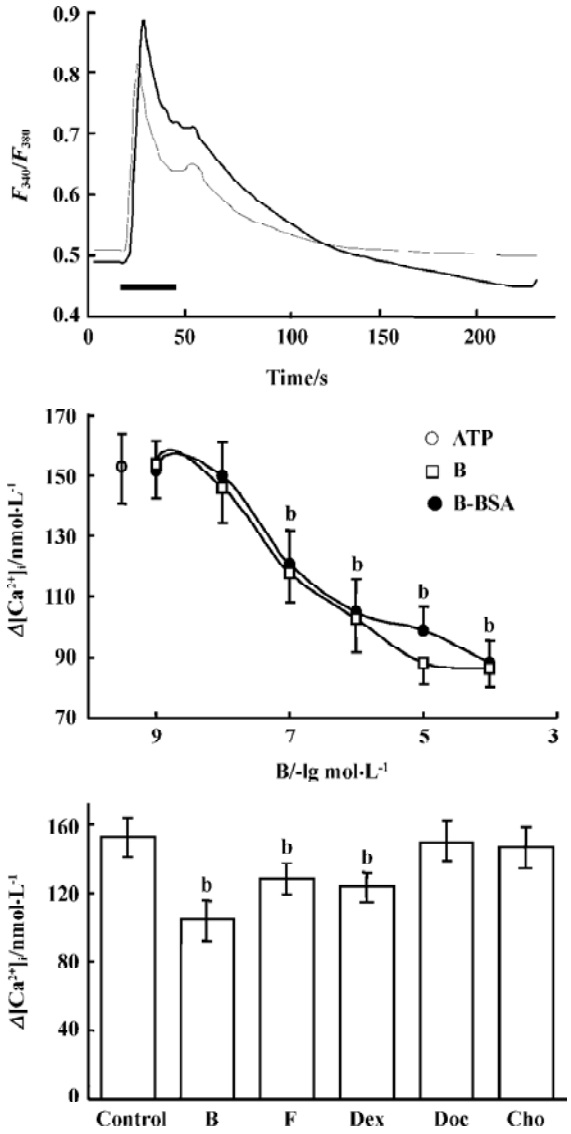

Figure 1. Inhibition of ATP-induced $[Ca^{2+}]_i$ increase by GCs in HT4 cells. (A) the $[Ca^{2+}]_i$ increase elicited by 100 μmol/L ATP in HEPES-buffered saline was measured after a 5-min pre-incubation with or without 1 μmol/L B. Traces from representative cells are shown and superimposed for ease of comparison (continuous trace: ATP only, dotted trace: B pretreated). The horizontal bar represents drug application. (B) Dose-response relationships of the B and B-BSA induced inhibition. (C) $[Ca^{2+}]_i$ increases elicited by 100 μmol/L ATP were measured after a 5-min pre-incubation with cortisol (F), dexamethasone (Dex), deoxycorticosterone (Doc), and cholesterol (Cho), respectively. All steroids were at 1 μmol/L in concentration. n=3 determinations. Mean±SD. $^bP<0.05$ *vs* control (100 μmol/L ATP only).

of B (1 μmol/L) (data not shown). Thus, the findings above imply that the action of B in HT4 cells is initiated at the plasma membrane and may not involve the nuclear receptors. Other GCs or analogs, such as cortisol and dexamethasone, were also tested and shown to be effective using the same experimental protocol. However, deoxycorticosterone and cholesterol were not effective (Figure 1C).

P2X receptor-mediated Ca^{2+} influx was affected by B In the absence of extracellular Ca^{2+}, ATP (100 μmol/L) was also capable of elevating $[Ca^{2+}]_i$ but with smaller amplitude. The $[Ca^{2+}]_i$ level dropped gradually to baseline even if ATP was not withdrawn. The subsequent introduction from the local superfusion system of 2.5 mmol/L Ca^{2+}-containing ATP solution to the same cells gave rise to a secondary calcium elevation (Figure 2A). These results suggest the generation of both Ca^{2+} influx across plasma membrane and Ca^{2+} release from intracellular stores upon ATP treatment. Using this experimental protocol, we investigated which component of the Ca^{2+} response was affected by the brief treatment of B. As shown in Figure 2A, the Ca^{2+} release evoked by ATP was not affected while the $[Ca^{2+}]_i$ increment during Ca^{2+} influx was significantly smaller after the pre-incubation of B (1 μmol/L). β,γ-meATP is a specific agonist for P2X receptors that has little effect on P2Y receptors[9]. The $[Ca^{2+}]_i$ increase induced by β,γ-meATP 10 μmol/L in HT4 cells was also inhibited by the pre-incubation of B (1 μmol/L) (Figure 2B and 2C). Taken together, the above results suggest that Ca^{2+} influx through P2X receptors was affected by B.

Effect of B on Ca^{2+} influx through SOC As shown earlier, ATP increases Ca^{2+} release from intracellular stores in HT4 cells. The depletion of the Ca^{2+} stores has been reported to trigger the opening of store-operated channels (SOC)[10,11]. We therefore examined whether B might exert its inhibitory effect by reducing Ca^{2+} influx through SOC. Thapsigargin (TG), a specific inhibitor of endoplasmic reticulum Ca^{2+}-ATPase, is widely used to activate SOC by depleting Ca^{2+} stores. In HT4 cells, exposure of TG (1 μmol/L) caused an initial spike followed by a sustained elevation at lower level that was indicative of the activation of SOC. Our results showed that the TG-induced plateau was insensitive to treatment of B (1 μmol/L), while ATP-induced further increase in $[Ca^{2+}]_i$ at this stage was still attenuated by B (Figure 3).

Rapid action of B was PKA-dependent Our previous observation found that ATP-induced $[Ca^{2+}]_i$ increase was negatively modulated by PKA or PKC in HT-4 cells[5]. Therefore we examined whether PKA or PKC related signaling pathways were involved in the rapid action of B. Effects of forskolin (1 μmol/L), PMA (0.5 μmol/L) on the $[Ca^{2+}]_i$ increase were studied and compared with that of B (1 μmol/L). There was no significant difference in the degrees of inhibition among groups pretreated with forskolin or B, or both, while the effect of a combination of PMA and B was addi-

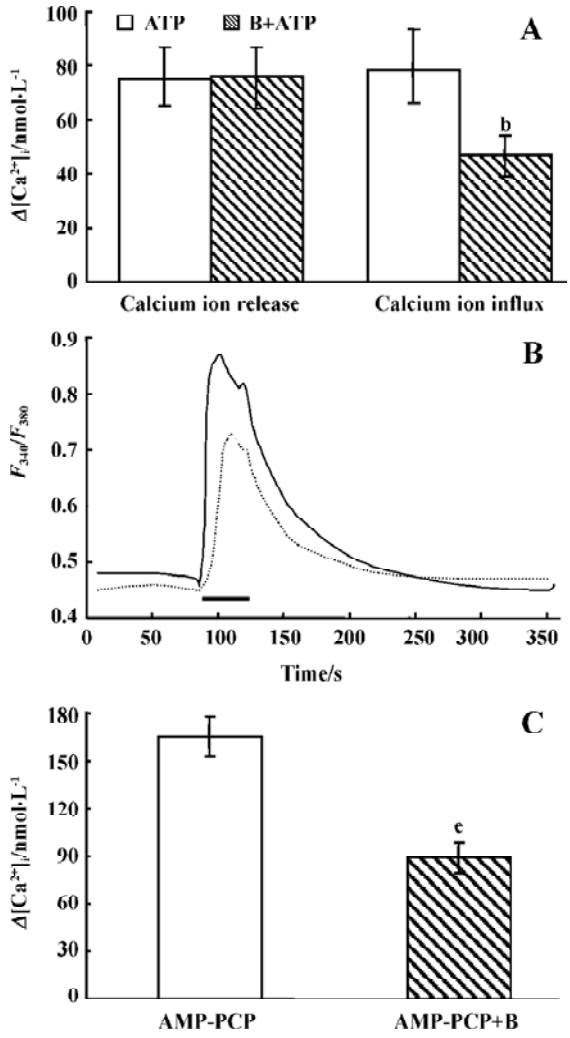

Figure 2. P2X receptor-mediated Ca^{2+} influx was affected by B. (A) using a Ca^{2+}-free and Ca^{2+}-reintroduction protocol, the ATP-evoked Ca^{2+}-influx was found to be suppressed by 5-min pretreatment of B (1 μmol/L). n=3 determinations. Mean±SD. ^bP<0.05 *vs* control (10 μmol/L β,γ-meATP only). (B) β,γ-meATP (10 μmol/L) caused a rapid increase in $[Ca^{2+}]_i$ (continuous trace), which was inhibited by pretreatment of the cells for 5 min with 1 μmol/L B (dotted trace). The horizontal bar represents drug application. (C) n=3 determinations. Mean±SD. ^eP<0.05 *vs* AMP-PCP group.

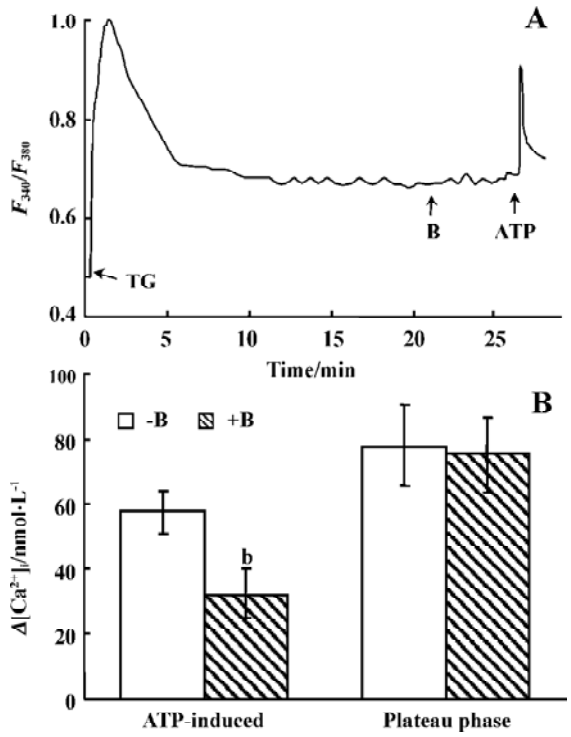

Figure 3. Effect of B on ATP-induced $[Ca^{2+}]_i$ increase after TG treatment. HT-4 cells were first exposed to TG (1 μmol/L) and subsequently stimulated with ATP (100 μmol/L) 25 min later. B (1 μmol/L) was applied 20 min after TG when the $[Ca^{2+}]_i$ levels reached a plateau. (A) a representative trace is presented to show the experimental protocol. (B) $\Delta[Ca^{2+}]_i$ values recorded immediately before ATP application represents the plateau phase Ca^{2+} levels. n=3–4 determinations. Mean±SD. ^bP<0.05 *vs* control (100 μmol/L ATP after TG treatment).

tive (Figure 4). These results imply that the forskolin-activated pathway is involved in the signaling of B-induced inhibition. However, PMA and B exerted their modulatory effects through distinct pathways. PKA inhibitor H89 (20 μmol/L), when applied 20 min before B, completely abrogated the inhibitory effect of B (1 μmol/L), while PKC inhibitors Ro31-8220 (0.5 μmol/L) and GF-109203X (0.5 μmol/L) had little influence (Figure 4). None of the drugs changed the basal $[Ca^{2+}]_i$ level in HT4 cells (data not shown).

Discussion

Pre-incubation with B inhibited the ATP-induced $[Ca^{2+}]_i$ increase in HT4 cells in a concentration-dependent manner. The minimum effective dose was 100 μmol/L, which falls below the peak-free B concentration (750 μmol/L) in serum during stress[12]. The pre-incubation time for B adopted in most of our experiments was 5 min. However, a 3-min pretreatment was found to be enough for B to take effect (data not shown). The very short latency is consistent with the criteria to define a rapid effect of steroid hormones[1]. Moreover, the rapid action was insensitive to treatment with nuclear receptor antagonist, further supporting the notion that this is a nongenomic effect of B.

Being large and predominantly hydrophilic molecules, steroid-BSA conjugates are thought to be membrane impermeable within 30 min[13]. However, they are biologically active and can reproduce the actions of free steroids[14]. In our study, B-BSA was found to be effective in inhibiting

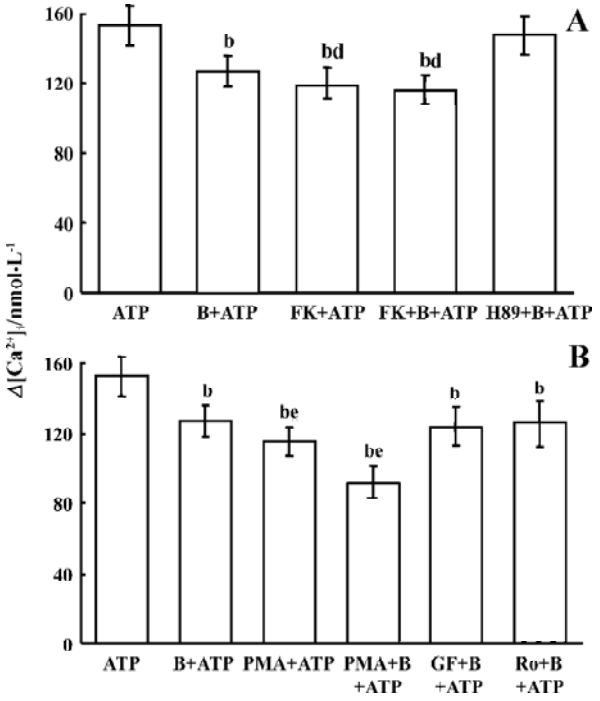

Figure 4. Rapid action of B was PKA-dependent. (A) before ATP (100 μmol/L) stimulation, HT4 cells were pretreated with B (1 μmol/L) for 5 min or forskolin (FK, 1 μmol/L) for 10 min or in combination. In experiments using H89 (20 μmol/L), the drug was applied 20 min before the addition of B. (B) before ATP (100 μmol/L) stimulation, HT4 cells were pretreated with PMA (0.5 μmol/L) for 5 min alone or in combination with B. In experiments using Ro31-8220 (Ro, 0.5 μmol/L) or GF109203X (GF, 0.5 μmol/L), the drugs were applied 20 min before the addition of B. n=3–4 determinations. Mean±SD. $^bP<0.05$ *vs* control (100 μmol/L ATP only). $^dP>0.05$, $^eP<0.05$ *vs* B+ATP group.

ATP-induced $[Ca^{2+}]_i$ increase, suggesting its action at the plasma membrane, where a signal was generated and transduced into the cells. Untill now, several specific membrane proteins have been reported as the receptors that mediate the rapid actions of GC[15,16]. It is interesting to note that they are different not only in molecular weight, but also in genetic identity. Being a splice variant of the nuclear GR, one membrane receptor has been reported to have cross-antigenicity with its nuclear counterpart, while others do not[17]. The identity of the membrane target in HT4 cells is not clear and needs to be elucidated.

The potency of B-BSA in this experimental model is almost the same as that of B. Previous work in our lab has revealed that both B and B-BSA activate PKC in PC12 cells, but the dose-dependence curve of the latter shifts rightward (ie, with lower potency)[6]. The reason for the difference is also unclear.

ATP, being a normal metabolite, exists in all living cells. In the nervous system, it is an important signaling molecule belonging to a class of fast excitatory transmitter in the brain[18,19]. Its signaling is mediated through the metabotropic P2Y and ionotropic P2X receptors[9]. In our experiment, the stable ATP analog β,γ-meATP was shown to be a potent agonist in HT4 cells. This result strongly implies actions at P2X receptors. Modulation of P2X purinoceptor-mediated Ca^{2+} responses by protein kinases has been well investigated[10,20–22]. In PC12 cells, for example, ATP-induced Ca^{2+} influx through P2X receptors is inhibited when PKC activity is enhanced[10].

It has been reported that PKA is involved in the GC rapid, nongenomic actions in many cell models[2]. It is interesting to note that the models are all pituitary-originated, such as rat pituitary cells in culture[23], cichlid fish pituitary *in vitro*[24], and mouse corticotroph tumor cell line AtT20[25]. In contrast, studies on rat brain synaptosomes, rat hippocampal neurons, PC12 cells, and glial cell lines reveal an alternative PKC pathway[2,26]. This prompted us to speculate that the protein kinases involved in GC rapid action could be predicted by cell type[2]. However, the present data we found in HT4 cells, a mouse hippocampus-derived cell line, show that such generalization is premature and open to further consideration.

Acknowledgment

We are grateful to Dr Zhuan ZHOU (Institute of Neuroscience, Chinese Academy of Sciences) for providing us the local superfusion apparatus from which our experiments greatly benefited.

References

1 Zakon H. The effects of steroid hormones on electrical activity of excitable cells. Trends Neurosci 1998; 21: 202–7.
2 Chen YZ, Qiu J. Pleiotropic signaling pathways in rapid, nongenomic action of glucocorticoid. Mol Cell Biol Res Commun 1999; 2: 145–9.
3 Watson CS, Gametchu B. Membrane-initiated steroid actions and the protein that mediate them. Proc Soc Exp Biol Med 1999; 220: 9–19.
4 Morimoto B, Koshland D Jr. Excitatory amino acid uptake and *N*-methyl-*D*-aspartate-mediated secretion in a neural cell line. Proc Natl Acad Sci USA 1990; 87: 3518–21.
5 Han JZ, Lin W, Chen YZ. Evoked intracellular Ca^{2+} elevations in HT4 neuroblastoma cells. Neuroreport 2002; 13: 1089–94.
6 Qiu J, Lou LG, Huang XY, Lou SJ, Pei G, Chen YZ. Nongenomic mechanisms of glucocorticoid inhibition of nicotine-induced calcium influx in PC12 cells: involvement of protein kinase C. Endocrinology 1998; 139: 5103–8.
7 Lou SJ, Chen YZ. The rapid inhibitory effect of glucocorticoid on cytosolic free Ca^{2+} increment induced by high extracellular K^+ and its underlying mechanism in PC12 cells. Biochem Biophys Res Commun 1998; 244: 403–7.
8 Grynkiewicz G, Poenie M, Tsien RY. A new generation of Ca^{2+} indi-

cators with greatly improved fluorescence properties. J Biol Chem 1985; 260: 3440–50.
9 Ralevic V, Burnstock G. Receptors for purines and pyrimidines. Pharmacol Rev 1998; 50: 413–92.
10 Park TJ, Song SK, Kim KT. A_{2A} adenosine receptors inhibit ATP-induced Ca^{2+} influx in PC12 cells by involving protein kinase A. J Neurochem 1997; 68: 2177–85.
11 Giniatullin R, Khiroug L, Talantova M, Nistri A. Fading and rebound of currents induced by ATP in PC12 cells. Br J Pharmacol 1996; 119: 1045–53.
12 Yeh KY. Corticosterone concentrations in the serum and milk of lactating rats parallel changes after induced stress. Endocrinology 1984; 15: 1364–70.
13 Blackmore P, Lattanzio G. Cell surface localization of a novel non-genomic progesterone receptor on the head of human sperm. Biochem Biophys Res Commun 1991; 181: 743–60.
14 Ramirez VD, Zheng J. Membrane sex-steroid receptors in the brain. Front Neuroendocrinol 1996; 17: 402–39.
15 Gametchu B. Glucocorticoid receptor-like antigen in lymphoma cell membranes: correlation to cell lysis. Science 1987; 236: 456–61.
16 Orchinik M, Murray TF, Moore FL. A corticosteroid receptor in neuronal membranes. Science 1991; 252: 1848–51.
17 Diba F, Watson CS, Gametchu B. 5'UTR sequences of the glucocorticoid receptor 1A transcript encode a peptide associated with translational regulation of the glucocorticoid receptor. J Cell Biochem 2001; 81: 149–61.
18 Edwards FA, Gibb AJ, Colquhoun D. ATP receptor mediated synaptic currents in the central nervous system. Nature 1992; 359: 144–6.
19 Nieber K, Poelchen W, Illes P. Role of ATP in fast excitatory synaptic potentials in locus coeruleus neurons of the rat. Br J Pharmacol 1997; 122: 423–30.
20 Chen C, Bobbin RP. P2X receptors in cochlear Deiters' cells. Br J Pharmacol 1998; 124: 337–44.
21 Boue-Grabot E, Archambault V, Seguela P. A protein kinase C site highly conserved in P2X subunits controls the desensitization kinetics of P2X(2) ATP-gated channels. J Biol Chem 2000; 275: 10190–5.
22 Seguela P, Haghighi A, Soghomonian JJ, Cooper E. A novel neuronal P2X ATP receptor ion channel with widespread distribution in the brain. J Neurosci 1996; 16: 448–55.
23 Rotsztejn W, Dussaillant M, Nobou F, Rosselin G. Rapid glucocorticoid inhibition of vasoactive intestinal peptide induced cyclic AMP accumulation and prolactin release in rat pituitary cells in culture. Proc Natl Acad Sci USA 1981; 78: 7584–8.
24 Borski RJ, Helms L, Richman N, Grau EG. Cortisol rapidly reduces prolactin release and cAMP and $^{45}Ca^{2+}$ accumulation in the cichlid fish pituitary *in vitro*. Proc Natl Acad Sci USA 1991; 88: 2758–62.
25 Iwasaki Y, Aoki Y, Katahira M, Oiso Y, Saito H. Non-genomic mechanisms of glucocorticoid inhibition of adrenocorticotropin secretion: possible involvement of GTP-binding protein. Biochem Biophys Res Commun 1997; 235: 295–9.
26 Han JZ, Lin W, Lou SJ, Qiu J, Chen YZ. A rapid, nongenomic action of glucocorticoids in rat B103 neuroblastoma cells. Biochim Biophys Acta 2002; 1591: 21–7.

Full-length article

Onychin inhibits proliferation of vascular smooth muscle cells by regulating cell cycle[1]

Ming YANG[2], Hong-lin HUANG[2], Bing-yang ZHU, Qin-hui TUO, Duan-fang LIAO[3]

Institute of Pharmacy and Pharmacology, Nanhua University, Hengyang 421001, China

Key words

onychin; vascular smooth muscle; cell cycle; retinoblastoma; cyclin D_1; cyclin E; tyrosine kinase; mitogen-activated protein kinase

[1] Project supported by grants from the State Key Basic Research and Development Program of China (973: No G2000056905), the National Natural Science Foundation of China (No 39970847, 30171084), and the Natural Science Foundation of Hunan (No 03JJY3037).
[2] These two authors contributed equally to the paper.
[3] Correspondence to Prof Duan-fang LIAO, MD, PhD.
Phn 86-734-828-1308.
Fax 86-734-828-1239.
E-mail dfliao66@yahoo.com.cn

Received 2004-09-20
Accepted 2004-11-15

doi: 10.1111/j.1745-7254.2005.00026.x

Abstract

Aim: To investigate the effects of onychin on the proliferation of cultured rat artery vascular smooth muscle cells (VSMCs) in the presence of 10% new-born calf serum (NCS). **Methods:** Rat VSMCs were incubated with onychin 1–50 μmol/L or genistein 10 μmol/L in the presence of 10% NCS for 24 h. The proliferation of VSMCs was measured by cell counting and MTS/PMS colorimetric assays. Cell cycle progression was evaluated by flow cytometry. Retinoblastoma (Rb) phosphorylation, and expression of cyclin D_1 and cyclin E were measured by Western blot assays. The tyrosine phosphorylation of ERK1/2 was examined by immunoprecipitation techniques using anti-phospho-tyrosine antibodies. **Results:** The proliferation of VSMCs was accelerated significantly in the presence of 10% NCS. Onychin reduced the metabolic rate of MTS and the cell number of VSMCs in the presence of 10% NCS in a dose-dependent manner. Flow cytometry analysis revealed that the G_1-phase fraction ratio in the onychin group was higher than that in the 10% NCS group (85.2% *vs* 70.0%, $P<0.01$), while the S-phase fraction ratio in the onychin group was lower than that in 10% NCS group (4.3% *vs* 16.4%, $P<0.01$). Western blot analysis showed that onychin inhibited Rb phosphorylation and reduced the expression of cyclin D_1 and cyclin E. The effects of onychin on proliferation, the cell cycle and the expression of cyclins in VSMCs were similar to those of genistein, an inhibitor of tyrosine kinase. Furthermore immunoprecipitation studies showed that both onychin and genistein markedly inhibited the tyrosine phosphorylation of ERK1/2 induced by 10% NCS. **Conclusion:** Onychin inhibits the proliferation of VSMCs through G_1 phase cell cycle arrest by decreasing the tyrosine phosphorylation of ERK1/2, and the expression of cyclin D_1 and cyclin E, and sequentially inhibiting Rb phosphorylation.

Introduction

Alterations in vascular smooth muscle cell (VSMC) proliferation plays an important role in the development of the pathological process that underlies restenosis, atherosclerosis, and vascular graft occlusion[1]. Despite intense efforts, no widely effective therapy exits for the prevention of such vascular diseases. Recently some agents have been shown to have potential value by virtue of their abilities to attenuate the proliferation of VSMCs[2–4]. Among them, genistein (4,5,7-trihydroxyisoflavone), a soybean-derived isoflavone, has been shown to inhibit platelet derived growth factor (PDGF)-induced proliferation and DNA synthesis of aortic smooth muscle cells in stroke-prone spontaneously hypertensive rats[5]. Moreover, epidemiological studies indicate that genistein has beneficial effects on cardiovascular disease[6,7], such as lowering total and low density lipoprotein (LDL)-cholesterol levels. More recently, onychin, a new compenent extracted from *Onychin lucidum* of sinopteridaceae, has attracted our interest because its structure is similar to genistein[8]. Interestingly, our previous results have shown that onychin protects the endothelium-dependent relaxation in rabbit aortic rings and inhibits oxidative stress-

induced apoptosis of endothelial cells, which is mediated by increasing NO release, regulating expression of caveolin-1 and activation of mitogen-activated protein kinases (MAPK)[9–13]. In the present study, we extend our investigation to the effects of onychin on the proliferation of rat VSMCs induced by 10% NCS.

Materials and methods

Materials Male Sprague-Dawley rats were obtained from the Experimental Animal Center of Nanhua University (Hengyang, China). Genistein, elastase, and monoclonal antibodies for α-actins of smooth muscle cells were obtained from Sigma (St Louis, USA). Dulbecco's modified Eagle's medium (DMEM) and NCS were from GibcoBRL (Maryland, USA). The Cell Titer 96 Aqueous Non-Radioactive Cell Proliferation Assay Kit (MTS/PMS) was purchased from Promega (WI, USA). Monoclonal mouse anti-ERK1/2, -pTyr, -cyclin D_1, -cyclin E, and polyclonal mouse anti-Rb were from Santa Cruz Biotechnology (Santa Cruz, USA).

Cell culture The thoracic aortas were isolated from the 150–200 g male Sprague-Dawley rats and cultured by using a novel enzymatic dispersion method[14]. Briefly, rat aortas were in sterile conditions removed from left subclavian origin to the point of diaphragmatic insertion. The vascular media was digested, and the cells were centrifuged and plated down in prepared flasks. VSMCs were cultivated in DMEM (containing 10% NCS) and in a 5% CO_2 humidified-atmosphere incubator until they displayed as a typical "hill and valley" morphology. The immunohistochemistry staining with a monoclonal antibody against α-actins showed that there were no co-cultured fibroblast cells. VSMCs from 5 to 15 passages were used for experimentation. Before mitogenic stimulation, subconfluent cells were arrested in a quiescent state with DMEM containing 0.1% NCS for 48 h.

Cell count VSMCs (2.5×10^4) were plated into a 24-well plate and grown in DMEM supplemented with 10% NCS for 24 h. In some experiments cells were growth-arrested by incubation in DMEM containing 0.1% NCS for 48 h and then exposed to different concentrations of onychin before treatment with 10% NCS for 24 h or 48 h. Genistein (10 μmol/L) was used as the positive control. The cells were then washed with phosphate-buffered saline (PBS), trypsinized, and diluted with isotonic solution. Cells were stained with Trypane blue and the viable cells were counted using a coulter counter.

MTS assay Cell growth was measured by using MTS assay according to the manufacture's instructions. Briefly, 3-(4,5-dimethylthiazol-2-yl)-5-(3-carboxymethoxyphenyl)-2-(4-sulfophenyl)-2*H*-tetrazolium (MTS) and phenazine methosulfate (PMS) were mixed at a ratio of 20:1 immediately before being added to the samples. The MTS/PMS solution (20 μL) was added to each well of the 96-well plate and and the plates were incubated at 37 ºC in a humidified 5% CO_2 atmosphere for 90 min. Absorbance was read at 490 nm using Bio-Tek's Power Wave X reader-assay system (BIO-TEK Instruments, USA). Each sample was read in triplicate.

Flow cytometry Cells were suspended in phosphate-buffered saline (PBS, pH 7.4), and fixed with 70% (v/v) ethanol at -20 ºC for 30 min. After the ethanol was removed, the cells were incubated with PBS containing RNase (172 MU/L) at 37 ºC for 30 min and then stained for 30 min with 0.005% propidium iodide. Fluorescence was measured by using Epics Altra Flow Cytometer (Beckman Coulter Co, USA).

Western blot analysis After treatment, VSMCs were washed twice with cold (4 ºC) PBS (pH 7.4) and harvested on ice in buffer A containing HEPES 20 mmol/L (pH 7.4), EDTA 2 mmol/L, glycerophosphate 50 mmol/L, dithiothreitol 1 mmol/L, Na_3VO_4 1 mmol/L, 1% Triton, 10% glycerol, leupeptin 1 mg/L, aprotinin 1 mg/L, and phenylmethylsulfonyl fluoride 100 μmol/L. The suspension was incubated on ice for 20 min and vortexed every 5 min. Cell lysates were then centrifuged at 13 000 r/min (Eppendorf centrifuge, Osterode, Germany) for 30 min at 4 ºC. The supernatants were collected, and protein concentration was measured by using the Bio-Rad assay. Forty micrograms of protein (40 μg) weas electrophoresed onto a 12% SDS-PAGE gel and transferred to a polyvinylidene difluoride membrane. The membrane was incubated for 1 h with primary antibodies followed by incubation with second antibodies (horseradish peroxidase-conjugated). Immunoactive bands were visualized using chemiluminescence (Amersham-Pharmacia Biotech, Piscataway, USA) and densitometric analysis was carried out using an imager and densitometer[15].

Immunoprecipitation Growth-arrested VSMCs were exposed to 0.1% NCS, 10% NCS, 10% NCS+10 μmol/L onychin, or 10% NCS+10 μmol/L genistein for 20 min. Cell lysates were prepared for immunoprecipitation as described previously[16]. Briefly, equal amounts of protein (500 μg) were immunoprecipitated with anti-ERK1/2 polyclonal antibodies overnight at 4 ºC. Immune complexes were collected by incubation with protein A-Sepharose beads for 2 h at 4 ºC. Immunoprecipitates were separated by using SDS-PAGE, and proteins were detected by immunoblotting as described above using anti-pTyr monoclonal antibodies.

Statistical analysis All values are expressed as mean±SD. Statistical significance was determined by one-way ANOVA. $P<0.05$ was considered significant.

Results

Effect of onychin on the proliferation of VSMCs Both cell counting and the MTS assay showed that onychin treatment for 24 h or 48 h significantly inhibited VSMC proliferation induced by 10% NCS. The inhibition was concentration-dependent with peak at 10 μmol/L (Table 1). The efficiency of 10 μmol/L onychin treatment for 24 h was similar to that of 10 μmol/L genistein. Therefore we chose 10 μmol/L onychin treating cells for 24 h in the following experiments.

Changes in the VSMC cycle induced by onychin treatment The percentages of G_0/G_1 or S phase cells in the 10% NCS-stimulated group were 70.0% and 16.4% respectively. In contrast, 10 μmol/L onychin and 10 μmol/L genistein treatments for 24 h led to a significant inhibition of DNA synthesis as evidenced by the fact that the percentages of G_0/G_1 phase cells increased to 85.2% and S phase cells decreased to 4.3% in the onychin group (Figure 1).

Decreased Rb phosphorylation induced by onychin treatment The cell cycle progression from G_1 to S phase is usually accompanied by Rb phosphorylation in the late G_1 phase. We therefore examined Rb phosphorylation in VSMCs by using Western blotting with anti-phospho Rb antibody. NCS (10%) stimulated Rb phosphorylation markedly and onychin and genistein inhibited Rb phosphorylation by 70.1% and 58.8%, respectively (Figure 2).

Onychin lowers the expression of cyclin D_1 and cyclin E To further explore the mechanism by which onychin inhibited Rb, we examined the expression of cyclin D_1 and cyclin E by Western blotting. Results showed that 10% NCS treatment significantly increased both expressions of cyclin D_1 and cyclin E and that pretreatment with onychin 10 μmol/L and genistein 10 μmol/L decreased the NCS-induced expression of these two proteins (Figure 3, 4).

Effect of onychin on the tyrosine phosphorylation of ERK1/2 ERK1/2 activation is at upstream of cyclins. It has been reported that the protein tyrosine inhibitor genistein is able to inactivate ERK1/2. To investigate whether the inhibitory effect of onychin on ERK1/2 is mediated by tyrosine kinase inhibition, we observed the phosphorylation of the tyrosine residue in ERK1/2. When growth-arrested VSMCs were treated with 10% NCS, a marked time-dependent tyrosine phosphorylation of ERK1/2 was observed, with peak at 20 min (data not shown). Pretreatment with genistein, as well as onychin, significantly inhibited the 10% NCS-induced

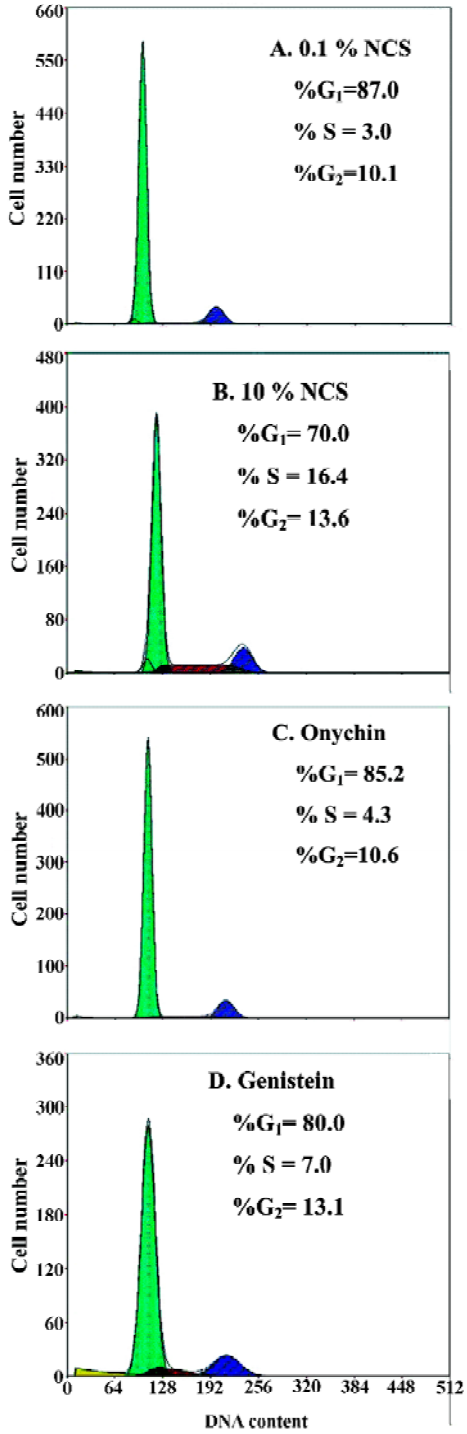

Figure 1. Effect of onychin 10 μmol/L on cell cycle progression induced by 10% NCS for 24 h in cultured vascular smooth muscle cells (VSMCs). Growth-arrested VSMCs were exposed to 0.1% NCS, 10% NCS, 10% NCS+10 μmol/L onychin or 10% NCS+10 μmol/L genistein for 24 h. Then cells were fixed with ethanol and incubated with PBS containing Rnase followed by staining with propidium iodide. Fluorescence was determined by using a flow cytometer.

Table 1. Inhibitory effect of onychin on the proliferation of rat VSMCs induced by 10% NCS. $n=8$. Mean±SD. $^{b}P<0.05$, $^{c}P<0.01$ *vs* 0.1 % NCS group. $^{e}P<0.05$ *vs* 10% NCS group.

		$10^{-7}\times$Cell counts/mL^{-1}		MTS measurement (*OD*)	
		24 h	48 h	24 h	48 h
Control	0.1% NCS	2.50±0.12	2.50±0.05	0.44±0.04	0.44±0.04
	10% NCS	7.74±0.57^{c}	13.68±0.96^{c}	1.04±0.06^{c}	1.94±0.06^{c}
Onychin	1 μmol/L	7.32±0.24	11.03±0.26	0.93±0.04	1.79±0.07
	5 μmol/L	6.36±0.20^{e}	9.88±0.13^{e}	0.85±0.07^{e}	1.47±0.07^{e}
	10 μmol/L	5.46±0.51^{e}	8.58±0.56^{e}	0.64±0.05^{e}	1.21±0.05^{e}
	50 μmol/L	5.74±0.21^{e}	8.75±0.23^{e}	0.69±0.03^{e}	1.34±0.04^{e}
Genistein	10 μmol/L	5.58±0.75^{b}	8.71±0.45^{b}	0.67±0.06^{b}	1.27±0.06^{b}

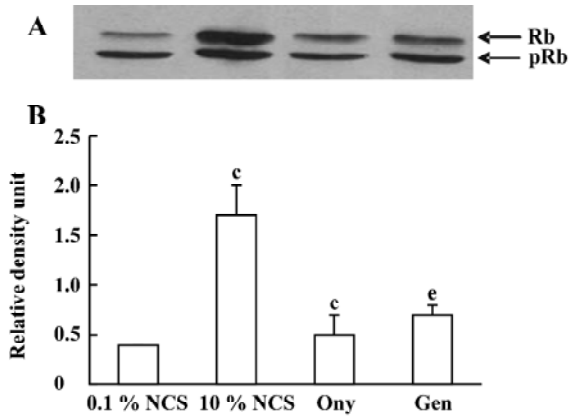

Figure 2. Inhibitory effect of onychin 10 μmol/L on phosphorylation of Rb induced by 10% NCS (24 h) in cultured vascular smooth muscle cells (VSMCs). A) Growth-arrested VSMCs were exposed to 0.1% NCS, 10% NCS, 10% NCS+10 μmol/L onychin or 10% NCS+10 μmol/L genistein for 24 h. Cells were harvested, and lysates were analyzed for Rb phosphorylation by Western blotting using anti-phosphor Rb antibodies. B) The relative expression of phosphorylated Rb over un-phosphorylated Rb was measured by using densitometry of autoradiograms in the linear range of film development. n=3 experiments. Mean±SD. $^{c}P<0.01$ *vs* 0.1% NCS group. $^{e}P<0.05$ *vs* 10% NCS group.

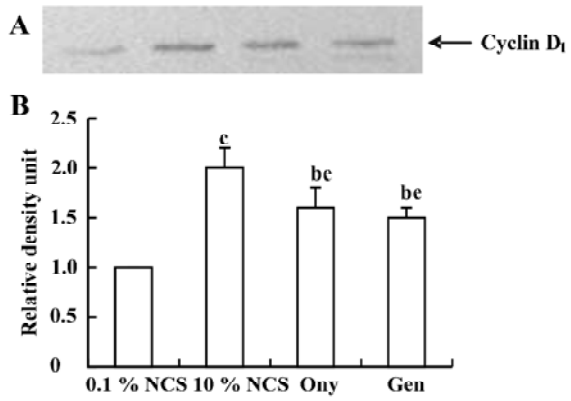

Figure 3. Inhibitory effect of onychin on cyclin D_1 expression in cultured VSMCs. A) Growth-arrested VSMCs were exposed to 0.1% NCS, 10% NCS, 10% NCS+10 μmol/L onychin, or 10% NCS+10 μmol/L genistein for 24 h. Cells were harvested, and lysates were analyzed for cyclin D_1 by using Western blotting. B) The relative expression of cyclin D_1 was measured by using densitometry of autoradiograms in the linear range of film development. The results of each experiment were normalized to the density of the control (0.1% NCS) sample, which was arbitrarily adjusted to 1.0. The response to 10% NCS, and 10% NCS+10 μmol/L onychin, 10% NCS+10 μmol/L genistein was then determined on a relative basis. n=3 experiments. Mean±SD. $^{b}P<0.05$, $^{c}P<0.01$ *vs* 0.1% NCS group. $^{e}P<0.05$ *vs* 10% NCS

tyrosine phosphorylation of ERK1/2, suggesting that onychin might be a potential inhibitor of tyrosine kinase (Figure 5).

Discussion

VSMC proliferation contributes to the remodeling of blood vessels and has been implicated in the pathogenesis of atherosclerosis. Phytoestrogens such as genistein can inhibit the proliferation of VSMC and have been implicated in the suppression of VSMC proliferation in neo-intima formation *in vivo*. Onychin, which has a similar structure to genistein, has been considered as a candidate for providing several cardiovascular protective effects[9–13]. To further investigate its actions in vascular biology, in the present study we studied the effect of onychin on the proliferation of rat VSMC induced by 10% NCS. The results showed that 1–50 μmol/L onychin inhibited the proliferation of VSMCs in a concentration-dependent manner, with a peak at 10 μmol/L.

Proliferating cells pass through several cell cycle checkpoints, mainly the G_1 to S and G_2 to M transitions. The former checkpoint is considered to be the most important one in the replication of DNA and mitosis. We thus

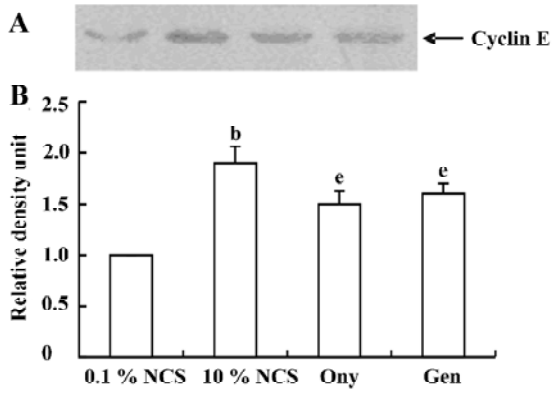

Figure 4. Inhibitory effect of onychin on cyclin E expression in cultured VSMCs. A. Growth-arrested VSMCs were exposed to 0.1% NCS, 10% NCS, 10% NCS+10 μmol/L onychin, or 10% NCS+10 μmol/L genistein for 24 h. Cells were harvested, and lysates were analyzed for cyclin E by Western blotting. B. The relative expression of cyclin E. The results of each experiment were normalized to the density of the control (0.1% NCS) sample, which was arbitrarily adjusted to 1.0. The response to 10% NCS, and 10% NCS+10 μmol/L onychin, 10% NCS+10 μmol/L genistein was then determined on a relative basis. n=3 experiments. Mean±SD. $^bP<0.05$ *vs* 0.1% NCS group. $^eP<0.05$ *vs* 10% NCS group.

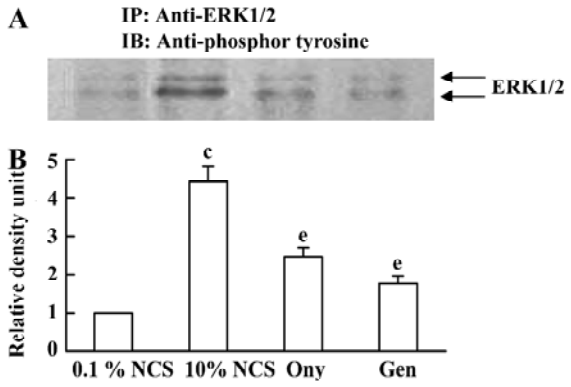

Figure 5. Inhibitory effect of onychin on the tyrosine phosphorylation of ERK1/2. A) Growth-arrested VSMCs were exposed to 0.1% NCS, 10% NCS, 10% NCS+10 μmol/L onychin, or 10% NCS+10 μmol/L genistein for 20 min. Cells lysates were immunoprecipitated with anti-ERK1/2 antibody, and Western blotting was performed with anti-phospho tyrosine antibodies. IP: immunoprecipitation; IB: immunoblot. B) The relative expression of tyrosine phosphorylation in ERK1/2 was measured by using densitometry of autoradiograms in the linear range of film development. The results of each experiment were normalized to the density of the control (0.1% NCS) sample, which was arbitrarily adjusted to 1.0. The response to 10% NCS, 10% NCS+10 μmol/L onychin, and 10% NCS+10 μmol/L genistein was then determined on a relative basis. n=3 experiments. Mean±SD. $^cP<0.01$ *vs* 0.1% NCS group. $^eP<0.05$ *vs* 10% NCS group.

logically speculate that onychin affects VSMC proliferation via alterations in the cell cycle progression. Indeed our data show that onychin blocks cell cycle progression at the G_1 transition and stops VSMCs entering the S phase from G_0/G_1, consequently inhibiting the replication of DNA and the growth of VSMCs.

Rb is a key modulator of cell-cycle transit because of its ability to control the G_1/S-phase transition[17]. Rb activity is related to its ability to modulate the activation of the E_2F family, which are required for S-phase progression[18]. Cell cycle progression from G_1 to S phase is usually accompanied by Rb phosphorylation, which is induced by the cyclin D_1-CDK_4 and the cyclin E-CDK_2 complexes in the late G_1 phase. Rb phosphorylation leads to E_2F release. Conversely, hypophosphorylated Rb sequesters E_2F and prevents transcription of the E_2F target genes. Recent evidence indicates that phosphorylated Rb (pRb) inactivation is a key molecular event leading to S-phase commitment at the G_1 restriction point in the cell cycle[19]. Therefore, deregulating pRb inactivation in the G_1 phase becomes a universal mechanism underlying cellular transformation. Recently, Chang *et al.* showed that a nonphosphorylatable, constitutive active form of murine Rb inhibited VSMC proliferation and reduced neointima formation in injured rat carotid arteries and porcine femoral artery models[20]. Growth factors such as platelet-derived growth factor, epidermal growth factor, and fibroblast growth factor have been shown to induce Rb phosphorylation in quiescent cells entering into the cell cycle[21]. In light of this broad spectrum of activity, Rb is a strong candidate for use as an anti-proliferative agent in a number of disorders that are characterized by inappropriate proliferate responses. To test the possible effects of onychin on Rb phosphorylation, we observed the relative amounts of hypophosphorylated and phosphorylated forms of Rb in VSMCs by using Western blotting. The results showed that onychin decreased the phosphorylation levels of Rb.

Progression through the mammalian mitotic cycle is coordinated by expression and/or activation of multiple holoenzymes composed of a catalytic cyclin-dependent kinase (CDK) and a cyclin-regulatory subunit[22]. Different cyclin/CDK complexes are temporally activated at specific phases of the cell cycle. Progression through the first gap phase (G_1) requires cyclin D-dependent kinase (CDK_4 and CDK_6) and cyclin E/CDK_2 activity[22,23], which results in Rb hyperphosphorylation. The association of CDK_4 or CDK_6 with D-type cyclins is critical for G1 phase progression, whereas the CDK_2-cyclin E complex is important for initiation of the S phase. It has been reported that administration

of genistein in rats with an acute renal injury decreases ERK activation and cyclin D_1 expression[24]. It has been reported that exposure of VSMC to 10% FCS causes a time-dependent increase in cyclin D1 and cyclin E[25]. In the present study, we also found that 10% FCS up-regulated the expression of cyclin D_1 and cyclin E, and onychin treatment inhibited the effects of NCS.

The MAPK family constitutes a major ubiquitous intracellular signaling system involved in the regulation of cell growth, differentiation, and survival[26]. To date, at least three distinct mammalian MAPKs have been characterized: the extracellular-regulated kinases (ERKs), Jun N-terminal kinases/stress-activated protein kinase (JNK/SAPK) and p38. Among of them, the mammalian ERKs (ERK1/p44 and ERK2/p42) are generally thought to play a role in cell proliferation and differentiation. ERK1/2 is serine/threonine kinase, which is activated by phosphorylation at both threonine and tyrosine residues. Evidence indicates that phosphorylation of the residues Thr 202/Tyr 204 (for human ERK, or Thr 185/Tyr 187 for bovine ERK) in the conserved Thr/Glu/Tyr ERK sequences is necessary and sufficient for full activation of these enzymes and serves as an indicator of their activation status[27]. In our experiments, we observed an obvious tyrosine phosphorylation of ERK1/2 in the 10% NCS group. Onychin, like genistein, markedly declined the phosphorylation level of tyrosine of ERK1/2.

In summary, onychin inhibits the proliferation of VSMCs through G_1 phase cell cycle arrest by decreasing the tyrosine phosphorylation of ERK1/2, decreasing the expression of cyclin D_1 and cyclin E, and sequentially inhibiting Rb phosphorylation.

Acknowledgement

The authors are indebted to Dr He-sheng OU (University of Chicago) for his critical discussion suggestions, and valuable help in the preparation of this manuscript.

References

1 Lin MW, Roubin GS, King SB III. Restenosis after coronary angioplasty. Potential biologic determinants and role of intimal hyperplasia. Circulation 1989; 79: 1374–87.

2 Ohlstein EH, Douglas SA, Sung CP, Yue T, Louden C, Arleth A, *et al*. Carvedilol, a cardiovascular drug, prevents vascular smooth muscle cell proliferation, migration, and neointimal formation following vascular injury. Proc Natl Acad Sci USA 1993; 93: 6189–93.

3 Corsini A, Bernini F, Quarato P, Donetti E, Bellosta S, Fumagalli R, *et al*. Non-lipid-related effects of 3-hydroxy-3-methylglutaryl coenzyme A reductase inhibitors. Cardiology 1996; 87: 458–68.

4 Bennett MR, Anglin S, McEwan JR, Jagoe R, Newby AC, Evan GI. Inhibition of vascular smooth muscle cell proliferation *in vitro* and *in vivo* by c-myc antisense oligodeoxy-nucleotides. J Clin Invest 1994; 93: 820–8.

5 Pan W, Ikeda K, Takebe M, Yamori Y. Genistein, daidzein and glycitein inhibit growth and DNA synthesis of aortic smooth muscle cells from stroke-prone spontaneously hypertensive rats. J Nutri 2001; 131: 1154–8.

6 Polkowski K, Mazurek AP. Biological properties of genistein. A review of *in vitro* and *in vivo* data. Acta Pol Pharm 2000; 57: 135–55.

7 Wang HK. The therapeutic potential of flavonoids. Expert Opin Investig Drugs 2000; 9: 2103-19.

8 Xu YL, Isao K, Ma YB. Acytotoxic flavanone glycoside from onychiun japonicum: structure of onychin. Phytochemistry 1993; 33: 510–1.

9 Tuo QH, Huang HL, Xie ZZ. Protection of onychin on injury of endothelium-dependent relaxion induced by lysophosphatidylcholine. Chin J Arterioscler 2001; 9: 27–30.

10 Tuo QH, Liao DF, Zhu BY, Yan FX. Protective effects of onychin on vascular endothelial cell injured by oxidative stress. Chin J Clin Pharmacol Ther 2003; 8: 381–4

11 Guo Y, Zhu BY, Yan FX, Liao DF. Protective action of onychin against growth inhibition of endothelial cell injured by oxidation and its mechanism. Chin Pharmacol Bull 2003; 19: 401–3.

12 Guo Y, Zhu BY, Yan FX, Huang HL, Liao DF. Protective effects of onychin on the human umbilical vein endothelial cell injured by menadione. Chin J Pathophysiol 2003; 19: 10–3.

13 Tuo QH, Wang C, Yan FX, Liao DF. MAPK pathway mediates the protective effects of onychin on oxidative stress-induced apoptosis in ECV304 endothelial cells. Life Sci 2004; 76: 487–97.

14 Tu YS, Huang HL, Zhu BY, Liao DF. Enzymatic dispersion method of primary culture of rat aortic vascular smooth muscle cells. Chin J Arterioscler 2001; 9: 438–40.

15 Liao DF, Monia B, Dean N, Berk BC. Protein kinase C-ζ mediates angiotensin II activation of ERK1/2 in vascular smooth muscle cells. J Biol Chem 1997; 272: 6146–50.

16 Liao DF, Jin ZG, Baas AS, Daum G, Gygi SP, Aebersold R, *et al*. Purification and identification of secreted oxidative stress-induced factors from vascular smooth muscle cells. J Biol Chem 2000; 275: 189–96.

17 Goodrich DW, Lee WH. Molecular characterization of the retinoblastoma susceptibility gene. Biochim Biophys Acta 1993; 1155: 43–61.

18 Hiebert SW. Regions of the retinoblastoma gene product required for its interaction with the E_2F transcription factor are necessary for E_2 promoter repression and pRb-mediated growth suppression. Mol Cell Biol 1993; 13: 3384–91.

19 King KL, Cidlowski JA. Cell cycle regulation and apoptosis. Annu Rev Physiol 1998; 60: 601–17.

20 Chang MW, Barr E, Seltzer J, Nabel GJ, Nabel GJ, Parmacek MS, *et al*. Cytostatic gene therapy for vascular proliferative disorders with a constitutively active form of the retinoblastoma gene product. Science 1995; 267: 518–22.

21 Slansky JE, Farnham PJ. Introduction to the E_2F family: protein structure and gene regulation. Curr Top Microbiol Immunol 1996; 208: 1–30.

22 Sherr CJ. G_1 phase progression: cycling on cue. Cell 1994; 79: 551–5.

23 Lu B, Dai YM. Abnormal cycle regulation of cells in the HCC. World

J Gastroenterol 2001; 9: 205–8.
24 Ishizuka S, Yano T, Hagiwara K, Sone M, Nihei H, Ozasa H, *et al*. Extracellular signal-regulated kinase mediates renal regeneration in rats with myoglobinuric acute renal injury. Biochem Biophys Res Commun 1999; 254: 88–92.
25 Kronemann N, Nockher WA, Busse R, Schini-Kerth VB. Growth-inhibitory effect of cyclic GMP- and cyclic AMP-dependent vasodilators on rat vascular smooth muscle cells: effect on cell cycle and cyclin expression. Br J Pharmacol 1999; 126: 349–57.
26 Seger R, Krebs EG. The MAPK signaling cascade. FASEB J 1995; 9: 726–35.
27 Huang CY, Ferrell JE Jr. Ultrasensitivity in the mitogen-activated protein kinase cascade. Proc Natl Acad Sci USA 1996; 93: 10078–83.

Full-length article

Effect of a single dose of mifepristone on expression of pinopodes in endometrial surface of mice[1]

Dong-mei HUANG, Luciano G NARDO[2], Guang-ying HUANG[3], Fu-er LU, Yan-juan LIU

Institute of Integrated Traditional and Western Medicine, Affiliated Tongji Hospital, Tongji Medical College, Huazhong University of Science and Technology, Wuhan 430030, China; [2]Department of Obstetrics and Gynaecology, Kingston University Hospital NHS Trust, Kingston upon Thames, Surrey, UK

Key words

mifepristone; endometrium; pinopode; embryo implantation; contraception

[1] Project supported by the National Natural Science Foundation of China (No 30171193).
[3] Correspondence to Dr Guang-ying HUANG.
Phn 86-27-8366-2577.
Fax 86-27-8364-0294.
E-mail GYhuang@tjh.tjmu.edu.cn

Received 2004-07-29
Accepted 2004-11-18

doi: 10.1111/j.1745-7254.2005.00036.x

Abstract

Aim: To investigate the effect of mifepristone (RU486) as a single dose on pinopodes expression in the endometrial surface of mice at the time of implantation. **Methods:** Pregnant mice in the treated four groups received mifepristone subcutaneously (0.1 mg) between 07:00 and 08:00 AM on Pd (day of pregnancy)1, Pd2, Pd3, and Pd4. Pregnant mice in the non-treated group were used as controls. The uterine horns were collected randomly from two mice in each group between 21:30 and 22:00 PM on Pd4, and from another two mice of the same group between 09:30 and 10:00 AM on Pd5. The specimens were examined by scanning electron microscopy for the detection of pinopodes. **Results:** When mifepristone was given on Pd1, developing and fully developed pinopodes were observed, but the expression was markedly reduced compared to the control group. When mifepristone was administered on Pd2, only a few developing pinopodes were present. When mifepristone was administered on Pd3, developing pinopodes were observed. When mifepristone was administered on Pd4, different development stage pinopodes were present in specimens collected between 21:30 and 22:00 PM on Pd4, but no pinopodes was observed in specimens taken between 09:30 and 10:00 AM on Pd5. **Conclusion:** These findings suggest that administration of a single dose of RU486 subcutaneously on Pd1, Pd2, Pd3, and Pd4 might play a role in inhibiting development and maturation of endometrium, hence affecting embryo implantation in mice.

Introduction

Mifepristone (RU486), a progesterone antagonist steroid, has been largely used for both planned and emergency contraception[1], as well as for termination of pregnancy[2]. Although the effect of RU486 for contraception has been described previously, its mechanism has not been completely elucidated. Anovulation, inhibition of fertilization and transportation of embryo through the Fallopian tube, and embryo implantation dysfunction have all been postulated. Recent data sustain the hypothesis that mifepristone reduces perivascular decidual haemostasis and increases extracellular matrix-degrading protease activity[3].

It is now well established that the cross-talk between the implanting embryo and the endometrial epithelium is a versatile and dynamic process, which requires a series of rather complicated and synchronous morphological and biochemical changes. Large and smooth membrane protrusions with pinocytotic function, known as pinopodes, have been observed in the endometrial surface during the window of implantation[4,5]. The formation and appearance of pinopodes appears to advance or regress, depending on hormonal milieu and other physiological modifications throughout the menstrual cycle[6]. Furthermore, a positive correlation between the pinopodes number and blastocyst implantation has been reported[7]. Fully developed pinopodes have been considered as the characteristic morphologic markers to assess endometrial receptivity and to locate the implantation win-

dow[8,9].

The aim of this experimental study was to investigate the timing of pinopodes expression in the endometrial surface epithelium of mice following a single dose administration of RU486.

Materials and methods

Animals and reagents Seventy female (weight: 28–30 g) and 15 male (weight: 40–45 g) adult Kunming mice (age 8–12 weeks) were provided by Sanitary Epidemic-Prevention Station of Hubei Province, China (Certificated No 19-082, China). Mifepristone tablets (Third Pharmaceutical Factory of Beijing, China) were ground carefully and dissolved in propylene glycol.

Animal treatment Female and male mice in a ratio of 2:1 were kept overnight in a cage for mating. The following morning, the display of a vaginal plug in female mice was designated as day 1 of pregnancy (Pd1). The pregnant mice were divided into five groups, as follows: a) non-treated group; b) treated group 1; c) treated group 2; d) treated group 3; and e) treated group 4. The non-treated group was considered the control. All mice in the treated groups received mifepristone subcutaneously (0.1 mL solution containing 0.1 mg mifepristone) between 07:00 and 08:00 AM on Pd1, Pd2, Pd3, and Pd4, respectively.

Scanning electron microscopy Two mice selected randomly from each group were killed by cervical dislocation between 21:30 and 22:00 PM on Pd4, and another two mice in the same group were killed between 09:30 and 10:00 AM on Pd5. All remaining mice were killed on Pd7 in order to observe the pregnancy and the average number of implanted embryos.

The murine uterine horns were excised and then cut open along the longitudinal axis. The endometrial tissue was rinsed in saline solution, fixed in 2.5% (w/v) glutaraldehyde solution in a sodium cacodylate buffer (0.15 mol/L, pH 7.3) and post-fixed in a 1% (w/v) osmium tetroxide solution in a sodium cacodylate buffer (0.15 mol/L, pH 7.3) containing sucrose (75 mmol/L). The specimens were dehydrated in a graded series of acetone, then dried in a critical-point drier with carbon dioxide, mounted on the specimen holder, coated with gold palladium, and observed by scanning electron microscopy (SEM) (S-520, Hitachi, Tokyo, Japan).

To avoid inter-observer bias, all specimens were analyzed by the same observer. Based on development stage and abundance, pinopodes were scored as developing, fully developed, or regressing, and then as few (<20%), moderate (20%–50%), or abundant (>50%), respectively. If different development stages were observed in the same specimen, only the commonest pattern was reported[6].

Statistical analysis Data were expressed as mean±SD. Unpaired *t*-test and χ^2-test were used. Software SPSS 11.0 for Windows was used. $P<0.05$ was considered to be statistically significant.

Results

Pregnancy rate and average implanted embryos No mice in treated groups 1, 2, or 3 conceived. In contrast, one mouse in group 4 achieved a pregnancy. Number of pregnant mice and average number of implanted embryos was significantly lower in treated group 4 as compared with controls (1 *vs* 9, $P<0.01$; 6 *vs* 14.67±1.35, $P<0.01$, respectively).

Pinopodes expression in endometrial surface In the control group, specimens collected between 21:30 and 22:00 PM on Pd4 showed abundant membrane projections widely distributed in the endometrial luminal surface. Clear, smooth, and slender projections were covered by short microvilli (developing pinopodes) (Figure 1). In specimens collected between 09:30 and 10:00 AM on Pd5, the endometrial surface was covered by membranous structures protruding and folding maximally (fully developed pinopodes). No microvilli were observed (Figure 2).

In treated group 1, the specimens collected between 21:30 and 22:00 PM on Pd4 showed smooth membrane projections. These structures, resembling developing pinopodes, were smaller, less abundant, and slightly lagged behind those present in controls (Figure 3). In specimens collected between 09:30 and 10:00 AM on Pd5, mainly fully developed pinopodes and developing pinopodes were present. Fully developed pinopodes were observed exclusively in epithelial cell depressions, while the neighboring surface was covered with short tips of microvilli (Figure 4).

In treated group 2, the specimens taken between 21:30 and 22:00 PM on Pd4 showed endometrial surface covered by scanty membrane projections. The endometrial luminal surface was relatively smooth with few and slender membranous projections (developing pinopodes) (Figure 5). These structures appeared slightly more pronounced in specimens collected between 09:30 and 10:00 AM on Pd5, but no fully developed pinopode was observed (Figure 6).

In treated group 3, no membrane projections were present in the endometrial surface of specimens collected between 21:30 and 22:00 PM on Pd4. The epithelial cells lining the luminal surface were rather smooth and covered by small tips of microvilli (Figure 7). The specimens taken between 09:30 and 10:00 AM on Pd5 showed smooth endometrial surface covered by normal epithelial cells and short microvilli in one case, while in the other there were slender membranous projections (developing pinopodes) which were much smaller

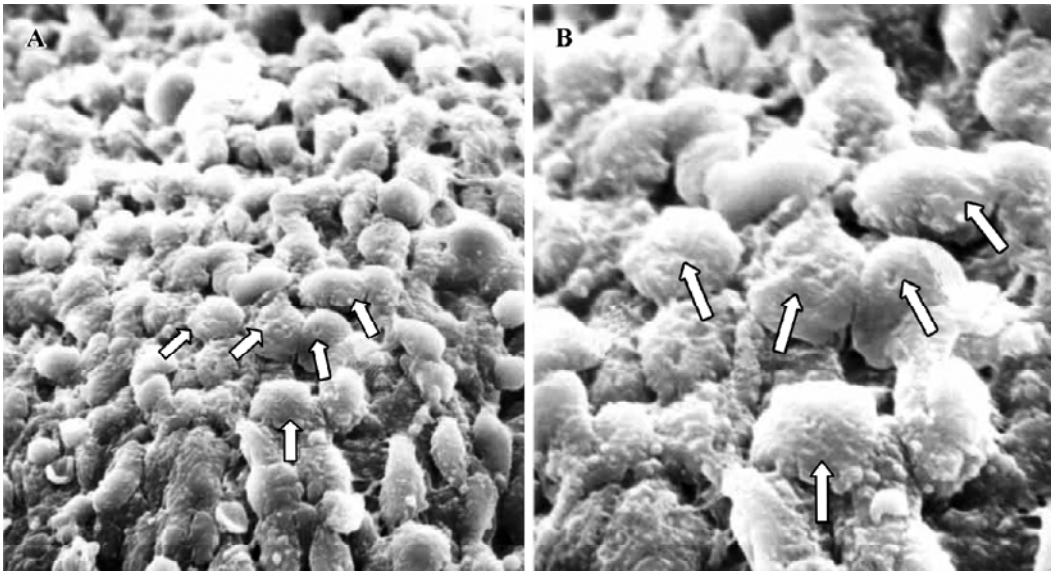

Figure 1. Pinopode expression in control group between 21:30 and 22:00 PM on Pd4. Smooth and slender membrane projections covered with short microvilli, almost the same shape and size, distributed over the whole endometrial luminal surface. (developing pinopodes: white arrow) (SEM, A×1500, B×3000).

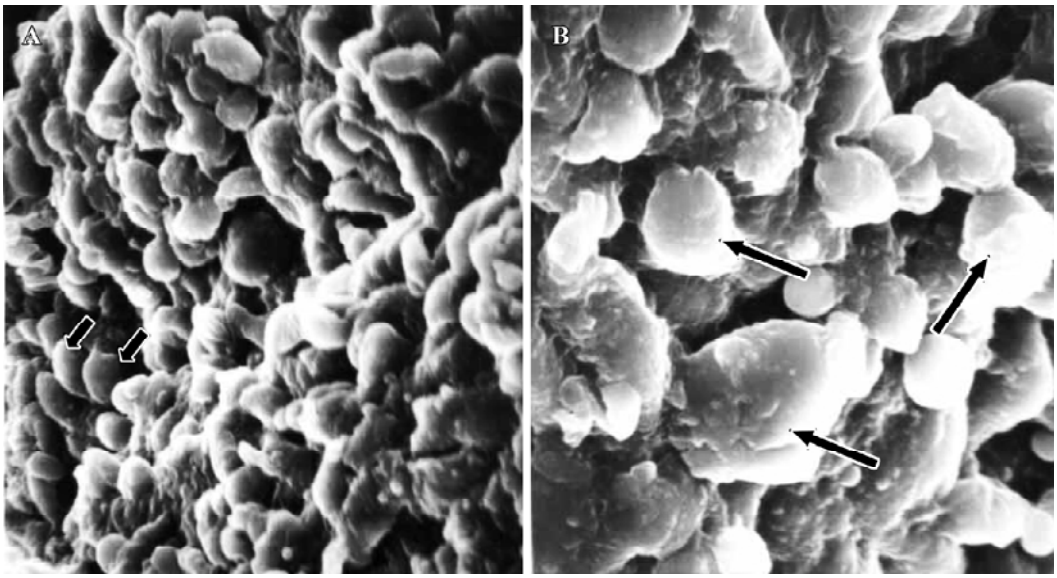

Figure 2. Pinopode expression in control group between 09:30 and 10:00 AM on Pd5. The endometrial surface was extensively covered with projections protruding and folding maximally (fully developed pinopodes: black arrow). No microvilli were observed. (SEM, A×1500, B×3000).

than those expressed in controls between 21:30 and 22:00 PM on Pd4 and between 09:30 and 10:00 AM on Pd5 (Figure 8).

Finally, in treated group 4, no synchronously developed structure was expressed in all specimens collected between 21:30 and 22:00 h on Pd4. Few pinopodes in different development stages were present. The majority of endometrial surface expressed no membrane projections and was covered by epithelial cells with short and thick microvilli. The boundaries of epithelial cells were not clear (Figure 9). Specimens collected between 09:30 and 10:00 AM on Pd5 had no pinopodes, but abundant microvilli and clear boundaries on the epithelial cells (Figure 10).

Figure 3. Pinopode expression in treated group 1 between 21:30 and 22:00 PM on Pd4. The specimens showed a lot of smooth membrane projections (developing pinopodes: white arrow) which were smaller, less abundant, and slightly lagged behind those in control group. (SEM, A×1500, B×3000).

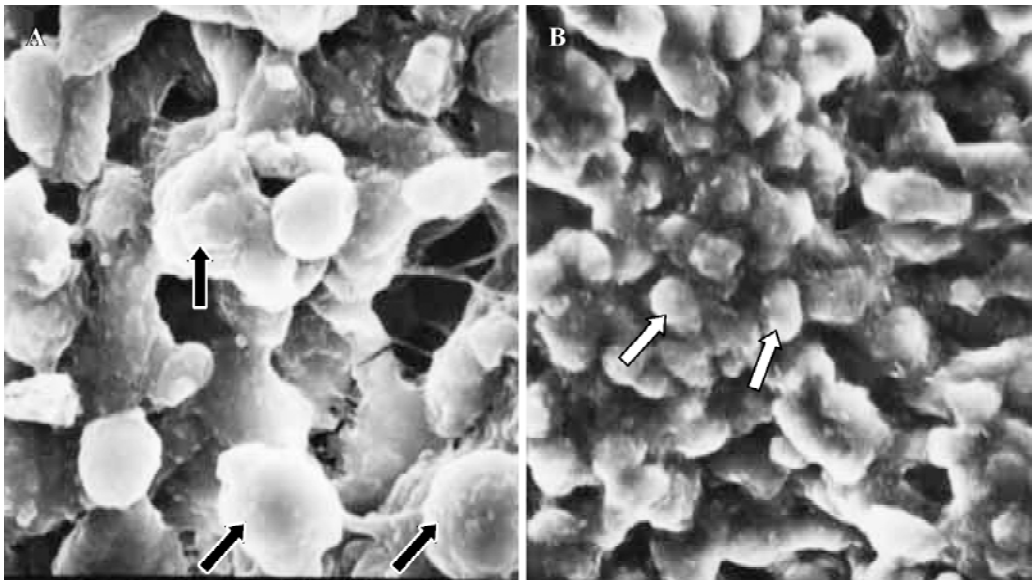

Figure 4. Pinopode expression in treated group 1 between 09:30 and 10:00 h on Pd5. Fully developed pinopodes (solid arrow) with many folds like a flower were observed in one specimen (SEM, A×3000), whereas another was mainly covered by abundant developing pinopodes (empty arrow) (SEM, B×1500).

Discussion

The use of mifepristone for emergency contraception has been widely accepted[1,3], however, a large number of prospective, randomized, double-blind studies are still in progress. Several clinical trials have shown that a single dose of mifepristone (10 mg) is effective for emergency contraception when given within 120 h from unprotected coitus, causing mild or

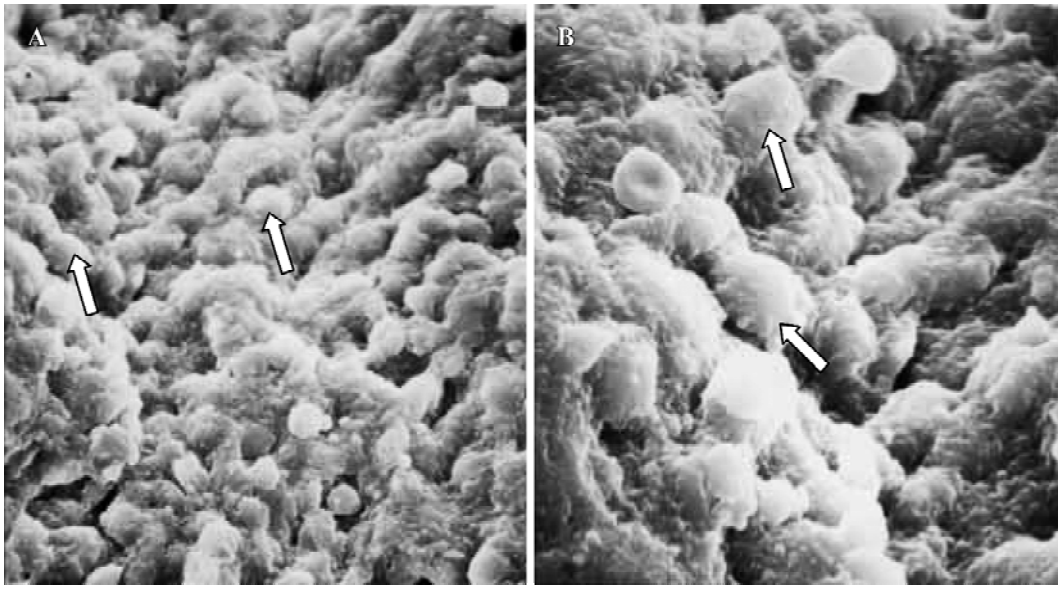

Figure 5. Pinopode expression in treated group 2 between 21:30 and 22:00 PM on Pd4. The endometrial luminal surfaces were relatively smooth with few and slender membranous projections (developing pinopodes: white arrow). (SEM, A×1500, B×3000).

Figure 6. Pinopode expression in treated group 2 between 09:30 and 10:00 AM on Pd5. These membrane projections (white arrow) appeared a little more pronounced in specimens, but no fully developed pinopodes were observed. (SEM, ×1500).

no side-effects[10,11]. However the biological mechanism of RU486 remains a matter of much debate.

Wang *et al*[12] investigated the effects of a single dose of mifepristone (10 mg) on the endometrial expressions of HOXA-11, progesterone receptors (PR), and leukaemia inhibitory factor (LIF). The found that following oral administration of mifepristone on d 2 post-ovulation (LH+2) the development of endometrium was quite delayed. In the glandular epithelium, the expressions of HOXA-11 and PR increased significantly and that of LIF decreased. Conversely, in the stromal epithelium, the expressions of these markers remained unchange.

More recently, it has been proved that mifepristone could inhibit the establishment of uterine receptivity in some animals[13,14]. Marions *et al*[15] reported that following mifepristone administration during early luteal phase in fertile women, down-regulation of PR was inhibited and no significant modifications of the remaining markers of endometrial receptivity, such as pinopodes, integrin dimmers α_4 and β_3, cyclooxygenase-1 and -2 were found. These authors[15] have also observed that the endometrial changes happened irrespective of embryo; however, its influence on implantation could not be ignored. Furthermore, they observed the influence of RU486 on endometrium only after RU486 was given on LH+2 whereas RU486 is effective for emergency contraception when given within 120 h from unprotected coitus.

A large consensus of opinion sustains that fully developed pinopodes represent specific morphological markers of endometrial receptivity[6,8,9]. The appearance and disappearance of fully developed pinopodes coincide with the nidation window both in humans and animals. Synchronous expressions of fully developed pinopodes and other markers of uterine receptivity such as integrins ($\alpha_v\beta_3$)[16], heparin-binding epidermal growth factor (HB-EGF)[17], LIF and

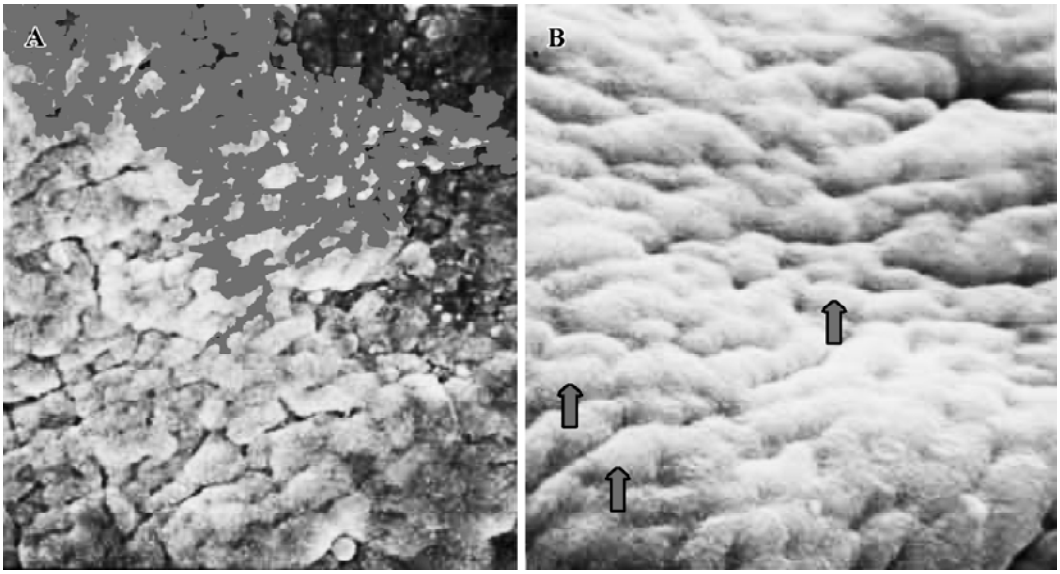

Figure 7. Pinopode expression in treated group 3 between 21:30 and 22:00 PM on Pd4. No membrane projections appeared. The epithelial cells (grey arrow) lining the luminal surface were rather smooth and covered by small tips of microvilli. (SEM, A×1500 B×3000).

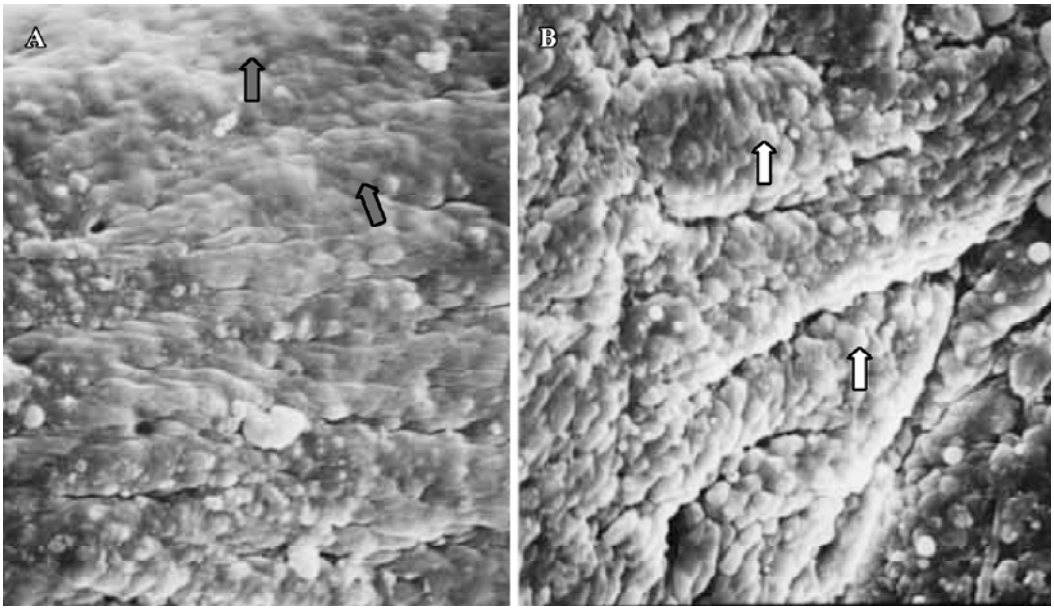

Figure 8. Pinopode expression in treated group 3 between 09:30 and 10:00 AM on Pd5. Smooth endometrial surface was covered by normal epithelial cells (grey arrow) and short microvilli in one case (SEM, A×1500), while in the other there were very slender membranous projections (developing pinopodes: white arrow) (SEM, B×1500).

LIF-receptor[18] have been noted. Therefore, it is plausible that morphological and biochemical changes during the menstrual cycle may be reliable in evaluating endometrial function and receptivity.

In this study, mifepristone as a single dose was administered straight away after the murine successful coitus was confirmed. When RU486 was given on Pd4, only one mouse conceived and the number of implanted embryos was significantly lower compared to controls (P<0.01). No mice conceived when RU486 was given on Pd1, Pd2, and Pd3. These data show that a single dose of RU486 is effective when given on Pd1, Pd2, Pd3, and Pd4.

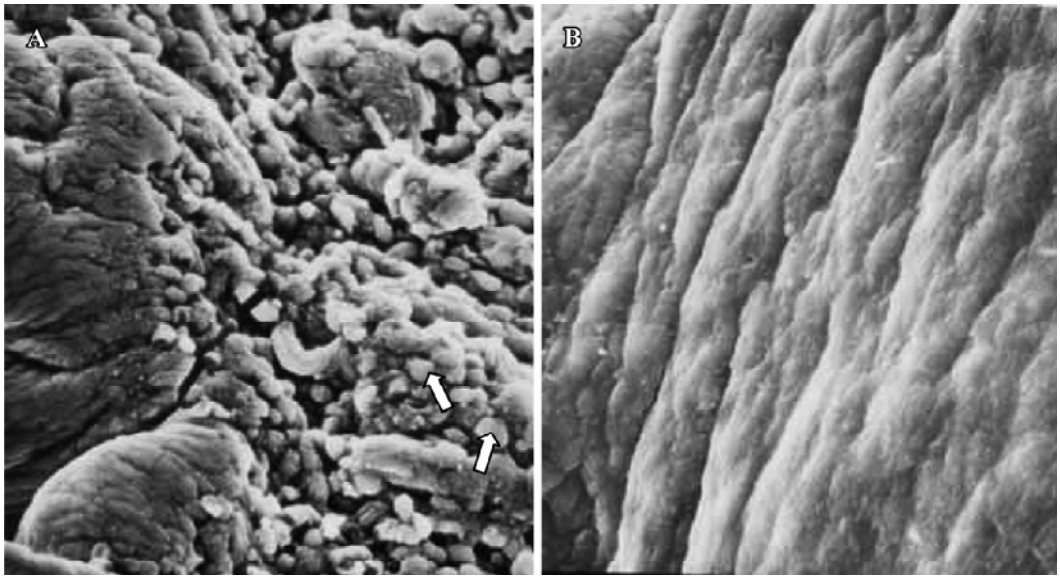

Figure 9. Pinopode expression in treated group 4 between 21:30 and 22:00 PM on Pd4. No synchronously developed structures were expressed in the samples. The pinopodes (white arrow) were few and with different development stages (SEM, A×1000). The majority of endometrial surface expressed no membrane projections and was covered by epithelial cells with short and thick microvilli. (SEM, B×1500).

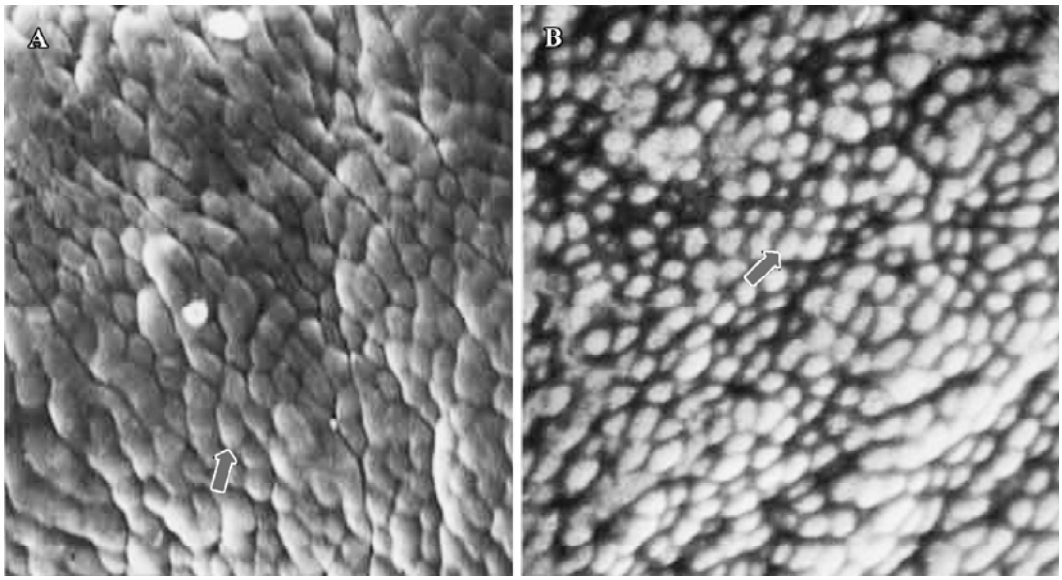

Figure 10. Pinopode expression in treated group 4 between 09:30 and 10:00 AM on Pd5. Specimens had no pinopodes, but abundant microvilli and clear boundaries on the epithelial cells (grey arrow) (SEM, ×1500).

When RU486 was administered on Pd1, developing and fully developed pinopodes were observed in the endometrial surface, but its expression was reduced compared to that of controls. It is therefore likely that mifepristone administration on Pd1 inhibits zygote development or embryo transportation through the Fallopian tube rather than having an effect on the endometrial surface. When mifepristone was given on Pd2, the uterine receptivity was significantly impaired, hence elucidating the effects of this antiprogestogenic steroid on the endometrium and its rationale for contraception. Likewise, administration of RU486 on Pd3 and Pd4 appeared to impair development and matura-

tion of pinopodes, so affecting endometrial receptivity and embryo implantation.

The effect of RU486 on the endometrium on Pd3 is stronger than that on Pd2 and Pd4. Conversely, the effect is relatively weak when this compound is given on Pd1. To our knowledge, this is the first report in the literature assessing pinopode expression as morphological marker of implantation window in mice following administration of mifepristone. Therefore, comparison with other data is not possible.

In conclusion, these findings suggest that mifepristone might inhibit endometrial receptivity and, to some extent, prevent embryo implantation as a result of morphological modifications of the luminal epithelial cells. Since the establishment of endometrial receptivity includes morphological immunological changes, further studies exploring the effects of RU486 on the expressions of cytokines, adhesion molecules and other immunological factors during the implantation window would provide new insights and improve our knowledge of implantation and early pregnancy.

References

1 Cameron ST, Critchley HO, Thong KJ, Buckley CH, Williams AR. Effects of daily low dose mifepristone on endometrial maturation and proliferation. Hum Reprod 1996; 11: 2518–26.

2 Basu R, Gundlach T, Tasker M. Mifepristone and misoprostol for medical termination of pregnancy: the effectiveness of a flexible regimen. J Fam Plann Reprod Health Care 2003; 29: 139–41.

3 Papp C, Schatz F, Krikun G, Hausknecht V, Lockwood CJ. Biological mechanisms underlying the clinical effects of mifepristone (RU486) on the endometrium. Early Pregnancy 2000; 4: 230–9.

4 Psychoyos A, Mandon P. Study of the surface of the uterine epithelium by scanning electron microscopy: observation in the rat at the 4th and 5th day of pregnancy. Crit Rev Acad Sci Paris 1971; 272: 2723–9.

5 Enders AC, Nelson DM. Pinocytotic activity of the uterus of the rat. Am J Anat 1973; 138: 277–99.

6 Nardo LG, Sabatini L, Rai R, Nardo F. Pinopode expression during human implantation. Eur J Obstet Gynecol Reprod Biol 2002; 10: 104–8.

7 Nikas G, Makrigiannakis A, Hovatta O, Jones HW Jr. Surface morphology of the human endometrium: basic and clinical aspects. Ann N Y Acad Sci 2000; 900: 316–24.

8 Psychoyos A, Nikas G. Uterine pinopodes as markers of uterine receptivity. Ass Reprod Rev 1994; 4: 26–32.

9 Bentin-Ley U, Sjogren A, Nilsson L, Hamberger L, Larsen JF. Presence of uterine pinopodes at the embryo-endometrial interface during human implantation *in vitro*. Hum Reprod 1999; 14: 515–20.

10 Von Hertzen H, Piaggio G, Ding J, Chen J, Song S, Bartfai G. Low dose mifepristone and two regimens of levonorgestrel for emergency contraception: a WHO multicentre randomized trial. Lancet 2002; 360: 1803–10.

11 Xiao BL, Von Hertzen H, Zhao H, Piaggio G. A randomized double-blind comparison of two single doses of mifepristone for emergency contraception. Hum Reprod 2002; 17: 3084–9.

12 Wang L, Wang H, Wu J, Luo HZ, Zhu ZM, Wang JD. The effect of low dose RU486 on the expression of HOXA11 in human endometrium during midluteal phase. J Reprod Med 2000; 9: 165–70. Chinese.

13 Gao F, Xu FH, Zhou XC, Han XB, Liu YX. Mifepristone regulates expression of apoptosis related genes fas and fasL in mouse endometrium. Acta Pharmacol Sin 2001; 22: 524–9.

14 Liu CQ, Wang ZX, Yuan Y. Effect of mifepristone on uterine receptivity in guinea pigs. Acta Pharmacol Sin 2002; 23: 177–82.

15 Marions L, Hultenby K, Lindell I, Sun X, Stabi B, Gemzell Danielsson K. Emergency contraception with mifepristone and levonorgestrel: mechanism of action. Obstet Gynecol 2002; 100: 65–71.

16 Nardo LG, Nikas G, Makrigiannakis A, Sinatra F, Nardo F. Synchronous expression of pinopodes and alpha v beta 3 and alpha 4 beta 1 integrins in the endometrial surface epithelium of normally menstruating women during the implantation window. J Reprod Med 2003; 48: 355–61.

17 Stavreus-Evers A, Aghajanova L, Brismar H, Eriksson H, Landgren BM, Hovatta O. Co-expression of heparin-binding epidermal growth factor-like growth factor and pinopodes in human endometrium at the time of implantation. Mol Hum Reprod 2002; 8: 765–9.

18 Aghajanova L, Stavreus-Evers A, Nikas Y, Hovatta O, Landgren BM. Co-expression of pinopodes and leukemia inhibitory factor, as well as its receptor, in human endometrium. Fertil Steril 2003; 79 (Suppl 1): 808–14.

Full-length article

Swietenia mahagony extract shows agonistic activity to PPARγ and gives ameliorative effects on diabetic *db/db* mice

Dan-dan LI[1,2,5], Jun-hua CHEN[1,4,5], Qing CHEN[1,4], Guo-wei LI[1,4], Jing CHEN[1,4], Jian-min YUE[1,4], Min-li CHEN[3], Xiao-ping WANG[2], Jian-hua SHEN[1,4,6], Xu SHEN[1,4,6], Hua-liang JIANG[1,4,6]

[1]Drug Discovery and Design Center, State Key Lab of Drug Research, Shanghai Institute of Materia Medica, Shanghai Institutes for Biological Sciences, Chinese Academy of Sciences, Shanghai 201203, [2]Chemistry Department, Tongji University, Shanghai 200092, [3]Animal Experiment Center, Zhejiang College of Traditional Chinese Medicine, Hangzhou 310053; [4]Graduate School of the Chinese Academy of Sciences, China

Key Words

Swietenia mahagony; diabetes mellitus; peroxisome proliferator-activated receptor γ; yeast-two hybrid

[5] These authors contributed equally to this work.
[6] Correspondence to Prof Jian-hua SHEN
E-mail jhshen@mail.shcnc.ac.cn;
Prof Xu SHEN
E-mail xshen@mail.shcnc.ac.cn;
Prof Hua-liang JIANG
hljiang@mail.shcnc.ac.cn
Phn 86-21-5080-6600.
Fax 86-21-5080-7088.

Received 2004-09-24
Accepted 2004-11-09

doi: 10.1111/j.1745-7254.2005.00027.x

Abstract

Aim: To search the peroxisome proliferator-activated receptor γ (PPARγ) agonists from *Swietenia mahagony* extract (*Sm*E) and observe the possible ameliorative effects of *Sm*E on diabetic *db/db* mice. **Methods:** The PPARγ agonistic activity of *Sm*E was screened by yeast-two hybrid system. The blood glucose levels of diabetic *db/db* mice were measured using a blood glucose level monitor and the data were statistically analyzed by NDST8.8W software. **Results:** By using the clinical drug rosiglitazone as a positive control, it was found that the PPARγ agonistic activity of *Sm*E at a concentration of 50 μg/L was approximately half that of 35.7 μg/L (0.1 μmol/L) of rosiglitazone. At the dose of 1000 mg/kg, *Sm*E remarkably decreased the blood glucose concentration of *db/db* mice from (15.26±2.98) to (7.58±2.20) mmol/L, and reduced the blood glucose levels by 55.49% compared with the control group ($P<0.01$). **Conclusion:** *Sm*E shows agonistic activity to PPARγ and can ameliorate the blood glucose levels of diabetic *db/db* mice. *Sm*E may be thus used as a potential agent for diabetes therapy.

Introduction

Peroxisome proliferator-activated receptor (PPAR) is a ligand-binding transcriptional regulatory factor, which belongs to the nuclear receptor superfamily and regulates the expression of a group of genes involving glucose and lipid metabolism. There are three PPAR subtypes, commonly designated as PPARα, PPARβ (δ), and PPARγ[1,2]. The functions of these PPAR isoforms, after activation by drugs (anti-inflammatory agents, fibric acids) and fatty acid derivatives (including prostaglandins and plasticizers), include an increase in lipid and cholesterol metabolism, adipocyte differentiation, and an improvement in insulin sensitivity[1,3,4]. PPARγ is the most extensively studied PPAR subtype. It has been demonstrated that PPARγ is the receptor of the thiazolidinedione (TZD) class ligands[5]. Among the TZD type antidiabetic drugs, rosiglitazone and troglitazone are potent adipocyte-differentiating agents, which activate *ap*2 gene expression in a PPARγ-dependent manner[6]. As PPARγ ligands may regulate the adipogenesis, they can be designed and modified for the treatment of cardiovascular disease and diabetes mellitus[1,7], and PPARγ has been an attractive target for new drug discovery. To date, several types of PPARγ agonist with new structures have been developed, as though few can be clinically used[8]. In fact, the search for new PPARγ agonists has long been an alluring project.

Nature remains as a source for organic structures with unparalleled diversity, and the enormous importance of natural product is obvious. In recent years, there has been growing interest in alternative therapies and the therapeutic use of natural products, especially those derived from plants. In fact, natural products, containing inherently more structural

diversity than synthetic compounds, have been the major resources of bioactive agents and will continue to play an important role in the discovery of new drugs[9]. Encouraged by these facts, we have recently focused on finding of PPARγ agonist on the basis of natural resource exploration. This present study was to test the PPARγ agonistic activity of *Sm*E and observe the ameliorative effects of *Smietenia mahagony* extract (*Sm*E) on diabetic *db/db* mice.

Materials and methods

Materials The plant material was purchased from Indonesia and the specimen (No 20030601) was deposited in Shanghai Institute of Materia Medica. OneTouch^R Ultra used for measuring the blood glucose level of diabetic *db/db* mice was purchased from Shanghai Qiangsheng Medical Treatment Equipment Ltd, Shanghai, China.

Animals The *db/db* mice were supplied by Shanghai BK Corporation. The male mice, 40–50 g, were sanitary, and allowed free access to water during the experiment.

Extract of *Swietenia mahagony* Powdered *S mahagony* seeds (0.8 kg) was refluxed with EtOH (95%, 2 L) for 2 h three times, then filtered. The combined filtrate was concentrated under reduced pressure and partitioned by EtOAc to obtain EtOAc fraction (40 g).

PPARγ agonists assay Yeast liquid synthetic dropout medium without leucine and tryptophan (T-L-) was prepared referring to Yeast Protocol Handbook[10]. *Sm*E (50 μg/L) and rosiglitazone (0.1 μmol/L) were dissolved in Me_2SO for assay use.

The yeast two-hybrid system was established for identifying PPARγ agonist by our laboratory[11]. The yeast strain AH109 named p1c2, harboring the expression plasmid pGADT7-CBP and PGBKT7-PPARγLBD, was used for PPARγ agonist screening[12].

Yeast clone p1c2 was inoculated into 2 mL T-L-liquid medium from a plate, then incubated at 30 ℃ overnight (16–18 h) with shaking (250 r/min). After vortexing and recording OD_{600}, the cell culture was diluted with T-L-liquid medium until its OD_{600} reached about 0.05. Subsequently 5 μL of Me_2SO or drug was added to 495 μL of diluted yeast culture, test cultures were incubated at 30 °C overnight (14–16 h), and then α-Galactosidase Assay was performed[10].

Blood glucose level measurement The basal blood glucose levels of 40 male *db/db* diabetic mice were measured everyday for 7 d, and 24 mice showing comparatively steady blood glucose level were screened out**.** These mice were divided into three groups (n=8) according to the blood glucose level. The mice were given 0.5% CMC-Na (10 mL/kg) in the control group, *Sm*E (1000 mg/kg) or rosiglitazone (10 mg/kg) in the treated group by ig everyday for 2 weeks. The blood glucose concentrations were measured using a blood glucose level monitor (OneTouch^R Ultra, Shanghai) every other day. Data were analyzed using the NDST8.8W analysis program.

Statistical analysis The results were expressed as mean±SD and analyzed by unpaired t-test.

Results

PPARγ ligand-binding activity of *Sm*E *Sm*E exhibited moderate agonistic activity to PPARγ, and its relative α-galactosidase intensity from the yeast two-hybrid assay was 2.13 at the concentration of 50 μg/L, which was approximately half that of rosiglitazone 35.7 μg/L (0.1 μmol/L), a potent synthetic PPARγ agonist (Figure 1), whose relative α-galactosidase intensity is around 4.29.

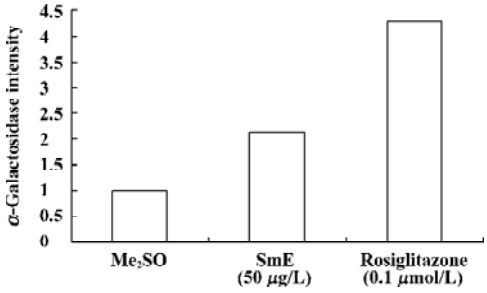

Figure 1. PPARγ agonistic activity was measured using a yeast two-hybrid system. All samples were dissolved in Me_2SO and the PPARγ agonistic activity was expressed as the relative α-galactosidase intensity. Data are means of three experiments performed in triplicate.

Effect of *Sm*E on diabetic *db/db* mice After 14 d of feeding, the blood glucose levels decreased markedly in the both *Sm*E- and rosiglitazone-treated groups compared with the control group. The blood glucose concentration of *db/db* mice in the control group was 17.03 mmol/L, yet in the treated groups 7.58 mmol/L and 6.98 mmol/L respectively (Table 1). In comparison with the control group, the blood glucose levels decreased 55.49 % (P<0.01) in the *Sm*E-treated group and 59% (P<0.01) in the rosiglitazone-treated group.

Discussion

Swietenia mahagony is a large, medicinally and economically important timber tree native to the West Indies. The seeds of this plant are used for the treatment of hypertension and malaria as a folk medicine in Indonesia[13]. In the present study, we tested the effect of *S mahagony* on the

Table 1. Ameliorative effects of *SmE* (1000 mg/kg, for 2 weeks) on diabetic *db/db* mice. n=8. Mean±SD. $^{b}P<0.05$, $^{c}P<0.01$ *vs* control group. $^{d}P>0.05$ *vs* Rosiglitazone group.

Group	Glucose concentration (mmol/L)						
	1 d	4 d	6 d	8 d	10 d	12 d	14 d
Control	15.04±2.33	15.04±2.16	16.00±2.23	17.01±2.92	16.92±2.76	17.70±2.55	17.03±4.55
Sm*E*	15.26±2.98	10.73±3.2^{bd}	9.53±2.43^{c}	11.37±3.54^{b}	8.76±2.52	8.4±2.26^{c}	7.58±2.20^{cd}
Rosiglitazone	14.59±1.90	10.54±3.18^{c}	7.38±0.74^{c}	9.53±0.78^{c}	7.21±0.68^{c}	7.02±0.3^{c}	6.98±2.31^{c}

PPARγ agonistic activity and the amelioration of the blood glucose level in type-II diabetic mice, a representative insulin resistance syndrome. With the help of the yeast two-hybrid system assay, the possible anti-diabetic mechanism of *Swietenia mahagony* was proposed. The results *in vivo* showed that *Sm E* exhibited moderate effects on decreasing the blood glucose levels of the diabetic *db/db* mice. These results may give us a new hint that *Sm*E might be used as a potential agent for diabetic therapy with its PPARγ transcriptional regulatory function as one of the *in vivo* mechanisms even though there may be existed other efficient components in *Sm*E against other targets for diabetic therapy.

Acknowledgement

Project supported by Kuancheng Wang Fundation of Chinese Academy of Sciences (2003), Shanghai Basic Research Project from the Shanghai Science and Technology Commission (No 02DJ14070), the National Natural Science Foundation of China (No 20372069, 29725203, and 20072042), and the State Key Program of Basic Research of China (No 2003CB514125, 2003CB514124, and 2002CB512807, 2002CB512802, 2002AA233011).

References

1 Willson TM, Brown PJ, Sternbach DD, Henke BR. The PPARs: from orphan receptors to drug discovery. J Med Chem 2000; 43: 527–50.

2 Kerstern S, Desverge B, Wahli W. Roles of PPARs in health and disease. Nature 2000; 405: 421–4.

3 Escher P, Wahli W. Peroxisome proliferator-activated receptors: insight into multiple cellular functions. Mutation Res 2000; 448: 121–38.

4 Vamecq J, Latruffe N. Medical significance of peroxisome proliferator-activated receptors. Lancet 1999; 354: 141–8.

5 Reginato MJ, Lazar MA. Mechanisms by which thiazolidinediones enhance insulin action. Trends Endoc Metab 1999; 10: 9–13.

6 Hulin B, McCarthy PA, Gibbs EM. The glitazone family of antidiabetic agents. Curr Pharm Des 1996; 2: 85–102.

7 Barry GS, William JH. Recent advances in peroxisome proliferator-activated receptor science. Curr Med Chem 2003; 10: 267–80.

8 Murphy GJ, Holder JC. PPARγ agonists: therapeutic role in diabetes, inflammation and cancer. Trends Pharm Sci 2000; 21: 469–74.

9 Shen JH, Xu XY, Cheng F, Liu H, Luo XM, Shen JK, *et al.* Virtual screening on natural products for discovering active compounds and target information. Curr Med Chem 2003; 10: 2327–42.

10 Yeast protocols handbook. Available from: http://www.bdbiosciences.com/clontech/techinfo/manuals/PDF/PT3024-1.pdf.

11 Chen Q, Chen J, Sun T, Shen JH, Shen X, Jiang HL. A yeast two-hybrid technology based system for the discovery of PPARγ agonist and antagonist. Anal Biochem 2004;335:253–9.

12 Taniguchi T, Mizukami J, inventors. Method for identifying or screening agonist and antagonist to PPAR. US patent 6 365 361. 2002 Aug 23.

13 Kadota S, Marpaaung L, Kikuchi T, Ekimoto H. Constituents of the seeds of *Swietenia mahagoni* JACQ. III. Structures of mahonin and secomahoganin. Chem Pharm Bull 1990; 38: 1495–500.

Full-length article

Triptolide suppresses CD80 and CD86 expressions and IL-12 production in THP-1 cells[1]

Jing LIU, Qing-li WU, Yong-hong FENG, Yi-fu YANG, Xiao-yu LI, Jian-ping ZUO[2]

State Key Laboratory of Drug Research, Shanghai Institute of Materia Medica, Shanghai Institutes for Biological Sciences, Chinese Academy of Sciences, Shanghai 201203, China

Key words

triptolide; CD80 antigens; CD86 antigens; interleukin-12

[1] Project supported by the National Natural Science Foundation of China (No A30171086) and the Knowledge Innovation Program of the Chinese Academy of Sciences (No KSCX2-SW-202).
[2] Correspondence to Dr Jian-ping ZUO. Phn/Fax 86-21-5080-6701. E-mail jpzuo@mail.shcnc.ac.cn

Received 2004-08-25
Accepted 2004-11-02

doi: 10.111/j.1745-7254.2005.00035.x

Abstract

Aim: To investigate the effects of triptolide, a diterpenoid triepoxide from *Tripterygium wilfordii* Hook F (TWHF), on the co-stimulatory molecule expression and interleukin-12 (IL-12) production from THP-1 cells. **Methods:** THP-1 cells were differentiated into macrophage-like cells by Me_2SO, and then cultured with IFN-γ (500 kU/L) and lipopolysaccharide (LPS) (1 mg/L) with or without triptolide. The surface molecule expressions were analyzed on a FACScan flow cytometer. IL-12p40, IL-12p70 were assayed by ELISA. **Results:** Tripolide suppressed CD80 and CD86 expressions on IFN-γ (500 kU/L) and LPS (1 mg/L) activated THP-1 cells at nontoxic dosages of 2.5–0.625 μg/L. Furthermore, the production of IL-12p40 and IL-12p70 were also significantly reduced in THP-1 cells exposed to triptolide. **Conclusion:** Triptolide impairs the antigen-presenting function by inhibiting CD80 and CD86 expressions and decreased IL-12p40 and IL-12p70 (bioactive form) productions from the activated THP-1 cells.

Introduction

Human cells of monocytic lineage, including monocytes, macrophages, and monocyte-derived dendritic cells, play an essential role in initiating and maintaining immune responses by acting as antigen-presenting cells (APC). They process and present antigenic peptides via the major histocompatibility complex (MHC) molecules and the expression of costimulatory molecules[1,2]. The best-characterized costimulatory molecules to date are two structurally related proteins, CD80 and CD86. Both provide costimulation to T-cells, leading to their proliferation, cytokine production, and development[2,3]. *In vivo* studies using anti-CD80 and anti-CD86 monoclonal antibodies or genetically manipulated animals have demonstrated that a blockade of CD80/CD86 costimulatory molecules can prolong allograft survival and reduce the severity of autoimmune diseases[4,5]. Preliminary clinical studies in human subjects also support this concept[6]. Therefore, pharmacological intervention in the upregulation of CD80/CD86 may therefore be useful in the treatment of autoimmune diseases or in transplantation.

Tripterygium wilfordii Hook F (TWHF) is a herb used in traditional Chinese medicine for the treatment of rheumatoid arthritis and other autoimmune diseases[7,8]. Triptolide, a highly oxygenated diterpenoid triepoxide, is the major component responsible for the immunosuppressive and anti-inflammatory effects of TWHF[9]. It is effective for the treatment of autoimmune diseases, prevention of allograft rejection, and graft-versus-host disease in animal experiments[10–13]. The inhibitory effect of triptolide on T-cell activation is stronger than cyclosporine[14] and FK-506[15] *in vitro*. Furthermore, it can induce activated T-cell apoptosis[16]. Thus, T-cells are considered to be the main target for triptolide. Recently, Hong *et al*[17] and Li *et al*[18] demonstrated that triptolide inhibited upregulation of B7 on activated human proximal tubular epithelial cells. These results suggest that triptolide may have suppressive effects on APC. In a further analysis of this theory, we used a human monocytic leukemia cell line (THP-1) that had been differentiated into macrophage-like cells by treatment with Me_2SO. The macrophage-like THP-1 cells were used to examine the influences of triptolide on the expression of CD80 and CD86 molecules and the production

of IL-12, an important cytokine that biases $CD4^+$ T-cells toward Th1 differentiation[19].

Materials and methods

Reagents Triptolide was provided by the Department of Chemistry, Shanghai Institute of Materia Medica. Lipopolysaccharide (LPS, Escherichia coli 055: B5), 3-[4,5-dimethylthylthiazol-2-yl]-2,5-diphenyl-tetrazolium bromide (MTT), and 3,3′,5,5′-tetramethylbenzidine (TMB) were from Sigma (St Louis, MO, USA). Recombined human IFN-γ was purchased from Shanghai Clonbiotech (Shanghai, China). PE-conjugated mAbs were used to detect cell surface expression of CD14, HLA-ABC, HLA-DR, CD80 and CD86 by flow cytometry, as well as isotype-matched mAbs,which were purchased from PharMingen (San Jose, CA, USA).

Cells The human monocytic THP-1 line (ATCC, Manassas, VA, USA) was maintained in suspension culture in RPMI1640 medium, supplemented with 10% FBS. Cultures were maintained at 37 ºC in a humidified atmosphere of 5% CO_2 and were subcultured at 1/10 dilution every 5–6 d. Cells were used to differentiate when seeded at a density of 5×10^8 cells/L in a 10-cm^2 culture dish for 24 h.

Flow cytometry analysis THP-1 cells were cultured in a screw cap container 2.4×10^6 cells in 4 mL of RPMI1640 medium with 10% FBS per-well. Cells were differentiated with 1.2% Me_2SO for 24 h, then pre-treated with IFN-γ (500 kU/L) for 16 h and stimulated by LPS (1 mg/L) for another 24 h. Various concentrations of triptolide were added at the initiation of the culture. Cells were collected and washed in an ice cold staining buffer (PBS containing 0.1% w/v sodium azide, 1% FBS, pH 7.2). Cells were then resuspended at $4.0–5.0\times10^9$/L in an ice-cold staining buffer. Optimal concentrations of each fluorochrome-labeled antibody were added. Cells were incubated at 4 ºC for 30 min, then washed twice and analyzed by flow cytometry using FACSCalibur (Becton Dickinson, San Jose, CA,USA). Data were illustrated by CELLQuest.

Cytokine analysis THP-1 cells were cultured in 24-well plates at 6.0×10^5 cells in 2 mL of RPMI1640 medium with 10% FBS and other treatments were the same as in the surface molecules analysis. Culture supernatants were harvested and stored at -20 ºC. Human IL-12p70 and IL-12p40 productions were measured using ELISA kits (PharMingen) according to the manufacturer's instructions.

MTT assay Cytotoxicity was assessed by MTT assay[20]. Me_2SO-differentiated THP-1 cells were incubated in a 96-well plate at 5.4×10^4 cells in 180 μL of RPMI1640 medium with 10% FBS per-well for 72 h with and without various concentrations of triptolide. MTT (5 g/L) 18 μL was added 5 h prior to the end of the culture, and then 90 μL solvent (10% SDS, 50% *N, N*-dimethy formamide, pH 7.2) was added. The cells were then incubated for another 7 h and value was measured at 570 nm by a microplate reader (Bio-Rad Model 550, Japan).

Statistical analysis Results were expressed as mean±SD. An independent two-tailed *t*-test was performed and $P<0.05$ was considered to be statistically significant.

Results

Triptolide influenced the surface molecule expressions on Me_2SO-differentiated THP-1 cells THP-1 cells are known to be activated by LPS stimulation and have been used as a surrogate for investigation of human monocytes[21]. When THP-1 cells are treated with Me_2SO, the cells differentiate into macrophage-like cells and proliferation is profoundly inhibited. IFN-γ pretreatment and LPS stimulation enhanced the expression of a variety of surface molecules such as HLA-ABC, HLA-DR, and B7 molecules on THP-1 cells. Tripolide could suppress CD80 and CD86 expressions on IFN-γ (500 kU/L) and LPS (1 mg/L)-activated THP-1 cells at 2.5–0.625 μg/L (Figure 1). Triptolide also weakly down-regulated the HLA-ABC expression, but it did not change the expressions of HLA-DR and CD14 on THP-1 cells.

Triptolide inhibited IL-12 production of Me_2SO-differentiated THP-1 cells IFN-γ pretreatment and LPS stimulation induced IL-12p40 and IL-12p70 production from Me_2SO-differntiated THP-1 cells. The productions of IL-12p40 and IL-12p70 in response to IFN-γ (500 kU/L) and LPS (1 mg/L) induction were significantly reduced in THP-1 cells exposed to triptolide in the concentration of 2.5–0.625 μg/L (Figure 2). IL-10 production was too low to be detected in this experiment system.

Cytotoxicity of triptolide on Me_2SO-differentiated THP-1 cells We examined whether the above suppressive effects of triptolide were due to its cytotoxicity to THP-1 cells. When Me_2SO-differentiated THP-1 cells were cultured with and without different concentrations of triptolide for 72 h, the cytotoxicity was monitored by MTT assay. As shown in Figure 3, triptolide did not exert any cytotoxic effect on the THP-1 cells from 2.5 μg/L to 0.625 μg/L in the present study.

Discussion

The immunosuppressive and therapeutic activity of triptolide upon systemic administration has been demonstrated in animal models for human-like diseases, such as in experimental autoimmune uveitis[22], collagen-induced arthritis[11], diabetes[12], nephrotic syndrome[13]. It also improves

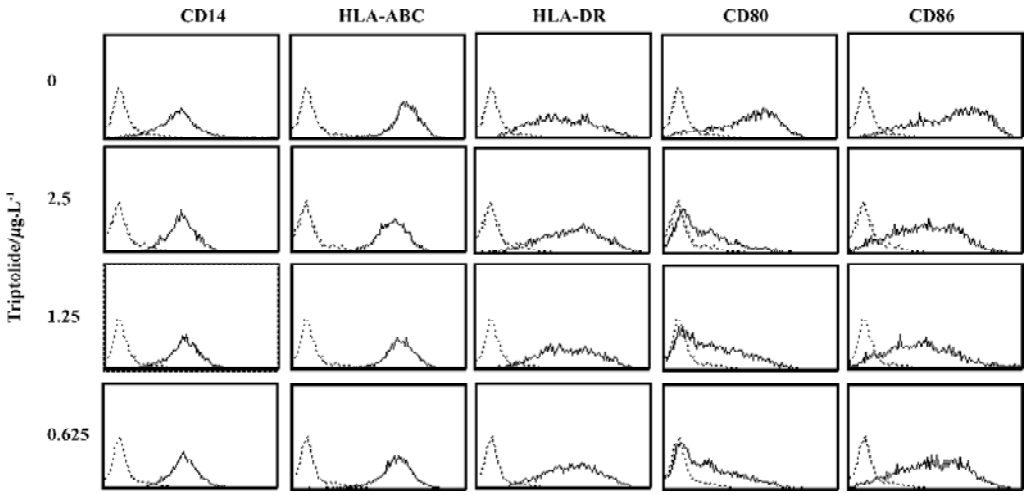

Figure 1. Suppressive effects of triptolide on the expression of CD80 and CD86 in THP-1 cells. Dotted line represents cells incubated with isotype-matched antibodies and solid line represents cells incubated with specific antibodies. Results were obtained from one of the three experiments performed.

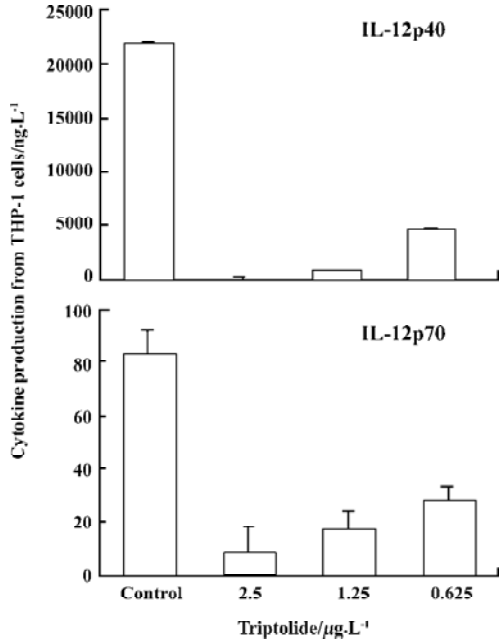

Figure 2. Analysis of IL-12p40 and IL-12p70 productions in THP-1 cells. Mean±SD. Results were obtained from one of the three experiments performed.

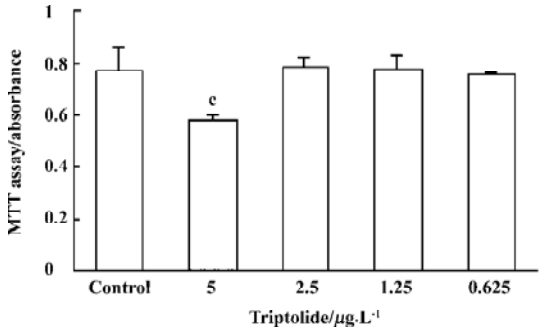

Figure 3. Cytotoxicity of triptolide on THP-1 cells. THP-1 cells (6.0×10^8/L) were differentiated with 1.2% Me_2SO. Compounds were added at the initiation of culture. Mean±SD. $^cP<0.01$ *vs* control. Results were obtained from one of the three experiments performed.

the survival rate of the heart[23] and kidney[24] allograft in the rat transplantation model and graft-versus-host disease in a murine allogeneic bone marrow transplantation model[25]. However the immunosuppressive mechanism of triptolide has not been completely delineated[26]. In the present study, we demonstrated a new finding that triptolide, an active component of TWHF, directly down-regulats the costimulation molecule CD80 and CD86 expressions on macrophages-like cells (Me_2SO-differentiated THP-1 cells), and inhibits the bioactive form of IL-12p70 production from Me_2SO-differentiated THP-1 cells by a dose-dependent manner.

CD80 and CD86 on APC delivered the critical costimulatory signals for optimal T-cell activation[3]. Blockade of CD80 and CD86 signaling resulted in ineffective T-cell activation. The implication is that reduced and blocked CD80/CD86 costimulations can prevent the induction of pathogenic T-cell responses in autoimmune disease and allow for prolonged acceptance of allografts in organ transplantation[4–6]. In addition to the processing and presentation of antigenic peptides via MHC molecules and the expression of costimulatory molecules, APC played a central role in driving $CD4^+$ T helper cell differentiation through the

production of critical cytokines, such as IL-12, IL-10, TGF-β and possibly IL-4. The production of bioactive form IL-12p70 by host antigen-presenting cells was a primary determinant in the differentiation of naive $CD4^+$ T cells into Th1 effector cells[19]. These suppressive effects of triptolide on CD80 and CD86 expressions, and IL12p70 production suggest an important therapeutic implication for multiple sclerosis and other abnormal immune response mediated diseases associated with the increased expression of CD80/CD86 and the production of IL-12[27].

Triptolide has been proven to be a potent immunosuppressive agent, although information on the molecular mechanism of triptolide is scarce. Recent studies have shown that triptolide inhibits T-cell activation and early cytokine gene transcription in T-cell at the purine-box/ARRE/NF-AT and NF-κB target sequence after specific DNA binding[28,29]. NF-κB is a family of transcription factors central to immunityand inflammation. It regulates expression of a number of genes, including cytokines, costimulatory molecules, nitric oxide, and susceptibility to apoptosis[30]. Therefore, the suppressive effects of triptolide on the co-stimulatory molecular expression and IL-12 production from THP-1 cells can result from the inhibition of NF-κB transcriptional activation.

In conclusion, we have demonstrated that triptolide downregulats the levels of CD80 and CD86 expressions in THP-1 cells. Production of bioactive form IL-12p70 in THP-1 cells was effectively inhibited by triptolide. These immunosuppressive activities of triptolide contribute, at least in part, to the therapeutic effect and mechanism of triptolide in the treatment of autoimmune diseases.

References

1 Schwartz RH. T-lymphocyte recognition of antigen in association with gene products of the major histocompatibility complex. Annu Rev Immunol 1985; 3: 237–61.

2 Greenfield EA, Nguyen KA, Kuchroo VK. CD28/B7 costimulation. Crit Rev Immunol 1998; 18: 389–418.

3 Salomon B, Bluestone JA. Complexities of CD28/B7: CTLA-4 costimulatory pathways in autoimmunity and transplantation. Annu Rev Immunol 2001; 19: 225–52.

4 Jonker M, Ossevoort And MA, Vierboom M. Blocking the CD80 and CD86 costimulation molecules: lessons to be learned from animal models. Transplantation 2002; 73: S23–6.

5 Anand S, Chen L. Control of autoimmune diseases by the B7-CD28 family molecules. Curr Pharm Des 2004; 10: 121–8.

6 Gottlieb AB, Lebwohl M, Totoritis MC, Abdulghani AA, Shuey SR, Romano P, *et al*. Clinical and histologic response to single-dose treatment of moderate to severe psoriasis with an anti-CD80 monoclonal antibody. J Am Acad Dermatol 2002; 47: 692–700.

7 Tao XL, Sun Y, Dong Y, Xiao YL, Hu DW, Shi YP, *et al*. A prospective, controlled, double-blind, cross-over study of tripterygium wilfodii hook F in treatment of rheumatoid arthritis. Chin Med J 1989; 102: 327–32.

8 Lipsky PE, Tao XL. A potential new treatment for rheumatoid arthritis: thunder god vine. Semin Arthritis Rheum 1997; 26: 713–23.

9 Qiu D, Kao PN. Immunosuppressive and anti-inflammatory mechanisms of triptolide, the principal active diterpenoid from the Chinese medicinal herb *Tripterygium wilfordii* Hook f. Drugs R D 2003; 4: 1–18.

10 Su D, Song Y, Li R. Comparative clinical study of rheumatoid arthritis treated by triptolide and an ethyl acetate extract of *Tripterygium wilfordii*. Chin J Integrated Trad West Med 1990; 10: 144–6.

11 Gu WZ, Brandwein SR. Inhibition of type II collagen-induced arthritis in rats by triptolide. Int J Immunopharmacol 1998; 20: 389–400.

12 Li L, Wakukami T, Teng WP, Di GX, Murakami K, Mimura G. The effect of triptolide on the development of insulitis in low-dose streptozotocin induced diabetic mice and on the beta-cells of normal mice. Chin J Diabetes 1994; 2: 69–75.

13 Yi ZW, Li L. Clinical study of nephrotic syndrome in children treated by triptolide. Hunan Med J 1994; 11: 284–5.

14 Lu H, Hachida M, Enosawa S, Li XK, Suzuki S, Koyanagi H. Immunosuppressive effect of triptolide *in vitro*. Transplant Proc 1999; 31: 2056–7.

15 Chan MA, Kohlmeier JE, Branden M, Jung M, Benedict SH. Triptolide is more effective in preventing T cell proliferation and interferon-gamma production than is FK506. Phytother Res 1999; 13: 464–7.

16 Yang Y, Liu Z, Tolosa E, Yang J, Li L. Triptolide induces apoptotic death of T lymphocyte. Immunopharmacology 1998; 40: 139–49.

17 Hong Y, Zhou W, Li K, Sacks SH. Triptolide is a potent suppressant of C3, CD40 and B7h expression in activated human proximal tubular epithelial cells. Kidney Int 2002; 62: 1291–300.

18 Li H, Liu ZH, Dai CS, Liu D, Li LS. Triptolide inhibits proinflammatory factor-induced over-expression of class II MHC and B7 molecules in renal tubular epithelial cells. Acta Pharmacol Sin 2002; 23: 775–81.

19 Gately MK, Renzetti LM, Magram J, Stern AS, Adorini L, Gubler U, *et al*. The interleukin-12/interleukin-12-receptor system: role in normal and pathologic immune responses. Annu Rev Immunol 1998; 16: 495–521.

20 Mosmann T. Rapid colorimetric assay for cellular growth and survival: application to proliferation and cytotoxicity assays. J Immunol Method 1983; 65: 55–63.

21 Kubin M, Chow JM, Trinchieri G. Differential regulation of interleukin-12 (IL-12), tumor necrosis factor alpha, and IL-1 beta production in human myeloid leukemia cell lines and peripheral blood mononuclear cells. Blood 1994; 83: 1847–55.

22 Wu Y, Wang Y, Zhong C, Li Y, Li X, Sun B. The suppressive effect of triptolide on experimental autoimmune uveoretinitis by down-regulating Th1-type response. Int Immunopharmacol 2003; 3: 1457–65.

23 Lin JF, Zhu H, Liu XQ, Zhen HP, Zheng YL. Triptolide prolong the survival of heart transplant in mice. Strait Pharmacentical J 1998; 10: 29–30.

24 Yang J, Fan Z, Dai C, Wang J, Liu Z, Li L. Antirenal allograft rejection effects of triptolide in rats. J Nephrol Dialy Trans-

plant 1997; 6: 214–20.
25 Chen BJ, Liu C, Cui X, Fidler JM, Chao NJ. Prevention of graft-versus-host disease by a novel immunosuppressant, PG490-88, through inhibition of alloreactive T cell expansion. Transplantation 2000; 70: 1442–7.
26 Du ZY, Li XY, Li YC, Wang SY. Analysis of triptolide-regulated gene expression in Jurkat cells by complementary DNA microarray. Acta Pharmacol Sin 2003; 24: 864–72.
27 Monteyne P, Guillaume B, Sindic CJ. B7-1 (CD80), B7-2 (CD86), interleukin-12 and transforming growth factor-beta mRNA expression in CSF and peripheral blood mononuclear cells from multiple sclerosis patients. J Neuroimmunol 1998; 91: 198–203.
28 Liu H, Liu ZH, Chen ZH, Yang JW, Li LS. Triptolide: a potent inhibitor of NF-kappa B in T-lymphocytes. Acta Pharmacol Sin 2000; 21: 782–6.
29 Qiu D, Zhao G, Aoki Y, Shi L, Uyei A, Nazarian S, *et al*. Immunosuppressant PG490 (triptolide) inhibits T-cell interleukin-2 expression at the level of purine-box/nuclear factor of activated T-cells and NF-kappaB transcriptional activation. J Biol Chem 1999; 274: 13443–50.
30 Caamano J, Hunter CA. NF-kappaB family of transcription factors: central regulators of innate and adaptive immune functions. Clin Microbiol Rev 2002; 15: 414–29.

Full-length article

RNA interference by expression of short hairpin RNAs suppresses *bcl*-xL gene expression in nasopharyngeal carcinoma cells[1]

Fang LIU[2], Cheng-wei HE, Yue-fei ZHANG[4], Ke-yuan ZHOU[3]

[2]*Institute of Biochemistry and Molecular Biology;* [4]*Department of Otorhinolaryngology, The First Affiliated Hospital, Guangdong Medical College, Zhanjiang 524023, China*

Key words

RNAi; plasmid; gene transfection; short hairpin RNA; *bcl*-xL; apoptosis; nasopharyngeal carcinoma cells

[1] Project supported by grants from the Natural Science Foundation of Guangdong Province (No 31962), the Special Funds for Major Research Program of Guangdong Province (No ZKM04205S), and the Special Funds for Major Subject Program of Guang dong Province (No 9906).
[3] Correspondence to Prof Ke-yuan ZHOU.
Phn 86-759-238-8301.
E-mail kyzhou@gdmc.edu.cn

Received 2004-09-24
Accepted 2004-10-22

doi: 10.1111/j.1745-7254.2005.00029x

Abstract

Aim: To evaluate a new plasmid mediated RNA interference (RNAi) system and investigate whether knock-down of *bcl*-xL by short hairpin RNA (shRNA) can induce apoptosis of human nasopharyngeal carcinoma (NPC) cell line CNE-2Z *in vitro*. **Methods:** The plasmid containing mU6 promoter was subcloned to yield the pmU6 plasmid, recombinant plasmid expressing shRNA targeting *bcl*-xL gene was designed and constructed, and were co-transfected cells with green fluorescence protein expressing plasmid. Flow cytometry was used to evaluate transfection efficiency, and RT-PCR and Western blot were applied to analyze *bcl*-xL mRNA and protein levels, respectively. **Results:** The shRNA expressed by the recombinant plasmid efficiently suppressed *bcl*-xL gene expression and induced apoptosis of NPC cells *in vitro*. **Conclusion:** The recombinant plasmid can sufficiently mediate RNAi in CNE-2Z cells, and knock-down of the *bcl*-xL expression by shRNA significantly induced apoptosis in CNE-2Z cells. The results suggest this new system, mediated RNAi can be used as a tool for the study of gene function and gene therapy.

Introduction

RNA interference (RNAi) is a ubiquitous mechanism of eukaryotic gene regulation that can be exploited for specific gene silencing. In 1998, Fire and his colleagues firstly named these phenomena as RNAi[1]. Recently, RNAi has emerged as a powerful reverse genetic tool to silence gene expression in multiple organisms including plants, *Caenorhabditis* elegans, and *Drosophila*[2].

The specificity of RNAi is determined by 21- to 23-nt RNA duplexes, referred to as micro-RNAs (miRNA) or small interfering RNAs (siRNA). miRNAs are generated from endogenous precursors, which form hairpin structures with stretches of double-stranded RNA (dsRNA). They are cleaved by the ribonuclease Dicer to produce mature miRNA. After unwinding, one of the strands becomes incorporated into the RNA-induced silencing complex (RISC) and guides the destruction or repression of complementary mRNA. siRNA arise from viral or other exogenous dsRNA, but they use the same mechanism to effect mRNA degradation[3].

Nasopharyngeal carcinoma (NPC) is a gene-related malignancy that threatens many people's lives in Southern China. Since its discovery, many people have lost their lives to this malignancy because of the lack of ideal therapeutics. Presently, overexpression of *bcl*-xL is widely considered as a poor prognosis in this cancer. In recent years, we have done much work to investigate its ideal therapeutics, including antisense gene therapy strategy. We found a favorable selectivity and high specificity of antisense RNA to treat NPC *in vivo*; however, the quick degradation of antisense RNA in cells and the unspecific toxicity limit its applications. RNA interference, a tool for inhibiting the overexpression of specific oncogenes, has been included in therapeutic studies of cancers in recent years[4].

One obstacle to achieve RNAi in mammals is that dsRNA longer than 30 nt will provoke an antiviral response, leading to the non-specific degradation of RNA transcripts and a global shutdown of host cell protein translation, known as a strong cytotoxic response. As a result, the long dsRNA

does not produce RNAi activity as expected. This obstacle has recently been solved by Elbashir *et al* who found that gene specific suppression in mammalian cells can be achieved by *vitro*-synthesized siRNA that are 21 nt in length, long enough to induce gene-specific suppression, but short enough to evade the host interferon response[2,5]. However, this gene-specific suppression is transient, which severely restricts its applications. To overcome this restriction, various kinds of vectors have been designed to express siRNA or hairpin RNA transcripts to suppress expression of endogenous genes in mammalian cells[6–8].

In this article, we constructed a plasmid to achieve RNAi in mammalian cells. With this plasmid, shRNA are predicted to be synthesized from a DNA template under the control of mU6 promoter (a kind of eukaryotic RNA polymerase III promoter) in transfected cells. This construction has two *BbsI* cloning sites under mU6 promoter to ensure the coding sequences for shRNA insert in the right direction and direct the synthesis of shRNA in cells. Also, this plasmid containing a neomycin resistance gene (neo^r) can be used for positive screening. These properties make it possible to use DNA templates to synthesize shRNA *in vivo* and produce RNAi activity to trigger silencing of homologous gene expression. Using this plasmid, we found that *bcl*-xL in NPC cells can be efficiently inhibited and then induce apoptosis in NPC cells.

Materials and methods

Construction of plasmid containing DNA template for synthesis of shRNA under the control of mU6 promoter mU6 promoter was obtained by cutting mU6pro (gift of Li-ping LI, Guangdong Medical College, Zhanjiang, China) with *Bbs*I and cloned into pcDNA3 instead of its CMV promoter to generate the plasmid pmU6. A general strategy for constructing an RNAi plasmid involved cloning an inverted repeat into pmU6 at the *Bbs*I site. The selection of the coding sequences for siRNA were empirically determined but were analyzed by BLAST search to ensure that they did not have significant sequence homology with other genes. To generate the pmU6 *bcl*-xL RNAi plasmid, a 21-nt oligo corresponding to nucleotides (605–625) of the *bcl*-xL coding region was designed together with the 9-nt spacer, five Ts and two *Bbs*I sites. They were then inserted into the pmU6 vector digested with *Bbs*I to generate pmU6 *bcl*-xL RNAi plasmid. This oligonucletide sequence encoding shRNA for the targeted gene *bcl*-xL coding region was taken from GenBank accession Z23115 L20121, GI-510900 (nucleotides 605–625)[9,10]. Primitive oligo is 5′-GGAGATGCAGGTATTGGTGAG-3′ (forward) and 5′-CTCACCAATACCTGCATCTCC-3′ (reverse). Modified oligos are primitive oligos plus the 9-nt spacer, five Ts and two *Bbs*I sites, Modified oligo is 5′TTTGGGAGATGCAGGTATTGGTGAGTTCAAGAGACTCACCAATA-CCTGCATCTCCTTTTT 3′ (forward) and 5′ GCTAAAAA-AGGAGATGCAGGTATTGGTGAGTCTCTTGAACTCAC-CAATACCTGCATCTCC 3′ (reverse).

Cell culture and transfections NPC cell line CNE-2Z cells were cultured in RPMI-1640 (GIBCO, NY , USA) complete culture medium which supplemented with 10% of heat-inactivated FBS (GIBCO, NY , USA), benzylpenicillin (100 kU/L) and streptomycin (100 mg/L) at 37 ºC in an incubator in a humidified atmosphere, with 5% CO_2 in air. The cells were routinely passaged every 1 or 2 d[11]. For transfection, 0.5×10^5 cells mixed with 500 μL RPMI-1640 (Invitrogen, Carlsbad, CA,USA, supplemented with 10% of heat-inactivated FBS, without any antibiotic) were seeded into a well of a 24-well plate and incubated at 37 ºC for 24 h. pmU6-RNAi plasmid and pTR-UF5 plasmid (gift of Dr Muzyczka, Florida University, USA) harboring green fluorescence protein (GFP) reporter gene were co-transfected using a Lipofectamine 2000 (Invitrogen, Carlsbad, CA, USA)-mediated method according to the manufacturer's protocol. Nearly confluent cells in 24-well plates were transfected with 2.0 μg of pmU6-RNAi plasmid and 0.2 μg of pTR-UF5 per well, the final concentration of plasmid was 0.4 μg/mL; the ratio of plasmid to lipofectamine was 1:1. After a 6 h-transfection, the medium was replaced by complete culture medium. Cells were continuously cultured untill harvest for analysis.

Transfection efficiency assay The procedure of transfection was the same as described above. Cells were harvested after 24 h by centrifugation for 5 min at 200×*g,* to remove cell debris and washed three times with phosphate buffered saline (PBS) by centrifugation for 5 min at 1000×*g* to remove culture medium. Cells were then suspended again in PBS again for analysis by flow cytometry (Coulter, Becton Dickinson, USA). For each samples, at least 1×10^4 cells were analyzed by flow cytometry. Results were presented as the number of green fluorescence cells versus the total cells detected by flow cytometry and repeated for at least 3 times[12] and analyzed by Student's *t*-test.

Hoechst 33258 fluorescence staining CNE-2Z cells (1×10^5) were seeded in a T-10 cm^2 cell culture plate and cultured in RPMI-1640 supplemented with 10% heat-inactivated FBS without antibiotic. After an incubation at 37 °C for 24 h, cells were transfected with 4.0 μg of pmU6-RNAi plasmid alone per plate. After a transfection for 6 h, the medium was changed to complete culture medium. Cells were collected

12 to 24 h after the transfection and centrifuged for 5 min at 200×*g* to remove cell debris, and cells were washed three time with 0.9% saline after a centrifugation for 5 min at 1000×*g* to remove culture medium. And then 10 μL of cell suspensions were treated with 10 μL of 10 mg/L Hoechst 33258 for 30 min in the dark. Ten μL of the stained cell suspensions were taken out and dripped on the slides and covered with a cover slip. The morphological changes of nuclei in CNE-2Z cells were observed by fluorescence microscope (×400) to discriminate native cells, apoptotic cells and necrotic cells. Cells were photographed and processed by Adobe PHOTOSHOP software.

Quantitative RT-PCR Cells were collected 12 to 48 h after transfection and washed with PBS (pH 7.3), homogenized once and centrifuged at 1000×*g* for 5 min to remove culture medium. One mL TRIzol (Gibco, NY , USA) was added to the cell pellets, total RNA was extracted from with or without pmU6-RNAi plasmid transfected CNE-2Z cells according to a single step method (One-Step RT-PCR Kit, Applied QIAGEN Inc, USA). After centrifugation, the supernatant was extracted once with 0.2 mL chloroform and 0.5 mL isopropanol respectively, then total RNA was precipitated with 75% ice-cold ethanol (diluted with DEPC water). The precipitate was centrifuged and dissolved with 100 μL RNase-free water, after purification by a LiCl precipitating method, UV spectrophotometer analysis at 260 nm and electrophoresis detection showed good quality of purified RNA[13]. The upperstream primer of *bcl*-xL (amplified products were 448 bp) was 5′-CCC AGA AAG GAT ACA GCT GG-3′, the downstream primer was 5′-GCG ATC CGA CTC ACC AAT AC-3′. The expression of house keeping gene, β-actin mRNA, was used as an internal standard[14]. The upperstream primer of β-actin (amplified products were 235 bp) is 5′-GGG AGC CAA AAG GGT CAT CAT CT-3′, the downstream primer was 5′-GAG GGG CCA TCC ACA GTC TTC T-3′ (primers were commercially available). PCR were run 30 cycles for *bcl*-xL and β-actin in Eppendorf Mastercycler. Denaturing, annealing, and extension reactions were performed at 94 ºC for 45 s, 55 ºC for 1 min, and 72 ºC for 1 min. The PCR pro-ducts were electrophoresed on 1% agarose gel, stained with ethidium bromide, and detected by UV irradiation. The levels of *bcl*-xL mRNA were expressed as the ratio of *bcl*-xL to β-actin.

Western blotting The cells were washed three times with PBS and collected by scraping and were lysed in150 μL of ice-cold Tris buffer (50 mmol/L, pH 7.5) containing edetic acid 5 mmol/L, NaCl 150 mmol/L, 0.1% NP-40, 0.1 % SDS, 2.0 g/L aprotinin, 0.02 % NaN_3, PMSF 0.2 mmol/L, and antiprotease mixture, sonicated, and centrifuged at 12 000×*g* for 15 min and the concentration of protein in each lysate was determined with Coomassie brilliant blue G-250. Loading buffer was added to each lysate, which was subsequently boiled for 3 min and then electrophoresed on a SDS-PAGE[15]. Before electrophoresis, the proteins were mixed with 2×loading buffer (containing Tris-HCl 100 mmol pH 6.8, 20% Glycerin, 4% SDS, tetrabromophenol-sulfonphthalein 0.05 g/L and 10% 2-β-mercaptoethanol) by the same volume. Proteins were transferred onto nitrocellulose and incubated with antibody and then with peroxidase-conjugated secondary antibody in the second reaction (The anti-*bcl*-xL antibody was used at a 1:500 dilution, the anti-β-actin antibody was used at a 1:400 dilution, the anti-HA mAb was used at a 1: 2500 dilution, all antibodies was obtained from Peking Zhongshan Biote-chnology, Beijing, China). Detection was performed with enhanced chemiluminescence agent. The electrochemi-luminescence (ECL) Test Kit-based detection was performed with Chemiluminescence Reagent (Sigma Life Science) according to the manufacturer's instructions. The results of Western blot analysis represented the average of three individual experiments.

Results analysis and statistics The electrophoregram of RT-PCR and Western blotting were scanned by Scanner and the optical density scores of bands were calculated to analyze the relative content of *bcl*-xL to β-actin. Differences between individual groups were analyzed by One-Way ANOVA with SPSS10.0 software, and the results was expressed as mean±SD.

Results

Analysis of transfection efficiency The expression of GFP in cells was detected by flow cytometry 24 h after co-transfection. Transfection efficiency was the rate of GFP expressing cells to the totally assayed cells; fluorescence index (FI) reflects the expression efficiency of the GFP gene[16]. The transfection efficiency of the untreated control group and pTR-UF5 group was (0.4±0.4)% and (50.7±4.4)% respectively, implying lipofectamine-2000 can efficiently introduce plasmid into cancer cells. The FI of the control group and pTR-UF5 group was negative (–) and 13.0±0.3 (P<0.01 *vs* control), respectively, showing GFP had a higher expression in NPC cells after introducing pTR-UF5 into cancer cells by lipofectamine-2000 (Figure 1).

Morphology of fluorescence staining cells Hoechst 33258 is a specific fluorescent stain. A small quantity of Hoechst 33258 will be allowed to enter normal cells because of its natural characteristics. Cell membrane permeability will be enhanced during apoptosis, which makes more Hoechst 33258 enter apoptotic cells than natural cells to bind

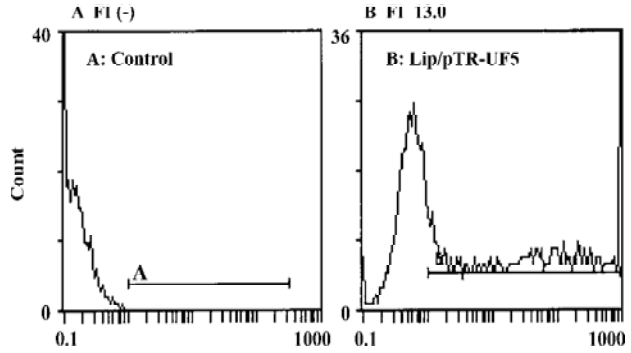

Figure 1. The fluorescence index of CNE-2Z cells transfected with lip-mediated plasmid of pTR-UF5. One of the three representatives.

with base regions of DNA. At disposal of Hoechst 33258, the apoptotic body or fragments of nuclei were stained a deep blue color, normal cells a light blue color, and the delimitation between cytoplasm and nuclei of necrotic cells became unclear for organelle swelling and lysis through fluorescence microscope. From the photographs (Figure 2), apoptotic cells were nearly invisible from the untreated group and the empty pmU6 group, whereas the pmU6-RNAi groups (12 h, 24 h, and 48 h after transfection) had more apoptotic cells compared to the above mentioned groups. These results showed that the pmU6-RNAi plasmid efficiently induced apoptosis in CNE-2Z cells by expressing shRNA.

Quantitative RT-PCR The reduction of mRNA was in a time-dependent manner (Figure 3) apart from the untreated and the pmU6 treated group. The mRNA was reduced by 90% to 99% 12 to 48 h after transfection with pmU6-RNAi, respectively (Figure 4). The results indicate that the shRNA expressed by the pmU6-RNAi plasmid in cells could efficiently suppress *bcl*-xL gene expression.

Western Blotting Western blot was used for the analysis of bcl-xL protein level. Compared with control, the pmU6-RNAi showed great capacities of inhibition at a protein level, and we also detected dramatic differences in the Bcl-xL protein levels between 24 h and 48 h after transfection, Bcl-xL protein was hardly measured after 48 h transfection (Figure 5, 6). This result suggested bcl-xL shRNA expressed by pmU6-RNAi could efficiently downregulate the protein level of Bcl-xL. Associated with the corresponding transfection time of bcl-xL mRNA levels and protein data, we found that *bcl*-xL shRNA could suppress *bcl*-xL gene expression, not only in transcript levels but also in protein levels.

Discussion

The expression level of some oncogenes such as *bcl*-2/*bcl*-xL, *survivin*, and *caspase* is significantly related to the prognosis of NPC. Particularly, overexpression of *bcl*-xL is widely considered as a poor prognosis following a tumor resection and might be associated with increased resistance to cancer chemotherapy[17,18]. Presently, radiotherapeutics and chemotherapeutics are the main therapies for this malignancy, and usually result in a favorable clinical response and a dramatic regression of NPC. But they have various kinds of unwanted side effects and locally advanced or metastatic NPC severely affect the prognosis in these patients and these therapies also fail to deliver a significant improvement in 5 year survival. It has been shown that specific suppression of over-expressed *bcl*-xL genes might result in an improvement in the therapy for this cancer. RNA interference, an useful tool for inhibiting the overexpression of specific oncogenes, was involved in the study of therapies for NPC in our study.

The Bcl-2 family of proteins play major role in regulating apoptosis and include both anti- and pro-apoptotic members[19]. The *bcl*-xL is an important anti-apoptotic member of the *bcl-2* family and it has 44% homology to *bcl-2*. Its function is similar to *bcl-2* in anti-apoptosis. Expression of this protein is significantly higher in NPC where it might play a pivotal role in tumor initiation, progression, and resistance to chemotherapy and radiotherapy[20,21]. In the present study, we constructed a plasmid expressing *bcl*-xL shRNA that could suppress *bcl*-xL gene expression in cells, and results indicated that *bcl*-xL shRNA could efficiently inhibit the expression of the target genes. According to the morphology of Hoechst 33258 staining cells, more apoptotic cells could be seen from the pmU6-RNAi transfected group than the empty plasmid group and the untreated group. RT-PCR analysis and Western-blot assay further indicated *bcl*-xL shRNA expressed by pmU6-RNAi had silenced the target gene and induced apoptosis in NPC cells.

Our results showed an obvious difference of time course between inducing of apoptotic cells by Hoechst 33258 analysis and decrease of *bcl*-xL mRNA by quantitative RT-PCR analysis (compare Figure 2 to Figure 3). The change at the mRNA level in pmU6-RNAi (12 h) transfected cells was obvious, whereas apoptotic cells were observed until 24 h after tranfection. This strongly suggested that down regulation of *bcl*-xL mRNA and protein, thereafter, by shRNA was the reason for apoptosis in NPC cells. The apoptosis occurred approximately 12 h after diminution of *bcl*-xL mRNA and finally the protein, to a definitive threshold.

Quantitative RT-PCR analysis of mRNA extracted from pmU6-RNAi transfected CNE-2Z cells was used to compare mRNA levels of *bcl*-xL with the corresponding protein data.

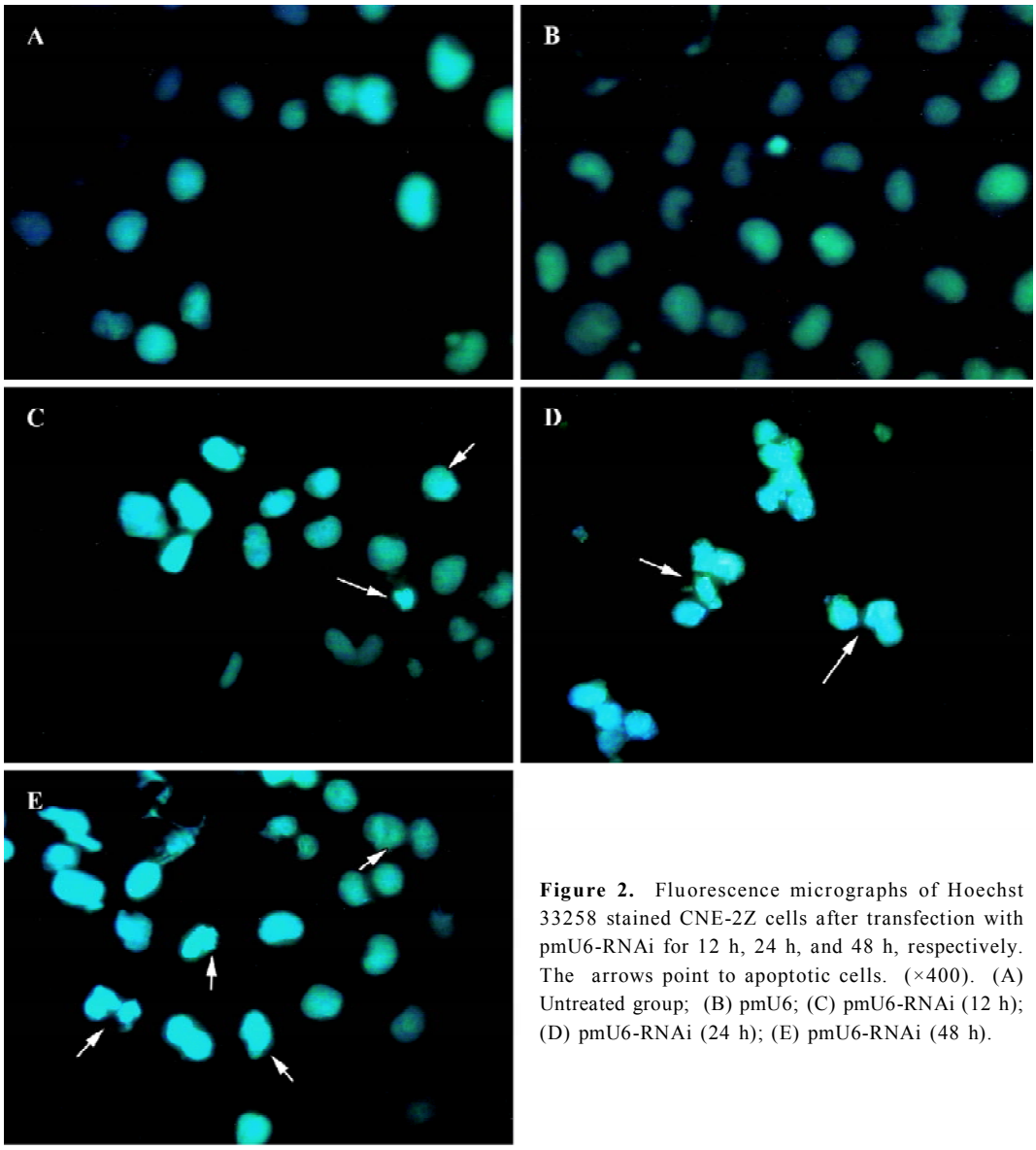

Figure 2. Fluorescence micrographs of Hoechst 33258 stained CNE-2Z cells after transfection with pmU6-RNAi for 12 h, 24 h, and 48 h, respectively. The arrows point to apoptotic cells. (×400). (A) Untreated group; (B) pmU6; (C) pmU6-RNAi (12 h); (D) pmU6-RNAi (24 h); (E) pmU6-RNAi (48 h).

From the analysis of RT-PCR, it showed that the *bcl*-xL mRNA levels between the empty plasmid group and the untreated group had no significant difference, and the results of quantitative RT-PCR analysis of *bcl*-xL revealed mRNA variations generally correlated with the Western blot data in our study. Another more interesting discovery was that pmU6-RNAi plasmid reduced *bcl*-xL mRNA levels by nearly 9.5-fold 12 h after transfection, almost equal to the decrease in the mRNA levels 24 h after transfection, despite significant and consistent changes were not always equal between mRNA and protein[22]. The tendency for variations between them was a common coincidence in our present study. For example, pmU6-RNAi treated for 24 h reduced mRNA levels by nearly 9.5-fold, and the reduction at the protein level was 8.5-fold. In another example, we detected a >9.9-fold decrease in the mRNA level by pmU6-RNAi (48 h) treated group, whereas the corresponding Western blots showed a 9.4-fold diminution in bcl-xL protein (compare Figure 4 to Figure 6). According to the above analysis, we presumed that there were similar changes between the protein level and the corresponding mRNA level of *bcl*-xL in pmU6-RNAi (12 h) treated group.

Based on the RNAi-mediated *bcl*-xL gene silencing in NPC cell line described above, we underlined the effects of *bcl*-xL shRNA to suppress *bcl*-xL gene expression. Taken together, these issues will have a profound influence on the use of RNAi technology, on a large scale, for functional

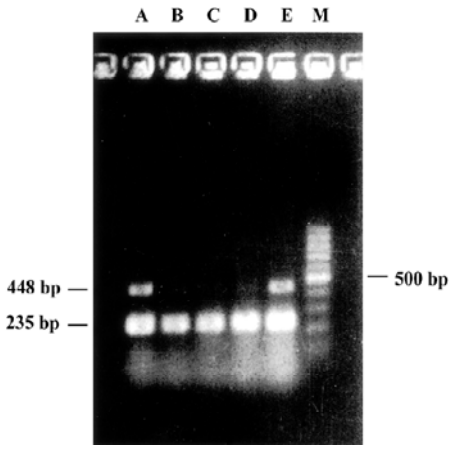

Figure 3. Quantitative RT-PCR analysis of *bcl*-xL mRNA level in CNE-2Z cells after transfection with plasmid pmU6-RNAi for 12 h, 24 h, and 48 h respectively. (A) Untreated group; (B) pmU6-RNAi (12 h); (C) pmU6-RNAi (24 h); (D) pmU6-RNAi (48 h); (E) pmU6; (M) 100 bp DNA marker.

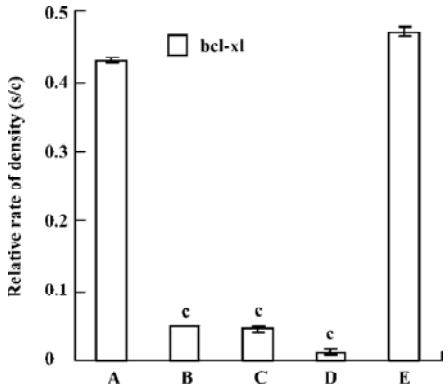

Figure 4. *Bcl*-xL mRNA level by image analysis. n=4. Mean±SD. ^cP<0.01 *vs* control. (A) Untreated group; (B) pmU6-RNAi (12 h); (C) pmU6-RNAi (24 h); (D) pmU6-RNAi (48 h); (E) pmU6.

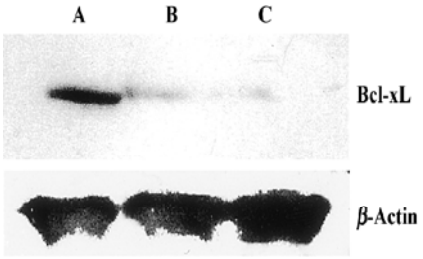

Figure 5. Western-blot analysis of Bcl-xL protein level in CNE-2Z cells after transfection with pmU6-RNAi for 24 h and 48 h respectively. (A) Untreated group; (B) pmU6-RNAi (24 h); (C) pmU6-RNAi (48 h).

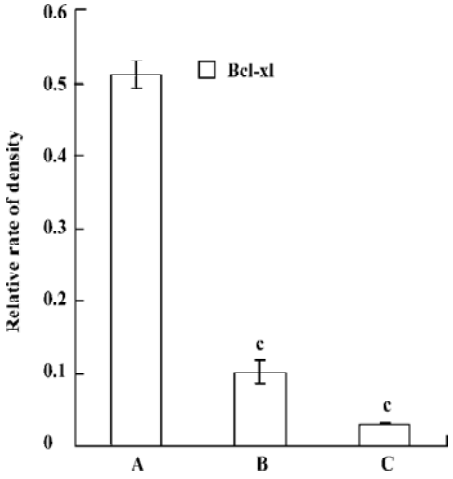

Figure 6. Bcl-xl protein level by image analysis. n=4. Mean±SD. ^cP<0.01 *vs* control. (A) Untreated group; (B) pmU6-RNAi (24 h); (C) pmU6-RNAi (48 h).

genomics studies and therapy of cancer.

References

1 Fire A, Xu S, Montgomery MK, Kostas SA, Driver SE, Mello CC. Potent and specific genetic interference by double-stranded RNA in *Caenorhabditis elegans*. Nature 1998; 391: 806-11.

2 Sui GC, Christina SH, Affar EB, Gay FR, Shi YJ, Forrester WC, *et al.* DNA vector-based RNAi technology to suppress gene expression in mammalian cells. Proc Natl Acad Sci USA 2002; 99: 515–20.

3 Schuck S, Manninen A, Honsho M, Joachim F, Simons K. Generation of single and double knockdowns in polarized epithelial cells by retrovirus-mediated RNA interference. Proc Natl Acad Sci USA 2004; 101: 4912–7.

4 Sunita G, Rebecca AS, James EE, Gregory JH, Vivek M. Inducible, reversible, and stable RNA interference in mammalian cells. Proc Natl Acad Sci USA 2004; 101: 1927–32.

5 Elbashir SM, Harborth J, Lendeckel W, Yalcin A, Weber K, Tuschl T. Duplexes of 21-nucleotide RNAs mediate RNA interference in cultured mammalian cells. Nature 2001; 411: 494–8.

6 Brummelkamp HR, Bernards R, Agami R. A system for stable expression of short interfering RNAs in mammalian cells. Science 2002; 296: 550–3.

7 Monika P, Michael M, Mark I, Michal M, Yen C, Aaron K. Inhibition of herpes simplex virus 1 gene expression by designer zinc-finger transcription factors. Proc Natl Acad Sci USA 2003; 100: 1621–6.

8 Zhang L, Yang N, Mohamed-Hadley A, Rubin SC, Coukos G. Vector-based RNAi, a novel tool for isoform-specific knockdown of VEGF and anti-angiogenesis gene therapy of cancer. Biochem Biophys Res Commun 2003; 303: 1169–78.

9 Boise LH, Gonzalez-Garcia M, Postema CE, Ding L, Lindsten T, Turka LA, *et al.* *Bcl*-x, a *bcl*-2-related gene that functions as a dominant regulator of apoptotic cell death. Cell 1993; 74: 597–608.

10 Altschul L, Stephen F, Thomas LM, Alejandro AS, Zhang JH, Zhang Z, *et al*. Gapped BLAST and PSI-BLAST: a new generation of protein database search programs. Nucleic Acids Res 1997; 25: 3389–402.
11 Xu F, Zhen YS. (-)-Epigallocatechin-3-gallate enhances antitumor effect of cytosine arabinoside on HL-60 cells. Acta Pharmacol Sin 2003; 24: 163–8.
12 Zheng XL, Sun HX, Liu XL, Chen YX, Qian BC. Astilbic acid induced COLO 205 cell apoptosis by regulating Bcl-2 and Bax expression and activating caspase-3. Acta Pharmacol Sin 2004; 25: 1090–5.
13 Wan YF, Guo XQ, Wang ZH, Ying K, Yao MH. Effects of paclitaxel on proliferation and apoptosis in human acute myeloid leukemia HL-60 cells. Acta Pharmacol Sin 2004; 25: 378–84.
14 Liu LH, Wang XK, Hu YD, Kang JL, Wang LL, Li S. Effects of a fatty acid synthase inhibitor on adipocyte differentiation of mouse 3T3-L1 cells. Acta Pharmacol Sin 2004; 25: 1052–7.
15 Li XH, Li JJ, Zhang HW, Sun P, Zhang YL, Cai SH, *et al*. Nimesulide inhibits tumor growth in mice implanted hepatoma: overexpression of Bax over Bcl-21. Acta Pharmacol Sin 2003; 24: 1045–50.
16 Liu RY, Luo HL, Feng HL, Peng JL, Cai TY, Huang WL, *et al*. A method to detect gene transfection efficacy by flow cytometry. Chin J Cancer 2002; 21: 267–71.
17 He GR, Zhou KY, Cai KR, Liang T, He CW, Zhang YF. Apoptotic effect of *bcl*-xL antisense oligodeoxynucleotide mediated by lipofectin on cell strain CNE-2Z. Chin J Cancer 2003; 22: 11–5.
18 Min L, Zhou KY, Liang T, Zhang YF. Inhibitory effects of *bcl*-xL antisense oligodeoxynucleotides on growth of human nasopharyngeal carcinoma in nude mice. Chin J Oncol 2004; 26: 14–6.
19 Yang SP, Song ST, Song HF. Advancements of antisense oligonucleotides in treatment of breast cancer. Acta Pharmacol Sin 2003; 24: 289–95.
20 He GR, Zhou KY, Zhang YF, Liang T, Min L. Effect of lipofectin-mediated *bcl*-xL antisense oligodeoxynucleotide on CNE-2Z cells. J Guangdong Med Coll 2003; 21: 1–4.
21 Reed JC. Prevention of apoptosis as a mechanism of drug resistance. Hem Onc Clinics North Am 1995; 9: 451–73.
22 Scacheri PC, Rozenblatt-Rosen O, Caplen NJ, Wolfsberg TG, Umayam L, Lee JC, *et al*. Short interfering RNAs can induce unexpected and divergent changes in the levels of untargeted proteins in mammalian cells. Proc Natl Acad Sci USA 2004; 101: 1892–7.

Full-length article

Synthesis and anti-tumor activity of alkenyl camptothecin esters[1]

Zhi-song CAO[2], John MENDOZA, Albert DEJESUS, Beppino GIOVANELLA

Stehlin Foundation for Cancer Research and St Joseph Hospital Cancer Laboratory, 1918 Chenevert Street, Houston, Texas 77003, USA

Key words

alkaloids; camptothecin; 9-nitrocamptothecin; structure-activity relationship

[1] Financial support from the Stehlin Foundation for Cancer Research.
[2] Correspondence to Dr Zhi-song CAO.
Phn 1-713-756-5750.
Fax 1-713-756-5783.
E-mail zcao@stehlin.org

Received 2004-07-02
Accepted 2004-10-27

doi:10.111/j.1745-7254.2005.00031.x

Abstract

Aim: To study the degrees of influence of changing side ester chains at position C20 of camptothecin on the anti-tumor activity of the molecules. **Methods:** The esterification reaction of camptothecin 1 and 9-nitrocamptothecin 2 with crotonic anhydride in pyridine gave the corresponding esters 3 and 4, respectively. The acylation of 1 and 2 with cinnamoyl chloride gave products 7 and 8. Epoxidation reaction of 3 and 4 with *m*-chloroperoxybenzoic acid in benzene solvent gave the products 5 and 6. Esters 3, 4, and 5 were tested for anti-tumor activity against 14 human cancer cell lines. **Results:** Both *in vitro* and *in vivo* anti-tumor activity studies for these esters were conducted and the data demonstrated positive results, that is, these esters were active against the tested tumor lines. **Conclusion:** Alkenyl esters 3 and 4 showed strong anti-tumor activity *in vitro* against 14 different cancer cell lines. Ester 3 was active against human breast carcinoma in mice and the toxicity of the agent was not observed in mice during the treatment, implying that this agent is effective for treatment with low toxicity.

Introduction

Camptothecin, a pentacyclic alkaloid derixxved from a Chinese tree *Camptotheca acuminata*, showed good anti-tumor activity against the mouse leukemia L1210 system[1]. Camptothecin itself is water-insoluble. The sodium form of this compound was prepared and used in early clinical trials. Unfortunately, this carboxylate form of the molecule did not show the inherent anti-tumor activity, but severe toxicity[2–6], which caused the discontinuation of human clinical trials in the 1970s. Pharmacology and activity studies conducted since then have demonstrated that the lactone form and the 20-S-OH group of the compound are the most important structural requirements for anti-cancer activity. For example, the carboxylate sodium salt form showed only one-tenth the potency of the lactone form in an anti-tumor assay (P388 rodent leukemia) conducted by Wani *et al*[7]. In order to increase the stability of the lactone form of the molecule, we previously reported the preparation of alkyl camptothecin esters (Scheme 1)[8]. These alkyl camptothecin esters substantially increase the stability of the lactone form of the drug in mouse and human plasmas, and also the biological life of the active form of the drug in body. Zhao *et al* also reports that the 20-acylation of camptothecin brings lactone stabilization[9]. It is established that the 20-acylation of camptothecin is an effective method of increasing the lactone stability of the molecule.

Our structure-activity relationship (SAR) studies of alkyl camptothecin esters indicated that the anti-tumor activity of alkyl camptothecin esters A depends on the geometric shape of their side alkyl chains. For example, of all alkyl camptothecin esters tested, the compound with a C_2 straight alkyl chain (R_1=CH_2CH_3) shows good anti-tumor activity[10,11]. The compound is less active when R_1 group in structure A becomes longer (C_3, or C_4), or bulkier (isopropyl group, or cyclic propyl group). The compound is inactive when the R_1 group in structure A becomes larger (C_5, C_6, *etc*). Based on these SAR studies we propose that the introduction of an unsaturated functional group such as a double-bond or an epoxy group into the side ester chain in structure A would have an effect on anti-tumor activity. We now wish to report the preparation of alkenyl camptothecin esters 3, 4, 7, and 8 and the corresponding epoxy derivatives 5-6 together with the pre-

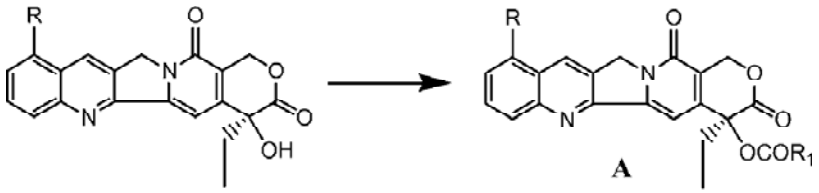

Scheme 1.

liminary results of biological studies with these new compounds.

Materials and methods

General Dry nitrogen was routinely used as the reaction atmosphere in all reactions. All glassware was baked at 70± 10 ºC for a minimum of 2 h before being used. Melting points were obtained with a MEL-TEMP melting point apparatus and were uncorrected. The ^{1}H NMR spectrums of approximately 10 % (w/v) solution in $CDCl_3$ were obtained at 270.05 MHz with a JEOL GX-270 WB NMR spectrometer. Chemical shifts are reported in parts per million (δ scale), employing tetramethylsilane as an internal standard. In reporting the NMR data, we have used the following abbreviations: coupling constants in Hertz (*J*), singlet (s), doublet (d), triplet (t), multiplet (m), and *etc*. Mass Spectra were recorded using a VG ZAB-SEQ mass spectrometer (VG Analytical Co, England) with a resolution of 10 000. Routinely used solvents such as THF and methylene chloride were dried and freshly distilled. Silica gel (230–400 mesh, Aldrich) for column chromatography was used for all product separations. TLC sheets (Silica gel with fluorescent indicator on polyethylene) employed in TLC (Thin-layer Chromatography) operations were purchased from Aldrich Chemical Co (Aldrich, Milwaukee, WI). The numbering system used in reporting NMR data were shown in Scheme 2. Camptothecin was purchased from China and purified before being used. Nine-nitrocamptothecin was prepared in our laboratory by using an established procedure[14].

Preparation of camptothecin-20-*O*-crotonate 3 Crotonic anhydride (40 mL) and pyridine (30 mL) were mixed in a 100 mL round-bottomed flask equipped with a magnetic stirrer. To this solution, 8 g (0.0230 mol) of the starting camptothecin 1 was added. The mixture was stirred at 110±10 ºC with a sand bath for 15 h. After cooling to room temperature, the reaction mixture was poured onto 1000 mL petroleum ether while stirring. The crude products precipitated from petroleum ether were collected by filtration and then separated by column chromatography with THF-CH_2Cl_2 (1:15) as eluent. Pure product 3 (3 g) was obtained as white powder after precipitation from 300 mL of petroleum ether, mp 218–220 ºC (deformed at 155 ºC), yield 31%, purity 99% (HPLC); ^{1}H NMR: δ; 1.00 (3H, t, *J* 7.51, C19-methyl protons), 1.94 (3H, dd, $J_{H25\text{-}H24}$ 6.96, $J_{H25\text{-}H23}$ 1.89 Hz, C25-methyl protons), 2.15–2.35 (2H, m, C18-methylene protons), 5.28 (2H, s, C5-methylene protons), 5.38–5.74 (2H, dd, *J* 17.22, 17.22, C17-methylene protons), 5.99 (1H, d, *J* 13.92, C23-H), 7.05–7.14 (1H, dq, $J_{H24\text{-}H23}$ 15.38, $J_{H24\text{-}H25}$ 6.96, C24-H), 7.24 (1H, s, C14-H), 7.67 (1H, t, *J* 6.96, C10-H), 7.83 (1H, t, *J* 6.96, C11-H), 7.94 (1H, d, *J* 7.70, C9-H), 8.21 (1H, d, *J* 8.43, C12-H), 8.39 (1H, s, C7-H); m/z (relative intensity) 416 (M^+, 20), 330 [M-86 (CH_3CH=CHCOOH), 100], 315 [M-101 (CH_3CH=CHCOOH+CH_3), 40)], 302 [M-114 (CH_3CH=CHCOOH+CO), 73)], 287 [M-129(CH_3CH=CHCOOH+CO_2+H), 30], 274 (10), 259 (9), 246 (9), 234 (3), 218 (5), 205 (4), 191 (3). HMRS ($C_{24}H_{20}N_2O_5$): Found: 416.137, required, 416.137.

Preparation of 9-Nitrcamptothecin-20-*O*-crotonate 4 Using 3.0 g (0.0076 mol) of 9-nitrocamptothecin 2 as the starting material, the reaction was carried out in the same manner as when preparing 3. Pure product 4 (2.5 g) was obtained as yellow powder, mp 224–225 ºC (deformed twice at 180 ºC and 203 ºC respectively), yield 71%, purity 99% (HPLC); ^{1}H NMR: δ; 1.01 (3H, t, *J* 7.48, C19-methyl protons), 1.94 (3H, dd, $J_{H25\text{-}H24}$ 7.00, $J_{H25\text{-}H23}$ 1.83, C25-methyl protons), 2.15–2.33 (2H, m, C18-methylene protons), 5.36 (2H, s, C5-methylene protons), 5.40–5.73 (2H, dd, *J* 7.20 and 17.20, C17-methylene protons), 6.01 (1H, d, *J* 13.93, C23-H), 7.08–7.24 (1H, dq, $J_{H24\text{-}H23}$ 15.35, $J_{H24\text{-}H25}$ 6.98, C24-H), 7.26 (1H, s, C14-H), 7.92 (1H, t, *J* 6.98, C11-H), 8.47–8.53 (2H, m, C10-H and C12-H), 9.26 (1H, s, C7-H); m/z (relative intensity) 461 (M^+, 15), 375 [M-86 (C+H_3CH=CHCOOH), 100], 360 [M-101 (CH_3CH=CHCOOH+CH_3), 32], 347 [M-114 (CH_3CH=CHCOOH+CO), 74], 332 [M-129 (CH_3CH=CHCOOH+CO+CH_3), 32], 319 (10), 302 (10), 286 (13), 274 (8), 216 (7). HMRS ($C_{24}H_{19}N_3O_7$): Found, 461.122, required, 461.122.

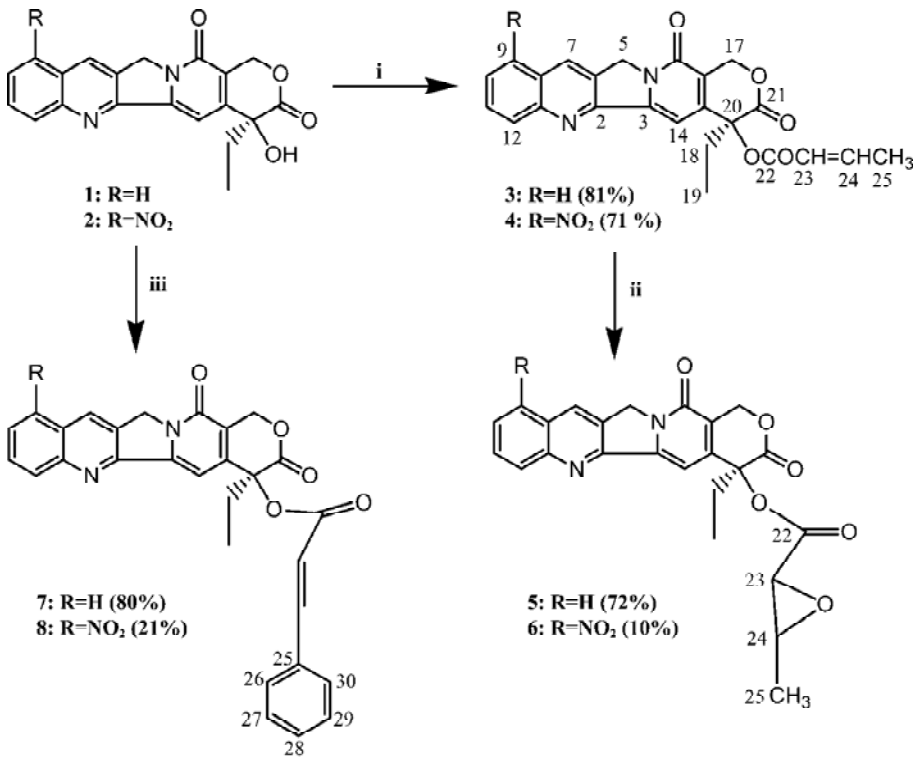

i. $(CH_3CH=CH-CO)_2O$/Pyridine/Heat; ii. m-$ClC_6H_4CO_3H$/rt; iii. $C_6H_4CH=CHCOCl$/Heat

Scheme 2.

Preparation of camptothecin 20-*O*-(2′,3′-epoxy)-butyrate 5 To 50 mL benzene in a 100-mL round-bottomed flask equipped with a magnetic stirrer 0.16 g (~0.0004 mol) of ester 3 and 150 mg of *m*-chloroperoxybenzoic acid (57%–86%, Aldrich Chemical) were added. The mixture was stirred at room temperature for a week. The solvent was removed by a rotary evaporator. The residue was chromatographically separated with THF-methylene chloride (1:10) as eluent. Pure product 5 (0.12 g) was obtained as white powder after precipitation from 100 mL of petroleum ether, mp 210–213 ºC (decomposition, the crystals deformed at 175 ºC), yield 72%, purity 99% (HPLC); ^{1}H NMR: δ; 0.99 (3H, t, *J* 7.51, C19-methyl protons), 1.90–1.94 (3H, dd, $J_{H25\text{-}H24}$ 6.96, $J_{H25\text{-}H23}$ 1.84, C25-methyl protons), 2.07–2.33 (2H, m, C18-methylene protons), 5.30 (2H, s, C5-methylene protons), 5.38–5.72 (2H, dd, *J* 17.59 and 17.95, C17-metnylene protons), 5.95-6.02 (1H, dq, $J_{H23\text{-}H24}$ 15.75, $J_{H23\text{-}H25}$ 1.83, C23-H), 7.04–7.12 (1H, dq, $J_{H24\text{-}H25}$ 6.59, $J_{H24\text{-}H23}$ 15.38, C24-H), 7.22 (1H, s, C14-H), 7.75-8.01 (4H, m, C9-C12 aromatic protons), 8.78 (1H, s, 7-H); m/z (relative intensity) 432 (M^+, 28), 416 [M-16 (O), 12], 346 [M-86 ($C_4H_6O_2$), 100], 331 [M-101 ($C_4H_5O_3$), 53], 318 [M-114 ($C_4H_6O_2$+CO), 75], 303 [M-129 ($C_4H_5O_3$+CO), 54], 287 [M-145 ($C_4H_5O_3$+CO_2), 27], 275 (15), 259 (7), 246 (8), 231 (5), 218 (8), 205 (10), 191 (5). HRMS ($C_{24}H_{20}N_2O_6$): Found, 432.132, required, 432.132.

Preparation of 9-Nitrocamptothecin-20-*O*-(2′,3′-epoxy)-butyrate 6 Using 0.9 g (~0.0020 mol) of 4 as starting material, the reaction was carried out in the same manner as when preparing 5. Pure product 6 (0.10 g) was obtained as yellow powders after precipitation from 100 mL of petroleum ether, mp 216–218 ºC(decomposition, deformed at ~196 ºC), yield 10%, purity 99% (HPLC); ^{1}H NMR: δ; 1.00 (3H, t, *J* 7.50, C19-methyl protons), 1.91–1.95 (3H, dd, $J_{H25\text{-}H24}$ 6.97, $J_{H25\text{-}H23}$ 1.85, C25-methyl protons), 2.05-2.31 (2H, m, C18-methylene protons), 5.31 (2H, s, C5-methylene protons), 5.39–5.74 (2H, dd, *J* 17.60 and 17.94, C17-methylene protons), 5.97–6.04 (1H, dq, $J_{H23\text{-}H24}$ 15.77, $J_{H23\text{-}H25}$ 1.81, C23-H), 7.02-7.14 (1H, dq, $J_{H24\text{-}H23}$ 15.40, $J_{H24\text{-}H25}$ 6.61, C24-H), 7.24 (1H, s, C14-H), 7.78–8.10 (3H, m, C10-H, C11-H, and C12-H), 9.25 (1H, s, C7-H); *m/z* (relative intensity) 477 (M^+, 30), 461 [M-16 (O), 10], 391 [M-86 ($C_4H_6O_2$), 100], 376 [M-101 ($C_4H_6O_3$), 55], 363 [M-114 ($C_4H_6O_2$+CO), 73], 348 [M-29 ($C_4H_6O_3$+CO), 51], 332 [M-145 ($C_4H_6O_3$+CO_2), 26], 320 (13), 314 (6), 301 (7), 286 (5), 273 (7), 268 (9), 254 (4). HRMS ($C_{24}H_{18}N_3O_8$): Found, 477.122, required, 477.121.

Preparation of camptothecin-20-*O*-cinnamate 7 Camptothecin 4.0 g (0.0115 mol) was added to 23 g (in excess) of cinnamoyl chloride in a 100 mL round-bottomed flask

equipped with a magnetic stirrer and a sand bath. The mixture was stirred at 110±10 ºC for 24 h. After cooling to 50 ºC, the reaction mixture was poured onto 400 mL petroleum ether portion by portion while stirring. The crude product was collected by filtration after precipitation from petroleum ether. The crude product was then added to 300 mL of acetone-petroleum ether mixture (100 mL acetone, 200 mL petroleum ether) and was refluxed for 1 h. The pure product was obtained as pale yellow crystals after precipitation from the acetone-petroleum ether solvent system, mp 268 ºC (deformed at 250 ºC), yield 80%, purity 99% (HPLC); ^{1}H NMR(Me_2SO-d_6): δ; 0.97 (3H, t, *J* 7.325, C19-methylprotons), 2.09–2.26 (2H, m, C18-methylene protons), 5.27 (1H, s, C5-methylene protons), 5.53 (2H, s, C17-methylene protons), 6.86 (1H, d, *J* 16.381, C23-H), 7.04 (1H, s, C14-H), 7.442–7.813 (8H, m, C10-H, C11-14, C24-C30-Hs), 8.09 (2H, t (d+d), *J* 8.545 and 9.156, C9H and C12-H), 8.66 (1H, s, C7-H); ^{13}C NMR (Me_2SO-d_6): δ; 7.68 (C19), 30.35 (C18), 50.30 (C5), 66.37 (C17), 75.87 (C20), 94.70 (C23), 116.64 (C14), 118.96, 127.75, 128.01, 128.53, 128.82, 128.92, 129.05, 129.84, 120.43, 131.09, 131.68, 133.69, 145.49, 146.04, 146.95, 147.81, 152.26, 156.63 (C2, C3, C6-C16a, C24-C30), 165.00, 167.32 (C21, C22); *m/z* (relative intensity) 478 (M^+, 26), 330 [M-148 (C_6H_5CH=$CHCOOH$), 100], 315 (42), 302 (63), 287 (12), 259 (8), 246 (7), 234 (5); HRMS ($C_{29}H_{22}N_2O_5$): Found: 478.138, required, 478.137.

Preparation of 9-nitrocamptothecin-20-*O*-cinnamate 8 Nine-nitrocamptothecin 1.4 g (50% pure, prepared in our laboratory) was added all in once to 6.0 g of cinnamoyl chloride in a 100 mL round-bottomed flask equipped with a magnetic stirrer and a sand bath. The mixture was stirred at 110±10 ºC for 24 h. After cooling to 50 ºC, the reaction mixture was poured onto 100 mL petroleum ether while stirring. The crude products were precipitated from the solvent. After filtration the crude products were chromatographically separated with THF-methylene chloride (1:15) as an eluent. The pure product was obtained as yellow powders after precipitation from petroleum ether, mp 282 ºC, yield 21%, purity 99% (HPLC); ^{1}H NMR: δ; 1.04 (3H, t, *J* 7.325, C19-methyl protons), 2.156–2.40 (2H, m, C18-methylene protons), 5.36 (2H, s, C5-methylene protons), 5.42–5.75 (2H, dd, *J* 17.09 and 17.70, C17-methylene protons), 6.57 (1H, d, *J* 5.87, C23-H), 7.25 (1H, s, C14-H), 7.40–7.55 (5H, m, C10-H, C11-H, C12-H, C27-H, and C29-H), 7.74 (1H, d, *J* 16.47, C24-H), 7.87 (1H, t, *J* 7.94, C28-H), 8.44–8.48 (2H, m, C26-H, C30-H), 9.245 (1H, s, C7-H); ^{13}NMR: d; 7.64 (C19), 31.91 (C18), 50.20 (C5), 67.07 (C17), 75.80 (C20), 97.08 (C23), 116.12 (C14), 120.90, 121.56, 125.80, 127.37, 128.38, 128.54, 128.90, 130.94, 131.48, 133.85, 136.48, 144.50, 145.96, 147.46, 157.60 (C2, C3, C6-C16a, C25-C30), 167.323 (C21 or C22, one of them not found); *m/z* (relative intensity) 523 (M^+, 12), 375 [M-148 (C_6H_5CH=$CHCOOH$), 100], 360 (30), 347 (71), 332 (30); HRMS ($C_{29}H_{21}N_3O_7$): Found, 523.124, required, 523.123.

Growth inhibition assay To assess the anti-proliferative activity of the various esters, identical cell cultures received equimolar concentrations of these esters and the cell number per ml was counted using the Trypan blue exclusion method. Cells were seeded at a concentration of 2.5×10^4 cells per well in a 48-microwell plate. Three such plates were seeded for end-point observation of cytotoxicity after 3, 5, and 7 d of treatment. Two concentrations of each test compound were used, one which was equal to the known cytotoxic level of the parent compound and one which was four times that amount. Stocks consisted of fine suspensions of esters in polyethylene glycol (PEG-400; Aldrich). Control cultures received only the carrier. The cell number was counted at time points of 72, 120, and 168 h, respectively. The targeted cells included 14 human malignant cell lines: CLO breast carcinoma, MDA 231 breast carcinoma, BRO melanoma, SCH melanoma, MiaPaCa2 pancreatic carcinoma, panc1 pancreatic carcinoma, HT 29 colon carcinoma, MCCN colon carcinoma, EFO27 ovarian carcinoma, 2774 ovarian carcinoma, DU145 prostate carcinoma, PC3 prostate carcinoma, DOY lung carcinoma, and SPA lung carcinoma.

HPLC procedure for purity analysis The purities of the ester products were determined by HPLC analysis. The procedure was previously reported[12].

***In vivo* toxicity and anti-tumor activity** All the animal experiments were performed on nude Swiss mice of the NIH, high-fertility strain. They were bred and raised in our laboratory under strict pathogen-free conditions. For the *in vivo* toxicity and anti-tumor activity determination, a tumor xenograft growing in a nude mouse, approximately 1 cm^3 in size, was surgically removed under sterile conditions, finely minced with iridectomy scissors, and suspended in cell culture medium at the ratio 1:10, v/v. One half of 1 mL of this suspension, containing about 50 mg of wet-weight tumor mince was subcutaneously inoculated on the upper half of the dorsal thorax of the mouse. Groups of four or five animals were used. The drug was finely suspended in cottonseed oil and then injected into the stomach cavity of the mouse through the anterior abdominal wall using a 26-gauge needle. The weekly schedule previously established for intragastric injection of 9NC was once a day, 5 on, and 2 off. This schedule was employed throughout all the animal experiments. Treatment was initiated when the tumor had reached a volume of approximately 200 mm^3, well-vascularized, measurable, and growing exponentially. Tumors growing in animals were checked and measured with a

caliper once a week.

Statistical analysis Data were expressed as mean±SD and compared with *t*-test.

Results and discussion

Chemistry A number of published reports have shown the methodologies for 20-OH acylation of camptothecins. Wall *et al* successfully prepared Camptothecin acetate by using the straight acylation reaction of camptothecin with acetic anhydride in pyridine[1]. This compound was also prepared by two other different methods, one using acetic acid (rather than the reactive anhydride) as acylating agent with nitronium tetrafluoroborate as the catalyst, and one using trichloroethane as acylating agent with concentrate sulfuric acid as the reaction solvent[12,13]. We used crotonic anhydride as acylating reagent to prepare alkenyl camptothecin esters 3 and 4. Camptothein 1 and 9-nitrocamptothecin 2 were allowed to react with a largely excessive amount of crotonic anhydride in pyridine to give the corresponding products 3 (31% yield) and 4 (71% yield), respectively. The reaction mixture was heated with a sand bath at 110±10 ℃ for 15 h. The products 3 and 4 were obtained respectively as white crystals (3) and yellow crystals (4) after separation by column and precipitation from petroleum ether. The subsequent epoxidation of 3 and 4 with *m*-chloroperoxybenzioc acid in benzene solvent gave the corresponding products 5 and 6 in yields of 70% and 10%, respectively (Scheme 2). Esters 7 and 8 were obtained in yields of 80% and 21%, respectively by heating the starting 1 or 2 in cinnamoyl chloride. The proton NMR spectra showed characteristic peaks at 1.00±0.05 ppm for C19-methyl protons of compounds. The C18-methylene protons of these compounds absorbed in the 2.05 to 2.35 ppm region with a multiplet peaks. The C25-methyl protons showed characteristic double doublets at 1.90±1.94 ppm for compounds 3–6. The alkenyl C23 proton of ester 3 and 4 showed characteristic peaks at 6.00±0.01 ppm; the other alkenyl C24 proton absorbed in the 7.04 to 7.24 ppm region. Esters 7 and 8 absorbed at 6.72±0.15 ppm for C23 proton. The C23 proton of esters 5 and 6 absorbed in the 5.95 to 6.04 ppm region with dq peaks because of the remote coupling between C23-proton and C25-methyl protons; the C24 proton of these two epoxy derivatives absorbed in the 7.02 to 7.14 ppm region. The mass spectra of these esters showed characteristic fragmentation pathway as depicted in Scheme 3.

Biological studies Cytotoxicity of these esters was observed *in vitro* by microwell plate screening as a first means of determining whether or not a compound warrants further evaluation. Standard microscopic observation of toxicity includes changes in morphology and the percent of cells remaining after specified amount of time in treated versus untreated cells. These esters were tested *in vitro* against 14 human malignant cell lines for anti-tumor activity. The experimental results were shown in Table 1. Table 2 showed the comparison of IC_{50} values of esters 3 and 4 to the commercially available comptothecin analogues, irinotecan (CPT-11) and topotecan. Figure 1 showed the anti-tumor activity of ester 3 against human breast carcinoma growing in nude mice as xenografts. Figure 2 showed the corresponding toxicity of ester 3 in mice. All esters tested in this study

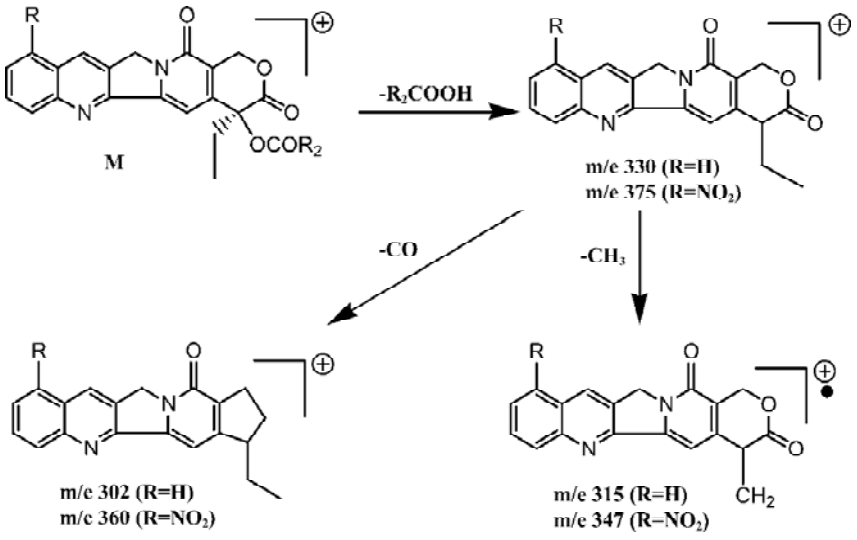

Scheme 3.

showed anti-tumor activity. However, larger doses were needed for these compounds in order to show the same strength of anti-tumor activity of their parent compounds, implying these esters are prodrugs. It is apparent from Table 1 that esters 3 and 4 are active against the tested cell lines and have almost the same strengths. It is also clear that from these tests that the activity of ester 5 is slightly higher than esters 3 and 4. Finally, the data in Table 1 showed that esters 6, 7, and 8 were only slightly active against those tested cell lines when comparing them to the control. We chose esters 3 and 4 for the further IC_{50} comparison studies because of the availability of the substances due to their easier syntheses. Irinotecan and topotecan are two camptothecin derivatives approved by FDA for treating cancer patients.

Table 1. Average response of 14 malignant cells to esters 3–8. n=3. Mean±SD. $^bP<0.05$, $^cP<0.01$ *vs* control.

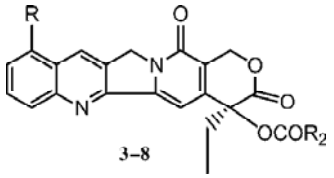

3–8

Compounds/mol·L^{-1}	Time/d		
	3	5	7
Control	4.0±0.0	4.0±0.0	4.0±0.0
Camptothecuin (200)	1.2±0.2^b	1.0±0.2^b	0.6±0.2^b
9-Nitrocamptothecin (200)	1.3±0.3^b	0.9±0.2^b	0.4±0.2^b
Ester 3 (200)	2.8±0.3^b	2.2±0.3^b	1.5±0.3^b
(800)	1.8±0.2^b	1.2±0.3^b	0.8±0.2^b
Ester 4 (200)	2.5±0.5^b	1.9±0.2^b	1.3±0.4^b
(800)	1.3±0.4^b	0.9±0.3^b	0.5±0.2^b
Ester 5 (200)	1.9±0.5^b	1.4±0.4^b	0.9±0.3^b
(800)	1.4±0.2^b	0.7±0.2^b	0.6±0.3^b
Ester 6 (200)	3.2±0.6^c	3.0±0.3^b	3.0±0.6
(800)	3.0±0.4^b	3.0±0.5^b	2.8±0.5^b
Ester 7 (200)	3.2±0.6^b	3.1±0.6^b	3.0±0.4^b
(800)	3.2±0.5^b	3.0±0.4^b	2.7±0.5^b
Ester 8 (200)	3.5±0.6	3.3±0.5^c	3.0±0.5^c
(800)	3.4±0.4^c	3.2±0.6^c	0.8±0.4^c

Number 4.00 represents the highest level of confluent cells at a given time point. A rating of 4.00 woulg be given to healthy dividing cells as seen in a control group and in a group treated with a drug which has no apparent cytotoxicic effect. Number 3.00 represents 75% of the cells remain as compared to level 4.00; and accordingly, numbers 2.00 and 1.00 represent 50% and 25%, respectively, of the cells remain as compared to level 4.00. The numbers represent the grouth inhibition. The smaller the number, the greater the inhibition.

The IC_{50} values of esters 3 and 4 are compared to the IC_{50} values of two marketed comptothecin analogues as shown in Table 2. In terms of IC_{50} values, ester 3 is 3 to 12 folds more potent than irinotecan against all testing cell lines and 1.3 to 3 folds more potent than topotecan against almost every testing cell line except for cell line McCain; ester 4 is 4 to 27 folds more potent than irinotecan and 1 to 4 folds more potent than topotecan against all testing cell lines. We also found that the anti-tumor activity of these new esters is same as or slightly higher than the corresponding alkyl derivatives when comparing the data in Table 1 to the data we previously reported for the corresponding alkyl ester compounds[10,11]. Thus, the introduction of an unsaturated double bond into the side ester chain of the molecule does not significantly alter the anti-tumor activity. We also chose ester 3 for the *in vivo* evaluation because of the availability of the

Table 2. Comparison of IC_{50} values of esters 3 and 4 to commercailly available anticancer agents irinotecan and topotecan. n=3. Mean±SD.

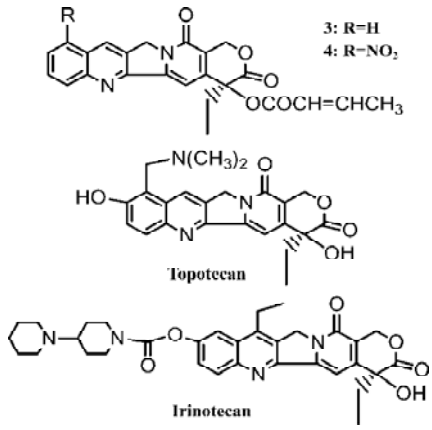

Cell lines	IC_{50} values in nmol/L			
	3	4	Irinotecan	Topotecan
HT29	91.5±0.8	40.0±0.5	1068.5±2.5	161.8±0.9
McCain	164.0±1.2	121.0±0.9	522.1±1.3	121.2±1.0
DU145	95.0±0.7	38.0±0.7	608.7±1.5	145.3±1.2
T47D	56.6±0.6	28.9±0.6	219.3±1.1	121.3±0.9
Kielty	103.0±0.9	44.1±0.6	1035.2±2.3	143.3±0.8
MPC2	119.8±1.1	73.5±0.8	646.6±2.0	155.6±1.2
DOY	51.5±0.5	34.9±0.8	585.1±1.9	165.7±1.3
SchC11	105.0±0.9	66.2±0.9	873.4±1.8	142.3±0.9
BRO	55.3±0.7	25.7±0.4	482.9±3.4	151.4±0.8

HT-29 and McCain: human collen cell lines; T47D and Kielty: human breast cell lines; DU-145: human prostate cell line; MPC2: Human pancrea cell line; DOY: human lung cell line; SchC11 and BRO: human melanoma cell lines.

larger scale synthesis of the molecule. Figure 1 shows the anti-tumor activity of ester 3 at a dose of 8 mg/kg against human breast carcinoma growing as xenografts in nude mice, and Figure 2 shows the corresponding toxicity of 3 at same dose level in mice. It is apparent form these *in vivo* studies that compound 3 completely inhibits the growth of human breast tumor in mice with no signs of toxicity as the bodyweight of mice increased slightly during the treatment.

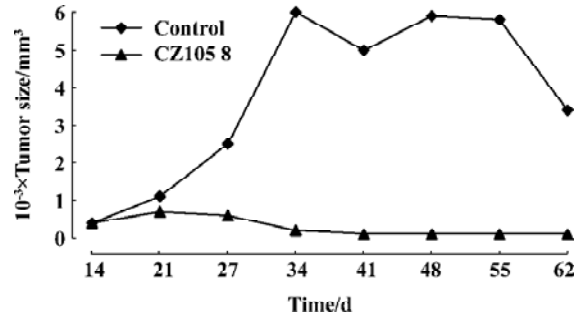

Figure 1. Anti-tumor activity of ester 3 against human breast cancer in mice. *n*=8.

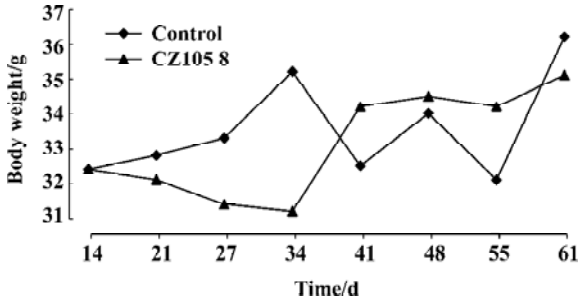

Figure 2. Toxicity of ester 3 in mice. *n*=8.

In conclusion, alkenyl campothecin esters 3 and 4 can be obtained by the straight esterification of the corresponding starting mother compounds with crotonic anhydride. These two compounds are more potent than the commercially available camptoxthecin analogues, irinotecan and topotecan, in terms of IC_{50} values. Furthermore, compound 3 shows strong *in vivo* anti-tumor activity against human breast carcinoma in mice with no signs of toxicity. Thus, these alkenyl camptothecin esters have great potential to be developed for human treatment.

Acknowledgement

The friends of the Stehlin Foundation are gratefully acknowledged.

References

1 Wall ME, Wani MC, Cook CE, Palmer KH, McPhail AT, Sim GA. Plant antitumor agents. I. The isolation and structure of camptothecin, a novel alkaloidal leukemia and tumor inhibitor from *camptotheca acuminata*. J Am Chem Soc 1966; 88: 3888–90.

2 Gottlieb JA, Guarino AM, Call JB, Oliverio VT, Block JB. Preliminary pharmacologic and clinical evaluation of camptothecin sodium (NSC-100880). Cancer Chemother Rep Part 1 1970; 54: 461–70.

3 Gottlieb JA, Luce JK. Treatment of malignant melanoma with camptothecin (NSC-100880). Cancer Chemother Rep 1972; 56: 103–5.

4 Muggia FM, Creaven PJ, Hansen HH, Cohen MH, Selawry OS. Phase I clinical trial of weekly and daily treatment with camptothecin (NSC-100880): correlation with preclinical studies. Cancer Chemother Rep 1972; 56: 515–21.

5 Moertel CG, Schutt AJ, Reitemeier RJ, Hahn RG. Phase II studies of camptothecin (NSC-100880) in the treatment of advanced gastrointestinal cancer. Cancer Chemother Rep 1972; 56: 95–101.

6 Schaeppi U, Fleishman RW, Cooney DA. Toxicity of camptothecin (NSC-100880). Cancer Chemother Rep 1974; 5: 25–36.

7 Wani MC, Ronman PE, Lindley LT, Wall ME. Plant antitumor agents. 18. Synthesis and biological activity of camptothecin analogs. J Med Chem 1980; 23: 554–60.

8 Cao Z, Harris N, Kozielski A, Vardeman D, Stehlin J, Giovanella B. Alkyl esters of camptothecin and 9-nitrocamptothecin: synthesis, *in vitro* pharmacokinetics, toxicity, and antitumor activity. J Med Chem 1998; 41: 31–7.

9 Zhao H, Lee C, Sai P, Choe Y, Boro M, Pendri A, *et al*. 20-*O*-Acylcamptothecin derivatives: evidence for lactone stablization. J Org Chem 2000; 65: 4601–6.

10 Cao Z, Mendoza J, Early J, Harris N, Kozieski A, Liehr J, *et al*. Structure-activity relationship of alkyl camptothecin esters. The Camptothecins: unfolding their anticancer potential. Ann NY Acad Sci 2000; 922: 122–35.

11 Cao Z, Mendoza J, Early J, Harris N, Kozieski A, Liehr J, *et al*. Structure-activity relationship of alkyl 9-nitrocamptothecin esters. Acta Pharmacol Sin 2003; 24: 109–19.

12 Cao Z, Armstrong K, Shaw M, Petry E, Harris N. Nitration of camptothecin with various inorganic nitrate salts in concentrated surfuric acid: a new preparation of anticancer drug 9-nitrocamptothecin. Synthesis 1998; 1724–30.

13 Cao Z. Preparation of 14-nitrocamptothecin derivatives by reactions of camptothecin with nitronium tetrofluoroborate in acidic solvents. J Chem Soc Perkin Trans 1 1996; 2629–32.

14 Cao Z. An alternative preparation of camptothecin 20(*S*)-acetate. Synth Commun 1997; 27: 2013–9.

Full-length article

Effect of MePEG molecular weight and particle size on *in vitro* release of tumor necrosis factor-α-loaded nanoparticles[1]

Chao FANG, Bin SHI, Yuan-ying PEI[2]

Department of Pharmaceutics, School of Pharmacy, Fudan University, Shanghai 200032, China

Key words

tumor necrosis factor-alpha; stealth; nanoparticles; polyethylene glycols; poly (methoxypolyethyleneglycol cyanoacrylate-co-*n*-hexadecyl cyanoacrylate)

[1] Project supported by the Science and Technology Development Foundation of Shanghai (No 0243nm067).

[2] Correspondence to Prof Yuan-ying PEI.
Phn/Fax 86-21-5423-7186.
E-mail yypei@shmu.edu.cn

Received 2004-06-07
Accepted 2004-09-21

doi: 10.111/j.1745-7254.2005.00037.x

Abstract

Aim: To study the *in vitro* release of recombinant human tumor necrosis factor-alpha (rHuTNF-α) encapsulated in poly (methoxypolyethyleneglycol cyanoacrylate-co-*n*-hexadecyl cyanoacrylate) (PEG-PHDCA) nanoparticles, and investigate the influence of methoxypolyethyleneglycol (MePEG) molecular weight and particle size. **Methods:** Three sizes (approximately 80, 170, and 240 nm) of PEG-PHDCA nanoparticles loading rHuTNF-α were prepared at different MePEG molecular weights (M_r=2000, 5000, and 10 000) using the double emulsion method. The *in vitro* rHuTNF-α release was studied in PBS and rat plasma. **Results:** A higher burst-release and cumulative-release rate were observed for nanoparticles with higher MePEG molecular weight or smaller particle size. A decreased cumulative release of rHuTNF-α following the initial burst effect was found in PBS, while the particle sizes remained constant and MePEG liberated. In contrast, in rat plasma, slowly increased cumulative-release profiles were obtained after the burst effect. During a 5-h incubation in rat plasma, more than 50% of the PEG-PHDCA nanoparticles degraded. **Conclusion:** The MePEG molecular weight and particle size had an obvious influence on rHuTNF-α release. rHuTNF-α released from PEG-PHDCA nanoparticles in a diffusion-based pattern in PBS, but in a diffusion and erosion-controlled manner in rat plasma.

Introduction

The rapid removal of colloidal drug carrier systems in blood by the mononuclear phagocytic system (MPS), which is comprised mainly of Kupffer cells of the liver and macrophages of the spleen, has been identified as major obstacle in the efficient targeting of colloidal particles in sites such as solid tumors and inflammatory regions[1,2]. Recently, a great deal of work has been devoted to developing "stealth" particles that are "invisible" to macrophages. Stealth nanoparticles (NP) are characterized by a prolonged half-life in the blood compartment that allows them to extravasate and accumulate more in pathological sites, such as tumors with leaky vasculature caused by the "enhanced permeability and retention effect"[3,4]. In our previous study, higher intratumoral drug accumulation and antitumor potency were achieved for recombinant human tumor necrosis factor-alpha (rHuTNF-α)-loaded stealth poly (methoxypolyethyleneglycol cyanoacrylate-co-*n*-hexadecyl cyanoacrylate) (PEG-PHDCA) NP with sizes of approximately 150 nm and methoxypolyethyleneglycol (MePEG) molecular weight of 5000[5].

It is known that surface properties, particle size, and drug release behavior are the key for the biological fate of stealth NP. However, no previous study has focused on the relationship between these characteristics and their ability to accumulate in tumors and antitumor efficacy. The aim of the present study is to investigate the influence of MePEG molecular weight and particle size on their long-circulating properties, tumor targeting, and antitumor efficacy. In this article, rHuTNF-α-loaded PEG-PHDCA NP with various MePEG molecular weights and particle sizes were elaborated. The particle physicochemical characteristics, drug release behaviors and mechanisms in PBS and rat plasma were determined. This work on the *in vitro* characteristics of

stealth NP might contribute to further understanding of their *in vivo* biological fate and tumor targeting properties.

Materials and methods

Reagents and drugs rHuTNF-α (M_r=17 000) was supplied by Shanghai Research Center of Biotechnology, Chinese Academy of Sciences (Shanghai, China). MePEG (M_r=2000, 5000), human serum albumin (HSA), and $Na^{125}I$ were obtained from Sigma Chemical (St Louis, MO, USA). MePEG (M_r=10 000) was donated by the Department of Polymer Material and Science of Fudan University. Cyanoacetic acid, 1,3-dicyclohexyl carbodiimide, 4-(dimethylamino) pyridine, and poly (vinylalcohol) (PVA) (M_r=16 000, 98% hydrolyzed) were purchased from Acros Organics (Geel, Belgium). All other reagents and solvents were of analytical grade.

Preparation and measurement of PEG-PHDCA polymers PEG-PHDCA was synthesized as described[6] in a previous study at an MePEG to *n*-hexadecyl ratio of 1:5 with appropriate modifications. The poly (*n*-hexadecyl cyanoacrylate) (PHDCA) was synthesized and used as a control.

^{1}H-NMR and ^{13}C-NMR spectra were recorded in $CDCl_3$ on a Mercury Plus 400 MHz spectrometer. Recognition of methyl, methylene, methane and quaternary carbon nuclei in ^{13}C-NMR spectra rested on the BB and DEPT-135. FTIR spectra (Avatar 360ESP) were obtained from a neat film cast from the chloroform copolymer solution between KBr tablets. GPC of polymers was performed in tetrahydrofuran with a Waters Associates Model ALC/GPC 244 apparatus. Molecular weight and molecular weight distribution of polymers were calculated by using polystyrene as the standard.

Preparation of rHuTNF-α-loaded nanoparticles rHuTNF-α was labeled with ^{125}I using the IODO-GEN procedure. Briefly, 100 μg of protein in 60 μL of potassium phosphate buffer (0.1 mol/L, pH 7.4) was layered over a freshly prepared film of IODO-GEN (100 μg) and incubated at 4 ºC for 10 min with 2 mCi of carrier-free $Na^{125}I$. The reaction mixture was made up to 0.5 mL volume with PBS, and the unreacted iodine was removed by gel filtration chromatography on a Sephadex G-25 PD10 column equilibrated with PBS. The specific radioactivity of the product was assessed in an autogamma (Packard Instruments, CT, Meriden, USA).

NP were prepared by an adjustment of the double emulsion ($w_1/o/w_2$) procedure as described in a previous study[7]. A w_1/o emulsion was prepared by sonicating 0.1 mL of a rHuTNF-α solution (w_1) containing HSA (2%, w/v) with a PEG-PHDCA or PHDCA solution in methylene chloride in an ice bath. The first emulsion was then poured into a PVA solution and sonicated in an ice bath. The double emulsion ($w_1/o/w_2$) obtained was diluted in 150 mL PVA solution (0.1%, w/v) and the organic solvent was evaporated at room temperature under reduced pressure. Finally, the NP were isolated and collected by two cycles of ultracentrifugation at 21 000×*g* for 40 min and washed three times with water.

Particle size and zeta potential measurement Particle size was determined in double distilled water by dynamic light scattering using Nicomp 380ZLS (NICOMP Particle Sizing Systems, Santa Barbara, CA, USA). Determinations were carried out at 23 ºC at a fixed angle of 90º. He-Ne laser was operated at 632.8 nm as light source.

Zeta potential of the NP was determined in double distilled water using electrophoretic light scattering technique on a Nicomp 380ZLS instrument.

Determination of entrapment efficiency and drug loading The NP containing rHuTNF-α and [^{125}I]-iodinated rHuTNF-α with HSA (2.0%) were centrifuged, washed and the supernatants were assessed for gamma emission. The amount of rHuTNF-α encapsulated in the NPs was calculated by the difference between the total amount used to prepare the NP and the amount of rHuTNF-α present in the aqueous phase. The rHuTNF-α loading of the NP, given as a percentage, indicates the amount of protein encapsulated per 100 mg of NP.

rHuTNF-α release and MePEG liberation in PBS *In vitro* release studies were performed in triplicate in 25 mL of phosphate buffered saline (PBS, 0.05 mol/L, pH 7.4) containing 0.2% (w/v) sodium azide. The NP suspensions were continuously stirred in a thermoshake (60 r/min) at 37 ºC in dark. At predetermined time intervals, 1 mL samples were withdrawn, centrifuged at 21 000×*g* for 40 min, and replaced by fresh release medium. The 0.5 mL supernatant was removed for measurement of the released rHuTNF-α fraction, by radioactivity counting.

For PEG-PHDCA NP, MePEG liberated during drug release in PBS was assayed using an iodine complexation method[8]. At preselected times, 0.8 mL of supernatant was collected by centrifugation of NP suspensions at 21 000×*g* for 40 min, diluted with 1.2 mL double-distilled water and then mixed with 50 μL of iodine solution composed of I_2 (10 g/L) and KI (20 g/L). After 5 min of incubation at room temperature in dark, the absorbance at 525 nm was read against a blank. In order to assay the total amount of MePEG in NP, the NP suspensions were digested by NaOH (2 mol/L) at 50 ºC for 5 d. The method was linear in the range of MePEG concentrations measured (1–25 mg/L).

rHuTNF-α release and nanoparticle degradation in rat plasma A total of 0.5 mL of each NP suspension was

incubated with equal volumes of fresh rat plasma in a water bath at 37 ºC in dark. At 0.5, 1, 2, 3, 4, and 5 h, the NP were separated from release medium by centrifugation at 21 000×*g* for 40 min. The drug release (%) was determined at each time point from the ratio of radioactivity associated with the pellet and the supernatant[9].

The degradation of the NP in rat plasma was performed by spectrophotometric measurements using a UV/VIS spectrophotometer (Shimadzu 2401) as described in a previous study[10]. The reduction in light transmission at 450 nm was recorded for evaluating the degradation of NP.

rHuTNF-α adsorption on PHDCA nanoparticles Blank PHDCA NP (approximately 25 mg of NPs in 25 mL of 0.05 mol/L phosphate buffer, pH 7.4, stabilized with 0.2% (w/v) sodium azide) were incubated at 37 ºC in a thermoshake (60 r/min) with an aqueous solution of rHuTNF-α (10 mg/L). At fixed time intervals, 1 mL of samples were centrifuged at 21 000×*g* for 40 min, and the amount of free rHuTNF-α in the supernatant was determined by radioactivity measurement. The amount of rHuTNF-α adsorbed on NP was determined using difference between the initial amount and the amount remaining in the supernatant.

Statistical analysis Physicochemical characteristics and *in vitro* release of NP were evaluated for statistical significance with analysis of variance (ANOVA) and Dunnett *t*-test.

Results

Characterization of PEG-PHDCA and PHDCA The ^{1}H-NMR, ^{13}C-NMR, and FTIR spectra were consistent with the structures of polymers (figures not shown). GPC showed that all polymers had narrow size distribution with an index of polydispersity less than 1.1 (Table 1).

Physicochemical characteristics of nanoparticles The basic characteristics of the eight types of NP formulations are summarized in Table 2.

rHuTNF-α release and MePEG liberation in PBS The influence of MePEG molecular weight on the protein release in PBS is shown in Figure 1. For each formulation, an initial burst release followed by a slow reduction of rHuTNF-α cumulative release was observed. More than 40% of rHuTNF-α released from the PEG-PHDCA NP during the first 1 h, but less than 10% of the drug released from the PHDCA NP during the same time. At d 8, PEG-PHDCA NP had a remarkably higher cumulative release ratio than PHDCA (P<0.01). As a whole, the cumulative release ratio increased with the increase of MePEG molecular weight (P<0.05). The effect of particle size on the rHuTNF-α release is compared in Figure 2. Each formulation showed burst effect followed by decreased rHuTNF-α cumulative release. For both PEG_{5000}-PHDCA and PHDCA NP, the NP of the smallest size showed the largest burst effect and highest cumulative release ratio (P<0.05).

In the study of rHuTNF-α release in PBS, MePEG detachment from PEG-PHDCA NP was observed (Figure 3). In 8 d, about 35% (w/w) of MePEG liberated. The evolution of the mean diameters of the NP during the 8-d *in vitro* release period was studied. The initial size of all the NP formulations remained constant and no new larger or smaller size populations were observed untill the end of this study.

rHuTNF-α release and nanoparticle degradation in rat plasma All NP formulations showed a greater burst effect in rat plasma than in PBS (P<0.05) (Figure 4). The amount of drug released increased with the increase of incubation time. The burst release amount depended on both the particle size and the MePEG molecular weight. It significantly varied in the following series: PEG_{5000}–PHDCA NP (80.0 nm)>PEG_{5000}–PHDCA NP (170.9 nm)>PEG_{5000}–PHDCA NP (242.9 nm) (P<0.01); PHDCA NP (85.2 nm)> PHDCA NP (173.1 nm)>PHDCA NP (242.3 nm) (P<0.01); PEG_{10000}–PHDCA NP (168.8 nm)>PEG_{5000}–PHDCA NP (170.9 nm)>PEG_{2000}–PHDCA NP (172.4 nm) (P<0.01).

In rat plasma, more than 50% of PEG-PHDCA NP were degraded in 5 h of incubation, while no degradation occurred

Table 1. Characterization of PEG-PHDCA and PHDCA polymers

Mole ratio feed	MePEG to *n*-hexadecyl polymer composition[1)]	Expected polymers	Theoretical MePEG M_n	MePEG M_n[2)]	Polymer M_n[3)]	Polymer M_w[4)]	PI[5)]
1:5	1:4.83	PEG_{2000}-PHDCA	2000	1570	3192	3341	1.05
1:5	1:4.74	PEG_{5000}-PHDCA	5000	4516	6162	6331	1.03
1:5	1:4.85	PEG_{10000}-PHDCA	10000	9353	10865	11408	1.05
–	–	PHDCA	–	–	1752	1891	1.08

[1)] Calculated from ^{1}H-NMR spectra. [2,3,4)] Determined by GPC. [5)] Polydispersity index=M_w/M_n

Table 2. Physicochemical properties of PEG-PHDCA and PHDCA NP containing rHuTNF-α. *n*=3. Mean±SD.

Size range	Polymers	Particle size/nm	Zeta potential/mV	Entrapment efficiency/%	Drug loading/%
Small (<100 nm)	PEG_{5000}-PHDCA	80.0±1.4	-3.19±0.09	37.6±3.2	0.83±0.04
	PHDCA	85.2±3.3	-17.27±0.25	45.2±4.6	0.85±0.03
Middle (100-200 nm)	PEG_{2000}-PHDCA	172.4±1.5	-14.82±0.23	49.8±2.7	0.88±0.02
	PEG_{5000}-PHDCA	170.9±2.3	-10.56±0.35	54.3±3.3	0.87±0.03
	PEG_{10000}-PHDCA	168.8±1.1	-3.77±0.49	57.0±1.8	0.92±0.03
	PHDCA	173.1±2.5	-22.4±0.24	60.1±2.9	0.88±0.02
Large (>200 nm)	PEG_{5000}-PHDCA	242.9±3.8	-13.73±0.18	46.7±2.2	0.86±0.03
	PHDCA	242.3±3.6	-23.4±0.51	55.5±3.7	0.84±0.04

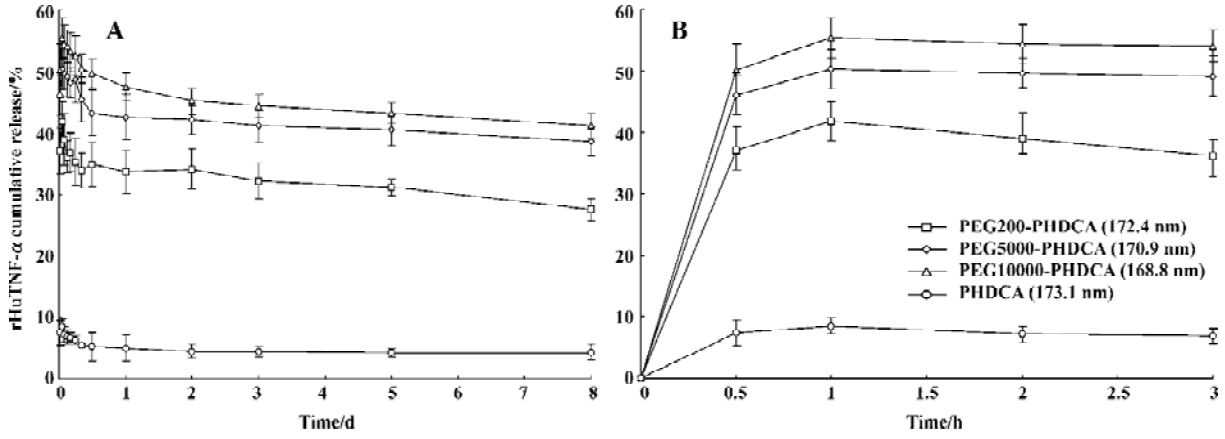

Figure 1. Influence of MePEG molecular weight on the rHuTNF-α release in PBS. (A) rHuTNF-α release over 8 d; (B) a close up of the first 3 h. *n*=3. Mean±SD.

to PHDCA NP during the same time (Figure 5). For PEG-PHDCA NP, the degradation rate increased with the increase of MePEG molecular weight ($P<0.01$).

Evaluation of rHuTNF-α adsorption on PHDCA nanoparticles The aim of the present study was to shed light on the adsorption of rHuTNF-α on the hydrophobic blank PHDCA NP surface and to better understand what happens during its release from NP. The adsorption was studied for 8 d (Figure 6). The adsorption of rHuTNF-α on PHDCA NP was very rapid, depending on the particle size. It was shown that the adsorption capacity varies in the series: 85.2 nm>173.1 nm>242.3 nm ($P<0.05$). The adsorption plateau was reached after approximately 1 to 2 d.

Discussion

Both particle size and MePEG coating influenced the zeta potential (Table 2). In the same size range, the significant lower negative potentials were obtained for PEG-PHDCA NP compared to PHDCA NP ($P<0.01$). This might be related to a shift of the hydrodynamic phase of shear to greater distance from the particle surface. The surface negative charge of PEG-PHDCA NP dramatically decreased with the increase of MePEG molecular weight. As for PEG_{5000}-PHDCA NP, the surface charge notably increased when the particle size increased ($P<0.05$), and the reason is now under investigation.

In the same size range, PEG-PHDCA NP showed lower entrapment efficiency compared with PHDCA NP ($P<0.01$). The same results were obtained in the comparison made of PEG-PLA and PLA[11] and those made of PEG-PLGA and PLGA NP[12]. The difference might come from the presence of MePEG in the PHDCA chains, but the mechanism was indistinct. For PEG-PHDCA NP, entrapment efficiency increased with the increase of MePEG molecular weight ($P<0.05$), and the influence of particle size on the entrapment efficiency was irregular. No regular change with re-

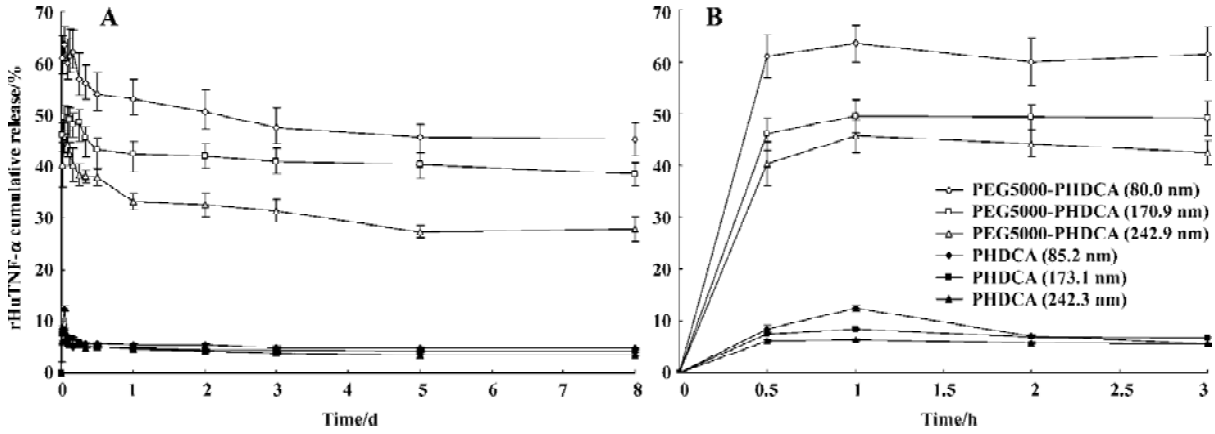

Figure 2. Influence of particle size on the rHuTNF-α release in PBS from PEG_{5000}-PHDCA and PHDCA NP (A) rHuTNF-α release over 8 d; (B) a close up of the first 3 h. n=3. Mean±SD.

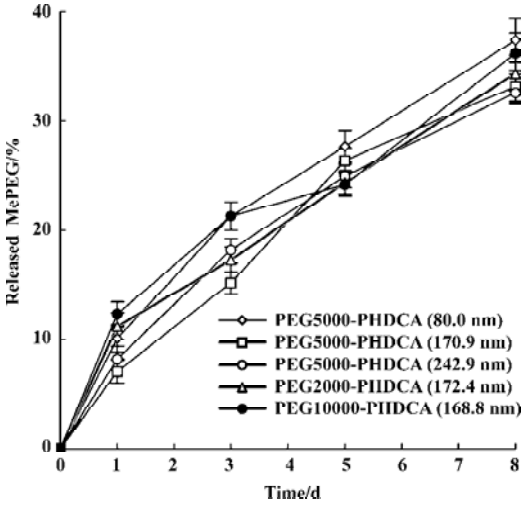

Figure 3. MePEG liberation during the study of rHuTNF-α release from PEG-PHDCA NP in PBS. n=3. Mean±SD.

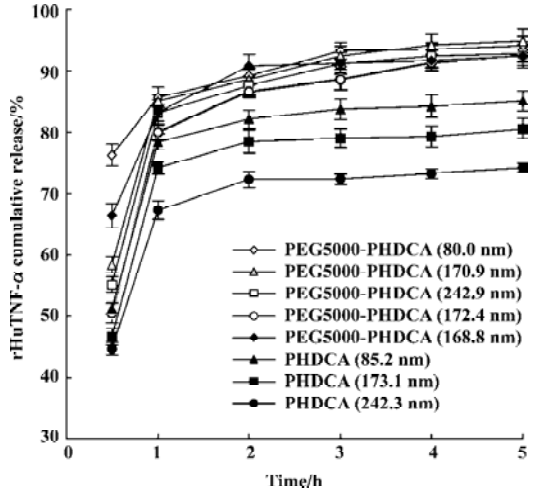

Figure 4. Release profiles of rHuTNF-α-loaded NP in rat plasma. n=3. Mean±SD.

spect to drug loading was found. And the differences of drug loading among PHDCA and PEG-PHDCA NP were not remarkable (P>0.05).

The burst release depended on MePEG molecular weight (Figure 1). It was shown that the higher the MePEG molecular weight, the more the rHuTNF-α burst release. It was reported that the faster release of tetanus toxoid from PLA-PEG microspheres than PLA could be related to their different inner structure and reduced protein-polymer interactions[11]. Similarly, the MePEG chains in NP orient not only towards the external aqueous medium but also towards the inner aqueous phase[13,14]. Thus the protein reservoirs are theoretically surrounded by a MePEG barrier, which reduces the interaction of rHuTNF-α with the PHDCA matrix[7]. The different burst effect might result from the different intensity of this interaction between rHuTNF-α and PHDCA. It is supposed that the longest chain (MePEG of 10 000) hindered the interaction between rHuTNF-α and PHDCA, and PEG_{10000}–PHDCA NP had the highest burst effect. Higher burst release of small size NP than middle and large NP could be related to their larger surface areas (Figure 2).

For PEG-PHDCA NP, a reduction of rHuTNF-α release percentage following burst effect was observed in PBS. This same phenomenon in the process of protein release from NP was reported in other articles[8,15]. MePEG chains can create a steric barrier around NP and repel proteins to some degree, in which the density of MePEG "brush" is of great importance[16]. MePEG chains are highly hydrophilic and can facilitate the penetration of incubation medium, and hydroly-

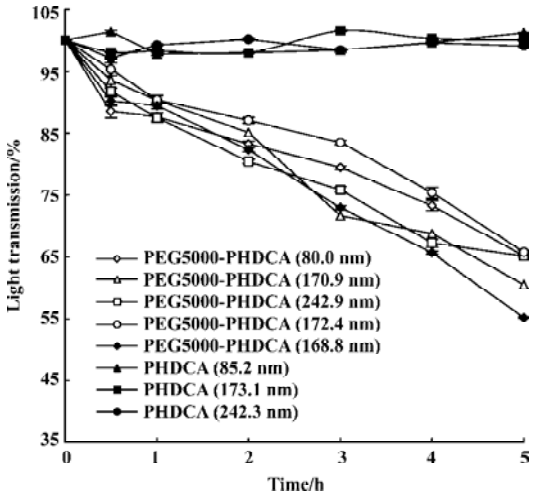

Figure 5. Degradation profiles of rHuTNF-α-loaded NP in rat plasma. *n*=3. Mean±SD.

sis of the ester bonds associated to them[10] (Figure 3). After partial MePEG detachment, the density of MePEG "brush" was not sufficient to repel proteins and rHuTNF-α was re-absorbed on the particle surface, which resulted in a decreased cumulative release ratio. The readsorption phenomenon is evidenced in the study of rHuTNF-α adsorption on blank PHDCA NP (Figure 6).

There might be competition between protein release from NPs and protein readsorption onto the NP surface[15]. It is reasonable that the amount of rHuTNF-α detected in the supernatant was the result of rHuTNF-α release and rHuTNF-α readsorption onto the NP surface, each process having its own rate that depended on the rHuTNF-α concentrations in NP and in release medium. After a certain time, the release plateau was reached, indicating that equilibrium was established between the release and readsorption of rHuTNF-α. Noticeably, the readsorption phenomenon in the present study did not occur in a previous study in our lab[7]. We hypothesized that the loading of the NP used here was lower than that of the PEG_{5000}-PHDCA NP (approximately 150 nm) prepared previously and relatively lower rHuTNF-α concentrations in NP were obtained in this study. Therefore it is possible that after a significant burst release, the rHuTNF-α concentration in NP is lower than that in the release medium and that a slow readsorption happened till the release plateau was reached. This could also be used to explain the readsorption of PHDCA NP.

The mean diameters of the eight types of NP remained constant during the 8-d release at 37 ºC in PBS. The ratios of particle size after incubation to its initial size for each NP formulation were all in the range of 1.0±0.3, indicating no significant aggregation or degradation occurred[17]. In summary, rHuTNF-α release was accompanied with constant particle size evolution and MePEG detachment from PEG-PHDCA NP in PBS. Combined with the known fact that polyalkylcyanoacrylate (PACA) polymer could be degraded mainly by enzymatic degradation[10], and PACA NP degraded mainly by surface erosion[18], it is hypothesized that rHuTNF-α release in PBS from PEG-PHDCA NP might follow a diffusion-based model.

Figure 5 showed that the presence of the MePEG chain greatly increased the degradation of PHDCA in rat plasma.

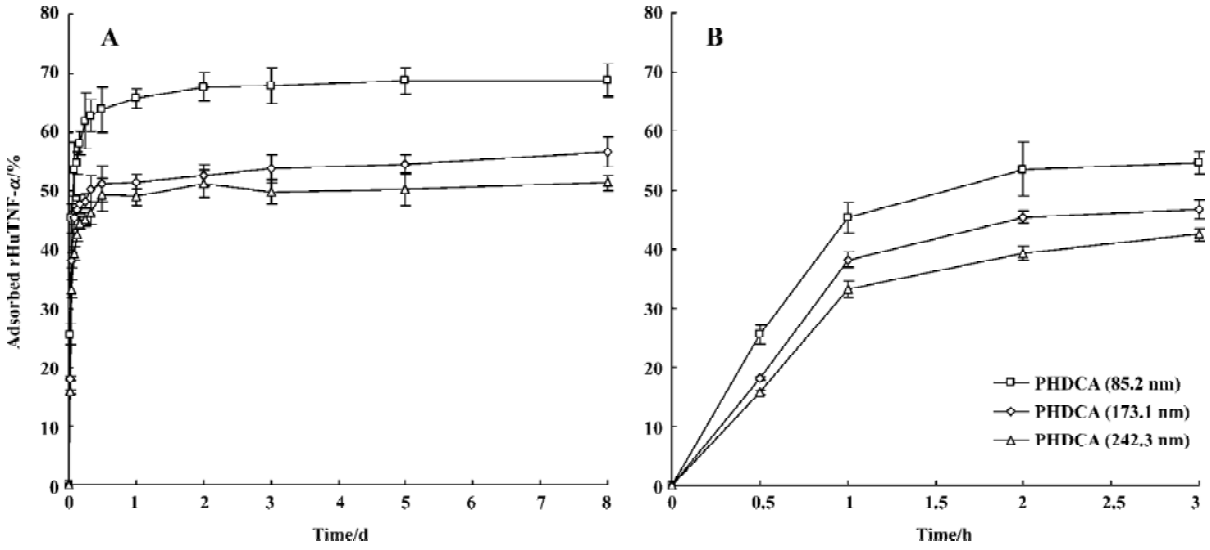

Figure 6. Adsorption kinetics of rHuTNF-α on blank PHDCA NP. (A) rHuTNF-α adsorption over 8 d; (B) a close up of the first 3 h. *n*=3. Mean±SD.

This might be a result of the enhanced penetration of the plasma and the esterase hydrolysis caused by the highly hydrophilic MePEG moieties in the polymer structure.

The influence of particle size and MePEG molecular weight on the release of rHuTNF-α in rat plasma was similar to that in PBS. But no decreased cumulative release profiles was observed. We supposed that a competitive readsorption existed between rHuTNF-α and the proteins in rat plasma. Relatively small amounts of rHuTNF-α in the supernatant could hardly be reabsorbed onto the NP surface with a great amount of plasma proteins. Thus, a slightly increased cumulative release percentage was obtained under this condition. The burst release of PEG-PHDCA NP was greater than that of PHDCA NP. This could be a result of PEG-PHDCA degradation and the hindrance of interaction between protein and PHDCA by MePEG chains. Combined with the NP degradation behavior in rat plasma, it can be expected that rHuTNF-α released in rat plasma in a diffusion-controlled pattern for PHDCA NP, but in a diffusion and erosion-controlled manner for PEG-PHDCA NP.

Compared with PHDCA NP, PEG-PHDCA NP had a much higher cumulative release ratio, but their burst effects were a bit larger, which was a disadvantage when designing a stealth delivery system. However, compared to the free drug, a markedly extended circulating time was still obtained for stealth NP with high burst release[19]. And it was reported that *in vitro* release behavior did not always coincide with *in vivo* circulation time of NP, which represented the more complex nature of the *in vivo* system[20]. Therefore, for the validation of the "stealth" property of NP, pharmacokinetic studies *in vivo* are necessary. In view of the lower burst release possessed by PHDCA NPs, we supposed NP made with a proper ratio of PEG-PHDCA: PHDCA might have a lower burst effect as well as satisfactory cumulative release characteristics. This needs to be studied further.

In summary, a higher MePEG molecular weight offered higher entrapment efficiency, lower zeta potential, faster rHuTNF-α release rate and a larger cumulative release ratio. Larger particle size provided relatively higher surface charge, slower drug release rate and a smaller cumulative release ratio. rHuTNF-α release from PEG-PHDCA NP follows a diffusion-based model in PBS while a diffusion and erosion-controlled pattern in rat plasma. The present results implied that these NP might have different biological fates. The relationship between their *in vitro* characteristics and *in vivo* intratumoral drug accumulation and antitumor potency is now under investigation.

Acknowledgment

We thank Prof Jian-hua ZHU (Department of Radiopharmacy, Fudan University, Shanghai, China) for the radiolabelling and measurement.

References

1 Dunn SE, Coombes AGA, Garnett MC, Davis SS, Davies MC, Illum L. *In vitro* cell interaction and *in vivo* biodistribution of poly (lactide-co-glycolide) nanospheres surface modified by poloxamer and poloxamine copolymers. J Control Release 1997; 44: 65–76.

2 Mosqueira VCF, Legrand P, Morgat JL, Vert M, Mysiakine E, Gref R, *et al*. Biodistribution of long-circulating PEG-grafted nanocapsules in mice: effects of PEG chain length and density. Pharm Res 2001; 18: 1411–19.

3 Moghimi SM, Hunter AC, Murray JC. Long-circulating and target-specific nanoparticles: theory to practice. Pharmacol Rev 2001; 53: 283–318.

4 Brigger I, Dubernet C, Couvreur P. Nanoparticles in cancer therapy and diagnosis. Adv Drug Del Rev 2002; 54: 631–51.

5 Li YP, Pei YY, Zhou ZH, Zhang XY, Gu ZH, Ding J, *et al*. Stealth polycyanoacrylate nanoparticles as tumor necrosis factor-alpha carriers: pharmacokinetics and anti-tumor effects. Biol Pharm Bull 2001; 24: 662–5.

6 Li YP, Zhou ZH, Pei YY, Zhang XY, Gu ZH, Yuan WF. PEGylated polycyanoacrylate nanoparticles as salvicine carriers: synthesis, preparation, and *in vitro* characterization. Acta Pharmacol Sin 2001; 22: 645–50.

7 Li YP, Pei YY, Zhou ZH, Zhang XY, Gu ZH, Ding J, *et al*. PEGylated polycyanoacrylate nanoparticles as tumor necrosis factor-alpha carriers. J Control Release 2001; 71: 287–96.

8 Zambaux MF, Bonneaux F, Gref R, Dellacherie E, Vigneron C. Protein C-loaded monomethoxypoly (ethylene oxide)-poly (lactic acid) nanoparticles. Int J Pharm 2001; 212: 1–9.

9 Redhead HM, Davis SS, Illum L. Drug delivery in poly (lactide-co-glycolide) nanoparticles surface modified with poloxamer 407 and poloxamine 908: *in vitro* characterisation and *in vivo* evaluation. J Control Release 2001; 70: 353–63.

10 Peracchia MT, Vauthier C, Desmaele D, Gulik A, Dedieu JC, Demoy M, *et al*. Pegylated nanoparticles from a novel methoxypolyethylene glycol cyanoacrylate-hexadecyl cyanoacrylate amphiphilic copolymer. Pharm Res 1998; 15: 550–6.

11 Tobio M, Gref R, Sanchez A, Langer R, Alonso MJ. Stealth PLA-PEG nanoparticles as protein carriers for nasal administration. Pharm Res 1998; 15: 270–5.

12 Li YP, Pei YY, Zhang XY, Gu ZH, Zhou ZH, Yuang WF, *et al*. PEGylated PLGA nanoparticles as protein carriers: synthesis preparation and biodistribution in rats. J Control Release 2001; 71: 203–11.

13 Brigger I, Chaminade P, Desmaele D, Peracchia MT, d'Angelo J, Gurny R, *et al*. Near infrared with principal component analysis as a novel analytical approach for nanoparticle technology. Pharm Res 2000; 17: 1124–32.

14 Quellec P, Gref R, Perrin L, Dellacherie E, Sommer F, Verbavatz JM, *et al*. Protein encapsulation within polyethylene glycol-coated nanospheres. I. Physicochemical characterization. J Biomed Mater Res 1998; 42: 45–54.

15 Quellec P, Gref R, Dellacherie E, Sommer F, Tran MD, Alonso MJ. Protein encapsulation within poly (ethylene glycol)-coated nanospheres. II. Controlled release properties. J Biomed Mater Res 1999; 47: 388–95.
16 Passirani C, Barratt G, Devissaguet JP, Labarre D. Interactions of nanoparticles bearing heparin or dextran covalently bound to poly (methyl methacrylate) with the complement system. Life Sci 1998; 62: 775-85.
17 Lin WJ, Juang LW, Lin CC. Stability and release performance of a series of pegylated copolymeric micelles. Pharm Res 2003; 20: 668–73.
18 Muller RH, Lherm C, Herbort J, Couvreur P. *In vitro* model for the degradation of alkylcyanoacrylate nanoparticles. Biomaterials 1990; 11: 590–5.
19 Avgoustakis K, Beletsi A, Panagi Z, Klepetsanis P, Karydas AG, Ithakissios DS. PLGA-PEG nanoparticles of cisplatin: *in vitro* nanoparticles degradation, *in vitro* drug release and *in vivo* drug residence in blood properties. J Control Release 2002; 79: 123–35.
20 Gaur U, Sahoo SK, De TK, Ghosh PC, Maitra A, Ghosh PK. Biodistribution of fluoresceinated dextran using novel nanoparticles evading reticuloendothelial system. Int J Pharm 2000; 202: 1–10.

4th National Congress of Chinese Society of Toxicology

2005 Sep 18-21 Shenyang, China

Info: Director Tian-en WANG
Chinese Toxicology Society
27 Taiping Road
Beijing 100850, China
Phn 86-10-6693-2387
Fax 86-10-6818-3899

Director Yu-hong SONG
National Shenyang Center for Safety Evaluation of New Drugs
8 Liaodong Road
Shenyang 110021, China
Phn 86-24-2581-2684
Fax 86-24-8935-3490

Full-length article

Pharmacokinetics and tissue distribution of 5-fluorouracil encapsulated by galactosylceramide liposomes in mice[1]

Yong JIN, Jun LI[2], Long-fu RONG, Xiong-wen LÜ, Yan HUANG, Shu-yun XU

Institute of Clinical Pharmacology, School of Pharmacy, Anhui Medical University, Hefei 230032, China

Key words

5-fluorouracil; galactosylceramide; liposomes; pharmacokinetics

[1] Project supported by Key Teacher Foundation of Ministry of Education of China (No 1869) and Young Teacher Foundation of Department of Education of Anhui Province (No 2000jg112).
[2] Correspondence to Prof Jun LI.
Phn/Fax 86-551-516-1001.
E-mail amuicplj@mail.hf.ah.cn

Received 2004-04-01
Accepted 2004-11-15

doi: 10.1111/j.1745-7254.2005.00030.x

Abstract

Aim: To study the pharmacokinetics and tissue distribution of 5-fluorouracil encapsulated by galactosylceramide liposomes (5-Fu-GCL) in mice. **Methods**: The concentration of 5-fluorouracil (5-Fu) in serum was detected by high performance liquid chromatography after 5-Fu-GCL (80, 40, 20 mg/kg) and free 5-Fu (40 mg/kg) were injected intravenously into mice. The tissue distribution of 5-Fu-GCL (40 mg/kg) and free 5-Fu (40 mg/kg) was investigated**,** and concentration-time profile of the two preparations in the liver were studied. Data were analyzed by 3p97 program. **Results**: Serum concentration-time curves of 5-Fu-GCL and free 5-Fu conformed to one compartment model of first order absorption. 5-Fu-GCL at 80, 40, and 20 mg/kg had $T_{1/2Ke}$ of 25.8±4.2, 27.3±4.4, and 28.2±5.6 min; C_0 of 24.9±4.9, 17.7±3.6, and 11.5±2.7 mg/L; and AUC of 990.0±45.2,622.5±38.3, and 340.4±25.6 mg·min·L^{-1}, respectively. In contrast free 5-Fu at 40 kg/mg had $T_{1/2Ke}$ of 15.8±2.2 min, C_0 of 35.8±6.2 mg/L, AUC of 639.0±35.9 mg·min·L^{-1}. The tissue distribution of 5-Fu-GCL in the liver and immune organs was significantly increased, while in heart and kidney it was remarkably decreased**.** The AUC of 5-Fu-GCL in the liver was 3 times higher than that of free 5-Fu. **Conclusion**: The pharmacokinetics and tissue distribution of 5-Fu-GCL appears to be linear-related and dose-dependent, and exhibits sustained-release and hepatic target characteristics.

Introduction

5-Fluorouracil (5-Fu) is a chemotherapeutic drug that is used widely for the treatment of malignant cancers, and is usually the first choice of drug for the treatment of hepatic cellular cancer. High doses of this drug are currently administered, mostly by continuous infusion, over 5 to 21 d[1]. But its use has been limited by its systemic toxicities, which have severe gastrointestinal toxicities, hematologic side effects, and severe disturbance in bone marrow[2]. Moreover, 5-Fu has a serum half-life of only 15 min, further limiting its usefulness[3]. Several studies have reported a relationship between 5-Fu plasma levels and its toxicity, and the response to treatment. 5-Fu is often monitored in serum by pharmacokinetic follow-up with liquid chromatography[4].

In order to maximize the therapeutic effect of 5-Fu and minimize its adverse effects, microsphere, liposome, implants, and nanoparticles were made[5–8]. But they were all passive for targeting preparations. Galactosylceramide (GC), as a novel membrane material, was adopted to envelop 5-Fu and form liposomes. This kind of 5-Fu preparation has not been previously reported. The purpose of this study was to measure the pharmacokinetic parameters and tissue distribution of 5-Fu-GCL in mice, which should supply evidence for its long effect and active targeting.

Materials and methods

Drugs and reagents 5-Fluorouracil encapsulated by galactosylceramide liposomes (5-Fu-GCL) (Batch No, 20020318, enveloped rate: 52%), was made in the Institute of Clinical Pharmacology, Anhui Medical University. Free 5-Fu (Batch No, 20020318, purity >99.3%), was obtained from Ji-nan Pharmaceutical Co (Ji-nan, China). Acetonitrile,

para-aminobenzoic acid and ethyl acetate was of analytical grade.

Apparatus Shimadzu LC-10A HPLC equipment consisted of LC-10A pumps, SCL-6A system controller, SPD-6AV ultraviolet spetrophotometric detector, ODS-C18 column(150 mm×4.6 mm) (Shimadzu Co, Japan), and V4.0$^+$ software on a computer.

Animals Balb/c mice (male and female, 18–22 g) in the study were provided by the Experimental Animal Center of Anhui Medical University (certifcate No 001). All animals were maintained at a controlled temperature (22±2 ºC), and a regular light/dark cycle (7:00 AM to 19:00 PM, light), and all animals had free access to food and water. All experimental protocols described in this study were approved by the Ethics Review Committee for Animal Experimentation of Anhui Medical University.

Liposome preparation 5-Fu was encapsulated in liposomes made of galactocerebroside, Lecithin Granules and cholesterin in a molar ratio of 6:3:1. Liposomes were prepared by combined calcium-induced fusion with reverse evaporation method. In brief, phospholipids were dissolved in 0.7 mL of carbinol and chloroform compound with 2:1 volume and subjected to rotary evaporation until the lipid membrane formed. Then 1.5 mL of chloroform, 250 μL of 5-Fu (10 g/L) and 250 μL of ultrasonic buffer were added to the dried phospholipids, to which ultrasonic vibrations and rotary evaporation were carried out to wipe off organic solvent until the gel formed. Ultrasonic buffer 1.5 mL was added and the compounds were rotated at room temperature after which 125 μL of calcium liquor was added to 0.5 mL of liposomes prepared through reverse-phase evaporation. After incubation at 37 ºC for 60 min, 12.5 μL of edetic acid (EDTA) was added to the compounds and shaken acutely, followed by incubation at 37 ºC for 15 min and at room temperature for another 30 min. Using an initial drug-to-lipid molar ratio of 5:1, the enveloped rate was 52%. After being stored at 4 ºC for 6 months, its permeability rate was less than 5%, which indicated the stability of 5-Fu-GCL was high. The recovery of 5-Fu-GCL was between 95.3% and 98.7%.

Pharmacokinetics of 5-Fu-GCL Two hundred and eighty-eight mice were randomly divided into four groups. Each group, which consisted of 36 males and 36 females, was injected with 5-Fu-GCL 20, 40, and 80 mg/kg or free 5-Fu 40 mg/kg through the tail vein. Before each injection and 2, 5, 10, 15, 20, 30, 45, 60, 90, 120, and 180 min later, 6 mice were anesthetized by diethyl ether, after which their eyeballs were excised and exsanguinated. Blood samples were centrifuged at 1400×*g* for 10 min to obtain 0.2 mL of serum each. Finally, mice were killed by dislocation of the cervical vertebra[9].

Tissue distribution of 5-Fu-GCL Twenty mice were stratified into two groups. Both groups including 5 males and 5 females were injected with 5-Fu-GCL 40 mg/kg and free 5-Fu 40 mg/kg through the caudal veins. Twenty minutes later, the mice were killed and the hearts, livers, spleens, lungs, kidneys, brains, lymph, thymuses, and marrow were removed, washed (except marrow), weighed, and homogenized using a tissue blender in 2 mL PBS solution. After extraction, concentrations in different tissues were detected by HPLC to study whether there were differences in distributions between the two groups[10].

Concentration-time course of 5-Fu-GCL in liver The livers from mice untreated and treated with 5-Fu-GCL 40 mg/kg or free 5-Fu 40 mg/kg at 2, 5, 10, 15, 20, 30, 45, 60, 90, 120, and 180 min were removed, washed, weighed, and homogenized using a tissue blender in 2 mL PBS solution. The sample was extracted and detected by HPLC.

Analytical method The drug concentration in serum and tissues were analyzed by HPLC. The mobile phase components were water and acetonitrile (99:1). Ultraviolet wavelength was 205 nm. The flow-rate was 1 mL/min[11,12].

The ratio of the peak area of 5-Fu to that of internal standard was plotted versus the concentration of the 5-Fu. Values of unknown serum drug concentrations were determined from calibration curve.

Standard solutions 5-Fu was dissolved in acetonitrile, then different amounts of this solution were added into blank 5-mL glass tubes and evaporated to dryness by nitrogen. The residues were dissolved with 0.2 mL mice serum or tissues to make 5-Fu of 0.313, 0.625, 1.25, 2.5, 5.0, 10.0, 20.0, and 40.0 mg/L, respectively, as serum standard solutions. The extraction of serum standard solutions was described in "Serum extraction procedure."

Sample extraction procedure Serum or tissue samples (0.2 mL) were added with 150 μL para-amino-benzoic acid (15 mg/L) as internal standard, distilled water (0.2 mL), and ethyl acetate (4 mL). They were then vortex-mixed in a 10-mL glass tube for 1 min. After centrifugation at 700×*g* for 20 min, the organic phase was aspirated. The remainder was extracted by addition of 4 mL ethyl acetate as described above. The two organic phases were mixed and evaporated until dry under a gentle stream of nitrogen at 35 ºC in a water bath. The residues were reconstituted with 200 μL ethanol, and 50 μL of extracted samples were injected into the chromatography of liquid. On account of its character of being collapsed by ethyl acetate, 5-Fu-GCL could be detected as free 5-Fu. Both 5-Fu-GCL and free 5-Fu were detected by HPLC in the study.

Recovery, accuracy, and precision of 5-Fu Different 5-Fu standards were added into blank glass tubes and evaporated to dryness by nitrogen. The residues were dissolved with 0.2 mL serum or tissues to make concentrations of 0.313, 1.25, 5, and 20 mg/L. The samples were handled referring to the "serum extraction procedure."

Five extracted samples of each concentration were determined. The recovery of 5-Fu in serum or tissues was assayed, and expressed as the percentage of detected concentrations to nominal concentration of standard (recovery). The accuracy of 5-Fu in serum or tissues was assayed, and expressed as the percentage of detected concentration to nominal concentration of serum or tissues (accuracy). Meanwhile, the inter-day and intra-day coefficient of variation of samples of different concentrations were measured 5 times on a single day and daily for a consecutive 5 d respectively (precision).

Pharmacokinetics calculations Phamacokinenic parameters were calculated by 3p97 program.

Statistical analysis Data were presented as mean±SD. Statistical analysis of the data was performed using the *t*-test. $P<0.05$ was considered statistically significant.

Results

Method validation In the conditions described above, no significant interfering peak was observed. The retention time of 5-Fu was 7.7 min (Figure 1). The calibration curve of 5-fluorouracil in serum or tissue was in good linearity over the concentration range of -0.313–40.000 mg/L, and the coefficient of correlation was 0.9992–0.9996. The regression equation was: A=0.10+2.18C (serum); A=0.11+2.17C (heart); A=0.11+2.19C (liver); A=0.09+2.18C (spleen); A=0.13+2.19C (lung); A=0.10+2.17C (kidney); A=0.11+2.18C (brain); A=0.13+2.21C (thymus); A=0.12+2.20C (lymph); A=0.12+2.19C (marrow). A: ratio of 5-Fu peak area to internal standard peak area; C: 5-Fu concentration. The limit of detection was 15.6 ng. The average recovery of 5-Fu was over the range of (80±3)%–(97±7)% (Table 1, 2) and the accuracy of 5-Fu was over the range of (93±4)%–(103±7)% (Table 3, 4). The inter-day and intra-day reproducibility of 5-Fu is shown in Table 5, 6, and the coefficient of variation was all below 10%. Meanwhile, the average recovery of internal standard was over the range of (88±4)%–(93±5)%. And the stability of internal standard was high because the deviation of it were all below 15%.

Table 1. Average recovery of 5-Fu in mice serum. n=5. Mean±SD.

Nominal concentration/mg·L^{-1}	Measurement concentration/mg·L^{-1}	Recovery/%
20.00	16.85±0.59	84±3
5.00	4.53±0.23	91±5
1.25	1.16±0.07	93±6
0.31	0.29±0.02	94±6

Pharmacokinetic parameters of 5-Fu-GCL in serum Data of drug serum concentrations at different time points in three 5-Fu-GCL groups (80, 40, and 20 mg/kg) and free 5-Fu group (40 mg/kg) are shown in Figure 2.

Pharmacokinetic parameters were calculated by 3p97 program. Drug serum concentration-time course of 5-Fu-GCL groups (80, 40, and 20 mg/kg) and free 5-Fu group (40 mg/kg) conformed to one compartment model of the first

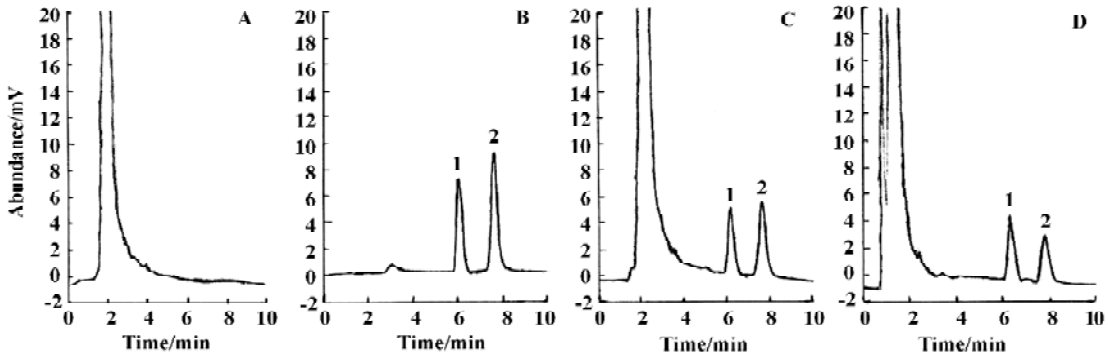

Figure 1. Separation of 5-Fu. (A) Blank serum; (B) 5-Fu standard; (C) 5-Fu+Blank serum; (D) Serum sample. (1) internal standard; (2) 5-Fu.

Table 2. Average recovery of 5-Fu in mice tissues. *n*=5. Mean±SD.

Tissues	Recovery/%			
	20.00 mg/L	5.00 mg/L	1.25 mg/L	0.31 mg/L
Heart	89±3	91±4	92±4	92±3
Liver	88±4	89±3	89±5	90±7
Spleen	80±3	85±4	88±3	94±4
Lung	90±4	92±5	95±6	96±5
Kidney	91±5	94±6	97±7	96±7
Brain	81±3	86±5	88±5	91±7
Thymus	83±4	84±5	89±5	92±6
Lymph	85±3	88±4	92±4	94±6
Marrow	82±4	85±3	90±5	92±5

Table 3. Accuracy of 5-Fu in mice serum. *n*=5. Mean±SD.

Nominal concentration/mg·L^{-1}	Measurement concentration/mg·L^{-1}	Accuracy/%
20.00	19.18±0.71	96±4
5.00	4.82±0.23	96±5
1.25	1.24±0.07	99±6
0.31	0.32±0.02	103±7

Table 4. Accuracy of 5-Fu in mice tissues. *n*=5. Mean±SD.

Tissues	Accuracy/%			
	20.00 mg/L	5.00 mg/L	1.25 mg/L	0.31 mg/L
Heart	95±4	97±4	99±6	102±7
Liver	97±5	96±4	98±7	99±5
Spleen	95±5	95±6	97±6	103±6
Lung	99±6	99±5	101±6	103±7
Kidney	96±4	94±4	97±5	99±6
Brain	93±4	96±5	98±5	101±7
Thymus	95±5	96±7	98±6	98±6
Lymph	95±6	98±5	100±5	101±7
Marrow	98±5	96±6	96±5	99±6

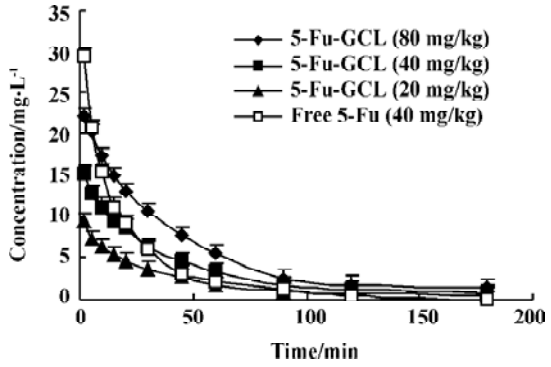

Figure 2. Serum concentration-time profile of 5-Fu after a single dose of 5-Fu-GCL or free 5-Fu. *n*=6. Mean±SD.

order absorption. Pharmacokinetic parameters of groups are shown in Table 7.

The results demonstrated that 5-Fu-GCL, in contrast to free 5-Fu, had delayed characteristics.

Concentration of 5-Fu-GCL in different tissue Distribution results showed that drug concentrations of 5-Fu-GCL in immune organs, which include the spleen, thymus, and lymph, but especially in the liver were remarkably higher than those of free 5-Fu at the same dose (40 mg/kg). Drug concentrations of 5-Fu-GCL in the heart and kidney were significant lower than that of free 5-Fu. In the brain, drug concentrations of both 5-Fu-GCL and free 5-Fu were not detected (Figure 3).

Concentration-time course of 5-Fu-GCL in liver The time course of drug concentration in the liver is shown in Figure 4. Area under time-concentration curve (AUC) of 5-Fu-GCL (485 mg·min·kg^{-1}) , which was calculated by 3p97 program, was three times higher than that of free 5-Fu (157

Table 5. Precision of 5-Fu in mice serum. *n*=5. Mean±SD.

Nominal concentration/mg·L^{-1}	Inter-day Measurement concentration/mg·L^{-1}	RSD/%	Intra-day Measurement concentration/mg·L^{-1}	RSD/%
20.00	18.66±0.56	3.0	18.22±0.74	4.1
5.00	4.72±0.15	3.2	4.64±0.30	6.5
1.25	1.17±0.06	5.1	1.16±0.07	6.0
0.31	0.28±0.01	3.6	0.30±0.02	6.7

Table 6. Precision of 5-Fu in mice tissues. *n*=5. Mean±SD.

Tissues	Inter-day RSD/%				Intra-day RSD/%			
	20.00 mg/L	5.00 mg/L	1.25 mg/L	0.31mg/L	20.00 mg/L	5.00 mg/L	1.25 mg/L	0.31 mg/L
Heart	2.9	3.4	4.4	3.9	4.3	6.4	5.9	6.8
Liver	3.1	3.2	4.2	3.3	4.0	6.2	6.3	6.7
Spleen	3.3	4.3	5.2	5.4	5.5	7.0	7.3	6.9
Lung	3.9	4.7	6.1	6.9	5.2	7.7	7.6	6.7
Kidney	4.0	4.8	5.8	6.2	5.8	8.4	8.3	7.0
Brain	2.9	3.3	4.2	4.7	4.1	8.2	8.4	7.0
Thymus	3.5	3.9	5.5	5.6	5.3	7.5	7.7	6.7
Lymph	3.1	4.4	6.3	6.5	5.5	7.2	7.9	6.9
Marrow	3.8	5.0	6.2	6.8	6.1	7.9	7.7	6.8

Table 7. Main pharmacokinetics parameters following iv 5-Fu-GCL (80, 40, 20 mg/kg) and free 5-Fu (40 mg/kg) in mice. *n*=6. Mean±SD. $^{c}P<0.01$ *vs* free 5- Fu (40 mg/kg).

Parameters	5-Fu-GCL 80 mg/kg	5-Fu-GCL 40 mg/kg	5-Fu-GCL 20 mg/kg	Free 5-Fu 40 mg/kg
$T_{1/2Ke}$/min	25.8±4.2	27.3±4.4^{c}	28.2±5.6	15.8±2.2
C_0/mg·L^{-1}	24.9±4.9	17.7±3.6^{c}	1.5±2.7	35.8±6.2
AUC/mg·min·L^{-1}	990.0±45. 2	622.5±38.3	340.4±25.6	639.0±35.9
Cl/L·min^{-1}	0.081±0.005	0.064±0.006	0.059±0.003	0.076±0.011
V/L	4.0±0.9	3.3±0.7	3.0±0.7	2.6±0.7

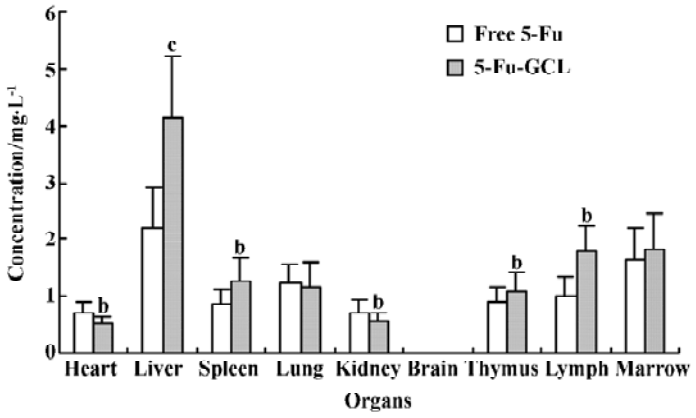

Figure 3. Concentration of 5-Fu in tissue samples collected at 20 min after a single dose of 5-Fu-GCL or free 5-Fu. *n*=10. Mean±SD. $^{b}P<0.05$, $^{c}P<0.01$ *vs* free 5-Fu in same tissue.

mg·min·kg^{-1}).

Discussion

In drug delivery[13], liposomes could congregate drugs in certain tissues, decrease poisonous effects and increase the curative effect. Lecithoid material is the primary liposome in common use.

As GC is a cerebroside containing galactose, liposomes made of GC also possess galactose. As a result, this kind of

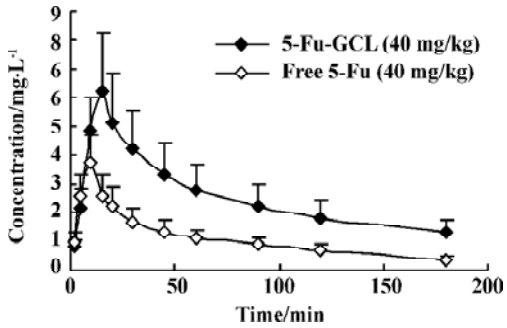

Figure 4. Liver concentration-time profile of 5-Fu after a single dose of 5-Fu-GCL or free 5-fluorouracil. n=6. Mean±SD.

liposome has a special bonding ability to salivary acid protein receptor located on the membrane of mammal[14,15]. Compared with lecithoid[16], GC has several advantages such as the stable chemical characters, the long retention in blood, the anti-oxide ability, and the unique directional trait. It could be developed to be a new kind of medicine carrier.

5-Fu is a dissoluble chemical with small molecules so it is difficult to achieve a highly enveloped rate. In a recent study, we applied combined calcium-induced fusion with reverse evaporation method to envelop 5-Fu, and the enveloped rate reached 52%.

Pharmacokinetic results showed that serum drug concentration curves of 5-Fu-GCL in single intravenous administration at 20, 40, and 80 mg/kg conformed to one compartment model of the first order absorption. Mean serum $T_{1/2Ke}$ of three dosage groups was similar. The pharmacokinetics of 5-Fu-GCL appeared to be linear over the doses. Both C_0 and AUC were enhanced as the dose increased. $T_{1/2Ke}$ of 5-Fu-GCL was much longer and the C_0 was strongly lower than those of free 5-Fu. All these results indicated that 5-Fu-GCL could be released much slower.

Because 5-Fu-GCL was injected through the vein and exhibited first order kinetic characteristics, it had no absorption or distribution phase and had only the elimination phase. For the study of tissue distribution one time point needed to be chosen. Tissue distribution results elucidated that the concentrations of 5-Fu-GCL in immune organs, especially in the liver, were remarkably higher than those of free 5-Fu with the same dose. Concentration-time course of 5-Fu-GCL in the liver showed that the AUC of 5-Fu-GCL was 3 times higher than that of free 5-Fu. This suggests that 5-Fu-GCL had a high selectivity to liver. In contrast, drug concentrations of 5-Fu-GCL in the heart and kidneys were significantly reduced, so we proposed that the toxicity of 5-Fu-GCL in the heart and kidneys were lower than that of free 5-Fu. Drug concentrations of both 5-Fu-GCL and free 5-Fu were not detected in the brain. The data indicate that they did not cross the blood brain barrier.

Previous studies showed that LD_{50} of 5-Fu-GCL was higher than that of free 5-Fu, indicating that toxicity of 5-Fu-GCL was lower than that of free 5-Fu. We, therefore conclude that 5-Fu-GCL could prospectively be used to develop a novel preparation for liver cancer therapy with long efficacy, low toxicity, and directional peculiarity.

References

1 Cao S, Rustum YM. Synergistic antitumor activity of irinotecan in combination with 5-fluorouracil in rats bearing advanced colorectal cancer: role of drug sequence and dose. Cancer Res 2000; 60: 3717–21.

2 Di Paolo A, Danesi R, Falcone A, Cionini L, Vannozzi F, Masi G, *et al*. Relationship between 5-fluorouracil disposition, toxicity and dihydropyrimidine dehydrogenase activity in cancer patients. Ann Oncol 2001; 12: 1301–6.

3 Schlemmer HP, Becker M, Bachert P, Dietz A, Rudat V, Vanselow B, *et al*. Alterations of intratumoral pharmacokinetics of 5-fluorouracil in head and neck carcinoma during simultaneous radiochemotherapy. Cancer Res 1999; 59: 2363–9.

4 Fraile RJ, Baker LH, Buroker TR, Horwitz J, Vaitkevicius VK. Pharmacokinetics of 5-fluorouracil administered orally, by rapid intravenous and by slow infusion. Cancer Res 1980; 40: 2223–8.

5 Hagiwara A, Sakakura C, Shirasu M, Yamasaki J, Togawa T, Takahashi T, *et al*. Therapeutic effects of 5-fluorouracil microspheres on peritoneal carcinomatosis induced by Colon 26 or B-16 melanoma in mice. Anticancer Drugs 1998; 9: 287–9.

6 Jing M, Xi S, Chen R. The inhibitory effect of tissue plasminogen activator combined with 5-fluorouracil polyphase liposome on the scar formation in experimental filtration surgery. Chin J Ophthalmol 1997; 33: 376–80. Chinese.

7 Wang G, Tucker IG, Roberts MS. *In vitro* and *in vivo* evaluation in rabbits of a controlled release 5-fluorouracil subconjunctival implants base on poly (*D*, *L*-lactide-co-glycoside). J Control Release 1996; 13: 1059–64.

8 Umejima H, Kikuchi A, Kim NS, Uchida T. Goto S. Preparation and evaluation of Eudragit gels. VIII. Rectal absorption of 5-fluorouracil from Eudispert hv gels in rats. J Pharm Sci 1995; 84: 199–202.

9 Kuan HY, Smith DE, Ensminger WD, Knol JA, De Remer SJ, Yang Z, *et al*. Regional pharmacokinetics of 5-fluorouracil in dogs: role of the liver, gastrointestinal tract, and lungs. Cancer Res 1998; 58: 1688–94.

10 Zhao MZ, Zhao YK, Zhu LY, Xu G, Wang S, Mi JB, *et al*. Pharmacokinetics and tissue distribution of iv injection of polyphase liposome-encapsulated cisplatin (KM-1) in rats. Acta Pharmacol Sin 2003; 24: 89–92.

11 Jung M, Berger G, Pohlen U, Pauser S, Reszka R, Buhr HJ. Simultaneous determination of 5-fluorouracil and its active metabolites in serum and tissue by HPLC. J Chromatogr B 1997; 702: 193–203.

12 Joulia JM, Pinguet F, Grosse PY, Astre C, Bressolle F. Determination of 5-fluorouracil and its main metabolites in plasma by high-performance liquid chromatography: application to a pharmacokinetic study. J Chromatogr B 1997; 692: 427–35.

13 Gregoriadis G. Engineering liposomes for drug delivery: progress and problems. Trends Biotechnol 1995; 13: 527–37.
14 Nishikawa M, Hirabayashi H, Takakura Y, Hashida M. Design for cell-specific targeting of proteins utilizing sugar-recognition mechanism: effect of molecular weight of proteins on targeting efficiency. Pharm Res 1995; 12: 209–14.
15 Murahashi N, Ishihara H, Sasaki A, Sakagami M, Hamana H. Hepatic accumulation of glutamic acid branched neogalactosyllipid modified liposomes. Biol Pharm Bull 1997; 20: 259–66.
16 Tsuji H, Osaka S, Kiwada H. Targeting of liposomes surface-modified with glycyrrhizin to the liver. I. Preparation and biological disposition. Chem Pharm Bull 1991; 39: 1004–8.

9th International Congress on Amino Acids and Proteins including brainprot

2005 Aug 8–12 Vienna, Austria

Please visit
http://www.iuphar.org/

Please contact
Robert Mostoegl
Department of Pediatrics, Medical University of Vienna
Währinger Gürtel 18–20
A 1090 Vienna, Austria
Fax +431 40400 3194
E-mail gert.lubec@meduniwien.ac.at

Acta Pharmacologica Sinica 2005 Mar; 26 (3): 257–258

Editorial

A new season of Chinese cardiovascular pharmacology research

Alex F CHEN[1,3], Ding-feng SU[2,3]

[1]*Department of Pharmacology and Toxicology, Michigan State University East Lansing, MI 48824-1317, USA;* [2]*Department of Pharmacology, Second Military Medical University, Shanghai 200433, China*

[3] Correspondence to Drs Alex F CHEN and Ding-feng SU.
Dr Alex F CHEN: Phn 1-517-432-2730. Fax 1-517-353-8915. E-mail chenal@msu.edu
Dr Ding-feng SU: Phn 86-21-2507-0323. Fax 86-21-6549-3951. E-mail dfsu@citiz.net

Received 2004-12-23
Accepted 2005-01-10

doi: 10.1111/j.1745-7254.2005.00060.x

In this issue of Acta Pharmacologica Sinica, we are proud to present to our readers and colleagues a series of review articles from several Chinese-American university laboratories in USA[1–6]. These reviews are a collection of the proceedings from the 8th Chinese Cardiovascular Pharmacology Conference held on July 23–26, 2004 in Urumchi, Xinjiang. As the first of its kind at any Chinese Pharmacological Society meeting, a half-day research symposium in English was held on the first day of this conference (an official meeting of the society held every three years for Chinese cardiovascular pharmacologists worldwide). The symposium was co-sponsored by the Cardiovascular Pharmacology Division of the Chinese Pharmacological Society and the Academy of Cardiovascular Research Excellence (ACRE), a non-profit academic organization in USA that includes many of prominent American faculties from mainland China in the field of cardiovascular research.

Like many other biomedical research areas in China, cardiovascular pharmacology research has experienced significant growth in recent years. The Cardiovascular Pharmacology Division is the largest division of the Chinese Pharmacological Society with the most registered members. Similarly, of all the original research articles published in Acta Pharmacologica Sinica, the premier pharmacology journal in China, the total number of cardiovascular pharmacology articles currently ranked first. An increasing number of cardiovascular pharmacology laboratories in China have recently begun to publish their original research findings in international journals, including some in the top-tier journals of cardiovascular research in the world[7,8]. More and more principal investigators have also developed research collaborations with a number of overseas laboratories. The aforementioned phenomena represent a promising trend towards a modernizing era of Chinese cardiovascular pharmacology in the early 21st century.

Despite the significant progress and growth, biomedical research in China still faces a number of major challenges as highlighted in two unprecedented "China voices" supplements recently published in Nature[9,10]. Among these problems, a major issue is a lack of impact in scientific publications. Although the total publications from China ranked the ninth in the world between the years 1997–2001, the citations per paper from China ranked only the nineteenth with a rate of 1.56 according to a most recent study based on the ISI Essential Science Indicators[11]. A prominent overseas Chinese-American scientist pointed out that as "measured by the number of original research papers published in internationally refereed high-impact journals", a productive scientist should have "published at least eight highly cited research papers in the past ten years … in a journal with an impact factor of at least two … and at least one should be published in a journal with an impact factor of five or above"[12]. If such a "not overly demanding standard"[12] would be used to judge research productivity, concrete efforts must be made by a majority of Chinese cardiovascular pharmacologists to meet it.

Chinese pharmacologists worldwide are eager and determined to make a significant contribution to the success of the 15th World Congress of Pharmacology (IUPHAR) to be hosted by the Chinese Pharmacological Society in Beijing on July 2–7, 2006. The primary authors of this review collection all grew up in China and now have all established their

independent research laboratories in several major universities across the United States. The research work they presented in these reviews spans from molecular cardiovascular biology to integrated physiology and pharmacology. As an internationally refereed pharmacology journal with increasing impact, Acta Pharmacologica Sinica would like to showcase the research of these overseas Chinese cardiovascular pharmacologists in this issue, and by doing so hopes to enhance not only the research exchange and collaboration between Chinese pharmacologists at home and overseas, but also the quality and impact of Chinese pharmacology research in the world.

References

1 Luo JD, Chen AF. Nitric oxide: a newly discovered function on wound healing. Acta Pharmacol Sin 2005; 26: 259–64.

2 Duan DY, Liu LL, Bozeat N, Huang ZM, Xiang SY, Wang GL, *et al*. Functional role of anion channels in cardiac diseases. Acta Pharmacol Sin 2005; 26: 265–78.

3 Ren J, Fang CX. Small guanine nucleotide-binding protein Rho and myocardial function. Acta Pharmacol Sin 2005; 26: 279–85.

4 Wang DH. The vanilloid receptor and hypertension. Acta Pharmacol Sin 2005; 26: 286–94.

5 Sun ZJ, Zhang ZE. Historic perspectives and recent advances in major animal models of hypertension. Acta Pharmacol Sin 2005; 26: 295–301.

6 Liao DF, Chen LL, Peng CY, Zhang J, Li K. Exo$^+$ proofreading polymerases mediate genetic analysis and its application in biomedical studies. Acta Pharmacol Sin 2005; 26: 302–6.

7 Wang GL, Wang XR, Lin MJ, He H, Lan XJ, Guan YY. Deficiency in ClC-3 chloride channels prevents rat aortic smooth muscle cell proliferation. Circ Res 2002; 91: E28–32.

8 Xu FP, Chen MS, Wang YZ, Yi Q, Lin SB, Chen AF, *et al*. Leptin induces hypertrophy via endothelin-1-reactive oxygen species pathway in cultured neonatal rat cardiomyocytes. Circulation 2004; 110: 1269–75.

9 Poo MM, Wu R, Chiew K, Chien L, Yang X, Wu CI, *et al*. China: views from the west. China voice I. Nature 2004; 428: 203–22.

10 China voice II. Nature 2004; 432 (Suppl): A5–55.

11 King DA. The scientific impact of nations. Nature 2004; 430: 311–6.

12 Wu R. Making an impact. Nature 2004; 428: 206–8.

Acta Pharmacologica Sinica 2005 Mar; 26 (3): 259–264

Invited review

Nitric oxide: a newly discovered function on wound healing

Jian-dong LUO[1,2], Alex F CHEN[1,3]

[1]*Departments of Pharmacology and Neurology and the Neuroscience Program, Michigan State University, East Lansing, MI 48824-1317, USA;*
[2]*Department of Pharmacology, Guangzhou Medical College, Guangzhou 510182, China*

Key words

angiogenesis; inflammation; nitric oxide; proliferation; wound healing

[3] Correspondence to Alex F CHEN.
Phn 1-517-432-2730.
Fax 1-517-353-8915.
E-mail chenal@msu.edu

Received 2004-08-14
Accepted 2004-12-14

doi: 10.1111/j.1745-7254.2005.00058.x

Abstract

Wound healing impairment represents a particularly challenging clinical problem to which no efficacious treatment regimens currently exist. The factors ensuring appropriate intercellular communication during wound repair are not completely understood. Although protein-type mediators are well-established players in this process, emerging evidence from both animal and human studies indicates that nitric oxide (NO) plays a key role in wound repair. The beneficial effects of NO on wound repair may be attributed to its functional influences on angiogenesis, inflammation, cell proliferation, matrix deposition, and remodeling. Recent findings from *in vitro* and *in vivo* studies of NO on wound repair are summarized in this review. The unveiled novel mechanisms support the use of NO-containing agents and/or NO synthase gene therapy as new therapeutic regimens for impaired wound healing.

Introduction

Wound repair is a well orchestrated and highly coordinated process that includes a series of overlapping phases: inflammation, cell proliferation, matrix deposition, and tissue remodeling. This involves a complex, dynamic series of events including clotting, inflammation, granulation tissue formation, epithelialization, neovascularization, collagen synthesis, and wound contraction[1]. Loss of a functional healing process could lead to severe disabilities. Accordingly, chronic, non-healing wound conditions represent a situation of major clinical importance. The series of pathological changes associated with several diseases ultimately leads to severely disturbed wound healing conditions[2]. Among those, the most prominent chronic wound impairments include decubitus or pressure ulcers, venous ulcers, and diabetic ulcers. The advent of molecular and cellular biology and the use of different modeling systems, most notably genetically engineered animals, have greatly extended our knowledge of wound repair. Inflammation, re-epithelialization, and granulation tissue formation are driven in part by a complex mixture of growth factors and cytokines, which are released coordinately into the wounds[1,2]. Besides these protein-type factors and mitogens, evidence is emerging for the important role of small diffusible molecules such as nitric oxide (NO) in wound repair[3]. In this review, we summarize the current knowledge of the modulating functions of NO on wound repair.

Chemistry and biosynthesis of nitric oxide

NO is a highly diffusible intercellular signaling molecule implicated in a wide range of biological effects. It is generated by the enzyme nitric oxide synthase (NOS), which catalyzes the conversion of *L*-arginine to *L*-citrulline[4]. Three NOS isoforms have been characterized, each encoded by different chromosomes. Two enzyme isoforms are constitutively expressed (endothelial and neuronal NOS), whereas one isoform is an inducible enzyme (iNOS), initially found in macrophages. All three NOS isoforms exist in their active form of homodimers of two domains: a C-terminal reductase domain, and an N-terminal oxygenase domain with molecular masses of approximately 135 kDa (eNOS), 150–160 kDa (nNOS), and 130 kDa (iNOS)[4]. The reductase domain contains binding sites for one molecule each of nicotinamide adenine dinucleotide phosphate (NADPH), flavin mononucleotide (FMN), and flavin dinucleotide (FAD), in close homology with cytochrome P-450 reductase, whereas the oxygen domain binds heme, the essential cofactor tetrahydrobiopterin (BH4), and the substrate *L*-arginine[4].

Between these two regions lies the calmodulin (CaM) binding site, which plays a key role in both the structure and function of the enzyme. The constitutive isoforms (eNOS and nNOS) are permanently active, generating low concentrations of NO (in nmol/L range). Their enzymatic activities are regulated by intracellular calcium fluxes or exogenous calmodulin. The expression, transcription, and function of the iNOS is induced by a variety of cytokines, growth factors, and inflammatory stimuli on target cells which lead to the release of much higher levels of NO (in μmol/L range), which is involved in host immune response.

All three NOS isoforms are expressed in skin tissue[3]. Expression of nNOS has been observed in keratinocytes and melanocytes; eNOS can be detected in keratinocytes of the basal epidermal layer, dermal fibroblasts, endothelial capillaries, and eccrine glands; and iNOS can be induced in keratinocytes, fibroblasts, Langerhans, and endothelial cells. Accordingly, NO participates in the regulation of skin homeostatic functions such as circulation, sunburn erythema, and maintenance of the protective barrier against microorganisms.

Nitric oxide and wound healing

L-Arginine, the substrate for NOS, was first noted to enhance wound healing in 1978[5]. Subsequently, dietary *L*-arginine intake has been shown to improve collagen deposition and wound strength in both animals and humans[6–8]. This effect of *L*-arginine may be due in part to its conversion to *L*-ornithine through the action of arginase, an enzyme that may compete with NOS for *L*-arginine and thereby help regulate NO production during wound healing[9]. However, the finding that *L*-arginine intake does not improve collagen deposition in iNOS-deficient mice to the same extent as in wild-type littermates implicates that part of *L*-arginine's effect involves NO directly[10].

Accumulating evidence indicates that NO plays a key role in normal wound repair (Figure 1)[11–18]. Production of nitrite (NO_2) and nitrate (NO_3), the stable NO metabolites, are elevated early in the fluid of subcutaneous wounds[11], and urinary nitrate excretion increases in a sustained manner after excisional wounding[12]. Furthermore, the presence of nitrite and nitrate is directly correlated with collagen deposition within the wound and in dermal fibroblasts, suggesting that NO synthesis is critical for wound collagen accumulation and acquisition of mechanical strength[11,13,14]. All three NOS isozymes are involved in the wound healing process. Both iNOS and nNOS mRNA and protein expression are increased in cutaneous wounds[15,16]. Our recent findings demonstrate that there is a significant increase of cutaneous eNOS protein expression as well as constitutive NOS enzymatic activity after excisional wounding in normal mice[17]. Consequently, an NO deficiency directly contributes to wound healing impairment. Inhibition of NOS by competitive inhibitors, either applied to the wound surface[18] or given systemically[11], decreases collagen deposition and breaking strength of incisional wounds and impairs the healing.

Consistent with these findings, studies with targeted disruption of NOS genes have revealed that the excisional wound closure is delayed by 30% in both eNOS and iNOS knockout mice compared to their wild-type littermates[19,20]. Conversely, adenoviral vector-mediated gene transfer of iNOS to the wound site of iNOS knockout mice completely reversed the delayed healing[20].

Finally, there are strong correlations between reduced cutaneous NO levels and impaired wound healing under disease conditions such as diabetes[11,14,17,21], malnutrition[13], and chronic steroid treatment[18]. Diabetic wound healing impairment is one of the most well-known chronic wound situations. Studies of ours and others demonstrate that cutaneous eNOS expression, constitutive NOS activity, and/or NO levels are significantly decreased in streptozotocin (STZ)-induced type 1 diabetic animals[11,14,17,21]. In fact, our findings indicate that the augmented cutaneous eNOS protein expression and constitutive NOS activity observed in normal animals in the healing process are absent in the type 1 diabetic mice[17]. These findings suggest that impairment of wound-induced endogenous NOS expression and NOS activity is responsible for reduced cutaneous NO bioavailability in type 1 diabetic animals (Figure 1). In agreement with the above notion, cutaneous gene therapy of eNOS or manganese superoxide dismutase (MnSOD) restored eNOS protein and NO levels and accelerated the wound healing rate in STZ-induced diabetic mice[17]. Similarly, the NO donor molsidomine (*N*-ethoxycarbomyl-3-morpholinyl-sidnonimine) or NO releasing poly (vinyl alcohol) hydrogel dressings are also shown to partially restore such healing impairment in STZ-induced diabetic rats[22,23]. Collectively, impairment of skin NO function represents an important factor for delayed wound healing in diabetes and strategies aimed at restoring cutaneous NO bioavailability with NO donors or NOS gene therapy may serve as effective means for diabetic wound healing.

Mechanisms of nitric oxide on wound healing

NO and angiogenesis Angiogenesis, the process of forming new microvessels, is an important component of normal

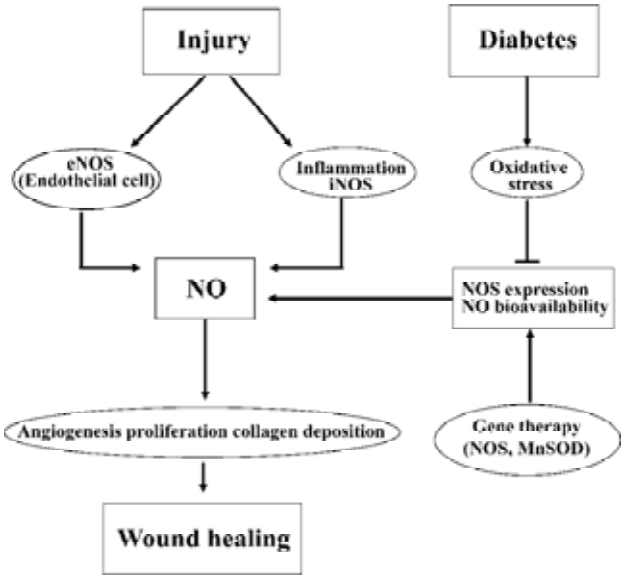

Figure 1. Nitric oxide (NO) as a signaling molecule accelerates wound healing. Abbreviations: eNOS, endothelial nitric oxide synthase; iNOS, inducible nitric oxide synthase; MnSOD, manganese superoxide dismutase; VEGF, vascular endothelium growth factor.

wound repair. NO plays a central role in this process[24] as it increases angiogenesis in ischemic murine tissues[25]. Conversely, NOS inhibitors impair angiogenesis in granulation tissue during gastric ulcer healing[26] and suppress capillary organization *in vitro*[27].

NO is also vital to the activity of pro-angiogenic cytokines. Vascular endothelial growth factor (VEGF) is a potent angiogenic factor which involves the modulation of NO generation[28]. VEGF increases NO production via upregulation of eNOS[29,30]. Conversely, the angiogenic effect of VEGF also depends on NO as pharmacological blockade of NOS prevent both VEGF-induced endothelial cell proliferation and mitogen-activated protein (MAP) kinase[31]. VEGF-stimulated endothelial cell migration, decreased adhesion, and organization are also dependent on NO[32,33]. Keratinocytes are the major source of VEGF expression upon cytokine stimulation[34], which is blocked by iNOS inhibitors both *in vitro* and *in vivo*[35]. NO has also been shown to downregulate protein kinase C (PKC)-induced VEGF expression in smooth muscle cells by interfering with the binding of AP-1[36] and to participate in the conversion of VEGF from an inert to an angiogenic form[37]. Interestingly, NO is also involved in VEGF-independent angiogenesis mechanisms. Evidence includes the role of NO in monocyte-induced angiogenesis induced by monocytes[38], substance P[39], and transforming growth factor (TGF)-β1[40]. Taken together, these studies suggest a vital role of NO in post-wound angiogenesis.

NO and inflammation NO has been shown to modulate chemoattractant cytokines that initiate post-wound inflammation, including interleukin (IL)-8[41], TGF-β1[42], monocytes, and neutrophils[43] that contribute to wound chemoattraction. Once monocytes and neutrophils are attracted to the site of a wound, they are activated and begin to produce TNF-α and IL-1, both of which are implicated in wound healing[33]. Because IL-1 is a potent chemoattractant for keratinocytes, the modulation of IL-1 by NO may usher keratinocyte recruitment, proliferation, and differentiation. Taken together, NO modulation of inflammation-associated cytokines may affect the inflammatory phase of wound healing.

NO and cell proliferation, differentiation, and apoptosis NO affects proliferation, differentiation, and apoptosis in a number of cell types involved in wound healing. The iNOS inhibitor N^{ω}-imino ethyl *L*-lysine (*L*-NIL) has been found to decrease proliferation in keratinocytes at the wound edge[44]. Indeed, treatment of murine wounds with *L*-NIL leads to delayed re-epithelialization with atrophied hyperproliferative epithelium seen at the wound edge[45]. Conversely, the NO donor sodium nitroprusside (SNP) significantly increases fetal bovine serum-induced thymidine incorporation into the DNA of human dermal fibroblasts and enhances fibroblast growth factor- or platelet-drived growth factor-induced DNA synthesis[46]. Furthermore, low levels of NO increase keratinocyte proliferation *in vitro*[44], an effect that is mimicked by 8-bromo-cGMP[33], an analog of NO second messenger cGMP. NO also modulates keratinocyte apoptosis induced by irradiation of keratinocytes with ultraviolet B light as addition of NOS inhibitors to irradiated keratinocytes increases apoptosis, an effect that is reversed by the NO donor *S*-nitroso-penicillamine[47]. It appears that both inducible and constitutive NOS are involved in this process. Furthermore, NO has been shown to stimulate the proliferation of endothelial cells, protect endothelial cells from apoptosis, and mediate VEGF production[34]. These effects of NO on endothelial cells may also be related to another facet of wound healing, namely angiogenesis. In contrast, NO may also affect fibroblast proliferation. For instance, NO donor SNAP has been reported to decrease the proliferation of normal dermal fibroblasts in rats[48] while increase their proliferation in mice[49], even though the reasons for such discrepancy are not clear. Altogether, the above studies suggest that NO affect the proliferative phase of wound healing.

NO and matrix deposition and remodeling The final phases of healing require increased collagen synthesis and

deposition, and a link between NO and collagen deposition has been described[11]. In most studies, treatment with NO donors, dietary *L*-arginine, or iNOS overexpression via gene therapy increased the collagen content of experimental wounds[10,11,50,51]. Indeed, treatment with a NO donor has been shown to increase collagen formation in fibroblasts derived from both normal and wound skin, which was decreased following NOS inhibition[51]. The effect of NO may primarily be due to the posttranslational enhancement of collagen synthesis rather than *de novo* transcription of the relevant collagen genes[51].

Mechanisms of wound nitric oxide dysfunction

Although impaired NO function contributes to delayed wound healing in diabetes, the mechanisms of cutaneous NO dysfunction in this setting is unclear. In diabetes, causative factors for hyperglycemia-induced organ damage include the activation of the polyol pathway, nonenzymatic glycation, activation of PKC pathway, and increased hexosamine pathway flux[52]. However, previously there was no apparent common element linking these mechanisms. Recent studies suggest that these different mechanisms may be linked by a single cellular process: an overproduction of superoxide induced by sustained hyperglycemia[53]. Sustained hyperglycemia is known to increase vascular superoxide levels, resulting in cardiovascular dysfunction[54]. Superoxide produced in the vasculature rapidly inactivates NO and thus reduces its bioavailability in diabetic vasculature[55]. Independent strategies aimed at reducing superoxide levels have been shown to prevent high glucose-induced PKC activation, formation of advanced glycation end-products (AGEs), sorbitol accumulation, and NFκB activation, resulting in improvement of endothelium-dependent NO-mediated vasodilation[53,54]. These results indicate that increased superoxide levels are a key factor in vascular NO dysfunction in diabetes. However, whether sustained hyperglycemia increases cutaneous O_2^- levels and the mechanisms by which cutaneous NO levels are decreased in diabetes is unknown. Our recent studies demonstrate that glucose concentration-dependently increases superoxide levels in normal mouse skin and there is a marked increase of cutaneous superoxide levels in streptozotocin-induced type 1 diabetic mice[17]. Furthermore, cutaneous gene therapy of MnSOD significantly reduced superoxide and increased NO levels, resulting in accelerated wound healing in this model. These results provide the direct evidence that increased cutaneous superoxide contributes to reduced NO bioavailability and wound healing impairment in diabetes (Figure 2).

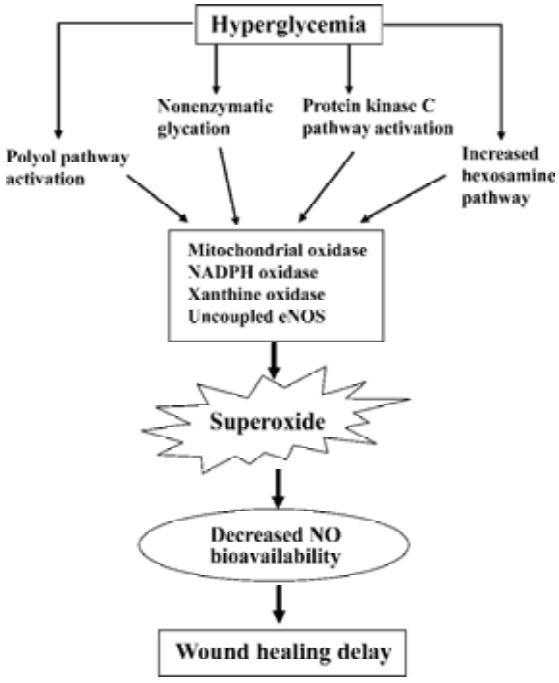

Figure 2. The proposed mechanism by which superoxide contributes to decreased NO bioavailability and wound healing impairment in diabetes.

Future directions

Although a central role for several protein-type growth factors and mitogens on wound repair has been well-established for many years, the application of these factors in the treatment of wound healing has not provided a breakthrough in the clinical arena[1,2]. One possible reason for the failure of markedly accelerating closure of chronic wounds may be due to increased protease activities in the wound fluids, which may impair the ability of endogenous and exogenously applied growth factor proteins to stimulate healing. In contrast, NO may represent a novel target molecule to circumvent these difficulties. Because NO is a short-lived gas molecule, maintaining an effective level of NO at the wound site is an obvious problem for clinical therapy. In recent studies we have demonstrated that gene therapy of NOS or SOD is effective in restoring cutaneous NO levels and accelerating wound healing in diabetic mice[17]. Gene therapy strategies aimed at increasing NO or reducing superoxide levels may represent an effective means of reversing cutaneous NO deficiency at the wound site for healing refractory wounds in diabetes and other diseases. Future preclinical studies are warranted to optimize the designs and regimens before clinical trails can be conducted and the ultimate translation of basic science to the clinical settings for human gene therapy.

Acknowledgements

This work was supported in part by the Juvenile Diabetes Research Foundation (JDRF) Innovative Grant 5-2001-311, American Diabetes Association (ADA) Regular Research Award 7-01-RA-10, American Heart Association (AHA) Grants 9806347X, 0130537Z and 0455594Z, and the Intramural Research Grants Program (IRGP) grant #41140 of the Michigan State University (all to Dr Alex F CHEN).

References

1 Singer AJ, Clark RA. Cutaneous wound healing. N Engl J Med 1999; 341: 738–46.
2 Bello YM, Phillips TJ. Recent advances in wound healing. JAMA 2000; 283: 716–8.
3 Frank S, Kampfer H, Wetzler C, Pfeilschifter J. Nitric oxide drives skin repair: novel functions of an established mediator. Kidney Int 2002; 61: 882–8.
4 Griffith OW, Stuehr DJ. Nitric oxide synthases: properties and catalytic mechanism. Annu Rev Physiol 1995; 57: 707–36.
5 Seifter E, Rettura G, Barbul A, Levenson SM. Arginine: an essential amino acid for injured rats. Surgery 1978; 84: 224–30.
6 Barbul A, Lazarou SA, Efron DT, Wasserkrug HL, Efron G. Arginine enhances wound healing and lymphocyte immune responses in humans. Surgery 1990; 108: 331–6.
7 Kirk SJ, Hurson M, Regan MC, Holt DR, Wasserkrug HL, Barbul A. Arginine stimulates wound healing and immune function in elderly human beings. Surgery 1993; 114: 155–9.
8 Arbss MA, Ferrando JM, Vidal J, Quiles MT, Huguet P, Castells J, *et al*. Early effects of exogenous arginine after the implantation of prosthetic material into the rat abdominal wall. Life Sci 2000; 67: 2493–512.
9 Albina JE, Mills CD, Henry WL Jr, Caldwell MD. Temporal expression of different pathways of *L*-arginine metabolism in healing wounds. J Immunol 1990; 144: 3877–80.
10 Shi HP, Efron DT, Most D, Tantry US, Barbul A. Supplemental dietary arginine enhances wound healing in normal but not inducible nitric oxide synthase knockout mice. Surgery 2000; 128: 374–8.
11 Schaffer MR, Tantry U, Gross SS, Wasserburg HL, Barbul A. Nitric oxide regulates wound healing. J Surg Res 1996; 63: 237–40.
12 Smith DJ, Dunphy MJ, Strag LN, Marletta MA. The influence of wound healing on urinary nitrate levels in rats. Wounds 1991; 3: 50–8.
13 Schaffer MR, Tantry U, Ahrendt GM, Wasserburg HL, Barbul A. Acute protein-calorie malnutrition impairs wound healing: a possible role of decreased wound nitric oxide synthesis. J Am Coll Surg 1997; 184: 37–43.
14 Schaffer MR, Tantry U, Efron PA, Ahrendt GM, Thornton FJ, Barbul A. Diabetes-impaired healing and reduced wound nitric oxide synthesis: a possible pathophysiologic correlation. Surgery 1997; 121: 513–9.
15 Frank S, Madlener M, Pfeilschifter J, Werner S. Induction of inducible nitric oxide synthase and its corresponding tetrahydrobiopterin-cofactor-synthesizing enzyme GTP-cyclohydrolase I during cutaneous wound repair. J Invest Dermatol 1998; 111: 1058–64.
16 Boissel JP, Ohly D, Bros M, Godtel-Armbrust U, Forstermann U, Frank S. The neuronal nitric oxide synthase is upregulated in mouse skin repair and in response to epidermal growth factor in human HaCaT keratinocytes. J Invest Dermatol 2004; 123: 132–9.
17 Luo JD, Wang YY, Fu W, Wu J, Chen AF. Gene therapy of eNOS and MnSOD restores delayed wound healing in type 1 diabetic mice. Circulation 2004; 110: 2484–93.
18 Bulgrin JP, Shabani M, Chakravarthy D, Smith DJ. Nitric oxide synthesis is suppressed in steroid-impaired and diabetic wounds. Wounds 1995; 7: 48–57.
19 Lee PC, Salyapongse AN, Bragdon GA, Shears LL, Watkins SC, Edington HDJ, *et al*. Impaired wound healing and angiogenesis in eNOS-deficient mice. Am J Physiol 1999; 277: H1600–8.
20 Yamasaki K, Edington HDJ, McClosky C, Tzeng E, Lizonova A, Kovesdi I, *et al*. Reversal of impaired wound repair in iNOS-deficient mice by topical adenoviral-mediated iNOS gene transfer. J Clin Invest 1998; 101: 967–71.
21 Stallmeyer B, Anhold M, Wetzler C, Kahlina K, Pfeilschifter J, Frank S. Regulation of eNOS in normal and diabetes-impaired skin repair: implications for tissue regeneration. Nitric Oxide 2002; 6: 168–77.
22 Witte MB, Kiyama T, Barbul A. Nitric oxide enhances experimental wound healing in diabetes. Br J Surg 2002; 89: 1594–601.
23 Masters KS, Leibovich SJ, Belem P, West JL, Poole-Warren LA. Effects of nitric oxide releasing poly(vinyl alcohol) hydrogel dressings on dermal wound healing in diabetic mice. Wound Repair Regen 2002; 10: 286–94.
24 Donnini S, Ziche M. Constitutive and inducible nitric oxide synthase: role in angiogenesis. Antioxid Redox Signal 2002; 4: 817–23.
25 Murohara T, Asahara T, Silver M, Bauters C, Masuda H, Kalka C, *et al*. Nitric oxide synthase modulates angiogenesis in response to tissue ischemia. J Clin Invest 1998; 101: 2567–78.
26 Konturek SJ, Brzozowski T, Majka J, Pytko-Polonczyk J, Stachura J. Inhibition of nitric oxide synthase delays healing of chronic gastric ulcers. Eur J Pharmacol 1993; 239: 215–7.
27 Papapetropoulos A, Garcia-Cardena G, Madri JA, Sessa WC. Nitric oxide production contributes to the angiogenic properties of vascular endothelial growth factor in human endothelial cells. J Clin Invest 1997; 100: 3131–9.
28 Zhang R, Wang L, Zhang L, Chen J, Zhu Z, Zhang Z, *et al*. Nitric oxide enhances angiogenesis via the synthesis of vascular endothelial growth factor and cGMP after stroke in the rat. Circ Res 2003; 92: 308–13.
29 Hood JD, Meininger CJ, Ziche M, Granger HJ. VEGF upregulates ecNOS message, protein, and NO production in human endothelial cells. Am J Physiol 1998; 274: H1054–8.
30 Gelinas DS, Bernatchez PN, Rollin S, Bazan NG, Sirois MG. Immediate and delayed VEGF-mediated NO synthesis in endothelial cells: role of PI3K, PKC and PLC pathways. Br J Pharmacol 2002; 137: 1021–30.
31 Ziche M, Morbidelli L, Choudhuri R, Zhang HT, Donnini S, Granger HJ, *et al*. Nitric oxide synthase lies downstream from vascular endothelial growth factor-induced but not basic fibroblast growth factor-induced angiogenesis. J Clin Invest 1997; 99: 2625–34.
32 Morbidelli L, Chang CH, Douglas JG, Granger HJ, Ledda F, Ziche M. Nitric oxide mediates mitogenic effect of VEGF on coronary venular endothelium. Am J Physiol 1996; 270: H411–5.

33 Schwentker A, Vodovotz Y, Weller R, Billiar TR. Nitric oxide and wound repair: role of cytokines? Nitric Oxide 2002; 7: 1–10.
34 Frank S, Kampfer H, Wetzler C, Pfeilschifter J. Nitric oxide drives skin repair: novel functions of an established mediator. Kidney Int 2002; 61: 882–8.
35 Frank S, Stallmeyer B, Kampfer H, Kolb N, Pfeilschifter J. Nitric oxide triggers enhanced induction of vascular endothelial growth factor expression in cultured keratinocytes (HaCaT) and during cutaneous wound repair. FASEB J 1999; 13: 2002–14.
36 Tsurumi Y, Murohara T, Krasinski K, Chen D, Witzenbichler B, Kearney M, *et al.* Reciprocal relation between VEGF and NO in the regulation of endothelial integrity. Nat Med 1997; 3: 879–86.
37 Xiong M, Elson G, Legarda D, Leibovich SJ. Production of vascular endothelial growth factor by murine macrophages: regulation by hypoxia, lactate, and the inducible nitric oxide synthase pathway. Am J Pathol 1998; 153: 587–98.
38 Leibovich SJ, Polverini PJ, Fong TW, Harlow LA, Koch AE. Production of angiogenic activity by human monocytes requires an *L*-arginine/nitric oxide-synthase-dependent effector mechanism. Proc Natl Acad Sci USA 1994; 91: 4190–4.
39 Ziche M, Morbidelli L, Masini E, Amerini S, Granger HJ, Maggi CA, *et al.* Nitric oxide mediates angiogenesis *in vivo* and endothelial cell growth and migration *in vitro* promoted by substance P. J Clin Invest 1994; 94: 2036–44.
40 Roberts AB, Sporn MB, Assoian RK, Smith JM, Roche NS, Wakefield LM, *et al.* Transforming growth factor type beta: rapid induction of fibrosis and angiogenesis *in vivo* and stimulation of collagen formation *in vitro*. Proc Natl Acad Sci USA 1986; 83: 4167–71.
41 Andrew PJ, Harant H, Lindley IJ. Nitric oxide regulates IL-8 expression in melanoma cells at the transcriptional level. Biochem Biophys Res Commun 1995; 214: 949–56.
42 Malik AA, Radhakrishnan N, Reddy K, Smith AD, Singhal PC. Tubular cell-*Escherichia coli* interaction products modulate migration of monocytes through generation of transforming growth factor-beta and macrophage-monocyte chemoattractant protein-1. J Endourol 2002; 16: 599–603.
43 Belenky SN, Robbins RA, Rubinstein I. Nitric oxide synthase inhibitors attenuate human monocyte chemotaxis *in vitro*. J Leukoc Biol 1993; 53: 498–503.
44 Stallmeyer B, Kampfer H, Kolb N, Pfeilschifter J, Frank S. The function of nitric oxide in wound repair: inhibition of inducible nitric oxide-synthase severely impairs wound reepithelialization. J Invest Dermatol 1999; 113: 1090–8.
45 Opal SM, DePalo VA. Anti-inflammatory cytokines. Chest 2000; 117: 1162–72.
46 Dhaunsi GS, Ozand PT. Nitric oxide promotes mitogen-induced DNA synthesis in human dermal fibroblasts through cGMP. Clin Exp Pharmacol Physiol 2004; 31: 46–9.
47 Seo SJ, Choi HG, Chung HJ, Hong CK. Time course of expression of mRNA of inducible nitric oxide synthase and generation of nitric oxide by ultraviolet B in keratinocyte cell lines. Br J Dermatol 2002; 147: 655–62.
48 Witte MB, Thornton FJ, Efron DT, Barbul A. Enhancement of fibroblast collagen synthesis by nitric oxide. Nitric Oxide 2000; 4: 572–82.
49 Schwentker A, Billiar TR. Inducible nitric oxide synthase: from cloning to therapeutic applications. World J Surg 2002; 26: 772–8.
50 Thornton FJ, Schaffer MR, Witte MB, Moldawer LL, MacKay SL, Abouhamze A, *et al.* Enhanced collagen accumulation following direct transfection of the inducible nitric oxide synthase gene in cutaneous wounds. Biochem Biophys Res Commun 1998; 246: 654–9.
51 Schaffer MR, Efron PA, Thornton FJ, Klingel K, Gross SS, Barbul A. Nitric oxide, an autocrine regulator of wound fibroblast synthetic function. J Immunol 1997; 158: 2375–81.
52 Brownlee M. Biochemistry and molecular cell biology of diabetic complications. Nature 2001; 414: 813–20.
53 Nishikawa T, Edelstein D, Du XL, Yamagishi S, Matsumura T, Kaneda Y, *et al.* Normalizing mitochondrial superoxide production blocks three pathways of hyperglycaemia damage. Nature 2000; 404: 787–90.
54 Kim YK, Lee MS, Son SM, Kim IJ, Lee WS, Rhim BY, *et al.* Vascular NADH oxidase is involved in impaired endothelium-dependent vasodilation in OLETF rats, a model of type 2 diabetes. Diabetes 2002; 51: 522–7.
55 Hink U, Li H, Mollnau H, Oelze M, Matheis E, Hartmann M, *et al.* Mechanisms underlying endothelial dysfunction in diabetes mellitus. Circ Res 2001; 88: E14–22.

Acta Pharmacologica Sinica 2005 Mar; 26 (3): 265–278

Blackwell Publishing

Invited review

Functional role of anion channels in cardiac diseases[1]

Da-yue DUAN[2], Luis LH LIU, Nathan BOZEAT, Z Maggie HUANG, Sunny Y XIANG, Guan-lei WANG, Linda YE, Joseph R HUME

Center of Biomedical Research Excellence, Department of Pharmacology, School of Medicine, University of Nevada, Reno, Nevada 89557-0270, USA

Key words

anion channel; cardiovascular system; physiology; heart disease; blood pressure

[1] Supported by National Center for Research Resources (NCRR) P-20 RR-15581 and National Heart, Lung, and Blood Institute Grant (HL63914).

[2] Correspondence to Da-yue DUAN, MD, PhD, FAHA.
Phn 1-775-784-4738.
Fax 1-775-784-1620.
E-mail dduan@med.unr.edu

Received 2004-12-22
Accepted 2005-01-11

doi: 10.1111/j.1745-7254.2005.00061.x

Abstract

In comparison to cation (K^+, Na^+, and Ca^{2+}) channels, much less is currently known about the functional role of anion (Cl^-) channels in cardiovascular physiology and pathophysiology. Over the past 15 years, various types of Cl^- currents have been recorded in cardiac cells from different species including humans. All cardiac Cl^- channels described to date may be encoded by five different Cl^- channel genes: the PKA- and PKC-activated cystic fibrosis tansmembrane conductance regulator (*CFTR*), the volume-regulated *ClC-2* and *ClC-3*, and the Ca^{2+}-activated *CLCA* or *Bestrophin*. Recent studies using multiple approaches to examine the functional role of Cl^- channels in the context of health and disease have demonstrated that Cl^- channels might contribute to: 1) arrhythmogenesis in myocardial injury; 2) cardiac ischemic preconditioning; and 3) the adaptive remodeling of the heart during myocardial hypertrophy and heart failure. Therefore, anion channels represent very attractive novel targets for therapeutic approaches to the treatment of heart diseases. Recent evidence suggests that Cl^- channels, like cation channels, might function as a multiprotein complex or functional module. In the post-genome era, the emergence of functional proteomics has necessitated a new paradigm shift to the structural and functional assessment of integrated Cl^- channel multiprotein complexes in the heart, which could provide new insight into our understanding of the underlying mechanisms responsible for heart disease and protection.

Introduction

Abnormalities of cardiac ion channels have been linked to a variety of inherited and acquired cardiac diseases including myocardial ischemia, hypertrophy, heart failure, and arrhythmias[1–5]. In addition, ion channels may also be mediators of the cardioprotective effects of ischemic preconditioning (IPC)[6,7]. While cation (K^+, Na^+, and Ca^{2+}) channels have received the most attention in the past four decades, the role of anion channels in the cardiovascular system has been largely ignored. Within the last 15 years, a re-surgence of interest in Cl^- channels in the cardiovascular system has led to the discovery of at least seven different types of Cl^- currents in cardiac cells from different regions of the heart and in different species[8]. Intensive efforts have been given to characterize the properties of these anion channels at the cellular and molecular levels. More details about the biophysical, pharmacological, and molecular properties of Cl^- channels in the heart can be found in several recent excellent review articles[8–11]. It has also been demonstrated in recent studies that Cl^- channels may be involved in the regulation of a large repertoire of cellular functions, including cellular excitability, cell volume homeostasis, intracellular organelles acidification, cell migration, proliferation and differentiation, and apoptosis[8,9,12]. With the recent identification of molecular entities responsible for cardiac Cl^- channels[8] and the genes mapped to specific human chromosomal locations[13], gene targeting and transgenic techniques have been used to delineate the functional role of Cl^- channels in the context of health and disease. It has been reported that Cl^- channels could contribute to: 1) arrhythmogenesis in myo-

cardial injury; 2) the adaptive remodeling of the heart during myocardial hypertrophy and heart failure; and 3) IPC. Therefore, anion channels represent very attractive novel targets for therapeutic approaches to the treatment of heart diseases. In this review, we will briefly summarize the major findings and recent advances in the study of functional role of anion channels in the heart.

Anion channels in the heart

Since the independent discovery of a cAMP-activated Cl^- current in the guinea pig heart by Bainski *et al*, Harvey and Hume in 1989[14,15], intensive efforts have been made to characterize Cl^- channels in the cardiovascular system at both the cellular and molecular levels. These have been

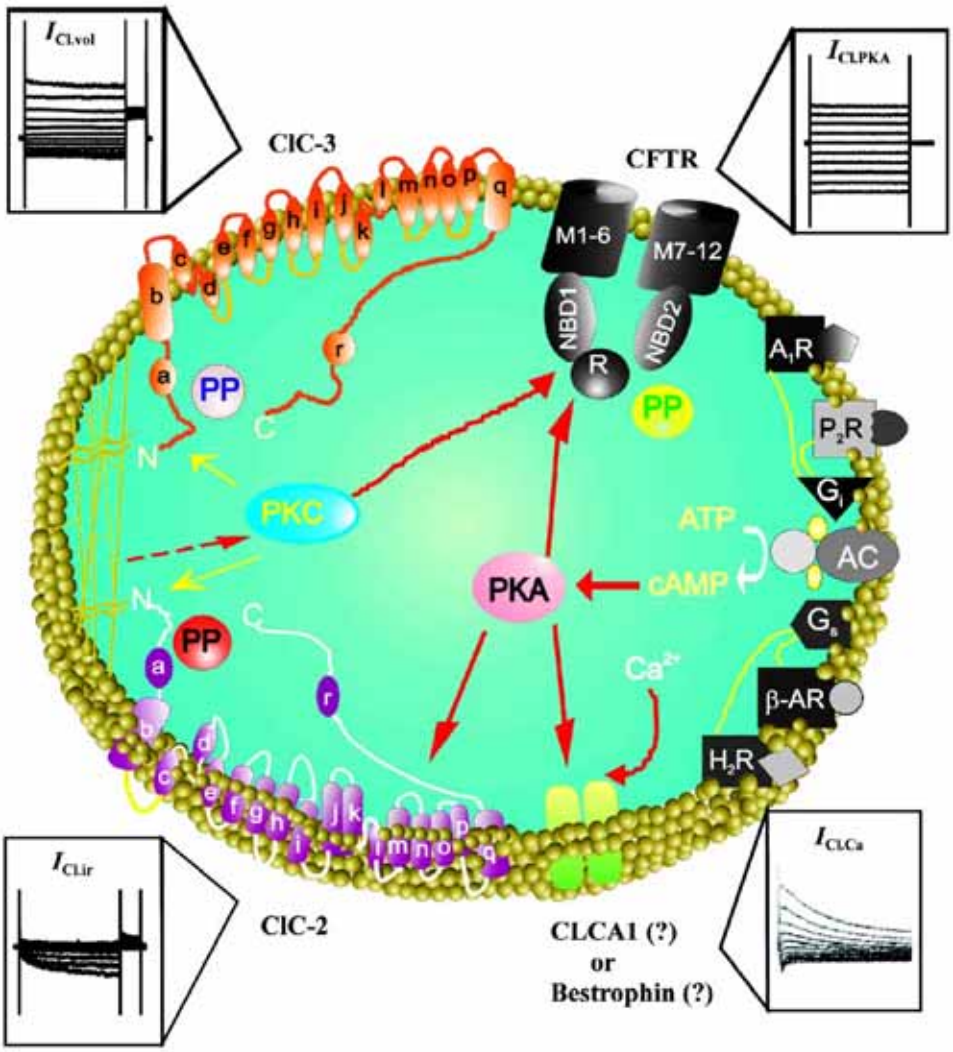

Figure 1. Schematic representation of anion channels in cardiac myocytes. Anion channels and their corresponding molecular entities or candidates are indicated in parentheses. I_{CLPKA}, Cl^- current regulated by adenylyl cyclasecAMP-protein kinase A pathway; CFTR, cystic fibrosis transmembrane conductance regulator; M1–6, CFTR transmembrane spanning segments 1–6; M7–12, CFTR transmembrane spanning segments 7–12; NBD1, nucleotide binding domain 1; NBD1, nucleotide binding domain 2; R, regulatory subunit; P, phosphorylation sites for protein kinase A (PKA) and protein kinase C (PKC); PP, serine-threonine protein phosphatases; Gi, heterodimeric inhibitory G protein; A_1R, adenosine type I receptor; M_2R, muscarinic type II receptor; AC, adenylyl cyclase; H_2R, histamine type II receptor; Gs, heterodimeric stimulatory G protein; β-AR, β-adrenergic receptor; P_2R, purinergic type 2 receptor; I_{Clvol}, Cl^- current regulated by cell volume; ClC-3, member of voltage-gated ClC Cl^- channel family; $I_{Cl\,Ca}$, Cl^- current regulated by intracellular Ca^{2+} concentration ($[Ca^{2+}]_i$); CLCA1, member of a Ca^{2+}-sensitive Cl^- channel family (CLCA); *Bestrophin*: the *Bestrophin* gene family; I_{Clir}, inward rectifying Cl^- current; ClC-2, member of voltage-gated ClC Cl^- channel family. Membrane topology models (α-helices A-X) for ClC-2 and ClC-3 are modified from Dutzler *et al*[125].

recently reviewed and thoroughly described elsewhere[8–11] and will not be repeated in this review. Briefly, at the molecular level, all cardiac Cl^- channels described so far may fall into the following Cl^- channel gene families (Figure 1): 1) the cystic fibrosis transmembrane conductance regulator (CFTR), which is a member of the adenosine triphosphate-binding cassette (ABC) superfamily and may be responsible for the Cl^- currents activated by protein kinase A (PKA) (I_{ClPKA})[14–16], protein kinase C (PKC) (I_{ClPKC})[17,18], and extracellular ATP (I_{CLATP}) in the heart[19–21]; 2) ClC voltage-gated Cl^- channel superfamily: a) *ClC-2*, which is responsible for the hyperpolarization- and cell swelling-activated inwardly rectifying Cl^-current (I_{Clir})[22–24]; b) *ClC-3*, which is responsible for the volume regulated outwardly rectifying Cl^- current (I_{Clvol}), including the basally-activated (I_{Clb})[25] and swelling-activated ($I_{Clswell}$) components[25–34]; 3) *CLCA-1*, which was thought to be responsible for the Ca^{2+}-activated Cl^- current (I_{ClCa})[35–38]; and 4) *Bestrophin*, a new candidate for I_{ClCa}[39–42]. Further studies on the molecular and functional properties of these Cl^- channel genes are necessary to define the structure of the channel proteins and to elucidate the physiological and clinical significance of these channels.

Functional role of Cl^- channels in cardiac diseases

Theoretically, Cl^- channels could be involved in the regulation of cellular excitability, cell volume homeostasis, intracellular organelles acidification, cell proliferation and differentiation, and apoptosis[12]. Thus, they may have important physiological and pathological significance in cardiac function under normal and pathological (hypoxia, ischemia, myocardial infarction, hypertrophy, and heart failure) conditions. Mutations in several Cl^- channels have been known to result in human inherited diseases[13]. But the exact role of Cl^- channels in human cardiovascular physiology and pathophysiology is still unclear[8]. The ability to examine the exact role of Cl^- channels in human cardiovascular physiology and pathology has been hampered by the lack of specific pharmacological and molecular tools. With the recent identification of the molecular entities responsible for Cl^- channels in the heart[8] and the genes mapped to specific human chromosomal locations[13], it is now possible to overcome these obstacles by use of gene targeting and transgenic animals. We have been using a multitude of approaches from traditional methodologies including biophysics, biochemistry, electrophysiology, and pharmacology to state-of-the-art technologies including telemetry system, echocardiography, genomics, and proteomics to effectively and accurately define the role of each Cl^- channel in heart function in the context of health and disease.

Functional role in electrophysiology and arrhythmogenesis

Estimates of intracellular Cl^- activity (a^i_{Cl}) in cardiac myocytes from ion-selective microelectrode studies indicate the equilibrium potential for Cl^- (E_{Cl}) be more positive than the resting membrane potential under normal physiological conditions with an extracellular Cl^- concentration ($[Cl^-]_o$) of 145 mmol/L and an intracellular Cl^- concentration ($[Cl^-]_i$) of 10 to 20 mmol/L[43–46]. Because the E_{Cl} is within a membrane potential range (usually –65 to –40 mV) that can be either negative or positive to the actual membrane potential during the normal cardiac cycle, activation of cardiac Cl^- channels can generate both inward and outward currents (Figure 2). Thus, compared with cationic channels, Cl^- channels have the unique ability to cause both depolarization as well as repolarization during the action potential and produce significant effects on cardiac pacemaker activity and action potential characteristics.

The degree to which activation of Cl^- currents depolarizes the resting membrane or accelerates the repolarization of action potential depends critically on the actual value of E_{Cl} and the magnitude of the Cl^- conductance relative to the total membrane conductance. Under physiological conditions the transmembrane Cl^- gradient is asymmetrical. Thus, the activation of CFTR and ClC-3 Cl^- channels in the heart will result in outwardly rectifying currents. This will have more significant effects at positive potentials to accelerate repolarization and shortening of the action potential duration compared with smaller depolarizing effects at negative potentials near the resting membrane potential (Figure 2). The ability of Cl^- current activation to depolarize cardiac cells is also opposed by the presence of a large background K^+ conductance that normally controls the resting membrane potential. Both abbreviation of APD and depolarization of E_m upon activation of Cl^- channels may play a role in rhythm disturbance and likely contribute to arrhythmogenesis under pathological conditions.

CFTR and arrythmogenesis CFTR channels are closed under basal conditions but can be open under conditions where intracellular PKA- and PKC-dependent phosphorylation activity is increased. A major physiological role of activation of CFTR channels may be to minimize (oppose) the significant action potential prolongation associated with β-adrenergic stimulation of I_{Ca}. This is expected to contribute to action potential shortening during strong adrenergic stimu-

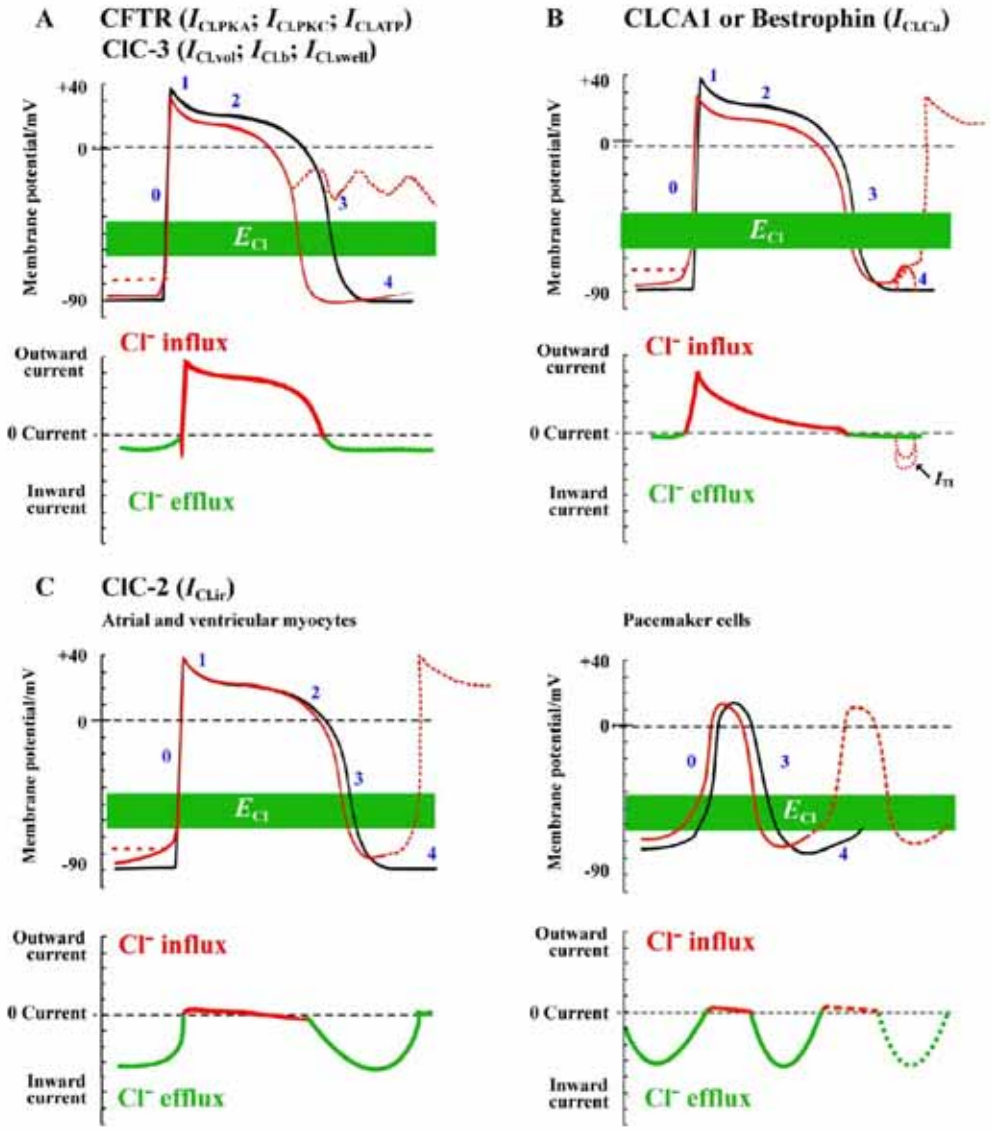

Figure 2. Modulation of cardiac electrical activity by sarcolemmal anion channels in cardiac myocytes. Changes in action potentials (top) and membrane currents (bottom) caused by activation of cystic fibrosis transmembrane conductance regulator (CFTR) and volume-regulated ClC-3 Cl^- channels (A), Ca^{2+}-activated Cl^- channels (B), ClC-2 channels (C) are depicted. $I_{Cl,CFTR}$ can be activated by stimulation of protein kinase A (PKA), protein kinase C (PKC), or purinergic receptors; $I_{Cl,vol}$ is activated by cell swelling induced by exposure to hypotonic extracellular solutions or possibly membrane stretch; $I_{Cl,Ca}$ is activated by elevation of localized $[Ca^{2+}]_i$. $I_{Cl,ir}$ is activated by hyperpolarization, cell swelling, acidosis. Range of estimates for normal physiological values for Cl^- equilibrium potential (E_{Cl}) is indicated in green in top panels in A–C; range of zero-current values corresponding to E_{Cl} is shown in green in bottom panels. Numbers in top panels of A–C illustrate conventional phases of a prototype ventricular action potential under control conditions (black) and after activation of I_{Cl} (red). In A, activation of I_{Cl} induces larger membrane depolarization and induction of early afterdepolarizations (EAD) under conditions where resting K^+ conductance is reduced (dashed red lines); in B, activation of $I_{Cl,Ca}$ during $[Ca^{2+}]_i$ overload results in oscillatory transient inward current (I_{Tl}) and induction of delayed afterdepolarization (DAD); in C, activation of $I_{Cl,ir}$ during hyperpolarization causes acceleration of phase 4 depolarization and automaticity (dashed red lines, left panel) and shortening of action potential duration, membrane depolarization and/or phase 4 depolarization and induction of abnormal electrical impulse (trigger activity) and automaticity (right panel).

lation and faster heart rates. Therefore, activation of CFTR channels may prevent excessive prolongation of APD and protect the heart against the development of early after depolarizations (EAD) and triggered activity caused by activation of Ca^{2+} channels in the presence of β-adrenergic stimulation. EAD arising from phase 2 and 3 underlie focal triggered tachyarrhythmias and repolarization abnormalities, which contribute to cardiac sudden death[47]. It is well-

established that APD prolongation favors EAD by allowing recovery of inward currents and, conversely, shortening of APD makes it more difficult to induce EAD. Therefore, activation of CFTR channels should protect against focal triggered arrhythmias. However, when background K^+ conductance is reduced in the case of myocardial hypokalemia, activation of CFTR channels will cause significant membrane depolarization and induce abnormal automaticity leading to the development of, EAD (dotted red lines in Figure 2A). These predicted effects of CFTR channel activation on APD and automaticity have been verified experimentally by manipulations of the Cl^- gradient or the use of Cl^- channel blockers[11,48–51]. Histamine was found to activate CFTR channels in ventricular myocytes and induce oscillatory activity and abnormal impulses in the heart, although the contribution of CFTR channels to these arrhythmogenic activities has not been further explored. It has been shown that activation of CFTR channels contributes to hypoxia-induced shortening in APD[52]. Activation of CFTR channels may accelerate the development of reentry because of the shortening of APD and refractoriness and a decrease in conduction velocity caused by a slight depolarization of diastolic potential leading to Na^+ channel inactivation.

ClC-3 and arrhythmogenesis The current through ClC-3 channels under basal or isotonic conditions is small, but can be further activated by stretching of the cell membrane by inflation and/or cell swelling induced by exposure to hypoosmotic solutions. Activation of ClC-3 channels is expected to induce a similar effect on cardiac action potentials as that of activation of CFTR channels (Figure 2A) because both Cl^- currents through both channels are relatively time- and voltage-independent over the physiological range of membrane potentials[53,54]. Activation of ClC-3 channels might produce more significant action potential shortening than CFTR channels because of its stronger outwardly rectifying property. Because myocardial cells swell during hypoxia and ischemia, and the washout of hyperosmotic extracellular fluid after reperfusion induces further cell swelling, activation of ClC-3 channels may also contribute to hypoxia, ischemia and reperfusion induced shortening in APD and arrhythmias[9,53,54]. Abbreviation of APD and, therefore, the effective refractory period reduces the length of the conducting pathway needed to sustain reentry (wavelength). In principle, this favors the development of atrial or ventricular fibrillation, which depends on the presence of multiple reentrant circuits or rotating spiral waves. $I_{Clswell}$ also may slow or enhance the conduction of early extrasystoles, depending on the timing. In the case of myocardial hypertrophy and heart failure, ionic remodeling is one of the major features of pathophysiological changes[55]. It has been found that the current densities and molecular expression of several major repolarizing K^+ channels (such as Kv4x) are significantly reduced, which may be responsible for the prolongation of APD and development of EAD[55]. However, under these conditions, I_{Clvol} is constitutively active[56]. The persistent activation of I_{Clvol} may limit the APD prolongation and make it more difficult to elicit EAD. Indeed, as shown in Figure 3, in myocytes from hearts in failure, block of I_{Clvol} by tamoxifen significantly prolonged APD and decreased the depolarizing current required to elicit EAD by about 50% (Figure 4B) and hyperosmotic cell shrinkage, which also inhibits I_{Clvol}, was almost equivalent to tamoxifen in causing EAD in these myocytes (Figure 4C)[9]. Therefore, the consequences of activation of I_{Clvol} are very complex. It may be detrimental, beneficial, or simultaneously both in different parts of the heart.

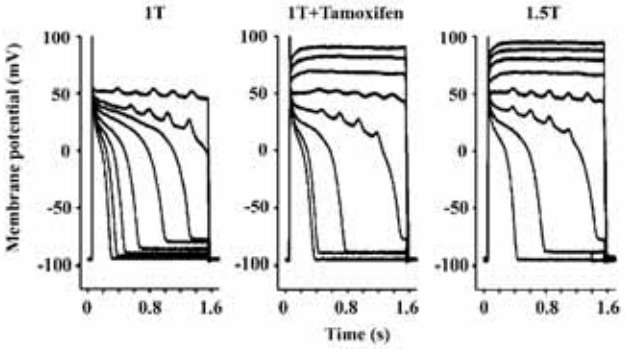

Figure 3. Activation of I_{Clvol} shortened APD and increased threshold for inducing early afterdepolarizations (EAD) in canine ventricular myocytes isolated from infarction and peri-infarction zones 30 days after left anterior descending artery ligation (MI). EAD were elicited with depolarizing pulses (20–200 pA) and current-voltage relationships were obtained from the same cells (not shown). Threshold for inducing EAD was 120 pA in a post-MI ventricular myocyte in 1T. Tamoxifen (10 μmol/L) reduced the threshold for induction of EAD in isotonic (1 T) solutions from 120 to 60 pA. Hyperosmotic shrinkage (in 1.5 T solutions), which also inhibits I_{Clvol}; reduced threshold for eliciting EAD to 40 pA. All panels from same cell under perforated patch conditions. (From Baumgarten and Clemo[9] with permission from Elsevier Science).

It has been shown that mechanical stretching or dilation of the atrial myocardium is able to cause arrhythmias. Since $I_{Clswell}$ was also found in sino-atrial (S-A) nodal cells, ClC-3 channels may serve as a mediator of mechanotransduction and play a significant role in the pacemaker function if they act as the stretch activated channels in these cells[9,57]. Baumgarten's laboratory has recently demonstrated that $I_{Clswell}$ in ventricular myocytes could be directly activated by

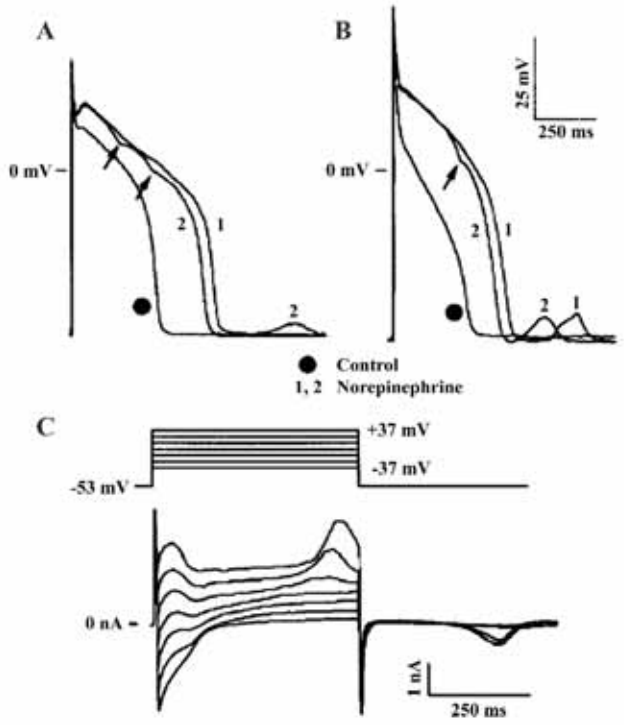

Figure 4. Contribution of I_{ClCa} to delayed afterdepolarization in ventricular and Purkinje myocytes. (A) Ventricular action potentials were recorded during control (•), 38 (1), and 45 (2) seconds after application of norepinephrine. Norepinephrine elevated the plateau and prolonged the action potential duration (1) and eventually caused delayed afterdepolarization (DAD) accompanied by transient repolarizations during the plateau (arrows). (B) Purkinje action potentials were recorded during control (•), 49 (1), and 52 (2) seconds after application of norepinephrine. Both action potentials recorded in the presence of norepinephrine were accompanied by DAD, but only the action potential recorded at (2) shows a transient repolarization (arrow) as well. (C) Membrane currents in ventricular myocyte activated by voltage steps from -53 mV to potentials between -23 and +37 mV in the presence of norepinephrine (1 mmol/L). Depolarization to -23 mV induced a large Ca^{2+} current which is superimposed with a transient outward current. This became more pronounced with stronger depolarization (From Verkerk *et al*[64] with permission from American Heart Association).

mechanical stretch through selectively stretching β1-integrins with mAb-coated magnetic bEAD[9,58,59]. Although it has been suggested that stretch and swelling activate the same anion channel in some non-cardiac cells, further study is needed to determine whether this is true in cardiac myocytes.

Ca^{2+}-activated Cl^- channel and arrhythmogenesis As illustrated in Figure 2B, the activation of I_{ClCa} will have considerably different effects on cardiac action potentials and resting membrane potential from those of CFTR and ClC-3 channels, even though I_{ClCa} is also expected to be outwardly rectifying under physiological conditions. This is because the kinetic behavior of I_{ClCa} is significantly determined by the time course of the $[Ca^{2+}]_i$ transient[60]. Normally, I_{ClCa} will have insignificant effects on the diastolic membrane potential, as resting $[Ca^{2+}]_i$ is low. When $[Ca^{2+}]_i$ is substantially increased above the physiological resting level, however, I_{ClCa} carries a significant amount of transient outward current. I_{ClCa} will be activated early during the action potential in response to an increase in $[Ca^{2+}]_i$ associated with Ca^{2+}-induced Ca^{2+} release (CICR). The time course of decline of the $[Ca^{2+}]_i$ transient will determine the extent to which I_{ClCa} contributes to early repolarization during phase 1 (Figure 2B). In the rabbit left ventricle, I_{ClCa} contributes to APD shortening in subendocardial myocytes but not in subepicardial myocytes. These differences in functional expression of I_{ClCa} may reduce the electrical heterogeneity in the left ventricle[61]. In Ca^{2+}-overloaded cardiac preparations, I_{ClCa} can contribute to the arrhythmogenic transient inward current (I_{Ti}, Figure 2B)[62]. I_{Ti} produces delayed after-depolarization (DAD)[63] and induces triggered activity (red dotted line in Figure 2B), which is an important mechanism for abnormal impulse formation. In sheep Purkinje and ventricular myocytes, activation of I_{ClCa} was found to induce DAD and plateau transient repolarization (Figure 4)[64]. Therefore, blockade of I_{ClCa} may be potentially antiarrhythmogenic by reducing DAD amplitude and triggered activity based on DAD. However, the role of I_{ClCa} in phase 1 repolarization and the generation of EAD and DAD of either normal or failing human heart seem very limited[65–67]. Therefore, the clinical relevance of I_{ClCa} blockers remains to be determined.

ClC-2 and arrhythmogenesis ClC-2 channels are activated by hyperpolarization, cell swelling, and acidosis and have an inwardly rectifying *I-V* relationship. During the cardiac action potential, therefore, the ClC-2 channel will conduct a mainly inward current as a result of Cl^- efflux at negative membrane potentials and cause a depolarization of the resting membrane potential of cardiac cells. At membrane potentials more positive than E_{Cl}, ClC-2 may conduct a small outward current as a result of Cl^- influx and may accelerate repolarization of the action potential. It is also possible that, in a manner analogous to the role and tissue distribution pattern of the cationic pacemaker channels (I_f), Cl.ir channels normally play a much more prominent role in the SA or AV nodal regions of the heart (Figure 2C). The hyperpolarization-activated inward rectifying Cl^- current (I_{Clir}) through ClC-2 channels under basal or isotonic conditions is small, but can be further activated by hypotonic cell swelling[22] and acidosis[23,24]. The volume-sensitivity of the channel also suggests its role in cell volume regulation. The sensitivity of ClC-2 to $[H^+]_o$ and cell volume may be of pathologi-

cal importance during hypoxia- or ischemia-induced acidosis or cell swelling. Therefore, it may be possible that the significance of $I_{Cl,ir}$ in the heart becomes more prominent under some pathological conditions (ischemia or hypoxia)[68]. As a matter of fact, ischemia and acidosis have consistently been shown to depolarize the resting membrane potential of cardiac myocytes, increase automaticity and cause lethal arrhythmias, although the mechanism has remained obscure[1,11]. It is reasonable to suggest that an increase in ClC-2 conductance could be responsible for these phenomena and be pro-arrhythmic. Drugs targeting ClC-2 channels could be anti-arrhythmic. Therefore, the ClC-2 channels could have important clinical significance for such cardiac diseases as arrhythmias, ischemia and reperfusion, and congestive heart failure. Activation of ClC-2 current should mainly cause a depolarization of the RMP and it is suggested that the acidosis-induced increase in $I_{Cl,ir}$ might underlay the depolarization of the resting membrane potential during acidosis or hypoxia[23,24].

It should be pointed out that prediction of the consequences of activation of Cl^- channels is complex. Most studies that have examined the contribution of Cl^- currents to the cardiac action potential and arrhythmias have relied on anion antagonist and substitution experiments. The pharmacological specificity of many of these anion channel antagonists can be problematic, and anion substitution, in addition to altering anion movement through channels, can have other unpredictable side effects on other transport proteins and signaling pathways[69,70]. With the recent identification of the molecular entities responsible for Cl^- channels in the heart, it is now possible to combine electrophysiological, molecular biological, and especially gene-targeting techniques in the study of cardiac Cl^- channels to effectively and accurately define the role of each Cl^- channel in heart function. However, as the distribution of various Cl^- channels in the heart varies among cell types and regions[8], activation of these channels may increase the dispersion of the electrophysiological properties and provide substrates for heart diseases involving cardiac arrhythmias and myocardial remodeling.

Functional role of Cl^- channels in cardiac IPC

Ischemia causes myocardial damage and leads to infarction through apoptosis (programmed cell death) and necrosis. IPC is a phenomenon in which brief ischemic episodes elicit protection of the heart against sustained ischemia. It has been suggested that both sarcolemmal and mitochondrial ATP-sensitive potassium channels (sarc-K_{ATP} and mito-K_{ATP}, respectively) may serve as triggers or end-effectors. PKC may link cellular signal events during ischemia to the activation of end-effectors, which will somehow prevent or delay apoptosis and protect the cardiac myocytes. The precise mechanism of IPC, however, remains to be elucidated. Several recent studies have pointed to a potential role of Cl^- channels in IPC.

$I_{Clswell}$ and ClC-3 in IPC It has been reported that the block of $I_{Clswell}$ in rabbit cardiac myocytes inhibits preconditioning by brief ischemia, hypoosmotic stress[71,72] and adenosine receptor agonists[73]. These studies are solely based on the use of several Cl^- channel blockers, such as anthracene-9-carboxylic acid (9-AC) and 4-acetamide-4'-isothiocyanato-stilbene-2,2'-disulfonic acid (SITS). As mentioned above, these pharmacological tools lack specificity to a particular Cl^- channel in the heart and may also act on other ion channels or transporters. Therefore it has been very difficult to confirm the causal role of $I_{Clswell}$ in IPC[74]. The exact role of $I_{Clswell}$ in IPC needs to be further determined adequately using more specific approaches. To specifically test whether the volume-regulated Cl^- channels are indeed involved in IPC, we have recently established *in vitro* and *in vivo* IPC models in *ClC-3* knockout mice ($ClCn3^{-/-}$). Our preliminary results indicate that targeted inactivation of *ClC-3* gene prevented protective effects of late IPC but not of early IPC, suggesting that $I_{Clswell}$ may contribute differently to early and late IPC[75]. The underlying mechanisms for these differential effects are currently unknown. Recent reports, however, suggest that $I_{Clswell}$ and ClC-3 might play an important role in apoptosis. Cl^- channel blockers 4,4'-diisothiocyano-stilbene-2,2'-disulphonate (DIDS) and 5-nitro-2-(3-phenylpropyllamino)-benzoic acid (NPPB) were as potent as a broad-spectrum caspase inhibitor in preventing apoptosis and elevation of caspase-3 activity and improved cardiac contractile function after ischemia and *in vivo* reperfusion[76]. Transgenic mice overexpressing Bcl-2 in the heart had significantly smaller infarct size and reduced apoptosis of myocytes after ischemia and reperfusion[77]. It has been shown that Bcl-2 induces up-regulation of I_{Clvol} by enhancing ClC-3 expression in human prostate cancer epithelial cells[78]. Cell shrinkage is an integral part of apoptosis, suggesting that I_{Clvol} and ClC-3 might be intimately linked to apoptotic events through regulation of cell volume homeostasis[78,79].

CFTR channels and IPC Several lines of evidence suggest that CFTR channels could be involved in IPC including: (1) sarc-K_{ATP} blockers, such as glibenclamide, which suppress IPC protection, also block CFTR channels in noncardiac[80,81] and cardiac cells[19,82]; (2) PKC and PKA, two essential second messengers in IPC[83,84] can activate CFTR

channels[8,19,85]; and (3) triggers of IPC (nitric oxide, opioids, and adenosine *etc*) can all regulate CFTR channel function[8]. We have directly tested whether activation of CFTR channels is involved in IPC by studying hemodynamics and tissue injury of hearts isolated from WT and two strains of *CFTR* knockout ($CFTR^{-/-}$) mice subjected to ischemia and reperfusion. In isolated mouse heart perfused in the Langendorff or working heart mode, we have recently found that targeted inactivation of *CFTR* gene prevented protection on cardiac function and myocardium injury against sustained ischemia by ischemic preconditioning (Figure 5)[86]. Our *in vivo* studies using both wild type and *CFTR* knockout mice also demonstrated that CFTR was an important mediator in both early and late ischemic preconditioning in the heart[87]. Several mechanisms may be responsible for a functional role of CFTR channels in mouse heart IPC: (1) It has been demonstrated that cardiac CFTR plays a role in early action potential shortening during hypoxia and ischemia[52]. Activation of CFTR will also decrease resting membrane potential and action potential duration, thereby limiting intracellular Ca^{2+} overload and cell damage[8]; (2) The CFTR channel is an important transporter of sphingosine 1-phosphate (S-1-P)[88], which has recently emerged as an important lipid messenger involved in IPC[89]; (3) CFTR is permeable not only to Cl^-, but also to larger organic ions, as well as reduced and oxidized forms of glutathione (GSH)[90]. Therefore CFTR may contribute to the control of oxygen stress-induced apoptosis and the regulation of inflammation and the immune responses; (4) CFTR might decrease intracellular pH and modulate apoptosis[91]; (5) CFTR functions as a regulator of volume-dependent homeostatic cell mechanisms in cell proliferation and apoptosis[92]. We are currently in the

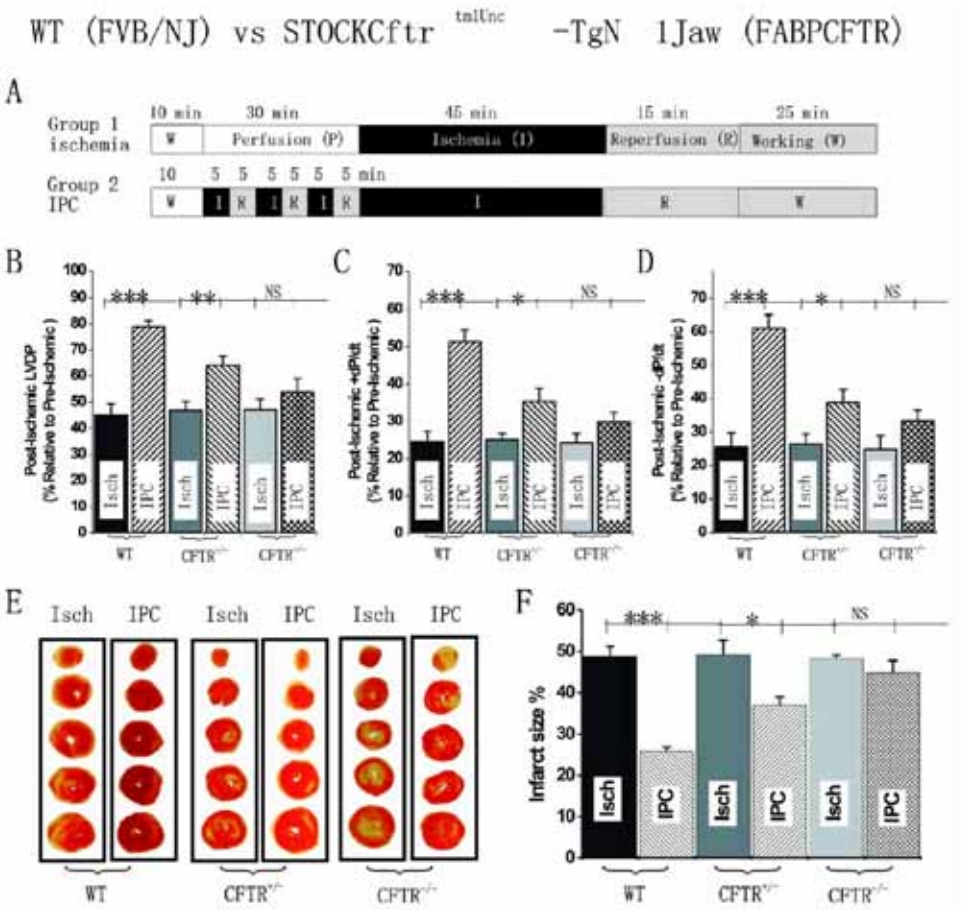

Figure 5. Effects of cystic fibrosis transmembrane conductance regulator (CFTR) gene knockout (FABPCFTR) on ischemic preconditioning (IPC) in isolated working mouse heart. (A) Experimental protocol. (B–D) Recovery of left ventricular contractile (B,C) and relaxation (D) function of WT (FVB/NJ), $CFTR^{-/+}$ and $CFTR^{-/-}$ (FABPCFTR) mice after 45 min of ischemia and 40 min of reperfusion. (E,F) IPC on infarct size of ventricles. (E) Representative ventricle transverse slices after ischemia (Isch) or IPC. (F) Mean infarct size measured from age-matched WT, $CFTR^{-/+}$, or $CFTR^{-/-}$ mouse heart after ischemia (Isch) or IPC (n=6 for each group). *P<0.05, **P<0.01, ***P<0.001. (From Chen *et al*[86] with permission from American Heart Association)

process of investigating these potential mechanisms and the relative role of CFTR in early and late preconditioning.

$I_{Cl,Ca}$ in IPC It has been well known that ischemia/reperfusion usually causes a cytosolic overload of Ca^{2+} in cardiac myocytes[93,94]. Therefore, it is very possible that $I_{Cl,Ca}$ may be activated during ischemia and reperfusion[38,62,64,95-98]. But, no information for the possible involvement of $I_{Cl,Ca}$ in IPC is currently available.

Functional role of Cl^- channels in myocardial hypertrophy and heart failure Myocardial hypertrophy and its progression to dilated cardiomyopathy or heart failure are characterized by not only structural remodeling, including hypertrophic growth of cardiac myocytes (changes in cell volume) and changes in the cytoskeleton and extracellular matrix (ECM)[99,100] but also ionic remodeling, that is, changes in expression and activity of many ion channels. It should be pointed out that ionic remodeling during the progression of hypertrophy to heart failure provides not only substrates for arrhythmias but also cellular mechanisms for structural remodeling. During the remodeling process, multiple neurohormonal and intracellular signaling cascades, including tyrosine kinases, PKA, PKC, protein phosphatases, MAP kinases, and endothelin, are activated[101]. These second messengers are well-known effective regulators of various ion channels. Indeed, it has been found that several cation channels, such as K^+ channels, Ca^{2+} channels, and stretch-activated non-selective channels, undergo significant changes. Recent evidence also supports possible involvement of anion channels in the remodeling process.

$I_{Clswell}$ and ClC-3 in myocardial hypertrophy and heart failure $I_{Clswell}$ is persistently activated in ventricular myocytes from a canine pacing-induced dilated cardiomyopathy model[102]. Using the perforated patch-clamp technique, Clemo *et al* found that, even in isotonic solutions, a large 9-AC-sensitive, outwardly rectifying Cl^- current was recorded in heart failure myocytes but not in normal myocytes. Graded hypotonic cell swelling (90%–60% hypotonic) failed to activate additional current while graded hypertonic cell shrinkage caused an inhibition of the "basal" Cl^- current in failure myocytes. Moreover, the maximum current density of the $I_{Clswell}$ in failure myocytes was about 40% greater than that in osmotically swollen normal myocytes. Constitutive activation of $I_{Clswell}$ is also observed in several other animal models of heart failure, such as a rabbit aortic regurgitation model of dilated cardiomyopathy[103,104] and a dog model of heart failure caused by myocardial infarction[105]. In human atrial myocytes obtained from patients with right atrial enlargement and/or elevated left ventricular end-diastolic pressure, a tamoxifen sensitive $I_{Clswell}$ was also found to be persistently activated[106]. It is not known at this time whether $I_{Clswell}$ is also persistently activated in hypertrophied non-failure (or non-dilated) myocytes in the above described models or in the human heart. In a rat aortic constriction model, however, a 9-AC-sensitive Cl^- current is present in hypertrophied ventricular myocytes but not in control myocytes, and this hypertrophy-activated Cl^- current seems to contribute to the shortening of APD in the hypertrophied cells[107]. It is not known, however, whether this hypertrophy-activated Cl^- current is the same as $I_{Clswell}$ because the volume-sensitivity of this Cl^- current was not assessed. Nevertheless, it is possible that persistent activation of $I_{Clswell}$ is a common response of cardiac myocytes to hypertrophy or heart failure-induced remodeling. The mechanism for this phenomenon is still not clear. Perhaps the cell volume increase caused by hypertrophy and cell membrane stretch caused by dilation, are both involved in the activation of $I_{Clswell}$. Alternatively, the persistent activation of $I_{Clswell}$ may be caused by signaling cascades activated during hypertrophy and heart failure independent of changes in cell length and volume, or both. $I_{Clswell}$ could be activated by direct stretching of β1-integrin through focal adhesion kinase (FAK) and/or Src[58]. Mechanical stretch of myocytes also releases angiotensin II (AngII), which binds to AT1 receptors (AT1R) and stimulates FAK and Src in an autocrine-paracrine loop. A recent study by Browe and Baumgarten suggests that the stretch of β1-integrin in cardiac myocytes activates $I_{Clswell}$ by activating AT1R and NADPH oxidase and, thereby, producing reactive oxygen species. In addition, NADPH oxidase may be intimately coupled to the channel responsible for $I_{Clswell}$, providing a second regulatory pathway for this channel through membrane stretch or oxidative stress[59]. This finding is very important for further understanding of the mechanism for hypertrophy activation of $I_{Clswell}$ and ClC-3 channels and their relationship to hypertrophy and heart failure as it is very well known that Ang II plays a crucial role in myocardial hypertrophy and heart failure[108].

The functional and clinical significance of $I_{Clswell}$ in the hypertrophied and dilated heart is currently unknown. Using a mouse aortic banding model of myocardial hypertrophy, we have recently found that targeted disruption of ClC-3 gene ($ClCn3^{-/-}$) accelerated the development of myocardial hypertrophy and the discompensatory process[109], suggesting that activation of I_{Clvol} might be important in the adaptive remodeling of the heart during pressure overload. Further studies on the mechanism for the ClC-3 channels' effects on hypertrophy and heart failure are in progress in our laboratory. It is well accepted that in most cells activation of I_{Clvol} represents one important trigger to initiate regula-

tory volume decrease (RVD) when cells swell[12]. Cell volume homeostasis, therefore, could be an important function of $I_{Clswell}$ activation in the heart. Activation of Cl^- conductance causes significant changes in APD and intracellular Ca^{2+} concentration, and should also affect excitation-contraction (E-C) coupling, contractility, and other hemodynamic functions of the heart[8,11]. Recent studies suggest that $I_{Clswell}$ and ClC-3 channels play important roles in cell proliferation[110], differentiation[111], migration[112], and apoptosis[78,79]. All of these have been demonstrated as important cellular processes in myocardial remodeling during hypertrophy and heart failure[113].

CFTR in myocardial hypertrophy and heart failure Remodeling of CFTR channels has been observed in myocardial hypertrophy and heart failure. Using *in situ* mRNA hybridization in a combined pressure and volume overload model of heart failure in the rabbit, Wong *et al* found that the normal epicardial to endocardial gradient of *CFTR* mRNA expression is reversed due to a significant decrease in epicardial expression of CFTR mRNA in the rabbit left ventricle[114]. A post-translational change in the CFTR expression could be responsible for this phenomenon[115]. The loss of the normal transmural gradient of repolarising ion channels is likely to contribute to instability of repolarisation in the hypertrophied heart and hence increased risk of cardiac arrhythmias in patients with heart failure. The exact functional and clinical significance of the changes in CFTR expression during hypertrophy and heart failure is currently not clear and merits further study.

I_{ClCa} in myocardial hypertrophy and heart failure The critical role of Ca^{2+} in cardiac development, function, and disease is undisputable. Despite the heterogeneous etiology and overt manifestations of heart failure, abnormalities in Ca^{2+} handling are prominent, and alterations in Ca^{2+} homeostasis are a hallmark of myocardial hypertrophy and heart failure[116]. Ca^{2+} transients in failing cardiac myocytes, for example, are characterized by diminished amplitude, elevated diastolic Ca^{2+} levels, and prolonged decay of the Ca^{2+} transients. In non-cardiac cells, I_{ClCa} could be an important mediator of apoptosis[117]. But, information on the possible involvement of I_{ClCa} in heart failure is currently very limited. It is reported that I_{ClCa} may play little, if any, role in the electrical remodeling of human end-stage failing heart[66,67,118].

Conclusions and future directions

Although the field of anion channels in cardiac physiology and pathophysiology lags significantly behind that of cation channels, the gap can now be narrowed with the recent identification of molecular entities responsible for cardiac Cl^- channels[8], their genes mapped to specific human chromosomal locations[13] and the use of gene targeting and transgenic animals. Recent efforts not only at the cellular and molecular levels but also the isolated organ and whole animal levels have provided strong evidence that Cl^- channels may play an important role in cardiac diseases, including arrhythmias, myocardial ischemia, hypertrophy, and congestive heart failure. Anion channels in the heart, therefore, may represent important novel targets for therapeutic agents against heart diseases.

Despite these exciting developments, further investigations of the cellular and molecular mechanisms by which the Cl^- channel proteins function to impart a physiological or a pathophysiological phenotype may require a multitude of approaches for the assessment of the Cl^- channel functions in healthy and diseased hearts. Although global knockout mice are invaluable experimental models and functional genomics remains a powerful approach to understanding the function of cardiac Cl^- channels, several theoretical and practical problems should be considered. First, homologous recombination gene targeting is based on the assumption that targeting will result in specific loss of the gene's product and will not directly affect the expression of other genes. In reality, however, even though the loss of the gene's product can be verified, the upregulation of another gene in the vicinity of the targeting can occur[119] and may readily escape detection. Such upregulation could have an important effect on the observed phenotype. Second, a knockout may not always be a knockout[120] such as when the targeted gene is widely or ubiquitously expressed, when alternative splicing variants of the gene exist[121], and when functional channels are actually heteromultimeric and the structure might be associated with modulatory subunits, such as Barttin for ClC channels[122]. Accessory proteins may be involved in the determination of the stability of the channel complex in the membrane and in the modulation of biophysical, pharmaco-logical, and regulatory properties of the channel. Recent evidence suggests that Cl^- channels, like cation channels[52,123,124], may function as a multiprotein complex or functional module. A functional anion channel module may be a complex composed of the following: (a) pore forming subunit for ion transportation; (b) auxiliary subunits for modulating pore gating; and (c) proteins as second messengers tightly coupled to channel function. These proteins might be intimately linked to certain physiological functions and belong to the same subproteome. Manipulation of one gene in the subproteome may cause changes in other proteins of the same subproteome. Therefore, the functional consequences of disrupting the specific gene are very difficult to

predict unless the changes in the entire subproteome are examined. Similar phenotypes can be attained from alternative protein pathways within cellular networks, which are influenced by disease, environmental, internal, and biochemical stimuli. Therefore, caution should be taken when conventional global gene knockout animals are used in functional studies. Alternatively, tissue-specific conditional or inducible knockout or knockin animal models may be more valuable in the phenotypic studies of specific genes by limiting the effect of upregulation or developmental compensation on the phenotype of manipulated genes. Many phenotypic changes may actually be a result of posttranslational changes caused by protein modifications such as phosphorylation or dephosphorylation. Therefore, it is clear that conventional functional genomics may provide only limited information on the functional module of multiprotein complexes. We are now facing the challenge of a major paradigm shift in the study of integrated anion channel functions. In the postgenomic era, the recent advances in the genome resources including genome-wide microarray profiling together with advancement in the application of functional proteomics and bioinformatics will certainly facilitate our understanding of the functions of anion channels in the cardiovascular system. It is feasible that anion channels may become novel targets for therapeutic approaches to the treatment of cardiovascular diseases.

Acknowledgements

The research in the Laboratory of Functional Genomics and Proteomics, Center of Biomedical Research Excellence and the Department of Pharmacology, University of Nevada, School of Medicine is supported by grants from the National Institutes of Health (R01-HL63914), National Center of Research Resources (NCRR, P20RR15581).

References

1 Carmeliet E. Cardiac ionic currents and acute ischemia: from channels to arrhythmias. Physiol Rev 1999; 79: 917–1017.
2 Marban E. Cardiac channelopathies. Nature 2002; 415: 213–8.
3 Nattel S, Khairy P, Schram G. Arrhythmogenic ionic remodeling: adaptive responses with maladaptive consequences. Trends Cardiovasc Med 2001; 11: 295–301.
4 Nattel S. New ideas about atrial fibrillation 50 years on. Nature 2002; 415: 219–26.
5 Nattel S. Human genetics: lost anchors cost lives. Nature 2003; 421: 587-90.
6 Gross GJ, Peart JN. K_{ATP} channels and myocardial preconditioning: an update. Am J Physiol Heart Circ Physiol 2003; 285: H921–30.
7 O'Rourke B. Evidence for mitochondrial K^+ channels and their role in cardioprotection. Circ Res 2004; 94: 420–32.
8 Hume JR, Duan D, Collier ML, Yamazaki J, Horowitz B. Anion transport in heart. Physiol Rev 2000; 80: 31–81.
9 Baumgarten CM, Clemo HF. Swelling-activated chloride channels in cardiac physiology and pathophysiology. Prog Biophys Mol Biol 2003; 82: 25–42.
10 Harvey RD. Cardiac chloride currents. News Phys Sci 1996; 11: 175–81.
11 Hiraoka M, Kawano S, Hirano Y, Furukawa T. Role of cardiac chloride currents in changes in action potential characteristics and arrhythmias. Cardiovasc Res 1998; 40: 23–33.
12 Lang F, Busch GL, Ritter M, Volkl H, Waldegger S, Gulbins E, *et al*. Functional significance of cell volume regulatory mechanisms. Physiol Rev 1998; 78: 247–306.
13 Lehmann-Horn F, Jurkat-Rott K. Voltage-gated ion channels and hereditary disease. Physiol Rev 1999; 79: 1317–72.
14 Bahinski A, Nairn AC, Greengard P, Gadsby DC. Chloride conductance regulated by cyclic AMP-dependent protein kinase in cardiac myocytes. Nature 1989; 340: 718–21.
15 Harvey RD, Hume JR. Autonomic regulation of a chloride current in heart. Science 1989; 244: 983–5.
16 Nagel G, Hwang TC, Nastiuk KL, Nairn AC, Gadsby DC. The protein kinase A-regulated cardiac Cl^- channel resembles the cystic fibrosis transmembrane conductance regulator. Nature 1992; 360: 81–4.
17 Collier ML, Hume JR. Unitary chloride channels activated by protein kinase C in guinea pig ventricular myocytes. Circ Res 1995; 76: 317–24.
18 Walsh KB, Long KJ. Properties of a protein kinase C-activated chloride current in guinea pig ventricular myocytes. Circ Res 1994; 74: 121–9.
19 Duan D, Ye L, Britton F, Miller LJ, Yamazaki J, Horowitz B, *et al*. Purinoceptor-coupled Cl^- channels in mouse heart: a novel, alternative pathway for CFTR regulation. J Physiol 1999; 521 Pt 1: 43–56.
20 Levesque PC, Hume JR. ATP_o but not $cAMP_i$ activates a chloride conductance in mouse ventricular myocytes. Cardiovasc Res 1995; 29: 336–43.
21 Yamamoto-Mizuma S, Wang GX, Hume JR. P2Y purinergic receptor regulation of CFTR chloride channels in mouse cardiac myocytes. J Physiol 2004; 556: 727–37.
22 Duan D, Ye L, Britton F, Horowitz B, Hume JR. A novel anionic inward rectifier in native cardiac myocytes. Circ Res 2000; 86: E63–E71.
23 Komukai K, Brette F, Orchard CH. Electrophysiological response of rat atrial myocytes to acidosis. Am J Physiol Heart Circ Physiol 2002; 283: H715–24.
24 Komukai K, Brette F, Pascarel C, Orchard CH. Electrophysiological response of rat ventricular myocytes to acidosis. Am J Physiol Heart Circ Physiol 2002; 283: H412–22.
25 Duan D, Fermini B, Nattel S. Sustained outward current observed after I_{to1} inactivation in rabbit atrial myocytes is a novel Cl^- current. Am J Physiol 1992; 263: H1967–71.
26 Duan D, Nattel S. Properties of single outwardly rectifying Cl^- channels in heart. Circ Res 1994; 75: 789–95.
27 Duan D, Fermini B, Nattel S. Alpha-adrenergic control of volume-regulated Cl^- currents in rabbit atrial myocytes. Characterization of a novel ionic regulatory mechanism. Circ Res 1995; 77: 379–93.
28 Duan D, Hume JR, Nattel S. Evidence that outwardly rectifying

Cl^- channels underlie volume-regulated Cl^- currents in heart. Circ Res 1997; 80: 103–13.

29 Duan D, Winter C, Cowley S, Hume JR, Horowitz B. Molecular identification of a volume-regulated chloride channel. Nature 1997; 390: 417–21.

30 Duan D, Cowley S, Horowitz B, Hume JR. A serine residue in ClC-3 links phosphorylation-dephosphorylation to chloride channel regulation by cell volume. J Gen Physiol 1999; 113: 57–70.

31 Duan D, Zhong J, Hermoso M, Satterwhite CM, Rossow CF, Hatton WJ, *et al*. Functional inhibition of native volume-sensitive outwardly rectifying anion channels in muscle cells and *Xenopus* oocytes by anti-ClC-3 antibody. J Physiol 2001; 531: 437–44.

32 Hermoso M, Satterwhite CM, Andrade YN, Hidalgo J, Wilson SM, Horowitz B, *et al*. ClC-3 is a fundamental molecular component of volume-sensitive outwardly rectifying Cl^- channels and volume regulation in HeLa cells and *Xenopus laevis* oocytes. J Biol Chem 2002; 277: 40066–74.

33 Wang GX, Hatton WJ, Wang GL, Zhong J, Yamboliev I, Duan D, *et al*. Functional effects of novel anti-ClC-3 antibodies on native volume-sensitive osmolyte and anion channels in cardiac and smooth muscle cells. Am J Physiol Heart Circ Physiol 2003; 285: H1453–63.

34 Yamamoto-Mizuma S, Wang GX, Liu LI, Schegg K, Hatton WJ, Duan D, *et al*. Altered properties of volume-sensitive osmolyte and anion channels (VSOACs) and membrane protein expression in cardiac and smooth muscle myocytes from $Clcn3^{-/-}$ mice. J Physiol 2004; 557: 439–56.

35 Britton FC, Ohya S, Horowitz B, Greenwood IA. Comparison of the properties of CLCA1 generated currents and $I_{Cl(Ca)}$ in murine portal vein smooth muscle cells. J Physiol 2002; 539: 107–17.

36 Collier ML, Levesque PC, Kenyon JL, Hume JR. Unitary Cl^- channels activated by cytoplasmic Ca^{2+} in canine ventricular myocytes. Circ Res 1996; 78: 936–44.

37 Zygmunt AC, Gibbons WR. Properties of the calcium-activated chloride current in heart. J Gen Physiol 1992; 99: 391–414.

38 Xu Y, Dong PH, Zhang Z, Ahmmed GU, Chiamvimonvat N. Presence of a calcium-activated chloride current in mouse ventricular myocytes. Am J Physiol Heart Circ Physiol 2002; 283: H302–14.

39 Hartzell C, Putzier I, Arreola J. Calcium-activated chloride channels. Annu Rev Physiol 2005; 67: 221–40.

40 Qu Z, Wei RW, Mann W, Hartzell HC. Two *Bestrophins* cloned from *Xenopus laevis* oocytes express Ca^{2+}-activated Cl^- currents. J Biol Chem 2003; 278: 49563–72.

41 Qu Z, Fischmeister R, Hartzell C. Mouse *Bestrophin*-2 is a bona fide Cl^- channel: identification of a residue important in anion binding and conduction. J Gen Physiol 2004; 123: 327–40.

42 Qu Z, Hartzell C. Determinants of anion permeation in the second transmembrane domain of the mouse *Bestrophin*-2 chloride channel. J Gen Physiol 2004; 124: 371–82.

43 Baumgarten CM, Fozzard HA. Intracellular chloride activity in mammalian ventricular muscle. Am J Physiol 1981; 241: C121–9.

44 Caille JP, Ruiz-Ceretti E, Schanne OF. Intracellular chloride activity in rabbit papillary muscle: effect of ouabain. Am J Physiol 1981; 240: C183–8.

45 Spitzer KW, Walker JL. Intracellular chloride activity in quiescent cat papillary muscle. Am J Physiol 1980; 238: H487–93.

46 Vaughan-Jones RD. Non-passive chloride distribution in mammalian heart muscle: micro-electrode measurement of the intracellular chloride activity. J Physiol (Lond) 1979; 295: 83–109.

47 Tomaselli GF, Beuckelmann DJ, Calkins HG, Berger RD, Kessler PD, Lawrence JH, *et al*. Sudden cardiac death in heart failure. The role of abnormal repolarization. Circulation 1994; 90: 2534–9.

48 Harvey RD, Clark CD, Hume JR. Chloride current in mammalian cardiac myocytes. Novel mechanism for autonomic regulation of action potential duration and resting membrane potential. J Gen Physiol 1990; 95: 1077–102.

49 Matsuoka S, Ehara T, Noma A. Chloride-sensitive nature of the adrenaline-induced current in guinea-pig cardiac myocytes. J Physiol (Lond) 1990; 425: 579–98.

50 Takano M, Noma A. Distribution of the isoprenaline-induced chloride current in rabbit heart. Pflugers Arch 1992; 420: 223–6.

51 Yamawake N, Hirano Y, Sawanobori T, Hiraoka M. Arrhythmogenic effects of isoproterenol-activated Cl^- current in guinea-pig ventricular myocytes. J Mol Cell Cardiol 1992; 24: 1047–58.

52 Ruiz PE, Ponce ZA, Schanne OF. Early action potential shortening in hypoxic hearts: role of chloride current(s) mediated by catecholamine release. J Mol Cell Cardiol 1996; 28: 279–90.

53 Du XY, Sorota S. Cardiac swelling-induced chloride current depolarizes canine atrial myocytes. Am J Physiol 1997; 272: H1904–16.

54 Vandenberg JI, Bett GC, Powell T. Contribution of a swelling-activated chloride current to changes in the cardiac action potential. Am J Physiol 1997; 273: C541–7.

55 Tomaselli GF, Marban E. Electrophysiological remodeling in hypertrophy and heart failure. Cardiovasc Res 1999; 42: 270–83.

56 Clemo HF, Stambler BS, Baumgarten CM. Swelling-activated chloride current is persistently activated in ventricular myocytes from dogs with tachycardia-induced congestive heart failure. Circ Res 1999; 84: 157–65.

57 Hagiwara N, Masuda H, Shoda M, Irisawa H. Stretch-activated anion currents of rabbit cardiac myocytes. J Physiol (Lond) 1992; 456: 285–302.

58 Browe DM, Baumgarten CM. Stretch of beta 1 integrin activates an outwardly rectifying chloride current via FAK and Src in rabbit ventricular myocytes. J Gen Physiol 2003; 122: 689–702.

59 Browe DM, Baumgarten CM. Angiotensin II (AT1) receptors and NADPH oxidase regulate Cl^- current elicited by β1 integrin stretch in rabbit ventricular myocytes. J Gen Physiol 2004; 124: 273–87.

60 Zygmunt AC, Gibbons WR. Calcium-activated chloride current in rabbit ventricular myocytes. Circ Res 1991; 68: 424–37.

61 Verkerk AO, Tan HL, Ravesloot JH. Ca^{2+}-activated Cl^- current reduces transmural electrical heterogeneity within the rabbit left ventricle. Acta Physiol Scand 2004; 180: 239–47.

62 Zygmunt AC. Intracellular calcium activates a chloride current in canine ventricular myocytes. Am J Physiol 1994; 267: H1984–95.

63 January CT, Fozzard HA. Delayed afterdepolarizations in heart muscle: mechanisms and relevance. Pharmacol Rev 1988; 40: 219–27.

64 Verkerk AO, Veldkamp MW, Bouman LN, van Ginneken AC. Calcium-activated Cl^- current contributes to delayed afterdepolarizations in single Purkinje and ventricular myocytes. Circulation 2000; 101: 2639–44.

65 Verkerk AO, Veldkamp MW, de Jonge N, Wilders R, van Ginneken AC. Injury current modulates afterdepolarizations in single human ventricular cells. Cardiovasc Res 2000; 47: 124–32.

66 Verkerk AO, Veldkamp MW, Baartscheer A, Schumacher CA,

Klopping C, van Ginneken AC, *et al*. Ionic mechanism of delayed afterdepolarizations in ventricular cells isolated from human end-stage failing hearts. Circulation 2001; 104: 2728–33.

67 Verkerk AO, Wilders R, Coronel R, Ravesloot JH, Verheijck EE. Ionic remodeling of sinoatrial node cells by heart failure. Circulation 2003; 108: 760–6.

68 Wright AR, Rees SA. Targeting ischaemia–cell swelling and drug efficacy [published erratum appears in Trends Pharmacol Sci 1997; 18: 345]. Trends Pharmacol Sci 1997; 18: 224–8.

69 Frace AM, Maruoka F, Noma A. Control of the hyperpolarization-activated cation current by external anions in rabbit sinoatrial node cells. J Physiol (Lond) 1992; 453: 307–18.

70 Nakajima T, Sugimoto T, Kurachi Y. Effects of anions on the G protein-mediated activation of the muscarinic K^+ channel in the cardiac atrial cell membrane. Intracellular chloride inhibition of the GTPase activity of GK. J Gen Physiol 1992; 99: 665–82.

71 Diaz RJ, Losito VA, Mao GD, Ford MK, Backx PH, Wilson GJ. Chloride channel inhibition blocks the protection of ischemic preconditioning and hypo-osmotic stress in rabbit ventricular myocardium. Circ Res 1999; 84: 763–75.

72 Diaz RJ, Batthish M, Backx PH, Wilson GJ. Chloride channel inhibition does block the protection of ischemic preconditioning in myocardium. J Mol Cell Cardiol 2001; 33: 1887–9.

73 Batthish M, Diaz RJ, Zeng HP, Backx PH, Wilson GJ. Pharmacological preconditioning in rabbit myocardium is blocked by chloride channel inhibition. Cardiovasc Res 2002; 55: 660–71.

74 Heusch G, Liu GS, Rose J, Cohen MV, Downey JM. No confirmation for a causal role of volume-regulated chloride channels in ischemic preconditioning in rabbits. J Mol Cell Cardiol 2000; 32: 2279–85.

75 Bozeat ND, Dwyer L, Ye L, Yao T, Duan D. The role of ClC-3 chloride channels in early and late ischemic preconditioning in mouse heart. FASEB J 2005; 32: in press.

76 Mizoguchi K, Maeta H, Yamamoto A, Oe M, Kosaka H. Amelioration of myocardial global ischemia/reperfusion injury with volume-regulatory chloride channel inhibitors *in vivo*. Transplantation 2002; 73: 1185–93.

77 Chen Z, Chua CC, Ho YS, Hamdy RC, Chua BH. Overexpression of Bcl-2 attenuates apoptosis and protects against myocardial I/R injury in transgenic mice. Am J Physiol Heart Circ Physiol 2001; 280: H2313–20.

78 Lemonnier L, Shuba Y, Crepin A, Roudbaraki M, Slomianny C, Mauroy B, *et al*. Bcl-2-dependent modulation of swelling-activated Cl^- current and ClC-3 expression in human prostate cancer epithelial cells. Cancer Res 2004; 64: 4841–8.

79 Wei L, Xiao AY, Jin C, Yang A, Lu ZY, Yu SP. Effects of chloride and potassium channel blockers on apoptotic cell shrinkage and apoptosis in cortical neurons. Pflugers Arch 2004; 448: 325–34.

80 Sheppard DN, Welsh MJ. Effect of ATP-sensitive K^+ channel regulators on cystic fibrosis transmembrane conductance regulator chloride currents. J Gen Physiol 1992; 100: 573–91.

81 Sheppard DN, Robinson KA. Mechanism of glibenclamide inhibition of cystic fibrosis transmembrane conductance regulator Cl^- channels expressed in a murine cell line. J Physiol (Lond) 1997; 503 (Pt 2): 333–46.

82 Yamazaki J, Hume JR. Inhibitory effects of glibenclamide on cystic fibrosis transmembrane regulator, swelling-activated, Ca^{2+}-activated Cl^- channels in mammalian cardiac myocytes. Circ Res 1997; 81: 101–9.

83 Lochner A, Genade S, Tromp E, Podzuweit T, Moolman JA. Ischemic preconditioning and the beta-adrenergic signal transduction pathway. Circulation 1999; 100: 958–66.

84 Ping P, Song C, Zhang J, Guo Y, Cao X, Li RC, *et al*. Formation of protein kinase C (epsilon)-Lck signaling modules confers cardioprotection. J Clin Invest 2002; 109: 499–507.

85 Yamazaki J, Britton F, Collier ML, Horowitz B, Hume JR. Regulation of recombinant cardiac cystic fibrosis transmembrane conductance regulator chloride channels by protein kinase C. Biophys J 1999; 76: 1972–87.

86 Chen H, Liu LL, Ye LL, McGuckin C, Tamowski S, Scowen P, *et al*. Targeted inactivation of cystic fibrosis transmembrane conductance regulator chloride channel gene prevents ischemic preconditioning in isolated mouse heart. Circulation 2004; 110: 700–4.

87 Ye L, Ge ZD, Liu L, Murray K, Hatton WJ, Auchampach JA, *et al*. *In vivo* study of the protective role of CFTR chloride channels in ischemic preconditioning. FASEB J 2003; 174: A106.

88 Boujaoude LC, Bradshaw-Wilder C, Mao C, Cohn J, Ogretmen B, Hannun YA, *et al*. Cystic fibrosis transmembrane regulator regulates uptake of sphingoid base phosphates and lysophosphatidic acid: modulation of cellular activity of sphingosine 1-phosphate. J Biol Chem 2001; 276: 35258–64.

89 Karliner JS. Lysophospholipids and the cardiovascular system. Biochim Biophys Acta 2002; 1582: 216–21.

90 Kogan I, Ramjeesingh M, Li C, Kidd JF, Wang Y, Leslie EM, *et al*. CFTR directly mediates nucleotide-regulated glutathione flux. EMBO J 2003; 22: 1981–9.

91 Barriere H, Poujeol C, Tauc M, Blasi JM, Counillon L, Poujeol P. CFTR modulates programmed cell death by decreasing intracellular pH in Chinese hamster lung fibroblasts. Am J Physiol Cell Physiol 2001; 281: C810–24.

92 Valverde MA, Vazquez E, Munoz FJ, Nobles M, Delaney SJ, Wainwright BJ, *et al*. Murine CFTR channel and its role in regulatory volume decrease of small intestine crypts. Cell Physiol Biochem 2000; 10: 321–8.

93 Piper HM, Meuter K, Schafer C. Cellular mechanisms of ischemia-reperfusion injury. Ann Thorac Surg 2003; 75: S644–8.

94 Piper HM, Abdallah Y, Schafer C. The first minutes of reperfusion: a window of opportunity for cardioprotection. Cardiovasc Res 2004; 61: 365–71.

95 Li GR, Du XL, Siow YL, O K, Tse HF, Lau CP. Calcium-activated transient outward chloride current and phase 1 repolarization of swine ventricular action potential. Cardiovasc Res 2003; 58: 89–98.

96 Li GR, Sun H, To J, Tse HF, Lau CP. Demonstration of calcium-activated transient outward chloride current and delayed rectifier potassium currents in Swine atrial myocytes. J Mol Cell Cardiol 2004; 36: 495–504.

97 Verkerk AO, Wilders R, Zegers JG, van Borren MM, Ravesloot JH, Verheijck EE. Ca^{2+}-activated Cl^- current in rabbit sinoatrial node cells. J Physiol 2002; 540: 105–17.

98 Zygmunt AC, Goodrow RJ, Weigel CM. $I_{Na(Ca)}$ and $I_{Cl(Ca)}$ contribute to isoproterenol-induced delayed after depolarizations in midmyocardial cells. Am J Physiol 1998; 275: H1979–92.

99 Laser M, Willey CD, Jiang W, Cooper G, Menick DR, Zile MR, *et al*. Integrin activation and focal complex formation in cardiac hypertrophy. J Biol Chem 2000; 275: 35624–30.

100 Weber KT, Sun Y, Guarda E. Structural remodeling in hypertensive heart disease and the role of hormones. Hypertension 1994; 23: 869–77.

101 Colucci WS. Molecular and cellular mechanisms of myocardial failure. Am J Cardiol 1997; 80: 15L–25L.

102 Clemo HF, Stambler BS, Baumgarten CM. Swelling-activated chloride current is persistently activated in ventricular myocytes from dogs with tachycardia-induced congestive heart failure. Circ Res 1999; 84: 157–65.

103 Clemo HF, Baumgarten CM. Protein kinase C activation blocks $I_{Cl(swell)}$ and causes myocyte swelling in a rabbit congestive heart failure model. Circulation 1998; 98: I-695.

104 Clemo HF, Danetz, JS, Baumgarten CM. Does ClC-3 modulate cardiac cell volume? Biophys J 1999; 76: A203.

105 Clemo HF, Rana J, Vaida AM, Tseng GN, Higgins RS, Baumgarten CM. Chronic activation of $I_{Cl,swell}$ in canine infarction model supressess inducibility of early afterdepolarizations. Circulation 2001; 104: II-624.

106 Patel DG, Higgins RS, Baumgarten CM. Swelling-activated Cl current, $I_{Cl,swell}$, is chronically activated in diseased human atrial myocytes. Biophys J 2003; 84: 233a.

107 Benitah JP, Gomez AM, Delgado C, Lorente P, Lederer, WJ. A chloride current component induced by hypertrophy in rat ventricular myocytes. Am J Physiol 1997; 272: H2500–6.

108 De Mello WC. Heart failure: how important is cellular sequestration? The role of the renin-angiotensin-aldosterone system. J Mol Cell Cardiol 2004; 37: 431–8.

109 Liu L, Ye L, McGuckin C, Hatton WJ, Duan D. Disruption of Clcn3 gene in mice facilitates heart failure during pressure overload. J Gen Physiol 2003; 122: 76.

110 Wondergem R, Gong W, Monen SH, Dooley SN, Gonce JL, Conner TD, *et al*. Blocking swelling-activated chloride current inhibits mouse liver cell proliferation. J Physiol 2001; 532: 661–72.

111 Duffy SM, Leyland ML, Conley EC, Bradding P. Voltage-dependent and calcium-activated ion channels in the human mast cell line HMC-1. J Leukoc Biol 2001; 70: 233–40.

112 Olsen ML, Schade S, Lyons SA, Amaral MD, Sontheimer H. Expression of voltage-gated chloride channels in human glioma cells. J Neurosci 2003; 23: 5572–82.

113 Paul S. Ventricular remodeling. Crit Care Nurs Clin North Am 2003; 15: 407–11.

114 Wong KR, Trezise AE, Crozatier B, Vandenberg JI. Loss of the normal epicardial to endocardial gradient of cftr mRNA expression in the hypertrophied rabbit left ventricle. Biochem Biophys Res Commun 2000; 278: 144–9.

115 Davies WL, Vandenberg JI, Sayeed RA, Trezise AE. Post-transcriptional regulation of the cystic fibrosis gene in cardiac development and hypertrophy. Biochem Biophys Res Commun 2004; 319: 410–8.

116 Houser SR, Piacentino V III, Weisser J. Abnormalities of calcium cycling in the hypertrophied and failing heart. J Mol Cell Cardiol 2000; 32: 1595–607.

117 Elble RC, Pauli BU. Tumor suppression by a proapoptotic calcium-activated chloride channel in mammary epithelium. J Biol Chem 2001; 276: 40510–7.

118 Verkerk AO, Tan HL, Kirkels JH, Ravesloot JH. Role of Ca^{2+}-activated Cl^- current during proarrhythmic early afterdepolarizations in sheep and human ventricular myocytes. Acta Physiol Scand 2003; 179: 143–8.

119 Moore RC, Lee IY, Silverman GL, Harrison PM, Strome R, Heinrich C, *et al*. Ataxia in prion protein (PrP)-deficient mice is associated with upregulation of the novel PrP-like protein doppel. J Mol Biol 1999; 292: 797–817.

120 London B. A knockout may not always be a knockout. Circulation 2000; 102: E122.

121 Jentsch TJ, Stein V, Weinreich F, Zdebik AA. Molecular structure and physiological function of chloride channels. Physiol Rev 2002; 82: 503–68.

122 Estevez R, Boettger T, Stein V, Birkenhager R, Otto E, Hildebrandt F, *et al*. Barttin is a Cl^- channel beta-subunit crucial for renal Cl^- reabsorption and inner ear K^+ secretion. Nature 2001; 414: 558–61.

123 Ardehali H, Chen Z, Ko Y, Mejia-Alvarez R, Marban E. Multiprotein complex containing succinate dehydrogenase confers mitochondrial ATP-sensitive K^+ channel activity. Proc Natl Acad Sci USA 2004; 101: 11880–5.

124 Ping P, Song C, Zhang J, Guo Y, Cao X, Li RC, *et al*. Formation of protein kinase C(epsilon)-Lck signaling modules confers cardioprotection. J Clin Invest 2002; 109: 499–507.

125 Dutzler R, Campbell EB, Cadene M, Chait BT, MacKinnon R. X-ray structure of a ClC chloride channel at 3.0 A reveals the molecular basis of anion selectivity. Nature 2002; 415: 287–94.

Acta Pharmacologica Sinica 2005 Mar; 26 (3): 279–285

Invited review

Small guanine nucleotide-binding protein Rho and myocardial function

Jun REN[1], Cindy X FANG

Center for Cardiovascular Research and Alternative Medicine & Division of Pharmaceutical Sciences, University of Wyoming, Laramie, WY 82071, USA

Key words

RhoA; Rho kinase; heart disease

[1] Correspondence to Dr Jun REN.
Phn 1-307-766-6131.
Fax 1-307-766-2953.
E-mail jren@uwyo.edu

Received 2004-08-14
Accepted 2004-12-14

doi: 10.1111/j.1745-7254.2005.00059.x

Abstract

RhoA and Rho-kinase (ROCK) participate in a wide variety of cell signal functions such as cell growth, smooth and cardiac muscle contraction, cytoskeleton rearrangement, cell migration and proliferation. In vascular smooth muscle cells, RhoA and ROCK play an important role in Ca^{2+} sensitization and regulate vascular smooth muscle tone. In the heart, RhoA and ROCK mediate hypertrophic response leading to cardiac hypertrophy. Recent cellular and molecular biology studies using ROCK inhibitors such as Y-27632 and fasudil have indicated a pivotal role of the RhoA-ROCK cascade in many aspects of cardiovascular function such as cardiac hypertrophy and ventricular remodeling following myocardial infarction. Inhibition of the RhoA-ROCK signaling pathway may be a suitable target for a number of cardiovascular diseases including hypertension, atherosclerosis, diabetes and hypertrophic heart failure. This review focuses on the current understanding of the RhoA-ROCK signal pathway in heart diseases and discusses the use of ROCK inhibitors as therapeutic agents for heart diseases ranging from hypertensive cardiomyopathy to heart failure.

Introduction

RhoA, along with RhoB, RhoC, Rac1, Rac2, Cdc42, RhoG, and TC10, belongs to the Ras family of small GTP-binding proteins. RhoA and Rho-kinase (ROCK), a downstream target protein of small GTP-binding protein Rho, are known to regulate a wide variety of cellular processes such as changes in cell morphology, cell motility, focal adhesions, light chain phosphorylation, and cytokinesis[1,2]. Inhibition of the RhoA/ROCK cascade has been demonstrated to elicit beneficial effects on function of both heart tissues and vasculature. RhoA is believed to play a key role in cell growth, myofibrillar assembly, cardiac hypertrophy, hypertension, vascular smooth muscle cell proliferation and migration in response to heterotrimeric G protein receptor stimulation and to mechanical strain or tyrosine kinase growth factors[3–8]. ROCK has been implicated to mediate the angiotensin II (Ang II)-induced hypertrophic responses of vascular smooth muscle cells and hypertensive vascular diseases in hypertension[9,10]. In addition to cardiovascular diseases, RhoA and ROCK also participate in normal physiological processes such as pregnancy and early heart development. The mRNA expression of RhoA and two types of ROCK (α and β) was found to be elevated in the pregnant myometrium[11], which may be responsible for the augmented myometrial contractility during pregnancy. Using the small interfering RNAs (siRNA) technique, it was reported that disruption of RhoA expression resulted in absence of heart tube fusion and abnormal head development in chick embryos, indicating the importance of RhoA for normal embryogenesis and early heart development[12]. Recent studies have indicated that inhibition of the RhoA-ROCK signal pathway may be a potential target for a number of cardiovascular diseases including hypertension, atherosclerosis, diabetes and hypertrophic heart failure[13]. This review will summarize the role of RhoA and ROCK in heart morphology and function, with a special focus on the pathogenesis of heart diseases associated with abnormal RhoA and ROCK signaling. As certain factors such as peripheral vascular resistance may affect cardiac afterload and subsequently cardiac contractile function, the effect of RhoA-ROCK on cardiac morphology and function appears to be more complex than originally thought and requires more

intensive research.

Role of RhoA in cardiac hypertrophy Cardiac hypertrophy is a cardiac physiological adaptation in response to pressure or volume overload. However, after a prolonged period of time, this initial adaptive response becomes maladaptive, thus switching the heart from a compensated to a decompensated state and ultimately increased cardiac mortality and morbidity. The Gq-RhoA-ROCK pathway, which may be activated by several neurohormonal factors such as angiotensin II, is believed to function as an important signaling pathway for cardiac hypertrophy or transition from left ventricular hypertrophy to heart failure. Activation of RhoA is essential for sensing externally applied force, subsequently relaying onto the actin cytoskeleton leading to translocation of extracellular signal-regulated kinase (ERK) *en route* to cardiac hypertrophy[14,15]. It is believed that hypertrophy-related gene expression in response to RhoA activation is mediated through cross-talk with β1 integrin signal pathway via an organized actin cytoskeleton[14,15]. In addition, transcription factor GATA-4, a key regulator of cardiac genes, may also be a nuclear mediator of RhoA participating in sarcomere assembly in cardiomyocytes. Both RhoA and GATA-4 are necessary for sarcomeric reorganization in response to hypertrophic stimuli. It has been demonstrated that overexpression of either protein alone is sufficient to trigger sarcomeric reorganization[16].

In a recent study of heart failure model in Dahl salt-sensitive rats fed an 8% NaCl diet from 8 weeks with or without the ROCK inhibitor Y-27632, Satoh and colleagues reported elevated left ventricular mass, cardiac myocyte cross-sectional area, interstitial fibrosis, and contractile dysfunction shown as reduced left ventricular ejection fraction and fractional shortening, as well as prolongation in contraction/relaxation duration associated with increased protein expression of Galphaq and ROCK in the Dahl salt-sensitive, salt intake Y-27632-untreated group. Interestingly, the degree of myocardial hypertrophy was significantly reduced in conjunction with improved contractile function but no change in interstitial fibrosis following Y-27632 treatment in Dahl salt-sensitive, salt intake rats[17]. These results suggest the possibility that the Gq-ROCK signal pathway plays an important role in the process of hypertension-induced left ventricular hypertrophy leading to contractile dysfunction. The notion of a key role for RhoA-ROCK in cardiac hypertrophy received convincing support from transgenic studies using mice overexpressing RhoA or a constitutively-activated RhoA mutant in atria and ventricles[18]. Heterozygotes displayed high premature mortality, ventricular dilatation (without change in mass) and dysfunction, changes in expression of hypertrophic index gene, increases in atrial mass, marked conduction abnormalities, and other signs of heart failure[18]. Nevertheless, the phenotype of cardiac anomalies in these transgenic mice is different from those commonly seen in compensated hypertrophy, thus precluding any firm conclusion to be drawn regarding the role of RhoA in cardiac hypertrophy. The possible role of RhoA in cardiac hypertrophy also received indirect evidence from the work related to 3-hydroxyl-3-methylglutaryl coenzyme A (HMG-CoA) reductase inhibitors, or statins. Statins have been shown to inhibit cardiac hypertrophy by cholesterol-independent mechanisms including inhibition of activation of RhoA and Rac1[19]. Since Rac1 is a crucial component of reduced nicotinamide adenine dinucleotide phosphate (NADPH) oxidase, which is a main source for reactive oxygen species (ROS) in the hearts, the fact that statins inhibit Rac1-mediated oxidative stress may contribute to their inhibitory effects on cardiac hypertrophy[19].

RhoA and cardiac electromechanical function Although there have been some indications that inhibition of RhoA-ROCK may benefit cardiac dysfunction under conditions such as heart failure or ischemia-reperfusion cardiac injury[20], the precise role of RhoA-ROCK on cardiac contractile function remains unclear. Using the Dahl salt-sensitive heart failure model, it was demonstrated that inhibition of ROCK with Y-27632 significantly improved cardiac contractile dysfunction in Dahl salt-sensitive high salt intake heart failure model including reconciling reduced in left ventricular ejection fraction and fractional shortening, prolonged duration of contraction and relaxation, associated with lessened cardiac hypertrophy. These authors also found that the upregulated proto-oncogene c-*fos* gene expression, but not that of ERK and p70S6 kinase phosphorylation, under heart failure rats was decreased by inhibiting ROCK, suggesting a differential activation of the Rho-ROCK and the ERK-p70S6 kinase pathways in the failing hearts of Dahl salt-sensitive hypertensive rats[20]. The observation that ROCK inhibition rescues cardiac contractile defects (reduced contractility and prolonged duration of contraction/relaxation) is supported by cardiac function assessment obtained from the RhoA transgenic mice. Cardiac-specific overexpression of RhoA triggered prolongation of action potential duration and reduction in ventricular contractility[18]. In a separate study, cardiac-specific inhibition of ROCK was achieved by expressing Rho GDIα, an endogenous specific GDP dissociation inhibitor for Rho family proteins, using the α-myosin heavy chain (α-MHC) promoter. Increased expression of Rho GDIα preserved the left ventricular systolic and diastolic function both before and after the development of cardiac hypertrophy,

indicating that Rho GTPases may not be required for maintenance of ventricular contractile function under basal physiological conditions[21]. The RhoA-ROCK also participates in the function of cardiac conducting system. Electrocardiography and intracardiac electrophysiological evidence suggest first- and second-degree atrioventricular (AV) block in cardiac-specific Rho GDIα (which inhibits Rho GTPase) transgenic hearts at 1 and 4 weeks of age, respectively, prior to the development of cardiac hypertrophy[21]. These results suggest that the RhoA-ROCK signal cascade is necessary for cardiac electrical conduction under normal physiological conditions. Further examination revealed that expression of connexin 40 was significantly decreased from 1 to 4 weeks of age in the Rho GDIα transgenic heart, which may contribute, at least in part, to the conduction defects in the Rho GDIα transgenic mice[21].

RhoA, hypertension, and cardiac afterload Regulation of vascular smooth muscle cell contractile state is critical for the maintenance of vascular tone. The RhoA-ROCK signal cascade may affect heart function indirectly through regulation of peripheral vascular resistance. The RhoA-ROCK pathway has been demonstrated to play an important role in a wide variety of cell functions in the vasculature including actin cytoskeleton organization and vascular smooth muscle contraction. The RhoA-ROCK pathway is constitutively active in a number of organs including vascular smooth muscle under physiological and pathophysiological conditions[22]. It is believed that upregulated RhoA-ROCK signal cascade promotes cytosolic Ca^{2+} sensitization and vascular tension in smooth muscles, leading to enhanced peripheral vascular resistance, vascular tone and subsequently hypertension[22,23]. Myosin phosphatase is the key enzyme responsible for myosin light chain (MLC) dephosphorylation that regulates smooth muscle cell contraction. Vasoconstrictors and vasodilators are expected to inhibit or promote the activity of myosin phosphatase, respectively. It was indicated that G-protein-coupled receptor agonists might inhibit the activity of myosin phosphatase leading to vasoconstriction through activation of RhoA-ROCK. However, nitric oxide (NO) may activate myosin phosphatase, leading to vasorelaxation through cGMP-dependent protein kinase. It has been postulated that RhoA regulates vascular smooth muscle contraction through interaction with myosin phosphatase-Rho interacting protein, a likely new member of the myosin phosphatase controlling myosin light chain dephosphorylation[24].

In addition to the peripheral effect, blockade of the RhoA-ROCK signal pathway in nucleus tractus solitarii (NTS) of brain stem decreased blood pressure, heart rate, and renal sympathetic nerve activity in both Wistar-Kyoto (WKY) rats and spontaneously hypertensive rats (SHR), suggesting a role of the RhoA-ROCK signal cascade in central regulation of blood pressure[7]. Interestingly, the magnitude of blood pressure, heart rate, and renal sympathetic nerve activity drop was much greater in SHR than in WKY rats. Furthermore, membrane RhoA expression and ROCK activity in NTS were enhanced in SHR compared with WKY rats, confirming the contribution of the NTS RhoA-ROCK pathway to blood pressure regulation via sympathetic nervous system[7]. Additional work from the same group suggested that activation of the RhoA-ROCK signal pathway might contribute to neurogenic hypertensive mechanisms caused by chronic inhibition of NO synthesis[8]. Chronic inhibition of NO synthesis by the NO synthase (NOS) inhibitor N^{ω}-nitro-*L*-arginine methyl ester (*L*-NAME) is known to trigger the onset of hypertension, which was alleviated by the ROCK inhibitor, Y-27632. Expression of membranous RhoA and phosphorylation of the target proteins of ROCK, the ERM (ezrin, radixin, moesin) family members, was significantly greater in the *L*-NAME-treated group than control group, indicating that activation of the RhoA-ROCK signal pathway contributes to neurogenic hypertension triggered by chronic NOS inhibition[8].

RhoA and diabetic cardiovascular complications Prolonged contraction and relaxation are hallmarks of diabetic cardiomyopathy, one of the most devastating complications in diabetes[25,26]. Studies from our laboratory depicted prolonged duration of contraction and relaxation associated with normal contractility and maximal rate of contraction and relaxation in diabetes[25–27]. Although several mechanisms have been postulated for the diabetes-related mechanical defects such as diabetes-induced myosin isozyme switch (from the fast type V_1 to the slow type V_3), impaired function of sarco (endo) plasmic reticulum Ca^{2+}-ATPase (SERCA) and Na^{+}/Ca^{2+} exchanger, as well as reduced myofilament Ca^{2+} sensitivity [26,28–30], the signaling mechanisms responsible for these cellular alterations remain poorly defined. Recently, we reported up-regulation of cardiac RhoA signaling in diabetic hearts[27]. RhoA expression has been demonstrated to be up-regulated in arteries from aged, hypertensive, or diabetic rats[27,31–33]. The dynamics of RhoA gene expression is sparsely documented although binding of transcription factor cAMP-responsive element binding (CREB) protein/ activating transcription factor-1 (ATF-1) has been shown to increase the RhoA promoter activity[34]. Hyperglycemia and reactive oxygen species, which often accompany hyperglycemia, have been shown to increase nuclear CREB activity through a p38 MAP kinase-dependent pathway[35,36]. Elevated oxidative stress in diabetic heart and enhanced p38

MAP kinase activation were observed in a preliminary study (Ren and colleagues, unpublished data), which may be related to enhanced expression of RhoA and activity of ROCK. Although there is little evidence depicting a direct regulation of RhoA signaling in cardiac excitation-contraction coupling, activation of ROCK, the Rho-dependent serine-threonine kinase, has been shown to regulate cardiac contractility and gene expression, probably mediated through the MAP kinase super-family[6,18,20]. One of the likely scenarios that RhoA may participate cardiac excitation-contraction coupling is speculated to be mediated through regulation of K^+ channel and action potential duration. Cardiac-specific overexpression of RhoA was reported to prolong action potential duration and to diminish ventricular contractility[18]. The RhoA-induced prolongation of action potential may be related to its ability to interrupt certain voltage-dependent K^+ channel(s)[37]. These speculations are supported by our recent observation of concurrent up-regulation of RhoA mRNA/protein and diminished Kv1.2 protein expression in diabetic hearts (Ren and colleagues, unpublished data). Depressed expression and function of voltage-dependent K^+ channels have also been implicated in prolonged phase 3 of action potential repolarization and thus lengthened relaxation duration in diabetic hearts[38]. The involvement of RhoA signaling in diabetic heart dysfunction was supported by our finding using the ROCK inhibitor Y27632. Incubation of Y-27632 with high extracellular glucose (25.5 mmol/L) for 12 h significantly reduced the compromised cardiac mechanical function elicited by high glucose toxicity (Figure 1), suggesting that RhoA-ROCK activation may be a permissive step in the development of cardiac mechanical defects in response to high extracellular glucose or diabetic environments.

Our recent study revealed that IGF-1 transgene protected diabetes-induced mechanical dysfunctions in cardiac myocytes[39] in parallel to its action on STZ-induced elevation of RhoA mRNA and protein expression, down-regulation of Kv1.2 channels and activation of p38 MAP kinase (Ren and colleagues, unpublished data). Our results did not favor any involvement of another MAP kinase signal molecule ERK1/2 in diabetes-induced cardiomyocyte dysfunction or the cardiac protective effect of IGF-1 (Ren and

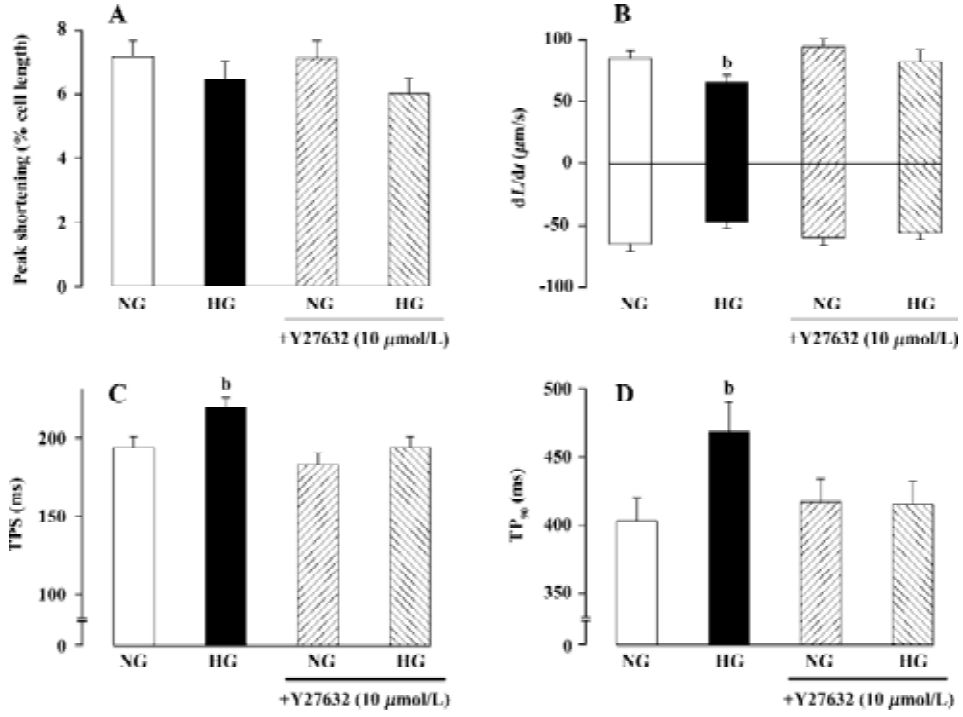

Figure 1. Effect of the ROCK-specific inhibitor Y27632 (10 μmol/L) on glucose toxicity (25.5 mmol/L)-induced mechanical defects in rat ventricular myocytes. Myocytes from normal adult male rats (225–250 g) were isolated and maintained under normal (NG, 5.5 mmol/L) or high (HG, 25.5 mmol/L) glucose medium for 12 h in the presence or absence of A27632. (A) Peak shortening (normalized to resting cell length); (B) Maximal velocity of shortening/relengthening ($\pm dL/dt$); (C) Duration of contraction: time-to-peak shortening (TPS); (D) Duration of relaxation time to 90% relengthening (TR_{90}). n=60–62 cells/group. Mean±SEM. $^bP<0.05$ *vs* NG group.

colleagues, unpublished data). Collectively, these data suggest that up-regulation of the RhoA-ROCK signal cascade may suppress the expression or function of voltage-dependent K^+ channel and p38 MAP kinase, an route to mechanical dysfunction in diabetes manifested as prolonged duration of contraction and relaxation, as well as reduced contractility. It is possible that the beneficial effects of IGF-1 on cardiac mechanical defects diabetes may be elicited though suppression of activation of the RhoA-ROCK signal cascade[40,41].

Results from our study suggested likely additional signaling mechanisms from RhoA and p38 MAP kinase (Ren and colleagues, unpublished data). Activation of p38 MAP kinase has been speculated to be down-stream of the ROCK signaling pathway[35]. However, current data failed to display that an enhanced ROCK I/II mRNA expression in diabetic groups, indicating that the activity rather than mRNA expression of ROCK I/II may be involved. Nevertheless, IGF-1 transgene reduced ROCK I/II mRNA, consistent with the notion that IGF-1 may inactivate RhoA signal cascade. The lack of effect on ERK1/2 phosphorylation in response to either diabetes or IGF-1 is somewhat consistent with our earlier report using the high glucose culture system[42].

RhoA and other cardiovascular complications Ample of evidence has demonstrated that the RhoA-ROCK mediated signaling pathway plays an important role in other cardiovascular complications such as ischemia/reperfusion heart injury and ventricular remodeling following myocardial infarction. It was reported that fasudil, a potent ROCK inhibitor, prevented occurrence of myocardial ischemia in patients with microvascular angina[43]. It was found that ischemia/reperfusion upregulated RhoA expression in ischemic myocardium and increased ROCK activity. Inhibition of ROCK with selective ROCK inhibitors protected the heart against ischemia injury and enhanced post-ischemia cardiac function. This cardioprotective effect may be attributed to an anti-apoptotic mechanism of ROCK inhibition since ROCK inhibitors may significantly attenuate the downregulation of Bcl-2 expression induced by ischemia/reperfusion injury. An alternative explanation for such cardioprotective property of the ROCK inhibitors may be associated with their ability to suppress ischemia/reperfusion-induced elevation in serum levels of proinflammatory cytokines[44]. Further studies have shown that RhoA may be a novel mediator of adenosine-induced cardiac protection against ischemia. The adenosine A_3 receptor mediated anti-ischemic function in the heart appeared to signal selectively through RhoA since overexpression the RhoA-noninteracting mutant caused significant reduction of A_3 agonist-induced anti-ischemic effect. It was suggested that RhoA was an important cardioprotective signaling molecule that interacted directly to phospholipase D (PLD) in cardiac myocytes[45]. Inhibition of ROCK attenuates production of superoxide, reduces generation of monocyte chemoattractant protein-1 or plasminogen activator inhibitor-1 (PAI-1), and inhibits activation of macrophages, neutrophils, and platelets, all of which are considered essential for inhibition of stress-induced regional inflammatory responses and diminished myocardial ischemia-reperfusion injury[46]. Furthermore, RhoA was found to mitigate the reperfusion-induced change in the shape of cardiac capillary endothelial cells *in situ* and thereby ameliorate the reperfusion injury[47].

Apart from cardiac ischemia/reperfusion injury, RhoA-ROCK has also been demonstrated to be involved in the process of myocardial infarction. It is generally accepted that inhibition of ROCK directly relaxes vascular smooth muscle and therefore increases regional myocardial blood flow at sites of major coronary artery stenosis by dilating abnormally narrowed or occulted artery. However, a recent study revealed that the infarct-limiting mechanism which involved ROCK inhibition could be independent of either a change in systemic hemodynamics or recruitment of collateral blood flow. Transient accumulation of cAMP was demonstrated in myocardium during ischemic preconditioning and may play a role to limit the size of infarction[48]. Other mechanisms such as down-regulating inflammatory responses mediated by cytokines and chemokines may also be involved in limiting the growth of infarct size[49] although further study is warranted to elucidate the therapeutic value of ROCK inhibitors in the management of myocardial infarction.

Summary and conclusion During the past few years, considerable progress has been made toward understanding the signaling pathways and the function of RhoA-ROCK in cardiovascular systems. These studies have convincingly revealed that RhoA-ROCK are versatile signaling molecules regulating diverse cellular functions including cytoskeletal rearrangement[50], Ca^{2+} sensitization[51], cytokinesis[52] and lineage commitment as well as fate of stem cells[53]. However, much remains to be learned about the detailed regulation mechanisms of RhoA-ROCK as well as its downstream signaling targets. It is imperative that future efforts be directed toward better defining and characterizing the signal pathways regulated by RhoA-ROCK in cardiovascular systems. Such efforts will likely yield new molecular targets for the RhoA-ROCK signal cascade and ultimately more effective therapies for preventing or ameliorating cardiovascular diseases such as cardiac hypertrophy, hypertension, diabetes

and atherosclerosis through either pharmacologically or genetic modulation of RhoA-ROCK regulated signaling.

Acknowledgement

The Ren laboratory has been supported by grants from the American Diabetes Association, the American Heart Association, the National Institute of Health, the North Dakota Max Baer Heart Fund, and a University of Wyoming Research Grant.

References

1 Amano M, Chihara K, Kimura K, Fukata Y, Nakamura N, Matsuura Y, *et al*. Formation of actin stress fibers and focal adhesions enhanced by Rho-kinase. Science 1997; 275: 1308–11.

2 Yasui Y, Amano M, Nagata K, Inagaki N, Nakamura H, Saya H, *et al*. Roles of Rho-associated kinase in cytokinesis: mutations in Rho-associated kinase phosphorylation sites impair cytokinetic segregation of glial filaments. J Cell Biol 1998; 143: 1249–58.

3 Hoshijima M, Sah VP, Wang Y, Chien KR, Brown JH. The low molecular weight GTPase Rho regulates myofibril formation and organization in neonatal rat ventricular myocytes: involvement of Rho kinase. J Biol Chem 1998; 273: 7725–30.

4 Majumdar M, Seasholtz TM, Goldstein D, de Lanerolle P, Brown JH. Requirement for Rho-mediated myosin light chain phosphorylation in thrombin-stimulated cell rounding and its dissociation from mitogenesis. J Biol Chem 1998; 273: 10099–106.

5 Seasholtz TM, Majumdar M, Kaplan DD, Brown JH. Rho and Rho kinase mediate thrombin-stimulated vascular smooth muscle cell DNA synthesis and migration. Circ Res 1999; 84: 1186–93.

6 Clerk A, Sugden PH. Small guanine nucleotide-binding proteins and myocardial hypertrophy. Circ Res 2000; 86: 1019-23.

7 Ito K, Hirooka Y, Sakai K, Kishi T, Kaibuchi K, Shimokawa H, *et al*. Rho/Rho-kinase pathway in brain stem contributes to blood pressure regulation via sympathetic nervous system: possible involvement in neural mechanisms of hypertension. Circ Res 2003; 92: 1337–43.

8 Ito K, Hirooka Y, Kishi T, Kimura Y, Kaibuchi K, Shimokawa H, *et al*. Rho/Rho-kinase pathway in the brainstem contributes to hypertension caused by chronic nitric oxide synthase inhibition. Hypertension 2004; 43: 156–62.

9 Yamakawa T, Tanaka S, Numaguchi K, Yamakawa Y, Motley ED, Ichihara S, *et al*. Involvement of Rho-kinase in angiotensin II-induced hypertrophy of rat vascular smooth muscle cells. Hypertension 2000; 35: 313–8.

10 Mukai Y, Shimokawa H, Matoba T, Kandabashi T, Satoh S, Hiroki J, *et al*. Involvement of Rho-kinase in hypertensive vascular disease: a novel therapeutic target in hypertension. FASEB J 2001; 15: 1062–4.

11 Nirro N, Nishimura J, Sakihara C, Nakano H, Kanaide H. Up-regulation of Rho A and Rho-kinase mRNAs in the rat myometrium during pregnancy. Biochem Biophys Res Commun 1997; 230: 356–9.

12 Kaarbo M, Crane DI, Murrell WG. RhoA is highly up-regulated in the process of early heart development of the chick and important for normal embryogenesis. Dev Dyn 2003; 227: 35–47.

13 Hu E, Lee D. Rho kinase inhibitors as potential therapeutic agents for cardiovascular diseases. Curr Opin Investig Drugs 2003; 4: 1065–75.

14 Wei L, Wang L, Carson JA, Agan JE, Imanaka-Yoshida K, Schwartz RJ. beta1 Integrin and organized actin filaments facilitate cardiomyocyte-specific RhoA-dependent activation of the skeletal alpha-actin promoter. FASEB J 2001; 15: 785–96.

15 Kawamura S, Miyamoto S, Brown JH. Initiation and transduction of stretch-induced RhoA and Rac1 activation through caveolae: cytoskeletal regulation of ERK translocation. J Biol Chem 2003; 278: 31111–7.

16 Charron F, Tsimiklis G, Arcand M, Robitaille L, Liang Q, Molkentin JD, *et al*. Tissue-specific GATA factors are transcriptional effectors of the small GTPase RhoA. Genes Dev 2001; 15: 2702–19.

17 Satoh S, Ueda Y, Koyanagi M, Kadokami T, Sugano M, Yoshikawa Y, *et al*. Chronic inhibition of Rho kinase blunts the process of left ventricular hypertrophy leading to cardiac contractile dysfunction in hypertension-induced heart failure. J Mol Cell Cardiol 2003; 35: 59–70.

18 Sah VP, Minamisawa S, Tam SP, Wu TH, Dorn GW, Ross J Jr, *et al*. Cardiac-specific overexpression of RhoA results in sinus and atrioventricular nodal dysfunction and contractile failure. J Clin Invest 1999; 103: 1627–34.

19 Nakagami H, Liao JK. Statins and myocardial hypertrophy. Coron Artery Dis 2004; 15: 247–50.

20 Kobayashi N, Horinaka S, Mita S, Nakano S, Honda T, Yoshida K, *et al*. Critical role of Rho-kinase pathway for cardiac performance and remodeling in failing rat hearts. Cardiovasc Res 2002; 55: 757–67.

21 Wei L, Taffet GE, Khoury DS, Bo J, Li Y, Yatani A, *et al*. Disruption of Rho signaling results in progressive atrioventricular conduction defects while ventricular function remains preserved. FASEB J 2004; 18: 857–9.

23 Somlyo AP, Somlyo AV. Ca^{2+} sensitivity of smooth muscle and nonmuscle myosin II: modulated by G proteins, kinases, and myosin phosphatase. Physiol Rev 2003; 83: 1325–58.

24 Surks HK, Richards CT, Mendelsohn ME. Myosin phosphatase-Rho interacting protein: a new member of the myosin phosphatase complex that directly binds RhoA. J Biol Chem 2003; 278: 51484–93

25 Ren J, Davidoff AJ. Diabetes rapidly induces contractile dysfunctions in isolated ventricular myocytes. Am J Physiol Heart Circ Physiol 1997; 272: H148–H158.

26 Ren J, Bode AM. Altered cardiac excitation-contraction coupling in ventricular myocytes from spontaneously diabetic BB rats. Am J Physiol Heart Circ Physiol 2000; 279: H238–44.

27 Duan J, Zhang HY, Adkins SD, Ren BH, Norby FL, Zhang X, *et al*. Impaired cardiac function and IGF-I response in myocytes from calmodulin-diabetic mice: role of Akt and RhoA. Am J Physiol Endocrinol Metab 2003; 284: E366–76.

28 Dillmann WH. Diabetes and thyroid-hormone-induced changes in cardiac function and their molecular basis. Annu Rev Med 1989; 40: 373–94.

29 Hofmann PA, Menon V, Gannaway KF. Effects of diabetes on isometric tension as a function of $[Ca^{2+}]$ and pH in rat skinned cardiac myocytes. Am J Physiol Heart Circ Physiol 1995; 269:

H1656–63.
30 Chattou S, Diacono J, Feuvray D. Decrease in sodium-calcium exchange and calcium currents in diabetic rat ventricular myocytes. Acta Physiol Scand 1999; 166: 137–44.
31 Miao L, Calvert JW, Tang J, Parent AD, Zhang JH. Age-related RhoA expression in blood vessels of rats. Mech Ageing Dev 2001; 122: 1757–70.
32 Seasholtz TM, Zhang T, Morissette MR, Howes AL, Yang AH, Brown JH. Increased expression and activity of RhoA are associated with increased DNA synthesis and reduced p27(Kip1) expression in the vasculature of hypertensive rats. Circ Res 2001; 89: 488–95.
33 Massey AR, Miao L, Smith BN, Liu J, Kusaka I, Zhang JH, *et al*. Increased RhoA translocation in renal cortex of diabetic rats. Life Sci 2003; 72: 2943–52.
34 Sauzeau V, Rolli-Derkinderen M, Marionneau C, Loirand G, Pacaud P. RhoA expression is controlled by nitric oxide through cGMP-dependent protein kinase activation. J Biol Chem 2003; 278: 9472–80.
35 Singh LP, Andy J, Anyamale V, Greene K, Alexander M, Crook ED. Hexosamine-induced fibronectin protein synthesis in mesangial cells is associated with increases in cAMP responsive element binding (CREB) phosphorylation and nuclear CREB: the involvement of protein kinases A and C. Diabetes 2001; 50: 2355–62.
36 Ichiki T, Tokunou T, Fukuyama K, Iino N, Masuda S, Takeshita A. Cyclic AMP response element-binding protein mediates reactive oxygen species-induced c-*fos* expression. Hypertension 2003; 42: 177–83.
37 Cachero TG, Morielli AD, Peralta EG. The small GTP-binding protein RhoA regulates a delayed rectifier potassium channel. Cell 1998; 93: 1077–85.
38 Shimoni Y, Firek L, Severson D, Giles W. Short-term diabetes alters K^+ currents in rat ventricular myocytes. Circ Res 1994; 74: 620–8.
39 Norby FL, Aberle NS 2nd, Kajstura J, Anversa P, Ren J. Transgenic overexpression of insulin-like growth factor I prevents streptozotocin-induced cardiac contractile dysfunction and beta-adrenergic response in ventricular myocytes. J Endocrinol 2004; 180: 175–82.
40 Kajstura J, Fiordaliso F, Andreoli AM, Li B, Chimenti S, Medow MS, *et al*. IGF-1 overexpression inhibits the development of diabetic cardiomyopathy and angiotensin II-mediated oxidative stress. Diabetes 2001; 50: 1414–24.
41 Norby FL, Wold LE, Duan J, Hintz KK, Ren J. IGF-I attenuates diabetes-induced cardiac contractile dysfunction in ventricular myocytes. Am J Physiol Endocrinol Metab 2002; 283: E658–66.
42 Ren J, Duan J, Hintz KK, Ren BH. High glucose induces cardiac insulin-like growth factor I resistance in ventricular myocytes: role of Akt and ERK activation. Cardiovasc Res 2003; 57: 738–48.
43 Mohri M, Shimokawa H, Hirakawa Y, Masumoto A, Takeshita A. Rho-kinase inhibition with intracoronary fasudil prevents myocardial ischemia in patients with coronary microvascular spasm. J Am Coll Cardiol 2003; 41: 15–9.
44 Bao W, Hu E, Tao L, Boyce R, Mirabile R, Thudium DT, *et al*. Inhibition of Rho-kinase protects the heart against ischemia/reperfusion injury. Cardiovasc Res 2004; 61: 548–58.
45 Mozzicato S, Joshi BV, Jacobson KA, Liang BT. Role of direct RhoA-phospholipase D1 interaction in mediating adenosine-induced protection from cardiac ischemia. FASEB J 2004; 18: 406–8.
46 Shimokawa H. Rho-kinase as a novel therapeutic target in treatment of cardiovascular diseases. J Cardiovasc Pharmacol 2002; 39: 319–27.
47 Glyn MC, Lawrenson JG, Ward BJ. A Rho-associated kinase mitigates reperfusion-induced change in the shape of cardiac capillary endothelial cells *in situ*. Cardiovasc Res 2003; 57: 195–206.
48 Sanada S, Asanuma H, Tsukamoto O, Minamino T, Node K, Takashima S, *et al*. Protein kinase A as another mediator of ischemic preconditioning independent of protein kinase C. Circulation 2004; 110: 51–7.
49 Hattori T, Shimokawa H, Higashi M, Hiroki J, Mukai Y, Tsutsui H, *et al*. Long-term inhibition of Rho-kinase suppresses left ventricular remodeling after myocardial infarction in mice. Circulation 2004; 109: 2234–9.
50 Ishizaki T, Morishima Y, Okamoto M, Furuyashiki T, Kato T, Narumiya S. Coordination of microtubules and actin cytoskeleton by the Rho effector mDial. Nature Cell Biol 2001; 3: 8–14.
51 Somlyo AV. New roads leading to Ca^{2+} sensitization. Circ Res 2002; 91: 83–4.
52 Glotzer M. Cytokinesis: progress on all fronts. Curr Opin Cell Biol 2003; 15: 684–90.
53 McBeath R, Pirone DM, Nelson CM, Bhadriraju K, Chen CS. Cell shape, cytoskeletal tension, and RhoA regulate stem cell lineage commitment. Dev Cell 2004; 6: 483–95.

Acta Pharmacologica Sinica 2005 Mar; 26 (3): 286–294

Blackwell Publishing

Invited review

The vanilloid receptor and hypertension[1]

Donna H WANG[2]

Department of Medicine, College of Human Medicine, Michigan State University, East Lansing, MI 48825, USA

Key words

TRP family; afferent neurons; capsaicin; calcitonin gene-related peptide; substance P; vanilloid receptor; renin-angiotensin-aldosterone system; endothelin, sympathetic nervous system; salt-sensitive hypertension

[1] This work was supported in part by National Institutes of Health (grants HL-52279 and HL-57853) and a grant from the Michigan Economic Development Corporation.
[2] Correspondence to Donna H WANG, MD.
Phn 1-517-432-0797.
Fax 1-517-432-1326.
E-mail donna.wang@ht.msu.edu

Received 2004-08-10
Accepted 2004-12-14

doi: 10.1111/j.1745-7254.2005.00057.x

Abstract

Mammalian transient receptor potential (TRP) channels consist of six related protein sub-families that are involved in a variety of pathophysiological function, and disease development. The TRPV1 channel, a member of the TRPV sub-family, is identified by expression cloning using the "hot" pepper-derived vanilloid compound capsaicin as a ligand. Therefore, TRPV1 is also referred as the vanilloid receptor (VR1) or the capsaicin receptor. VR1 is mainly expressed in a subpopulation of primary afferent neurons that project to cardiovascular and renal tissues. These capsaicin-sensitive primary afferent neurons are not only involved in the perception of somatic and visceral pain, but also have a "sensory-effector" function. Regarding the latter, these neurons release stored neuropeptides through a calcium-dependent mechanism via the binding of capsaicin to VR1. The most studied sensory neuropeptides are calcitonin gene-related peptide (CGRP) and substance P (SP), which are potent vasodilators and natriuretic/diuretic factors. Recent evidence using the model of neonatal degeneration of capsaicin-sensitive sensory nerves revealed novel mechanisms that underlie increased salt sensitivity and several experimental models of hypertension. These mechanisms include insufficient suppression of plasma renin activity and plasma aldosterone levels subsequent to salt loading, enhancement of sympathoexcitatory response in the face of a salt challenge, activation of the endothelin-1 receptor, and impaired natriuretic response to salt loading in capsaicin-pretreated rats. These data indicate that sensory nerves counterbalance the prohypertensive effects of several neurohormonal systems to maintain normal blood pressure when challenged with salt loading. The therapeutic utilities of vanilloid compounds, endogenous agonists, and sensory neuropeptides are also discussed.

Introduction

Mammalian transient receptor potential (TRP) channels consist of six related protein sub-families known as TRPV, TRPC, TRPM, TRPP, TRPML, and TRPA[1]. These channels are widely distributed and involved in sensing local stimuli ranging from changes in hemodynamics to pH and osmolarity. The TRPV1 channel, a member of the TRPV sub-family, was identified by expression cloning using the "hot" pepper-derived vanilloid compound capsaicin as a ligand. TRPV1 is therefore referred as the vanilloid receptor (VR1) or the capsaicin receptor. Capsaicin as well as other closely related vanilloid substances are principal constituents in the hot chilli peppers and responsible for the pungency of these spices[2].

Over the last several centuries, knowledge about the physiological actions of capsaicin has grown and capsaicin has become a powerful tool, as will be described, for studying mechanisms underlying hypertension. Ever since its isolation in the mid-nineteenth century, capsaicin has been documented to act on sensory fibers with neuroselectivity[3,4]. Nelson elucidated the structure of capsaicin, reporting it as 8-methyl-vannillyl-6-noneamide, an acylamide derivative of homovanillic acid[5]. The compound consists of three functional moieties: vannilyl, acylamide, and alkyl[2]. Jancso later showed that capsaicin-sensitive nerve endings could be

stimulated as well as destroyed by a sufficiently high dose of capsaicin[6]. The neurotoxicity effect of capsaicin is of paramount importance, for reasons that will become clear, to neurobiologists using capsaicin sensitive-sensory nerve degeneration to study blood pressure regulation. The review that follows outlines the advances that have been made since Jancso's publications, with regard to mechanisms of capsaicin's action, cardiovascular effects of select neuropeptides released by a subset of capsaicin-sensitive primary afferent neurons (CSPAN) innervating cardiovascular and renal tissues, and pathophysiologic mechanisms of hypertension elucidated by capsaicin sensitive sensory-nerve degeneration. Capsaicin pharmacology and the nature of capsaicin-sensitive sensory nerves are discussed in greater detail in a number of other excellent scholarly reviews[7–9]. This review is restricted to a discussion of the effects of capsaicin on the cardiovascular system. Other authors have reviewed the effects of capsaicin on the somatosensory, respiratory, thermoregulatory, and gastrointestinal systems[10–14].

VR1 positive sensory neurons

VR1-positive sensory neurons refer to a subset of primary afferent neurons that express the VR1 receptors which can be activated by capsaicin. The pharmacological property of sensitivity to capsaicin distinguishes these afferent neurons, mostly having unmyelinated (C fibers) or thinly myelinated axons (Aδ fibers), from other afferent neurons[15].

Maggi[15] has described the functional anatomy of the VR1-positive primary afferent neuron by identifying four sites from which neurotransmitter release may occur: (i) central terminals of the afferent neuron in contact with second-order neurons in the CNS; (ii) terminals distributed in the prevertebral ganglia; (iii) peripheral terminals distinct from the terminal at which the sensory stimulus is applied; and (iv) the same peripheral terminal at which the sensory stimulus is applied. Neurotransmitter release at sites (i) and (ii) accounts for the sensory function of CSPAN and is central to perception of somatic and visceral pain. In contrast, and as implied by neuropeptide release from peripheral terminals (iii) and (iv), CSPAN nerve endings not only serve as sensory receptors, but also as effector sites from which neurotransmitters are released. Thus, neurotransmitter release from sites (iii) and (iv) accounts for the "sensory-efferent" function of CSPAN, with release from site (iv) not even requiring neuronal conduction[15]. Accordingly, Maggi and Meli[11] have termed release from site (iv) the "sensory receptor potential-coupled efferent response." Local sensory stimuli that may induce neurotransmitter release are varied and include nerve growth factor[16], vascular wall tension[17], the sympathetic nervous system[18], bradykinin[19], and endothelin[20].

Efferent function of VR1-positive sensory neurons

VR1-positive sensory neurons have a dual function: sensory perception and sensory efferent function. Binding of capsaicin and capsaicin agonists to VR-1 leads to neuropeptide release from a subpopulation of neuropeptide-containing primary afferent neurons[15]. Binding to this receptor opens a receptor-operated permeable cation channel[21–25] that ultimately results in the influx of sodium and calcium ions. Sodium influx is sufficient for afferent impulse conduction. In sharp contrast, calcium influx, and thus extracellular calcium, is prerequisite for neuropeptide release. Without extracellular calcium, sensory neuropeptides are no longer released from sensory nerve endings when these endings are depolarized[15].

Given that the neuroselectivity of capsaicin is a reflection of the selective expression of the VR1 on a subpopulation of primary afferent neurons, a closer look at the VR1 is warranted. Initial evidence supporting a capsaicin-binding site on a subset of primary afferent neurons came from observations that capsaicin analogues are able to exert similar functional changes[26,27]. Additional support came from experimentation with resiniferatoxin, a phorbol ester derivative that has been shown to exhibit structural similarity [28,29] and densensitizing and excitatory properties homologous to those exhibited by capsaicin, albeit at 1000-fold lower doses[28–30]. Definitive support for the presence of a chemical moiety capable of binding to capsaicin and related agonists came with the development of capsazepine, experimentally shown to act as a competitive antagonist of vanilloid binding and activity[31]. The VR-1 has been reviewed in greater detail in an authoritative review by Caterina and Julius[32].

Concerning the nature of transmitters released from VR1-positive sensory neurons, Maggi and Meli[15] have reported that at least the following 12 different types of transmitters are present in capsaicin-sensitive sensory neurons: substance P (SP), neurokinin A, neuropeptide K, eledoisin-like peptide, somatostatin, vasoactive intestinal polypeptide, cholecystokinin-octapeptide, calcitonin gene-related peptide (CGRP), galanin, corticotrophin-releasing factor, arginin vasopressin, bombesin-like peptides. These authors also report that multiple neuropeptides can be simultaneously released from VR1-positive sensory nerve endings. However,

different neuropeptides may be preferentially released as a function of stimulus intensity[33].

It has been shown that plasma concentrations of CGRP rise transiently after administration of capsaicin in adult rats[3,4]. Given that capsaicin exerts its action through release of neuropeptides, acute administration of capsaicin produces functional changes related to the activity of the released neuropeptides[35]. In contrast, and of significance to elucidating mechanisms underlying hypertension, capsaicin administered systemically at a dose of 50 mg/kg of body weight to neonatal rats or mice leads to an irreversible loss of more than 80% of small-diameter sensory neuron cell bodies[36–41]. These observations indicate that high doses of capsaicin lead to neurotoxic effects including substantial depletion of stores of neuropeptides within VR-1 positive sensory neuron.

Innervation of cardiovascular tissue by VR1-positive sensory nerves

VR1-positive sensory nerves are found around blood vessels in virtually all vascular beds. CGRP, often co-localized with SP, is found in nerve endings of a subset of these sensory nerves[42–46]. Synthesis of these neuropeptides occurs in the dorsal root ganglia which contain cell bodies of the capsaicin-sensitive sensory nerves. CGRP, co-localized with SP, is also found in a subpopulation of VR1-positive sensory nerves innervating the hearts of rats, guinea pigs, and humans, though in a much lower density than around blood vessels[43].

CGRP is a potent vasodilator that also has positive chronotropic and ionotropic effects[43]. The coronary vasculature is a particularly susceptible target of the vasodilatory action of CGRP[47,48]. Of significance to understanding the pathogenesis of hypertension, systemic administration of CGRP decreases blood pressure in normotensive animals, normotensive humans, and spontaneously hypertensive rats[43,44]. This decrease is produced via peripheral arterial dilation mediated through nitric oxide-dependent and nitric oxide-independent mechanisms[43]. The fact that bolus injection of $CGRP_{8-37}$, a CGRP receptor antagonist, produces dose-dependent increases in mean arterial pressure in deoxycorticosterone-salt hypertensive rats indicates that CGRP-induced vasodilation may play a compensatory role in this model[49].

VR1-positive sensory nerves and established models of hypertension

At least two hypertensive models have been used for defining the role of VR1-positive sensory nerves. One is the one-kidney wrap (1K-WRAP) hypertensive model and the other the deoxycorticosterone (DOCA)-salt hypertensive model. Intrathecal administration of capsaicin to adult rats was used to deplete SP and CGRP within central processes of afferent renal nerves (ARN) within selective laminae of the dorsal horn for determining whether SP and/or CGRP localized in ARN play a role in the development of 1K-WRAP hypertension or DOCA-salt hypertension[50]. Capsaicin treatment enhanced the development of 1K-WRAP hypertension, considering that systolic blood pressure was greater in 1K-WRAP rats pretreated with capsaicin compared with vehicle-treated 1K-WRAP rats[50]. However, capsaicin pretreatment had no effect on systolic blood pressure in DOCA-salt rats, suggesting that the depletion of sensory neurotransmitters from ARN by capsaicin does not exacerbate DOCA-salt hypertension. Indeed, these authors concluded that "ARN did not play a major role in the development of DOCA-salt hypertension."[50]

Manzini and Bacciarelli[51] performed a similar study in which the effect of neonatal degeneration of VR1-positive sensory nerves on the development of DOCA-salt hypertension was investigated. As expected by the degeneration of sensory neurons in capsaicin-pretreated animals, substance P-like immunoreactivity was virtually undetectable in capsaicin-pretreated animals and blood pressure was much less responsive to acute administration to capsaicin as compared to control animals. DOCA-salt induced-hypertension was of quicker onset and of greater magnitude in the animals pretreated with capsaicin. Hypertensive rats pretreated with capsaicin also had a greater incidence of cardiac necrosis. These authors, in contrast to Burg *et al*, concluded that capsaicin-sensitive sensory fibers may underlie antihypertensive mechanisms and play a protective role in preventing the development of DOCA-salt hypertension[51].

VR1-positive sensory nerves and increased salt sensitivity

Though studies by Burg *et al*[50] and Manzini and Bacciarelli[51] have shown that VR1-positive sensory nerves are implicated in blood pressure regulation, these investigations have not shown whether impairment of the sensory nervous system is sufficient to produce hypertension. We showed for the first time in 1998 that neonatal degeneration of VR1-sensitive sensory nerves rendered an adult rat salt-sensitive[52]. We administered 50 mg/kg capsaicin or vehicle subcutaneously to newborn Wistar rats on the first and second days of life, and a high or normal sodium diet was given

immediately following the weaning period. We found that neonatal treatment with capsaicin led to elevation of blood pressure in rats fed a high sodium diet, but not in those fed a normal sodium diet. High salt intake increased urine volume and sodium excretion in both vehicle and capsaicin treated rats. However, these parameters were significantly lower in capsaicin treated rats fed a high-salt diet compared to vehicle treated rats fed a high-salt diet. These results suggest that capsaicin neonatal treatment might impair renal function when rats are loaded with salt.

Role of the renin-angiotensin-aldosterone system (RAAS) To define the molecular mechanisms underlying sensory nerve function involved in the pathogenesis of salt-sensitive hypertension, we[53] subsequently explored the role of the RAAS in the aforementioned salt-sensitive hypertensive model induced by sensory denervation. Capsaicin plus high-salt-treated rats were given losartan (a type I angiotensin II receptor blocker), prazosin (a selective α_1-adeno-receptor blocker), or hydralazine (a nonspecific vasodilator). Both tail-cuff systolic blood pressure and mean arterial blood pressure were higher in capsaicin-treated rats fed a high-salt diet and capsaicin treated rats fed a high-salt diet plus prazosin when compared to capsaicin treated-rats fed a high-salt diet plus losartan or hydralazine, the vehicle-treated rats fed a high-salt diet, or capsaicin-treated rats fed a normal salt diet. These results suggest that losartan and hydralazine, but not prazosin, are able to prevent the development of salt-induced hypertension in capsaicin-pretreated animals. Of significance to understanding the pathophysiology of salt-sensitive hypertension, these results revealed that there was an interaction between the sensory nervous system and the RAAS in a manner that prevents the development of salt-induced hypertension in sensory-intact rats. This study also confirmed that capsaicin might impair the natriuretic response to a high salt intake, as rats pretreated with capsaicin and fed a high-salt diet have decreased urinary volume and sodium excretion. Interestingly, losartan and hydralazine did not protect against the impaired natriuretic response, even though these agents did prevent the development of hypertension in salt-loaded capsaicin pretreated rats. These results indicate that intact sensory innervation is essential for the normal natriuretic response to sodium loading and that the antihypertensive effects of losartan and hydralazine may be mediated by mechanisms for example, vasodilatory mechanism, other than those that protect against the impairment of urinary sodium and water excretion in this model.

To further investigate the roles of the type 1 (AT1) and 2 (AT2) angiotensin II (AII) receptors in the development of salt-induced hypertension in capsaicin-pretreated rats, we[54] treated capsaicin-pretreated rats fed a high-salt diet with candesartan (a selective blocker of the AT1 receptor), PD 123319 (a selective blocker of the AT2 receptor), or a combination of these two drugs. Development of hypertension in capsaicin treated rats fed a high-salt diet was prevented or attenuated by candesartan and PD 123319, respectively, indicating that both of these antagonists were protective and effective in lowering increased blood pressure induced by a salt challenge in capsaicin-pretreated animals. The antihypertensive effect of PD 123319 is unexpected and the underlying mechanisms remain to be defined. Plasma renin activity (PRA) was suppressed by high salt intake in both vehicle- or capsaicin-treated rats, but it was significantly less suppressed in the latter than in the former. This observation suggests that PRA may be insufficiently suppressed in capsaicin-pretreated animals, likely contributing to hypertension in these animals.

We next studied aldosterone and its interaction with the sensory nervous system in the induction of salt-sensitive hypertension, in light of the aforementioned finding that PRA is insufficiently suppressed in neonatally capsaicin-pretreated rats challenged with a salt load[54,55]. Both vehicle- and capsaicin-treated rats fed a high-salt diet was given spironolactone, an aldosterone receptor antagonist for 3 weeks. We found that chronic spironolactone treatment appeared to restore renal functional impairment and prevented the development of hypertension in neonatally capsaicin-pretreated rats fed a high-salt diet[55]. This is in contrast to our previous report with losartan and hydralazine, which have been shown to attenuate elevated blood pressure in capsaicin pretreated rats challenged with a salt load, but not able to improve renal functional impairment[53]. These results indicate that the antihypertensive effect of spironolactone in this model is mediated by improving renal function, consistent with the role of aldosterone receptors in the kidney that cause sodium and water retention.

Albeit markedly suppressed by salt loading, plasma aldosterone levels (PAL) and PRA were significantly higher in capsaicin-pretreated rats challenged with salt load than sensory-nerve-intact rats fed the same high-salt diet[55]. This suggests PRA and PAL are insufficiently suppressed in sensory-denervated rats, contributing to increased salt sensitivity and renal functional impairment in these animals. Insufficiently suppressed PAL in response to salt loading can be attributed to one or both of the following: (i) increased circulating and/or tissue AII levels; and/or (ii) upregulation of the AII type I receptor in the zona glomerulosa of the adrenal gland, a receptor to which binding of AII increases aldosterone synthesis and secretion. We[55] found that the

AT1 receptor content in the adrenal gland was not altered in any of the experimental groups, strongly suggesting that insufficiently suppressed PAL is a reflection of insufficiently suppressed circulating and/or tissue AII levels.

In contrast to above mentioned studies that define the role of the RAAS in the development of hypertension in capsaicin treated rats fed a high-salt diet, we studied the role of sensory nerves in attenuating the development of hypertension induced by AII infusion[56]. AII or vehicle-infused rats were pretreated with capsaicin or vehicle. Mean arterial pressure was higher in rats infused with AII, and it was higher in AII-infused rats pretreated with capsaicin compared to rats infused with AII alone. Northern blot analysis revealed that AII-infused rats had an increase in the level of CGRP mRNA in the dorsal root ganglia, suggesting that subpressor infusion of AII either stimulates the synthesis of CGRP mRNA or retards its degradation. Taken together, these data suggest that neuropeptides released by sensory nerves attenuate elevated blood pressure induced by AII infusion and that the increase in CGRP synthesis appears to be a compensatory response to diminish increased blood pressure induced by AII infusion. Furthermore, 24-h urinary and sodium excretions were lower in AII-infused rats pretreated with capsaicin than they were in rats infused with AII alone. These results are consistent with the finding that degeneration of VR1 positive sensory nerves impairs the natriuretic response to a salt load[52–55].

Role of the sympathetic nervous system Defining the interaction between the sympathetic and sensory nervous systems, we found that sympathectomy produced by administration of guanethidine subcutaneously prevented the development of salt-sensitive hypertension induced by sensory nerve degeneration[57]. This finding suggests that: (i) enhanced sympathoexcitatory response occurs in capsaicin-pretreated rats fed a high-salt diet, which may contribute to increased salt sensitivity in these animals; and (ii) there is a balance between antihypertensive effects of sensory nerves and prohypertensive effects of the sympathetic nervous system in a normal rat. This balance is disrupted following capsaicin-pretreatment and consequential sensory nerve degeneration, such that the animal is salt-sensitive. Sympathectomy may also result in less renin release by withdrawing the stimulation of the α_1-adrenergic receptors.

These findings appear to be in contrast to our previous results in which prazosin is not able to prevent the development of salt-induced hypertension in capsaicin-pretreated animals[53]. To reconcile this finding about prazosin with the antihypertensive effect of sympathectomy, one should keep in mind the following considerations: (i) the dose of prazosin may not have been high enough to decrease blood pressure in neonatally capsaicin-pretreated rats challenged with a salt load, even though the same dose resulted in reduction in blood pressure in spontaneously hypertensive rats[58]; (ii) alpha-1 adrenoreceptors are necessary for preventing salt-induced hypertension, an idea supported by findings by Osborn *et al*[59] who have shown that blockade of the α_1-adrenoreceptor with prazosin renders the rat salt-sensitive and leads to the development of salt-sensitive hypertension; and (iii) the sympathetic nervous system may contribute to the development of salt-induced hypertension in neonatally capsaicin-pretreated rats via a non-α_1-adrenoreceptor mechanism.

Role of the endothelin system We investigated the role of endothelin-1 (ET-1) and its receptors in sensory-dependent salt-sensitive hypertension, in light of the finding that AII is a stimulus for ET-1 production[60–63]. We found that plasma ET-1 levels and blood pressure were elevated in sensory-denervated rats fed a high-salt diet. Moreover, development of salt-sensitive hypertension in these rats can be prevented by blockade of the ET_A receptor, just as it can be prevented with losartan[53] and candesartan[54], hydralazine[53], sympathectomy[57], and spironolactone[55]. Unlike chronic treatment with spironolactone[55], however, blockade of the ET_A receptor is not able to alleviate renal functional impairment in capsaicin-pretreated rats fed a high-sodium diet.

Furthermore, elevated plasma ET-1 levels may reflect one or both of the following: (i) decreased internalization by ET_B receptors, which have been shown to act as clearance receptors for ET-1[64–65]; or (ii) increased production. Because we observed that plasma ET-1 levels in sensory denervated rats that were salt loaded were unaffected by blockade of the ET_B clearance receptor[60], it is clear that elevated plasma ET-1 levels are indeed the result of increased production, consistent with the possibility of increased synthesis and release of ET-1 secondary to insufficiently suppressed PRA in these capsaicin-pretreated animals[54,55].

VR1-positive sensory nerves and pulmonary hypertension

The role of neuropeptides released by sensory nerves in hypoxic pulmonary hypertension have been studied[66,67]. Tjen-A-Looi revealed that rats pretreated with capsaicin and subsequently placed in hypobaric hypoxia (10% O_2, 16 d) had increased pulmonary artery pressure and right ventricular hypertrophy compared to sensory-nerve-intact rats subjected to the same hypoxia[66]. These investigators concluded that depleted stores of CGRP secondary to capsaicin

administration exacerbated hypoxic pulmonary hypertension. Interestingly, these authors reported that depletion of SP did not exacerbate pulmonary artery pressure and right ventricular hypertrophy. Regarding the latter observation, it follows that endogenous CGRP may indeed modulate pulmonary vascular tone and counterbalance hypoxic pulmonary vasoconstriction, reducing elevated pulmonary artery pressure and right ventricular hypertrophy in pulmonary hypertension.

In contrast to the protective effect of CGRP on pulmonary artery pressure observed by Tjen-A-Looi[66], Zhou and Lai[67] found that SP was implicated in pulmonary hypertension. Zhou and Lai induced ventilatory dysfunction and pulmonary hypertension in Sprague-Dawley rats by administering monocrotaline (MCT). SP levels were elevated 1–2 weeks after the administration of MCT. Compared to rats given MCT alone, rats given MCT plus capsaicin showed attenuated increases in pulmonary arterial pressure and the weight ratio of right ventricle/(left ventricle+septum). These data suggest that MCT produces pneumotoxicity that may be mediated or at least accompanied by elevated SP levels. Because capsaicin treatment depletes this neuropeptide, capsaicin attenuates MCT-induced pneumotoxicity[67].

Clinical and therapeutic implications

Given that excitation of VR1-positive sensory nerves is followed by a refractory state, capsaicin has being found to have therapeutic potential in the treatment of neuropathic pain[68]. But, and as has been suggested within this review, capsaicin has implications beyond the treatment of pain as an agent capable of acting on the cardiovascular system. The observation that capsaicin (an agonist of the VR1) is able to produce a hypotensive effect in SHR is an indication that activation of the VR1 may be an efficacious means of preventing the development of hypertension – a prospect with far-reaching therapeutic implications[69].

Of growing interest is the compelling evidence that vanilloid receptors on sensory nerves may mediate the vasodilator action of anandamide[70–74], which was originally isolated from the brain as an endogenous cannabinoid receptor ligand[75]. Indeed, our recent data indicate that administration of methanandamide caused a greater hypotensive effect in SHR rats as compared with control animals, suggesting that anandamide may serve as an endogenous compound able to stimulate VR1 and consequently produce a decrease in blood pressure[69]. It follows that changes in circulating or tissue anandamide levels under particular pathophysiological conditions may alter VR1 function and thereby regulate blood pressure. The search for endogenous VR1 activators and inhibitors is certainly motivated by the implications that such vanilloid therapy may treat hypertension.

In addition to vanilloid therapy, there are broad implications for the clinical application of neuropeptides stored in the endings of VR1-positive sensory nerves. In particular, the clinical utility of CGRP receptor agonists in the treatment of cardiovascular disorders is discussed below and in greater detail in a review by Feuerstein *et al*[76].

Considering its potent vasodilatory action, CGRP has been evaluated in the treatment of subarachnoid hemorrhage and shown to relax severely constricted vessels in animal models of this disorder[77]. However, the European CGRP in Subarachnoid Hemorrhage Study Group[78] was not able to produce definitive evidence supporting the use of this neuropeptide in the treatment of subarachnoid hemorrhage. Their study was complicated by almost two-thirds of patients in the treatment group not being able to complete the course of the trial because of frequent episodes of CGRP-induced hypotension. Perhaps this adverse systemic side effect could be minimized by intrathecal administration of CGRP.

Other studies have shown that CGRP has potential beneficial hemodynamic effects in congestive heart failure[79–80]. Shekhar *et al* observed that CGRP infusion over 8 h increased cardiac output by 72% while reducing right atrial and pulmonary wedge pressure[80]. Unfortunately, these favorable hemodynamic responses returned to pre-infusion levels once CGRP delivery was withdrawn. The need for continuous infusion of CGRP thus diminishes its clinical utility in the treatment of congestive heart failure.

Similarly, CGRP has been evaluated in the treatment of coronary heart disease. Indeed, it has been shown to improve exercise tolerance in patients with chronic stable angina[81]. But, specificity for CGRP or related agonists for the coronary vasculature has not been demonstrated and CGRP infusion for the treatment of coronary heart disease would thus be expected to produce systemic side effects, as it does in the treatment of heart failure.

As another example of the possible clinical utility of CGRP, it has been demonstrated that patients with Raynaud's disease are deficient in cutaneous CGRP-containing nerve fibers[82]. However, CGRP has not been shown to be useful in the treatment of this peripheral vascular disease.

Conclusion remarks

It is estimated that 50 million individuals in the United

States suffer from hypertension. The detrimental consequences of this disease involve myocardial infarction, congestive heart failure, stroke, and renal failure. Despite intensive research in this field, the molecular basis underlying human essential hypertension is largely unknown and pharmacologic prevention of end organ damage induced by hypertension is a challenge. Defining how sensory nerves sense changes in the environment, alter their afferent and efferent activities, and cross-talk with other systems to modulate cardiovascular and renal function and blood pressure may provide valuable new insight into the interactions that lead to hypertension and increased salt sensitivity. Such insight may unveil novel pharmacologic approaches to tackle hypertension and end organ damage. The study of abnormalities in VR1 expression, VR1-induced release of sensory neurotrans-mitters, and post-signaling pathways may also have significant impact in our understanding of the pathogenesis of hypertension and have far-reaching clinical and therapeutic implications.

Acknowledgement

Dr Wang is an American Heart Association Established Investigator and she would like to express her gratitude to all the research fellows, students, and visiting scientists who have participated and contributed to the aforementioned studies.

References

1 Clapham DE. TRP channels as cellular sensors. Nature 2003; 426: 517–24.
2 Nagy JI. Capsaicin: a chemical probe for sensory neuron mechanisms. In: Iversen LL, Iversen SD, Snyder SH, editors. Handbook of psychopharmacology; v 15. New York: Plenum Press; 1982. p 185–235.
3 Thresh LT. Isolation of capsaicin. Pharm J 1846; 6: 941.
4 Hogyes E. Beitrage zur physiologischen Wirkung der Bestandteile des Capsicum annuum. Arch Exp Pathol Pharmakol 1878; 9: 117–30
5 Nelson EK. The constitution of capsaicin, the pungent principal of capsicum. J Am Chem Soc 1919; 41: 1115–21.
6 Jancso N. Pharmacological analysis of the function and receptor structure of the pain-sensitive nerve endings. Acta Physiol Hung 1957; 11 (Suppl): 11–4.
7 Bevan S, Szolcsanyi J. Sensory neuron-specific actions of capsaicin: mechanisms and applications. Trends Pharmacol Sci 1990; 11:330–3.
8 Holzer P. Capsaicin: cellular targets, mechanisms of action, and selectivity for sensory neurons. Pharmacol Rev 1991; 43: 143–201.
9 Szolcsanyi J, Porszasz R, Petho G. Capsaicin and pharmacology of nociceptors. In: Besson JM, editor. Peripheral neurons in nociception: physio-pharmacological aspects. Paris: John Libbey; 1994. p 109–24.
10 Fitzgerald M. Capsaicin and sensory neurons: a review. Pain 1983; 15: 109–30.
11 Maggi CA, Meli A. The sensory-efferent function of capsaicin-sensitive neurons. Gen Pharmacol 1988; 19: 1–43.
12 Nagy JI. Capsaicin's action on the nervous system. Trends Neurosci 1982; 5: 362–5.
13 Szolcsanyi J. Forty years in capsaicin research for sensory pharmacology and physiology. Neuropeptides 2004; 38: 377–84.
14 Virus RR, Gebhart GF. Pharmacologic actions of capsaicin: apparent involvements of substance P and serotonin. Life Sci 1979; 25: 1273–84.
15 Maggi CA. The pharmacological modulation of neurotransmitter release. In: Wood John, editor. Capsaicin in the study of pain. New York: Harcourt Brace & Company; 1993. p 161–89.
16 Lindsay RM, Lockett C, Sternbeg J, Winter J. Neuropeptide expression in cultures of adult sensory neurons: modulation of substance P and calcitonin gene-related peptide levels by nerve growth factor. Neuroscience 1989; 33: 53–65.
17 Holzer P. Local effector functions of capsaicin-sensitive sensory nerve endings: involvement of tachykinins, calcitonin gene-related peptide, and other neuropeptides. Neuroscience 1988; 24: 739–68.
18 Kawasaki H, Nuki C, Saito A, Takasaki K. Adrenergic modulation of calcitonin gene-related peptide (CGRP) containing nerve-mediated vasodilation in the rat mesenteric resistance vessel. Brain Res 1990; 506: 287–90.
19 Vasko MR, Campbell WB, Waite KG. Prostaglandin E_2 enhances bradykinin stimulated release of neuropeptides from rat sensory neurons in culture. J Neurosci 1994; 14: 4987–97.
20 Dymshitz J, Vasko MR. Endothelin-1 enhances capsaicin-induced peptide release and cGMP accumulation in cultures of rat sensory neurons. Neurosci Lett 1994; 167: 128–32.
21 Winter J, Dray A, Wood JN, Yeats JC, Bevan S. Cellular mechanism of action of resiniferatoxin: a potent sensory neuron excitotoxin. Brain Res 1990; 520: 13–40.
22 Bevan S, Forbes CA. Membrane effects of capsaicin on rat dorsal root ganglion neurons in culture. J Physiol 1988; 398: 28.
23 Forbes CA, Bevan S. Single channels activated by capsaicin in patches of membrane from adult rat sensory neurons in culture. Neurosci Lett 1998; S3: 32.
24 Marsh SJ, Stansfeld CE, Brown DA, Davey R, McCarthy D. The mechanism of action of capsaicin on sensory C-type neurons and their axons *in vitro*. Neuroscience 1987; 23: 275–89.
25 Wood JN, Winter J, James IF, Rang HP, Yeats J, Bevan S. Capsaicin-induced ion fluxes in dorsal root ganglion cells in culture. J Neurosci 1988; 8: 3208–20.
26 Szolcsanyi J, Jancso-Gabor A. Sensory effects of capsaicin congeners. I. Relationship between chemical structure and pain-producing potency of pungent agents. Drug Res 1975; 25: 1877–81.
27 Szolcsanyi J, Jancso-Gabor A. Sensory effects of capsaicin congeners. II. Importance of chemical structure and pungency in desensitizing activity of capsaicin-like compounds. Drug Res 1976; 26: 33–7.
28 deVries DJ, Blumberg PM. Thermoregulatory effects of resiniferatoxin in the mouse: comparison with capsaicin. Life Sci

1989; 44: 711–5.
29 Szallasi A, Blumberg PM. Resiniferatoxin, a phorbol-related diterpene, acts as an ultrapotent analog of capsaicin, the irritant constituent in red pepper. Neuroscience 1989; 30: 515–20.
30 Winter J, Dray A, Wood JN, Yeats JC, Bevan S. Cellular mechanism of action of resiniferatoxin: a potent sensory neuron excitotoxin. Brain Res 1990; 520: 131–40.
31 Bevan S, Hothi S, Hughes G, James IF, Rang HP, Shah K, *et al*. Capsazepine: a competitive antagonist of the sensory neuron excitant capsaicin. Br J Pharmacol 1992; 107: 544–52.
32 Caterina MJ, Julius D. The vanilloid receptor: a molecular gateway to the pain pathway. Annu Rev Neurosci 2001; 24: 487–517.
33 Hua XY, Lundberg JM. Dual capsaicin effects on ureteric motility: low dose inhibition mediated by CGRP and high dose stimulation by tachykinins? Acta Physiol Scand 1986; 128: 453–65.
34 Bell D, McDermott B. Calcitonin gene-related peptide in the cardiovascular system: characterization of receptor populations and their (patho)physiological significance. Pharmacol Rev 1996; 48: 257.
35 Buck SH, Burks TF. The neuropharmacology of capsaicin: review of some recent observations. Pharmacol Rev 1986; 38: 179–226.
36 Jancso G, Kiraly E, Jancso-Gabor A. Pharmacologically induced selective degeneration of chemosensitive primary sensory neurons. Nature 1977; 270: 741–3.
37 Lawson SN, Nickels SM. The use of morphometric techniques to analyze the effect of neonatal capsaicin treatment on rat dorsal root ganglia and dorsal roots. J Physiol 1980; 303: 12.
38 Scadding JW. The permanent anatomical effects of neonatal capsaicin on somatosensory nerves. J Anat 1980; 131: 471–82.
39 Nagy JI, Iversen LL, Goedert M, Chapman D, Hunt SP. Dose-dependent effects of capsaicin on primary sensory neurons in the neonatal rat. J Neurosci 1983; 3: 399–406.
40 Jancso G, Karcsu S, Kiraly E, Szebeni A, Toth L, Bacsy E, *et al*. Neurotoxin induced nerve cell degeneration: possible involvement of calcium. Brain Res 1984; 295: 211-6.
41 Nagi JI, Hunt SP, Iversen LL, Emson PC. Biochemical and anatomical observations on the degeneration of peptide-containing primary afferent neurons after neonatal capsaicin. Neuroscience 1981; 6: 1923-34.
42 Breimer LH, MacIntyre I, Zaidi M. Peptides from the calcitonin genes: molecular genetics, structure, and function. Biochem J 1988; 255: 377–90.
43 Wimalawansa SJ. Calcitonin gene-related peptide and its receptors: molecular genetics, physiology, pathophysiology, and therapeutic potentials. Endocr Rev 1996; 17: 533–85.
44 Preibisz JJ. CGRP and regulation of human cardiovascular homeostasis. Am J Hypertens 1993; 6: 434–50.
45 Zaidi M, Moonga BS, Bevis PJ, Bascal ZA, Breimer LH. The calcitonin gene peptides: biology and clinical relevance. Crit Rev Clin Lab Sci 1999; 28: 109.
46 McEwan J, Legon S, Wimalawansa SJ, Zaida M, Dollery CT, MacIntyre I. Calcitonin gene-related peptide: a review of its biology and relevance to the cardiovascular system. In: Laragh JH, Brenner BN, Kaplan NM, editors. Endocrine mechanisms in hypertension. New York: Raven Press; 1989. p 287.
47 Asimakis GK, DiPette DJ, Conti VR, Holland OB, Zwischenberger JB. Hemodynamic action of calcitonin gene-related peptide in the isolated rat heart. Life Sci 1987; 41: 597.
48 DiPette DJ, Scwarzenberger K, Kerr N, Holland OB. Dose-dependent systemic and regional hemodynamic effects of calcitonin gene-related peptide. Am J Med Sci 1989; 297: 65.
49 Supowit SC, Zhao H, Hallman DM, DiPette DJ. Calcitonin gene-related peptide is a depressor of deoxycorticosterone-salt hyperten-sion. Hypertension 1997; 29: 945–50.
50 Burg M, Zahm DS, Knuepfer MM. Intrathecal capsaicin enhances one-kidney renal wrap hypertension in the rat. J Auton Nerv Syst 1994; 50: 180–99.
51 Manzini S, Bacciarelli C. Enhanced development of deoxycorticosterone-induced hypertension in neonatally capsaicin-pretreated rats. Regul Pept 1988; 22: 119.
52 Wang DH, Li J, Qiu J. Salt-sensitive hypertension induced by sensory denervation: introduction of a new model. Hypertension 1998; 32: 649–53.
53 Wang DH, Li J. Antihypertensive mechanisms underlying a novel salt-sensitive hypertensive model induced by sensory denervation. Hypertension 1999; 33: 499-503.
54 Huang Y, Wang DH. Role of AT1 and AT2 receptor subtypes in salt-sensitive hypertension induced by sensory nerve degeneration. J Hypertens 2001; 19: 1841–6.
55 Huang Y, Wang DH. Role of renin-angiotensin-aldosterone system in salt-sensitive hypertension induced by sensory denervation. Am J Physiol Heart Circ Physiol 2001; 281: H2143–9.
56 Wu W, Zhang Y, Ballew JR, Fink G, Wang DH. Development of hypertension induced by subpressor infusion of angiotensin II. Hypertension 2000; 36: 549.
57 Wang DH, Wu W, Lookingland KJ. Degeneration of capsaicin-sensitive sensory nerves leads to increased salt sensitivity through enhancement of sympathoexcitatory response. Hypertension 2001; 37: 440–3.
58 Lefevre-Borg F, Roach AG, Gomeni R, Cavero I. Mechanism of antihypertensive therapy of orally administered prazosin in spontaneously hypertensive rats. J Cardiovasc Pharmacol 1979; 1: 31–42.
59 Osborn JW, Provo BJ, Montana JS III, Trostel KA. Salt-sensitive hypertension caused by long-term α-adrenergic blockade in the rat. Hypertension 1993; 21: 995–9.
60 Ye DZ, Wang DH. Function and regulation of endothelin-1 and its receptors in salt sensitive hypertension induced by sensory nerve degeneration. Hypertension 2002; 39: 673.
61 Dohi Y, Hahn AW, Boulanger CM, Buhler FR, Luscher TF. Endothelin stimulated by angiotensin II augments contractility of spontaneously hypertensive rat resistance arteries. Hypertension 1992; 19: 131–7.
62 Imai T, Hirata Y, Emori T, Yanagisawa M, Masaki T, Marumo F. Induction of endothelin-1 gene by angiotensin and vasopressin in endothelial cells. Hypertension 1992; 19: 752–7.
63 Moreau P, d'Uscio LV, Shaw S, Takase H, Barton M, Luscher TF. Angiotensin II increases tissue endothelin and induces vascular hypertrophy: reversal by ET_A-receptor antagonist. Circulation 1997; 96: 1593–7.
64 Loffler BM, Breu V, Clozel M. Effect of different endothelin receptor antagonists and of the novel non-peptide antagonist R046-2005 on endothelin levels in rat plasma. FEBS Lett 1993; 333: 108–10.

65 Fukuroda T, Fujikawa T, Ozaki S, Ishikawa K, Yano M, Nishikibe M. Clearance of circulating ET-1 by ET_B receptor in rats. Biochem Biophys Res Commun 1994; 199: 1461–5.
66 Tjen-A-Looi S, Kraiczi H, Ekman R, Keith IM. Sensory CGRP depletion by capsaicin exacerbates hypoxia-induced pulmonary hypertension in rats. Regul Pept 1998; 74: 1–10.
67 Zhou KR, Lai YL. Capsaicin pretreatment attenuates monocrotaline-induced ventilatory dysfunction and pulmonary hypertension. J Appl Physiol 1993; 75: 2781–8.
68 Szallasi A. Vanniloid receptor ligands: hopes and realities for the future. Drugs Aging 2001; 18: 561–73.
69 Li J, Kaminski NE, Wang DH. Anandamide-induced depressor effect in spontaneously hypertensive rats: role of the vanilloid receptor. Hypertension 2003; 41 (3 Pt 2):757–62.
70 De Petrocellis L, Bisogno T, Maccarrone M, Davis JB, Finazzi-Agro A, Di Marzo V. The activity of anandamide at vanilloid VR1 receptors requires facilitated transport across the cell membrane and is limited by intracellular metabolism. J Biol Chem 2001; 276: 12856–63.
71 Smart D, Gunthorpe MJ, Jerman JC, Nasir S, Gray J, Miur AI, *et al*. The endogenous lipid anandamide is a full agonist at the human vanilloid receptor (hVR1). Br J Pharmacol 2000; 129: 227–30.
72 Zygmunt PM, Petersson J, Andersson DA, Chuang H, Sorgard M, Di Marzo V, *et al*. Vanilloid receptors on sensory nerves mediate the vasodilator action of anandamide. Nature 1999; 400: 452–7.
73 Zygmunt PM, Chuang H, Movahed P, Julius D, Hogestatt ED. The anandamide transport inhibitor AM404 activates vanilloid receptors. Eur J Pharmacol 2000; 396: 39–42.
74 Malinowska B, Kwolek G, Gothert M. Anandamide and methanandamide induce both vanilloid VR1- and cannabinoid CB1 receptor-mediated changes in heart rate and blood pressure in anesthetized rats. Naunyn Schmiedebergs Arch Pharmacol 2001; 364: 562–9.
75 Devane WA, Hanus L, Breuer A, Pertwee RG, Stevenson LA, Griffin G, *et al*. Isolation and structure of a brain constituent that binds to the cannabinoid receptor. Science 1992; 258: 1946–9.
76 Feuerstein G, Willette R, Aiyar N. Clinical perspectives of calcitonin gene-related peptide pharmacology. Can J Physiol Pharmacol 1995; 73: 1070–4.
77 Edvinsson L, Fredholm BB, Hamel E, Jansen I, Verrecchia C. Perivascular peptides relax cerebral arteries concomitant with stimulation of cyclic adenosine monophosphate accumulation or release of an endothelium derived relaxing factor. Neurosci Lett 1985; 58: 213–7.
78 European CGRP in Subarachnoid Hemorrhage Study Group. Effects of calcitonin gene-related peptide in patients with delayed post-operative cerebral ischemia after aneurysmal subarachnoid hemorrhage. Lancet 1992; 339: 831–3.
79 Gennari C, Nami R, Agnusdei D. Improved cardiac performance with human calcitonin gene-related peptide in patients with congestive heart failure. Cardiovasc Res 1990; 24: 239–41.
80 Shekhar YC, Anard IS, Sarma R, Ferrari R, Wahi PL, Poole-Wilson PA. Effects of prolonged infusion of human alpha CGRP on hemodynamics, renal blood flow, and hormone levels in congestive heart failure. Am J Cardiol 1991; 67: 732–8.
81 Uren NG, Seydoux D, Davies GJ. Effect of intravenous calcitonin gene-related peptide on ischaemia threshold and coronary stenosis severity in humans. Cardiovasc Res 1993; 27: 1477–81.
82 Shawket S, Dickerson C, Haxleman B, Brown MJ. Prolonged effect of CGRP in Raynaud's patients: a double blind randomized comparison with prostacyclin. Br J Clin Pharmacol 1991; 32: 209–13.

Acta Pharmacologica Sinica 2005 Mar; 26 (3): 295–301

Invited review

Historic perspectives and recent advances in major animal models of hypertension[1]

Zhong-jie SUN[2], Zhong-e ZHANG

Departments of Medicine and Physiology & Functional Genomics, College of Medicine, University of Florida, Gainesville, Florida FL32610-0274, USA

Key words

spontaneous hypertension; cold-induced hypertension; DOCA-salt-induced hypertension; renal-induced hypertension; cardiac hypertrophy; blood pressure

[1] Project supported by grant (No 0130387N) from the American Heart Association (National).
[2] Correspondence to Dr Zhong-jie SUN.
Phn 1-352-392-5815.
Fax 1-352-846-0270.
E-mail zsun@phys.med.ufl.edu

Received 2004-08-16
Accepted 2004-11-17

doi: 10.1111/j.1745-7254.2005.00054.x

Abstract

Hypertension and related cardiovascular diseases are the leading causes of death in many countries. The etiology of human essential hypertension is largely unknown. It is highly likely that hypertension is a complex and multifactorial disease resulting from the interaction of multiple genetic and environmental factors. Animal models of hypertension have been proved to be useful to study the pathogenesis of, and to find a new therapy for, hypertension. The aim of this article is to briefly review the most widely used rodent models of experimental hypertension, including history and recent advances. These models are classified as genetically-induced, environmentally-induced, pharmacologically-induced, and renal-induced hypertension according to the way of induction; the typical representatives of each of these major types of experimental hypertension are spontaneous hypertension, cold-induced hypertension, DOCA-salt-induced hypertension, and renal-induced hypertension, respectively. The processes of induction of hypertension, possible pathogenesis, characteristics, advantages, and limitations of these animal models are reviewed. In addition, the clinical implications of the above experimental models of hypertension are addressed.

Introduction

Hypertension is the prevalent cause of cardiovascular disease that leads to heart failure, stroke, renal failure, and, ultimately, to death. In the USA, approximately 50 million people have hypertension, according to Phase I estimates of the National Health and Nutrition Examination Survey III (NHANES III), from 1988 to 1991[1]. The prevalence is about 20%. According to a report[2], about 40% of white people and more than 50% of black people aged 65 or older suffer from some form of high blood pressure in the USA. Epidemiological surveys have demonstrated an increasing prevalence of hypertension in China, from 5.11% in 1958 to 7.73% in 1980 and 11.89% in 1991[3,4]. Although this incidence is lower than that in many developed countries such as the USA (20%)[1] and Canada[5], it represents 50 million people in 1980 and 90 million people in 1991 due to the size of the Chinese population. According to relevant reports[4,6], cardiovascular diseases are the leading causes of death in Chinese society.

The syndrome of hypertension is more than just an elevation of arterial pressure, although it is this aspect that the general public is most familiar with. Hypertension when fully developed is characterized by an increase in vascular resistance to blood flow, cardiac hypertrophy, often an increase in cardiac output, an increased output of sympathetic nervous system (SNS), changes within the vascular smooth muscles, often atherosclerosis, and abnormalities in renal function. Increased vascular resistance is due to constriction of the vascular smooth muscle, primarily in the high resistance vessels. The etiology of essential hypertension is not known and the causes of it may be multifactorial. It is generally believed that both genetic and environmental factors and their interactions play a critical role in the pathogenesis of hypertension and other cardiovascular diseases. Since hypertension and associated cardiovascular diseases are the leading causes of death of human beings, medical scientists are dedicated to elucidate the mechanism of and

explore the treatment for hypertension.

It is noticed that animal models of human disease have been widely used to study etiology and pathogenesis of human disease, to prevent disease or to find a therapy and identify risk factors contributing to the disease. This literature reviews briefly advances in the most widely used rodent models of hypertension, including advantages and limitations. Hopefully, this will be useful to those in choosing appropriate animal models of hypertension for their researches. This comprehensive review may help physicians and scientists understand the pathogenesis of hypertension and therefore optimize therapeutic approaches. It is our expectation that the creation and utilization of novel animal models of hypertension will fundamentally advance the fields of cardiovascular medicine and physiology.

The major animal models of hypertension

Basically, animal models of hypertension comprise primary and secondary hypertension according to hypertension etiology (Figure 1). The primary hypertension includes genetically-induced and environmentally-induced hypertension and the secondary hypertension includes pharmacologically-induced and renal-induced hypertension by the way of induction.

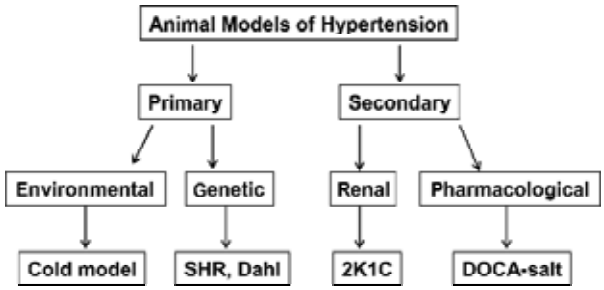

Figure 1. The classification of major animal models of hypertension.

Genetically-induced hypertension Animals that have undergone artificial genetic manipulation are predestined to become hypertensive. Some investigators believe that genetically hypertensive rats comprise the most popular models to study essential hypertension[7]. One example is the spontaneously hypertensive rat (SHR), originally inbred from Wistar stock by Okamoto and Aoki, and their WKY inbred nonhypertensive controls. These rats develop hypertension at about 4–6 weeks of age, largely independent of dietary levels of either Na^+ or Cl^-. Another model is the Dahl salt-sensitive rats, originally derived from Sprague-Dawley stock by Dahl on the basis of developing hypertension with high NaCl diet. When fed with normal salt diets, these rats become hypertensive, indicating that this is a genetic model of hypertension with the feature of salt sensitivity. O'Dowd and Rapp[8] have refined the genetic background of the original Dahl stock, and their salt-sensitive/Jr line is now preferred (along with their salt-resistant/Jr controls). Genetic analysis revealed linkage with loci close to the angiotensin converting enzyme (ACE) and guanylyl cyclase A (GCA)/ atrial natriuretic factor (ANF) receptor genes in Dahl salt-sensitive rats[9]. It was found that certain alleles at the GCA and ACE loci (or at loci closely linked to them) had a significant impact on blood pressure response to high salt in Dahl salt-sensitive rats.

The SHR was generated by inbreeding Wistar rats with the highest blood pressure[7]. The SHR develop many features of hypertensive end-organ damages including cardiac hypertrophy, heart failure, and renal dysfunction. According to relevant reports[11,12], the SHR is the most commonly used genetic model although the mechanisms for producing the hypertension are not clear. Overactivity of the brain renin-angiotensin system (RAS) appears to be involved in initiating the development of spontaneous hypertension based on the finding that central injections of angiotensin II (AngII) receptor antagonists cause greater reductions in systolic blood pressure in SHR than in normotensives[13,14]. However, DePasquale and colleagues[15] reported that central administration of AT_1 receptor blocker losartan (DuP 537) did not lower blood pressure in SHR. Thus, the above hypothesis needs further confirmation. Interestingly, some hemodynamic alterations which occur during the development of the disease are similar to human essential hypertension (ie, a high cardiac output early, and in the adult, a normal cardiac output and an increased vascular resistance)[16]. In this model, there is also an increase in the activity of the sympathetic nervous system as evidenced by increased renal sympathetic activity[16]. The renal blood flow and glomerular filtration rate are normal[17] and renal vascular resistance is increased[22]. The SHR stroke prone (SHR-SP) is a further developed sub-strain with even higher levels of blood pressure and a strong tendency to die from stroke[18]. The SHR has been used to evaluate genetic factors involved in hypertension. Although a wide variety of genes seems to cosegregate in various crosses[12], neither of these genes is confirmed to be the etiological gene for hypertension. The advantage of this model is that its pathophysiological changes are similar to those found in human essential hypertension[16,19]. A major drawback of this model is the lack of an appropriate control, which has been genetically altered

yet is free from the disease and the complexity of the genetic mutations which have affected not only blood pressure but many other regulatory systems as well.

Transgenic hypertension models can be generated by over-expressing a specific gene. This type of genetic model usually has a relatively good normotensive control, the same strain of animals without genetic alteration. It is an excellent model to study the role of a specific gene in the pathogenesis of hypertension. However, the transgenic model may not mimic human essential hypertension as well as the SHR does in terms of pathophysiology. A representative of this type of hypertension is the TGR (mREN2)27 transgenic rats[10]. In this genetic model, the introduction and overexpression of the mouse Ren-2 gene in Sprague-Dawley rats leads to severe hypertension[10]. The appropriate control is the age-, body weight-, and sex-matched normotensive Sprague-Dawley rats without renin transgene.

Environmentally-induced hypertension In recent years, the important role of environmental factors in the disease process has received great attention from scientists and physicians. The primary interest is focused on the area of cardiovascular disorders, particularly hypertension. To understand better the ways in which the environmental factors affect the cardiovascular functions, researchers have tried to produce experimental hypertension in animals by exposing them to different experimental paradigms.

Stress-induced hypertension Epidemiologists and clinicians have long suspected that stressful life events can be a sufficient trigger for the expression of hypertension in some individuals[20]. Attempts to induce hypertension in animals using sensory stimulation have generally employed loud noises, flashing lights, and oscillating cages, either separately or together. For example, in one early study rats were subjected to 20 weeks of randomized flashing lights, motion, and loud noises[21]. After 12 weeks on this schedule, systolic blood pressure (SBP) values reached approximately 150–160 mmHg. Perhaps a better example of this type of experiment is found in a study by Lin and Li[22]. Stressed rats developed hypertension within two weeks after irregular foot electric-shocks combined with buzzing noise. It is accepted that activation of sympathetic nervous system[23] and the RAS[24] play a role in the initiation of stress-induced hypertension. Li[25] found that increased activity of the cholinergic system in the rostral ventrolateral medulla (rVLM) was also involved in the development of stress-induced hypertension. Plasma catecholamine, corticosterone, angiotensin II, glucose, and lipids were found to be increased during stress. In this model, about 40%–50% of stressed rats failed to develop hypertension[26].

Diet-induced hypertension It is known that long-term exposure to a special diet (high salt, fat, or sugar) results in dietary hypertension in some animals or humans. For example, chronic fructose treatment in rats repeatedly has been shown to elevate blood pressure associated with insulin resistance and hyperinsulinemia[27,28]. Hyperactivity of the SNS and the RAS, vascular hypertrophy, and sodium retention by the kidney tubules have been proposed to be some of the mechanisms by which fructose induces hypertension. By degeneration of capsaicin-sensitive nerves, Wang and colleagues[29,30] developed a salt-sensitive model of hypertension. In this model, the increased salt sensitivity is mediated by the enhancement of the SNS[29].

Cold-induced hypertension: Fregly[31] and Sun[32–36] found that chronic exposure of rats to mild cold (41 °F or 5 °C) induced hypertension including cardiac hypertrophy within 3 weeks. This is presently the only "naturally-occurring" form of experimentally-induced hypertension that is induced without surgical intervention, administration of excessive doses of drugs or hormones, or genetic manipulation. It is interesting that the elevated blood pressure of rats after 7 weeks of exposure to cold does not return to pre-cold exposure level during the 4 weeks after removal from cold. Thus, an elevation of blood pressure induced by a longer period of cold exposure might not be reversible after return to thermoneutral temperature. Intermittent exposure of rats to cold also induces hypertension, with a sigmoid relationship between the hours per day exposed to cold and systolic blood pressure.

Cold-induced hypertension (CIH) is also demonstrable in humans. Epidemiological surveys and clinical observations have established that people who live and work in cold areas have a high incidence of hypertension and related cardiovascular diseases[37–39]. Cold temperature (weather) makes hypertension more severe in hypertensive patients[39,40]. The cold winter season has the highest mortality and morbidity of cardiovascular diseases in a year[39–42]. Donaldson[38], after studying the relationship between outdoor temperature and blood pressure in men in central London between 1986 and 1992, reported that cold exposure of normal life in winter is sufficient to induce significant and prolonged hypertension in the general population.

It was originally assumed that cold-induced elevation of blood pressure was a direct vasoconstrictive effect of sympathetic nervous system (SNS). Indeed, the SNS is activated by chronic cold exposure and the plasma and urine levels of catecholamines are increased significantly in cold-exposed rats[32–34,43]. However, the *in vitro* vascular contractile response to α_1-adrenoceptor agonist, phenylephrine, is

decreased significantly in cold-exposed rats[44]. The *in vivo* pressor response to phenylephrine is significantly reduced by chronic cold exposure[45]. Thus, the vascular α_1-adrenoceptors are down-regulated during cold exposure. Several studies[32,34,36,46] have shown that blockade of the RAS at different sites could attenuate or prevent the cold-induced elevation of blood pressure. Antisense oligodeoxynucleotides to angiotensinogen mRNA or AT_1-receptor mRNA reduce elevated blood pressure of cold-exposed rats[47]. Angiotensinogen gene knockout delays and attenuates CIH[48]. It has been therefore suggested elsewhere[32–34,36,48] that the hyperactivity of the SNS initiates CIH probably via activation of the RAS. Indeed, plasma renin activity (PRA) is increased during exposure to cold and abolishment of the rise in PRA by renal denervation prevents the development of CIH[32]. Cold-exposed rats had an elevation of blood pressure that was proportional to the concentration of NaCl in the diet[49], suggesting that CIH is sodium-dependent hypertension.

CIH is a prototypic model of environmentally-induced hypertension, which is similar in many ways to human hypertension. Induction of CIH requires a climate-controlled chamber, with a strict requirement of temperature and humidity. Perhaps, this is the limitation of this model.

Pharmacologically-induced hypertension The DOCA-salt-induced model of hypertension is a typical representative of pharmacologically-induced hypertension. A very high dose of deoxycorticosterone acetate (DOCA) ranging from about 300 to 1000 $mg \cdot kg^{-1} \cdot d^{-1}$ (sc) is required to induce hypertension in rats. Isotonic saline is the sole drinking fluid. This is an important co-factor because it expedites the development of hypertension and makes it more severe. Thus, this model is salt-dependent in its initiation. It often needs surgical reduction of renal mass or unilateral nephrectomy. The combination of DOCA-salt and unilateral nephrectomy results in hypertension, cardiac and renal hypertrophy, and nephrosclerosis[50]. DOCA-salt hypertension is a low renin and volume overloaded form of hypertension. There is evidence that arginine vasopressin (AVP) plays a role in both the development and maintenance of DOCA-salt hypertension[51,52]. It is believed that AVP is involved as a vasopressor hormone in the pathogenesis of malignant DOCA-salt hypertension[53]. The SNS also appears to be involved in the development of DOCA-salt hypertension[54]. The increased activity of the SNS may affect renal function through the renal nerve, as denervation of the kidneys delays the onset and decreases the severity of the disease[54,55]. Further studies[56] indicated that AngII receptor binding sites were increased in the brain, suggesting an up-regulation of AngII receptors. However, AngI converting enzyme inhibitors and AngII receptor blocker are ineffective in reducing blood pressure in low-renin, DOCA-salt hypertension[57,58]. In contrast, aldosterone receptor blockers and diuretics are effective in reducing blood pressure in this model[59]. Most recent studies indicate that the endothelin system plays an important role in the pathogenesis of DOCA-salt hypertension[60–65]. Oxidative stress may also be involved in DOCA-salt hypertension[65,66]. The major limitations of the DOCA-salt model are: 1) the pharmacological (large) doses of drug required; 2) requirement for surgical reduction of renal mass; and 3) ingestion of a large amount of NaCl required. The major advantage of this model is the potential to investigate the role of sodium in the developmental stages of hypertension.

Renal-induced hypertension The physiological function of the kidney includes maintenance of electrolyte and fluid balance and secretion of renin, an important component of the RAS. Thus, its involvement in the regulation of blood pressure and its important role in the development of hypertension are well accepted. Since 1934, when Goldblatt and his co-workers[67] induced an elevation of blood pressure by partial constriction of the renal artery of the dog, many renal-induced models of hypertension have been successfully established in rats, rabbits, sheep, and cats[68]. Generally, renal-induced experimental hypertension includes two-kidney Goldblatt hypertension (constriction of one renal artery while the contralateral kidney is left intact) and one-kidney Goldblatt hypertension (one renal artery is constricted and the contralateral kidney is removed).

In the rat, by clipping one renal artery (leaving the contralateral kidney untouched) with a clip which induced a severe hypertension, a biphasic course in the plasma renin activity was found. In the initial phase, sodium retention occurred and was associated with a transient increase in plasma renin activity returning to control levels within a week[69,70]. Thus, it has been suggested that the RAS plays a role in the development of two-kidney Goldblatt hypertension[69-71]. The sustained elevation of blood pressure may still be AngII-dependent since a sub-pressor dose of AngII would result in an elevation of blood pressure due to a shift in the dose-response curve of AngII[72]. This suggests, but does not prove, that AngII receptors are upregulated in this model of hypertension. The initial elevation of blood pressure in the one-kidney Goldblatt model is also AngII-mediated[73]. Due to the absence of the other normal kidney, no compensatory increase in sodium and water excretion can occur, and hence, fluid volume is retained[74]. This model is thus a sodium-fluid volume-dependent model. This would

be an ideal model for studying the role of volume expansion in the development of hypertension.

During the early developmental stage of these two renal-dependent models, when the clip is removed, arterial blood pressure returns to normal[70,75]. Thus, renal-induced hypertension is reversible and reproducible. Furthermore, these models provide a unique opportunity to investigate the changes which occur specifically at the level of the kidney, as well as the role of the kidney in the long-term blood pressure control. If the reversal of hypertension is time-dependent, it would suggest that relevant changes, perhaps structural, have developed.

Clinical implications of animal models of hypertension

It should be mentioned that each of the above models of experimental hypertension studies a specific aspect of hypertension. Neither of them encompasses all traits of human essential hypertension. Due to the unknown etiologies of hypertension, the use of various research models, each of which induces the disease by a different mechanism yet with the same end result, is advantageous. By using different types of experimental hypertension, scientists could identify and evaluate potential risk factors contributing to hypertension and related cardiovascular diseases. This would allow new and effective measures to be adopted for preventions and therapies. Usually, animal studies are essential to the success of clinical trials. It is noted that remarkable advances in cardiovascular medicine have been originated from experimental hypertension. Therefore, animal models of hypertension are very important approaches to the study of human hypertension.

Physicians and scientists could learn the developmental process and pathogenesis of hypertension from these animal models that are designed to mimic those of human hypertension. The induction of hypertension in animals could help understand the etiological factors that may be involved in essential hypertension. For example, hypertension and cardiovascular diseases (CVD) may have genetic predeterminants. There is a predisposition to hypertension and CVD in those patients with a positive family history. The notion of genetic predisposition for the development of hypertension has been strengthened by the development of genetic or spontaneous models of hypertension. The pathophysiological changes of spontaneous hypertension in animals are very similar to those of human essential hypertension. Also, transgenic models of hypertension induced by targeting different genes are excellent tools to study genes relevant to hypertension. An animal model of DOCA-induced hypertension is an ideal model for evaluating the role of sodium in hypertension. Studies from DOCA-induced hypertension have provided a strong basis for using spironolactone (aldosterone receptor blocker) to treat clinical hypertension. Because some special diets (high salt, fat, or sugar) could result in dietary hypertension, restriction of these diets has been suggested by clinicians for preventive and therapeutic purposes. The cause of hypertension varies with hypertensive patients. Thus, it is important to identify the potential cause of hypertension prior to treatment; which guarantees appropriate and effective treatment. For example, stenosis of the renal artery could cause hypertension as learned from an animal model of renal-induced hypertension. In this case, surgical correction of the stenosis of the renal artery may be more important than treatment with antihypertensive drugs. In addition, research findings from experimental hypertension may have clinical implications. For example, the RAS has been found to play a critical role in the pathogenesis of CIH in rats. This has led to a clinical trial which proves that the ACE inhibitor (captopril) or AT_1 receptor blocker (losartan) can control hypertension appropriately and effectively in hypertensive patients in winter. This also could help to control the high incidence of myocardial infarction and stroke during the cold season. In contrast, the use of animal models of hypertension would allow scientists to test new pharmacological treatments and gene therapy for hypertension and related CVD. Thus, what is learned from animal hypertension may reveal new insights into both preventive strategies and optimization of therapeutic approaches. It should be emphasized that any experimental data from animal models of hypertension must be tested and further validated in humans before they can be applied in hypertensive patients.

References

1 Burt VL, Whelton P, Roccela EJ, Brown C, Cutler JA, Higgins M, *et al*. Prevalence of hypertension in the US adult population. Results from the third national health and nutrition examination survey, 1988–1991. Hypertension 1995; 25: 305–13.

2 National Heart, Lung, and Blood Institute. Age Page. High blood pressure: a common but controllable disorder. Bethesda, MA, USA. Department of Health and Human Services and National Institute of Health. 1991.

3 Wu YK, Lu CQ, Gao RC, Yu JS, Liu GC. Nationwide hypertension screening in China during 1979–1980. Chin Med J 1982; 335: 101–5.

4 PRC National Blood Pressure Survey Cooperative Group. Prevalence and development trends of hypertension in China. Chin J Hypertens 1996; 3: 7–13.

5 Joffres MR, Hamet P, Rabkin SW, Gelskey D, Hogan K, Fodor G. Prevalence, control and awareness of high blood pressure among Canadian adults. Can Med Assoc J 1992; 146: 1997–2005.
6 Hamet P, Gong LS. Chinese contribution to trials on antihypertensive therapy. J Hypertens 1996; 14: S123–9.
7 Yagil Y, Yagil C. Genetic models of hypertension in experimental animals. Exp Nephrol 2001; 9: 1–9.
8. O'Dowd BF, Rapp JP. Heterogeneity of rennin alleles in outbred Dahl salt-sensitive (Brookhaven) rats. Hypertension 1991; 18: 9–11.
9. Deng Y, Rapp JP. Cosegregation of blood pressure with angiotensin converting enzyme and arterial natriuretic peptide receptor genes using Dahl salt sensitive rats. Nat Genet 1992; 1: 267–72.
10 Langheinrich M, Lee MA, Bohm M, Pinto YM, Ganten D, Paul M. The hypertensive Ren-2 transgenic rat TGR (mREN2)27 in hypertension research. Characteristics and functional aspects. Am J Hypertens 1996; 9: 506–12.
11 Pravenec M, Zidek V, Landa V, Kostka V, Musilova A, Kazdova L, *et al*. Genetic analysis of cardiovascular risk factor clustering in spontaneous hypertension. Folia Biol Praha 2000; 46: 233–40.
13 Yang RH, Jin H, Wyss JM, Oparil S. Depressor effect of blocking angiotensin subtype 1 receptors in the anterior hypothalamus. Hypertension 1992; 19: 475–81.
12 Pinto YM, Paul M, Ganten D. Lessons from rat models of hypertension: from Goldblatt to genetic engineering. Cardiovasc Res 1975; 39: 77–88.
14 Mann JF, Phillips MI, Dietz R, Haebara H, Ganten D. Effects of central and peripheral angiotensin blockade in hypertensive rats. Am J Physiol 1978; 234: H629–37.
15 DePasquale MJ, Fossa AA, Holt WF, Mangiapane ML. Central DuP 753 does not lower blood pressure in spontaneously hypertensive rats. Hypertension 1992; 19: 668–71.
16 Trippodo NC, Frohlich ED. Similarities of genetic (spontaneous) hypertension: man and rat. Circ Res 1981; 48: 309–19.
17 Arendshorst WJ, Beierwaltes D. Renal and nephron hemodynamics in spontaneously hypertensive rats. Am J Physiol 1979; 236: F246–51.
18 Yamori Y. Development of the spontaneously hypertensive rat (SHR) the stroke prone hypertensive SHR (SHRSP) and their various substrain models for hypertension-related cardiovascular diseases. In: Ganten D, de Jong W (volume editors) Birkenhager WH, Reid JT (series editors). Handbook of hypertension, v 16: Experimental and genetic models of hypertension. Amsterdam: Elsevier; 1994. p23–31.
19 Coleman TG, Guyton AC, Young DB. The role of the kidney in essential hypertension. Clin Exp Pharmacol Physiol 1975; 2: 571–81.
20 Zimmerman RS, Frohlich ED. Stress and hypertension. J Hypertens 1990; 8: S103–7.
21 Smookler HH, Buckley JP. Relationships between brain catecholamine synthesis, pituitary adrenal function and the production of hypertension during prolonged exposure to environmental stress. Int I Neuropharmacol 1969; 8: 33–41.
22 Lin Q, Li P. The effects of chronic stress on blood pressure and heart rate in rats. Chin J Physiol Sci 1990; 6: 101–7.
23 Smith PA, Graham LN, Mackintosh AF, Stoker JB, Mary DA. Sympathetic neural mechanisms in white-coat hypertension. J Am Coll Cardiol 2002; 40: 126-32.
24 Coste SC, Brooks VL, McCarron DA, Hatton DC. Captopril and stress-induced hypertension in the borderline hypertensive rat. J Hypertens 1995; 13(12 Pt 1): 1391–8.
25 Li P, Zhu DN, Kao KM, Lin Q, Sun SY. Role of acetylcholine, corticoids and opioids in the rostral ventrolateral medulla in stress-induced hypertensive rats. Biol Signals 1995; 4: 124–32.
26. Lin Q, Li P. Rostral medullary cholinergic mechanisms and chronic stress-induced hypertension. J Auton Nerv Syst 1990; 31: 211–8.
27 Hwang IS, Hwang WC, Wu JN. Effect of fructose-induced hypertension on the renin-angiotensin-aldosterone system and atrial natriuretic factor. Am J Hypertens 1989; 2: 424–7.
28 Iyer SN, Raizada MK, Katovich MJ. AT1 receptor density changes during development of hypertension in hyperinsulinemic rats. Clin Exper Hypertens 1996; 18: 793–810.
29 Wang DH, Wu W, Lookingland KJ. Degeneration of capsaicin-sensitive sensory nerves leads to increased salt sensitivity through enhancement of sympathoexcitatory response. Hypertension 2001; 37(2 Part 2): 440–3.
30 Huang Y, Wang DH. Role of AT1 and AT2 receptor subtypes in salt-sensitive hypertension induced by sensory nerve degeneration. J Hypertens 2001; 19: 1841–6.
31 Fregly MJ, Kikta DC, Threatte RM, Torres JL, Barney CC. Development of hypertension in rats during chronic exposure to cold. J Appl Physiol 1989; 66: 741–9.
32 Sun Z, Fregly MJ, Cade R. Effect of renal denervation on elevation of blood pressure in cold-exposed rats. Can J Physiol Pharmacol 1995; 73: 72–8.
33 Sun Z, Cade R, Tatum C. Central imidazoline and angiotensin II receptors in cardiovascular responses to chronic cold exposure in rats. J Therm Biol 2001; 26: 513–8.
34 Sun Z, Cade R, Morales C. Role of central angiotensin II receptors in cold-induced hypertension. Am J Hypertens 2002; 15: 85–92.
35 Sun Z, Cade R, Katovich MJ, Fregly MJ. Body fluid distribution in rats with cold-induced hypertension. Physiol Behav 1999; 65: 879–84.
36 Sun Z, Cade R. Cold-induced hypertension and diuresis. J Thermal Biol 2000; 25: 105–9.
37 Thorvaldsen P, Asplund K, Kuulasmaa K, Rajakangas AM, Schroll M. Stroke incidence, case fatality, and mortality in the WHO MONICA project: World Health Organization Monitoring Trends and Determinants in Cardiovascular Diseases. Stroke 1995; 26: 361–7.
38 Donaldson GC, Robinson D, Allaway SL. An analysis of arterial disease mortality and BUPA health screening data in men, in relation to outdoor temperature. Clin Sci Colch 1997; 92: 261–8.
39 Gyllerup S, Lanke J, Lindholm LH, Schersten B. Cold climate is an important factor in explaining regional differences in coronary mortality even if serum cholesterol and other established risk factors are taken into account. Scott Med J 1993; 38: 169–72.
40 Sheth T, Nair C, Muller J, Yusuf S. Increased winter mortality from acute myocardial infarction and stroke: the effect of age. J Am Coll Cardiol 1999; 33: 1916–9.
41 He BL. Epidemiological characteristic of stroke in 1985–1989, Beijing. Chin J Med 1993; 73: 104–8.

42 Marchant B, Ranjadayalan K, Stevenson R, Wilkinson P, Timmis AD. Circadian and seasonal factors in the pathogenesis of acute myocardial infarction: the influence of environmental temperature. Br Heart J 1993; 69: 385–7.
43 Papanek PE, Wood CE, Fregly MJ. Role of the sympathetic nervous system in cold-induced hypertension in rats. J Appl Physiol 1991; 71: 300–6.
44 Flaim SF, Hsieh C. Effect of cold acclimatization on rabbit carotid artery: altered response to norepinephrine. Gen Pharmacol 1978; 9: 437–42.
45 Fregly MJ, Brummermann M. Effect of chronic exposure to cold on vascular responsiveness to phenylephrine and angiotensin II. Pharmacology1993; 47: 237–43.
46 Shechtman O, Fregly MJ, van Bergen P, Papanek PE. Prevention of cold-induced increase in blood pressure of rats by captopril. Hypertension 1991; 17: 763–70.
47 Peng JF, Kimura B, Fregly MJ, Phillips MI. Reduction of cold-induced hypertension by antisense oligodeoxynucleotides to angiotensinogen mRNA and AT_1-receptor mRNA in brain and blood. Hypertension 1998; 31: 1317–23.
48 Sun Z, Cade R, Zhang Z, Alouidor J, Van H. Angiotensinogen gene knockout delays and attenuates cold-induced hypertension. Hypertension 2003; 41: 322–7.
49 van Bergen P, Fregly MJ, Papanek PE. Effect of a reduction in sodium intake on cold-induced elevation of blood pressure in the rat. Proc Soc Exp Biol Med 1992; 200: 472–9.
50 Sellye H. Production of nephrosclerosis by overdosage with deoxycorticosterone acetate. Can Med Assoc J 1942; 47: 515–9.
51 Crofton JT, Share L, Shade RE. The importance of vasopressin in the development and maintenance of DOC-salt hypertension in the rat. Hypertension 1978; 1: 31–8.
52 Intengan HD, Park JB, Schiffrin EL. Blood pressure and small arteries in DOCA-salt-treated genetically AVP-deficient rats. Role of endothelin. Hypertension 1999; 34 [part2]: 907–13.
53 Mohring J, Mohring B, Petri M, Haack D. Vasopressor role of ADH in the pathogenesis of malignant DOC hypertension. Am J Physiol 1977; 232: F260–9.
54 Katholi RE, Naftilan AJ, Oparil S. Importance of renal sympathetic tone in the development of DOCA-salt hypertension in the rat. Hypertension 1980; 2: 266–73.
55 O'Hagan KP, Thomas GD, Zambraski EJ. Renal denervation decreases blood pressure in DOCA-treated miniature swine with established hypertension. Am J Hypertens 1990; 3: 62–4.
56 Wilson KM, Sumners C, Hathaway S, Fregly MJ. Mineralocorticoids modulate central angiotensin II receptors in rats. Brain Res 1986; 382: 87–96.
57 French JF, Anderson BA, Downs TR, Dage RC. Dual inhibition of angiotensin-converting enzyme and neutral endopeptidase in rats with hypertension. J Cardiovasc Pharmacol 1995; 26: 107–13.
58 Wong PC, Price WA Jr, Chiu AT, Duncia JV, Carini DJ, Wexler RR. *In vivo* pharmacology of DuP 753. Am J Hypertens 1991; 4 (4 pt 2): S288–98.
59 Van den Berg DT, de Kloet ER, de Jong W. Central effect of mineralocorticoid antagonist RU-28318 on blood pressure of DOCA-salt hypertensive rats. Am J Physiol 1994; 267(6 Pt 1): E927–33.
60 Matsumura Y, Hashimoto N, Taira S, Kuro T, Kitano R, Ohkita M, *et al*. Different contribution of endothelin-A and endothelin-B receptors in the pathogenesis of deoxycorticosterone acetate-salt-induced hypertension in rats. Hypertension 1999; 33: 759–65.
61 Moreau P, Schifrin EL. Role of endothelins in animal models of hypertension: focus on cardiovascular protection. Can J Physiol Pharmacol 2003; 81: 511–21.
62 Schiffrin EL. Role of endothelin-1 in hypertension and vascular disease. Am J Hypertens 2001;14: S83–9.
63 van den Meiracker AH. Endothelins and venous tone in DOCA-salt hypertension. J Hypertens 2002; 20: 587–9.
64 Callera GE, Montezano AC, Touyz RM, Zorn TMT, Carvalho MHC, Fortes ZB, *et al*. ET_A receptor mediates altered leukocytes-endothelial cell interaction and adhesion molecules expression in DOCA-salt rats. Hypertension 2004; 43: 872–9.
65 Li L, Chu Y, Fink GD, Engelhardt JF, Heistad DD, Chen A. Endothelin-1 stimulates arterial VCAM-1 expression via NADPH oxidase-derived superoxide in mineralocorticoid hypertension. Hypertension 2003; 42: 997–1003.
66 Manning RD Jr, Meng S, Tian N. Renal and vascular oxidative stress and salt-sensitivity of arterial pressure. Acta Physiol Scand 2003; 179: 243–50.
67 Goldblatt H, Lynch J, Hanzel RF. Studies on experimental hypertension. The production of persistent elevation of systolic blood pressure by means of renal ischemia. J Exp Med 1934; 59: 347–79.
68 Zandberg P. Animal models in experimental hypertension: relevance to drug testing and discovery. In: van Zwieten PA, editor. Handbook of hypertension. Vol. 3: Pharmacology of antihypertensive drugs. New York: Elsevier Science Publishers; 1984. Chapter 2.
69 Leenen FHH, De Jong W. Plasma renin and sodium balance during development of moderate and severe renal hypertension in rats. Circ Res 1975; 36/37 (Suppl 1): 179–84.
70 Liard JF, Cowley AW Jr, McCaa RE, McCaa CS, Guyton AC. Renin, aldosterone body fluid volumes and the baroreceptor reflex in the development and reversal of Goldblatt hypertension in conscious dogs. Circ Res 1974; 34: 549–60.
71 Sawamura T, Nakada T. Role of dopamine in the striatum, renin-angiotensin system and renal sympathetic nerve on the development of two-kidney, one clip Goldblatt hypertension. J Urol 1996; 155: 1108–11.
72 Bean BL, Brown JJ, Casals-Stenzel J, Fraser R, Lever AF, Millar JA, *et al*. The relation of arterial pressure and plasma angiotensin II concentration. A change produced by prolonged infusion of angiotensin II in conscious dog. Circ Res 1979; 44: 452–8.
73 Freeman RH, Davis JO, Watkins BE. Effects of continuous converting enzyme blockade on renovascular hypertension in the rat. Am J Physiol 1979; 236: F221–4.
74 Brown JJ, Fraser R, Lever AF. Mechanism in hypertension: a personal view. In: Genest J, Koiw E, Kuchel O, editors. Hypertension. New York: McGraw-Hill; 1977. Chapter 12.1.
75 Ten Berg RGM, Leenen FHH, De Jong W. Plasma renin activity and sodium, potassium and water excretion during reversal of hypertension in the one-clip, two kidney hypertensive rat. Clin Sci 1979; 57: 7–15.

Acta Pharmacologica Sinica 2005 Mar; 26 (3): 302–306

Invited review

Exo$^+$ proofreading polymerases mediate genetic analysis and its application in biomedical studies[1]

Duan-fang LIAO[2], Lin-ling CHEN[2], Cui-ying PENG[2], Jia ZHANG[2], Kai LI[2,3,4]

[2]Division of Pharmacogenomics, SNP Institute, School of Life Science, Nanhua University, Hengyang 421001, China; [3]Department of Human Genetics, City of Hope National Medical Center, Duarte, CA, USA

Key words

single nucleotide polymorphism; DNA primers; DNA-directed DNA polymerase

[1] Project supported in part by the National Major Basic Research Program (973) of China (No G2000056905), the Natural Science Foundation of Hu-nan (No 03JJY4041) and the Key Project of Education Committee of Hu-nan.
[4] Correspondence to Dr Kai LI.
E-mail kaili34@yahoo.com

Received 2004-08-10
Accepted 2004-12-14

doi: 10.1111/j.1745-7254.2005.00056.x

Abstract

Polymerases with a proofreading function in their internal 3′ to 5′ exonuclease possess high fidelity for DNA replication both *in vivo* and *in vitro*. The obstacle facing Exo$^+$ polymerases for single nucleotide polymorphism (SNP) detection could be bypassed by using primer-3′-termini modification. This hypothesis has been well tested using three types of modified allele specific primers with: 3′ labeling, 3′ to 5′exonuclease resistance, and 3′dehydroxylation. Accordingly, three new SNP assaying methods have been developed to carry out genome-wide genotyping, taking advantage of the enzymatic properties of Exo$^+$ polymerases. These new mutation detection assays are widely adaptable to a variety of platforms, including multi-well plate and microarray technologies. Application of Exo$^+$ polymerases to genetic analysis, including genotyping that is mostly relevant to pharmacogenetics, high-fidelity gene expression profiling, rare mutation detection and mutation load assay, will help to accelerate the pace of personalized medicine. In this review paper, we will first introduce three new assays that we have recently developed, and then describe a number of their applications in pharmacogenetics and in other biomedical studies.

High-fidelity DNA polymerases mediate genotyping

3′Terminal-labeled primer extension Terminal-labeled primer extension is a single nucleotide polymorphism (SNP) assay consisting of 3′ terminal-labeled, allele-specific primers and DNA polymerases with proofreading activity. Both 3′ terminal [^{3}H]-labeled and fluorescent-labeled primers have been successfully applied in genotyping analyses. The 3′ terminal mismatched nucleotide that bears the signal to be detected was removed by the proofreading function, whereas the label was retained when the primer and template were perfectly matched. The terminal-labeled primer extension approach has several advantages over current SNP assays. The most significant advantage is that it greatly decreases false positive results by a direct consequence of the proofreading activity of Exo$^+$ polymerases. The second advantage of terminal-labeled primer extension is its high sensitivity. Terminally labeled primer extension harnesses the power of polymerase chain reaction (PCR) to improve the efficiency of genetic analysis[1–7].

SNP-triggered on/off switch Exo$^+$ polymerases together with 3′ phosphorothioate-modified mismatched primers work as an off switch in DNA polymerization. Phosphorothioate modification renders oligonucleotides nuclease–resistant, which blocks mismatch excision, a strategy widely used in antisense technology as well as in single base extension. For 3′ allele-specific primers with phosphorothioate modification, a perfectly matched primer turns on DNA polymerization, whereas mismatched primers turn it off, resulting in no product. This breakthrough observation of an on/off switch action has been repeatedly confirmed using either short artificial amplicons or natural genomic DNA templates. The off switch directly resulted from 3′exonuclease activity and has been well supported by comparisons of a variety of DNA polymerases in both linear and expo-

nential amplification with phosphorothioate-modified, allele-specific primers[3–13].

The crucial structural components of the on/off switch are: (i) allele-specific primers with 3′ terminal exonuclease-resistant modification; and (ii) DNA polymerases possessing 3′ exonuclease activity. In recent studies by Di Giusto *et al*[6,7,14], four types of DNA polymerases, $T4^+$, $T7^+$, KF^+ and Vent, were tested and similar off switches were observed when the polymerases were combined with 3′ phosphorothioate-modified primers. Based on the new model of this proofreading mechanism (Figure 1), polymerases with 3′ exonuclease function should have a higher base discrimination ability over exo-polymerases regardless of the properties of the substrates used. In addition to comparing nine different DNA polymerases, Di Giusto *et al*[6,7,14] evaluated the effect of dNTP(2′-deoxynucleotide-5′-triphosphate), ddNTP (2′,3′-dideoxynucleotide-5′-triphosphate), and acyNTP (acyclo-2′-deoxynucleotide-5′-triphosphate) on the accuracy of primer extension. The maintenance of high fidelity with ddNTP and acyNTP allows the Exo^+ polymerases to be applied in both exponential and linear primer extensions in SNP analysis. The latter was tested using MALDI-TOF MS (Matrix Assisted Laser Desorption/Ionization Time of Flight Mass Spectrometry) and is compatible with many other detection formats.

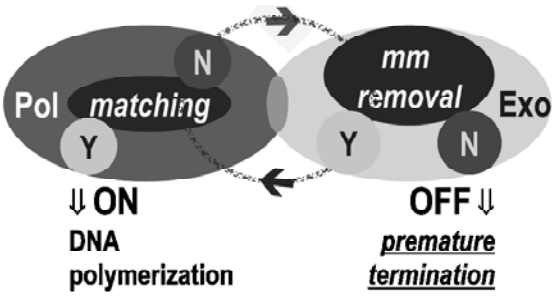

Figure 1. Mismatch primer extension model using Exo^+ polymerases based on results from phosphorothioate (PTO)-modified primers.

SNP-triggered reversed on/off switch or off/on switch The SNP triggered reversed on/off switch works in a way complementary to proofreading 3′ exonuclease-resistant or 3′ labeled primers. With the introduction of inert allele-specific primers or proprimers, matched amplicons turn off and mismatched amplicons turn on DNA polymerization. Inert primers of a perfectly matched amplicon are not processed by the 3′Exo domain of the high-fidelity DNA polymerases. In this circumstance, inert primers remain inactive and no DNA polymerization occurs. In contrast, the inert primers of mismatched amplicons trigger the 3′exonuclease excision process by which the mismatched 3′ terminal is removed and subsequent processes activate the 3′ hydroxyl group for DNA polymerization. One of the benefits of the reversed on/off switch is that positive results can screen all three mismatched nucleotides other than the complementary one, and this is a powerful tool in mutation detection.

To date two types of 3′ dehydroxylated primers, 3′ phosphorylated and 3′ hydrogenized, have been evaluated for use in the SNP-triggered reversed on/off switch. The 3′ phosphorylated primers can always be extended regardless of whether low-fidelity or high-fidelity polymerases are used. Fortunately, the 3′ hydrogenized primer works well as an inert primer that can not be extended without activation through removal of the 3′ terminal nucleotide residue. The SNP-operated reversed on/off switch is not a simple candidate method in mutation detection. One particularly important feature of the previously developed on/off switch and this new reversed on/off switch is the identical reaction conditions of the two types of Exo^+ DNA polymerases mediated by the primer extension. In large-scale SNP scanning, the application of two complementary assays within one platform, such as multi-well plates or microarrays, will help to minimize wrongly genotyped SNP sites resulting from special local sequence contents. With the application of the reversed on/off switch using the inert primers and the on/off switch using the 3′ exonuclease-resistant primers, their complementary effect will help to increase assay sensitivity and reliability in genetic analysis. The on/off switch provides assays for precise detection of the location and type of mutation, whereas the reversed on/off switch serves as a very powerful and efficient assay in unknown mutation scanning[11]. The reversed on/off switch was first described in 1998 as a proofreading PCR by Bi and Stambrook[15].

Genomapping applications other than SNP assay

The high-fidelity features of the Exo^+ polymerases mediated on/off and off/on switch can be widely used in a variety of genetic analysis, other than SNP assays. These include both genotyping and gene expression profiling. Genotyping focuses on the sequencing context and gene expression profiling evaluates both the sequence context and the functional levels of any specific isoforms of a given gene product. The Exo^+ polymerases mediated assays provide methods useful for these two types of genetic assays simultaneously, an advantage favor to pharmacogenetic studies. To simplify the terminology, we refer the combination of genotyping

and gene expression profiling as genomapping analysis.

Analysis of mutations with short deletion/insertion Most of the currently available SNP assays, such as the single base extension assay, can not discriminate between wild-type alleles and mutants with small insertions or deletions. The aforementioned data illustrates the powerful mutation detection ability of the novel on/off switch, indicating its potential in the analysis of both SNP and other types of mutations. Except for the deletion or insertion of identical short repeats, the application of this on/off switch provides an efficient and high throughput compatible assay for mutation analysis[4–11,16].

Detection of rare alleles using the novel on/off switch The novel SNP-operated on/off switch is more sensitive than many conventional mutation analysis methods, including preferential amplification of the mutant allele, preferential destruction of the wild-type allele and spatial separation of mutant from wild-type alleles, by virtue of its use of Exo^+ high-fidelity DNA polymerases. This breakthrough observation of an on/off switch action was repeatedly confirmed using either short artificial amplicons or natural genomic DNA templates[11]. Another outstanding feature of the novel on/off switch is its flexibility and its ability to apply double switches in a single reaction (for example both the forward and the reverse primers are 3′-phosphorothioate modified and allele specific). The double-switch approach does not compromise sensitivity as is the case in most other primer-extension-based SNP assays.

Allele frequency estimation in pooled DNA samples The application of pooled DNA samples in initial studies can help to identify significant divergence in allele frequencies between case and control populations for further, more extensive association studies or for haplotype analysis. Invader technology, Bi-PAP (double directions-pyrophosphorolysis activated polymerization), and the SNP-operated on/off switch can all be used in allele frequency estimation. Among these three assays, the on/off switch has the advantage of simplicity, sensitivity, and accuracy. The application of the novel on/off switch in allele frequency estimation is expected to lower the cost and increase the accuracy of allele estimation using pooled DNA samples. Because the analysis of pooled samples requires only a handful of reactions per SNP, low assay development cost becomes of paramount importance.

High-fidelity gene expression profiling with the novel on/off switch

In our SNP and mutation detection assays, we have shown that the on/off switch can recognize a single mismatch in six nucleotides upstream of the 3′terminus. In most circumstances, Exo^+ DNA polymerases can discriminate single mismatched nucleotides several bases upstream of the primer-3′-termini, but this varies according to the amplicons and the enzymes[3].

In the early stage of gene expression analysis, mRNA is the target material. Such methods include Northern blotting and ribonuclease protection assays. Although these methods could be compatible with high throughput scalability, the ribonuclease protection assay is still, to date, the most reliable method in gene expression profiling. Microarray technology has solved the high throughput issue for genome-wide gene expression profiling. However, cDNA is an indirect target because it cannot completely represent the type and abundance of mRNA. False positives are particularly high when post reverse transcription amplification by *Taq* polymerases is used. To minimize the errors introduced by *Taq* polymerase-mediated amplification, high-fidelity DNA polymerases have recently been used in genome-wide gene expression profiling. Because proofreading polymerases display up to two orders of magnitude better amplification fidelity, the application of high-fidelity polymerases has great potential in improving the reliability of microarray-based gene expression profiling.

In general, false positives in gene expression profiling arise from three sources: mismatched incorporation in reverse transcription, mismatched priming, and mismatched incorporation during primer extension. Although the high-fidelity gene expression assay described in the present study has nothing to do with the errors introduced from reverse transcription, it eliminated the mismatchedpriming error and greatly minimized the mismatched incorporation during primer extension. Increased fidelity in gene expression profiling not only benefits assay sensitivity and reliability, it also provides new applications in genetic analysis. The differential amplification of the on/off switch allows for the profiling of very rare abundant transcripts in normal tissues or cancer tissues. It also offers simple and convenient methods for comparing isoforms, inter-species or intra-species.

Suggested strategies for somatic mutation load assay

It was almost impossible to analyze rare mutations or mutation loads before the development of highly sensitive genotyping methods. The false positives recorded in conventional assay methods, in both hybridization-based and enzyme-based assays, are higher than the mutation rate. Theoretically, our recently developed Exo^+ polymerase-mediated on/off switch is a good method for examining rare

mutations because it almost eliminates false positives. However, assay sensitivity is another obstacle facing the detection of rare mutations. For example, for single-copy genes, 1 mg genomic DNA only contains 3×10^5 molecules of relevant genes. Theoretically, to detect a single mutant out of 1×10^9–1×10^{10} wild-type molecules (based on the mutation rate in human somatic cells per generation), at least mg scale genomic DNA is needed. These results in two immediate problems: technical difficulties in obtaining the large amount of human genomic DNA required, and the inhibitory effect of large amounts of DNA on PCR reactions.

An alternative approach in somatic mutation load analysis is to use genetic elements with high-copy numbers in the genome. As spontaneous mutation rates vary among genes and tissues, interspersed repeats might be a better choice than tandem repeats. A combination of highly sensitive SNP genotyping methods and a high-copy number of interspersed repeats may provide a practical and useful strategy for somatic mutation load assays at the genome level.

Selection of interspersed repeats for somatic mutation load analysis Short, interspersed nucleotide element (SINE) repeats, such as Alu elements with a high incidence of CpG dinucleotides in new Alu inserts, predisposes a higher mutation rate than long, interspersed nucleotide elements (LINE). Approximately half of the SNP in young Alu elements fall in the region of CpG dinucleotides. For somatic mutation load analysis, it appears that the targeting nucleotides to be chosen need to be carefully sorted. If too many targets are CpG dinucleotides, the overall estimated somatic mutation load might be biased and higher than the actual load.

In the case of this example, 1 ng of genomic DNA used in a somatic mutation load assay with a high-copy number repeat sequence will have the same power as approximately 1 mg of genomic DNA when targeting single-copy genes. Another issue regarding our strategies for somatic mutation load analysis is validation using genomic DNA samples that have different somatic mutations as expected, such as DNA from cancer tissue versus DNA from normal tissue, or DNA from cells in their early passages versus that from late passages.

Alternative opportunities from mitochondrial DNA The large number of mitochondria present in every mammalian cell (1000–10 000) makes this extra-nuclear genetic material very useful in somatic mutation analyses. Furthermore, studies have reported that mitochondrial DNA (mtDNA) has a mutation rate of one base mutation per 1500–3000 years of evolution, which is believed to be a higher rate than chromosomal DNA. The existence of homoplasmy and heteroplasmy in mitochondria mutation and their close relationship with the development of disease strongly suggests the value of testing the mutation load of mtDNA in future studies of personalized medicine. Some mtDNA somatic mutation showed a dose-dependent pattern in causing diseases[17,18]

One technical advantage of sequence comparisons is the very-low copy numbers of well-matched regions between mitochondrial and chromosomal DNA. This is especially true for mitochondrial tRNA genes, which are never observed in more than five copies in chromosomal DNA. This feature allows somatic mutation load assays to be separately designed for chromosomal and mitochondrial DNA without preparing separate DNA samples.

Target simplification by using *in vitro* amplified DNA Genomic DNA can be easily simplified and amplified using routine PCR technology. From a technical point of view, a combination of the PCR amplification of target DNA and a subsequent mutation load detection using one of the mutation quantitative analysis methods outlined can be viewed as a type of nested PCR. An advantage of this nested strategy is that any chromosomal region can be used as the target in somatic mutation load analysis.

In addition, many types of RNA are transcribed at highly abundant levels. Therefore, cDNA obtained immediately from *in vitro* reverse transcription or with a low-cycle-number PCR amplification can be a useful target in somatic mutation load analysis. A potential drawback of using RNA as the target in somatic mutation load analyses is that most mutated RNA are not as stable as their wild-type partners, which may decrease the opportunity for accurately detecting mutations. Therefore, RNA can act as one of the targets, but can not be used as the sole target in practical somatic mutation load analyses when a global approximate of the mutation load is required.

Conclusion

Significant advances after the completion of the Human Genome Project, including bioinformatic algorithms and highly sensitive SNP genotyping technologies, have provided great possibilities for studies relating genotype with phenotype. High-fidelity DNA polymerases have been approved for use as new and very attractive members among a variety of enzymes in genetic analysis. The three types of new methods mediated by proofreading polymerases provide sensitive and reliable tools for genomapping analyses consisting of genotyping, gene expression profiling, and mutation load assay. Genotyping, including SNP screening, is now widely used in pharmacogenetic studies. The most immediate tasks in somatic mutation load analysis are the selection of the genetic sequence set as representative tar-

gets for mutation assay, and the validation of these representative sequences using one or more of the three mutation analysis methods discussed. It is reasonable to expect that somatic mutation load analysis, especially the mitochondrial somatic mutation load, will have an important impact on both basic research and clinical practice.

References

1 Zhang J, Li K. The 3′ terminal labeled primer extension: a new method of high throughput screening for SNP analysis. Curr Drug Disc 2001; 9: 21–3.

2 Zhang J, Li K, Deng Z, Liao D, Fang W, Zhang X. Efficient mutagenesis method for producing the template of single nucleotide polymorphisms. Mol Biotechnol 2003; 24: 105–10.

3 Zhang J, Li K, Liao D, Pardinas JR, Chen L, Zhang X. Different application of polymerases with and without proofreading activity in single-nucleotide polymorphism analysis. Lab Invest 2003; 83: 1147–54.

4 Li K, Zhang J. New SNP assays from an old concept of proofreading. Curr Drug Disc 2003; 11: 37–9.

5 Cahill P, Bakis M, Hurley J, Kamath V, Nielsen W, Weymouth D, *et al*. Exo-proofreading, a versatile SNP scoring technology. Genome Res 2003; 13: 925-31.

6 King GC, Di Giusto DA, Wlassoff WA, Giesebrecht S, Flening E, Tyrelle GD. Proofreading genotyping assays and electrochemical detection of SNPs. Hum Mutat 2004; 23: 420-5.

7 Di Giusto DA, King GC. Strong positional preference in the interaction of LNA oligonucleotides with DNA polymerase and proofreading exonuclease activities: implications for genotyping assays. Nucleic Acids Res 2004; 32: e32.

8 Zhang J, Meng B, Liao D, Zhou L, Zhang X, Chen L, *et al*. *De novo* synthesis of PCR templates for the development of SARS diagnostic assay. Mol Biotechnol 2003; 25: 107–12.

9 Zhang J, Li K. Single base discrimination mediated by proofreading 3′ phosphorothioate-modified primers. Mol Biotechnol 2003; 25: 223–8.

10 Zhang J, Li K. On/off regulation of 3′ exonuclease excision to DNA polymerization by exo$^+$ polymerase. J Biochem Mol Biol 2003; 36: 525–8.

11 Zhang J, Chen LL, Guo ZF, Peng CY, Liao DF, Li K. On/off switch mediated by exo$^+$ polymerases: experimental analysis for its physiological and technological implications. J Biochem Mol Biol 2003; 36: 529–32.

12 Zhang J, Li K, Pardinas JR, Liao DF, Li HJ, Zhang X. SNP discrimination through proofreading and off-switch of Exo$^+$ polymerase. Mol Biotechnol 2004; 27: 75–80.

13 Gale JM, Tafoya GB. Evaluation of 15 polymerases and phosphorothioate primer modification for detection of UV-induced C:G to T:A mutations by allele-specific PCR. Photochem Photobiol 2004; 79: 461–9.

14 Di Giusto DA, King GC. Single base extension with proofreading polymerases and phosphorothioate primers: improved fidelity in single-substrate assays. Nucleic Acid Res 2003; 31: 7.

15 Bi W, Stambrook PJ. Detection of known mutation by proofreading PCR. Nucleic Acids Res 1998; 26: 3073–5.

16 Zhang J, Li K. New performance from an old member: SNP assay and *de novo* sequencing mediated by Exo$^+$ DNA polymerase. J Biochem Mol Biol 2004; 37: 269–74.

17 Li K, Chen LL, Peng CY, Wang C, Liao DF, Zhang J. Transgenic human assay and evolutionary role of mtDNA by mitochromic analysis. J Nanhua Univ 2004,32: 1–3.

18 Li K, Liao DF, Zhang J, Chen LL, Peng CY, Wang C. Mitochromics: a simplified transgenic human assay. Chin J Arterioscler 2003; 11: 601–2.

Acta Pharmacologica Sinica 2005 Mar; 26 (3): 307–314

Full-length article

Gene expression profile induced by oral administration of baicalin and gardenin after focal brain ischemia in rats[1]

Zhan-jun ZHANG[2], Zhong WANG[3], Xiao-yan ZHANG[4], Kang YING[5], Jian-xun LIU[3], Yong-yan WANG[6]

[2]The Clinical School of Beijing University of Traditional Chinese Medicine, Beijing 100029, China; [3]Xi-yuan Hospital of the Academy of Traditional Chinese Medicine, Beijing 100089, China; [4]Beijing Normal University, Beijing 100036, China; [5]BioStar Genechip Incorporated, Shanghai 200012, China; [6]The Academy of Traditional Chinese Medicine, Beijing 100059, China

Key words

microarray; gene expression; baicalin; gardenin; brain ischemia

[1] Project supported by the Major State Basic Research Development Program of the People's Republic of China (No G19990554).
[2] Correspondence to Dr Zhan-jun ZHANG.
Phn 86-10-6287-5599, ext 6114.
Fax 86-10-6287-4049.
E-mail zhangzhanjun1972@yahoo.com.cn

Received 2004-06-29
Accepted 2004-11-19

doi: 10.1111/j.1745-7254.2005.00051.x

Abstract

Aim: To investigate differential gene expression and the pharmacological mechanism of baicalin and gardenin in focal cerebral ischemia in rats with high-density cDNA microarray. **Methods:** Rat left middle cerebral arteries were occluded and treated with either baicalin or gardenin. The pharmacological effects were investigated using the difference in infarction areas before and after treatment, which were determined by 2,3,5-triphenyltetrazolium chloride (TTC) staining. Gene expression was demonstrated using a "Biostar40S" gene microarray. Semiquantitative reverse transcription-polymerase chain reaction (RT-PCR) was used to verify the result of the selected genes. **Results**: Both baicalin and gardenin reduced the infarction areas in focal cerebral ischemia rats ($P<0.05$). The differential genes were 211, 177, and 70 (upregulated or downregulated) in the model group, baicalin, and gardenin treatment groups compared with the sham-operated group, respectively. Gene expression of RpL19 and Csnk2 underwent an approximately 1.9 and 2.1-fold increase, respectively, verified by semiquantitative RT-PCR, which was the same trend as the cDNA microarray. **Conclusion:** Differential gene expression with respect to the pharmacological effects of baicalin and gardenin on focal cerebral ischemia by cDNA microarray revealed a number of clues with respect to the therapeutic mechanisms of Chinese traditional medicine. In addition, the present study provided theoretical and experimental evidence that will aid future studies examining cerebral ischemia.

Introduction

Stroke, mostly caused by cerebral ischemia, is a multifactorial disease involving the activation of myriads of death inducers, which leads to injury of neurons by eliciting cascades of signal transduction pathways[1]. The Qing Kai Ling injection (QKLI) is a modified preparation of the "An Gong Niu Huang" pill, a famous traditional Chinese medicament. In recent studies, QKLI showed strong therapeutic effects on stroke in clinical usage. However, this preparation is a compound comprising of many components. Its therapeutic mechanism is very complex, with regard to both individual and integrative effects. Baicalin and gardenin are two effective compounds of QKLI. Baicalin, known as an antioxidant flavonoid *in vitro*, functions as a biological response modifier[2,3], and has been investigated for its neuroprotective effects against glutamate/*N*-methyl-*D*-aspartate (Glu/NMDA) stimulation and glucose deprivation in primary cultured rat brain neurons. Baicalin was found to significantly reduce Glu/NMDA-increased lactate dehydrogenase (LDH) release[4]. Baicalin is also a potent inhibitor of endothelial cell proliferation, migration, and differentiation[5]. Gardenin can significantly decrease the content of transcription factor monocyte chemoattractant protein-1 (MCP-1) in rat brains suffering focal ischemia[6]. cDNA microarray possesses the ability to analyze the expression changes of hundreds, thousands, or even tens of thousands of genes simultaneously. Several waves of gene expression have been observed after focal cerebral ischemia[7]; however, a comparative study examin-

ing the pharmacological mechanisms of different drugs has not been reported in the literature. Results from the present study suggest that baicalin and gardenin play a pharmacological role in focal cerebral ischemia by regulating gene expression.

Materials and methods

Cerebral ischemia Forty-four Sprague-Dawley rats (250–280 g, supplied by Beijing Weitong-Lihua Experimental Animal Center, Beijing, China) were randomly divided into four groups: model, baicalin-treatment, gardenin-treatment, and sham-operated group, respectively. Under isofurane anesthesia, rats were subjected to occlusion of the left middle cerebral artery (MCAO) using an intraluminal filament as described by Haruo *et al*[8]. After 24 h of focal cerebral ischemia, the rats were deeply re-anesthetized using halothane and the left half of the brain was removed for total RNA isolation. In the sham-operated rats, all procedures except for MCAO were carried out. Baicalin or gardenin (National Institute for the Control of Pharmaceutical and Biological Products, Beijing, China) was given orally (40 mg/kg) 2 h after MCAO.

Measurement of cerebral infarction areas Eight rats from each group were used to calculate the infarction ratio. In brief, the cerebrum was removed and cut into five slices on the coronal section at the location from which the distance to the prefrontal is 1, 3, 5, and 7 mm, respectively. The slices were stained in 4% 2,3,5-triphenyltetrazolium chloride (TTC) solution for 10 min[9]. Images of the slices were captured using a digital camera (Color CCD camera TP-6001A, Topica Inc, Japan). We calculated the areas of the infarction region using a Pathology Image Analysis System (Topica Inc, Japan). The ratio of the infarction area to the total slice area was calculated.

Total RNA isolation The left half of the brain from the remaining three rats in each group was carefully dissected out from the re-anesthetized rats under RNAase-free conditions. The total RNA in each sample was extracted with Trizol reagent (Invitrogen, San Diego, CA, USA) using the procedure outlined in the manufacturer's protocol.

Microarrays Hybridization was carried out on the rat "Biostar40S" gene microarray (BioStar Genechip Incorporated, Shanghai, China), which contained 4096 elements. The array provided a broad overview of the rat genome, which was added to the high-quality array cDNA libraries, and the sequence information, maps, and expression data were placed into the public domain (NCBI, Nucleotide). All clones used for production of the microarrays were sequence verified. Three pieces of total RNA from the same group were pooled following transcription into cDNA and were labeled with Cy5 and Cy3, respectively, and hybridized on the array. Image files were processed using the Axon GenePix 4000B scanner(Axon, USA) and datasets were prepared according to the routine procedures using Genepix 4.0 software (Axon, USA).

Data analysis Data sheets derived from the results of the Genepix 4.0 analysis were further evaluated using Excel software (Microsoft, USA). The microarrays were hybridized in triplicate and each measurement containing the extracted total RNA from each group was used to analyze each gene, which had three data points of relative changes. Thus, a balance coefficient was calculated to correct variations resulting from unequal amounts of fluorescent dye fade; the average signal from all elements in the Cy3 channel was divided by the average signal from all elements in the Cy5 channel, which resulted in the balance coefficient. The Cy5 signal for each element was then multiplied by the balance coefficient, prior to calculating the expression ratio (Cy3/Cy5). A fold value of =2.0 or = -2.0 indicated that differences in the Cy3:Cy5 ratio were detected at a 99% confidence level (information provided by Incyte, USA). All probes fulfilling the criterion (=2.0 or = -2.0) were compiled[10–13].

Semiquantitative RT-PCR The procedures for isolating total RNA using Trizol reagent (Invitrogen, Life Technology, Incorporated, New York, NY, USA) and synthesizing first strand cDNA were exactly as previously described[14]. The optimal polymerase chain reaction (PCR) amplification conditions and cycle number were determined experimentally to ensure specific signal generation. Glyceraldehyde-3-phosphate dehydrogenase (GAPDH) was considered to be stably expressed after focal cerebral ischemia acted as an inter-reference gene. All amplifications were carried out on a Gradient PCR System (Biometra, USA). cDNA synthesis was carried out using 200 ng of mRNA with 5×10^6 U/L reverse transcriptase (TaKaRa, Japan) in a total 100 μL reaction mixture and incubated for 60 min at 48 °C. The primer pairs were for ribosomal protein L19 (Rpl19): AAC AGA TCA GGA AGC TGA TCA AGA; AGT CTT GAT GAT CTC CTC CTT CTT (NM 031103); casein kinase II beta subunit (Csnk2b): CGG ACA TAA AGA TGA GTA GCT CTG A; GTG GTG CCT AGA GGA CTT GGG TGT G (NM 031021); GAPDH: ACC ACA GTC CAT GCC ATC AC; TCC ACC ACC CTG TTG CTG TA (NM 008084.1). After heating to 95 °C for 5 min, each RT reaction mixture was used for PCR amplification. The PCR mixture started with in an initial step of 5 min at 95 °C followed by 35 cycles of 30 s at 95 °C and an annealing temperature of 1 min at 64.5 °C for Csnk2b mRNA, at 57.4 °C for

Rpl19 mRNA and GAPDH, followed by 72 °C for 10 min. Products of 5 μL from each PCR mixture were dyed with 1 μL SYBR Green I Nucleic Acid Gel stain (Cambrex Bio Science Rockland Incorporated, USA) and loaded on 2.5% agarose gels, which were evaluated according to the intensity differences of image electrophoresis using Gel Analyzing Imager (FuRi, Shanghai, China).

Results

TTC staining Both baicalin and gardenin reduced the infarction areas in cerebral ischemia rats by 6%–7% compared with the model group. The ratio of differences was tested using the Student *t*-test (Figure 1, Table 1).

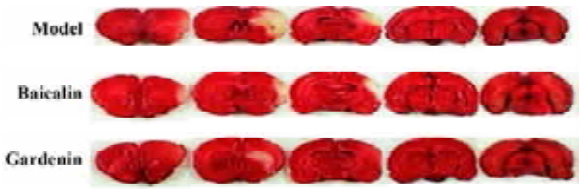

Figure 1. Cross-sections showing cerebral infaction areas (in white) of a number of samples stained with 2,3,5-triphenyltetrazolium chloride.

Table 1. Cerebral infarction areas from a number of samples stained with 2,3,5-triphenyltetrazolium chloride. n=8. Mean±SD. $^bP<0.05$ *vs* the model group.

Group	Percentage of infarcted area to cerebral area/%
Model	24.7±5.6
Baicalin	14.7±3.0^b
Gardenin	15.4±3.2^b

Changes in gene expression after MCAO occlusion Genes were classified into 12 categories by the International General Principle (www.geneontology.org). One hundred and ninety-nine genes were significantly upregulated which are involved in metabolism, signal transduction, cell organization, response to stress, cell adhesion, transport, apoptosis, and a variety of other processes. Another 12 genes showed downregulated expression under the same conditions (Table 2).

Metabolism The largest increases in gene expression were shown by genes involved in protein synthesis: the ribosomal proteins L10, S5, S3a, S24, S6, S11, and L19, glycoprotein 38, eukaryotic translation elongation factor 1 alpha and actin-related protein complex 1b. The expression of genes related to cell metabolism changed with increased expression of coenzyme A dehydrogenase, procollagen-lysine, lactate dehydrogenase and ubiquinone oxidoreductase subunit B13.

Cell organization and adhesion Cell organization and adhesion genes also showed prominent changes in expression. These included Fibronectin 1, Integrin, H2A histone family member and apolipoprotein M.

Signal transduction Increases in expression were shown by genes involved in cellular signal transduction: CDK5, pyruvate kinase 3, phosphatidylinositol 4-kinase, and casein kinase II. In addition, the G protein pathway suppressor showed decreased expression over this interval.

Response to stress Several "stress" genes involved in cellular responses to inflammation and injury were induced, including Cd63 antigen, MRC OX-45 surface antigen and immunoglobulin superfamily member. Another induced gene, glutathione peroxidase 1, was also upregulated after focal cerebral ischemia.

Apoptotic genes The expression of several apoptotic effector genes was altered. These included programmed-cell-death-8, Urmodulin, and tumor protein translationally controlled genes.

Effect of baicalin on gene expression Increases in gene expression were observed in 89 genes. These included genes involved in metabolism, signal transduction, cell organization, responses to stress, and transcription regulators. In addition to the induced genes, 88 genes simultaneously showed decreased expression (Table 3).

Metabolism Metabolism-related genes showed prominent changes in expression. These included ADP-ribosylation factor, enolase, adenine phosphoribosyltransferase, and palmitoyl-protein thioesterase. In addition, histamine *N*-methyltransferase simultaneously showed decreased expression.

Signal transduction The largest increases in expression were shown by genes involved in protein tyrosine phosphatase receptor type D and receptor type A. S100 calcium-binding protein A9 also showed prominent changes. In addition, the expression of protein kinase C-binding protein Zeta and surfactant-associated protein decreased. Protein kinase is controlled by specific binding proteins, which are believed to sequester each type of kinase to the region of a neuron, such as the postsynaptic specialization or cell nucleus, that requires its function[15]. The protein kinase C-binding protein Zeta is one of these proteins. Arachidonic acid epoxygenase, an adapter protein of the prostaglandin

Table 2. Partial differential genes in the model compared with the sham-operated group.

Accession number	Average microarray ratio	Definition	Classification
NM_024151	2.369	ADP-ribosylation factor 4	Metabolism
NM_012898	2.293	alpha-2-*HS*-glycoprotein	Metabolism
AW918082	3.201	Deoxyribose-phosphate aldolase	Metabolism
NM_012576	2.313	Nuclear receptor subfamily 3	Signal transduction
BE113312	2.127	Adapter-related protein complex 3 beta 1 subunit	Signal transduction
X79328	2.153	CaBP1 mRNA	Signal transduction
AI407932	3.301	Retinoid-inducible serine carbopeptidase precursor	Signal transduction
AF335277	2.371	Centrosomal protein centrin 3 mRNA	Cell cycle
NM_017082	2.327	Urmodulin (Tamm-Horsfall protein)	Apoptosis
AW918198	2.295	Myosin heavy chain mRNA	Cell mobility
L24897	3.528	TROPOMYOSIN BETA CHAIN	Cell mobility
NM_031509	3.132	Glutathione-S-transferase (Mu2)	Response to stress
NM_053440	2.908	Superiorcervical ganglia, neural specific 10	Others
AW915152	4.633	Hypothetical protein C32E8.9	Others
BF388747	2.172	ESTs	Others
AA893226	2.198	ESTs	Others
BI276980	2.485	ESTs	Others
BF391240	2.248	ESTs	Others
AI639155	2.512	ESTs	Others
BF556197	3.577	ESTs	Others
NM_031797	2.591	Suppression of tumorigenicity	Others
AW918368	3.391	Hypothetical protein	

and leukotriene family of intracellular messengers, also appears to play an important role in the regulation of signal transduction in the brain and elsewhere[14].

Cell organization The expression of nucleolar phosphoprotein p130, an adapter protein that participates in nucleolar disassembly and cell cycle, decreased after MCAO. In addition, peroxisomal membrane protein showed increased expression over this interval.

Transcription regulator Two genes related to the transcription regulator were altered. These were spliceosome-associated protein and DNA primase.

Effect of gardenin on gene expression Increases in gene expression were observed for 68 genes. These included genes involved in metabolism, signal transduction, cell organization, response to stress, cell cycle, and cell mobility. In addition, two genes showed decreased expression over this interval (Table 4).

Metabolism The expression of several genes involved in protein synthesis and cell metabolism was altered. These included ADP-ribosylation factor, HS-glycoprotein and deoxyribose-phosphate aldolase.

Signal transduction Changes in the expression of genes indirectly related to signal transduction were observed, and consisted of increased expression in nuclear receptor, adapter-related protein complex and retinoid-inducible serine carbopeptidase precursor.

Response to stress Several "stress" genes involved in cellular responses to oxidation were induced. The most striking was the increased expression of glutathione-*S*-transferase.

Cell mobility Myosin heavy chain and tropomyosin beta chain genes that participate in cell mobility and cell cycle were also induced.

Semiquantitative RT-PCR The outcome of this study showed that the expression of ribosomal protein RpL19 mRNA and Csnk2 mRNA were consistently upregulated in the individual samples from MCAO rats relative to sham-operated rats. Expression increased by 1.9- and 2.1-fold, respectively, and showed the same trend as the results of the microarray. The outcome of RT-PCR indicated that broad, array-based gene expression measurements were reliable for determining gene expression patterns in the brain (Figure 2).

Discussion

Messenger RNA is only an intermediate on the way to the production of the eventual protein products. In the present study we explored the potential role of cDNA

Table 3. Partial differential genes in the model compared with the baicalin-treatment group.

Accession number	Average microarray ratio	Definition	Classification
NM_019156	0.222	Vitronectin	Others
NM_022399	0.383	Calreticulin	Others
NM_023986	0.472	TEMO	Others
NM_031140	2.317	Vimentin	Others
NM_053372	3.058	Secretory leukocyte protease inhibitor	Others
NM_012559	3.359	Fibrinogen, gamma polypeptide	Others
NM_017131	2.848	Calsequestrin 2	Others
BI285007	0.271	Spliceosome-associated protein	Transcription regulator
U67994	0.441	DNA primase small subunit mRNA	Transcription regulator
NM_022869	0.327	Nucleolar phosphoprotein p130	Cell organization
NM_017234	3.408	Peroxisomal membrane protein 3	Cell organization
NM_031559	0.365	Carnitine palmitoyltransferase 1 alpha	Metabolism
NM_024152	0.402	ADP-ribosylation factor 6	Metabolism
NM_012554	0.405	Enolase 1, alpha	Metabolism
L04970	0.408	Adenine phosphoribosyltransferase	Metabolism
NM_022502	0.491	Palmitoyl-protein thioesterase	Metabolism
NM_031044	2.921	Histamine N-methyltransferase	Metabolism
[1609]	0.264	Protein kinase C-binding protein Zeta	Signal transduction
NM_017329	0.436	Surfactant-associated protein 1	Signal transduction
NM_053587	3.054	S100 calcium-binding protein A9	Signal transduction
NM_031839	4.286	Arachidonic acid epoxygenase	Signal transduction
NM_019140	7.844	Protein tyrosine phosphatase receptor type D	Signal transduction
NM_012763	6.988	Protein tyrosine phosphatase receptor type A	Signal transduction
NM_031140	2.317	Vimentin	Response to stress
NM_053372	3.058	Secretory leukocyte protease inhibitor	Response to stress
NM_012559	3.359	Fibrinogen, gamma polypeptide	Response to stress

microarrays for gene expression analysis after focal brain ischemia and examined the differences in gene expression after the action of different compounds of QKLI. An ischemia period of 24 h was used because this is the maximum period of cerebral ischemia that is compatible with neuroprotection[16–18]. To select results from microarray experiments with reliably altered ratios, we filtered the results using two criteria[10–13]: minimal fold-change values, and ratios reproducibly different from unity. The hybridization ratio had to be at least two-fold higher or lower than the control groups. Of these filters, the two-fold ratio filter was by far the most restrictive and there was no uniform standard across the different platforms of the arrays. We have listed the information of differential gene expression according to the functional classification of genes. In brief, baicalin and gardenin appear to have a profound influence on the model by regulating the expression of different genes or by acting on different metabolic pathways. The genes related to cell metabolism presented striking changes, and showed increased expression in both model and baicalin-treatment groups in contrast to the gardenin-treatment group. Baicalin appears to have a more prominent action on signal transduction in cells than gardenin, including activation of ion channels, regulation of kinase and phosphorylation of receptor proteins. In contrast, the effects of gardenin in stress responses and anti-oxidation appear to be more significant

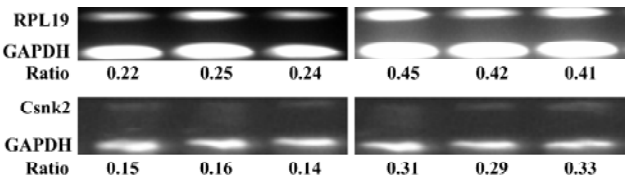

Figure 2. Some strongly regulated Rpl19 and Csnk2 genes are confirmed with RT-PCR. Size of the internal control is 550 bp, and that of the target genes are 350 and 320 bp. Ratios indicate the signal intensity of examined gene *vs* that of glyceraldehyde-3-phosphate dehydrogenase (GAPDH) at different groups. The bottom panel in each graph is a representative gel of the PCR products of three independent repeats.

Table 4. Partial differential genes in the model compared with the gardenin-treatment group.

Accession number	Average microarray ratio	Definition	Classification
NM_019156	0.222	Vitronectin	Others
NM_022399	0.383	Calreticulin	Others
NM_023986	0.472	TEMO	Others
NM_031140	2.317	Vimentin	Others
NM_053372	3.058	Secretory leukocyte protease inhibitor	Others
NM_012559	3.359	Fibrinogen, gamma polypeptide	Others
NM_017131	2.848	Calsequestrin 2	Others
BI285007	0.271	Spliceosome-associated protein	Transcription regulator
U67994	0.441	DNA primase small subunit mRNA	Transcription regulator
NM_022869	0.327	Nucleolar phosphoprotein p130	Cell organization
NM_017234	3.408	Peroxisomal membrane protein 3	Cell organization
NM_031559	0.365	Carnitine palmitoyltransferase 1 alpha	Metabolism
NM_024152	0.402	ADP-ribosylation factor 6	Metabolism
NM_012554	0.405	Enolase 1, alpha	Metabolism
L04970	0.408	Adenine phosphoribosyltransferase	Metabolism
NM_022502	0.491	Palmitoyl-protein thioesterase	Metabolism
NM_031044	2.921	Histamine *N*-methyltransferase	Metabolism
[1609]	0.264	Protein kinase C-binding protein Zeta	Signal transduction
NM_017329	0.436	Surfactant-associated protein 1	Signal transduction
NM_053587	3.054	S100 calcium-binding protein A9	Signal transduction
NM_031839	4.286	Arachidonic acid epoxygenase	Signal transduction
NM_019140	7.844	Protein tyrosine phosphatase receptor type D	Signal transduction
NM_012763	6.988	Protein tyrosine phosphatase receptor type A	Signal transduction
NM_031140	2.317	Vimentin	Response to stress
NM_053372	3.058	Secretory leukocyte protease inhibitor	Response to stress
NM_012559	3.359	Fibrinogen, gamma polypeptide	Response to stress

than those of baicalin.

Changes in gene expression after MCAO Prominent changes were recorded in the ribosomal proteins S6, L6, S3a, S24, L5, L10, L19, and S11 on the microarray[19]. In general, this finding supports previous studies[20], perhaps reflecting recovery from an early postischemic transcriptional defect. Integrin is a transmembrane protein, and the adhesion effects between leucocytes and cerebral micrangium cells mediated by integrin participated in the injury and destruction of inflammation factors to tissues. The increased expression of integrin after MCAO is, in general, in line with a preceding report[21]. The increased expression of protein kinase (PK) is mostly caused by the large amount of PK released as a result of metabolic dysfunction, necrosis, ischemia and hypoxia of cells, which occurs in acute cerebrovascular diseases, and this finding was in accordance with the clinical diagnosis. The increased expression of genes in the G protein pathway suppressor 1 may have contributed to the adaptive modulation of the body. In general, G protein plays a role in signal amplification and in switching the molecule on and off in the course of signal transduction. G protein pathway suppressor was upregulated after focal cerebral ischemia, which might occur in compensation for stress and signal transduction regulation in the body[22,23]. Casein kinase II is a necessary substance for cell survival, and increased expression of casein kinease II is correlated with hyperplasia and the proliferation of cells after cerebral ischemia. Cyclin-dependent kinase 5 (CDK5) mRNA was found to be downregulated after focal brain ischemia, whereas variable changes were noted at the protein level in focal ischemia[24]. Downregulation of phosphatases was noted, which would alter the balance of protein phosphorylation in several cellular signaling pathways; much more information is needed before any suggestions regarding functional effects can be made. As the oxidation of glutathione peroxidase might offer a new modulating mechanism of cellular signal transduction[25], it was suggested that its increased expression could provide a sign in response to stress in the body.

Effect of baicalin on gene expression Programmed-cell-death-8 was upregulated after MCAO with baicalin treatment.

Furthermore, novel mediators of cerebral ischemia inducing neuronal death have also been found using cDNA microarrays. All these studies reinforce the idea that common cell death pathways are activated in response to neurondeath inducers, which promise to serve as potential therapeutic targets for modulation to achieve neuroprotection[26]. The expression of the protein kinase C-binding protein Zeta was downregulated in rats treated with baicalin, which resulted in a decrease in the activity of protein kinase C (PKC). Aronowski *et al*[27] observed that the activity of PKC in the brain cortex and hippocampus decreased significantly after ischemia and this decrease could be alleviated by the pretreatment of the NMDA receptor antagonist. Further studies need to examine whether baicalin acts as an antagonist to the NMDA receptor. After all, the relationship between the changing activity of PKC and neuron injury has not been elucidated completely in many key pathophysiological procedures of ischemia, such as increment of fermentation, acidosis, and deficiency of ATP production. The prominent differential genes involved in protein tyrosine phosphatase receptor type D and A are central to the course of signal transduction, which has been implicated both in the regulation of cell growth and the rearrangement of actin that is mediated by several receptor tyrosine kinases. Differential gene expression showed that baicalin played an important role in cell signal transduction and protein phosphorylation after MCAO, and might act as a neuroprotectant.

Effect of gardenin on gene expression The differential genes in the gardenin-treatment group showed extreme variation compared with the baicalin-treatment group. Several genes encoding anti-oxidation were upregulated. For example, an increase in Mu2 suggested that Mu2 played an activation role in anti-oxidation responses, and was regarded as one of the markers of internal anti-injury because of its anti-oxidative and antidotal effects[25]. According to the actions of Mu2, the anti-oxidative and antidotal effects of gardenin might be one of the mechanisms of cerebral protection after MCAO.

The most interesting phenomenon observed was that there was no overlap in the genes showing differential expression in the three groups despite the similar trends in expression. The results suggest that there are considerable differences in the pharmacological effects of baicalin and gardenin at the molecular level after MCAO. Compared with the role of gardenin and bacalin, which are components of QKLI, it appears that QKLI plays an integral role and has important therapeutic effects requiring further investigation.

In conclusion, the cDNA microarray study not only confirmed that changes in many genes contributed to cerebral ischemia, but also suggested several potential targets for further investigation. Of course, global expression of genes measured at the levels of mRNA transcription obtained using microarray analysis should be viewed from two different standpoints. Looking from mRNA towards protein, one would ultimately like to test the increased production of the proteins encoded by the upregulated mRNA or demonstrate a loss of protein encoded by downregulated mRNA. Thus, it may be rewarding to reconstruct the networks of regulation in response to ischemia and, by inference, to hypoxia, using bioinformatic strategies[28]. Understanding such regulatory networks and the therapeutic mechanisms of QKLI for ischemia–hypoxia responsive gene expression in neurons may extend the relevance of these studies.

References

1 Hou ST, MacManus JP. Molecular mechanisms of cerebral ischemia-induced neuronal death. Int Rev Cytol 2002; 221: 93–148.

2 Chen X, Nishida H, Konishi T. Baicalin promoted the repair of DNA single strand breakage caused by H_2O_2 in cultured NIH3T3 fibroblasts. Biol Pharm Bull 2003; 26: 282–4.

3 Huang Y, Wong CM, Lau CW, Yao X, Tsang SY, Su YL, *et al*. Inhibition of nitric oxide/cyclic GMP-mediated relaxation by purified flavonoids, baicalin and baicalein in rat aortic rings. Biochem Pharmacol 2004; 67: 787–94.

4 Lee HH, Yang LL, Wang CC, Hu SY, Chang SF, Lee YH. Differential effects of natural polyphenols on neuronal survival in primary cultured central neurons against glutamate- and glucose deprivation-induced neuronal death. Brain Res 2003; 986: 103–15.

5 Liu JJ, Huang TS, Cheng WF, Lu FJ. Baicalein and baicalin are potent inhibitors of angiogenesis: inhibition of endothelial cell proliferation, migration and differentiation. Int J Cancer 2003; 106: 559–65.

6 Zhou JW. Gardenin and bacalin show the effect on MCP-1 of rat brain suffered focal ischemia. Chin Arch Tradit Chin Med 2004; 22:1016–7.

7 Sharp FR, Lu A, Tang Y, Millhorn DE. Multiple molecular penumbras after focal cerebral ischemia. J Cereb Blood Flow Metab 2000; 20: 1011–32.

8 Haruo N, Agasawa K, Yuya K. Correlation between cerebral blood flow and histologic changes in a new rat model of middle cerebral artery occlusion. Stroke 1989; 20: 1037–42.

9 Bederson JB. Evaluation of 2,3,5-triphenyltetrazolium chloride as a stain for detection and quantification of experimental cerebral infarction in rats. Stroke 1986; 17: 1304–8.

10 Jiang CH, Tsien JZ, Schultz PG, Hu Y. The effects of aging on gene expression in the hypothalamus and cortex of mice. Proc Natl Acad Sci USA 2001; 98: 1930–4.

11 Jin K, Mao XO, Eshoo MW, Nagayama T, Minami M, Simon RP, *et al*. Microarray analysis of hippocampal gene expression in global cerebral ischemia. Ann Neurol 2001; 50: 93–103.

12 Lee CK, Weindruch R, Prolla TA. Gene-expression profile of

the ageing brain in mice. Nat Genet 2000; 25: 294–7.
13 Sandberg R, Yasuda R, Pankratz DP, Barlow C. Regional and strain-specific gene expression mapping in the adult mouse brain. Proc Natl Acad Sci USA 2000; 97: 11038–43.
14 Hou ST, Callaghan D, Fournier MC, Hill I, Kang L, Massie B, *et al*. The transcription factor E2F1 modulates apoptosis of neurons. J Neurochem 2000; 75: 91–100.
15 Jaken S. An overlay assay for detecting protein kinase C-binding proteins and substrates. Methods Mol Biol 2003; 233: 359–68.
16 Belayev L, Liu Y, Zhao W, Busto R, Ginsberg MD. Human albumin therapy of acute ischemic stroke: marked neuroprotective efficacy at moderate doses and with a broad therapeutic window. Stroke 2001; 32: 553–60.
17 Huh PW, Belayev L, Zhao W, Koch S, Busto R, Ginsberg MD. Comparative neuroprotective efficacy of prolonged moderate intraischemic and postischemic hypothermia in focal cerebral ischemia. J Neurosurg 2000; 92: 91–9.
18 Belayev L, Zhao W, Busto R, Ginsberg MD. Transient middle cerebral artery occlusion by intraluminal suture: I. Three-dimensional autoradiographic image-analysis of local cerebral glucose metabolism-blood flow interrelationships during ischemia and early recirculation. J Cereb Blood Flow Metab 1997; 17: 1266–80.
19 Guhaniyogi J, Brewer G. Regulation of mRNA stability in mammalian cells. Gene 2001; 265: 11–23.
20 Schmidt-Kastner R, Zhang B, Belayev L, Khoutorova L, Amin R, Busto R, *et al*. DNA microarray analysis of cortical gene expression during early recirculation after focal brain ischemia in rat. Brain Res Mol Brain Res 2002; 108: 81–93.
21 Zhang ZG, Chopp M, Tang WX, Jiang N, Zhang RL. Postischemic treatment (2-4) with anti-CD11b and anti-CD18 monoclonal antibodies is neuroprotective after transient (2 h) focal cerebral ischemia in the rat. Brain Res 1995; 698: 79–85.
22 Bogousslavsky J, Paciaroni M, Gallai V. Glycoprotein (GP) IIb/IIIa inhibitors for acute stroke treatment. Clin Exp Hypertens 2002; 24: 603–10.
23 Wannier-Morino P, Rager G, Sonderegger P, Grabs D. Expression of neuroserpin in the visual cortex of the mouse during the developmental critical period. Eur J Neurosci 2003; 17: 1853–60.
24 Hayashi T, Warita H, Abe K, Itoyama Y. Expression of cyclin dependent kinase 5 and its activator p35 in rat brain after middle cerebral artery occlusion. Neurosci Lett 1999; 265: 37–40.
25 Paolicchi A, Dominici S, Pieri L, Maellaro E, Pompella A. Glutathione catabolism as a signaling mechanism. Biochem Pharmacol 2002; 64: 1027–35.
26 Read SJ, Parsons AA, Harrison DC, Philpott K, Kabnick K, O'Brien S, *et al*. Stroke genomics: approaches to identify, validate, and understand ischemic stroke gene expression. J Cereb Blood Flow Metab 2001; 21: 755–78.
27 Aronowski J, Waxham MN, Grotta JC. Neuronal protection and preservation of calcium/calmodulin-dependent PKII and PKC activity by dextrorphan treatment in lobal ischemia. J Cereb Blood Flow Metab 1993;13: 550–7.
28 Thieffry D. From global expression data to gene networks. Bioessays 1999; 21: 895–9.

Acta Pharmacologica Sinica 2005 Mar; 26 (3): 315–322

Full-length article

Inducible nitric oxide synthase contributes to intermittent hypoxia against ischemia/reperfusion injury[1]

Hai-lei DING[2], Hai-feng ZHU[2], Jian-wen DONG[2], Wei-zhong ZHU[2], Wei-wei YANG[3], Huang-tian YANG[3], Zhao-nian ZHOU[2,4]

[2]Physiological Laboratory of Hypoxia, Shanghai Institutes for Biological Sciences, Chinese Academy of Sciences, Shanghai 200031, China; [3]Laboratory of Molecular Cardiology, Health Science Center, Shanghai Institutes for Biological Sciences, Chinese Academy of Sciences and Shanghai Second Medical University, Shanghai 200025, China

Key words

intermittent hypoxia; ischemia/reperfusion; inducible nitric oxide synthase; aminoguanidine; rats

[1] Project supported by the National Natural Science Foundation of China (No 30393130) and the Science and Technology Committee of Shanghai Municipality (No 02JC14038).
[4] Correspondence to Prof Zhao-nian ZHOU.
Phn 86-21-5492-0305.
Fax 86-21-5492-0306.
E-mail znzhou@server.shcnc.ac.cn

Received 2004-05-13
Accepted 2004-11-03

doi: 10.1111/j.1745-7254.2005.00046.x

Abstract

Aim: To investigate the role of inducible nitric oxide synthase (iNOS)-derived nitric oxide (NO) in the cardioprotection of intermittent hypoxia (IH) against ischemia/reperfusion (I/R) injury. **Methods:** Langendorff-perfused isolated rat hearts were used to measure variables of left ventricular function during baseline perfusion, ischemia, and reperfusion period. Nitrate plus nitrite (NOx) content in myocardium was measured using a biochemical method. iNOS mRNA and protein expression in rat left ventricles were detected using reverse transcription polymerase chain reaction (RT-PCR) and Western blot, respectively. **Results:** Myocardial function recovered better in IH rat hearts than in normoxic control hearts. The iNOS-selective inhibitor aminoguanidine (AG) (100 μmol/L) significantly inhibited the protective effects of IH, but had no influence on normoxic rat hearts. The baseline content of NOx in IH hearts was higher than that in normoxic hearts. After 30 min ischemia, the NOx level in normoxic hearts increased compared to the corresponding baseline level, whereas there was no significant change in IH hearts. However, the NOx level in IH hearts was still higher than that of normoxic hearts during ischemia and reperfusion period. AG 100 μmol/L significantly diminished the NOx content in IH and normoxic hearts during ischemia and reperfusion period. The baseline levels of iNOS mRNA and protein in IH hearts were higher than those of normoxic hearts. Compared to the corresponding baseline level, iNOS mRNA and protein levels in normoxic rat hearts increased and those in IH rat hearts decreased after reperfusion. The addition of AG 100 μmol/L significantly decreased iNOS mRNA and protein expression in IH rat hearts after I/R. **Conclusion:** IH upregulated the baseline level of iNOS mRNA and protein expression leading to an increase in NO production, which may play an important role in the cardiac protection of IH against I/R injury.

Introduction

Intermittent hypoxia, or periodic exposure to hypoxia interrupted by a return to normoxia or less hypoxic conditions, is encountered more frequently in life than sustained hypoxia[1, 2]. Many studies have shown that intermittent hypoxia adaptation might have cardioprotective effects similar to those observed in ischemic preconditioning (IPC)[3–6]. To date, several potential factors have been proposed to be involved in the protective mechanisms afforded by IH[4–10]; however, the precise mechanisms in which IH increases resistance to myocardial ischemia remain far from clear.

Beall *et al* reported that exhalation of nitric oxide (NO) by chronically hypoxic populations of Tibetans and Bolivian Aymara is unexpectedly increased compared with low-alti-

tude populations[11]. The similar response of these two geographically separate high-altitude populations underlines the importance of NO for life under hypoxic stress. Beall *et al* speculated that one possible adaptation to maintaining high-output NO synthesis under hypoxia included increased expression of the synthase enzymes themselves. Nitric oxide synthase (NOS) are a family of three isozymes responsible for the production of NO: the constitutive endothelial (eNOS) and neuronal (nNOS) isozymes and the inducible isozyme. It is known that iNOS is expressed in a wide variety of cell types, including cardiac myocytes. iNOS is usually expressed in response to various physiological and pathophysiological stimuli, such as intense exercise and hypoxia. Recent studies have shown that NO plays an important role in protecting myocardium from I/R injury[12–14]. In addition, studies have indicated that the cardioprotective effects of late preconditioning observed after 24 h resulted from the upregulation of NOS and, more specifically, of iNOS[15,16]. Neckar *et al*[17] reported that the cardioprotective effects of chronic hypoxia and IPC were not additive, suggesting that the mechanisms of protection conferred by chronic hypoxia and preconditioning may share some common signaling pathways. At present, little is known about the role of iNOS-derived NO in the cardioprotection of IH and there is no evidence about the changes in iNOS mRNA and protein in IH rat hearts subjected to ischemia and reperfusion. The aim of the present study was to evaluate: (i) the effect of aminoguanidine (AG) on the post-ischemic recovery of left ventricular function in IH rat hearts, thereby determining the role of iNOS-derived NO in the cardioprotection afforded by IH; and (ii) the effect of IH on iNOS mRNA and protein expression in rat hearts during baseline perfusion, ischemia and reperfusion period.

Materials and methods

Animal preparation Adult male Sprague-Dawley rats (Clean grade, Shanghai Experimental Animal Center, Chinese Academy of Sciences, Shanghai, China), initially weighing 100–130 g and finally weighing 280–330 g, were exposed to intermittent high-altitude hypoxia of 5000 m in a hypobaric chamber for 6 h/day. Barometric pressure (p_B) was lowered to the level equivalent to an altitude of 5000 m (p_B=54 kPa; po_2=11.3 kPa). The total number of exposures was 42-day. The temperature in the chamber was maintained at 22–24 °C. The animals were examined the day after the last hypoxic exposure. The control group of animals was kept under normoxic environmental conditions. All animals were maintained with a natural light-dark cycle (12 h Light: 12 h Dark).

Isolated rat heart perfusion The rats were anesthetized with sodium pentobarbital (60 mg/kg, ip) as previously described[9]. Hearts were quickly excised and mounted on a Langendorff apparatus for a retrograde perfusion with Krebs–Henseleit solution (K-H buffer solution) at a constant pressure of 80 mmHg. K-H buffer solution contains (mmol/L): NaCl 118.0, KCl 4.7, $CaCl_2$ 2.5, $MgSO_4$ 1.2, $NaHCO_3$ 25.0, KH_2PO_4 1.2, glucose 11.0, and sodium pyruvate 2.0. The medium was continuously gassed with 95% O_2 and 5% CO_2 (pH 7.4) and maintained at 37 °C. A water-filled latex balloon connected to a pressure transducer (Gould P23Db) was introduced into the left ventricle via the mitral valve to record isovolumic left ventricular pressure. The balloon volume was adjusted to achieve a stable left ventricular end-diastolic pressure (LVEDP) of 5–10 mmHg during the initial equilibration. Heart rate (HR), left ventricular peak systolic pressure (LVPSP), LVEDP, left ventricular developed pressure (LVDP), coronary flow (CF), and the peak rate of pressure developed ($\pm dp/dt_{max}$) were monitored using a PowerLab system (AD Instrument Ltd, Castle Hill, Australia). LVDP=LVPSP–LVEDP. Pressure-rate product (PRP) was calculated, PRP = HR×LVDP.

Experimental protocol and groups We chose AG, an iNOS-specific inhibitor[18], to detect its effect on the cardioprotection of IH. Rats were divided into four groups: (1) corresponding control (CON) group; (2) CON+AG group; (3) IH group; and (4) IH+AG group. In the present study, we used 20 min baseline perfusion, 30 min no-flow global ischemia, followed by 30 min reperfusion protocol. The hearts of rats in the drug group were treated with AG 100 μmol/L for 5 min before ischemia and maintained during 30 min ischemia, followed by 30 min reperfusion with K-H buffer solution. To obtain samples for biochemical, RT-PCR, and Western-blot experiments, each group was further divided into three subgroups: (1) baseline perfusion group: 20 min baseline perfusion; (2) ischemia group: 20 min baseline perfusion followed by 30 min no-flow global ischemia; and (3) ischemia/reperfusion group: 20 min baseline perfusion, 30 min no-flow global ischemia, followed by 30 min reperfusion. At the end of baseline perfusion, ischemia, and reperfusion, respectively, the hearts were dissected into left and right ventricles, frozen in liquid nitrogen, and stored at –80 °C.

Nitrate plus nitrite (NOx) measurement NOx, the stable end product of NO, was assessed as nitrite concentration after conversion of nitrate to nitrite with nitrate reductase and measured using a commercial kit (Nanjing Jiancheng Bioengineering Institute, Nanjing, China). NOx was designated as μmol/g protein. Its concentration was determined

at an optical density of 550 nm in a spectrophotometric method. Protein determination was carried out according to the Bradford method using bovine serum albumin as the standard.

RNA isolation and semi-quantitative determination of iNOS using RT-PCR Total RNA was extracted from frozen ventricular tissue with Trizol reagent and quantified by absorption at 260 nm. Reverse transcription from 0.5 μg total RNA was incubated in a 20-μL mixture containing 40 U reverse transcriptase, 500 μmol/L of each dNTP, 500 ng oligo(dT) and reaction buffer at 42 °C for 50 min. The sequences of the iNOS primers were 5'-ACTGCTGGTGGTGACAAG-3' (forward) and 5'-CGTTGGAAGTGTA-GCGTT-3' (reverse), allowing the amplification of a 333-bp fragment; the sequences of the M28S primers were 5' AGCAGCCGACTTAGAACTGG-3' (forward) and 5'-TAGGGACAGTGGGAATCTCG-3' (reverse), allowing the amplification of a 250-bp fragment. The PCR contained 0.1 μmol/L of each primer, 200 μmol/L of each dNTP, 2.5 mmol/L $MgCl_2$ reaction buffer and 1 U *Taq* DNA polymerase in a final reaction volume of 20 μL. The reaction mixture was incubated in a thermocycler (Eppendorf Mastercycler gradient, Germany) programmed to predenature at 94 °C for 5 min, denature at 94 °C for 40 s, anneal at 60 °C for 40 s, and extend at 72 °C for 40 s for a total of 38 cycles. The last cycle was followed by a final elongation at 72 °C for 5 min and cooled to 4 °C. A pilot experiment had shown that this cycle number allowed product detection within the linear phase of amplification.

The amplified products were electrophoresced on a 1.0 % agarose gel stained with ethidium bromide, visualized under ultraviolet light, and scanned using Gel doc 2000 (Bio-Rad, Richmond, CA, USA). The results were expressed as the relative intensity of bands for iNOS PCR product normalized by the intensity of the band for M28S.

Preparation of protein extracts and Western blot analysis of iNOS isozyme The protein extracts were prepared by homogenizing the left ventricles in isotonic sucrose buffer A (mmol/L): Tris-HCl 20.0, sucrose 250.0, Na_3VO_4 0.03, $MgCl_2$ 2.0, edetic acid 2.0, egtazic acid 0.5, PMSF 2.0, DTT 1.0, protease inhibitor cocktail 0.02 % (v/v), pH 7.4. The homogenates were centrifuged at 100 000×*g* for 60 min at 4 °C to separate the particulate fraction from the cytosolic fraction. The supernatant containing soluble NOS, designated as cytosol, was used for the Western blot analysis of iNOS.

After boiling for 10 min, equivalent amounts of cytosolic protein (40 μg) were separated by 8% denaturing sodium dodecyl sulfate (SDS)-polyacrylamide gel electrophoresis (PAGE), electroblotted onto a nitrocellulose membrane and immunoreacted with iNOS primary antibody (Santa Cruz Biotech, Santa Cruz, CA, USA) overnight at 4 °C, followed by a 2-h incubation at room temperature with the second antibody (goat anti-rabbit IgG, Sigma Chemical Company, St Louis, MO, USA) conjugated with horseradish peroxidase. The iNOS isozyme was detected using enhanced chemiluminescence (ECL, Amersham Biosciences, UK) as 130-kDa bands. Each iNOS isozyme signal was normalized to the standard signal of the normoxic control heart. The scanned image was imported into Adobe Photoshop software; scanning densitometry was used for quantitative analysis of the data.

Materials and reagents AG was purchased from the Sigma Chemical Company; Trizol isolation reagent was from Invitrogen Life Technologies (San Diego, CA, USA); primers of iNOS and M28S were synthesized by Sangon Bioengineering Company (Shanghai, China); and the reverse transcription system was obtained from Promega (Madison, WI, USA).

Statistical analysis All data are expressed as mean±SD. Statistical analysis were carried out using one-way ANOVA or Student's *t* tests when appropriate. Differences were considered significant at $P<0.05$.

Results

Effects of AG on recovery of CF and ventricular function after I/R in IH and normoxic rats Our previous study showed that the ratio of whole ventricle weight to body weight of rats in IH groups was not significantly different from normoxic control animals, which meant that intermittent hypoxia in this experimental condition did not result in heart hypertrophy[6,19]. The present study demonstrated that CF was slightly but significantly higher in IH hearts during baseline perfusion (Table 1). CF dramatically decreased during reperfusion in all groups, but the improvement of CF during reperfusion was greater in the IH group compared with the normoxic control group. The addition of AG 100 μmol/L did not significantly change either pre-ischemic CF or LVDP, but inhibited pre-ischemic $\pm dp/dt_{max}$ in normoxic and IH hearts (data not shown). The addition of AG 100 μmol/L inhibited the improvement of CF during reperfusion in the IH group, but had no influence on normoxic hearts.

As shown in Table 1, HR did not change in any group and was not affected by AG 100 μmol/L. Baseline values of ventricular function variables did not differ in any group during baseline perfusion, except for CF, but the values of LVPSP, $\pm dp/dt_{max}$, and PRP were greatly decreased, whereas LVEDP significantly increased during reperfusion. During

Table 1. Hemodynamic parameters in normoxic and intermittent hypoxia hearts at baseline perfusion and after 30 min reperfusion. CON, normoxic control hearts (n=8), CON+AG, normoxic hearts pretreated with 100 μmol/L aminoguanidine (AG) for 5 min before ischemia and during ischemia (n=6); IH, intermittent hypoxia hearts (n=8), IH+AG, intermittent hypoxia hearts pretreated with 100 μmol/L AG for 5 min before ischemia and during ischemia (n=7). Mean±SD. $^{b}P<0.05$, $^{c}P<0.01$ *vs* corresponding baseline perfusion. $^{e}P<0.05$, $^{f}P<0.01$ *vs* corresponding of CON. $^{h}P<0.05$, $^{i}P<0.01$ *vs* corresponding of IH.

		CON	CON+AG	IH	IH+AG
Perfusion	CF (mL/min)	15.1±0.6	15.6±1.2	17.3±1.1^{f}	17.1±1.3^{e}
	LVPSP (mmHg)	114.8±9.3	112.2±8.6	112.8±15.3	113.9±7.9
	LVEDP (mmHg)	6.1±2.2	6.3±1.2	5.3±2.0	6.2±0.9
	HR (beat/min)	350±34	347±23	354±37	345±21
	+dp/dt_{max} (mmHg/s)	2832±274	2853±226	2947±168	2904±153
	-dp/dt_{max} (mmHg/s)	–2418±255	–2437±203	–2452±352	–2514±212
	10^{-3}×PRP (mmHg/min)	38.4±3.4	37.6±4.1	38.6±5.4	38.2±4.2
Reperfusion	CF (mL/min)	6.3±1.4^{c}	6.1±1.3^{c}	10.6±2.0^{cf}	6.4±1.2^{ci}
	LVPSP (mmHg)	92.7±7.4^{b}	93.6±7.1^{b}	93.8±6.5^{b}	91.9±6.9^{b}
	LVEDP (mmHg)	77.2±6.6^{c}	78.5±5.2^{c}	68.0±6.7^{ce}	79.0±5.8^{ch}
	HR (beat/min)	308±25	303±27	313±26	309±37
	+dp/dt_{max} (mmHg/s)	484±32^{c}	448±43^{c}	760±91^{cf}	397±52^{ci}
	-dp/dt_{max} (mmHg/s)	–437±39^{c}	–374±47^{c}	–662±68^{cf}	–336±47^{ci}
	10^{-3}×PRP (mmHg/min)	5.0±0.4^{c}	4.7±0.5^{c}	8.1±0.7^{cf}	3.9±0.8^{ci}

CF, coronary flow; LVPSP, left ventricular peak systolic pressure; LVEDP, left ventricular end-diastolic pressure; HR, heart rate; ±dp/dt_{max}, peak rate of pressure developed; PRP, pressure-rate product.

reperfusion, values of ±dp/dt_{max}, LVEDP, and PRP in the IH group were superior to the normoxic group, suggesting that left ventricular functional recovery was modestly facilitated by IH adaptation. AG significantly inhibited the recovery of IH hearts, whereas it had no effect on normoxic hearts during reperfusion (Figure 1).

Effects of AG on the nitrate/nitrite content of IH and normoxic rat hearts The biochemical experiment demonstrated that the baseline content of NOx in IH hearts was 30.4% higher than that in normoxic hearts (P<0.01). After 30 min ischemia, the NOx level in normoxic heart tissue increased from 0.608±0.060 to 0.747±0.062 μmol/g protein, whereas in IH heart tissue there was no significant change (P>0.05, 0.793±0.075 *vs* 0.837±0.054 μmol/g protein). The addition of AG 100 μmol/L significantly diminished the content of NOx in IH hearts from 0.837±0.054 to 0.606±0.070 μmol/g protein and from 0.747±0.062 to 0.541±0.062 μmol/g protein in normoxic hearts during the ischemia period. AG also significantly decreased the content of NOx in IH hearts from 0.742±0.062 to 0.535±0.072 μmol/g protein and from 0.617±0.072 to 0.519±0.059 μmol/g protein in normoxic hearts during the reperfusion period (Figure 2).

Effects of AG on iNOS mRNA expression in IH and normoxic rat hearts The expression of iNOS mRNA is shown in Figure 3A,3B. The baseline level of iNOS mRNA in IH hearts was higher than that in normoxic hearts by 50.2% (P<0.01). After reperfusion, iNOS mRNA level in normoxic hearts increased from 0.470±0.051 to 0.590±0.092 (P<0.05); however, the iNOS mRNA level in IH hearts decreased from 0.706±0.061 to 0.549±0.066 after reperfusion (P<0.05). The addition of 100 μmol/L AG significantly diminished iNOS mRNA level in normoxic and IH hearts after reperfusion; however, the reduced extent of IH hearts was higher than that of normoxic hearts (P<0.01).

Effects of AG on iNOS protein expression in IH and normoxic rat hearts The expression of iNOS protein is demonstrated in Figure 4A, 4B. In accordance with the changes at mRNA level, the baseline level of iNOS protein in IH hearts was 33.8% higher than that of normoxic hearts (P<0.05). After reperfusion, iNOS protein level in the normoxic hearts increased by 18.4% (from 100% ± 0.0% to 118.4%±8.4%, P<0.05); however, iNOS protein level in IH hearts decreased by 31.9% (from 133.8%±16.6% to 91.1%± 7.0%, P<0.01). After reperfusion, the level of iNOS protein between normoxic and IH hearts was significantly different (P<0.05). The addition of 100 μmol/L AG significantly decreased iNOS protein level in IH hearts; however, AG had no influence on iNOS protein expression in normoxic hearts after reperfusion. Ischemia significantly decreased iNOS protein expression in the different groups (P<0.05).

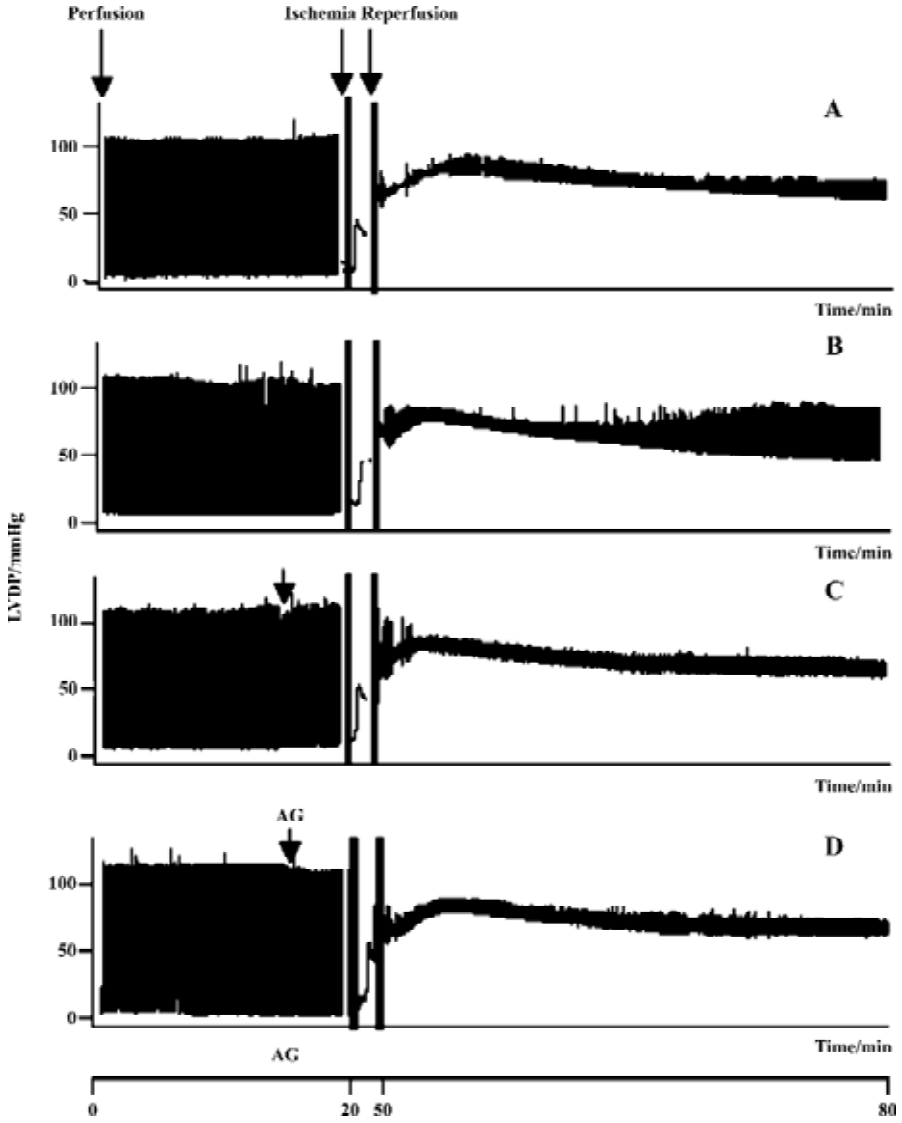

Figure 1. Original recording of left ventricular developed pressure in isolated Langendorff-perfused rat hearts in different groups during 20 min baseline perfusion, 30 min ischemia, and 30 min reperfusion. The arrow indicates the times of the different treatments. (A) normoxic control heart; (B) intermittent hypoxia (IH) heart; (C) normoxic heart pretreated with aminoguanidine (AG) 100 μmol/L for 5 min before ischemia and during ischemia; and (D) IH heart pretreated with AG 100 μmol/L for 5 min before ischemia and during ischemia.

Discussion

The present study showed that IH increased the tolerance of hearts to I/R injury, determined by improved recovery of post-ischemic ventricular function. This protective effect was abolished by AG, suggesting that iNOS-derived NO may participate in the cardioprotection of IH. Our results also showed that the baseline level and the recovery of CF after ischemia were higher in IH hearts compared with normoxic hearts. Zhong *et al*'s study revealed that capillary densities were increased in IH hearts, which contributed to better functional recovery when isolated rat hearts were subjected to an I/R injury[6]. The recovery of post-ischemic CF in IH hearts was abolished by AG, suggesting that iNOS-derived NO may be involved in the improvement of CF by IH.

The level of NOS expression relates directly to the quantity of NOx production. To examine the effect of IH on iNOS expression, we investigated NOx content, iNOS mRNA, and protein expression in normoxic and IH rat hearts during baseline perfusion. Providing important additional insights into IH against I/R injury, we also examined NOx content, iNOS mRNA and protein expression in IH and normoxic rat

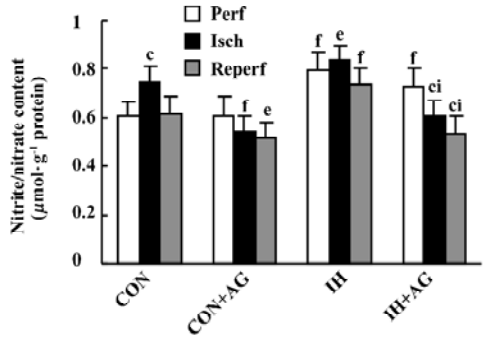

Figure 2. Nitrite/nitrate level in normoxic and intermittent hypoxia (IH) rat hearts treated with or without 100 μmol/L aminoguanidine (AG). *n*=6 rats. Mean±SD. Perf, perfusion; Isch, ischemia; Reperf, reperfusion. $^{c}P<0.01$ *vs* corresponding Perf. $^{e}P<0.05$, $^{f}P<0.01$ *vs* corresponding control (CON). $^{i}P<0.01$ *vs* corresponding IH.

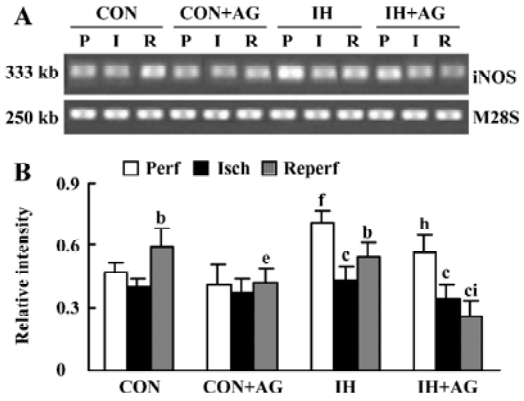

Figure 3. The mRNA expression of inducible nitric oxide synthase (iNOS) isozyme in normoxic and intermittent hypoxia (IH) rat hearts treated with or without 100 μmol/L aminoguanidine (AG). (A) Top panel shows mRNA levels of iNOS; bottom panel shows M28S mRNA, which was used as an internal control. (B) Relative intensity of iNOS mRNA was determined relative to M28S mRNA. *n*=5 rats. Mean±SD. P and Perf, perfusion; I and Isch, ischemia; R and Reperf, reperfusion. $^{b}P<0.05$, $^{c}P<0.01$ *vs* corresponding Perf. $^{e}P<0.05$, $^{f}P<0.01$ *vs* corresponding control (CON). $^{i}P<0.01$ *vs* corresponding IH.

hearts subjected to ischemia/reperfusion. This may help us to understand why IH could improve the post-ischemic recovery of left ventricular function. Our results showed that iNOS mRNA and protein were unregulated and that NOx content increased after IH adaptation in rat hearts. Palmer *et al* showed that hypoxia induced iNOS expression in cardiac myocytes and vascular endothelial cells[20,21]. Rouet-Benzineb *et al* also indicated that after 15 days of hypoxia there was a two-fold increase in iNOS protein abundance in rat left ventricles[22]. However, Baker *et al* demonstrated that

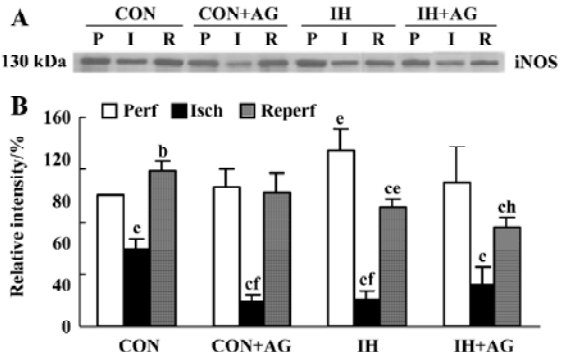

Figure 4. The protein expression of inducible nitric oxide synthase (iNOS) isozyme in normoxic and intermittent hypoxia (IH) rat hearts treated with or without 100 μmol/L aminoguanidine (AG). The immunoreactive band of iNOS was detected using Western blot. (A) The band shows protein expression of iNOS during various periods in different groups; (B) Relative intensity of iNOS protein level was determined relative to a selected standard signal of the normoxic control heart. P and Perf, perfusion; I and Isch, ischemia; R and Reperf, reperfusion. *n*=5 rats. Mean±SD. $^{b}P<0.05$, $^{c}P<0.01$ *vs* corresponding Perf. $^{e}P<0.05$, $^{f}P<0.01$ *vs* corresponding control (CON). $^{h}P<0.05$ *vs* corresponding IH.

increased tolerance to ischemia in rabbit hearts adapted to chronic hypoxia was associated with increased expression of eNOS isozymes, which led to an increase in myocardial nitrite/nitrate content and cGMP level[23]. The signaling functions of NO begin with its binding to protein receptors, such as guanylyl cyclase, which generates cGMP. In the present study, the elevated expression of myocardial iNOS in IH hearts compared to control hearts was also consistent with Zhong *et al*'s report[6], which showed that the myocardial cGMP level in IH rats increased compared to normoxia control rats. Baker *et al* suggested that a small increase in NO levels appears to be cardioprotective, whereas a large increase in NO production may be detrimental, resulting in vasodilation, decreased blood pressure and, perhaps, vascular leakage[23]. Importantly, in our study the magnitude of iNOS upregulation caused by IH was mild. This quantitative induction of iNOS may be critical in explaining the protective effects of iNOS following IH adaptation. The discrepancies between Baker *et al*'s study and ours lie in the age of the animals (adult *vs* neonatal), the species (rabbit *vs* rat), the experimental model, and the training duration and/or intensity.

In the present study, iNOS-derived NO was assessed by measuring the AG-inhibitable nitrite/nitrate content in IH and normoxia rat hearts. The addition of 100 μmol/L AG significantly decreased NOx content, iNOS mRNA and protein levels in IH hearts after reperfusion and abolished the protective effect of IH; AG also decreased NOx content and

iNOS mRNA expression in normoxic hearts; however, the inhibitory extent was lower in normoxic hearts compared with IH hearts. This result suggests that iNOS is tonically higher in IH hearts compared with normoxic hearts and that iNOS may play an important role in the cardioprotection of IH.

Studies examining the role of NO in modulating ischemia/reperfusion injury are complicated. There are conflicting reports about the changes in NO content during ischemia/reperfusion period. A number of studies have demonstrated that NO content increased in hearts subjected to ischemia[24,25]. Studies have also shown that short-term ischemia leads to an increase in iNOS activity and expression; however, iNOS activity and expression decreased with prolonged ischemia. This may be related to a deficiency in essential co-factors for protein synthesis and stability (eg, haem, FAD, FMN, calmodulin). In addition to NO production by specific NOS, Zweier *et al* also demonstrated that NO could be generated in tissues by either direct disproportionation or reduction of nitrite to NO under the acidic and highly reduced conditions that occur in disease states, such as ischemia[26]. Thus, we considered that the basal level of nitrite and nitrate was a better index of nitric oxide production from the aerobically perfused heart.

In addition, we found that iNOS mRNA and protein level in normoxic hearts increased after reperfusion; however, iNOS mRNA and protein level decreased in IH hearts. The results from Zingarelli *et al*'s study differed from our result in that iNOS mRNA in wild-type mice was significantly increased after 30 min reperfusion compared to the basal level[27]. In the present study, the level of iNOS protein in normoxic hearts was higher than the level in IH hearts after I/R. It is known that induction of high-output iNOS usually occurs in an oxidative environment, and thus high levels of NO have the opportunity to react with superoxide anion (O_2^-) leading to peroxynitrite ($ONOO^-$) formation and cell toxicity[28]. The generation of $ONOO^-$ can account for the toxicity of NO in biological systems. Yasmin *et al* and Wang and Zweier's studies indicated that generation of $ONOO^-$ at reperfusion contributed to the I/R injury in isolated rat hearts[29,30]. In general, O_2^- formation increases during the early period of reperfusion and reacts with NO to form $ONOO^-$, which results in amino acid nitration and cellular injury[30]. Our previous study suggested that an increase in antioxidant capacity might play an important role in the effect of IH reducing I/R injury[5]. Based on the above investigations, we propose that during reperfusion, normoxic hearts may be predisposed to produce more O_2^- and $ONOO^-$ than IH hearts, and thus produce more potent toxicity than IH hearts. Our results also suggest that during reperfusion after sustained ischemia, NO may have bidirectional effects on myocardium because of the coexistence of NO and O_2^-. AG significantly diminished NOx content, iNOS mRNA and protein level in IH hearts after reperfusion and led to the inhibitory effect of AG on the recovery of left ventricular function of IH rat hearts. As far as we know, NO is considered to play a pivotal role in numerous physiological and pathophysiological processes, with effects arising from both a lack and a surfeit of this chemically reactive molecule. This seemingly paradoxical behavior may be explained by the amount of NO generated, temporal-spatial intracellular compartmentalization of NO, and the intracellular redox environment.

The mechanisms leading to upregulation of iNOS after IH adaptation and the mechanism whereby iNOS-derived NO plays a role in the protection of IH have not been clarified and need to be further investigated. Mechanisms by which hypoxia induces gene expression include transcriptional and posttranscriptional regulation. The molecular mechanisms of hypoxia adaptations are centered on the activation of hypoxia-inducible factor 1 (HIF-1). During hypoxia, however, HIF-1α is stabilized, leading to accumulation of the active HIF-1α, HIF-1β heterodimer, which binds to specific recognition elements within promoter/enhancer regions of many target genes, the induction of which generates this cytoprotective process. The set of genes induced in this manner include iNOS[20,21], which drives cytoprotective events mediated by NO. At the same time, complex mechanisms may exist and interplay in the regulation of iNOS expression in the heart.

NO is an important endogenous regulatory molecule involved in a variety of biological functions. For example, it maintains coronary vasodilator tone, inhibits platelet aggregation and the adhesion of neutrophils to vascular endothelium[31]. It can also regulate myocardial contractile function. Studies have suggested that NO could also regulate oxygen demand and the delivery of oxygen[32]. Therefore, moderate increases in NO during intermittent hypoxia might be involved in the regulation of the above effects.

We concluded that IH upregulated the baseline level of iNOS mRNA and protein expression leading to an increase in NO production, which may play an important role in the cardiac protection of IH against I/R injury.

References

1 Powell FL, Garcia N. Physiological effects of intermittent hypoxia. High Altitude Med Biol 2000; 1: 125–36.

2 Prabhakar NR. Physiological and genomic consequences of intermittent hypoxia: invited review: oxygen sensing during intermittent hypoxia: cellular and molecular mechanisms. J Appl

Physiol 2001; 90: 1986–94.
3 Meerson FZ, Ustinova EE, Orlova EH. Prevention and elimination of heart arrhythmias by adaptation to intermittent high altitude hypoxia. Clin Cardiol 1987; 10: 783–9.
4 Asemu G, Papousek F, Ostadal B, Kolar F. Adaptation to high altitude hypoxia protects the rat heart against ischemia-induced arrhythmias. Involvement of mitochondrial K_{ATP} channel. J Mol Cell Cardiol 1999; 31: 1821–31.
5 Zhang Y, Zhong N, Zhu HF, Zhou ZN. Antiarrhythmic and antioxidative effects of intermittent hypoxia exposure on rat myocardium. Acta Physiol Sin 2000; 52: 89–92.
6 Zhong N, Zhang Y, Zhu HF, Wang JC, Fang QZ, Zhou ZN. Myocardial capillary angiogenesis and coronary flow in ischemia tolerance rat by adaptation to intermittent high altitude hypoxia. Acta Pharmacol Sin 2002; 23: 305–10.
7 Zhong N, Zhang Y, Fang QZ, Zhou ZN. Intermittent hypoxia exposure-induced heat-shock protein 70 expression increases resistance of rat heart to ischemic injury. Acta Pharmacol Sin 2000; 21: 467–72.
8 Neckar J, Szarszoi O, Koten L, Papousek F, Ost'adal B, Grover GJ, *et al*. Effects of mitochondrial K_{ATP} modulators on cardioprotection induced by chronic high altitude hypoxia in rats. Cardiovasc Res 2002; 55: 567–75.
9 Zhu HF, Dong JW, Zhu WZ, Ding HL, Zhou ZN. ATP-dependent potassium channels involved in the cardiac protection induced by intermittent hypoxia against ischemia/reperfusion injury. Life Sci 2003; 73: 1275–87.
10 Dong JW, Zhu HF, Zhu WZ, Ding HL, Ma TM, Zhou ZN. Intermittent hypoxia attenuates ischemia/reperfusion induced apoptosis in cardiac myocytes via regulating Bcl-2/Bax expression. Cell Res 2003; 13: 385–91.
11 Beall CM, Laskowski D, Strohl KP, Soria R, Villena M, Vargas E, *et al*. Pulmonary nitric oxide in mountain dwellers. Nature 2001; 414: 411–2.
12 Jones SP, Girod WG, Palazzo AJ, Granger DN, Grisham MB, Jourd'Heuil D, *et al*. Myocardial ischemia-reperfusion injury is exacerbated in absence of endothelial cell nitric oxide synthase. Am J Physiol 1999; 276: H1567–73.
13 Weiland U, Haendeler J, Ihling C, Albus U, Scholz W, Ruetten H, *et al*. Inhibition of endogenous nitric oxide synthase potentiates ischemia-reperfusion-induced myocardial apoptosis via a caspase-3 dependent pathway. Cardiovasc Res 2000; 45: 671–8.
14 Brunner F, Maier R, Andrew P, Wolkart G, Zechner R, Mayer B. Attenuation of myocardial ischemia/reperfusion injury in mice with myocyte-specific overexpression of endothelial nitric oxide synthase. Cardiovasc Res 2003; 57: 55–62.
15 Guo Y, Jones WK, Xuan YT, Tang XL, Bao W, Wu WJ, *et al*. The late phase of ischemic preconditioning is abrogated by targeted disruption of the inducible NO synthase gene. Proc Natl Acad Sci USA 1999; 96: 11507–12.
16 Bolli R. Cardioprotective function of inducible nitric oxide synthase and role of nitric oxide in myocardial ischemia and preconditioning: an overview of a decade of research. J Mol Cell Cardiol 2001; 33: 1897–918.
17 Neckar J, Papousek F, Novakova O, Ost'adal B, Kolar F. Cardioprotective effects of chronic hypoxia and ischaemic preconditioning are not additive. Basic Res Cardiol 2002; 97: 161–7.
18 Misko TP, Moore WM, Kasten TP, Nickols GA, Corbett JA, Tilton RG, *et al*. Selective inhibition of the inducible nitric oxide synthase by aminoguanidine. Eur J Pharmacol 1993; 233: 119–25.
19 Zhang Y, Zhong N, Zhou ZN. Effects of intermittent hypoxia on action potential and contraction on non-ischemic and ischemic rat papillary muscle. Life Sci 2000; 67: 2465–71.
20 Palmer LA, Semenza GL, Stoler MH, Johns RA. Hypoxia induces type II NOS gene expression in pulmonary artery endothelial cells via HIF-1. Am J Physiol 1998; 274: L212–19.
21 Jung F, Palmer LA, Zhou N, Johns RA. Hypoxic regulation of inducible nitric oxide synthase via hypoxia inducible factor-1 in cardiac myocytes. Circ Res 2000; 86: 319–25.
22 Rouet-Benzineb P, Eddahibi S, Raffestin B, Laplace M, Depond S, Adnot S, *et al*. Induction of cardiac nitric oxide synthase 2 in rats exposed to chronic hypoxia. J Mol Cell Cardiol 1999; 31: 1697–708.
23 Baker JE, Holman P, Kalyanaraman B, Griffith OW, Pritchard KA Jr. Adaptation to chronic hypoxia confers tolerance to subsequent myocardial ischemia by increased nitric oxide production. Ann N Y Acad Sci 1999; 874: 236–53.
24 Zweier JL, Wang PH, Kuppusamy P. Direct measurement of nitric oxide generation in the ischemic heart using electron paramagnetic resonance spectroscopy. J Biol Chem 1995; 270: 304–7.
25 Node K, Kitakaze M, Kosaka H, Komamura K, Minamino T, Inoue M, *et al*. Increased release of NO during ischemia reduces myocardial contractility and improves metabolic dysfunction. Circulation 1996; 93: 356–64.
26 Zweier JL, Samouilov A, Kuppusamy P. Non-enzymatic nitric oxide synthesis in biological systems. Biochim Biophys Acta 1999; 1411: 250–62.
27 Zingarelli B, Hake PW, Yang Z, O'Connor M, Denenberg A, Wong HR. Absence of inducible nitric oxide synthase modulates early reperfusion-induced NF-kappaB and AP-1 activation and enhances myocardial damage. FASEB J 2002; 16: 327–42.
28 Xie Q, Nathan C. The high-output nitric oxide pathway: role and regulation. J Leukoc Biol 1994; 56: 576–82.
29 Yasmin W, Strynadka KD, Schulz R. Generation of peroxynitrite contributes to ischemia-reperfusion injury in isolated rat hearts. Cardiovasc Res 1997; 33: 422–32.
30 Wang P, Zweier JL. Measurement of nitric oxide and peroxynitrite generation in the postischemic heart. Evidence for peroxynitrite-mediated reperfusion injury. J Biol Chem 1996; 271: 29223–30.
31 Kelly RA, Balligand JL, Smith TW. Nitric oxide and cardiac function. Circ Res 1996; 79: 363–80.
32 Brown GC. Nitric oxide and mitochondrial respiration. Biochim Biophys Acta 1999; 1411: 351–69.

Acta Pharmacologica Sinica 2005 Mar; 26 (3): 323–328

Full-length article

Regulation of intracellular Ca^{2+} and calcineurin by NO/PKG in proliferation of vascular smooth muscle cells

Shi-jun LI, Ning-ling SUN[1]

Department of Cardiology, People's Hospital, Peking University, Beijing 100044, China

Key words

calcium; calcineurin; nitric oxide; cGMP-dependent protein kinase; vascular smooth muscle

[1] Correspondence to Prof Ning-ling SUN.
Phn 86-10-6831-4422, ext 5563.
Fax 86-10-8836-1687.
E-mail lsj_020626@163.com or nlsun@medmail.com.cn

Received 2004-05-31
Accepted 2004-11-15

doi: 10.1111/j.1745-7254.2005.00049.x

Abstract

Aim: To determine whether Ca^{2+}/calcineurin mediated the inhibitory effects of nitric oxide /cGMP-dependent protein kinase (NO/PKG) on the proliferation of vascular smooth muscle cells (VSMC). **Methods:** Proliferation and viability of primary VSMC from rat aorta were measured using [3-(4,5-dimethyl thiazol-2-yl)-2, 5-diphenyl tetrazolium bromide] (MTT) assay and acridine orange and ethidium bromide staining, respectively. Cytosolic Ca^{2+} was determined by Fluo-3/AM. Calcineurin protein and its activity were assayed using immunoblotting and free inorganic phosphate analysis, respectively. **Results:** (±)-*S*-nitroso-*N*-acetyl-penicillamine (SNAP) and Sp-8-(4-chlorophenylthio)-guanosine-3',5'-cyclic monophosphorothioate (Sp-8-pCPT-cGMPS) decreased phenylephrine (PE)-induced proliferation of VSMC by 27.3% and 36.6%, respectively, but Rp-8-[(4-chlorophenyl)thio]-guanosine-3',5'-cyclic monophosphorothioate (Rp-8-pCPT-cGMPS) increased PE-induced proliferation of VSMC. SNAP, Sp-8-pCPT-cGMPS, and Rp-8-pCPT-cGMPS did not affect the viability of VSMC. Calcineurin protein was decreased by 63.1% and its activity was decreased by 59.7% in smooth muscle cells (SMC) pretreated with verapamil (Ver) and then stimulated by PE. In SMC pretreated with Ver, the absorbance of cells stimulated by PE decreased by 22.0% and was further inhibited by the additional treatment of SNAP and Sp-8-pCPT-cGMPS. In SMC pretreated with cyclosporin A (CsA), the absorbance of cells stimulated by PE decreased by 36.7%, but could not be further altered by the additional treatment of SNAP, Sp-8-pCPT-cGMPS, and Rp-8-pCPT-cGMPS. In addition, Ver inhibited PE-induced intracellular Ca^{2+} variations, which could be further inhibited by SNAP and Sp-8-pCPT-cGMPS, but not by Rp-8-pCPT-cGMPS. Moreover, the increase in calcineurin activity induced by PE was inhibited by SNAP and Sp-8-pCPT-cGMPS, but was promoted by Rp-8-pCPT-cGMPS. **Conclusion:** NO/PKG regulates calcineurin activity via the modulation of intracellular Ca^{2+} concentration, and thus partially inhibits the proliferation of VSMC without affecting their viability.

Introduction

Injuries to vascular endothelium induce the migration, hypertrophy, and proliferation of vascular smooth muscle cells (VSMC)[1]. Compelling evidence indicates that nitric oxide (NO) negatively regulates the proliferation of VSMC via the pathways of guanosine-3',5'-cyclic monophosphate (cGMP) and cGMP-dependent protein kinase (PKG). Ca^{2+}/calcineurin is involved in smooth muscle-specific transcription, and may be a potential target of smooth muscle cell proliferation[2–4]. However, the mechanisms by which NO/PKG inhibits VSMC proliferation remain unknown.

Therefore, it is proposed that NO/PKG can inhibit VSMC proliferation via modulation of Ca^{2+}/calcineurin. NO donor SNAP inhibited the intracellular Ca^{2+} response of SMC to acetylcholine (ACh). Caffeine[5] and cGMP can modulate

Ca^{2+} spark activity[6]. PKG regulates intracellular Ca^{2+} variations at multiple levels[7]. Inhibition of nuclear factors of activated T cells (NFAT) by NO-cGMP-PKG I is responsible for cardiac hypertrophy after α1-adrenoceptor stimulation[8]. However, whether or not NO/PKG inhibits the proliferation of VSMC via the modulation of Ca^{2+}/calcineurin is unclear. In the present study, we used VSMC from rat aorta and studied the activities of NO/PKG, intracellular Ca^{2+}, and calcineurin in VSMC proliferation.

Materials and methods

Materials NO donor (±)-*S*-nitroso-*N*-acetylpenicillamine (SNAP), phenylephrine (PE), cyclosporin A (CsA), and verapamil (Ver) were purchased from Sigma-Aldrich Corp. (St Louis, MO, USA). The PKG-selective cGMP analog Sp8-pCPT-cGMPS and PKG antagonist Rp-8-[(4-chlorophenyl) thio]-guanosine-3',5'-cyclic monophosphoro-thioate (Rp-8-pCPT-cGMPS) were from BioMol Company (Plymouth Meeting, PA, USA). Fluo-3/AM ester was obtained from Biotium Inc (Hayward, CA, USA). Rabbit anti-calcineurin Aα affinity-purified polyclonal antibody was from Chemicon Incorporated (Temecula, CA, USA). The biotinylated protein ladder detection pack was from Cell Signaling Technology, Inc (Beverly, MA, USA). The calcineurin assay kit was from Nanjing Jiancheng Bioengineering Institute (NJBI) (Nanjing, China). Dulbecco's modified Eagle's medium (DMEM) and fetal bovine serum (FBS) were obtained from Gibco/Life Technologies (Grand Island, NY, USA).

Culture of VSMC The medial layer of the thoracic aorta from 7-day-old Wistar rats was explanted and cultured in DMEM containing 5% FBS at 37 °C in 5% CO_2 atmosphere. The cells were spread onto six-well plates or 35-mm dishes and cultured to a near confluent condition. Primary VSMC (<4 passage) were used.

Intracellular Ca^{2+} by Fluo-3/AM staining The experiment was carried out at room temperature in a darkroom. Intracellular Ca^{2+} concentration in VSMC was monitored using the fluorescent Ca^{2+} indicator, Fluo-3/AM. In brief, cells growing in a special 35-mm culture dish were loaded with Fluo-3/AM 10 μmol/L (acetoxymethyl esters) in Krebs-Ringer solution (in mmol/L: NaCl 140, KCl 5, $MgCl_2$ 0.5, HEPES 5.5, glucose 10, $CaCl_2$ 1.2, pH 7.4) containing 0.05% pluronic acid at 37 ºC for 60 min. After being washed twice with Krebs-Ringer solution to remove unhydrolyzed indicator, the dish was transferred to a chamber to which the drugs were added. Fluorescence in cells was measured using a confocal microscope. The excitation wavelength was 488 nm, and the emission wavelength was 522 nm. Change in fluorescence was expressed as F/F_0, where F represents the fluorescence intensity (F) of each pixel in the original fluorescence image and F_0 is defined as the intensity at the beginning of the images when the cell was assumed to be in the resting state.

Calcineurin protein expression Protein was separated by 10% sodium dodecyl sulfate polyacrylamide gel electrophoresis (SDS-PAGE) and transferred to nitrocellulose membranes, and the membranes were incubated with rabbit anti-calcineurin Aα affinity-purified polyclonal antibody directed against the major calcineurin catalytic subunit, calcineurin A (CnA)-α. Additional procedures followed the methods of Hammes *et al*[9]. The blotted antibody was visualized using chemiluminescence, and a densitometric scanner determined the density of the band.

Calcineurin enzymatic activity The activity of calcineurin was determined using a calcineurin activity assay kit as described in the manufacturer's protocol. The RII-phosphopeptide (BioMol) was used as a highly specific substrate for calcineurin. The detection of free inorganic phosphate released from RII by calcineurin was based on the malachite green dye reaction. Reactions were terminated after 30 min, and absorption was read on an ultraviolet spectroscope at 660 nm. The activity was corrected for protein concentration. Calcineurin activity was expressed as a percentage compared with the control group.

Cell proliferation assay After VSMC were incubated at 37 °C for 48 h, stock [3-(4,5-dimethyl thiazol-2-yl)-2,5-diphenyl tetrazolium bromide] (MTT) solution was added and incubated with the cells for 4 h. The medium was then removed as completely as possible without disturbing the formazan crystals that had formed within the cells. After the addition of Me_2SO (Merck, Darmstadt, Germany) into the wells the plate was shaken for a short time, and optical density was measured at 570 nm.

Cell viability VSMC were cultured to 1×10^4 cells/well in six-well dishes and then incubated in the absence (control) or presence of PE 10 μmol/L, SNAP 250 μmol/L, Sp-8-pCPT-cGMPS 500 μmol/L, and Rp-8-pCPT-cGMPS 100 μmol/L, or various combinations for 48 h. At the end of the incubation, nucleic acid-binding fluorescent dyes, acridine orange and ethidium bromide (10 mg/L each per well), were added. Using fluorescent microscopy, viable cells with green fluorescent nuclei and non-viable cells with red or orange fluorescent nuclei were counted, and at least 200 cells were counted for each sample. Cell viability (%)=100×(number of viable cells)/(number of cells counted).

Statistical analysis Data were expressed as mean±SEM and statistical analysis were carried out using ANOVA followed by *Bonferroni* or *Dunn post-hoc* tests. $P<0.05$ was

considered significant.

Results

Effect of NO/PKG on the proliferation and viability of VSMC SNAP (250 μmol/L) and Sp-8-pCPT-cGMPS (500 μmol/L) decreased PE 10 μmol/L-induced proliferation of VSMC by 27.3% and 36.6%, respectively, and Rp-8-pCPT-cGMPS (100 μmol/L) increased PE-induced proliferation of VSMC. However, SNAP, Sp-8-pCPT-cGMPS, and Rp-8-pCPT-cGMPS did not affect the viability of VSMC compared with the control group (Figure 1).

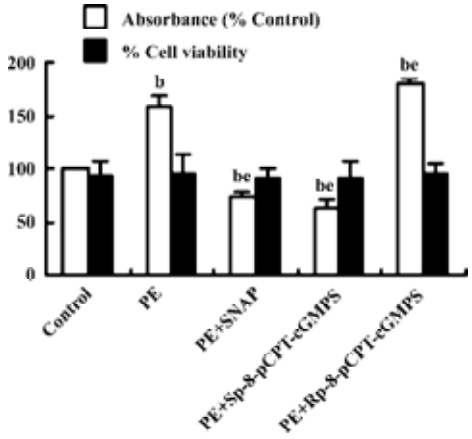

Figure 1. Effects of NO/PKG on PE-induced proliferation and the viability of vascular smooth muscle cells (VSMC). VSMC were stimulated in the absence (control) or presence of PE (10 μmol/L), SNAP (250 μmol/L), Sp-8-pCPT-cGMPS (500 μmol/L), and Rp-8-pCPT-cGMPS (100 μmol/L), or various combinations for 48 h. n=5 experiments. Mean±SEM. ^bP<0.05 *vs* control. ^eP<0.05 *vs* PE.

Effect of Ver on calcineurin protein expression and activity in VSMC After VSMC were pretreated with Ver (8 μmol/L) for 24 h and then incubated with PE (10 μmol/L) for another 24 h, calcineurin protein expression and its activity were decreased by 63.1% (Figure 2A) and 59.7% (Figure 2B) compared with the control group, respectively.

Effect of Ver and CsA on the downregulation of VSMC proliferation by NO/ PKG VSMC were pretreated with Ver (8 μmol/L) or CsA (500 μg/L) for 24 h to inhibit Ca^{2+} influx or calcineurin activity, respectively. The VSMC were then treated with SNAP (250 μmol/L), Sp-8-pCPT-cGMPS (500 μmol/L), or Rp-8-pCPT-cGMPS (100 μmol/L) for 12 h. Finally they were incubated with PE (10 μmol/L) for 12 h.

Pretreatment with Ver decreased PE-induced VSMC proliferation by 22.0% compared with the control group. Additional treatment with SNAP and Sp-8-pCPT-cGMPS further inhibited VSMC proliferation compared with the Ver pretreatment group (P<0.05, Figure 3A).

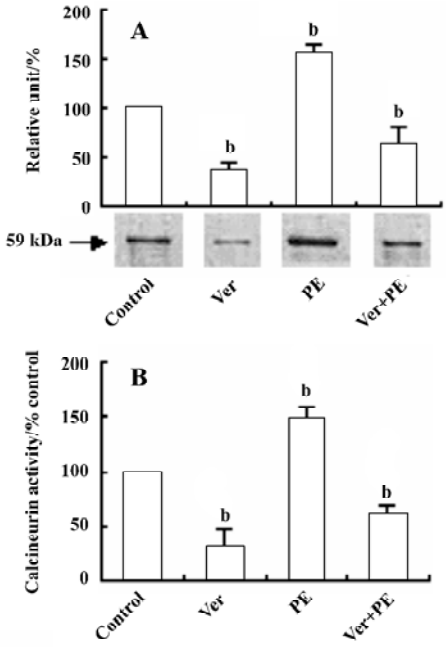

Figure 2. Effect of verapamil on the proliferation of vascular smooth muscle cells (VSMC) induced by PE. VSMC were pretreated in the absence (control) or presence of PE (10 μmol/L), Ver (8 μmol/L) or Ver and PE. n=5 experiments. Mean±SEM. ^bP<0.05 vs control.

Pretreatment with CsA decreased PE-induced VSMC proliferation by 36.7% compared with the control group. Additional treatment with SNAP, Sp-8-pCPT-cGMPS, or Rp-8-pCPT-cGMPS did not further affect VSMC proliferation compared with the CsA pretreatment group (P>0.05, Figure 3B).

Effects of Ver and NO/PKG on variations in intracellular Ca^{2+} induced by PE in VSMC VSMC were pretreated with Ver (8 μmol/L) for 30 min and then incubated with SNAP (250 μmol/L), Sp-8-pCPT-cGMPS (500 μmol/L), or Rp-8-pCPT-cGMPS (100 μmol/L) for 30 min. Finally the VSMC were stimulated with PE (10 μmol/L). Intracellular Ca^{2+} variation was inhibited by Ver. Additional treatment with SNAP and Sp-8-pCPT-cGMPS after Ver pretreatment further inhibited intracellular Ca^{2+} variation, but additional treatment with Rp-8-pCPT-cGMPS did not (Figure 4).

Effect of NO/PKG on calcineurin expression and activity in VSMC The increase in calcineurin protein expression and its activity induced by PE (10 μmol/L) for 24 h were inhibited by a 24-h pretreatment with SNAP (250 μmol/L) or Sp-8-pCPT-cGMPS (500 μmol/L), and was slightly promoted by a 24-h pretreatment with Rp-8-pCPT-cGMPS (100 μmol/L) (Figure 5).

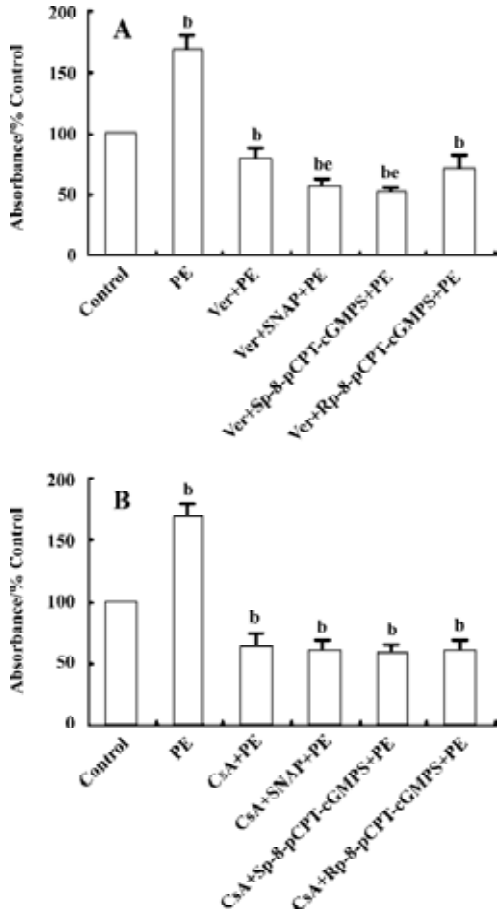

Figure 3. Role of Ca^{2+}/calcineurin in the regulation of vascular smooth muscle cells (VSMC) proliferation by NO/ PKG. VSMC were pretreated with Ver (8 μmol/L, A) or CsA (500 μg/L, B) for 24 h, and then incubated with SNAP (250 μmol/L), Sp-8-pCPT-cGMPS (500 μmol/L), and Rp-8-pCPT-cGMPS (100 μmol/L) for 12 h, respectively. PE was finally added to stimulate the VSMC for 12 h. n=5 experiments. Mean±SEM. $^bP<0.05$ *vs* control. $^eP<0.05$ *vs* Ver+PE group.

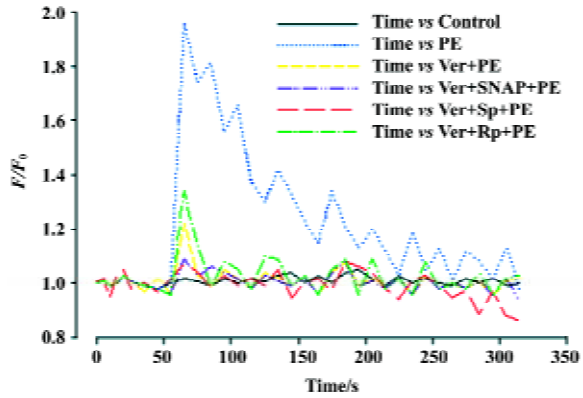

Figure 4. PE-induced intracellular Ca^{2+} variations by NO/PKG in vascular smooth muscle cells (VSMC). VSMC were first stimulated by Ver for 30 min, and then incubated with SNAP (250 μmol/L), Sp-8-pCPT-cGMPS (500 μmol/L), and Rp-8-pCPT-cGMPS (100 μmol/L) for 30 min, respectively. Finally PE (10 μmol/L) was added to the superfusion buffer (indicated by the arrow). n=5 experiments.

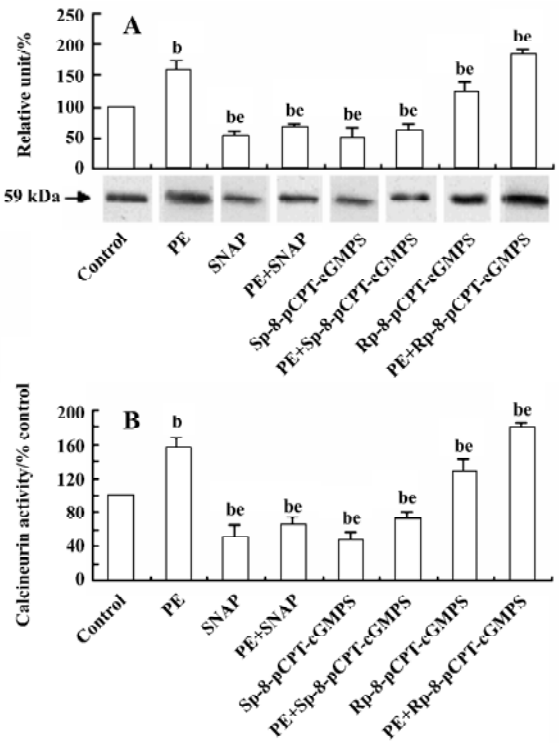

Figure 5. Effect of NO/PKG on calcineurin protein expression and activity in vascular smooth muscle cell (VSMC) proliferation. VSMC were stimulated in the absence (control) or presence of PE (10 μmol/L), SNAP (250 μmol/L), Sp-8-pCPT-cGMPS (500 μmol/L) and Rp-8-pCPT-cGMPS (100 μmol/L), or various combinations as indicated. n=5 experiments. Mean±SEM. $^bP<0.05$ *vs* control. $^eP<0.05$ *vs* PE.

Discussion

NO inhibits the proliferation of VSMC via the pathways of cGMP and PKG. NO/PKG modulates a large variety of physiological functions including vascular tone, platelet aggregation, apoptosis, and proliferation. However, the mechanisms by which NO/PKG inhibits VSMC proliferation are still unclear. The present study investigated the activities of NO/PKG, intracellular Ca^{2+}, and calcineurin in the proliferation of VSMC.

PE, a stimulator for Ca^{2+} oscillations and cell growth[10,11], is used to induce intracellular Ca^{2+} variations and the proliferation of VSMC. Our results show that the addition of SNAP and Sp-8-pCPT-cGMPS decreases cell proliferation in cells pre-stimulated with PE by 27.3% and 36.6%, respectively, whereas the addition of Rp-8-pCPT-cGMPS increases cell

proliferation. No significant changes in VSMC viability were found between the experimental groups**.** These results suggest that NO/PKG is involved in the inhibitory effects on SMC proliferation, but has no marked effects on SMC viability.

Ca^{2+} is an essential regulator of the cell cycle. The Ca^{2+} response control gene was expressed in various cell types[12]. In VSMC, when intracellular $[Ca^{2+}]_i$ level increases, calcineurin is activated. Its de-phosphorylated transcription factors, NFAT, in turn promote nuclear translocation of NFAT. The NFAT transcription factors then cooperate with nuclear transcription factors and stimulate the transcriptional activation of various genes that are involved in VSMC proliferation[13]. Our results confirm that intracellular Ca^{2+} variations play an important role in regulating VSMC proliferation.

Recent studies have shown that NO/PKG can regulate intracellular Ca^{2+} variations. NO reduces the intracellular Ca^{2+} concentration in SMC by inhibiting sarcoplasmic reticulum (SR). Ca^{2+} release through both IP3R and RyR[5], and Ca^{2+} influx through N-channel gating via cGMP and PKG[14]. cGMP can modulate Ca^{2+} spark activity by decreasing myofibrillar Ca^{2+} sensitivity and increasing Ca^{2+} uptake by the SR[6]. PKG has been proposed to regulate $[Ca^{2+}]_i$ variations in different cell types by different mechanisms[7]. For example, PKG can inhibit intracellular Ca^{2+} release from the endoplasmic reticulum by inhibition of IP_3 formation[15] and Ca^{2+} entry through plasma membrane Ca^{2+} channels[16,17] or stimulate its efflux across the membrane by activation of a Na^+/Ca^{2+} exchanger[18]. Bonnevier and Arner[19] reported that signals downstream of cGMP/PKG could reverse PKC-mediated Ca^{2+} sensitization in smooth muscle. However, whether or not NO/PKG inhibits VSMC proliferation via the regulation of intracellular Ca^{2+} movement has not been revealed. We found that Ver inhibited PE-stimulated intracellular Ca^{2+} variations, which could be further inhibited by SNAP and Sp-8-pCPT-cGMPS. These results suggest that NO/PKG can regulate PE-induced intracellular Ca^{2+} variations in VSMC, which is possibly achieved via regulation of Ca^{2+} release, Ca^{2+} efflux, and Ca^{2+} influx by NO/PKG. The definite mechanisms by which NO/PKG modulates intracellular Ca^{2+} variations of SMC will be studied in the future. For these reasons, we conclude that NO/PKG inhibits VSMC proliferation via modulation of intracellular Ca^{2+} variations.

Calcineurin is a heterodimer consisting of a 59-kDa subunit, CnA, and a 19-kDa subunit with calcineurin B (CnB) tightly bound to CnA. CnA consists of a catalytic and a regulatory domain. The regulatory domain contains the CnB binding domain, the calmodulin binding domain, and an autoinhibitory domain at the C-terminus. Ca^{2+} binds to both calmodulin and CnB displacing the inhibitory C-terminal peptide from the active site of CnA, thus activating phosphatase function[20]. So CnB acts as a sensor for changes in intracellular Ca^{2+}. Calcineurin is a downstream target of intracellular Ca^{2+}. Increase in intracellular Ca^{2+} concentration will activate calcineurin, thus inducing proliferation-related gene transcription. Our results further demonstrate that intracellular Ca^{2+} variation plays an important role in regulating the expression and activity of calcineurin in VSMC, and that calcineurin is a potential target for treatment of diseases related to SMC proliferation. However, it remains to be determined whether NO/PKG decreases the proliferation of VSMC via calcineurin. Our study shows that the pre-addition of CsA decreases PE-induced proliferation by 36.7% compared with controls. CsA had no influence on the inhibitory effects of SNAP, Sp-8-pCPT-cGMP, and Rp-8-pCPT-cGMPS. These results suggest that NO/PKG inhibits VSMC proliferation via calcineurin. Furthermore, our study demonstrates that SNAP and Sp-8-pCPT-cGMPS reduced, but Rp-8-pCPT-cGMPS increased, calcineurin protein expression and its activity in SMC stimulated by PE. Therefore, we conclude that NO/PKG inhibits VSMC proliferation by regulating calcineurin expression and its activity.

In addition, Sp-8-pCPT-cGMPS has the ability to stimulate both PKG and cAMP-dependent protein kinase (PKA) with similar potency. cAMP/PKA is able to induce Ca^{2+} desensitization by inhibition of the muscarinic receptor signaling upstream from Rho activation and preferentially reverse PKC-mediated Ca^{2+} sensitization in SMC[21]. It is possible that PKA is partially involved in the regulation of calcineurin by changing intracellular Ca^{2+} variations in SMC proliferation.

In conclusion, NO/PKG partially inhibits the proliferation of VSMC without affecting their viability. It is associated with the regulation of calcineurin activity by modulating intracellular Ca^{2+} concentration.

Acknowledgements

We thank Prof Chao-shu TANG, Prof Xian WANG, Prof Yuan-sheng GAO, Prof Ding-feng SU, and Prof Ding-fang BU for their kind help in preparing this manuscript.

References

1 Ross R. Atherosclerosis: an inflammatory disease. N Engl J Med 1999; 340: 115–26.

2 Chen Y, Zhao M, Xia C. Effect of urotensin II on the airway smooth muscle cell proliferation and its mechanism. Chin J Med 2000; 80: 928–30.

3 Wada H, Hasegawa K, Morimoto T, Kakita T, Yanazume T, Abe

M, *et al*. Calcineurin-GATA-6 pathway is involved in smooth muscle-specific transcription. J Cell Biol 2002; 156: 983–91.
4 Lipskaia L, Pourci ML, Delomenie C, Combettes L, Goudouneche D, Paul JL, *et al*. Phosphatidylinositol 3-kinase and calcium-activated transcription pathways are required for VLDL-induced smooth muscle cell proliferation. Circ Res 2003; 92: 1115–22.
5 Kannan MS, Prakash YS, Johnson DE, Sieck GC. Nitric oxide inhibits calcium release from sarcoplasmic reticulum of porcine tracheal smooth muscle cells. Am J Physiol 1997; 272 (1 Pt 1): L1–7.
6 Satoh S, Makino N. Intracellular mechanisms of cGMP-mediated regulation of myocardial contraction. Basic Res Cardiol 2001; 96: 652–8.
7 Hofmann F, Ammendola A, Schlossmann J. Rising behind NO: cGMP-dependent protein kinases. J Cell Sci 2000; 113: 1671–6.
8 Fiedler B, Lohmann SM, Smolenski A, Linnemuller S, Pieske B, Schroder F, *et al*. Inhibition of calcineurin-NFAT hypertrophy signaling by cGMP-dependent protein kinase type I in cardiac myocytes. Proc Natl Acad Sci USA 2002; 99: 11363–8.
9 Hammes A, Oberdorf-Maass S, Rother T, Nething K, Gollnick F, Linz KW, *et al*. Overexpression of the sarcolemmal calcium pump in the myocardium of transgenic rats. Circ Res 1998; 83: 877–88.
10 Hamada H, Damron DS, Hong SJ, Van Wagoner DR, Murray PA. Phenylephrine-induced Ca^{2+} oscillations in canine pulmonary artery smooth muscle cells. Circ Res 1997; 81: 812–23.
11 Shaw L, O'Neill S, Jones CJ, Austin C, Taggart MJ. Comparison of U46619-, endothelin-1- or phenylephrine-induced changes in cellular Ca^{2+} profiles and Ca^{2+} sensitisation of constriction of pressurised rat resistance arteries. Br J Pharmacol 2004; 141: 678–88.
12 Dolmetsch RE, Lewis RS, Goodnow CC, Healy JI. Differential activation of transcription factors induced by Ca^{2+} response amplitude and duration. Nature 1997; 386: 855–8.
13 Suzuki E, Nishimatsu H, Satonaka H, Walsh K, Goto A, Omata M, *et al*. Angiotensin II induces myocyte enhancer factor 2- and calcineurin/nuclear factor of activated T cell-dependent transcriptional activation in vascular myocytes. Circ Res 2002; 90: 1004–11.
14 D'Ascenzo M, Martinotti G, Azzena GB, Grassi C. cGMP/protein kinase G-dependent inhibition of N-type Ca^{2+} channels induced by nitric oxide in human neuroblastoma IMR32 cells. J Neurosci 2002; 22: 7485–92.
15 Furuichi T, Mikoshiba K. Inositol 1, 4, 5-trisphosphate receptor-mediated Ca^{2+} signaling in the brain. J Neurochem 1995; 64: 953–60.
16 Mery PF, Lohmann SM, Walter U, Fischmeister R. Ca^{2+} current is regulated by cyclic GMP-dependent protein kinase in mammalian cardiac myocytes. Proc Natl Acad Sci USA 1991; 88: 1197–201.
17 Clapp LH, Gurney AM. Modulation of calcium movements by nitroprusside in isolated vascular smooth muscle cells. Pflügers Arch 1991; 418: 462–70.
18 Furukawa KI, Ohshima N, Tawada-Iwata Y, Shigekawa M. Cyclic GMP stimulates Na^{+}/Ca^{2+} exchange in vascular smooth muscle cells in primary culture. J Biol Chem 1991; 266: 12337–41.
19 Bonnevier J, Arner A. Actions downstream of cyclic GMP/protein kinase G can reverse protein kinase C-mediated phosphorylation of CPI-17 and Ca^{2+} sensitization in smooth muscle. J Biol Chem 2004; 279: 28998–9003.
20 Klee CB, Ren H, Wang X. Regulation of the calmodulin-stimulated protein phosphatase, calcineurin. J Biol Chem 1998; 273: 13367–70.
21 Endou K, Iizuka K, Yoshii A, Tsukagoshi H, Ishizuka T, Dobashi K, *et al*. 8-Bromo-cAMP decreases the Ca^{2+} sensitivity of airway smooth muscle contraction through a mechanism distinct from inhibition of Rho-kinase. Am J Physiol Lung Cell Mol Physiol 2004; 287: L641–8.

Acta Pharmacologica Sinica 2005 Mar; 26 (3): 329–333

Full-length article

Protective effects of cariporide on endothelial dysfunction induced by high glucose[1]

Shuang-xi WANG, Xiao-ming XIONG, Tao SONG, Li-ying LIU[2]

Department of Pharmacology, Pharmaceutical College, Central South University, Changsha 410078, China

Key words

sodium-hydrogen antiporter; endothelium; glucose; nitric oxide; malondialdehyde; superoxide dismutase

[1] Project supported by the National Natural Science Foundation of China (No 39770857).
[2] Correspondence to Prof Li-ying LIU.
Phn 86-731-2355-077.
E-mail xjjz@public.cs.hn.cn

Received 2004-04-23
Accepted 2004-09-27

doi: 10.1111/j.1745-7254.2005.00042.x

Abstract

Aim: To explore the effects of cariporide, a selective sodium-hydrogen antiporter inhibitor, on endothelial dysfunction induced by high glucose. **Methods:** Acetylcholine (ACh)-induced endothelium-dependent relaxation (EDR), sodium nitroprusside (SNP)-induced endothelium-independent relaxation and biochemical parameters including malondialdehyde (MDA), superoxide dismutase (SOD), and nitric oxide (NO) were measured in rat isolated aorta. **Results:** A 6-h incubation of aortic rings with high glucose (44 mmol/L) resulted in a significant inhibition of EDR, but had no effects on endothelium-independent relaxation. After the 6-h incubation of aortic rings in the co-presence of cariporide (0.01, 0.1, and 1 μmol/L) with high glucose, cariporide prevented the inhibition of EDR caused by high glucose in concentration-dependent manners. Similarly, high glucose decreased SOD activity and contents of NO, and increased MDA concentration in aortic tissue. Cariporide (1 μmol/L) significantly resisted the decrease of NO content and SOD activity, and elevation of MDA concentration caused by high glucose in aortic tissues. Mannitol (44 mmol/L) or cariporide (1 μmol/L) alone had no effect on EDR, endothelium-independent relaxation and biochemical parameters. **Conclusion:** Cariporide significantly prevented endothelial dysfunction induced by high glucose. The mechanisms of endothelial dysfunction induced by high glucose may involve the activation of sodium-hydrogen antiporter and the generation of oxygen-free radicals, but it is not related to the change of osmolarity.

Introduction

The relation between diabetes and premature vascular disease has been well established[1]. One of the defects involves endothelial dysfunction characterized by impaired endothelium-dependent relaxation responses. Many metabolic disturbances of diabetes, hyperglycemia have been suggested to be the main cause of endothelial dysfunction. High glucose *in vitro* or *in vivo* has been reported to inhibit acetylcholine (ACh)-induced endothelium-dependent relaxation[2] responses, to impair the biological synthesis pathway of nitric oxide (NO)[3], and to generate reactive oxygen species[4].

It has been demonstrated that hyperactivity of sodium-hydrogen exchange subtype 1 (NHE-1) has been implicated in the vascular injury in diabetes mellitus[5]. Ganz *et al*[6] found that the activity and expression of NHE-1 significantly increased in mesangial cells after exposure to high glucose. Our previous experiments have demonstrated that the benzoylguanidine compound cariporide (4-isopropyl-3-methylsulfonyl-benzoylguanidine methanesulfonate), which is a selective NHE-1 inhibitor, protected against injuries of endothelial functions induced by high lipid diet in rabbits[7]. However, it is not known whether NHE-1 inhibitor protects against endothelial function affected by high glucose. The aim of this study is to explore the effect of cariporide against endothelial dysfunction of isolated rat aortic rings induced by high glucose and to investigate its mechanisms.

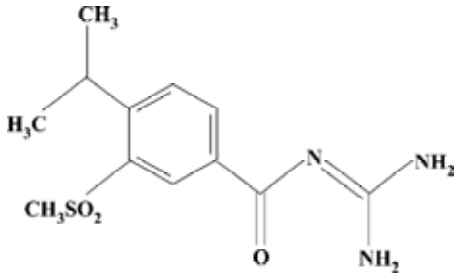

Chemical structure of cariporide

Materials and methods

Drugs and chemicals Cariporide was obtained from Hoechst Company (Frankfurt, Germany). SNP, ACh, and phenylephrine (Phe) were purchased from Sigma Chemical Co (Saint Louis, Mo, USA). The kits for measurement of nitrite/nitrate (NO), MDA, and SOD activity were purchased from Nanjing Jiancheng Bioengineering Institute (Jiangsu, China).

Animal Male Sprague-Dawley rats (No SCXK2003-0003; Grade II) weighing 180–200 g, supplied by the Animal Center of Xiangya Medical College (Central South University, China) were used.

Preparation of rat thoracic aorta rings The rats were killed by exsanguinations after an intraperitoneal anesthesia with pentobarbital sodium 30 mg/kg and intravenous anticoagulation with heparin sodium 150 U/kg. The descending thoracic aorta was rapidly dissected from the rats and immersed in Krebs' solution, composed of (mmol/L): NaCl, 118.3; KCl, 4.7; $MgSO_4 \cdot 7H_2O$, 1.2; KH_2PO_4, 1.2; $CaCl_2$, 2.5; $NaHCO_3$, 24.0; glucose, 11; and Na_2-EDTA, 0.026; and bubbled with 95% O_2+5% CO_2 (pH 7.4). After the perivascular tissue was carefully removed, the aortic rings (which were approximately 4 mm in length), were prepared.

Bioassay of vasoreactivity[8] For isometric force recording, the aortic rings were mounted between two stainless steel hooks and suspended in a 10 mL organ bath containing above Krebs' solution at 37 ºC bubbled with 95% O_2+5% CO_2 gas mixture (pH 7.4). An initial load of 2.0 g was applied, and the tension of the aortic ring was monitored by a force transducer and recorded on a polygraph (Model YL-1, Chengdu Instruments, China). After a 90-min equilibration period, the ring was precontracted by Phe 1 μmol/L. When the development tension attained its peak value, the ring was relaxed by ACh or SNP, respectively. Accumulative concentration-response curves to ACh (0.003, 0.01, 0.03, 0.1, 0.3, 1, and 3 μmol/L) or SNP (0.001-1 μmol/L) were recorded.

Determination of MDA concentration After a 6-h incubation of aortic segments, the aortic segments were blotted dry and weighed, then made into 5% tissue homogenate in ice-cold 0.9% NaCl solution. A supernatant was obtained from tissue homogenate by centrifugalization (1000×*g*, 4 ºC, 10 min). The MDA concentration (thiobarbituric acid reactive substances, TBARS) in the supernatant was measured. Briefly, 1.0 mL of 20% trichloroacetic acid and 1.0 mL of 1% TBARS reagent were added to 100 μL supernatant, then mixed and incubated at 100 ºC for 80 min. After cooling on ice, samples were centrifuged at 1000×*g* for 20 min and the absorbance of the supernatant was read at 532 nm. TBARS results were expressed as MDA equivalents using tetraethoxypropane as standard.

Assay of SOD activity in aortic rings The supernatant of tissue homogenate of the aortic rings were obtained as described earlier. A competitive inhibition assay was performed by using xanthine/xanthine oxidase reaction-generated superoxide radicals to reduce nitro blue tetrazolium (NBT) quantitatively to blue formazan. Conversion of superoxide radicals to hydrogen peroxide by superoxide dismutase inhibited dye formation and served as a measure of superoxide dismutase activity. Briefly, the supernatant of 0.5 mL with xanthine 50 μmol/L and xanthine oxidase 2.5 μmol/L in potassium phosphate buffer 50 mmol/L (pH 7.8, 37 ºC) were incubated for 40 min and NBT was added. Blue formazan was then monitored spectrophotometrically at 550 nm. The amount of protein that inhibited NBT reduction to 50% maximum was defined as 1 nitrite unit (NU) of SOD activity.

Assay of NO concentration of incubation medium The incubation medium of the aortic artery was centrifugated (1000×*g*, 15 min, 4 ºC) and the supernatant was used for NO measurement. NO was assayed by the Griess method. Because NO is a compound with a short half life and is rapidly converted to the stable end products nitrate (NO_3^-) and nitrite (NO_2^-), the principle of the assay is the conversion of nitrate into nitrite by cadmium and followed by color development with Griess reagent (sulfanilamide and *N*-naphthyl ethylenediamine) in acidic medium. The total nitrite was measured by Griess reaction. The absorbance was determined at 540 nm with a spectrophotometer.

Protocol of experiment The first series of experiments were designed in order to evaluate the protective effects of cariporide against ACh-induced endothelium-dependent and SNP-induced endothelium-independent relaxing response of isolating rat aortic rings affected by high glucose. The experiment was divided into 7 groups with 8 aortic rings from 8 rats in each group. First, a normal control bioassay of vasoreactivity was formed in normal Krebs' solution. The rings, of which a percentage of relaxation induced by ACh

3 μmol/L to the contraction elicited by Phe 1 μmol/L is more than 80%, were considered as intact endothelium and used in the study. The aortic rings of each group were then continually incubated for 6 h in the following medium: (1) control group: glucose 11 mmol/L in Krebs' solution[9]; (2) high glucose group: glucose 44 mmol/L in Krebs' solution[9]; (3)–(5) cariporide-treated groups: cariporide 0.01, 0.1, and 1 μmol/L in Krebs' solution with glucose 44 mmol/L, respectively; (6) cariporide alone group: cariporide 1 μmol/L in Krebs' solution; (7) mannitol group: mannitol 44 mmol/L in Krebs' solution. The incubation mediums were changed every 30 min and cariporide was present throughout the incubation. After a 6-h incubation of aortic rings, the perfusion solution was changed to Krebs' solution, and bioassay of vasoreactivity was performed.

The second series of experiments were designed to assay the effects of high glucose on SOD activity, MDA concentration, NO and the effects of cariporide on the biochemical parameters in rat aortic rings. The experiment was divided into 5 groups with 8 aortic segments of 2 cm from 8 rats in each group; control group, high glucose group, mannitol group, cariporide-treated group, and cariporide-alone group. The components of incubation medium were the same as described earlier except that cariporide only had a dose of 1 μmol/L. The incubations media were changed every 30 min. Cariporide was added throughout incubation. After a 6-h incubation, the segments were transfered to 1 mL normal Kreb's solution which contained ACh 1 μmol/L for 30 min. The aortic segments and the medium were then collected and frozen at -70 ºC until analyzed.

Data analysis The ACh (3 μmol/L) or SNP (1 μmol/L) -induced maximal relaxation (E_{max}) in aortic rings was calculated as a percentage of the contraction to Phe (1 μmol/L). The half maximum effective concentration (EC_{50}) was defined as a concentration of the ACh that induced 50% of maximum relaxation response to contraction elicited by Phe (1 μmol/L) and calculated from the concentration-response curve generated by linear regression analysis. All data were expressed as mean±SD. Statistical comparisons were made using one-way ANOVA followed by Newman–Keuls test. $P<0.05$ was statistically significant.

Results

Effects of high glucose on EDR and endothelium-independent relaxation in aortic rings There were no significant differences in ACh-induced relaxation responses of rat isolated aortic rings before the 6-h incubation among various groups (data not shown). After a 6-h incubation of aortic rings in control glucose (11 mmol/L) buffer, ACh (0.003-3 μmol/L) still evoked a normal concentration-dependent relaxation (Figure 1), the E_{max} of aortic rings reached 88.4%±12.3%, and the EC_{50} value was 94.5±10.8 nmol/L. After the 6-h incubation of the aortic rings and exposure to high glucose (44 mmol/L), the E_{max} fell to 43.7%±16.1% and the EC_{50} value increased to 154.8±22.9 nmol/L ($P<0.01$ *vs* control group, $n=8$). However, no significant changes of E_{max} and EC_{50} were shown in the rings incubated in the cariporide (1 μmol/L)-alone group or mannitol (44 mmol/L) group, compared with the control group (Figure 1).

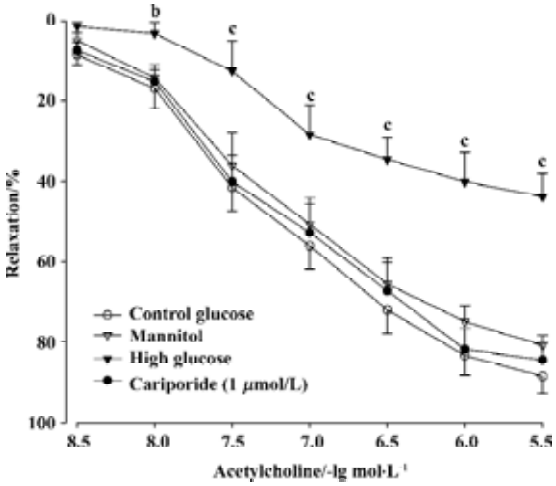

Figure 1. EDR induced by ACh in rat isolated aortic rings. After a 6-h incubation of aortic rings in control glucose (11 mmol/L), high glucose (44 mmol/L), mannitol (44 mmol/L), or cariporide (1 μmol/L) in Krebs' solution, the ACh (0.003-3 μmol/L)-induced EDR was measured and calculated as a percentage of the contraction to Phe (1 μmol/L). $n=8$. Mean±SD. $^bP<0.05$, $^cP<0.01$ *vs* control group.

The endothelium-independent relaxation induced by SNP (0.001-1 μmol/L) was not significantly different between the different treated groups (data not shown).

Effects of cariporide on the impairment of EDR induced by high glucose Treatment with cariporide in different concentration (0.01, 0.1, and 1 μmol/L, $n=8$, respectively) significantly prevented inhibition of EDR induced by high glucose (Figure 2). The E_{max} were 61.7%±10.5%, 76.0%±10.5%, and 83.4%±10.1%, and the EC_{50} value was 131.5±15.9 nmol/L, 117.1±13.7 nmol/L, and 109.6±10.5 nmol/L, respectively. There was a significant difference ($P<0.05$ or $P<0.01$), compared with those in the high glucose group (Figure 2).

Effects of cariporide on biochemical index in aortic segments A 6-h incubation of isolated aortic segments in high glucose resulted in an elevation of MDA content, decrease of SOD activity in aortic tissue, and reduction of NO

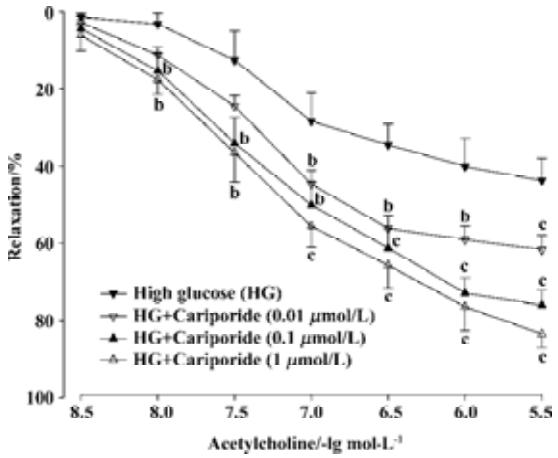

Figure 2. Effects of cariporide (0.01, 0.1, and 1 μmol/L) on EDR impaired by high glucose (44 mmol/L). After a 6-h incubation, ACh (0.003-3 μmol/L)-induced EDR were measured and calculated as a percentage of the contraction to Phe (1 μmol/L). n=8. Mean±SD. ^bP<0.05, ^cP<0.01 *vs* HG group.

releasing from aortic segments. Treatment with cariporide (1 μmol/L) in the high glucose (44 mmol/L) group significantly prevented the increase of MDA content, and protected the activity of SOD and release of NO in aortic segments (Table 1). Mannitol (44 mmol/L) or cariporide (1 μmol/L) alone had no effects on MDA, SOD, and NO, compared with the control group (Table 1).

Discussion

Diabetes mellitus is characterized by chronic hyperglycemia and associated with significant morbidity as a result of long-term complications, including diabetic nephropathy, atherosclerosis, and hypertension. High glucose had a lot of toxicity effects in endothelial cells, such as impairment of endothelial dependent relaxation[10], decrease of NO release, generation of free radicals, and increase in apoptosis[11]. The endothelial dysfunction has been thought to be the major cause of vascular disease due to hyperglycemia condition. It was reported that hyperglycemia resulted in an increase of NHE-1 activity in diabetes[12,13]. In addition, high glucose may induce the activation of NHE-1 and increase NHE-1 mRNA expression *in vitro* smooth muscle cells or myocytes [14,15]. However, there are no reports as to whether NHE-1 inhibitor is able to protect against the impairment of endothelial functions caused by high glucose. The present study explores the effects of cariporide against high glucose-induced endothelial dysfunction of rat isolated aorta and discusses its mechanisms.

In the present study, we employed a mimic pronounced hyperglycemia model in which the rat isolated aortic rings were exposed to high glucose for 6 h. High glucose significantly inhibited EDR and the release of NO in rat isolated aortic rings, but did not affect vasodilatation induced by SNP, a NO donor. It has been demonstrated that endothelium dysfunction induced by high glucose related to the release of NO from endothelial cells. The same concentration of mannitol had no effect on EDR of aortic rings, which showed that the damage of EDR of aortic rings induced by high glucose was not due to a hyperosmotic effect. These results in the present study were consistent with a previous study[2]. We also found that cariporide in dose-dependent manners prevented the inhibition of EDR induced by high glucose in rat isolated thoracic aorta (Figure 1), and simultaneously maintained SOD activity and NO release and decreased MDA concentration caused by high glucose in rat aortic segments (Table 1). It was reported that cariporide significantly inhibited the injuries of mitochondrial and pulmonary endothelial cells, and protected cardiac ischaemia and reperfusion *in vitro* by reducing intracellular pH and inhibiting NHE-1 activation, which simultaneously attenuated oxidant production[16-18]. The Na^+/H^+ exchanger inhibitor, amiloride, significantly reduced oxidant production of hepatic stellate cells including intracellular hydroperoxides and MDA induced by oxidant[19]. Accordingly, it is believed that the protective effects of cariporide against endothelial dysfunctions induced by high glucose may partly be due to anti-oxidation and pro-

Table 1. MDA concentration, SOD activity and NO content of isolated aortic segments in the different treated groups. n=8. Mean±SD. ^bP<0.05, ^cP<0.01 *vs* control glucose group. ^eP<0.05, ^fP<0.01 *vs* high glucose group.

Groups	MDA/μmol·g^{-1} protein	SOD activity/kNU·g^{-1} protein	NO/mmol·g^{-1} protein
Control glucose (11 mmol/L)	4.5±2.5	166±43	0.9±0.6
Mannitol (44 mmol/L)	4.3±1.7	167±73	0.8±0.5
Cariporide (1 μmol/L)	4.5±3.9	147±72	0.8±0.3
High glucose (44 mmol/L)	7.2±1.4^b	86±30^c	0.38±0.28^b
HG + Cariporide (1 μmol/L)	4.6±2.4^e	146±19^f	1.0±0.5^e

tective activity of anti-oxidative enzymes.

In the resting state, NHE-1 is relatively quiescent. When intracellular pH falls, the NHE-1 is activated, and the rate of H^+ efflux mediated by NHE-1 increases and causes intracellular alkalinization and Na^+ overload, which leads to intracellular Ca^{2+} overload through a mechanism of reverse Na^+-Ca^{2+} exchange. It is presumed that during high glucose condition, there is a metabolic mismatch between glycolysis and glucose oxidation that results in the accumulation of hydrogen ions, which, in turn, activates NHE-1, leading to intracellular alkalinization and Ca^{2+} overload. Therefore, we hypothesized that, in the present study, the mechanisms of cariporide against high glucose-induced endothelial dysfunction of rat isolated aortas might be also related to decreasing intracellular alkalinization and Ca^{2+} overload. Although intracellular pH and intracellular Ca^{2+} concentration were not assayed in the study, it has been reported that cariporide could protect from releasing NO in vascular endothelium through inhibiting activity of NHE-1, decreasing intracellular alkalinization and Ca^{2+} overload[17,20].

In conclusion, this study demonstrates that cariporide significantly prevents endothelial dysfunction, decreases NO release, elevates MDA concentration and reduces SOD activity induced by high glucose in rat isolated thoracic aorta. The mechanisms of protective effects of cariporide may be related to the inhibition of NHE-1 and the decrease of oxidative stress injury. These results provide a potential new target for intervention in the prevention of diabetic complications.

References

1 Najemnik C, Sinzinger H, Kritz H. Endothelial dysfunction, atherosclerosis and diabetes. Acta Med Austriaca 1999; 26: 148–53.

2 Guo X, Liu WL, Chen LW, Guo ZG. High glucose impairs endothelium-dependent relaxation in rabbit aorta. Acta Pharmacol Sin 2000; 21: 169–73.

3 Pieper GM. Enhanced, unaltered and impaired nitric oxide-mediated endothelium-dependent relaxation in experimental diabetes mellitus: importance of disease duration. Diabetologia 1999; 42: 204–13.

4 Friesen NT, Buchau AS, Schott-Ohly P, Lgssiar A, Gleichmann H. Generation of hydrogen peroxide and failure of antioxidative responses in pancreatic islets of male C57BL/6 mice are associated with diabetes induced by multiple low doses of streptozotocin. Diabetologia 2004; 47: 676–85.

5 Matteucci E, Giampietro. Sodium/hydrogen exchange activity in type 1 diabetes mellitus: the never-ending story. Diabetes Nutr Metab 2001; 14: 225–33.

6 Ganz MB, Hawkins K, Reilly RF. High glucose induces the activity and expression of Na^+/H^+ exchange in glomerular mesangial cells. Am J Physiol Renal Physiol 2000; 278: F91–6.

7 Tu JH, Liu LY, Zhang XH. Protective effect of Na^+/H^+ exchanger inhibitor cariporide on the injury of vascular endothelial function induced by hypercholesterolemia. Bull Hu-nan Med Univ 2002; 27: 13–6.

8 Ma FX, Liu LY, Xiong XM. Protective effects of lovastatin on vascular endothelium injured by low density lipoprotein. Acta Pharmacol Sin 2003; 24: 1027–32.

9 Tesfamariam B, Brown ML, Cohen RA. Elevated glucose impaired endothelium-dependent relaxation by activating protein kinase C. J Clin Invest 1991; 87: 1643–8.

10 Xu B, Rao MR. High concentration of glucose inhibits endothelium-dependent vasorelaxation of rabbit aortic artery. Acta Pharmacol Sin 2001; 22: 861–4.

11 Guo X, Liu WL, Chen LW, Guo ZG. High glucose enhances H_2O_2-induced apoptosis in bovine aortic endothelial cells. Acta Pharmacol Sin 2000; 21: 41–5.

12 Jandeleit-Dahm K, Hannan KM, Farrelly CA, Allen TJ, Rumble JR, Gilbert RE, *et al*. Diabetes-induced vascular hypertrophy is accompanied by activation of Na^+/H^+ exchange and prevented by Na^+/H^+ exchange inhibition. Circ Res 2000; 87: 1133–40.

13 Telejko B, Tomasiak M, Stelmach H, Kinalska I. Platelet sodium-proton exchanger and phospholipid-dependent procoagulant activity in patients with type 2 diabetes. Metabolism 2003; 52: 102–6.

14 Williams B, Howard RL. Glucose-induced changes in Na^+/H^+ antiport activity and gene expression in cultured vascular smooth muscle cells. Role of protein kinase C. J Clin Invest 1994; 93: 2623–31.

15 Siczkowski M, Ng LL. Glucose-induced changes in activity and phosphorylation of the Na^+/H^+ exchanger, NHE-1, in vascular myocytes from Wistar-Kyoto and spontaneously hypertensive rats. Metabolism 1996; 45: 114–9.

16 Scholz W, Albus U, Counillon L, Gogelein H, Lang HJ, Linz W, *et al*. Protective effects of HOE642, a selective sodium-hydrogen exchange subtype 1 inhibitor, on cardiac ischaemia and reperfusion. Cardiovasc Res 1995; 29: 260–8

17 Teshima Y, Akao M, Jones SP, Marban E. Cariporide (HOE642), a selective Na^+/H^+ exchange inhibitor, inhibits the mitochondrial death pathway. Circulation 2003; 108: 2275–81.

18 Cutaia M, Kroczynski J, Tollefson K. pH-dependent oxidant production following inhibition of the mitochondrial electron transport chain in pulmonary endothelial cells. Endothelium 2002; 9: 109–21.

19 Svegliati-Baroni G, Di Sario A, Casini A, Ferretti G, D'Ambrosio L, Ridolfi F, Bolognini L, *et al*. The Na^+/H^+ exchanger modulates the fibrogenic effect of oxidative stress in rat hepatic stellate cells. J Hepatol 1999; 30: 868–75.

20 Stromer H, de Groot MC, Horn M, Faul C, Leupold A, Morgan JP, *et al*. Na^+/H^+ exchange inhibition with HOE642 improves postischemic recovery due to attenuation of Ca^{2+} overload and prolonged acidosis on reperfusion. Circulation 2000; 101: 2749–55.

Acta Pharmacologica Sinica 2005 Mar; 26 (3): 334–338

Full-length article

Structural comparisons of meptazinol with opioid analgesics[1]

Wei LI, Jing-lai HAO, Yun TANG, Yan CHEN, Zhui-bai QIU[2]

Department of Medicinal Chemistry, School of Pharmacy, Fudan University, Shanghai 200032, China

Key words

meptazinol; tramadol; opioid analgesics; pharmacophore

[1] Project supported by the National Natural Science Foundation of China (No 30271539, 2003-2005).
[2] Correspondence to Prof Zhui-bai QIU.
Phn 86-21-5423-7595
Fax 86-21-5423-7264.
E-mail zbqiu@shmu.edu.cn

Received 2004-05-20
Accepted 2004-11-20

doi: 10.1111/j.1745-7254.2005.00045.x

Abstract

Aim: To investigate the mechanism of action of a potent analgesic, (±)-meptazinol. **Methods:** The structures of meptazinol enantiomers were compared with opioid pharmacophore and tramadol. **Results:** Neither enantiomer of meptazinol fitted any patterns among the opioid pharmacophore and tramadol, although they did share some structural and pharmacological similarities. However, the structure superpositions implied that both enantiomers of meptazinol might share some similar analgesic mechanisms with typical opiate analgesics. **Conclusion:** Meptazinol should have a different mechanism of action to known analgesics, which would be helpful in further investigations of meptazinol in the search for non-addictive analgesics.

Introduction

(±)-Meptazinol (Figure1), with one chiral center in the structure, is a potent analgesic similar to pethidine. Included in the British Pharmacopoeia in 1998[1], (±)-meptazinol was recommended by Hoskin and Hanks as one of six widely used agonist–antagonist analgesics[2]. However, to date its analgesic mechanism remains unknown. For example, we are still unsure if it is an agonist, an antagonist, or even a mixed agonist–antagonist, and whether it acts on one target or multiple targets.

During the early stages of development, meptazinol was regarded as a mixed agonist–antagonist opioid analgesic based on the following experimental evidence[3]: (i) the chemical structure of meptazinol is similar to that of morphine (Figure 1); (ii) meptazinol-induced analgesia is almost completely reversed by the opioid antagonist naloxone, although higher doses are required to reverse meptazinol compared to morphine; (iii) meptazinol is believed to be a selective μ opioid agonist[4]; and (iv) meptazinol reverses the signs of acute morphine overdose in animals and precipitates abstinence in animals rendered physically dependent on morphine.

However, unlike typical opiates whose notorious side-effects include respiratory depression and addiction, meptazinol induces little respiratory depression and has low addictive potential[5,6]. These properties make meptazinol

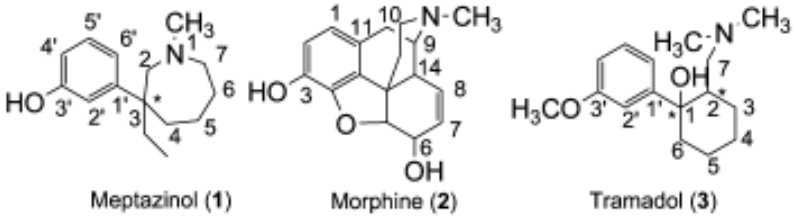

Figure 1. The structure of meptazinol, morphine, and tramadol.

quite similar to another analgesic, tramadol[7] (Figure 1), which is believed to have multiple analgesic mechanisms. Recent studies have also revealed that both tramadol and meptazinol differ from opioid analgesics in the lack of sensitization related to a low propensity to induce addition, which might greatly reduce the possibility of their abuse[8]. Furthermore, tramadol was found to induce its anti-nociceptive effects through monoamine neurotransmitters, whereas there was a cholinergic component in the action of meptazinol[9]. For example, the (–)-enantiomer of meptazinol was shown to be an inhibitor of acetylcholinesterase *in vitro* with potency 100-fold less than that of physostigmine[10]. All this evidence implies that there would be a unique analgesic mechanism for meptazinol.

Therefore, we are very interested in exploring the analgesic mechanism of meptazinol. Because the three-dimensional structures of opioid receptors are not available yet, as a first step of exploration we focused on structural comparisons of meptazinol with typical opiates and with tramadol. Our results will help elucidate the analgesic mechanism of meptazinol and will benefit the search for non-addictive analgesics.

Materials and methods

All calculations were carried out on a R14000 SGI Fuel workstation using the molecular modeling software package SYBYL version 6.9 (Tripos, St Louis, MO, USA).

Material preparation Both enantiomers of meptazinol were synthesized in our laboratory. Their analgesic activities were determined by observing the wrenching body reaction of mice after oral administration at the Shanghai Institute of Materia Medica, Chinese Academy of Sciences. Their absolute configurations were determined using x-ray crystallography, co-crystallizing with dibenzoyl tartaric acid (DBTA), in our previous work[11], which was used as a starting point for this study. For each enantiomer of meptazinol, a random search was carried out on the seven-member ring to ensure a stable ring conformation. Then, all of the other rotatable bonds (except bonds within the seven-member ring) were selected for a systematic search with an interval of 30º for each bond to obtain the lowest energy conformation. After the initial simple energy minimization, the lowest energy conformation of meptazinol was further optimized using a quantum chemical calculation [semi-empirical Austin Model 1 (AM1) method[12] available in SYBYL]. This final optimized geometry of meptazinol was used in the subsequent structural comparisons.

Nine typical opiates, including agonists, antagonists and partial agonists, were selected to generate the opioid pharmacophore according to previous literature [13]. The initial atomic coordinates for seven of these opiates (ie morphine[14], 3-*O*-methyletorphine[15], azidomorphine[16], *N*-allynormetazocine[17], cyclazocine[18], naloxone[19], and nalbuphine[20]) were obtained from published x-ray crystallographic data and modeled using the CRYSIN tool of SYBYL. The other two opiates, codeine and 6-hydroxylevalorphan, were constructed based on their analogues, the crystal structures of which were available in SYBYL.

The initial structure of (*R*,*R*)-tramadol, the active isomer of tramadol, was retrieved from the MDL Drug Data Report-3D database (MDDR-3D), and underwent a similar optimizing treatment to meptazinol with one exception. All the rotatable bonds of tramadol (except bonds within the six-member ring) underwent a genetic algorithm conformational search to find the corresponding lowest energy conformation.

All structures were energy minimized for 1000 steps using the Tripos force field and POWELL method and the termination setting was 0.001 kcal/(mol×A).

Analgesic pharmacophore generation The analgesic pharmacophore is defined in Figure 2. For comparison, related values were obtained from the literature[13] in which the pharmacophore was composed of four distances and two torsion angles. We extracted the common structures of nine opiates composed of a tyramine fragment considered to be the key pharmacophore according to the average values of the nine opiates. As shown in Figure 2, it should be noted that the hydroxyl group was located in the *para*-position of the phenyl ring in the opiates, but in the *meta*-position of the phenyl ring in meptazinol and tramadol (methoxyl instead of hydroxyl group in tramadol). Thus, we manually removed the two carbons between the nitrogen atom and the phenyl ring from the pharmacophore structure. The pharmacophore are composed of one protonated nitrogen atom and a phenol fragment. We superimposed all opiates to the pharmacophore template separately and calculated the average standard deviation value as shown in Table 1. In addition, we defined the pharmacophore for meptazinol and tramadol. One more torsion angle was defined in tramadol because the interval distance between the nitrogen atom and the phenyl ring is three carbon atoms in tramadol compared with two in the other compounds.

Structural superposition The method used to determine superposition was the database alignment facility in SYBYL, in which some or all of the molecules in the database were aligned with a template molecule also in the database. A common substructure was provided to evaluate the best "fit". Only rigid-body rotations and translations were supported.

For the comparison of meptazinol with the opioid pharmacophore, the generated pharmacophore were set as the common substructure for alignment. Both enantiomers of meptazinol were superimposed on each other first, and then superimposed with the other opiates separately.

Using the same pharmacophore, both meptazinol enantiomers and tramadol were superimposed onto the template.

Results and Discussion

The analgesic activities were determined as ED_{50} values for the two enantiomers of meptazinol, 14.583 μmol/kg for (+)-enantiomer and 31.333 μmol/kg for the (–)-enantiomer. The (+)-enantiomer is more potent than the (–)-enantiomer, although the difference between them was not significant.

Because the structures of morphine and its derivatives and analogs are fairly rigid, it is reasonable to assume that their x-ray structures are the same as the active conformations binding to opioid receptors. Therefore, our pharmacophore model was based on these rigid structures. According to the analgesic pharmacophore defined in Figure 2, we built this pharmacophore using the mean values of the nine opiates as the common substructure for superposition in SYBYL. For reasons mentioned above, we removed the two carbon atoms from the pharmacophore. We also measured the torsions of our pharmacophore structures without the removal of the carbon atoms to make our pharmacophore resemble the original one in the literature (Table 1).

The crystal structures of the meptazinol enantiomers were treated with a series of methods to determine the lowest energy conformer for each enantiomer. According to the systematic search results for both meptazinol enantiomers, we found the lowest energy conformations to be very similar. The lowest energy conformation was selected as the low energy conformer followed by semi-empirical AM1 geometry optimization.

Using the opiate pharmacophore as the overlap template we first superimposed both enantiomers of meptazinol onto each other. As illustrated in Figure 3, the pharmacophore elements of the meptazinol enantiomers superimposed well onto each other. Thus, both meptazinol enantiomers may induce a similar analgesic mechanism, at least in part. An experiment using electrical stimulation of guinea pig isolated ileum indicated that both enantiomers of meptazinol were μ-selective opioid receptor agonists[21]. And the similar pharmacology results from observing the mice wrenching body reaction of meptazinol enantiomers also supports this conclusion, although for the (–)-enantiomer there is another cholinergic component in the participating antinociceptive effect[10].

Table 1. Molecular parameters for the x-ray-determined crystals of opiates, meptazinol and tramadol (MDDR-3D).

	A (Å)	B (Å)	C (Å)	D (Å)	τ_1	τ'	τ_2
Mean values of nine opiates	7.0	4.4	1.1	4.3	173°		–89°
(–)-Meptazinol·(–),(–)DBTA	6.380	5.158	0.750	5.103	50.8°		169.0°
(+)-Meptazinol·(+),(+)DBTA	6.378	5.178	0.723	5.123	148.4°		–173.5°
(*R*,*R*)-Tramadol	4.510	2.960	2.581	1.449	62.1°	60.0°	–65.9°

DBTA, dibenzoyl tartaric acid; (*R*,*R*)-tramadol, the active isomer of tramadol. The molecular parameters are defined in Figure 2.

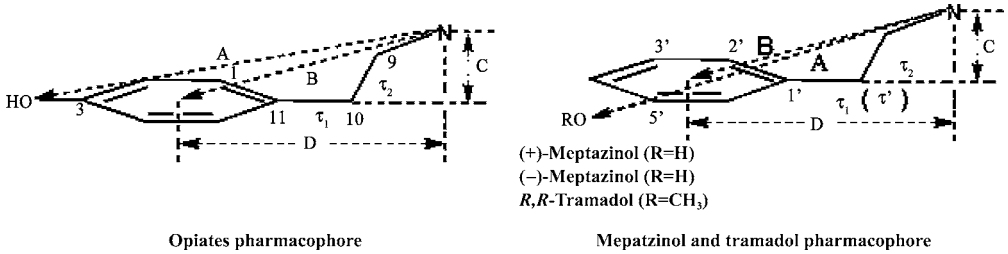

Figure 2. Diagrammatic illustration of the pharmacophores. (A) Distance between the N atom and the O atom; (B) Distance between the N atom and the center of the phenyl ring; (C) Vertical distance of the N atom to the plane of the phenyl ring; (D) Horizontal distance of the N atom to the center of the phenyl ring. Torsion angle definitions: τ_1: C_1-C_{11}-C_{10}-C_9, τ_2: C_{11}-C_{10}-C_9-N for opiates; τ_1: $C_{2'}$-$C_{1'}$-C_3-C_2, τ_2: $C_{1'}$-C_3-C_2-N for meptazinol; τ_1: $C_{2'}$-$C_{1'}$-C_1-C_2, τ_2: C_1-C_2-C_7-N, τ': $C_{1'}$-C_1-C_2-C_7 for tramadol.

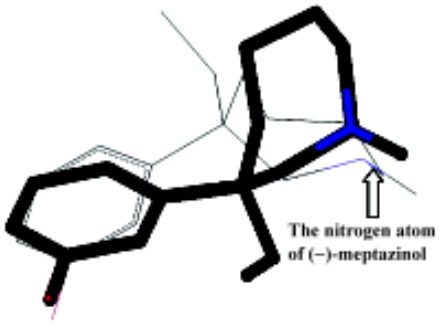

Figure 3. Superimposition of (-)-meptazinol (in thin sticks) and (+)-meptazinol (in thick sticks) based on the opiate pharmacophore.

However, as demonstrated in Figure 4, the meptazinol pharmacophore differed from the opiate pharmacophore, particularly in the position of the nitrogen atom. The overlap of (+)-meptazinol to the opiate pharmacophore is a little better than (–)-meptazinol in the region of the phenol fragment, which may account for the minor increase in analgesic effect of (+)-meptazinol. These differences were also reflected in related molecular parameters. From Table 1, we can see that distance A in the pharmacophore of meptazinol was about 0.6 Å shorter than that in the opiates examined. The nitrogen atom actually becomes further away (>0.7 Å) from the phenol fragment in meptazinol than in the opiates, which was confirmed by the increased B and D values in meptazinol. Both enantiomers of meptazinol did not fit the skeletons of the opiates particularly well. The azepane ring of meptazinol did not match the corresponding alkyl chain between the nitrogen atom and the phenol fragment in the opiates (Figure 4). Whether or not the azepane ring contributes to analgesic potency needs further investigation.

In addition, we compared meptazinol with tramadol because they share more common pharmacological effects with each other than with other opiates. It should be noted that we still used the pharmacophore model generated from the opiate structures because their pharmacology may be mediated by a similar mechanism. To determine the active conformation of (*R*,*R*)-tramadol, a series of methods were carried out. Twenty-four minimum energy conformations of tramadol were analyzed and found to be very similar to each other. Therefore, the lowest energy conformation was selected and geometrically optimized further using the quantum chemical calculation method AM1, which resulted in the active conformation of tramadol. The related molecular parameters of tramadol are also listed in Table 1, and the superposition of tramadol with meptazinol is shown in Figure 5. Although the pharmacophore of meptazinol enantiomers and tramadol occupied a similar region, poor overlap occurred between meptazinol enantiomers and tramadol in the phenol fragment and the protonated nitrogen atom. Although (*R*,*R*)-tramadol shares some similar pharmacological effects with meptazinol, our studies revealed that their pharmacophores might be different.

Conclusion

In summary, from the structural comparisons conducted in the present study we learned that both enantiomers of meptazinol differed from typical opiates and from (*R*,*R*)-tramadol. However, the pharmacophore of both enantiomers of meptazinol might be similar to each other, and this result is consistent with previous studies[21]. Therefore, we suggest that meptazinol has a unique analgesic mechanism that is different from known analgesics (ie meptazinol may not target opioid receptors only, and one of its enantiomers might

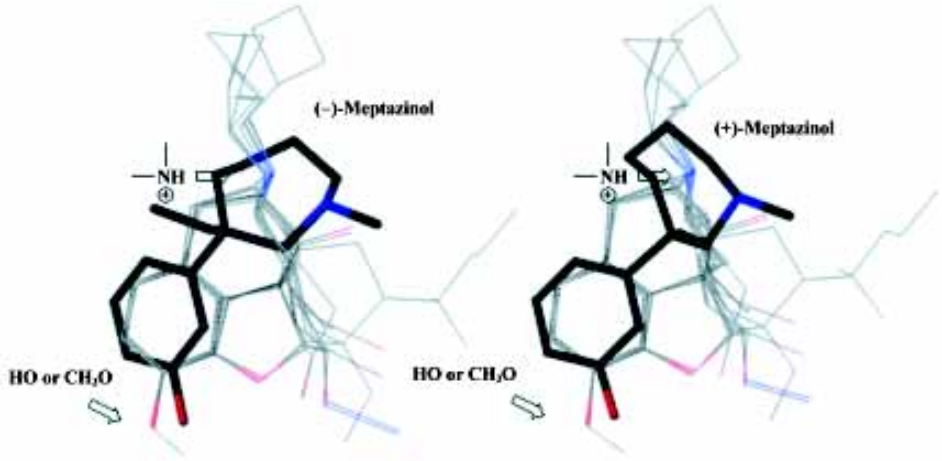

Figure 4. Superimposition of the nine opiates (in thin lines) with (+)- and (–)-meptazinol (in thick lines).

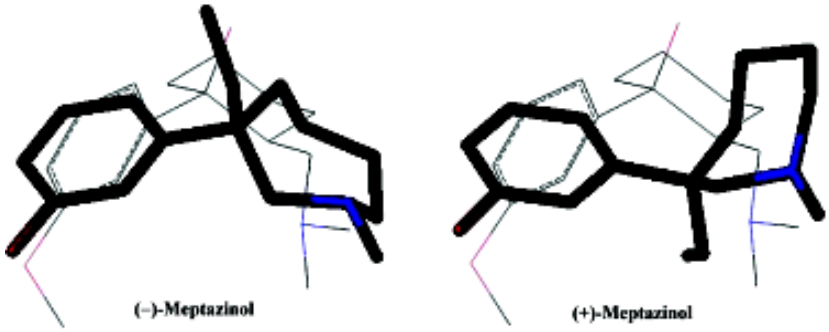

Figure 5. Superimposition of (+) or (–) meptazinol (thick lines) with (*R*, *R*)-tramadol (thin lines).

act on other targets in the cholinergic system). The antinociceptive targets and mechanism of meptazinol enantiomers needs to be investigated further.

Acknowledgements

We thank researchers from the Shanghai Institute of Materia Medica, Chinese Academy of Sciences for the pharmacological test of the meptazinol enantiomers.

References

1 Great Britain Medicines Commission. British Pharmacopoeia. London: Bernan Association; 1998. p 859.
2 Hoskin PJ, Hanks GW. Opioid agonist-antagonist drugs in acute and chronic pain states. Drugs 1991; 41: 326–44.
3 Green D. Current concepts concerning the mode of action of meptazinol as an analgesic. Postgrad Med J 1983; 59 (Suppl 1): 9–12.
4 Spiegel K, Pasternak GW. Meptazinol: a novel Mu-1 selective opioid analgesic. J Pharmacol Exp Ther 1984; 228: 414B.
5 Goode PG, Rhodes KF, Waterfall JF. The analgesic and respiratory effects of meptazinol, morphine and pentazocine in the rat. J Pharm Pharmacol 1979; 31: 793–5.
6 Johnson RE, Jasinski DR. Human pharmacology and abuse potential of meptazinol. Clin Pharmacol Ther 1987; 41: 426–33.
7 Dayer P, Collart L. Pharmacology of tramadol. Drugs 1997; 53 (Suppl 2): 18–24.
8 Tzschentke TM, Bruckmann W, Friderichs E. Lack of sensitization during place conditioning in rats is consistent with the low abuse potential of tramadol. Neurosci Lett 2002; 329: 25–8.
9 Holmes B, Ward A. Meptazinol. A review of its pharmacodynamic and pharmacokinetic properties and therapeutic efficacy. Drugs 1985; 30: 285–312.
10 Ennis C, Haroun F, Lattimer N. Can the effects of meptazinol on the guinea-pig isolated ileum be explained by inhibition of acetylcholinesterase? J Pharm Pharmacol 1986; 38: 24–7.
11 Chen Y. Studies on the synthesis, resolution and optical isomers of meptazinol. [Dissertation]. Shanghai: Fudan Univ; 2004. p 19–28.
12 Dewar MJS, Zoebisch EG, Healy EF, Stewart JJP. AM1: a new general purpose quantum mechanical model. J Am Chem Soc 1985; 107: 3902–9.
13 Horn AS, Rodgers JR. The enkephalins and opiates: structure-activity relations. J Pharm Pharmacol 1977; 29: 257–65.
14 Mackay M, Hodgkin DC. A crystallographic examination of the structure of morphine. J Chem Soc 1955; 3261.
15 Van Den Hende JH, Nelson NR. The crystal and molecular structure of 7.alpha.-(1-(*R*)-hydroxy-1-methylbutyl)-6,14-endo-ethenotetrahydrothebaine hydrobromide (19-propylthevinol hydrobromide) J Am Chem Soc 1967; 89: 2901–5.
16 Sasvari K, Simon K, Bognar R, Makleit S. The crystal and molecular structure of 6-deoxy-6-azido dihydroisomorphine, $C_{17}H_{20}N_4O_2$. Acta Cryst 1974; B30: 634–41.
17 Fedeli W, Giacomello G, Cerrini S, Vaciago A. Crystal and molecular structure of 2-allyl-2′-hydroxy-5,9-dimethyl-6,7-benzomorphan mydrobromide monohydrate. J Chem Soc (B). 1970: 1190–5.
18 Karle IL, Girardi RD, Fratini AV, Karle J. The crystal structures of *DL*-cyclazocine and *L*-cycla-zocine.HBr.H_2O, and the absolute configuration of *L*-cyclazocine.HBr.H_2O (2-cyclo-propyl-methyl-2′-hydroxy-5,9-dimethyl-6,7-benzomorphan). Acta Cryst 1969; B25: 146979.
19 Sime RL, Forehand R, Sime RJ. The crystal structure of a narcotic antagonist: naloxone hydrochloride dehydrate. Acta Cryst 1975; B31: 2326–30.
20 Sime RJ, Dobler M, Sime RL. The crystal structure of a narcotic agonist/antagonist: nalbuphine hydrochloride dehydrate. Acta Cryst 1976; B32: 809–12.
21 Duchesne RJ, Goodall J, Hughes IE. Pharmacological effects of meptazinol and its enantiomers on guinea-pig ileum and mouse vas deferens. J Pharm Pharmacol 1984; 36: 560–2.

Acta Pharmacologica Sinica 2005 Mar; 26 (3): 339–344

Blackwell Publishing

Full-length article

Development of a complex scintillation proximity assay for high-throughput screening of PPARγ modulators[1]

Bin WU, Jie GAO, Ming-wei WANG[2]

The National Center for Drug Screening, Shanghai Institute of Materia Medica, Shanghai Institutes for Biological Sciences, Chinese Academy of Sciences; Graduate School of Chinese Academy of Sciences, Shanghai 201203, China

Key words

peroxisome proliferator-activated receptor gamma; retinoid X receptor alpha; scintillation proximity assay; high-throughput screening

[1] Project supported by grants from the Ministry of Science and Technology of China (2002AA-2Z343A), Chinese Academy of Sciences (KSCX1-SW-11-2) and Shanghai Municipality Science and Technology Development Fund (03dz19224).
[2] Correspondence to Dr Ming-wei WANG.
Phn 86-21-5080-0598.
Fax 86-21-5080-0721.
E-mail mwwang@siniwest.com

Received 2004-09-06
Accepted 2004-11-26

doi: 10.1111/j.1745-7254.2005.00040.x

Abstract

Aim: To develop a complex high-throughput screening (HTS) assay based on scintillation proximity assay (SPA) technology for identification of novel peroxisome proliferator-activated receptor gamma (PPARγ) modulators. **Methods:** Full-length PPARγ and retinoid X receptor alpha (RXRα), biotinylated PPAR response element (PPRE), [^{3}H]BRL49653 and streptavidin-coated FlashPlate or microbead were used to develop an HTS assay based on SPA technology. This 'ABCDE' method was validated against conventional hydroxyapatite (HA) assay and applied to large-scale screening of 16 000 synthetic compounds and natural product extracts. **Results:** (1) IC_{50} values of positive control compounds (BRL49653 and troglitazone) obtained from the 'ABCDE' method and HA assay were comparable and consistent with those reported elsewhere; (2) Approximately 178 compounds, showing more than 70% competitive inhibition on BRL49653 binding to PPARγ, were identified initially by the 'ABCDE' method (microbead); (3) Secondary screening using FlashPlate and cross-reactivity studies with RARα, β, γ and RXRα, β, γ confirmed that 12 compounds possessed specific PPARγ binding properties including 2 with IC_{50} values less than 0.5 μmol/L and novel chemical structures. **Conclusions:** The 'ABCDE' method using either FlashPlate or microbead, is a highly efficient, automatable, and robust tool to screen potential PPARγ modulators in HTS setting. Its application may be expanded to other nuclear receptors that form heterodimers upon activation.

Introduction

Nuclear receptors (NRs) are a superfamily of ligand activated transcription factors that modulate specific gene expression. To date, more than 100 NRs have been identified including class I (ligand-dependent), class II (ligand-independent), and orphan receptors. A common feature of NRs is that they all contain a DNA binding domain that interacts with respective target genes to exert physiological functions[1]. Peroxisome proliferator-activated receptors (PPARs) with three isoforms (α, β, and γ) regulate gene transcription in response to small, lipophilic ligands[2-5]. PPARα is present in the liver, kidney, and heart, PPARβ (also known as PPARδ) is expressed ubiquitously, and PPARγ is mainly found in the adipose tissue and muscle. Upon ligand binding, PPARs release relevant co-repressors and form heterodimers with retinoid X receptors (RXRs)[6]. The heterodimers bind to peroxisome proliferator response elements (PPREs)[7,8] and recruit co-activators to initiate transcription of target genes. It is known that PPARγ is activated by fatty acids and prostaglandin J2 derivatives, although the identities of its physiologically relevant activators are not certain[9,10].

Because PPARγ activation can cause insulin sensitization, its synthetic agonists have been used in the treatment of type 2 diabetes[11,12]. Recently discovered liabilities of such therapy, namely, weight gain and edema, led to regulatory concerns on the long-term administration of drugs acting through PPARγ[13,14]. The elimination of such adverse effects may depend on the discovery of novel compounds with improved tissue selectivity while retaining insulin-sensitizing property.

Conventional methods to study and characterize NRs include non-homogeneous hydroxyapatite (HA) and gel shift assays which require a laborious separation procedure and thus, are not suitable for high-throughput screening (HTS). Scintillation proximity assay (SPA)[15] technology, howerer, provides a homogeneous screening approach that does not involve post-reaction liquid handling steps and is well-suited to automation and HTS. In the SPA system, an isotope (eg, [^{3}H]) is brought very close to a scintillant-impregnated microbead or FlashPlate by binding to its surface. Because the emitted β particles or augur electrons can only travel short distances in the bulk solution, the microbead or FlashPlate preferentially captures electrons from the bound radiolabeled ligand. Therefore, the amount of light emitted from the scintillant in the microbead or FlashPlate is directly proportional to the amount of bound radiolabeled ligand (Figure 1). Several SPA-based NR competitive binding assays were developed and applied to HTS using biotinylated receptor ligand binding domains (LBDs; 'ABC' method)[16,17]. In this paper, we describe a more complex SPA-based assay system which includes the full-length PPARγ and RXRα, biotinylated PPRE, [^{3}H]BRL49653 and streptavidin-coated FlashPlate or microbead in a homogeneous setting. This 'ABCDE' approach was fully validated and applied to HTS of a sizable compound library. A series of structurally diversified 'hits' were found, and subsequent characterization led to the discovery of two novel PPARγ binders with submicromolar potency and high specificity.

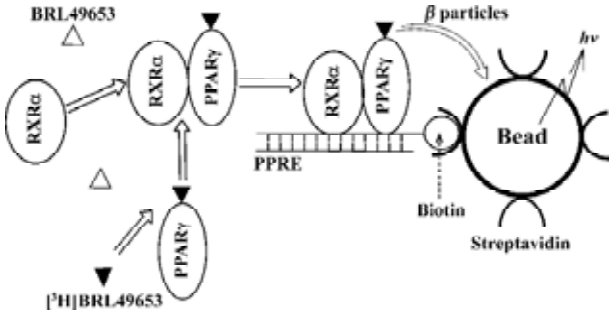

Figure 1. Principle of SPA: PPARγ forms a heterodimer with RXRα upon activation by BRL49653. The heterodimer binds to biotinylated PPRE via streptavidin-coated microbead. Because the distance between [^{3}H]BRL49653 and scintillant is short enough, the latter can be stimulated by [^{3}H] to release *hv*. In the case of FlashPlate, biotinylated PPRE, streptavidin and scintillant were immobilized on the surface of each well.

Materials and methods

Reagents Potassium chloride, sodium phosphate monobasic anhydrous, and magnesium chloride haxahydrate were purchased from Shanghai Chemical Co, Ltd. Edetic acid was purchased from Sigma-Aldrich (USA). BRL49653 and troglitazone were purchased from Cayman Chemical Co (USA). 3-[(3-Cholamidopropyl)dimethylammonio]-1-propane sulfonate (CHAPS) was purchased from Boehringer Mannheim GmbH (Germany). Dithiothreitol (DTT) was purchased from BioBasic Inc (Canada) and hydroxyapatite was obtained from Bio-Rad Laboratories (USA). Aprotinin and leupeptin were purchased from Merck KGaA (Germany). [^{3}H]BRL49653 (53 Ci/mmol) was obtained from American Radiolabeled Chemicals, Inc (USA), FlashPlate and flat-bottom Isoplate™ was obtained from PerkinElmer, Inc (USA), and streptavidin-coated microbead was obtained from Amersham Biosciences UK Ltd (England). The plasmids of human NRs used in this study were from Dr Shen X of Shanghai Institute of Materia Medica, Chinese Academy of Sciences and Dr Chen SJ of Shanghai Institute of Hematology. Full-length PPARγ, RARα, β, γ, and RXRα, β, γ were produced with a baculovirus expression system using IPLB-Sf-21 cells[18]. The stock solutions for PPARγ, RARα, β, γ and RXRα, β, γ extract proteins were at 7, 12–15, and 7–13 g/L, respectively. Double-strand 5′-biotinylated-PPRE (CCTTTGACCTATTGAACTATTACCT) was synthesized by Shanghai Sangon Biological Engineering Technology & Service Co, Ltd.

HA assay The assay buffer consists of 10% glycerol (v/v), NaH_2PO_4 25 mmol/L, $MgCl_2$ 0.5 mmol/L, DTT 1 mmol/L, edetic acid 1 mmol/L, CHAPS 5 mmol/L, aprotinin 2 mg/L and leupeptin 100 μmol/L. PPARγ 1 μL extract protein (70 mg/L) was loaded into each well of Isoplate™ containing the assay buffer, followed by [^{3}H]BRL49653 (1.2 μL, 10 nmol/L) and various concentrations of BRL49653 or troglitazone (2.5 μL), to give a final volume of 100 μL per well. The plates were sealed and incubated overnight at 4 °C. HA (25%, v/v) 25 mL was added to each well the next morning and the plates were gently agitated twice for 5 min each. Following centrifugation at 1200×*g* for 3 min, the supernatant was decanted and 100 μL assay buffer was added to each well. This washing procedure was repeated twice before adding 150 μL scintillation liquid (PerkinElmer), the plates were gently agitated to resuspend HA and counting was measured by a MicroBeta counter (PerkinElmer).

FlashPlate based SPA assay Biotinylated-PPRE (4 μL from a stock solution of 10 g/L) was mixed with the above assay buffer (20 mL) containing fish sperm DNA (Sangon; 20 μL from a 10 g/L stock solution), loaded to streptavidin-coated FlashPlate (200 μL/well) and incubated overnight at 4 °C. It was then washed three times with the assay buffer,

200 μL reaction solution containing 14 μg PPARγ extract protein (70 mg/L), 0.94 mg RXRα extract protein (4.7 mg/L), 10 nmol/L [^{3}H]BRL49653 and various concentrations of BRL49653 or troglitazone were added to each well. Following incubation at 4 °C for 4 h, the plates were counted by the MicroBeta counter. For validation purpose, various concentrations of PPARγ and RXRα extract proteins, as well as different reaction time lengths, were studied to determine an optimal assay condition.

Microbead based SPA assay Biotinylated-PPRE (2 μL from a stock solution of 10 g/L) was mixed with the assay buffer (10 mL) containing fish sperm DNA (Sangon; 10 μL from a 10 g/L stock solution) and 4 mg streptavidin-coated microbead in a conical polypropylene centrifuge tube (Corning Inc, USA) and incubated overnight at 4 °C. The mixture was centrifuged for 10 min at 1500×*g*. The supernatant was then removed and washed three times with the 10-mL assay buffer. Reaction solution 10 mL containing 700 μg PPARγ extract protein (70 mg/L), 47 μg RXRα extract protein (4.7 mg/L), 10 nmol/L [^{3}H]BRL49653 and various concentrations of BRL49653 or troglitazone were distributed to each well of a Isoplate™ (100 μL/well) and incubated at 4 °C for 4 h before counting by the MicroBeta counter. For validation purposes, various amounts of microbead were used to determine an optimal assay condition.

HTS studies The compound library used for screening consists of 16 000 pure synthetic compounds and extracts of natural products. A 10-compound pool per well mix was applied to the primary screening (microbead based SPA assay), with an average concentration of 7 μmol/L for each compound dissolved in 100% Me_2SO solution. This matrix system maximizes the advantage of HTS and allows duplicate screening of each compound[19]. In each 96-well Isoplate™, 16 wells were used as positive control (BRL-49653) and samples showing greater than 70% inhibition were considered 'hits'. Positive compounds were re-screened with FlashPlate based SPA assay and confirmed 'hits' studied for their binding cross-reactivities with RARα, β, γ and RXRα, β , γ using respective HA assay.

Results

Assay validation In the present study, we first assessed the kinetics of the signal strength generated by FlashPlate assay. Time-course experiment suggested that the equilibrium reached after 3.5 h of incubation at 4 °C and prolongation of the reaction time did not improve the assay efficiency (Figure 2A). Various concentrations of PPARγ and RXRα were used to establish the optimal assay condition. In the absence of unlabeled BRL49653, a maximum signal was detected with a combination of 140 mg/L (1:50 of the stock solution) PPARγ extract protein and 7 mg/L (1:1000 of the stock solution) RXRα (Figure 2B). The fully optimized assay possessed a signal to background ratio of 5. Thus, optimal receptor concentrations were determined for PPARγ (70 mg/L; 1:100) and RXRα (4.7 mg/L; 1:1500), respectively. Under this assay condition, IC_{50} values for the two PPARγ agonists, BRL49653 and troglitazone were measured (Figure 2C), and found to be comparable to those calculated from the HA assay (Figure 2D). Since the principle of microbead-based SPA assay is similar to that of FlashPlate, identical receptor concentrations were used with a reduced assay volume (100 μL/well). When different concentrations of microbead were used, a saturation reached between 2 and 4 g/L (Figure 3A) with a signal-to-background ratio equal to 5. The IC_{50} values for BRL49653 and troglitazone determined by this assay were within the range described earlier (Figure 3B).

Assay parameters In order to apply the microbead-based SPA assay to HTS, both non-specific binding (NSB; using 22.5 mmol/L BRL49653) and maximum binding (MB; using 0 mmol/L BRL49653) were studied. Coefficient of variation (*CV*) values were 8.5% for NSB and 6.2% for MB, respectively (Figure 3C). The Z' factor, which estimates the suitability to HTS[20], was calculated to be 0.71.

High-throughput screening Of the 16 000 samples initially screened, 178 'hits' (1.11%) showing greater than 70% competitive inhibition on BRL49653 binding to PPARγ were discovered (all synthetic compounds; Figure 4A). Secondary (single compound per well) screening confirmed that 24 of the above 'hits' displayed consistent inhibitory effects with IC_{50} values between 0.2 and 28.5 μmol/L. Cross-reactivity studies with RARα, β, γ and RXRα, β, γ revealed that 12 of these compounds possess specific PPARγ binding properties including 2 with IC_{50} values less than 0.5 μmol/L (Table 1). In this HTS campaign, the signal-to-noise ratio (10-to-15-fold), *CV* (5%–8%) (Figure 4B) and Z' factor (0.66–0.75) are of high quality nature.

Discussion

Three receptor binding assays were employed and compared side-by-side in the present study to measure specific binding properties of two known PPARγ agonists, namely, BRL49653 and troglitazone. Conventional HA assay is a non-homogeneous method widely used to assess competitive interaction between a testing agent and receptor in the presence of radiolabeled ligand. For PPARγ, such interaction involves additional components such as RXRα and

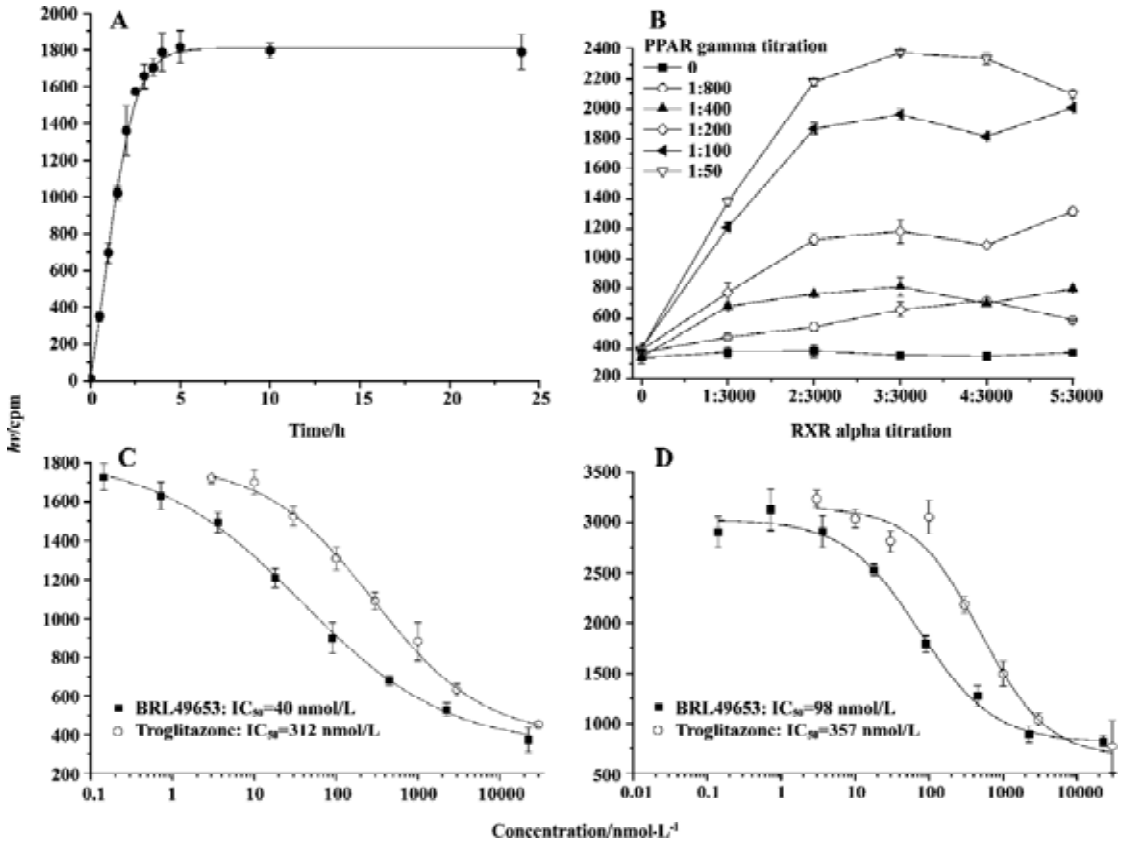

Figure 2. (A) Time-course study of FlashPlate assay. Equilibrium of PPARγ, RXRα, [^{3}H]BRL49653, unlabeled BRL49653, PPRE and streptavidin-coated FlashPlate was reached at 4 h. (B) Effects of different receptor concentrations on FlashPlate assay signal strength (the stock solution concentration is 7 g/L for both PPARγ and RXRα). (C) Dose-response curves of BRL49653 and troglitazone measured by FlashPlate assay from which IC_{50} values were calculated. (D) Dose-response curves of BRL49653 and troglitazone measured by HA assay. Data shown are duplicate samples with mean±SEM from at least two experiments.

PPRE. Therefore, the 'ABCDE' method utilizing either FlashPlate or microbead based on SPA technology was developed and validated to include both RXRα and PPRE in the assay system. The final readout is fully dependent upon specific binding of biotinylated PPRE to streptavidin-coated FlashPlate or microbead as addition of free biotin was able to block this interaction completely[16]. Although the IC_{50} values of BRL49653 and troglitazone generated by these three approaches were very similar and comparable to those reported previously with a relatively simple 'ABC' SPA method (BRL49653: K_d=26 nmol/L, IC_{50}=36 nmol/L; troglitazone: K_d=310 nmol/L, IC_{50}=320 nmol/L)[16], the 'ABCDE' model is obviously superior in terms of physiologic mimicry, easy to use, robustness and efficiency, largely due to its inclusiveness and homogenous nature.

We found that both FlashPlate and microbead-based SPA methods could be readily adapted to automated HTS. However, the cost of FlashPlate, including assay volume (200 μL), associated reagent consumption, and compound depletion, *etc*, is approximately 5 times greater than that of microbead (100 μL). This may constitute a major concern when implementing a large HTS campaign. All the key assay parameters, such as *CV* and Z' factor, obtained from our microbead-based SPA validation experiments, indicate that it is well suited to HTS[20]. Indeed, when employed in HTS of potential PPARγ modulators, this assay system demonstrated a consistently high quality in terms of the signal-to-noise ratio, *CV* and Z' factor in all the 40 pooled compound matrix plates. One implication of this is that microbead-based SPA technology may be expanded to other NRs that form heterodimers upon activation.

Following the initial screening of 16 000 samples, a "hit" rate of 1.11% was achieved, of which, only 13.5% of the 'hits' could be confirmed by secondary screening. They were further tested for cross-reactivities with both RARs and RXRs (defined as IC_{50} less than 70 μmol/L), and 12 compounds

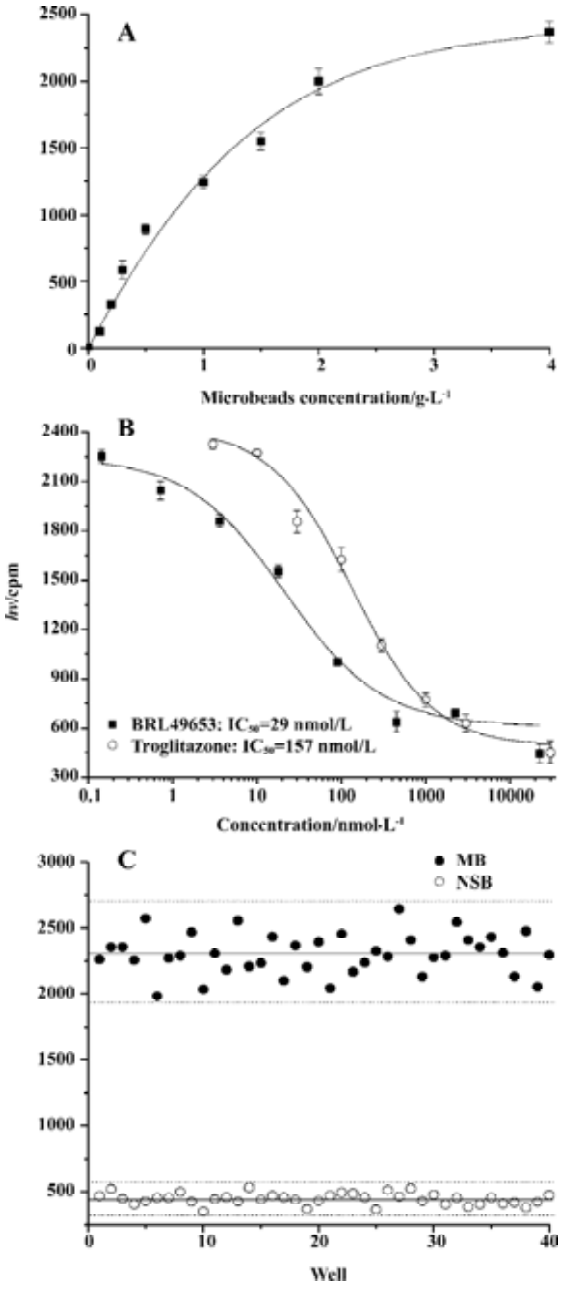

Figure 3. (A) Effects of different microbead concentrations on SPA assay signal strength. Saturation reached between 2 and 4 g/L. (B) Dose-response curves of BRL49653 and troglitazone measured by microbead based SPA assay from which IC_{50} values were calculated. Data shown are duplicate samples with mean±SEM from at least two experiments. (C) Intra-plate variation of microbead based SPA assay as demonstrated by MB and NSB.

showed high specificity for PPARγ with IC_{50} values ranging from 0.2 to 28.5 μmol/L. The IC_{50} for one thiazolidinedione-like compound is 0.2 μmol/L, better than several currently marketed PPARγ agonists. The other compound with an IC_{50} of 0.49 μmol/L belongs to the imide class. Both of them possess novel chemical structures (data not shown). If their activities could be demonstrated by cell-based functional assays, bioassay-guided structure modification and optimization may lead to the discovery of some entirely new PPARγ modulators.

Table 1. Receptor binding specificity and cross-activity of the confirmed 'hits'.

Compound	IC_{50} /μmol·L^{-1} PPARγ	RARα	RARβ	RARγ	RXRα	RXRβ	RXRγ
Thiazolidinedione class							
SH00013951	14.4	NB	NB	NB	NB	NB	NB
SH00012671	0.2	NB	NB	NB	NB	NB	NB
Imide class							
SH00017229	6.7	NB	NB	NB	NB	NB	NB
SH00013478	10.5	NB	NB	NB	NB	NB	NB
SH00012632	0.49	NB	NB	NB	NB	NB	NB
Other classes							
SH00017545	5.2	NB	NB	NB	NB	NB	NB
SH00010267	23.3	NB	NB	NB	NB	NB	NB
SH00017475	15.2	NB	NB	NB	NB	NB	NB
SH00015594	6.7	NB	NB	NB	NB	NB	NB
SH00012095	16.7	NB	NB	NB	NB	NB	NB
SH00013003	28.5	NB	NB	NB	NB	NB	NB
SH00010675	15.1	NB	NB	NB	NB	NB	NB

NB: No binding activity was detected at the concentration (70 μmol/L) tested. Secondary 'hits' showing binding activities of various degrees with RARs or RXRs were discared.

Acknowledgement

We thank Dr Dale E MAIS, Xin XIE, Na LI, and Chenghe JIN for their valuable discussions.

References

1 Mangelsdorf DJ, Thummel C, Beato M, Herrlich P, Schutz G, Umesono K, *et al*. The nuclear receptor superfamily: the second decade. Cell 1995; 83: 835–9.

2 Schmidt A, Endo N, Rutledge SJ, Vogel R, Shinar D, Rodan GA. Identification of a new member of the steroid hormone receptor superfamily that is activated by a peroxisome proliferators and fatty acids. Mol Endocrinol 1992; 6: 1634–41.

3 Sher T, Yi HF, McBride OW, Gonzalez FJ. cDNA cloning, chromosomal mapping and functional characterization of the human peroxisome proliferator activated receptor. Biochemistry 1993; 32: 5598–604.

4 Desvergne B, Wahli W. Peroxisome proliferator-activated receptors: nuclear control of metabolism. Endocr Rev 1999; 20: 649–88.

5 Wise H. Multiple signalling options for prostacyclin. Acta Pharmacol

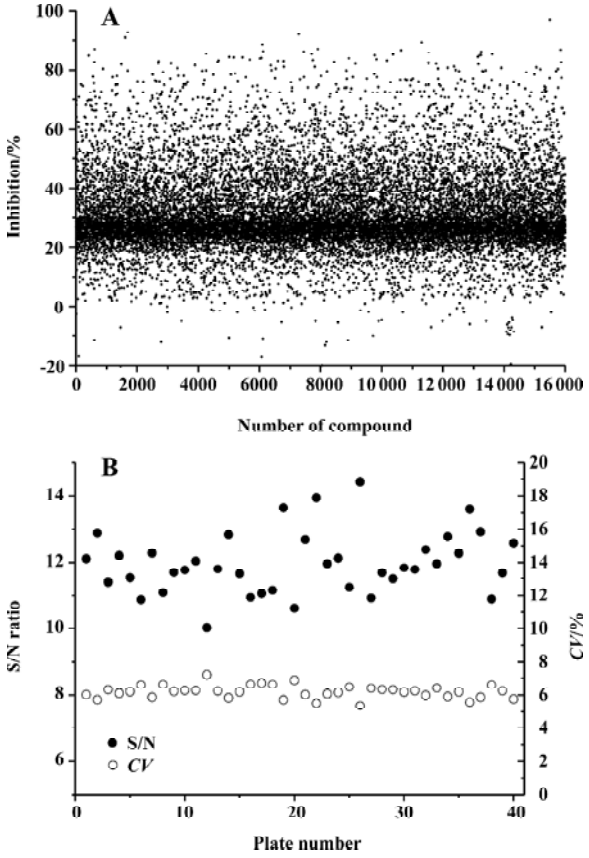

Figure 4. (A) High-throughput screening of 16 000 compounds using microbead-based SPA assay. Results are expressed as percentage inhibition of [^{3}H]BRL49653 binding to PPARγ. (B) Signal-to-noise (S/N) and coefficient of variation (*CV*) of the 10-compound pool per well matrix assay system.

Sin 2003; 24: 625–30.

6 Kliewer SA, Umesono K, Noonan DJ, Heyman RA, Evans RM. Convergence of 9-*cis* retinoic acid and peroxisome proliferator signalling pathways through heterodimer formation of their receptors. Nature 1992; 358: 771–4.

7 Ijpenberg A, Jeannin E, Wahli W, Desvergne B. Polarity and specific sequence requirements of PPAR-RXR heterodimer binding to DNA: a functional analysis of the malic enzyme gene PPRE. J Biol Chem 1997; 272: 20108–17.

8 Juge-Aubry C, Pernin A, Favez T, Burger AG, Wahli W, Meier CA, *et al*. DNA binding properties of peroxisome proliferator-activated receptor subtypes on various natural peroxisome proliferator response elements: importance of the 5' flanking region. J Biol Chem 1997; 272: 25252–9.

9 Yu K, Bayona W, Kallen CB, Harding HP, Ravera CP, McMahon G, *et al*. Differential activation of peroxisome proliferator-activated receptors by eicosanoids. J Biol Chem 1995; 270: 23975–83.

10 Kliewer SA, Lenhard JM, Willson TM, Patel I, Morris DC, Lehmann JM. A prostaglandin J2 metabolite binds peroxisome proliferator-activated receptor gamma and promotes adipocyte differentiation. Cell 1995; 83: 813–9.

11 O'Moore-Sullivan TM, Prins JB. Thiazolidinediones and type 2 diabetes: new drugs for an old disease. Med J Aust 2002; 176: 381–6.

12 Yang L, An HX, Deng XL, Chen LL, Li ZY. Rosiglitazone reverses insulin secretion altered by chronic exposure to free fatty acid via IRS-2-associated phosphatidylinositol 3-kinase pathway. Acta Pharmacol Sin 2003; 24: 429–34.

13 Camp HS. Thiazolidinediones in diabetes: current status and future outlook. Curr Opin Investig Drugs 2003; 4: 406–11.

14 Guan Y, Zhang Y, Davis L, Breyer MD. Expression of peroxisome proliferator-activated receptors in urinary tract of rabbits and humans. Am J Physiol 1997; 273: F1013–22.

15 Hart HE, Greenwald EB. Scintillation proximity assay of antigen-antibody kinetics: concise communication. J Nucl Med 1979; 20: 1062–5.

16 Nichols JS, Parks DJ, Consler TG, Blanchard SG. Development of a scintillation proximity assay for peroxisome proliferator-activated receptor gamma ligand binding domain. Anal Biochem 1998; 257: 112–9.

17 Henke BR, Consler TG, Go N, Hale RL, Hohman DR, Jones SA, *et al.* A new series of estrogen receptor modulators that display selectivity for estrogen receptor beta. J Med Chem 2002; 45: 5492-505.

18 Gearing KL, Göttlicher M, Teboul M, Widmark E, Gustafsson J. Interaction of the peroxisome proliferator-activated receptor and retinoid X receptor. Proc Natl Acad Sci USA 1993; 90: 1440–4.

19 Qian J, Voorbach MJ, Huth JR, Coen ML, Zhang HC, Ng SC, *et al*. Discovery of novel inhibitors of Bcl-xL using multiple high-throughput screening platforms. Anal Biochem 2004; 328: 131–8.

20 Zhang JH, Chung TD, Oldenburg KR. A simple statistical parameter for use in evaluation and validation of high-throughput screening assays. J Biomol Screen 1999; 4: 67–73.

Acta Pharmacologica Sinica 2005 Mar; 26 (3): 345–352

Full-length article

Hypoglycemic effect of *Astragalus* polysaccharide and its effect on PTP1B[1]

Yong WU[2,3], Jing-ping OU-YANG[2,5], Ke WU[2], Ya WANG[2], Yun-feng ZHOU[2], Chong-yuan WEN[4]

[2]*Department of Pathophysiology, Medical College of Wuhan University,* [3]*Department of Physiology, Hubei College of Traditional Chinese Medicine,* [4]*Department of Endocrinopathic Sciences, Renmin Hospital, Wuhan University, Wuhan 430060, China*

Key words

Astragalus membranaceus; polysaccharides; PTP1B; type II diabetes mellitus; insulin resistance; streptozotocin

[1] Project supported by the National Natural Science Foundation of China, No 30370673 and the Educational Bureau of Hubei, No 30113065.
[5] Correspondence to Jing-ping OU-YANG.
Phn 86-27-8733-1146.
Fax 86-27-8733-1077.
E-mail jpoy@163.com

Received 2004-07-12
Accepted 2004-12-03

doi: 10.1111/j.1745-7254.2005.00062.x

Abstract

Aim: To examine the effects of *Astragalus* polysaccharide (APS), a component of an aqueous extract of *Astragalus membranaceus* roots, on protein tyrosine phosphatase 1B (PTP1B), a negative regulator of insulin-receptor (IR) signal transduction, and its potential role in the amelioration of insulin resistance. **Methods:** Ten-week-old fat-fed streptozotocin (STZ)-treated rats, an animal model of type II diabetes mellitus (TIIDM), were treated with APS (400 mg/kg *po*) for 5 weeks. Insulin sensitivity was identified by the insulin-tolerance test. Further analyses on the possible changes in insulin signaling occurring in skeletal muscle and liver were performed by immunoprecipitation or Western blotting. PTP1B activity was measured by an assay kit. **Results:** The diabetic rats responded to APS with a significant decrease in body weight, plasma glucose, and improved insulin sensitivity. The activity and expression of PTP1B were elevated in the skeletal muscle and liver of TIIDM rats. Thus the insulin signaling in target tissues was diminished. APS reduced both PTP1B protein level and activity in the muscle, but not in the liver of TIIDM rats. Insulin-induced tyrosine phosphorylation of the IR β-subunit and insulin receptor substrate-1 (IRS-1) were increased in the muscle, but not in the liver of APS-treated TIIDM rats. There was no change in the activity or expression of PTP1B in APS-treated normal rats, and blood insulin levels did not change in TIIDM rats after treatment with APS. **Conclusion:** APS enables insulin-sensitizing and hypoglycemic activity at least in part by decreasing the elevated expression and activity of PTP1B in the skeletal muscles of TIIDM rats.

Introduction

Diabetes mellitus (DM) is a chronic disease characterized by high blood glucose levels. It can be broadly categorized into type I and type II. The former develops as a result of insulin deficiency and the latter is due to defects in pancreatic secretion of insulin and insulin action[1], and insulin resistance in target tissues, mainly muscle and liver. The biological effect of insulin is initiated with insulin binding to the α-subunit of insulin receptor (IR) and activating the intrinsic tyrosine kinase activity of the β-subunit of the receptor[2]. Activated IR results in the subsequent phosphorylation of intracellular substrates including insulin receptor substrates (IRSs) such as IRS-1 and -2, phosphatidylinositol (PI) 3-kinase, and protein kinase B (PKB)[3,4]. Normal insulin action leads to increased glycogen synthesis, glucose transport, and lipogenesis, and decreased gluconeogenesis, glycogenolysis, and lipolysis[5–7]. The net effect on glucose metabolism is that hepatic glucose production is reduced, whereas use of peripheral glucose is increased[6,7].

An exquisite balance is required between kinases, which are involved in transmitting signals to the downstream targets necessary for the processes described above, and phosphatases, which are required to shut down this signaling to prevent excessive or, in some cases, insufficient activation[8]. Insulin resistance and diabetes represent states in which the regulation of the signaling pathways is altered so that the intracellular actions of insulin are absent or reduced[9]. Overactivation of phosphatases is one possible means of

blocking the insulin signaling. One key phosphatase, protein tyrosine phosphatase 1B (PTP1B), which dephosphorylates the activated insulin receptor and IRS-1, has been shown to play a major role in insulin resistance and type II diabetes[10]. Recently, it was shown that PTP1B-knock-out mice become more insulin sensitive and fail to gain weight despite being fed with a fat-rich diet[11]. Moreover, the role for certain PTPs, including PTP1B, in the insulin resistance associated with diabetes and obesity, has been suggested by some clinical studies in which correlations between the levels of PTP1B expression in muscle and adipose tissue and insulin resistant states were found[12,13]. Therefore, PTP1B might be an attractive therapeutic target in the treatment of type II diabetes and obesity.

Plants have always been usable sources of drugs, and many currently available drugs are directly or indirectly derived from plants. Currently available therapies for diabetes include insulin and various oral anti-diabetic agents, such as sulfonylureas, metformin, α-glucosidase inhibitors, and rosiglitazone. These drugs are used as monotherapies or in combination to achieve better glycemic control. Each of these oral agents suffers from implication in a number of serious adverse effects[14]. Therefore, it is important to investigate the hypoglycemic actions of plants that were originally used in traditional medicine[15,16]. The biologically active components of plants with hypoglycemic actions include flavonoids, alkaloids glycosides, polysaccharides, and peptidoglycans[17,18]. *Astragalus* polysaccharides (APS) are one of the main efficacious principles of Radix Astragali (*Astragalus membranaceus*), which is reported to have antioxidant, anti-diabetic, anti-hypertensive, and immunomodulatory activities [19].

To study natural products with anti-diabetes activity, we screened our extract bank for inhibitors of PTP1B enzyme and found that a fraction from an aqueous extract of the roots of *A membranaceus* showed strong inhibitory bioactivity against PTP1B with IC_{50} equaling 7.50 μmol/L (positive control sodium orthovanadate IC_{50}=10 μmol/L). This study was to investigate the effects of APS on the activity and expression of PTP1B in the livers and skeletal muscles of non-diabetic rats and rats with high-fat streptozotocin-induced diabetes. The effects of APS on insulin sensitivity and insulin-induced tyrosine phosphorylation of IR β-subunit and IRS-1 in non-diabetic and diabetic rats were also studied in an effort to establish the mechanisms of its hypoglycemic actions.

Materials and methods

Plant materials and preparation of APS *Astragalus membranaceus* (Fisch) Bunge var *mongholicus* (Bunge) Hsiao was purchased from Shanghai Medicinal Materials Co (Shanghai, China), and identified by the Department of Authentication of Chinese Medicine, Hubei College of Chinese Traditional Medicine (Wuhan, China). A representative specimen has been kept in our laboratory for future reference.

APS were extracted with optimized techniques using direct water decoction, as described previously[20]. The yield of APS was 2.0%, and the total polysaccharide content was 38.5%. Three subtypes of APS are defined by phytochemical screening: APSI, II, and III (1.47:1.21:1). APSI consists of *D*-glucose, *D*-galactose, and *L*-arabinose in molar ratios of 1.75:1.63:1 and has an average molecular weight of 36 300. Both APSII and APSIII are dextrans, the linkage mode of which is mainly α-(1→4) linkages, and in which α-(1→6) linkages are exiguous.

APS is a *hazel*-colored and water-soluble powder. It was diluted to 20 g/L in distilled water before use.

Materials and chemicals The reagents for sodium dodecyl sulfate–polyacrylamide gel electrophoresis (SDS–PAGE) and immunoblotting were obtained from BioVision (Palo Alto, CA, USA) and the apparatus from Bio-Rad (Richmond, CA, USA). Streptozotocin (STZ), Tris, Nonidet P-40, porcine insulin, and nitrocellulose (NC) membranes were obtained from Sigma Chemical Co (St Louis, MO, USA). Protein A–Sepharose 6 MB was from Pharmacia (Uppsala, Sweden). The monoclonal anti-phosphotyrosine antibody (αPY, PY99) was purchased from Santa Cruz Biotechnology, Inc (Santa Cruz, CA, USA). Rabbit polyclonal anti-insulin receptor β-subunit (IRβ) antibody was purchased from Upstate Biotechnology Inc (Lake Placid, NY, USA). The anti-rat carboxy-terminal IRS-1 antibody (clone 8–63) was from NeoMarkers (Fremont, CA, USA). α-PTP1B polyclonal antibody was purchased from Upstate Biotechnology Inc. Enhanced chemiluminescence (ECL) detection reagents were from Kirkegaard & Perry Laboratories (Gaithersburg, MA, USA). All other chemicals were of the highest analytical grade.

Type II diabetic (TIIDM) rat model and treatment protocol Male Sprague-Dawley rats [from the experimental animal center of Wuhan University, certificate No SCXK (Hubei) 2003-0003], 8 weeks of age and weighing approximately 200 g, were used for all studies. All procedures were in accordance with the Institute Ethical Committee for the Experimental Use of Animals of Wuhan University. Rats were housed five per cage in a room with a 12:12 hour light: dark cycle and an ambient temperature of 22–25 °C. Animals were fed either a normal chow diet consisting (as a percentage of total kcal) of 12% fat, 60% carbohydrate, and

28% protein, or a high-fat diet (HFD) consisting of 41% fat, 41% carbohydrate, and 18% protein. After 2 weeks on either diet, animals (with the exception of noninjected controls) were anesthetized with ketamine (65 mg/kg) and xylazine (7 mg/kg) after an overnight fast and injected with STZ (30 mg/kg in 0.1 mol/L citrate-buffered saline, pH 4.5) into the tail vein via a temporary indwelling 24-gauge catheter. Animals had free access to food and water after the STZ injection, and both STZ-injected and noninjected animals continued on their original diets (chow or fat) for the duration of the study. After a 12-h fast, animals showing fasting glucose levels >6.7 mmol/L at 72 h after STZ injection were considered diabetic. The control rats were fasted in an identical manner and had a volume of citrate-buffered saline, equal to that of the STZ solution, injected by the same route.

The control and diabetic groups were then further subdivided into treated and untreated groups: control (n=10); control treated with APS (Control+APS, n=10); TIIDM (n=12); and TIIDM treated with oral APS (400 mg/kg) (TIIDM +APS, n=12). Treatment was given daily for 5 weeks. The control group received an equal volume of vehicle (saline). At the end of each week, individual body weights were recorded, and glucose and insulin levels were determined under fasting and nonfasting conditions. Glycemia was assessed on blood collected from the tail vein using an OneTouch Ultra blood glucose meter (LifeScan, Milpitas, CA, USA). Insulin levels were determined by radio-immunoassay (RIA) with a kit from Beifang Biotech Research Center (Beijing, China). Before necropsy, saline- and APS-treated animals were intraperitoneally administered insulin (5 U/kg) in saline with 0.1% bovine serum albumin (BSA) or vehicle (saline with 0.1% BSA) after a 10-h fast. Tissue samples from livers and soleus muscles were taken (10 min after treatment) from both vehicle- and insulin-treated animals and snap frozen in liquid nitrogen.

Insulin sensitivity Peripheral insulin resistance was assessed with an insulin-tolerance test (ITT) [21] that measured insulin sensitivity using K_{ITT} as an index of insulin-mediated glucose metabolism. Rats were fasted for 15 h before insulin challenge. Neutral insulin injections were diluted with 0.9% saline to a final concentration of 2 kU/L, and then administered at a dose of 2 U/kg body weight by slow intravenous injection through the tail vein. Blood samples were collected at 0, 10, 20, 30, and 60 min after the administration of insulin. Serum was separated and subjected to glucose estimation. Serum glucose concentrations were determined using a commercial assay kit (Sigma Diagnostics, St Louis, MO, USA) and 10 μL of serum was used for each assay. K_{ITT} was determined from the slope of a linear portion of the regression line of the natural logarithm of glucose versus time[21], and calculated using the formula[22]: K_{ITT}= $(0.693/t_{1/2})\times100$, where $t_{1/2}$ represents the half-life of plasma glucose decay, which was estimated by plotting plasma glucose concentration versus time on semilogarithmic graph paper. Lower insulin-sensitivity index (K_{ITT}) scores mean higher degrees of insulin resistance.

Lysate preparation and protein assays Frozen liver tissue (50 mg) was sonicated in 1 mL of lysis buffer (buffer A) containing Tris-HCl 20 mmol/L (pH 7.4), 1% Triton X-100, 10% glycerol, NaCl 150 mmol/L, edetic acid 2 mmol/L, β-glycerophosphate 25 mmol/L, sodium fluoride 20 mmol/L, sodium orthovanadate 1 mmol/L, sodium pyrophosphate 2 mmol/L, leupeptin 10 mg/L, benzamidine 1 mmol/L, 4-(2-aminoethyl) benzenesulfonyl fluoride hydrochloride 1 mmol/L, and microcystin 1 mmol/L, and rocked for 40 min at 4 °C. Detergent-insoluble material was sedimented by centrifugation at 12 000×g at 4 °C for 10 min. Muscle samples (50 mg) were homogenized and centrifuged at 1000 000×g for 1 h in ice-cold Hepes buffer 50 mmol/L (pH 7.4) containing NaCl 150 mmol/L, sodium pyrophosphate 10 mmol/L, Na_3VO_4 2 mmol/L, NaF 10 mmol/L, edetic acid 2 mmol/L, phenylmethylsulfonyl fluoride (PMSF) 2 mmol/L, leupeptin 5 mg/L, 1% Nonidet P-40, and 10% glycerol (buffer B).

Supernatants were collected, and protein concentrations were measured with Bradford protein assay reagent (Bio-Rad), using BSA as the standard.

Western blotting Aliquots (50 μg) of muscle or liver homogenates were subjected to SDS-PAGE (7.5% gel) and transferred electrophoretically onto nitrocellulose (NC) membranes for 5 h. NC membranes were then blocked for 2 h at room temperature with block solution provided in the ECL kits. This step was followed by overnight incubation at 4 °C with anti-α-PTP1B polyclonal antibody or anti-phosphotyrosine (PY99) as the primary antibodies, as described in the figure legends. The NC membranes were then washed for 30 min with wash solution (ECL kits), followed by a 1-h incubation with either anti-mouse or anti-rabbit IgG conjugated with horseradish-peroxidase in block solution. The NC membranes were washed for 30 min in wash solution, and the immunoreactive bands were detected with an enhanced chemiluminescence method.

Tyrosine phosphorylation of IR-subunit and IRS-1 Muscle or liver lysates (1 mg of protein) were immunoprecipitated overnight at 4 °C with 2 μg of anti-IRβ or anti-IRS-1 coupled to protein A–Sepharose. The immune complex was washed three times in phosphate-buffered saline (PBS) (pH 7.4) containing 1% Nonidet P-40 and Na_3VO_4

2 mmol/L, resuspended in Laemmli buffer, and boiled for 5 min. Proteins were resolved on SDS-PAGE (7.5% gel), then electrotransferred from the gel to nitrocellulose membranes. The nitrocellulose filters were incubated at 4 ºC overnight with 1 mg/L PY99. Subsequent steps were performed as described above.

PTP1B protein levels and activity The tissue homogenate was assayed in a microtiter plate at 27 °C. The PTP1B assay kit was obtained from Upstate Biotechnology Inc. The protocol outlined by the manufacturer was followed rigidly. PTP1B protein levels were assessed by immunoblotting using polyclonal antibodies directed against PTP1B, as described above.

Statistical analysis All values are expressed as mean± SEM. Statistical significance was determined using analysis of variance (ANOVA) followed by Tukey's test. $P<0.05$ was considered statistically significant.

Results

Characteristics of experimental animals The glucose levels of both fasting and fed rats were significantly higher ($P<0.05$) in HFD/STZ rats (TIIDM) than in normal control rats (Control) (Table 1). The levels of glucose in fasting and fed TIIDM rats were significantly reduced ($P<0.05$) after treatment with APS at a dose of 400 mg/kg *po* per day for 5 weeks (TIIDM+APS). It should be noted that insulin concentrations in type II diabetic rats were similar to values of control rats. Treatment with APS did not affect insulin levels in control or type II diabetic rats. HFD/STZ diabetic rats weighed 20 g more than the normal chow-fed controls ($P<0.05$). APS treatment could significantly reduce body weights in diabetic rats and had no effects on those of control rats. All data are mean±SEM calculated from 10 rats.

Table 1. Characteristics of the experimental animals. n=10. Mean±SEM. $^bP<0.05$ *vs* control group. $^eP<0.05$ *vs* TIIDM group.

	Control	Control+APS	TIIDM	TIIDM+APS
Plasma glucose (fasting)(mmol/L)	4.3±0.2	4.1±0.2	10.3±0.8^b	6.8±0.5^e
Plasma glucose (fed) (mmol/L)	6.6±0.5	6.2±0.3	15.6±1.2^b	9.8±0.7^e
Insulin (pmol/L)	162±13	168±15	178±20	171±18
Body weight (g)	200±2	202±2	220±5^b	205±3^e

Insulin sensitivity Insulin sensitivity in the TIIDM rats was significantly lower than that in the control group. The impaired insulin sensitivity in the TIIDM rats was improved following APS treatment (Figure 1).

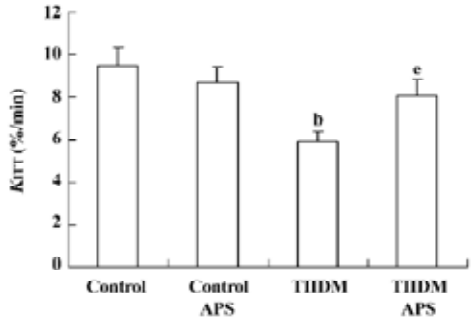

Figure 1. Effect of APS on insulin sensitivity in TIIDM rats. n=5–8. Mean±SEM. $^bP<0.05$ *vs* control. $^eP<0.05$ *vs* TIIDM group.

Effects of APS on PTP1B expression in muscles and livers of control and TIIDM rats PTP1B protein levels in the skeletal muscles of TIIDM rats were significantly increased (1.6-fold, $P<0.05$) compared with those of controls. In TIIDM rats, the level of PTP1B after treatment with APS was reduced by 30% ($P<0.05$), compared with that of the TIIDM rats (Figure 2A and C). PTP1B protein levels in the livers of TIIDM rats were also significantly increased (1.7-fold, $P<0.05$) compared with those of control rats. However, treatment with APS did not affect PTP1B protein levels in the livers of TIIDM rats (Figure 2B and D). PTP1B levels in the muscles and livers of normal control rats were not affected by APS treatment.

Effects of APS on PTP1B activity in muscles and livers of control and TIIDM rats There was a two-fold ($P<0.01$) increase in the activity of PTP1B in the skeletal muscles of TIIDM rats. APS reduced the activity of PTP1B by 25% ($P<0.05$) in APS-treated TIIDM rats (Figure 3A). PTP1B activity in the livers of TIIDM rats was significantly elevated (1.8-fold, $P<0.01$) compared with that of the controls. Treatment with APS did not change PTP1B activity in the livers of TIIDM rats (Figure 3B). Nor did APS affect the activity of PTP1B in the skeletal muscles or livers of APS-treated control rats.

Effects of APS on insulin-induced tyrosine phosphorylation of IR β-subunit In each group of animals, the administration of insulin resulted in an increase in the tyrosine phosphorylation of the IR β-subunit (Figure 4). However, the levels of IRβ tyrosine phosphorylation in the skeletal muscles and livers of TIIDM rats after stimulation with insulin were reduced by 47% ($P<0.05$) and 41% ($P<0.05$), respectively, compared with those of the control rats (Figure 4). Treatment with APS significantly increased the level of IRβ tyrosine phosphorylation stimulated by insulin in the skeletal muscles of TIIDM rats, but did not affect that in the livers of TIIDM rats. APS also did not affect the IRβ ty-

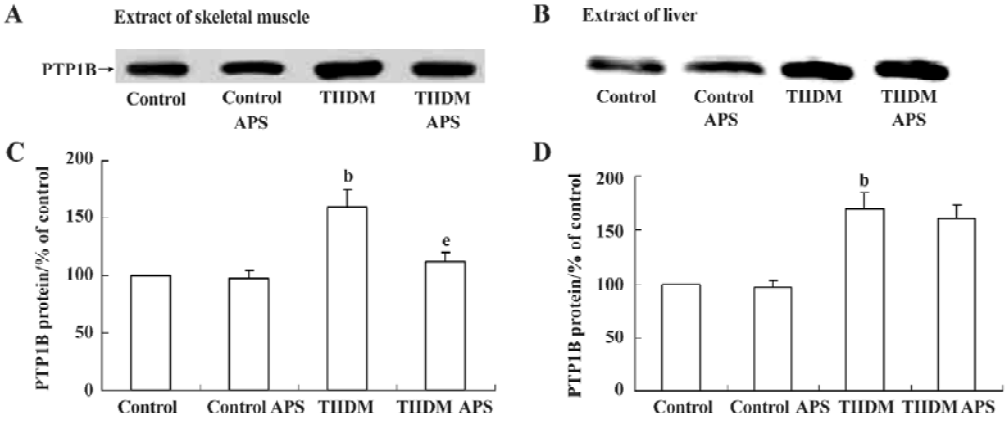

Figure 2. Effect of APS on PTP1B protein expression in skeletal muscle (A) and liver (B) from control and TIIDM rats. Corresponding band intensities were quantitated by scanning densitometry (C and D). n=3. Mean±SEM expressed as relative to normal values, which were set as 100%. ^{b}P<0.05 *vs* APS-untreated control rats. ^{e}P<0.05 *vs* APS-untreated TIIDM rats.

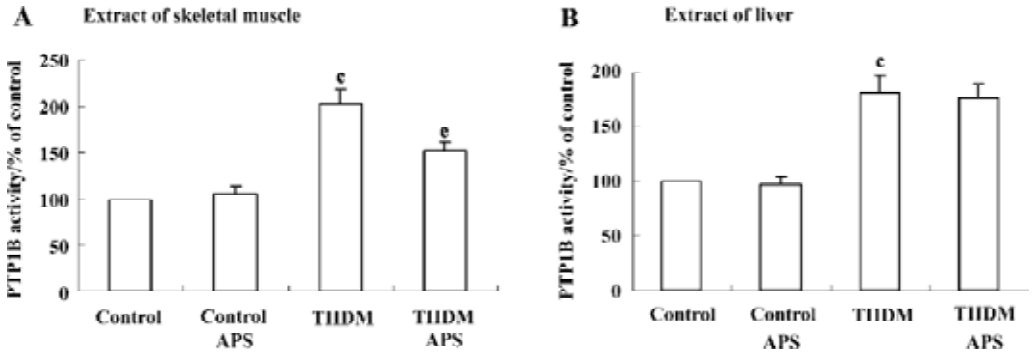

Figure 3. Effect of APS on PTP1B activity in muscle (A) and liver (B) from control and TIIDM rats. n=3–5. Mean±SEM expressed as relative to normal values (100%). ^{c}P<0.01 *vs* APS-untreated control rats. ^{e}P<0.05 *vs* APS-untreated TIIDM rats.

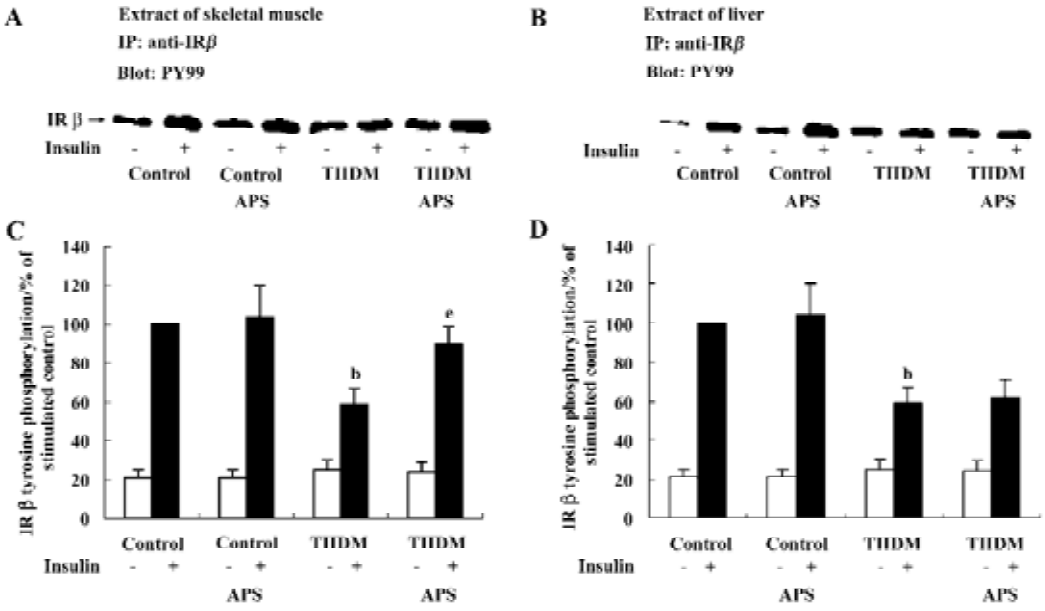

Figure 4. Effect of APS on insulin-induced tyrosine phosphorylation of IR β-subunit in muscle (A) and liver (B). Corresponding data quantification by scanning densitometry (C and D). n=3. Mean±SEM. IR β tyrosine phosphorylation is expressed as percentage, assigning a value of 100% to the mean of insulin-stimulated control rats. ^{b}P<0.05 *vs* APS-untreated control rats. ^{e}P<0.05 *vs* APS-untreated TIIDM rats.

rosine phosphorylation stimulated by insulin in the skeletal muscles or livers of APS-treated control rats, as evaluated by scanning densitometry.

Effects of APS on insulin-induced tyrosine phosphorylation of IRS-1 Insulin administration resulted in an increase in IRS-1 tyrosine phosphorylation in each group of animals (Figure 5). TIIDM rats exhibited a reduced response to insulin, and the levels of tyrosine phosphorylation of IRS-1 after insulin stimulation in skeletal muscles and livers were reduced by 37% and 35% ($P<0.05$), respectively, compared with the values measured in control rats (Figure 5). APS treatment did not increase the level of tyrosine phosphorylation of IRS-1 induced by insulin in the liver tissues of TIIDM rats, but significantly improved that in skeletal muscles ($P<0.05$) in TIIDM rats. APS had no effect on the tyrosine phosphorylation of IRS-1 stimulated by insulin in the skeletal muscles or livers of APS-treated control rats.

Discussion

In the present study, we developed an animal model for type II diabetes, the HFD/STZ rat. These rats constitute a relatively inexpensive and easily accessible rodent model that is not extremely obese and simulates the natural history and metabolic characteristics of patients with type II diabetes[23]. Recent reports[24] have indicated that insulin resistance may be caused by an excess nutrient supply. Both excess glucose and excess fat can cause insulin resistance in muscle and fat tissues, whereas excess fat can cause impaired suppression of endogenous glucose production. The present animal model was based on the rationale described above. At first, we used high-fat diets to induce insulin resistance in Sprague-Dawley rats. Plasma glucose concentrations were similar in chow-fed and HFD rats after two weeks of the high-fat diet, whereas insulin concentrations in the HFD rats were significantly higher than those in the chow-fed controls (HFD: 338±25 *vs* Control: 162±13 pmol/L, $P<0.05$). The association of normoglycemia and hyperinsulinemia suggested that the HFD rats were insulin-resistant. Conversion of pre-diabetes to frank hyperglycemia in patients with type II diabetes is associated with a decline in the secretory capacity of the pancreatic β-cells[25,26]. However, this failure in β-cell compensation is relative, not absolute[23]. We attempted to simulate this evolution from a state of insulin resistance and absolute hyperinsulinemia to a state of "relative" hypoinsulinemia by injecting insulin-resistant HFD rats with a moderate amount of STZ, which partly damaged β-cell and reduced the serum insulin concentration to a relatively lower level (178±20 pmol/L), which is approximately that of normal chow-fed rats. Comparison of the data in Table 1 indicates that we were successful in this attempt.

The signaling pathways affected by the inhibition of

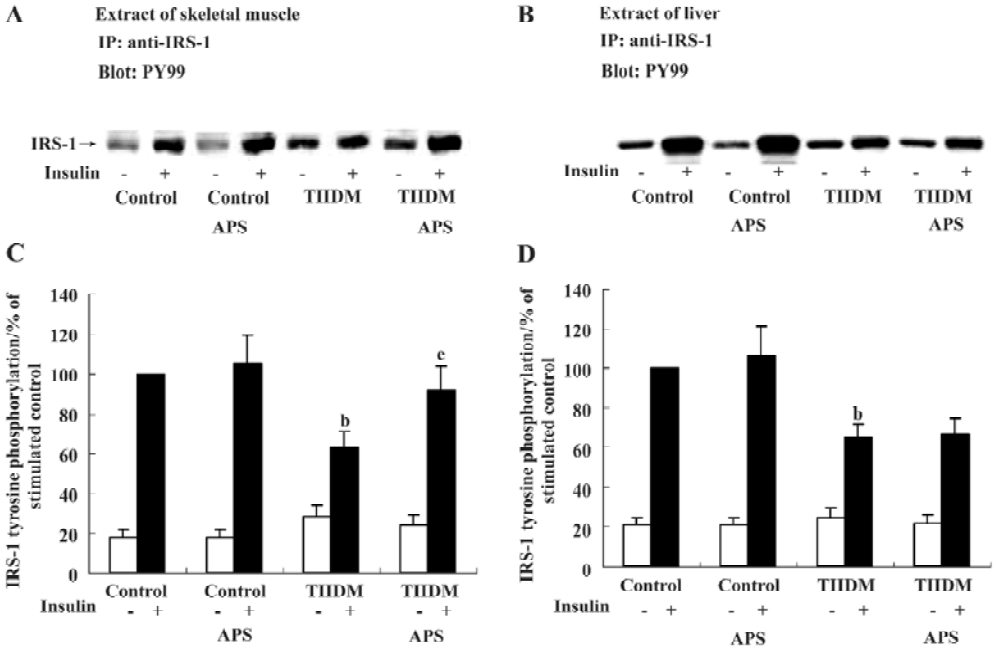

Figure 5. Effect of APS on insulin-induced tyrosine phophorylation of IRS-1 in muscle (A) and liver (B). Corresponding data quantification by scanning densitometry (C and D). $n=3$. Mean±SEM. IRS-1 tyrosine phosphorylation is expressed as relative to the mean of insulin-stimulated control rats, which was set as 100%. $^bP<0.05$ *vs* APS-untreated control rats. $^eP<0.05$ *vs* APS-untreated TIIDM rats.

PTP1B, particularly in a diabetic model, have been characterized. In this study, we observed increased PTP1B activity in skeletal muscle and liver tissues of HFD/STZ rats when *para*-nitrophenyl phosphate (*p*NPP) was used as substrate. These changes were similar to those in PTP1B protein levels in the tissues. Corresponding to these results, insulin-induced tyrosine phosphorylation of the IR β-subunit and IRS-1 were significantly decreased in muscle and liver tissues. This is the first study to demonstrate the *in vivo* effects of changes in PTP1B activity and expression on insulin signaling molecules in the skeletal muscles and livers of HFD/STZ rats.

Using reduced carboxymethylated-maleylated (RCM)-lysozyme as a substrate, Seiichi Tagami[27] and McGuire *et al*[28] found increases in PTP1B activity in the skeletal muscles of insulin-resistant Otsuka Long-Evans Tokushima fatty (OLETF) rats and insulin-resistant human subjects, relative to the activity in the corresponding control groups. Muscle PTP1B activity, measured with myelin basic protein and the insulin-receptor cytoplasmic domain as substrates, was also increased in an animal model of insulin-resistant obesity and DM[10]. Those findings accord with our results. It is reasonable to postulate that increased PTP1B activity in the muscle and liver contributes to insulin resistance and type II diabetes in HFD/STZ rats because PTP1B inhibits tyrosine phosphorylation of the insulin receptor and its substrates, including IRS-1.

Our own earlier ethnopharmacological studies of an aqueous extract of *Astragalus* confirm the data reported for the plant *A membranaceus*, which is traditionally used as an infusion of (mainly) roots by the Chinese population to treat type II diabetes. Most important of all, *A membranaeus* is an important component of the majority of traditional herbal blend prescriptions used to cure type II diabetes in traditional Chinese medicine. The unique nature of the *A membranaceus* extract inspired us to work towards the isolation of the active ingredient from the crude extract. When subjected to sequential extraction, maximum activity was found in APS. In the present study, we found that APS significantly reduced both PTP1B protein levels and activity in the skeletal muscles, but not in the livers of HFD/STZ rats. Consistent with this change, the insulin-induced tyrosine phosphorylation of the IR β-subunit and IRS-1 increased in the skeletal muscles, but not in the livers of APS-treated TIIDM rats. Furthermore, blood glucose levels were controlled and insulin sensitivity was apparently improved in APS-treated TIIDM rats when K_{ITT} was used as an index of glucose metabolism. This is a simple, reasonably accurate, and rapid method for screening insulin resistance[29], and indicates the net resistance to insulin at the target level, including receptor and post-receptor defects. The data collected in this study indicate that blood insulin levels are not altered by treatment with APS in TIIDM rats, suggesting that the hypoglycemic effects of APS are not mediated through insulin secretion. In addition, HFD/STZ rats had a higher body weight than that of normal rats. The effect of STZ injection plus high fat diet on body weight gain is in accordance with the earlier findings[23,30]. APS could decrease body weight in diabetic rats. It has been suggested that PTP1B can act as a negative regulator of leptin signaling by dephosphorylating the leptin receptor associated kinase Jak2[31,32]. So one can postulate that the obesity resistance effect of APS be associated with enhanced leptin sensitivity induced by its inhibitory action on PTP1B.

PTP1B is a well-established drug target in the treatment of TIIDM and obesity[33]. However, the PTP family of enzymes is large, and all are highly specific for charged phosphotyrosine residues. Finding a selective small-molecule inhibitor of PTP1B is therefore proving difficult. Numerous PTP1B-inhibiting candidates are undergoing trials, but significant success has yet to be achieved[34]. Our study showed that protein levels of PTP1B changed in parallel with changes in its activities in skeletal muscle and liver. The alterations in PTP1B activities may be partly due to changes in its protein levels. Therefore, we postulate that the inhibitory effect of APS on PTP1B activity is most likely mediated by the inhibition of PTP1B protein expression. Detailed studies are in progress in our laboratory to clarify the mechanism underlying the inhibitory action of APS on PTP1B. In the present study, our data suggest that APS induces normalization of PTP1B activity in the muscles, leading to an improvement in insulin sensitivity. However, changes in PTP1B activity alone may not account for the complete insulin-sensitizing effect of APS. Other possible mechanisms cannot be excluded.

In conclusion, we have presented evidence to substantiate the anti-diabetic and insulin-sensitizing effects of the *A membranaceus* extract, APS. The insulin-enhancing effects of APS are at least partially exerted through its effects on PTP1B in skeletal muscle. The results of this study support this hypothesis, at least in this animal model.

Acknowledgments

We thank R William CALDWELL, PhD, Ron DUNDORE, PhD, and Herman RHEE, PhD for valuable discussion and critical review of the manuscript. We also acknowledge the Young Investigator Award received by Yong

WU presented by the Division for Drug Discovery, Drug Development and Regulatory Affairs of the American Society for Pharmacology and Experimental Therapeutics.

References

1 Kahn BB. Type 2 diabetes: when insulin secretion fails to compensate for insulin resistance. Cell 1998; 92: 593–6.
2 Leng Y, Karlsson HK, Zierath JR. Insulin signaling defects in type 2 diabetes. Rev Endocr Metab Disord 2004; 5: 111–7.
3 White MF, Kahn CR. The insulin signaling system. J Biol Chem 1994; 269: 1–4.
4 Saltiel AR. Diverse signaling pathways in the cellular actions of insulin. Am J Physiol Endocrinol Metab 1996; 270: E375–85.
5 Kahn BB, Flier JS. Obesity and insulin resistance. J Clin Invest 2000; 106: 473–81.
6 Newsholme EA, Dimitriadis G. Integration of biochemical and physiologic effects of insulin on glucose metabolism. Exp Clin Endocrinol Diabetes 2001; 109(Suppl 2): S122–34.
7 Saltiel AR. New perspectives into the molecular pathogenesis and treatment of type 2 diabetes. Cell 2001; 104: 517–29.
8 Rebecca JG, Lori LG, Sandra LK, Matthew H, Jill EC, Bradley AZ, *et al.* Reduction of protein tyrosine phosphatase 1B increases insulin-dependent signaling in *ob/ob* mice. Diabetes 2003; 52: 21–8.
9 Steppan CM, Lazar MA. Resistin and obesity-associated insulin resistance. Trends Endocrinol Metab 2002; 13: 18–23.
10 Ahmad F, Goldstein BJ. Increased abundance of specific skeletal muscle protein-tyrosine phosphatases in a genetic model of insulin-resistant obesity and diabetes mellitus. Metabolism 1995; 44: 1175–84.
11 Elchebly M, Payette P, Michaliszyn E, Cromlish W, Collins S, Loy AL, *et al.* Increased insulin sensitivity and obesity resistance in mice lacking the protein tyrosine phosphatase-1B gene. Science 1999; 283: 1544–8.
12 Ahmad F, Azevedo JL, Cortright R, Dohm GL, Goldstein BJ. Alterations in skeletal muscle protein-tyrosine phosphatase activity and expression in insulin-resistant human obesity and diabetes. J Clin Invest 1997; 100: 449–58.
13 Kusari J, Kenner KA, Sub KI, Hill DE, Henry RR. Skeletal muscle protein-tyrosine phosphatase activity and tyrosine phosphatase 1B protein content are associated with insulin action and resistance. J Clin Invest 1994; 93: 1156–62.
14 Zhang BB, Moller DE. New approaches in the treatment of type 2 diabetes. Curr Opin Chem Biol 2000; 4: 461–7.
15 Alarcon-Aguilara FJ, Rornan-Ramos R, Perez-Gutierrez S. Study of the anti-hyperglycemic effect of plants used as antidiabetics. J Ethnopharmacol 1998; 61 (Pt 2): 101–10.
16 Wu YC, Hsu JH, Liu IM, Liou SS, Su HC, Cheng JT. Increase of insulin sensitivity in diabetic rats received die-huang-wan, a herbal mixture used in Chinese traditional medicine. Acta Pharmacol Sin 2002; 23: 1181–7.
17 Grover JK, Yadav S, Vats V. Medicinal plants of India with anti-diabetic potential. J Ethnopharmacol 2002; 81: 81–100.
18 Mao CP, Xie ML, Gu ZL. Effects of konjac extract on insulin sensitivity in high fat diet rats. Acta Pharmacol Sin 2002; 23: 855–9.
19 Wu F, Chen X. A review of pharmacological study on *Astragalus membranaceus* (Fisch) Bge. Zhong Yao Cai 2004; 27: 232–4.
20 Ni Y, Su Q, Liu X, Li XR. Experimental study of optimized techniques of water decoction extraction of *Astragalus* polysaccharide. Zhongguo Zhong Yao Za Zhi 1998; 23: 284–6.
21 Alford FP, Martin FIR, Pearson MJ. Significance and interpretation of mildly abnormal oral glucose tolerance test. Diabetalogia 1971; 7: 173–80.
22 Lundbaek K. Intravenous glucose tolerance as a tool in definition and diagnoses of diabetes mellitus. Br Med J 1962; 5291: 1507–13.
23 Reed MJ, Meszaros K, Entes LJ, Claypool MD, Pinkett JG, Gadbois TM, *et al*. A new rat model of type 2 diabetes: the fat-fed, streptozotocin-treated rat. Metabolism 2000; 49: 1390–6.
24 Proietto J, Filippis A, Nakhla C, Clark S. Nutrient-induced insulin resistance. Mol Cell Endocrinol 1999; 151: 143–9.
25 Lillioja S, Mott DM, Spraul M, Ferraro R, Foley JE, Ravussin E, *et al*. Insulin resistance and insulin secretory dysfunction as precursors of non-insulin-dependent diabetes mellitus. N Engl J Med 1993; 329: 1988–92.
26 Warram JH, Martin BC, Krowleski AS, Soelener JS, Kahn CR. Slow glucose removal rate and hyperinsulinemia precede the development of type II diabetes in the offspring of diabetic patients. Ann Intern Med 1990; 113: 909–15.
27 Tagami S, Sakaue S, Honda T, Yoshimura H, Homma H, Ohno K, *et al*. Effects of troglitazone on skeletal muscle and liver protein tyrosine phosphatase activity in insulin-resistant Otsuka Long-Evans Tokushima fatty rats. Curr Ther Res Clin 2002; 63: 572–86.
28 McGuire MC, Fields RM, Nyomba BL, Raz I, Bogardus C, Tonks NK, *et al*. Abnormal regulation of protein tyrosine phosphatase activities in skeletal muscle of insulin-resistant humans. Diabetes 1991; 40: 939–42.
29 Grulet H, Duriach V, Hecart AC, Gross A, Leutenegger M. Study of the rate of early glucose disappearance following insulin injection, insulin sensitivity index. Diabetes Res Clin Pract 1993; 20: 201–7.
30 Leng SH, Lu FE, Xu LJ. Therapeutic effects of berberine in impaired glucose tolerance rats and its influence on insulin secretion. Acta Pharmacol Sin 2004; 25: 496–502.
31 Myers MP, Andersen JN, Cheng A, Tremblay ML, Horvath CM, Parisien JP, *et al*. TYK2 and JAK2 are substrates of protein-tyrosine phosphatase 1B. J Biol Chem 2001; 276: 47771–4.
32 Zabolotny JM, Bence-Hanulec KK, Stricker-Krongrad A, Haj F, Wang Y, Minokoshi Y, *et al*. PTP1B regulates leptin signal transduction *in vivo*. Dev Cell 2002; 2: 489–95.
33 van Huijsduijnen RH, Bombrun A, Swinnen D. Selecting protein tyrosine phosphatases as drug targets. Drug Discov Today 2002; 7: 1013–9.
34 Brown M. A tale of two necessities: breakaway technology versus diabetes. Drug Discov Today 2003; 8: 561–2.

Acta Pharmacologica Sinica 2005 Mar; 26 (3): 353–358

Blackwell Publishing

Full-length article

Changes of 5-lipoxygenase pathway and proinflammatory mediators in cerebral cortex and lung tissue of sensitized rats[1]

Yang-mei DENG, Qiang-min XIE[2], Shui-juan ZHANG, Ji-qiang CHEN, Qiu-huo YANG, Ru-lian BIAN

Zhejiang Respiratory Drugs Research Laboratory of State Drugs Administration of China, Medical School of Zhejiang University, Hangzhou 310031, China

Key words

5-lipoxygenase; leukotriene A_4-hydrolase; cytokine; brain; lung; asthma

[1] Project supported by National Natural Science Foundation of China (No 30371314).
[2] Correspondence to Prof Qiang-min XIE.
Phn 86-571-8721-7380.
Fax 86-571-8721-7380.
E-mail Xieqm@zju.edu.cn

Received 2004-03-30
Accepted 2004-10-11

doi: 10.1111/j.1745-7254.2005.00043.x

Abstract

Aim: To explore the change of 5-lipoxygenase (5-LO) pathway expression and proinflammatory mediators level of lung tissue and cerebral cortex, and the possible regulatory mechanism through central nervous 5-LO pathways to pulmonary inflammatory status in antigen repeated challenged rats. **Methods:** Four groups of rats were treated as control, asthma model, asthma model treatment with dexamethasone (DXM, 0.5 mg/kg, ip) and ketotifen (5 mg/kg, ig). Tumor necrosis factor (TNF)-α, interleukin (IL)-4, interferon (IFN)-γ, and nitric oxide (NO) were detected by ELISA kits. The mRNA expression of 5-LO and LTA_4-hydrolase (LTA_4-H) was analyzed by reverse transcription-polymerase chain reaction (RT-PCR), and the protein content of 5-LO was measured by Western blot. **Results:** Increase of TNF-α, IL-4, NO level, and decrease of IFN-γ level in bronchoalveolar lavage fluid (BALF) and cerebral cortex in sensitized rats were shown after repeated antigen challenge. The expression of 5-LO and LTA_4-H mRNA, and 5-LO protein levels were increased in lung tissue and cerebral cortex in asthma rats. In comparison with the asthma model, DXM significantly inhibited the increase of cytokine levels and the expression of 5-LO pathway enzyme ($P<0.05$). Ketotifen also inhibited the increase of TNF-α level and 5-LO pathway enzyme expression in lung and cerebral cortex, but had no effect on the level of NO, IL-4, and IFN-γ. **Conclusion:** The correlative increase of 5-LO pathway enzyme expression and proinflammatory mediators of brain may have a regulatory effect on pulmonary inflammation in asthma.

Introduction

The interaction between central nervous-immune pathways or neuroendocrine-immune (NEI) networks in various disease states is affected by various pathophysiologic status. In the pathogenesis of allergic diseases, the abnormalities in immune function are mediated by the NEI network through overproduction of allergic mediators[1]. Undoubtedly, leukotrienes (LTs), the metabolites of 5-lipoxygenase (5-LO) pathways are thought to play crucial roles in the inflammatory network. Up to now, it is unclear how the metabolites of 5-LO pathways in the central nervous system regulate inflammation in lung tissue of asthma rats. From previous work, we found that the change of Th1/Th2 paradigm (ratio of interferon (IFN)-γ/interleukin (IL)-4 decreased and the content of LTB_4 in the cerebral cortex increased correspondent to that in bronchoalveolar lavage fluid (BALF) or lung tissue in inflammatory status of asthma rats[2,3]. These findings indicate that there is an interactive response of LTs and proinflammatory cytokines in the central nervous system, and the changes of these proinflammatory mediators in the central nervous system may have pathophysiologic effects in asthma rats. To explore these hypotheses and get a clearer understanding of the central nervous system changes of 5-LO pathway, Tumor necrosis factor (TNF)-α, IL-4, IFN-γ, and nitric oxide (NO) in asthma rats, we have further investigated the correlative alterations of proinflammatory mediators and the expression of 5-LO pathway enzyme in lung

tissue and cerebral cortex.

Materials and methods

Animal and reagent Sprague–Dawley rats of either sex weighing 180 g±20 g were purchased from the Laboratory Animal Center of Medical School of Zhejiang University (Grade II, Certificate No 220010014), and maintained on a regular 12-h daylight cycle with water and food available *ad libitum*. Dexamethasone sodium phosphate (DXM, Suzhou Sixth Pharmaceutical Factory, Suzhou), ketotifen (Shanghai Pharmaceutical Factory, Shanghai), egg albumin Grade V (Sigma, St louis, USA), heparin sodium (Xuzhou Biochemical Pharmaceutical Factory, Xuzhou), IFN-γ, TNF-α, NO, and IL-4 ELISA kit (Jinmei Biotech Co Ltd, Shenzhen, China) were commercially available. TRIzol reagent, SuperScript II reverse transcriptase, and *Taq* DNA polymerase were obtained from GIBCO BRL (Paisley, Scotland, UK).

Sensitization, treatment, and challenge regimens The sensitization procedure to induce IgE-mediated asthma response is as earlier described[3]. At d 14 after sensitization, the rats were placed in a 45 cm×45 cm×15 cm plastic box and challenged by exposure to an aerosol of ovalbumin (10 g/L in saline) which was generated in a jet nebulizer (partical size 1-5 μm; BARI, MASTER, Germany) for 20 min, and repeated daily for 6 d. Control rats were similarly exposed to an aerosol of saline. One hour before antigen challenge, the rats in the treatment groups were administered with DXM (0.5 mg/kg, ip) and ketotifen (5 mg/kg, ig), respectively. The rats in the control and model groups were administered with saline (ip). All the animals were studied on d 21 after the first sensitization.

BALF Bronchoalveolar lavage (BAL) was performed by flushing the airways with saline 5 mL containing 1% bovine serum albumin and 1 kU/L heparin sodium through the tracheal cannula three times. BAL fluid (BALF) were pooled and centrifuged (Eppendorf Centrifuge 5804R, Germany) at 500×*g* for 10 min at 4 ºC. The supernatant was collected and stored at -70 ºC for assaying IFN-γ, TNF-α, NO, and IL-4 level.

Brain homogenates preparation Blood cells in systemic circulation were removed by perfused with D-Hanks' liquid through ascending aorta cannula. The left cerebral cortex was then cut into 1 mm^3, homogenated (DY89-I Homogenater, Linbo Xinzhi SCI-TETH research Institute, Ningbo) in ice-cold Hanks' buffer (pH 7.5). Thereafter, the homogenates were centrifuged at 3000×*g* at 4 ºC for 10 min. The supernatant was collected and stored at -70 ºC for assaying IFN-γ, TNF-α, NO, and IL-4 level.

Assay of IFN-γ, TNF-α, NO, and IL-4 The IFN-γ, TNF-α, NO, and IL-4 levels in the BALF and cerebral cortex homogenates were measured according to the ELISA kit description. All measurements were carried out in duplicate.

Reverse transcription-polymerase chain reaction (RT-PCR) assay Total RNA was isolated from the cerebral cortex and lung tissue. Trizol 1 mL was added per 100 mg tissue and was homogenized; samples were left at 18–21 ºC for 3 min. Chloroform 0.2 mL was added to the homogenizer and mixed. After 10 min at 18–21 ºC, the samples were centrifuged at 15 000×*g* in a microcentrifuge at 4 ºC for 15 min. The upper phase was transferred to new tubes and the same volume isopropanol was added. RNA was allowed to precipitate at 18–21 ºC for 10 min and collected by centrifugation at 15 000×*g* at 4 ºC for 10 min. After washing precipitates in 75% ethanol and drying for 10 min, the RNA was dissolved in DEPC-treated water and quantified by the measurement of ultraviolet absorption at 260 nm (Eppendorf Biophotometer, Germany). All samples were kept at -70 ºC until use.

For the synthesis of the single-stranded cDNA (Eppendorf Mastercycler gradient, Germany), total RNA (4 μg) from each sample was reverse-transcripted using an antisense specific primer and 200 U of SuperScript II RT. Sequences of the PCR primers for 5-LO, LTA_4-H, and glyceraldehydes-3-phosphate dehydrogenase (GAPDH) were derived from published sequences as follows: 5-LO: sense 5´ AGG CTG CAG TGA GAA GCA TC 3´, antisense 5´ GCC AGT GGT TCT TGA CTC TC 3´, designed to amplify a fragment corresponding to nucleotides 181–770[4]; LTA_4-H: sense 5´CAG TCA CAG GAG GAT AAT 3´, antisense 5´ GGA GTG AGC CAC TGA AGG 3´, designed to amplify a fragment corresponding to nucleotides 131–363[5]; GAPDH: sense 5´ ACC ACC ATG GAG AAG GCT GG 3´, antisense 5´ CTC AGT GTA GCC CAG GAT GC 3´, designed to amplify a fragment corresponding to nucleotides 372–899. All amplified segments extended over at least 1 intron boundary of the genomic DNA. The reactants were cycled at 94 ºC 30 s, 59 ºC 20 s, 72 ºC 10 s for LTA_4-H, and 94 ºC 45 s, 58 ºC 30 s, 72 ºC 90 s for 5-LO and GAPDH. Reaction products were separated by electrophoresis using 1.5% standard agarose gel. Amplification of GAPDH was performed as a control. PCR products were analyzed by electrophoresis (CLP, USA), visualized by ultraviolet transillumination of ethidium bromide-stained gels, and the intensity of each band was measured by the UVP Image Analyzer (UVP, Inc Upland, CA). The expression of 5-LO and LTA_4-H were normalized to that of GAPDH.

5-LO Western immunoblotting The cerebral cortex and lung tissue were dissected and homogeniz-

ing buffer, containing Tris-HCl 20 mmol/L, egtazic acid 2 mmol/L, edetic acid 5 mmol/L, pepstatin 1.5 mmol/L, leupeptin 2 mmol/L, phenylmethylsulfonyl fluoride 0.5 mmol/L, aprotinin 0.2 kU/L, and dithiothreitol 2 mmol/L, using a Polytron. The homogenates were centrifuged at 100 000×*g* at 4 °C for 60 min . The resulting supernatant was a portion of the cytosol (S1) fraction, and the pellet was resuspended in the homogenizing buffer and centrifuged again at 100 000×*g* at 4 °C for 60 min. The resulting supernatant (S2) was combined with the S1 fraction, and the combination was used for analyses as the "cytosol" fraction. The concentration of protein in these two fractions was determined using the procedure of Lowry *et al*.

Equal volumes of protein samples (40 mg of protein) and gel loading solution (Tris-HCl 50 mmol/L pH 6.8, β-mercaptoethanol 4%, sodium dodecyl sulfate 1%, glycerol 40%, and a trace amount of bromphenol blue) were mixed, and the samples were boiled for 3 min and kept on ice for 10 min. The samples were placed onto 12.5% (w/v) acrylamide gel using the Mini Protean gel apparatus (CLP, USA). The gels were electrophoresed using Tris base 25 mmol/L, glycine 192 mmol/L, and sodium dodecyl sulfate 0.1% (w/v) at 150 V. The proteins were subsequently transferred electrophoretically to an ECL nitrocellulose membrane (Amersham) using the CLP semi-dry Electroblotter(CLP, USA) at 150 mA constant current. Membranes were washed with TBST buffer (Tris base 10 mmol/L, NaCl 0.15 mol/L, and Tween-20 0.05%) for 10 min.

The blots were blocked by incubating them with 5% (wt/vol) powdered non-fat milk in TBST buffer, Nonidet P-40 2 mL, and sodium dodecyl sulfate 0.02% (wt/vol) (pH 8.0). Thereafter, the blots were incubated overnight with the primary anti-5-LO antibody (rabbit polyclonal; cayman chemical, Ann Arbor, MI, USA) at a dilution of 1:1000. The blots were then washed with TBST buffer, incubated with horseradish peroxidase-linked secondary antibody (anti-rabbit IgG; 1:3000) for 4 h at room temperature, and processed with the ECL kit. The blots were then washed with TBST and exposed to ECL film. The UVP Image Analyzer was used to measure and analyze the band intensity.

Statistical analysis Data were presented as mean±SD. Statistical difference was determined using one-way analysis of variance followed by the Student-Newman-Keuls method for multiple comparisons between groups. All statistical calculations were performed using a Sigmastat statistical package.

Results

Antigen-induced changes of IL-4 and IFN-γ, TNF-α, and NO in BALF and cerebral cortex homogenate Amounts of IL-4, TNF-α, and NO from BALF and cerebral cortex homogenates in antigen-challenged rats were markedly higher compared with samples from normal rats ($P<0.05$). In contrast, amounts of IFN-γ in antigen-challenged rats were less (BALF $P<0.05$, cerebral cortex homogenates $P<0.01$). Therefore, the IFN-γ/IL-4 ratio was lowered. DXM-treated rats had less IL-4, TNF-α, and NO amounts in cerebral cortex homogenates and higher IFN-γ amounts compared with that of model rats. The down-regulation of IFN-γ/IL-4 ratio in antigen-challenged rats was recovered by DXM (BALF $P<0.05$ and cerebral cortex homogenates $P<0.01$). Ketotifen had no effect on the amount of IL-4, IFN-γ, and NO in BALF and cerebral cortex homogenates, but inhibited the TNF-α both in BALF and cerebral cortex homogenates in model rats ($P<0.05$) (Table 1).

5-LO and LTA_4-H mRNA expression in lung tissue and cerebral cortex Using GAPDH as the internal control, the band intensity of 5-LO and LTA_4-H mRNA is shown in Figures 1, 2. The expression of 5-LO and LTA_4-H mRNA in asthma rats were significantly higher than that in the control rats ($P<0.05$). Both DXM and ketotifen inhibited the 5-LO and LTA_4-H mRNA expression of lung and cerebral cortex in the asthma rats (Figures 1, 2).

Table 1. Changes of proinflammatory mediators content in BALF and cerebral cortex of sensitized rats after antigen-challenge. n=6. Mean±SD. $^bP<0.05$, $^cP<0.01$ *vs* control group; $^eP<0.05$ *vs* model group. DXM: dexamethasone, KF: Ketotifen.

Group	Cerebral cortex				BALF			
	IL-4/pg·g^{-1} wet weight	IFN-γ/pg·g^{-1} wet weight	TNF-α/pg·g^{-1} wet weight	NO/nmol·g^{-1} wet weight	IL-4/ pg·mL^{-1}	IFN-γ/ pg·mL^{-1}	TNF-α/ pg·mL^{-1}	NO/ nmol·mL^{-1}
Control	157±27	465±90	342±124	123±29	39±12	315±55	78±17	7.5±2.2
Model	215±34^b	318±39^c	793±160^b	169±28^b	68±22^b	170±72^b	112±24^b	12±3^b
Model+KF	297±99	333±59	501±141^e	158±47	64±26	180±60	83±21^e	10±4
Model+DXM	165±46^e	372±4^{be}	468±136^e	109±29^e	44±11^e	256±76^{be}	70±27^e	6±4^e

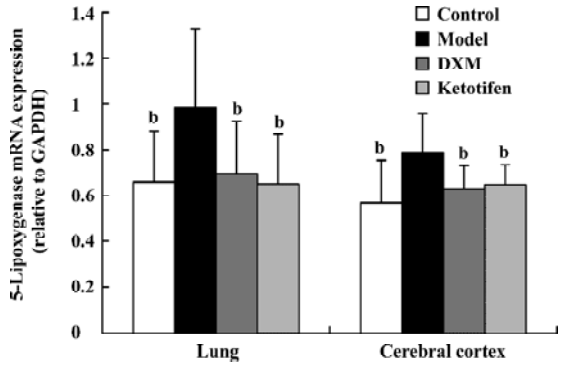

Figure 1. Changes of 5-LO mRNA expression in lung tissue and cerebral cortex of sensitized rats after antigen-challenge. Mean±SD. Lung: Control n=10, DXM n=11, Ketotifen and model n=9; brain: Control n=10, DXM n=8, ketotifen and model n=9. ^{b}P<0.05 *vs* model group.

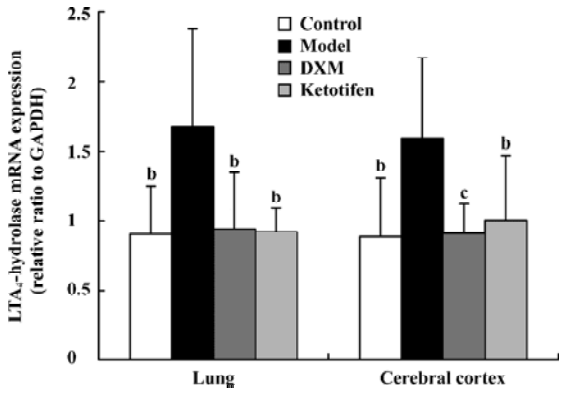

Figure 2. Changes of LTA_4-H mRNA expression in lung tissue and cerebral cortex of sensitized rats after antigen-challenge. n=9. Mean±SD. ^{b}P<0.05, ^{c}P<0.01 *vs* model group.

5-LO protein content Both 5-LO mRNA expression and the amount of cytosol 5-LO-immunoreactive protein in both cerebral cortex and lung tissue increased in the asthma rats compared with the control rats (P<0.05 and P<0.01 respectively; Figure 3). Both DXM and ketotifen significantly decreased the 5-LO protein level in cytosol of asthma rats (P<0.05).

Discussion

The first step in the production of all LTs, the oxygenation of arachidonic acid (AA) to form 5-hydroperoxyeicosatetranoic acid and the immediate dehydration of this unstable intermediate to LTA_4, is carried out by 5-LO. Metabolism of LTA_4 by LTA_4 hydrolase (LTA_4-H) results in the production of the potent chemoattractant LTB_4. Alternatively, LTA_4 can be conjugated with glutathione by LTC_4 synthase (LTC_4-S) to produce LTC_4 and its metabolites LTD_4 and E_4, collectively

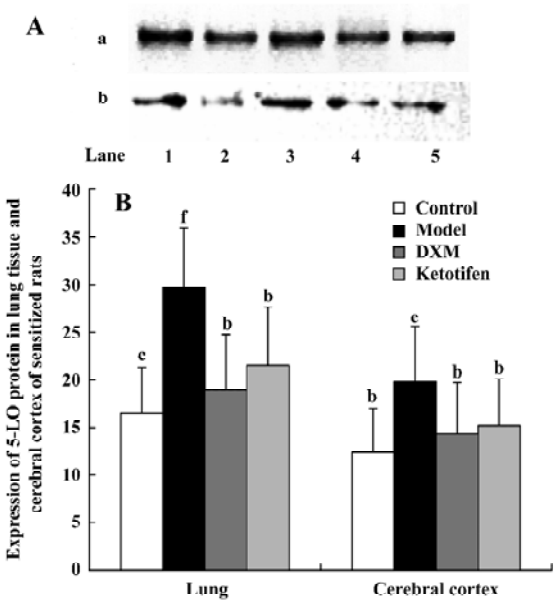

Figure 3. Changes of 5-LO protein expression in lung tissue and cerebral cortex in antigen-induced sensitized rats. n=10. Mean±SD. ^{b}P<0.05, ^{c}P<0.01 *vs* model group; ^{e}P<0.05, ^{f}P<0.01 *vs* control group. A: 5-LO protein production visualized by UVP system. (a) Lung tissue; (b) Cerebral cortex. Lane 1: model group; 2: normal control; 3: model group; 4: DXM group; 5: KF group. B: Densitometric analyses of the 5-LO protein production in lung and cerebral cortex.

referred to as the cysteinyl LTs[6].

The actions of 5-LO metabolites and Th1/Th2 paradigm in the pathogenesis of asthma and allergic disease have been understood[7,8]. In the present research, IL-4 level, the expression of 5-LO and LTA_4-H mRNA, and 5-LO protein are simultaneously increased in BALF and the cerebral cortex in asthma rats. We postulate that the increased expression of 5-LO pathway enzymes is partly due to the overproduction of proinflammatory cytokines, as heterogeneous profiles of eicosanoid generation would be determined by the absence or presence of additional local factors, particularly the Th2 cytokines that associate with mucosal surfaces in allergic diseases. Previous literature has shown that Th2 cytokines, thought to favor asthma and allergic diseases, upregulated LT synthesis. Recent findings showed that IL-4, IL-5, and IL-13 also upregulated cysteinyl LT1 receptor expression[9]. IL-4 priming dramatically induced the steady-state expression of LTC_4-S[10], and IL-5 supported the localization of 5-LO to the nucleus of human mast cells *in vivo*[11]. With immunologic disorders, inflammatory mediators interacted with one another, creating upregulatory cascades by various feedback mechanisms[12]. Conversely, the regulation of cytokine expression by LTs has also been explored:

cysteinyl LTs upregulated Th2 cytokine expression and decreased Th1 cytokine expression, favoring an allergic phenotype[13]. LTB_4 stimulated monocytes and T cell to produce IL-1, TNF-α, and IL-5[14]. However, it is unclear how it influences pulmonary function during the increase of expression of 5-LO, LTA_4-H mRNA, and LTB_4 level in the cerebral cortex. Recently, our group found exogenous LTB_4, by intercerebro-ventricularly injection, inhibited antigen-induced increase of lung resistance and decreased lung compliance in sensitized rats, and reduced antigen-induced eosinophils infiltration of airway in the sensitized mice (unpublished data). The results suggest the increase of 5-LO mRNA expression and metabolites in inflammatory status of asthma may be a negative feedback to relieve asthmatic inflammation.

Glucocorticoids are the most effective drugs to inhibit inflammatory reaction in asthma, but whether they are also able to inhibit the 5-LO pathway enzyme expression in sensitized rats after antigen challenge is still unclear. In our previous experiment, the effect of DXM in decreasing LTB_4 and IL-4 content was found to decrease the number of inflammatory cells in cerebral cortex and lung tissue of sensitized rats[2,3]. In this study, administration of DXM (0.5 mg/kg, ip) before each challenge fully inhibited the 5-LO and LTA_4-H mRNA expression. Conversely, Uz *et al*[15] found that DXM stimulated 5-LO mRNA expression in the brain of normal rats. These data suggest that glucocorticoid may be at least partly effective in regulating the metabolites of 5-LO pathways in the brain.

It is known that TNF-α is released in allergic responses from both mast cells and macrophages via IgE-dependent mechanisms, and elevated levels have been demonstrated in the BALF of asthmatic subjects undergoing allergen challenge[16]. In the present research, we found a coincidental increase of TNF-α between the cerebral cortex and lung tissue in asthma rats, which could be inhibited by DXM and ketotifen. Ketotifen, as the mast cell membrane stabilizer and H_1 receptor antagonist, can inhibit the release of mediators from inflammatory cells. Our previous study demonstrated that ketotifen inhibited the increase of LTB_4 level in the cerebral cortex and BALF in asthma rats[3]. In this study, ketotifen did not inhibit the downregulation of IFN-γ and upregulation of IL-4 but decreased 5-LO and LTA_4-H mRNA expression and TNF-α level in asthma rats. Canetti *et al*[17] found that using a neutralizing anti-TNF-α antibody could block IL-18 induced LTB_4 production, and Spanbroek *et al*[18] found granulocyte-macrophage colony-stimulating factor plus TNF-α promoted dendritic cells differentiation and induced a strong rise in 5-LO expression. The results suggest that ketotifen may not influence the Th1/Th2 paradigm but inhibits the release of mediators from mast cells. TNF-α may be also one of the proinflammatory mediators of regulating 5-LO and LTA_4-H mRNA expression.

NO can inhibit the secretion of IL-2 and IFN-γ by Th1 cells but has no effect on IL-4 production by Th2 cells. Thus, NO seems to exert a self-regulatory effect on Th1 cells implicated in immunopathology. NO derived from airway epithelial cells, macrophages, and Th1 cells plays an important role in amplifying and perpetuating the Th2 cell-mediated inflammatory response, both in allergic and non-allergic asthma[19]. Low concentrations of reactive oxygen intermediates in combination with NO were additive in suppressing 5-LO enzyme activity, possibly through peroxynitrite generation. The ability of peroxynitrite to suppress LT synthesis is associated with its ability to cause nitrotyrosination and *S*-nitrosylation of the 5-LO enzyme[20]. Contrary to the inhibitory effect of DXM on NO content in this research, ketotifen did not inhibit the increased NO level in the asthma rats. Therefore, the regulatory effect of NO on 5-LO and LTA_4-H requires elucidating.

In the present research, the correlative increase of 5-LO pathway and proinflammatory mediators between cerebral cortex and lung tissue were shown in sensitized rats after repeated antigen challenge. We postulate that an increase of 5-LO pathway expression and pro-inflammatory mediators of the brain may have regulatory effects on pulmonary inflammation of asthma.

References

1 Frieri M. Neuroimmunology and inflammation: implications for therapy of allergic and autoimmune diseases. Ann Allergy Asthma Immunol 2003; 90 (Suppl 3): 34–40.

2 Xie QM, Chen JQ, Shen WH, Bian RL. Correlative changes of interferon-γ and interleukin-4 between cerebral cortex and pulmonary airway of sensitized rats. Acta Pharmacol Sin 2002; 23: 248–52.

3 Deng YM, Xie QM, Chen JQ, Bian RL. Coincidental increase of leukotriene B_4 between cerebral cortex and lung tissue of sensitized rats. Acta Pharmacol Sin 2003; 24: 1039–44.

4 Shimada K, Navarro J, Goeger DE, Mustafa SB, Weigei PH, Weinman SA. Expression and regulation of leukotriene of leukotriene-synthesis enzyme in rat liver cells. Hepatology 1998; 28: 1275–81.

5 Nakao A, Watanabe T, Ohishi N, Toda A, Asano K, Taniguchi S, *et al*. Ubiquitous localization of leukotriene A_4 hydrolase in the rat nephron. Kidney Int 1999; 55: 100–8.

6 Werz O. 5-Lipoxygenase: cellular biology and molecular pharmacology. Curr Drug Targets Inflamm Allergy 2002; 1: 23–44.

7 Hsieh FH, Lam BK, Penrose JF, Austen KF, Boyce JA. T helper cell type 2 cytokines coordinately regulate immunoglobulin E-dependent cysteinyl leukotriene production by human cord blood-derived mast cells: profound induction of leukotriene C(4) synthase expression by interleukin 4. J Exp Med 2003; 193: 123–33.

8 Coffey M, Peters-Golden M. Extending the understanding of leukotrienes in asthma. Curr Opin Allergy Clin Immunol 2003; 3: 57–63.
9 Thivierge M, Stankova J, Rola-Pleszczynski M. IL-13 and IL-4 up-regulate cysteinyl leukotriene 1 receptor expression in human monocytes and macrophages. J Immunol 2001; 167: 2855–60.
10 Zaitsu M, Hamasaki Y, Matsuo M, Kukita A, Tsuji K, Miyazaki M, *et al*. New induction of leukotriene A4 hydrolase by interleukin-4 and interleukin-13 in human polymorphonuclear leukocytes. Blood 2000; 96: 601–9.
11 Cowburn AS, Holgate ST, Sampson AP. IL-5 increases expression of 5-lipoxygenase-activating protein and translocates 5-lipoxygenase to the nucleus in human blood eosinophils. J Immunol 1999; 163: 456–65.
12 Spanbroek R, Hildner M, Kohler A, Muller A, Zintl F, Kuhn H, *et al*. IL-4 determines eicosanoid formation in dendritic cells by down-regulation of 5-lipoxygenase and up-regulation of 15-lipoxygenase expression. Proc Natl Acad Sci USA 2001; 98: 5152–7.
13 Nag S, Lamkhioued B, Renzi PM. Interleukin-2-induced increased airway responsiveness and lung Th2 cytokine expression occur after antigen challenge through the leukotriene pathway. Am J Respir Crit Care Med 2002; 165: 1540–5.
14 Anthonsen MW, Andersen S, Solhaug A, Johansen B. Atypical lambda/iota PKC conveys 5-lipoxygenase/leukotriene B4-mediated cross-talk between phospholipase A2s regulating NF-kappa B activation in response to tumor necrosis factor-alpha and interleukin-1beta. J Biol Chem 2001; 276: 35344–51.
15 Uz T, Dwivedi Y, Savani PD, Impagnatiello F, Pandey G, Manev H. Glucocorticoids stimulate inflammatory 5-lipoxygenase gene expression and protein translocation in the brain. J Neurochem 1999; 73: 693–9.
16 Thomas PS. Tumour necrosis factor-α: the role of this multifunctional cytokine in asthma. Immunol Cell Biol 2001; 79: 132–40.
17 Canetti CA, Leung BP, Culshaw S, McInnes IB, Cunha FQ, Liew FY. IL-18 enhances collagen-induced arthritis by recruiting neutrophils via TNF-alpha and leukotriene B4. J Immunol 2003; 171: 1009–15.
18 Spanbroek R, Hildner M, Steinhilber D, Fusenig N, Yoneda K, Radmark O, *et al*. 5-Lipoxygenase expression in dendritic cells generated from CD34(+) hematopoietic progenitors and in lymphoid organs. Blood 2000; 96: 3857–65.
19 Ricciardolo FL. Multiple roles of nitric oxide in the airways. Thorax 2003; 58: 175–82.
20 Coffey MJ, Phare SM, Peters-Golden M. Interaction between nitric oxide, reactive oxygen intermediates, and peroxynitrite in the regulation of 5-lipoxygenase metabolism. Biochim Biophys Acta 2002; 1584: 81–90.

4th National Congress of Chinese Society of Toxicology

2005 Sep 18-21 Shenyang, China

Please contact
Director Tian-en WANG
Chinese Toxicology Society
27 Taiping Road
Beijing 100850, China
Phn 86-10-6693-2387
Fax 86-10-6818-3899

Director Yu-hong SONG
National Shenyang Center for Safety Evaluation of New Drugs
8 Liaodong Road
Shenyang 110021, China
Phn 86-24-2581-2684
Fax 86-24-8935-3490

Acta Pharmacologica Sinica 2005 Mar; 26 (3): 359–363

Full-length article

Diethyldithiocarbamate inhibits iNOS expression in human lens epithelial cells stimulated by IFN-gamma and LPS

De-xin LI, Si-ling WANG[1], Yoshimasa ITO[2,3], Jing-hai ZHANG, Chun-fu WU

Department of Pharmaceutics, College of Pharmacy, Shenyang Pharmaceutical University, Shenyang 110016, China; [2]School of Pharmacy, [3]Pharmaceutical Research and Technology Institute, Kinki University, Osaka 577-8502, Japan

Key words

human lens; epithelial cells; inducible nitric oxide synthase; interferon gamma; lipopolysaccharide; diethyldithiocarbamate

[1] Correspondence to Prof Si-ling WANG.
Phn 86-24-2384-3711, ext 3641.
E-mail silingwang@hotmail.com

Received 2004-05-06
Accepted 2004-10-29

doi: 10.1111/j.1745-7254.2005.00041.x

Abstract

Aim: To investigate the biological activity of human lens epithelial cells (HLEC) in producing inducible nitric oxide synthase (iNOS) and nitric oxide (NO), and to assesse the effect of diethyldithiocarbamate (DDC) on iNOS mRNA levels and expression of NOS. **Methods:** The human lens epithelial cell line SRA 01/04 was used in this experiment. Semi-quantitative reverse transcription polymerase chain reaction (RT-PCR) and Western blotting were used to detect, respectively, iNOS mRNA expression and protein production. **Results:** A costimulation by interferon gamma (IFN-γ) and lipopolysaccharide (LPS) was necessary for iNOS expression in HLEC. The expression of iNOS was significantly reduced in a dose-dependent manner by adding DDC from 10 μmol/L to 1 mmol/L. **Conclusion:** The expression of iNOS in HLEC needs co-stimulation with IFN-γ and LPS and it is inhibited by DDC.

Introduction

Cataracts are still the most important cause of blindness in the world and are a significant and increasing global problem. The mechanism of cataract development is complicated and involves many factors. For many years, we have been involved in the development of anti-cataract treatments and investigating the mechanisms of cataract development. Our previous studies on selenite-induced rat cataracts demonstrated that the NO concentration in ocular tissue was significantly higher than in normal rats. Inducible nitric oxide synthase (iNOS or NOS2) is thought to play a role in the initiation of cataracts, and the development of cataracts is prevented by NOS inhibitors[1]. We researched whether NO was produced by the ocular tissues or comes from other parts of the body, so we selected human lens epithelial cells (HLEC) for further study.

Inducible NOS, one of the three isoforms of NOS, catalyses the oxidization of *L*-arginine and generates large amounts of NO[2]; it does not require elevated intracellular Ca^{2+} levels for activation. In addition, its function lasts for a longer period than that of constitutive NOSs (endothelial NOS, eNOS; neural NOS, nNOS). Inducible NOS can be produced by treatment with agents, such as cytokines, interferons and bacterial lipopolysaccharide (LPS), in a wide variety of cell types such as macrophages, hepatocytes, keratinocytes, endothelial cells, and epithelial cells[3-7]. In the eye, eNOS and nNOS are localized in the retina, ciliary body and conjunctiva, and are thought to be involved in neurotransmission, regulation of intraocular pressure and vasodilation, while iNOS is involved in endotoxin-induced uveitis and inflammation of the anterior segment of the eye, and inhibits the cellular proliferation of retinal pigment epithelial cells[8,9]. Therefore, the purpose of this study is to investigate the biological activity of HLEC in iNOS expression and NO production.

Diethyldithiocarbamate (DDC), a potent free radical scavenger, has been found to prevent selenite-induced opacity in cultured rat lenses[10]. This was thought to be related to its anti-oxidant effect. It has been reported that both NO and its derivative peroxynitrite ($ONOO^-$) inhibit mitochondrial respiration and may increase oxygen radical production by mitochondria. Large or persistent levels of NO promote mitochondrial oxidant formation, and inhibit the respiratory chain complexes, probably by nitrosylating or oxidizing protein thiols and removing iron from the iron-sulphur centres.

Peroxynitrite causes irreversible inhibition of mitochondrial respiration and damage to a variety of mitochondrial components via oxidizing reactions, most notably at complexes I and II of the electron transport chain, ATPase, aconitases, and Mn-superoxide dismutase[11,12]. These damages lead to deficient energy metabolism. Usually, in the initiation of cataractogenesis, deficient energy metabolism occurs with mitochondria function disorder. Thus, the effect of DDC for the prevention of NO overproduction was also investigated in this study.

Materials and methods

Materials DDC and bovine serum albumin (BSA) were purchased from Wako Pure Chemical Industries Ltd (Osaka, Japan). Dulbecco's modified Eagle's medium (low glucose) (DMEM), fetal bovine serum (FBS), 0.05% trypsin-EDTA solution and phosphate buffered saline (PBS) were purchased from GIBCO^{TM} Invitrogen Co (Tokyo, Japan). Gentamicin reagent solution (10 g/L) was obtained from GIBCO BRL Life Technologies (Japan). Interferon-γ (IFN-γ) was purchased from PeproTech EC Ltd (London, UK). LPS purified from *Escherichia coli* was obtained from Sigma-Aldrich Co (St Louis, MO, USA). Protease inhibitor cocktail tablets were obtained from Complete Roche Applied Science (Japan). All the primers used were synthesized by Sigma Genosys (Sigma Genosys, Japan, KK). Alkaline phosphatase (AP)-conjugated anti-rabbit IgG and ProtoBlot II AP System with Stabilized Substrate (BCIP/NBT) were obtained from Promega Co. All other chemicals used, except where indicated, were of analytical grade.

Cell culture and treatments The human lens epithelial cell line SRA 01/04 was provided by Ibaraki Medical University, and maintained in DMEM supplemented with 10% (v/v) heat-inactivated FBS and 10 mg/L gentamicin at 37 °C in a humidified CO_2 incubator (ESPEC BNA-111, TABAI ESPEC CORP, Japan) with 5% CO_2. Culture medium was changed every other day. The confluent cells were separated and trypsinized with 0.05% trypsin-EDTA to produce single cells, after which they were seeded at 4×10^4 cm^{-2} and allowed to form subcultures. Cell viability was assessed by Trypan blue exclusion assay. Each treatment was carried out on d 3 after seeding, when the cells were 80% confluent. The culture medium was changed every other day for routine culture, and then 1 h before each experiment. All cultures were carried out in duplicate.

Semiquantitative reverse transcription-polymerase chain reaction (RT-PCR) for iNOS mRNA evaluation Total cellular RNA was extracted and purified from HLEC with the RNeasy Mini Kit and RNase-Free DNase Set (QIAGEN KK, Tokyo, Japan) according to the manufacturer's instructions. The RNA level was quantified by measuring the absorbance at 260 nm. The samples with a ratio of 260/280 nm greater than 1.8 were used. RT-PCR was performed using the RNA PCR Kit (AWV Ver 2.1, TAKARA BIO INC, Tokyo, Japan). As a control for calibrating an equivalent amount of input cDNA, the mRNA level of constitutively expressed G3PDH was determined in parallel aliquots of cDNA to control any differences in cDNA synthesis efficiency. In general, total RNA 1 μg was added to a 20 μL volume of reaction medium for reverse transcription, and all PCR procedures were performed using a volume of 50 μL according to the manufacturer's instructions. The primers used in this study were as follows: iNOS (sense, 5′-CCAGT GACAC AGGAT GACCT TCAG-3′ and antisense, 5′-TGCCA TTGTT GGTGG AGTAA CG-3′), and human G3PDH (sense, 5′-CATCA CCATC TTCCA GGAGC GAGA-3′ and antisense, 5′-CCACC ACCCT GTTGC TGTAG CCA-3′). The cycling conditions were: 35 cycles for iNOS and 20 cycles for G3PDH at 94 °C for 30 s, 65 °C for 30 s, and 72 °C for 1 min for amplifying 603 bp and 752 bp products, respectively. Finally, the extension of products was performed at 72 °C for 10 min. PCR-amplified samples were run on 1.5% agarose gel and visualized using ethidium bromide, and then photographed (ImageMaster VDS-CL, Amersham Biosciences) under UV light.

Western blotting for determination of iNOS protein At the end of the treatment, cells were washed with ice-cold phosphate buffer and removed from plates by a cell scraper and centrifuged at 200×*g* for 5 min. The cell pellets were then suspended in 200 μL lysis buffer (Tris·HCl 50 mmol/L, pH 7.6, protease inhibitor cocktail tablet in PBS 150 mmol/L, Triton X-100 0.5%) and lysed for 30 min on ice. The cell debris was removed by centrifugation at 12 000×*g* at 4 °C for 20 min. The protein concentration was determined using a protein assay kit (Bio-Rad Laboratories, CA, USA) with BSA as the standard. A sample of total protein (20 μg) was separated on an 8% polyacrylamide sodium dodecyl sulfate (SDS) gel. The proteins were then transferred to polyvinylidene difluoride (PVDF) membranes (BIO-RAD, CA, USA), using a semi-dry transfer cell (TRans-Blot SD Semi-Dry Electrophoretic Transfer Cell, BIO-RAD, CA, USA). The transfer buffer used in the system contained Tris·HCl 25 mmol/L, glycine 192 mmol/L, methanol 20%, and SDS 0.0375%. After transfer, nonspecific sites on the membranes were blocked with 5% non-fat dry milk in PBS. The blots were probed with 1 mg/L rabbit anti-human iNOS polyclonal antibody (Santa Cruz Biotechnology Inc, CA, USA) overnight at

4 ºC followed by washing several times with PBS-0.1% Tween 20 (PBST). A secondary alkaline-phosphatase conjugated anti-rabbit IgG (1:7500 dilutions) was added, and incubated for 1 h at room temperature. After washing several times in PBST, iNOS proteins were visualized by BCIP/NBT kit.

Results

Induction of iNOS mRNA The expression of iNOS has been studied in most detail in murine macrophages where maximum expression can be induced by a combination of IFN-γ and LPS[16]. Figure 1 showed that non-stimulated HLEC had undetectable levels of iNOS mRNA (lane 1). Stimulation with LPS or IFN-γ alone for 3 h had a negligible effect on iNOS mRNA induction (lanes 2 and 3). HLEC, pretreated with IFN-γ for 3 h, then washed twice with PBS, followed by an incubation with LPS for 3 h, had a very thin band (lane 4), whereas, cells treated with IFN-γ for 3 h followed by co-incubation with LPS and IFN-γ, produced a substantial amount of iNOS mRNA (lane 5).

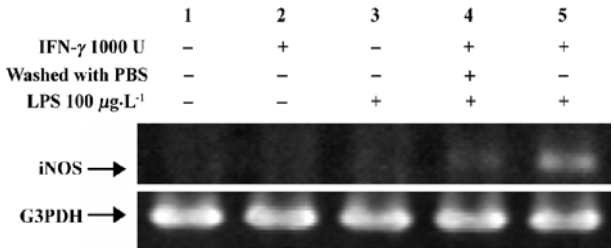

Figure 1. Transcription of iNOS mRNA in HLEC treated with/without IFN-γ and LPS. Representative results of the 3 independent experiments are shown.

Increasing the amount of LPS from 1 μg/L to 1 mg/L resulted in a corresponding increase of iNOS mRNA levels (Figure 2A). With the co-incubation time increase, the intensity of the iNOS bands tended to increase (Figure 2B). On the contrary, extending the pretreatment time of IFN-γ from 1 d to 2 d did not produce a stronger iNOS band (Figure 2C, lane 5 *vs* 3).

Inhibitory effect of DDC on iNOS expression Figure 3 shows the effect of DDC on iNOS mRNA expression. Incubation with LPS, IFN-γ, or DDC alone failed to produce iNOS mRNA or protein, while the combination of LPS and IFN-γ resulted in the expression of iNOS (lane 4), and the expression was inhibited by adding DDC to the culture medium (lane 5). However, the induction of iNOS by LPS and

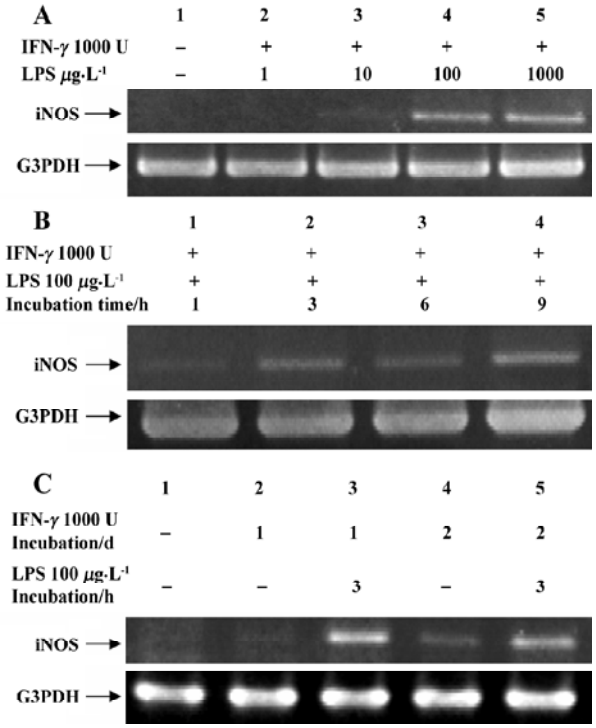

Figure 2. Transcription of iNOS mRNA in HLEC. HLEC were pretreated with IFN-γ for 3 h followed by co-incubation (A) with LPS at different concentrations, (B) with LPS for indicated time intervals, and (C) pretreated with IFN-γ for 1 day or 2 day followed by a coincubation with/without LPS for another 3 h. Representative results of the 3 independent experiments are shown.

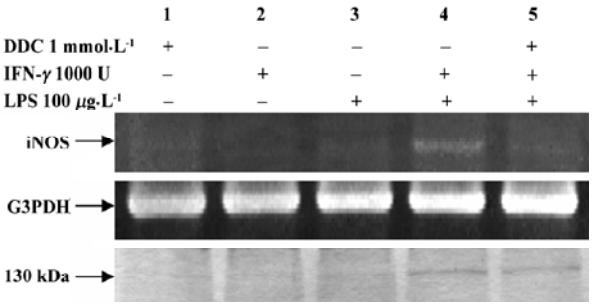

Figure 3. Inhibitory effect of DDC on iNOS mRNA transcription and protein production. HLEC were pretreated with/without IFN-γ in the presence/absence of DDC for 3 h, followed by a 24-h coincubation with/without LPS. Representative results of the 3 independent experiments are shown.

IFN-γ was attenuated in HLEC that had been loaded with DDC. In addition, the inhibitory effect was enhanced at increased DDC concentrations from 10 μmol/L to 1 mmol/L (Figure 4).

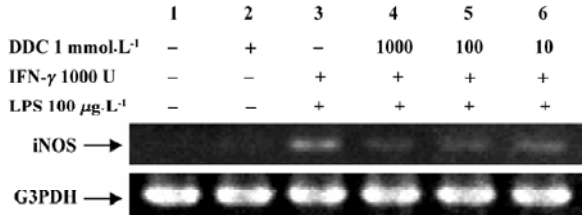

Figure 4. Relationship between DDC concentrations and inhibitory effect on iNOS mRNA transcription. HLEC were treated with/without IFN-γ in the presence/absence of DDC for 3 h, followed by a 24-h coincubation with/without LPS. Representative results of the 3 independent experiments are shown.

Discussion

The present research reports the expression of iNOS mRNA in HLEC stimulated with LPS and IFN-γ. The coincubation of both factors is needed for a quick cellular response and large amount of iNOS mRNA production, compared with stimulation with LPS or IFN-γ alone or successively. The synergistic effect between LPS and IFN-γ, as far as the transcription of iNOS mRNA is concerned, has been extensively investigated in mouse macrophages[15-17]. LPS is a common initiator of inflammation, triggering tyrosine phosphorylation and activation of mitogen-activated protein kinases (MAPKs)[18]. MAPKs phosphorylate and regulate a variety of transcription factors, leading to inflammatory gene expression[19]. In several cell types, LPS also activates transcription nuclear factor kappa B (NF-κB) and regulates iNOS gene expression[20]. The synthesis of iNOS is mainly regulated at the transcriptional level. The promoter region of the iNOS gene from different species has been reported to contain binding sites for several transcription factors. Those known to be active include κB sites located both in the enhancer and basal promoter[20,21], two juxtaposed enhancer-linked IFN-stimulated response elements (ISREs), the distal one of which is a strong activator[20,21], while the proximal one is a weak activator of transcription[22] , and an octamer element in the basal promoter[21]. An IFN-γ activated site (GAS) is necessary for full expression of the mouse iNOS gene in response to IFN-γ and LPS. The binding of Stat1α to the GAS of the iNOS promoter is required for optimal induction of the iNOS gene by IFN-γ and LPS[23]. Also, iNOS gene expression appears to require the simultaneous presence of all transcription factors binding to their enhancers. When all are present, transcription is enhanced; when any one of them is absent, the transcription level is reduced or completely stopped. In the case of humans, transcriptional regulation is a crucial factor in the initiation of cytokine-stimulated NO production by human iNOS[24]. The two activator protein-1 sites, as well as the upstream NF-κB site, are important for LPS and IFN-γ stimulation of human iNOS induction.

Activation of NF-κB seems to be an essential step for iNOS induction in most cell types, and the inhibitory effect of DDC on the transcriptional activity of the iNOS gene may be due to an effect on the activation of transcription factor NF-κB, which regulates the expression of a variety of genes essential for cellular immune response, inflammation, growth, and development. Because dithiocarbamates are well-known antioxidants and NF-κB inhibitors[25,26], and DDC, a dithiocarbamate analogue, exhibits concentration-dependent biphasic effects in inhibiting NF-κB activation in cerebral endothelial cells[27], that is, it inhibits NF-κB activation at low but not high concentrations (>500 μmol/L). The present studies investigated the inhibitory effect of DDC at concentrations ranging from 10 μmol/L to 1 mmol/L, and no biphasic effect was observed. If a biphasic effect does exist in HLEC, the "high concentration" should be more than 1 mmol/L. Our previous studies on the ocular bioavailability of disulfiram (DSF), which is a dimer of DDC and quickly converted into DDC by catalysis of the protein mercapto group in the cornea and aqueous humor, demonstrated that the concentration of DDC in the aqueous humor was not more than 100 μmol/L after topical administration. Thus, if DSF is used as an anticataract agent for the prevention and treatment of cataracts, the main problem we need to consider is how to enhance the corneal permeability and bioavailability of DSF preparations. Whether the anticataract effect of DDC is due to its inhibition of NF-κB or not, the signal transduction pathway linking stimulation of iNOS mRNA in HLEC needs to be clarified by further investigations.

In conclusion, the present study reports the expression of iNOS in HLEC, which shows that co-stimulation of IFN-γ and LPS is required, while the expression is inhibited by DDC.

Acknowledgment

We are most grateful to Dr David JACK for comments and suggestions on our manuscript.

References

1 Ito Y, Nabekura T, Takeda M, Nakao M, Terao M, Hori R, *et al*. Nitric oxide participates in cataract development in selenite-treated rats. Curr Eye Res 2001; 22: 215–20.

2 Moncada S, Higgs A. The *L*-arginine-nitric oxide pathway. N Engl J Med 1993; 329: 2002–12.

3 Griffth OW, Stuehr DJ. Nitric oxide synthases: properties and cata-

lytic mechanism. Annu Rev Physiol 1995; 57: 707–36.
4 Asano K, Chee CB, Gaston B, Lilly CM, Gerard C, Drazen JM, *et al*. Constitutive and inducible nitric oxide synthase gene expression, regulation, and activity in human lung epithelial cells. Proc Natl Acad Sci USA 1994; 91: 10089–93.
5 Fimiani C, Magazine H, Welters ID, Bilfinger TV, Salsano F, Tonnesen E, *et al*. Antagonism of LPS and IFN-gamma induced iNOS expression in human atrial endothelia by morphine, anandamide, and estrogen. Acta Pharmacol Sin 2000; 21: 405–9.
6 Salzman AL, Eaves-Pyles T, Linn SC, Denenberg AG, Szabo C. Bacterial induction of inducible nitric oxide synthase in cultured human intestinal epithelial cells. Gastroenterology 1998; 114: 93–102.
7 Hussaini IM, Zhang YH, Lysiak JJ, Shen TY. Dithiolane analogs of lignans inhibit interferon-gamma and lipopolysaccharide-induced nitric oxide production in macrophages. Acta Pharmacol Sin 2000; 21: 897–904.
8 Jacquemin E, de Kozak Y, Thillaye B, Courtois Y, Goureau O. Expression of inducible nitric oxide synthase in the eye from endotoxin-induced uveitis rats. Invest Ophthalmol Vis Sci 1996; 37: 1187–96.
9 Goureau O, Lepoivre M, Becquet F, Courtois Y. Differential regulation of inducible nitric oxide synthase by fibroblast growth factors and transforming growth factor γ in bovine retinal pig mented epithelial cells: inverse correlation with cellular proliferation. Proc Natl Acad Sci USA 1993; 90: 4276–80.
10 Ito Y, Cai H, Terao M, Tomohiro M. Preventive effect of diethyldithiocarbamate on selenite-induced opacity in cultured rat lenses. Ophthalmic Res 2001; 33: 52–9.
11 Brown GC. Nitric oxide and mitochondrial respiration. Biochim Biophys Acta 1999; 1411: 351–69.
12 Radi R, Cassina A, Hodara R. Nitric oxide and peroxynitrite interactions with mitochondria. Biol Chem 2002; 383: 401–9.
13 Moncada S, Palmer RM, Higgs EA. Nitric oxide: physiology, pathophysiology, and pharmacology. Pharmacol Rev 1991; 43: 109–42.
14 Lorsbach RB, Murphy WJ, Lowenstein CJ, Snyder SH, Russell SW. Expression of the nitric oxide synthase gene in mouse macrophages activated for tumor cell killing. Molecular basis for the synergy between interferon-gamma and lipopolysaccharide. J Biol Chem 1993; 268: 1908–13.
15 Xie QW, Whisnant R, Nathan C. Promoter of the mouse gene encoding calcium-independent nitric oxide synthase confers inducibility by interferon gamma and bacterial lipopolysaccharide. J Exp Med 1993; 177: 1779–84.
16 Lowenstein CJ, Alley EW, Raval P, Snowman AM, Snyder SH, Russell SW, *et al.* Macrophage nitric oxide synthase gene: two upstream regions mediate induction by interferon gamma and lipopolysaccharide. Proc Natl Acad Sci USA 1993; 90: 9730–4.
17 Gao J, Morrison DC, Parmely TJ, Russell SW, Murphy WJ. An interferon-γ-activated site (GAS) is necessary for full expression of the mouse iNOS gene in response to interferon-γ and lipopolysaccharide. J Biol Chem 1997; 272: 1226–30.
18 Weinstein SL, Sanghera JS, Lemke K, DeFranco AL, Pelech SL. Bacterial lipopolysaccharide induces tyrosine phosphorylation and activation of mitogen-activated protein kinases in macrophages. J Biol Chem 1992; 267: 14955–62.
19 Neary JT. MAPK cascades in cell growth and death. News Physiol Sci 1997; 12: 286–93.
20 Xie Q, Kashiwabara Y, Nathan C. Role of transcription factor NF-κB/Rel in induction of nitric oxide synthase. J Biol Chem 1994; 269: 4705–8.
21 Goldring CE, Reveneau S, Algarte M, Jeannin JF. *In vivo* footprinting of the mouse inducible nitric oxide synthase gene: inducible protein occupation of numerous sites including Oct and NF-IL6. Nucleic Acids Res 1996; 24: 1682–7.
22 Kamijo R, Harada H, Matsuyama T, Bosland M, Gerecitano J, Shapiro D, *et al*. Requirement for transcription factor IRF-1 in NO synthase induction in macrophages. Science 1994; 263: 1612–5.
23 Martin E, Nathan C, Xie QW. Role of interferon regulatory factor 1 in induction of nitric oxide synthase. J Exp Med 1994; 180: 977–84.
24 de Vera ME, Shapiro RA, Nussler AK, Mudgett JS, Simmons RL, Morris SMJ, *et al*. Transcriptional regulation of human inducible nitric oxide synthase (NOS2) gene by cytokines: initial analysis of the human NOS2 promoter. Proc Natl Acad Sci USA 1996; 93: 1054–9.
25 Moellering D, McAndrew J, Jo H, Darley-Usmar VM. Effects of pyrrolidine dithiocarbamate on endothelial cells: protection against oxidative stress. Free Radic Biol Med 1999; 26: 1138–45.
26 Schreck R, Meier B, Mannel DN, Droge W, Baeuerle PA. Dithiocarbamates as potent inhibitor of nuclear factor kB activation in intact cells. J Exp Med 1992; 175: 1181–94.
27 Kim CH, Kim JH, Moon SJ, Hsu CY, Seo JT, Ahn YS. Biphasic effect of dithiocarbamates on the activity of nuclear factor-κB. Eur J Pharmacol 2000; 392: 133–6.

Acta Pharmacologica Sinica 2005 Mar; 26 (3): 364–368

Blackwell Publishing

Full-length article

Antisense oligodeoxynucleotides targeting the serine/threonine kinase Pim-2 inhibited proliferation of DU-145 cells

Jin-ming DAI, Shu-qun ZHANG[1], Wei ZHANG, Ru-xian LIN, Zong-zheng JI[1], Sheng-qi WANG[2]

Beijing Institute of Radiation Medicine, Beijing 100850, China; [1]Department of Oncology, the Second Hospital of Xi'an Jiaotong University, Xi'an 710004, China

Key words

antisense oligodeoxynucleotide; Pim-2; cell proliferation; DU-145

[2] Correspondence to Prof Sheng-qi WANG.
Phn 86-10-6693-2211.
Fax 86-10-6821-4653.
E-mail sqwang@nic.bmi.ac.cn

Received 2004-06-14
Accepted 2004-11-24

doi: 10.1111/j.1745-7254.2005.00050.x

Abstract

Aim: To investigate the effect of antisense oligodeoxynucleotides (ASODN) targeting Pim-2 on cell proliferation of DU-145 cells. **Methods:** Three ASODN targeting Pim-2 were designed and synthesized. After transfection with ASODN, cell proliferation was analyzed using an MTS [3-(4,5-dimethylthiazol-2-yl)-5-(3-carboxymethoxyphenyl)-2-(4-sulfophenyl)-2*H*-tetrazolium, inner salt] assay. In addition, Pim-2 mRNA, protein levels, and cell cycles were examined. **Results:** The ASODN designed and synthesized by our laboratory significantly reduced Pim-2 mRNA level and protein content in DU-145 cells. After transfection with ASODN for 48 h, a marked reduction in cell viability was observed in DU-145 cells in a dose-dependent manner. No remarkable apoptosis occurred in cells treated with ASODN compared with control cells. However, it should be noted that G_1 phase arrest was clearly observed in ASODN-treated cells. **Conclusion:** ASODN targeting Pim-2 resulted in a marked reduction in DU-145 cell proliferation, and induction of G_1 phase cell cycle arrest is one of the important mechanisms for ASODN to reduce cell growth. Moreover, antisense inhibition of Pim-2 expression provides a new promising therapy target for prostate cancer.

Introduction

Prostate cancer is the most frequent non-cutaneous malignancy and the second leading cause of cancer death among males in the western world. It has long been recognized that cancer arises as a result of somatic mutations; and a concept dramatically reinforced by the demonstration that a cellular "proto-oncogene" is mutationally involved in prostate cancer formation. To date a number of the genes associated with prostate cancer formation and progression have been identified, which are deregulated or abnormally overexpressed contributing to tumor formation. Recent technological developments have paved the way for the identification of the genes PRC17, Stat3, and Pim[1–5]. Identification of these genes provides a new target for prostate cancer therapy.

The Pim serine/threonine kinase family was first identified as a common proviral insertion site in T and B-cell lymphomas in mice[6]. To date, three family members have been identified: Pim-1, Pim-2, and Pim-3. These related enzymes show substantial homology, but differ in their tissue expression[7]. It is unknown to what extent the various family members differ in their biochemical effects. The Pim-2 gene encodes a cytoplasmic serine/thronine kinase whose expression is regulated by hematopoietic cytokines[8,9]. There are multiple isoforms of Pim-2 protein resulting from the use of the alternative translation start codon, CTG[10]. Among these isoforms, the short Pim-2 (34 kDa) form is the most active at enhancing survival of FDCP1 cells after cytokine withdrawal. The Pim-2 transgene induces lymphoid tumors, and exhibits potent synergy with c-*myc*[9]. Recent studies have indicated that Pim-2 kinase could phosphorylate the pro-apoptotic protein Bard on serine 112, and thus inhibit cell apoptosis[11]. Although the contribution of Pim-2 to cancer formation and progress is relatively unknown, Pim-2 has been recognized as a procongene, and procongenes are associated with many types of cancer formation.

At present, more and more patients are being diagnosed with early stage prostate cancer because of improvements in

diagnostic techniques. Although surgery and chemotherapy are effective on patients with localized tumors, the prognosis of patients with advanced or metastatic tumors is not ideal. It is clear that novel treatment approaches to prostate cancer are urgently needed. It is now accepted that antisense oligodeoxynucleotides have sequences that are complementary to specific strands of RNA. Once delivered into a target cell, the oligodeoxynucleotides hybridise with its RNA complement and inhibit expression of the corresponding disease-relevant protein. More and more data demonstrate that antisense therapy for cancer is a very promising strategy. Consequently, the aim of our paper is to investigate whether inhibition of Pim-2 expression using antisense oligodeoxynucleotides can reduce proliferation of DU-145 cells.

Materials and methods

Antisense oligodeoxynucleotides The antisense sequences used in these experiments were designed using a computational neural network model[12]. BLAST confirmed that they were specific for the Pim-2 gene. Eicosomer ASODN were synthesized in our laboratory using an Applied Biosystems 391 DNA synthesizer and purified by OPC (Oligonucleotide Purification Cartrigde) (Perkin-Elmer, Foster City, CA, USA). Table 1 shows the sequence of ASODN.

Table 1. The sequence of antisense oligodeoxynucleotides (ASODN).

No	Position	Sequence (5′–3′)
ASODN 1	4–23	CGCCGCGCGCTCGTGCCGAA
ASODN 2	123–142	CCTCGAACGCTTCCCGATCC
ASODN 3	344–363	TGGCCACCTGGAGTCGATCT

Cell line and culture Human prostate cancer cell lines, DU-145, were obtained from the Chinese Academy of Medical Sciences (Beijing, China). Cells were cultured in RPMI-1640 medium (Invitrogen, San Diego, CA, USA) supplemented with 10% fetal bovine serum (GIBCO BRL, Grand Island, NY, USA), 100 kU/L benzylpenicillin and 100 mg/L streptomycin. All cultures were incubated at 37 °C in a 5% CO_2 atmosphere.

Cell viability The effects of ASODN on cellular viability were determined using an MTS [3-(4,5-dimethylthiazol-2-yl)-5-(3-carboxymethoxyphenyl)-2-(4-sulfophenyl)-2*H*-tetrazolium, inner salt] assay. In brief, 3×10^3 cells were seeded in 96-well microtiter plate and allowed to attach overnight. Cells were then transfected with different concentrations (0.1 μmol/L, 0.2 μmol/L, 0.4 μmol/L, 0.8 μmol/L) of ASODN. After 48 h of incubation, 20 mL of MTS (Sigma Chemical Company, St Louis, MO, USA) was added to each well. The 96-well microtiter plate was incubated for 2 h at 37 °C, and a 490 nm absorbance value was determined using an MR 600 Microplate reader (Wallac, Turku, Finland). Each assay was carried out in quadruplicate. Cellular proliferation inhibition rate is calculated as: $(A_{control}–A_{sample})/(A_{control}–A_{blank})\times100\%$.

Lip-mediated transfection of antisense oligodeoxynucleotides Cells were plated in six-well plates at a density of 1×10^5 cells per well. Transfections were carried out after plating for 24 h, when cells reached a confluence of (50–80)%. Lipofectamine 2000 (Invitrogen) was used for transfection in this experiment and transfection was carried out according to the manufacturer's instructions. ASODN concentrations were selected as 0.1 μmol/L, 0.2 μmol/L, 0.4 μmol/L, 0.8 μmol/L, respectively. After transfection (incubation for 6 h at 37 °C), the cells were washed with phosphate-buffered saline (PBS) and incubated in fresh culture medium.

Reverse transcription-polymerase chain reaction (RT-PCR) After transfection for 48 h, total RNA was extracted using TRIzol (Invitrogen) by a single-step phenol extraction. Subsequent RT-PCR was carried out using a reverse transcription system (RT-PCR kit, Promega, Madison, WI, USA). In brief, first strand cDNA was synthesized using an Oligo $(dT)_{15}$ primer at 42 °C for 30 min. The PCR reaction for Pim-2 and β-actin was carried out in a single reaction of 20 mL volume. The latter served as a control following 32 cycles of denaturing at 95 °C for 45 s, annealing at 55 °C for 40s, and extending at 72 °C for 40 s. Under this reaction condition, the amplification showed linearity (data not shown). PCR products were run on a 3.0% agarose gel and visualized using ethidium bromide staining, and the intensities were measured by scanning the gel with Gel Doc 1000 (Bio-Rad, Hercules, CA, USA). Inhibition of Pim-2 mRNA was calculated according to the following formula:

$$\text{Inhibition percentage (\%)} = \left(\frac{1-A_{sample}\times A_{0control}}{A_{control}\times A_{0sample}}\right)\times100$$

where A_{sample} is the intensity of Pim-2 PCR product in cells transfected with ASODN and lipofectamine, $A_{0sample}$ is the intensity of Pim-2 PCR product in cells transfected with lipofectamine alone, $A_{control}$ is the intensity of β-actin product in cells transfected with ASODN and lipofectamine, and $A_{0control}$ is the intensity of β-actin product in cells transfected with lipofectamine alone.

Western blot analysis After 72 h of transfection with

ASODN, cells were lysed in RIPA buffer [10 mmol Tris-HCL (pH 7.4), 1% deoxycholate, 1% NP40, 150 mmol NaCl, 0.1% SDS, 0.2 mmol phenylmethyl sulfonyl fluoride, 1 mg/L aprotinin and 1 mg/L leupeptin] for 30 min on ice. The lysates were centrifuged at 12000×*g* for 15 min to remove debris. Protein samples (30 μg) were separated using 12% sodium dodecyl sulfate-polyacrylamide gel electrophoresis (SDS-PAGE) gel and transferred onto hybond-polyvinylidene difluoride (PVDF) membranes (Schleicher & Schuell Biosciences, Inc, Keene N H, USA). Pim-2 protein was identified using anti-Pim-2 primary and peroxidase-conjunct secondary antibody (Santa Cruz Biotechnology, Santa Cruz, CA, USA). Finally, the reactive band was visualized using an ECL-plus Detection Kit (Amersham Biosciences) and scanned by Gel Doc 1000 (Bio-Rad).

Cell cycle and apoptosis analysis Cell cycle assays were carried out as described previously[13]. In brief, cells were harvested after transfection with 0.4 μmol/L ASODN for 48 h, and fixed with 70% ethanol at -20 °C overnight. Fixed cells were washed twice again with PBS, and stained with 50 mg/L propidium iodide (PI) in the presence of RNase A. The stained cells were analyzed for DNA content by fluorescence-activated cell sorting (FACS) in a FACScan (SOBR model, Becton-Dickinson, San Jose, CA, USA). Cell cycle fractions were quantified with CellQuest (Becton Dickinson), and apoptosis was estimated using the fraction of sub-G_1 phase cells.

Statistics Data were expressed as mean±SD. Statistical analysis were carried out using Student's *t*-tests (two-tailed). $P<0.05$ indicates statistical significance.

Results

Effects of ASODN on Pim-2 expression After transfection of ASODN targeting Pim-2, semi-quantitative RT-PCR was used to determine the inhibitory effects on Pim-2 mRNA transcription. ASODN 1–3 examined in the present study exerted different inhibitory effects on mRNA transcription (Figure 1A). The Pim-2 transcription level was decreased by 64.5%, 56.8%, and 55.2% ($P<0.05$) in DU-145 cells by ASODN1-3, respectively (Figure 1B). In addition, the Pim-2 protein amount was diminished by treatment with ASODN compared with the control (Figure 2).

Effects of ASODN on cell viability As shown in Figure 3, all of the ASODN targeting Pim-2 gene treatment significantly decreased cell viability, and the inhibition rate was dose-dependent.

Effects of ASODN on DU-145 cell growth arrest and apoptosis Flow cytometry was used to quantify changes in

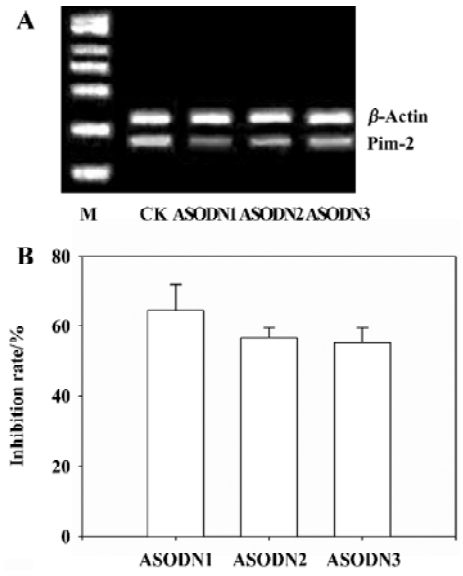

Figure 1. Effects of antisense oligodeoxynucleotides (ASODN) on mRNA level of Pim-2 in DU-145 cells. (A) Electrophoresis of reverse transcription–polymerase chain reaction products of the Pim-2 gene and β-actin gene in DU-145 cells transfected with ASODN1, 2 and 3. (B) Quantification of the data presented in (A). Data are expressed as mean±SD from four independent experiments. $P<0.05$ *vs* the cells transfected with lipofectamine alone.

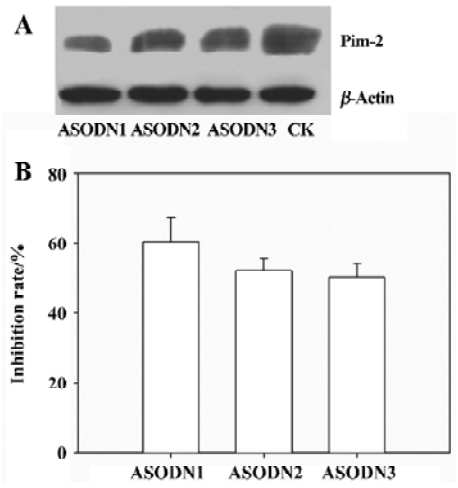

Figure 2. Inhibition of Pim-2 protein expression in DU-145 cells after transfection with antisense oligodeoxynucleotides (ASODN) 1, 2, and 3. (A) Cell extracts were separated using sodium dodecyl sulfate gel electrophoresis, transferred to a membrane and blotted with anti-Pim-2 goat polyclonal antibody. Anti-β-actin rabbit polyclonal antibodies were used as loading control. (B) Quantification of the data presented in (A). Data are expressed as mean±SD from four independent experiments. $P<0.05$ *vs* the cells (CK) transfected with lipofectamine alone.

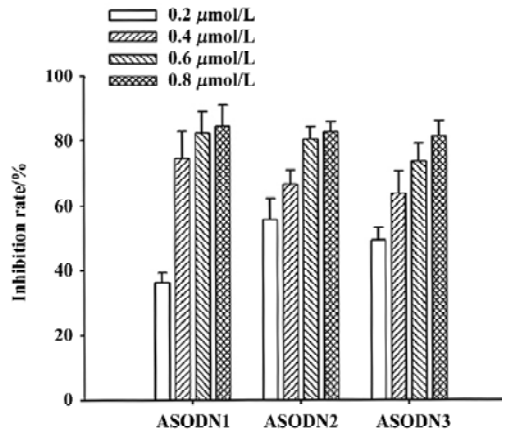

Figure 3. Effects of antisense oligodeoxynucleotides (ASODN) on the proliferation of DU-145 cells. Data are expressed as mean±SD from four independent experiments.

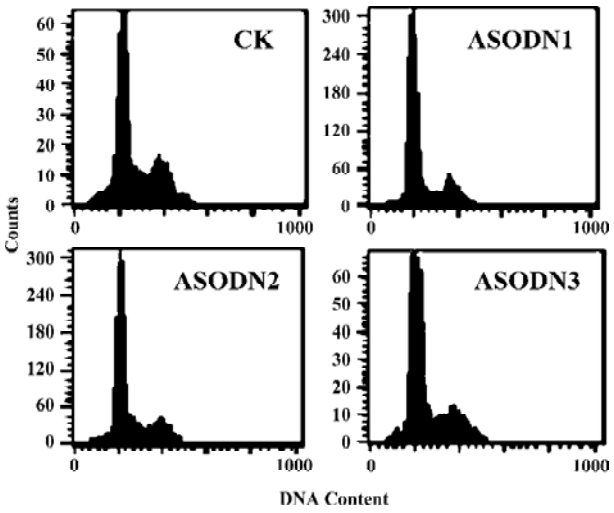

Figure 4. Analysis of cell apoptosis after transfection with antisense oligodeoxynucleotides (ASODN) in DU-145 cells. Cells transfected with lipofectamine alone were used as a control.

cell cycle and apoptosis 48 h after treatment with Pim-2 ASODN. All of the ASODN targeting Pim-2 increased the fraction of cells undergoing growth arrest at G_0/G_1 in DU-145 cells, and the inhibitory effect of ASODN1 was greater than the others (Table 2). It should be noted that no apparent apoptosis occurred in cells after treatment with any of the ASODN (Figure 4).

Table 2. Cell cycle distribution of DU-145 cells (%) treated with antisense oligodeoxynucleotides (ASODN). $^bP<0.05$ *vs* the control group.

Cell cycle (phase)	ASODN1	ASODN2	ASODN3	Control
G_0/G_1	71.68^b	69.78^b	65.72^b	51.76
G_2/M	7.06	8.13	8.26	9.26
S	21.26^b	22.09^b	26.02^b	38.98

Discussion

The balance between cell death and cell proliferation determines cells survive or die. Although the detailed mechanism and function of Pim-2 in cells are still unknown, research suggests that Pim-2 acts as an important factor to mediate cell survival. Consequently, ASODN against Pim-2 are anticipated to restrain cell proliferation. In this experiment, three ASODN targeting Pim-2 were designed and synthesized by our laboratory. Results indicated that all three ASODN could specifically reduce the mRNA transcription and protein expression level of Pim-2 in DU-145 cells (Figures 1, 2).

Prostate cancer is the most frequently diagnosed cancer in men. The incidence of prostate cancer rose in the late 1980s and early 1990s as a result of increased life expectancy, earlier and more accurate diagnosis, and increased public awareness of the disease. Nowadays, prostate cancer is believed to be the second leading cause of cancer related death in men. Thus, there is an urgent need to develop efficient therapy approaches to prostate cancer. Data presented here indicate that our ASODN could repress DU-145 cells growth to varying extents, and inhibitory effects were dose-dependent (Figure 3).

Despite extensive investigation, the physiological substrates of the Pim-2 kinase remain unknown. However, ASODN against Pim-2 induced marked G_1 phase cell cycle arrest in DU-145 prostate cancer cells (Table 2). This result implies that a number of proteins that are associated with cell cycle control are substrates of Pim-2 kinase. Similarly, Pim-1, its homological gene, was found to phosphorylate the cell cycle inhibitor p21Cip1/WAF1 and abrogate G_1 phase cell cycle arrest[14]. Taken together, these results offer evidence that the Pim serine/threonine kinase family show substantial homology, which can mediate the activity of a number of cell cycle related proteins. This experiment, implies that, in DU-145 cells, Pim-2 kinase is not the essential factor determining cell survival. In addition, abrogation of G_1 phase cell cycle arrest by Pim-2 serine/threonine kinase may be an important mechanism for prostate cell proliferation.

Antisense therapeutics for cancer are, after decades of difficulties, finally close to fulfilling their promise in the clinic.

Antisense compounds targeting certain genes, such as HER-2, VEGF, IGF-IR, and protein kinase C, were reported to efficiently inhibit target gene expression[15–18]. Advances in defining molecular abnormalities in prostate cancer offer the hope of improving both the diagnosis and therapy of the disease. It is now well established that the progression of epithelial cells in the prostate from normal to dysplastic or adenomatous epithelium to carcinoma *in situ* and finally to invasive carcinoma is the result of the sequential accumulation of genetic abnormalities involving oncogenes and tumor suppressor genes. A number of genetic mutations are found in prostate cancer, including activating mutations of the Pim-2 oncogene and loss of the tumor suppressor gene P_{53}[1–5]. In the present study, our antisense compounds could downregulate the expression of target mRNA level *in vitro*, as well as display certain antitumor activity. It is possible that antisense or other small molecule approaches to inhibit Pim-2 signaling may play a role in the treatment of patients with prostate cancer. In addition, a significant fraction of non-prostate tumors, including many colon, gastric, and testis carcinomas express elevated Pim-2 levels[19,20]. Whether or not antisense ODN targeting Pim-2 can also show antitumor activity against such neoplasm requires further study.

In summary, ASODN designed and synthesized by our laboratory against Pim-2 can efficiently suppress target gene expression and inhibit the growth of DU-145 cells, providing a new promising therapy target for prostate cancer.

References

1 Gonzalgo ML, Isaacs WB. Molecular pathways to prostate cancer. J Urol 2003; 170: 2444–52.

2 Maitland NJ, Stanbridge LJ, Dussupt V. Targeting gene therapy for prostate cancer. Curr Pharm Des 2004; 10: 531–55.

3 Hernandez I, Maddison LA, Wei Y, DeMayo F, Petras T, Li B, *et al*. Prostate-specific expression of p53 (R172L) differentially regulates p21, Bax, and mdm2 to inhibit prostate cancer progression and prolong survival. Mol Cancer Res 2003; 1: 1036–47.

4 Pei L, Peng Y, Yang Y, Ling XB, Van Eyndhoven WG, Nguyen KC, *et al*. PRC17, a novel oncogene encoding a Rab GTPase activating protein, is amplified in prostate cancer. Cancer Res 2002; 62: 5420–54.

5 Mora LB, Buttner R, Seigne J, Diaz J, Ahmad N, Garica R, *et al*. Constitutive activation of stats in human prostate tumors and cell lines: direct inhibition of Stat3 signalling induces apoptosis of prostate cancer cells. Cancer Res 2002; 62: 6659–66.

6 Cuypers HT, Selten G, Quint W, Zijlstra M, Maandag ER, Boelens W, *et al*. Murine leukemia virus-induced T-cell lymphomagenesis: integration of proviruses in a distinct chromosomal region. Cell 1984; 37: 141–50.

7 Eichmann A, Yuan L, Breant C, Alitalo K, Koskinen PJ. Developmental expression of Pim kinases suggests functions also outside of the hematopoietic system. Oncogene 2000; 19: 1215–24.

8 van der Lugt NM, Domen J, Verhoeven E, Linders K, van der Gulden H, Allen J. Proviral tagging in E mu-myc transgenic mice lacking the Pim-1 proto-oncogene leads to compensatory activation of Pim-2. EMBO J 1995; 14: 2536–44.

9 Allen JD, Verhoeven E, Domen J, vanderValk M, Berns A. Pim-2 transgene induces lymphoid tumors, exhibiting potent synergy with c-myc. Oncogene 1997; 15: 1133–41.

10 Saris CJ, Domen J, Berns A. The Pim-1 oncogene encodes two related protein-serine/threonine kinases by alternative initiation at AUG and CUG. EMBO J 1991; 10: 655–64.

11 Yan B, Zemskova, Holder S, Chin V, Kraft A. The PIM-2 kinase phosphorylates BAD on seine 112 and reverses BAD-induced cell death. J Biol Chem 2003; 46: 45358–67.

12 Chalk AM, Sonnhammer EL. Computational antisense oligo prediction with a neural network model. Bioinformatics 2002; 18: 1567–75.

13 Shao RG, Cao CX, Shimizu T, O'Connor PM, Kohn KW, Pommier Y. Abrogation of an S-phase checkpoint and potentiation of camptothecin cytotoxicity by 7-hydroxystaurosporine (UCN-01) in human cancer cell lines, possibly influenced by p53 function. Cancer Res 1997; 57: 4029–35.

14 Wang Z, Bhattacharya N, Mixter PF, Wei W, Sedivy J, Magnuson NS. Phosphorylation of the cell cycle inhibitor p21Cip1/WAF1 by Pim-1 kinase. Biochim Biophys Acta 2002; 1593: 45–55.

15 Yang SP, Song ST, Tang ZM, Song HF. Optimization of antisense drug design against conservative local motif in simulant secondary structures of HER-2 mRNA and QSAR analysis. Acta Pharmacol Sin 2003; 24: 897–902.

16 Zheng SX, Zhou LJ, Zhu XZ, Jin YX. Antisense oligodeoxynucleotide inhibits vascular endothelial growth factor in human glioma cells. Acta Pharmacol Sin 2000; 21: 211–4.

17 Sun HZ, Wu SF, Tu ZH. Knockdown of IGF-IR by antisense oligodeoxynucleotide auguments the sensitivity of bladder cancer cells to mitomycin. Acta Pharmacol Sin 2001; 22: 841–6.

18 Lahn M, Sundell K, Moore S. Targeting protein kinase C-alpha (PKC-alpha) in cancer with the phosphorothioate antisense oligonucleotide aprinocarsen. Ann NY Acad Sci 2003; 1002: 263–70.

19 Datta SR, Ranger AM, Lin MZ, Sturgill JF, Ma YC, Cowan CW, *et al*. Survival factor-mediated BAD phosphorylation raises the mitochondrial threshold for apoptosis. Dev Cell 2002; 3: 631–43.

20 Plas DR, Thompson CB. Cell metabolism in the regulation of programmed cell death. Trends Endo Met 2002; 13: 74–8.

Acta Pharmacologica Sinica 2005 Mar; 26 (3): 369–376

Full-length article

Effects of spider *Macrothele raven* venom on cell proliferation and cytotoxicity in HeLa cells[1]

Li GAO[2,3,9], Bao-en SHAN[4], Jing CHEN[5], Jiang-hui LIU[6], Da-xiang SONG[2], Bao-cheng ZHU[2,7,8]

[2]College of Life Science, Hebei University, Baoding 071002, China; [3]College of Life Science, Hebei Normal University, Shijiazhuang 050016, China; [4]Research Centre, The Fourth Hospital of Hebei Medical University, Shijiazhuang 050011, China; [5]Clinical Laboratory, Bethune International Peace Hospital, Shijiazhuang 050082, China; [6]Hebei Provincial Tumor Institute, Shijiazhuang 050011, China; [7]College of Life Science, Agricultural University of Hebei, Baoding 071001, China

Key words

HeLa cells; spider venom; cell proliferation; cytotoxicity; cell cycle; caspase-3 expression

[1] Project supported by the National Natural Science Foundation of China (No 30371753).
[8] Correspondence to Prof Bao-cheng ZHU.
Phn/Fax 86-312-507-9718.
E-mail zhu5079718@163.com
[9] Now in *College of Life Science, Hebei Normal University, Shijiazhuang 050016, China.*

Received 2004-07-15
Accepted 2004-11-10

doi: 10.1111/j.1745-7254.2005.00052.x

Abstract

Aim: To examine the effect of venom from the spider *Macrothele raven* on cell proliferation and cytotoxicity in human cervical carcinoma, HeLa cells. **Methods:** Morphological and biochemical signs of apoptosis appeared using acridine orange-ethidium bromide (AO/EB) staining. Marked morphological changes in HeLa cells after treatment with spider venom were observed using scanning electron microscopy (SEM) and transmission electron microscopy (TEM). Cell proliferation and cytotoxicity were determined by [*methyl*-^{3}H] thymidine assay ([^{3}H]TdR) and lactate dehydrogenase (LDH) release, respectively. DNA fragmentation and cell cycle distribution were monitored using flow cytometry. In addition, Western blot analysis was used to evaluate the level of caspase-3 expression. *In vivo* examination of the inhibition of the size of tumors in nude mice treated with spider venom was measured. **Results**: Marked morphological changes were observed using AO/EB staining, SEM and TEM assay. Spider venom at concentrations of 10–40 mg/L caused dose- and time-dependent inhibition of HeLa cell proliferation. The ratio of apoptosis and necrosis increased. The activity of caspase-3 was upregulated after spider venom treatment. *In vivo* study of tumor size revealed that tumors significantly decreased in size from controls to tumors treated for 3 weeks with spider venom (P<0.05). **Conclusion:** The inhibition of HeLa cells by the venom of the spider *Macrothele raveni* was carried out in three ways: induction of apoptosis, necrosis of toxicity damage and direct lysis. Spider venom is a novel anti-tumor material both *in vitro* and *in vivo*.

Introduction

Spider venoms are biochemically and biologically well studied world-wide and we know as much about spider venoms as we know about other animal venoms, such as snake venoms, bee venoms, and scorpion venoms. In general, the main toxin components of most spider venoms have been well identified as a complex mixture of proteins, polypeptides, polyamine neurotoxins, nucleic acids, free amino acids, monoamines, and inorganic salts that cause a wide range of effects in both vertebrates and invertebrates[1–3].

As far as the pharmacology and biochemistry of spider venom is concerned, spider venom represents a wide variety of ion channel toxins, novel non-neurotoxins, enzymes and low molecular weight compounds[4].

A number of studies have examined the anti-tumor substances found in snake venom[5–9], bee venom[10–12], and scorpion venom[13]. Many toxins isolated from spider venom have been invaluable in helping to determine the role and diversity of neuronal ion channels and the process of exocytosis[14–16]. Six peptide toxins (Magi 1–6) were isolated from the Hexathelidae spider, *Macrothele gigas*, dealing with sodium channel (Magi 1–5) and high toxicity in lepidoptera larvae of 3.1 nmol/g (Magi 6)[17]. Toxicological assays

showed diverse lethal or paralytic activities of Magi 7–16 in mice and/or insects[18]. The spider *Macrothele raveni* was indentified as a new species in the genus *Macrothele*[19]. There have been two papers published about raven toxin tests in mice in which the toxins acted as a neurotoxic peptide and blocked neuromuscular transmission[20,21]. To date there has been no study examining the venom of the spider *Macrothele raveni*. In the present study, the effects of *M raveni* spider venom on HeLa cells and possible mechanisms of action were evaluated.

Materials and methods

Reagents RPMI-1640 (Gibco Laboratories, Grand Island, NY, USA) dissolved in double distilled water with the pH value adjusted to 7.0 using $NaHCO_3$, was disinfected and stored at - 20 ºC. Fetal calf serum was purchased from Sijiqing Biological Engineering Company (Hangzhou, China), sterilized, and stored at -20 ºC. [^{3}H]TdR was purchased from the Atomic Energy Institute of China (Beijing, China). Verapamil, streptomycin, penicillin and 0.5% hydrocortisone were purchased from North China Pharmaceutical Company (Shijiazhuang, China). Propidium iodide (PI), bovine serum albumin (BSA), and Triton X-100 were purchased from Sigma Company (St Louis, MO, USA). The rabbit polyclonal antibody against caspase-3 and rodamine-labeled secondary antibody were purchased from Santa Cruz Biotech (Santa Cruz, CA, USA).

Spider venom Pure spider *Macrothele raveni* venom was collected by electrical stimulation of 15 spiders *M raveni* (the weight of each spider was approximately 60 g)[22]. Spider venom was dissolved in phosphate buffered saline (PBS) and centrifuged at 8000×*g* for 10 min to remove insoluble materials. The concentration of spider venom was adjusted to 0 (control group), 10, 20, 40 mg/L. The spider venom was freeze-dried and stored at -80 ºC until required.

Cell culture The human cervical carcinoma cell line HeLa was obtained from the Cellular Biology Institute of the Chinese Academy of Sciences (Shanghai, China). The frozen cells were defrosted, transferred into the culture medium RPMI-1640 supplemented with 10% fetal calf serum, 100 kU/L streptomycin, and 100 kU/L benzyl penicillin. The cells were grown at 37 °C under a humidified atmosphere of 5% CO_2 .

Determination of apoptosis Morphological evidence of apoptosis was obtained using acridine orange-ethidium bromide (AO/EB) staining. Monolayer cell cultures in 96-well plates were used for these studies. After removal of the incubation medium, the cells were rinsed and treated with a solution composed of AO/EB (100 mg/L PBS of each dye). Cells were examined using fluorescence microscopy and photographed (Olympus, Tokyo, Japan). Viable cells were colored green with intact nuclei. Non-viable cells had bright orange chromatin. Apoptosis was demonstrated by the appearance of cell shrinkage with condensation and fragmentation of nuclei. Apoptotic cells were easily distinguished from necrotic cells because the latter appeared orange with a normal nuclear structure. This procedure was used to quantify the number of apoptotic cells after treatment with spider venom. Apoptosis was also quantified using an enzyme-linked immunosorbent assay (ELISA) kit (Bindazyme; the Binding Site, Birmingham, UK) that measured the amounts of mono- and oligo-nucleosomes produced in the cytoplasmic fraction of lysed cells as a consequence of DNA fragmentation[23]. After treatment with spider venom, cells were collected and lysed according to the manufacturer's instructions. After centrifugation at 11 000×*g* for 15 min, equal amounts (0.3 μg of protein) of the cytosolic fractions were used for the assays.

Specimens for electron microscopy HeLa cells in the exponential phase were used and cultivated with various concentrations of spider venom for 24 h. The cells were harvested and fixed with 25 mL/L glutaraldehyde in 0.1 mol/L phosphate buffer (pH 7.4) for 2 h at 4 °C. For scanning electron microscopy (SEM) examination, the specimens were postfixed for 1 h in 2% OsO_4, dehydrated by adding a series of graded ethanol solutions to the filtration system and then slowly dried over the course of 24 h by evaporation. The filter was removed from the filtration apparatus and mounted on an aluminum stub, after which the cells were gold sputter coated. Specimens were examined with a STEREOSCAN 260 SEM at 25 kV. For transmission electron microscopy (TEM) examination, cells corresponding to each population were collected in Haemoline (BioChem Pharma, Allentown, PA, USA), transferred to microcentrifuge tubes, pelleted, and fixed in 1% OsO_4 (in distilled H_2O). A total of 4×10^7 cells were sorted to collect 2×10^6 cells representative of each of the individual populations. After dehydration through a series of graded alcohol and propylene oxide solutions, the cells were infiltrated with Epon (epoxy resin) and polymerized. Ultra-thin sections were cut, recovered on Formvar-coated copper grids, stained with uranyl acetate and lead citrate, and then examined with a 100 CXII transmission electron microscope (Jeol, Tokyo, Japan) operated at 80 kV.

Cell proliferation assay The inhibition of [^{3}H]TdR incorporation into DNA was examined using the pulse-labeling method. Proliferating HeLa cells were seeded onto 96-well plates and incubated for 16 h. HeLa cells were treated with different concentrations of spider venom (0, 10, 20,and

40 mg/L) for the next 24, 48, or 72 h. [^{3}H]TdR (37 MBq/L) was added and HeLa cells were exposed to [^{3}H]TdR for 16 h. The cells were then washed three times with PBS, lysed with 1 mol NaOH. After that the cells were harvested onto glass fiber filters with an automatic harvester. Filters were dried and radioactivity was quantified using liquid scintillation counter (Beckman LS6500, Fullerton, CA, USA). Results were expressed as the percent of specific lysis. Percent of specific lysis=100×[percent released from the target in the presence of effectors (experimental release)–percent released from the target in the presence of medium only (spontaneous release)]/(maximal release–spontaneous release).

Cell cytotoxicity assay Lactate dehydrogenase (LDH) release from cells was used as an index of cytotoxicity or necrosis. The quantity of LDH released by the cells into the medium was measured by the decrease in the absorbance at 340 nm for NADH disappearance within 5 min[13]. After incubation with various concentrations of spider venom (0, 10, 20, and 40 mg/L) for 24 h, the cell culture supernatant and medium (100 mL) were mixed with 900 mL PBS and 20 mg/L BSA. The percentage of LDH release (n=6) was equal to LDH activity in the medium divided by activity in both the cell culture supernatant and the medium×100%.

Cell cycle distribution using flow cytometry Bivariant flow cytometry was carried out on cells grown in the presence (control group) or absence of spider venom (10, 20, and 40 mg/L) after 24 h. Cells were collected and washed in cold PBS twice and resuspended in 100 mL of binding buffer (HEPES containing 2.5 mmol/L $CaCl_2$). Fluorescein-labeled annexin V and PI were added to the cell suspension. Cells were then analyzed using flow cytometry (Becton Dickinson, Mountain View, CA, USA). The DNA content of the cells was determined by staining with PI. The cells were incubated in 100 mL of fixing solution (PBS containing 4% formaldehyde) for 15 min at 4 ºC, washed in PBS, resuspended in permeabilizing solution (PBS containing 0.1% saponin and 0.1% sodium azide) in the presence of 10 mL of PI, and incubated at 4 ºC for 15 min. The cells were then washed with PBS and immediately analyzed using flow cytometry.

Western blot analysis HeLa cells exposed to different concentrations of spider venom (10, 20, 40 mg/L and control) were incubated in six-well plates at a density of 2.5×10^5 cells/well for 48 h, followed by a further cultivation of 48 h with the culture medium replaced with 1 mL of serum-free RPMI-1640. The serum-free medium was totally collected. Equal amounts of proteins in each sample were resolved in 10% sodium dodecyl sulfate-polyacrylamide gel electrophoresis (SDS-PAGE) and the proteins were transferred onto nitrocellulose membranes. After being washed in 10 ml/L fat-free milk, the membranes were incubated with the appropriate dilution of rabbit polyclonal caspase-3 antibody and glyceraldehyde-3-phosphate dehydrogenase (GAPDH) antibody. The membranes were then incubated with a horseradish peroxidase-conjugated secondary antibody. Proteins were detected using an enhanced chemiluminescence (ECL) kit according to the manufacturer's protocol (Amersham, Amersham, Buckinghamshire, UK).

***In vivo* reduction in tumor size in nude mice using spider venom** We induced cervical tumors by injecting HeLa cells (200 μL) under the skin of nude mice with a concentration of 4×10^9 cells/L. Three weeks after tumor growth was established, treatment was initiated. Nude mice with tumors were randomly placed into three groups (10 mice/group) and treated with spider venom, 1.0, 2.0, 4.0 μg/g body weight of mice three times per week for 3 weeks by tail vein injections. The control group of 10 mice received distilled water only as a placebo. The mice were killed and tumor size was evaluated by caliper measurements, and tumor volume was calculated as length×width×depth.

Statistical analyses Significant differences between groups were tested using Mann-Whitney U tests with a significance level of 95%. Differences between groups were considered statistically significant at P<0.05. Analyses were carried our using the Prism software package (GraphPad, San Diego, CA, USA).

Results

Effects of spider venom on viability and apoptosis in HeLa cells Our study was carried out using HeLa cells grown in serum-free monolayer cultures. We observed using light microscopy that treatment with spider venom (10, 20, and 40 mg/L) initially produced clusters of packed cells (data not shown). After 24 h of treatment, the bulk of the cells appeared to be seriously damaged. To investigate the type of cell death induced by spider venom, the cells were stained with AO/EB, which allows the identification of viable, apoptotic and necrotic cells based on color and appearance. Staining with AO/EB of the samples treated with different concentrations of spider venom (Figure 1) showed different percentages of orange-stained cells. Viable cells were green with intact nuclei. Non-viable cells had bright orange chromatin. Apoptosis was demonstrated by the appearance of cell shrinkage with condensation and breaking up of the nuclei. Apoptotic cells were easily distinguished from necrotic cells because the latter appeared orange with a normal nuclear structure. This procedure was used to quantify the number of apoptotic cells after treatment with spider venom.

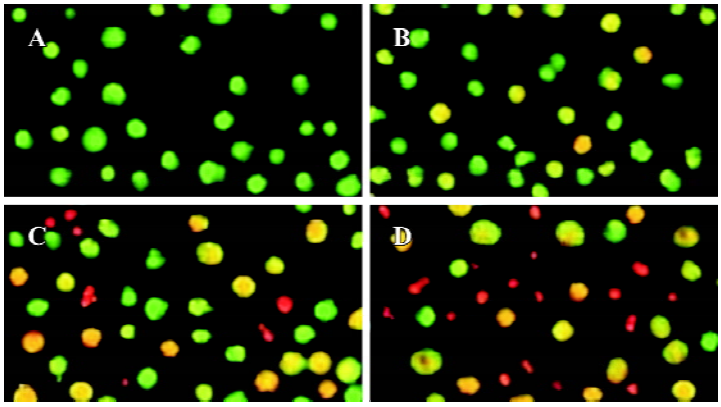

Figure 1. Identification of apoptotic cells using acridine orange-ethidium bromide staining and the effect induced by spider venom (10, 20, and 40 mg/L). Untreated cells (A) compared with cells treated with spider venom at 10 mg/L (B), at 20 mg/L (C) or at 40 mg/L (D) (×200)

A number of cells exhibited a flattened polygonal morphology, whereas other cells showed morphological features of apoptosis, consisting of a decrease in cell volume, membrane broken, and breaking up of the nuclei. Moreover, the majority of these non-viable cells, together with a number of viable cells, showed broken nuclei and other signs of apoptosis.

Morphological observations After exposure to spider venom for 24 h, SEM confirmed that HeLa cells treated with spider venom had morphological features indicative of apoptosis (Figure 2A,2B). Compared to cells treated with

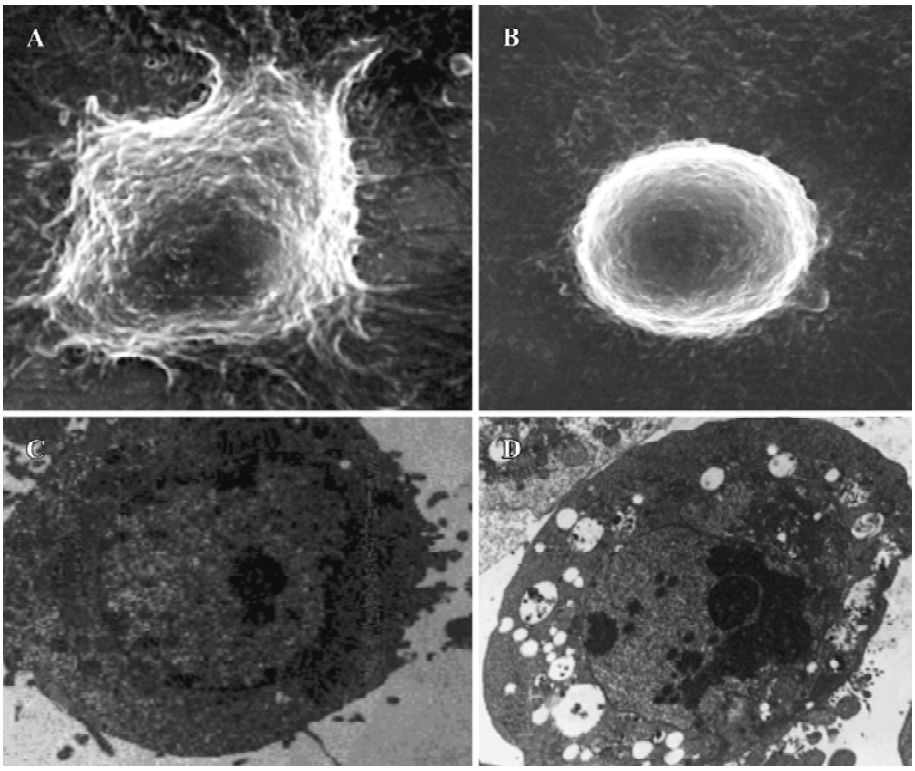

Figure 2. Morphological observations using scanning electron microscopy. (A) Control cells (×8000); (B) Spider-venom-treated cells (20 mg/L, 24 h) (×8000); Morphological observations using transmission electron microscopy; (C) Control cells (×10 500); (D) Spider-venom-treated cells (20 mg/L, 24 h) (×10 500).

control supernatants, approximately 25% of cells exposed to spider venom (20 mg/L) for 24 h appeared to be markedly reduced in size. These cells were devoid of the villous projections found on the surfaces of control cells. In addition, many of the spider-venom-treated cells exhibited perturbations of their plasma membranes as evidenced by membrane smoothing. Ultrastructural characterization of cells representative of the individual populations was achieved through cell sorting and subsequent evaluation using TEM. Cells treated with spider venom possessed well-defined plasma membranes and contained intact organelles with no evidence of nuclear condensation (Figure 2C). In contrast, the majority of cells in the venom-treated group exhibited morphological characteristics typical of cells in the early stages of apoptosis. These characteristics included a decrease in cell size, intact cell membranes, and flocculation of the nucleus (Figure 2D). None of these characteristics were present in untreated cells.

Effect of spider venom on [^{3}H]TdR incorporation in HeLa cells Inhibition of DNA synthesis was examined in the presence of spider venom (Figure 3). Proliferating HeLa cells were exposed to different concentrations of spider venom for 24, 48, or 72 h. The cells were then treated with [^{3}H]TdR for 12 h. Synthesis of DNA in these cells was inhibited, with IC_{50} ranging from 20 to 30 mg/L after 24 h, 48 h, 72 h. The degree of growth inhibition of HeLa cells in the presence of spider venom was dose-dependent. Spider venom significantly decreased cell proliferation, but the degree differed with the variant concentrations (P<0.01). The spider-venom-induced inhibition of cell proliferation was also time dependent. Spider venom significantly decreased cell proliferation, and again the decrease differed with time (P< 0.01).

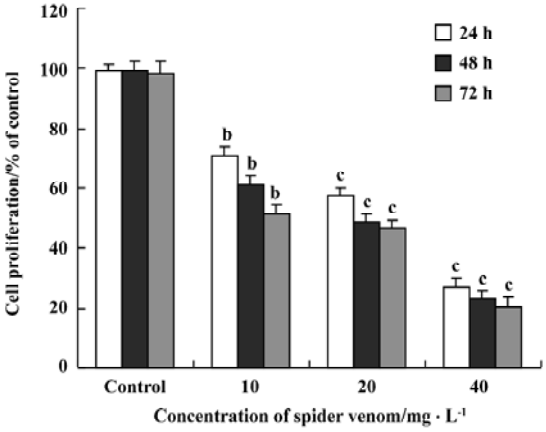

Figure 3. Effect of spider venom (10, 20 and 40 mg/L) on the proliferation of cells measured by [^{3}H]TdR assay. Results are expressed as % of control cells (n=6. Mean±SD. ^bP<0.05, ^cP<0.01 *vs* control group) using an ANOVA with subsequent multiple comparison tests.

Cell cytotoxicity of spider venom on HeLa cells Cell cytotoxicity was directly measured by LDH release (Figure 4). After 24 h incubation, spider venom (0, 10, 20, and 40 mg/L) significantly increased cell cytotoxicity (P<0.05) compared with the control group (5.95%). Increased cell cytotoxicity occurred with increased concentrations of spider venom. The activity is to be time- and dose-dependent.

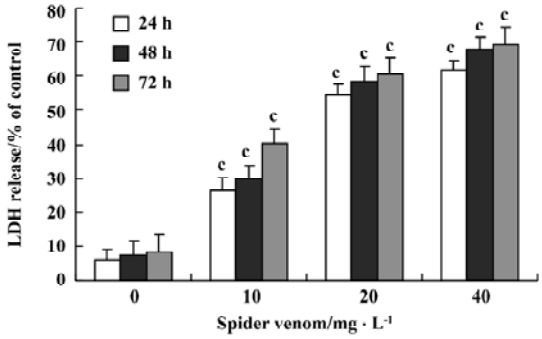

Figure 4. Effects of spider venom (10, 20, and 40 mg/L) on cell cytotoxicity in Hela cells determined by lactate dehydrogenase (LDH) release. Values not sharing the same letter differed significantly (n=6. Mean±SD. ^cP<0.01 *vs* control group) using an ANOVA with subsequent multiple comparison tests.

Effect of spider venom on apoptosis, necrosis ratio, and cell cycle Cells were exposed to different concentrations of spider venom (10, 20, and 40 mg/L). Cells in the early phase of apoptosis were labeled using single annexin V fluorescence. The ratio of apoptosis and necrosis in the cells increased with increasing venom concentrations. The early stages of apoptosis and necrosis started 5 h after treatment of HeLa cells with 40 mg/L spider venom (Table 1).

Cell cycle distribution, cell proliferation and apoptotic

Table 1. Effects of spider venom on the ratio of apoptosis and necrosis in Hela cells. n=6. Mean±SD. ^bP<0.05, ^cP<0.01 *vs* control.

Group/mg·L^{-1}		Ratio of apoptosis and necrosis/%			
		5 h		15 h	
		Apoptosis	Necrosis	Apoptosis	Necrosis
Control	0	0.20±0.01	0	1.10±0.14	0
Spider	10	5.7±0.2^b	7.1±0.3^c	8.2±1.9^b	12.9±1.0^c
venom	20	16.6±1.2^c	20.4±2.0^c	19.2±1.0^c	34.5±2.3^c
	40	20.8±2.8^c	40.6±0.4^c	25.1±2.4^c	61.3±2.6^c

damage of DNA were determined using a flow cytometer. Results showed the accumulation of cells in S and G_2/M, and a corresponding reduction in the percentages of cells in G_0/G_1 (Table 2).

Table 2. Effect of spider venom on cell cycle distribution and apoptosis in cells. n=10. Mean±SD. $^bP<0.05$, $^cP<0.01$ *vs* control.

Group/mg·L^{-1}		Cell cycle distribution/%		
		G_0/G_1	S	G_2/M
Control	0	59.3±1.2	28.9±0.5	10.7±1.4
Spider	10	63.2±2.1^c	26.8±3.9^b	9.8±0.6^b
venom	20	68.6±3.7^c	22.1±0.4^c	9.3±1.5^b
	40	74.1±2.7^c	19.7±1.8^c	6.1±1.3^c

Effects of spider venom on the activitiy of caspase-3 To elucidate the pathway leading to apoptosis, we examined the activation of caspase-3, which was reported to initiate apoptosis after various stimuli. HeLa cells treated with spider venom (10, 20, and 40 mg/L) for 48 h were analyzed for enzymatic activity using a Western blot analysis. Caspase-3 activity changed at 48 h in HeLa cells (Figure 5). The activity

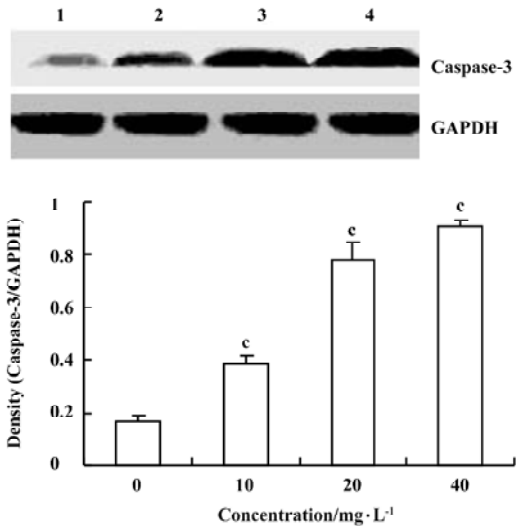

Figure 5. Effects of spider venom on the levels of caspase-3 protein in HeLa cells after treatment for 48 h. As an internal control, GAPDH protein was blotted concurrently. (A) Caspase-3 protein expression in control group (lane 1), and in the spider venom treatment groups (10 mg/L, lane 2; 20 mg/L, lane 3; 40 mg/L, lane 4). (B) Densitometric analysis of the levels of caspase-3 using an image analysis system. Data are expressed as the ratio to the internal standard. n=6. Mean±SD. $^cP<0.01$ *vs* control group. ANOVA with subsequent multiple comparison tests.

was enhanced significantly (1.7-, 2.2-, and 4.3-fold, respectively, versus controls, $P<0.01$). Western blotting analysis, revealed that the exposure of HeLa cells to spider venom enhanced the activity of caspase-3, which became four-fold higher than that in the control cells (Figure 5).

***In vivo* reduction in tumor size in nude mice using spider venom** We have investigated the effect of spider venom in nude mice with tumors. Mice were killed 21 d after treatment and tumor size was determined. In the groups injected with various concentrations of spider venom by the tail vein, the size of the tumor inside the skin was significantly smaller ($P<0.01$) than in untreated mice (Table 3).

Table 3. Effect of spider venom on size of tumor cells in nude mice. n=10. Mean±SD. $^cP<0.01$ *vs* control.

Group/μg·g^{-1}		Size of the tumor/mm^3
Control	0	55.5±0.4
Spider venom	1.0	39.7±0.6^c
	2.0	24.7±0.5^c
	4.0	12.2±0.2^c

Discussion

A number of possible biological and biochemical effects of spider venom were investigated in the present study.

Cells excluding vital dyes were considered to be viable. However, our current results suggest that many of these cells are actually undergoing apoptotic cell death despite having relatively intact cell membranes. Spider venom at doses of 40, 20, and 10 mg/L significantly decreased cell proliferation in HeLa cells, in a dose-dependent and time-dependent manner.

Aside from the inhibitory effect of spider venom on cell proliferation, spider venom at the same doses (10, 20, and 40 mg/L) significantly increased cytotoxicity determined by LDH release in the cells. The cytotoxic effect of spider venom reached a plateau at doses over 160 mg/L. The cytotoxic effect of spider venom could be attributed to necrosis[24]. The total number of cells present will be directly proportional to the background-subtracted fluorescence values, which represent LDH activity. It is relatively easy to distinguish between complete cell lysis occurring at time zero versus 50% cell lysis at 24 h, 48 h, and 72 h and this result was observed in the "lysed"data (Figure 4).

Meanwhile, we directly measured apoptosis using flow cytometry. Apoptosis in HeLa cells was increased in the spider venom-treated groups. It is possible that apoptosis

contributes to the cytotoxic effect of spider venom. Changes in cells associated with the early phases of apoptosis include a loss of cell membrane phospholipid symmetry. The effect of spider venom on HeLa cells was analyzed using fluorescein-labelled annexin V-stained and PI-stained cells (Table 1). Thus, our findings revealed that spider venom resulted in direct necrosis and indirect apoptosis (Table 1) to kill HeLa cells.

To examine whether growth inhibition of HeLa cells by spider venom resulted from cell cycle arrest, cell cycles treated with spider venom were analyzed using flow cytometry. The inhibitory effect of spider venom on growth of the cells may result from G_0/G_1 cell cycle arrest.

Caspases are common and critical components of the cell death pathway. Among these caspases, caspase-3-like proteases mediate the initiation and/or execution stages of programmed cell death[25,26]. The active enzyme takes part in the execution phase of apoptosis and it has been demonstrated that a high level of activity of effector caspase-3 in tumor cells plays a decisive role in their commitment to apoptosis[27–30]. Caspase-3 is a key executioner of apoptosis, whose activation is mediated by the initiator caspases, such as caspase-9[31]. Spider-venom-induced apoptosis was preceded by the activation of caspase-3, which was clearly observed after 48 h of treatment by direct estimation of its activity and by Western blotting analysis, which showed the conversion of procaspase-3 to the active form of the enzyme. This result is the same as norcantharidin-induced HeLa cell apoptosis resulting from an increase in caspase-3 activity[32].

All these events preceded the appearance of the morphological signs of apoptosis, which were observed in a large percentage of cells only after 48 h of treatment (Figure 5). The results from the present study suggested that the cytotoxic effect of spider venom on the cells was related to the induction of apoptosis.

Importantly, the anti-tumor *in vivo* action of spider venom resulted in either complete or significant regression of the human cervical tumors established in nude mice. Our *in vivo* results demonstrate that spider venom confers a systemic effect of tumor regression in a xenograft in a dose-dependent manner.

In conclusion, we demonstrated that spider venom caused an inhibition of cell growth in HeLa cells as a result of cycle arrest and apoptosis. Moreover, a large part of our study essentially focused on the mitochondrial pathway and we determined that one action of spider venom was caspase-3 dependent. These new findings suggest that spider-venom-induced effects may have novel applications for the treatment of cancer.

Acknowledgements

We are indebted to Jun-xin LI (Research Centre, the Fourth Hospital of Hebei Medical University) for equipment and technical assistance. We are also grateful to Ji-biao LI for technical assistance with the SEM; Jian ZHANG for molecular technical assistance and sharing his expertise (Hebei Normal University, Shijiazhuang, China). I thank Dr James P KEHRER (University of Texas at Austin,TX, USA) for helping us improve the manuscript.

References

1 Schanbacher FL, Lee CK, Hall JE, Wilson IB, Howell DE, Odell GV. Composition and properties of tarantula *Dugesiella hentzi* (Girard) venom. Toxicon 1973; 11: 21–4.

2 Jackson H, Parks TN. Spider toxins: recent applications in neurobiology. Annu Rev Neurosci 1989; 12: 405–14.

3 Ori M, Ikeda H. Spider venoms and spider toxins. J Toxicol 1998; 17: 405–26.

4 Rash LD, Hodgson WC. Pharmacology and biochemistry of spider venoms. Toxicon 2002; 40: 225–54.

5 Abu-Sinna G, Esmat AY, Al-Zahaby AA, Soliman NA, Ibrahim TM. Fractionation and characterization of *Cerastes cerastes* snake venom and the antitumor action of its lethal and non-lethal fractions. Toxicon 2003; 42: 207–15.

6 Swenson S, Costa F, Minea R, Sherwin RP, Ernst W, Fujii G, *et al* Intravenous liposomal delivery of the snake venom disintegrin contortrostatin limits breast cancer progression. Mol Cancer Ther 2004; 3: 499–511.

7 Correa MC Jr, Maria DA, Moura-da-Silva AM, Pizzocaro KF, Ruiz IR. Inhibition of melanoma cell tumorigenicity by the snake venom toxin jararhagin. Toxicon 2002; 40: 739–48.

8 de Carvalho DD, Schmitmeier S, Novello JC, Markland FS. Effect of BJcuL (a lectin from the venom of the snake *Bothrops jararacussu*) on adhesion and growth of tumor and endothelial cells. Toxicon 2001; 39: 1471–6.

9 Schmitmeier S, Markland FS, Chen TC. Anti-invasive effect of contortrostatin, a snake venom disintegrin, and TNF-alpha on malignant glioma cells. Anticancer Res 2000; 20: 4227–33.

10 Orsolic N, Sver L, Verstovsek S, Terzic S, Basic I. Inhibition of mammary carcinoma cell proliferation *in vitro* and tumor growth *in vivo* by bee venom. Toxicon 2003; 41: 861–70.

11 Shaposhnikova VV, Kublik LN, Narimanov AA, Levitman MKh, Orlova OE, Kudriavtsev AA,*et al*. Growth inhibition and induction of tumor cell death by phospholipase A2 and lipoxygenase inhibitors. Izv Akad Nauk Ser Biol 2001; (2): 249–52.

12 Liu X, Chen D, Xie L, Zhang R. Effect of honey bee venom on proliferation of K1735M2 mouse melanoma cells *in-vitr*o and growth of murine B16 melanomas *in-vivo*. J Pharm Pharmacol 2002; 54: 1083–9.

13 Liu YF, Ma RL, Wang SL, Duan ZY, Zhang JH, Wu LJ, *et al*. Expression of an antitumor-analgesic peptide from the venom of Chinese scorpion *Buthus martensii* karsch in *Escherichia coli*. Protein Expr Purif 2003; 27: 253–8.

14 Szeto TH, Birinyi-Strachan LC, Smith R, Connor M, Christie MJ, King GF, *et al*. Isolation and pharmacological characterisation of delta-atracotoxin-Hv1b, a vertebrate- selective sodium channel toxin. FEBS Lett 2000; 470: 293–9.
15 Stotz SC. Block of voltage-dependent calcium channel by the green mamba toxin calcicludine. J Membrane Biol 2000; 174: 157–65.
16 Marvin L, De E, Cosette P, Gagnon J, Molle G, Lange C. Isolation, amino acid sequence and functional assays of SGTx1. The first toxin purified from the venom of the spider *Scodra griseipes*. Eur J Biochem 1999; 265: 572–9.
17 Corzo G, Gilles N, Satake H, Villegas E, Dai L, Nakajima T, *et al*. Distinct primary structures of the major peptide toxins from the venom of the spider *Macrothele gigas* that bind to sites 3 and 4 in the sodium channel. FEBS Lett 2003; 547: 43–50.
18 Satake H, Villegas E, Oshiro N, Terada K, Shinada T, Corzo G. Rapid and efficient identification of cysteine-rich peptides by random screening of a venom gland cDNA library from the hexathelid spider *Macrothele gigas*. Toxicon 2004; 44: 149–56.
19 Zhu MS, Li TH, Song DX. A species of genus macrothele (araneae: hexathekidae) from China. J Hebei Univ (Natural Science Edition) 2000; 4: 358–61.
20 Zheng XZ, Liang SP. Purification and preliminary toxin research of raventoxin-II, a neurotoxic peptide from the venom of the spider *Macrothele raveni*. Life Sci Res 2001; 3: 217–20.
21 Zeng XZ, Xiao QB, Liang SP. Purification and characterization of raventoxin-I and raventoxin-III, two neurotoxic peptides from the venom of the spider *Macrothele raveni*. Toxicon 2003; 41: 651–6.
22 Friedel T, Nentwig W. Immobilizing and lethal effects of spider venoms on the cockroach and the common mealbeetle. Toxicon 1989; 27: 305–16.
23 Giuliano M, Lauricella M, Vassallo E, Carabillò M, Vento R, Tesoriere G. Induction of apoptosis in human retinoblastoma cells by topoisomerase inhibitors. Invest Ophthalmol Vis Sci 1998; 39: 1300–11.
24 Zhang Y, Wu LJ, Tashiro S, Onodera S, Ikejima T. Evodiamine induces tumor cell death through different pathways: apoptosis and necrosis. Acta Pharmacol Sin 2004; 25: 83–9.
25 Qi H, Chen HZ, Jin ZJ. Caspase 3 gene expression and $[Ca^{2+}]_i$ homeostasis underlying desipramine-induced C6 glioma cell apoptosis. Acta Pharmacol Sin 2002; 23: 803–7.
26 Lan H, Lu YY. Allitridi induces apoptosis by affecting Bcl-2 expression and caspase-3 activity in human gastric cancer cells. Acta Pharmacol Sin 2004; 25: 219–25.
27 Alnemri ES, Livingston DJ, Nicholson DW, Salvesen G, Thornberry NA, Wong WW, *et al*. Human ICE/CED-3 protease nomenclature. Cell 1996; 87: 171.
28 Chae HJ, Park KM, Lee GY, Jeong GS, Park HR, Kim HM, *et al*. Je-chun-jun induced apoptosis of human cervical carcinoma HeLa cells. Acta Pharmacol Sin 2004; 25: 1372–9.
29 Liu DC, Zang CB, Liu HY, Possinger K, Fan SG, Elstner E. A novel PPAR alpha/gamma dual agonist inhibits cell growth and induces apoptosis in human glioblastoma T98G cells. Acta Pharmacol Sin 2004; 25: 1312–19.
30 Hou R, Zhou QL, Wang BX, Tashiro S, Onodera S, Ikejima T. Diosgenin induces apoptosis in HeLa cells via activation of caspase pathway. Acta Pharmacol Sin 2004; 25: 1077–82.
31 Salvesen GS, Dixit VM. Caspases: intracellular signaling by proteolysis. Cell 1997; 91: 443–6.
32 An WW, Gong XF, Wang MW, Tashiro S, Onodera S, Ikejima T. Norcantharidin induces apoptosis in HeLa cells through caspase, MAPK, and mitochondrial pathways. Acta Pharmacol Sin 2004; 25: 1502–8.

Acta Pharmacologica Sinica 2005 Mar; 26 (3): 377–383

Full-length article

Inhibition of STAT3 expression by siRNA suppresses growth and induces apoptosis in laryngeal cancer cells

Li-fang GAO[1], De-qi XU[2], Lian-ji WEN[3], Xing-yi ZHANG[4], Yue-ting SHAO[1], Xue-jian ZHAO[1,5]

[1]Department of Pathophysiology, Basic School of Medicine, Jilin University, Changchun 130021, China; [2]Laboratory of Enteric and Sexually Transmitted Diseases, Center for Biologics Evaluation and Research, Food and Drug Administration, Bethesda MD, 20892, USA; [3]Departments of ENT and [4]Thoracic and Cardiovascular Surgery, the Second Hospital of Jilin University, Changchun 130021, China

Key words

STAT3; RNA interference; laryngeal neoplasms; apoptosis

[5] Correspondence to Prof Xue-jian ZHAO.
Phn/Fax 86-431-563-2348.
E-mail pro_2@jlu.edu.cn

Received 2004-07-22
Accepted 2004-11-10

doi: 10.1111/j.1745-7254.2005.00053.x

Abstract

Aim: To determine the inhibitory effect of the synthetic STAT3 siRNA on the expression of STAT3 gene in human laryngeal cancer cell lines Hep2 and to investigate the effect of STAT3 siRNA on growth and apoptosis in Hep2 cells. **Methods:** A pair of DNA templates coding siRNA against STAT3-mRNA was synthesized to reconstruct plasmid of pSilencer1.0-U6 siRNA-STAT3. Hep2 cells were transfected with RPMI-1640 media (untreated), plasmid (empty), and STAT3 siRNA, respectively. Northern blot and Western blot analysis of STAT3 and pTyr-STAT3 expression in Hep2 cells and Western blot analysis of Bcl-2 expression in the Hep2 cell was performed 72 h after transfection. MTT, flow cytometry, and AO/EB assay were used for determination of cells proliferation and apoptosis in Hep2 cells. **Results:** pTyr-STAT3 was markedly expressed in untreated Hep2 cells and the vector-treated Hep2 cells, whereas pTyr-STAT3 expression was significantly reduced in STAT3 siRNA-transfected Hep2 cells, indicating that STAT3 siRNA inhibited the activity of STAT3. Transfection of Hep2 cells with STAT3 siRNA significantly inhibited STAT3 expression at both mRNA and protein level in Hep2 cells and the inhibition was characterized by time-dependent transfection. Treatment of Hep2 cells with STAT3 siRNA resulted in dose-dependent growth inhibition of Hep2, this significantly increased apoptotic cell rate, and decreased Bcl-2 expression level in Hep2 cells. STAT3 siRNA had an effect on induction of either early or late stage apoptosis. **Conclusion:** This study demonstrates that STAT3 siRNA effectively inhibits STAT3 gene expression in Hep2 cells leading to growth suppression and induction of apoptosis in Hep2 cells. The use of siRNA technique may provide a novel therapeutic approach to treat laryngeal cancer and other malignant tumors expressing constitutively activated STAT3.

Introduction

Laryngeal carcinoma especially at late-stage is associated with high morbidity and poor long-term survival due to the absence of effective treatment methods. Better understanding of molecular mechanisms underlying proliferation, differentiation, and survival of laryngeal carcinoma is critical for the development of optimal therapeutic modalities. Recent studies suggest that signal transducers and activator of transcription (STATs) have the potential as novel molecular targets for the development and survival of laryngeal carcinomas.

STATs are latent cytoplasmic transcription factors that function as intracellular effectors of cytokine and growth factor signaling pathways . Among the STAT family, STAT3 plays a key role in promoting proliferation, differentiation, anti-apoptosis, or cell cycle progression. Constitutive activation of STAT3 is implicated in a variety of tumor cell lines[1–5], thereby suggesting that STAT3 is an important molecular target for tumor therapy.

In vitro studies have shown that inhibition of STAT3 activity in human tumor cells induces apoptosis and/or growth arrest. In human head and neck squamous carcinoma cells, blocking of STAT3 signaling by decoy oligonucleotide or antisense oligonucleotides abrogates transforming growth factor and suppresses oncogenic growth of these cells[6,7]. STAT3β is a naturally accruing dominant-negative STAT3 variant that is identical to STAT3 except for the absence of the transactivation domain[8]. Bowman *et al*[2] have reported that blockade of STAT3 signaling by STAT3β in human myeloma cells down-regulates IL-6-induced expression of the antiapoptotic gene, Bcl-x_L, resulting in a dramatic sensitization of cells to Fas-mediated apoptosis *in vitro*. STAT3β can promote apoptosis in breast cancer cells, inhibit Bcl-x_L expression, and induce apoptosis[9]. Overall, these raise the possibility that targeting STAT3 may enhance antitumor responses *in vivo* in a variety of human cancers.

A relatively new technique using RNA interference (RNAi) provides a novel approach of experimental inhibition of gene expression. RNAi is triggered by the presence of double-stranded RNA (dsRNA) in the cell and results in rapid degradation of the targeted mRNA with homology to the double strand leading to potent and selective silencing of genes. This phenomenon was first observed from studies in *Caenorhabditis* elegans and *Drosophila* melanogaster and subsequently, in other organisms[10]. Recent studies have shown that short interfering (21–25 bp) RNA molecules (siRNA), but not long dsRNA (greater than 30 bp), are key elements of RNAi. Only recently has the use of RNAi in mammalian studies been established by introducing siRNA[14]. At present, siRNA has been adapted as a functional genomic tool and has potential as a therapeutic approach in cancer.

Intriguingly, blocking of STAT3 signaling pathways by siRNA has been shown to suppress growth and induce apoptosis in prostate cancer cell lines and astrocytoma cells[15,16]. However, to date no studies have studied the effect of inhibition of STAT3 gene expression by siRNA on laryngeal cancer. Since STAT3 signaling is critical for the regulation of proliferation, differentiation, and apoptosis of tumor cells, we hypothesize that knockdown of STAT3 gene expression by siRNA should suppress tumor growths and induce apoptosis in laryngeal carcinoma that observed in models of prostate cancer and astrocytoma[16,17].

The objectives of the present study were (1) to determine the inhibitory effect of the synthetic STAT3 siRNA on the expression of STAT3 gene in laryngeal carcinoma cells and (2) to investigate the effect of STAT3 siRNA on the growths and apoptosis in laryngeal carcinoma cells.

Materials and methods

Construction of plasmids that contain DNA templates for the synthesis of siRNAs were constructed under the control of the U6 promoter The pSilencer1.0-U6 (Ambion Inc Austin, TX, USA) was used for DNA vector-based siRNA synthesis under the control of U6 promoter *in vivo*. In brief, first, the double stranded DNA template encoding siRNA oligonucleotides (GeneBank: access numbers for the human STAT3: NM003150) that contained a sense strand of 19 nucleotide sequences followed by a short space (TTCAAGAGA), the reverse complement of the sense strand, and five thymidines as a RNA polymerase III transcriptional stop signal were synthesized. The sequences were forward 5´-GCAGCAGCTGAACAACATGTTCAAGAGACATGTTGTTCAGCTGCTGCTTTTTT3´ and reverse 5´AATTAAAAAAGCAGCAGCTGAACAACATGTCTCTTGAACATGTTGTTCAGCTGCTGCGGCC3´ (locate on SH2 domain). The oligo nucleotides were annealed in a buffer (potassium actate 100 mmol/L , 30 mmol/L HEPES-KOH pH 7.4, and magnesium acetate 2 mmol/L) and the mixture was incubated at 90 ºC for 3 min and then at 37 ºC for 1 h. The double stranded oligos were cloned into the *Apa*I–*Eco*R I sites of the pSilencer 1.0-U6 vector (Ambion Inc) where short hairpin RNAs (shRNA) were expressed under the control of the U6 promoter.

Cell culture and transfections The human laryngeal cancer cell lines Hep2 were obtained from ATCC. Hep2 cells were cultured in medium RPMI-1640 (Invitrogen, Inc Carlsbad, CA, USA) supplemented with 10% fetal bovine serum (FBS) and penicillin (100 kU/L) and streptomycin (100 mg/L) at 37 ºC in a humidified incubator with 5% CO_2. For cell transfection, lipofectamine 2000 (Invitrogen) was used for transfecting the plasmids following the manufacturer instructions. In brief, pEGFP was cotransfected with pSilencer1.0-U6-siRNA-STAT3 or pSilencer empty vector at ratio of 1:20 to mark the positive transfected cells, respectively. The cells were cultured for 5–20 h and then transferred to fresh medium with 10% FBS and lysed for 24–72 h after transfection.

Northern blot Total RNA was extracted from cell samples with Trizol (Invitrogen, Carlsbad, CA, USA). Equal amounts of 20 μg total RNA were electrophoresed on 1.2% agarose gel with formaldehyde 2.2 mol/L and transferred onto nylon membranes (Hybond-N, Amersham Pharmacia Biotech). Blots were incubated with ^{32}P-labeled cDNA against STAT3 and actin with Hyb and washed according to the manufacture directions. Visualization of blots was performed by overnight exposure to Kodak MS film. Quantification of blots developed on films was accomplished with a

Molecular Dymanics phosphorimager.

Western blot Total protein was extracted from the harvested sample cells with protein lysis buffer (5 mol/L edetic acid, 300 mmol/L NaCl, 0.1% Igepal, 0.5 mmol/L NaF, 0.5 mmol/L Na_3VO_4, 0.5 mmol/L PMSF, and antiprotease mixture) using sonication. The lysates were centrifuged at 15 000×g for 30 min. Determination of protein concentrations of the supernatants was performed by the Bradford procedure (Bio-Rad Laboratory, Hercules, CA, USA). For STAT3 and pTry-stat3 analysis, the supernatant with 50 μg total protein was separated by electrophoresis on 10% SDS-Polyacrylamide gels and transferred onto PVDF membranes (Milipore, Bedford, MA) and blocked with 5% nonfat dry milk in PBS with 0.1% Tween-20. Blots were incubated with specific rabbit antibodies against STAT3 and pTry-stat3 and anti-β-actin antibody (Santa Cruz Biotech, Inc, Santa Cruz, CA, USA) and washed with TBST and subjected to corresponding HRP-conjugated secondary antibodies as indicated. For Bcl-2 analysis, 50 μg of total protein was electrophoresed on 12% SDS/PAGE gels and transferred onto PVDF membranes (Milipore, Bradford, MA,USA). The membranes were probed with mouse polyclonal antibodies against Bcl-2 antibody (Dako Biotech, Inc, Glostrup, Denmark) and washed with TBST and subjected to corresponding HRP-conjugated secondary antibodies as indicated. Blots were washed again with TBST and visualized by enhanced chemiluminescence detection system (Amersham Pharmacia Biotech, Uppsala, Sweden).

Proliferation and apoptosis assays *in vitro* Hep2 cells were incubated in 96-well plates. Cell proliferation was determined by 3-(4,5-dimethylthiazol-2-y1)-2,5-diphenyltetrazolium bromide (MTT, Sigma) assay whereby cell numbers were counted by hemocytometer 72h after transfection. The absorbance values at 570 nm (A_{570}) were determined on a multiwell plate reader. Cell growth inhibition rate was calculated according to the following formula:

Growth inhibition rate (%)=$[(A_{570c}-A_{570e})/A_{570c}]\times 100\%$

A_{570c}: A_{570} in control group; A_{570e}: A_{570} in experimental group.

For FACS analysis of apoptosis, Hep2 cells were transfected with siRNA-STAT3 or pSilencer empty vector. After 72 h, cells were collected and washed with cold PBS containing edetic acid 4 mmol/L. Cells were fixed in 70% cold ethanol, collected by centrifugation, and washed once again with PBS containing edetic acid 4 mmol/L. Cells were resuspended in PBS containing edetic acid 4 mmol/L, 20 mL/L of propidium iodide (Sigma), 0.2% Triton X-100, 40 mg/L RNase A, and incubated for at least 30 min at 4 ºC. The cells were then analyzed by flow cytometry (FACScan, Becton Dickinson, Franklin Lakes, NJ, USA), using Cell Quest software. For fluoromicroscopic determination of positive apoptosis cells, 95 μL floating cells were mixed with 0.1% AO/EB [acridine orange (Sigma)/ethidium bromide (Sigma)] and observed under microscope.

Statistical analysis Data were expressed as mean±SD. The square χ^2 analysis was performed to evaluate the significance of inter-group differences. Student's *t* test was used for single comparison between two groups. Two-way ANOVA using the Student-Newman-Keuls method was adopted for comparison of variables after treatment. $P<0.05$ was considered significant. All statistical calculations were performed using SigmaStat statistical software package (SPSS10.0, Chicago, IL,USA).

Results

STAT3 RNAi by siRNA specifically reduces STAT3 expression in Hep2 cells Since STAT3 levels are significantly higher in tumor cells (including laryngeal tumor) than that in normal cells, we attempted to determine whether the synthetic STAT3 siRNA could inhibit the expression of STAT3 gene in Hep2 cells. Treatment of Hep2 cells with siRNA-STAT3 resulted in a significant decrease of STAT3 expression at both mRNA (Figure 1) and protein (Figure 2A) level

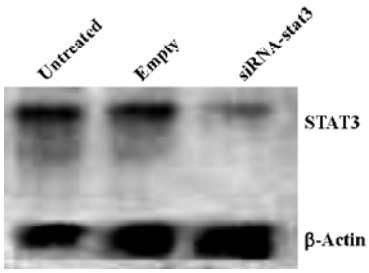

Figure 1. Northern blot analysis of STAT3 mRNA expression in Hep2 cells in the untreated, empty (vector), and STAT3 siRNA groups 72 h after transfection.

compared to the untreated Hep2 cells and the vector-treated Hep2 cells, respectively. STAT3 expression was specifically targeted by STAT3 siRNA, since STAT3 siRNA unchanged the expression of β-actin (Figure 1, 2A). Of note is that pTyr-STAT3 was markedly expressed in untreated Hep2 cells and the vector-treated Hep2 cells (Figure 2B), indicating that the detected STAT3 was indeed in the form of tyrosine-phosphorylated(ie, activated) form. In the STAT3 siRNA Hep2 cells, Tyr-STAT3 expression was significantly reduced, indicating that STAT3 siRNA also inhibited the activity of STAT3. Furthermore, as shown by Figure 2C treatment of

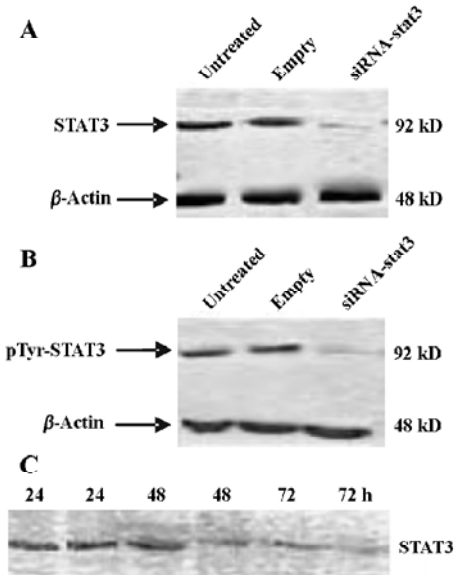

Figure 2. Western blot analysis of STAT3 and pTyr-STAT3 protein expression in Hep2 cells. (A) STAT3 protein expression in Hep2 cells in the untreated, empty (vector), and STAT3 siRNA groups 72 h after transfection. (B) pTyr-STAT3 protein expression in Hep2 cells in the untreated, empty (vector), and STAT3 siRNA groups 72 h after transfection. (C) STAT3 protein expression in the STAT3 siRNA-treated Hep2 cells at different transfection time.

Hep2 cells with STAT3 siRNA caused time-dependent inhibitory effect on STAT3 expression in Hep2 cells.

STAT3 siRNA down-regulates Bcl-2 expression in Hep2 cells Recent data indicate that constitutive activation of STAT3 induces the expression of anti-apoptotic genes including Bcl-2[17]. In order to determine whether Bcl-2 was involved in the STAT3-mediated apoptotic block in Hep2 cells, in this study Western blot analysis was performed. Figure 3 showed that Bcl-2 was remarkably expressed in the untreated Hep2 cells and the vector-treated Hep2 cells, whereas treatment of Hep2 cells with STAT3 siRNA significantly reduced the expression levels.

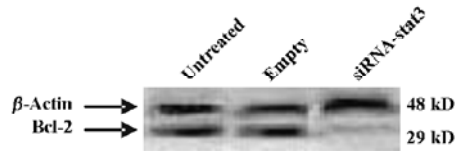

Figure 3. Western blot analysis of Bcl-2 protein expression in Hep2 cells in the untreated, empty (vector), and STAT3 siRNA groups 72 h after transfection.

STAT3 siRNA inhibits growth and survival of Hep2 cells and induces apoptosis of Hep2 cells *in vitro* To determine whether synthetic STAT3 siRNA had an inhibitory effect on Hep2 cells growths, we accomplished determination of cell proliferation with MTT assay. Table 1 showed that treatment of Hep2 cells with STAT3 siRNA contributed to dose-dependent inhibition of Hep2 cells, whereas no inhibitory effect was observed in the untreated Hep2 cells and the vector-treated Hep2 cells.

Two different methods including flow cytometry analysis and AO/EB staining (nucleus condensation) were adopted for determination of apoptosis in Hep2 cells (Table 2 and Figure 4). Flow cytometry analysis showed that in the STAT3

Table 1. Inhibitory effect of pSilencer1.0-U6 STAT3 siRNA on the growth of Hep2 cells. n=4. Mean±SD. $^bP<0.05$ *vs* the untreated and empty groups.

Group	$A_{570\ nm}$	Inhibition rate/%
Untreated	0.65±0.05	0.0
Empty	0.61±0.03	6.1
Stat3-siRNA 10 μg	0.54±0.12	16.9
Stat3-siRNA 15 μg	0.46±0.023^b	29.1
Stat3-siRNA 20 μg	0.29±0.06^b	45.5
Stat3-siRNA 30 μg	0.102±0.03^b	84.3

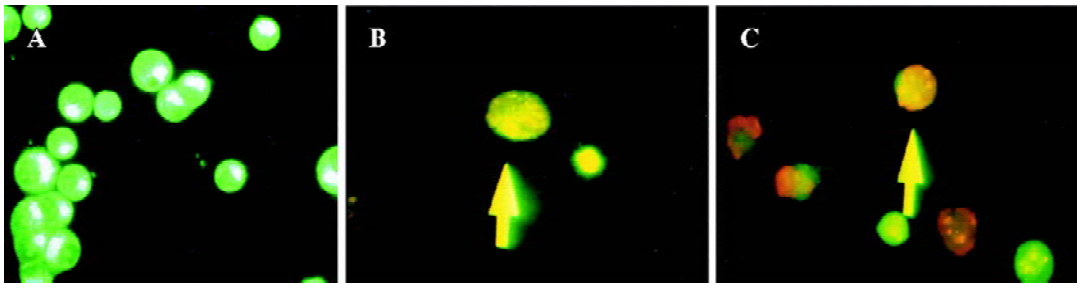

Figure 4. Representative fluoromicrographs of apoptosis detected by AO/EB assay in control and STAT3 siRNA-treated cells. (A): normal Hep2 cells. (B): arrow indicating early stage apoptotic cell. (C): arrow indicating late stage apoptotic cell.

siRNA treated cells the apoptosis rate was significantly higher than that in the untreated Hep2 cells and the vector-treated Hep2 cells, whereas the apoptosis rate in the vector treated Hep2 was slightly higher than that in the untreated Hep2 cells but no significance was achieved (Table 2), indicating that siRNA-STAT3 induced apoptosis in Hep2 cells. Moreover, AO/EB staining revealed that both early apoptotic and late apoptotic Hep2 cells were seen in the cells treated with STAT3 siRNA, suggesting that STAT3 siRNA had not only an effect on induction of early apoptosis but also late apoptosis in Hep2 cells (Figure 3).

Table 2. Percentage of apoptotic cells 72 h after transfection. n=3. Mean±SD. $^bP<0.05$ *vs* untreated groups.

Group	Apoptosis ratio/%
Untreated	0.42±0.01
Empty	2.87±1.67
STAT3-siRNA 20 μg	18.6±4.3^b

Discussion

Constitutively activated STAT3 is critical to STAT3 signaling pathway-dependent mechanism of malignancies[7,8,16]. A possible mechanism underlying transformation by activated STAT3 is the transcriptional upregulation of genes known to be involved in proliferation and apoptosis in laryngeal carcinomas and other malignant carcinomas. Under physiological conditions, STAT3 activation is transient and lasts from several minutes to several hours due to the transient nature of cytokine and growth factor signaling and the presence of proteins such as suppressor of cytokine signaling (SOCS) and PIAS (STAT blockade) that contribute to inhibition of STAT3 signaling. However, constitutive activation of protein tyrosine kinase (PTKs) occurs frequently during tumorigenesis due to activated mutations or aberrant growth factor or cytokine signaling, which results in constitutive activation of STAT3. Therefore, it is not surprising that constitutive activation of STAT3 is ubiquitous in human carcinomas[3,17,18]. In most instances, STAT3 that is capable of regulating growth, differentiation, and survival of cells is characterized by growth promoting manner[19–21]. At present, STAT3 has been recognized as an important oncogene[2,21].

STAT3 is implicated in both embryogenesis and tummorigenesis. This may raise the question as to whether blocking STAT3 is beneficial for malignant carcinoma cells but harmful to normal cells. Takeda *et al* revealed that homozygous deletion of STAT3 was embryonically lethal[22]. Biochemical studies have shown that disruption of STAT3 signaling with dominant-negative approaches in murine fibroblasts does not inhibit normal cell growth[23,24]. Also, blockade of STAT3 signaling by decoy oligonucleotides in head and neck cancer cells only decreases the amount of STAT3 in normal cell but has no significant effect on cell viability.

Grandis *et al*[15] have reported that constitutive activation of STAT3 signaling abrogates apoptosis in squamous cell carcinogenesis *in vivo*. Treatment of tumor cells with inhibitors of STAT signaling results in decreased cell viability and induces apoptosis. Accumulated evidence has suggested that apoptotic regulatory proteins are implicated in STAT3 associated-apoptosis inhibition. It has been demonstrated that STAT3 regulates transcription from the Bcl-x promoter. Moreover, elevated expression levels of Bcl-x_L mRNA in cells transformed by constitutively active STAT3 are observed[25].

Although the recently established approach of applying RNAi in mammalian studies by introducing siRNA can effectively inhibit gene expression[14,26,27], siRNA at present has been adopted as a promising genomic tool[17]. Such an approach overcomes many of the shortcomings previously experienced with approaches such as antibodies, antisense oligonucleotides, and pharmacological inhibitors. Intriguingly, RNAi targeting STAT3 by siRNA inhibits growth and induces apoptosis of prostate cancer and astrocytoma cells have been reported from different groups, however to date no one has known the effect of STAT3 siRNA on laryngeal cancer. Consequently, we have attempted to investigate the potential use of siRNA to block the expression of gene encoding STAT3 in laryngeal cancer.

To our knowledge we have successfully determined the inhibitory effect of the synthetic STAT3 siRNA on STAT3 expression in Hep2 cells at both mRNA and protein level (Figure 1, 2). We found that STAT3 was remarkably expressed in Hep2 cells, and treating Hep2 cells with STAT3 siRNA significantly reduced STAT3 expression levels characterized by a time-dependent inhibition of the gene expression. Increased STAT3 activation can occur through potential pathway of elevated constitutive levels of STAT3 protein and increased STAT3 tyrosine phosphorylation. In this study, the use of specific antibody of pTyr-STAT3 reveals that STAT3 siRNA inhibits not only STAT3 expression but also the activities of STAT3 in Hep2 cells (Figure 2), thereby confirming that the synthetic STAT3 siRNA can effectively inhibit STAT3 gene expressions in human laryngeal carcinoma

cells. Our results are consistent with others who have shown the potent inhibitory effect of STAT3 siRNA on STAT3 expression in the models of prostate cancer and astrocytoma cell lines[16,17]. Moreover, other studies have shown that ubiquitous expression of STAT3 gene exhibits in a variety of human tumors and can be effectively inhibited by the introduction of STAT3 inhibitors, dominant negative STAT3, and/or blockade of tyrosine kinases besides STAT3 siRNA whereby treatment of tumors is achieved.

Recent data indicate that constitutive activation of STAT3 induces expression of anti-apoptotic genes including Bcl-2[17]. In the present study, to determine whether STAT3-mediated cell apoptosis in Hep2 cells exists, Western blot analysis was used for the measurement of Bcl-2 protein expression. Additionally, quantification of apoptotic cells by flow cytometry was also performed in this study. We found that apoptosis in Hep2 cells was arrested as evidenced by low percentages of apoptotic cells (0.42%±0.01% and 2.87%±1.67%) and remarkable expression levels of Bcl-2 protein, whereas treatment of Hep2 cells with STAT3 siRNA significantly increased the number of apoptotic cells (18.6%±4.3%, $P<0.05$) and decreased Bcl-2 protein expression levels (Table 2 and Figure 3). This suggests that STAT3 gene expression is an important implication in the regulation of apoptosis in Hep2 cells. Furthermore, visualization of nucleus condensation using AO/EB dyes suggests that the synthetic STAT3 siRNA has an effect on both early and late apoptosis. Our study is consistent with two recent intriguing reports where STAT3 siRNA was also adopted for the study of astrocytomas and human prostate cancer[16,17]. All are supportive for the proposed mechanism underlying STAT3 participating in oncogenesis is by inhibiting apoptosis through the induction of anti-apoptotic genes. Konnikova *et al*[17] have demonstrated that STAT3 is required for the expression of the anti-apoptotic genes survivin and Bcl-x_L (a member of the Bcl-2 family of proteins) in astrocytoma cells. Likewise, Lee *et al*[16] have also shown that inhibition of STAT3 gene expression by siRNA induces apoptosis of human prostate cancer. Moreover, emerging evidence suggests that constitutive activation of STAT3 appears to be ubiquitous in tumors, which renders tumors cells resistant to apoptotic death caused by unbalanced expression level between anti-apoptotic genes and apoptotic genes[15,17,25]. Consistent with this, our recent work also has shown that human breast cancer cells implanted into nude mice exhibit remarkable expression of anti-apoptotic genes *Bcl*-2 but weak expression of apoptotic gene *Bax* accompanied by over-expression of *STAT3* gene (Data not shown). The context is altered by treatment of the breast cancer with STAT3 siRNA characterized by unchanged expression of *Bcl*-2 genes, increased expression of apoptotic *Bax* gene, and significant inhibition of expression of *STAT3* gene, and suppression of tumor growth (Data not shown).

siRNA has been effectively used *in vivo* to suppress gene expression in rats and adult mice whereby it achieves effective treatment of various organ and/or tissue disorders, including hepatitis, liver ischemia-reperfusion injury, allogeneic transplanted hepatocytes rejection, and CNS disorders[27-29]. This study also represents the first report that the synthetic STAT3 siRNA effectively suppresses Hep2 cells growths as evidenced by elevated inhibitory rate of Hep2 cell by STAT3 siRNA transfection (Table 1). In this study, an unexpected finding is that treatment of Hep2 cells with STAT3 siRNA is dose-dependent. Our results are consistent with other's reports that STAT3 has the potential as a promising therapeutic molecular target in tumors including laryngeal cancer, astrocytomas, and human prostate cancer, thereby extrapolating that STAT3 siRNA may represent a novel approach in tumor gene therapy.

Strategies for producing siRNA duplexes include direct chemical synthesis, transcription with T7 promoter *in vitro* and recombinant DNA construction by vector with U6 promoter. Our results demonstrate that pSilencer1.0-U6 STAT3 siRNA can result in a long-term target-gene inhibition in Hep2 cells leading to growth suppression and induction of apoptosis in Hep2 cells. The STAT3 signaling pathway has been shown to be critical for the survival of a number of human tumors. This therefore raises the possibility that STAT3 siRNA could become an effective therapeutic agent for STAT3-dependent tumors.

Conclusion

This study represents the first report that demonstrates that STAT3 siRNA effectively inhibits STAT3 gene expression in Hep2 cells leading to growth suppression and induction of apoptosis in Hep2 cells. The use of siRNA technique may provide a novel therapeutic approach to treatment of laryngeal cancer and other malignant tumors expressing constitutively activated STAT3.

Acknowledgments

We thank Dr Bao-xue YANG from UCLA, CA, USA, for Northern blot analysis and Dr Yan MENG in the Department of Pathophysiology at the Basic School of Medicine of Jilin University for her assistance in siRNA design.

References

1 Garcia R, Yu CL, Hudnall A, Catlett R, Nelson KL, Smithgall T, *et al*. Constitutive activation of STAT3 in fibroblasts transformed by diverse oncoproteins and in breast carcinoma cells. Cell Growth Differ 1997; 8: 1267–76.

2 Garcia R, Bowman TL, Niu G, Yu H, Minton S, Muro-Cacho CA, *et al*. Constitutive activation of STAT3 by the Src and JAK tyrosine kinases participates in growth regulation of human breast carcinoma cells. Oncogene 2001; 20: 2499–513.

3 Grandis JR, Drenning SD, Chakraborty A, Zhou MY, Zeng Q, Pitt AS, *et al*. Requirement of STAT3 but not stat1 activation for epidermal growth factor receptor-mediated cell growth *in vitro*. J Clin Invest 1998; 102: 1385–92.

4 Takemoto S, Mulloy JC, Cereseto A, Migone TS, Patel BK, Matsuoka M, *et al*. Proliferation of adult T cell leukemia/lymphoma cells is associated with the constitutive activation of JAK/STAT proteins. Proc Natl Acad Sci USA 1997; 94: 13897–902.

5 Gouilleux-Gruart V, Gouilleux F, Desaint C, Claisse JF, Capiod JC, Delobel J, *et al*. STAT-related transcription factors are constitutively activated in peripheral blood cells from acute leukemia patients. Blood 1996; 87: 1692–7.

6 Leong PL, Andrews GA, Johnson DE, Dyer KF, Sichuan Xi, Mai JC, *et al*. Targeted inhibition of STAT3 with a decoy oligonucleotide abrogates head and neck cancer cell growth. Proc Natl Acad Sci USA 2003; 100: 4138–43.

7 Mora LB, Buettner R, Seigne J, Diaz J, Ahmad N, Garcia R, *et al*. Constitutive activation of STAT3 in human prostate tumors and cell lines: direct inhibition of STAT3 signaling induces apoptosis of prostate cancer cells. Cancer Res 2002; 62: 6659–66.

8 Catlett-Falcone R, Landowski TH, Oshiro MM, Turkson J, Levitzki A, Savino R, *et al*. Constitutive activation of STAT3 signaling confers resistance to apoptosis in human U266 myeloma cells. Immunity 1999; 10: 105–15.

9 Caldenhoven E, van Dijk TB, Solari R, Armstrong J, Raaijmakers JA, Lammers JW, *et al*. STAT3 beta, a splice variant of transcription factor STAT3, is a dominant negative regulator of transcription. J Biol Chem 1996; 271: 13221–7.

10 Fire A, Xu S, Montgomery MK, Kostas SA, Driver SE, Mello CC. Potent and specific genetic interference by double-strand RNA in *Caenorhabditis* elegans. Nature 1998; 391: 806–11.

11 Hammond SM, Bernstein E, Beach D, Hannon GJ. An RNA-directed nuclease mediates post-transcriptional gene silencing in *Drosophila* cells. Nature 2000; 404: 293–6.

12 Sharp PA, Zamore PD. Molecular biology: RNA interference. Science 2000; 287: 2431–3.

13 Wianny F, Zernicka-Goetz M. Specific interference with gene function by double-strand RNA in early mouse development. Nat Cell Biol 2000; 2: 70–5.

14 Elbashir S, Harborth J, Lendeckel W, Yalcin A, Weber K , Tuschl T. Duplexes of 21-nucleotide RNAs mediate RNA interference in cultured mammalian cells. Nature 2001; 411: 494–8.

15 Grandis JR, Drenning SD, Zeng Q, Watkins SC, Melhem MF, Endo S, *et al*. Constitutive activation of that stat3 signaling abrogates apoptosis in squamous cell carcinogenesis *in vivo*. Proc Natl Acad Sci USA 2000; 97: 4227–32.

16 Lee SO, Lou W, Qureshi KM, Mehraein-Ghomi F, Trump DL, Gao AC. RNA interference targeting Stat3 inhibits growth and induces apoptosis of human cancer cells. Prostate 2004; 64: 303–9.

17 Konnikova L, Kotecki M, Kruger MM, Cochran BH. Knockdown of STAT3 expression by RNAi induces apoptosis in astrocytoma cells. BMC Cancer 2003; 3: 23.

18 Weber-Nordt RM, Mertelsmann R, Finke J. The JAK-STAT pathway: signal transduction involved in proliferation, differentiation and transformation. Leuk Lymphoma 1998; 28: 459–67.

19 Takeda K, Clausen BE, Kaisho T, Tsujimura T, Terada N, Forster I, *et al*. Enhanced Th1 activity and development of chronic enterocolitis in mice devoid of STAT3 in macrophages and neutrophils. Immunity 1999; 10: 39–49.

20 Kaplan DH, Shankaran V, Dighe AS, Stockert E, Aguet M, Old LJ, *et al*. Demonstration of an interferon gamma-dependent tumor surveillance system in immunocompetent mice. Proc Natl Acad Sci USA 1998; 95: 7556–61.

21 Bromberg JF, Wrzeszczynska MH, Devgan G, Zhao Y, Pestell RG, Albanese C, *et al*. STAT3 as an oncogene. Cell 1999; 98: 295–303.

22 Takeda K, Noguchi K, Shi W, Tanaka T, Matsumoto M, Yoshida N, *et al*. Targeted disruption of the mouse STAT3 gene leads to early embryonic lethality. Proc Nat1 Acad Sci USA 1997; 94: 3801–4.

23 Niu G, Heller R, Catlett-Falcone R, Coppola D, Jaroszeski M, Dalton W, *et al*. Gene therapy with dominant-negative STAT3 suppresses growth of the murine melanoma B16 tumor *in vivo*. Cancer Res 1999; 59: 5059–63.

24 Hammond SM, Boettcher S, Caudy AA, Kobayashi R, Hannon GJ. Argonaute 2, a link between genetic and biochemical analyses of RNAi. Science 2001; 293: 1146–50.

25 Scott S, Higdon R, Beckett L, Shi XB, deVere White RW, Earle JD, *et al*. Bcl 2 antisense reduces prostate cancer cell survival following irradiation. Cancer Biother Radiopharm 2002; 17: 647–56.

26 Xia H, Mao QW, Paulson HL, Davidson BL. siRNA-mediated gene silencing *in vitro* and *in vivo*. Nat Biotechnol 2002; 20: 1006–10.

27 Lewis DL, Hagstrom JE, Loomis AG, Wolff JA, Herweijer H. Efficient delivery of siRNA for inhibition of gene expression in postnatal mice. Nat Gen 2002; 32: 107–8.

28 Song E, Lee SK, Wang J, Ince N, Ouyan N, Min J, *et al*. RNA interference targeting Fas protects mice from fulminant hepatitis. Nat Med 2003; 9: 347–51.

29 Contreras JL, Vilatoba M, Eckstein C, Bilbao G, Thompson JA, Eckhoff DE. Caspase-8 and caspase-3 small interfering RNA decreases ischemia/reperfusion injury to the liver in mice. Surgery 2004; 136: 390–400.

Acta Pharmacologica Sinica 2005 Mar; 26 (3): 384–388

Full-length article

Pharmacodynamic effects and kinetic disposition of rabeprazole in relation to CYP2C19 genotype in healthy Chinese subjects[1]

Yong-mei HU[2,3], Jian-ming XU[3,5], Qiao MEI[3], Xin-hua XU[3], Shu-yun XU[4]

[2]*Anhui Geriatric Institute;* [3]*Department of Gastroenterology, First Affiliated Hospital of Anhui Medical University;* [4]*Clinical Pharmacology Institute, Anhui Medical University, Hefei 230022, China*

Key words

polymorphism (genetics); pharmacokinetics; pharmacodynamics; rabeprazole

[1] Supported by the Natural Science Foundations of the Ministry Education of Anhui Province of China (No 2003kj199).
[5] Correspondence to Dr Jian-ming XU.
Phn 86-551-292-2039.
E-mail huyongmei1013@yahoo.com.cn

Received 2004-04-26
Accepted 2004-11-11

doi: 10.1111/j.1745-7254.2005.00047.x

Abstract

Aim: To investigate whether the pharmacodynamics and pharmacokinetics of rabeprazole are dependent on CYP2C19 genotype status in healthy Chinese Han subjects. **Methods**: The CYP2C19 genotype status of healthy Chinese Han volunteers was determined using the polymerase chain reaction-restriction fragment length polymorphism method. Twenty healthy subjects volunteered to participate in the study. There were seven homozygous extensive metabolizers (homEM), six heterozygous extensive metabolizers (hetEM), and seven poor metabolizers (PM). All subjects were *Helicobactor pylori*-negative, which was determined by serology and ^{13}C-urea breath tests. Rabeprazole (20 mg) was taken orally once daily in the morning for 8 days, and intragastric pH values were monitored for 24 h by Digitrapper pH after day 1 (single dose) and day 8 (repeated dose). Meanwhile, blood samples were collected at various time-points for 24 h after administration. The serum concentrations of rabeprazole were measured using high-performance liquid chromatography. **Results**: The mean area under the curve (AUC) values for rabeprazole differed among the three different genotype groups, with a relative ratio of 1.0, 1.3, and 1.8 after a single dose and 1.0, 1.1, and 1.7 after repeated doses in the homEM, hetEM, and PM groups, respectively. Mean AUC values for rabeprazole after a single dose and after repeated doses were significantly different between the homEM and PM groups, but not between the homEM and hetEM or hetEM and PM groups. No significant differences in intragastric pH median, pH>4 total time, and pH>4 time percentage of 24 h, were observed among the three different genotype groups after a single dose or after repeated doses of rabeprazole. **Conclusion**: In healthy Chinese Han subjects, the pharmacokinetics of rabeprazole are dependent on a certain degree on CYP2C19 genotype status; however, the acid-inhibitory efficacy of rabeprazole is not influenced significantly by CYP2C19 genetic polymorphism.

Introduction

S-Mephenytoin-4'-hydroxylase (CYP2C19) is a genetically determined enzyme and its phenotypes can be classified as poor metabolizer (PM) and extensive metabolizer (EM) [1,2]. When CYP2C19 is the main metabolism enzyme of a drug, the pharmacokinetics of the drug are different between the PM and EM phenotypes, such as proton pump inhibitors (PPI). Recently, rabeprazole (RPZ) has been reported to be metabolized mainly via a non-enzymatic pathway, with only minor CYP2C19 and CYP3A4 involvement[3–6]. The pharmacokinetics of RPZ are assumed to be less influenced by the CYP2C19 phenotype. The incidence of PM for CYP2C19 in the Chinese population is very high (17.4%)[7]. However, it is not clear whether the pharmacokinetics and pharmacodynamics of RPZ depend on the CYP2C19 genotype status in Chinese people. Thus, studies examining the effects of CYP2C19 genetic polymorphism on the metabolism of RPZ

in Chinese people are important. In the present study we observed the metabolic disposition characteristics and pharmacodynamics of RPZ after a single dose and after 8 days of repeated doses with reference to different CYP2C19 genotype groups to provide valuable data that should be considered when selecting PPI for patients with acid-related diseases with reference to the CYP2C19 genotype status.

Materials and methods

Subjects and CYP2C19 genotypes *Helicobacter pylori* (*H pylori*) infection was screened using a serological test (Dot-immunogold kit, Lanbo Bio-Tech Institute, China) and a ^{13}C-urea breath test. DNA was extracted from each individual's leucocytes using a commercially available kit (Promega, Madison, WI, USA). Genotyping procedures for identifying the CYP2C19 wild-type (CYP2C19*1) and the two mutated alleles, CYP2C19*2 and CYP2C19*3, were carried out using the polymerase chain reaction and restriction fragment length polymorphism method[8].

A total of 20 *H pylori-negative* healthy volunteers participated in this study. Seven subjects were classified as homozygous extensive metabolizers (homEM). Six were heterozygous for exon 5 mutation of CYP2C19 (*1/*2) or heterozygous for the exon 4 mutation (*1/*3) and were classified as heterozygous extensive metabolizers (hetEM). The remaining seven subjects were homozygous for the exon 5 mutation (*2/*2) and were classified as the PM group (Table 1).

Table 1. Demographic characteristics of subjects enrolled in the study with different CYP2C19 genotypes. Mean±SD.

CYP2C19 genotype	*n*	Sex	Age/a	Body weight/kg
homEM (*1/*1)	7	Male	23.5±0.6	62.1±1.3
hetEM (*1/*2 *n*=4) (*1/*3 *n*=2)	6	Male	22.5±0.8	60.5±2.6
PM (*2/*2)	7	Male	22.8±0.7	61.8±2.8

None of the subjects consumed alcohol or smoking. None of the subjects had taken any drugs for at least 4 weeks before or during the study. The Ethics Committee of Anhui Medical University approved the protocol in advance. Written informed consent was obtained from each subject before participation in the study.

Study protocol All healthy volunteers were orally treated with 20 mg RPZ (Pariet, Eisai Company, Tokyo, Japan) for an 8-day period. The medication was taken once daily at 8:00. The 24-h intragastric pH monitoring and the measurement of serum levels of RPZ were carried out on day 1 and day 8. Two standard meals (12:00, 18:00), prepared at the hospital, were provided for each subject.

Intragastric pH measurement After overnight fasting, a glass electrode was inserted transnasally and placed approximately 5 cm below the cardia. The electrode was calibrated with standard buffers (pH 1.07 and 7.01) before recording the pH with a Digitrapper pH (Medtronic, Watford, UK). Intragastric pH recordings started after the oral dose of RPZ at 8:00 on d 1 and d 8.

Sample collection and concentration assays of rabeprazole Blood samples were collected before and 0.5, 1, 1.5, 2, 3, 5, 7, 10, 12, and 24 h after RPZ administration on day 1 and day 8. After collection, the blood samples were immediately centrifuged at 4000 r/min for 10 min and 100 μL of 1% diethylamine solution was added to the 1 mL sample of RPZ plasma. All samples were stored at –80°C until assayed. Plasma levels of RPZ were measured using high performance liquid chromatography[9,10]. The lower detection limit for RPZ was 0.01 mg/L. A good linearity is obtained from 0.01–0.75 mg/L of RPZ with r=0.999. The standard curve of RPZ in serum is Y=124950X – 806.05 (n=5). The recoveries of three concentra-tions, 0.05, 0.1, 0.5 mg/L are 75.2%, 84.2%, and 91.0%, respectively. The RSD of intra-day variation of RPZ are 5.1%, 9.2%, and 6.8% and the RSD of inter-day variation are 8.2%, 3.5%, and 4.2% for the three concentrations, respectively.

Statistical analysis Intragastric pH characters were described by the median, mean, pH>4 total time and the pH>4 time proportion of 24 h from the raw pH values. The values for the areas under the serum concentration-time curves (AUC) from 0 to 24 h for RPZ were calculated using the 3P87 software. All P values are two-sided, and P<0.05 indicated statistical significance. Data were expressed as mean±SD. Statistically significant differences in the mean AUC values for RPZ and intragastric pH values between the three different CYP2C19 genotype groups were compared using a one-way analysis of variance (ANOVA) combined with the least significant method (LSD). Paired t-tests were used to determine whether there were differences in the AUC values and intragastric pH values for RPZ between single and repeated doses. Statistical calculations were carried out using SPSS 11.0 software (SPSS Inc, Chicago, USA).

Results

Role of the CYP2C19 genotype on the acid-inhibitory efficacy of rabeprazole Raw data on the mean intragastric

pH-time curves after single and repeated doses of RPZ in the three different genotype groups are shown in Figure 1. The characteristic values of the 24-h intragastric pH after single and repeated doses of RPZ in the three different genotype groups are summarized in Table 2. The median intragastric pH value of the PM group was the highest, followed by the hetEM group, and the homEM group had the lowest value.

No significant differences in intragastric pH values were observed between the three groups after a single dose or after repeated doses for 8 days of RPZ. In addition, no significant increments in intragastric pH values from single to repeated doses were observed in the three different genotype groups.

Role of the CYP2C19 genotype on the kinetic disposition of rabeprazole The pharmacokinetic parameters are shown in Table 3. The mean AUC values for RPZ after a single dose differed among the three different genotype groups, with a relative ratio of 1.0, 1.3, and 1.8 in the homEM, hetEM and PM groups, respectively. The mean AUC values for RPZ after repeated doses also differed among the three groups, with a relative ratio of 1.0, 1.1, and 1.7 in the homEM, hetEM and PM groups, respectively. The mean AUC values for RPZ after single and repeated doses were significantly different between the homEM and PM groups, but not between the homEM and hetEM or between the hetEM and PM groups. No significant increase in the mean AUC values for RPZ from single to repeated doses was observed in any

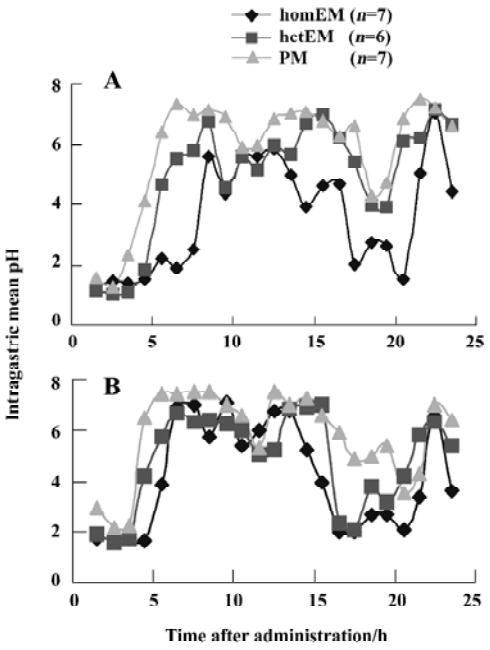

Figure 1. Intragastric pH 24-h profiles in the different CYP2C19 genotype groups after administration of a single dose (A) and repeated doses (B) of 20 mg rabeprazole.

Table 2. Intragastric pH values after a single dose (day 1) and repeated doses (day 8) of rabeprazole. homEM, homozygous extensive metabolizers; hetEM, heterozygous extensive metabolizers; PM, poor metabolizers.

	Day 1			Day 8		
	homeEM (n=7)	hetEM (n=6)	PM (n=7)	homEM (n=7)	hetEM (n=6)	PM (n=7)
pH>4 total time of 24 h/min	758.4±191.8	845.6±238.0	1011.0±104.2	841.3±178.1	763.0±95.9	977.5±128.9
pH>4 time percentage of 24 h/%	52.7±13.3	58.7±16.5	70.2±7.2	58.4±12.4	53.0±6.6	67.9±9.0
Mean	4.1±0.6	4.4±0.8	5.2±0.5	4.4±0.5	4.2±0.2	5.1±0.4
Median	3.8±1.1	4.4±1.6	6.1±0.7	4.5±1.0	4.4±1.3	5.7±0.6

Table 3. Pharmacokinetic characteristics of rabeprazole after single and repeated doses. $^{b}P<0.05$ *vs* homEM. $^{e}P<0.05$ *vs* hetEM. homEM, homozygous extensive metabolizers; hetEM, heterozygous extensive metabolizers; PM, poor metabolizers.

	Day 1			Day 8		
	homeEM (n=7)	hetEM (n=6)	PM (n=7)	homEM (n=7)	hetEM (n=6)	PM (n=7)
AUC/mg·h·L^{-1}	1.15±0.33	1.54±0.19	2.02±0.59^{b}	1.45±0.21	1.64±0.25	2.50±0.74^{b}
C_{max}/mg·L^{-1}	0.15±0.09	0.21±0.12	0.63±0.23^{be}	0.19±0.09	0.37±0.12	0.61±0.19^{be}
T_{max}/h	2.69±0.36	2.80±0.41	3.45±0.50	3.14±0.23	3.05±0.40	2.95±0.51
$T_{1/2}$/h	1.80±0.25	2.03±0.21	2.41±0.49	2.04±0.32	2.43±0.34	2.37±0.36

of the three different genotype groups. The C_{max} values were significantly different between the homEM and PM groups, and the hetEM and PM groups after single and repeated doses of RPZ. Whereas T_{max} and $T_{1/2}$ did not differ significantly between the three groups on day 1 and day 8.

Discussion

Proton pump inhibitors, such as omeprazole, lansoprazole, pantoprazole, and rabeprazole, have been used widely in the treatment of acid-related diseases. Recent research has paid more attention to the inhibitory effects of PPI in relation to the genetic polymorphism of CYP2C19, a major enzyme for the metabolism of PPI in the liver[11]. These studies have shown that CYP2C19 genetic polymorphism has a significant influence on acid-inhibitory efficacy and the metabolism of omeprazole in healthy Chinese Han subjects. However, to date no studies examining the relationship between the CYP2C19 genotype and the metabolism of RPZ has been carried out in the Chinese Han population. *In vitro* human liver microsomal and *in vivo* human pharmacology studies have shown that RPZ is metabolized mainly via a non-enzymatic reduction to RPZ thioether, and that CYP2C19 and CYP3A4 are partially involved in the metabolism of RPZ[3-6]. The existence of CYP3A4-related PM has not been reported in any Chinese population. Therefore, we did take into account CYP2C19-related genotyping factors in our study.

Rabeprazole has a rapid and powerful onset of pharmacological action[12]. Our study showed that the AUC for RPZ after a single dose exceeded 80% of the AUC after repeated doses and there were no significant increments from single to repeated doses, which was consistent with Yasuda *et al*[9]. In addition, we found that no significant increment in intragastric pH values was observed from single to repeated doses. These results suggest that the metabolism of RPZ after a single dose could attain maximum acid-inhibitory efficacy. And this appears to be the reason for pH values remaining elevated for more than 50% of the time, even with very modest exposures, and when the pharmacokinetic results on day 1 are consistent with the results on day 8.

Adachi and other researchers[3-6] have found that the acid-inhibitory efficacy and metabolism of RPZ are not dependent on CYP2C19 genotype status. However, Horai *et al* and Inaba *et al*[13,14] and Ieiri *et al*[15] reported that CYP2C19 genotypic differences affected the metabolism and kinetics process of RPZ, and influenced gastric pH values and gastrin level in plasma. In the present study, we found that the AUC for RPZ differed markedly only between homEM and PM, and the intragastric pH, the best and most direct pharmacological index when using PPI, was not significantly different among the different genotypes after a single or repeated doses of RPZ. As for the discrepancy between the kinetics and dynamics of RPZ, first we may hypothesize that the acid-inhibitory effect of RPZ is powerful and rapid, and that the serum levels of 20 mg RPZ are sufficient for acid-inhibitory efficacy in Chinese subjects, even in homEM subjects. Second, no direct and simple relationship between the serum concentration–time profile of the drug and the pharmacodynamic response has been reported because of the irreversible blockade of the therapeutic target by PPI. However, Hussein *et al*[16] have shown a clear relationship using the maximum effect (E_{max}) model. According to the model, our study suggests a lower half-maximal effective AUC value ($EAUC_{50}$) for RPZ than 2 mg·L^{-1}·h. As shown in Table 3, the mean AUC values of RPZ corresponding to the maximum acid-inhibitory effect of RPZ in this study may be greater than this threshold. Therefore, there were no significant differences for intragastric pH among the three genotypes.

In conclusion, our study focused on investigating the pharmacodynamic and pharmacokinetic effect of RPZ with reference to different CYP2C19 genotypes. The acid-inhibitory effects of RPZ were independent on their pharmacokinetic characteristics as well as an individual's CYP2C19 genotype status. Therefore, RPZ may be a more effective PPI for treating acid-related disease in relation to CYP2C19 genotype status.

References

1 Andersson T, Regardh CG, Dahl-Puustinen ML, Bertilsson L. Slow omeprazole metabolizers are also poor *S*-mephenytoin hydroxylators. Ther Drug Monit 1990; 12: 415–6.

2 Chiba K, Kobayashi K, Manabe K, Tani M, Kamataki T, Ishizaki T. Oxidative metabolism of omeprazole in human liver microsomes: cosegregation with *S*-mephenytoin 4'-hydroxylation. J Pharmacol Exp Ther 1993; 266: 52–9.

3 Adachi K, Katsube T, Kawamura A, Takashima T, Yuki M, Amano K, *et al*. CYP2C19 genotype status and intragastric pH during dosing with lansoprazole or rabeprazole. Aliment Pharmacol Ther 2000; 14: 1259–66.

4 Sakai T, Aoyama N, Kita T, Sakaeda T, Nishiguchi K, Nishitora Y, *et al*. CYP2C19 genotype and pharmacokinetics of three proton pump inhibitors in healthy subjects. Pharm Res 2001; 18: 721–7.

5 Hokari K, Sugiyama T, Kato M, Saito M, Miyagishima T, Kudo M, *et al*. Efficacy of triple therapy with rabeprazole for *Helicobacter pylori* infection and CYP2C19 genetic polymorphism. Aliment Pharmacol Ther 2001; 15: 1479–84.

6 Miyoshi M, Mizuno M, Ishiki K, Nagahara Y, Maga T, Torigoe

T, *et al*. A randomized open trial for comparison of proton pump inhibitors, omeprazole versus rabeprazole, in dual therapy for *Helicobacter pylori* infection in relation to CYP2C19 genetic polymorphism. J Gastroenterol Hepatol 2001; 16: 723–8.
7 Shu Y, Zhou HH. Individual and ethnic differences in CYP2C19 activity in Chinese populations. Acta Pharmacol Sin 2000; 21: 193–9.
8 de Morais SM, Goldstein JA, Xie HG, Huang SL, Lu YQ, Xia H, *et al*. Genetic analysis of the *S*-mephenytoin polymorphism in a Chinese population. Clin Pharmacol Ther 1995; 58: 404–11.
9 Yasuda S, Ohnishi A, Ogawa T, Tomono Y, Hasegawa J, Nakai H, *et al.* Pharmacokinetic properties of E3810, a new proton pump inhibitor, in healthy male volunteers. Int J Clin Pharmacol Ther 1994; 32: 466–73.
10 Ishizaki T, Chiba K, Manabe K, Koyama E, Hayashi M, Yasuda S, *et al*. Comparison of interaction potential of a new proton pump inhibitor, E3810, versus omeprazole with diazepam in extensive and poor metabolizers of *S*-mephenytoin 4'-hydroxylation. Clin Pharmacol Ther 1995; 58: 155–64.
11 Ishizaki T, Horai Y. Review article: cytochrome P450 and the metabolism of proton pump inhibitors–emphasis on rabeprazole. Aliment Pharmacol Ther 1999; 13 (Suppl 3): 27–36
12 Williams MP, Sercombe J, Hamilton MI, Pounder RE. A placebo-controlled trial to assess the effects of 8 days of dosing with rabeprazole versus omeprazole on 24-h intragastric acidity and plasma gastrin concentrations in young healthy male subjects. Aliment Pharmacol Ther 1998; 12: 1079–89.
13 Horai Y, Kimura M, Furuie H, Matsuguma K, Irie S, Koga Y, *et al*. Pharmacodynamic effects and kinetic disposition of rabeprazole in relation to CYP2C19 genotypes. Aliment Pharmacol Ther 2001; 15: 793–803.
14 Inaba T, Mizuno M, Kawai K, Yokota K, Oguma K, Miyoshi M, *et al*. Randomized open trial for comparison of proton pump inhibitors in triple therapy for *Helicobacter pylori* infection in relation to CYP2C19 genotype. J Gastroenterol Hepatol 2002; 17: 748–53.
15 Ieiri I, Kishimoto Y, Okochi H, Momiyama K, Morita T, Kitano M, *et al*. Comparison of the kinetic disposition of and serum gastrin change by lansoprazole versus rabeprazole during an 8-day dosing scheme in relation to CYP2C19 polymorphism. Eur J Clin Pharmacol 2001; 57: 485–92.
16 Hussein Z, Granneman GR, Mukherjee D, Samara E, Hogan DL, Koss MA, *et al*. Age-related differences in the pharmacokinetics and pharmacodynamics of lansoprazole. Br J Clin Pharmacol 1993; 36: 391-8.

Acta Pharmacologica Sinica 2005 Apr; 26 (4): 389–395

Invited review

Role of amygdala in mediating sexual and emotional behavior via coupled nitric oxide release[1]

Elliott SALAMON[2], Tobias ESCH[2,3], George B STEFANO[2,4]

[2]Neuroscience Research Institute, State University of New York, College at Old Westbury, Old Westbury, New York 11568, USA; [3]Charité University Medicine Berlin, Institute for General Practice and Family Medicine, Schumannstrasse, 10117 Berlin, Germany

Key words

amygdala; sex; nitric oxide; morphine; emotion

[1] This work in part was supported by grants DA09010 and MH47392.
[4] Correspondence to Dr George B STEFANO.
Phn 1-516-876-2732.
Fax 1-516-876-2727.
E-mail gstefano@sunynri.org

Received 2004-11-30
Accepted 2005-01-06

doi: 10.1111/j.1745-7254.2005.00083.x

Abstract

Although the anatomical configuration of the amygdala has been studied a great deal, very little research has been conducted on understanding the precise mechanism by which this emotional regulatory center exerts its control on emotional and sexual behavior. By applying research methodology from the Neuroscience Research Institute, State University of New York, College at Old Westbury, we intended to demonstrate that much of the mediated effects of the amygdala, specifically the regulation of the male and female sexual response cycles, as well as related emotional considerations, exert their effects coupled to nitric oxide (NO) release. Furthermore, by using current anatomical and histological data, we demonstrated that amygdalar tissue rich in endocannabinoid and opiate, as well as catecholamine, receptors could exert its neurochemical effects within an NO-mediated paradigm. This paradigm, together with the existence of estrogen and androgen signaling within the amygdala, further lends credence to our theoretical framework. We begin with a brief anatomical and functional review of amygdalar function, and then proceed to demonstrate its relationship with NO.

Introduction to the structure and function of the amygdala

The region of the human brain commonly referred to as the amygdala comprises an area of approximately 3 cm^3 [1,2]. At the dorsal base of the brain, the elevation of the parahippocampus at the uncus is in part a result of the amygdala, which resides dorsal to it. Although neuro-anatomists often make reference to this portion as a single unitary structure, the amygdala is actually three distinct collections of nuclei. The largest portion of the amygdaloid complex is the basolateral nuclear group, consisting of the lateral nucleus, the irregular basal nucleus, and the accessory basal nucleus. The other major portion consists of the centro-medial group, which comprises the central nucleus and the medial nucleus. The centromedial group communicates via fibers of the stria terminalis to the bed nucleus of the stria terminalis (BST)[2] (Figure 1). Cell types in the BST are identical to those in the centromedial, causing the BST to be included in the classification of amygdalar tissue. The BST lies in the basal forebrain, which also contains the basal nucleus of Meynert, the nucleus accumbens, and the ventral portions of the putamen and globus pallidus. Anatomically, the smallest portion of the amygdaloid complex is the cortical nucleus; with primary input originating from the olfactory bulb and olfactory cortex, undoubtedly this plays a role in emotion-associated olfaction[2].

Nitric oxide correlates amygdalar function When we examine nitric oxide (NO) signaling, we notice two constitutive enzymatic components, the constitutive NO synthase (cNOS), including endothelial (eNOS) and neuronal (nNOS) isoforms. cNOS, as the name implies, is always expressed. When cNOS is stimulated, NO release occurs for a short period of time, but this level of NO can exert profound physiological actions for a long period of time[3]. NO not only is an immune, vascular, and neural autoregulatory signaling molecule, but also performs vital physiological activities via

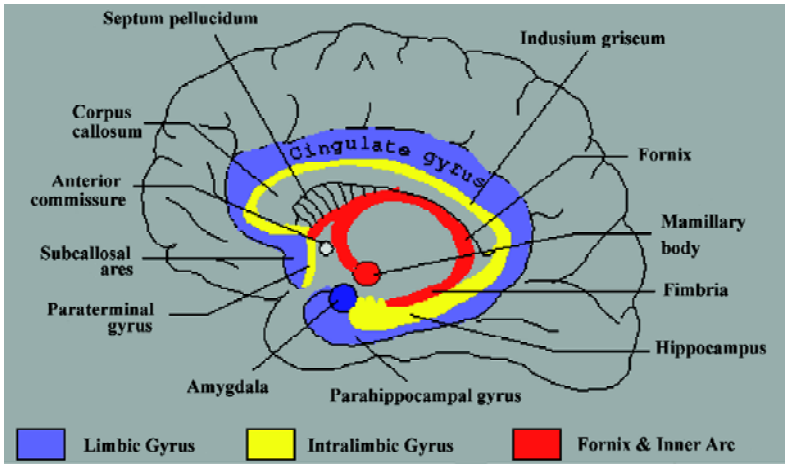

Figure 1. The limbic system.

its constitutive expression[4,5].

Both the amygdala and the hippocampus contain numerous receptors for varying neurotransmitters. The central nucleus of the amygdala is most strongly modulated by dopamine, norepinephrine (NE), epinephrine, and serotonin[6,7]. The basal nuclei receive moderately high inputs of dopamine, NE, and serotonin[6,7], each of which has been demonstrated to exert their desired effect via NO[4]. Taken together, we surmise that NE initially promotes a slight vasoconstriction of the artery during the amygdalar compensatory response, which is defined as the limbic system's inherent mechanism to maintain homeostasis and lower stress levels. This mechanism is indicated by a slight enhancement of sympathetic activity on stimulation (ie, emotional), and is immediately followed by the release of NO from the peripheral nitroxidergic nerve, which mediates a concentration-dependent vasodilation[5]. In primates, the cerebral arterial diameter, under resting conditions, is maintained by tonic release of NO from the nerve (10%–20%), or from the nerve and endothelium (30%)[8]. This observation is supported by other data from our laboratory because of the fact that basal NO is cNOS-derived and keeps particular types of cells in a state of inhibition[5]. Endogenous superoxide dismutase in the cerebral artery appears to protect the relaxation induced by NO from perivascular nerves from the NO scavenger action of superoxide anions[9]. This NO then produces the longer-lived phenomenon of smooth muscle relaxation. In another report, it was found that NE vascular hyperresponsiveness in hypertension was dependent on an impairment of NO activity that was realized through NE-induced oxygen free radical production[10], providing an important contribution to the understanding of this regulatory process.

Amygdalar NO release and its relationship to sexual behavior

In addition to NO and the amygdala, new knowledge has emerged concerning the role of hypothalamic, limbic, and brainstem structures, neuropeptides, and brain monoamines in the control of partner preference, sexual desire, erection, copulation, ejaculation, orgasm, and sexual satiety – the details of which are discussed below. At least one important sex difference exists between the male and female amygdala of many species. Owing to the interplay of the differing sex hormones, males and females will experience pleasure from differing experiences (eg, it has been shown that males are more visually stimulated than females[7,11]). In addition, modulating the concentration of testosterone may cause a male to partake in stereotypical "male behavior." Likewise, modifying the concentration of estrogen may cause the female to partake in specified, stereotypical "female behavior"[7,11]. The amygdala is intimately involved in sex and sexuality. It is important to note that the male amygdala is slightly bigger than that of the female. The medial part of the female amygdala plays an important role in pregnancy and appropriate coordination of the endocrine system. Stimulation of the amygdala will produce penile erection, sexual sensation, representations/memories of intercourse, and orgasm[7,12,13]. Furthermore, precortical region epilepsy has been shown to elicit spontaneous sexual arousal and orgasm, thus clearly demonstrating the role of the amygdala in sexual pleasure[12,13].

Stimulation of the corticomedial amygdala has been shown to induce ovulation in the female, and cutting the stria terminalis abolishes this effect. The introduction of tract lesions to the rat amygdala, including the medial nucleus, eliminates male libido, but not female libido[2,7,11,14]. In humans, temporal lobe epilepsy has been associated with sexual

arousal in women to the point of orgasm; however, evidence of this in men is unsubstantiated[12,13].

Nitric oxide release has been demonstrated as the critical link between corticomedial stimulation and its relationship with the densely packed estrogen/androgen regions within the amygdala[15–19]. NO has been shown to be crucial for the occurrence of basal luteinizing hormone (LH) release in males[15], and for the LH surge in ovariectomized females treated with estradiol plus progesterone[16–18]. Furthermore, NO donors induce an LH surge in estradiol-treated ovariectomized females[16–20], and thus, have a progesterone-like effect. Concomitant findings show that estradiol stimulates nNOS expression in the preoptic area and exerts a helping influence on NO-producing neurons[17]. The released NO appears to be able to modulate the activity of gonadotrophic releasing hormone neurons (GnRH)[17]. These observations implicate neuronal NO in the regulation of GnRH cell activity in the preoptic area[20–23]. It is important to note that some studies suggest that at the median eminence (ME) level, the NO implicated in the modulation of GnRH release is endothelial in origin, rather than neuronal[23]. This is consistent with the fact that, unlike in the preoptic area where GnRH perikarya are surrounded by nNOS-containing cells, nNOS fibers and GnRH fibers in the ME are distributed separately in the internal and external zones, respectively[19]. Furthermore, in the ME, eNOS immunoreactivity is observed in endothelial cells of the pituitary portal blood vessels[20], located in immediate proximity to the GnRH terminals[21]. The endothelial origin of NO secreted from ME fragments is further substantiated by the results of prior reports that show that central administration of eNOS antisense is more efficacious than nNOS antisense administration in suppressing an estradiol-/progesterone-induced LH surge in ovariectomized females[21]. These findings are directly related to amygdalar function by way of neuronal projections extending from the amygdala precortical region to the ME (interestingly, this relationship can be made without regard to whether ME signaling occurs via neuronal or endothelial NO). Thus, we can hypothesize a more robust signaling system involving both NO from amygdalar origins, as well as hypothalamic hormonal relationships.

Emotional stressors mediated via amygdalar NO release

Morphine and related compounds mediating NO release within the amygdala The endocannabinoids, anandamide, and 2-arachidonyl glycerol, are naturally occurring, constitutively expressed, NO-stimulating signaling molecules[24]. Anandamide and morphine can also cause NO release from human immune cells, neural tissues, and human vascular endothelial cells[25]. Moreover, both anandamide and morphine can initiate invertebrate immune cell cNOS-derived NO[26]. Additionally, estrogen can stimulate cNOS-derived NO in human immune and vascular cells[27,28]. Anandamide, as part of the ubiquitous arachidonate and eicosanoid signaling cascade, serves to maintain and augment tonal NO in vascular tissues[24].

Both the hippocampus and the amygdala (particularly the lateral nucleus) contain high concentrations of receptors for the endocannabinoids[29,30]. In fact, reports have found endogenous morphine within the structure of the hippocampus[29,30]. In addition, this morphine activates pleasure pathways via NO and has been shown to do so in the rat brain hippocampus and amygdala[31–34]. Studies from our laboratory confirm the mediated release of NO via real-time amperometric measurement from the rat brain hippocampus[34] and amygdala[31]. This information can further be used to understand some of the pleasurable aspects of sexual activity that, indeed, are often found to have morphine-like properties and, perhaps, are mediated via these endocannabinoid and morphine laden amygdalar pathways[31,35]. Further credence to these findings stems from lesional data. Humans with amygdala lesions show a decrease in emotional tension and related sexual dysfunction[6,7]. It has been postulated that endocannabinoids and endogenous morphine may act on the lateral nucleus to prevent the linkage of sexual significance to sensory stimuli prior to conscious processing, thus interfering with the perception of sexually and emotionally charged stimuli[36].

Estrogen mediates NO release within the amygdala Estrogen, through NO release, provides an additional pathway by which the system can downregulate immunocyte and vascular function in women[37]. This may be because of both the immune and vascular trauma associated with cyclic reproductive activities, such as endometrial buildup, when a high degree of vascular and immune activities occur. Given the extent of proliferative growth capacity during peak estrogen levels in this cycle, NO may function to enhance down regulation of the immune system to allow for these changes. Therefore, enhanced cNOS activity would be a beneficial effect within the concept and time framework of amygdalar compensation (as defined earlier) and the subsequent sense of calm it induces. Thus, these signal molecules, especially endocannabinoid and opiate alkaloids, have the potential to make you "feel" good and relax[38] by releasing NO, which may once again be part of the sexual resolution (post coitus) phase of the sexual cycle.

Emotionally charged events mediating NO release within the amygdala Within this context of varying stimuli evoking

NO release, emotional stresses such as fear and anxiety can induce cardiovascular alterations, such as cardiac dysrhythmias. These are some of the same events that occur when one is exposed to sexually charged stimulus, or engaged in a sexual act[39–42]. These cardiovascular events are initiated at the level of the cingulated, amygdalar, and hypothalamic processes, as well as their projection into the higher level cerebral cortex, further altering the heart rate under stressful or sexually aroused conditions[43]. Neurons in the insular cortex, the central nucleus of the amygdala, and the lateral hypothalamus, owing to their role in the integration of emotional and ambient sensory input, may be involved in the emotional link to the cardiovascular phenomenon[44]. These include changes in cardiac autonomic tone with a shift from the cardioprotective effects of parasympathetic predominance to massive cardiac sympathetic activation[45]. This autonomic component, carried out with parasympathetic and sympathetic preganglionic cells via subcortical nuclei from which descending central autonomic pathways arise, may therefore be a major pathway in how emotional state may affect cardiovascular function. The importance of an elicited emotional response (and therefore limbic activation) was further demonstrated in ischemic heart disease when patients with frequent and severe ventricular ectopic rhythms were subjected to psychological stress[46]. The frequency and severity of ventricular ectopic beats increased dramatically during emotional activation of sympathetic mechanisms, but not during reflexively induced increased sympathetic tone. Perhaps we can even relate this mechanism to sexual orgasm, a process dominated by increased sympathetic tone.

The hard-wiring of emotional and sexual sensations coupled to cardiovascular neural processes probably involves many subcortical descending projections from the forebrain, midbrain, and, specifically, the amygdala[47–50]. Cardiovascular changes were observed in experiments where the motor cortex surface was stimulated, eliciting tachycardia accompanied by and independent of changes in arterial blood pressure[51]. The "sigmoid" cortex[52] and frontal lobe[53–55], and, in particular, the medial agranular region[56], subcallosal gyrus[57], septal area[58], temporal lobe[59], and cingulate gyrus[60–62] appear to be involved. The insular cortex in cardiac regulation is important because of its high connectivity with the limbic system, suggesting that the insula is involved in cardiac rate and rhythm regulation under emotional stress[53,54]. This form of regulation is mediated via a parasympathetic response, and is probably active in the resolution phase following orgasm[2,6,12,13].

The amygdala, with respect to autonomic-emotional integration[63,64], is composed of numerous subnuclei, which play a major role in the elaboration of autonomic responses[65]. There are profuse inputs to this region from the insular and orbitofrontal cortices, the parabrachial nucleus, and the nucleus tractus solitarius[66]. Amygdalo-tegmental projections are viewed as a critical link in cerebral cortical control of autonomic function[8,67]. This level of input allows for cerebral control of sexual behavior, such as showing sexual restraint and the ability to pass on sexual gratification. Indeed, a great deal of research center on sex-offenders' inability for, or lack of, the above-mentioned amygdalo-tegmental projections[68,69].

Mechanisms of amygdala-induced emotional compensation

As noted above, once individuals are exposed to sexually explicit or emotionally charged information, they experience peripheral vasodilation: warming of the skin, an increase in heart rate, and an ensuing sense of agitation[5,70]. This experience is remarkably similar to the physiological state that exists throughout the sexual cycle, from initial arousal through to resolution. It is the function of the amygdala to aid in the relief of these altered states, through the amygdalar primary compensatory response as defined above[2,6,7,53]. In examining a potential mechanism for this relief, besides the overriding central nervous system output via the autonomic nervous system, peripheral neuro-vascular processes would appear to be important. We surmise that NO is of fundamental importance in this response because of the increase in peripheral temperature (ie, vasodilation[5]). For a complete review of possible related mechanisms as well as the related mechanisms outlined above, see the studies by Toda *et al*[8], Lembo *et al*[10], Okamura *et al*[66], and Toda[67].

We also surmise, based on current studies, that endothelial-derived NO, released through normal pulsations as a result of vascular dynamics responding to heart beat[38], as well as acetylcholine-stimulated endothelial NO release, may contribute to the effect of NO in inducing smooth muscle relaxation[5,70]. Furthermore, vascular pulsations may be of sufficient strength to also stimulate nNOS-derived NO release, limiting any basal NE actions[5,70]. Interestingly, nitrosative stress, mediated by involvement of the reactive nitrogen oxide species, N_2O_3, does inhibit dopamine hydroxylase, which, in turn, inhibits NE synthesis and contributes to the regulation of neurotransmission and vasodilation[5,70]. This system may provide an autoregulatory mechanism involved in the neuronal control of peripheral vasomotor responses and may, once again, aid in the resolution phase of sexual intercourse (Figure 2).

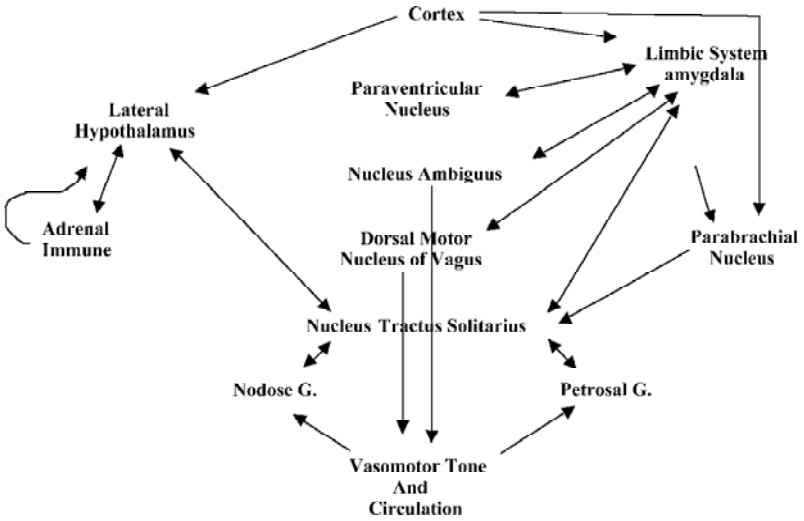

Figure 2. Summary of amygdalar projections involved in the amygdalar-induced compensatory response.

Conclusion

Our conclusion is two-fold. We demonstrate that amygdalar regulation of the male and female sexual cycle is medicated by estrogen-/androgen-related signaling molecules, both of which exert their respective influences on ovulation and sexual behavior via coupled NO release. Furthermore, we propose that amygdalar-induced homeostatic control mechanisms acting in response to emotionally charged stimuli, including sexually stimulating sensations, appear to be mediated by a system of regulation involving NO as a neurotransmitter and as a locally acting hormone. Hence, these two principal roles of the amygdala exert their respective behaviors via NO.

In final summary, we have demonstrated numerous mechanisms and neurochemical pathways with regard to both emotion and sexual behavior (ovulation, arousal, *etc*), and we have shown a link between each of these complex pathways systems, as well as the use of NO as a major biochemical messenger. Moreover, throughout each of the aforementioned pathways, we have attempted to offer a possible relationship to sex, either as a mediator of direct sexual activity, or as a mediator of an individual aspect of the sexual cycle.

Acknowledgment

We thank John R HESSELINK, Professor of Radiology and Neurosciences at University of California San Diego Medical Center, San Diego, CA, for permission to use his figure of the limbic system (Figure 1).

References

1 Kier EL, Staib LH, Davis LM, Bronen RA. MR imaging of the temporal stem: anatomic dissection tractography of the uncinate fasciculus, inferior occipitofrontal fasciculus, and Meyer's loop of the optic radiation. AJNR Am J Neuroradiol 2004; 25: 677–91.

2 Thomas A, Woolsey JH, Mokhtar HG. The brain atlas. 2nd ed. New York: Wiley-Liss; 2002.

3 Frank M. MAL, a proteolipid in glycosphingo lipid enriched domains: functional implications in myelin and beyond. Prog Neurobiol 2000; 60: 531–44.

4 Cadet P, Zhu W, Mantione K, Rymer M, Dardik I, Reisman S, *et al.* Cyclic exercise induces anti-inflammatory signal molecule increases in the plasma of Parkinson's patients. Int J Mol Med 2003; 12: 485–92.

5 Stefano GB, Fricchione GL, Slingsby BT, Benson H. The placebo effect and relaxation response: neural processes and their coupling to constitutive nitric oxide. Brain Res Brain Res Rev 2001; 35: 1–19.

6 Joseph JT, Cardozo DL. Functional neuroanatomy: an interactive text and manual. New York: Wiley-Liss; 2004.

7 Smith CM. Elements of molecular neurobiology. 3rd ed. New York: Wiley-Liss; 2002.

8 Toda N, Tanaka T, Ayajiki K, Okamura T. Cerebral vasodilatation induced by stimulation of the pterygopalatine ganglion and greater petrosal nerve in anesthetized monkeys. Neuroscience 2000; 96: 393–8.

9 Tanaka T, Okamura T, Handa J, Toda N. Neurogenic vasodilation mediated by nitric oxide in porcine cerebral arteries. J Cardiovasc Pharmacol 1999; 33: 56–64.

10 Lembo G, Vecchione C, Izzo R, Fratta L, Marino G, Pilato G, *et al.* Noradrenergic vascular hyper-responsiveness in human hypertension is dependent on oxygen free radical impairment of nitric oxide activity. Circulation 2000; 102: 552–7.

11 McClure EB, Monk CS, Nelson EE, Zarahn E, Leibenluft E, Bilder RM, *et al.* A developmental examination of gender differences in brain engagement during evaluation of threat. Biol Psychiatry 2004; 55: 1047–55.

12 Janszky J, Szucs A, Halasz P, Borbely C, Hollo A, Barsi P, *et al.* Orgasmic aura originates from the right hemisphere. Neurology

2002; 58: 302–4.
13 Tanuri FD, Thomaz RB, Tanuri JA. Temporal lobe epilepsy with aura of pleasure. Arq Neuropsiquiatr 2000; 58: 178–80.
14 Rasia-Filho AA, Fabian C, Rigoti KM, Achaval M. Influence of sex, estrous cycle and motherhood on dendritic spine density in the rat medial amygdala revealed by the Golgi method. Neuroscience 2004; 126: 839–47.
15 Rettori V, Belova N, Dees WL, Nyberg CL, Gimeno M, McCann SM. Role of nitric oxide in the control of luteinizing hormone-releasing hormone release *in vivo* and *in vitro*. Proc Natl Acad Sci USA 1993; 90: 10 130–4.
16 Bonavera JJ, Sahu A, Kalra PS, Kalra SP. Evidence that nitric oxide may mediate the ovarian steroid-induced luteinizing hormone surge: involvement of excitatory amino acids. Endocrinology 1993; 133: 2481–7.
17 Bonavera JJ, Sahu A, Kalra PS, Kalra SP. Evidence in support of nitric oxide (NO) involvement in the cyclic release of prolactin and LH surges. Brain Res 1994; 660: 175–9.
18 Bonavera JJ, Kalra PS, Kalra SP. *L*-Arginine/nitric oxide amplifies the magnitude and duration of the leuteinizing hormone surge induced by estrogen: involvement by neuropeptide Y. Endocrinology 1996; 137: 1956–62.
19 Pu S, Kalra PS, Kalra SP. Ovarian steroid-independent diurnal rhythm in cyclic GMP/nitric oxide efflux in the medial preoptic area: possible role in preovulatory and ovarian steroid-induced LH surge. J Neuroendocrinol 1998; 10: 617–25.
20 Prevot V, Rialas C, Croix D, Salzet M, Dupouy JP, Puolain P, *et al.* Morphine and anandamide coupling to nitric oxide stimulated GnRH and CRF release from rat median eminence: neurovascular regulation. Brain Res 1998; 790: 236–44.
21 Herbison AE, Simonian SX, Norris PJ, Emson PC. Relationship of neuronal nitric oxide synthase immunoreactivity to GnRH neurons in the ovariectomized and intact female rat. J Neuroendocrinol 1996; 8: 73–82.
22 Yamada K, Emson P, Hokfelt T. Immunohistochemical mapping of nitric oxide synthase in the rat hypothalamus and colocalization with neuropeptides. J Chem Neuroanat 1996; 10: 295–316.
23 Prevot V, Dutoit S, Croix D, Tramu G, Beauvillain JC. Semiquantitative ultrastructural analysis of the localization and neuropeptide content of gonadotropin releasing hormone nerve terminals in the median eminence throughout the estrous cycle of the rat. Neuroscience 1998; 84: 177–91.
24 Stefano GB, Salzet M, Magazine HI, Bilfinger TV. Antagonist of LPS and IFN-γ induction of iNOS in human saphenous vein endothelium by morphine and anandamide by nitric oxide inhibition of adenylate cyclase. J Cardiovasc Pharmacol 1998; 31: 813–20.
25 Stefano GB, Salzet M, Bilfinger TV. Long-term exposure of human blood vessels to HIV gp120, morphine and anandamide increases endothelial adhesion of monocytes: uncoupling of nitric oxide. J Cardiovasc Pharmacol 1998; 31: 862–8.
26 Stefano GB, Salzet B, Salzet M. Identification and characterization of the leech CNS cannabinoid receptor: coupling to nitric oxide release. Brain Res 1997; 753: 219–24.
27 Stefano GB, Cadet P, Breton C, Goumon Y, Prevot V, Dessaint JP, *et al.* Estradiol-stimulated nitric oxide release in human granulocytes is dependent on intracellular calcium transients: evidence for a cell surface estrogen receptor. Blood 2000; 95: 3951–8.
28 Stefano GB, Goumon Y, Casares F, Cadet P, Fricchione GL, Rialas C, *et al.* Endogenous morphine. Trends Neurosci 2000; 9: 436–42.
29 Bianchi E, Guarna M, Tagliamonte A. Immunocytochemical localization of endogenous codeine and morphine. Adv Neuroimmunol 1994; 4: 83–92.
30 Spector S, Munjal I, Schmidt DE. Endogenous morphine and codeine. Possible role as endogenous anticonvulsants. Brain Res 2001; 915: 155–60.
31 Zhu W, Ma Y, Bell A, Esch T, Guarna M, Bilfinger TV, *et al.* Presence of morphine in rat amygdala: evidence for the 3 opiate receptor subtype via nitric oxide release in limbic structures. Med Sci Monit 2004; 10: BR433–9.
32 Steffens M, Engler C, Zentner J, Feuerstein TJ. Cannabinoid CB1 receptor-mediated modulation of evoked dopamine release and of adenylyl cyclase activity in the human neocortex. Br J Pharmacol 2004; 141: 1193–203.
33 Castellano C, Rossi-Arnaud C, Cestari V, Costanzi M. Cannabinoids and memory: animal studies. Curr Drug Targets CNS Neurol Disord 2003; 2: 389–402.
34 de la Torre JC, Pappas BA, Prevot V, Emmerling MR, Mantione K, Fortin T, *et al.* Hippocampal nitric oxide upregulation precedes memory loss and A beta I-40 accumulation after chronic brain hypoperfusion in rats. Neurol Res 2003; 25: 635–41.
35 Esch T, Guarna M, Bianchi E, Zhu W, Stefano GB. Commonalities in the central nervous system's involvement with complementary medical therapies: limbic morphinergic processes. Med Sci Monit 2004; 10: MS6–17.
36 Azad SC, Zieglgansberger W. What do we know about the state of chronic pain? Schmerz 2003; 17: 441–4.
37 Stefano GB. Endocannabinoid immune and vascular signaling. Acta Pharmacol Sin 2000; 21: 1071–81.
38 Stefano GB, Prevot V, Cadet P, Dardik I. Vascular pulsations stimulating nitric oxide release during cyclic exercise may benefit health: a molecular approach. Int J Mol Med 2001; 7: 119–29.
39 Lown B, DeSilva RA. Roles of psychologic stress and autonomic nervous system changes in provocation of ventricular premature complexes. Am J Cardiol 1978; 41: 979–85.
40 Lown B, Verrier RL. Neural activity and ventricular fibrillation. N Engl J Med 1976; 294: 1165–70.
41 Wellens HJ, Vermeulen A, Durrer D. Ventricular fibrillation occurring on arousal from sleep by auditory stimuli. Circulation 1972; 46: 661–5.
42 Schiffer F, Hartley LH, Schulman CL, Abelmann WH. Evidence for emotionally-induced coronary arterial spasm in patients with angina pectoris. Br Heart J 1980; 44: 62–6.
43 Holstege G. Some anatomical observations on the projections from the hypothalamus to brainstem and spinal cord: an HRP and autoradiographic tracing study in the cat. J Comp Neurol 1987; 260: 98–126.
44 Holstege G, Meiners L, Tan K. Projections of the bed nucleus of the stria terminalis to the mesencephalon, pons, and medulla oblongata in the cat. Exp Brain Res 1985; 58: 379–91.
45 Hopkins DA. Amygdalotegmental projections in the rat, cat and rhesus monkey. Neurosci Lett 1975; 1: 263–70.
46 Hopkins DA, Holstege G. Amygdaloid projections to the mesencephalon, pons and medulla oblongata in the cat. Exp

Brain Res 1978; 32: 529–47.
47 Kuypers HGJM, Maisky VA. Retrograde axonal transport of horseradish peroxidase from spinal cord to brainstem cell groups in the cat. Neurosci Lett 1975; 1: 9–14.
48 Swanson LW, Kuypers HG. The paraventricular nucleus of the hypothalamus: cytoarchitectonic subdivisions and organization of projections to the pituitary, dorsal vagal complex, and spinal cord as demonstrated by retrograde fluorescence double-labeling methods. J Comp Neurol 1980; 194: 555–70.
49 de la Torre JC, Stefano GB. Evidence that Alzheimer's disease is a microvascular disorder: the role of constitutive nitric oxide. Brain Res Rev 2000; 34: 119–36.
50 Deutsch DG, Goligorsky MS, Schmid PC, Krebsbach RJ, Schmid HHO, Das SK, *et al*. Production and physiological actions of anandamide in the vasculature of the rat kidney. J Clin Invest 1997; 100: 1538–46.
51 MacLean PD. Discussion. Physiol Rev 1960; 40: 113–4.
52 Smith WK. The functional significance of the rostral cingular cortex as revealed by its responses to electrical excitation. J Neurophysiol 1945; 8: 241–54.
53 Ueda H. Arrhythmias produced by cerebral stimulation. Jpn Circ J 1962; 26: 225–30.
54 Fimiani C, Liberty T, Aquirre AJ, Amin I, Ali N, Stefano GB. Opiate, cannabinoid, and eicosanoid signaling converges on common intracellular pathways: nitric oxide coupling. Prostaglandins Other Lipid Mediat 1999; 57: 23–34.
55 Russchen FT. Amygdalopetal projections in the cat. I. Cortical afferent connections. A study with retrograde and anterograde tracing techniques. J Comp Neurol 1982; 206: 159–79.
56 Calaresu FR, Ciriello J. Projections to the hypothalamus from buffer nerves and nucleus tractus solitarius in the cat. Am J Physiol 1980; 239: R130–6.
57 Bonvallet M, Bobo EG. Changes in phrenic activity and heart rate elicited by localized stimulation of amygdala and adjacent structures. Electroencephalogr Clin Neurophysiol 1972; 32: 1–16.
58 Allen GV, Saper CB, Hurley KM, Cechetto DF. Organization of visceral and limbic connections in the insular cortex of the rat. J Comp Neurol 1991; 311: 1–16.
59 Kapp BS, Schwaber JS, Driscoll PA. Frontal cortex projections to the amygdaloid central nucleus in the rabbit. Neuroscience 1985; 15: 327–46.
60 Beattie J, Brow GR, Long CNH. Physiological and anatomical evidence for the existence of nerve tracts connecting the hypothalamus with spinal sympathetic centres. Proc R Soc Lond B Biol Sci 1930; 106: 253–75.
61 Magoun HW, Ranson SW, Heatherington A. Descending connections from the hypothalamus. Arch Neurol Psychiatry 1938; 39: 1127–49.
62 Saper CB, Swanson LW, Cowan WM. An autoradiographic study of the efferent connections of the lateral hypothalamic area in the rat. J Comp Neurol 1979; 183: 689–706.
63 Hurley KM, Herbert H, Moga MM, Saper CB. Efferent projections of the infralimbic cortex of the rat. J Comp Neurol 1991; 308: 249–76.
64 Hosoya Y, Matsushita M. Brainstem projections from the lateral hypothalamic area in the rat, as studied with autoradiography. Neurosci Lett 1981; 24: 111–6.
65 ter Horst GJ, Luiten PG, Kuipers F. Descending pathways from hypothalamus to dorsal motor vagus and ambiguus nuclei in the rat. J Auton Nerv Syst 1984; 11: 59–75.
66 Okamura T, Ayajiki K, Uchiyama M, Uehara M, Toda N. Neurogenic vasodilatation of canine isolated small labial arteries. J Pharmacol Exp Ther 1999; 288: 1031–6.
67 Toda N. Mediation by nitric oxide of neurally-induced human cerebral artery relaxation. Experientia 1993; 49: 51–3.
68 Dressing H, Obergriesser T, Tost H, Kaumeier S, Ruf M, Braus DF. Homosexual pedophilia and functional networks: an fMRI case report and literature review. Fortschr Neurol Psychiatr 2001; 69: 539–44.
69 Howard RC. The neurophysiology of sexual desire, with particular reference to paedophilia. Ann Acad Med Singapore 1995; 24: 724–7.
70 Salamon E, Kim M, Beaulieu J, Stefano GB. Sound therapy induced relaxation: down regulating stress processes and pathologies. Med Sci Monit 2003; 9: RA96–101.

Acta Pharmacologica Sinica 2005 Apr; 26 (4): 396–404

Blackwell Publishing

Invited review

Development of *Caenorhabditis elegans* pharynx, with emphasis on its nervous system

Marc PILON[1], Catarina MÖRCK

Lundberg Laboratory, Chalmers University, Göteborg S-405 30, Sweden

Key words

Caenorhabditis elegans; pharynx; axon; growth cones; morphogenesis; heart

[1] Correspondence to Dr Marc PILON.
Phn 46-31-773-3279.
Fax 46-31-773-3801.
E-mail marc.pilon@molbio.gu.se

Received 2004-11-14
Accepted 2004-12-14

doi: 10.1111/j.1745-7254.2005.00070.x

Abstract

The *Caenorhabditis elegans* pharynx is a neuromuscular tube of which the function is to pump and crush bacteria, and inject them into the intestine. The 80-cell pharynx develops via the morphogenesis and differentiation of the cells that compose its semi-spherical primordium, and requires the activity of several evolutionarily conserved genes, such as *pha-4* (the homolog to the *Drosophila forkhead* and vertebrate FoxA), *ceh-22* (the homolog to the *Drosophila tinman* and vertebrate Nkx2.5), and *pha-2* (the homolog to the vertebrate Hex). There are 20 neurons in the pharynx, each with a reproducible unique trajectory. Developmental genetic analysis of axon guidance in the pharynx indicates that some axon trajectories are in part established without growth cones, whereas other parts necessitate growth cone function and guidance. Here we provide an overview of the developmental genetics of the *Caenorhabditis elegans* pharynx, with an emphasis on its nervous system.

Introduction

Caenorhabditis elegans (*C elegans*) is a 1-mm long free-living nematode that currently has tremendous popularity as a model organism, especially regarding questions of interest to developmental biologists. Given its ease of culture (it is typically grown on *Escherichia coli* lawns), a 3-d life cycle from egg to egg, a transparent body that allows visualization of any cell of interest, a fully described cell lineage, and the ease with which genetic screens can be carried out at low costs, it is no wonder that *C elegans* is such a versatile and popular laboratory model organism. The 97 Mb genome of *C elegans* is also completely sequenced, and computer algorithms predict nearly 20 000 functional genes. Furthermore, the *C elegans* research community has a traditional helpfulness and openness: thousands of mutants are freely available to academic laboratories from the *C elegans* Genetics Center (http://biosci.umn.edu/CGC/CGChomepage.htm), and public databases of anatomical and molecular information are available on the internet (http://www.wormatlas.org/; http://www.wormbase.org/).

Here, we review the developmental genetics of the *C elegans* pharynx, with an emphasis on the development of its small 20-neuron network. However, here is one last introductory note: several lines of evidence suggest that the *C elegans* pharynx evolved from an organ that was also the common ancestor to the vertebrate heart. This evidence consists mostly of physiological and molecular similarities: (i) like the heart, the pharynx is a rhythmically contracting neuromuscular pump[1]; (ii) the muscle cells of the pharynx have autonomous contractile activity reminiscent of cardiac myocytes[2]; and (iii) *ceh-22*, the *C elegans* homolog to the homeobox gene NK2.5 that plays an important role in heart development in vertebrates, participates in pharyngeal development, and can partially be replaced functionally by the zebrafish NK2.5[3]. The evolutionary relatedness of the *C elegans* pharynx and the vertebrate heart suggest that insights regarding heart development and function may be gained by studying the simpler and experimentally more convenient *C elegans* pharynx.

Pharynx form and function

The pharynx represents the foregut of the nematode digestive tract (Figure 1). Food (typically *E coli* in the laboratory) is pumped through the mouth by the action of the mus-

cular pharynx, ground by specialized cuticle lining the pharynx (the "grinder" in the posterior bulb), and transferred to the intestine via a pharyngeal-intestinal valve. The main anatomical features of the pharynx are, from anterior to posterior, the procorpus, the metacorpus, the isthmus, and the posterior bulb in which the grinder is located (Figure 1). The mature pharynx is composed of 62 cells (for a total of 80 nuclei, since several of the cells are binucleate as a result of cell fusion). These cells can be categorized into 5 types: neurons (20), muscles (20 cells; 37 nuclei), marginal cells (9), epithelial cells (9), and gland cells (4 cells; 5 nuclei). The muscle cells and marginal cells constitute a single-cell-thick tube, continuous at its anterior end with the tube of the hypodermis that encloses the worm. Muscle and marginal cells are joined by tight junctions, which divide the membrane into apical and basal surfaces. The apical surfaces face the lumen and secrete cuticle, continuous with the cuticle made by the hypodermis. The basal surfaces face a basal lamina that is continuous with the basal lamina that separates the hypodermis and intestine from the pseudocoelom (fluid-filled body cavity) and mesoderm. Components of this basal lamina are likely produced by body-wall muscles[4,5]. The 9 epithelial cells are arranged so as to form a narrow ring at the anterior end of the pharynx, where it connects with the buccal cavity. There is otherwise no epithelial sheet covering the bulk of the pharynx. Precise knowledge of pharyngeal anatomy is available at the ultrastructural level, thanks to detailed electron microscopy studies[6].

Pharyngeal neurons lie deep within folds of the basal membrane of pharyngeal muscle cells (note that this is not a "basal lamina" or "basement membrane", but is that part of the muscle cell membranes that is on the "basal" side), between the muscle and basal lamina, just as the extrapharyngeal nervous system is between the basal membrane of the hypodermis and the basal lamina. No basal lamina separates pharyngeal motor neuron presynaptic terminals from the post-synaptic muscle membrane. In contrast, extrapharyngeal motor neurons are separated from the muscle cells on which they synapse by the basal lamina that separates the mesodermal muscle cells from the ectodermal neurons.

The role of the pharyngeal nervous system in regulating pumping is somewhat of a mystery. Normal feeding consists of two primary motions: pumping and isthmus peristalsis[1]. A pump is a near-simultaneous contraction of the muscles of the corpus, anterior isthmus, and terminal bulb, followed by a near-simultaneous relaxation. The contractile fibers of the pharyngeal muscles are radially oriented, so contraction pulls the lumen open from its resting closed Y-shape to a triangular shape. The second motion, isthmus peristalsis, occurs after the main relaxation is complete. It is a peristaltic wave of contraction in the posterior isthmus that carries bacteria trapped in the anterior isthmus back to the grinder. Typically, only every fourth pump is followed by an isthmus peristalsis. The nervous system is not essential for pumping; pumping continues even when the entire pharyngeal nervous system is killed[2]. However, many neurons are important; efficient pumping and trapping of bacteria by the pharynx requires the presence of the neurons I5, MC, M3, M4, and NSM[2,7,8].

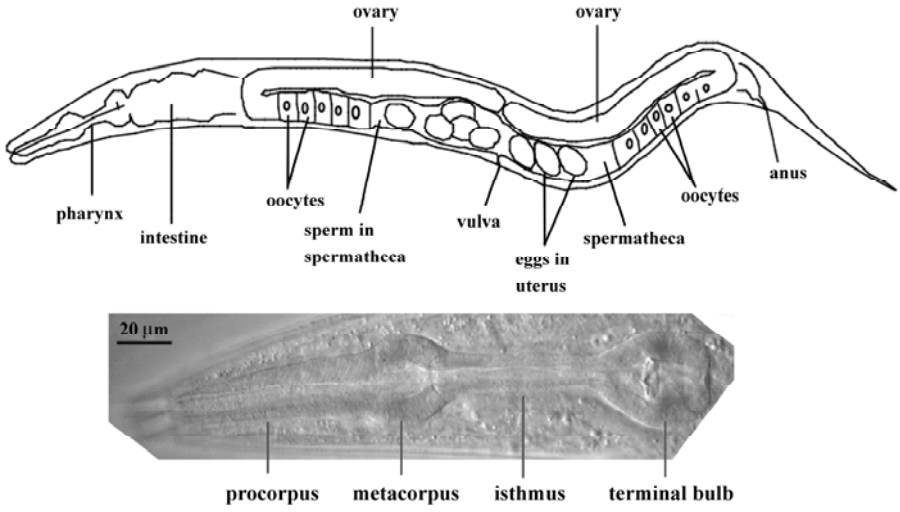

Figure 1. Diagram showing the main anatomical features of the *Caenorhabditis elegans* hermaphrodite (top) and Nomarski image of the *C elegans* pharynx (bottom). Anterior is to the left.

Development of the pharynx

In order to begin understanding how the pharyngeal neurons develop, it is necessary first to describe pharyngeal development itself (Figure 2). The *C elegans* pharynx offers a very simple model to understand morphogenesis and differentiation. The pharynx develops through the morphogenesis of a primordium composed of 80 undifferentiated cells (plus many apoptotic cells; there are 19 apoptotic cells that are sisters to final pharyngeal cells and that die within 350– 420 min of development[9]). Morphogenesis is accompanied by differentiation but not by new cell divisions, so the mature pharynx contains 80 nuclei but only 62 cells as a result of cell fusion among some of the muscle and two gland cells; these fusions occur around the time of hatching and seem irrelevant to the developmental process[9], although it would be interesting to understand how these fusions are regulated.

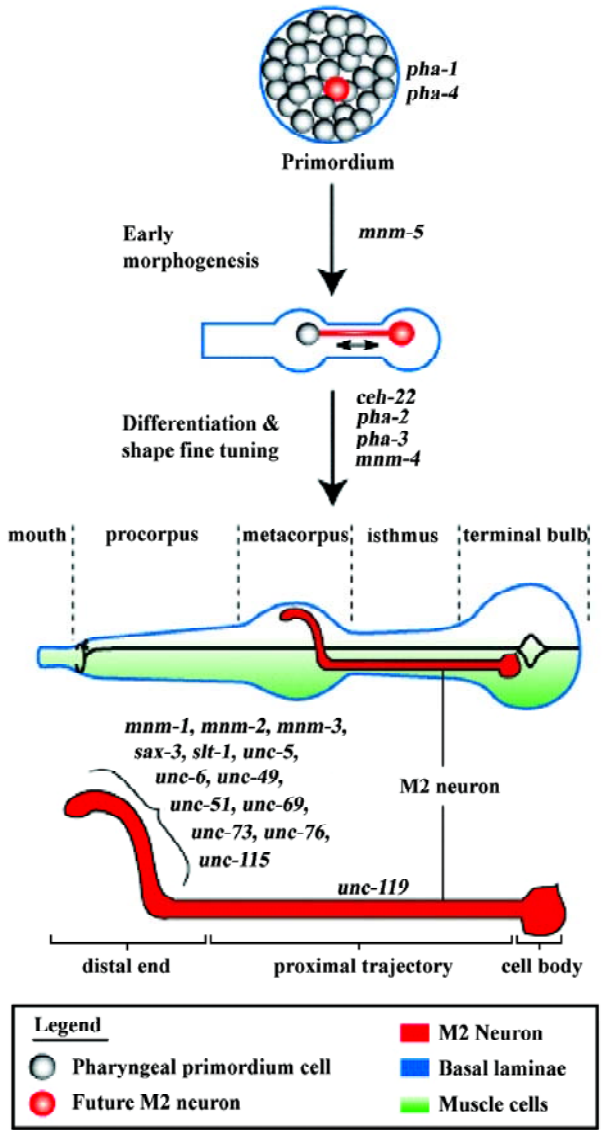

Figure 2. General overview of pharyngeal anatomy and developmental genetics with the M2 neuron trajectory described in detail at bottom. Gene name explanation: *ceh, Caenorhabditis* elegans homeobox; *mnm*, M neuron morphology abnormal; *pha*, defective pharynx development; *sax*, sensory axon guidance; *slt*, slit (*Drosophila*) homolog; and *unc*, uncoordinated.

0–100 min: early cell divisions and establishment of main lineages The cells that make up the pharyngeal primordium originate from two early embryonic blastomeres: the ABa and the MS blastomeres. This is quite remarkable: members of two distinct lineages are recruited to form one organ. Not only that, but cells with these two very different ancestries may end up adopting nearly identical fates. For example, the muscle cell m3VL has the ancestry ABalpappppp, whereas the identical cell m3DL has the ancestry Msaaapaaa (these two cells will fuse later). Note that even though each cells is normally specific to adopt a developmental fate, there is some degree of developmental plasticity. For example, Avery and Horvitz showed that the pharyngeal neuron M4 is essential for feeding in wild-type *C elegans*, but that in a *ced-3* mutant (in which the sister cell of M4 does not die of apoptosis), the now viable sister of M4 can sometimes take over the function of M4[10].

The respective contributions of the ABa and MS lineages are more or less spatially consistent with their initial positions within the 8-cell embryo. For example, the anterior cell ABa contributes cells of the anterior pharynx, whereas the more posterior MS cell contributes mostly posterior pharyngeal cells. This observation holds true for later descendents and narrower scopes of spatial contributions. Figure 3 shows the adult pharyngeal contributions from the pharyngeal precursors of the 100-cell stage embryo, and emphasizes the preservation of spatial relationships during development. Thus, ABalpa contributes mostly to the anterior left subventral area, *etc*.

100–250 min: gastrulation At 100 min after first cleavage, when the egg comprises 28 cells, gastrulation begins. During gastrulation, several cells enter deep into the embryo through a ventral cleft. The first cells to enter are the gut precursor cells Ea and Ep. Next are the P4 and MS progeny at 120–200 min of development, and the AB-derived pharyngeal precursors enter more anteriorly at 210–250 min. The ventral cleft closes from posterior (230 min) to anterior (290 min). As gastrulation proceeds, the E cell descendents and the pharyngeal precursors form a central cylinder. Note that as gastrulation proceeds, so do cell divisions. Active pre-pharyngeal cell divisions continue until approximately

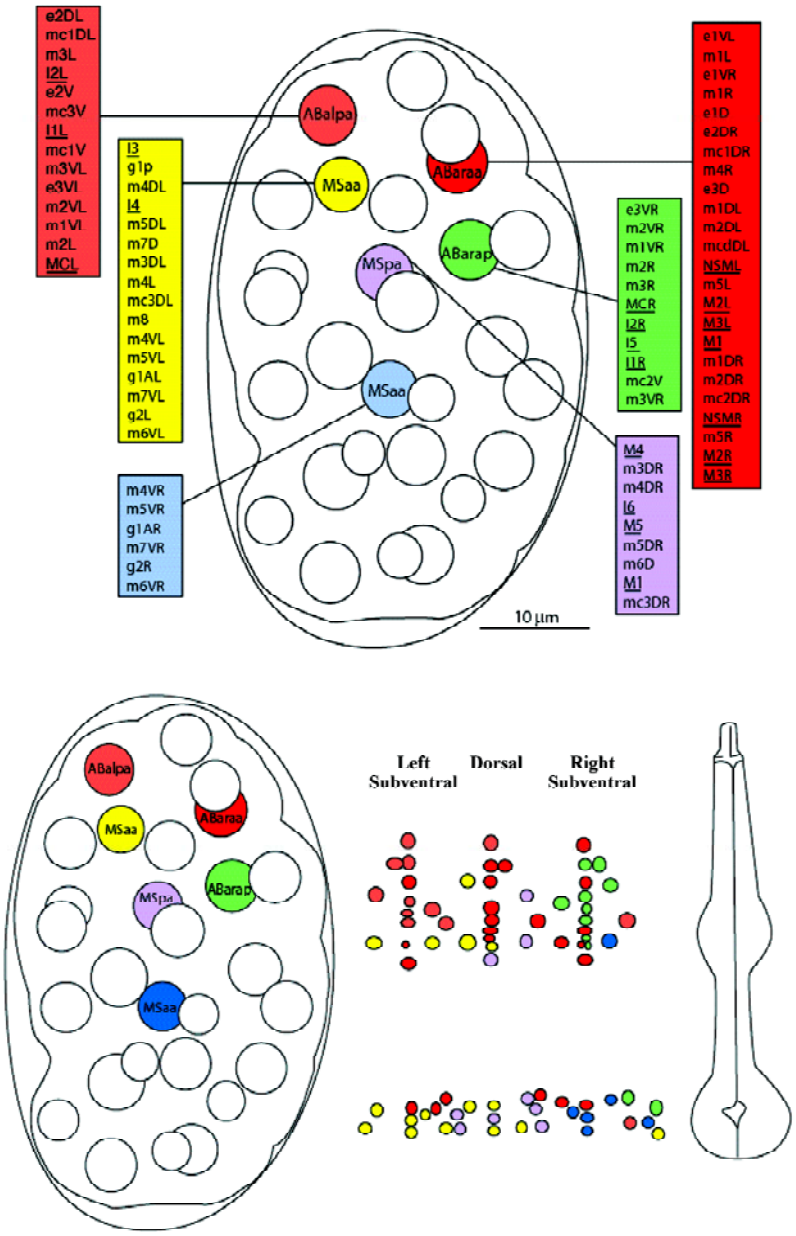

Figure 3. Color-coded cell fates of the pharyngeal precursor cells in the 28-cell embryo (A) and the location of their nuclei in the mature pharynx (B). Note preservation of spatial relationships in the mature pharynx, and absence of nuclei in the isthmus. Adapted from Sulston *et al*[9] and Albertson and Thomson[6].

350 min of development, and some late divisions occur until approximately400 min.

250–400 min: compaction of pharyngeal primordium Between 250 min and 400 min the pharyngeal primordium becomes clearly defined. The non-pharyngeal precursor cells are somehow excluded from the pharyngeal primordium. Perhaps they are squeezed out in a process by which the pharyngeal cells have more adhesive affinity to each other than to any other cell (in line with the theory of Malcolm Steinberg; eg see Duguay *et al*[11]). This aspect of primordium formation has not been investigated experimentally.

400–430 min: extension of pharyngeal primordium The approximately 400-min-old primordium is insulated by a basement membrane (present at or before 400 min[9]), such that the pharynx develops autonomously, perhaps with no extrapharyngeal cues, or with very few. Such autonomous development is also true of the 20-cell intestine that, together with the pharynx, makes up the entire *C elegans* gut[12]. At

approximately 400 min, the pharyngeal primordium is approximately spherical, and most of the cell nuclei appear located in spatial relationships that are consistent with their final positions, at least along the anterior-posterior axis, although the relative distances between these nuclei can be very different from those of the mature organ. For example, at approximately 430 min, the sister cells M2 and M3 have their nuclei next to each other, whereas in the final pharynx M2 has its nucleus in the posterior bulb and M3 in the metacorpus. It therefore seems that development of the pharynx is mostly a question of cell differentiation and morphogenesis, not of active cell migration. However, some cells do migrate within the developing pharynx. For example, Sulston *et al* observed that the 3 g1 gland cells migrate in a reproducible way. They wrote: "Their movements approximately follow the subsequent course of their secretory processes, and may be responsible for laying down the latter"[9].

Beginning at approximately 400 min, the primordium elongates anteriorly then posteriorly. The primordium develops into a tube connected anteriorly to the buccal cavity and posteriorly to the midgut. The adherens junctions that connect many pharyngeal cells with each other form simultaneously with the process of elongation. Note that there is no evidence of any basement membrane within the elongated pharynx during or after elongation or at any other stage of development or adulthood[5]. Portereiko and Mango have studied the morphogenesis of the pharyngeal primordium and divided the process into three stages: (i) lengthening of the nascent pharyngeal lumen by reorientation of the apicobasal polarity of anterior pharyngeal cells ("Reorientation"); (ii) formation of an epithelium by the buccal cavity cells, which mechanically couples the buccal cavity to the pharynx and anterior epidermis ("Epithelialization"); and (iii) a concomitant movement of the pharynx anteriorly and the epidermis of the mouth posteriorly to bring the pharynx, buccal cavity, and mouth into close apposition ("Contraction")[4].

430–800 min: completion of functional pharynx Between 430 min and 490 min, as elongation proceeds, the pharyngeal bulbs and isthmus become apparent. It is probably at this time that the pharyngeal cells interpret their final differentiation programs and adopt their final shapes. Between 600 min and 650 min, the pharyngeal cuticle is produced and the lumen becomes distinct. The pharyngeal glands are active by 720 min and the pharynx is pumping by 750 min. Hatching occurs at approximately 800 min following first cleavage.

Genetics of pharyngeal development

What follows is a brief overview of some of the genes that have been shown to play a role in pharyngeal development.

pha-4 *pha-4* encodes the *C elegans* homolog of FoxA, a fork-head transcription factor[13]. The *pha-4* gene is expressed in all pharyngeal cells, and also in some cells of the rectum[13]. Expression of PHA-4 is detected in all pharyngeal precursor cells beginning from at least 200 min of development (and perhaps even earlier). By the comma stage (~430 min), all the pharyngeal cells are present and express PHA-4. PHA-4 is also expressed in the 6 cells of the pharyngeal intestinal valve, which is not considered a part of the pharynx *per se*. At 430 min, PHA-4 expression is also found in 6–8 rectal cells, including the 2 rectal valve cells and the 3 rectal epithelial cells. This expression pattern is therefore conserved with that of the *Drosophila forkhead* gene (high levels in the foregut/pharynx and hindgut/rectum). The *pha-4* mutants completely lack all pharyngeal cells, even though the AB and MS lineages are otherwise completely normal[14]. It seems that *pha-4* acts as an organ identity factor. Indeed, Gaudet and Mango have proposed that the PHA-4 protein may directly activate most or all pharyngeal genes, with the expression timing being regulated by the presence of binding sites of varying affinity: poor binding sites will have delayed expression, as they will require higher levels of PHA-4 before becoming activated[15]. The consensus binding site for PHA-4 has been defined as: TRTTKRY (R=A/G, K=T/G, Y=T/C). This site is present in the *myo-2* gene, a pharyngeal-specific muscle myosin that is a confirmed direct target of PHA-4[13]. Ectopic expression of PHA-4 causes ectopic expression of *myo-2*, *ceh-22* (a homeodomain protein that is also a coactivator of the *myo-2* gene), *pha-2* (another homeodomain protein important for pharynx development, see below), and most likely other otherwise pharyngeal specific genes[13,16].

pha-1 In *pha-1* mutants, the pharyngeal primordium appears to form normally, with a full complement of nuclei and surrounded by a basal membrane. In these mutants, elongation also appears normal up to at least 420 min of development, including the expression of an antigenic marker for the pharyngeal muscle cell precursors detected with the monoclonal antibody 3NB12[17,18]. After elongating and contacting the buccal cavity, the developing organ detaches from the buccal cavity and retracts, causing a "Pun" (pharynx unattached) phenotype. The end result is a worm in which the incompletely formed pharynx is slightly elongated, surrounded by the visible basement membrane and unattached to the mouth. It is difficult to determine if all pharyngeal cell differentiation events take place in the *pha-1* mutant, but expression of

MYO-2::GFP is detected and a pharyngeal lumen forms[17]. Thus *pha-1* affects pharynx development after pharynx cells are committed to a specific cell fate, but before terminal differentiation/morphogenesis of the different pharyngeal cell types occurs[17,18].

Initial analysis of the PHA-1 amino acid sequence suggested that it was a basic leucine zipper (bZIP) transcription factor. Expression of a PHA-1::LacZ reporter also suggested restricted expression in pharyngeal cells as well as in body muscle cells[18]. However, a more recent evaluation of the PHA-1 amino acid sequence indicates that *pha-1* actually does not encode a bZIP transcription factor[17]. Consistent with this last analysis, a rescue-competent PHA-1::GFP fusion protein suggests that PHA-1 is a cytosolic protein[17] that is widely expressed (essentially in all cells by the 100-cell stage). Because the biochemical function of PHA-1 is unknown at present, little can be said about its actual mechanism of action. However, genetic interaction experiments have shown that *pha-1*, *lin-35* (the *C elegans* Retinoblastoma protein homolog), and *ubc-18* (a ubiquitin-conjugating enzyme) play partially redundant functions to control pharyngeal morphogenesis[17]. Indeed, *lin-35*/Rb; *ubc-18* double mutants exhibit a synthetic pharyngeal phenotype; that is, failure to undergo pharyngeal primordium elongation, typically failing already at the reorientation step during which the anterior epithelial cells of the primordium should align their long axis with the dorsoventral axis of the embryo[19]. The *ubc-18* and *pha-1* also both show strong synthetic pharyngeal phenotypes when combined with class B synthetic multivulval (SynMuv) genes. The SynMuv genes form two molecularly heterogeneous classes (class A and B) of genes that contribute redundantly to vulva development; class B SynMuv genes obviously also play a hitherto unknown role in pharyngeal development that is redundant with both *ubc-18* and *pha-1*[17,19].

pha-2 The *pha-2* mutant worms exhibit a late defect in pharyngeal morphogenesis that results in the two pharyngeal bulbs being next to each other rather than being separated by a narrow, nucleus-free isthmus. We cloned the *pha-2* gene and found that it encodes a homeobox gene most homologous to the vertebrate Hex gene[16]. Using a PHA-2::GFP translational fusion reporter in which a *pha-2* genomic fragment containing 2.7 kb of pha-2 5'UTR plus the entire gene fused to GFP at its C-terminal codon, we observed expression in several pharyngeal cells: the pm5 muscle cells that form the isthmus but have their cell bodies within the posterior bulb; the pm4 cells that make up the bulk of the metacorpus; and pharyngeal epithelial cells. As this translational fusion reporter was able to rescue the mutant phenotype, we are relatively confident that the expression profile of the reporter reflects normal PHA-2 expression. We hypothesize that PHA-2 confers an isthmus cell identity to the pm5 muscle pharyngeal cells that express it and that form the isthmus. The main characteristic of isthmus cells is that they have a long elongated shape extending into the isthmus, but that their cell bodies are embedded within the metacorpus or posterior bulb. This isthmus cell shape likely results from directional growth of the cells occurring after the comma stage (~430 min), because at this stage there is no nuclear-free zone along the length of the elongated primordium. As Sulston *et al* documented, it is during the 430–490 min interval, as the emerging pharynx continues its elongation, that the pharyngeal bulbs become apparent[9].

What are the genes regulated by *pha-2*? Experimental evidence suggests that *pha-2* acts as a repressor of *ceh-22* in the pm5 cells. In wild-type animals, expression of a CEH-22::GFP reporter is downregulated in the isthmus by late embryogenesis. In contrast, in *pha-2* mutants the expression of the CEH-22::GFP reporter persists and even increases in the isthmus during late embryogenesis, and also post-embryonically. Because of the late effects of the *pha-2* mutation, we also surmise that at some downstream level, *pha-2* acts via genes that implement the differentiation program by driving the final cell shape changes, such as cytoskeletal genes. It is perhaps worth noting that located just next to the *pha-2* gene is the intermediate filament 2c gene, IF-C2 (M6.1), which is expressed in pharyngeal and intestinal desmosomes and thus likely plays a role in cell-cell connections[20]. Given that intermediate filaments are important in several morphogenesis processes, including cell elongation[21,22], there is a possibility that M6.1 contributes to pharyngeal morphogenesis. Consistent with this line of reasoning, the expression of IF-C2 begins in the late embryo, when final pharyngeal morphogenesis occurs.

ceh-22 Like vertebrate cardiac and smooth muscles, the pharyngeal muscles of *C elegans* do not express any of the known members of the MyoD family of myogenic factors. In addition, like vertebrate cardiac muscle cells, the pharyngeal muscles exhibit an intrinsic rhythmic contraction activity that does not depend on any neuronal input. Two myosin heavy chain genes *myo-1* and *myo-2* are specifically expressed in pharyngeal muscles. In 1994, Okkema and Fire characterized the *myo-2* promoter and identified a transcription factor that binds this promoter and regulates its expression in pharyngeal muscles[23]. This transcription factor was CEH-22, a homeobox protein most homologous to the vertebrate Nkx2.5 and the *Drosophila tinman*, which regulate heart development in their respective organisms. Furthermore, expression

of the zebrafish *nkx2.5* gene in *C elegans* can activate *myo-2* and can rescue the *ceh-22* mutant, suggesting that *ceh-22* and *nkx2.5* share a conserved molecular function[3]. Somewhat confusingly, the phenotype of the *ceh-22* mutant includes a slightly abnormal pharyngeal shape (slight thickening of the isthmus), but no defect in the expression of *myo-2*, suggesting that other regulatory pathways act in parallel with *ceh-22* to regulate *myo-2*[24]. Okkema *et al* showed that PHA-1 itself also directly regulates the *myo-2* gene, and that a *pha-1*; *ceh-22* double mutant is more severe than either mutant alone; the early pharyngeal 3NB12 antigen is not even expressed[24].

Development of the pharyngeal neurons

Pharyngeal nervous system overview The mature pharynx contains 20 neurons. Each establishes a unique and predictable morphology that is reproducible from worm to worm. The pharyngeal nervous system is organized into four general structures: two subventral nerve cords, one dorsal nerve cord, and one circular pharyngeal ring, which is located within the posterior half of the metacorpus and to which 12 neurons contribute processes[6]. The synapses and gap junctions made by the pharyngeal neurons have also been described and thus a basic wiring diagram of the pharyngeal network exists[6]. Speculations that the pharyngeal neural network plays an important role in regulating the pumping activity, as has been postulated for the intrinsic cardiac ganglia in the vertebrate heart[25], are stunted by the above-mentioned observation that most of the pharyngeal neurons can be laser-ablated without visible effects on pharyngeal behavior.

How does the intricate network of axon trajectories and synapses become established within the small cramped space of the developing pharynx? In particular, it is important to re-emphasize that the pharyngeal neurons, in contrast to body neurons, are not projecting between a basal lamina and an epithelial cell. Rather, they project within muscle cell folds, directly in contact with the muscle cell surface. Does this rather unique substrate for the neurons involve guidance cues different from those guiding body neurons? Also of importance is the fact that the pharyngeal neuron cells are already present in undifferentiated form within the spherical pharyngeal primordium. This offers intriguing developmental possibilities. For example, the pharyngeal neurons can take advantage of instructive interactions between cells that are neighbors within the primordium but are widely separated in the mature pharynx.

Establishing axon trajectories without growth cones We have shown that the M2 pharyngeal axons establish their trajectories via at least two independent mechanisms[26]. The straight proximal M2 trajectory (between the cell body, through the isthmus, and reaching into the metacorpus; Figure 2) does not depend on genes that act as axon guidance cues or that are important for growth cone functions. Thus, this proximal straight trajectory is established in a growth-cone-independent manner. We have suggested that the M2 cell forms, within the primordium, a physical connection with some neighboring cell that is ultimately located within the metacorpus, and that these connections elongate to form the proximal M2 axon trajectory as the primordium undergoes morphogenesis. It is a long-standing observation that mechanical tension exerted on neuronal cells can induce formation of a projection that can elongate rapidly as tension is maintained, "as a fishing line from a reel"[27,28]. Such mechanically induced axon formation and elongation can take place even when growth cone function is impaired[29]. This would be a process similar to the scenario that Sulston *et al* described for the pharyngeal gland cell g1 (discussed earlier), and also similar to the immature sensilla neurons that, after contacting the tip of the head, move posteriorly while laying down their dendritic processes[9]. The ability of a neuronal cell body to migrate and leave an extending axon behind has also been attributed to vertebrate facial motorneurons, although that particular case involves the movement of the cell nucleus ("nucleokinesis") into a dendrite[30]. In *Drosophila*, the larval optic nerve undergoes a period of elongation by intercalation of membrane as the neuron cell body and a distant guidepost cell move away from each other; later, a growth-cone-dependent process completes the establishment of the distal trajectory[31]. Similarly, neurons of the larval imaginal leg disc also lengthen axons in keeping with the vast leg morphogenesis process[32].

Distal ends are established using a growth cone Axon trajectories are usually established by specialized structures at their growing ends, the growth cones, that sense the molecular environment and interpret guidance cues so as to migrate along the correct paths[33]. The distal end of the M2 axon, which exhibits a complex trajectory within the metacorpus (first turning outward laterally, then dorsally, before extending towards the midline to establish a gap junction with the contralateral M2 neuron), depends on basic growth cone function genes (*unc-73*, *unc-51*) as well as several well-known axon guidance cues and receptors for these cues (*sax-3, slt-1, unc-6, unc-5, unc-40*)[26]. It is therefore our conclusion that the rough trajectories of pharyngeal neurons may be established during morphogenesis in the absence of growth cones, relying instead on cell-cell contacts

that are stretched to form axons during cell movements, but that fine-tuning of the ends of the trajectories depends on functional growth cones and multiple guidance cues. A screen for mutants with abnormal M2 trajectories allowed the isolation of several *mnm* (M neuron morphology abnormal) mutants, three of which specifically affected the formation of the distal M2 ends (Figure 2)[26]. These mutations likely affect the function of genes important for the function/guidance of the M2 growth cones.

An instructive developmental role for neurons? Interestingly some of the pharyngeal neurons themselves may act as sources of guidance cues. At least 2 of the pharyngeal neurons likely play developmental roles. The interneuron I5 is a source of UNC-6[34] that is likely to be important for the guidance of other axons, notably M2, which exhibits abnormal trajectories in a *unc-6* mutant background. The interneuron I4 expresses UNC-129[35], also a secreted guidance molecule. Hence, it seems likely that many of the apparently unimportant pharyngeal neurons (most neurons of the pharynx can be ablated in the adult worm without impairing pharyngeal function) play an important role during development. It would be interesting to ablate the neuronal precursor in the embryo prior to pharyngeal morphogenesis end, and thus test directly the hypothesis that these neurons play an instructive developmental role. It would also be interesting to determine whether this is a function that neurons play in other developing organs and other organisms.

References

1 Avery L, Shtonda BS. Food transport in the *C. elegans* pharynx. J Exp Biol 2003; 206: 2441–57.

2 Avery L, Horvitz HR. Pharyngeal pumping continues after laser killing of the pharyngeal nervous system of *C. elegans*. Neuron 1989; 3: 473–85.

3 Haun C, Alexander J, Stainier D, Okkema PG. Rescue of *Caenorhabditis elegans* pharyngeal development by a vertebrate heart specification gene. Proc Natl Acad Sci USA 1998; 95: 5072–5.

4 Portereiko MF, Mango SE. Early morphogenesis of the *Caenorhabditis elegans* pharynx. Dev Biol 2001; 233: 482–94.

5 Graham PL, Johnson JJ, Wang S, Sibley MH, Gupta MC, Kramer JM. Type IV collagen is detectable in most, but not all, basement membranes of *Caenorhabditis elegans* and assembles on tissues that do not express it. J Cell Biol 1997; 137: 1171–83.

6 Albertson DG, Thomson JN. The pharynx of *Caenorhabditis elegans*. Philos Trans R Soc Lond B Biol Sci 1976; 275: 299–325.

7 Avery L, Thomas JH. Feeding and defecation. In: Riddle DL, Blumenthal T, Meyer BJ, Priess JR, editors. *C. elegans* II. New York: Cold Spring Harbor Laboratory Press; 1997. p 679–716.

8 Avery L. Motor neuron M3 controls pharyngeal muscle relaxation timing in *Caenorhabditis elegans*. J Exp Biol 1993; 175: 283–97.

9 Sulston JE, Schierenberg E, White JG, Thomson JN. The embryonic cell lineage of the nematode *Caenorhabditis elegans*. Dev Biol 1983; 100: 64–119.

10 Avery L, Horvitz HR. A cell that dies during wild-type *C. elegans* development can function as a neuron in a *ced-3* mutant. Cell 1987; 51: 1071–8.

11 Duguay D, Foty RA, Steinberg MS. Cadherin-mediated cell adhesion and tissue segregation: qualitative and quantitative determinants. Dev Biol 2003; 253: 309–23.

12 Leung B, Hermann GJ, Priess JR. Organogenesis of the *Caenorhabditis elegans* intestine. Dev Biol 1999; 216: 114–34.

13 Kalb JM, Lau KK, Goszczynski B, Fukushige T, Moons D, Okkema PG, *et al*. *pha-4* is *Ce-fkh-1*, a *fork head*/HNF-3α, β, γ homolog that functions in organogenesis of the *C elegans* pharynx. Development 1998; 125: 2171–80.

14 Mango SE, Lambie EJ, Kimble J. The pha-4 gene is required to generate the pharyngeal primordium of *Caenorhabditis elegans*. Development 1994; 120: 3019–31.

15 Gaudet J, Mango SE. Regulation of organogenesis by the *Caenorhabditis elegans* FoxA protein PHA-4. Science 2002; 295: 821–5.

16 Mörck C, Rauthan M, Wågberg F, Pilon M. *pha-2* encodes the *C. elegans* ortholog of the homeodomain protein HEX and is required for the formation of the pharyngeal isthmus. Dev Biol 2004; 272: 403–18.

17 Fay DS, Qiu X, Large E, Smith CP, Mango S, Johanson BL. The coordinate regulation of pharyngeal development in *C. elegans* by *lin-35/Rb*, *pha-1*, and *ubc-18*. Dev Biol 2004; 271: 11–25.

18 Granato M, Schnabel H, Schnabel R. Genesis of an organ: molecular analysis of the *pha-1* gene. Development 1994; 120: 3005–17.

19 Fay DS, Large E, Han M, Darland M. *lin-35*/Rb and *ubc-18*, an E2 ubiquitin-conjugating enzyme, function redundantly to control pharyngeal morphogenesis in *C. elegans*. Development 2003; 130: 3319–30.

20 Karabinos A, Schulze E, Klisch T, Wang J, Weber K. Expression profiles of the essential intermediate filament (IF) protein A2 and the IF protein C2 in the nematode *Caenorhabditis elegans*. Mech Dev 2002; 117: 311–4.

21 Ding M, Woo WM, Chisholm AD. The cytoskeleton and epidermal morphogenesis in *C. elegans*. Exp Cell Res 2004; 301: 84–90.

22 Coulombe PA, Wong P. Cytoplasmic intermediate filaments revealed as dynamic and multipurpose scaffolds. Nat Cell Biol 2004; 6: 699–706.

23 Okkema PG, Fire A. The *Caenorhabditis elegans* NK-2 class homeodomain CEH-22 is involved in combinatorial activation of gene expression in pharyngeal muscle. Development 1994; 120: 2175–86.

24 Okkema PG, Ha E, Haun C, Chen W, Fire A. The *Caenorhabditis elegans* NK-2 homeobox gene *ceh-22* activates pharyngeal muscle gene expression in combination with *pha-1* and is required for normal pharyngeal development. Development 1997; 124: 3965–73.

25 Randall DC. Towards an understanding of the function of the

intrinsic cardiac ganglia. J Physiol 2000; 528: 406.
26 Mörck C, Axäng C, Pilon M. A genetic analysis of axon guidance in the *C. elegans* pharynx. Dev Biol 2003; 260: 158–75.
27 Bray D. Axonal outgrowth in response to experimentally applied tension. Dev Biol 1984; 102: 379–89.
28 Zheng J, Lamoureux P, Santiago V, Dennerll T, Buxbaum RE, Heidemann SR. Tensile regulation of axonal elongation and initiation. J Neurosci 1991; 11: 1117–25.
29 Lamoureux P, Altun-Gultekin ZF, Lin C, Wagner JA, Heidemann SR. Rac is required for growth cone function but not neurite assembly. J Cell Science 1997; 110: 635–41.
30 Lambert de Rouvroit C, Goffinet AM. Neuronal migration. Mech Dev 2001; 105: 47–56.
31 Schmucker D, Jäckle H, Gaul U. Genetic analysis of the larval optic nerve projection in Drosophila. Development 1997; 124: 937–48.
32 Jan YN, Ghysen A, Christoph I, Barbel S, Jan LY. Formation of neuronal pathways in the imaginal discs of *Drosophila melanogaster*. J Neurosci 1985; 5: 2453–64.
33 Dickson BJ. Molecular mechanisms of axon guidance. Science 2002; 298: 1959–64.
34 Wadsworth WG, Bhatt H, Hedgecock EM. Neuroglia and pioneer neurons express UNC-6 to provide global and local netrin cues for guiding migrations in *C. elegans*. Neuron 1996; 16: 35–46.
35 Colavita A, Krishna S, Zheng H, Padgett RW, Culotti JG. Pioneer axon guidance by UNC-129, a *C. elegans* TGF-β. Science 1998; 281: 706–9.

Welcome a new Advisory Board Member at Acta Pharmacologica Sinica!

Acta Pharmacologica Sinica is pleased to announce a new member of the advisory board, **Prof Demetrios A SPANDIDOS**, who brings wonderful insights from their research fields to the articles published in Acta Pharmacologica Sinica.

Demetrios A SPANDIDOS is Professor of Virology (since 1988) at the Medical School, University of Crete; Director of Clinical Virology Laboratory (since 1990) at the University Hospital in Heraklion, Crete, and he was Research Professor and Director of the Laboratory of Molecular Oncology and Biotechnology (1988–1998) at the Institute of Biological Research and Biotechnology at the National Hellenic Research Foundation in Athens, Greece. He is the founder and Editor of the International Journal of Oncology, Oncology Reports and International Journal of Molecular Medicine.

Dr Spandidos obtained his BSc in Chemistry from the University of Thessaloniki, Greece in 1971, a PhD in Biochemistry from McGill University in Montreal, Canada in 1976 and a DSc in Genetics from the University of Glasgow, UK in 1989. He is Fellow of the Royal Society of Health (1994) London, UK, Fellow of the Royal College of Pathology (1997) London, UK and corresponding Member of the Academia National de Medicina de Buenos Aires, Argentina (1999). He has received the degrees of doctor honoris causa from the Universities of Bucharest (2002) and Cluj-Napoca (2004) Romania.

Dr Spandidos was the first scientist in the field of oncology to develop and apply the gene transfer technique, which has become a most potent tool to investigate oncogenes. Thus, his work assisted in development of the gene transfer technology that has been of paramount importance in revealing new oncogenes, as well as implementing the molecular understanding of oncogenes and how the normal proto-oncogenes become activated into their malignant transforming cognates. This field has expanded tremendously over the past twenty years and Dr Spandidos has continued to contribute actively, playing a major role in his scientific investigations on the ras oncogene. While at the Beatson Institute for Cancer Research in Glasgow he performed notable and important investigations on the nature of transformation of normal cells by introduction of single ras genes using retroviral LTRs and other strong promoters.

Acta Pharmacologica Sinica 2005 Apr; 26 (4): 405–416

Inivted review

Baculovirus as a highly efficient expression vector in insect and mammalian cells

Yu-chen HU[1]

Department of Chemical Engineering, National Tsing Hua University, Hsinchu, Taiwan, China

Key words

baculovirus; insect cell; mammalian cell; gene therapy; vaccine; recombinant protein

[1] Correspondence to Dr Yu-chen HU.
Phn 886-3-571-8245.
Fax 886-3-571-5408.
E-mail ychu@mx.nthu.edu.tw

Received 2004-11-24
Accepted 2004-12-24

doi: 10.1111/j.1745-7254.2005.00078.x

Abstract

Baculovirus has been widely used for the production of recombinant proteins in insect cells. Since the finding that baculovirus can efficiently transduce mammalian cells, the applications of baculovirus have been greatly expanded. The prospects and drawbacks of baculovirus-mediated gene expression, either in insect or in mammalian cells, are reviewed. Recent progresses in expanding the applications to studies of gene regulation, viral vector preparation, *in vivo* and *ex vivo* gene therapy studies, generation of vaccine vectors, *etc* are discussed and the efforts directed towards overcoming the existing bottlenecks are particularly emphasized.

Introduction

Baculoviruses make up a family of viruses and are grouped into nuclear polyhedrosis viruses (NPV) and granulosis viruses. More than 500 different types of baculoviruses have been discovered and the host range is restricted to invertebrates, mostly to insects (eg, moths and butterflies); thus, several baculoviruses (eg, *Helicoverpa zea, Orgya pseudotsugata*, and *Lymantria dispar*) have been registered for use as biological pesticides by the US Environmental Protection Agency[1]. Among the numerous baculoviruses, *Autographa californica* multiple NPV (AcMNPV) is the most well studied and most extensively used. AcMNPV has a circular double-stranded DNA genome of approximately 130 kb, which is condensed with a protamine-like protein into the core and packed into the nucleocapsids. Nucleocapsids are synthesized in the nucleus of infected cells (typically 40 nm–50 nm in diameter and 200 nm–400 nm in length). Membrane-enveloped nucleocapsids are referred to as virus particles or virions. In nature, AcMNPV are occluded in a polyhedron (2 μm–15 μm in size) mainly consisting of polyhedrin protein. After ingestion by insects, the polyhedrin matrix is dissolved in the alkaline midgut, thus releasing the embedded virions, which subsequently infect the epithelial cells of the intestine. Early in the infection cycle, the DNA genome is replicated and transcribed in the nucleus and the nucleocapsids are assembled. The budding of nucleocapsids through plasma membrane results in the release of budded virus, which is responsible for systemic transmission within an infected insect. Late in the infection cycle, progeny nucleocapsids become membrane-bound within the nucleus and are embedded into the polyhedra. After cell death and lysis, the polyhedra are released in the wild to spread the infection. Budded virus is highly infectious to cultured insect cells and is the primary form used in the laboratory as an expression vector.

Baculovirus infection of insect cells

The baculovirus has been widely used for the production of numerous recombinant proteins in insect cells[2–4] because it has the following advantages: (i) proper post-translational modification, because insect cells are higher eukaryotes; (ii) a high capacity for multiple genes or a large insert, because of the huge and flexible viral genome (130 kb); (iii) biosafety, because baculovirus naturally does not infect humans; and (iv) a very high yield driven by the strong promoters polyhedrin or p10. Among the natural host cells, Sf-9 and Sf-21, derived from the ovarian tissue of *Spodoptera frugiperda*, and BTI-TN-5B1-4 (High-Five; Invitrogen,

Carlsbad, CA, USA), derived from *Trichoplusia ni*, which is suitable for the expression of secreted proteins[5], are most popular. In addition to cultured cell lines, insect larvae are also excellent hosts for protein production. For example, *T ni* insect larvae can be readily infected by recombinant AcMNPV[6,7], and silkworms can be readily infected by recombinant *Bombyx mori* NPV[8]. Both systems have been employed for the production of numerous recombinant proteins[6,9]. The products synthesized in insect larvae are almost identical to those produced in insect cells and mammalian cells and the yields are generally very high (eg 13 mg luciferase per larva[10]). Therefore, baculovirus infection of live insects may represent an inexpensive and rapid approach for protein production[11], but consistent infection and quality control are more difficult to achieve.

The large cloning capacity renders baculovirus an ideal tool for the synthesis of virus-like particles (VLP), which generally require simultaneous expression of multiple viral structural proteins for self-assembly. VLP are empty particles composed of viral structural proteins but devoid of viral nucleic acids; thus, they are non-infectious. VLP can generally induce broad and strong immune responses thanks to the preservation of many essential epitopes[12,13]; therefore, VLP have gained increasing attention as potential vaccine candidates[14,15] or diagnostic reagents[16]. Extended applications of VLP as gene delivery vehicles have also been reported[17,18]. To date, numerous VLP of different viruses, including HIV[19], herpes simplex virus[20], human papillomavirus[21], polyomavirus[22], parvovirus[23], infectious bursal disease virus[24], hepatitis C virus (HCV)[16], and enterovirus 71[25], have been expressed using the baculovirus/insect cell expression system. Very recently, the synthesis of severe acute respiratory syndrome coronavirus (SARS-CoV) VLP using the baculovirus/insect cell system has also been reported[26,27]. The assembly of VLP using baculovirus enables the investigation of virus assembly process as well as the minimal requirements for viral capsid assembly. For example, Mortola and Roy demonstrated that coexpression of SARS-CoV envelope and membrane proteins is required and sufficient for the assembly of spikeless VLP[27], yet additional coexpression of the spike (S) protein results in the incorporation of the S protein. The resultant VLP possesses distinctive spike projections, making it morphologically indistinguishable from the authentic virus. Through co-infection with different recombinant baculoviruses, one can manipulate the composition of the particles, obtaining higher specific immunogenicity[28], or other biological functions by incorporating enzymes[29] or affinity tags for downstream purification[24]. In this regard, Conner *et al* successfully demonstrated chimeric VLP formed by structural proteins of viruses isolated from different animals (bovine and simian)[30]. By including viral proteins from different strains, referred to as phenotypic mixing, one can broaden the spectrum of the chimeric particles as a vaccine[31].

There are drawbacks associated with the baculovirus/insect cell expression system. First, baculovirus infection ultimately results in cell death and lysis in a few days. Because the expression driven by a polyhedrin or p10 promoter usually reaches the maximum near the death of infected cells, protein processing is likely to be suboptimal at that time because of the compromise of post-translational machinery and secretory pathway. This may seriously affect the processing of proteins destined for plasma membrane or for secretion. Efforts have been directed towards alleviating this problem by the use of early baculovirus promoters (eg, IE1) in either transiently or stably transformed cells[32]. The expression driven by early promoters is continuous and stable, and confers more efficient processing of the glycoprotein (eg tissue plasminogen activator), but the expression level is lower than those obtained with the lytic baculovirus system. Such a system is a feasible approach for expression in insect cells for products that are relatively poorly processed in lytic insect cells, and may be useful for functional studies of recombinant receptor proteins. To circumvent the protein degradation problem associated with cell lysis, a novel non-lytic baculovirus has recently been developed by random mutagenesis of viral genomes[33] and subsequent selection. At 5 d post-infection, the non-lytic baculovirus shows only 7% cell lysis, in contrast to 60% cell lysis by lytic baculovirus. This system is thus a convenient alternative for the production of proteins vulnerable to degradation using lytic baculoviruses.

The second disadvantage is that glycosylation in insect cells differs in many aspects from in mammalian cells. For example, truncated oligosaccharides containing just 3 or even 2 mannose residues and sometimes fucose have been found on proteins expressed in insect cells. Besides, there appears to be no significant sialylation of *N*-glycans in insect cells[34]. The glycoproteins lacking sialic acids have extremely short half-lives *in vivo*; therefore, the truncated *N*-glycans of glycoproteins produced in insect cells constitute a barrier to their use as therapeutics. One example to engineer the *N*-glycosylation pathway is the construction of transformed Sf-9 cells that constitutively express bovine β1, 4-galactosyltransferase under *hr5-ie1* control[35,36]. Baculo-virus infection of this cell line results in the production of terminally galactosylated recombinant proteins. Other attempts and strategies to "mammalianize" or "humanize" the

N-glycosylation capacity of insect cells have been reviewed previously[37–39]. Another limitation of the baculovirus/insect cell system is its inefficiency to properly process proteins that are initially synthesized as large inactive precursor proteins, such as peptide hormones, matrix metalloproteases, and fusogenic viral envelope glycopro-teins. A family of mammalian proprotein convertases has been characterized to be involved in the cleavage, and it has been shown that coexpression of the prohormone convertase furin with transforming growth factor β1 (TGF β1) results in a 7.8-fold increase in the production of mature TGF β1[40].

Baculovirus transduction of mammalian cells

Baculovirus was originally regarded as infecting solely insects and invertebrates; but in 1983 Volkman and Goldsmith found that baculovirus can be internalized by non-target vertebrate cells (eg, human lung carcinoma cell line A427)[41]. Carbonell *et al* further confirmed the entry of baculovirus into mammalian cells and very low level reporter gene expression under the control of polyhedrin and Rous sarcoma virus (RSV) promoters in mammalian cells[42]. However, virus replication was not detected in either study. Their discovery was not widely noted until 10 years later when two pioneer groups reported that recombinant baculoviruses harboring a cytomegalovirus (CMV) promoter-luciferase gene cassette[43] or an RSV long terminal repeat (LTR) promoter-β galactosidase (β-gal) gene cassette[44] can efficiently transduce mammalian cells. Their data indicate a strong preference for baculovirus to enter hepatocytes of different origins, and suggest that the block to expression in less susceptible cells does not appear to result from the ability to be internalized by the target cells but rather by events subsequent to viral entry because high and low expressing cell lines internalize similar amounts of virus[44]. One factor accounting for the low apparent transduction efficiency in other cell types is promoter strength. Shoji *et al* showed that cells that are not transduced by a baculovirus expressing β-gal under the control of a CMV promoter can be efficiently transduced by a baculovirus expressing the same reporter protein under the transcriptional control of a stronger CAG promoter[45] (a composite promoter consisting of the CMV immediate early enhancer, chicken β-actin promoter and rabbit β-globin polyadenylation signal). Thus, it is of interest to examine different promoters of viral and cellular origins in the baculovirus context in mammalian cells. Following these findings, subsequent studies have rapidly expanded the list of permissive cells that include cell lines originating from human (eg, HeLa, Huh-7, HepG2, keratinocytes, and bone marrow fibroblasts), rodent (eg, CHO, BHK), porcine (eg, CPK, PK-15), bovine (eg, BT)[46], and even fish sources (eg, EPC, CHH-1)[47]. Besides, baculovirus is capable of transducing non-dividing cells[48]. Transduction of primary cells, such as human neural cells[49], pancreatic islet cells[50], and rat articular chondrocytes[51], has also been observed. In addition, Wagle and Jesuthasan recently showed that baculovirus can successfully transduce the embryos of zebrafish[52]. By injecting the baculovirus expressing ephrinB2a into specific tissues, ephrinB2a is normally expressed in the posterior region of developing somite and baculovirus-mediated misexpression causes abnormal somite boundary formation. Despite the rapidly growing list of susceptible cells, however, baculovirus transduction of cell lines of hematopoietic origin, such as U937, K562, Raw264.7[53], LCL-cm, and Raji[54], is inefficient.

The transduction efficiencies vary considerably depending on cell types and can be up to 95% for BHK cells or lower than 10% for NIH-3T3 cells[54]. One possibility accounting for the high transduction efficiency in certain cell lines is the activation of mammalian promoters (eg, CMV promoter and heat shock promoter) by a DNA sequence upstream from the polyhedrin (*pu*) and a homologous region (*hr*) of AcMNPV[55]. The *hr*1 sequence enhances transcription from polyhedrin and *Drosophila* heat shock protein (*hsp70*) promoter in Sf cells[56] and functions as an origin of replication (*ori*), but does not support *ori* activities in mammalian cells[57]. *pu* and *hr* together function synergistically, resulting in as much as 18 000-fold promoter activation[55]. The *hr*1 can also function in mammalian cells as an enhancer when present *in trans* [57]. The insertion of an additional copy of the *hr*1 region in the AcMNPV genome thus represents an attractive approach to promoting overexpression of foreign proteins in mammalian cells as has been demonstrated in insect cells[56]. The additional *hr*1 can also help maintain the genetic stability of the bacmid-derived baculoviruses, because spontaneous deletion of the heterologous gene(s) in the foreign bacterial artificial chromosome sequences readily occurs[58,59].

The transduction efficiency can be markedly enhanced by the addition of sodium butyrate, trichostatin A[53], and valproic acid[60]. These compounds are histone deacetylase inhibitors, inducing a hyperacetylation of the chromatin and enhancement of transcription, thus highlighting the importance of the chromatin state of the baculovirus genome in the transduced cells for transgene expression. However, cytotoxicity is often associated with the use of these drugs[60]. Another approach to enhance the transduction efficiency is to alter the transduction protocol. For transduction, typically the virus is concentrated by ultracentrifugation and

resuspended in phosphate-buffered saline (PBS). The cells are then incubated with the virus for 1 h at 37 °C using growth medium (eg, DMEM) as the surrounding solution[44,45,61]. Recently, we found that incubation of the unconcentrated virus (ie virus supernatant) at a lower temperature (eg, 25 °C) for 4 h–6 h using PBS as the surrounding solution results in gene transfer into HeLa and chondrocytes[51,62] with efficiencies comparable or superior to those using the traditional protocols. This is in part because of prolonged virus uptake provided that sufficient amount of the virus is present. One key determinant accounting for the high transduction efficiency is PBS, which is superior to DMEM or TNM-FH (the medium for baculovirus production) as the surrounding solution in terms of enhancing the transduction efficiency and transgene expression[51,62], although the exact mechanism awaits further elucidation. The same protocol also confers gene delivery into human mesenchymal stem cells (MSC) isolated from umbilical cord blood (uMSC) and bone marrow (bMSC) with efficiencies of up to approximately 72.8% and 41.1%, respectively[63] (Figure 1). This protocol eliminates the need for virus ultracentrifugation; thus, it not only represents a simpler approach, but also considerably reduces possible virus inactivation during ultracentrifugation.

Baculovirus transduction is generally considered nontoxic to mammalian cells and does not hinder cell growth even at high multiplicity of infection[43,64]. Our recent studies again confirm this notion because transduction with a wild-type baculovirus does not cause any observable adverse effect to chondrocytes or MSC[51,63]. From the growth curves, however, we noted a slower cell proliferation on expression of enhanced green fluorescent protein (EGFP) under the transcriptional control of a CMV promoter. The slightly retarded cell growth is attributed to the EGFP overexpression because: (i) EGFP overexpression could be toxic and might even induce apoptosis in some cells[65,66]; and (ii) the transcriptional activation of CMV promoter could repress other viral or cellular gene expression[67]. Fortunately, the cell growth rate may be restored after several passages, as EGFP expression attenuates[63].

Mechanisms of baculovirus entry into mammalian cells Baculovirus enters insect cells via endocytosis followed by low pH-induced fusion of a viral envelope protein with the endosomal membrane, thus allowing viral entry into the cytoplasm and nucleus[68]. Likewise, baculovirus is generally considered to follow the same route to enter mammalian cells, as gene expression is inhibited by lysosomotropic agents (eg, chloroquine), which block endosomal maturation[43,44]. Initially it was suggested that the transduction is liver specific and the asialoglycoprotein could be involved in virus binding[43,44]. However, van Loo *et al* showed that Pk1 cells, which do not express the asialoglycoprotein receptors, could be successfully transduced, thus asialoglycoprotein is not a key determinant[48]. It was also shown that electrostatic interactions and the heparan sulfate moieties might be necessary for baculovirus binding to the mammalian cell surface[69]. However, no follow-up report has confirmed their findings and the nature of the receptors remains unclear. In contrast, the viral envelope glycoprotein gp64 is shown to be essential for virus attachment and endosomal escape[70]. Supporting this is the finding that a baculovirus over-expressing gp64 in addition to the endogenous copy of gp64 can incorporate approximately 1.5-fold the normal amount of gp64 on the virion surface and exhibit 10- to 100-fold more reporter gene expression in a variety of mammalian cells compared with similar viruses with a normal amount of gp64[71]. In the same study, phospholipids on the cell surface are

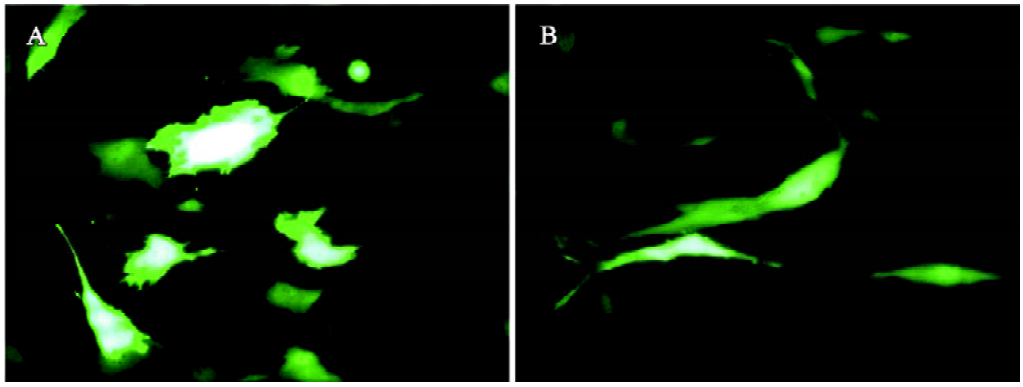

Figure 1. Efficient transduction of human mesenchymal stem cells isolated from umbilical cord blood (A) and mesenchymal stem cells isolated from bone marrow (B) by a recombinant baculovirus expressing enhanced green fluorescent protein under the control of a cytomegalovirus promoter. The cells cultured on 6-well plates (5×10^5 cells/well) were transduced with 100 μL unconcentrated virus (2×10^8 plaque forming units per milliliter) with 400 μL phosphate-buffered saline as the surrounding solution for 4 h at 25 °C.

suggested to serve as an important docking point for gp64, thus facilitating viral entry into mammalian cells. By transient depletion of calcium using EGTA pretreatment, Bilello *et al* demonstrated that paracellular junction complexes are important for baculoviral entry into primary hepatocytes[72].

It is generally assumed that the escape from the endosomes sets the block for transduction of some mammalian cells by baculovirus[44,73]; however, a recent study showed that the transduction block lies not in the endosomal escape, but rather in the cytoplasmic trafficking or nuclear import of the virus capsids[74]. In the cytoplasm, the nucleocapsids appear to induce formation of actin filaments, which probably facilitate the transport of viral nucleocapsids into the nucleus, as cytochalasin D strongly reduces the transduction efficiency but not the delivery of nucleocapsids to the cytoplasm[48]. In contrast, we recently found that incubation of cells with PBS during transduction results in significantly higher virus entry and higher transduction efficiency compared with incubation with DMEM[63], suggesting that virus internalization may be a bottleneck as well. Overall, the events responsible for virus uptake and detailed mechanisms of intracellular movement and nuclear entry of the virus are still largely unknown.

Baculovirus display The tropism and transduction efficiency of baculovirus has been manipulated by modifying the envelope protein. The modification can be performed by fusing a heterologous protein (or peptide) in-frame at the N-terminus of the gp64 gene under the control of a polyhedrin or p10 promoter. The fusion protein, after expression as an additional copy, is translocated to the plasma membrane and incorporated into the viral envelope on virus budding. Proof of this principle was first approached by fusing HIV-1 envelope proteins; the modified virus binds the CD4 receptor on T cells[75]. A similar strategy has been applied to construct avidin-displaying baculovirus, which shows a 5-fold increase in transduction efficiency in rat malignant glioma cells and a 26-fold increase in rabbit aortic smooth muscle cells compared with the wild-type baculovirus[76]. Baculovirus displaying heterologous envelope proteins, such as vesicular stomatitis virus G protein (VSVG), has also been constructed, which transduces human hepatoma and rat neuronal cells at efficiencies roughly 10- to 100-fold greater than baculovirus lacking VSVG[73]. This pseudotyped virus also transduces cell lines that are transduced at very low levels or not at all by the unmodified baculovirus, thus broadening the tropism. The enhanced transduction efficiency and wider tropism are attributed to increasing transport of baculovirus DNA into nuclei rather than to increasing cell binding or virus uptake[73]. In contrast, specific targeting of baculovirus to mammalian cells by displaying a single-chain antibody fragment specific for the carcinoembryonic antigen (CEA) or synthetic IgG binding domains is also demonstrated[77,78]. In addition, the baculovirus display technology has been utilized to construct and screen a eukaryotic epitope library[79]. In this context, the HIV-gp41 epitope "ELDKWA" specific for the neutralizing MAb 2F5 is inserted into the antigenic site of influenza virus hemagglutinin, flanked by additional random amino acids. This pool of hemagglutinin genes is cloned into baculovirus, and an individual clone displaying the epitope with markedly increased binding capacity out of a pool of 8000 variants is screened rapidly by fluorescence activated cell sorting.

Note, however, that the expression of gp64-fusion under the control of a late promoter may lead to a heterogeneous virus population that possesses various amounts of fusion protein and hence varied properties. This might be resolved by: (i) inserting the gp64 fusion gene into the genomic gp64 locus so that all gp64 copies contain the fusion partner; and (ii) expressing the gp64 fusion protein under an early promoter. More recently, baculovirus capsid display has also been developed in which the fusion can be made to the N- or C-terminus of the major capsid protein vp39 rather than to gp64 without compromising the viral titer or functionality[74]. It has been demonstrated that the incorporation of green fluorescent protein (GFP) into the virus capsid does not interfere with the capsid assembly and allows for visualization of the virus biodistribution *in vivo*[74]. This capsid-modified baculovirus holds great promise for the nuclear and subcellular targeting of the transgenes.

Viral vector generation and viral protein production Thanks to the large DNA genome, recombinant baculovirus offers an attractive means for the production of other viral vectors for gene delivery/gene therapy purposes because the production of many viral vectors requires either plasmid transfection into producer cell lines or helper virus infection. For instance, all genes essential for replication and packaging of the adenoviral vector (38 kb) can be delivered and expressed by a single baculovirus, which is co-transfected with a plasmid vector harboring only the inverted terminal repeats (ITR) and packing signal of the wild-type virus as well as a reporter gene[80]. The co-delivery results in the generation of a fully deleted adenovirus vector free of helper virus. This technique is also exploited for the production of adeno-associated virus (AAV), whose use is hampered by the lack of a simple and efficient vector production method. The mammalian producer cells are co-transduced with 3 viruses: 1 baculovirus harboring the reporter gene flanked by AAV ITR, 1 baculovirus expressing the AAV *rep* gene,

and a helper adenovirus expressing the AAV *cap* gene[81]. The simultaneous delivery produces infectious recombinant AAV particles and constitutes an option for improving large-scale recombinant AAV vector production. Besides virus preparation, Ramos *et al* recently investigated the feasibility of using the baculovirus/mammalian cell system for protein production. They investigated two protocols for optimal cell culture and virus transduction and achieved volumetric yields for 3 secreted proteins (SAF-3-Fc, CD40-hexa his, and Asp 2-Fc) at 4 mg/L–25 mg/L[82]. In our laboratory, the application of baculovirus is further expanded to the production of hepatitis delta virus (HDV) VLP. HDV can not replicate in cultured cell lines, and thus is difficult to propagate; therefore, studies of HDV particle assembly mainly rely on cDNA transfection, which suffers, however, from low efficiency and hinders subsequent structural and immunological studies of HDV VLP. We demonstrated that the co-transduction of hepatoma cell lines with 2 recombinant baculoviruses, one expressing hepatitis large delta antigen and another expressing hepatitis B surface antigen (HBsAg), leads to self-assembly and secretion of the HDV VLP[83]. The yield (~150 ng HBsAg per mL in the secreted particle) is approximately 2-fold of that achieved by plasmid transfection. VLP synthesis has also been demonstrated in BHK cells and the process is transferred to a novel oscillating bioreactor for production on a larger scale[84]. One bioreactor run (500 mL working volume) can yield over 400 μg HBsAg, which substantially increases the total particle yield and thus enables future structural and immunological studies of the VLP. In comparison with stable cell lines, the gene expression levels and the VLP composition can be easily manipulated simply by varying the virus concentration. In addition, the expressed proteins are obtained in a few days; therefore, this baculovirus/mammalian cell expression system may serve as a transient expression system for early evaluation of proteins of interest while stable cell lines are being generated and evaluated.

Studies of gene functions and viral infections Gene delivery into primary cells using transfection or electroporation either suffers from low efficiency or causes extensive membrane damage. Because baculovirus is generally non-toxic and non-replicative in mammalian cells, and the transduction efficiencies into various human primary cells are high, cell-based assays have been developed for gene function studies. Clay *et al* demonstrated that co-transduction of cells with 2 recombinant baculoviruses, one expressing an estrogen receptor and another expressing a reporter gene controlled by an estrogen receptor-responsive promoter, results in ligand-induced reporter gene activity, and this approach is successfully applied to assay development in Saos-2 human osteosarcoma (HOS) cells[85]. Similarly, a cell/cell fusion assay that mimics the HIV viral/cell fusion process was developed based on the baculovirus system[86]. In the assay, HOS cells stably expressing CCR5, CD4, and LTR-luciferase serve as the recipient host cell. An HEK-293 cell line transduced with a baculovirus expressing the viral proteins gp120, gp41, tat, and rev represents the virus. Interaction of gp120 with CCR5/CD4 results in the fusion of 2 cells and transfer of tat to the cytoplasm of the HOS cell; tat, in turn, binds to the LTR region on the luciferase reporter and activates transcription, leading to an increase in cellular luciferase activity. This assay has been demonstrated to be a robust and reproducible high-throughput surrogate assay for evaluating the effects of compounds on gp120/CCR5/CD4-mediated viral fusion into host cells[86]. This system could also facilitate the assessment of different promoters for their strength as well as temporal and spatial regulation across mammalian cells of different origins.

Similar to HDV, hepatitis B virus (HBV) and HCV are not capable of replication in cultured cells; thus, the evaluation of novel antiviral strategies have been hindered by the lack of a convenient and reliable *in vitro* culture system. To overcome this problem, recombinant baculoviruses are constructed to carry and deliver the genomes of HBV[87] and HCV[88] into hepatoma cells lines. With this approach, replication of HBV DNA and RNA, and expression of viral genes are detected[87]. Viral replication is evidenced by the presence of high levels of intracellular replicative intermediates and protected HBV DNA in the medium. The successful HBV replication thus allows for the establishment of a highly flexible system for studying: (i) the effects of (-)-β-2',3'-dideoxy-3'-thiacytidine on HBV replication and accumulation of covalently closed circular DNA[89]; and (ii) the cross-resistance profiles of HBV mutants against antihepadnaviral compounds[90]. The HCV full-length and minigenome under the tetracycline-inducible promoter are also delivered into HepG2 cells and regulable transcription and viral polypeptide processing are demonstrated[91], thus providing a novel tool for the analysis of HCV replication and host-cell interactions.

Generation of stable cell lines Normally, baculovirus-mediated gene expression lasts approximately 1–2 weeks as a result of cell division. The gradual extinction of transgene expression is also attributed to the degradation of baculoviral DNA, as degradation has been revealed in hepatoma cells[83] and articular chondrocytes[51]. However, it was found that transduction of CHO cells with a baculovirus expressing neomycin phosphotransferase results in the isolation of CHO

cells stably expressing GFP by selection using the antibiotic G418[53]. The frequency of G418 resistant colony formation is approximately 1 in 50–100 of the transduced cells. The same group further confirmed that discrete portions of baculovirus DNA are randomly integrated as single-copy fragments ranging in size from 5 kb to 18 kb[92]. Periodic assays on the stable clones show no loss of transgene expression over a 5 month period. Coupled with high transduction efficiency, the high frequency of emergence of stable transductants makes baculovirus a valuable tool to derive human cell lines that are either difficult to isolate in large numbers or are difficult to transfect by other methods.

***In vivo* gene therapy** Thanks to highly efficient gene delivery, baculovirus has captured increasing interest as a vector for *in vitro* and *in vivo* gene delivery. However, reports of successful *in vivo* applications are limited. The complement system appears to be a potent barrier for *in vivo* gene therapy because the efficiency of gene transfer into hepatocytes of complement-deficient mice is greatly enhanced[70]. Inactivation of baculovirus in human plasma and whole blood is prevented by treatment with cobra venom factor[93]. An alternative approach is adopted by avoiding contact of baculovirus vectors with blood components. By using a silastic collar, transduction of adventitial cells in rabbit carotid arteries is achieved and the efficiencies are comparable to those obtained with adenoviral vectors[94]. The gene expression is transient and the arterial structure and endothelium remain intact after baculovirus transduction, although signs of inflammation are detected. Unmodified baculovirus vectors have also been injected into the rodent brain where the complement proteins may not reach in the presence of an intact blood-brain barrier and/or the complement level in the brain is insufficient to affect the gene transfer[95]. After *in vivo* injection into the brain, baculovirus specifically transduces the epithelium of the choroids plexus in ventricles and the transduction efficiency is as high as 76%±14%; thus, baculovirus seems to be especially useful for the targeting of choroids plexus cells[95].

A more cutting-edge approach to alleviate the complement inactivation problem is the generation of complement-resistant baculovirus by displaying decay-accelerating factor, a regulator that blocks complement at the central step of both the classical and alternative pathways[96]. Such a complement-resistant baculovirus vector expressing additional human coagulation factor IX (hFIX) allows for a substantial improvement of gene transfer into complement-sufficient neonatal rats *in vivo* after local injection into the liver parenchyma. Gene expression is transient probably as a result of the generation of antibodies directed against the transgene product hFIX, which might lead to clearance of either expressed hFIX protein and/or positively transduced cells. Alternatively, baculovirus can be pseudotyped by displaying VSVG on the envelope. The VSVG-modified virus enhances gene transfer efficiencies into mouse skeletal muscle *in vivo* and the transgene expression lasts 178 d in DBA/2J mice and 35 d in BALB/c and C57BL/6 mice[97]. The VSVG-modified baculovirus also exhibits greater resistance to inactivation by animal sera and can transduce the cerebral cortex and testis of mice by direct inoculation *in vivo*[61].

Another potential barrier may be the presence of heparin or heparin-like factors, which block baculovirus-mediated gene delivery in cell culture[93]. Intercellular junctions may be an additional hurdle because transient disruption of these junctions by EDTA treatment prior to transduction improves the gene delivery efficiency into long-term cultures of primary hepatocytes but does not lead to permanent alternations in hepatocyte ultrastructure, albumin mRNA, and protein expression profiles[98]. Their studies also suggest the importance of the basolateral surface for virus entry at least for some cell types[72]. In our laboratory, however, the transient disruption of cell junctions fails to effectively enhance the baculovirus-mediated gene transfer into chondrocytes and HepG2 cells that are cultured to over-confluence, implying that other factors in addition to the paracellular junction complexes might be involved in the transduction of these cells.

Another problem associated with baculovirus as a gene delivery vector is that purification by ultracentrifugation often leads to virus aggregation[99]. In addition, the ultracentrifugation process is time-consuming, labor intensive, and difficult to scale up. To resolve these problems, we construct a recombinant baculovirus with a hexahistidine (His_6) tag displayed on the viral envelope, which enables virus purification by a simple immobilized metal affinity chromatography with high purity (~87%). This methodology obviates the need for successive ultracentrifugation steps[100] and may be employed to purify other viral vectors for gene therapy studies.

***Ex vivo* gene therapy** To date, most gene therapy studies using baculovirus vectors have focused on *in vivo* experiments, yet relatively little is known about the potential of baculovirus for *ex vivo* therapy. One relevant report was published by Sandig *et al*[101] who established an *ex vivo* perfusion model for human liver segments. The recombinant baculovirus is perfused through the liver segments for 15 min and reasonable transduction rates are achieved in all perfused parts of the liver tissue. This study verifies for the first time that baculovirus-mediated gene transfer is pos-

sible in the liver tissue and encourages future studies including *in situ* perfusion of intact livers with baculovirus vectors in animal models.

Recently, we have also demonstrated the highly efficient baculovirus-mediated gene transfer into articular chondrocytes[51] and human MSC[63], both being candidate cell sources for cartilage tissue engineering. Importantly, normal differentiation states of chondrocytes and MSC are retained on baculovirus transduction. Our experiments regarding MSC suggest that the phenotypic changes along the adipogenic differentiation pathway positively influence the baculovirus transduction and may implicate two possible applications: (i) MSC may be transduced with baculovirus expressing specific factors (eg b-FGF or BMP-2) to promote the expansion or regulate the differentiation via autocrine and paracrine effects of the factors so that supplementation of these factors in the medium may be omitted; and (ii) differentiation of MSC towards a specific lineage pathway may be induced first and the committed progenitor cells can be transduced *ex vivo* by the recombinant baculovirus expressing appropriate growth factors (eg TGFβ1 or IGF-1), seeded onto polymeric scaffolds, and implanted into animal models for tissue regeneration. Although sustained transgene expression is restricted by the degradation of baculoviral DNA within the cells, the non-replication and degradation characteristics prove that baculovirus may be a safe gene delivery vehicle for tissue engineering in which long-term expression is not critical.

Immunological response and potential as a vaccine vector Host responses to baculovirus uptake, either *in vitro* or *in vivo*, were not evaluated until Gronowski *et al* reported that administration of baculovirus *in vitro* induces interferon (IFN) production from human and murine cell lines and induces *in vivo* protection of mice from encephalomyocarditis virus infection[102]. A more recent study discovered that the presence of baculovirus disrupts the phenobarbital gene induction, a potent transcriptional activation event characteristic of highly differentiated hepatocytes, and represses expression of the albumin gene, but neither cAMP nor PKA activities are affected by the virus[102]. Baculovirus transduction also induces expression of cytokines such as TNF-α, IL-1α, and IL-1β in primary hepatocytes[103]. These findings raise concerns as to whether these properties will compromise the use of baculovirus vectors for *in vivo* gene therapy in humans, and more investigations will be needed to ensure the safety of baculovirus vectors. Despite these, the ability of baculovirus to induce immune responses has been exploited by Abe *et al*, who found that intranasal inoculation with a wild-type baculovirus elicits a strong innate immune response that protects mice from a lethal challenge of influenza virus[104]. The feasibility of using baculovirus as a vaccine carrier was also demonstrated by Aoki *et al*[105], who found that a recombinant baculovirus expressing glycoprotein gB of pseudorabies virus induces antibodies against gB protein in mice, thus suggesting that this recombinant baculovirus could serve as a vaccine candidate for pseudorabies. Similarly, *in vivo* administration of a baculo-virus expressing hFIX elicits antibodies against hFIX. The antibody titers are proportional to the amount of protein produced by the virus[96]. More recently, Facciabene *et al* demonstrated that the intramuscular injection of a baculovirus expressing CEA induces measurable anti-CEA-specific $CD4^+$ T-cell response[106]. The immunogenic property of baculovirus is not restricted to CEA because the intramuscular injection of another baculovirus (Bac-E2) expressing E2 glycoprotein of HCV induces anti-E2 $CD8^+$ T-cell response[106]. Interestingly, when Bac-E2 is pseudotyped to display VSVG on the envelope, the minimal dose required to elicit a measurable T-cell response is 10-fold less, indicating that the VSVG-pseudotyped Bac-E2 appears to be a more potent immunogen than the unmodified virus. This finding agrees with the previous statement that baculovirus displaying VSVG confers a more efficient immunogen expression in transduced cells.

It is also likely that baculovirus can mediate an immune response against an antigen when it is displayed on the viral surface. In this regard, the immunodominant antigenic site of foot-and-mouth disease virus (FMDV) has been displayed on the baculovirus envelope[107], which is able to bind a panel of FMDV-specific MAb and indicates the preservation of antigenic epitopes on the virus envelope. A more recent study further showed that immunization with adjuvant-free baculovirus displaying rodent malaria *Plasmodium berghei* circumsporozoite protein (PbCSP) on the envelope induces high levels of antibodies and γ-interferon-secreting cells against PbCSP, and protects 60% of mice against sporozoite challenge[108]. These studies substantiate the potential of baculovirus displaying immunogens as a vaccine candidate.

Conclusions and future prospects

The values of baculovirus for recombinant protein expression in insect cells have long been proven. The extremely high yield by baculovirus-infected insect cells or larvae makes it an attractive tool for pharmaceutical protein production. Despite its inability to process some proteins correctly, rapid advances in cell engineering may overcome these drawbacks and render baculovirus a proper system for

large-scale protein production. To the best of my knowledge, no insect cell-derived recombinant protein has gained official approval from the US Food and Drug Administration. Nonetheless, more and more proteins are produced in insect cells in the preclinical stage. Particularly promising is the field of viral vaccines, where the formation of virus-mimicking multimers can be essential for eliciting protective immune responses. An HCV vaccine might be the first human therapeutic expressed in insect cells[109].

The broad range of susceptible mammalian cells, coupled with its non-toxic and non-replication nature, makes baculovirus a useful tool for studying the expression and function of gene products. As a gene therapy vector, baculovirus possesses the following extra advantages: (i) the AcMNPV genome is large, thus rendering the virus flexible to carry multiple genes or large inserts; (ii) recombinant baculoviruses are easy to construct and produce to high titers simply by infecting insect cells; and (iii) the purification of baculovirus can be readily performed by ultracentrifugation[110] or, alternatively, by a newly developed affinity chromatographic technique[100]. The last two features greatly simplify the large-scale preparation of high titer baculoviral vectors. In addition to therapeutic genes, baculovirus may serve as a promising vector for the delivery of cDNA of infectious RNA viruses towards antisense therapy approaches. The same concept may be applied to the delivery of siRNA to silence specific target genes. The combination of *ex vivo* gene transfer and tissue engineering holds great promise as well. One bottleneck to the application of baculovirus lies in the short duration of transgene expression. This may be overcome by selecting a proper promoter that is not silenced, and developing a proper superinfection protocol that can effectively deliver fresh genes into cells. The baculovirus may also be applied in conjunction with other viral vectors to escape either pre-existing or therapy-induced antiviral immunity. In summary, baculovirus can be used as an efficient vector for gene delivery into insect and mammalian cells for a wide variety of applications.

Acknowledgment

The author gratefully acknowledges the financial support of the National Science Council (Grant NSC 93-2214-E-007-016) and Ministry of Economic Affairs (Technology Development Program for Academia Grant 93-EC-17A-17S1-0009), Taiwan, China.

References

1 Wood HA. Development and testing of genetically improved baculovirus insecticides. In: Shuler ML, Wood HA, Granados RR, Hammer DA, editors. Baculovirus expression systems and biopesticides. New York: Wiley-Liss; 1995. p91–102.
2 Patterson RM, Selkirk JK, Merrick BA. Baculovirus and insect cell gene expression-review of baculovirus biotechnology. Environ Health Perspect 1995; 103: 756–9.
3 Luckow VA, Summers MD. Trends in the development of baculovirus expression vectors. Biotechnology 1988; 6: 47–55.
4 Beljelarskaya SN. A baculovirus expression system for insect cells. Mol Biol 2002; 36: 281–92.
5 Ikonomou L, Schneider YJ, Agathos SN. Insect cell culture for industrial production of recombinant proteins. Appl Microbiol Biotechnol 2003; 62: 1–20.
6 Cha HJ, Pham MQ, Rao G, Bentley WE. Expression of green fluorescent protein in insect larvae and its application for heterologous protein production. Biotechnol Bioeng 1997; 56: 239–47.
7 Cha HJ, Dalal NG, Pham MQ, Vakharia VN, Rao G, Bentley WE. Insect larval expression process is optimized by generating fusions with green fluorescent protein. Biotechnol Bioeng 1999; 65: 316–24.
8 Lihoradova OA, Bachurina EY, Azimova SS. Biosynthesis of the recombinant middle surface antigen of the human hepatitis B virus in silkworm larvae. Mol Biol 2004; 38: 603–7.
9 Maeda S. Expression of foreign genes in insects using baculovirus vectors. Ann Rev Entomol 1989; 34: 351–72.
10 Palhan VB, Sumathy S, Gopinathan KP. Baculovirus mediated high-level expression of luciferase in silkworm cells and larvae. Biotechniques 1995; 19: 97–104.
11 Medin JA, Hunt L, Gathy K, Evans RK, Coleman MS. Efficient, low-cost protein factories: expression of human adenosine deaminase in baculovirus-infected insect larvae. Proc Natl Acad Sci USA 1990; 87: 2760–4.
12 Casal JI. Use of parvovirus-like particles for vaccination and induction of multiple immune responses. Biotechnol Appl Biochem 1999; 29: 141–50.
13 Lenz P, Day PM, Pang YYS, Frye SA, Jensen PN, Lowy DR, *et al*. Papillomavirus-like particles induce acute activation of dendritic cells. J Immunol 2001; 166: 5346–55.
14 Schiller JT, Lowy DR. Papillomavirus-like particle based vaccines: cervical cancer and beyond. Expert Opin Biol Ther 2001; 1: 571–81.
15 Roy P. Genetically engineered particulate virus-like structures and their use as vaccine delivery systems. Intervirology 1996; 39: 62–71.
16 Xiang J, Wunschmann S, George SL, Klinzman D, Schmidt WN, LaBrecque DR, *et al*. Recombinant hepatitis C virus-like particles expressed by baculovirus: utility in cell-binding and antibody detection assays. J Med Virol 2002; 68: 537–43.
17 Touze A, Bousarghin L, Ster C, Combita AL, Roingeard P, Coursaget P. Gene transfer using human polyomavirus BK virus-like particles expressed in insect cells. J Gen Virol 2001; 82: 3005–9.
18 Tegerstedt K, Andreasson K, Vlastos A, Hedlund KO, Dalianis T, Ramqvist T. Murine pneumotropic virus VP1 virus-like particles (VLPs) bind to several cell types independent of sialic acid residues and do not serologically cross react with murine polyomavirus VP1 VLPs. J Gen Virol 2003; 84: 3443–52.

19 Luo L, Li Y, Cannon P, Kim S, Kang CY. Chimeric gag-V3 virus-like particles of human immunodeficiency virus induce virus-neutralizing antibodies. Proc Natl Acad Sci USA 1992; 89: 10527–31.
20 Tatman JD, Preston VG, Nicholson P, Elliott RM, Rixon FJ. Assembly of herpes simplex virus type 1 capsids using a panel of recombinant baculoviruses. J Gen Virol 1994; 75: 1101–13.
21 Volpers C, Schirmacher P, Streeck RE, Sapp M. Assembly of the major and the minor capsid protein of human papillomavirus type 33 into virus-like particles and tubular structures in insect cells. Virology 1994; 200: 504–12.
22 Gillock ET, Rottinghaus S, Chang D, Cai X, Smiley SA, An K, *et al*. Polyomavirus major capsid protein VP1 is capable of packaging cellular DNA when expressed in the baculovirus system. J Virol 1997; 71: 2857–65.
23 Kajigaya S, Fujii H, Field A, Anderson S, Rosenfeld S, Anderson L, *et al*. Self-assembled B19 parvovirus capsids, produced in a baculovirus system, are antigenically and immunogenically similar to native virions. Proc Natl Acad Sci USA 1991; 88: 4646–50.
24 Hu YC, Bentley WE, Edwards GH, Vakharia VN. Chimeric infectious bursal disease virus-like particles expressed in insect cells and purified by immobilized metal affinity chromatography. Biotechnol Bioeng 1999; 63: 721–9.
25 Hu YC, Hsu TA, Huang JH, Ho MS, Ho YC. Formation of enterovirus-like particle aggregates by recombinant baculoviruses co-expressing P1 and 3CD in insect cells. Biotechnol Lett 2003; 25: 919–25.
26 Ho Y, Lin PH, Liu CYY, Lee SP, Chao YC. Assembly of human severe acute respiratory syndrome coronavirus-like particles. Biochem Biophys Res Commun 2004; 318: 833–8.
27 Mortola E, Roy P. Efficient assembly and release of SARS coronavirus-like particles by a heterologous expression system. FEBS Lett 2004; 576: 174–8.
28 Tsao E, Mason M, Cacciuttolo M, Bowen S, Wassweman G. Production of parvovirus B19 vaccine in insect cells co-infected with double baculovirus. Biotechnol Bioeng 1996; 49: 130–8.
29 Wang C, Olsen J, Zhang Y, Barklis E. Assembly of HIV GAG-βgalactosidase fusion proteins into virus particles. Virology 1994; 200: 524–34.
30 Conner M, Zarley C, Hu B, Parsons S, Drabinski D, Greiner S, *et al*. Virus-like particles as a rotavirus subunit vaccine. J Infect Dis 1996; 174: S88–S92.
31 Gerhardt E, Bruss V. Phenotypic mixing of rodent but not avian hepadnavirus surface proteins into human hepatitis B virus particles. J Virol 1995; 69: 1201–8.
32 Jarvis DL, Fleming J, Kovacs GR, Summers MD, Guarino LA. Use of early baculovirus promoters for continuous expression and efficient processing of foreign gene products in stably transformed lepidopteran cells. Biotechnology 1990; 8: 950–55.
33 Ho Y, Lo HR, Lee TC, Wu CP, Chao YC. Enhancement of correct protein folding *in vivo* by a non-lytic baculovirus. Biochem J 2004; 382: 695–702.
34 Raju TS, Lerner L, O'Connor JV. Glycopinion: biological significance and methods for the analysis of complex carbohydrates of recombinant glycoproteins. Biotechnol Appl Biochem 1996; 24: 191–4.
35 Hollister JR, Shaper JH, Jarvis DL. Stable expression of mammalian beta 1,4-galactosyltransferase extends the *N*-glycosylation pathway in insect cells. Glycobiology 1998; 8: 473–80.
36 Hollister JR, Jarvis DL. A stably-transformed insect cell line engineered to support asialoglycoprotein production by baculovirus expression vectors. Glycobiology 1999; 9: 1124.
37 Altmann F, Staudacher E, Wilson IBH, Marz L. Insect cells as hosts for the expression of recombinant glycoproteins. Glycoconj J 1999; 16: 109–23.
38 Jarvis DL. Developing baculovirus-insect cell expression systems for humanized recombinant glycoprotein production. Virology 2003; 310: 1–7.
39 Jarvis DL, Aumiller JJ, Hollister JR, Kawar ZS, Pilon J, Vadaie N. Analysis and manipulation of the protein *N*-glycosylation pathway in the baculovirus-insect cell system. Glycobiology 2004; 14: 1059–60.
40 Laprise M-H, Grondin F, Dubois CM. Enhanced TGFβ1 maturation in high five cells coinfected with recombinant baculovirus encoding the convertase furin/pace: improved technology for the production of recombinant proproteins in insect cells. Biotechnol Bioeng 1998; 58: 85–91.
41 Volkman LE, Goldsmith PA. *In vitro* study of *Autographa californica* nuclear polyhedrosis virus interaction with nontarget vertebrate host cells. Appl Environ Microbiol 1983; 45: 1085–93.
42 Carbonell LF, Klowden MJ, Miller LK. Baculovirus-mediated expression of bacterial genes in dipteran and mammalain cells. J Virol 1985; 56: 153–60.
43 Hofmann C, Sandig V, Jennings G, Rudolph M, Schlag P, Strauss M. Efficient gene-transfer into human hepatocytes by baculovirus vectors. Proc Natl Acad Sci USA 1995; 92: 10 099–103.
44 Boyce FM, Bucher NLR. Baculovirus-mediated gene transfer into mammalian cells. Proc Natl Acad Sci USA 1996; 93: 2348–52.
45 Shoji I, Aizaki H, Tani H, Ishii K, Chiba T, Saito I, *et al*. Efficient gene transfer into various mammalian cells, including non-hepatic cells, by baculovirus vectors. J Gen Virol 1997; 78: 2657–64.
46 Kost TA, Condreay JP. Recombinant baculoviruses as mammalian cell gene delivery vectors. Trends Biotechnol 2002; 20: 173–80.
47 Leisy DJ, Lewis TD, Leong JAC, Rohrmann GF. Transduction of cultured fish cells with recombinant baculoviruses. J Gen Virol 2003; 84: 1173–8.
48 van Loo ND, Fortunati E, Ehlert E, Rabelink M, Grosveld F, Scholte BJ. Baculovirus infection of nondividing mammalian cells: mechanisms of entry and nuclear transport of capsids. J Virol 2001; 75: 961–70.
49 Sarkis C, Serguera C, Petres S, Buchet D, Ridet JL, Edelman L, *et al*. Efficient transduction of neural cells *in vitro* and *in vivo* by a baculovirus-derived vector. Proc Natl Acad Sci USA 2000; 97: 14638–43.
50 Ma L, Tamarina N, Wang Y, Kuznetsov A, Patel N, Kending C, *et al*. Baculovirus-mediated gene transfer into pancreatic islet cells. Diabetes 2000; 49: 1986–91.
51 Ho YC, Chen HC, Wang KC, Hu YC. Highly efficient baculovirus-mediated gene transfer into rat chondrocytes. Biotechnol Bioeng 2004; 88: 643–51.
52 Wagle M, Jesuthasan S. Baculovirus-mediated gene expression in

zebrafish. Marine Biotechnol 2003; 5: 58–63.
53 Condreay JP, Witherspoon SM, Clay WC, Kost TA. Transient and stable gene expression in mammalian cells transduced with a recombinant baculovirus vector. Proc Natl Acad Sci USA 1999; 96: 127–32.
54 Cheng T, Xu CY, Wang YB, Chen M, Wu T, Zhang J, *et al*. A rapid and efficient method to express target genes in mammalian cells by baculovirus. World J Gastroenterol 2004; 10: 1612–18.
55 Lo HR, Chou CC, Wu TY, Yuen JP, Chao YC. Novel baculovirus DNA elements strongly stimulate activities of exogenous and endogenous promoters. J Biol Chem 2002; 277: 5256–64.
56 Venkaiah B, Viswanathan P, Habib S, Hasnain SE. An additional copy of the homologous region (hr1) sequence in the *Autographa californica* multinucleocapsid polyhedrosis virus genome promotes hyperexpression of foreign genes. Biochemistry 2004; 43: 8143–51.
57 Viswanathan P, Venkaiah B, Kumar MS, Rasheedi S, Vrati S, Bashyam MD, *et al*. The homologous region sequence (hr1) of *Autographa californica* multinucleocapsid polyhedrosis virus can enhance transcription from non-baculoviral promoters in mammalian cells. J Biol Chem 2003; 278: 52 564–71.
58 Pijlman GP, de Vrij J, van den End FJ, Vlak JM, Martens DE. *Evaluation* of baculovirus expression vectors with enhanced stability in continuous cascaded insect-cell bioreactors. Biotechnol Bioeng 2004; 87: 743–53.
59 Pijlman GP, van den Born E, Martens DE, Vlak JM. Autographa californica baculoviruses with large genomic deletions are rapidly generated in infected insect cells. Virology 2001; 283: 132–8.
60 Hu YC, Tsai CT, Chang YJ, Huang JH. Enhancement and prolongation of baculovirus-mediated expression in mammalian cells: Focuses on strategic infection and feeding. Biotechnol Prog 2003; 19: 373–9.
61 Tani H, Limn CK, Yap CC, Onishi M, Nozaki M, Nishimune Y, *et al*. *In vitro* and *in vivo* gene delivery by recombinant baculoviruses. J Virol 2003; 77: 9799–808.
62 Hsu CS, Ho YC, Wang KC, Hu YC. Investigation of optimal transduction conditions for baculovirus-mediated gene delivery into mammalian cells. Biotechnol Bioeng 2004; 88: 42–51.
63 Ho YC, Chung YC, Hwang SM, Wang KC, Hu YC. Transgene expression and differentiation of baculovirus-transduced human mesenchymal stem cells. J Gene Med 2005; in press.
64 Gao R, McCormick CJ, Arthur MJP, Ruddle R, Oakley F, Smart DE, *et al*. High efficiency gene transfer into cultured primary rat and human hepatic stellate cells using baculovirus vectors. Liver 2002; 22: 15–22.
65 Detrait ER, Bowers WJ, Halterman MW, Giuliano RE, Bennice L, Federoff HJ, *et al*. Reporter gene transfer induces apoptosis in primary cortical neurons. Mol Ther 2002; 5: 723–30.
66 Liu HS, Jan MS, Chou CK, Chen PH, Ke NJ. Is green fluorescent protein toxic to the living cells? Biochem Biophys Res Commun 1999; 260: 712–17.
67 Wang YC, Huang CF, Tung SF, Lin YS. Competition with TATA box-binding protein for binding to the TATA box implicated in human cytomegalovirus IE2-mediated transcriptional repression of cellular promoters. DNA Cell Biol 2000; 19: 613–19.
68 Dee KU, Shuler ML. A mathematical model of the trafficking of acid-dependent enveloped viruses: application to the binding, uptake, and nuclear accumulation of baculovirus. Biotechnol Bioeng 1997; 54: 468–90.
69 Duisit G, Saleun S, Douthe S, Barsoum J, Chadeuf G, Moullier P. Baculovirus vector requires electrostatic interactions including heparan sulfate for efficient gene transfer in mammalian cells. J Gene Med 1999; 1: 93–102.
70 Hofmann C, Lehnet W, Strauss M. The baculovirus system for gene delivery into hepatocytes. Gene Ther Mol Biol 1998; 1: 231–9.
71 Tani H, Nishijima M, Ushijima H, Miyamura T, Matsuura Y. Characterization of cell-surface determinants important for baculovirus infection. Virology 2001; 279: 343–53.
72 Bilello JP, Cable EE, Myers RL, Isom HC. Role of paracellular junction complexes in baculovirus-mediated gene transfer to non-dividing rat hepatocytes. Gene Ther 2003; 10: 733–49.
73 Barsoum J, Brown R, McKee M, Boyce FM. Efficient transduction of mammalian cells by a recombinant baculovirus having the vesicular stomatitis virus G glycoprotein. Hum Gene Ther 1997; 8: 2011–8.
74 Kukkonen SP, Airenne KJ, Marjomaki V, Laitinen OH, Lehtolainen P, Kankaanpaa P, *et al*. Baculovirus capsid display: a novel tool for transduction imaging. Mol Ther 2003; 8: 853–62.
75 Boublik Y, Di Bonito P, Jones IM. Eukaryotic virus display: engineering the major surface glycoprotein of the *Autographa californica* nuclear polyhedrosis virus (AcNPV) for the presentation of foreign proteins on the virus surface. Biotechnology 1995; 13: 1079–84.
76 Raty JK, Airenne KJ, Marttila AT, Marjomaki V, Hytonen VP, Lehtolainen P, *et al*. Enhanced gene delivery by avidin-displaying baculovirus. Mol Ther 2004; 9: 282–91.
77 Mottershead DG, Alfthan K, Ojala K, Takkinen K, Oker-Blom C. Baculoviral display of functional scFv and synthetic IgG-binding domains. Biochem Biophys Res Commun 2000; 275: 84–90.
78 Ojala K, Mottershead DG, Suokko A, Oker-Blom C. Specific binding of baculoviruses displaying gp64 fusion proteins to mammalian cells. Biochem Biophys Res Commun 2001; 284: 777–84.
79 Ernst W, Grabherr R, Wegner D, Borth N, Grassauer A, Katinger H. Baculovirus surface display: construction and screening of a eukaryotic epitope library. Nucleic Acids Res 1998; 26: 1718–23.
80 Cheshenko N, Krougliak N, Eisensmith RC, Krougliak VA. A novel system for the production of fully deleted adenovirus vectors that does not require helper adenovirus. Gene Ther 2001; 8: 846–54.
81 Sollerbrant K, Elmen J, Wahlestedt C, Acker J, Leblois-Prehaud H, Latta-Mahieu M, *et al*. A novel method using baculovirus-mediated gene transfer for production of recombinant adeno-associated virus vectors. J Gen Virol 2001; 82: 2051–60.
82 Ramos L, Kopec LA, Sweitzer SM, Fornwald JA, Zhao HZ, McAllister P, *et al*. Rapid expression of recombinant proteins in modified CHO cells using the baculovirus system. Cytotechnology 2002; 38: 37–41.
83 Wang KC, Wu JC, Chung YC, Ho YC, Chang MD, Hu YC. Baculovirus as a highly efficient gene delivery vector for the expression of hepatitis delta virus antigens in mammalian cells. Biotechnol Bioeng 2005; 89: 464-73.
84 Chen YH, Wu JC, Wang KC, Chiang YW, Lai CW, Chung YC, *et al*. Baculovirus-mediated production of HDV-like particles in

BHK cells using a novel oscillating bioreactor. J Biotechnol 2005; in press.
85 Clay WC, Condreay JP, Moore LB, Weaver SL, Watson MA, Kost TA, *et al*. Recombinant baculoviruses used to study estrogen receptor function in human osteosarcoma cells. Assay Drug Dev Technol 2003; 1: 801–10.
86 Jenkinson S, McCoy DC, Kerner SA, Ferris RG, Lawrence WK, Clay WC, *et al*. Development of a novel high-throughput surrogate assay to measure HIV envelope/CCR5/CD4-mediated viral/cell fusion using BacMam baculovirus technology. J Biomol Screen 2003; 8: 463–70.
87 Delaney WE, Isom HC. Hepatitis B virus replication in human HepG2 cells mediated by hepatitis B virus recombinant baculovirus. Hepatology 1998; 28: 1134–46.
88 Fipaldini C, Bellei B, La Monica N. Expression of hepatitis C virus cDNA in human hepatoma cell line mediated by a hybrid baculovirus-HCV vector. Virology 1999; 255: 302–11.
89 Delaney WE, Miller TG, Isom HC. Use of the hepatitis B virus recombinant baculovirus-HepG2 system to study the effects of (-)-beta-2',3'-dideoxy-3'-thiacytidine on replication of hepatitis B virus and accumulation of covalently closed circular DNA. Antimicrob Agents Chemother 1999; 43: 2017–26.
90 Delaney WE, Edwards R, Colledge D, Shaw T, Torresi J, Miller TG, *et al*. Cross-resistance testing of antihepadnaviral compounds using novel recombinant baculoviruses which encode drug-resistant strains of hepatitis B virus. Antimicrob Agents Chemother 2001; 45: 1705–13.
91 McCormick CJ, Rowlands DJ, Harris M. Efficient delivery and regulable expression of hepatitis C virus full-length and minigenome constructs in hepatocyte-derived cell lines using baculovirus vectors. J Gen Virol 2002; 83: 383–94.
92 Merrihew RV, Clay WC, Condreay JP, Witherspoon SM, Dallas WS, Kost TA. Chromosomal integration of transduced recombinant baculovirus DNA in mammalian cells. J Virol 2001; 75: 903–9.
93 Hofmann C, Strauss M. Baculovirus-mediated gene transfer in the presence of human serum or blood facilitated by inhibition of the complement system. Gene Ther 1998; 5: 531–6.
94 Airenne KJ, Hiltunen MO, Turunen MP, Turunen AM, Laitinen OH, Kulomaa MS, *et al*. Baculovirus-mediated periadventitial gene transfer to rabbit carotid artery. Gene Ther 2000; 7: 1499–1504.
95 Lehtolainen P, Tyynela K, Kannasto J, Airenne KJ, Yla-Herttuala S. Baculoviruses exhibit restricted cell type specificity in rat brain: a comparison of baculovirus- and adenovirus-mediated intracerebral gene transfer *in vivo*. Gene Ther 2002; 9: 1693–9.
96 Huser A, Rudolph M, Hofmann C. Incorporation of decay-accelerating factor into the baculovirus envelope generates complement-resistant gene transfer vectors. Nature Biotechnol 2001; 19: 451–5.
97 Pieroni L, Maione D, La Monica N. *In vivo* gene transfer in mouse skeletal muscle mediated by baculovirus vectors. Hum Gene Ther 2001; 12: 871–81.
98 Bilello JP, Delaney WE, Boyce FM, Isom HC. Baculovirus entry into nondividing hepatocytes is enhanced by transient disruption of intercellular junctions. Hepatology 2001; 34: 834.
99 Barsoum J. Concentration of recombinant baculovirus by cation-exchange chromatography. Biotechniques 1999; 26: 834–40.
100 Hu YC, Tsai CT, Chung YC, Lu JT, Hsu JT. Generation of chimeric baculovirus with histidine-tags displayed on the envelope and its purification using immobilized metal affinity chromatography. Enzyme Microb Technol 2003; 33: 445–52.
101 Sandig V, Hofmann C, Steinert S, Jennings G, Schlag P, Strauss M. Gene transfer into hepatocytes and human liver tissue by baculovirus vectors. Hum Gene Ther 1996; 7: 1937–45.
102 Gronowski AM, Hilbert DM, Sheehan KCF, Garotta G, Schreiber RD. Baculovirus stimulates antiviral effects in mammalian cells. J Virol 1999; 73: 9944–51.
103 Beck NB, Sidhu JS, Omiecinski CJ. Baculovirus vectors repress phenobarbital-mediated gene induction and stimulate cytokine expression in primary cultures of rat hepatocytes. Gene Ther 2000; 7: 1274–83.
104 Abe T, Takahashi H, Hamazaki H, Miyano-Kurosaki N, Matsuura Y, Takaku H. Baculovirus induces an innate immune response and confers protection from lethal influenza virus infection in mice. J Immunol 2003; 171: 1133–9.
105 Aoki H, Sakoda Y, Jukuroki K, Takada A, Kida H, Fukusho A. Induction of antibodies in mice by a recombinant baculovirus expressing pseudorabies virus glycoprotein B in mammalian cells. Vet Microbiol 1999; 68: 197–207.
106 Facciabene A, Aurisicchio L, La Monica N. Baculovirus vectors elicit antigen-specific immune responses in mice. J Virol 2004; 78: 8663–72.
107 Tami C, Farber M, Palma EL, Taboga O. Presentation of antigenic sites from foot-and-mouth disease virus on the surface of baculovirus and in the membrane of infected cells. Arch Virol 2000; 145: 1815–28.
108 Yoshida S, Kondoh D, Arai E, Matsuoka H, Seki C, Tanaka T, *et al*. Baculovirus virions displaying *Plasmodium berghei* circumsporozoite protein protect mice against malaria sporozoite infection. Virology 2003; 316: 161–70.
109 Baumert TF, Ito S, Wong DT, Liang TJ. Hepatitis C virus structural proteins assemble into viruslike particles in insect cells. J Virol 1998; 72: 3827–36.
110 O'Reilly D, Miller L, Luckow V. In: Baculovirus expression vectors: a laboratory manual. New York: WH Freeman and Co; 1992.

Acta Pharmacologica Sinica 2005 Apr; 26 (4): 417–422

Full-length article

Novel role for gabapentin in neuroprotection of central nervous system in streptozotocine-induced diabetic rats[1]

Giyasettin BAYDAS[2,3], Ertugrul SONKAYA[4], Mehmet TUZCU[5], Abdullah YASAR[3], Emir DONDER[4]

[3]Department of Physiology; [4]Department of Internal Medicine, College of Medicine, Firat University; [5]Department of Biology, Faculty of Science, Firat University, Elazig 23119, Turkey

Key words

gabapentin; glial fibrillary acidic protein; neurotrophic protein S100beta; phosphopyruvate hydratase; lipid peroxidation

[1] Study supported by the Firat University Research Foundation (FUBAP Project number 831).
[2] Correspondence to Prof Giyasettin BAYDAS.
Phn 90-424-237-0000.
Fax 90-424-233-3770.
E-mail baydas@hotmail.com

Received 2004-07-02
Accepted 2005-12-09

doi: 10.1111/j.1745-7254.2005.00072.x

Abstract

Aim: To investigate the effect of gabapentin on neural [neuron-specific enolase (NSE)] and glial markers [glial fibrillary acidic protein (GFAP) and S100B] in different brain regions of diabetic rats. **Methods:** Diabetes was induced by a single intraperitoneal injection of streptozotocine (50 mg/kg body weight). Rats in one diabetic group received gabapentin (50 $mg \cdot kg^{-1} \cdot d^{-1}$) and rats in the other diabetic group received vehicle only for 6 weeks. The levels of GFAP, S100B, and NSE were determined by immunoblotting in the hippocampus, cortex, and cerebellum. Lipid peroxidation (LPO as malondialdehyde+ 4-hydroxyalkenals) and glutathione (GSH) levels were also determined in the same brain parts. **Results:** Total and degraded GFAP content and S100B protein expression in different areas of brain tissues significantly increased in diabetic rats compared to control rats. Similarly, NSE levels were also significantly elevated in hyperglycemic rats. In addition, there was a significant increase in LPO levels in the diabetic rat brain compared to control rat brains. Pretreatment with gabapentin prevented the upregulation of GFAP, S100B, and NSE in all brain regions of diabetic rats. The level of LPO was reduced, but not completely halted, by treatment with gabapentin. **Conclusion:** These results suggest that diabetes causes glial and neuronal injury, possibly as a result of elevated oxidative stress, and that gabapentin protects neurons and glial cells. Thus, we predict that gabapentin treatment will attenuate the hippocampal and cortical neurodegeneration observed during diabetes mellitus in rats.

Introduction

Diabetes mellitus is a common metabolic disorder that affects the peripheral as well as the central nervous system. Animal models of diabetes can make an important contribution to understanding the pathology of the effects of diabetes on the brain. Hyperglycemia provides more substrate for anaerobic glycolysis in the brain, resulting in lactic acidosis and enhanced damage to both glial and neuronal cells[1]. Furthermore, enhanced formation of oxygen free radicals occurs in the tissues during hyperglycemia[2]. These oxidant radicals also contribute to increased neuronal death by oxidizing proteins damaging DNA and inducing the lipoperoxidation of cellular membranes[3].

One of the complications of diabetes is neuropathy. Gabapentin (GBP) is used to treat diabetic neuropathy. GBP is an anticonvulsant that reduces pain in peripheral neuropathy, including diabetic neuropathy[4]. GBP is a hydrophilic analogue of the inhibitory neurotransmitter gamma aminobutyric acid (GABA). It readily penetrates the blood-brain barrier via an L-system amino acid transporter system[5]. In addition, GBP has been shown to be neuroprotective in animals[6]. However, to date, no study has examined the effects of GBP on neural and glial markers.

S100B and neuron-specific enolase protein (NSE), distributed mainly in the central nervous system, can provide qualitative information about the extent of brain injury and are sensitive markers of brain damage after stroke and cere-

bral hypoxia[7,8]. NSE is a glycolytic enzyme that is a soluble cytoplasmatic protein localized principally in neurons. Recent evidence has shown that NSE is a marker of neuronal damage following cerebral ischemia[8,9]. S100B is an acidic Ca^{2+} binding protein, present mainly in astrocytes, that exerts paracrin trophic effects on several neuronal populations[10]. Brain injury causes a selective leakage of S100B into the cerebrospinal fluid and blood so that serum S100B levels were found to be good indicators for the assessment of patients with cerebral ischemia[11,12].

Glial fibrillary acidic protein (GFAP) is another astrocytic marker. GFAP is an intracellular intermediate filament protein of glial cells. It has been suggested that GFAP is essential for the formation of stable astrocytic processes in response to neuronal damage and this may be critical for morphogenesis of the central nervous system[13]. Chemical or mechanical insults to the brain cause permanent changes, with astrocytes responding via a variety of reactions called reactive gliosis[14]. A key indicator of glial reactivity is the increased synthesis of GFAP. Increases in GFAP are commonly used to examine the distributions of glial cells in response to neural injury[14,15]. Recently, we have demonstrated that streptozotocine (STZ)-induced diabetes causes reactive gliosis[15,16]. In the present study we aimed to examine the effects of GBP on neural and glial markers in STZ-induced diabetic rats.

Materials and methods

Sixty adult male Wistar rats (Animal Research Unit, Firat University, Elazig, Turkey) weighing 200–250 g were used in this study. The rats were housed in a temperature-controlled room (22–25 ºC) with a 12/12 h light/dark cycle. Water and food were given *ad libitum*. Animals were assigned into a diabetic group (n=30) or an age-matched control group (n=30). Diabetes was induced by a single intraperitoneal (ip) injection of 50 mg/kg body weight STZ. STZ (Sigma Chemical Company, St Louis, MO, USA) was dissolved in sodium citrate buffer (pH 4.5). Blood glucose concentrations were determined 3 d after STZ injection. Rats with a blood glucose concentration above 250 mg/dL were declared diabetic. Diabetic rats were randomly assigned to two groups: the first group received GBP (Sigma) diluted in sterile physiological saline and administered ip (50 $mg \cdot kg^{-1} \cdot d^{-1}$) in a volume of 1 mL/kg. (STZ-GBP group, n=15). The second group received the vehicle alone (STZ group; n=15). Control rats were injected with the vehicle alone (n= 15) or with the same dose of GBP (GBP group; n=15). Each animal's body weight and diabetic state were reassessed after 6 weeks just prior to killing the animals. All animals were killed by decapitation after 5 weeks of treatment by GBP. The brain tissues were removed; the hippocampus, cortex, and cerebellum were dissected. Samples were used fresh or kept at -70 ºC. All protocols described were reviewed and approved by the local Institutional Committee for the Ethical Use of Animals.

Western blotting Tissue samples were homogenized in Tris-HCl 10 mmol/L (pH 7.4), NaCl 0.1 mmol/L, phenylmethylsulphonyl fluoride 0.2 mmol/L, edetic acid 5 mmol/L, β-mercaptoethanol 2 mmol/L, and 1% Triton X-100 containing proteinaze inhibitors, and centrifuged at 40 000×g at 4 ºC for 60 min. Supernatants were collected, aliquoted, and stored at -70 ºC until required.

Sodium dodecyl sulfate (SDS)-polyacrylamide gradient gel electrophoresis was carried out as previously described[17]. Samples and standard protein markers were submitted to the SDS-polyacrylamide gradient gel and the separated proteins were transferred to nitrocellulose filters (Schleicher & Schuell Incorporated, Keene, NH, USA). Non-specific binding was blocked by incubation with 1% bovine serum albumin. The blots were then incubated with primary antibodies (Santa Cruz Biotechnology Incorporated, Santa Cruz, CA, USA) as follows: GFAP 1:2 000; S100 1:1000; NSE 1:1000. After a 1-h incubation the blots were washed extensively in TBS-Tween (Tris-HCl 25 mmol/L, NaCl 0.2 mmol/L, 0.1% Tween-20). The blots were then incubated for 1 h with a secondary antibody, a goat anti-rabbit Ig peroxidase conjugated (Sigma, Dorset, UK). Specific binding was detected using diaminobenzidine and H_2O_2 as the substrates. The relative amounts of immunoreactive GFAP, S100B, and NSE were quantified in arbitrary units by scanning blots using a computerized software program (LabWorks 4.0; UVP Incorporated, Cambridge, UK).

Levels of tissue protein, glutathione, and LPO Protein determinations were carried out according to the Lowry procedure using a protein assay kit (Sigma Chemical Company, Deisenhofen, Germany). Tissue lipid peroxidation (malondialdehyde+4-hydroxyalkenals) was determined using a LPO-586 kit (Oxis International Incorporated, Corvallis, OR, USA); the method is based on the reaction of *N*-methyl-2-phenylindole with malondialdehyde and 4-hydroxyalkenals at 45 °C. Glutathione (GSH) levels were determined using the method of Ellman[18]. Tissue homogenates were centrifuged with 5% trichloroacetic acid to centrifuge out the proteins. Two milliliters of phosphate buffer, 0.5 mL of 5,5' dithiobis (2-nitrobenzoic acid) and 0.4 mL of distilled water was added to 0.1 mL of this homogenate. The mixture was vortexed and the absorbance was read at 412 nm.

Statistical analysis Results were expressed as mean±SD and significant differences between groups were evaluated

using ANVOA followed by a *post-hoc* Bonferroni test. A level of significance of $P<0.05$ was considered to be statistically significant.

Results

Estimation of glial and neuronal markers A common marker for reactive gliosis is an increase in GFAP. GFAP showed many immunopositive protein bands with relative molecular weights of 49 kDa (main band) and several small molecular weight bands at roughly 42–47 kDa (degraded product of GFAP), respectively (Figure 1). Although Western blot measurement of brain 49 kDa GFAP contents after 6 weeks of STZ-induced diabetes showed no significant difference, the amount of degraded GFAP product increased significantly compared with the non-diabetic controls. The beneficial effects of the repeated administration of GBP were manifested by downregulation of the degradation products of GFAP (Figure 1, Table 1).

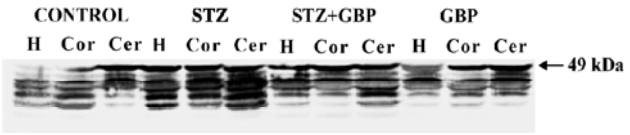

Figure 1. Western blot analysis of GFAP protein from hippocampal, cortical, and cerebellar homogenates of control, STZ, and GBP groups. H, hippocampus; Cor, cortex; Cer, cerebellum.

The immunoblots of the brain homogenates showed a single S100B-immunoreactive polypeptide band with a molecular weight of approximately 11 kDa. The levels of S100B protein in the hippocampus, cortex, and cerebellum were significantly higher in STZ-treated rats than that in the control group. Similarly, GBP prevented the increase of S100B protein in all studied brain areas (Figure 2, Table 1).

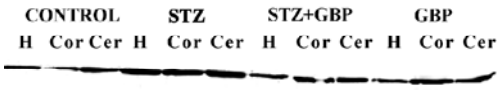

Figure 2. Western blot detection of S100B protein from the hippocampus, cortex, and cerebellum of control, STZ, and GBP groups. H, hippocampus; Cor, cortex; Cer, cerebellum.

In the brain regions of STZ-treated rats, the NSE contents showed a significant increase compared with the controls. Similarly to GFAP and S100B, NSE levels were reduced by treatment with GBP (Figure 3, Table 1).

Estimation of LPO and GSH Likewise, STZ-induced diabetes led to a marked elevation in the levels of malondialdehyde+4-hydroxyalkenals in the cortex, hippocampus, and

Table 1. Densitometric results (as arbitrary units) of GFAP, S100B, and NSE and the levels of LPO and GSH in the hippocampus, cortex and cerebellum of control, diabetic and GBP-treated rats. n=15. Mean±SD. $^bP<0.05$, $^cP<0.01$ *vs* control. $^eP<0.05$, $^fP<0.01$ *vs* STZ-diabetic group.

	Control	STZ	STZ+GBP	GBP
Hippocampus				
GFAP (au)	1.0±0.1	2.2±0.2^c	1.2±0.1	0.80±0.09
S100B (au)	1.0±0.09	2.1±0.2^c	1.10±0.09^f	0.80±0.09
NSE (au)	1.0±0.1	2.0±0.2^c	1.2±0.1^f	1.3±0.1
LPO (nmol/mg protein)	3.2±0.3	4.9±0.5^c	4.1±0.3^e	3.1±0.2
GSH (μg/g protein)	375±42	348±38	335±42	350±35
Cortex				
GFAP (au)	1.0±0.09	2.0±0.2^c	0.80±0.09^e	0.90±0.09
S100B (au)	1.0±0.09	3.4±0.4^c	1.1±0.09^f	1.8±0.2^c
NSE (au)	1.0±0.1	2.2±0.2^c	1.1±0.1^f	1.2±0.1
LPO (nmol/mg protein)	3.2±0.3	4.8±0.5^c	3.8±0.3^e	3.0±0.3
GSH (μg/g protein)	360±40	325±30^b	310±30	342±34
Cerebellum				
GFAP (au)	1.0±0.1	2.8±0.3^c	1.3±0.1	1.1±0.1
S100B (au)	1.0±0.08	1.8±0.2	0.80±0.09	0.80±0.08
NSE (au)	1.0±0.09	2.4±0.3	1.2±0.1	0.9±0.1
LPO (nmol/mg protein)	3.3±0.4	4.8±0.5^c	3.9±0.3^e	3.2±0.3
GSH (μg/g protein)	362±42	322±38^b	315±35	340±36

au, arbitrary units; GBP, gabapentin; LPO, lipid peroxidation as malondialdehyde plus 4-hydroxyalkenals; STZ, streptozotocine.

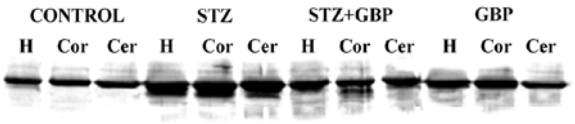

Figure 3. Western blot of NSE protein from the hippocampus, cortex, and cerebellum of control, STZ, and GBP groups. H, hippocampus; Cor, cortex; Cer, cerebellum.

cerebellum compared with the control group. A significant positive correlation was found between the levels of malondialdehyde +4-hydroxyalkenals and the GFAP contents in the cortex and hippocampus (r=0.625, P<0.01; r=0.604, P<0.01, respectively). Treatment with GBP significantly reduced the levels of malondialdehyde+4-hydroxyalkenals in the brain homogenates of diabetic rats compared to the controls (Table 1).

In the present study we measured the amount of GSH in the homogenates of cortex, hippocampus and cerebellum. In each of these brain parts, the levels of GSH were lower in the STZ-diabetic rats than in the control animals. Treatment with GBP led to a slight but non-significant reduction in the levels of GSH compared with the levels in the STZ group (Table 1).

Discussion

In the experiment reported here, we investigated the effects of GBP on glial and neuronal markers in different brain regions of diabetic rats. We found that diabetes induced overexpression in both glial and neuronal markers and GBP prevented the elevation of these markers. Interestingly, treatment with GBP did not change the levels of both neuronal and glial markers in non-diabetic rats. Furthermore, GBP treatment moderately inhibited, but did not completely reverse, the elevation in LPO induced by STZ diabetes. GFAP and S100B can be trophic or toxic depending on their concentrations. Over production of both glial markers causes glial and neuronal death, whereas in low concentrations they can act as neurotrophic factors, which may be important during both development and nerve regeneration[19,20].

Herein we report a new role for GBP that is associated with neuroprotection. These data provide the first indication that GBP regulates the expression of neural and glial markers. Although the mechanism of action of GBP was not specifically investigated in this study, the present findings provide some clues.

It has been reported that GBP is neuroprotective in chronic neural diseases[21]. Current findings appear to support this idea. The mechanism by which GBP reduced LPO levels and inhibited the expression of neuronal and glial markers is not known. This process may occur through a free radical mediated pathway. Tissue damage is observed during untreated diabetes with very high glucose levels and this is attributed to oxidative injury resulting from the production of free radicals[2,22]. One of the consequences of such damage is the depletion of the cellular antioxidant, GSH. A decreased defense system against free radicals and elevated glutamatergic activity in diabetes may cause glial sensitivity[23]. Diabetes-related sensitivity to oxidative stress of astrocytes makes neurons more susceptible to injury. Neuronal and glial injury leads to the over production of NSE, GFAP, and S100B. In agreement with the present findings we recently hypothesized that glial reactivity was closely related to the oxidative environment[15].

The current results show that treatment with GBP significantly prevents glial reactivity by reducing the over production of GFAP and S100B. Similarly GBP inhibited the elevation of NSE, a neuronal marker. The exact mechanism by which GBP inhibits reactive gliosis is not entirely clear; however, one possible explanation is that GBP may reduce oxidative stress via an unknown mechanism. Oxidative stress is known to exacerbate glial reactivity[15,16]. Decreased LPO levels as a result of GBP treatment in the present study supports this explanation.

Hyperglycemia causes a reduction in extracellular GABA, which exacerbates neuronal injury by reducing generalized neuroinhibition[23,24]. Reduced GABAergic action in the cerebral cortex in diabetes has been shown to be increased by GBP treatment[25]. Several investigations have confirmed that GBP has the ability to increase the GABA content of the brain, influence GABA receptor activity, and exhibit anticonvulsant activity[26,27]. An increase in GABAergic activity by GBP would promote inhibitory neurotransmission in the central nervous system. This is a potent mechanism by which GBP acts as a neuroprotector.

The other possible explanation for the effect of GBP is a drug-induced decrease in glutamatergic neurotransmission[28]. Glutamate neurotoxicity has been implicated in the neurodegeneration associated with several neurodegene-rative diseases. Diabetes may increase the release of glutamate and activate NMDA receptors[29]. Glutamate causes a transmembrane ion imbalance, in particular a calcium influx, which in turn generates reactive oxygen species. These free radicals actively attack macromolecules within neuron and glial cells, resulting in structural and functional changes in proteins. Glial cells respond to the oxidative insult by producing GFAP and S100B[30,31]. The present findings are in agreement with recent reports that clearly show that reactive

gliosis occurs in diabetes, possibly as a result of oxidative stress. This is consistent with our previous studies in diabetic rats in which the protective effects of antioxidants against reactive gliosis were attributed to their free radical scavenging properties[15,16]. As we previously described, antioxidant vitamin E[32] and melatonin[15] treatment improved reactive gliosis induced by hyperglycemia via a dramatic reduction in oxidative stress. Compared with antioxidants, the effect of GBP on oxidative stress is considerably more modest. The present results suggest that GBP prevents reactive gliosis and oxidative stress in an indirect way, possibly by reducing glutamate neurotoxicity, which causes free radical production in brain tissue. Previous studies have shown that repeated administration of GBP inhibits excitatory glutamatergic neurotransmission via direct blockage of excitatory receptors or alteration of glutamate metabolism or release[32]. In the present study we have shown that the production of glial and neuronal markers is increased in the brain by hyperglycemia and that this increase is attenuated by treatment with GBP. Thus, we predict that GBP treatment will attenuate the hippocampal and cortical neurodegeneration observed during diabetes mellitus in rats.

References

1 Biessels GJ, Kappelle AC, Bravenboer B, Erkelens DW, Gispen WH. Cerebral function in diabetes mellitus. Diabetologia 1994; 37: 643–50.

2 Baydas G, Canatan H, Turkoglu A. Comparative analysis of the protective effects of melatonin and vitamin E on streptozocin-induced diabetes mellitus. J Pineal Res 2002; 32: 225–30.

3 Hawkins CL, Davies MJ. Generation and propagation of radical reactions on proteins. Biochim Biophys Acta 2001; 1504: 196–219.

4 Field MJ, McCleary S, Hughes J, Singh L. Gabapentin and pregabalin, but not morphine and amitriptyline, block both static and dynamic components of mechanical allodynia induced by streptozocin in the rat. Pain 1999; 80: 391–8.

5 Su TZ, Lunney E, Campbell G, Oxender DL. Transport of gabapentin, a gamma-amino acid drug, by system l alpha-amino acid transporters: a comparative study in astrocytes, synaptosomes, and CHO cells. J Neurochem 1995; 64: 2125–31.

6 Lagreze WA, Müler-Valten R, Feuerstein TJ. The neuroprotective properties of gabapentin-lactam. Graef's Arch Clin Exp Ophthalmol 2001; 239: 845–9.

7 Buttner T, Lack B, Jager M, Wunsche W, Kuhn W, Muller T, *et al.* Serum levels of neuron-specific enolase and S-100 protein after single tonic-clonic seizures. J Neurol 1999; 246: 459–61.

8 Hatfield RH, McKernan RM. CSF neuron-specific enolase as a quantitative marker of neuronal damage in a rat stroke model. Brain Res 1992; 577: 249–52.

9 Persson L, Hardemark HG, Gustafsson J, Rundstrom G, Mendel-Hartvig I, Esscher T, *et al.* S-100 protein and neuron-specific enolase in cerebrospinal fluid and serum: markers of cell damage in human central nervous system. Stroke 1987; 18: 911–8.

10 Kligman D, Marshak DR. Purification and characterisation of a neurite extension factor from bovine brain. Proc Natl Acad Sci USA 1985; 82: 7136–9.

11 Heizmann CW, Fritz G, Schafer BW. S-100 proteins: structure, functions and pathology. Front Biosci 2002; 7: 1356–67.

12 Misler U, Wiesmann M, Friedrich C, Kaps M. S-100 protein and neuron-spesific enolase concentrations in blood as indicators of infarction volume and prognosis in acute ischemic stroke. Stroke 1997; 28: 1956–60.

13 Liedtke W, Edelmann W, Bieri PL, Chiu FC, Cowan NJ, Kucherlapati R, *et al.* GFAP is necessary for the integrity of CNS white matter architecture and long-term maintenance of myelination. Neuron 1996; 17: 607–15.

14 Kunkler PE, Kraig RP. Reactive astrocytosis from excitotoxic injury in hippocampal organ culture parallels that seen *in vivo*. J Cereb Blood Flow Metab 1997; 17: 26–43.

15 Baydas G, Reiter RJ, Yasar A, Tuzcu M, Akdemir I, Nedzvetskii VS. Melatonin reduces glial reactivity in the hippocampus, cortex, and cerebellum of streptozotocin-induced diabetic rats. Free Radic Biol Med 2003; 35: 797–804.

16 Baydas G, Reiter RJ, Nedzvetskii VS, Yasar A, Tuzcu M, Ozveren F, *et al.* Melatonin protects the central nervous system of rats against toluene-containing thinner intoxication by reducing reactive gliosis. Toxicol Lett 2003; 137: 169–74.

17 Laemmli UK. Cleavage of structural proteins during the assembly of the head of bacteriophage T4. Nature 1970; 227: 680–5.

18 Ellman GL. Tissue sulphydryl groups. Arch Biochem Biophys 1959; 82: 70–7.

19 Fano G, Mariggio MA, Angelella P, Nicoletti I, Antonica A, Fulle S, *et al.* The S-100 protein causes an increase of intracellular calcium and death of PC12 cells. Neuroscience 1993; 53: 919–25.

20 Donato R. S100: a multigenic family of calcium-modulated proteins of the EF-hand type with intracellular and extracellular functional roles. Int J Biochem Cell Biol 2001; 33: 637–68.

21 Rothstein JD, Kuncl RW. Neuroprotective strategies in a model of chronic glutamate-mediated motor neuron toxicity. J Neurochem 1995; 65: 643–51.

22 Ercel E, Baydas G, Akyol A, Eksioglu E, Canpolat L. The effect of vitamin E on the sciatic nerve lipid peroxidation in streptozotocin induced diabetes mellitus. Biomed Res 1999; 10: 95–101.

23 Guyot LL, Diaz FG, O'Regan MH, Song D, Phillis JW. The effect of topical insulin on the release of excitotoxic and other amino acids from the rat cerebral cortex during streptozotocin-induced hyperglycemic ischemia. Brain Res 2000; 872: 29–36.

24 Malcangio M, Tomlinson DR. A pharmacologic analysis of mechanical hyperalgesia in streptozotocin/diabetic rats. Pain 1998; 76:151–7.

25 Petroff OA, Rothman DL, Behor KL, Lamoureux D, Mattson RH. The effect of gabapentin on brain gamma-aminobutyric acid in patients with epilepsy. Ann Neurol 1996; 39: 95–9.

26 Cutrer FM. Antiepileptic drugs: how they work in headache. Headache 2001; 41: S3–10.

27 Petroff OA, Hyder F, Rothman DL, Mattson RH. Effects of gabapentin on brain GABA, homocarnosine, and pyrrolidinone in epilepsy patients. Epilepsia 2000; 41: 675–80.

28 Shimoyama M, Shimoyama N, Hori Y. Gabapentin affects glutamatergic excitatory neurotransmission in the rat dorsal horn.

Pain 2000; 85: 405–14.
29 Gupta M, Singh J, Sood S, Arora B. Mechanism of antinociceptive effect of nimodipine in experimental diabetic neuropathic pain. Methods Find Exp Clin Pharmacol 2003; 25: 49–52.
30 Kaneko K, Nakamura A, Yoshida K, Kametani F, Higuchi K, Ikeda S. Glial fibrillary acidic protein is greatly modified by oxidative stress in aceruloplasminemia brain. Free Radic Res 2002; 36:303–6.
31 Baydas G, Nedzvetskii VS, Tuzcu M, Yasar A, Kirichenko SV. Increase of glial fibrillary acidic protein and S-100B in hippocampus and cortex of diabetic rats: effects of vitamin E. Eur J Pharmacol 2003; 462: 67–71.
32 Fink K, Dooley DJ, Meder WP, Suman-Chauhan N, Duffy S, Clusmann H, *et al.* Inhibition of neuronal Ca^{2+} influx by gabapentin and pregabalin in the human neocortex. Neuropharmacology 2002; 42: 229–36.

The First Scientific Meeting of the Asian Society for Vascular Biology

October 8–11, 2005 Shanghai, China

Info: Yu Huang
Department of Physiology
Chinese University of Hong Kong
Hong Kong SAR, China
Phn: 852-2609-6787
Fax: 852-2603-5022
E-Mail: yu-huang@cuhk.edu.hk
Http:// www.sbsonline.org/sbscon/2005/index.php

Acta Pharmacologica Sinica 2005 Apr; 26 (4): 423–427

Blackwell Publishing

Full-length article

Influence of low dietary histamine on the seizure development of chemical kindling induced by pentylenetetrazol in rats[1]

Chun-lei JIN[2], Eiko SAKURAI[3], Yoshinobu KISO[4], Jian-hong LUO[2], Kazuhiko YANAI[2,3], Zhong CHEN[2,3,5]

[2]Department of Pharmacology, School of Medicine, Zhejiang University, Hangzhou 310031, China; [3]Department of Pharmacology, Tohoku University School of Medicine, Sendai 980-8575, Japan; [4]Institute for Health Care Science, Suntory Limited, Shimamoto-cho, Osaka 618-0012, Japan

Key words

seizures; pentylenetetrazol; brain; histamine; diet

[1] Project supported by the National Natural Science Foundation of China (No 30371638) and by the Grants-in-Aid for Scientific Research B (No 14370027) from the Ministry of Education, Culture, Sports, Science and Technology, Japan; in part by a grant from the Zhejiang Provincial Scientific Foundation of China (2004C34002).
[5] Correspondence to Prof Zhong CHEN.
Phn/Fax 86-571-8721-7446.
E-mail chenzhong@zju.edu.cn

Received 2004-11-25
Accepted 2005-01-12

doi: 10.1111/j.1745-7254.2005.00097.x

Abstract

Aim: To determine the role of dietary low histamine on the seizure development of pentylenetetrazol (PTZ)-induced kindling in rats. **Methods:** After 14 d of feeding on a low histamine diet (LH, containing 0.145 μmol/g of histamine), the rats were chemically kindled by repeated intraperitoneal injection of a subconvulsant dose of PTZ (35 mg/kg) once every 48 h, and seizure activity of kindling was recorded for 30 min. Histamine in brain samples was analyzed using a high performance liquid chromatography system with a fluorescence spectrofluorometer. **Results:** The LH diet induced an increase in seizure response (seizure susceptibility) to the first trial of PTZ, and resulted in facilitation of subsequent PTZ kindling process (seizure development). The histamine levels in the cortex, hippocampus, and hypothalamus of LH-treated rats decreased significantly and these changes correlated well with seizure behavior (r = 0.875, 0.651, and 0.796, respectively). In addition, chronic kindled seizures resulted in a significant increase of the histamine content in the cortex and hypothalamus in the LH-fed groups. **Conclusion:** These findings indicate that the histamine in daily food could influence the brain histaminergic function, and play an important role in regulating seizure susceptibility.

Introduction

Since Churchill first described certain antihistaminics enhance epileptic extent[1], a number of studies have indicated that brain histamine is involved in mechanisms regulating seizure susceptibility, and the anticonvulsant action of histamine has been well documented[2–5]. Histamine increases the threshold for amygdaloid kindling and pentylenetetrazol (PTZ)-induced seizures[6,7]. A marked increase in H_1-receptor binding has been observed around the epileptic foci of complex partial seizures and may be involved in inhibiting the spread of seizure activity[8]. In addition, we have recently reported severe seizure development of PTZ-induced kindling in H_1 receptor knockout mice (H_1R KO) and histidine decarboxylase-deficient (HDC $^{-/-}$) mice[9].

It has recently been reported that long-term treatment with high histamine level diets could increase brain histamine levels in HDC $^{-/-}$ mice, which lack the ability to synthesize histamine[11,12]. These results suggest that histamine can be absorbed from the digestive tract and distributed to the brain[12]; furthermore, histamine levels in various diets might influence the histaminergic system and so affect certain neuronal functions, such as epilepsy. Yet, so far there is only limited information about the effects of dietary histamine on these neurotransmitters.

Kindling has been accepted as an experimental animal model for analyzing epilepsy and epileptogenesis, and estimating the effectiveness of antiepileptic drugs. It is generally known that PTZ-induced kindling creates proconflict and convulsant effects in rodents, and is considered as an adequate model of human absence epilepsy and myoclonic, generalized tonic-clonic seizure[13]. We therefore designed the present study to further elucidate the possible relationship between the appearance of seizures and histamine in daily diet.

Materials and methods

Animals Male Sprague-Dawley rats (4–5 weeks old) were purchased from Japan SLC (Shizuoka, Japan), and were maintained in individual cages under constant temperature (22–24 °C) and humidity (40%–70%) with a 12-h light/dark cycle (lights on from 6:00 AM–18:00 PM). The rats were fed with basal histamine diets (BH, containing 79.6 nmol/g of histamine, Nihon Nosan Kogyo KK, Yokohama, Japan) or low histamine diets (LH, containing 1.45 nmol/g of histamine, Ver 3 from Nihon Nosan Kogyo KK, Yokohama, Japan), and water was given *ad libitum*. Behavioral studies were carried out each day between 10.00 AM and 17.00 PM. All experiments were carried out in accordance with the National Institutes of Health Guide for the Care and Use of Laboratory Animals.

Chemical kindling After 2 weeks of LH feeding, the rodents were intraperitoneally injected with PTZ (35 mg/kg) every 48 h until the animals were fully kindled[4,5,14]. After PTZ injections, the seizure intensity was scored for 30 min using the following scale: Stage 0, no response; Stage 1, ear and facial twitching; Stage 2, myoclonic body jerks; Stage 3, clonic forelimb convulsions; Stage 4, generalized clonic convulsions, turn over on to side position; Stage 5, generalized clonic-tonic convulsions or died within 30 min. In addition, the latency to the onset of myoclonic jerks were measured and analyzed statistically. In the absence of seizures within 30 min, the latency was taken as 1800 s. When the rat had a seizure score of 4 or 5 at three consecutive injections, it was defined as fully kindled.

Measurements of brain histamine The rodents were killed by decapitation. The brain was quickly removed, and placed on an ice-cold stainless steel plate, and dissected according to the methods of Glowinski and Iversen[15]. These tissues were stored at -80 ℃ until assayed. The brain tissue was weighed and homogenized in 3% perchloric acid. The homogenate was centrifuged at 15 000×*g* for 20 min at 4 ℃ to obtain a clear supernatant. After filtration (0.22 μm), histamine was analyzed fluorometrically with *o*-phthaladehyde after separation on an HPLC system (CCP & 8010 series, Tosoh, Tokyo, Japan, particle size 5 μm). The fluorescence intensity was measured at 450 nm with excitation at 360 nm in a spectrofluorometer (model C-R3A, Shimadzu, Kyoto, Japan)[9,10].

Statistical analysis All data were expressed as mean± SEM. One-way analysis of variance with Dunnetts test was used for calculating a significant difference. Statistical significance was set at $P<0.05$.

Results

Effects of LH diet on seizure development induced by PTZ-kindling After 2 weeks on a LH diet, compared with BH, histamine levels significantly decreased in the cortex (23.2%), hippocampus (16.5%), and hypothalamus (43.7%) ($P<0.05$) (Figure 1). Rats fed with the LH diet for 2 weeks showed greatly enhanced development of PTZ-induced kindled seizures (Figure 2). They were fully kindled through less chemical stimuli compared with those fed with the BH diet. Rats fed with the LH diet and control rats fed with the BH diet became fully kindled at d 8 and d 14, respectively. In addition, rats fed with the LH exhibited more severe seizure stages than rats fed with the BH diet ($P<0.05$ for the first 8 d of PTZ injection). The latency to the onset of seizures was also significantly shorter in the LH group ($P<0.05$ for the first 3 d of PTZ injection).

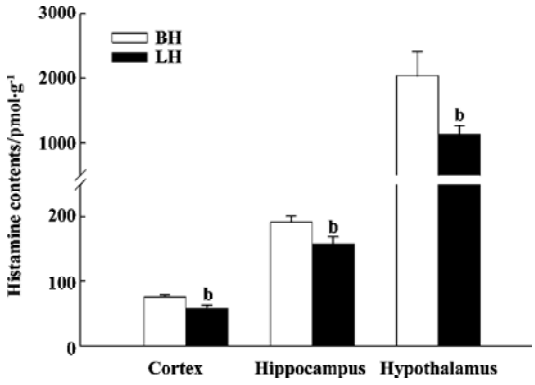

Figure 1. Changes of histamine levels in the brain of rats after 2 weeks on the LH diet. BH: basal histamine diets; LH: laohistamine diets. n=10–12. Mean±SEM. $^bP<0.05$ *vs* BH-fed group.

Correlation between the decrease in brain histamine levels and the increase in seizure stage after the first PTZ injection To investigate the relationship between the increase in seizure scores and the decrease in the histamine levels in the brain induced by the LH diet, the regression line of Y (decrease in histamine levels of the cortex, hippocampus, and hypothalamus) on X (increase in seizure scores) and the correlation coefficient (r) were calculated (Figure 3). The correlation coefficients of the cortex, hippocampus, and hypothalamus were 0.875, 0.651, and 0.796, respectively.

Effects of chronic kindled seizures on levels of histamine in the brain of rats Twenty-four hours after fully kindled, the rats were killed by decapitation. The histamine in the brain tissues was measured. Compared with control rats fed

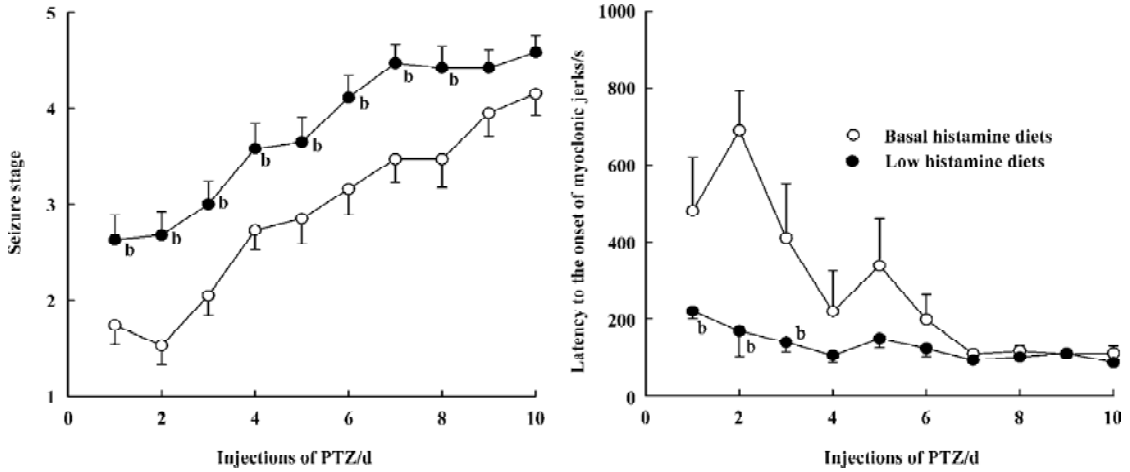

Figure 2. Effects of LH diet on seizure development induced by PTZ-kindling. n=15–16 rats. Mean±SEM. $^bP<0.05$ *vs* BH-fed group.

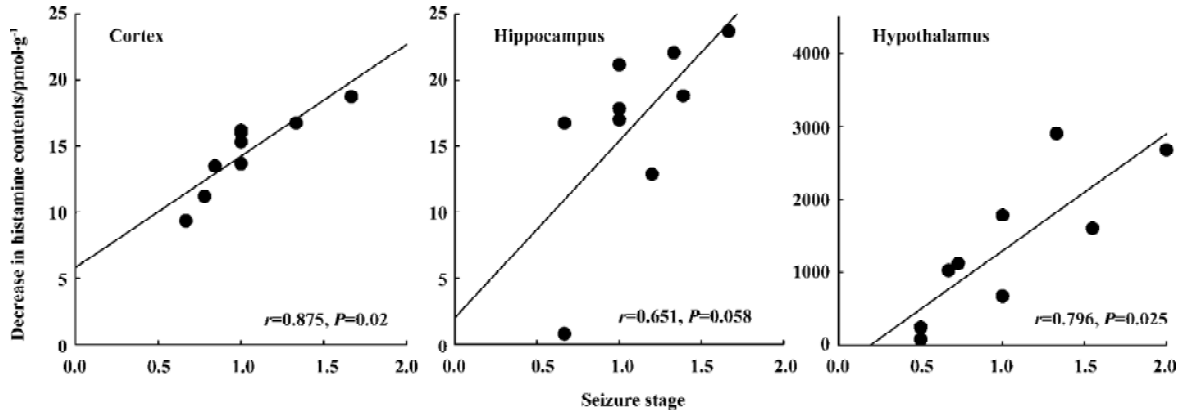

Figure 3. Correlation between the decrease in brain histamine levels and the increase in the scores of seizure stage after the first PTZ injection. n=9. Mean±SEM.

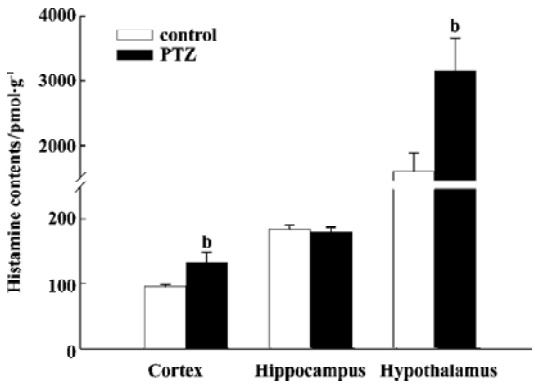

Figure 4. Effect of chronic PTZ administration on brain histamine levels in rats fed with the LH diet. n=10–11. Mean±SEM. $^bP<0.05$ *vs* the control group.

the LH diet without PTZ treatment, chronic PTZ kindled elicited significant increases in histamine levels both in the cortex (137.6%) and hypothalamus (195.7%), but not in the hippocampus (Figure 4).

Discussion

The interactions between histamine levels in food and normal physiological functions have recently excited interest[11,12]. This study provides the first evidence that dietary histamine affects the onset and development of seizures induced by chronic PTZ kindling in rats. Relative to BH diets, LH diets significantly augmented the onset of seizures induced by chronic PTZ-kindling, and further resulted in facilitation of subsequent PTZ kindling process. Meanwhile, significant decreases in histamine levels in the cortex,

hippocampus, and hypothalamus were observed following the 2-week LH diets. Interestingly, a strong correlation was found between decreased histamine levels in the cortex and hypothalamus and increased seizure scores following PTZ treatment. It is therefore likely that the reduced histamine plays an important role in the seizure susceptibility. We previously reported that α-fluoromethylhistidine, an inhibitor of HDC, accelerates seizure development induced by PTZ- kindling in rats[4].

The chronic kindled seizures markedly increased histamine levels in the cortex and hypothalamus in rats fed with the LH diet. It has been reported that increased histamine levels in the cortex and hypothalamus are induced by PTZ kindling seizures in H1R KO mice[9], and by maximal electroshock in mice[16]. However, the histamine levels significantly decrease in the amygdala of electrical stimulation site after the development of amygdaloid kindling[6,17,18] and in the cortex and hypothalamus following acute PTZ kindled seizure[16]. These differences might be due to variations in the experimental methods, the species used, drug dosages, or routes of administration. PTZ kindling is the animal model for human primary generalized (or absence) epilepsy. Our data at least suggest that the chronic development of this epileptic seizure is different from the acute one[16], and other epilepsy styles, such as temporal lobe epilepsy, generalized seizure, and so on[16,17]. At present, we have no explanation for why chronic kindling could increase histamine levels in rats fed with LH diets. Further experiments are needed to elucidate its mechanism. An increase in histamine levels in the cortex and hypothalamus might reflect a compensating and protective physiological mechanism after long-term low levels of histamine induced by LH diets. These results further support the concept of histamine as an endogenous anticonvulsant.

An interesting finding in the present study is that there was no significant changes of histamine levels in the hippocampus in the fully PTZ-kindled rats. This suggests that once it is fully kindled by PTZ, the type of seizure is less sensitive to histamine levels in the hippocampus, although it is well known that the hippocampus plays an important role in electrically kindled seizures[17,19,20]. Furthermore, we have also reported that PTZ-kindled is independent of the hippocampal *N*-methyl-*D*-aspartate receptor subunit 2B, which was strongly associated with amygdaloid kindled seizures in rats[9]. These results suggest that the different types of kindled seizures may be associated with region-dependent foci and circuits, and therefore results from different mechanisms. For example, Mirski *et al* found that separate neuronal circuits mediate PTZ and maximal electroshock seizures[21].

Therefore, the present study indicates that histamine in daily food can influence histaminergic function in the brain, and may play an important role in regulating human primary generalized (or absence) epilepsy. These findings further suggest that more attention should be paid to daily dietary containing low and high histamine, and their possible influence on seizure susceptibility of human primary generalized (or absence) epilepsy.

Acknowledgement

The authors thank Dr Iain C BRUCE for critically reading this paper.

References

1 Churchill JA, Gammon JD. The effect of antihistaminic drugs on convulsive seizures. J Am Med Assoc 1949; 141: 18–21.

2 Lintunen M, Sallmen T, Karlstedt K, Fukui H, Eriksson KS, Panula P. Postnatal expression of H1-receptor mRNA in the rat brain: correlation to *L*-histidine decarboxylase expression and local upregulation in limbic seizures. Eur J Neurosci 1998; 10: 2287–301.

3 Toyota H, Ito C, Yanai K, Sato M, Watanabe T. Histamine H1 receptor binding capacities in the amygdala of the amygdaloid kindled rat. J Neurochem 1999;72: 2177–80.

4 Zhang LS, Chen Z, Huang YW, Hu WW, Wei EQ, Yanai K. Effects of endogenous histamine on seizure development of pentylenetetrazole-induced kindling in rats. Pharmacology 2003; 69: 27–32.

5 Zhang LS, Chen Z, Ren KM, Leurs R, Chen JC, Zhang WB, *et al*. Effects of clobenpropit on pentylenetetrazole- kindled seizures in rats. Eur J Pharmacol 2003; 482: 169–75.

6 Kamei C, Ishizawa K, Kakinoki H, Fukunaga M. Histaminergic mechanisms in amygdaloid-kindled seizure in rats. Epilepsy Res 1998; 30: 187–94.

7 Scherkl R, Hashem A, Frey HH. Histamine formation in rat brain: its role in regulation of seizure susceptibility. Epilepsy Res 1991; 10: 111–8.

8 Iinuma K, Yokoyama H, Otsuki T, Yanai K, Watanabe T, Ido T, *et al*. Histamine H_1 receptors in complex partial seizure. Lancet 1993; 341: 238.

9 Chen Z, Li ZY, Sakurai E, Mobarakeh JI, Ohtsu H, Watanabe T, *et al*. Chemical kindling induced by pentylenetetrazol in histamine H_1 receptor gene knockout mice (H_1KO), histidine decarboxylase-deficient mice ($HDC^{-/-}$) and mast cell-deficient W/W^v mice. Brain Res 2003; 968: 162–6.

10 Yamatodani A, Fukuda H, Wada H, Iwaeda T, Watanabe T. High-performance liquid chromatographic determination of plasma and brain histamine without previous purification of biological samples: cation-exchange chromatography coupled with post-column derivatization fluorometry. J Chromatogr 1985; 344: 115–23.

11 Ohtsu H, Kuramasu A, Tanaka S, Terui T, Hirasawa N, Hara M, *et al*. Plasma extravasation induced by dietary supplemented histamine in histamine-free mice. Eur J Immunol 2002; 32: 1698–708.

12 Watanabe T, Yanai K. Studies on functional roles of the histaminergic neuron system by using pharmacological agents, knockout mice

and positron emission tomography. Tohoku J Exp Med 2001; 195: 197–217.
13 Morimoto K, Fahnestock M, Racine R J. Kindling and status epilepticus models of epilepsy: rewiring the brain. Prog Neurobiol 2004; 73: 1–60.
14 Chen Z, Li WD, Zhu LJ, Shen YJ, Wei EQ. Effects of histidine, a precursor of histamine, on pentylenetetrazole-induced seizures in rats. Acta Pharmacol Sin 2002; 23: 361–6.
15 Glowinski J, Iversen LL. Regional studies of catecholamines in the rat brain. I. The disposition of [^{3}H]norepinephrine, [^{3}H]dopamine and [^{3}H]dopa in various regions of the brain. J Neurochem 1966; 13: 655–69.
16 Vohora D, Pal SN, Pillai KK. Histamine and selective H3-receptor ligands: a possible role in the mechanism and management of epilepsy. Pharmacol Biochem Behav 2001; 68: 735–41.
17 Toyota H, Ito C, Ohsawa M, Sakurai E, Sato M, Watanabe T. Decreased central histamine in the amygdaloid kindling rats. Brain Res 1998; 802: 241–6.
18 Chen Z, Sakurai E, Hu WW, Jin CL, Kiso Y, Kato M, *et al*. Pharmacological effects of carcinine on histaminergic neurons in the brain. Br J Pharmacol 2004; 143: 573–80
19 Simonato M, Hosford DA, Labiner DM, Shin C, Mansbach HH, McNamara JO. Differential expression of immediate early genes in the hippocampus in the kindling model of epilepsy. Brain Res Mol Brain Res 1991; 11: 115–24.
20 Vaidya VA, Siuciak JA, Du F, Duman RS. Hippocampal mossy fiber sprouting induced by chronic electroconvulsive seizures. Neuroscience 1999; 89: 157–66.
21 Mirski MA, McKeon AC, Ferrendelli JA. Anterior thalamus and substantia nigra: two distinct structures mediating experimental generalized seizures. Brain Res 1986; 397: 377–80.

Acta Pharmacologica Sinica 2005 Apr; 26 (4): 428–434

Full-length article

Bradykinin potentiates 5-HT$_3$ receptor-mediated current in rat trigeminal ganglion neurons

Wang-ping HU[1,2], Xue-mei LI[2], Ji-liang WU[3], Min ZHENG[3], Zhi-wang LI[4]

[2]Department of Physiology, [3]Department of Pharmacology, Xianning College, Xianning 437100, China; [4]Department of Neurobiology, Tongji Medical College of Huazhong University of Science and Technology, Wuhan 430030, China

Key words

bradykinin; 5-HT3 serotonin receptor; regulation; patch-clamp techniques; trigeminal ganglion

[1] Correspondence to Prof Wang-ping HU.
Phn 86-715-826-0754.
Email huwangping@21cn.com

Received 2004-10-29
Accepted 2004-12-09

doi: 10.1111/j.1745-7254.2005.00074.x

Abstract

Aim: To explore the modulatory effect of bradykinin (BK) on 5-HT$_3$ receptor-mediated current in trigeminal ganglion (TG) neurons in rats. **Methods:** The whole-cell patch-clamp technique was used to record 5-HT-activated currents ($I_{5\text{-HT}}$) in neurons freshly dissociated from rat TG. Drugs were applied by rapid solution exchange. **Results:** The majority of the neurons examined responded to 5-HT applied externally with an inward current (76.3%, 74/97) that could be blocked by the 5-HT$_3$ receptor antagonist, ICS-205,930 (1×10^{-6} mol/L). In 66 of the 74 cells sensitive to 5-HT (89.2%), pretreatment for 30 s with BK (1×10^{-6}–1×10^{-10} mol/L) could potentiate $I_{5\text{-HT}}$ with the maximal modulatory effect occurring at 10^{-7} mol/L BK (71.6%±4.9%). BK shifted the 5-HT concentration-response curve upwards with an increase of 68.9%±7.2% in the maximal current response, but with no significant change in the EC_{50} value (19.1±3.2 μmol/L *vs* 20.9±3.5 μmol/L; *t*-test, $P>0.05$; $n=8$). BK potentiated $I_{5\text{-HT}}$ in a holding potential-independent manner and did not alter the reverse potential of $I_{5\text{-HT}}$. This BK-induced potentiation of $I_{5\text{-HT}}$ was almost completely blocked by Hoe 140 (5×10^{-7} mol/L), a selective B_2 BK receptor antagonist, and was removed after intracellular dialysis of GF-109203X (2 μmol/L), a selective protein kinase C (PKC) inhibitor, with the re-patch clamp. **Conclusion:** Pre-application of BK exerts an enhancing effect on $I_{5\text{-HT}}$ via a PKC-dependent pathway in rat TG neurons, which may explain the peripheral mechanism of pain and hyperalgesia caused by, for example, tissue damage and inflammation.

Introduction

Serotonin (5-HT), a major component of the inflammatory chemical milieu, is released from platelets, mast cells, or basophils that infiltrate an area of tissue damage[1]. Once released, 5-HT is free to interact with a number of molecularly distinct receptor subtypes, including the 5-HT$_3$ receptor expressed in primary afferent nociceptors[2,3], and is capable of evoking pain and hyperalgesia[4]. To date, receptors for 5-HT can be classified into seven types and can be further distinguished into at least 13 subtypes. Unlike all other known 5-HT receptor subtypes, which are G-protein coupled, the 5-HT$_3$ receptor is a member of the excitatory ligand-gated ion channel (LGIC) superfamily[5,6]. Researchers believe that 5-HT$_3$ receptors located on sensory nerve terminals are mainly responsible for 5-HT-induced pain and hyperalgesia, although other subtypes of 5-HT receptors are also involved[4,7–10]. Recently we have demonstrated the potentiation of 5-HT$_3$ receptor function by substance P and α-methyl-5-HT, an agonist of 5-HT$_2$ receptor, through a protein kinase C (PKC)-dependent pathway in primary sensory neurons[11,12].

Bradykinin (BK) is an inflammatory mediator that plays a pivotal role in pain and hyperalgesia by exciting nociceptors and sensitizing them through activation of PKC[13]. BK responses are mediated by BK receptors. There are two main types of BK receptors, B_1 and B_2. B_2 BK receptors are constitutively and abundantly expressed in primary sensory neu-

rons[14]. The B_2 BK receptor has been implicated in BK-induced nociceptor activities and nociceptive behaviors[15–17], and animals deficient in B_2 BK receptors show hypoalgesia and reduced inflammatory responses[18,19]. The cDNA of the B_2 BK receptor has already been cloned[20] and evidence for the contribution of the PKC pathway to the B_2 BK receptor-mediated algesic action of BK has accumulated[17,21]. Thus, it is highly possible that 5-HT_3 receptor function is also enhanced by BK through a PKC-dependent pathway. The present study aimed to explore whether the modulation of BK in 5-HT_3 receptor-mediated current could occur in trigeminal ganglion (TG) neurons.

Materials and methods

Isolation of TG neurons Spraque-Dawley rats, 2–3 weeks old, were anesthetized with ether and decapitated. The TG were removed and transferred immediately into Dulbecco's modified Eagle's medium (DMEM, Sigma, St Louis, MO, USA) at pH 7.4. After removal of the surrounding connective tissues the TG were minced with fine spring scissors and the ganglion fragments were placed in a flask containing 5 mL DMEM in which trypsin (type II-S, Sigma) 0.5 g/L, collagenase (type I-A, Sigma) 1.0 g/L, and DNase (type IV, Sigma) 0.1 g/L had been dissolved, and incubated at 35 °C in a shaking water bath for 30–35 min. Soybean trypsin inhibitor (type II-S, Sigma) 1.25 g/L was added to stop trypsin digestion. Dissociated neurons were placed into a 35 mm Petri dish and kept for at least another 30 min before electrophysiological recording. The neurons selected for the patch-clamp experiment measured 20–45 μm in diameter.

Electrophysiological recordings Whole-cell patch-clamp recordings were carried out at room temperature (22–24 ºC) using a whole-cell patch-clamp amplifier (CEZ-2400, Nihon Kohden, Tokyo, Japan). Pipettes were filled with internal solution containing (in mmol/L): KCl 140, $CaCl_2$ 1, $MgCl_2$ 2.5, HEPES 10, egtazic acid 11, and ATP 5; the pH was adjusted to 7.2 with KOH and the osmolarity was adjusted to 310 mOsm/L with sucrose. Cells were bathed in an external solution containing (in mmol/L): NaCl 150, KCl 5, $CaCl_2$ 2.5, $MgCl_2$ 2, HEPES 10, and *D*-glucose 10; the osmolarity was adjusted to 340 mOsm/L with sucrose and the pH was adjusted to 7.4 with NaOH. The resistance of the recording pipette was in the range of 2–5 MΩ. A small patch of membrane underneath the tip of the pipette was aspirated to form a gigaseal and then more negative pressure was applied to rupture it, thus establishing a whole-cell configuration. The adjustment of capacitance compensation and series resistance compensation was done before recording the membrane currents. The holding potential was set at -60 mV, unless otherwise indicated. Membrane currents were filtered at 10 kHz (-3 dB), and the data were stored and analyzed in a computer with data acquisition software and hardware systems (Huazhong University of Science and Technology, Wuhan, China) and recorded using a pen recorder (Nihon Kohden).

Drug application Drugs used in the experiments included: serotonin hydrochloride (5-HT, Sigma), bradykinin (BK, Sigma), 2-methyl-5-hydroxytryptamine maleate (Research Biochemicals Incorporated, Natick, MA, USA), ICS -205,930 (Research Biochemicals Incorporated), Hoe 140 (Sigma), and GF 109203X (Research Biochemicals Incorporated). All drugs except GF 109203X were dissolved in the external solution just prior to use and held in a linear array of fused silica tubes (od/id=500/200 μm) connected to a series of independent reservoirs. The distance from the tube mouth to the cell examined was approximately 100 μm. The application of each drug was driven by gravity and controlled by the corresponding valve, and rapid solution exchange could be achieved by shifting the tubes horizontally with a micromanipulator. Cells were constantly bathed in normal external solution flowing from one tube connected to a larger reservoir between drug applications. In a number of the experiments GF 109203X needed to be applied intracellularly and was dissolved in the internal solution.

Data analysis Data were statistically analyzed using Student's *t*-test or analysis of variance (ANOVA). Statistical analysis of the concentration-response data was carried out using the non-linear, curve-fitting program ALLFIT. Current values were expressed as mean±SEM.

Results

Current mediated by the 5-HT_3 receptor in rat TG neurons In our experiments neurons freshly isolated from rat TG were round or elliptic in shape under light microscopy. The majority of the cells examined responded to 5-HT applied externally with a concentration (1×10^{-3}–1×10^{-6} mol/L)-dependent inward current (76.3%, 74/97). This 5-HT-activated current ($I_{5\text{-HT}}$, 1×10^{-4} mol/L) could be mimicked by 2-methyl-5-HT (1×10^{-4} mol/L), a specific 5-HT_3 receptor agonist, and could be blocked by ICS-205,930 (1×10^{-6} mol/L), a selective antagonist of 5-HT_3 receptor, indicating that this current was mediated by the 5-HT_3 receptor (Figure 1A).

When 5-HT was applied regularly for 3-s durations with 3-min intervals, the $I_{5\text{-HT}}$ was repeated stably within at least 90 min, and the change in amplitude was within 8% (data not shown). Thus, we used this pattern of 5-HT applications in the following experiments.

Potentiation of $I_{5\text{-HT}}$ by pre-application of BK BK applied for 30 s prior to the application of 5-HT (1×10^{-4} mol/L)

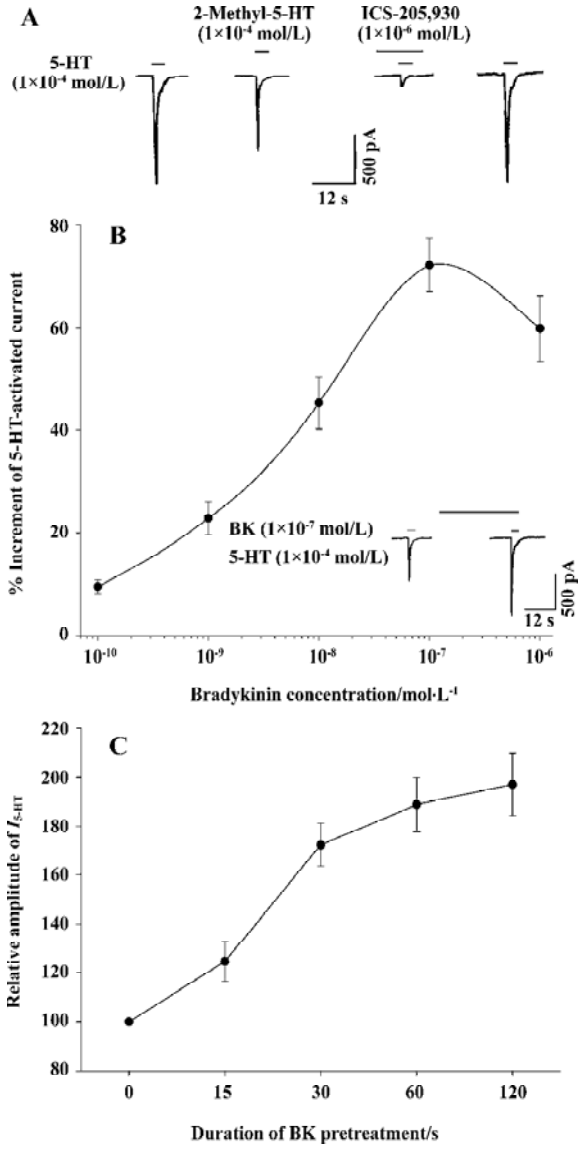

Figure 1. Potentiation of $I_{5\text{-HT}}$ by BK. (A) The current traces show that 5-HT (1×10^{-4} mol/L) activated an inward current in TG neurons, which could be mimicked by the application of 2-methyl-5-HT (1×10^{-4} mol/L), and blocked by ICS-205,930 (1×10^{-6} mol/L) (n=7). All current traces were recorded from the same neuron. (B) BK potentiated $I_{5\text{-HT}}$ in a concentration-dependent manner. The duration of BK pre-application lasted for 30 s. Each point represents the mean±SEM of 7–9 neurons. The current traces in the inset show that BK (1×10^{-7} mol/L) potentiated $I_{5\text{-HT}}$. (C) The enhancing effect of BK (1×10^{-7} mol/L) on $I_{5\text{-HT}}$ (1×10^{-4} mol/L) increased with increments in BK pre-application duration from 0 to 120 s (n=6–9).

potentiated $I_{5\text{-HT}}$ reversibly in the majority of the neurons examined (66/74, 89.2%). In 18 of the 74 (24.3%) cells sensitive to 5-HT there was also a response to BK with a very small inward or outward current (<150 pA), which showed slow desensitization (data not shown). The BK potentiation of $I_{5\text{-HT}}$ was observed irrespective of whether BK evoked an inward or outward current, or no response. The $I_{5\text{-HT}}$ was potentiated by the pre-application of BK (1×10^{-6}–1×10^{-10} mol/L) in a concentration-dependent manner. Figure 1B shows that with an increase in BK concentration from 1×10^{-10} to 1×10^{-6} mol/L, the amplitude of $I_{5\text{-HT}}$ (1×10^{-4} mol/L) increased stepwise until it reached its maximum at a concentration of 1×10^{-7} mol/L BK (71.6±4.9%). Thereafter this potentiating effect did not increase further, but rather decayed with further increases in BK concentration until 10^{-6} mol/L (Figure 1B).

Effect of the duration of BK pre-application on $I_{5\text{-HT}}$ To explore the relationship between the effect of BK on $I_{5\text{-HT}}$ and the duration of the pre-application of BK, different BK pre-application durations ranging from 15 to 120 s were tested. Figure 1C illustrates that the amplitude of $I_{5\text{-HT}}$ (1×10^{-4} mol/L) increased with increasing BK (1×10^{-7} mol/L) pre-application durations. With the duration of BK pre-application at 120 s, the amplitude of $I_{5\text{-HT}}$ increased (1.97±0.13)-fold compared with that of the control. However, there was no enhancing effect observed when 5-HT and BK were co-applied for 3 s (n=7; data not shown).

Effect of the B_2 BK receptor antagonist Hoe 140 on BK potentiation of $I_{5\text{-HT}}$ To verify whether the BK potentiation of $I_{5\text{-HT}}$ was mediated by the receptor for BK, we examined the effect of the pre-application of both BK and Hoe 140, a selective B_2 BK receptor antagonist, on $I_{5\text{-HT}}$. The pre-application of both BK and Hoe 140 abolished BK-induced potentiation of $I_{5\text{-HT}}$ significantly (Figure 2A,B, paired t-test, P<0.01, n=7).

Concentration-response relationship for 5-HT with and without BK pre-application Figure 3A demonstrates the concentration-response curves for 5-HT with or without the pre-application of BK (1×10^{-7} mol/L). The threshold concentrations of 5-HT in the two concentration-response curves for 5-HT with or without BK pre-application were similar at approximately 3×10^{-6} mol/L; and the EC_{50} values were also very similar (19.1±3.2 μmol/L and 20.9±3.5 μmol/L; t-test; P>0.05; n=8); whereas the maximal response induced by 5-HT with BK pre-application increased by 68.9%±7.2% of that without BK pre-application. The present results reveal that the concentration-response curve for 5-HT pretreated with BK shifts upwards compared with the curve for 5-HT alone.

Current-voltage (*I-V*) relationship for $I_{5\text{-HT}}$ with or without BK pre-application $I_{5\text{-HT}}$ (1×10^{-4} mol/L) with or without the pre-application of BK (1×10^{-7} mol/L) was recorded at different holding potentials. All current values from the same cell were normalized to the current response induced by

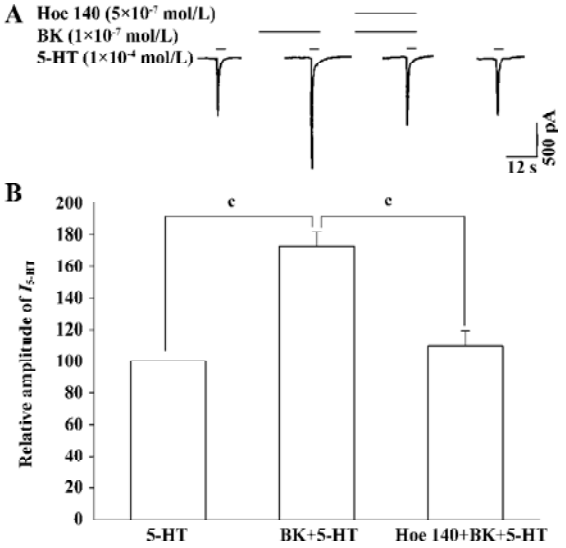

Figure 2. Blockade of BK-induced potentiation of $I_{5\text{-HT}}$ by the B_2 BK receptor antagonist Hoe 140. The current traces in (A) and the bar graph in (B) show that the potentiation of $I_{5\text{-HT}}$ by BK pre-applied alone was abolished by the co-application of BK and Hoe 140, a selective B_2 BK receptor antagonist (paired *t*-test, $^cP<0.01$ *vs* BK+5-HT).

5-HT alone at a holding potential of -60 mV when *I-V* curves were drawn (Figure 3B). The reverse potential values for the two curves were essentially the same at 0 mV. The amplitude of $I_{5\text{-HT}}$ with BK pre-application was greater than that without BK pre-application at all holding potentials from -80 to +40 mV, and the BK-induced alteration of $I_{5\text{-HT}}$ did not correlate with the change in holding potential (ANOVA; $P>0.05$, $n=8$), which suggests that the potentiation of $I_{5\text{-HT}}$ by BK occurs in a voltage-independent manner and the reverse potential of $I_{5\text{-HT}}$ is unchanged by BK.

Intracellular signal transduction mechanism underlying BK potentiation of $I_{5\text{-HT}}$ To explore whether this enhancing effect is mediated through BK-receptor-induced intracellular signal transduction, for example, activating PKC, GF-109203X, a selective PKC inhibitor[22], was included in the recording pipette for intracellular dialysis using the re-patch technique. In the control experiment with the pipette filled with normal internal solution, the BK-induced potentiation of $I_{5\text{-HT}}$ was 72.2%±5.2%. In contrast, when using a pipette filled with GF-109203X (2 μmol/L) containing internal solution the BK-induced potentiation of $I_{5\text{-HT}}$ was 13.5%±4.3%. It is evident that GF-109203X applied intracellularly removes the enhancing effect of BK on $I_{5\text{-HT}}$ (Figure 4).

Discussion

The 5-HT-activated current we recorded from TG neu-

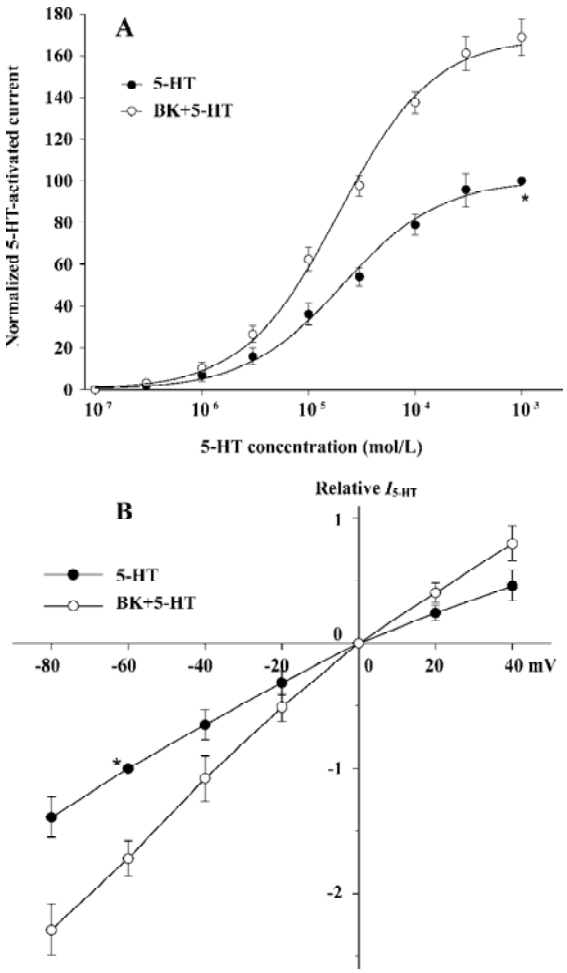

Figure 3. Concentration-response and current-voltage relationships for 5-HT with or without the pre-application of BK. (A) The concentration-response curves for 5-HT with or without BK (1×10^{-7} mol/L) pre-application, each point represents the mean±SEM of 7–11 neurons. All 5-HT-induced currents were normalized to the response induced by 10^{-4} mol/L 5-HT applied alone (marked with asterisk). The holding potential was set at -60 mV. The data for 5-HT alone is a good fit to the logistic equation $I=I_{max}/[1+(EC_{50}/C)^n]$, where C is the concentration of 5-HT, I is the normalized $I_{5\text{-HT}}$ value, and EC_{50} is the concentration of 5-HT for half maximal current response. The Hill coefficients (n) for the cases with and without BK pre-application were 0.98 and 0.96, respectively. It is evident that the curve for 5-HT with BK pre-application shifts upwards compared with the curve for 5-HT applied alone. (B) The *I-V* curves for 5-HT (1×10^{-4} mol/L)-activated current with or without BK (1×10^{-7} mol/L) pre-application. BK did not alter the reverse potential of $I_{5\text{-HT}}$ (0 mV in both cases). All current values from the same cell were normalized to the current response induced by 5-HT (1×10^{-4} mol/L) alone at the holding potential of -60 mV (marked with asterisk). BK pre-application potentiated $I_{5\text{-HT}}$ at all holding potentials from -80 to +40 mV. Each point represents the mean±SEM of 7–9 neurons. This experiment was carried out using recording pipettes filled with CsCl containing internal solution.

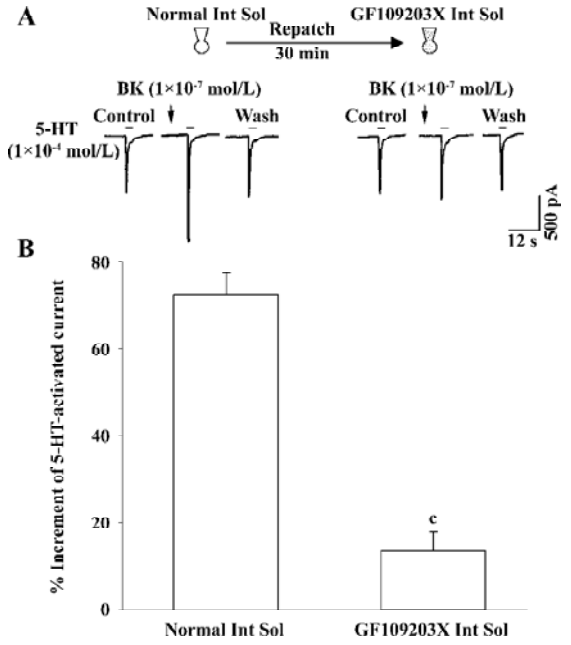

Figure 4. Reversal of the BK potentiation of $I_{5\text{-HT}}$ by intracellular dialysis of GF-109203X. The diagram in the upper row in (A) schematically shows the experiment of intracellular dialysis of GF-109203X, a selective PKC inhibitor, on an individual cell. The current traces in the lower row in (A) demonstrate that intracellular dialysis of GF-109203X (2 μmol/L) markedly reversed the potentiating effect of BK on $I_{5\text{-HT}}$. The bar graph in (B) shows the percentage increases in the $I_{5\text{-HT}}$ induced by BK pre-application with recording pipettes filled with the normal internal solution or with GF-109203X containing internal solution. n=7. Mean±SEM. (paired t-test, $^cP<0.01$ *vs* normal).

rons was mediated by the 5-HT_3 receptor, the sole ligand-gated ion channel (LGIC) in the family of 5-HT receptors, because it was blocked by ICS-205,930, a selective antagonist of the 5-HT_3 receptor (Figure 1A). There was evidence to indicate that 5-HT_3 receptors were present in rat TG neurons[23]. Similarly, B_2 BK receptors were also expressed in TG neurons[14]. In the present study we recorded both B_2 BK receptors and 5-HT_3 receptors in TG neurons, and in the majority of these neurons (89.2%, 66/74) the pre-application of BK (1×10^{-7} mol/L) potentiated $I_{5\text{-HT}}$ (1×10^{-3}–1×10^{-6} mol/L). This potentiation was mediated by B_2 BK receptors because the selective B_2 BK receptor antagonist Hoe 140 blocked this potentiating effect, obviously and reversibly (Figure 2). However, a previous study has reported that the inflammatory mediators BK, 5-HT, and prostaglandin E_2 do not cooperate to elevate intracellular calcium concentration when applied simultaneously for 10 s in cultured dorsal root ganglion neurons[24]. The distinction possibly results from different observation indices and specimens, or may be caused by the different treatment of BK. In the present experiment, there was also no enhancing effect observed when 5-HT and BK were co-applied for 3 s, whereas $I_{5\text{-HT}}$ was potentiated by the pre-application of BK for more than 15 s (Figure 1C).

It is evident from Figure 1B that the enhancement of amplitude of $I_{5\text{-HT}}$ increased gradually with incremental increases in the concentration of BK from 10^{-10} to 10^{-7} mol/L. However, when the concentration of BK increased to 10^{-6} mol/L the modulatory effect of BK on $I_{5\text{-HT}}$ did not increase further. The decrease in potentiation of $I_{5\text{-HT}}$ by BK (10^{-6} mol/L) might be a non-specific action of the agonist that emerges at high concentrations because very high concentrations of drug or ligand may block the channel and/or shelter the binding site of the receptor[25].

From the comparison between the concentration-response curves for 5-HT with and without the pre-application of BK (Figure 3A) it is clear that: (i) pre-application of BK shifted the curve upwards; (ii) the maximal response induced by 5-HT with BK pre-application increased by 68.9%, whereas the threshold concentrations of 5-HT in both cases were similar; and (iii) the EC_{50} values of the two curves were very close (19.1±3.2 μmol/L *vs* 20.9±3.5 μmol/L). This implies that the intrinsic efficacy of the 5-HT_3 receptor increases after pretreatment with BK; however, its affinity does not change.

From the *I-V* curves for $I_{5\text{-HT}}$ with and without BK pretreatment, it can be seen that the reverse potentials were the same (0 mV), indicating that there was no change in the ionic components mediating this current. This enhancement was not caused by the release of the channel blocker, as is the case in the voltage-dependent Mg^{2+} block of NMDA-gated ion channel, because the BK-induced alteration of $I_{5\text{-HT}}$ was not correlated with the change in holding potential (Figure 3B). This implies that the potentiation of $I_{5\text{-HT}}$ by BK occurs in a voltage-independent manner.

The potentiation of $I_{5\text{-HT}}$ by BK may involve intracellular signal transduction because there was no enhancing effect observed when 5-HT and BK were co-applied; nevertheless, BK applied prior to 5-HT application induced the enhancement of $I_{5\text{-HT}}$ and this effect was positively related to the duration of BK pretreatment, implying that this enhancement is a time-consuming process. Furthermore, this potentiation was blocked by Hoe 140, a selective B_2 BK receptor antagonist. B_2 BK receptors belong to the superfamily of G-protein-coupled receptors (GPCR)[20]. When activated by BK, the B_2 BK receptor is coupled to $PLC_{\beta1}$ via $G_{q/11}$ protein; which in turn catalyzes PIP_2 into secondary messengers, IP_3 and DAG. The latter activates PKC. Reports have shown

that 5-HT_3 receptor function is enhanced by the activation of PKC[26,27]. In the present experiment, the enhancing effect of BK on $I_{5\text{-}HT}$ was evidently blocked by intracellular dialysis of GF-109203X, a selective PKC inhibitor[22], indicating that potentiation occurs via a PKC-dependent pathway. How does PKC affect the function of 5-HT_3 receptors? Recently, a novel mechanism for 5-HT_3 receptor modulation by the activation of PKC was demonstrated[28]; that is, the PKC-induced potentiation of 5-HT_3 receptor mediated current in *Xenopus* oocytes and mouse NIE-115 neuroblastoma cells resulted from the enhancement of F-actin-dependent trafficking of 5-HT_3 receptors instead of direct phosphorylation of the 5-HT_{3A} receptor protein.

What is the physiological significance of this BK modulation on $I_{5\text{-}HT}$ or 5-HT_3 receptor function? In this work we used the cell body of TG neurons as a simple and accessible model to examine the characteristics of the membrane of peripheral terminals. The nerve endings of the peripheral axon of primary sensory neurons, including TG neurons, are sensitive to many inflammatory chemical mediators, of which BK and 5-HT are two potent stimulating mediators. In the case of inflammation and/or tissue damage these two substances are released. On the one hand, they exert a stimulating effect on the nerve endings and initiate nociceptive information through their corresponding receptors located on the membranes of separate nerve endings. On the other hand, in the present study we found that in the case of coexistence of B_2 BK receptors and 5-HT_3 receptors in TG neurons the inward current mediated by the 5-HT_3 receptor could be strengthened by pretreatment with BK, indicating that B_2 BK receptors and 5-HT_3 receptors may "cross-talk" in producing algesic information at nociceptors. Behavioral experiments have also demonstrated that 5-HT causes marked potentiation of BK-induced pain responses through 5-HT_3 receptors[29]. The present study may provide a hint for explaining the peripheral mechanism of pain and hyperalgesia caused by, for example, tissue damage and inflammation.

References

1 Dray A. Inflammatory mediators of pain. Br J Anaesth 1995; 75: 125–31.

2 Martin GR, Eglen RM, Hamblin MW, Hoyer D, Yocca F. The structure and signaling properties of 5-HT receptors: an endless diversity? Trends Pharmacol Sci 1998; 19: 2–4.

3 Hamon M, Bourgoin S. Serotonin and its receptors in pain control. In: Sawynok J, Cowan A, editors. Novel aspects of pain management: opioids and beyond. New York: Wiley; 1999. p 203–28.

4 Dock GJ, Sawynok J. Formalin-induced nociceptive behavior and edema: involvement of multiple peripheral 5-hydroxytryptamine receptor subtypes. Neuroscience 1997; 80: 939–49.

5 Maricq AV, Peterson AS, Brake AJ, Myers RM, Julius D. Primary structure and functional expression of the 5-HT_3 receptor, a serotonin-gated ion channel. Science 1991; 254: 432–7.

6 Davies PA, Pistis M, Harma MC, Peters JA, Lambert JJ, Hales TG, *et al*. The 5-HT_3B subunit is a major determinant of serotonin–receptor function. Nature 1999; 397: 359–63.

7 Orwin JM, Fozard JR. Blockade of the flare response to intradermal 5-hydroxytryptamine in man by MDL72222, a selective antagonist at neuronal 5-hydroxytryptamine receptors. Eur J Clin Pharmacol 1986; 30: 209–12.

8 Eschalier A, Kayser V, Guilbaud G. Influence of a specific 5-HT_3 antagonist on carrageenan-induced hyperalgesia in rats. Pain 1989; 36: 249–55.

9 Giordano J, Rogers LV. Perpherally administered serotonin 5-HT_3 receptor antagonists reduce inflammatory pain in the rats. Eur J Pharmacol 1989; 170: 83–6.

10 Zeitz KP, Guy N, Malmberg AB, Dirajlal S, Martin WJ, Sun L, *et al*. The 5-HT_3 subtype of serotonin receptor contributes to nociceptive processing via a novel subset of myelinated and unmyelinated nociceptors. J Neurosci 2002; 22: 1010–9.

11 Hu WP, You XH, Guan BC, Ru LQ, Chen JG, Li ZW. Substance P potentiates 5-HT_3 receptor mediated current in rat trigeminal ganglion neurons. Neurosci Lett 2004; 365: 147–52.

12 Hu WP, Guan BC, Ru LQ, Chen JG, Li ZW. Potentiation of 5-HT_3 receptor function by the activation of coexistent 5-HT_2 receptor in trigeminal ganglion neurons of rats. Neuropharmacology 2004; 47:833–40.

13 Sugiura T, Tominaga M, Katsuya H, Mizumura K. Bradykinin lowers the threshold temperature for heat activation of vanilloid receptor 1. J Neurophysiol 2002; 88: 544–8.

14 Steranka LR, Manning DC, DeHaas CJ, Ferkany JW, Borosky SA, Connor JR, *et al*. Bradykinin as a pain mediator: receptors are localized to sensory neurons, and antagonists have analgesic actions. Proc Natl Acad Sci USA 1988; 85: 3245–9.

15 Ferreira J, da Silva GL, Calixto JB. Contribution of vanilloid receptor to the overt nociception induced by B_2 kinin receptor activation in mice. Br J Pharmacol 2004; 141: 787–94.

16 Dray A, Perkins M. Bradykinin and inflammatory pain. Trends Neurosci 1993; 16: 99–104.

17 Mizumura K. Natural history of nociceptor sensitization: the search for a peripheral mechanism of hyperalgesia. Pain Rev 1998; 5: 59–82.

18 Boyce S, Rupniak NM, Carlson EJ, Webb J, Borkowski JA, Hess JF, *et al*. Nociception and inflammatory hyperalgesia in B_2 bradykinin receptor knockout mice. Immunopharmacology 1996; 33: 333–5.

19 Seabrook GR, Bowery BJ, Heavens R, Brown N, Ford H, Sirinathsinghi DJ, *et al*. Expression of B_1 and B_2 bradykinin receptor mRNA and their functional roles in sympathetic ganglia and sensory dorsal root ganglia neurons from wild-type and B_2 receptor knockout mice. Neuropharmacology 1997; 36: 1009–17.

20 Ma JX, Wang DZ, Chao L, Chao J. Cloning, sequence analysis and expression of the gene encoding the mouse bradykinin B_2 receptor. Gene 1994; 149: 283–8.

21 Cesare P, Dekker LV, Sardini A, Parker PJ, McNaughton PA. Specific involvement of PKC-epsilon in sensitization of the neuronal response to painful heat. Neuron 1999; 23: 617–24.

22 Toullec D, Pianetti P, Coste H, Bellevergue P, Grand-Perret T, Ajakane M, *et al*. The bisindolylmaleimide GF 109203X is a potent and selective inhibitor of protein kinase C. J Biol Chem 1991; 266: 15771–81.
23 Zhu M, Wu SX, Wang W, Li YQ. Expression of 5-HT receptor subtype mRNAs in the rat trigeminal and spinal dorsal root ganglia: a polymerase chain reaction study. Chin J Neuroanat 2000; 16: 107–12.
24 Linhart O, Obreja O, Kress M. The inflammatory mediators serotonin, prostaglandin E2 and bradykinin evoke calcium influx in rat sensory neurons. Neuroscience 2003; 118: 69–74.
25 Arias HR. Binding sites for exogenous and endogenous non-competitive inhibitors of the nicotinic acetylcholine receptor. Biochim Biophys Acta 1998; 1376: 173–220.
26 Coultrap SJ, Machu TK. Enhancement of 5-hydroxytryptamine$_{3A}$ receptor function by phorbol 12-myristate, 13-acetate is mediated by protein kinase C and tyrosine kinase activity. Receptor Channels 2002; 8: 63–70.
27 Zhang L, Oz M, Weight FF. Potentiation of 5-HT$_3$ receptor-mediated responses by protein kinase C activation. Neuroreport 1995; 6: 1464–8.
28 Sun H, Hu XQ, Moradel EM, Weight FF, Zhang L. Modulation of 5-HT$_3$ receptor-mediated response and trafficking by activation of protein kinase C. J Biol Chem 2003; 278: 34150–7.
29 Richardson BP, Engel G, Donatsch P, Stadler PA. Identification of serotonin M-receptor subtypes and their specific blockade by a new class of drugs. Nature 1985; 316: 126–31.

Acta Pharmacologica Sinica 2005 Apr; 26 (4): 435–440

Full-length article

ONO-1078 reduces NMDA-induced brain injury and vascular cell adhesion molecule-1 expression in rats[1]

Li-hui ZHANG[2,3], Er-qing WEI[2,4]

[2]Department of Pharmacology, School of Medicine, Zhejiang University, Hangzhou 310031; [3]Medical School, Hangzhou Normal University, Hangzhou 310018, China

Key words

leukotriene antagonists; pranlukast; *N*-methylaspartate; vascular cell adhesion molecule-1; neurotoxicity; brain injuries

[1] Project supported by the National Natural Science Foundation of China (No 30271498).
[4] Correspondence to Prof Er-qing WEI.
Phn 86-571-8721-7391.
Fax 86-571-8721-7044.
E-mail weieq2001@yahoo.com

Received 2004-08-09
Accepted 2004-11-10

doi: 10.1111/j.1745-7254.2005.00063.x

Abstract

Aim: To determine whether ONO-1078 (pranlukast), a potent cysteinyl leukotriene receptor 1 ($CysLT_1$) antagonist, has an effect on *N*-methyl-*D*-aspartate (NMDA)-induced brain injury and vascular cell adhesion molecule-1 (VCAM-1) expression in rats. **Methods:** Brain injury was induced by direct microinjection of NMDA (0.3 μmol in 1 μL of sterile 0.1 mol/L PBS, pH 7.4) into the cerebral cortex. The lesion volume (area), brain edema and neuron density were assessed by an image analyzer and the expression of VCAM-1 in the cortex was detected by Western blot 24 h after NMDA injection. ONO-1078 (0.03, 0.1, or 0.3 mg/kg) and edaravone (MCI-186, 10 mg/kg), a neuroprotective agent, were ip injected 30 min before and after NMDA injection. **Results:** NMDA microinjection produced well-defined focal lesions (Figure 1) dose- and time-dependently. ONO-1078 (0.1, 0.3 mg/kg) and edaravone (10 mg/kg) decreased the total lesion volume, lesion area and brain edema induced by NMDA. Furthermore, ONO-1078 (0.1, 0.3 mg/kg) significantly inhibited the enhanced expression of VCAM-1 in the injured cortices, but edaravone did not have this effect. **Conclusion:** $CysLT_1$ receptor antagonist ONO-1078 attenuates NMDA-induced brain damage in rats, and this might relate to the attenuation of NMDA receptor-dependent neurotoxicity and the inhibition of the upregulation of VCAM-1 expression.

Introduction

It is well known that *N*-methyl-*D*-aspartate (NMDA) receptors play a critical role in the initiation of cerebral ischemic injury[1]. The excitotoxicity mediated by NMDA receptors contributes to the damage that occurs in the early stages (min to h), and inflammation and programmed cell death in the late stages (h to weeks) of cerebral ischemia[1,2]. Among many factors involved in inflammation, adhesion molecules, including vascular cell adhesion molecule 1 (VCAM-1), can modulate ischemic injury in the brain[3,4]. However, cysteinyl leukotrienes (CysLTs, including LTC_4, LTD_4, and LTE_4), 5-lipoxygenase (5-LOX) metabolites of arachidonic acid, are potent inflammatory mediators[5] that are also involved in pathogenic processes of cerebral ischemia. CysLT levels were elevated after global and focal cerebral ischemia and 5-lipoxygenase inhibitor attenuated CysLT production and ischemic brain injury[6–8]. Furthermore, we have previously found that ONO-1078 {pranlukast, 4-*oxo*-8-[*p*-(4-phenylbutyloxy)benzoyl-amono]-2-(tetrazol-5-yl)-4H-1-benzopyran hemihydrate}, a $CysLT_1$ receptor antagonist, protects rats and mice against focal cerebral ischemic injury[9,10].

Recently, we reported that global cerebral ischemia induces brain injury and time-dependently increases the expressions of NMDA receptor subunit proteins and VCAM-1 in different regions of the brain in rats[11]. We also found that ONO-1078 attenuates ischemic injury and inhibits the increased expressions of NMDA receptor subunit NR2A and VCAM-1[12]. However, whether ONO-1078 protects rats from chemically induced injury, and if NMDA receptor activation directly links to the increased VCAM-1 expression, remains unknown. Thus, in the present study, we induced cortical injury by NMDA microinjection to evaluate the

protective effect of ONO-1078. Also, we observed VCAM-1 expression after NMDA receptor activation and the influence of ONO-1078. Edaravone (MCI-186, 3-methyl-1-phenyl-2- pyrazolin-5-one), a novel neuroprotective agent for ischemic stroke[13,14], was used as a control drug.

Materials and methods

Drugs and reagents NMDA was purchased from Sigma (St Louis, MO, USA); ONO-1078 was provided by Dr Masami TSUBOSHIMA (Ono Pharmaceutical Co, Osaka, Japan). This compound was dissolved in 100% ethanol (10 g/L), and freshly diluted with saline before use. Edaravone injection was obtained from Hangzhou Conba Pharmaceutical Co; polyclonal goat antibody against VCAM-1 from Santa Cruz, CA, USA; rabbit anti-goat IgG-HRP was obtained from Zhong-Shan Biotech Co, Beijing; enhanced chemiluminescence (ECL) reagent was obtained from Renaissance, New England Nuclear-Dupont. Other reagents were commercial products with analytic purity.

NMDA microinjection in neocortex Male Sprague-Dawley rats weighting 250–300 g were from the Experimental Animal Center of Zhejiang Academy of Medical Sciences (Grade II, Certificate No 2001001). Rats were housed in groups of 4 per cage at a constant temperature (25 ºC) and allowed free access to laboratory chow and water. In chloral hydrate-anesthetized (350 mg/kg, ip) rats, the dura overlying the parietal cortex was exposed, and a microinjector was inserted into the parietal cortex at a site 3.0 mm caudal to bregma, 5.0 mm from the midline, and 1.5 mm below the dural surface. NMDA (0.1, 0.2, and 0.3 μmol in 1 μL of sterile 0.1 mol/L PBS, pH 7.4) or 0.1 mol/L PBS alone (control) was injected according to the method described by Iadecola *et al*[15]. The microinjector was left in place for 10 min, to minimize the back-flux of NMDA, and then removed.

After these procedures, the incisions were closed and rats were returned to their cages. ONO-1078 (0.03, 0.1, and 0. 3 mg/kg), edaravone (10 mg/kg) or the same volumes of saline were ip injected 30 min before and after NMDA injection.

Evaluation of tissue injury Twenty-four hours after NMDA microinjection, the rats were anesthetized with chloral hydrate again and decapitated. Brains were removed immediately and sectioned coronally into 6 slices (2 mm-thick). Brain slices were stained in 0.5% 2,3,5-triphenyl tetrzolium chloride at 37 ºC for 30 min, followed by fixation with 10% formalin, overnight. All the brain slices were photographed using a CCD camera (MV-CP-230, Panasonic, Japan) on an anatomy microscope (XTL 2600, Shanghai, China). The volume and area of NMDA-injured cortex were measured by an image analyzer (AnalyPower1.0, Zhejiang University, Hangzhou, China).

Histopathological assessment Under chloral hydrate anesthesia, the rats were infused with 100 mL of heparinized saline followed by 300 mL of 10% formalin, before being decapitated. Brains were removed and fixed in 10% formalin for 7 d; paraffin sections (5 μm) were then cut and stained with hematoxylin and eosin. The densities of survival neurons in the cortex were counted using the image analyzer (AnalyPower1.0, Zhejiang University, Hangzhou, China).

Western blot analysis Western blot analysis was performed as described by Kang *et al*[16]. The injured and contralateral cortices were dissected and homogenized in buffer A (10 mmol/L Tris-HCl, pH 7.4, containing 320 mmol/L sucrose). The homogenate was centrifugated at 700×*g* for 10 min at 4 ºC, and the supernatant was further centrifuged at 37 000×*g* for 40 min at 4 ºC. The resultant pellet was resuspended in buffer B (10 mmol/L Tris-HCl, pH 7.4), and protein concentration was determined by the Lowry method.

The protein samples of 7.5 μg were separated by 7.5% SDS-PAGE and transferred to a nitrocellulose membrane in transfer buffer (Tris 25 mmol/L, glycine 192 mmol/L, 20% methanol, 0.05% SDS, pH 8.3). The nonspecific binding was blocked in 5% fat-free dry milk in TBST (Tris-HCl 20 mmol/L, NaCl 140 mmol/L, 0.1% Tween-20, pH 7.4) for 30 min at room temperature. The membrane was incubated with polyclonal goat antibody against VCAM-1 (1:500) overnight at 4 ºC. After washing with TBTS, the membrane was then incubated with HRP-conjugated rabbit anti-goat IgG (1:2000) for 2 h at room temperature followed by repeated washing with TBST. At the end, the membrane was incubated in enhanced chemiluminescence (ECL) solution for 1 min and then exposed to X-ray film. The protein bands on an X-ray film were scanned by a GS-800 Laser Densitometer (Bio-Rad, USA) and analyzed by Met Imaging Series 5.0 (Bio-Rad, USA). As a standard, a protein sample from normal rat brains was used and the relative expression of VCAM-1 was calculated as the ratio of tested/standard sample densities.

Statistical analysis Data were reported as mean±SD. Statistical evaluation was carried out by the independent-sample *t*-test or one-way ANOVA (SPSS 11.0 for Windows, SPSS Inc, USA), according to the experimental design. $P<0.05$ was considered statistically significant.

Results

NMDA-induced injury *in vivo* NMDA microinjection produced well-defined focal lesions (Figure 1) dose- and time-dependently in TTC-stained brain slices. The lesion volumes induced by NMDA 0.3 μmol (32.4±10.7, n=5) were

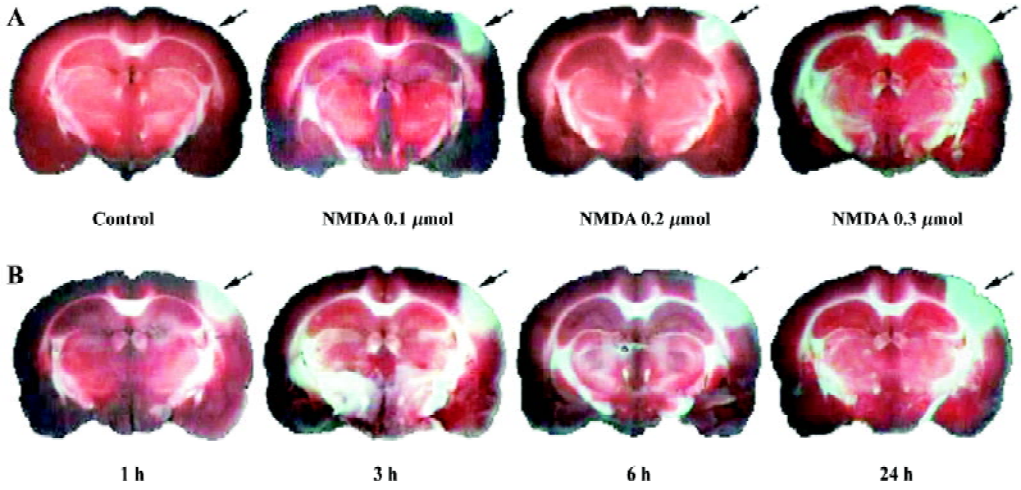

Figure 1. TTC-stained brain slices after direct microinjection of NMDA into the cerebral cortex in rats. A: brain slices 24 h after NMDA microinjection with various dose; B: brain slices 1–24 h after NMDA microinjection (0.3 μmol). Arrowheads show the injection sites.

significantly larger than those by 0.1 and 0.2 μmol (11.1±5.5 and 15.6±7.6, n=5, P<0.01, respectively) 24 h after NMDA injection. The lesion volumes at 24 h after NMDA (0.3 μmol) microinjection (35.4±7.0, n=4) were larger than those at 1, 3, or 6 h after injection (21.8±8.0, 25.1±8.8, or 30.7±9.2, respectively, n=4, P<0.05).

Histopathological changes in the lesion regions 24 h after NMDA (0.3 μmol) injection were characterized by neuronal damage with eosinophilic cytoplasm and serious pyknotic nucleus, and survival neuron decreased markedly in the injured cortices; however, no cell damage was observed in the contralateral cortices or in PBS-injected control cortices (Figure 2).

Effects of ONO-1078 and edaravone on NMDA-induced injury ONO-1078 at 0.1 and 0.3 mg/kg significantly reduced the lesion volume (P<0.05 or P<0.01, Table 1) and the lesion

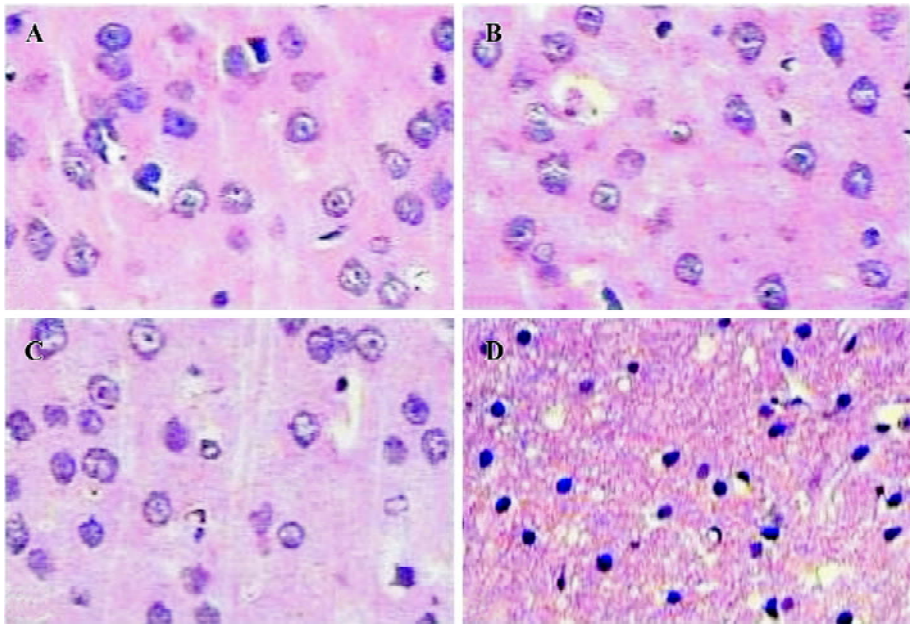

Figure 2. Histopathologic changes 24 h after direct microinjection of PBS (control) or NMDA into the cerebral cortex in rats. A: contralateral cortex of control rat; B: PBS-injected cortex of control rat; C: contralateral cortex of NMDA-injected rat; D: NMDA (0.3 μmol)-injected cortex. (HE staining, ×250).

areas in individual 2 mm-thick consecutive slices (P<0.05 or P<0.01, Table 2), and the enlargement of injected cortices (indicated as I/C ratio) at 0.1 mg/kg (P<0.05, Table 1). The survival neuron densities in NMDA-injured regions showed a tendency to increase in the rats treated with ONO-1078, but no significant difference was found among these groups (P>0.05, Table 1). Edaravone (10 mg/kg) exhibited a similar effect to ONO-1078 (Tables 1, 2).

Effects of ONO-1078 and edaravone on VCAM-1 expression in NMDA-injected cortex To assess the relation between the protection of ONO-1078 and the expression of inflammatory adhesion molecule VCAM-1, we detected the local expression of VCAM-1 in contralateral and injured cortices 24 h after NMDA injection. VCAM-1 level did not remarkable change among the groups in the contralateral cortices without damage. In the injured cortices, however, VCAM-1 expression was up-regulated. ONO-1078 (0.1 and 0.3 mg/kg) significantly inhibited the increased VCAM-1 expression (P<0.05 or P<0.01), however, edaravone did not show a significant effect (P>0.05, Figure 3).

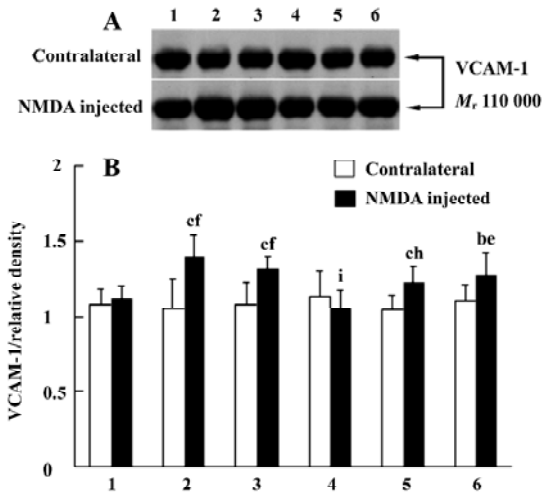

Figure 3. Effects of ONO-1078 and edaravone on VCAM-1 expression in rat cerebral cortex 24 h after NMDA microinjection. A: Western blot results; B: statistical analysis of VCAM-1 expression. 1: control rats with PBS-injected; 2: saline-treated rats with NMDA-injected; 3: ONO-1078 0.03 mg/kg; 4: ONO-1078 0.1 mg/kg; 5: ONO-1078 0.3 mg/kg; 6: edaravone 10.0 mg/kg. n=6–8. Mean±SD. ^{b}P<0.05, ^{c}P<0.01 *vs* contralateral. ^{e}P<0.05, ^{f}P<0.01 *vs* control. ^{h}P<0.05, ^{i}P<0.01 *vs* saline.

Table 1. Effects of ONO-1078 and edaravone on the lesion volume, the ratio of I/C cortex area and viable neuron counts (10^3 cells per mm^2) in cerebral cortex 24 h after NMDA microinjection in rats. Mean±SD. ^{c}P<0.01 *vs* control. ^{e}P<0.05, ^{f}P<0.01 *vs* saline. ^{i}P<0.01 *vs* contralateral cortices. I: NMDA injected, C: contralateral.

Drug/mg·kg^{-1}	n	Lesion volume (mm^3)	Ratio of I/C cortex area	Neuron densities in cortex	
				Contralateral	NMDA injected
Control	6	0±0	0.99±0.04	0.68±0.07	0.65±0.07
Saline	8	35.75±10.36^{c}	1.15±0.08^{c}	0.63±0.11	0.14±0.04^{c,i}
ONO-1078 0.03	8	29.92±12.26	1.12±0.09	0.64±0.12	0.15±0.04^{i}
0.1	8	21.12±7.10^{f}	1.05±0.06^{e}	0.66±0.07	0.19±0.07^{i}
0.3	8	23.74±10.76^{e}	1.08±0.06	0.65±0.10	0.18±0.06^{i}
Edaravone 10.0	8	21.46±7.57^{f}	1.06±0.07^{e}	0.64±0.10	0.17±0.05^{i}

Table 2. Effects of ONO-1078 and edaravone on lesion area in 2 mm-thick consecutive brain slices 24 h after NMDA microinjection in rats. Mean±SD. ^{b}P<0.05, ^{c}P<0.01 *vs* saline.

Drug/mg·kg^{-1}	n	Lesion area (mm^2)/slice number			
		3	4	5	6
Control	6	0±0	0±0	0±0	0±0
Saline	8	1.93±3.50	11.61±2.48	4.16±4.90	0.19±0.52
ONO-1078 0.03	8	3.23±2.75	9.87±1.67	1.87±3.15	0±0
0.1	8	0±0	7.86±2.04^{c}	2.70±1.98	0±0
0.3	8	0.83±2.35	8.53±1.82^{b}	2.52±2.25	0±0
Edaravone 10.0	8	1.64±3.19	7.80±1.94^{c}	1.30±2.02	0±0

Discussion

The findings in the present study show that NMDA microinjection produces serious neocortical damage and a $CysLT_1$ receptor antagonist ONO-1078 possessed protective effect on NMDA-induced brain injury. This effect of ONO-1078 on chemically-induced brain injury is consistent with its protective effect on brain ischemic injuries discussed in our previous studies[12]. Furthermore, the results of the present study indicates that NMDA microinjection up-regulates the local expression of VCAM-1, and ONO-1078 inhibits the enhanced VCAM-1 expression in the injured cortices.

The excessive release of excitory amino acids and activation of NMDA receptor are important events in cerebral ischemia and other brain injuries. NMDA receptor activation has been reported to be related to CysLT production in focal cerebral ischemia because NMDA receptor antagonist MK 801 reduces both CysLT production and ischemic injury[17]. Also, LTC_4 synthesis inhibitor azelastine protects cultured hippocampal slices from hypoxic or NMDA-induced injury *in vitro*[18]. Therefore, the protective effect of ONO-1078 in this study might be via antagonizing the actions of resultant CysLTs after NMDA receptor activation.

However, the increased VCAM-1 expression by NMDA injection suggests a possibility that excitotoxicity might initiate inflammation in the brain. It has been reported that NMDA receptor activation can up-regulate the expression of inflammatory cytokines, such as TNF-α and MCP-1[19,20], and induce neuronal signal transduction-associated adhesion molecules, such as PSA-NCAM and NCAM-180[21,22]. Our results further confirmed that NMDA increases the expression of inflammatory adhesion molecule VCAM-1. Evidence has shown the involvement of VCAM-1 in cerebral ischemic injury and inflammation. Serum level of soluble VCAM-1 increased in patients with ischemic stroke, at its peak 5 d after ischemia[4]. VCAM-1 expression also increased in astrocytes and endothelial cells from the infarcted brain areas in patients who died of acute ischaemic stroke[23], and in cultured human cerebromicrovascular endothelial cells after being subjected to ischemia-like insults or inflammatory cytokinins (IL-1 and TNF-α)[24]. VCAM-1 promotes intracerebral inflammation by affecting leukocyte rolling, adhesion[25] or earlier steps of interaction between inflammatory cells (such as T lymphocytes) and microvascular endothelial cells[26]. Furthermore, we found that ONO-1078 inhibits NMDA-increased VCAM-1 expression. In other reported studies, CysLTs only slightly augmented VCAM-1 expression in human umbilical vein endothelial cells[27]; $CysLT_1$ receptor antagonist ONO-1078[16, 28] and montelukast[29] suppressed VCAM-1 expression in the lung after allergen challenge. Based on these findings, we hypothesized that NMDA receptor activation induces CysLT production, CysLTs activate their receptors followed by VCAM-1 expression. This might partially explain our previous results that ONO-1078 reduces VCAM-1 expression in rat global ischemia[12].

As a control drug used in this study, edaravone protected NMDA-induced injury but did not reduce VCAM-1 expression compared with ONO-1078. Edaravone is a scavenger reacting with hydroxyl radical (OH)[30] and might act on the signal pathways other than those of ONO-1078. In cultured human dermal microvascular endothelial cells, antioxidants show different actions on TNF-α-induced expressions of VCAM-1, ICAM-1 and E-selectin: pyrrolidine dithiocarbamate had inhibiting effects, but N-acetylcysteine did not[31]. In our previous study of rat global ischemia, edaravone also did not significantly inhibit VCAM-1 expression[12]. Its neuroprotective effect might be mediated by other actions, such as inhibition of mitochondrial permeability transition pore, upregulation of Bcl-2[32], normalization of irradiation-reduced endothelial nitric oxide synthase expression[33], and protection against hypoxia/ischemia-induced endoplasmic reticulum dysfunction[34].

In the present study, we found that ONO-1078 reduced NMDA-induced lesion size, but did not increase survival neurons in the lesion, suggesting incomplete protection. We have not yet explained the details of NMDA receptor activation in CysLTs production, VCAM-1 expression and brain injury, however, the results of the present study indicate that $CysLT_1$ receptor antagonist ONO-1078 inhibits NMDA-induced brain injury and pro-inflammatory VCAM-1 expression, supplying further evidence for its neuroprotective effect on ischemic brain injury.

Acknowledgment

We thank Dr Masami TSUBOSHIMA of Ono Pharmaceutical Co Ltd, Osaka, Japan, for providing us with ONO-1078.

References

1 Lee JM, Zipfel GJ, Choi DW. The changing landscape of ischaemic brain injury mechanisms. Nature 1999; 399: A7–14.

2 Dirnagl U, Simon RP, Hallenbeck JM. Ischemic tolerance and endogenous neuroprotection. Trends Neurosci 2003; 26: 248–54.

3 Zaremba J, Losy J. Adhesion molecules of immunoglobulin gene superfamily in stroke. Folia Morphol (Warsz) 2002; 61: 1–6.

4 Bitsch A, Klene W, Murtada L, Prange H, Rieckmann P. A longitudinal prospective study of soluble adhesion molecules in acute stroke. Stroke 1998; 29: 2129–35.

5 Stewart LR, White AR, Jobling MF, Needham BE, Maher F, Thyer J, *et al*. Involvement of the 5-lipoxygenase pathway in the neurotoxicity of the prion peptide PrP106–126. J Neurosci Res 2001; 65: 565–72.

6 Rao AM, Hatcher JF, Kindy MS, Dempsey RJ. Arachidonic acid and leukotriene C_4: role in transient cerebral ischemia of gerbils. Neurochem Res 1999; 24: 1225–32.

7 Shishido Y, Furushiro M, Hashimoto S, Yokokura T. Effect of nordihydroguaiaretic acid on behavioral impairment and neuronal cell death after forebrain ischemia. Pharmacol Biochem Behav 2001; 69: 469–74.

8 Baskaya MK, Hu Y, Donaldson D, Maley M, Rao AM, Prasad MR, *et al*. Protective effect of the 5-lipoxygenase inhibitor AA-861 on cerebral edema after transient ischemia. J Neurosurg 1996; 85: 112-6.

9 Zhang WP, Wei EQ, Mei RH, Zhu CY, Zhao MH. Neuroprotective effect of ONO-1078, a leukotriene receptor antagonist, on focal cerebral ischemia in rats. Acta Pharmacol Sin 2002; 23: 871–7.

10 Zeng LH, Zhang WP, Wang RD, Wang LP, Wei EQ. Protective effect of ONO-1078, a leukotriene antagonist, on focal cerebral ischemia in mice. Acta Pharm Sin 2001; 36: 148–50.

11 Zhang LH, Wei EQ. Time course of brain damage and expression of related molecules in rats with transient global cerebral ischemia. J Zhejiang Univ Med Sci 2002; 31: 77–80.

12 Zhang LH, Wei EQ. Neuroprotective effect of ONO-1078, a leukotriene receptor antagonist, on transient global cerebral ischemia in rats. Acta Pharmacol Sin 2003; 24: 1241–7.

13 Toyoda K, Fujii K, Kamouchi M, Nakane H, Arihiro S, Okada Y, *et al*. Free radical scavenger, edaravone, in stroke with internal carotid artery occlusion. Neurol Sci 2004; 221: 11–7.

14 Yasuoka N, Nakajima W, Ishida A, Takada G. Neuroprotection of edaravone on hypoxic-ischemic brain injury in neonatal rats. Dev Brain Res 2004; 151: 129–39.

15 Iadecola C, Niwa K, Nogawa S, Zhao X, Nagayama M, Araki E, *et al*. Reduced susceptibility to ischemic brain injury and *N*-methyl-*D*-aspartate-mediated neurotoxicity in cyclooxygenase-2-deficient mice. Proc Natl Acad Sci USA 2001; 98: 1294–9.

16 Kang H, Wei EQ, Yang XH, Zhang WP, Shen JZ. VCAM-1 expression, eosinophil infiltration, and pharmacological modulation in rat allergic airway inflammation. Acta Pharmacol Sin 2002; 23: 157–61.

17 Ciceri P, Rabuffetti M, Monopoli A, Nicosia S. Production of leukotrienes in a model of focal cerebral ischaemia in the rat. Br J Pharmacol 2001; 133: 1323–9.

18 Wallis RA, Panizzon KL. Protection from hypoxic and *N*-methyl-*D*-aspartate injury with azelastine, a leukotriene inhibitor. Eur J Pharmacol 1993; 238: 165–71.

19 Block F, Loos M, Frohn C, Schwarz M. Association between inflammation and nigral neuronal damage following striatal excitotoxic lesion. Brain Res 2004; 998: 29–35.

20 Katayama T, Minami M, Nakamura M, Ito M, Katsuki H, Akaike A, *et al*. Excitotoxic injury induces production of monocyte chemoat-tractant protein-1 in rat cortico-striatal slice cultures. Neurosci Lett 2002; 328: 277–80.

21 Bouzioukh F, Tell F, Jean A, Rougon G. NMDA receptor and nitric oxide synthase activation regulate polysialylated neural cell adhesion molecule expression in adult brainstem synapses. J Neurosci 2001; 21: 4721–30.

22 Hoffman KB, Murray BA, Lynch G, Munirathinam S, Bahr BA. Delayed and isoform-specific effect of NMDA exposure on neural cell adhesion molecules in hippocampus. Neurosci Res 2001; 39: 167–73.

23 Blann A, Kumar P, Krupinski J, McCollum C, Beevers DG, Lip GY. Soluble intercelluar adhesion molecule-1, E-selectin, vascular cell adhesion molecule-1 and von Willebrand factor in stroke. Blood Coagul Fibrinolysis 1999; 10: 277–84.

24 Stanimirovic DB, Wong J, Shapiro A, Durkin JP. Increase in surface expression of ICAM-1, VCAM-1 and E-selectin in human cerebromicrovascular endothelial cells subjected to ischemia-like insults. Acta Neurochir Suppl (Wien) 1997; 70: 12–6.

25 James WG, Bullard DC, Hickey MJ. Critical role of the alpha 4 integrin/VCAM-1 pathway in cerebral leukocyte trafficking in lupus-prone MRL/fas(lpr) mice. J Immunol 2003; 170: 520–7.

26 Laschinger M, Engelhardt B. Interaction of alpha4-integrin with VCAM-1 is involved in adhesion of encephalitogenic T cell blasts to brain endothelium but not in their transendothelial migration *in vitro*. J Neuroimmunol 2000; 102: 32–43.

27 Saito H, Shimizu H, Mita H, Maeda Y, Akiyama K. Histamine augments VCAM-1 expression on IL-4- and TNF-alpha-stimulated human umbilical vein endothelial cells. Int Arch Allergy Immunol 1996; 111: 126–32.

28 Yang XH, Wei EQ. Expression of vascular cell adhesion molecule-1 in lung slices from antigen sensitized rats and pharmacological modulation. J Zhejiang Univ Med Sci 2003; 32: 319–22.

29 Wu AY, Chik SC, Chen AW, Li Z, Tsang KW, Li W. Anti-inflammatory effects of high-dose montelukast in an animal model of acute asthma. Clin Exp Allergy 2003; 33: 359–66.

30 Abe S, Kirima K, Tsuchiya K, Okamoto M, Hasegawa T, Houchi H, et al. The reaction rate of edaravone (3-methyl-1-phenyl-2-pyrazolin-5-one (MCI-186)) with hydroxyl radical. Chem Pharm Bull (Tokyo) 2004; 52: 186–91.

31 Jiang MZ, Tsukahara H, Ohshima Y, Todoroki Y, Hiraoka M, Maeda M, *et al*. Effects of antioxidants and nitric oxide on TNF-alpha-induced adhesion molecule expression and NF-kappaB activation in human dermal microvascular endothelial cells. Life Sci 2004; 75: 1159–70.

32 Rajesh KG, Sasaguri S, Suzuki R, Maeda H. Antioxidant MCI-186 inhibits mitochondrial permeability transition pore and upregulates Bcl-2 expression. Am J Physiol Heart Circ Physiol 2003; 285: H2171–8.

33 Zhang XH, Matsuda N, Jesmin S, Sakuraya F, Gando S, Kemmotsu O, *et al*. Normalization by edaravone, a free radical scavenger, of irradiation-reduced endothelial nitric oxide synthase expression. Eur J Pharmacol 2003; 476: 131–7.

34 Qi X, Okuma Y, Hosoi T, Nomura Y. Edaravone protects against hypoxia/ischemia-induced endoplasmic reticulum dysfunction. J Pharmacol Exp Ther 2004; 311: 388–93.

Acta Pharmacologica Sinica 2005 Apr; 26 (4): 441–446

Blackwell Publishing

Full-length article

Down regulation of cyclooxygenase-2 is involved in delayed neuroprotec-tion by ischemic preconditioning in rats

Liang XIAO, Fei-li ZHAO, Xing-zu ZHU[1]

Department of Pharmacology II, Shanghai Institute of Materia Medica, Shanghai Institutes for Biological Sciences, Chinese Academy of Sciences, Shanghai 201203, China

Key words

ischemic preconditioning; brain ischemia; prostaglandins; cyclooxygenase-2

[1] Correspondence to Prof Xing-zu ZHU.
Phn/Fax 86-21-5080-6096.
E-mail xzzhu@mail.shcnc.ac.cn

Received 2004-08-18
Accepted 2005-01-18

doi: 10.1111/j.1745-7254.2005.00064.x

Abstract

Aim: To examine whether the prostaglandins (PGs) pathway is involved in triggering delayed neuroprotection by ischemic preconditioning (IPC) and evaluate the effects of IPC on cyclooxygenase-2 (COX-2) expression following focal cerebral ischemia and reperfusion in rats. **Methods:** IPC was induced by 10 min of saline infusion into the left internal carotid artery with the right common carotid artery clamped at the same time. Middle cerebral artery occlusion (MCAO) and reperfusion model was produced using intraluminal filament method. **Results:** IPC 48 h prior to MCAO significantly reduced infarct area as compared with MCAO alone. A nonselective inhibitor of COX indomethacin (3 mg/kg ip) applied 1 h prior to or 1 h after IPC failed to affect its protective effects. IPC had no direct effect on the cortex COX-2 mRNA and protein expression 72 h later, but decreased the expression of COX-2 mRNA and protein following ischemia and reperfusion insult. **Conclusion:** PGs pathways was not involved in triggering delayed neuroprotection by IPC, and IPC induced down-regulation of COX-2 following focal cerebral ischemia and reperfusion in rats *in vivo*.

Introduction

A short period of ischemia is known to increase tolerance of the brain to a subsequent prolonged ischemia by reducing brain infarction and apoptosis, this phenomenon is termed as ischemic preconditioning (IPC) or ischemic tolerance[1]. The neuroprotection of cerebral ischemic preconditioning is divided into acute and delayed effects[2]. Delayed neuroprotection occurs 24 h after IPC, then becomes manifest thereafter and lasts up to 7 d.

Recently, it has been reported that indomethacin, a nonselective inhibitor of cyclooxygenase (COX), applied 1 h prior to lipopolysaccharide (LPS) treatment abolished the LPS-induce delayed neuroprotection against focal cerebral ischemia and reperfusion injury[3]. The results suggested that PGs pathway or inflammatory pathway might be involved in triggering delayed neuroprotection by LPS[3]. It has also been reported that PGs increased to a high level in the brain tissues within hours following a short period of ischemia[4]. However it is still unknown whether a rise of PGs in the brain is involved in the delayed neuroprotection induced by IPC.

COX, also known as prostaglandin H2 synthase, is the rate-limiting enzyme in the metabolism of arachidonic acid into prostanoids (PGs and thromboxanes). COX-2, which is normally expressed in the neurons of the brain, is inducible in response to mitogen, endotoxin, and cytokines. Previous studies have demonstrated that focal cerebral ischemia induced strongly expressed COX-2 in neurons in penumbra and contributed significantly to enlargement of infarction[5]. Since IPC limits infarction induced by ischemia and reperfusion injury, it may prevent the up-regulation of COX-2 following focal cerebral ischemia and reperfusion insult. Recently it was shown that IPC stimulus reprogrammed the response of gene transcription to subsequent ischemia and reperfusion insult in mice. It was found that COX-2 showed lower expression of mRNA by IPC using a microarray analysis[6].

In the present study, the PGs pathway was examined to evaluate whether it is involved in triggering cerebral IPC, and effects of IPC on COX-2 expression were evaluated fol-

lowing focal cerebral ischemia and reperfusion.

Material and methods

Materials Indomethcin (Sigma-Aldrich, St Louit, MO, USA) was dissolved in Me_2SO. The compound 2,3,7-triphenyltetrazolium chloride (TTC, Sigma-Aldrich, St Louis, USA) was dissolved in saline. TRI-REAGENT-LS extraction kit was purchased from Molecular Research Center, Inc (Cincinnati, USA). RNasin, dNTP, oligo (dT) 18 primer, and *Taq* DNA polymerase were obtained from Sangon Biotechnology Co (Shanghai, China). M-MuLV reverse transcriptase was from Fermentas Inc (Vilnius, Lithuania). The DNA Master SYBR Green I was from Roche Co (Mannheim, Germany). BCA protein assay kit and ECL chemiluminescence system were purchased from Pierce Co (Rockford, USA). Goat Polyclonal antibody specific for COX-2 was from Santa Cruz Biotechnology, Inc (Santa Cruz, USA, working concentration 1:500). Rat mono-antibody specific for beta-actin was from Sigma-Aldrich (St Louis, USA, working concentration 1:5000). Supersignal West Pico Trial Kit was from Pierce Co (Rockford, USA).

Animals and experiment design Male Sprague-Dawley rats weighing 220–250 g (the Shanghai Experimental Animal Center of Chinese Academy of Sciences) were used in this study. The rats were randomly divided into six groups (n=8 each). In the sham group (sham), the left common carotid artery was exposed, and the external carotid artery and its branches were isolated and coagulated without middle cerebral artery occlusion (MCAO). The rats of the ischemia and reperfusion group (I/R) were subjected to MCAO (90 min) and reperfusion (24 h). For the IPC group (IPC), IPC was applied 48 h before MCAO and reperfusion. For indomethacin group 1 (Indo1+IPC+I/R), the rats were treated with indomethacin (3 mg/kg ip) 1 h prior to IPC, and MCAO and reperfusion was applied 48 h later. For indomethacin group 2 (Indo2+IPC+I/R), the rats were treated with indomethacin (3 mg/kg ip) 1 h after IPC, and MCAO and reperfusion were applied 48 h later. The last group was used to exclude the effects of indomethacin itself on injuries of MCAO and reperfusion. The rats were treated with indomethacin (3 mg/kg ip) 48 h before MCAO and reperfusion (Indo+I/R).

COX-2 mRNA and protein expression Another series of experiments were performed. The rats were divided into four groups (n=6 each). In the sham operation group, the left common carotid artery was exposed, and the external carotid artery and its branches were isolated and coagulated without MCAO. The rats of the ischemia and reperfusion group were subjected to MCAO (90 min) and reperfusion (24 h). In the third group, IPC was applied 48 h before MCAO and reperfusion. In the last group, only IPC was applied.

Model of IPC IPC was induced as described previously with minor modification[7]. Briefly, the left common carotid artery was exposed, and the external carotid artery and its branches were isolated and coagulated. A branch of the left internal carotid artery (the left pterygopal artery) was isolated and coagulated. The right common carotid artery was exposed. Then a cannula was inserted into the external carotid artery stump and advanced into the internal carotid artery to infuse saline into the brain. The saline infusion rate was 12 mL/h, which was controlled by a Harvard apparatus compact infusion pump (USA). A surgery artery nip was used to clamp the right common carotid artery. To achieve marked neuroprotection, we chose 48 h after IPC as the time interval to apply ischemia and reperfusion insult.

Evaluation of infarct area Coronal sections of the brain (2 mm thick) were cut and immersed in a 1% solution of TTC. The stained slices were then fixed by immersion in phosphate-buffered 10% formaldehyde. The infarct area and hemispheric area of each section were photographed by a digital camera and quantitated using the public domain image processing and analysis program developed at the National Institute of Health, USA. The infarct area was expressed as percentage to the contralateral hemisphere.

Real-time reverse transcription PCR The expression of RNAs was determined by quantitative real-time RT-PCR using a Continuous Fluorescence Detector (MJ Research Incorporated, DNA Engine Opticn 2) with the DNA Master SYBR Green I. Animals were killed 24 h after reperfusion and their brains removed. A 4-mm-thick coronal brain slice was cut at the levels of the optic chiasm, and the infarcted cortex was dissected using the corpus callosum as a ventral landmark[8]. Total RNA was prepared from the samples with TRI-REAGENT-LS extraction kit according to manufacture's instructions. Complementary DNA was created from RNA using TrueScript MMLV reverse transcriptase and oligo d $(T)_{18}$ primers. A 0.2 μg amount of RNA was included in each reaction in a total volume of 20 μL. The reaction was performed at 42 ºC for 2 h. Thereafter the mix was diluted five-fold, and 2 μL was added to the PCR reaction mixture to yield a total volume of 20 μL. The COX-2 primers were forward, 5'-CCA TGT CAA AAC CGT GGT GAA TG-3'; reverse: 5'-ATG GGA GTT GGG CAG TCA TCA G-3', which result in a PCR product of 374 bp. The amplification reaction consisted of 35 cycles of denaturation (94 ºC, 30 s), annealing (64 ºC, 30 s), and elongation (72 ºC, 45 s). The beta-actin primers were forward, 5'AAG ATG ACC CAG ATC ATG TT3'; reverse: 5'TTA ATG TCA CGC ACG ATT T3', which resulted in a PCR

product of 286 bp. The amplification reaction consisted of 35 cycles of denaturation (94 ℃, 30 s), annealing (56 ℃, 30 s), and elongation (72 ℃, 45 s). Cycle numbers (crossing points, when amplification starts its exponential phase) were used for statistical analysis. The lower the cycle number indicates the higher the amount of initial template. The PCR products were verified by agarose gel electrophoresis.

Western blot analysis A 4-mm-thick coronal brain slice was cut at the levels of the optic chiasm, and the infarcted cortex was dissected using the corpus callosum as a ventral landmark[8]. The isolated cortex was homogenized in ice-cold lysis buffer. The protein content was determined by BCA protein assay. Equal amounts of protein per lane (50 μg) were loaded onto an 8 % polyacrylamide gel and separated by electrophoresis at 120 V. Proteins were then transferred to PVDF membrane at 25 mA for 90 min, and the membrane was blocked with 5% nonfat dry milk in 1X TBS, 0.1% Tween-20 at 25 ℃ with gentle shaking, overnight. The PVDF membrane was then incubated with a goat polyclonal antibody specific for COX-2 (1:500) 1 h at 25 ℃ followed by horseradish peroxidase-conjugated secondary antibody (rabbit anti-goat) for 1 h at 25 ℃. Antibody labeling was detected by Supersignal West Pico Trial Kit. After being stripped, the same PVDF membrane was incubated with mono-antibody specific for beta-actin (1:5000) as an internal control. Western blot results were quantified by density.

Data analysis All data were expressed as mean±SD. Differences between different groups were assessed by a one-way analysis of variance and Student-Newman-Keuls test. A value of $P<0.05$ was considered statistically significant.

Results

Protective effects of IPC At 24 h after operation, sham-operated rats did not show any cerebral tissue damage in TTC staining (not shown). IPC reduced the infarct area by 63% as compared with the MCAO alone group. Indomethacin (3 mg/kg ip), a nonselective inhibitor of COX, applied 1 h prior to or 1 h after IPC failed to affect these protective effects. Indomethacin itself had no effect on infarction by ischemia and reperfusion injury (Figure 1).

Effects of IPC on COX-2 mRNA expression In agreement with previous study, low levels of COX-2 PCR products were observed in the brain of sham-operated rats (to achieve the crossing points, the cycle number 25.8±2.4 was needed). After transient 90 min MCAO and 24 h reperfusion, COX-2 mRNA expression was significantly up regulated (the cycle number decreased to 19.9±1.9, $P<0.01$). IPC significantly prevented the up-regulation of COX-2 mRNA expression following ischemia and reperfusion injury (the cycle number decreased to 23.7±2.4, $P<0.01$), while IPC itself had no effect on the expression of COX-2 mRNA 72 h later (Figure 2).

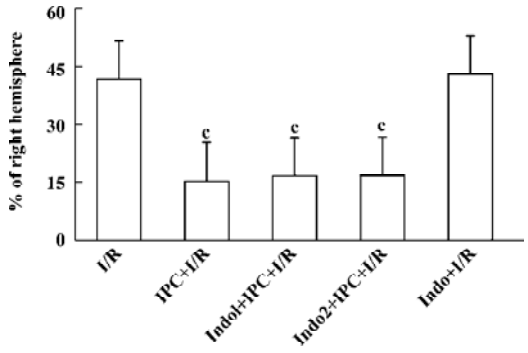

Figure 1. Effects of IPC and indomethacin on brain infarct area. I/R: 90 min ischemia and 24 h reperfusion, IPC+I/R: 10 min of ischemic preconditioning and 48 h later I/R was applied, Indo1+IPC+I/R: indomethacin 3 mg/kg ip1 h prior to IPC+I/R, Indo2+IPC+I/R: indomethacin 3 mg/kg ip 1 h after induction of IPC and 48 h later I/R was applied, Indo+I/R: indomethacin 3 mg/kg ip 48 h prior to I/R. n=8. Mean±SD. $^cP<0.01$ *vs* I/R.

Effects of IPC on COX-2 protein expression COX-2 protein was expressed at a low level in the brain of sham-operated rats (132±35). IPC itself had no effects on expression of COX-2 protein 72 h later (135±32). Ischemia and reperfusion markedly increased COX-2 protein expression (362±28, $P<0.01$). IPC prevented the up regulation of COX-2 protein following ischemia and reperfusion injury (225±21, $P<0.01$) (Figure 3).

Discussion

IPC is a fundamental adaptive response of organisms against deleterious stress such as ischemia and other severe stimuli. In fact, this phenomenon exists in most organs such as brain, heart, skeletal muscle, lung, liver, stomach, intestine, and kidney. IPC shares some common mechanisms in different organs. The elements that constitute this molecular cascade of delayed IPC can be conceptually subdivided into three major components: (i) "triggers" or sensors, (ii) "effectors" or mediators, and (iii) "transducers", signaling pathways that connect these two groups of molecules[1,9]. Endogenous active substances and bio-synthesized proteins have been suggested as triggers and end effectors of brain IPC, respectively. Adenosine, glutamate, oxygen free radical, and nitric oxide (NO) are these candidate substances that trigger brain IPC[1].

PGs are endogenous active substances that are suggested to be involved in IPC in the heart. It has been reported that pretreatment with indomethacin attenuated PGs release and abolished acute cardioprotection by IPC in

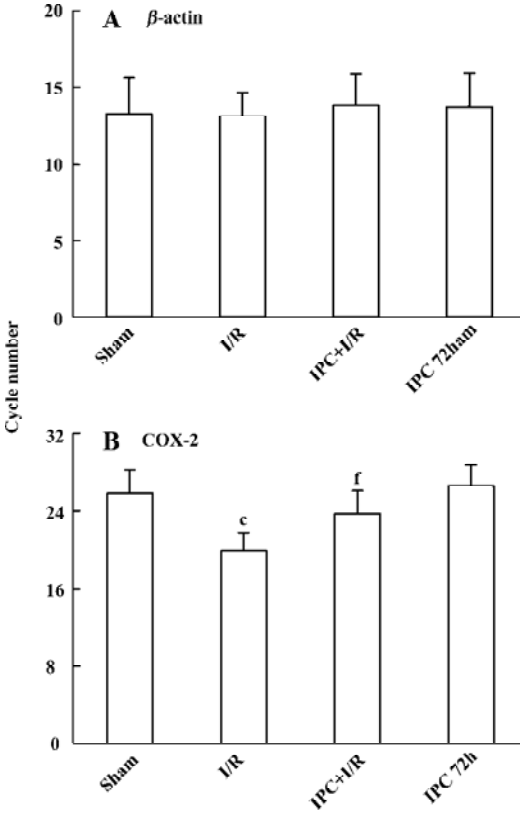

Figure 2. Effects of ischemic preconditioning on COX-2 mRNA expression following ischemia and reperfusion injury in cortex of rats detected by real-time PCR. Sham: sham group, I/R: 90 min ischemia and 24 h reperfusion, IPC + I/R: 10 min of ischemic preconditioning and 48 h later I/R was applied, IPC72h: 72 h after IPC. n=6. Mean±SD. ^{c}P<0.01 *vs* sham. ^{f}P<0.01 *vs* I/R.

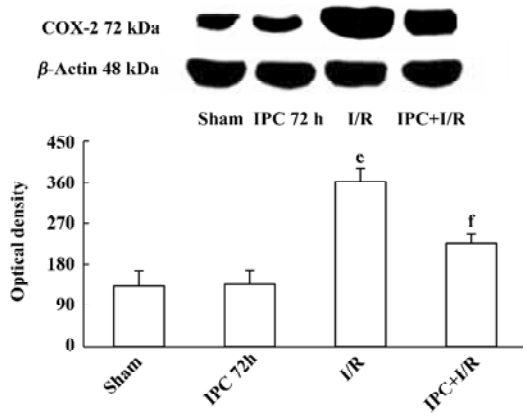

Figure 3. Effects of ischemic preconditioning on COX-2 protein expression following ischemia and reperfusion injuries in cortex of rats detected by western blot. Sham: sham group, IPC 72 h: 72 h after IPC, I/R: 90 min ischemia and 24 h reperfusion, IPC+I/R: 10 min of ischemic preconditioning and 48 h later I/R was applied. n=5. Mean±SD. ^{c}P<0.01 *vs* sham. ^{f}P<0.01 *vs* I/R.

different animal models *in vivo* or *in vitro*[10,11]. Exogenous PGs perfusion in isolated hearts mimicked cardioprotection induced by cardiac IPC[12]. The mechanisms of cardio-protection mediated by PGs are mainly related to the direct effects of PGs on the heart, including antagonism of adenylyl cyclase, activation of ATP-sensitive potassium channels, inhibition of calcium influx, and attenuation of neutrophil infiltration[13]. However, there was no study on the role of PGs in neuroprotection induced by IPC. A period of ischemia as short as 5 min can induce an early increase in PGs levels after 2 h of reperfusion in the brain[4]. However, cerebral IPC dose not seem to be triggered by increased PGs, since indomethacin failed to affect the protective effects of IPC. The negative role for PGs pathway may be attributed to the specific model of focal cerebral ischemia used for preconditioning. Saline infusion compromised oxygen and glucose supply, however, inflammatory response could be smaller, due to maintained idle perfusion at least partial being able to prevent from disturbed microcirculation and reduce leukocyte-endothelial cell adhesive interaction and so on. This in turn potentially diminished the inflammatory signal (including PGs pathway) as a trigger for preconditioning mechanisms. The result suggested the delayed neuroprotection by our model of IPC has different triggering mechanisms from that of delayed ischemic tolerance induced by LPS.

Three types of COX isoforms have been documented: COX-1, COX-2, and COX-3. COX-1 is constitutively expressed under physiological conditions. COX-3 is identical in sequence to COX-1 except for the in-frame retention of intron 1. Like its counterpart COX-1, COX-3 does not generally appear to be induced by acute inflammatory stimulation[14]. Several studies have demonstrated that COX-2 played an important role in the development of ischemic injury. In rodents as well as in humans, cerebral ischemia up-regulated COX-2 in neurons, blood vessels, and inflammatory cells in the injured brain[4,15,16]. Although COX-2 mRNA was not induced in the ischemic core, it was induced in the penumbral area in permanent or transient MCAO in rats. The up regulation of COX-2 began 6 h after ischemia, reached a maximum at 12–24 h and subsided at 48 h[4,8,17]. NS398, a selective COX-2 inhibitor, decreased infarction volume when administered 6 h after induction of ischemia[18]. In COX-2-deficient mice, there was a significant reduction in the MCAO-induced brain injury[19,20]. Our results that COX-2 mRNA and protein in the MCA cortex increased at 24 h after reperfusion in the rats of MCAO and reperfusion group were consistent with these previous studies. The mechanisms of the cytotoxicity of COX-2 induction may be related to the excessive release of arachidonic acid, and its products

such as PGs, thromboxane and free oxygen radicals. These factors may act as the major inflammatory substances involved in the pathogenesis of ischemia and reperfusion[8]. COX-2 reaction products may also contribute to NMDA-induced neuronal injury and the pathogenesis of nitric oxide after ischemia[21,22].

Evidence has shown that COX-2 was an obligatory effector in delayed IPC in the heart[13]. Increased expression of COX-2 protein was observed 24 h after IPC with an increased enzymatic activity[23]. NS-398 and celecoxib, two selective inhibitors of COX-2, abolished the cardioprotection conferred by IPC [24]. It was also demonstrated that the expression of COX-2 subsided 48 h after a short period of ischemia in the brain[4,8,17]. Since the delayed neuroprotection produced by IPC lasts as long as 7 d and is much longer than that of delayed cardioprotection (72 h), the up-regulated COX-2 does not seem to be the effector of delayed neuroprotection by IPC in the brain. In the present study, we examined the expression of COX-2 after IPC or IPC followed by ischemia and reperfusion injury. Our results demonstrated that IPC had no direct effect on the cortex COX-2 mRNA and protein expression 72 h later. Thus, it is not likely that an up-regulation of COX-2 contributes to the delayed neuroprotection by IPC in the brain. In the present study, we demonstrated that IPC significantly prevented the up-regulation of COX-2 mRNA and protein expression with a reduced infarction of the brain following ischemia and reperfusion injury. These results are similar to the previous finding that hyperbaric oxygen confers neuroprotection by depressing COX-2 expression and activity following ischemia and reperfusion injury[8]. So we speculate that while the up-regulation of COX-2 contributes to the delayed cardioprotection by IPC in the heart, it is probably that COX-2 takes an inverse role in delayed neuroprotection by IPC in the brain. Our results are consistent with the recent observation that COX-2 expression was down-regulated by ischemic preconditioning in the gerbil brain[25].

Recently, it has been shown that preconditioning stimulus reprogrammed the response of gene transcription to subsequent ischemia and reperfusion injury in mice. This feature mimics specific adaptive neuroprotective strategies seen in hibernation[6]. Depressed protein synthesis may be mediated in part via translational mechanisms that affect both initiation and elongation[6,26]. Since IPC confers robust neuroprotection, one presumption is that ischemic preconditioning may induce pro-survival factors that would negatively regulate COX-2. To date, three major mechanisms have been suggested to contribute to the neuroprotection by IPC, including anti-excitotoxic mechanisms, anti-apoptosis mechanisms, and anti-inflammatory mechanisms[1]. COX-2 has been verified to take an important role in pro-inflammatory action. We speculate that down-regulation of COX-2 may cooperate with other protective mechanisms and ultimately result in neuroprotection. However, more studies are needed to verify this hypothesis.

References

1 Dirnagl U, Simon RP, Hallenbeck JM. Ischemic tolerance and endogenous neuroprotection. Trends Neurosci 2003; 26: 248–54.

2 Perez-Pinzon MA, Xu GP, Dietrich WD, Rosenthal M, Sick TJ. Rapid preconditioning protects rats against ischemic neuronal damage after 3 but not 7 days of reperfusion following global cerebral ischemia. J Cereb Blood Flow Metab 1997; 17: 175–82.

3 Bordet R, Deplanque D, Maboudou P, Puisieux F, Pu Q, Robin E, *et al.* Increase in endogenous brain superoxide dismutase as a potential mechanism of lipopolysaccharide-induced brain ischemic tolerance. J Cereb Blood Flow Metab 2000; 20: 1190–6.

4 Candelario-Jalil E, Gonzalez-Falcon A, Garcia-Cabrera M, Alvarez D, Al-Dalain S, Martinez G, *et al.* Assessment of the relative contribution of COX-1 and COX-2 isoforms to ischemia-induced oxidative damage and neurodegeneration following transient global cerebral ischemia. J Neurochem 2003; 86: 545–55.

5 Koistinaho J, Chan PH. Spreading depression-induced cyclooxygenase-2 expression in the cortex. Neurochem Res 2000; 25: 645–51.

6 Stenzel-Poore MP, Stevens SL, Xiong Z, Lessov NS, Harrington CA, Mori M, *et al.* Effect of ischaemic preconditioning on genomic response to cerebral ischaemia: similarity to neuroprotective strategies in hibernation and hypoxia-tolerant states. Lancet 2003; 362: 1028–37.

7 Zhang FY, Cheng XC, Reng HM, Wu JS, Bao WM. A novel model of cerebral ischemic preconditioning in rats. Chin Clin Neurosci 2001; 9: 82–4.

8 Yin W, Badr AE, Mychaskiw G, Zhang JH. Down regulation of COX-2 is involved in hyperbaric oxygen treatment in a rat transient focal cerebral ischemia model. Brain Res 2002; 926: 165–71.

9 Bolli R. The late phase of preconditioning. Circ Res 2000; 87: 972–83.

10 Song QJ, Xiao J, Deng HW, Li YJ. Role of calcitonin gene-related peptide in prostaglandins-mediated ischemic preconditioning in guinea pig hearts. Acta Pharmacol Sin 2001; 22: 3–9.

11 Ma SG, Fu RF, Feng GQ, Wang ZJ, Ma XQ, Weng SA. Effect of G (alphaq/11) protein and ATP-sensitive potassium channels on prostaglandin E(1) preconditioning in rat hearts. Acta Pharmacol Sin 2004; 25: 587–92.

12 Bouchard JF, Chouinard J, Lamontagne D. Participation of prostaglandin E2 in the endothelial protective effect of ischaemic preconditioning in isolated rat heart. Cardiovasc Res 2000; 45: 418–27.

13 Bolli R, Shinmura K, Tang XL, Kodani E, Xuan YT, Guo Y, *et al.* Discovery of a new function of cyclooxygenase (COX)-2: COX-2 is a cardioprotective protein that alleviates ischemia/reperfusion injury and mediates the late phase of preconditioning. Cardiovasc Res 2002; 55: 506–19.

14 Shaftel SS, Olschowka JA, Hurley SD, Moore AH, O'Banion MK.

COX-3: a plice variant of cyclooxygenase-1 in mouse neural tissue and cells. Brain Res Mol Brain Res 2003; 119: 213–5.

15 Nogawa S, Zhang F, Ross ME, Iadecola C. Cyclo-oxygenase-2 gene expression in Neurons contributes to ischemic brain damage. J Neurosci 1997; 17: 2746–55.

16 Ohtsuki T, Kitagawa K, Yamagata K, Mandai K, Mabuchi T, Matsushita K, *et al*. Induction of cyclooxygenase-2 mRNA in gerbil hippocampal neurons after transient forebrain ischemia. Brain Res 1996; 736: 353–6.

17 Yokota C, Kaji T, Kuge Y, Inoue H, Tamaki N, Minematsu K. Temporal and topographic profiles of cyclooxygenase-2 expression during 24 h of focal brain ishemia in rats. Neurosci Lett 2004; 357: 219–22.

18 Nagayama M, Niwa K, Nagayama T, Ross ME Iadecola C. The cyclooxygenase-2 inhibitor NS-398 ameliorates ischemic brain injury in wild-type mice but not in mice with deletion of the inducible nitric oxide synthase gene. J Cereb Blood Flow Metab 1999; 19: 1213–9.

19 Sasaki T, Kitagawa K, Yamagata K, Takemiya T, Tanaka S, Omura-Matsuoka E, *et al*. Amelioration of hippocampal neuronal damage after transient forebrain ischemia in cyclooxygenase-2-deficient mice. J Cereb Blood Flow Metab 2004; 24: 107–13.

20 Iadecola C, Niwa K, Nogawa S, Zhao X, Nagayama M, Araki E, *et al*. Reduced susceptibility to ischemic brain injury and *N*-methyl-*D*-aspartate-mediated neurotoxicity in cyclooxygenase-2-deficient mice. Proc Natl Acad Sci USA 2001; 98: 1294–9.

21 Hewett SJ, Uliasz TF, Vidwans AS, Hewett JA. Cyclooxygenase-2 contributes to *N*-methyl-*D*-aspartate-mediated neuronal cell death in primary cortical cell culture. J Pharmacol Exp Ther 2000; 293: 417–25.

22 Kittaka M, Giannotta SL, Zelman V, Correale JD, DeGiorgio CM, Weiss MH, *et al*. Attenuation of brain injury and reduction of neuron-specific enolase by nicardipine in systemic circulation following focal ischemia and reperfusion in a rat model. J Neurosurg 1997; 87: 731–7.

23 Xuan YT, Guo Y, Zhu Y, Han H, Langenbach R, Dawn B, *et al*. Mechanism of cyclooxygenase-2 upregulation in late preconditioning. J Mol Cell Cardiol 2003; 35: 525–37.

24 Shinmura K, Tang XL, Wang Y, Xuan YT, Liu SQ, Takano H, *et al*. Cyclooxygenase-2 mediates the cardioprotective effects of the late phase of ischemic preconditioning in conscious rabbits. Proc Natl Acad Sci USA 2000; 97: 10197–202.

25 Colangelo V, Gordon WC, Mukherjee PK, Trivedi P, Ottino P. Downregulation of COX-2 and JNK expression after induction of ischemic tolerance in the gerbil brain. Brain Res 2004; 1016: 195–200.

26 Frerichs KU, Smith CB, Brenner M, DeGracia DJ, Krause GS, Marrone L, *et al*. Suppression of protein synthesis in brain during hibernation involves inhibition of protein initiation and elongation. Proc Natl Acad Sci USA 1998; 95: 14511–6.

Acta Pharmacologica Sinica 2005 Apr; 26 (4): 447–452

Full-length article

Ascorbic acid improves impaired venous and arterial endothelium-dependent dilation in smokers[1]

Márcio Gonçalves de SOUSA[2], Juan Carlos YUGAR-TOLEDO[2], Marcelo RUBIRA[3], Sílvia Elaine FERREIRA-MELO[2], Rodrigo PLENTZ[3], Deise BARBIERI[2], Fernanda CONSOLIM-COLOMBO[3], Maria Cláudia IRIGOYEN[3], Heitor MORENO Jr[2,4]

[2]Cardiovascular Pharmacology and Cardiology, Clinical Hospital of Campinas and Faculty of Medical Sciences, State University of Campinas, 13081-970, Campinas, São Paulo, Brazil; [3]Hypertension Unit, InCor, Clinical Hospital of São Paulo, Faculty of Medicine of São Paulo University, 05403-000, São Paulo, Brazil

Key words

ascorbic acid; vasodilation; vascular endothelium; arterioles; venules; dorsal hand vein; flow-mediated dilation

[1] Project supported by Fundação de Amparo à Pesquisa do Estado de São Paulo (FAPESP), São Paulo, Brazil.
[4] Correspondence to Dr Heitor MORENO Jr. Fax 55-19-3289-2968.
E-mail hmoreno@uol.com.br

Received 2004-09-03
Accepted 2004-12-01

doi: 10.1111/j.1745-7254.2005.00069.x

Abstract

Aim: To compare the acute effects of ascorbic acid on vasodilation of veins and arteries *in vivo*. **Methods:** Twenty-six healthy non-smokers and 23 healthy moderate smokers were recruited in this study. The dorsal hand vein compliance technique and flow-mediated dilation were used. Dose-response curves to bradykinin and sodium nitroprusside were constructed to test the endothelium-dependent and -independent relaxation before and after acute infusion of ascorbic acid. **Results:** Smokers had an impaired venodilation with bradykinin compared with non-smokers (68.3%±13.2% *vs* 93.7%±20.1%, respectively; $P<0.05$). Ascorbic acid administration in the dorsal hand vein significantly increased the venodilation with bradykinin in smokers (68.3%±13.2% *vs* 89.5%±6.3% before and after infusion, respectively; $P<0.05$) but not in non-smokers (93.7%±20.1% *vs* 86.4%±12.4% before and after infusion, respectively). Similarly, the arterial response in smokers had an impaired endothelium-dependent dilation compared with that in non-smokers (8.8%±2.7% *vs* 15.2%±2.3%, respectively; $P<0.05$) and ascorbic acid restored this response in smokers (8.8%±2.7% *vs* 18.7%±6.5% before and after infusion, respectively; $P<0.05$), but no difference was seen in non-smokers (15.2%±2.3% *vs* 14.0%±4.4% before and after infusion, respectively). The endothelium-independent dilation did not differ in both the groups studied. No important hemodynamic change was detected using the Portapress device. **Conclusion:** Smokers had impaired endothelium-dependent vasodilation responsiveness in both arterial and venous systems. Ascorbic acid restores this responsiveness in smokers.

Introduction

Chronic cigarette smoking is a major risk factor for cardiovascular disease and is associated with dose-dependent arterial endothelial dysfunction and hemodynamic changes[1–3]. The cause of endothelial dysfunction in smokers is not known. Carbon monoxide and nicotine have been implicated[4–6], but the mechanism that seems to have the greatest effect is oxidant injury[7,8].

Although probably multifactorial, it has been hypothesized that the adverse effects of smoking may result from an accumulation of oxidative damage caused by the reactive oxygen species (ROS) on endothelial cells[9]. Low plasma concentrations of nitric oxide (NO)[10], which is a possible sign of endothelial dysfunction, along with low plasma concentrations of ascorbic acid (AA) have been reported in long-term habitual smokers[11]. AA has a broad spectrum of antioxidant activities because of its ability to react with numerous aqueous free radicals and ROS and it effectively protects lipids in human plasma against peroxidative damage[12]. It has been demonstrated that the administration of AA in arterial beds markedly improves endothelium-mediated vasodilation in chronic smokers[13], but its *in vivo* effect in veins has not been studied yet.

In contrast to the continuous production of NO in the arterial endothelium, a very low basal production of NO has been demonstrated in the venous endothelium[14,15]. In contrast, in the cultured endothelial cells of rats, higher en-

dothelial isoform of the nitric oxide synthase (NOS) protein levels, nitric oxide synthase (NOS) activity, and intracellular *L*-arginine have been found in veins compared with that in arteries[16]. There is considerable evidence of heterogeneity between the arterial and the venous endothelium[17]. The goal of the present study was to compare the acute response of AA in both vascular beds in smokers.

Materials and methods

Study population The volunteers for this study were as follows: the control group comprised 26 healthy subjects without familial history of coronary artery disease or arterial hypertension (blood pressure<140/90 mmHg), who were also non-hypercholesterolemic, non-diabetic and non-smokers without a history of being regular passive smokers. The smoker group comprised 23 regular smokers (normally 20 cigarettes daily) without familial history of coronary artery disease or arterial hypertension, who were also non-hypercholesterolemic and non-diabetic.

None of the subjects was taking regular medications and all were clinically well. Subjects with cardiac or cerebral ischemic vascular disease, impaired renal function, or other major pathologies were excluded from the study. In accordance with current legislation, all patients were aware of the investigational nature of the study and gave their written informed consent before participating. The Institutional Committee for Ethics in Research approved this study.

Experimental procedure All studies were initiated at 8:00 AM after overnight fasting, with the subjects lying in the supine position in a quiet air-conditioned room (22–24 °C). The subjects were admitted in the outpatient clinic of the Campinas State University Hospital (HC-UNICAMP)on 2 different occasions for 4 h studies. During the first study, measurements were performed after infusion of saline solution at a rate of 75 mL/h, iv. The second study was performed with infusion of saline solution (75 mL/h, iv) plus AA at a rate of 25 mg/min, iv.

Dorsal hand vein technique The dorsal hand vein technique, previously modified by Aellig[18], as used in our laboratory has been described in detail[5]. Briefly, a 23 G butterfly needle was inserted into a suitable vein on the back of the hand, with the arm positioned at an upward angle of 30 ° to allow the complete emptying of the veins. A tripod, holding a linear variable differential transformer (LVDT; Schaevitz Engineering, Pennsauken, New Jersey, USA) was mounted on the back of the hand with its central aperture, containing a movable metal core, at a distance of 10 mm downstream from the tip of the needle. The signal output of the LVDT, which is linearly proportional to the vertical movement of the core, gave a measurement of the diameter of the vein. Readings were taken under a congestive pressure of 40 mmHg by inflating a blood pressure cuff placed on the upper portion of the arm under study. Results were presented as normalized dose-response curves in which the diameter of the vein during saline infusion is defined as 100% dilation. The vein was pre-constricted to 20% of the baseline size by infusing increasing doses of phenylephrine (12–3166 ng/min). This dose rate of phenylephrine was defined as the ED_{80} dose and this degree of constriction was defined as 0% dilation for the purposes of subsequent calculations. The vasodilation effects expressed in this study were calculated as a percentage in the range between 0% and 100% dilation. Drugs were infused using a Harvard infusion pump (Harvard Apparatus, South Natick, MA, USA) at a flow rate of 0.3 mL/min. Blood pressure and heart rate were monitored in the opposite arm with a Dynamap Blood Pressure Monitor (Critikon, Tampa, FL, USA). After pre-constriction of the vein by phenylephrine, dose-response curves of bradykinin (1–278 ng/min) and sodium nitroprusside (0.0187 ng/min–3166 ng/min) were constructed with 5 ng/min infusion rates in both smoker and non-smoker volunteers. AA (25 mg/min) was co-infused during the second study of each volunteer. Infusions at each rate lasted for 5 min with the sphygmomanometer cuff inflated to 45 mmHg for the last 2 min of the infusion.

Flow-mediated dilation Brachial artery flow-mediated dilation was measured with a 7.0 MHz linear array transducer and an ATL HDI system (Advanced Technology Laboratories, Seattle, WA, USA) according to the manufacturer's instructions[19]. The brachial artery was scanned longitudinally 5–10 cm above the elbow and a holder probe was used to hold the transducer in the same position throughout the procedure. The focus zone was set to the depth of the near wall of the artery. Depth and gain settings were set to optimize images of the lumen-arterial wall interface. The images were magnified by a resolution box function and measurements were taken from the anterior to posterior "m" line at the R-wave peak of the electrocardiogram. The brachial artery diameter was measured by identifying a clear section of the vessel in B-mode.

After the baseline-resting scan, a pneumatic cuff, placed at the wrist, was inflated to 300 mmHg for 5 min. The second scan was performed 45–120 s after cuff deflation. Fifteen minutes were allowed for vessel recovery, after which a second baseline scan was performed. Glyceryl trinitrate (0.4 mg; Nitrostat, Parke-Davis, Morris Plainf , New Jersey, USA) was then administered and the 4th scan of the brachial artery was undertaken. When the brachial artery diameter and blood flow had returned to baseline, flow-mediated dilation was determined after AA infusion (25 mg/min, iv; 10 min). Blood flow and brachial artery diameter data for glyceryl trinitrate and vitamin C represent measurements during the last minute

of each infusion[20]. Two independent observers unaware of the subjects' clinical details, and the type and stage of the study measured the vessel diameter. Repeated measurements in individuals using this technique are consistent and reproducible.

Statistical analysis Descriptive data were expressed as mean±SD. The dose-response curves were fitted to a sigmoid model[21], and the maximum effect (E_{max}) and the dose that causes 50% of the E_{max} (ED_{50}), were determined. Parametric tests (Student's paired and unpaired *t*-tests) were used to compare the E_{max} and $lgED_{50}$ values. The sample size was calculated for a power of 0.80. $P<0.05$ was considered to be statistically significant.

Results

Clinical characteristics No statistical difference between smokers and non-smokers in terms of clinical characteristics was detected (Table 1). Chronic smokers had a history of 23.1±6.1 cigarettes a day. No side-effect was observed during the studies.

Table 1. Clinical characteristics of the participants in the study. Mean±SD. BMI, body mass index; F, female; M, male; MBP, mean blood pressure.

	Control	Smokers
Sex (M/F)	12/14	13/10
Age (years)	36.1±6.4	39.0±8.4
BMI (kg/m^2)	23.8±5.0	22.5±2.5
Daily cigarettes	–	23.1±6.1
MBP (mmHg)	83.1±4.7	86.9±6.6
Glycemia (mg/dL)	97.3±6.4	88.1±7.2
Total cholesterol (mg/dL)	171.0±38.3	181.2±32.3
Triglyceride (mg/dL)	112.3±47.2	103.2±41.4
Creatinine (mg/dL)	0.7±0.3	0.9±0.1

Dorsal hand vein Smokers had an impaired endothelium-dependent venodilation with bradykinin compared with non-smokers (68.3%±13.2% and 93.7%±20.1%, respectively; $P<0.05$) (Table 2; Figure 1). AA administration significantly increased the venodilation to bradykinin in smokers (68.3% ±13.2% and 89.5%±6.3% before and after AA infusion, respectively; $P<0.05$), restoring it to levels similar to those observed in non-smokers (93.7%±20.1% and 86.4%±12.4% before and after AA infusion, respectively; $P>0.05$) (Table 2). The endothelium-independent venodilation response did not show significant differences (Table 3; Figure 1).

Flow-mediated dilation The arterial response measured by flow-mediated dilation showed an impaired endothelium-dependent vasodilation in smokers compared with non-smokers (8.8%±2.7% *vs* 15.2%±2.3%, respectively; $P<0.05$). AA administration significantly increased the endothelium-dependent vasodilation in response to reactive hyperemia in smokers (8.8%±2.7% *vs* 18.7%±6.5% before and after AA infusion, respectively; $P<0.05$), restoring it to similar levels

Table 2. The maximum effect (E_{max}), the bradykinin dose that causes 50% of the E_{max} (ED_{50}), and $lgED_{50}$ in control and smoker subjects, before and after ascorbic acid (AA) administration to bradykinin infusion. Mean±SD. $^bP<0.05$ *vs* controls; $^eP<0.05$ *vs* smokers before ascorbic acid.

	Controls before AA (n=12)	Controls after AA (n=14)	Smokers before AA (n=13)	Smokers after AA (n=10)
E_{max}/%	93.7±20.1	86.4±12.4	68.3±13.2^b	89.5±6.3^e
ED_{50}/μg·L^{-1}	41.2±10.2	18.5±8.2	17.1±7.3	15.0±2.8
$lgED_{50}$	1.4±0.5	1.1±0.1	1.0±0.2	1.2±0.1

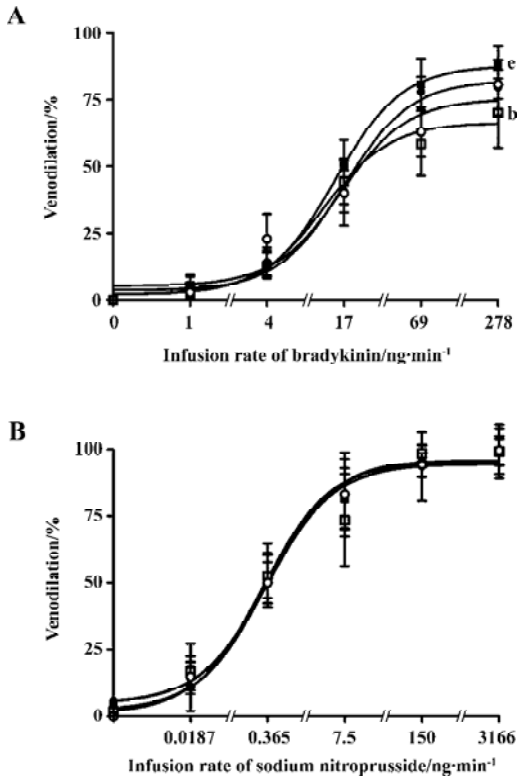

Figure 1. Dose-response curve to bradykinin (A) and sodium nitroprusside (B) of the dorsal hand veins pre-constricted with phenylephrine. The venodilation was expressed as a percentage of the baseline (pre-phenylephrine) vein diameter. Mean±SD. Controls before ascorbic acid (AA; n=12, open circle); controls after AA (n=14, closed circles); smokers before AA (n=13, open squares); smokers after AA (n=10, closed squares). $^bP<0.05$ *vs* controls; $^eP<0.05$ *vs* smokers before AA.

Table 3. The maximum effect (E_{max}), the dose of sodium nitroprusside that causes 50% of the E_{max} (ED_{50}), and $lgED_{50}$ in control and smoker subjects, before and after ascorbic acid (AA) administration to sodium nitroprusside infusion. Mean±SD.

	Controls before AA (n=12)	Controls after AA (n=14)	Smokers before AA (n=13)	Smokers after AA (n=10)
E_{max}/%	106.0±8.1	98.6±14.6	114.2±13.8	101.4±6.2
ED_{50}/μg·L^{-1}	0.5±0.3	0.4±0.2	0.4±0.2	0.6±0.4
$lgED_{50}$	-1.0±0.9	-0.5±0.3	-0.9±0.2	-1.7±0.4

Table 4. Brachial artery diameter in non-smokers and smokers, before and after ascorbic acid (AA) administration through flow-mediated dilation. Mean±SD. ^bP<0.05 *vs* control; ^eP<0.05 *vs* smokers before vitamin C. GTN, glyceryl trinitrate of vascular reactivity (brachial artery diameter % changes).

Change/%	Controls before AA (n=12)	Controls after AA (n=14)	Smokers before AA (n=13)	Smokers after AA (n=10)
Hyperemia	15.2±2.3	14.0±4.4	8.8±2.7^b	18.7±6.5^e
GTN	25.9±5.7	27.1±6.4	21.7±4.3	28.9±8.6

to those observed in non-smokers (15.2%±2.3% *vs* 14.0%±4.4% before and after AA, respectively). The endothelium-independent vasodilation response did not show significant difference (Table 4).

Hemodynamic findings Infusion of AA in smokers and non-smokers did not cause significant vascular changes, as evidenced using Portapress (TNO BMI, Amsterdam, Netherlands) device (Tables 5, 6), excepting a mild increase in the heart rate.

Discussion

The present study demonstrates that impaired endothelium-dependent vasodilation in chronic smokers could be markedly improved in both arterial and venous endothelium beds by acute administration of the anti-oxidant AA. In contrast to the continuous production of NO by the arterial

Table 5. Hemodynamic variables in control group before and after infusion of ascorbic acid (AA) in different stages. Mean±SD. ^bP<0.05 *vs* basal. RH, reactive hyperemia (brachial artery diameter % changes); GTN, glyceryl trinitrate vascular reactivity (brachial artery diameter % changes); CO, cardiac output (L/min); SVR, systemic vascular resistance (dyne·s·cm^{-5}); DP, diastolic pressure (mmHg); SP, systolic pressure (mmHg); MAP, mean arterial pressure (mmHg); HR, heart rate (beat/min).

	Control before AA (n=12)			Control after AA (n=14)		
	Basal	RH	GTN	Basal	RH	GTN
CO	6.0±1.7	5.4±1.2	5.7±1.2	6.4±1.9	6.1±1.8	5.8±1.5
SVR	1287±373	1267±325	1306±343	1189±484	1203±337	1390±543
SP	117±8	107±9	122±6	117±13	108±8	127±14
DP	70±5	66±4	74±4	64±17	65±5	76±10
MAP	86±5	80±5	91±4	82±15	80±5	93±11
HR	64±9	62±10	76±11^b	60±8	62±10	72±11^b

Table 6. Hemodynamic variables in smoker group before and after infusion of ascorbic acid (AA) in different stages of vascular reactivity. Mean±SD. RH, reactive hyperemia (brachial artery diameter % changes); GTN, glyceryl trinitrate vascular reactivity (brachial artery diameter % changes); CO, cardiac output (L/min); SVR, systemic vascular resistance (dyne·s·cm^{-5}); SP, systolic pressure (mmHg); DP, diastolic pressure (mmHg); MAP, mean arterial pressure (mmHg); HR, heart rate (beat/min).

	Smokers before AA (n=13)			Smokers after AA (n=10)		
	Basal	HR	GTN	Basal	HR	GTN
CO	4.5±0.9	4.3±1.1	4.3±0.8	4.9±0.7	4.8±1.0	4.2±0.4
SVR	1804±666	1536±282	1971±789	1562±244	1938±999	1829±387
SP	127±16	119±17	131±16	128±18	121±14	131±23
DP	77±12	72±11	79±11	73±7	70±5	77±10
MAP	93±12	88±12	91±4	92±10	87±7	95±14
HR	63±5	62±6	77±8	62±7	61±8	75±9

endo-thelium, the basal production of NO from the venous endothelium is very low[22]. However, its production from the venous endothelium can be increased in response to bradykinin or other molecules[23]. Recently, Wagner *et al* found higher eNOS protein levels, NOS activity, and intracellular *L*-arginine levels exhibited in cultured venular endothelial cells from rat mesenteric circulation compared with cultured endothelial cells from their paired arterioles[16]. Bohlen reported that, although the mean NO concentration was not significantly different between vessel types because of the high variability in absolute values, the venous wall NO concentration was higher than the arterial wall NO concentration in approximately 80% in terms of small mesenteric artery vein pairs studied *in vivo*[24]. Other studies have suggested that the venous endothelium does not have a larger capacity for NO synthesis than the arterial endothelium and in some cases may generate less NO. For example, shear stress and acetylcholine stimulate less NO release from the jugular vein than from the nearby carotid artery[25] and shear stress elicits a smaller NO-dependent dilation in coronary venules than in their respective arterioles[26].

Many studies have demonstrated the superior long-term patency of arterial grafts compared with the saphenous vein, based on endothelial function[27]. A higher basal release of NO and endothelium-derived hyperpolarizing factor in arterial grafts[15], intact endothelial function and absence of intimal thickening in arterial grafts when compared with saphenous grafts[28], and the maintenance of the physiological NO and prostacyclin metabolisms, both soon after surgery and in long-term follow up, in arterial rather than venous grafts[29] suggest a higher bioavailability of NO in arterial beds. All these findings highlight the growing consensus that there is a marked regional and segmental heterogeneity in vascular endothelial function, with NO release and/or its vascular effects varying between and within specific vascular beds[17].

Previously, we demonstrated an impaired vasodilation in smokers using the dorsal hand vein technique[30] and flow-mediated dilation[31]. Now, our data show that acute AA administration reverses this abnormal response caused by cigarette smoking in both vascular beds. Clinical observations have shown oxygen-derived free radicals as mediators of smoking-induced endothelial dysfunction. Ascorbate improves or reverses endothelial dysfunction suggesting that there is a link between this and NO production or its metabolism. Depleted levels of AA, have been demonstrated in chronic smokers[11,32]. Ascorbate has been shown to reverse NO-dependent endothelial dysfunction present in the coronary arteries of patients with atherosclerosis[33], hyperhomocysteinemia[34], hypercholesterolemia[35], hypertension[36], and diabetes[37]. There are many mechanisms for the improvement of endothelial function by ascorbate[38]: (i) prevention of endothelial dysfunction induced by oxidized cholesterol low-density lipoproteins; (ii) ascorbate-induced release of NO from *S*-nitrosothiols in plasma; (iii) reduction of nitrite to NO; (iv) scavenging of superoxide by ascorbate; (v) thiol-dependent redox regulation of eNOS interaction with ascorbate; (vi) regulation of eNOS through tetra-hydrobiopterin; (vii) ascorbate as a cofactor for eNOS; and (viii) effects on stimulation of guanylyl cyclase by NO. Many studies have shown these improvements in the arterial beds of regular smokers using flow-mediated dilation, impedance plethysmography, and intra-arterial infusions, but not in venous vascular beds.

Our findings demonstrate that endothelial dysfunction in smokers can be reversed by AA in venous and arterial vascular beds. Arteries and veins have different biological activities in terms of the endothelium, probably by marked regional and segmental heterogeneity in vascular endothelial function, but we have demonstrated similar findings in this specific vascular bed. The precise mechanism for this needs further investigation. Because veins are not susceptible to atherosclerosis, we have demonstrated that the dorsal hand vein technique can be used as a tool to assess vascular responsiveness in smokers.

These results show that there is a similar impaired responsiveness in arterial and venous endothelial-dependent vascular reactivity in smokers, and that after acute infusion of AA there is an improved responsiveness in both vascular beds.

Acknowledgments

This study, Heitor MORENO Jr, Maria Cláudia IRIGOYEN and Fernanda CONSOLIN-COLOMBO were supported by CNPq (São Paulo, Brasil). Márcio Gonçalves de SOUSA, Marcelo RUBIRA, Sílvia Elaine FERREIRA-MELO, Rodrigo PLENTZ and Deise BARBIERI thank FAPESP (São Paulo, Brasil) and CNPq (Brasília, Brasil).

References

1 Celermajer DS, Sorensen KE, Georgakopoulos D, Bull C, Thomas O, Robinson J, *et al*. Cigarette smoking is associated with dose-related and potentially reversible impairment of endothelium-dependent dilation in healthy young adults. Circulation 1993; 88 (5 Pt 1): 2149–55.

2 Benowitz NL. Cigarette smoking and cardiovascular disease: pathophysiology and implications for treatment. Prog Cardiovasc Dis 2003; 46: 91–111.

3 Tanus-Santos JE, Toledo JC, Cittadino M, Sabha M, Rocha JC, Moreno H Jr. Cardiovascular effects of transdermal nicotine in mildly hypertensive smokers. Am J Hypertens 2001; 14 (7 Pt 1): 610–4.

4 Samet JM. The 1990 report of the surgeon general: the health

benefits of smoking cessation. Am Rev Respir Dis 1990; 142: 993–4.
5 Sabha M, Tanus-Santos JE, Toledo JC, Cittadino M, Rocha JC, Moreno H Jr. Transdermal nicotine mimics the smoking-induced endothelial dysfunction. Clin Pharmacol Ther 2000; 68: 167–74.
6 Neunteufl T, Heher S, Kostner K, Mitulovic G, Lehr S, Khoschsorur G, *et al*. Contribution of nicotine to acute endothelial dysfunction in long-term smokers. J Am Coll Cardiol 2002; 39: 251–6.
7 Kalra J, Chaudhary AK, Prasad K. Increased production of oxygen free radicals in cigarette smokers. Int J Exp Pathol 1991; 72: 1–7.
8 Morrow JD, Frei B, Longmire AW, Gaziano JM, Lynch SM, Shyr Y, *et al*. Increase in circulating products of lipid peroxidation (F2-isoprostanes) in smokers. Smoking as a cause of oxidative damage. N Engl J Med 1995; 332: 1198–203.
9 Reilly M, Delanty N, Lawson JA, FitzGerald GA. Modulation of oxidant stress *in vivo* in chronic cigarette smokers. Circulation 1996; 94: 19–25.
10 Node K, Kitakaze M, Yoshikawa H, Kosaka H, Hori M. Reversible reduction in plasma concentration of nitric oxide induced by cigarette smoking in young adults. Am J Cardiol 1997; 79: 1538–41.
11 Tsuchiya M, Asada A, Kasahara E, Sato EF, Shindo M, Inoue M. Smoking a single cigarette rapidly reduces combined concentrations of nitrate and nitrite and concentrations of antioxidants in plasma. Circulation 2002; 105: 1155–7.
12 Frei B, England L, Ames BN. Ascorbate is an outstanding antioxidant in human blood plasma. Proc Natl Acad Sci USA 1989; 86: 6377–81.
13 Heitzer T, Just H, Munzel T. Antioxidant vitamin C improves endothelial dysfunction in chronic smokers. Circulation 1996; 94: 6–9.
14 Luscher TF, Diederich D, Siebenmann R, Lehmann K, Stulz P, von Segesser L, *et al*. Difference between endothelium-dependent relaxation in arterial and in venous coronary bypass grafts. N Engl J Med 1988; 319: 462–7.
15 Liu ZG, Ge ZD, He GW. Difference in endothelium-derived hyperpolarizing factor-mediated hyperpolarization and nitric oxide release between human internal mammary artery and saphenous vein. Circulation 2000; 102 (19 Suppl 3): III296–301.
16 Wagner L, Hoey JG, Erdely A, Boegehold MA, Baylis C. The nitric oxide pathway is amplified in venular *vs* arteriolar cultured rat mesenteric endothelial cells. Microvasc Res 2001; 62: 401–9.
17 Boegehold MA. Heterogeneity of endothelial function within the circulation. Curr Opin Nephrol Hypertens 1998; 7: 71–8.
18 Aellig WH. A new technique for recording compliance of human hand veins. 1981. Br J Clin Pharmacol 2004; 58: S768–74.
19 Corretti MC, Anderson TJ, Benjamin EJ, Celermajer D, Charbonneau F, Creager MA, *et al*. Guidelines for the ultrasound assessment of endothelial-dependent flow-mediated vasodilation of the brachial artery: a report of the International Brachial Artery Reactivity Task Force. J Am Coll Cardiol 2002; 39: 257–65.
20 Landmesser U, Merten R, Spiekermann S, Buttner K, Drexler H, Hornig B. Vascular extracellular superoxide dismutase activity in patients with coronary artery disease: relation to endothelium-dependent vasodilation. Circulation 2000; 101: 2264–70.
21 Mackay D. A generally useful modification of ALLFIT that facilitates the fitting of null equations to dose-response curves. Trends Pharmacol Sci 1988; 9: 121–2.
22 Vallance P, Collier J, Moncada S. Nitric oxide synthesised from *L*-arginine mediates endothelium dependent dilation in human veins *in vivo*. Cardiovasc Res 1989; 23: 1053–7.
23 Bedarida GV, Kim D, Blaschke TF, Hoffman BB. Characterization of an inhibitor of nitric oxide synthase in human-hand veins. Horm Metab Res 1994; 26: 109–12.
24 Bohlen HG. Mechanism of increased vessel wall nitric oxide concentrations during intestinal absorption. Am J Physiol 1998; 275 (2 Pt 2): H542–50.
25 Fukaya Y, Ohhashi T. Acetylcholine- and flow-induced production and release of nitric oxide in arterial and venous endothelial cells. Am J Physiol 1996; 270 (1 Pt 2): H99–106.
26 Kuo L, Arko F, Chilian WM, Davis MJ. Coronary venular responses to flow and pressure. Circ Res 1993; 72: 607–15.
27 Mangoush O, Nakamura K, Al-Ruzzeh S, Athanasiou T, Chester A, Amrani M. Effect of ascorbic acid on endothelium-dependent vasodilation of human arterial conduits for coronary artery bypass grafting. Eur J Cardiothorac Surg 2003; 24: 541–6.
28 Komori K, Inoguchi H, Kume M, Shoji T, Furuyama T. Differences in endothelial function and morphologic modulation between canine autogenous venous and arterial grafts: endothelium and intimal thickening. Surgery 2002; 131 (1 Suppl): S249–55.
29 Yang ZH, von Segesser L, Bauer E, Stulz P, Turina M, Luscher TF. Different activation of the endothelial *L*-arginine and cyclooxygenase pathway in the human internal mammary artery and saphenous vein. Circ Res 1991; 68: 52–60.
30 Moreno H Jr, Chalon S, Urae A, Tangphao O, Abiose AK, Hoffman BB, *et al*. Endothelial dysfunction in human hand veins is rapidly reversible after smoking cessation. Am J Physiol 1998; 275 (3 Pt 2): H1040–45.
31 Yugar-Toledo JC, Tanus-Santos JE, Sabha M, Sousa MG, Cittadino M, Tacito LH, *et al*. Uncontrolled hypertension, uncompensated type II diabetes, and smoking have different patterns of vascular dysfunction. Chest 2004; 125: 823–30.
32 Schectman G, Byrd JC, Gruchow HW. The influence of smoking on vitamin C status in adults. Am J Public Health 1989; 79: 158–62.
33 Heitzer T, Schlinzig T, Krohn K, Meinertz T, Munzel T. Endothelial dysfunction, oxidative stress, and risk of cardiovascular events in patients with coronary artery disease. Circulation 2001; 104: 2673–8.
34 Chambers JC, McGregor A, Jean-Marie J, Obeid OA, Kooner JS. Demonstration of rapid onset vascular endothelial dysfunction after hyperhomocysteinemia: an effect reversible with vitamin C therapy. Circulation 1999; 99: 1156–60.
35 Perticone F, Ceravolo R, Maio R, Cloro C, Candigliota M, Scozzafava A, *et al*. Effects of atorvastatin and vitamin C on endothelial function of hypercholesterolemic patients. Atherosclerosis 2000; 152: 511–8.
36 Sherman DL, Keaney JF Jr, Biegelsen ES, Duffy SJ, Coffman JD, Vita JA. Pharmacological concentrations of ascorbic acid are required for the beneficial effect on endothelial vasomotor function in hypertension. Hypertension 2000; 35: 936–41.
37 Hirai N, Kawano H, Hirashima O, Motoyama T, Moriyama Y, Sakamoto T, *et al*. Insulin resistance and endothelial dysfunction in smokers: effects of vitamin C. Am J Physiol Heart Circ Physiol 2000; 279: H1172–8.
38 May JM. How does ascorbic acid prevent endothelial dysfunction? Free Radic Biol Med 2000; 28: 1421–9.

Acta Pharmacologica Sinica 2005 Apr; 26 (4): 453–461

Full-length article

Identification and classification of all potential hemolysin encoding genes and their products from *Leptospira interrogans* serogroup Icterohaemorrhagiae serovar Lai[1]

Yi-xuan ZHANG[2,3,4,5], Yan GENG[2,3,4,5], Bo BI[2,4], Jian-yong HE[4], Chun-fu WU[4], Xiao-kui GUO[3], Guo-ping ZHAO[2,4,6,7]

[2]*Research Center of Biotechnology, Shanghai Institutes for Biological Sciences, Chinese Academy of Sciences, Shanghai 200233, China;* [3]*Department of Microbiology and Parasitology, Shanghai Second Medical University, Shanghai 200025, China;* [4] *The School of Pharmaceutical Engineering,Shenyang Pharmaceutical University, Shenyang 110016, China;* [6]*Chinese National Human Genome Center at Shanghai, ZhangJiang High Tech Park, Shanghai 201203, China*

Key words

hemolysin; *Leptospira interrogans;* sphingomyelinase

[1] Project supported by the National Natural Science Foundation of China (No 30370071) and the National High Technoogy Research and Development Program of China (863 Program, No 2003, AA223030).
[5] The two authors contributed equally to this work.
[7] Correspondence to Prof Guo-ping ZHAO.
Phn 86-21-5080-1919.
Fax 86-21-5080-1922.
E-mail gpzhao@sibs.ac.cn

Received 2004-11-18
Accepted 2005-01-06

doi: 10.1111/j.1745-7254.2005.00075.x

Abstract

Aim: To identify and classify all potential hemolysin candidates of *Leptospira interrogans* serogroup Icterohaemorrhagiae serovar Lai. **Methods:** All of the potential hemolysin encoding genes were characterized *in silico*. These genes were cloned and expressed in *Escherichia coli*. The hemolytic activities of the expressed proteins were assayed observing the hemolysis on sheep blood agar plates. Sphingomyelinase activities of the hemolysin candidates were measured by thin-layer chromatography (TLC) and HPLC for sphingomyelin-hydrolysis. Expression and secretion of the hemolysins in *L interrogans* were studied by reverse transcription polymerase chain reaction, Western blot, and enzyme-linked immunosorbent assays. **Results and Conclusion:** The hemolytic activities of hemolysin candidates (LA0327, LA0378, LA1027, LA1029, LA1650, LA3050, LA3937, LA4004) from *L interrogans* strain Lai were confirmed. They were further divided into two groups, sphingomyelinase hemolysins and non-sphingomyelinase hemolysins, based on their ability to hydrolyze sphingomyelin. Most of these hemolysins were actually expressed in living *L interrogans* and some of them were secreted into the environment. This study establishes an essential and complete basis for further studying the contribution of hemolysins to the pathogenesis of *L interrogans.*

Introduction

Leptospirosis is a worldwide zoonosis caused by pathogenic species of *Leptospira*, particularly, *Leptospira interrogans*[1]. Pathogenic *Leptospira* infection causes leptospirosis (Weil's syndrome), which manifests with jaundice and renal failure[2–4] along with prominent respiratory symptoms. In some cases, severe pulmonary hemorrhages may happen, which may lead to sudden death. Although potential virulence factors, such as hemolysin, lipopolysaccharide (LPS), and heat shock proteins, are suggested for leptospiral infection, the pathogenetic mechanism of leptospirosis is yet to be clarified.

Among these suggested virulence factors, bacterial hemolysin has been demonstrated in several pathogenic bacteria[5,6] and a limited number of them have been identified in *L interrogans*[7]. Annotation of the complete genomic sequence of *L interrogans* serogroup Icterohaemorrhagiae serovar Lai[8] indicated that there were ten putative hemolysin genes located on the large chromosome (CI, GB: AE010300), of which, one (LA3540) had been previously identified[7]. Our current work characterized all the other genes, except LA0177 because of its extremely short nucleotide sequence. The classification of the hemolytic activities and their expression and secretion in *L interrogans* were investigated.

Materials and methods

Bacterial strains and plasmids The virulent *L interrogans* serogroup Icterohaemorrhagiae serovar Lai type strain 56601 used in this study was maintained by the Institute for Infectious Disease Control and Prevention, Beijing, China. The avirulent strain of *L interrogans* serogroup Icterohaemorrhagiae serovar Lai (strain IPAV) was given as a gift by Dr PICARDEAU, M (Institute Pasteur, Paris, France). Strains were grown in liquid Ellinghausen-McCullough-Johnson-Harris (EMJH) medium[1] at 28 °C under aerobic conditions and collected at a density of approximately 1×10^8 bacteria per mL. *Escherichia coli* DH5α and BL21 (DH3) were used for the cloning and expression of hemolysin candidates, respectively. The pUCm-T and pET28b plasmids were served as the vectors for cloning and expression, respectively.

Characterization of hemolysin candidates First, coding sequences (CDSs) potentially encoding hemolysin candidates were identified during the genomic annotation[8]. Second, amino acid sequences of those hemolysin candidates were analyzed with the SWISS-PROT/TrEMBL non-redundant databases[9] to obtain homologous proteins, which were further compared with BioEdit (Tom Hall, North Carolina State University, Carolina, USA). Third, the domain structures of the hemolysin candidates were predicted by Pfam[10], PROSITE[11] or ProDom[12]. The secondary structures of the proteins were predicted by Jpred^2 [13]. Finally, multiple sequence alignments were made for sphingomyelinase-like hemolysin homologous proteins using clustW, and Mega^2 (Sudhir Kumar, Arizona State University, Arizona, USA) was used to establish their phylogenetic tree.

Cloning, expression, and purification of the recombinant hemolysin candidates in *E coli* Genomic DNA was isolated from *L interrogans* strain 56601 cultivated in EMJH medium. The hemolysin candidate genes were obtained by polymerase chain reaction (PCR), ligated with pUCm-T vector and transformed into DH5α cells. The confirmed recombinant plasmids were digested with corresponding enzymes, ligated with pET28b vector and then transformed into BL21 (DH3) cells. *E coli* cells were grown in Luria-Bertani medium supplemented with kanamycin at 50 mg/L at 37 °C. Protein expression was induced at A_{600} of 0.6 by addition of isopropyl-beta-*D*-thiogalactopyranoside (IPTG) at 0.6 mmol/L for 3 h. The harvested cells were suspended in Tris-HCl buffer (20 mmol/L Tris-HCl, pH 7.9) and lysed by sonication. The insoluble inclusion bodies were dissolved in the buffer (Tris-HCl 20 mmol/L, pH 7.9, NaCl 0.5 mol/L, 10% glycerol, guanidium HCl 6 mol/L) and then centrifuged at 20 000×*g* for 20 min. The soluble supernatant was applied to Ni-NTA His-Bind resin and the His-tag fusion protein was eluted by an imidazole gradient from 10 mmol/L to 1000 mmol/L in the elution buffer (20 mmol/L Tris-HCl pH 7.9, 0.5 mol/L NaCl, 10% glycerin). The purified proteins were analyzed by sodium dodecyl sulphate polyacrylamide gel electrophoresis (SDS-PAGE) with coomassie brilliant stain.

Hemolytic activity assay on sheep blood agar plates Sheep blood plates, 10% (v/v) supplemented with 25 mmol/L $MgCl_2$ and 100 mg/L kanamycin, were used to measure hemolytic activities. Lysate of *E coli* cells expressing hemolysin candidate proteins (100g/L) was dropped onto the plates, and the plates were incubated at 37 °C for 16 h, and then placed at 4 °C for 30 min. Sphingomyelinase C (0.1 U, Sigma, St Louis, MO, USA) and lysate of *E coli* cells harboring pET28b (100 g/L) were used as positive and negative controls, respectively.

Sphingomyelinase assay by thin-layer chromatography and HPLC The biphasic system consisted of an ether: methanol (9:1 v/v) organic phase containing sphingomyelin (2 g/L) and a water phase (25 mmol/L $MgCl_2$) containing the lysate of *E coli* cells expressing hemolysin candidate proteins (100 g/L). This biphasic solution was shaken at 37 °C for 4 h. After that, the organic phase (15 μL) was applied on a silica gel-60 coated glass plate. The chromatogram was developed with a mobile phase (chloroform:methanol:water: 25% ammonia 58.0:35.0:3.5:3.5 v/v). Lipids were visualized by spraying on a plate with 30% H_2SO_4 at 110 °C for 10 min. For HPLC, sphingomyelinase activity was determined in a biphasic system as described above, except for the organic phase containing sphingomyelin (1 g/L). The organic phase (7.5 μL) was applied to HPLC (YWG C_{18} 5 μm, 200 mm×4.6 mm, China) and the elutes were monitored by absorption at 207 nm. The mobile phase was a mixture of acetonitrile: methanol:water (154:45:81 v/v). The flow rate was 1 mL/min. Sphingomyelinase C (0.1 U) and lysate of *E coli* cells harboring pET28b (100 g/L) were used as positive and negative controls, respectively.

Validation of hemolysin encoding gene expressions in *Leptospira interrogans* strain Lai by reverse transcription RCR and Western blot According to the manufacturer's instructions, total RNA was extracted with TRIzol reagent (Invitrogen, Carlsbad, California, USA) from *L interrogans* strain Lai cultivated in EMJH medium. Total RNA (1 μg) from each sample was reverse-transcribed into cDNA according to the instructions provided with the cDNA Synthesis Kit (Invitrogen, Carlsbad, California, USA). Equal amounts of the product of the reverse transcription reaction were subjected to PCR amplification. The primers and related infor-

Table 1. Primers of hemolysin candidate genes in reverse transcription polymerase chain reaction (RT–PCR) assay and the product information. Tm, temperature.

Gene ID	RT-PCR sense primer (5'–3')	RT-PCR antisense primer (5'–3')	Product length (bp)	Tm (°C)
LA1027	CAT ATG TAC CCA TAC CAA ACC AAC	CCG TAT ACC GGA TAA CGA TCT GAA A	665	50
LA1029	TGG GAC ACG ATG AAA GAG C	ATC CAG ATA CGG TCC AAG TTT	750	52
LA4004	GTT TAC GCC GAC CCT TCC ACT CC	CTA ACG ATA AAT TAG ATC CTT GCT CCA	569	52
LA3050	CAT ATG TCT AAA ACG ACA CGA AAA	AAA GTT TCG GTT GGT GGT	501	50
LA0327	CAT ATG CTT CTT TTT GAA AGG GGA T	ATC CGA CTT AAC TCT ATA AGT TCC A	763	54
LA3937	CAT ATG CTT TTG AAG CTG ATT GGA	AAG AAG ACC CGC AAC TCC ACC	495	54
LA1650	AGA GGT GCT GAT TGT TGG G	CTA GAG CAA ATT AGA TTT GTC TGG	504	52
LA0378	AAG ATC CTG AAA ATG TAA AA	AAC AAT GCG ATT TGG TTT TGT GGA G	659	50

mation are shown in Table 1. After amplification, 5 μL of each PCR reaction product was electrophoresed on a 1.5% (w/v) agarose gel containing ethidium bromide (0.5 mg/L). For Western blot analysis, *L interrogans* strains cultivated in EMJH medium were harvested by centrifugation at 14 600×*g* for 10 min, electrophoresed on 10% SDS-PAGE gels and electrotransferred to nitrocellulose membrane under a constant voltage of 5 mA/cm^2 for 1 h. The blot was first masked by the blotting buffer (10% skim milk in 10 mmol/L Tris-HCl buffer with NaCl 150 mmol/L and 0.1% Tween-20) for 2 h and then incubated with rabbit anti-hemolysin antibody (1:5000) for 2 h. After being washed with TBST 3 times, the blot was incubated for 1 h with alkaline phosphatase (AP)-conjugated goat anti-rabbit IgG antibody (1:7500) and the color was developed by addition of bromo-chloro-indoryl phosphate/nitroblue tetrazolium (BCIP/NBT) for AP reaction.

Detection of hemolysin secretion in *L interrogans* Briefly, the culture supernatant (100 ng/well) of *L interrogans* in Korthof[11] was coated onto 96-well ELISA plates by incubation at 37 °C for 2 h. After the removal of blocking solution and washing 3–5 times with phosphate-buffered saline buffer (PBS) containing 0.1% Tween (PBS-Tween), anti-hemolysin antibodies were incubated in the plate at 37 °C for 2 h. The plate was washed 3–5 times with PBS-Tween and then incubated with AP-conjugated goat anti-rabbit IgG antibody (1:1500) at 37 °C for 1 h. The plate was washed 3–5 times with PBS-Tween and incubated with the BCIP/NBT for 20 min in the dark. Absorbance at 492 nm was recorded using an automated ELISA microplate reader.

Results

The *in silico* structural analysis indicated that there were at least two kinds of hemolysin candidates from *L interrogans* Genomic annotation of *L interrogans* strain Lai indicated that there were 10 genes putatively encoding proteins highly similar to hemolysins reported in the NCBI/Genbank and SwissProt/TrEMBL databases (Table 2).

Domain structure analysis of the candidate proteins indicated that 5 of them had barring of the characteristic domains of the phosphatase family. Specifically, the Pfam-based domain analysis indicated that all of LA1027, LA1029, LA4004, and LA3050 barred a conserved domain PF03372 of the phosphatase family. The ProDom-based analysis showed that all of the proteins, except LA3050, were highly similar to *L interrogans* serovar hardjo sphingomyelinase-like hemolysin (SP17627/SwissProt), barring phosphatase domains of PD011673, PD447657, and PD041204 in similar regions of the proteins. Although LA3050 was reasonably similar to SP17627 (67%) and also had the PD041204 domain, it lacks the other two domains mainly because of its short primary peptide sequence. Although LA3540 had PD011673, PD041204, and the phosphatase conserved domain PF03372, LA3540 had previously been identified as a pore-forming hemolysin[5].

Amino acid sequence analysis of these sphingomyelinase-like hemolysin candidates indicated that the conserved Mg^{2+}-complexing glutamic acid and asparagine involved in substrate binding were identified in LA1029, Glu^{200}, and Asn^{343}, corresponding to the Glu^{131} and Asn^{274} of SP17627, respectively. For LA4004, only Asn^{267} was identified as corresponding to the conserved Asn^{274} of SP17627. Protein secondary structures were predicted by Jpred[2], and their similarities are shown in Figure 1.

The remaining 5 candidate proteins have little sequence similarity to those of sphingomyelinase-hemolysin proteins. Based on the *in silico* analysis, they do not have any phosphatase family domains or share any common domains. Therefore, these hemolysin candidates, if they are active, may function based on the mechanism of pore formation and

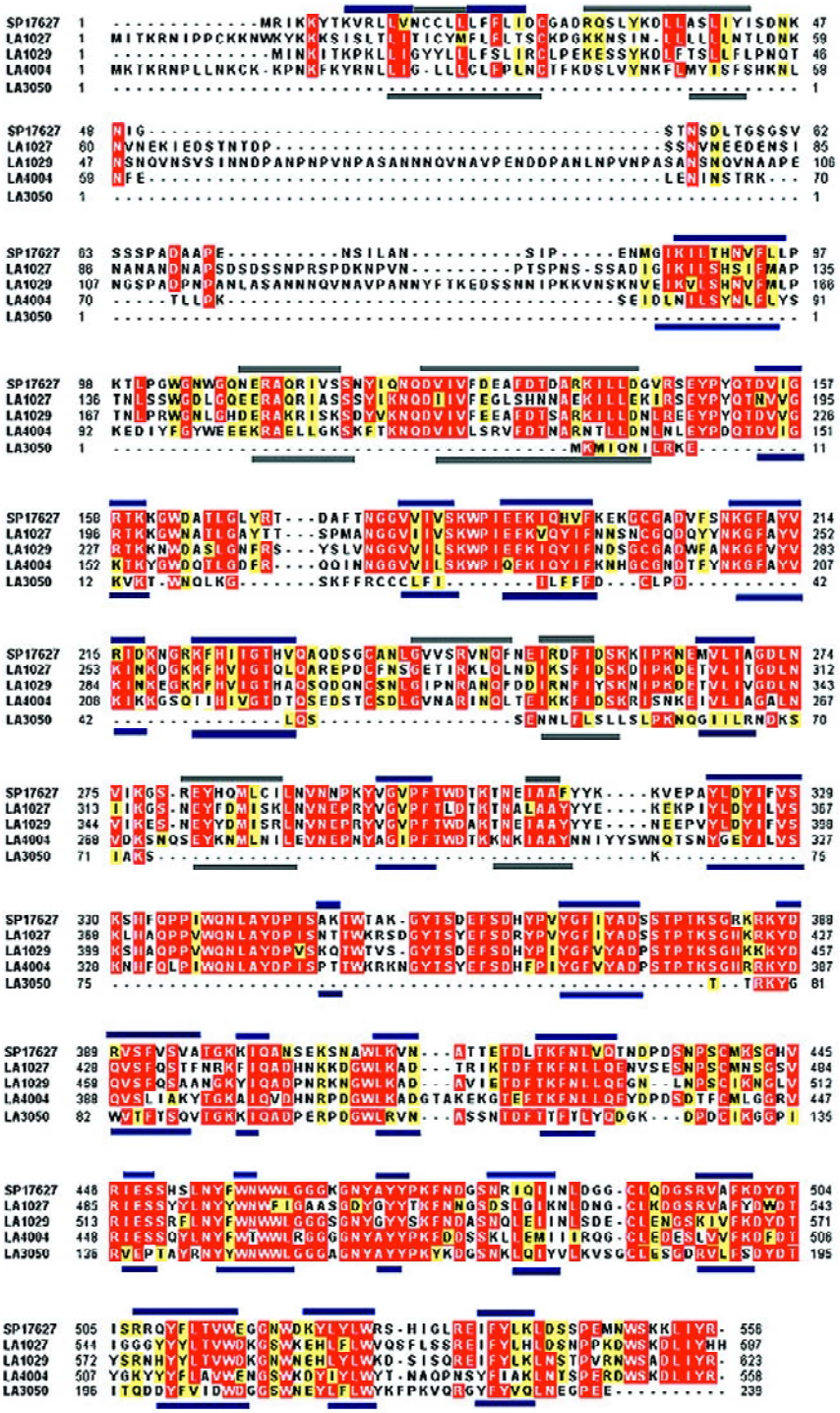

Figure 1. Primary and secondary structure comparisons of SP17627 and *Leptospira interrogans* sphingomyelinase-like hemolysins. Multiple amino acid sequence alignment was performed using BioEdit. Identical amino acids are shaded in red. Similar amino acids are shaded in yellow. The Mg^{2+}-complexing glutamic acid and asparagine involved in substrate binding are indicated by arrows; these were Glu^{131} and Asn^{274} in SP17627. Correspondingly, the conserved sites were found at Glu^{200} and Asn^{343} in LA1029, and Asn267 in LA4004. Protein secondary structures were predicted by Jpred[2], and only the results of SP17627 (up) and LA1029 (down) are shown (the grey belts are alpha-helices and the black belts are beta-sheets).

Table 2. Hemolysin candidate genes of *Leptospira interrogans*.

Groups	Gene identity	Gene name	Gene length (bp)	Transcription orientation	Product	Molecular weight (Da)	Isoelectric point
Sphingomyelinase	LA1027	*sph1*	1794	Reverse (R)	Sphingomyelinase C precursor	68 192	8.15
	LA1029	*sph2*	1872	R	Sphingomyelinase C precursor	71 030	5.95
	LA4004	*sph3*	1665	Forward (F)	Sphingomyelinase C precursor	64 433	7.94
	LA3050	*sph4*	720	R	Sphingomyelinase C precursor	27 926	8.73
Non-sphingomyelinase	LA3540	*sphH*	1677	R	Sphingomyelinase C precursor	65 336	8.84
	LA0327	*tlyA*	831	F	Hemolysin	31 670	9.54
	LA0378	*hlyX*	1179	R	TPR-repeat-containing protein	44 956	6.17
	LA1650	*hlpA*	942	F	Hemolysin hemolytic protein	36 534	8.52
	LA3937	*hlyC*	1335	R	Similar to hemolysin	50 431	5.04
	LA0177	*hlyA*	225	F	Alpha-hemolysin	8 590	9.64

other mechanisms.

Phylogenetic analysis was performed on the sphingomyelinase-hemolysin proteins. An neighbor-joining unrooted phylogenetic tree was established including sequences of SP17627, LA1027, LA1029, LA4004, LA3050, and other similar proteins, with a cut-off amino acid identity of 53% and similarity of 67%. Hemolysins from *Staphylococcus aureus, Bacillus cereus, Listeria ivanovii*, and *Pseudomonas* sp strain TK4 made up one branch of the tree, and the sphingomyelinase-like proteins of *L interrogans* made up another branch (Figure 2).

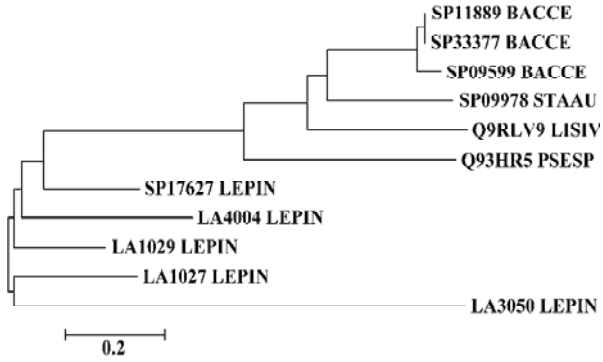

Figure 2. Comparison of sphingomyelinase-hemolysin protein sequences by neighbor-joining method shown in unrooted tree. STAAU, *Staphylococcus aureus*; BACCE, *Bacillus cereus*; LISIV, *Listeria ivanovii*; PSESP, *Pseudomonas* sp strain TK4; LEPIN, *Leptospira interrogans*.

The hemolytic activities of the recombinant hemolysin candidates from *L interrogans* were determined Among the 10 hemolysin candidates from *L interrogans*, LA3540 had previously been identified[7], whereas LA0177 is extremely short in its sequence and has no detectable phosphatase domain. Therefore, only the remaining 8 hemolysin candidate genes were cloned into *E coli* and the recombinant proteins were purified to homogeneity determined by

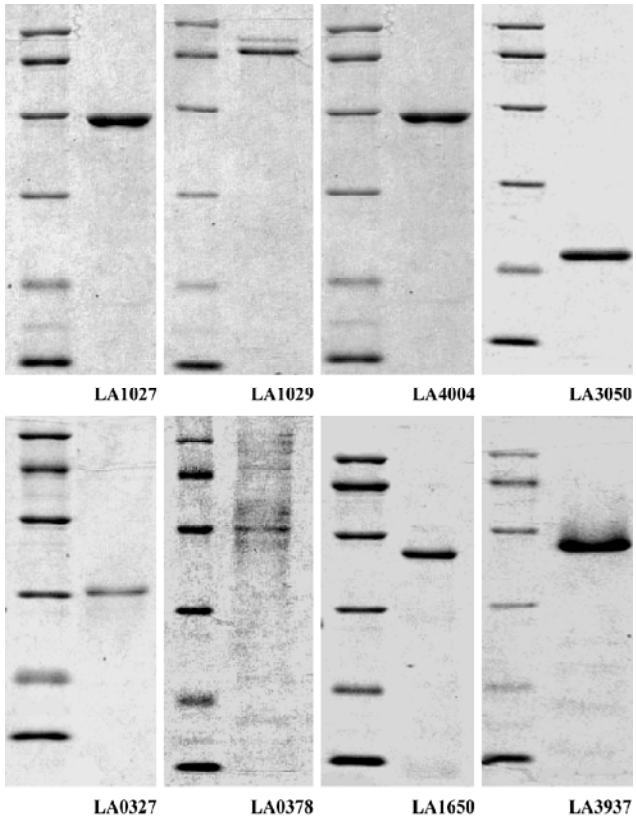

Figure 3. Purification of recombinant hemolysins. Protein markers: 97 400 Da, 66 200 Da, 43 000 Da, 31 000 Da, 20 100 Da, 14 400 Da.

SDS-PAGE followed by coomassie brilliant stain (Figure 3).

Crude cell lysates of *E coli* expressing cloned hemolysin candidates were spotted onto sheep blood agar plates and, after incubation at 37 ºC for 16 h, clear hemolytic zones were observed for all the candidates via a cold-warm hemolytic procedure (Figure 4). The hemolytic zone of LA1029 appeared at first and the area of hemolysis was the biggest. Clear hemolytic zones of LA1027 and LA4004 appeared a little later. Hemolysis caused by LA3050 appeared last and the area of the hemolytic zone was the smallest. For those predicted to be in the non-sphingomyelinase-hemolysin family, hemolytic abilities were also different: LA3937 was the highest and LA0327, LA0378, and LA1650 were second highest, third highest, and lowest, respectively.

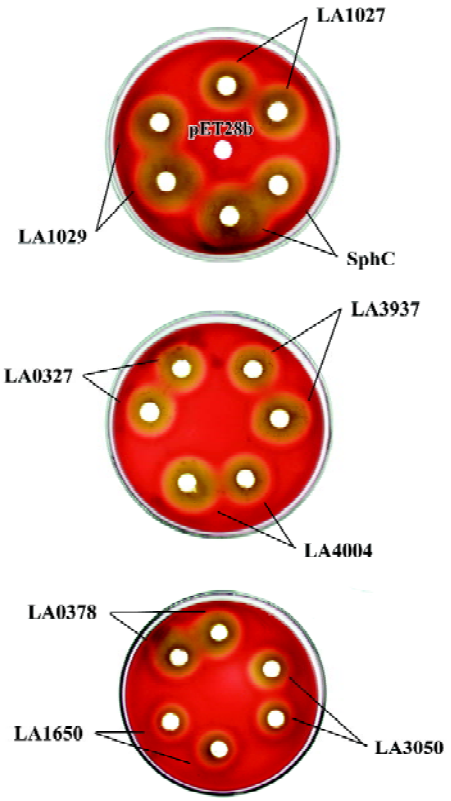

Figure 4. Hemolysis of recombinant hemolysin candidates on sheep blood planes.

The sphingomyelinase activities of hemolysin candidates were detected The sphingomyelinase activities of recombinant hemolysin candidates were detected by TLC assay. Results showed that only LA1027, LA1029, LA4004, and LA3050 could hydrolyze sphingomyelin. These results were confirmed by HPLC assay. The peak area of sphingomyelin was diminished after hemolysin treatment and the percentages of hydrolyzed sphingomyelin are displayed in Table 3. The percentages of hydrolyzed sphingomyelin of sphingomyelinase (SphC), LA1029, LA1027, LA4004, and LA3050 were 73.99%, 68.87%, 61.10%, 56.52%, and 48.04%, respectively. LA3937, LA0327, LA0378, and LA1650 could not hydrolyze sphingomyelin under the same condition.

Hemolysin gene expression and hemolysin secretion in *L interrogans* RT-PCR analysis indicated that all the 8 candidates, LA0327, LA0378, LA1027, LA1029, LA1650, LA3050, LA3937, and LA4004, were transcribed in *L interrogans* strain Lai and strain IPAV cultivated in EMJH or Korthof culture medium (Figure 5). The transcription levels of some hemolysin encoding genes, LA0378, LA0327, and LA3050, were higher in *L interrogans* cultivated in Korthof medium than those in the EMJH medium. Western blot can detect hemolysin proteins in strain Lai cell crude extracts for all the candidates except LA1027 (Table 4). In addition, we failed to detect this protein by Western blot in the strain IPAV cultured in EMJH medium. In addition, we failed to detect LA3050 under the same condition, whereas the other 6 hemolysin candidates were all detected. LA1029, LA4004, LA3050, LA1650, and LA3937 were secreted into the environment, as determined by ELISA, and the secretion levels were higher in strain Lai than those in strain IPAV (Figure 6). LA0327 was secreted into the environment both in strain Lai and in strain IPAV. LA1027 was not secreted either in strain Lai or in strain IPAV.

Discussion

In 1956, Alexander *et al*[14], for the first time, discovered that *L interrogans* had a hemolysin-like substance that could hemolyze red blood cells of ruminants, such as sheep, cows,

Table 3. Percentage of hydrolyzed sphingomyelin after reaction with hemolysins for 4 h.

	SMaseC	LA1029	LA1027	LA4004	LA3050
Peak area before reaction	317 274	317 274	317 274	317 274	317 274
Peak area after reaction	82 498	98 754	123 410	137 946	164 836
Hydrolyzed sphingomyelin (%)	73.99	68.87	61.10	56.52	48.04

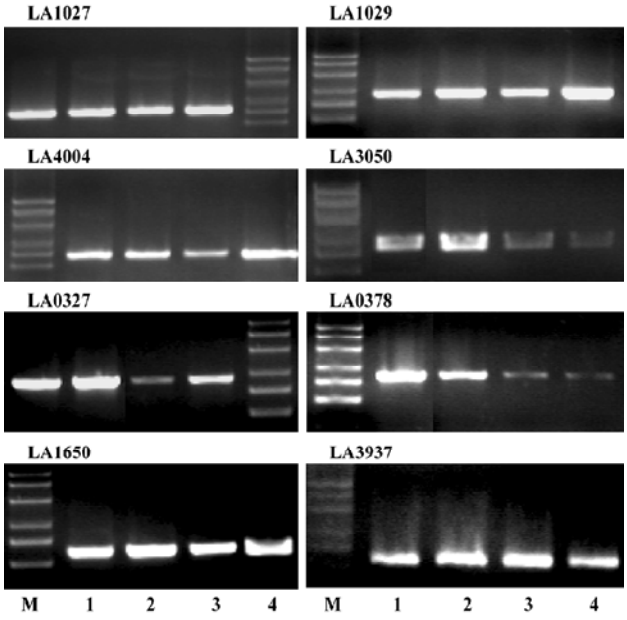

Figure 5. Transcription of hemolysin candidate genes encoded by *L interrogans* chromosome by reverse transcription polymerase chain reaction detection. 1, virulent strain Lai cultivated in Korthof (KV); 2, avirulent strain IPAV cultivated in Korthof (KNV); 3, avirulent strain IPAV cultivated in EMJH medium (ENV); 4, virulent strain Lai cultivated in EMJH medium (EV). DNA markers: 400 bp, 600 bp, 800 bp, 1200 bp, 1600 bp, 2000 bp.

Table 4. Hemolysin candidate gene expression in *L interrogans*. ELISA, enzyme-linked immunosorbent assay; NV, avirulent strain IPAV; V, virulent strain Lai.

Gene ID	Western blot assay	
	V	NV
LA1027	–	–
LA1029	+	+
LA4004	+	+
LA3050	+	–
LA0327	+	+
LA0378	+	+
LA1650	+	+
LA3937	+	+

and goats. Its hemolytic activity was completely lost after being heated at 56 °C for 5 min, indicating its heat-labile character. Later, hemolysins were detected in many pathogenic *L interrogans*[15].

L interrogans gene encoding hemolysin was first cloned from the pathogenic serovar hardjo. This protein obviously possessed both hemolytic and sphingomyelinase C activities[16]. The only hemolysin gene cloned from serovar lai before our efforts was CDS LA3540[7]. Although this gene encoded a hemolytically active protein with a phosphatase-like domain, the purified protein did not have any detectable sphingomyelinase activity. Therefore, it was proposed that it was a transmembrane pore formation protein. The concept of transmembrane pore formation by bacterial protein toxins was first brought forward by Fussle *et al*[17] to explain the mechanism of action of staphylococcal alpha-toxin and it is apparent today that the majority of medically relevant pathogens produce pore-forming proteins[18]. Many of these toxins have been designated as hemolysins because of their lytic action on red blood cells.

Our studies have proven experimentally that, besides the previously characterized LA3540 and the very short hemolysin candidate gene, LA0177, the recombinant proteins encoded by the candidate genes from *L interrogans* strain Lai (LA0327, LA0378, LA1027, LA1029, LA1650, LA3050, LA3937, LA4004) were hemolysin. According to the *in silico* structure analysis, LA1027, LA1029, LA4004, and LA3050 are highly similar to SP17627, the hemolytic sphingomyelinase C from serovar hardjo, with respect to domain organizations, amino acid sequences, and the predicted secondary structures. These predictions were further confirmed by sphingomyelinase assays. Other candidates, LA0327, LA0378, LA1650, and LA3937, were confirmed to be non-sphingomyelinase hemolysins. They are likely either to be pore-forming proteins or to have other mechanisms of hemolytic activity.

Spirochetes are evolutionarily primitive and *L interrogans* is a facultative free-living pathogen possessing a large number of different kinds of hemolysins. Therefore, questions about the possibilities of convergence, divergence, or other models of evolution should be addressed in the future. In this study, the phylogenetic analysis of sphingomyelinase from *L interrogans*, both serovar lai and serovar hardjo, with those from other bacteria indicated that the sphingomyelinase hemolysins of *L interrogans* are closely related but distantly different from those of the others. Thus, this group of hemolysins is more likely to be evolved from a common ancestor with a divergence mechanism. For the other group of hemolysins, because of their high level of diversity, the possibility of horizontal gene transfer cannot be excluded.

Almost all of these hemolysins were expressed *in vivo* under normal culture conditions. Among them, LA1029, LA4004, LA1650, and LA3937 were secreted into the environment and the secretion level was significantly higher ($P<0.01$) in the virulent strain Lai than in the avirulent strain IPAV (Figure 6). LA0327 was secreted into the environment both in strain Lai and IPAV without significant difference.

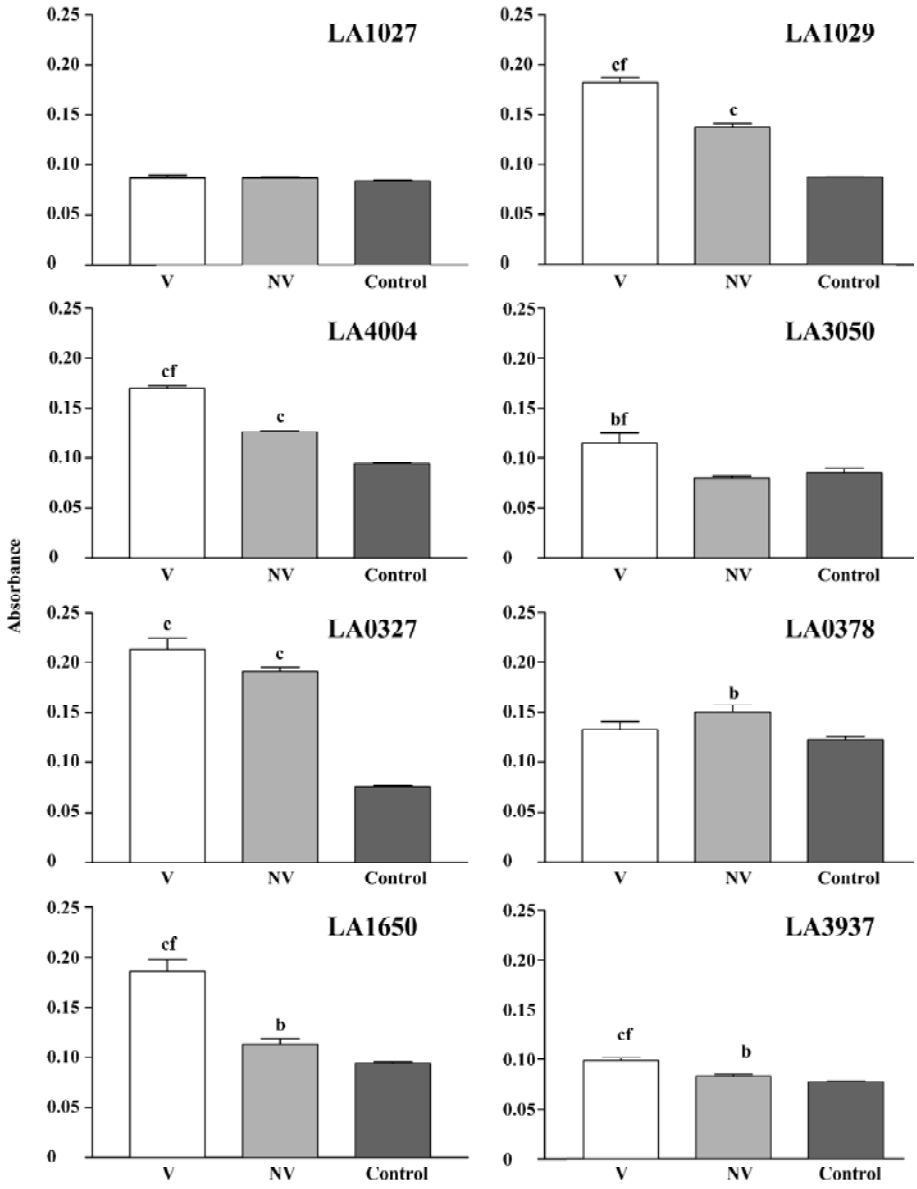

Figure 6. Secretion of hemolysin candidates in *Leptospira interrogans* by enzyme-linked immunosorbent assay. C, control (blank Korthof medium); NV, avirulent strain IPAV; V, virulent strain Lai. $^{b}P<0.05$; $^{c}P<0.01$ *vs* control. $^{e}P<0.05$, $^{f}P<0.01$ *vs* NV.

LA1027 was not expressed or secreted in either strain Lai or IPAV, which was testified by ELISA and Western blot assay (Figure 6, Table 4). The significant difference in hemolysin expression and secretion between the virulent strain Lai and the avirulent strain IPAV may suggest that hemolysins might play an important role in the pathogenesis of *Leptospira*.

Acknowledgment

We thank Shuang-xi REN for suggestions and comments, and Bao-yu HU and Xiu-gao JIANG for help in bacterial culture preparation.

References

1 Faine S. Leptospira and leptospirosis. New York: CRC Press; 1994.
2 Kmety E, Dikken H. Classification of the species *Leptospira interrogans* and history of its serovars. Groningen: University Press; 1993.
3 Ramadass P, Jarvis BD, Corner RJ, Penny D, Marshall RB. Genetic characterization of pathogenic *Leptospira species* by DNA hybridization. Int J Syst Bacteriol 1992; 42: 215–9.
4 Ozdemir V, Erol E. Leptospirosis in Turkey. Vet Rec 2002; 150:

248–9.
5 Lee SH, Kim S, Park SC, Kim MJ. Cytotoxic activities of *Leptospira interrogans* hemolysin SphH as a pore-forming protein on mammalian cells. Infect Immun 2002; 70: 315–22.
6 Sakurai J, Honda T, Jinguji Y, Arita M, Miwatani T. Cytotoxic effect of the thermostable direct hemolysin produced by *Vibrio parahaemolyticus* on FL cells. Infect Immun 1976; 13: 876–83.
7 Lee SH, Kim KA, Park YG, Seong IW, Kim MJ, Lee YJ. Identification and partial characterization of a novel hemolysin from *Leptospira interrogans* serovar lai. Gene 2000; 254: 19–28.
8 Ren SX, Fu G, Jiang XG, Zeng R, Miao YG, Xu H, *et al*. Unique physiological and pathogenic features of *Leptospira interrogans* revealed by whole genome sequencing. Nature 2003; 422: 888–93.
9 SWISS-PROT/TrEMBL databases. Europe: Swiss Institute of Bioinformatics. c2004. Available from: http://www.expasy.org/sprot and http://www.expasy.org/TrEMBL
10 Pfam database. St Louis: Washington University in St Louis. c2004. Available from: http://pfam.wustl.edu/hmmsearch.shtml
11 PROSITE database. Europe: Swiss Institute of Bioinformatics. c2004. Available from: http://us.expasy.org/prosite
12 ProDom database. Europe: Laboratoire des Interactions Plantes Microorganismes. c2004. Available from: http://prodes.toulouse.inra.fr/prodom/current/html/home.php
13 Jpred^2 database. Scotland: University of Dundee. c2004. Available from: http://www.compbio.dundee.ac.uk/~www-jpred/submit.html
14 Alexander AD, Smith OH, Hiatt CW, Gleiser CA. Presence of hemolysin in cultures of pathogenic leptospires. Proc Soc Exp Biol Med 1956; 91: 205–11.
15 Bauer DC, Morse EV. Variation and hemolysin production in relation to virulence of *Leptospira pomona*. Proc Soc Exp Biol Med 1958; 98: 505–8.
16 Cloning of a hemolysin gene from *Leptospira interrogans* serovar hardjo. Infect Immun 1989; 57: 2588–90.
17 Fussle R, Bhakdi S, Sziegoleit A, Tranum-Jensen J, Kranz T, Wellensiek HJ. On the mechanism of membrane damage by *Staphylococcus aureus* alpha-toxin. J Cell Biol 1981; 91: 83–94.
18 Bhakdi S, Tranum-Jensen J. Damage to cell membranes by pore-forming bacterial cytolysins. Prog Allergy 1988; 40: 1–43.

Acta Pharmacologica Sinica 2005 Apr; 26 (4): 462–468

Blackwell Publishing

Full-length article

Identification of a novel splice variant of human *PD-L1* mRNA encoding an isoform-lacking Igv-like domain[1]

Xian-hui HE[2], Li-hui XU, Yi LIU[3]

Key Laboratory of Ministry of Education for Tissue Transplantation and Immunology, Ji-nan University, Guangzhou 510632, China

Key words

costimulatory molecules; PD-L1; RNA splice sites; subcellular localization

[1] Project supported by grants from the National Natural Science Foundation of China (No 30230350 and No 30371651) and Major State Basic Research Development Program of China (No G2000057006).
[2] Correspondence to Dr Xian-hui HE.
Phn/Fax 86-20-8522-0679.
E-mail thexh@jnu.edu.cn
[3] Now in *Department of Dermatology, First Affiliated Hospital, Zhengzhou University, Zhengzhou 450052, China*.

Received 2004-11-12
Accepted 2005-01-10

doi: 10.1111/j.1745-7254.2005.00086.x

Abstract

Aim: To investigate the expression and regulation of PD-1 ligand 1 (PD-L1) in peripheral blood mononuclear cells (PBMC). **Methods**: The cDNA encoding human PD-L1 precursor was cloned from the total RNA extracted from the resting and phorbol dibutyrate plus ionomycin- or phytohemagglutinin-activated PBMC, by reverse transcription polymerase chain reaction (RT-PCR), and independent clones were sequenced and analyzed. The expression and subcellular localization were examined in transiently transfected cells. The *PD-L1* gene expression in different PBMC was also analyzed by RT-PCR. **Results**: A novel human *PD-L1* splice variant was identified from the activated PBMC. It was generated by splicing out exon 2 encoding an immunoglobulin variable domain (Igv)-like domain but retaining all other exons without a frame-shift. Consequently, the putative translated protein contained all other domains including the transmembrane region except for the Igv-like domain. Furthermore, the conventional isoform was expressed on the plasma surface whereas the novel isoform showed a pattern of intracellular membrane distribution in transiently transfected K562 cells. In addition, the expression pattern of the PD-L1 splice variant was variable in different individuals and in different cellular status. **Conclusion**: PD-L1 expression may be regulated at the posttranscriptional level through alternative splicing, and modulation of the PD-L1 isoform expression may influence the outcome of specific immune responses in the peripheral tissues.

Introduction

The signals provided by B7 family members are critical for both stimulating and inhibiting T-cell activation[1]. In conjunction with signaling through the T-cell receptor, CD28 ligation by B7 molecules stimulates antigen-specific proliferation of T cells and enhances production of cytokines, differentiation, and the effector function of T cells[2]. In contrast, B7 interaction with cytotoxic T-lymphocyte-associated antigen 4 (CTLA-4, or CD152) delivers a negative signal that inhibits T-cell proliferation, IL-2 production, and cell cycle progression[3]. In addition to CTLA-4, several studies have indicated that PD-1, a member of the immunoglobulin (Ig) superfamily and a CD28 homolog, functions as an important negative regulator of the immune system[2]. The ligands of PD-1, PD-L1 (B7-H1), and PD-L2 (B7-DC) have recently been identified[4–6], which deliver an inhibitory signal by binding to the common receptor PD-1[4], although some studies suggest a stimulatory signal is delivered by the PD ligand (PD-L) through a putative receptor other than PD-1[2,5]. PD-L1 and PD-L2 are homologous to B7 molecules and belong to the Ig superfamily[2]. Despite their homology with B7 molecules, PD-L1 and PD-L2 do not bind to CD28 or CTLA-4[5,6], suggesting that they possess different roles from B7 molecules.

Because of their important roles in the immune response, the expression of the B7 family is strictly regulated. Moreover, their expression is further modulated by alternative splicing of the transcripts[2]. Some of these alternatively spliced isoforms play an important part in the modulation of

immune responses. Study on CTLA-4 isoforms, for instance, indicates an association of lower mRNA levels of the soluble alternative splice form with susceptibility to autoimmune disease[7]. Similarly, differential splice variants have also been identified for B7-1 and B7-2 genes and its receptor CD28[8–10]. It has been demonstrated that a soluble B7-2 is a costimulatory molecule for human T cells[9]. Recently, we have identified two alternatively spliced variants of human PD-L2[11], although their functional implications remain to be discovered.

The present study reports the identification of a novel splicing variant of human *PD-L1* mRNA, which encodes an isoform lacking immunoglobulin variable domain (Igv)-like domain in the extracellular region. The expression and subcellular localization of this isoform was compared with the conventional product. Differential expression patterns of PD-L1 variants of different statuses suggest alternative splicing of PD-L1 may modulate the immune response in peripheral tissues.

Materials and methods

Cell preparation and activation To prepare peripheral blood mononuclear cells (PBMC), heparinized human peripheral blood was collected from two adult volunteers by venipuncture. Blood samples were diluted 1:2 with phosphate-buffered saline (PBS) and a mononuclear cell fraction was obtained by centrifugation over a Ficoll-Hypaque density gradient (Lymphoprep; NYCOMED, Elverum, Norway). PBMC were collected from the interface and washed twice with PBS and resuspended in RPMI-1640 medium supplemented with 10% (v/v) fetal bovine serum, 10 mmol/L glutamine, 2-mercaptoethanol 50 μmol/L , benzylpenicillin 100 kU/L , and streptomycin 100 mg/L (Invitrogen, Carlsbad, CA, USA) at a final concentration of 2×10^9 cells/L. The cells were incubated in a humidified atmosphere with 5% CO_2 for 48 h at 37 ℃ in the presence of 1×10^{-7} mol/L phorbol 12,13-dibutyrate (PDB; Calbiochem, San Diego, CA, USA) and 0.5 μg/mL ionomycin (Sigma, St Louis, MO, USA) or 10 mg/L phytohemagglutinin (PHA; Sigma).

Reverse transcription polymerase chain reaction amplification (RT-PCR) of PD-L1 cDNA Heparinized human peripheral blood was collected from two donors by venipuncture. Total RNA was extracted from freshly isolated and activated PBMC using TRIzol reagent (Invitrogen). cDNA were synthesized from the isolated RNA using the ThermoScript RT-PCR system according to the recommended procedure (Invitrogen). RNA integrity was verified by both electrophoresis in 1% (w/v) agarose gels and PCR amplification of the cDNA of a house-keeping gene, glyceraldehyde-3-phosphate dehydrogenase (GAPDH). PCR amplification of the resultant cDNA was performed in a total volume of 50 μL containing high fidelity DeepVent *Taq* polymerase (New England Biolabs, Beverly, MA, USA). For amplification of PD-L1, PCR was performed with an initial denaturation for 2 min at 94 ℃, followed by 35 cycles of 94 ℃ for 30 s, 50 ℃ for 30 s, and 72 ℃ for 1 min, and a final extension for 10 min at 72 ℃. The primers (5'-CCG CGA ATT CAT GAG GAT ATT TGC TGT CTT TA-3' and 5'-ATC AGG TAC CTT ACG TCT CCT CCA AAT GTG TAT C-3') were designed to amplify the entire coding sequence of human PD-L1 cDNA[4]. For amplification of the GAPDH cDNA, PCR was performed as above, except that the annealing temperature was 60 ℃ and the primers (5'-AAG GCT GAG AAC GGG AAG CTT GTC ATC AAT-3' and 5'-TTC CCG TCT AGC TCA GGG ATG ACC TTG CCC-3') were designed to amplify the target sequence. All primers were synthesized at BioAsia (Shanghai, China).

Cloning and sequencing of PD-L1 cDNA The PCR products were separated by electrophoresis in 1% (w/v) agarose gels containing ethidium bromide and recovered from the gel using a QIAquick Gel Extraction kit (QIAGEN, Hilden, Germany). The fragments of 873 bp and 532 bp were digested separately with *Eco*RI and *Kpn*I, and cloned into a pEGFP-N1 vector (ClonTech, Palo Alto, CA, USA). Randomly selected transformed DH5α clones were screened with *Eco*RI and *Kpn*I cutting for the presence of a correctly sized insert. Nucleotide sequences of independent clones from the samples of 2 donors were determined using dye-labeled deoxy-terminator, a 377 automated DNA sequencer (Applied Biosystem, Foster City, CA, USA).

Expression of PD-L1-EGFP fusion proteins in K562 cells PD-L1 type I or type II cDNA containing the sequence encoding signal peptide was separately subcloned into the mammalian expression vector pEGFP-N1 to construct the vectors for the fusion proteins of PD-L1 isoforms with enhanced green fluorescent protein (EGFP). These vectors were named pEGFP/PD-L1I (for the type I isoform) and pEGFP/PD-L1II (for the type II isoform). A Kozak sequence was included at the translational initiation region and the stop codon was deleted. EGFP was thus fused at the C-terminus of the PD-L1 isoform. For transient transfection, K562 cells were grown in RPMI-1640 supplemented with 10% (v/v) fetal bovine serum at 37 ℃ in a CO_2 incubator. Cells were transfected using a Cell Line Nucleofector kit V and Nucleofector Device (Amaxa, Cologne, Germany) according to the recommended protocol with 2 μg of the expression vector pEGFP/PD-L1I, pEGFP/PD-L1II, or empty vector pEGFP-N1, respectively, and left for 24 h in a CO_2 incubator.

These cells were subsequently stained with phycoerythrin (PE)-labeled mouse-antihuman PD-L1 monoclonal antibody (PE-PD-L1, *e*-Bioscience, San Diego, CA) and fixed with 4% (w/v) paraformaldehyde. The fluorescence of EGFP and PE was then analyzed by flow cytometry (FACSCalibur; Becton Dickinson, San Jose, CA, USA) and confocal microscopy (Spinning Disk Confocal Microscope; Perkin Elmer, Wellesley, MA, USA).

Western blot Cells (1×10^6) were dissolved in loading buffer and separated using sodium dodecyl sulfate-polyacrylamide gel electrophoresis (10% w/v) according to Laemmli's discontinuous system[12]. After electrophoresis, the gels were blotted onto nitrocellulose paper (Bio-Rad, Hercules, CA, USA) for Western blot analysis to visualize the specific protein bands. The Western blots were incubated with the goatantihuman PD-L1 antibody (R&D, Minneapolis, MN, USA). Horseradish peroxidase-conjugated rabbit-antigoat antibody (Jackson ImmuneResearch, West Grove, PA, USA) was used as the secondary reagent, and the color reaction was developed using 4-chloro-1-naphthol as a substrate. The molecular mass was evaluated with a software package (PhotoCapt Ver11.01; Vilber Lourmat, Marne La Vallée, France).

Bioinformatics Homology analyses of the cloned sequences were performed using a BLAST[13] search on the NCBI website and a PROSIS software package (Hitachi Software, Yokohama, Japan). The human genomic DNA sequence (submitted to the GenBank database under accession number AL162253) from clone RP11-574F11 on chromosome 9, which contains the *PD-L1* gene, was used to analyze exon-intron junction sequences. The transmembrane regions were predicted using TMpred, a web-based program[14]. SignalP[15] was used to identify the potential signal peptide.

Results

Cloning and sequence analysis of a *PD-L1* splice variant RT-PCR was performed to amplify the full coding sequence of *PD-L1* mRNA with specific primers. PCR product resolution on agarose gel revealed that the product of activated PBMC had one main band of 873 bp and a minor band of 532 bp (Figure 1A, lane 3), whereas that of freshly isolated PBMC only had the shorter one (Figure 1A, lane 2). The fragments of 873 bp and 532 bp were inserted separately into the pEGFP-N1 vector. Nine independent transformed DH5a clones were identified to have the expected inserts. DNA sequencing of these clones showed that 5 clones contained the 873 bp DNA fragment, which was the complete

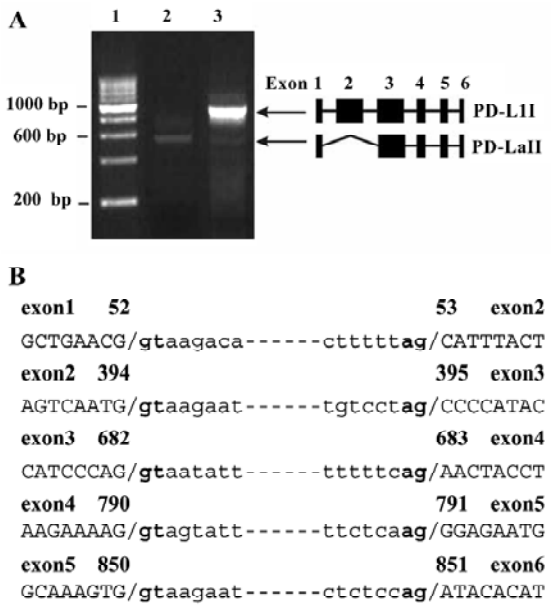

Figure 1. Reverse transcription polymerase chain reaction amplification and cloning of *PD-L1* mRNA from human leukocytes. (A) RT-PCR products with the exons depicted at the right. Lane 1, 200 bp DNA ladder; lane 2, RT-PCR product of total RNA from fresh peripheral blood mononuclear cells (PBMC); lane 3, RT-PCR product of total RNA from phorbol dibutyrate+ionomycin-activated PBMC. (B) Exon-intron junction sequences are indicated with the nucleotide numbers of human *PD-L1* cDNA, which are based on the DNA sequence AL162253.

coding sequence for conventional PD-L1 (designated PD-L1I, submitted to the GenBank database under accession number AY254342), and which was identical to the previously reported cDNA of human PD-L1 (submitted to the GenBank database under accession number AF233516[4]). The other 4 clones contained the 532 bp fragment and were identical to PD-L1 cDNA except for a deletion of a 341 bp fragment as revealed by BLAST analysis. Sequence homology searches performed with the BLASTn algorithm[13] revealed that this sequence might be an alternatively spliced variant of *PD-L1* mRNA.

To examine how this variant was generated, the exon-intron junction sequences (Figure 1B) were analyzed based on the DNA sequence containing the *PD-L1* gene (submitted to the GenBank database under accession number AL162253). The result showed that this variant was an alternatively spliced variant, which was produced by splicing out exon 2 to the canonical acceptor site at the 5' end of exon3 while retaining all other exons (Figure 1A). This splice variant was designated PD-L1II (submitted to the GenBank database under accession number AY291313).

Analysis of amino acid sequence deduced from *PD-L1* splice variant To analyze the putative translated protein of the PD-L1II, the deduced amino acid sequence was aligned with the conventional product PD-L1I using the PROSIS program. PD-L1I and PD-L1II variants contain open reading frames of 290 and 176 amino acid residues, respectively (Figure 2). Both of them contain the transmembrane domain as predicted with the TMpred program[14], and the signal peptide identified with the SignalP program[15], whereas the alternatively spliced isoform PD-L1II lacks an IgV-like domain but retains all other domains.

Expression and subcellular localization of the PD-L1II isoform fused with EGFP PD-L1 is a transmembrane protein, which would be expressed on the plasma surface, but direct visualization of its subcellular localization has not been reported. To determine whether the conventional product, PD-L1I, was located at the cell surface, and to investigate the distribution of PD-L1II, we examined the subcellular localization of their proteins in K562 cells transfected with pEGFP/PD-L1I or pEGFP/PD-L1II by flow cytometry and confocal microscopy. The expression of PD-L1I-EGFP and PD-L1II-EGFP fusion proteins was verified by Western blot (Figure 3). The estimated molecular masses of these two products were 74.3 kDa and 52.3 kDa, respectively, which were larger than the theoretical molecular masses of PD-L1I-EGFP (60 kDa) and PD-L1II-EGFP (47 kDa), probably because of posttranslational glycosylation. Thus, the glycosylation extent of PD-L1II was likely to be lower than that of PD-L1I. Moreover, flow cytometry analysis revealed that only the cells transfected with pEGFP/PD-L1I expressed PD-L1 on the

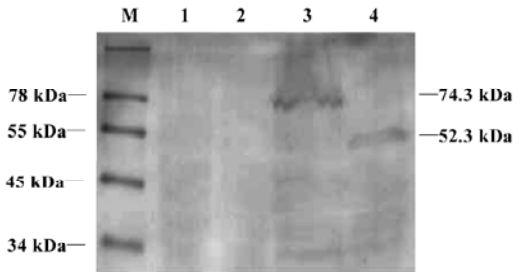

Figure 3. Western blot analysis of PD-L1-enhanced green fluorescent protein (EGFP) fusion proteins expressed in transiently transfected K562 cells. M, molecular weight marker; lane 1, control cells; lane 2, pEGFP-N1; lane 3, pEGFP/PD-L1I; lane 4, pEGFP/PD-L1II.

cell surface, whereas no PD-L1 could be detected on the surface of the cells transfected with pEGFP/PD-L1II using antihuman PD-L1 antibody (Figure 4). To further investigate the subcellular distribution of the fusion proteins, confocal microscopy showed that PD-L1I-EGFP was largely located on the plasma membrane in the pEGFP/PD-L1I transfected cells, which could be stained by the specific monoclonal antibody for human PD-L1, indicating that it could be transported to the cell surface. Interestingly, PD-L1II-EGFP showed a pattern of intracellular membrane distribution as revealed by EGFP fluorescence, and those cells transfected with pEGFP/PD-L1II could not be stained by the specific antibody (Figure 5).

Differential expression of *PD-L1* variants To compare the expression pattern of these *PD-L1* mRNA variants in the resting and activated PBMC, total RNA of freshly isolated (resting) and activated PBMC of two unrelated donors were

```
          10         20         30         40         50         60
I   MRIFAVFIFM TYWHLLNAFT VTVPKDLYVV EYGSNMTIEC KFPVEKQLDL AALIVYWEME   Signal peptide
II  MRIFAVFIFM TYWHLLNA-- ---------- ---------- ---------- ----------   (1-18aa)
          70         80         90        100        110        120
I   DKNIIQFVHG EEDLKVQHSS YRQRARLLKD QLSLGNAALQ ITDVKLQDAG VYRCMISYGG   IgV-like
II  ---------- ---------- ---------- ---------- ---------- ----------   (19-132aa)
         130        140        150        160        170        180
I   ADYKRITVKV NAPYNKINQR ILVVDPVTSE HELTCQAEGY PKAEVIWTSS DHQVLSGKTT   IgC-like
II  ---------- --PYNKINQR ILVVDPVTSE HELTCQAEGY PKAEVIWTSS DHQVLSGKTT   (133-238aa)
         190        200        210        220        230        240
I   TTNSKREEKL FNVTSTLRIN TTTNEIFYCT FRRLDPEENH TAELVIPELP LAHPPNERTH   TM
II  TTNSKREEKL FNVTSTLRIN TTTNEIFYCT FRRLDPEENH TAELVIPELP LAHPPNERTH   (239 258aa)
         250        260        270        280        290
I   LVILGAILLC LGVALTFIFR LRKGRMMDVK KCGIQDTNSK KQSDTHLEET*              Cytoplasmic tail
II  LVILGAILLC LGVALTFIFR LRKGRMMDVK KCGIQDTNSK KQSDTHLEET*              (259-290aa)
```

Figure 2. Alignment of the deduced amino acid sequences of human PD-L1 variants. Amino acid sequences were deduced from the cDNA and aligned by PROSIS program. Gaps have been introduced for best-fit alignment and are indicated by dashes. The signal peptide is in bold. The transmembrane regions were predicted using the TMpred program[14] and are indicated by single underlining. Translational stop sites are indicated by asterisks. IgV, immunoglobulin (Ig) variable-like domain; IgC, Ig constant-like domain; TM, transmembrane domain.

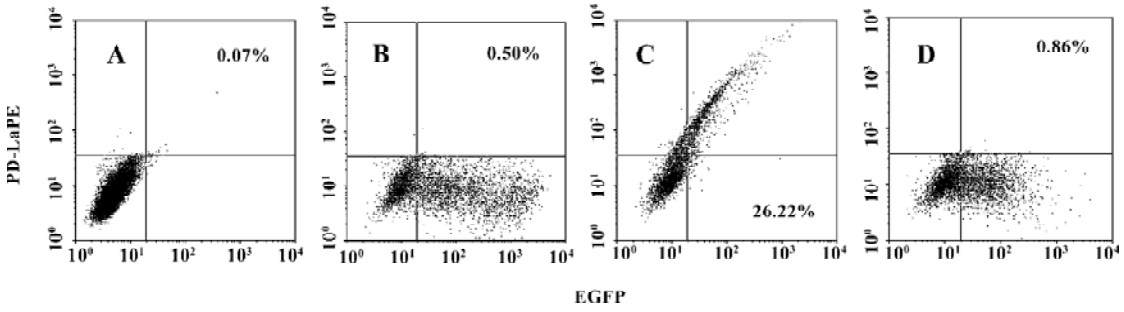

Figure 4. Flow cytometry analysis of the expression of PD-L1-enhanced green fluorescent protein (EGFP) fusion proteins in transiently transfected K562 cells. The percentages of PD-L1$^+$ and EGFP$^+$ cells are shown in the upper right quadrant. Data represent one of three independent experiments: (A) control; (B) pEGFP-N1; (C) pEGFP/PD-L1I; (D) pEGFP/PD-L1II.

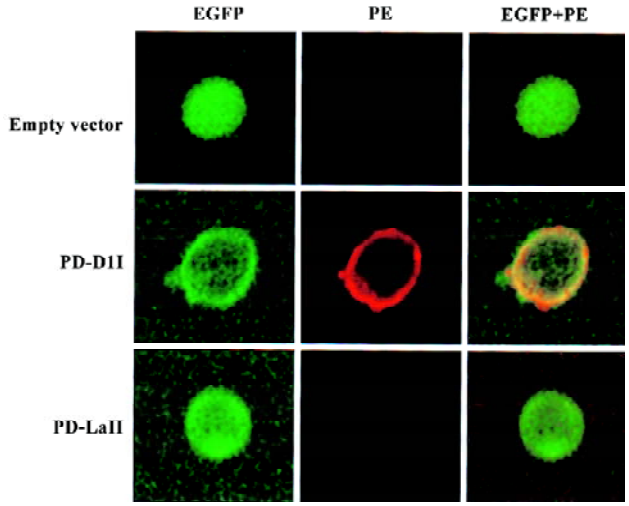

Figure 5. Confocal microscopy analysis of the subcellular distribution of PD-L1I-enhanced green fluorescent protein (EGFP; middle panels) and PD-L1II-EGFP (bottom panels) in transiently transfected K562 cells (×200). Left panels, EGFP fluorescence; middle (vertical) panels, phycoerythrin (PE) fluorescence; right panels, overlay of EGFP and PE fluorescence.

examined by RT-PCR (Figure 6). There was only the *PD-L1II* mRNA variant in the resting PBMC from donor 1, whereas both *PD-L1I* and *PD-L1II* variants existed in the PDB plus ionomycin-activated cells of the same donor, although the level of the *PD-L1II* variant was much lower. However, only the PD-L1I variant was detected in PHA-activated cells. In contrast, only the *PD-L1I* mRNA variant was amplified in the activated PBMC from donor 2 and there was a very low level of the PD-L1II mRNA variant in the resting cells from donor 2.

Discussion

Alternative splicing of costimulatory molecules is a common phenomenon and probably an important mechanism for regulating their function during immune responses. For instance, the splice variants of both CD28/CTLA-4 and their ligands B7-1/B7-2 have been identified, and these isoforms have been shown to play a role in regulating T-cell responses[7–10]. Recently, an alternative variant of *PD-L2* that lacks an Igv-like domain has been identified in mice[6], and a human *PD-L2* variant lacking an Igc-like domain has also been described[11]. However, no such splice variant of human *PD-L1* has been reported to our knowledge. In the present study, we identified an alternatively spliced variant of *PD-L1* mRNA encoding an isoform lacking the Igv-like domain. The novel variant was generated through splicing out exon 2, encoding an Igv-like domain but retaining all other exons without a frame-shift. The PD-L1II isoform was located at an intracellular compartment, which was likely to be the endoplasmic reticulum. In contrast, the conventional product of PD-L1 was located on the plasma membrane. Moreover, *PD-L1II* mRNA was expressed in resting PBMC but diminished or was absent in activated cells dependent on stimulating mitogens. Our results suggest that alternative splicing may be one of the mechanisms for modulating *PD-L1* expression and function in peripheral blood cells.

As the Igv-like domain of PD-L1/PD-L2 is critical for binding to PD-1[2], any isoform of PD-1 ligands lacking the Igv-like domain does not bind to PD-1. For instance, Latchman *et al* found that an alternatively spliced variant of murine PD-L2, with the Igv-like exon being deleted, did not bind to PD-1-Ig, indicating that the Igv-like domain is necessary for ligand binding[6]. Moreover, molecular modeling and site-directed mutagenesis indicates that the binding sites of PD-L1/PD-L2 for PD-1 are largely located within the Igv-like domain[16]. Therefore, the novel PD-L1II isoform identified in this study would not bind to the receptor PD-1 because of the absence of the Igv-like domain, although direct measure-

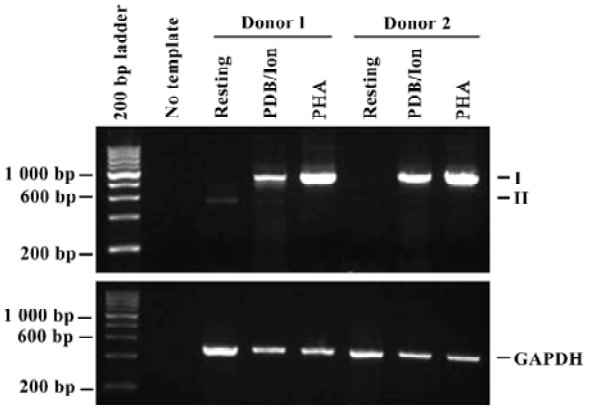

Figure 6. Reverse transcription polymerase chain reaction (RT-PCR) analysis of *PD-L1* splice variant expression in freshly isolated and mitogen-activated human peripheral blood mononuclear cells. The cDNA of the house-keeping gene, glyceraldehyde-3-phosphate dehydrogenase (GAPDH), was amplified as a control. Ion, ionomycin; PDB, phorbol dibutyrate; PHA, phytohemagglutinin.

ment needs to be carried out. In addition, this isoform was located in the intracellular compartment and was unable to be transported onto the cell surface, suggesting that it would not function properly because only those expressed on the cell surface can interact with receptors. We have found similar results for the PD-L2 isoform lacking the Igc-like domain, which is also located mainly in intracellular compartments[11]. Why these isoforms could not be transported to the cell surface was unclear when the study was carried out, but this was probably a result of incorrect folding and/or defects in glycosylation of the *PD-L1*II isoform in the endoplasmic reticulum. The present study shows that the glycosylation extent of PD-L1II is lower than that of PD-L1I, suggesting that potential glycosylation sites on the Igv-like domain may be important for PD-L1 transportation to the cell surface.

PD-L1 and PD-L2 are two ligands for PD-1, a costimulatory molecule that plays an inhibitory role in regulating T-cell activation in the periphery[4,6,17,18]. Their expression is thus modulated precisely during immune responses[2]. PD-L1 and PD-L2 share 40% amino acid identity and are more homologous to each other than to other ligands of the B7 family[2]. However, the expression pattern of these molecules is significantly broader than that of other B7 family ligands. The transcripts of both *PD-L1* and *PD-L2* were detected at high levels in the placenta and at low levels in the spleen, lymph nodes, and thymus, and were absent in the brain[4–6]. Expression of *PD-L1* and *PD-L2* in both lymphoid and nonlymphoid tissues suggests that the PD-1/PD-1 ligand pathway may modulate immune responses in secondary lymphoid organs as well as in peripheral sites. We[19] and other investigators[5] have found that the resting T cells do not express PD-L1, but mitogen activation of human T cells results in cell surface expression of PD-L1 in addition to PD-1. Similarly activated B cells express PD-L1 and PD-L2 in addition to PD-1[4,6,20]. This suggests that at the interface of T and B contact, antigen signals can be modulated bidirectionally through PD-1, thereby limiting T-cell-receptor and B-cell-receptor signaling after activation. However, the results presented here show that the PD-L1II splice variant can be detected by RT-PCR in the resting PBMC, suggesting that the mRNA transcripts of *PD-L1* were actually produced in the resting cells, but may be alternatively spliced to generate a variant encoding the PD-L1II isoform. Because of its intracellular localization as revealed by an EGFP tag, the PD-L1II isoform could not be detected using surface staining. Thus, alternative splicing prevented PD-L1 from expression on the surface of the resting cells, thereby blocking its function. Although the expression of PD-L1II at the protein level in PBMC awaits confirmation, our results suggest that PD-L1 expression may be modulated at the posttranscriptional level through alternative splicing of its transcript.

To conclude, we identified an mRNA variant encoding a novel isoform of PD-L1, which was localized in the intracellular compartment, probably the endoplasmic reticulum. Our data also demonstrate the importance of the Igv-like domain of PD-L1 for targeting it to the cell surface.

References

1 Mueller DL, Jenkins MK, Schwartz RH. Clonal expansion versus functional inactivation: a costimulatory signaling pathway determines the outcome of T cell antigen receptor occupancy. Annu Rev Immunol 1989; 7: 445–80.

2 Carreno BM, Collins M. The B7 family of ligands and its receptors: new pathways for costimulation and inhibition of immune responses. Annu Rev Immunol 2002; 20: 29–53.

3 Krummel MF, Allison JP. CD28 and CTLA-4 have opposing effects on the response of T cells to stimulation. J Exp Med 1995; 182: 459–65.

4 Freeman GJ, Long AJ, Iwai Y, Bourque K, Chernova T, Nishimura H, *et al*. Engagement of the PD-1 immunoinhibitory receptor by a novel B7 family member leads to negative regulation of lymphocyte activation. J Exp Med 2000; 192: 1027–34.

5 Dong H, Zhu G, Tamada K, Chen L. B7-H1, a third member of the B7 family, co-stimulates T-cell proliferation and interleukin-10 secretion. Nat Med 1999; 5: 1365–9.

6 Latchman Y, Wood CR, Chernova T, Chaudhary D, Borde M, Chernova I, *et al*. PD-L2 is a second ligand for PD-I and inhibits T cell activation. Nat Immunol 2001; 2: 261–8.

7 Ueda H, Howson JM, Esposito L, Heward J, Snook H, Chamberlain G, *et al*. Association of the T-cell regulatory gene *CTLA4* with susceptibility to autoimmune disease. Nature 2003; 423:

506–11.

8 Faas SJ, Giannoni MA, Mickle AP, Kiesecker CL, Reed DJ, Wu D, *et al*. Primary structure and functional characterization of a soluble, alternatively spliced form of B7-1. J Immunol 2000; 164: 6340–8.

9 Jeannin P, Magistrelli G, Aubry JP, Caron G, Gauchat JF, Renno T, *et al*. Soluble CD86 is a costimulatory molecule for human T lymphocytes. Immunity 2000; 13: 303–12.

10 Magistrelli G, Jeannin P, Elson G, Gauchat JF, Nguyen TN, Bonnefoy JY, *et al*. Identification of three alternatively spliced variants of human CD28 mRNA. Biochem Biophys Res Commun 1999; 259: 34–7.

11 He XH, Liu Y, Xu LH, Zeng YY. Cloning and identification of two novel splice variants of human PD-L2. Acta Biochim Biophys Sin 2004; 36: 284–9.

12 Laemmli UK. Cleavage of structural proteins during the assembly of the head of bacteriophage T4. Nature 1970; 227: 680–5.

13 National Center for Biotechnology Information [homepage on the Internet]. Bethesda: USA. National Library of Medicine; c2005 [updated 2005 Jan 19; cited 2004 Oct 13]. Available from: http://www.ncbi.nih.gov/BLAST

14 Swiss EMBnet Node [homepage on the Internet]. Epalinges: Swiss Institute of Bioinformatics; [updated 2004 Dec 20; cited 2004 Oct 14]. TMpred Server; [about 2 screens]. Available from: http://www.ch.EMBnet.org/software/TMPRED_form.html

15 Bendtsen JD, Nielsen H, von Heijne G, Brunak S. Improved prediction of signal peptides: SignalP 3.0. J Mol Biol 2004; 340: 783–95.

16 Wang S, Bajorath J, Flies DB, Dong H, Honjo T, Chen L. Molecular modeling and functional mapping of B7-H1 and B7-DC uncouple costimulatory function from PD-1 interaction. J Exp Med 2003; 197: 1083–91.

17 Wiendl H, Mitsdoerffer M, Schneider D, Chen L, Lochmuller H, Melms A, *et al*. Human muscle cells express a B7-related molecule, B7-H1, with strong negative immune regulatory potential: a novel mechanism of counterbalancing the immune attack in idiopathic inflammatory myopathies. FASEB J 2003; 17: 1892–4.

18 He YF, Zhang GM, Wang XH, Zhang H, Yuan Y, Li D, *et al*. Blocking programmed death-1 ligand-PD-1 interactions by local gene therapy results in enhancement of antitumor effect of secondary lymphoid tissue chemokine. J Immunol 2004; 173: 4919–28.

19 He XH, Xu LH, Liu Y, Cai XC, Zeng YY. Cloning of the cDNA of human PD-L1 gene and the expression of its extracellular domain in *Escherichia coli*. Chin J Cell Mol Immun 2004; 20: 659–63.

20 Agata Y, Kawasaki A, Nishimura H, Ishida Y, Tsubata T, Yagita H, *et al*. Expression of the PD-1 antigen on the surface of stimulated mouse T and B lymphocytes. Int Immunol 1996; 8: 765–72.

Acta Pharmacologica Sinica 2005 Apr; 26 (4): 469–476

Blackwell Publishing

Full-length article

Hepatocyte-like cells from directed differentiation of mouse bone marrow cells *in vitro*[1]

Xiao-lei SHI[2], Yu-dong QIU[2], Qiang LI[2], Ting XIE[2], Zhang-hua ZHU[2], Lei-lei CHEN[3], Lei LI[3], Yi-tao DING[2,4]

[2]Department of Hepatobiliary Surgery; [3]Scientific Research Department, Affiliated Drum Tower Hospital, Medical College of Nanjing University, Nanjing 210008, China

Key words

bone marrow cells; hepatocytes; cell differentiation; stem cells

[1] Project supported by the National Natural Science Foundation of China (No 30371391) and the National Natural Science Foundation of Jiangsu Province, China (No BK2003008).
[4] Correspondence to Prof Yi-tao DING.
Phn 86-25-8330-4616, ext 66866.
Fax 86-25-8331-7016.
E-mail yitaoding@hotmail.com

Received 2004-11-22
Accepted 2005-01-19

doi: 10.1111/j.1745-7254.2005.00093.x

Abstract

Aim: To design the effective directed differentiation medium to differentiate bone marrow cells into hepatocyte-like cells. **Methods:** Bone marrow cells were cultured in the directed differentiation media including fibroblast growth factor-4 (FGF-4) and oncostatin M (OSM). Hepatocyte-like cells from directed differentiation of bone marrow cells were identified through cell morphology, RNA expressions by reverse transcriptase-polymerase chain reaction (RT-PCR), protein expressions by Western blot, and hepatocellular synthesis and metabolism functions by albumin ELISA, Periodic acid-Shiff staining and urea assay. **Results:** Some epithelial-like cells or polygonal cells appeared and increased in the course of the cell directed differentiation. Hepatocyte nucleur factor-3β (HNF-3β), albumin (ALB), cytokeratin 18 (CK18), transthyretin (TTR), glucose-6-phosphate (G-6-Pase), and tyrosine aminotransferase (TAT) mRNA were expressed in the course of the directed differentiation. The directed differentiated cells on d 21 expressed HNF-3β, ALB, and CK18 proteins. The directed differentiated cells produced albumin and synthesized urea in a time-dependent manner. They could also synthesize glycogen. **Conclusion:** Our differentiation media, including FGF-4 and OSM, are effective to differentiate bone marrow cells into hepatocyte-like cells, which could be used for hepatocyte resources for bioartificial liver or hepatocyte transplantation.

Introduction

Liver transplantation is one of the most effective treatments for patients with acute and chronic liver failure[1]. However, since donor livers are scare, only a small number of patients can receive a replacement liver in time. Thus, it is necessary to seek alternative therapies to replace liver transplantation.

Bioartificial liver or hepatocyte transplantation, serving as temporary liver support, can provide necessary liver functions[2-3]. The functional hepatocyte is the core of the temporary liver support. Since donor hepatocytes are limited, it is imperative to explore ways to gain functional hepatocytes. Stem cells are defined as cells that have clonogenic and self-renewing capabilities, and can differentiate into multiple different cell types that make up the organ under the right condition or given the right signals[4]. Thus, stem cell can be an ideal resource of functional hepatocytes.

Hepatocytes originating from bone marrow stem cells were first observed in rats after combined bone marrow transplantation and liver damage. In rats, a combination of hepatotoxin, which induces widespread liver damage, and 2-acetylaminofluorine, which prevents endogenous liver repair, were used. Then, a combination of Y chromosome fluorescence *in situ* hybridization (FISH) and transgene expression were used to confirm that bone marrow stem cells were the source of resultant hepatocytes[5]. The same results were demonstrated in mice[6] and humans[7,8]. In a later study, Lagasse *et al* demonstrated that transplantation of xc-kit^{high}Thy1^{low} Lin^{-}Sca-1^{+}(KTLS) bone marrow cells to irradiated hosts could treat an inborn error of hepatic metabolism[9]. Multipotent adult progenitor cells (MAPCs), a sub-

population of mesenchymal stem cells in the bone marrow, were found to differentiate into many kinds of cells including hepatocytes[10]. Recently, it has been reported that bone marrow stromal cells can develop into hepatocyte-like cells[11]. Thus, we can confirm from these findings that stem cells in bone marrow exist and can differentiate into hepatocytes *in vivo* and *in vitro*.

The differentiation processes of stem cells are likely to be complex, but must exist in the microenvironment of the cells, the signals which originate from the extracellular matrix through adhesion-related events[12], and the cocktail of soluble ligands now known to control cell growth, differentiation, and morphogenesis[13]. In the course of hepatic differentiation, some cytokines, including fibroblast growth factor-4 (FGF-4)[14], oncostatin M (OSM)[15], hepatocyte growth factor (HGF)[16] and epithermal growth factor (EGF)[17], control the hepatic differentiation and maturation. In the present study, we used the cell directed differentiation medium including FGF-4 and OSM, to investigate hepatocyte-like cells from the directed differentiation of mouse bone marrow cells *in vitro*.

Materials and methods

Materials C57BL/6 mice (3–4 weeks old) were purchased from the Model Animal Research Center of Nanjing University (Grade: SPF, No 041117035). The mice were kept individually in pathogen-free conditions with a 12-h light/dark cycle and were fed sterile food and water. All animals were treated in accordance with the guidelines of the European Community Standards on the Care and Use of Laboratory Animals (No 28871-22A9).

Dulbecco's modified essential media-low glucose (DMEM-LG), Iscove's modified Dulbecco's medium (IMDM), *L*-glutamine, and fetal calf serum (FCS) were obtained from Hyclone Laboratories (South Logan, UT84321, USA). MCDB-201, insulin-transferrin-selenium (ITS), dexamethasone, ascorbic acid 2-phosphate, benzylpenicillin, streptomycin, and fibronectin were obtained from Sigma-Aldrich (Saint Louis, Missouri 63103, USA). FGF-4 and OSM were obtained from R&D Systems (Minneapolis, MN 55413, USA).

The antibody against mouse albumin was obtained from Dako Systems (DK-2600, Glostrup, Denmark). The antibody against mouse cytokeratin18 was obtained from Chemicon (Temecula, Ca 92590, USA). Fluorescein (FITC)-conjugated secondary antibody, phycoerythrin (PE)-conjugated secondary antibody, and rhodamine (TRITC)-conjugated secondary antibody were obtained from Sigma-Aldrich (Saint Louis, Missouri 63103, USA). Trizol reagent was also purchased from Sigma-Aldrich. A TITANIUM^{TM} one-step RT-PCR kit was purchased from Clontech (Palo Alto, CA 94303-4230, USA). Periodic acid-Shiff (PAS) staining solution was purchased from Shanghai Bioengineer Company (590 Zhaojiabang Road, Shanghai, China). A Colorimetric assay kit was purchased from Randox Laboratories (Randox Laboratories, Antrim, UK).

Preparation of bone marrow cells Bone marrow cells were prepared as previously described[18]. Fresh bone marrow aspirate extracted from the tibias and the femora of the C57BL/6 mice was suspended in DMEM-LG media and was centrifuged to pellet the cells, and the fat was removed. The cell pellet was resuspended in DMEM-LG media and fractionated on a density gradient generated by centrifugation of 1.077 g/L percoll solution at 1150×*g* for 30 min at the room temperature. The cells in the percoll interface were then collected and rinsed twice. Cell viability was determined by the trypan blue exclusion test. Only suspensions with cell viability of 95% were used.

Directed differentiation of bone marrow cells Bone marrow cells were inoculated in bone marrow cells' directed differentiation media at 5×10^5 cells/cm^2 in 10 mg/L fibronectin-coated culture flasks. Bone marrow cells' directed differentiation media consisted of the following: 54% DMEM-LG, 36% MCDB-201, 10% FCS with 1×ITS, 1×10^{-8} mol/L dexamethasone, 1×10^{-4} mol/L ascorbic acid 2-phosphate, 100 U/L benzylpenicillin, 100 mg/L streptomycin, 30 μg/L FGF-4, 30 μg/L OSM. As a negative control, bone marrow cells' culture medium was similar to the directed differentiation medium but without FGF-4 and OSM. Cells were cultured in a humidified atmosphere of 5% CO_2 and 95% air at 37 °C. After 72 h, non-adherent cells and debris were removed, and the adherent cells were cultured continuously. Cultures were maintained by media exchange every 3 d.

Cell morphology was observed under Olympus phase contrast microscope (CX40RF200, Olympus optical Co LTD, Japan). On d 0, 3, 6, 9, 12, 15, 18, 21, some cells were detached with 0.25% trypsin-EDTA solution and collected for RNA extraction. Cells on d 21 were detached with the same method and used for experiments. Cell supernatant on d 0, 3, 6, 9, 12, 15, 18, 21 were collected for albumin ELISA.

Hepatocyte isolation and culture Hepatocytes were isolated from 3–4 weeks old C57BL/6 mice by a conventional two-step collagenase liver perfusion[19] and cultured on fibronectin-coated flasks 10 mg/L in IMDM containing 10% FCS, *L*-glutamine 2 mmol/L, dexamethasone 1 μmol/L, insulin 1 μmol/L, benzyl penicillin 100 U/L, and streptomycin 100 mg/L. Cultures were maintained by media exchange every 3 d.

RNA extraction and RT-PCR analysis Total RNA was

extracted by using Trizol reagent from C57BL/6 mouse hepatocytes, fresh bone marrow cells, cultural bone marrow cells, and directed differentiated bone marrow cells. In total, 1 μg RNA was used for cDNA synthesis and amplification by one-step RT-PCR kit. For hepatocyte nuclear factor-3β (HNF-3β), albumin (ALB), cytokeratin18 (CK18) and transthyretin (TTR), the following reaction conditions were used: reverse transcription at 50 °C for 1 h, denaturation of RNA/DNA hybrid and inactivation of reverse transcriptase at 94 °C for 5 min. Polymerase chain reaction (PCR) was used for 40 cycles, denaturation at 94 °C for 30 s, annealing at 60 °C for 1 min, extension at 72 °C for 1 min, final extension at 72 °C for 5 min. For glucose-6-phosphatase (G-6-Pase) and tyrosine aminotransferase (TAT), the following reaction conditions were used: reverse transcription at 50 °C for 1 h, denaturation of RNA/DNA hybrid and inactivation of reverse transcriptase at 94 °C for 5 min. PCR was used for 30 cycles, denaturation at 94 °C for 1 min, annealing at 55 °C for 1 min, extension at 72 °C for 1 min, final extension at 72 °C for 5 min.

Primers used for amplification are listed in Table 1. All primers were synthesized by Shanghai Sangon Biological Engineering Technology & Service Co Ltd , (Shanghai, China). mRNA levels were normalized using β-actin as a housekeeping gene. The amplified products were subjected to electrophoresis in 1% agarose gels and stained with ethidium bromide.

Western blot analysis Cells, including C57BL/6 mouse hepatocytes, fresh bone marrow cells, cultural bone marrow cells, and directed differentiated bone marrow cells, were washed with 0.01 mol/L PBS and lysed with lysis buffer. About 50 ug of proteins in each supernatant were boiled for 5 min in a sodium dodecyl sulfate (SDS) sample buffer and subjected to electrophoresis on 10% SDS-PAGE gels. The proteins were transferred to Polyvinylidene Fluoride (PVDF) membrane through semidry transfer at 210 mA for 0.5 h. The membrane was blocked for 30 min at room temperature in 3% nonfat milk in Tris-buffered saline (TBS) with 0.05% Tween20, and incubated with primary antibodies against mouse ALB (1:1000), mouse HNF-3β (1:500), and mouse CK18 (1:500) at room temperature for 1 h. The membrane was rinsed and washed 3 times in TBS-Tween20 for 10 min each, and then incubated at room temperature for 1 h with a Horseradish peroxidase (HRP)-conjugated second antibody (1:1000). After adequate washes with TBS, the membrane was stained with diaminiobenzidene (DAB) stain at room temperature for 2–3 min, and then washed with PBS.

Table 1. Primer sequences used for RT-PCR.

Gene	Primer	Length
HNF-3β	5'-AGACTCCGGCGGGCACCGAG-3' 5'-GTGGTTGAAGGCGTAATGGT-3'	276 bp
CK18	5'-TGGTACTCTCCTCAATCTGCTG-3' 5'-CTCTGGATTGACTGTGGAAGTG-3'	128 bp
ALB	5'-TCAACTGTCAGAGCAGAGAAGC-3' 5'-AGACTGCCTTGTGTGGAAGACT-3'	149 bp
TTR	5'-TCTCTCAATTCTGGGGGTTG-3' 5'-TTTCACAGCCAACGACTCTG-3'	105 bp
G-6-Pase	5'-CAGGACTGGTTCATCCTT-3' 5'-GTTGCTGTAGTAGTCGGT-3'	210 bp
TAT	5'-ACCTTCAATCCCATCCGA-3 5'-TCCCGACTGGATAGGTAG-3'	206 bp
β-actin	5'-CCAAGGCCAACCGCGAGAAGATGAC-3' 5'-AGGGTACATGGTGGTGCCGCCAGAC-3'	587 bp

Albumin ELISA Cell culture media at various time points were collected as samples for ALB ELISA. One microlitre of a monoclonal antibody against mouse ALB was diluted with 100 μL coating buffer for each well and incubated for 60 min. After incubation, the capture antibody solution was aspirated and washed with wash solution. Total 200 μL of blocking solutions were added to each well and incubated for 30 min. After incubation, the blocking solution was removed and each well was washed. One hundred microlitre standards or samples were transferred to assigned wells and incubated for 60 min. After incubation, standards or samples were removed, and each well was washed. 100 uL HRP conjugate (1:10000) were transferred to each well and incubated for 60 min. After incubation, the HRP conjugate were removed and each well was washed. Tetramethylbenzidine (TMB) 100 μL were transferred to each well and incubated for 30 min. To stop the TMB reaction, 100 μL of H_2SO_4 2 mmol/L were applied to each well. The plate was read at the wavelength 450 nm for TMB through the microtitration plate reader (TECAN A-S002, Austria).

Periodic acid-Shiff (PAS) staining Cells were fixed with 20% formaldehyde and intercellular glycogen was stained with PAS staining solution according to the standard protocol.

Urea assay Urea concentrations were measured through a colorimetric assay kit. The mouse bone marrow cells were plated at 5×10^5 cells/cm^2 on 1 mg/L fibronectin (FN)-coated 6-well plates in bone marrow cells' directed differentiated medium or cultural medium. The cells (on d 3, 6, 9, 12, 15, 18, and 21) were incubated in 2 mL medium containing 5 mmol/L NH_4CL for 24 h in 5% CO_2 at 37 °C. After incubation, the urea concentrations in the supernatant were measured. Mouse hepatocytes grown in the monolayer with the same density was used as positive control and culture medium used as

nega tive control. No urea was detected in culture medium alone.

Results

Changes of cell amount and morphology The changes in cell amount and morphology could be seen in the course of the cell-directed differentiation. Bone marrow cells were inoculated at the density of 5×10^5 cells/cm^2. However, when the nonadherent cells were removed 3 d later, we found that the adherent cells' density was suitable for the adherent cells to grow well. On d 12, we could see some epithelial-like cells or polygonal cells in the directed differentiation medium, and the number and sizes of colonies of epithelial-like cells or polygonal cells increased in the course of the cell directed differentiation. On d 21, cells were detached and counted. The yield of the cells was approximately 8×10^3/cm^2. In the negative group, we could see many fibroblast-like cells or fusiform cells, and only slight polygonal cells (Figure 1).

Gene expressions of liver specific markers To assess the directed differentiation of bone marrow cells into hepatic lineages, we first examined mRNA expressions of endodermal and liver specific genes including HNF-3β, ALB, CK18, TTR, G-6-Pase, and TAT, which could not be detected in fresh bone marrow cells and cultural bone marrow cells (Figure 2). In the bone marrow cells' directed differentiation culture group, HNF-3β, ALB, and CK18 mRNA expressions first appeared within 6 d, and lasted throughout the later directed differentiation. TTR mRNA was expressed within 9 d, and its expression lasted throughout the later directed differentiation. From our research, we found that G-6-Pase and TAT mRNA expressions could be detected within 12 d, and their expressions lasted in the course of the later directed differentiation (Figure 2).

Protein expressions of liver specific markers We found that fresh bone marrow cells and cultural bone marrow cells on d 21 did not express any HNF-3β, ALB or CK18, but directed differentiated bone marrow cells on d 21 expressed HNF-3β, ALB, and CK18 (Figure 3).

Hepatocyte functional activity ALB secretion was measured at various times throughout the cell differentiation. Undifferentiated bone marrow cells and cultural bone marrow cells did not secret any ALB. Following treatment with FGF-4 and OSM, directed differentiated bone marrow cells

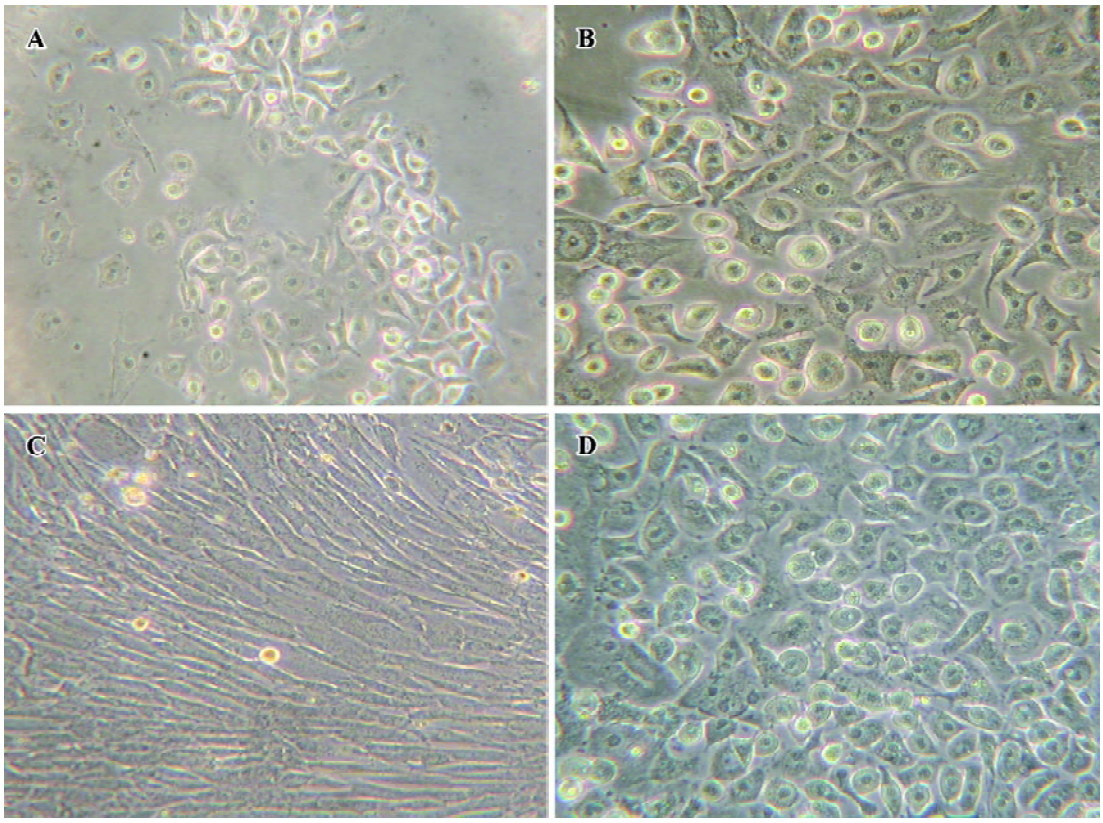

Figure 1. Cell morphology was observed with an Olympus phase contrast microscope. (A) Directed differentiated bone marrow cells on d 12; (B) directed differentiated bone marrow cells on d 21; (C) cultural bone marrow cells in the culture media; and (D) mouse hepatocytes. (×200).

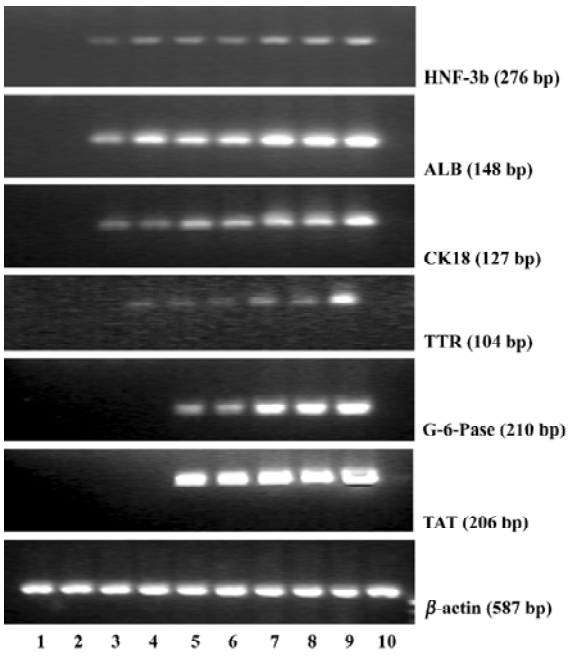

Figure 2. Some genes were selected and reverse transcriptase-polymerase chain reaction was performed. Lane 1-Lane 8 presented respectively: directed differentiated bone marrow cells on d 0, 3, 6, 9, 12, 15, 18, 21; Lane 9: mouse hepatocytes; Lane 10: cultural bone marrow cells in the culture media.

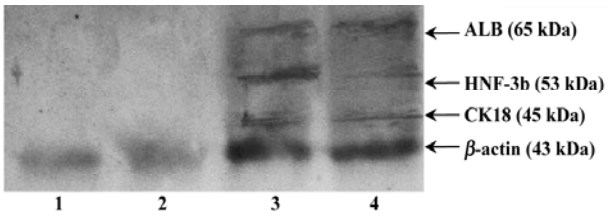

Figure 3. Protein expression was confirmed by Western blot analysis. Lane 1: fresh bone marrow cells; Lane 2: cultural bone marrow cells in the culture media; Lane 3: mouse hepatocytes; Lane 4: directed differentiated bone marrow cells on d 21.

produced ALB in a time-dependent manner. On d 15, the amount of secreted albumin reached the maxium amount (Figure 4).

Intracellular glycogen accumulation, one feature of adult liver, was analyzed by staining the cells with the PAS reagent. A slight accumulation of glycogen was detected in the course of directed differentiation, while no accumulation of glycogen was found in the culture media without FGF-4 and OSM (Figure 5).

We then assessed urea production at various time point throughout the differentiation. Undifferentiated bone marrow cells and cultural bone marrow cells did not produce

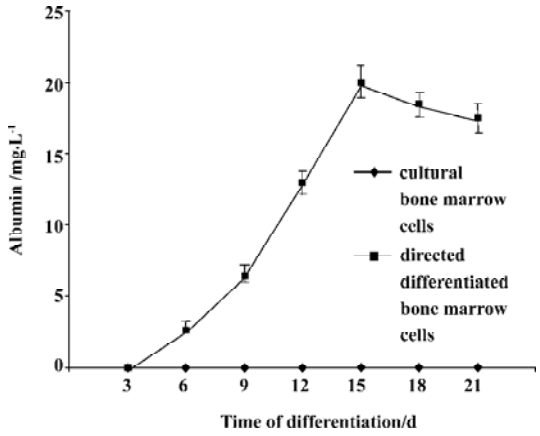

Figure 4. Albumin secretion by directed differentiated or cultural bone marrow cells were measured by albumin ELISA. Mean±SD. n=5.

urea. In the directed differentiated group, directed differentiated bone marrow cells produced urea 3 d later, and in a time-dependent manner. On d 15, the amount of urea produced by directed differentiated bone marrow cells reached the maxium amount (Figure 6).

Discussion

In the present study, we selected bone marrow cells for further differentiation study because no matter hematopoietic stem cells, multipotent progenitor cells, and bone marrow stromal cells, they share common aspects. As bone marrow cells, they exist in the same bone marrow cell-cell microenvironment. They share the same character-stem cell plasticity, which means they have the ability to differentiate into cells of different tissue under certain microenvironments[20]. It has recently been founded by reseachers that there are ways of seperating hematopoietic stem cells and multipotent progenitor cells from bone marrow, but there is no good way to propagate hematopoietic stem cells *in vitro*. The multipotent progenitor cells could be propagated *in vitro*, but its cultural condition or requirement is very harsh [10]. In the present study, bone marrow stromal cells were shown to differentiate into hepatocyte-like phenotypes given the HGF induction, but these hepatocyte-like cells only expressed ALB and α-fetoprotein[11]. Furthermore, in the course of the organ development including the developing liver, cell-cell interactions are very important for modulating cell growth, migration, and/or differentiation, and are imperative for coordinated organ function[21]. A directed differentiated culture system, in which all bone marrow stem cells could differentiate into hepatocytes would be beneficial. From our study, we found that bone marrow cells grow easily and differentiate well in the induction of differentiation into

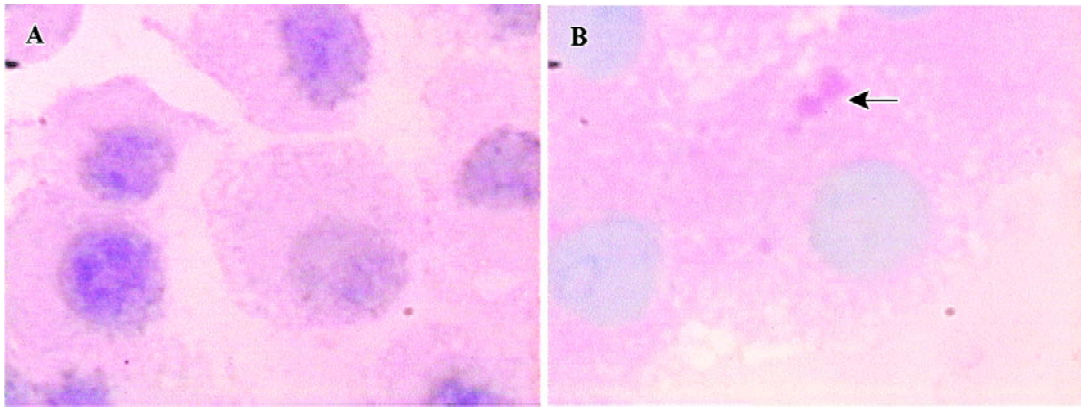

Figure 5. Intracellular glycogen accumulation was analyzed by PAS staining. (A) No glycogen particles could be seen in the cytoplasm of cultural bone marrow cells. (B) Some glycogen particles could be seen in the cytoplasm of directed differentiated bone marrow cells on d 21. (×1000).

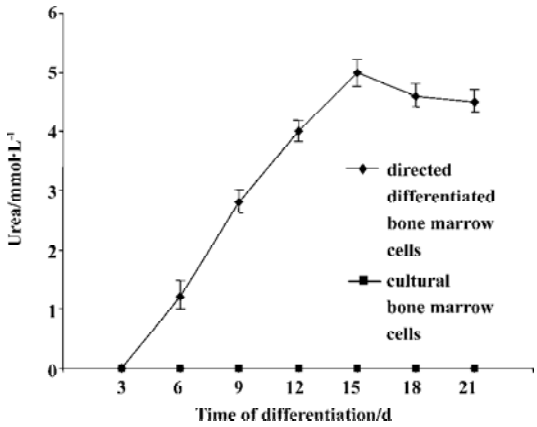

Figure 6. Urea production by directed differentiated or cultural bone marrow cells, were measured through a colorimetric assay kit. Mean±SD. n=5.

hepatocytes.

Liver development is known to proceed through several distinct steps and many growth factors and cytokines are involved in each step. In mice, the initial event in liver development occurs at E9. The foregut endoderm becomes the liver through interaction with the cardiogenic mesoderm[22,23]. FGF-4 is involved in endoderm specification and hepatic differentiation in this step[14]. OSM, an interleukin (IL)-6 family cytokeratin, is a paracrine factor produced by hematopoietic cells and plays an important role in hepatic maturation during the mid to late fetal stages[15]. HGF has been shown to be important components of liver development and the differentiation process. However, HGF is different from OSM in inducing hepatic maturation, as it seems to be a paracrine factor that is involved in postnatal hepatic maturation[16]. Some other cytokines, including (EGF), insulin, TGF, appear to play important roles in liver development and regeneration[17]. The question is asked: *in vitro*, which cytokines will affect hepatocyte from the directed differentiation of stem cells? Some answers include: HGF [11,24,25], HGF and EGF[26], HGF and FGF[27]. We established a differentiation culture system including FGF-4, HGF, OSM, and EGF, where hepatocytes were in the presence of FGF-4, HGF, OSM and EGF in the cell culture system. (SHI *et al*, unpublished data). We then adopted a uniform design method to research the most effective density of each cytokine and get the most effective match of these cytokines. We have sifted through the most effective directed differentiation culture system including FGF-4 and OSM (SHI *et al*, in press). From our research, we used the most effective directed differentiation culture system and researched the differentiation of bone marrow cells into hepatocytes.

In the present study, we found that these hepatocyte-like cells expressed HNF-3β, ALB, CK18, TTR, G-6-Pase, and TAT at the gene level and/or protein level. HNF-3β is a hepatocyte nuclear factor, which occurs in the cell nucleus of the premature or mature hepatocyte. Expression of ALB, the abundant protein synthesized by mature hepatocytes, starts in early fetal hepatocytes and reaches the maximal level in adult hepatocytes[28]. CK18 is a cytoskeletal protein and is expressed in mature hepatocytes. TTR represents endodermal differentiation and is expressed throughout liver maturation[29]. G-6-Pase is predominantly expressed in the liver [28]. TAT represents an excellent enzymatic marker for peri- or postnatal hepatocyte-specific differentiation. Since hormone-regulated TAT activity is strictly limited to the parenchymal cells of the adult liver, it has been used extensively for monitoring cellular differentiation in experimental models

for liver development/maturation *in vitro*[30]. Furthermore, these hepatocyte-like cells had some hepatocellular synthesis and metabolism functions, which would be used for hepatocyte transplantation or bioartificial liver.

Bone marrow stem cell can differentiate into hepatocytes, which is referred to as stem cell plasticity. There are many published studies explaining stem cell plasticity. First, multiple stem cells can coexist in multiple tissues, even after birth, and they proliferate and differentiate in respond to local stimulation[31]. Second, multipotent stem cells, which are akin to ES cells, persist past initial lineage specification[10]. Third, cells can undergo de- and re-differentiation[32]. Cell fusion has recently been suggested as another explanation of stem cell plasticity[33]. Irrespective of the explanations of stem cell plasticity, the fact that bone marrow stem cell can differentiate into hepatocyte *in vitro* holds great promise for the treatment of inherited and degenerative liver diseases.

From our research, we can conclude that our differentiation media, including FGF-4 and OSM, are effective for differentiating bone marrow cells into hepatocyte-like cells, which were identified at the gene level and protein level and had some hepatocellular synthesis and metabolism functions. Thus, we will serve these functional hepatocyte-like cells as hepatocyte resources for bioartificial liver or hepatocyte transplantation.

References

1 Everhart JE, Lombardero M, Detre KM, Zetterman RK, Wiesner RH, Lake JR, *et al*. Increased waiting time for liver transplantation results in higher mortality. Transplantation 1997; 64: 1300–6.

2 Suh KS, Lilja H, Kamohara Y, Eguchi S, Arkadopoulos N, Neuman T, *et al*. Bioartifical liver treatment in rats with fulminant hepatic failure: effect on DNA-binding activity of liver-enriched and growth-associated transcription factors. J Surg Res 1999; 85: 243–50.

3. Malhi H, Gupta S. Hepatocyte transplantation: new horizons and challenges. J Hepatobiliary Pancreat Surg 2001; 8: 40–50.

4. Weissman IL. Stem cells: units of development, units of regeneration, and units in evolution. Cell 2000; 100: 157–68.

5 Petersen BE, Bowen WC, Patrene KD, Mars WM, Sullivan AK, Murase N, *et al*. Bone marrow as a potential source of hepatic oval cells. Science 1999; 284: 1168–70.

6 Theise ND, Badve S, Saxena R, Henegariu O, Sell S, Crawford JM, *et al*. Derivation of hepatocytes from bone marrow cells in mice after radiation-induced myeloablation. Hepatology 2000; 31: 235–40.

7 Alison MR, Poulsom R, Jeffery R, Dhillon AP, Quaglia A, Jacob J, *et al*. Hepatocytes from non-hepatic adult stem cells. Nature 2000; 406: 257.

8 Theise ND, Nimmakayalu M, Gardner R, Illei PB, Morgan G, Teperman L, *et al*. Liver from bone marrow in humans. Hepatology 2000; 32: 11–6.

9 Lagasse E, Connors H, Al-Dhalimy M, Reitsma M, Dohse M, Osborne L, *et al*. Purified hematopoietic stem cells can differentiate into hepatocytes *in vivo*. Nat Med 2000; 6: 1229–34.

10 Jiang Y, Jahagirdar BN, Reinhardt RL, Schwartz RE, Keene CD, Gonzalea XR, *et al*. Pluripotency of mesenchymal stem cells derived from adult marrow. Nature 2002; 418: 41–9.

11 Wang PP, Wang JH, Ya ZP, Hu MY, Lau GK, Fan ST, *et al*. Expression of hepatocyte-like phenotypes in bone marrow stromal cells after HGF induction. Biochem Biophys Res Commun 2004; 320: 712–6.

12 Hemler ME, Rutishauser U. Cell-to-cell contact and extracelluar matrix. Curr Opin Cell Biol 2000; 12: 539–41.

13 Birchmeier C, Brohmann H. Genes that control the development of migrating muscle precursor cells. Curr Opin Cell Biol 2000; 12: 725–30.

14 Wells, J.M., Melton, DA. Vetebrate endoderm development. Annu Rev Cell Dev Biol 1999; 15: 393–410.

15 Taga T, Kishimoto T. Gp130 and the interleukin-6 family of cytokines. Annu Rev Immunol 1997; 15: 797–819.

16 Kamiya A, Kinoshita T, Miyajima A. Oncostatin M and hepatocute growth factor induce hepatic maturation via distinct signaling pathways. FEBS Lett 2001; 492: 90–4.

17 Michalopeulos GK, DeFrances MC. Liver regeneration. Science 1997; 276: 60–6.

18 Levite M, Meshorer A, Reisner Y. A rapid method for obtaining murine bone marrow cells in high yield. Bone Marrow Transpl 1991; 8: 225–7.

19 Seglen PO. Preparation of isolated rat liver cells. Methods Cell Biol 1976; 13: 23–28.

20 Verfaillie CM, Pera MF, Lansdorp PM. Stem cells: hype and reality. Hematology 2002: 369–91.

21 Bhatia SN, Balis UJ, Yarmush ML, Toner M. Effect of cell-cell interactions in preservation of cellular phenotype: cocultivation of hepatocytes and nonparenchymal cells. FASEB J 1999; 13: 1883–900.

22 Zaret KS. Liver specification and early morphogenesis. Mech Dev 2000; 92: 83–8.

23 Zaret KS. Hepatocyte differentiation: from the endoderm and beyond. Curr Opin Genet Dev 2001; 11: 568–74.

24 She HO, Masahiro M, Hirosuke K, Yusuke I, Masakiyo S, Toshiya T, *et al*. Hepatocyte growth factor induces differentiation of adult rat bone marrow cells into a hepatocyte lineage *in vitro*. Biochem Biophys Res Commun 2000; 279: 500–4.

25 Henning CF, Michael VL, Lourdes CD, Claudia L, Dietrich K, Boris F, *et al*. Liver-specific gene expression in cultured human hematopoietic stem cells. Stem Cells 2003; 21: 98–104.

26 Masahiro M, Ichiro A, Masakiyo S, Emiko N, Mayumi O, Ken K, *et al*. Improved conditions to induce hepatocytes from rat bone marrow cells in culture. Biochem Biophys Res Commun 2002; 298: 24–30.

27 Robert ES, Morayma R, Lisa K, Yuehua J, Mark B, Troy L, *et al*. Multipotent adult progenitor cells from bone marrow differentiate into functional hepatocyte-like cells. J Clin Invest 2002; 109: 1291–302.

28 Pan CJ, Lei KJ, Chen H, Ward JM, Chou JY. Ontogeny of the murine glucose-6-phosphatase system. Arch Biochem Biophys 1998; 358: 17–24.

29 Makover A, Soprano DR, Wyatt ML and Goodman DS. An in

situ-hybridization study of the localization of retinol-binding protein and transthyretin messenger RNAs during fetal development in the rat. Differentiation 1989; 40: 17–25.
30 Shelly LL, Tynan W, Schmid W, Schutz G, Yeoh GC. Hepatocyte differentiation *in vitro*: initiation of Tyrosine amino transferase expression in cultured fetal rat hepatocytes. J Cell Biol 1989; 109: 403–10.
31 Kawada H, Ogawa M. Bone marrow origin of hematopoietic progenitors and stem cells in murine muscle. Blood 2001; 98: 2008–13.
32 Wilmut I, Schnieke AE, Mcwhir J, Kind AJ, Campbell KH. Viable offspring derived from fetal and adult mammalian cells. Nature 1997; 385: 810–3.
33 Ying QY, Nichols J, Evans EP, Smith AG. Changing potency by spontaneous fusion. Nature 2002; 416: 545–8.

Acta Pharmacologica Sinica 2005 Apr; 26 (4): 477–485

Blackwell Publishing

Full-length article

Inducible effects of icariin, icaritin, and desmethylicaritin on directional differentiation of embryonic stem cells into cardiomyocytes *in vitro*[1]

Dan-yan ZHU, Yi-jia LOU[2]

Department of Pharmacology and Toxicology, College of Pharmaceutical Sciences, Zhejiang University, Hangzhou 310031, China

Key words

embryonic stem cells; directional differentiation; cardiomyocytes; icariin; icaritin; desmethylicaritin; α-major histocompatibility complex; myosin light chain 2v; cell cycle; apoptosis

[1] Project supported by the National Natural Science Foundation of China (No 30171121), by the Key Grant Project of the Chinese Ministry of Education (No 03088), and by the Key Grant Project of the International Joint Key Grant Project of Zhejiang Province (No 2003C24005).
[2] Correspondence to Prof Yi-jia LOU.
Phn/Fax 86-571-8721-7206.
E-mail yijialou@zju.edu.cn

Received 2004-09-05
Accepted 2005-12-21

doi: 10.1111/j.1745-7254.2005.00076.x

Abstract

Aim: To investigate the possible inducible effects of icariin, icaritin, and desmethylicaritin on the directional differentiation of embryonic stem (ES) cells into cardiomyocytes *in vitro*. **Methods:** ES cells were cultivated as embryoid bodies (EBs) in hanging drops with icariin, icaritin, or desmethylicaritin. ES cells treated with retinoic acid and with solvent were used as positive and negative controls, respectively. The cardiomyocytes derived from the ES cells were verified using immunocytochemistry. The expression of cardiac developmental-dependent genes was detected using the reverse transcription-polymerase chain reaction (RT-PCR) method. Cell cycle distribution and apoptosis were analyzed using flow cytometry to determine the partly inducible effect mechanisms involved. **Results:** The total percentage of beating EBs treated with 1×10^{-7} mol/L icariin, icaritin, or desmethylicaritin was 87% ($P<0.01$), 59% ($P<0.01$), and 49%, respectively. All the beating cardiomyocytes derived from the ES cells expressed cardiac-specific proteins for α-actinin and troponin T. Among them, 1×10^{-7} mol/L icariin treatment resulted in a significantly advanced and increased mRNA level of α-cardiac major histocompatibility complex (MHC) and myosin light chain 2v (MLC-2v) in EBs in the early cardiac developmental stage. Before shifting to the cardiomyocyte phenotype, icariin could evoke the accumulation of ES cells in G_0/G_1 and accelerate apoptosis of the cell population ($P<0.05$). **Conclusion:** Icariin facilitated the directional differentiation of ES cells into cardiomyocytes at a concentration of 1×10^{-7} mol/L. The promoting effect of icariin on cardiac differentiation was related to increasing and accelerating gene expression of α-cardiac MHC and MLC-2v, as well as regulating the cell cycles and inducing apoptosis.

Introduction

Embryonic stem (ES) cells are pluripotent cells derived from the inner cell mass of the pre-implantation blastocyst[1]. These cells can proliferate in an undifferentiated state and remain totipotent when grown on a suitable fibroblast feeder layer. Under certain conditions ES cells are capable of differentiating into a variety of cell types *in vitro*, including spontaneously beating cardiac myocytes[2,3]. The entire differentiating process is rich in developmental-dependent biological information, for example, the sequence of expression of cardiac-specific genes and proteins during differentiation of ES cells *in vitro* accords with that *in vivo*[4]. Control of the ES cell mitotic cycle displays an unusual feature, and regulation of the cell cycle is critical in maintaining the transition towards differentiation[5,6]. The apoptotic signaling potential of ES cells is necessary to trigger ES cell differentiation[7,8]. Therefore, the system of ES cells can provide a platform for studying the effects of drugs on differentiation and detecting the specific or unique targets of drug action.

Up to now, the interfering effects of the traditional Chinese medicine on ES cells and their directional differentiation *in vitro* have not been investigated. Icariin (ICA), icaritin (ICT), and desmethylicaritin (DICT) (Figure 1) are constituents of *Epimedium*, a traditional Chinese herbal medicine that has

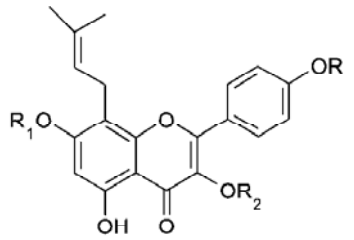

	R1	R2	R
Icariin	Glc	Rha	CH_3
Icaritin	H	H	CH_3
Desmethylicaritin	H	H	H

Figure 1. Molecular structure of related compounds.

many biological functions, particularly in cardiovascular function improvement, hormone regulation, immunological function modulation, and antitumor activity[9]. Our former work has shown that icariin can be metabolized to icartin and demethylicartin by human intestinal bacteria *in vitro*[10]. Furthermore, icaritin and desmethylicaritin, but not icariin, exert estrogen-like activity using the estrogen receptor-positive human breast adenocarcinoma MCF-7 cell proliferation assay[11]. In addition, icariin is the major active part in "Xinshen-ning" tablets, which are used for the treatment of heart disease[12]. However, the pharmacological effects and mechanism of the icariin series on the cardiovascular system are not yet known.

In the present study, the inducible effects of icariin, icaritin, and desmethylicaritin on the directional differentiation of ES cells into cardiomyocytes were examined *in vitro*. The cardiomyocytes derived from ES cells were verified using immunocytochemistry. The possible mechanisms of inducible action in transcription level, cell cycle distribution and apoptosis were investigated using reverse transcription-polymerase chain reaction(RT-PCR) and cell cycle analysis, with a view to detecting the targets of drug action on promoting ES cells to differentiate in this culture system.

Materials and methods

Animals and cells NIH mice (male, weighing 24±2 g; female, weighing 22±2 g) were obtained from the Experimental Animal Center, Zhejiang University, Hangzhou, China (Grade II, Certificate No 22-9601018). Mice were housed under 12-h light/12-h dark and 21±1 ºC conditions. To obtain fetuses, mice (3 female and 1 male) were housed together at 17:00. The following morning, when a copulation plug was detected, was defined as d 0 of gestation. The permanent ES cell line D3 (ES-D3) was obtained from the American Type Culture Collection (CRL-1934)[2].

Drugs and reagents Icariin was obtained from the Drug Biology Product Examination Bureau, Beijing, China (Batch No 0737-200011, purity 99%); icaritin was prepared using the cellulose hydrolysis method from icariin, and icaritin was demethyled using boron tribromide to obtain desmethylicaritin[6]. Purification was carried out by preparative high-performance liquid chromatography (HPLC) and identification was conducted using liquid chromatography/electrospray ionization mass spectrometry (LC/ESI-MS). The purities of these compounds were above 98%. Retinoic acid (RA), β-mercaptoethanol, and the antibodies were from Sigma Corproration, St Louis, Missouri, USA; Dulbecco's modified Eagle's minimal essential medium (DMEM) and fetal calf serum (FCS) were from Gibco Invitrogen Corporation, Grand Island, NY USA; the non-essential amino acids (NEAA) were from Hyclone Logan UT, USA; mitomycin C was from Kyowa Hakko Kogyo (Tokyo, Japan); and recombinant mouse leukemia inhibitory factor (LIF) was from Chemicon International Inc, Temecula, CA, USA. The reagents for the RT-PCR were purchased from the Shanghai Sangon Biological Engineering and Technological & Service Company (Shanghai, China).

Cultures of undifferentiated ES cells Fetuses were obtained from the mice on d 13 of gestation for the preparation of embryonic fibroblast (MEF) cells[13]. The MEF cells of generation three to generation five were used as feeder cells, which were treated with 1 mg/L mitomycin C for 1 h and plated at an appropriate density. ES-D3 cells were maintained in an undifferentiated state by culturing on a monolayer of MEF feeders in DMEM, supplemented with 10% FCS, 0.1 mmol/L β-mercaptoethanol, NEAA, and 1×10^6 U/L LIF.

Differentiation determination of cardiomyocytes and icariin, icaritin or desmethylicaritin treatment For differentiation of ES cells, EBs were generated using the hanging drop method[14,15]. Thirty microlitre of drops containing approximately 600 ES-D3 cells were placed on the lids of Petri dishes filled with *D*-Hanks solution, and cultivated in hanging drops for 3 d followed by another 2 d in the Petri dishes. On d 5, EBs were plated separately onto gelatin-coated 24-well culture plates in differentiation medium that consisted of DMEM, 20% FCS, 0.1 mmol/L β-mercaptoethanol, and NEAA. Icariin, icaritin, or desmethylicaritin were added to the differentiation medium at a concentration of 1×10^{-7} mol/L according to the preliminary test. Our previous study examining the concentration-effect relationship of icariin revealed that treatment with icariin 1×10^{-7} mol/L significantly enhanced cardiac differentiation (unpublished data). Thus, a concen-

tration of 1×10^{-7} mol/L was used in the present experiment. ES-D3 cells treated with RA 1×10^{-8} mol/L and with 0.1% Me_2SO were used as positive and negative controls, respectively.

In the experiment, d 1 referred to the day of dissociation of ES cells from MEF and the initiation of differentiation by the formation of EBs. EBs were observed with light microscopy every day to record the morphology and the number of the spontaneously beating EBs from d 7 to d 7+23. According to the percentage of the beating EBs, the inducing effects of icariin, icaritin, or desmethylicaritin on the directional differentiation of ES-D3 cells into cardiomyocytes were evaluated using the time-effect relationship curve. Rhythmically beating EBs were considered to be spontaneously beating cardiomyocytes in EB outgrowths, and were defined as the marker of successful differentiation[14,15].

Expression of cardiac-specific proteins analyzed using immunocytochemistry Cardiomyocytes were isolated from the beating areas of EBs using a modified procedure described by Maltsev *et al*[16,17]. For immunostaining, cells were rinsed twice with PBS, and fixed with cold acetone for 10 min. After being treated with goat serum for 30 min, specimens were incubated at 4 ºC overnight with the primary antibody, monoclonal anti-sarcomeric-actinin (clone number EA-53, 1:200 dilution, Sigma) or monoclonal anti-troponin T (clone number JLT-12, 1:100 dilution, Sigma). The following day, the specimens were washed with PBS three times and incubated with the fluorescent antibody: FITC-conjugated $F(ab)_2$ fragment of affinity-purified goat anti-mouse IgG (1:1000 dilution, Rockland Inc Gilbertsville, PA, USA) for 1.5 h at 37 ºC. Specimens were then rinsed in PBS, mounted onto a coverslip with 90% glycerol in PBS and examined using a fluorescence microscope (Leica DMIL,California Nevada, Germany).

Expression of cardiac-specific genes using semi-quantitative RT-PCR The expression of the cardiac-specific α-myosin heavy chain (α-MHC) gene and myosin light chain-2v (MLC-2v) in EBs was confirmed using semi-quantitative RT-PCR. Total RNA was isolated from EBs (n=20) induced by 1×10^{-7} mol/L icariin, icaritin, or desmethylicaritin, and 1×10^{-8} mol/L RA or solvent, respectively, at d 7+0, d 7+5, d 7+9 using the Trizol reagent according to the manufacturer's instructions. After extraction, mRNA was precipitated using the recommended procedures and dissolved in 0.1% diethylpyrocarbonate solution. To synthesize first strand cDNA, 7 μL total RNA was incubated in 0.5 μg of oligo (dT) 6 primer and 5 μL deionized water at 65 ºC for 15 min. Reverse transcription reactions were carried out with 200 U of M-MuLV reverse transcriptase in 5×reaction buffer and 1 mmol/L dNTP mixture for 1 h at 42 ºC. Multiplex polymerase chain reactions of 50 μL contained 1 μL of the RT reaction product, 10×PCR buffer, 25 U *Taq* polymerase, 1 μL of 10 mmol/L dNTP mixtures, and 30 pmol of each primer. The specific primer pairs were designed as follows: the cardiac-specific α-MHC gene (5'-CTGCTGGAGAGGTTATTCCTCG-3',5'-GGAAGAGTGAGCGGCGCATCAAGG-3'; 301 bp)[18] and MLC-2v(5'-TGTGGGTCACCTGAGGCTGTGGTTCAG-3',5'-GAAGGCTGACTATGTCCGGGAGATGC-3'; 189 bp)[18], and the housekeeping gene β-actin was used as an internal standard (5'-TGACGGGGTCACCCACACTGTGCCCATCTA-3', 5'-CTAGAAGCATTTGCGGTGGACGATGGAGGG-3'; 660 bp).

For the semi-quantitative determination of α-MHC and MLC-2v mRNA levels, the products of the reverse transcription reactions were denatured for 3 min at 94 ºC, followed by 40 cycles (α-MHC), 45 cycles (MLC-2v), and 30 cycles (β-actin) of amplification in the reaction with Ampli *Taq* DNA polymerase: 45 s denaturation at 94 ºC, 40 s annealing at 66.4 ºC (α-MHC) or 61.1 ºC (MLC-2v) or 55 ºC (β-actin) and 45 s elongation at 72 ºC. The PCR products were analyzed using 1.5% agarose gel electrophoresis, visualized with ethidium bromide staining, and quantified using a bio-imaging analyzer (Bio-Rad, Hercules, CA, USA), and the density of the products was quantified using Quantity One version 4.2.2 software (Bio-Rad).

Analysis of cell cycle and apoptosis by flow cytometry To analyze the cell cycle distribution of ES cells and apoptosis as parameters in the early differentiation phase, ES-D3 cells were cultivated without MEF feeders and LIF, and treated with 1×10^{-7} mol/L icariin, icaritin, or desmethyl-icaritin, or 1×10^{-8} mol/L RA. After 48 h, the cells were harvested and 1×10^{6} cells were placed into a polypropylene tube and centrifuged at 90×g. The supernatant was removed and 70% EtOH 1 mL in 4 ºC was dropped into the cell pellet while vortexing. The cells were kept at 4 ºC until the DNA was stained. Fixed cells were treated with RNase A in PBS for 1 h, followed by staining with 50 mg/L propidium iodide in PBS. Flow cytometric analysis of the cell cycle distribution and apoptosis was carried out using a BD FACSCalibur with a 488 nm (blue) argon (Becton Dickinson, San Jose, CA, USA). Data acquisition was carried out with CellQuest 3.1 software and the data were analyzed with ModFit LT 3.0 software (Variety Software House, Topsham, ME, USA).

Statistical analysis Each data point represents the mean±SD. At least three independent experiments were carried out. Statistical significance was evaluated using one-way ANOVAS with SPSS 10.0 for WINDOWS software. P<0.05 was considered statistically significant.

Results

Apparent cell morphological changes during the course of differentiation ES-D3 cells grew aggregates with clear boundaries and appeared ovoid or nodule shaped on MEF feeder cells (Figure 2A). Representative EBs at 5 d after the initiation of differentiation, and just prior to plating onto gelatin-coated 24-well culture plates, were formed by hanging drop cultures. EBs kept globular shaped structure. (Figure 2B). After plating for 2 d, cells started outgrowing from the EBs, and cardiomyocytes appeared as spontaneously contracting cell clusters[14] (Figure 2C). One EB contained one or more beating areas in which the enlarged size, increased contracting strength, and beating frequency were observed during the subsequent differentiation phase.

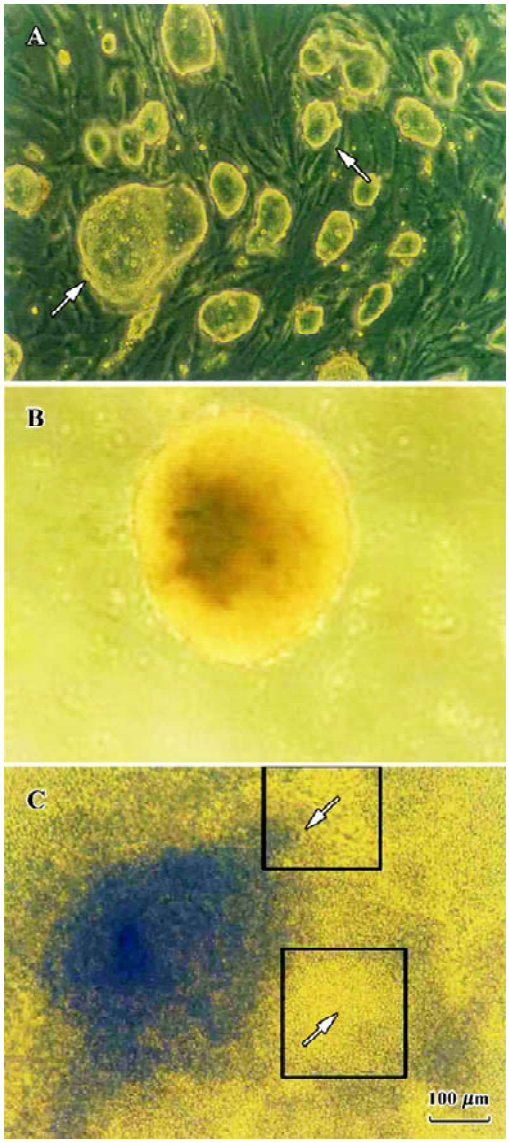

Figure 2. Cell apparent morphological changes during the course of differentiation. (A) Colonies of ES-D3 cells on a feeder layer of murine embryonic fibroblasts (arrows refer to colonies of ES-D3 cells). (B) Embryoid body before plating onto gelatin-coated 24-well culture plates. (C) Synchronously contracting, functional syncytium of cardiac clusters derived from EBs treated with icariin 1×10^{-7} mol/L at d 7+5 (rectangular frames refer to the contracting areas; arrows point to contraction foci).

Inducible effect of icariin, icaritin, and desmethylicaritin on the directional differentiation of ES-D3 cells into cardiomyocytes Icariin, icaritin, and desmethylicaritin influenced the degree of cardiac differentiation of ES-D3 cells. During the course of differentiation (from d 7+2 to d 7+23), the total percentage of beating EBs treated with 1×10^{-7} mol/L icariin, icaritin, and desmethylicaritin was 87% ($P<0.01$), 59% ($P<0.01$), and 49%, respectively. In particular, in the case of icariin at a concentration of 1×10^{-7} mol/L the inducing effect on the directional differentiation of ES-D3 cells into cardiomyocytes was remarkable compared with the control ($P<0.05$). Although only 46% of the EBs in control samples contained beating clusters, 68% of the EBs treated with 1×10^{-8} mol/L RA differentiated into beating cardiac clusters (Figure 3A).

The results of the time-effect relationship revealed that the percentage of differentiation cultures containing contracting EBs with icariin 1×10^{-7} mol/L reached a peak level of 85% at d 7+10 and 10% at terminal stages. The potential of EBs treated with icariin 1×10^{-7} mol/L undergoing cardiac differentiation was enhanced compared with control cells over the period from d 7+5 to d 7+23 ($P<0.05$). Treatment of EBs with icaritin 1×10^{-7} mol/L also resulted in a remarkable increase in the number of EBs with spontaneously beating cardiomyocytes between d 7+9 and d 7+17 ($P<0.05$), whereas the differentiation effect of EBs induced by desmethylicaritin 1×10^{-7} mol/L was only prominent from d 7+9 to d 7+11 ($P<0.05$) (Figure 3B).

If culture of differentiation was continued, the numbers of spontaneously beating foci increased and the spontaneously contractile activity of cardiac myocytes strengthened[19].

Detection of cardiac-specific proteins during the differentiation phases of ES-D3 cells into cardiomyocytes To identify whether the observed cell types derived from ES-D3 cells expressed cardiac-specific proteins, indirect immunofluorescence was carried out. The results verified that differentiated beating cardiac cells stained positively with anti-α-actinin mAb and anti-troponin T mAb, and these results support previous studies[20] (Figure 4).

Effect of icariin, icaritin, and desmethylicaritin on the level of α-cardiac MHC and MLC-2v mRNA during the early cardiac developmental stage To explore whether icariin,

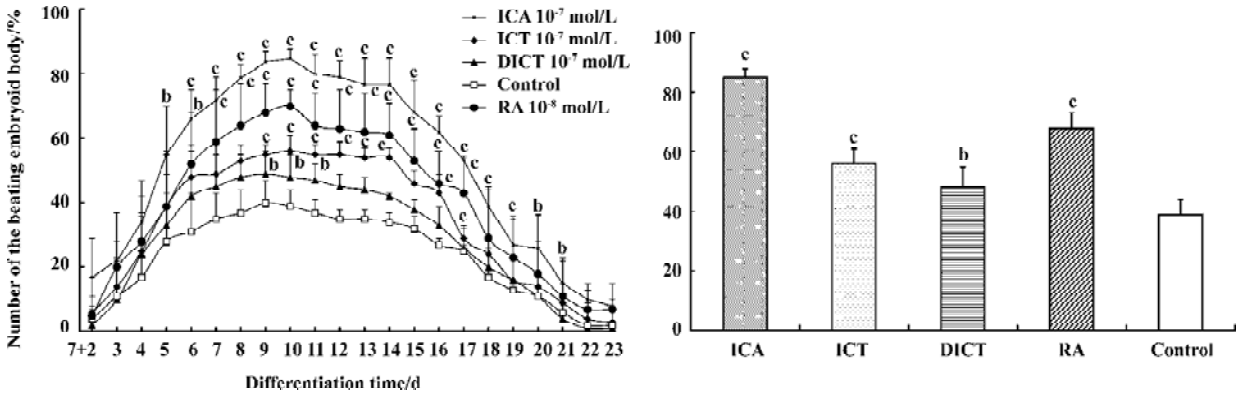

Figure 3. (A) Curve of the time-effect relationship. EBs were plated at d 5 and the number of beating EBs was evaluated every day during cultivation from 2 d up to 25 d after plating. EBs were treated with icariin (ICA) 1×10^{-7} mol/L , icaritin (ICT), desmethylicaritin (DICT), RA 1×10^{-8} mol/L , or Me_2SO 0.1% . (B) Percentage of beating EBs on d 7+10. Mean±SD. n=4 independent experiments. $^bP<0.05$, $^cP<0.01$ *vs* control.

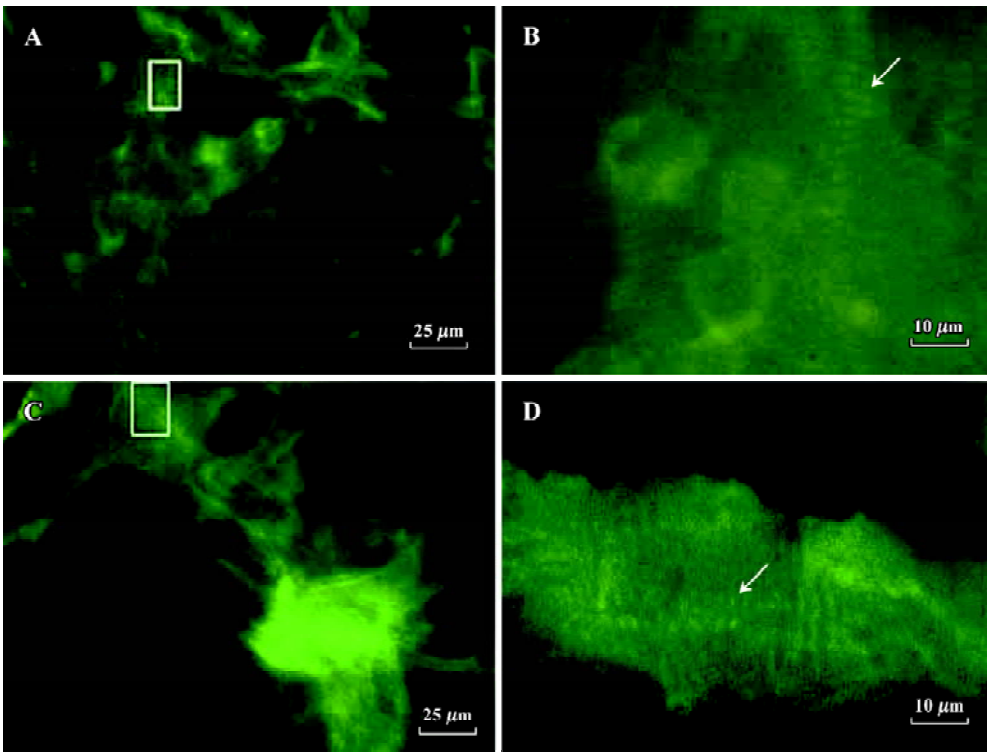

Figure 4. Positive immunostaining of dispersed cardiomyocytes from beating EBs treated with ICA 1×10^{-7} mol/L on d 7+11. The cardiomyocytes were verified by the expression of cardiac-specific sarcomeres. (A) Positive staining with anti-sarcomeric α-actinin mAb. The rectangular frame indicates the part magnified in panel B. (B) Higher magnification of sarcomeric α-actinin staining (arrow). (C) Positive staining with anti-cardiac-troponin T mAb. The rectangular frame indicates the part magnified in panel D. (D) Higher magnification of sarcomeric troponin T staining (arrow).

icaritin, and desmethylicaritin influence the expression level of a-cardiac MHC and MLC-2v mRNA during cardiomyocyte differentiation, the beating EBs outgrowths differentiated from ES-D3 cells were studied using semi-quantitative RT-

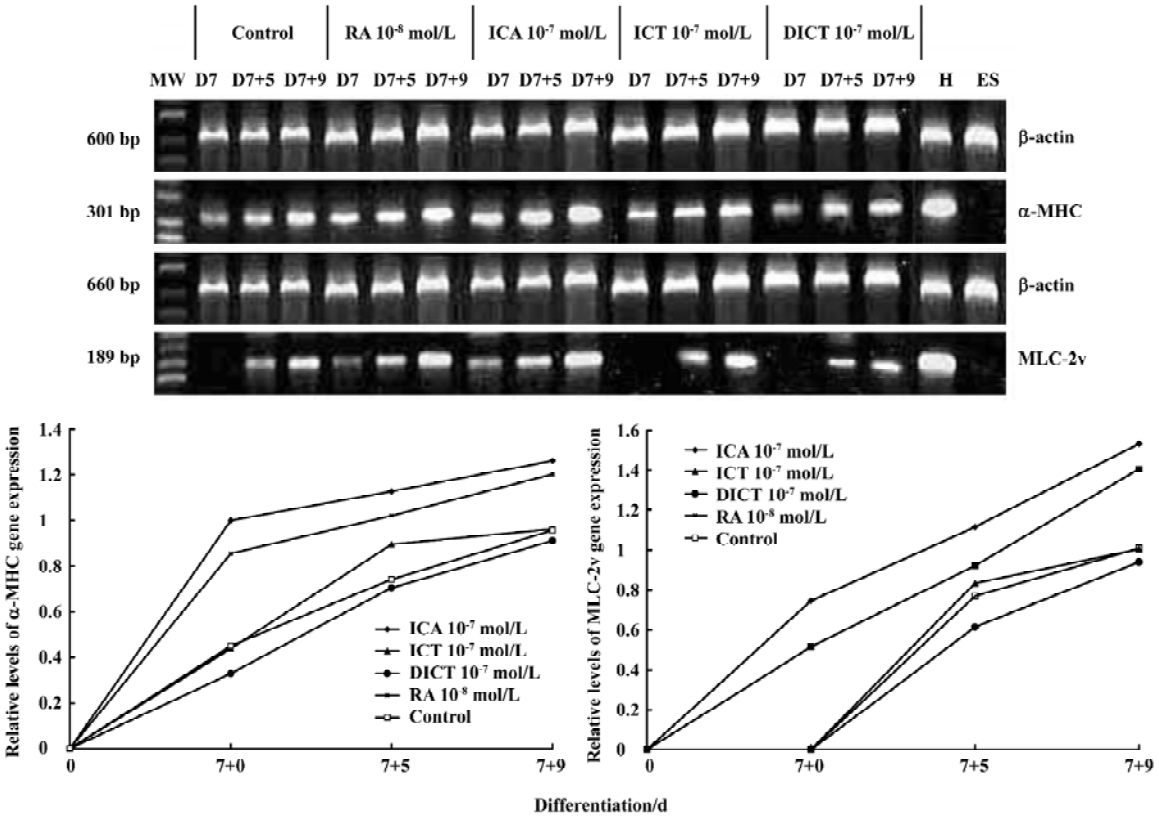

Figure 5. The mRNA level of α-MHC and MLC-2v in icariin (ICA), icaritin (ICT), and desmethylicaritin (DICT)-treated EBs compared with control cells analyzed using semi-quantitative RT-PCR. The ethidium-bromide-stained gels of PCR products (A) were analyzed using computer-assisted densitometry and the data are plotted for α-MHC (B) and MLC-2v (C) genes in relation to β-actin gene expression. Similar data were obtained in three independent RT-PCR experiments. MW, molecular weight; ES, embryonic stem cells; H, 16-d-old embryonic heart of mouse.

PCR analysis. mRNA expression levels of α-MHC by 1×10^{-7} mol/L icariin, icaritin, and of MLC-2v by 1×10^{-7} mol/L icariin increased during an early cardiac developmental stage for the period between d 7+0 and d 7+9. In particular, 1×10^{-7} mol/L icariin-induced MLC-2v expression was detected as early as d 7+0, whereas increased expression in control cells was not observed until d 7+5. The experiments also revealed that there was almost no difference between 1×10^{-7} mol/L desmethylicaritin treated cells and control cells from d 7+0 to d 7+9 (Figure 5).

Analysis of cell cycles and apoptosis using flow cytometry The cell cycle distribution of ES-D3 cells was considered to be a parameter of their differentiation state[5,6], which enabled us to determine the effect of icariin, icaritin, and desmethylicaritin on early differentiation events before a shift to the cardiomyocyte phenotype. The results of the cell cycle analysis on propidium-iodide-stained cells showed a smaller percentage of ES-D3 cells in the G_0/G_1 phase compared with differentiation cells in control samples (approximately 30% and 40%, respectively). Icariin, icaritin, and desmethylicaritin 1×10^{-7} mol/L induced the accumulation of cells in G_0/G_1 (approximately 44%, 40%, and 35%, respectively). In particular, the effect of icariin on the G_0/G_1 was remarkable compared with control cells ($P<0.05$). Treatment of 1×10^{-8} mol/L RA let ES cells present a similar effect on the accumulation of cells in G_1 (48%). Proportions of S phase cells in either 1×10^{-7} mol/L icariin-treated cells or 1×10^{-8} mol/L RA-treated cells were remarkably reduced (29% and 27%, respectively, versus 47% of S phase in ES-D3 cells; $P<0.05$) (Figure 6).

Apoptosis plays a vital role in development by removing unwanted cells[21], which is a possible checkpoint for the transition towards differentiation of ES cells. In the present study, ES-D3 cells induced by icariin 1×10^{-7} mol/L for 48 h showed greater levels of apoptosis (10%) than control cells (4%) ($P<0.05$). In contrast, treatment with icaritin 1×10^{-7} mol/L or desmethylicaritin resulted in apoptosis levels of approximately 9% and 8%, respectively. RA 1×10^{-8} mol/L treatment for 48 h also led to 8% apoptosis ($P<0.05$; Figure 6).

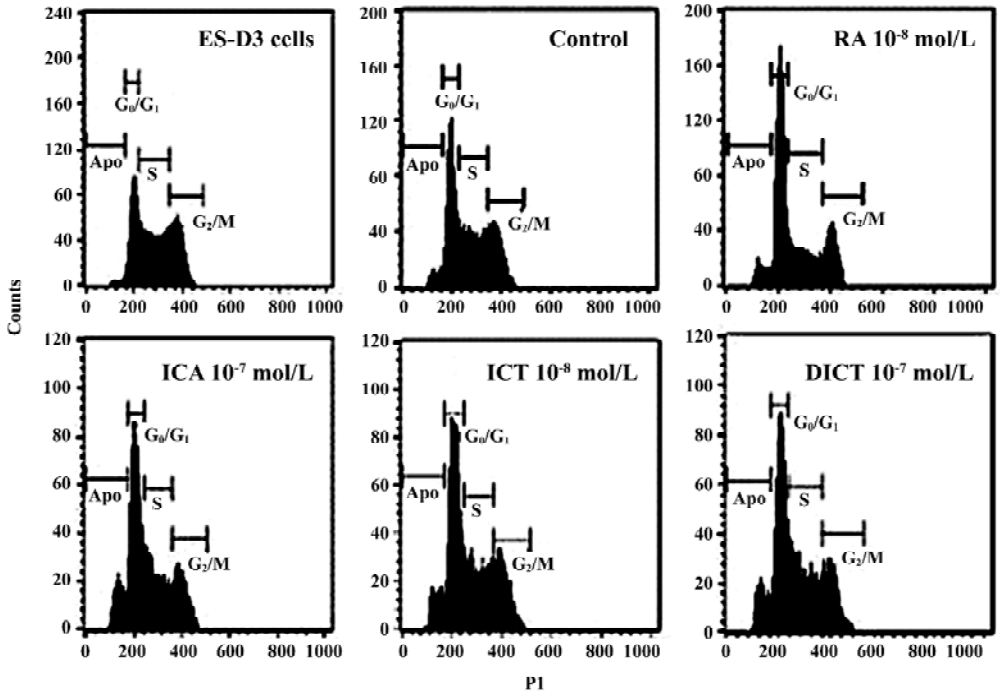

Cell cycle phase	G_0/G_1 (%)	S (%)	G_2/M (%)	Apoptosis (%)
ES-D3 cells	30.8±2.2	46.6±6.4	21.8±6.3	1.6±0.3
Control	39.7±1.3^{c}	33.5±4.9^{b}	23.6±6.3	3.6±1.2^{b}
RA 10^{-8} mmol/L	48.3±0.6^{cf}	26.7±0.4^{c}	16.8±1.0	8.5±1.5^{ce}
ICA 10^{-7} mol/L	43.9±1.2^{ce}	28.7±0.2^{c}	17.4±1.4	10.1±2.5^{ce}
ICT 10^{-7} mol/L	41.8±4.4^{b}	31.3±3.8^{b}	18.7±2.4	9.0±4.0^{b}
DICT 10^{-7} mol/L	35.5±2.2	37.0±5.9	18.9±2.6	8.8±3.2^{b}

Figure 6. Cell cycle analysis of icariin (ICA), icaritin (ICT), and desmethylicaritin (DICT)-treated ES-D3 cells for 48 h by flow cytometry (FCM). The table shows the percentage of G_0/G_1, S, G_2/M phase and apoptosis populations of cells under each treatment condition. n=3 independent experiments. Mean±SD. $^{b}P<0.05$, $^{c}P<0.01$ *vs* ES-D3 cells. $^{e}P<0.05$, $^{f}P<0.01$ *vs* control.

Discussion

ES cell differentiation into cardiomyocytes *in vitro* is a unique system that not only provides opportunities to study cardiomyocyte differentiation, but also offers a platform for evaluating the effects of drugs and detecting the specific targets of drug action during cardiogenesis. In the present study, the possible inducible effects of icariin, icaritin, and desmethylicaritin on the directional differentiation of ES cells into cardiomyocytes *in vitro* were explored. To investigate the partly inducible effect mechanisms of the three compounds involved in ES cell differentiation, the expression of cardiac developmental-dependent genes was detected using RT-PCR. Cell cycle distribution and apoptosis were analyzed using flow cytometry.

Our results revealed that treatment of EBs with icariin resulted in increased and accelerated differentiation into beating cardiomyocytes. The degree of the inducible effect of icaritin was less than that of icariin, and desmethylicaritin had the least inducing effect on the directional differentiation of ES cells into cardiomyocytes *in vitro*. Moreover, cardiac-specific sarcomeric proteins in the cardiomyocytes derived from ES-D3 cells were identified, since one of the major questions in muscle development is how a large number of protein subunits assembles into the remarkably regular structure known as the sarcomere[20]. Our results confirmed that the cardiomyocytes were derived from ES-D3 cells.

ES-cell-derived cardiomyocytes express the cardiac genes in a developmentally controlled manner, that is, atrial natriuretic factor (ANF), α-MHC, β-MHC, and MLC-2v[4]. In our

experiment, α-MHC and MLC-2v were chosen as the evaluation targets for the directional differentiation. Our experiments demonstrated that icariin significantly advanced and increased the mRNA levels of α-MHC and MLC-2v at an early stage of differentiation, which suggested a partial mechanism for icariin involving in differentiation could be related to the expression of the cardiac developmental-dependent genes[4,22,23]. However, icaritin and desmethylicaritin had less effect on improving the mRNA level of α-MHC and MLC-2v during cardiac differentiation. Other studies have shown that α-MHC is expressed relatively early during the course of cardiogenesis[24]; however, MLC-2v mRNA is highly expressed relatively late in the process and is spatially restricted to the ventricular portion[25,26]. Our results support these studies. One of the mechanisms of icariin in differentiation is to increase and accelerate the mRNA level of α-MHC and MLC-2v at an early stage of differentiation.

Icariin is a new type of biological response modifier and differentiation agent[27] and can induce some cells to differentiate by regulating the cell cycle[27,28]. The cell cycle distribution of ES cells was considered to be a parameter of their differentiation state[5,6]. This system of ES cell differentiation could recapitulate the *in vivo* differentiation process, including the occurrence of apoptosis accompanying differentiation. Furthermore, the potential in ES cell apoptotic signals is necessary to trigger ES cell differentiation. Alternatively, it is possible that some cells enter apoptosis and the remainder differentiate, and this may depend on their stage in the cell cycle[7,8]. To elucidate the mechanism of icariin action on differentiation before a shift to the cardiomyocyte phenotype, we examined the distribution of the ES cell cycle and apoptosis using flow cytometry. Our experiment showed that the induction of icariin was associated with remarkable enrichment of ES-D3 cells in the G_0/G_1 phase and a significant reduction in cells in the S phase. In addition, icariin-mediated differentiation leads to higher apoptosis. These results suggest that the effect of icariin is associated with cell cycle arrest and apoptosis. The balance between positive and negative regulators of the ES cell cycle is important in maintaining the transition towards differentiation. The apoptotic signal in ES cells also triggers the differentiation of ES cells[7].

In conclusion, ES-D3 cells could be remarkably induced to directionally differentiate into cardiomyocytes by icariin at a concentration of 1×10^{-7} mol/L. The promoting effect of icariin on cardiac differentiation depended on the advancing and increasing gene expression of α-cardiac MHC and MLC-2v. At an early differentiation stage, the inducible effect of icariin was related to the regulation of the cell cycle and the induction of apoptosis.

References

1 Evans MJ, Kaufman MH. Establishment in culture of pluripotential cells from mouse embryos. Nature 1981; 292: 154–6.

2 Doestschman TC, Eistetter H, Katz M, Schmidt W, Kemler R. The *in vitro* development of blastocyst-derived embryonic stem cell lines: formation of visceral yolk sac, blood islands and myocardium. J Embryol Exp Morph 1985; 87: 27–45.

3 Robbins J, Doetschman T, Jones WK, Sanchez A. Embryonic stem cells as a model for cardiogenesis. Trends Cardiovasc Med 1992; 2: 44–50.

4 Hescheler J, Fleischmann BK, Lentini S, Maltsev VA, Rohwedel J, Wobus AM, *et al*. Embryonic stem cells: a model to study structural and functional properties in cardiomyogenesis. Cardiovasc Res 1997; 136: 149–62.

5 Rohwedel J, Sehlmeyer U, Shan J, Meister A, Wobus AM. Primordial germ cell-derived mouse embryonic germ (EG) cells *in vitro* resemble undifferentiated stem cells with respect to differentiation capacity and cell cycle distribution. Cell Biol Int 1996; 20: 579–87.

6 Ludmila J, Marielle A, Stephanie GG, Suzy M, Pierre S. Differential contributions of ERK and PI3-kinase to the regulation of cyclin D1 expression and to the control of the G1/S transition in mouse embryonic stem cells. Oncogene 2002; 21: 5515–28.

7 Kanaga S, Martina K, Rudolf J, Erwin FW. Regulation of ES cell differentiation by functional and conformational modulation of p53. EMBO J 1997; 16: 6217–29.

8 Sarkar SA, Sharma RP. All-tras-retinoic acid-mediated modulation of p53 during neural differentiation in murine embryonic stem cells. Cell Biol Toxicol 2002; 18: 243–57.

9 He W, Sun H, Yang B, Zhang D, Kabelitz D. Immunoregulatory effects of the herb *Epimediia* glycoside icariin. Arzneimittelforschung 1995; 45: 910–3.

10 Liu J, Lou YJ. Determination of icariin and metabolites in rat serum by capillary zone eletrophoresis: rat pharmacokinetic studies after administration of icariin. J Pharmaceut Biomed 2004; 29: 365–70.

11 Wang ZQ, Lou YJ. Proliferation-stimulating effects of icaritin and desmethylicaritin in MCF-7 cells. Eur J Pharmacol 2004; 504: 147–53.

12 Zhang YW, Morita I, Shao G, Yao XS, Murota SI. Screening of anti-hypoxia/reoxygenation agents by an *in vitro* model. Part 1: Natural inhibitors for protein tyrosine kinase activated by hypoxia/reoxygenation in cultured human umbilical vein endothelial cells. Planta Med 2000; 66: 114–8.

13 Qiu GT, Huang B, Tang SB, Hu J, Liu ZX. The investigation of cell culture conditions maintained embryonic stem cells as totipotent cells. Acad J SUMS 2000; 21: 100–3.

14 Metzger JM, Lin WI, Johnston RA, Westfall MV, Samuelson LC. Myosin heavy chain expression in contracting myocytes isolated during embryonic stem cell cardiogenesis. Circ Res 1995; 76: 710–9.

15 Scholz G, Pohl I, Genschow E, Klemm M, Spielmann H. Embryotoxicity screening using embryonic cells *in vitro*: correlation to *in vivo* teratogenicity. Cells Tissues Organs 1999; 165: 203–11.

16 Maltsev VA, Rohwedel J, Hescheler J, Wobus AM. Embryonic stem cells differentiation *in vitro* into cardiomyocytes representing sinusnodal, atrial and ventricular cell type. Mech Dev 1993; 44: 41–50.
17 Maltsev VA, Wobus AM, Rohwedel J, Bader M, Hescheler J. Cardiomyocytes differentiated *in vitro* from embryonic stem cells developmentally express cardiac-specific genes and ionic currents. Circ Res 1994; 75: 233–44.
18 Wobus AM, Kaomei G, Shan J, Wellner M, Rohwedel J, Guanju J, *et al*. Retinoic acid accelerates embryonic stem cell-derived cardiac differentiation and enhances development of ventricular cardiomyocytes. J Mol Cell Cardiol 1997; 29: 1525–39.
19 Boheler KR, Czyz J, Tweedie D, Yang HT, Anisimov SV, Wobus AM. Differentiation of pluripotent embryonic stem cells into cardiomyocytes. Circ Res 2002; 91: 189–201.
20 Guan K, Furst DO, Wobus AM. Modulation of sarcomere organization during embryonic stem cell-derived cardiomyocyte differentiation. Eur J Cell Biol 1999; 78: 813–23.
21 Uren AG, Vaux DL. Molecular and clinical aspects of apoptosis. Pharmacol Ther 1996; 72: 37–50.
22 Wobus AM, Guan K. Embryonic stem cell-derived cardiac differentiation: modulation of differentiation and 'loss of function' analysis *in vitro*. Trends Cardiovasc Med 1998; 8: 64–74.
23 Miller-Hance WC, LaCorbiere M, Fuller SJ, Evans SM, Lyons G, Schmidt C, *et al*. *In vitro* chamber specification during embryonic stem cell cardiogenesis. Expression of the ventricular myosin light chain-2 gene is independent of heart tube formation. J Biol Chem 1993; 268: 25244–52.
24 Lyons GE, Schiaffino S, Sassoon D, Barton P, Buckingham M. Developmental regulation of myosin gene expression in mouse cardiac muscle. J Cell Biol 1990; 111: 2427–36.
25 Franz W-M, Breves D, Klingel K, Brem G. Heart-specific targeting of firefly luciferase by the myosin light chain-2 promoter and developmental regulation in transgenic mice. Circ Res 1993; 73: 629–38.
26 O'Bruen TX, Kee K, Chien KR. A morphogenetic field of MLC-2v gene expression in the primordial heart tube of normal and MLC-luciferase transgenic mice. Proc Natl Acad Sci USA 1993; 90: 5157–61.
27 Mao H, Zhang L, Wang Y, Li X. Experimental studies of icariin on anticancer mechanism. J Chin Med Mater 2000; 23: 554–6.
28 Di KJ, Zhang JB. An outline of icariin pharmacological study. J Nature 2003; 25: 191–6. Chinese.

Acta Pharmacologica Sinica 2005 Apr; 26 (4): 486–491

Blackwell Publishing

Full-length article

Engagement of membrane immunoglobulin enhances Id3 promoter activity in WEHI-231 B lymphoma cells

Xiao-jun LI[1,2,3], Kikumi HATA[3], Junichiro MIZUGUCHI[3]

[2]*Department of Medical Laboratory Science, Jinling Hospital, School of Medicine, Nanjing University, Nanjing, 210002, China;*
[3]*Department of Immunology and Intractable Disease Research Center, Tokyo Medical University, 6-1-1 Shinjuku, Shinjuku-ku, 160-8402, Tokyo, Japan*

Key words

B lymphoma cells; inhibitor of differentiation; CD40L anti-IgM; transcriptional control

[1] Correspondence to Prof Xiao-jun LI.
Phn 86-25-8086-0177.
Fax 86-25-8480-3061.
E-mail lixiaojun62@yahoo.com.cn

Received 2004-07-15
Accepted 2004-11-26

doi: 10.1111/j.1745-7254.2005.00067.x

Abstract

Aim: We have recently shown that engagement of membrane immunoglobulin (mIg) induced upregulation of inhibitor of differentiation 3 (Id3) mRNA, resulting in growth arrest at G1 phase in WEHI-231 cells. In the present study, we examined whether engagement of mIg will affect promoter activity of the Id3 gene in WEHI-231 cells. **Methods:** DNA fragments corresponding to the 5'-flanking region of mId3 gene were amplified by polymerase chain reaction (PCR) using genomic DNA as the template. Three DNA fragments upstream of the transcription start site (+1) of the mId3 gene were subcloned into the luciferase reporter vector PGV-B2. The recombinant constructs were transiently transfected into WEHI-231 cells by an electroporation method. After incubation for 24 h, WEHI-231 cells were stimulated with 10 mg/L anti-IgM or irradiated CD40L-expressing NIH3T3 cells or control NIH3T3 cells for further 24 h, followed by assay for luciferase activity. **Results:** The luciferase analysis demonstrated that basal promoter activity of the Id3 gene was found in the region between -200 and +54. The Id3 promoter activity was increased 2-fold following stimulation with anti-IgM, but not CD40L, compared with medium alone. **Conclusion:** The mIg-mediated upregulation of Id3 expression is controlled, at least in part, through transcriptional regulation, as assessed by luciferase assay.

Introduction

Signalling transduction molecule(s) through B cell antigen receptor (BCR) are considered to play a crucial role in the regulation of B cell fate. The engagement of BCR leads to activation or inactivation of B cells, depending on B cell developmental stage as well as interaction with other cells including T cells expressing CD40 ligand (CD40L)[1–3]. The molecular mechanisms underlying BCR-mediated activation and/or inactivation remain largely unresolved. WEHI-231 B lymphoma cells, representing immature stage of B cells, have been widely used as an *in vitro* model system to analyze B cell-unresponsiveness[4–6], since costimulation with CD40L rescues anti-IgM-induced growth arrest and/or apoptosis[7,8].

The basic helix-loop-helix (bHLH) family of transcription factors including E2A play a key role in proliferation and/or differentiation in a variety of cell types[9,10]. The E protein contains a highly conserved HLH dimerization domain and a DNA-binding basic region that binds a conserved E-box. Another category of HLH protein, the inhibitor of differentiation (Id) family possess homologous HLH domain, but not DNA-binding domain[11,12]. Thus, Id proteins function as a dominant-negative (dn) regulator of transcription upon binding with other HLH proteins. The Id proteins are thought to promote cell cycle progression from G1 to S phase, while E2A proteins are thought to prevent it[9,13]. These findings indicate that E2A/Id proteins function to promote or inhibit proliferation in a context of cell types in divergent stimuli. For example, mature B cells from Id3-deficient mice failed to proliferate in response to anti-IgM[14]. Contrary to this current notion, we have recently demonstrated that anti-

IgM-induced G1 arrest appears to result from the anti-IgM-induced upregulation of Id3 expression at both mRNA and protein levels in WEHI-231 cells[15], as reported in other cell types[16]. In the present study, we examined whether anti-IgM-induced upregulation of Id3 mRNA resulted from transcriptional regulation of the Id3 gene.

Materials and methods

Cell culture WEHI-231 B lymphoma cells were maintained in RPMI-1640 medium supplemented with 10% fetal bovine serum (FBS), 2-mercaptoethanol 50 μmol/L, and kanamycin 100 mg/L at 37 ℃ in 5% CO_2.

Isolation of 5'-flanking region of mouse Id3 Genomic DNA was extracted from WEHI-231 cells using QIAGEN Genomic DNA Kit according to the manufacturer's instruction. DNA fragments corresponding to the 5'-flanking region of the mouse Id3 gene were isolated from the genomic DNA by polymerase chain reaction (PCR) using Id3-specific primers and high fidelity KOD DNA polymerase (Toyobo Co, Ltd, Japan) (Figure 1), based on the reported nucleotide sequences (GenBank accession number, AL935264). The nucleotide sequences of the primers were the following: forward with a *Kpn* I restriction enzymatic site underlined, Id3 -1981/+54, (5'-CGGGGTACCCATACAGAAGTCTTCACGAGAG-3); Id3-1012/+54 (5'-CGGGGTACCTGGCTGCCCTTCCACAACAG-3'); Id3 -200/+54 (5'-CGG GGTACC TCCTCGCATCCGAGGCTCC-3'). Reverse for the three fragments with a *Hind* III restriction enzymatic site underlined, (5'-CGGAAGCTTGAGAGTAGAGATAGAGAGGGAG-3'). The DNA fragments Id3 -1981/+54 (Id3/2k), Id3 -1012/+54 (Id3/1k), and Id3 -200/+54 (Id3/254) were cloned into pCR-Blunt II-TOPO vector by Zero Blunt PCR Cloning Kit (Invitrogen, USA). The nucleotide sequences of the fragments were confirmed to be identical to the reported sequences (GenBank) using ABI PRISM BigDyeTM Terminator Cycle Sequencing Ready Reaction Kits (Applied Biosystems, USA).

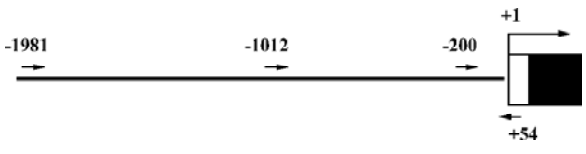

Figure 1. Isolation of DNA fragments containing 5'-flanking region of the Id3 gene by PCR. The DNA fragments containing Id3 promoter were amplified by PCR using the Id3-specific primers. To obtain three different fragments, sets of primers (forward, → and reverse, ←) were employed.

Plasmid construction for transient transfection assay The fragments of the Id3 promoter spanning nucleotides -1981/+54, -1012/+54, and -200/+54 were subcloned into the firefly luciferase reporter PGV-B2 vector lacking the promoter and enhancer (Tokyo-Inki, Tokyo, Japan) (Id3/PBV-B2), as previously described[17], resulting in Id3/2k-Luc, Id3/1k-Luc, and Id3/254-Luc, respectively.

Transient transfection of WEHI-231 cells was carried out by an electroporation method[17]. WEHI-231 cells (1.2×10^7 per 0.7 mL) containing 20 μg of the reporter constructs and 400 ng of internal control pRL-CMV Renilla luciferase vector were pulsed (400 V, 500 μF) using Gene Pulser (Bio-rad, USA). Following a 24-h incubation, the cells were further stimulated with 10 mg/L anti-IgM mAb or medium alone for 24 h, or cocultured with irradiated CD40L-expressing NIH3T3 cells or control NIH3T3 cells. The cells were harvested and lysed in lysis buffer (Promega, USA), followed by an assay for luciferase activity using a Dual-Luciferase Reporter Assay System (Promega), according to the manufacturer's instructions. Both firefly and Renilla luciferase activities were monitored with a Lumat LB9507 luminometer (Bert-hold). The ratio of firefly/renila values was caculated to normalize report activity. Normalized data are expressed as relative luciferase activity compared with that seen for PGV-B2 vector alone.

Statistical analysis Data were expressed as mean±SD. For single comparison, statistical significance between groups was determined by Student's *t*-test. Significance for multiple comparisons was determined by one-way ANOVA. $P<0.05$ was considered to indicate statistically significant differences.

Results

Structure of the functional Id3 locus We have recently found that anti-IgM upregulated Id3 mRNA expression, while CD40L downregulated it in WEHI-231 cells[15]. To analyze whether engagement of mIg influences transcriptional regulation of the Id3 gene, the three fragments containing the 5'-flanking region of the murine Id3 gene were isolated by PCR using Id3-specific primers. These fragments were subcloned into PGV-B2 vector to measure the promoter activity of the Id3 gene (Figure 2). Nucleotide sequence analysis confirmed the fidelity of the all constructs generated.

Basal promoter activity in the 5'-flanking region of the Id3 gene WEHI-231 cells were transfected with the constructs Id3/2k-Luc, Id3/1k-Luc, or Id3/254-Luc in combination with internal control vector and incubated with medium alone for 24 h, followed by assay for luciferase activity (Figure

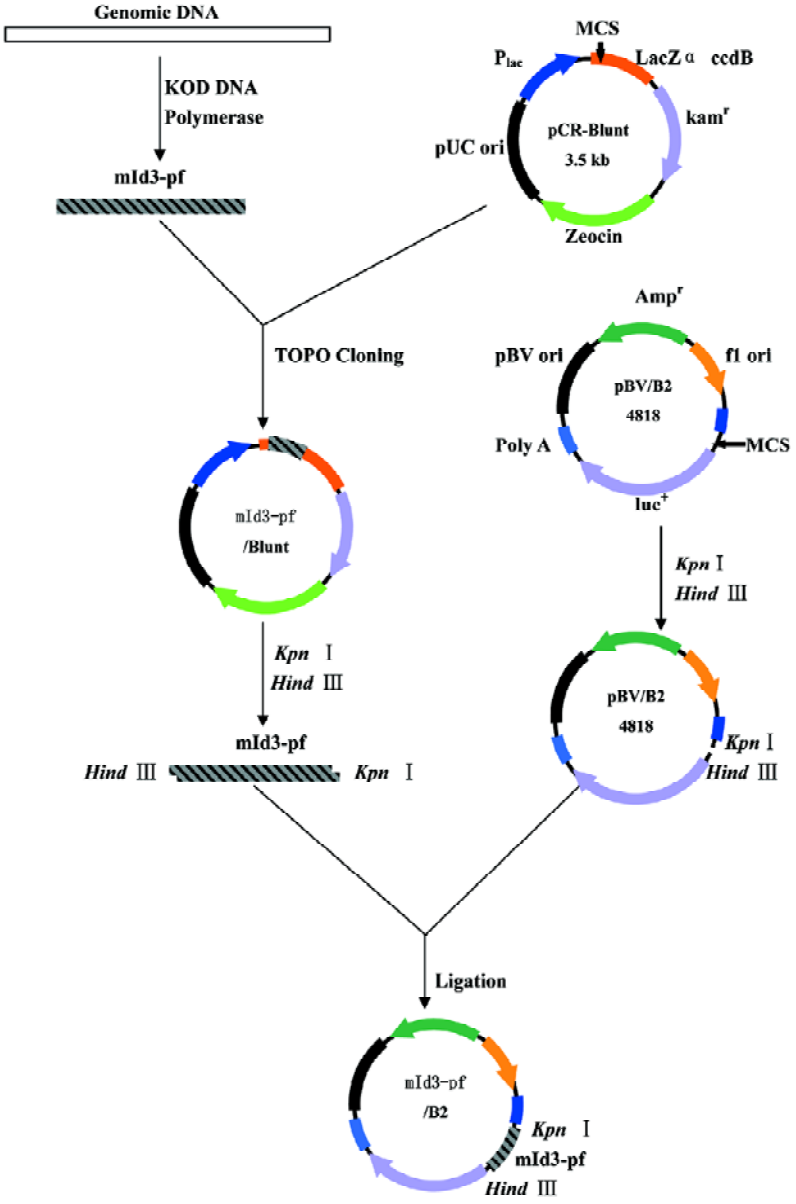

Figure 2. Procedures to create luciferase reporter vectors. The three distinct DNA fragments (Id3/2k, Id3/1k, and Id3/254) generated by PCR were cloned into pCR-Blunt II-TOPO, followed by digestion at sites (*Kpn* I/*Hind* III) to subclone into the luciferase reporter vector PGV-B2, resulting in Id3/2k-Luc, Id3/1k-Luc, and Id3/254-Luc, respectively.

3A, 3B). The basal promoter activity in these fragments Id3/2k, Id3/1k, or Id3/254 was increased 24-fold, 36-fold, and 54-fold, respectively, compared with the control vector (Figure 3B). These results suggest that the 254-bp fragment contains some positive regulatory element(s) of the Id3 gene, as reported by Yeh and Lim[18]. It is also possible that there are putative negative regulatory elements in the region from -1981 to -201.

Anti-IgM, but not CD40L, upregulates the promoter activity of the Id3 gene To examine whether transcriptional regulation is involved in the anti-IgM-induced upregulation of the Id3 gene, the WEHI-231 cells co-transfected with the Id3/2k-Luc, Id3/1k-Luc, Id3/254-Luc constructs and internal control vector were stimulated with 10 mg/L anti-IgM for 24 h, followed by assay for luciferase activity. The stimulation with anti-IgM enhanced the promoter activity of the Id3

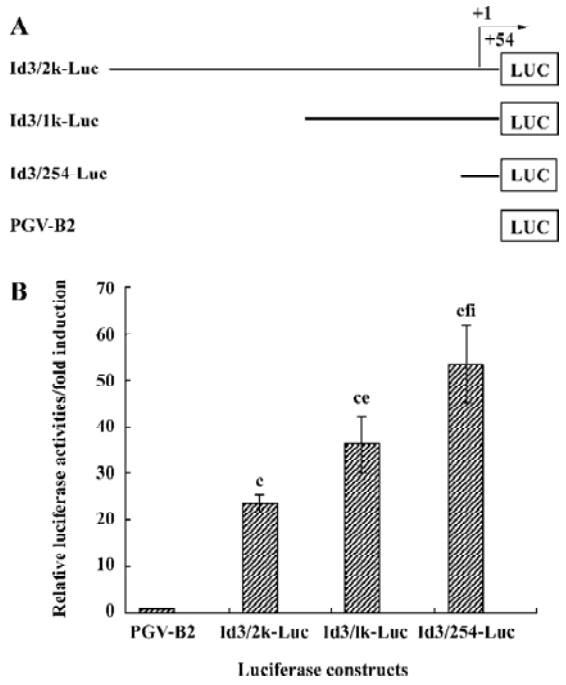

Figure 3. Basal promoter activity in the 5'-upstream region of the Id3 gene. (A) Structure of the reporter plasmids. The transcription start site is indicated by +1. (B) WEHI-231 cells were transfected with 20 mg/L Id3/2k-Luc, Id3/1k-Luc, Id3/254-Luc, or control vector alone, in combination with internal control vector. Following 24-h incubation, extracts were taken, and dual luciferase assay was carried out. The results were presented as the means±SD from three independent experiments. $^{c}P<0.01$ *vs* PGV-B2 control. $^{e}P<0.05$, $^{f}P<0.01$ *vs* Id3/2k-Luc. $^{i}P<0.05$ *vs* Id3/1k-Luc.

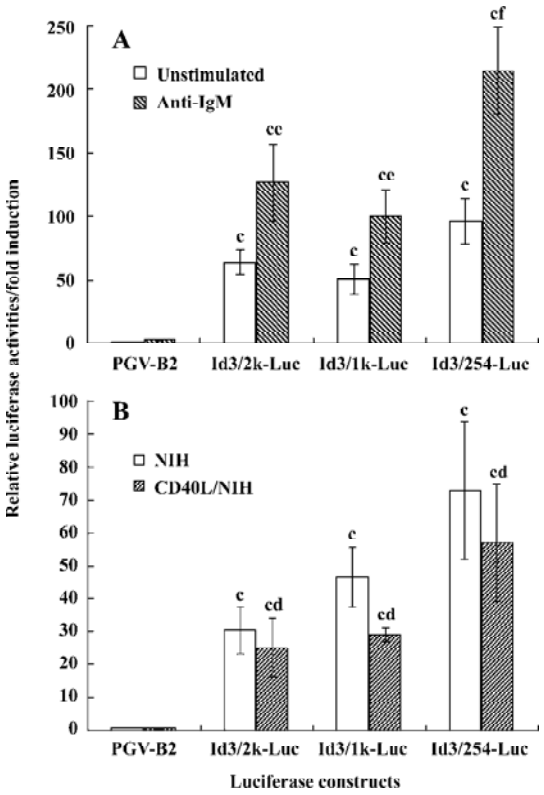

Figure 4. Upregulation of the Id3 promoter activity following stimulation with anti-IgM, but not CD40L. Twenty four hours after transfection of the Id3-Luc constructs, the cells were stimulated with 10 mg/L anti-IgM (A), or cocultured with CD40L-expressing NIH3T3 or control NIH3T3 cells (B). Following further 24-h incubation, the lysates were assayed for luciferase activity. The results were presented as the mean±SD from three independent experiments. $^{c}P<0.01$ *vs* PGV-B2 control. $^{d}P>0.05$, $^{e}P<0.05$, $^{f}P<0.01$ *vs* unstimulated cells.

gene which increased up to two-fold as compared with the activities in unstimulated cells, as assessed by luciferase activity (Figure 4A). The CD40L stimulation slightly decreased it, but the difference was not statistically significant (Figure 4B).

In our previous study, with Northern blot assay we observed an upregulation of Id3 mRNA expression in WEHI-231 cells after anti-IgM stimulation to reach levels 5-fold greater than that seen in unstimulated cells. There are many reasons to explain the inconsistent results between luciferase activity assay and northern blot. Besides the stability of the luciferase and mRNA, additional mechanisms may exist that contribute to the upregulation of Id3 expression at transcription level following anti-IgM stimulation. These results suggest that the mIg-mediated upregulation of Id3 expression is controlled, at least in part, through transcriptional regulation, as assessed by luciferase assay.

Discussion

Id proteins, a member of the HLH family proteins, play a crucial role in proliferation, differentiation, and apoptosis in a variety of cells including lymphocytes[9–11]. The mature B cells from Id3-deficient mice failed to proliferate in response to anti-IgM, whereas they showed proliferation comparable to those from control mice in response to LPS or CD40L[14], suggesting that Id3 promotes mIg-mediated B cell growth, as demonstrated in some cell types[11]. However, WEHI-231 cells, representing immature B cells, displayed growth arrest at the G1 phase of the cell cycle, accompanied by upregulation of Id3 mRNA following stimulation with anti-IgM[15]. In this study we examined whether the mIg-mediated upregulation of Id3 mRNA expression resulted from transcriptional activation and found that anti-IgM upregulated Id3 expression at least through transcriptional activation.

The nucleotide sequences of the 5'-upstream fragments isolated from WEHI-231 genomic DNA were confirmed to be identical with the published sequences[18] (GenBank accession number, AL935264). Consistent with the observation

of Yeh and Lim[18] using C2C12 muscle cells, the 254-bp fragment had substantial basal promoter activity of the Id3 gene (Figure 3). Indeed, several putative binding sites (*ATF*, *Sp1*, *Egr1*, *Cre*) for transcription factors were found using TRANSFAC databases[18]. Interestingly, when the longer fragments Id3/2k-Luc or Id3/1k-Luc was used, the basal promoter activity decreased compared with Id3/254-Luc (Figure 3B). These results might suggest that the promoter activity of the Id3 gene be regulated by both positive and negative regulatory elements, as reported in the transcriptional regulation of a variety of genes in eukaryotes[19]. A sufficient promoter activity was also found in other several B lymphoid lineage cell lines BAL17 and J558L (Li and Hata unpublished observation, 2003), although it is not dependent on B cell development.

The promoter activity of the Id3 gene was increased following engagement of mIg, but not CD40 (Figures 4A and 4B), resulting in the upregulation of the Id3 mRNA in WEHI-231 B lymphoma cells[15]. Although the Id3 upregulation through engagement of T cell receptor for antigen was abrogated by MEK1 inhibitor PD98059[20], the mIg-mediated upregulation of the Id3 message was not affected (Li and Hata, unpublished observation), suggesting that antigen receptor-mediated upregulation of Id3 expression is differently regulated between T and B cells.

In contrast to anti-IgM, CD40L decreased Id3 mRNA levels in WEHI-231 cells[15]. The promoter activity of the Id3 gene in response to CD40L was somewhat low, but not significant, compared with medium alone, suggesting that CD40-mediated down-regulation of Id3 mRNA expression is controlled post-transcriptionally. In our preliminary experiments, pretreatment with proteasomal inhibitor lactacystin restored CD40L-mediated down-regulation of Id3 protein expression (Li and Hata, unpublished observation), as suggested by Bounpheng *et al*[21]. These findings suggest that CD40-mediated down-regulation is controlled post-translationally.

Following an encounter with antigen, immature B cells undergo growth arrest/apoptosis unless T cell-derived signals such as CD40L are provided[7, 22]. Since transduction of Id3 gene into WEHI-231 cells results in growth arrest at the G1 phase of the cell cycle[15], Id3 appears to contribute to G1 arrest in immature B cells. The cell cycle progression from G1 to S phase in mammalian cells is tightly regulated by a cyclin-dependent kinase (CDK) and cyclin[23]. CDK activity is controlled by CDK inhibitors (CKIs) including $p21^{Cip1}$ and $p27^{Kip1}$[24]. Anti-IgM induced growth arrest through an upregulation of $p27^{Kip1}$ and down-regulation of cyclins[25]. It remains unclear how Id3 relates to $p27^{Kip1}$-mediated signalling pathway in B cells.

In contrast to our findings, Pan *et al* reported that anti-IgM-induced proliferative responses were severely reduced in mature B cells from Id3-deficient mice, compared with those from control mice[14]. Id3 appears to promote cell cycle progression in mature B cells upon encounter with antigen, whereas it prevents cell cycle progression in immature B cells, which could be accounted for by differential target(s) of Id3 molecule between mature and immature B cells. Experiments to examine this possibility are in progress.

In the present study, we clarified that engagement of mIg increased the promoter activity of the Id3 gene, probably resulting in an enhanced Id3 expression. The mIg-mediated Id3 upregulation appears to contribute to growth arrest, which could be reversed by the addition of CD40L, at least in part, through down-regulation of Id3 expression. Our results would be valuable for analysis of mIg-mediated unresponsiveness in B cells.

References

1 Nossal GJ. Immunologic tolerance: collaboration between antigen and lymphokines. Science 1989; 245: 147–53.

2 Klaus GG, Choi MS, Lam EW, Johnson-Leger C, Cliff J. CD40: a pivotal receptor in the determination of life/death decisions in B lymphocytes. Int Rev Immunol 1997; 15: 5–31.

3 DeFranco AL. The complexity of signaling pathways activated by the BCR. Curr Opin Immunol 1997; 9: 296–308.

4 Donjerkovic D, Scott DW. Activation-induced cell death in B lymphocytes. Cell Res 2000; 10: 179–92.

5 Benhamou LE, Cazenave PA, Sarthou P. Anti-immunoglobulins induce death by apoptosis in WEHI-231 B lymphoma cells. Eur J Immunol 1990; 20: 1405–7.

6 Scott DW, Livnat D, Pennell CA, Keng P. Lymphoma models for B cell activation and tolerance. III. Cell cycle dependence for negative signalling of WEHI-231 B lymphoma cells by anti-mu. J Exp Med 1986; 164: 156–64.

7 Scott DW, Chace JH, Warner GL, O'Garra A, Klaus GG, Quill H. Role of T cell-derived lymphokines in two models of B-cell tolerance. Immunol Rev 1987; 99: 153–71.

8 Tsubata T, Wu J, Honjo T. B-cell apoptosis induced by antigen receptor crosslinking is blocked by a T-cell signal through CD40. Nature 1993; 364: 645–8.

9 Massari ME, Murre C. Helix-loop-helix proteins: regulators of transcription in eucaryotic organisms. Mol Cell Biol 2000; 20: 429–40.

10 Engel I, Murre C. The function of E- and Id proteins in lymphocyte development. Nat Rev Immunol 2001; 1: 193–9.

11 Norton JD, Deed RW, Craggs G, Sablitzky F. Id helix-loop-helix proteins in cell growth and differentiation. Trends Cell Biol 1998; 8: 58–65.

12 Benezra R, Davis RL, Lockshon D, Turner DL, Weintraub H. The protein Id: a negative regulator of helix-loop-helix DNA binding proteins. Cell 1990; 61: 49–59.

13 Norton JD. ID helix-loop-helix proteins in cell growth, differ-

entiation and tumorigenesis. J Cell Sci 2000; 113 (Pt 22): 3897–905.
14 Pan L, Sato S, Frederick JP, Sun XH, Zhuang Y. Impaired immune responses and B-cell proliferation in mice lacking the Id3 gene. Mol Cell Biol 1999; 19: 5969–80.
15 Hata K, Yoshimoto T, Mizuguchi J. CD40 ligand rescues inhibitor of differentiation 3-mediated G1 arrest induced by anti-IgM in WEHI-231 B lymphoma cells. J Immunol 2004; 173: 2453–61.
16 Zhao F, Vilardi A, Neely RJ, Choi JK. Promotion of cell cycle progression by basic helix-loop-helix E2A. Mol Cell Biol 2001; 21: 6346–57.
17 Hata K, Mizuguchi J. Genomic organization and characterization of the promoter for the E2A gene. Gene 2004; 325: 53–61.
18 Yeh K, Lim RW. Genomic organization and promoter analysis of the murine Id3 gene. Gene 2000; 254: 163–71.
19 Ogbourne S, Antalis TM. Transcriptional control and the role of silencers in transcriptional regulation in eukaryotes. Biochem J 1998; 331 (Pt 1): 1–14.
20 Bain G, Cravatt CB, Loomans C, Alberola-Ila J, Hedrick SM, Murre C. Regulation of the helix-loop-helix proteins, E2A and Id3, by the Ras-ERK MAPK cascade. Nat Immunol 2001; 2: 165–71.
21 Bounpheng MA, Dimas JJ, Dodds SG, Christy BA. Degradation of Id proteins by the ubiquitin-proteasome pathway. FASEB J 1999; 13: 2257–64.
22 DeFranco AL, Gold MR, Jakway JP. B-lymphocyte signal transduction in response to anti-immunoglobulin and bacterial lipopolysaccharide. Immunol Rev 1987; 95: 161–76.
23 Morgan DO. Cyclin-dependent kinases: engines, clocks, and microprocessors. Annu Rev Cell Dev Biol 1997; 13: 261–91.
24 Sherr CJ, Roberts JM. CDK inhibitors: positive and negative regulators of G1-phase progression. Genes Dev 1999; 13: 1501–12.
25 Ezhevsky SA, Toyoshima H, Hunter T, Scott DW. Role of cyclin A and p27 in anti-IgM induced G1 growth arrest of murine B-cell lymphomas. Mol Biol Cell 1996; 7: 553–64.

Acta Pharmacologica Sinica 2005 Apr; 26 (4): 492–499

Blackwell Publishing

Full-length article

Effect of 7-hydroxystaurosporine on glioblastoma cell invasion and migration[1]

Qing-hui MENG[2], Li-xin ZHOU[3], Jia-lin LUO[4], Jian-ping CAO[4], Jian TONG[4], Sai-jun FAN[2,4,5]

[2]Department of Oncology, Lombardi Comprehensive Cancer Center, Georgetown University, Washington DC 20057, USA; [3]Institute of Medicine and Biotechnology, Chinese Academy of Medical Sciences, Beijing 100050, China; [4]School of Radiation Medicine and Public Health, Soochow University, Suzhou 215007, China

Key words

7-hydroxystaurosporine; protein kinase C; cell movement; cadherins; BRCA1 protein

[1] Project supported in part by a National Institutes of Health Grant (R21AA13122) and by the National Natural Science Foundation of China (No 30128018).

[5] Correspondence to Saijun FAN, MD, PhD.
Phn 86-512-6512-5142.
Fax 86-512-6530-4830.
E-mail sjfan@suda.edu.cn
sf88@georgetown.edu

Received 2004-10-25
Accepted 2005-01-10

doi: 10.1111/j.1745-7254.2005.00087.x

Abstract

Aim: To investigate the effect of 7-hydroxystaurosporine (UCN-01), a selective protein kinase C (PKC) inhibitor, on cell growth, migration, and invasion in invasive human glioblastoma U-87MG cells. **Methods:** PKC activity was determined based on the PKC-catalyzed transfer of the ^{32}P-phosphate group from [g-^{32}P]ATP into a PKC-specific peptide substrate. Cell viability was measured by MTT assay. Cell invasion and migration were evaluated by a Boyden chamber assay and scratch wound assay, respectively. Protein expression was analyzed using Western blot assay. The formation of 3-dimensional cellular aggregates was examined by a cell-cell aggregation assay. **Results:** UCN-01 treatment resulted in concentration- and time-dependent inhibition of U-87MG cell growth at higher doses (> 100 nmol/L), and reduced cell invasion and migration capability at less cytotoxic doses (<100 nmol/L). UCN-01 significantly repressed PKC activity. Consistent with this result, UCN-01 blocked cell invasion stimulated by phorbel 12-myristate-13-acetate (PMA) and ethanol (EtOH), 2 PKC activators. Enforced expression of the tumor suppressor genes BRCA1 and PTEN increased the anti-invasion potential of UCN-01. Exposure to UCN-01 caused a dose-dependent increase in cell adhesion molecule E-cadherin. The effect of UCN-01 on the formation of cell-cell aggregation was significantly reduced by the addition of an anti-E-cadherin antibody. **Conclusion:** UCN-01 inhibits the invasion and migration of human glioma cells. Accordingly, UCN-01 can have potential clinical applications for the treatment of human glioma metastasis.

Introduction

Protein kinase C (PKC) is a family of serine/threonine protein kinases that transduce signals for tumorigenesis, tumor cell invasion, and metastasis, and has thus been newly targeted for use in cancer treatment[1]. Activation of PKC augments tumor cell metastatic potential, whereas suppression of PKC activity through PKC inhibitors reduces tumor cell invasion and migration[1,2]. 7-Hydroxystaurosporine (UCN 01) is a selective PKC inhibitor derived from the non-selective protein kinase inhibitor staurosporine[3]. A number of studies, including some conducted in our own laboratories, have revealed that UCN-01 holds promise for use as a single agent or in combination with other chemotherapeutic agents, such as camptothecin, 5-fluorouracil, tamoxifen, and ionizing radiation, in inhibiting tumor cell growth *in vitro* and *in vivo*[3–9].

Our previous studies corroborate other studies, which indicate that the anti-tumor activities of UCN-01 are associated with arrest of cell cycle progression, including G1/S and/or G2/M[4,5], apoptosis induction[5–7,10], and the inhibition of DNA repair[11,12]. Most notably, UCN-01 abrogates the S or G2 arrest caused by chemotherapeutic agents[4]. It has also been found that UCN-01 inhibits microvessel formation (angiogenesis), which is required for tumor formation and growth[13,14]. Taken together, these studies indicate

that UCN-01 is a profound anti-tumor agent in several different tumors, including glioma. Moreover, UCN-01 has entered Phase I trials as a single agent in the USA and Japan[3,15].

In the present study, the effects of UCN-01 on cell growth, invasion, and migration were investigated in U-87MG, an invasive human glioblastoma cell line. The purpose of this study is to explore whether UCN-01 can be used as a new therapeutic agent in the treatment of glioblastoma growth and invasion.

Materials and methods

Cell culture and chemicals The human glioblastoma cell line U-87MG was purchased from the American Type Culture Collection (ATCC, Manassas, VA, USA) and maintained as monolayer cultures in D-MEM supplemented with 10% fetal calf serum (FCS), glutamine 2 mmol/L , streptomycin 100 mg/L , and 100 kU/L benzylpenicillin G (BioWhittaker, Walkersville, MD, USA). Cell number and viability were determined by staining a small volume of cell suspension with 0.4% trypan blue saline solution and examining the cells using a haemocytometer. The doubling time of U-87MG cell was approximately 30 h under our culture conditions. UCN-0 was obtained from the Laboratory of Molecular Pharmacology, Division of Basic Science, NCI, NIH (Bethesda, MD, USA) and stored at -20 ºC as a 10 mmol/L stock solution in 20% Me_2SO. Phorbel 12-myristate-13-acetate (PMA) and ethanol (EtOH) were purchased from Sigma Chemical Company (St Louis, MO, USA). PMA was dissolved in 20% Me_2SO and frozen at -20 ºC for storage purposes. UCN-01, PMA, and EtOH were further diluted in 2% medium prior to use.

Expression vectors and transfection A full-length BRCA1 or PTEN cDNA was expressed in a pCMV-Tag2B vector (Stratagene, La Jolla, CA, USA), which allows for the expression of proteins with an N-terminal FLAG sequence, as described previously[16]. Transfection of BRCA1 or PTEN was performed using a transfection reagent, Lipofect-Amin 2000, according to the manufacturer's instructions (Invitrogene, Gaithersburg, MD, USA) as described previously[16]. The efficiency of gene transfer was determined by a β-galactosidase assay using co-transfection with plasmid pRSV-β-gal.

Measurement of PKC activity Aliquots of 4×10^6 untreated and treated cells were washed with ice-cold Dulbecco's phosphate-buffered saline (PBS), suspended in a homogenization buffer (0.05 mol/L Tris-HCl, pH 7.5, containing EDTA 5 mmol/L , EGTA 10 mmol/L , β-mercaptoethanol 0.6 g/L , leupeptin 10 mmol/L , PMSF 1 mmol/L), and broken by probe sonication. The nuclei and unbroken cells were removed using low-speed spin, and the resulting supernatant was spun at 100 000×*g* for 30 min. The nuclear pellet was resuspended in HB and was referred to as a whole cell lysate. The 100 000×g supernatant was termed the soluble or cytosolic fraction. The 100 000×*g* pellet was washed with homogenization buffer, suspended by probe sonication in homogenization buffer containing 0.1% Triton X-100, incubated on ice for 1 h, and spun again at 100 000×*g*. The resulting supernatant was termed the particulate or membrane fraction.

Total PKC activity in the three fractions was estimated using a commercially available assay system (Amersham Life Science, Arlington Heights, IL, USA) according to the manufacturer's instructions. This assay is based on the PKC-catalyzed transfer of the ^{32}P-phosphate group from [γ-^{32}P] ATP into a PKC-specific peptide substrate (amino acids 65-658 of the EGF receptor with the phosphorylation site on Thr-654) in the presence of Ca^{2+} phosphatidylserine, and phorbol 12-myristate 13-acetate. All 3 fractions were diluted with 0.05 mol/L Tris-HCl (pH 7.5), and 25 μg of each were added to equal volumes of reaction solution (consisting of Tris-HCl 0.05 mol/L, $CaCl_2$ 1.5 mmol/L, dithiothreitol 7.5 mmol/L, PKC peptide substrate 45 mmol/L, and dioleoyl-glycerol 82 mmol/L) as provided by the manufacturer. Reactions were carried out at 37 ºC for 15 min. After 15 min, the reactions were stopped using a stop reagent (provided by the manufacturer); one hundred microlitre of each were blotted on glass fiber filters and extensively washed with 0.1% orthophosphoric acid. The bound radioactivity was counted using liquid scintillation spectroscopy. The protein content in each of the 3 fractions was measured. Radioactivity values resulting from the phosphorylation of endogenous substrates were subtracted from all determinations. Reactions were performed in triplicate and the values were averaged. Each assay was performed at least 3 times.

Measurement of cell viability Cell viability, an indicator of cytotoxicity, was evaluated using an MTT assay as described previously[17]. Four sets of experiments were performed in 10 wells for each treatment.

***In vitro* invasion assay** *In vitro* invasion assay was performed with a modified Boyden chamber[17]. The surfaces of filter (0.8 μm pore size) were coated with 25 μg Matrigel of uniform thickness for 1 h at room temperature. The uniformity of the coating was checked by Coomassie blue staining and low-power microscope observation. The lower chamber was filled with 10% FCS medium containing fibronectin (16 μg per chamber) as the chemoattractant. Cells (1×10^8 cells/L) re-suspended in the medium containing 2% FCS and 50 or

100 nmol/L UCN-01 were carefully transferred onto the upper surface of the filters in the chamber. After a 48-h incubation, the filter was gently removed from the chamber. The cells on the upper surface were removed with a cotton swab, cells that had passed through the Matrigel and attached themselves to the lower surface of the filter were fixed, stained with hematoxylin and eosin, and counted in 15 randomly selected microscopic fields (×400) per filter. Experiments were performed at least 3 times, independently. In the trials for determining the effect of UCN-01 on the PMA- and EtOH-promoted cell invasion, fibronectin was not added to the lower chamber.

Scratch wound assay The spreading and migration capabilities of U-87MG cells were assessed using a scratch wound assay[17] which measures the expansion of a cell population on surfaces. The cells were seeded into 6-well tissue culture dishes at a concentration of 2.5×10^5 cells and cultured in medium containing 10% FCS to nearly confluent cell monolayers, which were then carefully wound using 1-mL sterile pipette tips. Any cellular debris was removed by washing with PBS. The wounded monolayers were then incubated in 10% FCS medium containing UCN-01 (50 or 100 nmol/L) for 24 h or 48 h, then photographed under a light microscope (×200). The experiments were repeated in quadruplicate wells at least 3 times.

Immunoblot assay Protein expression was assessed using an immunoblot assay as described previously[16]. A monoclonal E-cadherin antibody was purchased from Transduction Laboratories (Lexington, KY, USA). A mouse monoclonal anti-FLAG antibody M2 (Stratagene, La Jolla, CA, USA) was used to detect expression of the FLAG-tagged BRCA1 and PTEN proteins. Equal protein loading and the protein transfer were confirmed by immunoblotting for the determination of α-actin protein using a polyclonal α-actin antibody (I-19, Santa Cruz, Hercule, CA, USA) on the same Western blots stripped. A colored marker (Bio-Rad Laboratories, Hercules, CA, USA) was used as a molecular size standard.

Reverse transcription-polymerase chain reaction (RT-PCR) mRNA was assayed by RT-PCR as described in previous studies[16]. cDNA was synthesized from 2 μg of total RNA in a 30-μL reaction mixture containing 5×reverse transcriptase reaction buffer (Life Technologies, Inc, Gaithersburg, MD, USA), dNTP 200 μmol/L, 100 μmol/L solution of primers, 50 units of RNasin (Promega, Madison, WI, USA), dithiotheithol 10 mmol/L , and 100 units of reverse transcriptase (Life Technologies, Inc). The mixture was incubated at 37 °C for 60 min, heated to 95 °C for 10 min, and then chilled on ice. PCR was carried out in a 50-μL volume containing 10–20 ng cDNA, chelating buffer (Perkin-Elmer/Cetus, Norwalk, CT, USA), 20 μmol/L dNTP mixture, 1.5 units of *Taq* DNA polymerase (Perkin-Elmer/Cetus), and 0.5 μmol/L of the following E-cadherin-specific primer pairs: 5'-CAATCTCAAGCTCATGG-3' (forward) and 5'-CCATTCGTTCAAGTAGTC-3' (backward). The PCR was processed at 94 °C for 1 min, 54 °C for 1 min, and 72 °C for 1 min. To ensure that the RNA was of sufficient purity to undergo RT-PCR, a PCR assay using primers specific for the β-actin gene cDNA was performed for each sample through the same PCR process. β-Actin specific primer pairs were as follows: 5'-GTC AAC GGA TTT GGT CTG TAT T-3' (forward); 5'-AGT CTT CTG GGT GGC AGT GAT-3' (backward). Semi-quantitative PCR conditions for E-cadherin and β-actin are 28 cycles and 22 cycles, respectively. The PCR products were electrophoresed on a 5% nondenaturing polyacrylamide gel. The gel was then dried and exposed to an imaging plate, and the radioactivity was determined using a Bioimage Analyzer (Bas1000; Fuji, Kanagawa, Japan).

Cell-cell aggregation assay Cells were harvested using HBSS buffer containing 0.01% trypsin and centrifuged at 100 000×*g* for 5 min. Cell pellets were re-suspended in a HCMF buffer (NaCl 160 mmol/L, Na_2HP_4 0.6 mmol/L , 0.1% w/v glucose, and 0.01% HEPES, pH 7.4) containing $CaCl_2$ 4 mmol/L at a cell density of 1×10^5 cell/ml. Total 1 mL aliquots of a single cell suspension were transferred to microcentrifuge tubes. UCN-01 (50 or 100 nmol/L), anti-E-cadherin antibody (0.5 mg/L, Transduction Laboratories, Lexington, KY, USA), or a combination of both was added. The cell cultures were then put on a shaker maintained at 37 °C for 60 min and 0.02 mL aliquots from all cell cultures were removed and fixed in 0.060 mL of glutaraldehyde. The total number of particles (that is, cells or aggregates) were counted by two investigators, using a haemocytometer. The degree of aggregation is represented by the aggregation index calculated by $N_{t=60}/N_{t=0}$, where $N_{t=0}$ is the number of single cells before the incubation and $N_{t=60}$ is the number of single cells after the incubation for 60 min. $N_{t=x60}/N_{t=0}>1$=no cell-cell adhesion; $N_{t=60}/N_{t=0}<1$=specific cell-cell adhesion.

Statistical analysis Each assay was performed at least 3 times. Statistical significance for the results was assessed using Student's *t*-test. $P<0.05$ suggests a statistically significant difference.

Results

Effect of UCN-01 on proliferation of U-87MG cells Using an MTT assay, we determined the cell viability of U-87MG glioblastoma cells after treatment with various doses of UCN-01 for 24 or 48 h. As shown in Figure 1A, exposure

to UCN-01 resulted in a loss of cell viability in a concentration- and time-dependent manner. ID_{50}, a dose at which 50% of the cells lost their viability, was approximately 400 nmol/L and 260 nmol/L after the 24-h and 48-h treatments, respectively (P<0.01). At UCN-01<100 nmol/L doses, no significant effect on cell viability was observed at any exposure time points (P>0.01). UCN-01 doses of <100 nmol/L were thus selected for use in further studies. We also determine the cytotoxicity of UCN-01.

Effect of UCN-01 on PKC activity of U-87MG cells Subconfluent cells were left untreated or treated with 100 nmol/L UCN-01 for 4 h and then harvested for assay of PKC activity . The membranous fractions (404±23 pmol ^{32}P/min, P<0.01) and cytosolic factions (114±46 pmol ^{32}P/min, P<0.01) were significantly inhibited in the cells treated with UCN-01 compared to the untreated control cells (885±42 pmol ^{32}P/min for the membranous fractions, 289±65 pmol ^{32}P/min for the cytosolic fractions). Similarly, reduced PKC activity was also observed after treatment with 50 nmol/L UCN-01 (data not shown).

Effect of UCN-01 on invasion and motility of U-87MG cells Cell invasion and migration are crucial processes in tumor metastasis. A modified Boyden chamber assay was performed in order to determine the ability of U-87MG cells to invade through biological matrices *in vitro*, based on the percentage of cells able to penetrate the reconstituted base-

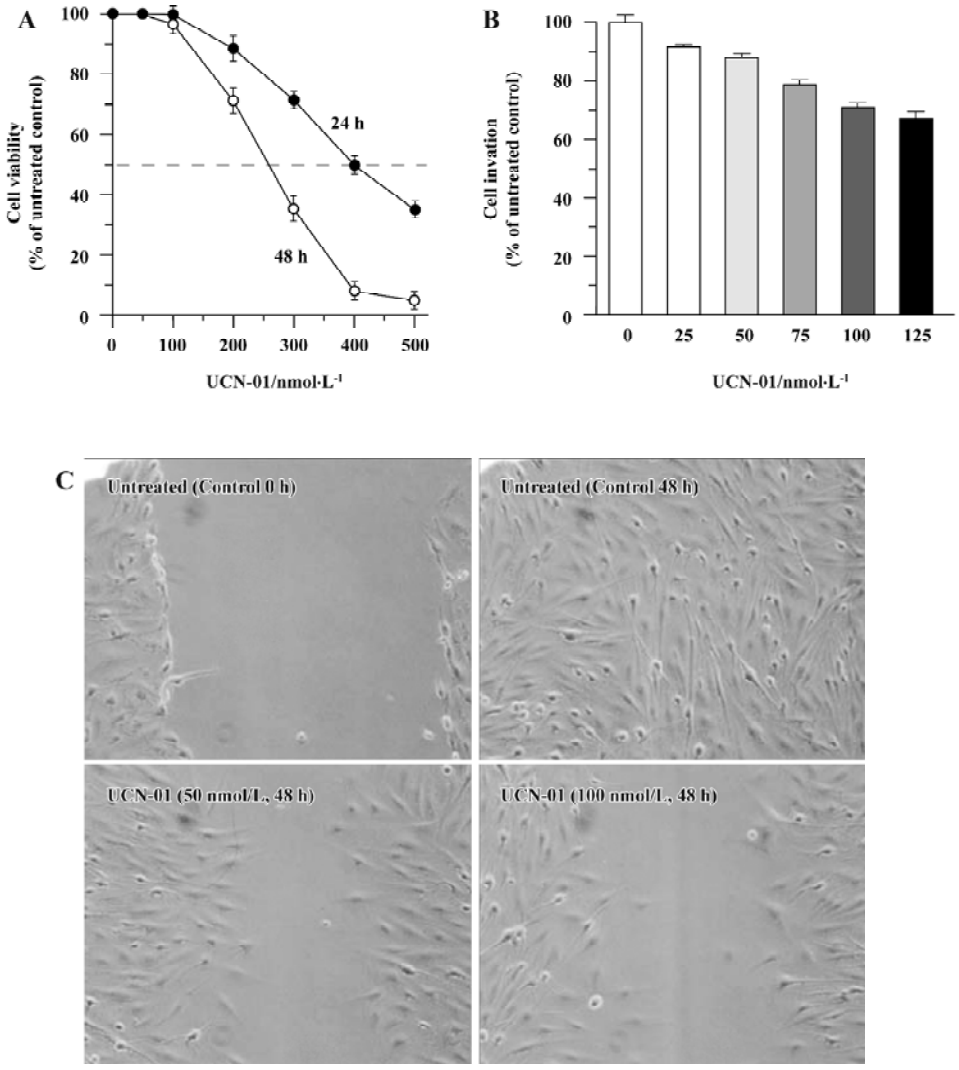

Figure 1. Effect of UCN-01 on U-87MG cell viability, invasion, and migration. (A) MTT assays of cell viability. Mean±SEM. n=3. (B) *In vitro* invasion assay. Data (mean±SEM) are expressed as the percentage of the control response from 3 independent experiment assays that yielded similar results. (C) Scratch wound assay

ment membrane-coated filters and attach to the lower surface of filter. As shown in Figure 1B, the invasion capacity of U-87MG cells was markedly inhibited when UCN-01 was present in the upper chamber; a reduction of approximately 12% and 25% (P<0.01) was observed for 50 and 100 nmol/L UCN-01 after 48-h treatment, respectively. A similar inhibition of cell invasion activity by UCN-01 was also observed in U-373, another glioblastoma cell line (data not shown).

To examine whether UCN-01 anti-invasion potential is associated with its ability to suppress cell spreading and migration, the effect of UCN-01 on U-87MG cell motility was also analyzed using a scratch wound assay. As demonstrated by the representative fields shown in Figure 1C, 50 nmol/L UCN-01 markedly inhibited the flattening and spread of both cell lines along the edges of the wound compared to the untreated control cells. When this experiment was repeated using a UCN-01 dosage of 100 nmol/L instead of 50 nmol/L, the anti-migration observed was more significant.

Effect of UCN-01 on PMA- and EtOH-stimulated cell invasion We determined the effect of UCN-01 on the stimulation of cell invasion caused by PMA and EtOH, two PKC activators. U-87MG cells spontaneously penetrated through an artificial basement membrane, and the number of invading cells significantly increased when PMA or EtOH was included in the cell suspension [invasion index 58±4 (PMA), 62±6 (EtOH) versus the untreated control, 46±3; P<0.01]. However, both spontaneous invasion and PMA- or EtOH-promoted cell invasion were markedly inhibited by UCN-01(Figure 2A). The ability of UCN-01 to suppress PMA- and EtOH-promoted cell invasion could not be attributed to increased cytotoxicity, since UCN-01 did not significantly affect the cytotoxicity of PMA or EtOH (Figure 2B).

Effect of BRCA1 and PTEN on anti-invasion activity of UCN-01 To determine the effect of the tumor suppressor genes BRCA1 and PTEN on the anti-invasion potential of UCN-01, we compared the invasion behavior of U-87MG cells that had been transiently transfected with the BRCA1 or PTEN gene in the presence and absence of UCN-01 (100 nmol/L). The full-length BRCA1 or PTEN cDNA was expressed in a pCMV-Tag2B vector, which allows for the expression of proteins with an N-terminal FLAG sequence. Exponentially growing cells (3×10^5 cell/well) in 6-well tissue culture dishes were transfected with either the BRCA1 or PTEN vector (5 μg/well) overnight, washed, and then incubated for 48 h. Overexpression of the BRCA1 or PTEN transgene was confirmed by the determination of BRCA1 or PTEN protein using an anti-FLAG antibody (M2). Significant expression levels of the BRCA1 (220 kDa) and PTEN (67 kDa) proteins were observed in U-87MG cells 48 h after transfections (Figure 3A). The transfected cells were collected and subjected to the *in vitro* invasion assay. As shown in Figure 3B, the transfection with the "empty" pCMV-Tag2B control vector had no effect on UCN-01 modulation of cell invasion, whereas overexpression of the BRCA1 or PTEN transgene significantly enhanced the anti-invasion potential of UCN-01. BRCA1 or PTEN transfection alone caused a 20% reduction in cell invasion; 100 nmol/L UCN-01 inhibited 30% of cell invasion. However, UCN-01 caused an 87% and a 90% inhibition in invasion in cells transfected with BRCA1 and PTEN, respectively. These results suggest that a combination of UCN-01 and BRCA1 or PTEN transgene synergistically inhibits the invasive behavior of glioblastoma cells.

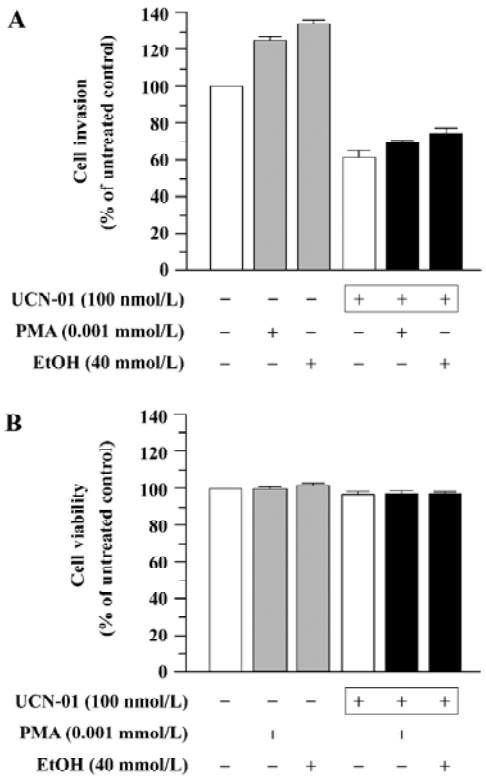

Figure 2. Effect of UCN-01 on PMA- and EtOH-induced promotion of cell invasion. (A) Subconfluent U-87MG cells were trypsized and counted. Cell viability was also assessed using the MTT assay 48 h after treatment with UCN-01 (100 nmol/L) and/or PMA (1 μmol/L) or EtOH (40 mmol/L) in 96-well tissue culture plates (B) Mean±SEM. n=3 independent experiments.

UCN-01 increases E-cadherin expression To explore the mechanism(s) underlying the effect of UCN-01 on U-87MG cell invasiveness and migration, we analyzed the expression of E-cadherin protein, an adhesion molecule, by an immunoblot assay, following treatment with UCN-01. As illustrated in Figure 4A, U-87MG cells contained a low basal

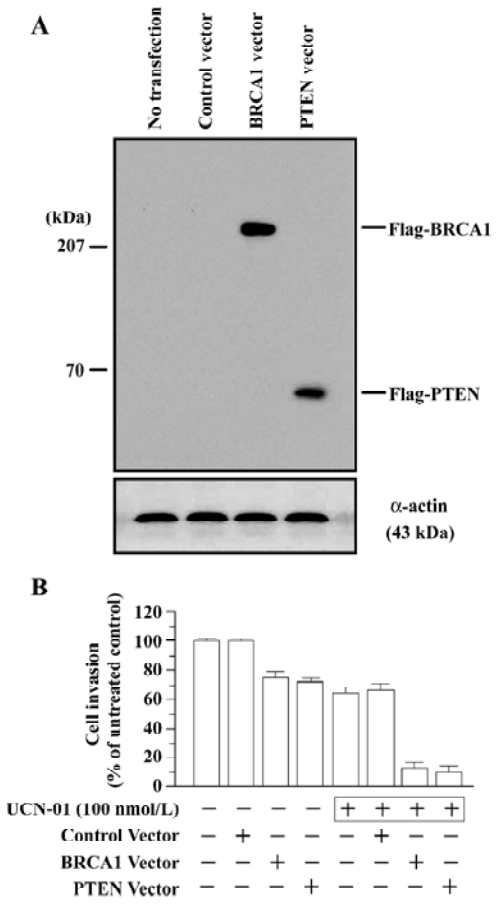

Figure 3. Effect of BRCA1 or PTEN on anti-invasion potential of UCN-01. Cells harvested and subjected to the immunoblot assay (A) and the *in vitro* invasion assay (B) 48 h after transfections. A representative set of experiments from 3 individual transfections is shown.

level of the endogenous E-cadherin protein. Forty-eight hours exposure to UCN-01 resulted in a significant dose-dependent increase. UCN-01(50 and100 nmol/L resulted in approximate 2.2- and 6.3-fold increases in the E-cadherin protein. Similar results were obtained for E-cadherin mRNA expression in response to UNC-01 treatment (Figure 4C).

Effect of UCN-01 and anti-E-cadherin antibody on formation of cell-cell aggregates To ascertain whether E-cadherin plays an important role in the protection of UCN-01 against the migration and invasion activity of U-87MG cells, we examined the effect of UCN-01 on the formation of cell-cell aggregates. UCN-01 100 nmol/L significantly inhibited the formation of 3-dimensional cellular aggregates (aggregation index=1.3, $P<0.01$) compared to the untreated control U-87MG cells, which showed a significant degree of cell-cell aggregation (aggregation index=0.65). However, in the presence of the E-cadherin antibody, the protective ability of UCN-01 against the formation of cell-cell aggregates was

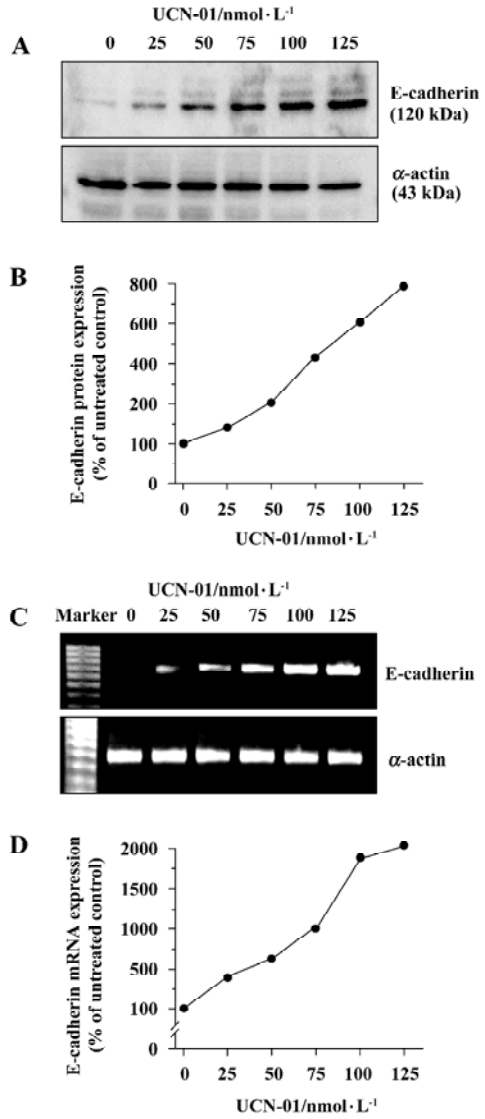

Figure 4. Effect of UCN-01 on E-cadherin expression. Cells were treated with indicated concentration of UCN-01 for 24 h and subjected to Western blotting for protein expression (A) and RT-PCR (C) for mRNA expression. Protein expression (B) and mRNA (D) expression bands were quantitated by densitometry and expressed relative to the α-actin bands and the untreated control band from 2 experiments, respectively. Standard errors were less than 5%.

markedly reduced (aggregation index=0.8). Similar results were observed in another human glioblastoma cell line, U-373 (data not shown). These results suggest that E-cadherin can play a critical role in the anti-invasion potential of UCN-01.

Discussion

PKC is viewed as a new target for suppressing tumor cell

invasion and migration, and therefore metastasis[1,2]. In the present study we found that in human gliocarcinoma U-87MG cells, UCN-01 inhibits cell proliferation in a concentration- and time-dependent fashion at higher doses (>100 nmol/L). Furthermore, at less cytotoxic doses (<100 nmol/L), UCN-01 reduces the PKC activity and suppresses the cell invasion and migration capabilities. The anti-invasion and anti-migration potential of UCN-01 was confirmed by further experiments in which the PMA- or EtOH-promoted activities of cell invasion were blocked by UCN-01. Both PMA and EtOH are potent activators of PKC[1,18]. These findings corroborate previous observations that PKC plays a central role in the invasion of glioblastoma-derived cell lines[19]. Therefore, the profound inhibition of tumor cell invasion and migration are novel features that contribute to the anti-tumor properties of UCN-01.

Although the mechanisms by which suppression of cell invasion and migration by UCN-01 have yet to be discovered, our study has revealed an important finding: despite the inhibition of PKC activity, up-regulated expression of the cell adhesion E-cadherin protein accompanies UCN-01-modulated cell invasion and migration activity. Moreover, a significant reduction of UCN-01 resulted in increased formation of cell-cell aggregates by the E-cadherin antibody. E-cadherin, a transmembrane glycoprotein, is a key mediator of cell-cell adhesion, which acts via the formation of a complex with 3 major cytoplasmic catenins (α, β, and γ), and reportedly plays a key role in controlling the invasive and metastatic progression of a variety of human carcinoma cells, including glioblastoma[20]. Disruption of the E-cadherin/catenin complex, due primarily to decreased or lost expression of E-cadherin, is shown to be correlated with increased cell proliferation, motility, and invasiveness associated with the progression of tumors[21]. Moreover, it is also found that tamoxifen, a PKC inhibitor, blocks the invasion and migration of tumor cells by increasing the expression and functions of E-cadherin/catenin complexes[1]. Therefore, E-cadherin is believed to be a critical mediator of the anti-tumor invasion and migration potential of UCN-01, although further experiments are needed for clarification of the relationship between E-cadherin expression and PKC activity.

In addition, we also found that the enforced expression of two tumor suppressor genes, BRCA1 or PTEN, by a transient transfection assay significantly affects the inhibition potential of UCN-01 on U-87MG glioblastoma cell invasion in a synergistic manner. BRCA1 (Breast Cancer susceptibility gene 1) is located at human chromosome 17q21, and mutations of BRCA1 are known to confer an added risk for breast and ovarian cancers in women, and for prostate cancer in men[22]. Increasingly, evidence indicates that invasive breast tumors show decreased BRCA1 mRNA expression and a loss of BRCA1 immunochemical staining relative to non-invasive tumors and benign tissues[23]. A clinical observation suggests that E-cadherin expression is potentially correlated with BRCA1-associated breast cancer[24]. Our recent studies also found that indole-3carbinol, a promising phytochemical produced by cruciferous vegetables, results in up-regulation of BRCA1 and E-cadherin/catenin complex expression, which results in the suppression of tumor invasion and migration[17]. In addition, we also found that alcohol promotes tumor cell invasion and migration and is associated with down-regulation of BRCA1[24].

Phosphatase and tensin homologue deleted from chromosome 10 (PTEN) was identified in the 10q23 chromosome region and is often found in mutated forms in a wide range of human malignancies, including glioblastoma[25]. The restoration of the PTEN gene into U-87MG cells has been found to markedly suppress cell migration and invasion by negative regulation of the signals generated at the focal adhesions, and by the direct dephosphorylation and inhibition of FAK, which is involved in the cell's interactions with extracellular matrix proteins responsible for the migration and enhancement of cell spreading through phosphorylation of its tyrosine[26]. Loss of PTEN expression and inactivation of wild-type PTEN function can often be observed in advanced or invasive tumors. Accordingly, these findings suggest that both BRCA1 and PTEN can function as inhibitors of tumor invasion and metastasis. Thus, our present findings provide *in vitro* evidence to suggest that a combination of UCN-01 function along with BRCA1 or PTEN gene therapy could be potentially useful in the clinical prevention and treatment of glioblastoma, although it is evident that for this to occur, further studies are required.

In conclusion, we discovered that UCN-01, as a selective PKC inhibitor, suppressed the cell migration and invasion and inhibits the PMA- and EtOH-promoted cell invasion in human glioblastoma U-87MG cells. Moreover, this inhibition of glioblastoma cell invasion and migration by UCN-01 is characterized by an enhanced expression of cell adhesion molecule E-cadherin. Therefore, UCN-01 can be a potent anti-tumor agent in the therapy of glioblastoma, not only via the suppression of proliferation of glioblastoma cells, but also via the inhibition of cell invasion and metastasis. Our results, which support previous studies[19], also indicate that the PKC signal transduction pathway can play an important role in glioblastoma cell invasion and metastasis, and that the suppression of this pathway may significantly impair the malignant progression of human glioblastoma.

References

1 Caponigro F, French RC, Kaye SB. Protein kinase C: a worthwhile target for anticancer drugs? Anticancer Drugs 1997; 8: 26–33.

2 Gomez DE, Skilton G, Alonso DF, Kazanietz MG. The role of protein kinase C and novel phorbol ester receptors in tumor cell invasion and metastasis. Oncol Rep 1999; 6: 1363–70.

3 Akinaga S, Sugiyama K, Akiyama T.UCN-01(7-hydroxystaurosporine) and other indolocarbazole compounds: a new generation of anti-cancer agents for the new century? Anticancer Drug Des 2000; 15: 43–52.

4 Wang Q, Fan S, Eastman A, Worland PJ, Sausville EA, O'Connor PM. UCN-01: a potent abrogator of G2 checkpoint function in cancer cells with disrupted p53. J Natl Cancer Inst 1996; 88: 956–65.

5 Shao RG, Cao CX, Pommier Y. Activation of PKCalpha downstream from caspases during apoptosis induced by 7-hydroxystaurosporine or the topoisomerase inhibitors, camptothecin and etoposide, in human myeloid leukemia HL60 cells. J Biol Chem 1997; 272: 31321–5.

6 Shao RG, Shimizu T, Pommier Y. 7-Hydroxystaurosporine (UCN-01) induces apoptosis in human colon carcinoma and leukemia cells independently of p53. Exp Cell Res 1997; 234: 388–97.

7 Shimizu, T, Cao CX, Shao RG, Pommier Y. Lamin B phosphorylation by protein kinase calpha and proteolysis during apoptosis in human leukemia HL60 cells. J Biol Chem 1998; 273: 8669–74.

8 Koh J, Kubota T, Koyama T, Migita T, Hashimoto M, Hosoda Y, *et al*. Combined antitumor activity of 7-hydroxystaurosporine (UCN-01) and tamoxifen against human breast carcinoma *in vitro* and *in vivo*. Breast Cancer 2003; 10: 260–7.

9 Koh J, Kubota T, Migita T, Abe S, Hashimoto M, Hosoda Y, *et al*. UCN-01 (7-hydroxystaurosporine) inhibits the growth of human breast cancer xenografts through disruption of signal transduction. Breast Cancer 2002; 9: 50–4.

10 Bozko P, Larsen AK, Raymond E, Skladanowski A. Influence of G2 arrest on the cytotoxicity of DNA topoisomerase inhibitors toward human carcinoma cells with different p53 status. Acta Biochim Pol 2002; 49: 109–19.

11 Jones CB, Clements MK, Redkar A, Daoud SS. UCN-01 and camptothecin induce DNA double-strand breaks in p53 mutant tumor cells, but not in normal or p53 negative epithelial cells. Int J Oncol 2000; 17: 1043–51.

12 Yamauchi T, Keating MJ, Plunkett W. UCN-01 (7-hydroxystaurosporine) inhibits DNA repair and increases cytotoxicity in normal lymphocytes and chronic lymphocytic leukemia lymphocytes. Mol Cancer Ther 2002; 1: 287–94.

13 Kruger EA, Blagosklonny MV, Dixon SC, Figg WD. UCN-01, a protein kinase C inhibitor, inhibits endothelial cell proliferation and angiogenic hypoxic response. Invasion Metastasis 1998; 18: 209–18.

14 Kruger EA, Figg WD. Protein binding alters the activity of suramin, carboxyamidotriazole, and UCN-01 in an *ex vivo* rat aortic ring angiogenesis assay. Clin Cancer Res 2001; 7: 1867–72.

15 Nahta R, Hortobagyi GN, Esteva FJ. Signal transduction inhibitors in the treatment of breast cancer. Curr Med Chem Anti-Cancer Agents 2003; 3: 201–16.

16 Fan S, Ma YX, Wang C, Yuan RQ, Meng Q, Wang JA, *et al*. Role of direct interaction in BRCA1 inhibition of estrogen receptor activity. Oncogene 2001; 20: 77–87.

17 Meng Q, Qi M, Chen DZ, Yuan R, Goldberg ID, Rosen EM, *et al*. Suppression of breast cancer invasion and migration by indole-3-carbinol: associated with up-regulation of BRCA1 and E-cadherin/catenin complexes. J Mol Med 2001; 78: 155–65.

18 Stubbs CD, Slater SJ. Ethanol and protein kinase C. Alcohol Clin Exp Res 1999; 23: 1552–60.

19 Zhang W, Law RE, Hinton DR, Couldwell WT. Inhibition of human malignant glioma cell motility and invasion in vitro by hypericin, a potent protein kinase C inhibitor. Cancer Lett 1997; 120: 31–8.

20 Frixen UH, Behrens J, Sachs M, Eberle G, Voss B, Warda A, *et al*. E-cadherin-mediated cell-cell adhesion prevents invasiveness of human carcinoma cells. J Cell Biol 1991; 113: 173–85.

21 Meng Q, Gao B, Goldberg ID, Rosen EM, Fan S. Stimulation of invasion and migration by alcohol in breast cancer cells. Biochem Biophys Res Commun 2000;273: 448–53.

22 Zheng L, Li S, Boyer TG, Lee WH. Lessons learned from BRCA1 and BRCA2. Oncogene 2000; 19: 6159–75.

23 Seery LT, Knowlden JM, Gee JM, Robertson JF, Kenny FS, Ellis IO, *et al*. BRCA1 expression levels predict distant metastasis of sporadic breast cancers. Int J Cancer 1999; 84: 258–62.

24 Jacquemier J, Eisinger F, Nogues C, Sun ZZ, Guinebretiere JM, Peyrat JP, *et al*. Histological type and syncytial growth pattern affect E-cadherin expression in a multifactorial analysis of a combined panel of sporadic and BRCA1-associated breast cancers. Int J Cancer 1999; 83: 45–9.

25 Li J, Yen C, Liaw D, Podsypanina K, Bose S, Wang SI, *et al*. PTEN, a putative protein tyrosine phosphatase gene mutated in human brain, breast, and prostate cancer. Science 1997; 275: 1943–7.

26 Tamura M, Gu J, Matsumoto K, Aota S, Parsons R, Yamada KM. Inhibition of cell migration, spreading, and focal adhesions by tumor suppressor PTEN. Science 1998; 280: 1614–7.

Acta Pharmacologica Sinica 2005 Apr; 26 (4): 500–512

Blackwell Publishing

Full-length article

Predictive model of blood-brain barrier penetration of organic compounds[1]

Xiao-lei MA, Cheng CHEN, Jie YANG[2]

State Key Laboratory of Pharmaceutical Biotechnology, School of Life Science, Nanjing University, Nanjing 210093, China

Key words

blood-brain barrier; quantitative structure-activity relationship; theoretical models

[1] Project supported by the National Natural Science Foundation of China (No 30171094, 30271497).
[2] Correspondence to Dr Jie YANG.
Phn 86-25-8359-4060. Fax 86-25-8332-4605.
E-mail luckyjyj@sina.com.cn

Received 2004-10-11
Accepted2004-12-06

doi: 10.1111/j.1745-7254.2005.00068.x

Abstract

Aim: To build up a theoretical model of organic compounds for the prediction of the activity of small molecules through the blood-brain barrier (BBB) in drug design. **Methods:** A training set of 37 structurally diverse compounds was used to construct quantitative structure-activity relationship (QSAR) models. Intermolecular and intramolecular solute descriptors were calculated using molecular mechanics, molecular dynamics simulations, quantum chemistry and so on. The QSAR models were optimized using multidimensional linear regression fitting and stepwise method. A test set of 8 compounds was evaluated using the models as part of a validation process. **Results:** Significant QSAR models (R=0.955, s=0.232) of the BBB penetration of organic compounds were constructed. BBB penetration was found to depend upon the polar surface area, the octanol/water partition coefficient, Balaban Index, the strength of a small molecule to combine with the membrane-water complex, and the changeability of the structure of a solute-membrane-water complex. **Conclusion:** The QSAR models indicate that the distribution of organic molecules through BBB is not only influenced by organic solutes themselves, but also relates to the properties of the solute-membrane-water complex, that is, interactions of the molecule with the phospholipid-rich regions of cellular membranes.

Introduction

The two barriers separating the central nervous system (CNS) from the periphery are the blood-brain barrier (BBB), located at the endothelial cells of the brain tissue capillaries, and the blood-cerebrospinal fluid barrier (B-CSF-B), at the choroids plexus and the circumventricular organs[1]. Formed by complex tight junctions of the brain capillary endothelial cells, the BBB segregates the circulating blood from interstitial fluid in the brain[2]. The capillary endothelial cells regulate the permeability property of the BBB. However, there are at least four kinds of cells that comprise the brain microvasculature, and all contribute to the regulation of the cerebral microvasculature and, indirectly, to the regulation of BBB permeability. The endothelial cell and the pericyte share a common capillary basement membrane. There is approximately one pericyte for every two to four endothelial cells[3]. Also, immunohistochemistry is a widely used research technique in BBB research for the cellular localization of proteins of interest in normal vessels and the documentation of altered expression following disease states, for the identification of cultured cells and for the spatial localization of novel gene products[4].

Although the BBB was thought to act as a static wall protecting the brain, application of recent advanced methodologies to study the BBB has led to the new concept that the BBB acts as a dynamic regulatory interface. Using primary cultured bovine brain capillary endothelial cells, Tsuji *et al*[5,6] have found that P-glycoprotein (ABCB1) acts as an efflux pump for the anti-cancer drugs, vincristine, at the BBB. Schinkel *et al*[7–9] have developed the *mdr* 1*a* gene knockout mouse and proved that P-glycoprotein (ie, *mdr* 1*a* gene products) plays a key role in restricting the apparent cerebral distributed vinblastine (a substrate of P-glycoprotein)

across the BBB. However, several hydrophilic substrates such as metabolites of cerebral neurotransmitters are present in the brain, which reduce the cerebral concentration, and as a result, could play an important role in CNS detoxification.

To be effective, CNS therapeutic agents must have the ability to cross over the BBB whereas peripherally acting drugs should hardly be able to pass the BBB. The uptake of a compound into the brain is a complex process. The moderately lipophilic drugs can pass the BBB by passive diffusion and the hydrogen bonding properties of drugs significantly influence their particular CNS uptake profiles. Polar molecules are generally poor CNS agents unless they undergo active transport to pass the CNS. Size, ionization properties, and molecular flexibility are other factors observed to influence transport of an organic compound across the BBB[10–13]. Recently, there has been a surge in computational efforts to evaluate absorption, distribution, metabolism, excretion, and toxicity (ADME/T) properties of drugs. These new computational approaches remain to focus on modeling structurally diverse data sets by dealing with the properties of the solutes. These properties are limited to relative lipophilicity indices, solvation and hydrogen bond parameters, topological indices, and limited three-dimensional solute properties[14–19]. Iyer *et al*[20] have developed a methodology called membrane-interaction (MI)-QSAR analysis, where structure-based design methodology is combined with classic intramolecular QSAR analysis to model different compounds interacting with cellular membranes. They have also built a predictive model of BBB penetration of organic compounds by simulating the interaction of an organic compound with the phospholipide-rich region of cellular membranes. As a result, they indicated that BBB penetration of an organic compound depended upon PSA, ClogP, and the conformational flexibility of the compounds as well as the strength of their "binding" to the model biologic membrane. The BBB penetration process can be reliably described for structurally diverse molecules whose interactions with the phospholipide-rich regions of cellular membranes are explicitly considered. There are other important applications of MI-QSAR analysis. For example, it can be used as a computational approach to estimate ADME properties such as the transport of organic solutes through biological membranes; and by this way, we can forecast intestinal absorption[21] of drugs and construct MI-QSAR model for skin irritation[22], and eye irritation[23]. However, as a prediction measure, the MI-QSAR computational model is itself somewhat inconvenient. It is quite easily susceptible to manipulation during the prediction process, and so models with more reliability can still have a reasonable-looking MI-QSAR model. Moreover, there are several non-MI-QSAR computational models including other descriptors besides PSA and ClogP reported to describe and predict BBB penetration. Lombardo and colleagues[17] reported about computing BBB penetration of organic solutes via free energy calculations. Keseru *et al*[24] clarified a high-throughput prediction of BBB penetration of organic molecules using a thermodynamic approach. Crivori *et al*[25] elucidated a method to predict BBB penetration from a three-dimensional molecular structure. Their research results showed that the BBB penetration only relies on one or two descriptors, which leads to the simplification of the prediction model of BBB.

In this article, we focus on constructing the predictive models of BBB penetration of organic compounds on the basis of QSAR analysis and MI-QSAR analysis.

Materials and methods

Building solute molecules A training set of 37 organic compounds[26,27] (Table 1) and a test set of 8 organic compounds (Table 2) were selected. These compounds had ranges in molecular weights from 16.03 to 448.58, whose concentrations in blood and brain (C_{blood} and C_{brain}) were measured in units of mmol/L, and there were variations in net charge at pH 7.4[26]. The dependent variable used in this theoretical model was the logarithm of the BBB partition coefficient, log BB=log (C_{brain}/C_{blood})[27]. Experimental values of log BB published to date covered the range of about -2.00 to +1.04. Within this range, compounds with log BB> 0.30 cross the BBB readily while compounds with log BB< -1.00 are poorly distributed to the brain[20,27]. All these compounds were built on a PC computer using the Build module of the commercial software packages Hyperchem 6[28]. First, the geometry of these compounds were opitimized using the Amber 94 force field in gas state. Second, they were placed in a periodic solvent box whose volume was X=16Å, Y=10 Å, Z=18Å, which included 96 water molecules. Here, temperature was 300 K and pressure was 101.325 kPa. Then the compounds in water were minimized by the above method. Third, the compounds in water were simulated by the Monte Carlo method and minimized by the above method.

Molecular modeling of a DMPC membrane monolayer complex with a layer of water (DMPC-water model) A model of dimyristoylphosphatidylcholine (DMPC) membrane monolayer was constructed using the software Material Studio[29], and minimized for 200 steps with the smart minimizer. According to the work done by van der Ploeg and Berendsen[30], the DMPC monolayer was composed of 25 DMPC molecules (5×5×1).

Table 1. The structure, molecular weight, formula, and log BB of 37 organic compounds in the training set[20].

ID	Structure	M_r	Formula	Log BB
1	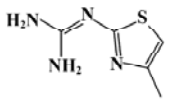	156.21	$C_5H_8N_4S$	-0.04
2	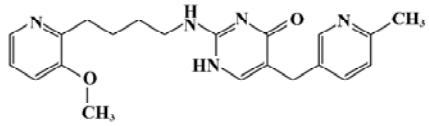	379.46	$C_{21}H_{25}N_5O_2$	-2.00
3	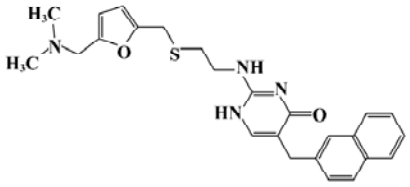	448.58	$C_{25}H_{28}N_4O_2S$	-1.30
4	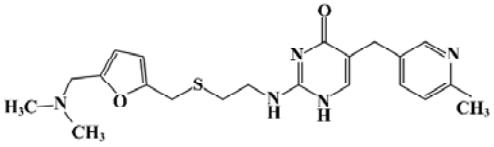	413.54	$C_{21}H_{27}N_5O_2S$	-1.06
5	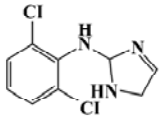	230.1	$C_9H_9C_{12}N_3$	0.11
6	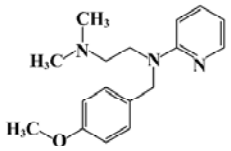	285.39	$C_{17}H_{23}N_3O$	0.49
7	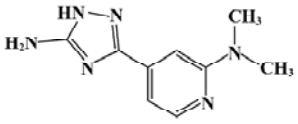	204.23	$C_9H_{12}N_6$	-1.17
8	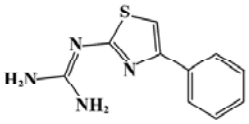	218.28	$C_{10}H_{10}N_4S$	-0.18
9	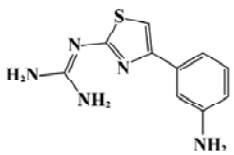	233.29	$C_{10}H_{11}N_5S$	-1.15
10	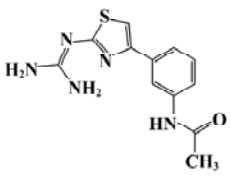	275.33	$C_{12}H_{13}N_5OS$	-1.57

(Continued)

ID	Structure	M_r	Formula	Log BB
11	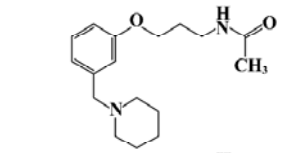	290.41	$C_{17}H_{26}N_2O_2$	-0.46
12	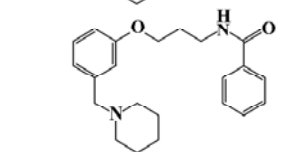	352.48	$C_{22}H_{28}N_2O_2$	-0.24
13	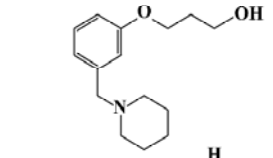	249.35	$C_{15}H_{23}NO_2$	-0.02
14	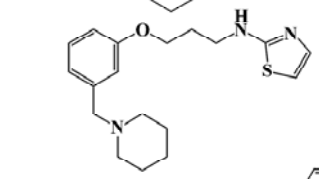	331.48	$C_{18}H_{25}N_3OS$	0.44
15	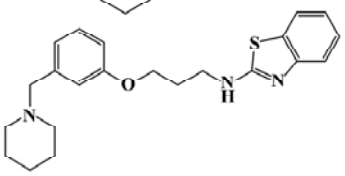	381.54	$C_{22}H_{27}N_3OS$	0.14
16	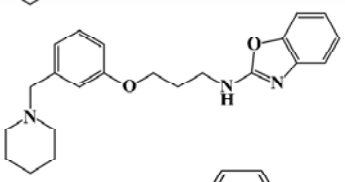	365.47	$C_{22}H_{27}N_3O_2$	0.22
17	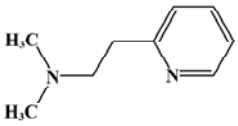	150.22	$C_9H_{14}N_2$	-0.06
18	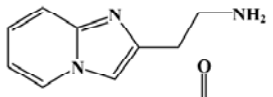	161.21	$C_9H_{11}N_3$	-1.40
19	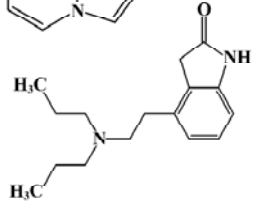	260.38	$C_{16}H_{24}N_2O$	0.25
20	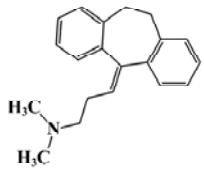	277.41	$C_{20}H_{23}N$	0.85

(Continued)

ID	Structure	M_r	Formula	Log BB
21		8.01	N_2	0.03
22	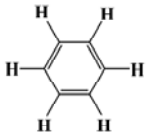	78.11	C_6H_6	0.37
23	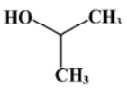	60.1	C_3H_8O	-0.15
24	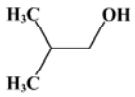	74.12	$C_4H_{10}O$	-0.17
25	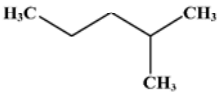	86.18	C_6H_{14}	0.97
26	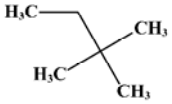	86.18	C_6H_{14}	1.04
27	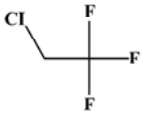	118.49	$C_2H_2ClF_3$	0.08
28		133.41	$C_2H_3Cl_3$	0.40
29	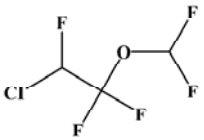	184.49	$C_3H_2ClF_5O$	0.24
30	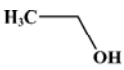	46.07	C_2H_6O	-0.16
31	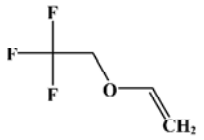	126.08	$C_4H_5F_3O$	0.13
32	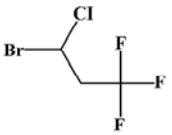	211.41	$C_3H_3BrClF_3$	0.35

(Continued)

ID	Structure	M_r	Formula	Log BB
33	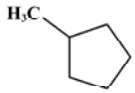	84.16	C_6H_{12}	0.93
34	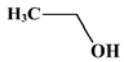	46.07	C_2H_6O	-0.16
35	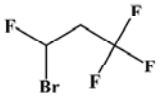	194.95	$C_3H_3BrF_4$	0.27
36	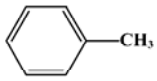	92.14	C_7H_8	0.37
37	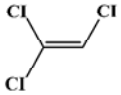	31.39	C_2HCl_3	0.34

Table 2. The structure, molecular weight, formula, and log BB of 8 organic compounds in the test set[20].

ID	Structure	M_r	Formula	Log BB
T1	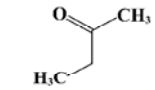	72.11	C_4H_8O	-0.08
T2	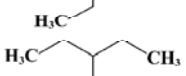	86.18	C_6H_{14}	1.01
T3	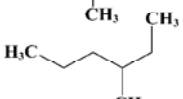	100.20	C_7H_{16}	0.90
T4	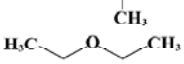	74.12	$C_4H_{10}O$	0.00
T5		100.20	C_7H_{16}	0.81
T6		16.04	CH_4	0.04
T7	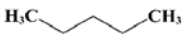	72.15	C_5H_{12}	0.76
T8	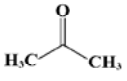	58.08	C_3H_6O	-0.15

Here, the unit cell parameters used for building the DMPC monolayer were a=8Å, b=8Å, and γ=96.0º, which yield an average surface area per phospholipid of 64Å^2 that was similar to Stouch's research results[31]. Moreover, we added a layer of water (40×40×10) including 529 water molecules to the polar side of the DMPC monolayer.

Molecular dynamic simulation (MDS) of a solute-membrane-water complex In order to prevent unfavorable van der Waals interactions between a solute molecule and the membrane DMPC molecules, one of the "center" DMPC molecules was removed from the DMPC-water model and an organic compound (solute) was inserted in the space cre-

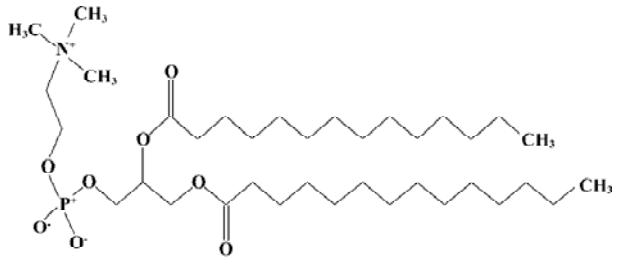

Structure of a single DMPC molecule

ated by the missing DMPC molecule to form a solute-membrane-water complex. The solute was inserted at three different positions in the DMPC-water model and three corresponding MDS models were generated for each compound. MDS of the complex was performed for 1000 steps using Material Studios[29] with a Compass force field. Here, the three-dimensional volume was restricted to a boundary of X=40Å, Y=40Å, Z=91.76Å, and γ=96.0°.

Calculation of descriptors Most of the intramolecular solute descriptors were calculated by the commercial software packages CS Chem3D Ultra7.0[32], which included molecular mechanism (MM) parameters, quantum chemistry parameters, hydrophobic parameters (such as ClogP), stereo parameters (such as Es and Balaban Index) and so on. The MM parameters comprised bending energy, stretch-bend energy, torsion energy, total energy, van der Waals energy and others. The quantum chemistry parameters consisted of electronic energy, HOMO energy, LUMO energy, total energy, and so on. The data of molecular PSA (polar surface area) came from Iyer and colleagues[20].

The intermolecular solute-membrane interaction descriptors were extracted directly from the MDS trajectories in which the solute-membrane-water complex had the lowest energy geometry. These descriptors were mainly energy parameters. The total energy of a system could be expressed as follows[20]:

$$E_{total}=E_{valence}+E_{crossterm}+E_{nonbond}$$

Here, the valence interactions include bond stretching (bond), valence angle bending (angle), dihedral angle torsion (torsion), and inversion, also called out-of-plane interactions (oop) terms, which are part of nearly all forcefields for covalent systems. In addition, a Urey-Bradley term (UB) may be used to account for interactions between atom pairs involved in 1, 3 configurations (ie, atoms bound to a common atom). $E_{valence}=E_{bond}+E_{angle}+E_{torsion}+E_{oop}+E_{up}$. Modern (second-generation) forcefields generally achieve higher accuracy by including crossterms to account for such factors as bond or angle distortions caused by nearby atoms. Crossterms can include the following terms: stretch-stretch, stretch-bend-stretch, bend-bend, torsion-stretch, torsion-bend-bend, bend-torsion-bend and stretch-torsion-stretch. The interaction energy between non-bonded atoms is accounted by van der Waals, electrostatic (Coulomb), and hydrogen bond terms in some older forcefields. $E_{non\text{-}bond}=E_{van\text{-}der\text{-}Waals}+E_{Coulomb}+E_{hydrogen\text{-}bond}$. Restraints that can be added to an energy expression include distance, angle, torsion, and inversion restraints. Restraints are useful if you, for example, are interested in only part of a structure for information on restraints and their implementation, use, and also the documentation for the particular simulation engine.

Construction and testing of MI-QSAR models MI-QSAR models of some organic compounds through BBB were constructed by partial sum of squares for regression using software SPSS. A training set of 37 structurally diverse compounds whose BBB partition coefficients had been measured was used to construct MI-QSAR models. MDSs were used to determine the explicit interaction of each test compound with the DMPC-water model. An additional set of intramolecular solute descriptors were computed and considered in the trial pool of descriptors for building MI-QSAR models. The QSAR models were optimized using multidimensional linear regression fitting and stepwise method. A test set of 8 compounds was evaluated using the MI-QSAR models as part of a validation process.

Results

Building solute molecules A training set of 37 organic compounds and a test set of 8 organic compounds were built and minimized, dissolved in liquid, and optimized by Monte Carlo method and MM. Finally, the dominant conformations of these compounds were obtained (Figure 1).

MDS of a solute-membrane-water complex The result revealed that the energy of a solute inserted at the middle position of the DMPC-water model was lower than that of the other two positions. Figure 2 shows the dominant conformation of a solute-membrane-water complex in the MDS.

Construction and testing of MI-QSAR models MI-QSAR analysis was used to develop predictive models of some organic compounds through BBB and to simulate the interaction of a solute with the phospholipide-rich regions of cellular membranes surrounded by a layer of water. Molecular descriptors of 37 compounds in the training set were listed in Table 3. Six MI-QSAR equations were constructed based on Table 3 and were listed as follows:

$$\log BB=0.552-1.73\times10^{-2}PSA$$
$$n=37 \quad R=0.835 \quad S=0.398 \qquad (1)$$
$$\log BB=0.229-1.70\times10^{-2}\,PSA+0.131\,Clog\,P$$

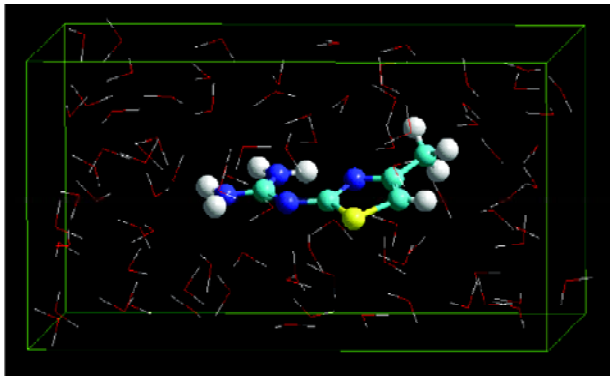

Figure 1. The dominant conformation of Number 1 compound labeled by balls and cylinders in water. The box denotes the water solvent box defined in Monte Carlo simulation.

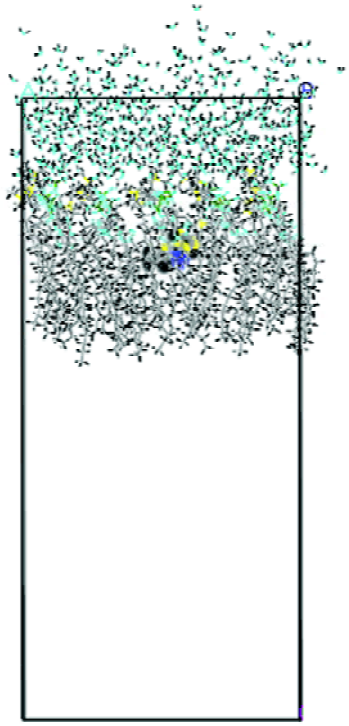

Figure 2. The dominant conformation of a solute-membrane-water complex in the MDS. The DMPC molecules appear as black stick. The upper molecules show water molecules. The center ball molecule expresses organic compound. The black box displays the border of volume.

n=37 R=0.878 S=0.352 (2)

$\log BB = 4.965\times10^{-2} - 1.28\times10^{-2}\,PSA + 0.211\,ClogP - 6.40\times10^{-7}\,BIndx$

n=37 R=0.924 S=0.285 (3)

$\log BB = 6.262\times10^{-2} - 1.36\times10^{-2}\,PSA + 0.205\,ClogP - 7.11\times10^{-7}\,BIndx - 0.185E_{sb}$

n=37 R=0.938 S=0.264 (4)

$\log BB = 6.580\times10^{-2} - 1.21\times10^{-2}\,PSA + 0.206\,ClogP - 7.77\times10^{-7}\,BIndx - 0.197E_{sb} + 1.330\times10^{-3}\Delta E_{total}$

n=37 R=0.947 S=0.248 (5)

$\log BB = 8.730\times10^{-2} - 1.04\times10^{-2}\,PSA + 0.222\,ClogP - 9.60\times10^{-7}\,BIndx - 0.183E_{sb} + 1.364\times10^{-3}\Delta E_{total} - 2.68\times10^{-3}\Delta E_{torsion}$

n=37 R=0.955 S=0.232 (6)

where PSA is the polar surface area, ClogP is the calculated logP (the logarithm of the partition coefficient for octanol/water), BIndx is the Balaban Index, namely connective index of molecular average total distance (relative covalent radius), and E_{sb} is the stretch-bend energy of a molecule. These intramolecular solute descriptors came from CS calculation. In addition, calculated from the MDS, intermolecular descriptors ΔE_{total} and $\Delta E_{torsion}$ are related to interactions between a solute and the DMPC-water model. They display the change in the total potential energy and the dihedral torsion energy of the solute-membrane-water complex comparing with that of the DMPC-water model, respectively. Here, n is the number of organic compounds, R is the correlation coefficient, and S is the standard deviation.

With the increase of the variable from one to six, the relativity of MI-QSAR equations was also improved, and the predictive ability of the models was enhanced. Figure 3 displaye a diagnostic plot of the MI-QSAR models. Here, equation 6 was the most significant, which means that the capability of an organic compound through BBB depends upon PSA, ClogP, BIndx, E_{sb}, ΔE_{total}, and $\Delta E_{torsion}$. Moreover, the potential of an organic compound through BBB is directly proportional to ClogP and ΔE_{total}, but inversely proportional to PSA, BIndx, E_{sb}, and $\Delta E_{torsion}$. The observed and predicted log BB values of the training set are listed in Table

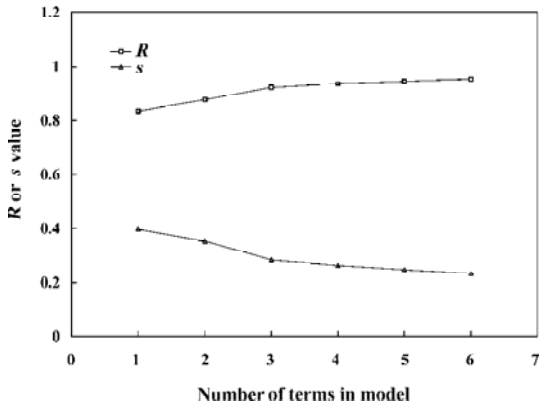

Figure 3. A diagnostic plot of the MI-QSAR models. R is the correlative coefficient and s is the standard deviation of the best x-term model, where x is plotted on the X-axis for the 37 compounds of the training set.

Table 3. The values of molecular descriptors of 37 organic compounds in the training set.

ID	PSA (Å^2)	ClogP	BIndx (Å)	E_{sb} (kcal/mol)	E_{total} (kcal/mol)	$E_{torsion}$ (kcal/mol)	ΔE_{total} (kcal/mol)	$\Delta E_{torsion}$ (kcal/mol)
1	78.90	1.20	12378.00	–1.3550	–298.30	–1713.11	42.46	11.30
2	94.00	1.98	1101758.00	–0.1560	–406.08	–1789.81	–65.32	–65.39
3	73.00	3.79	1738650.00	–1.4847	–256.30	–1703.14	84.46	21.27
4	87.00	1.63	1346396.00	–1.3911	–302.75	–1841.56	38.00	–117.15
5	39.00	1.02	41807.00	0.5813	–226.38	–1734.75	114.38	–10.33
6	26.80	3.23	305770.00	–0.0926	–228.29	–1679.46	112.47	44.96
7	88.80	1.01	58510.00	0.7104	–279.08	–1671.34	61.68	53.07
8	76.60	2.80	62216.00	–0.3833	–309.30	–1654.67	31.46	69.74
9	104.40	1.77	83798.00	–0.3560	–313.42	–1639.99	27.34	84.43
10	108.80	2.00	193593.00	–0.5217	–548.56	–1640.92	–207.80	83.49
11	47.90	2.51	352512.00	–0.0950	–312.12	–1656.75	28.64	67.67
12	45.20	4.27	779210.00	0.0048	–163.80	–1716.31	176.96	8.11
13	38.50	2.61	158640.00	–0.0949	–170.33	–1716.72	170.43	7.70
14	40.00	4.28	431722.00	–1.3051	–247.10	–1748.02	93.66	–23.61
15	39.20	5.88	766256.00	0.0991	–289.28	–1735.40	51.48	–10.98
16	54.90	5.14	766256.00	–0.1422	–181.06	–1743.61	159.70	–19.19
17	18.80	0.62	20863.00	0.1807	–331.70	–1695.70	9.05	28.72
18	46.70	0.27	20264.00	–1.3684	–209.47	–1644.68	131.29	79.74
19	44.10	2.80	190375.00	–2.9778	–311.92	–1713.89	28.84	10.52
20	5.40	4.85	210631.00	–0.0608	–235.72	–1704.34	105.03	20.08
21	0.00	–0.47	4.00	0.0000	–407.32	–1729.38	–66.56	–4.96
22	0.00	2.14	972.00	–0.0001	–239.88	–1675.18	100.88	49.23
23	23.40	0.07	213.00	0.0000	–160.13	–1672.39	180.63	52.03
24	22.60	0.69	712.00	0.0000	–319.07	–1742.70	21.69	–18.28
25	0.00	3.74	1899.00	0.0007	–282.37	–1751.62	58.39	–27.20
26	0.00	3.61	1661.00	0.0000	–285.71	–1731.95	55.05	–7.54
27	0.00	1.43	1661.00	–0.0001	–238.72	–1731.31	102.03	–6.89
28	0.00	2.48	633.00	0.0000	–291.56	–1725.74	49.20	–1.32
29	11.60	2.46	21380.00	–0.0001	–418.03	–1682.71	–77.27	41.70
30	24.40	–0.24	47.00	0.0000	–329.32	–1704.62	11.44	19.80
31	10.70	1.27	7864.00	–0.0000	–253.35	–1747.7	87.41	–23.29
32	0.00	2.37	7322.00	–0.0000	–268.83	–1714.25	71.93	10.17
33	0.00	3.31	931.00	0.0257	–353.84	–1739.77	–13.08	–15.35
34	24.40	–0.24	47.00	0.0000	–187.45	–1720.55	153.31	3.87
35	0.00	1.93	7322.00	–0.0000	–177.49	–1728.86	163.27	–4.45
36	0.00	2.64	2050.00	–0.0234	–220.39	–1681.15	120.36	43.26
37	0.00	2.63	712.00	–0.0000	–231.58	–1722.26	109.18	2.16

5 and plotted in Figure 4. The predicted log BB value of compound 18 in the training set was much higher than observed, and this molecule has also been identified as an outlier in other studies[20]. Protonation of the molecule could account for its low log BB value.

A test set of 8 organic compounds was constructed as a way to attempt to validate the MI-QSAR models given by the six equations mentioned. The compounds of the test set were selected so as to span almost the entire range in BBB penetration. The observed and predicted log BB values for this test set are given in Table 6 and plotted in Figure 5. It seems that the 5–6 terms MI-QSAR models could predict log BB for other compounds in drug design.

Discussion

We have built up a theoretical model of BBB penetration of organic compounds by simulating the interaction of an organic compound with the phospholipid-rich regions of cellular membranes. The family of these MI-QSAR models

Table 4. The values of molecular descriptors of 8 organic compounds in the test set.

ID	PSA (Å^2)	ClogP	BIndx (Å)	E_{sb} (kcal/mol)	E_{total} (kcal/mol)	$E_{torsion}$ (kcal/mol)	ΔE_{total} (kcal/mol)	$\Delta E_{torsion}$ (kcal/mol)
T1	22.70	0.32	712.00	0.0000	–274.72	–1713.74	66.04	10.68
T2	0.00	3.74	1838.00	0.0000	–225.63	–1716.62	115.13	7.79
T3	0.00	4.27	4150.00	0.0000	–331.38	–1700.64	9.38	23.78
T4	11.30	0.87	791.00	0.0000	–181.6	–1700.84	159.16	23.57
T5	0.00	4.40	4650.00	0.0000	–404.29	–1741.24	–63.53	–16.83
T6	0.00	1.10	0.00	0.0000	–282.94	–1746.19	57.82	–21.77
T7	0.00	3.34	791.00	0.0006	–271.93	–1681.94	68.84	42.47
T8	22.70	–0.21	213.00	0.0000	–364.89	–1695.36	–24.13	29.06

Table 5. The experimental value of log BB and the predictive value of log BB of 37 organic compounds in the training set.

ID	Experimental value of log BB	Predictive value of log BB					
		TERM1	TERM2	TERM3	TERM4	TERM5	TERM6
1	–0.04	–0.81	–0.95	–0.71	–0.52	–0.33	–0.20
2	–2.00	–1.07	–1.11	–1.44	–1.56	–1.57	–1.39
3	–1.30	–0.71	–0.51	–1.20	–1.11	–0.98	–1.17
4	–1.06	–0.95	–1.04	–1.58	–1.49	–1.37	–1.13
5	0.11	–0.12	–0.30	–0.26	–0.40	–0.19	–0.06
6	0.49	0.09	0.20	0.19	0.16	0.34	0.28
7	–1.17	–0.98	–1.15	–0.91	–1.11	–0.90	–0.86
8	–0.18	–0.77	–0.71	–0.38	–0.38	–0.22	–0.22
9	–1.15	–1.25	–1.31	–0.97	–0.99	–0.79	–0.81
10	–1.57	–1.33	–1.36	–1.05	–1.05	–1.16	–1.20
11	–0.46	–0.28	–0.26	–0.26	–0.31	–0.21	–0.32
12	–0.24	–0.23	0.02	–0.13	–0.23	0.03	0.04
13	–0.02	–0.11	–0.08	0.01	–0.02	0.26	0.34
14	0.44	–0.14	0.11	0.17	0.33	0.51	0.64
15	0.14	–0.13	0.33	0.30	0.17	0.26	0.33
16	0.22	–0.40	–0.03	–0.06	–0.15	0.10	0.22
17	–0.06	0.23	–0.01	–0.07	–0.11	–0.07	–0.09
18	–1.40	–0.26	–0.53	–0.50	–0.28	–0.02	–0.14
19	0.25	–0.21	–0.15	–0.05	0.45	0.59	0.62
20	0.85	0.46	0.77	0.87	0.85	0.99	1.01
21	0.03	0.55	0.17	–0.05	–0.03	–0.12	–0.10
22	0.37	0.55	0.51	0.50	0.50	0.64	0.57
23	–0.15	0.15	–0.16	–0.23	–0.24	0.04	–0.03
24	–0.17	0.16	–0.06	–0.09	–0.10	–0.04	0.08
25	0.97	0.55	0.72	0.84	0.83	0.91	1.07
26	1.04	0.55	0.70	0.81	0.80	0.88	0.98
27	0.08	0.55	0.42	0.35	0.35	0.49	0.56
28	0.40	0.55	0.55	0.57	0.57	0.64	0.71
29	0.24	0.35	0.35	0.41	0.39	0.31	0.27
30	–0.16	0.13	–0.22	–0.31	–0.32	–0.26	–0.26
31	0.13	0.37	0.21	0.18	0.17	0.31	0.43
32	0.35	0.55	0.54	0.55	0.54	0.64	0.68
33	0.93	0.55	0.66	0.75	0.74	0.73	0.84
34	–0.16	0.13	–0.22	–0.31	–0.32	–0.07	–0.02
35	0.27	0.55	0.48	0.45	0.45	0.68	0.74
36	0.37	0.55	0.57	0.61	0.61	0.77	0.72
37	0.34	0.55	0.57	0.60	0.60	0.75	0.81

Table 6. The experimental value of log BB and the predictive value of log BB of 8 organic compounds in the test set.

ID	Experimental value of log BB	Predictive value of log BB					
		TERM1	TERM2	TERM3	TERM4	TERM5	TERM6
T1	–0.08	0.16	–0.11	–0.17	–0.18	–0.06	–0.02
T2	1.01	0.55	0.72	0.84	0.83	0.99	1.05
T3	0.90	0.55	0.79	0.95	0.93	0.95	0.98
T4	0.00	0.36	0.15	0.09	0.09	0.32	0.32
T5	0.81	0.55	0.81	0.97	0.96	0.88	1.02
T6	0.04	0.55	0.37	0.28	0.29	0.37	0.47
T7	0.76	0.55	0.67	0.75	0.75	0.84	0.81
T8	–0.15	0.16	–0.18	–0.28	–0.29	–0.28	–0.31

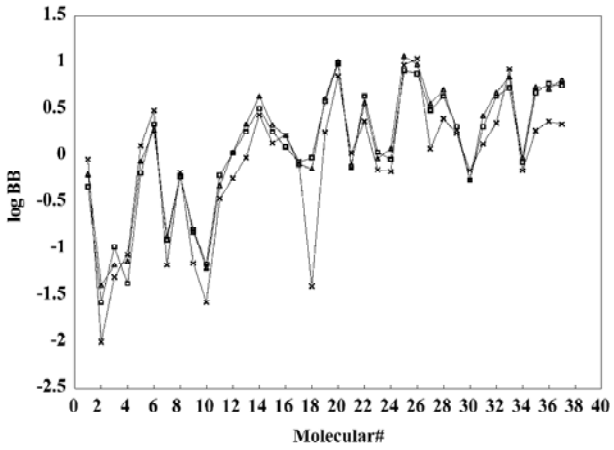

Figure 4. Comparison of the experimental log BB values (–×–) with the corresponding predicted log BB as predicted by the 5-term MI-QSAR model (– □ –) and by the 6-term MI-QSAR model (– △ –) for all the molecules of the training set.

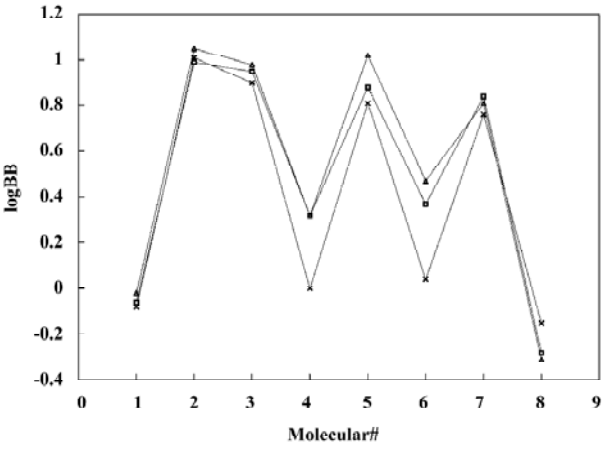

Figure 5. Comparison of the experimental log BB values (–×–) with the corresponding predicted log BB as predicted by the 5-term MI-QSAR model (– □ –) and by the 6-term MI-QSAR model (– △ –) for all the molecules of the test set.

reveal that the capability of an organic compound through BBB focus on six significant features, which are PSA, ClogP, BIndx, E_{sb}, ΔE_{total}, and $\Delta E_{torsion}$. The descriptor PSA is found as a dominant descriptor in these MI-QSAR models, which is related to the aqueous solubility of the solute and can be used as a direct lipophilicity descriptor[19]. When the value of PSA lessens within the range from 0 to 108.80 Å^2, the value of log BB will increase. This is consistent with the experimental result that the higher polarity it possesses, the more difficultly a molecule enters the hydrophobic environment of BBB[31]. Along with PSA, many descriptors can display various other kinds of the hydrophobic parameters of compounds, such as ClogP. In some cases it may be appropriate to display the parameter in the form of meshes, such as PSA. The higher the hydrophobic property, the greater the value of ClogP is. And the value of log BB of a molecule increases with the increase of ClogP. It means that the hydrophobic molecule can pass through BBB more easily than the hydrophilic molecule does, which is supported by the experimental results[33]. As stated, BIndx is the connective index of molecular average total distance, which pertains to the volume parameter. Our research result reveals that with the accretion of its bulk, a molecule becomes more and more difficult to cross over BBB by diffusion. The presence of the descriptor E_{sb} suggests that with the decrease of the stretch-bend energy the value of log BB increases.

Interestingly, the other two descriptors, ΔE_{total}, and $\Delta E_{torsion}$, reflect the interaction of the solute with the membrane and the behavior of the entire membrane-solute complex. Here, the more the value of ΔE_{total} changes, the more the value of log BB increases. This is because that small molecule acrossing the BBB membrane leads to the change in the structure of the complex, which therefore, results in a greater change of total potential energy, and the accretion of the energy change is the most important cause

for the increase of BBB penetration of small molecules. In contrast, the less the difference in the torsion energy is, the larger the value of log BB is. It displays that a small molecule tightly combined with the membrane-water complex has a higher value of log BB. The relationship suggests that as the solute becomes more flexible within the membrane-water complex, its log BB value would increase, which is in agreement with the research results by Iyer *et al*[20].

As an extra bonus of our work, we have developed an extension of traditional computational approaches that combines QSAR with solute-membrane-water complex. There is an obvious difference between our method and Iyer's method, which is the addition of a layer of water on the hydrophilic side of the DMPC membrane monolayer. So it is more analogous to the true BBB environment. Our results revealed that the distribution of organic molecules through BBB was not only influenced by the properties of organic solutes, but also related to the property of the solute-membrane-water complex. The former involves the polarity, hydrophobicity, size, and conformational freedom degree of organic molecules. The latter deals with the strength of an organic molecule to combine with the BBB membrane and the structural changeability of a solute-membrane-water complex. Moreover, the capability of a small molecule across BBB is mainly related to four physicochemical factors, which are the relative polarity of a small molecule, the molecular volume, the strength of a small molecule to combine with DMPC-water model, and the changeability of the structure of a solute-membrane-water complex. The MI-QSAR model shows that, relatively, less polar and more hydrophobic small molecules, which tightly combine with the membrane-water complex and are more flexible within the complex, can easily pass through BBB and enter the brain to be effective. In drawing conclusions from our model, it seldom matters if one or two parameters are slightly off (eg, *BIndx*), but it is often critical if some parameters are actually in the wrong value (eg, ClogP*, PSA,* or E_{sb}): that will change which molecules are in a position to penetrate through BBB.

Incidentally, since the molecular structures in the training set are not very comparable, our MI-QSAR equations possess universal significance. Nevertheless, the precision of the MI-QSAR equation is so low that there is still some time before it can be applied. If a series of organic compounds with similar structures were chosen to construct a training set, the precision of MI-QSAR simulation may be largely increased, while the prediction of the analogues through BBB will be greatly improved.

In conclusion, we have developed an extension of traditional computational approaches that combines QSAR with solute-membrane-water complex to simulate the BBB environment, which resembles Iyer's method, but differs from it by adding a layer of water on the hydrophilic side of the DMPC membrane monolayer. Our modified MI-QSAR method is more approximate to the body condition than Iyer's MI-QSAR analysis and possesses higher ability to predict organic compounds across BBB. Moreover, while still applying the structural information in a two-dimensional, "structure-function relationship" fashion, this method also takes into account the powerful three-dimensional information displayed by membrane structures, and thus improves existing MI-QSAR method. The MI-QSAR models indicate that the distribution of organic molecules through BBB was not only influenced by organic solutes themselves, but also related to the properties of the solute-membrane-water complex, that is, interactions of the molecule with the phospholipid-rich regions of cellular membranes.

References

1 Bickel U, Yoshikawa T, Pardridge WM. Delivery of peptides and proteins through the blood-brain barrier. Adv Drug Deliv Rev 2001; 46: 247–79.

2 Hosoyo K, Ohtsuki S, Terasaki T. Recent advances in the brain-to-blood efflux transport across the blood/brain barrier. Int J Pharm 2002; 248: 15–29.

3 Pardridge WM. Molecular biology of the blood-brain barrier. Methods Mol Med 2003; 89: 385–99.

4 Nag S. Immunohistochemical detection of endothelial proteins. Methods Mol Med 2003; 89: 489–502.

5 Tsuji A, Tamai I. Carrier-mediated or specialized transport of drugs across the blood-brain barrier. Adv Drug Deliv Rev 1999; 36: 277–90.

6 Tamai I, Tsuji A. Drug delivery through the blood-brain barrier. Adv Drug Deliv Rev 1996; 19: 401–2.

7 Jette L, Murphy GF, Leclerc JM, Beliveau R. Interaction of drugs with P-glycoprotein in brain capillaries. Biochem Pharmacol 1995; 50: 1701–9.

8 Chen W, Mehta SC, Lu DR. Selective boron drug delivery to brain tumors for boron neutron capture therapy. Adv Drug Deliv Rev 1997; 26: 231–47.

9 Friden PM. Utilization of an endogenous cellular transport system for the delivery of therapeutics across the blood-brain barrier. J Control Release 1997; 46: 117–28.

10 Begley DJ. The blood-brain barrier: Principles for targeting peptides and drugs to the central nervous system. J Pharm Pharmacol 1996; 48: 136–46.

11 Anderson BD. Prodrugs for improved CNS delivery. Adv Drug Deliv Rev 1996; 19: 171–202.

12 Pardridge WM. CNS drug design based on principles of blood-brain barrier transport. J Neurochem 1998; 70: 1781–92.

13 Cornford EM, Hyman S. Blood-brain barrier permeability to small and large molecules. Adv Drug Deliv Rev 1999; 36: 145–63.

14 Liu R, Sun H, So SS. Development of quantitative structure-property relationship models for early ADME evaluation in drug

discovery. 2. Blood-brain barrier penetration. J Chem Inf Comput Sci 2001; 41: 1623–32.
15 Rogers D, Hopfinger AJ. Applications of genetic function approximation to quantitative structure-activity relationships and quantitative structure-property relationships. J Chem Inf Comput Sci 1994; 34: 854–66.
16 Abraham MH, Chadha HS, Mitchell RC. Hydrogen bonding factors that influence the distribution of solutes between blood and brain. J Pharm Sci 1994; 83: 1257–68.
17 Lombardo F, Blake JF, Curatolo WJ. Computation of brain-blood partitioning of organic solutes via free energy calculations. J Med Chem 1996; 39: 4750–5.
18 Luco JM. Prediction of brain-blood distribution of a large set of drugs from structurally derived descriptors using partial least squares (PLS) modeling. J Chem Inf Comput Sci 1999; 39: 396–404.
19 Clark DE. Rapid calculation of polar molecular surface area and its application to the prediction of transport phenomena. 2. Prediction of blood-brain barrier penetration. J Pharm Sci 1999; 88: 815–21.
20 Iyer M, Mishra R, Han Y, Hopfinger AJ. Predicting blood-brain barrier partitioning of organic molecules using membrane-interaction QSAR analysis. Pharm Res 2002; 19: 1611–21.
21 Kulkarni A, Han Y, Hopfinger AJ. Predicting Caco-2 cell permeation coefficients of organic molecules using membrane-interaction QSAR analysis. J Chem Inf Comput Sci 2002; 42: 331–42.
22 Kodithala K, Hopfinger AJ, Thompson ED, Robinson MK. Prediction of skin irritation from organic chemicals using membrane-interaction QSAR analysis. Toxicol Sci 2002; 66: 336–46.
23 Kulkarni A, Hopfinger AJ, Osborne R, Bruner LH, Thompson ED. Prediction of eye irritation from organic chemicals using membrane-interaction QSAR analysis. Toxicol Sci 2001; 59: 335–45.
24 Keseru GM, Molnar L. High-throughput prediction of blood-brain partitioning: A thermodynamic approach. J Chem Inf Comput Sci 2001; 41: 120–8.
25 Crivori P, Cruciani G, Carrupt PA, Testa B. Predicting blood-brain barrier permeation using three-dimensional molecular structure. J Med Chem 2000; 43: 2204–16.
26 Abraham MH, Chadha HS, Mitchell RC. Hydrogen bonding. Part 36. Determination of blood-brain barrier distribution using octanol-water partition coefficients. Drug Des Discov 1995; 13: 123–31.
27 Abraham MH, Takacs-Novak K, Mitchell RC. On the partition of ampholytes: Application to blood-brain distribution. J Pharm Sci 1997; 86: 310–5.
28 Hyperchem HyperChem. Release 6.0 for MS Windows. Waterloo, Ontario, Hypercube Inc, 2001.
29 Materials Studios. San Diego, USA, Accelrys Inc, 2001
30 van der Ploeg P, Berendsen HJC. Molecular dynamics simulation of a bilayer membrane. J Chem Phys 1982; 76: 3271–6.
31 Stouch TR. Lipid membrane structure and dynamics studied by all atom molecular dynamics simulations of hydrated phosphatidylcholine vesicles. Mol Simulation 1993; 1: 335–62.
32 Chemoffice 2002 CS Chem3D Ultra7.0. Cambridge, USA, Cambridgesoft Inc, 2002
33 Kaliszan R, Markuszewski M. Brain-blood distribution described by a combination of partition coefficients and molecular mass. Int J Pharm 1996; 45: 9–16.

Acta Pharmacologica Sinica 2005 May; 26 (5): 513–518

Invited review

Telomere and telomerase as targets for anti-cancer and regeneration therapies[1]

Yi-hsin HSU, Jing-jer LIN[2]

Institute of Biopharmaceutical Science, National Yang-Ming University, Taipei, Taiwan, China

Key words

telomere; telomerase; cancer; regenerative disease; gene therapy

[1] Project supported by National Science Council grants (NSC 93-2311-B-010-001 and NSC 93-3112-B-010-010)
[2]Correspondence to Prof Jing-jer LIN
Phn 886-2-2826-7258
Fax 886-2-2825-0883
E-mail jjlin@ym.edu.tw

Received 2004-12-30
Accepted 2005-01-18

doi: 10.1111/j.1745-7254.2005.00098.x

Abstract

Telomerase is a ribonucleoprotein that directs the synthesis of telomeric sequence. It is detected in majority of malignant tumors, but not in most normal somatic cells. Because telomerase plays a critical role in cell immortality and tumor formation, it has been one of the targets for anti-cancer and regeneration drug development. In this review, we will discuss therapeutic approaches based mainly on small molecules that have been developed to inhibit telomerase activity, modulate telomerase expression, and telomerase directed gene therapy.

Introduction

Telomeres are specialized protein-DNA structures at the end of eukaryotic chromosomes. They protect chromosomes from end-to-end fusion and nuclease degradation. In humans, telomeres consists of approximately 4–14 kb of TTAGGG duplex repeats and 150–200 bases of single-stranded DNA overhang running 5' to 3' toward the end of chromosome[1]. Because of the end replication problem[2,3], telomeres in human cells erode by approximately 100 bp with each cell division[4]. Telomerase is the key enzyme for the stabilization of telomere by adding TTAGGG repeats to telomere ends[5]. It is a ribonucleoprotein that utilizes its RNA component as the template to synthesis telomere repeats. In humans, telomerase activity is not detected in most somatic cells[6,7]. Progressive telomere shortening after each cell division leads to cellular senescence after 60–80 population doublings[4]. Escaping senescence leads to further shortening of telomeres and can eventually cause cells to enter crisis and cell death[8]. Cells at this stage appear aneuploidy because telomere loss induces chromosome instability through the breakage/fusion/bridge cycles[9]. Few cells stabilize telomere length through activating telomerase activity[10]. Indeed, telomerase activity is detected in approximately 90% to 95% of human immortal cell lines and up to 85% of cancers[6,7]. In the remaining 5% to 10% immortal cells, telomerase-independent telomere maintenance mechanism, also known as the alternative lengthening of telomeres (ALT), were used to maintain telomere length[11]. These cells could then divide with great capacity.

Because telomerase is an essential component for the proliferation of cancer cells, targeting telomere and telomerase has drawn the interests of scientists in anti-cancer and regeneration drug development. In the present study, we discuss various approaches used including the small molecules that have been developed using telomere and telomerase as targets for chemotherapeutic developments.

Inhibition of telomerase activity

Although tumors are caused by mutations that activate oncogenes and repress tumor suppressor genes, they still need to overcome telomere-dependent senescence for their indefinite divisions. Because telomerase activity is crucial for supporting indefinite proliferation of most tumor cells, selective inhibition of telomerase activity only limits the proliferation capacity of tumor cells[12]. In principle, a telomerase-specific inhibitor is expected to affect telomere maintenance. It has been proposed that a telomerase inhibitor can be utilized as complementary therapy in cancer chemotherapeutics[12,13]. However, more and more studies indicate that telomerase also plays an important role in the telomere-cap-

ping function[14]. Inhibition of telomerase can affect the survival of cancer cells. Indeed, several published reports have found that the inhibition of telomerase can cause apoptosis without long-term treatment of the cells[15–17]. Thus, it is expected that the inhibition of telomerase activity in cells produces different effects depending on the means of inhibition. Because telomerase activities are also presented in human germline cells, stem cells, peripheral blood mononuclear cells, and normal fibroblasts[6,18,19], it is likely that telomerase inhibition also affects these cells. The potential risks of telomerase inhibition have to be carefully evaluated in these cells.

Targeting telomerase Telomerase is a unique reverse transcriptase consisting of two major components, the RNA template (*hTR*) and the catalytic subunit (hTERT). Both components have been used as targets for telomerase inhibition. The first successful case was reported in 1995 where antisense RNA against the first 185 nucleotides of the *hTR* molecule was introduced into HeLa cells and caused progressive telomere shortening and eventually cell crisis[20]. Similarly, short peptide nucleic acid (PNA) or 2'-*O*-methyl-RNA (2'-*O*-meRNA) oligomers with enhanced binding properties to *hTR* efficiently inhibit telomerase activity, and lead to progressive telomere shortening in immortal breast epithelial cells[21]. Synthetic oligonucleotides applying 2–5A (5'-phosphorylated 2'-5'-linked oligoadenylate)-linked antisense approaches were used to degrade *hTR* and caused apoptosis in several cancer models including glioma[15]. Utilizing ribozymes to cleave *hTR* has also been reported in several published studies[13,22]. These small catalytically-active RNA molecules cleave their RNA substrate in a sequence-dependent manner. Interestingly, the inhibition of telomerase activity using hammerhead ribozyme against *hTR* appears to sensitize the breast epithelial cells to topoisomerase inhibitors[13]. Another approach is to target the catalytic subunit of telomerase hTERT. A dominant negative mutant of hTERT was identified that caused complete inhibition of telomerase activity, telomere shortening, and increased cell apoptosis when introduced into cancer cells[16,17]. This dominant negative-hTERT also reduced tumorigenicity in nude mice[16].

Even though antisense, ribozyme, and dominant negative approaches showed promising results in inhibiting telomerase activity, these approaches were less applicable because the techniques for effective and convenient delivery of RNA or proteins were not available for clinical settings. Thus, small molecule compounds that inhibit telomerase activity appear to be more suited. There were several types of compounds identified, including nucleotide analogs that inhibit the catalytic activity of the enzyme and non-nucleotide analogs that have inhibitory effects less characterized. As these molecules have been extensively reviewed recently[23,24], they will not be discussed further here. However, it is worthy of noting that compound BIBR1532 was shown to inhibit telomerase non-competitively[25] and cause telomere shortening and senescence in cancer cells[26]. Moreover, cancer cells pretreated with BIBR1532 showed a reduced tumorigenic potential in the mouse xenograft model[26]. With the IC_{50} value at nanomolar concentration, BIBR1532 and several other compounds should have the potential for further developments[26–28].

Targeting telomeres In humans, the G-rich telomeric DNA tails are capable of forming a planar structure, termed G-quadruplexes, through non-Watson-Crick Hoogsteen hydrogen bonding *in vitro*[29]. A recent study has detected the G-quadruplex-induced fluorescence in telomeres of metaphase chromosomes using a G-quadruplex-selective fluorescent compound BMVC [3,6-*bis*(1-methyl-4-vinylpyridinium) carbazole diiodide], providing the first evidence for the presence of G-quadruplexes inside human cells[30]. In addition to telomeres, the G-quadruplex structure was also reported in the transcriptional regulatory region of several important oncogenes that their expression could be regulated by them[31]. Thus, even though telomeres in human cells were shown to form T-looped structures[32], it appears that human telomeres could also form G-quadruplex structures inside cells. The function of G-quadruplex structure in telomeres is not clear. However, because G-quadruplexes formed by telomeric DNA sequences were not the substrates for telomerase[33], the G-quadruplex structure might have a role in telomere maintenance and transcriptional regulation of oncogene expression. Agents that stimulate the formation or stabilize G-quadruplexes become important targets for drug design.

Several researchers have adopted a structure-based design and synthesis approach to identify lead compounds that interact with G-quadruplexes[24]. Successful lead compounds that were identified include derivatives of proflavins[28], porphyrins[34], acridines[35], anthraquinones[36], triazines[37], and carbazoles[27]. All of these identified compounds have planar aromatic rings. Molecular modeling studies have indicated that these planar structures bind to the G-quadruplexes through a series of interactions to the planar and loop structures of G-quadruplexes[28,38,39]. These interactions stabilize the structure of G-quadruplexes and increase the melting temperature upon binding. For example, a carbazole derivative BMVC increases the melting temperature (Tm) of G-quadruplexes formed by human telomeric DNA by as much as 13 ºC[40]. It is interesting to note that these planar compounds appear to be very effective in affecting telomerase

as several of these compounds have the IC_{50} at the range of nanomolar concentration[27,28,37].

Modulation of telomerase expression

Direct inhibition of telomerase at the activity level provides a simpler mean to target telomerase for cancer therapy. In recent years, several reports have also attempted to target the expression of telomerase at the gene level. Repression of telomerase expression in cancer cells would have applications in anti-cancer chemotherapies whereas activation of telomerase expression in normal cells would have applications in regeneration therapies.

Repressing hTERT expression in cancer cells In human cells, the expressing of telomerase catalytic enzyme hTERT correlates well with the telomerase activity[41]. It also appears that regulation at the transcriptional level was the most important step for hTERT expression[42] even though regulation at the splicing[43,44], post-translational modification[45–48], or subcellular localization[49] were also reported. Thus, targeting hTERT transcription is the focus for developing agents that repress hTERT expression. However, there were only a limited number of reports targeting hTERT expression. Retinoic acid represents the most characterized small molecule in this category. Retinoic acid at the micromolar concentration down-regulates telomerase activity in human leukemia cells[50,51]. Long-term treatment of leukemia cells with retinoic acid leads to telomere shortening and eventually cell death[50]. The specificity of retinoic acid is a concern in future drug development. An ideal compound should only affect the expression of the hTERT gene. Nevertheless, repressing hTERT expression is an effective way to limit the proliferation capacity of cancer cells. Recently, a cell-based system was developed that enables the screening of small molecule compounds for repressing hTERT expression[52]. The hTERT promoter was ligated downstream to a reporter gene, GFP or SEAP (secreted alkaline phosphatase), and introduced into human cancer cells. The expression of hTERT could then be monitored by the reporter genes. A series of anthraquinone derivatives were tested for their ability to repress hTERT expression using this cell-based system[52]. Even though anthraquinone derivatives did not repress hTERT expression, it is anticipated that small molecule compounds that repress hTERT expression could be screened and identified using this approach.

Activating hTERT expression in normal cells While telomerase inhibition or hTERT repression could have applications in anticancer therapeutics, telomerase activation could serve as a mean to extend the lifespan of normal cells and to treat degenerative diseases. For example, liver cirrhotic pathology is caused by continual hepatocyte destruction over many years. The end-stage of cirrhosis is characterized by extensive fibrotic replacement and cessation of hepatocyte proliferation. In a mouse experimental liver cirrhosis model, the pathology is alleviated through activation of telomerase activity[53]. Also in Werner syndrome cells, the accelerated aging phenotype is reversed by telomerase activation[54]. Moreover, the life span of human bone marrow stromal stem cells are achieved by telomerase expression[55,56]. These *ex vivo* expanded stem cells could have profound applications in, for instance, tissue engineering.

Ectopically expressed hTERT by introducing a virus promoter-driven hTERT gene into normal human cells has been found to be very effective in increasing hTERT mRNA expression and telomerase activity, and extending the life span of normal cells[10,57]. For example, the replication capacity of skin fibroblasts[10] and adult mesenchymal stem cells[58] could be expanded with the introduction of a viral promoter driven hTERT gene. However, given the role of telomerase in cancer and the introduced DNA which integrates randomly into chromosomes, this type of approach might cause some risks. Although some reports indicated that ectopic expression of telomerase did not cause transformation phenotypes or cancer-associated changes[59,60], more and more studies raise concerns about the future application of cells immortalized by ectopic hTERT expression in normal cells. Telomerase overexpression in mice has been found to increase epidermal tumors and promote mammary carcinomas[58,61,62] and that expressing hTERT in human mesenchymal stem cells renders these cells tumorigenic[58]. Thus, the ideal situation would be controlled expression of hTERT in target cells to avoid unnecessary side-effects. One approach is using small molecules that activate telomerase upon addition and return to the repressed state upon removal which might provide the solution for controlled expression of hTERT. This approach also avoids the uncertainty concerning the integration of DNA into chromosomes.

There are several molecules which have been identified that affect hTERT expression through inhibiting DNA methylation or histone deacetylation. Normal human fibroblast treated with 5-azacytidine (5-AZC) can cause demethylation of the CpG islands within hTERT promoter. It then turns on hTERT mRNA expression and activates telomerase activity[63,64]. Similarly, histone deacetylase inhibitor tricostain A (TSA) causes activation of hTERT mRNA expression and telomerase activity in human normal cells[65,66]. However, because both DNA methylation and histone deacetylation are general mechanisms in controlling gene expression in human cells, the treatment of 5-AZC or TSA would have

broad effects on cellular gene expressions. To achieve selective activation of hTERT expression, a more specific promoter-targeted agent is desired. Sequence analysis of hTERT promoter reveals an estrogen response element (ERE) located upstream to the transcription start site. The function of ERE is established in normal human ovary epithelium cells where the addition of 17â-estradiol activates the expression of hTERT and telomerase activity[67]. Thus, telomerase activity could be activated by estrogen in cells with estrogen receptors. However, since estrogens also activate the telomerase activities in cancer cells with estrogen receptor[67–69], the applicability of estrogen or its analogs in clinics remains to be evaluated. Similar to the approach used in identifying small molecule compounds, a cell-based reporter system was developed in normal human cells that enabled the identification of several *bis*-substituted derivatives of anthraquinones that activate hTERT[52]. Unlike inhibitors of DNA methylation or histone deacetylation, the repression of hTERT expression by these anthraquinones appears to be specific as they do not activate the expression of reporter gene driven by a virus promoter. Using a similar cell-based chemical screening strategy, compound CGK1026 was also identified to activate hTERT expression in normal human fibroblasts[70]. CGK1026 activates hTERT expression by affecting the interaction between E2F-pocket protein and histone deacetylase. The effect of CGK1026 on other promoters is still unclear.

Telomerase-directed tumor gene therapy

One of the major goals in anticancer therapies is to target toxic agents to tumor cells specifically to minimize the effects toward normal cells. The specific expression of telomerase hTERT in most types of tumors provides a good discrimination between cancer and normal cells[6,7]. Deletion analysis of the hTERT promoter reveals a core promoter region located approximately 200 bp upstream of the transcription start site, and is sufficient to confer its specific expression in cancer cells[71]. The property of hTERT promoter has been applied to restrict the expression of therapeutic genes in tumors. The therapeutic genes utilized include apoptosis-inducing[72–74], toxin-encoding[75], chemotherapeutic sensitizer[71], xenoantigen[76] genes, or genes used in gene-directed enzyme prodrug therapy (GDEPT)[77,78]. These hTERT promoter-driven therapeutic genes were introduced into tumor cells through liposome- or virus-mediated pathways. As expected from the expression pattern of telomerase, this type of approach selectively kills virtually all types of telomerase-positive cancer cells without affecting the viability of telomerase-negative cells in both cellular and animal xenograft models. Thus, hTERT directed tumor gene therapy appears to be a promising approach in treating telomerase-positive tumors. Because hTERT expression varies in different telomerase-positive cells[72–74], it is anticipated that telomerase-directed tumor gene therapy would work better in cancer cells with high levels of hTERT expression.

Summary

Because of the unique property of telomere and telomerase in cancer and the aging process, they have been the targets for new drug developments toward anticancer or regenerative disease therapeutics. In addition to various approaches that have been described here, other approaches based on the property of telomerase have also been reported. For example, hTERT has been reported as a tumor-associated antigen in a wide range of tumors. These hTERT-derived tumor antigens could be recognized by cytotoxic T lymphocytes that could then be applied in designing anticancer immunotherapeutic strategies[79,80]. It is anticipated that other novel approaches based on telomere functions will be developed.

Acknowledgement

We thank Yu-ling LEE for reading the manuscript.

References

1 Zakian VA. Telomeres: beginning to understand the end. Science 1995; 270: 1601–7.
2 Olovnikov AM. A theory of marginotomy. The incomplete copying of template margin in enzymatic synthesis of polynucleotides and biological significance of the phenomenon. J Theor Biol 1973; 41: 181–90.
3 Watson JD. Origin of concatemeric DNA. Nature (New Biol) 1972; 239: 197–201.
4 Harley CB, Futcher AB, Greider CW. Telomeres shorten during ageing of human fibroblasts. Nature 1990; 345: 458–60.
5 Morin GB. The human telomere terminal transferase enzyme is a ribonucleoprotein that synthesizes TTAGGG repeats. Cell 1989; 59: 521–9.
6 Kim NW, Piatyszek MA, Prowse KR, Harley CB, West MD, Ho PL, *et al*. Specific association of human telomerase activity with immortal cells and cancer. Science 1994; 266: 2011–5.
7 Shay JW, Bacchetti S. A survey of telomerase activity in human cancer. Eur J Cancer 1997; 33: 787–91.
8 Shay JW, Roninson IB. Hallmarks of senescence in carcinogenesis and cancer therapy. Oncogene 2004; 23: 2919–33.
9 Gisselsson D, Jonson T, Petersen A, Strombeck B, Dal Cin P, Hoglund M, *et al*. Telomere dysfunction triggers extensive DNA fragmentation and evolution of complex chromosome abnormalities in human malignant tumors. Proc Natl Acad Sci USA 2001; 98: 12683–8.
10 Bodnar AG, Ouellette M, Frolkis M, Holt SE, Chiu CP, Morin GB, *et al*. Extension of life-span by introduction of telomerase into normal human cells. Science 1998; 279: 349–52.
11 Henson JD, Neumann AA, Yeager TR, Reddel RR. Alternative

lengthening of telomeres in mammalian cells. Oncogene 2002; 21: 598–610.
12 Shay JW, Wright WE. Telomerase: a target for cancer therapeutics. Cancer Cell 2002; 2: 257–65.
13 Ludwig A, Saretzki G, Holm PS, Tiemann F, Lorenz M, Emrich T, *et al*. Ribozyme cleavage of telomerase mRNA sensitizes breast epithelial cells to inhibitors of topoisomerase. Cancer Res 2001; 61: 3053–61.
14 Blackburn EH. Switching and signaling at the telomere. Cell 2001; 106: 661–73.
15 Kondo S, Kondo Y, Li G, Silverman RH, Cowell JK. Targeted therapy of human malignant glioma in a mouse model by 2-5A antisense directed against telomerase RNA. Oncogene 1998; 16: 3323–30.
16 Hahn WC, Stewart SA, Brooks MW, York SG, Eaton E, Kurachi A, *et al*. Inhibition of telomerase limits the growth of human cancer cells. Nature Med 1999; 5: 1164–70.
17 Zhang X, Mar V, Zhou W, Harrington L, Robinson MO. Telomere shortening and apoptosis in telomerase-inhibited human tumor cells. Genes Dev 1999; 13: 2388–99.
18 Bodnar AG, Kim NW, Effros RB, Chiu CP. Mechanism of telomerase induction during T cell activation. Exp Cell Res 1996; 228: 58–64.
19 Masutomi K, Yu EY, Khurts S, Ben-Porath I, Currier JL, Metz GB, *et al*. Telomerase maintains telomere structure in normal human cells. Cell 2003; 114: 241–53.
20 Feng J, Funk WD, Wang SS, Weinrich SL, Avilion AA, Chiu CP, *et al*. The RNA component of human telomerase. Science 1995; 269: 1236–41.
21 Herbert BS, Pitts AE, Baker SI, Hamilton SE, Wright WE, Shay JW, *et al*. Inhibition of human telomerase in immortal human cells leads to progressive telomere shortening and cell death. Proc Natl Acad Sci USA 1999; 96: 14276–81.
22 Yokoyama Y, Takahashi Y, Shinohara A, Lian Z, Wan X, Niwa K, *et al*. Attenuation of telomerase activity by a hammerhead ribozyme targeting the template region of telomerase RNA in endometrial carcinoma cells. Cancer Res 1998; 58: 5406–10.
23 Rezler EM, Bearss DJ, Hurley LH. Telomeres and telomerases as drug targets. Curr Opin Pharmacol 2002; 2: 415–23.
24 Neidle S, Parkinson G. Telomere maintenance as a target for anticancer drug discovery. Nat Rev Drug Discov 2002; 1: 383–93.
25 Pascole E, Wenz C, Lingner J, Hauel N, Priepke H, Kauffmann I, *et al*. Mechanism of human telomerase inhibition by BIBR1532, a synthetic, non-nucleosidic drug candidate. J Biol Chem 2002; 277: 15566–72.
26 Damm K, Hemmann U, Garin-Chesa P, Hauel N, Kauffmann I, Priepke H, *et al*. A highly selective telomerase inhibitor limiting human cancer cell proliferation. EMBO J 2001; 20: 6958–68.
27 Chang CC, Kuo IC, Lin JJ. A novel carbazole derivative, BMVC: a potential antitumor agent and fluorescence marker of cancer cells. Chem Biodivers 2004; 1: 1377–84.
28 Read M, Harrison RJ, Romagnoli B, Tanious FA, Gowan SH, Reszka AP. Structure-based design of selective and potent G-quadruplex-mediated telomerase inhibitors. Proc Natl Acad Sci USA 2001; 98: 4844–9.
29 Sen D, Gilbert W. The structure of telomeric DNA: DNA quardruplex formation. Curr Opin Struct Biol 1991; 1: 435–8.
30 Chang CC, Kuo IC, Ling IF, Chen CT, Chen HC, Lou PJ. Detection of quadruplex DNA structures in human telomeres by a fluorescent carbazole derivative. Anal Chem 2004; 76: 4490–4.
31 Siddiqui-Jain A, Grand CL, Bearss DJ, Hurley LH. Direct evidence for a G-quadruplex in a promoter region and its targeting with a small molecule to repress c-MYC transcription. Proc Natl Acad Sci USA 2004; 99: 11593–8.
32 Griffith JD, Comeau L, Rosenfield S, Stansel RM, Bianchi A, Moss H, *et al*. Mammalian telomeres end in large duplex loop. Cell 1999; 97: 503–14.
33 Zahler AM, Williamson JR, Cech TR, Prescott DM. Inhibition of telomerase by G-quartet DNA structure. Nature 1991; 350: 718–20.
34 Wheelhouse RT, Sun D, Han H, Han FX, Hurley LH. Cationic porphyrins as telomerase inhibitors: the interaction of tetra-(*N*-methyl-4-pyridyl)porphine with quadruplex DNA. J Am Chem Soc 1998; 120: 3261–2.
35 Heald RA, Modi C, Cookson JC, Hutchinson I, Laughton CA, Gowan SM, *et al*. Antitumor polycyclic acridines. 8. Synthesis and telomerase-inhibitory activity of methylated pentacyclic acridinium salts. J Med Chem 2002; 45: 590–7.
36 Sun D, Thompson B, Cathers BE, Salazar M, Kerwin SM, Trent JO, *et al*. Inhibition of human telomerase by a G-quadruple-interactive compound. J Med Chem 1997; 40: 2113–28.
37 Riou JF, Guittat L, Mailliet P, Laoui A, Renou E, Petitgenet O, *et al*. Cell senesscence and telomere shortening induced by a new series of specific G-quadruplex DNA ligands. Proc Natl Acad Sci USA 2002; 99: 2672–7.
38 Perry PJ, Read MA, Davies RT, Gowan SM, Reszka AP, Wood AA, *et al*. 2,7-Disubstituted amidofluorenone derivatives as inhibitors of human telomerase. J Med Chem 1999; 42: 2679–84.
39 Cairns D, Michalitsi E, Jenkins TC, Mackay SP. Molecular modeling and cytotoxicity of substituted anthraquinones as inhibitors of human telomerase. Bioorgan Med Chem 2002; 10: 803–7.
40 Chang CC, Wu JY, Chang TC. A carbazole derivative synthesis for stabilizing the quadruplex structure. J Chin Chem Soc 2003; 50: 185–8.
41 Nakamura TM, Morin GB, Chapman KB, Weinrich SL, Andrews WH, Lingner J, *et al*. Telomerase catalytic subunit homologs from fission yeast and human. Science 1997; 277: 955–9.
42 Ducrest AL, Szutorisz H, Lingner J, Nabholz M. Regulation of the human telomerase reverse transcriptase gene. Oncogene 2002; 21: 541–52.
43 Ulaner GA, Hu JF, Vu TH, Oruganti H, Giudice LC, Hoffman AR. Regulation of telomerase by alternate splicing of human telomerase reverse transcriptase (hTERT) in normal and neoplastic ovary, endometrium and myometrium. Int J Cancer 2000; 85: 330–5.
44 Yi X, White DM, Aisner DL, Baur JA, Wright WE, Shay JW. An alternate splicing variant of the human telomerase catalytic subunit inhibits telomerase activity. Neoplasia 2000; 2: 433–40.
45 Ku WC, Cheng AJ, Wang TCV. Inhibition of telomerase activity by PKC inhibitors on human nasopharyngeal cancer cells in culture. Biochem Biophys Res Commun 1997; 241: 730–6.
46 Li H, Zhao LL, Funder JW, Liu JP. Protein phosphatase 2A inhibits nuclear telomerase activity in human breast cancer cells. J Biol Chem 1997; 272: 16729–32.
47 Li H, Zhao L, Yang Z, Funder JW, Liu JP. Telomerase is controlled by protein kinase Ca in human breast cancer cells. J Biol Chem 1998; 273: 33436–42.
48 Kang SS, Kwon T, Kwon DY, Do SI. Akt protein kinase enhances human telomerase activity through phosphorylation of telo-merase reverse transcriptase subunit. J Biol Chem 1999; 274: 13085–90.
49 Wong JMY, Kusdra L, Collins K. Subnuclear shuttling of human telomerase induced by transformation and DNA damage. Nature

Cell Biol 2002; 4: 731–6.
50 Pendino F, Flexor M, Delhommeau F, Buet D, Lanotte M, Segal-Bendirdjian E. Retinoids down-regulate telomerase and telomere length in a pathway distinct from leukemia cell differentiation. Proc Natl Acad Sci USA 2001; 98: 6662–7.
51 Mano Y, Shimizu T, Tanuma S, Takeda K. Synergistic down-regulation of telomerase activity and hTERT mRNA expression by combination of retinoic acid and GM-CSF in human myeloblastic leukemia ML-1 cells. Anticancer Res 2000; 20: 1649–52.
52 Huang HS, Chiou JF, Fong Y, Hou CC, Lu YC, Wang JY, *et al*. Activation of human telomerase reverse transcriptase expression by some new symmetrical *bis*-substituted derivatives of the anthraquinone. J Med Chem 2003; 46: 3300–7.
53 Rudolph KL, Chang S, Millard M, Schreiber-Agus N, DePinho RA. Inhibition of experimental liver cirrhosis in mice by telomerase gene delivery. Science 2000; 287: 1253–8.
54 Wyllie FS, Jones CJ, Skinner JW, Haughton MF, Wallis C, Wynford-Thomas D, *et al*. Telomerase prevents the accelerated cell ageing of Werner syndrome fibroblasts. Nat Genet 2000; 24: 16–7.
55 Shi S, Gronthos S, Chen S, Reddi A, Counter CM, Robey PG, *et al*. Bone formation by human postnatal bone marrow stromal stem cells is enhanced by telomerase expression. Nat Biotechnol 2002; 20: 587–91.
56 Simonsen JL, Rosada C, Serakinci N, Justesen J, Stenderup K, Rattan SI, *et al*. Telomerase expression extends the proliferative life-span and maintains the osteogenic potential of human bone marrow stromal cells. Nat Biotechnol 2002; 20: 592–6.
57 Counter CM, Meyerson M, Eaton EN, Ellisen ZW, Caddle SD, Haber DA, *et al*. Telomerase activity is restored in human cells by ectopic expression of hTERT (hEST2), the catalytic subunit of telomerase. Oncogene 1998; 16: 1217–22.
58 Serakinci N, Guldberg P, Burns JS, Abdallah B, Schrodder H, Jensen T, *et al*. Adult human mesenchymal stem cell as a target for neoplastic transformation. Oncogene 2004; 23: 5095–8.
59 Jiang XR, Jimenez G, Chang E, Kaur KJ, Yan Y, Wilson KS, *et al*. Telomerase expression in human somatic cells does not induce changes associated with a transformed phenotype. Nat Genet 1999; 21: 111–4.
60 Morales CP, Holt SE, Ouellette M, Kaur KJ, Yan Y, Wilson KS, *et al*. Absence of cancer-associated changes in human fibroblasts immortalized with telomerase. Nat Genet 1999; 21: 115–8.
61 Gonzalez-Suarez E, Samper E, Ramirez A, Flores JM, Martin-Caballero J, Jorcano JL, *et al*. Increased epidermal tumors and increased skin wound healing in transgenic mice overexpressing the catalytic subunit of telomerase, mTERT, in basal keratinocytes. EMBO J 2001; 20: 2619–30.
62 Artandi SE, Alson S, Tietze MK, Sharpless NE, Yes, Greenberg RA, *et al*. Constitutive telomerase expression promotes mammary carcinomas in aging mice. Proc Natl Acad Sci USA 2002; 99: 8191–6.
63 Devereux TR, Horikawa I, Anna CH, Annab LA, Afshari CA, Barrett JC, *et al*. DNA methylation analysis of the promoter region of the human telomerase reverse transcriptase (hTERT) gene. Cancer Res 1999; 59: 6087–90.
64 Dessain SK, Yu H, Reddel RR, Beijersbergen RL, Weinberg RA. Methylation of the human telomerase gene CpG island. Cancer Res 2000; 60: 537–41.
65 Cong YS, Bacchetti S. Histone deacetylation is involved in the transcriptional repression of hTERT in normal human cells. J Biol Chem 2000; 275: 35665–8.
66 Takakura M, Kyo S, Sowa Y, Wang Z, Yatabe N, Maida Y, *et al*. Telomerase activation by histone deacetylase inhibitor in normal cells. Nucleic Acids Res 2001; 29: 3006–11.
67 Misiti S, Nanni S, Fontemaggi G, Cong YS, Wen J, Hirte HW, *et al*. Induction of hTERT expression and telomerase activity by estrogens in human ovary epithelium cells. Mol Cell Biol 2000; 20: 3764–71.
68 Kyo S, Takakura M, Kanaya T, Cong YS, Wen J, Hirte HW, *et al*. Estrogen activates telomerase. Cancer Res 1999; 59: 5917–21.
69 Wang Z, Kyo S, Takakura M, Tanaka M, Yatabe N, Maida Y, *et al*. Progesterone regulates human telomerase reverse transcriptase gene expression via activation of mitogen-activated protein kinase signaling pathway. Cancer Res 2000; 60: 5376–81.
70 Won J, Chang S, Oh S, Kim TK. Small-molecule-based identification of dynamic assembly of E2F-pocket protein-histone deacetylase complex for telomerase regulation in human cells. Proc Natl Acad Sci USA 2004; 101: 11328–33.
71 Nakamura M, Kyo S, Kanaya T, Yatabe N, Maida Y, Tanaka M, *et al*. hTERT-promoter-based tumor-specific expression of MCP-1 effectively sensitizes cervical cancer cells to a low dose of cisplatin. Cancer Gene Ther 2004; 11: 1–7.
72 Gu J, Kagawa S, Takakura M, Kyo S, Inoue M, Roth JA, *et al*. Tumor-specific transgene expression from the human telomerase reverse transcriptase promoter enables targeting of the therapeutic effects of the Bax gene to cancers. Cancer Res 2000; 60: 5359–64.
73 Komata T, Kondo Y, Kanzawa T, Hirohata S, Koga S, Sumiyoshi H, *et al*. Treatment of malignant glioma cells with the transfer of constitutively active caspase-6 using the human telomerase catalytic subunit (human telomerase reverse transcriptase) gene promoter. Cancer Res 2001; 61: 5796–802.
74 Koga S, Hirohata S, Kondo Y, Komata T, Takakura M, Inoue M, *et al*. A novel telomerase-specific gene therapy: gene transfer of caspase-8 utilizing the human telomerase catalytic subunit gene promoter. Hum Gene Ther 2000;11: 1397–406.
75 Abdul-Ghani R, Ohana P, Matouk I, Ayesh S, Ayesh B, Laster M, *et al*. Use of a transcriptional regulatory sequences of telomerase (hTER and hTERT) for selective killing of cancer cells. Mol Ther 2000; 2: 539–44.
76 Sawada T, Yamada O, Yoshimura N, Hatori K, Fuchinoue S, Teraoka S, *et al*. Xenoantigen, an aGal epitope-expression construct driven by the hTERT-promoter, specifically kills human pancreatic cancer cell line. Cancer Cell Int 2002; 2: 14–20.
77 Majumdar AS, Hughes DE, Lichtsteiner SP, Wang Z, Lebkowski JS, Vasserot AP, *et al*. The telomerase reverse transcriptase promoter drives efficacious tumor suicide gene therapy while preventing hepatotoxicity encountered with constitutive promoters. Gene Ther 2001; 8: 568–78.
78 Song JS, Kim HP, Yoon WS, Lee KW, Kim MH, Kim KT, *et al*. Adenovirus-mediated suicide gene therapy using the human telomerase catalytic subunit (hTERT) gene promoter induced apoptosis of ovarian cancer cell line. Biosci Biotechnol Biochem 2003; 67: 2344–50.
79 Vonderheide RH, Hahn WC, Schultze JL, Nadler LM. The telomerase catalytic subunit is a widely expressed tumor-associated antigen recognized by cytotoxic T lymphocytes. Immunity 1999; 10: 673–9.
80 Vonderheide RH. Telomerase as a universal tumor-associated antigen for cancer immunotherapy. Oncogene 2002; 21: 674–9.

Acta Pharmacologica Sinica 2005 May; 26 (5): 519–526

Full-length article

Effects of melatonin on wortmannin-induced tau hyperphosphorylation[1]

Yan-qiu DENG, Guo-gang XU, Ping DUAN, Qi ZHANG, Jian-zhi WANG[2]

Department of Pathophysiology, Institute of Neuroscience, Tongji Medical College, Huazhong University of Science and Technology, Wuhan 430030, China

Key words

Alzheimer disease; wortmannin; mela-tonin; tau protein

[1] Project supported in part by grants from the National Natural Science Foundation of China (No 30170221, 30430270, 30328007, and 30400068).

[2] Correspondence to Dr Jian-zhi WANG.
Phn 86-27-8369-2625.
Fax 86-27-8369-3883.
E-mail wangjz@mails.tjmu.edu.cn

Received 2004-12-17
Accepted 2005-01-31

doi: 10.1111/j.1745-7254.2005.00102.x

Abstract

Aim: To explore the underlying mechanism of tau hyperphosphorylation in an Alzheimer's-affected brain and the possible arresting strategies. **Methods:** MTT (3-[4,5-dimethylthiazol-2-yl]-2,5-diphenyl-tetrazolium bromide), crystal violet assay, phase-contrast, dead end colorimetric apoptosis detection system (TUNEL) and electron microscopy were used to detect cell viability, morphology and apoptosis. Western blot, ^{32}P-labeling and the detection of malondialdehyde level and superoxide dismutase activity were used respectively for the phosphorylation level of tau, the activity of glycogen synthase kinase (GSK-3), and oxidative stress measurement. **Results:** Exposure of the cells to wortmannin resulted in an obvious lipid peroxidation, reduction of cell viability, cell process retraction, and plasma vacuolation, but with no obvious cell apoptosis. We also found that preincubation of the cells with melatonin or vitamin E attenuated differentially wortmannin-induced oxidative stress as well as GSK-3 overactivation and tau hyperphosphorylation. **Conclusion:** Wortmannin is an effective tool for reproducing Alzheimer-like tau hyperphosphorylation cell model and melatonin/vitamin E can effectively protect the cells from wortmannin-induced impairments.

Introduction

Alzheimer disease (AD) is neuropathologically characterized by cell loss and formation of amyloid plaques and neurofibrillary tangles (NFTs), which are composed of paired helical filaments formed by abnormally hyperphosphorylated microtubule associated protein tau[1]. Studies have shown that tau regulates microtubule dynamics, axonal transport, and neuronal morphology by binding and stabilizing the microtubule structure[2,3]. In AD, abnormally phosphorylated tau associated with paired helical filaments decreases affinity in binding to the microtubules and balks its normal microtubule-related function[4]. Therefore, understanding the regulatory mechanism for tau hyperphosphorylation and aggregation is critical in designing the strategies to arrest it.

A defect in the regulation of protein kinases/protein phosphatases is responsible for tau hyperphosphorylation. Among them, glycogen synthase kinase-3 (GSK-3) is a recognized tau kinase that plays a crucial role in AD pathology[5]. GSK-3 phosphorylates tau both *in vivo* and in intact cells, and enhanced expression of GSK-3 leads to tau hyperphosphorylation[6,7]. In an Alzheimer's-affected brain, GSK-3 is activated in pretangle neurons and accumulates in paired helical filaments[8]. We also found that the activation of GSK-3 by brain injection of wortmannin led to hyperphosphorylation of tau and spatial memory impairment in a rat brain[9]. These data together indicate that GSK-3 can serve as a crucial target for reproducing an AD-like experimental modal and for screening potential therapeutic reagents. However, it is not known whether wortmannin also induces tau hyperphosphorylation in neuroblastoma N2a cells, and whether wortmannin treatment affects cell viability, what kind of cell death wortmannin might induce, and if melatonin, as an effective antioxidant secreted from pineal gland [10], which has been used in our previous studies[11–13], influences wortmannin-induced alterations in N2a cell and by which mechanism melatonin works.

Therefore, in the present study, we examined the effect of wortmannin, an indirect GSK-3 activator, on cell viability and tau phosphorylation, and the effect and mechanism of

melatonin on wortmannin-induced cytotoxicities in N2a cells. We found that the treatment of cells with 1 μmol/L wortmannin induced GSK-3 activation and tau hyperphosphorylation. Although reduced cell viability and increased cell retraction were observed, no obvious cell apoptosis was detected. Melatonin not only attenuated wortmannin-induced lipid peroxidation but also counteracted wortmannin-induced GSK-3 overactivation and tau hyperphosphorylation.

Materials and methods

Measurement of cell viability and metabolism N2a cell, a gift from Dr HX XU (The Burnham Institute, San Diego, USA), was propagated in Dulbecco's modified Eagle's medium with 5% fetal bovine serum (5% CO_2 and 95% air) (GIBCO, NY, USA). The cells were then grown and differentiated in 96-well culture plates at density of 1.5×10^5 cells in 100 μL. Cells were exposed to various concentrations of wortmannin for 2 h at 37 ºC in the presence or absence of a 12-h-preincubation with melatonin 25, 50, and 100 μmol/L or Vitamin E (VE). Dimethylsulfoxide (Me_2SO, 0.01%), in which wortmannin, melatonin and VE were dissolved, served as a vehicle control. Then, 0.2% crystal violet or 1% MTT (3-(4, 5-dimethylthiazol-2-yl)-2,5-diphenyl-tetrazolium bromide) in phosphate-buffered saline (PBS) were added and incubated for 3 min or 4 h at dark and read at 570 nm (TECAN Austria, Salzburg, Austria). All assays were performed with five repeats. Wortmannin, Me_2SO and melatonin were purchased from Sigma (St Louis, MO, USA).

Morphology features of N2a cells with phase-contrast and electron microscopy Morphology changes of N2a cells treated by wortmannin with or without preincubation of melatonin or VE were examined under phase-contrast microscope. For electron microscopy, cultures were fixed in 2.5% glutaraldehyde/0.2% tannic acid in 0.1 mol/L cacodylate buffer (pH 7.4) overnight at 4 ºC and then post-fixed in 1% osmium tetroxide/1.5% ferrocyanide solution for 30 min at room temperature. Cells were dehydrated in ethanol, embedded in Epon resin, and heat polymerized. Epon blocks were cut, double stained with uranyl acetate and lead citrate, and observed under an Opton EN/l0C electron microscope (Opton, Oberkochen, Germany).

TUNEL assay and cleavage of caspases-3 To determine the form of cell death in wortmannin-treated cells and relationship of tau phosphorylation and apoptosis, we used the Dead End TM Colorimetric Apoptosis detection system (TUNEL) (Promega Corp, Madison, USA) and immunofluorescence of cleaved caspase-3 to measure DNA fragmentation and caspase-3 activation. Positive control of apoptosis was treated with 1 μmol/L staurosporine, an apoptosis inducer for 3 h. For TUNEL, cells were fixed in 4% paraformaldehyde solution for 25 min at room temperature, rinsed in phosphate buffered saline (PBS), and permeabilized by immersing the slides in 0.2% Triton X-100 solution. Cells were incubated with terminal deoxynucleotidyl transferase (TdT) reaction mixture containing biotinylated nucleotides and TdT at 37 ºC for 60 min, rinsed with SSC (Sodium Chloride-Sodium Citrate Buffer) and PBS. Streptavidin HRP (Horseradish Peroxidase) was added to cells. Slides were then stained with diaminobenzidine system (DAB).

For caspases-3 immunofluorescence assay, cells were fixed for 15 min with 4% paraformaldehyde in 0.1 mol/L phosphate buffer and immunostained by sequential reaction with a rabbit polyclonal antibody caspase-3 (1:200) (Cell Signaling Technology Inc, Beverly, MA, USA), followed by FITC (Fluorescein isothiocyanate)-conjugated goat anti-rabbit IgG (Dianova GmbH, Hamburg, Germany). Sections were analyzed with a 525-nm filter (FITC staining) with a fluorescence microscope (Olympus, Hamburg, Germany).

Western blot Total cell lysates of N2a from each treatment were separated on 10% SDS-PAGE (PolyAcrylamide Gel Electrophoresis) and the protein were transferred onto the nitrocellulose membranes. Membranes were blocked in Tris-buffered saline containing 5% non-fat milk followed by incubation with primary antibody at 4 ºC for 24 h. Primary mouse monoclonal antibodies including Tau-1 and PHF-1 and rabbit polyclonal antibodies 92e which recognized phosphorylated tau and non-phosphorylated tau were gifts from Dr BINDLE (North Western University, Chicago, Illinois), Dr DAVIES (Albert Einstein College of Medicine, Bronx, NY), and Drs Iqbal and Grundke-Iqbal (NYS Institute for Basic Research, Staten Island, NY, USA). GSK3β and phospho-GSK3β (serine9) were obtained from Cell Signaling Technology Inc (Beverly, MA, USA). The blots were developed by enhanced chemiluminescence (Santa Cruz Biotechnology Inc, Santa Cruz, CA, USA) and computer image analysis software (Image-Pro Plus, Media Cybernetics, Silver Spring, MD) was used for quantitative analysis of the blots.

Kinase assay Activity of GSK-3 was measured using phospho-GS (Upstate Biotechnology, Lake Placid, NY, USA) as substrate. Cells were treated with factors as described earlier and lysed at 4 ºC in a solution containing (in mmol/L) Tris-HCl 10 (pH 7.4), edetic acid 10, NaCl 0.15, NaF 50, Na_3VO_4 0.2, 1% NP40, phenylmethylsulfonyl fluoride 1, and 2 μg/μL aprotinin. Cell lysates were clarified by centrifugation at 15 000×*g* at 4 ºC for 10 min. The samples were incubated with the substrates in buffer containing 30 mmol/L Tris-HCl (pH 7.4), 10 mmol/L $MgCl_2$, 10 mmol/L NaF,

1 mmol/L Na_3VO_4, 2 mmol/L Na_4EGTA, 10 mmol/L β-mercaptoethanol, 0.2 mmol/L (1500 cpm/pmol) [γ-^{32}P] ATP (Beijing Yahui Biologic and Medicinal Engineering Co, Beijing, China) at 30 ºC for 30 min. Reaction was stopped by adding 12.5 μL *o*-phosphoric acid (300 mmol/L). A total of 20 μL of incubation mixture was applied in duplicates to phosphor cellulose units. The filters were washed 3 times with 75 mmol/L *o*-phosphoric acid and then dried. The radioactivity incorporated into the substrates was analyzed by liquid scintillation counting at 30 ºC. The protein concentration of the cell lyses was estimated by bicinchoninic acid (BCA) method (Micro BCA Protein Assay Reagent Kit, Pierce Biotechnology, Rockford, IL, USA). GSK-3 activity was expressed as nmol·min^{-1}·g^{-1} protein at 30 ºC.

Assay of malondialdehyde (MDA) and superoxide dismutase (SOD) The amount of MDA was measured by the thiobarbituric acid (TBA) assay, which is based on the reaction of MDA with TBA to produce a red species with excitation at 515 nm and emission at 553 nm measured in Schimadzu-RF-5000 (Kyoto, Japan)[14]. The activity of SOD was measured according to the method established previously[15].

Data analysis Data were expressed as mean±SD and analyzed using SPSS 10.0 statistical software (SPSS Inc, Chicago, Illinois, USA). The one-way ANOVA procedure followed by Student's *t*-test was used to determine the differences among groups.

Results

Effect of wortmannin, melatonin, and VE on cell viability and morphology Wortmannin induced decreased cell viability in a concentration-dependent manner from 0.1 μmol/L to 10 μmol/L in 2 h (Figure 1A). Therefore, 1 μmol/L wortmannin, represented 20%–30% inhibition of MTT and crystal violet, was used for all subsequent experiments. Exposure of the cells to 50 μmol/L melatonin (Figure 1B) or 50 μmol/L VE (Figure 1C) before administration of wortmannin resulted in protective effects. However, the premixing of melatonin or VE with wortmannin did not show protection in cell viability (data not shown).

By phase-contrast microscopy, we observed that in the control group the border of the cells was clear with plenty of processes, and treatment of the cells with 1 μmol/L wortmannin induced retraction of cell processes, with some cells detaching from the plate. Preincubation of the cells with 50 μmol/L melatonin or 50 μmol/L VE protected against the morphology changes induced by wortmannin, although the cell body was still larger than normal cells (Figure 2). With electron

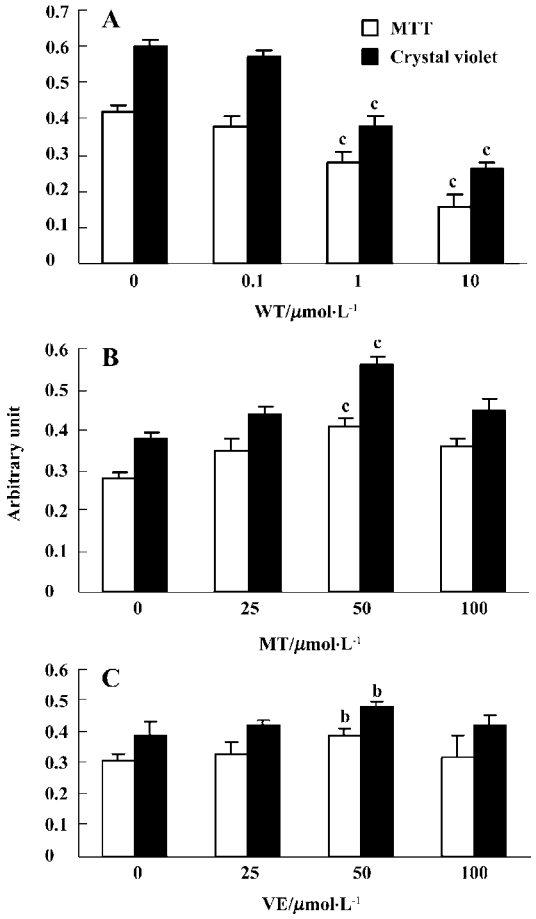

Figure 1. Effect of wortmannin, melatonin and VE on cell viability and metabolism measured by MTT and crystal violet staining. A dose-dependent decrease of cell viability and metabolism was observed when the cells were exposed to 0.1 μmol/L, 1 μmol/L or 10 μmol/L wortmannin for 2 h (A). These cytotoxicities were inhibited by pretreatment of the cells with melatonin (B) or VE (C) for 12 h. n=5. Mean±SD. $^bP<0.05$, $^cP<0.01$ *vs* control.

microscopy, we found that treatment of cells with wortmannin induced organelle vacuolation and mitochondrial swelling (markers of degeneration), but no cellular shrinkage and chromatin condensation (markers of apoptosis) was observed. Pretreatment with melatonin or VE partly protected cells from the degeneration induced by wortmannin (Figure 3).

Effect of wortmannin on cell apoptosis Very few positive cells were detected in the 1 μmol/L wortmannin-treated samples. However, numerous apoptotic cells were seen in positive control of 1 μmol/L staurosporine-treated cells (Figure 4).

Effect of wortmannin, melatonin, and VE on tau phosphorylation, and the activity of GSK-3β Tau was hyperphosphorylated at both tau-1 (recognized non-phosphorylated tau at Ser-199/202) and PHF-1 (recognized phos-

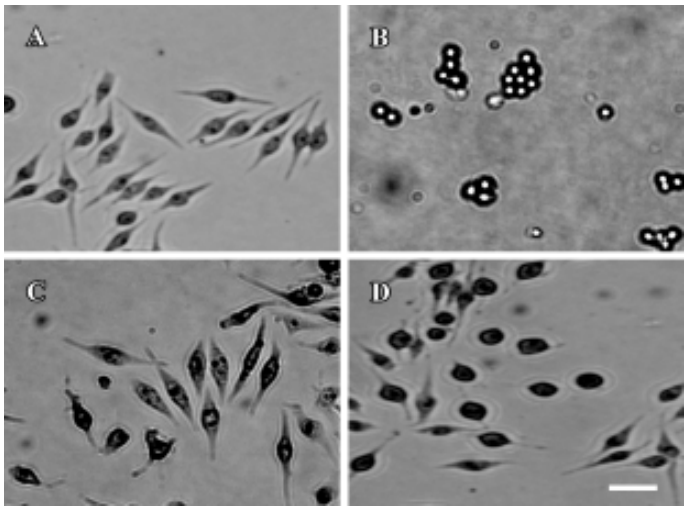

Figure 2. Effect of wortmannin, melatonin and VE on cell morphology measured by phase-contrast microscopy. Most of the normal cells showed bipolar and long-cylindrical processes (A). Cells exposed to 1 μmol/L wortmannin for 2 h revealed loss of neurites with nuclear pyknosis, some of them detached from the plate (B). Cells were partially rescued from wortmannin exposure by pretreatment with 50 μmol/L melatonin (C) or 50 μmol/L VE (D) for 12 h. (Scale Bar 15 μm).

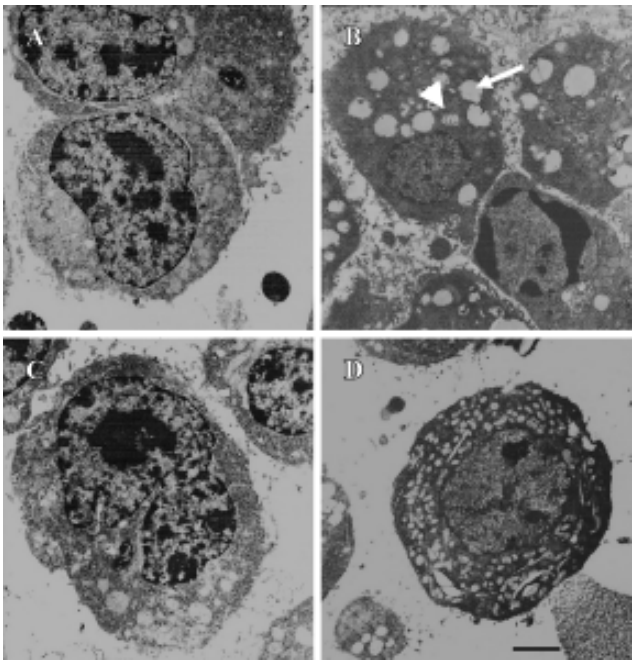

Figure 3. Effect of wortmannin, melatonin and VE on the ultrastructure of the cells. Compared with control (A), treatment of the cells with 1 μmol/L wortmannin for 2 h (B) induced organelle vacuolation (arrow) and mitochondrial swelling (arrow head), but pretreatment of the cells with 50 μmol/L melatonin (C) or 50 μmol/L VE (D) for 12 h partly protected cells from wortmannin-induced alterations (Scale Bar 1 μm).

phorylated tau at Ser-396/404) epitopes by treatment with wortmannin for 2 h. The hyperphosphorylation of tau was blocked by preincubation of the cells with melatonin and VE. Melatonin showed a more efficient protective effect than VE (Figure 5). We also found that wortmannin increased activity of GSK-3, pretreatment with melatonin almost completely reversed wortmannin-induced activation of GSK-3, and preincubation of VE partially restored the activity of GSK-3 (Figure 6).

As GSK-3β activity is regulated by the phosphorylation and dephosphorylation on its serine-9 (Ser-9)[16], we further detected the expression of total and phosphorylated GSK-3β. We found that wortmannin treatment did not change the expression of the total GSK-3β, but markedly decreased the expression of phosphorylated-GSK-3 at Ser-9. We also demonstrated that preincubation of melatonin or VE obviously arrested wortmannin-induced decrease of phosphorylated GSK-3β at Ser-9 (Figure7A, 7B).

Effect of wortmannin, melatonin, and VE on lipid peroxidation The level of MDA was significantly higher, but the activity of SOD was significantly lower in wortmannin-treated cells than the vehicle control samples. After preincubation of 50 μmol/L melatonin or VE, the MDA level and SOD activity was partially restored, and the protective effect of melatonin was stronger than that of VE at the same concentration (Table 1).

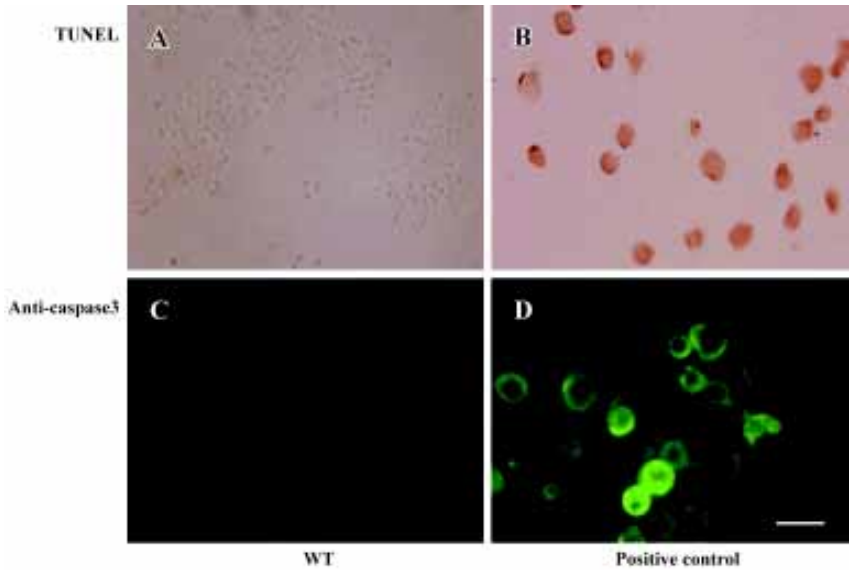

Figure 4. Effect of wortmannin on cell apoptosis. Apoptosis was not detected by TUNEL (A) nor by activated caspases-3 staining (C) in wortmannin-treated cells, but it did show in the positive control cells treated with 1 μmol/L of staurosporine (B and D) (Scale Bars 15 μm).

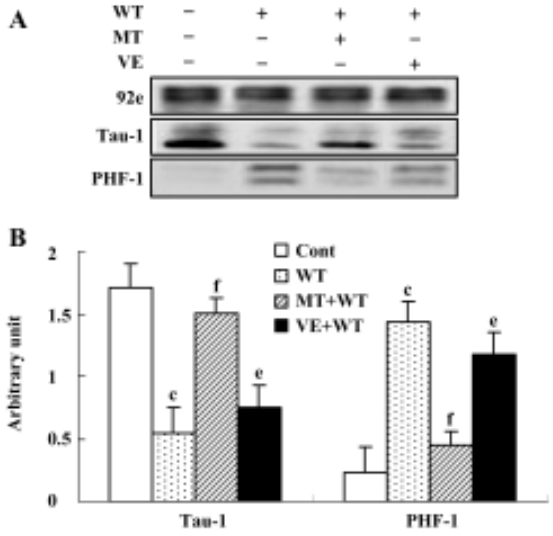

Figure 5. Effect of wortmannin, melatonin, and VE on tau phosphorylation. Representative Western blots (A) and quantitative analysis (B) of tau phosphorylation at Tau-1 and PHF-1 sites, which was normalized by the total tau (probed by 92e). n=5. Mean±SD. ^{b}P<0.05, ^{c}P<0.01 *vs* control. ^{e}P<0.05, ^{f}P<0.01 *vs* wortmannin-treated cells.

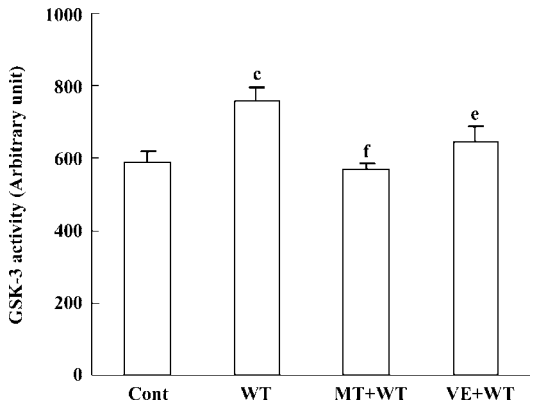

Figure 6. Effect of wortmannin, melatonin, and VE on the activity of GSK-3. GSK-3 activity was measured by ^{32}P-labeling in wortmannin-treated cells with or without preincubation of melatonin or VE. n=5. Mean±SD. ^{c}P<0.01 *vs* control. ^{e}P<0.05, ^{f}P<0.01 *vs* wortmannin-treatment.

Discussion

Abnormal hyperphosphorylation of tau is a recognized pathological process, which might be responsible for the disruption of microtubules and thus neurodegeneration seen in the brain of patients with Alzheimer's disease (AD). Many

Table 1. Malondialdehyde level and superoxide dismutase activity. ^{c}P<0.01 *vs* control. ^{e}P<0.05, ^{f}P<0.01 *vs* WT-treated cells.

Groups	MDA/U·L^{-1}	SOD/U·L^{-1}
Cont	1.45±0.08	40.25±4.40
WT	3.30±0.44^{c}	20.35±4.59^{c}
MT 50 μmol/L+WT	1.55±0.22^{f}	34.24±1.84^{f}
VE 50 μmol/L+WT	2.02±0.25^{e}	28.11±1.42^{e}

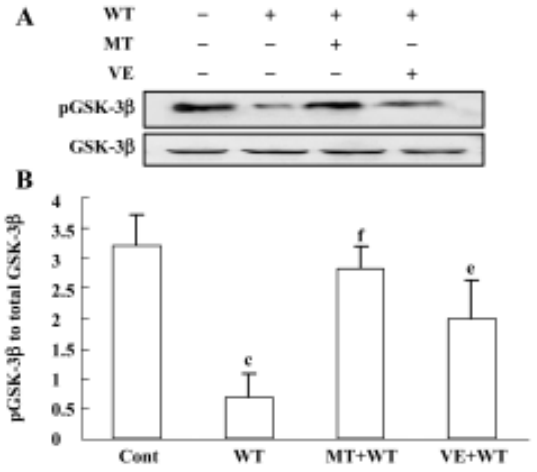

Figure 7. Effect of wortmannin, melatonin and VE on the expression of GSK-3β protein. Western Blots (A) and quantitative analysis (B) of Ser-9-phosphorylated GSK-3β and the total level of GSK-3β, or ratio of Ser-9-phosphorylated GSK-3β to total GSK-3β in cells treated as indicated. n=5. Mean±SD. ^{c}P<0.01 *vs* control. ^{e}P<0.05, ^{f}P<0.01 *vs* wortmannin-treatment.

protein kinases are reported to phosphorylate tau at some of the AD sites and can lead to the dysfunction of tau in maintaining stability of cytoskeleton. Among them, GSK-3, a major tau kinase, is a leading candidate for initiating pathologic tau hyperphosphorylation[5,7]. GSK-3 forms a complex with tau in the microtubule fraction from the bovine brain and it is co-localized with phosphorylated tau during development[17]. Hyperphosphorylation of tau by GSK-3 accelerates neurodegeneration and induces fibrillary tau inclusions both *in vivo* and *in vitro*[18]. As direct GSK-3 activator is not commercially available at the moment, wortmannin, an inhibitor of phosphatidylinositol 3-kinase (PI3K), has been widely used in activating GSK-3 indirectly through protein kinase B (PKB)-mediated signal transduction pathway; that is, wortmannin turns down PKB through inhibiting PI3K and thus activates GSK-3 by decreasing the phosphorylation level of GSK-3 at its serine residues[6,18,19]. We previously reported that wortmannin could induce Alzheimer's-like hyperphos-phorylation of cytoskeleton proteins in a rat brain[9,20]. To further explore the mechanism of how wortmannin influences tau phosphorylation, and thus to establish an AD-like cell model, we used wortmannin to treat N2a, a neuroblastoma cell line widely used in the AD field[21–23], in the present study. We have found that wortmannin activates GSK-3 and leads to tau hyperphosphorylation in N2a cell line, demonstrating that wortmannin can be used for reproducing a cell model with AD-like tau hyperphosphorylation. We have also observed that wortmannin treatment induces oxidative stress as displayed by the increase of MDA level and the decrease of SOD activity. This suggests the crucial role of oxidative stress in wortmannin-induced tau hyperphosphorylation.

Although the treatment of the cells with wortmannin led to significantly decreased cell viability, we did not see a typical cell apoptosis in the present study. The cells show evident hyperphosphorylation of tau, which is considered to be one of the earliest signs of neuronal degeneration and appears to precede tau aggregation or amyloid formation[24]. Tau abnormality provides the basis for the unequivocal diagnosis. However, its role in AD pathogenesis, especially in cell loss, is still not understood. The results observed in this study are consistent with the observations of SY5Y cells that tau phosphorylation can be an anti-apoptosis[25]. In another project, we also found that treatment of cells with calyculin A (a protein phosphatase inhibitor) led to neurofilament hyperphosphorylation and aggregation with minimal apoptosis[12]. Neurons in AD were not co-labeled with AT8 (an antibody that probes phosphorylated tau) and an antibody to activate caspase-3[26]. Similarly, activated JNK, p38, and ERK1/2 (phosphorylated forms of these proteins) co-localized with hyperphosphorylated tau in an AD brain, but not with markers of apoptosis[27,28], indicates that increased tau phosphorylation seems to resist apoptotic stimuli. Therefore, although many *in vivo* and *in vitro* data support the involvement of apoptosis in neurodegenerative processes, there is considerable evidence suggesting that very complex events can contribute to neuronal death with possible repair mechanisms[29], elucidation of which could prove useful for future investigation of the mechanisms of cell death in these disorders and their relations to cytoskeletal abnormalities, as well as prevention and therapy of neurodegenerative disorders.

AD is the most common cause of dementia and there is no specific and effective cure for this disorder to date. Recently, increasing data suggests that melatonin might play an important role in the development of AD and serve as a candidate for arresting AD-like pathological processes[30,31]. Patients with AD have a more profound reduction of melatonin in the brain and in cerebrospinal fluid[31,32]. The efficacy of melatonin in inhibiting oxidative damage has been tested in a variety of neurodegenerative disease models, including Huntington's disease, Parkinson's disease and AD, induced with quinolinic acid, MPTP, β-amyloid, and OA (okadaic-acid) respectively in rat brain or in cultured cells[33–36]. In the present study, we have found that melatonin rescues cell viability and reverses tau hyperphosphorylation induced by wortman-nin in N2a neuroblastoma cells. At the same time,

melatonin decreases the level of lipid peroxide and increases the activity of antioxidant enzymes. This is consistent with previous findings that melatonin prevents oxidative damage to the cell membrane, organelles, nuclear and mitochondrial DNA by donating electrons[37]. From this data, we speculate that melatonin might prevent wortmannin-induced tau hyperphosphorylation through its antioxidant effects. We have also found that melatonin obviously inhibits wortmannin-induced activation of GSK-3, suggesting that melatonin might act not only against free radicals, but also indirectly as an enzyme modulator[31] in rescuing wortmannin-induced tau hyperphosphorylation; further study is needed to explore the mechanism. We also observed that melatonin acted more efficiently than vitamin E not only as an antioxidant but also in restoring GSK-3 activity and tau hyperphosphorylation. Melatonin is a small amino acid hormone secreted mainly in the pineal gland. Specific characters of melatonin, such as its solubility in both lipids and water that allow it to be easily penetrated into the cells and pass through the blood brain barrier, can make it totally different from other antioxidant. In addition to its role in rescuing AD-like tau abnormalities, melatonin is also reported to protect β-amyloid peptide-induced cell injuries[38,39]. Therefore, melatonin might become a promising candidate thwarting the two hallmark abnormalities in AD patients.

Melatonin could function through its membranous and nuclear receptors in peripheral tissues; melatonin receptors are widely expressed in different organs, such as the brain hippocampus, retina, lung, liver, and kidney[40]. Melatonin could also function through non-receptor mediated pathways[41]. In N2a cells, whether melatonin functions through the receptor-dependent pathway or receptor-independent pathway, needs further study.

Taken together, we have found in the present study that wortmannin induces overactivation of GSK-3 and tau hyperphosphorylation with a concurrent lipid peroxidation and reduction of cell viability in the N2a cell line. Melatonin rescues not only wortmannin-induced oxidative stress, but also GSK-3 overactivation and tau hyperphosphorylation.

References

1 Lee VM, Goedert M, Trojanowski JQ. Neurodegenerative tauopathies. Annu Rev Neurosci 2001; 24: 1121–59.

2 Johnson GV, Hartigan JA. Tau protein in normal and Alzheimer's disease brain: an update. J Alzheimers Dis 1999; 1: 329–51.

3 Billingsley ML, Kincaid RL. Regulated phosphorylation and dephosphorylation of tau protein: effects on microtubule interaction, intracellular trafficking and neurodegeneration. Biochem J 1997; 323: 577–91.

4 Maas T, Eidenmuller J, Brandt R. Interaction of tau with the neural membrane cortex is regulated by phosphorylation at sites that are modified in paired helical filaments. J Biol Chem 2000; 275: 15733–40.

5 Bhat RV, Budd Haeberlein SL, Avila J. Glycogen synthase kinase 3: a drug target for CNS therapies. J Neurochem 2004; 89: 1313–7.

6 Li X, Bijur GN, Jope RS. Glycogen synthase kinase-3β, mood stabilizers, and neuroprotection. Bipolar Disord 2002: 4: 137–44.

7 Bhat RV, Budd SL. GSK-3beta signalling: casting a wide net in Alzheimer's disease. Neurosignals 2002; 11: 251–61.

8 Pei JJ, Braak E, Braak H, Grundke-Iqbal I, Iqbal K, Winblad B, *et al*. Distribution of active glycogen synthase kinase 3beta (GSK-3beta) in brains staged for Alzheimer disease neurofibrillary changes. J Neuropathol Exp Neurol 1999; 58: 1010–9.

9 Liu SJ, Zhang AH, Li HL, Wang Q, Deng HM, Netzer WJ, *et al*. Overactivation of glycogen synthase kinase-3 by inhibition of phosphoinositol-3 kinase and protein kinase C leads to hyperphosphorylation of tau and impairment of spatial memory. J Neurochem 2003; 87: 1333–44.

10 Reiter RJ. Pineal melatonin: cell biology of its synthesis and of its physiological interactions. Endocr Rev 1991; 12: 151–80.

11 Zhang YC, Wang ZF, Wang Q, Wang YP, Wang JZ. Melatonin attenuates beta-amyloid-induced inhibition of neurofilament expression. Acta Pharmacol Sin 2004; 25: 447–51.

12 Li SP, Deng YQ, Wang XC, Wang YP, Wang JZ. Melatonin protects SH-SY5Y neuroblastoma cells from calyculin A-induced neurofilament impairment and neurotoxicity. J Pineal Res 2004; 36: 186–91.

13 Wang DL, Ling ZQ, Cao FY, Zhu LQ, Wang JZ. Melatonin attenuates isoproterenol-induced protein kinase an overactivation and tau hyperphosphorylation in rat brain. J Pineal Res 2004; 37: 11–6.

14 Kim BC, Shon BS, Ryoo YW, Kim SP, Lee KS. Melatonin reduces X-ray irradiation-induced oxidative damages in cultured human skin fibroblasts. J Dermatol Sci 2001; 26: 194–200.

15 Marklund S, Marklund G. Involvement of the superoxide anion radical in the autoxidation of pyrogallol and a convenient assay for superoxide dismutase. Eur J Biochem 1974; 47: 469–74.

16 Lee CW, Lau KF, Miller CC, Shaw PC. Glycogen synthase kinase-3 beta-mediated tau phosphorylation in cultured cell lines. Neuroreport 2003; 14: 257–60.

17 Sun W, Qureshi HY, Cafferty PW, Sobue K, Agarwal-Mawal A, Neufield KD, *et al*. Glycogen synthase kinase-3beta is complexed with tau protein in brain microtubules. J Biol Chem 2002; 277: 11933–40.

18 Eldar-Finkelman H. Glycogen synthase kinase 3: an emerging therapeutic target. Trends Mol Med 2002; 8: 126–32.

19 Krasilnikov MA. Phosphatidylinositol-3 kinase dependent pathways: the role in control of cell growth, survival, and malignant transformation. Biochemistry (Mosc) 2000; 65: 59–67.

20 Liu SJ, Wang JZ. Alzheimer-like tau phosphorylation induced by wortmannin *in vivo* and its attenuation by melatonin. Acta Pharmacol Sin 2002; 23: 183–7.

21 Wang YP, Wang ZF, Zhang YC, Tian Qing, Wang JZ. Effect of amyloid peptides on serum withdrawal-induced cell differentiation and cell viability. Cell Res 2004; 14: 467–72.

22 Stamer K, Vogel R, Thies E, Mandelkow E, Mandelkow EM. Tau

blocks traffic of organelles, neurofilaments, and APP vesicles in neurons and enhances oxidative stress. J Cell Biol 2002; 156: 1051–63.
23 Munoz JP, Alvarez A, Maccioni RB. Increase in the expression of the neuronal cyclin-dependent protein kinase cdk-5 during differentiation of N2A neuroblastoma cells. Neuroreport 2000; 11: 2733–8.
24 Brandt R. Cytoskeletal mechanisms of neuronal degeneration. Cell Tissue Res 2001; 305: 255–65.
25 Lesort M, Blanchard C, Yardin C, Esclaire F, Hugon J. Cultured neurons expressing phosphorylated tau are more resistant to apoptosis induced by NMDA or serum deprivation. Brain Res Mol Brain Res 1997; 45: 127–32.
26 Jellinger KA. Cell death mechanisms in neurodegeneration. J Cell Mol Med 2001; 5: 1–17.
27 Atzori C, Ghetti B, Piva R, Srinivasan AN, Zolo P, Delisle MB, *et al*. Activation of the JNK/p38 pathway occurs in diseases characterized by tau protein pathology and is related to tau phosphorylation but not to apoptosis. J Neuropathol Exp Neurol 2001; 60: 1190–7.
28 Ferrer I, Blanco R, Carmona M, Ribera R, Goutan E, Puig B, *et al*. Phosphorylated map kinase (ERK1, ERK2) expression is associated with early tau deposition in neurones and glial cells, but not with increased nuclear DNA vulnerability and cell death, in Alzheimer disease, Pick's disease, progressive supranuclear palsy and corticobasal degeneration. Brain Pathol 2001; 11: 144–58.
29 Marx J. Neuroscience. New leads on the 'how' of Alzheimer's disease. Science 2001; 293: 2192–4.
30 Grundman M, Grundman M, Delaney P. Antioxidant strategies for Alzheimer's disease. Proc Nutr Soc 2002; 61: 191–202.
31 Matsubara E, Shoji M, Murakami T, Kawarabayashi T, Abe K. Alzheimer's disease and melatonin. Int Congress Series 2003; 1252: 395–98.
32 Beyer CE, Steketee JD, Saphier D. Antioxidant properties of melatonin–an emerging mystery. Biochem Pharmacol 1999; 57: 1077.
33 Guillemin GJ, Brew BJ. Implications of the kynurenine pathway and quinolinic acid in Alzheimer's disease. Redox Rep 2002; 7: 199–206.
34 Cabrera J, Reiter RJ, Tan DX, Qi W, Sainz RM, Mayo JC, *et al*. Melatonin reduces oxidative neurotoxicity due to quinolinic acid: *in vitro* and *in vivo* findings. Neuropharmacology 2000; 39: 507–14.
35 Miranda S, Opazo C, Larrondo LF, Munoz FJ, Ruiz F, Leighton F, *et al*. The role of oxidative stress in the toxicity induced by amyloid beta-peptide in Alzheimer's disease. Prog Neurobiol 2000; 62: 633–48.
36 Montilla-Lopez P, Munoz-Agueda MC, Feijoo Lopez M, Munoz-Castaneda JR, Bujalance-Arenas I, Tunez-Finana I. Comparison of melatonin versus vitamin C on oxidative stress and antioxidant enzyme activity in Alzheimer's disease induced by okadaic acid in neuroblastoma cells. Eur J Pharmacol 2002; 451: 237–43.
37 Reiter RJ. Melatonin. Lowering the high price of free radicals. News Physiol Sci 2000; 15: 246–50.
38 Matsubara E, Bryant-Thomas T, Pacheco Quinto J, Henry TL, Poeggeler B, Herbert D, *et al*. Melatonin increases survival and inhibits oxidative and amyloid pathology in a transgenic model of Alzheimer's disease. J Neurochem 2003; 85: 1101–8.
39 Reiter RJ, Tan DX, Sainz RM, Mayo JC, Lopez-Burillo S. Melatonin: reducing the toxicity and increasing the efficacy of drugs. J Pharm Pharmacol 2002; 54: 12299–321.
40 Naji L, Carrillo-Vico A, Guerrero JM, Calvo JR. Expression of membrane and nuclear melatonin receptors in mouse peripheral organs. Life Sci 2004; 74: 2227–36.
41 Pappolla MA, Simovich MJ, Bryant-Thomas T, Chyan YJ, Poeggeler B, Dubocovich M, *et al*. The neuroprotective activities of melatonin against the Alzheimer beta-protein are not mediated by melatonin membrane receptors. J Pineal Res 2002; 32: 135–42.

Acta Pharmacologica Sinica 2005 May; 26 (5): 527–532

Full-length article

Pharmacological profiles of an anticholinergic agent, phencynonate hydrochloride, and its optical isomers[1]

Li-yun WANG, Yun WANG, Jian-quan ZHENG[2], Bo-hua ZHONG, He LIU, Si-jian DONG, Jin-xiu RUAN, Ke-liang LIU

Beijing Institute of Pharmacology and Toxicology, Beijing 100850, China

Key words

optical isomers; muscarinic acetylcholinic receptors; pharmacological profiles; radioligand binding assay

[1] Project supported by the Major Program of National Natural Science Foundation of China (No 203900508).
[2] Correspondence to Prof Jian-quan ZHENG.
Phn 86-10-6693-1635.
Fax 86-10-6821-1656.
E-mail jqzh@yahoo.com

Received 2004-10-25
Accepted 2005-01-10

doi: 10.1111/j.1745-7254.2005.00089.x

Abstract

Aim: To comparatively study the pharmacological profiles of 3-methyl-3-azabicyclo (3,3,1)nonanyl-9-α-yl-α-cyclopentyl-α-phenyl-α-glycolate (phencynonate hydrochloride, CPG), an anticholinergic agent, and its enantiomers [*R*(–)- and *S*(+)-CPG]. **Methods:** The affinity and relative efficacy were tested using radioligand-binding assay with muscarinic acetylcholine receptors from rat cerebral cortex. The pharmacological activities were assessed in three individual experiments: (1) potentiating the effect of subthreshold hypnotic dose of sodium pentobarbital; (2) inhibiting oxotremorine-induced salivation; and (3) inhibiting the contractile response to carbachol. **Results:** The order of potency of phencynonate hydrochloride and its optical isomers to inhibit the binding of [^{3}H]quinuclidinyl benzilate ([^{3}H]QNB) was *R*(–)-CPG (K_i=46.49±1.27 nmol/L)>CPG (K_i=271.37±72.30 nmol/L)>*S*(+)-CPG (K_i=1263.12±131.64 nmol/L). The results showed that *R*(–)-CPG had the highest affinity to central muscarinic receptors among the three compounds, but did not show any central depressant effects at dose from 10.00 to 29.15 mg/kg. CPG increased the effects of subthreshold hypnotic dose of sodium pentobarbital induced-sleeping [the ED_{50}±95% LC value was 21.06±3.04 mg/kg]. CPG and *R*(–)-CPG displayed nearly equipotent effect in depressing oxotremorine-induced salivation [the ED_{50} ±95% LC for *R*(–) and CPG were 1.10±0.28 and 1.07±0.15 mg/kg, respectively], and the contractile response to carbachol (pA_2 values for *R*(–) and CPG were 6.84 and 6.80, respectively). *S*(+)-CPG presented the lowest anticholinergic profiles, but could potentate effects of its enantiomers in some manner. **Conclusions:** These data suggested that *R*(–)-CPG acted as an eutomer in racemate and a competitive antagonist to acetylcholine muscarinic receptors, but *S*(+)-CPG was less active in comparison to *R*(–)-CPG and its racemate. The central depressant effects of *R*(–)-CPG and *S*(+)-CPG were lower in comparison to its racemate.

Introduction

Molecular handedness is a crucial structural feature of biologically active compounds, since opposite configurations at pharmacophoric groups frequently influence the biological response, mainly in terms of affinity, toxicity, and receptor subtype selectivity[1]. Therefore, the stereoisomeric composition of drugs is currently receiving considerable attention owing to its pharmacological as well as industrial and regulatory implications[2,3].

3-Methyl-3-azabicyclo(3,3,1)nonanyl-9-α-yl-α-cyclopentyl-α-phenyl-α-glycolate (phencynonate hydro-chloride, CPG) is a central anticholinergic agent synthesized at the Beijing Institute of Pharmacology and Toxicology. It has been developed as a new medicine for motion sickness. Our previous studies revealed that CPG prevented motion sickness with higher efficacy and lower central inhibitory side effects compared to other motion sickness drugs, such as dimenhydrinate and scopolamine HBr[4]. There is one chiral carbonic atom in the molecular structure of CPG (Figure 1).

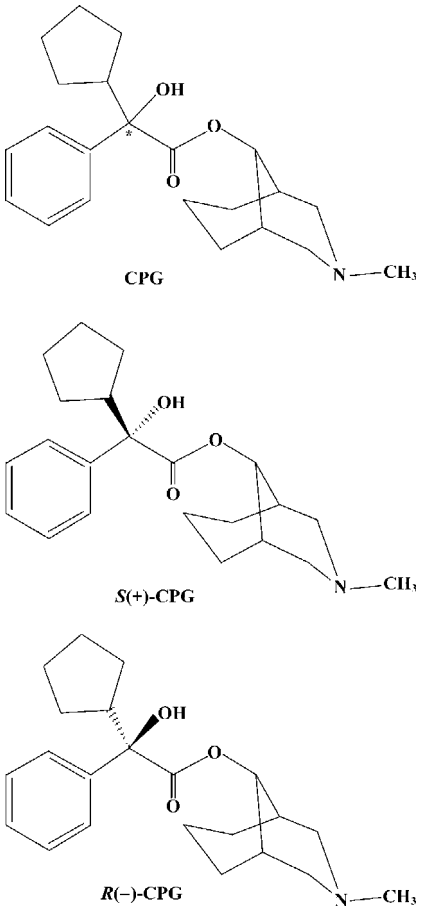

Figure 1. Chemical structure of CPG and its optical isomers.

Thus, there were two optical isomers of CPG with *R*(–)- and *S*(+)-different configurations. The pharmacological effects of these isomers remained unknown. In order to study the pharmacological differences between the stereoisomers and develop more safe drugs, we investigated the pharmacological characteristics of these two chiral muscarinic antagonists by comparing their effects on muscarinic receptors *in vivo* and *in vitro*.

Materials and methods

Chemicals [^{3}H]QNB [^{3}H-quinuclindiny benzilate] (43.3 Ci/mmol) was purchased from Amersham Co (Uppsala, Sweden) (TRK604). CPG and its isomers were synthesized at our institute. CPG comprised nearly the same proportion for *R*(–)- and *S*(+)-CPG. Atropine, pentobarbital sodium, oxotremorine, and carbachol were from Sigma Co (St Lowis, USA).

Animals The experiments were carried out in accordance with the Guide for the Care and Use of Laboratory Animals, National Research Council, 1996. Animals used in the study were: male or female Wistar rats weighing 180–220 g, [Grade II, Certificate No scxk (Jing) 2002-0003] and male guinea pigs (200–300 g, Grade II, Certificate No (Jing) 2003-0005), which were purchased from Lianhelihua Co (Beijing, China); Kunming species mice [18–22 g, Grade II, Certificate No SCXK-(Army) 2002-001] were provided from the animal center at our institute.

Binding assays on rat cerebral cortex homogenate Male or female Wistar rats were killed by decapitation. The cerebral cortex was immediately removed and processed as described by Yamamura and Snyder[5]. Protein concentration was determined by the method of Lowry *et al*[6]. Homogenate (50 mg of protein) was incubated for at 37 ºC for 30 min in 0.5 mL of assay buffer containing 6 nmol/L [^{3}H]QNB and various concentrations of drugs. In saturation binding assays, the homogenate was incubated in the presence of [^{3}H]QNB (0.25–20 nmol/L). Non-specific binding was defined as binding in presence of atropine (1 μmol/L). Each sample was filtered through GF/C glass fibers with a vacuum. The filters were rinsed three times with 3 mL cold buffer, and placed in scintillation vials containing 3 mL of scintillation fluid. Radioactivity trapped on the filters was determined by liquid scintillation spectrometry at approximately 40%–50% efficiency.

Carbachol-induced contraction Male guinea pigs were killed by cervical dislocation. The organs required were set up rapidly under 1 g of tension in 20 mL organ baths containing physiological salt solution (PSS), which was kept at 37 ºC and aerated with 5% CO_2 and 95% O_2. Two-centimeter-long portions of terminal ileum were taken at about 5 cm from the ileum-cecum junction and mounted in PSS at 37 ºC. The composition of PSS was as the following (mmol/L): NaCl (118), $NaHCO_3$ (23.8), KCl (4.7), $MgSO_4 \cdot 7H_2O$ (1.18), KH_2PO_4 (1.18), $CaCl_2$ (2.52), and glucose (11.7). Tension changes were recorded isotonically. Tissues were equilibrated for 90 min before the experiments began.

The concentration was increased in a stepwise manner after the response to the previous concentration had reached a plateau to make concentration-response curve for carbachol. After cumulative concentration-response curves were generated in the absence of any antagonist, the ileum strips were washed several times with PSS and allowed to relax to baseline. After 60 min, the strips were incubated with *R*(–)-, *S*(+)-, or CPG for 10–15 min. The concentration-response curves for carbachol were then obtained in the presence of increasing concentrations of different antagonists.

To assess the potency of the antimuscarinic action, the ratio of the ED_{50} values for the carbachol-induced contrac-

tions in the presence and in the absence of antagonist were obtained. Schild plots were obtained by plotting logarithmic (dose ratio-1) against the logarithmic molar concentration of the antagonist, and pA_2 values were derived from the Schild plots according to the method described by Arunlakshana and Schild[7].

Effect on sub-threshold hypnotic dose of sodium pentobarbital induced-sleeping Four dosage groups were used for each drug and each group consists of 10 mice of each sex. CPG and its optical isomers were injected intra-peritoneally (ip). Fifteen minutes later, subthreshold hypnotic dose of sodium pentobarbital (30 mg/kg) was applied ip and lossing in the righting reflex was observed as the score to present the central inhibitory effect of the drugs. The ED_{50} values of these three drugs were estimated to compare the central inhibitory effect of the indicated agents.

Inhibiting oxotremorine-induced salivation Four dosage groups were used for each compound and each group consisted of 10 mice of each sex. CPG and its optical isomers were applied ip 15 min prior to the use of oxotremorine (3 mg/kg) subcutaneously (sc). ED_{50} values were utilized to evaluate the anti-secretive potencies of above described compounds.

Statistics

Binding assay The IC_{50} values were obtained from at least three separate experiments performed in triplicate with between 6 and 8 different concentrations of drugs. Hill coefficients and IC_{50} values were determined using the ORIGIN6.0 software program and inhibition constants (K_i values) were calculated utilizing the Cheng-Prusoff equation[8].

Functional assay In carbachol induced-contraction, the E_{max} value (the maximum contractile response) was obtained from the maximum stress developed, and the ED_{50} value was calculated from a semi-logarithmic plot of the percentage of the maximum response versus drug concentration. Statistical analyses for comparison between groups and between concentration-response curves were performed using analysis of variance (ANOVA). $P<0.05$ was considered statistically significant. In the experiments for observing the effects of CPG and its optical isomers on salivation and sedation induced by oxotremorine and sodium pentobarbital, ED_{50} values were calculated utilizing the Bliss method. Data were shown as mean±SD.

Results

Competitive binding of CPG and its optical isomers to rat central muscarinic acetylcholine receptors The K_d values for [^{3}H]QNB binding to receptors were 6.66±0.95 nmol/L. The B_{max} values were 0.758± 0.086 fmol/mg. The competition binding potency of *R*(–)-CPG for [^{3}H]QNB corresponded to a K_i value of 46.49±1.27 nmol/L (n=4). An average Hill coefficient (n_H) was 1.54±0.06. The affinity of *R*(–)-CPG at central muscarinic acetylcholine receptors was greater than that of CPG (K_i=271.37±72.3 nmol/L, n_H=1.48). *S*(+)-CPG displayed the lowest affinity to muscarinic receptor (K_i=1263.12±131.64 nmol/L, n_H=1.12). The results showed that the isomer with *R*(–)-configuration was more potent than the isomer with *S*(+)-configuration and CPG (Figure 2).

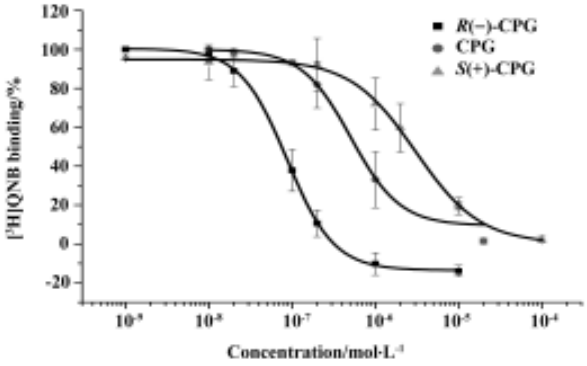

Figure 2. Effects of CPG and its optical isomers on the binding of [^{3}H]QNB to rat central muscarinic acetylcholine receptors. Rat cerebral cortex homogenate was incubated with 6 nmol/L [^{3}H]QNB at 37 °C for 30 min in the absence and presence of increasing concentrations of different drugs. Data were the means from four independent experiments performed in duplicate.

Effect of CPG and its optical isomers on carbachol-induced contraction Carbachol (1×10^{-8}–1×10^{-2} mol/L) caused concentration-dependent contraction of guinea pig ileum. The E_{max} values for the carbachol-induced contractions were 2.9±0.2 g (n=30). CPG and *R*(–)-configuration (1×10^{-8}–1×10^{-7} mol/L) caused typical rightward shifts in the concentration-response curves for carbachol, except for a higher concentration (1×10^{-6} mol/L) of *R*(–)- and CPG, which caused decreases of about 80% of the maximum contractile responses to carbachol. However, *S*(+)-CPG only caused decreases of about 10%–20% of the maximum contractile effects induced by carbachol at the dose of 1×10^{-6} mol/L, the difference was not significant ($P>0.05$). All slopes of the regression lines of Schild plots were close to unity in Figure 3. The IC_{50} value of *R*(–)- and CPG are shown in Figure 4. The rank order of pA_2 values was: CPG (6.80)≈*R*(–)-CPG (6.84) (Table 1).

Potentiating the effect of sub-threshold hypnotic dose of sodium pentobarbital Pentobarbital (ip 30 mg/kg) alone did not cause loss in righting reflex in mice (n=50). Pretreatment

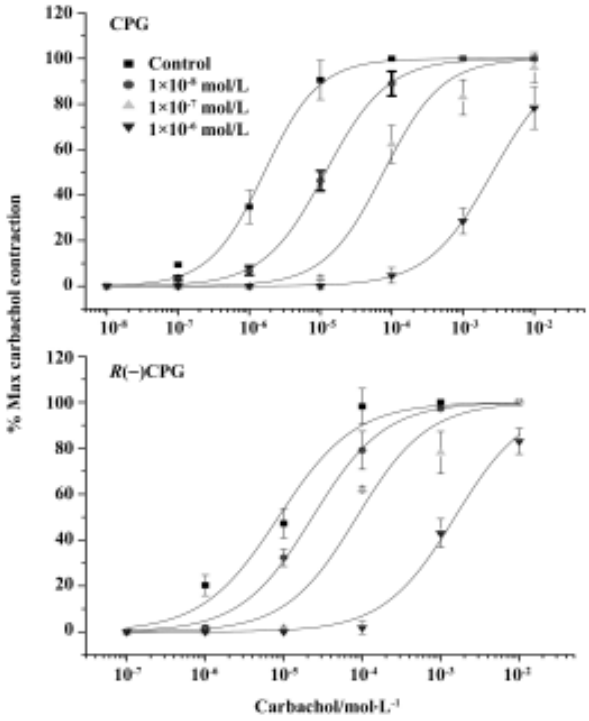

Figure 3. Effects of CPG and *R*(–)-CPG 1 (1×10^{-8}, 1×10^{-7}, and 1×10^{-6} mol/L) on the concentration-response curves for carbachol in guinea ileum. For each experiment, contractile responses were expressed as percentages of the maximum contractile response in the absence of any antagonist. Each point represented the mean±SD of the results from six separate experiments.

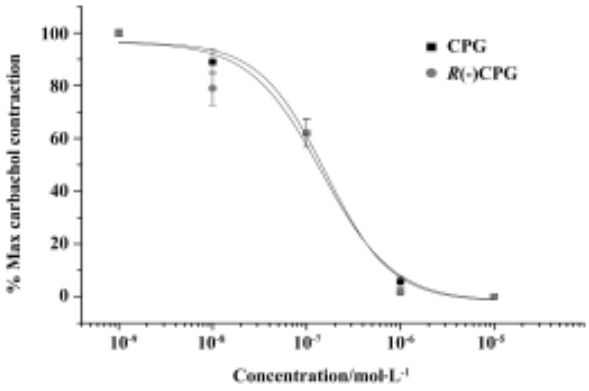

Figure 4. Concentration-response curves for *R*(–)-CPG and CPG (1×10^{-9}–1×10^{-5} mol/L) on the maximum contractile response induced by carbachol (1×10^{-4} mol/L) in guinea pig ileum. For each experiment, contractile responses were expressed as percentages of the maximum contractile response in the absence of any antagonist. Each point represented the mean±SD of the results from six separate experiments; if not shown, SD bars fall within the size of the symbol.

with CPG (14.28–41.64 mg/kg) at 15 min intervals potentiated

Table 1. pA_2 Values and slopes of CPG and *R*(–)-CPG inhibiting carbachol-induced contraction in guinea pig ileum. *n*=6. Mean±SD.

Chiral compound	pA_2	Slopes
CPG	6.80±0.22	1.00±0.05
R(–)-CPG	6.84±0.24	0.95±0.01

the effect of sub-threshold hypnotic dose of sodium pentobarbital in a dose-dependent manner (Table 2). The ED_{50} value and its 95% confident limits of CPG was 21.06 (18.02–24.10) mg/kg. The isomer with *R*(–)- and *S*(+)-configuration did not show any effects on pentobarbital induced-sleeping at the dose from 10.00–29.15 mg/kg. The result suggested that the central depressant effect of CPG was more potent than the other two isomers used separately.

Table 2. The effect of CPG and its optical isomers on sub-threshold hypnotic dose of sodium pentobarbital induced-sleeping. For each experiment, the rate of loss in righting reflex was expressed in the ratio of mice lost in righting reflex to 10 mice.

Chiral compound	Dose /mg·kg^{-1}	The rate of loss in right reflex /%	ED_{50}±95% LC /mg·kg^{-1}
CPG	14.28	1	21.06±3.04
	20.40	0.8	
	29.15	0.5	
	41.64	0.1	
R(–)CPG	10.00	0	
	14.28	0	
	20.40	0	–
	29.15	0	
S(+)CPG	10.00	0	
	14.28	0	
	20.40	0	–
	29.15	0	

Oxotremorine (sc 3mg/kg) induced an obvious salivation in mice (*n*=50). Whereas, CPG and its optical isomers showed antagonistic effects on oxotremorine-induced salivation in dose-dependent manner when pre-administered. The ED_{50}±95% LC for CPG, *R*(–)-, and *S*(+)-configuration were 1.07±0.15, 1.10±0.28, and 16.69±4.82 mg/kg, respectively, which indicated that CPG was equivalent to *R*(–)-CPG and more potent than *S*(+)-CPG in inhibiting glandular secretion (Table 3).

Table 3. Effect of CPG and its optical isomers on oxotremorine-induced salivation. (For each experiment, the rate of anti-salivation was expressed as the ratio of mice lost in righting reflex to 10 mice).

Chiral compound	Dose /mg·kg^{-1}	The rate of anti-salivation	ED_{50}±95% LC /mg·kg^{-1}
CPG	1.68	0.90	1.07±0.15
	1.18	0.70	
	0.82	0.30	
	0.58	0.00	
R(–)-CPG	1.68	0.70	1.10±0.28
	1.18	0.60	
	0.82	0.40	
	0.58	0.10	
S(+)-CPG	20.4	0.80	16.69±4.82
	14.28	0.50	
	10.00	0.30	
	7.00	0.00	

Discussion

Motion sickness is a common disease in modern society. The pathogenic mechanism inducing the sickness is not fully understood. However, the etiologic theory that cholinergic hyperfunction of the vestibular system excites the vomiting center and the central cholinergic neuron system plays an important role in the neural mechanism of motion sickness is generally accepted[9,10]. The anticholinergic agents, such as scopolamine, when used for preventing motion sickness, present some disadvantages at the effective dose, especially the troublesome central inhibitory effect[11].

The new central anticholinergic drug CPG has been widely used in clinic. Animal experiments and clinic research have demonstrated that CPG was more potent and had lesser central inhibitory side effects in the prevention of motion sickness (airsickness and seasickness) than those of central cholinergic drugs, such as scopolamine HCl and dimenhydrinate[12]. There was the same proportion of two enantiomers in the race mixture of CPG. In order to illuminate the pharmacological profiles of its optical isomers, we compared the affinity of CPG and its optical isomers to muscarinic acetylcholine receptors. In the competitive binding assay, it was found that *R*(–)-CPG inhibited the binding of [^{3}H]QNB with the highest potency (K_i=46.49±1.27 nmol/L) compared with CPG (K_i=271.37±72.3 nmol/L) and *S*(+)-CPG (K_i= 1263.12±131.64 nmol/L). In the functional study, CPG and *R*(–)-CPG (1×10^{-8}–1×10^{-6} mol/L) caused parallel rightward shifts of the concentration-response curves for carbachol-induced ileum contraction. All the slopes of the regression lines of Schild plots were close to unity, which implied a competitive antagonism. *S*(+)-configuration slightly decreased the maximum contractile response at the dose of 1×10^{-6} mol/L. The order of potencies of these agents to inhibit the contractile responses was *R*(–)-CPG≈CPG>*S*(+)-CPG. The same result was obtained in inhibiting glandular secretion. These results revealed that *R*(–)-CPG acted as an active composition of racemate with competitive antagonistic mechanism to muscarinic acetylcholine receptors, but *S*(+)-CPG less bioactivity. It also had been to be noted that there was 50% of *S*(+)-CPG with lower binding affinity in racemate CPG; according to binding assay, CPG should less potent in suppressing smooth muscle contraction and glandular secretion. These results suggest that *S*(+)-configuration may increase the potencies of its enantiomer in some manner. Furthermore, at the same dose, *S*(+)- and *R*(–)-configuration did not display any synergestic effect on sub-threshold hypnotic dose of sodium pentobarbital, but their racemate, CPG, revealed remarkable central sedation effects. One possible explanation for these results was that *S*(+)-configuration might play a role in modulating the binding of *R*(–)-configuration by allosteric mechanism. In contrast, muscarinic acetylcholine receptors (mAChRs) modulate the activity of an extraordinarily large number of physiological functions. Individual members of the mAChR family (M_1–M_5) are expressed in a complex, overlapping fashion in most tissues and cell types. The M_1 and M_3 subtypes are the major muscarinic acetylcholine receptors in the salivary gland and M_3 is reported to be more abundant[13,14]. Guinea pig ileum smooth muscle is enriched with muscarinic receptors, the majority of which are of the M_2 subtype whereas the remaining minority belongs to the M_3 subtype[15,16]. The M_1, M_2, and M_4 subtypes of mAChRs are the predominant receptors in the CNS[17]. Our experiments were performed in different species and tissue *in vivo* and *in vitro*, preferential binding of one isomer to muscarinic subtype receptor may cause differences in pharmacological action. Drug enantiomers have identical properties in an achiral environment, but should be considered as different chemical compounds. This is because they often differ considerably in potency, pharmacological activity, and pharmacokinetic profile, since the modules with which they interact in biological systems are also optically active. Interactions of both isomers may differ at the active sites through which pharmacological action is mediated. For this, there were possible subtype and sterochemical selective mechanisms that account for the different actions and levels of activity of the CPG and its enantiomers. Hence, further studies were necessary to resolve the underlying mechanisms of muscarinic receptor with these compounds.

Taken together, the present work demonstrated that *R*(–)-CPG acted as an active component in racemate and a competitive antagonist to acetylcholine muscarinic receptors, but *S*(+)-CPG displayed less activities in comparison to *R*(–)-CPG and its racemate. In contrast to its racemate, both of the enantiomers showed lower central depressant effects.

References

1 Ariens EJ, Wuis EW, Veringa EJ. Stereoselectivity of bioactive xenobiotics. A pre-Pasteur attitude in medicinal chemistry, pharmacokinetics and clinical pharmacology. Biochem Pharmacol 1988; 37: 9–18.

2 Birkett DJ. Racemates or enantiomers: regulatory approaches. Clin Exp Pharmacol Physiol 1989; 16: 479–83.

3 Ariens EJ. Stereochemistry: a source of problems in medicinal chemistry. Med Res Rev 1986; 6: 451–66.

4 Dai JG, Liu CG, Yu LS, Yang AZ, Jia HB, Wang KN. Antimotion sickness effect of phencynonate hydrochloride in man. Chin J Aerospace Med 1997; 8: 10–4.

5 Yamamura HI, Snyder SH. Muscarinic cholinergic binding in rat brain. Proc Natl Acad Sci USA 1974; 71: 1725–9.

6 Lowry OH, Rosebrough NJ, Farr AL, Randall RJ. Protein measurement with the Folin phenol reagent. J Biol Chem 1951; 193: 265–75.

7 Arunlakshana O, Schild HO. Some quantitative uses of drug antagonists. Br J Pharmacol 1959; 14: 48–58.

8 Cheng Y, Prusoff WH. Relationship between the inhibition constant (K_i) and the concentration of inhibitor which causes 50 percent inhibition (I_{50}) of an enzymatic reaction. Biochem Pharmacol 1973; 22: 3099–108.

9 Yates BJ, Miller AD, Lucot JB. Physiological basis and pharmacology of motion sickness: an update. Brain Res Bull 1998; 47: 395–406.

10 Kohl RL, Homick JL. Motion sickness: a modulatory role for the central cholinergic nervous system. Neurosci Biobehav Rev 1983; 7: 73–85.

11 Taillemite JP, Devaulx P, Bousquet F. Motion sickness. Med Trop 1997; 57: 483–7.

12 Deng YJ, Zhang YM. Study on the efficacy of phencynonate hydrochloride tablets in prevention of motion sickness. Chin J New Drugs 2001; 10: 453–4

13 Nakamura T, Matsui M, Uchida K, Futatsugi A. M (3) muscarinic acetylcholine receptor plays a critical role in parasympathetic control of salivation in mice. J Physiol 2004; 558: 561–75.

14 Gautam D, Heard TS, Cui Y, Miller G, Miller G, Bloodworth L, Wess J. Cholinergic stimulation of salivary secretion studied with M1 and M3 muscarinic receptor single- and double-knockout mice. Mol Pharmacol 2004; 66: 260–7

15 Ehlert FJ, Thomas EA. Functional role of M2 muscarinic receptors in the guinea pig ileum. Life Sci 1995; 56: 965–71.

16 Honda K, Takano Y, Kamiya H. Pharmacological profiles of muscarinic receptors in the longitudinal smooth muscle of guinea pig ileum. Jpn J Pharmacol 1993; 62: 43–7.

17 Volpicelli LA, Levey AI. Muscarinic acetylcholine receptor subtypes in cerebral cortex and hippocampus. Prog Brain Res 2004; 145: 59–66.

Acta Pharmacologica Sinica 2005 May; 26 (5): 533–538

Full-length article

Effects of *l*-tetrahydropalmatine on locomotor sensitization to oxycodone in mice

Yan-li LIU[1, 2], Jian-hui LIANG[3], Ling-di YAN[1], Rui-bin SU[1], Chun-fu WU[2], Ze-hui GONG[1,4]

[1]*Beijing Institute of Pharmacology and Toxicology, Beijing 100850, China;* [2]*Department of Pharmacology, Shenyang Pharmaceutical University, Shenyang 110016, China;* [3]*Department of Neuropharmacology, National Institute on Drug Dependence, Peking University, Beijing 100083, China*

Key words

l-tetrahydropalmatine; oxycodone; locomotor sensitization

[4] Correspondence to Prof Ze-hui GONG.
Phn 86-10-6693-1620.
E-mail Gongzeh@yahoo.com.cn

Received 2004-07-17
Accepted 2004-12-30

doi: 10.1111/j.1745-7254.2005.00101.x

Abstract

Aim: Recent studies have shown that l-tetrahydropalmatine (*l*-THP), an active component of *Corydolis yanhusuo*, can inhibit the development of the conditional place preference induced by opioid receptor agonists, but the effects of *l*-THP on locomotor sensitivity induced by opioid receptor agonists have not been documented. In the present study, the effects of *l*-THP on locomotor sensitization to oxycodone, which is an opioid receptor agonist, were studied. **Methods:** Mice treated daily for 7 d with 5 mg/kg oxycodone and challenged with the same dose after 5 days of washout showed locomotor sensitization. In order to study the effects of *l*-THP on locomotor sensitization induced by oxycodone, *l*-THP was administered at doses of 6.25, 12.5, and 18.75 mg/kg, 40 min prior to treatment of oxycodone. **Results:** *l*-THP *per se* did not affect the locomotor activity at the doses of 6.25, 12.5, and 18.75 mg/kg, but could antagonize the hyperactivity induced by oxycodone (5 mg/kg). Co-administration of *l*-THP (18.75 mg/kg), 40 min prior to oxycodone, could inhibit the development of sensitization to oxycodone. In addition, *l*-THP (6.25, 12.5, and 18.75 mg/kg, ig) dose-dependently prevented the expression of oxycodone sensitization. **Conclusion:** These results suggested that *l*-THP could attenuate the locomotor-stimulating effects of oxycodone and inhibit the development and expression of oxycodone behavioral sensitization.

Introduction

The term 'behavioral sensitization' is used to describe the augmented behavior activity produced by a given dose of an opioid-drug after repeated intermittent injections[1]. Recently, the importance of behavioral sensitization in drug abuse research has been realized. Studies have shown that behavioral sensitization has a close relationship with relapse, compulsive drug-seeking and drug-taking behaviors[2–5]. Investigation of sensitization may be helpful for better understanding of the relapse mechanisms and for providing new strategies for the treatment of drug addiction.

Oxycodone (4,5-epoxy-14-hydroxy-3-methoxy-17-methylmorphinan-6-one) is a semi-synthetic derivative of the naturally occurring opium alkaloid, thebaine. Oxycodone is an opioid receptor agonist similar to morphine[6–8]. It is reported that the abuse potential of oxycodone is equivalent to that of morphine[9]. It has been found that withdrawal syndrome may occur in patients when high doses or the chronic treatment of oxycodone is broken or weakened, but the effects of oxycodone on locomotor behavior sensitivity in animals has not been documented. Therefore, the present study was designed to investigate whether acute injection of oxycodone would induce hyperlocomotor activity and chronic administration of oxycodone would induce locomotor sensitization in mice.

l-Tetrahydropalmatine (*l*-THP) is an active principle of *Corydolis yanhusuo*, a Chinese traditional herb used as an analgesic[10]. It is reported that *l*-THP possesses a blocking effect on dopamine D_1 and D_2 receptors and voltage-sensitive Ca^{2+} channels[11]. It has been suggested in recent studies that *l*-THP can inhibit physical dependence in morphine-

dependent mice and significantly reduce the development of the conditional place preference induced by morphine in mice[12,13]. However, no research has been carried out on the effects of *l*-THP on locomotor sensitization. Therefore, it is interesting to determine whether pretreatment with *l*-THP prior to administration of oxycodone would inhibit the hyperactivity induced by oxycodone and prevent the development and expression of locomotor activity to oxycodone.

Materials and methods

Animals Kunming mice, initially weighing 18–22 g, were purchased from the Experimental Animal Center of Beijing Institute of Pharmacology and Toxicology. The animals were fed *ad libitum* and were housed in a room with a controlled ambient temperature (22±2 ºC), humidity (50%±10%), and a 12-h light/dark cycle. Animals were acclimated to the housing conditions and handled for 3–4 d before experiments. All experiments were performed between 08.00 h and 16.00 h. All experiments were conducted according to the NIH Guide for the Care and Use of Laboratory Animals (NIH Publications No. 80-23, revised 1996). The experimental procedures were approved by the local Committee on Animal Care and Use.

Drugs Oxycodone, obtained from Beijing Four-Ring Pharmaceutical Factory (Beijing), was dissolved in 0.9% saline injected subcutaneously. *l*-THP, kindly provided by Professor Guo-zhang JIN (Shanghai Insititute of Materia Medica, Chinese Academy of Sciences), was dissolved in distilled water and administered intragastrically.

Apparatus Locomotor activity was counted automatically with Small Animal Locomotion Recording Apparatus (Institute of Materia Medica, Chinese Academy of Medical Science), which consisted of four boxes (20 cm in diameter and 15 cm in height) with six photoelectric infrared sensors 2 cm above the floor of each box. The sensors detect the movements of the mice through infrared radiation.

Experimental procedures

Acute effects of oxycodone on locomotor activity in mice Mice were put into the test boxes immediately after treatment with saline or oxycodone (1.25, 2.5, and 5.0 mg/kg, sc). Locomotor counts were measured every 10 min for 90 min.

Development of locomotor sensitivity to oxycodone in mice Two groups of 10 mice each were given oxycodone or saline for 7 consecutive days, and their activity was measured for 60 min immediately after each administration. The experimental period for the 7 d remained at approximately the same time everyday during the daytime.

Effects of acute and chronic *l*-THP on locomotor activity in mice Four groups of mice were given *l*-THP (6.25, 12.5, and 18.75 mg/kg) or saline, respectively, once per day for 7 consecutive days, followed by a 5-d withdrawal period. On d 13, all animals were challenged with saline. On d 1, 7, and 13, after 40-min treatment with *l*-THP or saline, the mice were put into the test boxes and locomotor activity was monitored for 60 min.

Effects of *l*-THP on the acute oxycodone-induced hyperactivity in mice Five groups of mice were administered with one of the following drug pairs: saline+saline, saline+oxycodone, and *l*-THP (6.25, 12.5, and 18.75 mg/kg)+oxycodone with a 40-min interval between the two treatments. After the second treatment, the mice were put into the test boxes to record their locomotor activity for 60 min.

Effects of *l*-THP on the development of oxycodone sensitization To assess the effects of *l*-THP on the development of oxycodone sensitization, five groups of mice were administered for 7 consecutive days with one of the following drug pairs: saline+saline, saline+oxycodone, and *l*-THP (6.25, 12.5, and 18.75 mg/kg)+oxycodone. The interval between *l*-THP and oxycodone injections was 40 min, with *l*-THP given prior to the oxycodone. After 5 washout periods, all animals were injected with oxycodone (5 mg/kg) and then put into the test chambers to record their locomotor activity for 60 min.

Effects of *l*-THP on the expression of oxycodone sensitization Mice were injected with 5 mg/kg oxycodone for 7 consecutive days to induce locomotor sensitization. After 5 days of washout, the mice were challenged with 5 mg/kg oxycodone, and with either saline or *l*-THP (6.25, 12.5, and 18.75 mg/kg), given 40 min prior to the oxycodone challenge. The locomotor activity of the mice was then measured for 60 min.

Statistics The results were expressed as the mean±SEM. In experiment acute effects of oxycodone on locomotor activity in mice and development of locomotor sensitivity to oxycodone in mice locomotor activity was analyzed using a two-way ANOVA. *Post hoc* comparisons were performed using Tukey's test. For the other experiments, statistical analyses were performed using one-way ANOVA and a *post hoc* Tukey's test. $P<0.05$ was considered statistically significant. Calculations were performed using the SPSS statistical package.

Results

Acute effects of oxycodone on locomotor activity in mice Mice were given saline, oxycodone (1.25, 2.5, or 5 mg/kg), then locomotor activity was monitored for 90 min. Locomotor acounts showed a great difference between saline-treated

mice and oxycodone-treated mice. Oxycodone dose-dependently induced locomotor response in mice during the 90-min test session [F (treatment) (3, 33)=16.598, P<0.01; F (treatment×time) (24, 424)=6.080, P<0.01]. During the first and the last 10 min, there was a significant difference between the saline-treated and oxycodone-treated group (5 mg/kg, sc). The climax of oxycodone-induced hyperactivity appeared approximately 30–40 min after the treatment of oxycodone. The psychomotor effect of 5 mg/kg oxycodone lasted about 90 min, and 1.25, 2.5 mg/kg oxycodone increased locomotor activity only at some time points (Figure 1).

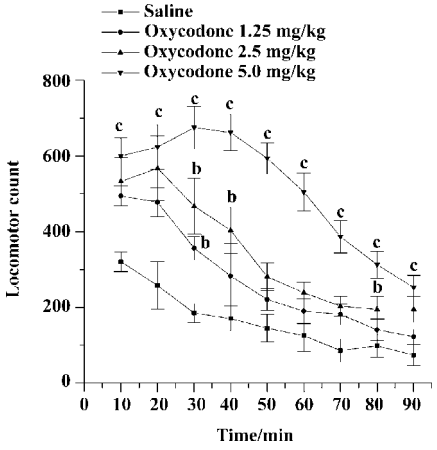

Figure 1. Acute effects of oxycodone on locomotion in mice. Mice were put into the test boxes immediately after treatment with saline or oxycodone (1.25, 2.5, and 5.0 mg/kg, sc). Locomotor counts were measured for 90 min. Mean±SEM. n=10–12. ^bP<0.05, ^cP<0.01 *vs* saline group.

Development of locomotor sensitivity to oxycodone in mice Figure 2 showed the total 60-min activity counts after 7 repeated administrations of oxycodone or saline to the mice in the test boxes. The activity counts were dependent on the drug [F (1,126) =20.764, P<0.01] and number of administrations [F (6,126)=73.246, P<0.01]. There was a significant interaction between the drug given and the number of administrations [F (6,126)=45.00, P<0.01]. The locomotor activity showed significant enhancement in the fourth injection compared to the initial injection. There was no significant difference among saline groups.

Effects of acute and chronic *l*-THP on locomotor activity in mice Mice were given *l*-THP (6.25, 12.5, and 18.75 mg/kg, ig) for 7 consecutive days, then subjected to withdrawal from *l*-THP for 5 d. On d 13, all animals were challenged with saline. On d 1, 7, and 13, 40 min after injection of *l*-THP or saline, the mice were put into the test boxes and locomotor counts were measured for 60 min. On d 1 and 7, there was no difference

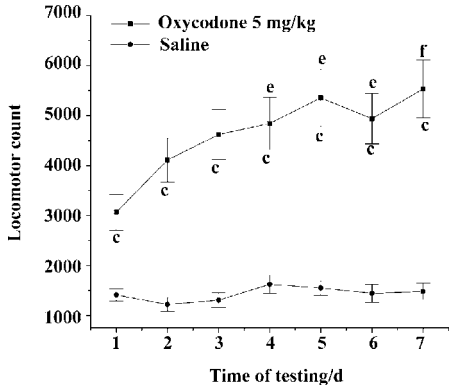

Figure 2. The development of locomotion sensitivity to oxycodone in mice. Two groups of 10 mice each were given oxycodone or saline for 7 consecutive days and their locomotor activity was measured immediately for 60 min after each administration. The experimental time remained approximately at the same time everyday during the daytime. Mean±SEM. n=10. ^cP<0.01 *vs* saline group. ^eP<0.05, ^fP<0.01 *vs* the first administration within group.

between the l-THP groups (6.25, 12.5, and 18.75 mg/kg) and saline group [F (3, 37)=1.360, P>0.05, F (3, 37)=0.348, P> 0.05, respectively]. On d 13, there was also no significant difference between *l*-THP groups and saline groups after administration of saline [F (3, 37)=1.532, P>0.05]. These results indicated that acute or chronic pretreatment with *l*-THP at the dose of 6.25, 12.5, and 18.75 mg/kg might not affect locomotor activity in mice (Figure 3).

Effects of *l*-THP on acute oxycodone-induced hyperactivity in mice Locomotor counts were greatly increased in the oxycodone group compared with the saline group. *l*-THP at doses of 6.25, 12.5, and 18.75 mg/kg antagonized hyperactivity induced by oxycodone [F (4, 60)=15.76, P<0.01] (Figure 4).

Effects of *l*-THP on the development of oxycodone sensitization Figure 5 showed that the psychomotor effect of oxycodone was significantly enhanced in mice pretreated with oxycodone (5 mg/kg×7, sc), 5 d cessation of treatment. *l*-THP (6.25, 12.5 mg/kg) did not affect the magnitude of sensitization, but there was a marked difference between oxycodone+oxycodone group and *l*-THP (18.75 mg/kg) +oxycodone+oxycodone group, indicating that *l*-THP (18.75 mg/kg) greatly inhibited the development of oxycodone sensitization [F (4, 62) =8.766, P<0.01].

Effects of *l*-THP on expression of oxycodone sensitization Our protocol induced great locomotor sensitization to oxycodone in oxycodone+oxycodone group compared to the saline+oxycodone group. There were great differences between oxycodone+oxycodone group and *l*-THP (6.25, 12.5, 18.75 mg/kg)+oxycodone+oxycodone groups [F (4, 65)=

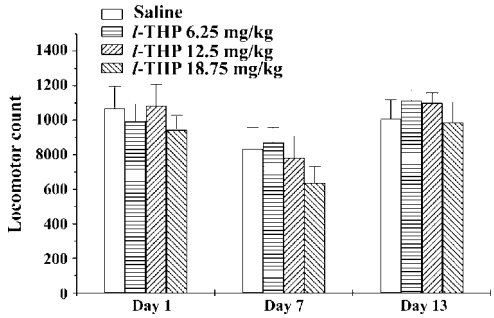

Figure 3. Effects of acute and chronic *l*-THP on locomotor activity in mice. Mice were given *l*-THP (6.25, 12.5, and 18.75 mg/kg) or saline once per day for 7 consecutive days, followed by a 5-d withdrawal period. On d 13, all mice were challenged with saline. On d 1, 7, and 13, 40 min after treatment with *l*-THP or saline, the mice were put into test boxes and locomotor activity was monitored for 60 min. n=10 in each group. Mean±SEM.

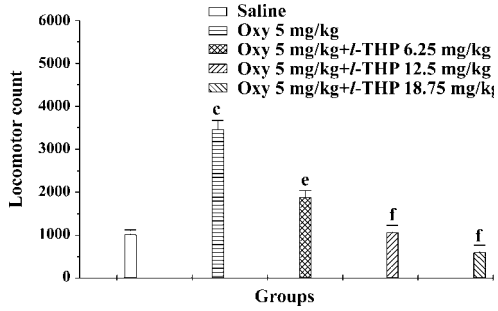

Figure 4. Effects of *l*-THP on the acute oxycodone-induced hyperactivity in mice. Five groups of mice were administered with one of the following drug pairs: saline+saline, saline+oxycodone, and *l*-THP (6.25, 12.5, and 18.75 mg/kg)+oxycodone with a 40-min interval between the two treatments. After the second treatment, the mice were put into the test boxes for recording of their locomotor activity for 60 min. n=10–12. Mean±SEM. ^{c}P<0.01 *vs* saline+saline group. ^{e}P<0.05, ^{f}P<0.01 *vs* saline+oxycodone group.

24.128, P<0.01]. In all, *l*-THP (6.25, 12.5, and 18.75 mg/kg), administered 40 min before the challenge doses of oxycodone, inhibited the expression of oxycodone sensitization (Figure 6).

Discussion

In our research, acute administration of oxycodone increased locomotor activities in mice and those effects were progressively enhanced by the repeated injection of oxycodone, indicated by the development of behavioral locomotor activity (Figure 1). In addition, locomotor activities were increased when the mice were treated with oxycodone after a 7-d period of washout, which attributed to the expression phase (Figure 2). Oxycodone has been used clinically for

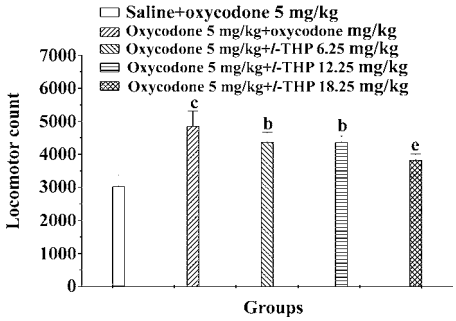

Figure 5. Effects of *l*-THP on the development of oxycodone locomotor sensitization. Mice were administered for 7 consecutive days with one of the following drug pairs: saline+saline, saline+oxycodone, and *l*-THP (6.25, 12.5, and 18.75 mg/kg)+oxycodone. The interval between *l*-THP and oxycodone injections was 40 min, with *l*-THP given prior to the oxycodone. After 5 washout period, all animals were injected with oxycodone (5 mg/kg) and then put into the test chambers to record their locomotor activity for 60 min. n=12–14. Mean±SEM. ^{b}P<0.05, ^{c}P<0.01 *vs* saline+oxycodone group. ^{e}P<0.05 *vs* oxycodone+oxycodone group.

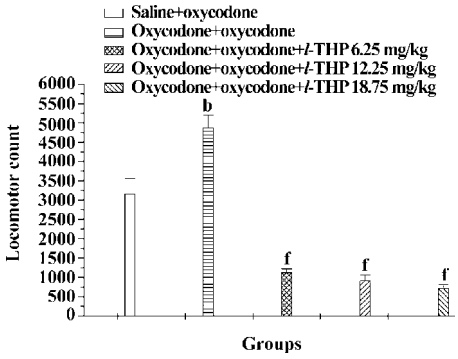

Figure 6. Effects of *l*-THP on the expression of oxycodone sensitization. Mice were injected with 5 mg/kg oxycodone for 7 consecutive days to induce behavioral sensitization. After 5 d of washout, all mice were challenged with 5 mg/kg oxycodone, and with either saline or *l*-THP (6.25, 12.5, 18.75 mg/kg), given 40 min prior to the oxycodone challenge. The locomotor activity of the mice was then measured for 60 min. n=12–14. Mean±SEM. ^{b}P<0.05 *vs* saline+oxycodone group. ^{f}P<0.01 *vs* oxycodone+oxycodone group.

over 80 years, but its pharmacological properties are still poorly characterized. The present results showed that the repeated administration of oxycodone in mice induced behavioral locomotor sensitization similar to morphine.

l-THP, an active principle of *Corydolis yanhusuo*, at doses of 6.25, 12.5, and 18.75 mg/kg *per se* did not affect locomotor activity in mice treated with acute or chronic administration, but inhibited hyperactivity, and the development and expression of locomotor sensitivity induced by oxycodone (5 mg/kg, sc).

Behavioral sensitization consists of two phases: development/induction and expression. There is evidence suggesting that the induction and the expression of sensitization to opioids involve different anatomical and physiological mechanisms. The development of sensitization consists of the immediate molecular and/or cellular effects that induce behavioral sensitization and are altered by drug actions in the somatodendritic regions of the A10/A9 dopamine neurons[14]. Changes in dopamine transmission within the nucleus accumbens seems to be responsible for the expression of sensitization, which refers to the long-term consequences of molecular and/or cellular effects that induce behavioral sensitization[14]. The present results demonstrated that pretreatment with *l*-THP not only inhibited the development, but also inhibited the expression of oxycodone.

It has been hypothesized that dopamine (DA) is one of the important neurotransmitters involved in locomotion. Measurement of spontaneous locomotor activity has been used to obtain preliminary information on the behavioral properties of drugs acting on dopaminergic system[15,16]. Morphine is known to activate ventral tegmental area dopamine neurons indirectly as a consequence of inhibiting non-dopamine, presumably γ-GABA, neurons of the ventral tegmental area, leading to increased dopamine release in the nucleus accumbens[17]. Direct infusions of morphine or μ-receptor-selective peptides into the ventral tegmental area elicit locomotion, which can be blocked by DA receptor antagonist administration into the nucleus accumbens. Following repeated administration of morphine, there is a marked increase in the induction of locomotor-stimulating effects of morphine, there is general agreement that the mesoaccumbens DA system is the anatornical locos for sensitized locomotion[18]. Kalivas and Stewart (1991) presented preliminary results showing that either systemic or intra-ventral tegmental area administration of sch23390 prevented sensitization to systemic morphine, when the combinations were given every other day for 8 d. They also suggested DA D_1 receptor involvement in the development of morphine sensitization[14]. In other studies, the blockade of the dopamine D_2 receptor by haloperidol significantly antagonized the effects of opioid on locomotor activity[19]. Thus, dopamine D_1 and D_2 receptors play important roles in the acceleration of opioid sensitization[20]. Although the mechanisms of action through which *l*-THP attenuates the psychomotor effect of oxycodone are not clear, one reason maybe relevant to dopamine D_1 and D_2 receptors, which are involved in oxycodone-induced hyperactivity and locomotor sensitivity. *l*-THP, which has affinity for D_1 as well as D_2 receptors, is a dopamine receptor antagonist[11]. *l*-THP may inhibit mesolimbic dopamine D_1 and D_2 receptors and attenuate psychomotor effects of oxycodone. Our recent studies also showed that oxycodone (2.5 mg/kg, sc) increased dopamine-concentrations of dialysates with microdialysis in the striatum of rat. *l*-THP (25 mg/kg, ig) *per se*, did not affect dopamine release, but pretreatment of rats with *l*-THP (25 mg/kg, ig) significantly inhibited oxycodone-induced increases in extraceullar dopamine concentrations [$F_{(3,18)}$=5.068, P<0.05] (Liu *et al*, unpublished data, 2004). These results indicate that the inhibiting locomotor sensitivity effect of *l*-THP might be connected with the DA system. *l*-THP could inhibit dopamine release in the mesolimbic system, induced by oxycodone, and then inhibit the development and expression of locomotor sensitization.

Another reason might be connected with L-type Ca^{2+} channels. Recent reports show that L-type Ca^{2+} channels may play an important role in the development of morphine behavioral sensitization. Co-administration with L-type Ca^{2+} channel blockers attenuates the development of morphine tolerance, dependence, and sensitization, suggesting that the L-type Ca^{2+} channel might play a role in morphine-induced neural and behavioral plasticity[21,22]. In contrast, L-type Ca^{2+} channel blockers have antidopaminergic properties[23]. L-type Ca^{2+} channel blockers such as nimodipine, nifedipine, and verapamil, dose-dependently antagonize apomorphine-induced yawning and penile erections in rats[24,25]. Nimodipine and verapamil inhibits locomotor activity induced by morphine[26]. Therefore, L-type Ca^{2+} channel blockers could attenuate morphine-induced hyperactivity through an antidopaminergic action. The inhibitory effect of *l*-THP on the development and expression of sensitivity of oxycodone might also be a result of the inhibitory effect of *l*-THP on L-type Ca^{2+} channel. Previous studies show that *l*-THP is also an L-type calcium antagonist. Using the patch-clamp technique, *l*-THP causes both tonic and use-dependent reduction of Ca^{2+} current in single ventricular myocytes of guinea pigs, has a moderate inhibitory effect on L-type Ca^{2+} current, and has inhibitory effects on $[Ca^{2+}]_i$ in myocytes by blocking voltage-dependent calcium channels similar to verapamil[27–29]. Therefore, the inhibitory effect of *l*-THP on L-type Ca^{2+} channel might be included in mechanisms of action through which *l*-THP attenuated locomotor sensitization to oxycodone.

In conclusion, the present data indicates that *l*-THP attenuated psychomotor effects of oxycodone, and the development and expression of locomotor sensitivity of oxycodone. The exact mechanisms of the inhibitory effect of *l*-THP on oxycodone sensitivity need further investigation.

Acknowledgement

We thank Prof Guo-zhang JIN for kindly providing *l*-THP.

References

1 Spyraki C, Fibinger HC, Phillips AG. Attenuation of heroin reward in rats by disruption of the mesolimbic dopamine system. Psychopharmacology 1983; 79: 278–83.
2 De Vries TJ, Schoffelmeer AN, Binnekade R, Mulder AH, Vanderschuren LJ. Drug-induced reinstatement of heroin- and cocaine-seeking behaviour following long-term extinction is associated with expression of behavioural sensitization. Eur J Neurosci 1998; 10: 3565–71.
3 Kalivas PW, Pierce RC, Cornish J, Sorg BA. A role for sensitization in craving and relapse in cocaine addiction. J Psychopharmacol 1998; 12: 49–53.
4 Robinson TE, Berridge KC. The neural basis of drug craving: an incentive-sensitization theory of drug addiction. Brain Res Brain Res Rev 1993; 18: 247–91.
5 Robinson TE, Berridge KC. The psychology and neurobiology of addiction: an incentive-sensitization view. Addiction 2000; 95: S91–117.
6 Kalso E, Vainio A. Morphine and oxycodone hydrochloride in the management of cancer pain. Clin Pharmacol Ther 1990; 47: 639–46.
7 Glare PA, Walsh TD. Dose-ranging study of oxycodone for chronic pain in advanced cancer. J Clin Oncol 1993, 11: 973–8.
8 Mather LE. Analgesic drug. In: Anaesthesia. Nimmo WS, Smith G, editors. Oxford: Blackwell Scientific Publications; 1989. p 73–104.
9 Fishbain DA, Goldberg M, Rosomoff RS, Rosomoff H. Atypical withdrawal syndrome (organic delusional syndrome) secondary to oxycodone detoxification. J Clin Psychopharmacol 1988; 8: 441–2.
10 Chen MX, Jin GZ. Role of *d*-tetrahydropalmatine in the inhibition of dopamine and serotonin uptake of synaptosomes in the rat brain. Chin J Physiol Sci 1996; 12: 25–30.
11 Jin GZ. (-)-Tetrahydropalmatine and its analogues as new dopamine receptor antagonists. TIPS 1987; 8: 81–2.
12 Ge XQ, Zhang HQ, Zhou HZ, Xu ZG, Bian CF. Experimental study of tetrahydroprotoberberines inhibiting morphine withdrawal syndromes. Chin J Drug Depend 1999; 8: 178–84.
13 Jin GZ. Discoveries in the voyage of *Corydalis* reseach. Shanghai: Shanghai Scientific & Technical Publishers; 2001. p351-2.
14 Kalivas PW, Stewart J. Dopamine transmission in the initiation and expression of drug- and stress-induced sensitization of motor activity. Brain Res Rev 1991; 16: 223–44.
15 Kalivas PW, Duffy P. Sensitization to repeated morphine injection in the rat: possible involvement of A 10 dopamine neurons. J Pharmacol Exp Ther 1987; 241: 204–12.
16 Vezina P, Stewart J. The effect of dopamine receptor blockade on the development of sensitization to the locomotor activating effects of amphetamine and morphine. Brain Res 1989; 499: 108–20.
17 Scheel-Kruger J. Dopamine-GABA interactions: evidence that GABA transmits, modulates and mediates dopaminergic functions in the basal ganglia and the limbic system. Acta Neuron Scand 1986; Suppl 107: 1–54.
18 Kalivas PW, Duffy P. Time course of extracellular dopamine and behavioral sensitization to cocaine. I. Dopamine axon terminals. J Neurosci 1993; 13: 266–75.
19 Magnus-Ellenbroek B, Havemann-Reinecke U. Morphine-induced hyperactivity in rats-a rebound effect? Naunyn Schmiedebergs Arch Pharmacol 1993; 347: 635–42.
20 Kuribara H. Modification of morphine sensitization by opiod and dopamine receptor antagonists: evaluation by studying ambulation in mice. Eur J Pharmacol 1995; 275: 251–8.
21 Martin MI, Lizasoain L, Leza JC. Calcium channel blockers: effects on morphine-induced hyperactivity. Psychopharmacol 1990; 101: 267–70.
22 Michaluk J, Karokewicz B, Antkiewicz-Michaluk L, Vetulani J. Effects of various Ca^{2+} channel antagonists on morphine analgesia, tolerance and dependence and on blood pressure in the rat. Eur J Pharmacol 1998; 352: 189–97.
23 Pucilowski O. Psychopharmacological properties of calcium channel inhibitors. Psychopharmacology 1992; 109: 12–29.
24 Argiolas A, Melis MR, Gessa GL. Calcium channel inhibitors prevent apomorphine- and oxytocin-induced penile erection and yawning in male rats. Eur J Pharmacol 1989; 166: 515–8.
25 Czyrak A, Mogilnicka E, Maj J. Some central pharmacological effects of the calcium channel antagonist flunarizine. J Neural Transm Gen Sect 1990; 83: 179–88.
26 Zhang Q, Li JX, Zheng JW, Lliu RK, Liang JH. L-type Ca^{2+} channel blockers inhibit the development but not the expression of sensitization to morphine in mice. Eur J Pharmacol 2003; 467: 145–50.
27 Huang K, Dai GZ, Li XH, Fan Q, Cheng L, Feng YB, *et al*. Blocking L-calcium current by *l*-tetrahydropalmatine in single ventricular myocyte of guinea pigs. Acta Pharmacol Sin 1999; 20: 907–11.
28 Li XT, Wang YL, Wang JX, Yang SJ. Effects of tetrahydroprotoberberines on cytosolic free calcium in cultured rat single myocardial cells. Acta Pharm Sin 1995; 30: 567–72.
29 Sun F, Li DX. Effects of *l*-tetrahydropalmatine on isolated rabbit arterial strips. Acta Pharmacol Sin 1989; 10: 30–3.

Acta Pharmacologica Sinica 2005 May; 26 (5): 539–545

Full-length article

Action of aluminum on high voltage-dependent calcium current and its modulation by ginkgolide B

Lei CHEN, Chang-jin LIU[1], Ming TANG, Ai LI, Xin-wu HU, Yi-mei DU, Jing-jing SHEN, Yong-li LU, Jurgen HESCHLER[2]

Department of Physiology, Tongji Medical College, Huazhong University of Science and Technology, Wuhan 430030, China;[2]Institute of Neurophysiology, University of Cologne, Cologne D-50931, Germany

Key words

hippocampus; aluminum; voltage-dependent calcium channels; ginkgolide B; patch-clamp technique

[1] Correspondence to Prof Chang-jin LIU.
Phn 86-27-8369-1545.
Fax 86-27-8369-2608.
E-mail tjchangjinliu@hotmail.com

Received 2004-09-20
Accepted 2004-12-09

doi: 10.1111/j.1745-7254.2005.00073.x

Abstract

Aim: To investigate the effect of aluminum (Al) on high voltage-dependent calcium current (I_{HVA}) and its modulation by ginkgolide B (Gin B). **Methods:** The whole-cell, patch-clamp technique was used to record I_{HVA} from acutely isolated hippocampal CA1 pyramydal neurons in rats. **Results:** Al 0.1 mmol/L (low concentration) reduced I_{HVA}; Al 0.75 and 1.0 mmol/L (high concentrations) increased I_{HVA}, and Al decreased and increased I_{HVA} at intermediate concentrations of 0.25 and 0.5 mmol/L. The increase of I_{HVA} by Al 1.0 mmol/L was enhanced by the adenylyl cyclase (AC) agonist forskolin and was partly abolished by the cyclic adenosine monophosphate (cAMP)-dependent protein kinase A (PKA) antagonist H-89, whereas the decrease observed with Al 0.1 mmol/L was neither reversed by forskolin nor affected by H-89. Gin B had no effect on I_{HVA} in normal neurons, but canceled the increase in I_{HVA} by 1.0 mmol/L Al. **Conclusion:** The results indicate that the mechanism of Al affecting I_{HVA} differs at different concentrations, and this may be attributed to its complex actions. Gin B could prevent neurons from injury by inhibiting calcium influx.

Introduction

The accumulation of aluminum (Al) within the body can result in many mental diseases. For example, Al is concentrated in the neurofibrillary tangles and senile plaques of patients with Alzheimer disease (AD)[1]. Al can be attributed to several neurological disorders, such as dialysis syndrome and Guamanian amylotrophic lateral sclerosis-Parkinson's dementia[2]. A number of studies have implicated that Al has no effect on long-term potentiation (LTP)[3]. However, more and more studies have shown that Al can impair LTP[4] and evoke potential in the hippocampus[5]. Studies have also shown that Al affects amino acid neurotransmitters in the hippocampus and enhances glutamate-mediated excitotoxicity, which may be one of the causes of its toxicity[6]. Reports about its mechanism involving ion channels are few and controversial[7–9].

Extracts from leaves of *Ginkgo biloba* (*EG*b) and one of its constituents ginkgolide B have been demonstrated to protect cardiomyocytes and cultured neurons from the injury induced by hypoxia, ischemia, and the neurotoxicity induced by Aβ[10–12]. However, it is not known whether the mechanism of this protection of neurons involves ion channels, such as voltage-dependent calcium channels (VDCC).

The present study investigated the actions of Al on I_{HVA} and its modulation by Gin B to examine the neurotoxic mechanisms of Al and the neuroprotective mechanisms of Gin B.

Materials and methods

Reagents Pronase E, forskolin, TEA-Cl, H-89, and HEPES were purchased from Sigma Chemical Company (St Louis, MO, USA). H-89 was dissolved in pipette solution and stored at -20°C. After the whole-cell configuration was constructed, H-89 was dialyzed into the cell through the pipette. Ginkgolide B (BN52021, purity 98.2%) was from the Wuhan Institute of Botany, Chinese Academy of Sciences (Wuhan, China). $AlCl_3$ was from Jinghua Chemical Company (Beijing, China). The remaining chemicals, unless otherwise

stated, were all purchased from the Shanghai Chemical Reagent Plant (Shanghai, China).

Cell isolation Animals were provided by the experimental animal center of Tongji Medical College (Grade II, Certificate No 19-050). Hippocampal CA1 neurons were acutely isolated by enzymatic digestion and mechanical dispersion from 7 to 10-d-old Wistar rats as described in a previous study[13], with a few modifications. After the animals were killed, the hippocampi were removed and coronary slices were cut at a thickness of approximately 500 μm in ice-cold oxygenated incubation solution within 30 s. The slices were incubated in an external solution saturated with pure O_2 at 32 °C for 1 h, treated with Pronase E 6.0–7.0 kU/L for 25 min in the oxygenated external solution at 32 °C. After digestion the slices were washed six times with external solution and incubated in the same solution saturated with pure O_2 at room temperature. CA1 regions were dissected out and transferred into centrifuge tubes. Hippocampal neurons were dispersed by gentle pipetting using fine glass tubes. After 5 min, the cell suspension was transferred into the recording chamber with a glass coverslip filled with external solution. The cells were left for approximately 30 min before beginning the experiments.

Electrophysiology The cells were placed in a recording chamber mounted on the stage of an inverted microscope (Carl Zeiss, Germany) and superfused with extra cellular solution at room temperature (21–22 °C). Extracellular solution for recording I_{HVA} was composed of (mmol/L): NaCl 150, KCl 5, $MgCl_2$ 1.1, $CaCl_2$ 2.5, HEPES 10, glucose 10, TTX 0.001, and the pH was adjusted to 7.4 with NaOH. Extracellular application of drugs was carried out by perfusing cells with extracellular solution containing the drugs.

Whole-cell patch experiments were carried out using an Axopatch 200A amplifier (Axon Instruments, Foster City, CA, USA) driven by ISO2 software (MFK, Frankfurt, Germany). In the voltage-clamp experiments, the cells were stepped from -80 mV (50 ms) to -40 mV (200 ms), and then depolarized to 0 mV (200 ms) after briefly hyperpolarizing the membrane potential for 10 ms to -45 mV. The I_{HVA} was activated by the second depolarization. The protocol was applied every 5 s. For analysis of the current-voltage (*I–V*) relationship, voltage steps (200 ms) were used to depolarize from -40 mV to +40 mV in 10 mV increments. Glass pipettes were used with a resistance of about 3–5 MΩ when filled with a pipette solution composed of (mmol/L): CsCl 140, $MgCl_2$ 2, Mg-ATP 4, TEA-Cl 2, HEPES 10, egtazic acid 11, and the pH was adjusted to 7.2 with CsOH.

Data were acquired at a sampling rate of 10 kHz, filtered at 2 kHz, stored on hard disk and analyzed off-line using the ISO2 analysis software package (MFK, Frankfurt, Germany).

Data analysis The amplitude of I_{HVA} was calculated as the difference between the instantaneous current at the beginning of the experiment and the maximum activating current. Currents were normalized to membrane capacitance to calculate current densities ($pA \cdot pF^{-1}$). Cell membrane capacitance (Cm) was determined online using the ISO2 software program. The activation rate constant and inactivation rate constant were obtained using the ISO2 analysis software. Graphical and statistical data analyses were carried out using Sigmaplot 2001 (SPSS, Chicago, IL, USA) and Origin 6.0 (Microcal Software, Inc, Northampton, MA01060, USA). Data were presented as mean±SEM where appropriate. Statistical analysis were carried out using Student's paired and unpaired *t*-tests and values of $P<0.05$ were considered statistically significant.

Results

Action of Al on I_{HVA} Bath application of $AlCl_3$ 0.01 mmol/L had no effect on I_{HVA}. The current densities before and after $AlCl_3$ application were 18.5±2.4 $pA \cdot pF^{-1}$ and 18.5±2.2 $pA \cdot pF^{-1}$, respectively (n=11, $P>0.05$) (Figure 1A).

Bath application of $AlCl_3$ 0.1 mmol/L caused a reduction in I_{HVA} from 17.7±1.6 $pA \cdot pF^{-1}$ to 12.7±1.4 $pA \cdot pF^{-1}$ (n=27, $P<0.01$), that is, a reduction of 30.5%± 4.1%. The reduction of I_{HVA} by $AlCl_3$ did not recover after the $AlCl_3$ was washed out (Figure 1B).

$AlCl_3$ 0.25 mmol/L caused a reduction in I_{HVA} in 80% (8/15) of the neurons, and an increase in 20% (4/15) of the neurons. $AlCl_3$ 0.50 mmol/L caused a reduction in I_{HVA} in 50% (7/14) of the neurons, and an increase in I_{HVA} in 50% (7/14) of the neurons. In contrast, $AlCl_3$ 0.75 mmol/L increased I_{HVA} by 30.8%±5.2% (n=15, $P<0.01$) in all neurons tested (from 17.8± 1.8 $pA \cdot pF^{-1}$ to 23.0±2.5 $pA \cdot pF^{-1}$). $AlCl_3$ 1.0 mmol/L increased I_{HVA} by 37.3%±7.8% (from 19.6±3.1 $pA \cdot pF^{-1}$ to 26.2±4.3 $pA \cdot pF^{-1}$) (n=21, $P<0.01$). I_{HVA} increased by $AlCl_3$ was irreversible after $AlCl_3$ was washed out (Figure 1C).

At both low and high concentrations, $AlCl_3$ inhibited or increased the maximum amplitude of I_{HVA}, but had no effect on the activation threshold potential of I_{HVA} in the *I–V* relationship (Figure 2A, B). The *G-V* curve was unaffected by $AlCl_3$ 0.1 mmol/L (n=5, $P>0.05$) or $AlCl_3$ 1.0 mmol/L (n=5, $P>0.05$) (control: $V_{0.5}$=-12.8 mV±4.4 mV, k=5.5±3.8; $AlCl_3$ 0.1 mmol/L: $V_{0.5}$=-12.0 mV±4.5 mV, k=5.0±4.0; $AlCl_3$ 1.0 mmol/L: $V_{0.5}$=-13.6 mV±5.3 mV, k=5.2±4.4) (Figure 2C). In addition, AlCl3 had no effect on the activation rate constants at concentrations of 0.1 mmol/L (n=8, $P>0.05$) or 1.0 mmol/L (n=9, $P>0.05$).

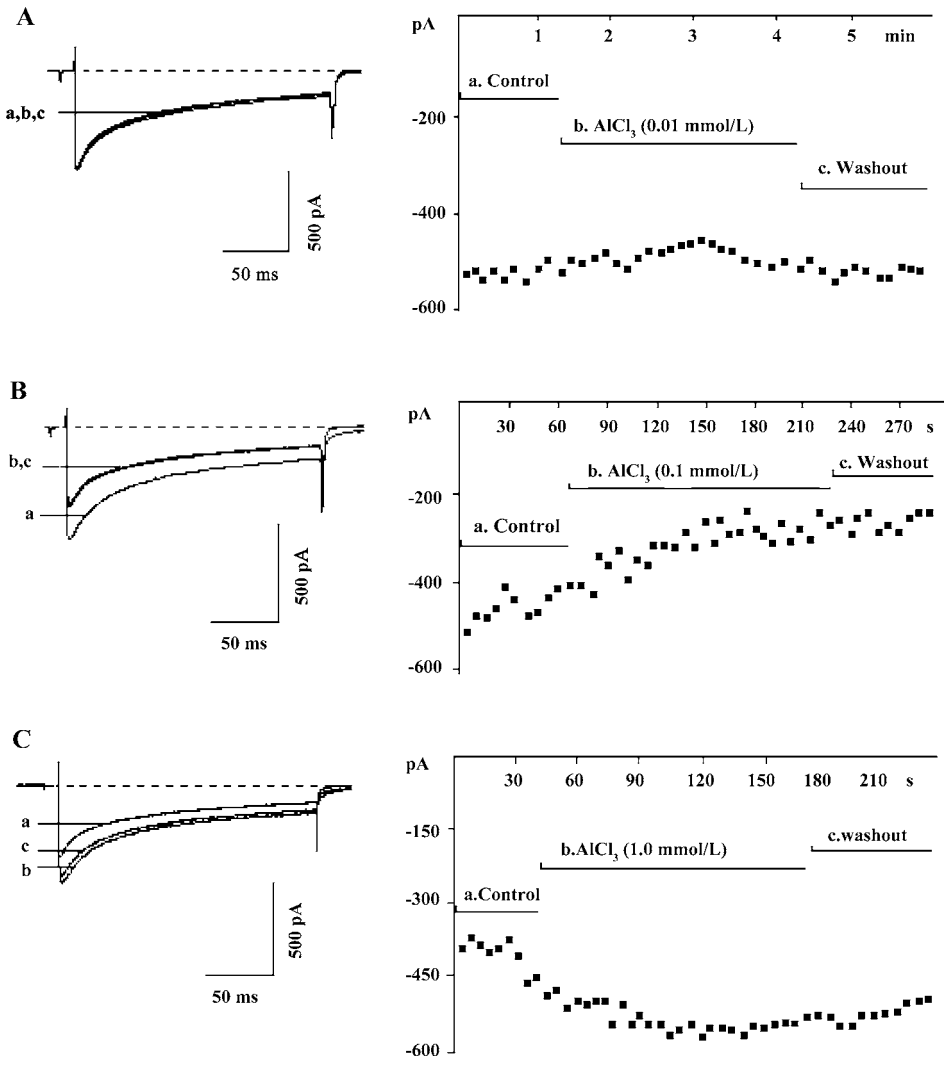

Figure 1. Effect of $AlCl_3$ on I_{HVA} at concentrations of 0.01, 0.1 and 1.0 mmol/L (A, B, C, respectively). I_{HVA} current was recorded at different concentrations of $AlCl_3$ (left). (a) Before the application of $AlCl_3$; (b) Application of $AlCl_3$; (c) washout. The time course of the experiment corresponding to left-hand panels (right).

To gain a better understanding of the action of Al on I_{HVA}, we explored its action on the steady-state inactivation curve of I_{HVA}. $AlCl_3$ shifted the curve to a depolarizing voltage at 1.0 mmol/L (n=5, P<0.05), whereas it shifted the inactivation curve to a hyperpolarizing voltage at 0.1 mmol/L (n=5, P< 0.05). (Control: $V_{0.5}$=-35.4±3.3 mV, k=-14.3±2.5; 0.1 mmol/L $AlCl_3$: $V_{0.5}$=-41.1±2.7 mV, k=-9.2±2.0; 1.0 mmol/L $AlCl_3$: $V_{0.5}$= -29.8±6.9 mV, k=-10.8±2.4). $AlCl_3$ 0.1 mmol/L decreased the inactivation rate constant by 27.3%±6.3% (n=5, P<0.01), whereas 1.0 mmol/L $AlCl_3$ increased the inactivation rate constant by 44.7%±3.4% (n=7, P<0.01) (Figure 3).

Effect of Gin B on I_{HVA} in hippocampal neurons Gin B at doses of 0.01–20 μmol/L had no effect on I_{HVA} in normal hippocampal neurons (P>0.05) (Table 1). Gin B inhibited the increase of I_{HVA} by $AlCl_3$ 1.0 mmol/L. After a steady increase in the action of $AlCl_3$, Gin B at concentrations of 0.01 μmol/L,

Table 1. Effect of Gin B at different concentrations (0.01, 0.1, 1.0, 10, and 20 μmol/L) on the amplitude of I_{HVA}. n=6. Mean±SD.

Gin B/μmol·L^{-1}	I_{HVA}/pA·pF^{-1}	
	Control	Gin B
0.01	19.6±2.9	19.1±3.9
0.1	19.1±3.2	19.6±2.2
1.0	19.4±1.9	18.8±1.6
10	20.0±1.2	18.7±0.8
20	17.2±0.9	17.2±1.3

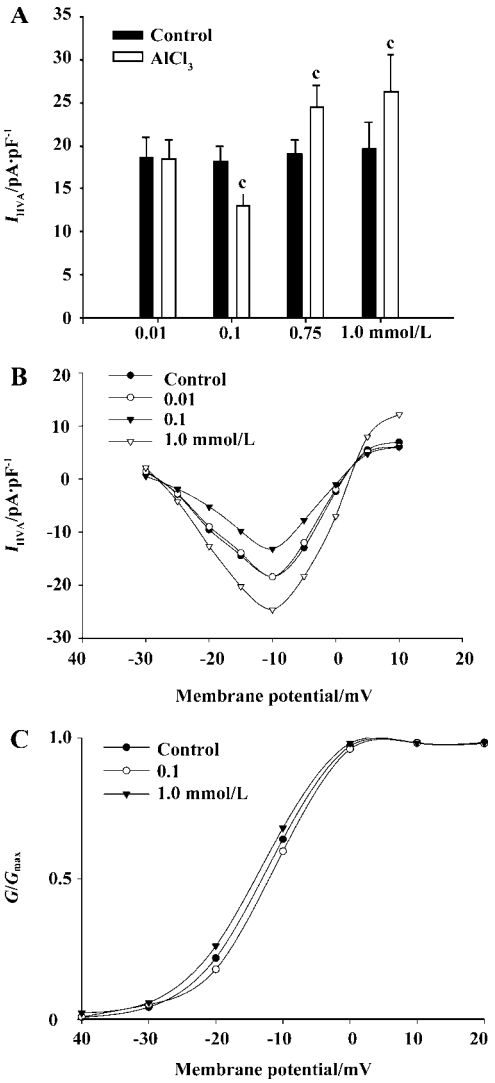

Figure 2. (A) Effect of Al at different concentrations on the amplitude of I_{HVA}. $^cP<0.01$ *vs* control. (B) Effect of Al at different concentrations on the current-voltage (*I–V*) relationship of HVA. (C) Effect of Al at different concentrations on the steady-state conductance (G) and voltage (V) curve. Data were transformed from the *I–V* data shown in B. *G–V* parameters were fitted to the Boltzman equation: $G/G_{max}=1/[1+\exp(V_m-V_{1/2})/k]$, where G_{max} is the maximum conductance, $V_{1/2}$ is the membrane potential at which 50% of activation was observed, and *k* is the slop of the function.

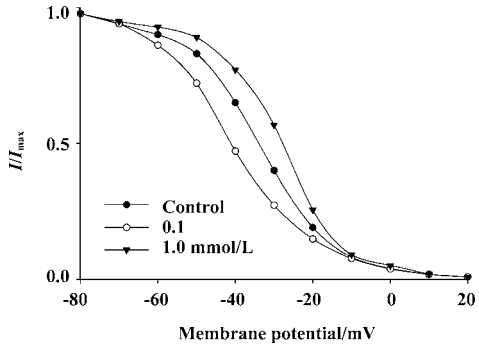

Figure 3. Effects of Al at different concentrations on the steady-state inactivation curve. I_{HVA} was measured using a 200 ms test pulse to 10 mV by 3 s conditioning prepulse ranging from -80 mV to +20 mV, with 10 mV increments. Data were fitted to the Boltzman equation: $I/I_{max}=1/[1+\exp(V_{1/2}-V_m)/k]$, where $V_{1/2}$ is the membrane potential at which 50% of activation was observed, and *k* is the slop of the function.

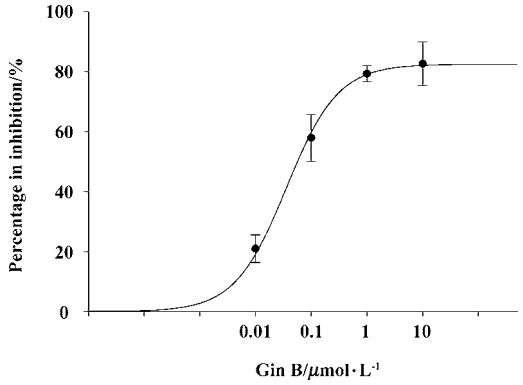

Figure 4. Concentration-response relationship for the inhibition of Gin B on the action of $AlCl_3$ (1.0 mmol/L) in hippocampal neurons. In the concentration-response curve for Gin B each point represents the mean±SEM of the percentage inhibition of Gin B from six to seven cells. The curve shown is the fit of the data to the logistic equation $Y=Y_{max}/[1+(IC_{50}/C)^n]$, where *C* is the concentration of Gin B, *Y* is the fraction of the maximal inhibition response value, *n* is the Hill coefficient, and IC_{50} is the concentration of Gin B producing 50% inhibition on the increase in I_{HVA} by 1.0 mmol/L Al.

0.1μmol/L, 1.0 μmol/L, and 10 μmol/L reduced I_{HVA} by 21.0%±4.6% (*n*=7, *P*<0.05), 57.9%±7.8% (*n*=6, *P*<0.01), 79.3%±2.7% (*n*=6, *P*<0.01), and 82.4%±7.3% (*n*=6, *P*<0.05), respectively. The concentration producing 50% inhibition by Gin B of Al 1.0 mmol/L is 0.0359 μmol/L±0.0038 μmol/L (Figure 4).

Co-superfusion $AlCl_3$ 0.1 mmol/L plus Gin B 10 μmol/L was applied in the same way as $AlCl_3$ 1.0 mmol/L. For all tested neurons (*n*=15), there was no change in I_{HVA} in 53.3% of the neurons and a slight increase in I_{HVA} in the remaining neurons (*P*>0.05). This result indicated that Gin B had no effect on the action of Al 0.1 mmol/L .

Mechanism of action of high concentrations of Al on I_{HVA} Application of forskolin 10 μmol/L (an agonist of adenylyl cyclase) increased I_{HVA} by 30.8%±7.5% (*n*=14, *P*< 0.05). Bath application of forskolin 10 μmol/L in combination with Al 1.0 mmol/L increased I_{HVA} by 68.3%±8.7% (*n*=31, *P*< 0.05) (Figure 5A).

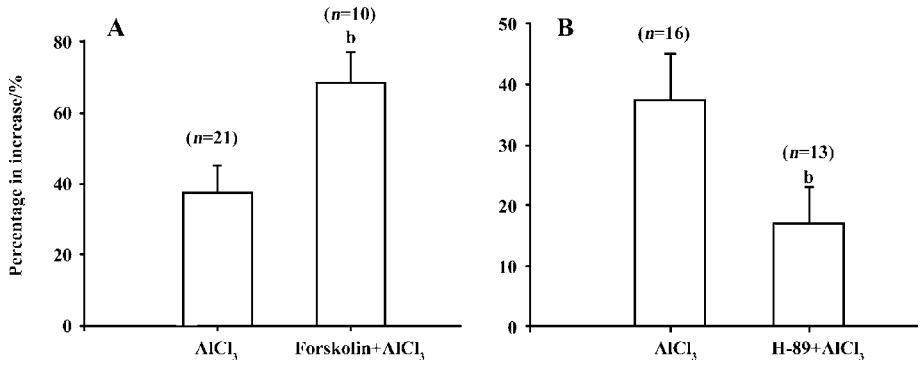

Figure 5. (A) Percentage of increased action by $AlCl_3$ 1.0 mmol/L and $AlCl_3$ co-superfusion with forskolin. (B) Percentage of increased action by $AlCl_3$ 1.0 mmol/L in the presence and the absence of H-89. $^bP<0.05$ *vs* $AlCl_3$ 1.0 mmol/L.

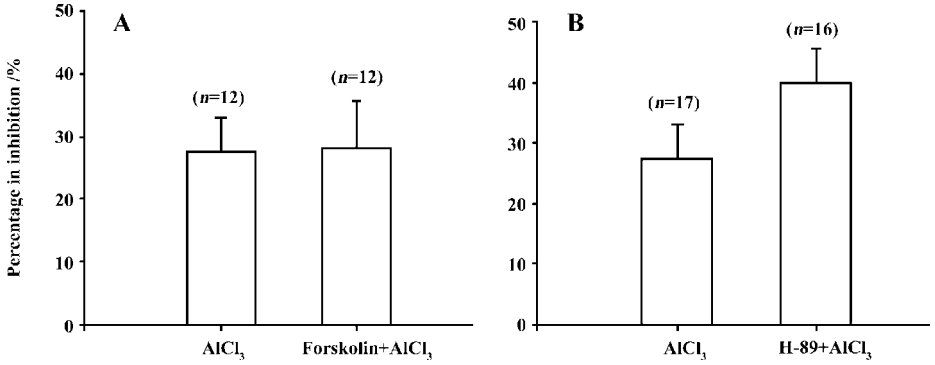

Figure 6. (A) Percentage of inhibitory action by $AlCl_3$ 0.1 mmol/L (27.5%±5.6%) and $AlCl_3$ co-superfusion with forskolin (28.2%± 7.3%). (B) Percentage of inhibitory action by $AlCl_3$ 0.1 mmol/L in the presence (39.9%±5.7%) and absence of H-89 (27.5%±5.6%).

H-89 is a selective antagonist of PKA. In this study, adding H-89 in the pipette solution reduced the amplitude of I_{HVA} by 42.0%±4.1% (from 20.2±3.3 pA·pF^{-1} to 13.9±3.1 pA·pF^{-1}, n=6, P<0.01) within approximately 80–100 s. $AlCl_3$ 1.0 mmol/L was bath applied in the presence of H-89 (10 μmol/L) in the pipette solution. Aluminum increased I_{HVA} by 17.2%±5.8% (n=10, P<0.05). Compared with the effect of Al 1.0 mmol/L on I_{HVA} without H-89 (n=29, P<0.05), the reduction in I_{HVA} in the presence of H-89 was significant, indicating that H-89 could, in part, abolish the increase in I_{HVA} by Al at high concentrations (Figure 5B).

Mechanism of action of low concentrations of Al on I_{HVA} To investigate the mechanism by which Al inhibited I_{HVA} at low concentrations, $AlCl_3$ 0.1 mmol/L was applied first and I_{HVA} was reduced to 12.9±1.1 pA·pF^{-1} from 18.5±1.7 pA·pF^{-1} (n=12, P<0.01). After the current was stable, forskolin 10 μmol/L and $AlCl_3$ 0.1 mmol/L were co-applied. Forskolin did not cancel the inhibition of I_{HVA} by 0.1 mmol/L $AlCl_3$. The I_{HVA} after forskolin application was 12.5±0.9 pA·pF^{-1} (n=12, P>0.05) (Figure 6A).

In the presence of H-89 (10 μmol/L), I_{HVA} was reduced to 13.1±2.5 pA·pF^{-1} from 20.1±4.2 pA·pF^{-1} (n=8, P<0.01). After the current was stable, $AlCl_3$ 0.1 mmol/L was bath applied, and I_{HVA} was reduced to 12.5±2.5 pA·pF^{-1}. There was no difference in the percentage inhibition with and without H-89 application (n=33, P>0.05) (Figure 6B).

Discussion

VDCC in hippocampal neurons are divided into high voltage-dependent channels (HVA) and low voltage-dependent channels (LVA) according to the difference in activation threshold. In the present study we demonstrated that the effect of Al on I_{HVA} differed at different concentrations. Al reduced the amplitude of I_{HVA} irreversibly at low concentrations (0.1 mmol/L). This result supports a previous report on dorsal root ganglion (DRG) neurons[7]. However, Al inhibited and enhanced I_{HVA} as Al concentrations increased

(between 0.25 mmol/L and 0.50 mmol/L), and the percentage of enhanced I_{HVA} by Al in the neurons examined increased with increased Al concentrations. When 0.75 mmol/L and 1.0 mmol/L Al were bath applied, the amplitude of I_{HVA} in all neurons tested increased.

The toxic effect of Al in humans is chronic and accumulative and leads to degradation and apoptosis of cells[14]. Acute application of Al inhibits LTP on hippocampal slices of rats as well as *in vivo* by intracerebroventricular injection. Studies have shown that a series of molecular mechanisms involved in synaptic plasticity, including protein phosphorylation, gene expression, and neurotransmitter release, were regulated by VDCC[15]. LTP induced in different areas of the hippocampus has an intimate relationship with VDCC[16]. The inhibition of I_{HVA} by Al at low concentrations could lead to a reduction in calcium influx, resulting in the reduced release of some neurotransmitters, which might explain impaired LTP in this concentration range. Aluminum increased the amplitude of I_{HVA} at high concentrations and, thus, led to increased calcium influx, resulting in a series of pathological changes, which could cause impairment of LTP and neuronal damage.

In our study, the actions of Al on I_{HVA} differed at different concentrations; thus, it is possible that the mechanism of action is different at different Al concentrations. Protein phosphorylation modulates the function of VDCC and the AC-cAMP-PKA system plays a key role[17]. Thus, forskolin and H-89 were used to investigate whether the action of Al on I_{HVA} is involved in this mechanism. H-89 markedly abolished the increase of I_{HVA} by Al 1.0 mmol/L. Co-superfusion with forskolin plus Al at high concentrations caused more Ca^{2+} influx. Together these results indicate that an Al-induced increase in I_{HVA} possibly results from activating cAMP-PKA. However, H-89 did not reverse the action of $AlCl_3$ totally, suggesting that other mechanisms must contribute to its action on I_{HVA} at high concentrations.

Platt[7] reported that the interactions of aluminum with two different binding sites (within and outside) of calcium channels might contribute to the reduction of VDCCs on DRG neurons. Al has been reported to inhibit Mg-dependent enzymes and to interact with phosphorylation sites[18]. In the present study, the co-application of forskolin and Al did not cancel the reduction and the action of 0.1 mmol/L Al was not affected by H-89, indicating that the mechanism by which Al reduces I_{HVA} at low concentrations might not be involved in the cAMP-PKA system. In addition, Gin B effectively canceled the increase of I_{HVA} by Al at high concentrations, but had almost no effect on the reduction of I_{HVA} by Al at low concentrations, further suggesting that the action of Al at low concentrations on I_{HVA} occurs via a different mechanism. The mechanism by which Al reduced I_{HVA} requires further examination. At intermediate concentration ranges, Al both reduced and enhanced I_{HVA}. The mechanism is not known, but may result from a difference in neurons or from the concentration of Al itself, which indicated that this concentration might be the point at which I_{HVA} moves from being inhibited to enhanced and this might be the reason for its complexity and diversity.

*EG*b is a complex mixture containing 24% flavonoid glycosides, 6% terpene lactones, such as ginkgolide A, B, C, J and bilobalide, a number of organic acids, and various other constituents. Studies have shown that Gin B has many pharmacological effects (ie preventing atherosclerosis, diminishing coagulation of platelets, ameliorating the circulation system) and has a distinctively protective effect on the central nerve and cardiovascular systems. Clinical studies have shown that oral administration of *EG*b in human patients with dementia is effective[19]. Gin B can protect cardiocmyocytes and cultured neurons from injury by hypoxia and ischemia through many pathways, for example, by acting as an anti-oxidant[20], acting as the antagonist of platelet-activating factor[21] and by inhibiting NO-stimulated PKC activity[22]. Furthermore, Gin B has been shown to prevent neurons from glutamate excitoxicity through a reduction in $[Ca^{2+}]_i$[23] and to have an effect on the glycine-gated chloride channel[24]. The present study provides the first evidence that Gin B can cancel the increase of I_{HVA} by Al, and that Gin B can protect neurons by inhibiting I_{HVA}, providing a possible mechanism for clinical treatment in a number of nervous system diseases. The detailed mechanism by which Gin B inhibits I_{HVA} remains to be investigated.

References

1 Tokutake S, Nagase H, Morisaki S, Oyanagi S. Aluminium detected in senile plaques and neurofibrillary tangles is contained in lipofuscin granules with silicon, probably as aluminosilicate. Neurosci Lett 1995; 185: 99–102.

2 Wisniewski HM. Aluminum, tau protein, and Alzheimer's disease. Lancet 1994; 344: 204–5.

3 Gilbert ME, Shafer TJ. *In vitro* exposure to aluminum does not alter long-term potentiation or glutamate release in rat hippocampal slices. Neurotoxicol Teratol 1996; 18: 175–80.

4 Platt B, Carpenter DO, Busselberg D, Reymann KG, Riedel G. Aluminum impairs hippocampal long-term potentiation in rats *in vitro* and *in vivo*. Exp Neurol 1995; 134: 73–86.

5 Zou BD, Xiao HM, Zhang ZD, Li A. Effect of aluminum on evoked potential on hippocampal CA3 area in rats. J Tongji Med Univ 1998; 27: 15–18.

6 Matyja E. Aluminum enhances glutamate-mediated neurotoxicity in organotypic cultures of rat hippocampus. Folia Neuropathol

2000; 38: 47–53.
7 Platt B, Büsselberg D. Actions of aluminium on voltage-activated calcium channel currents. Cell Mol Neurobiol 1994; 14: 819–29.
8 Trombley, PQ. Selective modulation of $GABA_A$ receptors by aluminum. J Neurophysiol 1998; 80: 755–61.
9 Platt B, Haas H, Büsselberg D. Aluminum reduces glutamate-activated currents of rat hippocampal neurons. Neuroreport 1994; 5: 2329–32.
10 Zhang ZX, Qi XY, Xu YQ. Effect of ginkgolide B on L-type calcium current and cytosolic $[Ca^{2+}]_i$ in guinea pig ischemic ventricular myocytes. Acta Physiol Sin 2003; 55: 24–8.
11 Bastianetto S, Quirion R. EGb 761 is a neuroprotective agent against beta-amyloid toxicity. Cell Mol Biol 2002; 48: 693–7.
12 Wu XF, Wang QJ, Lou FC. Protective effect of *Ginkgolides* on rat focal brain ischemia. J China Pharm Univ 2001; 32: 141–5.
13 Xu CQ, Zhang ZM, Xia ZL, Wu CH, Zhou PA. Acute isolation and identification of CA1 pyramidal neurons in hippocampus of rats. Chin J Appl Physiol 1999; 15: 189–91.
14 Savory J, Herman MM, Ghribi O. Intracellular mechanisms underlying aluminum-induced apoptosis in rabbit brain. J Inorg Biochem 2003; 97: 151–4.
15 Deisseroth K, Heist EK, Tsien RW. Translocation of calmodulin to the nucleus supports CREB phosphorylation in hippocampal neurons. Nature 1998; 392: 198–202.
16 Morgan SL, Teyler TJ. VDCCs and NMDARs underline two forms of LTP in CA1 hippocampus *in vivo*. J Neurophysiol 1999; 82: 736–40.
17 Kavalali ET, Hwang KS, Plummer MR. cAMP-dependent enhancement of dihydropyridine-sensitive calcium channel availability in hippocampal neurons. J Neurosci 1997; 17: 5334–48.
18 Macdonald TL, Martin RB. Aluminum ion in biological systems. Trends Biochem Sci 1988; 13: 15–19.
19 Le Bars PL, Katz MM, Berman N, Itil TM, Freedman AM, Schatzberg AF. A placebo-controlled, doubled-blind, randomized trial of an extract of *Ginkgo biloba* for dementia. J Am Med Assoc 1997; 278: 1327–32.
20 Lenoir M, Pedruzzi E, Rais S, Drieu K, Perianin A. Sensitization of human neutrophil defense activities through activation of platelet-activating factor receptors by ginkgolide B, a bioactive component of the *Ginkgo biloba* extract EGB 761. Biochem Pharmacol 2002; 63: 1241–9.
21 Bastianetto S, Zheng WH, Quirion R. The *Ginkgo biloba* extract (EGb 761) protects and rescues hippocampal cells against nitric oxide-induced toxicity: involvement of its flavonoid constituents and protein kinase C. J Neurochem 2000; 74: 2268–77.
22 Zhu L, Wu J, Liao H, Gao J, Zhao XN, Zhang ZX. Antagonistic effects of extract from leaves of *Ginkgo biloba* on glutamate neurotoxicity. Acta Pharmacol Sin 1997; 18: 344–7.
23 Kondratskaya EL, Lishko PV, Chatterjee SS, Krishtal OA. BN52021, a platelet activating factor antagonist, is a selective blocker of glycine-gated chloride channel. Neurochem Int 2002; 40: 647–53.
24 Chatterjee SS, Kondratskaya EL, Krishtal OA. Structure-activity studies with *Ginkgo biloba* extract constituents as receptor-gated chloride channel blockers and modulators. Pharmacopsychiatry 2003; 36: S68–77.

Acta Pharmacologica Sinica 2005 May; 26 (5): 546–550

Full-length article

Remifentanil mimics cardioprotective effect of ischemic preconditioning via protein kinase C activation in open chest of rats

Ye ZHANG[1,3], Zhi-wu CHEN[2,5], Michael G IRWIN[3], Tak-ming WONG[4]

[1]Department of Anesthesiology, the Affiliated Hospital of Anhui Medical University, Hefei 230022; [2]Department of Pharmacology, Anhui Medical University, Hefei 230022; [3]Department of Anesthesiology; [4]Department of Physiology, the University of Hong Kong, Hong Kong, China

Key words

remifentanil; myocardial ischemia preconditioning; myocardial reperfusion injury; protein kinase C; chelerythrine; GF109203X

[5] Correspondence to Prof Zhi-wu CHEN.
Phn 86-551-516-1133.
Fax 86-551-292-2026.
E-mail wuzhichen@mail.hf.ah.cn

Received 2004-08-29
Accepted 2004-12-08

doi: 10.1111/j.1745-7254.2005.00100.x

Abstract

Aim: To examine whether the protective effect of remifentanil preconditioning (RPC) on postischemic hearts is mediated by protein kinase (PKC) activation in comparison with ischemic preconditioning (IPC). **Methods:** Male Sprague-Dawley rats were anesthetized and their chests were opened. The experiment was performed with chelerythrine (CHE, 2 mg/kg), GF109203X (0.05 mg/kg) protein kinase C (PKC) inhibitors administered before RPC (remifentanil 6 $\mu g \cdot kg^{-1} \cdot min^{-1} \times 3$ cycle) or IPC, respectively. Infarct size (IS), as a percentage of the area at risk (AAR), was determined by triphenyltetrazolium staining. **Results:** In groups subjected to IPC and RPC the IS/AAR were significantly reduced (IS/AAR from 52.7%±5.5% to 12.9%±3.4%, $P<0.01$ *vs* CON and 16.2%±6.4%, $P<0.01$ *vs* CON), respectively. CHE and GF, both PKC inhibitors, administered 5 min before RPC or IPC completely abolished the cardioprotective effect of RPC (IS/AAR: CHE+RPC 51.2%±5.0%, GF+RPC 53.6%±6.1%, $P>0.05$ *vs* CON) or IPC (CHE+IPC 53.7%±4.3%, GF+IPC 54.1%±6.2%, $P>0.05$ *vs* CON). The difference was not significant in any of the hemodynamic parameters between control and treatment groups during ischemia and reperfusion. **Conclusion:** Remifentanil confers myocardial protection against ischemic injury through a mechanism that is similar to IPC and involves PKC activation.

Introduction

Several studies found opioids preconditioning had a protective effect on the postischemic heart[1–5]. Remifentanil has been demonstrated to mimic the cardioprotective effect of ischemic preconditioning (IPC) in anesthetized open-chest rats, which reduced infarct size (IS) dose-dependently[5].

Remifentanil is an ultra-short-acting phenylpiperidine opioid analgesic agent, which is rapidly metabolized by nonspecific blood and tissue esterases[6]. It has an analgesic potency similar to fentanyl and 100 times greater than morphine[7]; the opioids that have been most extensively studied in cardioprotection. The effect of remifentanil preconditioning (RPC) was abolished by blockade of any one of the μ-, δ-, and κ-opioid receptors (OR). This means all three OR are involved in cardioprotection by RPC[5].

Opioid-induced cardioprotection and IPC seem to share a common pathway[8,9]. Several studies have demonstrated that fentanyl and morphine significantly reduced IS, and that this effect was blocked by the protein kinase C (PKC) inhibitor chelerythrine (CHE)[4,10]. However, no study has examined the role of PKC in the protection conferred by remifentanil-induced preconditioning.

Therefore, we decided to examine whether the protection effect of RPC on postischemic hearts was mediated by PKC in comparison with IPC.

Materials and methods

Surgical preparation Our preparation and measurements have been described previously in detail[5]. Briefly, male Sprague-Dawley rats weighing 300 to 350 g were used. The rats were anesthetized by intraperitoneal administration of pentobarbitone (50 mg/kg bodyweight) and maintained by

repeat doses of 25 mg/kg every 60–90 min. All of the animals underwent tracheotomy and endotracheal intubation. Mechanical ventilation was provided with a Harvard Apparatus Rodent Respirator (Boston, MA, USA) and the rats were ventilated with room air at 60 to 70 breaths per min. Body temperature was monitored and maintained at 37±1 °C (mean±SD) using a heating pad. The carotid artery was cannulated to measure mean blood pressure (MBP) via a pressure transducer, and a Lead-II electrocardiogram, via subcutaneous stainless steel electrodes, monitored heart rate (HR). These were connected to a PowerLab monitoring system (ML750 PowerLab/4sp with MLT0380 Reusable BP Transducer, AD Instruments, USA). The right jugular vein was cannulated to infuse saline or drugs. A left thoracotomy was performed to expose the heart at the fifth intercostal space. After removing the pericardium, a 6-0 Prolene loop, along with a snare occluder, was placed at the origin of the left coronary artery (LCA). Regional ischemia was achieved by pulling the snare and securing the threads with a mosquito hemostat. Ischemia was confirmed by a substantial fall in left ventricular pressure, ECG changes, and cardiac cyanosis. After surgical preparation, the rat was allowed to stabilize for 15 min.

Study groups and experimental protocol Rats were randomly assigned to one of nine groups. All animals received 30 min of occlusion of the left coronary artery followed by 2-h reperfusion: Group 1, Control (CON, saline vehicle); Group 2, chelerythrine[11,12], (CHE, a PKC inhibitor, Sigma Chemical Co, Saint Louis, USA) 2 mg/kg iv 5 min before ischemia; Group 3, GF109203X[12], (GF, another potent and selective PKC inhibitor, Tocris Cookson Ltd, Bristol, UK) 0.05 mg/kg iv 5 min before ischemia; Group 4, RPC, RPC hearts were subject to three 5-min cycles of infusion of remifentanil (Glaxo Wellcome Operations, Greenford, Middlesex, UK) at 6 $\mu g \cdot kg^{-1} \cdot min^{-1}$ interspersed with 5-min drug-free periods before 30 min of occlusion of the left coronary artery and 2 h of reperfusion; Group 5, IPC, before the 30-min occlusion, rats were subjected to preconditioning by ischemia (IPC, 5-min occlusion, 5-min reperfusion×3); Group 6, CHE+RPC; Group 7, CHE+IPC (2 mg/kg, iv, 5 min before RPC or IPC); Group 8, GF +RPC; and Group 9, GF+IPC (0.05 mg/kg, iv, 5 min before RPC or IPC).

Determination of infarct size On completion of the reperfusion period, the heart was excised, transferred to a Langendorff apparatus, and perfused with normal saline for 1 min at a pressure of 100 cmH_2O to flush out blood. The snare was securely re-tightened and 0.25% Evans blue dye was injected to stain the normally perfused region of the heart. This procedure allowed visualization of the normal, non-ischemic region and the area at risk (AAR). The heart was then weighed, frozen, and cut into 2-mm slices. Thereafter, the slices were stained by incubation at 37 °C for 20 min in 1% 2,3,5- triphenyltetrazolium (TTC, Sigma Chemical Co, Saint Louis, USA)[1,13,14] in phosphate buffer (pH 7.4), and then were immersed in 10% formalin, to enhance the contrast of the stain. The areas of infarct (TTC negative) and risk zone (TTC stained) for each slice were traced and digitized using a computerized planimetry technique (SigmaScan 4.0, Systat Software Inc, CA, USA). The volumes of the left ventricles, IS and AAR were calculated by multiplying each area with slice thickness and summing the product. The IS was expressed as a percentage of the AAR (IS/AAR).

Statistical analysis Data analysis was performed with a personal computer statistical software package (Prism v4.0, GraphPad Software, San Diego, USA). Data were expressed as mean±SD. Hemodynamics were analyzed using 2-way analysis of variance (ANOVA) with *Bonferroni post-hoc* test for multiple comparisons if significant *F* ratios were obtained. IS (expressed as percentage of the area at risk) were analyzed between groups using ANOVA with a Student-Newman-Keuls *post-hoc* test for multiple comparisons. Statistical differences were considered significant if $P<0.05$.

Results

Effects of RPC and IPC on cardiac morphology LV+ RV volume average was 0.99±0.22 cm^3 and the AAR ranged from 0.378±0.061 to 0.440±0.056 cm^3. There was no difference in LV+RV and AAR between the control and treatment groups (Table 1). The IS, expressed as a percentage of the AAR, of the control group was 52.7%± 5.5%. In groups subjected to IPC and RPC the infarct sizes were significantly reduced. IPC and RPC markedly reduced IS/AAR from 52.7%±5.5% to 12.9%±3.4% ($P<0.01$ *vs* CON) and 16.2%±6.4% ($P<0.01$ *vs* CON), respectively. CHE 2 mg/kg, a PKC inhibitor, or GF 0.05 mg/kg, another selective PKC inhibitor, administered 5 min before RPC or IPC completely abolished the cardioprotective effect of RPC (IS/AAR: CHE+RPC 51.2%±5.0%, GF+RPC 53.6%±6.1%, $P>0.05$ *vs* CON) or IPC (CHE+IPC 53.7%±4.3%, GF+IPC 54.1%±6.2%, $P>0.05$ *vs* CON). Neither CHE nor GF by itself modified IS in non-PC hearts (Figure 1).

Effects of RPC and IPC on hemodynamics As shown in Table 2, administration of remifentanil at 6 $\mu g \cdot kg^{-1} \cdot min^{-1}$ significantly reduced the HR, MBP, and RPP ($P<0.01$ *vs* baseline). HR in CHE+RPC or GF+RPC group was not reduced significantly after pretreated with remifentanil, and the difference was significant compared with RPC group ($P<0.05$, respec-

Table 1. Morphometrics after remifentanil preconditioning and ischemia preconditioning and the effects of chelerythrine (CHE) and GF109203X (GF). Mean±SD. $^{c}P<0.01$ *vs* Control. $^{f}P<0.01$ *vs* RPC. $^{i}P<0.01$ *vs* IPC.

	n	Body weight/g	Heart weight/g	LV+RV volume/cm^3	AAR volume/cm^3	IS volume/cm^3
Control	9	326±18	1.36±0.31	1.08±0.32	0.384±0.051	0.202±0.045
CHE	6	331±15	1.38±0.32	1.11±0.20	0.394±0.052	0.201±0.062
GF	6	326±15	1.18±0.27	0.99±0.21	0.382±0.063	0.205±0.028
RPC	7	324±19	1.33±0.27	1.15±0.28	0.434±0.071	0.068±0.024^{c}
CHE+RPC	6	313±15	1.13±0.21	0.93±0.19	0.406±0.072	0.204±0.034^{f}
GF+RPC	6	315±18	1.08±0.27	0.88±0.21	0.378±0.061	0.197±0.043^{f}
IPC	9	321±18	1.32±0.26	1.14±0.31	0.440±0.054	0.056±0.018^{c}
CHE+IPC	6	323±15	1.24±0.29	1.05±0.31	0.433±0.072	0.233±0.061^{i}
GF+IPC	6	312±18	1.19±0.27	0.99±0.27	0.387±0.063	0.209±0.062^{i}

LV, left ventricle volume; RV, right ventricle volume; IS, infarct size; AAR, area at risk.

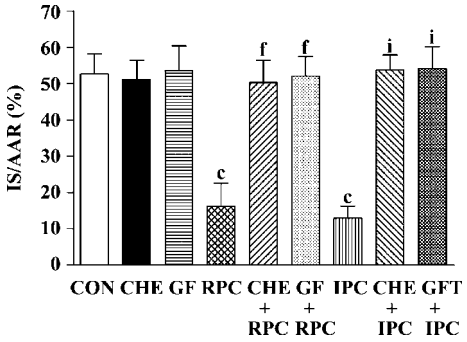

Figure 1. The effect of PKC inhibitors on remifentanil preconditioning. Infarct size (IS) expressed as a percentage of the area-at-risk (AAR). Infarct sizes in rat hearts subjected to control (CON), remifentanil preconditioning (RPC), ischemic preconditioning (IPC), chelerythrine (2 mg/kg, iv, CHE+RPC or CHE+IPC) given 5 min before the RPC, GF109203X (0.05 mg/kg, iv, GF+RPC or GF+IPC) given 5 min before the RPC or IPC. Mean±SD. $^{c}P<0.01$ *vs* Control. $^{f}P<0.01$ *vs* RPC. $^{i}P<0.01$ *vs* IPC.

tively). The bradycardia produced by remifentanil was abolished with pretreatment of CHE or RPC. There was no difference in any of the hemodynamic parameters between control and treatment groups during ischemia and reperfusion.

Discussion

The present results demonstrated that remifentanil conferred cardioprotection against injury induced by ischemic reperfusion, which was completely abolished by CHE and GF, both PKC inhibitors, and suggests that RPC, like IPC, protects myocardium by a mechanism that involves PKC activation.

Miki *et al*[10] found that the cardioprotective effect of morphine could be blocked by the PKC inhibitor CHE and OR participate in the triggering effect of IPC through activation of PKC. Also, Kato *et al*[4] suggested that fentanyl limited infarction size through meditation by PKC activation. Our data showed that CHE or GF abolished the protective effect of RPC, suggesting that like morphine and fentanyl, the protective effect of RPC on postischemia myocardial injury is mediated by a PKC activated pathway. In agreement with previous studies, we also found blockade of PKC abolished the effect of IPC.

The cellular mechanisms by which RPC exerts its postischemic protective action are unknown. Ligand-binding data show that remifentanil has a high degree of μ-opioid receptor selectivity (EC_{50}=2.6 nmol/L) with a lower affinity for δ (EC_{50}=66 nmol/L) and κ (EC_{50} = 6.1 μmol/L) opioid receptors. Previously, we found remifentanil reduced IS dose-dependently in open chest anesthetized rats[5]. The protective effect of RPC was abolished by all three OR antagonists CTOP, naltrindole, and nor-binaltorphinmine, indicating that the effect of remifentanil is mediated via μ-, δ-, and κ-OR[5]. The OR are known to couple to pertussis toxin sensitive G proteins such as G_i or G_o[15,16]. If opioid receptors act by activation of PKC, then they must couple to a phospholipse. In the heart, δ- and κ-OR stimulation could increase the level of inositol 1,4,5-triphosphate, suggesting phospholipase C or D-mediated turnover of phosphatidylinositol[17]. Opioids are linked to PKC and are therefore putative mediators in RPC or IPC.

Furthermore, intracellular signaling pathways, which mediate subtype of the OR-induced cardioprotection have been studied previously. Fryer *et al*[12] found that TAN-67, a selective δ_1-OR agonist, had an IS reduction effect that was abolished by CHE and GF, two PKC inhibitors that act on different binging sites on PKC to produce an inhibitory effect. In contrast, our lab showed that the cardioprotection of

Table 2. Hemodynamic parameters. Mean±SD. $^{c}P<0.01$ *vs* baseline. $^{e}P<0.05$ *vs* RPC

		Baseline			Treatment			30-min occlusion			2-h reperfusion		
	n	HR	MBP	RPP	HR	MBP	RPP	HR	MBP	RPP	HR	MBP	RPP
Control	9	435±54	82±16	47±10				446±52	79±13	45±8	474±52	63±15	45±13
CHE	6	432±51	87±18	47±9	388±64	83±10	42±8	444±58	81±17	45±10	440±46	74±11	43±12
GF	6	427±76	84±10	48±11	410±71	73±11	41±9	461±63	73±7	44±8	453±61	75±12	44±11
RPC	7	414±28	70±10	40±4	324±113^{c}	64±12^{c}	28±11^{c}	425±28	69±13	38±6	423±25	68±16	37±6
CHE+RPC	6	404±45	82±11	44±5	384±43^{e}	67±10	35±7	435±44	67±16	39±3	438±46	68±10	36±5
GF+RPC	6	411±78	90±18	48±12	404±65^{e}	82±12	43±10	449±50	85±19	46±10	452±43	67±18	37±8
IPC	9	428±70	82±14	44±9	423±40	88±10	46±10	435±24	83±8	43±14	463±29	81±15	46±10
CHE+IPC	6	427±48	88±16	48±10	447±46	87±13	52±11	468±43	80±9	52±8	478±37	77±9	53±7
GF+IPC	6	402±54	80±9	43±7	414±67	81±14	44±8	439±56	76±12	44±9	447±65	75±11	44±9

HR, heart rate (beats/min); MBP, mean arterial blood pressure (mmHg); RPP, rate-pressure product (mmHg/min per 1000). Baseline, 15 min after surgery procedures; Treatment, after remifentanil preconditioning (RPC) or ischemia preconditioning (IPC). 30-min occlusion, 30 min after regional ischemia; 2-h reperfusion, 2 h after reperfusion.

activation of κ-OR and IPC was significantly attenuated by blockade of PKC with PKC inhibitor CHE in the isolated rat heart[14,18,19] and myocytes[19]. These results provided evidence that the effect of RPC on postischemic hearts was partially mediated via a PKC activated pathway.

The role of PKC in IPC and opioid-induced PC is not fully understood[20,21]. Generally, opioids activate δ-and κ-OR, which lead to PKC activation. Activated PKC acts as an amplifier of the preconditioning stimulus and stabilizes, by phosphorylation, the open state of the mitochondrial K_{ATP} channel and the sarcolemmal K_{ATP} channel. PKC-δ translation seems to be responsible for activating mitochondrial K_{ATP} channels and PKC-ε translocation for the establishment of late preconditioning by phosphorylating nuclear targets. The opening of K_{ATP} channels ultimately elicits cytoprotection by decreasing cytosolic and mitochondrial Ca^{2+} overload[22].

Although our data also show that pretreatment with PKC inhibitor CHE or GF could prevent HR from decreasing led by RPC, the difference was significant among all treatment groups and control. It suggests that PKC is also involved in the bradycardia response of remifentanil.

We conclude that RPC limits infarction in open chest rat hearts via PKC activation mechanism, which mimics the effect of IPC.

Acknowledgments

The authors thank CP MOK for technical assistance.

References

1 Schultz JE, Hsu AK, Gross GJ. Morphine mimics the cardioprotective effect of ischemic preconditioning via a glibenclamide-sensitive mechanism in the rat heart. Circ Res 1996; 78: 1100–4.

2 Schultz JJ, Hsu AK, Gross GJ. Ischemic preconditioning and morphine-induced cardioprotection involve the delta (delta)-opioid receptor in the intact rat heart. J Mol Cell Cardiol 1997; 29: 2187–95.

3 Kato R, Ross S, Foex P. Fentanyl protects the heart against ischaemic injury via opioid receptors, adenosine A1 receptors and K_{ATP} channel linked mechanisms in rats. Br J Anaesth 2000; 84: 204–14.

4 Kato R, Foex P. Fentanyl reduces infarction but not stunning via delta-opioid receptors and protein kinase C in rats. Br J Anaesth 2000; 84: 608–14.

5 Zhang Y, Irwin M, Wong TM. Remifentanil preconditioning protects against ischemic injury in the intact rat heart. Anesthesiology 2004; 101: 918–23.

6 James MK, Feldman PL, Schuster SV, Bilotta JM, Brackeen MF, Leighton HJ. Opioid receptor activity of GI 87084B, a novel ultra-short acting analgesic, in isolated tissues. J Pharmacol Exp Ther 1991; 259: 712–8.

7 Egan TD, Minto CF, Hermann DJ, Barr J, Muir KT, Shafer SL. Remifentanil versus alfentanil: comparative pharmacokinetics and pharmacodynamics in healthy adult male volunteers. Anesthesiology 1996; 84: 821–33.

8 Schultz JE, Gross GJ. Opioids and cardioprotection. Pharmacol Ther 2001; 89: 123–37.

9 Gross GJ. Role of opioids in acute and delayed preconditioning. J Mol Cell Cardiol 2003; 35: 709–18.

10 Miki T, Cohen MV, Downey JM. Opioid receptor contributes to ischemic preconditioning through protein kinase C activation in rabbits. Mol Cell Biochem 1998; 186: 3–12.

11 Fryer RM, Schultz JE, Hsu AK, Gross GJ. Pretreatment with tyrosine kinase inhibitors partially attenuates ischemic preconditioning in rat hearts. Am J Physiol 1998; 275: H2009–15.

12 Fryer RM, Wang Y, Hsu AK, Gross GJ. Essential activation of PKC-delta in opioid-initiated cardioprotection. Am J Physiol Heart Circ Physiol 2001; 280: H1346–53.

13 Schultz JE, Hsu AK, Gross GJ. Ischemic preconditioning in the intact rat heart is mediated by delta1- but not mu- or kappa-opioid receptors. Circulation 1998; 97: 1282–9.
14 Wang GY, Wu S, Pei JM, Yu XC, Wong TM. Kappa- but not delta-opioid receptors mediate effects of ischemic preconditioning on both infarct and arrhythmia in rats. Am J Physiol Heart Circ Physiol 2001; 280: H384–91.
15 Aghajanian GK, Wang YY. Pertussis toxin blocks the outward currents evoked by opiate and alpha 2-agonists in locus coeruleus neurons. Brain Res 1986; 371: 390–4.
16 Burns DL, Hewlett EL, Moss J, Vaughan M. Pertussis toxin inhibits enkephalin stimulation of GTPase of NG108-15 cells. J Biol Chem 1983; 258: 1435–8.
17 Ventura C, Spurgeon H, Lakatta EG, Guarnieri C, Capogrossi MC. Kappa and delta opioid receptor stimulation affects cardiac myocyte function and Ca^{2+} release from an intracellular pool in myocytes and neurons. Circ Res 1992; 70: 66–81.
18 Cao CM, Xia Q, Tu J, Chen M, Wu S, Wong TM. Cardioprotection of interleukin-2 is mediated via {kappa}-opioid receptors. J Pharmacol Exp Ther 2004; 309: 560–7.
19 Wu S, Li HY, Wong TM. Cardioprotection of preconditioning by metabolic inhibition in the rat ventricular myocyte. Involvement of kappa-opioid receptor. Circ Res 1999; 84: 1388–95.
20 Armstrong SC. Protein kinase activation and myocardial ischemia/reperfusion injury. Cardiovasc Res 2004; 61: 427–36.
21 Simkhovich BZ, Przyklenk K, Kloner RA. Role of protein kinase C as a cellular mediator of ischemic preconditioning: a critical review. Cardiovasc Res 1998; 40: 9–22.
22 Zaugg M, Lucchinetti E, Uecker M, Pasch T, Schaub MC. Anaesthetics and cardiac preconditioning. Part I. Signalling and cytoprotective mechanisms. Br J Anaesth 2003; 91: 551–65.

The First Scientific Meeting of the Asian Society for Vascular Biology

October 8–11, 2005 Shanghai, China

Info: YuHUANG
Department of Physiology
Chinese University of Hong Kong
Hong Kong SAR, China
Phn: 852-2609-6787
Fax: 852-2603-5022
E-mail: yu-huang@cuhk.edu.hk
Http:// www.sbsonline.org/sbscon/2005/index.php

Acta Pharmacologica Sinica 2005 May; 26 (5): 551–558

Full-length article

Modulating effect of ginseng saponins on heterologously expressed HERG currents in *Xenopus* oocytes[1]

Cuk-seong KIM[2], Sook-jin SON[2], Hyo-shin KIM[2], Yong-duk KIM[2], Kyu-seung LEE[2], Byeong-hwa JEON[2], Kwang-jin KIM[2], Jin-kyu PARK[3], Jin-bong PARK[2,4]

[2]Department of Physiology, College of Medicine, Chungnam National University, Daejeon 301-131, Korea; [3]Korea Ginseng and Tobacco Research Institute, Daejeon 305-805, Korea

Key words

Ginseng saponins; *Xenopus* laevis; potassium channels; action potentials; patch-clamp techniques

[1] Project supported by a grant from Korea Research Foundation (2000-002-E00005).
[4] Correspondence to Jin-bong PARK, DVM, PhD.
Phn 82-42-580-8212.
Fax 82-42-545-8440.
E-mail jinbong@cnu.ac.kr

Received 2005-01-05
Accepted 2005-03-02

doi: 10.1111/j.1745-7254.2005.00116.x

Abstract

Aim: To examine the effects of ginseng saponins on the heterologously expressed human ether-a-go-go related gene (HERG) that encodes the rapid component of the delayed rectifier K^+ channel. **Methods:** A two-electrode voltage clamp technique was used. HERG currents were recorded in *Xenopus* oocytes injected with HERG cRNA. **Results:** Crude saponins of Korean red ginseng (GS) induced a minimal increase of the maximal HERG conductance without changes in the voltage-dependent HERG current activation and inactivation curves. GS, however, decelerated HERG current deactivation in a concentration-dependent manner, which was more noticeable with panaxitriol (PT) than panaxidiol (PD). Consistently, ginseng saponins increased the HERG deactivation time constants with the order of potency of Rg_1 (a major component of PT)>Rf_1>Rb_1 (a major component of PD). Re had little effect on HERG deactivation. During a cardiac action potential, GS increased the outward HERG current. **Conclusion:** Ginseng saponins enhance HERG currents, which could be in part a possible mechanism of the shortening cardiac action potential of ginseng saponins.

Introduction

Ginseng, the root of *Panax ginseng* CA Meyer, has been used for more than 2 000 years as a general tonic and restorative agent. Ginseng saponins, also called ginsenosides, are one of the main molecular ingredients responsible for the actions of ginseng. Ginseng saponins have beneficial effects on cardiovascular functions[1,2], including the antihypertensive effect[3], the protective effect against ischemia/reperfusion injury[4], the negative chronotropic and inotropic effects[5], and the antiarrhythmic effect[6,7].

The delayed rectifier K^+ current is critical for repolarization of cardiac action potential[8], which represents the sum of two components; the rapidly (I_{Kr}) and slowly activating components (I_{Ks})[9]. The human ether-a-go-go-related gene (HERG) is expressed in the heart of mammalian species including humans[10]. It encodes the pore-forming subunit of I_{Kr}[11,12], which initiates repolarization and terminates the plateau phase of the cardiac action potential. Heterologously expressed HERG currents share pharmacological and biophysical properties with I_{Kr}. It has been shown that channels formed by coexpression of MinK-related protein, MiRP1 and HERG resemble native cardiac I_{Kr} channels[13]. Mutations in the HERG channel gene cause inherited long QT syndrome (LQT), a disorder of cardiac repolarization that predisposes affected individuals to lethal arrhythmias[11,14]. Acquired LQT is far more common and is most often caused by commonly used medications blocking cardiac HERG channels[15–18]. Thus I_{Kr}/HERG is especially relevant to both acquired and inherited forms of LQT[19, 20].

Ginseng saponins decreased the action potential duration of cardiac myocytes[21,22] and showed antiarrhythmic effects[6,7]. HERG/I_{Kr} has been regarded as a common target of pro- and anti-arrhythmic drugs[19]. Therefore, it can be assumed that ginseng saponins may shorten action potential duration and exert antiarrhythmic effects by altering HERG channel activities. To investigate the possibility, we examined the effect of ginseng saponins on the HERG current

expressed in *Xenopus* oocytes. We found that ginseng saponins enhanced the HERG current in a concentration- and structure-dependent manner during cardiac action potential.

Materials and methods

Oocyte preparation Ovarian lobes were excised from anesthetized *Xenopus laevis* (Xenopus I, Dexter, MI, USA) through a small abdominal incision and were treated with Ca^{2+}-free Barth's solution containing 0.2% collagenase (type II, Sigma-Aldrich, St Louis, MO, USA) for 1–2 h and then the remaining inner ovarian epithelium, theca, and follicular cell layers were removed with fine forceps. The composition of Ca^{2+}-free Barth's solution was as follows (mmol/L): NaCl 88.7, KCl 1.0, $NaHCO_3$ 2.4, $MgSO_4 \cdot 7H_2O$ 0.8, HEPES 5 (pH=7.5). Only healthy, stage V or VI oocytes were selected for cRNA injection. cRNA of HERG was synthesized from the linearized cDNA using an *in vitro* transcription kit (Ambion, Austin, TX, USA) and stored at -80 °C until used. Denuded oocytes were then injected manually with 50 nL cRNA (0.3–1.0 g/L) using a glass capillary connected with a microdispenser (VWR Scientific, West Chester, PA, USA). For controls, oocytes were either injected with 50 nL distilled water or left uninjected. After injection, oocytes were cultured at 18 °C in Barth's solution containing (mmol/L): NaCl 88.0, KCl 1.0, $NaHCO_3$ 2.4, $MgSO_4 \cdot 7H_2O$ 0.8, $Ca(NO_3)_2 \cdot 4H_2O$ 0.3, $CaCl_2$ 0.4, HEPES 5 (pH=7.5), supplemented with pyruvate 2 mmol/L and gentamicin sulfate 50 mg/L. The culture medium was changed daily. Currents were recorded 2–7 d after injection.

Whole cell current recording in *Xenopus* oocytes HERG currents were recorded using a two-electrode voltage-clamp amplifier (OC-725C; Warner Instruments, Hamden, CT, USA) from the oocytes placed in the recording chamber (2.0 mL) superfused with Oocyte-Ringer solution containing (mmol/L): NaCl 96.0, KCl 2.0, $MgCl_2$ 1.0, $CaCl_2 \cdot 2H_2O$ 1.8, HEPES 5.0 (pH=7.5). Stimulation and data acquisition were controlled with Digidata 1200 (Axon Instruments, Union City, CA, USA) and pClamp 6.04 (Axon Instruments). Electrodes were fabricated from glass capillaries containing an inner filament (OD 1.5 mm, ID 1.12 mm; WPI, Sarasota, FL, USA). Electrodes filled with 3 mol/L KCl had a resistance of 1–2 MΩ for current-passing electrodes and 2–4 MΩ for voltage-recording electrodes.

Data analysis The voltage dependence of HERG current activation was determined for each oocyte by fitting peak values of tail current (I_{tail}) versus test potential (V_t) to Boltzmann's function:

$$I_{tail} = \frac{I_{tail}^{max}}{1+\exp\left(\frac{V_{1/2}-V_t}{k}\right)}$$

where I_{tail}^{max} is maximum tail current, $V_{1/2}$ is the voltage at which 50% of the channels are activated, and k is the slope factor. To examine steady-state inactivation, conditioning pulses between -130 and +20 mV in 10-mV increments for 60 ms were applied after a depolarizing pulse to +20 mV for 900 ms, followed by a common test pulse to +20 mV. The peak current amplitudes during test pulses were plotted as a function of the previous conditioning pulses. Normalized steady-state inactivation as a function of prepulse of test potential was also fitted to Boltzmann's function. The data were expressed as mean±SEM. Statistical analysis were carried out using one-way ANOVA or Student *t*-test when appropriate.

Drugs All drugs except ginsenosides were purchased from Sigma. Lyophilized ginsenosides were kindly donated by Dr PARK of Korean Tobacco and Ginseng Institute.

Results

The HERG potassium current was recorded by a two-electrode voltage-clamp from the *Xenopus* oocyte expression system. Steady-state current was recorded by depolarization to potentials between -60 and 40 mV and the holding potential was maintained at -80 mV for 4 s. Tail currents were recorded upon repolarization to -60 mV. This voltage protocol was repeated and the amplitude of the current was monitored until no changes in current amplitude could be recorded for 3 min. Figure 1 shows current records obtained in the absence or the presence of 30 mg/L crude saponin of Korean red ginseng (GS). HERG current amplitudes and deactivation kinetics were changed by bath application of GS, but not by intraoocyte injection of the same concentration of GS (30 mg/L).

Figure 2A shows the effect of extracellular GS (30 mg/L) on the amplitude of steady-state current that was measured at the end of depolarizing pulse and peak tail current. The steady-state current first appears at -50 mV test potential, and the peak tail current is maximal at +10 mV test potential. GS (30 mg/L) induced a minimal increase in steady-state current and peak tail currents (Figure 2A, 2B). The increase of steady-state currents were observed only at more negative membrane voltages than 0 mV, where HERG channel inactivation was observed, while the increase of peak tail currents were observed at all tested voltages. Drugs that changed ion channel activities often alter the voltage dependence of channel kinetics. Therefore, we analyzed the

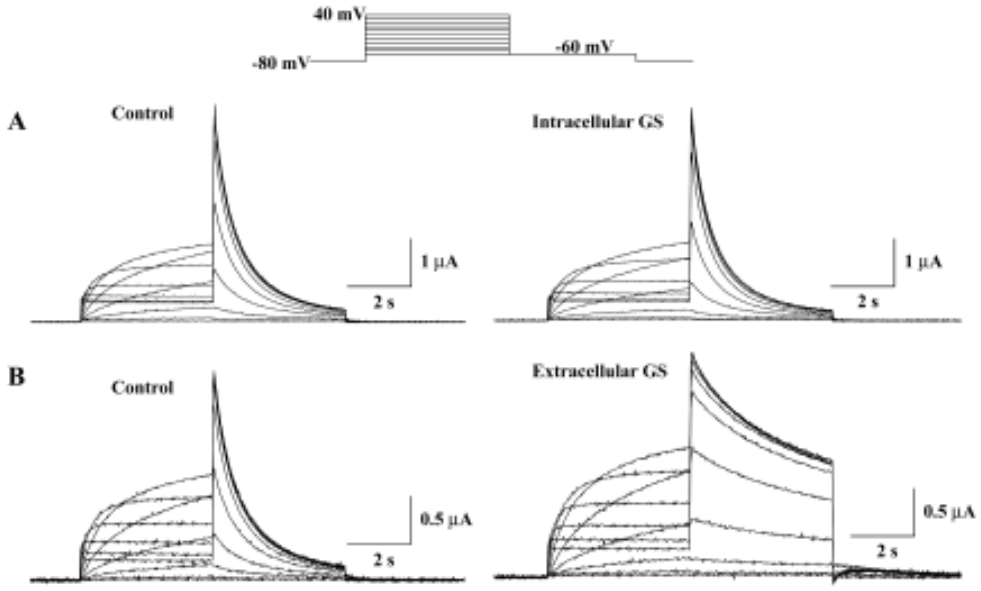

Figure 1. Selective effect of ginseng saponins (GS) on HERG current expressed in *Xenopus* oocyte. Traces of HERG current were recorded before and after exposure to 30 mg/L GS for 10 min with intra-oocyte injection (A) and bath application (B). Voltage protocol consisted of depolarizing steps from a holding potential of -80 mV in 10 mV increments from –60 to +40 mV for 4 s and repolarizing step to -60 mV for 6 s (inset). Steps were repeated at 30 s intervals.

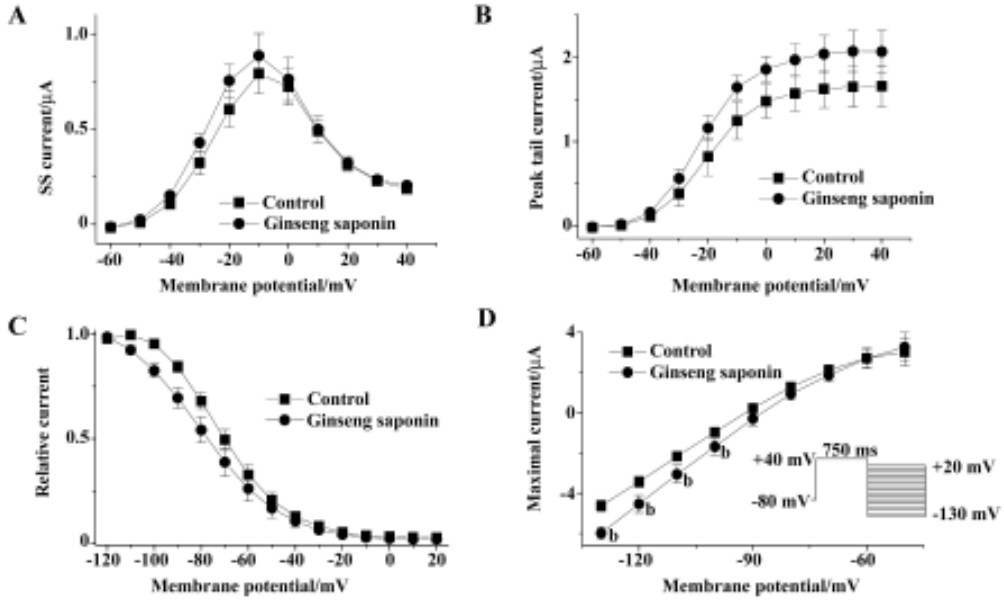

Figure 2. Effect of ginseng saponins (GS) on voltage-dependent kinetics and maximal conductance of HERG current. (A) Current-voltage relation curves were plotted from the current measured at the end of depolarizing test pulse ranging from –60 to +40 mV (4 s in 10 mV increments) from a holding potential of -80 mV (n=6). (B) Voltage-dependent activation curves plotted from peak tail currents during a repolarizing step to -60 mV after depolarizing to various voltages (n=6). (C) Steady-state inactivation curves of HERG channels before and after GS exposure. Solid lines indicate the product of the fitted steady-state inactivation curves with Boltzmann's equation on experimental data. (D) Current-voltage plot was obtained from peak tail currents ranging from -130 to +20 mV following a 750-ms prepulse to +40 mV from a holding potential of -80 mV. To clarify the change of slope conductance, current amplitudes were plotted between -130 and -50 mV. n=6. Mean±SEM. $^bP<0.05$ *vs* control.

voltage dependence of activation of the HERG current in the absence or presence of GS. Peak amplitudes of tail currents were plotted as a function of test potential as shown in Figure 2B, and were fitted with Boltzmann's function. In the control experiment, the activation curve had a mid-point of -18.1±2.2 mV and a slope factor of 6.5±0.2 mV (n=6), which is similar to previous reports[12,23]. In the presence of GS (30 μmol/L), a mid-point of -19.6±1.9 mV and a slope factor of 7.1±0.2 mV (n=6) , the difference compared with control was not significant.

We also analyzed the steady-state HERG inactivation in the absence and presence of GS. Steady-state inactivation currents were measured with the following protocol: channels were inactivated at a holding potential of +20 mV before short test pulses. Potentials ranging from -120 mV to +20 mV (15 ms, 10 mV-increments) were applied to recover the channels from inactivation. Membrane potential returned to a holding potential of +20 mV after these test pulses evoked large outward inactivating currents. After having obtained a measurement under control conditions, the oocyte was clamped at a holding potential of -80 mV during a 10-min wash (30 mg/L GS), which was necessary to avoid destruction of the cell. Peak outward current amplitudes after the return to the holding potential were normalized and fitted to Boltzmann's function, which elicited significant left shift in the steady-state inactivation curve (n=6, Figure 2C). In the absence of GS, the inactivation curve had a mid-point of -69.7±2.8 mV and a slope factor of -11.6±0.8 mV (n=6). These values were -78.7±4.5 mV and -15.3±0.7 mV (n=6), respectively, in the presence of GS (30 mg/L, 10 min).

To examine whether the increase in HERG current represents the change in HERG conductance, we measured maximal HERG conductance in the absence or presence of GS. For this purpose, we studied the fully activated *I-V* relationships by applying various test potentials after a depolarizing conditioning pulse (Figure 2D). A conditioning pulse to +40 mV, which induced a full activation, for 750 ms was applied from a holding potential of -80 mV, followed by test pulses to various potentials between -130 and +20 mV in 10-mV increments. The amplitude of the current was measured at its peak before the time-dependent change proceeded, and plotted as a function of test potential. GS increased maximal HERG conductance obtained from the slope of the curve (Figure 2D). The slope conductance was obtained from the slope of the *I-V* curves between -130 and -110 mV. The value of the slope was 0.11±0.01 and 0.14±0.01 for control and 30 mg/L GS (Figure 2D).

To evaluate the most prominent effect of GS on HERG current, decelerating current deactivation, we analyzed the time constant for the deactivation of HERG tail current. For this purpose, we used long hyperpolarizing test pulses following a depolarizing conditioning pulse (Figure 3A). Deactivating currents during test pulses were well fitted to a double-exponential function. GS (3–30 mg/L) increased both fast and slow deactivation time constants of HERG tail current in a concentration-dependent change at all repolarizing tested voltage. The fast deactivation time constants at repolarizing test voltage of -60 mV were increased from 1.5± 0.3 s of control to 2.2±1.1, 3.2±1.0, 4.1±1.0, and 5.1±1.2 s by GS 3, 10, 30, and 100 mg/L, respectively (Figure 3B). The slow deactivation time constants at -60 mV of control were increased from 6.0±1.4 s to 7.0±0.3, 9.2±1.0, 11.1±1.2, and 17.0±2.7 s by GS 3, 10, 30, and 100 mg/L, respectively (Figure 3B).

GS may include many different ginsenosides classified into panaxadiol (PD) and panaxatriol (PT) saponins according to their chemical structures. To know the possible structure-dependent effect of ginsenosides on HERG current, we examined the effect of PD and PT on the deactivation of the HERG tail current. PT evoked more potent deceleration of the HERG deactivation than PD did (Figure 4A). Consistently, deceleration of HERG current was more pronounced by ginsenoside Rg_1 and Rf_1 the major components of Korean red ginseng (KRG) PT than by ginsenoside Rb_1, the major component of PD (Figure 4B). Interestingly, another PT ginsenoside, Re had little effect on HERG current.

To evaluate the physiological significance of enhancement of HERG by ginsenoside, we examined the effects of GS on repolarizing currents with ramp pulses. In the ramp protocol that involved an initial step depolarization from -80 to +10 mV, followed by a slow ramp (1.7 s) to -80 mV, GS (10 mg/L), induced a significant enhancement of the outward current upon slow repolarization (Figure 5).

Finally, we investigated the possible subcellular mechanism of GS effects on HERG currents. We used PTX to test the possible involvement of PTX-sensitive G-protein in GS effects on HERG currents. Pretreatment with PTX (2 mg/L, 16 h), however, did not affect HERG current modulation by GS (Figure 6A). To examine whether the intracellular Ca^{2+} was involved in the modulation of HERG current, we used intracellular Ca^{2+} buffer, BAPTA. Intraoocyte injection of BAPTA had no effect on GS modulation of the HERG current (Figure 6B).

Discussion

We have shown that ginsenosides enhance the HERG current expressed in *Xenopus* oocytes. Ginsenosides are

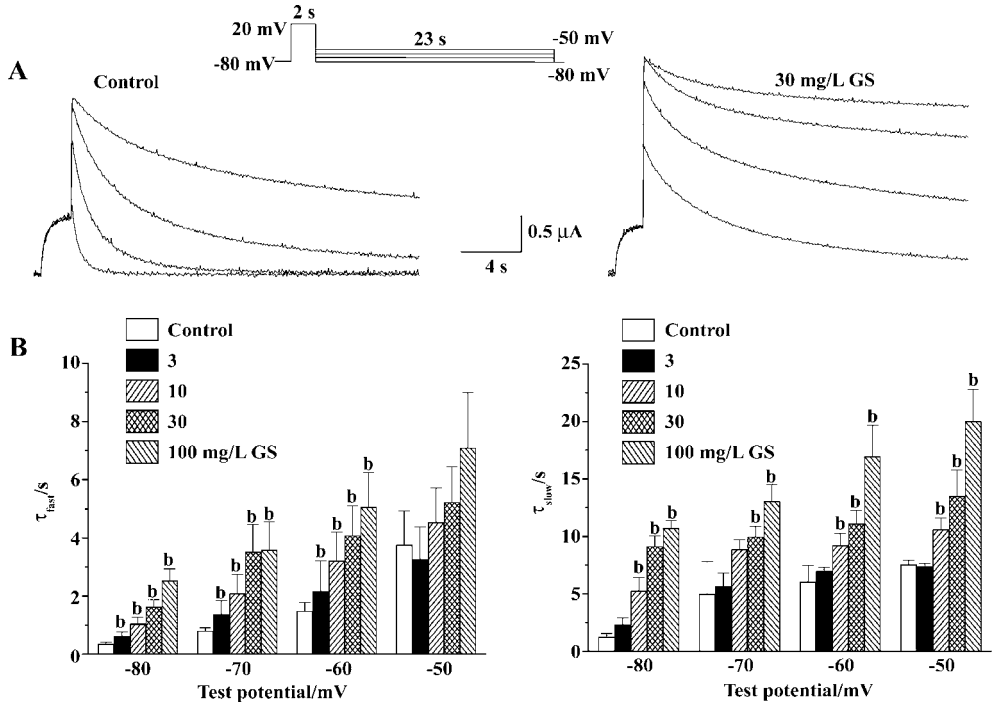

Figure 3. Effects of ginseng saponin on HERG current deactivation. (A) Representative HERG deactivation before and after exposure to GS. Currents were stimulated by a 2 s prepulse to +20 mV followed by test pulses ranging from -80 to -50 mV for 23 s. (B) Effects of different concentrations (3–100 mg/L) of ginseng saponin on HERG deactivation time constants. The deactivation time constants were determined from tail currents recorded during the long-lasting test potentials. Current decay was fitted with a double exponential function. n=7 experiments. Mean±SEM. $^bP<0.05$ *vs* control.

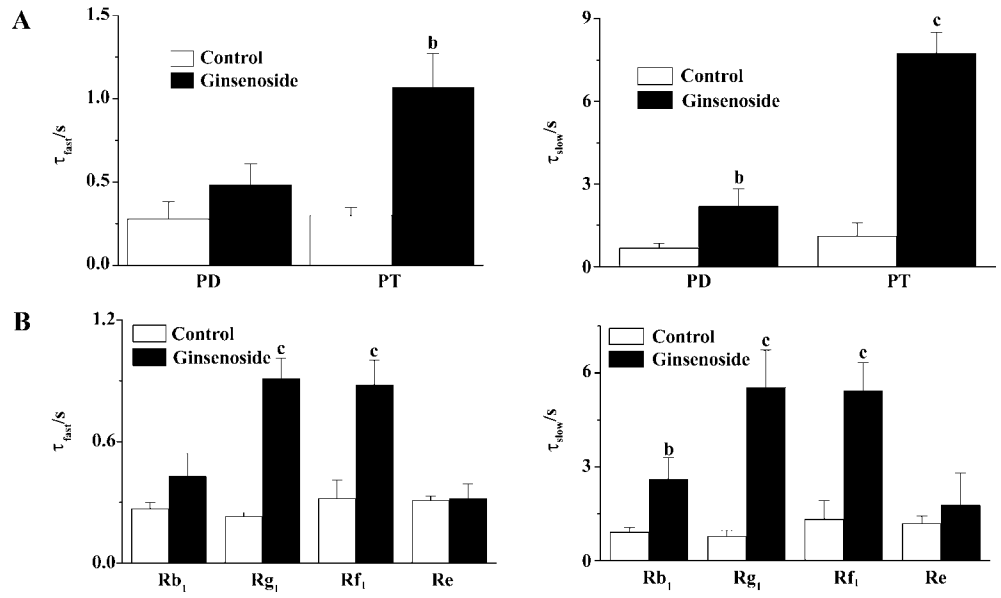

Figure 4. Effects of various ginsenosides on HERG current deactivation. Effects of panaxadiol (PD) and panaxatriol (PT) saponins (A), and ginsenoside Rg_1, Rf_1, Re, and Rb on HERG current deactivation (B). The pulse protocol is the same as in Figure 3. The fast and slow deactivation time constants of HERG were shown before and after the application of ginsenosides (30 mg/L). n=4–6 experiments. Mean±SEM. $^bP<0.05$, $^cP<0.01$ *vs* control.

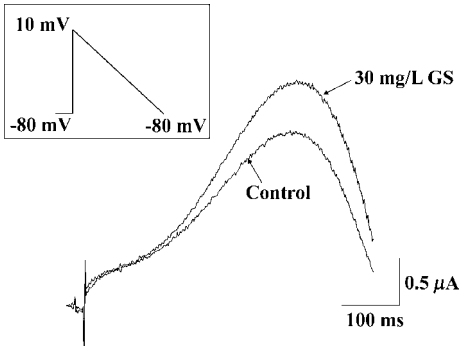

Figure 5. Effects of ginseng saponin (GS) on the HERG current during cardiac action potential. Representative current traces recorded during voltage protocol mimicked cardiac action potential in the absence and presence of GS (30 mg/L). HERG currents were stimulated by depolarization pulse to +10 mV following repolarization pulse to -80 mV for 500 ms (inset).

known to be effective against cardiac arrhythmias and elicit APD shortening and I_K inhibition[21]. It is well known that heterologously expressed HERG currents share pharmacological and biophysical properties with I_{Kr} [11,12,24,25]. The characteristics of the current recorded in the present study correspond to HERG current; slow current activation at negative potentials, large long-lasting tail currents on repolarization, strong inward rectification and sensitivity to class III methanesulfonanilides (data not shown). The present study is the first to characterize the interaction between ginsenosides and the HERG channels. The major finding of the present study was that ginsenosides enhanced HERG channel activities in a structure- and concentration-dependent manner. Considering all of this, ginsenosides may induce APD shortening partly through enhancement of HERG/I_{Kr} as well as I_{Ks} [21]. This finding provides a clearer ionic mechanism of the antiarrhythmic effect of ginsenosides. That is, HERG is another target of ginsenosides.

Mutations in HERG that cause LQT can reduce the amplitude of I_{Kr} by several different mechanisms. The most common mechanism is a loss of channel function and a dominant negative effect[26]. Therefore mutation in HERG also accelerated the rate of channel deactivation and would cause a net reduction in outward current during slow repolarization typical of a cardiac action potential. In the present study, we have shown that GS increased the maximal conductance of HERG potassium channel and it also increased the deactivation time constants of HERG potassium current. Our results, therefore, indicate that the effects of GS on HERG potassium channel may improve the LQT through speed repolarization and shorten the action potential.

To clarify the biophysical mechanism of HERG potentiation by ginsenosides, we analyzed the effect of ginsenosides on HERG current using various pulse protocols. The results suggest that ginsenosides affect preferentially the deactivation of HERG channels with a maximal conductance increase. The rate of recovery from inactivation and the rate

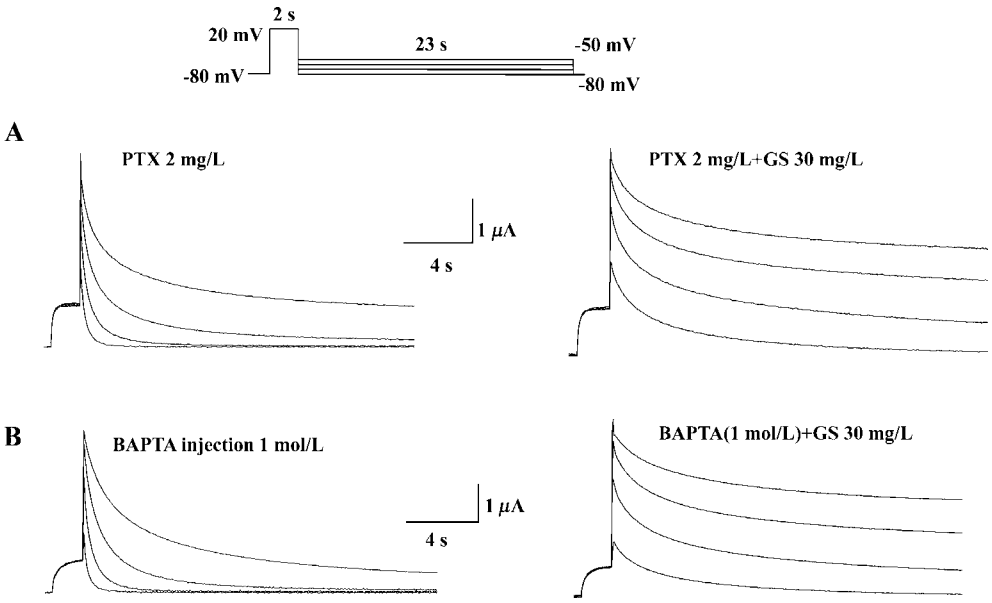

Figure 6. Effect of ginseng saponin (GS) on HERG current in different conditions. Deceleration of HERG current deactivation by GS was not altered by extracellular PTX pretreatment (2 mg/L, 16 h) (A) or by intra-oocyte injection of BAPTA (1 mmol/L) (B). Representative currents stimulated by a series of step pulses. The pulse protocol is the same as in Figure 4.

of deactivation are major HERG channel kinetic factors determining the duration of the action potential[27]. HERG modulation is expected to speed repolarization and shorten the action potential, which could decrease the inter-spike interval and accelerate the heart rate.

How might a GS contribute to the enhancement of HERG potassium current? The heart is presented with continually varying cardiovascular demands that require dynamic responses, both inotropic and chronotropic. Most cardiac adaptation that occurs is the result of changes in autonomic/hormonal stimulation involving G-protein-coupled receptors[28]. In a previous study, ginsenosides were shown to increase the Ca^{2+}-activated Cl^- current in *Xenopus* oocytes through a signaling pathway linked to the muscarinic ACh receptor, which involves G protein-coupled PLC activation and Ca^{2+} mobilization from IP_3-sensitive intracellular store[29]. In our experiments, the effects of GS on HERG potassium currents were not blocked by intracellular Ca^{2+} chelation and intraoocyte injection of BAPTA nor pretreatment with PTX (2 mg/L, 16 h) (Figure 6A, 6B). Therefore, it should be noted that ginsenoside Rf could regulate GIRK channels with unidentified proteins derived from the rat brain through PTX-insensitive G proteins[30]. However, we still cannot exclude the possibility of direct interaction between ginsenosides and HERG channel proteins.

Approximately 30 different ginsenosides have now been isolated and identified from *Panax ginseng*. Studies have shown that certain ginsenosides are more potent than others[31]. It should be noted that ginsenoside Re had no effect on HERG currents, showing the structure-dependence of HERG modulations by ginsenosides. HERG currents were enhanced by PT and PD as well as by ginsenoside Rb_1, Rg_1, and Rf with different potency. Crude saponin of KRG used in this experiment contained 56.3% of ginsenosides. Therefore, the effect of KRG-CS on the HERG potassium current was mainly a result of the saponin fraction of KRG.

Synthetic molecules such as fenamates and other openers of the K^+ channel offer a novel therapeutic approach to stabilizing and controlling cellular function[32]. Our results, demonstrate for the first time a link between ginseng saponin and the electrophysiological properties of the HERG channel. The positive regulation by ginseng saponin on HERG and the previously described effects on I_{Ks}[21,22], suggest a potential role for ginseng saponin in the prevention or treatment of long QT syndrome.

References

1 Chen X. Cardiovascular protection by ginsenosides and their nitric oxide releasing action. Clin Exp Pharmacol Physiol 1996; 23: 728–32.

2 Zhang JM, Matsuura Y, Sueda T, Orihashi K. Beneficial effects of ginsenosides of stems and leaves on cardiac and coronary vascular functions after 12-hour rat heart preservation. Transplant Proc 1999; 31: 2175–8.

3 Jeon BH, Kim CS, Kim HS, Park JB, Nam KY, Chang SJ. Effect of Korean red ginseng on blood pressure and nitric oxide production. Acta Pharmacol Sin 2000; 21: 1095–100.

4 Zhan Y, Xu XH, Jiang YP. Protective effects of ginsenoside on myocardiac ischemic and reperfusion injuries. J Natl Med J China 1994; 74: 626–8.

5 Wu JX, Chen JX. Negative chronotropic and inotropic effects of *Panax notoginseng* saponins. Acta Pharmacol Sin 1988; 9: 409–12.

6 Li XJ, Zhang BH. Studies on anti-arrhythmia effects of panaxatriol saponins isolated from *Panax notoginseng*. Acta Pharm Sin 1988; 23: 168–73.

7 Zhang RB, Li ZY, Shi HY. Cardiac arrhythmia induced by hypothalamic stimulation in cardiac ischemic rabbits and the antiarrhythmic action of *Panax* ginseng. Acta Pharmacol Sin 1982; 3: 226–30.

8 Carmeliet E. K^+ channels and control of ventricular repolarization in the heart. Fundam Clin Pharmacol 1993; 7: 19-28

9 Sanguinetti MC, Jurkiewicz NK. Two components of cardiac delayed rectifier K^+ current. Differential sensitivity to block by class III antiarrhythmic agents. J Gen Physiol 1990; 96: 195–215.

10 Wymore RS, Gintant GA, Wymore RT, Dixon JE, McKinnon D, Cohen IS. Tissue and species distribution of mRNA for the I_{Kr}-like K^+ channel, erg. Circ Res 1997; 80: 261–8.

11 Sanguinetti MC, Jiang C, Curran ME, Keating MT. A mechanistic link between an inherited and an acquired cardiac arrhythmia: HERG encodes the I_{Kr} potassium channel. Cell 1995; 81: 299–307.

12 Wang S, Liu S, Morales MJ, Strauss HC, Rasmusson RL. A quantitative analysis of the activation and inactivation kinetics of HERG ex pressed in *Xenopus* oocytes. J Physiol 1997; 502: 45–60.

13 Abbott GW, Sesti F, Splawski I, Buck ME, Lehmann MH, Timothy KW, *et al*. MiRP1 forms I_{Kr} potassium channels with HERG and is associated with cardiac arrhythmia. Cell 1999; 97: 175–87.

14 Curran ME, Splawski I, Timothy KW, Vincent GM, Green ED, Keating MT. A molecular basis for cardiac arrhythmia: HERG mutations cause long QT syndrome. Cell 1995; 80: 795–803.

15 Suessbrich H, Waldegger S, Lang F, Busch AE. Blockade of HERG channels expressed in *Xenopus* oocytes by the histamine receptor antagonists terfenadine and astemizole. FEBS Lett 1996; 385: 77–80.

16 Rampe D, Roy ML, Dennis A, Brown AM. A mechanism for the proarrhythmic effects of cisapride (Propulsid): high affinity blockade of the human cardiac potassium channel HERG. FEBS Lett 1997; 417: 28–32.

17 Drolet B, Vincent F, Rail J, Chahine M, Deschenes D, Nadeau S, *et al*. Thioridazine lengthens repolarization of cardiac ventricular myocytes by blocking the delayed rectifier potassium current. J Pharmacol Exp Ther 1999; 288: 1261–8.

18 Volberg WA, Koci BJ, Su W, Lin J, Zhou J. Blockade of human cardiac potassium channel human ether-a-go-go-related gene (HERG) by macrolide antibiotics. J Pharmacol Exp Ther 2002; 302: 320–7.

19 Mitcheson JS, Chen J, Lin M, Culberson C, Sanguinetti MC. A structural basis for drug-induced long QT syndrome. Proc Natl Acad Sci USA 2000; 97: 12329–33.

20 Tseng GN. I_{Kr}: the hERG channel. J Mol Cell Cardiol 2001; 33:

835–49.

21 Bai CX, Sunami A, Namiki T, Sawanobori T, Furukawa T. Electrophysiological effects of ginseng and ginsenoside Re in guinea pig ventricular myocytes. Eur J Pharmacol 2003; 476: 35–44.

22 Bai CX, Takahashi K, Masumiya H, Sawanobori T, Furukawa T. Nitric oxide-dependent modulation of the delayed rectifier K^+ current and the L-type Ca^{2+} current by ginsenoside Re, an ingredient of *Panax ginseng*, in guinea-pig cardiomyocytes. Br J Pharmacol 2004; 142: 567–75.

23 Park JB, Choe H, Lee YK, Ha KC, Rhee KS, Ko JK, *et al.* Open channel block by KCB-328 [1-(2-amino-4-methanesulfonamidophenoxy)-2-[*N*-(3,4-dimethoxyphenethyl)-*N*-methylamino]ethane hydrochloride] of the heterologously expressed human ether-a-go-go-related gene K^+ channels. J Pharmacol Exp Ther 2002; 302: 314–9.

24 Kiehn J, Wible B, Ficker E, Taglialatela M, Brown AM. Cloned human inward rectifier K^+ channel as a target for class III methanesulfonanilides. Circ Res 1995; 77: 1151–5.

25 Spector PS, Curran ME, Keating MT, Sanguinetti MC. Class III antiarrhythmic drugs block HERG, a human cardiac delayed rectifier K^+ channel. Open-channel block by methanesulfonanilides. Circ Res 1996; 78: 499–503.

26 Sanguinetti MC. Dysfunction of delayed rectifier potassium channels in an inherited cardiac arrhythmia. Ann N Y Acad Sci 1999; 868: 406–13.

27 Zhou Z, Gong Q, Epstein ML, January CT. HERG channel dysfunction in human long QT syndrome. Intracellular transport and functional defects. J Biol Chem 1998; 273: 21061–6.

28 Bian J, Cui J, McDonald TV. HERG K^+ channel activity is regulated by changes in phosphatidyl inositol 4,5-bisphosphate. Circ Res 2001; 89: 1168–76.

29 Choi S, Rho SH, Jung SY, Kim SC, Park CS, Nah SY. A novel activation of Ca^{2+}-activated Cl^- channel in *Xenopus* oocytes by *Ginseng saponins*: evidence for the involvement of phospholipase C and intracellular Ca^{2+} mobilization. Br J Pharmacol 2001; 132: 641–8.

30 Choi S, Jung SY, Ko YS, Koh SR, Rhim H, Nah SY. Functional expression of a novel ginsenoside Rf binding protein from rat brain mRNA in *Xenopus* laevis oocytes. Mol Pharmacol 2002; 61: 928–35.

31 Nah SY, Park HJ, McCleskey EW. A trace component of ginseng that inhibits Ca^{2+} channels through a pertussis toxin-sensitive G protein. Proc Natl Acad Sci USA 1995; 92: 8739–43.

32 Lawson, K. Potassium channel openers as potential therapeutic weapons in ion channel disease. Kidney Int 2000; 57: 838–45.

Acta Pharmacologica Sinica 2005 May; 26 (5): 559–562

Blackwell Publishing

Full-length article

Effects of AMP579 and adenosine on L-type Ca^{2+} current in isolated rat ventricular myocytes

Xiong WANG[1], Bo-wei WU, Dong-mei WU

Department of Physiology, Shanxi Medical University, Taiyuan 030001, China

Key words

AMP579; adenosine; heart ventricles; cardiac myocytes; L-type calcium channels; patch-clamp techniques

[1] Correspondence to Prof Xiong WANG.
Phn 86-351-469-0162.
E-mail Wxiong@public.ty.sx.cn

Received 2004-08-23
Accepted 2004-12-11

doi: 10.1111/j.1745-7254.2005.00107.x

Abstract

Aim: To compare the effects of AMP579 and adenosine on L-type Ca^{2+} current ($I_{Ca\text{-}L}$) in rat ventricular myocytes and explore the mechanism by which AMP579 acts on $I_{Ca\text{-}L}$. **Methods:** $I_{Ca\text{-}L}$ was recorded by patch-clamp technique in whole-cell configuration. **Results:** Adenosine (10 nmol/L to 50 μmol/L) showed no effect on basal $I_{Ca\text{-}L}$, but it inhibited the $I_{Ca\text{-}L}$ induced by isoproterenol 10 nmol/L in a concentration-dependent manner with the IC_{50} of 13.06 μmol/L. Similar to adenosine, AMP579 also showed an inhibitory effect on the $I_{Ca\text{-}L}$ induced by isoproterenol. AMP579 and adenosine (both in 10 μmol/L) suppressed isoproterenol-induced $I_{Ca\text{-}L}$ by 11.1% and 5.2%, respectively. In addition, AMP579 had a direct inhibitory effect on basal $I_{Ca\text{-}L}$ in a concentration-dependent manner with IC_{50} (1.17 μmol/L). PD116948 (30 μmol/L), an adenosine A_1 receptor blocker, showed no action on the inhibitory effect of AMP579 on basal $I_{Ca\text{-}L}$. However, GF109203X (0.4 μmol/L), a special protein kinase C (PKC) blocker, could abolish the inhibitory effect of AMP579 on basal $I_{Ca\text{-}L}$. So the inhibitory effect of AMP579 on basal $I_{Ca\text{-}L}$ was induced through activating PKC, but not linked to adenosine A_1 receptor. **Conclusion:** AMP579 shows a stronger inhibitory effect than adenosine on the $I_{Ca\text{-}L}$ induced by isoproterenol. AMP579 also has a strong inhibitory effect on basal $I_{Ca\text{-}L}$ in rat ventricular myocytes. Activation of PKC is involved in the inhibitory effect of AMP579 on basal $I_{Ca\text{-}L}$ at downstream-mechanism.

Introduction

Recent studies showed that AMP579 was a novel adenosine agonist with high affinity for adenosine A_1 and A_2 receptors[1,2]. Experiments in animal models have demonstrated that AMP579 reduced infarct size by 50% to 98% when administered before a final ischemic event (mediation of ischemic preconditioning) or just before reperfusion (attenuation of reperfusion injury)[3,4]. Further experiments on pigs, dogs, and rabbits suggested that AMP579 was more powerful than adenosine in attenuating polymorphonuclear neutrophil-mediated inflammatory responses, dilating the coronary artery, reducing myocardial contracture and limiting infarct size[5,6]. Although the protective effect of AMP579 required adenosine receptor activation, adenosine could not duplicate the effects.

The difference between pharmacologic effect of AMP579 and adenosine might reflect the differences in ionic mechanisms. It has been established that adenosine could cause an attenuation of basal $I_{Ca\text{-}L}$ only in unstimulated atrial myocytes, but under conditions of isoproterenol stimulation, adenosine could markedly attenuate isoproterenol induced-$I_{Ca\text{-}L}$ in both atrial and ventricular myocytes. However, little is known about the electrophysiological effects of AMP579 so far. This study will examine the effects of AMP579 and adenosine on L-type calcium channel and elucidate the mechanisms underlying the cardioprotective effect of AMP579 and its utility in treatment of myocardial ischemia-reperfusion injury.

Materials and methods

Rat myocardial cell isolation Ventricular myocytes were obtained from Wistar male rats (250–300 g) by enzymatic

isolation procedure. In brief, rats were killed by cervical dislocation and the heart was then immediately removed, cannulated through the aorta and perfused through the coronary artery with Ca^{2+}-free Tyrode's solution for 10 min. The composition of Ca^{2+}-free Tyrode's solution was: NaCl 140.0 mmol/L, KCl 5.4 mmol/L, $MgCl_2$ 1.0 mmol/L, NaH_2PO_4 0.3 mmol/L, glucose 10.0 mmol/L, HEPES 5.0 mmol/L; pH adjusted to 7.4 with NaOH at room temperature. The heart was then perfused with enzymatic solution, which was low Ca^{2+} ($CaCl_2$ 150 μmol/L) Tyrode's solution with collagenase P (0.3g/L) for about 8−10min. The left ventricle was then removed. The cells were isolated by gentle agitation and kept in Krebs buffer (KB) solution, which contained: KOH 85.0 mmol/L, *L*-glutamic acid 50.0 mmol/L, KCl 30.0 mmol/L, taurine 20.0 mmol/L, KH_2PO_4 30.0 mmol/L, $MgCl_2$ 1.0 mmol/L, HEPES 10.0 mmol/L, glucose 10.0 mmol/L and egtazic acid 0.5 mmol/L; pH adjusted to 7.4 by KOH.

Electrophysiological measurement Whole-cell patch-clamp was used to record $I_{Ca\text{-}L}$ (L-type Ca^{2+} currents) and membrane capacitance was measured with a P-clamp 5.51 software package (Axon Instruments, USA). Patch electrodes were made from thin-walled glass capillaries (1.5 mm outside diameter) using a two-stage vertical microelectrode puller (model PP-83, Narishige Scientific Instruments, Japan). The electrode resistance ranges 3 MΩ, when filled with pipette solution.

For the measurement of $I_{Ca\text{-}L}$, the extracellular solution contained: NaCl 140.0 mmol/L, $CaCl_2$ 1.8 mmol/L, $MgCl_2$ 1.0 mmol/L, KCl 5.4 mmol/L, glucose 10.0 mmol/L, NaH_2PO_4 0.3 mmol/L, and HEPES 10.0 mmol/L; pH adjusted to 7.4 with NaOH. The pipette solution contained: egtazic acid 10.0 mmol/L, KCl 140.0 mmol/L, Na_2ATP 2.0 mmol/L, HEPES 5.0 mmol/L, 4-AP 5.0 mmol/L, $MgCl_2$ 1.0 mmol/L; pH adjusted to 7.4 with KOH. The calcium current was expressed as membrane current density (pA/pF). The cell capacitance was measured by the method previously described by Coetzee *et al*[9]. $I_{Ca\text{-}L}$ was measured according to the method described by Hartzell *et al*[10]. The AMP579 was a gift from Department of Cardiothoracic Surgery Research Laboratory, Emory University School of Medicine, USA. AMP579 was dissolved in small volumes of Me_2SO, then diluted to the desired final concentration before each experiment.

Statistic analysis Data were expressed as mean±SD. Statistical significance was determined by Student's *t*-test and $P<0.05$ was considered significant.

Results

Detection of L-type calcium channel current The calcium current was activated by depolarizing pulse from a holding potential of -40 mV to +10 mV at 50 mV step-voltage. This inward current could be completely inhibited by 1 μmol/L verapmil, the basic characteristics indicated that the current present in rat ventricular myocytes was L-type Ca^{2+} current .

Effect of AMP579 and adenosine on L-type calcium current In the presence of adenosine at 10 nmol/L, 1, 10, and 50 μmol/L, $I_{Ca\text{-}L}$ varied from 4.9±0.9 to 4.8±0.9, 4.9±0.9, 4.9±0.9, 4.7±0.9 pA/pF, respectively (n=5, $P>0.05$). Adenosine had no effect on basal $I_{Ca\text{-}L}$. However, when $I_{Ca\text{-}L}$ was augmented to 2.7±0.6 pA/pF by 10 nmol/L isoproterenol, adenosine at 10 nmol/L, 1, 10, and 50 μmol/L significantly reduced it to 2.4±0.6, 2.1±0.6, 2.0±0.5, and 1.9±0.5 pA/pF, respectively (n=4, $P<0.05$). Adenosine showed an inhibitory effect on isoproterenol-induced $I_{Ca\text{-}L}$ in a concentration-dependent manner with the IC_{50} of 13.06 μmol/L (Figure 1, 2).

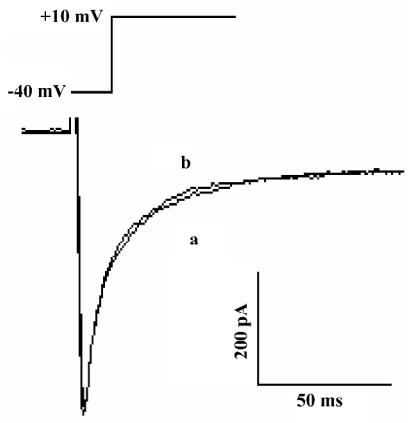

Figure 1. Effect of adenosine on $I_{Ca\text{-}L}$ in isolated rat ventricular myocytes. (a) Control; (b) 50 μmol/L adenosine.

Effect of AMP579 on $I_{Ca\text{-}L}$ Isoproterenol 10 nmol/L augmented $I_{Ca\text{-}L}$ to 3.8±0.7 pA/pF. AMP579 10 μmol/L reduced $I_{Ca\text{-}L}$ to 2.4±0.1 pA/pF ($P<0.05$, n=3, Figure 3), AMP579 also showed an inhibitory effect on isoproterenol-induced $I_{Ca\text{-}L}$. AMP579 and adenosine (both 10 μmol/L) suppressed isoproterenol-induced $I_{Ca\text{-}L}$ by 11.1% and 5.2%, respectively. AMP579 had a stronger inhibitory effect. In contrast to adenosine, AMP579 possessed a direct inhibitory effect on basal $I_{Ca\text{-}L}$ in a concentration-dependent manner with the IC_{50} of 1.17 μmol/L (Table 1, Figure 4).

AMP579 10 μmol/L markedly reduced basal $I_{Ca\text{-}L}$ from 2.5±1.2 to 2.0±1.0 pA/pF (n=5, $P<0.05$). Infusion of PD116948 30 μmol/L, an adenosine A_1 receptor blocker, did not abolish the inhibitory effects of AMP579 on $I_{Ca\text{-}L}$ (1.9±0.6 *vs* 2.0±1.0 pA/pF, $P>0.05$). But under the same conditions AMP579 10

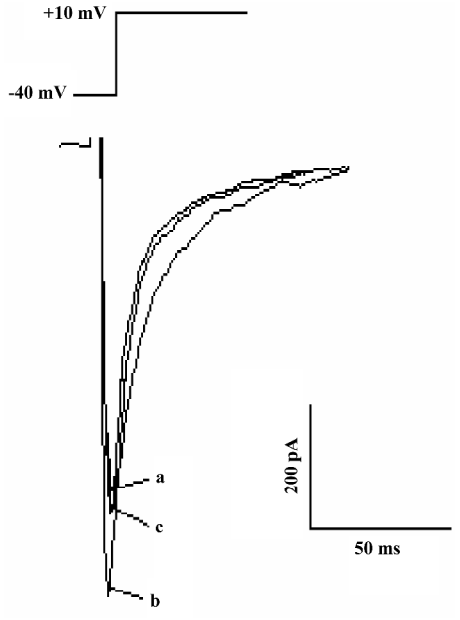

Figure 2. The inhibitory effect of adenosine on $I_{Ca\text{-}L}$ induced by isoproterenol in isolated rat ventricular myocytes. (a) Control; (b) isoproterenol 10 nmol/L; (c) adenosine 50 μmol/L.

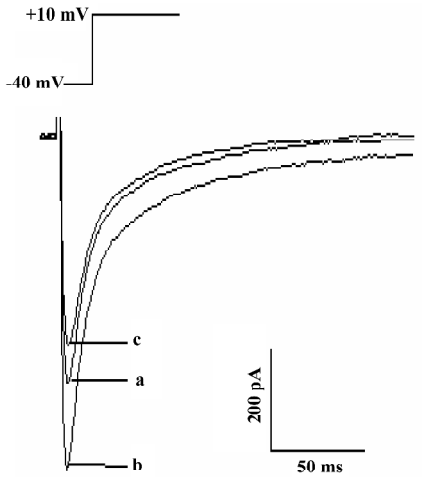

Figure 3. The inhibitory effect of AMP579 on $I_{Ca\text{-}L}$ induced by isoproterenol in isolated ventricular myocytes. (a) Control; (b) isoproterenol 10 nmol/L; (c) AMP579 10 μmol/L.

μmol/L markedly reduced the $I_{Ca\text{-}L}$ from 2.4±0.4 to 1.8±0.4 pA/pF (n=4, P<0.01). Infusion of 0.4 μmol/L GF109203X, a PKC blocker, significantly reversed it to 2.2±0.4 pA/pF (P< 0.05, Figure 5). So GF109203X could abolish the inhibitory effect of AMP579, indicating that the inhibitory effect on basal $I_{Ca\text{-}L}$ by AMP579 was induced through activating PKC but not linked to the adenosine A_1 receptor.

Table 1. Effect of AMP579 on basal $I_{Ca\text{-}L}$ in rat ventricular myocytes. n=5. Mean±SD. ^bP<0.05, ^cP<0.01 *vs* corresponding control group.

AMP579 concentration	$I_{Ca\text{-}L}$ value/ pA·pF^{-1}	Change rate/ %
0 (Control)	2.80±0.75	
10 nmol/L	2.66±0.75^b	-5.0
1 μmol/L	2.36±0.71^b	-15.7
10 μmol/L	2.03±0.72^c	-27.5
50 μmol/L	1.78±0.70^c	-36.4

Change rate=(the current value after administration of drug−control value)/control value×100%

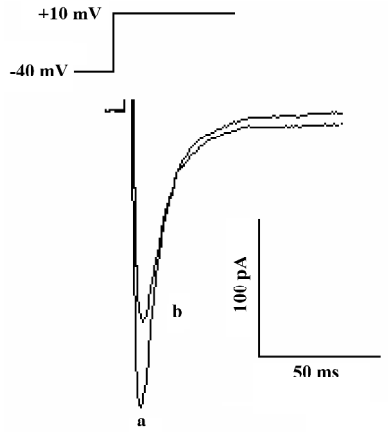

Figure 4. Effect of AMP579 on $I_{Ca\text{-}L}$ in isolated rat ventricular myocytes. (a) Control; (b) AMP579 50 μmol/L.

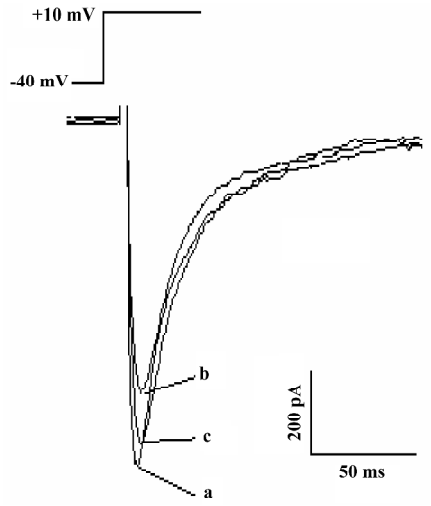

Figure 5. Abolition of inhibitory effects of AMP579 on $I_{Ca\text{-}L}$ by a PKC blocker in isolated rat ventricular myocytes. (a) Control; (b) AMP579 10 μmol/L; (c) GF109203X 0.4 μmol/L.

Discussion

In cardiac tissue, a direct inhibition of basal $I_{Ca\text{-}L}$ by adenosine has only been demonstrated in guinea-pig atrial and ferret ventricular myocytes[11,12]. But in the presence of isoproterenol stimulation, adenosine has prominent inhibitory effects on $I_{Ca\text{-}L}$ in ventricular myocytes[13]. These may reflect differences in receptor-effector coupling mechanisms, the level of basal adenylate cyclase activity, the basal phosphorylated state of Ca^{2+} channels and/or the effect of phosphorylation on the gating of L-type Ca^{2+} channel. Consistent with previous reports, our experiment shows that adenosine has no direct inhibitory effect on basal $I_{Ca\text{-}L}$ in the rat ventricle, but in the condition that isoproterenol was previously administered, adenosine shows an inhibitory effect on the $I_{Ca\text{-}L}$ induced by isoproterenol with an IC_{50} of 13.06 μmol/L, suggesting that adenosine exerts an indirect inhibitory effect on $I_{Ca\text{-}L}$ in the rat ventricle by inhibition of isoproterenol stimulation.

In contrast to adenosine, AMP579 shows a direct inhibitory effects on basal $I_{Ca\text{-}L}$ in the rat ventricle with IC_{50} of 1.17 μmol/L. The blocking of Ca^{2+} influx by L-type Ca^{2+} channel could serve as an efficient method for protecting the ischemic myocyte by minimizing ischemia-induced Ca^{2+} overload and irreversible cell contracture and autodigestion by Ca^{2+}-dependent proteases[14]. Therefore, by reducing both basal $I_{Ca\text{-}L}$ and isoproterenol-induced $I_{Ca\text{-}L,}$ AMP579 will play a more important role in negative chronotropic and negative dromotropic effects. These action mechanism differences between AMP579 and adenosine may account for the contribution of AMP579 in reducing neutrophil-mediated inflammatory reaction, inhibiting cardiac contraction, dilating coronary vessels, attenuating ischemia and reperfusion injury.

Our study does not show that adenosine A_1 receptor is linked to inhibition of AMP579 on basal $I_{Ca\text{-}L}$. At present, available data indicate that three pathways are involved in receptor-linked downstream mechanisms for inhibition of $I_{Ca\text{-}L}$ by adenosine. The first is cAMP-PKA, as PKA increase $I_{Ca\text{-}L}$ by phosphorylation on the gating of the L-type calcium channel, inhibitions of adenylate cyclase and reductions of cAMP and PKA levels by adenosine result in attenuation on $I_{Ca\text{-}L}$[12]. Second is that activation of guanylate cyclase results in increments of intracellular cGMP and PKG concentration, which in turn inhibits phosphorylation on the gating of the L-type calcium channel[15]. The third is modulated by PKC, because there are different PKC subunits which result in different effects[16]. Our experiment finds that special PKC antagonist GF109203X can totally eliminate inhibitory effects of AMP579 on $I_{Ca\text{-}L}$, suggesting that AMP579 exerts a direct inhibitory effects on the L-type calcium channel through the PKC pathway.

References

1 Nakamura M, Zhao ZQ, Clark KL, Velez DV, Guyton RA, Vinter-Johansen J. A novel adenosine analog, AMP579, inhibits neutrophil activation, adherence and neutrophil-mediated injury to coronary vascular endothelium. Eur J Pharmacol 2000; 397: 197–205.

2 Sledeski AW, Kubiak GG, O'Brien MK, Powers MR, Powener TH, Truesssdale LK. Efficient synthesis of AMP579, a novel adenosine A_1/A_2 receptor agonist. J Org Chem 2000; 65: 8114–9.

3 Budde JM, Velez DA, Zhao ZQ, Clark KL, Morris CD, Muraki S, *et al*. Comparative study of AMP579 and adenosine inhibition of neutrophil-mediated vascular and myocardial injury during 24 h of reperfusion. Cardiovasc Res 2000; 47: 294–305.

4 Xu Z, Downey JM, Cohen MV. AMP579 reduces contracture and limits infarction in rabbit heart by activating adenosine A_2 receptors. J Cardiovasc Pharmacol 2001; 38: 474–81.

5 Mcvey MJ, Smiths GJ, Cox BF, Kitzen JM, Clark KL, Perrone MH. Cardiovascularpharmacology of the adenosine A_1/A_2-receptor agonist AMP579: coronary hemodynamic and cardioprotective effects in the canine myocardium. J Cardiovasc Pharmacol 1999; 33: 701–10

6 Smits GJ, Mcvey M, Cox BF, Perrone MH, Clark KL. Cardioprotective effects of the novel A_1/A_2 receptor agonist AMP579 in a porcine model of myocardial infarction. J Pharmacol Exp Ther 1998; 286: 611–8.

7 Pelleg A, Belardinelli C. Cardiac electrophysiology and pharmacology of adenosine: basic and clinical aspects. Cardiovasc Res 1993; 27: 54–61.

8 Belardinelli L, Linden J, Berne RM. The cardiac effects of adenosine. Prog Cardiovasc Dis 1989; 32; 73–97.

9 Coetzee WA, Ichikawa H, Hearse DJ. Oxidant stress inhibits Na^+/Ca^{2+} exchange in cardiac myocytes: mediation by sulfhydryl groups? Am J Physiol 1994; 266; H909–19.

10 Hartzell HC, Simmons MA. Comparison of effects of acetylcholine on calcium and potassium currents in frog atrium and ventricle. J Physiol 1987; 89: 411–22.

11 Cerbai E, Klockner U, Isenberg G. Ca^{2+}-antagonistic effects of adenosine in guinea-pig atrial cell. Am J Physiol 1988; 255: H872–8.

12 Qu Y, Campbell DL, Whorton AR, Strauss HC. Modulation of basal L-type Ca^{2+} current by adenosine in ferret isolated right ventricular myocytes. J Physiol 1993; 471: 269–93.

13 Isenberg G, Belardinelli L. Ionic basis for the antagonism between adenosine and isoproterenol on isolated mammalian ventricular myocytes. Circ Res 1984; 55: 309–25.

14 Eckert R, Utz J, Trautwin W, Mentzer RM, Wis M, Saar H. Involvement of intracellular Ca^{2+} release mechanism in adenosine-induced cardiac Ca^{2+} current inhibition. Surgery 1993; 114: 334–42.

15 Shen JB, Pappano AJ. On the role of phosphatase in regulation of cardiac L-type calcium current by cyclic GMP. J Pharmacol Exp Ther 2002; 301: 501–6.

16 Kameyama M, Hofmann F, Trautwein W. On the mechanism of beta-adrenergic regulation of the Ca^{2+} channel in the guinea-pig heart. Pflugers Arch 1985; 405: 285–93.

Acta Pharmacologica Sinica 2005 May; 26 (5): 563–567

Full-length article

5-Hydroxytryptamine-induced proliferation of pulmonary artery smooth muscle cells are extracellular signal-regulated kinase pathway dependent[1]

Dan SONG, Huai-liang WANG[2], Shuang WANG, Xin-hua ZHANG

Department of Clinical Pharmacology, China Medical University, Shenyang 110001, China

Key words

antisense oligodeoxyribonucleotides; serotonin; membrane transport proteins; pulmonary hypertension; vascular smooth muscle; fluxetine; mitogen-activated protein kinases

[1] Project supported in part by National Natural Science Foundation of China (No 0271510) and the Science and Technology Committee of China (No 9690105274).
[2] Correspondence to Prof Huai-liang WANG.
Phn 86-24-2325-6666, ext 5547.
Fax 86-24-2324-6666, ext 5547.
E-mail hlwang@mail.cmu.edu.cn

Received 2004-07-15
Accepted 2004-11-10

doi: 10.1111/j.1745-7254.2005.00071.x

Abstract

Aim: To investigate the effect of 5-hydroxytryptamine transporter (5-HTT) inhibitor fluoxetine and antisense oligodeoxynucleotide (ODN) to extracelluar signal-regulated kinases (ERKs) on pulmonary arterial smooth muscle cells (PASMCs) proliferation induced by 5-HT. **Methods:** Liposomal transfection was used to introduce ODNs to ERK1/2 into cultured rat PASMCs and the transfection efficiency was measured by observing the uptake of the fluorecein isothiocynate (FITC)-labeled antisense ODN in PASMCs. The effects of 5-HTT selective inhibitor fluoxetine and ODNs on the proliferation of PASMCs were evaluated by cell number counting and cell cycle analysis, and measured by microculture tetrazolium (MTT) assay and flow cytometry (FCM), respectively. **Results:** Liposomes mediated the transfection of ODNs into PASMCs with high efficiency. MTT assay showed fluoxetine (10 μmol/L, 1 μmol/L, and 100 nmol/L) concentration dependently inhibited the proliferation of PASMCs induced by 5-HT (1 μmol/L) *in vitro*. The proliferation rate of PASMCs by 5-HT was significantly inhibited by pretreatment with ERK1/2 antisense ODN (0.2 μmol/L) from 251%±18% to 86%±5% ($P<0.01$). Flow cytometric analysis of cell cycle distribution showed that the increase of 5-HT induced S phase fraction (SPF) and proliferation index (PI) were significantly inhibited by fluoxetine (1 μmol/L) or antisense ODN with SPF from 36%±4% to 26%±3% and 24%±4%, and PI from 34%±2% to 29%±2% and 24%±2%, respectively. **Conclusion:** 5-HTT mediates the mitogenic effect of 5-HT on PASMCs and the proliferation of PASMCs induced by 5-HT is dependent on ERKs signal pathway.

Introduction

Exposure to acute or chronic hypoxia leads to the development of pulmonary arterial hypertension (PAH). The cardinal features of PAH are persistent vasoconstriction and structural remodeling of the pulmonary vessels[1]. Hyperplasia of pulmonary artery smooth muscle cells (PASMCs) is the main component of pulmonary vascular remodeling which is associated with progressive elevation in pulmonary arterial pressure[2]. However, the exact mechanism of the proliferation of PASMCs was unclear.

Several studies have shown that 5-hydroxytryptamine (5-HT), endothelin-1 (ET), platelet derived growth factors (PDGF), angiotensin II (Ang II), and epidermal growth factor (EGF) participate in the regulation of proliferation in PASMCs[3]. Among these mediators, 5-HT plays an important role in the pathogenesis of PAH. 5-HT exerts potent mitogenic and comitogenic effects on PASMCs, and these effects are associated with cellular internalization of 5-HT mediated by the 5-hydroxytryptamine transporter (5-HTT)[4,5]. Yet, it is not clear if inhibition of 5-HTT may abolish the proliferation of PASMCs to 5-HT.

Furthermore, mitogen activated protein kinases (MAPKs) are a superfamily of serine/threonine protein kinases distributed extensively in cytoplasm. Many stimuli resulting in cell

growth, differentiation, and vascular contraction may activate MAP kinase-dependent signaling pathways.

Among this family, extracelluar signal-regulated kinases (ERKs) are activated in response to growth and differentiation factors[6–8]. Previous studies have shown that 5-HT induced ERK1/2 activation in rat aortic smooth muscle cells and rabbit isolated renal artery smooth muscle cells[9,10]. However, whether the intracelluar signal pathway of 5-HT in PASMCs is dependent on the ERKs activation is largely unconcerned. Therefore, the present study was designed to observe the effect of fluoxetine, a selective inhibitor of 5-HTT, on the proliferation of PASMCs in response to 5-HT, and then to study the effect of downregulation of ERK1/2, using antisense oligodeoxynucleotides (ODNs), on the proliferation of 5-HT-stimulated PASMCs *in vitro*.

Materials and methods

Drugs and reagents Dulbecco's modified Eagle's medium (DMEM), fetal bovine serum (FBS), and trypsin were purchased from Gibco Co (Grand Island, New York, USA). 5-HT and propidium iodide (PI) were purchased from Sigma Co (St Louis, USA). Lipofectin reagent was from Life Technologies Inc, Ltd (Rockville, USA). Fluoxetine hydrochloride was from Eli Lilly Co (Indianapolis, USA). ODNs were synthesized by Sangon (Shanghai, China).

Pulmonary artery smooth muscle cell culture Lungs were removed from male Wistar rats weighing 250–300 g (supplied by the Animal Center of China Medical University, Grade II, Certificate No LN 03-0009). Under aseptic conditions, proximal pulmonary arteries were isolated. After removing the tissue around the arteries, the pulmonary arteries were cut into small pieces about 1 mm^2 and then seeded into 30-mm Petri dishes and cultured in DMEM (containing 20% FBS, 100 kU/L of penicillin and 100 mg/L of streptomycin, pH 7.2). Then these explants were incubated at the atmosphere of 37 °C and 95% O_2/5% CO_2[11]. When the cells had grown out from the explants and reached the confluence of more than 70%, cells were passaged to T25 flasks. Cells used in experiments were from passages 3 to 9.

Oligodeoxynucleotides On account of GCG package locating in the translation initiation region of rat ERK1/2 mRNA, the sequences of antisense ODN were designed as follows: 5'-GCC GCC GCC GCC GCC AT. This ODN has been used successfully to downregulte ERK1/2 in VSMCs, rat cardiac myocytes and rat cardiac fibroblasts[12]. Sense ODN (5'-AT GGC GGC GGC GGC GGC), random ODN (5'-CGC GCG CTC GCG CAC CC) were used as controls. All bases were protected by phosphorothioation. One batch of antisense ODN was labeled with fluorecein isothiocyanate (FITC) used in fluorescence microscopy experiments.

Microculture tetrazolium (MTT) assay Cells were seeded into 96-well plates at a density of 1×10^4 cells/well. The cells were then incubated in medium containing vehicle (5% FCS DMEM) and 5-HT (1 μmol/L) for 24 h with or without fluoxetine (10 μmol/L, 1 μmol/L, and 100 nmol/L) added 30 min before 5-HT. The effect of different ODNs (0.2 μmol/L) on the proliferation induced by 5-HT was also observed after transfection. The group with the cells incubated in serum-free medium was used as the control. At the end of this period, MTT (5 g/L) was added to each well, and incubation proceeded at 37 °C for 4 h. Thereafter, the medium was removed and the cells were solubilized in 150 μL Me_2SO. Optical density (*OD*) of each well was determined by enzyme-linked ELISA at 490 nm of wavelength. Then the proliferation rates (PR) of each group were calculated.

$$PR=(OD_{experiment}-OD_{control})/OD_{control}$$

Flow cytometry (FCM) PASMCs grown in T25 plates were treated with fluoxetine or antisense ODN (0.2 μmol/L) before 5-HT was added. The cells were harvested by trypsinization, washed twice with PBS, and the pellets were resuspended in 0.5 mL of PBS containing 100 mg/L RNase for incubation at 37 °C for 30 min. Then, 0.5 mL of PI solution (100 mg/L in PBS) was added, and the mixture was incubated in the dark at 4 °C for 30 min. The cells were analyzed with a FACScan flow cytometer. Then S-phase cell fractions (SPF) and proliferation index (PI) of each group were calculated. $SPF=S/(G_0G_1+S+G_2M)$; $PI=(G_2M+S)/(G_0G_1+S+G_2M)$.

Liposomal transfection Prior to transfection, PASMCs were cultured in serum-free medium for 24 h. ODNs were mixed with antibiotic- and serum-free medium to a concentration of 0.8 μmol/L, then mixed with equal volume of medium containing 80 mg/L of lipofectin and incubated at room temperature for 15 min. ODN/lipofectin mix 20 μL was added to each well of a 96-well plate, 200 μL to each well of a 12-well plate, and 1000 μL to the T25 plates, with equal volume of antibiotic- and serum-free medium. The cells were incubated for a further 6 h with gentle agitation every 2 h. The medium was then replaced with the same volume of liposome-free medium containing the same concentration of ODN and 5% FBS. Cells were incubated for another 24 h before MTT assay and FCM.

Fluorescence microscopy PASMCs were seeded into 12-well plate and transfected using FITC-labeled antisense ODN. After 24 h and 48 h of incubation, the cells were viewed by fluorescence microscopy.

Statistical analysis All the data are presented as mean±SD, and assessed by ANOVA and *t*-test. $P<0.05$ was

considered significant.

Results

Uptake of ODNs by PASMCs Twenty four hours after liposomal transfection, FITC-labeled antisense ODN were observed in both cytoplasm and the nuclei of PASMCs (Figure 1). More than 90% of the cells exhibited fluorescence.

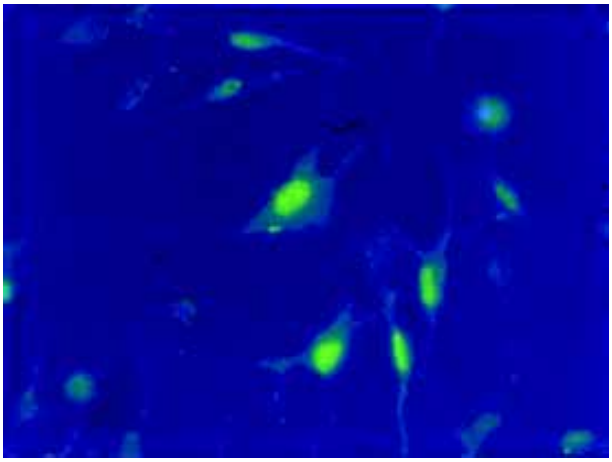

Figure 1. Fluorescence photomicrograph of PASMCs taken 24 h after transfection with the FITC-labeled antisense ODN (× 400). Fluorescence were observed in both cytoplasm and the nuclei of PASMCs.

Effect of fluoxetine and ODNs on the proliferation of PASMCs induced by 5-HT MTT assay showed that 5-HT (1 μmol/L) induced increased proliferation of PASMCs and the PR in response to 5-HT increased from 172%±5% to 217%±4% compared with the vehicle. Pretreatment of the cells with fluoxetine (10 μmol/L, 1 μmol/L, and 100 nmol/L) could produce a concentration-dependent reduction in PR (Figure 2). According to these results, 1 μmol/L was chosen as the concentration of fluoxetine used in following experiments.

Pretreatment of PASMCs with ERK1/2 antisense ODN resulted in a significant inhibition of 5-HT-induced PASMCs proliferation (Figure 3) and this inhibitory effect is rather more potent than fluoxetine. In contrast, sense ODN and random ODN did not have such effect.

Effect of fluoxetine and antisense ODN on cell cycle Flow cytometric analysis of cell cycle distribution showed that the cells treated with 5-HT had larger values of S-phase cell fraction (SPF) and PI than the vehicle. But pretreatment with fluoxetine or antisense ODN decreased these values (Figures 4, 5). These results indicated that 5-HT promoted the PASMCs from the G_0/G_1 phase of the cell cycle into S phase and this effect was inhibited by fluoxetine and antisense ODN.

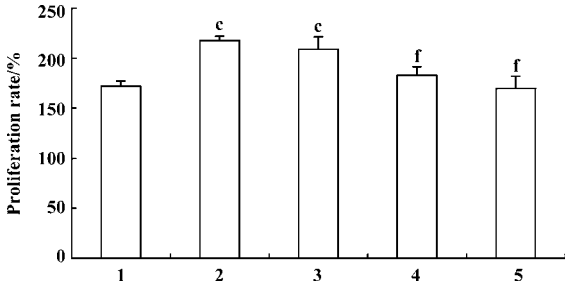

Figure 2. Effect of different concentrations of fluoxetine on the proliferation of PASMCs induced by 5-HT. Experimental groups: 1) vehicle (5% FBS DMEM); 2) 5-HT (1 μmol/L); 3) 5-HT (1 μmol/L) +fluoxetine (100 nmol/L); 4) 5-HT (1 μmol/L)+fluoxetine (1 μmol/L); 5) 5-HT (1 μmol/L)+fluoxetine (10 μmol/L). n=3. ^cP<0.01 *vs* control. ^fP<0.01 *vs* 5-HT (1 μmol/L).

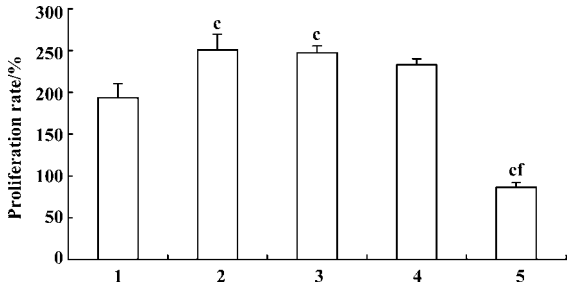

Figure 3. Effect of different ODNs on the proliferation of PASMCs induced by 5-HT. Experiment groups: 1) vehicle (5% FBS DMEM); 2) 5-HT (1 μmol/L); 3) 5-HT (1 μmol/L)+random ODN (0.2 μmol/L); 4) 5-HT (1 μmol/L)+sense ODN (0.2 μmol/L); 5) 5-HT (1 μmol/L) +antisense ODN (0.2 μmol/L). n=3. ^cP<0.01 *vs* control. ^fP<0.01 *vs* 5-HT (1 μmol/L).

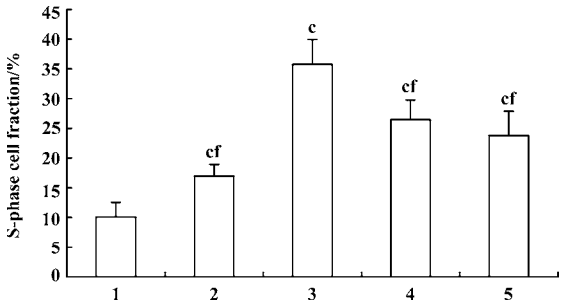

Figure 4. Effect of fluoxetine and antisense ODN on S-phase cell fraction of PASMCs. Experiment groups: 1) control; 2) vehicle (5% FBS DMEM); 3) 5-HT (1 μmol/L); 4) 5-HT (1 μmol/L)+fluoxetine (1 μmol/L); 5) 5-HT (1 μmol/L)+antisense ODN (0.2 μmol/L). n=3. ^cP<0.01 *vs* control. ^fP<0.01 *vs* 5-HT(1 μmol/L).

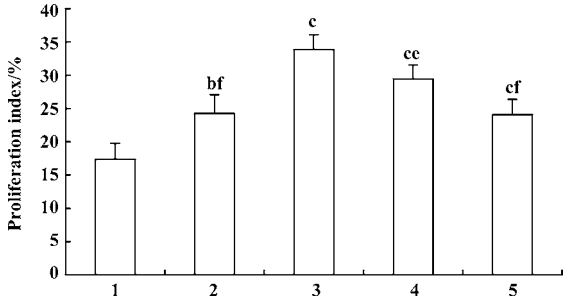

Figure 5. Effect of fluoxetine and antisense ODN on proliferation index of PASMCs. Experiment groups: 1) control; 2) vehicle (5% FBS DMEM); 3) 5-HT (1 μmol/L); 4) 5-HT (1 μmol/L)+fluoxetine (1 μmol/L); 5) 5-HT (1 μmol/L)+antisense ODN (0.2 μmol/L). n=3. $^{b}P<0.05$, $^{c}P<0.01$ *vs* control. $^{e}P<0.05$, $^{f}P<0.01$ *vs* 5-HT (1 μmol/L).

Discussion

Results from the present study demonstrated that 5-HTT played a key role in the mitogenic effect of 5-HT on PASMCs. Fluoxetine, a highly selective inhibitor of 5-HTT inhibited the proliferation of PASMCs induced by 5-HT *in vitro*. Meanwhile, antisense ODN to ERK1/2 inhibited 5-HT-induced proliferation of PASMCs. These findings suggest that 5-HT-induced proliferation of PASMCs is 5-HTT and ERK pathway dependent.

In response to hypoxia, 5-HT is released from pulmonary neuroendocrine cells and neuroepithelial bodies distributed throughout the airways. An increase in 5-HT may contribute to secondary pulmonary artery hypertension[13]. The proliferation of PASMCs induced by 5-HT is an important component of pulmonary arterial remodeling. RT-PCR analyses of PASMCs indicated the presence of 5-$HT_{1B/1D}$, 5-HT_2 receptors and 5-HTT mRNA[14,15]. The present results show that the proliferation of PASMCs induced by 5-HT is inhibited by fluoxetine in a manner that is concentration-dependent. In contrast, the 5-$HT_{1B/1D}$ receptor antagonist GR127935, the 5-HT_{2A} receptor antagonist ketanserin, or the 5-$HT_{2B/2C}$ receptor antagonist SB206553 had no this effect[16]. It has been recently reported that exposure of PASMCs to hypoxia increased 5-HTT expression and activity, and this effect was associated with potentiation of the mitogenic action of 5-HT[5,17]. Some scholars found that mice deficient in 5-HTT or treated with selective inhibitors of 5-HTT developed less PAH than controls when exposed to hypoxia[18,19]. These evidences suggest that 5-HTT in PASMCs may be a key determinant of pulmonary arterial remodeling and the development of PAH. Therefore, our result means that 5-HTT is one of the important mechanisms of PAH and this may provide a novel therapeutic target for PAH.

The uptake of FITC-labeled antisense ODN by PASMCs with liposomes proved the high efficiency of transfection. In the present study, the antisense ODN to ERK1/2 delivered by lipofectin resulted in an effective suppression of the proliferative response to 5-HT in PASMCs. Meanwhile, the effect of antisense ODN stronger than fluoxetine suggests that antisense ODN to ERK1/2 could inhibit the proliferation of PASMCs not only induced by 5-HT, but also by the serum[20]. The present study proves that 5-HT induced the proliferation of PASMCs and is dependent on the activation of ERK1/2. Therefore, it is reasonable to consider that 5-HT induced activation of ERKs through 5-HTT in PASMCs. Previous studies showed that 5-HT induced the Tyr phosphorylation of GTPase-activating protein (GAP) and the effect was mediated by 5-HTT, which was the upstream of the ERK pathway, not by 5-HT receptors[21]. The mechanism of 5-HT signaling for PASMCs through 5-HTT has also been shown to involve the production of reactive oxygen species (ROS) such as superoxide and H_2O_2 via the activation of NAD(P)H oxidase, and the activation of the ERK pathway occurs secondary to ROS formation[22,23]. Therefore, the activation of ERKs induced by 5-HT is mediated by 5-HTT.

The present study showed that fluoxetine concentration-dependently inhibited 5-HT-induced proliferation of PASMCs *in vitro*, and demonstrated that antisense ODN to ERK1/2 significantly inhibited mitogenesis of PASMCs. Therefore, we concluded that 5-HT-induced mitogenesis of PASMCs was mediated by 5-HTT, in which the signal transduction for 5-HT was dependent on ERKs signal pathway.

References

1 Fishman AP. Clinical classification of pulmonary hypertension. Clin Chest Med 2001; 22: 385–91.
2 Jeffery TK, Morrell NW. Molecular and cellular basis of pulmonary vascular remodeling in pulmonary hypertension. Prog Cardiovasc Dis 2002; 45: 173–202.
3 Eddahibi S, Morrell N, d'Ortho MP, Maeije R, Adnot S. Pathobiology of pulmonary arterial hypertension. Eur Respir J 2002; 20: 1559–72.
4 Lee SL, Wang WW, Lanzillo JJ, Fanburg BL. Serotonin produces both hyperplasia and hypertrophy of bovine pulmonary artery smooth cells in culture. Am J Physiol 1994; 266: L46–52.
5 Eddahibi S, Fabre V, Boni C, Martres MP, Raffestin B, Hamon M, *et al*. Induction of serotonin transporter by hypoxia in pulmonary vascular smooth muscle cells. Relationship with the mitogenic action of serotonin. Circ Res 1999; 84: 329–36.
6 Robinson MJ, Cobb MH. Mitogen-activated protein kinase pathways. Curr Opin Cell Biol 1997; 9: 180–6.
7 Force T, Bonventre JV. Growth factors and mitogen-activated protein kinases. Hypertension 1998; 31: 152–61.
8 Florian JA, Watts SW. Integration of mitogen-activated protein

kinase kinase activation in vascular 5-hydroxytryptamine2A receptor signal transduction. J Pharmacol Exp Ther 1998; 284: 346–55.
9 Watts SW, Yang P, Banes AK, Baez M. Activation of Erk mitogen-activated protein kinase proteins by vascular serotonin receptors. J Cardiovasc Pharmacol 2001; 38: 539–51.
10 Hinton JM, Hill P, Jeremy J, Garland C. Signalling pathways activated by 5-HT_{1B}/5-HT_{1D} receptors in native smooth muscle and primary cultures of rabbit renal artery smooth muscle cells. J Vasc Res 2000; 37: 457–68.
11 Rothman A, Kulik TJ, Taubman MB, Berk BC, Smith CW, Nadal-Ginard B. Development and characterization of a cloned rat pulmonary arterial smooth muscle cell line that maintains differentiated properties through multiple subcultures. Circulation 1992; 86: 1977–86.
12 Huang SL, Ding B, Yu QS, Guo ZG. Effect of antisense mitogen-activated protein kinase oligonucleotides on rat vascular smooth muscle cell proliferation induced by EGR *in vitro*. Acta Pharmacol Sin 1998; 19: 489–93.
13 MacLean MR, Herve P, Eddahibi S, Adnot S. 5-Hydroxytryptamine and the pulmonary circulation: receptors, transporters and relevance to pulmonary arterial hypertension. Br J Parmacol 2000; 131: 161–8.
14 Ullmer C, Schmuck K, Kalkman HO, Lubbert H. Expression of serotonin receptor mRNAs in blood vessels. FEBS Lett 1995; 370: 215–21.
15 Ramamoorthy S, Bauman AL, Moore KR, Han H, Yang-Feng T, Chang AS, *et al*. Antidepressant- and cocaine-sensitive human serotonin transporter: molecular cloning expression and chromosomal location. Proc Natl Acad Sci USA 1993; 90: 2542–6.
16 Marcos E, Adnot S, Pham MH, Nosjean A, Raffestin B, Hamon M, *et al*. Serotonin transporter inhibitors protect against hypoxic pulmonary hypertension. Am J Respir Crit Care Med 2003; 168: 487–93.
17 Eddahibi S, Humbert M, Fadel E, Raffestin B, Darmon M, Capron F, *et al*. Serotonin transporter overexpression is responsible for pulmonary artery smooth muscle hyperplasia in primary pulmonary hypertension. J Clin Invest 2001; 108: 1141–50.
18 Marcos E, Adnot S, Pham MH, Nosjean A, Raffestin B, Hamon M, *et al*. Serotonin transporter inhibitors protect against hypoxic pulmonary hypertension. Am J Respir Crit Care Med 2003; 168: 487–93.
19 Eddahibi S, Hanoun N, Lanfumey L, Lesch KP, Raffestin B, Hamon M, *et al*. Attenuated hypoxic pulmonary hypertension in mice lacking the 5-hydroxytryptamine transporter gene. J Clin Invest 2000; 105: 1555–62.
20 Fisher M, Liu B, Glennon PE, Southgate KM, Sale EM, Sale GJ, *et al*. Downregulation of the ERK 1 and 2 mitogen activated protein kinases using antisense oligonucleotides inhibits proliferation of porcine vascular smooth muscle cells. Atherosclerosis 2001; 156: 289–95.
21 Lee SL, Wang WW, Fanburg BL. Association of Tyr phosphorylation of GTPase-activating protein with mitogenic action of serotonin. Am J Physiol 1997; 272: C223–30.
22 Lee SL, Wang WW, Finlay GA, Fanburg BL. Serotonin stimulates mitogen-activated protein kinase activity through the formation of superoxide anion. Am J Physiol 1999; 277: L282–91.
23 Lee SL, Simon AR, Wang WW, Fanburg BL. H_2O_2 signals 5-HT-induced ERK MAP kinase activation and mitogenesis of smooth muscle cells. Am J Physiol 2001; 281: L646–52.

Acta Pharmacologica Sinica 2005 May; 26 (5): 568–574

Full-length article

Activation of human tonsil and skin mast cells by agonists of proteinase activated receptor-2[1]

Shao-heng HE[2], Hua XIE, Yi-ling FU

Allergy & Inflammation Research Institute, Shantou University Medical College, Shantou 515031, China

Key words

tryptase; histamine; mast cells; proteinase activated receptor-2; anti-IgE; tonsil; skin

[1] Project supported by the Planned Science and Technology Project of Guangdong Province, China, No 2003B31502, and the Li Ka Shing Foundation, Hong Kong, China, No C0200001.
[2] Correspondence to Prof Shao-heng HE.
Phn 86-754-890-0407.
Fax 86-754-890-0405.
E-mail shoahenghe@hotmail.com

Received 2004-06-02
Accepted 2004-12-20

doi: 10.1111/j.1745-7254.2005.00079.x

Abstract

Aim: To investigate the effects of the agonists of proteinase activated receptor (PAR)-2, and histamine on degranulation of human mast cells. **Methods:** Human mast cells were enzymatically dispersed from tonsil and skin tissues. The dispersed cells were then cultured with various stimuli, and tryptase and histamine levels in cell supernatants collected from challenge tubes were measured. **Results:** PAR-2 agonist peptide SLIGKV provoked a dose-dependent release of histamine from skin mast cells. It also induced tryptase release from tonsil mast cells. tc-LIGRLO appeared less potent than SLIGKV in induction of release of histamine and tryptase. Trypsin was able to induce a "bell" shape increase in tryptase release from tonsil mast cells. It was also able to induce a dose-dependent release of histamine from both tonsil and skin mast cells. The actions of trypsin on mast cells were inhibited by soy bean trypsin inhibitor (SBTI) or α_1-antitrypsin (α_1-AT). Time course study revealed that both stimulated tryptase or histamine release initiated within 10 s and reached their peak release between 4 and 6 min. Pretreatment of cells with metabolic inhibitors or pertussis toxin reduced the ability of mast cells to release tryptase or histamine. **Conclusion:** It was demonstrated that the *in vitro* tryptase release properties of human tonsil and skin mast cells suggested a novel type of mast cell heterogeneity. The activation of mast cells by PAR-2 agonists indicated a self-amplification mechanism of mast cell degranulation.

Introduction

Recently, it was summarized that apart from allergic disease, mast cells were associated with at least 35 different non-allergic clinical disorders[1]. The increased numbers of mast cells or mast cell degranulation being observed in these diseases implied that this cell type was most likely involved in the pathogenesis of these diseases. Since mast cells carry out their functions mainly through their released mediators including histamine, tryptase, chymase, heparin, cytokines, and other products[2,3], the understanding of mediator release properties of mast cells is crucial for our study on the roles of mast cells in diseases.

Tryptase is a tetrameric serine proteinase that constitutes some 20% of the total protein within human mast cells and is stored almost exclusively in the secretory granules of mast cells[4] in a catalytically active form[5]. Upon degranulation, tryptase is released from mast cells along with histamine and other mast cell products.

For more than four decades, histamine has been widely used as a marker of mast cell degranulation *in vitro*, and numerous anti-allergic drugs such as sodium cromoglycate, lodoxamide, salbutamal, ketotifen, terfenadine, and cetirizine[6,7], and salmeteral[8] were reported to inhibit anti-IgE induced histamine release from human tonsil, skin, or lung mast cells. Therefore, both tryptase and histamine were used as markers of mast cell degranulation in the current study.

In recent years, it was found that PAR-2, a receptor of trypsin and tryptase[9] was expressed on human mast cells[10] and PAR-2 agonists were reported to be capable of activating rat peritoneal mast cells[11] and human gut mast cells[12]. However, the potential effects of PAR-2 agonists including trypsin, SLIGKV, and tc-LIGRLO[13] on human tonsil and skin mast cells have not been examined. Therefore, the actions of

these PAR-2 agonists on tonsil and skin mast cells were investigated in the current study. We reported that histamine was able to activate gut mast cells, which presents a self-amplification mechanism of mast cell degranulation[14]. Since human mast cells from different anatomical sources may respond to a stimulus to different extents, which has long been known as mast cell heterogeneity[15], the effect of histamine on tryptase release from human tonsil and skin mast cells was also examined in this study.

Materials and methods

Dispersion of mast cells Human tonsil and skin tissue were obtained at tonsillectomy and circumcision, from the Pathology Department of Shantou University Medical College (Shantou, China). Informed consent from the patients and agreement of the Ethical Committee of the college were obtained. Only macroscopically normal tissues were used for the study. The mast cell dispersion procedures employed were similar to that described previously[16]. Briefly, finely chopped tissue was incubated with 1.5 g/L collagenase (Sigma, USA) and 0.75 g/L hyaluronidase (Sigma) in minimum essential medium (MEM, Gibco, Invitrogen Corporation, USA) containing 25 mmol/L *N*-2-hydroxylethyl-piperazine-*N*'-2-ethane sulphonic acid (HEPES) and 2% foetal calf serum (FCS, 1 g tonsil/10 mL buffer and 1 g skin/15 mL buffer) at 37 °C for 60–70 min. Dispersed cells were separated from undigested tissue by filtration through nylon gauze (pore size 100 μm diameter), washed and maintained in MEM (containing 10% FCS, 200 kU/L benzylpenicillin, and 200 mg/L streptomycin) on a roller overnight at room temperature. Mast cell purity, as determined by light microscopy after staining by alcine blue, ranged from 0.5% to 1.1% for tonsil cells and 3.5% to 5.8% for skin cells.

Mast cell challenge Dispersed cells were resuspended in HEPES buffered salt solution (HBSS, pH 7.4) with $CaCl_2$ and $MgCl_2$ (complete HBSS). Aliquots of 100 μL containing 4×10^3–6×10^3 mast cells were added a 50-μL of tc-LIGRLO (Meilian, GuZhen Town, China), tc-OLRGIL (Meilian), SLIGKV (Meilian), VKGILS (Meilian), trypsin (Sigma), tryptase (self-prepared[17]), histamine (Sigma), anti-IgE antibody (Serotec, Oxford, UK), calcium ionophore (CI) (Sigma), SBTI (Sigma), or α_1-AT (Sigma), and incubated at 37 °C for 15 min. The reaction was terminated by addition of 150 μL ice cold incomplete HBSS and tubes were centrifuged immediately (500×*g*, 10 min, 4 °C). All experiments were performed in duplicate. For measuring of total histamine or tryptase concentrations, four tubes were either boiled for 6 min or the freeze-thaw cycle was repeated five times. Supernatants were stored at -20 °C until tryptase and histamine concentrations were determined (in duplicate for each tube).

Inhibition of release of tryptase or histamine When added, SBTI or α_1-AT were incubated with trypsin for 20 min on ice before adding to cells. Data were expressed as the percentage inhibition of tryptase or histamine release, taking into account histamine or tryptase release in presence and absence of the inhibitor. When the experiments with pertussis toxin were performed, cells were incubated with 1.0 mg/L pertussis toxin at 37 °C for 4 h, and then washed with HBSS before stimulus being added. When the experiments with metabolic inhibitors were performed, cells were incubated with 2-deoxy-*D*-glucose (10 mmol/L, Sigma) and antimycin A (1 μmol/L, Sigma) at 37 °C for 40 min before being challenged with stimulus.

Tryptase and histamine measurement Tryptase concentrations were measured with a sandwich ELISA procedure with a specific polyclonal antibody against human tryptase as the capture antibody and AA5 a monoclonal antibody specific for human tryptase (both donated by Dr Andrew FW, University of Southampton, UK) as the detecting antibody[18]. Histamine concentrations were determined using a glass fibre-based fluorometric assay[16].

Statistical analysis Statistical analysis were performed by using SPSS software. Data were expressed as mean±SD. Where analysis of variance indicated significant differences between groups with ANOVA, for the preplanned comparisons of interest, Student's *t*-test was applied. $P<0.05$ was taken as a statistically significant difference.

Results

Effect of PAR-2 agonists and their reverse peptides on tryptase and histamine release from tonsil and skin mast cells PAR-2 agonist peptide SLIGKV at the concentrations of 1, 10, and 100 $\mu mol\cdot L^{-1}$ was able to induce a dose-dependent release of histamine (ranging from 8.9% to 13.8% net histamine release), but not tryptase (data not shown) from skin mast cells. However, SLIGKV at 300 $\mu mol\cdot L^{-1}$ failed to induce histamine release from skin mast cells. In the same experiments, a reverse peptide of SLIGKV, VKGILS had little effect on histamine release. In contrast to skin mast cells, tonsil mast cells released more tryptase, but not histamine (data not shown) in response to SLIGKV. In the same experiments, VKGILS induced significantly less tryptase release from tonsil cells than SLIGKV did. Another PAR-2 agonist peptide tc-LIGRLO was able to induce significant release of histamine from skin mast cells and release of tryptase from tonsil mast cells, but the extent of histamine and tryptase release induced by tc-LIGRLO appeared less than that induced by its reverse peptide tc-OLRGIL (Table 1).

Table 1. Effects of PAR-2 agonists and their reverse peptides on tryptase release from human tonsil mast cells and histamine release from human skin mast cells. n=4. Mean±SD. $^bP<0.05$ *vs* baseline release. $^eP<0.05$ *vs* the corresponding concentration of the reverse peptide.

Peptide concentration/ μmol·L^{-1}		Net tryptase release/% Tonsil	Net histamine release/% Skin
tc-LIGRLO	0.1	4.0±3.2	1.9±1.3
	1.0	4.7±4.3	3.6±0.5
	10	2.5±1.9	2.2±2.0
	100	4.9±0.8^b	7.2±1.0^b
	300	0.3±1.6	9.9±1.7^{be}
tc-OLRGIL	0.1	1.1±1.7	4.0±2.4
	1.0	10.2±1.8^b	9.7±4.1^b
	10	7.7±1.4^b	15.3±0.9^b
	100	5.2±0.5^b	12.8±3.0^b
	300	4.3±1.7	4.4±2.4
SLIGKV	0.1	3.1±1.9	2.9±1.2
	1.0	16.9±3.2^{be}	8.9±3.0^{be}
	10	13.1±3.6^{be}	9.1±2.6^{be}
	100	11.0±0.7^{be}	13.8±1.5^{be}
	300	6.2±2.3^b	3.9±2.5
VKGILS	0.1	3.6±2.4	1.5±2.3
	1.0	8.0±1.4^b	0.2±1.2
	10	7.0±0.7^b	1.0±0.6
	100	3.3±2.2	1.5±1.0
	300	4.5±3.2	4.6±1.4

Cells were incubated with peptides at 37 ºC for 15 min.

Effects of trypsin, anti-IgE, CI, and histamine on tryptase release from tonsil and skin mast cells Trypsin was able to induce a "bell" shape increase in tryptase release from tonsil mast cells. The maximum of net tryptase release was 19.4% induced by 1 mg/L trypsin (Figure 1). With the same experimental procedure, trypsin failed to induce significant tryptase release from skin mast cells (Figure 2). Anti-IgE was able to stimulate tryptase release from both tonsil and skin mast cells (Figure 1, 2). The maximum release of tryptase from tonsil cells was 17.7% induced by 10 mg/L anti-IgE. CI at the concentrations of 0.1, 0.3, and 1 mg/L was able to provoke a dose-dependent release of tryptase from tonsil mast cells (Figure 1). The maximum release of tryptase from tonsil cells was 22.8% induced by 1 mg/L CI (Figure 1). CI at the concentration of 1 mg/L was also able to induce significant tryptase release from skin mast cells (Figure 2).

Effects of trypsin, anti-IgE, CI, and tryptase on histamine release from tonsil and skin mast cells Trypsin at the concentrations of 0.1, 1.0, 10, and 100 mg/L was able to induce a dose-dependent release of histamine from skin mast cells (Figure 2). The maximum of histamine release was 13.9% induced by100 mg/L trypsin. Trypsin at the concentrations of 10 and 100 mg/L was also able to induce significant histamine release from tonsil mast cells (Figure 3).

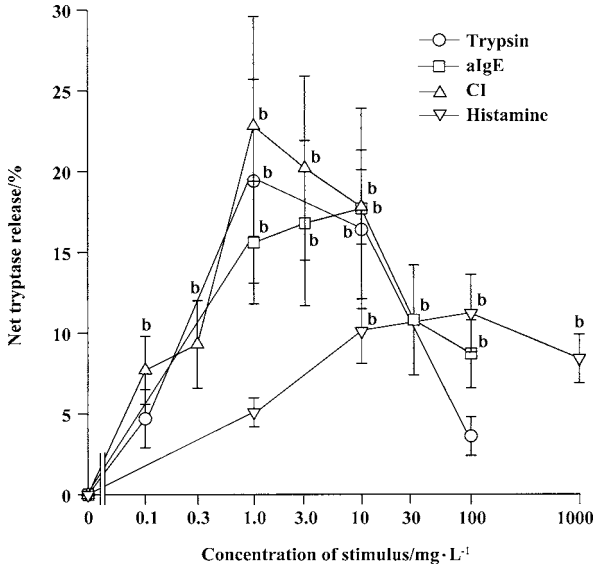

Figure 1. Induction of tryptase release from tonsil mast cells by trypsin, anti-IgE antibody (aIgE), calcium ionophore (CI), and histamine. n=4. Mean±SD. $^bP<0.05$ *vs* baseline. Stimulus or HBSS alone was incubated with cells for 15 min before termination of the reactions.

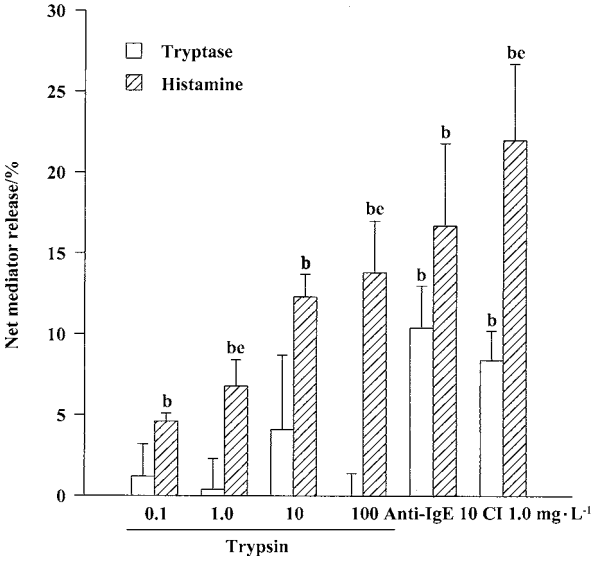

Figure 2. Induction of tryptase or histamine release from skin mast cells by trypsin, anti-IgE, and calcium ionophore (CI). n=4. Mean±SD. $^bP<0.05$ *vs* control. $^eP<0.05$ *vs* the corresponding tryptase release. Stimulus or HBSS alone was incubated with cells for 15 min before termination of the reactions.

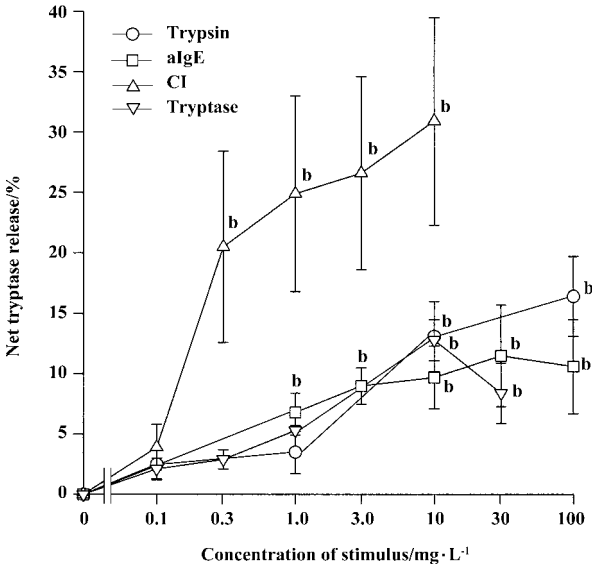

Figure 3. Induction of histamine release from tonsil mast cells by trypsin, anti-IgE, CI, and tryptase. n=4. Mean±SD. $^bP<0.05$ *vs* control. Stimulus or HBSS alone was incubated with cells for 15 min before termination of the reactions.

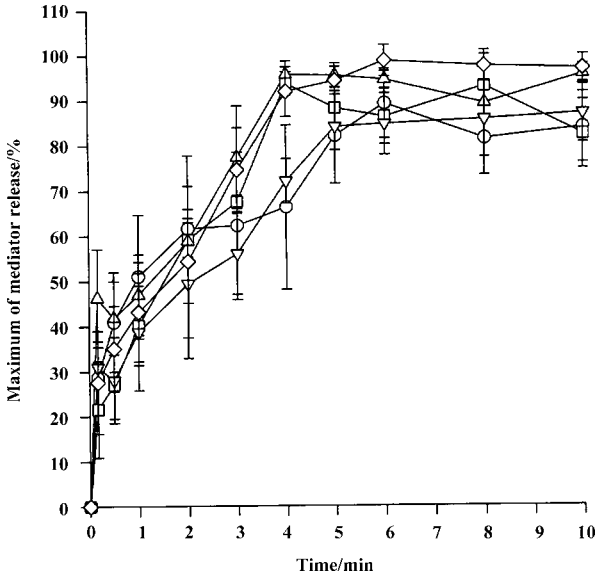

Figure 4. Time course for anti-IgE antibody (10 mg/L, – ○ –), calcium ionophore (1 mg/L, – □ –) and histamine (10 mg/L, –Δ–)-induced release of tryptase, and anti-IgE antibody (10 mg/L, –∇–) and calcium ionophore (1 mg/L, – ◇ –)-induced release of histamine from tonsil mast cells. n=4. Mean±SD.

Similarly, anti-IgE and CI were able to induce a dose-dependent release of histamine from tonsil mast cells. Up to12.8% release of histamine from tonsil mast cells was observed when cells were incubated with tryptase 10 mg/L (Figure 3).

Time course for tryptase and histamine release from tonsil mast cells Time course study revealed that both tryptase and histamine release induced by anti-IgE, histamine, and CI from tonsil mast cells initiated within 10 s when cells were incubated with stimulus. Up to 45% and 31% of the maximum tryptase and histamine release were observed 10 s after cells were incubated with stimulus. The peak tryptase release from tonsil cells occurred at 4 min for CI and histamine, and 6 min for anti-IgE following incubation (Figure 4). In comparison, the peak of histamine release induced by anti-IgE or CI occurred at 5 min and 6 min, respectively (Figure 4). Similarly, tc-LIGRLO, trypsin, and CI-induced histamine release from skin mast cells all started within 10 s of stimulation. But the peak histamine release occurred at 4 min for CI and 6 min for tc-LIGRLO and trypsin (Figure 5).

Inhibition of trypsin-induced tryptase and histamine release by trypsin inhibitors The trypsin-induced tryptase release from tonsil mast cells was inhibited by approximately 65.1% and 62.2% by SBTI or α_1-AT, respectively (Table 2). Similarly, the trypsin-induced histamine release from tonsil mast cells was inhibited by approximately 82.4% and 80.4% by SBTI or α_1-AT, respectively (Table 2). SBTI or α_1-AT

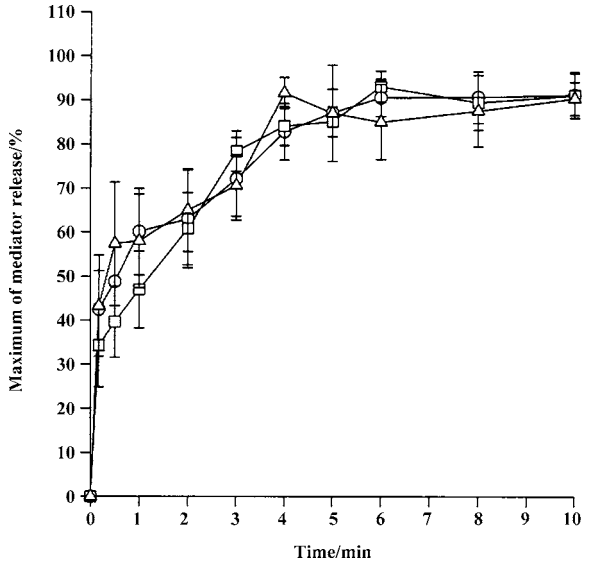

Figure 5. Time course for tc-LIGRLO (100 μmol/L, – ○ –), trypsin (10 mg/L, – □ –) and calcium ionophore (1 mg/L, –Δ–)-induced release of histamine from skin mast cells. n=4. Mean±SD.

were also able to inhibit trypsin-induced histamine release from skin mast cells by 77.2% and 63.2%, respectively (Table 2).

Inhibition of tryptase and histamine release by pertussis toxin and metabolic inhibitors Pretreatment of cells with metabolic inhibitors (10 mmol/L of 2-deoxy-*D*-glucose and 1

Table 2. Inhibition of trypsin-induced tryptase and histamine release from tonsil and skin mast cells by trypsin inhibitors. n=4. Mean±SD. $^bP<0.05$ *vs* trypsin alone.

Concentration of compound/mg·L^{-1}		Inhibition of tryptase release/%		Inhibition of histamine release/%	
		Tonsil	Skin	Tonsil	Skin
Trypsin 10+SBTI	30	65.1±9.3^b	nd	82.4±13.5^b	77.2±11.8^b
Trypsin 10+a_1-AT	30	62.2±10.1^b	nd	80.4±11.6^b	63.2±2.2^b

Cells were incubated with trypsin and inhibitors at 37 ºC for 15 min.

μmol/L of antimycin A) reduced trypsin-induced tryptase release from tonsil cells and histamine release from skin cells by 79.4% and 61.9%, respectively. Metabolic inhibitors were also able to inhibit histamine-induced tryptase release from tonsil mast cells, and tc-LIGRLO and SLIGKV-induced histamine release from skin mast cells. Pretreatment of cells with 1 mg/L pertussis toxin diminished both trypsin and histamine-induced tryptase release from tonsil mast cells, and trypsin, tc-LIGRLO, and SLIGKV-provoked histamine release from skin mast cells. Similarly, metabolic inhibitors and pertussis toxins were able to inhibit both anti-IgE and CI-induced tryptase and histamine release from both tonsil and skin mast cells (Table 3).

Discussion

We have reported the *in vitro* tryptase release properties of human tonsil and skin mast cells. This was particularly important when tryptase and histamine, the two major mast cell mediators were investigated in parallel in the same experiments, which not only proved that the quantities of the two mediators released from mast cells were in an inconstant ratio, but also revealed that the pace of release was different between histamine and tryptase upon mast cell degranulation. These phenomena were similar to our previous findings with human colon mast cells[12].

Trypsin at 1 mg/L was able to stimulate the maximum tryptase release (19.4%), but not significant histamine release from tonsil mast cells. In contrast, trypsin at 100 mg/L was able to stimulate 16.4% histamine release, but not significant tryptase release from tonsil mast cells. These are surprising observations, which suggests strongly that tryptase and histamine release from tonsil mast cells induced by trypsin may be involved in different mechanisms. Since anti-IgE and CI also showed “bell” shape tryptase release and dose-dependent histamine release patterns in the same experimental system, these observations may reflect a common phenomenon of tonsil mast cell degranulation. It is most likely that tryptase release pathway of tonsil mast cells has the ability to prevent itself from strong stimulation. However, more experiments are needed to prove this. In contrast to mast cells from tonsil, mast cells from skin released only histamine, but not tryptase in response to trypsin, which indicated further that tryptase and histamine release from human mast cells induced by trypsin was through different mechanisms. The difference in the ability of trypsin inhibitors to inhibit trypsin induced histamine release (up to 82.4%) and tryptase release (up to 65%) may also suggest the different mechanisms involved in tryptase and histamine release from tonsil mast cells.

Moreover, PAR-2 agonist peptides SLIGKV and tc-LIGRLO showed different effects on tryptase and histamine release from mast cells. As for trypsin, SLIGKV was also able to stimulate histamine release, but not tryptase release

Table 3. Effects of pertussis toxin (1 mg/L) and metabolic inhibitors (antimycin A 1 μmol/L+2-deoxy-*D*-glucose 10 mmol/L) on trypsin-, histamine-, tc-LIGRLO-, SLIGKV-, anti-IgE-, and CI-induced tryptase or histamine release from tonsil and skin mast cells. n = 4. Mean±SD. $^bP<0.05$ *vs* control.

Stimulus	Inhibition of tryptase release/%				Inhibition of histamine release/%			
	Pertussis toxin		Metabolic inhibitors		Pertussis toxin		Metabolic inhibitors	
	Tonsil	Skin	Tonsil	Skin	Tonsil	Skin	Tonsil	Skin
Trypsin/10 mg·L^{-1}	78.6±11.5^b	ns	79.4±9.6^b	ns	nd	65.7±12.5^b	nd	61.9±6.1^b
Histamine/100 mg·L^{-1}	65.3±12.7^b	nd	69.0±5.2^b	nd	na	na	na	na
tc-LIGRLO/100 μmol·L^{-1}	nd	ns	nd	ns	ns	62.6±13.1^b	ns	82.6±13.4^b
SLIGKV/100 μmol·L^{-1}	nd	ns	nd	ns	ns	70.4±13.2^b	ns	70.1±11.9^b
Anti-IgE/10 mg·L^{-1}	80.7±9.8^b	68.0±6.4^b	90.7±5.6^b	85.4±8.1^b	81.4±6.4^b	63.3±8.2^b	72.7±9.5^b	72.1±4.0^b
CI/1.0 mg·L^{-1}	76.9±9.4^b	77.5±11.2^b	75.7±10.5^b	72.3±6.9^b	79.6±8.3^b	70.1±11.5^b	94.7±3.2^b	84.0±5.7^b

nd=not done; na=not applicable; ns=no stimulation before pertussis toxin and metabolic inhibitor treatment.

from skin mast cells. The extent of histamine release induced by SLIGKV was similar to that induced by trypsin, indicating that the actions of trypsin on skin mast cells may be through PAR-2. Because VKGILS (a reversed peptide of SLIGKV) had little effect on tryptase and histamine release from skin mast cells, the action of SLIGKV on skin mast cells was a specific one. Different from skin mast cells, tonsil mast cells released tryptase but not histamine in response to SLIGKV. This suggested that trypsin induced histamine release from tonsil mast cells might not be through a PAR-2 related mechanism. It suggested also that release of tryptase and histamine from tonsil mast cells upon stimulation might not occur simultaneously. Another PAR-2 agonist peptide tc-LIGRLO had a similar effect to SLIGKV on skin mast cells, confirming further the functional expression of PAR-2 on these cells. Interestingly, tc-OLRGIL a reversed peptide of tc-LIGRLO appeared a potent stimulus of histamine release from skin mast cells, and a secretagogue of tryptase release from tonsil mast cells. The physiological or pathophysiological meaning of the action of tc-OLRGIL on mast cells requires further investigation to be understood.

Consistent with our previous findings[14,15], histamine exhibited its ability to stimulate tryptase release from tonsil mast cells, and tryptase showed its ability to provoke histamine release from mast cells. These implicated that there were at least two self-amplification mechanisms of mast cell degranulation in the human tonsil; the histamine associated mechanism and the tryptase associated mechanism.

Approximately 30% tryptase and histamine release occurred within 10 s of IgE-dependent stimulation, suggesting that tonsil mast cells were able to quickly respond to allergen challenge, but to reach their full capacity (maximum histamine or tryptase release) a minimum of 5 min was required. The time courses for CI were similar to those for anti-IgE, except for a minimum 4 min being required to reach the full tryptase and histamine release capacity. The reasons for the relatively slow release of mediators from human mast cells remain unclear. Approximately 45% tryptase release induced by histamine was completed within the first 10 s of stimulation, indicating that the process may be different from the one induced by anti-IgE or CI. The time courses for histamine release from skin mast cells induced by CI and tc-LIGRLO were quite similar, indicating tc-LIGRLO may act like CI on induction of mast cell degranulation.

Pretreatment of cells with metabolic inhibitors abolished the actions of anti-IgE and CI on mast cells, indicating that tryptase and histamine release induced by them was a non-cytotoxic process, and was dependent on cell energy supply. The inhibition of tryptase and histamine release by pertussis toxin suggested that the release process was associated with activation of G-protein coupled receptors.

In conclusion, it was found that tryptase release properties of human tonsil and skin mast cells were similar to the histamine release properties of these cells in response to anti-IgE and CI. In contrast, tryptase release properties were quite different from histamine release properties in response to PAR-2 agonists including trypsin, tc-LIGRLO, and SLIGKV, which uncovered a novel type of mast cell heterogeneity in response to different stimulation. The activation of mast cells by PAR-2 agonists may indicate a self-amplification mechanism of mast cell degranulation in humans.

References

1 He S. The key role of mast cells and their major secretory products in inflammatory bowel disease. World J Gastroenterol 2004; 10: 309–18.

2 Walls AF, He S, Buckley MG, McEuen AR. Roles of the mast cell and basophil in asthma. Clin Exp Allergy Rev 2001; 1: 68–72.

3 He S, Chen HQ, Zheng J. Inhibition of tryptase and chymase induced nucleated cell infiltration by proteinase inhibitors. Acta Pharmacol Sin 2004; 25: 1677–84.

4 Schwartz LB. Preformed mediators of human mast cells and basophils. In: Holgate ST, editor. Mast cells, mediators and disease. Dordrect: Kluwer Academic Publishers; 1988. p 129–47.

5 McEuen AR, He S, Brander ML, Walls AF. Guinea pig lung tryptase: Localisation to mast cells and characterisation of the partially purified enzyme. Biochem Pharmacol 1996; 52: 331–40.

6 Okayama Y, Church MK. Comparison of the modulatory effect of ketotifen, sodium cromoglycate, procaterol and salbutamol in human skin, lung and tonsil mast cells. Int Arch Allergy Appl Immunol 1992; 97: 216–25.

7 Okayama Y, Benyon RC, Lowman MA, Church MK. *In vitro* effects of H_1-antihistamine and PGD_2 release from mast cells of human lung, tonsil, and skin. Allergy 1994; 49: 246–53.

8 Butchers PR, Vardey CJ, Johnson M. Salmeterol: a potent and long-acting inhibitor of inflammatory mediator release from human lung. Br J Pharmacol 1991; 104: 67–26.

9 Molino M, Barnathan ES, Numerof R, Clark J, Dreyer M, Cumashi A, *et al*. Interactions of mast cell tryptase with thrombin receptors and PAR-2. J Biol Chem 1997; 272: 4043–9.

10 D'Andrea MR, Rogahn CJ, Andrade-Gordon P. Localization of protease-activated receptors-1 and -2 in human mast cells: indications for an amplified mast cell degranulation cascade. Biotech Histochem 2000; 75: 85–90.

11 Stenton GR, Nohara O, Dery RE, Vliagoftis H, Gilchrist M, Johri A, *et al*. Proteinase-activated receptor (PAR)-1 and -2 agonists induce mediator release from mast cells by pathways distinct from PAR-1 and PAR-2. J Pharmacol Exp Ther 2002; 302: 466–74.

12 He S, He Y, Xie H. Activation of human colon mast cells through proteinase activated receptor-2 (PAR-2). World J Gastroenterol 2004; 10: 327–31.

13 Hollenberg MD, Saifeddine M, al-Ani B, Kawabata A. Proteinase-activated receptors: structural requirements for activity, re-

ceptor cross-reactivity, and receptor selectivity of receptor-activating peptides. Can J Physiol Pharmacol 1997; 75: 832–41.
14 He S, Xie H. Modulation of tryptase secretion from human colon mast cells by histamine. World J Gastroenterol 2004; 10: 323–26.
15 He S, Gaça MDA, Walls AF. A role for tryptase in the activation of human mast cells: modulation of histamine release by tryptase and inhibitors of tryptase. J Pharmacol Exp Ther 1998; 286: 289–97.
16 He S, Xie H, Zhang XJ, Wang XJ. Inhibition of histamine release from human mast cells by natural chymase inhibitors. Acta Pharmacol Sin 2004; 25: 822–6.
17 He S, Chen P, Chen HQ. Modulation of enzymatic activity of human mast cell tryptase and chymase by proteinase inhibitors. Acta Pharmacol Sin 2003; 24: 923–9.
18 Buckley MG, Walters C, Brander M, Wong WM, Cawley MI, Ren S, *et al*. Mast cell activation in arthritis: detection of α- and β-tryptase, histamine and eosinophil cationic protein in synovial fluid. Clin Sci 1997; 93: 363–70.

Congratulations to Dr Hua-liang JIANG, an Editorial Board member of Acta Pharmacologica Sinica, for his extraordinary career accomplishment!

It is time to celebrate!

We are very proud to announce that, since 2003, Dr Hua-liang JIANG have had 27 citations to his article, **A 3D MODEL OF SARS_COV 3CL PROTEINASE AND ITS INHIBITORS DESIGN BY VIRTUAL SCREENING** [by Bin XIONG, Chun-shan GUI , Xiao-ying XU, Cheng LUO, Jing CHEN, Hai-bin LUO, Li-li CHEN, Guo-wei LI, Tao SUN, Chang-ying YU, Li-duoYUE, Wen-hu DUAN, Jin-kang SHEN, Lei QIN, Tei-liu SHI, Yi-xue LI, Kai-xian CHEN, Xiao-min LUO, Xu SHEN, Jian-hua SHEN, Hua-liang JIANG. Acta Pharmacol Sin 2003, 24 (6): 497–504. Received 2003-05-16 Accepted 2003-05-18].

What's more, the number of citations of this article received has placed it in the top 1% within its field according to ***Essential Science Indication***[SM]. His work is highly influential and is making a significant impact among his colleagues in his field of study.

It is worth pointing out that it were Dr Jiang HL *et al* who firstly constructed a three-dimensional model for the 3C like proteinase of SARS coronavirus and designed anti-SARS drugs by virtual screening. Based on the finding published in Acta Pharmacologica Sinica, Dr Jiang managed to find a new strategy to discover anti-SARS compounds from the existing drugs by combining computationally virtual screening with bioassay. His latest work has been accepted by *Journal of Virology* recently and will be published as a Spotlight Paper soon.

Acta Pharmacologica Sinica 2005 May; 26 (5): 575–580

Full-length article

Pioglitazone can ameliorate insulin resistance in low-dose streptozotocin and high sucrose-fat diet induced obese rats

Shi-ying DING, Zhu-fang SHEN[1], Yue-teng CHEN, Su-juan SUN, Quan Liu, Ming-zhi XIE

Institute of Materia Medica, Chinese Academy of Medical Sciences and Peking Union Medical College, Beijing 100050, China

Key words

insulin resistance; pioglitazone; thiazolidinedione; obesity; glucose transporter; insulin receptor substrate-1

[1] Correspondence to Prof Zhu-fang SHEN.
Phn/Fax 86-10-8317-2669.
E-mail shenzhf@imm.ac.cn

Received 2004-12-20
Accepted 2005-01-10

doi: 10.1111/j.1745-7254.2005.00090.x

Abstract

Aim: To investigate the effect of the peroxisome proliferator-activator receptor (PPAR)-γ agonist, pioglitazone, on insulin resistance in low-dose streptozotocin and high sucrose-fat diet induced obese rats. **Methods:** Normal female Wistar rats were injected intraperitoneally with low-dose streptozotocin (STZ, 30 mg/kg) and fed with a high sucrose-fat diet for 8 weeks. Pioglitazone (20 mg/kg) was administered orally to the obese and insulin-resistant rats for 28 d. Intraperitoneal glucose tolerance tests, insulin tolerance tests and gluconeogenesis tests were carried out over the last 14 d. At the end of d 28 of the treatment, serums were collected for biochemical analysis. Glucose transporter 4 (GLUT4) and insulin receptor substrate-1 (IRS-1) protein expression in the liver and skeletal muscle were detected using Western blotting. **Results:** Significant insulin resistance and obesity were observed in low-dose STZ and high sucrose-fat diet induced obese rats. Pioglitazone (20 mg/kg) treatment significantly decreased serum insulin, triglyceride and free fatty acid levels, and elevated high density lipoprotein-cholesterol (HDL-C) levels. Pioglitazone also lowered the lipid contents in the liver and muscles of rats undergoing treatment. Gluconeogenesis was inhibited and insulin sensitivity was improved markedly. The IRS-1 protein contents in the liver and skeletal muscles and the GLUT4 contents in skeletal muscle were elevated significantly. **Conclusion:** The data suggest that treatment with pioglitazone improves insulin sensitivity in low-dose STZ and high sucrose-fat diet induced obese rats. The insulin sensitizing effect may be associated with ameliorating lipid metabolism, reducing hyperinsulinemia, inhibiting gluconeogenesis, and increasing IRS-1 and GLUT4 protein expression in insulin-sensitive tissues.

Introduction

Insulin resistance is a major characteristic of various metabolic disorders, including type 2 diabetes and obesity[1]. There is strong evidence that an important factor leading to obesity and insulin resistance is an increase in energy intake[2]. Our previous study demonstrated that high-fat, high-sucrose feeding led to insulin resistance and impaired glucose tolerance in female Wistar rats[3]. In our study, female rats were given a relatively low-dose of streptozotocin (STZ), followed by a high sucrose-fat diet containing 52% sucrose, 24% fat, and 18% protein (4.8 cal/g chow). Compared to the control group, which did not receive either STZ or a high sucrose-fat diet, the treatment group showed obvious obesity and impaired glucose tolerance after 8 weeks. Fasting blood glucose levels increased slightly or moderately, and were accompanied by hyperinsulinemia, dyslipidemia, enhanced gluconeogenesis, and reduced insulin tolerance. These characteristics indicated insulin resistance and obesity with mild β-cell dysfunction, which was further induced by the high sucrose-fat diet. A similar result is observed in humans. Our results suggested that this model was a successful insulin-resistant rat model and is useful in the study of insulin resistance and insulin sensitivity.

Thiazolidinediones (TZDs), a new class of insulin sensitizing drugs including troglitazone, pioglitazone, and rosiglitazone, provide an effective approach for treating type 2 diabetes. TZDs improve insulin sensitivity, impair glucose tolerance and dyslipidemia in type 2 diabetics[4], as well as in obese non-diabetic subjects[5]. Similar findings have been demonstrated in a number of genetic and non-genetic animal models of diabetes/insulin resistance[6,7]. TZDs elicit their effects through activating the peroxisome proliferator–activator receptor (PPAR)-γ, a nuclear hormone receptor. When ligands stimulate the PPAR-γ nuclear receptor, a variety of response genes are stimulated or repressed. The TZD PPAR-γ agonists improve insulin sensitivity via multiple mechanisms. Although the exact target genes for insulin sensitization remain unknown, it has been demonstrated *in vitro* and *in vivo* that treatment with TZDs affects a variety of factors involved in lipid metabolism, insulin signal pathways, glucose phosphorylation, and glucose transport.

In the present study, we evaluated the effect of pioglitazone, a PPAR-γ agonist, on insulin resistance and related abnormalities in low-dose STZ and high sucrose-fat diet induced obese rats. Our findings demonstrated that PPAR-γ agonist treatment reduced circulating and stored lipids and improved the insulin-resistant status in model rats.

Materials and methods

Animals Thirty female Wistar rats, weighing 225–250 g, were obtained from the Experimental Animal Center, Chinese Academy of Medical Sciences, Beijing, China [Certificate No SCXK(Jing)2000-0006], and maintained in individual cages with a 12-h/12 h light-dark cycle. All animals were allowed free access to water. At the beginning of the study, rats were randomly assigned to control (n=8) and experimental groups (n=22). Experimental groups were injected intraperitoneally with low-dose STZ, 30 mg/kg (Sigma, St Louis, MO, USA). After 2 weeks, a glucose tolerance test was carried out and 15 rats that had developed impaired glucose tolerance in the STZ-treated group were selected and received a high sucrose-fat diet (containing 52% sucrose, 24% fat, 18% protein, and 4.8 cal/g chow). Rats in the control group were fed *ad libitum* on a standard chow.

After 8 weeks on a high sucrose-fat diet, weight-matched, fasting-blood-glucose-matched STZ rats were randomly divided into two groups, a STZ group and a pioglitazone group. STZ rats (n=8) were given vehicle solution and pioglitazone rats (n=7) were orally administered pioglitazone (20 $mg \cdot kg^{-1} \cdot d^{-1}$; the pioglitazone was a gift from Prof Yu-ling LIU) as a suspension in 1% Tween 80 solution (the high sucrose-fat diet was given to the rats during this period). Rats in each group were treated for 28 d. Glucose tolerance tests, insulin tolerance tests and gluconeogenesis tests were carried out over the last 14 d of the experiment. At the end of the treatment period, all animals were decapitated after a 4-h fast. Blood samples were collected and serum was prepared and kept at -20 ºC for the determination of serum lipids and immunoreactive insulin. Celiac fats were excised for weighing. Skeletal muscles and livers were separated and frozen immediately in liquid nitrogen, and stored at -70 ºC for further analysis of GLUT4 and IRS-1.

Biochemical analysis Serum glucose levels were assayed using the glucose oxidase method. Serum insulin was determined using a radioimmunoassay kit (China Institute of Atomic Energy, Beijing, China). Free fatty acid (FFA) concentrations were measured using the Cu^{2+} reagent method. Triglyceride (TG), total cholesterol (TC), and HDL-cholesterol (HDL-C) levels were determined using the colorimetric method with commercial kits (Zhong sheng bei kong Bio-Technology and Science, Beijing, China).

Intraperitoneal glucose tolerance test (IPGTT) Baseline glucose levels were determined after a 4-h fast, after which glucose (2 g/kg body wt) was administered intraperitoneally to non-sedated animals. Tail vein blood was sampled for glucose determination 30 and 120 min after glucose administration.

Insulin tolerance test (ITT) Baseline glucose levels were determined after a 4-h fast. Insulin (0.4 U/kg body wt) was injected subcutaneously. Blood was sampled from the tail tip 40 and 90 min after insulin administration, and the glucose concentration was determined. Insulin injections and blood glucose sampling took approximately the same amount of time per animal (ie 25 animals were injected in 12 min and blood glucose sampling of those same 25 animals also took approximately 12 min), so that the sample times are accurate for each animal.

Gluconeogenesis test Baseline glucose levels were determined after an overnight fast. *DL*-alpha alanine was injected intraperitoneally. Blood was sampled from the tail and glucose levels were determined at 0 and 60 min. The percent increase in glucose level at 60 min was calculated. Higher values indicated higher levels of gluconeogenesis.

GLUT4 and IRS-1 protein expression Protein extractions and immunoblots for the determination of GLUT4 were carried out on frozen skeletal muscle from 12 rats using a modified Klip's method[8]. Skeletal muscle (1 g) was powdered under liquid nitrogen and homogenized for 20 s in buffer (pH 7.4) containing sucrose 250 mmol/L, Tris 50 mmol/L and edetic acid 0.2 mmol/L. The homogenates were centrifuged

at 9000×*g* for 10 min (4 ºC) and the supernatants were reserved. The pellet was cleaned with buffer and centrifuged three times. All three supernatants were mixed and centrifuged at 190 000×*g* for 60 min (4 ºC). The resulting pellet was resuspended in a small amount of buffer (about 0.5 mL) as a total membrane fraction. Protein concentrations of the suspensions were determined using the Coomasine brilliant blue method[8] prior to Western blot analysis.

Frozen tissues (100 mg liver, 100 mg skeletal muscle) were ground into a fine powder with a mortar and pestle and homogenized in the buffer (1% Triton X-100, sodium pyrophosphate 100 mmol/L, HEPES 50 mmol/L, pH 7.4, NaF 100 mmol/L, PMSF 2 mmol/L, 0.1% aprotinin, sodium edetic acid 10 mmol/L, Na_3VO_4 10 mmol/L) with a polytron homogenizer at 4 ºC for 6 (for muscle) or 10 (for liver) times[9,10]. The homogenates were centrifuged at 10 000×*g* at 4 ºC for 60 min and the supernatants were collected for IRS-1 analysis.

Protein extracts were resuspended in Laemmli buffer and separated using sodium dodecylsulfate-polyacrylamide gel electrophoresis (SDS-PAGE) on 10% (for GLUT4) or 7.5% (for IRS-1) polyacrylamide gels. Proteins were electrophoretically transferred to nitrocellulose membranes. The nitrocellulose membranes were incubated in phosphate buffer saline contained 0.1% Tween-20 overnight at 4 ºC to reduce non-specific binding and blotted with GLUT4 (anti-rabbit carboxy-terminal GLUT4, Santa Cruz Biotechnology, California, USA 1:1000) and IRS-1 (anti-rabbit carboxy-terminal IRS-1, Santa Cruz Biotechnology) antibodies according to the manufacturer's instructions. After incubation with peroxidase-conjugated secondary antibodies (1:2500, Santa Cruz Biotechnology), proteins were visualized using enhanced chemiluminescence. Band intensities were quantified by densitometry.

Statistical analysis The values presented are expressed as mean±SD. Statistical analyses were carried out using ANOVA. $P<0.05$ was considered to be statistically significant.

Results

Effect of pioglitazone on body weight, adipose weight, fasting blood glucose (FBG), fasting blood insulin (FBI), and insulin sensitivity index (ISI) STZ rats had significantly elevated levels of glucose and insulin compared with control rats ($P<0.01$) (Table 1). Reduced ISI (1/FBG×FBI) values revealed that insulin resistance developed in STZ rats. Treatment with pioglitazone for 28 d significantly lowered fasting glucose and insulin levels, and improved insulin sensitivity. STZ rats had significantly increased body weight and mass of celiac fat ($P<0.01$). There was no significant difference in body weight and adipose tissue weight between STZ animals and pioglitazone-treated animals (Table 1).

Table 1. Effects of pioglitazone (20 mg/kg, *po*) on body weight (BW), adipose tissue weight (AW) in the abdominal cavity, FBG, FBI and ISI in low-dose STZ rats. n=7–8. Mean±SD. $^cP<0.01$ *vs* control group. $^eP<0.05$, $^fP<0.01$ *vs* STZ group.

Group	BW/g	AW/g	FBG/ mmol·L^{-1}	FBI/ mU·L^{-1}	10^4×ISI
Control	270±7	8.4±2.9	3.8±0.5	37±9	77±23
STZ	322±42^c	29±10^c	4.6±0.3^c	61±27^c	42±16^c
Pioglitazone	322±36	30±12	4.2±0.3^e	32± 9^e	81±20^f

Effect of pioglitazone on glucose tolerance in STZ rats The IPGTT results revealed that rats in the STZ group had significantly impaired glucose tolerance compared with those in the control group. Surprisingly, the area under the curve (AUC) indicated that no effect attributable to pioglitazone administration on glucose tolerance was observed in the pioglitazone-treated group, although fasting glucose was slightly but significantly decreased (Table 2).

Table 2. Effect of pioglitazone (20 mg/kg, *po*) on glucose tolerance in low-dose STZ rats. n=7–8. Mean±SD. $^bP<0.05$, $^cP<0.01$ *vs* control group. $^fP<0.01$ *vs* STZ group.

Group	Blood glucose/mmol·L^{-1}			AUC/
	0 min	30 min	120 min	mmol·L^{-1}·min
Control	4.2±0.4	6.8±0.7	4.9±0.6	691±58
STZ	5.0±0.4	11.9±2.6^c	7.1±1.8^b	1107±200^c
Pioglitazone	4.3±0.5^f	12.4±1.4	6.1±1.2	1083±127

Effect of pioglitazone on insulin tolerance in STZ rats The results of the ITT showed that insulin resistance had developed significantly in STZ rats. Treatment with pioglitazone for 19 d markedly decreased glucose levels at every point, including AUC, indicating that insulin sensitivity was improved. In particular, the data suggested a prolongation in insulin action (Table 3).

Effect of pioglitazone on gluconeogenesis in STZ rats Under conditions of insulin resistance, gluconeogenesis from non-glucose substrates was always elevated in STZ rats. Our results showed that pioglitazone significantly reduced glucose production from alanine, which was assessed by a percentage increase in blood glucose levels at 60 min (Table 4).

Effect of pioglitazone on lipid profiles in serum, liver, and muscle The changes in lipid contents in these three

Table 3. Effect of pioglitazone (20 mg/kg, *po*) on insulin tolerance in low-dose STZ rats. n=7–8. Mean±SD. ^{b}P<0.05, ^{c}P<0.01 *vs* control group. ^{f}P<0.01 *vs* STZ group.

Group	Blood glucose/mmol·L^{-1}			AUC
	0 min	40 min	90 min	mmol·L^{-1}·min
Control	4.3±0.3	2.9±0.5	3.8±0.8	314±14
STZ	5.0±0.4^{c}	3.6±0.4^{b}	4.1±0.6	366±24^{c}
Pioglitazone	4.6±0.5	2.9±0.2^{f}	2.8±0.5^{f}	298±20^{f}

Table 4. Effect of pioglitazone (20 mg/kg, *po*) on gluconeogenesis ability from alanine in STZ rats. n=7–8. Mean±SD. ^{c}P<0.01 *vs* control group. ^{e}P<0.05 *vs* STZ group.

Group	Blood glucose/mmol·L^{-1}		Blood glucose increase/%
	0 min	60 min	
Control	3.8±0.4	5.4±0.7	31±10
STZ	5.3±0.4^{c}	8.6±1.0^{c}	65±20^{c}
Pioglitazone	4.8±0.7	7.0±1.3^{e}	42±16^{e}

groups (Table 5) indicated that the serum TG, TC, and FFA levels were all elevated significantly in the untreated STZ group, whereas HDL-C decreased. Pioglitazone treatment decreased TG, TC, and FFA and increased HDL-C levels significantly. Elevated liver TG, TC, FFA levels and muscle TG were observed in STZ rats and were normalized by pioglitazone treatment. These findings may indicate that tissue lipid levels are closely associated with insulin sensi-tivity. The TC/HDL-C ratio is considered to be a predictor of cardiovascular disease (CVD). TC/HDL-C values suggested that pioglitazone diminished the potential risk of CVD by correcting dyslipidemia.

Table 5. Effect of pioglitazone (20 mg/kg, *po*) on lipid contents in serum, liver, and muscle in STZ rats. n=7–8. Mean±SD. ^{b}P<0.05 ^{c}P<0.01 *vs* control group. ^{e}P<0.05, ^{f}P<0.01 *vs* STZ group.

	Control	STZ	Pioglitazone
Serum TG/mmol·L^{-1}	1.3±0.1	3.7±1.3^{c}	1.8±0.7^{f}
Serum HDL-C/mmol·L^{-1}	0.59±0.16	0.39±0.10^{b}	0.65±0.21^{e}
Serum TC/mmol·L^{-1}	2.1±0.4	3.5±0.7^{c}	3.0±0.3
TC/HDL-C	3.6±0.8	9.1±2.2^{c}	5.2±1.7^{f}
Serum FFA/mmol·L^{-1}	1.1±0.1	1.3±0.2^{b}	1.2±0.1^{e}
Liver TG/mg·g^{-1} tissue	15±3	34±4^{c}	20±4^{f}
Liver TC/mg·g^{-1} tissue	3.6±0.3	9.3±2.4^{c}	6.5±1.8^{e}
Liver FFA/μmol·g^{-1} tissue	65±10	78±5^{c}	68±4^{f}
Muscle TG/mg·g^{-1} tissue	2.4±0.6	3.5±0.6^{b}	2.5±0.8^{e}

Effect of pioglitazone on GLUT4 content in skeletal muscle membrane Membrane GLUT4 protein content was decreased by 68.7% in skeletal muscles from untreated STZ rats compared with control rats (Figure 1). Pioglitazone treatment increased GLUT4 protein levels significantly.

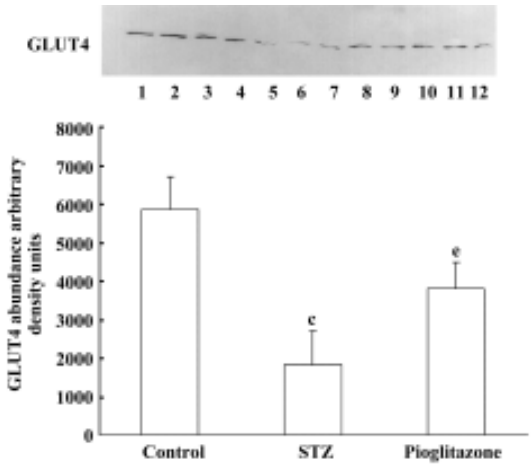

Figure 1. GLUT4 protein content in skeletal muscle membrane using Western blot analysis. GLUT4 protein was detected using rabbit polyclonal antibody. Control, lanes 1–4; STZ, lanes 5–8; pioglitazone, lanes 9–12. Blots were quantified using densitometry and expressed as mean±SD (n=4). ^{c}P<0.01 *vs* control group. ^{e}P<0.05 *vs* STZ group.

Effect of pioglitazone on IRS-1 expression in liver and skeletal muscle Statistically significant (A, 26.7%; B, 28.6%) decreases in IRS-1 proteins were observed in untreated STZ rats compared with control rats (Figure 2). Pioglitazone treatment for 28 d increased IRS-1 protein expression in liver and skeletal muscle significantly.

Discussion

Insulin resistance is a characteristic feature of type 2 diabetes and other pathophysiological states in humans. Therefore, amelioration of insulin sensitivity is an important therapeutic goal. Diet plays an important role in the development of insulin resistance and type 2 diabetes. An excessive intake of fat and sugar can lead to obesity and diabetes[11]. Previous studies have shown that high fat (59%) feeding for 24 d leads to significant insulin resistance. Euglycemic clamp revealed that glucose disposal rate (GDR) decreased by 50%; however, hyperglycemia was not observed[12]. Pascoe and Storlien reported that low-dose STZ (45 mg/kg body wt) administration to neonatal rats caused no change in glucose and insulin levels after 8 weeks; however, hyperglycemia

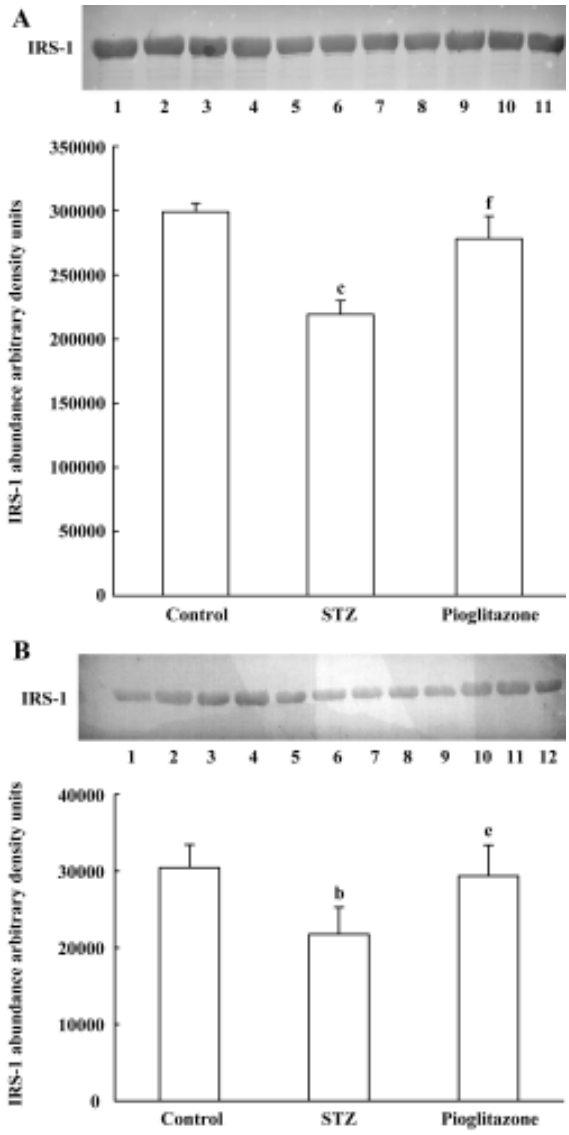

Figure 2. IRS-1 protein expressions in liver and skeletal muscle using Western blot analysis. IRS-1 protein was detected using rabbit polyclonal antibody. Blots were quantified using densitometry and expressed as mean±SD (n=3–4). $^{b}P<0.05$, $^{c}P<0.01$ *vs* control group. $^{e}P<0.05$, $^{f}P<0.01$ *vs* STZ group. (A) IRS-1 protein in liver. Control, lanes 1–4; STZ, lanes 5–8; pioglitazone, lanes 9–11. (B) IRS-1 protein in muscle. Control, lanes 1–4; STZ, lanes 5–8; pioglitazone, lanes 9–12.

and insulin resistance developed after high-fat feeding for 1 week[13]. In the present study, we injected STZ at low doses to Wistar rats to induce light damage of islet cells, leading to glucose intolerance. On this basis, a high sucrose-fat diet was followed to induce obesity. Our previous study reported that glucose infusion rate (GIR) decreased significantly in model rats compared with control rats (15.1±4.8 *vs* 27.3±2.9 mg/kg per min, $P<0.01$)[14]. This model is similar to the genetically insulin-resistant obese Zucker rats, which are characterized by a range of metabolic abnormalities including severe hyperinsulinemia, dyslipidemia and adipocyte hypertrophy; however, they possess normal blood glucose levels[15]. The precise mechanisms responsible for this defect remain unknown.

Major progress has been made in understanding the mechanisms that causally underlie the metabolic actions of TZDs. Although the exact mechanisms remain uncertain, it has been widely reported that TZDs activate PPAR-γ and stimulate adipocyte differentiation, which might modulate the glucose metabolism of other tissues.

In the present study, we investigated the effects of a particular TZD, pioglitazone, on insulin resistance induced by low-dose STZ and a high sucrose-fat diet in Wistar rats. The model rats showed significant elevation in fasting blood glucose and insulin levels, as well as in circulating TG, TC, and FFA levels. Pioglitazone treatment markedly normalized serum lipid contents and decreased lipid storage in insulin-sensitive tissues. In our previous study, a strong correlation was found between circulating triglycerides and *in vivo* insulin resistance as assessed by the hyperinsulinemic-euglycemic clamp. Evidence from other studies also suggests an important role for tissue lipid levels in insulin action[16]. It was, therefore, suggested that regulating lipid metabolism might play an important role in the insulin sensitizing effect of pioglitazone.

Studies *in vitro* have shown that a major effect of TZDs is the inhibition of gluconeogenesis in isolated hepatocytes[17]. Our gluconeogenesis test revealed that pioglitazone significantly inhibited the impaired gluconeogenesis in STZ rats.

Our study also shed some light on the potential molecular mechanisms underlying amelioration of insulin resistance. We focused on the insulin sensitive tissues, that is, liver and skeletal muscle. It has been reported that glucose transport decreases in the skeletal muscle of high-fat or high-sucrose induced insulin-resistant rats, and that GLUT4 mRNA and protein expression also decrease[18]. In insulin-deficient type 1 diabetic rats, GLUT4 expression also decreased[19]. Our results are consistent with these reports and show a 68.7% decrement in skeletal GLUT4 protein content in STZ rats compared with control rats, although we did not measure plasmid membrane GLUT4 content during insulin stimulation, which reflects GLUT4 translocation. Although it is unlikely that changes in GLUT4 content entirely explain the insulin sensitizing effects of pioglitazone treatment because of various defects in the intracellular insulin-signaling pathway, GLUT4 is contributing to a certain extent.

IRS-1 is a well-described insulin receptor substrate that, after tyrosine phosphorylation, is associated with and activates PI3-kinase, and plays an important role in insulin signaling[20]. Our results showed a marked deficiency in IRS-1 protein content in untreated STZ rats, with a significant improvement towards normal levels after pioglitazone treatment. Pioglitazone induced increases in GLUT4 and IRS-1 protein expression, which were associated with improvements in glucose transport and insulin signaling pathways, and this may explain the effects of pioglitazone in improving insulin resistance in the model animals.

In the present study, pioglitazone treatment improved insulin sensitivity as assessed by both ISI and ITT; however, pioglitazone had no effect on glucose intolerance in STZ rats. Glucose intolerance pre-existed prior to high sucrose-fat diet feeding, which means that the impaired glucose tolerance was originally caused by STZ administration, and developed gradually with feeding. The reasons for this remain uncertain and require further investigation, particularly the effects on β-cell function.

In conclusion, our studies showed a marked state of insulin resistance and obesity in STZ rats that is associated with various defects in glucose and lipid metabolism, including the insulin signaling–glucose transport pathway. Despite the persistence of obesity in these animals, pioglitazone treatment led to an apparent improvement in overall insulin sensitivity by ameliorating dyslipidemia, hyperinsulinemia, and gluconeogenesis, as well as affecting glucose transport and insulin signaling.

References

1 Defronzo RA, Bonadonna RC, Ferrannini E. Pathogenesis of NIDDM. A balanced overview. Diabetes Care 1992; 15: 318–68.

2 Hallfrisch J, Lazar F, Jorgensen C, Reiser S. Insulin and glucose responses in rats fed sucrose or starch. Am J Clin Nutr 1979; 32: 787–93.

3 Xie MZ, Liu HF, Zhang LY, Shen ZF, Chen QM. An experimental rat model of obesity and diabetes. Acta Pharm Sin 1985; 20: 801–6.

4 Suter SL, Nolan JJ, Wallace P, Gumbiner B, Olefsky JM. Metabolic effects of new oral hypoglycemic agent CS-045 in NIDDM subjects. Diabetes Care 1992; 15: 193–203.

5 Nolan JJ, Ludvik B, Beerdsen P, Joyce M, Olefsky J. Improvement in glucose tolerance and insulin resistance in obese subjects treated with troglitazone. N Engl J Med 1994; 331: 1188–93.

6 Ikeda H, Taketomi S, Sugiyama Y, Shimura Y, Sohda T, Meguro K, *et al*. Effects of pioglitazone on glucose and lipid metabolism in normal and insulin resistant animals. Arzneimittelforschung 1990; 40: 156–62.

7 Oakes ND, Camilleri S, Furler SM, Chisholm DJ, Kraegen EW. The insulin sensitizer, BRL 49653, reduces systemic fatty acid supply and utilization and tissue lipid availability in the rat. Metabolism 1997; 46: 935–42.

8 Klip A, Ramlal T, Young DA, Holloszy JO. Insulin-induced translocation of glucose transporters in rat hindlimb muscles. FEBS Lett 1987; 224: 224–30.

9 Hotamisligil GS, Budavari A, Murray D, Spiegelman BM. Reduced tyrosine kinase activity of the insulin receptor in obesity-diabetes. Central role of tumor necrosis factor-alpha. J Clin Invest 1994; 94: 1543–9.

10 Saad MJ, Folli F, Kahn JA, Kahn CR. Modulation of insulin receptor, insulin receptor substrate-1, and phosphatidylinositol 3-kinase in liver and muscle of dexamethasone-treated rats. J Clin Invest 1993; 92: 2065–72.

11 Perriello G, Misericordia P, Volpi E, Pampanelli S, Santeusanio F, Brunetti P, *et al*. Contribution of obesity to insulin resistance in noninsulin-dependent diabetes mellitus. J Clin Endocrinol Metab 1995; 80: 2464–9.

12 Kraegen EW, James DE, Storlien LH, Burleigh KM, Chisholm DJ. *In vivo* insulin resistance in individual peripheral tissues of the high fat fed rat: assessment by euglycaemic clamp plus deoxyglucose administration. Diabetologia 1986; 29: 192–8.

13 Pascoe WS, Storlien LH. Inducement by fat feeding of basal hyperglycemia in rats with abnormal β-cell function: model for study of etiology and pathogenesis of NIDDM. Diabetes 1990; 39: 226–33.

14 Ding SY, Shen ZF, Chen YT, Xie MZ. Evaluation on two insulin resistance rat models by euglycemic clamp technique. Chin J Diabetes 2001; 9: 286–90.

15 Terrettaz J, Assimacopoulos-Jeannet F, Jeanrenaud B. Severe hepatic and peripheral insulin resistance as evidenced by euglycemic clamps in genetically obese fa/fa rats. Endocrinology 1986; 118: 674–8.

16 Kim JK, Fillmore JJ, Chen Y, Yu C, Moore IK, Pypaert M, *et al*. Tissue-specific overexpression of lipoprotein lipase causes tissue-specific insulin resistance. Proc Natl Acad Sci USA 2001; 98: 7522–7.

17 Ciaraldi TP, Gilmore A, Olefsky JM, Goldberg M, Heidenreich KA. *In vitro* studies on the action of CS-045, a new antidiabetic agent. Metabolism 1990; 39: 1056–62.

18 Sevilla L, Guma A, Enrique-Tarancon G, Mora S, Munoz P, Palacin M, *et al*. Chronic high-fat feeding and middle-aging reduce in an additive fashion Glut4 expression in skeletal muscle and adipose tissue. Biochem Biophys Res Commun 1997; 235: 89–93.

19 Garvey WT, Huecksteadt TP, Birnbaum MJ. Pretranslational suppression of an insulin-responsive glucose transporter in rats with diabetes mellitus. Science 1989; 245: 60–3.

20 Kanai F, Ito K, Todaka M, Hayashi H, Kamohara S, Ishii K, *et al*. Insulin-stimulated GLUT4 translocation is relevant to the phosphorylation of IRS-1 and the activity of PI-3 kinase. Biochem Biophys Res Commun 1993; 195: 762–8.

Acta Pharmacologia Sinica 2005 May; 26 (5): 581–586

Full-length article

Inhibitory effects of idoxifene on hepatic fibrosis in rats[1]

Ya-jun ZHOU[2], Dong-mei YIN, Hong-shan CHEN, Jian-hua SHI, Bao-xi SHA, Xing WANG

Department of Biochemistry & Molecular Biology, Medical College, Nan Tong University, Nantong 226001, China

Key words

fibrosis; idoxifene; oxidative stress; hepatic stellate cell; liver

[1] Project supported by fund from Ministry of Education of China (No 02KJB310003), Jiangsu Province of China (No 2002247) and Medical College, Nan Tong University.
[2] Correspondence to Dr Ya-jun ZHOU.
Phn 86-513-583-0994.
Fax 86-513-505-1533.
E-mail zhouyajun64@hotmail.com

Received 2004-08-02
Accepted 2004-11-05

doi: 10.1111/j.1745-7254.2005.00082.x

Abstract

Aim: To investigate the effects of a tissue-specific selective estrogen receptor modulator, idoxifene, on hepatic fibrosis in rats. **Methods:** Hepatic fibrosis was induced by dimethylnitrosamine (DMN) in male rats. The DMN model of hepatic fibrosis and the hepatocytes undergoing oxidative stress were treated with idoxifene respectively. The effect of idoxifene on hepatic fibrosis in the DMN model was examined by immunohistochemistry. Effects of idoxifene on antioxidant enzyme levels of copper, zinc-dependent superoxide dismutase (CuZn-SOD), and cellular glutathione peroxidase (GSHPx) were measured by ELISA. Effects of idoxifene on activation, proliferation, and apoptosis of culture-activated hepatic stellate cells (HSC) were analysed by immunohistochemistry, bromodeoxyuridine (BrdU) uptake, and flow cytometry, respectively. **Results:** Idoxifene could markedly suppress DMN-induced hepatic fibrosis in male rats. A treatment of 0.4 $mg\cdot kg^{-1}\cdot d^{-1}$ of idoxifene reduced the protein levels of collagen in the DMN model by 41.19% ($P<0.05$). Protein level of CuZn-SOD and activitiy of GSHPx in liver treated with DMN plus 0.4 $mg\cdot kg^{-1}\cdot d^{-1}$ of idoxifene were 2.65 times ($P<0.05$) and 2.08 times greater ($P<0.05$) than that of liver treated with DMN alone respectively. The protein level of CuZn-SOD and activity of GSHPx in cultured rat hepatocytes treated with ferric nitrilotriacetate (FeNTA) plus 1×10^{-7} mol/L of idoxifene were 3.43 times ($P<0.05$) and 2.52 times ($P<0.05$) greater than that treated with FeNTA alone. Idoxifene could inhibit HSC activation. Compared with the control, the uptake of BrdU in HSC cultured with 1×10^{-7} mol/L of idoxifene was reduced by 51.87 % ($P<0.05$), and the number of apoptotic HSCs cultured with 1×10^{-7} mol/L of idoxifene increased by 94.52% ($P<0.05$). **Conclusion:** Idoxifene showed inhibitory action on hepatic fibrosis in male rats.

Introduction

Chronic injury leading to liver fibrosis occurs in response to a variety of insults, including viral hepatitis, alcohol abuse, drugs, metabolic diseases due to overload of iron, *etc*. Hepatic fibrosis is reversible, whereas cirrhosis, the end-stage consequence of fibrosis, is generally irreversible. Suppression of hepatic fibrogenesis and prevention of cirrhosis has attracted the attention of researchers from a therapeutic perspective. Hepatic fibrosis induced by dimethylnitrosamine (DMN) in rats is generally used as a model of hepatic fibrosis[1,2]. Female hormone 17β-estradiol possesses inhibitory effect on DMN-induced hepatic fibrosis in rats[1]. However, administration of estrogen leads to some potential risks including breast cancer.

Idoxifene (*E*-1-[2-[4-[1-(4-iodophenyl)-2-phenyl-1-butenyl]-phenoxy] ethyl] pyrrolidine) is a novel tissue-specific selective estrogen receptor modulator (SERM). Idoxifene was originally developed for the treatment of advanced breast cancer[3] and had no side effects of estrogen[4]. Idoxifene possessed the protective roles in vascular smooth muscle cells by its blunting the angiotensin II-induced production of reactive oxygen species (ROS)[5]. Chronic liver injury causes overproduction of ROS which result in oxidative stress and oxidative stress is a link between chronic liver injury and hepatic fibrosis. Moreover, idoxifene could also protect hepa-

tocytes from inflammatory cell injury[6].

Based on the information**,** the aim of present study is to ascertain the effect of idoxifene on DMN-induced hepatic fibrosis in rats.

ROS are by-products of the inflammatory response, and contribute to both onset and progession of hepatic fibrosis[7]. Copper,zinc-dependent superoxide dismutase (CuZn-SOD) and cellular glutathione peroxidase (GSHPx) are important enzymatic antioxidants in cells. Hepatic stellate cells (HSCs) play a central role in the development and resolution of hepatic fibrosis[8–10]. In response to liver damage, HSCs "activate" to a myofibroblast-like (α-SMA-expressing) phenotype. Activation of HSCs is a critical step in hepatic fibrogenesis. Culturing quiescent HSC on plastic plates causes spontaneous activation leading to a myofibroblast-like phenotype, mimicking the process seen *in vivo*. This provides a simple and useful model for studying HSC activation. Therefore, in this report the impacts of idoxifene on enzymatic antioxidant and on cultured HSCs were explored.

Materials and methods

DMN model Thirty male Wistar rats (200±6 g, provided by the Animal Center of Nan Tong Medical College) were used for the DMN model of hepatic fibrosis (five groups of six each). The animals, were administered a single intraperitoneal injection of DMN (Sigma, St Louis, MO) (diluted with saline) at a dose of 40 mg/kg body weight[1]. After the DMN treatments, the rats received daily oral gavage of idoxifene (synthesized at SmithKline Beecham Pharmaceuticals, King of Prussia, PA) in a dosing vehicle (methylcellulose) at a dose of 0.02 $mg\cdot kg^{-1}\cdot d^{-1}$, 0.1 $mg\cdot kg^{-1}\cdot d^{-1}$, or 0.4 $mg\cdot kg^{-1}\cdot d^{-1}$ respectively for two weeks[1]. The controls received vehicle. After two weeks, the livers were removed and the protein levels of collagen were measured; hepatic fibrosis was shown by immunohitochemistry using an antibody against type I collagen. The protein levels of CuZn-SOD and the activities of cellular GSHPx in the liver were also detected.

Cell culture Hepatocytes were isolated from the livers of male Wistar rats (500–550 g) as described previously[11]. Approximately 5×10^5 cells were introduced into 20-mm diameter plastic dishes. Cells were cultured in 1 mL Williams medium E supplemented with 5% fetal bovine serum (FBS), penicillin 100 kU/L, streptomycin 0.1 g/L, and *L*-glutamine 2 mmol/L at 37 °C in 5% CO_2 atmosphere and 100% humidity. Overnight, the cell medium was removed, and the serum-free medium with 1×10^{-9}, 1×10^{-8}, or 1×10^{-7} mol/L of idoxifene was added to the cells respectively. After incubation for 1 h, FeNTA was added into the wells at a final concentration of 100 μmol/L which is generally used to cause oxidative stress in cultured hepatocytes[6,12,13]. After 24 h[12], the cells were collected and the protein levels of CuZn-SOD and the activities of cellular GSHPx were measured.

Isolation of HSCs from the liver of male Wistar rats (500–550 g) and the assay of purity and viability of isolated HSCs were performed as described previously[14]. Both cell purity and viability was in excess of 90%. After HSCs were cultured in Dulbecco's modified Eagle's medium (DMEM) supplemented with 10% FBS on uncoated plastic culture dishes for 5 d, the activation of HSCs occurred[2]. In present experiment, HSCs were initially cultured in DMEM supplemented with 10% FBS on uncoated plastic culture dishes for several days, then the culture medium was removed and the same medium with or without idoxifene was added to the cells which were cultured for an additional time. After the time, examination of activation, proliferation, and apoptosis of HSCs were performed.

Collagen determination Protein levels of collagen were determinated as described previously[2]. A portion of each liver was homogenized in 35 volumes (mL/g) of 0.5 mol/L acetic acid at 4 °C; homogenates were disrupted by freeze-thawing and sonicated for 2 min for collagen determination. The fraction of insoluble collagen after the acid extraction was then heated at 80 °C for 60 min and then converted into soluble gelatin. The collagen and gelatin contents of the acid extract were assayed using the Sircol collagen assay kit (Biocolor, Belfast, Northern Ireland) according to the manufacturer's directions.

Immunohistochemistry Immunohistochemical examination of the liver fibrosis was performed using polyclonal antibody against type I collagen (Chemicon International, Temecula, CA, diluted 1:100) as described previously[2]. Briefly, after incubation with the antibody against type I collagen, liver samples were washed and were incubated with the biotin-conjugated IgG $F(ab')_2$ (DAKO, diluted 1:200), and finally with the avidin-biotin complex (Vectastain ABC reagent, Vector Laboratories, Burlingame, CA). Reaction products were visualized with diaminobenzidine and photographed.

For immunohistochemical examination of α-SMA, HSCs were initially cultured for 2 d in DMEM supplemented with 10% FBS. The culture medium was then removed and the same medium with or without 1×10^{-7} mol/L of idoxifene was added to the cells and the cells were cultured for an additional 4 d. During this period, the medium was replaced every other day. An immunohistochemical examination of α-SMA was performed as described previously[14]. Briefly, after incubation with the a monoclonal antibody against α-

SMA (DAKO, diluted 1:50), cells were washed and were incubated with the biotin-conjugated IgG F(ab')$_2$ (DAKO, diluted 1:200), and finally with the avidin-biotin complex (Vectastain ABC reagent, Vector Laboratories, Burlingame, CA). Reaction products were visualized with diaminobenzidine and were photographed.

Antioxidant enzyme assays Liver tissues were washed with a 0.5% heparin sodium solution in PBS, and were then homogenized on ice in 6 volumes (mL/g) of Tris buffer (50 mmol/L Tris-HCl, pH 7.5, 5 mmol/L ethylenediaminetetraacetic acid and 1 mmol/L diethiothreitol). Cultured hepatocytes were washed twice with ice-cold PBS, and lysed directly in 150 μL of Tris buffer. The resulting homogenate and cells were disrupted by sonication for 1 min. The suspension was then centrifuged at 14 000×*g* at 4 ºC for 30 min. Aliquot samples of the supernatants were analyzed for antioxidant enzymes. Protein level of CuZn-SOD was detected using an enzyme-linked immunosorbent assay (ELISA) system kit (Amersham, Little Chalfont, UK). GSHPx activities were determined using a cellular glutathione peroxidase assay kit (Calbiochem, San Diego, CA). Enzyme assays were performed according to each manufacturer's recommendation protocol.

Cell proliferation assays DNA synthesis in cultured HSCs was measured using a Cell Proliferation Biotrack ELISA system (Amersham, Little Chalfont, UK). HSCs were cultured in DMEM supplemented with 10% FBS in 96-well plate for 4 d. In the period, the medium was replaced every other day. After 4 d, the culture medium was removed and the same medium with or without 1×10^{-9}, 1×10^{-8}, or 1×10^{-7} mol/L of idoxifene was added to the cells respectively. After the cells were cultured for an additional 24 h, bromodeoxyuridine (BrdU) was added into each well at a final concentration of 10 μmol/L and the cells were incubated with BrdU for 24 h. The incorporated BrdU was detected according to the manufacturer's recommended protocol.

Early apoptosis detection A combination of FITC-conjugated annexin V and propidium iodide (PI) is a powerful and selective tool for measuring early apoptosis by flow cytometry. HSCs cultured in DMEM supplemented with 10% FBS in 6-well plates for 5 d. In the period, the medium was replaced every other day. After 5 d, the cultured medium was removed and the same medium with or without 1×10^{-7} mol/L of idoxifene was added to the cells. The apoptotic cells were detected using an ANNEXIN V FITC kit (Immunotech, Marseille, France) according to the manufacturer's recommended protocol. Flow cytometric analysis was performed on an ELICS XL flow cytometer (Coulter, Hialeah, FL).

Statistical analysis Data were expressed as mean±SD. Comparisons among groups were performed by an analysis of variance and Scheffe's test. $P<0.05$ was considered statistically significant.

Results

Effects of idoxifene on hepatic fibrosis The protein level of collagen increased in rat liver treated with DMN; 0.1 mg·kg^{-1}·d^{-1} or 0.4 mg·kg^{-1}·d^{-1} of idoxifene could inhibit the production of collagen induced by DMN in liver and 0.4 mg·kg^{-1}·d^{-1}of idoxifene reduced the protein level of collagen induced by DMN in liver by 41.19% ($P<0.05$, Table 1). Immunohistochemistry study indicated that in DMN model, 0.4 mg·kg^{-1}·d^{-1}of idoxifene markedly suppressed the expression of type I collagen (Figure 1) which is the most excessive extracellular matrix protein in hepatic fibrosis.

Table 1. Effects of idoxifene on protein levels of collagen in DMN model of rat hepatic fibrosis. n=6. Mean±SD. $^bP<0.05$ *vs* Normal; $^eP<0.05$ *vs* DMN ; $^hP<0.05$ *vs* DMN+idoxifene.

Groups	Idoxifene mg·kg^{-1}·d^{-1}	Collagen /mg·mg^{-1} liver
Normal		7.26±3.13
DMN		15.22±4.12^b
DMN+idoxifene	0.02	14.10±3.85
DMN+idoxifene	0.1	10.58±2.87^{eh}
DMN+idoxifene	0.4	8.95±2.62^{eh}

Effects of idoxifene on antioxidant enzymes Compared with the normal (control), the protein levels of CuZn-SOD and the activities of GSHPx both in liver treated with DMN alone and in hepatocytes cultured with FeNTA alone evidently declined, whereas all the decline were inhibited by idoxifene (Table 2, 3). The protein level of CuZn-SOD and the activity of GSHPx in the liver treated with DMN plus 0.4 mg·kg^{-1}·d^{-1} of idoxifene were 2.65 ($P<0.05$) and 2.08 ($P<0.05$) times greater than that in liver treated with DMN alone (Table 2). The protein level of CuZn-SOD and the activity of GSHPx in hepatocytes cultured with FeNTA plus 1×10^{-7} mol/L of idoxifene were 3.43 ($P<0.05$) and 2.52 ($P<0.05$) times greater than that in hepatocytes cultured with FeNTA alone (Table 3).

Effects of idoxifene on culture-activated HSCs Idoxifene evidently suppressed HSC activation (Figure 2), inhibited culture-activated HSC proliferation in a dose-dependent manner (Figure 3), and induced culture-activated HSC apoptosis in a time-dependent manner (Figure 4). Compared with the control, the uptake of BrdU in HSCs cultured with

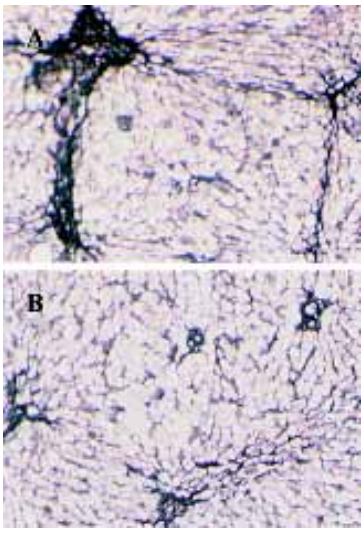

Figure 1. Effects of idoxifene on hepatic fibrosis shown by immunohistochemistry using antibody against type I collagen in a DMN model of rat hepatic fibrosis. A) DMN; B) DMN+idoxifene (0.4 mg·kg^{-1}·d^{-1}). (ABC stain, ×50).

Table 2. Effects of idoxifene on protein levels of CuZn-SOD and on activities of GSHPx in DMN model of rat hepatic fibrosis. n=6. Mean±SD. ^{b}P<0.05 *vs* Normal; ^{e}P<0.05 *vs* DMN; ^{h}P<0.05 *vs* DMN+idoxifene.

Groups	Idoxifene /mg·kg^{-1}·d^{-1}	CuZn-SOD /ng·mg^{-1} liver	GSHPx /U·mg^{-1}liver
Normal		l 3.78±0.49	0.79±0.13
DMN		1.13±0.15^{b}	0.37±0.12^{b}
DMN+idoxifene	0.02	2.11±0.31^{eh}	0.42±0.08^{eh}
DMN+idoxifene	0.1	2.49±0.37^{e}	0.68±0.09^{e}
DMN+idoxifene	0.4	2.99±0.43^{e}	0.77±0.09^{e}

Table 3. Effects of idoxifene on protein levels of CuZn-SOD and on activities of GSHPx in cultured rat hepatocytes undergoing oxidative stress. n=6. Mean±SD. ^{b}P<0.05 *vs* Normal; ^{e}P<0.05 *vs* FeNTA; ^{h}P<0.05 *vs* FeNTA+idoxifene .

Groups	Idoxifene /mol·L^{-1}	CuZn-SOD /ng·mg^{-1} liver	GSHPx /U·mg^{-1}liver
Normal		8.86±1.81	1.49±0.33
FeNTA		2.11±0.83^{b}	0.50±0.16^{b}
FeNTA+idoxifene	1×10^{-9}	3.23±1.35^{h}	0.52±0.18^{h}
FeNTA+idoxifene	1×10^{-8}	6.28±1.40^{e}	0.84±0.19^{e}
FeNTA+idoxifene	1×10^{-7}	7.23±1.74^{e}	1.26±0.25^{e}

1×10^{-7} mol/L of idoxifene was reduced by 51.87% (P<0.05) (Figure 3) and the number of apoptotic HSCs cultured with

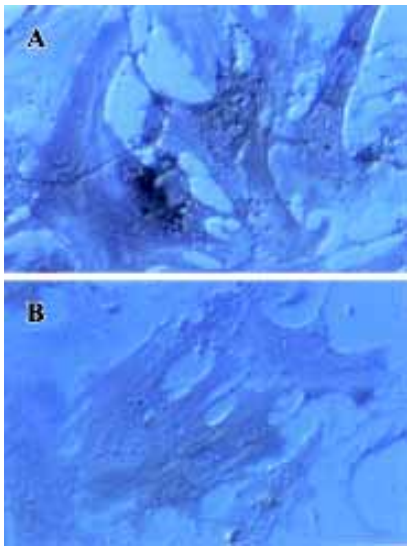

Figure 2. Effects of idoxifene on the activation of cultured rat HSCs. After cultured for 2 d, HSCs were incubated without (A) or with (B) idoxifene (1×10^{-7} mol/L) for additional 4 d. Immunohistochemical examination of HSC activation was performed using the antibody against α-SMA. (ABC stain, ×400).

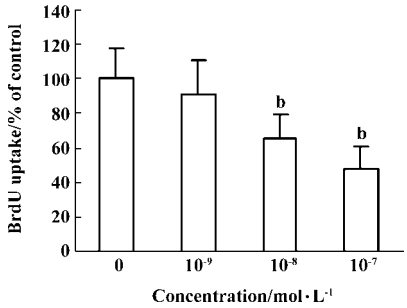

Figure 3. Effects of idoxifene on DNA synthesis in cultured rat HSCs. After cultured for 4 d, HSCs were incubated in the medium with or without 1×10^{-7}, 1×10^{-8}, or 1×10^{-9} mol/L of idoxifene for additional 24 h before being labeled with BrdU for 24 h. The incorporated BrdU was detected. n=4. Mean±SD. ^{b}P<0.05 *vs* the 0 mol/L (control).

1×10^{-7} mol/L of idoxifene increased by 94.52% (P<0.05) (Figure 4D).

Discussion

Hepatic fibrogenesis is a process where production of extracellular matrix surpasses degradation. Collagen is the main component of extracellular matrix. Abnormal accumulation of collagen in chronic liver injury is a direct index that indicates the hepatic fibrogenesis. Data in this report showed that idoxifene could reduce the protein level of

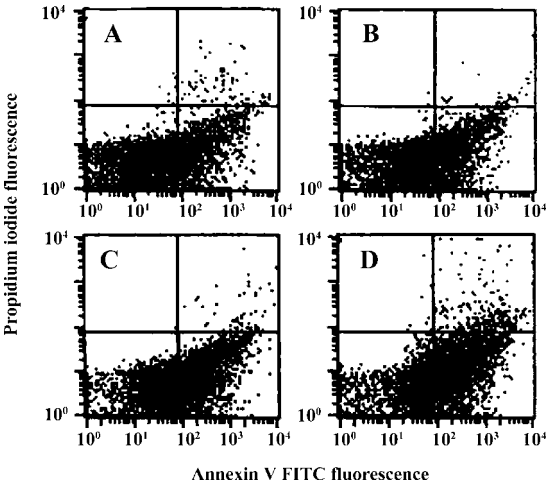

Figure 4. Effects of idoxifene on apoptosis of cultured rat HSCs. After cultured for 5 d, HSCs were incubated without (A, control) or with (B, C, D) idoxifene (1×10^{-7} mol/L) for additional 0 (A), 1 (B), 2 (C), 3 (D) d, respectively. Flow cytometric analysis of the apoptotic cells was performed. Total numbers of cells examined in each sample was 25 000. In each panel (A, B, C, D), the lower right quadrant demonstrated the apoptotic cells. The ratios of apoptotic cell numbers to total cell numbers: A (26.84%), B (33.5%), C (42.44%), D (52.21%).

collagen in DMN model of hepatic fibrosis in a dose-dependent manner. Immunohistochemical studies directly showed that idoxifene markedly suppressed hepatic fibrosis induced by DMN. Together, these data demonstrated the inhibitory effect of idoxifene on hepatic fibrosis in rats.

ROS mainly include superoxide anion and its metabolin such as hydrogen peroxide and lipid peroxide. Since overproduction of ROS results in oxidative stress which is a link between chronic liver injury and hepatic fibrosis, reduction of oxidative stress by antioxidants can prevent hepatic fibrogenesis. Idoxifene evidently inhibited the decline in enzymatic antioxidant levels of CuZn-SOD and GSHPx, which can neutralize the effects of ROS, both in DMN model of hepatic fibrosis and in hepatocytes undergoing oxidative stress. CuZn-SOD can eliminate superoxide anion and GSHPx can eliminate hydrogen peroxide and lipid peroxide. The data partly suggested the inhibitory mechanisms of idoxifene on rat hepatic fibrosis.

Activated HSCs are proliferative and are responsible for the majority of extracellular matrix protein deposition that forms scar tissue during liver fibrogenesis. Idoxifene clearly suppressed HSC activation and culture-activated HSC proliferation. The data were consistent with the inhibitory effect of idoxifene on rat hepatic fibrosis.

Accumulating evidence has indicated that oxidative stress plays critical roles in activation of HSC[8,15,16]. Hepatocytes and Kupffer cells after chronic liver injury are a potent source of reactive oxygen intermediates[17]. These compounds exert paracrine stimulation of stellate cells. In cultured stellate cells, conditioned medium from hepatocytes undergoing oxidative stress increases proliferation and collagen synthesis[18]. Thereby the effects of idoxifene on the antoxidant enzymes (CuZn-SOD, GSHPx) *in vivo* and *in vitro* as shown in results suggested that idoxifene could inhibit HSCs activation at least through indirectly blunting the roles of ROS.

Recovery from established experimental fibrosis can occur through apoptosis of activated HSCs and is associated with reductions in liver collagen[10,19]. The result that idoxifene effectively induced culture-activated HSC apoptosis further supported the inhibitory effect of idoxifene on hepatic fibrosis in rats.

Oxidative stress in liver causes hepatocyte apoptosis[20] which promotes the activation of HSCs and hepatic fibrogenesis[21–23]. Our recent results showed that idoxifene at 1×10^{-7} mol/L could markedly inhibit oxidative stress-induced hepatocyte apoptosis[24]. Those results demonstrated the protective effect of idoxifene on hepatocytes and implied another inhibitory mechanism of idoxifene on hepatic fibrosis in rats.

Collectively, our data provides evidence that idoxifene possesses the inhibitory effect on hepatic fibrosis in rats. The inhibitory effect of idoxifene on hepatic fibrosis in rats was, at least in part, through maintaining antioxidant enzyme levels (CuZn-SOD and GSHPx).

SERMs are a diverse group of compounds that bind with specific, high-affinity binding to the estrogen receptor (ER) and can act as either ER agonists or antagonists. Tamoxifen, one of SERMs, increases fibrogenesis in CCl_4-induced liver fibrosis, showing estrogen antagonist activity[25]. The data presented in the present study demonstrates the inhibitory effect of idoxifene on DMN-induced liver fibrosis in rats, showing the potential of idoxifene as an estrogen agonist in rat liver. The different biologic actions can be related to the ER subtype involved, different conformational changes of the ER according to the ligand, and steroil receptor coactivators and corepressors that modulate the cellular response to the ER-ligand complex[26]. It is known that the alterations in the conformation of receptors influence their abilities to interact with coactivators and corepressors[27].

Estrogen can suppress the hepatic fibrosis[1], but it leads to serious side effects which restricts its application. The side effects of idoxifene is presently unknown. Idoxifene has been used for the treatment of advanced breast cancer

and also has no side effects of estrogen[4], the findings in this report suggest that idoxifene might be useful in developing new therapeutic strategies for the treatment and prevention of hepatic fibrogenesis.

References

1 Yasuda M, Shimizu I, Shiba M, Ito S. Suppressive effects of estradiol on dimethylnitrosamine-induced fibrosis of the liver in rats. Hepatology 1999; 29: 719–27.

2 Shimizu I, Ma YR, Mizobuchi Y, Liu F, Miura T, Nakai Y, *et al*. Effects of Sho-saiko-to, a japanese herbal madicine, on hepatic fibrosis in rats. Hepatology 1999; 29: 149–60.

3 Johnston SR, Boeddinghaus IM, Riddler S, Haynes BP, Hardcastle IR, Rowlands M, *et al*. Idoxifene antagonizes estradiol-dependent MCF-7 breast cancer xenograft growth through sustained induction of apoptosis. Cancer Res 1999; 59: 3646–51.

4 Hirsimaki P, Aaltonen A, Mantyla E. Toxicity of antiestrogens. Breast J 2002; 8: 92–6.

5 Baumer AT, Wassmann S, Ahlbory K, Strehlow K, Muller C, Sauer H, *et al*. Reduction of oxidative stress and AT1 receptor expression by the selective oestrogen receptor modulator idoxifene. Br J Pharmacol 2001; 134: 579–84.

6 Omoya T, Shimizu I, Zhou Y, Okamura Y, Inoue H, Lu G, *et al*. Effects of idoxifene and estradiol on NF-kappaB activation in cultured rat hepatocytes undergoing oxidative stress. Liver 2001; 21: 183–91.

7 Poli G. Pathogenesis of liver fibrosis: role of oxidative stress. Mol Aspects Med 2000; 21: 49–98.

8 Friedman SL. Molecular regulation of hepatic fibrosis, an integrated cellular response to tissue injury. J Biol Chem 2000; 275: 2247-50.

9 Alcolado R, Arthur MJ, Iredale JP. Pathogenesis of liver fibrosis. Clin Sci (Lond) 1997; 92: 103–12.

10 Iredale JP, Benyon RC, Pickering J, McCullen M, Northrop M, Pawley S, *et al*. Mechanisms of spontaneous resolution of rat liver fibrosis. Hepatic stellate cell apoptosis and reduced hepatic expression of metalloproteinase inhibitors. J Clin Invest 1998; 102: 538–49.

11 Shimizu I, Ichihara A, Nakamura T. Hepatocyte growth factor in ascites from patiens with cirrhosis. J Biochem 1991; 109: 14–8.

12 Morel I, Lescoat G, Cillard J, Pasdeloup N, Brissot P, Cillard P. Kinetic evaluation of free malondialdehyde and enzyme leakage as indices of iron damage in rat hepatocyte cultures. Biochem Pharmacol 1990; 39: 1647–55.

13 Liu Y, Shimizu I, Omoya T, Ito S, Gu XS, Zuo J. Protective effects of estradiol on hepatocytic oxidative damage. World J Gastroenterol 2002; 8: 363–6.

14 Zhou YJ, Yin DM, Chen HS, Zhu HX, Wan X. Effects of blocking transforming growth factor signaling on culture-activated rat hepatic stellate cells. Chin J Hepatol 2003; 11: 282–4.

15 Lee KS, Buck M, Houglum K, Chojkier M. Activation of hepatic stellate cells by TGF α and collagen type I mediated by oxidative stress through c-*myb* expression. J Clin Invest 1995; 96: 2461–6.

16 Fernandez-Checa JC, Kaplowitz N, Garcia-Ruiz C, Colell A. Mitochondrial glutathione: importance and transport. Semin Liver Dis 1998; 18: 389–401.

17 Maher JJ. Leukocytes as modulators of stellate cell activation. Alcohol Clin Exp Res 1999; 23: 917–21.

18 Svegliati Baroni G, D'Ambrosio L, Ferretti G, Casini A, Di Sario A, Salzano R, *et al*. Fibrogenic effect of oxidative stress on rat hepatic stellate cells. Hepatology 1998; 27: 720–6.

19 Wright MC, Issa R, Smart DE, Trim N, Murray GI, Primrose JN, *et al*. Gliotoxin stimulates the apoptosis of human and rat hepatic stellate cells and enhances the resolution of liver fibrosis in rats. Gastroenterology 2001; 121: 685–98.

20 Czaja MJ. Induction and regulation of hepatocyte apoptosis by oxidative stress. Antioxid Redox Signal 2002; 4: 759–67.

21 Canbay A, Guicciardi ME, Higuchi H, Feldstein A, Bronk SF, Rydzewski R, *et al*. Cathepsin B inactivation attenuates hepatic injury and fibrosis during cholestasis. J Clin Invest 2003; 112: 152–9.

22 Canbay A, Higuchi H, Bronk SF, Taniai M, Sebo TJ, *et al*. Fas enhances fibrogenesis in the bile duct ligated mouse: a link between apoptosis and fibrosis. Gastroenterology 2002; 123: 1323-30.

23 Faouzi S, Burckhardt BE, Hanson JC, Campe CB, Schrum LW, Rippe RA, *et al*. Anti-Fas induces hepatic chemokines and promotes inflammation by an NF-kappa B-independent, caspase-3-dependent pathway. J Biol Chem 2001; 276: 49077–82.

24 Zhou YJ, Chen HS, Sha BX. Antiapoptotic mechanisms of idoxifene on cultured rat hepatocytes undergoing oxidative stress. Chin Pharm J 2005; 40: 278–81.

25 Xu JW, Gong J, Chang XM, Luo JY, Dong L, Hao ZM, *et al*. Estrogen reduces CCl_4-induced liver fibrosis in rats. World J Gastroenterol 2002; 8: 883–7.

26 Burger HG. Selective oestrogen receptor modulators. Horm Res 2000; 53 Suppl 3: 25–9.

27 Smith CL, O'Malley BW. Coregulator function: a key to understanding tissue specificity of selective receptor modulators. Endocr Rev 2004; 25: 45–71.

Acta Pharmacologica Sinica 2005 May; 26 (5): 587–592

Full-length article

Effect of *Oenanthe javanica* flavone on human and duck hepatitis B virus infection[1]

Wei-na WANG[2], Xin-bo YANG[3,6], He-zhi LIU[4], Zheng-ming HUANG[5,6], Guang-xia WU[2]

[2]Research Center for Eco-Environmental Sciences, Chinese Academy of Sciences, Beijing 100084; [3]Institute of Gerontology, General Hospital of PLA, Beijing 100853; [4]Insititute for Drug and Instrument Control of Health Dept GLD of PLA, Beijing 100071; [5]The 302th Hospital of PLA, Beijing 100039, China

Key words

Oenanthe javanica; flavones; hepatitis B virus; 2.2.15 cells; Duck hepatitis B virus; antiviral agents

[1] Project supported by the National New Drug Research Foundation of China (No 96-901-05-016).
[6] Correspondence to Prof Xin-bo YANG.
Phn 86-10-6693-7576.
E-mail Yang_xinbo@yahoo.com
Prof Zheng-ming HUANG
Phn 86-10-6693-3233
Email huang_zhengming@sohu.com

Received 2004-07-02
Accepted 2004-09-17

doi: 10.1111/j.1745-7254.2005.00055.x

Abstract

Aim: To study the antiviral effect of *Oenanthe javanica* flavones (*Oj*F) on human hepatoma HepG2.2.15 culture system and duck hepatitis B virus (DHBV) infection. **Methods:** (1) After incubation for 24 h, the 2.2.15 cells were treated with different concentrations of *Oj*F for 12 d. The cell alteration was observed by microscope. The presence of HBsAg and HBeAg were measured using the enzyme immunoassay kit after 2.2.15 cells were treated with *Oj*F for 9 d. (2) Ducklings infected with DHBV intravenously were divided into 5 groups and treated with *Oj*F, acyclovir (ACV), and normal saline respectively for 10 d. All the ducklings were bled before, during, and after treatments at different times, and serum levels of DHBV-DNA were detected by a dot-blot hybridization assay. **Results:** (1) The 50% toxic concentration (TC_{50}) of *Oj*F was 2.28 g/L. The maximum nontoxic concentration (TC_0) was 1.00 g/L. In nontoxic concentrations, *Oj*F significantly inhibited HBsAg and HBeAg in 2.2.15 cells after 9 d of treatment ($P<0.05$, $P<0.01$). (2) The DHBV-DNA levels decreased significantly after the treatment with 0.50 and 1.00 g/kg of *Oj*F ($P<0.01$). The inhibition of the peak of viremia was maximum at a dose of 1.00 g/kg and reached 54.3% on d 5 and 64.5% on d 10, respectively. **Conclusion:** The results demonstrate that *Oj*F is a strong inhibitor of HBsAg and HBeAg secretion in 2.2.15 cells and DHBV-DNA levels in the HBV-infected duck model.

Introduction

Oenanthe javanica (*Oj*), umbelliferate, has been widely used in traditional Chinese medicine for treatment of jaundice, hypertension, and polydipsia diseases for many years[1]. Previous studies have shown that it has liver-protective[2], hypotensive[3], anti-arrhythmic[4], anti-anaphylactic[5], and antidiabetic[6] effects. Recent studies also show that *Oj* was helpful in treatment of hepatitis B virus (HBV) infection in clinical trials[7], and had an inhibitory effect on duck hepatitis B virus (DHBV)-induced hepatitis in Nestling ducks *in vivo*[8] and *in vitro*[9]. However, which is the active part and what are the active components of *Oj* in inhibiting HBV remain unclear. Using modern techniques, it has been revealed that *Oj*F is one of the main active parts against HBV and it comprises approximately 2.2% of the whole plant content. The present study aimed to investigate the anti-hepatitis activity of *Oj*F in 2.2.15 cells *in vitro* and duck HBV infection in a duck model *in vivo.*

Materials and methods

Preparation of *Oj*F *Oj* was collected from the Yanbian Autonomus Region in autumn and identification was performed by Prof Hui-zhong XIAO, Department of Phytochemistry, Yanbian Medical University. Dried whole plant was pulverized and extracted with 80% ethanol, and subsequently partitioned in ethyl acetate. The ethyl acetate soluble materials were fractionated by ethanol and distilled water gradient of column chromatography in polyamide. *Oj*F was eluted and the content was determined according to aluminium nitrate reagent method. The content of hyperoside,

the major ingredient of *Oj*F, was determined by reverse phase-high performance liquid chromatography (RP-HPLC)[10,11]. The contents of *Oj*F and hyperoside were 51.67% and 7% in whole extracts, respectively. The concentration used in the experiment was based on the dry weight of the extract.

Experimental animals Beijing ducklings within 1 d of hatching were obtained from an animal breeding farm, Chinese Academy of Medical Sciences [SCXK- (Beijing) 2002-001].

Reagents Minimum essential medium (MEM) was obtained from Gibco BRL (Gaithersburg, MD, USA). Fetal bovine serum (FBS) and G-418 were purchased from HyClone (Logan, Utah, USA). *L*-glutamine was obtained from Sigma (St Louis, MO, USA). HBsAg and HBeAg enzyme immunoassay (EIA) kits were purchased from China Isotope Co (Beijing, China).

Cell culture and treatment HepG2.2.15 cells (clonal cells derived from human hepatoma cell line G_2) were from the Institute of Medicinal Biotechnology, Chinese Academy of Medical Sciences. The 2.2.15 cells were cultured in complete MEM (containing 10% FBS, 100 kU/L benzylpenicillin, streptomycin, G-418, *L*-glutamine 0.03%, pH 7.0) in 75-cm^2 tissue culture flasks at 37 ºC in a humidified 5% CO_2.

Cytotoxic studies The 2.2.15 cells were first seeded into 96-well plates (Corning Inc, Corning, NY, USA) at a density of 1.0×10^5 cells per mL and cultured in 200 μL complete MEM containing 10% FBS. After 24 h of incubation, cells were washed three times with phosphate-buffered |saline (pH 7.0) and treated with different concentrations (0.125, 0.25, 0.50, 1.00, 2.00, and 4.00 g/L) of *Oj*F in serum-free medium for 12 d. The medium was replaced every 4 d in MEM supplemented with various concentrations of *Oj*F. Untreated cells were used as control. The cell pathological changes (CPE) were observed by microscope. The degree of CPE was graded as: all positive cells (–), the number of negative cells <25% (+), 25%–49% (++), 50%–75% (+++), and >75% (++++).

Determination of HBsAg and HBeAg The 2.2.15 cells were incubated in 24-well plates at a density of 1.0×10^5 cells per mL in 1 L MEM medium containing 10% FBS. After 24 h, the 2.2.15 cells were treated with different concentrations of *Oj*F (0.125, 0.25, 0.50, and 1.00 g/L) in serum-free medium. Cells grew in the presence of drugs for 9 d with changes of medium every 3 d. After 6 and 9 d, supernatant was collected and performed at -20 °C. The HBsAg and HBeAg in culture medium were simultaneously measured by EIA kits on d 6 and d 9.

Experimented animals infection and drug treatment Beijing ducklings within 1 d of hatching were inoculated intravenously with DHBV-DNA-positive serum from Shanghai ducks (0.2 mL/animal). Seven days after infection, ducklings were divided into five groups: the control group (normal saline); the positive drug group (ACV, 0.1 $g\cdot kg^{-1}\cdot d^{-1}$); and the *Oj*F 0.25, 0.50, and 1.00 $g\cdot kg^{-1}\cdot d^{-1}$ groups. Drugs were administered orally, bid for 10 d. Serum samples were obtained before treatment (d 0), d 5, and d 10 during treatment, and d 3 (d 13) after the cessation of treatment. The serums were stored at -70 °C for future analysis.

Viremia analysis Viremia was assessed throughout the treatment and follow-up period by a semi-quantitative detection of DHBV-DNA in duck serum using a dot-blot hybridization. Fifty microliters of serum was spotted directly onto nitrocellulose filters. After denaturation and neutralization, the filters were hybridized with a full-length DHBV genomic DNA probe labeled with ^{32}P. The filters were autoradiographed and the spots were counted in a scintillation counter.

Histopathological examination of hepatocytes On d 13, each duckling was laparotomized to obtain the liver immediately after collecting blood from the leg vein. Fragments of the ducklings liver were fixed in 10% formalin solution, dehydrated with ethanol solution from 50% to 100%, embedded in paraffin and cut into 5 μm sections, and stained using haematoxylin-eosin dye for photomicroscopic observations.

Statistics The data were expressed as mean±SD, and analyzed by one-way repeated-measure ANOVA and *t*-test for comparisons between groups. $P<0.05$ was considered statistically significant.

Results

The cytotoxicity of *Oj*F in 2.2.15 cells *Oj*F-induced cytotoxicity was observed by microscope. After 12 d of incubation with 1.00 g/L *Oj*F, no significant difference was found from that of the control. However, when *Oj*F concentration increased, cell injury caused by *Oj*F was observed (Table 1). The 50% toxic concentrations (TC_{50}) was 2.28±0.13 g/L and the maximum nontoxic concentrations (TC_0) was 1.00 g/L.

Inhibition of HBsAg and HBeAg production in 2.2.15 cells After 9 d of incubation, HBsAg and HBeAg production in the culture medium were determined (Table 2). The results showed that *Oj*F suppressed HBsAg and HBeAg production in the 2.2.15 cells with median effective concentration (IC_{50}) of about 0.56 and 0.41 g/L respectively on d 6, 0.64 and 0.30 g/L respectively on d 9 (Table 3). *Oj*F-induced suppression of HBsAg and HBeAg production in 2.2.15 cells was also reflected by the inhibition rate percentage (Figure 1, 2). The inhibitory effects appeared when cells were treated with 0.25 g/L *Oj*F. A substantial increase of

Table 1. Cell toxicity of *Oj*F on cultured 2.2.15 cells at d 12.

	Parameter	Dose/g·L^{-1} 4.00	2.00	1.00	0.50	0.25	0.125	0	TC_{50} /g·L^{-1}
1	CPE	++++	+	–	–	–	–	–	2.41
		++++	+	–	–	–	–	–	
		++++	++	–	–	–	–	–	
		++++	+	–	–	–	–	–	
	CPE %	100	31.25						
2	CPE	++++	+	–	–	–	–	–	2.29
		++++	++	–	–	–	–	–	
		++++	+	–	–	–	–	–	
		++++	++	–	–	–	–	–	
	CPE %	100	37.50						
3	CPE	++++	+ +	–	–	–	–	–	2.15
		++++	++	–	–	–	–	–	
		++++	++	–	–	–	–	–	
		++++	+	–	–	–	–	–	
	CPE %	100	43.75						
Mean									2.28

Positive cells (-); number of negative cells <25% (+), 25%–49% (++), 50%–75% (+++), and >75% (++++) in three experiments.
CPE: cell pathological changes. TC_{50} was the 50% toxic concentrations.

Table 2. HBsAg and HBeAg levels in 2.2.15 cells treated with *Oj*F . n=9. Mean±SD. ^{b}P<0.05, ^{c}P<0.01 *vs* control.

Dose/g·L^{-1}	10^{-3}×Radioactivity/Bq d 6 HBsAg	d 6 HBeAg	d 9 HBsAg	d 9 HBeAg
0	3.44±0.24	7.13±1.34	2.66±0.16	7.47±1.43
0.25	2.34±0.17^{c}	3.88±0.95^{c}	1.90±0.11^{b}	2.83±0.44^{c}
0.50	1.59±0.05^{c}	2.93±0.86^{c}	1.47±0.07^{c}	1.78±0.28^{c}
1.00	1.32±0.07^{c}	1.50±0.23^{c}	0.94±0.11^{c}	1.09±0.29^{c}

inhibitory effects was observed from 0.50 g/L *Oj*F. When treated with 1.00 g/L *Oj*F, the inhibition rate percentage on HBsAg and HBeAg in 2.2.15 cells were both more than 50%. The inhibition rate percentage on HBsAg was dose-dependent, and the inhibition rate percentage on HBeAg was both time- and dose-dependent.

Inhibitory effect of *Oj*F on DHBV-DNA During the course of this study, no obvious side effects were observed in animals receiving antiviral therapy or in control animals.

The effects of *Oj*F and ACV, which were used for comparison, on DHBV replication *in vivo* were determined

Table 3. Inhibitory effect on HBsAg and HBeAg in 2.2.15 cells treated with *Oj*F.

	HBsAg IC_{50}/g·L^{-1} d 6	d 9	TI[1)] d 6	d 9	HBeAg IC_{50}/g·L^{-1} d 6	d 9	TI d 6	d 9
1	<0.25	0.62	9.64	3.91	0.56	0.25	4.33	>9.64
2	1.00	0.71	2.29	3.22	0.42	0.25	5.42	>9.16
3	0.43	0.59	5.00	3.67	0.25	0.41	>8.60	5.28
Mean±SD	0.56±0.39	0.64±0.06	5.64±3.72	3.60±0.35	0.41±0.15	0.30±0.09	6.12±2.22	8.03±2.39

[1] TI, therapeutic indices. The values were determined by IC_{50} *vs* TC_{50}. The more the value of TI, the more suppression activity of *Oj*F.

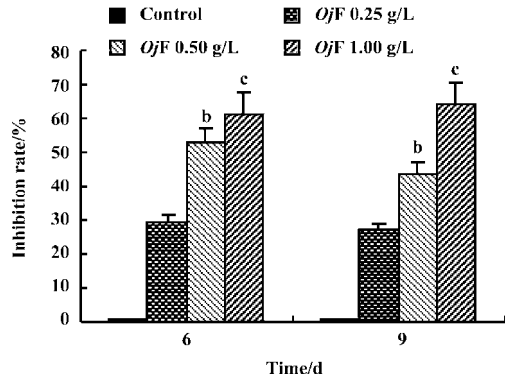

Figure 1. The inhibition rate percentage of *Oenanthe javanica* flavones (*Oj*F) on HBsAg production in 2.2.15 cells. n=9. Mean±SD. ^bP<0.05, ^cP<0.01 *vs* control.

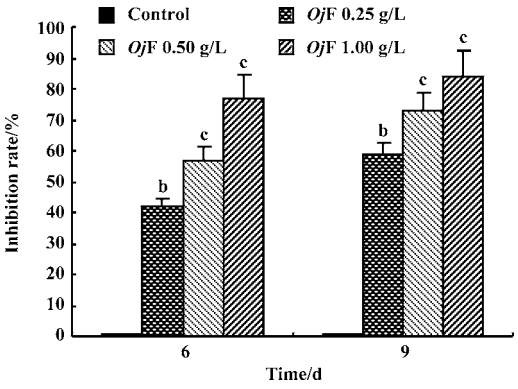

Figure 2. The inhibition rate percentage of *Oj*F on HBeAg production in 2.2.15 cells. n=9. Mean±SD. ^bP<0.05, ^cP<0.01 *vs* control.

by quantification of DHBV-DNA by dot-blot hybridization. The levels of serum viral DNA were recorded in the 5 groups before the experiment. During treatment, serum levels of DHBV-DNA decreased in all 16 ducks treated with *Oj*F 0.50 and 1.00 g·kg^{-1}·d^{-1} (Table 4). The mean percentage inhibition of viral DNA levels with *Oj*F 0.50 and 1.00 g·kg^{-1}·d^{-1} was 54.3% and 64.5% respectively on the last day of treatment

Table 5. The inhibition rate percentage of *Oj*F on DHBV-DNA. n=16. Mean±SD. ^cP<0.01 *vs* control.

Dose/g·kg^{-1}·d^{-1}	Inhibition rate percentage/%		
	d 5	d 10	d 13
0	0	0	0
0.25	14.1±0.16	15.2±0.08	8.2±0.11
0.50	42.4±0.13^c	39.2±0.10^c	43.5±0.07^c
1.00	54.3±0.11^c	64.5±0.06^c	61.1±0.05^c

(Table 5). But 3 days after the cessation of treatment with ACV, the viral replication level returned to the pretreatment baseline. In ducks treated with *Oj*F, the effect of DHBV-DNA inhibition lasted. No significant decrease of serum DHBV-DNA was observed during treatment with *Oj*F 0.25 g·kg^{-1}·d^{-1}. In the control group, serum DHBV-DNA remained unaffected during the course of the study.

Histopathological features Histopathological profiles of the liver from model group ducklings revealed necrosis, steatosis, and often swelling of the hepatic cytoplasm. The protective effect of *Oj*F was confirmed by histopathological examinations. Administration of *Oj*F to the experimental animals (1.00 g·kg^{-1}·d^{-1}) showed a significant improvement of the hepatocellular architecture over the model group, as evident from a considerable reduction in necrosis and vacuolation (Figure 3).

Discussion

Hepatitis B virus causes acute and chronic hepatitis, which affects nearly 360 million people worldwide[12]. Chronic infection with HBV has been associated with a high risk for the development of primary hepatocellular carcinoma[13,14]. Effective antiviral therapy against HBV infection has not been fully developed. Studies have been hampered by the extremely narrow host range and limited access to experimental culture systems. Fortunately, techniques have been

Table 4. Mean changes of serum DHBV-DNA level in treated duck. n=16. Mean±SD. ^bP<0.05, ^cP<0.01 *vs* control. ^eP<0.05, ^fP<0.01 *vs* ACV.

Group	Dose/ g·kg^{-1}·d^{-1}	Absorbance			
		d 0	d 5	d 10	d 13
Control	-	0.88±0.10	0.92±0.10	0.79±0.04	0.85±0.08
ACV	0.1	0.87±0.06	0.27±0.16^c	0.32±0.09^c	0.74±0.14
*Oj*F	0.25	0.83±0.17	0.79±0.21^{bf}	0.67±0.11^{cf}	0.78±0.12
	0.50	0.92±0.11	0.53±0.15^{cf}	0.48±0.10^{cf}	0.48±0.05^{cf}
	1.00	0.85±0.09	0.42±0.15^{ce}	0.28±0.05^c	0.33±0.03^{cf}

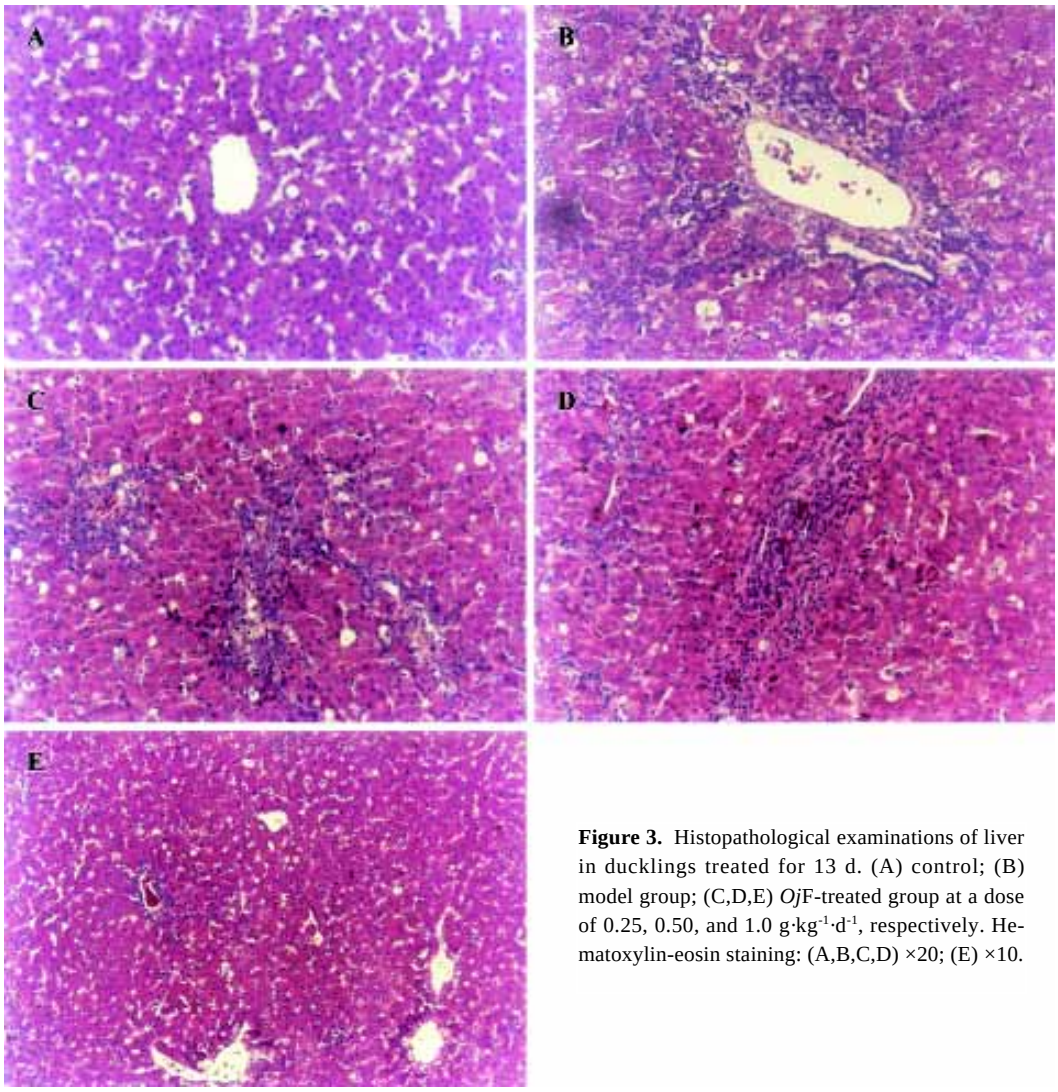

Figure 3. Histopathological examinations of liver in ducklings treated for 13 d. (A) control; (B) model group; (C,D,E) *Oj*F-treated group at a dose of 0.25, 0.50, and 1.0 $g \cdot kg^{-1} \cdot d^{-1}$, respectively. Hematoxylin-eosin staining: (A,B,C,D) ×20; (E) ×10.

developed to propagate hepadnaviridae in tissue culture[15,16] and animal systems[17]. The 2.2.15 cells contain all HBV particles, and the Peking ducks allow multiplication of the HBV-like virus, which make it possible to study the various aspects of the viral life cycle and to examine the effectiveness of potential antiviral drugs.

In a previous study, we have shown that the acid-base extracts of *Oj* could protect hepatic cells, decrease the content of ALT, AST, and BiliT on a liver damage model caused by carbon tetrachloride (CCl_4) in rats[18], and inhibit DHBV[7,8]. Similar results of the inhibitory effect of *Oj* extracts on HBsAg and HBeAg production in cultured 2.2.15 cells was also observed[19]. However, what the active part of *Oj* against HBV is is still unknown. *Oj*F was obtained through extraction and separation, which made up more than 50% in the whole extracts. It might be an active part against HBV. Through subsequent purification of *Oj*F, hyperoside, persicarin, isorhamnetin, and quercetin were obtained. Among them, the assay of hyperoside was the highest (purity>96%) , which was used as the criterion to control the quality of *Oj*F.

This study demonstrated the inhibitory effect of *Oj*F on HBsAg and HBeAg secretion by human hepatoma 2.2.15 cells and on serum DHBV-DNA levels of ducklings infected with hepatitis B virus. TC_{50} of *Oj*F was 2.28 g/L and TC_0 was 1.00 g/L in 2.2.15 cells, which suggested that the inhibitory action of *Oj*F had no cytotoxicity. In nontoxic concentrations, *Oj*F significantly inhibited the secretion of HBsAg and HBeAg. With *Oj*F concentration increasing, a dose-dependent response was observed. At a TC_0 of 1.00 g/L, the inhibition rate percentage of *Oj*F on HBsAg and HBeAg in 2.2.15 cells were both more than 50%, and the inhibition rate per-

centage on HBsAg exceeded that of *Oj*F on HBeAg.

These results clearly illustrate an inhibitory effect of *Oj*F on HBsAg and HBeAg production in 2.2.15 cells, which provide strong evidence to evaluate the effect of drugs against HBV in a cellular model, but it is still necessary to verify this in an animal model. Therefore, the inhibitory effect of *Oj*F in the duck HBV model was investigated. Our experiments with *Oj*F (0.50 and 1.00 $g \cdot kg^{-1} \cdot d^{-1}$) in ducklings pointed to a suppressive action on DHBV replication *in vivo*. With *Oj*F 1.00 $g \cdot kg^{-1} \cdot d^{-1}$, the therapy caused a more pronounced decrease (64.5%) in viremia. It was well known that most antivirus medicines had the inevitable rebound effect after drug cessation. This shortcoming had limited the therapy to those diseases infected by viruses such as HB or AIDS. The similar phenomena appeared in the positive control drug ACV in the present study. *Oj*F showed therapeutic effects as well as ACV, and no difference was observed after cessation of *Oj*F therapy compared to *Oj*F-treated animals. It suggested that *Oj*F could maintain for a long time in treating viremia of HBV and the effect of DHBV-DNA inhibition showed a concentration-dependent response. Histopathological examination also confirmed the function of *Oj*F protecting the liver in DHBV-infected ducklings. Xiong Q *et al*[19] reported that *Apocynum ventun* extracts containing hyperoside and quercetin had hepatoprotective activity, and *Oj*F contained these two compounds. These results demonstrated the antihepatitis B virus effect of *Oj*F, which were consistent with antiviral activity of *Oj*[7,8], making *Oj*F a candidate for future evaluation in patients with HBV infection.

In order to elucidate the possible mechanism of *Oj*F towards DHBV-DNA on DHBV-infected ducklings, the effect of *Oj*F on DHBV-DNA was investigated (data not shown). Our results indicate that *Oj*F might inhibit the DNA-dependent DNA polymerase reaction, which results in the termination of replication of DHBV-DNA. This hypothesis is currently under investigation in our laboratory.

In conclusion, *Oj*F possessed the significant antiviral activity *in vitro* and *in vivo*, and it was one of the main active parts of *Oj* against HBV. Elucidation of the mechanism of its antiviral activity and identification of the active components in *Oj*F will greatly enhance the understanding of viral gene expressions and provide new clues to assist in the development antiviral agents in the future.

Acknowledgement

The authors wish to thank Zhuang LI for his excellent technical support in this study. This research was supported by Institute of Medicinal Biotechnology, Chinese Academy of Medical Sciences.

References

1 Huang ZM, Yang XB, Cao WB. Modern study and clinic application of *Oenanthe javanica*. Pharm J Chin PLA 2001; 17: 266–9.
2 Huang ZM, Zhang ZM, Yang XB, Cao WB. Study of Shui Qin on antihepatitis. Pharmacol Clin Chin Mat Med 1991; 7: 11–3.
3 Yang XB, Huang ZM, Cao WB. Effect of an aqueous extract from *Oenanthe javanica* on rat cardiovascular system. Chin Tradit Herb Drugs 1998; 10: 47–9.
4 Ji GJ, Cao WB, Huang ZM. Anti-arrhythmic effect of injections of SQ. Chin Pharm J 1990; 15: 134–8.
5 Zhang JZ, Cao WB,Yang XB, Huang ZM. Anti-anaphylactic effect of the decoction of SQ. Pharmacol Clin Chin Mat Med 1992; 8(suppl): 29–32.
6 Yang XB, Huang ZM, Cao WB. Antidiabetic effect of *Oenanthe javanica* flavone. Acta Pharmacol Sin 2000; 21: 239–42.
7 Huang ZM, Yang XB, Cao WB. Effects of Qin ling ke li in the treatment of 90 patients with chronic hepatitis B. Pharm J Chin PLA 2001; 17: 41–4.
8 Huang ZM, Yang XB, Cao WB. Inhibition of shuiqin on DHBV *in vitro*. Chin Pharm J 1997; 32: 720–3.
9 Huang ZM, Yang XB, Cao WB. Study of inhibition of duck hepatitis B virus by extract from *Oenanthe javanica*. Chin Sci Bull 1997; 42: 1863–7.
10 Sha M, Cao A, Wang B. Determination of Hyperin in *Sanguisorba officinalis* L by high performance liquid chromatography. Chin J Chromatogr 1998; 16: 226–8.
11 Wu Y, Zhou SD, Li P. Determination of flavonoids in *Hypericum perforatum* by HPLC analysis. Acta Pharm Sin 2002; 37: 280–2.
12 Lamivudine Clinical Practice Group. Lamivudine treatment consensus from relative experts in 2004. Chin J Hepatol 2004; 12: 425–7.
13 Hantz O, Perigaud C, Borel C, Jamard C, Zoulim F. The SATE pronucleotide approach applied to acyclovir Part II. Effect of *bis*(SATE)phosphotriester derivatives of acyclovir on duck hepatitis B virus replication *in vitro* and *in vivo*. Antiviral Res 1999; 40: 179–87.
14 Liu J, Shen HM, Ong CN. *Salvia miltiorrhiza* inhibits cell growth and induces apoptosis in human hepatoma HepG2 cells. Cancer Lett 2000; 153: 85–93.
15 Sells MA, Chen ML, Acs G. Production of hepatitis B virus particles in $HepG_2$ cells transfected with cloned hepatitis B virus DNA. Proc Natl Acad Sci USA 1987; 84: 1005–9.
16 Wu B, Wang CN, Xu JR. Effect of epidermal growth factor on cultured rat hepatocytes poisoned by CCl_4. Acta Pharmacol Sin 1997; 18: 176–9.
17 Liu J, Liu YP, Curtis DK. Protective effect of oleanolic acid against chemical-induced acute necrotic liver injury in mice. Acta Pharmacol Sin 1995; 16: 97–102.
18 Chen HY, Liu J, Zhu HF, Xu L. Action of acid-base extract of *Oenanthe javanica* on mice models of CCl_4 hepatic injury. Pharm J Chin PLA 2001; 17: 22–4.
19 Xiong QB, Fan WZ, Tezuka YH. Hepatoprotective effect of *Apocynum ventun* and its active constituents. Planta Med 2000; 66: 127–33.

Acta Pharmacologica Sinica 2005 May; 26 (5): 593–597

Full-length article

The anti-endotoxic effect of *o*-aminobenzoic acid from Radix Isatidis[1]

Jian-guo FANG[2], Yun-hai LIU, Wen-qing WANG, Wei XIE, Shu-xian FANG, Hong-gang HAN

Department of Pharmacy, Tongji Hospital, Tongji Medical College, Huazhong University of Science and Technology, Wuhan 430030, China

Key words

Radix Isatidis (Banlangen); *o*-aminobenzoic acid; endotoxin; lipopolysaccharides; Tachypleus Amebocyte Lysale; tumor necrosis factor-α; nitric oxide

[1] Project was supported by the National Natural Science Foundation of China (No 39170877, 39800193, and 39870872) and the Foundation of Ministry of Health People's Republic of China (No 98-2-110).
[2] Correspondence to Jian-guo FANG.
Phn 86-27-8364-9095.
Fax 86-27-8362-4090.
E-mail fjg3560@sina.com

Received 2004-09-27
Accepted 2004-01-06

doi: 10.1111/j.1745-7254.2005.00080.x

Abstract

Aim: To study the anti-endotoxic effect of *o*-aminobenzoic acid (OABA) isolated from Banlangen(BLG). **Methods:** OABA was extracted and isolated from BLG and diluted into 0.5% solution. The concentration of endotoxin (ET) pretreated with OABA was quantitatively detected using Limulus test. The inhibition of ET-induced fever by OABA was measured in rabbits. The rates of lipopolysaccharides (LPS)-induced death in mice pretreated with or without OABA were then compared. The influence of OABA on the release of TNF-α and NO from macrophages induced by LPS was examined in mice. **Results:** After pretreatment with OABA, 84.4% of ET was destroyed. The ET-induced fever in rabbits decreased significantly and the rate of LPS-induced death in mice dropped from 70% to 20%. The release of TNF-α and NO induced by LPS in mice was inhibited dose-dependently when the concentration of OABA was between 0.125% and 0.5%. **Conclusion:** OABA isolated from BLG has an anti-endotoxic effect.

Introduction

The pharmacological action of antipyretic and detoxicant materials is mainly related to their antibiotic and anti-endotoxic effects. It has been reported that Radix Isatidis (Banlangen, BLG) has antagonistic effects on endotoxin (ET) produced by *E Coli* $O_{111}B_4$[1–6]. In all chemical constituents, the *o*-aminobenzoic acid (OABA) represented 70% of the total five organic acids[7]. The Tachypleus Amebocyte Lysale (TAL) test *in vitro* showed that OABA had the strongest anti-endotoxin action[8]. In the present study, the anti-endotoxic effect of the OABA was studied.

Materials and methods

Extraction and isolation of OABA BLG, which was grown in Xingtai, Hebei, China and identified as the root of *Isatis indigotica* Fort belonging to *Cruciferae*, was infused in ethanol for 72 h and percolated by ethanol after being powdered. Being concentrated in depression, the extract formed was extracted repeatedly by petroleum ether. When the petroleum ether was removed, the remaining was extracted by chloromethane so the F_{02} part was obtained (0.8%). To get a purer active ingredient, the F_{02} part was isolated on silica gel column chromatography and the mobile phase was a mixture of $CHCl_3$-CH_3OH with different proportions. Four different polar fractions were obtained. By doing tests *in vitro* and *in vivo*, the F_{022} part was found to have the strongest anti-endotoxic activity with a productivity of 0.31%[9,10]. By further isolation with other proportions of $CHCl_3$-CH_3OH, we got another 14 components. Using the same method, we found that the part of F_{02209} whose productivity was 0.093% had the strongest activity among the 14 parts. The component was identified as OABA by Shanghai Institute of Materia Medica, Chinese Academy of Sciences (purity 99.7%).

Preparation of OABA solution With some flux being added, 0.5 g OABA was heated in a water bath until melted, then diluted in distilled water to 100 mL and adjusted to pH 6–7 with NaOH solution kept for later use after disinfection.

Reagents and instruments Lipopolysaccharides (LPS, *E Coli* $O_{26}B_6$, 5 mg each unit) were purchased from Sigma (St Louis, MO, USA). Working standard materials of Bacterial Endotoxin (Endotoxin, ET, *E Coli* $O_{111}B_4$, 120 EU each unit, batch No 2000-4) were supplied by the National Institute for the Control of Pharmaceutical and Biological Products

(Beijing, China). Tachypleus Amebocyte Lysale (TAL, with a sensitivity of 0.05 EU/mL, batch No 0008152) and water for bacterial endotoxin test (BET water, with the content of endotoxins below 0.015 EU/mL, batch No 000308) were the products of Zhanjiang A&C Biological Ltd (Guangdong Zhanjiang). Bacillus Calmette-Guerin (BCG, 50 mg per unit) was provided by Shanghai Institute of Biologicals (Shanghai, China). TNF-α reagent box (Biotinge Biomedicine Limited Company (Peking, China); N-1 Naphthalene ethylenediamine (the pure analysis, Chemical Reagent Research Institute, Tianjing, China); $NaNO_2$ (Germany, loaded separately, in chemical factory of Hubei University); sulfanilic amine(pure of analysis, FangCao Chemical Research Company in Beijing).

EDS98-Bacterial ET Detector was provided by Beijing Jinshan Science Development Co Ltd (Beijing, China). DG3022A type of enzyme-linked immunodetection instrument (Huangdong Radio Tube Company, Nanjing); 1815 TC type of the CO_2 cultivated box (Shel-Lab Company, USA); and XW-Vortex mixer from Instrumental Factory of Shanghai Medical University (Shanghai, China).

Animals Japanese big-ear rabbits of both sexes (weighing 2.0–2.5 kg) and Kunming strain mice of both sexes (weighing 16–18 g) were provided by the Experimental Animal Center of Tongji Medical College, Huazhong University of Science and Technology.

Quantitative determination of ET after being destroyed by *o*-aminobenzoic acid (OABA)

Preparation of ET solution One unit of ET (120 EU each unit) was dissolved in BET water to 1 mL, and spun homogeneously on XW-Vortex mixer for 30 s with concentration of 120 EU/mL.

Calibration curve A series of ET solution of 5.0, 2.5, 1.0, 0.5, 0.25, and 0.1 EU/mL were prepared. For every concentration, two tubes of TAL were used (two-tube method) and 0.2 mL solution was moved into either of them. When air bubbles disappeared by vibrating, the two tubes were rapidly inserted into the access holes of quantitative detector for bacterial endotoxins and the formation time of gel (Tg) was recorded. Correlation between Tg and lg*C* was analyzed with linear regression. The regression equation was: Tg=2.80049–0.23326 lg*C*, and the regression coefficient (r) was 0.9905. If the concentration of ET was in the range of 5.0–0.1 EU/mL, the linearity was fine and the lowest detecting limit was 0.05 EU/mL.

Recovery rate Tg of 4 EU/mL ET was determined in the same way as described above. When the data were put into the regression equation, the result was 4.218±0.243 EU/mL and the recovery ratio was (105.45±10.52)%.

Measurement of samples OABA solution 0.5 mL (0.5%) was homogenized with 0.1 mL ET (4 EU/mL), spun for 30 s, incubated in water bath at 37±1 ºC for 60±2 min. Then 0.1 mL of the mixture was diluted in 0.4 mL fresh BET water. The final concentrations of OABA and ET were adjusted to 0.833 g/L and 4 EU/mL, respectively, serving as sample groups. We used 0.833 g/L OABA as a negative control and 4 EU/mL ET as a positive control. Tg of each group was determined and put into the regression equation, so concentrations of ET in each group and the destroy rate of OABA against ET could be obtained. The basal destroying rate was calculated according to the formula: r=[1-(Sample group-Negative group)/(Positive group-Negative group)]×100%[11].

Effects of OABA on ET-induced fever in rabbits

Preparation of reagent One unit of ET (120 EU) was diluted to 6 mL with sodium chloride injection and the concentration was 20 EU/mL.

Operation Before the experiment, rabbits were placed in the experimental environment and fed for a week. Three days before the experiment, anal temperatures of the rabbits were measured twice a day. The rabbits were fed only water as of the afternoon before the experiment day. Before administration, anal temperature was measured every 30 min. Fifteen rabbits whose anal-temperature fluctuations were below 0.2 ºC were divided into three groups at random. Each group had five rabbits of both sex. Rabbits in the sample group and the negative group were given OABA (0.5%) 5 mL/kg via the marginal ear-vein. At the same time, the rabbits in the positive group were given a sodium chloride injection 5 mL/kg. Ten minutes later, the rabbits in the sample group and the positive group were injected with ET (20 EU/mL) at a dose of 2 mL/kg. Half an hour after the injection, the anal temperature of each rabbit was measured every 0.5 h for 4 h[12].

Protective effect of OABA on LPS-induced toxicity in mice

BCG-induced enhancement of endotoxin sensitivity BCG (50 mg) was dissolved with sodium chloride injection and diluted to 5 mL (10 g/L). According to the method previously reported[13], each mouse was intraperitoneally injected with BCG at a dose of 0.4 mL, then reared in the conventional way. Nine days after the injection the mice were given water, but no food. The experiment began on the tenth day.

Operation After fasting for 16 h, the mice were randomly divided into three groups (n=20; in each group, either sex). The mice in the OABA group and the negative control group were given OABA (0.5%) at a dose of 0.4 mL/20 g. The mice in the LPS model group were all intraperitoneally injected with the same dose of sodium chloride injection at the start of the

experiment. An hour and a half later, they were injected with the same dosage of injection again. Half an hour after this injection, the OABA and the LPS groups were injected with LPS at a dose of 0.2 mL/20 g. Time of death for all mice was observed over the next 72 h .

Effect of OABA on the LPS-induced release of TNF-α and NO in the serum of mice

Preparation of sample solution OABA solution was diluted with BET water from 0.5% to 0.25% and 0.125%.

Prepration of LPS solution One unit of LPS (5 mg) was dissolved in BET water to 10 mL (500 mg/L), spun for 30 s; then 0.8 mL was diluted in fresh BET water to 100 mL (4 mg/L).

Preparation of serum samples Thirty mice, each ip BCG 3 mg, were fasted without water for 12 h before the experiment. They were randomly divided into five groups, six mice per group in each experiment. The three experiment groups were ig 0.5%, 0.25%, 0.125% of sample solution at dose of 0.4 mL respectively. The control group and model group were administered NS. After 0.5 h the experiment group and the model group were iv LPS 0.2 mL/20 g from tail vein, 9 h later, they were anaesthetized with ether and blood was taken from the eye sockets. The serum were kept in -20 ºC.

TNF-α examination Using the ELISA method, we proceeded examination according to the instruction in reagent box. On the enzyme-marked single quilted plank with anti-human cell factor, we added standard solution with which we acquired a series of concentration and 100 μL serum sample. In the meantime, we established the blank group (double tube method), and added TMB substrate to display the color for 15 min after function for 60 min at 37 ºC. The absorbance at 450 nm was checked, and the standard curve was drawn. As a result, the curve was in linearity at 10–1000 ng/L. We also tested the serum sample by using the same method, and calculated the concentration of TNF-α according to the standard curve.

NO examination Using the Griess reagent method, we took $NaNO_2$ 1 g precisely in a 100 mL volumetric flask and dissolved it with water. Then we took precisely 1 mL of this, and added water to 100 mL (100 mg/L) and diluted it to obtain a series of solutions. Each solution was 50 μL and the Griess liquid was added (containing 1% Sulfanilic amine, 0.1% N-1 Naphthalene ethylenediamine, 2.5% phosphoric acid) 50 μL, respectively, placed at room temperature (20 ºC) for 10 min, and the absorbance value was tested at 550 nm. On the enzyme-linked immunodetection instrument, a standard curve was drawn. As a result, the curve had a line behavior at 1–100 mg/L. We added Griess liquid at the same volume to 50 μL serum of mice, tested in the same way, and calculated the concentration of NO according to the standard curve.

Results

Destroying rate of OABA against ET The concentrations of ET were 0.668 EU/mL in the sample group, 4.036 EU/mL in the positive group, and 0.045 EU/mL in the negative group. We concluded that 0.833 g/L OABA could destroy ET directly and the destroy rate was [1-(0.668-0.045)/(4.036-0.045)]×100%=84.4%.

The ability to induce fever by ET after pretreatment with OABA If the average body temperature before injection was taken as basal body-temperature and the difference between the maximum body-temperature and basal body-temperature was taken as maximum rising temperature, the average DT_{max} of each group could be obtained. The temperature reaction index in 4 h (TRI_4) and DT_{max} are listed in Table 1.

Table 1. Restraining action of OABA to ET-induced fever in rabbits. n=5. Mean±SD. $^bP<0.05$ *vs* positive group.

Groups	Basal body-temperature/ºC	TRI_4/cm^2	DT_{max}/ºC
Sample group	39.16±0.28^b	1.26±0.18^b	0.32±0.14^b
Positive control	39.04±0.18	3.28±0.42	1.21±0.32
Negative control	39.32±0.36	0.63±0.15	0.26±0.12

Table 1 shows that typical fever reaction occured in rabbits given ET (40 EU/kg), while the TRI_4 and DT_{max} dropped when the rabbits were given the OABA solution (5 mL/kg) before the same dosage of ET was administered. The difference between the two groups was significant and OABA did not have the activity to induce fever.

The mortality rate of mice treated with OABA Four of the 20 mice died within 10 h in the OABA group with a mortality rate of 20%. Fourteen of 20 mice died within 5 h in the ET model group with a mortality rate of 70%. In the negative control group, all of the 20 mice survived after 72 h. There was a significant difference in mortality between the OABA group and the LPS group.

The inhibitory function of OABA on the excessive release of TNF-α and NO in the serum of mice induced by LPS Administering different concentrations of F022 part to mice, then also giving LPS at equal dosage, the TNF-α and NO in the serum and the percentage of inhibition were shown in Table 2. The formula of inhibitory percentage follows[11]: IP%=[1-(specimen group-blank control group)/(model group-

Table 2. Inhibitory influence of OABA from Radix Isatidis on the level of TNF-α and NO in mice serum induced by LPS. n=6. Mean±SD. $^bP<0.05$ *vs* LPS model group.

Groups	Concentration (%)	LPS (mL/20 g)	TNF-α ($ng \cdot L^{-1}$)	Percentage of inhibition (%)	NO ($mg \cdot L^{-1}$)	Percentage of inhibition (%)
Experimental group	0.5	0.2	126.6±12.3^b	85.44	13.5±4.2^b	90.73
	0.25	0.2	213.5±58.6^b	70.88	36.3±9.5^b	62.16
	0.125	0.2	587.1±123.3	8.25	73.8±20.5	15.16
Model group	–	0.2	636.3±215.3	–	85.9±21.4	–
Control group	–	–	39.8±5.4	–	6.1±3.3	–

blank control group)]×100%

Table 2 shows OABA from Radix Isatidis had inhibitory function on the release of TNF-α and NO induced by LPS in mice, the percentage of inhibition was dependent on the dosage when the concentration was between 0.125% and 0.5%.

Discussion

The chemical components of traditional Chinese medicine (TCM) were the substance basis of its pharmacology. Studying the Radix Isatidis's traditional function of reducing heat and detoxification was to study TCM with modernization research. Further study showed that organic acids of Radix Isatidis (quinazolinone acid, OABA, syringic acid, salicylic acid, and benzoic acid) had anti-endotoxic effects *in vitro*[14–19]. The study showed that OABA had anti-endotoxic effect *in vivo* and *in vitro*. The OABA content in the Radix Isatidis was higher than other organic acids and had strong anti-endotoxic activity. It could be taken as a single active anti-endotoxic ingredient. The OABA could be used in the quality control production of Radix Isatidis medicinal materials, technology of preparation, and manufacture.

The dynamic color matrix method has many merits such as simple procedures, economy, high sensitivity, and wide detectable area. Normally, ET content between 0.05–300 EU/mL can be quantitatively measured. The content of ET was decreased to 0.668 g/L with the destroying rate being up to 84.4% when 4 EU/mL ET reacted with 0.833 g/L OABA.

One of the features of ET is its ability to induce fever. Rabbits are often used to screen antipyretic drugs because they are sensitive to ET. The dosages reported to induce fever in rabbits were not consistent, and we found that the results between the positive control group given *E Coli* $O_{111}B_4$ endotoxin at 40 EU/kg and the negative control group given 0.5% OABA solution was comparable well.

The sensitivity of different kinds of experimental animals to LPS varies greatly. The lethal dose of 50% (LD_{50}) in mice was 25 mg/kg[13]. After being sensitized by BCG, 2.42 mg/kg LPS could induce fatalities in 70% of mice. As BCG could stimulate T-cells to activate macrophages, the mitosis and metabolism in macrophages were strengthened substantially and the recognition ability of macrophages increased, so the quantity of LPS decreased. We also found that if OABA was given before LPS, OABA could exert a protective action on mice, while if OABA given after LPS, the protective action of OABA disappeared. The results showed that the action of OABA on LPS happened before the immune system was activated.

There is more and more evidence about the function of excessive release of TNF-α and NO in the disease process of shock induced by LPS. Some measures of anti-TNF-α will become important pathways of prevention and cure for LPS-induced shock. The release of a large quantity of NO is the main factor of endotoxin shock, low blood pressure, and exhausted function of many organs. It could cause tissues and organs to be scathed when NO was combined with anion of oxidated subnitryl. In the shock and exhaustion of many visceras, inhibiting the release of a large quantity of NO could prevent low blood pressure and alleviate the oxidized harm of tissues. Radix Isatidis was able to inhibit the function of the excessive release of TNF α and NO induced by endotoxin in mice macrophages.

References

1 Liu YH. Experimental study on the antiendotoxin of dyers woad (*Isatis tinctoria*) injection. Chin J Herb Med 1993; 24: 413–4.

2 Li YW, Zhang SM. Influence of γ ray radiation on the anti-endotoxin effect of Radix Isatidis. China Pharm 1995; 6: 9–10.

3 Li BH, Zhang HM, Wang Y, Ding RX, Xu TF. Antiendotoxic action of hairy roots of autotetraploid *Isatis indigotica* Fort. Acad J Sec Milit Med Univ 2000; 21: 201–3.

4 Li BH, Zhang HM, Fan GR, Yin C, Ding RX, Xu TF, Qiao CZ. Studies on culture of hairy roots of autotetraploid *Isatis indigotoca* and analysis of its antiendotoxic active components. Chin Pharm

J 2000; 35: 728–31.
5 Wang Y, Qiao CZ, Yin C, Zhang HM. Determination of organic acids of Tetraploid *Isatis indigotica* with high performance capillary electrophoresis. J Chin Med Meter 2000; 23: 204–6.
6 Liu ZF, Li GS, Fu FH, Liu K. Studies of anti-endotoxin effect of eight Chinese herb injections *in vitro*. Chin Trad Herb Drugs 2002; 33: 58–9.
7 Wang Y, Qiao CZ. Determination of anthranilic acid in the leaves of *Isatidis indigotica* by first order derivative UV spectrophotometry. Chin J Herb Med 2000; 31: 664–5.
8 Zhang HM, Zhang G, Qiao ZZ. Detection of indigo and indirubin in different part of Radix Isatidis and Folium Isatidis and anti-endotoxic action comparison of some ingredients (abstract). J Pharm Pract 2000; 18: 347.
9 Liu YH, Lin AH, Ding SP, Fang JG, Li J, Chen X. Study on anti-endotoxin of chloroform extract from Radix Isatidis. Chin J Hosp Pharm 2001; 21: 326–8.
10 Liu YH, Ding SP, Lin AH, Fang JG, Shi SP. The protective effects of different polar fractions from Radix Isatidis on endotoxin challenged mice. Acta Univ Med Tongji 2001; 30: 272–3.
11 Du GH, Li XJ, Zhang YX. Guide of pharmacological experiments — drug discovery and evaluation pharmacological assays. Beijing: Beijing Science and Technology Publishing House; 2001. p 528–9
12 The National Pharmacopoeia Commission. The Chinese Pharmacopoeia (part II). Beijing: Chemical Industry Press; 2000. Supplement, p 85–6.
13 Vogel SN, Moore RN, Sipe JD. BCG-induced enhancement of endotoxin sensitivity in C3H/ HeJ mice. J Immunol 1980; 124: 2004.
14 Wu XY, Liu YH, Sheng WY, Sun J, Qin GW. Chemical constituents of *Isatis indigotica*. Planta Med 1997; 63: 55–7.
15 Liu YH, Liu YF, Guo XX. Current studes on anti-endotoxic chemical components of traditional Chinese medicine in China. Acta Pharmacol Sin 2001; 22: 1071–7.
16 Liu YH, Du G, Han HG, Tan LX. Study on the anti-endotoxic effect of Radix Isatidis. Herald Med 2001; 29: 547–8.
17 Liu YH, Qin GW, Fang JG, Wu XY. Screening of chemical constituents with antiendotoxin activity from Radix Isatidis. Heral Med 2002; 21: 74–5.
18 Liu YH, Wu XY, Fang JG, Xie W. Chemical constituents from Radix Isatidis. Central South Pharm 2003; 1: 302–5.
19 Michael JP. Quinoline, quinazoline and acridone alkaloids. Nat Prod Rep 1998; 15; 595–606.

Acta Pharmacologica Sinica 2005 May; 26 (5): 598–602

Full-length article

Mycophenolate mofetil as a treatment for refractory idiopathic thrombocytopenic purpura[1]

Wang-gang ZHANG[2], Lei JI, Xing-mei CAO, Yin-xia CHEN, Ai-li HE, Jie LIU, Wan-hong ZHAO, San-peng ZOU

[2]*Department of Hematology, the 2nd Hospital of Xi'an Jiaotong University, Xi'an 710004, China*

Key words

mycophenolate acid; idiopathic thrombocytopenic purpura; male; female; apoptosis

[1] Project supported by a grant from the Clinical Key Programmer Foundation of the Ministry of Public Health of China (No 20012131).
[2] Correspondence to Prof Wang-gang ZHANG.
Phn 86-29-8767-9457.
Fax 86-29-8767-8634.
E-mail wanggang_zhang@yahoo.com.cn

Received 2004-06-08
Accepted 2004-12-02

doi: 10.1111/j.1745-7254.2005.00088.x

Abstract

Aim: To determine whether mycophenolate mofetil (MMF) has beneficial effects on refractory idiopathic thrombocytopenic purpura (ITP) and the corresponding cellular mechanism. **Methods:** Twenty refractory ITP patients resistant to corticosteroid and/or splenectomy and chemical therapy were given MMF 1.5–2.0 g/d orally for a 2 to 4-month period. Serum immunoglobulin was detected by rate nephelometry. Platelet-associated antibodies (PAIgG) were assayed by enzyme-linked immunosorbant assay. The immunophenotypic analysis was performed on a flow cytometer and cell apoptosis was detected with transferase mediated dUTP biotin nick end labeling (TUNEL) method. **Results:** Sixteen of the 20 (80%) patients had responses to MMF treatment; 9 (45%) achieved a complete response, 4 (20%) achieved a partial response, and 3 (15%) achieved a minor response. The therapeutic effects were found to be better in male patients than female patients. The number of $CD3^+$ peripheral blood cells (PBCs) and $CD4^+$ PBCs increased and the number of $CD8^+$ PBCs decreased. The plasma level of IgG, IgM, IgA and platelet associated IgG (PAIgG) decreased in 86% of the patients. TUNEL assay showed that mycophenolate acid (MPA) 0.1 mmol/L induced apoptosis of peripheral blood mononuclear cells isolated from refractory ITP patients. The apoptosis rate was increased in male patients after treatment with MPA, but was unchanged in female patients. **Conclusion:** Therapy for a period of 8 to 16 weeks with median-dose of MMF was valuable for the treatment of refractory ITP.

Introduction

Idiopathic thrombocytopenic purpura (ITP) is a common autoimmune hemorrhagic disorder, and the treatments are based on individual experience[1]. In the clinic, the first line treatment is steroid therapy, and splenectomy is recommended as an alternative. However, 20% to 30% of ITP patients failed to respond to these two treatments, especially patients with refractory ITP[2]. As the new immunosuppressive agent, mycophenolate mofetil (MMF) is widely used in renal transplantations and its relative safety has already been confirmed[3,4]. In recent times, MMF has been used in the treatment of autoimmune disorders such as nephrotic syndrome[5], Crohn's disease[6], and autoimmune myasthenia gravis. The immunosuppressive ability of MMF is mainly derived from the inhibition of inosine monophosphate dehydrogenase[7]. It has been reported that MMF can selectively inhibit the proliferation of T and B-lymphocytes, the generation of the antibodies, and the production of the cytotoxic T cells induced by immune stimuli. This also provided a strong basis for MMF as a novel therapeutic agent to treat refractory ITP. Here we reported the long-term therapy with MMF of 20 patients with refractory chronic ITP.

Materials and methods

Patients Twenty patients (12 males and 8 females), aged between 11 and 80 years (median 44.3 years) participated in the study; each patient gave their informed consent. The Ethics Committee of the 2nd Hospital of Xi'an Jiaotong University approved the study. Each patient was diagnosed as

refractory ITP in accordance with the following criteria: (1) thrombocytopenia (a platelet count<50×10^9/L) over 6 months, unrelated to any underlying viral infection, collagen vascular diseases, malignancy, or medications; (2) without or with slight splenomegaly, with a normal or increased number of megakaryocytes in bone marrow, and no failure of maturing; (3) the failure of drug treatment and surgery treatment (prednisone, vincristine, danazol, long-term use of traditional Chinese medicine or intravenous injection of high doses of immunoglobulin G and splenectomy) (Table 1).

Therapeutic regimen MMF (250 mg/capsule, Shanghai Roche Pharmaceuticals Ltd, Shanghai, China) was taken orally at a dosage of 1.5–2.0 g/d for 4 weeks as 1 period of treatment. Patients who had responses to MMF continued taking MMF for another 2–4 periods. The therapy was discontinued in patients who achieved complete response during therapeutic period and in all patients after 16 weeks. Patients were given prednisone (1 $mg\cdot kg^{-1}d^{-1}$) orally and hemostasia therapy concurrently with MMF. Follow-up was performed on each patient for 2–6 months (median, 3 months). Full blood platelet count was evaluated before and after MMF treatment in every period. Serum immunoglobulin IgG, IgM, and IgA were detected by rate nephelometry with the Array 360 system and associated reagents (Beckman Coulter Inc, Fullerton, CA, USA). Platelet-associated antibodies (PAIgG) were assayed by enzyme-linked immunosorbant assay (ELISA, PeproTech Inc, Rocky Hill, NJ, USA). The normal value of PAIgG is <60 μg/L. Peripheral blood mononuclear cells (PBMNCs) were isolated by a Ficoll gradient (Ficoll-Hypaque, Density=1.077 g/L, Amersham-Pharmacia, Piscataway, NJ, USA). Fluorescein-conjugated monoclonal antibodies against CD3 (SK7 clone) and CD4 (SK3 clone) and phycoerythrin (PE)-conjugated monoclonal antibodies against CD8 (SK1 clone) were obtained from Becton Dickinson (Mountain View, CA, USA). Appropriate isotype-matched controls were included. PBMNCs were incubated with the monoclonal antibodies on ice for half an hour, then washed in phosphate buffered solution (PBS) three times, and suspended in PBS supplemented with 0.5% bovine serum albumin (BSA). A phenotypic analysis of cell populations was performed on a FACScan flow cytometer by using LYSIS software (Becton Dickinson, Franklin Lakes, NJ, USA). The criteria for response were defined as follows: (1) complete response: thrombocyte count rose above 300×10^9/L, and blood platelet count rose above 100×10^9/L. There was no bleeding for at least 3 months and no relapse for 2 years; (2) partial response: blood platelet count was above 50×10^9/L or 30×10^9/L higher than that before MMF treatment. There

Table 1. Characteristics and previous treatments of the 20 patients with refractory idiopathic thrombocytopenic purpura.

Case	Age	Sex	Course of ITP	Symptoms	Previous therapies	Response
1	37	F	14 months	Menorrhagia, petechia	Pred, VCR, CsA, splenectomy	No
2	55	M	26 months	Petechia	Pred, ivIgG	No
3	48	M	30 months	Petechia, gum bleeding	Pred, VCR, CsA, ivIgG	No
4	80	M	6 months	Petechia, epistaxis	Pred, CsA, TCM	No
5	50	F	24 months	Menorrhagia, petechia	Pred, CsA, ivIgG, CTX	No
6	20	M	8 months	Petechia, epistaxis	Pred, ivIgG, splenectomy	No
7	11	M	3 months	Petechia	Pred, ivIgG	No
8	62	F	19 months	Petechia, gum bleeding	Pred, VCR, CsA, TCM	No
9	33	F	28 months	Menorrhagia, petechia	Pred, VCR, danazol	No
10	29	M	12 months	Petechia, epistaxis	Pred, VCR, ivIgG	No
11	26	F	9 months	Menorrhagia, petechia	Pred, VCR, CsA, danazol	No
12	49	F	18 months	Menorrhagia, petechia, gum bleeding	Pred, CsA, CTX, splenectomy	No
13	56	M	21 months	Petechia, gum bleeding	Pred, VCR, CsA	Minor
14	28	F	16 months	Menorrhagia	Pred, CTX	No
15	57	M	19 months	Petechia, gum bleeding	Pred, VCR, CsA,TCM, danazol	No
16	70	M	28 months	Petechiagum bleeding, epistaxis	Pred, VCR, CsA, TCM	No
17	65	F	23 months	Petechiagum bleeding	Pred, VCR, CsA, danazol	No
18	35	M	11 months	Petechia, epistaxis	Pred, CsA, ivIgG, CTX	No
19	24	M	29 months	Petechia	Pred, ivIgG,	No
20	44	M	21 months	Petechia, gum bleeding	Pred, VCR, CsA	No

Pred: prednisone; CsA: cyclosporine; VCR: vincristine; CTX: cyclophosphamide; IVIgG: intravenous immunoglobulin G; TCM: traditional Chinese medicine; F: female; M: male.

was no bleeding for 2 months; (3) minor response: increase in blood platelet count not exceeding 30×10^9/L after MMF treatment. Bleeding symptoms were improved for 2 weeks; (4) no response: blood platelet was unchanged and bleeding symptoms were neither improved or worsened.

TUNEL assay Peripheral blood lymphocytes isolated from 20 refractory ITP patients were grown with or without mycophenolic acid 0.1 μmol/L (MPA, Sigma, St Louis, USA) for 3 d. The apoptosis was analyzed by transferase-mediated dUTP-biotin nick-end labeling (TUNEL) using a TUNEL kit (Boster Co, Wuhan, China). TUNEL assay were performed at room temperature unless indicated. Cells were fixed in 4% paraformaldehyde/1×PBS at for 10 min. After pouring off paraformaldehyde cells were incubated with PBS containing glycine 50 mmol/L for 10 min. Cells were permeabilized by 0.5% Triton X-100 in PBS for 10 min. After washing thrice in PBS, cells were equilibrated in equilibration buffer [200 mL of 1×terminal deoxynucleotidyl transferase (TdT) buffer+1 mmol/L cobalt chloride) under a 60 mm×24 mm coverslip for 5 min. Cells were incubated in 1×TdT buffer containing cobalt chloride1 mmol/L, 25 units TdT 100 μL, and 0.25 nmol/L biotin labeled dATP 100 μL at 37 °C for 1 h in humidified chamber (petri dish, lined with filter paper, soaked PBS). The tailing reaction was terminated by 4×standard saline citrate (SSC). After applying 200 μL of 4× SSC with 2 g/L BSA and 1:100 dilution of fluorochrome-avidin under a coverslip, cells were incubated at 37 °C for 1 h in humidified chamber. Then cells were washed in dark in 4×SSC for 5 min, 4×SSC/0.1% Tween 20 with 0.01 g/L DAPI for 5 min, and 4×SSC for 5 min, respectively. The TUNEL-positive cells were analyzed by fluorescence microscopy.

Statistical analysis Statistic analysis was performed by the χ^2 test and the paired *t*-test. All data are expressed as the mean±SD. $P<0.05$ was considered to be significant.

Results

Therapeutic effects of MMF Sixteen of the 20 (80%) patients had responses to MMF treatment; 9 (45%) achieved a complete response, 4 (20%) achieved a partial response, and 3 (15%) achieved a minor response. The platelet count increased in 4 patients after 2 weeks of MMF treatment; it was above 50×10^9/L in 7 patients after 4 weeks of MMF treatment and was above 100×10^9/L in 10 patients after 6 weeks of MMF treatment. The responses of the 16 patients were sustained overtime after the withdrawal of MMF for 1 month, but less patients had a relapse after treatment discontinuation.

Twelve men had responses to MMF treatment; 8 (66.7%) achieved a complete response, 2 (16.7%) achieved a partial response, and 2 (16.7%) achieved a minor response. From the 8 women, only 1 (12.5%) achieved a complete response, 2 (25%) achieved a partial response, 1 (12.5%) achieved a minor response, and 4 (50%) had no response. These results indicate that the therapeutic effects of MMF are relatively better in male patients than female patients.

Side effects of MMF During the early stages of treatment, 7 patients experienced transient adverse reactions such as abdominal distension, anorexia, and nausea; these symptoms were later treated. No blood infection, bone marrow suppression, hypertension, severe headache, or muscle pain was observed in the 20 patients after MMF treatment. All of the patients completed the scheduled treatment suggesting that these patients had no tolerarance of MMF.

Effect of MMF on immunophenotypics The percentage of $CD3^+$ and $CD4^+$ lymphocytes increased, but the percentage of $CD8^+$ lymphocytes decreased. Thus, the $CD4^+/CD8^+$ ratio elevated after MMF treatment (Table 2). The plasma levels of IgG, IgM, IgA, and PAIgG were markedly reduced in 17 patients after more than 2 weeks of MMF treatment (Table 3).

Table 2. Effect of mycophenolate mofetil on immunophenotypes of peripheral blood mononuclear cells in patients with refractory idiopathic thrombocytopenic purpura. n=20. Mean±SD. $^bP<0.05$ *vs* before treatment.

	Before	After
$CD3^+$ (%)	65±5	69±4^b
$CD4^+$ (%)	32±4	39±4^b
$CD8^+$ (%)	34±3	30±5^b
$CD4^+/CD8^+$ (%)	0.95±0.15	1.31±0.22^b

Table 3. Effect of mycophenolate mofetil on serum immunoglobulin and platelet associated antibodies (PAIgG) in patients with refractory idiopathic thrombocytopenic purpura. n=20. Mean±SD. $^bP<0.05$ *vs* before treatment.

	Before	After
IgG/g·L^{-1}	14±5	11.8±2.9^b
IgA/g·L^{-1}	3.3±1.8	2.4±1.0^b
IgM/g·L^{-1}	2.0±1.0	1.6±0.6^b
PAIgG/μg·L^{-1}	202±147	102±109^b

Effect of MPA on cell apoptosis After the peripheral blood mononuclear cells isolated from the patients were incubated with MPA 0.1 μmol/L for 3 d, a number of TUNEL-positive mononuclear cells were observed in male patients, ($P<0.05$), indicating that the peripheral blood mononuclear

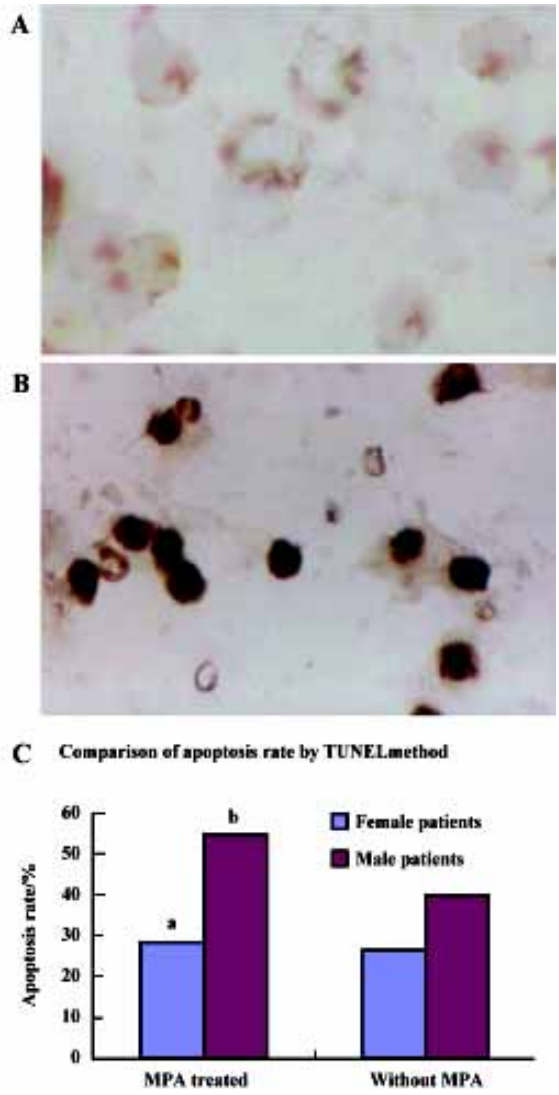

Figure 1. Effects of mycophenolic acid 0.1 μmol/L on apoptosis of peripheral blood mononuclear cells *in vitro* by TUNEL assay. (×1000). (A) Without MPA for 3 d *in vitro.* (B) MPA 0.1 μmol/L was incubated with peripheral blood mononuclear cells for 3 d *in vitro*. (C) Apoptosis rate in male and female patients before and after treatment. n=12 (male). n=8 (female). ^{a}P>0.05, ^{b}P<0.05 *vs* without MPA.

cells underwent apoptosis. The difference in apoptosis rate in female patients before and after MPA treatment was not significant (P>0.05).

Discussion

ITP is a common immune disorder caused by platelet-reactive autologous antibodies. In some patients, platelet production is decreased as well. ITP in adults does not generally remit spontaneously, and most patients need hemostasia therapy. Corticosteroids, danazol, immunoglobulin, anti-D antibody, and several other agents inhibit clearance of the antibody-coated platelets, but the effect is not sufficient. Most patients will sustain a hemostatic response after splenectomy, although relapses can occur at any time[8]. Refractory idiopathic thrombocytopenic purpura represents a life-threatening condition that fails to respond to a variety of therapeutic measures[9]. In recent years, immunosuppressive agents such as cyclosporine A and MMF were used to treat refractory ITP as second line drugs. However, cyclosporine A has apparent side effects including hypertension, headache, and muscle pain. Thus, splenectomy could not be avoided, but could only be postponed in refractory ITP patients after they received cyclosporine A treatment. Howard *et al* reported that 4 patients with autoimmune haemolytic anemia and 5 of the 6 patients with autoimmune thrombocytopenia purpura showed a complete or good partial response to MMF[10], confirming the beneficial effects of MMF on refractory ITP. However, only 6 patients participated in the study. In the present study, MMF treatment was sustained for at least 1 month. Sixteen of the 20 (80%) patients had responses to MMF treatment; 9 (45%) achieved a complete response, 4 (20%) achieved a partial response, and 3 (15%) achieved minor response. The curative rate was 80%. The results indicated that MMF could be used as a second line agent for the treatment of refractory ITP. We also found that men achieved better response to MMF than women which was not been reported in other published studies[12]. The cell apoptosis rate was consistent with this conclusion. In long-term clinical observations, we also found that female ITP patients did not achieve better responses than male patients. We speculated that the difference might be related to different hormone levels and different MMF metabolization. However, the mechanism requires further study. MMF selectively inhibited the proliferation and survival of lymphocytes by inducing apoptosis and suppressing glycosylation and expression of adhesion molecules such as P-selectin, etc, which were over-expressed in ITP[13]. Our result that MPA induced apoptosis of PB lymphocytes from ITP patients *in vitro* was consistent with a previous report[14].

In contrast to MMF, we found that prednisone caused a significant increase in the number of myocarditis lesions. This is consistent with earlier studies that corticosteroids increased the severity of the disease during the acute phase of viral myocarditis in murine models[15]. In conclusion, long-term therapy with a median-dose of MMF is valuable for the treatment of refractory ITP. Randomized clinical trials need to be performed in the future.

References

1 Cines DB, Blanchette VS. Immune thrombocytopenic purpura. N Engl J Med 2002; 346: 995–1008.

2 Bussel JB. Novel approaches to refractory immune thrombocytopenic purpura. Blood Rev 2002; 16: 31–6.

3 Becker BN. Mycophenolate mofetil. Transplant Proc 1999; 31: 2777–8.

4 Glander P, Hambach P, Braun KP, Fritsche L, Waiser J, Mai I, *et al*. Effect of mycophenolate mofetil on IMP dehydrogenase after the first dose and after long-term treatment in renal transplant recipients. Int J Clin Pharmacol Ther 2003; 41: 470–6.

5 Gellermann J, Querfeld U. Frequently relapsing nephrotic syndrome: treatment with mycophenolate mofetil. Pediatr Nephrol 2004; 19: 101–4.

6 Wenzl HH, Hinterleitner TA, Aichbichler BW, Fickert P, Petritsch W. Mycophenolate mofetil for Crohn's disease: short-term efficacy and long-term outcome. Aliment Pharmacol Ther 2004; 19: 427–34.

7 Srinivas TR, Kaplan B, Meier-Kriesche HU. Mycophenolate mofetil in solid-organ transplantation. Expert Opin Pharmacother 2003; 4: 2325–45.

8 Cines DB, McKenzie SE, Siegel DL. Mechanisms of action of therapeutics in idiopathic thrombocytopenic purpura. J Pediatr Hematol Oncol 2003; 25 Suppl 1: S52–6.

9 Narang M, Penner JA, Williams D. Refractory autoimmune thrombocytopenic purpura: responses to treatment with a recombinant antibody to lymphocyte membrane antigen CD20 (rituximab). Am J Hematol 2003; 74: 263–7.

10 Howard J, Hofferand AV, Prentice HG, Mehta A. Mycophenolate mofetil for the treatment of refractory auto immune haemolytic anemia and auto immune thrombocytopenia purpura. Br J Haematol 2002; 117: 712–5.

11 Kneitz C,Wilhelm M,Tony HP. Effective B cell depletion with rituximab in the treatment of autoimmune disease. Immunobiology 2002; 206: 519–27.

12 Hou M, Peng J, Shi Y, Zhang C, Qin P, Zhao C, *et al*. Mycophenolate mofetil for the treatment of steroid resistant idiopathic thrombocytopenic purpura. Eur J Hematol 2003; 70: 353–7.

13 Goldsmith D, Carrey EA, Edbury S, Smolenski RT, Jagodzinski P, Simmonds HA. Mycophenolate mofetil, an inhibitor of IMP dehydrogenase, causes paradoxical elevation of GTP in erythrocytes of renal transplant patients. Clin Sci (Lond) 2004; 107: 63–8.

14 Cohn RG, Mirkovich A. Mycophenolic acid increases apoptosis lysosomes and lipid droplets in human lymphoid and monocytic cell lines. Transplantation 1999; 68: 411–8.

15 Padalko E, Verbeken E, Matthys P, Aerts JL, Clercq ED, Neyts J. Mycophenolate mofetil inhibits the development of *Coxsackie* B3-virus-induced myocarditis in mice. BMC Microbiol 2003; 3: 25–8.

Acta Pharmacologica Sinica 2005 May; 26 (5): 603–609

Full-length article

Curcumin, a potent anti-tumor reagent, is a novel histone deacetylase inhibitor regulating B-NHL cell line Raji proliferation[1]

Hong-li LIU[2], Yan CHEN[2,3], Guo-hui CUI[2], Jian-feng ZHOU[4]

[2]*Department of Hematology, Union Hospital, Tongji Medical College, Huazhong University of Science and Technology, Wuhan 430022, China;* [4]*Department of Hematology, Tongji Hospital, Tongji Medical College, Huazhong University of Science and Technology, Wuhan 430030, China*

Key words

curcumin; histone deacetylase; acetylated-histone H4; Raji

[1] Project supported by the National Natural Science Foundation of China (No 30271672).
[3] Correspondence to Prof Yan CHEN.
Phn 86-27-6604-6609.
Fax 86-27-8572-6387.
Email liuhl60@tom.com

Received 2004-10-15
Accepted 2004-12-20

doi: 10.1111/j.1745-7254.2005.00081.x

Abstract

Aim: To investigate curcumin (diferuloylmethane) induced apoptosis and its molecular mechanism of action in B-NHL cell line Raji cells. **Methods:** Raji cells were cultured in RPMI-1640 medium and treated with curcumin in different concentrations. 3-(4,5-Dimethyl-2-thiazolyl)-2,5-diphenyl-2*H*-tetrazolium (MTT) assay was used to detect growth inhibition and Hoechst 33258 staining was used to detect apoptosis. Immunocytochemistry and Western blot were used to detect the expressions of histone deacetylase 1, 3, and 8 (HDAC1, HDAC3, and HDAC8) and acetylated histone H4 (Ac-histone H4) protein. **Results:** Curcumin inhibited the proliferation of B-NHL cell line Raji cells with a 36-h IC_{50} value of 24.1±2.0 μmol/L. Hoechst 33258 staining showed that curcumin could induce Raji cell apoptosis. The expression levels of HDAC1, HDAC3, and HDAC8 proteins were downregulated following curcumin treatment in Raji cells, whereas Ac-histone H4 protein expression was upregulated after treatment with curcumin. **Conclusion:** Curcumin, as a new member of the histone deacetylase inhibitors, can inhibit the expression of class I HDACs (HDAC1, HDAC3, and HDAC8), and can increase the expression of Ac-histone H4 in Raji cells. Curcumin plays an important role in regulating B-NHL cell line Raji cell proliferation and apoptosis.

Introduction

Histone acetylation/deacetylation is a key mechanism for regulating transcription. Acetylation of the ε-amino group of specific lysine residues within the N-terminal tail of core histones results in location chromatin relaxation. In general, histone acetylase activity is correlated with transcription activation, whereas histone deacetylase activity is correlated with transcription repression[1,2]. Significant progress has been made in the use of histone deacetylase inhibitors as antineoplastic drugs. Several reagents have been shown to be histone deacetylase inhibitors (HDACIs), including TSA (Trichostatin A), butyrate, FR90228, and sulindac[3,4]. The mechanism of HDACIs relates to inducing cell cycle arrest and apoptotic responses, and is regulated by changes in histone acetylation and deacetylation. Emerging evidence suggests that a family of histone deacetylases may exist to regulate diverse cellular functions, including chromatin structure, gene expression, cell cycle progression, and oncogenesis[5].

Curcumin, the major component of the spice turmeric and the yellow pigment in curry powder, has been widely used in India and other parts of South-East Asia as a spice and a coloring agent in cooking. Many studies have shown that curcumin (diferuloylmethane) has significantly antiproliferative and apoptotic effects for cancer treatment, including pancreatic carcinoma, liver carcinoma, and leukemia[6,7]. Experimental studies have also revealed that curcumin regulates molecules in the cell signal transduction pathways, including NF-kappaB, Akt, MAPK, p53, AR, Ras, and ER pathways[8,9]. Research has shown that curcumin is structurally related to sulindac, and the latter is a member of HDACs. Sulindac exerts significant chemopreventive activity, which is related to cell cycle arrest and the histone acetylation/

deacetylation state[10]. In a previous study we revealed that curcumin inhibited K562 cell proliferation by Janus kinase-signal transducer and by activating transcription and activator protein-5 signaling pathways[11]. In the present study, we chose the B-NHL cell line as the target. We assumed that curcumin could inhibit carcinoma cell proliferation by regulating Raji cells and we explored the underlying mechanism of curcumin regulating the histone acetylation/deacetylation pathway.

Materials and methods

Drugs and reagents Curcumin was purchased from Sigma Chemical Company (St Louis, MO, USA) and initially dissolved in dimethylsulfoxide (Me_2SO), stored at -20 °C, and thawed before use. 3-(4,5-Dimethyl-2-thiazolyl)-2,5-diphenyl-2*H*-tetrazolium (MTT) was purchased from Janssen Chimica Company (New Brunswick, NJ), and RPMI-1640 medium, Hoechst 33258, and Me_2SO were purchased from Sigma. Anti-HDAC1, anti-HDAC3, anti-HDAC8, and anti-Ac-histone H4 were purchased from Santa Cruz (California, USA). Streptavidin peroxidase (SP) reagent kits were purchased from Zhongshan Company (Beijing, China). Chemiluminescence (ECL) reagent kits were purchased from Pierce Biotechnology, Inc (Rockford, IL). The Raji cell line was obtained from China Center for Typical Culture Collection (Wuhan, China). The following treatments were applied: untreated Raji cells and Raji cells treated with 6.25 μmol/L, 12.5 μmol/L, and 25 μmol/L of curcumin for 24 h. All cell groups were grown in RPMI-1640 culture medium containing 10% fetal calf serum (FCS) and 2 mmol/L *L*-glutamine at 37 ºC in a 5% CO_2 incubator.

MTT assay The antiproliferative effects of curcumin against different cell groups were determined using the MTT dye uptake method. In brief, the cells (40 000 per well) were incubated in triplicate in a 96-well plate. Different concentrations of curcumin were added, and the final concentrations were 6.25, 12.5, 25, 50, and 100 μmol/L. The plates were in the presence or absence of the indicated test samples for 0, 24, 36, 48, 60, and 72 h. The largest Me_2SO dissolved concentration group acted as the control group. Thereafter, 20 μL MTT solution (5 g/L in phosphate-buffered saline [PBS]) was added to each well. After 4 h at 37 °C, the supernatant was removed and 150 μL Me_2SO was added. When the blue crystal was dissolved, the optical density (*OD*) was detected in the microplate reader at 570 nm wavelength using a 96-well multiscanner autoreader (Biotech Instruments, New York, USA). The following formula was used: Cell proliferation inhibited (%)=[1–(*OD* of the experimental samples/*OD* of the control)]×100%.

Apoptosis assay Curcumin-induced apoptosis was monitored by the extent of nuclear fragmentation. Nuclear fragmentation was visualized by Hoechst 33258 staining of apoptotic nuclei. Apoptotic cells were collected by centrifugation, washed with PBS, and fixed in 4% paraformaldehyde for 20 min at room temperature. Subsequently the cells were washed and resuspended in 20 μL PBS before being deposited on poly lysine-coated coverslips and left to adhere to the cover slips for 30 min at room temperature, after which the cover slips were washed twice with PBS. The adhered cells were then incubated with 0.1% Triton X-100 for 5 min at room temperature and rinsed with PBS three times. The coverslips were treated with Hoechst 33258 at 37°C for 30 min, rinsed with PBS, and mounted on slides with glycerol-PBS. The cells were viewed with an Olympus BH-2 fluorescence microscope (Japan).

Immunocytochemistry analysis Curcumin-treated cells were plated onto a glass slide, air dried for 1 h at room temperature, and fixed with cold acetone. After brief washing in PBS, the slides were blocked with 5% normal goat serum for 1 h and incubated with HDAC1, HDAC3, HDAC8, and Ac-histone H4 (dilution 1:100, respectively). After being left overnight at 4 ºC the cells were treated with biotinylated link secondary antibody and peroxidase-labeled streptavidin followed by diaminobenzidine (DAB). The cells were viewed with an Olympus microscope and their individual *OD* values were recorded using an HPIAS 1000 Image Analysis System (High Resolution Pathological Image & Word Analysis System, Bejing, China).

Western blot analysis Lysates were prepared from 1×10^7 cells by dissolving cell pellets in 100 μL of lysis buffer (Na_2PO_4 (pH 7.4) 20 mmol/L, NaCl 150 mmol/L, Triton X-100 1%, aprotinin 1%, phenylmethylsulfonyl fluoride 1 mmol/L, leupeptin 10 g/L, NaF 100 mmol/L, and Na_3VO_4 2 mmol/L). Lysates were centrifuged at 18 000×*g* for 15 min and the supernatant was collected. Protein content was determined using a Bio-Rad protein assay (Bio-Rad Laboratories, Hercules, CA, USA). Sodium dodecylsulfate-polyacrylamide gel electrophoresis (SDS-PAGE) sample buffer (10 mmol/L Tris-HCl, pH 6.8, 2% SDS, 10% glycerol, 0.2 mol/L DTT) was added to the lysates. Lysates were heated to 100 ºC for 5 min, and 80 μg of protein was loaded into each well of a 10% SDS-PAGE gel. Resolved proteins were electrophoretically transferred to nitrocellulose and blocked with 5% non-fat milk, and the primary antibodies HDAC1, HDAC3, HDAC8, and Ac-histone H4 were added. After overnight incubation at 4 °C the blots were washed, exposed to HRP-conjugated corresponding secondary antibodies for 1 h, and finally detected by ECL.

Quantification of the bands was carried out using densitometric analysis software, Quantity One (Bio-Rad), and processed as described previously[12].

Statistical analysis All data were expressed as mean±SD using SPSS 10.0 for windows 98. Using linear *t*-tests for statistics analysis, *P* values of less than 0.01 or 0.05 were considered to be statistically significant.

Results

Effects of curcumin on the proliferation of Raji cells by MTT Raji cells treated with different concentrations of curcumin for 0, 24 , 36, 48, 60, and 72 h resulted in the inhibition of cell proliferation in a dose- and time-dependent manner. The *OD* value of curcumin-treated groups decreased significantly compared with the untreated group. Results reveal great differences between curcumin-treated groups and the untreated group (Figure 1). The IC_{50} of 36 h is 24.1± 2.0 μmol/L.

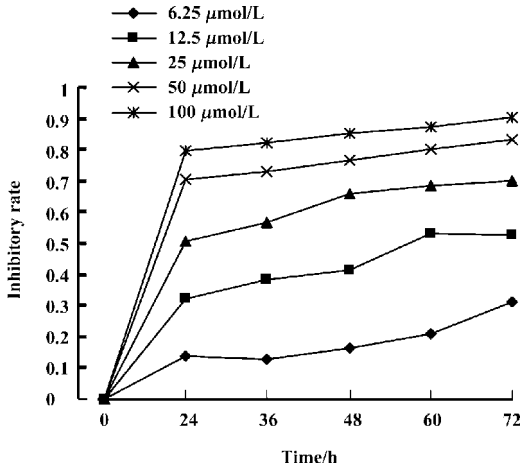

Figure 1. Antiproliferation effect of curcumin in Raji cells. Raji cells were treated with various concentrations of curcumin as indicated for 0, 24, 36, 48, 60, and 72 h. Growth inhibition was determined using a MTT assay and shown as inhibitory rate.

Nuclear damage observed using Hoechst 33258 staining Apoptotic nuclear morphology was assessed using Hoechst 33258 staining. Hoechst 33258 staining of untreated Raji cells and cells treated with 25 μmol/L curcumin for 24 h was conducted. Curcumin permeates the cell and is known to play a role in cancer chemoprevention and tumor growth suppression. Exposure of tumor cells to curcumin *in vitro* results in the inhibition of cell proliferation and the induction of apoptosis. Consistent with previous reports on other cell lines[9,11], treatment of Raji cells with curcumin (24 h exposure to 25 μmol/L curcumin) induces apoptosis (Figure 2).

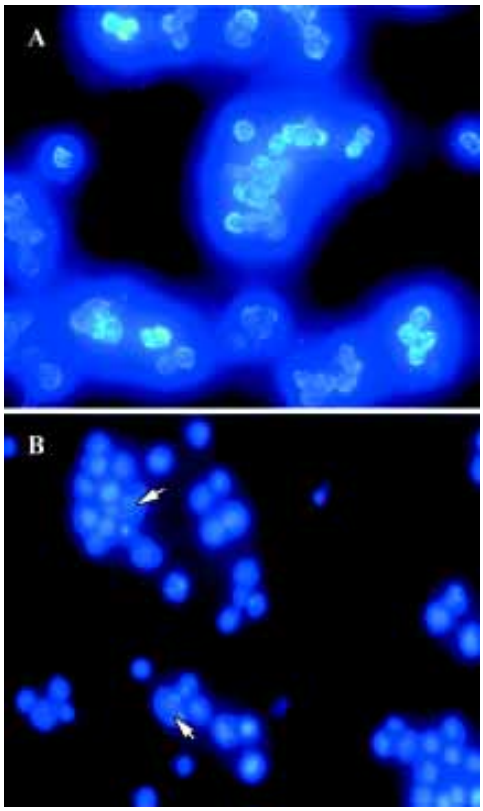

Figure 2. (A) Untreated Raji cells. (B) Cells treated with 25 μmol/L curcumin for 24 h. Photographs were taken under an Olympus BH-2 fluorescence microscope (×40). Arrows indicate apoptotic nuclear fragmentation.

Expression of HDACs and Ac-histone H4 on Raji cells and curcumin-treated cells using immunocytochemistry Our results reveal that the expression of HDAC1, HDAC3, and HDAC8 was significantly higher in Raji cells compared with curcumin-treated cells (25 μmol/L for 24 h)(P<0.05). The expression of Ac-histone H4 was significantly higher in curcumin-treated cells (25 μmol/L for 24 h) than in Raji cells (P<0.05)(Figure 3). Photos were analyzed using a HPIAS 1000 Image Analysis System and *OD* values were recorded (Figure 4).

Expression of HDAC1, HDAC3, and HDAC8 on Raji cells and curcumin-treated cells using Western blot Our results reveal that curcumin can induce antiproliferation and apoptosis in Raji cells. However, it is unclear how curcumin induces this antiproliferation and apoptosis. Cells treated with 6.25, 12.5, and 25 μmol/L of curcumin for 24 h were lysed and resolved in 10% SDS-PAGE, and Western blot analysis was carried out using anti-HDAC1, anti-HDAC3, and anti-HDAC8. Figure 5 shows considerable changes in HDAC1, HDAC3, and HDAC8 following curcumin treatment.

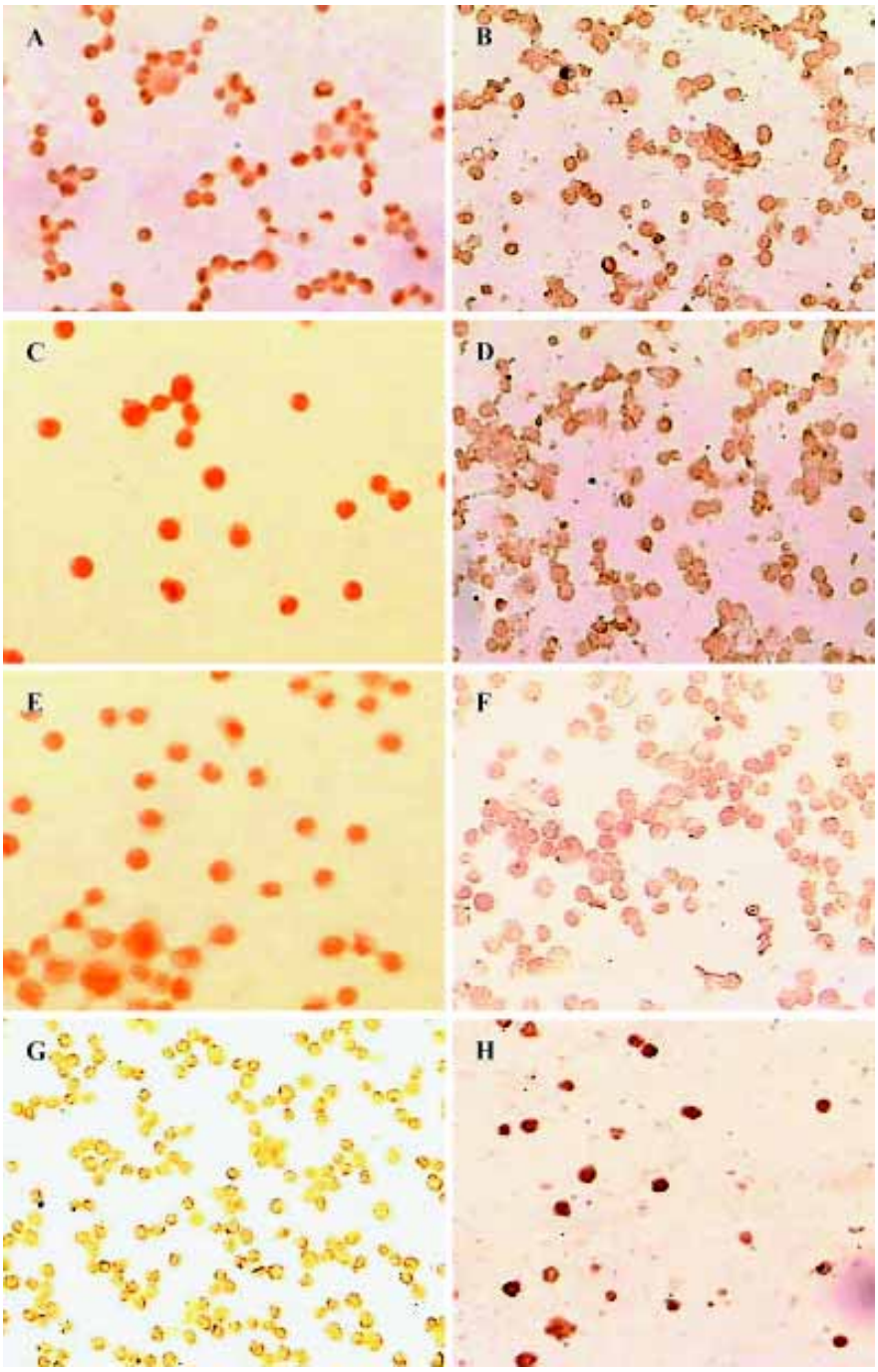

Figure 3. (A, B) Expression of HDAC1 in control and curcumin-treated cells; (C, D) Expression of HDAC3 in control and curcumin-treated cells; (E, F) Expression of HDAC8 in control and curcumin-treated cells; (G, H) expression of Ac-histone H4 in control and curcumin-treated cells.

These results indicate that HDAC1, HDAC3, and HDAC8 are related to curcumin-mediated apoptosis. The levels of HDAC1, HDAC3 and HDAC8 protein decreased in a dose-dependent manner (Figure 5).

Expression of Ac-histone H4 in Raji cells and curcumin-treated cells The expression of Ac-histone H4 was significantly greater in curcumin-treated Raji cells (6.25, 12.5, and 25 μmol/L, for 24 h) than that in Raji cells (P<0.05, Figure 6).

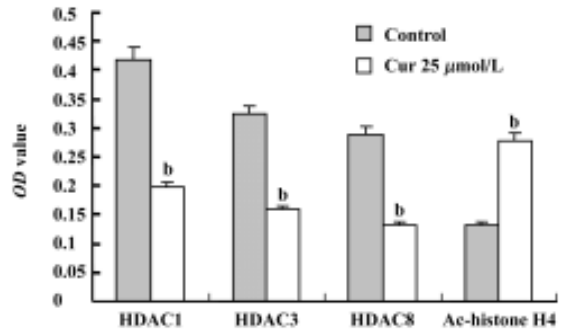

Figure 4. *OD* value of HDAC1, HDAC3, HDAC8, and Ac-histone H4 in Raji cells and curcumin-treated Raji cells (25 μmol/L, 24 h). $^{b}P<0.05$ *vs* control.

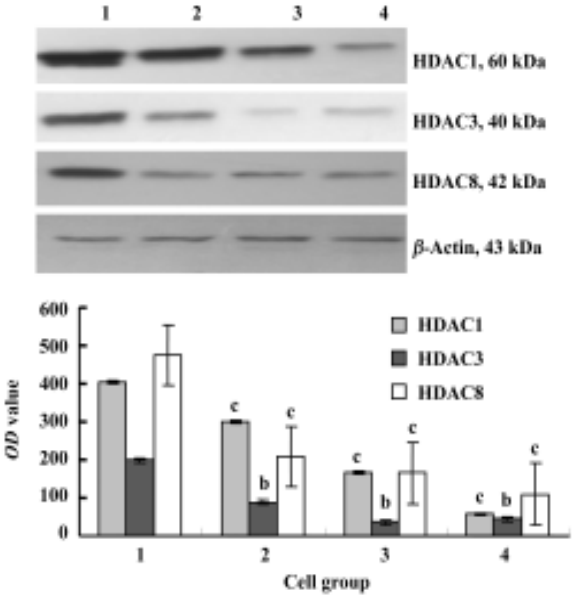

Figure 5. Effects of curcumim on the expression of HDACs in Raji cells. Cells were treated with different concentrations of curcumin for 24 h and HDACs expression was tested using Western blot analysis. 1, 2, 3, and 4 are the control, and curcumim 6.25, 12.5, and 25 μmol/L, respectively. n=3. Mean±SD. $^{b}P<0.05$, $^{c}P<0.01$ compared with the control.

Discussion

Reversible histone acetylation occurs in the ε-amino group of the specific internal lysine residues located at the highly basic N-terminal domains of core histones. Histone acetyltransferase (HAT) and HDAC control the addition and removal of acetyl groups on proteins and maintain a dynamic balance of steady-state acetylation[13]. A balance between the acetylation and deacetylation states of these proteins forms the basis for the regulation of transcription. Research has shown that HDACs have wide ranges of effects on cell function. These effects include specific gene activation, inhibition of cell proliferation and cell cycle arrest, as well as induction of cell differentiation[14]. Multiple forms of HDACs have been identified in mammalian cells. In humans, at least 11 HDACs have been uncovered. They are classified into three general classes: class I (HDAC1, 2, 3, 8, and 11), class II (HDAC4, 5, 6, 7, 9, and 10) and class III[15]. Class I enzymes are smaller polypeptides of approximately 500 amino acids, whereas class II HDACs are much larger proteins with approximately 100 amino acids. Most class II HDACs shuttle between the cytoplasm and nucleus and regulate myogenesis. HDACs can react with co-repressor (Mad/Max, N-CoR, SMRT) to regulate cell proliferation and change the dynamics of chromatin structure[16]. In general, HDAC1, HDAC3, and HDAC8 are located in the cell nucleus. Many signal transfer pathways (RAS/MAPK, JAK-STAT) and transcriptional factors related to hematopoietic stem cells are regulated by HDACs and HATs.

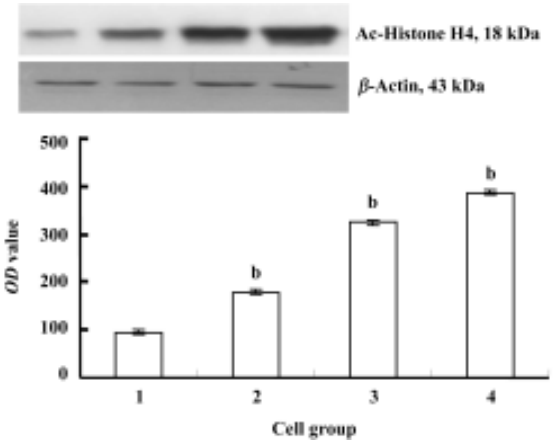

Figure 6. Effect of curcumim on the expression of Ac-histone H4 in Raji cells. Cells were treated with different concentrations of curcumin for 24 h and Ac-histone H4 expression was tested using Western blot analysis. 1, 2, 3, and 4 are the control, and curcumin 6.25, 12.5, and 25 μmol/L, respectively. n=3. Mean±SD. $^{b}P<0.05$ compared with the control.

B-NHL plays an important role in blood system tumors. We chose the Burkkit lymphoma cell line Raji as the research target. Previous studies have revealed that lymphoma is related to the rearrangement of BCL6. Several studies have shown that BCL6 is rearranged in 30%–40% of diffuse large cell lymphoma (DCLC) and 6%–14% of follicular lymphomas (FL). In addition, the chromosomal band 3q27 affects IG gene loci that lead to lymphoma. Abnormal BCL6 can regulate cell-cycle factors (pRB, PLZF) by recruiting HDACs,

and can affect the cell cycle. As the result of an abnormal recruiting function, many transcriptional factors can suppress specific genes, which can lead to carcinogenesis. HDACIs can cure cancer by inhibiting HDACs and blocking abnormal recruitment.

Chemoprevention is a rapidly growing field in cancer research that focuses on inhibiting and delaying the onset of carcinogenesis. A large number of natural products have been evaluated as potential chemopreventive agents. Numerous studies have shown that curcumin could suppress the proliferation of many cancer cells. In the present study, we found that curcumin could inhibit the proliferation of Raji cells, and that the effects were time- and dose-dependent. The 36 h IC_{50} of curcumin was 24.1±2.0 μmol/L. Curcumin can lead to the apoptosis of Raji cells, and can affect cell cycles. The cell cycle was arrested in G_0/G_1 and G_2/M phases, and the S phase also decreased (data not shown). However, the mechanisms of apoptosis and cell cycle arrest are not clear. In our study, the expression of HDAC1, HDAC3, HDAC8 and Ac-histone H4 on B-NHL cell line Raji and curcumin-treated Raji cells (different concentrations for 24 h) was examined using immunocytochemistry and Western blot analysis. The expression of HDAC1, HDAC3, and HDAC8 proteins on Raji cells decreased compared with the control Raji group, whereas Ac-histone H4 expression increased compared with the control Raji group in a dose-dependent way.

Trichostatin (TSA) was the first discovered HDAC inhibitor (HDACI), followed by sodium butyrate, sulindac, MS-27-275, and FR90228[10]. *In vitro* and *in vivo* studies examining HDACIs reveal that HDACIs affect many cell functions, such as cell proliferation, chromosome remodeling, and gene transcription. The mechanism of action relates to inhibiting HDACs, increasing the function of HATs, and increasing histone deacetylation. Hu *et al*[15] found that TSA decreased the expression of HDAC1, HDAC3, and HDAC8 in SW620 in a dose-dependent way. The IC_{50} was approximately 0.1–0.3 nmol/L. In addition, TSA can increase the expression of Ac-histone H4 and lead to apoptosis, which is related to the SV40 promotor. Balasubramanyam *et al*[13] reported that curcumin was a specific inhibitor of p300/CBP HAT activity, but not of PCAF, *in vitro* and *in vivo*. Furthermore, curcumin can also inhibit the p300-mediated acetylation of p53 *in vivo*. Curcumin specifically represses the p300/CBP HAT activity-dependent transcriptional activation from chromatin, but not from a DNA template.

Thus, we believe that curcumin, as a new member of the HDACIs, can inhibit the expression of HDAC1, HDAC3, and HDAC8 in curcumin-treated Raji cells and can increase the expression of Ac-histone H4. In addition, curcumin can inhibit cell proliferation and induce apoptosis. Dysfunction of histone acetyltransferases and histone deacetylases is often associated with the manifestation of several different types of cancer. These enzymes, therefore, are potential new targets for therapy. However, the mechanism by which the abnormal function of HDAC1, HDAC3, and HDAC8 regulates gene transcription remains to be determined. The increase in Ac-histone H4 highlights whose gene will be opened and provides a new field to examine the action mechanism of curcumin.

Acknowledgements

Thanks to the Tumour Biology Laboratory, Center of Gynaecology, Tongji Hospital, Huazhong University of Science and Technology for offering relevant experimental facilities and technical support. We wish to particularly thank Prof Jian-feng ZHOU and Yun-ping LU for their guidance and help with the experiment.

References

1 Secrist JP, Zhou X, Richon VM. HDAC inhibitors for the treatment of cancer. Curr Opin Invest Drugs 2003; 12: 1422–7.
2 Hu E, Dul E, Sung CM, Chen Z, Kirkpatrick R, Zhang GF, *et al*. Identification of novel isoform-selective inhibitors within class I histone deacetylases. J Pharmacol Exp Ther 2003; 307: 720–8.
3 Buggy JJ, Sideris ML, Mak P, Lorimer DD, McIntosh B, Clark JM. Cloning and characterization of a novel human histone deacetylase, HDAC8. Biochem J 2000; 350: 199–205.
4 Murata M, Towatari M, Kosugi H. Apoptotic cytotoxic effects of a histone deacetylase inhibitor, FK228, on malignant lymphoid cells. Jpn J Cancer Res 2000; 91: 1154–60.
5 Graessle S, Loidl P, Brosch G. Histone acetylation: plants and fungi as model systems for the investigation of histone deacetylases. Cell Mol Life Sci 2001; 58: 704–20.
6 Aggarwal BB, Kumar A, Bharti AC. Anticancer potential of curcumin: preclinical and clinical studies. Anticancer Res 2003; 23: 363–98.
7 Leu TH, Maa MC. The molecular mechanisms for the antitumorigenic effect of curcumin. Curr Med Chem Anti-Cancer Agents 2002; 2: 357–70.
8 Ranjan D, Chen C, Johnston TD, Jeon H, Nagabhushan M. Curcumin inhibits mitogen stimulated lymphocyte proliferation, NFkappaB activation, and IL-2 signaling. J Surg Res 2004; 121: 171–7.
9 Wu L, Xu J, Wu G, Chen Y. Inhibitory effect of curcumin on proliferation of K562 cells involves down-regulation of p210bcr/abl-initiated Ras signal transduction pathway. Acta Pharmacol Sin 2003; 24: 1155–60.
10 Mariadason JM, Corner GA, Augenlicht LH. Genetic reprogramming in pathways of colonic cell maturation induced by short chain fatty acids: comparison with trichostatin A, sulindac, and curcumin and implications for chemoprevention of colon cancer.

Cancer Res 2000; 60: 4561–72.
11 Chen W, Chen Y, Gu J, He J. Effects of curcumin on proliferation of K562 cells involves STAT5 signal transduction pathway. Chin J Hematol 2004; 25: 151–3.
12 Zhou N, Zhu X, Zhou J, Li M, Zhang X, Huang P, *et al*. 2-Methoxyestradiol induces cell cycle arrest and apoptosis of nasopharyngeal carcinoma cells. Acta Pharmacol Sin 2004; 25: 1515–20.
13 Balasubramanyam K, Varier RA, Altaf M, Swaminathan V, Siddappa NB, Ranga U, *et al*. Curcumin, a novel p300/CBP specific inhibitor of acetyltransferase, represses the acetylation of histones/nonhistone proteins and HAT dependent chromatin transcription. J Biol Chem 2004; 279: 51163-71.
14 Sullivan SA, Landsman D. Characterization of sequence variability in nucleosome core histone folds. Proteins 2003; 52: 454–65.
15 Hu E, Chen Z, Fredrickson T, Zhu Y, Kirkpatrick R, Zhang GF, *et al*. Cloning and characterization of a novel human class I histone deacetylase that functions as a transcription repressor. J Biol Chem 2000; 20: 15254–64.
16 Yamashita Y, Shimada M, Harimoto N, Rikimaru T, Shirabe K, Tanaka S, *et al*. Histone deacetylase inhibitor trichostatin A induces cell-cycle arrest/apoptosis and hepatocyte differentiation in human hepatoma cells. Int J Cancer 2003; 103: 572–6.

Acta Pharmacologica Sinica 2005 May; 26 (5): 610–615

Full-length article

Transfection of promyelocytic leukemia in retrovirus vector inhibits growth of human bladder cancer cells[1]

Lei LI, Da-lin HE[2]

Institute of Urology, First Hospital of Xi'an Jiaotong University, Xi'an 710061, China; Key Laboratory of Environment and Genes Related to Diseases of Ministry of Education, Xi'an Jiaotong University, Xi'an 710061, China

Key words

promyelocytic leukemia protein; retrovirus; gene therapy

[1] Project supported by the National Natural Science Foundation of China, No 30170937.
[2] Correspondence to Da-lin HE.
Phn 86-29-8532-4008.
Fax 86-29-8525-1632.
E-mail hedalin@yahoo.com.cn

Received 2004-08-23
Accepted 2005-11-09

doi: 10.1111/j.1745-7254.2005.00065.x

Abstract

Aim: To construct a recombinant retrovirus vector carrying human promyelocytic leukemia (PML) cDNA and identify its expression and biology role in bladder cancer UM-UC-2 cells for future gene therapy. **Methods:** PML full-length cDNA was inserted into the *Eco*R I and *Bam*H I site of pLXSN vector containing the long terminal repeat (LTR) promoter. The vector was identified by restriction enzyme digestion and then transfected into PA317 packaging cell line by calcium phosphate coprecipitation. PML cDNA was detected by polymerase chain reaction (PCR) and the protein was identified by laser confocal microscopy and Western blot in bladder cancer cells, respectively. The morphology was observed by inverted phase contrast microscope, and MTT assay determined growth curve of the bladder cancer cells. **Results:** Restriction enzyme digestion proved that a 2.1 kb PML cDNA was inserted into the pLXSN vector. PCR assay demonstrated that 304 bp fragments were found in UM-UC-2/pLPMLSN transfects. Laser confocal microscopy showed speck dots fluorescence in the UM-UC-2/pLPMLSN nucleus. A 90 kD specific brand was found by Western blot. MTT assay demonstrated the UM-UC-2/pLPMLSN bladder cancer growth inhibition. **Conclusion:** The retrovirus pLPMLSN vector was successfully constructed and could generate high effective expression of human PML in bladder cancer cell UM-UC-2, suggesting that PML recombinant retrovirus have potential utility in the gene therapy for bladder cancer.

Introduction

Promyelocytic leukemia (PML), which encodes a growth transformation suppressor[1] and pro-apoptosis factor, mediating cell death by apoptosis[2], is disrupted by 15:17 chromosomal translocation in acute promyelocytic leukemia. The physical function of the PML gene was complicated and the PML gene has an altered expression during human oncogenesis. Its expression was reduced dramatically when cancer turned invasive[3]. Cells deficient in PML are resistant to apoptosis by multiple apoptotic stimuli, suggesting that PML is a pro-apoptosis factor[2]. Overexpression of PML protein could inhibit various human tumor growth *in vitro* and *in vivo*, such as in Hela cell[4], prostate cancer cells (PC-3,DU145, LNCaP)[5], breast cancer[6], and bladder cancer cells (5637; UM-UC-2 unpublished data)[7]. This evidence suggests that PML could be a candidate gene for human tumor gene therapy.

In this study, we further detected whether the PML as a growth suppressor could be a potential candidate gene for bladder cancer gene therapy. We constructed a recombinant retrovirus carrying the PML gene, which was controlled by long terminal repeat (LTR) promoter, and we want to study whether recombinant PML retrovirus has a high level PML protein expression in bladder cancer UM-UC-2 cells and whether overexpression of PML could inhibit bladder cancer cell growth.

Materials and methods

Cell culture and reagents UM-UC-2 cells[8] were cultured in Dulbecco's modified Eagle's medium (DMEM) at

37 °C supplemented with 10% fetal calf serum (FCS). PA317 packaging cells and NIH3T3 cell were maintained in RPMI-1640 medium supplemented with 10% fetal bovine serum (FBS). Each medium was supplemented with penicillin (50 kU/L) and streptomycin (50 kU/L). The GST-PML antibody and PGS5-PML vector were obtained from Dr K S CHANG (MD Anderson Cancer Center, The University of Texas, USA). The PLXSN vector was purchased from Clontech Company.

Construction and amplification of pLPMLSN The PML retroviral vector pLPMLSN was constructed by inserting the full-length PML cDNA[1] into the *Eco*R I and *Bam*H I restriction site of the pLXSN retroviral vector. The reconstructed plasmid DNA used for transfection was purified by the plasmid purification kit (Huashun Inc, Shanghai, China) according to the manufacturers' instruction. DNA concentration was determined by UV spectrophotometer[4].

Generation of viral particles and infection to target cells pLXSN and pLPMLSN were transfected into the PA317 packaging cell lines by calcium phosphate coprecipitation[9]. PA317 packaging cells were split and grew in the selective medium with 800 mg/L of G418. After 2 weeks, G418 resistant colonies were picked and expanded in medium with 200 mg/L G418 and the supernatant viral particles were collected. The titer of viral stocks was calculated by infection of mouse fibroblast NIH 3T3 cell[11]. The titer of pPMLSN and pLXSN retrovirus was 1.3×10^9 CFU/L and 2.1×10^9 CFU/L, respectively.

The UM-UC-2 cells, as target cells, were infected with recombinant PML retrovirus and the control virus respectively by the supernatant gene transfer technique, as previously described[10]. In brief, UM-UC-2 cells in exponential growth were plated in 60-mm culture dishes 1 day before recombinant virus infection. Each culture dish was then fed with 10 mL of recombinant viral supernatant containing polybrene at a final concentration of 8 mg/L. The UM-UC-2 cells were then infected with viral particles for 48 h. The viral supernatant was prepared by incubating fresh medium for 1 day with the growth-accelerated viral producer and then used directly for further experiments.

Identification of PML cDNA in transfected cells Genomic DNA was prepared from UM-UC-2, UM-UC-2/pPMLSN, UM-UC-2/pLXSN cells and used for polymerase chain reaction (PCR) with primers specific for PML (forward 5'-CTT GAA CCT CCT CGT TCG ACC-3' reverse 5'-GTA CAA CAG GTA GCG GAT CCC-3'). The forward primer was specifically designed for pLXSN vector, and the reverse primer was for PML cDNA. The reaction mixture for PCR amplification was subjected to 30 cycles of denaturation (95 ºC, 60 s), annealing (56 ºC, 60 s), and extension (72 ºC, 60 s). The amplification products were identified by 2% agarose-gel electrophoresis.

Identification of PML protein expression in transfected cells by immunofluorescence staining and Western blot Western blot and immunofluorescence staining of bladder cancer UM-UC-2 cells infected with recombinant PML retrovirus and control virus were carried out as described in our previous report[5]. Briefly, UM-UC-2 cells were seeded on coverslides for at least 4 h, and then recombinant PML retrovirus was added and incubated at 37 ºC for 24 h. Cells were washed in phosphate-buffered saline (PBS) twice and fixed in 4% paraformaldehyde for 20 min and 0.1% Triton X-100 for 10 min, followed with three washes in PBS containing 0.1% BSA. Cells were then incubated in the washing buffer for 20 min at room temperature. Immunofluorescence staining was performed using the affinity-purified antipeptide polyclonal antibody GST-PML at dilution of 1:2000 for 1 h at 37 ºC, and then goat anti-rabbit IgG-fluorescein isothiocyanate secondary antibody (Sabc Inc, Beijing, China) was added for another 1 h. Confocal microscopy analysis was performed by using a Zeiss (New York, NY, USA) laser scanning confocal microscope at 494-nm stimulated wavelength.

Western blot of PML protein was performed using RIPA lysis buffer and 8% SDS-PAGE gel electrophoresis. Proteins were transferred to NC filter (Bio-Rad) and blocked with 5% non-fat milk for 1.5 h. The filters were then incubated for 2 h with a dilution of 1:2000 GST-PML antibody and then for 1 h with the secondary antibody at dilution of 1:500. Immunodetection was performed using the ECL Western blot detection system.

Cell viability UM-UC-2 Cell viability was evaluated by 3-(4,5-dimethylthiazol-2-yl)-2,5-diphenyltetrazolium bromide (MTT) assay. In brief, we selected 1 d, 2 d, 3 d, and 4 d as different times for observation points. Bladder cancer cells (1×10^4) were plated in 96-well tissue culture plates in DMEM containing 10% FBS in a final volume of 0.2 mL. When the cells reached 50% confluence, they were treated with recombinant PML retrovirus and control virus. After 24 h of culture, cell proliferation was assessed by directly adding 50 μL of 3-(4,5-dimethylthiazol-2-yl)-2,5-diphenyltetrazolium bromide 7 dye (0.005 mg/L) to the medium for another 4 h, and then bladder cancer cells were solubilized in Me_2SO (150 μL/well) on a shaker at room temperature for 10 min before reading the absorbance at 570 nm using a Biorad Technologies Microplate Reader.

Statistical analysis The experimental results shown were repeated three times, unless otherwise indicated. Results are expressed as mean±SD. Statistical analysis was carried

out using Student's *t*-test and one-way ANOVA. Significance was set at $P<0.05$. Statistical analyses were performed using SPSS10.0 (SPSS Inc, Chicago, IL, USA).

Results

Identification of the recombinant retrovirus vector pLPMLSN The full-length PML cDNA was excised by *Eco*R I and *Bg*L II from the plasmid pSG5PML[1], and then ligated into the *Eco*R I and *Bam*H I digested restriction site, for *Bg*L II and *Bam*H I are isocaudamers, which have the same cohesive terminus. The constructed plasmid was digested with *Kpn* I, and three fragments of 2.0 kb, 2.9 kb, and 3.1 kb are acquired on agarose-gel electrophoresis. Two 2.3 kb and 5.7 kb fragments were obtained by *Eco*R I and *Hind* III (Figure 1). It suggests that PML cDNA had been inserted into retrovirus vector pLXSN successfully.

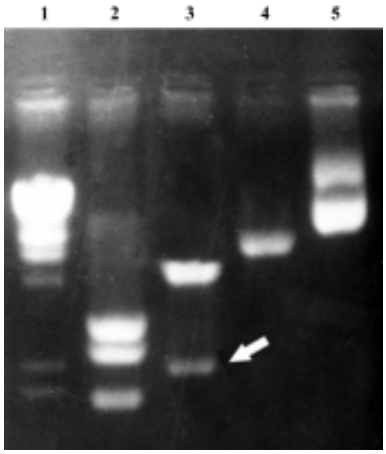

Figure 1. Identification of the recombinant retro-virus vector pLPMLSN. Lane 1: λ DNA/*Hind* III marker. Lane 2: pPMLSN digested with *Kpn* I, three fragments of 2.0 kb, 2.9 kb, and 3.1 kb acquired. Lane 3: 2.3 kb and 5.7 kb fragments digested by *Eco*R I and *Hind* III as shown by the arrow. Lane 4: linear by single *Eco*R I site. Lane 5:control plasmid.

Identification of PML cDNA in transfected cells PCR was performed using total DNA samples prepared from UM-UC-2 cell culture after the recombinant retrovirus particles were transducted into the cultured cells. The PCR products of 304 bp fragments for PML were amplified from UM-UC-2/pLPMLSN cells but not from control cells infected with UM-UC-2/pLXSN and UM-UC-2 parental cells (Figure 2).

Determination of PML expression after recombinant PML retrovirus infection by immunofluorescence Immunofluorescence staining was performed to confirm whether the reconstructed retrovirus could infect and express PML protein in bladder cancer cells UM-UC-2. As shown in Figure 3, both the number and intensity of PML specific nuclear speckle significantly increased in UM-UC-2/pPMLSN cells, while in parental cells only a little poor and nonspecific signal was detected.

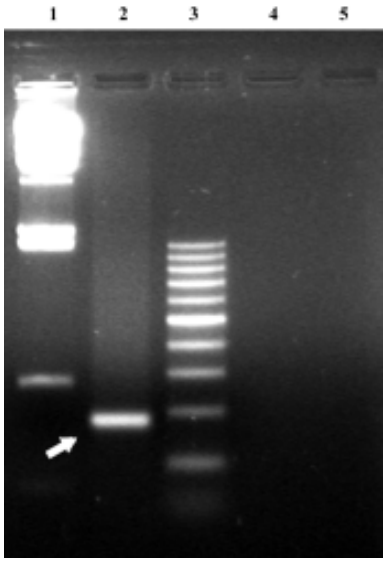

Figure 2. IPML cDNA in transfected cells determined by PCR. Lane 1: λDNA/*Hind* III marker. Lane 2: UM-UC-2/pLPMLSN cell, 304 bp PCR product as indicated by arrow. Lane 3: 200 bp ladder marker. Lanes 4 and 5: the UM-UC-2 cells infected with the pLXSN control retrovirus and parental UM-UC-2 cells, respectively.

Demonstration of PML expression after recombinant PML retrovirus infection by Western blot Western blot analysis showed that the bladder cancer UM-UC-2 cells infected with recombinant PML retrovirus expressed a high level of 90 kDa PML protein. The protein was undetectable in the parental bladder cancer UM-UC-2 cells by Western blot (Figure 4).

Effect of PML overexpression on cell growth We had previously shown that PML could repress the growth of prostate cancer LNcap, DU145, and PC-3 cells[5]. Now, to further test the effect of increased expression of PML on bladder cancer UM-UC-2 cell growth, MTT assay was used. As shown in Figure 5, UM-UC-2/pLPMLSN grew significantly more slowly than the parental UM-UC-2 and control UM-UC-2/pLXSN cells ($P<0.05$).

Morphological changes were also observed under phase contrast and light microscopes. As shown in Figure 6A and 6B, UM-UC-2 and UM-UC-2/pLXSN control cells showed

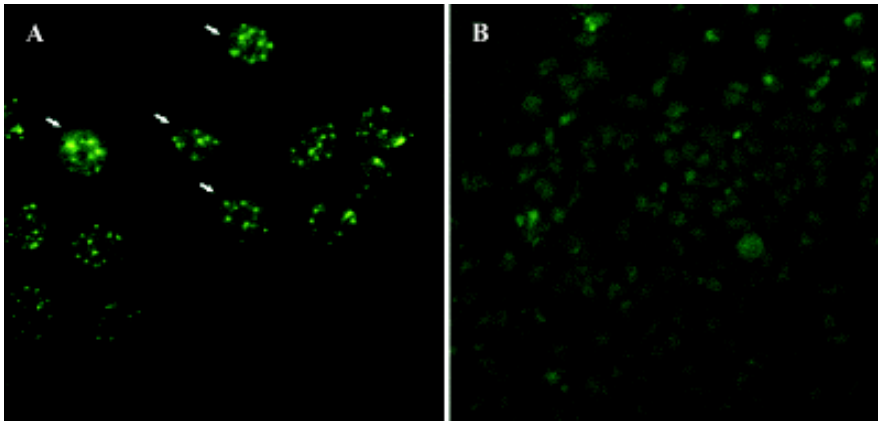

Figure 3. Expression of PML protein in UM-UC-2 cells infected with retro-PML detected by immunofluorescence staining. (A) FITC labelling immunofluorescence staining of PML protein in UM-UC-2 cells infected with retro-PML as indicated by arrows. (B) parental UM-UC-2 cells.

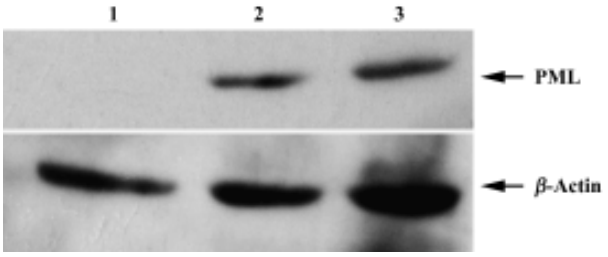

Figure 4. Detected PML expression after recombinant PML retrovirus infection by Western blot. Lane 1: control bladder cancer UM-UC-2 cells. Lanes 2 and 3: bladder cancer UM-UC-2 cells infected with recombinant PML retrovirus.

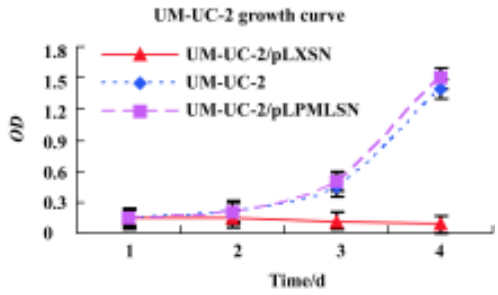

Figure 5. The effect of PML on the growth inhibition of UM-UC-2 cells. Growth rate of UM-UC-2, UM-UC-2/pLXSN and UM-UC-2/pLPMLSN cell were determined by MTT assay. Results presented in each group represent the average of three independent experiments.

normal morphology. In contrast, UM-UC-2/pLPMLSN cells were shrunk, lost cell-to-cell contact, and in part detached from the plate (Figure 6C). These characteristics suggested apoptotic morphology feature.

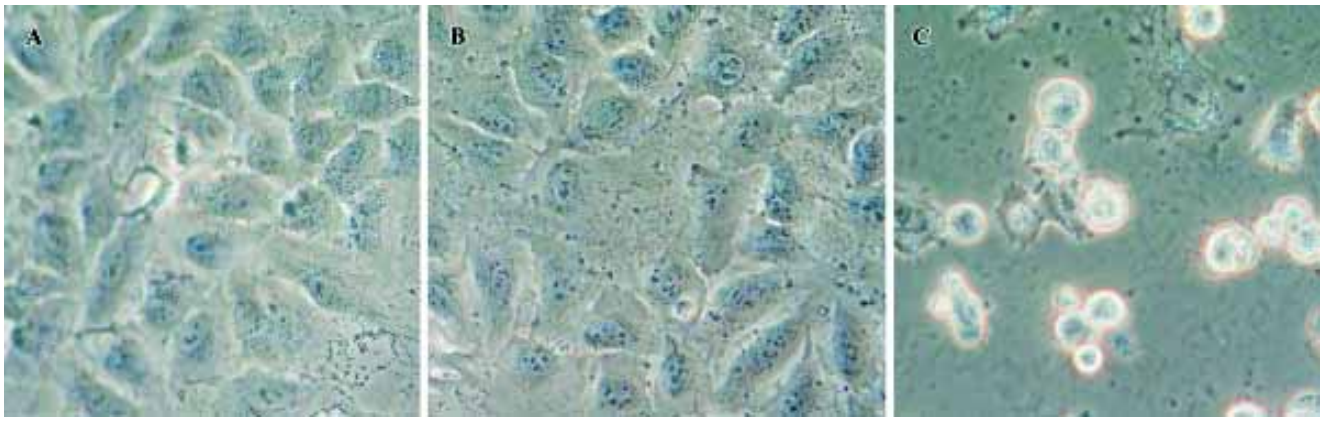

Figure 6. Identification of the morphology alteration in bladder cancer cells. (A) the parental UM-UC-2 cells (×40 magnification). (B) UM-UC-2/pLXSN bladder cells (×40 magnification). (C) UM-UC-2/pLPMLSN easily detaching from the plate surface (×40 magnification). Remaining cells are shrunk.

Discussion

In recent years, studies have been provided that activated oncogene or loss of tumor suppressor leads to the development of human cancer. Based on this concept, new effective therapeutic regimens have been developed as alternatives to conventional cancer therapy. One field that most scientists focused on is gene therapy, which is to suppress the overexpressed oncogene or rebuild the function of tumor suppressor[12]. To deliver a gene into tumor cells, two major vector systems, such as viral system and non-viral system, have been thrown into research studies and clinical trials. The latter has relative low transduction efficacy and required some special equipment, therefore was not widely used. Compared to the adenovirus system, the retrovirus systems have some advantages in tumor gene therapy because of the following reasons. First, infection by retrovirus depends on host cell division. Most tumor cells are active in cell mitosis, which made wide range infection to carrier cells[13]. Second, retrovirus can integrate into host genome, which can stably and continuously express targeting protein as host cell growth[13]. Third, a recent study demonstrated that the entrance of adenovirus to the host cell must be mediated by the specific receptor. For example coxsackie and adenovirus receptor (CAR), whose protein expression level is reduced and even lost when breast cancer[14], urothelial cancer[15,16], head, and neck cancers[17] are in high-grade or become invasive as adenovirus mediated gene therapy is not adapt to high-grade, late-stage invasive tumor[14–17]. While the retrovirus does not have these limitations. This is one good reason why we constructed the recombinant PML retrovirus. Finally, when adenovirus infects the host cells for gene therapy, frequent administration of recombinant adenovirus were required to achieve therapeutic efficacy. Because of a strong immunological response, it could not operate repeatedly[5]. In contrast, the retrovirus did not have the adverse immunological response.

We constructed recombinant retrovirus vector carrying PML gene, which was involved in the 15:17 translocation in acute promyelocytic leukemia (APL), and is a growth and transformation suppressor and plays an essential role in multiple pathways of apoptosis[1,2]. PML is lost or reduced in solid tumor of several histological origins[4–7] and is found to be more frequently lost in late-stage or metastatic cancer[3]. Our previous study demonstrated that endogenous PML expression was related to the stage, grade, and invasiveness of bladder cancer. Stably overexpressed PML protein leads to decreased cell growth and tumorigenicity of bladder cancer *in vivo*[7] and prostate cells *in vitro* and *in vivo*[5]. Overexpression of PML induced G1 cell cycle arrest and subsequently triggered cell death by apoptosis in breast cancer cells[6].

In addition, PML is a much more stable protein with long half-life of about 6 h compared to other tumor suppressor genes such as p53 which has a half-life of 1.5 h. This suggest that long-time and high concentration of protein could accumulate in tumor cells and a better therapeutic effect could be obtained[5].

These results strongly indicate that PML has therapeutic potential in the gene therapy of human tumors.

In conclusion, we constructed recombinant retrovirus stable expressed PML. PCR confirmed that the recombinant retrovirus could infect bladder cancer cells. Laser scanning confocal microscope and Western blot showed high level PML protein could be expressed. Overexpression of PML could inhibit the growth of bladder cancer. It may be an attempt for human tumor gene therapy in future.

References

1 Mu ZM, Chin KV, Liu JH, Lozano G, Chang KS. PML, a growth suppressor disrupted in acute promyelocytic leukemia. Mol Cell Biol 1994; 14: 6858–67.

2 Wang ZG, Ruggero D, Ronchetti S, Zhong S, Gaboli M, Rivi R, *et al*. PML is essential for multiple apoptotic pathways. Nat Genet 1998; 20: 266–72.

3 Koken MH, Linares-Cruz G, Quignon F, Viron A, Chelbi-Alix MK, Sobczak-Thepot J, *et al*. The PML growth-suppressor has an altered expression in human oncogenesis. Oncogene 1995; 10: 1315–24.

4 Mu ZM, Le XF, Vallian S, Glassman AB, Chang KS. Table overexpression of PML alters regulation of cell cycle progression in HeLa cells. Carcinogenesis 1997; 18: 2063–9.

5 He D, Mu ZM, Le X, Hsieh JT, Pong RC, Chung LW, *et al*. Adenovirus-mediated expression of PML suppresses growth and tumorigenicity of prostate cancer cells. Cancer Res 1997; 57: 1868–72.

6 Le XF, Vallian S, Mu ZM, Hung MC, Chang KS. Recombinant PML adenovirus suppresses growth and tumorigenicity of human breast cancer cells by inducing G1 cell cycle arrest and apoptosis. Oncogene 1998; 16: 1839–49.

7 He D, Nan X, Chang KS, Wang Y, Chung LW. Overexpression of the promyelocytic leukemia gene suppresses growth of human bladder cancer cells by inducing G1 cell cycle arrest and apoptosis. Chin Med J 2003; 116: 1394–8.

8 Grossman HB, Wedemeyer G, Ren L. UM-UC-1 and UM-UC-2: characterization of two new human transitional cell carcinoma lines. J Urol 1984; 132: 834–7.

9 Jseph S, Daivd WR. Laboratory manual. 3rd ed. Cold Spring, NY: Cold Spring Laboratory; 2001. p 1282–6.

10 Miller AD, Miller DG, Garcia JV, Lynch CM. Use of retroviral vectors for gene transfer and expression. Methods Enzymol 1993; 217: 581–99.

11 Bodine DM, McDonagh KT, Seidel NE, Nienhuis AW. Development of a high-titer retrovirus producer cell line and strategies for retrovirus-mediated gene transfer into rhesus monkey he-

matopoietic stem cells. Ann N Y Acad Sci 1990; 612: 415–26.
12 Friedmann T. Progress toward human gene therapy. Science 1989; 244: 1275–81.
13 Sokol DL, Gewirtz AM. Gene therapy: basic concepts and recent advances. Crit Rev Eukaryot Gene Expr 1996; 6: 29–57.
14 Shayakhmetov DM, Li ZY, Ni S, Lieber A. Targeting of adenovirus vectors to tumor cells does not enable efficient transduction of breast cancer metastases. Cancer Res 2002; 62: 1063–8.
15 Li Y, Pong RC, Bergelson JM, Hall MC, Sagalowsky AI, Tseng CP, *et al*. Loss of adenoviral receptor expression in human bladder cancer cells: a potential impact on the efficacy of gene therapy. Cancer Res 1999; 59: 325–30.
16 Rauen KA, Sudilovsky D, Le JL, Chew KL, Hann B, Weinberg V, *et al*. Expression of the Coxsackie adenovirus receptor in normal prostate and in primary and metastatic prostate carcinoma: potential relevance to gene therapy. Cancer Res 2002; 62: 3812–8.
17 Kasono K, Blackwell JL, Douglas JT, Dmitriev I, Strong TV, Reynolds P, *et al*. Selective gene delivery to head and neck cancer cells via an integrin targeted adenoviral vector. Clin Cancer Res 1999; 5: 2571–9.

Acta Pharmacologica Sinica 2005 May; 26 (5): 616–622

Full-length article

Inhibitory effect of agmatine on proliferation of tumor cells by modulation of polyamine metabolism[1]

Ji-fang WANG[2], Rui-bin SU[2], Ning WU, Bo XU, Xin-qiang LU, Yin LIU, Jin LI[3]

Beijing Institute of Pharmacology and Toxicology, Beijing 100850, China

Key words

agmatine; polyamine; tumor cell; proliferation

[1] Project supported by the Hi-Tech Research Program of China (2002AA2Z3028) and the National Basic Scientific Research and Development Program of China (2003CB-515400).
[2] The two authors did the same contribution for the paper.
[3] Correspondence to Prof Jin LI.
Phn 86-10-6693-1603.
Fax 86-10-6693-2681.
E-mail jinli9802@yahoo.com

Received 2004-10-04
Accepted 2005-01-09

doi: 10.1111/j.1745-7254.2005.00084.x

Abstract

Aim: To assess the inhibitory effect of agmatine on tumor growth *in vivo* and tumor cell proliferation *in vitro*. **Methods:** The transplanted animal model, [^{3}H]thymidine incorporation assay, 3-[4,5-dimethythiazol-2-yl]-2,5-diphenyltetrazolium assay, and lactate dehydrogenase (LDH) release assay were performed. **Results:** Agmatine, at doses of 5–40 mg/kg, suppressed the S_{180} sarcoma tumor growth dose-dependently in mice *in vivo* and the highest inhibitory ratio reached 31.3% in Kunming mice and 50.0% in Balb/c mice, respectively. Similar results were obtained in the transplanted B_{16} melanoma tumor model. Agmatine (1–1000 μmol/L) was able to attenuate the proliferation of cultured MCF-7 human breast cancer cells in vitro in a concentration-dependent manner and the highest inhibitory ratio reached 50.3% in the [^{3}H]thymidine incorporation assay. Additionally, in the LDH release assay, spermine (20 μmol/L) and spermidine (20 μmol/L) increased the LDH release significantly, but agmatine (1–1000 μmol/L) did not, indicating that the inhibitory effect of agmatine on the proliferation of MCF was not related to cellular toxicity. In the [^{3}H]thymidine incorporation assay, putrescine (12.5–100.0 μmol/L) could reverse the inhibitory effect of agmatine on the proliferation of MCF concentration-dependently, suggesting that the inhibitory effect of agmatine on the proliferation of MCF might be associated with a decreased level of the intracellular polyamines pool. **Conclusion:** Agmatine had significant inhibitory effect on transplanted tumor growth *in vivo* and proliferation of tumor cells *in vitro*, and the mechanism might be a result of inducing decrease of intracellular polyamine contents.

Introduction

Polyamines, including putrescine, spermidine, and spermine, are required for cell proliferation and homeostasis. The intracellular pool of polyamines is precisely regulated through their biosynthesis, degradation, uptake, and excretion[1]. The disorder of intracellular polyamines plays an important role in carcinogenesis. Polyamines can promote the neoplastic transformation of normal cells, stimulate the proliferation of tumor cells, and facilitate angiogenesis in tumor tissues. Therefore, their metabolism pathway is an interesting anticancer drug target[2].

Agmatine, one of the analogs of polyamines, is the product of *L*-arginine decarboxylation and was initially believed to be present only in bacteria, plants, and invertebrates. Now it has been shown to be present in mammals[3]. The accumulated results show that agmatine has some important biological activities[4]. Among them, the inhibitory effect of agmatine on cell proliferation is of great interest.

The current results show that agmatine is able to modulate the cellular concentration of polyamines[5]. Agmatine can be hydrolyzed to putrescine and urea. Putrescine is then converted into spermidine and spermine by spermidine/spermine synthases[6]. So agmatine might have the capacity to increase the level of intracellular polyamines. In addition, agmatine has been postulated to decrease the cellular level of polyamines. There is much evidence to support this hypothesis. First, because agmatine and polyamines are

structurally analogous and derived from same precursor, *L*-arginine[7], administration of exogenous agmatine would be able to reduce the synthesis of polyamines by a back-feed way. Second, as a competitor, agmatine can retard putrescine intake by the same carrier[8]. Most importantly, besides polyamines, agmatine is the only known molecule that has the capacity to induce antizyme[9]. Antizyme is the only known endogenous protein that binds to ornithine decarboxylase, inhibiting its activity and accelerating its degradation. Indeed, when tested *in vitro*, agmatine inhibited DNA synthesis and proliferation in some cell lines[10]. Moreover, Regunathan *et al*[11] reported that agmatine inhibited proliferation of human coronary artery vascular smooth muscle cells by stimulation of imidazoline receptors. Satriano *et al*[12] claimed that agmatine dramatically decreased the ratio of DNA synthesis on mouse kidney proximal tubule cells by attenuation of the cellular polyamine level. In 2003, Gardini *et al*[13] found that agmatine inhibited the proliferation of rat hepatoma cells. These results indicate that agmatine might be an endogenous anti-proliferation factor, and whether the pharmacological effect of exogenous agmatine on cells *in vivo* is the same as *in vitro* is an interesting question.

In the present study, we investigated the inhibitory effects of agmatine on several classical tumor cells *in vivo* and *in vitro* and explored its possible mechanisms *in vitro.*

Materials and methods

Reagents and drugs Agmatine sulfate was obtained from the Beijing Institute of Pharmacology and Toxicology; cyclophosphamide was manufactured by Hengrui Pharmaceutical Co (Lianyungang, Jiangsu, China); spermine, spermidine, putrescine, 3-(4,5-dimethylthiazol-2-yl)-2,5-diphenyltetrazolium bromide (MTT), and sodium dodecylsulfonate (SDS) were obtained from Sigma Chemical (St Louis, MO, USA); Roosevelt Park Memorial Institute medium (RPMI-1640) was purchased from Gibco (Carlsbad, CA, USA); and [^{3}H]thymidine was obtained from DuPont/NEN Company (Boston, MA, USA).

Animals Male Kunming, Balb/c, and C_{57} mice [20±2 g, Grade II, Certificate No SCXK (Jun) 2002-001, Experimental Animal Center of Academy of Military Medical Sciences] were used. After transplanted with tumor cells, animals were randomly distributed into different groups. The control group was administered with saline alone and the others were treated with different drugs. All drugs were dissolved in normal saline and freshly prepared on the experimental day. Both normal saline and agmatine were administered subcutaneously (sc) and cyclophosphamide was injected intraperitoneally (ip) in a volume of 10 mL/kg. All of the animals were housed and maintained in a temperature-controlled room (22 °C–24 °C) with free access to qualified food and water at all times.

Cell culture MCF-7 human breast cancer cells were maintained in RPMI-1640 medium with 10% fetal bovine serum (FBS), 100 kU/L penicillin and 100 kU/L streptomycin. Cells were incubated at 37 °C in a humidified 5% CO_2 atmosphere and subcultured every 3 d.

Evaluation of agmatine's inhibitory effects on the growth of tumor cells *in vivo* S_{180} sarcoma and B_{16} melanoma cells were subcultured in the abdominal cavity of mice for 8 d. The resulting ascites were diluted with saline to form a suspension containing 2×10^{10} cells/L. Aliquots of cell suspensions (0.2 mL) were injected (sc) into the right armpit of the mice. From the 1st day after implantation, saline, agmatine (5–40 mg/kg, tid, sc), or cyclophosphamide (20 mg/kg, qd, ip) were administered for 10 d. At d 10, the animals were killed and the tumors were chipped from their armpits. The tumor weights (g) were measured and the mean tumor weight of every group was calculated. The anti-tumor activities of the drugs were determined by a comparison between the inhibitory ratios obtained from the treated groups and the control group. The inhibitory ratio of drugs was expressed as [(average tumor weights in saline group–average tumor weights in drug treated group)/(average tumor weights in saline group)×100].

Measurement of proliferation *in vitro* in [^{3}H]thymidine incorporation assay Proliferation of the MCF cells was assessed by [^{3}H]thymidine incorporation assay. Briefly, cells suspended in RPMI-1640 medium with 10% FBS were seeded into a 96-well cell culture plate (80 μL/well) at a density of 6000 cells/well. Then they were treated with saline (control), or different concentrations of agmatine (1, 10, 100, 200, 500, or 1000 μmol/L), respectively, at a volume of 20 μL. Drugs were added for a total period of 48 h and [^{3}H]thymidine (3.7×10^4 Bq/well) was added at 36 h of incubation. The medium was removed and the cells were washed three times with phosphate-buffered saline and then twice with ice-cold 10% trichloroacetic acid. Fixed cells were then solubilized in 0.2 mol/L NaOH (100 μL/well) and sonicated for 15 min. After mixing with scintillant liquid (1 mL) for 24 h, an aliquot (90 μL/well) was used for scintillation counting. Then the radioactivity was determined with a Multi-purpose Scintillation Counter (Columbus Instruments, Columbus, OH, USA). The mean cpm value of every group was calculated. The anti-proliferation potency of the drugs was determined by a comparison between the inhibitory ratios obtained from the

treated groups and the control. The inhibitory ratio of the drugs was expressed as [(average cpm value in control group–average cpm value in drug treated group)/(average cpm value in control group)×100%].

Measurement of proliferation *in vitro* Cell proliferation was also confirmed again by measuring with MTT assay based on the colorimetric measurement of formazan dye formed from MTT by mitochondrial dehydrogenases. Exponentially growing cells were plated at a seeding density of 7.5×10^4 cells/mL in 96-well plates (80 μL/well). Then they were treated with saline (control), or different concentrations of agmatine (100, 200, 500, or 1000 μmol/L), respectively, at a volume of 20 μL. After they were incubated with or without drugs for 44 h, 20 μL of MTT reagent (0.5 g/L) was added to each well. The plates were incubated at 37 °C for an another 4 h. At the end of the incubation, the formazan crystals formed by MTT metabolism were solubilized by the addition of 100 μL of 10% SDS to each well. After 16 h, the absorbance of the solubilized product was measured at 570 nm in a Micro-plate Reader (Molecular Devices Corporation, Sunnyvale, CA, USA). The anti-proliferation potency of the drug was determined by a comparison between the inhibitory ratios. The percentage of growth inhibition was calculated by comparison of the absorbance of the treated group versus the control [(average absorbance value in control group-average absorbance value in drug treated group)/(average absorbance value in control group)×100].

Lactate dehydrogenase release assay To assess whether the reduction of cell numbers was attributable to the cellular toxicity of polyamines or agmatine, we measured the release of lactate dehydrogenase (LDH) in cell medium after drug treatment. Cells were cultured at a seeding density of 7.5×10^4 cells/mL in 24-well plates (800 μL/well). They were treated with saline, a range of concentrations of agmatine, spermidine, or spermine, respectively, at a volume of 200 μL and incubated at 37 °C and 5% CO_2 for 48 h. Then 0.8 mL of the supernatant of each well was used for analysis by an Automatic Biochemical Analyzer (Hitachi7020, Tokyo, Japan). The release of LDH from the treated cells was compared to the control.

Statistical analysis Data were expressed as mean±SD. SAS software (SAS Inc, Raleigh, NC) was used to conduct a one-way ANOVA. $P<0.05$ was considered statistically significant.

Results

Inhibitory effects of agmatine on the growth of S_{180} sarcoma tumor cell lines in Kunming and Balb/c mice In Kunming mice transplanted with S_{180} sarcoma tumor cell lines, the S_{180} cells grew well and the average tumor weight reached 1.6 g in the normal, saline-treated group. Meanwhile, cyclophosphamide, a clinically approved anticancer agent, exhibited significant anti-tumor activity. In the cyclophosphamide-treated group (20 mg/kg, qd, ip), the average tumor weight was only 0.7 g and the inhibitory ratio was 56.3%. Agmatine also exerted a remarkable inhibitory effect on tumor growth. In the agmatine-treated groups (5–40 mg/kg, tid, sc), the tumor weights were significantly reduced (n=27, $P<0.05$) in a dose-dependent manner. The inhibitory ratio of tumor growth reached 31.3% at a dose of 40 mg/kg (Table 1).

Table 1. Anti-tumor activity of agmatine on S_{180} in Kunming mice. The S_{180} sarcoma tumor cells were inoculated (sc) into Kunming mice on d 0. The bearing mice were randomly distributed into 6 groups. Each group contained 27 mice. From d 1, they were injected with saline, cyclophosphamide, or differeent doses of agmatine, respectively, at a volume of 0.1 mL/10 g. After 10 d, tumor weight was measured. n=27. Mean±SD. $^cP<0.01$, compared with the saline-treated group. "–" represents 0.1 mL/10 g saline.

	Dose /mg·kg^{-1}	Tumor weight /g	Ratio of inhibition/%
Saline	–	1.6±0.9	
Cyclophosphamide	20	0.7±0.2^c	56.3
Agmatine	5	1.7±0.4	-6.3
	10	1.3±0.7	18.8
	20	1.1±0.6^c	31.3
	40	1.1±0.8^c	31.3

In Balb/c mice transplanted with S_{180} sarcoma tumor cell lines, we obtained similar results. The average tumor weight was 1.0 g in the normal, saline-treated group. Cyclophosphamide (20 mg/kg, qd, ip) inhibited tumor growth significantly, and the inhibitory ratio reached 50.0%. Agmatine also inhibited the growth of tumors in a dose-dependent manner (n=10, $P<0.05$). The inhibitory ratio of agmatine on tumor growth was 50.0% at a dose of 40 mg/kg (Table 2).

Inhibitory effects of agmatine on the growth of B_{16} melanoma tumor cell lines in C_{57} mice In C_{57} mice transplanted with B_{16} melanoma tumor cells, the tumor weight was 1.8 g in the normal, saline-treated group. In the cyclophosphamide-treated group (20 mg/kg, qd, ip), the tumor weight decreased to 1.0 g and the inhibitory ratio reached 44.4%. Agmatine (2.5–20.0 mg/kg, tid, sc) significantly suppressed the growth of the tumor (n=10, $P<0.05$), but the effect did not exhibit an obvious dose-dependent relationship (Table 3).

Inhibitory effect of agmatine on the proliferation of MCF cells *in vitro* In the [^{3}H]thymidine incorporation assay, the

Table 2. Anti-tumor activity of agmatine on S_{180} cell growth in Balb/c mice. In Balb/c mice transplanted with S_{180} sarcoma tumor cell lines as well, we acquired similar results. On d 0, the S_{180} sarcoma cells were inoculated (sc). The 60 bearing mice were reandomly distributed into 6 groups. Each group contained 10 mice. From d 1, they were injected with saline, cyclophosphamide, or different doses of agmatine, respectively, at a volume of 0.1 mL/10 g. After 10 d, tumor weight was measured. n=10. Mean±SD. $^bP<0.05$, $^cP<0.01$, compared with the saline-treated group. "–" represents 0.1 mL/10 g saline.

	Dose /mg·kg^{-1}	Tumor weight /g	Ratio of inhibition/%
Saline	–	1.0±0.3	
Cyclophosphamide	20	0.5±0.3^c	50.0
Agmatine	5	0.8±0.3	20.0
	10	0.6±0.2	40.0
	20	0.5±0.2^b	50.0
	40	0.5±0.3^c	50.0

Table 3. Anti-tumor activity of agmatine on B_{16} cell growth in C_{57} mice. The B_{16} melanoma cell lines were inoculated (sc) into C_{57} mice on d 0. The 60 bearing mice were randomly distributed into 6 groups. Each group contained 10 mice. From d 1, they were injected with saline, cyclophosphamide, or different doses of agmatine, respectively, at a volume of 0.1 mL/10 g. After 10 d, tumor weight was measured. n=10. Mean±SD. $^bP<0.05$, compared with the saline-treated group. "–" represents 0.1 mL/10 g saline.

	Dose /mg·kg^{-1}	Tumor weight /g	Ratio of inhibition/%
Saline	–	1.8±0.3	
Cyclophosphamide	20.0	1.0±0.4^b	44.4
Agmatine	2.5	0.9±0.5	50.0
	5.0	0.6±0.3^b	66.7
	10.0	0.9±0.6^b	50.0
	20.0	0.8±0.6^b	55.6

MCF cells grew well and the average cpm value was 3143.8 in the normal, saline-treated group after a 48-h incubation. Agmatine showed anti-proliferation activity compared with the saline-treated group in a concentration-dependent manner. The cpm value was significantly reduced (n=8, P<0.05) after pretreatment with agmatine (1–1000 μmol/L). The inhibitory ratio of cell proliferation was 50.3% at a concentration of 1000 μmol/L (Table 4).

This effect of agmatine on cellular proliferation was further proved with the MTT assay. The MCF cells grew well and the absorbance value was 0.99 in the normal, saline-treated group after a 48-h incubation. Agmatine showed anti-proliferation activity compared with the saline-treated group in a concentration-dependent manner. The absorbance value was significantly reduced (n=8, P<0.05) after the cells were administered with agmatine (100–1000 μmol/L). The inhibitory ratio of cell growth was 23.8% at a concentration of 1000 μmol/L (Table 5).

Table 4. Effect of agmatine on MCF-7 human breast cancer cells proliferation in a [^{3}H]thymidine incorporation assay. In the assay, the cells were seeded into a 96-well cell culture plate at a density of approximately 6000 cells/well. Then they were treated with saline (control), or different concentrations of agmatine (1, 10, 100, 200, 500, or 1000 μmol/L), respectively, at a volume of 20 μL. Each group contained 8 wells. Drugs were added for a total period of 48 h, and [^{3}H]thymidine (3.7×10^4 Bq/well) was added at 36 h of incubation. To evaluate the anti-proliferation effect, the cpm value was counted and the inhibitory ratio was calculated. n=8. Mean±SD. $^bP<0.05$, compared with control.

	Concentration /μmol·L^{-1}	[^{3}H]thymidine incorporation/cpm	Inhibitory ratio/%
Saline		3143.8±506.5	0
Agmatine	1	2776.8±662.3	11.7
	10	2610.0±940.3	17.0
	100	2576.3±345.3	18.1
	200	2380.0±533.8	24.3
	500	2080.0±327.0^b	33.8
	1000	1562.5±264.0^b	50.3

Table 5. Effect of agmatine on MCF-7 human breast cancer cells proliferation by MTT. The cells were seeded into a 96-well cell culture plate at a density of approximately 6000 cells/well. Then they were treated with saline (control), or different concentrations of agmatine (100, 200, 500, or 1000 μmol/L), respectively, at a volume of 20 μL. Each group contained 8 wells. Drugs were added for a total period of 48 h and MTT (2.5 g/L, 20 μL/well) was added at 44 h of incubation. To evaluate the anti-proliferation effect, the absorbance of the solubilized product was measured at 570 nm on a Micro-plate Reader (Molecular Devices Corporation, Sunnyvale, CA, USA). The percentage of inhibition was calculated by comparison of the absorbance of the treated group versus the control. n=8. Mean±SD. $^bP<0.05$, $^cP<0.01$ *vs* control.

	Concentration /μmol·L^{-1}	Absorbance	Inhibitory ratio/%
Saline		1.01±0.02	
Agmatine	100	0.97±0.03^b	4.0
	200	0.91±0.03^c	9.9
	500	0.86±0.03^c	14.9
	1000	0.77±0.02^c	23.8

We then investigated the time-dependent effect of agmatine on MCF cell proliferation. MCF cells were cultured for different lengths of time in the presence of 1 mmol/L agmatine, and cell viability was evaluated by a [^{3}H]thymidine incorporation assay. Over 48 h, the inhibitory potency of agmatine strengthened gradually with prolonged time (n=8, P<0.01). The inhibitory ratio was 10%, 17%, 38%, and 62% at 12 h, 24 h, 36 h and 48 h, respectively (Figure 1).

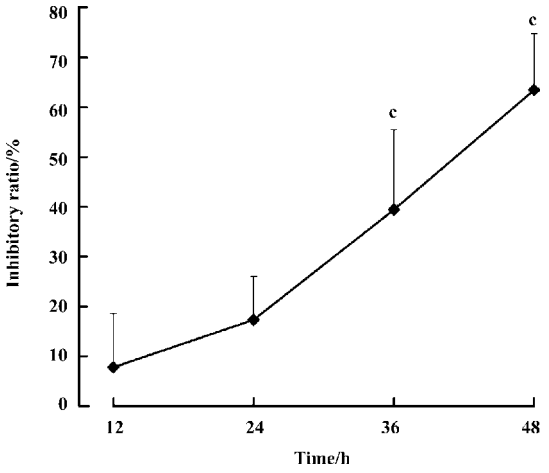

Figure 1. Time-dependent effect of agmatine on MCF-7 human breast cancer cells proliferation. MCF cells were cultured for different lengths of time in the presence of 1 mmol/L agmatine, and cell viability was evaluated by [^{3}H]thymidine incorporation assay. Over 48 h, the inhibitory potency of agmatine strengthened gradually with prolonged time. Mean±SD for 4 experiments. n=8. ^cP<0.01, compared with the saline-treated group.

Effect of agmatine on LDH release in the medium To assess whether the reduction of cell numbers was attributable to toxicity of polyamines or agmatine, we measured the release of LDH in cell medium after drug treatment. Administration on MCF cells for 48 h, spermine (20 μmol/L) or spermidine (20 μmol/L) significantly increased the activity of LDH in the medium, but agmatine (1–1000 μmol/L) did not. At a concentration of 1000 μmol/L, agmatine decreased the LDH activity significantly (n=8, P<0.05; Table 6).

Putrescine reverses agmatine's inhibitory effect on MCF cell proliferation As polyamines are essential growth factors, their dramatic intracellular decrease may be the main mechanism of the anti-proliferation action of agmatine. To check whether this is the mechanism involved, MCF cells were treated simultaneously with agmatine (1 mmol/L) and putrescine (12.5–100.0 μmol/L). Putrescine counteracted the inhibitory effect of agmatine on MCF cell proliferation in a concentration-dependent manner (n=8, P<0.05; Table 7).

Table 6. Effect of agmatine, spermidine, or spermine on lactate dehydrogenase (LDH) release in MCF-7 human breast cancer cells. To assess whether the reduction of cell numbers was attributable to toxicity of polyamines or agmatine, we measured the release of LDH in cell medium after drug treatment. The cells were plated at a seeding density of 7.5×10^4 cells/mL in 24-well plates. Then they were treated with saline (control), spermine (20 μmol/L), spermidine (20 μmol/L), or different concentrations of agmatine (1, 10, 100, or 1000 μmol/L), respectively, at a volume of 200 μL. Each group contained 8 wells. Drugs were added for a total period of 48 h and then 0.8 mL of the supernatant of each well was used for analysis by the Automatic Biochemical Analyzer (Hitachi7020, Tokyo, Japan). The percentage release of LDH from the treated cells was calculated by comparing it to the control cells. n=8. Mean±SD. ^bP<0.05, ^cP<0.01, compared with control.

	Concentration /μmol·L^{-1}	LDH release /U·L^{-1}
Saline		26.0±1.6
Agmatine	1	25.8±0.9
	10	27.0±1.2
	100	25.8±1.3
	1000	22.3±0.9^b
Spermine	20	51.0±2.2^c
Spermidine	20	28.8±0.5^c

Table 7. Reversal of agmatine's effect on MCF-7 human breast cancer cells proliferation by putrescine. The cells were seeded into a 96-well cell culture plate at a density of approximately 6000 cells/well. Then they were treated with saline (control), putrescine (100 μmol/L), agmatine (1000 μmol/L), or different concentrations of putrescine (12.5, 50.0, or 100.0 μmol/L), and agmatine (1000 μmol/L), respectively, at a volume of 20 μL. Each group contained 8 wells. Drugs were added for a total period of 48 h, and [^{3}H]thymidine (3.7×10^4 Bq/well) was added during the last 12 h of incubation. To evaluate the anti-proliferation effect, the cpm value was counted and the inhibitory ratio was calculated. n=8. Mean±SD. ^bP<0.05, ^cP<0.01, compared with control. ^eP<0.05, ^fP<0.01, compared with agmatine 1000 μmol/L. "–" represents 0.1 mL/10 g saline.

	Concentration /μmol·L^{-1}	[^{3}H]thymidine incorporation/cpm	Inhibitory ratio/%
Saline	–	2584.5±503.8	–
Putrescine	100	2960.8±1090.3	-14.6
Agmatine	1000	1224.5±241.3^c	52.6
Agmatine+putrescine	1000+12.5	1513.5±288.0^c	41.4
	1000+50	1673.3±335.8^{ce}	35.3
	1000+100	2005.0±395.5^{bf}	22.4

Discussion

The present study demonstrated the inhibitory properties of agmatine toward S_{180} sarcoma and B_{16} melanoma cells in vivo. We found that, at doses of 5–40 mg/kg, agmatine suppressed S_{180} and B_{16} cell growth in three kinds of mice *in vivo*. The highest inhibitory ratio was more than 50.0%. We applied for a Chinese patent with these results in 2002 (02125495.8). Although Gardini *et al* reported that agmatine inhibited the proliferation of rat hepatoma cells *in vitro* by modulation of polyamine metabolism in 2003[13], they did not report anything related to the inhibitory effects of agmatine on the growth of transplanted tumors *in vivo*; in addition, the paper by Gardini *et al*[13] was published much later than when we applied for the Chinese patent. It is reasonable to state, therefore, that our current results demonstrate for the first time that agmatine has an inhibitory effect on S_{180} and B_{16} cell lines *in vivo*.

Polyamines play an essential role in proliferation, differentiation, and neoplastic transformation in mammalian cells[1]. Indeed, cellular polyamine levels are higher in tumor cell lines. Conversely, the depletion of polyamines results in growth arrest of neoplastic cells *in vitro*. The polyamine-biosynthetic pathway is an inviting target for the development of agents inhibiting carcinogenesis and tumor growth. The present therapeutic agents acting on this pathway are α-difluoromethylornithine (DFMO) and polyamine analogs[2]. They influence both polyamine synthesis and degradation and are now being used in clinical trials.

Agmatine is an analog of polyamines and can modulate the cellular concentration of polyamines[14]. As an intermediate of putrescine, agmatine may be a factor for increasing the cellular concentration of polyamines. Although tumor cells and tissues have been reported to have increased polyamines levels compared with normal cells, this increase is often in the range of 2- to 3-fold. When putrescine levels are approximately 10-fold higher than those present in cancer cells, the cells undergo apoptosis[15]. It has also been reported that overloaded polyamines have toxic effects on some normal cells. The toxicity of polyamines was studied in a well-characterized neuronal system of cerebellar granule cells *in vitro*. Twenty-four-hour exposure to spermine (1–500 μmol/L) resulted in a concentration-dependent death of granule cells, with the half of lethal dose (LD_{50}) being reached at a concentration below 50 μmol/L. Putrescine was moderately toxic, with the LD_{50} at a concentration of only 500 μmol/L. The LD_{50} of spermidine was tested between concentrations of 50 and 100 μmol/L and its toxicity has been evaluated to be approximately 50% of that of spermine[16]. This was consistent with our results (data not shown). In contrast, agmatine has been postulated to decrease the cellular level of polyamines by inducing antizyme, competing with putrescine on transporter and other mechanisms.

So, in theory, agmatine might have double-edged effects on cell growth. But, to date, there has been no report that agmatine can enhance the proliferation of cells. Conversely, there is much evidence that agmatine can suppress cell proliferation, including different cells and malarial parasites[17,18]. Consistent with these studies, the present study proves agmatine has a significant inhibitory effect on cell proliferation in several classical solid tumors in a transplanted model *in vivo* and in an MCF model *in vitro*. Putrescine prevented the effect of agmatine on [^{3}H]thymidine incorporation in MCF cells. This effect of agmatine is similar to that of DFMO, which can block the synthesis of polyamines significantly. These results suggest that the effect of agmatine might be related to its influence on the synthesis of polyamine.

In addition, polyamines can interact with DNA directly[19], so, in our experiments, the decreased [^{3}H]thymidine incorporation may be caused by the inhibitory synthesis of DNA. As putrescine plays a partial role in energy supply[20], the results of the MTT assay indicate that agmatine might inhibit MCF cell proliferation by influence on energy metabolism. In addition, the effect on LDH activity in the medium showed that agmatine (1–1000 μmol/L) exhibited no cellular toxicity, whereas spermidine (20 μmol/L) and spermine (20 μmol/L) did. To sum up, these results partly demonstrate that agmatine does not increase the level of cellular polyamines and supports the conclusion that the anti-proliferation effect of agmatine is a result of polyamine limitation.

Currently, we know that agmatine's toxicity is low and its effects on tumor cells are not similar to those of classical chemotherapeutical drugs. Regarding its low toxicity, its enhancement of opioid analgesia, and its antidepressant effect[21,22], we hope that agmatine could efficiently improve life quality of cancer patients. There are still many issues to be explored, and further experiments should be carried out to confirm our results.

In conclusion, agmatine has significant inhibitory effects on transplanted tumor growth *in vivo* and proliferation of tumor cells *in vitro*. The possible mechanisms might be related to inducing decrease of intracellular polyamine contents.

References

1 Tabor CW, Tabor H. Polyamines. Annu Rev Biochem 1984; 53: 749–90.

2 Seiler N. Pharmacological properties of the natural polyamines

and their depletion by biosynthesis inhibitors as a therapeutic approach. Prog Drug Res 1991; 37: 107–59.
3 Raasch W, Regunathan S, Li G, Reis DJ. Agmatine, the bacterial amine, is widely distributed in mammalian tissues. Life Sci 1995; 56: 2310–30.
4 Gabrielson EW, Pegg AE, Casero RA Jr. The induction of spermidine/spermine *N*1-acetyl transferase (SSAT) is a common event in the response of human primary non-small cell lung carcinomas to exposure to the new anti-proliferation polyamine analogue *N1*, *N11-bis* (ethyl) norspermine. Clin Cancer Res 1999; 5: 1638–41.
5 Satriano J, Kelly CJ, Blantz RC. An emerging role for agmatine. Kidney Int 1999; 56: 1252–3.
6 Vargiu C, Cabella C, Belliardo S, Cravanzola C, Grillo MA, Colombatto S. Agmatine modulates polyamine content in hepatocytes by inducing spermidine/spermine acetyltransferase. Eur J Biochem 1999; 259: 933–8.
7 Cabella C, Gardini G, Corpillo D, Testore G, Bedino S, Solinas SP, *et al*. Transport and metabolism of agmatine in rat hepatocyte cultures. Eur J Biochem 2001; 268: 940–47.
8 Satriano J, Isome M, Casero RA Jr, Thomson SC, Blantz RC. Polyamine transport system mediates agmatine transport in mammalian cells. Am J Physiol Cell Physiol 2001; 281: C329–34.
9 Gardini G, Cabella C, Cravanzola C, Vargiu C, Belliardo S, Testore G, *et al*. Agmatine induces apoptosis in rat hepatocyte cultures. J Hepatol 2001; 35: 482–9.
10 Li G, Regunathan S, Barrow CJ, Eshragi J, Cooper R, Reis DJ. Agmatine: an endogenous clonidine displacing substance in the brain. Science 1994; 263: 966–9.
11 Regunathan S, Reis DJ. Stimulation of imidazoline receptors inhibits proliferation of human coronary artery vascular smooth muscle cells. Hypertension 1997; 30: 295–300.
12 Satriano J, Matsufuji S, Murakami Y, Lortie MJ, Schwartz D, Kelly CJ, *et al*. Agmatine suppresses proliferation by frameshift induction of antizyme and attenuation of cellular polyamine levels. J Biol Chem 1998; 273: 15 313–5.
13 Gardini G, Cravanzola C, Autelli R, Testore G, Cesa R, Morando L, *et al*. Agmatine inhibits the proliferation of rat hepatoma cells by modulation of polyamine metabolism. J Hepatol 2003; 39: 793–9.
14 Ishizuka S, Cunard R, Poucell-Hatton S, Wead L, Lortie M, Thomson SC, *et al*. Agmatine inhibits cell proliferation and improves renal function in anti-Thy-1 glomerulonephritis. J Am Soc Nephrol 2000; 11: 2256–64.
15 Thomas T, Thomas TJ. Polyamines in cell growth and cell death: molecular mechanism and therapeutic applications. Cell Mol Life Sci 2001; 58: 244–58.
16 Sparapani M, Dall'Olio R, Gandolfi O, Ciani E, Contestabile A. Neurotoxicity of polyamines and pharmacological neuroprotection in cultures of rat cerebellar granule cells. Exp Neurol 1997; 148: 157–66.
17 Su RB, Wei XL, Liu Y, Li J. Antimalarial effect of agmatine on plasmodium berghei K173 strain. Acta Pharmacol Sin 2003; 24: 918–22.
18 Babal P, Ruchko M, Campbell CC, Gilmour SP, Mitchell JL, Olson JW, *et al*. Regulation of ornithine decarboxylase activity and polyamine transport by agmatine in rat pulmonary artery endothelial cells. J Pharmacol Exp Ther 2001; 296: 372–7.
19 D'Agostino L, Di Luccia A. Polyamines interact with DNA as molecular aggregates. Eur J Biochem 2002; 269: 4317–25.
20 Rustenbeck I, Eggers G, Reiter H, Munster W, Lenzen S. Polyamine modulation of mitochondrial calcium transport. Biochem Pharmacol 1998; 56: 977–85.
21 Su RB, Li J, Qin BY. A biphasic opioid function modulator: agmatine. Acta Pharmacol Sin 2003; 24: 631–6.
22 Li YF, Gong ZH, Cao JB, Wang HL, Luo ZP, Li J. Antidepressant-like effect of agmatine and its possible mechanism. Eur J Pharmacol 2003; 469: 81–8.

Acta Pharmacologica Sinica 2005 ; 26 (5): 623–628

Full-length article

Induction of leukemia cell apoptosis by cheliensisin A involves down-regulation of *Bcl-2* expression[1]

Li ZHONG, Chao-ming LI[2], Xiao-jiang HAO[2], Li-guang LOU[3]

Shanghai Institute of Materia Medica, Shanghai Institutes for Biological Sciences, Shanghai 201203, China; [2]Kunming Institute of Botany, Chinese Academy of Sciences, Kunming 650204, China

Key words

Goniothalamus cheliensis; cheliensisin A; apoptosis; HL-60 cells; *bcl-2* genes; cyclic AMP-dependent protein kinases, caspases

[1] Project supported by grants from the Chinese Academy of Sciences (KSCX1-09-01-1) and from the Shanghai Science and Technology Committee (No 014319313).
[3] Correspondence to Prof Li-guang LOU.
Phn 86-21-5080-6056.
Fax 86-21-5080-7088.
E-mail lglou@mail.shcnc.ac.cn

Received 2004-10-21
Accepted 2004-12-13

doi: 10.1111/j.1745-7254.2005.00077.x

Abstract

Aim: To investigate the apoptosis-inducing effect of cheliensisin A (GC-51), a novel styryl-lactone isolated from *Goniothalamus cheliensis*, on human promyelocytic leukemia HL-60 cells and the mechanism of action involved. **Methods:** Apoptotic cell death was determined by morphological examination and DNA agarose gel electrophoresis. The activity of caspase-3 was assessed using Western blotting and the expression of *Bcl-2* and *Bax* genes was analyzed using the reverse transcription-polymerase chain reaction (RT-PCR) method. **Results:** GC-51 significantly inhibited the proliferation of HL-60 cells with an IC_{50} of 2.4±0.2 ìmol/L and effectively induced apoptosis in HL-60 cells. Exposure of HL-60 cells to 10 ìmol/L GC-51 for 8 h resulted in approximately 53% of the cells undergoing apoptosis. Caspase-3 was activated in GC-51-treated cells, which was manifested by the appearance of the 17 kDa active form of caspase-3 and the cleavage of poly(ADP-ribose) polymerase (PARP). Meanwhile, GC-51 markedly reduced the expression of the anti-apoptotic gene *Bcl-2* and increased the expression of the pro-apoptotic gene *Bax*. The apoptosis-inducing effect of GC-51 was cAMP-dependent protein kinase (PKA) dependent because PKA, but not the protein kinase C, specific inhibitor H-89, blocked the induction of apoptosis by GC-51 in HL-60 cells. **Conclusion:** The results demonstrate that GC-51 effectively induces apoptosis in HL-60 cells and that this effect is PKA-dependent and involves the downregulation of *Bcl-2* expression and the activation of caspase-3.

Introduction

Apoptosis is defined by distinct morphological and biochemical changes, mediated by a family of cysteine aspases (caspases) that are expressed as inactive zymogens and are proteolytically processed to an active state following an apoptotic stimulus[1]. Two pathways leading to caspase cascade activation, including an intrinsic pathway and an extrinsic pathway, have been characterized[2,3]. Both pathways may involve the release of mitochondrial proteins, such as cytochrome c, Smac/DIABLO, and HtRA2, into the cytosol to trigger the activation of caspases, including initiator caspase-9 and effector caspase-3. The release of mitochondrial proteins into the cytosol usually depends on mitochondrial membrane permeabilization, which is regulated by pro- and anti-apoptotic *Bcl-2* family members[1]. In theory, factors capable of regulating the activities of caspases and/or the functions of *Bcl-2* family members are able to induce or prevent apoptotic cell death.

Styryl-lactones are a new class of compounds with potential anti-tumor activities[4,5]. Most styryl-lactones are isolated from the genus *Goniothalamus* (Annonaceae)[4]. The mechanisms of action by which styryl-lactones exert their anti-tumor activity are currently unknown. The suggested mechanisms include non-steroid, receptor-mediated anti-proliferative effects[6], disruption of mitochondrial transmembrane potential[7], and the induction of apoptosis[8]. GC-51, a novel styryl-lactone isolated from *Goniothalamus cheliensis*, has previously been shown in our laboratory to

possess potent cytotoxicity against human promyelocytic leukemia HL-60 cells[9]. In the present study, we investigated the potential apoptosis-inducing effect of GC-51 and the possible mechanism of action involved.

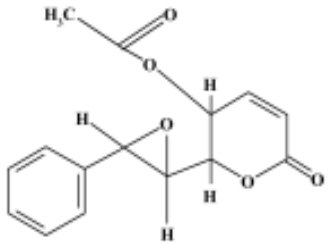

Figure 1. Chemical structure of GC-51.

Materials and methods

Chemicals GC-51 [6(7,8-epoxy-styryl)-5-acetoxy-5,6-dihydro-2-pyrone] was purified from *Goniothalamus cheliensis* at the Kunming Institute of Botany, Chinese Academy of Sciences, Kunming, China, as previously described[9] (Figure 1). GC-51 is a white crystal powder and its purity is greater than 99.0%. H-89 and chelerythrine chloride were purchased from Calbiochem (San Diego, USA). Propidium iodide and 4',6'-diamino-2-phenylindole (DAPI) were purchased from Sigma (St Louis, USA). RNase, polyclonal antibodies against caspase-3 and PARP were purchased from Becton Dickinson (Franklin Lakes, USA). Trizol and RPMI-1640 medium were purchased from Gibco (Grand Island, New York, USA).

Cell culture and treatment Human promyelocytic leukemia HL-60 cells were from the American Type Culture Collection (Manassas, VA 20108 USA). HL-60 cells were maintained in RPMI-1640 medium containing 10% heat-inactivated fetal bovine serum, 100 kU/L penicillin, and 100 mg/L streptomycin. Cells were cultured in a humidified incubator at 37 °C in 5% CO_2/air. GC-51 was dissolved in dimethylsulfoxide and diluted in culture medium just prior to use. The final concentration of dimethylsulfoxide was less than 0.1% which had no effect on cell proliferation and the assay system.

Morphology staining Morphological changes in HL-60 cells were determined by staining the cells with DNA-specific dye, DAPI, after the GC-51-treated cells were fixed with methanol for 10 min at room temperature. Stained cells were observed under a fluorescence microscope (Olympus, Tokyo, Japan).

Cell cycle analysis The DNA content of the cells was analyzed as previously described[10,11]. In brief, untreated and treated cells were harvested by centrifugation, washed in phosphate-buffered saline (PBS containing 137 mmol/L NaCl, 2.7 mmol/L KCl, 10 mmol/L Na_2HPO_4, 1.8 mmol/L KH_2PO_4, pH 7.4), and fixed in ice-cold 70% ethanol overnight. Following fixation, the cells was stained with PBS containing 50 mg/L propidium iodide, 0.1% Triton X-100, and 20 mg/L RNase. The fluorescence of individual cells was measured using FACStar plus flow cytometer (Becton Dickinson, Franklin Lakes, USA).

DNA agarose gel electrophoresis Analysis of DNA fragmentation was carried out using DNA agarose gel electrophoresis as described previously[11]. In brief, DNA extracted from untreated and treated cells was loaded onto a 1.8% agarose gel in TBE (Tris 45 mmol/L borate buffer, edetic acid 1 mmol/L, pH 8.0), and electrophoresed at 40 V for 5 h. DNA in the gels was visualized under UV light after staining with ethidium bromide 5 mg/L.

Western blotting Western blot analysis was carried out as described previously[12,13]. After treatment with GC-51, cells were washed twice with ice-cold PBS and total cell lysates were collected in sodium dodecylsulfate (SDS) sample buffer (50 mmol/L Tris-HCl, pH 6.8, 100 mmol/L DTT, 2% SDS, 0.1% bromophenol blue, 10% glycerol). Cell lysates containing equal amounts of protein were separated by sodium dodecylsulfate–polyacrylamide gel electrophoresis (SDS-PAGE) and transferred to polyvinylidine difluoride membranes. After blocking in 5% non-fat milk in TBST (Tris-buffered saline with 0.1% Tween 20, pH 8.0), the membranes were incubated with the appropriate primary antibodies at 4°C overnight. Membranes were washed three times in TBST and exposed to secondary antibodies for 2 h at room temperature, and then washed four times in TBST. Immunoreactive proteins were visualized using the enhanced chemiluminescence system from Pierce (Rockford, IL, USA).

RNA isolation and RT-PCR Total mRNA was prepared from HL-60 cells using Trizol (Sangon, Shanghai, China). The cDNA was synthesized using random hexamers from 1 ìg of mRNA. To amplify the cDNAs, a 2 ìL aliquot of the reverse-transcribed cDNA was subject to 29 cycles of PCR in 50 ìL of 1×buffer (10 mmol/L Tris·HCl, pH 8.3, 1.5 mmol/L $MgCl_2$, 50 mmol/L KCl, 50 ìmol/L dNTP, three units of *Taq* DNA polymerase and 0.2 ìmol/L specific primers). Each cycle consisted of denaturation at 94 °C for 30 s, annealing at 60 °C for 40 s, and extension at 72 °C for 40 s. The amplified products were separated by electrophoresis on 1.0% agarose gel. Each RT-PCR was repeated three times using different preparations of RNA. The RT-PCR of GAPDH was used as an internal control with all samples. The PCR primers used are

listed in Table 1.

Table 1. The primer sequences used for amplifying the desired genes

Genes	PCR primers	Product size/bp
Bcl-2	5'TGC ACC TGA CGC CCT TCA C 3' (sense) 5'AGACAAGGAGAAATCAAACAG 3' (antisense)	293
Bax	5'ACCAAGAAGCTGAGCGAGTGTC 3' (sense) 5'ACAAAGATGGTCACGGTCTGCC 3 (antisense)	265
GAPDH	5'TCATCATCTCTGCCCCCTCTG 3' (sense) 5'GCCTGCTTCACCACCTTCTTG 3' (antisense)	459

Statistical analysis Data were analyzed using Student's *t*-tests. *P* values less than 0.05 were considered significant.

Results

Inhibition of cell proliferation and induction of cell apoptosis by GC-51 The effect of GC-51 on cell proliferation was determined by counting the cell number using the Trypan blue exclusion method. After a 48-h treatment, GC-51 markedly inhibited the proliferation of HL-60 cells in a concentration-dependent manner with an IC_{50} of 2.4±0.2 ìmol/L (95% confidence: 1.5–3.3 μmol/L, Figure 2A). The inhibition of cell proliferation was also time-dependent (data not shown).

To further identify the inhibitory effect of GC-51 on cell proliferation, we examined the apoptosis-inducing effect of GC-51 on HL-60 cells. Incubation of HL-60 cells with GC-51 (2.5–10 ìmol/L) for various times (2–8 h) resulted in dramatic morphological changes in the treated cells typical of apoptosis, such as cell shrinkage, chromatin condensation, and nuclear fragmentation (Figure 2B). Treatment of cells with 10 ìmol/L GC-51 for 4 h was enough to induce cell apoptosis.

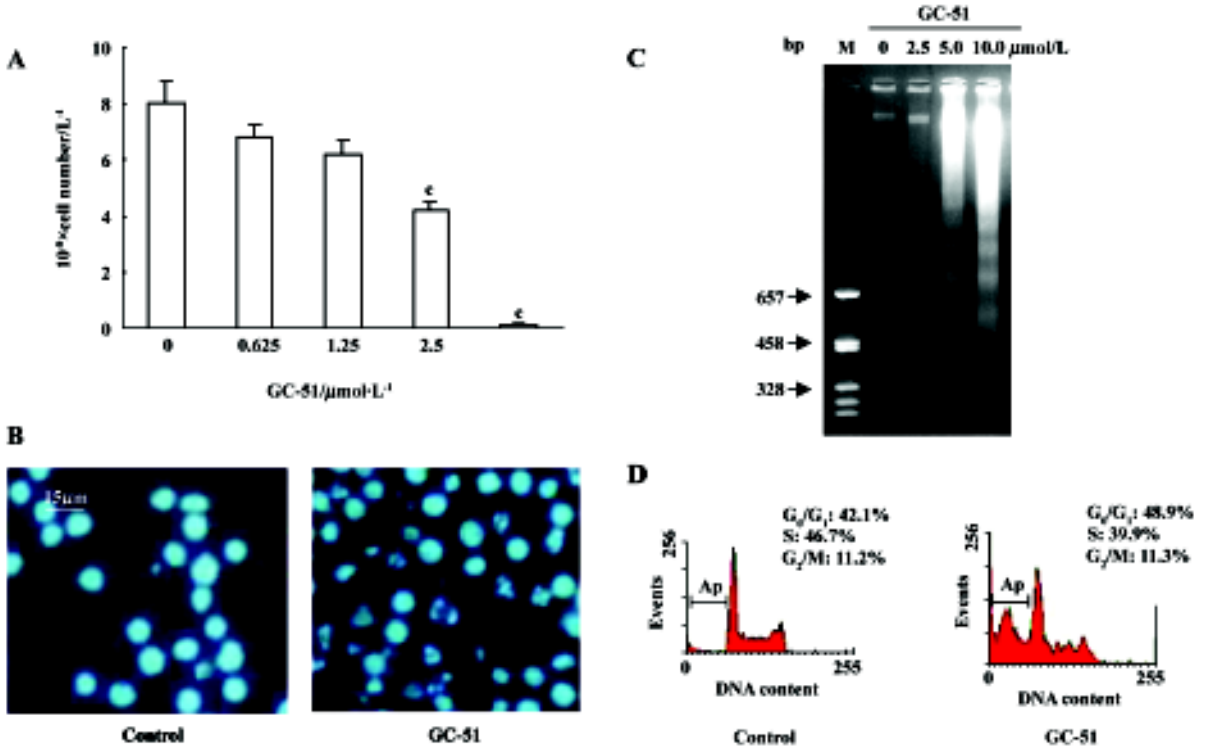

Figure 2. GC-51 inhibited HL-60 cell proliferation (A) and induced HL-60 cell apoptosis (B, C, D). (A) Cells were treated with different concentrations of GC-51 for 48 h, and the cell number was counted using the Trypan blue exclusion method. n=3. Mean±SD. $^cP<0.01$ *vs* control. (B) Cells untreated (left) or treated with 10 ìmol/L GC-51 for 8 h (right) were stained with DAPI and observed under fluorescence microscope (×200). (C) Agarose gel electrophoresis of DNA extracted from cells treated with 10 ìmol/L GC-51 for 8 h. (D) DNA content analysis using flow cytometry of the cells untreated (left) or treated with 10 ìmol/L GC-51 for 8 h (right). B, C, D represent at least three independent experiments with identical results. Ap, apoptotic cells.

The apoptosis-inducing effect of GC-51 was confirmed by the appearance of a DNA "ladder", another major hallmark of apoptosis (Figure 2C).

It is widely accepted that apoptotic cells have reduced DNA stainability following staining with a variety of fluorochromes, including propidium iodide. Thus, the appearance of cells with low stainability (ie sub-G_1 peak) in cultures has been considered to be another marker of apoptosis and has been used to quantify the extent of apoptosis. GC-51 treatment led to the formation of a "sub-G_1" peak in the DNA content frequency distribution (Figure 2D) and caused apoptosis in a concentration- and time-dependent manner. Exposure of HL-60 cells to 10 ìmol/L GC-51 for 2 h, 6 h, and 8 h resulted in 3.5%±3.0%, 26.2%±4.3%, and 53.0%±7.2% cells undergoing apoptosis, respectively, whereas GC-51 treatment for 8 h at concentrations of 5, 10, and 25 μmol/L led to apoptotic cell death in 7.3%±3.5%, 54.2% ±9.2%, and 78.7%±10.2% cells, respectively.

Activation of caspase-3 in GC-51-treated apoptotic cells Cell death is executed by effector caspases such as caspases-3, thus, the activation of caspase-3 is the critical cellular event during apoptosis. Intact caspase-3 was a 32 kDa protein as detected in control cells and was processed into its catalytically active p17 subunits in GC-51-treated HL-60 cells (Figure 3A). To confirm the activation of caspase-3, we evaluated the cleavage of PARP, a major substrate of caspase-3. GC-51 treatment caused the cleavage of 116 kDa PARP into a 85 kDa form (Figure 3B), indicating that caspase-3 was indeed activated during GC-51-induced HL-60 cell apoptosis.

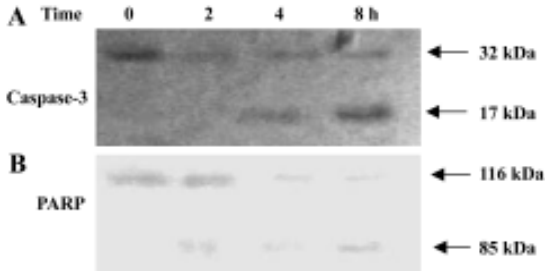

Figure 3. GC-51 activated caspase-3 (A) and stimulated the cleavage of PARP (B). Cells treated with 10 ìmol/L GC-51 for different time periods were lysed, and the proteins were separated by SDS-PAGE and detected by Western blotting using specific antibodies against caspase-3 and PARP, respectively.

Downregulation of *Bcl-2* mRNA expression by GC-51 Caspase-3 activation requires the release of a number of proteins, including cytochrome c, from mitochondria and this release is, in general, determined by the permeability of the mitochondrial membrane. Members of the *Bcl-2* family regulate the release of cytochrome c from mitochondria, primarily by affecting the permeability of the mitochondrial membrane. Thus, we tested the effect of GC-51 on the expression of the anti-apoptotic gene *Bcl-2* and the pro-apoptotic gene *Bax*. Exposure of HL-60 cells to 10 ìmol/L GC-51 for 8 h led to a significant reduction in *Bcl-2* gene expression. In contrast, the expression of the *Bax* gene markedly increased after GC-51 treatment. As a control, GC-51 had no effect on the expression of the GAPDH gene (Figure 4). Regulation by GC-51 of the expression of the *Bcl-2* and *Bax* genes resulted in a decrease in the ratio of *Bcl-2/Bax*, which will make the cells more susceptible to apoptosis inducers.

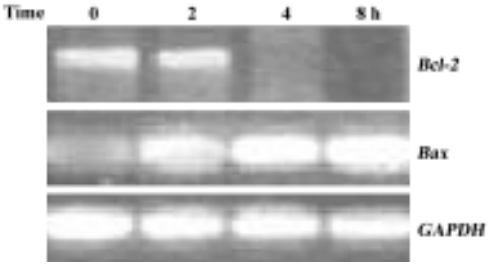

Figure 4. GC-51 reduced the expression of the *Bcl-2* gene and increased the expression of the *Bax* gene. Cells were treated with 10 ìmol/L GC-51 for 8 h and the total mRNA from treated cells was extracted and the expression of *Bcl-2*, *Bax*, and *GAPDH* genes was detected using RT-PCR with specific primers.

Induction of apoptosis by GC-51 in HL-60 cells was PKA dependent Bullatacin, a bioactive component isolated from *Annonaceous*, induces cell apoptosis by reducing the intracellular cAMP level[14]. Thus, we tested the role of cAMP in GC-51-induced HL-60 cell apoptosis. If induction of HL-60 cell apoptosis by GC-51 occurs via a similar mechanism to that of bullatacin, forskolin, an adenylate cyclase activator that effectively increases intracellular cAMP level, should block the apoptosis-inducing effect of GC-51. We did not record a significant effect of forskolin on induction of apoptosis by GC-51 in HL-60 cells (Figure 5A). To our surprise, H89, a PKA-specific inhibitor, blocked induction of HL-60 apoptosis by GC-51, whereas chelerythrine, a protein kinase C inhibitor, had no effect on the action of GC-51 (Figure 5B), suggesting that GC-51 induction of HL-60 apoptosis is specifically dependent on PKA activity.

Discussion

Defects in apoptosis underpin both tumorigenesis and drug resistance, and most anticancer drugs exert their che-

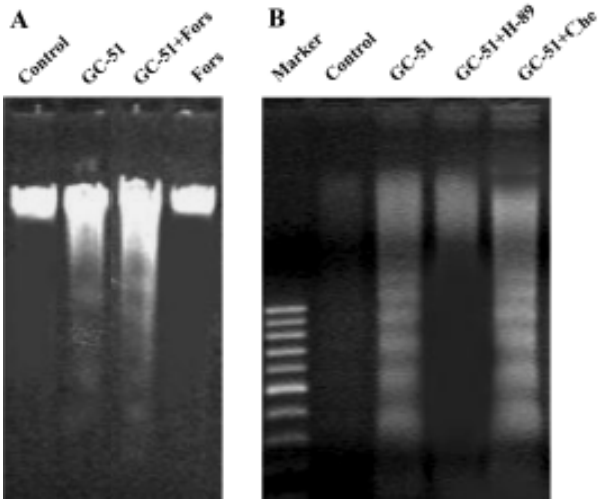

Figure 5. GC-51 induced apoptosis in HL-60 cells in a PKA-dependent manner. Cells were treated with 10 μmol/L GC-51 for 8 h in the presence of 10 ìmol/L forskolin (Fors), 1 ìmol/L H-89, or 10 ìmol/L chelerythrine chloride (Che), respectively, and DNA was extracted from treated cells and subject to DNA agarose gel electrophoresis.

motherapeutic effect by inducing tumor cell apoptosis[1]. Therefore, the discovery and development of drugs targeting the apoptotic pathway represent a novel and rational strategy for the treatment of cancers.

GC-51 a novel styryl-lactone isolated from *Goniothalamus cheliensis*, which is a widely occurring plant in Southwest China, exhibits a potent cytotoxicity in HL-60 cells[9]. In the present study, GC-51 significantly inhibited HL-60 cell proliferation, which is consistent with a previous report[9]. GC-51 inhibits cell proliferation or induces cell apoptosis based on the concentrations applied (low *vs* high concentrations). Induction of apoptosis by GC-51 was confirmed by the appearance of characteristic morphological changes, including a DNA "ladder" and a "sub-G_1 peak" in DNA content frequency distribution. Our results demonstrate that GC-51, like other styryl-lactones, is a potent inducer of cell apoptosis.

Caspase-3 is an effector caspase whose activation is critical for the execution of apoptotic death of tumor cells. We clearly showed in the present study that caspase-3 was activated during GC-51-induced HL-60 cell apoptosis and the activation was further verified by the cleavage of PARP, a preferred substrate of caspase-3 in apoptotic cells. Our results combined with findings from other laboratories[7,8] suggest that the activation of caspase-3 is a common mechanism responsible for styryl-lactone-induced apoptosis.

It is generally accepted that the ratio of *Bcl-2/Bax* determines the permeability of mitochondrial transmembranes, and this permeability controls the release of a number of proteins, such as cytochrome c, from the mitochondria into the cytosol[1]. GC-51 treatment significantly inhibited the expression of anti-apoptotic gene *Bcl-2* and increased the expression of the pro-apoptotic gene *Bax*. This effect of GC-51 on the expression of members of the *Bcl-2* family is, at least in part, contributing to the activation of caspase-3 and the subsequent apoptosis of HL-60 cells. To our knowledge, this is the first study to show that GC-51, a styryl-lactone compound, induces HL-60 cell apoptosis via reduction of the expression of the *Bcl-2* gene.

cAMP is a critical mediator of apoptosis[15-18]. cAMP triggers apoptosis by stimulating its major effector protein PKA, which phosphorylates the cAMP response element-binding protein (CREB), activates caspase-3, and induces apoptosis[18]. Kim *et al*[19] showed that 8-Cl-cAMP, an analogue of cAMP, induced cell-cycle-specific apoptosis in HL-60 cells. In contrast, PKA phosphorylates Bad, a member of the *Bcl-2* family, to prevent apoptosis[1]. Bullatacin induces hepatoma cell apoptosis by decreasing the intracellular cAMP level[14]. In the present study, we examined whether GC-51 induced HL-60 cell apoptosis via a similar mechanism. The data showed that forskolin had no significant effect on induction of cell apoptosis by GC-51, whereas in contrast H-89, the PKA-specific inhibitor, blocked the apoptosis-inducing effect of GC-51. Our results suggest that GC-51 induction of apoptosis is dependent on PKA. The opposite effects of GC-51 and bullatacin on intracellular cAMP levels is not surprising considering that these two compounds are totally different in structure: GC-51 is a styryl-lactone compound, whereas bullatacin is an annonaceous acetogenin compound. In addition, the cells used in these two experiments were also different, leukemia HL-60 cells compared with hepatoma 2.2.15 cells, and it is well known that effect of cAMP on cell apoptosis is cell-type specific[18]. We postulate that GC-51 induces HL-60 cell apoptosis via a similar mechanism to that demonstrated by Zhang and Insel[18]. However, further investigations are needed to confirm this hypothesis.

In conclusion, GC-51 effectively induces HL-60 apoptosis. The apoptosis-inducing effect of GC-51 is PKA-dependent and involves the downregulation of anti-apoptotic *Bcl-2* gene expression and the activation of caspase-3.

References

1 Johnstone R, Ruefli AA, Lowe SW. Apoptosis: a link between cancer genetics and chemotherapy. Cell 2002; 108: 153–64.
2 Green DR. Apoptotic pathways: paper wraps stone blunts scissors. Cell 2000; 102: 1–4.

3 Wang X. The expanding role of mitochondria in apoptosis. Genes Dev 2001; 15: 2922–33.
4 Mereyala HB, Joe M. Cytotoxic activity of styryl lactones and their derivatives. Curr Med Chem Anti-Canc Agents 2001; 1: 293–300.
5 Mu Q, Tang WD, Liu RY, Li CM, Lou LG, Sun HD, *et al*. Constituents from the stems of *Goniothalamus griffithii*. Planta Med 2003; 69: 826–30.
6 Pihie AH, Stanslas J, Din LB. Non-steroid receptor-mediated antiproliferative activity of styrylpyrone derivative in human breast cancer cell lines. Anticancer Res 1998; 18: 1739–43.
7 Inayat-Hussain SH, Annuar BO, Din LB, Ali AM, Ross D. Loss of mitochondrial transmembrane potential and caspase-9 activation during apoptosis induced by the novel styryl-lactone goniothalamin in HL-60 leukemia cells. Toxicol *in vitro* 2003; 17: 433–9.
8 Inayat-Hussain SH, Osman AB, Din LB, Ali AM, Snowden RT, MacFarlane M, *et al*. Caspases-3 and -7 are activated in goniothalamin-induced apoptosis in human Jurkat T-cells. FEBS Lett 1999; 456: 379–83.
9 Li CM, Mu Q, Sun HD, Xu B, Tang WD, Zheng HL, *et al*. A new anti-cancer constituent of *Goniothalamus cheliensis*. Acta Bot Yunnan 1998; 20: 102–4.
10 Lou LG, Xu B. Induction of apoptosis of human leukemia cells by α-anordrin. Chin J Cancer Res 1997; 9: 1–5.
11 Lou LG, Xu B. Induction of apoptosis in human leukemia K562 cells by α-anordrin. Acta Pharmacol Sin 1996; 17: 255–8.
12 Lou LG, Urbani J, Riberio-Neto F, Altschuler DL. cAMP inhibition of Akt is mediated by activated and phosphorylated Rap1b. J Biol Chem 2002; 277: 32799–806.
13 Ribeiro-Neto F, Urbani J, Lemee N, Lou L, Altschuler DL. On the mitogenic properties of Rap1b: cAMP-induced G1/S entry requires activated and phosphorylated Rap1b. Proc Natl Acad Sci USA 2002; 99: 5418–23.
14 Chiu HF, Chih TT, Hsian YM, Tseng CH, Wu MJ, Wu YC. Bullatacin, a potent antitumor *Annonaceous acetogenin*, induces apoptosis through a reduction of intracellular cAMP and cGMP levels in human hepatoma 2.2.15 cells. Biochem Pharmacol 2003; 65: 319–27.
15 Muhl H, Nitsch D, Sandau K, Brune B, Varga Z, Pfeilschifer J. Apoptosis is triggered by cyclic AMP signaling pathway in renal mesangial cells. FEBS Lett 1996; 382: 271–5.
16 Lomo J, Blomhoff HK, Beiske K, Stokke T, Smeland EB. TGF-â1 and cyclic AMP promote apoptosis in resting human B lymphocytes. J Immunol 1995; 154: 1634–43.
17 Aharoni D, Dantes A, Oren M, Amsterdam A. cAMP-mediated signals as determinants for apoptosis in primary granulosa cells. Exp Cell Res 1995; 218: 271–82.
18 Zhang L, Insel PA. The pro-apoptotic protein Bim is a convergence point for cAMP/protein kinase A-and glucocorticoid-promoted apoptosis of lymphoid cells. J Biol Chem 2004; 279: 20858–65.
19 Kim SN, Ahn YH, Kim SG, Park SD, Cho-Chung YS, Hong SH. 8-Cl-cAMP induces cell cycle-specific apoptosis in human cancer cells. Int J Cancer 2001; 93: 33–41.

Acta Pharmacologica Sinica 2005 May; 26 (5): 629–634

Full-length article

Antitumor effect of cytosine deaminase/5-fluorocytosine suicide gene therapy system mediated by *Bifidobacterium infantis* on melanoma[1]

Cheng YI[2], Ying HUANG[3], Zhi-ying GUO[3], Shu-ren WANG[3,4]

[2]*Cancer Center, West China Hospital, Sichuan University, Chengdu, 610041, China;* [3]*Department of Pathophysiology, West China School of Preclinical and Forensic Medicine, Sichuan University, Chengdu 610041, China*

Key words

Bifidobacterium infantis; cytosine deaminase; gene therapy

[1] Supported by CMB project (MERF-2002)
[4] Correspondence to Shu-ren WANG.
Phn 86-28-8550-1268.
Fax 86-28-8550-3204.
E-mail wansuren@mail.sc.cninfo.net

Received 2004-08-11
Accepted 2005-01-04

doi: 10.1111/j.1745-7254.2005.00094.x

Abstract

Aim: To construct a *Bifidobacterium infantis*/CD targeting gene therapy system and observe the antitumor effect of cytosine deaminase/5-fluorocytosine (CD/5-FC) suicide gene therapy system mediated by *Bifidobacterium infantis* on melanoma *in vitro* and *in vivo*. **Methods:** A recombinant CD/pGEX-1LamdaT plasmid was transfected into *Bifidobacterium infantis* by electroporation. *Bifidobacterium infantis* transfected by recombinant CD/pGEX-1LamdaT plasmid was incubated with 5-FC anaerobically. Then the supernatant fluid was collected and added to melanoma B16-F10 cells to observe the killing effect for B16-F10 cells. Mice were inoculated with melanoma B16-F10 cells to establish animal models. The mice were then injected with 5-FC and *Bifidobacterium infantis* transfected by recombinant CD/pGEX-1LamdaT plasmid. **Results:**Two segments of approximate 4.9 kb and 1.3 kb were extracted from the 6.2 kb recombinant plasmid, which were equal to the size of the pGEX-1LamdaT plasmid and CD gene, respectively. Sequencing results showed that the full length and sequence of nucleotide acid of the inserted gene in extracted recombinant plasmid was completely identical to the CD gene. *In vitro*, B16-F10 cells treated by supernatant fluid were remarkably damaged morphologically, and the cell growth was significantly inhibited. Experiments on the mice melanoma model showed that after treatment with a combination of transfected *Bifidobacterium infantis* and 5-FC, the tumor volume was significantly inhibited compared with controls. **Conclusion:** The foreign gene, CD gene, was correctly inserted into pGEX-1LambdaT plasmid and transferred into *Bifidobacterium infantis*. CD/5-FC suicide gene therapy system mediated by *Bifidobacterium infantis* demonstrated a good antitumor effect on melanoma *in vitro* and *in vivo*.

Introduction

Suicide gene therapy is a highlight in tumor gene therapy at present. Therapy using cytosine deaminase/5-fluorocytosine (CD/5-FC) is one of the most widely studied systems, in which CD can convert relatively nontoxic 5-fluorocytosine (5-FC) into a toxic metabolite 5-fluorouracil(5-FU) and kill tumor cells[1–4].

Transfer vectors are a key factor in the tumor gene therapy system, which directly influences tumor targeting. It is evident that most of the interest and effort in cancer gene therapy in the coming years should be focused on transfer vectors. So far viruses are the most widely used suicide gene vectors. However, viruses are relatively poor in tumor targeting and safety, which has badly impeded tumor gene therapy[5,6]. It is crucial to search for a novel gene vector that has good tumor targeting and is relatively safe.

It is evident that the center of a solid tumor is generally found at a low level of oxygen, and anaerobic bacteria tend to colonize in a low oxygen environment. Therefore, anaero-

bic bacteria is a potential vector for tumor gene therapy[7–9]. In a previous study, our laboratory selected a strain of Bifidobacterium Infantis proven to be good for targeting solid tumors and non-pathogenic[10]. The aim of the present study was to transfer the CD gene into *Bifidobacterium infantis* to construct a *Bifidobacterium infantis*/CD targeting gene therapy system and observe the antitumor efficacy of a CD/5-FC suicide gene therapy system mediated by *Bifidobacterium infantis* on melanoma *in vitro* and *in vivo*.

Materials and methods

Materials pGEX-1LamdaT plasmid was kindly provided by Research Unit of Infection & Immunity, West China School of Preclinical and Forensic Medicine, Sichuan University, China. Strains of *E Coli* K12λ were purchased from Chengdu Institute of Biological Products, China. Strains of Bifidobacterium Infantis 2001 were obtained from West China School of Stomatology, Sichuan University, China.

LA *Taq* DNA polymerase, T4 DNA ligase and λ-*Eco*T14 I digest DNA Marker were purchased from TaKaRa, Japan. 200 bp DNA Ladder Marker was purchased from Sino-American Biotechnology, China. Purification kit of plasmid, Wizard PCR Preps DNA Purification Resin, *Eco*R I and *Bam*H I were purchased from Promega (Madison, WI, USA).

Mouse melanomacytes B16-F10 were provided by China Center for Typical Culture Collection. Female C57BL/6 mice (class 1, aged 6–8 weeks) were provided by the Experimental Animal Center of Sichuan University.

Methods

Amplification of CD gene Strains of *E Coli* K12λ were inoculated into 5 mL LB liquid medium with shaking, overnight at 37 ºC. The next day, genomic DNA was prepared by phenol/chloroform method and used as template DNA to perform PCR for the amplification of CD gene. Specific primers of CD gene were designed based on published sequences (Genebank, NC-0009131). The upstream primer is 5'-ATG GAT CCG GAG GCT AAC AAT G-3' and the downstream primer is 5'-GGG GAA TTC TGT AAC CCA GTC GT-3'. The amplification cycle was repeated 35 times with the condition of denaturation at 94 ºC for 30 s, annealing at 55 ºC for 30 s and extension at 72 ºC for 2 min. Amplified products were purified with Wizard PCR Preps DNA Purification Resin and separated with electrophoresis of 0.8% agarose gel to confirm whether amplified products had the desired size of 1.3 kb.

Digestion of CD gene and pGEX-1LamdaT plasmid CD gene 1 μg and pGEX-1 LamdaT plasmid 1 μg were added into 10 μL 10×Buffer E reactions, separately. The plasmid and CD gene were digested with dual restriction endonucleases (1 μL *Eco*R I+1 μL *Bam*H I) for 3 h. Once the digestion was complete, the DNA fragments were separated by electrophoresis with 0.8% agarose gel. The desired bands of 4.9 kb and 1.3 kb were cut out from the gel. The DNA fragments in the gel were extracted and recovered with gel extraction kit. Recovered pGEX-1LamdaT plasmid vector fragment was dephosphorylated with calf intestinal phosphatase.

Ligation of plasmid vector fragment and CD gene fragment Recovered CD gene fragment 10 μL, recovered pGEX-1LamdaT plasmid vector fragment 10 μL, and 1U T4 DNA ligase were added into the microfuge tube. The reactions were incubated at 16 ºC overnight. Then the ligation products, recombinant CD/pGEX-1LamdaT plasmid were separated by electrophoresis to confirm whether the ligation products had the desired size.

Transfection of *Bifidobacterium infantis* Suspensions of *Bifidobacterium infantis* 10 mL were washed with ice-cold pure water and resuspended in 40 μL ice-cold 10% glycerol. Recombinant CD/pGEX-1LamdaT plasmid 5 μL was added to the bacterial suspensions, then mixed and transferred to electroporation cuvette. Electroporation was carried out to transfect recombinant CD/pGEX-1LamdaT into *Bifidobacterium infantis* at 2.0 kV for 10 ms.

Culture of transfected *Bifidobacterium infantis* and detection of positively transfected bacterial colony When electroporation was completed, 1 mL MRS liquid medium was added into the electroporation cuvette to resuspend bacteria. Then the bacteria suspensions were transferred into a 1.5 mL EP tube and incubated in an anaerobic jar at 37 ºC. Two hours later, bacteria suspensions were plated on MRS solid medium with ampicillin and incubated in an anaerobic jar at 37 ºC. After 72 h, a single positively transfected bacterial colony of *Bifidobacterium infantis* was picked up and inoculated into 5 mL MRS liquid medium. Two to three drops of liquid paraffin was added to the medium and then the cultures were incubated overnight at 37 ºC. The next day, recombinant plasmid was extracted from the incubated bacteria using Purification kit of plasmid. Extracted recombinant plasmid was separated with electrophoresis to confirm whether the recombinant plasmid is the recombinant CD/pGEX-1LamdaT plasmid. In addition, the extracted recombinant plasmid from positively transfected bacterial colony was digested with dual restriction endonucleases of *Eco*R I and *Bam*H I as described previously. The size of digested segments were analyzed by electrophoresis with 0.8% agarose gel.

Sequencing of inserted gene segment in recombinant

plasmid Sequencing of inserted gene segment in recombinant plasmid extracted from positively transfected bacteria was performed according to the method of Sanger dideoxynucleotide triphosphate chain termination. Shanghai Genebase Gen-tech (Shanghai, China) carried out the sequencing.

Processing of positively transfected *Bifidobacterium infantis* Suspension of positively transfected *Bifidobacterium infantis* 20 mL was incubated at 37 ºC anaerobically overnight. The next day, 5-FC with final concentration 1 mmol/L was added and then the incubation continued. After 24 h, 10 mL bacteria suspension was taken and centrifuged for 5 min. The supernatant fluid was collected and 2 mL ethyl acetate was added and mixed to make the supernatant fluid suspension in ethyl acetate properly. The mixture was centrifuged (150×*g*) at 4 ºC for 10 min. The organic fluid was transferred to EP pipette and dried in a vacuum. The dried product was resolved in 1 mL 0.9% saline to be used as the positive treatment fluid. Suspension of untransfected *Bifidobacterium infantis* was processed with the same method and used as the negative treatment fluid.

Killing effects of treatment fluid on melanomacyte B16-F10 Melanomacytes B16-F10 were first digested with 0.125% trypsin and counted. They were then diluted to a final concentration of 1.5×10^5 cells/mL and inoculated into six wells at 1.8 mL/well in 6-well cell culture cluster. The six wells were randomized into two groups with three wells in each group. When 50%–60% of the wells were covered by cells, 200 μL positive treatment fluid and 200 μL negative treatment fluid were separately added to the two groups with one well from each group added with saline as the control. The cell culture cluster was placed in a 5% CO_2 incubator at 37 ºC. After 24 h, the morphology of cells was observed and the number of cells was counted using trypan blue dye exclusion method to calculate the suppression rate of each test group, namely; Suppression rate=$(N_n–N)/(N_n–N_0)\times100\%$ (N_0: number of inoculated cells; N: number of cells in test well after 24 h; N_n: number of cells in control well after 24 h).

Antitumor effect *in vivo* Mouse melanomacytes B16-F10 were inoculated in the muscle of the right thigh of the female C57BL/6 mice at 5×10^6 cells/mouse to establish a melanoma model. The experiment was initiated when the tumor grew to 0.8–1.0 cm in diameter (d 10 after inoculation). Twenty tumor-bearing mice were divided into test group (n=10) and control group (n=10) randomly. Diluted suspension 0.2 mL of positively transfected *Bifidobacterium infantis* containing 5×10^6–6×10^6 bacteria was injected into the mice in the test group through the tail vein. The control group were injected with the same volume and number of untransfected *Bifidobacterium infantis*. After 7 d, 5-FC was injected intraperitoneally for each mouse in both groups at a dose of 500 mg each day, consecutively for 7 d. From the first day of 5-FC injection, the length and width of the tumor were measured every two days. The volume was calculated using the formula $V=1/2\times A\times B^2$ (A: length; B: width) and the measurement continued for 21 d.

Statistic methods Comparison of tumor growth suppression rates was examined by chi-square test of four-fold table. Tumor volume was compared by *t*-test. The results were analyzed using statistic software STATA5.0.

Results

Detection of positively transfected *Bifidobacterium infantis* colony Electroporation method was used to transfect recombinant CD/pGEX-1LamdaT plasmid into *Bifidobacterium infantis*. After 72 h, sparse bacterial colonies were observed on MRS solid medium containing ampicillin. A single positively transfected bacterial colony was picked up and cultured, then the recombinant plasmid in the positively transfected *Bifidobacterium infantis* was extracted. The size of extracted recombinant plasmid was approximately 6.2 kb (Figure 1, lane A), which was equal to the size of recombinant CD/pGEX-1LamdaT plasmid.

Detection of recombinant plasmid digested with dual restriction endonucleases After the recombinant plasmid extracted from the positively transfected bacteria was digested with dual restriction endonucleases of *Bam*H I and *Eco*R I, two fragments with sizes of approximately 1.3 kb and 4.9 kb were obtained, which were consistent with the sizes of CD gene and pGEX-1LamdaT plasmid, respectively (Figure 1, lane B).

Sequencing of inserted gene segment in recombinant plasmid extracted from positively transfected *Bifidobacterium infantis* Sequencing results showed that the size and sequence of nucleotide acid of inserted gene segment were completely consistent with the size and sequence of nucleotide acid of CD gene (Genebank: NC-000913). The full length of inserted gene fragment was 1309 bp. The sequence of two ends of the inserted gene was also consistent with *Bam*H I site and *Eco*R I site. The sequencing identified that the foreign gene, CD gene, was correctly inserted into pGEX-1LambdaT plasmid and transferred into Bifidobacterium Infantis. Targeting gene therapy system of Bifidobacterium Infantis/CD was successfully constructed.

Morphologic changes of B16-F10 cells after treatment After being treated with the positive treatment fluid for 24 h, most B16-F10 cells were killed and only a few grew along the wall.

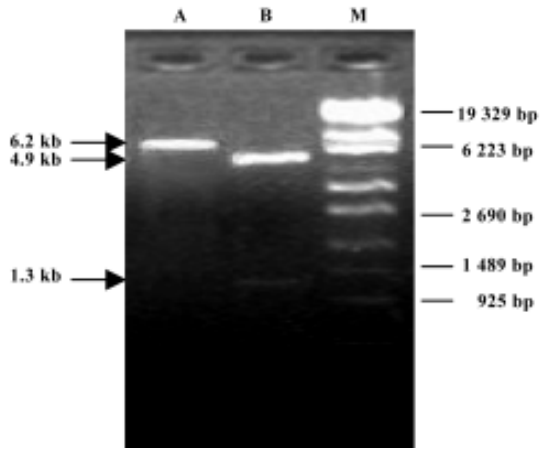

Figure 1. The electrophoregram of recombinant plasmid (0.8% agarose gel). Lane A: recombinant plasmid extracted from positively transfected *Bifidobacterium infantis* (approximately 6.2 kb). Lane B: digested fragments with dual restriction endonucleases of recombinant plasmid extracted from positively transfected bacteria (approximately 4.9 kb and 1.3 kb, respectively). Lane M: λ-*Eco*T14 I digest DNA Marker

Most cells floated and quantities of cell debris were observed in the medium. The cells left on the wall underwent significant changes in morphology; the original shape was gone, cytoplasm became rougher, the nucleus showed pycnosis and the refraction decreased (Figure 2), demonstrating obvious cellular damages. In contrast, B16-F10 cells treated with negative treatment fluid did not appear to have obvious morphologic changes compared with the control (Figures 3, 4).

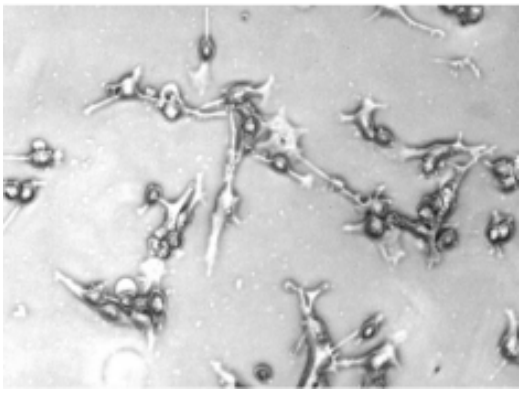

Figure 2. B16-F10 cells treated with positive treatment fluid (×100).

Examination of tumor cell growth suppression rate The negative treatment fluid had no significant effects on tumor cell growth. The cells growth suppression rate was 4.8%. The B16-F17 cells treated with positive treatment fluid grew at a critically lower rate. The cells growth suppression rate

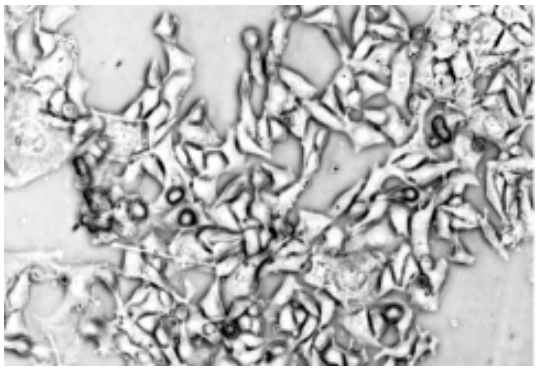

Figure 3. Control B16-F10 cells without any treatment (×100).

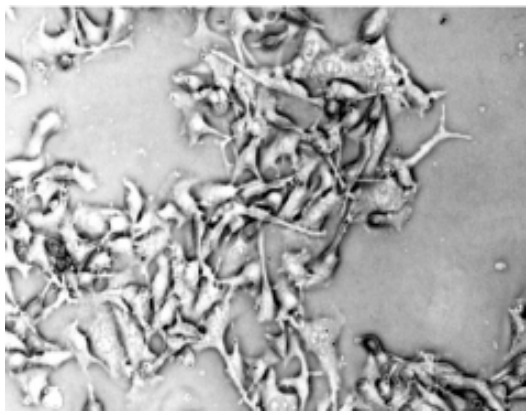

Figure 4. B16-F10 cells treated by negative treatment fluid (×100).

was 80%, which was significantly higher than that of group treated with negative treatment fluid (chi-square test: $\chi^2=7.02$, $\upsilon=1$, $P<0.01$) (Table 1).

Antitumor effects *in vivo* There was no significant difference between the tumor volumes in the test group and control group before treatment. On the d 7 after 5-FC injection, tumor volumes in the test group were considerably smaller than those in the control group ($P<0.05$), and the difference became greater over time until the end of observation (Figure 5).

Discussion

It has been proved that a hypoxic region exists in many human and mouse tumors, especially in solid tumors, which kill over 90 % of cancer patients. Vaupel[11] made his study on cancer patients using oxygen electrode measurement. In his study, Vaupel found the average oxygen partial pressure in normal tissues read 24–66 mmHg, whereas the readings dropping to 10–30 mmHg in a tumor tissue with a marked central region where the readings went below 2.5 mmHg.

Table1. Effects of treatment fluid on the growth of B16-F10 cells χ^2=7.02, υ=1, ^cP<0.01.

Group	10^{-8}×Cells of control well/L^{-1}	10^{-8}×Cells of test well/L^{-1}	Suppression rate/%
A	6.8	28	80^c
B	30	31	4.8

A: group treated with positive treatment fluid. B: group treated with negative treatment fluid.

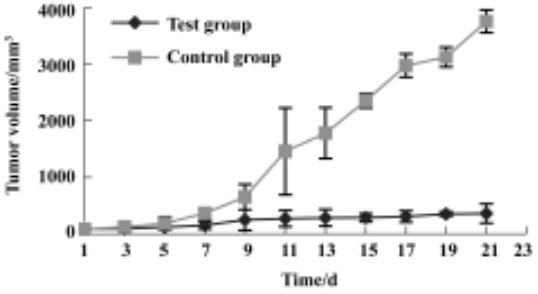

Figure 5. Tumor volume changes of test group and control group.

Based on the presence of a hypoxic metabolic region in a solid tumor and tendency of anaerobic bacteria to hypoxic environment, anaerobic bacteria can be used as transfer vectors for tumor targeting gene therapy.

Compared with viral or other non-viral vectors, the anaerobic bateria is advantageous for tumor targeting[13–17]. Yazawa *et al*[9] injected non-pathological strains of *Bifidobacterium* 105-A and 108-A into mice bearing lung cancer. After 168 h, both strains of bacteria were observed to have targeted and colonized in the tumors, whereas no bacteria were found in the liver, spleen, kidney, normal lung tissues or other normal tissues. When the anaerobic bacteria were used as the gene transfer vector, it could specifically proliferate and directly express foreign gene products in tumor tissues. There is no need to transform cancer cells, which highly improves the gene expression[9,13,14] . Most of the transfer vectors used in current studies are strains of *Bifidobacterium. Bifidobacteriu*m is a non-pathogenic anaerobic bacteria. It resides in the lower section of the small intestine and in the large intestine of humans or rodent animals, and is good for the health of its host and widely used in food manufacturing and medicine[9,12–15]. It has been proved in animal experiments that Bifidobacterium has no obvious influence on body weight, peripheral leukocytes, temperature, or survival time of mice, hamsters, guinea pigs or rabbits[13]. Moreover, anaerobic bacteria are highly vulnerable to antibiotics and very low doses of antibiotics are enough to kill them. Even in the case of overgrowth, the bacteria can be easily controlled by antibiotics, which further the safety.

In the present study, we used *Bifidobacterium infantis* as a CD gene transfer vector, then transferred the CD gene into *Bifidobacterium infantis* and successfully constructed a *Bifidobacterium infantis*/CD targeting gene therapy system.

In the *in vitro* experiment, positively transfected *Bifidobacterium infantis* was incubated anaerobically with 5-FC overnight. The supernatant fluid of the bacteria culture was extracted and resolved in saline. The final solution was added to the melanomacyte B16-F10 and it was observed that the growth of melanomacyte B16-F10 was obviously suppressed at a rate of 80% and the morphology of the cells was also damaged. It was also observed in our study that the growth of tumors were greatly inhibited on mice that were injected with 5-FC and positively transfected *Bifidobacterium infantis*. These results indicate that positively transfected with *Bifidobacterium infantis* can express CD *in vitro* and *in vivo*, which can convert 5-FC into 5-FU to inhibit tumor growth.

CD/5-FC suicide gene therapy system mediated by *Bifidobacterium infantis* has primarily demonstrated its antitumor effects *in vivo* and *in vitro* in this experiment. This system shows promise as a novel tumor targeting gene therapy system and is worthy of further study.

References

1 Miller CR, Gustin AN, Buchsbaum DJ, Vickers SM, Manne U, Grizzle WE, *et al*. Quantitation of cytosine deaminase mRNA by real-time reverse transcription polymerase chain reaction: a sensitive method for assessing 5-fluorocytosine toxicity *in vitro*. Anal Biochem 2002; 30: 189–99.

2 Miyagi T, Koshida K, Hori O, Konaka H, Katoh H, Kitagawa Y, *et al*. Gene therapy for prostate cancer using the cytosine deaminase/uracil phosphoribosyltransferase suicide system. J Gene Med 2003; 5: 30–7.

3 Plumb JA, Bilsland A, Kakani R, Zhao J, Glasspool RM, Knox RJ, *et al*. Telomerase-specific suicide gene therapy vectors expressing bacterial nitroreductase sensitize human cancer cells to the pro-drug CB1954. Oncogene 2001; 20: 7797–803.

4 Brown NL, Lemoine NR. Clinical trials with GDEPT: cytosine deaminase and 5-fluorocytosine. Methods Mol Med 2004; 90: 451–7.

5 Xu G, McLeod HL. Strategies for enzyme/prodrug cancer therapy. Clin Cancer Res 2001; 7: 3314–24.

6 Denny WA. Prodrug strategies in cancer therapy. Eur J Med Chem 2001; 36: 577–95.

7 Liu SC, Minton NP, Giaccia AJ, Brown JM. Anticancer efficacy

of systemically delivered anaerobic bacteria as gene therapy vectors targeting tumor hypoxia/necrosis. Gene Ther 2002; 9: 291–6.
8 Nuyts S, Van Mellaert L, Theys J, Landuyt W, Lambin P, Anne J. Clostridium spores for tumor-specific drug delivery. Anticancer Drugs 2002; 13: 115–25.
9 Yazawa K, Fujimori M, Amano J, Kano Y, Taniguchi S. Bifidobacterium longum as a delivery system for cancer gene therapy: selective localization and growth in hypoxic tumors. Cancer Gene Ther 2000; 7: 269–74.
10 Wu Y, Yi C, Wang S, Zhang M, Zhang J. Investigation on tumor-targeting characteristics of *Bifidobacterium infantis* toward melanoma in mice. J Sichuan Univ 2003; 34: 435–8.
11 Vaupel PW. Oxygenation of solid tumors in drug resistance in oncology. In: Teicher BA, editor. New York: Marcel Dekker; 1993, p53–85.
12 Nagy H, Panis Y, Fabre M, Perrin H, Klatzmann D, Houssin D. Are hepatomas a good target for suicide gene therapy? An experimental study in rats using retroviral-mediated transfer of thymidine kinase gene. Surgery 1998; 123: 19–24.
13 Fujimori M, Amano J, Taniguchi S. The genus *Bifidobacterium* for cancer gene therapy. Curr Opin Drug Discov Devel 2002; 5: 200–3.
14 Yazawa K, Fujimori M, Nakamura T, Sasaki T, Amano J, Kano Y, *et al*. *Bifidobacterium longum* as a delivery system for gene therapy of chemically induced rat mammary tumors. Breast Cancer Res Treat 2001; 66: 165–70.
15 Nakamura T, Sasaki T, Fujimori M, Yazawa K, Kano Y, Amano J, *et al*. Cloned cytosine deaminase gene expression of *Bifidobacterium longum* and application to enzyme/pro-drug therapy of hypoxic solid tumors. Biosci Biotechnol Biochem 2002; 66: 2362–6.
16 Kim TB, Song SH, Kang SC, Oh DK. Quantitative comparison of lactose and glucose utilization in *Bifidobacterium longum* cultures. Biotechnol Prog 2003; 19: 672–5.
17 Makelainen H, Tahvonen R, Salminen S, Ouwehand AC. *In vivo* safety assessment of two *Bifidobacterium longum* strains. Microbiol Immunol 2003; 47: 911–4.

Acta Pharmacologica Sinica 2005 May; 26 (5): 635–640

Full-length article

Effects of {2-[(3-carboxy-1-oxoprogy1)amino]-2-deoxy-*D*-glucose} on human hepatocellular carcinoma cell line[1]

Jing WU[2,3], Wei KOU[4], Ming-tai GAO[5], Yong-ning ZHOU[3], Ai-qin WANG[2], Qun-ji XUE[2], Liang QIAO[6]

[2]Lanzhou Institute of Chemical Physics, Chinese Academy of Sciences, [3]Department of Gastroenterology and Hepatology, First Teaching Hospital of Lanzhou Medical College, [4]Medical College of Northwest University for Nationalities, [5]Department of Surgery, First Teaching Hospital of Lanzhou Medical College, Lanzhou 730000, China; [6]Storr Liver Unit, Westmead Millennium Institute, Department of Gastroenterology and Hepatology, University of Sydney at Westmead Hospital, Westmead, NSW 2145, Australia

Key words

apoptosis; hepatoma; HepG$_2$; 2-[(3-carboxy-1-oxoprogy1)amino]-2-deoxy-*D*-glucose

[1] Project supported by the Creative Engineering Realm the Item of Chinese Academia of Sciences, CX805.
[3] Correspondence to Jing WU.
Phn 86-931-861-9605.
Fax 86-931-861-9797.
E-mail wujing36@163.com

Received 2004-08-13
Accepted 2004-11-15

doi: 10.1111/j.1745-7254.2005.00066.x

Abstract

Aim: To study the effects of {2-[(3-carboxy-1-oxoprogy1)amino]-2-deoxy-*D*-glucose (COPADG) on cultured human hepatocellular carcinoma cells (HepG2). **Methods:** HepG2 cells were cultured in RPMI-1640 medium. Cell proliferation was determined by MTT assay. Apoptosis was determined by fluorescence microscopy, transmission electron microscopy, agarose gel electrophoresis of DNA fragmentation, and flow cytometry. **Results:** At the concentration ranging between 1–30 μmol/L, COPADG potently inhibited the growth and induced apoptosis of HepG2 cells. **Conclusion:** COPADG could effectively induce apoptosis in human hepatocellular carcinoma cells. More investigations are warranted for the potential use of this compound as a new agent for the non-surgical management of human hepatocellular carcinoma.

Introduction

Apoptosis is a cellular suicidal process that plays an important role in the elimination of unwanted or damaged cells. Under the physiological condition, apoptosis counteracts with cellular proliferation to maintain homeostasis. Dysregulated apoptotic response has been associated with certain diseases such as neural degenerative disorders and cancers. Many chemotherapeutic agents, radiation therapy, and therapeutic cytokines are known to induce apoptosis. Thus, apoptosis has been recognized as one of the major modes of cell death in cancer therapy. Resistance to undergo apoptosis is one of the important mechanisms that leads to treatment failure in cancer[1–2].

In recent years, agents or treatment modalities that result in apoptosis have become a new focus in cancer therapy[3–5]. {2-[(3-carboxy-1-oxoprogy1)amino]-2-deoxy-*D*-glucose} (COPADG)[6] is a derivative of *D*-glucose (molecular structure shown in Figure 1). *D*-amino-glucose is a monose that comes from the chitosan's degradation. Previous studies by others have discovered that some *D*-amine-glucose derivatives were able to induce leukemia cells K562 to differentiate into macrophages[7]. However, it is still unknown whether derivatives of *D*-amine-glucose can induce apoptosis in tumor cells. In this study, we aimed to determine whether COPADG could induce apoptosis on human hepatocellular carcinoma cells (HepG2).

Materials and methods

Materials Human hepatocellular carcinoma cells (HepG2) were provided by the Department of Pathology, Fourth Military Medical University, China. COPADG was newly synthesized by the Lanzhou Institute of Chemical Physics, Academy of Sciences, China, and was dissolved in distilled water, filter-sterilized with 0.22 μm filter disc, and stored at 4 ºC until use. The structure of COPADG is shown in Figure 1. RPMI-1640 medium was purchased from Invitrogn (Invitrogen Corporation, CA, USA). MTT, agarose, and all routine chemicals were purchased from Sigma-Aldrich (Sigma-Aldrich Chemicals, Louis Mo, USA). Trypsin, acridine orange, and fetal calf serum were purchased from Shanghai Biological

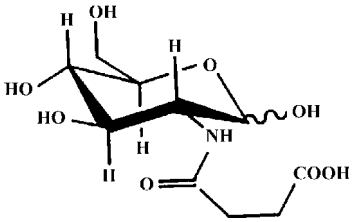

Figure 1. Chemical structure of 2-[(3-carboxy-1-oxoprogy1)amino]-2-deoxy-*D*-glucose.

Engineering Limited (Shanghai, China).

Cell culture HepG2 cells were cultured in RPMI-1640 medium supplemented with heat inactivated 10% fetal calf serum (FCS), streptomycin 100 mg/mL and benzylpenicillin 100 mg/mL . Cells were maintained in a humidified atmosphere of 5% CO_2 with 95% air at 37 °C. Medium is changed every 48 h.

MTT colorimetric assay The MTT test is based on the enzymatic reduction of the tetrazolium salt MTT in viable/metabolically active cells. Cells at approximately 85%–90% confluency were harvested with 0.25% Trypsin/0.02% edetic acid solution and seeded into a 96-well plate at a density of 4×10^3 cells/well. Cells were incubated with various concentrations (1–30 μmol/L) of COPADG for indicated time (24–96 h). Control cells were treated in the same way except that COPADG was replaced by sterile PBS. After treatment, medium was changed to fresh medium, and cells were incubated with 5 g/L of MTT for 4 h. MTT was then dissolved with 150 μL of 10% Me_2SO for 1 h. The optical densities (*OD*) in the 96-well plates were determined using a microplate reader at 490 nm. Cell growth inhibition was estimated by using the following formula:

% Growth inhibition=1–*OD* (treated cells)/*OD* (control cells)×100%

Morphological study of apoptosis by acridine orange Acridine orange (AO) is a membrane-permeable fluorescent dye. It is specific for apoptotic cell death and does not significantly stain necrotic cells[8]. Apoptotic nuclei exhibiting typical changes such as nuclear condensation and segmentation will be stained yellow by AO. Cells (2×10^5/well) were seeded into 6-well plate, grown to approximately 85% confluency, treated with various concentrations of COPADG for various durations, fixed in methanol: glacial acetic acid (3:1) for 30 min at room temperature, washed in PBS, and stained with 0.01% AO. Stained cells were washed with distilled water, viewed under a fluorescence microscope. Apoptotic cells were counted and expressed as a percentage of the total number of cells counted.

Transmission electron microscopies (TEM) Cells were processed for TEM to further evaluate apoptosis. Cells of logarithmic growth were treated as described above, harvested by trysinization, fixed in 3% glutaraldehyde for 1 h. After removal of the primary fixative, cells were washed three times in MOPS buffer, post fixed in 1% osmium tetroxide (OsO_4), dehydrated in graded alcohol, and embedded in epoxy resin. Ultra thin sections were double-stained with lead citrate/uranyl acetate before being examined using JEF-100CX transmission electron microscope (Japan).

Agarose gel electrophoresis for detection of DNA fragmentation Upon completion of treatment, cells were processed for DNA fragmentation analysis by agarose gel electrophoresis as described previously[9]. Briefly, cells (detached and attached) were incubated in 400 μL of lysis buffer (Trinton X-100, 10 mmol/L Tris, 1 mmol/L edetic acid, pH 8.0) for 30 min. The whole cell lysates were centrifugated at 12 000 rpm at 4 °C for 15 min . The supernatants were then incubated with 1 g/L proteinase K at 56 °C for 3 h followed by incubation with 2 g/L RNase A for 2 h. The solution was then sequentially extracted with an equal volume of phenol (pH 8.0), phenol/chloroform (1:1), and chloroform/isoamyl alcohol (24:1). Total genomic DNA was precipitated by adding 1/10 volume of 3 mol/L sodium acetate (pH 5.2) and 2 volumes of ice-cold ethanol for overnight at -20 °C. DNA was collected by centrifugation at 13 000 rpm at 4 °C for 10 min. The pellets were washed once with 70% alcohol and air-dried before being dissolved in TE buffer (10 mmol/L Tris-HCl, pH 8.0, 1 mmol/L edetic acid). DNA concentration was measured at *OD* 260 nm, and 5 μg was loaded onto a 1.5% agarose gel in TAE buffer. Electrophoresis was performed at 35 V for 4 h, the gel was stained with ethidium bromide, viewed under UV illumination, and photographed.

Flow cytometry analysis Following treatment, cells were rinsed with PBS, trypsinized by 0.25% trypsin/0.02% EDTA solution, and collected by centrifugation at 1000 rpm at 4 ºC for 5 min . The cell pellets were fixed in 70% ethanol at 4 °C for at least 1 h. The fixed cells were washed twice with PBS, resuspended in PBS containing 50 g/L RNase A and 50 mg/L of propidium iodide (PI). The suspension was incubated at 37°C for 30 min, filtered through 200 μm nylon mesh, and were analyzed by flow cytometer (Coulter EPICS XL). The apoptotic population was identified as cells appeared in sub-G_0/G_1 peak. Multicycle software was used for data analysis.

Statistical analysis The results are presented as mean±SD. Each experiment was repeated at least three times. Statistical differences between each group were determined by single factor analysis of variance and correlation analysis.

Results

Proliferation inhibition of HepG$_2$ cells by COPADG As indicated by MTT assay results, proliferation of HepG2 cells was significantly inhibited by COPADG in a dose-dependent manner (Figure 2A). The inhibitory effect started at 24 h, and reached maximum at 48 h (Figure 2B).

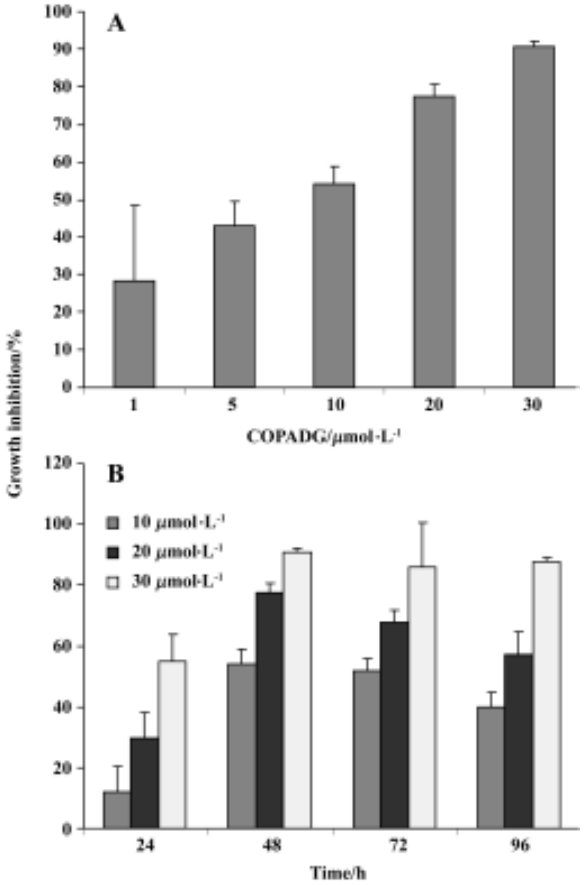

Figure 2. Inhibition of HepG2 cell growth by COPADG. (A) HepG2 cells were treated with various concentrations of COPADG for 48 h. (B) HepG2 cells were treated with 10, 20, and 30 μmol/L of COPADG for 24, 48, 72, and 96 h. The results shown were the averages of three separate experiments. Mean±SD.

Apoptosis inhibition in HepG2 cells by COPADG

Apoptosis morphology by acridine orange fluorescence staining Apoptosis was first detected by typical morphology after staining with acridine orange (AO), one of the early techniques used for apoptosis detection. When HepG2 cells were treated with 20 μmol/L of COPADG for 48 h, cells with condensed or fragmented chromatin indicative of apoptosis were frequently observed, as compared to control cells which showed evenly distributed yellowish-green fluorescent chromatin (Figure 3).

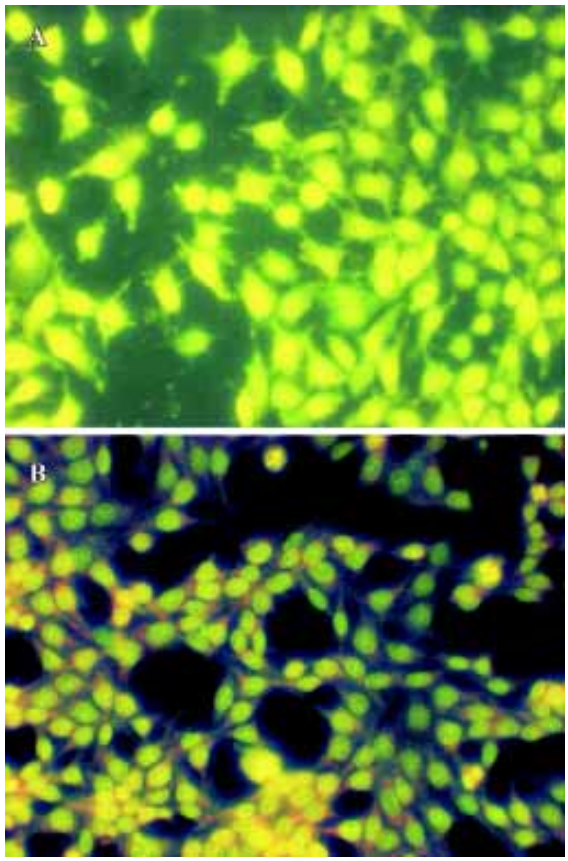

Figure 3. Fluorescence microscopy of HepG2 cells treated with (B) or without (A) COPADG and stained with acridine orange. In panel B, HepG2 cells were treated with 20 μmol/L of COPADG for 48 h. Note the presence of chromatin condensation and nuclear fragmentation indicative of apoptosis, as compared to untreated HepG2 cells in panel A. The results shown were representatives of three separate experiments. (Magnification: ×200).

Induction of apoptosis by COPADG was in a dose- as well as a time-dependent manner, with 30 mmol/L of COPADG induced approximately 60% of apoptosis at 48 h. Figure 4 showed the quantitative results of COPADG-induced apoptosis in HepG2 cells.

Ultrastructure of apoptosis by transmission electron microscopy (TEM) At the ultrastructural level, features of apoptosis were also observed by TEM. In HepG2 cells treated with 20 μmol/L of COPADG for 48 h, some nuclei displayed characteristic changes of apoptosis: chromatin condensation and margination, as well as nuclear fragmentation, cell shrinkage and cell blebbing (Figure 5). The intracellular organelles such as endoplasmic reticulum become loose and fuse with cell membrane resulting in vacuolation. These

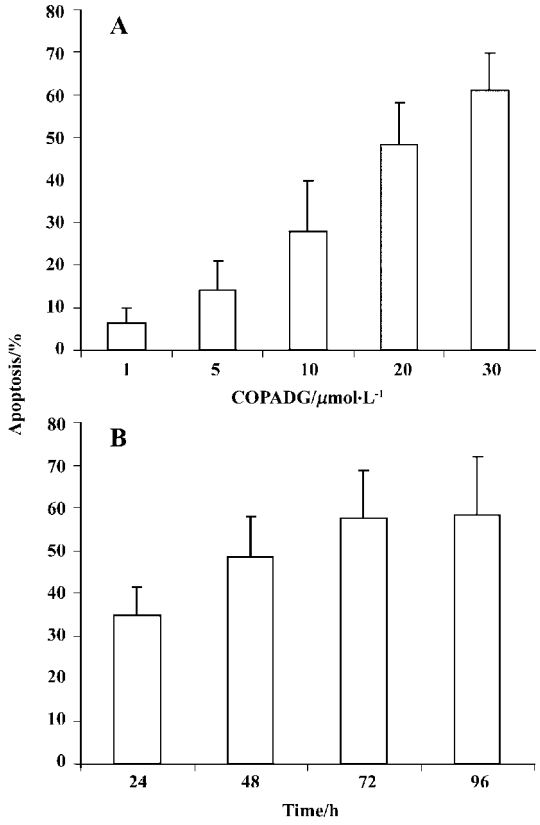

Figure 4. Quantitative analysis of apoptosis of HepG2 cells treated with COPADG. Cells were either treated with various concentrations of COPADG for 48 h (A), or treated with 20 μmol/L of COPADG for various durations (B). The results were mean values of three separate experiments.

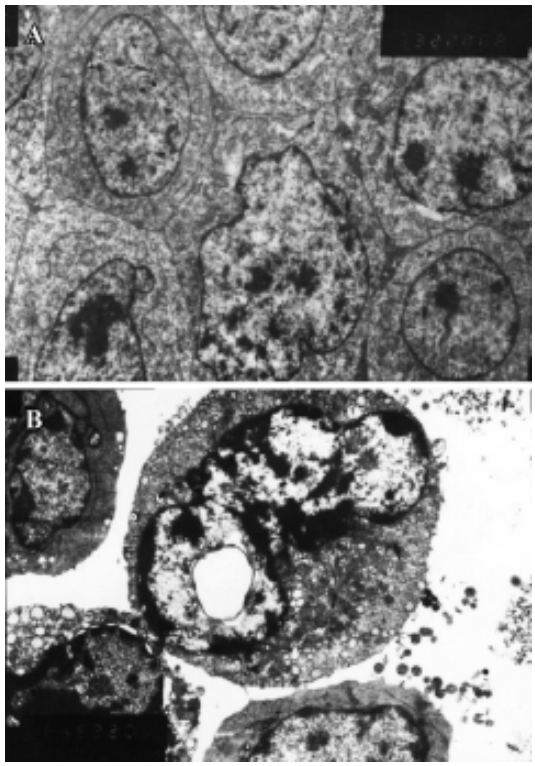

Figure 5. Transmission electron microscopy of HepG2 cells treated with 20 μmol/L of COPADG for 48 h (B). Cells displayed chromatin condensation and fragmentation. The fragmented and condensed chromatin marginate around the nuclear envelope, forming crescent-like structures. In certain fields, pyknotic apoptotic bodies were observed. The micrograph was representative of three separate experiments. (A) untreated control cells.

changes were in sharp contrast to untreated HepG2 cells, which showed normal cell membrane and nuclei with evenly distributed chromatin, as well as intact intracellular organelles.

DNA fragmentation by agarose gel electrophoresis In order to investigate whether COPADG kills HepG2 cells by apoptosis, agarose gel electrophorsis of genomic DNA from COPADG-treated HepG2 cells were performed. As shown in Figure 6, typical DNA laddering patterns suggestive of apoptosis were observed when HepG2 cells were treated with 20–30 μmol/L of COPADG for 48 h (lanes 4 and 5, respectively).

FACS analysis of apoptosis These biochemical features were verified by FACScan analysis, in which apoptosis was indicated by the presence of cells in the sub-G_0/G_1 peak. As shown in Figure 7 and Table 1, $HepG_2$ cells treated with 10 μmol/L, 20 μmol/L, and 30 μmol/L of COPADG for 48 h displayed a dose-dependent accumulation of cells in the apoptosis peak (panel B, 17.4%; panel C, 26.8%; and panel D, 34.3%, respectively), as compared to untreated control (panel A).

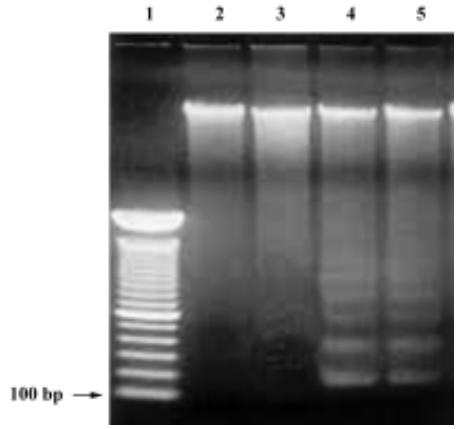

Figure 6. DNA fragmentation analysis by agarose gel electrophoresis. HepG2 cells were either treated with 0 μmol/L (lane 2, control), 10 μmol/L (lane 3), 20 μmol/L (lane 4), and 30 μmol/L (lane 5) of COPADG for 48 h. Lane 1 was molecular marker. The result was representative of three separate experiments.

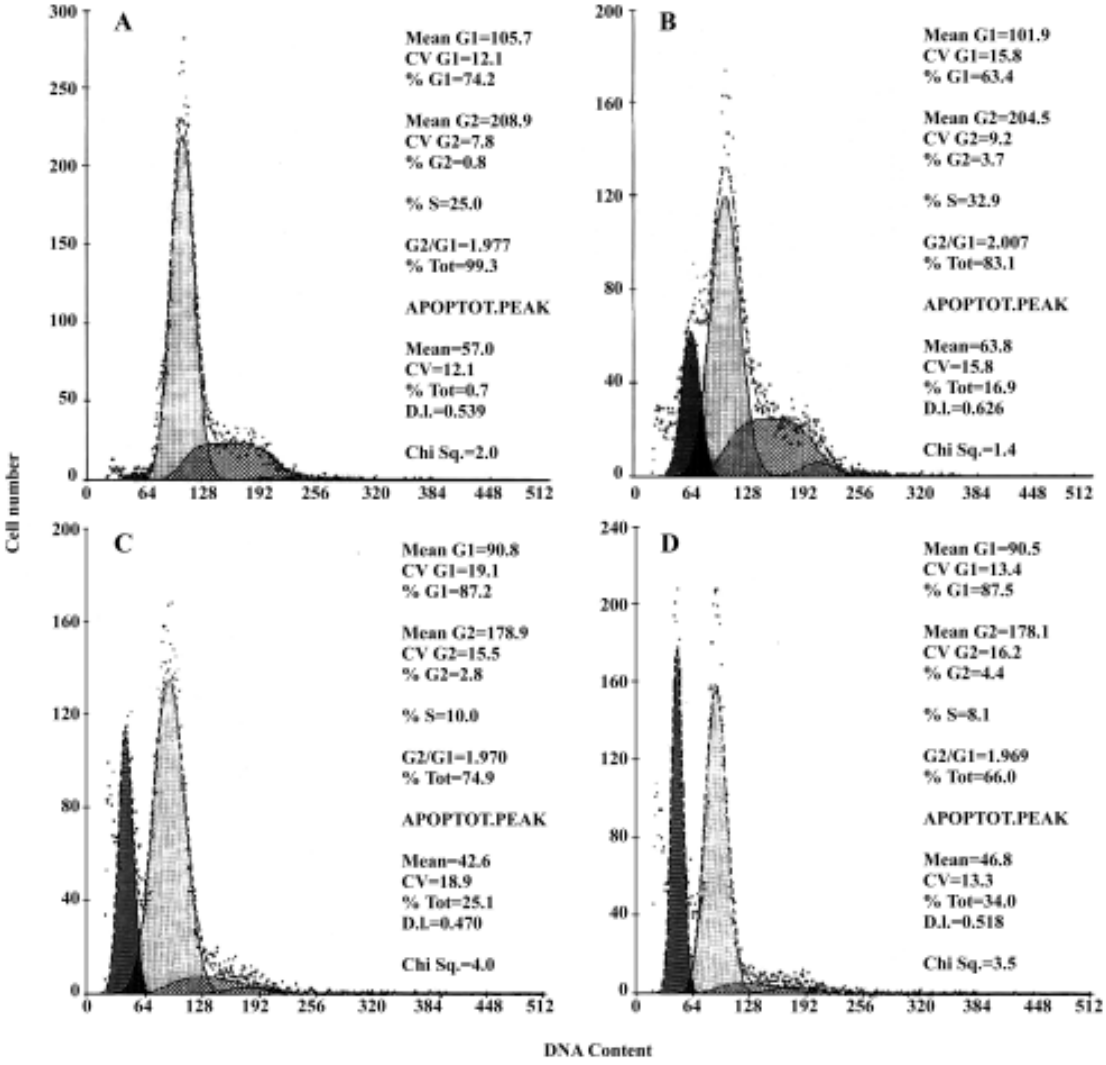

Figure 7. FACS analysis of HepG2 cells by PI staining. HepG2 cells were exposed to 0 μmol/L (A, control), 10 μmol/L (B), 20 μmol/L (C), and 30 μmol/L (D) of COPADG for 48 h. Apoptotic cells with a subdiploid amount of DNA appeared on the left side of the $G_{0/1}$ peak (sub-$G_{0/1}$) as a result of loss of internucleosomal DNA cleavage fragments. The values represent the percentage of cells in the sub-$G_{0/1}$ phase of the cell cycle. The result was representative of three separate experiments.

Table 1. FACScan analysis of HepG2 cells by PI staining. HepG2 cells were exposed to 0, 10, 20, and 30 μmol/L of COPADG for 48 h. Apoptosis is indicated by the presence of $G_{0/1}$ peak (sub-$G_{0/1}$) as a result of loss of internucleosomal DNA cleavage fragments. The result is the average of three separate experiments.

COPADG /μmol·L^{-1}	G1	S	G2	Sub-$G_{0/1}$ peak /%
0 (control)	74.9±0.81	24.0±0.38	1.10±0.12	1.70±0.32
10	64.4±2.30	33.1±2.10	2.50±0.80	17.4±1.21
20	84.2±3.82	12.0±1.83	3.80±0.85	26.8±2.18
30	87.5±2.95	8.10±1.01	4.40±0.75	34.3±1.80

Discussion

D-glucose is a low molecular weight compound with multiple biological activities. Studies also have shown that *D*-glucose could inhibit tumor cell growth; some of the partial derivatives of *D*-glucose could potently induce the differentiation of tumor cells[10]. Our study was aimed to test whether the newest derivative of *D*-glucose (COPADG) had any effect on the proliferation and apoptosis in human hepatoma cells. We utilized several different methods to measure the effect of COPADG on cell proliferation and apoptosis. By MTT assay, it was shown that COPADG could effectively inhibit HepG2 cell proliferation in a dose-depen-

dent manner. The inhibition of cell proliferation was associated with profound induction of cell apoptosis, as demonstrated by a series of complementary techniques for apoptosis detection, including morphologic study by acridine orange fluorescence staining and TEM, both showed typical morphology of apoptosis: cell pyknosis, chromatin condensation, and nuclear fragmentation. The nature of apoptotic cell death was also demonstrated by the presence of its biochemical feature (ie, typical "DNA ladder" on agarose gel electrophoresis indicating internucleosomal DNA fragmentation). These characteristics were further verified by FACScan analysis, which showed the presence of apoptotic peak in subG_0/G_1 peak. These results suggest that COPADG exerts its anti-tumor effects via two fundamental processes: suppression of cell proliferation and induction of apoptosis.

Under the physiological conditions, apoptosis is programmed cell dying process controlled by numerous genes[11–13]. The balance between well-controlled apoptosis and cell proliferation is an important determinant of cell fate. Thus, impaired apoptotic response or overactive proliferation is among the mechanisms of cancer initiation and progression. Human hepatocellular carcinoma (HCC) is one of the most common and chemoresistant cancers. At the present, there is no effective therapy against this deadly cancer, especially when it reaches advanced stage. Thus, novel and effective treatments are desperately needed. Agents or treatments that inhibit proliferation and /or promote apoptosis are under intensive investigation for their potential use in liver cancer therapy.

Our preliminary *in vitro* study suggested that COPADG could potently suppress proliferation and induce apoptosis in HepG2 cells. However, further studies are necessary to test the effect of this agent on other HCC cell lines or other types of cancer cells to make sure the effects we observed were not cell line specific. Studies are also warranted to elucidate the underlying mechanisms by which COPADG inhibits proliferation and induces apoptosis in HCC cells. *In vivo* studies in HCC-bearing nude mice may be also necessary to test the toxicity of this agent.

In conclusion, our current study has demonstrated that COPADG is a potent antiproliferative and proapoptotic agent against HepG2 cells. More studies are currently underway to expand these results to other cell lines.

References

1 Thompson CB. Apoptosis in the pathogenesis and treatment of disease. Science 1995; 10; 267: 1456–62.

2 Carson DA, Riberio JM. Apoptosis and disease. Lancet 1993; 341: 1251–4.

3 Kerr JF, Winterford CM, Harmon BV. Apoptosis. Its significance in cancer and cancer therapy. Cancer 1994; 73: 2013–26.

4 Dive C, Hickman JA. Drug-target interactions: only the first step in the commitment to a programmed cell death? Br J Cancer 1991; 64: 192–6.

5 Thompson HJ, Strange R, Schedin PJ. Apoptosis in the genesis and prevention of cancer. Cancer Epidemiol Biomarkers Prev 1992; 1: 597–602.

6 Qiao Y, Wang AQ, Wang Z, Huang GS. The synthesis of 2-[(3-carboxy-1-oxoprogy1)amino]-2-deoxy-*D*-glucose. Chem Reagents 2004; 26:107–8.

7 Wang Z, Qiao Y, Huang GS, Wang AQ, Zhang YQ, Feng JL, *et al*. Glucosamine and glucosamine hydrochloride induced leukemia cell line K562 differentiation into macrophage. Chin Pharmacol Bull 2003; 19: 290–3.

8 Abrams JM, White K, Fessler LI, Steller H. Programmed cell death during *Drosophila embryogenesis*. Development 1993; 117: 29–43.

9 Qiao L, Farrell GC. Reciprocal control of apoptosis and proliferation in cultured rat hepatoma arl-6 cells: roles of nutrient supply, serum, and oxidative stress. *In Vitro* Cell Dev Biol Anim 2000; 36: 465–75.

10 Mc Donnel TJ, Meyn RE, Robertson LE. Implications of apoptotic cell death regulation in cancer therapy. Semin Cancer Biol 1995; 6: 53–60.

11 Castaneda F, Kinne RK. Apoptosis induced in HepG2 cells by short exposure to millimolar concentrations of ethanol involves the Fas-respector pathway. J Cancer Res Clin Oncol 2001: 127; 418–24.

12 Eichhorst ST, Muller M, Li-Weber M, Schulze-Bergkamen H, Angek P, Krammer PH. A novel AP-1 element in the CD95 ligand promoter is required for induction of apoptosis in hepatocellular carcinoma cells upon treatment with anticancer drugs. Mol Cell Biol 2000; 20: 7826–37.

13 Lin HL, Liu TY, Chau GY, Lui WY, Chi CW. Comparison of 2-methoxyestradiol-induced, docetaxel-induced, and paclitaxel-induced apoptosis in hepatoma cells and its correlation with reaction oxygen species. Cancer 2000; 89: 983–94.

Acta Pharmacologica Sinica 2005 Jun; 26 (6): 641–648

Invited Review

Antibody engineering: facing new challenges in cancer therapy[1]

Laura SANZ, Ángel M CUESTA, Marta COMPTE, Luis ÁLVAREZ-VALLINA[2]

Servicio de Inmunología, Hospital Universitario Puerta de Hierro, Madrid, Spain

Key words

immunoglobulin fragments; monoclonal antibodies; antibody formation; gene therapy; recombinant proteins; biomedical engineering

[1] Project supported by grants from the Fondo de Investigación Sanitaria (grant 02/1144), from the Comunidad Autónoma de Madrid (grant GR/SAL/0214/2004) and from the 5th framework of the European Community (grant EC QLK3-CT-1999-00386).
[2] Correspondence to Prof Luis ÁLVAREZ-VALLINA.
Phn/Fax 34-9-1316-0644.
E-mail lalvarezv.hpth@salud.madrid.org

Received 2005-03-08
Accepted 2005-03-28

doi: 10.1111/j.1745-7254.2005.00135.x

Abstract

Antibody-based therapeutics are beginning to realize the promise enclosed in their early denomination as "magic bullets". Initial disappointment has turned into clinical and commercial success, and engineered antibodies currently represent over 30% of biopharmaceuticals in clinical trials. Recent structural and functional data have allowed the design of a new generation of therapeutic antibodies, with strategies ranging from complement-mediated and antibody-dependant cellular cytotoxicity enhancement to improved cytotoxic payloads using toxins, drugs, radionucleids and viral delivery. This review considers the structure of different types of recombinant antibodies, their mechanism of action and how their efficacy has been increased using a broad array of approaches. We will also focus on the additional benefits offered by the use of gene therapy methods for the *in vivo* production of therapeutic antibodies.

Introduction

Monoclonal antibodies (mAb) are unique and versatile molecules that have been found applications in research, diagnosis, and in the treatment of multiple diseases, including cancer. The advent of hybridoma technology for mAb production in 1975[1] was a breakthrough in the field of biomedicine; 30 years later, a plethora of biotech companies produces thousands of mAb, and at least 17 of them have FDA (US Food and Drug Administration) approval for therapeutic use in patients, with hundreds of them still in the pipeline.

However promising their future is, the development of therapeutic mAb suffered a number of serious drawbacks, which considerably reduced faith in their clinical applicability. These disappointments were caused by their inability to trigger human effector functions, and because repeated administration provoked an immune response against murine antibody (Ab) domains (HAMA, human anti-murine Abs)[2]. Recently developed technologies (phage display and transgenic mice) allow the selection and identification of fully human Ab, as well as the improvement of Ab affinity[3]. The ability to generate human mAb achieved 2 important goals: it overcame most host anti-Ab responses, and it extended the half-life of the reagent to something closer to that of normal IgG. As a result of these advances, mAb are starting to fulfill their potential as therapeutics.

Not surprisingly, Ab engineering has constituted its own field. Mutations can be introduced in the variable regions to increase the affinity of the Ab for its antigen or in the constant region to enhance its natural effector functions. Pharmacokinetics and avidity are improved by multimerization of Ab fragments. Ab molecules have been dissected to their basic elements, and then rearranged to produce a variety of formats not found in nature that display new properties. Moreover, these "building blocks" have been incorporated into multiple types of fusion proteins, soluble (immunocytokines, immunotoxins), as well as part of artificial cell surface receptors and viral envelopes for the retargeting of both effector cells and virus particles (Figure 1).

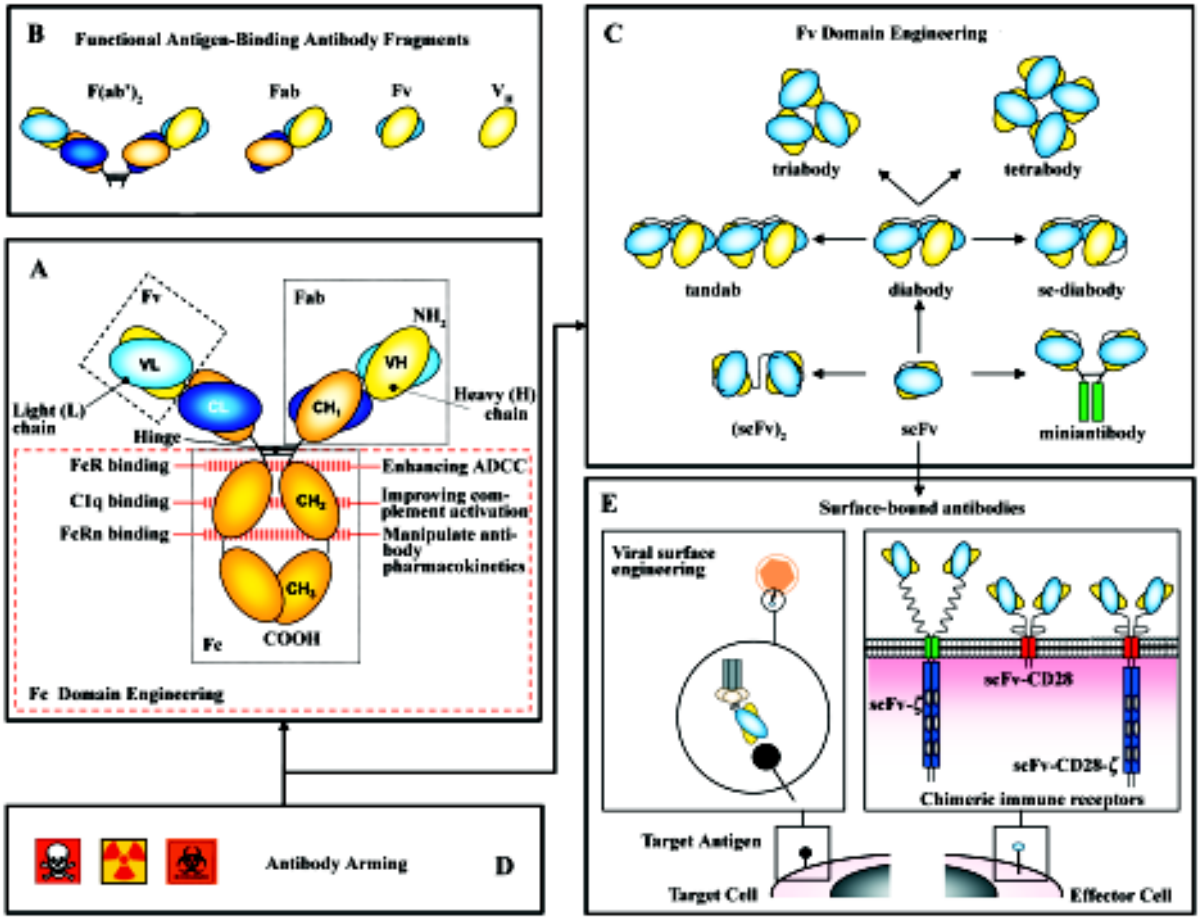

Figure 1. (A) Schematic representation of an intact IgG molecule. All Ig monomers are composed of 2 identical light chains (L) and 2 identical heavy chains (H). The 4 chains are covalently bonded together by disulfide bonds. Light chains are composed of 1 constant domain (CL) and one variable domain (VL), whereas heavy chains consist of 3 constant domains (CH1, CH2 and CH3) and 1 variable domain (VH). Ab functions can be separated into 2 proteolytic fragments by cleavage with the enzyme papain in the hinge region. The Fab fragment (fragment antigen binding) retains the antigen-binding activity, whereas the Fc fragment (fragment crystalizable) mediates effector functions. The minimal fragment that still contains the whole antigen-binding site is composed of both V_H and V_L domains. This heterodimer, called Fv fragment (for fragment variable) is still capable of binding the antigen. Bottom: strategies for enhancing the potency of therapeutic Ab by Fc domain manipulation. Key Fc regions can be engineered to enhance efector functions or to increase the Ab half-life. (B) Dissection of the binding region of an Ab in progressively smaller fragments. F(ab´)2 and Fab fragments are obtained by proteolysis with pepsin and papain, respectively. (C) Using scFv (single-chain Fv, obtained by linking VH y VL with a flexible polypeptide) as building blocks, different multivalent Ab fragments can be engineered. Shortening the intradomain linker connecting the VH and VL chains results in the formation dimers, (diabodies), trimers (triabodies) and tetramers (tetrabodies). To create a miniantibody, a scFv is genetically linked to the IgG1 CH3 domain via connecting peptides. A bispecific and tetravalent recombinant Ab can be constructed by linking four Ab variable domains (V_H and V_L) of 2 different specificities into a single chain construct. They can either form bivalent bispecific Abs by diabody-like folding (sc-diabodies) or dimerize with the formation of tetravalent bispecific Abs (tandem diabodies). The efficacy of tandem diabody (tandab) formation is dependent on the length of the linker between 2 halves of the molecule. (D) Ab can be “armed” by incorporation (by chemical conjugation or at genetic level) of a variety of moieties, including radionuclides, chemotherapeutics, toxins and cytokines. (E) Surface-bound, scFv-based molecules comprise chimeric immune receptors (CIR) and engineered viral surfaces. CIR comprise a recognition unit (the Ab fragment) attached to the transmembrane and intracytoplasmic sequences of a signaling molecule. Viral envelopes or capsides can be designed to incorporate scFvs for virus retargeting.

Making better mAb: how to improve their "natural" effector functions

Ab contains two functionally and molecularly separable modules (Figure 1A): one module for antigen binding (Fab) and another for triggering effector functions (Fc). The antigen-binding region can be manipulated to increase both binding affinity and specificity. Methods of Ab affinity maturation are based on the principle of changing parts of the variable domains while keeping the specificity. Different approaches are: chain-shuffling (substitution of the native light chain with a new light-chain repertoire, but retaining the variable heavy chain), randomization of complementarity determining regions (CDR), and generation of Ab libraries with mutations within the variable regions by error-prone PCR, and *E coli* mutator strains or site-specific mutagenesis[4].

Fragment cystalizable (FC) domains contain motifs for the activation of both effector immune cells and the classical pathway of the complement (C1q) responsible, respectively, for Ab-dependent cellular cytotoxicity (ADCC) and complement-dependent cytotoxicity (CDC). A variety of immune cells express on their surface receptors for the Fc domain of IgG1 and IgG3: FcγRI, FcγRIIa, FcγRIII are stimulatory and FcγRIIb is inhibitory. The Fc domain sequence can be manipulated (Figure 1A) to increase its affinity for the stimulatory receptors or to decrease its binding to the inhibitory one, modulating the activity of the whole Ab[5]. Similarly, point mutations in the Fc domain can increase the binding to C1q, improving complement activation[6]. Modification of Fc glycosylation can also enhance its ability to support ADCC[7].

The Fc region of human Ab also contains a binding motif for the receptor FcRn that protects immunoglobulins (Ig) from intracellular degradation (Figure 1A). By contrast, rodent mAb fail to bind to FcRn and are rapidly removed from the circulation. Using combinatorial phage display libraries, mutations in the Fc region have been identified with higher binding affinity to FcRn, implying longer half-life of the mAb[8].

New formats, new functions

The domain architecture of Ig has facilitated the creation of both smaller and larger forms with variable valency for one or more target antigens and pharmacokinetic properties that are tunable to specific settings[9]. Non-natural Ab formats (Figure 1C), such as the single-chain fragment variable (scFv) and the diabody, are rapidly emerging as key players in the engineered Ab field. A scFv (~30 kDa) comprises the V domains of the heavy and light chains (VH and VL) of a mAb joined by a linker sequence[3]. A diabody (~60) kDa is produced when scFv contain short interdomain linkers (5 aminoacids or less)[10]. This prevents intramolecular pairing of the VH and VL domains on the same chain, but allows interchain pairing to form dimers. Reducing further the linker length promotes the assembly of scFv into trimers (triabodies, ~90 kDa) or tetramers (tetrabodies, ~120 kDa). The increased binding valency of these multimers results in high avidity and low off-rates.

Given that Ab fragments lack the Fc region, their biological effects can not be attributed to CDC or ADCC. In this context, the nature of the target is crucial, as Ab fragments function by blocking the action of specific molecules or by acting as signaling molecules. The blocking activity is achieved by preventing growth factors, cytokines or other soluble mediators reaching their target receptors, accomplished either by the Ab binding to the factor itself or to its receptor. The signaling effect is based on the crosslinking of receptors that are, in turn, connected to mediators of cell division or programmed cell death[4].

Diabodies constitute the most effective way to generate bispecific Ab fragments through their ability to bind to 2 different antigens and used to crosslink various cells and molecules. Bispecific Ab offer a variety of new effector mechanisms: retargeting of effector cells (cytotoxic T cells, NK cells, and macrophages), recruitment of effector molecules (toxins, drugs, prodrugs, cytokines, radioisotopes, and complement system) and retargeting of carrier systems (viral vectors for gene therapy)[11].

Ab fragments as Fab and scFv offer several advantages because of their small size when compared to parental Ig (150 kDa): (i) they are easy to produce in bacterial systems; (ii) extravasate more efficiently; and (iii) their tissue penetration ability is higher. However, recombinant proteins that are smaller than 60 kDa are taken up by the kidney and excreted into the urine. Therefore, these molecules tend to have a short circulating half-life. As Fab and scFv fragments lack the Fc region altogether, they can not be saved from degradation by FcRn. Multimerization is an obvious strategy to increase the size, and therefore, the half-life of Ab fragments (triabodies, tetrabodies). The use of bispecific Ab fragments for retargeting serum Ig provides with the Fc-associated effector functions and prolongs the residence time in serum. A new approach is the pegylation of Ab fragments, achieved by chemical coupling of polyethylene glycol (PEG) to amino groups in the protein structure, increasing the size of the molecule above the glomerular filtration limit[12].

Naked versus armed mAb: acquisition of new effector functions

In cancer therapy, Ab fragments are fused (chemically or at genetic level) with a range of molecules to introduce different functionalities, including cytotoxic drugs, toxins, or radionuclides for cancer cell killing, enzymes for prodrug therapy and cytokines to stimulate the antitumor immune response (Figure 1D). These "armed" Ab exhibit considerably better therapeutic performance than their "naked" counterparts (for a review on the topic, see Ref [2]).

Incorporation of agents with direct toxic effect The most widely explored strategy for enhancing the efficacy of antitumor Ab is direct arming by linkage to cytotoxic agents or radionuclides. In fact, 3 of the approved mAb for use in patients belong to this group: gemtuzumab ozogamicin was the first (2000), followed by ibritumomab tiuxetan and tositumomab (2002 and 2003, respectively). Gemtuzumab ozogamicin is an anti-CD33 (antigen expressed in 90% of acute myeloid leukemias) mAb conjugated to calicheamicin. Calicheamicins and maytansinoids are (100–1000)-fold more potent than conventional chemotherapeutics and constitute the most extensively evaluated small-molecule toxins used for Ab arming[2]. Biological toxins, such as ricin or diphtheria toxin, can be attached to an Ab (native Ig or recombinant fragments), although their clinical application has been hampered by their high toxicity. It has recently been published that a single point mutation in ricin toxin can eliminate vascular damage without compromising its action[13].

Ibritumomab tiuxetan and tositumomab are anti-CD20 mAb conjugated, respectively, to ^{90}Y and ^{131}I, and approved for non-Hodgkin lymphoma treatment. Radioimmunotherapy (RAIT/RIT) has the advantage to kill bystander cells, especially interesting when not all the tumor cells express the antigen recognized by the Ab[14].

ADEPT: Ab-directed enzyme prodrug therapy ADEPT involves the pre-targeting of prodrugs to tumors. An Ab-enzyme fusion protein is first administered and allowed to localize to the tumor, followed by the administration of the prodrug which is activated by the enzyme at the tumor site[15,16]. This strategy has proven highly effective in preclinical tumor models, allowing 4–12 fold higher intratumor drug concentrations and up to 5-fold lower extratumor drug concentration[2]. An interesting approach is the use of Abs with inherent catalytic activity, so the conjugation to an enzyme is not required[17].

Immunocytokines Several cytokines have demonstrated their potent antitumoral effect, but unfortunately their side effects limit their administration. In order to accumulate preferentially the cytokine in the tumor, fusion proteins (immunocytokines) consisting of a targeting mAb specific for a tumor antigen and the selected cytokine (IL-2, IL-12, TNF-α and GM-CSF) have been designed[18]. These immunocytokines allow the local activation of the antitumoral immune response, avoiding the toxicity associated with systemic cytokine administration[19,20]. A different approach is based on the targeting of tumor vasculature using cytokines with recognized antiangiogenic effect, as IL-12[21].

Gene therapy: new scenarios

The practical utility of Ab fragments has been limited by problems related to large-scale production and biodistribution. Monovalent Ab fragments exhibit rapid blood clearance and poor retention time on the target, which results in the necessity of frequent delivery of such Ab fragments. To circumvent these limitations, Ab-based gene therapy approaches have been developed. *In vivo* production makes the Abs less immunogenic and better tolerated and results in effective and persistent levels of Ab fragments, compensating for the rapid blood clearance of scFvs. Moreover, genetic approaches provide Ab molecules with new functions in unexpected scenarios[22].

Secretion of soluble Abs by genetically modified cells *In vivo* production of therapeutic mAb by genetically engineered cells could advantageously replace the injection of purified Ab in cancer treatment. The feasibility of the *in vivo* production and systemic delivery of mAb by different cells/tissues has now been demonstrated using different techniques, as *ex vivo* genetically modified autologous or encapsulated heterologous cells and *in vivo* gene transfer using viral vectors[23].

In the first work reporting a therapeutic effect associated to *in vivo* mAb production, an anti-erbB-2 scFv was expressed using an adenoviral vector. In this model, a human ovarian cancer cell line erbB-2$^+$ was established in the context of athymic nude mice. Whereas exponential growth in tumor volumes was noted in the control groups, a clear inhibition of tumor growth was observable for the animals treated with the adenoviral vector encoding anti-erbB-2 scFv[24].

We have demonstrated that both monospecific and bispecific Ab can be efficiently produced by mammalian cells with a clear therapeutic effect. Using an anti-laminin scFv with antiangiogenic activity[25,26], we assessed that gene-modified human fibrosarcoma cells failed to grow to detectable tumors when inoculated in athymic mice[27]. In another set of experiments, functionally active diabody (anti-CEA x anti-CD3) was secreted from stably transfected human cells and promoted unstimulated human primary T cells to proliferate and kill CEA-expressing cancer cells. Importantly,

locally produced diabodies showed significant cytotoxic activity *in vivo* against established tumors and only required the infusion of small numbers of functional T cells[28].

Surface-bound Abs: chimeric immune receptors Adoptive cellular immunotherapy of cancer has been limited mostly because of the poor immunogenicity of tumor cells and the difficulties in obtaining tumor-specific MHC-restricted cytotoxic T lymphocytes (CTL) in large numbers[29]. To circumvent these limitations, new strategies have been designed in order to target CTL to relevant tumor cell surface antigens, including genetic manipulation of T cells to graft them with new recognition specificities[30].

Chimeric immune receptors (CIR) genes are composed of a recognition unit attached to the transmembrane and intracytoplasmic sequences of a signaling molecule. Most Ab-derived CIR use scFvs as recognition domains. Signaling molecules belong to a family of structurally and functionally related proteins that include TCR-associated polypeptides and some Fc receptors. As the requirements of MHC restriction are bypassed, the tumor cell recognition of CTL grafted with CIR is not hampered by the down-regulation of HLA class I molecules usually found in tumors[30].

The utility and effectiveness of the CIR approach has been demonstrated in a variety of animal models where tumor-specific CIR drove the adoptive transferred autologous T-lymphocytes to accumulate at the tumor site *in vivo* and prevented the growth of syngenic tumors that grow rapidly in the native host. Target antigens include CEA (colorectal cancer), PSMA (prostate cancer), erbB-2 (breast and others), CD19 and CD20 (B-cell malignancies), CD30 (lymphomas), GD2 (neuroblastoma) and the tumor neovasculature receptor VEGFR-2[22]. Recently, human peripheral blood leukocytes genetically modified to target CD19 were shown to eliminate systemic B-cell tumors in immunodeficient mice[31]. Primarily investigated in T cells, CIR have also proven useful in the retargeting of NK cells[32].

Recent studies have established that the provision of additional or co-stimulatory signals is essential for the expansion and activity of adoptively transferred T cells. We have reported that CD28-based CIRs were stably expressed as functional cell surface receptors and that Ag-specific costimulatory signals could synergize with signals mediated through the native TCR/CD3 complex or TCRz-based CIR to produce optimal levels of IL-2[33]. Moreover, CIR providing both primary and costimulatory signaling in T cells from a single gene product have been described[34].

Viral surface engineering Most of the viral vectors developed for gene therapy have a broad tissue tropism. The development of viral vectors targeted into a selected type of cell or tissue, without losing virus infection efficiency or causing toxicity, is critical for their clinic application. Cancer cells represent major targets in this strategy, as they often express lower levels of viral receptors compared to normal cells[35].

Using Ab directed against tumor-associated antigens expressed on the cell surface for virus pseudotyping has been successfully associated with different viral vectors in directing them to cancer cells. Adenovirus (AdV) has been extensively studied in this approach, especially in the context of capsid engineering. The most recent developments in this approach have overcome several limitations in this strategy, including the need for correct ligand folding, the structural and biosynthetic compatibility of ligands with the AdV, along with the fact that in this strategy, viruses have to be specifically engineered for each particular targeting situation. Thus, several groups have used similar strategies by incorporating an IgG-binding domain of staphylococcal protein A into the AdV fiber protein, allowing the vectors to form a stable complex with either full size mAb or fusion proteins consisting of a targeting scFv fused to an Ig Fc domain[36,37].

Another group of preferred vectors in preclinical and clinical settings for cancer gene therapy are the murine leukemia virus (MLV)-based retroviral vectors. Several groups have inserted a scFv moiety in the virus envelop to obtain cell-specificity[38–41]. Using a different strategy, the IgG-binding domain of protein A was inserted into the envelope, allowing the redirecting lentiviral vectors to target cells through adaptors as described for AdV[42].

The attenuated measles virus (MV) is another vector with great therapeutic potential in gene therapy. The feasibility to expand MV tropism by virtue of a scFv displayed on its H protein was demonstrated using an anti-CEA scFv[43]. Replicating MV have been obtained which are capable of entering $CD20^+$ or $CD38^+$ target cells through interaction between either an anti-CD20 or anti-CD38 scFv and the cognate antigen molecules on the cell surface. Both studies have shown significant antitumor effects *in vivo*[44,45].

Intrabodies Intracellular Ab (intrabodies) constitute neutralizing molecules with a great potential in gene therapy and represent an alternative to other methods of gene inactivation as antisense RNA and RNA interference (RNAi). When provided with the corresponding protein trafficking signals, intrabodies can be directed to endoplasmic reticulum via addition of a SEKDEL retention signal, nucleus via the SV40-derived nuclear localization signal, inner face of the plasma membrane by the addition of farnesylation signals or cytoplasm simply by the deletion of the leader peptide. Although

classically designed to divert proteins from their usual cellular compartment or to block protein-protein or protein-nucleic acid interactions, this concept is currently in expansion, with intrabodies capable of directly inhibiting the function of an enzyme, activating intracellular proteins, as caspase-3, or leading proteins to degradation in the ubiquitin-proteasome pathway using F-box-intrabody fusions[46].

ScFvs are the preferred format for intrabodies, but their stability is affected by the reducing conditions inside the cell, which prevent the formation of intradomain disulphide bonds and blocks their proper folding. Efforts to generate functional intrabodies include the isolation of naturally occurring intrabodies from large libraries and the creation of an artificial intrabody framework that relies on the pre-determined ability of certain scFv to fold adequately and remain stable in the cellular milieu[46,47]. While scFv intrabodies are the most common, alternative formats have been shown to be equally effective, including single Ab domains ("camelized" or not) and bispecific Ab, known as "intra-diabodies" which are able to downregulate simultaneously 2 cell surface receptors[48].

Regarding their application in cancer therapy, intrabodies are suitable to downregulate proteins overexpressed in tumors, such as EGFR, erbB-2, cathepsin L[49], and cyclin E or to target mutant oncogenic forms of Ras and p53 and fusion proteins as BCR-ABL. Apoptosis of tumor cells can be promoted by downregulation of Bcl-2 or activation of caspase-3, and the uptake of cytotoxic drugs can be increased blocking the multidrug resistance (MDR) gene product[22]. Inhibition of tumor neovascularization is a promising approach for cancer therapy. Recently, an adenoviral vector was used to deliver a scFv capable of blocking surface expression of an endothelial cell-specific receptor and significantly inhibited growth of human xenografts in a murine model[50].

Conclusions

Antibody engineering represents an emerging technology that holds great promise for medical science. With the plethora of new molecular techniques at hand, many innovative approaches to diagnostics and therapeutics applications are under consideration. The development of protein engineering techniques to reduce immunogenicity, alter half-life, improve efficacy, and increase tumor targeting has provided the new types of antibodies that are moving rapidly from the bench to the clinic. In fact, engineered antibodies now represent over 30% of biopharmaceuticals in clinical trials. Furthermore, genetic approaches provide antibody molecules with new functions in unexpected scenarios: expression of antibody domains in precise intracellular locations and grafting of new binding activities to engineered cells. Further improvement will require the design of *in vivo* selection systems to generate antibodies fully active in specific cellular compartments, and the use of antibodies as tools for functional gene identification and drug target validation (genomics- and proteomics-based high-throughput systems) and for better understanding of disease pathways.

References

1 Kohler G, Milstein C. Continuous cultures of fused cells secreting antibody of predefined specificity. Nature 1975; 256: 495–7.

2 Carter P. Improving the efficacy of antibody-based cancer therapies. Nat Rev Cancer 2001; 1: 118–29.

3 Hudson PJ, Souriau C. Engineered antibodies. Nat Med 2003; 9: 129–34.

4 Brekke OH, Sandlie I. Therapeutic antibodies for human diseases at the dawn of the twenty-first century. Nat Rev Drug Disc 2003; 2: 52–62.

5 Shields RL, Namenuk AK, Hong K, Meng YG, Rae J, Briggs J, *et al*. High resolution mapping of the binding site on human IgG1 for Fc gamma RI, Fc gamma RII, Fc gamma RIII, and FcRn and design of IgG1 variants with improved binding to the Fc gamma R. J Biol Chem 2001; 276: 6591–604.

6 Idusogie EE, Wong PY, Presta LG, Gazzano-Santoro H, Totpal K, Ultsch M, *et al*. Engineered antibodies with increased activity to recruit complement. J Immunol 2001; 166: 2571–5.

7 Umaña P, Jean-Mairet J, Moudry R, Amstutz H, Bailey JE. Engineered glycoforms of an antineuro-blastoma IgG 1 with optimized antibody-dependent cellular cytotoxic activity. Nat Biotechnol 1999; 17: 176–80.

8 Ghetie V, Popov S, Borvak J, Radu C, Matesoi D, Medesan C, *et al*. Increasing the serum persistence of an IgG fragment by random mutagenesis. Nat Biotechnol 1997; 15: 637–40.

9 Pluckthun A. Mono- and bivalent antibody fragments produced in *Escherichia coli*: engineering, folding and antigen binding. Immunol Rev 1992; 130: 151–88.

10 Holliger P, Prospero T, Winter G. "Diabodies": small bivalent and bispecific antibody fragments. Proc Natl Acad Sci USA 1993; 90: 6444–8.

11 Kontermann RE. Recombinant bispecific antibodies for cancer therapy. Acta Pharmacol Sin 2005; 26: 1–9.

12 Natarajan A, Xiong CY, Albrecht H, DeNardo GL, DeNardo SJ. Characterization of site-specific ScFv PEGylation for tumor-targeting pharmaceuticals. Bioconjug Chem 2005; 16:113–21.

13 Smallshaw JE, Ghetie V, Rizo J, Fulmer JR, Trahan LL, Ghetie MA, *et al*. Genetic engineering of an immunotoxin to eliminate pulmonary vascular leak in mice. Nat Biotechnol 2003; 21: 387–91.

14 Goldenberg DM. Advancing role of radiolabeled antibodies in the therapy of cancer. Cancer Immunol Immunother 2003; 52: 281–96.

15 Xu G, McLeod HL. Strategies for enzyme/prodrug cancer therapy. Clin Cancer Res 2001; 7: 3314–24.

16 Sharma SK, Pedley RB, Bhatia J, Boxer GM, El-Emir E, Qureshi

U, *et al*. Sustained tumor regression of human colorectal cancer xenografts using a multifunctional mannosylated fusion protein in antibody-directed enzyme prodrug therapy. Clin Cancer Res 2005; 11: 814–25.
17 Shabat D, Lode HN, Pertl U, Reisfeld RA, Rader C, Lerner RA, *et al*. *In vivo* activity in a catalytic antibody-prodrug system: antibody catalyzed etoposide prodrug activation for selective chemotherapy. Proc Natl Acad Sci USA 2001; 98: 7528–33.
18 Nissim A, Gofur Y, Vessillier S, Adams G, Chernajovsky Y. Methods for targeting biologicals to specific disease sites. Trends Mol Med 2004; 10: 269–74.
19 Hombach A, Heuser C, Abken H. Simultaneous targeting of IL2 and IL12 to Hodgkin's lymphoma cells enhances activation of resting NK cells and tumor cell lysis. Int J Cancer. 2005; 115: 241–7.
20 Gillies SD, Lan Y, Williams S, Carr F, Forman S, Raubitschek A, *et al*. An anti-CD20-IL-2 immunocytokine is highly efficacious in a SCID mouse model of established human B lymphoma. Blood. 2005; 105: 3972–8.
21 Halin C, Rondini S, Nilsson F, Berndt A, Kosmehl H, Zardi L, *et al*. Enhancement of the antitumor activity of interleukin-12 by targeted delivery to neovasculature. Nat Biotechnol 2002; 20: 264–9.
22 Sanz L, Blanco B, Alvarez-Vallina L. Antibodies and gene therapy: teaching old 'magic bullets' new tricks. Trends Immunol 2004; 25: 85–91.
23 Pelegrin M, Gros L, Dreja H, Piechaczyk M. Monoclonal antibody-based genetic immunotherapy. Curr Gene Ther 2004; 4: 347–56.
24 Arafat WO, Gomez-Navarro J, Buchsbau DJ, Xiang J, Wang M, Casado, *et al*. Effective single chain antibody (scFv) concentrations *in vivo* via adenoviral vector mediated expression of secretory scFv. Gene Ther 2002; 9: 256–62.
25 Sanz L, Kristensen P, Russell SJ, Ramirez Garcia JR, Alvarez-Vallina L. Generation and characterization of recombinant human antibodies specific for native laminin epitopes: potential application in cancer therapy. Cancer Immunol Immunother 2001; 50: 557–65.
26 Sanz L, Garcia-Bermejo L, Blanco FJ, Kristensen P, Feijoo M, Suarez E, *et al*. A novel cell binding site in the coiled-coil domain of laminin involved in capillary morphogenesis. EMBO J 2003; 22: 1508–17.
27 Sanz L, Kristensen P, Blanco B, Facteau S, Russell SJ, Winter G, *et al*. Single-chain antibody-based gene therapy: inhibition of tumor growth by *in situ* production of phage-derived human antibody fragments blocking functionally active sites of cell-associated matrices. Gene Ther 2002; 9: 1049–53.
28 Blanco B, Holliger P, Vile R, Alvarez-Vallina L. Induction of human T lymphocyte cytotoxicity and inhibition of tumor growth by tumor-specific diabody-based molecules secreted from gene-modified bystander cells. J Immunol 2003; 171: 1070–7.
29 Baxenavis CN, Papamichail M. Targeting of tumor cells by lymphocytes engineered to express chimeric receptor genes. Cancer Immunol Immunother 2004; 53: 893–903.
30 Álvarez-Vallina L. Genetic approaches for antigen-selective cell therapy. Curr Gene Ther 2001; 4: 385–97.
31 Brentjens RJ, Latouche JB, Santos E, Marti F, Gong MC, Lyddane C *et al*. Eradication of systemic B-cell tumors by genetically targeted human T lymphocytes co-stimulated by CD80 and interleukin-15. Nat Med 2003; 9: 279–86.
32 Uherek C, Tonn T, Uherek B, Becker S, Schnierle B, Klingemann HG, *et al*. Retargeting of natural killer-cell cytolytic activity to ErbB2-expressing cancer cells results in efficient and selective tumor cell destruction. Blood 2002; 100: 1265–73.
33 Alvarez-Vallina L, Hawkins RE. Antigen-specific targeting of CD28-mediated T cell co-stimulation using chimeric single-chain antibody variable fragment-CD28 receptors. Eur J Immunol 1996; 26: 2304–9.
34 Finney HM, Lawson AD, Bebbington CR, Weir AN. Chimeric receptors providing both primary and costimulatory signaling in T cells from a single gene product. J Immunol 1998; 161: 2791–7.
35 Sanz L, Qiao J, Vile R, Alvarez-Vallina L. Antibody engineering, virus retargeting and cellular immunotherapy: one ring to rule them all? Curr Gene Ther 2005; 5: 63–70.
36 Korokhov N, Mikheeva G, Krendelshchikov A, Belousova N, Simonenko V, Krendelshchikov V, *et al*. Targeting of adenovirus via genetic modification of the viral capsid combined with a protein bridge. J Virol 2003; 77: 12931–40.
37 Volpers C, Thirion C, Biermann V, Hussmann S, Kewes H, Dunant P, *et al*. Antibody-mediated targeting of an adenovirus vector modified to contain a synthetic immunoglobulin g-binding domain in the capsid. J Virol 2003; 77: 2093–104.
38 Russell SJ, Hawkins RE, Winter G. Retroviral vectors displaying functional antibody fragments. Nucleic Acids Res 1993; 21: 1081–5.
39 Somia NV, Zoppe M, Verma IM. Generation of targeted retroviral vectors by using single-chain variable fragment: an approach to *in vivo* gene delivery. Proc Natl Acad Sci USA 1995; 92: 7570–4.
40 Chu TH, Dornburg R. Toward highly efficient cell-type-specific gene transfer with retroviral vectors displaying single-chain antibodies. J Virol 1997; 71: 720–5.
41 Martin F, Neil S, Kupsch J, Maurice M, Cosset F, Collins M. Retrovirus targeting by tropism restriction to melanoma cells. J Virol 1999; 73: 6923–9.
42 Morizono K, Xie Y, Ringpis GE, Johnson M, Nassanian H, Lee B, *et al*. Lentiviral vector retargeting to P-glycoprotein on metastatic melanoma through intravenous injection. Nat Med 2005; 11: 346–52.
43 Hammond AL, Plemper RK, Zhang J, Schneider U, Russell SJ, Cattaneo R. Single-chain antibody displayed on a recombinant measles virus confers entry through the tumor-associated carcinoembryonic antigen. J Virol 2001; 75: 2087–96.
44 Bucheit AD, Kumar S, Grote DM, Lin Y, von Messling V, Cattaneo RB, *et al*. An oncolytic measles virus engineered to enter cells through the CD20 antigen. Mol Ther 2003; 7: 62–72.
45 Peng KW, Donovan KA, Schneider U, Cattaneo R, Lust JA, Russell SJ. Oncolytic measles viruses displaying a single-chain antibody against CD38, a myeloma cell marker. Blood 2003; 101: 2557–62.
46 Lobato MN, Rabbits TH. Intracellular antibodies and challenges facing their use as therapeutic agents. Trends Mol Med 2003; 9: 390–6.
47 Stocks MR. Intrabodies: production and promise. Drug Discov Today 2004; 9: 960–6.
48 Jendreyko N, Popkov M, Beerli RR, Chung J, McGavern DB,

Rader C *et al*. Intra-diabodies: bispecific, tetravalent antibodies for the simultaneous functional knockout of two cell surface receptors. J Biol Chem 2003; 278: 47812–9.

49 Rousselet N, Mills L, Jean D, Tellez C, Bar-Eli M, Frade R. Inhibition of tumorigenicity and metastasis of human melanoma cells by anti-cathepsin L single chain variable fragment. Cancer Res 2004; 64: 146–51.

50 Popkov M, Jendreyko N, McGavern DB, Rader C, Barbas CF III. Targeting tumor angiogenesis with adenovirus-delivered anti-Tie-2 intrabody. Cancer Res 2005; 65: 972–81.

The 15th World Congress of Pharmacology (IUPHAR-2006)

2006, July 2-7 Beijing International Convention Center, China

Info: Ms Xiao-dan Zhao
Chinese Pharmacological Society
1, Xian Nong Tan St
Beijing 100050, China
Phn/Fax 86-10-6316-5211
E-mail zhxd@imm.ac.cn
http://www.cnphars.org

Acta Pharmacologica Sinica 2005 Jun; 26 (6): 649–658

Invited Review

Recombinant approaches to IgG-like bispecific antibodies

Jonathan S MARVIN, Zhenping ZHU[1]

Department of Antibody Technology, ImClone Systems Incorporated, New York, NY 10014, USA

Key words

bispecific antibodies; single chain Fv; diabody; immunoglobulin G; biomedical engineering

[1] Correspondence to Dr Zhenping ZHU.
Phn 1-646-638-5190.
Fax 1-212-645-2054.
E-mail zhenping.zhu@imclone.com

Received 2005-03-01
Accepted 2005-03-18

doi: 10.1111/j.1745-7254.2005.00119.x

Abstract

One of the major obstacles in the development of bispecific antibodies (BsAb) has been the difficulty of producing the materials in sufficient quality and quantity by traditional technologies, such as the hybrid hybridoma and chemical conjugation methods. In contrast to the rapid and significant progress in the development of recombinant BsAb fragments (such as diabody and tandem single chain Fv), the successful design and production of full length IgG-like BsAb has been limited. Compared to smaller fragments, IgG-like BsAb have long serum half-life and are capable of supporting secondary immune functions, such as antibody-dependent cellular cytotoxicity and complement-mediated cytotoxicity. The development of IgG-like BsAb as therapeutic agents will depend heavily on our research progress in the design of recombinant BsAb constructs (or formats) and production efficiency. This review will focus on recent advances in various recombinant approaches to the engineering and production of IgG-like BsAb.

Introduction

Antibodies quickly evolve by recombination, somatic mutation, and clonal selection *in vivo* to acquire the exquisite specificity and high affinity needed for an effective immune response. The modular structure of antibodies that permits *in vivo* reorganization also makes them exceptionally amenable to molecular manipulation, and facilitates the development of desirable properties. As a result, the field of antibody engineering has developed rapidly in recent years, as researchers exploit the ease with which antibodies can be genetically modified to develop ever more powerful therapeutics. So far, 18 antibody-based products have been approved by the FDA for therapeutic applications, including 8 for oncology indications. While the inoculation of animals with antigen and high-throughput screening of hybridoma clones is still common practice, *in vitro* selection is rapidly becoming the norm. Through the use of synthetic or semi-synthetic libraries in microscopic selection techniques (such as phage display[1], yeast surface display[2], and ribosomal display[3]), identifying an antibody to a given target has become a routine, although by no means trivial, matter.

Once an antibody specific to a particular antigen is identified, numerous mechanisms of action can be exploited for therapy. These mechanisms include: (1) as an antigen (growth factor or cytokine) sequestrant, the antibody binds a soluble antigen and prevents it from interacting with other molecules, such as its receptors. Avastin (Genentech, South San Francisco, CA), an anti-angiogenic therapy for colon cancer, binds vascular endothelial growth factor (VEGF) and blocks its interaction with the receptors[4]. Remicade (Centocor, Malvern, PA), a treatment for auto-immune disorders such as Crohn's disease and rheumatoid arthritis, works by sequestering tumor necrosis factor-α[5]. A number of antibodies to sequester anthrax toxin[6] and botulinum toxin[7] are also being developed; (2) as a receptor antagonist, the antibody binds a cell surface receptor and inactivates it by blocking the binding site of an activating ligand. Erbitux (ImClone, New York, NY), an antibody for the treatment of colon cancer, binds epidermal growth factor receptor (EGFR) at the EGF-binding site and blocks activation by both EGF and transforming growth factor-α[8]. Alternatively, the antibody may not directly block ligand/receptor interaction but rather exerts its effects by preventing receptor dimerization/multimerization, which is required for activation. For example, Omnitarg, also known as 2C4 (Genentech), an anti-HER2 antibody currently under clinical development, is believed

to inhibit tumor cell growth by blocking HER2 from dimerizing with EGFR and HER3 (there is no ligand identified so far for HER2)[9]; (3) as an agonist, the antibody binds to and cross-links multiple membrane bound receptors, mimicking the function of a natural ligand, and activating the receptor. There are a number of antibodies that mimic the function of Apo2L (ligand) and trigger apoptosis by activation of death receptor 5[10,11]; (4) as an effector function activator, the antibody binds a cell surface target and acts as an immune system identifier for antibody dependent cellular cytotoxicity (ADCC) or complement-mediated cytotoxicity (CMC). Rituxan (Genentech), an antibody for the treatment of CD20-positive, B-cell non-Hodgkin's lymphoma[12], and Herceptin (Genentech), an antibody for the treatment of HER2 positive metastatic breast cancer[13,14], are postulated to exert their effect in part by this mechanism[15]; (5) as a chemotherapy or radiotherapy adjunct, the antibody acts as a carrier molecule to deliver an attached chemotherapeutic agent or toxin, or radioisotope to cells displaying a specific antigen. A number of antibody conjugates have been approved by the FDA for oncology indications, including Mylotarg (Wyeth, Madison, NJ), an anti-CD33 antibody-calicheamicin conjugate for the treatment of CD33 positive acute myeloid leukemia; Zevalin (Biogen Idec, Cambridge, MA), a ^{90}Y-labeled anti-CD20 antibody, and Bexxar (GlaxoSmithKline, Brentford, UK), an ^{131}I-labeled anti-CD20 antibody for non-Hodgkin's lymphoma[16]; (6) as a means to redirect cytotoxic agents or immune effector cells to target sites, such as tumors, in the form of a bispecific antibody (BsAb), which is discussed in detail in the present paper.

Bispecific antibodies

BsAb are antibody-based molecules that can simultaneously bind two separate and distinct antigens (or different epitopes of the same antigen). The primary use of BsAb has been to redirect cytotoxic immune effector cells for enhanced killing of tumor cells by ADCC. In this context, one arm of the BsAb binds an antigen on the tumor cell, and the other binds a determinant expressed on effector cells, such as CD3, CD16, or CD64, which are expressed on T lymphocytes, natural killer (NK) cells, or other mononuclear cells[17–20]. By cross-linking tumor and effector cells, the BsAb not only brings the effector cells within the proximity of the tumor cells but also simultaneously triggers their activation, leading to effective tumor cell-killing. Preliminary but promising clinical benefits have been observed in a number of early stage trials[21]. In addition, BsAb has also been used to enrich the tumor/normal tissue localization ratio of chemo- or radiotherapeutic agents. In this setting, one arm of the BsAb binds an antigen expressed on the cell targeted for destruction, and the other arm binds a chemotherapeutic drug, radioisotope, or toxin. The naked BsAb is administered first, and after sufficient time has passed for the BsAb to bind tumor cells and to clear from normal tissue, the cytotoxic molecule is delivered, with rapid accumulation in the tumor, because of its affinity for the tumor bound BsAb[21–25]. Recently, a novel concept has emerged - the development of BsAb that target two tumor-associated antigens (eg, growth factor receptors) for down-regulation of multiple distinct cell proliferation/survival pathways, which provides enhanced antitumor activity[26–28].

A major obstacle in the general development of BsAb has been the difficulty of producing materials of sufficient quality and quantity for both preclinical and clinical studies. Initially, the main route to the production of BsAb was by co-expression of both the light chains (LC) and both the heavy chains (HC) of two parent antibodies of different specificities (antibody A and antibody B) in a single cell through either the hybrid hybridoma technique[29] or DNA co-transfection. Unfortunately, assuming that all the four polypeptide chains are equally expressed and there is no pairing preference between any particular LC and HC, in addition to the desired heterodimeric BsAb product (LC_A-HC_A plus LC_B-HC_B), there is also a large number of undesired products formed from the ten molecules that result from the 16 permutations LC and HC pairings (Figure 1). Consequently, the desired binding-competent BsAb are a minor product (in theory, an eighth of the total), and purification from the other products is very difficult. Another traditional method for BsAb production is chemical conjugation of two antibodies (or their fragments) of different specificities[30], although this method is by no means simple. Furthermore, the chemical modification process may inactivate the antibody or promote aggregation. As purification from undesired products remains difficult, the resulting low yield and poor quality BsAb makes this process, like the hybrid hybridoma and DNA co-transfection, unsuitable for the large scale production required for clinical development.

Thus the major requirements of efficient BsAb production are: (1) a novel structural format that promotes or obligates the formation of homogenous, bispecific proteins; and (2) an efficient expression system in prokaryotic or eukaryotic cells that leads to high-level production. Significant progress has been made in the past decade towards the development of BsAb fragments[31,32], which have various advantages and disadvantages. Firstly, they are smaller than full length IgG, so they have better solid tumor penetration

rates, but their small size and lack of an intact Fc also results in rapid clearing from circulation, leading to a short *in vivo* half-life. Secondly, the BsAb fragments do not require glycosylation, so they can be produced in high yield in bacteria. Compared to the full length IgG-like BsAb, these fragments are, however, incapable of promoting effector function such as ADCC and CMC (unless one arm of the BsAb fragments is specifically targeted to bind an effector cell determinant or certain components of the complement proteins, eg, C1q). The engineering and application of various BsAb fragments have been discussed in a recent review by Kontermann[33]. Our review will thus focus on the latest advancements and ongoing developments in recombinant production of full-length, IgG-like BsAb.

Recombinant approaches to IgG or IgG-like BsAb

Increasing heterodimer : homodimer ratio

"Knobs-into-holes" BsAb IgG Because one of the major barriers to the production of BsAb in a single cell system, such as hybrid hybridoma, is the undesired formation of HC homodimers (Figure 1), a first and obvious solution is to re-engineer the CH3 domain of the Fc so as to favor HC heterodimerization over homodimerization. This concept, first developed by Carter *et al* at Genentech[34], is based on the idea that simple mutations can be introduced into one half of the CH3 dimer, such that the steric complementarity required for CH3/CH3 association obligates the mutated CH3 domain to pair with a CH3 domain that has different, accommodating mutations (Figure 2). Specifically, a "knob" mutation (T366W in the CH3 domain, chosen by inspection of the crystal structure of the Fc[35]) is made into one HC to introduce a larger residue at the CH3 dimer interface and create a steric barrier to homodimerization. To promote heterodimerization, an accommodating "hole" (Y407A) mutation is engineered into the CH3 domain of the other HC. Co-expression of these two HC results in the formation of a mostly (92%) heterodimeric product, but with a stability that is significantly lower than that of the wild-type (knob: T366W+ hole: Y407A mutant, T_m=65.4°C; wild-type, T_m=80.4°C). To optimize and stabilize the heterodimerized molecules, variants with enhanced stability were selected from a phage display library in which residues near the "hole" (T366, L368, Y407) were randomized[36]. The resulting variant (knob: T366W; hole: T366S, L368A, Y407V) has an increased T_m (69.4°C) and formed predominantly heterodimers, when co-transfected in 293 cells. This example clearly demonstrates the utility of the knob-into-holes approach. It is possible there are other sets of residues within the CH3 domains that could be mutated/optimized to further increase BsAb stability and the heterodimer: homodimer ratio.

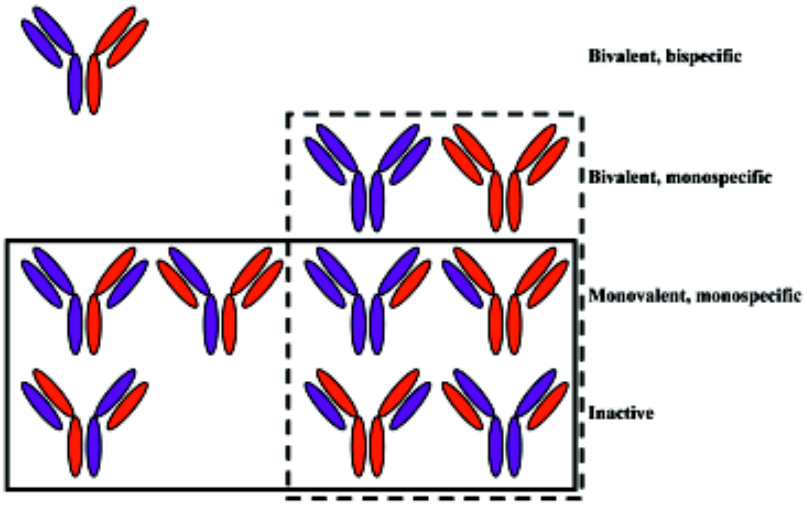

Figure 1. Chain mispairing is a major obstacle to BsAb production using both the hybrid hybridoma and DNA co-transfection methods. Random pairings of the two heavy and the two light chains from two different antibodies results in 10 possible combinations, only one of which is the desired bivalent, bispecific product. The use of knob-into-holes technology disfavors the formation of the six possible HC homodimeric products (dashed box). Use of a common LC eliminates all the LC/HC mispairings (solid box), and when combined with knob-into-holes engineered HC, renders all LC/HC pairings binding competent, and results in the preferential formation of the bivalent, bi-specific molecule (top row).

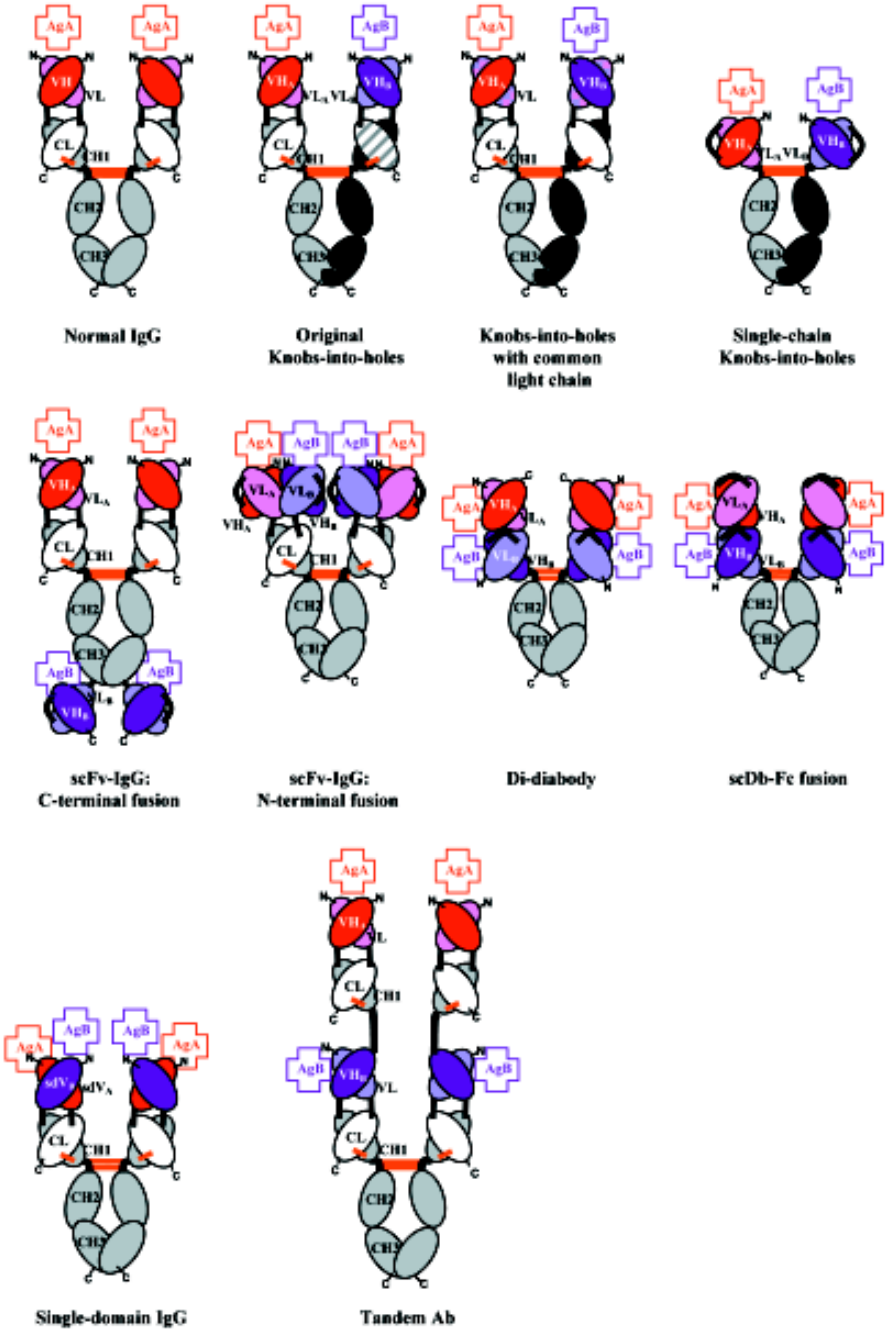

Figure 2. Schematic of recombinant BsAb formats. Details of each construct are described in text. HC constant domains, grey (and dark grey for knobs-into-holes); LC constant domain, white (and diagonal hashed for knobs-into-holes IgG); VH binding to antigen A, red; VL binding to antigen A, light red; common LC for knobs-into-holes, patched light red and light purple; VH binding to antigen B, purple; VL binding to antigen B, light purple; covalent polypeptide linkers, black; interchain disulfide bonds, orange; antigens A and B are indicated by colored crosses, red and purple, respectively. N- and C-terminal are indicated for each polypeptide chain.

While this approach solves the HC homodimerization problem, and reduces the total number of potential LC/HC pairings in a co-transfected single host from ten to four (Figure 1) thus, in theory, increasing the production of the functional BsAb from 12.5% to 25%, it does not address the equally problematic mispairing of LC and HC from two differ-

ent antibodies (eg, LC_A-HC_B and LC_B-HC_A mispairing, instead of the correct LC_A-HC_A and LC_B-HC_B pairing). This can be resolved by similarly redesigning the LC-HC interaction to incorporate knobs and holes at the VL-VH interface[37]. Based on inspection of the VL-VH interface of the anti-HER2 Fab fragment, 4D5 Fab[38], knob mutations and the complementary hole mutations were designed for a diabody fragment containing the Fvs of 4D5 and an anti-CD3 antibody. For one of the variants (termed "v5"; knob: VH-V37F, L45W; hole: VL-Y87A, F98M) 92% of the products were heterodimers, and near wild-type affinity for antigens was retained. Although these mutations were used to promote heterodimerization in a bispecific diabody, the principle should translate easily to a full length IgG format.

Common light chain BsAb IgG An alternative approach to solve the LC-HC mispairing problem is to construct BsAb using two antibodies of different specificities that share an identical LC[39] (Figures 1, 2). In a "proof-of-concept" study, a large scFv phage display library was used to screen for antibodies to a variety of antigens. The VL fragments of selected scFv were compared and those with identical amino acid sequences, but paired with different VH fragments for different antigen binding specificity, were selected to create BsAb. Functional IgG-like BsAb were formed with high yield (>95% of total IgG products) when a single LC was co-transfected in a host with two different HC that were engineered to incorporate the original knobs and holes mutations (knob: T366W, hole: T366S, L368A, Y407V) and a heterodimer promoting/stabilizing disulfide bond (S354C, Y349'C).

This highly engineered system demonstrates that the knobs-into-holes principle, when combined with a common light chain, can be used to effectively produce a near homogenous population of BsAb IgG. It also suggests that there are multiple ways in which the knob-into-holes approach can be applied, and that BsAb with even higher ratios of heterodimer formation may be achieved with further engineering. However, an obvious drawback of this method is that the inclusion of multiple mutations in the CH3 domains might pose an immunogenic risk in a therapeutic setting. Furthermore, it requires the identification of antibodies with common LC, which is rare, particularly for high-affinity antibodies.

Single chain Fv-Fc "knobs-into-holes" BsAb The LC-HC mispairing problem may also be circumvented by fusing the VL and VH in a single-chain Fv (scFv) format[40]. In this construct, an anti-HER2 scFv is fused to an Fc with the "knob" mutation T366Y, and an anti-CD16 scFv is fused to an Fc with the "hole" mutation Y407T (Figure 2). Efficient pairing of the two chains, through the knobs-into-holes mechanism, was demonstrated (but not quantitated), and specificity for both antigens was confirmed by cell surface binding analysis. The scFv-Fc knobs-into-holes molecule is also able to crosslink the two target antigens, as shown by its ability to induce higher NK cell-mediated cytotoxicity than a monospecific anti-HER2 antibody alone. One could hypothesize that this format, which is slightly smaller (120 kDa) than a normal IgG (150 kDa), might provide slight gains in tumor penetration, while maintaining the longer half-life and effector functions provided by the intact Fc region.

IgG-scFv fusions To circumvent the LC-HC mispairing and HC homodimerization issues completely, a number of formats have been developed to construct and produce BsAb that achieve their bi-specificity and product homogeneity not by molecular alteration of the component domains, but by direct addition of a new antigen binding specificity to a fully functional antibody or an antibody-like molecule,such as an IgG antibody or a scFv-Fc fusion protein (Figure 2).

C-terminal scFv fusion One approach is to fuse a scFv specific for one antigen to the carboxy terminus of a full-length IgG antibody specific for another antigen, creating a tetravalent bispecific IgG-like antibody[41] (Figure 2). The specificity at the N-terminal end (in this case, for dextran) is defined by a normal Fab. The specificity at the C-terminal end (in this case, for dansyl) is conferred by an anti-dansyl scFv. The fusion construct has an affinity approximately 10-fold lower for dansyl than expected (as compared to its parent IgG), primarily because of a slower on-rate. This may be a result of steric hindrance from the rest of the IgG, an inability of both scFv fragments to bind antigen simultaneously (whether all four binding sites were occupied was not tested), or an artifact resulting from conversion of the original anti-dansyl IgG to scFv format. Regardless, the constructs in both a full-length IgG-like format (VL_A-CL plus VH_A-CH1-CH2-CH3-$scFv_B)_2$ and a F(ab')2-like format (VL_A-CL plus VH_A-CH1-$scFv_B)_2$ were capable of binding both target antigens. Furthermore, the IgG-like version is capable of binding C1q, presumably through the intact Fc fragment, although it is unable to trigger a complete complement cascade. This format has the potential to allow the creation of tetravalent molecules with some effector function, but the full potential of the latter remains to be investigated.

N-terminal scFv fusion In an alternative approach, the two scFv of different specificities are fused, respectively, to the N-termini of the constant light (CL) and the first-constant heavy (CH1) domains of an IgG: ($scFv_A$)-CL and ($scFv_B$)-CH1-CH2-CH3. Co-expression of the two polypeptide chains in a single host results in the formation of a tetravalent bispecific molecule, $Bs(scFv)_4$-IgG (Figure 2)[42]. Only ho-

mogenous BsAb are generated as a result of the natural heterodimerization between the CL and the CH1 domains. Similar to the C-terminal fusion, this molecule is also amenable to truncation: a bivalent bispecific Fab-like molecule can be created without the Fc fragment. The ability of this construct to crosslink antigen (in this case, two distinct epitopes on vascular endothelial growth factor receptor 2 (VEGFR2) was demonstrated, but it is not clear whether all four binding sites are or can be occupied simultaneously.

Two other Bs(scFv)$_4$-IgG molecules were recently constructed, using the same two scFv fragments directed against EGFR and insulin-like growth factor receptor (IGFR), but in different fusion orientations[28]. Both constructs, scFv$_{anti\text{-}EGFR}$-CL plus scFv$_{anti\text{-}IGFR}$-CH1-CH2-CH3, or scFv$_{anti\text{-}IGFR}$-CL plus scFv$_{anti\text{-}EGFR}$-CH1-CH2-CH3, blocked EGF and IGF from binding their respective receptors and inhibited signal transduction pathways activated by both EGF and IGF, whereas a monospecific antibody only inhibited the pathway stimulated by a single ligand. In addition, the BsAbs inhibited tumor cell proliferation *in vitro* at a level that is on par with the combination of the two parental IgG antibodies. Furthermore, both Bs(scFv)$_4$-IgG demonstrated very good stability when incubated *in vitro* in mouse serum at 37 ºC for 7 d. We believe that this Bs(scFv)$_4$-IgG format should be applicable to BsAb construction from two antibodies directed against any pair of antigens. A drawback of the format is its low expression level in mammalian cells, probably because of both its large size (~ 200kDa) and structural complexity.

Diabody-Fc fusions Another method by which homogenous populations of IgG-like BsAb can be constructed is by replacement of the Fab fragment with a bispecific diabody. Diabodies are a derivative of the scFv construct[43]. An scFv is composed of a VH and a VL domain connected by a flexible linker of approximately 15 amino acids, such as (Gly$_4$Ser)$_3$, that permits self assembly into an antigen binding competent form. If the linker is shortened to 5 amino acids, such as Gly$_4$Ser, self assembly is impossible, and two scFv interact with each other to form a bivalent molecule of two interlinked polypeptides, the VL of one chain associating with the VH of the other. If VL and VH with specificities for different antigens comprise the diabody; namely, VH$_A$-VL$_B$ and VH$_B$-VL$_A$ (the two so-called "cross-over" scFv), bispecific bivalent diabodies are formed, with one binding site for each antigen. In addition to assembling as functional heterodimers, the cross-over scFv can also assemble as non-functional homodimers. Fortunately, purification of properly heterodimerized molecules can easily be achieved by one round of affinity chromatography. And as noted earlier, the knobs-into-holes technique can be used to re-engineer the Fv interface to promote the correct heterodimeric VH-VL pairing[37]. Diabodies have shown to be useful for antigen cross linking[43,44], and their small size is valuable for tumor penetration[45]. However, like many other smaller bispecific fragments, diabodies lack functional Fc domains and the corresponding effector function[46]. Recently, they have been fused to the Fc domain of an IgG to create tetravalent IgG-like BsAb.

Single chain diabody-Fc fusion Kipriyanov *et al* have developed a "single chain" diabody (scDb) by fusing both "cross-over" scFv of a bispecific diabody with a flexible linker[47]. This construct is fused to an Fc fragment (or just a CH3 domain) to create a tetravalent bispecific IgG-like molecule (Figure 2). In this format, one polypeptide with six domains is produced: VH$_A$-VL$_B$-VH$_B$-VL$_A$-CH2-CH3, which then assembles into IgG-like dimers through the Fc domains[48]. The scDb-Fc is bispecific and bivalent for both antigens, and has a full Fc (although effector function activity was not tested). The stability of the scDb-Fc fusion was not reported, but the multiple exposed non-human polypeptide linkers within the molecule may not only subject the BsAb to proteolytic cleavage, but may also introduce a potential immunogenic risk, thus lowering the utility of the molecule *in vivo*. Finally, this format lacks sufficient levels of expression (~5 mg/L) to make a practical transition to a therapeutic molecule.

Di-diabody An alternative diabody-Fc fusion format is the so-called "di-diabody". In this construct, one half of a diabody; namely, one "cross-over" scFv, is fused to the Fc domain, creating a "heavier chain" (VL$_A$-VH$_B$-CH2-CH3) and the other "cross-over" scFv associates with it as a "lighter chain" (VL$_B$-VH$_A$)[27]. The heavier and lighter chains assemble with each other through the VH-VL interfaces, and two heavier chains homodimerize through the Fc regions to form an IgG-like tetravalent BsAb (Figure 2). Although lighter chains can homodimerize to form non-functional diabodies, they are easily removed when the full length functional di-diabody is purified by protein A chromatography. A similar but smaller di-diabody construct can also be created by just using the CH3 domain for dimerization, namely, VL$_B$-VH$_A$ plus VL$_A$-VH$_B$-CH3[49]. As a precautionary measure to avoid potential immunogenicity in human therapy, a human sequence, the first 5 amino acids of the human IgG CL(Kappa) domain, is used as the linker between the variable domains[44], instead of a "standard" Gly$_4$Ser linker. A di-diabody that binds both EGFR and IGFR was constructed using the variable domains of an anti-EGFR and an anti-IGFR antibody. The di-diabody has affinity for its antigens, EGFR and IGFR, similar

to that of the parental antibodies from which the VL and VH were derived. The di-diabody blocks both EGF and IGF from binding their respective receptors and down-regulates the signal transduction pathways activated by each ligand. In addition, the di-diabody induces efficient ADCC activity against tumor cells that express EGFR and/or IGFR, indicating that the di-diabody possesses an intact and unhindered Fc domain. It also has an *in vivo* half-life that is equivalent to that of an intact human IgG. Finally, the di-diabody effectively inhibits the growth of two different human tumor xenografts in nude mice. Unlike the Bs(scFv)$_4$-IgG format discussed previously, the di-diabody construct is expressed in mammalian cells at much higher levels (>400 mg/L in unoptimized conditions), which could greatly facilitate the transition from "proof-of-concept" to therapeutic application. Unfortunately, the di-diabody construct has a tendency to form inactive molecules *in vivo* that lack the lighter chain, a result of dissociation between the heavier and the lighter chains (caused by the inherent instability of diabodies) followed by the rapid clearance of the lighter chain from the circulation. Hopefully, this shortcoming will be surmounted by either the introduction of disulfide bonds[37,50,51] or improved packing[52] to stabilize the VL-VH interfaces in the diabody.

Future perspective

Other novel IgG-like BsAb constructs

BsAb IgG using single domain antibodies as building blocks The aforementioned methods use some form of Fv, comprised of a VL and a VH, to bind antigen. An emerging and promising novel approach in which BsAb can be constructed is to use the VL and VH as independent binding units. It has been observed that some camel antibodies are composed of only heavy chains[53]. This observation has led to the development of human "single domain" antibody fragments, in which a VL or a VH alone comprises the binding unit[54,55]. These fragments can then be used to construct tetravalent IgG-like BsAb by fusing a single domain of one specificity to CL and a single domain of a different specificity to the CH1 of an IgG. Preferably, one single domain would be derived from a VL, and the other from a VH, to provide increased stability using a VL-VH interface, in addition to that of the CL-CH1 interface (ie, VL_A-CL plus VH_B-CH1-CH2-CH3) (Figure 2), but an IgG-like molecule with bispecific binding capacity derived from any single domain combination could be imagined (ie, VL_A-CL plus VL_B-CH1-CH2-CH3, or VH_A-CL plus VH_B-CH1-CH2-CH3).

Tandemabs An interesting application of antibody engineering that could readily be applied to the construction of BsAb is an expansion of the multivalent Fab constructs developed by Presta *et al* at Genentech[56]. Based on the observation that cross-linking increases the biological efficacy of some antibodies, a series of multivalent antibody constructs were developed from the interaction of an identical LC with tandem repeats of the VH-CH1 unit fused to the Fc. If one were to construct a pseudo-tandem repeat of the form VH_A-CH1-VH_B-CH1-CH2-CH3, and pair that with a common LC unit VL-CL, one could achieve tetravalent (or possibly higher order) bispecific (or tri-specific) antibodies (Figure 2). Again, the challenge here is to identify antibodies of different specificities that share identical LC.

Novel applications of BsAb As noted earlier, most of the efforts in BsAb development have been focused on the use of BsAb as means to redirect either effector cells or cytotoxic agents, including chemotherapeutic drugs, radioisotopes, and toxins, to the sites of destruction, such as tumors. There are a number of novel benefits of BsAb that can be exploited for more efficacious human therapy.

Binding avidity enhancement One very valuable benefit of BsAb is the enhanced avidity they pose for their antigen[57]. In addition to having intrinsic high affinity on a binding unit (ie, a Fab) to antigen basis, normal IgG antibodies also exploit the avidity effect to increase their association with antigens as a result of their bivalent binding towards the targets. Except for the knob-into-holes BsAb format, which is monovalent for each antigen, all the IgG-like BsAb discussed here are bivalent for each antigen. Consequently, these IgG-like BsAb, once bound to cell-surface antigens, are expected to dissociate at a very slow rate: two dissociation events must occur simultaneously for the BsAb to be free from the cell. High binding affinity (or avidity) is usually beneficial and, in some cases, may even be required for the biological activity of a therapeutic antibody. In addition, bivalent binding to a target, particularly a cell-surface receptor, is under many circumstances a prerequisite for antibody function, such as cross-linking the receptors in order to stimulate activation, to induce apoptosis, or to promote receptor internalization.

Epitope cross-linking for acquired antagonistic activity A BsAb directed against two separate epitopes on the same antigen molecule may not only provide the benefit of enhanced binding avidity (because of bivalent binding), but may also acquire novel properties that are not associated with either of the parent antibodies. For example, we have demonstrated that a bispecific diabody that binds two distinct epitopes on VEGFR2 cross-links the epitopes and effectively blocks the binding of VEGF to the receptor, whereas

the parent scFv from which the bispecific diabody is derived do not, on their own or in combination, block VEGF binding[57]. Cross-linking two separate epitopes within the same receptor molecule may introduce new steric hindrance for ligand binding, and/or induce conformation changes in the receptor, preventing it from binding ligand. It will be interesting to see if this principle is applicable to antibodies to other receptors for which ligand-blocking antibodies are difficult to identify.

Fine-tuning antibody specificity towards tumor cells

An emerging and intriguing concept is the use of BsAb to further fine-tune the specificity of antitumor antibodies to target cells. In this context, a BsAb is constructed from two antibodies directed against different tumor antigens, each of low to moderate binding affinity. Only simultaneous binding (or cross-linking) to the two target antigens on the same tumor cell surface by BsAb leads to strong association (ie, high avidity resulting from bivalency), which is required to trigger biological processes, such as ADCC, CMC, and down-regulation of signaling pathways. In contrast, weak association, which may not be sufficient to induce any meaningful cellular activity, would result from monovalent binding of the BsAb to cells that only express one of the target antigens. This is significant as most of the targets currently being used as tumor cell identifiers are, in fact, not truly "tumor-specific" but rather "tumor-associated", that is, they are also expressed in certain normal tissues/cells, albeit at lower density than in tumor cells. By identifying and constructing BsAb to pairs of targets simultaneously expressed on a given type of tumor, one could expect enhanced antibody specificity towards the targeted cells while sparing normal cells of unwanted side effects.

Simultaneous blockade of two signaling pathways

Perhaps the most promising application of BsAb is the ability to simultaneously block the signaling pathways of two targets with one molecule[26–28,58]. As demonstrated with the anti-EGFR×anti-IGFR BsAb, either in the form of di-diabody or Bs(scFv)4-IgG[27,28], it is possible to achieve the effects of administering two antibodies with one IgG-like BsAb. This provides a promising alternative to the development of antibody combination therapies, as in the latter each antibody has to be approved separately by regulatory agencies before being approved as a combination. Furthermore, if BsAb can be produced in similar quantities as normal IgG, then significant cost savings can be achieved.

Conclusion

Recently, developments in the design of IgG-like BsAb have provided some success in overcoming the major obstacles to BsAb production. It is now possible to use a novel structural format that promotes or obligates the formation of homogenous, bispecific proteins, and some of these constructs can be efficiently produced in eukaryotic cells in quantities sufficient for clinical development. Furthermore, IgG-like BsAb offer the benefits of normal IgG, including long half-life and native effector function, along with the additional capability of being able to act as two drugs in one by simultaneously addressing two disease-relevant targets in a highly specific manner, thus making them in many ways superior to BsAb fragments. We believe that IgG-like BsAb will undoubtedly challenge monospecific antibodies as the champion of therapeutic proteins in coming years.

Abbreviations

ADCC, antibody-dependent cellular cytotoxicity; BsAb, bispecific antibody; CL, constant domain of light chain; CH, constant domain of heavy chain; CMC, complement-mediated cytotoxicity; Fab, antigen binding fragment; Fc, crystallized fragment; Fv, variable fragment (VL+VH); EGFR, epidermal growth factor receptor; HC, heavy chain; IGFR, insulin-like growth factor receptor; LC, light chain; scFv, single-chain variable fragment (VL and VH tethered by a 15 amino acid linker); VEGF, vascular endothelial growth factor; VEGFR2, vascular endothelial growth factor receptor 2; VH, variable heavy domain; VL, variable light domain.

References

1 Sidhu SS. Phage display in biotechnology and drug discovery. New York (NY): Marcel Dekker; 2005.
2 Colby DW, Kellogg BA, Graff CP, Yeung YA, Swers JS, Wittrup KD. Engineering antibody affinity by yeast surface display. Methods Enzymol 2004; 388: 348–58.
3 Lipovsek D, Pluckthun A. *In-vitro* protein evolution by ribosome display and mRNA display. J Immunol Methods 2004; 290: 51–67.
4 Ferrara N, Hillan KJ, Gerber HP, Novotny W. Discovery and development of bevacizumab, an anti-VEGF antibody for treating cancer. Nat Rev Drug Discov 2004; 3: 391–400.
5 Knight DM, Trinh H, Le J, Siegel S, Shealy D, McDonough M, *et al*. Construction and initial characterization of a mouse-human chimeric anti-TNF antibody. Mol Immunol 1993; 30: 1443–53.
6 Maynard JA, Maassen CB, Leppla SH, Brasky K, Patterson JL, Iverson BL, *et al*. Protection against anthrax toxin by recombinant antibody fragments correlates with antigen affinity. Nat Biotechnol 2002; 20: 597–601.
7 Nowakowski A, Wang C, Powers DB, Amersdorfer P, Smith TJ, Montgomery VA, *et al*. Potent neutralization of botulinum neurotoxin by recombinant oligoclonal antibody. Proc Natl Acad Sci USA 2002; 99: 11346–50.
8 Li S, Schmitz K, Jeffery PD, Wiltzius J, Kussie P, Ferguson KM. Structural basis for inhibition of the epidermal growth factor

receptor by cetuximab/Erbitux. Cancer Cell 2005; in press:
9 Franklin MC, Carey KD, Vajdos FF, Leahy DJ, de Vos AM, Sliwkowski MX. Insights into ErbB signaling from the structure of the ErbB2-pertuzumab complex. Cancer Cell 2004; 5: 317–28.
10 Ichikawa K, Liu W, Zhao L, Wang Z, Liu D, Ohtsuka T, *et al*. Tumoricidal activity of a novel anti-human DR5 monoclonal antibody without hepatocyte cytotoxicity. Nat Med 2001; 7: 954–60.
11 Yagita H, Takeda K, Hayakawa Y, Smyth MJ, Okumura K. TRAIL and its receptors as targets for cancer therapy. Cancer Sci 2004; 95: 777–83.
12 McLaughlin P, Grillo-Lopez AJ, Link BK, Levy R, Czuczman MS, Williams ME, *et al*. Rituximab chimeric anti-CD20 monoclonal antibody therapy for relapsed indolent lymphoma: half of patients respond to a four-dose treatment program. J Clin Oncol 1998; 16: 2825–33.
13 Cobleigh MA, Vogel CL, Tripathy D, Robert NJ, Scholl S, Fehrenbacher L, *et al*. Multinational study of the efficacy and safety of humanized anti-HER2 monoclonal antibody in women who have HER2-overexpressing metastatic breast cancer that has progressed after chemotherapy for metastatic disease. J Clin Oncol 1999; 17: 2639–48.
14 Slamon DJ, Leyland-Jones B, Shak S, Fuchs H, Paton V, Bajamonde A, *et al*. Use of chemotherapy plus a monoclonal antibody against HER2 for metastatic breast cancer that overexpresses HER2. N Engl J Med 2001; 344: 783–92.
15 Clynes RA, Towers TL, Presta LG, Ravetch JV. Inhibitory Fc receptors modulate *in vivo* cytoxicity against tumor targets. Nat Med 2000; 6: 443–6.
16 Silverman DH, Delpassand ES, Torabi F, Goy A, McLaughlin P, Murray JL. Radiolabeled antibody therapy in non-Hodgkins lymphoma: radiation protection, isotope comparisons and quality of life issues. Cancer Treat Rev 2004; 30: 165–72.
17 Xiong D, Xu Y, Liu H, Peng H, Shao X, Lai Z, *et al*. Efficient inhibition of human B-cell lymphoma xenografts with an anti-CD20×anti-CD3 bispecific diabody. Cancer Lett 2002; 177: 29–39.
18 Kipriyanov SM, Cochlovius B, Schafer HJ, Moldenhauer G, Bahre A, Le Gall F, *et al*. Synergistic antitumor effect of bispecific CD19×CD3 and CD19×CD16 diabodies in a preclinical model of non-Hodgkin's lymphoma. J Immunol 2002; 169: 137–44.
19 James ND, Atherton PJ, Jones J, Howie AJ, Tchekmedyian S, Curnow RT. A phase II study of the bispecific antibody MDX-H210 (anti-HER2×CD64) with GM-CSF in HER2+ advanced prostate cancer. Br J Cancer 2001; 85: 152–6.
20 Baeuerle PA, Kufer P, Lutterbuse R. Bispecific antibodies for polyclonal T-cell engagement. Curr Opin Mol Ther 2003; 5: 413–9.
21 Cao Y, Lam L. Bispecific antibody conjugates in therapeutics. Adv Drug Deliv Rev 2003; 55: 171–97.
22 Corvalan JR, Smith W, Gore VA. Tumour therapy with Vinca alkaloids targeted by a hybrid-hybrid monoclonal antibody recognising both CEA and Vinca alkaloids. Int J Cancer Suppl 1988; 2: 22–5.
23 Ford CH, Osborne PA, Rego BG, Mathew A. Bispecific antibody targeting of doxorubicin to carcinoembryonic antigen-expressing colon cancer cell lines *in vitro* and *in vivo*. Int J Cancer 2001; 92: 851–5.
24 Ferrini S, Sforzini S, Canevari S. Bispecific monoclonal antibodies for the targeting of type I ribosome-inactivating proteins against hematological malignancies. Methods Mol Biol 2001; 166: 177–92.
25 Chang CH, Sharkey RM, Rossi EA, Karacay H, McBride W, Hansen HJ, *et al*. Molecular advances in pretargeting radioimunotherapy with bispecific antibodies. Mol Cancer Ther 2002; 1: 553–63.
26 Lu D, Jimenez X, Zhang H, Wu Y, Bohlen P, Witte L, *et al*. Complete inhibition of vascular endothelial growth factor (VEGF) activities with a bifunctional diabody directed against both VEGF kinase receptors, fms-like tyrosine kinase receptor and kinase insert domain-containing receptor. Cancer Res 2001; 61: 7002–8.
27 Lu D, Zhang H, Koo H, Tonra J, Balderes P, Prewett M, *et al*. A fully human recombinant IgG-like bispecific antibody to both the epidermal growth factor receptor and the insulin-like growth factor receptor for enhanced antitumor activity. J Biol Chem 2005; March 9 [Epub ahead of print].
28 Lu D, Zhang H, Ludwig D, Persaud A, Jimenez X, Burtrum D, *et al*. Simultaneous blockade of both the epidermal growth factor receptor and the insulin-like growth factor receptor signaling pathways in cancer cells with a fully human recombinant bispecific antibody. J Biol Chem 2004; 279: 2856–65.
29 Milstein C, Cuello AC. Hybrid hybridomas and their use in immunohistochemistry. Nature 1983; 305: 537–40.
30 Brennan M, Davison PF, Paulus H. Preparation of bispecific antibodies by chemical recombination of monoclonal immunoglobulin G1 fragments. Science 1985; 229: 81–3.
31 Carter P, Ridgway J, Zhu Z. Toward the production of bispecific antibody fragments for clinical applications. J Hematother 1995; 4: 463–70.
32 Todorovska A, Roovers RC, Dolezal O, Kortt AA, Hoogenboom HR, Hudson PJ. Design and application of diabodies, triabodies and tetrabodies for cancer targeting. J Immunol Methods 2001; 248: 47–66.
33 Kontermann RE. Recombinant bispecific antibodies for cancer therapy. Acta Pharmacol Sin 2005; 26: 1–9.
34 Ridgway JB, Presta LG, Carter P. 'Knobs-into-holes' engineering of antibody CH3 domains for heavy chain heterodimerization. Protein Eng 1996; 9: 617–21.
35 Deisenhofer J. Crystallographic refinement and atomic models of a human Fc fragment and its complex with fragment B of protein A from Staphylococcus aureus at 2.9- and 2.8-A resolution. Biochemistry 1981; 20: 2361–70.
36 Atwell S, Ridgway JB, Wells JA, Carter P. Stable heterodimers from remodeling the domain interface of a homodimer using a phage display library. J Mol Biol 1997; 270: 26–35.
37 Zhu Z, Presta LG, Zapata G, Carter P. Remodeling domain interfaces to enhance heterodimer formation. Protein Sci 1997; 6: 781–8.
38 Eigenbrot C, Randal M, Presta L, Carter P, Kossiakoff AA. X-ray structures of the antigen-binding domains from three variants of humanized anti-p185HER2 antibody 4D5 and comparison with molecular modeling. J Mol Biol 1993; 229: 969–95.
39 Merchant AM, Zhu Z, Yuan JQ, Goddard A, Adams CW, Presta LG, *et al*. An efficient route to human bispecific IgG. Nat Biotechnol 1998; 16: 677–81.

40 Xie Z, Guo N, Yu M, Hu M, Shen B. A new format of bispecific antibody: highly efficient heterodimerization, expression and tumor cell lysis. J Immunol Methods 2005; 296: 95–101.
41 Coloma MJ, Trinh KR, Wims LA, Morrison SL. The hinge as a spacer contributes to covalent assembly and is required for function of IgG. J Immunol 1997; 158: 733–40.
42 Zuo Z, Jimenez X, Witte L, Zhu Z. An efficient route to the production of an IgG-like bispecific antibody. Protein Eng 2000; 13: 361–7.
43 Holliger P, Prospero T, Winter G. "Diabodies": small bivalent and bispecific antibody fragments. Proc Natl Acad Sci USA 1993; 90: 6444–8.
44 Zhu Z, Zapata G, Shalaby R, Snedecor B, Chen H, Carter P. High level secretion of a humanized bispecific diabody from Escherichia coli. Biotechnology (NY) 1996; 14: 192–6.
45 Colcher D, Bird R, Roselli M, Hardman KD, Johnson S, Pope S, *et al*. *In vivo* tumor targeting of a recombinant single-chain antigen-binding protein. J Natl Cancer Inst 1990; 82: 1191–7.
46 Kipriyanov SM. Generation of bispecific and tandem diabodies. Methods Mol Biol 2002; 178: 317–31.
47 Kipriyanov SM, Moldenhauer G, Schuhmacher J, Cochlovius B, Von der Lieth CW, Matys ER, *et al*. Bispecific tandem diabody for tumor therapy with improved antigen binding and pharmcokinetics. J Mol Biol 1999; 293: 41–56.
48 Alt M, Muller R, Kontermann RE. Novel tetravalent and bispecific IgG-like antibody molecules combining single-chain diabodies with the immunoglobulin gamma1 Fc or CH3 region. FEBS Lett 1999; 454: 90–4.
49 Lu D, Jimenez X, Zhang H, Atkins A, Brennan L, Balderes P, *et al*. Di-diabody: a novel tetravalent bispecific antibody molecule by design. J Immunol Methods 2003; 279: 219–32.
50 Jung SH, Pastan I, Lee B. Design of interchain disulfide bonds in the framework region of the Fv fragment of the monoclonal antibody B3. Proteins 1994; 19: 35–47.
51 FitzGerald K, Holliger P, Winter G. Improved tumour targeting by disulphide stabilized diabodies expressed in Pichia pastoris. Protein Eng 1997; 10: 1221–5.
52 Worn A, Pluckthun A. Stability engineering of antibody single-chain Fv fragments. J Mol Biol 2001; 305: 989–1010.
53 Muyldermans S, Atarhouch T, Saldanha J, Barbosa JA, Hamers R. Sequence and structure of VH domain from naturally occurring camel heavy chain immunoglobulins lacking light chains. Protein Eng 1994; 7: 1129–35.
54 Riechmann L, Muyldermans S. Single domain antibodies: comparison of camel VH and camelised human VH domains. J Immunol Methods 1999; 231: 25–38.
55 Els Conrath K, Lauwereys M, Wyns L, Muyldermans S. Camel single-domain antibodies as modular building units in bispecific and bivalent antibody constructs. J Biol Chem 2001; 276: 7346–50.
56 Miller K, Meng G, Liu J, Hurst A, Hsei V, Wong WL, *et al*. Design, construction, and *in vitro* analyses of multivalent antibodies. J Immunol 2003; 170: 4854–61.
57 Lu D, Kotanides H, Jimenez X, Zhou Q, Persaud K, Bohlen P, *et al*. Acquired antagonistic activity of a bispecific diabody directed against two different epitopes on vascular endothelial growth factor receptor 2. J Immunol Methods 1999; 230: 159–71.
58 Lu D, Jimenez X, Zhang H, Bohlen P, Witte L, Zhu Z. Fab-scFv fusion protein: an efficient approach to production of bispecific antibody fragments. J Immunol Methods 2002; 267: 213–26.

Acta Pharmacologica Sinica 2005 Jun; 26 (6): 659–665

Invited review

Cytogenetic and molecular genetic alterations in hepatocellular carcinoma

Sze-hang LAU, Xin-yuan GUAN[1]

Department of Clinical Oncology, Faculty of Medicine, The University of Hong Kong, Hong Kong, China

Key words

hepatocellular carcinoma; chromosome aberrations; oncogenes; tumor suppressor genes

[1] Correspondence to Dr Xin-yuan GUAN.
Fax 852-2816-9126.
E-mail xyguan@hkucc.hku.hk

Received 2005-02-17
Accepted 2005-03-25

doi: 10.1111/j.1745-7254.2005.00126.x

Abstract

Specific chromosome aberrations are frequently detected during the development of hepatocellular carcinoma. Molecular cytogenetic approaches such as comparative genomic hybridization and loss of heterozygosity analyses have provided fruitful information on changes in HCC cases at the genomic level. Mapping of chromosome gains and losses have frequently resulted in the identification of oncogenes and tumor suppressors, respectively. In this review, we summarize some frequently detected chromosomal aberrations reported for hepatocellular carcinoma cases using comparative genomic hybridization and loss of heterozygosity studies. Focus will be on gains of 1q, 8q, and 20q, and losses of 4q, 8p, 13q, 16q, and 17p. We then examine the candidate oncogenes and tumor suppressors located within these regions, and explore their possible functions in hepatocarcinogenesis. Finally, the impact of microarray-based screening platforms will be discussed.

Introduction

Hepatocellular carcinoma (HCC) is one of the most common human malignant neoplasms, with a particularly high incidence in Chinese and African populations[1]. In 2000, HCC ranked as the fifth most frequent cancer, but the third leading cause of cancer death worldwide[2]. Unlike other cancers, the main causative agents for HCC, hepatitis B virus (HBV), hepatitis C virus (HCV) and aflatoxin (AFB), are well studied. Yet little is known about the molecular pathogenesis of HCC[3]. In fact, the majority of HCC are associated with a background of chronic liver disease. Therefore, hepatocarcinogenesis is believed to be a long-term process that involves multiple genetic alterations.

Recurrent chromosome alterations

Chromosome aberrations are a hallmark of solid tumors and it has been known for decades that chromosome rearrangements exist in most if not all human tumors[4]. Additionally, cytogenetic study followed by molecular analysis of recurring chromosome changes has greatly facilitated the identification of crucial oncogenes and tumor suppressors[5]. For example, the tumor suppresor gene Rb was identified based on the observation of chromosome deletion del(13)(q14) in retinoblastoma[6] and the proto-oncogene myc was shown to be involved in the chromosome translocation t(8;14) in human Burkett's lymphoma[7]. The conventional comparative genomic hybridization (CGH) method provides a powerful means of global analysis of segmental chromosome gains or losses[8]. Since it was developed, CGH has been widely applied to the detection of recurrent chromosomal alterations in various cancers, including HCC[9–13]. Frequent non-random chromosomal gains and losses detected by CGH are summarized in Table 1, including gains of 1q, 6p, 8q, 17q, and 20q, and losses of 1p, 4q, 5q, 6q, 8p, 9p, 10q, 13q, 16q, 17p, 19p, and 22q[9–13]. In addition, the loss of heterozygosity (LOH) assay is used to define chromosomal regions with allelic deletions, and results revealed that LOH was frequently detected in 1p, 4q, 6q, 8p, 13q, 16q, and 17p[14–16]. These studies suggest the presence of multiple oncogenes or tumor suppressor genes in regions of recurrent gain or loss, respectively.

To avoid overlap with comprehensive reviews that have been published recently[3,17], this review will mainly focus on chromosomal gains on 1q, 8q, and 20q, and losses on 4q, 8p, 13q, 16q, and 17p in HCC. For simplicity, gene symbols will

Table 1. Summary of chromosomal gains and losses revealed by comparative genomic hybridization analyses

	Marchio *et al*[9]	Wong *et al*[10]	Kusano *et al*[11]	Guan *et al*[12]	Chang *et al*[13]
Gains					
1q	25/43 (58%)	48/67 (72%)	32/41 (78%)	33/50 (66%)	19/22 (86%)
8q	26/43 (60%)	32/67 (48%)	27/41 (66%)	24/50 (48%)	17/22 (77%)
20q	10/43 (23%)	25/67 (37%)	6/41 (14%)	10/50 (20%)	1/22 (5%)
Losses					
4q	30/43 (70%)	29/67 (43%)	13/41 (32%)	20/50 (40%)	13/22 (59%)
8p	28/43 (65%)	25/67 (37%)	12/41 (29%)	16/50 (32%)	17/22 (77%)
13q	16/43 (37%)	25/67 (37%)	15/41 (37%)	8/50 (16%)	6/22 (27%)
16q	23/43 (54%)	20/67 (30%)	19/41 (46%)	35/50 (70%)	11/22 (50%)
17p	22/43 (51%)	7/67 (10%)	21/41 (51%)	26/50 (52%)	10/22 (45%)

be used for all genes described throughout the review (details for all genes are summarized in Table 2).

Chromosome gains

Gain of 1q Gain of 1q is one of the most frequently detected alterations in HCC and has been suggested as an early genomic lesion in the process of HCC development[18], although the target oncogene within the amplified region has not been identified. CGH studies showed that the gain of 1q was detected in 58%–86% of HCC cases[9–13], with about 10% high-copy number amplification[12]. Several minimal amplifying regions (MAR) were mapped including 1q12-q22[12,19], 1q23.3-q25.3[20] and 1q24.2-1q43[21]. In an attempt

Table 2. Summary of candidate cancer-related genes within abnormal chromosomal regions

Gene name	Symbol	Locus	Reference
Oncogenes			
Jumping translocation breakpoint	JTB	1q21-q22	22
SHC (Src homology 2 domain containing) transforming protein 1	SHC1	1q21-q22	22
Chaperonin containing TCP1, subunit 3 (gamma)	CCT3	1q21-q22	22
Coatomer protein complex, subunit alpha	COPA	1q21-q22	22
V-myc myelocytomatosis viral oncogene homolog (avian)	c-Myc	8q24.12-q24.13	18
Protein tyrosine kinase 2	PTK2	8q23-q24	29
Eukaryotic translation initiation factor 3, subunit 3 gamma	EIF3S3	8q23-q24	29
Nuclear receptor coactivator 3	AIB1	20q12	18, 31
Tumor suppressors			
PR domain containing 5	PRDM5	4q25-q26	37
PIN2-interacting protein 1	PINX1	8p23	38
Fibrinogen-like 1	FGL1	8p22-p21.3	39
Deleted in liver cancer 1	DLC1	8p22	40–42
Platelet-derived growth factor receptor-like	PDGFRL	8p22-p21.3	43
Tumor suppressor candidate 3	TUSC3	8p22	44
Retinoblastoma 1 (including osteosarcoma)	RB	13q14.2	6
Inhibitor of growth family, member 1	P33ING1	13q34	45, 46
START domain containing 13 (Deleted in liver cancer 2)	DLC2	13q12-q13	47
Cadherin 1, type 1, E-cadherin (epithelial)	CDH1	16q22.1	49, 50
HSV-1 stimulation-related gene 1	HSRG1	16q23.1	51
WW domain containing oxidoreductase	WWOX	16q23.3-q24.1	52
Tumor protein p53 (Li-Fraumeni syndrome)	TP53	17p13.1	53
Chromosome 17 open reading frame 25	C17orf25	17p13.3	58

to identify candidate oncogene(s) at 1q12-q22, Wong *et al* examined the expression level of several candidate oncogenes in this region using reverse transcription-polymerase chain reaction (RT-PCR). Significant overexpression of 4 genes known as *JTB*, *SHC1*, *CCT3*, and *COPA* were observed in tumors as compared with paired adjacent liver tissues[22].

Gain of 8q Gain of 8q is frequently observed in HCC (48%–77%)[9–13]. The gain of 8q is also frequently detected in many other solid tumors including those of the prostate[23], lung[24], esophagus[25], nasopharynx[26], ovary[27] and breast[28]. Amplification and overexpression of the c-myc oncogene has been reported in various solid tumors, including HCC. In our recent study, amplification of *c-myc* was correlated with HCC tumor size, tumor metastasis and recurrence. Amplification of *c-myc* was found in 11/13 (85%), 9/25 (36%) and 4/12 (33%) cases of large HCC (>9 cm), medium HCC (4–9 cm) and small HCC (<4 cm), respectively. In addition, a higher frequency of c-myc amplification was detected in metastatic tumors (45%) than in their primary HCC (29%), and in recurrent tumors (60%) than in their primary HCC (38%)[18]. Because the gain of 8q involved the entire long arm in this study, it is highly likely that one or more novel oncogenes are involved in HCC development apart from *c-myc*. In a recent report, Okamoto *et al* suggested 2 candidate oncogenes as amplification targets at 8q23-q24 known as *PTK2* and *EIF3S3*. *PTK2* encodes focal adhesion kinase, while *EIF3S3* encodes the p40 subunit of eukaryotic translation initiation factor 3. Overexpression of these genes may be involved in HCC progression[29].

Gain of 20q Gain of 20q was detected in 3/5 CGH studies with a frequency of 20%–37% [9,10,12]. Gain of 20q was also frequently detected in breast cancer, and a steroid receptor coactivator, *AIB1*, has been identified within the commonly amplified region at 20q12[30,31]. Interestingly, gain of 20q is significantly associated with clinical stages and tumor size of HCC. Guan *et al* reported that gain of 20q occurred in 10/40 (25%) of stage II and III HCC but in 0/10 stage I HCC[12]. In addition, Wong *et al* reported that significantly more 20q gain was found in non-cirrhotic HCC. Strikingly, gain of 20q was observed in 9/12 (75%) non-cirrhotic, while only in 16/55 (29%) cirrhotic HCC (P=0.003)[10]. In our recent study, amplification of the *AIB1* gene was correlated with HCC metastasis and recurrence. The amplification frequency of AIB1 was significantly higher in metastatic HCC (41%) than in matched primary HCC (23%), as well as being higher in recurrent HCC (60%) than in matched primary HCC (29%) ($P < 0.05$)[18].

Chromosome losses

Loss of 4q Loss of chromosome 4q was detected by CGH in 32%–70% of HCC cases[9–13]. Deletion of 4q has been well described because of its specificity for HCC. Several minimal deletion regions (MDR) on 4q have been detected by LOH including 4q12-q23, 4q13.1-q21.23, 4q13-q34, 4q21-q25, 4q24-q28, 4q28.2-q34.3, and 4q35[32–34]. In addition, Yeh *et al* reported recently the mapping of a 17.5 cM MDR between D4S1534 and D5S1572 by screening 149 HCC: a few candidate genes were found to be downregulated[35]. Biological evidence for tumor suppressor genes on 4q comes from a study that reversed the tumorigenic phenotype of a teratoma cell line by introducing a normal chromosome 4 into malignant teratoma cells using microcell-mediated chromosome transfer[36]. To date, candidate tumor suppressor genes correlated with 4q loss have remained unidentified. A recent report by Deng *et al* described the role of *PRDM5* at 4q26 as a suppressor in various tumors including HCC. *PRDM5* encodes a protein belonging to the PR-domain protein family. Epigenetic silencing was evident for this gene and its overexpression resulted in proapoptotic and growth suppressive functions[37].

Loss of 8p Loss of 8p is well documented in HCC with a frequency of 29%–77%[9–13]. By analyzing 50 HCC cases, we observed a correlation of 8p loss with advanced stage of disease and tumor size; most strikingly, 8p loss was present in 8/13 (62%) of large, 7/25 (28%) of medium, but only 1/12 (8%) of small HCC cases (P=0.014)[12]. Furthermore, 8p deletion was associated with HCC metastasis, suggesting the presence of one or more candidate gene(s) are involved in HCC progression[19]. Using the high-resolution LOH strategy, Jou *et al* reported that 50% of HCC showed LOH in chromosome 8p and the percentages of 3 MDR at 8p23.3-p23.1 (D8S504–D8S277), 8p22-p21.3 (D8S1106–D8S258) and 8p21.3-p12 (D8S258–D8S283) were 71%, 69%, and 63%, respectively[34]. Several candidate tumor suppressors have been isolated within these regions, including *PINX1* at 8p23[38], *FGL1* at 8p22[39] and *DLC1*[40] at 8p22-p21.3 regions. In the 8p23 region, Liao *et al* observed the under-expression of *PINX1* (*LPTS*) in HCC cells and tissues, while ectopic expression of this gene in liver cancer cells SMMC-7721 resulted in growth suppression[38]. At 8p22, Yan *et al* reported reduced or undetectable expression of *FGL1* in HCC specimens, and found a significant correlation with tumor differentiation[39]. Interestingly, Wong *et al* reported the significant under-expression of DLC1 mRNA and promoter hypermethylation was found in 24% of primary HCC cases, suggesting a role of epigenetic silencing in *DLC1* downregulation[41]. *DLC-1* belongs to the rho family GTPase-activating proteins (RhoGAP) specific to RhoA and cdc42, which are implicated in cell migration control. Re-expression of *DLC1*

in HCC cells resulted in caspase-3-dependent apoptosis, inhibition of cell growth and invasiveness *in vitro*, and reduction of tumor formation in nude mice[42]. Furthermore, candidate tumor suppressors known as *PDGFRL*[43] and *TUSC3*[44] were identified in the 8p22-p21.3 region.

Loss of 13q Loss of 13q was detected in 16%–37% of HCC cases[9–13]. LOH analyses also showed a high percentage of allelic deletion on 13q (40%–55%)[14–16]. Jou *et al* identified 5 MDR with high frequencies of LOH including 13q12.11-q12.3 (71%), 13q13.1-q22.1 (79%), 13q31.3-q32.2 (67%), 13q32.2-q33.3 (73%) and 13q33.3-q34 (75%)[34]. MDR in 13q13.1-q22.1 (D13S171–D13S156) showed the highest frequency of LOH, and well-documented tumor suppressors including *BRCA2* and *RB* are located in this region. In 13q33.3-q34 MDR, one candidate tumor suppressor known as *P33ING1* has been isolated[45]. Overexpression of *p33ING1* inhibited cell cycle progression and the repression function of *p33ING1* was enhanced by the Ras/Raf pathway[46]. Recently, another candidate tumor suppressor known as deleted in liver cancer 2 (*DLC2*) was identified on 13q12.3. It shows homology to tumor suppressor gene *DLC1* located at 8p22-p21.3. *DLC2* encodes a protein with RhoGAP, SAM and START domains and is significantly underexpressed in only 8 of 45 (18%) HCC, as compared with its ubiquitous expression in normal tissues[47].

Loss of 16q One of the most frequent losses in HCC cases is located in the long arm of chromosome 16. Loss of 16q was detected in 30%–70% of HCC cases by CGH studies[9–13]. LOH also revealed allelic deletions in 55%–59 % of HCC[14–16]. Two MDR at 16q in HCC have been reported to include 16q12.1-q23.1 (71%) and 16q23.1-q24.1 (71%)[33]. Several candidate tumor suppressors have been reported in recent publications. The loss of 16q has also been reported as a frequent genomic alteration in ovarian[27] and prostate cancer[48]. The loss of 16q24.1-q24.2 in prostate cancer has been associated with aggressive behavior of the disease, recurrent growth, poor differentiation of the tumor, and a poor prognosis for the patient[48]. The best-studied tumor suppressor gene is E-cadherin (*CDH1*) at 16q22.1. Interestingly, expression of the E-cadherin gene is reduced by a hypermethylation mechanism although no somatic mutations of the E-cadherin gene in HCC have yet been described[49,50]. Bando *et al* identified a distinct commonly deleted region at 16q24.1-24.2 (D16S534 and D16S3091) near novel sequence *HSRG1*[51]. Another candidate tumor suppressor known as WWOX was identified at 16q23.3-q24.1: absence or reduced expression of WWOX was observed in 60% of HCC cell lines compared with normal liver[52].

Loss of 17p Loss of 17p is one of the most frequent chromosomal alterations in HCC as determined by both CGH[2,11–13] and LOH[14–16]. Deletion of 17p is common in various cancers including breast[53] and colon cancer[54]. The frequent deletion of 17p may affect the tumor suppressor gene *TP53* on 17p13.1. *TP53* is frequently inactivated in various types of malignant tumors, including HCC[55]. However, Yumoto *et al* showed that loss of 17p occurred in 18/31 HCC cases (58%) by LOH, whereas *TP53* mutation was only observed in 8/31 HCC cases (26%)[56]. Our recent study revealed that loss of one allele at 17p13.3 distal to the *TP53* gene was observed in 48/94 HCC (51%), whereas LOH at 17p13.1, near the *TP53* gene, was detected in 30/94 HCC (32%) and p53 mutation was only detected in 22/94 HCC (23%)[57]. These results suggest that another tumor suppressor gene at 17p13.3 may be involved in the pathogenesis of HCC. One candidate suppressor, *C17orf25*, has been isolated from this region[58]. Downregulated expression of *C17orf25* was found in HCC samples matched to adjacent non-tumor liver tissues. Furthermore, transfection of *C17orf25* into the hepatocellular carcinoma cell SMMC-7721 inhibited cell growth[58].

Conclusion

Molecular cytogenetic approaches such as CGH and LOH provide important clues to the identification of novel genes involved in the multistage development of HCC. In this review, we discussed some of the most common chromosome aberrations, including gains of 1q, 8q, and 20q, and loss of 4q, 8p, 13q, 16q, and 17p, followed by candidate oncogenes and tumor suppressors that may be involved within these regions. Due to the heterogeneity of HCC, it has been suggested that gains or losses of specific chromosomal loci rarely affect more than half of them, and specific HCC-related genes have not been identified in most of the above-mentioned chromosomal regions[3]. Results obtained with traditional approaches such as cytogenetic CGH and LOH studies are relatively low in resolution and are labor intensive. Advances in microarray-based approaches are beginning to reverse this situation by providing an integrated view of genetic alterations during tumorigenesis and progression[59].

Different microarray-based CGH (aCGH) platforms are emerging that allow high-resolution genomic profiling[60–62]. For instance, Hashimoto *et al* reported the use of cytogenetic CGH and aCGH in the identification of genes involved in HCV-related HCC[63]. In a recent article, Ishkanian *et al* reported the construction of submegabase resolution tiling genomic arrays (SMRT arrays) containing 32 433 overlapping BAC clones. This allows the detection of cryptic chro-

mosomal changes down to microgain and microloss resolution[64]. In addition, some groups have used oligonucleotide arrays for high-resolution CGH and LOH studies. Single nucleotide polymorphism (SNP) arrays have been employed for high-resolution LOH studies in small cell lung cancer samples[65] and have permitted the simultaneous detection of copy number changes and LOH in a single experiment[66].

In another approach, chromosomal bias of gene expression signature was studied in HCC cases[67,68]. Using a recently developed technique known as expression balance map analysis, Midorikawa *et al* identified regions with frequent chromosomal aberrations in HCC based solely on expression data. Common alterations, including gain of 1q21-q23 and loss of 4q13, were found in 74% and 48% of HCC cases, respectively[67]. These matched well with previous CGH analyses. In conclusion, a combination of these powerful technologies provides a more comprehensive view of the development of HCC, and identification of novel gene candidates may provide better diagnosis and prognostication of HCC.

References

1 Arbuthnot P, Kew M. Hepatitis B virus and hepatocellular carcinoma. Int J Exp Pathol 2001; 82: 77–100.
2 Block TM, Mehta AS, Fimmel CJ, Jordan R. Molecular viral oncology of hepatocellular carcinoma. Oncogene 2003; 22: 5093–107.
3 Thorgeirsson SS, Grisham JW. Molecular pathogenesis of human hepatocellular carcinoma. Nat Genet 2002; 31: 339–46.
4 Miteiman F, Kaneko Y, Trent J. Human gene mapping 11: report of the committee on chromosome changes in neoplasia. Cytogenet Cell Genet 1991; 58: 1053–79.
5 Albertson DG, Collins C, McCormick F, Gray JW. Chromosome aberrations in solid tumors. Nat Genet 2003; 34: 369–76.
6 Yunis JJ, Ramsay N. Retinoblastoma and subband deletion of chromosome 13. Am J Dis Child 1978; 132: 161–3.
7 Zech L, Haglund U, Nilsson K, Klein G. Characteristic chromosomal abnormalities in biopsies and lymphoid-cell lines from patients with Burkitt and non-Burkitt lymphomas. Int J Cancer 1976; 17: 47–56.
8 Kallioniemi A, Kallioniemi OP, Sudar D, Rutovitz D, Gray JW, Waldman F, *et al*. Comparative genomic hybridization for molecular cytogenetic analysis of solid tumors. Science 1992; 258: 818–21.
9 Marchio A, Meddeb M, Pineau P, Danglot G, Tiollais P, Bernheim A, *et al*. Recurrent chromosomal abnormalities in hepatocellular carcinoma detected by comparative genomic hybridization. Genes Chromosomes Cancer 1997; 18: 59–65.
10 Wong N, Lai P, Lee SW, Fan S, Pang E, Liew CT, *et al*. Assessment of genetic changes in hepatocellular carcinoma by comparative genomic hybridization analysis: relationship to disease stage, tumor size, and cirrhosis. Am J Pathol 1999; 154: 37–43.
11 Kusano N, Shiraishi K, Kubo K, Oga A, Okita K, Sasaki K. Genetic aberrations detected by comparative genomic hybridization in hepatocellular carcinomas: their relationship to clinicopathological features. Hepatology 1999; 29: 1858–62.
12 Guan XY, Fang Y, Sham JS, Kwong DL, Zhang Y, Liang Q, *et al*. Recurrent chromosome alterations in hepatocellular carcinoma detected by comparative genomic hybridization. Genes Chromosomes Cancer 2000; 29: 110–6.
13 Chang J, Kim NG, Piao Z, Park C, Park KS, Paik YK, *et al*. Assessment of chromosomal losses and gains in hepatocellular carcinoma assessment of chromosomal losses and gains in hepatocellular carcinoma. Cancer Lett 2002; 182: 193–202.
14 Nishida N, Fukuda Y, Kokuryu H, Sadamoto T, Isowa G, Honda K, *et al*. Accumulation of allelic loss on arms of chromosomes 13q, 16q and 17p in the advanced stages of human hepatocellular carcinoma. Int J Cancer 1992; 51: 862–8.
15 Nagai H, Pineau P, Tiollais P, Buendia MA, Dejean A. Comprehensive allelotyping of human hepatocellular carcinoma. Oncogene 1997; 14: 2927–33.
16 Piao Z, Park C, Park JH, Kim H. Allelotype analysis of hepatocellular carcinoma. Int J Cancer. 1998; 75: 29–33.
17 Grisham JW. Molecular genetic alterations in primary hepatocellular neoplasms: hepatocellular adenoma, hepatocellular carcinoma, and hepatoblastoma. In: Coleman WB, Tsongalis GJ, editors. The Molecular Basis of Human Cancer. Totowa, NJ: Humana Press; 2001. p 269–346.
18 Wang Y, Wu MC, Sham JS, Zhang W, Wu WQ, Guan XY. Prognostic significance of c-myc and AIB1 amplification in hepatocellular carcinoma. A broad survey using high-throughput tissue microarray. Cancer 2002; 95: 2346–52.
19 Qin LX, Tang ZY, Sham JS, Ma ZC, Ye SL, Zhou XD, *et al*. The association of chromosome 8p deletion and tumor metastasis in human hepatocellular carcinoma. Cancer Res 1999; 59: 5662–5.
20 Nishimura T, Nishida N, Itoh T, Komeda T, Fukuda Y, Ikai I, *et al*. Discrete breakpoint mapping and shortest region of overlap of chromosome arm 1q gain and 1p loss in human hepatocellular carcinoma detected by semiquantitative microsatellite analysis. Genes Chromosomes Cancer 2004; 42: 34–43.
21 Nishimura T, Nishida N, Itoh T, Kuno M, Minata M, Komeda T, *et al*. Comprehensive allelotyping of well-differentiated human hepatocellular carcinoma with semiquantitative determination of chromosomal gain or loss. Genes Chromosomes Cancer 2002; 35: 329–39.
22 Wong N, Chan A, Lee SW, Lam E, To KF, Lai PB, *et al*. Positional mapping for amplified DNA sequences on 1q21-q22 in hepatocellular carcinoma indicates candidate genes overexpression. J Hepatol 2003; 38: 298–306.
23 Sattler HP, Rohde V, Bonkhoff H, Zwergel T, Wullich B. Comparative genomic hybridization reveals DNA copy number gains to frequently occur in human prostate cancer. Prostate 1999; 39: 79–86.
24 Tai ALS, Yan WS, Fang Y, Xie D, Sham JST, Guan XY. Recurrent chromosomal imbalances in non small cell lung cancer: the association of 1q amplification and tumor recurrence. Cancer 2004; 100: 1918–27.
25 Kwong D, Lam A, Guan XY, Law S, Tai A, Sham J. Chromosomal aberrations in esophageal squamous cell carcinoma among Chinese: gain of 12p predicts poor prognosis after surgery. Human Pathol 2004; 35: 309–16.

26 Fong Y, Guan XY, Guo Y, Deng M, Liang Q, Li H, *et al*. Analysis of genetic alterations in primary nasopharyngeal carcinoma by comparative genomic hybridization (CGH). Genes Chromosomes Cancer 2001; 30: 254–60.

27 Sham JST, Tang TCM, Fang Y, Sun L, Qin LX, Xie D, Guan XY. Recurrent chromosome alterations in primary ovarian carcinoma of Chinese women. Cancer Genet Cytogenet 2002; 133: 39–44.

28 Tirkkonen M, Tanner M, Karhu R, Kallioniemi A, Isola J, Kallioniemi OP. Molecular cytogenetics of primary breast cancer by CGH. Genes Chromosomes Cancer 1998; 21: 177–84.

29 Okamoto H, Yasui K, Zhao C, Arii S, Inazawa J. PTK2 and EIF3S3 genes may be amplification targets at 8q23-q24 and are associated with large hepatocellular carcinomas. Hepatology 2003; 38: 1242–9.

30 Guan XY, Xu J, Anzick SL, Zhang H, Trent JM, Meltzer PS. Hybrid selection of transcribed sequences from microdissected DNA: isolation of genes within amplified region at 20q11-113.2 in breast cancer. Cancer Res 1996; 56: 3446–50.

31 Anzick SL, Kononen J, Walker RL, Azorsa DO, Tanner MM, Guan XY, *et al*. AIB1, a novel estrogen receptor co-activator amplified in breast and ovarian cancer. Science 1997; 277: 965–8.

32 Piao Z, Park C, Park JH, Kim H. Deletion mapping of chromosome 4q in hepatocellular carcinoma. Int J Cancer 1998; 79: 356–60.

33 Bando K, Nagai H, Matsumoto S, Koyama M, Kawamura N, Onda M, *et al*. Identification of a 1-cM region of common deletion on 4q35 associated with progression of hepatocellular carcinoma. Genes Chromosomes Cancer 1999; 25: 284–9.

34 Jou YS, Lee CS, Chang YH, Hsiao CF, Chen CF, Chao CC, *et al*. Clustering of minimal deleted regions reveals distinct genetic pathways of human hepatocellular carcinoma. Cancer Res 2004; 64: 3030–6.

35 Yeh SH, Lin MW, Lu SF, Wu DC, Tsai SF, Tsai CY, *et al*. Allelic loss of chromosome 4q21 approximately 23 associates with hepatitis B virus-related hepatocarcinogenesis and elevated alpha-fetoprotein. Hepatology 2004; 40: 847–54.

36 McGowan-Jordan IJ, Speevak MD, Blakey D, Chevrette M. Suppression of tumorigenicity in human teratocarcinoma cell line PA-1 by introduction of chromosome 4. Cancer Res 1994; 54: 2568–72.

37 Deng Q, Huang S. PRDM5 is silenced in human cancers and has growth suppressive activities. Oncogene 2004; 23: 4903–10.

38 Liao C, Zhao M, Song H, Uchida K, Yokoyama KK, Li T. Identification of the gene for a novel liver-related putative tumor suppressor at a high-frequency loss of heterozygosity region of chromosome 8p23 in human hepatocellular carcinoma. Hepatology 2000; 32: 721–7.

39 Yan J, Yu Y, Wang N, Chang Y, Ying H, Liu W, *et al*. LFIRE-1/HFREP-1, a liver-specific gene, is frequently downregulated and has growth suppressor activity in hepatocellular carcinoma. Oncogene 2004; 23: 1939–49.

40 Yuan BZ, Miller MJ, Keck CL, Zimonjic DB, Thorgeirsson SS, Popescu NC. Cloning, characterization, and chromosomal localization of a gene frequently deleted in human liver cancer (DLC-1) homologous to rat RhoGAP. Cancer Res 1998; 58: 2196–9.

41 Wong CM, Lee JM, Ching YP, Jin DY, Ng IO. Genetic and epigenetic alterations of DLC-1 gene in hepatocellular carcinoma. Cancer Res 2003; 63: 7646–51.

42 Zhou X, Thorgeirsson SS, Popescu NC. Restoration of DLC-1 gene expression induces apoptosis and inhibits both cell growth and tumorigenicity in human hepatocellular carcinoma cells. Oncogene. 2004; 23: 1308–13.

43 Fujiwara Y, Ohata H, Kuroki T, Koyama K, Tsuchiya E, Monden M, *et al*. Isolation of a candidate tumor suppressor gene on chromosome 8p21.3-p22 that is homologous to an extracellular domain of the PDGF receptor beta gene. Oncogene 1995; 10: 891–5.

44 Levy A, Dang UC, Bookstein R. High-density screen of human tumor cell lines for homozygous deletions of loci on chromosome arm 8p. Genes Chromosomes Cancer 1999; 24: 42–7.

45 Garkavtsev I, Grigorian IA, Ossovskaya VS, Chernov MV, Chumakov PM, Gudkov AV. The candidate tumour suppressor p33ING1 cooperates with p53 in cell growth control. Nature 1998; 391: 295–8.

46 Goeman F, Thormeyer D, Abad M, Serrano M, Schmidt O, Palmero I, *et al*. Growth inhibition by the tumor suppressor p33ING1 in immortalized and primary cells: involvement of two silencing domains and effect of Ras. Mol Cell Biol 2005; 25: 422–31.

47 Ching YP, Wong CM, Chan SF, Leung TH, Ng DC, Jin DY, *et al*. Deleted in liver cancer (DLC) 2 encodes a RhoGAP protein with growth suppressor function and is underexpressed in hepatocellular carcinoma. J Biol Chem 2003; 278: 10 824–30.

48 Elo JP, Harkonen P, Kyllonen AP, Lukkarinen O, Vihko P. Three independently deleted regions at chromosome arm 16q in human prostate cancer: allelic loss at 16q24.1-q24.2 is associated with aggressive behaviour of the disease, recurrent growth, poor differentiation of the tumour and poor prognosis for the patient. Br J Cancer 1999; 79: 156–60.

49 Yoshiura K, Kanai Y, Ochiai A, Shimoyama Y, Sugimura T, Hirohashi S. Silencing of the E-cadherin invasion-suppressor gene by CpG methylation in human carcinomas. Proc Natl Acad Sci USA 1995; 92: 7416–9.

50 Wei Y, Van Nhieu JT, Prigent S, Srivatanakul P, Tiollais P, Buendia MA. Altered expression of E-cadherin in hepatocellular carcinoma: correlations with genetic alterations, beta-catenin expression, and clinical features. Hepatology 2002; 36: 692–701.

51 Bando K, Nagai H, Matsumoto S, Koyama M, Kawamura N, Tajiri T, *et al*. Identification of a 1-Mb common region at 16q24.1-24.2 deleted in hepatocellular carcinoma. Genes Chromosomes Cancer 2000; 28: 38–44.

52 Park SW, Ludes-Meyers J, Zimonjic DB, Durkin ME, Popescu NC, Aldaz CM. Frequent downregulation and loss of WWOX gene expression in human hepatocellular carcinoma. Br J Cancer 2004; 91: 753–9.

53 Cornelis RS, van Vliet M, Vos CB, Cleton-Jansen AM, van de Vijver MJ, Peterse JL, *et al*. Evidence for a gene on 17p13.3, distal to TP53, as a target for allele loss in breast tumors without p53 mutations. Cancer Res 1994; 54: 4200–6.

54 He QJ, Zeng WF, Sham JST, Xie D, Yang XW, Lin HL, *et al*. Recurrent genetic alterations in 26 colorectal carcinomas and 21 adenomas from Chinese patients. Cancer Genet Cytogenet 2003; 144: 112–8.

55 Bressac B, Kew M, Wands J, Ozturk M. Selective G to T mutations of p53 gene in hepatocellular carcinoma from southern Africa. Nature 1991; 350: 429–31.
56 Yumoto Y, Hanafusa T, Hada H, Morita T, Ooguchi S, Shinji N, *et al*. Loss of heterozygosity and analysis of mutation of p53 in hepatocellular carcinoma. J Gastroenterol Hepatol 1995; 10: 179–85.
57 Guan XY, Sham JST, Tai LS, Fang Y, Li H, Liang Q. Evidence for another tumor suppressor gene at 17p13.3 distal to p53 in hepatocellular carcinoma. Cancer Genet Cytogenet 2003; 140: 45–8.
58 Qin WX, Wan F, Sun FY, Zhang PP, Han LW, Huang Y, *et al*. Cloning and characterization of a novel gene (C17orf25) from the deletion region on chromosome 17p13.3 in hepatocellular carcinoma. Cell Res 2001; 11: 209–16.
59 Pollack JR, Iyer VR. Characterizing the physical genome. Nat Genet 2002; 32: 515–21.
60 Pinkel D, Segraves R, Sudar D, Clark S, Poole I, Kowbel D, *et al*. High resolution analysis of DNA copy number variation using comparative genomic hybridization to microarrays. Nat Genet 1998; 20: 207–11.
61 Albertson DG, Pinkel D. Genomic microarrays in human genetic disease and cancer. Hum Mol Genet 2003; 12: R145–52.
62 Mantripragada KK, Buckley PG, de Stahl TD, Dumanski JP. Genomic microarrays in the spotlight. Trends Genet 2004; 20: 87–94.
63 Hashimoto K, Mori N, Tamesa T, Okada T, Kawauchi S, Oga A, *et al*. Analysis of DNA copy number aberrations in hepatitis C virus-associated hepatocellular carcinomas by conventional CGH and array CGH. Mod Pathol 2004; 17: 617–22.
64 Ishkanian AS, Malloff CA, Watson SK, DeLeeuw RJ, Chi B, Coe BP, *et al*. A tiling resolution DNA microarray with complete coverage of the human genome. Nat Genet 2004; 36: 299–303.
65 Lindblad-Toh K, Tanenbaum DM, Daly MJ, Winchester E, Lui WO, Villapakkam A, *et al*. Loss-of-heterozygosity analysis of small-cell lung carcinomas using single-nucleotide polymorphism arrays. Nat Biotechnol 2000; 18: 1001–5.
66 Zhao X, Li C, Paez JG, Chin K, Janne PA, Chen TH, *et al*. An integrated view of copy number and allelic alterations in the cancer genome using single nucleotide polymorphism arrays. Cancer Res 2004; 64: 3060–71.
67 Midorikawa Y, Tsutsumi S, Nishimura K, Kamimura N, Kano M, Sakamoto H, *et al*. Distinct chromosomal bias of gene expression signatures in the progression of hepatocellular carcinoma. Cancer Res 2004; 64: 7263–70.
68 Patil MA, Chua MS, Pan KH, Lin R, Lih CJ, Cheung ST, *et al*. An integrated data analysis approach to characterize genes highly expressed in hepatocellular carcinoma. Oncogene 2005; 21: 1–11.

Acta Pharmacologica Sinica 2005 Jun; 26 (6): 666–672

Blackwell Publishing

Full-length article

Gene expression profile of amyloid beta protein-injected mouse model for Alzheimer disease

Ling-na KONG, Ping-ping ZUO[1], Liang MU, Yan-yong LIU, Nan YANG

Department of Pharmacology, School of Basic Medicine, Peking Union Medical College and Chinese Academy of Medical Sciences, Beijing 100005, China

Key words

Alzheimer disease; dementia; amyloid beta-protein; cDNA microarray

[1] Correspondence to Prof Ping-ping ZUO.
Phn/Fax 86-10-6529-6404.
E-mail zuopp@public3.bta.net.cn

Received 2004-11-25
Accepted 2005-03-14

doi: 10.1111/j.1745-7254.2005.00129.x

Abstract

Aim: To investigate the gene expression profile changes in the cerebral cortex of mice injected icv with amyloid beta-protein (Aβ) fragment 25-35 using cDNA microarray. **Methods:** Balb/c mice were randomly divided into a control group and Aβ-treated group. The Morris water maze test was performed to detect the effect of Aβ-injection on the learning and memory of mice. Atlas Mouse 1.2 Expression Arrays containing 1176 genes were used to investigate the gene expression pattern of each group. **Results:** The gene expression profiles showed that 19 genes including *TBX1*, *NF-κB*, *AP-1/c-Jun*, *cadherin*, *integrin*, *erb-B2*, and *FGFR1* were up-regulated after 2 weeks of icv administration of Aβ; while 12 genes were down-regulated, including *NGF*, *glucose phosphate isomerase 1*, *AT motif binding factor 1*, *Na^+/K^+-ATPase*, and *Akt*. **Conclusions:** The results provide important leads for pursuing a more complete understanding of the molecular events of Aβ-injection into mice with Alzheimer disease.

Introduction

Alzheimer disease (AD) is the most common cause of dementia in the elderly, affecting 7%–10% of individuals over 65 years of age and approximately 40% of persons over 80 years old[1]. The disease is characterized behaviorally by global cognitive decline, and defined histologically by two distinguishing pathologies: amyloid plaques, which are extracellular deposits consisting mainly of aggregated amyloid beta-protein (Aβ), and neurofibrillary tangles (NFT), which are intracellular deposits consisting predominantly of hyperphosphorylated tau protein[2]. Epidemiological and molecular studies suggest that AD has multiple etiologies, including genetic mutations, susceptibility genes and environmental factors that promote formation and accumulation of insoluble Aβ and hyperphosphorylated tau. An animal model that mimics the progression of AD was developed using icv injection of Aβ into mice[3–5]. This was accompanied by impairment in learning and memory in addition to biochemical changes and neuronal degeneration.

Recently, a high-throughput technique was developed using cDNA microarrays, in which labeled RNA hybridizes to DNA molecules attached at specific locations on the surface of micrarray membrane[6]. One of the most attractive applications of microarrays is in the study of differential gene expression in disease and animal models. Microarrays are extensively employed to study global changes in gene expression in post-mortem tissues, cultured cells, animal models, and in response to drug treatment. The expression pattern of a gene provides indirect information about function, drug target and cause of a disease. In this study we used cDNA microarrays (Clontech Laboratories, Palo Alto, CA, USA) to investigate gene expression patterns in an icv Aβ mouse model for AD in the cerebral cortex. This approach provided an additional insight into gene processes, which occur not only in AD animal model but also in other neurodegenerative disorders. The knowledge of specific cascades of events leading and causing neurodegeneration will be the key factor in developing and using neuroprotective drugs.

Materials and methods

Reagents $A\beta_{25\text{-}35}$ (Sigma Chemical, St Louis, MO, USA)

was dissolved in sterile normal saline at a concentration of 1 g/L and aggregated by incubation at 37 ºC for 72 h. Sodium Dodecyl Sulfate (SDS) was also the product of Sigma. Trizol Reagent was purchased from Gibco-BRL (New York, NY, USA). [α-^{32}P]-dATP was from Amersham Pharmacia Biotech (Piscataway, NJ, USA). MMLV reverse transcriptase was from Promega (Madison, WI, USA). Polyclonal integrin αM, c-Jun, and phosphor-c-Jun antibody were purchased from Santa Cruz Biotechnology (Santa Cruz, CA, USA). Atlas Mouse 1.2 Expression Arrays and Atlas cDNA Expression Array Kit were provided by Clontech Laboratories. On each array membrane there are 1176 gene cDNA fragments with lengths of 200–600 bp. The name, coordinate, Gene-Bank Number, and other related information for these genes are available on Clontech's homepage (www.clontech.com).

Animals Male Balb/c mice weighing 22–24 g (Institute of Experimental Animal of Chinese Academy of Medical Sciences, Certificate No SCXK11-00-0006) were maintained in a climate-controlled room at 22±1 ºC on a 12 h light/dark cycle with free access to food and water. They were acclimatized to laboratory conditions for 5 d before experiments.

Aggregated Aβ_{25-35} was icv injected into mice according to the method described by Maurice *et al*[3]. In brief, a 28-gauge stainless-steel needle was inserted unilaterally 1 mm to the right of the midline point, equidistant from each eye, at an equal distance between the eyes and the ears and perpendicular to the plane of the skull. Aβ_{25-35} or sterile normal saline at a volume of 5 μL was delivered gradually within 15 s.

Water maze task The Morris water maze test began on d 11 after Aβ-injection as described[7]. The experimental apparatus consisted of a circular water tank (diameter=80 cm) filled to a depth of 15 cm with water maintained at 23±1 ºC. The water was made opaque by adding black ink. A platform (diameter=8 cm) was submerged 0.5 cm below the water surface and placed at the midpoint of one quadrant. Two training trials each day were conducted for 4 consecutive days. On each trial, the mice were placed in the pool at one starting position. They were allowed to swim freely or until they found the platform. The time required to escape onto the hidden platform was recorded. Mice that found the platform were allowed to remain on the platform for 10 s and were then returned to the home cage. If a mouse did not reach the platform within 120 s, it was gently guided to platform by the experimenter, where it remained for 10 s. Statistic comparison of the water maze test between the Aβ-treated and control group was analyzed by two-way analysis of variance (ANOVA).

RNA preparation Mice were killed after the water maze test. Total RNA was extracted from the cerebral cortex with Trizol according to the manufacturer's instructions. RNA extracts from 10 mice of each group were pooled to provide sufficient material for both cDNA microarray and reverse transcription-PCR analysis. Total RNA was treated with RNase-free DNase at 37 ºC for 20 min to avoid contamination of genomic DNA. The RNA quality and concentration were assessed using agarose gel electrophoresis and spectrophotometric reading.

Probe preparation and hybridization Total RNA (5 μg) was reverse transcribed using reagents provided in the Atlas cDNA Expression Array Kit and radiolabeled with [α-^{32}P]-dATP. The array membranes were prehybridized for 1 h at 68 ºC in ExpressHyb solution containing 100 mg/L of heat-denatured salmon testis DNA. The denatured ^{32}P-labeled cDNA was added to Express Hyb hybridization solution at a final concentration of 4.0 MBq/L and array membranes were hybridized with the labeled cDNA overnight at 68 ºC. The next day, the membranes were washed three times for 30 min with pre-warmed (68 ºC) washing solution 1 [2×SSC (1×SSC is 15 mmol/L sodium chloride, 15 mmol/L sodium citrate), 1% SDS] and once for 30 min with pre-warmed (68 ºC) washing solution 2 (0.1×SSC, 0.5% SDS) with continuous agitation at 68 ºC. After a final wash with 2×SSC at room temperature for 10 min, the membrane was immediately wrapped in plastic film and exposed to X-ray film at -70 ºC.

Detection and analysis Gene expression levels were assessed according to autoradiographic intensity of hybridization signals by software. Only those autoradiograms with similar background and identical signal intensity of housekeeping genes were comparable. Genes that showed an increase or decrease of 2.0-fold or greater were considered as differentially expressed genes. Each group sample was carried out three times, those genes that were all differentially expressed in the three hybridizations were reported as mean±SEM.

Semi-quantitative RT-PCR Expressions of 6 genes were randomly selected to be further confirmed by RT-PCR. Primers were designed using DNA Star software (Perkin Elmer, Norwalk, Conn, USA) and synthesized by Sbs Bio Inc (Beijing, China). Reverse transcription reaction was catalysed by MMLV. PCR was performed for 30 s at 94 ºC, 30 s at 55 ºC, and 1 min at 70 ºC for a cycle, 32 cycles were completed (25 cycles for *GAPDH* gene), and finally 10 min at 72 ºC. The RT-PCR products were subjected to electrophoresis in 1% agarose gels and quantitative analysis was carried out using the YLN 2000 Gel Analysis System (Yalien, Beijing, China). The gene expression levels were assessed according to the gray ratio value of the target genes and housekeeping gene, *GAPDH*. The PCR primers used were as follows: *GAPDH*,

forward primer, 5'-CAG CAA CTC CCA CTC TTGCC CCT CCT GTT ATT AT-3'; *AP-1*, forward primer, 5'-AGGCAGAGA-GGAAGCGCAT-3', reverse primer, 5'-TGGCACCCACTGTTA-ACGTG-3'; *NF-κB*: forward primer, 5'-GCAGCCTATCACCA-ACTCT-3' , reverse primer, 5'-TACTCCTTCTTCTCCACCA-3'; *integrin αM*, forward primer, 5'-TTAATGACTCTGCGTTT-GCCC-3', reverse primer, 5'-TCATGTCCTTGTACTGCCGCT-3'; *ATPase*, forward primer, 5'-CCATCTTCTGCACCATC-GTTC-3', reverse primer, 5'- AGACGCCCTGCCTCTTTCAG-3'; *nerve growth factor α* (*NGF α*), forward primer, 5'-ACTGG-GTTCTCACAGCTGCC-3', reverse primer, 5'-CGCAGCA-GCATCAGGTCAT-3'; *Akt*, forward primer, 5'-CCTGTCTCGA-GAGCGTGTGTT-3', reverse primer, 5'-CATAGTGGCACCGT-CCTTGA-3'.

Western blot analysis After decapitation, the cerebral cortex from 5 mice were immediately homogenized in 5 volumes of homogenization buffer [Tris-HCl 50 mmol/L (pH 7.5), NaCl 150 mmol/L, 1 % Triton-X 100, 1 % sodium deoxycholate, 0.1 % SDS]. After sonication and centrifugation at 4 ºC (10 min, 10 000×*g*), the supernatant was used for determination of protein concentrations, and the equal amounts of total solubilized proteins were eluted by heating with SDSPAGE sample buffer and separated by SDS-polyacrylamide gel electrophoresis. Proteins were then transferred to the nitrocellulose membrane. The membrane was blocked at room temperature with 5 % non-fat dry milk in Tris-buffered saline with 0.1 % (v/v) Tween-20 (TBST) and incubated with polyclonal integrin αM, c-Jun and phosphor-c-Jun antibody (1:1000) overnight at 4 ºC. After washing, the membrane was incubated with horseradish-labeled secondary antibody for 1 h. After five additional washes in TBST, the membrane was incubated with an enhanced chemiluminescence detecting reagent according to the manufacturer's protocols and exposed to X-ray film.

Results

Effects of icv injection of $A\beta_{25-35}$ on performance of the Morris water maze task Effect of Aβ-injection on learning and memory revealed a significant difference between the two groups. Aβ-injected mice exhibited an obvious learning deficit compared to the saline-injected mice. ANOVA analysis showed a significant decrease in the latency time for the control group during the 8 training trials, but not for the experimental group (Figure 1).

Gene expression analysis of mice cerebral cortex after icv injection of $A\beta_{25-35}$ The human cerebral cortex serves to control functions such as speech, memory, logical and emotional response, as well as consciousness, interpretation of

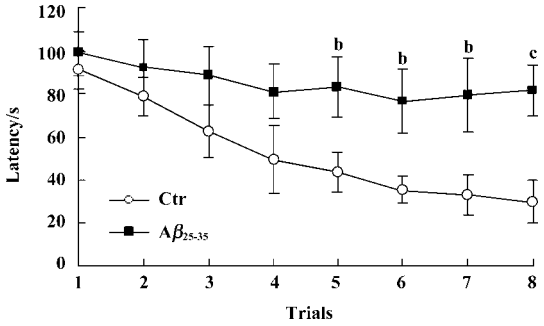

Figure 1. $A\beta_{25-35}$ induced impairment on learning and memory in mice in the Morris water maze task. Ten days after icv administration of the sterile normal saline (Ctr) or the aggregated $A\beta_{25-35}$, mice were subjected to the Morris water maze test. The training trials were carried out on d 11–14. n=10. Mean±SEM. $^bP<0.05$, $^cP<0.01$ *vs* Ctr group.

sensation, coordination of voluntary movement, and these are all greatly involved and damaged in AD. In our study, we used cDNA microarray to investigate the molecular events of neuronal toxicity induced by $A\beta_{25-35}$ in the cerebral cortex of mice. We compared the gene expression levels in the cerebral cortex of Aβ-injected mice and saline-injected mice. Of 1176 known mouse genes represented on the array, we detected 31 genes differentially expressed in the mice cerebral cortex. Among them 19 genes showed up-regulation in expression after injection of Aβ, including *TBX1*, *NF-κB*, *AP-1/c-Jun*, *cadherin*, *integrin*, *erb-B2*, and *FGFR1*; while expression of 12 genes were down-regulated, including *NGF*, *glucose phosphate isomerase 1*, *AT motif binding factor 1*, *Na^+/K^+-ATPase*, and *Akt*. All differentially expressed genes were functionally characterized as a diverse spectrum of the biologic process, including transcription factor, cell cycle protein, cytokines, signal transduction, energy metabolism, neurotrophic factor, and so on (Table 1).

Semi-quantitative RT-PCR To confirm the results of cDNA array, RT-PCR analysis was performed to examine the expression level of 6 genes that were up-regulated or down-regulated in the cerebral cortex of mice. The RT-PCR results indicated that 6 genes showed identical results to that of the microarray (Figure 2).

Western blot analysis The expression of integrin αM and activated AP-1/c-Jun of the cerebral cortex were investigated by Western blot analysis. Although total c-Jun was unchanged in intensity between the two groups, the increased expression of integrin αM and phosphorylated c-Jun were found in the cerebral cortex of Aβ-treated mice (Figure 3).

Table 1. Differentially expressed genes in the cerebral cortex of Aβ-treated mice. *n*=3. Mean±SEM.

Gene code	Protein/gene	Gene classification	Ratio
U57327	T-box 1 (TBX 1)	Basic transcription factors	11.73±1.84
AB009453	Transcription factor 21	Basic transcription factors	5.80±0.56
M61909	NF-κB p65	Transcription activators and repressors	3.17±0.86
J04115	Transcription factor AP-1; c-Jun	Transcription activators and repressors	2.78±0.34
X83974	Transcription termination factor 1	Oncogenes and tumor suppressors	2.35±0.29
M83749	Cyclin D2753	Cyclins	2.58±0.11
X07640	Integrin alpha M	Cell-cell adhesion receptors	6.27±0.99
M31131	Cadherin 2; neural-cadherin (NCAD)	Cell-cell adhesion receptors	3.14±0.72
M60778	Integrin alpha L	Intracellular transducers /modulators	2.74±0.66
L47239	erb-B2 proto-oncogene;neuro/glioblastoma derived oncogene homolog	Growth factor & chemokine receptors	4.37±1.01
M28998	Fibroblast growth factor receptor 1	Growth factor & chemokine receptors	2.04±0.21
AB010833	Patched homolog 2 (PTC2; PTCH2)	Intracellular transducers/modulators	5.00±0.38
U43320	Frizzled homolog 7 (FZD7; FZ7)	Intracellular transducers/modulators	3.62±1.40
AF080215	Coagulation factor II receptor-like 3	Intracellular transducers/modulators	3.24±0.55
U43205	Frizzled homolog 3 (FZD3; FZ3)	Intracellular transducers/modulators	2.94±0.18
X54924	Neurofibromatosis 1	Intracellular transducers/modulators	2.02±0.23
J05154	Lecithin cholesterol acyltransferase	Extracellular transport/carrier proteins	2.19±0.72
X15830	Secretory granule neuroendocrine protein 1, 7B2 protein	Neuropeptides	6.29±1.66
X02165	Neurofilament, light polypeptide	Cytoskeleton/motility proteins	2.58±0.48
L12703	Engrailed homeobox protein 1	Transcription activators and repressors	0.20±0.06
AF005772	Paired-like homeodomain transcription factor 3	Basic transcription factors	0.37±0.14
U43788	POU domain class 2-associating factor 1; Oct-1	Transcription activators and repressors	0.44±0.08
D26046	AT motif binding factor 1	Telomere-associated proteins	0.49±0.17
AF053471	Sodium/potassium-transporting ATPase isoform 2β polypeptide 2 (Na^+/K^+-ATPase 2β2)	Membrane channels and transporters	0.23±0.05
M11434	Nerve growth factor α (NGF α)	Growth factors, cytokines	0.35±0.11
M14220	Glucose phosphate isomerase 1	Growth factors, cytokines	0.41±0.19
U15159	LIM-domain containing protein kinase 1	Intracellular kinase network members	0.29±0.06
M33960	Serine (or cysteine) proteinase inhibitor, clade E, member 1	Inhibitors of proteases	0.26±0.10
D89076	Transthyretin	Extracellular transport/carrier proteins	0.45±0.16
M94335	Akt proto-oncogene; protein kinase B (PKB)	Apoptosis associated proteins	0.38±0.04
M29855	Interleukin 3 receptor	Interleukin and interferon receptors	0.32±0.14

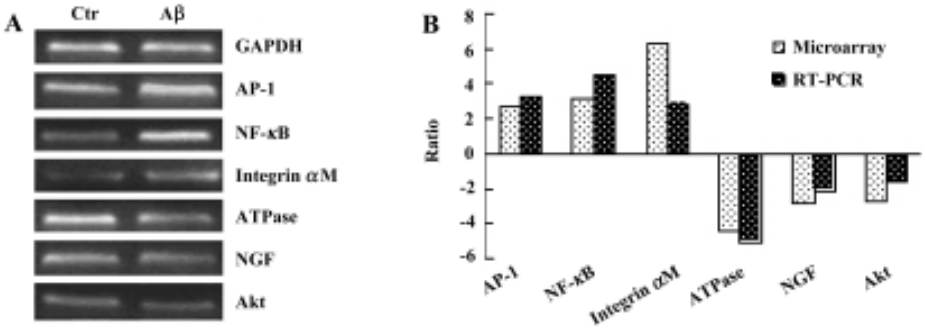

Figure 2. RT-PCR analysis of 6 gene expressions of the cerebral cortex of control (Ctr) or Aβ-treated mice (Aβ). (A) Agarose electrophoresis of PCR products; (B) Comparison of differential expression of 6 genes obtained from microarray and RT-PCR. The levels of gene expression were standardized against that of GAPDH as an internal control. The positive or negative ratios indicated the increase or decrease of gene expression in Aβ-treated mice compared with the control.

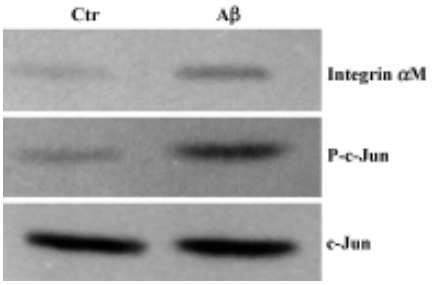

Figure 3. The expression of integrin αM and activated c-Jun in the cerebral cortex of control (Ctr) or Aβ-injected mice (Aβ). The experiment shown is a representative of three independent experiments showing similar results.

Discussion

Ample experimentation indicates that icv injection of Aβ to rodents can induce learning and memory impairments as well as neurodegeneration in brain areas related to cognitive function[3–5]. This model of Aβ exposure is a useful model *in vivo* for AD. In the present study, we used the Morris water maze test to detect the effect of aggregated $A\beta_{25\text{-}35}$ injection on the learning and memory of mice. Our results corresponded to previous reports that $A\beta_{25\text{-}35}$ could significantly impair the spacial learning ability and memory of mice.

Microarray provides a promising approach to explore novel molecular and cellular mechanisms that may contribute to some diseases. Gene expression changes in the mice cerebral cortex between icv injection of $A\beta_{25\text{-}35}$ and sterile normal saline were analyzed by using cDNA microarray. In total, 31 genes were differentially expressed, of which 19 genes were increased and 12 were decreased. This implies that only a small fraction of the surveyed genes were affected by $A\beta_{25\text{-}35}$, while most stayed at a stable expression level. The up-regulation or down-regulation of these genes may be responsible for Aβ-induced memory impairment in mice.

In the present study, we found that several genes encoding transcription and chromatin-modifying factors were differentially expressed after icv administration of $A\beta_{25\text{-}35}$. For example, *TBX1, transcription factor 21, transcription factor AP-1/c-Jun*, and *NF-κB* showed an increased expression level, while *engrailed homeobox protein 1* and *Oct-1* were decreased in expression. *AP-1* complex is composed of a heterodimer *Fos* and *Jun*, the latter is involved in p38/c-Jun N-terminal MAPK pathway (JNK) and considered as a major regulator of both neuronal death and regeneration[8,9]. A number of reports indicate that *NF-κB* regulates the expression of various genes that play critical roles in apoptosis, viral replication, tumorigenesis, various autoimmune diseases, and inflammation[10, 11]. Studies of postmortem brain tissue from patients with AD have revealed increased NF-κB activity in cells involved in the neurodegenerative process. This is consistent with increased p65 immunoreactivity in neurons and astrocytes in the immediate vicinity of amyloid plaques in brain sections from AD patients[12]. It is reported that Aβ can activate *NF-κB* in the cultured neurons[13], suggesting a molecular mechanism by which Aβ may act during AD pathogenesis. We also noticed that the most dramatic change in gene expression was for the transcript encoding for *TBX1*, a member of the T-box binding gene family[14]. There are at least 21 members of this gene family. The T-box region, which mediates DNA binding, is highly conserved from *Drosophila* to humans. Human and mice TBX1 proteins share 98% amino acid identity overall and are identical except for 2 residues within the T-box domain. Expression of human *TBX1* in adult and fetal tissues, as determined by Northern blot analysis, were similar to that found in the mice[15]. These transcription factors are involved in the regulation of developmental processes, where they seem to be required for tissue-specific development. In particular, the *TBX1* gene is a major genetic determinant in Del22q11.2 syndrome in human beings, which is characterized by a 3-Mb deletion on chromosome 22q11.2, cardiac abnormalities, T-cell deficits, cleft palate facial anomalies, and hypocalcemia[16]. However, there is little known about specific target genes for TBX1 proteins and the relationship between this gene and AD. The function of the most up-regulated gene, *TBX1*, in the Aβ-injection mice should be further studied.

Integrin αM and *integrin αL*, two cell adhesion receptors with an Aβ binding site and involved in the uptake of Aβ in neurons and glial cells[17], were observed to be up-regulated in the Aβ-treated mice. Adhesion proteins usually transduce the extracellular signal into cells and change the cell cytoskeleton. It is very possible that Aβ binds to integrin proteins and activates the focal adhesion (FA) proteins, paxillin and focal adhesion kinase (FAK). In this regard, fibrillar Aβ could promote dystrophy by aberrantly activating FA signal transduction cascades that would be involved in Aβ-induced neuronal dystrophy or cell death[18,19]. Moreover, the binding of Aβ to integrin proteins would induce sustained activation of MAPK pathways followed by neurite degeneration and hyperphosphorylation of tau proteins[20]. N-cadherin, another cell-adhesion protein, also showed an increase in expression after Aβ-injection. It is a cell surface glycoprotein that mediates calcium-dependent adhesion between neural cells and affects a wide range of cellular processes, including cell adhesion**,** cell morphogenesis and cell migration.

Two protein tyrosine kinases, *erb-B2*, and *FGF receptor 1*, were increased in expression after Aβ-injection. Erb-B2 is the receptor of neuregulin, and overexpression has been demonstrated to activate mitogenic signal transduction and enhance proliferative, prosurvival, and metastatic signals in cell lines. The activity of the MAPK pathway is up-regulated in cells overexpressing erb-B2[21,22]. However, the understanding of the function of erb-B2 in neural cells is very limited. This basic growth factor has pleiotropic effects and plays a regulatory role in angiogenesis, smooth muscle cell growth and wound healing through fibroblast growth factor receptors (FGFR)[23]. FGFR1 activation is followed by intracellular signaling cascades involving Ca^{2+} channels, phospholipase C, src family kinases, mitogen-activated kinases and the Grb2/Sos signaling complex[24,25]. An increase of FGFR2 in brain neurons and retinal pigment epithelial cells can lead to the activation of L-type channels of neuroendocrine and induce gene expression through the phosphorylation of CREB (cyclic AMP-responsive element binding protein)[26]. Whether the up-regulation of neuroendocrine protein 1 resulted from the increase of FGFR 1 in our study still needs to be studied further.

It is well known that Aβ can impair mitochondria energy metabolism and selectively inhibit Na^+/K^+-ATPase activity both *in vivo* and *in vitro*. From our present results, we found that two Na^+/K^+-ATPase related genes, *AT motif-binding factor 1 (ATBF1)*, and *Na^+/K^+-ATPase 2β2*, were down-regulated. This is consistent with previous studies. ATBF1 is a large transcription factor protein containing four homeodomains and 23 zinc finger motifs. It also includes several motifs that were found in ATPases[27]. The ATPase activity has been reported to be associated with ATBF1 activity in a unique DNA/RNA-dependent manner that requires both homeodomain and zinc finger motifs[28].

Interleukin 3 receptor has been reported to have a neurotrophic effect on central cholinergic neurons[29]. Down-regulation of this gene may be responsible for cholinergic dysfunction induced by Aβ. Another two growth factors, *NGF* and *glucose phosphate isomerase 1*, were also down-regulated. A large number of reports have shown that these neurotrophic factors have beneficial effects on neural cell survival both *in vivo* and *in vitro*.

The expression of an apoptosis associated protein, *Akt*, decreased in the Aβ-injected mice. This protein can protect cells from a variety of death-promoting insults in several different cell types, including Aβ toxicity[30]. Activated Akt would lead to phosphorylation of the proapoptotic protein Bad, stimulate Bcl-2 and Bax expression, decrease the interaction of Bad with Bcl-xL, increase the Bcl-xL/Bad ratio, eventually promoting cell survival[31].

In summary, we observed extensive activation of transcription factors and the signal transduction system, which may result in neuron apoptosis, energy metabolism and calcium ion homeostasis dysfunction, cell adhesion and neuronal dystrophy. A number of the candidate genes we describe have not been linked to AD in previous publications, and define novel injury pathways warranting further studies. The genes found from the cDNA microarray provide some clues for pursuing a more complete understanding of the molecular mechanism of Aβ-induced neural degeneration and memory impairment.

References

1 Price DL, Sisodia SS. Mutant genes in familial Alzheimer's disease and transgenic models. Annu Rev Neurosci 1998; 21: 479–505.

2 Cummings BJ, Pike CJ, Shankle R, Cotman CW. β-Amyloid deposition and other measures of neuropathology predict cognitive status in Alzheimer's disease. Neurobiol Aging 1996; 17: 921–33.

3 Maurice T, Lockhart BP, Privat A. Amnesia induced in mice by centrally administered β-amyloid peptides involves cholinergic dysfunction. Brain Res 1996; 706: 181–93.

4 Yamada K, Tanaka T, Han D, Senzaki K, Kameyama T, Nabeshima T. Protective effects of idebenone and α-tocopherol on β-amyloid-(1-42)-induced learning and memory deficits in rats: implication of oxidative stress in β-amyloid-induced neurotoxicity *in vivo*. Eur J Neurosci 1999; 11: 83–90.

5 Flood JF, Morley JE, Roberts E. Amnestic effects in mice of four synthetic peptides homologous to amyloid β protein from patients with Alzheimer disease. Proc Natl Acad Sci USA 1991; 88: 3363–6.

6 Lockhart DJ, Winzeler EA. Genomics, gene expression and DNA arrays. Nature 2000; 405: 827–36

7 Morris R. Developments of a water-maze procedure for studying spatial learning in the rat. J Neurosci Methods 1984; 11: 47–60.

8 Behrens A, Sibilia M, Wagner EF. Amino-terminal phosphorylation of c-Jun regulates stress-induced apoptosis and cellular proliferation. Nat Genet 1999; 21: 326–9.

9 Crocker SJ, LambaWR, Smith PD, Callaghan SM, Slack RS, Anisman H, *et al*. c-Jun mediates axotomy-induced dopamine neuron death *in vivo*. Proc Natl Acad Sci USA 2001; 98: 13385–90.

10 Baeuerle PA, Baichwal VR. NF-κB as a frequent target for immunosuppressive and anti-inflammatory molecules. Adv Immunol 1997; 65: 111–37.

11 Baichwal VR, Baeuerle PA. Activate NF-κB or die? Curr Biol 1997; 7: R94–6.

12 O'Neill LA, Kaltschmidt C. NF-κB: a crucial transcription factor for glial and neuronal cell function. Trends Neurosci 1997; 20: 252–8.

13 Barger SW, Horster D, Furukawa K, Goodman Y, Krieglstein J, Mattson MP. Tumor necrosis factors α and β protect neurons against amyloid β-peptide toxicity: evidence for involvement of

a κB-binding factor and attenuation of peroxide and Ca^{2+} accumulation. Proc Natl Acad Sci USA 1995; 92: 9328–32.
14 Papaioannou VE, Silver LM. The T-box gene family. Bioessays 1998; 20: 9–19.
15 Chieffo C, Garvey N, Gong W, Roe B, Zhang G, Silver L, *et al*. Isolation and characterization of a gene from the DiGeorge chromosomal region homologous to the mouse Tbx1 gene. Genomics 1997; 43: 267–77.
16 Yagi H, Furutani Y, Hamada H, Sasaki T, Asakawa S, Minoshima S, *et al*. Role of TBX1 in human del22q11.2 syndrome. Lancet 2003; 362: 1366–73.
17 Bi X, Gall CM, Zhou J, Lynch G. Uptake and pathogenic effects of amyloid beta peptide 1-42 are enhanced by integrin antagonists and blocked by NMDA receptor antagonists. Neuroscience 2002; 112: 827–40.
18 Berg MM, Krafft GA, Klein WL. Rapid impact of β-amyloid on paxillin in a neural cell line. J Neurosci Res 1997; 50: 979–89.
19 Williamson R, Scales T, Clark BR, Gibb G, Reynolds CH, Kellie S, *et al*. Rapid tyrosine phosphorylation of neuronal proteins including tau and focal adhesion kinase in response to amyloid-β peptide exposure: involvement of Src family protein kinases. J Neurosci 2002; 22: 10–20.
20 Anderson KL, Ferreira A. α1 integrin activation: a link between β-amyloid deposition and neuronal death in aging hippocampal neurons. J Neurosci Res 2004; 75: 688–97.
21 Wen D, Peles E, Cupples R, Suggs SV, Bacus SS, Luo Y, *et al*. Neu differentiation factor: a transmembrane glycoprotein containing an EGF domain and an immunoglobulin homology unit. Cell 1992; 69: 559–72.
22 Tari AM, Lopez-Berestein G. Serum predominantly activates MAPK and Akt kinases in EGFR- and erbB2-over-expressing cells, respectively. Int J Cancer 2000; 86: 295–7.
23 Bikfalvi A, Klein S, Pintucci G, Rifkin DB. Biological roles of fibroblast growth factor-2. Endocr Rev 1997; 18: 26–45.
24 Koike H, Saito H, Matsuki N. Effect of fibroblast growth factors on calcium currents in acutely isolated neuronal cells from rat ventromedial hypothalamus. Neurosci Lett 1993; 150: 57–60.
25 Williams EJ, Furness J, Walsh FS, Doherty P. Characterization of the second messenger pathway underlying neurite outgrowth stimulated by FGF. Development 1994; 120: 1685–93.
26 Rosenthal R, Thieme H, Strauss O. Fibroblast growth factor receptor 2 (FGFR2) in brain neurons and retinal pigment epithelial cells act via stimulation of neuroendocrine L-type channels ($Ca_v1.3$). FASEB J 2001; 15: 970–7
27 Miura Y, Tam T, Ido A, Morinaga T, Miki T, Hashimoto T, *et al*. Cloning and characterization of an ATBF1 isoform that expresses in a neuronal differentiation-dependent manner. J Biol Chem 1995; 270: 26840–8.
28 Kawaguchi M, Miura Y, Ido A, Morinaga T, Sakata N, Oya T, *et al*. DNA/RNA-dependent ATPase activity is associated with ATBF1, a multiple homeodomain-zinc finger protein. Biochim Biophys Acta 2001; 1550: 164–74.
29 Tabira T, Chui DH, Fan JP, Shirabe T, Konishi Y. Interleukin-3 and interleukin-3 receptors in the brain. Annal NY Acad Sci 1998; 840: 107–16.
30 Martin D, Salinas M, Lopez-Valdaliso R, Serrano E, Recuero M, Cuadrado A. Effect of the Alzheimer amyloid fragment Aβ (25-35) on Akt/PKB kinase and survival of PC12 cells. J Neurochem 2001; 78: 1000–8.
31 Seo JH, Rah JC, Choi SH, Shin JK, Min K, Kim HS, *et al*. α-Synuclein regulates neuronal survival via Bcl-2 family expression and PI3/Akt kinase pathway. FASEB J 2002; 16: 1826–8.

Acta Pharmacologica Sinica 2005 Jun; 26 (6): 673–678

Full-length article

Effects of huperzine A on secretion of nerve growth factor in cultured rat cortical astrocytes and neurite outgrowth in rat PC12 cells[1]

Li-li TANG, Rui WANG, Xi-can TANG[2]

State Key Laboratory of Drug Research, Shanghai Institute of Materia Medica, Shanghai Institutes for Biological Sciences, Chinese Academy of Sciences, Shanghai 201203, China

Key words

huperzine A; nerve growth factor; neurite outgrowth; acetylcholinesterase inhibitors

[1] Project supported by the National Natural Science Foundation of China (No 30123005) and the Ministry of Science and Technology of China (No 2004CB518907).
[2] Correspondence to Prof Xi-can TANG.
Phn 86-21-5492-0510
Fax 86-21-5080-7088
E-mail xctang@mail.shcnc.ac.cn

Received 2004-12-27
Accepted 2005-03-15

doi: 10.1111/j.1745-7254.2005.00130.x

Abstract

Aim: To study the effects of huperzine A (HupA) on neuritogenic activity and the expression of nerve growth factor (NGF). **Methods:** After being treated with 10 μmol/L HupA, neurite outgrowth of PC12 cells was observed and counted under phase-contrast microscopy. Mitogenic activity was assayed by [^{3}H]thymidine incorporation. Cell cytotoxicity was evaluated by lactate dehydrogenase (LDH) release. AChE activity, mRNA and protein expression were measured by the Ellman's method, RT-PCR, and Western blot, respectively. NGF mRNA and protein levels were determined by RT-PCR and ELISA assays. **Results:** Treatment of PC12 cells with 10 μmol/L HupA for 48 h markedly increased the number of neurite-bearing cells, but caused no significant alteration in cell viability or other signs of cytotoxicity. In addition to inhibiting AChE activity, 10 μmol/L HupA also increased the mRNA and protein levels of this enzyme. In addition, following 2 h exposure of the astrocytes to 10 μmol/L HupA, there was a significant up-regulation of mRNA for NGF and P75 low-affinity NGF receptor. The protein level of NGF was also increased after 24 h treatment with HupA. **Conclusion:** Our findings demonstrate for the first time that HupA has a direct or indirect neurotrophic activity, which might be beneficial in treatment of neurodegenerative disorders such as Alzheimer disease.

Introduction

Nerve growth factor (NGF) is a member of the neurotrophin family that promotes the survival and outgrowth of central cholinergic neurons[1]. The decrease in trophic support for the neurons in the aging brain is associated with neuronal death and appearance of neurodegenerative disorders such as Alzheimer disease (AD)[2]. A case study showed that topical application of NGF into the brain of one AD patient relieved symptoms of dementia[3]. However, the clinical utility of NGF is limited by an inability to cross the blood-brain barrier, necessitating invasive neurosurgical procedures for administration. In contrast, pharmacological stimulation of endogenous NGF synthesis or mimicking of NGF activity by compounds that penetrate membrane barriers may provide an alternative means to provide equivalent trophic actions in the central nervous system.

Accumulated data suggest that cholinergic mechanisms are involved in the regulation of NGF synthesis and release. It has been suggested that cholinergic activity in basal forebrain neurons may stimulate NGF synthesis in appropriate target areas during early postnatal development[4]. Additionally, substances that augment cholinergic function, such as nicotine, muscarinic receptor agonists, and acetylcholine-releasing agents, can increase NGF expression and synthesis[5,6]. Although there have been no reports that acetylcholinesterase (AChE) inhibitors elevate NGF production, some AChE inhibitors are known to exert NGF-like activity by potentiating the neuritogenic effect of NGF[7] or increasing choline acetyltransferase (ChAT) activity[8]. These actions appear to be independent of AChE inhibition. Such findings led us to suspect that the neurotrophic effects of huperzine A (HupA), a novel acetylcholinesterase inhibitor isolated from the Chinese herb *Huperzia serrata*, involve

NGF-like activity, directly or indirectly.

HupA has been proved to be one of the most promising new agents for AD therapy[9]. Our previous studies showed that, in addition to its potent inhibition of AChE, HupA exhibited neuroprotective effects both *in vivo* and *in vitro*[10,11]. For example, just as NGF can ameliorate neuronal degeneration in rat cerebral cortex and hippocampus after ischemic insult[12], HupA will attenuate ischemic damage from transient global ischemia in gerbils and hypoxic-ischemia (HI) in neonatal rats[13,14]. A multicenter, randomized, double-blind, placebo-controlled clinical trial in China proved that HupA markedly improved the cognitive function of vascular dementia (VD)[15–17]. In view of these findings it is natural to ask if HupA might influence intrinsic neurotrophic factors. The aim of this study was to examine the effects of HupA on neuritogenesis in rat pheochromocytoma cells and on the expression and secretion of NGF in primary cultures of rat cortical astrocytes.

Materials and methods

Materials HupA, provided by the Department of Phytochemistry at Shanghai Institute of Materia Medica is a colorless powder with mp 230 °C, and purity >99%. It was dissolved and diluted in phosphate-buffered saline (PBS). RPMI-1640 medium, DMEM/F12 medium, fetal bovine serum, horse serum, and N-2 supplement were purchased from Gibco (CA, USA). Cell cytotoxicity Kit, NGF $E_{max}^{®}$ Immunoassay System, Reverse Transcription System were purchased from Promega (Madison, WI, USA). Mouse monoclonal anti-AChE antibody was purchased from BD Biosciences (CA, USA). TRIzol reagent was purchased from Invitrogen (CA, USA). ECL kit was purchased from Pierce (Rockford, USA).

PC12 cell culture and neurite outgrowth assay Undifferentiated PC12 rat pheochromocytoma cells were obtained from ATCC. The cells were maintained in RPMI-1640 media containing 10% FCS, 5% HS, 100 kU/L penicillin, and 100 kU/L streptomycin in a humidified atmosphere of 95% air and 5% CO_2 at 37 °C. For each experiment, cells (3.5×10^4 cells/well) were seeded into a 12-well collagen-coated plate and cultured overnight. Subsequently the cells were washed once with PBS and transferred to fresh serum-free DMEM containing an N-2 supplement. After a 2-h incubation with serum-free DMEM, NGF or HupA was added to the cultures, which were incubated for a further 48 h. Neurite formation was examined under a phase-contrast microscope, and processed longer than one cell diameter were scored as neurites. The percentage of neurite-bearing cells in relation to the total number of cells was examined in four fields from each of the eight culture wells per treatment condition.

Mitogenic activity and cytotoxicity assay To analyze the effects of HupA on mitogenic activity, PC12 cells were seeded into 96-well plate at a density of 1×10^4 cell/well. After incubation of the cells with 10 μmol/L HupA for 48 h at 37 °C, [^{3}H]thymidine (37 000 Bq) was added to the cultures and incubation was continued for another 8 h. The cells were harvested onto filters using a cell harvester and the retained radioactivity was determined in a scintillation counter. HupA cytotoxicity was evaluated by an assay kit, following the manufac-ture's protocol to detect lactate dehydrogenase (LDH) release.

AChE activity assay AChE activity was measured by a standard spectrophotometric method[18].

Western blot analysis Changes in AChE levels were assessed by Western blot. For this purpose, cultured cells harvested 48 h after treatment with HupA were lysed in 1×SDS PAGE gel loading buffer [Tris-HCl 50 mmol/L pH 6.8, DTT 100 mmol/L, 2% (w/v) SDS, 10% (w/v) glycerol, 0.1% Bromophenol Blue] and boiled in a water bath for 10 min. Equal amounts of protein (40 μg) were loaded in each gel lane and, after electrophoresis, proteins were transferred to a nitrocellulose membrane. The membranes were blocked with TBST containing 5% non-fat milk and then were incubated at 4 °C overnight with primary antibody (a mouse monoclonal antibody raised against human AChE and crossreactive with rat AChE). Finally the blots were incubated with HRP-conjugated anti-mouse IgG at 37 °C for 2 h and target protein bands were detected by the ECL method according to the manufacture's instruction.

Astrocytes cultures and experimental treatment For studies of NGF expression, primary cultures of astrocytes were prepared from 1-day-old neonatal Sprague-Dawley rats. Cerebral cortices were stripped of meninges and dissected in Ca^{2+}-, Mg^{2+}-free D-Hanks' solution. Next the samples were trypsinized and passed through a monofilament mesh (pore size 80 μm). Cells were collected by centrifugation and resuspended in DMEM/F12 containing 10% FCS, 100 kU/L penicillin and 100 kU/L streptomycin for culture in a humidified atmosphere (95% air and 5% CO_2) at 37 °C. Astrocytes were grown to confluence and oligodendrocyte and microglial cells were removed by shaking and washing with cold D-Hanks' solution. The astrocytes were then trypsinized and plated onto 24-well plates at a density of 1×10^4 cell/cm^2, washed with D-Hanks' solution, and exposed for 24 h to serum-free medium. After this incubation, culture medium was collected and centrifuged to remove cell debris.

NGF content assay Released NGF was measured in the supernatant by a two-site enzyme-linked immunosorbent

assay (ELISA) using the NGF E_{max}® Immunoassay system.

RT-PCR analysis RT-PCR was performed to determine the expression of mRNA for AChE in PC12 cells and for NGF and $P75^{NTR}$ in astrocytes. Total cellular RNA was isolated using TRIzol reagent following the manufacturer's protocols and quantified by absorbance at 260 nm. RNA purity was determined using the A_{260}/A_{280} ratio (average ratio > 1.85). Total RNA of each sample was reverse-transcribed into cDNA using Reverse Transcription System. The cDNAs were amplified with the following specific primers. AChE: 5'-TCTTTGCTCAGCGACTTA-3' (upstream), 5'-GTCACAGGTCTGAGCATCT-3' (downstream); NGF: 5'-CTTCAGCATTCCCTTGACAC-3'(upstream),5'-AGCCTTCCTGCTGAGCACACA-3' (downstream); $P75^{NTR}$: 5'-AGCCAACCAGACCGTGTGTG-3' (upstream), 5'-TTGCA GCTGTTCCACCTCTT-3' (downstream); β-actin: 5'-CCTGCGTCTGGACCTG GCTG-3' (upstream), 5'-CTCAGGAGGAGCAATGATCT-3' (downstream). Amplifications were performed as follows: AChE: 30 cycles, 94 °C for 45 s, 56 °C for 45 s, 72 °C for 45 s; NGF: 24 cycles, 94 °C for 30 s, 60 °C for 30 s, and 72 °C for 60 s; $P75^{NTR}$: 25 cycles, 94 °C for 45 s, 55 °C for 30 s, and 72 °C for 90 s; β-actin: 30 cycles, 94 °C for 45 s, 57 °C for 45 s, and 72 °C for 60 s. The PCR products were normalized in relation to standards of β-actin mRNA.

Statistical analysis Data were expressed as mean±SEM. Statistical analysis was performed by one-way analysis of variance (ANOVA) followed by Duncan's multiple-range test, with $P<0.05$ as the significant level.

Results

Mitogenic activity and cytotoxicity of HupA on PC12 cells There was no effect on cell proliferation during a 48-h exposure of PC12 cells to HupA 10 μmol/L. Likewise, measures of LDH release showed that HupA 10 μmol/L did not induce any cytotoxic effects (Figure 1).

Effects of HupA on neurite outgrowth Most PC12 cells displayed a flat, polygonal, undifferentiated morphology after incubation under control conditions for 48 h, and only 5.5% of them exhibited neurites. However, after incubation with HupA 10 μmol/L for 48 h more cells differentiated and nearly twice as many (10.4%) were found to bear neuritis. Moreover, 14.2% of PC12 cells exhibited neuritis after incubation with 2 μg/L NGF (Figure 2).

Effects of HupA on activity, expression, and protein levels of AChE In PC12 cells the activity of AChE was inhibited substantially by HupA treatment. The expression of AChE was also affected. AChE mRNA was increased at 6 h and 10 h. Consistent with the late rise in mRNA, AChE protein levels rose after a 48-h incubation with HupA (Figure 3).

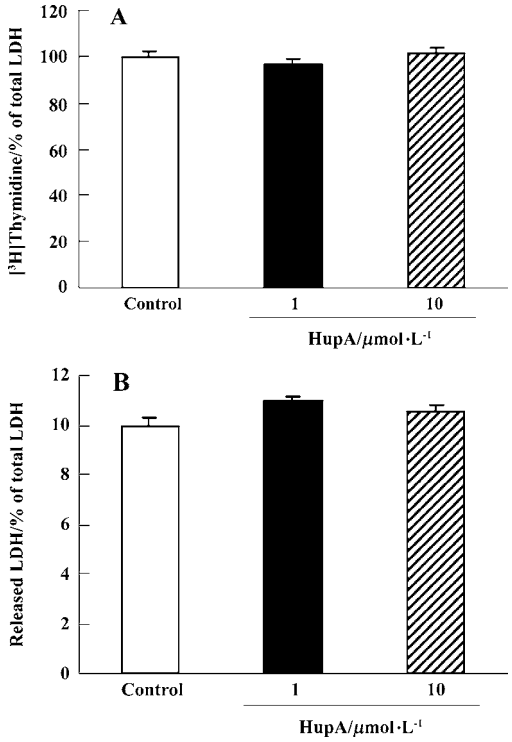

Figure 1. Effects of huperzine A on PC12 cell proliferation and viability. (A) Proliferation was measured by [^{3}H]thymidine incorporation. The [^{3}H]thymidine incorporation of control cells was 62690±1242 cpm per 1×10^4 cells. n=33. (B) Cytotoxicity was assessed by the release of LDH. The average absorbance of control cell supernatant was 0.214±0.009; of total control cell lysate was 2.68±0.11. n=18. Mean±SEM.

Effects of HupA on the expression and secretion of NGF Effects of HupA on NGF and $P75^{NTR}$ mRNA were determined by RT-PCR in primary rat cortical astrocytes, a cell type known to express the corresponding proteins. Figure 4A represents an example of RT-PCR products visualized after electrophoresis in 1.5% agarose gel containing ethidium bromide. The results suggested that NGF mRNA transcripts were slightly upregulated at 2, 4, and 6 h, while the levels of mRNA for $P75^{NTR}$ appeared greatly increased. Moreover, an ELISA for NGF protein showed a large and statistically significant increase in cultures incubated with HupA 10 μmol/L for 24 h when compared to controls incubated for the same length of time in normal medium (Figure 4B).

Discussion

PC12 cells cannot secret NGF, but they have NGF receptors and can respond to NGF. In the presence of NGF, PC12 cells cease cell division, differentiate into sympathetic neuron-like cells, and extend neuritis. So it is a putative model to

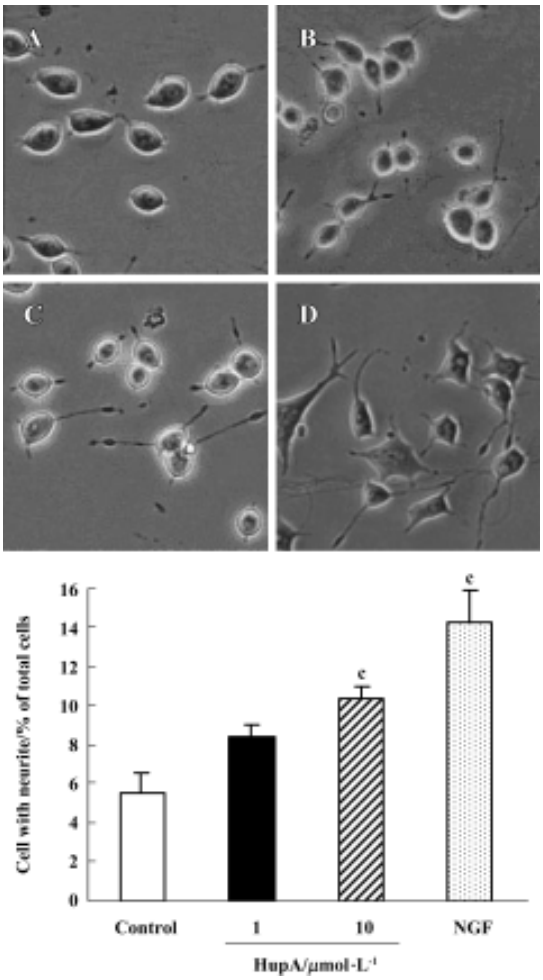

Figure 2. Effects of huperzine A on neurite outgrowth in PC12 cells. Top panels, representative phase contrast micrographs (×200). PC12 cells were incubated for 48 h under control conditions (A), with 1 μmol/L HupA (B), with 10 μmol/L HupA (C), and with 2 μg/L NGF (D). Bottom panels, quantitative effects of HupA on neurite outgrowth. Three independent experiments were carried out. n=8 for each independent experiment. Mean±SEM. ^cP<0.01 *vs* control.

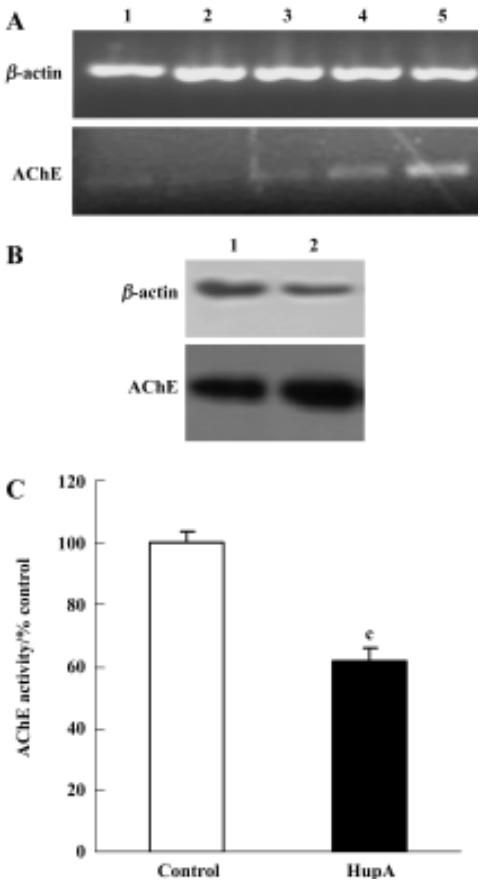

Figure 3. Effects of huperzine A on AChE mRNA expression and immunoreactive protein levels and inhibition of AChE activity. (A) Representative RT-PCR pattern. Lane 1, control; lanes 2–5: 10 μmol/L HupA incubated for 2, 4, 6 and 10 h, respectively. (B) Representative Western blot pattern. Lane 1: control; lane 2: treated with 10 μmol/L HupA for 48 h. (C) Inhibition of AChE activity in PC12 cells after treatment with 10 μmol/L huperzine A for 48 h. AChE activity of control was (1.80±0.15) OD_{440} values per mg protein. n=6. Mean±SEM. Note that the true level of inhibition during incubation is probably underestimated, owing to the reversible nature of HupA interaction with AChE. ^cP<0.01 *vs* control.

determine the neuritogenic activity[19]. Different from PC12 cells, astrocytes can secret NGF. In the injured brain, for example, astrocytes play an important role in neurotrophic support[20]. So the two different cells were used to determine the direct or indirect neurotrophic activity of HupA. In the present study, HupA was demonstrated to increase neurite outgrowth from undifferentiated PC12 cells and to enhance the expression and secretion of NGF in primary astrocytes. These findings indicate that HupA is not only an effective AChE inhibitor, but it also possesses NGF-inducing activity and an ability to induce certain NGF-like effects. The question arises whether these effects are closely linked, and what kind of relation they have to AChE. It has been reported that AChE plays an important role in neuronal proliferation and differentiation during early development of the central and peripheral nervous system. Neural AChE typically appears while axons are growing and before synaptic connections form[21]. Accumulating evidence indicates that AChE may influence neurite outgrowth through a non-catalytic mechanism such as cell-cell or cell-substratum adhesion[22]. It has been observed that the trophic activity of AChE is blocked by inhibitors that interact with the peripheral anionic site (PAS) but not by inhibitors that interact only with the active site, deep within the catalytic gorge[23,24]. Such findings sug-

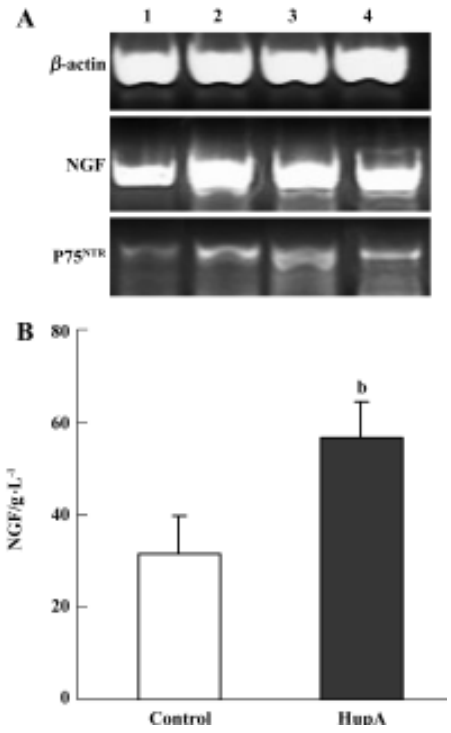

Figure 4. Effects of huperzine A on NGF and $P75^{NTR}$ mRNA expression and NGF secretion in rat cortical astrocytes. (A) Representative RT-PCR pattern. Lane 1: control; Lanes 2–4: 10 μmol/L HupA incubated for 2, 4, and 6 h, respectively. The PCR products were normalized with reference to β-actin mRNA. (B) Huperzine A enhances NGF protein level in rat cortical astrocytes. Astrocytes serum deprived for 24 h were incubated with vehicle or 10 μmol/L HupA for another 24 h. NGF protein level was determined directly in the culture medium by NGF-ELISA. n=9. Mean±SEM. $^{b}P<0.05$ *vs* control.

gest strongly that surface features of AChE rather than catalytic activity are responsible for its trophic effect. Hence, it is not contradictory to find that HupA affected neurite outgrowth in a positive rather than negative manner despite causing marked AChE inhibition. In fact, the differentiation-promoting effect of HupA may well reflect increased amounts of AChE protein. In other cell lines and to some extent *in vivo*, increased neurite outgrowth has been seen to parallel the level of AChE expression[25–27]. Conversely, decreasing expression of AChE expression, using antisense techniques, reduced outgrowth[28]. Our present results showed that AChE mRNA expression and protein levels were significantly up-regulated after treatment with HupA. This finding is consistent with other reports of increased AChE gene expression after exposure to AChE inhibitors[29,30]. It remains to be determined whether feedback regulation of AChE synthesis is involved in these changes.

Previous observations suggest that NGF regulates the phenotype and survival of basal forebrain cholinergic neurons[31] and protects hippocampal and cortical neurons against excitotoxic and ischemic damage[32]. Neurons surviving from transient ischemia highly expressed $P75^{NTR}$, suggesting that this low affinity neurotrophin receptor could contribute to the cytoprotective effect of NGF[33]. Our results showed that HupA enhanced the expression and secretion of NGF as well as increasing $P75^{NTR}$ mRNA level in astrocytes. We conclude that these two responses may be key to the neuroprotective effects that have been observed *in vitro* and *in vivo* after treatment with HupA.

The exact mechanism by which HupA increases NGF secretion remains to be determined. There is evidence that cholinergic and adrenergic mechanisms as well as PKC activation all affect NGF gene expression in astrocytes. Our previous studies have demonstrated that HupA has enhancing effects on PKC[34], and on cholinergic and adrenergic systems[35]. Such effects may participate in the modulation of NGF synthesis. This provides another possible mechanism for HupA to promote survival of damaged neurons, which may interact synergistically with other pathways to exert the neuroprotective effect of this drug.

In the present study, HupA induced the NGF synthesis of cultured astrocytes and enhanced the neurite outgrowth of undifferentiated PC12 cells *in vitro*. These effects provide the possibility that HupA increase NGF-induced enhancement of neurons survival and their function improvement that was helpful in the rescue of injured neurons.

In summary, our study has demonstrated for the first time that HupA induces neurite outgrowth in PC12 cells and stimulates expression of NGF, P75 mRNA, and secretion of NGF in cultured rat cortical astrocytes. These effects might be helpful to restore and maintain neural cells in neurodegenerative disease.

Acknowledgement

The authors wish to thank Prof Stephen BRIMIJOIN (Mayo Clinic, USA) for helpful discussion and English revision to the manuscript.

References

1 Hefti F, Hartikka J, Knusel B. Function of neurotrophic factors in the adult and aging brain and their possible use in the treatment of neurodegenerative disease. Neurobiol Aging 1989; 10: 515–33.

2 Mufson EJ, Bothwell M, Kordower JH. Loss of nerve growth factor receptor-containing neurons in Alzheimer's disease: a quantitative analysis across subregions of the basal forebrain. Exp

Neurol 1989; 105: 221–32.
3 Olson L, Nordberg A, von Holst H. Nerve growth factor affects [^{11}C]nicotine binding, blood flow, EEG, and verbal episodic memory in an Alzheimer patient (case report). J Neural Transm (P-D Sect) 1992; 4: 79–95.
4 da Penha Berzaghi M, Cooper J, Castren E, Zafra F, Sofroniew M, Thoenen H, *et al*. Cholinergic regulation of brain-derived neurotrophic factor (BDNF) and nerve growth factor (NGF) but not neurotrophin-3 (NT-3) mRNA levels in the developing rat hippocampus. J Neurosci 1993; 13: 3818–26.
5 French SJ, Humby T, Horner CH, Sofroniew MV, Rattray M. Hippocampal neurotrophin and trk receptor mRNA levels are altered by local administration of nicotine, carbachol and pilocarpine. Brain Res Mol Brain Res 1999; 67: 124–36.
6 Ghelardini C, Galeotti N, Bartolini A, Furukawa S, Nitta A, Manetti D, *et al*. Memory facilitation and stimulation of endogenous nerve growth factor synthesis by the acetylcholine releaser PG-9. Jpn J Pharmacol 1998; 78: 245–51.
7 Shigeta K, Ootaki K, Tatemoto H, Nakanishi T, Inada A, Muto N. Potentiation of nerve growth factor-induced neurite outgrowth in PC12 cells by a Coptidis Rhizoma extract and protoberberine alkaloids. Biosci Biotech Biochem 2002; 66: 2491–4.
8 Kato K, Hayako H, Ishihara Y, Marui S, Iwane M, Miyamoto M. TAK-147, an acetylcholinesterase inhibitor, increases choline acetyltransferase activity in cultured rat septal cholinergic neurons. Neurosci Lett 1999; 260: 5–8.
9 Tang XC, He XC, Bai DL. Huperzine A : a novel acetylcholinesterase inhibitor. Drugs Fut 1999; 24: 647–63.
10 Xiao XQ, Wang R, Tang XC. Huperzine A and tacrine attenuate beta-amyloid peptide-induced oxidative injury. J Neurosci Res 2000; 61: 564–9.
11 Wang R, Zhang HY, Tang XC. Huperzine A attenuates cognitive dysfunction and neuronal degeneration caused by beta-amyloid protein (1-40) in rat. Eur J Pharmacol 2001; 421: 149–56.
12 Buchan AM, Williams L, Bruederlin B. Nerve growth factor: pretreatment ameliorates ischemic hippocampal neuronal injury. Stroke 1990; 21: 177.
13 Zhou J, Zhang HY, Tang XC. HupA attenuates cognitive deficits and hippocampal neuronal damage after transient global ischemia in gerbils. Neurosci Lett 2001; 313: 137–40.
14 Wang LS, Zhou J, Shao XM, Tang XC. Huperzine A attenuates cognitive deficits and brain injury in neonatal rats after hypoxia-ischemia. Brain Res 2002; 949: 162–70.
15 Li HN, Min QY. Huperzine A improved the cognition of vascular dementia: a report of 30 patients in therapeutics. Chin J Clin Rehabil 2001; 5: 59.
16 Ma YX, Zhu Y, Gu YD, Yu ZY, Y SM, Ye YZ. Double-blind trial of huperzine-A (HUP) on cognitive deterioration in 314 cased of benign senescent forgetfulness, vascular dementia, and Alzheimer's disease. Ann NY Acad Sci 1998; 854: 506–7.
17 Pi X, Liu Y, Jiang ZY, Hu XQ, Zhu GZ. Clinical observation on treatment of light and moderate vascular dementia with meclofenoxate plus huperzine A. Shanghai Med Pharm J 2004; 255: 409–11.
18 Wang YE, Yue DX, Tang XC. Anti-cholinesterase activity of huperzine A. Acta Pharmacol Sin 1986; 7: 110–3.
19 Greene LA, Tischler AS. PC12 pheochromocytoma cultures in neurobiological research. Adv Cell Neurobiol 1982; 3: 373–414
20 Lu B, Yokoyama M, Dreyfus CF, Black IB. NGF gene expression in actively growing brain glia. J Neurosci 1991; 11: 318–26.
21 Drews U. Cholinersterase in embryonic development. Prog Histochem Cytochem 1975; 7: 1–53
22 Brimijoin S, Koenigsberger C. Cholinesterases in neural development: new findings and toxicologic implications. Environ Health Perspect 1999; 107 (Suppl 1): 59–64.
23 Munoz FJ, Aldunate R, Inestrosa NC. Peripheral binding site is involved in the neurotrophic activity of acetylcholinesterase. Neuroreport 1999; 10: 3621–5.
24 Sharma KV, Koenigsberger C, Brimijoin S, Bigbee JW. Direct evidence for an adhesive function in the noncholinergic role of acetylcholinesterase in neurite outgrowth. J Neurosci Res 2001; 63: 165–75.
25 Karpel R, Sternfeld M, Ginzberg D, Guhl E, Graessmann A, Soreq H. Overexpression of alternative human acetylcholinesterase forms modulates process extensions in cultured glioma cells. J Neurochem 1996; 66: 114–23.
26 Koenigsberger C, Chiappa S, Brimijoin S. Neurite differentiation is modulated in neuroblastoma cells engineered for altered acetylcholinesterase expression. J Neurochem 1997; 69: 1389–97.
27 Layer PG, Willbold E. Novel functions of cholinesterases in development, physiology and disease. Prog Histochem Cytochem 1995; 29: 1–94.
28 Grifman M, Soreq H. Differentiation intensifies the susceptibility of pheochromocytoma cells to antisense oligodeoxynucleotide-dependent suppression of acetylcholinesterase activity. Antisense Nucleic Acid Drug Dev 1997; 7: 351–9.
29 Kaufer D, Friedman A, Seidman S, Soreq H. Acute stress facilitates long-lasting changes in cholinergic gene expression. Nature 1998; 393: 373–7.
30 Chiappa S, Padilla S, Koenigsberger C, Moser V, Brimijoin S. Slow accumulation of acetylcholinesterase in rat brain during enzyme inhibition by repeated dosing with chlorpyrifos. Biochem Pharmacol 1995; 49: 955–63.
31 Whittemore SR, Seiger A. The expression, localization and functional significance of beta-nerve growth factor in the central nervous system. Brain Res 1987; 434: 439–64.
32 Semkova I, Wolz P, Schilling M, Krieglstein J. Selegiline enhances NGF synthesis and protects central nervous system neurons from excitotoxic and ischemic damage. Eur J Pharmacol 1996; 315: 19–30.
33 Lee TH, Abe K, Kogure K, Itoyama Y. Expressions of nerve growth factor and p75 low affinity receptor after transient forebrain ischemia in gerbil hippocampal CA1 neurons. J Neurosci Res 1995; 41: 684–95.
34 Zhang HY, Yan H, Tang XC. HupA enhances the level of secretory amyloid precursor protein and protein kinase C-alpha in intracerebroventricular beta-amyloid-(1-40) infused rats and human embryonic kidney 293 Swedish mutant cells. Neurosci Lett 2004; 360: 21–4.
35 Ou LY, Tang XC, Cai JX. Effect of HupA on working memory in reserpine- or yohimbine-treated monkeys. Eur J Pharmacol 2001; 433: 151-6.

Acta Pharmacologica Sinica 2005 Jun; 26 (6): 679–684

Full-length article

Overexpression of dishevelled-1 attenuates wortmannin-induced hyperphosphorylation of cytoskeletal proteins in N2a cell[1]

Hai-hong WANG, Ai-hong ZHANG, Ling-qiang ZHU, Qun WANG, Jian-zhi WANG[2]

Department of Pathophysiology, Tongji Medical College, Huazhong University of Science and Technology, Wuhan 430030, China

Key words

Alzheimer disease; tau proteins; neurofilament; wortmannin; dishevelled-1

[1] Project supported in part by grants from the National Natural Science Foundation of China (No 30170221 and No 30430270).
[2] Correspondence to Dr Jian-zhi WANG.
Phn 86-27-8369-2625.
Fax 86-27-8369-3883.
E-mail wangjz@mails.tjmu.edu.cn

Received 2005-01-03
Accepted 2005-03-15

doi: 10.1111/j.1745-7254.2005.00131.x

Abstract

Aim: To investigate the effect of dishevelled-1 (DVL-1) on wortmannin-induced Alzheimer-like hyperphosphorylation of cytoskeletal proteins in mouse neuroblastoma 2a (N2a) cells. **Methods:** Cultured N2a cells were transitorily transfected with DVL-1 expression plasmid using Lipofectamine™ 2000. Western blot and immunofluorescence microscopy were used to measure the phosphorylation of neurofilament and tau. **Results:** Level of phosphorylated neurofilament at SMI31 epitope and phosphorylated tau determined by PHF-1 was increased at 1 h and 3 h and back to normal at 6 h after wortmannin 1 μmol/L treatment. The highest level of phosphorylated neurofilament and phosphorylated tau was seen at 1 h and 3 h after wortmannin treatment, respectively. When DVL-1 protein was overexpressed, the hyperphosphorylation of neurofilament at SMI31 and SMI32 epitopes and tau at PHF-1 (Ser-396/404), M4 (Thr-231/Ser-235), and Tau-1 (Ser-198/199/202) epitopes was attenuated. **Conclusion:** Overexpression of mouse DVL-1 protein inhibits wortmannin-induced hyperphosphorylation of neurofilament and tau in N2a cells.

Introduction

Abnormally phosphorylated microtubule-associated protein tau is the major protein subunit of paired helical filaments (PHF) in the brain of Alzheimer disease (AD) patients, and accumulation of PHF in affected neurons leads to formation of neurofibrillary tangles (NFT)[1]. In addition, neurofilament, another neurospecific intermediate filament, is also hyperphosphorylated and accumulated in AD brain[2,3]. Although the precise mechanism for cytoskeleton hyper-phosphorylation is not currently understood, it is widely recognized that an imbalanced regulation in phosphorylation (catalyzed by protein kinases) and dephosphorylation (catalyzed by protein phosphatases) system may play an important role in this pathological process.

Studies have shown that various protein kinases, such as mitogen-activated protein kinases (MAPK), protein kinase A (PKA), cyclin-dependent kinase (CDK), and glycogen synthase kinase-3 (GSK-3), phosphorylate tau at several sites found in AD brain. Among them, GSK-3 is one of the most implicated[4]. Recent studies have shown that tau becomes a more favorable substrate for GSK-3 when it is prephosphorylated in rat brain[5]. GSK-3 is co-localized with hyperphosphorylated tau in degenerating neurons in AD brain[6]. It also phosphorylates neurofilament proteins[7,8]. GSK-3 is a downstream element of phosphatidylinositol-3 kinase (PI-3K), and it is inhibited by protein kinase B (PKB)-catalyzed phosphorylation at Ser-9 of GSK-3β and Ser-21 of GSK-3α. PKB in activity is stimulated by PI-3K-mediated phosphorylation[9]. As there is no direct GSK-3 activator available now, wortmannin is generally used to activate GSK-3 indirectly through inhibiting PI-3K[10] and overactivated GSK-3 phosphorylates tau in rat brain[11,12]. Based on the above information, we used wortmannin to produce a cell model with hyperphosphorylation of cytoskeletal proteins in the present study.

To search for the strategies in arresting Alzheimer-like hyperphosphorylation of cytoskeletal proteins, we used overexpression of dishevelled (DVL) protein. DVL is a cytoplasmic protein involved in the wingless signaling (Wnt) pathways[13]. Studies have shown that Wnt signaling pathways play important roles in AD. Overexpression of DVL-1

protein inhibits GSK-3β-mediated phosphorylation of tau in transfected CHO cells[14] and increases secreted amyloid precursor protein α (sAPPα) production in transfected HEK293 cells[15]. There is no report about the role of DVL-1 on neurofilament phosphorylation, and the role of DVL-1 on tau phosphorylation in neuronal cells is also not known.

In the present study, we used wortmannin to produce hyperphosphorylation of neurofilament and tau in N2a cells and then determined the effect of mouse DVL-1 protein overexpression on neurofilament and tau hyperphosphorylation.

Materials and methods

Chemicals Polyclonal antibody 111e against total tau, monoclonal antibody PHF-1 against PHF-tau phosphorylated at Ser396/404, monoclonal antibody M4 against PHF-tau phosphorylated at Thr231/Ser235, and monoclonal antibody Tau-1 against PHF-tau unphosphorylated at Ser198/199/202 were gifts from Dr Grundke-Iqbal (New York State Institute for Basic Research, Staten Island, NY, USA), Dr Davies (Albert Einstein College of Medicine, Bronx, NY, USA), and Dr Binder (Northwestern University, Chicago, IL, USA). Monoclonal antibodies SMI31 against phosphorylated neurofilament and SMI32 against unphosphorylated neurofilament were purchased from Sternberger Monoclonals, Inc (Baltimore, MD, USA). Oregon Green 488-conjugated goat anti-mouse IgG (H+L) was from Molecular Probes (Eugene, OR, USA). Mouse monoclonal antibody c-Myc Ab-2 and wortmannin were purchased from Sigma Chemical Co (St Louis, MO, USA). Bicinchoninic acid (BCA) protein detection kit was obtained from Pierce Chemical Company (Rockford, IL, USA).

Cell culture, plasmid and transfection Mouse neuroblastoma 2a (N2a) cells were obtained from Dr Hua-xi XU (Rockefeller University, NY, USA). The cells were cultured in a medium containing 50% Dulbecco's modified Eagle's medium (DMEM) and 50% Opti-MEM, supplemented with 5% fetal bovine serum (Gibico BRL, Gaithersburg, USA) in 5% CO_2 at 37 °C.

Mouse DVL-1 subcloned into the ClaI site of pCS2+ in frame with 6-Myc epitope at the C termini was a gift from Dr Lin MEI (University of Alabama at Birmingham, USA). The plasmid and the vector as a control were prepared using a maxi-prep endotoxin-free kit (Qiagen, Crawley, West Sussex, UK) and transfected into N2a cells using Lipofectamine™ 2000 (Invitrogen, Carlsbad, California, USA) in a 6-well format. The amounts and volumes were given on a per well basis. One day before transfection, about $(2–8)\times10^5$ cells were plated in 2 mL of growth medium without antibiotics and the confluence of the cells was about 90%–95% at the time of transfection. For each transfection, 4.0 μg DNA in 250 μL of Opti-MEM medium and 10 μL Lipofectamine™ 2000 in 250 μL of Opti-MEM medium were prepared and incubated for 5 min at room temperature. Then, the diluted DNA and the diluted Lipofectamine™ 2000 were mixed gently and incubated for another 20 min at room temperature. The mixture was then added to each well and incubated with the cells at 37 °C in a CO_2 incubator for 48 h prior to determination of the expression of transfected genes. Then the cells were treated with wortmannin 1 μmol/L[16] and harvested at 0, 1, 3, or 6 h after the treatment.

Western blot Cultures were homogenized in the buffer containing 50 mmol/L Tris-HCl (pH 8.0), 150 mmol/L sodium chloride, 1% NP-40, 0.5% sodium deoxychlolate, 0.1% sodium dodecyl sulfate, 0.02% sodium azide, 0.1 g/L phenylmethysulfonyl fluoride, and 1 mg/L aprotinin. Protein concentration was determined with BCA Protein Assay Reagent. A middle-molecule weight protein marker was used (Pierce, USA). Equal amounts of protein were separated on either 7.5% or 10% SDS-polyacrylamide gel and transferred onto nitrocellulose membranes (Amersham Pharmacia Biotech, USA). The membranes were blocked with 3% BSA in TBS at room temperature for 1 h, then incubated with primary antibodies and secondary antibodies, and finally developed using the Enhanced Chemiluminescence (ECL) detection system (Amersham Pharmacia Biotech, USA).

Immunofluorescence microscopy Culture medium was carefully removed. After two rinses in PBS, the cells were fixed in a freshly prepared solution of 4% paraformaldehyde for 1.5 h. After two more rinses in PBS, the cells were permeabilized in 1% Triton X-100 in PBS for 15 min. Then the cells were incubated in 3% BSA in PBS for 1 h and incubated with primary antibody at 4 °C overnight. After three rinses with PBS, cells were incubated in Oregon Green 488-conjugated secondary antibody (1:1000; Molecular Probes) for 1 h at room temperature. After three more rinses in PBS, fluorescence was observed using a fluorescence microscope (BX60; Olympus, Tokyo, Japan) with appropriate filter sets.

Statistical analysis All data were presented as mean±SD and analyzed by ANOVA followed by Student-Newman-Keuls test to determine the differences among groups.

Results

Wortmannin induces transient hyperphosphorylation of neurofilament and tau in N2a cells Phosphorylation of neurofilament and tau in N2a cells were measured by Western blot. The level of phosphorylated neurofilament determined by SMI31 antibody was increased at 1 h and at 3 h,

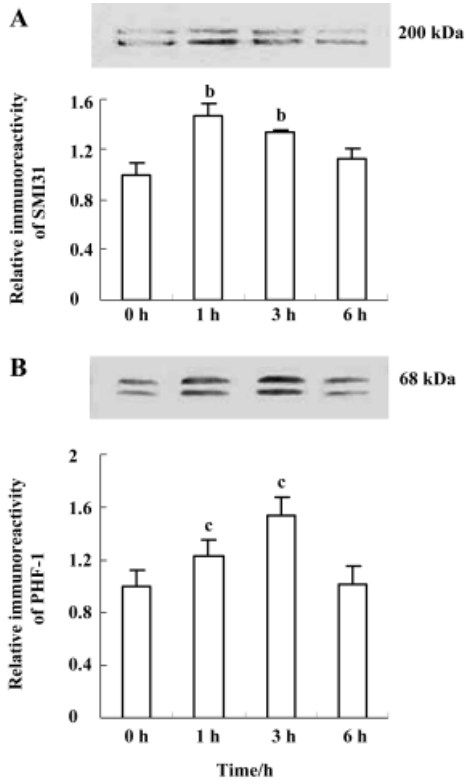

Figure 1. Wortmannin induced transient hyperphosphorylation of neurofilament (A) and tau (B) in N2a cells. N2a cells were cultured in the presence of 1 μmol/L wortmannin, harvested at different time points as indicated, and the supernatant was analyzed by Western blotting for neurofilament and tau phosphorylation. The intensity of immunoreactivity was quantitated by densitometry and presented under each blot. The highest phosphorylation of neurofilament and tau was detected at 1 h and 3 h, respectively. The data (mean±SD) were from three to five independent experiments. $^{b}P<0.05$; $^{c}P<0.01$ *vs* 0 h control group.

and it was restored to normal level at 6 h (Figure 1A); phosphorylation of tau recognized by PHF-1 antibody was elevated at 1 h, peaked at 3 h, and then back to the normal level at 6 h (Figure 1B) after treatment of the cells with wortmannin (1 μmol/L). The highest level of neurofilament and tau phosphorylation was seen at 1 h and 3 h, respectively (Figure 1). These data demonstrate that wortmannin can induce hyperphosphorylation of neurofilament and tau in N2a cells.

Overexpression of mouse DVL-1 protein inhibits wortmannin-induced neurofilament and tau hyperphosphorylation in N2a cells As wortmannin induces neurofilament and tau hyperphosphorylation most efficiently at 1 h and 3 h, respectively, in N2a cells, we investigated the effect of mouse DVL-1 protein overexpression on neurofilament and tau hyperphosphorylation at these two time points. The enhanced SMI31 (recognizes phosphorylated epitope) and the dimmed SMI32 (recognizes unphosphorylated epitope) immunoreactivity induced by wortmannin were efficiently attenuated when DVL-1 protein was overexpressed (Figure 2A, 2B), suggesting the role of DVL-1 in arresting wortmannin-induced neurofilament hyperphosphorylation. DVL-1 overexpression also efficiently arrested wortmannin-induced tau hyperphosphorylation at PHF-1 (recognizes phosphorylated epitope, Figure 2C), M4 (recognizes phosphorylated epitope, Figure 2D), and Tau-1 (recognizes unphos-phorylated epitope, Figure 2E) sites. Neither wortmannin alone nor wortmannin in combination with DVL-1 or with vector changed the level of total tau determined by 111e antibody (Figure 2F). The overexpression of DVL-1 protein was confirmed with anti-c-Myc tag antibody (Figure 2G). Inhibition of wortmannin-induced tau hyperphosphorylation at both PHF-1 and Tau-1 sites was also observed by immunofluoresce staining of the cells (Figure 3). We also noticed that the immunostaining pattern of Tau-1 antibody was different from that of PHF-1 and 111e and the distribution of Tau-1 staining was more concentrated into the cell membrane, especially in the cells transfected with DVL-1 and treated with wortmannin (Figure 3).

Discussion

Abnormal hyperphosphorylation and accumulation of tau protein in the affected neurons are recognized early pathological processes in AD brain. Several protein kinases are reported to hyperphosphorylate tau at some of the AD epitopes and GSK-3 is one of them[4]. In addition, GSK-3 also phosphorylates neurofilament in vitro[7] and in transfected cells[8]. As there is no direct activator for GSK-3, wortmannin, a specific inhibitor of PI3K[10], has been used to stimulate GSK-3 indirectly to phosphorylate tau *in vivo*[11,12]. In the present study, we used wortmannin to treat N2a cells and observed that wortmannin induced neurofilament and tau hyperphosphorylation, thus a cell model with Alzheimer-like hyperphosphorylation was established. We also noticed that the number of positive staining bands for tau and neurofilament was different when different antibodies were used. It is known that tau has at least six isoforms by alternative splicing[17]. The number of isoforms of tau and neurofilament shown on the blots depends on the species of the samples, the exposure of epitopes, and the degree of posttranslational modifications, such as phosphorylation.

Though hyperphosphorylation of cytoskeletal proteins plays a critical role in AD pathogenesis, there is no effective tool to arrest the pathological processes. In the present

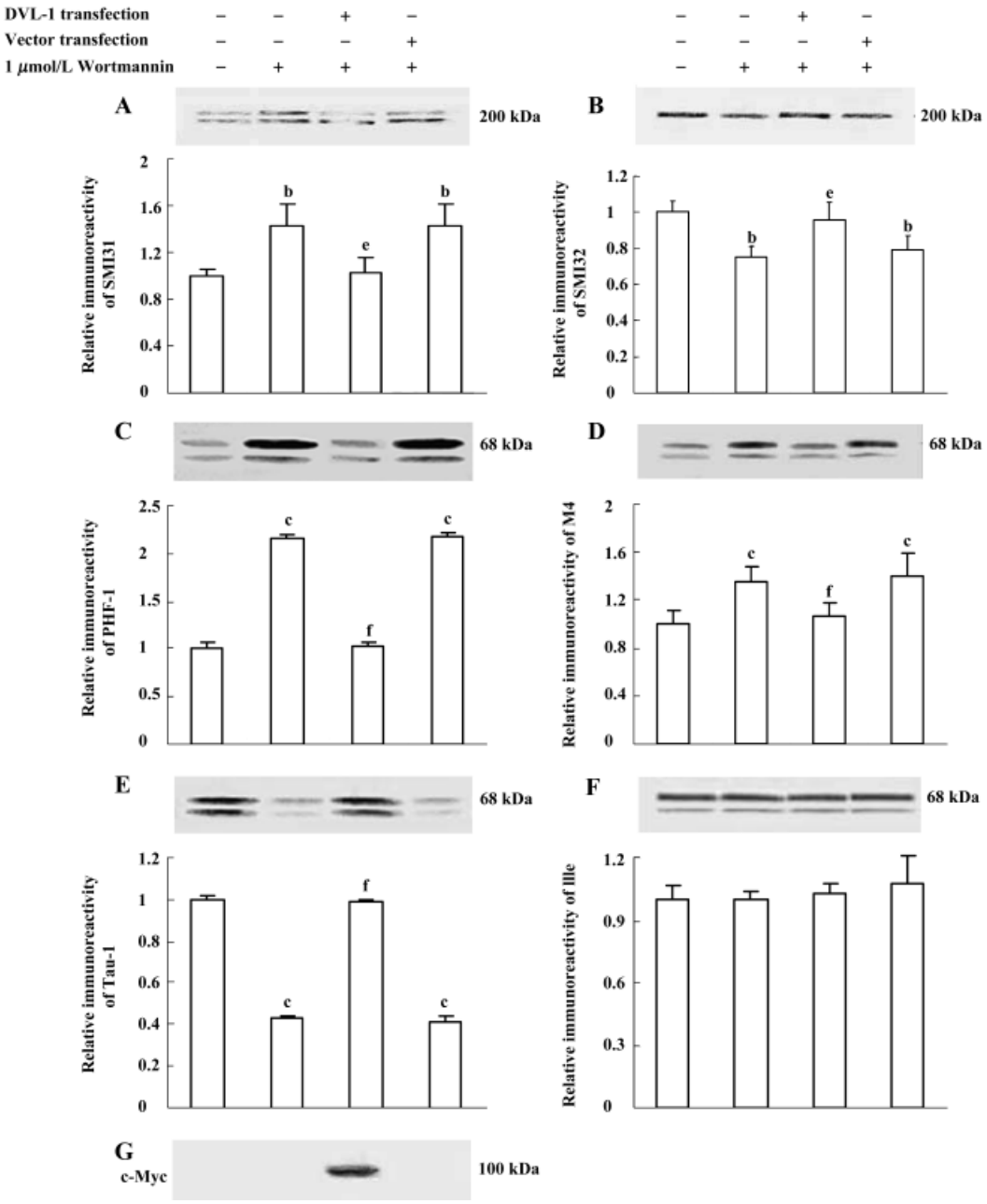

Figure 2. Overexpression of mouse DVL-1 protein inhibited neurofilament and tau hyperphosphorylation induced by wortmannin in N2a cells. DVL-1 protein overexpression attenuated neurofilament hyperphosphorylation examined at 1 h by SMI31 (A) and SMI32 (B). Similarly, DVL-1 protein overexpression efficiently arrested wortmannin-induced tau hyperphosphorylation examined at 3 h at PHF-1 (C), M4 (D) and tau-1 (E) sites. The phosphorylation level of tau was normalized by total tau (F). The expression of DVL-1 protein was determined with anti-c-Myc tag antibody (G). The intensity of immunoreactivity was quantitated by densitometry and presented under each blot. The data (mean±SD) were from three to five independent experiments. $^{b}P<0.05$, $^{c}P<0.01$ *vs* untreated group. $^{e}P<0.05$, $^{f}P<0.01$ *vs* wortmannin treated group.

study, we observed that mouse DVL-1 protein overexpression efficiently inhibited wortmannin-induced hyperphosphorylation of neurofilament at SMI31 and SMI32 epitopes and tau at PHF-1 (Ser-396/404), M4 (Thr-231/Ser-235) and Tau-1 (Ser-198/199/202) epitopes in N2a cells. As wortmannin is an indirect activator of GSK-3, we speculate that DVL-1

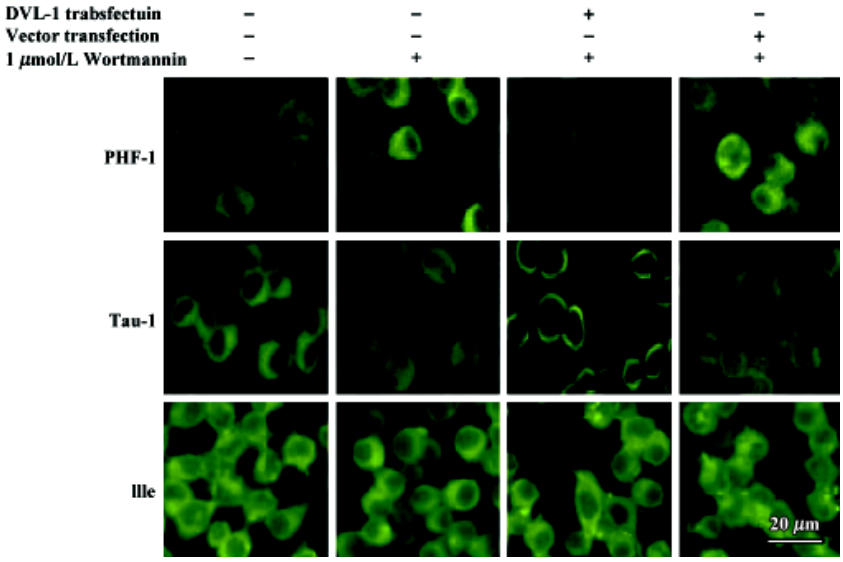

Figure 3. DVL-1 protein overexpression inhibited tau hyperphosphorylation induced by wortmannin in N2a cells by immunofluorescence. DVL-1 protein overexpression attenuated wortmannin-induced tau hyperphosphorylation examined at 3 h at PHF-1 and tau-1 sites as indicated. Neither wortmannin alone nor wortmannin in combination with DVL-1 or with vector changed the level of total tau determined by 111e antibody. The data represents three to five independent experiments. Bar: 20 μm.

may function through arresting the activity of GSK-3. DVL-1 is a component of the wingless pathway (Wnt signaling) and activation of wingless results in inhibition of GSK-3[18] and tau dephosphorylation in hippocampal neurons[19]. In Drosophila imaginal disc cells, overexpression of DVL-1 mimics the wingless signal[20]. These data suggest that loss of function of Wnt signaling may be involved in the pathological process of AD and that inhibition of GSK-3 activity by overexpression of DVL-1 may be useful in antagonizing Alzheimer-like hyperphosphorylation of cytoskeletal proteins. It was also reported that inactivation of GSK-3 induced by wingless may involve activation of PKC[18]. The precise mechanism through which DVL-1 functions is complex and further study is needed to illustrate the underlying mechanisms. Additionally, we also noticed that Tau-1 staining was more concentrated into the cell membrane after DVL-1 transfection and wortmannin treatment in immunocytochemistry study. We currently do not understand the meaning and the mechanism for this translocation of tau.

Taken together, we have found that overexpression of DVL-1 protein effectively attenuates wortmannin-induced neurofilament and tau hyperphosphorylation in N2a cells.

References

1 Iqbal K, Grundke-Iqbal I, Smith AJ, George L, Tung YC, Zaidi T. Identification and localization of a tau peptide to paired helical filaments of Alzheimer disease. Proc Natl Acad Sci USA 1989; 86: 5646–50.

2 Wang JZ, Tung YC, Wang YP, Li XT, Iqbal K, Grundke-Iqbal I. Hyperphosphorylation and accumulation neurofilament proteins in Alzheimer disease brain and in okadaic acid-treated SY5Y cells. FEBS Lett 2001; 507: 81–7.

3 Gong CX, Wang JZ, Iqbal K, Grundke-Iqbal I. Inhibition of protein phosphatase 2A induces phosphorylation and accumulation of neurofilaments in metabolically active rat brain slices. Neurosci Lett 2003; 340: 107–10.

4 Wang JZ, Wu Q, Smith A, Grundke-Iqbal I, Iqbal K. Tau is phosphorylated by GSK-3 at several sites found in Alzheimer disease and its biological activity markedly inhibited only after it is prephosphorylated by A-kinase. FEBS Lett 1998; 436: 28–34.

5 Liu SJ, Zhang JY, Li HL, Fang ZY, Wang Q, Deng HM, *et al*. Tau becomes a more favorable substrate for GSK-3 when it is prephosphorylated by PKA in rat brain. J Biol Chem 2004; 279: 50078–88.

6 Pei JJ, Tanaka T, Tung YC, Braak E, Iqbal K, Grundke-Iqbal I. Distribution, levels, and activity of glycogen synthase kinase-3 in the Alzheimer disease brain. J Neuropathol Exp Neurol 1997; 56: 70–8

7 Guan RJ, Khatra BS, Cohlberg JA. Phosphorylation of bovine neurofilament proteins by protein kinase FA (glycogen synthase kinase 3). J Biol Chem 1991; 266: 8262–7

8 Guidato S, Tsai LH, Woodgett J, Miller CC. Differential cellular phosphorylation of neurofilament heavy side-arms by glycogen synthase kinase-3 and cyclin-dependent kinase-5. J Neurochem 1996; 66: 1698–706

9 Cross DA, Alessi DR, Cohen P, Andjelkovich M, Hemmings BA. Inhibition of glycogen synthase kinase-3 by insulin mediated by protein kinase B. Nature 1995; 378: 785–9.

10 Welsh GI, Foulstone EJ, Young SW, Tavare JM, Proud CG. Wortmannin inhibits the effects of insulin and serum on the activities of glycogen synthase linase-3 and mitogen-activated protein kinase. Biochem J 1994; 303: 15–20.
11 Liu SJ, Wang JZ. Alzheimer-like tau phosphorylation induced by wortmannin *in vivo* and its attenuation by melatonin. Acta Pharmacol Sin 2002; 23: 183–7.
12 Liu SJ, Zhang AH, Li HL, Wang Q, Deng HM, Netzer WJ, *et al*. Overactivation of glycogen synthase kinase-3 by inhibition of phosphoinositol-3 kinase and protein kinase C leads to hyperphosphorylation of tau and impairment of spatial memory. J Neurochem 2003; 87: 1333–44.
13 Klingensmith, J Nusse R, Perrimon N. The Drosophila segment polarity gene dishevelled encodes a novel protein required for response to the wingless signal. Genes Dev 1994; 8: 118–30
14 Wagner U, Brownlees J, Irving NG, Lucas FR, Salinas PC, Miller CC. Overexpression of the mouse dishevelled-1 protein inhibits GSK-3β-mediated phosphorylation of tau in transfected mammalian cells. FEBS Lett 1997; 411: 369–72.
15 Mudher A, Chapman S, Richardson J, Asuni A, Gibb G, Pollard C, *et al*. Dishevelled regulates the metabolism of amyloid precursor protein via protein kinase C/mitogen-activated protein kinase and c-Jun terminal kinase. J Neurosci 2001; 21: 4987–95
16 Yu J, Deng YQ, Yang Y, Zhang JY, Zhang YP, Zhang SH, *et al*. Activation of glycogen synthase kinase 3 induces Alzheimer-like hyperphosphorylation of cytoskeleton protein and cell damage. Prog Biochem Biophys 2004; 31: 532–7
17 Andreadis A, Broderick JA, Kosik KS. Relative exon affinities and suboptimal splice site signals lead to non-equivalence of two cassette exons. Nucleic Acids Res 1995; 23: 3585–93
18 Cook D, Fry MJ, Hughes K, Sumathipala R, Woodgett JR, Dale TC. Wingless inactivates glycogen synthase kinase-3 via an intracellular signalling pathway which involves a protein kinase C. EMBO J 1996;15: 4526–36.
19 Alvarez AR, Godoy JA, Mullendorff K, Olivares GH, Bronfman M, Inestrosa NC. Wnt-3a overcomes beta-amyloid toxicity in rat hippocampal neurons. Exp Cell Res 2004; 297: 186–96.
20 Yanagawa S, Van Leeuwen F, Wodarz A, Klingensmith J, Nusse R. The dishevelled protein is modified by wingless signaling in Drosophila. Genes Dev 1995; 9: 1087–97.

Acta Pharmacologica Sinica 2005 Jun; 26 (6): 685–690

Full-length article

Distribution of cysteinyl leukotriene receptor 2 in human traumatic brain injury and brain tumors[1]

Hua HU[2,3], Gao CHEN[2], Jian-min ZHANG[2], Wei-ping ZHANG[3], Lei ZHANG[3], Qiu-fu GE[3], Hong-tian YAO[4], Wei DING[4], Zhong CHEN[3], Er-qing WEI[3,5]

[2]*Department of Neurosurgery, the Second Affiliated Hospital, School of Medicine, Zhejiang University, Hangzhou 310009*; [3]*Department of Pharmacology, School of Medicine, Zhejiang University, Hangzhou 310031*; [4]*Department of Pathology, the First Affiliated Hospital, School of Medicine, Zhejiang University, Hangzhou 310003, China*

Key words

cysteinyl leukotriene receptor 2; brain injuries; brain neoplasms; vascular smooth muscle cell

[1] Project supported by the National Natural Science Foundation of China (No 30271498) and the National Basic Research Program of China (No G1999054000).
[5] Correspondence to Prof Er-qing WEI.
Phn 86-571-8721-7391.
Fax 86-571-8721-7044.
E-mail weieq2001@yahoo.com

Received 2004-11-01
Accepted 2005-04-05

doi: 10.1111/j.1745-7254.2005.00092.x

Abstract

Aim: To determine the distribution of cysteinyl leukotriene receptor 2 ($CysLT_2$), one of the cysteinyl leukotriene receptors, in human brains with traumatic injury and tumors. **Methods:** Brain specimens were obtained from patients who underwent brain surgery. $CysLT_2$ in brain tissues was examined using immunohistochemical analysis. **Results:** $CysLT_2$ was expressed in the smooth muscle cells (not in the endothelial cells) of arteries and veins. $CysLT_2$ was also expressed in the granulocytes in both vessels and in the brain parenchyma. In addition, $CysLT_2$ was detected in neuron- and glial-appearing cells in either the late stages of traumatic injury or in the area surrounding the tumors. Microvessels regenerated 8 d after trauma and $CysLT_2$ expression was recorded in their endothelial cells. **Conclusion:** $CysLT_2$ is distributed in vascular smooth muscle cells and granulocytes, and brain trauma and tumor can induce its expression in vascular endothelial cells and in a number of other cells.

Introduction

Cysteinyl leukotrienes (CysLTs), including LTC_4, LTD_4 and LTE_4, are potent inflammatory mediators. In peripheral inflammatory diseases such as asthma and rhinitis, CysLTs can induce smooth muscle constriction, microvascular leakage, eosinophilic recruitment and other responses[1–3]. In the central nervous system (CNS), the level of CysLTs increases after brain injuries such as cerebral ischemia, brain trauma and tumors[4–6]. The increase in CysLTs after traumatic brain injury peaks at 4 h and again at 7 d, and is related to edema and cellular inflammatory responses in the rat brain[5]. In addition, the increase in CysLTs in metastatic tumors and gliomas is considered to be a factor promoting peritumoural edema[4,7].

The cloned CysLT receptors include $CysLT_1$ and $CysLT_2$, both of which are classic G protein-coupled receptors with seven transmembrane domains[8,9]. Human $CysLT_2$ is highly expressed in the spleen, placenta, heart, and peripheral blood leukocytes, and weakly expressed in the brain, prostate, skeletal muscle, kidney and ovary[8–10]. Using a ribonuclease protection assay, the highest expression of murine $CysLT_2$ was detected in the spleen, adrenal gland and thymus, and weaker expression was recorded in the kidney, brain and peripheral blood leukocytes[11]. In human and murine brains $CysLT_2$ is expressed much more than $CysLT_1$ using Northern blot and RT-PCR[11,12]. However, the distribution of $CysLT_2$ in the brains of animals including humans is still unknown.

Recently, we examined $CysLT_1$ expression in human brain specimens from patients with traumatic brain injury and brain tumors[13]. We found that $CysLT_1$ is mainly distributed in the vascular endothelium, which is consistent with the inhibiting effects of $CysLT_1$ antagonists on plasma extravasation and brain edema in the brains of focal cerebral ischemic rats[14]. In the present study, we examined the distribution of $CysLT_2$ in human brains after traumatic injury and in brains with tumors.

Materials and methods

Human brain specimens This study was approved by the ethics committee of the Second Affiliated Hospital, School of Medicine, Zhejiang University, Hangzhou, China. Brain specimens were obtained from 24 patients who underwent brain surgery because of traumatic brain injury, brain tumors, or benign meningioma (Table 1). The diagnosis of each patient with brain tumor was based on criteria pertaining to the clinical MRI picture, appropriate laboratory data and biopsy findings. Astrocytomas and gangliogliomas were classified as low (grades I–II) or high (grades III–IV) grade according to the Daumas-Duport criteria.

Immunohistochemistry Brain tissues were fixed in 4% formaldehyde for 24–48 h, and then embedded in paraffin. A 6 μm thick paraffin section was stained with hematoxylin and eosin (HE). Another section was incubated with a primary polyclonal antibody against $CysLT_2$ for 1 d at 4 °C (5 mg/L, rabbit IgG, Cayman, USA). This section was sequentially treated with anti-rabbit IgG biotinylated secondary antibody and avidin biotin complex (Zymed, USA). Finally, the section was visualized with 0.01% diaminobenzidine tetrahydrochloride (DAB) and 0.005% H_2O_2 in 50 mmol/L Tris-HCl, pH 7.6. Control sections were treated with normal goat serum instead of the primary antibody to test the specificity of the immunohistochemical reaction. Nuclei of cells were counter stained using hematoxylin.

Results

The control sections treated with normal goat serum showed no positive immunostaining (data not shown). $CysLT_2$ was highly expressed in the smooth muscle cells of both arteries and veins, but not in the endothelial cells (Figure 1A,1B). Brain tissues surrounding benign meningioma appeared relatively normal using MRI and HE staining (data not shown). In such relatively normal brain tissues, $CysLT_2$ was not detected in microvascular endothelial cells or in other cells (Figure 1C, Table 1).

$CysLT_2$ expression in human brains after traumatic injury Within 3 d after traumatic brain injury, mild expression of $CysLT_2$ was frequently detected in the neuron- and glial-appearing cells in a number of human brain specimens (Figure 2A, Table 1), but rarely in the microvascular endothelial cells (Figure 2B, Table 1). However, 8 d after trauma, microvascular regeneration was observed and $CysLT_2$ was highly expressed in the regenerated microvascular endothelial cells and glial-appearing cells (Figure 2C, Table 1), but no $CysLT_2$ positive cell was found in the necrotic regions (Figure 2D). In addition, in one patient, MPO-positive granulocytes were found within vessels and in the brain parenchyma (data not shown), and $CysLT_2$ was highly expressed in the granulocytes both within vessels (Figure 2E) and in the brain parenchyma (Figure 2F).

$CysLT_2$ expression in human brain tumors In brain tumors, no $CysLT_2$ was detected in the center of glioma, ganglioglioma and metastatic carcinomas (Figure 3A,3B, Table 1), but strong $CysLT_2$ immunostaining was found in neuron- and glial-apprearing cells surrounding tumors (Figure 3C, Table 1).

Discussion

In this study, the first finding is the specific distribution pattern of $CysLT_2$ in brain vessels. $CysLT_2$ was highly ex-

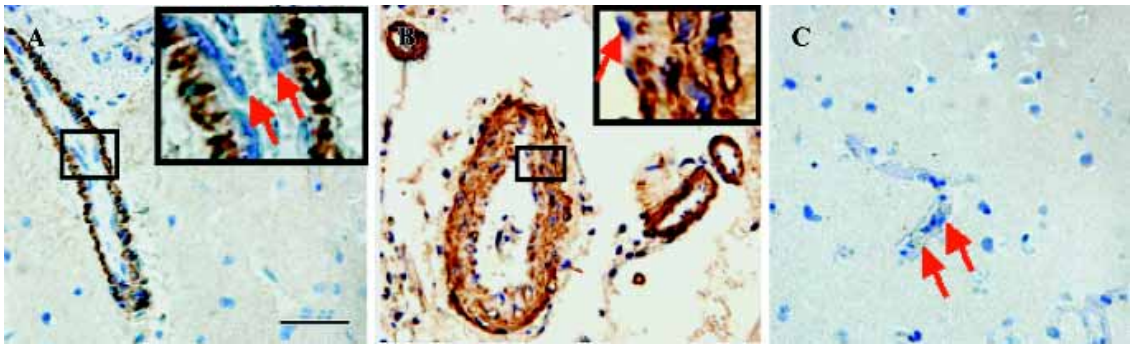

Figure 1. $CysLT_2$ expression in the vessels of the human brain. Brain samples were obtained from two patients with astrocytoma (Patient numbers 21 and 22 from Table 1 in A and B, respectively) and one patient with benign meningioma (Patient number 1 from Table 1 in C). $CysLT_2$ expression was detected using immunohistochemistry. $CysLT_2$ immunoreactivity (brown) was found in the smooth muscle cells of veins (A) and arteries (B), but not in endothelial cells (red arrows), microvascular endothelial cells (C, red arrows) or other cells within the brain tissues. The inserts are amplifications from the black boxes in A and B. Scale bar is 50 μm.

Table 1. Patient profiles and the immunohistochemical results for $CysLT_2$. NA, not applicable; -, absent; ±, weak or few; +, mild; ++, marked; ?, not detected; L, left; R, right; T, temporal lobe; F, frontal lobe; P, parietal lobe. Samples were from the tissues surrounding (*) and within (**) the injured regions or the tumors; NAC, neuron-appearing cells; GAC, glial-appearing cells; VEC, microvascular endothelial cells.

	Patient number	Age/sex	Duration from onset	Side/ lobes	Grade	Adjacent to lesions*			Center of lesions**		
						NAC	GAC	VEC	NAC	GAC	VEC
Control samples											
Beside benign meningioma	1	51/F	NA	L/T	NA	-	-	-	NA	NA	NA
Traumatic brain injury	2	55/M	6 h	R/T	NA	NA	NA	NA	-	-	-
	3	15/F	9h	L/T	NA	NA	NA	NA	-	-	-
	3	51/M	9 h	L/T	NA	NA	NA	NA	±	±	-
	4	26/F	9h	R/F	NA	NA	NA	NA	-	-	-
	5	30/M	14 h	R/P	NA	NA	NA	NA	±	±	-
	6	52/M	15 h	R/T	NA	NA	NA	NA	-	-	±
	7	49/M	20 h	R/L/F	NA	NA	NA	NA	-	-	-
	8	52/M	24 h	R/L/F	NA	NA	NA	NA	-	-	±
	9	21/M	24 h	R/L/F	NA	NA	NA	NA	±	±	-
	10	41/M	24 h	R/F	NA	NA	NA	NA	-	-	-
	11	51/M	24 h	R/F	NA	NA	NA	NA	-	-	-
	12	57/F	30 h	L/F	NA	NA	NA	NA	±	±	-
	13	71/M	2.5 d	R/T	NA	NA	NA	NA	±	±	-
	14	21/F	3 d	L/T	NA	NA	NA	NA	±	±	-
	15	39/M	8 d	R/T	NA	NA	NA	NA	?	++	++
Astrocytoma	16	42/F	NA	L/P	II	++	++	?	?	-	-
	17	38/F	NA	R/T	III	++	++	?	?	-	-
	18	82/M	NA	L/T	III	++	++	?	?	-	-
	19	64/M	NA	L/P	II	++	++	?	?	-	-
	20	29/F	NA	L/F	II	++	++	?	?	-	-
	21	38/M	5 y	L/T	II	++	++	?	?	-	-
	22	71/M	2 y	L/T	II	++	++	?	?	-	-
Ganglioglioma	23	52/M	NA	L/T	II	++	++	?	?	-	-
Metastatic carcinoma	24	55/M	NA	L/T	NA	++	++	?	-	-	-

pressed in the smooth muscle cells of arteries and veins, but rarely in vascular and microvascular endothelial cells in relatively normal brain tissues or in tissues within 3 d of brain trauma. This pattern is different from that of $CysLT_1$, which is primarily expressed in endothelial cells as found in our previous study[13]. However, strong expression of $CysLT_2$ was found in the regenerated microvascular endothelial cells 8 d after trauma, suggesting an inducible $CysLT_2$ expression. This result is similar to that of the human heart, in which $CysLT_2$ mRNA has been detected in myocytes, fibroblasts and vascular smooth muscle cells, but not in endothelial cells[15]. Moreover, $CysLT_2$ has been reported to be expressed primarily in human umbilical vein endothelial cells (HUVECs)[16], and may play a role in inflammation during atherogenesis or leukocyte infiltration into tissues[17]. A recent study using $CysLT_2$-deficient mice confirmed that $CysLT_2$ mediates an increase in vascular permeability in IgE-dependent passive cutaneous anaphylaxis[18]. Our present results showed that unlike peripheral tissues (HUVECs), $CysLT_2$ was only expressed in the endothelial cells of injured brain tissues after a longer duration. This result implies that $CysLT_2$ might be involved in inflammatory responses in the CNS.

The second finding of this study is the inducible $CysLT_2$ expression in neuron- and glial-appearing cells after brain trauma and in brain tumors. We have recently reported inducible $CysLT_1$ expression in neuron- and glial-appearing

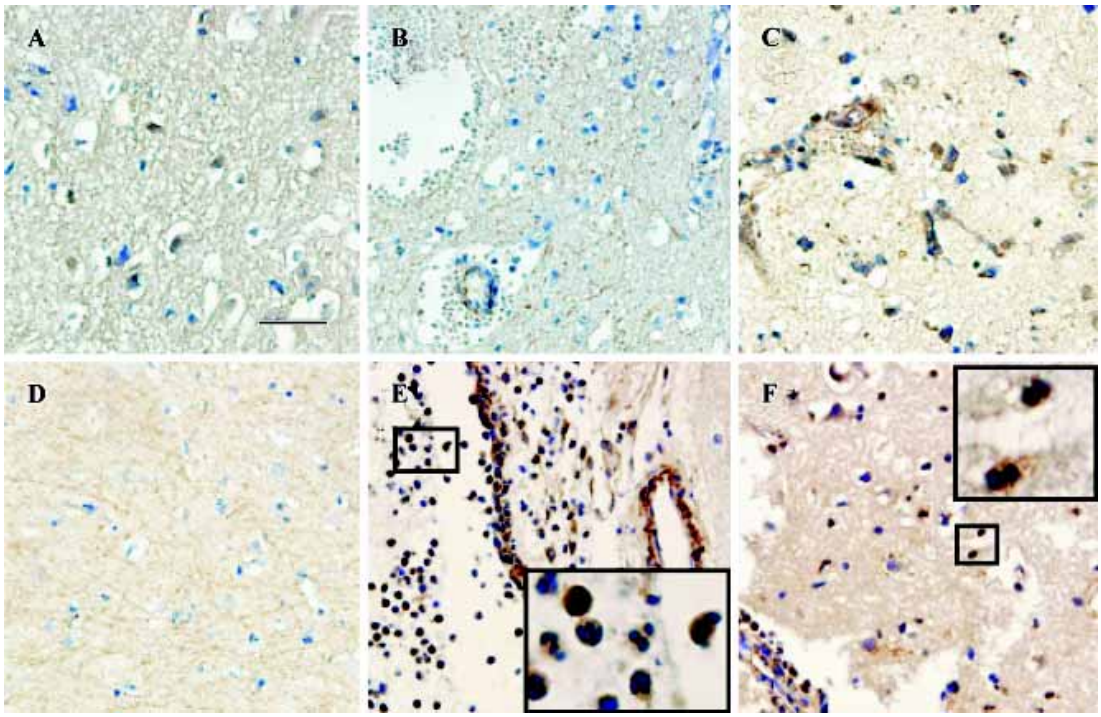

Figure 2. CysLT2 expression in human brains after traumatic brain injury. Brain samples were from patients 14 h (A; patient number 5), 15 h (B, E, F; patient number 6), or 8 d (C, D; patient number 15) after traumatic brain injury. At 14 or 15 h after injury, mild expression of CysLT2 were found in neuron- and glial-appearing cells (A), and in microvascular endothelial cells (B). At 8 d after injury, microvessels had regenerated, and CysLT2 was highly expressed in the microvascular endothelial cells, glial-appearing cells and granulocytes (C), but not in the necrotic region (D). CysLT2 was also highly expressed in granulocytes both within vessels (E) and within brain tissues (F). The inserts are amplifications from the black boxes in E and F. Scale bar is 50 μm.

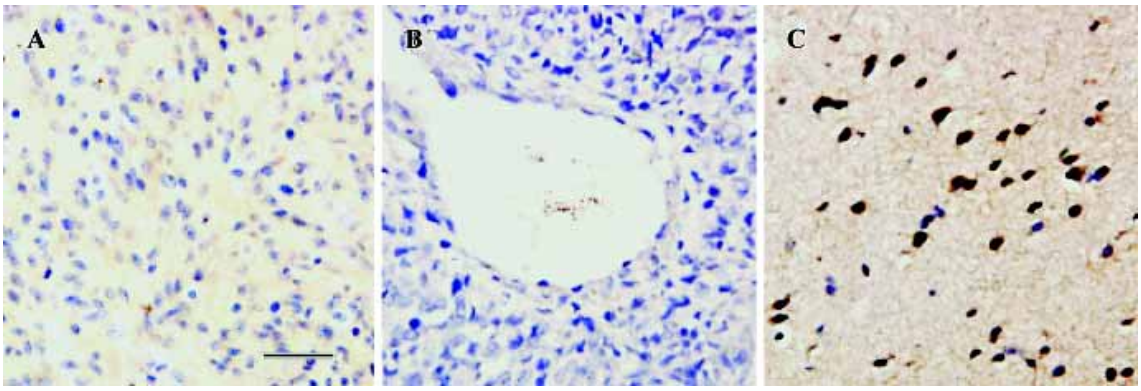

Figure 3. $CysLT_2$ expression in human brains with tumors. Samples were obtained from patients with astrocytoma (A, C; patient number 19) or metastatic carcinoma (B; patient number 24). $CysLT_2$ was not found within astrocytomas (A) or metastatic carcinomas (B), but was highly expressed in neuron- and glial-appearing cells surrounding the astrocytoma (C). Scale bar is 50 μm.

cells after traumatic brain injury and brain tumors[13]. Unlike $CysLT_1$, the inducible $CysLT_2$ expression in these cells was much reduced within 3 d after trauma, but was strong 8 d after trauma and surrounding the tumors. The pathophysiological implications of $CysLT_2$ in the brain are unknown, but $CysLT_2$ may be involved in intracerebral cell proliferation because CysLTs can promote astrocyte and intestinal epithelial cell proliferation[19,20]. Recently it has been reported that bleomycin-induced pulmonary fibrosis is increased in $CysLT_1$-deficient mice, but decreased in $CysLT_2$-deficient-

mice [18,21]. Therefore, the inducible $CysLT_2$ expression 8 d after trauma might be responsible for cell regeneration and/or proliferation.

In addition, $CysLT_2$ was highly expressed in the granulocytes in both vessels and brain tissues. This result is consistent with previous reports that show that $CysLT_2$ is expressed in peripheral blood leukocytes[10] and is responsible for chemotaxis[22]. However, according to the results of guinea pig brain perfusion with human neurtrophils, Di Gennaro *et al*[23] hypothesized that $CysLT_1$ in leukocytes and $CysLT_2$ in endothelial cells might be involved in the adherence and intrusion of leukocytes in brain inflammatory reactions. However, our results examining the distributions of $CysLT_1$ and $CysLT_2$ in human brains do not support their hypothesis.

In summary, we found that $CysLT_2$ was expressed in smooth muscle cells and granulocytes, suggesting that $CysLT_2$ might play a role in cerebral circulation and the inflammatory response that occurs in human brains after injury. The induced $CysLT_2$ expression in microvascular endothelial cells, and neuron- or glial-appearing cells after traumatic injury and in brain tumors requires further investigation.

Acknowledgment

We thank Prof Pei-hui CHEN from the Department of Pathology, the Second Affiliated Hospital, School of Medicine, Zhejiang University, for his help with the analysis of brain sections.

References

1 Borish L. The role of leukotrienes in upper and lower airway inflammation and the implications for treatment. Ann Allergy Asthma Immunol 2002; 88: 16–22.

2 Fujita M, Yonetomi Y, Shimouchi K, Takeda H, Aze Y, Kawabata K, *et al*. Involvement of cysteinyl leukotrienes in biphasic increase of nasal airway resistance of antigen-induced rhinitis in guinea pigs. Eur J Pharmacol 1999; 369: 349–56.

3 Storms WW. Minimal persistent inflammation, an emerging concept in the nature and treatment of allergic rhinitis: the possible role of leukotrienes. Ann Allergy Asthma Immunol 2003; 91: 131–40.

4 Shinonaga M, Chang CC, Kuwabara T. Relation between macrophage infiltrates and peritumoral edema. Adv Neurol 1990; 52: 475–81.

5 Schuhmann MU, Mokhtarzadeh M, Stichtenoth DO, Skardelly M, Klinge PM, Gutzki FM, *et al*. Temporal profiles of cerebrospinal fluid leukotrienes, brain edema and inflammatory response following experimental brain injury. Neurol Res 2003; 25: 481–91.

6 Ciceri P, Rabuffetti M, Monopoli A, Nicosia S. Production of leukotrienes in a model of focal cerebral ischaemia in the rat. Br J Pharmacol 2001; 133: 1323–9.

7 Inamura T, Abe M, Ikezaki K, Fukui M. Leukotriene C_4 contents, synthase and catabolic activity in human meningiomas. Neurol Res 1992; 14: 405–10.

8 Lynch KR, O'Neill GP, Liu Q, Im DS, Sawyer N, Metters KM, *et al*. Characterization of the human cysteinyl leukotriene $CysLT_1$ receptor. Nature 1999; 399: 789–93.

9 Sarau HM, Ames RS, Chambers J, Ellis C, Elshourbagy N, Foley JJ, *et al*. Identification, molecular cloning, expression, and characterization of a cysteinyl leukotriene receptor. Mol Pharmacol 1999; 56: 657–63.

10 Takasaki J, Kamohara M, Matsumoto M, Saito T, Sugimoto T, Ohishi T, *et al*. The molecular characterization and tissue distribution of the human cysteinyl leukotriene $CysLT_2$ receptor. Biochem Biophys Res Commun 2000; 274: 316–22.

11 Hui Y, Yang G, Galczenski H, Figueroa DJ, Austin CP, Copeland NG, *et al*. The murine cysteinyl leukotriene 2 $CysLT_2$ receptor. cDNA and genomic cloning, alternative splicing, and *in vitro* characterization. J Biol Chem 2001; 276: 47489–95.

12 Heise CE, O'Dowd BF, Figueroa DJ, Sawyer N, Nguyen T, Im DS, *et al*. Characterization of the human cysteinyl leukotriene 2 receptor. J Biol Chem 2000; 275: 30531–6.

13 Zhang WP, Hu H, Zhang L, Ding W, Yao HT, Chen KD, *et al*. Expression of cysteinyl leukotriene receptor 1 in human traumatic brain injury and brain tumors. Neurosci Lett 2004; 363: 247–51.

14 Zhang WP, Wei EQ, Mei RH, Zhu CY, Zhao MH. Neuroprotective effect of ONO-1078, a leukotriene receptor antagonist, on focal cerebral ischemia in rats. Acta Pharmacol Sin 2002; 23: 871–7.

15 Kamohara M, Takasaki J, Matsumoto M, Matsumoto S, Saito T, Soga T, *et al*. Functional characterization of cysteinyl leukotriene $CysLT_2$ receptor on human coronary artery smooth muscle cells. Biochem Biophys Res Commun 2001; 287: 1088–92.

16 Sjostrom M, Johansson AS, Schroder O, Qiu H, Palmblad J, Haeggstrom JZ. Dominant expression of the $CysLT_2$ receptor accounts for calcium signaling by cysteinyl leukotrienes in human umbilical vein endothelial cells. Arterioscler Thromb Vasc Biol 2003; 23: e37–41.

17 Lotzer K, Spanbroek R, Hildner M, Urbach A, Heller R, Bretschneider E, *et al*. Differential leukotriene receptor expression and calcium responses in endothelial cells and macrophages indicate 5-lipoxygenase-dependent circuits of inflammation and atherogenesis. Arterioscler Thromb Vasc Biol 2003; 23: e32–6.

18 Beller TC, Maekawa A, Friend DS, Austen KF, Kanaoka Y. Targeted gene disruption reveals the role of the cysteinyl leukotriene 2 receptor in increased vascular permeability and in bleomycin-induced pulmonary fibrosis in mice. J Biol Chem 2004; 279: 46129–34.

19 Ciccarelli R, D'Alimonte I, Santavenere C, D'Auro M, Ballerini P, Nargi E, *et al*. Cysteinyl-leukotrienes are released from astrocytes and increase astrocyte proliferation and glial fibrillary acidic protein via $CysLT_1$ receptors and mitogen-activated protein kinase pathway. Eur J Neurosci 2004; 20: 1514–24.

20 Paruchuri S, Hallberg B, Juhas M, Larsson C, Sjolander A. Leukotriene D_4 activates MAPK through a ras-independent but PKC ε-dependent pathway in intestinal epithelial cells. J Cell Sci 2002; 115: 1883–93.

21 Beller TC, Friend DS, Maekawa A, Lam BK, Austen KF, Kanaoka Y. Cysteinyl leukotriene 1 receptor controls the severity of chronic pulmonary inflammation and fibrosis. Proc Natl Acad Sci USA 2004; 101: 3047–52.
22 Evans JF. Cysteinyl leukotriene receptors. Prostaglandins Lipid Mediators 2002; 68–69: 587–97.
23 Di Gennaro A, Carnini C, Buccellati C, Ballerio R, Zarini S, Fumagalli F, *et al*. Cysteinyl-leukotrienes receptor activation in brain inflammatory reactions and cerebral edema formation: A role for transcellular biosynthesis of cysteinyl-leukotrienes. FASEB J 2004; 18: 842–4.

The First Scientific Meeting of the Asian Society for Vascular Biology

October 8–11, 2005 Shanghai, China

Info: Yu HUANG
Department of Physiology
Chinese University of Hong Kong
Hong Kong SAR, China
Phn 852-2609-6787
Fax 852-2603-5022
E-mail yu-huang@cuhk.edu.hk
http://www.sbsonline.org/sbscon/2005/index.php

Acta Pharmacologica Sinica 2005 Jun; 26 (6): 691–695

Full-length article

Fibrin(ogen)olytic character of FII_a isolated from *Agkistrodon acutus* venom[1]

Yi-wen WANG, Xiu-xia LIANG, Jia-shu CHEN[2], Qi CHEN, Peng-xin QIU, Xi LIN, Guang-mei YAN

Department of Pharmacology, Zhongshan Medical College, Sun Yat-sen University, Guangzhou 510080, China

Key words

snake venoms; *Agkistrodon acutus*; urokinase; fibrinolysis; carotid artery thrombosis

[1] Project supported by Guangdong Science and Technology Commission, (No 203059).
[2] Correspondence to Prof Jia-shu CHEN.
Phn 86-20-8733-0553.
Fax 86-20-8733-1577.
E-mail jiashu@gzsums.edu.cn

Received 2004-11-07
Accepted 2005-03-07

doi: 10.1111/j.1745-7254.2005.00099.x

Abstract

Aim: To investigate the fibrin(ogen)olytic character of FII_a isolated from *Agkistrodon acutus* venom *in vitro* and *in vivo*. **Methods:** ^{125}I-labeled human plasma clot lysis was measured *in vitro* and rabbit carotid artery thrombosis was as an *in vivo* model. **Results:** *In vitro*, urokinase (UK) at 25, 35, 40, 45, 60 kU/L and FII_a at 0.08, 0.23, 0.4, 0.5, and 0.7 g/L resulted an equivalent clot lysis (20%, 40%, 50%, 60%, and 80%). UK at 25–60 kU/L induced 27.3%±3.6%, 35.2%±2.3%, 39.3%±2.4%, 44.2%±4.6%, and 51.1%±1.2% fibrinogen degradation. But FII_a at 0.08–0.7 g/L induced 95.4%±0.3%, >95.6%, >95.6%, >95.6%, >95.6% fibrinogen degradation respectively. *In vivo*, UK 40 kU/kg and FII_a 1.0 mg/kg reduced the weight of residual thrombus to 9.0±2.5 mg and 7.8±3.5 mg compared with negative control group (30.0±5.4 mg). But the fibrinogen degradation rate after UK 40 kU/kg and FII_a 1.0 mg/kg treatment was 24.4%±6.2% and 4.1%±7.8%, respectively ($P<0.05$, $n=6$). The order of the lysis speed after UK 125 kU/L treatment was platelet poor plasma (PPP) clots>the whole blood clots>platelet rich plasma (PRP) clots. The sequence for FII_a 0.4 g/L was PRP>PPP>whole blood clots. **Conclusion:** At the same percentage of clot lysis, FII_a degraded more fibrinogen than UK did *in vitro* but less fibrinogen than UK did *in vivo*. The order of the lysis speed was PPP>whole blood clots>PRP clots for UK and PRP>PPP>whole blood clots for FII_a.

Introduction

Fibrin-specific clot lysis was initially the major goal to offer the opportunity for effective lysis of pathological thrombus without the risks of a systemic haemorrhagic diathesis[1]. But clinical studies show that even tissue plasminogen activator (t-PA), which exhibits strict selectivity toward fibrin-bound plasminogen, is associated with a significant although variable degree of fibrinogeno-lysis[2–4].

In our previous studies, fibrinolytic enzyme FII_a from *Agkistrodon acutus* venom was shown to dissolve both fibrin and fibrinogen *in vitro*. *In vivo*, FII_a was able to dissolve thrombus without hemorrhage at an effective dose for thrombolysis[5–7]. A few experiments were performed to investigate the fibrin(ogen)olytic character of FII_a such as the specificity to fibrin and fibrinogen and the specificity to different types of clots.

In this study, we compared fibrin(ogen)olytic character of FII_a with urokinase (UK) *in vitro* and *in vivo*.

Materials and methods

Snake venoms *Agkistrodon acutus* venom was collected in Yuanling, Hu-nan Province and lyophilized and stored in desiccator.

Reagents DEAE-Sephadex A-50 and Sephadex G-75 were from Pharmacia (Uppsala, Sweden); human fibrinogen (95% clottable) and bovine fibrinogen (70% clottable) was from Sigma (Saint Louis, USA); aprotinin was from Dadeli Biochemistry and Pharmaceutical Co Ltd (Lanzhou, China); thrombin was from Zhuhai Biochemical Pharmaceutical Factory (Zhuhai, China); UK was from Tianpu Biochemistry and Pharmaceutical Co Ltd (Guangzhou, China); ^{125}I-labeled fibrinogen was from the Department of Experimental Nuclear Medicine of our college by the method of chloramines-T; fibrinogen concentration determination reagent pack (Clauss

method) was from Sun Biotechnology Company (Shanghai, China); human plasma was from Guangzhou Blood Center was centrifugated at 3800×*g* for 8 min; whole blood was collected from healthy volunteers (n=5 male, age 24.0±4.2 a, weighing 61±2.4 kg). All materials were of analytical grade from commercial sources.

Animals Male New Zealand white rabbits (3–4 months old, weighing 2.2±0.1 kg, Grade II, certificate No 2001A033) were provided by the Experimental Animal Center of Zhongshan Medical College.

Purification of the enzyme FII_a, the fibrinolytic enzyme from *Agkistrodon acutus* venom was prepared according to the method described by Chen *et al*[7].

Lysis of ^{125}I-labeled human plasma clots *In vitro*, ^{125}I-labeled clots were prepared by the modified method of Gurewich *et al*[8]. Human plasma 5.5 mL were mixed with ^{125}I-labeled fibrinogen (6.105×10^4 Bq) plus 55 μL $CaCl_2$ (1 mol/L). This solution (0.5 mL) was added to 5-mm (ID) glass tube in the presence of 5 μL thrombin (100 kU/L). The clots were incubated at 37 ºC for 30 min and kept overnight at room temperature. All the clots were washed three times with 0.9% saline and the total radioactivity was measured before being transferred to 10-mm (ID) test tubes.

Plasma (4 mL) were incubated (37 ºC, 6 h) with radiolabeled clots in the presence of UK 20, 30, 40, 60, and 80 kU/L or FII_a 0.05, 0.1, 0.2, 0.4, and 0.8 g/L, respectively. The reaction was terminated by adding aprotinin (1×10^6 kU/L final concentration) into test tubes containing different concentrations of UK or edetic acid (5 μmol/L final concentration) into test tubes containing different concentrations of FII_a. Aliquots (1 mL) were removed for the measurement of radioactivity.

Clot lysis was calculated according to the formula: Clot lysis=Radioactivity in aliquot (modified volume)/total radioactivity×100%. The concentrations of UK or FII_a which could induce 20%, 40%, 50%, 60%, and 80% clot lysis were determined based on the concentration-response curve.

The same experiments were repeated with UK and FII_a at the concentrations that could induce 20%, 40%, 50%, 60%, and 80% clot lysis. Aliquots were removed for the measurement of fibrinogen concentration to get the fibrinogen degradation at the same percent of clot lysis.

Each experiment was performed three times.

Fibrinogen degradation Fibrinogen degradation was performed according to the reagent pack instruction by the Clauss method.

Carotid artery thrombosis The rabbit carotid artery thrombosis model was established according to the method of Wang *et al*[9]. Forty-eight rabbits were randomly divided into 8 groups (n=6): 0.9% saline 1 mL/kg, as the negative control group; UK 5, 10, 20, and 40 kU/kg group; FII_a 0.5, 1.0, and 2.0 mg/kg group.

Two hours after the initiation of the carotid thrombosis, UK and FII_a were administered via ear-edge vein of rabbit. One hour later, the residual thrombus within the carotid artery was excised and blotted. The wet weight was measured. Blood was drawn from the right femoral artery cannula before and 1 h after administration for the measurement of plasma fibrinogen concentration. The blood sample was drawn into a plastic syringe containing 3.8% sodium citrate as the anticoagulant (1: 9 *v*/*v*, citrate/blood) and was centrifuged at 1500×*g* 4 ºC for 15 min. The platelet-free plasma was stored at -70 ºC until assayed.

Lysis of platelet-rich plasma (PRP) clots, platelet-poor plasma (PPP) clots, and whole-blood clots Whole blood from healthy volunteers was mixed with 3.8% sodium citrate (1:9 *v*/*v*, citrate/blood) and immediately centrifuged at room temperature at 250×*g* for 10 min to obtain PRP. PPP was obtained by centrifuging the original blood sample at 1500×*g* for 10 min[10]. ^{125}I-labeled clots made from PRP, PPP, and whole blood were prepared as described above.

Plasma (4 mL) were incubated with these three types of radiolabeled clots in the presence of FII_a 0.4 g/L or UK 125 kU/L (final concentration) at 37 ºC. Aliquots were removed for the measurement of radioactivity in plasma at subsequent times during a course of 12 h. The time-response relationship of FII_a and UK for these three types of clots were compared. Each experiment was perfomed three times[11].

Data analysis Values were expressed as mean±SD. Analysis of variance and *t*-test was used for comparisons of the mean values. P<0.05 was considered significant.

Results

Fibrin(ogen)olytic character of FII_a *in vitro* *In vitro* both UK and FII_a dose-dependently dissolved clots. Based on the dose-effect relationship of UK and FII_a, UK at 25, 35, 40, 45, 60 kU/L and FII_a at 0.08, 0.23, 0.4, 0.5, and 0.7 g/L caused an equivalent clot lysis (20%, 40%, 50%, 60%, and 80%, Figure 1, 2).

At the calculated concentration, which could induce the same clot lysis, the fibrinogen degradation induced by FII_a was much higher than that induced by UK. In the negative control group, the fibrinogen degradation was 0.01%±0.02% (0.02±0.05 g/L).

Fibrin(ogen)olytic character of FII_a in rabbit carotid artery thrombosis UK or FII_a reduced the weight of residual thrombus and the level of fibrinogen in plasma in a

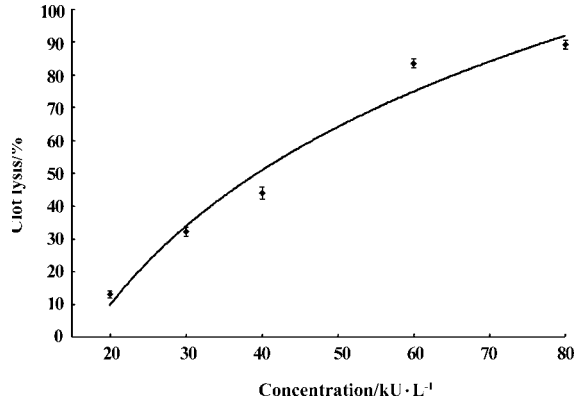

Figure 1. UK dose-dependently dissolved ^{125}I-labeled human plasma clots. In the negative control group, the clot lysis was 11.0%±1.0%.

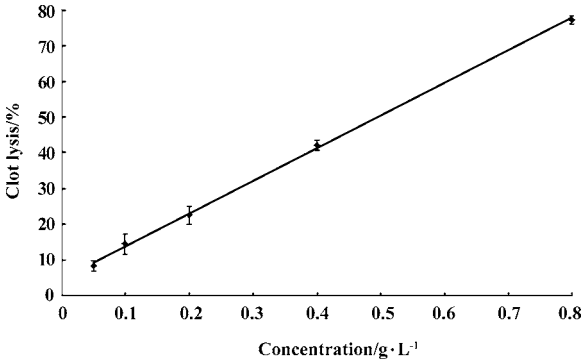

Figure 2. FII_a dose-dependently dissolved ^{125}I-labeled human plasma clots. In the negative control group, the clot lysis was 11.0%±1.0%.

dose-dependent manner. In the group treated with UK 40 kU/kg, the weight of residual thrombus was 9.0±2.5 mg. In the group treated with FII_a 1.0 mg/kg, the weight of residual thrombus was 7.8±3.5 mg. The fibrinolytic effects of these two groups were approximately the same, but the fibrinogen degradation of these two groups were 24.4%±6.2% and 4.1%±7.8%, respectively (P<0.05, n=6). In the negative control group, the weight of residual thrombus was 30.0±5.4 mg, and the fibrinogen degradation was 2.7%±2.7%. The difference between UK and control or FIIa and control was statistically significant (P<0.01, n=6, Table 3, 4).

Fibrin(ogen)olytic character of FII_a in lysis of platelet-rich clots, platelet-poor clots and whole-blood clots The kinetics of FII_a-induced lysis were characterized by an initial lag phase followed by an accelerated lysis, whereas lysis by UK lacked the lag phase. The order of the lysis speed after UK 125 kU/L treatment PPP clots>the whole blood clots> PRP clots. The sequence for FII_a 0.4 g/L was PRP clots>PPP clots>whole blood clots. The clot lysis of these three types of clots with saline was below 10% during the course of 12 h (Figure 3 and 4).

Table 1. Fibrin(ogen)olytic effects of UK on ^{125}I-labeled human plasma clots *in vitro*. n=3. Mean±SD. ^cP<0.01 *vs* control.

Concentration/ kU·L^{-1}	Fibrinogen degradation/%	Fibrinogen degradation/g·L^{-1}
25	27.3±3.6^c	0.88±0.12^c
35	35.2±2.3^c	1.10±0.07^c
40	39.3±2.4^c	1.26±0.08^c
45	44.2±4.6^c	1.42±0.15^c
60	51.1±1.2^c	1.64±0.04^c

Table 2. Fibrin(ogen)olytic effects of FII_a on ^{125}I-labeled human plasma clots *in vitro*. n=3. Mean±SD. ^cP<0.01 *vs* control.

Concentration/ g·L^{-1}	Fibrinogen degradation/%	Fibrinogen degradation/g·L^{-1}
0.08	95.44±0.28^c	3.07±0.01^c
0.23	>95.62	>3.07
0.4	>95.62	>3.07
0.5	>95.62	>3.07
0.7	>95.62	>3.07

Table 3. The thrombolysis and fibrinogen degradation by FII_a in rabbit carotid thrombosis model. n=6. Mean±SD. ^cP<0.01 *vs* control.

Dosage/ mg·kg^{-1}	Residual thrombus/mg	Fibrinogen degradation/%
0.5	12.5±3.9^c	1.2±9.9^c
1.0	7.8±3.5^c	4.1±7.8^c
2.0	3.4±2.2^c	6.8±5.2^c

Table 4. The thrombolysis and fibrinogen degradation by UK in rabbit carotid thrombosis model. n=6. Mean±SD. ^cP<0.01 *vs* control.

Dosage/ kU·kg^{-1}	Residual thrombus/mg	Fibrinogen degradation/%
5	21.1±3.8^c	10.3±9.9^c
10	17.2±2.5^c	15.2±6.3^c
20	12.2±2.8^c	19.9±7.0^c
40	9.0±2.5^c	24.4±6.2^c

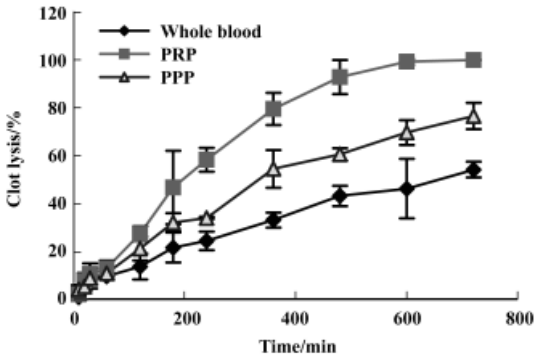

Figure 3. The clot lysis of human whole blood, platelet rich plasma (PRP), and platelet poor plasma (PPP) by FII_a 0.4 g/L. *n*=6. Mean±SD.

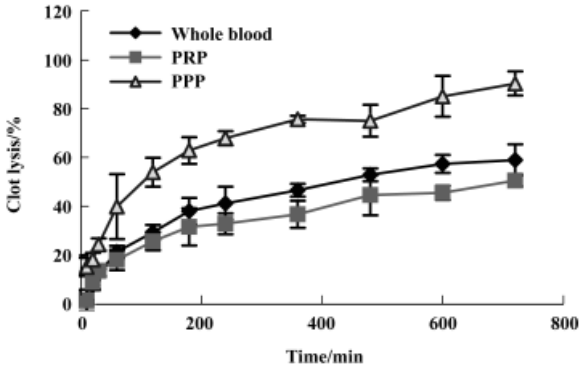

Figure 4. The clot lysis of human whole blood, platelet rich plasma (PRP), and platelet poor plasma (PPP) by UK 125 kU/L. *n*=6. Mean±SD.

Discussion

In this paper, the fibrin(ogen)olytic character of FII_a was studied and compared with UK. The *in vitro* results showed that both FII_a and UK degraded clots and fibrinogen in a dose-dependent manner. FII_a degraded 95.4%±0.3% fibrinogen when the clot lysis was 20% and UK degraded 51.1%± 1.2% fibrinogen when the clot lysis was 80%. *In vitro*, FII_a degraded more fibrinogen than UK did at the same percentage of clot lysis.

The *in vivo* results showed that both FII_a and UK could dose-dependently dissolve clots and fibrinogen. The fibrinolytic effects of UK 40 kU/kg or FII_a 1.0 mg/kg were approximately the same, but the fibrinogen degradation effects were 24.4%±6.2% and 4.1%±7.8%, respectively (P<0.05, n=6). *In vivo*, FII_a degraded less fibrinogen than UK did at the same percentage of clot lysis. The *in vivo* and *in vitro* results of the experiments are in accordance with the data of our previous studies[5,6,12].

UK and FII_a have different sensitivity and kinetics to different types of clots. UK dissolved most effectively the PPP clots, then the whole blood clots and PRP clots. The sequence for FII_a was PRP>PPP>whole blood clots.

Attention should be paid as to why the conclusion *in vitro* did not accord with the conclusion *in vivo*. It could be explained that the dosage of FII_a was much higher *in vitro* than that used *in vivo*, while the dosage of UK was opposite. The dosage was at least one of the causes of the inconsistency.

The main component of thrombus in rabbit carotid artery thrombosis model was platelet[9] and the main component in *in vitro* clots was fibrin. FII_a dissolves most effectively the platelet rich clots compared with UK that dissolves most effectively fibrin rich clots (Figure 3 and 4), which could explain why FII_a dissolved clot at less dosage *in vivo* than *in vitro* but the clot lysis effect of UK was just the opposite.

Our previous study showed that FII_a influenced blood coagulation by inhibiting platelet aggregation induced by ADP in rat PRP and degrading factor X and prothrombin[12]. It is also one of the reasons in the dosage inconsistency.

There are two opinions about the mechanism of the fibrinolytic enzyme from snake venom inhibiting platelet aggregation. (1) Fibrinolytic enzymes inhibit platelet aggregation by hydrolyzing α-fibrinogen to prevent fibrinogen from combining with fibrinogen receptor (GPIIb-IIIa), such as α-fibrinolytic enzyme from *Agkistrodon contortrix contortrix*[13], *A rhodostoma*[14], and *T mucrosquamatus*[15]. (2) The disintegrin-like domain may target the fibrinolytic enzyme to a particular site such as platelets where the metalloproteinase domain may cleave relevant substrates including integrins, coagulant proteins, matrix, or other latent proteins[16]: such as collagen receptor antagonist *Jararhagin* from *Bothrops jararaca*[17], *Mutalysin* I from *Lachesis muta muta*[16], *Crovidisin* from *C viridis*[18]; such as GPIIb-IIIa antagonist *Barbourin*[19] with KGD sequence. Our previous study showed FII_a degraded α and β chains of fibrinogen[5]. Is there any relationshiop between the inhibitory activity of FII_a on platelet aggregation and the proteolytic activity of FII_a on fibrinogen or membrane protein? This topic will be further explored in the near future.

References

1 Verstraete M, Lijnen HR, Collen D. Thrombolytic agents in development. Drugs 1995; 50: 29–42.

2 Collen D, Verstraete M. Systematic thrombolytic therapy of acute myocardial infarction. Circulation 1983; 68: 462–5.

3 Rao AK, Pratt C, Berke A, Jaffe A, Ockene I, Schreiber TL, *et al*. Thrombolysis in myocardial infarction (TIMI) trial-phase I:

hemorrhagic manifestations and changes in plasma fibrinogen and the fibrinolytic system in patients treated with recombinant tissue plasminogen activator and streptokinase. J Am Coll Cardiol 1988; 11: 1–11.

4 Stump DC, Califf RM, Topol EJ, Sigmon K, Thornton D, Masek R, *et al*. Pharmacodynamics of thrombolysis with recombinant tissue-type plasminogen activator: correlation with characteristics of and clinical outcomes in patients with acute myocardial infarction. Circulation 1989; 80: 1222–30.

5 Liang XX, Chen JS, Zhou YN, Qiu PX, Yan GM. Purification and biochemical characterization of FIIa, a fibrinolytic enzyme from *Agkistrodon acutus* venom. Toxicon 2001; 39: 1133–9.

6 Chen JS, Liang XX, Qiu PX, Yan GM. Thrombolysis effect with FIIa from *Agkistrodon acutus* venom in different thrombosis model. Acta Pharmacol Sin 2001; 22: 420–2.

7 Chen JS, Liang LG, Sun JJ. The pharmacology characterizations of fibrinolytic fraction II from five-pace snake venom. Chin Pharmacol Bull 1993; 9: 22–5.

8 Gurewich V, Pannell R, Louis S, Kelley P, Robert L, Suddith RL, *et al*. Effective and fibrin-specific clot lysis by a zymogen precursor from a study *in vitro* and in tow animal species. J Clin Invest 1984, 73: 1731–9.

9 Wang QC, Xu YL, Liu GF. A simple rabbit carotid thrombus model and the fibrinolytic effect of acutinase. Chin Pharmacol Bull 1993, 9: 228–9.

10 Datta G, Dong A, Witt J, Tu AT. Biochemical characterization of basilase, a fibrinolytic enzyme from *Crotalus basiliscus* basiliscus. Arch Biochem Biophys 1995, 317: 365–73.

11 Gurewich V, Pannell R. A comparative study of the efficacy and specificity of tissue plasminogen activator and pro-urokinase: demonstration of synergism and of different thresholds of non-selectivity. Throm Res 1986, 44: 217–28.

12 Wang QQ, Chen JS, Liang XX, Qiu PX, Wang YW, Yan GM. Hemorrhagic activity and mechanism of FIIa, a fibrinolytic enzyme from *Agkistrodon acutus* venom. Acta Pharmacol Sin 2004; 25: 514–21.

13 Manning MC. Sequence analysis of fibrolase, a fibrinolytic metalloproteinase from *Agkistrodon contortrix contortrix*. Toxin 1995; 33: 1189–200.

14 Huang TF, Chang MC, Peng HC, Teng CM. A novel alphatype fibrinogenase from *Agkistrodon rhodostoma* snake venom. Biophim Biophys Acta 1992; 1160: 262–8.

15 Sugihara H, Mori N, Nikai T, Kishida M, Akagi M. Comparative study of three proteinases from the venom of the Chinese hahu snake (*Trimeresurus mucrosquamatus*). Comp Biochem Physiol B 1985; 82: 29–35.

16 Estêvão-costa MI, Diniz CR, Magalhães A, Markland FS, Sanchezâ EF. Thromb Res 2000; 99: 363–76.

17 Kamiguti AS, Hay CRM, Zuzel M. Inhibition of collagen-induced platelet aggregation as the result of cleavage at $\alpha 2\beta 1$-integrin by the snake venom metalloproteinase jararhagin. Biochem J 1996; 320: 635–C41.

18 Liu CZ, Huang TF. Crovidisin, a collagen-binding protein isolated from snake venom of *Crotalus viridid*, prevents platelet-collagen interaction. Arch Biochem Biophys 1997; 337: 291–9.

19 Perutelli P. Disintegrins: potent inhibitors of platelet aggregation. Recent Prog Med 1995; 86: 168–74.

Acta Pharmacologica Sinica 2005 Jun; 26 (6): 696–704

Full-length article

Effects of simvastatin on cardiac performance and expression of sarcoplasmic reticular calcium regulatory proteins in rat heart[1]

Xia ZHENG, Shen-jiang HU[2]

The First Affiliated Hospital, College of Medicine, Zhejiang University, Hangzhou 310003, China

Key words

simvastatin; Ca^{2+}-transporting ATPase; endoplasmic reticulum; calcium regulatory protein; myocardial contraction; ryanodine receptor calcium release channel; reverse transcriptase polymerase chain reaction

[1] Project supported by grants from Health Bureau of Zhejiang Province, China (No 2004A035).
[2] Correspondence to Prof Shen-jiang HU.
Phn 86-571-8723-6569.
E-mail s0hu0001@hotmail.com

Received 2004-09-22
Accepted 2005-01-14

doi: 10.1111/j.1745-7254.2005.00105.x

Abstract

Aim: To investigate the effect of simvastatin on the cardiac contractile function and the alteration of gene and protein expression of the sarcoplasmic calcium regulatory proteins, including sarcoplasmic reticulum Ca^{2+}-ATPase (SERCA), phospholamban (PLB), and ryanodine receptor 2 (RyR2) in rat hearts. **Methods:** Langendorff-perfused rat hearts were subjected to 60-min perfusion with different concentrations of simvastatin (1, 3, 10, 30, or 100 μmol/L), and the parameters of cardiac function such as left ventricular developed pressure (LVDP), $+dp/dt_{max}$, and $-dp/dt_{max}$ were determined. The cultured neonatal rat ventricular cardiomyocytes were incubated with simvastatin (1, 3, 10, 30, and 100 μmol/L) for 1 h or 24 h. The levels of SERCA, PLB, and RyR2 expression were measured by reverse transcription-polymerase chain reaction and Western blot. Cytotoxic effect of simvastatin on ventricular cardiomyocytes was assessed by the MTT colorimetric assay. **Results:** LVDP, $+dp/dt_{max}$, and $-dp/dt_{max}$ of hearts were increased significantly after treatment with simvastatin 3, 10, and 30 μmol/L. In simvastatin-treated isolated hearts, the levels of mRNA expression of SERCA and RyR2 were elevated compared with the control ($P<0.05$), while the mRNA expression of PLB did not change. After the cultured neonatal rat ventricular cardiomyocytes were incubated with 3, 10, 30, and 100 μmol/L simvastatin for 1 h, SERCA and RyR2 mRNA expressions of cardiomyocytes rose, but there was no alteration in protein expressions. However, with the elongation of simvastatin treatment to 24 h, the protein expression of SERCA and RyR2 were also elevated. Additionally, simvastatin (1–30 μmol/L) had no influence on cell viability of cultured cardiac myocytes, but simvastatin 100 μmol/L inhibited the cell viability. **Conclusion:** Simvastatin improved cardiac performance accompanied by the elevation of SERCA and RyR2 gene and protein expression.

Introduction

There is evidence that early initiation of statins, HMG-CoA reductase inhibitors, in patients is associated with markedly reduced fatal or non-fatal myocardial infarction and the mortality of cardiovascular event. Scandinavian Simvastatin Survival Study (4S) and Heart Protect Study (HPS) test have demonstrated that simvastatin could decrease the incidence of ischemic stroke, myocardial infarction, and the mortality of severe cardiovascular events in atherosclerotic and hypercholesterolemic patients[1,2]. However, it is unclear whether treatment with simvastatin would influence cardiac function.

It is well known that Ca^{2+} plays a central role in excitation-contraction coupling of myocardium. Intracellular Ca^{2+} ($[Ca^{2+}]_i$) is from both of release of Ca^{2+} from intracellular Ca^{2+} stores and influx of extracellular Ca^{2+} across the plasma membrane. Several main proteins in sarcoplasmic reticulum (SR), such as SERCA and RyR2, are involved in the release, uptake, and storage of cardiac muscle Ca^{2+}. Contraction is mediated through the release of Ca^{2+} from the SR by IP_3R (Ca^{2+} pool sensitive to IP_3) and RyR (Ca^{2+} pool insensitive to

IP_3), while relaxation involves the active re-uptake of Ca^{2+} into the SR lumen by sarcoplasmic reticulum Ca^{2+}-ATPase (SERCA). In cardiac muscle, the SERCA activity is under reversible regulation by phospholamban (PLB).

As previous studies revealed, simvastatin induced an increase in $[Ca^{2+}]_i$ through two different pathways (*ie* the Ca^{2+} release from intracellular stores sensitive to thapsigargin and ryanodine and the Ca^{2+} influx from extracellular solution in endothelial cells[3,4], L6 rat myoblasts[5], or cultured cardiomyocytes[6]). In some pathophysiological conditions, statins can prevent Ca^{2+} overload. For example, liposoluble HMG-CoA reductase inhibitors could markedly inhibit $[Ca^{2+}]_i$ induced by angiotensin II, LPC, and noradrenaline[7–9]. Atrovastatin prevented the enhanced uptake of Ca^{2+} by sarcoplasmic reticulum (SR) and non-SR Ca^{2+} stores in diabetic dyslipidemic pigs[10]. However, it is still unclear whether simvastatin can induce the alteration of expression of SERCA, PLB, and RyR2. Thus, the present study was designed to evaluate the effect of simvastatin on cardiac contractile function and gene and protein expression of SR calcium regulatory proteins, such as SERCA, PLB, and RyR2, which are related with the alteration of $[Ca^{2+}]_i$.

Materials and methods

Drugs Simvastatin (gifted by Merck Sharp & Dohme, Hertfordshire, UK), a lactone prodrug, was diluted in 0.5 mL of 100% ethanol, mixed with 0.75 mL of 0.1 mol/L NaOH, heated at 50 °C for 2 h, neutralized with 0.1 mol/L HCl to pH 7.2, adjusted with deionized water to a final concentration of 5 mmol/L, sterilized by filtration, and stored in aliquots at -20 °C[11]. Other main reagents in this experiment include: Trizol (Invitrogen, CA, USA); MMLV and pUC19 DNA/*Msp*I (HpaII) Marker (MBI Fermentas, Vilnius, Lithuania); *Taq* plus DNA polymerase and primers (Sangon, Shanghai, China); DMEM (Gibco, Invitrogen); trypsin 1:250 (Amresco, Solon OH, USA); collagenase I (Sigma, St Louis, MO, USA); 5-bromo-2-deoxyuridine (Sigma); fetal bovine serum (Hangzhou-Sijiqing Biological Engineering Materials Co Ltd, China); rabbit anti-rat myosin heavy chain antibody (Novocastia Lab Ltd, USA); FITC-conjugated goat anti-rabbit IgG (Amersham, Buckinghamshire, UK); monoclonal mouse antibody to SERCA, PLB and RyR2 (ABR corporation); secondary anti-goat antibody (Beijing Zhongshan Biotechnology, Beijing, China); MTT (Sigma); EZ-ECL Chemiluminescence Detection Kit for HRP (Biological Industries, Haemek, Israel).

Animals Male Sprague-Dawley (SD) rats (240–270 g) and 1–3 d old SD rats were purchased from the Experimental Animal Center, Chinese Academy of Sciences (Shanghai, China) and all procedures in our experiments were approved by the Animal Care and Use Committee of Zhejiang University.

Isolated heart perfusion Rats were anesthetized with sodium pentobarbital (60 mg/kg), then the hearts were excised and perfused in a non-recirculating Langendorff apparatus with modified Krebs-Henseleit (KH) solution (in mmol/L: NaCl 118, KCl 4.7, $CaCl_2$ 1.5, KH_2PO_4 1.2, $MgSO_4$ 1.2, $NaHCO_3$ 25.2, and glucose 11.1, pH 7.4). The coronary perfusion pressure was 100 mmHg and KH solution was bubbled with 95% O_2:5% CO_2 at 37 °C. A water-filled latex balloon-tipped catheter was inserted into the left ventricle via the left atrium and connected to a computer coupled with MedLab software (Nanjing MedEase Science & Technology Co Ltd, China) through a pressure transducer. The volume of the balloon was adjusted to a left ventricular end-diastolic pressure of 6–8 mmHg during the initial equilibration, then remained constant throughout the experiment. Left ventricular developed pressure (LVDP) and the maximum rate of intraventricular pressure development and relaxation ($\pm dp/dt_{max}$) were measured during perfusion.

All hearts were equilibrated for 15 min for baseline measurements, and were then subjected to 60 min of reperfusion with or without simvastatin at 1, 3, 10, 30, or 100 μmol/L. After perfusion, the hearts were removed with the right ventricle and connective tissues, freeze-clamped into liquid nitrogen, then stored at -80 °C.

Cell culture Primary cultures of neonatal rat ventricular cardiomyocytes from 1–3 d old SD rats were performed as described previously[12]. Briefly, the ventricle was dissociated with the admixture of 0.25% trypsin and 0.1% collagenase I, then cell suspensions were washed with DMEM supplemented with 20% fetal bovine serum (FBS) and centrifuged at 1000 rpm for 6 min. The centrifuged cells were then resuspended in 10% FBS containing DMEM. These cells were preplated for 1 h in order that nonmyocyte readily attached to the bottom of the culture dishes. Unattached cells, which were enriched with cardiac myocytes, were plated onto 6-well dishes at a density of 0.5×10^6 cells/well. BrdU (0.01 mmol/L) was added during the first 72 h to prevent proliferation of nonmyocytes[12] (Figure 1).

Myocardial cells were incubated in DMEM containing non-bovine serum albumin for 24 h prior to respective simvastatin (1, 3, 10, 30, or 100 μmol/L) treatment for 1 h or 24 h.

RT-PCR Total RNA was extracted using TRIzol reagent from rat heart tissues and cultured neonatal rat ventricular cardiomyocytes according to the manufacturer's instruction. First-strand cDNA was generated by adding 2 μg total RNA,

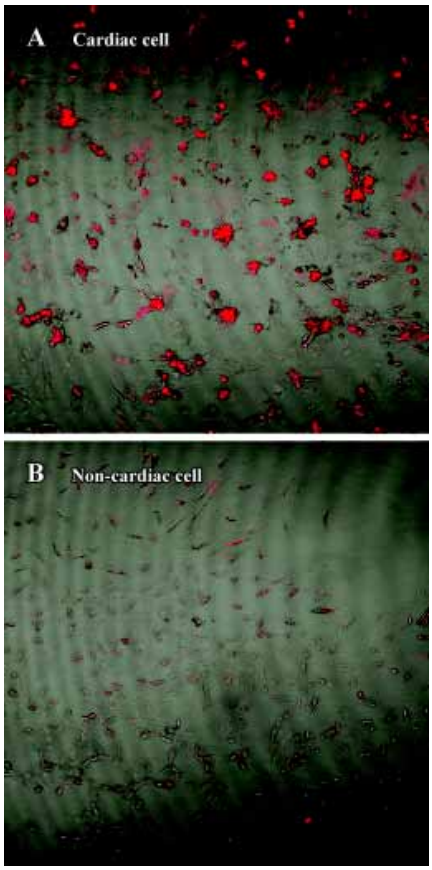

Figure 1. The identification of cultured neonatal rat ventricular cardiomyocytes. Confocal micrographs of the cultured cardiomyocytes. Immunofluorescence with FITG labeled anti-rat Myosin Heavy Chain (slow) antibody (red). (A) cultured neonatal rat ventricular cardiomyocytes; (B) non-cardiac cell from neonatal rat heart (×100).

5 μL of 5×reverse transcriptase buffer, 3 μL (0.5 μg/μL) randomhexamer primers, 2 μL (10 mmol/L) dNTP, 1 μL (200 U/μL) M-MLV reverse transcriptase and autoclaved water in a final volume of 20 μL. Reverse transcription was carried out at 42 °C for 90 min, followed by heat inactivation at 70 °C for 5 min, terminated at 70 °C for 10 min. Then, PCR was run in a DNA thermal cycler (PTC150 Thermo-Cycler, MJ Research, Inc, Waltham, MA, USA). The primers were up primer 5'-AAG-CAG-TTC-ATC-CGC-TAC-CT-3' and down primer 5'-AGA-CCA-TCC-GTC-ACC-AGA-TT-3' for SERCA; up primer 5'-TAC-CTT-ACT-CGC-TCG-GCT-ATC -3' and down primer 5'-CAG-AAG-CAT-CAC-AAT-GAT-GCA-G-3' for PLB; and up primer 5'-ACT-GCT -AAA-GTG-ACC-AAC-AG-3' and down primer 5'-TTG-CAT-CGC-TGA-AAT-CTA-GT-3' for RyR2. The β-actin gene (up primer 5'-GAG-ACC-TTC-AAC-ACC-CCA-GCC-3', down primer 5'-GGC-CAT-CTC-TTG-CTC-GAA-GTC-3') was used as control. *Taq* polymerase 1.5 units, 2 μL cDNA, 1 μL (10 μmol/L) each primer, 1 μL (10 μmol/L) β-actin, 1 μL of 10 mmol/L dNTP solution, 2.5 μL PCR buffer solution and ultrapure autoclaved water were used to reach a total reaction volume of 25 μL. The cycling parameters were as follows: 5 min of 1 cycle at 94 °C, 45 s at 94 °C, 1 min at 57°C, and 1 min of 23 cycles at 72 °C (SERCA); 30 sec at 94 °C, 1 min at 55 °C, and 1 min of 24 cycles at 72 °C (PLB); 45 s at 94 °C, 1 min at 57 °C, and 1 min of 27 cycles at 72 °C (RyR2); and 10 min of 1 cycle at 72 °C. The gray scales of absorbance in goal gene and β-actin gene were determined and assayed with Kodak digital science Electrophoresis Documentation and Analysis System120.

Western blot Heart tissue 50 mg was homogenized in 1 mL modified tonic sucrose[13] (0.3 mol/L sucrose, 10 mmol/L imidazole,10 mmol/L sodium metabisulfite, 1 mmol/L DTT, 0.3 mmol/L PMSF) and centrifuged at 13000×*g* at 4 °C for 15 min. Cultured cells were scraped in ice-cold RIPA solubilization buffer consisting of 50 mmol/L Tris-HCl (pH 7.4), 150 mmol/L NaF, 1% sodium deoxycholate, 1% Nodinet-P40, 0.1% sodium dodecylsulfate, 2.5 mmol/L pretreated sodium orthovanadate, 125 μmol/L phenylarsine oxide, and 2 mmol/L phenylmethyl sulphonyl fluoride[14] and centrifuged at 14 000×*g* for 30 min. The protein concentration was determined by the Brandford method.

Aliquots containing 24 μg of protein for SERCA or 10 μg of protein for PLB were loaded on the SDS-polyacrylamide gel and separated by electrophoresis (6% or 10% acrylamide separating gel, respectively, for 30 min). The separated proteins were electrophoretically transferred onto nitrocellulose membranes (Amersham) at 200 mA at 4 °C for 90 min in a buffer containing 25 mmol/L Tris base, 192 mmol/L glycine, and 20% methanol by using the Bio-Rad Trans-Blot electrophoretic transfer system (Bio-Rad). Aliquots of 6 μg RyR2 SDS-digested homogenate protein were loaded on the SDS-polyacrylamide gel, separated by electrophoresis (4% acrylamide stacking gel and 6% acrylamide separating gel), and were electrophoretically transferred onto polyvinylidene difluoride membranes (Bio-Rad) at 250 mA at 4 °C for 3 h and then at 50 V for about 12 h. These membranes were incubated at 4 °C overnight with mouse-anti-SERCA, mouse-anti-PLB, or mouse-anti-ryanodine receptor at 1:1000 dilution in 5% Carnation instant milk/TBS. After incubation with a secondary anti-goat antibody at a 1:500 dilution in 5% Carnation instant milk-TBS-Tween 20, the blot was developed using enhanced chemiluminescence according to the manual (Beit Haemek LTD) and exposed to X-ray film[11].

MTT assay Cells were incubated in the absence or presence of simvastatin for 24 h, and then the cytotoxic effect was assessed using MTT assay method. Each well of plates

was added with 10 μL MTT (5 g /L) per 100 μL of medium, and were incubated at 37 °C for 4 h. Then, the medium in each well was replaced with 100 μL dimethylsulfoxide and the plates were incubated for 5–10 min at room temperature for color development. Finally, 96-well of plates was read by enzyme-linked immunosorbent assay (ELISA) reader (570 nm) to get the absorbance density values[15].

Statistics Data were presented as mean±SD. To correct for variability in basal values, changes in left ventricular development pression, +dp/dt_{max} and -dp/dt_{max} were calculated as a percent of the initial basal values for each heart. Various kinds of indexes between the control group and simvastatin-treated groups were analyzed by one way ANOVA with SPSS 10.0 software. P<0.05 was considered the threshold for statistical significance between the control group and the experimental groups.

Results

Effect of simvastatin on cardiac performance To determine whether simvastatin exerted any direct cardiodynamic effect, the isolated rat hearts were initially perfused without or with simvastatin for 60 min in this experiment. The results showed that simvastatin 1 μmol/L had no impact on cardiac performance in the isolated rat hearts compared with control (LVDP: 68.9%±17.0% *vs* 71.7%±10.6%, P>0.05; +dp/dt_{max}: 69.3%±5.3% *vs* 72.1%±7.5%, P>0.05; -dp/dt_{max}: 67.3%±5.5% *vs* 68.5%±6.1%, P>0.05). However, simvastatin 3, 10, and 30 μmol/L significantly increased the levels of LVDP and ±dp/dt_{max} of rat hearts compared with those of control (LVDP: 95.8%±17.4%, 85.9%±8.6%, 96.9%±7.0% *vs* 71.7%±10.6%, P<0.01, 0.05, 0.01; +dp/dt_{max}: 89.5%±4.4%, 97.2%±10.8%, 89.8%±6.7% *vs* 72.1%±7.5%, P<0.01 all; -dp/dt_{max}: 82.9%±4.7%, 88.6%±11.0%, 79.6%±6.6% *vs* 68.5%±6.1%, P<0.01 all, respectively).

When 100 μmol/L simvastatin was applied in isolated rat hearts, sudden arrest of the isolated heart, following transient increased contractile performance, occurred. The scope of sudden death time interval was from 14 to 20 min. Thus, the measurement of LVDP% and ±dp/dt_{max}% were recorded every 2 min until 14 min (Figure 2).

Gene expression of SR protein in isolated rat hearts and cultured cardiomyocytes After being treated with simvastatin at different concentrations (3, 10, and 30 μmol/L), SERCA and RyR2 mRNA levels of isolated heart tissue were increased. However, no alteration was found in heart tissue after simvastatin 1 or 100 μmol/L treatment. There was no difference in PLB mRNA levels of rat hearts between the control group and simvastatin-treatment groups (Figure 3).

Simvastatin 3–100 μmol/L had no influence on PLB gene expression of neonatal rat ventricular cardiomyocytes, but markedly increased SERCA and RyR2 gene expression (Figure 4).

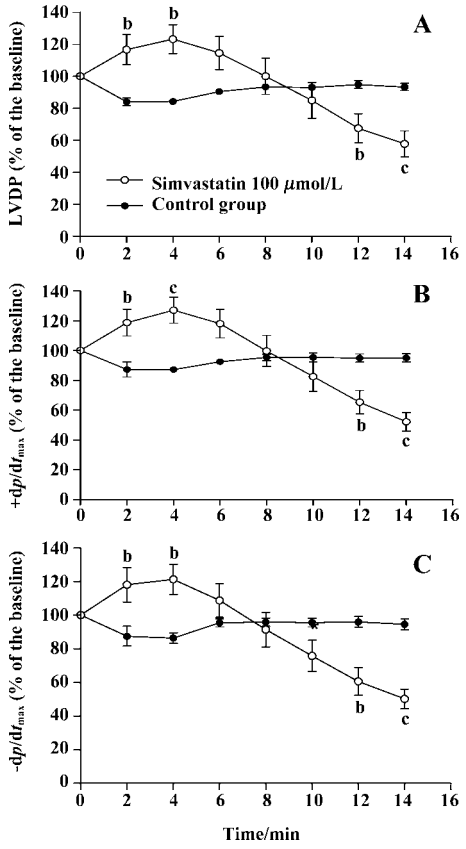

Figure 2. Alterations of LVDP (A), +dp/dt_{max} (B), and -dp/dt_{max} (C) of the isolated hearts after simvastatin 100 μmol/L treatment. The rat hearts received 14-min exposure to Kreb-Henseleit solution with simvastatin after 15-min stabilization. n=8 in control group. n=5 in simvastatin group. Mean±SD. ^bP<0.05, ^cP<0.01 *vs* the baseline.

Additionally, sequencing analysis showed 100% coincidence rates of SERCA, PLB, and RyR2 cDNA sequences, which came from the final products of RT-PCR compared with those in GeneBank, indicating that the amplified fractions had high specificity.

Expression of SR protein in isolated rat hearts and cultured cardiomyocytes No alteration in the protein levels of SERCA, PLB, and RyR2 was found after simvastatin 1, 3, 10, 30, or 100 μmol/L treatment (Figure 5).

In order to test whether the changes in protein levels occurred with the elongation of simvastatin treatment, we supplied cultured cardiomyocytes with different concentration simvastatin for 1 h and 24 h. The results showed that incubation with simvastatin for 1 h in the cultured cardiomyocytes had no effect on the protein expression of

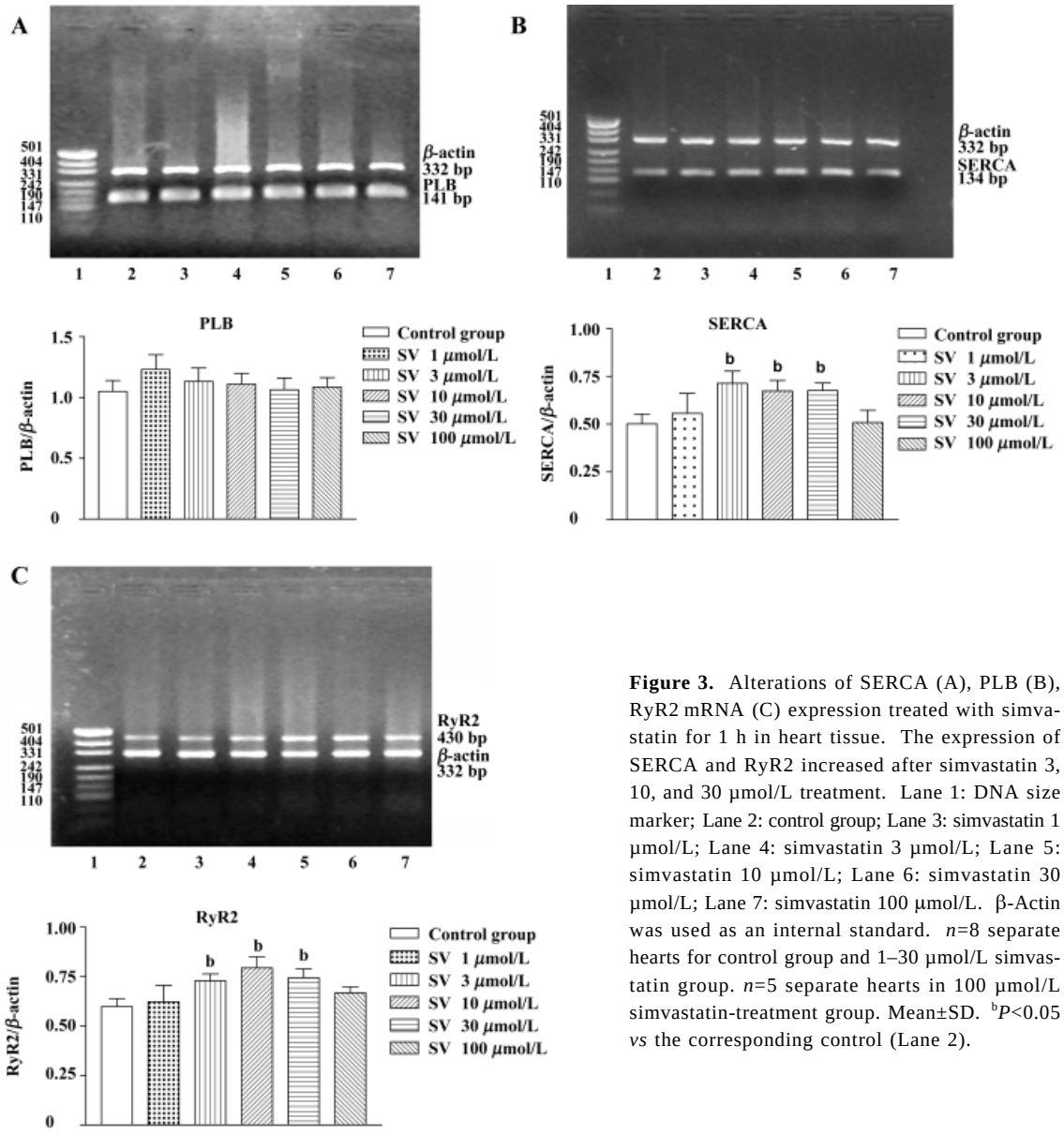

Figure 3. Alterations of SERCA (A), PLB (B), RyR2 mRNA (C) expression treated with simvastatin for 1 h in heart tissue. The expression of SERCA and RyR2 increased after simvastatin 3, 10, and 30 μmol/L treatment. Lane 1: DNA size marker; Lane 2: control group; Lane 3: simvastatin 1 μmol/L; Lane 4: simvastatin 3 μmol/L; Lane 5: simvastatin 10 μmol/L; Lane 6: simvastatin 30 μmol/L; Lane 7: simvastatin 100 μmol/L. β-Actin was used as an internal standard. n=8 separate hearts for control group and 1–30 μmol/L simvastatin group. n=5 separate hearts in 100 μmol/L simvastatin-treatment group. Mean±SD. $^bP<0.05$ *vs* the corresponding control (Lane 2).

SR calcium regulatory protein, whereas longer period (24 h) of simvastatin 3–100 μmol/L treatment increased SERCA and RyR2 protein level, except PLB protein levels of cardiomyocytes (Figure 6).

Effect of simvastatin on the cytotoxicity in cultured neonatal rat ventricular cardiomyocytes Simvastatin 1–30 μmol/L did not induce alteration of mitochondrial activity, whereas simvastatin 100 μmol/L produced a rapid drop of mitochondrial activity (Table 1).

Table 1. Effects of simvastatin (1–100 μmol/L) on neonatal cultured cardiomyocytes after a 24-h incubation. n=8 in each group. Mean±SD. $^cP<0.01$ *vs* control.

Group	Concentration/μmol·L^{-1}	$OD_{570\ nm}$
Control		1.19±0.13
Simvastatin	1	1.27±0.07
	3	1.16±0.14
	10	1.18±0.07
	30	1.12±0.06
	100	0.78±0.04^c

Discussion

It is well known that simvastatin can produce some

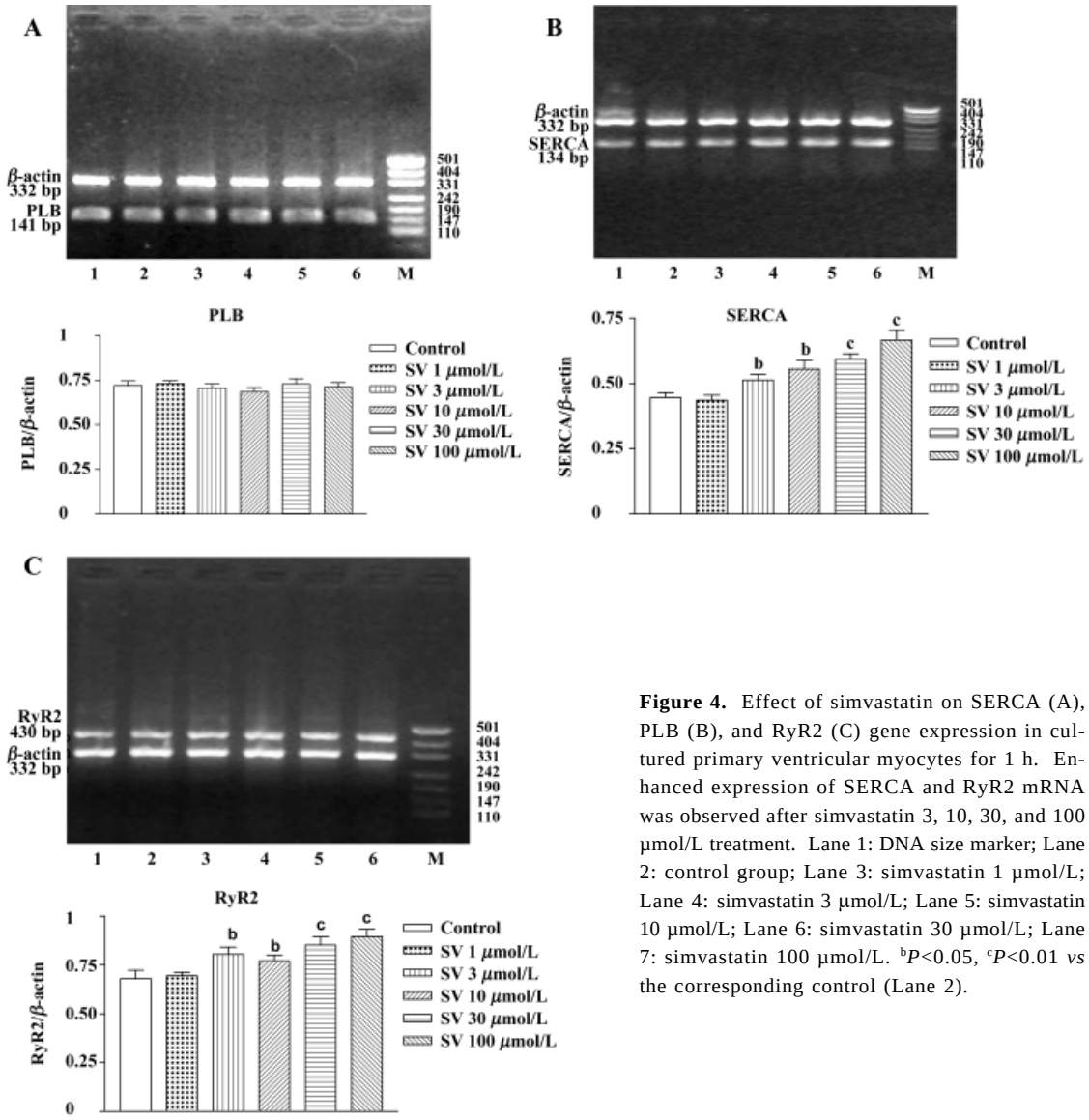

Figure 4. Effect of simvastatin on SERCA (A), PLB (B), and RyR2 (C) gene expression in cultured primary ventricular myocytes for 1 h. Enhanced expression of SERCA and RyR2 mRNA was observed after simvastatin 3, 10, 30, and 100 μmol/L treatment. Lane 1: DNA size marker; Lane 2: control group; Lane 3: simvastatin 1 μmol/L; Lane 4: simvastatin 3 μmol/L; Lane 5: simvastatin 10 μmol/L; Lane 6: simvastatin 30 μmol/L; Lane 7: simvastatin 100 μmol/L. $^{b}P<0.05$, $^{c}P<0.01$ *vs* the corresponding control (Lane 2).

beneficial effects independent of the lowering cholesterol level[16–19], so the direct pharmacological effect of simvastatin on the initial management and prevention of the disease are paid more attention. Our study was performed to identify whether simvastatin induced intrinsic alteration of cardiomyocyte contraction and related calcium regulatory protein, which might explain the effect of simvastatin on cardiac performance.

The present study demonstrated that simvastatin treatment (3, 10, and 30 μmol/L) resulted in the increase of LVDP, $+dp/dt_{max}$, and $-dp/dt_{max}$ in isolated perfused hearts, while simvastatin 100 μmol/L induced sudden heart related death. It has been shown that an increase of nitrogen monoxide (NO) and a decrease of ubiquinone and oxygen-derived free radicals were involved in the possible protective mechanism in isolated rat hearts[20–22], while impairment of mitochondria was associated with injury mechanism in ischemic rat hearts[23]. Previous studies also reported[6] that under normoxic conditions simvastatin caused an increase in $[Ca^{2+}]_i$, which is the key event in excitation-contraction coupling in cardiac myocytes. Therefore, the improvement of cardiac performance in isolated rat hearts during 1 h of perfusion can be explained by NO elevation, decrease of oxygen-derived free radicals, and an increase of $[Ca^{2+}]_i$ and so on.

Using RT-PCR assay, we found the elevation of RyR2 and SERCA mRNA in isolated hearts treated with simvastatin for 1 h and not in those treated with vehicle. Similar to these results, in neonatal cultured cardiac myocytes, the gene

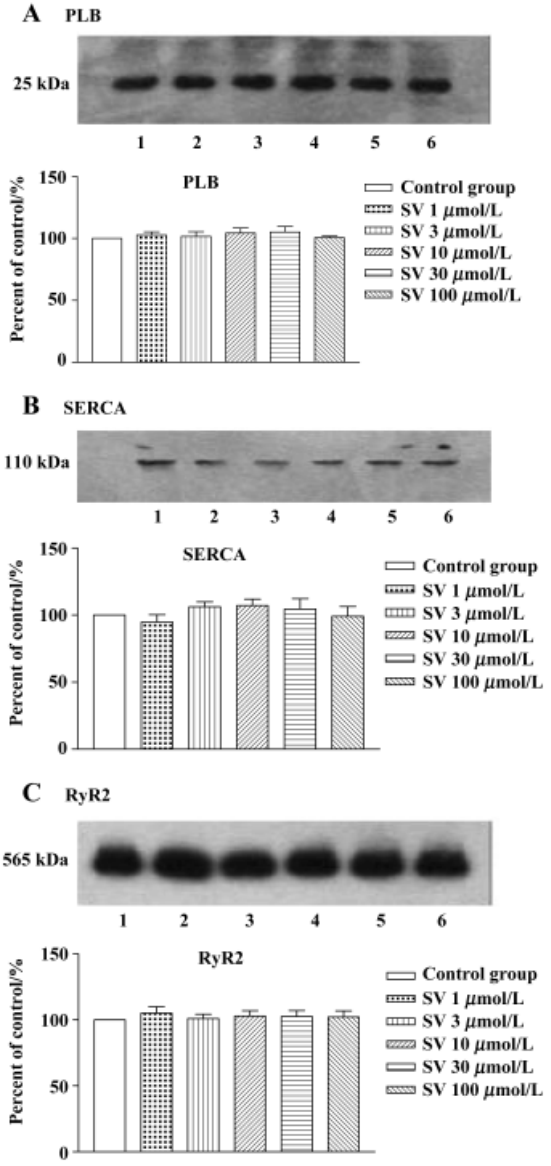

Figure 5. Western blot of PLB (A), SERCA (B), and RyR2 (C) protein levels in isolated heart after 1 h of simvastatin treatment. No alteration of the protein levels was shown after simvastatin treatment at different concentrations. Bars represent cumulative data of Mean±SD from eight hearts (1–30 μmol/L simvastatin groups) and five hearts (100 μmol/L simvastatin group). $^{b}P<0.05$ *vs* control.

levels of RyR2 and SERCA were both elevated after a 1-h incubation. As intracellular second messenger of the organism information transmission, Ca^{2+} is involved in some gene expression. Even transient calcium transport elevation can induce mRNA transcription for a long time. Therefore, the results in our experiment suggested that simvastatin-induced SERCA and RyR2 expression were involved in the mechanisms mentioned above. However, a 1-h treatment with simvastatin (1, 3, 10, 30, or 100 μmol/L) in the isolated hearts and cultured cardiomyocytes did not influence the protein levels of SERCA, PLB, or RyR2, while a 24-h incubation of simvastatin in cultured cardiomyocytes increased SERCA and RyR2 protein level, except PLB protein. It has been shown that several main proteins in SR, such as SERCA and RyR2, are implicated in the release, uptake, and storage of calcium in cardiac muscle. Contraction is mediated through the release of Ca^{2+} from the SR by ryanodine receptor, while relaxation involves the active re-uptake of Ca^{2+} into the SR lumen by SERCA. The SERCA activity is under reversible regulation by PLB[24]. Thereby, it is possible that although the expression of RyR2, SERCA, and PLB were not directly correlated with the cardiodynamic increase of isolated perfused hearts, simvastatin-induced SERCA and RyR2 expression may influence cardiac performance during extended periods of perfusion. Thus, there is reason to believe that alteration of gene and protein expression of SERCA and RyR2 might be a prophetic index of cardioprotective effect of simvastatin. Furthermore, the effect of simvastatin on SR calcium regulation protein gave a clue that the molecular biological mechanism could be a new approach to explain the alteration of cardiac performance affected by simvastatin in future.

In the meantime, the present study discovered that elevation of SERCA and RyR2 mRNA were shown in cultured cardiomyocytes, but not found in isolated rat hearts in the presence of simvastatin 100 μmol/L. We suspect that the result was due to insufficient expression time due to the cardiac sudden death in isolated rat hearts. The MTT assay, as an index of cell viability and cell growth[25,26], revealed that the survival rate of cardiac cells was markedly reduced with simvastatin 100 μmol/L treatment, while cell viability was not influenced by simvastatin 1, 3, 10, 30 μmol/L. Perhaps the toxic effect of overdose simvastatin promoted decrease of cardiac cells, which may indirectly explain the sudden arrest of isolated hearts with simvastatin 100 μmol/L.

Based on our research, it is concluded that simvastatin, at reasonable pharmacological concentration, would enhance cardiac performance concomitant with gene expression increase of calcium regulatory protein. Meanwhile, it should be noted that overdose of simvastatin (100 μmol/L) can produce a deterioration effect on hearts.

References

1 The Scandinavian Simvastatin Survival Study Group. Randomized trial of cholesterol lowering in 4444 patients with coronary heart disease: the Scandinavian Simvastatin Survival Study (4S). Lancet 1994; 344: 1383–9.

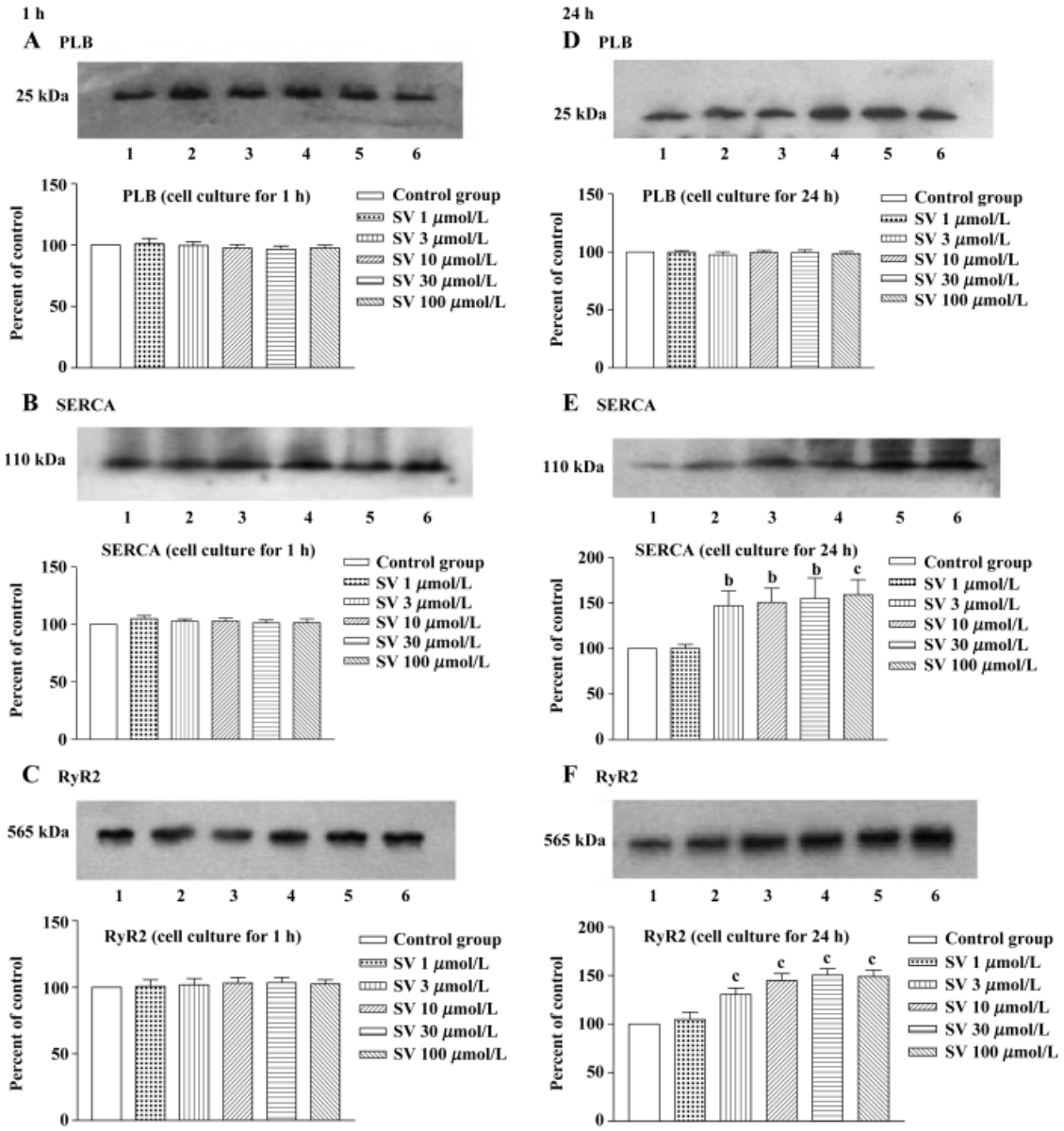

Figure 6. Western blot of PLB (A), (D), SERCA2 (B), (E), and RyR2 (C), (F) protein level after 1-h and 24-h simvastatin treatment in cultured neonatal rat ventricular cardiomyocytes. Incubation with simvastatin for 1 h in the cultured cardiomyocytes had no effect on the protein expression, whereas a 24-h simvastatin treatment increased SERCA and RyR2 protein level. n=8 well cultured cardiomyocytes in each concentration simvastatin group. Mean±SD. $^{b}P<0.05$, $^{c}P<0.01$ *vs* control.

2 Heart Protection Study Collaborative Group. MRC/BHF Heart Protection Study of cholesterol lowering with simvastatin in 20, 536 high-risk individuals: a randomised placebo-controlled trial. Lancet 2002; 360: 7–22.

3 Escobales N, Castro M, Altieri PI, Sanabria P. Simvastatin releases Ca^{2+} from a thapsigargin-sensitive pool and inhibits InsP3-dependent Ca^{2+} mobilization in vascular smooth muscle cells. J Cardiovasc Pharmacol 1996; 27: 383–91.

4 Alvarez de Sotomayor M, Andriantsitohaina R. Simvastatin and Ca^{2+} signaling in endothelial cells: involvement of Rho protein. Biochem Biophys Res Commun 2001; 280: 486–90.

5 Nakahara K, Yada T, Kuriyama M, Osame M. Cytosolic Ca^{2+} increase and cell damage in L6 rat myoblasts by HMG-CoA reductase inhibitors. Biochem Biophys Res Commun 1994; 202: 1579–8.

6 Bastiaanse EM, Atsma DE, Kuijpers MM, Van der Laarse A. Simvastatin-sodium delays cell death of anoxic cardiomyocytes by inhibition of the Na^{+}/Ca^{2+} exchanger. FEBS Lett 1994; 343: 151–4.

7 Tesfamariam B, Frohlich BH, Gregg RE. Differential effects of

pravastatin, simvastatin, and atorvastatin on Ca^{2+} release and vascular reactivity. J Cardiovasc Pharmacol 1999; 34: 95–101.
8 Alvarez de Sotomayor M, Perez-Guerrero C, Herrera MD, Marhuenda E. Effect of simvastatin on vascular smooth muscle responsiveness: involvement of Ca^{2+} homeostasis. Eur J Pharmacol 2001; 415: 217–24.
9 Yokoyama K, Ishibashi T, Ohkawara H, Kimura J, Matsuoka I, Sakamoto T. HMG-CoA reductase inhibitors suppress intracellular calcium mobilization and membrane current induced by lysophosphatidylcholine in endothelial cells. Circulation 2002; 105: 962–7.
10 Hill BJ, Dixon JL, Sturek M. Effect of atorvastatin on intracellular calcium uptake in coronary smooth muscle cells from diabetic pigs fed an atherogenic diet . Atherosclerosis 2001; 159: 117–24.
11 Llorente-Cortes V, Martinez-Gonzalez J, Badimon L. Differential cholesteryl ester accumulation in two human vascular smooth muscle cell subpopulations exposed to aggregated LDL: effect of PDGF-stimulation and HMG-CoA reductase inhibition. Atherosclerosis 1999; 144**:** 335–42.
12 Kurosaki K, Ikeda U, Maeda Y, Shimpo M, Ueno S, Shimada K. Effects of vesnarinone on nitric oxide synthesis in rat cardiac myocytes. Cardiovasc Res 1998; 38: 192–7.
13 Zhong Y, Ahmed S, Grupp IL, Matlib MA. Altered SR protein expression associated with contractile dysfunction in diabetic rat hearts. Am J Physiol Heart Circ Physiol 2001; 281: H1137–47.
14 Kwak BR, van Kempen MJ, Theveniau-Ruissy M, Gros DB, Jongsma HJ. Connexin expression in cultured neonatal rat myocytes reflects the pattern of the intact ventricle. Cardiovasc Res 1999; 44: 370–80.
15 Huang YT, Chueh SC, Teng CM, Guh JH. Investigation of ouabain-induced anticancer effect in human androgen-independent prostate cancer PC-3 cells. Biochem Pharmacol 2004; 67: 727–33.
16 Endres M, Laufs U, Huang Z, Nakamura T, Huang P, Moskowitz MA. Stroke protection by 3-hydroxy-3-methylglutaryl (HMG) CoA reductase inhibitors mediated by endothelial nitric oxide synthase. Proc Natl Acad Sci USA 1998; 95: 8880–5.
17 Lefer AM, Campbell B, Shin YK, Scalia R, Hayward R, Lefer DJ. Simvastatin preserves the ischemic-reperfused myocardium in normocholesterolemic rat hearts. Circulation 1999; 100: 178–84.
18 Wagner AH, Kohler T, Ruckschloss U, Just I, Hecker M. Improvement of nitric oxide-dependent vasodilation by HMG-CoA reductase inhibitors through attenuation of endothelial superoxide anion formation. Arterioscler Thromb Vasc Biol 2000; 20: 61–9.
19 Bourcier T, Libby P. HMG-CoA reductase inhibitors reduce plasminogen activator inhibitor-1 expression by human vascular smooth muscle and endothelial cells. Arterioscler Thromb Vasc Biol 2000; 20: 556–62.
20 Di Napoli P, Antonio Taccardi A, Grilli A, Spina R, Felaco M, Barsotti A. Simvastatin reduces reperfusion injury by modulating nitric oxide synthase expression: an *ex vivo* study in isolated working rat hearts. Cardiovasc Res 2001; 51: 283–93.
21 Jones SP, Trocha SD, Lefer DJ. Pretreatment with simvastatin attenuates myocardial dysfunction after ischemia and chronic reperfusion. Arterioscler Thromb Vasc Biol 2001; 21: 2059–64.
22 Wassmann S, Laufs U, Baumer AT, Muller K, Ahlbory K, Linz W. HMG-CoA reductase inhibitors improve endothelial dysfunction in normocholesterolemic hypertension via reduced production of reactive oxygen species. Hypertension 2001; 37: 1450–7.
23 Satoh K, Ichihara K. Effects of 3-hydroxy-3-methylglutaryl coenzyme A reductase inhibitors on mitochondrial respiration in ischemic rat hearts. Eur J Pharmacol 1995; 292: 271–5.
24 Arai M, Otsu K, MacLennan DH, Alpert NR, Periasamy M. Effect of thyroid hormone on the expression of mRNA encoding sarcoplasmic reticulum proteins. Circ Res 1991; 69: 266–76.
25 Kong JY, Rabkin SW. Mitochondrial effects with ceramide-induced cardiac apoptosis are different from those of palmitate. Arch Biochem Biophys 2003; 412: 196–206.
26 Balligand JL, Ungureanu-Longrois D, Simmons WW, Pimental D, Malinski TA, Kapturczak M. Cytokine-inducible nitric oxide synthase (iNOS) expression in cardiac myocytes. Characterization and regulation of iNOS expression and detection of iNOS activity in single cardiac myocytes *in vitro*. J Biol Chem 1994; 269: 27580–8.

Acta Pharmacologica Sinica 2005 Jun; 26 (6): 705–713

Full-length article

Differential regulation of cadherin expression by osteotropic hormones and growth factors *in vitro* in human osteoprogenitor cells

Peng LIU[2,3], Jian-hao LIN[1,3], Bin ZHANG[1]

[1]Arthritis Clinic and Research Center, People's Hospital, Medical Health Center, Peking University, Beijing 100044, China; [2]Department of Genetics and Developmental Biology, University of Connecticut Health Center, Farmington, CT 06030, USA

Key words

cadherins; stromal cells; cell differentiation; dexamethasone; prostaglandin E_2; tumor necrosis factor; basic fibroblast growth factor; estradiol; parathyroid hormone

[3] Correspondence to Dr Peng LIU.
Phn 1-86-679-2461. Fax 1-86-679-2125.
E-mail p.liu@neuron.uchc.edu
Prof Jian-hao LIN.
Phn 86-10-6831-4422, ext 3600.
Fax 86-10-6831-8386.
E-mail jianhao_lin@yahoo.com

Received 2004-11-19
Accepted 2005-02-18

doi: 10.1111/j.1745-7254.2005.00114.x

Abstract

Aim: To examine if cadherins are expressed constitutively in human bone marrow stromal cells (hBMSC) and investigate the regulation of cadherin expression by various osteotropic hormones and local factors. **Methods:** Cadherin expression was examined in first passaged (secondary) hBMSC as well as in the conditionally-immortalized human osteoprogenitor cell line (hOP-7). Using a monoclonal antibody (MoAb C-1821) to a cytoplasmic domain common to all known cadherins (pan-cadherin MoAb), cadherins were immunolocalized in first passaged hBMSC as well as in hOP-7 cells. In addition, intense immunostaining for cadherin expression was associated with alkaline phosphatase (ALP) in nodules formed in the high density cultures of hOP-7 cells. Human E-cadherin (HECD) was specifically detected by Western blotting in extracts of untreated hBMSC using an anti-HECD MoAb 004FD. **Results:** Differential regulation of cadherin expression by various osteotropic hormones and local factors (parathyroid hormone, dexamethasone, estradiol, prostaglandin E_2, basic fibroblast growth factor, and tumor necrosis factor-β) was also observed. In addition, blocking cadherins with the MoAb C-1821 increased basal ALP activity and had an additive effect on 1, 25$(OH)_2D_3$-induced ALP activity. **Conclusion:** Cadherins are expressed in human osteoprogenitor cells and are involved in the osteogenic differentiation. The differential modulation of cadherin expression by osteotropic agents indicates that these agents may regulate osteoprogenitor cells through different cadherins and these cadherins may play different roles.

Introduction

Cell adhesion molecules (CAM) are believed to play a key role in morphogenesis by modulating cellular proliferation and differentiation through cell-cell interaction and/or cell-matrix interactions[1]. In bones, the differentiation of human bone marrow stromal cells (hBMSC) into mature osteoblasts is essential for bone formation[2]. However, the mechanisms by which CAM modulate this process are still poorly understood. Cadherins, a family of transmembrane glycoproteins, are calcium-dependent homophilic cell-cell adhesion molecules, which have been shown to play an important role in the differentiation of a wide variety of cells and tissues[3].

Cadherins are divided into subclasses, all of which share a common basic structure. Four subclasses have been well characterized at the molecular level and they have about 50% amino acid sequence identity. These include E-cadherin, P-cadherin, and N-cadherin[3]. The extent of conservation varies depending on the region of the molecule with the cytoplasmic domain being the most conserved. A monoclonal antibody to this cytoplasmic domain designated pan-cadherin MoAb was produced, which can be used to recognize novel cadherins in a variety of cells and tissues and displays a broad interspecies cross-reactivity[4]. The evidence that cadherin-mediated interactions can actually modulate cell differentiation has been accumulated[5].

For example, N-cadherin has been demonstrated to be present in the limb mesenchyme in a development-specific manner *in vivo* and *in vitro*. In addition, functional N-cadherin is necessary for limb mesenchymal cells to undergo condensation and progress through chondrogenesis *in vitro* and *in vivo*[6].

Cadherin has recently been found in the cells of osteoblastic lineage[7]. E-cadherin is expressed by the UMR 106-H5 rat osteoblastic osteosarcoma cells as well as by the mouse calvarial MC3T3-E1 cells, and its expression is regulated by PTH in the UMR 106-H5 cells[8]. E-cadherin also plays a role in the generation of multinucleated osteoclasts by mediating fusion of mononuclear cells in murine marrow[9]. In addition, specific osteoblast-like cadherin (OB-cadherin) has been found to be expressed in osteoblasts[10]. However, it remains unclear whether these or other ubiquitous cell adhesion molecules are involved in the differentiation of human osteoblast precursors, which are derived mainly from hBMSC[2]. For better understanding of osteoblast lineage differentiation, this study was to examine the cadherins expression pattern and their regulation by osteotropic agents including systemic hormones and local growth factors in hBMSC.

Materials and methods

Antibodies and chemicals Mouse monoclonal antibody to pan-cadherins (MoAb C-1821) (mouse IgG_1 isotype) was purchased from Sigma Chemical Co (St Louis, USA); Mouse monoclonal antibody to human E-cadherin (MoAb 004FD) (mouse IgG_1 isotype) was purchased from R & D Systems Europe Ltd (Oxon, UK). Recombinant human (rh)-tumor necrosis facotr (TGF)-β was a gift from Genentech Inc (CA, USA). Recombinant human basic fibroblast growth factor (bFGF) was a gift from Schering Research Laboratories (Berlin, Germany). Stock concentration: 1 mg/L and it was diluted into 1 μg/L in PBS containing 0.1% BSA and aliquots of this was stored at -70 ºC. $1,25(OH)_2D_3$ was a gift from Hoffmann-La Roche, Inc (Nutley, NJ, USA). Dexamethasone (Dex), parathyroid hormone (PTH) and estradiol (E_2) were purchased from Sigma Chemical Co. Other chemicals were purchased from Sigma Chemical Co.

Cultures of human bone marrow stromal cells Primary cultures of hBMSC were described previously[11]. Briefly, when the cells became confluent (3-4 weeks after seeding) in the primary cultures, they were subcultured onto glass coverslips, Petri dishes, or into flasks as necessary. At confluence, first passage cells were treated with $1,25(OH)_2D_3$ (50 nmol/L), PTH (100 nmol/L), E_2 (10 nmol/L), Dex (10 nmol/L), prostaglandin E_2 (PGE_2 10 nmol/L), bFGF (1 and 10 μg/L), and TGF-β (1 and 10 μg/L) for 7 d. The doses for the tested agents were selected based on our previous works and others were used for examining osteogenic differentiation of hBMSC[2,7,12–18]. The cell lysates were extracted with RIPA buffer containing 1% NP-40, 1% Triton X-100, 2 mmol/L $CaCl_2$, 0.5% NaCl, 0.1% SDS in PBS with fresh protease inhibitors, including phenyl methyl sulfonyl fluoride (PMSF), pepstatin, 1,10-phenantroline and E-64.

Cultures of conditionally immortalized hBMSC hBMSC were transfected with a viral vector coding a temperature-sensitive mutant of the SV40 large T antigen. The growth characteristic of this immortalized hBMSC is controlled by this temperature-sensitive large T antigen. The large antigen expression was activated at 33 ºC and this allowed the cells to proliferate, producing a large population of homogenous hBMSC. While, the large T antigen was disabled at 39 ºC allowing these immortalized hBMSC to undergo osteogenic differentiation. One of nine clones obtained, hOP-7, was well characterized for osteogenic differentiation . These cells were induced to differentiate into osteoblasts by Dex and $1,25(OH)_2D_3$ at 39 ºC. Therefore, this cell line is thought to be a good model for the study of osteogenic differentiation[19].

hOP-7 cells were seeded onto LabTek chamber slides and maintained for 1–2 d at 33 ºC before being switched to 39 ºC to allow osteogenic differentiation. In some cases, cultures were plated out initially at a higher density to allow formation of nodules. These were also maintained at 33 ºC and thereafter switched to 39 ºC for a further 5 d.

Immunolocalization of cadherin expression Cells on coverslips or on chamber slides fixed with 4% paraformaldehyde were incubated with 5% goat serum for 30 min to block non-specific binding, followed by incubation with a murine monoclonal anti-pan-cadherin antibody (MoAb C-1821) (diluted 1:200 or 1:500) or a mouse monoclonal antibody to human E-cadherin (MoAb 004FD) (diluted 1:200) for 1 h at room temperature. The mouse cavarial cell line MC3T3-E1 was used as a positive control for pan-cadherin immunostaining[8], and MDCK cells for E-cadherin[20]. Mouse ascites fluid and PBS were used to substitute primary antibodies as negative controls. Then, these cells were washed with high salt buffer for 10 min, and twice with TBS for 15 min each. Thereafter, these cells were incubated with biotinylated secondary antibody for 45 min at room temperature and then washed as before. Immunoreactivity was detected using the Vectastain ABC-AP kit. Incubation was for 45 min at room temperature, followed by staining for alkaline phosphatase in the presence of 1 mmol/L levamisole, to block endogenous

alkaline phosphatase. The cells were washed again with TBS and the nuclei was stained with DAPI. After the coverslips and chamber slides were mounted with Kaiser's glycerol jelly, immunostaining was visualized under fluorescence-microscopy using a filter appropriate for rhodamine and another for ultraviolet, and then photographed. Cadherin antigenicity appears as a red coloration, while the nuclei are blue.

Histological staining for alkaline phosphatase (ALP) and biochemical determination of its activity in cultured hBMSC

Histochemical staining of ALP At the end of the culture period, cells on chamber slides were washed twice with PBS and fixed with 4% paraformaldehyde at 4 ºC for 30 min, washed three times with distilled water and then air-dried for 10 min. The cells were then stained for ALP for 30 min with fresh naphthol AS-MX phosphatase solution (0.2 g/L) containing fast red violet B salt (0.42 g/L) in 100 mmol/L Tris-HCl (pH 0.9) at room temperature and then photographed. Under these conditions, ALP-positive cells were stained pink or red.

Biochemical determination of ALP activity At the end of the incubation period, the culture medium was removed from wells, and the cell layers were washed three times with ice cold PBS (pH 7.4). The cells were scraped off the plates into 300–500 μL ice-cold 0.1% Triton-X100 using a 'rubber policeman'. The cell lysates were transferred into plastic tubes (LP4) on ice and subjected to mild sonication (3×5 s bursts, peak amplitude 10 μm at a frequency of 20 kHz) to completely solubilize these cells. The cell lysates were stored at -20 ºC until they were assayed. ALP activity was measured using 2 mmol/L para-nitrophenyl phosphate (*p*-NPP) in assay buffer (0.1 mol/L diethanolamine+1 mmol/L $MgCl_2$+2 mmol *p*-NPP, pH 10.5) at 37 ºC for 10–60 min. Protein content was determined using the Bio-Rad protein assay kit using BSA as a standard according to the manufacturer's manual. ALP activity was expressed as $\mu mol \cdot h^{-1} \cdot g^{-1}$ protein.

Western blot analysis At the end of incubation with the various hormones and/or growth factors, media were removed from Petri dishes and cells were washed with PBS at room temperature, after which the cells were scraped into RIPA buffer (PBS, 1% NP40, 0.5% sodium deoxycholate, 0.1% SDS, 2 mmol/L $CaCl_2$) containing fresh protease inhibitors on ice. Cell lysates were then passed repeatedly through a 21-gauge needle, incubated for 30 min on ice, and then centrifuged for 20 min at 4 ºC. Thereafter, the supernatants were harvested and the protein content was determined using the Bio-Rad protein assay.

Protein 10 μg was loaded into each lane, separated on a 7.5% SDS polyacrylamide gel and transferred onto nitrocellulose membrane in transblotting buffer containing 20 mmol/L Tris, 150 mmol/L glycine, and 20% methanol (pH 8.0). The membranes were blocked with blocking buffer consisting of 1% non-fat dry milk, 1% BSA, 0.05% Tween-20 in TBS buffer for 30 min and immunoblotted with the MoAb C-1821 diluted 1:3000 in blocking solution (Blotto B) for 45 min at room temperature. Thereafter, the membranes were washed three times, incubated with biotin-conjugated rabbit anti-mouse Ig G for 45 min, followed by incubation with streptavidin-conjugated horseradish peroxidase (HRP) for 30 min.

At the end of this incubation, the membranes were washed again three times and incubated with Amersham enhanced chemiluminesence (ECL) reagents for exactly 1 min. Excess ECL reagents were removed and the membranes were sealed in plastic wrap and exposed to ECL hyperfilms in a darkroom for 30 s. Then, the films were developed as for autoradiograph. Finally, the intensity of the two major cadherin bands on the hyperfilms was analyzed by scanning laser densitometry (discovery pDi densitometer, Pharmacia, Uppsala, Sweden). The intensity of control bands is expressed as 100%, and the others are expressed as percentage of respective control bands.

Membranes were also stripped of bound antibodies and re-probed by submerging them in stripping buffer (100 mmol/L 2-mercaptoethanol, 2% SDS, 62.5 mmol/L Tris-HCl, pH 6.7) and incubating at 50 °C for 30 min with occasional agitation. Then, the membranes were washed twice with TBS-Tween-20 at room temperature for 10 min. Following this, the membranes were blocked in blocking solution for 1 h after which immunodetection of HECD was performed using MoAb 004FD as described previously.

Statistical analysis Results of representative experiments are presented except where otherwise indicated. Biochemical determinations of ALP were performed in triplicate or quadruplicate and specific enzyme activity were presented as mean±SEM.

Statistical significance of difference within experiments was assessed using one factor analysis of variance (one way ANOVA). Values of *P* refer to a comparison of measured activity with that of control.

Results

Detection of cadherins expression in human bone marrow stromal cells Immunolocalization was performed to determine whether human bone-derived cells expressed cadherins using MoAb C-1821 in first passaged hBMSC and in hOP-7. Under fluorescence microscopy, there was no

staining for cadherins in the negative controls (such as mouse ascites fluid and PBS), while MC3T3-E1 cells were found to be stained for cadherin expression as a positive control (Figure 1B). Interestingly, strong cadherin expression was observed in first passaged hBMSC (Figure 1D) and hOP-7 (Figure 1F).

In the high-density cultures of hOP-7 cells, discrete nodules were formed and there were focal areas of intense immunostaining for cadherins in these nodules. However, staining at the periphery of the nodules was much weaker than at the center of the nodules. In addition, there was positive staining for ALP in the center of these nodules, while sparse ALP staining at the periphery of the nodules. This suggests an association between the expression of cadherins and ALP (Figure 1G and H), in which a close interaction of cells at the center of the nodules stimulates osteo-

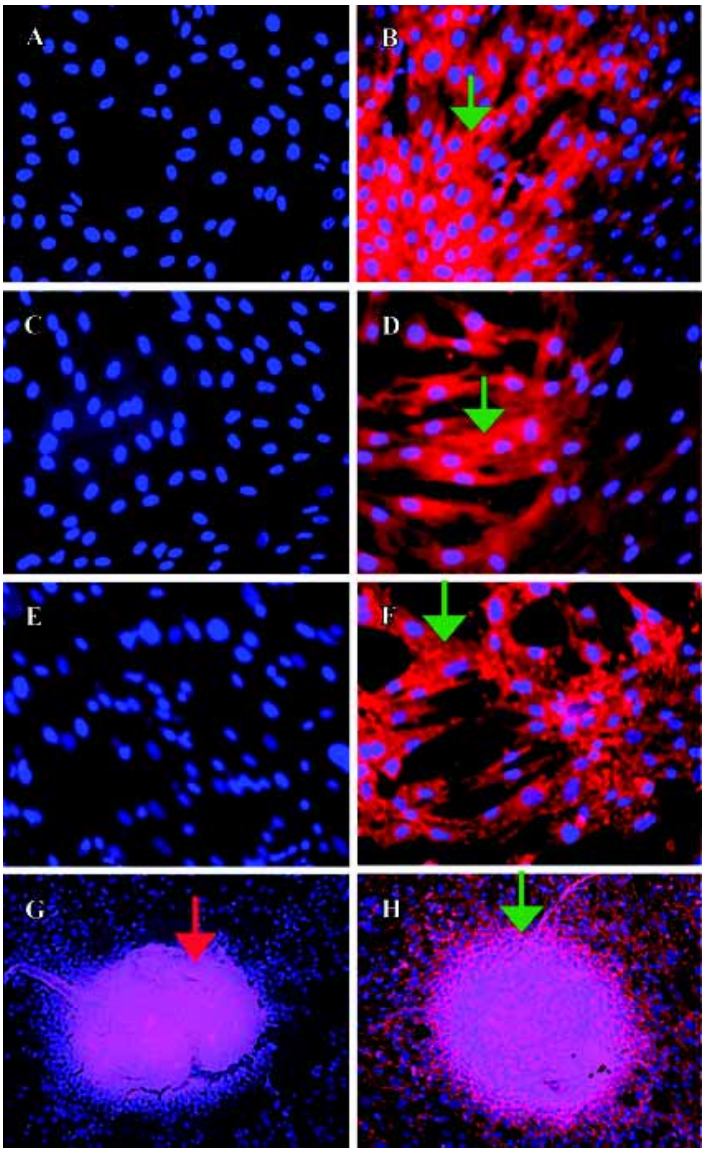

Figure 1. Expression of cadherins in MC3T3-E1 cells, hBMSCs, and hOP-7 cells. Cells cultured in coverslips or LabTek chamber slides were fixed with 4% paraformaldehyde, and immunolocalization was performed as described in 'Materials and methods'. In MC3T3 cells (A and B), hBMSC cells (C and D), and hOP-7 cells (E and F), an irrelevant isotype-matched antibody CB11 was used as control (A, C, and E) and cadherin expression was detected by MoAb C-1821 (B, D, and F). Associated expressions of ALP and cadherins were found in the nodules formed in the high density cultures of hOP-7 cell line. Histochemical staining for ALP (G) and immunolocalization of cadherin expression (H) using the MoAb C-1821 were carried out in these nodules. The green arrow points to the staining for cadherin expression and the red arrow indicates the ALP staining in a nodule. ×100

blast differentiation. Human E-cadherin (HECD) expression was confirmed in the positive control cells, MDCK cells. However, HECD was not detectable by immunolocalization in hBMSC (Figure 2D). To clarify the expression of cadherins in these cells identified by immmunolocalization as described above, Western blotting was performed using MoAb C-1821 in untreated hBMSC extracts and this revealed the presence of two bands (139.7 kDa and 118.6 kDa), associated with several small bands (Figure 3B).

After being stripped, the membranes previously used for detection of cadherins were immunoblotted again with mouse anti-human E-cadherin (MoAb 004FD). Although human E-cadherin was not detectable in hBMSC by immunocytochemistry using MoAb 004FD, it was demonstrated by Western blot using the same antibody (MoAb 004FD) and there was only one band with a M_r of approximately 118.6 kDa, which was corresponding to the major band detected using anti-pan-cadherin antibody and was different from that of cadherins (Figure 3D). This indicates that MoAb 004FD specifically recognizes human E-cadherin.

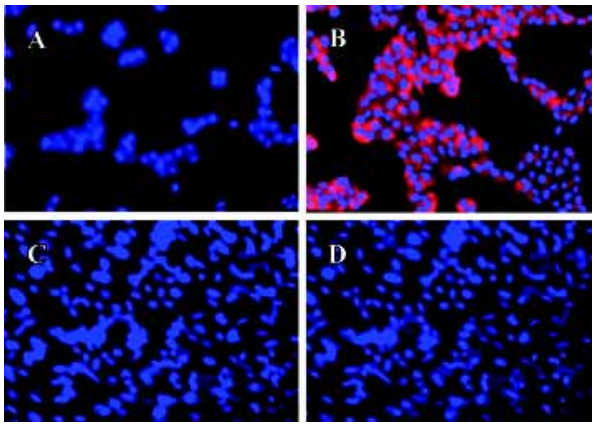

Figure 2. Expression of human E-cadherin in the kidney epithelium cell line MDCK (A and B) and lack of expression in hBMSCs (C and D). MDCK cells and hBMSCs cultured in coverslips were fixed with 4% paraformaldehyde, and immunolocalization was performed using anti-human E-cadherin MoAb 004FD. An irrelevant isotype-matched antibody CB11 was used as control (A and C) and anti-human E-cadherin MoAb 004FD was applied to detect human E-cadherin expression (B and D).

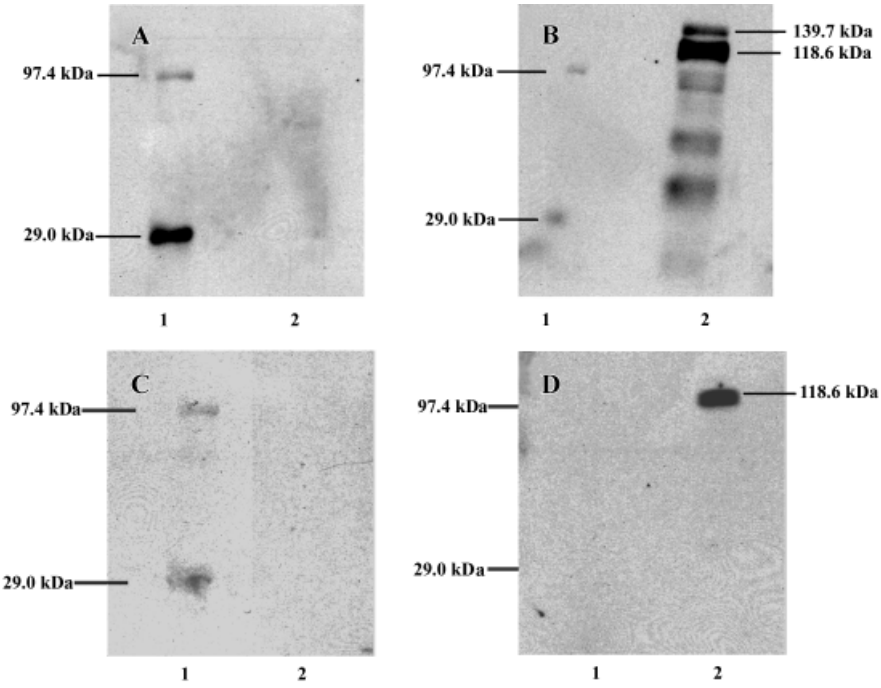

Figure 3. Detection of cadherin expression in hBMSCs by Western blot analysis. The cell layer was extracted with RIPA buffer and 10 μg proteins/lane were separated by 7.5% SDS-PAGE, and immunoblotted with either MoAb C-1821 or control antibody. After detection of cadherins using the anti-pan-cadherins MoAb, the membranes (A and B) were stripped of bound antibodies with a stripping buffer, and then immunoblotted for human E-cadherin expression. An irrelevant isotype-matched antibody CB11, which recognizes a fragment of denatured type II collagen, was used as a negative control (A and C). The anti-pan-cadherin MoAb C-1821 was applied to blot for cadherin expression (B) and the anti-human E-cadherin MoAb 004FD for human E-cadherin expression (D). Lane 1: molecular weight marker and Lane 2: cell lysates from untreated first passaged hBMSC.

Regulation of cadherins expression by osteotropic hormones and local growth factors hBMSC were treated with different agents for 7 d and the cell lysates were examined by Western blot. Using the ECL system, two major bands of cadherins with M_r 139.7 kDa and 118.6 kDa were examined using MoAb C-1821. These two bands were diminished in the 50 nmol/L $1,25(OH)_2D_3$-treated cellular extracts, in comparison to the control (Figure 4A). Similarly, in Dex-treated-cellular extracts, the two major bands were also abolished (Figure 4B). This suggests that $1,25(OH)_2D_3$ and Dex inhibit cadherin expression. With regards to 10 nmol/L PGE_2, band a (M_r about 139.7 kDa) was inhibited, but band b (M_r about 118.6 kDa) was increased nearly 1.5-fold. The expression of cadherins was also found an increase by PTH, E_2, bFGF, and TGF-β. All these agents increased band a more than band b in comparison to respective controls. PTH increased band a by more than 5-fold relative to the control and increased band b by only 1-fold. TGF-β enhanced band a by up to 3-fold and slightly stimulated band b. bFGF increased band a by up to 2-fold and also slightly enhanced band b (Figures 4C and D).

Effect of pan-cadherin MoAb on ALP activity To investigate a possible role of cadherins in the osteogenic differentiation of hBMSC, cadherins were blocked with MoAb C-

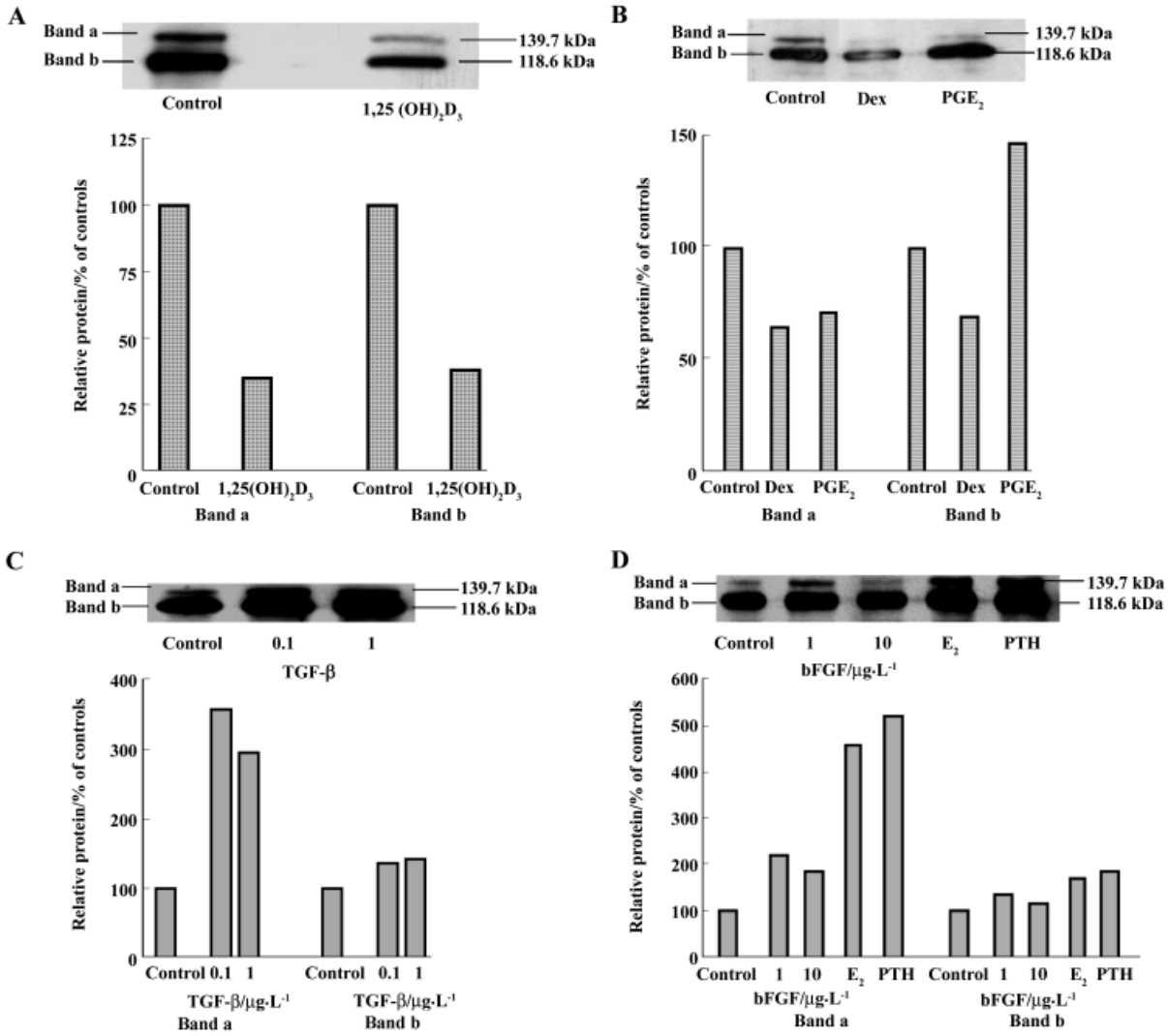

Figure 4. Regulation of cadherin expression by $1,25(OH)_2D_3$, dexamethasone (Dex), prostaglandin E2 (PGE_2), tumor necrosis factor (TGF)-β, basic fibroblast growth factor (bFGF), estradiol(E_2), and parathyroid hormone (PTH) in human bone marrow stromal cells. First passaged human bone marrow stromal cells were treated with $1,25(OH)_2D_3$ (50 nmol/L) (A), dexamethasone (10 nmol/L), PGE_2 (10 nmol/L) (B), TGF-β (0.1 and 1 μg/L) (C), bFGF (1 and 10 μg/L), estradiol (10 nmol/L), PTH (100 nmol/L) (D) for 7 d. Two major bands of cadherins (a and b) were examined using MoAb C-1821.

1821 and ALP activity was examined. In these experiments, treatment of hBMSC with MoAb C-1821 for 48 h increased the level of ALP activity to about 125.9% of control ($P<0.05$ *vs* control), and it also enhanced the effect of $1,25(OH)_2D_3$ on ALP activity ($P<0.05$ in experiment 1 and $P<0.01$ in experiment 2, compared to $1,25(OH)_2D_3$-treated cells) (Figure 5).

Discussion

There is a repertoire of cadherins expressed in osteoblasts. There are several subclasses of cadherins previously reported in cells of the osteoblast lineage, including E-cadherin[8], cadherin-4, cadherin-8, cadherin-11, protocadherin-43[14], and specific osteoblast-cadherin (OB-cadherins)[10]. In the present study, we demonstrated that cadherins were expressed in human osteoprogenitors. Cadherin expression was found to be associated with that of ALP in higher density cultures of hOP-7 cells. Furthermore, their expressions are regulated by osteotropic agents. These suggest that cadherins are involved in the process of osteogenic differentiation and some of the effects of these agents on bone are mediated, in part, via regulation of cadherins and possibly other cell adhesion molecules.

In the immunoblotting experiments, there were two major bands identified in hBMSC with molecular weights approximately 139.7 kDa and 118.6 kDa, along with several small bands using the anti-pan cadherin MoAb C-1821 (Figure 1), and this observation was consistent with a previous report using the same MoAb[4]. There was only one band with a M_r of 118.6 kDa using anti-human E-cadherin MoAb 004FD, which was in close agreement with human E-cadherin size (120 kDa)[21]. In this case, one of two major bands demonstrated by MoAb C-1821 may be human E-cadherin, another may be other cadherins, for example, osteoblast-like cadherin or N-cadherin, which was demonstrated to be specific for osteoblasts and its expression in the osteoblastic cells was up-regulated during differentiation, indicating an important role in osteogenic differentiation[10]. The results presented here are supported by a previous report in osteoblastic UMR106-H5 rat osteosarcoma cells[8]. It is necessary to determine whether all the polypeptides identified by the anti-pan cadherin MoAb C-1821 represent cadherin products encoded by distinct genes. Although roles of N-cadherin and osteoblast-like cadherins remains unknown, our data and others strongly suggest they are important regulators of osteoblast differentiation and osteogenesis and play a role in normal and pathological bone formation[8,10,13–18, 22].

On the basis of detecting cadherin expression in hBMSC, we investigated the regulation of cadherin expression by osteotropic hormones and local growth factors. All of these factors are thought to play important roles in bone remodeling[23]. Up until now, little was known of the role of cadherins in bone remodeling, particularly in osteogenic differentiation and whether osteotropic hormones and local growth factors regulate the expression of cadherin. With treatments of hBMSC with various hormones and growth factors for 7 d, it was observed that both $1,25(OH)_2D_3$ and dexamethasone inhibited the expression of cadherins. In contrast, PTH, PGE_2, estradiol, bFGF, and TGF-β increased the expression. However, these agents are found to differentially modulate these two bands. In these experiments, band a was enhanced more by certain agents than band b, and PGE_2 inhibited band

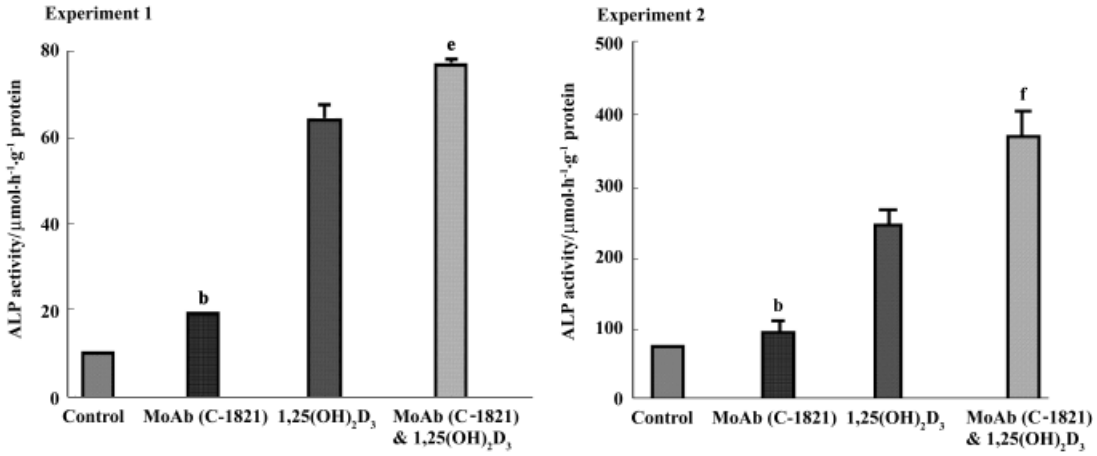

Figure 5. Effect of pan-cadherin antibody (MoAb C-1821) on alkaline phosphatase (ALP) activity in human bone marrow stromal cells (hBMSC). First passaged hBMSC were treated with the anti-pan-cadherin MoAb (1:200 dilution), in the presence or absence of $1,25(OH)_2D_3$ (50 nmol/L) for 48 h, in MEM containing 2% FCS. $^bP<0.05$ *vs* control. $^eP<0.05$, $^fP<0.01$ *vs* $1,25(OH)_2D_3$ treatment.

a, but increased band b. These results suggest that there may be more than one subclass of cadherins expressed in hBMSC and osteotropic hormones and growth factors may differentially regulate these individual cadherins. Certain factors, such as TGF-β, PTH, and E_2, had more specific effects on Band a, and these two bands may represent different cadherin expressions. PTH was shown to increase the expression of E-cadherin in mouse MC3T3-E1 osteoblastic cells[8] and increase mRNA level of the neural-cadherin-like adhesion molecule (N-CAD) *in vitro* and *in vivo*[15]. Dexamethasone was shown to decrease N-CAD and to completely inhibit cadherin mRNA in rats[15]. In addition, dexamethasone was also found to increase steady state mRNA for cadherin-4, but decrease mRNA expression for N-cadherin[14]. However, steady-state mRNA expression for protocadherin and cadherin-11 was not affected by dexamethasone[14]. Estradiol was shown to cause a rapid and significant increase in the ovarian E- and N-cadherin mRNA levels in mice *in vivo*[24]. It was reported that TGF-β up-regulated N-cadherin expression at mRNA level in mesenchymal cells obtained from early chick limb bud, which can differentiate into chondrocytes when plated at a high density[25].

It was known that osteogenic differentiation of hBMSC was stimulated by $1,25(OH)_2D_3$[12] and dexamethasone[11], and the proliferation of these cells is inhibited by the two agents[11,12]. PTH was shown to be mitogenic for human osteoblast-like cells[26]. Estradiol stimulates the proliferation of osteoblast-like cells derived from explants of rat trabecular bone and the immortalized rat calvarial RCT-3 cell line[27], mouse MC3T3-E1 osteoblastic cells[28] and human osteoblastic osteosarcoma SAOS-2 cell line[29]. The local factor PGE_2 was demonstrated to stimulate the proliferation of bone cells[30]. In addition, TGF-β and bFGF inhibit osteogenic differentiation of hBMSC and stimulate cell proliferation[12,31]. Taken together, it seems likely that the agents that promote osteogenic differentiation and inhibit cell proliferation may decrease certain cadherin expression, while other agents that inhibit osteogenic differentiation and stimulate cell proliferation may increase certain cadherin expressions, indicating that an increase in cadherin expression is associated with cell proliferation and a decrease in cadherin expression with osteogenic differentiation at a 'specific stage' of differentiation.

Because the C-terminal regions of cadherins are essential domains for function, and the anti-pan cadherin MoAb C-1821 recognizes this site, this MoAb was used as a function-perturbing antibody for examining a possible role for cadherins in osteogenic differentiation of hBMSC. A perturbing function of the cadherins with the MoAb caused the fibroblast-like hBMSC to become more or less ploygonal observed under microscope (data not shown here). It was also observed that this block with the MoAb significantly increased alkaline phosphatase activity, and enhanced 1,25 $(OH)_2D_3$-induced increase in ALP activity in which first passaged hBMSC were induced for osteogenic differentiation. This indicates that cadherins may play a role in differentiation of hBMSC. Based on 1:500 dilution used in immunolocalization described previously, a 1:200 dilution was used in these experiments. It remains possible that ALP activity may be increased more if higher concentrations of the MoAb are used. However, the MoAb C-1821 is expensive, so reasonable dilution 1:200 was applied to the experiments. As mentioned above, $1,25(OH)_2D_3$ inhibited the cadherin expression in hBMSC and $1,25(OH)_2D_3$ promoted osteogenic differentiation[12], including enhancement of ALP activity and osteocalcin expression. These suggest that the role of $1,25(OH)_2D_3$ on osteoblast differentiation may be partially through mediating the cadherin expression. There may be other cell adhesion molecules involved in the mediation of $1,25(OH)_2D_3$-induced effect on ALP activity. A role for E-cadherin in osteogenic differentiation had also been indicated in the fetal rat calvarial (FRC) osteoblast system. In these FRC cultures, treatment of FRC osteoblasts with polyclonal antibodies to murine E-cadherin significantly increased mineralized bone nodule formation[32]. Taken together, these data indicate that some specific cadherins may negatively regulate osteogenic differentiation at a 'specific stage' during osteogenic differentiation.

In conclusion, the effects of osteotropic hormones and local growth factors on osteogenic differentiation of hBMSC may be, at least, partially via regulation of cell adhesion molecules, such as cadherins. Cadherins may function as mediators of transition between proliferation and differentiation and then negatively regulate osteogenic differentiation.

References

1 Edelman GM, Crossin KL. Cell adhesion molecules: implications for a molecular histology. Annu Rev Biochem 1991; 60: 155–90.
2 Aubin JE. Advances in the osteoblast lineage. Biochem Cell Biol 1998; 76: 899–910.
3 Takeichi M. Cadherin cell adhesion receptors as a morphogenetic regulator. Science 1991; 251: 1451–5.
4 Geiger B, Volberg T, Ginsberg D, Bitzur S, Sabanay I, Hynes RO. Broad spectrum pan-cadherin antibodies, reactive with the C-terminal 24 amino acid residues of N-cadherin. J Cell Sci 1990; 97 (Pt 4): 607–14.
5 Geiger B, Ayalon O. Cadherins. Annu Rev Cell Biol 1992; 8: 307–32.
6 Oberlender SA, Tuan RS. Spatiotemporal profile of N-cadherin

expression in the developing limb mesenchyme. Cell Adhes Commun 1994; 2: 521–37.
7 Ahdjoudj S, Lasmoles F, Holy X, Zerath E, Marie PJ. Transforming growth factor beta2 inhibits adipocyte differentiation induced by skeletal unloading in rat bone marrow stroma. J Bone Miner Res 2002; 17: 668–77.
8 Babich M, Foti LR. E-cadherins identified in osteoblastic cells: effects of parathyroid hormone and extracellular calcium on localization. Life Sci 1994; 54: PL201–8.
9 Mbalaviele G, Chen H, Boyce BF, Mundy GR, Yoneda T. The role of cadherin in the generation of multinucleated osteoclasts from mononuclear precursors in murine marrow. J Clin Invest 1995; 95: 2757–65.
10 Okazaki M, Takeshita S, Kawai S, Kikuno R, Tsujimura A, Kudo A, *et al*. Molecular cloning and characterization of OB-cadherin, a new member of cadherin family expressed in osteoblasts. J Biol Chem 1995; 269: 12092–8.
11 Cheng SL, Yang JW, Rifas L, Zhang SF, Avioli LV. Differentiation of human bone marrow osteogenic stromal cells *in vitro*: induction of the osteoblast phenotype by dexamethasone. Endocrinology 1994; 134: 277–6.
12 Liu P, Oyajobi BO, Russell RG, Scutt A. Regulation of osteogenic differentiation of human bone marrow stromal cells: interaction between transforming growth factor-beta and 1,25(OH)(2) vitamin D(3) *in vitro*. Calcif Tissue Int 1999; 65: 173–80.
13 Castro CH, Shin CS, Stains JP, Cheng SL, Sheikh S, Mbalaviele G, et al. Targeted expression of a dominant-negative N-cadherin *in vivo* delays peak bone mass and increases adipogenesis. J Cell Sci 2004; 117(Pt 13): 2853–4.
14 Cheng SL, Lecanda F, Davidson MK, Warlow PM, Zhang SF, Zhang L, *et al*. Human osteoblasts express a repertoire of cadherins, which are critical for BMP-2-induced osteogenic differentiation. J Bone Miner Res 1998; 13: 633–4.
15 Ferrari SL, Traianedes K, Thorne M, Lafage-Proust MH, Genever P, Cecchini MG, *et al*. A role for N-cadherin in the development of the differentiated osteoblastic phenotype. J Bone Miner Res 2000; 15: 198–208.
16 Kawaguchi J, Azuma Y, Hoshi K, Kii I, Takeshita S, Ohta T, *et al*. Targeted disruption of cadherin-11 leads to a reduction in bone density in calvaria and long bone metaphyses. J Bone Miner Res 2001; 16: 1265–71.
17 Marie PJ, Debiais F, Hay E. Regulation of human cranial osteoblast phenotype by FGF-2, FGFR-2, and BMP-2 signaling. Histol Histopathol 2002; 17: 877–85.
18 Marie PJ. Role of N-cadherin in bone formation. J Cell Physiol 2002; 190: 297–305.
19 Houghton A, Oyajobi BO, Foster GA, Russell RG, Stringer BM. Immortalization of human marrow stromal cells by retroviral transduction with a temperature sensitive oncogene: identification of bipotential precursor cells capable of directed differentiation to either an osteoblast or adipocyte phenotype. Bone 1998; 22: 7–16.
20 Vandenbossche GM, De Bruyne GK, Bruyneel EA, Clemminck G, Vleminckx K, *et al*. Micro-encapsulation of MDCK-ras-e cells prevents loss of E-cadherin invasion-suppressor function *in vivo*. Int J Cancer 1994; 57: 73–80.
21 Wheelock MJ, Knudsen KA. Cadherins and associated proteins. In Vivo 1991; 5: 505–13.
22 Nagahata M, Tsuchiya T, Ishiguro T, Matsuda N, Nakatsuchi Y, Teramoto A, *et al*. A novel function of N-cadherin and connexin 43: marked enhancement of alkaline phosphatase activity in rat calvarial osteoblast exposed to sulfated hyaluronan. Biochem Biophys Res Commun 2004; 315: 603–11.
23 Canalis E. Insulin like growth factors and the local regulation of bone formation. Bone 1993; 14: 273–6.
24 MacCalman CD, Farookhi R, Blaschuk OW. Estradiol regulates *N*-cadherin mRNA levels in the mouse ovary. Dev Genet 1995; 16: 20–4.
25 Tsonis PA, Del Rio-Tsonis K, Millan JL, Wheelock MJ. Expression of N-cadherin and alkaline phosphatase in chick limb bud mesenchymal cells: regulation by 1,25-dihydroxyvitamin D3 or TGF-beta 1. Exp Cell Res 1994; 213: 433–7.
26 MacDonald BR, Gallagher JA, Russell RG. Parathyroid hormone stimulates the proliferation of cells derived from human bone. Endocrinology 1986; 118: 2445–9.
27 Ernst M, Heath JK, Rodan GA. Estradiol effects on proliferation, messenger ribonucleic acid for collagen and insulin-like growth factor-I, and parathyroid hormone-stimulated adenylate cyclase activity in osteoblastic cells from calvariae and long bones. Endocrinology 1989; 125: 825–33.
28 Masuyama A, Ouchi Y, Sato F, Hosoi T, Nakamura T, Orimo H. Characteristics of steroid hormone receptors in cultured MC3T3-E1 osteoblastic cells and effect of steroid hormones on cell proliferation. Calcif Tissue Int 1992; 51: 376–81.
29 Slootweg MC, Ederveen AG, Schot LP, Schoonen WG, Kloosterboer HJ. Oestrogen and progestogen synergistically stimulate human and rat osteoblast proliferation. J Endocrinol 1992; 133: R5–8.
30 Somjen D, Waisman A, Weisman J, Kaye AM. Nonhypercalcemic analogs of vitamin D stimulate creatine kinase B activity in osteoblast-like ROS 17/2.8 cells and up-regulate their responsiveness to estrogens. Steroids 1998; 63: 340–3.
31 Pri-Chen S, Pitaru S, Lokiec F, Savion N. Basic fibroblast growth factor enhances the growth and expression of the osteogenic phenotype of dexamethasone-treated human bone marrow-derived bone-like cells in culture. Bone 1998; 23: 111–7.
32 Kato Y, Boskey A, Spevak L, Dallas M, Hori M, Bonewald LF. Establishment of an osteoid preosteocyte-like cell MLO-A5 that spontaneously mineralizes in culture. J Bone Miner Res 2001; 16: 1622–33.

Acta Pharmacologica Sinica 2005 Jun; 26 (6): 714–720

Full-length article

Transforming growth factor-β1 gene polymorphisms associated with chronic obstructive pulmonary disease in Chinese population[1]

Zhi-guang SU[2], Fu-qiang WEN, Yu-lin FENG, Min XIAO, Xiao-ling WU

Laboratory of Pulmonary Medicine, West China Hospital, Sichuan University; Key Laboratory of Biotherapy of Human Disease, Ministry of Education, Chengdu 610041, China

Key words

chronic obstructive pulmonary disease; transforming growth factor-β1; single nucleotide polymorphisms; haplotypes

[1] Project supported by the National Natural Science Foundation of China (No 30200161 and No 30370628).
[2] Correspondence to Dr Zhi-guang SU.
Phn 86-28-8542-3484
E-mail zhiguang_su@hotmail.com

Received 2004-11-01
Accepted 2005-01-07

doi: 10.1111/j.1745-7254.2005.00085.x

Abstract

Aim: To determine the frequencies of polymorphism and haplotype in the transforming growth factor-beta 1 (TGF-β1) gene promoter in the Chinese population and to investigate the susceptibility of this population to chronic obstructive pulmonary disease (COPD). **Methods:** The target fragments of the TGF-β1 gene promoter were amplified and analyzed by polymerase chain reaction-restriction fragment length polymorphism technique in 84 COPD patients and 97 age- and sex-matched healthy controls. The test for Hardy-Weinberg equilibrium was performed using HWE program of the LINKUTIL package and statistical analysis was carried out with the SPSS statistical package. An expectation maximization algorithm was used for the pairwise linkage disequilibrium test and haplotype analysis. **Results:** More carriers of the -800A allele, or fewer carriers of the -509T allele, were detected in the COPD patients compared with the non-symptomatic control subjects [for the -800A allele, 29.8% *vs* 14.4%, respectively, χ^2=6.257, degrees of freedom (df)=1, *P*=0.012; for the -509T allele, 27.3% *vs* 44.3%, respectively, χ^2=5.582, df=1, *P*=0.018]. The prevalence of the -800A allele was significantly higher in the COPD patients than in control subjects (*P*=0.009), whereas the frequency of the -509T allele was significantly higher in control subjects than in the COPD patients (*P*=0.008). In addition, this distribution tendency for the -800A or -509T allele was similar in heavy smokers (smoking history ≥20 pack years); (number of packs of cigarettes per day multiplied by the number of years of smoking) χ^2=7.235, *P*=0.007, and χ^2=5.636, *P*=0.018, respectively). The linkage disequilibrium was found between -800 G→A and -509 C→T (*D*>0.60, *P*<0.0001), and the frequency of the AC haplotype, consisting of the least common base at -800 and the most common base at -509, was significantly higher in patients with COPD than in controls (0.056 *vs* 0.021, *P*<0.05). **Conclusions:** The single nucleotide polymorphism (SNP) in the TGF-β1 gene promoter might be associated with COPD, and the -800A/-509C haplotype is possibly one of the susceptibility factors for COPD.

Introduction

Chronic obstructive pulmonary disease (COPD) is currently the leading cause of disability-adjusted life years. Globally, it is projected to be the 3rd most important cause of death by the year 2020, and it is estimated that the national prevalence is up to 3.1% in the Chinese adult population. Cigarette smoking is the major risk factor for COPD; however, only approximately 15% of smokers develop clinically relevant airflow obstruction[1]. This variation in the susceptibility to cigarette smoke in combination with the familiar aggregation of COPD suggests that there may be a genetic component to the development of COPD. Multiple studies in diverse populations have shown evidence for a large

genetic contribution to the variability in pulmonary function and for the familial aggregation of COPD patients[2,3]. As expected, segregation analysis suggests that multiple genes may be involved. At present, however, only a single gene, α1-antitrypsin, a potent inhibitor of inflammatory cell protease in the lung, has been unequivocally implicated in the development of COPD. The association between the ZZ type polymorphism of this gene and COPD has been established[4]. Furthermore, the associations between COPD and polymorphisms in several other genes of potential importance to COPD pathogenesis also have been studied. These include α1-antichymotrypsin[5], microsomal epoxide hydrolase[6], vitamin D-binding protein[7], and tumor necrosis factor-α[8].

Transforming growth factor-β (TGF-β) is a multifunctional cytokine that regulates the proliferation and differentiation of a wide variety of cell types *in vitro*. In humans, the TGF-β family includes 3 isoforms (TGF-β1, TGF-β2, and TGF-β3) with great structural and functional similarities[9]. TGF-β1 is the most abundant isoform and is highly conserved in primary sequence through evolution. It is synthesized as precursor latent forms (390 amino acids long), which have no known biological activity[10]. The active form of TGF-β1 is released proteolytically from the precursor form[11] and consists of a disulphide-linked 25 kDa homodimer of two 112 amino acid peptides. The coding region of the TGF-β1 gene consists of 7 exons and 6 introns[12].

The expression of TGF-β1 is influenced by polymorphisms in the TGF-β1 gene, and some of these polymorphisms may be associated with COPD and other diseases[13–15]. Wu *et al* investigated the association between the single nucleotide polymorphism T+869C (Leu10Pro) at exon 1 of the TGF-β1 gene with COPD in a Caucasian Americans white population[16]. There are several registered polymorphisms within the TGF-β1 gene that might be functional and might be associated with COPD. In particular, a promoter polymorphism at -509 C/T is associated with the diagnosis of asthma and may enhance TGF-β1 gene transcription[17], but whether there is an association between the -509 C/T polymorphism and COPD has not yet been investigated. The aim of present study was to screen for DNA sequence variants in the TGF-β1 promoter, to establish the prevalence of each genotype in individuals with COPD and controls in a Chinese population, and to identify any haplotypes associated with a predisposition to COPD.

Materials and methods

Subjects Eighty-four patients with COPD were recruited from the West China Hospital, Sichuan University, Chengdu, China. The definition of COPD was consistent with that in the American Thoracic Society (ATS) consensus statement. The patients had a history of chronic or recurrent productive cough for >2 years and decreased maximum expiratory flow, which had been slowly progressive and irreversible. The presence of other lung or cardiac diseases as the cause of patient symptoms was excluded by clinical and radiographic examinations. The criteria for enrolment were as follows: (i) individuals with a forced expiratory volume in 1 s (FEV_1)<70% of predicted, an FEV_1/forced vital capacity (FVC) ratio of <70%, and an increase in FEV_1 of <12% 15 min after the inhalation of 400 μg Fenoterol HBr MDI (Berotec; Boehringer Ingelheim, Ridgefield, CT, USA); and (ii) patient consent to participate in the study. Most of the patients were receiving oral methylxanthine, inhaled anticholinergic agents, and inhaled β2-agonists as needed. The patient's name, age, sex, family history, smoking habits, the number of cigarettes smoked, the duration of diseases, and chest radiographic findings were recorded. Pulmonary function testing (CHESTAC-33-8800, Chest Ltd, Tokyo, Japan) was performed according to the ATS performance requirements. Ninety-seven unrelated, age-matched healthy subjects, who had no known medical illness or family disorders and were not taking any medications, acted as control subjects. This study was approved by the Internal Review Board of the West China Hospital, Sichuan University, and signed informed consent forms were obtained from all subjects.

DNA preparation and polymerase chain reaction amplification Genomic DNA was prepared from peripheral blood leukocytes using the "salting-out"[18] procedure and stored at 4 °C. Fragments containing the single nucleotide polymorphism (SNP) G-800A or T-509C were amplified by polymerase chain reaction (PCR). The primer sequence was based on the DNA sequence from GenBank accession numbers NM_000660 and X05839. For the detection of polymorphism at nucleotide acid -800, the primer pairs were 5'-CTGGCAGTTGGCGAGAACA-3' (sense) and 5'-TAGAAAGGACAGAAGCGGTG-3' (antisense); and the generated PCR product size was 326 base pairs (bp). The primer pairs for delineating the polymorphism at nucleotide acid -509 were 5'-CCAGCTAAGGCATGGC ACCG-3' (sense) and 5'-GCGGTGTGGGTCACCAGAGA-3' (antisense); the PCR product size from these primers was 300 bp. Each PCR amplification mixture contained 0.1 μg genomic DNA, 0.2 μmol/L primers, 50 μmol/L deoxyribonucleotide triphosphate (dNTP), and standard PCR buffer in a total volume of 50 μL. The reaction mixture was preheated at 94 °C for 4 min. Subsequently, 0.4 units of *Taq* polymerase was added. The 30 cycles of PCR amplification

were performed with a temperature profile consisting of denaturation at 94 °C for 45 s, annealing at 58 °C and 61 °C for 30 s, extension at 72 °C for 30 s, and final extension at 72 °C for 10 min. The reactions were carried out in a PTC-200 Programmable Thermal Controller (MJ Research, Watertown, MA, USA).

Genotyping Genotyping for the -800G/A and -509C/T polymorphisms was performed by digestion of PCR product with the restriction enzymes MaeIII and SauI (Amersham Biosciences, Piscataway, NJ, USA), respectively. After PCR, 10 μL of the reaction mixture was digested with 1 U MaeIII or SauI in 1×buffer M (Amersham Biosciences) for 3 h at 37 ºC. The digest mixture was resolved on a 2.0% agarose gel stained with ethidium bromide. For the -800G/A polymorphism, DNA from individuals with the homozygous G genotype (GG) produced 1 band at 326 bp; the homozygous A genotype (AA) produced 2 bands, 1at 206 bp and 1 at 120 bp; and the heterozygous genotype (GA) produced all 3 bands. A gel of the restriction fragment length polymorphism digestion products is shown in Figure 1A. For the -509C/T polymorphism, individuals with the homozygous C genotype (CC) produced 1 band at 300 bp; the homozygous T genotype (TT) produced 2 bands, 1 at 202 bp and 1 at 98 bp; and the heterozygous genotype (CT) produced all 3 bands, as shown in Figure 1B. Control DNA samples representative of each of the different genotypes were included in each digestion. Repeat genotyping was performed on 5 of every 100 samples chosen by random selection. Genotyping errors are estimated to have occurred at a frequency of <1%.

Statistical analysis Data analyses were performed with the Statistical Package for the Social Science (SPSS, version 10.0, Inc in Chicago, Illinois, USA). Data were expressed as mean±SEM. The significance level for statistical tests was taken to be 0.05. Deviation of the genotype counts from the Hardy-Weinberg equilibrium was tested using a χ^2 test with 1 degree of freedom (df). Differences between the patients with COPD and the controls with respect to the allele frequencies and genotype distributions were analyzed by χ^2 test or Fisher's exact test when necessary. Haplotype frequencies for pairs of alleles, as well as χ^2 values for allele associations, were estimated by the Estimating Haplotype-frequencies software program[19–20]. Linkage disequilibrium coefficients $D'=D/D_{max}$ (D is the difference between the observed and the expected gamete frequency, D_{max} is the maximum disequilibrium, which occurs when all double heterozygotes are either in linkage phase (AB/ab) or in repulsions phase (Ab/aB). were calculated by the 2LD program[21].

Results

General characteristics The study population consisted of 84 patients with COPD and 97 control subjects (Table 1).

Table 1. General characteristics of the study population (mean±SEM). FEV_1, forced expiratory volume in 1 s; FVC, forced vital capacity.

Variable	Controls (*n*=97)	COPD (*n*=84)	*P*
Age/years	65±8	63±9	>0.1
No. men/%	83 (85.6)	74 (88.1)	>0.1
Smoking history			
0–20 pack years[1]	26	17	>0.05
≥20 pack years	71	67	>0.05
FEV_1	1.87±0.60	0.97±0.32	<0.01
FEV_1/Predicted/%	93.7±3.4	49.0±0.4	<0.01
FEV_1/FVC	78.0±4.6	59.2±8.3	<0.01

[1] Pack years: number of packs of cigarettes per day multiplied by the number of years of smoking.

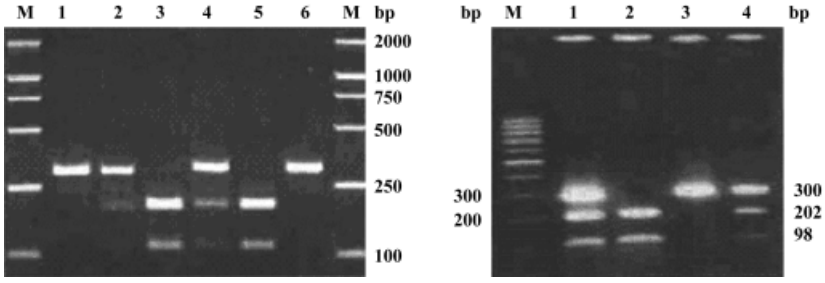

Figure 1. Agarose gel showing restriction fragment length polymorphism for polymorphisms in the transforming growth factor-β1 gene at nucleotide -800 (A) and nucleotide -509 (B). (A) M: marker, 250 bp DNA ladder; lanes 1 and 6 show the GG genotype; lanes 2 and 4 show the GA genotype, and lanes 3 and 5 show the AA genotype. (B) M, 100 bp DNA ladder; lane 2 shows the TT genotype; lane 3 shows the CC genotype; and lanes 1 and 4 show the TC genotype.

The COPD cases and control subjects did not differ significantly in sex, age, and smoking history characteristics. The parameters used for FEV_1, FEV_1/predicted, and FEV_1/FVC were significantly decreased in the COPD case subjects compared with the controls (Table 1, $P<0.01$).

Distribution of the G-800A and C-509T in COPD patients and controls To determine the prevalence of the SNP G-800A and C-509T, we screened them in all the 84 COPD patients and in the 97 controls. The genotype distribution and allele frequencies are listed in Table 2. No deviation from Hardy-Weinberg equilibrium (for SNP G-800A, χ^2= 1.379, df=1, P=0.240 in the COPD group, χ^2=1.737, df=1, P= 0.188 in controls; for SNP C-509T, χ^2=1.488, df=1, P=0.222 in the COPD group, χ^2=2.400, df=1, P=0.121 in controls) was noted in the COPD or control groups. As a result, more carriers of the -800A allele, or fewer carriers of -509T allele, were detected in the COPD patients compared with in the control subjects (for the -800A allele, 29.8% *vs* 14.4%, χ^2= 6.257, df=1, P=0.012; for the -509T allele, 27.3% *vs* 44.3%, χ^2=5.582, df=1, P=0.018). The prevalence of the -800A allele was significantly higher in COPD patients than in control subjects (P=0.009), whereas the frequency of -509T allele was significantly decreased in COPD patients compared with that in control subjects (P=0.008).

Relationship between cigarette smoking and the distribution of *TGF-β1* gene polymorphisms The allele and genotype distributions were compared in heavy smokers (smoking history ≥20 pack years (number of packs of cigarettes per day multiplied by the number of years of smoking) to determine whether the prevalence of different alleles or genotypes was associated with smoking. Results showed that the frequency of the -800A allele was still significantly higher and the frequency of the -509T allele was significantly decreased in patients with COPD (group A) than in control subjects (group B) (χ^2=7.235, P=0.007, and χ^2=5.636, P= 0.018, respectively; Table 3).

Linkage disequilibrium between -800G/A and -509C-T polymorphisms in the *TGF-β1* gene We analyzed the relationship between -800G/A and -509C-T polymorphisms and their effects on COPD. The extent of D in pairwise combinations of alleles in loci at the *TGF-β1* promoter was estimated by means of maximum likelihood from the frequency of diploid genotypes in the patients with asthma and controls. Haplotype frequencies and the coefficient of linkage disequilibrium (D') are given in Table 4. It was clear that the D' values for polymorphisms at nucleotides -800 bp and -509 bp

Table 2. Frequency distributions of the transforming growth factor-β1 gene in patients with chronic obstructive pulmonary disease versus controls.

SNP[1]	Genotype	Control *n* (%)	Case *n* (%)	χ^2	*P*	Allele	Control *n* (%)	Case *n* (%)	χ^2	*P*
-800 G/A	GG	83 (85.6)	59 (70.2)	6.47	0.039	GA	179 (92.3)	140 (83.3)	6.866	0.009
	GA	13 (13.4)	22 (26.2)				15 (7.7)	28 (16.7)		
	AA	1 (1)	3 (3.6)							
-509 C/T	CC	54 (55.7)	61 (72.6)	6.627	0.036	CT	143 (73.7)	143 (85.1)	7.064	0.008
	CT	35 (36.1)	21 (25.0)				51 (26.3)	25 (14.9)		
	TT	8 (8.2)	2 (2.4)							

[1]SNP: single nucleotide polymorphism age (years).

Table 3. Distribution of the alleles and genotypes of the transforming growth factor-β1 gene in smokers with or without chronic obstructive pulmonary disease.

Group	*n*	-800 G/A					-509 C/T				
		Genotypes (*n*/%)			Alleles (*n*/%)		Genotypes (*n*/%)			Alleles (*n*/%)	
		GG	GA	AA	G	A	CC	CT	TT	C	T
A	67	44 (65.7)	21 (31.3)	2 (3.0)	109 (81.3)	25 (18.7)	47 (70.1)	19 (28.4)	1 (1.5)	103 (72.5)	21 (15.7)
B	71	60 (84.5)	11 (15.5)	0 (0.0)	131 (92.3)	11 (7.7)	37 (52.1)	29 (40.8)	5 (7.1)	113 (84.3)	39 (27.5)

Table 4. Estimate of pairwise haplotype frequencies and disequilibrium statistics.

Polymorphic sites and subjects	Estimated haplotype frequency				D (difference between observed and expected gamete frequency)	D_{max} (maximum disequilibrium)	*D'* (linkage disequilibrium coefficients)	*P*
G-800A/C-509T	GC	AC	GT	AT				
COPD patients	0.795	0.056	0.088	0.061	0.086	0.124	0.691	<0.0001
Controls	0.716	0.021	0.207	0.056	0.036	0.057	0.632	<0.0001

differ significantly from zero, and the frequency of the AC haplotype, consisting of the least common base at -800 and the most common base at -509, was significantly higher in patients with COPD than in controls (0.056 *vs* 0.021, respectively, $P<0.05$).

Discussion

We have shown that the A allele at position -800 in the promoter region of the TGF-β1 gene is more common and the T allele at position -509 is less common in subjects with COPD than in control subjects. Some evidence has shown a correlation between the 2 polymorphisms (G-800A, C-509T) and the concentration of TGF-β1 in human plasma[22]. The G-800A substitution is thought to disrupt a consensus half-site for the binding of the nuclear transcription factor CRE (cyclic AMP-responsive element)-binding protein, and it was found that the presence of the A allele is significantly associated ($P<0.05$) with lower levels of total TGF-β1 in the circulation[22]. Conversely, the -509T allele has been shown to be associated with higher levels of TGF-β1 in serum and increased TGF-β1 mRNA in peripheral blood mononuclear cells[22]. These findings indicate that the G-800A and C-509T polymorphisms may be involved in the modulation of expression of the TGF-β1 gene and therefore a predisposition for COPD could be linked to particular alleles of this gene. The high producer genotype for TGF-β1 may protect against the development of COPD. A recent study by Wu *et al* has shown that the +869Pro allele, associated with higher serum concentrations of TGF-β1, was less common in subjects with COPD than in control subjects[16].

A recent study using an animal model of emphysema adds plausibility to the suggestion that increased production of TGF-b1 can protect against the development of COPD. The integrin $\alpha_v\beta_6$ activates latent TGF-β[23]. Mice that lack this integrin (Itgb6 null mice) develop age-related emphysema. When transgenes for TGF-β1 were inserted into these mice so that they constitutively expressed active TGF-β1, the changes in the lung associated with the deletion of the integrin gene no longer occurred. In these mice, the productive effects of TGF-β1 appear to be related to inhibition of macrophage metalloelastase (MMP12), which degrades elastin.

More than 100 SNP and other genetic variants have been identified in genes of the TGF-β1 signaling pathway, and a few of these have been associated with disease[13]. C-509T was chosen as the sole candidate SNP because previous studies suggest that it is associated with altered serum levels of TGF-β1, asthma diagnosis, asthma severity, and serum IgE levels[22,24,25]. For example, in a study involving 84 monozygous and 86 dizygous twins, Grainger *et al* showed that TGF-β1 levels in plasma were under genetic control (heritability estimate 0.54) with the C-509T SNP being responsible for 8.2% of the additive genetic variance[22]. The T allele was associated with higher levels of TGF-β1 than the C allele was, and there was an allele dose effect, with the highest levels in TT individuals (7.62 ng/mL), intermediate levels in CT individuals (5.06 ng/mL), and the lowest levels in CC individuals (3.83 ng/mL)[25].

A wide variety of functions have been attributed to TGF-β1 (such as reduction of inflammation and promotion of wound healing[26], immunosuppression[27], regulation of cell proliferation, differentiation and migration[9]), and regulation of extracellular matrix production[28,29]. Some of these functions could protect against the development of COPD. TGF-β1 can inhibit matrix metallopro-teinases that may contribute to the development of emphysema through the digestion of elastic fibers[30,31]. It also promotes the formation of elastin[32,33] and this could help repair damage to the lungs of individuals who are smokers and who are risk of developing COPD. Recently, TGF-β1 was located on chromosome 19q, a genomic region linked to the diagnosis of COPD in some genome-wide scans[34]. Our study strengthens this association between TGF-β1 and COPD.

In summary, our results suggest that genetic variation at

the promoter of the TGF-β1 gene might be associated with TGF-β1 levels and predisposition to the complex COPD. The distributions of TGF-β1 polymorphisms are different between different ethnic groups. Further replication is essential for the validation of this association in Caucasian, African, or other ethnic populations, and, to elucidate the role of TGF-β1 in COPD, future work is needed to establish the exact effect of TGF-β1 polymorphisms on the activation process of the protein and its function.

References

1 Davis RM, Novotny TE. The epidemiology of cigarette smoking and its impact on chronic obstructive pulmonary disease. Am Rev Respir Dis 1989; 140: S82–S84.

2 Molfino NA. Impact of basic research on tomorrow's medicine: genetics of COPD. Chest 2004; 125: 1929–40.

3 Kauffmann F, Tager IB, Munoz A, Speizer FE. Familial factors related to lung function in children aged 6–10 years. Results from the PAARC epidemiologic study. Am J Epidemiol 1989; 129: 1289–99.

4 Poller W, Meison C, Olek K. DNA polymorphisms of the α1-antitrypsin gene region in patients with chronic obstructive pulmonary disease. Eur J Clin Invest 1990; 20: 1–7.

5 Samilchuk EI, Chuchalin AG. Mis-sense mutation of α1-antichymotrypsin gene and chronic lung disease [letter]. Lancet 1993; 342: 624.

6 Smith CAD, Harrison DJ. Association between polymorphism in gene for microsomal epoxide hydrolase and susceptibility to emphysema. Lancet 1997; 350: 630–33.

7 Schellenberg D, Pare PD, Weir TD, Spinelli JJ, Walker BAM, Sandford AJ. Vitamin D binding protein variants and the risk of COPD. Am J Respir Crit Care Med 1998; 157: 957–61.

8 Huang SL, Su CH, Chang SC. Tumor necrosis factor-agene polymorphism in chronic bronchitis. Am J Respir Crit Care Med 1997; 156: 1436–9.

9 Massague, J. The transforming growth factor-β family. Annu Rev Cell Biol 1990; 6: 597–641.

10 Lyons RM, Gentry LE, Purchio AF, Moses HL. Mechanism of activation of latent recombinant transforming growth factor beta 1 by plasmin. J Cell Biol 1990; 110: 1361–7.

11 Lyons RM, Keski-Oja J, Moses HL. Proteolytic activation of latent transforming growth factor-beta from fibroblast conditioned medium. J Cell Biol 1988; 106: 1659–65.

12 Derynck R, Jarrett JA, Chen EY, Eaton DH, Bell JR, Assoian RK, *et al*. Human transforming growth factor-β complementary DNA sequence and expression in normal and transformed cells. Nature 1985; 316: 701–5.

13 Watanabe Y, Kinoshita A, Yamada T, Ohta T, Kishino T, Matsumoto N, *et al*. A catalog of 106 single-nucleotide polymorphisms (SNPs) and 11 other types of variations in genes for transforming growth factor-β1 (TGF-β1) and its signaling pathway. J Hum Genet 2002; 47: 478–83.

14 Cambien F, Ricard S, Troesch A, Mallet C, Generenaz L, Evans A, *et al*. Polymorphisms of the TGF-β1 gene in relation to myocardial infarction and blood pressure. The Etude Cas-Temoin de l'Infarctus du Myocarde (ECTIM) Study. Hypertension 1996; 28: 881–7.

15 Syrris P, Carter ND, Metcalfe JC, Kemp PR, Grainger DJ, Kaski JC, *et al*. Transforming growth factor-β1 gene polymorphisms and coronary artery disease. Clin Sci 1998; 95: 659–67.

16 Wu L, Chau J, Young RP, Pokony V, Mills GD, Hopkins R, *et al*. Transforming growth factor-beta1 genotype and susceptibility to chronic obstructive pulmonary disease. Thorax 2004; 59: 126–9.

17 Silverman ES, Palmer LJ, Subramaniam V, Hallock A, Mathew S, Vallone J, *et al*. Transforming growth factor-β1 promoter polymorphism C-509T is associated with asthma. Am J Respir Crit Care Med 2004; 169: 214–19.

18 Miller SA, Dykes DD, Polesky HF. A simple salting-out procedure for extracting DNA from human nucleated cells. Nucleic Acids Res 1988; 16: 1215.

19 Xie X, Ott J. Testing linkage disequilibrium between a disease gene and marker loci. Am J Hum Genet 1993; 53: 1107

20 Zhao JH, Curtis D, Sham PC. Model-free analysis and permutation test for allelic associations. Hum Hered 2000;50:133-39

21 Zhao JH. 2LD- two-locus linkage disequilibrium (LD) calculator. [cited 2002] Available from: http://www.iop.kcl.ac.uk/IoP/Departments/PsychMed/GEpiBSt/software.shtml

22 Grainger DJ, Heathcote K, Chiano M, Snieder H, Kemp PR, Metcalfe JC, *et al*. Genetic control of the circulating concentration of transforming growth factor type β1. Hum Mol Genet 1999; 8: 93–7.

23 Morris DG, Huang X, Kaminski N, Wang Y, Shapiro SD, Dolganov G, *et al*. Loss of integrin $\alpha_v\beta_6$ mediated TGF-β activation causes MMP12-dependent emphysema. Nature 2003; 422: 169–73.

24 Hobbs K, Negri J, Klinnert M, Rosenwasser LJ, Borish L. Interleukin-10 and transforming growth factor-β promoter polymorphisms in allergies and asthma. Am J Respir Crit Care Med 1998; 158: 1958–62.

25 Pulleyn LJ, Newton R, Adcock IM, Barnes PJ. TGFβ1 allele association with asthma severity. Hum Genet 2001; 109: 623–7.

26 Pratsinis H, Giannouli CC, Zervolea I, Psarras S, Stathakos D, Kletsas D. Differential proliferative response of fetal and adult human skin fibroblasts to transforming growth factor-beta. Wound Repair Regen 2004; 12: 374–83.

27 Derynck R, Akhurst RJ, Balmain A. TGF-beta signaling in tumor suppression and cancer progression. Nat Genet 2001; 29: 117–29.

28 Ravanti L, Häkkinen L, Larjava H, Saarialho-Kere U, Foschi M, Han J, *et al*. Transforming growth factor-beta induces collagenase-3 expression by human gingival fibroblasts via p38 mitogen-activated protein kinase J Biol Chem 1999; 274: 37 292–300.

29 Leivonen SK, Chantry A, Häkkinen L, Han J, Kähäri VM. Smad3 mediates transforming growth factor-beta-induced collagenase-3 (matrix metalloproteinase-13) expression in human gingival fibroblasts. J Biol Chem 2002; 277: 46 338–46.

30 Eickelberg O, Kohler E, Reichenberger F, Bertschin S, Woodtli T, Erne P, *et al*. Extracellular matrix deposition by primary human lung fibroblasts in response to TGF-beta1 and TGF-beta3. Am J Physiol 1999; 276 (5 Pt 1): L814–24.

31 Fang KC, Wolters PJ, Steinhoff M, Bidgol A, Blount JL, Caughey

GH. Mast cell expression of gelatinases A and B is regulated by kit ligand and TGF-beta. J Immunol 1999; 162: 5528–35.
32 McGowan SE, Jackson SK, Olson PJ, Parekh T, Gold LI. Exogenous and endogenous transforming growth factors-beta influence elastin gene expression in cultured lung fibroblasts. Am J Respir Cell Mol Biol 1997; 17: 25–35.
33 Kucich U, Rosenbloom JC, Abrams WR, Rosenbloom J. Transforming growth factor-beta stabilizes elastin mRNA by a pathway requiring active Smads, protein kinase C-delta, and p38. Am J Respir Cell Mol Biol 2002; 26: 183–8.
34 Celedon JC, Lange C, Raby BA, Litonjua AA, Palmer LJ, DeMeo DL, *et al*. The transforming growth factor-beta1 (TGFB1) gene is associated with chronic obstructive pulmonary disease (COPD). Hum Mol Genet 2004; 13: 1649–56.

SBS 11th Annual Conference and Exhibition Drug Discovery: From Targets to Candidates

September 11–15, 2005 Geneva, Switzerland

Info: The Society for Biomolecular Screening
36 Tmarack Avenue, #348
Danbury, CT06811, USA
Phn 1(203) 743-1336
Fax 1(203) 748-7557
E-mail email@sbsonline.org
Http://www.sbsonline.org/sbscon/2005/index.php

Acta Pharmacologica Sinica 2005 Jun; 26 (6): 721–728

Full-length article

Protective effects of bendazac lysine on early experimental diabetic nephropathy in rats

Xiao-xing YIN[1], Yin-di ZHANG[1,2], Jian-ping SHEN[1], Hai-wei WU[3], Xiang ZHU[3], Li-min LI[1], Jun QIU[1], Shao-jun JIANG[4], Xiao-gang ZHENG[4]

[1]Department of Pharmacology and [3]Department of Pathogenic Biology, Nanjing Medical University, Nanjing, 210029; [4]Department of Pathology, Nanjing Jing Ling Hospital, Nanjing 210002, China

Key words

bendazac lysine; diabetic nephropathies; blood glucose; oxidative stress

[2] Correspondence to Prof Yin-di ZHANG.
Phn/Fax 86-25-8686-3159.
E-mail ydzhang@njmu.edu.cn
yinxx@vip.sina.com

Received 2004-11-30
Accepted 2005-02-18

doi: 10.1111/j.1745-7254.2005.00111.x

Abstract

Aim: To investigate the preventive and protective effects of bendazac lysine (BDL) on experimental early diabetic nephropathy (DN) rats. **Methods:** After an early DN model was induced by streptozotocin, rats were administered BDL at doses of 100, 200, and 400 mg/kg for 8 weeks. Blood glucose, microalbuminuria, kidney index, total antioxidative capacity, laminin, advanced glycation end products (AGE), aldose reductase (AR) activity, and the relative quantity of transforming growth factor β1 (TGF-β1) mRNA were measured by different methods. The ultrastructural morphology was observed by transmission electron microscope. **Results:** The physical behaviors of early DN rats were hypopraxia, cachexia, and polyuria, while those treated with high doses of BDL were vibrant and vigorous. For BDL-treated DN rats, when compared with vehicle-treated DN rats, the blood glucose level and the intensity of oxidative stress were ameliorated. Also, the microalbuminuria level, AGE either in serum or in renal, and AR activity were significantly reduced. Furthermore, the expression of TGF-β1 mRNA in the kidney cortex was declined and the thickness of glomerular base membrane was decreased significantly. The ultrastructure of glomerulus and mesangial matrix of BDL-treated DN rats were ameliorated. **Conclusion:** BDL has protective effects on several pharmacological targets in the progress of DN and is a potential drug for the prevention of early DN.

Introduction

Diabetic nephropathy (DN) is now a leading cause of end-stage renal failure in many countries. More than 30% of diabetes mellitus patients develop clinically evident DN 10 to 20 years after the onset of diabetes mellitus. DN seems to occur as a result of interaction of metabolic and hemodynamic factors. Several biochemical pathways, such as increased oxidative stress and advanced glycation end-products (AGE)[1,2], hyperactivity of aldose reductase (AR) in the polyol pathway[3], and hyperactivity of pro-sclerotic cytokine, such as transforming growth factor-β1 (TGF-β1)[4] and connective tissue growth factor (CTGF)[5], have been proposed as candidates for explaining the mechanism of the progressive cause of DN. For the complexity of mechanism, there is still no definitive therapy halting the development of DN that afflicts diabetic patients. Therefore, it is necessary to develop a novel therapy strategy for DN that can deal with more than one pharmacological target in this intricate mechanism.

Bendazac lysine (BDL) is one of agents that have been introduced for the management of cataracts, protecting the level of vision in patients, thus delaying the need for surgical intervention. Its principal effects are to inhibit the denaturation of proteins and AR activity, responsible for the accumulation of sorbitol and water retention in the lens fibers[6]. Several studies show that BDL has an inhibitive effect on AR[7], a main enzyme in the polyol pathway, an antioxidative effect[8], and an inhibitive effect on glycosylation[9], all of which are included in the progression of DN. Since there are

still very few published reports focused on the effects of BDL on DN. Therefore, it is worthwhile for us to explore its potential effects on preventing the progression of DN.

To evaluate the effects of BDL on DN, we studied the possible influence of BDL on the parameters that indicate protective effects against the progress of DN, such as blood glucose level, AR activity, AGE level, laminin level in the kidney cortex, thickness of the glomerular base membrane (GBM) and expression of TGF-β1 mRNA in the kidney cortex on early experimental DN rats, and observe their morphological changes.

Materials and methods

Drugs BDL was synthesized by Supereyes (Lot No 020818, Zhejiang, China), and was dissolved in 1% carboxymethyl cellulose (CMC) solution. Streptozotocin (STZ) (Lot No P5639) was purchased from Biomol Research Lab (Plymouth Meeting, PA, USA). Epalrestat (Lot No 990921), an aldose reductase inhibitor, serving as a positive control drug, was kindly presented by Shanghai Institute of Materia Medica and suspended in 1% CMC solution.

Animals Male Sprague-Dawley rats (Grade I, Certificate No SYXK 2001-0010), weighing 162.5±6.7 g (150–175 g) were obtained from Laboratory Animal Center of Nanjing Medical University. Animal expeiments followed the Guidline Principles for Care and Use of Laboratory Animals of Nanjing Medical University.

Induction of DN model and study protocol Diabetic rats were induced with an ip injection of 60 mg/kg of STZ (dissolved in pH 4.5 citrate buffer immediately before injection), while controlled normal standard rats (NS group, *n*=10) received 2.5 mL/kg of citrate buffer. Induction of the diabetic state was confirmed by measuring the blood glucose level at the 72 h after the injection of STZ. The rats whose blood glucose concentrations were ≥13.88 mmol/L were randomly allotted into 5 groups: DN rats treated with 1% CMC solution (DN group, *n*=10); DN rats treated with 100, 200, and 400 mg/kg of BDL for BL group (low dose, *n*=10), BM group (moderate dose, *n*=11), and BH group (high dose, *n*=10), respectively; and DN rats treated with 100 mg/kg of epalrestat (EPS group, *n*=10). The same volume of CMC solution was administered to the NS group (*n*=10). The animals were housed in a controlled environment (24±1 °C, 12-h light: 12-h dark cycle, onset of light at 07:00 AM) and were allowed food and water *ad libitum*. After 8 weeks, urine and blood samples were collected. After animals were sacrificed, fresh kidney cortices were stored in formaldehyde solution for light microscopic observation, and 1 mm×1 mm×1 mm cubes of kidney cortices were fixed in 2.5% glutaraldehyde for electron microscopic measurement. The rest of the kidneys were stored at -75 °C for the later analysis.

Measurement of renal function and biochemical parameters Kidney index was the ratio of kidney weight versus body weight. Blood glucose was measured by the glucose oxidase method with kits purchased from Dong-Ou Bioengineering (No 2002110002, Wenzhou, China). The value of microalbuminuria was represented by the ratio of urinary albumin versus creatinine measured in urine, where urinary albumin was determined by the radioimmunoassay method, whose reagent kit was purchased from the Department of Isotope, China Institute of Atomic Energy (No 20021203, Beijing, China), and creatinine was assayed by the picric acid method.

To analyze the total antioxidative capability, 2.0 mL of ABTS [2,2'-azinobis-(3-ethylbenzothiazoline-6-sulphonic acid]/myoglobin reagent was mixed with 20 μL of sample and a further 180 μL of diluent, which flushed the sample probe. The initiator of the reaction, hydrogen peroxide (0.675 mmol/L, 250 μL), was added last to get a final concentration in the cuvette of 75 μmol/L. After a 6-min incubation, the optical density (OD) of $ABTS^{\cdot+}$ was read at 734 nm by spectrophotometer (UV-1600, Beijing, China), and the value of total antioxidative capability was calculated[10].

The AR activity was measured by fluorospectrophotometer (Shimadzu, RF-5300, Kyoto, Japan) with reagents of β-NADPH (Lot No 81k7059, Sigma, St Louis, MO, USA) and DL-glyceraldehyde (Lot No 120k2618, Sigma) and its activity is defined as the amount of micromole of β-NADPH oxidized per minute at 37 ºC[11].

Laminin, a main component of the extracellular matrix, was determined by the radioimmunoassay method, using kits from Shanghai High Biotech Center (No 20021201, Shanghai, China). AGE either in renal cortex or in serum was measured by fluorescence spectrophotometry (fluorospectrophotometer, Shimadzu) and the concentration of AGE was represented by the fluorescence optical density (OD). The final value of AGE in tissue was modulated by the total protein in tissue which was measured by biuret colorimetry.

RT-PCR for the relative quantity of TGF-β1 mRNA in kidney cortex RT- PCR was performed to determine the relative quantity of TGF-β1 mRNA in the kidney cortex, whereas β-actin mRNA, a housekeeping gene, was used as an internal control[12]. Briefly, total RNA was extracted from the kidney cortex with TRIzol (Lot No 1134369, Invitrogen, Carlsbad, CA, USA). First-strand cDNA synthesis was reversely transcribed from 2 μg of mRNA in transcription buffer and 200U MMLV reverse transcriptase (System Lot No

160419, Promega, Madison, WI, USA) at 42 °C for 1 h, followed by immediate cooling on ice. PCR amplification was performed using *Taq* polymerase (Lot No 101405, Promega, Shanghai, China) in a total volume of 50 μL. The upstream and downstream primers for rat TGF-β1 mRNA were 5'-CCCGCATCCCAGGACCTCTCT-3' and 5'-CGGGGGACTGGCGAGCCTTAG-3', yielding a 519 bp product, whereas those for β-actin were 5'-GCTGCGTGTGGCCCCTGAG-3' and 5'-ACGCAGGATGGCATGAGGGA-3', yielding a 252 bp product. PCR conditions were as follows: 35 cycles, denaturating at 94 °C for 30 s, annealing at 54 °C for 60 s and extending at 72 °C for 60 s with initial heating at 94 °C for 5 min and final extending at 72 °C for 7 min. The PCR products were separated by 1% agarose (Lot No 051363, Biowest, Miami, FL, USA) electrophoresis and the band densities were analyzed using laser densitometry (Gel Doc 1000, Bio-Rad, Richmond, CA, USA). The relative quantity of TGF-β1 mRNA in the kidney cortex was represented by the ratio of band density of TGF-β1 versus that of β-actin.

Morphological observation and measurement of thickness of GBM Kidney cortex samples stored in formaldehyde solution were embedded with paraffin and stained with HE. Each HE-stained sample in each group was observed under light microscope. Three kidney samples from each experimental group were randomly chosen for electron microscopic observation. Specimens were embedded in epoxy resin and cut into ultrathin sections and then stained with plumbum citrate for ultrastructural observation under transmission electron microscope (JEM 1200EX, Jeol, Tokyo, Japan). Five photos were taken at different views for each kidney sample. The images were amplified 10K and the photos were scanned into a computer to measure the thickness of GBM using an image analysis system (Leica Qwin Standard V2.6, Leica Microsystems, Welzlar, Germany).

Statistical analyses Statistical analysis was performed to compare the effects of BDL on early DN rats using one-way analysis of variance (ANOVA) and Dunnett's *t*-test (2-side) for the different groups using SPSS 10.0. Data were expressed as mean±SD. $P<0.05$ was considered statistically significant.

Results

Effects of BDL on physical behaviors, blood glucose, microalbuminuria, and kidney index In our experiment, rats in the DN group displayed the following physical characteristics: hypopraxia, cachexia, yellowish and damp fur, kyphosis, body shake, ptosis, polyuria polydipsia and tardy weight gain; while rats in NS and BH groups were vibrant, vigorous, with white and tidy fur, and weight gain.

The blood glucose level, microalbuminuria, and kidney index of the DN group were significantly higher than those of NS group ($P<0.01$), indicating that our early DN model was successful. Low doses of BDL slightly reduced blood glucose in DN rats, but greatly reduced microalbuminuria ($P<0.01$). High doses of BDL significantly reduced blood glucose and microalbuminuria level in DN rats ($P<0.01$). BDL (low, moderate and high doses) and epalrestat slightly reduced the kidney index, but differences were not significant (Table 1).

Table 1. Effects of bendazac lysine(BDL) on blood glucose, microalbuminuria, and kidney index of rats. Mean±SD. $^{c}P<0.01$ *vs* NS group. $^{f}P<0.01$ *vs* DN group.

Group	*n*	Blood glucose /mmol·L^{-1}	Microalbuminuria /μg·(molCr)$^{-1}$	Kidney index (×1000)
NS	10	4.58±0.75	3.39±1.93	6.61±0.52
DN	10	18.26±6.98^{c}	29.07±9.98^{c}	11.54±3.85^{c}
BL	10	17.65±3.42	9.72±3.30^{f}	9.12±1.44
BM	11	14.48±2.53	6.56±2.95^{f}	10.46±2.82
BH	10	10.28±3.82^{f}	4.22±2.34^{f}	10.68±1.94
EPS	10	17.10±5.62	6.19±2.40^{f}	9.72±4.37

Effects of BDL on laminin level in kidney cortex and thickness of GBM The level of laminin in the kidney cortex of early DN rats significantly increased, when compared with that of normal rats ($P<0.01$). Three doses of BDL caused a decrease in the level of laminin, but a greatly significant decrease can be found only in high doses ($P<0.01$) (Figure 1A).

There was a significant difference in the thickness of GBM between the NS group and DN group ($P<0.01$). The thickness of GBM decreased with increasing doses of BDL. Compared with the DN group, there were significant differences in the thickness of GBM of BL, BM, BH and EPS groups ($P<0.05$, or $P<0.01$) (Figure 1B).

Effect of BDL on AR activity in erythrocyte AR activities in the erythrocyte of NS and DN groups were 6.90 and 27.29 U, respectively ($P<0.01$). Significant differences of AR activities at low, moderate, and high dose BDL-treated rats existed when compared with CMC-treated DN rats ($P<0.01$). Furthermore, AR activity and BDL doses showed good dose-dependence. Epalrestat, an AR inhibitor, also significantly reduced AR activity from 27.29 to 11.07 U, showing a very significant difference ($P<0.01$) (Figure 2).

Effects of BDL on AGE and oxidative stress AGE levels

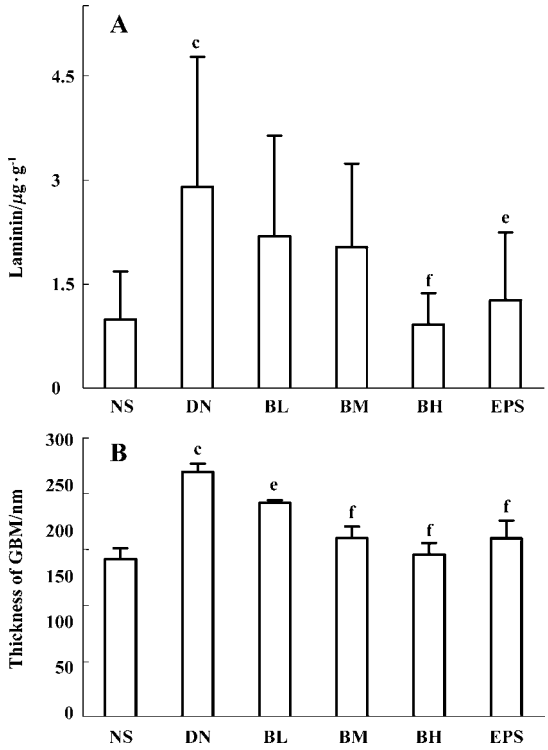

Figure 1. Effects of BDL on (A): laminin level in kidney cortex and (B): glomerular base membrane (GBM) of rats. NS, DN, BL, BM, BH, EPS represent normal standard rats, CMC treated DN rats, 100 mg/kg of BDL treated DN rats, 200 mg/kg of BDL treated DN rats, 400 mg/kg of BDL treated DN rats, 100 mg/kg of epalrestat treated DN rats, respectively. Mean±SD. $^{c}P<0.01$ *vs* NS group. $^{e}P<0.05$, $^{f}P<0.01$ *vs* DN group.

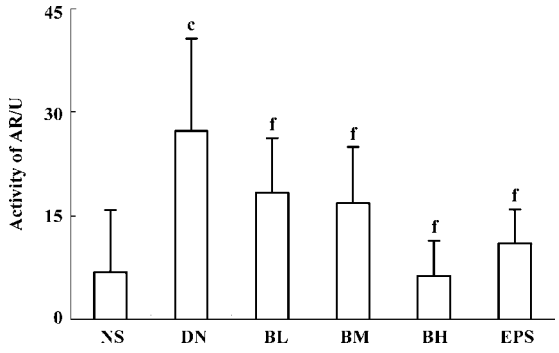

Figure 2. Effect of BDL on aldose reductase (AR) activity in erythrocyte of rats. NS, DN, BL, BM, BH, EPS represent normal standard rats, CMC treated DN rats, 100 mg/kg of BDL treated DN rats, 200 mg/kg of BDL treated DN rats, 400 mg/kg of BDL treated DN rats, 100 mg/kg of epalrestat treated DN rats, respectively. Mean±SD. $^{c}P<0.01$ *vs* NS group. $^{f}P<0.01$ *vs* DN group.

in the kidney cortex and in the serum of DN rats were greatly higher than those of normal rats ($P<0.01$). Both in the kidney cortex and in serum, there were significant decreases in AGE levels for BL, BM, and BH groups when compared with the DN group ($P<0.05$, or $P<0.01$), whereas epalrestat had the same significant difference ($P<0.01$). In contrast, the total antioxidative capability in serum, which expresses the antioxidative status of animals, was reduced significantly in DN rats. Three doses of BDL and epalrestat significantly enhanced the total antioxidative capability of DN rats ($P<0.01$) (Table 2).

Table 2. Effects of BDL on advanced glycation end products (AGE) and total antioxidative capability (T-AOC) in serum of rats. Mean±SD. $^{c}P<0.01$ *vs* NS group. $^{e}P<0.05$, $^{f}P<0.01$ *vs* DN group.

Group	*n*	AGE in kidney cortex/ AUF·mg cortex^{-1}	AGE in serum /AUF·mg protein^{-1}	T-AOC /kU·L^{-1}
NS	10	0.54±0.18	4.70±0.94	15.85±0.99
DN	10	2.30±0.71^{c}	17.25±2.50^{c}	6.94±1.81^{c}
BL	10	1.74±0.31^{e}	11.05±0.98^{f}	10.45±0.85^{f}
BM	11	1.45±0.44^{f}	7.85±2.65^{f}	11.13±1.37^{f}
BH	10	0.95±0.23^{f}	5.03±1.35^{f}	12.46±1.23^{f}
EPS	10	1.60±0.36^{e}	8.46±2.07^{f}	9.00±0.70^{f}

Effect of BDL on the relative quantity of TGF-β1 mRNA in kidney cortex After the RT-PCR procedure, the amplified products of TGF-β1 mRNA were completely separated by electrophoresis (Figure 3A). The relative quantity of TGF-β1 mRNA in the kidney cortex of the DN group significantly increased when compared with that of NS group ($P<0.01$). Low, moderate, and high dose BDL caused the level of TGF-β1 mRNA to decrease, and statistical differences existed when compared with CMC-treated DN rats ($P<0.01$). Epalrestat had the same effect as a moderate dose of BDL ($P<0.01$) (Figure 3B).

Effects of BDL on morphological change in kidney The light microphotograph showed that glomerular mesangial hyperplasia existed (Figure 4). In the transmission electron micrographs, the ultrastructure of glomerulus of the CMC-treated DN rat was changed. The GBM was wrinkled and partly thickened, with effacement of some visceral epithelial cell foot processes and microvillus transformation. After 8 weeks of treatment with 400 mg/kg of BDL, the glomerular capillary loops, GBM, pedicelsa and mesangial matrix of rats appeared to be almost normal (Figure 5).

Discussion

Oxidative stress plays an important role in the etiology

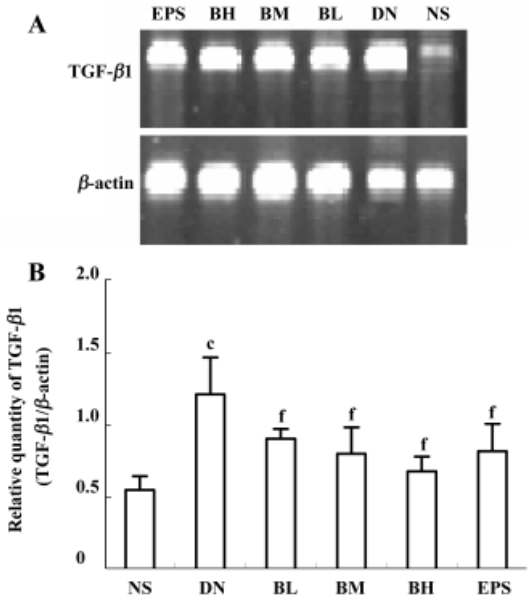

Figure 3. Effect of BDL on the relative quantity of TGF-β1 mRNA in kidney cortex of rats. NS, DN, BL, BM, BH, EPS represent normal standard rats, CMC treated DN rats, 100 mg/kg of BDL treated DN rats, 200 mg/kg of BDL treated DN rats, 400 mg/kg of BDL treated DN rats, 100 mg/kg of epalrestat treated DN rats, respectively. (A): cDNA samples obtained from kidney cortex of each rats were amplified for the detection of TGF-β1 mRNA. β-Actin was used as the internal standard in each sample. (B): RT-PCR data for relative quantity of TGF-β1 mRNA performed by densitometric analysis. Mean±SD. $^{c}P<0.01$ *vs* NS group. $^{f}P<0.01$ *vs* DN group.

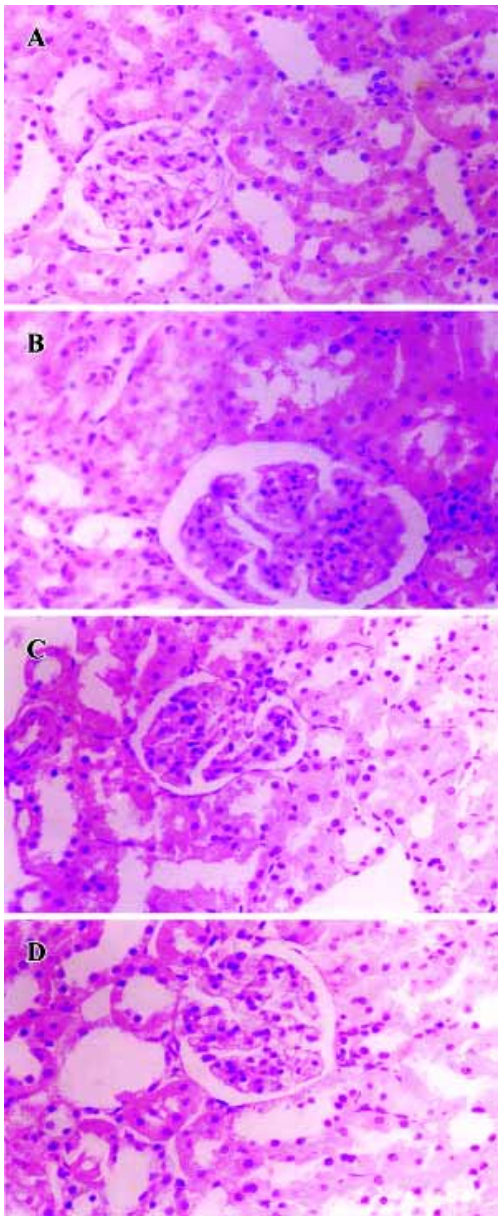

Figure 4. Representative light microphotographs showing the glomerular mesangial hyperplasia (HE stain, ×40). (A): The glomerulus of normal standard rat: the capillary loops are opened and portion of the glomerular is relatively small; (B): The glomerulus of CMC treated DN rat: the capillary loops are opened but narrowed and portion of the glomerular is relatively large. The mesangial hyperplasia is moderate-grade; (C): The glomerulus of 400 mg/kg of BDL treated DN rats: the mesangial hyperplasia is low-grade; (D): The glomerulus of 100 mg/kg of EPS treated DN rats: the mesangial hyperplasia is moderate-grade.

of diabetic complications[13], and the formation of reactive oxygen species is a direct consequence of hyperglycemia. In our study, we found that the total antioxidative capability (a common indicator for changes in the antioxidation system), which includes ascorbate, protein thiols, bilirubin, urate and α-tocopherol, was significantly increased by BDL, strongly suggesting that BDL has an effect on antioxidative capability *in vivo*. This result is consistent with a former report, in which BDL inhibited *in vitro* depolymerisation of hyaluronic acid by free hydroxyl and superoxide radicals from a sodium ascorbate system[14]. Furthermore, we also found that BDL, even in low doses, significantly decreased AGE levels either in the kidney cortex or in serum. Thus, the antioxidative effect of BDL is very important and can be of great clinical significance for DN.

The status of oxidative stress in intensity and durability facilitates the formation of AGE, which is the result of a reaction between carbohydrates and free amino group of proteins. AGE accumulates in extracellular matrix proteins as a physiological process during ageing. However, this accumulation happens earlier, and with an accelerated rate, in diabetes mellitus than in non-diabetic individuals[15]. AGE also enhances the susceptibility of LDL to oxidation[16] and induces apoptosis in cultured human umbilical vein endothe-

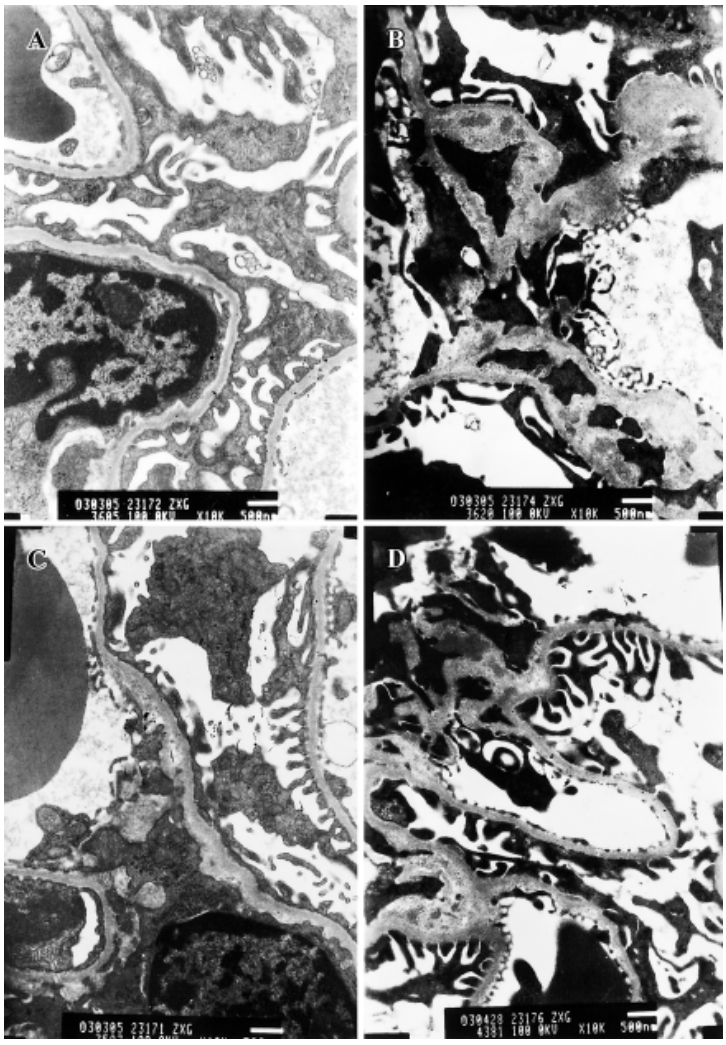

Figure 5. Transmission electron micrographs showing the ultrastructure of rat glomerulus as below (×10 k). (A): Normal control group of rats: illustrating a portion of the glomerular tuft, the thickness of glomerular basement membrane was normal, and pedicels embedded in the lamina rara externa. (B): CMC treated DN rats: the glomerular basement membrane was wrinkled, and thickened partly, with effacement of some visceral epithelial cell foot processes and microvillous transformation. (C): 400 mg/kg of BDL treated DN rats: the glomerular capillary loops, glomerular basement membrane, pedicelsa and mesangial matrix were normal. (D): 100 mg/kg of EPS treated DN rats. Bar=500 nm.

lial cells[17]. In reverse, the interaction between AGE and their specific receptor (RAGE) induces the activation of oxidative stress, and stimulates the production and release of cytokines, amplifying the tissue damage[2]. It can be concluded that oxidative stress and AGE interact with and upregulate each other. As already stated, the major metabolite of bendazac inhibited glycosylation by sugar in a dose-dependent manner[18], and also bendazac and its metabolite (5-hydroxybendazac) inhibit the carbamylation of soluble lens proteins *in vitro*[19]. Furthermore, in our study, BDL significantly decreased AGE levels both in the kidney cortex and in serum. These data strongly suggest the anti-AGE character of BDL and this could be of benefit for the prevention of DN.

Our data shows that BDL has an inhibitory effect on the relative quantity of TGF-β1 mRNA in the kidney cortex of DN rats, which is commonly considered as a pivotal cytokine in mediating the progression of DN. In vitro, studies have shown that a range of stimuli increase TGF-β1 expression, such as hyperglycemia, AGE, and various products of oxidative stress[20,21]. Indeed, TGF-β1 seems to be an important site of interaction between hemodynamic and metabolic pathways, playing a key role in the synergy between hypertension and hyperglycemia in mediating DN[22]. Therefore,

having an inhibitory effect on TGF-β1, BDL affects the regulation of several cytokine in the progression of DN, and is a prime candidate for developing appropriate agents in the prevention and treatment of DN.

Laminin, kidney index and the thickness of GBM are usually enlarged during the progression of DN and serve as persuasive parameters for describing glomerular hypertrophy. Although a decrease in the kidney index for 3 doses of BDL were not defined significantly in our experiment, the thickness of GBM, another significantly decreased morphological parameter in our study, together with laminin, which describes the level of extracellular matrix, still suggest that BDL can aid in preventing renal hypertrophy.

The accumulation of polyols in the kidney has been suggested to be involved in the development of DN. In diabetic patients, AR activity is greatly enhanced by high glucose and accumulated sorbitol, which is associated with the depletion of myoinositol and changes in the cellular redox potential[23], resulting in deteriorative function in nephropathy, retinopathy, and neuropathy. The importance of AR relevant to DN has also been emphasized with the demonstration that the increase of AR activity is associated with enhanced protein kinase C activation and TGF-β1 production in human mesangial cells in response to glucose[24]. In experimental diabetes, several studies have examined the effects of AR inhibition on various functional and structural markers of DN. In an in vitro experiment, the AR inhibitor, epalrestat, effectively corrected glucose-induced imbalances of the polyol pathway and myo-inositol uptake in neutrophils and was capable of ameliorating the neutrophil dysfunction[25]. Also, epalrestat lowers the level of Nepsilon-(carboxymethyl)lysine (CML) and associated variables, and polyol metabolites are correlated with CML in the erythrocytes of diabetic patients[26]. In a clinical study, the effects of epalrestat on autonomic and somatic neuropathy were assessed, suggesting that epalrestat has therapeutic value at early stages of DN[27]. In our current experiment, we found that BDL significantly lowered AR activities in rats from 27.29 U to 18.38 U (low dose), 16.92 U (moderate dose), and 6.39 U (high dose), while epalrestat lowered AR activities to 11.07 U (100 mg/kg). The effect of high doses of BDL on AR activity was stronger than that of a common dose of typical AR inhibitor, epalrestat, and therefore, testifying that BDL is a strong inhibitor for AR. Hence, besides its recognized cataract delaying effect on the communal pathway in the pathology of cataracts, BDL can be justified in its clinical application for DN treatment.

BDL is an oxyacetic acid with protein antidenaturant, anti-inflammatory, antinecrotic, choleretic and antilipidemic properties. *In vitro*, BDL inhibited the carbamylation of soluble lens proteins, and the depolymerisation of hyaluronic acid by free hydroxyl and superoxide radicals from a sodium ascorbate system[14]. Bendazac also has scavenger-like activity as a result of its interaction with protein molecules[6]. In our experiment, BDL and epalrestat (a commonly used DN-treatment agent) ameliorated the physical morbidity, reduced microalbuminuria, laminin level, thickness of GBM, AGE level, total antioxidative capability, AR activity, and TGF-β1 mRNA levels in DN rats. What must be pointed out is that BDL significantly decreased blood glucose and ameliorated the persuasive pathological changes by light and electron micrograph, while epalrestat has no effect on them. In the complicated mechanisms of DN development, the pathway of hyperglycemia-oxidative stress-AGE/TGF-β1 is assuredly very important. Many renal changes are the consequences of changes in blood glucose levels, and many ameliorative effects of BDL on DN may be closely dependant on its effect on the blood glucose level. Therefore, compared with epalrestat, BDL might have more widely therapeutic points for DN.

To sum up, in our STZ induced early DN rat model, BDL decreased the blood glucose level, reduced the level of AGE, the intensity of oxidative stress, AR activity, and the relative level of TGF-β1 mRNA and, furthermore, lowered the laminin level in the kidney cortex and decreased the thickness of GBM, and therefore ameliorated the morbidity in physical behavior, morphology, and microalbuminuria. In conclusion, BDL has protective effects on several pharmacological targets in the complicated pathology mechanism of DN. It is therefore worthwhile to study further its potential protective effects on early DN.

References

1 Catherwood MA, Powell LA, Anderson P, McMaster D, Sharpe PC, Trimble ER. Glucose-induced oxidative stress in mesangial cells. Kidney Int 2002; 61: 599–608.

2 Wautier JL, Guillausseau PJ. Advanced glycation end products, their receptors and diabetic angiopathy. Diabetes Metab 2001; 27: 535–42.

3 Cooper ME. Interaction of metabolic and haemodynamic factors in mediating experimental diabetic nephropathy. Diabetologia 2001; 44: 1957–72.

4 Sharma K, McGowan Tracy A. TGF-β in diabetic kidney: role of novel signaling pathways. Cytokine Growth Factor Rev 2000; 11: 115–23.

5 Liu BC, Chen Q, Luo DD, Sun J, Phillips AO, Ruan XZ, *et al*. Mechanisms of irbesartan in prevention of renal lesion in streptozotocin-induced diabetic rats. Acta Pharmacol Sin 2003; 24: 67–73.

6 Balfour JA, Clissold SP. Bendazac lysine: a review of its pharma-

cological properties and therapeutic potential in the management of cataracts. Drugs 1990; 39: 575–96.
7 Inliano G, Menzion M, Apponi-Battini G, Costagliola C. Inhibition of rat lens aldose reductase by bandazac-L-lysine salt. Enzyme 1989; 42: 235–7.
8 Schmut O, Hofmann H. Studies on the activity of bendalina (bendazac L-lysine salt) as a scavenger of hydroxyl and superoxide radials. Wien Klin Wochenschr 1985; 97: 819–22.
9 Marques C, Ramalho JS, Pereira P, Mota MC. Bendazac decreases *in vitro* glycation of human lens crystallins. Decrease of *in vitro* protein glycation by bendazac. Doc Ophthalmol 1995; 90: 395–404.
10 Miller NJ, Rice-Evans C, Davies MJ, Gopinathan V, Milner A. A novel method for measuring antioxidant capacity and its application to monitoring the antioxidant status in premature neonates. Clin Sci 1993; 84: 407–12.
11 Das B, Srivastava SK. Purification and properties of aldose reductase and aldehyde reductase II from human erythrocyte. Arch Biochem Biophy 1985; 238: 670–9.
12 Kaneto H, Morrissey J, Klahr S. Increased expression of TGF-β1 mRNA in the obstructed kidney of rats with unilateral ureteral ligation. Kidney Int 1993; 44: 313–21.
13 Ceriello A, Giugliano D, Quatraro A, Dello Russo P, Lefebvre PJ. Metabolic control may influence the increased superoxide generation in diabetic serum. Diabetic Med 1991; 8: 540–2.
14 Schmut, Fellinger C, Hofmann H. Bendazac lysine: a protective substance against oxygen-free radicals. In: D'Ermo F. Recent developments in the pharmacological treatment of cataract. Amsterdam: Kugler Publications; 1987. p 69–72.
15 Schleicher ED, Wagner E, Nerlich AG. Increased accumulation of the glycoxidation product N^{ε}-(carboxymethyl) lysine in human tissues in diabetes and aging. J Clin Invest 1997; 99: 457–68.
16 Ihm SH, Yoo HJ, Park SW, Ihm J. Effect of aminiguanidine on lipid peroxidation in streptozotocin-induced diabetic rats. Metabolism 1999; 48: 1141–5.
17 Min C, Kang E, Yu SK, Shinn SH, Kim YS. Advanced glycation end products induce apoptosis and procoagulant activity in cultured human umbilical vein endothelial cells. Diab Res Clin Pract 1999; 46: 197–202.
18 Lewis BS, Harding JJ. The major metabolite of bendazac inhibits the glycosylation of soluble lens proteins: a possible mechanism for a delay in cataractogenesis. Exp Eye Res 1988; 47: 217–25.
19 Lewis BS, Rixon KC, Harding JJ. Bendazac prevents cyanate binging to soluble lens proteins and cyanate-induced phase-separation opacities *in vitro*: a possible mechanism by which bendazac could delay cataract. Exp Eye Res 1986; 43: 973–9.
20 Jandeleit-Dahm K, Cao ZM, Cox AJ, Kelly DJ, Gilbert RE, Cooper ME. Role of hyperlipidemia in progressive renal disease: focus on diabetic nephropathy. Kidney Int 1999; 56 (Suppl 71): S31–6.
21 Montero A, Munger KA, Khan RZ, Valdivielso JM, Morrow JD, Guasch A, *et al*. F-2-isoprostanes mediate high glucose-induced TGF-beta synthesis and glomerular proteinuria in experimental type I diabetes. Kidney Int 2000; 58: 1963–72.
22 Yin XX, Zhang YD, Wu HW, Zhu X, Zheng XG, Jiang SJ, *et al*. Protective effects of Astragalus Sapoonin I on early stage of diabetic nephropathy in rats. J Pharmacol Sci 2004; 95: 256–66.
23 Greene DA, Lattimer SA, Sima AAF. Sorbitol, phosphoinositides, and sodium-potassium-ATPase in the pathogenesis of diabetic complicatins. N Engl J Med 1987; 316: 599–606.
24 Ishii H, Tada H, Isogai S. An aldose reductase inhibitor prevents glucose-induced increase in transforming growth factor-beta and protein kinase C activity in cultured human mesangial cells. Diabetologia 1998; 41: 362–4.
25 Suzuki K, Kawamura T, Sakakibara F, Sasaki H, Sano T, Sakamoto N, *et al*. Effect of aldose reductase inhibitors on glucose-induced changes in sorbitol and myo-inositol metabolism in human neutrophils. Diabet Med 1999; 16: 67–73.
26 Hamada Y, Nakamura J, Naruse K, Komori T, Kato K, Kasuya Y, *et al*. Epalrestat, an aldose reductase inhibitor, reduces the levels of Nepsilon-(carboxymethyl)lysine protein adducts and their precursors in erythrocytes from diabetic patients. Diabetes Care 2000; 23: 1539–44.
27 Nakayama M, Nakamura J, Hamada Y, Chaya S, Mizubayashi R, Yasuda Y, *et al*. Aldose reductase inhibition ameliorates papillary light reflex and F-wave latency in patients with mild diabetic neuropathy. Diabetes Care 2001; 24: 1093–8.

Acta Pharmacologica Sinica 2005 Jun; 26 (6): 729–736

Full-length article

Inhibitory effect of picroside II on hepatocyte apoptosis[1]

Hua GAO, Ya-wei ZHOU[2]

College of Chemistry and Molecular Engineering, Peking University, Beijing 100871, China

Key words

picroside II; hepatocytes; apoptosis; oxidative stress; *bcl-2* genes; *bax* genes

[1]Project supported by China Postdoctoral Science Foundation and the National Natural Science Foundation of China (No 90209046).
[2]Correspondence to Prof Ya-wei ZHOU.
Phn 86-01-6253-8501.
Fax 86-01-6253-8495.
E-mail zhouyawe@public.bta.net.cn

Received 2004-12-14
Accepted 2005-03-07

doi:10.1111/j.1745-7254.2005.00121.x

Abstract

Aim: To investigate the influence of picroside II on hepatocyte apoptosis and its mechanism. **Methods:** Morphological changes and quantification of apoptotic cells were determined under transmission electron microscopy and flow cytometry respectively. DNA fragmentation was visualized by agarose gel electrophoresis. Semi-quantitative reverse transcription-PCR (RT-PCR) was used to analyze the expression of *bcl-2* and *bax* genes. The content of manganese-superoxide dismutase (SOD) in liver mitochondria was detected by the Marland method. The content of malonic aldehyde (MDA) and the protein level in liver tissue were determined by thiobarbituric acid colorimetry and Lowry method. **Results:** Picroside II decreased the levels of alanine aminotransferase and aspartate aminotransferase in the serum resulting from acute-liver injured mice induced with *D*-GalN and LPS; it also reduced the content of MDA, and thus, enhanced the activity of SOD. Picroside II 10 mg/kg was found to protect hepatocytes against apoptosis in a dose-dependent manner; it up-regulated the expression of *bcl-2* genes, thus increased the *bcl-2/bax* ratio. **Conclusion:** Picroside II can protect hepatocytes against injury and prevent hepatocytes from apoptosis. It might by upregulating the *bcl-2* gene expression and antioxidation.

Introduction

Picrorhiza scrophulariiflora belongs to the plant family, scrophularia. Dried rhizome from *Picrorhiza scrophulariiflora* is used for medicine benefits. Many published studies have found that it can protect hepatocytes from many kinds of injury, but the mechanism has not been clearly elucidated. Picroside II is one of the most effective components extracted from *Picrorhiza scrophulariiflora*. To investigate the mechanism of picroside II's protective effects on hepatocytes, we have established hepatocyte apoptosis models *in vivo* and *in vitro*. Transmission electron microscopy, agarose gel electrophoresis of DNA and flow cytometry were used to evaluate apoptosis of hepatocytes. Semi-quantitative RT-PCR together with image manipulation were used to analyze *bcl-2* and *bax* mRNA which are highly related to apoptosis; immunohistochemistry was used to observe the protein expression of Bcl-2 and Bax. Together with several other oxidation indexes, we tried to demonstrate the mechanisms of picroside II's effect on liver protection in apoptosis.

Materials and methods

Animals Seventy-two mice of Kunming strain (20±2 g) and 2 SD rats (70±10 g) were supplied by the Animal Center of Academy of Military Medical Sciences (Beijing China), with the number of males and females being equivalent.

Materials Picroside II was supplied by the Bescholor Research Center of Peking University (Beijing China). Dicarboxylate pilules (DDB) were obtained from Beijing Union Pharmaceutical Factory (Beijing China). *D*-galactosamine (*D*-GalN), lipopolysaccharide (LPS), actinomycin-D (Act-D), and tumor necrosis factor-α (TNF-α) were purchased from Sigma (St Louis, Mo, USA). RNase A, diethylpyrocarbonate (DEPC), fetal bovine serum (FBS), and Trizol reagent were purchased from Gibco/BRL (California, USA). The *Bcl-2* monoclonal and *Bax* polyclonal antibodies were purchased from Santa Cruz Biotechnology (California,USA). Reverse Transcriptional kit was obtained from Promega Chemical Co (Wisconscin,

medison,USA). Alanine aminotransferase (ALT) and aspartate aminotransferase (AST) detection kits, malondialdehy (MDA, Mn-Super oxide dismutase (Mn-SOD), and streptavidin-peroxidase (SP) were all domestic products.

Models establishing and treatment

In vivo Before experiments were started, 72 mice were divided into 6 groups randomly. Five groups were treated with *D*-GalN (700 mg/kg, ip) and LPS (1 μg/kg, ip) to establish hapatocyte apoptosis model *in vivo*, among which the 4 groups were infused (ig) with picroside II 5 mg/kg, 10 mg/kg, 20 mg/kg, or vehicle (0.9 % NaCl) 10 min before and 4 h after the *D*-GalN and LPS administration, respectively. One group received biphenyl dimethyl dicarboxylate pilules (DDB) (200 mg/ kg) with the same manipulation acts as a positive control. The remained group was the negative control. Five hours after the model was established, the blood of 6 mice from each group was sampled though eye socket veins. ALT and AST in serum were then monitored (by continuously using the monitoring method, recommended by National Clinical Chemistry League). Cut sections of liver tissue (left part) of the remaining 6 mice of each group were prepared for pathology evaluation and immunohistochemistry detection of Bcl-2/Bax proteins. The liver suspending liquid (20%) was made from the rest of the liver and stored at under -20 ºC, in order to detect SOD in liver mitochondria (by the Marland method), protein level (by the Lowry method) and the content of MDA of liver tissue (by TBA colorimetry). Another 1 mL of liver suspending liquid was centrifuged at 12 000×*g* for 20 min. 400 μL upper liquid, 1 mL ethanol and 50 μL (5 mol/L) was mixed together and stored at under -20 ºC for DNA fragmentation analysis.

In vitro Primary culture of hepatocytes from rats were isolated as previously described[1]. Rats were decapitated under anesthesia. *In situ* perfusion was then performed with calcium and magnesium-free Hanks' salt solution followed by a medium containing collagenase through the hepatic portal vein of rats, the suspending liquid containing rat liver cells were collected. The suspending liquid was then centrifuged at 120×*g* at 4 ºC for 5 min. The cell pellets were washed twice with cold Hanks' solution and the cell concentration was modulated to 1×10^9/L. The cells were seeded in 24-well culture plates in the growth medium consisting of DMEM with 20% FBS, at 37 ºC in a water-saturated atmosphere of 5% CO_2. After 24 h, the culture medium was abandoned, and cells were exposed to a series of concentrations of picroside II (0.005, 0.01, and 0.02 mmol/L). After 1 h, Act-D 50 μg/L was added, and 30 min later TNF-α 3000 kU/L was added consecutively to the well for another 24 h. A negative control group was set which was exposed to the normal culture medium. An assessment of hepatocyte apoptosis and apoptosis-related genes *bcl-2* and *bax* mRNA extraction was then performed.

The Marland method was used to detect the content of SOD in liver mitochondria. MDA content of liver tissue was detected by TBA colorimetry and the protein level of liver was analyzed using Lowry method . ALT and AST in serum were detected by the continuous monitoring method (recommended by International Clinical Chemistry League).

Immunohistochemistry analysis Liver tissues were fixed in 4% formaldehyde for 24 h and embedded in paraffin routinely, followed by 5 μm slicing up. The streptavidin-peroxidase (SP) method was assumed. The bcl-2 monoclonal antibody (1:50) or Bax polyclonal antibody (1:50) as primary antibodies was applied and incubated overnight at 4 ºC or for 60 min at room temperature. The slices were observed and photographed through light microscope and the percentage of the positive staining area of bcl-2 or bax were semiquantitatively analyzed by using CMIAS-008 Image Analyser (Beijing, China).

Reverse transcriptase polymerase chain reaction assay Total cytoplasmic RNA of each group was isolated from 1.5×10^7 cultured cells by the TRIZOL method (according to GIBCO specification). The concentration of RNA was determinated by absorbance at 260 nm, and its integrity was confirmed by means of electrophoresis on 1% agarose gels, and then stained with 0.1 mg/L ethidium bromide (EB). A total of 1 μg of RNA was converted to complementary DNA (cDNA) using 15 U reverse transcriptase in 20 μL buffer, which contained 1 mmol/L deoxy-NTP, 1 U RNase inhibitor and 0.5 μg oligo (deoxythymidine)$_{15}$ primer. An aliquot (5%) of cDNA was amplified using the reverse (5'-AGA GGG GCT ACG AGT GGG AT-3') and forward primer (5'-CTC AGT CAT CCA CAG GGC GA-3') to yield 450 bp polymerase chain reaction (PCR) product for *bcl-2*, the reverse (5'-GGT TTC ATC CAG GAT CGA GAC GG-3') and forward primer (5'-ACA AAG ATG GTC ACG GTC TGC C-3') to yield a 429 bp PCR product for *bax*. In order to verify the equal amounts of cDNA were presented in the PCR reaction, β-actin was separately co-amplified with the *bcl-2* and *bax* cDNA, with the reverse (5'-TAA AGA CCT CTA TGC CAA CAC AGT-3') and forward primer (5'-CAC GAT GGA GGG GCC GGA CTC ATC-3') to yield a 240 bp PCR product. The PCR conditions were as follows: pre-denaturation at 94 ºC for 5 min, denaturation at 94 ºC for 30 s, annealing at 60 ºC (*bcl-2* and β-actin) or 64 ºC (*bax*) for 40 s, and polymerisation at 72 ºC for 40 s with *Taq* DNA polymerase. After 28 cycles, 20 μL *bcl-2* or *bax* PCR product together with the β-actin PCR product of the same template were separated by electrophoresis and

revealed by EB staining. Then each band of the electrophoresis gel was semiquantitatively analyzed using Imagemaster and Software Image Analyser (Beijing,China). The *bcl-2* and *bax* mRNA levels were expressed as the ratio of signal intensity for the target genes in relation to that for the coamplified β-actin.

Flow cytometry analysis Cultured hepatocytes 1×10^9/L of each group were harvested, washed with PBS at 4 ºC, and exposed to pre-chilled ethanol at 4 ºC for 30 min. They were then washed again with PBS, exposed to PI 50 mg/L, 0.1% TritonX-100, 0.01 mmol/L EDTA $(Na)_2$ and RNase 50 mg/L at normal temperature in darkness for 12–24 h. Specimen were then presented to the FACS-420 Flow Cytometry Analyser (New York, Becton Dickinson and Company, American) to evaluate apoptosis levels.

DNA fragmentation analysis The cultured hepatocytes of each group were lysed in Tris-HCl 20 mmol/L (pH 8.0), EDTA 10 mmol/L, and 0.5% lauryl sarcosyl containing 200 mg/L of proteinase K. DNA was extracted by supercentrifugation, precipitation with ethanol and was treated with RNase. The DNA was then loaded onto 1%–2% agarose gel containing ethidium bromide (EB), which was observed and photographed under UV transillumination.

Morphological evaluation light microscope assay Serial slices of liver tissues were prepared from mice in each group and stained with hematoxyline-eosin (HE) and then observed under light microscope at 200× or 400×magnification.

Transmission electron microscopy assay Liver tissue specimen were fixed and postfixed with glutaraldehyde and osmium troxide respectively, dehydrated by acetone, imbedded in eposy resin. Ultrathin sections were collected and counterstained with lead citrate and viewed with a JEM100CXtransmission electron microscope (Tokyo, Japan).

Statistical analysis All results were expressed as mean±SD. Data were assessed by using *t*-test, and $P<0.05$ was considered stastically significant.

Results

Effects of picroside II on ALT and AST in serum of mice suffered from acute liver injury induced by *D*-GalN and LPS ALT and AST values were markedly higher in the model group than those in negative control ($P<0.01$). Picroside II decreased ALT and AST values in a dose-dependent manner ($P<0.05$ or $P<0.01$ *vs* model control). ALT and AST values of the positive control group treated with DDB 200 mg/kg also decreased, especially ALT. The results revealed that picroside II can protect liver tissue from *D*-GalN and LPS-induced acute injury, and it was more powerful than DDB (Table 1).

Table 1. Effects of picroside II on ALT and AST in serum of mice suffering from acute liver injury induced by D-Galn and LPS. n=12. Mean±SD. $^bP<0.05$, $^cP<0.01$ *vs* model control. $^fP<0.01$ *vs* negative control.

Group	Dose/mg·kg^{-1}	ALT/U·L^{-1}	AST/U·L^{-1}
Negative control		48±15	130±74
Model control		512±256^f	563±19^f
Positive control	200	270±138^c	378±190^b
Picroside II	5	404±21	416±230
Picroside II	10	294±177^b	402±181^b
Picroside II	20	242±164^c	277±85^c

Effects of picroside II on MDA and SOD content of mice suffered from acute liver injury induced by *D*-GalN and LPS The SOD value of model group decreased, but the MDA value increased compared with negative group ($P<0.01$). The content of MDA of all groups exposed to picroside II markedly decreased, whereas SOD increased compared with the model group. This effect suggested a dose-dependent manner ($P<0.05$ or $P<0.01$) (Table 2).

Table 2. Effects of picroside II on MDA and SOD in liver of mice suffered from acute liver injury induced by *D*-GalN and LPS. n=12. Mean±SD. $^bP<0.05$, $^cP<0.01$ *vs* model control. $^fP<0.01$ *vs* negative control.

Group	Dose/mg·kg^{-1}	SOD/kNU·L^{-1}	MDA/nmol·L^{-1}
Negative control		256.8±14.9	4.51±0.66
Model control		222.7±18.3^f	8.64±1.69^f
Positive control	200	241.5±14.1^b	5.80±1.00^c
Picroside II	5	237.2±11.6^b	6.77±1.26^c
Picroside II	10	247.2±13.1^c	5.47±0.67^c
Picroside II	20	249.2±11.7^c	4.51±0.89^c

Immunohistochemistry analysis of Bcl-2 and Bax A few pale yellow granula (Bcl-2 protein) were detected in hepatocytes cytoplasm of the negative group. There were more granula in the model group and the most were found in the groups treated with picroside II (Figure 1A). Little buff granula (Bax protein) was detected in normal hepatocytes. The amount of the granula was more in the model group, and existed dispersedly or in focus with the color more heavily than others. Bax protein expression in groups treated with picroside II decreased (Figure 1B). The difference between

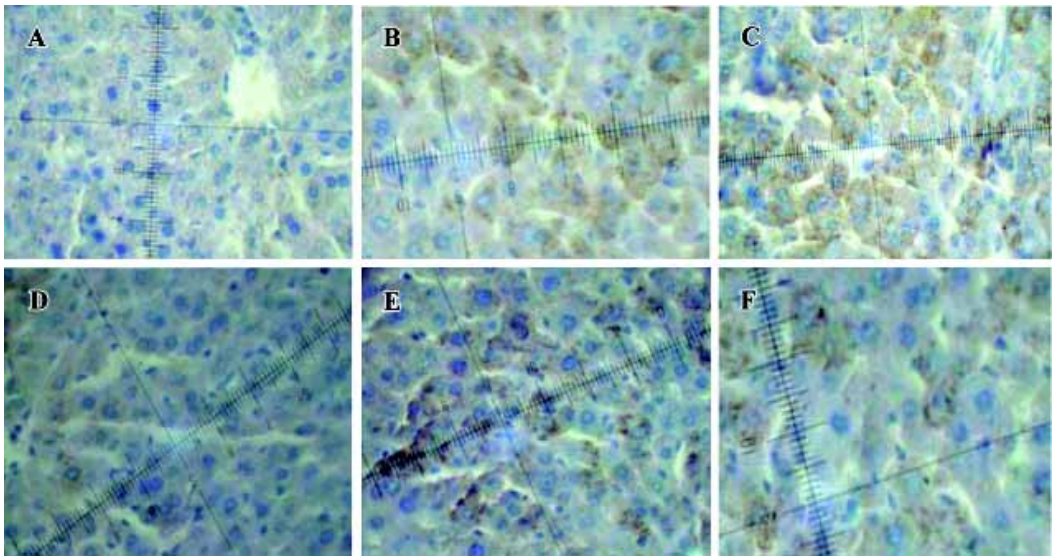

Figure 1. The Bcl-2 and Bax expression of each group (×400). Bcl-2 expression of negative group (A), Bcl-*2* expression of model group (B), Bcl-2 expression of groups treated with picroside II (C); Bax expression of negative group (D), Bax expression of model group (E), Bax expression of groups treated with picroside II (F).

groups treated with picroside II and the group of negative control was evidently significant (P<0.05 or P<0.01). The difference between picroside II groups and model control group was also significant (P<0.05 or P<0.01, Table 3).

Table 3. Bcl-2 and Bax protein expression levels of each group. n=10. Mean±SD. ^{b}P<0.05, ^{c}P<0.01 *vs* negative control. ^{f}P<0.01 *vs* model control.

Group	Bcl-2 protein/%	Bax protein/%
Negative control	4.82±0.26	4.76±0.16
Model control	5.26±0.34^{b}	7.24±0.38^{c}
Picroside II group	9.42±0.36^{ce}	6.22±0.24^{b}

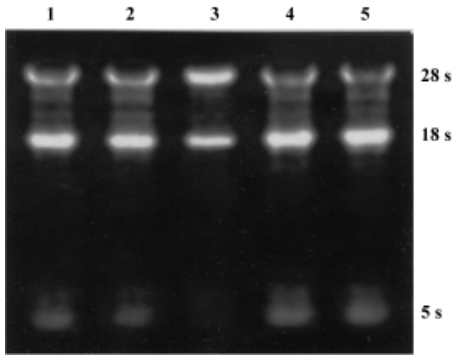

Figure 2. Total RNA of groups with different doses of Picriside II. 1: negative group; 2: model group; 3: treated with picroside II 20 mg·mL^{-1}; 4: treated with picroside II 10 mg·mL^{-1}; 5: treated with picroside II 5 mg·mL^{-1}.

These results suggested that picroside II could effectively up-regulate the expression of apoptosis-related gene *bcl-2* and inhibit *bax* expression. The increased *bcl-2*/*bax* ratio, thereby counteracted the hepatocyte apoptosis.

Semiquantitative RT-PCR analysis of apoptosis-related genes *bax* and *bcl-2* mRNA The total RNA extracted from each group were loaded onto 1% agarose gel; 28 s, 18 s, and 5 s bands could be clearly observed, which confirmed the integrity of the total RNA (Figure 2). In the present study, 20 μL *bcl-2* or *bax* PCR product together with β-actin PCR product of the same template were separated by electrophoresis and revealed by EB staining. PCR products of *bcl-2*, *bax*, and β-actin were 450 bp, 429 bp, 240 bp, respectively (Figure 3). The *bcl-2* mRNA was the most in the group treated with picroside II 20 g/L, and the least in the negative group; *bax* mRNA was the most in model group, followed by the negative group, and the least in the groups treated with picroside II.

Morphological evaluation by light microscope assay Hepatocytes exhibited acidophilic trait induced by *D*-GalN and LPS, and there were acidophilic bodies in cytoplasm. There was no obvious pathological change observed in groups treated with picroside II 10 and 20 g/L (Figure 4).

Transmission electron microscopy assay Normal hepatocyte was capsule intact, cytoplasm well-diffused, and karyotheca distinct and bears large nuclei. Apoptotic cells

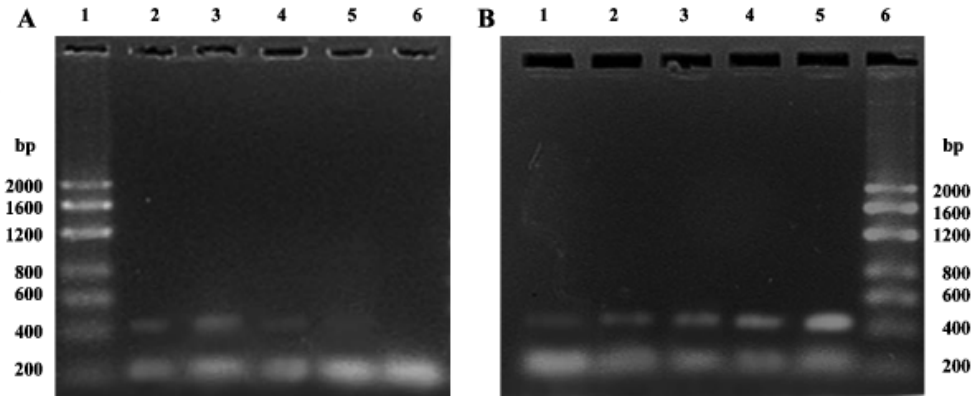

Figure 3. Semiquantitatively RT-PCR analysis of *bax* mRNA (A) and *bcl-2* mRNA (B). (A) 1, DNA marker; 2, negative group; 3, model group; 4, picroside II 20 mg·mL^{-1}; 5, picroside II 10 mg·mL^{-1}; 6, picroside II 5 mg·mL^{-1}. (B) 1, negative group; 2, model group; 3, picroside II 5 g·L^{-1}; 4, picroside II 10 g·L^{-1}; 5, picroside II 20 g·L^{-1}; 6, DNA marker.

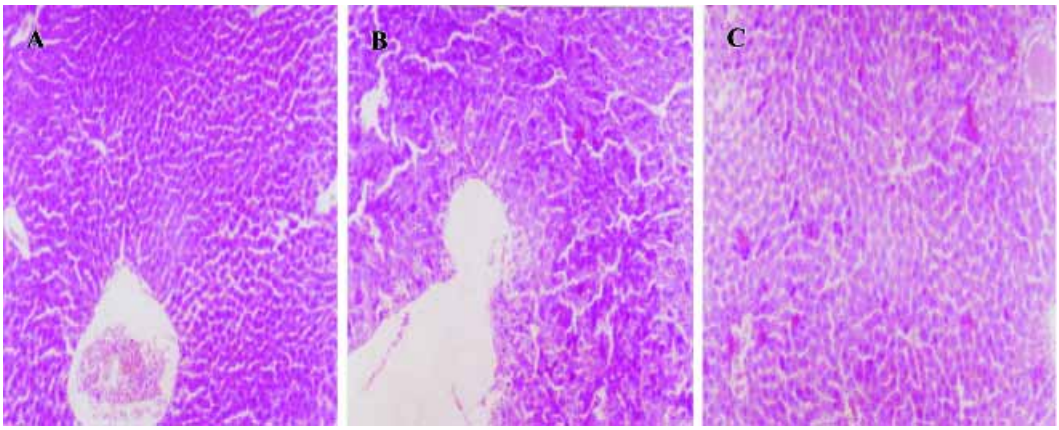

Figure 4. Liver tissue of each groups. (A) negative group; (B) model group; (C) Picroside II-treated group. HE, ×200.

in the initial stages had shrunken and compacted with condensed or marginal chromatin. Chromatin spalls to pieces or semilunar body gradually and cytoplasm becomes condensation. In addition, blebbing of the plasmalemma, forming apoptosis body, a hall marker of apoptosis was then be observed (Figure 5).

DNA fragmentation analysis Figure 6 shows that the model groups (lanes 2 and 7) exhibited the characteristic DNA ladder. In the groups treated with picroside II 5, 10, 20 g/L (lane 6, 5 and 4, respectively), the DNA ladder became less characteristic. Groups treated with picroside II 20 g/L (lane 4) were similar to negative group (lane 3).

Flow cytometry analysis of apoptosis Apoptosis rate of primary hepatocytes of the negative group was 4.1%, the model group was 22.3%, groups treated with picroside II 20, 10, 5 g/L were 6.9 %, 10.7 % and 15.1 %, respectively, which suggested that picroside II could protect hepatocyte against apoptosis, and it acted in a dose-dependent manner (Figure 7).

Discussion

The pathogenesis mechanisms of viral hepatitis is closely related to hepatocyte necrosis as well as apoptosis closely. Invasion of hepatitis virus to liver or hepatocytes canceration will result in hepatocyte apoptosis[9–11]. In inflammtory hepatitis, acidophilic body (shrunken necrosis, apoptosis corpuscula) and piece-meal necrosis were the characteristic morphological manifestation of apoptotic hepatocytes. Apoptosis of hepatocytes infected by virus can be a protective mechanism of the host to protect against virus replication and distribution from the infected cells[12]. Apoptotic cell death contributes to the removal of infected or cancerized cells, but over-apoptosis results in fulminate hepatitis[13,14]. Commonly, drugs are used to block hepatocyte apoptosis in

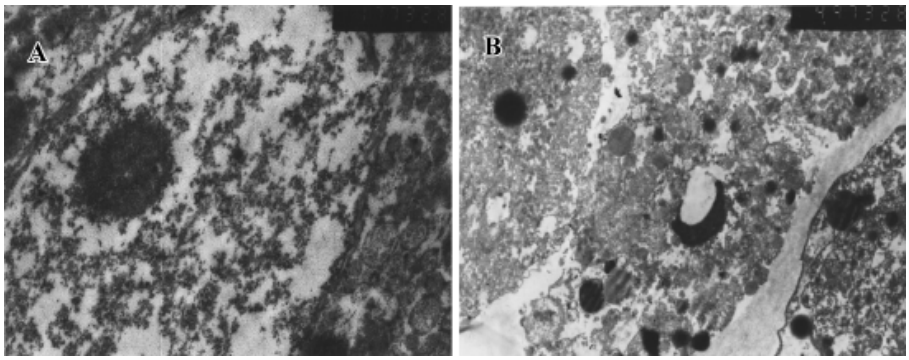

Figure 5. Transmission electron microscopy assay. (A): negative primary hepatocytes (×26500); (B): apoptotic primary hepatocytes (×7350).

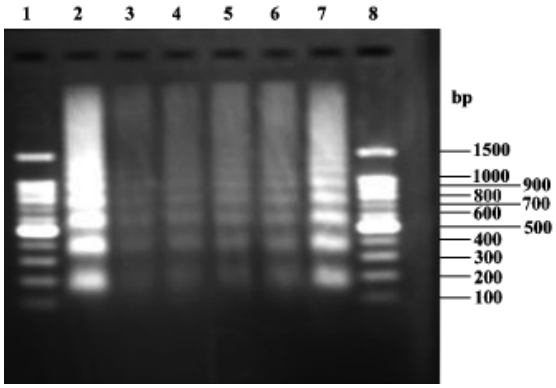

Figure 6. Agarose gel electrophoresis of DNA fragmentation. 1: DNA molecular weight marker. 2: model group. 3: negative group. 4: treated with picroside II 20 g·L^{-1}. 5:treated with picroside II 10 g·L^{-1}. 6: treated with picroside II 5 g·L^{-1}. 7: model group. 8: DNA molecular weight marker.

order to cure hepatitis gravis, and to induce hepatocyte apoptosis for removing infected and cancerized cells[15–20].

One important molecular mechanism for cell apoptosis might be the modulation of the expression of *bcl-2* gene family, which plays a critical role for the common pathway of apoptosis. Previous studies showed that proteins of Bcl-*2* family could inhibit apoptosis of chronic infective hepatocytes, marrow stem cells, and nerve cells. The biological function of Bcl-2 is to increase the power to resist many apoptotic factors, counteract the effect of apoptosis, and extend lifespan. Bax, another important apoptosis-modulating gene product, is highly related to Bcl-2. Bax inactivates Bcl-2 by binding it to form a heterogeneous dimer. The mRNA and protein ratio of Bcl-2 to Bax is a pivotal factor in determine whether or not apoptosis can happen to cells exposed to many injuries [21]. Studidies have revealed that

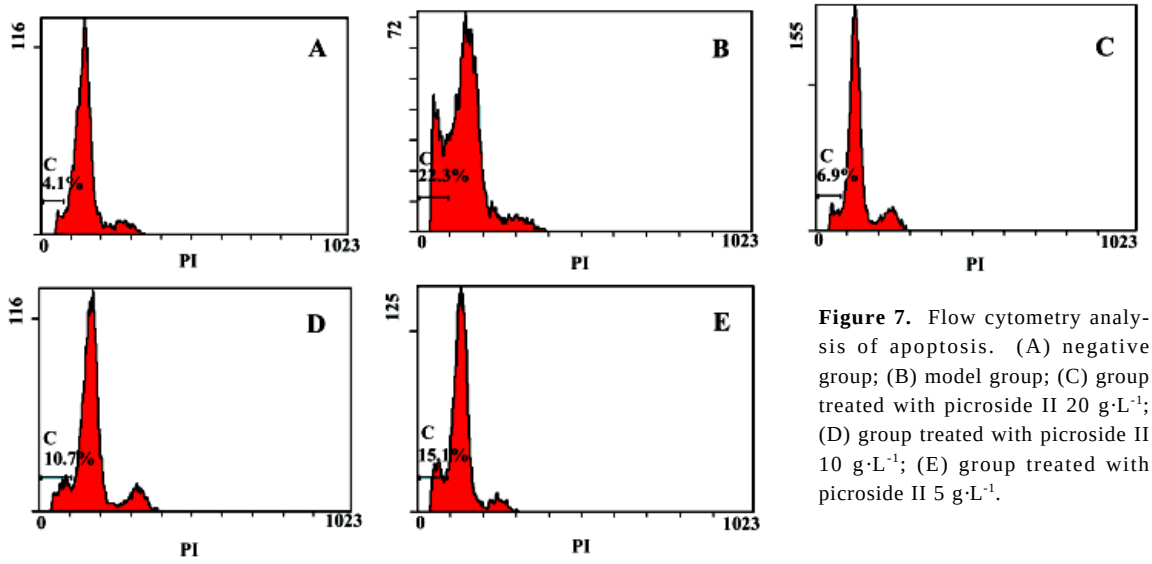

Figure 7. Flow cytometry analysis of apoptosis. (A) negative group; (B) model group; (C) group treated with picroside II 20 g·L^{-1}; (D) group treated with picroside II 10 g·L^{-1}; (E) group treated with picroside II 5 g·L^{-1}.

TNF-α could induce hepatocyte apoptosis, thus to participate in the onset of liver diseases. However, TNF-α itself dose not act *in vivo* and *in vitro* unless it is used together with Act-D and *D*-GalN[22]. Act-D is an inhibitor of RNA transcription, and could sensitize cells to the toxicity of TNF-α[23]. Therefore, the combination of Act-D and TNF-α is frequently used to establish models of hepatocyte apoptosis *in vivo* as well as *in vitro*[24]. The present study assumed that Act-D together with TNF-α to the establish experimental apoptosis model, agarose gel electrophoresis of DNA, and flow cytometry were used to evaluate hepatocyte apoptosis; light and transmission electron microscopy were used to observe morphological changes of cells and tissues; and quantitatively analysed the hepatocytes apoptosis. These results indicated that Picroside II evidently inhibited the morphological changes of hepatocytes, DNA fragmentation, and the increase of sub-G1 spike (represents proportion of apoptosis). Immunohistochemistry and semi-quantitative RT-PCR analysis of the Bcl-2 and Bax expression and mRNA of *bcl-2* and *bax* genes suggested that both *bcl-2* and *bax* increased after hepatocyte injury, especially *bax*. The *bcl-2* level and the ratio of *bcl-2/bax* increased markedly in groups treated with picroside II and apoptosis changes were also inhibited.

MDA is a lipid peroxide, whose content usually reflects the level of lipid peroxidation and indirectly reflects the extent of injury *in vivo*. SOD is a pivotal factor influencing the balance of oxidation and antioxidation, and its activity could indirectly reflect the capability of removing oxygen free radical. Biomembrane is the main place to undertake lipid peroxidation injury. Active oxygen from inflammatory cells could induce apoptosis in cells when lipid peroxidation injury occurs to the membranes of mitochondria and microsome. Changes of cell phenotype through gene transcription might be one of the mechanisms of apoptosis induced by oxidation injury. The present study also suggested that picroside II could simultaneously decrease the level of MDA, ALT, AST, and increase the activity of SOD in liver mitochondria.

In conclusion, we have shown for the first time that picroside II is able to protect hepatocytes against injury and counteract apoptosis through its anti-oxidation effect, and it can act by decreasing MDA level, increasing the activity of SOD in liver mitochondria and upregulating *bcl-2* gene expression.

References

1 Ansari RA, Aswal BS, Chander R, Dhawan BN, Garg NK, Kapoor NK, *et al*. Hepatoprotective activity of kutkin, the iridoid glycoside mixture of *Picrorhiza kurroa*. Indian J Med Res 1998; 87: 401–4.

2 Chander R, Wivedi Y, Rastogi R, Sharma SK, Garg NK, Kapoor NK, *et al*. Evaluation of hepatoprotective activity of Picroliv (from *Picrohiza kurroa*) in *Mastomys natalensis* infected with *Plasmodium berghei*. Indian J Med Res 1990; 92: 34–7.

3 Dwivedi Y, Rastoui R, Chander R, Sharma SK, Garg NK, Dhawan BN. Hepatoprotective activity of Picroliv against carbon tetrachloride induced damage in rats. Indian J Med Res 1990; 92: 195–200.

4 Saksena S, Rastogi R, Garg NK, Dhawan BN. Rifampicin induced hepatotoxicity in rats: protective effect of Picroliv. Drug Dev Res 1994; 33: 46–50.

5 Saraswat B, Visen P KS, Patnaik GK, Dhawan BN. Hepatoprotective activity of Picroliv against rifampicin induced toxicity. Drug Dev Res 1997; 40: 299–303.

6 Marland S, Marklund G. Involvement of the superoxide anion radical in the autoxidation of pyrogollol and a convenient assay for superoxide dismutase. Eur J Biochem 1974; 47: 469–74.

7 Lowry OH, Rosebrough NJ, Farr AL. Protein measurement with the Folin phenol reagent. J Biol Chem 1951; 193: 265–75.

8 Yagi K. A simple fluorometric assay for lipoperoxide in blood plasma. Biochem Med 1976; 15: 212–5.

9 Guo JT, Zhou H, Liu C, Aldrich C, Saputelli J, Whitaker T, *et al*. Apoptosis and regeneration of hepatocytes during recovery from transient hepadnavirus infections. J Virol 2000; 74: 1495–505.

10 Honda A, Hatano M, Kohara M, Arai Y, Hartatik T, Moriyama T, *et al*. HCV-core protein accelerates recovery from the insensitivity of liver cells to Fas-mediated apoptosis induced by an injection of anti-Fas antibody in mice. J Hepatol 2000; 33: 440–7.

11 Gu XH, Li QF, Wang YM. Expression of *bcl-2*, *bax* and hepatocyte apoptosis in the liver tissues of hepatitis D patients. Chin J Hepatol 2001; 9: 81–3.

12 Williams GT, Smith CA. Molecular regulation of apoptosis: genetic controls on cell death. Cell 1993; 74: 777.

13 Tokushige K, Yamaguchi N, Ikeda I, Hashimoto E, Yamauchi K, Hayashi N. Significance of soluble TNF receptor-1 in acute-type fulminant hepatitis. Am J Gastroenterol 2000; 95: 2040–6.

14 Ryo K, Kamogawa Y, Ikeda I, Yamauchi K, Yonehara S, Nagata S, *et al*. Significance of Fas antigen-mediated apoptosis in human fulminant hepatic failure. Am J Gastroenterol 2000; 95: 2047–55.

15 Van Molle W, Berghe JV, Brouckaert P, Libert C. Tumor necrosis factor-induced lethal hepatitis: pharmacological intervention with verapamil, tannic acid, picotamide and K76COOH. FEBS Lett 2000; 467: 201–5.

16 Okamoto T. The protective effect of glycyrrhizin on anti-Fas antibody-induced hepatitis in mice. Eur J Pharmacol 2000;387: 229–32.

17 Fiorucci S, Mencarelli A, Palazzetti B, Soldato PD, Morelli A, Ignarro LI. An NO derivative of ursodeoxycholic acid protects against Fas-mediated liver injury by inhibiting caspase activity. Proc Natl Acad Sci USA 2001; 98: 2652–7.

18 Yamamoto M, Miura N, Ohtake N, Amagaya S, Ishige A, Sasaki H, *et al*. Genipin, a metabolite derived from the herbal medicine Inchin-ko-to, and suppression of Fas-induced lethal liver apoptosis in mice. Gastroenterology 2000; 118: 380–9.

19 Liu J, Shen HM, Ong CN. *Salvia miltiorrhiza* inhibits cell growth and induces apoptosis in human hepatoma HepG(2) cells. Can-

cer Lett 2000; 153: 85–93.
20 Shimizu I. Sho-saiko-to: Japanese herbal medicine for protection against hepatic fibrosis and carcinoma. J Gastroenterol Hepatol 2000; 15: D84–90.
21 Amato D, Zwain I, Reed J. Expression of bcl-2 and bax in human placenta. J Soc Gynecol Invest 1996; 3 (Suppl): 226.
22 Zhang GQ, Yu H, Zhou XQ, Liao D, Xie Q, Wang B. TNF-α induced apoptosis and necrosis of mice hepatocytes. World Chin J Diges 2000; 8: 303–6.
23 Xu Y, Blalik S, Jones BE, Iimuro Y, Kitsis RN, Srinivasan A, *et al.* NF-κB inactivation converts a hepatocyte cell line TNF-α response from proliferation to apoptosis. Am J Physiol 1998; 275: C1058–66.
24 Leist M, Gantner F, Bohlinger I. Murine hepatocyte apoptosis induced *in vitro* and *in vivo* by TNF-α requires transcriptional arrest. J Immunol 1994; 153: 1778–88.

Acta Pharmacologica Sinica 2005 Jun; 26 (6): 737–744

Full-length article

Altered expression of cytochrome P450 and possible correlation with preneoplastic changes in early stage of rat hepatocarcinogenesis[1]

Lin-lin LIU[2,3], Li-kun GONG[2,3], Xin-ming QI[2,3], Yan CAI[2,3], Hui WANG[2], Xiong-fei WU[2,3], Ying XIAO[2,3], Jin REN[2,4]

[2]*State Key Laboratory of Drug Research, Shanghai Institute of Materia Medica, Shanghai Institutes for Biological Sciences, Chinese Academy of Sciences, Shanghai 201203, China;* [3]*Graduate School of the Chinese Academy of Sciences, Shanghai 201203, China*

Key words

cytochrome P450; preneoplastic changes; hepatocarcinogensis

[1]Project supported by the National Natural Science Foundation of China (No 30271558).
[4]Correspondence to Dr Jin REN.
Phn/Fax 86-21-5080-6031.
E-mail jren@mail.shcnc.ac.cn

Received 2005-01-11
Accepted 2005-03-07

doi: 10.1111/j.1745-7254.2005.00120.x

Abstract

Aim: Correlation of cytochrome P450 (CYPs) with preneoplastic changes in the early stage of hepatocarcinogenesis is still unclear. To detect the expression of carcinogen-metabolizing related microsomal P450 enzymes, namely the CYP1A1, CYP1A2, CYP2B1/2, CYP2E1, and CYP3A, we performed the medium-term bioassay of Ito's model in Sprague-Dawley rats. **Methods:** The amount and activity of CYP were assessed by biochemical and immunohistochemical methods in week 8. The correlation between CYP expression and microsomal oxidative stress was investigated by comparing the generation of microsomal lipid peroxidation in the presence or absence of specific CYP inhibitor. **Results**: In the DEN-2-AAF and 2-AAF alone groups, the expression of CYP1A1 and CYP2E1 were up-regulated and the expression of CYP2B1/2 and CYP1A2 were quite the contrary. Strong staining of CYP2E1 and CYP2B1/2 was found around the centrolobular vein and weak staining in the altered hepatic foci revealed by immunohistochemical procedure. There was no significant change in the activity of CYP3A among the 4 groups. Altered hepatic tissue bore more microsomal NADPH (nicotinamide adenine dimucleotide phosphate,reduced form)-dependent lipid peroxidation than normal tissue. And the difference among the 4 groups disappeared when CYP2E1 was inhibited. More microsomal lipid peroxidation was generated when incubated with CYP1A inhibitor α-naphthoflavone. **Conclusion**: CYP altered their expression levels and these alterations can play important roles in the alteration of cell redox status of preneoplastic tissue in the early stage of hepatocarcinogenesis.

Introduction

Cytochrome P450 (CYP) plays a pivotal role in oxidative metabolism of lipophilic drugs and xenobiotics (some of them are carcinogens), which will then be transformed into more polar water soluble molecule[1]. During these processes, activation or detoxicitation takes place. A prominent phenomenon during hepatocarcinogenesis is an alternation of the expression of drug metabolism enzymes[2]. CYP can be influenced by a number of exogenous and endogenous factors and its induction is of the utmost interest in carcinogenesis[3,4].

The underlying mechanisms by which CYP enzymes involved in the process of hepatocarcinogenesis have not been elucidated clearly or in detail. Some probable mechanisms have been suggested including the metabolism of exogenous chemicals involved in the generation of reactive oxygen species and oxidative DNA damage, which are associated with apoptosis and cell cycle arrest[5]. Moreover, alteration of the activities of CYP in rats could be an important factor in determining resistance or susceptibility to xenobiotics in the early stage of hepatocarcinogenesis[6].

Preneoplastic and neoplastic lesions induced by various different treatment regimens have a decrease in expression of phase I enzymes and an increase in expression of phase II enzymes in common[7]. The decrease in expression of CYP in preneoplastic lesions could alter the synthesis and/or inactivate endogenous and/or exogenous substance, which act as tumor promoters or comitogens, thus resulting in the selective growth of a subset of hepatic hyperplastic lesions [7,8].

CYP1A family might be marker enzymes that indicat the carcinogenic potential of xenobiotics. Most polyhalogenated aromatic hydrocarbons that have proven to be carcinogen have a common induction of CYP1A1. A previously published study demonstrated that the level of N-nitrosodimethylamine demethylase activities (mainly catalysed by CYP2E1) and CYP2E1 protein content were lower in hepatomas than in the corresponding host liver[9]. However, the change of CYP2E1 expression in the early stage of hepatocarcinogenesis and the probable role in the process of hepatocarcinogenesis was unclear.

Oxidative stress interacts with all 3 stages of the cancer process. Higher levels of reactive oxygen species (ROS) have been found in neoplastic nodules of rat liver than in the surrounding normal tissue. ROS can be generated from several intracellular locations including microsomal pathway and the mitochondrial electron transport chain. Microsomal generated ROS is one of the most significant causes of liver injury[10]. The existence of NADPH-dependent production of ROS by animal liver microsomes has been linked to CYP. The uncoupling of electron transfer and oxygen reduction from monooxygenation by CYP2B1 and CYP2E1 could result in the release of O_2^- and H_2O_2. A recent study has demonstrated that this step is also involved in CYP1A1, CYP3A, and CYP4A isoforms[11]. Within these isozymes, CYP2E1 is a major inducible hepatic microsomal CYP involved in the hydroxylation of fatty acids, and can initiate the autopropagative process of lipid peroxidantion if they are not countered efficiently by antioxidants. In the present paper, a reconstituted mircrosomal lipid peroxidation system consisting of rat liver microsomal NADPH-cytochrome P450 reductase and cytochrome P450 incorporated into phospholipids vesicles was developed to investigate the possible role of the specific CYP to generate microsomal lipid peroxidation that resulted in the different cell redox status among the 4 groups.

The medium-term bioassay, which was developed by Ito *et al* in 1989 to detect the carcinogenic potential and their postinitiation modifying effects[12], is of relatively short duration, but results in sufficient lesions to allow statistical comparisons[13]. To investigate the induction and inhibiton of CYP in the early stage of hepatocarcinogenesis induced by DEN and 2-AAF, we performed the medium-term bioassay. In the present study, we investigated the major carcinogenesis related to CYP isozymes, namely CYP1A1, CYP1A2, CYP2B1/2, CYP3A, CYP2E1, and indicated their respective role in the formation of hyperplastic foci.

Materials and methods

Chemicals Diethylnitrosamine (DEN), 2-acetylaminofluorene (2-AAF), α-naphthoflavone, 8-methoxypsoralen were purchased from Sigma Chemical Co. Ethoxyresorufin and resorufin were obtained from Molecular Probes. Erythromycin was purchased from Shanghai Sangon Co Ltd. All the antibodies, except those mentioned (later), were purchased from Chemicon International Institute. Enhancing chemiluminescence (ECL) was obtained form Amersham Life Sciences (Amersham, United Kingdom).

Animal experiment Sixty male pathogen-free Sprague–Dawley rats (70–80 g) were obtained at 6 weeks of age from the Shanghai Laboratory Animal Center, Chinese Academy of Sciences (Shanghai, China), and housed in plastic cages with wood chips for bedding in a temperature and humidity-controlled animal facility center with a daily photoperiod of 12 h of light and 12 h of darkness. Forty rats which had no abnormal findings after a 1-week acclimatization period, were randomly divided into 4 groups referred to as group A, B, C, and D, each consisting of 10 animals. Group D (control) was maintained on a basal diet without carcinogen treatment; group A received a single ip injection of DEN (200 mg/kg) in 0.9% NaCl, and 2 weeks later were placed on a diet containing 2-AAF (100 ppm) for 6 weeks. Group B received a single ip injection of DEN (200 mg/kg) dissolved in 0.9% NaCl and was then maintained on the basal diet for 8 weeks; group C were placed on a diet containing 2-AAF (100 ppm) from week 2 to week 8 without DEN initiation. All groups received partial hepatectomy (two-thirds of the total liver) in the third week. At week 8 all the rats were anesthetized with diethyl ether; liver perfusion was performed with ice-cold perfusion buffer [1.15% KCl, 1 mmol/L^{-1} EDTA, 0.25 mmol/L phenylmethylsulfonyl fluoride (PMSF)] at room temperature. Separate portions were fixed in 10% phosphate-buffered formalin, partially frozen in liquid nitrogen and stored at liquid nitrogen for molecular assessment. Microsomes were prepared by differential centrifugations as described previously and stored at -80 °C until use.

Biochemical assay

Ethoxy O-dealkylase activity assay The metabolism of ethoxyresorufin is associated with CYP1A1 and CYP1A2, with CYP1A1 metabolizing ethoxyresorufin to a much greater extent than CYP1A2 when both CYP are present. The dealkylation of ethoxyresorufin by microsomes was quantified by measurements of increased resorufin fluorescence over time using a Polar star* fluorescence microplate reader (BMG labtechnologies Pty Ltd, Melbourne, Australia). Microsome protein (50–150 μg) was added to 0.1 mol/L potas-

sium phosphate buffer pH 7.6, along with 2 μmol/L ethoxyresorufin in the total reaction volume of 2.0 mL. This microsome substrate solution was incubated at 37 ºC for 3 min prior to initiation of the reaction with 0.5 mmol/L NADPH. The reaction continued for the next 5 min, the formation of resorufin was measured at the excitation wavelength of 535 nm and emission wavelength of 590 nm. The standard curve was performed with the known amounts of resorufin.

p-Nitrophenol hydroxylase (PNPH) assay PNPH was assayed as described previously. The reaction mixtures contained a 0.1 mol/L potassium phosphate buffer, pH 6.8, 1.0 mmol/L ascorbic adid, 0.1 mmol/L *p*-nitrophenol, 100 μL 25% microsome protein and 1mmol/L NADPH in a total volume of 1.0 mL. The reaction was initiated by adding NADPH after incubation at 37 ºC for 3 min. After a 10-min incubation at 37 ºC, the reaction was stopped by adding 0.5 mL 0.6 mol/L $HClO_4$. The 4-nitrocatechol formed was determined spectrally at 510 nm in 1.0 mL of the supernatant at 546 nm after the addition of 0.1 mL 10 mol/L NaOH.

Erythromycin N-demethylase activity assay The microsomal erythromycin N-demethylase activity was performed as previouly described. The reaction mixture included 0.6 mL 50 mmol/L potassium phosphate buffer (pH 7.25), 0.1 mL 150 mmol/L magnesium chloride, 0.1 mL 10 mmol/L erythromycin and 0.1mL microsomal suspension. After adding NADPH to initiate the reaction, the reaction mixture was incubated at 37 ºC for 10 min. The reaction was then terminated by 0.5 mL ice-cold 12.5% (w/v) trichloroacetic acid. After centrifuge, the same volume of NASH reagent (NASH reagent containing 150 g ammonium acetate, 3.0 mL glacial acetic acid and 2.0 mL acetylacetone per liter of aqueous solution)was added to supernatant. The formaldehyde formed was determined spectrally at 412 nm after heating at 50 ºC for 30 min.

Western Blot Microsomal fractions of the liver samples were separated by SDS-PAGE and electrophoretically transferred to polyvinylidene fluoride (PVDF) membranes, incubation with rabbit anti-rat CYP1A1, CYP1A2, CYP2B1/2, CYP2E1 (1:1000) at 4 ºC overnight, followed by peroxidase-conjugated goat anti-rabbit IgG (1:4000) at room temperature for 1 h. Binding was visualized with an enchanced chemiluminescence.

Immunohistochemistry

glutathione *S*-transferase placental (GST-P) immunohistochemistry Immunhistochemical staining using rabbit anti-GST-P IgG (ready to use; Medical Biological Laboratories Co, Nagoya, Japan), was performed by avidin-biotin complex method. Quantitation of GST-P-positive foci was performed using 2-dimension evaluation only. The areas of GST-P-positive foci greater than 0.2 mm in diameter and the total areas of the liver sections were measured using Leica QFAB Image Processing (Leica Imaging Systems Ltd, Cambridge, England) and analysis system to give values per cm^2 of liver section.

Immunohistochemistry of proliferating cell nuclear antigen (PCNA) PCNA was detected from formalin-fixed paraffin-embedded tissue sections. Immunohistochemical staining using monoclonal mouse anti-PCNA IgG (1:100 diluted in 0.01 mmol/L PBS, pH 7.2) and biotinylated rabbit anti-mouse immunoglobulins (1:300 diluted in 0.01mmol/L PBS, pH 7.2) was performed by avidin-biotin complex method. Antigen retrieval was performed by boiling for 10 min in a microwave oven (600W). The number of nuclei and PCNA-positive nuclei were counted under a light microscope. Ten random fields (approximately 2000 nuclei) per section were assessed under 40×objective lens.

Liver microsomal NADPH-dependent lipid oxidation: thiobarbitric acid reactive substances (TBARS) assay Fe^{3+}/ADP-induced: liver microsomes (300 μg of protein per mL) were preincubated in 150 mmol/L Tris/HCl buffer, pH 7.4. After 10 min incubation at 37 ºC, lipid peroxidation was initiated by the addition of 2 μmol/L $FeCl_3$/200 μmol/L ADP (previously complexed), and 200 μmol/L NADPH. The total volume was 0.5 mL, and all additions expressed earlier were final concentration in the incubation system. Incubations were carried out at 37 ºC. Lipid peroxidation was monitored by the formation of TBARS reactions.

Not Fe^{3+}/ADP-induced: the microsomal protein (200 μg in 50 mmol/L phosphate buffer saline, pH 7.4) was incubated in the presence of 0.23 mmol/L NADPH at 37 ºC for 10 min before analysis of thiobarbitric acid (TBA) reactive substances. For pharmacological inhibition studies, microsomal protein was pre-incubated for 10–30 min at room temperature in the presence of either diethyldithiocarbamate (CYP2E1 inhibitor, 50 μmol/L) or α-naphthoflavone (CYP1A inhibitor, 10 μmol/L), 8-methoxypsoralen (CYP1A and CYP2A6 inhibitor, 1 μmol/L). α-Naphthoflavone is 10 times more potent as an inhibitor of CYP1A2 than CYP1A1. 8-Methoxypsoralen has a similar inhibition of CYP1A1 and CYP1A2. The microsomal NADPH-dependent lipid peroxidation was performed as described earlier.

Glutathione assay Glutathione level in the homogenates was assayed with a microplate reader using the GSH test kit. The GSH test kit was obtained from the Nanjing Jiancheng Bioengineering Institute (Nanjing, China).

Statistical methods Data were expressed as mean±SEM. After homogenetic analysis, homogeneous data were analyzed with one-way analysis of variance and a post hoc test

of least significant difference. Heterogeneous data were analyzed using the *t*-test. $P<0.05$ was considered significant.

Results

Body and liver weights The toxicity and abnormal proliferation induced by DEN and 2-AAF was evident in data for body or relative liver weights. The body weights of both groups A and B decreased significantly compared with that of group D. There were no significant alteration in absolute liver weight in all 4 groups. But the relative liver weights (relative to body weights) significantly ($P<0.05$, $n=5$) increased in DEN+2-AAF, DEN, and 2-AAF group (Table 1).

Table 1. Body and liver weights. $n=5$. Mean±SEM. $^bP<0.05$ *vs* control group.

Group	Body weight/g	Liver weight	
		Absolute/g	Relative/%
DEN+2-AAF	360±25[b]	13.5±1.3	3.78±0.49[b]
DEN	379±35[b]	13.0±1.6	3.44±0.43[b]
2-AAF	412±44	13.3±1.3	3.22±0.20
Control	452±52	13.0±0.7	2.87±0.25

Carcinogenic potential assay: GST-P and PCNA immunohistochemistry Carcinogenic potential assay was performed by comparing the numbers and areas of GST-P-positive foci. The numbers and areas of GST-P-positive foci significantly increased in group A as compared with that of groups B and D (Figure 1A, Table 2). With the present carcinogenic protocol, treatment of rats with single injection of DEN alone did not induce altered hepatic foci but treatment with DEN plus 2-AAF induced many altered hepatic foci in the liver.

PCNA was used as an indicator of cell proliferation. Immunohistochemistry detection of PCNA is a common method used to grade proliferative activity in a given tissue. The number of PCNA-positive cells in groups A and C were remarkably ($P<0.05$, $n=5$) more than that of control group (Table 2, Figure 1B).

Western blot analysis of Cytochrome P450 isozymes In the present experiments, we used liver samples without isolation of hyperplastic nodules for the analyses of CYP enzymes, because each hyperplastic nodule was too small to isolate. Western blot analysis revealed a slight increase of CYP2E1, significant decrease of CYP1A2 and CYP2B1/2 in both groups A and C. There was no detectable difference of CYP2E1, CYP1A2, and CYP2B1/2 between the DEN-PH group and the control group. CYP1A1 was almost undetectable in the control group, but the induction of CYP1A1 in group C was greater than DEN+2-AAF group and DEN group (Figure 2).

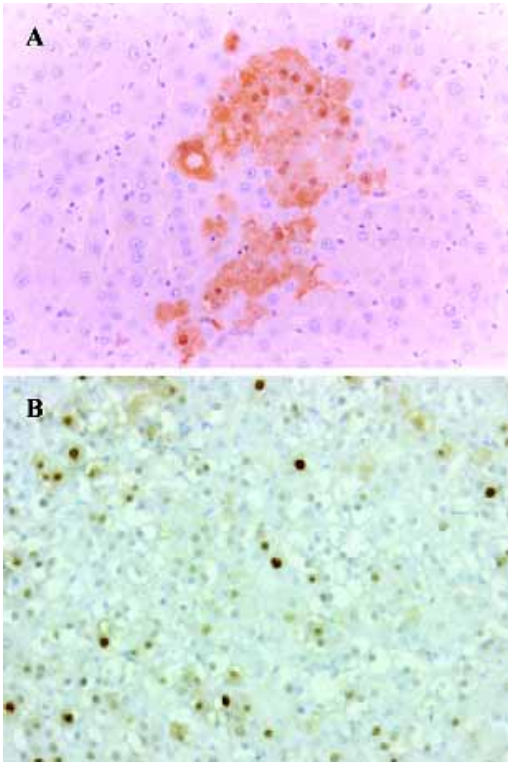

Figure 1. Immunohistochemical staining of GST-P and PCNA in the tissue of group A. (A) GST-P (×15); (B) PCNA (×30).

Table 2. Carcinogenic potential assay. Total areas of GST-P-positive foci and the number of PCNA positive nuclei per 1000 cells. $^cP<0.01$ *vs* control group. $^eP<0.05$, $^fP<0.01$ *vs* group DEN group.

Group	GST-P foci area/ $mm^2 \cdot cm^{-2}$	PCNA (+) nuclei (1000 cells)
DEN+2-AAF	17.13[c]	135±30[c,f]
DEN	1.16	68±45
2-AAF	1.08	115±28[c,e]
Control	Not detectable	32±13

Measurement of ethoxy-O-dealkylase activity, *p*-nitrophenol hydroxylase (PNPH) activity, and erythromycin N-demethylase activity assay The results of these experiments showed that treatment of DEN-PH-2-AAF statistically ($P<0.01$, $n=5$) increased the liver microsomal PNPH activity approximately 40% more than that of control group; treatment of 2-AAF-PH-2-AAF increased PNPH activity by

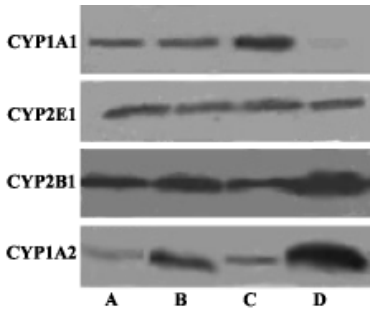

Figure 2. Western blot analysis of CYP1A1, CYP1A2, CYP2E1, CYP2B1/2. Lane A: group DEN+2-AAF; lane B, group DEN; lane C, group 2-AAF; lane D, group control. Microsomal protein 80 μg consisting of 3 samples of different rats was loaded into each band.

approximately 30%, but the treatment of a single injection of DEN had no influence on the PNPH activity. These results were in accordance with our Western blot analysis and immunohistochemisty results (Table 3).

Treatment with 2-AAF dramatically increased the ethoxy-O-dealkylase activity approximatley 7 times than that of control group. However, treatment with DEN-PH-2-AAF only increased the ethoxy-O-dealkylase activity 1.6 times more (Table 3).

There were no differences of the liver microsomal erythromycin N-demethylase activity among the 4 experiment groups (Table 3).

Immunohistochemistry of CYP2E1 and CYP2B1/2 In the normal liver tissue, immunohistochemical staining of CYP2E1 showed moderate or weak staining around the centrolobular vein (Figure 3C, 3D). In the DEN-2-AAF group

Table 3. Biochemical assay of hepatic microsomal CYP enzymes. Metabolism of *p*-nitrophenol is associated with CYP2E1. Metabolism of ethoxyresorufin is associated with CYP1A1 and CYP1A2, with CYP1A1 metabolizing ethoxyresorufin to a much greater extent than CYP1A2 when both CYP are present. n=5. Mean±SEM. $^{b}P<0.05$, $^{c}P<0.01$ *vs* control group. $^{e}P<0.05$ *vs* group 2-AAF group. $^{h}P<0.05$ *vs* group DEN group.

Group	PNPH activity/ mmol·g^{-1}·min^{-1}	Ethoxyresorufin O-dealkylase activity/nmol·g^{-1}·min^{-1}	Erythromycin N-demethylase activity/pmol·g^{-1}·min^{-1}
DEN+2-AAF	2.88±0.61^{ce}	61335±10334^{c}	1.56±0.35
DEN	2.22±0.26	126771±18071^{c}	1.42±0.30
2-AAF	2.75±0.27^{bh}	174533±54160^{c}	1.54±0.16
Control	2.12±0.26	23667±4616	1.46±0.15

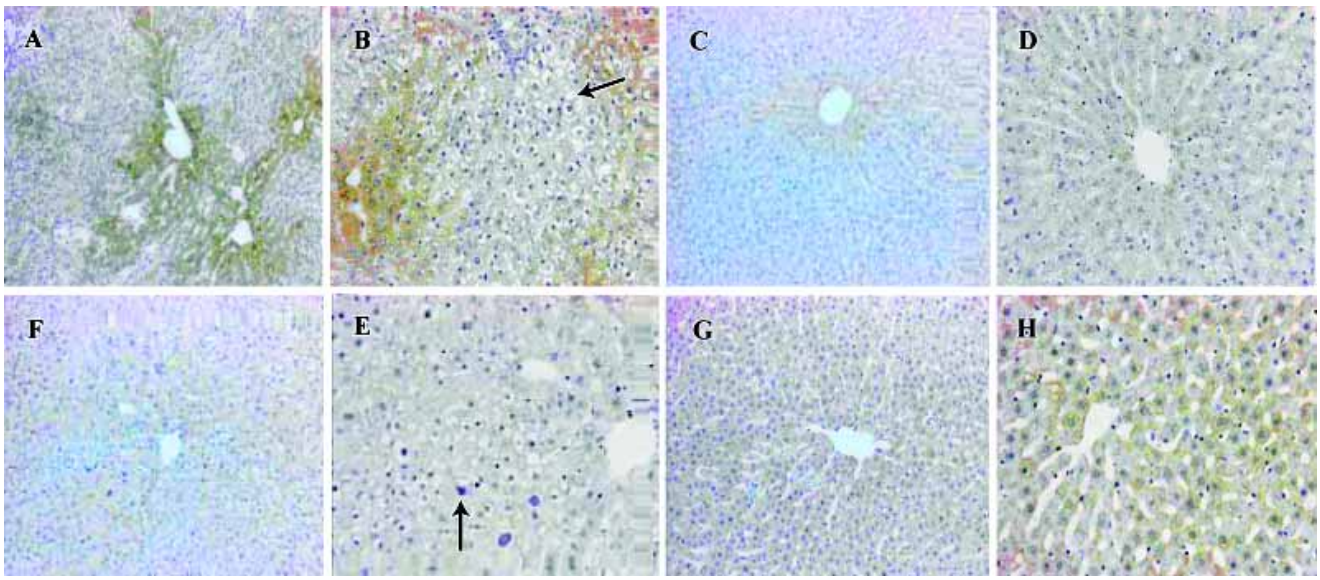

Figure 3. Immunohistochemistry staining of CYP2E1 and CYP2B1/2. (A) CYP2E1, group A (×15); (B) CYP2E1, group A. Preneoplastic foci is indicated by the arrow (×30); (C) CYP2E1, group D (×15); (D) CYP2E1, group D (×30); (E) CYP2B1/2, group D (×15); (F) CYP2B1/2, group D (×30); (G) CYP2B1/2, group A (×30); (H) CYP2B1/2, group A. Preneoplastic foci is indicated by the arrow (×15).

and 2-AAF alone group, the positive staining area was extended and the staining was stronger than that of the control group (Figure 3A). The staining of CYP2E1 was also not seen in the hepatocytes within the altered hepatic foci (Figure 3B).

In the normal liver tissue, immunohistochemical staining of CYP2B1/2 showed a strong centrolobular staining pattern; no staining of CYP2B1/2 was found in the periportal area (Figure 3G, 3H). In the liver treated with DEN-2-AAF, centrolobular staining of CYP2B1/2 was relatively weak and the number of positive hepatocytes was less than that in the normal tissue (Figure 3E). There was no staining of CYP2B1/2 in the altered hepatic foci hepatocytes, except some positive staining hepatocytes scattered among the negative hepatocytes (Figure 3F).

Liver microsomal lipid peroxidation and glutathione level

Treatment with DEN/PH/2-AAF significantly ($P<0.01$, $n=5$) increased the ability of liver microsome to generate the lipid peroxidation whether in the presence or absence of Fe^{3+}/ADP. Treatment with 2-AAF or a single injection of DEN could also increase the generation of lipid peroxidation without the presence of Fe^{3+}/ADP. However, in the presence of Fe^{3+}/ADP, no remarkable alteration existed between the groups DEN, 2-AAF, and control group, probably because Fe^{3+}/ADP presence could increase the normal liver microsomal lipid peroxidation and obliterate the difference. In the presence of CYP2E1 inhibitor diethyl-dithiocarbamate, the generation of lipid peroxidation decreased remarkably ($P<0.01$, $n=5$) in all 4 groups. The difference between the groups was obliterated. All 4 groups bore the higher lipid peroxidation in the presence of CYP1A inhibitor α-naphthoflavone and Fe^{3+}/ADP, than in the absence of α-naphthoflavone (Figure 4). This can indicate the specific role of CYP2E1 and CYP1A2 in the generation of microsomal lipid peroxidation.

Glutathione depletion in the DEN-2-AAF group was evident in the data of the glutathione level in the liver homogenization (Table 4).

Discussion

With the present carcinogenic protocol, treatment of rats with single injection DEN or 2-AAF alone for 6 weeks only induced sporadic, little-altered hepatic foci or GST-P positive cells, but treatment of DEN as initiator and 2-AAF as promoter induced many altered hepatic foci in the liver. It has been demonstrated that neoplastic or preneoplastic changes of the liver results in a decrease in the amount of total P450 and the altered expression of CYP isozymes in the liver[14]. Some isozymes can be overexpressed, at the same

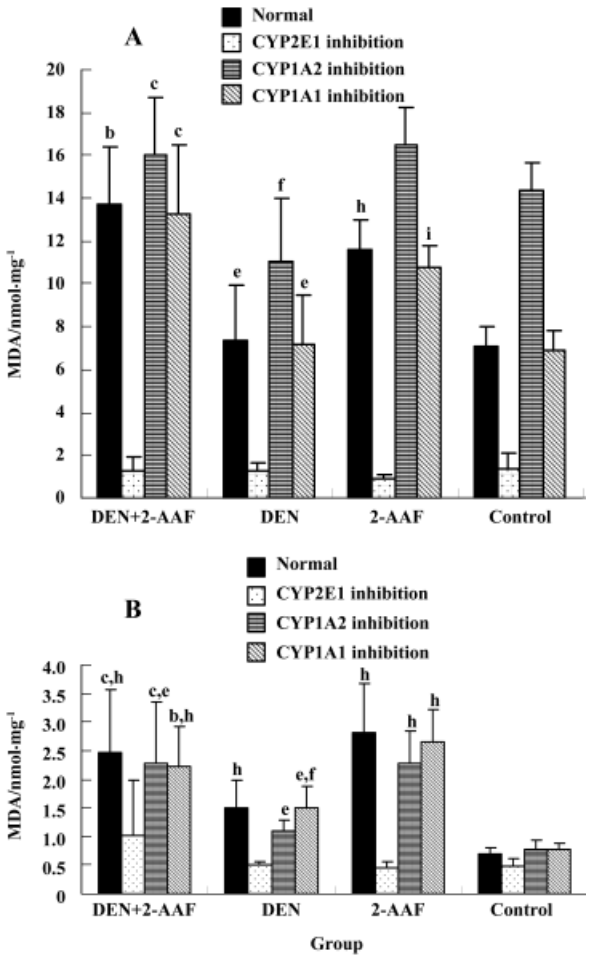

Figure 4. Effect of P450 enzyme inhibitor on microsomal NADPH-dependent lipid peroxidation in 4 groups with Fe^{2+} induction (A) or no Fe^{2+} induction (B). Before the reaction, microsome was incubated with or without specific P450 inhibitor for 10–30 min. Diethyldithiocarbamate is a CYP2E1 inhibitor; naphthoflavone is a CYP1A inhibitor (mainly CYP1A2); 8-methoxypsoralen is a CYP1A (with a similar effect on CYP1A1 and CYP1A2) and CYP2A6 inhibitor. The lipid peroxidation was measured by the formation of thiobarbituric acid reactive substances (TBARS). TBARS are reported in terms of malondialdehyde (MDA). $^{b}P<0.05$, $^{c}P<0.01$ *vs* DEN; $^{e}P<0.05$, $^{f}P<0.01$ *vs* 2-AAF; $^{h}P<0.05$, $^{i}P<0.01$ *vs* control.

Table 4. Glutathione level in the homogenate. $n=5$. Mean±SEM. $^{b}P<0.05$, $^{c}P<0.01$ *vs* control group.

Group	GSH/mg·g^{-1} protein
DEN+2-AAF	46.03±2.90^{c}
DEN	53.25±2.33^{b}
2-AAF	55.12±2.21^{b}
Control	65.82±5.02

time, other isozymes are downregulated expressed. The present work confirmed the alteration expression of CYP1A1, CYP1A2, CYP2B1/2 and CYP2E1. As we expected, CYP1A2 was down-regulated in groups A and C. As the previous report demonstrated[15], the expression of CYP1A2 was reduced preferentially in the liver bearing hyperplastic nodules. CYP1A1 which was undetectable in control rat liver, appeared in the groups A, B, and C. It was not expected that treatment with DEN alone significantly increased ethoxy-O-dealkylase activity, as DEN has no capacity for inducing CYP1A1 *in vitro*. This unexpected change was similar to those observed previously in the treatment of rats with DEN alone[15]. The mechanism of the unexpected appearance of CYP1A1 in the liver treated with DEN alone remains unclear and requires further study. It has been proposed that a link exists between the capacity of agents and their ability to promote hepatocarcinogenesis[16]. The altered hepatic foci that shows reduction of expression of CYP2B1/2 might have more potential to grow into hyperplastic nodules [17]. In the present study, CYP2B1/2 was down-regulated in groups A and C. However, CYP2B1/2 was down-regulated expression in the cells within the altered hepatic foci the same as the previous report .

CYP2E1 is a major microsomal source of hydrogen peroxide and NADPH-dependent lipid peroxidation[18]. In the present study, CYP2E1 inhibitor inhibited most microsomal lipid peroxidation production in all 4 groups and obliterated the difference among the groups. Thus, the increasing lipid microsomal peroxidation might be induced by overexpression of CYP2E1. This result was in accordance with the major role of CYP2E1 in the generation of microsomal hydrogen peroxide. Immunohistochemical assay indicated that CYP2E1 mainly expressed around the centrolobular vein and most of hepatocytes in the altered hepatic foci were negative. Thus, the hepatocytes within the altered hepatic foci might bear less peroxidation injury than that in the surrounding area. This could contribute to the formation of a resistant phenotype. Studies *in vitro* have indicated that CYP2E1 overexpression has left cells vulnerable to death from GSH depletion[19]; the different susceptibilities to ROS between hepatocytes within the altered hepatic foci and surrounding tissue can be partially explained by the depletion of glutathione, which was confirmed by the present assay of glutathione in the liver.

The previous study demonstrated that xenobiotic AHR (Aryl Hydrocarbon Receptor) ligands were mechanistically involved in toxicological processes of oxidative stress, generally resulting in increasing ROS production in microsomes[20]. The specific role of CYP1A1 and CYP1A2 that contributed to the generation of microsomal lipid peroxidation seemed to be contrary. CYP1A1 appeared to be an important contributor to a microsomal oxidative stress response. However, CYP1A2 decreased the microsomal hydrogen peroxidation generated by CYP2E1 and CYP1A1 by acting as an electron acceptor to prevent the uncoupled electron transferring from NADPH to O_2[21]. The present results indicate that CYP1A inhibitor α-naphthoflavone promotes the generation of lipid peroxidation in the presence of Fe^{3+}/ADP and did not effect the generation of lipid peroxidation in the absence of Fe^{3+}/ADP. Because α-naphthoflavone is a more potent inhibitor of CYP1A2 than CYP1A1, and CYP1A2 was an antioxidant enzyme, we proposed that more lipid peroxidation production in groups A and C could result not only from overexpression of CYP2E1 and CYP1A1, but also from decreased expression of CYP1A2.

Changes in CYP isozymes expression can directly produce interindividual differences in susceptibility to carcinogenic compounds; toxicities are modulated by these enzymes. N-nitrosodiethylaminie (DEN) is a widely occurring carcinogenic nitrosamine that requires oxygenation of the α-carbon catalyzed by CYP (mainly by CYP2E1) for its DNA-damaging activity[22]. The first necessary step for 2-AAF activation is N-hydroxylation mediated by CYP1A to form the proximate carcinogen N-OH-AAF[23]. In normal rat livers, the relevant isozyme mediated N-hydroxylation of 2-AAF is CYP1A2, but in the liver in which CYP1A1 was induced, we speculated that this step was mediated primarily by CYP1A1, because CYP1A1 N-hydroxylated 2-AAF 6 times more rapidly than CYP1A2. Therefore, in the present study, DEN+2-AAF, DEN, and 2-AAF group, in which CYP1A1 was induced, might have more susceptibility to 2-AAF. Although we are unable to explain the high induction of CYP1A1 in the rat liver of the DEN-PH group, the induction of CYP1A1 after a single injection of DEN might result in more 2-AAF being transformed to N-OH-AAF. Based on this proposal, it can be concluded that alteration of expression of CYP1A1/2 contributed to the hepatocytes within the preneoplastic foci acquisition of resistance to 2-AAF.

In conclusion, the expression of CYP was altered in the early stage of hepatocarcinogenesis and these alterations have an affect on the alteration of cell redox status and the metabolism of carcinogen.

Acknowledgment

We would like to thank Ms Hua SHENG, Ms Xing-ju YUAN, Ms Mei-ying WANG, Mr Ming DU, and Mr Jun-liang WU for their assistance in the experiments.

References

1 Lim JH, Lu AYH. Inhibition and induction of cytochrome P450 and the clinical implications. Clin Pharmacokinet 1998; 35: 361–90.

2 Yu MW, Gladek-Yarborough A, Chiamprasert S, Santella RM, Liaw YF, Chen CJ. Cytochrome P450 2E1 and glutathione S-transferase M1 polymorphisms and susceptibility to hepatocellular carcinoma. Gastroenterology 1995; 109: 1266–73.

3 Han XM, Zhou HH. Polymorphism of CYP450 and cancer susceptibility. Acta Pharmacol Sin 2000; 21: 673–9.

4 Toussaint C, Albin N, Massaad L, Grunenwald D. Main drugs and carcinogen-metabolizing enzyme systems in human non-small cell lung cancer and peritumoral tissues. Cancer Res 1993; 53: 4608–12.

5 Puga A, Marlowe J, Knudsen ES. Role of the aryl hydrocarbon receptor in cell cycle regulation. Toxicology 2002; 181-182: 171–7.

6 Maliakal PP, Coville PF, Wanwimolruk S. Decreased hepatic drug-metabolizing enzyme activity in rats with nitrosamine-induced tumours. Drug Metabol Drug Interact 2002; 19: 13–27.

7 Roomi MW, Ho RK, Farber E. A common biochemical pattern in preneoplastic nodules induced by 2-acetylaminofluorene in rat liver. Cancer Res 1985; 45: 564–71.

8 Rinaudo JAS, Farber E. The pattern of metabolism of 2-acetylaminofluorene in carcinogen-induced hepatocyte nodules in comparison to normal liver. Carcinogenesis 1986; 7: 523–8.

9 Hu JJ, Hong JY, Lea MA, Yang CS. Differential expression of cytochrome P4502E1 (CYP2E1) in Morris hepatomas and livers of tumor bearing rats. Int J Oncol 1998; 12: 1049–53.

10 Klaunig JE, Xu Y, Isenberg JS. The role of oxidative stress in chemical carcinogenesis. Environ Health Perspect 1998; 106: 289–95.

11 Sapone A, Affatato A, Canistro D, Broccoli M, Trespidi S, Pozzetti L, *et al*. Induction and suppression of cytochrome P450 isoenzymes and generation of oxygen radicals by procymidone in liver, kidney and lung of CD1 mice. Mutat Res 2003; 527: 67–80.

12 Ito N, Imaida K, Shirai T. Early detection of carcinogenic substances and modifiers in rats. Mutation Research 2000; 462: 209–17.

13 Ito N, Hasegawa R, Hagiwara A. Medium-term rat liver bioassay for rapid detection of hepatocarcinogenic substances. J Toxicol Pathol 1997; 10: 1–11.

14 Degawa M, Miura S, Hashimoto Y. Expression and induction of cytochrome P450 isozymes in hyperplastic nodules of rat liver. Carcinogenesis 1991; 12: 2151–6.

15 Degawa M, Miura S, Hashimoto Y. Altered expression of hepatic CYP1A Enzymes in rat hepatocarcinogenesis. Jpn J Cancer Res 1995; 86: 535–9.

16 Chen ZY, Eaton DL. Differential regulation of cytochrome (s) P4502B1/2 by phenobarbital, hepatic hyperplastic nodules induced by aflatoxin B1, or diethylnitrosamine plus 2-acetylaminofluorene in male F344 rats. Toxicol Appl Pharmacol 1991; 111: 132–44.

17 Chen ZY, Farin F, Eaton DL. Association between growth stimulation by phenobarbital and express of cytochromes P450 1A1, 1A2, 2B1/2 and 3A1 in hepatic hyperplastic nodules in male F344 rats. Carcinogenesis 1992; 13: 675–82.

18 Leclercq IA, Farrell GC, Field J, Bell DR, Gonzalez FJ, Robertson GR. CYP2E1 and CYP4A as microsomal catalysts of lipid peroxides in murine nonalcoholic steatohepatitis. J Clin Invest 2000; 105: 1067–75.

19 Jones BE, Liu H, Lo CR, Koop DR, Czaja MJ. Cytochrome P450 2E1 expression induces hepatocyte resistance to cell death from oxidative stress. Antioxid Redox Signal 2002; 4: 701–9.

20 Dalton TP, Puga A, Shertzer HG. Induction of cellular oxidative stress by aryl hydrocarbon receptor activation. Chem Biol Interact 2002; 141: 77–95.

21 Shertzer HG, Clay CD, Genter MB, Schneider SN, Nebert DW, Dalton TP. CYP1A2 protects against reactive oxygen production in mouse liver microsomes. Free Radical Biol Med 2004; 36: 605–17.

22 Suzuki T, Imagawa M, Yamada R, Yokoyama K, Kondo S, Itakura K, *et al*. Acute changes in liver gene expression in the N-nitrsodiethylamine-treated rat. Carcinogenesis 1994; 15: 1759–61.

23 Schrenk D, Gant TW, Michalke A, Orzechowski A, Silverman JA, Battula N, *et al*. Metabolic activation of 2-acetyl-aminofluorene is required for induction of multidrug resistance gene expression in rat liver cells. Carcinogenesis 1994; 15: 2541–6.

Acta Pharmacologica Sinica 2005 Jun; 26 (6): 745–752

Full-length article

Melatonin-selenium nanoparticles protects liver against immunological injury induced by bacillus Calmette-Guérin and lipopolysaccharide[1]

Hua WANG, Wei WEI[3], Sheng-yi ZHANG[2], Yu-xian SHEN, Ni-ping WANG, Li YUE, Shu-yun XU

Institute of Clinical Pharmacology, Anhui Medical University, Hefei 230032, China; [2]*Department of Chemistry, Anhui University, Hefei 230039, China*.

Key words

melatonin; selenium; liver; superoxide dismutase; glutathione peroxidase; nitric oxide; tumor necrosis factor; interleukin-1

[1] Project supported by the Key Project of the Natural Science Foundation of the Department of Education, Anhui Province (No 98JL0130Z).
[3] Correspondence to Prof Wei WEI.
Phn 86-551-516-1208.
E-mail wwei@ahmu.edu.cn

Received 2004-11-19
Accepted 2005-02-05

doi: 10.1111/j.1745-7254.2005.00110.x

Abstract

Aim: Melatonin-selenium nanoparticle (MT-Se), a novel complex, was synthesized by preparing selenium nanoparticles in a melatonin medium. The present investigation was designed to determine the protective effects of MT-Se against immunological liver injury in mice induced by bacillus Calmette-Guérin (BCG)/lipopolysaccharide (LPS). **Methods:** The model of immunological liver injury in mice was prepared. The levels of alanine aminotransferase, aspartate aminotransferase, nitric oxide (NO) in serum, malondialdehyde content, superoxide dismutase (SOD), and glutathione peroxidase (GSH-px) activities in a liver homogenate were assayed by spectrophotometry. The content of tumor necrosis factor-α (TNF-α) and interleukin-1 (IL-1) were determined by ELISA. The splenocyte proliferation was assayed by 3-[4,5-dimethylthiazol-2-yl]-2,5-diphenyltetra-zolium bromide (MTT) dye reduction. Meanwhile, a hepatic pathological examination was observed. **Results:** In the BCG/LPS-induced hepatic injury model, MT-Se administered at doses of 5, 10, or 20 mg/kg to the BCG/LPS-treated mice for 10 d significantly reduced the increase in serum aminotransferase, reduced the severe extent of hepatic cell damage and the immigration of inflammatory cells. It also attenuated the increase in the content of thiobarbituric acid-reactive substances and enhanced the decrease in activities of SOD and GSH-px. In contrast, the treatment with MT-Se suppressed the increase in NO level in both the serum and liver tissue. Furthermore, MT-Se significantly lowered an increase in TNF-α and IL-1β levels in the liver and inhibited the production of TNF-α and IL-1β by peritoneal macrophages. A downregulation effect of MT-Se on splenocyte proliferation was also observed. **Conclusion:** MT-Se showed a hepatic protective action on immunological liver injury in mice.

Introduction

Hepatic damage, both acute and chronic, is a common pathology worldwide quite often characterized in its chronic evolution by a progressive process from steatosis to hepatocellular carcinoma through chronic hepatitis, fibrosis, and cirrhosis. The main etiology is represented by viral infections (HBV, HDV, and HCV) and alcohol abuse[1]. The injection of bacillus Calmette-Guérin (BCG) followed by lipopolysaccharide (LPS) is useful for the creation of experimental models of immunological hepatic damage[2]. It is known that *Propionibacterium acnes* or BCG priming and LPS challenge in mice causes massive liver injury, which consists of priming and eliciting phases. *P acnes* or BCG priming induces mononuclear cell infiltration into the liver lobules and granuloma formation. The subsequent LPS injection elicits acute and massive hepatic injury, with a host release of reactive oxygen species, nitric oxide (NO) and pro-inflammatory cytokines such as tumor necrosis factor α (TNF-α), interleukin-1β (IL-1β)[3-5].

Melatonin participates in many important physiological

processes, including anti-inflammatory[6] and immunoregulatory[7] processes, as well as acting as an antioxidant[8,9]. It not only functions as a direct antioxidant; that is, as a scavenger of various oxygen free radicals including hydroxyl radical, singlet oxygen, hydrogen peroxide (H_2O_2) and peroxyl radical, but it also functions as an indirect antioxidant through the enhancement of antioxidant enzyme activities in tissues such as the liver and the brain. Furthermore, melatonin also neutralizes $ONOO^-$ and inhibits the production of NO. In addition, our and other published reports have shown that melatonin protects against liver injury through its antioxidant action[10,11].

Selenium (Se) is an essential element for humans and can improve the activity of the seleno-enzyme and glutathione peroxidase (GSH-px), and can also prevent free radicals from damaging cells and tissues *in vivo*. One of its best-understood functions is that it is present in the active center of GSH-px, an antioxidant enzyme that scavenges various peroxides and protects membrane lipids and macromolecules from oxidative damage[12]. The supplementation of food with selenium is usually limited to selenium-containing compounds, such as sodium selenite (Na_2SeO_3), ebselen, and other organoselenium compounds. However, several studies have been focused on the elemental selenium (Se^0). It is currently known that gray and black elemental Se is biologically inert. However, there is one kind of red elemental particulate selenium, observed in several bacteria, which could provide environmental protection from pollution caused by excessive selenium[13]. These elemental selenium particles are formed in the bacteria to detoxify the excess selenium. In the work of Zhang *et al*[14], it was found that selenium nanoparticles had a higher bioavailability, much less acute toxicity and better scavenging effect compared with organic and other inorganic selenium-containing compounds.

In the present paper, based on the antioxidant and immunoregulatory actions of melatonin and elemental selenium nanoparticles, we combined selenium nanoparticles with melatonin in order to obtain useful materials for medication. Melatonin-selenium nanoparticle (MT-Se), a novel complex, was synthesized by preparing selenium nanoparticles in melatonin medium. In this study, the mechanisms of the protective effects of MT-Se on immunological liver injury induced by BCG plus LPS were investigated.

Materials and methods

Preparation of melatonin-selenium nanoparticle MT-Se was prepared by reducing selenious acid with ascorbic acid in the presence of melatonin. In a synthetic process, the appropriate amount of selenious acid (the water solution of SeO_2) was thoroughly mixed with melatonin. Then excessive ascorbic acid was added into the selenious acid/melatonin mixture to initiate redox reaction[15].

After the reaction mixture was mixed for approximately 30 min, the product showing light red was obtained. In the reaction process, melatonin molecules could be strongly absorbed on the surface of nascent selenium seeds. Melatonin not only served as a seed growth controller, but also prevented selenium nanoparticles from congregating. Transmission electron microscopy (TEM) images of the product, as shown in Figure 1, were captured on a JEOL-JEM 200CX instrument (JEOL Company, Japan) at an accelerating voltage of 100 kV. From the image, it can be seen that uniform spherical selenium nanoparticles were produced. The final product prepared for medicine application was the complex made up of 95% melatonin, 1% elemental selenium, and 4% ascorbic acid/dehydroascorbic acid. It was dissolved with absolute ethanol and then stabilized and suspended briefly in 0.5% carboxymethylcellulose (CMC) before use.

Materials MT-Se, provided by the Department of Chemistry, Anhui University, was dissolved with absolute

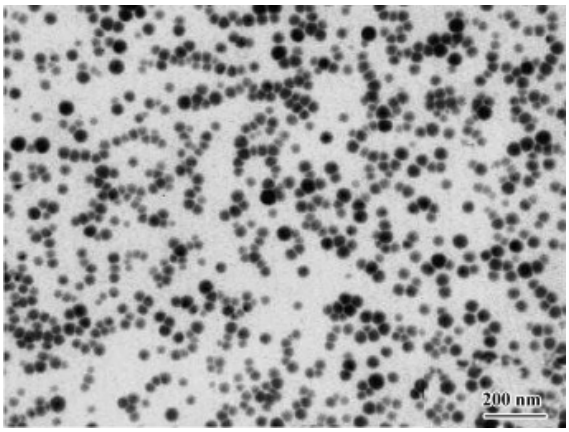

Figure 1. Transmission electron microscopy images of melatonin-selenium nanoparticles.

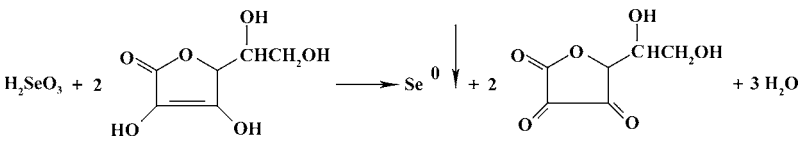

ethanol and then stabilized and suspended briefly in 0.5% CMC. Melatonin, purchased from Sigma Chemical (St Louis, MO, USA), was suspended in 0.5% CMC with absolute ethanol (≤0.01%, v/v) and stored at -20 ºC. LPS from *Escherichia coli* were obtained from Sigma Chemical. Commercial kits used for determining lipid peroxidation (TBRAS), GSH-px and superoxide dismutase (SOD) activity were obtained from the Jiancheng Institute of Biotechnology (Nanjing, China). Other chemicals used in these experiments were analytical grade from commercial sources.

Animals Male Kunming mice (20±2 g), obtained from the Animal Department of Anhui Medical University, were maintained on a 12 h light/12 h dark cycle from 6:00 AM to 18:00 PM under a regulated environment (20±1 ºC). Animals were housed in plastic cages with free access to food and water. All procedures followed the guidelines for human treatment of animals set by the Association of Laboratory Animal Sciences and the Center for Laboratory Animal Sciences at Anhui Medical University.

Establishment of acute liver injury model BCG (viable bacilli), 2.5 mg suspended in 0.2 mL saline, was injected through the tail vein in mice, and 10 d later they were injected with 7.5 μg LPS dissolved in 0.2 mL saline. The mice were anesthetized with ether then killed 16 h after LPS injection by cervical dislocation. The trunk blood was collected into heparinized tubes (50 kU/L) and centrifuged (1500×*g*, 10 min, 4 ºC). Serum was aspirated and stored at -70 ºC until assayed as described below. The liver was also removed and stored at -70 ºC until required[2, 10].

Drug treatment Seven groups of mice, 10 in each, were arranged as follows: (1) normal untreated mice; (2) model mice; (3) model mice treated with different drugs: (a) three MT-Se groups (5, 10, and 20 mg/kg respectively); (b) bifendate group (100 mg/kg). In the treatment groups, different drugs were administered orally by gastric intubation 10 d prior to LPS injection. The mice in normal and model control groups were fed the same volume of vehicle only.

Measurement of serum alanine aminotransferase and aspartate aminotransferase Serum alanine aminotransferase (ALT) and aspartate aminotransferase (AST) were determined using commercial kits produced by Jiancheng Institute of Biotechnology (Nanjing, China). Their activities were expressed as an international unit (U/L).

Histological analysis Formalin-fixed specimens were embedded in paraffin and stained with hematoxylin and eosin for conventional morphological evaluation. After decapitation of rats, small hepatic specimens were placed in 10% (v/v) formalin solution and processed routinely by embedding in paraffin. Tissue sections (4–5 μm) were stained with hematoxylin and eosin and examined under light microscope (Olympus IX70, Japan). An experienced histologist, who was unaware of the treatment conditions, made histological assessments.

Measurement of malondialdehyde, SOD, and GSH-px in liver homogenate Lipid peroxidation production in the liver tissue was determined by measuring thiobarbituric acid-reactive substances (TBARS)[16]. TBARS were measured using the thiobarbituric acid method, with 1,1,3,3-tetramethoxypropane as a standard. Hepatic protein was assayed by the method of Lowry *et al* using bovine serum albumin as a standard[17]. The amount of TBARS was expressed as nmol malondialdehyde (MDA)/mg protein. The assay for total SOD was based on its ability to inhibit the oxidation of oxymine by the xanthine-xanthine oxidase system[18]. Results were expressed as U per microgram protein. The activity of GSH-px was determined by quantifying the rate of H_2O_2-induced oxidation of GSH to oxidized glutathione (GSSH). A yellow product with absorbance at 412 nm was formed as GSH reacted with dithionitrobenzoic acid[19]. One unit of GSH-px was defined as the amount that reduced the level of GSH by 1 μmol/L in 1 min/mg protein.

Measurement of NO in serum and liver NO in the serum and the liver was measured by a microplate assay using Griess reagent, which produces a chromophore with the nitrite[20]. Briefly, 100 μL of supernatants were removed and incubated with 100 μL of Griess reagent (1% sulfanilamide and 0.1% *N*-1-naphthylethylenediamine dihydrochloride in 2.5% phosphoric acid) in a 96-well plate. The plate was incubated for 10 min at room temperature. Nitrite production was quantified spectrophotometrically using an automated colorimetric procedure. Absorbance at 540 nm was measured using a microplate reader (318MC, Shanghai Sanco). The nitrite concentration was calculated by comparing samples with standard solutions of sodium nitrite produced in the culture medium. All samples were assayed in triplicate. Results were expressed as μmol/L.

Splenocytes proliferation assay Mice were killed by cervical dislocation. Spleens were removed in sterile conditions and splenocytes were collected. Then the cells were suspended in RPMI-1640 medium at a concentration of 1×10^7 cell/L. The cell suspension (100 μL) and concanavalin A (ConA) (100 μL with final concentration of 3 mg/L) or LPS (100 μL with final concentration of 4 mg/L) were seeded to a 96-well culture plate simultaneously. Triplicates were designed. The cultures were incubated at 37 ºC in an atmosphere of 5% CO_2 for 48 h. Two hours before completion, 10 μL of MTT (5 g/L) was added to each well. The absorbance was measured on an EJ301 ELISA Microwell Reader (Wuxi

Keda, China) at 570 nm. The results were described as the average of triplicate A.

Preparation of peritoneal macrophages and induction of TNF-α and IL-1β Mice PMΦ were collected in D-Hanks' medium by routine method. Then PMΦ was resuspended in RPMI-1640 medium at 1×10^9 cell/L and the cell suspension was seeded into a 24-well culture plate, 1 mL per well. After incubation at 37 ºC for 2 h in 5% CO_2 atmosphere, supernatants were removed and the adherent cells were washed 3 times with Hanks' medium, which contained 5% neonatal bovine serum. Thus, the monolayer of PMΦ was obtained. LPS, with a final concentration of 4 mg/L, was added to each well and RPMI-1640 was also added to make a final volume per well of up to 1 mL. The plate was then incubated at 37 ºC in air with 5% CO_2 for 48 h. After being centrifuged (500×*g*, 10 min), all the supernatants containing extracellular TNF-α and IL-1β were collected and stored at -20 ºC until assay.

Measurement of TNF-α and IL-1β in liver and culture supernatants The TNF-α and IL-1β levels in the liver homogenate and culture supernatants were determined using rat ELISA kits. Their levels were expressed as ng/L.

Statistical analysis All values are presented as mean±SD. A two-tailed, non-paired, Student's *t*-test was used to evaluate differences between means. Statistical significance was set at $P<0.05$.

Results

Effect of MT-Se on serum ALT and AST concentration The model group (treated with BCG plus LPS) manifested severe liver damage with an elevation of serum aminotransferase, compared with the normal group. In the group of mice treated with MT-Se (5, 10, and 20 mg/kg), serum levels of liver enzymes were significantly decreased as compared with BCG plus LPS-treated mice. Similarly, bifendate (100 mg/kg) reduced the levels of liver enzymes as opposed to BCG plus LPS-treated mice (Table 1).

Effect of MT-Se on liver histology No histological abnormalities were observed in normal mice. There was severe necrosis of hepatocytes with marked mononuclear infiltration, seen after LPS injection in the BCG-primed mice. In the MT-Se (5, 10, and 20 mg/kg) treated groups, the area and extent of necrosis was attenuated and the immigration of inflammatory cells was reduced (Figure 2).

Effect of MT-Se on liver homogenate MDA content and SOD, GSH-px activities Injection of LPS after BCG priming in mice caused a significant elevation in MDA levels in the liver tissue. MT-Se (5, 10 and 20 mg/kg) reduced the elevation of MDA levels in the liver. The activities of antioxidant enzymes including GSH-px and SOD were significantly inhibited in the liver tissues of mice injected with LPS after BCG priming. Treatment with MT-Se (10 and 20 mg/kg) increased the activity of GSH-px and MT-Se at doses of 10 and 20 mg/kg elevated the activity of SOD (Table 2).

Table 1. Effect of MT-Se on serum ALT and AST activities in mice with immunological hepatic injury induced by BCG plus LPS. n=10. Mean±SD. $^cP<0.01$ *vs* normal. $^eP<0.05$, $^fP<0.01$ *vs* model.

Group	Doses/mg·kg^{-1}	ALT/U·L^{-1}	AST/U·L^{-1}
Normal	–	25±4	24±9
Model	–	139±34^c	101±14^c
MT-Se	5	102±17^f	80±18^e
	10	96±25^f	75±15^f
	20	95±24^f	67±16^f
Bifendate	100	95±22^f	66±17^f

MT-Se: Melatonin-selenium nanoparticles, ALT: alanine aminotransferase, AST: aspartate aminotransferase; BCG: bacillus Calmette-Guerin; LPS: lipopolysaccharide.

Effect of MT-Se on serum and liver levels of NO The levels of NO in serum and liver tissue were significantly increased in BCG-primed mice challenged with LPS. MT-Se (5, 10, and 20 mg/kg) reduced the elevation of NO levels in serum and liver tissue (Figure 3).

Effect of MT-Se on TNF-α and IL-1β concentration in the liver As shown in Table 3, when mice were first injected with BCG and then challenged with LPS, the proinflammatory cytokines, such as TNF-α and IL-1β, were significantly elevated. MT-Se (5, 10, and 20 mg/kg) decreased the levels of TNF-α and IL-1β in a liver homogenate. Bifendate had no effect on TNF-α and IL-1β (Table 3).

Effect of MT-Se on splenocyte proliferation in mice with immunological liver injury Treatment with MT-Se suppressed the accentuation of splenocyte proliferation induced by LPS or ConA (Figure 4).

Effect of MT-Se on production of TNF-α and IL-1β by PMΦ The levels of TNF-α and IL-1β in culture supernatants of PMΦ were significantly increased in immunological liver injury mice. MT-Se (5, 10, and 20 mg/kg) inhibited the production of TNF-α and IL-1β (Table 4).

Discussion

The findings of the present study showed that MT-Se, a new chemical compound that is composed of melatonin and red elemental selenium particles, prevented the development of immunological liver injury induced by BCG plus LPS. It markedly reduced the severe liver injury in mice as demon-

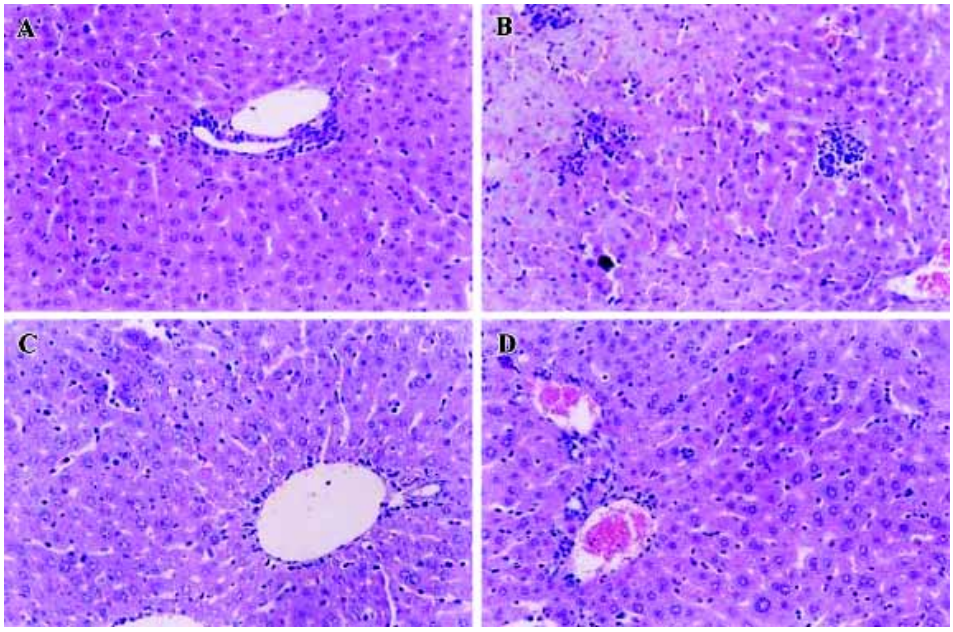

Figure 2. Histologic examination of liver sections (hematoxylin and eosin stains, ×200) from: (A) a normal mouse showing no histological abnormality; (B) a BCG-primed and LPS-treated mouse showing severe degeneration of hepatocytes with marked mononuclear infiltration; (C, D) a mouse treated with melatonin-selenium nanoparticle (MT-Se) and bifendate, respectively. Images show the area and extent of necrosis was attenuated and the immigration of inflammatory cells was reduced compared to BCG-primed and LPS-treated mouse.

Table 2. Effects of MT-Se on MDA levels, SOD, and GSH-px activities in hepatic homogenate of immunological hepatic injury. n=10. Mean±SD. ^{c}P<0.01 *vs* normal. ^{e}P<0.05, ^{f}P<0.01 *vs* model.

Groups	Doses/mg·kg^{-1}	MDA/mmol·g^{-1}protein	SOD/kU·g^{-1} protein	GSH-px/kU·g^{-1} protein
Normal	–	4.0±0.8	243±47	76±15
Model	–	6.9±1.7^{c}	122±59^{c}	40±17^{c}
MT-Se	5	5.1±1.2^{f}	173±33	49±12
	10	4.7±1.2^{f}	198±5^{e}	59±17^{e}
	20	4.1±0.9^{f}	202±68^{f}	69±2^{f}
Bifendate	100	4.4±1.1^{f}	131±36	37±10

MT-Se: Melatonin-selenium nanoparticle; MDA: malondialdehyde; SOD: superoxide dismutase; GSH-px: glutathione peroxide.

strated by a significant reduction in the serum transaminase levels and amelioration of severe hepatic pathological abnormalities. Meanwhile, MT-Se decreased MDA content and NO levels, and increased the antioxidant capacity, including SOD and GSH-px activity. In addition, MT-Se played an immunoregulatory role in decreasing proinflammatory cytokines and inhibiting splenocyte proliferation. We propose that oxidative stress and proinflammatory cytokine overproduction imposed on the liver play an important role in the pathogenesis of hepatic damage, and these results are attenuated by the antioxidant and immunoregulatory activity of MT-Se.

The current results confirmed that MT-Se's protection against hepatic injury was associated with the antioxidant property of melatonin and selenium. Melatonin combined with selenium could induce synergistic effects, indicated by improved free radical scavenging activity of MT-Se. Selenium, an integral part and located at the catalytic site of GSH-px, is now known to be of fundamental importance to human health[21]. Recent evidence has shown that treatment with selenium and other antioxidants results in positive clinical responses in various liver diseases associated with increased oxidative damage[22]. GSH-px and some seleno-compounds such as ebselen have also been shown to protect

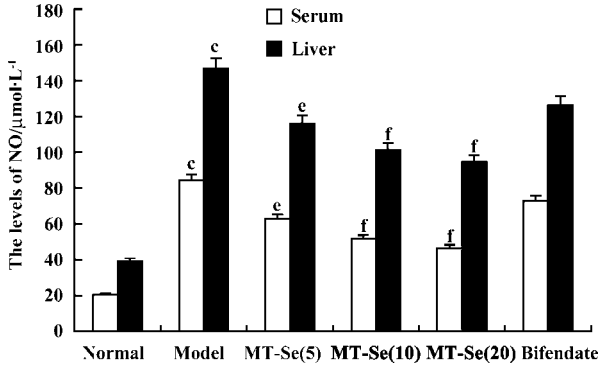

Figure 3. Effect of melatonin-selenium nanoparticle (MT-Se) administration on serum and hepatic NO levels in mice injected with BCG plus LPS. n=10. Mean±SD. ^cP<0.01 *vs* normal. ^eP<0.05, ^fP<0.01 *vs* model.

Table 3. Effect of MT-Se on TNF-α and IL-1β level in liver homogenate of mice with immunological hepatic injury. n=10. Mean±SD. ^cP<0.01 *vs* normal. ^eP<0.05, ^fP<0.01 *vs* model.

Groups	Dose/mg·kg^{-1}	TNF-α/ng·L^{-1}	IL-1β/ng·L^{-1}
Normal	–	1.6±0.8	1.3±0.7
Model	–	4.8±1.6^c	4.2±1.5^c
MT-Se	5	3.4±1.1^e	2.9±0.9^f
	10	3.3±0.7^f	2.6±0.7^f
	20	2.6±0.7^f	2.0±0.5^f
Bifendate	100	3.9±1.4	3.2±1.0

MT-Se: Melotonin-selenium nanoparticle; TNF: tumor necrosis factor; IL-1: interleukin-1

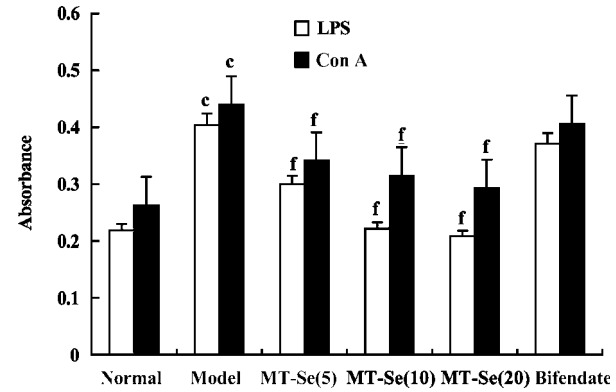

Figure 4. Effect of MT-Se on splenocyte proliferation in mice with immunological liver injury. n=5. Mean±SD. ^cP<0.01 *vs* normal. ^eP<0.05, ^fP<0.01 *vs* model.

against hepatic injury[23,24]. Selenium also appears to be protective for individuals infected with the hepatitis virus (B or C) against the progression of the condition to liver cancer[25]. These effects may prove selenium to be beneficial as an adjuvant therapy for liver disease. However, it must be remembered that selenium is a toxic mineral with a fairly small therapeutic window. Seleno-compounds, especially inorganic selenium, could be hepatotoxic and teratogenic in animals and humans. In some sensitive individuals, the maximum safe dietary intake may be as low as 600 μg per day. It would therefore seem prudent to restrict adult intake from all sources to an upper limit of 400–450 μg/day as recommended by several expert panels[26]. Although the toxic effect of elemental selenium nanoparticles is less, the selenium contents percentage in MT-Se is only 1% and the dose of selenium less than 200 μg in our experimental design. The current study confirmed that selenium at doses of 50 to 200 μg reinforced the endogenous anti-oxidative systems in comparison with melatonin or selenium alone; suggested by MT-Se blunting of lipid peroxidation and increased GSH-px activity.

Table 4. Effect of MT-Se on production of TNF-α and IL-1β by PMΦ. n=5. Mean±SD. ^cP<0.01 *vs* normal. ^eP<0.05, ^fP<0.01 *vs* model.

Groups	Dose/mg·kg^{-1}	TNF-α/ng·L^{-1}	IL-1β/ng·L^{-1}
Normal	–	0.77±0.26	0.8±0.4
Model	–	3.1±0.6^c	2.5±0.3^c
MT-Se	5	2.0±0.4^e	1.5±0.3^e
	10	1.90±0.23^e	1.3±0.4^f
	20	1.8±0.7^f	0.7±0.6^f
Bifendate	100	2.3±0.7	1.9±0.6

MT-Se: Melatonin-selenium nanoparticle; TNF: tumor necrosis factor; IL-1: interleukin-1; PMΦ: peritoneal macrophage.

Melatonin is also well known to be a multi-faceted free radical scavenger and antioxidant[8,9]. Previous studies have shown that melatonin could protect against several models of liver injury by inhibiting oxidative and nitrosative damage. Calvo *et al* found that melatonin protected against alpha-naphthylisothiocyanate (ANIT)-induced liver injury with cholestasis in rats, and suggested that this protective effect was a result of its antioxidative properties and above all to its capacity to inhibit liver neutrophil infiltration, a critical factor in the pathogenesis of ANIT-induced liver injury[27]. Melatonin at high doses (10–100 mg/kg) could also dose-dependently reduce liver lipid peroxide content in CCl_4-treated rats. This indicates that melatonin exerts a therapeutic effect on CCl_4-induced acute liver injury in rats, possibly through its antioxidant action[28]. Melatonin plays a cytoprotective role in the liver affected by ischemia and reperfusion through its ability to prevent hepatic malfunction and inhibit the gen-

eration of free radicals and accumulation of neutrophils in the damaged hepatic tissue[29]. Moreover, melatonin appeared to be significantly more potent than N-acetylcysteine in reversing the oxidative damage induced by ischemia and reperfusion[30]. In bile duct ligated rats, melatonin was much more effective than vitamin E in reducing liver injury and oxidative stress[31]. Acetaminophen at high doses can cause fulminant hepatic necrosis and nephrotoxic effects, and melatonin can reverse these effects with its higher efficacy in scavenging various free radicals and also because of its ability in stimulating the antioxidant enzymes[32]. In our previous study, we also observed that pretreatment with melatonin had a protective effect on immunological hepatic damage induced by BCG and LPS. In this study, it is confirmed that MT-Se also had a hepatic protective effect through the synergistic antioxidant effect of melatonin and selenium.

As is well known, TNF-α is considered to be a common early effector molecule for liver injury, in addition to its direct cytotoxic effects, this cytokine is able to induce chemokines, macrophage chemotactic protein-1, and adhesive molecules (vascular-cell adhesion molecule-1), which are key to inflammation and consequent liver damage. The prevention of liver injury has been observed upon neutralization of TNF-α with anti-TNF-α antibody, prevention of translation of primary RNA transcript of TNF-α by antisense oligonucleotide and interaction of TNF-α with soluble TNF-α receptors. Although IL-1 itself does not damage the liver, its elevation could stimulate inflammatory cells to excrete many other cytokines including TNF-α, IL-6, and IL-8. Our results suggest that the elevation of inflammatory cytokines, including TNF-α and IL-1β, in the liver tissue and PMΦ cell culture supernatants are contributing to the mechanisms of immunological liver injury. MT-Se decreased TNF-α and IL-1β levels in the liver inhibiting their production by PMΦ. These results are consistent with the literature suggesting melatonin's immunosuppressive effect on the production of inflammatory cytokines. Shin *et al*[33] found that low levels of Bacillus anthracis were known to induce the release of cytokines such as TNF-α, and thereby exposure of melatonin (1×10^{-7}–1×10^{-6}mol) to anthrax lethal toxin-treated macrophages also decreased the release of TNF-α to the extracellular medium as compared with the control. Sacco *et al*[34] found that the administration of melatonin to mice (5 mg/kg, sc, 30 min before or simultaneously with LPS) inhibited serum TNF-α levels by 50%–80% and improved the survival of mice treated with a lethal dose of LPS. It was also previously reported that melatonin had a protective role in LPS-induced septic shock by suppressing proinflammatory cytokines, prostaglandins and NO production[35]. Thus, the present study revealed that MT-Se had an immunoregulatory effect on immunological liver injury in mice by inhibiting proinflammatory cytokine production. Moreover, in our *in vivo* experiment, MT-Se suppressed the proliferation of spleen cells induced by ConA or LPS. These findings suggest that MT-Se may alleviate immunological liver injury not only through inhibiting the activation of PMΦ, but also by inducing the dysfunction of activated lymphocytes.

In summary, the results obtained in the present study indicate that the mode of MT-Se's hepatic protective action is, at least in part, related to its antioxidant properties, such as inhibiting lipid peroxidation and NO production, as well as increasing the antioxidant enzyme capacity. Furthermore, we found that it appeared that MT-Se had an immunoregulatory effect on inhibiting proinflammatory cytokines and activated lymphocytes. MT-Se, a novel complex, may be beneficial as a valuable drug for protection against liver injury. However, further investigation is required to clarify the detailed mechanism of the therapeutic effect of MT-Se on liver injury.

References

1 Hoek JB, Pastorino JG. Ethanol, oxidative stress, and cytokine-induced liver cell injury. Alcohol 2002; 27: 63–8.

2 Wang GS, Liu GT. Influences of Kupffer cell stimulation and suppression on immunological liver injury in mice. Acta Pharmacol Sin 1997; 18: 173–6.

3 Guler R, Olleros ML, Vesin D, Parapanov R, Vesin C, Kantengwa S, *et al*. Inhibition of inducible nitric oxide synthase protects against liver injury induced by mycobacterial infection and endotoxins. J Hepatol 2004; 41: 773–81.

4 Nagakawa J, Hishinuma I, Hirota K, Miyamoto K, Yamanaka T, Tsukidate K, *et al*. Involvement of tumor necrosis factor-α in the pathogenesis of activated macrophage mediated hepatitis in mice. Gastroenterology 1990; 99: 758–65.

5 Tsuji H, Harada A, Mukaida N, Nakanuma Y, Bluethmann H, Kaneko S, *et al*. Tumor necrosis factor receptor p55 is essential for intrahepatic granuloma formation and hepatocellular apoptosis in a murine model of bacterium-induced fulminant hepatitis. Infect Immun 1997; 65: 1892–8.

6 Cuzzocrea S, Reiter RJ. Pharmacological actions of melatonin in acute and chronic inflammation. Curr Top Med Chem 2002; 2: 153–65.

7 Guerrero JM, Reiter RJ. Melatonin-immune system relationships. Curr Top Med Chem 2002; 2: 167–79.

8 Reiter RJ, Tan DX, Mayo JC, Sainz RM, Leon J, Czarnocki Z. Melatonin as an antioxidant: biochemical mechanisms and pathophysiological implications in humans. Acta Biochim Pol 2003; 50: 1129–46.

9 Rodriguez C, Mayo JC, Sainz RM, Antolin I, Herrera F, Martin V, *et al*. Regulation of antioxidant enzymes: a significant role for melatonin. J Pineal Res 2004; 36: 1–9.

10 Wang H, Wei W, Shen YX, Dong C, Zhang LL, Wang NP, *et al*.

Protective effect of melatonin against liver injury in mice induced by Bacillus Calmette-Guerin plus lipopolysaccharide. World J Gastroenterol 2004; 10: 2690–6.
11 Bruck R, Aeed H, Avni Y, Shirin H, Matas Z, Shahmurov M, *et al*. Melatonin inhibits nuclear factor kappa B activation and oxidative stress and protects against thioacetamide induced liver damage in rats. J Hepatol 2004; 40: 86–93.
12 Jozanov-Stankov O, Demajo M, Djujic I, Mandic M. Selenium intake as a modulator of responsiveness to oxidative stress. J Environ Pathol Toxicol Oncol 1998; 17: 251–7.
13 Tomei FA, Barton LL, Semanski CL. Transformation of selenate and selenite to elemental selenium by *Desulfovibrio* desulfuricans. J Ind Microbiol 1995; 14: 329–36.
14 Zhang JS, Gao XY, Zhang LD, Bao YP. Biological effects of a nano red elemental selenium. Biofactors 2001; 15: 27–38.
15 Mees DR, Pysto W, Tarcha PJ. Formation of selenium colloids using sodium ascorbate as the reducing agent. J Colloid Interface Sci 1995; 170: 254–90.
16 Shechter I, Fogelman AM, Haberland ME, Seager J, Hokom M, Edwards PA. Effect of polyunsaturated fatty acids and antioxidants on lipid peroxidation in tissue cultures. J Lipid Res 1981; 22: 63–9.
17 Lowry OH, Rosebrough NJ, Farr AL, Randall RJ. Protein measurement with the Folin-phenol reagent. J Biol Chem 1951; 193: 265–73.
18 Sykes JA, McCormack FX Jr, O'Brien TJ. A preliminary study of the superoxide dismutase content of some human tumors. Cancer Res 1978; 38: 2759–62.
19 Paglia DE, Valentine WN. Studies on the quantitative and qualitative characterization of erythrocyte glutathione peroxidase. J Lab Clin Med 1967; 70: 58–169.
20 Kiechle FL, Malinski T. Nitric oxide. Biochemistry, pathophysiology, and detection. Am J Clin Pathol 1993; 100: 567–75.
21 Rotruck JT, Pope AL, Ganther HE, Swanson AB, Hafeman DG, Hoekstra WG. Selenium: biochemical role as a component of glutathione peroxidase. Science 1973; 179: 588–90.
22 Sakaguchi S, Iizuka Y, Furusawa S, Tanaka Y, Takayanagi M, Takayanagi Y. Roles of selenium in endotoxin-induced lipid peroxidation in the rats liver and in nitric oxide production in J774A.1 cells. Toxicol Lett 2000; 118: 69–77.
23 Ozdil S, Bolkent S, Yanardag R, Arda-Pirincci P. Protective effects of ascorbic acid, *dl*-alpha-tocopherol acetate, and sodium selenate on ethanol-induced liver damage of rats. Biol Trace Elem Res 2004; 97: 149–62.
24 Kono H, Arteel GE, Rusyn I, Sies H, Thurman RG. Ebselen prevents early alcohol-induced liver injury in rats. Free Radic Biol Med 2001; 30: 403–11.
25 Yu MW, Horng IS, Hsu KH, Chiang YC, Liaw YF, Chen CJ. Plasma selenium levels and the risk of hepatocellular carcinoma among men with chronic hepatitis virus infection. Am J Epidemiol 1999; 150: 367–74.
26 Rayman MP. The importance of selenium to human health. Lancet 2000; 356: 233–41.
27 Calvo JR, Reiter RJ, Garcia JJ, Ortiz GG, Tan DX, Karbownik M. Characterization of the protective effects of melatonin and related indoles against alpha-naphthylisothiocyanate-induced liver injury in rats. J Cell Biochem 2001; 80: 461–70.
28 Ohta Y, Kongo-Nishimura M, Matsura T, Yamada K, Kitagawa A, Kishikawa T. Melatonin prevents disruption of hepatic reactive oxygen species metabolism in rats treated with carbon tetrachloride. J Pineal Res 2004; 36: 10–7.
29 Okatani Y, Wakatsuki A, Reiter RJ, Enzan H, Miyahara Y. Protective effect of melatonin against mitochondrial injury induced by ischemia and reperfusion of rat liver. Eur J Pharmacol 2003; 469: 145–52.
30 Sener G, Tosun O, Sehirli AO, Kacmaz A, Arbak S, Ersoy Y, *et al*. Melatonin and N-acetylcysteine have beneficial effects during hepatic ischemia and reperfusion. Life Sci 2003; 72: 2707–18.
31 Ohta Y, Kongo M, Kishikawa T. Melatonin exerts a therapeutic effect on cholestatic liver injury in rats with bile duct ligation. J Pineal Res 2003; 34: 119–26.
32 Sener G, Sehirli AO, Ayanoglu-Dulger G. Protective effects of melatonin, vitamin E and N-acetylcysteine against acetaminophen toxicity in mice: a comparative study. J Pineal Res 2003; 35: 61–8.
33 Shin S, Hur GH, Kim YB, Yeon GB, Park KJ, Park YM, *et al*. Dehydroepiandrosterone and melatonin prevent Bacillus anthracis lethal toxin-induced TNF production in macrophages. Cell Biology Toxicol 2000; 16: 165–74.
34 Sacco S, Aquilini L, Ghezzi P, Pinza M, Guglielmotti A. Mechanism of the inhibitory effect of melatonin on tumor necrosis factor production *in vivo* and *in vitro*. Eur J Pharmacol 1998; 343: 249–55.
35 Maestroni G.J. Melatonin as a therapeutic agent in experimental endotoxic shock. J Pineal Res 1996; 20: 84–9.

Acta Pharmacologica Sinica 2005 Jun; 26 (6): 753–761

Full-length article

Peroxisome proliferator-activated receptor γ ligands induce cell cycle arrest and apoptosis in human renal carcinoma cell lines[1]

Feng-guang YANG[2], Zhi-wen ZHANG[3], Dian-qi XIN[2], Chang-jin SHI[2], Jie-ping WU[2], Ying-lu GUO[2,4], You-fei GUAN[3,4]

[2]Department of Molecular Biology, Institute of Urology, Peking University First Hospital; [3]Department of Physiology and Pathophysiology, Peking University Health Science Center, Beijing 100034, China

Key words

renal cell carcinoma; peroxisome proliferator-activated receptor γ; cell cycle; apoptosis; cyclin; cdk

[1] Project partly supported by National Natural Science Foundation of China (No 30250002 to Yin-lu GUO and No 30271521, No 30340084 and No G2000056908 to You-fei GUAN) and a grant from Peking University "211" Program (to You-fei GUAN).
[4] Correspondence to Dr You-fei GUAN and Ying-lu GUO.
Phn 86-10-8280-1447.
E-mail youfeiguan@bjmu.edu.cn

Received 2004-12-08
Accepted 2005-02-05

doi: 10.1111/j.1745.7254.2005.00103.x

Abstract

Aim: To study the effect of peroxisome proliferator-actived receptor γ (PPARγ) ligands on cell proliferation and apoptosis in human renal carcinoma cell lines. **Methods:** The expression of PPARγ was investigated by reverse transcriptase polymerase chain reaction (RT-PCR), Western blot and immunohistochemistry. The effect of thiazolidinedione (TZD) PPARγ ligands on growth of renal cell carcinoma (RCC) cells was measured by MTT assay and flow cytometric analysis. Cell death ELISA, Hoechst 33342 fluorescent staining and DNA ladder assay were used to observe the effects of PPARγ ligands on apoptosis. Regulatory proteins of cell cycle and apoptosis were detected by Western blot analysis. **Results:** PPARγ was expressed at much higher levels in renal tumors than in the normal kidney (2.16±0.85 *vs* 0.90±0.73; $P<0.01$). TZD PPARγ ligands inhibited RCC cell growth in a dose-dependent manner with IC_{50} values of 7.08 μmol/L and 11.32 μmol/L for pioglitazone, and 5.71 μmol/L and 8.38 μmol/L for troglitazone in 786-O and A498 cells, respectively. Cell cycle analysis showed a G_0/G_1 arrest in human RCC cells following 24-h exposure to TZD. Analysis of cell cycle regulatory proteins revealed that TZD decreased the protein levels of proliferating cell nuclear antigen, pRb, cyclin D_1, and Cdk4 but increased the levels of p21 and p27 in a time-dependent manner. Furthermore, high doses of TZD induced massive apoptosis in renal cancer cells, with increased Bax expression and decreased Bcl-2 expression. **Conclusion:** TZD PPARγ ligands showed potent inhibitory effect on proliferation, and could induce apoptosis in RCC cells. These results suggest that ligands for PPARγ have potential antitumor effects on renal carcinoma cells.

Introduction

Peroxisome proliferator-activated receptor γ (PPARγ) belongs to the superfamily of nuclear hormone receptor transcription factors[1–3]. PPARγ forms a heterodimer with another nuclear receptor, retinoid X receptor α (RXRα)[4]. In the presence of their ligands, PPARγ/RXRα heterodimer binds to a specific DNA sequence designated peroxisome proliferating response element (PPRE) located in the promoter region of PPARγ target genes and modulates their transcription[5]. Thus far, hundreds of PPARγ target genes have been identified and most of them are involved in adipogenesis[6], glucose metabolism[7] and angiogenesis[8]. Since the discovery of specific ligands for PPARγ, including synthetic antidiabetic thiazolidinediones (TZD) and endogenous 15-deoxy-$D^{12,14}$-PGJ2 (15dPGJ2) and some polyunsaturated fatty acids, accumulating evidence using many experimental systems suggests that PPARγ plays an important role in carcinogenesis in both adipose and nonadipose cells. It has been known that PPARγ expression is up-regulated in many tumor tissues and its ligands, including pioglitazone, troglitazone and roglitazone, can induce apoptosis and exert antiproliferative effects in human colon cancer[9], breast cancer[10], pituitary adenomas[11], gastric cancer[12] and bladder cancer[13]. Moreover, PPARγ may play an important role in inducing cell differentiation or growth inhibition in patients

with liposarcoma[14] and prostate cancer[15]. Therefore activation of PPARγ seems to be a potential approach for treatment of some malignant tumors.

Renal cell carcinoma (RCC) is the most common renal tumor and the third malignancy within urological oncology. It makes up approximately 2%–3% of all adult malignancies. At present, more than 50% of all RCC are found incidentally, which results in a high proportion of patients with progressive metastasis at the time of diagnosis[16,17]. Surgery remains the only effective therapeutic option. Although combination of chemotherapy and/or radiotherapy might help in survival rate, it is considered to be of limited value for the treatment of RCC. Therefore, improvement of life span in patients with renal cell carcinoma greatly depends on the identification of novel treatment strategies. An alternative treatment may include activation of PPARγ, as PPARγ has been shown to be expressed in the kidney[18], and its ligands can induce cell growth inhibition and terminal differentiation in many other maliganancies[9–14].

In the present study, we examined the expression of PPARγ in human primary RCC and RCC cell lines, and determined the biological events of PPARγ activation in inducing RCC cell cycle arrest and apoptosis. We have also explored the molecular mechanism through which PPARγ agonists inhibit cell growth and induce cell death in RCC cell lines.

Materials and methods

Chemicals Pioglitazone and troglitazone were kindly gifted by Park-Davis Pharmaceutical Research (Ann Arbor, MI, USA) and Takeda Chemical Industries (Osaka, Japan). All other chemicals were purchased from Sigma (St Louis, MO, USA). Stock solutions of pioglitazone or troglitazone were made at 100 mmol/L concentration in dimethyl sulfoxide and added to the culture medium at the final concentration of less than 0.1%.

Cell lines and culture conditions Human RCC-derived cell lines 786-O and A498, human proximal tubular cell line (HK-2), and human mesangium cell line (HMCL) were cultured in Hepes-buffered RPMI-1640 medium (Gibco BRL, Grand Island, NY, USA) supplemented with 10% FBS, 100 kU/mL penicillin G, 100 g/L streptomycin, and 2 mmol/L *l*-glutamine in a humidified 5% CO_2 atmosphere at 37 ºC. The media were changed every 3 d, and the cells were separated by trypsinization using trypsin/edetic acid when they reached 90% confluence.

Tumor specimens and immunohistochemistry Specimens were obtained from 120 patients with RCC and 20 patients with normal kidney (NK) who underwent total nephroureterectomy as a result of ureteral cancer or trauma. All patients were treated at the Institute of Urology in Peking University between June 1999 and June 2001. No patients had received irriadiation or chemotherapy prior to surgery. Tumor samples with the highest nuclear grade were selected. All tissues were preserved in 10% formalin serially sectioned onto microscope slides with a thickness of 4 μmol/L. Sections were immunostained with polycolonal antibody to human PPARg (1:100, Santa Cruz Biotechonology, Santa Cruz, CA, USA) using avidin-biotin-complex-peroxidase and counterstained with hematoxylin. Negative control slides were prepared by omitting the primary antibody. The intensity of immunostaining and the ratio of the positive cells were roughly graded into four scores (0, 1, 2, 3, and 4) by two observers who did not know the origin of the samples on two occasions. The score 4 was defined as maximum intensity of immunostaining throughout the section, while the score 0 implied that staining was absent throughout the specimen.

Measurement of PPARγ mRNA by reverse transcription-polymerase chain reaction Total RNA from 15 RCC tissues, 10 NK tissues, RCC cell lines 786-O and A498, HK-2 cells and HMCC (normal kidney derived mesangium cell line). Cells was isolated using TRIzol reagent (Invitrogen, Carlsbad, CA, USA). Contaminated genomic DNA in total RNA was removed by RNase-free DNase I digestion. Reverse transcription was performed in a total volume of 25 μL using 3 μg of total RNA, oligo-dT primer and MMLV reverse transcriptase (Amersham, Buckinghamshire, UK). Primers used for the amplification of PPARγ cDNA were synthesized at the SBS Gene Company (Beijing, China). The sense primer was 5'-AGAGATGCCATTCTGGCC-3' and antisense primer was 5'-GTGGAGTAGAAATGCTGGAGA-3'. Polymerase chain reaction (PCR) amplification yielded a PCR product of 130 bp. Primers used for amplifying a 500-bp of β-actin cDNA as an internal control were as follows: 5'-ACTGACTACCTCATGAAGATC-3' (sense) and 5'-CGTCATACTCCTGCTTGC-3' (anti-sense). The PCR condition was 40 s (denaturation) at 94 °C, 35 s (annealing) at 60 °C and 35 s (extension) at 72 °C for 33 cycles. PCR products were separated in 1.5% agarose gel and visualized after ethidium bromide staining.

Growth inhibition of RCC cell lines by PPARγ agonists The effect of PPARγ ligands on cell proliferation of RCC cells was determined using MTT assay[13]. Briefly, cells of 0.5×10^4 cells/well were inoculated into a 96-well plate (Costar, Cambridge, MA, USA), treated with pioglitazone or troglitazone at various concentrations. After an incubation for 24 h, 20 μL/well 3-(4,5-dimethylthiazol-2-yl)-2,5-diphenyl tetrazolium bromide (MTT, 5 g/L) was added to each well, the me-

dium was then removed, and 200 μL of 0.04 mol/L HCl in isopropanol was added to dissolve the reduced formazan product. The plate was read in a microplate reader (model 3550, BIO-RAD, Richmond, CA, USA) at 590 nm.

Flow cytometry assay RCC cell lines 786-O and A498 treated with pioglitazone (20 μmol/L) and troglitazone (30 μmol/L) for 24 h were harvested and washed with PBS. Cells of 1×10^6 were fixed in 75% ethanol at 4 °C for 24 h, washed in PBS, resuspended in 0.5–1.0 mL PBS containing 100 mg/L RNase A at 37 °C for 30 min, incubated in 10 mg/L propidium iodide in dark at 4 °C for 30 min, and sorted in a Coulter EPICS-XL Cytometer (Becton Dickinson and Beckman-Coulter, San Jose, CA, USA).

Apoptosis assay Cytosolic histon-bound DNA fragments caused by apoptosis were detected using a cell death ELISA kit (Roche Applied Science, Mannheim, Germany) according to manufacturer's protocol. Briefly, 1×10^4 cells were seeded in a 96-well microplate and incubated for 4 h at 37 °C. Pioglitazone 0–100 μmol/L or troglitazone was added and incubated for 48 h. Cells were then lysed with lysis buffer for 30 minutes at 25 °C. Supernatant 20 μL was transferred into the streptavidin coated multiplate, 4 μL anti-histon-biotin and 4 μL anti-DNA-POD were added to each well, and the plate was shaken for 2 h. After being washed with incubation buffer, 100 μL ABTS (2,2'-Azino-di[3-ethylbenzthiazoline-sulfonate]) solution was pipetted into each well. The absorbance was read immediately in a microplate reader (BIO-RAD, model 3550) at 405 nm. Furthermore, apoptosis of RCC cell lines induced by 70 μmol/L troglitazone or 80 μmol/L pioglitazone was also assayed using two other methods. Morphological changes resulting from apoptosis were determined by Hoechst 33342 staining. Cells suspended in PBS were stained with 2 mg/L Hoechst33342 and observed under fluorescence microscope using a blue filter. Cells showing cytoplasmic and nuclear shrinkage and chromatin condensation or fragmentation were defined as apoptotic cells. DNA fragmentation manifested as laddering in agarose gel was also examined. After drug treatment, the cells pellet was lysed in 10 mmol/L Tris-HCl pH 8.0, 150 mol/L NaCl, 10 mmol/L edetic acid and 0.5% SDS on ice for 10 min, and treated with RNase A and proteinase K for 1 h. Following DNA precipitation with ethanol and ammonium acetate at -20 °C for 10 h, DNA was dissolved in TE buffer, electrophoresed in 1.8% agarose gel, and visualized under UV light.

Western blot analysis Cells before and after drug treatment were extracted with lysis buffer containing 50 mmol/L Tris-HCL, pH 8.0, 150 mmol/L sodium chloride, 1% TritonX-100, 0.02% sodium azide, 100 mg/L phenylmethylsulfony fluoride and 1 mg/L aprotinin. The protein content in cell lysate was determined by bicichoninic acid assay using bovine serum albumin as the standard. Cell lysate containing 50–60 μg protein was resolved by SDS-polyacrylamide gel electrophoresis and electrophoretically transferred onto a polyvinylidene difluoride membrane (Millipore, Bedford, MA, USA). The membrane was blotted by antibodies against human PPARγ (1:500), proliferating cell nuclear antigen (PCNA; 1:1500), pRb (1:1000), p21 (1:1000), p27 (1:1000), cyclinD_1 (1:1000), Cdk_4 (1:1000), Bcl-2 (1:1000) and Bax (1:800) (Santa Cruz Biotechnology). Blotted antibody was developed by horseradish peroxidase-conjugated secondary antibody and enhanced chemiluminescence detection system (Amersham Pharmacia Biotech, Uppsala, Sweden).

Statistical analysis The experimental results shown were repeated twice or three times, unless otherwise indicated. Results are expressed as mean±SD. Statistical analysis was carried out using Student's *t*-test and one-way ANOVA. Significance was set at $P<0.05$. Statistical analyses were performed using SPSS10.0 (SPSS Inc, Chicago, IL, USA)

Results

PPARγ expression in human RCC tissue and RCC cell lines Using RT-PCR and Western blot analysis PPARγ mRNA expression was detected in 15 human RCC tissues, 10 normal kidney tissues, 2 RCC cell lines (786-O and A498) and 2 normal kidney cell lines (HK-2 and HMCL). PPARγ expression at both mRNA (Figure 1A) and protein level (Figure 1B) was detected in all tissues and cell lines examined. Much higher PPARγ expression levels were observed in human RCC tissues and cell lines (786-O and A498) compared to normal renal tissues and cell lines (Figure 1A, 1B). Immunostaining analysis further demonstrated that PPARγ immunoreactivity was much higher over cancer cells in human RCC tissues compared to adjacent normal tissues and normal renal tissues (Figure 1C).

Strong staining of PPARγ was observed in 118 out of 120 human RCC tissues. PPARγ protein was predominantly localized to nucleus and cytoplasm areas of the cells. In contrast, although 16 out of the 20 normal renal samples showed PPARγ protein expression, only weak PPARγ expression was observed in cytoplasm of the medullary collecting duct cells. Statistically, the intensity of PPARγ immunoreactivity was much higher in human RCC tissues than in normal renal tissues (2.16±0.85 *vs* 0.90±0.73; $P< 0.01$).

PPARγ agonists inhibited proliferation of RCC cell lines To determine the effect of PPARγ ligands on growth of human RCC cell lines, the exponentially growing 786-O and A498 cells were treated with 0–50 μmol/L pioglitazone and

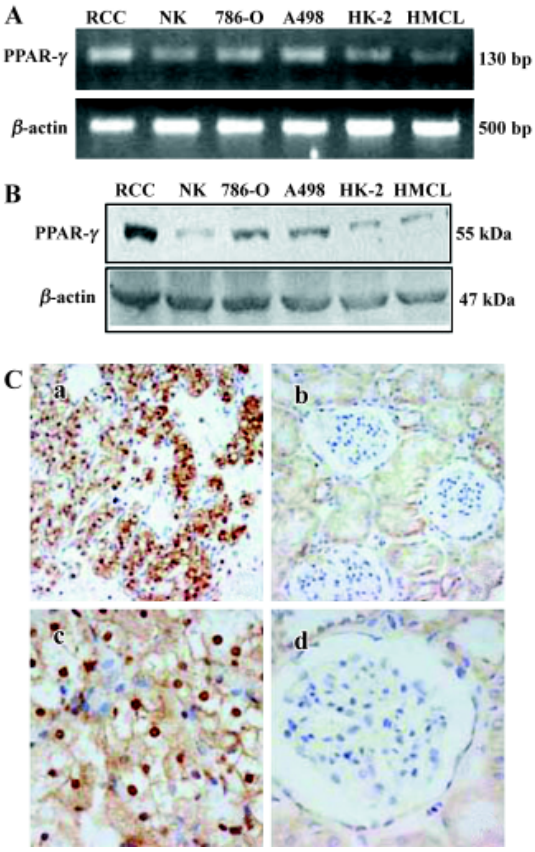

Figure 1. (A) RT-PCR analysis showing expression of PPARγ mRNA in human RCC tissues, normal kidney (NK) tissues, RCC cell lines 786-O and A498, and normal renal cell lines HK-2 and HMCL. β-actin was used as an internal control for RNA loading. (B) Immunoblotting analysis showing that PPARγ protein (55 kDa) was detected in all tissues and cell lines. β-Actin (47 kDa) was used as a protein loading control. Note: higher levels of PPARγ mRNA and protein in human RCC tissues and cell lines. (C) Immunohistochemistry analysis of PPARγ in human RCC tissues (a and c) and normal kidneys (b and d). The slides were counterstained with hematoxylin; a and b (×100) and c and d (×400). Note much higher staining of PPARγ in human RCC tissues than normal kidneys and intense immunoreactivity was observed over malignant cells with little staining in surrounding non-tumor cells (a&c).

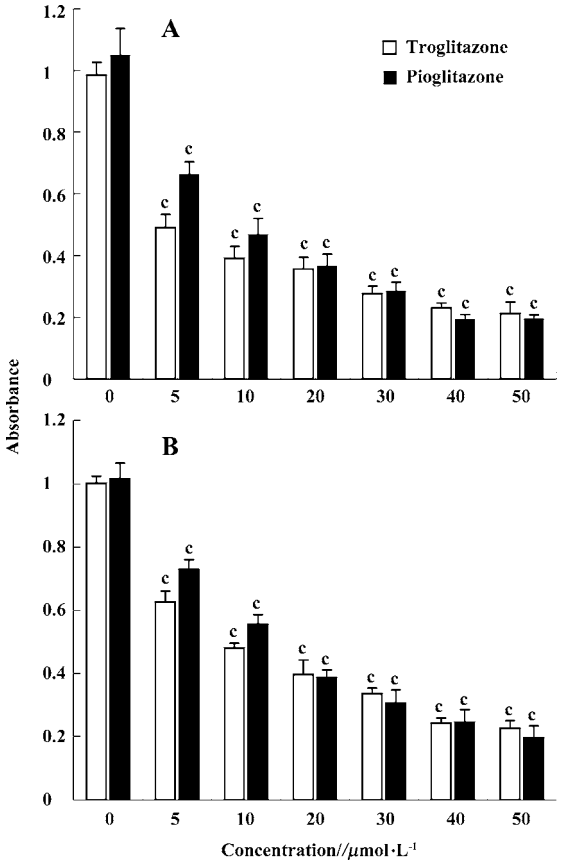

Figure 2. MTT assay showing effect of two TZD PPARγ agonists, pioglitazone and troglitazone, on the growth of human RCC cell lines. RCC 786-O cells (A) and A498 cells (B) were cultured and treated with pioglitazone and troglitazone at various concentrations. Cell growth of both 786-O and A498 cells was determined by MTT assay. Both TZD compounds inhibited cell proliferation of RCC cells in a dose-dependent manner. n=8. Mean±SD. $^cP<0.01$ versus corresponding control group.

troglitazone for 24 h. Cell growth was determined by an MTT assay. Figure 2 showed that two TZD PPARγ agonists pioglitazone and troglitazone significantly inhibited the cell growth of RCC in a dose-dependent manner, with the calculated IC_{50} values of 7.08 and 11.32 μmol/L for pioglitazone and 5.71 and 8.38μmol/L for troglitazone in 786-O and A498 cells, respectively.

Effect of PPARγ agonists on cell cycle of RCC cell lines Cell cycle analysis was performed in two RCC cell lines after exposure to 20–30 μmol/L pioglitazone and troglitazone for 24 h. In both cell lines, pioglitazone and troglitazone caused a dose-dependent increase in the G_0/G_1 phase and decrease in the S phase (Figure 3).

Effect of PPARγ ligands on cell cylce protein expression in human RCC cell lines The cell cycle is tightly regulated through a complex network of positive and negative regulatory molecules including cyclin dependent kinases (Cdks), cyclins, and Cdk inhibitors (Cdkis). To elucidate the role of these molecules in the inhibition of cell cycle induced by pioglitazone and troglitazone in RCC cell lines, protein extract was prepared from the cells treated with 30 μmol/L pioglitazone or troglitazone for 0, 12, and 24 h. Immunoblotting was performed using antibodies against human PCNA, pRb, cyclin D_1, p21, p27, and Cdk4. As shown in Figure 4, pioglitazone and troglitazone treatment time-dependently caused a marked decrease in PCNA, pRb, Cyclin

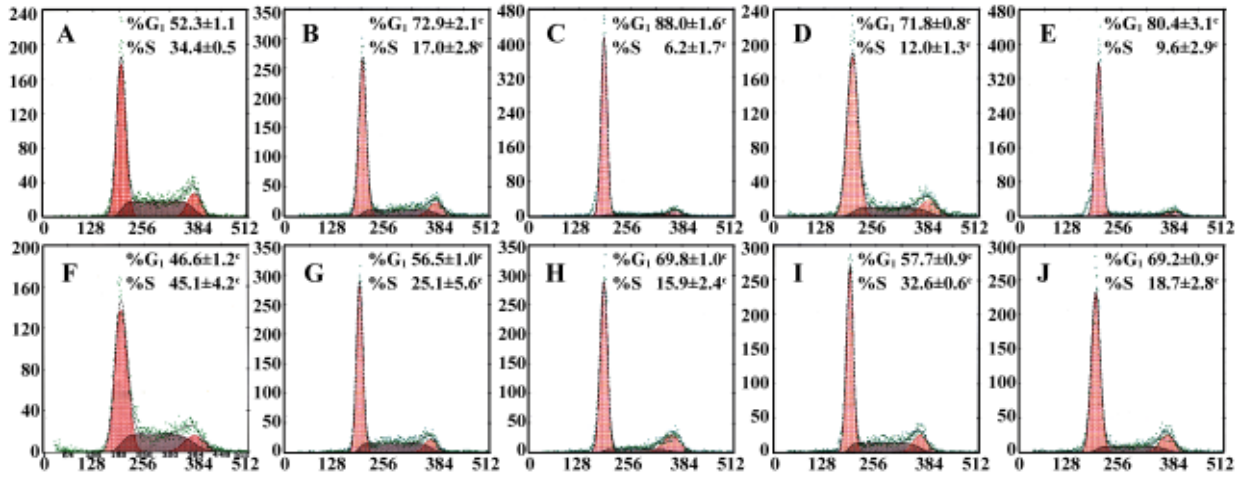

Figure 3. Flow cytometry analysis demonstrating the effect of pioglitazone and troglitazone on cell cycle of two RCC cell lines, 786-O cells (A–E) and A498 cells (F–J). (A) and (F), control cells; (B) and (G), cells treated with 20 μmol/L troglitazone; (C) and (H), cells treated with 30 μmol/L troglitazone; (D) and (I), cell treated with 20 μmol/L pioglitazone; (E) and (J), cells treated with 30 μmol/L pioglitazone. The two TZD PPARγ ligands induced the G_0/G_1 phase proportion and decreased the S phase proportion in both RCC cell lines. n=3. Mean±SD. $^cP<0.01$ *vs* control cells.

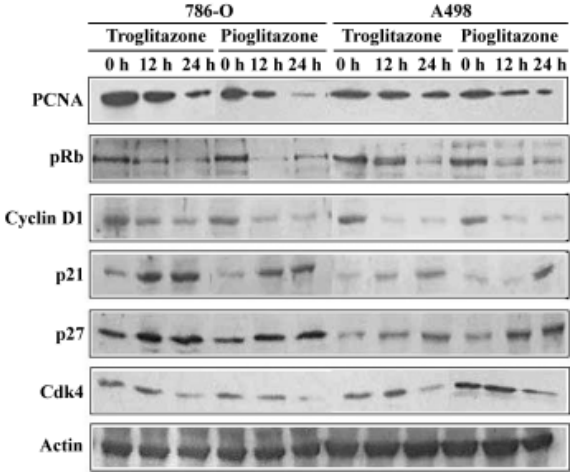

Figure 4. Western blot analysis showing the effect of PPARγ activation on the levels of proteins involved in cell cycle regulation in RCC cells. 786-O and A498 cells were treated with 30 μmol/L pioglitazone and troglitazone for 0, 12, and 24 h. Equal amount of cell lysate containing 50 μg protein was separated and blotted by specific antibodies as described in "Materials and Methods". Actin was used as a sample loading control.

D_1 and Cdk4 expression and a significant increase in p21 and p27 expression.

PPARγ agonist induced apoptosis in human RCC cell lines The ability of pioglitazone and troglitazone to induce apoptosis in two RCC cell lines was initially determined by the cytosolic histon-bound DNA fragments and cell death ELISA assay. We found that pioglitazone and troglitazone treatment for 48 h significantly increased apoptotic cell numbers in a dose-dependent manner, with IC_{50} values of 67.73 μmol/L and 78.12 μmol/L for pioglitazone and 65.11 μmol/L and 63.91μmol/L for troglitazone in 786-O and A498 cells, respectively (Figure 5). When 786-O and A498 cells were exposed to either 80 μmol/L pioglitazone or 70 μmol/L troglitazone for 48 h, they exhibited typical morphological changes of apoptosis including cytoplasmic and nuclear shrinkage, chromatin condensation and fragmentation after staining with Hoechst 33342 (Figure 6). The genomic DNA of treated cells exhibited a characteristic ladder pattern after electrophoresis in agarose gel (Figure 7). To further explore the mechanisms involved in PPARγ agonist-induced apoptosis, the expression of proteins involved in the Bcl-2 apoptotic pathway was examined in RCC cell lines. Treatment of RCC cells with pioglitazone or troglitazone for 48 h decreased the levels of Bcl-2 expression in a time-dependent manner in both 786-O and A498 cells. In contrast, the expression of Bax was increased following TZD treatment (Figure 8).

Discussion

PPARγ is a nuclear receptor transcription factor and plays an important role in many biological processes including adipogenesis, cell growth regulation, and cell differentiation. The synthetic TZD class of compounds, including pioglitazone and troglitazone, are originally developed as therapeu-

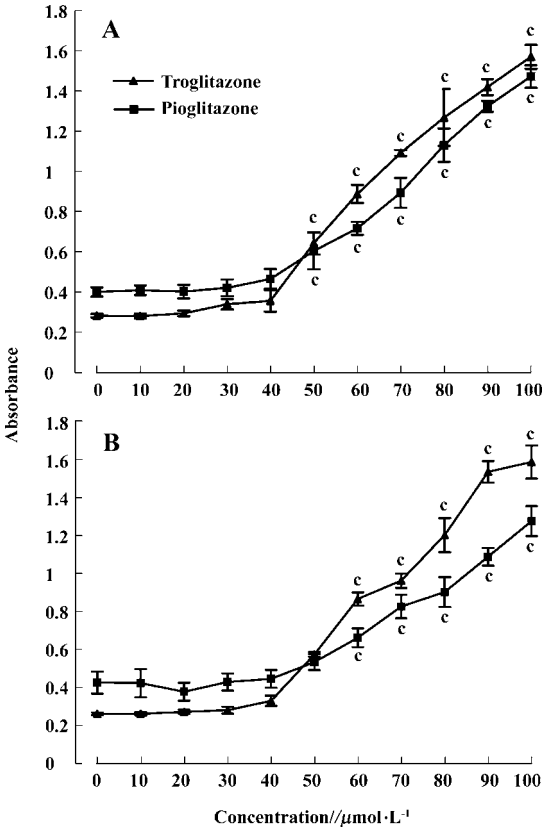

Figure 5. Cell death ELISA assay showing apoptosis of RCC cells induced by pioglitazone and troglitazone. (A) 786-O cells treated with two PPARγ ligands at various concentrations; (B) A498 cells treated with pioglitazone and troglitazone. Note low concentrations of the ligands had no apoptotic effect on both 786-O and A498 cells, but at concentrations exceeding 50 μmol/L, pioglitazone and troglitazone markedly induced apoptosis in the cells in a dose dependent manner. Experiments were carried out in triplicate. n=3. Mean±SD. $^{c}P<0.01$ versus corresponding baseline (0 μmol/L).

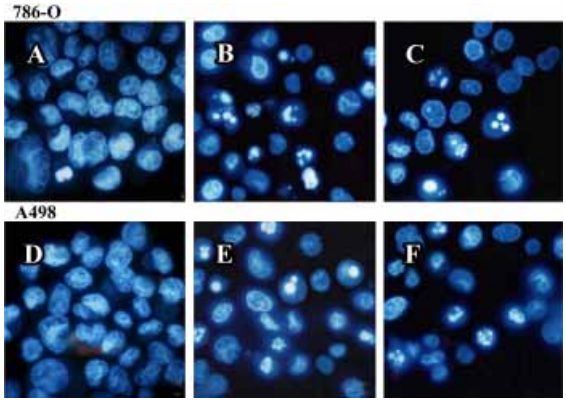

Figure 6. Fluorescence micrographs of 786-O and A498 cells stained with Hoechst 33342 (×400). Cells were treated with 80 μmol/L pioglitazone or 70 μmol/L troglitazone for 48 h. (A) and (D), control cells; (B) and (E), treated with 70 μmol/L troglitazone; (C) and (F) treated with 80 μmol/L pioglitazone. The PPARγ ligand-induced apoptosis was characterized by nuclear condensation and fragmentation.

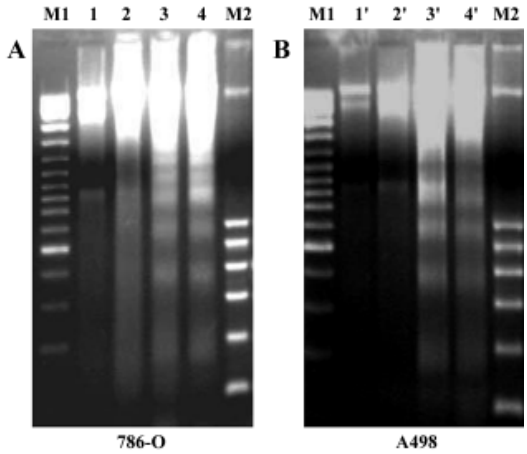

Figure 7. Agarose gel pictures showing DNA fragmentation in 786-O (A) and A498 cells (B) after treatment with 70–80 μmol/L pioglitazone or troglitazone for 48 h. Lanes M1 and M2, DNA molecular standards; lanes 1, 2, 1', and 2', untreated cells; lanes 3 and 3', after treatment with 70 μmol/L troglitazone, respectively; lanes 4 and 4', after treantment with 80 μmol/L pioglitazone, respectively. Note DNA ladder was observed in lanes 3, 4, 3', and 4'.

tic agents for diabetes mellitus and have been recently found to be specific ligands for PPARγ with high affinity. In the past decade, evidence began to emerge suggesting TZD PPARγ agonists not only exert antidiabetic effect in type II diabetes mellitus but also induce cell growth arrest, apoptosis and terminal differentiation in many human malignant tumors including colon cancer, breast cancer, pituitary adenomas, pancreatic carcinoma and esophageal cancer[9–11,19,20], suggesting PPARγ may be a potential therapeutic target for treatment of certain human cancers. The present study provides evidence that high expression of PPARγ was observed in human RCC tissues and cell lines, and activation of PPARγ resulted in G_0/G_1 cell cycle arrest and apoptosis involved Bcl-2 pathway.

In the present study, we observed that PPARγ was abundantly expressed in almost all high-grade human RCC specimens (98.3%), and two RCC cell lines were examined. Its intracellular distribution was mainly localized in nuclear area. In contrast, although PPARγ immunostaining was also positive in most normal renal tissues, its expression was much lower than that in RCC tissues and limited in medullary collecting duct cells in the kidney. Furthermore, its subcellular localization was predominantly in the cytoplasm. The differ-

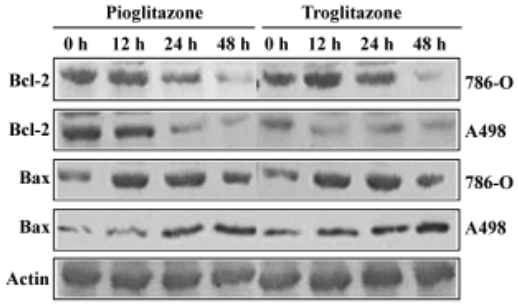

Figure 8. Western blot analysis showing Bcl-2 and Bax expression in 786-O and A498 RCC cells. Cells were exposed to 70 μmol/L troglitazone or 80 μmol/L pioglitazone for 0, 12, 24, and 48 h. Cell lysate containing 50 μg protein was separated and blotted with the antibodies. Actin was used as a sample loading control.

ences of PPARγ in quantity and intracellular distribution between human RCC and normal kidney tissues may implicate an important role of PPARγ in tumorigenesis of renal cell carcinoma.

Consistent with a previous study[21], activation of PPARγ in two human RCC cell lines resulted in inhibition of RCC cell growth as assessed using MTT assay and Flow Cytometry. As seen in other tumor cells, treatment of RCC cells lines with pioglitazone and troglitazone for 24 h caused G_0/G_1 phase arrest and blocked cells from entering the S phase[13,19,22–24]. To explore the mechanism involved in PPARγ-induced cell growth arrest, RCC cells were treated with pioglitazone and troglitazone and expression of cell cycle proteins was examined. We observed a marked reduction in PCNA, pRb, Cdk4 and Cyclin D1 expression and a dramatic increase in p21 and p27 expression in TZD-treated RCC cells. Down-regulation of PCNA, a nuclear protein essential for DNA replication and repair by DNA polymerase δ[25], is in agreement to the low proliferation rate observed in these treated RCC cells. Proliferation of eukaryotic cells is tightly regulated by expression and sequential activation of cell cycle-dependent cyclins, Cdks and CdkIs[26]. pRb, a key regulator of G_1 cell cycle progression, is phosphorylated by a set of Cyclin-Cdk complexes, such as the complexes of Cyclin D and Cdk4/6 or cyclin E and Cdk2[27,28]. In its dephosphorylated state, pRb binds to E2F and inhibits G_1-S phase transi-tion. In contrast, phosphorylation of pRb causes breakdown of E2F/pRb complex, and initiates DNA synthesis. In the present study, Decreased expression of phosphorylated pRb was found in these treated cells. CdkIs are cell cycle regulatory molecules having negative effects on cell cycle machinery by binding to various cyclin-Cdk complexes and inhibiting their activities. In mammals, there are two structurally defined classes of CdkIs, the INK4 family and the KIP/CIP family[29]. The KIP/CIP family, including $p21^{CIP}$, $p27^{KIP1}$, and $p57^{KIP2}$, interacts with cyclin E-Cdk2, cyclin D-Cdk4, cyclin D-Cdk6, and cyclin A-Cdk2 complexes, and inhibits their activities[28]. The decrease of cyclin D1 and Cdk4 and increased expression of CdkI proteins including p21 and p27 strongly suggest TZD PPARγ agonists induced the overexpression of the members of KIP/CIP family which sequentially inhibited the activities of cyclin D1-Cdk4 complex, the phosphorylation of pRb, and the G_1-S phase transition. These findings are consistent with the observation that two TZD PPARγ agonists decreased cell proliferation in MTT assay and arrested cells in G_0/G_1 phase by flow cytometry.

Cell cycle status and cell programmed death are usually closely associated[13]. Besides the cell cycle arrest, the inhibition of cell growth observed in RCC cells treated with pioglitazone and troglitazone may also be a result of the increase in apoptosis[30]. Cells failing to progress to mitosis phase are destined for apoptosis. TZD have been reported to be potent agents in inducing apoptosis in many human tumors including breast cancer, pituitary tumors and gastric cancer[10–12]. In the present study, we clearly demonstrated that at high concentrations PPARγ agonists pioglitazone and troglitazone caused marked apoptosis in human RCC cells as assessed by morphological change, DNA fragmentation and the cell death ELISA assay. These studies suggest that TZD may exert pro-apoptotic effect on human RCC cells.

Multiple pathways are involved in apoptosis including Bcl-2 system, fas/fasL pathway, and caspase cascade[31–33]. To explore the molecular mechanism through which TZD PPARγ agonist induces apoptosis in human RCC cells, we examined Bcl-2 and Bax expression following pioglitazone and troglitazone treatment in 786-O cells and A498 cells. We observed for the first time that activation of PPARγ by both TZD markedly decreased Bcl-2 protein expression but increased Bax protein expression. Because Bcl-2 protects cells from apoptosis, while the increase of Bax induces apoptosis[34,35], our findings suggest that decreased Bcl-2 expression and increased Bax expression may participate in TZD PPARγ agonist-induced apoptosis in human RCC cells.

PPARγ agonists, such as 15-dPGJ_2, troglitazone, have been shown to possess effects not involving PPARγ[36,37], For instance, the potencies for inhibition of cholesterol synthesis by troglitazone is mechanistically distinct from the transcriptional regulation by PPARγ[38] . In the present study, low doses of TZD fail to induce RCC cell death. It has been reported that TZD promote T cell survival at doses that induce optimal PPARγ transcriptional activity[39], and cell deaths induced by TZD always use concentrations of TZD several

orders of magnitude higher than K_D for PPARγ[39,40]. Moreover, troglitazone could induce apoptosis of rat hepatoma cells, but rosiglitazone, a potent PPARγ agonist, did not have the same effect[41], indicating that PPARγ independent pathways, such as TZD-induced loss of mitochondrial membrane potential[42], may be involved in the mechanisms of TZD induced cell apoptosis. Furthermore, it has also been reported that PPARγ agonists could induce apoptosis in non-malignant cells, including isolated rat mesangial cells[43]. Thus the mechanisms of anticaner effect of TZD need to be further explored.

In summary, the present study provides evidence that PPARγ is highly expressed in human renal cell carcinoma cells. Activation of PPARγ by TZD PPARγ agonists results in inhibition of cell proliferation, likely by arresting the cells in G_0/G_1 cell cycle phase. In addition, PPARγ agonists also induce marked apoptosis partly through decreased Bcl-2 and enhanced Bax protein expression in human RCC cells. Additional research will need to be performed to explore the mechanism of TZD which induced cell apoptosis, and the potential therapeutic value of PPARγ agonists in renal cell carcinoma.

References

1 Issemann I, Green S. Activation of a member of the steroid hormone receptor superfamily by peroxisome proliferators. Nature 1990; 347: 645–50.

2 Schoonjans K, Martin G, Staels B, Auwerx J. Peroxisome proliferator-activated receptors, orphans with ligands and functions. Curr Opin Lipidol 1997; 8: 159–66.

3 Kliewer SA, Umesono K, Noonan DJ, Heyman RA, Evans RM. Convergence of 9-*cis* retinoic acid and peroxisome proliferator signaling pathways through heterodimer formation of their receptors. Nature 1992; 358: 771–4.

4 Kliewer SA, Lehmann JM, Milburn MV, Willson TM. The PPARs and PXRs: nuclear xenobiotic receptors that define novel hormone signaling pathways. Recent Prog Horm Res 1999; 54: 345–67.

5 Palmer CN, Hsu MH, Griffin HJ, Johnson EF. Novel sequence determinants in peroxisome proliferator signaling. J Biol Chem 1995; 270: 16114–21.

6 Camp HS, Ren D, Leff T. Adipogenesis and fat-cell function in obesity and diabetes. Trends Mol Med 2002; 8: 442–7.

7 Rangwala SM, Lazar MA. Peroxisome proliferator-activated receptor gamma in diabetes and metabolism. Trends Pharmacol Sci 2004; 25: 331–6.

8 Fauconnet S, Lascombe I, Chabannes E, Adessi GL, Desvergne B, Wahli W, *et al*. Differential regulation of vascular endothelial growth factor expression by peroxisome proliferator-activated receptors in bladder cancer cells. J Biol Chem 2002; 277: 23534–43.

9 Sarraf P, Mueller E, Jones D, King FJ, DeAngelo DJ, Partridge JB, *et al*. Differentiation and reversal of malignant changes in colon cancer through PPARgamma. Nat Med 1998; 4: 1046–52.

10 Elstner E, Muller C, Koshizuka K, Williamson EA, Park D, Asou H, *et al*. Ligands for peroxisome proliferator-activated receptor-gamma and retinoic acid receptor inhibit growth and induce apoptosis of human breast cancer cells *in vitro* and in BNX mice. Proc Natl Acad Sci USA 1998; 95: 8806–11.

11 Heaney AP, Fernando M, Melmed S. PPAR-gamma receptor ligands: novel therapy for pituitary adenomas. J Clin Invest 2003; 111: 1381–8.

12 Takahashi N, Okumura T, Motomura W, Fujimoto Y, Kawabata I, Kohgo Y. Activation of PPARgamma inhibits cell growth and induces apoptosis in human gastric cancer cells. FEBS Lett 1999; 455: 135–9.

13 Guan YF, Zhang YH, Breyer RM, Davis L, Breyer MD. Expression of peroxisome proliferator-activated receptor gamma (PPARgamma) in human transitional bladder cancer and its role in inducing cell death. Neoplasia 1999; 1: 330–9.

14 Demetri GD, Fletcher CD, Mueller E, Sarraf P, Naujoks R, Campbell N, *et al*. Induction of solid tumor differentiation by the peroxisome proliferator-activated receptor-γ ligand troglitazone in patients with liposarcoma. Proc Natl Acad Sci USA 1999; 96: 3951–6.

15 Mueller E, Smith M, Sarraf P, Kroll T, Aiyer A, Kaufman DS, *et al*. Effects of ligand activation of peroxisome proliferator-activated receptor gamma in human prostate cancer. Proc Natl Acad Sci USA 2000; 97; 10990–5.

16 Golimbu M, Joshi P, Sperber A, Tessler A, Al-Askari S, Morales P. Renal cell carcinoma: survival and prognostic factors. Urology 1986; 27: 291–301.

17 Flanigan RC, Campbell SC, Clark JI, Picken MM. Metastatic renal cell carcinoma. Curr Treat Options Oncol 2003; 4: 385–90.

18 Guan Y, Zhang Y, Schneider A, Davis L, Breyer RM, Breyer MD. Peroxisome proliferator-activated receptor-gamma activity is associated with renal microvasculature. Am J Physiol Renal Physiol 2001; 281: 1036–46.

19 Motomura W, Okumura T, Takahashi N, Obara T, Kohgo Y. Activation of peroxisome proliferator-activated receptor gamma by troglitazone inhibits cell growth through the increase of p27KiP1 in human pancreatic carcinoma cells. Cancer Res 2000; 60: 5558–64.

20 Hashimoto Y, Shimada Y, Itami A, Ito T, Kawamura J, Kawabe A, *et al*. Growth inhibition through activation of peroxisome proliferator-activated receptor gamma in human oesophageal squamous cell carcinoma. Eur J Cancer 2003; 39: 2239–46.

21 Inoue K, Kawahito Y, Tsubouchi Y, Kohno M, Yoshimura R, Yoshikawa T, *et al*. Expression of peroxisome proliferator-activated receptor gamma in renal cell carcinoma and growth inhibition by its agonists. Biochem Biophys Res Commun 2001; 287: 727–32.

22 Heaney AP, Fernando M, Yong WH, Melmed S. Functional PPAR-gamma receptor is a novel therapeutic target for ACTH-secreting pituitary adenomas. Nat Med 2002; 8: 1281–7.

23 Mossner R, Schulz U, Kruger U, Middel P, Schinner S, Fuzesi L, *et al*. Agonists of peroxisome proliferator-activated receptor gamma inhibit cell growth in malignant melanoma. J Invest Dermatol 2002; 119: 576–82.

24 Brockman JA, Gupta RA, Dubois RN. Activation of PPARgamma leads to inhibition of anchorage-independent growth of human

colorectal cancer cells. Gastroenterology 1998; 115: 1049–55.
25 Luo Y, Hurwitz J, Massague J. Cell-cycle inhibition by independent CDK and PCNA binding domains in p21Cip1. Nature 1995; 375: 159–61.
26 Pines J. Four-dimensional control of the cell cycle. Nat Cell Biol 1999; 1: 73–9.
27 Bartek J, Bartkova J, Lukas J. The retinoblastoma protein pathway in cell cycle control and cancer. Exp Cell Res 1997; 237: 1–6.
28 Sherr CJ. Mammalian G1 cyclins. Cell 1993; 73: 1059–65.
29 Aprelikova O, Xiong Y, Liu ET. Both p16 and p21 families of cyclin-dependent kinase (CDK) inhibitors block the phosphorylation of cyclin-dependent kinases by the CDK-activating kinase. J Biol Chem 1995; 270: 18195–7.
30 Shi C, Yu L, Yang F, Yan J, Zeng H. A novel organoselenium compound induces cell cycle arrest and apoptosis in prostate cancer cell lines. Biochem Biophys Res Commun 2003; 309: 578–83.
31 Zhang CL, Wu LJ, Tashiro S, Onodera S, Ikejima T. Oridonin induces apoptosis of HeLa cells via altering expression of Bcl-2/Bax and activating caspase-3/ICAD pathway. Acta Pharmacol Sin 2004; 25: 691–8.
32 Filippova M, Parkhurst L, Duerksen-Hughes PJ. The human papillomavirus 16 E6 protein binds to Fas-associated death domain and protects cells from Fas-triggered apoptosis. J Biol Chem 2004; 279: 25729–44.
33 Orrenius S. Mitochondrial regulation of apoptotic cell death. Toxicol Lett 2004; 149: 19–23.
34 Li XH, Li JJ, Zhang HW, Sun P, Zhang YL, Cai SH, *et al*. Nimesulide inhibits tumor growth in mice implanted hepatoma: overexpression of Bax over Bcl-2. Acta Pharmacol Sin 2003; 24: 1045–50.
35 Salomons GS, Brady HJ, Verwijs-Janssen M, Van Den Berg JD, Hart AA, Van Den Berg H, *et al*. The Bax alpha:Bcl-2 ratio modulates the response to dexamethasone in leukaemic cells and is highly variable in childhood acute leukaemia. Int J Cancer 1997; 71: 959–65.
36 Chawla A, Barak Y, Nagy L, Liao D, Tontonoz P, Evans RM. PPAR-gamma dependent and independent effects on macrophage-gene expression in lipid metabolism and inflammation. Nat Med 2001; 7: 48–52.
37 Davies GF, Khandelwal RL, Wu L, Juurlink BH, Roesler WJ. Inhibition of phosphoenolpyruvate carboxykinase (PEPCK) gene expression by troglitazone: a peroxisome proliferator-activated receptor-gamma (PPARgamma)-independent, antioxidant-related mechanism. Biochem Pharmacol 2001; 62: 1071–9.
38 Wang M, Wise SC, Leff T, Su TZ. Troglitazone, an antidiabetic agent, inhibits cholesterol biosynthesis through a mechanism independent of peroxisome proliferator-activated receptor-gamma. Diabetes 1999; 48: 254–60.
39 Wang YL, Frauwirth KA, Rangwala SM, Lazar MA, Thompson CB. Thiazolidinedione activation of peroxisome proliferator-activated receptor gamma can enhance mitochondrial potential and promote cell survival. J Biol Chem 2002; 277: 31781–8.
40 Yu C, Chen L, Luo H, Chen J, Cheng F, Gui C, *et al*. Binding analyses between human PPARgamma-LBD and ligands. Eur J Biochem 2004; 271: 386–97.
41 Bae MA, Rhee H, Song BJ. Troglitazone but not rosiglitazone induces G1 cell cycle arrest and apoptosis in human and rat hepatoma cell lines. Toxicol Lett 2003; 139: 67–75.
42 Bova MP, Tam D, McMahon G, Mattson MN. Troglitazone induces a rapid drop of mitochondrial membrane potential in liver HepG2 cells. Toxicol Lett 2005; 155: 41–50.
43 Tsuchiya T, Shimizu H, Shimomura K, Mori M. Troglitazone inhibits isolated cell proliferation, and induces apoptosis in isolated rat mesangial cells. Am J Nephrol 2003; 23: 222–8.

Acta Pharmacologica Sinica 2005 Jun; 26 (6): 762–768

Full-length article

Inhibition of tumor growth and metastasis with antisense oligonucleotides (Cantide) targeting hTERT in an *in situ* human hepatocellular carcinoma model[1]

Ru-xian LIN[2], Chao-wei TUO[3], Qiu-jun LÜ[2], Wei ZHANG[2], Sheng-qi WANG[2,4]

[2]*Beijing Institute of Radiation Medicine, Beijing 100850, China,* [3]*Department of Pathology, PLA 202 Hospital, Shenyang 110001, China*

Key words

telomerase; Cantide; hepatocellular carcinoma; recurrence; neoplasm metastasis

[1] Project supported by the National High Technology Program of China (No 2004AA-215150).
[4] Correspondence to Prof Sheng-qi WANG.
Phn 86-10-6693-2211.
Fax 86-10-6821-4653.
E-mail sqwang@nic.bmi.ac.cn

Received 2005-02-23
Accepted 2005-03-09

doi: 10.1111/j.1745-7254.2005.00112.x

Abstract

Aim: To evaluate the *in vivo* antitumor effects of Cantide and the combined effect with 5-fluorouracil. **Methods:** An *in situ* human hepatocellular carcinoma model was established in mice livers orthotopically. Drugs were administered intravenously and tumor sizes were monitored with calipers. Plasma alpha-fetoprotein (AFP) were detected by radiation immunoassay. Morphology of tumors was evaluated by hematoxylin-eosin (H&E) staining of histological sections. Human telomerase reverse transcriptase (hTERT) protein levels were detected by Western blotting. **Results:** Cantide significantly inhibit *in situ* human hepatocellular carcinoma growth in mice with a 75 and 50 $mg \cdot kg^{-1} \cdot d^{-1}$ administration of Cantide compared to the saline group in a dose-dependent manner, which included injecting Cantide 25 $mg \cdot kg^{-1} \cdot d^{-1}$–75 $mg \cdot kg^{-1} \cdot d^{-1}$ by iv for 20 d after surgically removing the tumor in liver. Cantide was also found to prevent tumor recurrence in the liver and metastasis in the lung, showing a dose-dependent response. When Cantide was administered by iv combined with 5-fluorouracil, it resulted in a significant reduction in tumor growth compared to either agent alone treatment group. After the treatment with Cantide alone or combined with 5-fluorouracil, plasma AFP concentration decreased in a dose-dependent manner. **Conclusion:** These results demonstrated that Cantide was an effective antitumor antisense oligonucleotide *in vivo* and has the potential to be developed into a clinical anti-cancer drug.

Introduction

Telomerase is a unique ribonucleoprotein enzyme responsible for adding telomeric repeats onto the 3' ends of chromosomes[1,2]. Telomerase plays an important role in the development of cellular immortality and oncogenesis. Previous published studies have shown that telomerase activity is found in 85%–90% of all human tumors, but not in their adjacent normal cells. This makes telomerase a good target not only for cancer diagnosis, but also for the development of novel therapeutic agents[3,4].

A series of experimental strategies have been employed to block either telomerase function or expression, both *in vitro* and *in vivo* in several tumor cell lines derived from a number of species[5,6]. Antisense oligonucleotide (ASODN) is a new class of antineoplastic agents that can prevent the initiation and progression of specific human cancers when targeted to appropriate molecular targets[7,8]. Since the first antisense drug Vitravene was approved by the American Food and Drug Administration (FDA) in 1998, it has been our hope that this class of compound will represent a whole new class drug with potential therapeutic application against a variety of disease, including cancer. Human telomerase reverse transcriptase (hTERT) is a catalytic subunit of telomerase. There are many published studies which have found that more than 90% of examined tumors show telomerase activity in connection with the expression of the activity-limiting component hTERT[9,10]. The inhibition of telomerase activity in tumor cells can lead to telomere destabilization and consequently to growth inhibition and cell death. Therefore, targeting the catalytic subunit of hTERT represents a promis-

ing approach for diminishing telomerase function. Phosphoro-thioate antisense oligonucleotides targeted to hTERT had been studied and has been found to have growth inhibitory efficacy to cancer cells *in vitro*[11,12], but only few detected ASODN activity in animal models[13,14]. Our previous study had shown that an ASODN complementary to hTERT, Cantide, had a specific inhibitory effect on tumor cell growth after *in vitro* treatment, down-regulated hTERT mRNA expression and telomerase activity, and triggered apoptosis through the activation of the caspase family[15].

In the present study, we used an *in situ* human hepatocellular carcinoma (HCC) model to further assess the effect of Cantide in *in vivo* growth of HCC in mice and the combined effect of Cantide with 5-fluorouracil (5-FU). Our findings demonstrated that systemic administration of phosphorothioate antisense ODN to hTERT mRNA resulted in a significant growth inhibition of *in situ* HCC tumors and prevented tumor recurrence in the liver and metastasis in the lung.

Materials and methods

Oligonucleotides and drug Antisense phosphorothioate oligonucleotide Cantide (5'-ACTCACTCAGGCCTCAGACT-3') and sense phosphorothioate oligonucleotide (5'-AGTCT-GAGGCCTGAGTGAGT-3') were synthesized by an Applied Biosystems Model 391 DNA synthesizer on solid supports using Oligo Pilot II DNA (Amersham-Pharmacia, Piscataway, NJ, USA) and purified by high-performance liquid chromatography (HPLC) (Waters Delta Prep 4000, Milfordd, MA, USA) with SOURCE 15Q (Amersham Pharmacia, Piscataway, NJ, USA), the purity of oligonucleotides was over 95%. The sense sequence was used as a control. 5-Fluorouracil was purchased from the Shanghai Donghaipu Pharmaceuticals Company (Shanghai, China) as a positive control. An radiation immunoassay (RIA) kit was purchased from the China Institute of Atomic Energy (Beijing, China).

Animals and *in situ* human hepatocellular carcinoma model Experiments were carried out in virgin female Balb/c mice raised at the PLA 202 hospital. All animal studies were conducted in accordance with the highest standards of animal care as outlined in the NIH guide for the Care and Use of Laboratory Animals. Human hepatocellular carcinoma (HCC) high metastasis tumor line HCM-Y89, established in 1989 by PLA 202 Hospital, was derived from a HCC surgical specimen, and has been maintained by serial transplantation in animals. Briefly, the HCM-Y89 tumor was cut into 1 mm×1 mm×1 mm tissues, BALB/c mice (4–6 weeks old, weighing 18–22 g) were anesthetized with propofol (2 mg/kg, intra-venously). A small incision was made in the left liver and a fragment of tumor was implanted. The incision was closed using a Ethicon black braided silk suture. Twenty days later, the mice were killed by cervical dislocation and the tumors were removed. A histological evaluation of tumor tissues was performed, organs were fixed in neutral buffered 10% formalin, processed by standard methods, embedded in paraffin, sectioned and stained with H&E. This model showed various features in clinical liver cancer patients including local growth, regional invasion, spontaneous intrahepatic, lymph nodes and pulmonary metastasis, peritoneal seeding with bloody ascites, and secretion of alpha-fetoprotein in recipient animals.

Treatment of *in situ* HCC xenograft with cantide and anticancer drug Two days after the *in situ* HCC models were established, mice were injected by iv with saline (vehicle control), Cantide with 12.5 , 25, 50 , 75 $mg\cdot kg^{-1}\cdot d^{-1}$ or 5-FU 10 $mg\cdot kg^{-1}\cdot d^{-1}$ for 20 d, either alone or in combination. The body weight and general physical status of the animal were recorded daily. At the endpoint of the study, mice were killed by cervical dislocation and the tumors were removed and weighed. Tumor sizes were monitored with calipers, the tumor volume (V, mm^3) was calculated as $(L\times W^2)/2$, where L=length (mm) and W=width (mm). The percentage of tumor growth inhibition was calculated as:

Inhibitory rate (%)=$(W_{control}-W_{treat})/W_{control}\times 100$. Tissues for histopathological analysis were fixed in 10% buffered formalin.

Determination of tumor recurrence and metastasis The *in situ* HCC model was established according to above method, when the xenograft tumor had grown to 5 mm×5 mm×5 mm. An operation was then performed to remove the tumor. Three days later, saline and Cantide at 12.5, 25, 50, 75 $mg\cdot kg^{-1}\cdot d^{-1}$, or 5-FU 10 $mg\cdot kg^{-1}\cdot d^{-1}$ were administered by iv for 20 d. Tumor sizes were recorded as mentioned earlier. A histological evaluation of microscopic recurrence and metastasis was performed for the liver and lung, and tissues were fixed in 10% buffered formalin.

Histophatological analysis Tissues were excised and fixed in 10% buffered formalin. Representative fragments were embedded in paraffin, 5-μm sections were obtained and stained with H&E for microscopic observations.

Detection of plasma AFP concentration Animal serum was collected after the mice were killed. The plasma AFP concentrations were detected by RIA according to the manufacturer's instructions.

Statistical analysis Results of the quantitative studies were expressed as mean±SD. Student's *t*-test was used to determine the significance of differences between the 2 treat-

ment groups. Multiple comparisons were made using one-way analysis of variance (ANOVA), and post-tests comparing different treatment means were conducted using Fisher's test. Differences were considered significant for $P<0.01$

Results

***In vivo* effects of Cantide treatment on *in situ* hepatocellular carcinoma xenograft growth** The proposed role of the telomerase hTERT subunit has led us to investigate the pharmacological activity of phosphorothioate oligonucleotides targets to hTERT in animal models on tumor growth. In the present study, we used an *in situ* human hepatocellular carcinoma model in mice to evaluate the activity of Cantide. In order to exclude the nonspecific effect of oligonucleotides, we used sense sequence as a control. After establishing the model 2 d later, Cantide with different doses, sense oligonucleotide with 50 mg·kg^{-1}·d^{-1}, 5-Fu with 10 mg·kg^{-1}·d^{-1} and saline were administered by intravenous (iv) for 20 d. Tumors were removed after the mice were killed. The tumors were then measured and weighed. The results showed that 75 and 50 mg·kg^{-1}·d^{-1} Cantide treatment resulted in a significant inhibition of tumor growth compared to sense or saline-treated mice. The highest inhibitory efficacy was a 69.55% contrast to the saline group, but for the sense oligonucleotide , the inhibitory rate was only a 19.26% contrast to the saline group. The inhibitory rate of 50 mg·kg^{-1}·d^{-1} was 57.77% compared to the sense treatment group ($P<0.01$). The effect of Cantide was dose-dependent (Table 1). The mean body weight of the mice were not significantly different from the beginning of the study and between the groups (data not shown). Figure 1 shows the final tumor volumes after a 20-d treatment, which showed a significant decrease in the Cantide treatment group compared to the saline control group ($P<0.01$). However for the sense oligonucleotide treatment group, there was no significant decrease in tumor volume compared to the saline group ($P>0.05$). No inflammatory infiltrate was noted surrounding the solid tumor (data not shown).

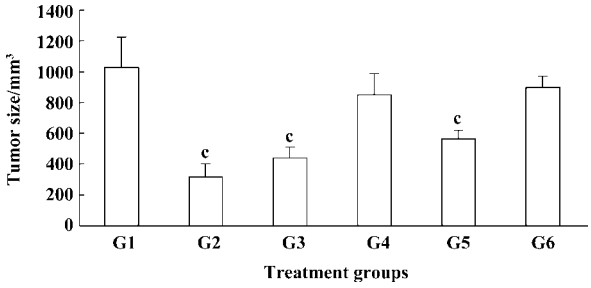

Figure 1. Effect of Cantide on tumor growth in *in situ* human hepatocellular carcinoma in the tested mice. G1: Saline; G2: Cantide 75 mg·kg^{-1}·d^{-1}; G3: Cantide 50 mg·kg^{-1}·d^{-1}; G4: Cantide 25 mg·kg^{-1}·d^{-1}; G5: 5-FU 10 mg·kg^{-1}·d^{-1}; G6: Sense SODN 50 mg·kg^{-1}·d^{-1}. n=8. Mean±SD. $^bP<0.05$, $^cP<0.01$ *vs* the control group.

To determine the effect of Cantide on preventing tumor recurrence and metastasize after surgical removal of the tumors, a highly metastatic HCC model was established in the mice liver according to the above method. When the xenograft tumor had grown to 5 mm×5 mm×5 mm, the mice underwent an operation to remove the tumors; 3 d later, animals were injected with different doses of Cantide or saline by iv for 20 d and then checked for a relapse in the liver. Table 2 shows how the Cantide 75 and 50 mg·kg^{-1}·d^{-1} treatment group could significantly inhibit tumor recurrence in livers after operation. However, there was no statistically significant difference in tumor recurrence in livers treated with 25 mg·kg^{-1}·d^{-1} and 12.5 mg·kg^{-1}·d^{-1} in the Cantide treatment group compared to the saline treatment group. 5-FU could not prevent tumor relapse after operation. The relapse tumor volumes also decreased significantly in the Cantide treatment group compared to the Saline control group (Figure 2). No signs of treatment-related toxicity such as inflammation,

Table 1. Effect of Cantide on tumor weight and inhibitory rate in mice with *in situ* HCC. n=8. Mean±SD. $^bP<0.05$, $^cP<0.01$ *vs* the control group.

Treatment group /mg·kg^{-1}·d^{-1}	Tumor weight/g	Inhibitory rate/%
Saline	1.35±0.35	–
Cantide 25	0.74±0.21^c	45.19
Cantide 50	0.57±0.12^c	57.77
Cantide 75	0.41±0.15^c	69.55
5-Fu 10	0.70±0.24^c	48.14
Sense SODN 50	1.09±0.12^b	19.26

Table 2. Inhibition of hepatocelluar carcinoma local relapse after surgical removal of tumors in mice with Cantide treatment.

Treatment group /mg·kg^{-1}·d^{-1}	No mice	No relapse	Liver relapse/%
Saline	24	24	100.0
Cantide 12.5	24	24	100.0
Cantide 25	24	22	91.7
Cantide 50	24	18	75.0
Cantide 75	24	15	62.5
5-Fu 10	24	24	100.0

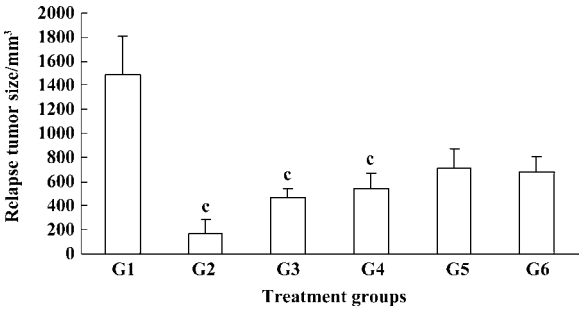

Figure 2. Effect of Cantide on preventing local recurrence of high metastatic human hepatocellular carcinoma after operation. G1: Saline; G2: Cantide 75 mg·kg^{-1}·d^{-1}; G3: Cantide 50 mg·kg^{-1}·d^{-1}; G4: Cantide 25 mg·kg^{-1}·d^{-1}; G5: 5-FU 12.5 mg·kg^{-1}·d^{-1}; G6: 5-FU 10 mg·kg^{-1}·d^{-1}. n=8. Mean±SD. ^{c}P<0.01 *vs* the control group.

bleeding, hepatomegaly and splenomegaly or weight loss was observed in the animals over the course of the study.

Inhibitory effects of Cantide on tumor metastasis in lung Tumor metastasis in the lung was also monitored after surgical removal of the tumors from the mice livers and treatment with Cantide or saline for 20 d. Cantide can also prevent tumor metastasis in the lung after operating on the liver. The results found that only 10 and 14 of the 24 mice tested showed evidence of tumor metastasis in the lung with 75 and 50 mg·kg^{-1}·d^{-1} in the Cantide treatment groups, respectively (Table 3). A histological analysis of the lungs showed that the metastatic areas markedly decreased in mice treated with 75 and 50 mg·kg^{-1}·d^{-1} Cantide compared to the other group, where 5-FU had no effect on tumor metastasis (data not shown).

Table 3. Inhibition of lung metastasis of HCC after operation and Cantide treatment. n=24. Mean±SD.

Treatment group /mg·kg^{-1}·d^{-1}	No mice	No metastasis	Metastasis rates/%
Saline	24	24	100.0
Cantide 12.5	24	24	100.0
Cantide 25	24	21	87.5
Cantide 50	24	14	58.3
Cantide 75	24	10	41.7
5-Fu 10	24	24	100.0

Effects of Cantide combined with 5-FU on xenograft tumor growth Several studies have shown that antisense oligonucleotides combined with chemotherapeutics can increase drug sensitivity[16,17]. In order to evaluate whether a combination effect would occur when Cantide was combined with a chemotherapy drug, Cantide was co-administered with 5-FU by iv for 20 d to mice bearing with *in situ* HCC tumors. The mice were killed and tumor volumes and weight were measured after the 20-d treatment. Table 4 shows that after the 20-d treatment, the tumor weight decreased in the combination treatment group compared to either agent alone treatment group. The tumor growth inhibitory rate also showed significant difference compared to either agent alone treated group (Table 4). Figure 3 shows that at the endpoint of treatment in the combination treatment group, a significant decrease in tumor volumes with respect to tumors growth in either Cantide or the 5-FU alone treatment group was induced.

Table 4. Combined treatment with Cantide and 5-FU on xenograft weights and inhibitory rates. n=8. Mean±SD. Combined group 1: 5-FU 10 mg·kg^{-1}·d^{-1}+Cantide 50 mg·kg^{-1}·d^{-1}; Combined group 2: 5-FU 10 mg·kg^{-1}·d^{-1}+Cantide 75 mg·kg^{-1}·d^{-1}. ^{c}P<0.01 *vs* the control group. ^{f}P<0.01 *vs* Cantide 50 mg·kg^{-1}·d^{-1} and ^{i}P<0.01 *vs* Cantide 75 mg·kg^{-1}·d^{-1}.

Treatment group /mg·kg^{-1}·d^{-1}	Tumor weights /g	Inhibitory rates/%
Saline	1.40±0.17	–
Cantide 50	0.81±0.05^{c}	42.14
Cantide 75	0.53±0.09^{c}	62.14
Combined group 1	0.45±0.08^{cf}	67.85
Combined group 2	0.36±0.05^{ci}	74.29
5-Fu 10	1.01±0.10	27.85

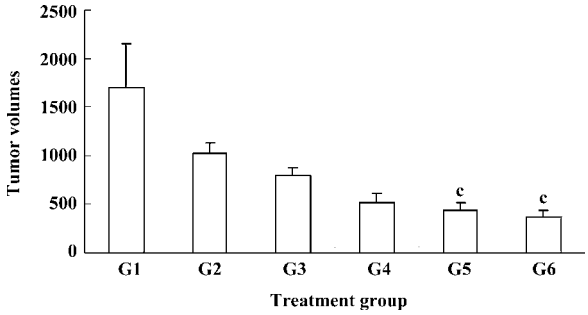

Figure 3. *In vivo* effects on tumor growth of 5-FU combined with Cantide. G1: Saline; G2: 5-FU 10 mg·kg^{-1}·d^{-1}; G3: Cantide 50 mg·kg^{-1}·d^{-1}; G4: Cantide 75 mg·kg^{-1}·d^{-1}; G5: 5-FU 10 mg·kg^{-1}·d^{-1}+Cantide 50 mg·kg^{-1}·d^{-1}; G6: 5-FU 10 mg·kg^{-1}·d^{-1}+Cantide 75 mg·kg^{-1}·d^{-1}. n=8. Mean±SD. ^{c}P<0.01 *vs* the control group.

Histopathological analysis Morphology of tumors from antisense ODN, sense ODN or saline-treated mice was evaluated by H&E staining of histological sections. Tumors were excised at the endpoint of treatment of each protocol. Figure

4 shows representative sections of tumors from each experimental protocol. Tumors from mice treated with Cantide or combined with 5-FU, showed a marked increase in the necrotic area and tumor cells fibrosis compared to saline-treated or normal animals. A large percentage of tumor mass from combination-treated mice was necrotic and fibrotic compared to either agent alone treated mice.

Inhibition of plasma AFP secretion with Cantide treatment Alpha-fetoprotein (AFP) is usually expressed at high concentrations in fetal liver, gastrointestinal tract and the yolk sack. It is transcriptionally down-regulated after birth, frequently re-expressed in HCC,and is a good tumor marker of HCC[13]. We used RIA to detect serum AFP concentration at the endpoint of treatment. Figure 5 shows how Cantide can significantly decrease AFP secretion at 75, 50, and 25 mg·kg^{-1}·d^{-1} compared to the saline group. AFP concentration was also correlated with tumor size (data not shown). The plasma AFP was also detected after treatment with Cantide combined with 5-FU. Figure 6 shows how Cantide combined with 5-FU could increase AFP secretion in plasma. In the two combination treatment groups, plasma AFP concentration decreased compared to either the Cantide or 5-FU alone treatment groups, possibly because there were fewer liver tumor cells in the combined treated mice and reduced circulating AFP.

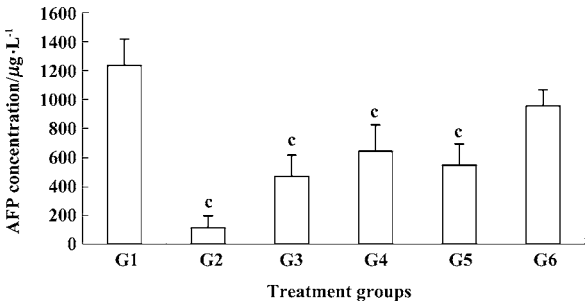

Figure 5. Serum AFP concentration at the endpoint after the treatment. G1: Saline; G2: Cantide 75 mg·kg^{-1}·d^{-1}; G3: Cantide 50 mg·kg^{-1}·d^{-1}; G4: Cantide 25 mg·kg^{-1}·d^{-1}; G5: 5-FU 10 mg·kg^{-1}·d^{-1}; G6: Sense SODN 50 mg·kg^{-1}·d^{-1}. n=8. Mean±SD. ^{b}P<0.05, ^{c}P<0.01 *vs* the control group.

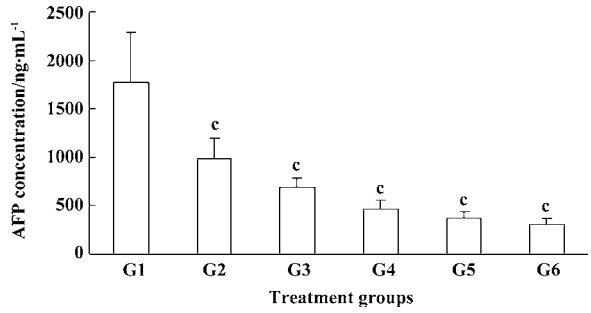

Figure 6. Inhibitory efficacy on AFP secretion of 5-FU in combination with Cantide. G1: Saline; G2: 5-Fu 10 mg·kg^{-1}·d^{-1}; G3: Cantide 50 mg·kg^{-1}·d^{-1}; G4: Cantide 75 mg·kg^{-1}·d^{-1}; G5: 5-FU 10 mg·kg^{-1}·d^{-1}+Cantide 50 mg·kg^{-1}·d^{-1}; G6: 5-FU 10 mg·kg^{-1}·d^{-1}+Cantide 75 mg·kg^{-1}·d^{-1}. n=8. Mean±SD. ^{c}P<0.01 *vs* the control group.

Discussion

In the present study we have demonstrated that systemic administration of phosphorothioate antisense ODNs to hTERT mRNA results in a significant growth inhibition of

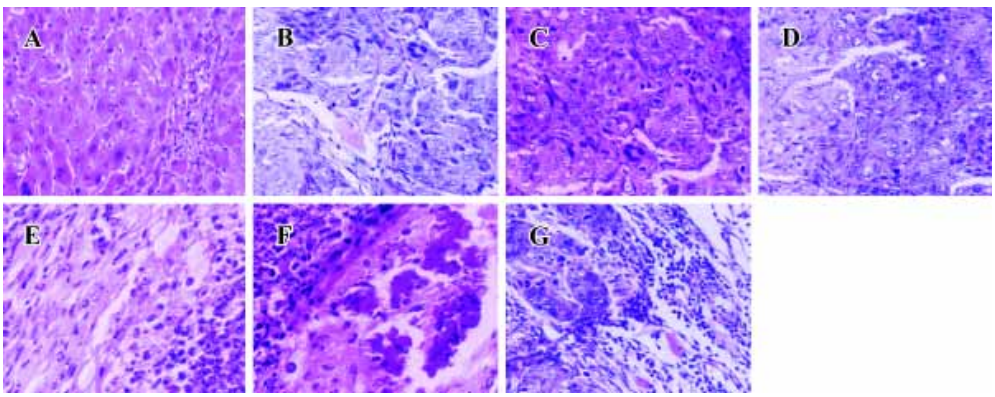

Figure 4. Histopathological analysis (×200). A: Tissue sections of liver from normal mouse; B: Tissue sections of tumor from *in situ* xenograft HCC; C and D: Tissue sections from 50 and 75 mg·kg^{-1}·d^{-1} Cantide-treated tumors, respectively; G: Tissue sections from 10 mg·kg^{-1}·d^{-1} 5-FU-treated tumors; E and F: Tissue sections of tumors from 50 mg·kg^{-1}·d^{-1} Cantide+10 mg·kg^{-1}·d^{-1} 5-FU and 75 mg·kg^{-1}·d^{-1} Cantide+10 mg·kg^{-1}·d^{-1} 5-FU-treated tumors, respectively. Increased regions of necrosis and fibrosis were observed in the combined treatment group compared with the agent alone treatment group.

the *in situ* HCC model in mice. It is worth noting that our experimental model of HCC has some advantages compared to the tumor cell inoculation model. First, the tumor line originated from human HCC; it completely kept the human HCC tissue structure and retained its AFP secretion ability. It also retained the original sensitivity to the antitumor drug, simulated the clinical features of patients with HCC such as the liver, lung and lymph nodes metastasis, and bloody ascites. Second, the pathological evidence suggests that this model exhibits various features seen in clinical HCC patients, so the reaction to antitumor drug can reflect the true clinic results by this model and more accurately to reflect the clinical results of patients. Therefore, our model system has provided a unique tool for exploring *in vivo* antitumor activity of ODN.

We have demonstrated that the antitumor effect of Cantide was because of a specific antisense effect. The inhibition of tumor growth by Cantide was dose-dependent and no abrogation of tumor proliferation was observed in any of the control groups. Another important finding of our present study is that Cantide can effectively prevent tumor recurrence and metastasis. Tumor recurrence and metastasis is a problem encountered during tumor treatment. At present, very few chemotherapeutics can prevent tumor relapse and metastasis after an operation. Pastorino's[18] study indicates that an antisense targeting to c-*myc* can inhibit tumor growth and metastasis. In the present study we demonstrated that Cantide effectively suppressed tumor metastasis in lungs with 75 $mg \cdot kg^{-1} \cdot d^{-1}$ treatment. Lung metastasis was found in only 10 mice of the 24 mice (41.7%). Cantide can also prevent local recurrence after an operation. An important factor contributing to these results is that Cantide might inhibit telomerase activity[15], thus the residue of tumor cells after an operation has less ability to proliferate.

AFP is a secretary protein that is heterogeneously glycosylated. AFP is usually expressed at high concentrations in fetal liver, gastrointestinal tract, and the yolk sack. It is transcriptionally down-regulated after birth and frequently re-expressed in HCC, therefore used as a diagnostic marker for the tumor. Serum AFP is useful not only for diagnosis, but also as a prognostic indicator for HCC patients. AFP mRNA has been proposed as a predictive marker of HCC cells disseminated into the serum circulation and for metastatic recurrence[19,20]. We detected serum AFP concentration after the surgical removal of tumors and their treatment with Cantide. The results showed that serum AFP secretion was significantly inhibited in a dose-dependent manner in the Cantide treatment groups compared to the saline group. The AFP concentration was also lower than 5-FU group. The serum AFP concentration and the relapse of tumor volume had a good dependent relationship, which was correlated with AFP as a marker for HCC recurrence and metastasis.

In the past decade, several ASODN have been developed and tested in preclinical and clinical studies. Many have found convincing *in vitro* reduction in target gene expression and promise activity against a wide variety of tumors[21,22]. However, because of the multigenic alterations of tumors, the use of ASODN as a single agent does not seem to be effective in the treatment of malignancies. Antisense therapy that interferes with signaling pathways involved in cell proliferation and apoptosis are particularly promising in combination with conventional anticancer treatment; several preclinical studies have also been performed using antisense oligonucleotides in combination therapy on human tumors[23,24]. Our previous study showed that Cantide inhibited tumor cells growth through triggered tumor cells apoptosis[15], and increasing 5-FU sensitivity in HepG2 cells *in vitro* (data not shown). Zhang and He also show an increased sensitivity to cisplatin caused by hTERT ASODN treatment in leukemia cells[25]. However, to our knowledge, no published studies have been performed to detect the *in vivo* activity of hTERT ASODN in combination with chemotherapy drugs. We investigated the combinational activity of Cantide with 5-FU in the *in situ* HCC model. The results indicate that 75 or 50 $mg \cdot kg^{-1} \cdot d^{-1}$ Cantide combined with 10 $mg \cdot kg^{-1} \cdot d^{-1}$ 5-FU significantly suppresses *in situ* HCC growth in mice. At the endpoint of the treatment, the tumor weight was much lighter than either agent alone treatment (Table 4). These results suggest that the combination of Cantide with 5-FU might sensitize patients with late-stage HCC to chemotherapy.

In summary, we have for the first time directly addressed the potential therapeutic role of Cantide in an *in situ* human HCC model. Significant inhibition of HCC growth was achieved by combining Cantide with 5-FU, indicating that combined targeted therapy with conventional cytotoxic agents are required for the prevention of tumor growth.

References

1 Holt SE, Shay JW. Role of telomerase in cellular proliferation and cancer. J Cell Physiol 1999; 180: 10–8.
2 Shen ZY, Xu LY, Li EM, Cai WJ, Chen MH, Shen J, *et al*. Telomere and telomerase in the initial stage of immortalization of esophageal epithelial cell. World J Gastroenterol 2002; 8: 357–62.
3 Granger MP, Wright W, Shay JW. Telomerase in cancer and aging. Crit Rev Oncol Hematol 2002; 41: 29–40.
4 Shay JW, Bacchetti S. A survey of telomerase activity in human cancer. Eur J Cancer 1997; 33: 787–91.
5 Norton JC, Piatyszek MA, Wright WE, Shay JW, Corey DR.

Inhibition of human telomerase activity by peptide nucleic acids. Nat Biol 1996; 14: 615–9.
6 Zhang RG, Wang XW, Yuan JH, Xie H. Human hepatoma cell telomerase activity inhibition and cell cycle modulation by its RNA component antisense oligodeoxyribonucleotides. Acta Pharmacol Sin 2000; 21:742–6.
7 Bennett CF, Cowsert LM. Application of antisense oligonucleotides for gene functionalization and target validation. Curr Opin Mol Ther 1999; 1: 359–71.
8 Banerjee D. Technology evaluation: G-3139. Curr Opin Mol Ther 1999; 1: 404–408.
9 Counter CM, Meyerson M, Eaton EN, Euisen LW, Caddle SD, Haber DA, *et al*. Telomerase activity is restored in human cells by ectopic expression of hTERT (hEST2), the catalytic subunit of telomerase. Oncogene 1998; 16: 1217–22.
10 Yang Y, Chen Y, Zhang C, Huang H, Weissman SM. Nucleolar localization of hTERT protein is associated with telomerase function. Exp Cell Res 2002, 277: 201–9.
11 Pang JX, Cheng XY, Xu W, Wu SG. Antisense Sp1 oligodeoxynucleotide decreases telomerase activity by inhibiting hTERT mRNA expression in Jurkat T cells. Acta Pharmacol Sin 2003; 24: 91–6.
12 Kraemer K, Fuessel S, Schmidt U, Kotzsch M, Schwenzer B, Wirth MP, *et al*. Antisense-mediated hTERT inhibition specifically reduces the growth of human bladder cancer cells. Clin Cancer Res 2003; 3794: 3794–800
13 Wang SQ, Lin L, Chen ZB, Lin RX, Chen SH, Guan W, *et al*. Effect of antisense oligonucleotides targeting telomerase catalytic subunit on tumor cell proliferation *in vitro*. Chin Sci Bull 2002; 47: 993–7.
14 Nguyen MH and Keeffe EB. Screening for hepatocellular carcinoma. J Clin Gastroenterol 2002; 35: s86–91.
15 Du QY, Wang XB, Chen XJ, Zhang W, Wang SQ. Antitumor mechanism of antisense Cantide targeting human telomerase reverse transcriptase. World J Gastroenterol 2003; 9: 2030–5.
16 Hu YP, Cherton-Horvat G, Dragowska V, Baird S, Korneluk RG, Durkin JP, *et al*. Antisense oligonucleotides targeting XIAP induce apoptosis and enhance chemotherapeutic activity against human lung cancer cells *in vitro* and *in vivo*. Clin Cancer Res 2003; 9: 2826–36.
17 Daniel E, Menezes L, Mayer LD. Pharmacokinetics of *Bcl*-2 antisense oligonucleotide (G3139) combined with doxorubicin in SCID mice bearing human breast cancer solid tumor xenografts. Cancer Chemother Pharmacol 2002; 49: 57–68.
18 Pastorino F, Brignole C, Marimpietri D, Paolo D, Zancolli M, Pagnan G, *et al*. Targeted liposomal c-*myc* antisense oligodeoxynucleotides induce apoptosis and inhibit tumor growth and metastases in human melanoma models. Clin Cancer Res 2003; 9: 4595–605.
19 Ijichi M, Takayama T, Matsumura M, Shiratori Y, Omata M, Makuuchi M, *et al*. Alpha-fetoprotein mRNA in the circulation as a predictor of postsurgical recurrence of hepatocellular carcinoma: a prospective study. Hepatology 2002; 35: 853–60.
20 He P, Tang ZY, Ye SL, Liu BB. Relationship between expression of alpha-fetoprotein messenger RNA and some clinical parameters of human hepatocellular carcinoma. World J Gastro enterol 1999; 5: 111–5.
21 Konopleva M, Tari AM, Estrov Z, Harris D, Xie Z, Lopez-Berestein G, *et al*. Liposomal *Bcl*-2 antisense oligonucleotides enhance proliferation, sensitize acute myeloid leukemia to cytosine-arabinoside, and induce apoptosis independent of other antiapoptotic proteins. Blood 2000; 95: 3929–39.
22 Luger SM, O'Brien SG, Ratajczak J, Ratajczak MZ, Mick R, Stadtmauer EA, *et al*. Oligodeoxynucleotide-mediated inhibition of c-*myb* gene expression in autografted bone marrow: a pilot study. Blood 2002; 99: 1150–8.
23 Zellweger T, Chi K, Miyake H, Adomat H, Kiyama S, Skov K, *et al*. Enhanced radiation sensitivity in prostate cancer by inhibition of the cell survival protein clusterin. Clin Cancer Res 2002; 8: 3276–84.
24 Wang H, Cai Q, Zeng X, Yu D, Agrawal S, Zhang R, *et al*. Antitumor activity and pharmacokinetics of a mixed-backbone antisense oligonucleotide targeted to the R I alpha subunit of protein kinase A after oral administration. Proc Natl Acad Sci USA 1999; 96: 13989–94.
25 Zhang Y, He DM. Effect of antisense hTERT mRNA oligodeoxynucleotide on telomerase activity of leukemic cells. Cell Biol Int 2002; 26: 427–31.

Acta Pharmacologica Sinica 2005 Jul; 26 (7): 769–779

Invited review

Plastins: versatile modulators of actin organization in (patho)physiological cellular processes

Veerle DELANOTE, Joël VANDEKERCKHOVE, Jan GETTEMANS[1]

Department of Medical Protein Research, Flanders Interuniversity Institute for Biotechnology (VIB), Ghent University, Faculty of Medicine and Health Sciences, Albert Baertsoenkaai 3, B-9000 Ghent, Belgium

Key words

actin; actin-binding protein; plastin; fimbrin; cytoskeleton

[1] Correspondence to Jan GETTEMANS.
Phn 32-9-264-9340.
Fax 32-9-264-9490.
E-mail jan.gettemans@ugent.be

Received 2005-03-21
Accepted 2005-04-08

doi: 10.1111/j.1745-7254.2005.00145.x

Abstract

Many actin-binding proteins are expressed in eukaryotic cells. These polypeptides assist in stabilizing and rearranging the organization of the actin cytoskeleton in response to external stimuli, or during cell migration and adhesion. Here we review a particular set of actin-binding proteins called plastins. Plastins (also called fimbrins) belong to a subclass of actin-binding proteins known as actin bundling proteins. Three isoforms have been characterized in mammals: T-plastin is expressed in cells from solid tissue, whereas L-plastin occurs predominantly in hematopoietic cells. The third isoform, I-plastin, is specifically expressed in the small intestine, colon and kidney. These proteins share the unique property of cross-linking actin filaments into tight bundles. Although plastins are primarily involved in regulation of the actin cytoskeleton, they possess some unique features. For instance, they are implicated in invasion by pathogenic bacteria such as *Shigella flexneri* and *Salmonella typhimurium*. Also, L-plastin plays an important role in leukocyte function. T-plastin, on the other hand, is possibly involved in DNA repair. Finally, both T- and L-plastin are implicated in several diseases, and L-plastin is considered to be a valuable marker for cancer.

Introduction

The actin cytoskeleton of eukaryotic cells is a dynamic meshwork that is involved in many biological phenomena, such as cell motility, cell substrate adhesion, intracellular transport, endo-, and exocytosis, cytokinesis, and cell morphology. The overall organization of the actin cytoskeleton is controlled by a plethora of actin-binding proteins[1]. Plastins belong to a class of actin-bundling proteins, and they are conserved from lower eukaryotes to humans. In vertebrates, three different plastin isoforms are expressed in a cell-type-specific manner, and these isoforms display distinct properties. Here we review the discovery, biological properties and regulation of plastin isoforms, and, where appropriate, discuss their interest from a medical perspective.

Discovery

The first plastin isoform was discovered in 1979[2] in microvilli isolated from chicken intestinal brush border as a 68 kDa polypeptide involved in microfilament organization of the microvilli core bundle. This protein was named fimbrin because it was associated with surface structures such as membrane ruffles, microvilli, microspikes and focal adhesions in chicken embryo fibroblasts and cultured rat mammary cells[3]. Chicken fimbrin was characterized as a monomeric cytoskeletal protein able to bind and cross-link F-actin filaments[4,5], promoting the formation of rigid straight bundles in which all actin filaments have the same polarity.

Meanwhile, a 68 kDa protein was identified in transformed human fibroblasts (neoplastic cells, hence the name)[6,7]. This isoform, L-plastin, is also abundantly expressed in untransformed lymphocytes[8]. Molecular cloning of their corresponding cDNAs and amino acid sequence comparison revealed two highly related proteins with a predicted molecular weight of 64 kDa. These two human cell type-specific isoforms, L- and T-plastin (80% amino acid identity), are expressed in hematopoietic cells and in cells derived from solid tissue, respectively[9]. In 1990, it was observed that an

amino-terminal sequence containing a potential calcium binding domain was missing in the sequences reported earlier[10,11]. A third human plastin isoform, called I-plastin, was discovered as a polypeptide that is specifically expressed in the small intestine, colon and kidney, and is 86% identical to the chicken fimbrin (plastin) isoform[12,13].

Plastin structure

Plastins have a modular structure consisting of 2 amino-terminal EF-hands, variably implicated in Ca^{2+}-binding, and two tandem actin-binding domains, each divided into two calponin homology (CH) domains[14–16] (Figure 1). These CH domains are shared by both signaling and cytoskeletal proteins such as dystrophin, α-actinin, and spectrin, and a tandem CH domain is generally involved in actin-binding.

Each CH domain is composed of four α-helical segments, in which three form a loose bundle of helices, with the fourth α-helix perpendicular to the major bundle. These segments are connected by extended and variable loops and sometimes 2 additional short helices. The complete crystal structure of plastin has not yet been resolved, but the structure of the N-terminal actin-binding domain 1 (ABD1) of T-plastin and the complete cross-linking core of *Arabidopsis thaliana* plastin and of *Schizosaccharomyces pombe* plastin have been solved[17,18]. Additional methods, such as electron microscopy, image analysis and homology modeling, have led to a general model of the plastin structure and to a view of how this protein cross-links actin filaments.

The actin cross-linking core of plastin has a compact architecture[17], and the ABDs pack in such a way that the CH1 domain and the CH4 domain make contact, involving conserved residues on the molecular surface of the CH1–CH4 interface. Electron density in regions connecting the CH domains is poorly defined, indicating that these segments are highly dynamic. The potential structural plasticity of ABD1 by reorganization of the CH domains is also confirmed by other crystal structures of utrophin, dystrophin, plectin and α-actinin[19–22].

The binding sites of plastin ABD1 on actin are located in two different subdomains (2 and 1) of the actin molecule[23]. The crystal structure also suggests that the two ABDs have non-identical interactions with F-actin because they each expose different surfaces to the solvent. This suggestion is consistent with the two different actin affinities found in L-plastin[24], in AtFim1[25] and in *S pombe* Fim1[26], and with the finding that the same mutations in both ABDs have different phenotypes in budding yeast[27]. Very recently, evidence has been put forward indicating that ABD1 of T-plastin is not only involved in actin-bundling, but may also control

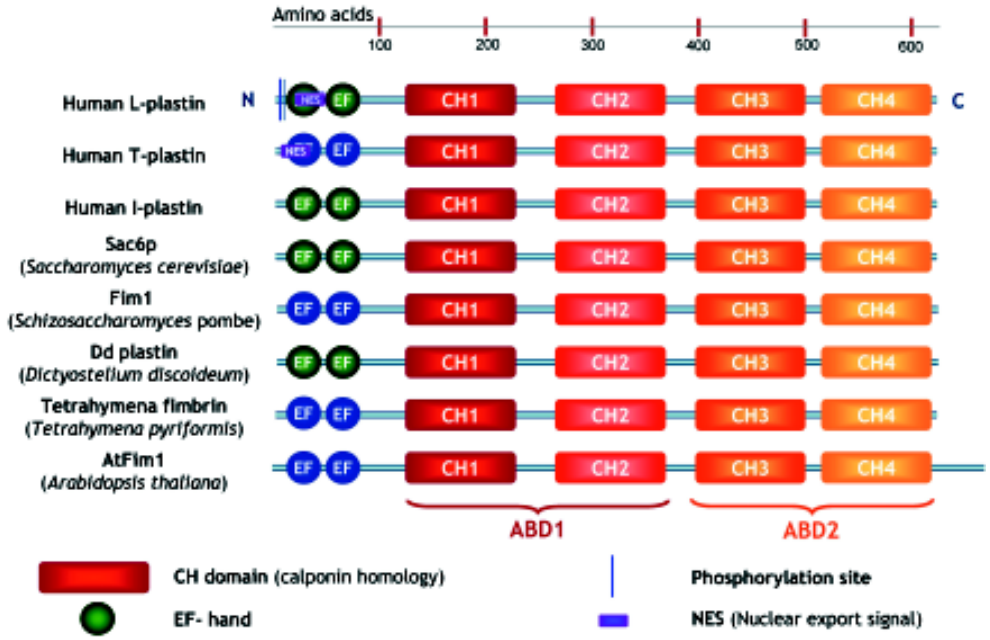

Figure 1. Domain organization in plastin isoforms from different species. A scale (in amino acids) is drawn on top of the figure. Domains in blue have no or less functionality. ABD=actin-binding domain. Note that each actin-binding domain consists of two CH domains. Human T- and L-plastin contain an NES, but it is unknown if plastins from other species are also endowed with a similar targeting signal.

actin turnover, stabilization and assembly, independently of its bundling capacity[28].

Plastins in other organisms

Using an actin affinity matrix to identify actin-binding proteins in the budding yeast *Saccharomyces cerevisiae*, the Sac6 protein was identified, which localizes with cytoplasmic actin cables and cortical actin patches[29]. Its actin regulatory role was confirmed when the gene encoding this protein was found to suppress an actin mutation[30]. Sac6p shows 43% and 36% identity with chicken plastin and human plastin, respectively. Mutant budding yeast cells lacking this gene display temperature sensitivity defects in growth, morphology, endocytosis and sporulation[31,32]. Surprisingly, overexpression of Sac6p is lethal[33]. This could be explained by competition with an essential actin-binding protein, or by titrating out some other essential factor for growth. Next to stabilizing actin filaments, yeast plastin also has a role in the polymerization of G-actin[34,35]. Adams and colleagues demonstrated a high degree of functional conservation between evolutionarily divergent plastins[36]. They demonstrated that human T- and L-plastin could both substitute for yeast plastin in a *Sac6* null mutant, and restore functional defects. However, the third isoform, I-plastin, could not complement this temperature sensitive growth defect, illustrating the functional differences between human isoforms. The fission yeast *Schizosaccharomyces pombe* also contains a plastin homologue, called Fim1. It is not essential for viability but has a role in cell morphogenesis. In mitotic cells, Fim1 plays a role in formation of the actin ring during cytokinesis[26]. *Dictyostelium discoideum* plastin shows 48%–50% identity with human plastins, and localizes to cortical structures associated with cell surface extensions[37].

In the ciliate *Tetrahymena*, plastin is localized in the cleavage furrow bundle during cytokinesis of dividing cells[38]. This protein cross-links actin filaments in a calcium-insensitive manner[39,40]. *Tetrahymena plastin* has a higher affinity for actin than the other plastin forms[39].

At least 3 plastin-like proteins may exist in the plant model system *Arabidopsis thaliana*[25,41]. The AtFim1 isoform contains an additional 65 amino acids at its carboxy-terminal end, and is Ca^{2+} insensitive because of less conserved Ca^{2+}-binding domains. AtFim1 inhibits *Zea mays* profilin-induced actin depolymerization *in vitro* and *in vivo*[25].

L-plastin is often used as a myeloid lineage protein marker in zebrafish (*Danio rerio*)[42]. Spatio-temporal expression of the L-plastin zebrafish homologue reveals a high level of conservation between zebrafish and mammals. Thus zebrafish constitutes an informative model system for the study of normal and anomalous human myelopoiesis[43].

Expression and localization

The three plastin isoforms share approximately 70% homology in their amino acid sequences but are encoded by three distinct genes located on chromosomes 3 (I-plastin), 13 (L-plastin) and X (T-plastin). Analysis of the exon–intron junction sequences of all three human plastin genes indicates that they evolved from a common ancestor[12] (our unpublished observations). Their tissue-specific expression is strictly regulated: L-plastin expression is controlled by its strong promoter, regulated by its upstream repressor and by steroid hormone receptors[44,45]; the T-plastin promoter has a weak basal activity, and expression may be controlled by upstream enhancer elements and by methylation of a CpG island[46].

Generally, plastins are located in focal adhesions, ruffling membranes, lammellipodia, filopodia, or in specialized surface structures with highly ordered microfilament bundles such as microvilli and stereocilia. Sometimes they co-localize with stress fibers.

In adherent macrophages, L-plastin co-localizes with actin in podosomes and filopodia, and also exhibits a punctuate distribution in the cytoplasm that overlaps with actin. L-plastin is constitutively phosphorylated, and phosphorylated plastin is concentrated in the insoluble cytoskeletal fraction[47]. Overexpression of T- or L-plastin in a fibroblast-like cell line induces cell rounding and simultaneous actin stress fiber rearrangements. Both proteins promoted a reduction in the number and size of focal contacts in comparison to untransfected cells. In polarized epithelial cells, overexpression of T-plastin increases the length and density of microvilli. Because both isoforms can associate with different actin structures, they may play different roles in actin filament organization in a cell type-specific fashion[48].

Plastin is often found in stereocilia. Thus actin bundles formed by plastin may also have a mechano-sensory function by transforming mechanical alterations in signals during chemosensory signal transduction. T-plastin and I-plastin, but not L-plastin, are expressed in rat cochlea auditory hair cell stereocilia[49]. During postnatal development of the rat organ of Corti, T-plastin is detected in the core of stereocilia from the early stages of hair cell differentiation, and its expression gradually increases in stereocilia as hair cells mature. However, T-plastin is absent from mature hair cell stereocilia. In contrast, I-plastin is expressed in stereocilia and the cuticular plate from the early stages of hair cell differentiation[50] up to the adult stage[51–53]. The expression

pattern of T-plastin in hair cell stereociliary bundles seems to be related to the location-specific length of hair cell stereocilia along the cochlear duct. Such temporally restricted expression strengthens the idea of functional differences between plastin isoforms, and suggests that T-plastin could have a specific role in sterocilia formation. Furthermore, plastin is also found in the microvilli of chicken photoreceptors[54], in microvillar projections in taste receptor cells of the mammalian taste bud[55], in microvilli from rat vomeronasal sensory epithelium[56], and in brush cells of the alimentary and respiratory system[57,58].

In general, it can be concluded that members of the plastin family have been identified in cellular regions containing polarized actin filaments, and in regions with a high actin filament turnover.

During differentiation of mouse intestine epithelium, three plastin isoforms are expressed in a cell-specific manner[59]. T- and L-plastin are present during the early stages of intestinal epithelial cell differentiation and localize to the apical and basal surface, respectively, until day 14.5, but disappear after day 16.5. I-plastin is first detected from day 14.5 at the apical surface. These findings suggest that plastin isoforms play different roles during epithelial cell differentiation. T- and I-plastin expression could be decisive for the formation and extension of the microvilli, whereas expression of L-plastin might play a role in controlling cell adhesion.

Because all plastin isoforms regulate the actin cytoskeleton, they have always been considered as cytoplasmic proteins. Very recently, however, we reported that endogenous as well as overexpressed T- and L-plastin were able to shuttle between nucleus and cytoplasm in HeLa and Jurkat cells. In most cells investigated, T-plastin is found exclusively in the cytoplasm, whereas L-plastin is located in the nucleus and cytoplasm[60]. We identified a strong leucine-rich nuclear export signal (NES) in T-plastin that was less conserved in L-plastin. This is due, in part, to lack of a phenylalanine residue in the weak NES of L-plastin. This particular residue forms part of the core amino acids that constitute the strong NES of T-plastin. When phenylalanine is inserted into the NES of L-plastin, we observed enhanced export activity of L-plastin from the nucleus. It is likely that shuttling occurs in other cell types as well, but this has not yet been demonstrated. The functional relevance of this nucleo-cytoplasmic shuttling of T- and L-plastin remains unclear at present. L-plastin could be implicated in the regulation of nuclear actin. Indeed, actin is an essential component of the pre-initiation complex and cooperates with polymerase I, II, and III in gene expression[61–63].

Regulation of plastin function

Calcium The two calmodulin-like calcium-binding domains in plastins, the so-called EF-hands, suggest that calcium could regulate actin-binding or other functions of plastins. The rather weak homology in the calcium binding domains of plastin isoforms may suggest that their actin-binding activities are differentially regulated by calcium. Human L-plastin is the only isoform that possesses all the conserved amino acids essential for calcium binding and, indeed, human L-plastin bundles actin filaments in a strictly calcium-regulated manner. Bundles are formed at pCa 7, but not at pCa 6 (free calcium concentration)[64]. I-plastin bundling activity is also inhibited by calcium[13]. The calcium sensitivity of T-plastin has not been studied thoroughly in the past, although some reports mention this[65,23,66]. Recently, this aspect was investigated by Giganti and colleagues, who showed that co-sedimentation of actin with T-plastin was not affected by free calcium concentrations of up to 2.2 μmol/L, in contrast to L-plastin activity, which was inhibited by calcium[28]. Similarly, in an F-actin depolymerization assay, no effect of T-plastin was observed in a free calcium concentration range of 4.6 nmol/L–1.6 μmol/L. Strangely, yeast plastin, Sac6p, is regulated by Ca^{2+}, although it does not contain the conserved residues required for calcium binding[35]. The *Tetrahymena* plastin, Arabidopsis Atfim1 and fission yeast Fim1 bundle actin filaments in a calcium-insensitive manner[65,26,39]. In contrast, *Dictyostelium discoideu*m plastin bundles actin in a calcium-sensitive manner[37].

Phospholipids Using solid-phase immunoassays it was found that increasing amounts of phospholipids affected the binding between monomeric actin and L-plastin. In the presence of PIP_2, and to a smaller extent phosphatidylinositol, the level of actin-L-plastin interaction decreases steadily. The observed inhibitory effect reaches 50% at 50 μg/mL PIP_2. However, diacylglycerol did not produce such an effect[24]. It remains to be demonstrated if this also applies to other plastin isoforms, and if the plastin-F-actin interaction would also be affected. Nevertheless, these findings may suggest that plastin activity is also susceptible to regulation by phospholipids, and this would tie in with many reports detailing modulation of the cytoskeleton through phospholipid interaction with actin-binding proteins.

Phosphorylation Only L-plastin has been reported to be phosphorylated *in vitro* and *in vivo*. Phosphorylation occurs particularly in hematopoietic cells, although this modification may also take place in malignant cells that express L-plastin. Two amino-terminally located serine residues, Ser5 and Ser7, are involved[67]. Protein kinase A (PKA) can

phosphorylate plastin *in vitro*[68,69]. In T-plastin, the Ser-7 residue is conserved, but has never been observed to be phosphorylated.

Ser5 is phosphorylated in HeLa cells. It is possible that Ser 7 is also phosphorylated but only after phosphorylation of Ser 5[70]. Another intensive study on L-plastin phosphorylation was done by Lin and colleagues[71]. They used fibroblasts stably transfected with wild type plastin and mutant plastins, in which each of the serines were mutated. Only the wild type was phosphorylated, but not the mutants, pointing to a possible phosphorylation zipper mechanism. All the data available so far point out that phosphorylation of L-plastin involves a complex mechanism that is not yet completely understood. L-plastin phosphorylation is also dependent on cell type and stimulus. Phosphorylation may regulate actin-binding/bundling, or interactions between plastin and other proteins.

Binding partners

Apart from actin, there have not been many plastin-binding partners characterized yet. However, L-plastin has been reported to be in complex with several proteins in hematopoietic cells. Grancalcin is a Ca^{2+}-binding protein, which is abundant in human neutrophils. Both proteins interact in hematopoietic cells and their interaction is negatively regulated by Ca^{2+} [72]. In adherent macrophages, L-plastin binds vimentin and Hsp70[73]. Only the L-plastin-vimentin interaction was further characterized. Plastin forms an adhesion-dependent complex with a vimentin subunit tetramer, but not with vimentin intermediate filaments. Both proteins interact with an affinity of 0.25 μmol/L (K_d) and co-localize in podosomes, filopodia and retraction fibers. Co-localization in or around the nucleus was also occasionally observed. The amino-terminal domain of vimentin was identified as the plastin-binding site, and the vimentin-binding site localizes to the first CH domain of plastin. Phosphorylation of plastin is probably not involved in complex formation. The interaction may play a role in directing the assembly of the vimentin cytoskeleton at cell adhesion sites.

L-plastin also interacts with Iba1, a microglia/macrophage-specific calcium-binding and actin-bundling protein[74]. In response to stimuli, L-plastin co-localizes with Iba1 and F-actin in membrane ruffles and phagocytic cups. The interaction is direct and independent of Ca^{2+}. Furthermore, Iba1 increases the actin-bundling activity of L-plastin.

Cellular functions of plastin isoforms

Phosphorylation and leukocyte function Leukocyte activation is an important aspect of inflammation and immunity. Quite a number of studies have addressed the phosphorylation of L-plastin during the activation of hematopoietic cells in response to a variety of signals.

In polymorphonuclear (PMN) leukocytes, L-plastin phosphorylation is induced by IL-1 after glucocorticoid treatment and this is blocked by inhibitors of adenylyl cyclase and protein kinase A, but not by a PKC inhibitor[75]. In stimulated cells, phosphorylation of L-plastin increases from 5% to 30%[68]. TNF treatment of peripheral blood mononuclear cells also induces the phosphorylation of L-plastin, but activators of protein kinase A fail to increase phosphorylation, suggesting that other kinases could be involved[76]. IL-8 and the chemotactic peptide fMLP (both chemoattractants for PMN) also promote phosphorylation of L-plastin. In this study, phosphorylation was inhibited by PKA inhibitors, whereas phorbol 12-myristate 13-acetate (PMA, a direct activator of PKC) stimulated phosphorylation significantly[77]. However, there is little evidence to support L-plastin phosphorylation by PKC *in vivo*. Nevertheless, these few examples illustrate that several stimulatory signals induce phosphorylation of L-plastin through distinct pathways in which PKA can sometimes act as a direct kinase, with PKC acting as an indirect effector. Bacterial lipopolysaccharide (LPS) also induces phosphorylation of L-plastin in murine peritoneal macrophages[78]. Phosphorylation closely correlated with cellular responses such as the production of inflammatogenic substances such as TNF, IL-1 and arachidonic acid, a precursor for prostaglandin synthesis in T-lymphocytes. Phosphorylation of L-plastin was discovered as an accessory receptor-mediated co-stimulatory event[79].

Apart from the phosphorylation of L-plastin induced by chemoattractants, interleukins, PMA or fMLP in various hematopoietic cells, L-plastin function and phosphorylation in leukocyte activation was also studied by ligation of IgGFc receptors. Ligation of FcγR in PMN by immune complexes leads to several effector events, including the secretion of inflammatory cytokines and vasoactive lipids, phagocytosis, antibody-dependent cell cytotoxicity and a respiratory burst[80]. Early events following ligation also include the polymerization of actin. More specifically, FcγRII adhesion and phagocytosis of IgG-opsonized particles induces L-plastin phosphorylation and L-plastin localization to the podosomes. L-plastin phosphorylation is not blocked by cytochalasin D[81], suggesting that phosphorylation does not require an intact actin cytoskeleton.

Integrin aMb2 (CD18) activation in PMN is necessary for sustained adhesion and involves L-plastin phosphorylation. To find out if the N-terminal region of L-plastin is

sufficient for regulating adhesion, L-plastin-derived (mutant) peptides (amino acids 2–19) were used in PMN following fusion with the Tat peptide[70]. These studies showed that wild type and the Ser5-phosphorylated peptide induced adhesion to serum-coated surfaces, but not activation of the respiratory burst or an increase in $[Ca^{2+}]_{ic}$. A corresponding T-plastin peptide or the L-plastin Ser5/Ala mutant peptide were inactive. Strangely, the activating peptides also induce phosphorylation of endogenous L-plastin. Phosphorylation could be blocked by PKC and PI3K inhibitors, but again L-plastin could not be phosphorylated *in vitro* by PKC.

Interestingly, PMN leukocytes lacking L-plastin are defective for killing pathogens *in vivo* and *in vitro*, even though they show normal migration to the site of infection, adhesion and spreading, and normal phagocytosis. Although L-plastin phosphorylation is known to be implicated in integrin activation[70,82], it seems not to be required here. L-plastin is involved in activation of the adhesion-dependent respiratory burst by signaling to NADPH oxidase[83]. L-plastin-deficient PMN cells had no altered morphology, which could be due to redundancy in actin-binding proteins.

Anti-leukoproteinase is a physiological inhibitor of granulocytic serine proteases. Anti-protease treatment reduces the incidence and severity of arthritis, and has a protective effect against cartilage and bone erosion. Anti-leukoproteinase binds to L-plastin and downregulates filamentous actin assembly in response to stimulation with IgG-coated latex beads in granulocytes. Anti-leukoproteinase also exerts additional inhibitory effects on neutrophil functions, such as phagocytosis and oxidative bursts[84]. Thus anti-leukoproteinase has anti-arthritis potential because of the modulation of L-plastin in neutrophils.

A role for T-plastin during invasion of bacteria T-plastin is involved in invasion by at least two enteropathic bacteria: *Shigella flexneri* and *Salmonella typhimurium*. These two bacteria have different mechanisms for entering non-phagocytic cells by using specific effector proteins. In both cases, T-plastin is involved in cytoskeletal rearrangements during bacterial invasion. These rearrangements consist of distinct nucleation zones involving strong actin polymerization in close proximity to the contact site between bacterium and cell. These structures then push cellular protrusions outward that engulf the entering bacterium. T-plastin is concentrated in the protrusions during invasion of *Shigella flexneri*[85,86]. Through transfection experiments it can be shown that T- and L-plastin are differentially recruited into *Shigella* entry zones, reflecting their distinct binding specificities. Transient expression of a dominant negative truncated T-plastin mutant decreased *Shigella* entry by 64%, indicating that T-plastin has a functional role in *Shigell*a entry into HeLa cells[85].

During *Salmonella typhimurium* invasion, T-plastin is first recruited to membrane ruffles induced by the bacterium via a Cdc42-dependent signaling process that is activated by the bacterial secreted protein SopE. Then another secreted bacterial effector protein, SipA, forms a complex with T-plastin and F-actin, which results in a marked increase in the actin-bundling activity of T-plastin. SipA also inhibits actin depolymerization. This leads to stabilization of actin filaments at the point of bacterium-host cell contact, which leads to more efficient *Salmonella* internalization[66].

Plastins and DNA repair Several independent reports indicate that plastin is involved in the cellular response to DNA-damaging agents and toxins. First of all, T-plastin expression is enhanced in cisplatin-resistant human bladder, prostatic, head and neck cancer cell lines, in comparison to their cisplatin-sensitive counterparts. Cisplatin is an anticancer agent that acts by binding to DNA and interfering with DNA repair. T-plastin mRNA is 12-fold more abundant in cisplatin-resistant cells in comparison to parental cells[87]. Furthermore, T-plastin is also upregulated in UV radiation-resistant cells[88]. In addition, downregulation of T-plastin expression is associated with increased sensitivity to cisplatin[87]. Increased expression of T-plastin has been observed in Chinese hamster ovary (CHO) cells in which G2 arrest has been induced by X-radiation and by a topoisomerase II inhibitor, etoposide[89]. In contrast, when T-plastin expression was downregulated, radiation-induced G2 arrest decreased in CHO cells, indicating a correlation between T-plastin expression and G2/M cell-cycle control.

Vinca alkaloids such as vincristin and vinblastin are chemotherapeutic agents used in the treatment of both childhood and adult cancers. Their main cellular target is the β-tubulin subunit of α/β-tubulin heterodimers, and they inhibit cell division by disrupting microtubule dynamics. Interestingly, L-plastin is downregulated in response to the vincristin treatment of drug-sensitive human leukemia cells and in vinblastin-resistant cells[90]. These alterations in expression could be involved in several protector functions specific for each drug. For example, T-plastin could play a role in alteration of the intracellular distribution of the drug[87]. Alternatively, the drug might be trapped in the cytoplasm by plastin-associated actin. T-plastin could also have a direct or indirect role in DNA repair. In UV radiation-resistant cells, this last possibility is a good candidate because these cells have a greater capacity to repair DNA[91]. Furthermore, T-plastin expression is suppressed in a human colorectal cancer cell line, SW948, because of promoter-specific DNA

methylation[89], which might be explained by T-plastin's possible role in checkpoint function. Taking everything into consideration, it seems likely that the protecting role of plastin is due to its involvement in DNA repair. Our finding that plastins can shuttle between nucleus and cytoplasm may strengthen this hypothesis[60].

Cancer A very interesting and uncommon finding is that L-plastin is specifically expressed in many transformed cells but absent in their normal cell counterparts[6,7]. Indeed, L-plastin has been described as a marker for many human cancer cells of non-hematopoietic origin[92]. Lin *et al* found that 68% of epithelial carcinomas investigated and 53% of non-epithelial mesenchymal tumors examined expressed L-plastin (remember that L-plastin is normally expressed only in cells of the hematopoietic lineage)[12]. In addition, examination of human neoplastic cell lines revealed that more than 90% of the cell lines surveyed exhibited widely varying degrees of L-plastin expression[93]. In particular, cells derived from the reproductive tract expressed L-plastin. In normal cells of reproductive tissues (which are responsive to ovarian steroids), L-plastin synthesis is induced by female hormones. During malignancy, expression becomes hormone-independent[94]. The L-plastin promoter harbors several hormone receptor-responsive elements; that is, one estrogen-responsive element and three imperfect androgen-responsive elements[44,45]. Estrogen receptor binding[95] and cooperative androgen receptor binding have been demonstrated[45].

In 1997, Zheng and colleagues[96] found that expression of L-plastin in prostatic epithelial cells was linked to the malignant state. Using antisense L-plastin constructs in prostate carcinoma cell lines (PC-3 and PC-3M cells, the metastatic variant), it was demonstrated that cell proliferation and invasion were drastically reduced[97].

Because L-plastin expression is generally considered to be a marker for many cancers[92], new therapeutic tools have been developed aimed at slowing down cancer progression *in vivo* based on the L-plastin gene. Gene therapy experiments in an animal model of colon cancer[98,99] involving a pro-drug approach have shown promising results: the cytosine deaminase gene, driven by an L-plastin tumor-specific promoter, modifies 5-fluorocytosine into a toxic derivative, fluorouracil. These vectors induced significant toxicity in carcinomas of the breast, ovary and colon *in vitro* and *in vivo*: tumor size as well as tumor cell growth decreased significantly. Mice injected with the expression vector and 5-fluorocytosine lived much longer than their untreated litter mates[98,99].

Although these approaches are promising, we still lack fundamental molecular data showing how increased (or ectopic) plastin expression contributes to tumor formation. In the same line, a clear causal relationship between plastin expression and invasion/metastasis, the hallmarks of malignant tumors, needs to be established and worked out at the molecular level. This will allow models to be put forward and thoroughly tested *in vitro* and in animal models. These approaches could help resolve the question of whether plastins could be valuable targets for drug development in the treatment of cancer.

Other diseases In an animal model of the auto-immune disease systemic lupus erythematosus (SLE, a chronic rheumatic disease) and in human patients, antibodies against T- and L-plastin were found in serum[100,101,102]. The presence of T- and L-plastin antibodies is correlated with the presence of the anti-Sm antibody, a typical SLE auto-antibody that recognizes a nuclear antigen. The stimulus for production of L- and T-plastin auto-antibodies may derive from the destruction of plastin-containing cells, such as replicating white blood cells (L-plastin), or epithelial and mesenchymal surfaces (T-plastin). It remains to be determined if L- and T-plastin antibodies contribute to the loss of cell function or other aspects of lupus. L-plastin has also been identified as a self-antigen associated with Vogt-Koyanagi's syndrome, an autoimmune disease[103].

Expression of a chimeric mRNA transcript between the LAZ3 gene and the L-plastin gene, resulting from chromosomal translocation, was observed in two B-cell non-Hodgkin-lymphomas. The 13q14 chromosome region, where the L-plastin gene is located, is frequently disrupted in various proliferative disorders, and defines a breakpoint site[104].

Finally, minimal change nephrotic syndrome (MCNS) is the most frequent glomerular disease in children, and is characterized by heavy proteinuria[105]. MCNS results from a systemic disorder of T cell function[106]. Expression levels of L-plastin and grancalcin are increased during the period of disease relapse[107]. A truncated protein, Tc-mip, was detected in peripheral blood mononuclear cells from MCNS patients. Overexpression of this truncated protein in T cell Jurkat cells induced redistribution of L-plastin, in addition to Src phosphorylation and T cell clustering[108]. Increased expression and redistribution of L-plastin may result in T-cell dysfunction, causing MCNS. These fragmentary data suggest that plastins contribute to the onset or progression of certain diseases, but it is clear that much more work needs to be done to ascertain their true role in these syndromes.

Concluding remarks and future directions

Although plastins have a clear role in actin-binding, there

is sometimes apparently incongruent information as to their exact actin-binding properties. Actin-bundling activity by mammalian plastins has been clearly established, but there is additional evidence for actin filament stabilization[26] and for filament anti-depolymerization activities[109,24,28,27]. In some organisms (yeast and plants), there is even indication that plastin has actin polymerization ability[35,25].

The depletion of plastin does not promote severe deficiencies at first glance, because the knockout of L-plastin has no influence on embryonic and neonatal development[83]. However, a lack of L-plastin could lead to immunological problems in a broad sense or complications involving inflammation.

Some culture cells overexpressing T- or L-plastin loose their adhesion properties and round up[48,110]. It is hard to generate stable cell lines overexpressing plastin[71,93], and this could be related to the observed invasive behavior of tumor cells (over)expressing plastin.

Future studies are expected to provide more clarity with respect to the functional significance of cell-type-specific expression of the three human plastin isoforms, each with its individual properties and functional regulation. In addition, nucleocytoplasmic shuttling of plastin isoforms elicits the question of what their true function in the nucleus is.

Acknowledgements

This work was supported by the Belgian Federation Against Cancer, the Fund for Scientific Research-Flanders (FWO-Vlaanderen), the IUAP and Fortis Bank Verzekeringen. VD is supported by a PhD grant from the Institute for the Promotion of Innovation through Science and Technology in Flanders (IWT-Vlaanderen).

We apologize to those colleagues whose work has not been mentioned in the text.

References

1 Dos Remedios CG, Chhabra D, Kekic M, Dedova IV, Tsubakihara M, Berry DA, *et al*. Actin binding proteins: Regulation of cytoskeletal microfilaments. Physiol Rev 2003; 83: 433–73.

2 Matsudaira PT, Burgess DR. Identification and organization of the components in the isolated microvillus cytoskeleton. J Cell Biol 1979; 83: 667–73.

3 Bretscher A, Weber K. Fimbrin, a new microfilament-associated protein present in microvilli and other cell-surface structures. J Cell Biol 1980; 86: 335–40.

4 Bretscher A. Fimbrin is a cytoskeletal protein that crosslinks F-actin *in vitro*. Proc Natl Acad Sci USA 1981; 78: 6849–53.

5 Glenney JR, Kaulfus P, Matsudaira P, Weber K. F-Actin binding and bundling properties of fimbrin, a major cytoskeletal protein of microvillus core filaments. J Biol Chem 1981; 256: 9283–8.

6 Leavitt J, Kakunaga T. Expression of a variant form of actin and additional polypeptide changes following chemical induced *in vitro* neoplastic transformation of human fibroblasts. J Biol Chem 1980; 255: 1650–61.

7 Leavitt J, Goldman D, Merril C, Kakunaga T. Changes in gene expression accompanying chemically induced malignant transformation of human fibroblasts. Carcinogenesis 1982; 3: 61–70.

8 Goldstein D, Djeu J, Latter G, Burbeck S, Leavitt J. Abundant synthesis of the transformation induced protein of neoplastic human fibroblasts, plastin, in normal lymphocytes. Cancer Res 1985; 45: 5643–7.

9 Lin CS, Aebersold RH, Kent SB, Varma M, Leavitt J. Molecular cloning and characterization of plastin, a human leukocyte protein expressed in transformed human fibroblasts. Mol Cell Biol 1988; 8: 4659–68.

10 Lin CS, Aebersold RH, Leavitt J. Correction of the N-terminal sequences of the human plastin isoforms by using anchored polymerase chain-reaction: identification of a potential calcium-binding domain. Mol Cell Biol 1990; 10: 1818–21.

11 Zu YL, Shigesada K, Nishida E, Kubota I, Kohno M, Hanaoka M, *et al*. 65-Kilodalton protein phosphorylated by interleukin-2 stimulation bears 2 putative actin-binding sites and 2 calcium-binding sites. Biochemistry 1990; 29: 8319–24.

12 Lin CS, Park T, Chen ZP, Leavitt J. Human plastin genes. Comparative gene structure, chromosome location, and differential expression in normal and neoplastic cells. J Biol Chem 1993; 268: 2781–92.

13 Lin CS, Shen WY, Chen ZP, Tu YH, Matsudaira P. Identification of I-plastin, a human fimbrin isoform expressed in intestine and kidney. Mol Cell Biol 1994; 14: 2457–67.

14 De Arruda MV, Watson S, Lin CS, Leavitt J, Matsudaira P. Fimbrin is a homologue of the cytoplasmic phosphoprotein plastin and has domains homologous with calmodulin and actin gelation proteins. J Cell Biol 1990; 111: 1069–79.

15 Gimona M, Djinovic-Carugo K, Kranewitter WJ, Winder SJ. Functional plasticity of CH domains. FEBS Lett 2002; 513: 98–106.

16 Korenbaum E, Rivero F. Calponin homology domains at a glance. J Cell Sci 2002; 115: 3543–5.

17 Klein MG, Shi WX, Ramagopal U, Tseng Y, Wirtz D, Kovar DR *et al*. Structure of the actin crosslinking core of fimbrin. Structure 2004; 12: 999–1013.

18 Goldsmith SC, Pokala M, Shen WY, Fedorov AA, Matsudaira P, Almo SC. The structure of an actin-crosslinking domain from human fimbrin. Nat Struct Biol 1997; 4: 708–12.

19 Garcia-Alvarez B, Bobkov A, Sonnenberg A, de Pereda JM. Structural and functional analysis of the actin binding domain of plectin suggests alternative mechanisms for binding to F-actin and integrin beta 4. Structure 2003; 11: 615–25.

20 Keep NH, Winder SJ, Moores CA, Walke S, Norwood FLM, Kendrick-Jones J. Crystal structure of the actin-binding region of utrophin reveals a head-to-tail dimer. Structure Fold Des 1999; 7: 1539–46.

21 Liu J, Taylor DW, Taylor KA. A 3-D reconstruction of smooth muscle alpha-actinin by CryoEm reveals two different conformations at the actin-binding region. J Mol Biol 2004; 338: 115–25.

22 Norwood FLM, Sutherland-Smith AJ, Keep NH, Kendrick-Jones J. The structure of the N-terminal actin-binding domain of human dystrophin and how mutations in this domain may cause Duchenne or Becker muscular dystrophy. Structure Fold Des 2000; 8: 481–91.
23 Hanein D, Volkmann N, Goldsmith S, Michon AM, Lehman W, Craig R *et al*. An atomic model of fimbrin binding to F-actin and its implications for filament crosslinking and regulation. Nat Struct Biol 1998; 5: 924.
24 Lebart MC, Hubert F, Boiteau C, Venteo S, Roustan C, Benyamin Y. Biochemical characterization of the L-plastin-actin interaction shows a resemblance with that of alpha-actinin and allows a distinction to be made between the two actin-binding domains of the molecule. Biochemistry 2004; 43: 2428–37.
25 Kovar DR, Staiger CJ, Weaver EA, McCurdy DW. AtFim1 is an actin filament crosslinking protein from *Arabidopsis thaliana*. Plant J 2000; 24: 625–36.
26 Nakano K, Satoh K, Morimatsu A, Ohnuma M, Mabuchi I. Interactions among a fimbrin, a capping protein, and an actin-depolymerizing factor in organization of the fission yeast actin cytoskeleton. Mol Biol Cell 2001; 12: 3515–26.
27 Brower SM, Honts JE, Adams AEM. Genetic-analysis of the fimbrin-actin binding interaction in *Saccharomyces cerevisiae*. Genetics 1995; 140: 91–101.
28 Giganti A, Plastino J, Janji B, Van Troys M, Lentz D, Ampe C *et al*. Actin-filament cross-linking protein T-plastin increases Arp2/3-mediated actin-based movement. J Cell Sci 2005; 118: 1255–65.
29 Drubin DG, Miller KG, Botstein D. Yeast actin-binding proteins: Evidence for a role in morphogenesis. J Cell Biol 1988; 107: 2551–61.
30 Adams AEM, Botstein D, Drubin DG. A yeast actin-binding protein is encoded by sac6, a gene found by suppression of an actin mutation. Science 1989; 243: 231–3.
31 Kubler E, Riezman H. Actin and fimbrin are required for the internalization step of endocytosis in yeast. Embo J 1993; 12: 2855–62.
32 Adams AEM, Botstein D, Drubin DG. Requirement of yeast fimbrin for actin organization and morphogenesis *in vivo*. Nature 1991; 354: 404–8.
33 Sandrock TM, Brower SM, Toenjes KA, Adams AEM. Suppressor analysis of fimbrin (Sac6p) overexpression in yeast. Genetics 1999; 151: 1287–97.
34 Cheng DM, Rubenstein PA. Interaction of yeast fimbrin (Sac6p) with a polymerization-defective (GG) actin. Mol Biol Cell 1998; 9: 269A.
35 Cheng DM, Marner J, Rubenstein PA. Interaction *in vivo* and *in vitro* between the yeast fimbrin, SAC6P, and a polymerization defective yeast actin (V266G and L267G). J Biol Chem 1999; 274: 35: 873–80.
36 Adams AEM, Shen WY, Lin CS, Leavitt J, Matsudaira P. Isoform specific complementation of the yeast Sac6 null mutation by human fimbrin. Mol Cell Biol 1995; 15: 69–75.
37 Prassler J, Stocker S, Marriott G, Heidecker M, Kellermann J, Gerisch G. Interaction of a *Dictyostelium* member of the plastin/fimbrin family with actin filaments and actin-myosin complexes. Mol Biol Cell 1997; 8: 83–95.
38 Watanabe A, Kurasawa Y, Watanabe Y, Numata O. A new Tetrahymena actin-binding protein is localized in the division furrow. J Biochem 1998; 123: 607–13.
39 Shirayama S, Numata O. *Tetrahymena* fimbrin localized in the division furrow bundles actin filaments in a calcium-independent manner. J Biochem 2003; 134: 591–8.
40 Watanabe A, Yonemura I, Gonda K, Numata O. Cloning and sequencing of the gene for a Tetrahymena fimbrin-like protein. J Biochem 2000; 127: 85–94.
41 McCurdy DW, Kim M. Molecular cloning of a novel fimbrin-like cDNA from *Arabidopsis thaliana*. Plant Mol Biol 1998; 36: 23–31.
42 Herbomel P, Thisse B, Thisse C. Ontogeny and behaviour of early macrophages in the zebrafish embryo. Development 1999; 126: 3735–45.
43 Bennett CM, Kanki JP, Rhodes J, Liu TX, Paw BH, Kieran MW, *et al*. Myelopoiesis in the zebrafish, *Danio rerio*. Blood 2001; 98: 643–51.
44 Lin CS, Chen ZP, Park T, Ghosh K, Leavitt J. Characterization of the human L-plastin gene promoter in normal and neoplastic cells. J Biol Chem 1993; 268: 2793–801.
45 Lin CS, Lau A, Yeh CC, Chang CH, Lue TF. Upregulation of L-plastin gene by testosterone in breast and prostate cancer cells: identification of three cooperative androgen receptor-binding sequences. DNA Cell Biol 2000; 19: 1–7.
46 Lin CS, Lau A, Huynh T, Lue TF. Differential regulation of human T-plastin gene in leukocytes and non-leukocytes: identification of the promoter, enhancer, and CpG island. DNA Cell Biol 1999; 18: 27–37.
47 Messier JM, Shaw LM, Chafel M, Matsudaira P, Mercurio AM. Fimbrin localized to an insoluble cytoskeletal fraction is constitutively phosphorylated on its headpiece domain in adherent macrophages. Cell Motil Cytoskeleton 1993; 25: 223–33.
48 Arpin M, Friederich E, Algrain M, Vernel F, Louvard D. Functional differences between L-plastin and T-plastin isoforms. J Cell Biol 1994; 127: 1995–2008.
49 Daudet N, Lebart MC. Transient expression of the T-isoform of plastin/fimbrin in the stereocilia of developing auditory hair cells. Cell Motil Cytoskeleton 2002; 53: 326–36.
50 Zine A, Hafidi A, Romand R. Fimbrin expression in the developing rat cochlea. Hearing Res 1995; 87: 165–9.
51 Flock A, Bretscher A, Weber K. Immunohistochemical localization of several cytoskeletal proteins in inner-ear sensory and supporting cells. Hearing Res 1982; 7: 75–89.
52 Sobin A, Flock A. Immunohistochemical identification and localization of actin and fimbrin in vestibular hair cells in the normal guinea-pig and in a strain of the Waltzing guinea-pig. Acta Otolaryngol 1983; 96: 407–12.
53 Slepecky N, Chamberlain SC. Immunoelectron microscopic and immunofluorescent localization of cytoskeletal and muscle like contractile proteins in inner-ear sensory hair cells. Hearing Res 1985; 20: 245–60.
54 Hofer D, Drenckhahn D. Molecular heterogeneity of the actin filament cytoskeleton associated with microvilli of photoreceptors, Muller glial-cells and pigment epithelial-cells of the retina. Histochemistry 1993; 99: 29–35.
55 Hofer D, Drenckhahn D. Localisation of actin, villin, fimbrin, ezrin and ankyrin in rat taste receptor cells. Histochem Cell Biol 1999; 112: 79–86.

56 Hofer D, Shin DW, Drenckhahn D. Identification of cytoskeletal markers for the different microvilli and cell types of the rat vomeronasal sensory epithelium. J Neurocytol 2000; 29: 147–56.

57 Hofer D, Drenckhahn D. Identification of brush cells in the alimentary and respiratory system by antibodies to villin and fimbrin. Histochem 1992; 98: 237–42.

58 Hofer D, Drenckhahn D. Cytoskeletal markers allowing discrimination between brush cells and other epithelial cells of the gut including enteroendocrine cells. Histochem Cell Biol 1996; 105: 405–12.

59 Chafel MM, Shen WY, Matsudaira P. Sequential expression and differential localization of I-fimbrin, L-fimbrin, and T-fimbrin during differentiation of the mouse intestine and yolk-sac. Dev Dyn 1995; 203: 141–51.

60 Delanote V, Van Impe K, De Corte V, Bruyneel E, Vetter G, Boucherie C *et al*. Molecular basis for dissimilar nuclear trafficking of the actin-bundling protein isoforms T- and L-plastin. Traffic 2005; 6: 335–45.

61 Hofmann WA, Stojiljkovic L, Fuchsova B, Vargas GM, Mavrommatis E, Philimonenko V *et al*. Actin is part of pre-initiation complexes and is necessary for transcription by RNA polymerase II. Nat Cell Biol 2004; 6: 1094–101

62 Hu P, Wu S, Hernandez N. A role for beta-actin in RNA polymerase III transcription. Genes Dev 2004; 18: 3010–5.

63 Philimonenko V, Zhao J, Iben S, Dingova H, Kysela K, Kahle M *et al*. Nuclear actin and myosin I are required for RNA polymerase I transcription. Nat Cell Biol 2004; 6: 1165–72.

64 Namba Y, Ito M, Zu YL, Shigesada K, Maruyama K. Human T-cell L-plastin bundles actin-filaments in a calcium-dependent manner. J Biochem 1992; 112: 503–7.

65 Kovar DR, Gibbon BC, McCurdy DW, Staiger CJ. Fluorescently-labeled fimbrin decorates a dynamic actin filament network in live plant cells. Planta 2001; 213: 390–5.

66 Zhou DG, Mooseker MS, Galan JE. An invasion-associated Salmonella protein modulates the actin-bundling activity of plastin. Proc Natl Acad Sci USA 1999; 96: 10 176–81.

67 Shinomiya H, Hagi A, Fukuzumi M, Mizobuchi M, Hirata H, Utsumi S. Complete primary structure and phosphorylation site of the 65-kDa macrophage protein phosphorylated by stimulation with bacterial lipopolysaccharide. J Immunol 1995; 154: 3471–8.

68 Matsushima K, Shiroo M, Kung HF, Copeland TD. Purification and characterization of a cytosolic 65-kilodalton phosphoprotein in human-leukocytes whose phosphorylation is augmented by stimulation with interleukin-1. Biochemistry 1988; 27: 3765–70.

69 Wang J, Brown EJ. Immune complex-induced integrin activation and L-plastin phosphorylation require protein kinase A. J Biol Chem 1999; 274: 24 349–56.

70 Jones SL, Wang J, Turck CW, Brown EJ. A role for the actin-bundling protein L-plastin in the regulation of leukocyte integrin function. Proc Natl Acad Sci USA 1998; 95: 9331–6.

71 Lin CS, Lau A, Lue TF. Analysis and mapping of plastin phosphorylation. DNA Cell Biol 1998; 17: 1041–6.

72 Lollike K, Johnsen AH, Durussel I, Borregaard N, Cox JA. Biochemical characterization of the penta-EF-hand protein grancalcin and identification of L-plastin as a binding partner. J Biol Chem 2001; 276: 17762–9.

73 Correia I, Chu D, Chou YH, Goldman RD, Matsudaira P. Integrating the actin and vimentin cytoskeletons: adhesion-dependent formation of fimbrin-vimentin complexes in macrophages. J Cell Biol 1999; 146: 831–42.

74 Ohsawa K, Imai Y, Sasaki Y, Kohsaka S. Microglia/macrophage-specific protein Iba1 binds to fimbrin and enhances its actin-bundling activity. J Neurochem 2004; 88: 844–56.

75 Matsushima K, Kobayashi Y, Copeland TD, Akahoshi T, Oppenheim JJ. Phosphorylation of a cytosolic 65-kDa protein, induced by interleukin-1 in glucocorticoid pretreated normal human peripheral-blood mononuclear leukocytes. J Immunol 1987; 139: 3367–74.

76 Shiroo M, Matsushima K. Enhanced phosphorylation of 65 and 74 kDa proteins by tumor necrosis factor and interleukin-1 in human peripheral blood mononuclear cells. Cytokine 1990; 2: 13–20.

77 Shibata M, Yamakawa Y, Ohoka T, Mizuno S, Suzuki K. Characterization of a 64-kD protein phosphorylated during chemotactic activation with IL-8 and fMLP of human polymorphonuclear leukocytes . Purification and aminoacid analysis of phosphorylated 64-kD protein. J Leukoc Biol 1993; 54: 10–6.

78 Shinomiya H, Hirata H, Nakano M. Purification and characterization of the 65-kD protein phosphorylated in murine macrophages by stimulation with bacterial lipopolysaccharide. J Immunol 1991; 146: 3617–25.

79 Henning SW, Meuer SC, Samstag Y. Serine phosphorylation of a 67-kD protein in human T-lymphocytes represents an accessory receptor-mediated signaling event. J Immunol 1994; 152: 4808–15.

80 Schubert J, Hundt M, Schmidt R. Fc gamma receptor mediated activation of human polymorphonuclear neutrophils (PMN). Arch Immunol Ther Exp 1992; 40: 65–6.

81 Jones SL, Brown EJ. Fc gamma RII-mediated adhesion and phagocytosis induce L-plastin phosphorylation in human neutrophils. J Biol Chem 1996; 271: 14623–30.

82 Wang J, Chen H, Brown EJ. L-plastin peptide activation of alpha(v)beta(3)-mediated adhesion requires integrin conformational change and actin filament disassembly. J Biol Chem 2001; 276: 14474–81.

83 Chen H, Mocsai A, Zhang H, Ding RX, Morisaki JH, White M, *et al*. Role for plastin in host defense distinguishes integrin signaling from cell adhesion and spreading. Immunity 2003; 19: 95–104.

84 Sehnert B, Cavcic A, Bohm B, Kalden JR, Nandakumar KS, Holmdahl R, *et al*. Antileukoproteinase: modulation of neutrophil function and therapeutic effects on anti-type II collagen antibody-induced arthritis. Arthritis Rheum 2004; 50: 2347–59.

85 Adam T, Arpin M, Prevost MC, Gounon P, Sansonetti PJ. Cytoskeletal rearrangements and the functional role of T-plastin during entry of Shigella flexneri into Hela-cells. J Cell Biol 1995; 129: 367–81.

86 Prevost MC, Lesourd M, Arpin M, Vernel F, Mounier J, Hellio R, *et al*. Unipolar reorganization of F-actin layer at bacterial division and bundling of actin-filaments by plastin correlate with movement of Shigella flexneri within Hela cells. Infect Immun 1992; 60: 4088–99.

87 Hisano T, Ono M, Nakayama M, Naito S, Kuwano M, Wada M. Increased expression of T-plastin gene in cisplatin-resistant human cancer cells: Identification by mRNA differential display. FEBS Lett 1996; 397: 101–7.
88 Higuchi Y, Kita K, Nakanishi H, Wang XL, Sugaya S, Tanzawa H *et al*. Search for genes involved in UV-resistance in human cells by mRNA differential display: Increased transcriptional expression of nucleophosmin and T-plastin genes in association with the resistance. Biochem Biophys Res Commun 1998; 248: 597–602.
89 Sasaki Y, Itoh F, Kobayashi T, Kikuchi T, Suzuki H, Toyota M, *et al*. Increased expression of T-fimbrin gene after DNA damage in CHO cells and inactivation of T-fimbrin by CpG methylation in human colorectal cancer cells. Int J Cancer 2002; 97: 211–6.
90 Verrills NM, Walsh BJ, Cobon GS, Hains PG, Kavallaris M. Proteome analysis of Vinca alkaloid response and resistance in acute lymphoblastic leukemia reveals novel cytoskeletal alterations. J Biol Chem 2003; 278: 45 082–93.
91 Suzuki N, Kurata T. Studies on the repair capacity of a UV-resistant human cell strain, Uvr-1. J Radiat Res 1982; 23: 63.
92 Leavitt J. Discovery and characterization of 2 novel human cancer-related proteins using 2-dimensional gel-electrophoresis. Electrophoresis 1994; 15: 345–57.
93 Park TS, Chen ZP, Leavitt J. Activation of the leukocyte plastin gene occurs in most human cancer cells. Cancer Res 1994; 54: 1775–81.
94 Leavitt J, Chen ZP, Lockwood CJ, Schatz F. Regulation of synthesis of the transformation-induced protein, leukocyte plastin, by ovarian-steroid hormones. Cancer Res 1994; 54: 3447–54.
95 Lin CS, Lau A, Huynh T. Differential regulation of L- and T-plastin genes by steroid receptors and upstream enhancers. FASEB J 1997; 11: 3203.
96 Zheng JP, Rudra-Ganguly N, Miller GJ, Moffatt KA, Cote RJ, Roy-Burman P. Steroid hormone induction and expression patterns of L-plastin in normal and carcinomatous prostate tissues. Am J Pathol 1997; 150: 2009–18.
97 Zheng JP, Rudra-Ganguly N, Powell WC, Roy-Burman P. Suppression of prostate carcinoma cell invasion by expression of antisense L-plastin gene. Am J Pathol 1999; 155: 115–22.
98 Akbulut H, Zhang LX, Tang YC, Deisseroth A. Cytotoxic effect of replication-competent adenoviral vectors carrying L-plastin promoter regulated E1A, cytosine deaminase genes in cancers of the breast, ovary and colon. Cancer Gene Ther 2003; 10: 388–95.
99 Akbulut H, Tang YC, Maynard J, Zhang LX, Pizzorno G, Deisseroth A. Vector targeting makes 5-fluorouracil chemotherapy less toxic and more effective in animal models of epithelial neoplasms. Clin Cancer Res 2004; 10: 7738–46.
100 Mine M, Koarada S, Sai T, Miyake K, Kimoto M. Peptide-binding motifs of the mixed haplotype A beta(z)/A alpha(d) major histocompatibility complex class II molecule: a restriction element for auto-reactive T cells in (NZBxNZW)F-1 mice. Immunology 1998; 95: 577–84.
101 Shinomiya H, Nagai K, Hirata H, Kobayashi N, Hasegawa H, Liu FZ, *et al*. Preparation and characterization of recombinant murine p65/L-plastin expressed in *Escherichia coli* and high-titer antibodies against the protein. Biosci Biotech Biochem 2003; 67: 1368–75.
102 Neto ECD, Kumar A, Shadick NA, Michon AM, Matsudaira P, Eaton RB, *et al*. Antibodies to T-isoform and L-isoform of the cytoskeletal protein, fimbrin, in patients with systemic lupus-erythematosus. J Clin Invest 1992; 90: 1037–42.
103 Kobayashi H, Kokubo T, Abe K, Sato K, Kimura S, Miyokawa N, *et al*. Analysis of anchor residues in a naturally processed HCA-DR53 ligand. Immunogenetics 1996; 44: 366–71.
104 Galiegue-Zouitina S, Quief S, Hildebrand MP, Denis C, Detourmignies L, Lai JL *et al*. Nonrandom fusion of L-plastin (LCPI) and LAZ3(BCL6) genes by t(3;13)(q27;q14) chromosome translocation in two cases of B-cell non-Hodgkin lymphoma. Genes Chromosomes Cancer 1999; 26: 97–105.
105 Niaudet P. Nephrotic syndrome in children. Curr Opin Pediatr 1993; 5: 174–9.
106 Shalhoub RJ. Pathogenesis of lipoid nephrosis. Disorder of T-cell function. Lancet 1974; 2: 556–60.
107 Sahali D, Pawlak A, Valanciute A, Grimbert P, Lang P, Remy P, *et al*. A novel approach to investigation of the pathogenesis of active minimal-change nephrotic syndrome using subtracted cDNA library screening. J Am Soc Nephrol 2002; 13: 1238–47.
108 Grimbert P, Valanciute A, Audard V, Pawlak A, Le Gouvelo S, Lang P, *et al*. Truncation of C-mip (Tc-mip), a new proximal signaling protein, induces c-maf Th2 transcription factor and cytoskeleton reorganization. J Exp Med 2003; 198: 797–807.
109 Belmont LD, Drubin DG. The yeast V159N actin mutant reveals roles for actin dynamics *in vivo*. J Cell Biol 1998; 142: 1289–99.
110 Timmers ACJ, Niebel A, Balague C, Dagkesaruanskaya A. Differential localisation of GFP fusions to cytoskeleton-binding proteins in animal, plant, and yeast cells. Protoplasma 2002; 220: 69–78.

Acta Pharmacologica Sinica 2005 Jul; 26 (7): 780–788

Invited review

Dissecting role of regulatory factors in NF-κB pathway with siRNA[1]

Jun GUO[2], Yu-cai FU[3], Carlos R BECERRA[2,4]

[2]Division of Hematology-Oncology, Department of Medicine, Harold Simmons Cancer Center, University of Texas Southwestern Medical Center, Dallas, Texas 75390, USA; [3]Laboratory of Cell Senescence, Shantou University Medical College, Shantou 515041, China

Key words

NF-κB pathway; small interfering RNA; RNA interference

[1] Project supported by the Helen and Alden Wagner Cancer Fund and the Nasher Cancer Research Program.
[4] Correspondence to Dr Carlos BECERRA.
Phn 1-214-648-1929.
Fax 1-214-648-1955.
E-mail carlos.becerra@utsouthwestern.edu

Received 2005-03-18
Accepted 2005-04-07

doi: 10.1111/j.1745-7254.2005.00140.x

Abstract

NF-κB, a family of related transcription factors, has been a focus of intense scientific research during the past decade. Multiple stimuli, both extracellular and intracellular, lead to its activation. The NF-κB pathway regulates expression of a diverse array of genes involved in different biological processes. Various pathological states are characterized by the dysregulated NF-κB pathway. Recently, NF-κB activation has been connected with multiple aspects of oncogenesis and serves as an important mechanism to regulate cell survival in response to chemotherapy by activating different genes that inhibit apoptosis. Several methods of inhibiting NF-κB activation, such as antisense oligonucleotides, proteosome inhibitors and RNA interference (RNAi) are currently under investigation. RNAi represents a powerful tool to better define the role of specific genes in different signal transduction pathways and has recently been used to define the function of genes that regulate the NF-κB pathway. This review discusses the emerging role of RNAi to dissect the function of regulatory factors in the NF-κB pathway and its potential use as a targeted therapy.

Introduction

The NF-κB family is comprised of a variety of homo- and hetero-dimers formed by p50, p52, RelA (p65), RelB, and c-Rel subunits[1–4]. The best-described form of NF-κB is constituted by the p50 and p65 heterodimer. This heterodimer is sequestered in the cytoplasm bound to a family of inhibitory proteins known as IκB[5,6]. Following cell stimulation, the IκB proteins become phosphorylated by IκB kinase (IKK), a large kinase complex consisting of 2 catalytic subunits, IKKα and IKKβ, and the regulatory subunit, IKKγ/NEMO[7–9]. Phosphorylation of IκB targets this inhibitor for ubiquitination and degradation, which results in the release and subsequent translocation of NF-κB to the nucleus to activate transcription of a variety of genes[10] (Figure 1). In this review, we first discuss the current understanding of why RNA-mediated gene silencing by small interfering RNA (siRNA) is important in NF-κB pathway and then focus on the use of siRNA to analyze the role of cellular factors in regulating the NF-κB pathway and its potential use as a targeted therapy to inhibit the NF-κB pathway.

The NF-κB pathway: mechanisms leading to activation

NF-κB can be activated by a variety of stimuli, including inflammatory cytokines, such as TNF-α and IL-1, and growth factors as a result of stress response. Intra-cellular events such as DNA damage by radiation or chemotherapy serve as potent stimulus to activate NF-κB as well. TNF-α and IL-1 are important to the generation of a systemic and local response to infection, injury, and immunological challenges[2]. The signals from the TNF receptor (TNFR) and IL-1 receptor (IL-1R) are transduced through the TNF receptor-associated factor2 (TRAF2) and 6 (TRAF6), respectively[11]. These TRAF are believed to function 'upstream' of the cascades of IKK and NF-κB[12,13]. Many members of the mitogen-activated protein kinase kinase kinase (MAP3K) family including MEKK1[14], MEKK2, MEKK3[15], TGF-β-activating kinase1 (TAK1)[16] and NF-κB-inducing kinase (NIK)[17] also activate IKK when overexpressed. However, MEKK3 is an essential signal transducer in both TNFR- and IL-1R-induced NF-κB activation[11,18-22].

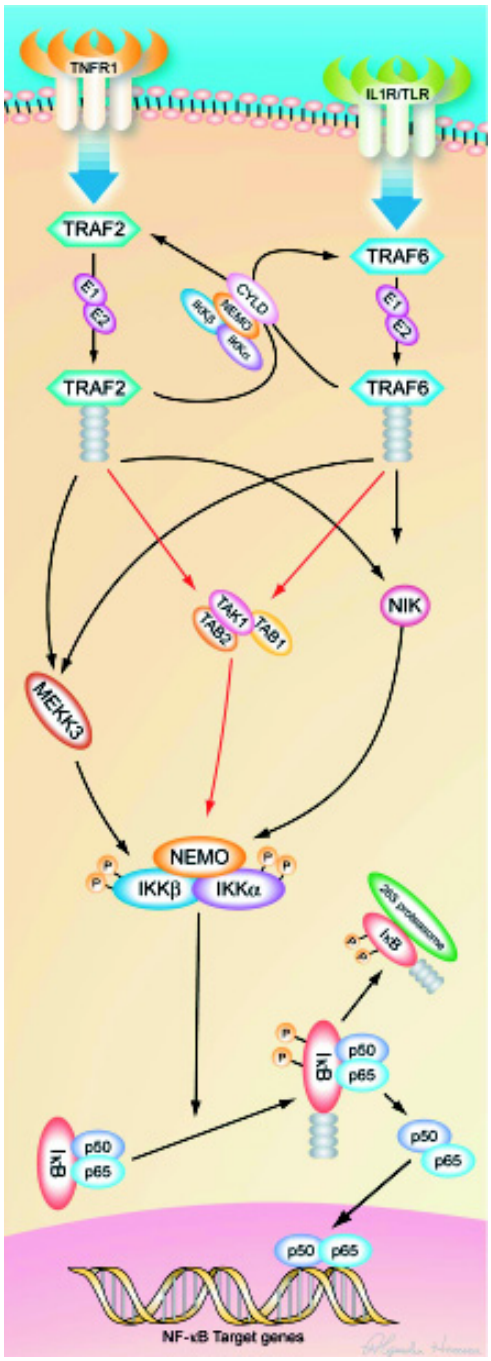

Figure 1. TRAF2 and TRAF6 mediated NF-κB activation. Both of the TRAF2 and TRAF6 are ubiquitinated in the presence of ubiquitin-activating enzyme (E1) and ubiquitin-conjugating enzyme (E2). Ubiquitinated TRAF2 and TRAF6 bind to TAB2 and activate TAK1. Activated TAK1 leads to IKK activation. In turn, activated IKK results in IκB phosphorylation. Phosphorylated IκB will be rapidly degraded after ubiquitination, and NF-κB (shown as the p65/p50 heterodimer) is translocated into the nucleus. TRAF2 and TRAF6 may also associate with NIK and MEKK3 to activate IKK complex. CYLD binds to NEMO and facilitates the disassembly of K63-linked polyubiquitin chains on TRAF2, TRAF6.

Initial studies on the structure of TRAF showed that the C-terminal domain for TRAF was responsible for protein-protein interactions and the N-terminal region of TRAF, including a RING finger and a variable number of Zn finger domains, was necessary for TRAF mediated activation of downstream signaling pathways[23,24]. A RING finger with ubiquitin ligase activity[25] is critical for NF-κB activation by TRAF[26–28]. TRAF2 and TRAF6 were shown to be able to function as ubiquitin ligases that autoubiquitinate resulting in a lysine-63 (K63)-linked polyubiquitination[29–31]. Ubiquitinated TRAF can bind to the TAK1, and its adapter proteins TAB1 and TAB2[18,32,33]. TAB1 binds to TAK1 and is involved in regulating its activity, while TAB2 binds preferentially to K63-linked polyubiquitin chains[12], resulting in the activation of TAK1[34]. Activated TAK1 can phosphorylate IKK directly or act on the NF-κB-inducing kinase (NIK), which in turn activates IKK[16,35]. Thus, the TAK1 complex is an important link between TRAF and the NF-κB pathway (Figure 1). TRAF7 also plays an important role in regulating activation of NF-κB and it can act like TRAF6 in relaying signals and activating the NF-κB pathway[18].

IKK activation by the TNF-α and IL-1 is a rapid, but transient process, implying a negative feedback regulation of IKK following its activation. This negative regulation of IKK is controlled, at least in part, by deubiquitination, as shown in recent studies on the tumor suppressor cylindromatosis protein CYLD[36,37]. Loss of CYLD has been linked to a predisposition to cylindromas, a syndrome characterized by benign tumors of the skin appendages. Interestingly, CYLD contains cysteine and histidine boxes found in the ubiquitin-specific protease (UBP) family of deubiquitination enzymes[38]. Moreover, a portion of the histidine box of CYLD is deleted in some cylindromatosis patients, suggesting a link between the deubiquitination activity of CYLD and its tumor suppressor function. Three independent studies have shown that CYLD binds to NEMO and facilitates the disassembly of K63-linked polyubiquitin chains on TRAF2 and TRAF6[36,37]. Thus, a critical function of CYLD is to down-regulate NF-κB activation through its deubiquitinating activity[31].

RNAi-mediated gene silencing

RNAi is associated with a number of practical and theoretic advantages over pre-existing methods of suppressing gene expression (Table 1)[39–44] and thus provides a useful mean to dissect the role of various factors that regulate the NF-κB pathway. RNAi also has the potential to be developed as a therapeutic modality to knock-down gene products that are important in activating the NF-κB pathway[45].

Table 1. Advantages and disadvantages of different gene suppression strategies.

Gene suppression	Advantages	Disadvantages
RNAi	Potent, specific and simple Post-transcriptional gene silencing	Transfection-dependent Knock-down not knock-out
Antisense technology	Simple	Efficacy and specificity variable
Knockout mouse	Complete gene silencing.	Time-consuming and laborious to produce
Transfection of dominant negative mutant gene	Ability to determine functions of discrete regions of a protein	Transfection-dependent Variable specificity
Small molecule inhibitors	Simple	Often nonspecific

Several lines of evidence support a role for RNAi in a cell-based defense mechanism that protects the genome against mobile genetic elements such as viruses and transposons[46,47]. There are 2 classes of small RNA that can silence gene expression. One class is processed from double-stranded (dsRNA) precursor molecules into small interfering RNA (siRNA) by the RNAase III-like nuclease called Dicer; these siRNA act as guides for the siRNA-induced silencing complex (siRISC) to target and cleave complementary mRNA[48]. Dicer processes another class of small RNA from pre-microRNA into microRNA. These micro RNA act as guides for a multiprotein complex (miRISC) which identifies mRNA and silences gene expression either via destruction of the mRNA or by blocking its translation[47,49,50]. Dicer was first isolated from extracts of *Drosophila*, but was later shown to exist in a large variety of species ranging from fungi to man[51]. Two Dicers, Dcr-1 and Dcr-2 were found in *Drosophila*. Dcr-1 processes pre-miRNA[52,53], while Dcr-2 processes dsRNA. In contrast to their processing specificities, both Dcr-1, Dcr-2 and its associated factor R2D2 are required for assembly of siRNA into siRISC (Figure 2)[47,54]. Synthetic 21-23 nucleotide double stranded siRNA were synthesized to resemble Dicer cleavage products and could be directly incorporated in the mammalian RISC to target mRNA for degradation[55]. Another approach relies on stable expression of short hairpin RNA from a plasmid vector down stream from a pol III or U6 promoter to result in a reproducible reduction of target gene expression in mammalian cells[45]. Various strategies including retroviral, adenoviral and lentiviral vectors have been developed that allow the introduction of siRNA encoding vectors at high efficiency in primary cells. With these technologies, it is now possible to obtain effective gene silencing in transgenic embryos and adult mice[48]. There have been several reports of successful use of *in vivo* siRNA in different animal models of human diseases; for example, microinjection of siRNA directed against zebrafish dystrophin gene into zebrafish embryos demonstrates the efficacy of siRNA-based gene silencing in this model and illustrates the potential of this approach to determine the roles of multiple protein products expressed by a single gene during the early stages of development[56]. Delivery of siRNA directed against either caspase 8 or hepatitis B virus (HBV) by mouse tail vein have been effective in suppressing specific gene expression[57,58]. In addition, Verma *et al* demonstrated that siRNA directed against β-catenin reduced tumor growth in nude mice when administered by either intravenous or intraperitoneal injections, which suggests that siRNA could have therapeutic potential for inhibiting the expression of genes that enhance the growth of tumors[59]. RNAi also holds great promise for the treatment of CNS diseases in which neurodegeneration is linked to overproduction of endogenous protein or to synthesis of aberrant proteins coded by dominant mutant alleles[60].

More recently, many researchers have used plasmid and viral vectors for transcription of short-hairpin RNA (shRNA) that efficiently deliver siRNA into both dividing and non-dividing cells, stem cells, zygotes, and their differentiated progeny. Gene expression was more stably inhibited with these expression systems than with the transient knockdown recorded with chemically synthesised siRNA. A number of groups have used shRNA instead of siRNA to obtain relatively long-lived gene silencing *in vivo*[61]. The libraries of retroviruses expressing shRNA designed to silence large fractions of all expressed human genes have been produced. These shRNA libraries have the potential to provide mammalian biologists for the first time with a genetic screening tool similar to that which has been used in more primitive organisms.

RNAi is an important tool for analyzing the NF-κB pathway

Signal transduction pathways, such as the NF-κB pathway, are modular composites of functionally interde-

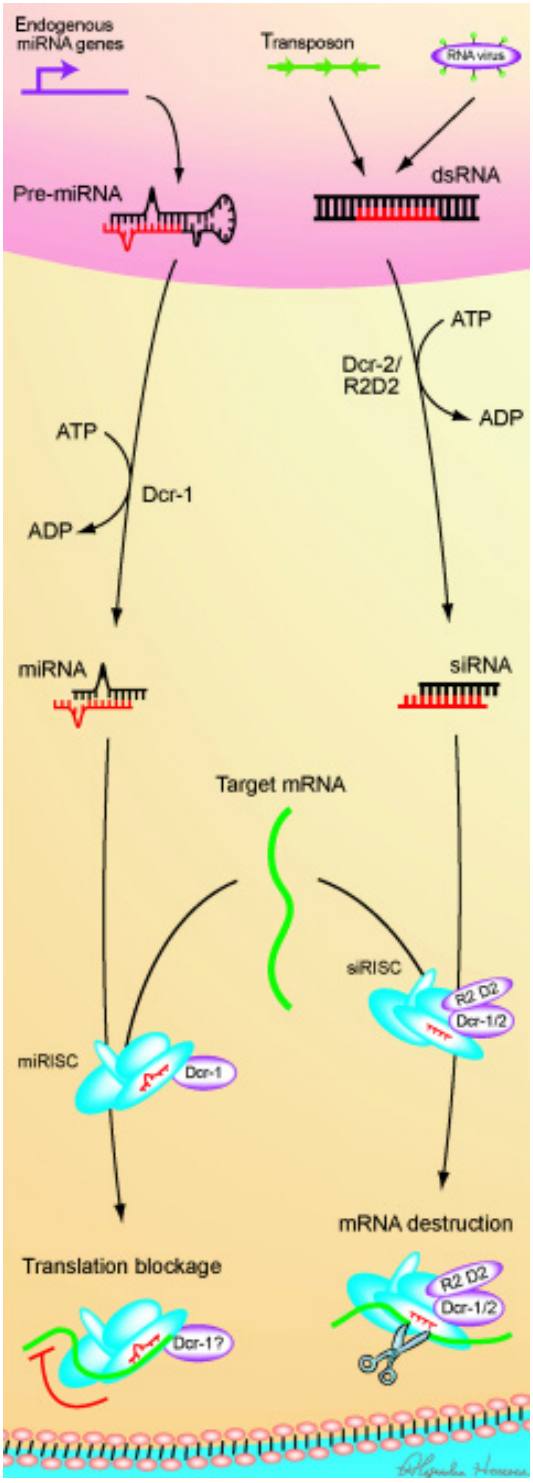

Figure 2. siRNA pathways. Long dsRNA is processed by the RNAase III-like nuclease called Dicer2/R2D2 into siRNAs, while pre-miRNA is processed by the RNAase III-like nuclease called Dicer1 into miRNA. The 2 strands of the siRNAs or miRNA are unwound by the siRISC or miRISC, 1 strand is selected to identify a complementary target mRNA which in turn is cleaved by an endonuclease in siRISC or blocking translation in miRISC.

pendent sets of proteins that act in a coordinated fashion to transform environmental information into a phenotypic response. Several mechanisms that cause constitutive NF-κB activity can be found in different epithelial tumors, tumor cell lines and lymphoid malignancies[62]. Many different inhibitors affecting the NF-κB activation pathway that have beneficial effects on tumor development or that increase the response to radiation and chemotherapy have been described. However, most of these inhibitors are not specific and inhibit many other pathways as well[63]. Using RNAi to stably knock out specific gene expression and function is a highly effective and novel method that is rapidly gaining ground because of an explosion of new and improved techniques. The exquisite sequence specificity of RNAi provides a promising approach to address the complex interactions of viral and cellular regulatory proteins involved in NF-κB pathway[64]. As potent small-molecule inhibitors to any gene expression, siRNA can be used to specifically analyze the role of single gene products in NF-κB pathway to emphasize the selectivity of RNAi-based therapy. Direct evidence, using both *in vitro* and *in vivo* models, indicates that RNAi is a critical tool to inhibit the NF-κB pathway at multiple levels and study the transmission of signals in both physiologic and pathologic states[36,37,65–68].

TAK1 is an important upstream mediator of the NF-κB pathway[16,34,46]. siRNA directed against TAK1 decreased the amount of both IL-1 and TNFα-induced phospho-IκBα expression and prevented IκBα degradation. The loss of endogenous TAK1 by siRNA resulted in impaired DNA-binding of NF-κB. These results provide the first genetic evidence that supports a role of TAK1 as a critical upstream kinase for IKKα or IKKβ in IL-1 and TNFα-induced activation of the NF-κB pathway[69]. Takaesu *et al* also reported that endogenous IKKα and IKKβ co-immunoprecipitated with TAK1 upon TNFα stimulation. siRNA directed against IKKα and IKKβ reduced IL-1 and TNFα-induced activation of the NF-κB pathway. Simultaneous transfection of both IKKα and IKKβ siRNA resulted in further decreases in NF-κB activation as compared to transfection of each of these individual siRNA. These findings suggest that in addition to IKKα and IKKβ, TAK1 is important for NF-κB activation challenging previous result that only IKKβ was involved in NF-κB activation[28,70–72].

Bcl-10, a cellular homolog of the equine herpesvirus-2 E10 gene[73], was found over-expressed in some lymphomas of the mucosa-associated lymphoid tissue (MALT). Bcl-10 has been shown to physically associate with MALT1, which is a member of the paracaspase family and also involved in MALT lymphoma. Bcl-10 and MALT1 are essential for the

activation of IKK and NF-κB in response to T cell receptor stimulation[74]. Sun *et al* presented evidence that TRAF2 and TRAF6 mediated IKK activation by Bcl-10 and T cell receptor stimulation. TRAF6 siRNA reduced the activation of IKK by 50% and the same percentage of reduction in IKK activation was observed by TRAF2 siRNA. However, the combination of TRAF2 and TRAF6 siRNA reduced IKK activation by approximately 80%. Thus in T cells, both TRAF2 and TRAF6 are involved in upstream regulation of the NF-κB pathway in response to T cell receptor stimulation[64]. In addition, TAK1 siRNA transfection also dramatically reduced IKK activation by T cell receptor stimulation in T cells. Moreover, MALT1 and Bcl-10 have been shown to mediate IKK activation by facilitating the K63 polyubiquitination of NEMO. siRNA that reduced the expression of paracaspase and Ubc13 abrogated the effects of Bcl-10, which indicates that Bcl-10 promotes activation of IKK and NF-κB through paracaspase- and Ubc13-dependent ubiquitination of NEMO[75].

The tumor suppressor cylindromatosis protein CYLD belongs to a subfamily of enzymes with deubiquitinase activity[76,77]. A collection of shRNA that suppress 50 human de-ubiquitinating enzymes were used to identify deubiquitination enzymes and study the mechanism for human cylindromatosis[36] in the NF-κB pathway[45]. The studies from this and other groups show that CYLD binds to NEMO, and appears to regulate its activity through deubiquitination of TRAF2[38,78]. They also demonstrated that inhibition of CYLD by siRNA enhanced NF-κB activation and prevented apoptosis, suggesting a mechanism through which loss of CYLD contributes to oncogenesis[36]. In independent studies, Trompouki *et al*[37] also used the siRNA method and demonstrated that CYLD interacted with NEMO and negatively regulated NF-κB signaling by deubiquitination of TRAF2. They have now started to investigate the use of CYLD inhibitors in clinical trials.

Potential therapeutic uses of NF-κB inhibition by siRNA

The NF-κB signaling pathway is important in the generation of the monocyte-derived dendritic cells and regulates their functional maturation and activation[79–81]. Dendritic cells play a prominent role in infectious diseases, immune disorders, and in cancer immunology[82]. In mammalian cells, NF-κB/Rel proteins are involved in regulating survival, differentiation, and activation of the dendritic cells[80,81,83]. Targeted mutations in mice demonstrate that deficits in RelB, cRel, p50, or p52 lead to various immune impairments that directly implicate dendritic cells. Transfection of dendritic cells with p50 siRNA was tested by Diego[88] and his colleagues as a way of performing loss-of-function analysis *in vitro* and the results showed strong and specific down-regulation of both p50 mRNA and protein levels. Such interference impaired p50 nuclear localization and DNA-binding in response to CD40 Ligand (CD40L) and IL-1 activation. The cytosolic fraction also showed reduced p50 activity after p50 siRNA transfection[88].

IL-12 is a cytokine pivotal for the development of cellular immunity and production of high levels of IFN-γ by T cells. A biologically active form of IL-12 (IL-12α and IL-12β heterodimer) is produced from the transcription of separate genes which are regulated independently[89]. Prior results have shown that CD40L alone or in combination with IL-1 induces high levels of IL-12β transcription[90]. However, a significantly reduced IL-12β mRNA level and reduction of the secretion of IL-12αβ heterodimer was observed after p50 siRNA, which suggests that p50 siRNA down-regulated the production of IL-12 in response to CD40L and IL-1. These results are consistent with studies of the promoter of the IL-12β gene, which is NF-κB inducible and contains sites for the binding of p50 in B cells[91].

It has been reported that p65 can stimulate HIV-1 transcriptional elongation by binding to the HIV-1 long terminal repeat (LTR)[92,93]. The use of siRNA directed against p65 resulted in reduced HIV-1 replication, which correlated with the decrease in HIV-1 virons in supernatants from MAGI cells[66]. CD4-positive human T-lymphocyte cell lines including MAGI have been used to study different aspects of the HIV-1 life cycle. These cells, which stably express CD4 receptors on the cell surface, can be infected by HIV-1. Since they contain a HIV-1 LTR fused to the β-galactosidase gene, infectious virus can transactivate the LTR-β-galactosidase reporter and increase β-galactosidase activity. Thus, staining of MAGI cells to determine β-galactosidase activity makes these cells an excellent indicator to determine the number of HIV-1 infectious particles[94]. It has been observed that more than 90% of the infected cells transfected with control siRNA demonstrated marked β-galactosidase positivity. In contrast, only a few cells had β-galactosidase activity when the MAGI cells were transfected with p65 siRNA, which indicate that inhibition of HIV-1 replication by p65 siRNA resulted in very low levels of HIV-1 infectious particles[66]. This finding highlights the importance that NF-κB plays in the life cycle of HIV-1.

Tumors that have constitutive NF-κB activity show increased resistance to chemotherapy. Inhibition of NF-κB does not only lead to enhanced apoptosis but also to in-

creased sensitivity to radiation or chemotherapy in several tumor cells such as fibrosarcoma and colorectal cancer cell lines, as well as xenograft models or pancreatic carcinoma cells[63]. CPT-11 is a topoisomerase I inhibitor which has efficacy in the treatment of certain neoplasms including colorectal cancer. In spite of the initial response to therapy[81], most tumors from patients treated with CPT-11 become resistant and exhibit tumor progression[95]. However, inducible chemotherapy resistance to CPT-11 has been shown to be reversed by inhibiting NF-κB[83,96]. More recent studies from Guo *et al*[65] demonstrate that NF-κB activation induced by CPT-11 in the relatively resistant HCT116 cell line is effectively inhibited by p65 siRNA both *in vitro* and *in vivo*. Transfection of p65 siRNA into HCT116 cells dramatically reduced the expression of p65. In addition, they found that loss of p65 did not impact cell viability on its own, but p65 siRNA in conjunction with CPT-11 increased tumor cell sensitivity to the cytotoxic effects of CPT-11. P65 siRNA increased apoptosis and reduced NF-κB-binding activity. The effect on apoptosis could be partly explained by down-regulation of the NF-κB target genes c-IAP1 and c-IAP2[65]. These results are consistent with the role that NF-κB plays in the inhibition of CPT-11 mediated cell killing[2,97]. Importantly, transient exposure of HCT116 cells to p65 siRNA in cell culture altered the ability of these cells to proliferate following injection into nude mice in the presence of CPT-11 treatment. Systemic therapy with intravenous injection of p65 siRNA did not limit tumor growth. However, when combined with CPT-11, intravenous injection of p65 siRNA significantly delayed tumor growth with dramatic reductions in tumor volume[65]. These studies demonstrate that delivery of siRNA to tumor cells *in vivo* is feasible and that inhibition of NF-κB-mediated transcription by p65 siRNA holds therapeutic promise in cancer[98].

Questions to the safety and efficacy of using RNAi as a therapeutic strategy

Interest in RNAi initially was restricted to basic researchers to study gene function. The subsequent finding that *in vivo* delivery of siRNA to induce RNAi in mammalian cells has generated excitement regarding its potential therapeutic applications. Various approaches have been shown to improve cell and tissue delivery of siRNA and shRNA[61,99].

A major obstacle to the development of siRNAi as a therapeutic tool is its delivery to the desired cell type in the correct tissue or organ. Hydrodynamic delivery of siRNA that involves the intravascular injection of large fluid volumes in order to locally increase intravascular pressure[100,101] might be adapted for local administration of siRNA by arterial or venous catheters in organs such as liver, kidney, heart or lungs, but cannot be utilized for systemic treatment. Intravenous injection of siRNA in large volumes of saline solution, works by creating a back-flow in the venous system that forces the siRNA solution into several organs with lesser efficiency[102,103]. Using RNAi to silence genes is also limited by the stability of siRNA molecules *in vivo* and the efficiency with which they are taken up by target cells and tissues[104]. An additional obstacle in exploring siRNA as a therapeutic tool is toxicity. siRNA have the potential to induce a concentration- and cell-type-dependent cell death[105]. In mammalian cells, the utility of RNAi has been limited by the innate immune response triggered by dsRNA. Long dsRNA induce an interferon response usually resulting in a generalized inhibition of gene expression. However, this response can usually be avoided in mammalian cell cultures by using synthetic siRNA with a length of 21 nt[105].

Inhibition of viral replication by RNAi has been demonstrated *in vitro* for a variety of viruses, including RNA viruses such as HIV, respiratory syncytial virus, influenza virus, poliovirus, West Nile virus, dengue virus, and foot and mouth disease virus. However, some viruses are resistant to RNAi; for example, although siRNA can inhibit the production of progeny virus, the genomic RNA of respiratory syncytial virus, hepatitis delta virus, and rotavirus are resistant to RNAi, either because of tight shielding by proteins or to sequestration in compartments inaccessible to siRNA[106–108]. Moreover, some viruses such as influenza and vaccinia produce proteins that actively suppress silencing by RNAi[109]. Adenovirus was recently shown to block the processing of shRNA in mammalian cells by expressing a viral noncoding RNA at such high levels that it binds most of the available RNAi processing machinery[110].

Summary

The discovery of RNAi has already provided a powerful tool for basic science researchers to study gene function. More recently the use of RNAi for genetic-based therapies has been widely studied, especially in viral infections, cancers, and inherited genetic disorders. Combined with genomics data, RNAi-directed gene-silencing could allow functional determination of any gene expressed in a cell or pathway. Thus, the therapeutic potential for RNAi is enormous, but the ability to efficiently and stably produce and deliver sufficient amounts of siRNA to the target tissues require refinement before this new technology can be tried clinically[111].

Acknowledgments

We thank Richard GAYNOR and Udit VERMA for their helpful comments during the preparation of the manuscript. We also thank Janice BOX for the preparation of the manuscript and Alejandra HERRERA for graphical support.

References

1 Perkins ND. The Rel/NF-kappa B family: friend and foe. Trends Biochem Sci 2000; 25: 434–40.
2 Baldwin AS. Control of oncogenesis and cancer therapy resistance by the transcription factor NF-kappaB. J Clin Invest 2001; 107: 241–6.
3 Baeuerle PA, Baltimore D. κB: Ten years after. Cell 1996, 87: 13–20.
4 Ghosh S, May MJ, Kopp EB. κB and Rel proteins: evolutionarily conserved mediators of immune responses. Annu Rev Immunol 1998; 16: 225–60.
5 Ghosh S, Karin M. Missing pieces in the NF-kappaB puzzle. Cell 2002; 109: S81–S96.
6 Verma IM, Stevenson JK, Schwartz EM, Van Antwerp D, Miyamoto S. κB/IκB family: intimate tales of association and dissociation. Genes Dev 1995; 9: 2723–35.
7 DiDonato JA, Hayakawa M, Rothwarf DM, Zandi E, Karin M. κB kinase that activates the transcription factor NF-κB. Nature 1997; 388: 548–54.
8 Mercurio F, Zhu H, Murray BW, Shevchenko A, Bennett BL, Li J, *et al*. κB kinases essential for NF-κB activation. Science 1997; 278: 860–6.
9 Li Y, Kang J, Friedman J, Tarassishin L, Ye J, Kovalenko A, *et al*. κB activity and as a target of an adenovirus inhibitor of tumor necrosis factor α-induced apoptosis. Proc Natl Acad Sci USA 1999; 96: 1042–7.
10 Stancovski I, Baltimore D. NF-kappaB activation: the I kappaB kinase revealed? Cell 1997; 91: 299–303.
11 Baud V, Liu ZG, Bennett B, Suzuki N, Xia Y, Karin M. Signaling by proinflammatory cytokines: oligomerization of TRAF2 and TRAF6 is sufficient for JNK and IKK activation and target gene induction via an amino-terminal effector domain. Genes Dev 1999; 13: 1297–308.
12 Sun L, Chen ZJ. The novel functions of ubiquitination in signaling. Curr Opin Cell Biol 2004; 16: 339–40.
13 Wajant H, Scheurich P. Analogies between Drosophila and mammalian TRAF pathways. Prog Mol Subcell Biol 2004; 34: 47–72.
14 Lee FS, Peters RT, Dang LC, Maniatis T. MEKK1 activates both IkappaB kinase alpha and IkappaB kinase beta. Proc Natl Acad Sci USA 1998; 95: 9319–24.
15 Zhao Q, Lee FS. Mitogen-activated protein kinase/ERK kinase kinases 2 and 3 activate nuclear factor-kappaB through IkappaB kinase-alpha and IkappaB kinase-beta. J Biol Chem 1999; 274: 8355–8.
16 Ninomiya-Tsuji J, Kishimoto K, Hiyama A, Inoue J, Cao Z, Matsumoto K. The kinase TAK1 can activate the NIK-I kappaB as well as the MAP kinase cascade in the IL-1 signalling pathway. Nature 1999; 398: 252–6.
17 Woronicz JD, Gao X, Cao Z, Rothe M, Goeddel DV. κB kinase-β: NF-κB activation and complex formation with IκB kinase-α and NIK. Science 1997; 278: 866–9.
18 Bouwmeester T, Bauch A, Ruffner H, Angrand PO, Bergamini G, Croughton K, *et al*. A physical and functional map of the human TNF-alpha/NF-kappa B signal transduction pathway. Nat Cell Biol 2004; 6: 97–105.
19 Malinin NL, Boldin MP, Kovalenko AV, Wallach D. κB induction by TNF, CD95 and IL-1. Nature 1997; 385: 540–8.
20 Song HY, Regnier CH, Kirschning CJ, Goeddel DV, Rothe M. Tumor necrosis factor (TNF)-mediated kinase cascades: bifurcation of nuclear factor-kappaB and c-jun N-terminal kinase (JNK/SAPK) pathways at TNF receptor-associated factor 2. Proc Natl Acad Sci USA 1997; 94: 9792–6.
21 Yang J, Lin Y, Guo Z, Cheng J, Huang J, Deng L, *et al*. The essential role of MEKK3 in TNF-induced NF-kappaB activation. Nat Immunol 2001; 2: 620–4.
22 Huang Q, Yang J, Lin Y, Walker C, Cheng J, Liu ZG, *et al*. Differential regulation of interleukin 1 receptor and Toll-like receptor signaling by MEKK3. Nat Immunol 2004; 5: 98–103.
23 Cheng G, Cleary AM, Ye ZS, Hong DI, Lederman S, Baltimore D. Involvement of CRAF1, a relative of TRAF, in CD40 signaling. Science 1995; 267: 1494–8.
24 Rothe M, Sarma V, Dixit VM, Goeddel DV. κB by TNF receptor 2 and CD40. Science 1995; 269: 1424–7.
25 Pickart CM. Mechanisms underlying ubiquitination. Annu Rev Biochem 2001; 70: 503–33.
26 Takeuchi M, Rothe M, Goeddel DV. Anatomy of TRAF2. Distinct domains for nuclear factor-kappaB activation and association with tumor necrosis factor signaling proteins. J Biol Chem 1996; 271: 19935–42.
27 Dadgostar H, Cheng G. An intact zinc ring finger is required for tumor necrosis factor receptor-associated factor-mediated nuclear factor-kappaB activation but is dispensable for c-Jun N-terminal kinase signaling. J Biol Chem 1998; 273: 24775–80.
28 Hu Y, Baud V, Delhase M, Zhang P, Deerinck T, Ellisman M, *et al*. A subunit of IκB kinase. Science 1999; 284: 316–20.
29 Deng L, Wang C, Spencer E, Yang L, Braun A, You J, *et al*. Activation of the IkappaB kinase complex by TRAF6 requires a dimeric ubiquitin-conjugating enzyme complex and a unique polyubiquitin chain. Cell 2000; 103: 351–61.
30 Wajant H, Henkler F, Scheurich P. The TNF-receptor-associated factor family: scaffold molecules for cytokine receptors, kinases and their regulators. Cell Signal 2001; 13: 389–400.
31 Wilkinson KD. Signal transduction: aspirin, ubiquitin and cancer. Nature 2003; 424: 738–9.
32 Shibuya H, Yamaguchi K, Shirakabe K, Tonegawa A, Gotoh Y, Ueno N, *et al*. TAB1: an activator of the TAK1 MAPKKK in TGF-beta signal transduction. Science 1996; 272: 1179–82.
33 Wang C, Deng L, Hong M, Akkaraju GR, Inoue J, Chen ZJ. TAK1 is a ubiquitin-dependent kinase of MKK and IKK. Nature 2001; 412: 346–51.
34 Takaesu G, Kishida S, Hiyama A, Yamaguchi K, Shibuya H, Irie K, *et al*. TAB2, a novel adaptor protein, mediates activation of TAK1 MAPKKK by linking TAK1 to TRAF6 in the IL-1 signal transduction pathway. Mol Cell 2000; 5: 649–58.
35 Shirakabe K, Yamaguchi K, Shibuya H, Irie K, Matsuda S, Moriguchi T, *et al*. TAK1 mediates the ceramide signaling to stress-activated protein kinase/c-Jun N-terminal kinase. J Biol Chem 1997; 272: 8141–4.
36 Brummelkamp TR, Nijman SM, Dirac AM, Bernards R. Loss of the cylindromatosis tumour suppressor inhibits apoptosis by ac-

tivating NF-kappaB. Nature 2003; 424: 797–801.
37 Trompouki E, Hatzivassiliou E, Tsichritzis T, Farmer H, Ashworth A, Mosialos G. CYLD is a deubiquitinating enzyme that negatively regulates NF-kappaB activation by TNFR family members. Nature 2003; 424: 793–6.
38 Bignell GR, Warren W, Seal S, Takahashi M, Rapley E, Barfoot R, *et al*. Identification of the familial cylindromatosis tumour-suppressor gene. Nat Genet 2000; 25: 160–5.
39 Dave RS, Pomerantz RJ. RNA interference: on the road to an alternate therapeutic strategy. Rev Med Virol 2003; 13: 373–85.
40 Schmidt CW. Therapeutic interference: small RNA molecules act as blockers of disease metabolism. Modern Drug Disc 2003: 37–42.
41 Arenz C, Schepers U. RNA interference: from an ancient mechanism to a state of the art therapeutic application? Naturwissenschaften 2003; 90: 345–59.
42 Fire A, Xu S, Montgomery MK, Kostas SA, Driver SE, Mello CC. Potent and specific genetic interference by double-stranded RNA in Caenorhabditis elegans. Nature 1998; 391: 806–11.
43 Hohmann HP, Brockhaus M, Baeuerle PA, Remy R, Kolbeck R, van Loon AP. Expression of the types A and B tumor necrosis factor (TNF) receptors is independently regulated, and both receptors mediate activation of the transcription factor NF-kappa B. TNF alpha is not needed for induction of a biological effect via TNF receptors. J Biol Chem 1990; 265: 22409–17.
44 Boutla A, Delidakis C, Livadaras I, Tsagris M, Tabler M. Short 5'-phosphorylated double-stranded RNAs induce RNA interference in Drosophila. Curr Biol 2001; 11: 1776–80.
45 Brummelkamp TR, Bernards R, Agami R. A system for stable expression of short interfering RNAs in mammalian cells. Science 2002; 296: 550–3.
46 Waterhouse PM, Wang MB, Lough T. Gene silencing as an adaptive defence against viruses. Nature 2001; 411: 834–42.
47 Pham JW, Pellino JL, Lee YS, Carthew RW, Sontheimer EJ. A Dicer-2-dependent 80s complex cleaves targeted mRNAs during RNAi in Drosophila. Cell 2004; 117: 83–94.
48. Medema RH. Optimizing RNA interference for application in mammalian cells. Biochem J 2004; 380: 593–603.
49 Lee YS, Nakahara K, Pham JW, Kim K, He Z, Sontheimer EJ, *et al*. Distinct roles for Drosophila Dicer-1 and Dicer-2 in the siRNA/miRNA silencing pathways. Cell 2004; 117: 69–81.
50 Murchison EP, Hannon GJ. miRNAs on the move: miRNA biogenesis and the RNAi machinery. Curr Opin Cell Biol 2004; 16: 223–9.
51 Hannon GJ. RNA interference. Nature 2002; 418: 244–51.
52 Hutvagner G, Zamore PD. A microRNA in a multiple-turnover RNAi enzyme complex. Science 2002; 297: 2056–60.
53 Doench JG, Petersen CP, Sharp PA. siRNAs can function as miRNAs. Genes Dev 2003; 17: 438–42.
54 Liu Q, Rand TA, Kalidas S, Du F, Kim HE, Smith DP, *et al*. R2D2, a bridge between the initiation and effector steps of the Drosophila RNAi pathway. Science 2003; 301: 1921–5.
55 Tomari Y, Zamore PD. Perspective: machines for RNAi. Genes Dev 2005; 19: 517–29.
56 Dodd A, Chambers SP, Love DR. Short interfering RNA-mediated gene targeting in the zebrafish. FEBS Lett 2004; 561: 89–93.
57 Zender L, Hutker S, Liedtke C, Tillmann HL, Zender S, Mundt B, *et al*. Caspase 8 small interfering RNA prevents acute liver failure in mice. Proc Natl Acad Sci USA 2003; 100: 7797–802.
58 Klein C, Bock CT, Wedemeyer H, Wustefeld T, Locarnini S, Dienes HP, *et al*. Inhibition of hepatitis B virus replication *in vivo* by nucleoside analogues and siRNA. Gastroenterology 2003; 125: 9–18.
59 Verma UN, Surabhi RM, Schmaltieg A, Becerra C, Gaynor RB. Small interfering RNAs directed against beta-catenin inhibit the *in vitro* and *in vivo* growth of colon cancer cells. Clin Cancer Res 2003; 9: 1291–300.
60 Forte A, Cipollaro M, Cascino A, Galderisi U. Small interfering RNAs and antisense oligonucleotides for treatment of neurological diseases. Curr Drug Targets 2005; 6: 21–9.
61 Zhang Y, Boado RJ, Pardridge WM. *In vivo* knockdown of gene expression in brain cancer with intravenous RNAi in adult rats. J Gene Med 2003; 5: 1039–45.
62 Gilmore T, Gapuzan ME, Kalaitzidis D, Starczynowski D. Rel/NF-kappa B/I kappa B signal transduction in the generation and treatment of human cancer. Cancer Lett 2002; 181: 1–9.
63 Greten FR, Karin M. The IKK/NF-kappaB activation pathway-a target for prevention and treatment of cancer. Cancer Lett 2004; 206: 193–9.
64 Sun L, Deng L, Ea CK, Xia ZP, Chen ZJ. The TRAF6 ubiquitin ligase and TAK1 kinase mediate IKK activation by BCL10 and MALT1 in T lymphocytes. Mol Cell 2004; 14: 289–301.
65 Guo J, Verma UN, Gaynor RB, Frenkel EP, Becerra CR. Enhanced chemosensitivity to irinotecan by RNA interference-mediated down-regulation of the nuclear factor-kappaB p65 subunit. Clin Cancer Res 2004; 10: 3333–41.
66 Surabhi RM, Gaynor RB. RNA interference directed against viral and cellular targets inhibits human immunodeficiency virus type 1 replication. J Virol 2002; 76: 12963–73.
67 Brisibe EA, Okada N, Mizukami H, Okuyama H, Fujii YR. RNA interference: potentials for the prevention of HIV infections and the challenges ahead. Trends Biotechnol 2003; 7: 306–11.
68 Lee NS, Rossi JJ. Control of HIV-1 replication by RNA interference. Virus Res 2004; 102: 53–8.
69 Takaesu G, Surabhi RM, Park KJ, Ninomiya-Tsuji J, Matsumoto K, Gaynor RB. TAK1 is critical for IkappaB kinase-mediated activation of the NF-kappaB pathway. J Mol Biol 2003; 326: 105–15.
70 Takeda K, Takeuchi O, Tsujimura T, Itami S, Adachi O, Kawai T, *et al*. Science 1999; 284: 313–6.
71 Li Q, Van Antwerp D, Mercurio F, Lee KF, Verma IM. κB kinase 2 gene. Science 1999; 284: 321–5.
72 Li ZW, Chu W, Hu Y, Delhase M, Deerinck T, Ellisman M, *et al*. kB kinase (IKK) is essential for nuclear factor kappa B activation and prevention of apoptosis. J Exp Med 1999; 189: 1839–45.
73 Willis TG, Jadayel DM, Du MQ, Peng H, Perry AR, Abdul-Rauf M, *et al*. Bcl10 is involved in t(1;14)(p22;q32) of MALT B cell lymphoma and mutated in multiple tumor types. Cell 1999; 96: 35–45.
74 Lucas PC, McAllister-Lucas LM, Nunez G. NF-kappaB signaling in lymphocytes: a new cast of characters. J Cell Sci 2004; 117: 31–9.
75 Zhou H, Wertz I, O'Rourke K, Ultsch M, Seshagiri S, Eby M, *et al*. Bcl10 activates the NF-kappaB pathway through ubiquitination of NEMO. Nature 2004; 427: 167–71.
76 Wilkinson KD. Regulation of ubiquitin-dependent processes by deubiquitinating enzymes. FASEB J 1997; 11: 1245–56.
77 D'Andrea A, Pellman D. Deubiquitinating enzymes: a new class

of biological regulators. Crit Rev Biochem Mol Biol 1998; 33: 337–52.
78 Chen G, Goeddel DV. TNF-R1 signaling: a beautiful pathway. Science 2002; 296: 1634–5.
79 Yoshimura S, Bondeson J, Brennan FM, Foxwell BM, Feldmann M. Role of NFkappaB in antigen presentation and development of regulatory T cells elucidated by treatment of dendritic cells with the proteasome inhibitor PSI. Eur J Immunol 2001; 31: 1883–93.
80 Yoshimura S, Bondeson J, Foxwell BM, Brennan FM, Feldmann M. Effective antigen presentation by dendritic cells is NF-kappaB dependent: coordinate regulation of MHC, co-stimulatory molecules and cytokines. Int Immunol 2001; 13: 675–83.
81 O'Sullivan BJ, Thomas R. CD40 ligation conditions dendritic cell antigen-presenting function through sustained activation of NF-kappaB. J Immunol 2002; 168: 5491–8.
82 Silverman N, Maniatis T. κB signaling pathways in mammalian and insect innate immunity. Genes Dev 2001; 15: 2321–42.
83 Neumann M, Fries H, Scheicher C, Keikavoussi P, Kolb-Maurer A, Brocker E, *et al*. Differential expression of Rel/NF-kappaB and octamer factors is a hallmark of the generation and maturation of dendritic cells. Blood 2000; 95: 277–85.
84 Burkly L, Hession C, Ogata L, Reilly C, Marconi LA, Olson D, *et al*. Expression of relB is required for the development of thymic medulla and dendritic cells. Nature 1995; 373: 531–6.
85 Kontgen F, Grumont RJ, Strasser A, Metcalf D, Li R, Tarlinton D, *et al*. Mice lacking the c-rel proto-oncogene exhibit defects in lymphocyte proliferation, humoral immunity, and interleukin-2 expression. Genes Dev 1995; 9: 1965–77.
86 Sha WC, Liou HC, Tuomanen EI, Baltimore D. κB leads to multifocal defects in immune responses. Cell 1995; 80: 321–30.
87 Franzoso G, Carlson L, Poljak L, Shores EW, Epstein S, Leonardi A, *et al*. κB/p52 present with defects in humoral responses, germinal center reactions, and splenic microarchitecture. J Exp Med 1998; 187: 147–59.
88 Laderach D, Compagno D, Danos O, Vainchenker W, Galy A. RNA interference shows critical requirement for NF-kappa B p50 in the production of IL-12 by human dendritic cells. J Immunol 2003; 171: 1750–7.
89 Trinchieri G. Interleukin-12: a cytokine at the interface of inflammation and immunity. Adv Immunol 1998; 70: 83–243.
90 Wesa AK, Galy A. IL-1 beta induces dendritic cells to produce IL-12. Int Immunol 2001; 13: 1053–61.
91 Gri G, Savio D, Trinchieri G, Ma X. Synergistic regulation of the human interleukin-12 p40 promoter by NFkappaB and Ets transcription factors in Epstein-Barr virus-transformed B cells and macrophages. J Biol Chem 1998; 273: 6431–8.
92 Barboric M, Nissen RM, Kanazawa S, Jabrane-Ferrat N, Peterlin BM. κB binds P-TEFβ to stimulate transcriptional elongation by RNA polymerase II. Mol Cell 2001; 8: 327–37.
93 West MJ, Lowe AD, Karn J. Activation of human immunodeficiency virus transcription in T cells revisited: NF-kappaB p65 stimulates transcriptional elongation. J Virol 2001; 75: 8524–37.
94 Kimpton J, Emerman M. Detection of replication-competent and pseudotyped human immunodeficiency virus with a sensitive cell line on the basis of activation of an integrated beta-galac tosidase gene. J Virol 1992; 66: 2232–9.
95 Hannon GJ, Conklin DS. RNA interference by short hairpin RNAs expressed in vertebrate cells. Methods Mol Biol 2004; 257: 255–66.
96 Hilliard B, Samoilova EB, Liu TS, Rostami A, Chen Y. Experimental autoimmune encephalomyelitis in NF-kappa B-deficient mice: roles of NF-kappa B in the activation and differentiation of autoreactive T cells. J Immunol 1999; 163: 2937–43.
97 Wang CY, Mayo MW, Korneluk RG, Goeddel DV, Baldwin Jr AS. κB anti-apoptosis: induction of TRAF1 and TRAF2 and c-IAP1 and c-IAP2 to suppress caspase-8 activation. Science 1998; 281: 1680–3.
98 Veiby OP, Read MA. Chemoresistance: impact of nuclear factor (NF)-kappaB inhibition by small interfering RNA. Commentary re J. Guo *et al*. Enhanced chemosensitivity to irinotecan by RNA interference-mediated down-regulation of the NF-kappaB p65 subunit. Clin Cancer Res 2004; 10: 3333–41.
99 Muratovska A, Eccles MR. Conjugate for efficient delivery of short interfering RNA (siRNA) into mammalian cells. FEBS Lett 2004; 558: 63–8.
100 Song E, Lee SK, Wang J, Ince N, Ouyang N, Min J, *et al*. RNA interference targeting Fas protects mice from fulminant hepatitis. Nat Med 2003; 9: 347–51.
101 Yokota T, Sakamoto N, Enomoto N, Tanabe Y, Miyagishi M, Maekawa S, *et al*. Inhibition of intracellular hepatitis C virus replication by synthetic and vector-derived small interfering RNAs. EMBO Rep 2003; 4: 602–8.
102 McCaffrey AP, Meuse L, Pham TT, Conklin DS, Hannon GJ, Kay MA. RNA interference in adult mice. Nature 2002; 418: 38–9.
103 Lewis DL, Hagstrom JE, Loomis AG, Wolff JA, Herweijer H. Efficient delivery of siRNA for inhibition of gene expression in postnatal mice. Nat Genet 2002; 32: 107–8.
104 Dillon CP, Sandy P, Nencioni A, Kissler S, Rubinson DA, Van Parijs L. RNAi as an experimental and therapeutic tool to study and regulate physiological and disease processes. Annu Rev Physiol 2005; 67: 147–73.
105 Achenbach TV, Brunner B, Heermeier K. Oligonucleotide-based knockdown technologies: antisense versus RNA interference. Chembiochemistry 2003; 4: 928–35.
106 Silvestri LS, Taraporewala ZF, Patton JT. Rotavirus replication: plus-sense templates for double-stranded RNA synthesis are made in viroplasms. J Virol 2004; 78: 7763–74.
107 Chang J, Provost P, Taylor JM. Resistance of human hepatitis delta virus RNAs to dicer activity. J Virol 2003; 77: 11910–17.
108 Bitko V, Barik S. Phenotypic silencing of cytoplasmic genes using sequence-specific double-stranded short interfering RNA and its application in the reverse genetics of wild type negative-strand RNA viruses. BMC Microbiol 2001; 1: 34.
109 Li WX, Li H, Lu R, Li F, Dus M, Atkinson P, *et al*. Interferon antagonist proteins of influenza and vaccinia viruses are suppressors of RNA silencing. Proc Natl Acad Sci USA 2004; 101: 1350–5.
110 Lu S, Cullen BR. Adenovirus VA1 noncoding RNA can inhibit small interfering RNA and MicroRNA biogenesis. J Virol 2004; 78: 12868–76.
111 Shankar P, Manjunath N, Lieberman J. The prospect of silencing disease using RNA interference. JAMA 2005; 293: 1367–73.

Acta Pharmacologica Sinica 2005 Jul; 26 (7): 789–798

Full-length article

Activation of ERK/CREB pathway in spinal cord contributes to chronic constrictive injury-induced neuropathic pain in rats[1]

Xue-song SONG[2], Jun-li CAO[3,4,5], Yan-bing XU[3], Jian-hua HE[3], Li-cai ZHANG[3], Yin-ming ZENG[3,4]

[2]Department of Anesthesiology, First Clinical College of N.Bethune Centre of Health Sciences, Jilin University, Changchun 130021, China; [3]Department of Anesthesiology, Affiliated Hospital of Xuzhou Medical College, Xuzhou 221002, China; [4]Jiangsu Institute of Anesthesiology, Xuzhou 221002, China

Key words

extracellular signal-regulated kinases; cyclic AMP-response DNA-binding protein; pain; hyperalgesia; spinal cord

[1] Project supported by an Open Project Grant from the Jiangsu Province Key Laboratory of Anesthesiology (No KSJ03081) and in part supported by the National Natural Science Foundation of China (No 30200267).
[5] Correspondence to Jun-li CAO.
Phn 86-516-580-2018.
Fax 86-516-570-8135.
E-mail caojl0310@yahoo.com.cn

Received 2004-12-06
Accepted 2005-03-10

doi: 10.1111/j.1745-7254.2005.00123.x

Abstract

Aim: To investigate whether activation and translocation of extracellular signal-regulated kinase (ERK) is involved in the induction and maintenance of neuropathic pain, and effects of activation and translocation of ERK on expression of pCREB and Fos in the chronic neuropathic pain. **Methods:** Lumbar intrathecal catheters were chronically implanted in male Sprague-Dawley rats. The left sciatic nerve was loosely ligated proximal to the sciatica's trifurcation at approximately 1.0 mm intervals with 4-0 silk sutures. The mitogen-activated protein kinase kinase (MEK) inhibitor U0126 or phosphorothioate-modified antisense oligonucleotides (ODN) were intrathecally administered every 12 h, 1 d pre-chronic constriction injury (CCI) and 3 d post-CCI. Thermal and mechanical nociceptive thresholds were assessed with the paw withdrawal latency (PWL) to radiant heat and von Frey filaments. The expression of pERK, pCREB, and Fos were assessed by both Western blotting and immunohistochemical analysis. **Results:** Intrathecal injection of U0126 or ERK antisense ODN significantly attenuated CCI-induced mechanical allodynia and thermal hyperalgesia. CCI significantly increased the expression of p-ERK-IR neurons in the ipsilateral spinal dorsal horn to injury, not in the contralateral spinal dorsal horn. The time courses of pERK expression showed that the levels of both cytosol and nuclear pERK, but not total ERK, were increased at all points after CCI and reached a peak level on postoperative d 5. CCI also significantly increased the expression of pCREB and Fos. Phospho-CREB-positive neurons were distributed in all laminae of the bilateral spinal cord and Fos was expressed in laminae I and II of the ipsilateral spinal dorsal horn. Intrathecal injection of U0126 or ERK antisense ODN markedly suppressed the increase of CCI-induced pERK, pCREB and c-Fos expression in the spinal cord. **Conclusion:** The activation of ERK pathways contributes to neuropathic pain in CCI rats, and the function of pERK may partly be accomplished via the cAMP response element binding protein (CREB)-dependent gene expression.

Introduction

Peripheral nerve injury induced in various ways may produce chronic pain states characterized by hyperalgesia, allodynia and spontaneous pain. To date, there is no effective treatment for releasing neuropathic pain. Recently, the synaptic plasticity of spinal cord neurons induced by long-lasting nociceptive stimulation (also called central sensitization) has been under intensive investigation[1–3]. Several studies have suggested that central sensitization related to pain, and hippocampal long term potentiation (LTP) associated with learning and memory, may share certain mechanisms[4,5]. For example, activation of *N*-methyl-*D*-aspartate

(NMDA) receptor and the subsequent associated intracellular signal transduction cascades are involved in the induction, development and maintenance of synaptic plasticity in the spinal cord and hippocampus. Like the consolidation of early-phase LTP into late-LTP in the hippocampus, activity-dependent gene expression or transcription, which can increase the expression of pain-related receptors and signal proteins, plays an important role in conversion from acute nociceptive injury to chronic pain states[6,7]. The transcription factor cAMP response element binding protein (CREB), which can be phosphorylated by multiple intracellular kinases in response to a vast range of physiological and pathological stimuli, is critical for activity-dependent gene expression. Genetic studies have shown that CREB contributes to hippocampal late-LTP and memory consolidation, and CREB activation may serve as a molecular switch to transform short-lasting into long-lasting synaptic plasticity in the hippocampus[8,9]. Similarly, CREB has been suggested to contribute to the central sensitization associated with persistent pain states[10–12]. It has been proposed that NMDA activation-induced Ca^{2+} influx can trigger an early phase of CREB phosphorylation and a persistent phase of CREB phosphorylation is mediated by a delayed extracellular signal-regulated kinase (ERK) signal cascade, which is important to the development and maintainment of chronic pain.

ERK, one member of the mitogen-activated protein kinase (MAPK) family, transduces a broad range of extracellular stimuli into diverse intracellular responses by producing changes in the level of gene expression or transcription. Activated ERK translocates from the cytosol into the nucleus and in turn phosphorylates CREB at serine residue 133. Phosphorylation of CREB binding to the cAMP response element (CRE) of the target gene regulates gene expression and mediates the roles of ERK. Many studies found that ERK-mediated CREB phosphorylation is required for the induction of stable, late-phase LTP and long-term memory[13–15]. It has been reported that ERK may be involved in the modulation of nociceptive information and central sensitization produced by intense noxious stimuli and/or peripheral tissue inflammation[16–21]. However, few studies have focused on the roles of ERK and the relationship between ERK and CREB in neuropathic pain produced by nerve injury, such as chronic constriction injury (CCI) of the sciatic nerve.

In the present study, we used a CCI model to investigate whether activation and translocation of ERK were involved in the induction and maintenance of chronic neuropathic pain, and to observe the effect of ERK on the expression of pCREB in chronic neuropathic pain.

Materials and methods

Animals One hundred and seventy-four male Sprague-Dawley rats (200–250 g) provided by the Experimental Animal Center of Xuzhou Medical College were kept under a 12 h/12 h light-dark cycle regimen, with free access to food and water. All experiments were approved by the Animal Care and Use Committee at the Xuzhou Medical College and were in accordance with the college's guidelines for the care and use of laboratory animals.

Implantation of intrathecal catheter For intrathecal drug administration, rats were implanted with catheters as described by Yaksh and Rudy[22]. In brief, under anesthesia with pentobarbital sodium (40 mg/kg, ip), rats were fixed, the occipital muscles were bluntly separated, then the cisternal membrane was exposed. Polyethylene catheters (PE-10) were inserted via an incision in the cisterna magna, and advanced 7.0–7.5 cm caudally to the level of the lumbar enlargement. Correct intrathecal placement was confirmed by injection of 10 μL 2% lidocaine through the catheter. The catheter was judged to be intrathecal if paralysis and dragging of bilateral hind limbs occurred within 30 s of this injection. Animals with signs of motor dysfunction were excluded from the experiment. The rats were housed individually after surgery and allowed to recover 5–7 d before the CCI test.

Chronic constrictive injury CCI of the sciatic nerve was performed as previously described by Bennett and Xie[23]. Briefly, under anesthesia with isoflurane, the left sciatic nerves of rats were exposed at the level of the middle of the thigh, and then four ligatures (4–0, silk thread) were tied loosely around proximal to the sciatica's trifurcation at 1.0-mm intervals. Sham surgery was done by exposing the left sciatic nerve without ligation.

Drug administration Intrathecal drug administration was accomplished using a microinjection syringe connected to the intrathecal catheter in awake, briefly restrained rats. The injection was performed manually over a 30 s period in a single injection volume of 10 μL followed by a flush with 10 μL physiological saline.

U0126 (Biomol Research Laboratories, Pennsylvania, USA), an MEK inhibitor [dissolved in 5% dimethylsulfoxide (Me_2SO), 0.5 g/L] or ODN (1 g/L) were administered every 12 h, 1 d pre-CCI and 3 d post-CCI. Me_2SO and mis-sense ODN were injected as control.

The sequence of ERK antisense ODN was designed as reported previously[24]; antisense: 5'-GCCGCCGCCGCC-GCCAT-3', directed against the initiation of the translation start site of rat ERK1 and ERK2 mRNA; mis-sense: 5'-CGCGCGCTCGCGCACCC-3'. ODN was synthesized by Shanghai Sangon (Shanghai, China) and modified with

phosphorothioate. The efficacy of the antisense oligonucleotide in inhibiting ERK expression was confirmed at the protein level by Western blotting. Twelve hours after the last administration of the antisense oligonucleotide, the expression of the ERK protein was reduced by approximately 70% in the rat spinal cord (Figure 1).

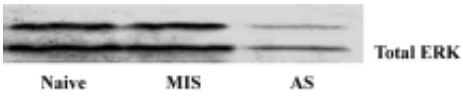

Figure 1. Expression of ERK in rat spinal cords after the intrathecal injection of the ERK antisense oligonucleotide. Phosphorothioate-modified antisense oligonucleotides (AS group) (1 g/L) were administered every 12 h for 4 d. Mis-sense oligonucleotides (MIS group) were injected as a control.

Behavioral studies Mechanical allodynia was assessed by using von Frey filaments. Animals were placed on a wire mesh platform and covered with a transparent plastic dome (20 cm×25 cm×15 cm), and the animals were allowed to acclimate to their surrounds for 30 min before testing. Each filament was applied perpendicularly to the plantar surface of the hindpaw (ipsilateral to the side of surgery in nerve-injured animals). The paw withdrawal threshold (PWT) was determined by sequentially increasing and decreasing the stimulus strength (the "up- and-down" method), and the data were analyzed using the nonparametric method of Dixon, as described by Chaplan *et al*[25].

Thermal hyperalgesia was assessed with the paw withdrawal latency (PWL) to radiant heat according to the protocol of Hargreaves *et al*[26]. Rats were placed in clear plastic cages on an elevated glass plate and allowed to acclimate to their surrounds for 30 min before testing. A high intensity light beam was focused onto the plantar surface of the hindpaw through the glass plate. The nociceptive endpoints in the radiant heat test were the characteristic lifting or licking of the hindpaw; the time to the endpoint was considered the PWL. To avoid tissue damage, a cut-off time of 30 s was used. There were 3 trials per rat and 5 min intervals between trials.

The tests were performed on each of 3 successive days prior to surgery and alternate days up to 15 d after surgery. Eight animals per group were used for behavior tests.

To study the effect of U0126 and antisense-ODN on the rat's motor function, motor functions were evaluated by the observation of placing/stepping reflexes and righting reflexes and were conducted 5 min before the assessment of nociceptive responses.

Immunohistochemistry Immunohistochemical studies were performed as previously described[27,28]. Briefly, the spinal cord was cut into 40 μm-thick segments. After washing in phosphate buffer saline, the tissue sections were incubated in phosphate-buffered saline containing 5% normal goat serum and 0.3% TritonX-100 at room temperature for 30 min, followed by primary polyclonal mouse-anti-pERK antibody (1:200), primary polyclonal rabbit-anti-ser133-pCREB (1:400) antibody or primary polyclonal rabbit-anti-Fos antibody (1:1000) at 4 °C for 48 h (all antibodies were from Santa Cruz Biotechnology, California, USA). The sections were then incubated in biotinylated goat anti-rabbit or -mouse IgG (1:200) at 37 °C for 1 h and in avidin-biotin-peroxidase complex (1:100) (Vector Labs, California, USA) at 37 °C for 2 h. Finally, the sections were reacted with diaminobenzidine (DAB) for 5–10 min. Sections were rinsed in phosphate-buffered saline to stop the reaction, mounted on gelatin-coated slides, air-dried, dehydrated with 70%–100 % alcohol, cleared with xylene, and cover-slipped for microscopic examination.

We selected 5 spinal cord sections per animal, selecting sections that had the greatest number of positive neurons. For each animal, two measurements were made: (1) total number of positive neurons in the spinal cord dorsal horn ipsilateral to injury; (2) total number of positive neurons in the spinal cord dorsal horn contralateral to injury. All positive neurons were counted without considering the intensity of the staining.

Western blotting The lumbosacral spinal cords of the rats were extracted and stored in liquid nitrogen. Tissue samples were homogenized in lysis buffer A (in mmol/L): HEPES 10.0, Na_3VO_4 1.0, $MgCl_2$ 1.5, KCl 10.0, NaF 50.0, edetic acid (EDTA) 0.1, egtazic acid (EGTA) 0.1, phenylmethylsulfonyl fluoride (PMSF) 0.5, dithiothreitol (DDT) 1.0 and 0.02% protease inhibitor cocktail (pH 7.9). After the addition of 90 μL NP-40 (10%), the homogenates were vortexed for 30 s and then centrifuged at 800×*g* for 15 min at 4 °C. The supernatants were used for Western blot analysis as cytosolic proteins. The nuclear pellets were resuspended in buffer B (in mmol/L): HEPES 20.0, NaCl 420.0, $MgCl_2$ 1.5, EDTA 1.0, EGTA 1.0, PMSF 0.5, DDT 1.0, 20 % glycerol, and 0.02% protease inhibitor cocktail (pH 7.9). The homogenates were incubated for 30 min in ice-cold water with constant agitation and then centrifuged at 13 000×*g* for 15 min at 4 °C to separate the nuclear proteins. Protein concentrations were determined using the Bradford method and the protein samples were stored at -80 °C.

Protein samples were dissolved in 4×sample buffer [in mmol/L: Tris-HCl 250.0, sucrose 200.0, DDT 300.0, 0.01% Coomassie brilliant blue-G, and 8% sodium dodecyl sulfate

(SDS), pH 6.8], and denatured at 95 °C for 5 min, then the equivalent amounts of proteins were separated by using 10% SDS-polyacrylamide gel electrophoresis (PAGE) and transferred onto a nitrocellulose membrane. The membranes were incubated overnight at 4 °C with the following primary antibodies: mouse polyclonal anti-pERK antibody and rabbit polyclonal anti-ser133-pCREB. The membranes were extensively washed with Tris-Buffered Saline Tween-20 (TBST) and incubated for 1 h with the secondary antibody conjugated with alkaline phosphatase (AP) at room temperature. The immune complexes were detected by using a NBT/BCIP assay kit (Promega, Shanghai, China). The scanned images were imported into Adobe Photoshop software (Adobe, California, USA). Scanning densitometry was used for semiquantitative analysis of the data.

Experimental groups Rats were divided into six groups in the behavior test: the sham group, CCI group, U0126 group, Me_2SO group, antisense ODN group and mis-sense ODN group. Four groups were included in the immunohistochemistry studies and the Western blot testing: the sham group, CCI group, U0126 group, and antisense ODN group. Because few pERK, pCREB and Fos-positive neurons were expressed in the spinal dorsal horn of sham group rats, these data are not shown in results.

Statistical analysis All data are expressed as mean±SD Statistical analysis was carried out using one-way ANOVA or Student's *t*-test. $P<0.05$ was considered statistically significant.

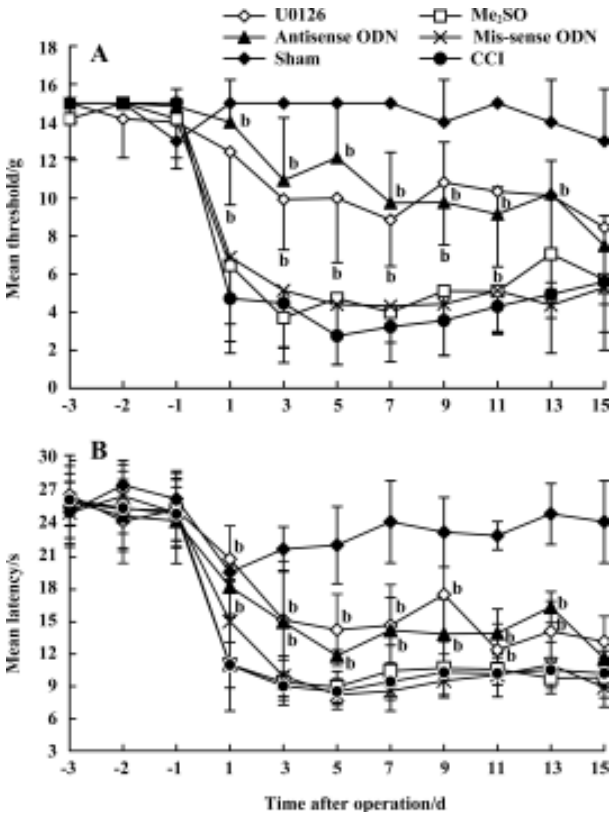

Figure 2. Intrathecal administration of U0126 or ERK antisense oligonucleotides prevented chronic constriction injury-induced mechanical allodynia (A) and thermal (B) hyperalgesia. Mean±SD. n=8. $^bP<0.05$ *vs* CCI group.

Results

Effects of U0126 or ERK antisense ODN on CCI-induced mechanical allodynia and thermal hyperalgesia Intrathecal administration of U0126 or ERK antisense-ODN did not affect the mechanical PWT, the thermal PWL, or motor function in the rats that received implanted intrathecal catheters. CCI, and not sham surgery, produced significant mechanical allodynia and thermal hyperalgesia. The time course of PWT and PWL is presented in Figure 2. Intrathecal injection of U0126 or ERK antisense ODN, and not Me_2SO or mis-sense ODN, attenuated CCI-induced mechanical allodynia and thermal hyperalgesia.

Effects of U0126 or ERK antisense ODN on CCI-induced pERK expression in the spinal cord CCI significantly increased the expression of pERK-IR neurons in the spinal cord dorsal horn ipsilateral to injury. The pERK positive neurons were distributed mainly in laminae I and II of the spinal dorsal horn. Few positive neurons were distributed in other laminae or the contralateral spinal cord. Intrathecal injection of U0126 or ERK antisense ODN inhibited the increase in pERK expression in the spinal dorsal horn on postoperative d 3 and d 5 (Figure 3).

CCI-induced ERK activation was also confirmed by Western blot analysis. Compared with sham group rats, the levels of both phospho-ERK1 (44 kDa) and phospho-ERK2 (42 kDa), not unphospho-ERK (data not shown), were increased at all measured time points after CCI (Figures 4, 5). The expression of pERK reached a peak level on postoperative d 5. The increase in the nuclear fraction of pERK expression indicated that pERK was translocated into the nucleus from the cytoplasm. Intrathecal injection of U0126 or ERK antisense ODN markedly inhibited the increase in both cytosolic and nuclear pERK expression.

Effects of U0126 or ERK antisense ODN on CCI-induced pCREB expression in the spinal cord The immunohistochemical results revealed that CCI significantly increased the expression of pCREB, and pCREB-positive neurons were distributed in all laminae of the bilateral spinal cord. Expressions in the ipsilateral and contralateral spinal

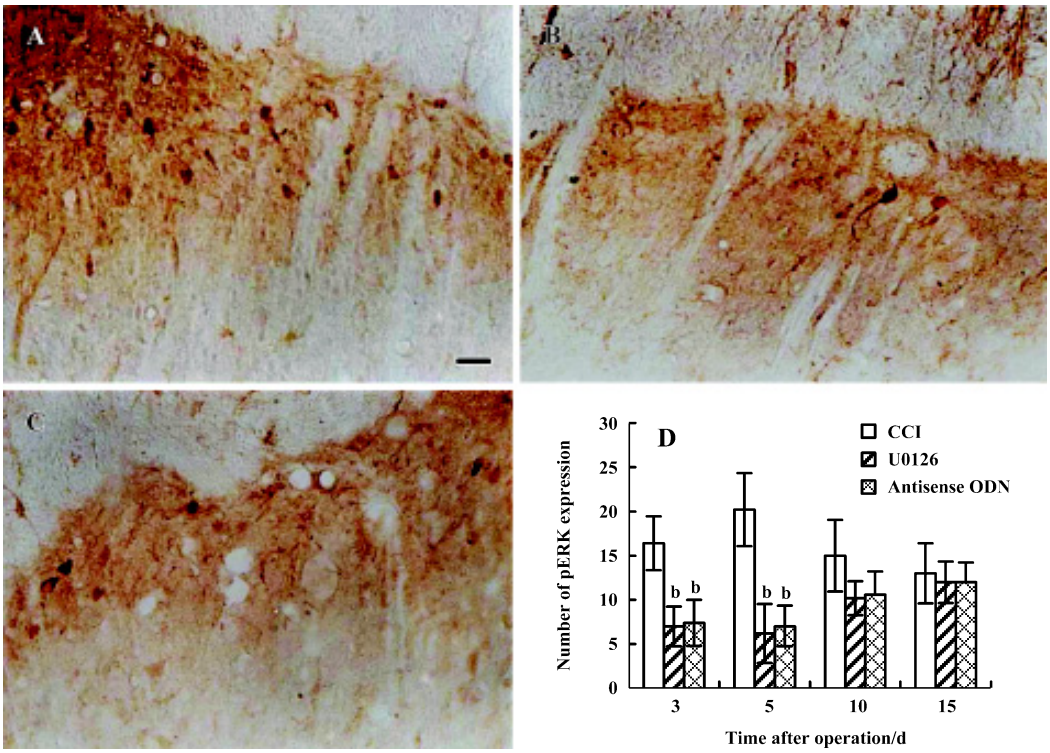

Figure 3. Effects of intrathecal administration of U0126 or ERK antisense ODN on CCI-induced pERK expression in the ipsilateral spinal dorsal horn. Representative immunohistochemical staining for pERK in the ipsilateral spinal dorsal horn of rats in the CCI group (A), U0126 group (B) and antisense ODN group (C) 5 d post-CCI. (D) Quantitative data indicating the number of pERK immunoreactivity neurons. n=6. Mean±SD. ^{b}P<0.05 *vs* CCI group. bar=25 μm.

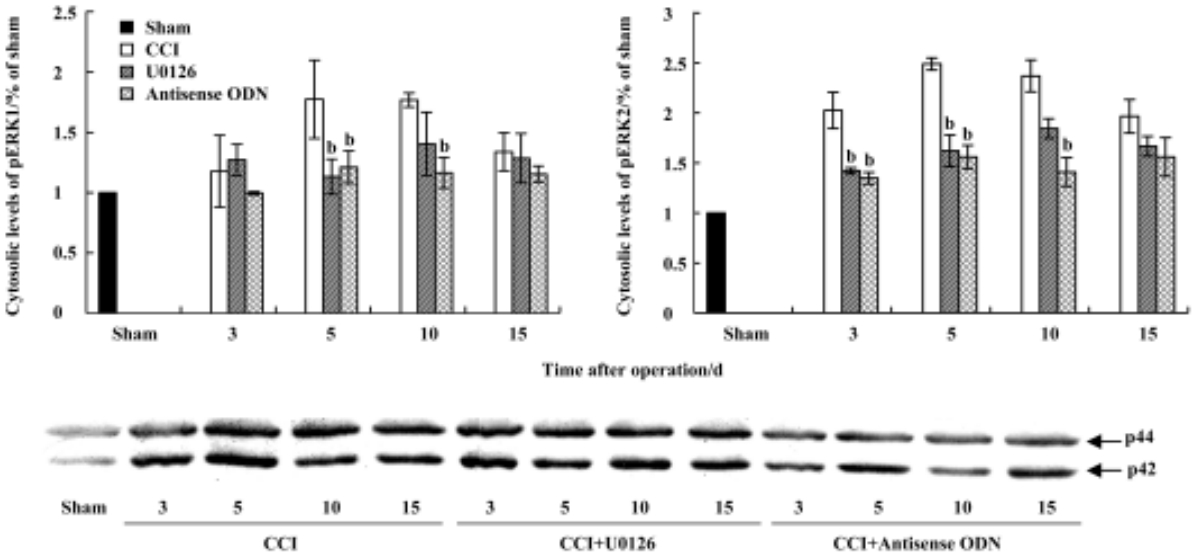

Figure 4. Western blot analysis of the effect of intrathecal administration of U0126 or ERK antisense ODN on CCI-induced cytosolic pERK expression in the rat spinal cord. (Middle) A representative Western blot band for pERK. (Top and bottom) Quantitative data indicating the expression of pERK. ERK expression in the sham group is set at 100%. n=4. Mean±SD. ^{b}P<0.05 *vs* CCI group.

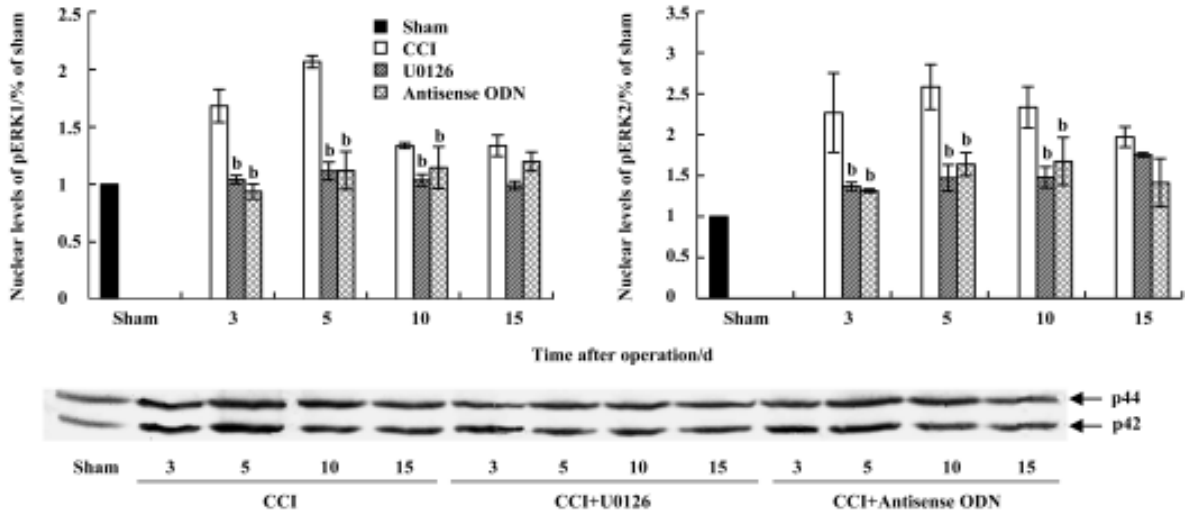

Figure 5. Western blot analysis on the effect of intrathecal administration of U0126 or ERK antisense ODN on CCI-induced nuclear pERK expression in the rat spinal cord. (Middle) A representative Western blot band for pERK. (Top and bottom) Quantitative data indicating the expression of pERK. The expression of pERK in the sham group is set at 100%. n=4. Mean±SD. $^bP<0.05$ *vs* CCI group.

cord were not significantly different. Intrathecal injection of U0126 or ERK antisense ODN markedly inhibited pCREB expression in both sides of the spinal cord (Figure 6). Few pCREB positive neurons were found in the sham group rats (data not shown).

Similar to the results of the immunohistochemical studies, the Western blot results showed that nuclear pCREB was highly expressed on postoperative d 3 and d 5. Intrathecal administration of U0126 or ERK antisense ODN significantly inhibited the increase of pCREB expression, especially on postoperative d 5 (Figure 7). These data suggest that activation of ERK contributes to increased pCREB expression in the spinal cords of CCI rats.

Effects of U0126 or ERK antisense ODN on CCI-induced Fos expression in the spinal cord CCI significantly increased the expression of Fos in laminae I and II of the ipsilateral spinal dorsal horn. Dissimilar to the findings for pCREB, few c-Fos positive neurons were found in the contralateral spinal cord. Intrathecal administration of U0126 or ERK antisense ODN also significantly reduced the expression of Fos-positive neurons (Figure 8A, 8B, 8C, and 8D).

Discussion

Central sensitization, an activity-dependent functional plasticity, is one of the main causes of behavior hyperalgesia under pathological conditions. Activation of postsynaptic membrane receptors or ion channels, intracellular kinase cascades and intranuclear gene expression contributes to the induction, development and maintainment of central sensitization. Intracellular kinase cascades, as the linkage bridge, transduce noxious stimuli into diverse intracellular responses, including changes in the levels of gene expression or transcription. A large number of studies have implicated several protein kinases, for example, protein kinases A (PKA), protein kinases C (PKC) and calcium/calmodullin-dependent protein kinase II (CaMKII), in central sensitization[29–31]. Recently, several studies have reported that ERK, a mitogen-activated protein kinase, contributes to pain hypersensitivity and central sensitization. Acute noxious stimuli, such as formalin or capsaicin, induce ERK phosphorylation in spinal dorsal horn neurons, and MEK inhibitor PD 98059 or U0126 reduces acute pain behavior after subcutaneous injection of formalin or capsaicin[16–21]. In agreement with previous reports using other pain models, the present studies indicate that activation of ERK in rat spinal cord contributes to CCI-induced allodynia and hyperalgesia. We demonstrated here, the time course of pERK and the relationship between pERK and pCREB expression in a CCI model. CCI induces long-lasting ERK phosphorylation and nuclear translocation in the spinal cord. The time course of changes in pERK expression, at least in part, correlated significantly with behavior hyperalgesia. Intrathecal injection of U0126 or ERK antisense ODN markedly attenuated CCI-induced mechanical allodynia and thermal hyperalgesia.

Nerve fibers display abnormal ectopic excitability at or near the site of nerve ligation after CCI. The local persistent abnormal excitation of sensory nerves can spread to the pe-

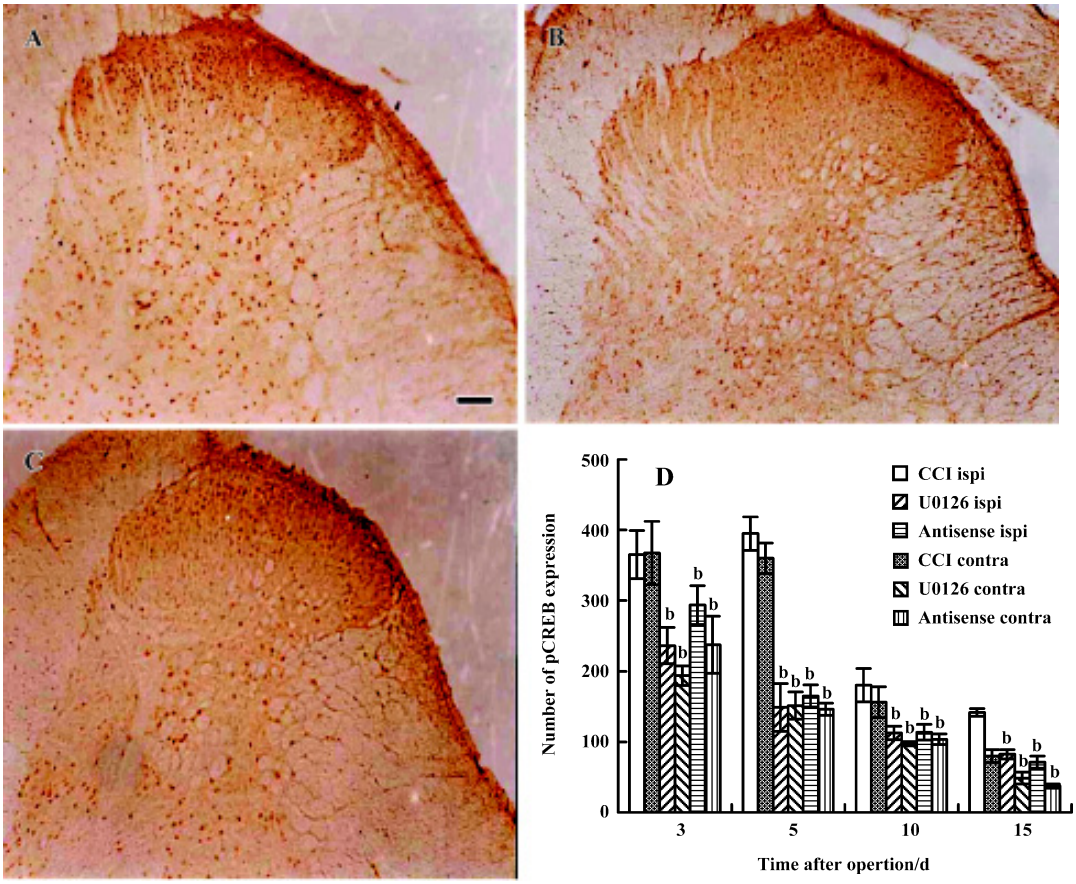

Figure 6. Intrathecal administration of U0126 or ERK antisense ODN markedly inhibited the increase of CCI-induced pCREB expression in the ipsilateral and contralateral rat spinal dorsal horn. Representative immunohistochemical staining for pCREB in the ipsilateral spinal dorsal horn of the CCI group (A), the U0126 group (B) and the antisense ODN group rats (C) 5 d post-CCI. (D) Quantitative data indicating the number of pCREB immunoreactive neurons. n=6. Mean±SD. ^{b}P<0.05 *vs* CCI group. bar=100 μm.

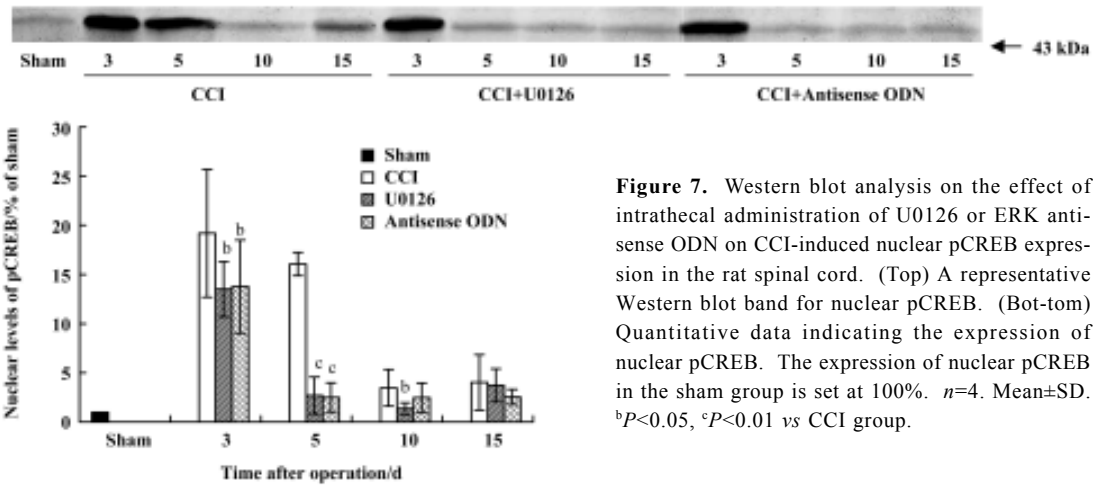

Figure 7. Western blot analysis on the effect of intrathecal administration of U0126 or ERK antisense ODN on CCI-induced nuclear pCREB expression in the rat spinal cord. (Top) A representative Western blot band for nuclear pCREB. (Bot-tom) Quantitative data indicating the expression of nuclear pCREB. The expression of nuclear pCREB in the sham group is set at 100%. n=4. Mean±SD. ^{b}P<0.05, ^{c}P<0.01 *vs* CCI group.

ripheral nerve bodies in the dorsal root ganglion (DRG) and central nervous system. Repeated or prolonged noxious stimulation and the persistent abnormal input following nerve injury increase the release of nociceptive neurotransmitters,

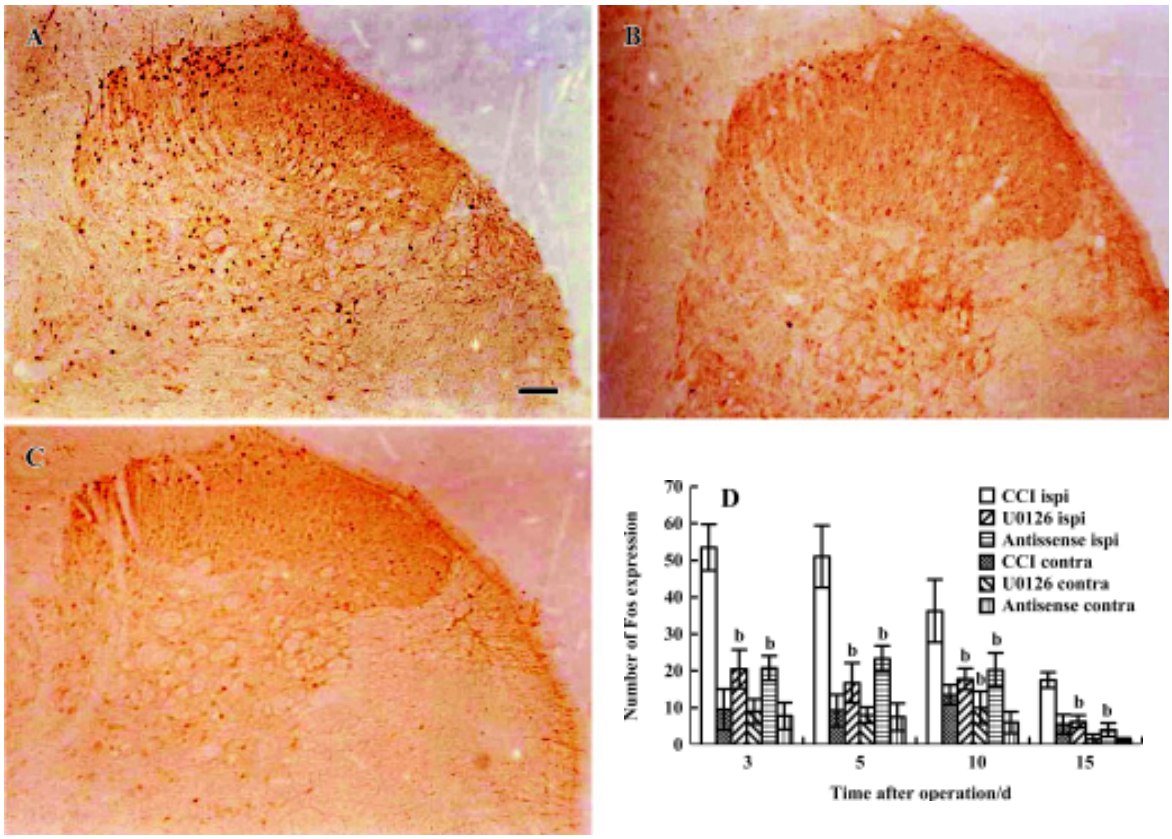

Figure 8. Effects of intrathecal administration of U0126 or ERK antisense ODN on CCI-induced Fos expression in the ipsilateral dorsal horn. Representative immunohistochemical staining for Fos in the ipsilateral spinal dorsal horn of the CCI group (A), the U0126 group (B) and the antisense ODN group (C) 5 d post-CCI. (D) Quantitative data indicating the number of Fos immunoreactivity neurons. n=6. Mean±SD. $^{b}P<0.05$ *vs* CCI group (ipsilateral). bar=100 μm.

such as glutamate, substance P, and calcitonin gene-related peptide (CGRP) in the central terminals of primary sensory afferents and then activate NMDA and neurokinin (NK) receptors in spinal dorsal horn neurons. Calcium influx through NMDA receptors triggers an increase in the levels of Ras-GTP and in turn leads to the activation of raf/MEK/ERK cascades.

ERK mediates central sensitization by phosphorylating the effector protein. Two potential effectors of ERK related to central sensitization are the potassium channel Kv4.2 and the transcription factor CREB. Recent evidence has shown that ERK integrates PKA and PKC to modulate the K^+ channel Kv4.2 and A-type K^+ currents (I_A) in superficial dorsal horn neurons. Kv4.2 and I_A are critical determinants of neuronal excitability in central sensitization[32–34]. It is possible that modulation of potassium channels may be involved in the short-term or acute effect of pERK. Our unpublished data show that CCI-induced hyperalgesia is reversed 30 min after intrathecal administration of U0126 on postoperative d 5.

Importantly, pERK is able to translocate from the cytoplasm into the nucleus and in turn phosphorylate the transcriptional factor CREB on serine 133. In the current study, CCI significantly increased the expression of pCREB in the rat spinal cord. The time course of pCREB expression correlates with the activation of ERK and behavioral hyperalgesia. Intrathecal injection of U0126 or ERK antisense ODN markedly inhibited the increase in pCREB expression. This suggests that activation of ERK may contribute to increased pCREB expression in the spinal cord of CCI rats, and that the function of pERK is partly accomplished via CREB-dependent gene expression. Phosphorylation of CREB on serine 133 recruits the CREB binding protein, CBP, to the complex and promotes the transcription of downstream genes. Many "pain genes", which may contribute to central sensitization, are activated by CREB, including the immediate early gene c-fos, BDNF, CGRP, the alpha subunit of CaMKII, and the neurokinin 1 receptor. A considerable amount of evidence has indicated that CREB-dependent gene expression is re-

quired for long-term changes in the synaptic plasticity induced by various nociceptive stimuli[10–12, 35–37].

We found that increases in pCREB expression occurred bilaterally in all laminae of the spinal cord in CCI rats. Expression levels in the ipsilateral and the contralateral sides were not significantly different. Fos protein was expressed only in the ispilateral spinal dorsal horn. Similar results have been reported in other pain models, for example, formalin injection and carrageenan injection[11,12,38,39]. However, few interpreted this result consistently. Ji and Rupp speculated that signal strength might affect gene expression differentially with respect to protein phosphorylation[38]. We, however, favor the explanation that different intracellular signal transduction pathways contribute to pCREB expression in the ispilateral and the contralateral spinal cords. In the present study, pCREB was expressed in both sides of the spinal cord, but pERK only in the ipsilateral side. These results suggest that pERK contributed to pCREB expression in the ipsilateral spinal cord, but not in the contralateral spinal cord. Intrathecal injection of U0126 or ERK antisense ODN inhibited pCREB expression not only in the ispilateral spinal cord, but also in the contralateral spinal cord. This suggests that activation of ERK in the ispilateral spinal cord is also involved in pCREB expression in the contralateral spinal cord. CCI induces ipsilateral primary afferent terminals to release nociceptive neurotransmitters, which induces the NMDA receptor-dependent activation of intracellular kinase cascades, including the ERK pathway, in the spinal cord. Furthermore, cross-talk between intracellular kinase cascades can produce strong activation of signal pathways. Then some kinases phosphorylate CREB and regulate noxious-induced target gene expression, such as c-fos, in a pCREB-dependent manner. But how should we interpret pCREB expression in the contralateral spinal cord, which did not receive noxious inputs? Numerous lines of evidence have shown that unilateral noxious stimuli can indirectly induce the activation of several intracellular signal pathways in the bilateral spinal cord. For example, Solodkin *et al* reported that unilateral hindpaw inflammation produced a bilateral increase in NADPH-diaphorase in rat lumbar spinal cord[40]. Noxious stimuli also induce glial activation, and excitation of glia at one site can activate distant and even the contralateral dorsal horn glia via gap junctions and propagated calcium waves[41]. The ipsilateral noxious stimuli-induced activation of several intracellular signal pathways in the contralateral spinal cord may indeed be a critical factor in pCREB expression in the contralateral spinal cord. Because CREB phosphorylation in the contralateral spinal cord does not result from direct extracellular noxious inputs, it cannot upregulate the expression of the noxious marker gene, c-fos.

In summary, the present study found that activation of the ERK/CREB pathway in the spinal cord contributed to chronic constrictive injury-induced neuropathic pain.

Acknowledgements

We gratefully acknowledge technical assistance from Dr Hai-lei DING. We also thank Steve PILLING for editing the English of this manuscript.

References

1 Ikeda H, Heinke B, Ruscheweyh R, Sandkuhler J. Synaptic plasticity in spinal lamina. I projection neurons that mediate hyperalgesia. Science 2003; 299: 1237–40.
2 Melzack R, Coderre TJ, Katz J, Vaccarino AL. Central neuroplasticity and pathological pain. Ann NY Acad Sci 2001; 933: 157–74.
3 Wolpaw JR, Tennissen AM. Activity-dependent spinal cord plasticity in health and disease. Annu Rev Neurosci 2001; 24: 807–43.
4 Ji RR, Kohno T, Moore KA, Woolf CJ. Central sensitization and LTP: do pain and memory share similar mechanisms? Trends Neurosci 2003; 26: 696–705.
5 Rygh LJ, Tjolsen A, Hole K, Svendsen F. Cellular memory in spinal nociceptive circuitry. Scand J Psychol 2002; 43: 153–9.
6 Messaoudi E, Ying SW, Kanhema T, Croll SD, Bramham CR. Brain-derived neurotrophic factor triggers transcription-dependent, late phase long-term potentiation *in vivo*. J Neurosci 2002; 22: 7453–61.
7 Woolf CJ, Costigan M. Transcriptional and posttranslational plasticity and the generation of inflammatory pain. Proc Natl Acad Sci USA 1999; 96: 7723–30.
8 Chen A, Muzzio IA, Malleret G, Bartsch D, Verbitsky M, Pavlidis P, *et al*. Inducible enhancement of memory storage and synaptic plasticity in transgenic mice expressing an inhibitor of ATF4 (CREB-2) and C/EBP proteins. Neuron 2003; 39: 655–69.
9 Ho N, Liauw JA, Blaeser F, Wei F, Hanissian S, Muglia LM, *et al.* Impaired synaptic plasticity and cAMP response element-binding protein activation in Ca^{2+}/calmodulin-dependent protein kinase type IV/Gr-deficient mice. J Neurosci 2000; 20: 6459–72.
10 Hoeger-Bement MK, Sluka KA. Phosphorylation of CREB and mechanical hyperalgesia is reversed by blockade of the cAMP pathway in a time-dependent manner after repeated intramuscular acid injections. J Neurosci 2003; 23: 5437–45.
11 Ma W, Hatzis C, Eisenach JC. Intrathecal injection of cAMP response element binding protein (CREB) antisense oligonucleotide attenuates tactile allodynia caused by partial sciatic nerve ligation. Brain Res 2003; 988: 97–104.
12 Ma W, Quirion R. Increased phosphorylation of cyclic AMP response element-binding protein (CREB) in the superficial dorsal horn neurons following partial sciatic nerve ligation. Pain 2001; 93: 295–301.
13 Kelleher RJ, Govindarajan A, Jung HY, Kang H, Tonegawa S. Translational control by MAPK signaling in long-term synaptic

plasticity and memory. Cell 2004; 116: 467–79.
14 Morozov A, Muzzio IA, Bourtchouladze R, Van-Strien N, Lapidus K, Yin D, *et al*. Rap1 couples cAMP signaling to a distinct pool of p42/44MAPK regulating excitability, synaptic plasticity, learning, and memory. Neuron 2003; 39: 309–25.
15 Thomas GM, Huganir RL. MAPK cascade signalling and synaptic plasticity. Nature Rev Neurosci 2004; 5: 173–83.
16 Aley KO, Martin A, McMahon T, Mok J, Levine JD, Messing RO. Nociceptor sensitization by extracellular signal-regulated kinases. J Neurosci 2001; 21: 6933–9.
17 Ciruela A, Dixon AK, Bramwell S, Gonzalez MI, Pinnock RD, Lee K. Identification of MEK1 as a novel target for the treatment of neuropathic pain. Br J Pharmacol 2003; 138: 751–6.
18 Galan A, Cervero F, Laird JM. Extracellular signaling-regulated kinase-1/2 (ERK1/2) mediate referred hyperalgesia in a murine model of visceral pain. Mol Brain Res 2003; 116: 126–34.
19 Ji RR, Baba H, Brenner GJ, Woolf CJ. Nociceptive-specific activation of ERK in spinal neurons contributes to pain hypersensitivity. Nat Neurosci 1999; 2; 1114–9.
20 Ji RR, Befort K, Brenner GJ, Woolf CJ. ERK MAP kinase activation in superficial spinal cord neurons induces prodynorphin and NK-1 upregulation and contributes to persistent inflammatory pain hypersensitivity. J Neurosci 2002; 22; 478–85.
21 Wang H, Dai Y, Fukuoka T, Yamanaka H, Obata K, Tokunaga A, *et al*. Enhancement of stimulation-induced ERK activation in the spinal dorsal horn and gracile nucleus neurons in rats with peripheral nerve injury. Eur J Neurosci 2004; 19: 884–90.
22 Yaksh TL, Rudy TA. Chronic catheterization of the subarachnoid space. Physiol Behav 1976; 7: 1032–6.
23 Bennett GJ, Xie YK. A peripheral mononeuropathy in rat that produces disorder of pain sensation like those seen in man. Pain 1988; 33: 87–107.
24 Sale EM, Atkinson PG, Sale GJ. The requirement of MAP kinase for the differentiation of fibroblasts to adipocytes, for insulin activation of p90 S6 kinase and for insulin or serum stimulation of DNA synthesis. J EMBO 1995; 14: 674–84.
25 Chaplan SR, Bach FW, Pogrel JW, Chung JM, Yaksh TJ. Quantitative assessment of tactile allodynia in the rat paw. J Neurosci Methods 1994; 53: 55–63.
26 Hargreaves K, Dubner R, Brown F, Flores C, Joris J. A new and sensitive method for measuring thermal nociception in cutaneous hyperalgesia. Pain 1988; 32: 77–88.
27 Cao JL, Zeng YM, Zhang LC, Gu J, Liu HF, Zhou WH, *et al*. NO mediated the increase of Fos protein and $NDMA_{1A}R$ mRNA expression in the rat spinal cord during morphine withdrawal. Acta Pharmacol Sin 2001; 22: 505–11.
28 Cao JL, Ding HL, Zhang LC, Duan SM, Zeng YM. Pretreatment with midazolam suppresses morphine withdrawal response in mice and rats. Acta Pharmacol Sin 2002; 23: 685–90.
29 Aley KO, Levine JD. Role of protein kinase A in the maintenance of inflammatory pain. J Neurosci 1999; 19: 2181–6.
30 Fang L, Wu J, Lin Q, Willis WD. Calcium-calmodulin-dependent protein kinase II contributes to spinal cord central sensitization. J Neurosci 2002; 22: 4196–204.
31 Zimmermann M. Pathobiology of neuropathic pain. Eur J Pharmacol 2001; 429: 23–37.
32 Hu HJ, Glauner KS, Gereau IV RW. ERK integrates PKA and PKC signaling in superficial dorsal horn neurons. I. Modulation of A-type K^+ currents. J Neurophysiol 2003; 90: 1671–9.
33 Hu HJ, Gereau IV RW. ERK integrates PKA and PKC signaling in superficial dorsal horn neurons. II. Modulation of neuronal excitability. J Neurophysiol 2003; 90: 1680–8.
34 Adams JP, Anderson AE, Varga AW, Deneley KT, Cook RG, Pfaffinger PJ, *et al*. The A-type potassium channel KV4.2 is a substrate for the mitogen-activated protein kinase ERK. J Neurochem 2000; 75: 2277–87.
35 Lewin MR, Walters ET. Cyclic GMP pathway is critical for inducing long-term sensitization of nociceptive sensory neurons. Nat Neurosci 1999: 2: 18–23.
36 Miletic G, Pankratz MT, Miletic V. Increases in the phosphorylation of cyclic AMP response element binding protein (CREB) and decreases in the content of calcineurin accompany thermal hyperalgesia following chronic constriction injury in rats. Pain 2002; 99: 493–500.
37 White DM, Walker S, Brenneman DE, Gozes I. CREB contributes to the increased neurite outgrowth of sensory neurons induced by vasoactive intestinal polypeptide and activity-dependent neurotrophic factor. Brain Res 2000; 868: 31–8.
38 Ji RR, Rupp F. Phosphorylation of transcription factor CREB in rat spinal cord after formalin-induced hyperalgesia: relationship to c-fos induction. J Neurosci 1997; 17: 1776–85.
39 Messersmith DJ, Kim DJ, Iadarola MJ. Transcription factor regulation of prodynorphin gene expression following rat hindpaw inflammation. Mol Brain Res 1998; 53: 260–9.
40 Solodkin A, Traub RJ, Gebhart GF. Unilateral hindpaw inflammation produces a bilateral increase in NADPH-diaphorase histochemical staining in the rat lumbar spinal cord. Neuroscience 1992; 51: 495–9.
41 Milligan ED, Twining C, Chacur M, Biedenkapp J, O'Connor K, Poole S, *et al*. Spinal glia and proinflammatory cytokines mediate mirror-image neuropathic pain in rats. J Neurosci 2003; 23: 1026–40.

Acta Pharmacologica Sinica 2005 Jul; 26 (7): 799–805

Full-length article

6-Hydroxydopamine-induced glutathione alteration occurs via glutathione enzyme system in primary cultured astrocytes[1]

Ji ZHANG, Jun HU, Jian-hua DING, Hong-hong YAO, Gang HU[2]

Department of Pharmacology, Nanjing Medical University, Nanjing 210029, China

Key words

6-hydroxydopamine; glutathione; oxidative stress; glutamate-cysteine ligase; gamma-glutamyltransferase

[1] Project supported by the National Natural Science Foundation of China (No 39970846).
[2] Correspondence to Prof Gang HU.
Phn 86-25-8686-3169.
Fax 86-25-8686-3108.
E-mail ghu@njmu.edu.cn

Received 2005-01-14
Accepted 2005-03-10

doi: 10.1111/j.1745-7254.2005.00124.x

Abstract

Aim: To define the role of enzymes involved in glutathione metabolism in 6-hydroxydopamine (6-OHDA)-induced glutathione alteration in primary cultured astrocytes. **Methods:** Total glutathione (GSx) levels were determined using the modified enzymatic microtiter plate assay. The mRNA levels of γ-glutamylcysteine synthetase (γGCS), γ-glutamyltransferase (γGT), glutathione peroxidase (GPx), GR (glutathione reductase), and glutathione transferases (GST) were determined using RT-PCR. γGT activity was determined using γGT assay kits. **Results:** In primary cultured astrocytes, 6-OHDA induced a significant elevation of cellular GSx levels after treatment for 24 h. However, the GSx levels decreased after 24 h and the values were even lower than the value in the control group without 6-OHDA at 48 h. RT-PCR data showed that the mRNA levels of γGCS, the rate-limiting enzyme of γ-*L*-glutamyl-*L*-cysteinylglycine (GSH) synthesis, were increased by 6-OHDA after treatment for 24 h and 48 h; the mRNA levels of GPx, GR, and GST did not alter in 6-OHDA-treated astrocytes after treatment for 24 h and 48 h; and 6-OHDA increased the mRNA levels and the activity of γGT after treatment for 48 h, which induced a decrease in GSx levels, despite the up-regulation of γGCS after exposure to 6-OHDA for 48 h. **Conclusion:** The change in γGCS correlated with the increase in GSH levels induced by 6-OHDA after treatment for 24 h. GSx levels decreased because of increased γGT mRNA levels and γGT activity induced by 6-OHDA after treatment for 48 h.

Introduction

Parkinson's disease is characterized by the selective demise of dopaminergic neurons. Recent findings in molecular genetics and neurochemistry have suggested that oxidative stress is possibly involved in the aging process and is one of the pathogenic mechanisms of Parkinson's disease[1].

6-Hydroxydopamine (6-OHDA) is one of the most common neurotoxins used to model nigral degeneration experimentally *in vitro* as well as *in vivo*. 6-OHDA, like dopamine (DA), is a substrate for monoamine oxidase (MAO). This enzymatic reaction gives rise to hydrogen peroxide[2]. Astrocytes are essential for the cellular defense against reactive oxygen species (ROS)[3], within which there is a high concentration of the tripeptide glutathione (GSH; γ-*L*-glutamyl-*L*-cysteinylglycine)[4].

Glutathione in astrocytes is very important for cellular defense against ROS. Alterations of the GSH metabolism in the brain have been implicated in oxidative stress and neurodegenerative diseases such as Parkinson's disease[5]. Sian *et al* found that GSH levels were reduced in substantia nigra in patients with Parkinson's disease (reduced by 40% compared with control subjects)[6]. This depletion in GSH may increase the susceptibility of brain cells to other harmful events, such as the reduction of mitochondrial energy production.

In addition to the GSH levels, alterations in the specific activities of enzymes involved in GSH metabolism and defense against ROS have been reported. They are[7]: (1) γ-glutamylcysteine synthetase (γGCS), the rate-limiting enzyme and the first enzyme used in GSH synthesis, which converts glutamate and cysteine to γ-glutamylcysteine. (2) The

ectoenzyme γGT (γ-glutamyltransferase), which converts GSH to cysteinylglycine (CysGly) and γ-glutamyl[8]. CysGly is a precursor for *de novo* GSH synthesis in both astrocytes and neurons[9]. Inhibition of γGT prevents the astroglia-induced effect on GSH levels in neurons[9]. (3) Glutathione peroxidase (GPx) and glutathione reductase (GR), which catalyze the SH/S-S exchange reactions and contribute to protein thiol protection. (4) Glutathione transferases (GST), which use GSH to detoxify peroxides and carbonyl-containing products of lipid peroxidation.

In the present study, we investigated the role of 6-OHDA in astroglial GSH metabolism, and the expression of glutathione-related enzymes, especially γGCS and γGT in primary cultured astrocytes induced by 6-OHDA.

Materials and methods

Materials Glutathione reductase, β-NADPH-Na_4, and 6-OHDA were obtained from Sigma (St Louis, MO, USA). Dulbecco's modified Eagle's medium (DMEM) was obtained from Gibco (Grand Island, NY, USA). γGT assay kits were purchased from Nanjing Jiancheng Biological Co (Nanjing, China). All PCR primers were purchased from Sangon (Shanghai, China). All reagents for RT-PCR were purchased from Promag (Madison, WI, USA). All other chemicals were obtained from standard commercial sources.

Cell culture Astrocyte-rich primary cultures obtained from the whole brains of neonatal Sprague-Dawley rats were prepared and maintained as described previously[10]. Briefly, the cortex was incubated in 0.125% trypsin at 37 °C for 8 min and mechanically disrupted by passing the tissue through nylon mesh. After centrifugation (1500×*g*, 5 min), the cell pellet was gently resuspended in a small volume of tissue growth medium (DMEM containing 10% fetal bovine serum, 100 kU/L penicillin and 100 mg/L streptomycin) and plated in the same medium at a density of 1×10^7 cells/L in 12-well plates precoated with poly-lysine for the GSH assay.

GSx assay GSH was assayed as total glutathione (GSx), which was the sum of the reduced and oxidized forms [GSH+2×glutathione disulfide (GSSG)] by a modified enzymatic recycling method of Tietze[11]. Cells were washed in PBS, dissolved in 200 μL PBS buffer (0.05 mmol/L edetic acid; 0.05% Triton-X 100, pH 8.0), and centrifuged to remove protein. According to the Bradford method[12], we used a volume of 50 μL of supernatant for assessing protein by using bovine serum albumin as a standard. A volume of 100 μL of supernatant was neutralized with 50 μL of a 5% (w/v) salicylsalicylic acid (SSA) solution. The solution was centrifuged, then the GSH content was determined after the addition of 4 μL 10 mmol/L β-NADPH, 3 μL 10 mmol/L 5, 5'-dithio-*bis*-2-nitrobenzoic acid (DTNB), 2 kU/L GSH reductase. The GSH content was determined by kinetic measurement of the absorbance changes at 412 nm for 5 min and calculated by comparison with standards.

RNA preparation and semiquantitative RT-PCR Semiquantitative RT-PCR with β-actin as an internal control was performed to examine the expression of messenger RNA for the γGCS, γGT, and other GSH enzymes in glial-rich primary cultures. Total RNA (2 μg) from primary cultured astrocytes was reverse transcribed into single-stranded cDNA in a 20-μL reaction mixture containing: 10 mmol/L dNTP, 1 μg oligo (dT) primer, 20 IU RNasin and 200 IU M-MLV reverse transcriptase. The mixture was incubated at 42 °C for 1 h and then the reverse transcriptase was inactivated by heating the reaction mixture to 95 °C for 10 min. PCR amplification was carried out with 1.5 μL cDNA product in a 30 μL reaction volume containing 3 pmol of each specific oligonucleotide primer, 10 mmol/L dNTP, and 1.5 IU *Taq* DNA polymerase. For all of the reactions, preliminary experiments were performed to determine the number of PCR cycles at which saturation occurred, and the experiments mentioned were carried out with a number of cycles that precedes saturation. The sequences of the primers, product size, and optimized number of PCR cycles for GSH-related enzymes and β-actin expression analyses were: (1) γGCS, forward primer: 5'-AGACACGGCATCCTCCAGTT-3'; reverse primer: 5'-CTGACACGTAGCCTCGGTAA-3' (GenBank accession no: NM_012815; product size: 801 bp). The thermal cycler unit was programmed for 30 cycles at 95 °C for 1 min, 60 °C for 1 min, then 72 °C for 1 min. (2) γGT: we used nested RT-PCR for γGT, in which the reverse transcriptase reaction and two sequential PCR procedures were carried out. The first-round primer pairs were designed from the target mRNA, and the second-round primers were designed from the first-round amplified PCR products. Forward and reverse primers were selected from the coding domain to identify any γGT mRNA nonselectively; the first-round primers were 5'-GCTTTGTGCGAGGTGTTCTG-3' and 5'-CCATCGTCTGGAAGGTAGA-3'; the second-round primers were 5'-CTCAGCGGGCCCGTGCTG-3' and 5'-GGCGGTTGGGTGAGTGGT-3', in the primary and the secondary PCR reactions, respectively (GenBank accession no: BC078768; product size: 261 bp). The thermal cycler unit was programmed for 30 cycles at 95 °C for 1 min, 55 °C for 1 min, and 72 °C for 1.5 min. (3) GPx, forward primer: 5'-GTATGTCTGCTGCTCGGCTCTC-3'; reverse primer: 5'-AAATGATGTACTTGGGGTCGGTC-3' (GenBank accession no: NM_030826; product size: 450 bp). The thermal cycler unit was programmed for 26 cycles at 94 °C for 45 s, 61 °C for

45 s, and 72 °C for 45 s. (4) GR, forward primer: 5'-ACGAGGAAGACGAAATGCGTGATG-3'; reverse primer: 5'-AGGATGAATGGCGACCCTATTGTC-3' (GenBank accession no: U73174; product size: 171 bp). The thermal cycler unit was programmed for 24 cycles at 94 °C for 1 min, 56 °C for 1 min, and 72 °C for 1 min. (5) GST, forward primer: 5'- CCAAATTGAGAATTCCACAGCGC-3'; reverse primer: 5'- TGCCTGCAGGATCCAATGTGGA-3' (GenBank accession no: NM_017014; product size: 205 bp). The thermal cycler unit was programmed for 22 cycles at 95 °C for 30 s, 63 °C for 45 s, and 72 °C for 30 s. (6) β-actin, forward primer: 5'-CACGATGGAGGGGCCGGACTCATC-3'; reverse primer: 5'-TAAAGACCTCTATGCCAACACAGT-3' (GenBank accession no: NM_031144; product size: 240 bp). The thermal cycler unit was programmed for 24 cycles at 94 °C for 30 s, 61 °C for 30 s, and 72 °C for 30 s. PCR products were separated by electrophoresis on a 2% agarose gel and visualized after ethidium bromide staining over UV light.

Determination of γGT activity After removal of the medium, cells were washed twice with 4 mL ice-cold PBS [10 mmol/L potassium phosphate buffer containing 150 mmol/L NaCl (pH 7.4)] and were lysed by incubation with 500 μL 20 mmol/L potassium phosphate buffer (pH 7.0) containing 0.2 mmol/L edetic acid for 10 min on ice. The cell lysates were scraped off the flask and transferred to Eppendorf tubes. After centrifugation (15 000×*g*, 5 min, 4 °C), the supernatant was discarded and the pellets were resuspended in 100 μL of 20 mmol/L potassium phosphate buffer (pH 7.0) containing 200 μmol/L edetic acid and 1% (w/v) Triton X-100. During 20-min incubation on ice the lysates were resuspended several times. After centrifugation (15 000×*g*, 5 min, 4 °C) the activity of γGT was measured in 50 μL aliquots of the supernatants according to the method described by Meister *et al*[8]. The samples were determined by γGT assay kits from the Nanjing Jiancheng Biological Co. The protein content of the cultured cells was determined using the Bradford method[12].

Data analysis All values were presented as mean±SD. The *t*-test was used for comparisons and differences were considered significant if $P<0.05$.

Results

Effect of 6-OHDA on endogenous GSx contents in astrocytes To elucidate the relationship between endogenous GSx and 6-OHDA-induced cell damage, we measured the GSx content of astrocytes. The GSx concentration increased from 14.62 μmol·g^{-1}·protein to 24.02 μmol·g^{-1} protein after incubation of the astrocytes with 6-OHDA for 24 h (Figure 1) and decreased to 10.35 μmol·g^{-1} protein after exposure to 6-OHDA for 48 h (Figure 1). The GSx content further reduced to 20% of control levels when cells were incubated with 0.13 mmol/L 6-OHDA for 48 h (Figure 1).

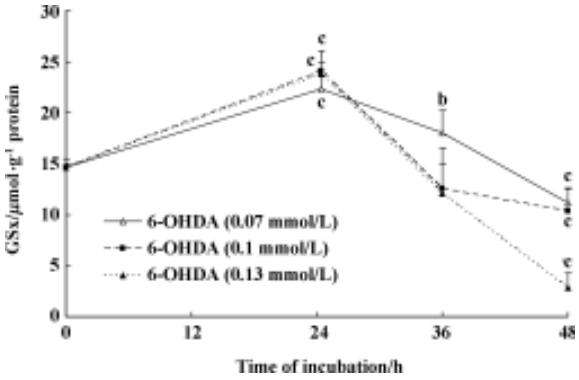

Figure 1. Effect of 6-OHDA on GSx production over time in primary astrocytes. n=6. Mean±SD. $^bP<0.05$, $^cP<0.01$ *vs* the corresponding value at 0 h.

Effect of 6-OHDA on glutathione enzyme expression in astrocytes To further address whether the 6-OHDA had an effect on glutathione enzymes, we detected the mRNA expression of glutathione enzymes. In this study, all RT-PCR data were normalized relative to levels of β-actin mRNA. Astrocytes were exposed to 6-OHDA for 24 h or 48 h. We found that the levels of cellular GSx and γGCS mRNA were increased after the cells were incubated with 6-OHDA for 24 h; however, the levels of cellular GSx decreased markedly, whereas γGCS mRNA expression increased again after exposure for 48 h (Figure 2). However, 6-OHDA failed to alter the levels of GPx, GR, and GST mRNA, after exposure for both 24 h and 48 h (Figure 3). The levels of γGT mRNA expression in astrocytes were up-regulated after exposure to 6-OHDA for 48 h, but not for 24 h (Figure 4).

Measurement of γGT activity in astrocytes Specific γGT activity was measured in astrocytes in the presence and absence of 6-OHDA. We treated astrocytes with 100 μmol/L 6-OHDA for 24 h or 48 h. γGT activity did not alter after treatment with 6-OHDA for 24 h, but it increased significantly from an initial value of 0.08 kU·g^{-1} protein to a plateau value of 0.17 kU·g^{-1} protein after exposure to 6-OHDA for 48 h. The increase in γGT activity in astrocytes correlated well with the levels of γGT mRNA expression in cells (Figure 5).

Discussion

A high intracellular concentration of glutathione protects against a variety of different ROS. GSH reacts directly with

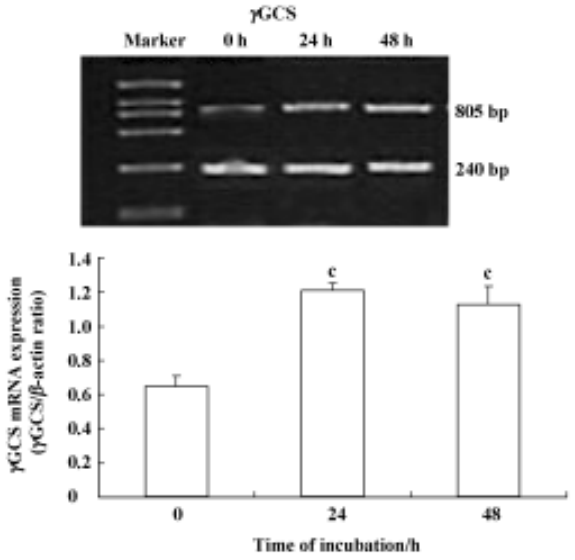

Figure 2. Effects of 6-OHDA (0.1 mmol/L) on γGCS mRNA expression in astrocytes. The top panel shows the results of RT-PCR, which demonstrates the effect of 6-OHDA on γGCS mRNA levels (805 bp). The bottom panel shows the mRNA levels of β-actin (240 bp). DNA markers: 2000, 1000, 750, 500, 250, 100 bp. n=3. Mean±SD. $^cP<0.01$ *vs* the value at 0 h.

radicals in nonenzymatic reactions. It should be noted that GSx, including GSH and GSSG, is very important for cellular defense against ROS. Glutathione levels in the substantia nigra pars compacta of patients with Parkinson's disease is significantly reduced, but the levels do not change in patients with multiple system atrophy or progressive supranuclear palsy[13]. It has been found that oxidative stress might originate in astrocytes rather than in neurons. Astrocytes surrounding dopaminergic neurons in the brain may be involved in the selective vulnerability of these neurons by scavenging ROS and releasing CysGly by using γGT, and CysGly is the precursor for GSH synthesis in neurons. Hence, astrocyte function is an important contributor to the pathogenesis of Parkinson's disease.

6-OHDA is known to cause oxidative stress to DA neurons, and it is usually thought to cross cell membrane through dopamine transporters, to inhibit mitochondrial respiration and to generate intracellular ROS[14]. A previous study has shown that in 6-OHDA-treated rats, the decreased levels of GSH could be due to an increased level of free radical-generated lipid peroxidation[15].

To investigate the relationship between glutathione and 6-OHDA-induced cell damage, we measured the GSx content of cells by using the enzymatic recycling method with some modifications[11]. We found that in primary cultured astrocytes, the cytosolic GSx content increased in response

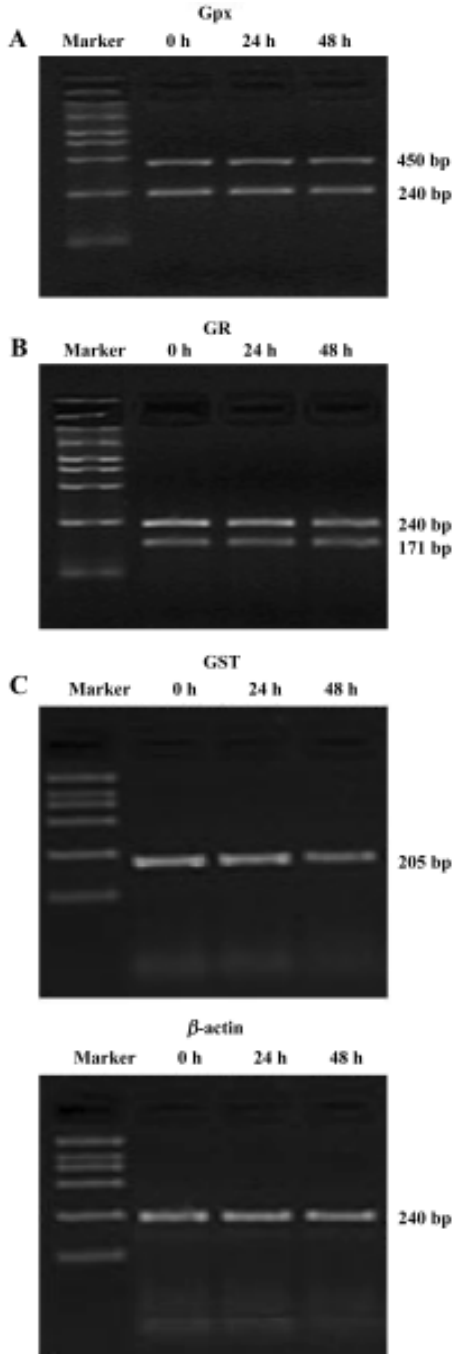

Figure 3. Effects of 6-OHDA 0.1 mmol/L on GPx, GR, and GST mRNA expression in astrocytes. (A) The top panel shows the results of RT-PCR, demonstrating the effect of 6-OHDA on GPx (450 bp); the bottom panel shows the mRNA levels of β-actin (240 bp). (B) The bottom panel shows the results of RT-PCR, demonstrating the effect of 6-OHDA on GR (171 bp); the top panel shows the mRNA levels of β-actin (240 bp). (C) The upper panel shows the results of RT-PCR, demonstrating the effects of 6-OHDA on GST (205 bp); the bottom panel shows the mRNA levels of β-actin (240 bp). DNA markers: 2000, 1000, 750, 500, 250, 100 bp.

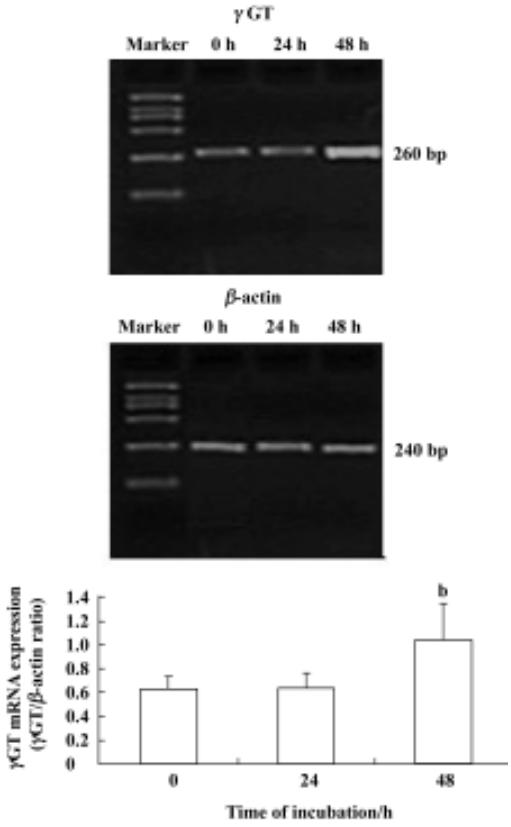

Figure 4. Effects of 6-OHDA 0.1 mmol/L on γGT mRNA expression in astrocytes. The top panel shows the results of RT-PCR, demonstrating the effects of 6-OHDA on γGT mRNA levels (260 bp). The bottom panel shows the mRNA levels of β-actin (240 bp). DNA markers: 2000, 1000, 750, 500, 250, 100 bp. n=4. Mean±SD. ^bP<0.05 *vs* the value at 0 h.

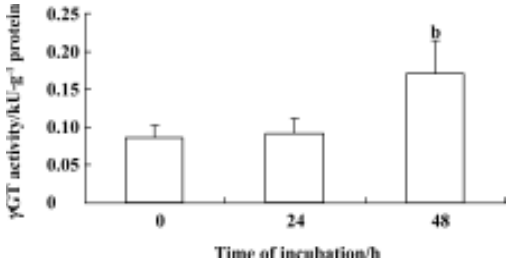

Figure 5. Activity of γGT following 48-h exposure to 6-OHDA 0.1 mmol/L in primary cultured astrocytes. n=4. Mean±SD. ^bP<0.05 *vs* the value at 0 h.

to treatment with different concentrations of 6-OHDA (0.07, 0.1, and 0.13 mmol/L) after incubation for 24 h, but decreased significantly after incubation for 48 h (Figure 1). The data presented here are consistent with the previous findings that treatment with 6-OHDA for 24 h induced up-regulation of GSx levels in astrocytes[15]. Shimizu *et al* also found a delayed increase in GSH levels after the addition of 6-OHDA in human neuroblastoma SK-N-SH cells[16]. However, the mechanism by which GSx fluctuates in primary culture astrocytes in response to 6-OHDA is not clear. Some investigators have suggested that in the primary astrocytes, 6-OHDA toxicity may not result from the inhibition of mitochondrial respiration, but may be secondary to auto-oxidation and ROS generation[17].

More importantly, our results showed that the mRNA expression of γGCS was up-regulated significantly after incubation of the astrocytes with 6-OHDA for 24 h, which correlated well with the alteration of GSx in the presence of 6-OHDA in astrocytes (Figure 2). A previous study has shown that 6-OHDA induced an elevation of GSx contents in astrocyte cells because of an increase of the expression of γGCS mRNA[16]. It is well known that γGCS is the first and the rate-limiting enzyme in the synthesis of GSH. Induction of γGCS by oxidative stress could play a key role in determining cellular glutathione content[16]. Recent studies have demonstrated that the antioxidant response element (ARE), a cis-acting enhancer sequence, mediates the transcriptional activation of genes in cells exposed to oxidative stress. The 5'-flanking region of the γGCS gene also contains several transcription binding sites, including the ARE[18,19]. These findings support the idea that transcriptional regulation of the γGCS gene is involved in the antioxidant system of astrocyte cells. Hence, the increased γGCS levels in 6-OHDA-treated astrocytes may occur by activating ARE, and regulating the γGCS gene, thereby activating the antioxidative system including GSx. Therefore, the elevation of GSx in astrocytes appears to reflect the resistance and defense mechanisms of astrocytes in the brain against oxidative stress in the early stages. If the toxicity of 6-OHDA continues, massive production of ROS may contribute to the decline in GSx levels in cells.

However, our results showed that γGCS mRNA expression did not decrease after 48-h incubation with 6-OHDA (Figure 2). This finding was not consistent with the change in GSx in 6-OHDA-treated astrocytes. GSH redox-system genes play a key role in the control of the oxidation and reduction of the SH groups of proteins. For this reason, we detected the mRNA expression levels of other glutathione enzymes, including GPx, GR, GST, and γGT in astrocytes treated with 6-OHDA for 24 h and 48 h. Our finding that 6-OHDA failed to alter the mRNA levels of GPx, GR, and GST (Figure 3) confirmed the previous finding that the expression levels of GPx mRNA were not changed in astrocytes after paraquat exposure[20]. However, other studies have shown that GPx and GR expression increased after the expo-

sure of cultured astrocytes to H_2O_2. With regard to this experimental result, we believe that the different results may be related to differences in preparation techniques, to differences in experimental methods, or to differences in culture conditions.

For further investigation, we measured the activity of γGT in astrocytes treated with 6-OHDA for 24 h and 48 h. The increase in γGT activity after 6-OHDA treatment for 48 h (Figure 5) was consistent with the change in γGT mRNA levels. A previous study reported that the activities of enzymes involved in the glutathione cycle were normal with the exception of γGT, the activity of which was increased in Parkinson's disease[21]; this was a similar finding to our results. So we conclude that the increase in mRNA levels and the activity of γGT induced GSx loss after exposure to 6-OHDA for 48 h. The dipeptide CysGly, which is generated from extracellular GSH by a γGT reaction, may be the most important among the exogenous precursors of GSH, because it is efficiently utilized by neurons in micromolar concentrations. However, dipeptides could be hydrolyzed by neuronal ectopeptidase-generating amino acids such as cystein, glutamate, and glycine[22]. Many such amino acids possibly also have toxic effects on neurons[28].

It has been found that γGT activity increases in astroglial cultures treated with an nitric oxide donor for 24 h[23]. Ruedig *et al* suggested that TNFα synthesis in the brain also induced γGT expression in astrocytes[24]. Such a scenario can be considered for Parksinson's disease, where an elevated level of TNFα in the substantia nigra and increased immunoreactivity for TNFα in astrocytes[25] is accompanied by an elevated specific γGT activity[6]. Previous findings have shown that 6-OHDA can increase the generation of NO and TNFα in mesencephalic cells[26,27]. Thus, 6-OHDA may up-regulate γGT via the activation of the NO or TNFα signaling pathway followed by GSH loss. Increased intracellular GSH content and γGT activity in astrocytes exposed to 6-OHDA may help to protect neurons *in vitro* by supplying more GSH precursors, and thus elevating neuronal GSH levels.

In the present study, we found that glutathione played an important role in mediating 6-OHDA-induced cell damage in a Parkinson's disease model. We also found that an increase in γGCS, the rate-limiting enzyme in GSH synthesis, correlated with an increase in GSx after exposure of the cells to 6-OHDA for 24 h. Interestingly, GSx levels decreased because of increased γGT mRNA levels and γGT activity, despite up-regulated γGCS mRNA levels after 48-h incubation with 6-OHDA. The findings in this study may provide useful information for identifying new therapeutic targets for neurodegenerative diseases such as Parkinson's disease.

References

1 Jenner P. Oxidative stress in Parkinson's disease. Ann Neurol 2003; 53: S26–S38.

2 Blum D, Torch S, Lambeng N, Nissou M, Benabid AL, Sadoul R, *et al*. Molecular pathways involved in the neurotoxicity of 6-OHDA, dopamine and MPTP: contribution to the apoptotic theory in Parkinson's disease. Prog Neurobiol 2001; 65: 135–72.

3 Cooper AJL. Role of astrocytes in maintaining cerebral glutathione homeostasis and in protecting the brain against xenobiotics and oxidative stress. In: Shaw CA, editor. The role of glutathione in the nervous system. Washington: Taylor and Francis; 1998. p 91–115.

4 Halliwell B, Gutteridge JMC. Free radicals in biology and medicine. New York: Oxford University Press; 1999.

5 Bains JS, Shaw CA. Neurodegenerative disorders in humans: the role of glutathione in oxidative stress-mediated neuronal death. Brain Res Rev 1997; 25: 335–58.

6 Sian J, Dexter DT, Lees AJ, Daniel S, Agid Y, Javoy-Agid F, *et al*. Alteration in glutathione levels in Parkinson's disease and other neurodegenerative disorders affecting basal ganglia. Ann Neurol 1994; 36: 348–55.

7 Aksenov MY, Markesbery WR. Changes in thiol content and expression of glutathione redox system genes in the hippocampus and cerebellum in Alzheimer's disease. Neurosci Lett 2001; 302: 141–5.

8 Anderson ME, Meister A. Transport and direct utilization of γ-glutamylcyst(e)ine for glutathione synthesis. Proc Natl Acad Sci USA 1983; 80: 707–11.

9 Dringen R, Kranich O, Hamprecht B. The 7-glutamyl transpeptidase inhibitor acivicin preserves glutathione released by astroglial cells in culture neurochemical research. Neurochem Res 1997; 22: 727–33.

10 Hamprecht B, Loffler F. Primary glial cultures as a model for studying hormone action. Methods Enzymol 1985; 109: 341–5.

11 Tietze F. Enzymic method for quantitative determination of nanogram amounts of total and oxidized glutathione: applications to mammalian blood and other tissues. Anal Biochem 1969; 27: 502–22.

12 Kruger NJ. The Bradford method for protein quantitation. Methods Mol Biol 1994; 32: 9–15.

13 Uitti RJ, Calne DB. Pathogenesis of idiopathic Parkinsonism. Eur Neurol 1993; 33 (Suppl l): 6–23.

14 Dringen R. Metabolism and functions of glutathione in brain. Prog Neurobiol 2000; 62: 649–71.

15 Iwata-Ichikawa E, Kondo Y, Miyazaki I, Asanuma M, Ogawa N. Glial cells protect neurons against oxidative stress via transcriptional up-regulation of the glutathione synthesis. J Neurochem 1999; 72: 2334–44.

16 Shimizu E, Hashimoto K, Komatsu N, Iyo M. Roles of endogenous glutathione levels on 6-hydroxydopamine induced apoptotic neuronal cell death in human neuroblastoma SK-N-SH cells. Neuropharmacology 2002; 43: 434–43.

17 Sagara J, Miura K, Bannai S. Cysteine uptake and glutathione level in fetal brain cells in primary culture and in suspension. J Neurochem 1993; 61: 1667–71.

18 Nguyen T, Sherratt PJ, Pickett CB. Regulatory mechanisms

controlling gene expression mediated by the antioxidant response element. Annu Rev Phamacol Toxicol 2003; 43: 233–60.
19 Mulcahy RT, Gipp JJ. Identification of a putative antioxidant response element in the 5'-flanking region of the human gamma-glutamylcysteine synthetase heavy subunit gene. Biochem Biophys Res Commun 1995; 209: 227–33.
20 Schmuck G, Rohrdanz E, Tran-Thi QH, Kahl R, Schluter G. Oxidative stress in rat cortical neurons and astrocytes induced by paraquat *in vitro*. Neurotox Res 2002; 4: 1–13.
21 Owen AD, Schapira AH, Jenner P, Marsden CD. Oxidative stress and Parkinson's disease. Ann NY Acad Sci 1996; 786: 217–23.
22 Dringen R, Pfeiffer B, Hamprecht B. Synthesis of the antioxidant glutathione in neurons: supply by astrocytes of CysGly as precursor for neuronal glutathione. J Neurosci 1999; 19: 562-69.
23 Gegg ME, Beltran B, Salas-Pino S, Bolanos JP, Clark JB, Moncada S, *et al*. Differential effect of nitric oxide on glutathione metabolism and mitochondrial function in astrocytes and neurones: implications for neuroprotection/neurodegeneration. J Neurochem 2003; 86: 228–37.
24 Ruedig C, Dringen R. TNFα increases the activity of γ-glutamyl transpeptidase in cultured rat astroglial cells. J Neurosci Res 2004; 75: 536–43.
25 Boka G, Anglade P, Wallach D, Javoy-Agid F, Agid Y, Hirsch EC. Immunocytochemical analysis of tumor necrosis factor and its receptors in Parkinson's disease. Neurosci Lett 1994; 172: 151–54.
26 Nobre HV Jr, Cunha GM, Maia FD, Oliveira RA, Moraes MO, Rao VS. Catechin attenuates 6-hydroxydopamine (6-OHDA)-induced cell death in primary cultures of mesencephalic cells. Comp Biochem Physiol C Toxicol Pharmacol 2003; 136: 175–80.
27 Mogi M, Togari A, Tanaka K, Ogawa N, Ichinose H, Nagatsu T. Increase in level of tumor necrosis factor (TNF)-alpha in 6-hydroxydopamine-lesioned striatum in rats without influence of systemic *L*-DOPA on the TNF-alpha induction. Neurosci Lett 1999; 268: 101–4.
28 Puka-Sundvall M, Eriksson P, Nilsson M, Sandberg M, Lehmann A. Neurotoxicity of cysteine: interaction with glutamate. Brain Res 1995; 705: 65–70.

Acta Pharmacologica Sinica 2005 Jul; 26 (7): 806–812

Full-length article

Phosphorylated heat shock protein 27 is involved in enhanced heart tolerance to ischemia in short-term type 1 diabetic rats[1]

Hong CHEN[2,4,5], Xing-jun WU[2], Xi-yuan LU[3], Liang ZHU[2], Li-ping WANG[2], Huang-tian YANG[3], Hong-zhuan CHEN[2,6], Wen-jun YUAN[4,6]

[2]Department of Pharmacology, Shanghai Second Medical University, Shanghai 200025; [3]Laboratory of Molecular Cardiology, Health Science Center, Shanghai Second Medical University, Shanghai Institute for Biological Sciences, Chinese Academy of Sciences, Shanghai 200025; [4]Department of Physiology, Second Military Medical University, Shanghai 200433, China

Key words

type 1 diabetes mellitus; ischemia; reperfusion; heart; heat shock proteins

[1] Project supported by Major State Basic Research Development Program of China (Grant No G2000056905).
[5] Now in *Department of Pharmacology at Shanghai Second Medical University, Shanghai 200025, China*.
[6] Correspondence to Prof Hong-zhuan CHEN and Wen-jun YUAN.
Phn 86-21-6384-6590, ext 776449.
Fax 86-21-6467-1610.
E-mail hchen100@hotmail.com

Received 2005-02-03
Accepted 2005-02-24

doi: 10.1111/j.1745-7254.2005.00113.x

Abstract

Aim: To examine the tolerance of type 1 diabetic hearts to ischemia and reperfusion injury. Myocardial contents of 27-kDa and 70-kDa heat shock proteins (hsp) as well as phosphorylated hsp27 were also determined. **Methods:** Hearts from hyperglycemic rats 3 weeks after streptozocin injection and age-matched normal rats were subjected to ischemia and reperfusion *in vitro*. Cardiac function and electrocardiogram were recorded throughout experiments. Myocardial heat shock proteins were detected with Western blot. **Results:** Despite depressed systolic function at the baseline, diabetic hearts exhibited considerable enhancement in post-ischemic heart function, manifested by an increase in the maximal rate of left ventricular pressure rise and fall (post-ischemic dp/dt_{max} and dp/dt_{min} were 560±117 and -313±68 mmHg/s in control, n=7, 1249±57 and -1204±36 mmHg/s in diabetes, n=10, P<0.01). Reperfusion ventricular fibrillation in the diabetic group were attenuated compared with controls (1.5±0.3 *vs* 7.2±2.1 min in control, P<0.01). The increased heart resistance to ischemia in diabetes was associated with hyperglycemia and accompanied by enhanced expression of myocardial phosphorylated hsp27 with normal aortic vessel relaxation. Cardioprotection was abrogated by metabolic correction with insulin and accompanied by phospho-hsp27 reduction. **Conclusion:** Heart resistance to ischemia is increased in type 1 diabetes, and hyperglycemia may present a mild yet stressful stimulus leading to upregulation of endogenous stress protein, which may play a potential role in cardioprotection and compensate for detrimental effects of hyperglycemia in diabetes.

Introduction

It is well known that cardiovascular disease is the major cause of morbidity and mortality in diabetic patients. However, there exists considerable debate over the causal relationship between diabetes *per se* and cardiovascular disease[1]. Unlike classical microvascular complications, large vessel atherosclerosis is not correlated with duration and severity of hyperglycemia[2,3]. Some studies demonstrate that cardiovascular disease prevalence remains constant despite different levels of glycohemoglobin. Furthermore, intensive control of hyperglycemia is not consistently effective in reducing cardiovascular complications[4], leaving unanswered the question of whether hyperglycemia contributes to cardiovascular disease in diabetes.

In addition to clinical debates, experimental studies also show inconsistent results regarding the role of hyperglycemia in myocardial ischemia. Studies of animals with type 1 diabetes demonstrate either increased or decreased sensitivity of diabetic hearts to ischemia[5–7]. Suggested mechanisms for decreased sensitivity include attenuated Na^+-H^+ exchanger activity, inhibited glycolysis, and reduced Ca^{2+} overload during reperfusion[7–9]. Studies demonstrating the detrimental effects of hyperglycemia on ischemia suggest

roles of pseudohypoxia and reactive oxygen species[6]. Regardless of whether hyperglycemia is the cause of increased cardiovascular disease, it is generally agreed that experimental type 2 diabetes has a detrimental effect on myocardial ischemia[10] and coexisting cardiovascular risk factors like hypertension and elevated cholesterol contribute significantly to the poor outcome in type 2 diabetes as seen in clinical settings[11,12]. Type 1 diabetes, however, has severe hyperglycemia and relatively less coexisting cardiovascular disease. Thus, type 1 diabetic animals provide good models for investigating hyperglycemia influence on ischemic outcomes.

The present study was designed to observe heart sensitivity to ischemia in type 1 diabetic rats using functional recovery and creatine phosphokinase as measures of ischemic injury, in addition to arrhythmias. Aortic vessel function was also examined to test whether there was functional impairment of large vessels. As circulating antibody titers to some of heat shock proteins family are increased in type 1 diabetic patients[13], we observed whether these powerful protective proteins were upregulated in diabetic hearts. Our data indicate that type 1 diabetic hearts are resistant to ischemia/reperfusion with no obvious impairment of large vessel relaxation. The study also reveals increased expression of myocardial phosphorylated heat shock protein 27 (phospho-hsp27) in diabetes. To further examine the association of hyperglycemia and heat shock proteins with heart sensitivity to ischemia, we observed the effects of insulin treatment on ischemic outcomes and phospho-hsp27 by the correction of hyperglycemia.

Materials and methods

Animals Male Sprague-Dawley rats (originally weighing 200–220 g) were injected intraperitoneally with 60 mg/kg of streptozocin (Sigma, St Louis, USA) in citrate buffer (pH 4.5). Age-matched control rats received an injection of citrate buffer. The onset of diabetes was confirmed by measuring blood glucose within 72 h after injection. Rats had free access to tap water and standard laboratory chow and were maintained until the *in vitro* experiment began after 3 weeks of hyperglycemia induction. Another experiment was carried out with one group of rats treated with subcutaneous injection of protamine zinc insulin (9 units/kg) 3 weeks after diabetes induction and a heart ischemia experiment was carried out after 2 d of complete correction of hyperglycemia (duration of insulin administration was 5.1±0.7 d). All experiments conformed to the Guide for the Care and Use of Laboratory Animals (NIH Publication No 85–23, revised 1996).

Isolated heart preparation and ischemia/reperfusion The hearts were excised under anesthesia with sodium pentobarbital 60 mg/kg, ip, and perfused retrogradely (Langendorff apparatus, IPH-W2, Labo Support, Osaka, Japan) through the aorta with Krebs-Henseleit buffer (KHB) containing: NaCl 118.0 mmol/L, KCl 4.7 mmol/L, $CaCl_2$ 2.5 mmol/L, $MgSO_4$ 1.2 mmol/L, KH_2PO_4 1.2 mmol/L, $NaHCO_3$ 25.0 mmol/L, glucose 11.0 mmol/L, Na_2-EDTA 0.5 mmol/L. After cannulation of the left atrium the hearts were switched to antegrade perfusion (working heart). Perfusate was kept at 37 ºC and bubbled with 95% O_2 and 5% CO_2. Aortic perfusion pressure was set at 60 mmHg and the left atrium at 10 mmHg at the beginning of each experiment. All hearts were allowed to beat spontaneously.

With a catheter inserted into the left ventricular cavity, left ventricular pressure (LVP), left ventricular end-diastolic pressure (LVEDP) and maximal rate of LVP rise (dp/dt_{max}) and fall (dp/dt_{min}) were recorded with a data acquisition system (MPA 2000, Alcott Biotech, Shanghai, China). The hearts were subjected to 30-min global ischemia by clamping both atrial inflow and aortic outflow and followed by 40 min of reperfusion.

Two silver electrodes were inserted into the myocardium and electrocardiogram was recorded continuously. Premature ventricular beats, ventricular tachycardia and fibrillation during reperfusion were recorded. The severity of arrhythmias was scored on a 0 to 9 scale[14]. The time from the cessation of perfusion to the cessation of heart contraction was recorded as time to arrest.

Creatine phosphokinase and norepinephrine assay Creatine phosphokinase (CPK) was measured in coronary effluent with assay kits (Jian-Cheng Biomedical Engineering, Nanjing, China) according to the manufacturer's protocols. Coronary norepinephrine was determined with high performance liquid chromatography coupled with electrochemical detection (Neurochem Model 5500, ESA, Bedford, MA, USA).

Vessel tension recording Aortic rings were suspended in an organ bath (PowerLab ML0140, ADInstruments, Castle Hill, NSW, Australia) containing KHB. The buffer was bubbled with 95% O_2 and 5% CO_2 and kept at 37 ºC. Aortic rings were allowed to equilibrate for 90 min before tension recording. After precontraction with 1×10^{-7} mol/L of norepinephrine, acetylcholine (ACh) was added in a cumulative manner and aorta relaxation was recorded. Vasodilation in the presence of nitric oxide synthase inhibitor, N^{ω}-nitro-*L*-arginine methyl ester (*L*-NAME, 1×10^{-4} mol/L) was also measured.

Western blot analysis Left ventricles before and after ischemia were freeze-clamped and homogenized in lysis buffer (pH 7.4) containing: Tris/HCl 50 mmol/L, sucrose 150 mmol/L,

edetic acid-Na_2 5 mmol/L, egtazic acid 2 mmol/L, Na_3VO_4 1 mmol/L, NaF 50 mmol/L, phenylmethanesulfonyl fluoride 0.1 mmol/L, leupeptin 1 mg/L. Protein samples were loaded onto 12% SDS-PAGE acrylamide gels and transferred to polyvinylidene difluoride membrane. Blots were incubated with antibodies to either hsp27 or phosphorylated hsp27 at serine 15 and inducible hsp70 (Santa Cruz, Santa Cruz, CA, USA). The immunoreactive bands were visualized using enhanced chemiluminescence detection, and relative levels of heat shock proteins were semiquantified with densitometry (QuantityOne software, Bio-Rad, Hercues, CA, USA) normalizing to actin band.

Statistical analysis Data were expressed as mean±SEM. Parameters were compared with analysis of variance (ANOVA) for repeated measures followed by Student-Newman-Keuls test. The relationship between blood glucose level and ischemic outcomes (arrhythmia score and time to arrest) was evaluated with multiple regression analysis. $P<0.05$ was considered statistically significant.

Results

Effects of diabetes on baseline and post-ischemic heart function A significant elevation in blood glucose was accompanied by a reduction in contractility of the diabetic heart, represented by lower dp/dt_{max} and lower heart work (lower left ventricular developed pressure, LVDP; the difference between LVP and LVEDP). Diabetic hearts also exhibited reduced heart rate and normal LVEDP at baseline perfusion (Table 1).

Although depressed at the baseline, post-ischemic recovery of dp/dt_{max}, dp/dt_{min} and LVDP in diabetic hearts was enhanced significantly as compared with controls (Table 1). Coronary perfusion and cardiac output also recovered to better levels after ischemia in diabetes (Table 1). Reperfusion arrhythmias, cardiac CPK release, as well as cardiac norepinephrine release, were reduced in diabetic hearts (Table 2).

Table 2. Duration of arrhythmias, cardiac CPK and norepinephrine released from streptozocin-induced diabetic rat hearts underwent ischemia and reperfusion. Mean±SEM. $^bP<0.05$, $^cP<0.01$ *vs* control.

	Control (n=7)	Diabetes (n=10)
Duration of VT and VF/min	7.2±2.1	1.5±0.3^c
Coronary CPK/IU·g^{-1} wet weight	642±73	349±90^c
Coronary norepinephrine/ pmol·g^{-1} wet weight	258±44	121±37^b

VT and VF, ventricular tachycardia and fibrillation; CPK, creatine phosphokinase.

Ischemic outcome and correlation with blood glucose level Subgroups of mild or severe hyperglycemia (blood glucose <19 or >20 mmol/L) exhibited different post-ischemic outcomes (Figure 1A). Higher glucose within each group was accompanied by longer time to arrest and less arrhythmias (Figure 1B, 1C).

Aortic relaxation Normal vessel relaxation was found in the diabetic aorta (Figure 2), indicating no obvious impairment of large vessel function in this type of diabetic rat. The ACh-induced relaxation was abrogated by 1×10^{-4} mol/L

Table 1. Characteristics, basal and post-ischemic heart function of streptozocin-induced diabetic rats and age-matched control rats. n=7 in control group. n=10 in diabetes group. Mean±SEM. $^bP<0.05$, $^cP<0.01$ *vs* respective controls; $^eP<0.05$ *vs* values in diabetes group before I/R.

	Before I/R		After I/R	
	Control	Diabetes	Control	Diabetes
Body weight (g)	306±9	198±14^c	–	–
Blood glucose (mmol/L)	4.8±0.3	18.0±1.6^c	–	–
Heart rate (beat/min)	219±15	163±23^c	121±23	97±14^e
Coronary flow (mL·min^{-1}·g^{-1})	14.4±0.7	13.6±1.1	6.2±0.6	8.1±0.5^e
Cardiac output (mL·min^{-1}·g^{-1})	41.5±2.3	38.5±3.8	9.1±2.3	15.3±1.6^e
LVDP (mmHg)	96±2	85±4^b	38.7±11.2	64.3±5.4^e
LVEDP (mmHg)	8.2±2.0	9.5±1.1	21.4±2.1	16.5±1.8^e
dp/dt_{max} (mmHg/s)	2297±306	1603±117^b	560±117	1249±57^e
dp/dt_{min} (mmHg/s)	-1491±178	-1418±108	-313±68	-1204±36^e

I/R, ischemia/reperfusion; LVDP, left ventricular developed pressure; LVEDP, left ventricular end-diastolic pressure.

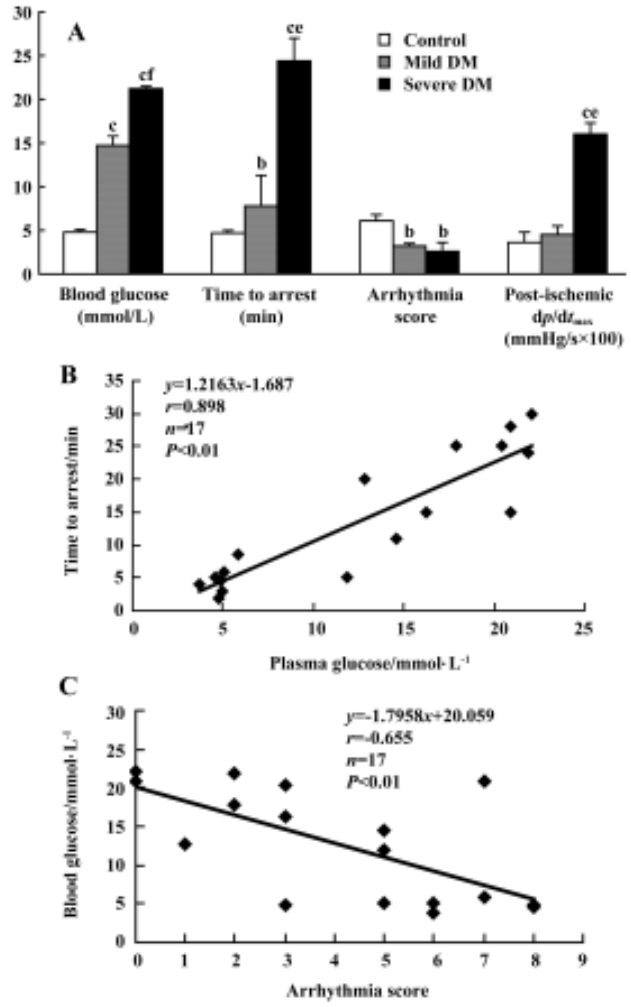

Figure 1. Stratification of hyperglycemia and its relationship with ischemic outcomes. Higher blood glucose was associated with longer time to arrest, and higher post-ischemic dp/dt_{max} for diabetic rats (A, n=5–7. Mean±SEM). Time to arrest was positively related to blood glucose levels *in vivo* (B) and arrhythmia score negatively related to glucose levels (C). Mild DM or severe DM, diabetic rats with blood glucose <19 or >20 mmol/L. ^{b}P<0.05, ^{c}P<0.01 *vs* age-matched controls; ^{e}P<0.05, ^{f}P<0.01 *vs* age-matched mild DM.

L-NAME to similar extents in 2 groups.

Myocardial expression of heat shock proteins There were no differences in basal amounts of total hsp27 or inducible hsp70 between diabetic and control groups (Figure 3A, 3B). Because the protective ability of hsp27 depends on its phosphorylation state, we also analyzed phosphorylated hsp27 in the myocardium. Phospho-hsp27 content was found to be significantly higher in diabetic hearts before (Figure 3C) and after ischemia (Figure 3D). To eliminate the possible role of streptozocin in inducing expression of phospho-

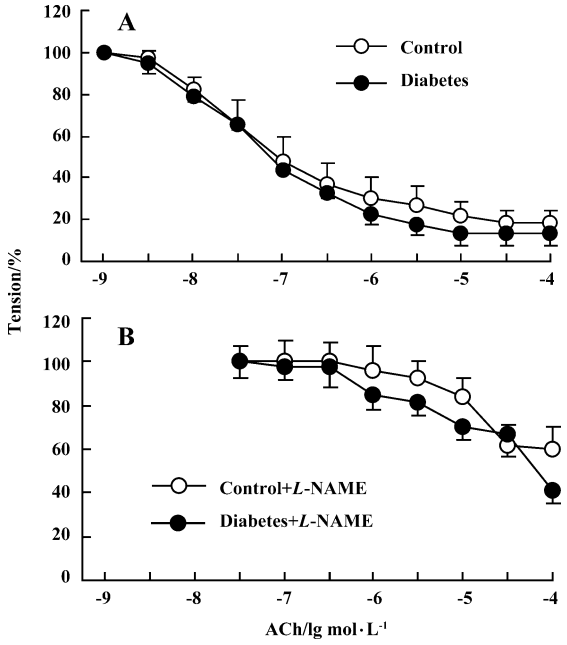

Figure 2. Aortic vasodilation in 3-week streptozocin-induced diabetic (DM) and age-matched control rats. There was no significant difference in aortic relaxation in response to acetylcholine (ACh) between diabetic and control rats (A). The vasodilation to ACh was partly abrogated by nitric oxide synthase inhibitor, N^{ω}-nitro-*L*-arginine methyl ester (*L*-NAME, 1×10^{-4} mol/L) to a similar extent in both groups (B). n=5. Mean±SEM.

hsp27, we also examined the content of phospho-hsp27 in rats that failed to develop diabetes after streptozocin injection (15 % of animals receiving streptozocin did not show significant elevation of blood glucose in this study and served as non-diabetic controls). There was no significant change of phospho-hsp27 in those animals (relative density values for myocardial phospho-hsp27 before ischemia were 5.4±0.9 in normal controls *vs* 6.2±1.0 in non-diabetic controls receiving streptozocin, n=4, P>0.05).

Ischemic outcomes after metabolic correction Further intervention experiments were carried out with complete correction of hyperglycemia for 2 d prior to the ischemia experiment (Figure 4A). Cardioprotection was abrogated in blood glucose-controlled diabetes, demonstrated by increased reperfusion arrhythmias (Figure 4B) and reduced post-ischemic dp/dt_{max} (Figure 4C). Abrogation of cardioprotection through metabolic control was accompanied by reduction of myocardial phospho-hsp27 (Figure 4D).

Discussion

The present study demonstrated significantly enhanced resistance to ischemia/reperfusion in type 1 diabetic hearts,

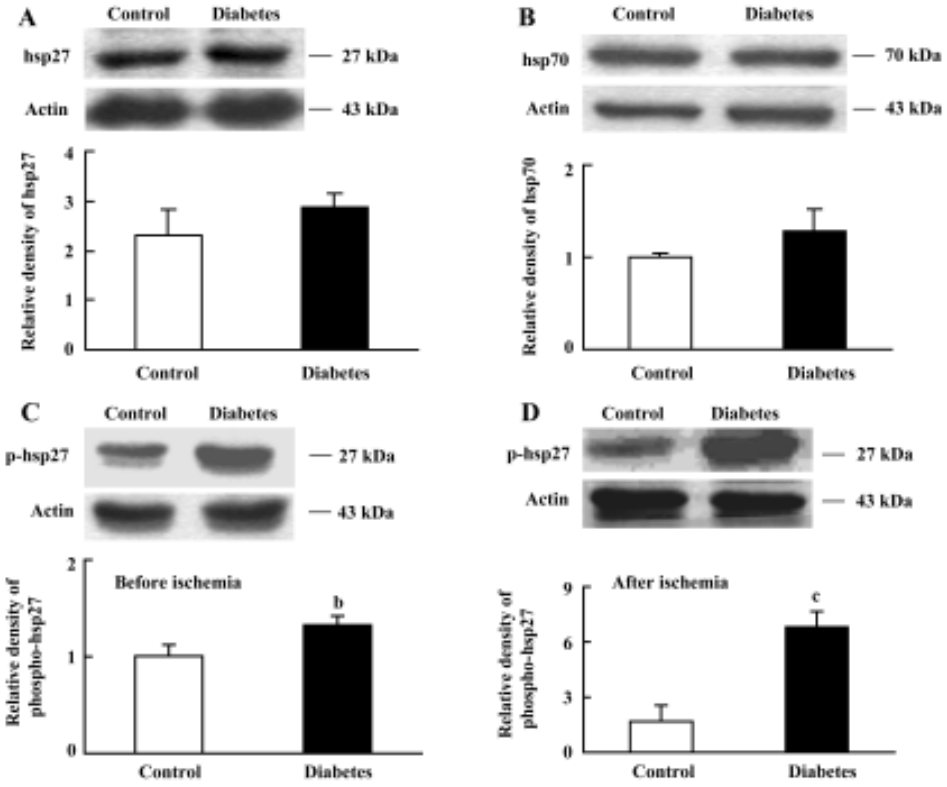

Figure 3. Western blot analysis of heat shock proteins in left ventricles of 3-week diabetic rats. There was no significant difference in total hsp27 (A) and inducible hsp70 (B) between diabetic and control hearts before ischemia. Diabetic hearts showed higher levels of phospho-hsp27 before (C) and after (D) ischemia. Densitometric data are mean±SEM of 4 to 5 hearts. $^{b}P<0.05$, $^{c}P<0.01$ *vs* controls.

manifested by improved post-ischemic mechanical function, prolonged time to arrest, attenuated reperfusion arrhythmias and reduced CPK release. Furthermore, there was a significantly increased amount of phospho-hsp27 in diabetic hearts compared with non-diabetic hearts. The reduction of phospho-hsp27 in correlation to hyperglycemia was effective in abrogating heart tolerance to ischemia in diabetes.

Although there is controversy over the effects of hyperglycemia on cardiovascular outcomes, it is important to note that increased tolerance to ischemia is almost exclusively found in type 1 diabetic hearts[8,9,15,16]. In contrast to decreased sensitivity to ischemia of type 1 diabetic hearts, increased sensitivity to myocardial ischemia was found in type 2 diabetic Otsuka Long-Evans Tokushima Fatty rats[17]. It is of interest that higher blood glucose induced by sucrose feeding in type 2 diabetes paradoxically attenuated post-ischemic cardiac dysfunction[17]. There is also a study showing that the correction of metabolic state alone in type 2 diabetes did not improve heart function recovery from ischemia[10]. These data from type 1 and type 2 diabetes indicate that factors other than hyperglycemia increase heart sensitivity to ischemia in type 2 diabetes, and marked high glucose or other factors secondary to elevated glucose can participate in preconditioning hearts to resist ischemia insult in type 1 diabetes.

A striking finding of the present study is that increased myocardial resistance to ischemia was accompanied by increased amounts of phospho-hsp27 in diabetic hearts. Because there is no significant change in myocardial phospho-hsp27 of rats that failed to develop diabetes after injection of streptozocin, the increase of phospho-hsp27 in streptozocin-induced diabetes is not likely to be induced by this toxic agent used for destroying pancreas beta-cells and induction of type 1 diabetes. Here we suggest for the first time that hyperglycemia can present a chronic and mild, yet stressful, stimulus to myocardium inducing upregulation of some stress proteins in diabetic hearts, which may in turn enhance heart tolerance to ischemia.

Elevated levels of hsp27 are reported to participate in cardioprotection by maintaining the integrity of microtubules and actin cytoskeleton, and can protect endothelium from ischemia[18]. The phosphorylation and translocation of hsp27 from cytosol to myofibril or nucleus is found to be especially important for protecting actin fragmentation and microtu-

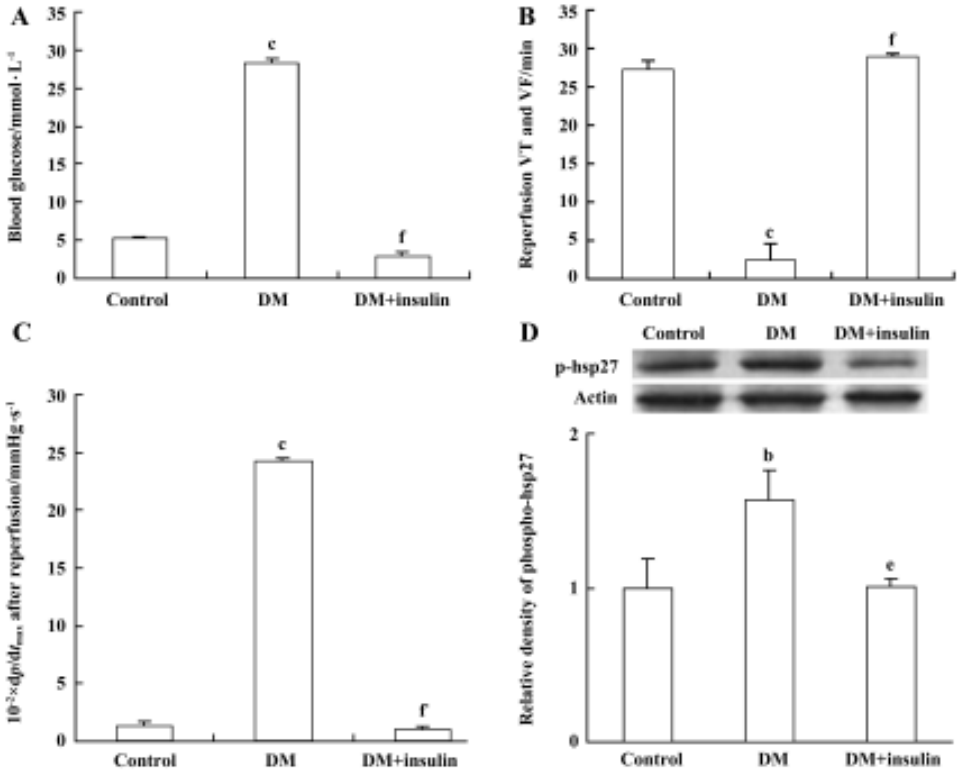

Figure 4. Ischemic outcomes after insulin treatment. Complete correction of hyperglycemia with insulin (A) for 2 d abrogated protection in 3-week diabetic hearts subjected to ischemia as shown by increased arrhythmias (B) and reduced post-ischemic dp/dt_{max} (C) in insulin-treated diabetic rats (DM+Insulin). There was concomitant reduction of phospho-hsp27 as compared with diabetes control without insulin injection (DM) (D). n=5–6. Mean±SEM. $^bP<0.05$, $^cP<0.01$ *vs* controls; $^eP<0.05$, $^fP<0.01$ *vs* DM without insulin.

bule degradation[19]. In the present study, hyperglycemia did not affect total hsp27 but significantly increased the amount of phosphor-hsp27, indicating the potential cardioprotective role of phospho-hsp27 during ischemia and reperfusion of diabetic hearts. The elevated lipid peroxidation product found in our previous work and other works[6,20] indicates higher oxidative stress in type 1 diabetes, while upregulation of protective proteins may compensate for such detrimental effects of hyperglycemia.

Inhibited glycolysis could result in myocardial salvage as a result of less accumulation of lactate during ischemia[21]. In accordance with previous published reports, we also found decreased lactate production from diabetic hearts[20], which possibly contributed to the observed cardioprotection. In addition to the above mechanisms, decreased cardiac norepinephrine may also account for improved mechanical function, in accordance with our previous finding that norepinephrine reduction conferred significant cardioprotection during ischemia[22]. Because Na^+-H^+ exchanger enhances norepinephrine release, diminished activation of Na^+-H^+ exchanger in diabetic hearts[8] may be one explanation for reduced norepinephrine release. This needs further investigation.

There is a report that early type 1 diabetes was found to have increased aortic relaxation[23]. In this study, no significant large vessel dysfunction was found in this early stage of type 1 diabetes. The relatively higher post-ischemic coronary flow in the diabetic group also indicated no impairment of coronary vessel function. The elevated coronary perfusion may be a result of myogenic dilation, a main determinant for myocardial perfusion, as during reperfusion the diabetic hearts relaxed significantly more than the controls. The improved coronary perfusion in turn enhanced myocardial salvage during reperfusion.

In summary, the present study reveals that the hearts of early-stage type 1 diabetes are resistant to ischemic injury. The concomitant upregulation of phospho-hsp27, in addition to inhibited glycolysis and reduced norepinephrine release, may participate in protecting diabetic hearts from ischemia. Hyperglycemia may contribute to the induction of the stress protein. However, caution should be taken when extrapolating the present results to clinical settings as most

diabetic patients have type 2 diabetes commonly associated with other risk factors. Further investigation on the combination of hyperglycemia and other conventional risk factors will lead to a better understanding of the complex pathogenesis of diabetes mellitus.

References

1 Buse JB. Should postprandial glucose be routinely measured and treated to a particular target? No! Diabetes Care 2003; 26: 1615–8.

2 Balkau B, Forhan A, Eschwege E. Two hour plasma glucose is not unequivocally predictive for early death in men with impaired fasting glucose: more results from the Paris Prospective Study. Diabetologia 2002; 45: 1224–30.

3 Jarrett RJ. Type 2 (non-insulin-dependent) diabetes mellitus and coronary heart disease – chicken, egg or neither? Diabetologia 1984; 26: 99–102.

4 Meigs JB, Singer DE, Sullivan LM, Dukes KA, D'Agostino RB, Nathan DM, *et al*. Metabolic control and prevalent cardiovascular disease in non-insulin-dependent diabetes mellitus (NIDDM): The NIDDM Patient Outcome Research Team. Am J Med 1997; 102: 38–47.

5 Liu Y, Thornton JD, Cohen MV, Downey JM, Schaffer SW. Streptozotocin-induced non-insulin-dependent diabetes protects the heart from infarction. Circulation 1993; 88: 1273–8.

6 Marfella R, D'Amico M, Di Filippo C, Piegari E, Nappo F, Esposito K, *et al*. Myocardial infarction in diabetic rats: role of hyperglycaemia on infarct size and early expression of hypoxia-inducible factor 1. Diabetologia 2002; 45: 1172–81.

7 Feuvray D, Lopaschuk GD. Controversies on the sensitivity of the diabetic heart to ischemic injury: the sensitivity of the diabetic heart to ischemic injury is decreased. Cardiovasc Res 1997; 34: 113–20.

8 Ramasamy R, Schaefer S. Inhibition of Na^+-H^+ exchanger protects diabetic and non-diabetic hearts from ischemic injury: insight into altered susceptibility of diabetic hearts to ischemic injury. J Mol Cell Cardiol 1999; 31: 785–97.

9 Tani M, Neely JR. Hearts from diabetic rats are more resistant to *in vitro* ischemia: possible role of altered Ca^{2+} metabolism. Circ Res 1988; 62: 931–40.

10 Aasum E, Hafstad AD, Severson DL, Larsen TS. Age-dependent changes in metabolism, contractile function, and ischemic sensitivity in hearts from d*b*/d*b* mice. Diabetes 2003; 52: 434–41.

11 Stern MP. Diabetes and cardiovascular disease. The "common soil" hypothesis. Diabetes 1995; 44: 369–74.

12 Sowers JR, Epstein M, Frohlich ED. Diabetes, hypertension, and cardiovascular disease: an update. Hypertension 2001; 37: 1053–9.

13 Weitgasser R, Lechleitner M, Koch T, Galvan G, Muhlmann J, Steiner K, *et al*. Antibodies to heat shock protein 65 and neopterin levels in patients with type 1 diabetes mellitus. Exp Clin Endocrinol Diabetes 2003; 111: 127–31.

14 Curtis MJ, Walker MJ. Quantification of arrhythmia using scoring systems: an examination of seven scores in an *in vivo* model of regional myocardial ischaemia. Cardiovasc Res 1988; 22: 656–65.

15 Ravingerova T, Neckar J, Kolar F, Stetka R, Volkovova K, Ziegelhoffer A, *et al*. Ventricular arrhythmias following coronary artery occlusion in rats: is the diabetic heart less or more sensitive to ischaemia? Basic Res Cardiol 2001; 96: 160–8.

16 Ramasamy R, Oates PJ, Schaefer S. Aldose reductase inhibition protects diabetic and nondiabetic rat hearts from ischemic injury. Diabetes 1997; 46: 292–300.

17 Chen H, Higashino H, Kamenov ZA, Azuma M, Lee WH, Yang XQ, *et al*. Preserved postischemic heart function in sucrose-fed type 2 diabetic OLETF rats. Life Sci 2003; 72: 2839–51.

18 Latchman DS. Heat shock proteins and cardiac protection. Cardiovasc Res 2001; 51: 637–46.

19 Dana A, Skarli M, Papakrivopoulou J, Yellon DM. Adenosine A_1 receptor induced delayed preconditioning in rabbits: induction of p38 mitogen-activated protein kinase activation and Hsp27 phosphorylation via a tyrosine kinase- and protein kinase C-dependent mechanism. Circ Res 2000; 86: 989–97.

20 Wang LP, Liu T, Chen H, Chen HZ, Gao PJ, Zhu DL. Experimental study on paradoxical phenomenon in type 1 diabetic heart: increased resistance to ischemia/reperfusion injury. Shanghai Med J 2004; 91: 300–6.

21 Finegan BA, Lopaschuk GD, Gandhi M, Clanachan AS. Ischemic preconditioning inhibits glycolysis and proton production in isolated working rat hearts. Am J Physiol 1995; 269: H1767–H1775.

22 Chen H, Higashino H, Maeda K, Zhang Z, Ohta Y, Wang Z, *et a*l. Reduction of cardiac norepinephrine improves postischemic heart function in stroke-prone spontaneously hypertensive rats. J Cardiovasc Pharmacol 2001; 38: 821–32.

23 Shen B, Ye CL, Ye KH, Liu JJ, Sun P, Jiang JH. Mechanism underlying enhanced endothelium-dependent vasodilation in thoracic aorta of early stage streptozotocin-induced diabetic mice. Acta Pharmacol Sin 2003; 24: 422–8.

Acta Pharmacologica Sinica 2005 Jul; 26 (7): 813–820

Full-length article

Isoflurane preconditioning protects against ischemia-reperfusion injury partly by attenuating cytochrome c release from subsarcolemmal mitochondria in isolated rat hearts[1]

Li-ping QIAN, Shan-shan ZHU[2], Jun-li CAO, Yin-ming ZENG

Jiangsu Provincial Key Lab of Anesthesiology, Jiangsu Institute of Anesthesiology, Xuzhou Medical College, Xuzhou 221002, China

Key words

isoflurane; reperfusion injury; cytochrome c; mitochondria

[1] Project supported by the Natural Science Foundation of Jiangsu Province (No BK2002139).
[2] Correspondence to Dr Shan-shan ZHU.
Phn 86-516-580-2231.
Fax 86-516-570-8135.
E-mail xzzss2004@yahoo.com.cn

Received 2004-12-03
Accepted 2005-03-03

doi: 10.1111/j.1745-7254.2005.00117.x

Abstract

Aim: To examine if isoflurane preconditioning can attenuate ischemia/reperfusion injury by reducing cytochrome c release from inner mitochondrial membrane. **Methods:** Isolated hearts of Sprague-Dawley rats were perfused on Langendorff apparatus. Hearts were randomly assigned to a non-treated group (CON group, n=12) or three isoflurane preconditioning groups (0.5% ISC group, 1.0% ISC group, and 2.0% ISC group; n=12). In the latter three groups, isoflurane was given at concentrations of 0.5%, 1.0%, and 2.0% for 15 min with 15-min washout before 30-min ischemia. Subsarcolemmal mitochondria of the myocardium were isolated after 60-min reperfusion. Hemodynamics of the each heart was recorded, infarct size of the hearts and contents of cytosolic cytochrome or mitochondrial cytochrome c were measured at the end of reperfusion. Morphology of isolated mitochondria in the four groups was evaluated, respectively. **Results:** Compared with the CON group, cytosolic cytochrome c in 0.5% ISC group, 1.0% ISC group, and 2.0% ISC group were significantly decreased along with a significant increase of mitochondrial cytochrome c. Infarct size of the hearts in the four groups were 56%±12%, 41%±12%, 32%±7% and 33%±11%, respectively. The values of the three isoflurane preconditioning groups were significantly lower than that of the CON group (P<0.05). Isoflurane exposure before ischemia can attenuate the change of morphology of mitochondria after reperfusion. The effects of 2.0% isoflurane on reducing cytochrome c release were more remarkable than 0.5% and 1.0% concentrations of isoflurane. **Conclusion:** Myocardioprotective effects of isoflurane preconditioning were associated with attenuation of cytochrome c loss from the inner membrane of subsarcolemmal mitochondria.

Introduction

Volatile anesthetics can protect against reperfusion injury after myocardial ischemia *in vitro* and *in vivo*[1–4]. And isoflurane is one of the drugs most commonly used to maintain the state of general anesthesia. Isoflurane preconditioning, a temporary exposure to isoflurane followed by its complete washout, can protect against cardiac ischemia-reperfusion injury. It has been reported that isoflurane preconditioning can mimic ischemia preconditioning to protect against reperfusion injury after myocardial ischemia *in vitro* and *in vivo*[3,4]. However, to date, the mechanism of isoflurane preconditioning remains unclear. It has been reported that ischemic preconditioning can induce mitochondrial tolerance by using the loss of cytochrome c as an indication of mitochondrial dysfunction[5]. It is not known whether the cardioprotective effect of isoflurane preconditioning can also be achieved by inducing mitochondrial tolerance.

Mitochondria sustains progressive damage during ischemia. Cardiac mitochondria exist in two functionally distinct populations. Subsarcolemmal mitochondria (SSM) are located beneath the plasma membrane, whereas interfibrillar

mitochondria (IFM) are located between the myofibrils. These two mitochondria are affected differently in myocardiopathy and ischemia. The progression of ischemic damage is more rapid in SSM[6,7]

In the present study, we examined if isoflurane preconditioning protected against a detrimental ischemic insult by attenuating cytochrome c release from the inner membrane of subsarcolemmal mitochondria

Materials and methods

Isolated heart preparation and measurements Experiments were performed on adult male Sprague-Dawley rats weighing 230–300 g. The rats were housed in plastic cages with soft bedding and free access to food and water under a 12-h day/12-h night cycle. Rats were supplied by the Experimental Animal Center of Xuzhou Medical College. All experiments were approved by the Animal Care and Use Committee at the college and were in accordance with the Guidelines for Care and Use of Laboratory Animals. Pentobarbital 40 mg/kg and heparin 500 U/kg were injected intraperitoneally into 44 Sprague-Dawley rats weighing 250–300 g. After thoracotomy, the hearts were isolated and immediately placed in 4 °C Krebs-Henseleit (K-H) solution, then rapidly prepared using the Langendorff method and perfused at 55 mmHg with K-H solution at 37 °C. The perfusate was equilibrated with mixed gas of 95% O_2 and 5% CO_2 to meet standards (pH, 7.4±0.02; carbon dioxide partial pressure, 25±4 mmHg; oxygen partial pressure, 570±20 mmHg). The composition of K-H perfusate was as follows: NaCl 118 mmol/L, KCl 4.7 mmol/L, KH_2PO_4 1.2 mmol/L, $CaCl_2$ 2.5 mmol/L, $MgSO_4$ 1.2 mmol/L, $NaHCO_3$ 25 mmol/L, glucose 11.1 mmol/L, Na_2-EDTA 0.125 mmol/L.

Left ventricular pressure (LVP) and d*p*/d*t* were measured isovolumetrically with a saline-filled latex balloon inserted into the left ventricle through a cut in the left atrium. At the beginning of the experiment, the balloon volume was adjusted to achieve a diastolic LVP of 0 mmHg, so that any subsequent increase in diastolic LVP indicated an increase in left ventricular wall stiffness or diastolic contracture. Baseline hemodynamics were recorded 20 min after stabilization. Hearts were randomly assigned to a non-treated group (CON group, n=12) or three isoflurane preconditioning groups (0.5% ISC group, 1.0% ISC group and 2.0% ISC group; n=12) and were perfused with K-H solution saturated with 0.0%, 0.5%, 1.0%, and 2.0% isoflurane, respectively, for 15 min and followed by a 15-min washout with normal K-H solution before 30 min ischemia and 60 min reperfusion. Isoflurane was bubbled into the perfusate with an isoflurane vaporizer (Ohmeda, West Yorkshire, England) placed in the oxygen-carbon dioxide gas mixture line. Vapour concentrations were measured continuously by an anesthetic gas detector (Capnomac; Ultima, Datex-Engstrom, Helsinki, Finland). LVP, d*p*/dt, and HR were monitored continuously during the whole experiment using Maclab 4.0 software (AD Instruments, Australia).

Measurement of infarct size The 2,3,5-triphenyltetrazolium chloride (TTC) staining technique was used to determine infarct size after 60-min reperfusion. Fresh TTC was prepared in 0.1 mol/L phosphate buffer adjusted to pH 7.4. TTC stained the non-infarcted myocardium a bright red color, caused by reduction of TTC by dehydrogenases present in viable tissues. Hearts stored at -70 °C after each experiment were taken up and sliced into 4–6 transverse sections (3-mm thickness). The sections were immersed in 1% TTC solution and incubated for 30 min at 37 °C. All slices were digitally imaged by a photoscanner[8], and the infarcted areas of each slice were measured in a blinded fashion by planimetry using Imagemaster VDS (Pharmacia Bioter, USA).

Isolation of subsarcolemmal rat heart mitochondria and cytosolic fractions Subsarcolemmal mitochondria were isolated from the ventricles as follows: the ventricles were rapidly dissected and rinsed in ice-cold homogenization buffer (CP1: KCl 100 mmol/L, MOPS 50 mmol/L, $MgSO_4$ 5.0 mmol/L, edetic acid 1.0 mmol/L, ATP 1.0 mmol/L, at pH 7.4). The ventricles were blotted dry, weighed, minced, and washed with CP1. The mince was homogenized at 20 mL/g tissue in cold CP2 (CP1+BSA 2.0 g/L). The homogenate was then centrifuged at 584×*g* for 10 min. The supernatant was filtered through double layer gauze and centrifuged at 3015×*g* for 10 min. The mitochondrial pellet was resuspended in 5 mL CP2 per gram of heart and centrifuged at 3015×*g* for 10 min, and finally subsarcolemmal mitochondria were resuspended in 2.5 mL KME (100 mmol/L KCl, 50 mmol/L MOPS, 5 mmol/L egtazic acid) per gram of heart and centrifuged at 3 015×*g* for 10 min. Subsarcolemmal mitochondria was resuspended into KME at a final protein concentration of approximately 1.5 g/L. The first 3015×*g* supernatant represented the cytosolic fraction (protein concentration of approximately 2.0 g/L). All manipulations were carried out at 4 °C. Protein concentration was determined using Bradford assay, with BSA as standard.

Detection of cytochrome c by Western blotting Mitochondria prepared from isolated rat hearts were added 0.25% volume of 2×sample buffer (250 mmol/L Tris-HCl, 8.0% SDS, 700 mmol/L sucrose, 300 mmol/L DTT, 0.01% bromophenol blue, at pH 6.8). Samples were loaded onto 15% Tris-buffered polyacrylamide gels and component proteins resolved

by SDS-PAGE. Proteins were electroblotted onto a nitrocellulose membrane and cytochrome c was detected using monoclonal anti-cytochrome c (Santa Cruz Biotechnology, Inc, USA) as primary antibody and anti-mouse IgG conjugated to alkaline phosphatase as secondary antibody. Primary antibody binding was visualized with an alkaline phosphatase based chemiluminescence system.

Electron microscopy Mitochondria isolated from the myocardium in several kinds of buffer by density centrifugation was resuspended and fixed with 2% glutaraldehyde in 0.1 mol/L PBS buffer. Mitochondria were post-fixed using 1% OsO_4. En bloc staining with uranyl acetate was followed by dehydration and embedding. Embedded samples were sectioned and affixed to grids according to standard protocols. Mitochondrial ultrastructure was then evaluated by transmission electron microscopy.

Statistical analysis All data were expressed as mean± SD. Statistical analysis of data within and between groups was performed with analysis of variance (ANOVA) for repeated measures followed by Turkey multiple-comparison *post-hoc* test. $P<0.05$ was considered statistically significant.

Results

Changes in hemodynamics Figures 1–3 show changes in LVP, dp/dt_{min}, dp/dt_{max}, and HR of hearts in each of the four groups during the time course of the experiment. There was no difference in baseline hemodynamics among experimental groups. A concentration-dependent depression of left ventricular systolic pressure (LVSP), dp/dt_{max}, and heart rate was observed after 15 min of isoflurane treatment. After 60 min of reperfusion, hemodynamic function decreased in each group compared with baseline values. Left ventricular end diastolic pressure (LVEDP) was lower in the three isoflurane-preconditioning groups than in the CON group at 30 and 60 min reperfusion, but there was no significant difference in LVSP, dp/dt_{min}, dp/dt_{max}, and HR among the four groups.

Infarct size Figure 4 shows that the infarct size of the CON group was 56%±12%, isoflurane-preconditioning (0.5%,1.0%, and 2.0 %) significantly reduced infarct size to 41%± 12%, 32%±7%, and 33%±11%, respectively ($P<0.05$). But there was no significant difference among the three isoflurane-preconditioning groups.

Morphology of isolated mitochondria Electron microscopy analysis (×10 000) reveals basically formed membranes and clearly discernable cristae in the mitochondria isolated from hearts. The outer membranes of mitochondria isolated from CON groups were partly disrupted, and mitochondria were severely swollen, with fragmentation of the cristae. Isoflurane preconditioning attenuated morphological changes of mitochondria after ischemia and reperfusion. Mitochondria in the 2% isoflurane-preconditioned group appeared to

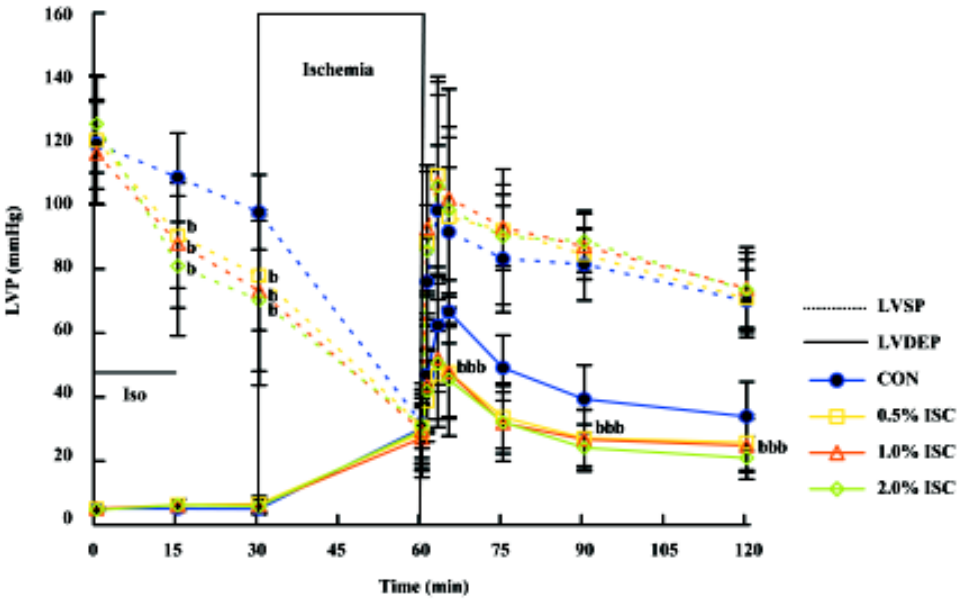

Figure 1. Time course of left ventricular pressure (LVP) and left ventricular end diastolic pressure (LVEDP) in CON group and isoflurane preconditioning groups. Isoflurane caused a significant decrease in systolic LVP in a concentration-dependent manner, but after reperfusion no difference between groups was observed. Isoflurane preconditioning group showed a lower elevation of LVEDP *vs* untreated control hearts after 15 min of reperfusion, whereas there was no difference among the isoflurane preconditioning groups. n=10. Mean±SD. $^bP<0.05$ *vs* CON.

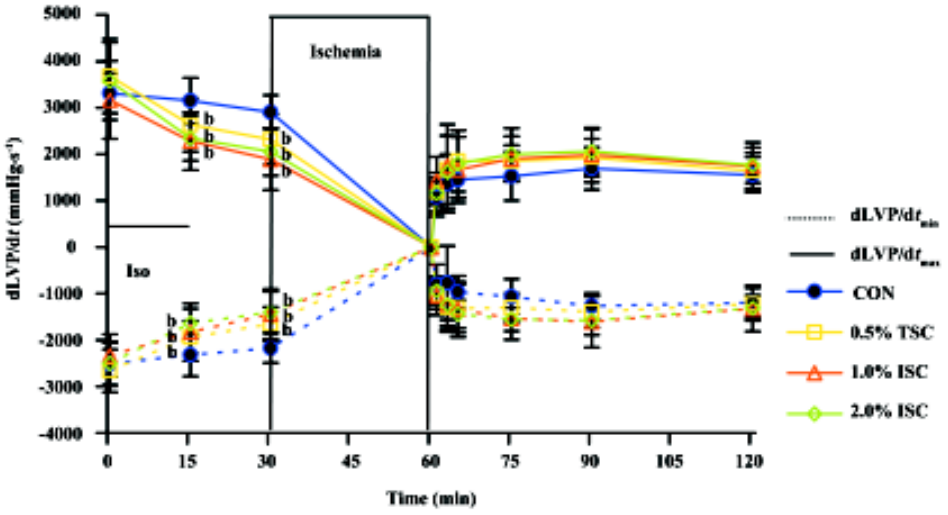

Figure 2. Time course of dp/dt_{max} (contractility) and dp/dt_{min} (relaxation) in CON group and isoflurane preconditioning groups. dp/dt_{max} and dp/dt_{min} were depressed during isoflurane exposure. During the early reperfusion, the contraction and relaxation indices were improved in isoflurane preconditioning group compared with non-treated ischemia hearts, but no significant difference between the isoflurane preconditioning groups was observed at the end of the experiments. n=10. Mean±SD. ^bP<0.05 *vs* CON.

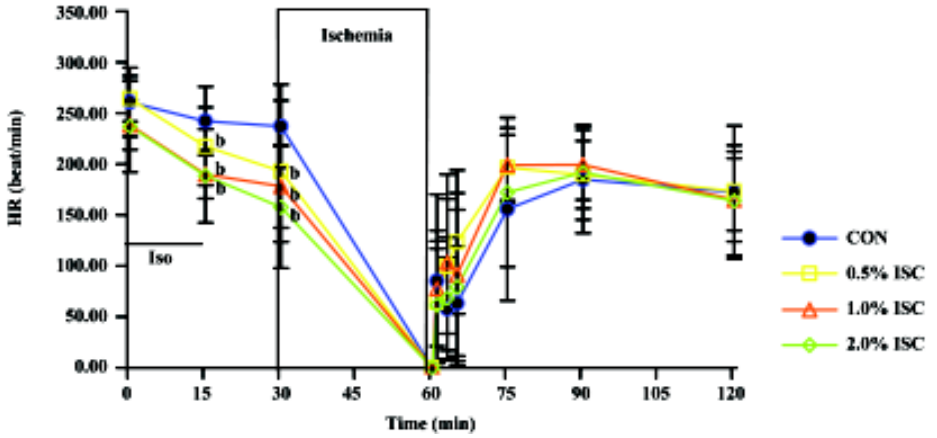

Figure 3. Time course of heart rate (HR) in CON group and isoflurane preconditioning groups. Isoflurane exposure caused a decrease of HR in a concentration-dependent manner. After the onset of reperfusion among the four groups there was no significant difference. n=10. Mean±SD. ^bP<0.05 *vs* CON.

be morphologically better than those of the other preconditioning groups.

Western blot analysis of the release of mitochondrial cytochrome c Isoflurane-preconditioning reduces ischemia reperfusion-induced cytochrome c release from the mitochondria in a concentration-related manner. The results showed the amounts of cytosolic cytochrome c significantly decreased (P<0.05 *vs* CON group) in an isoflurane concentration-related manner, while the amounts of mitochondrial cytochrome c markedly increased (P<0.05 *vs* CON group). The results indicate that mitochondrial dysfunction occurred after reperfusion and was attenuated by isoflurane-precon-

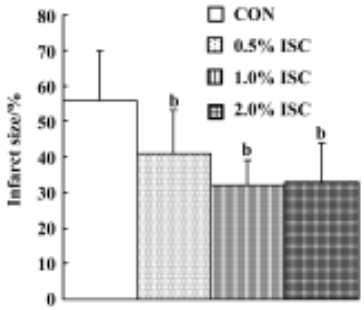

Figure 4. Effects of isoflurane preconditioning on the infarct size of hearts at the end of reperfusion in CON group and isoflurane preconditioning groups. n=6. Mean±SD. ^bP<0.05 *vs* CON.

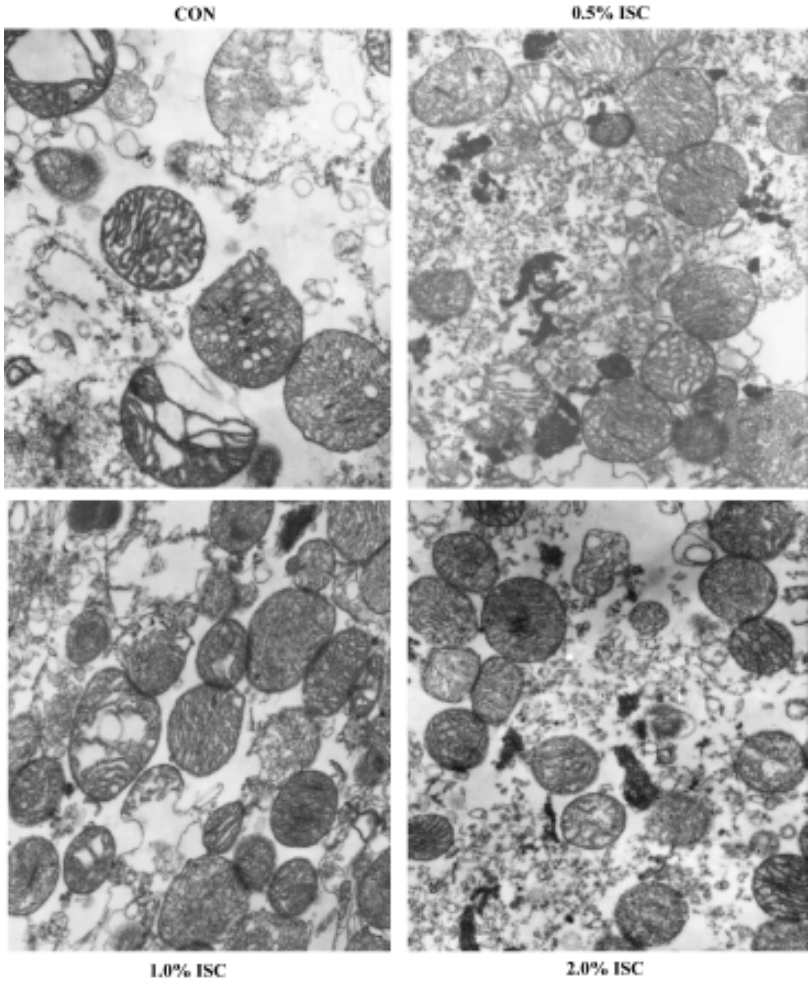

Figure 5. Electronic micrographs of mitochondria isolated from myocardium of CON group and isoflurane preconditioning groups. ×10 000.

ditioning (Figure 6).

Discussion

In the present study, by Western blot examining of cytochrome c in mitochondria and cytosol, we observed that isoflurane increased the content of cytochrome c in mitochondria while reduced it in cytosol in a concentration-dependent manner. Isoflurane at concentration of 2% showed the most significant effect on cytochrome c loss in the mitochondria. Furthermore, mitochondria isolated from three isoflurane preconditioning groups were morphologically better than that isolated from CON. Similarly, isoflurane preconditioning significantly reduced the infarct size of hearts at the end of reperfusion. Therefore, we concluded that cytochrome c release from the mitochondria played a key role in the pathogenesis of ischemia/reperfusion injury and myocardioprotective effects of isoflurane preconditioning were associated with the attenuation of cytochrome c loss from the inner membrane of subsarcolemmal mitochondria.

Cytochrome c is a 12-kDa protein which functions in the mitochondrial electron transport chain. At physiological ionic strength, cytochrome c diffuses in the aqueous phase between the inner and outer membranes (outer compartment) and between complex III (cytochrome bc_1) and complex IV (cytochrome aa_3). But as a small and water-soluble molecule, cytochrome c is easier to be released from mitochondria than other mitochondrial proteins. Studies have shown that the loss of cytochrome c from mitochondria could occur during ischemia and after reperfusion[9,10]. Ischemia tolerance induced by sublethal ischemia is associated with mitochondrial protection (attenuating cytochrome c release from mitochondria) *in vitro* and *in vivo*[5].

Increasing evidence suggests that lethal reperfusion injury possibly consists of two forms of cell death, necrosis and apoptosis. The apoptotic process is initiated shortly

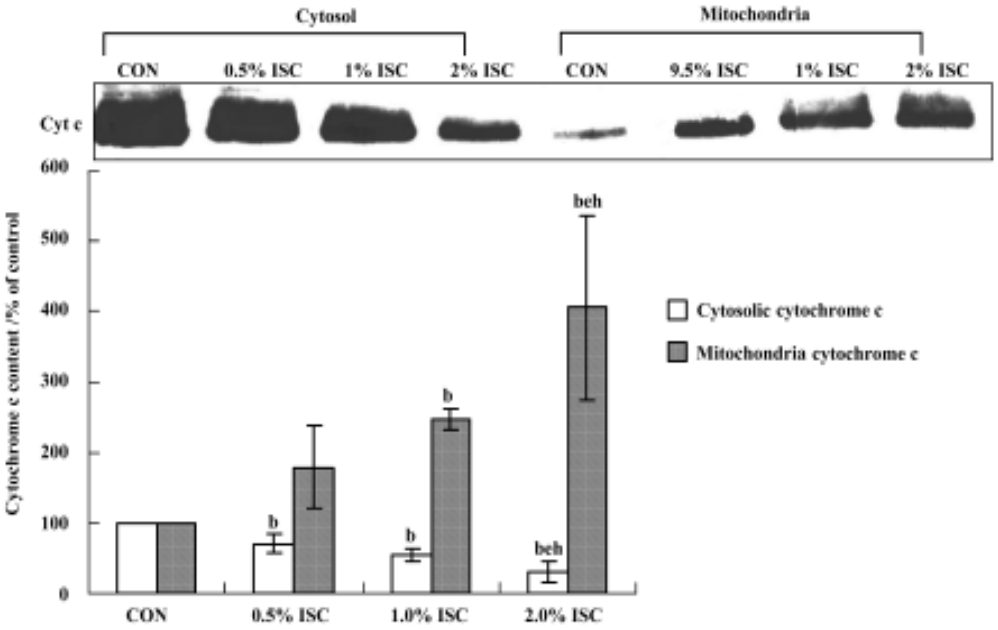

Figure 6. Western blot analysis of cytosolic and mitochondrial cytochrome c in CON group and isoflurane preconditioning groups. Left, cytochrome c from the cytosolic fraction in the control and three isoflurane preconditioning (0.5%, 1.0%, and 2.0%) groups. Right, cytochrome c from the mitochondrial fraction. The results show the amount of cytosolic cytochrome c significantly decreased by isoflurane in a concentration-dependent manner, while the amounts of mitochondrial cytochrome c markedly increased. n=4. Mean±SD. ^{b}P<0.05 *vs* CON. ^{e}P<0.05 *vs* 0.5% ISC. ^{h}P<0.05 *vs* 1.0% ISC.

after the onset of ischemia, and becomes markedly enhanced during reperfusion. Inhibition of the apoptotic process can then attenuate irreversible injury in connection with reperfusion[11]. One of the main mechanisms of cellular death induced by ischemia/reperfusion appears to be mitochondrial dysfunction. The cytochrome c release from mitochondria is a rapid and apoptosis-specific process within 1 h after the induction of apoptosis[12]. In the process of apoptosis, cytochrome c is released from the mitochondria to cytosol and caspase-3 is activated[13]. At the same time, the loss of cytochrome c could also lead to the formation of free radicals, and disturbances of oxidative phosphorylation. Whether the release of cytochrome c leads to necrotic or apoptotic cellular death depends largely on intracellular ATP levels. Most of this protein release from mitochondria to cytosol results in ATP depletion associated with necrotic cell death. Therefore, loss of cytochrome c is considered to be an indication of mitochondrial dysfunction[14,15]. Our results show a possible involvement of mitochondria in the cellular death pathway that is initiated during ischemia/reperfusion. Compared with the other groups, more cytochrome c of CON group was released from mitochondria to cytosol. Also the infarct size in the CON group was higher than those of the isoflurane preconditioning groups. Isoflurane preconditioning attenuated cytochrome c release along with reduced infarct size. Our study demonstrates for the first time in isolated hearts that isoflurane preconditioning is able to attenuate cytochrome c release from mitochondria in a concentration-dependent manner. Meanwhile, isoflurane preconditioning significantly deceased infarct size and morphologically ameliorated mitochondria injury suffered from ischemia and reperfusion. This result also indicated that the redistribution of cytochrome c was highly correlated with cellular death.

The mechanism by which isoflurane preconditioning induces mitochondrial tolerance via attenuating cytochrome c loss is not clear. The effect of preconditioning may first be on cytosolic factors, which lead to mitochondrial tolerance that persists until mitochondria were isolated for testing. Mitochondrial ATP-sensitive potassium (K_{ATP}) channels appear to be involved in the process of anesthetics-preconditioning[15–21]. Recent studies have shown that activation of K_{ATP} channels reduces the loss of mitochondrial cytochrome c through the protein kinase C signaling[22]. Anesthetic-induced preconditioning reduced cytosolic Ca^{2+} loading, one factor of cytochrome c release, in part through mitochondrial K_{ATP} channels[15,23]. Furthermore, Bcl-2 family proteins are important endogenous factors in regulating cytochrome c release from mitochondria, in which antiapoptotic proteins (eg, Bcl-2, Bcl-X_L, *etc*) inhibit, but proapoptotic proteins (eg,

Bax, Bad, *etc*) enhance, cytochrome c release[24,25]. Therefore, the expression and redistribution of Bcl-2 family proteins is possibly another important factor of isoflurane preconditioning inducing mitochondria tolerance by attenuating cytochrome c release. There is evidence that ischemia and some pharmacological preconditioning are able to induce transcription and expression of Bcl-2 and Bcl-X_L without changing transcription and the expression of Bax[26–28].

In the present study, isoflurane preconditioning reduced cytochrome c loss from mitochondria in a concentration-dependent manner. There was a remarkable reduction in cytochrome c release associated with higher concentrations of isoflurane preconditioning. However, infarct size was no further reduced by 2.0% isoflurane, which indicated that isoflurane preconditioning reduced infarct size with a peak effect at a concentration of approximately 1%. Although the release of cytochrome c from mitochondria is the main pathway of cellular death, it is not the only one. For example, members of the death receptor family, such as the Fas receptor and the tumor necrosis factor receptor also play a role in cellular death. Isoflurane preconditioning significantly attenuated cytochrome c release, but the effects of isoflurane preconditioning on other cell death signaling pathways is unclear. It is possible that other pathways of inducing cellular death contributed to the myocardial infarct in 2.0% ISC group. In the present study, however, it can be inferred that isoflurane preconditioning can protect against myocardial ischemic/reperfusion injury in part through attenuating cytochrome c loss. At the same time, it is not appropriate to tell directly whether the cytochrome c release from mitochondrial is likely to be a final step or trigger factor of myocardial injury from the present study. Further studies should be taken to examine if blocking of isoflurane preconditioning could abolish the attenuated release of cytochrome c.

In conclusion, the present study demonstrated that isoflurane preconditioning was capable of protecting against myocardium ischemia/reperfusion injury in part by attenuating the release of cytochrome c from the mitochondria.

Acknowledgement

The authors are grateful to Dr Qun CHEN for his helpful instruction on the experiment.

References

1 Kehl F, Krolikowski JG, Mraovic B, Pagel PS, Warltier DC, Kersten JR. Is isoflurane-induced preconditioning dose related? Anesthesiology 2002; 96: 675–80.

2 Obal D, Preckel B, Scharbatke H, Miillenheim J, Hoterkes F, Thamer V, *et al*. One MAC of sevoflurane provides protection against reperfusion injury in the rat heart *in vivo*. Br J Anaesth 2001; 87: 905–11.

3 Martini N, Preckel B, Thämer V, Schlack W. Can isoflurane mimic ischemia preconditioning in isolated rat? Br J Anaesth 2001; 86: 269–71.

4 Belhomme D, Peynet J, Louzy M, Launay JM, Kitakaze M, Menasché P. Evidence for precondition by isoflurane in coronary artery bypass graft surgery. Circulation 1999; 100: II–340.

5 Zhan RZ, Fujihara H, Baba H, Yamakura T, Shimoji K. Ischemic preconditioning is capable of inducing mitochondrial tolerance in the rat brain. Anesthesiology 2002; 97: 896–901.

6 Lesnefsky EJ, Tandler B, Ye J, Slabe TJ, Turkaly J, Hoppel CL. Myocardial ischemia decreases oxidative phosphorylation through cytochrome oxidase in subsarcolemmal mitochondria. Am J Physiol 1997; 273: H1544–54.

7 Lesnefsky EJ, Slabe TJ, Stoll MS, Minkler PE, Hoppel CL. Myocardial ischemia selectively depletes cardiolipin in rabbit heart subsarcolemmal mitochondria. Am J Physiol Heart Circ Physiol 2001; 280: H2770–8.

8 Riess ML, Novalija E, Camara AKS, Eells JT, Chen Q, Stowe DF. Preconditioning with sevoflurane reduces changes in nicotinamide adenine dinucleotide during ischemia-reperfusion in isolated hearts. Anesthesiology 2003; 98: 387–95.

9 Soeda J, Miyagawa S, Sano K, Masumoto J, Taniguchi SI, Kawasaki S. Cytochrome c release into cytosol with subsequent caspase activation during warm ischemia in rat liver. Am J Physiol Gastrointest Liver Physiol 2001; 281: G1115–23.

10 Czerski LW, Szweda PA, Szweda LI. Dissociation of cytochrome c from the inner-mitochondrial membrane during cardiac ischemia. J Biol Chem 2003; 278: 34499–504.

11 Ji ES, Yue H, Wu YM, He RR. Effects of phytoestrogen genistein on myocardial ischemia/reperfusion injury and apoptosis in rabbits. Acta Pharmacol Sin 2004; 25: 306–12.

12 Renz A, Berdel WE, Kreuter M, Bleka C, Schulze-Osthoff K, Los M. Rapid extracellular release of cytochrome c is specific for apoptosis and marks cell death *in vivo*. Blood 2001; 98: 1542–8.

13 Hu XM, Zhang Y, Zeng FD. Effects of β-aescin on apoptosis induced by transient focal cerebral ischemia in rats. Acta Pharmacol Sin 2004; 25: 1267–75.

14 Shiraishi J, Tatsumi T, Keira N, Akashi K, Mano A, Yamanaka S, *et al*. Important role of energy-dependent mitochondrial pathways in cultured rat cardiac myocyte apoptosis. Am J Physiol Heart Circ Physiol 2001; 281: H1637–47.

15 Leist BM, Single B, Castoldi AF, Kühnle S, Nicotera P. Intracellular adenosine triphosphate (ATP) concentration: a switch in the decision between apoptosis and necrosis. J Exp Med 1997; 185: 1481–6.

16 Chen Q, Camara A, An JZ, Novalija E, Riess ML, Stowe DF. Sevoflurane preconditioning before moderate hypothermic ischemia protects against cytosolic [Ca^{2+}] loading and myocardial damage in part via mitochondrial K_{ATP} channels. Anesthesiology 2002; 97: 912–20.

17 Rourke BO. Myocardial K_{ATP} channels in preconditioning. Circ Res 2000; 87: 845.

18 Shimizu J, Sakamoto A, Ogawa R. Activation of the adenosine triphosphate sensitive mitochondrial potassium channel is involved in the cardioprotective effect of isoflurane. J Nippon

Med Sch 2001; 68: 238–44.
19 Tanaka K, Weihrauch D, Ludwig LM, Kersten JR, Pagel PS, Warltier DC. Mitochondrial adenosine triphosphate-regulated potassium channel opening acts as a trigger for isoflurane-induced preconditioning by generating reactive oxygen species. Anesthesiology 2003; 98: 935–43.
20 Lim KH, Javadov SA, Das M, Clarke SJ, Suleiman MS, Halestrap AP. The effects of ischaemic preconditioning, diazoxide and 5-hydroxydecanoate on rat heart mitochondrial volume and respiration. J Physiol 2002; 545: 961–74.
21 Shen YL, Chen YY, Wu XD, Bruce IC, Xia Q. Activation of mitochondrial ATP-sensitive potassium channels delays ischemia-induced cellular uncoupling in rat heart. Acta Pharmacol Sin 2004; 25: 22–8.
22 Takashi E, Wang Y, Ashraf M. Activity of mitochondrial K_{ATP} channel elicits late preconditioning against myocardial infarction via protein kinase C signaling pathway. Circ Res 1999; 85: 1146–53.
23 AN J, Varadarajan SG, Novalija E, Stowe DF. Ischemic and anesthetic preconditioning reduces cytosolic [Ca^{2+}] and improves Ca^{2+} responses in intact hearts. Am J Physiol Heart Circ Physiol 2001; 281: 1508–23.
24 Finucane DM, Bossy-Wetzel E, Waterhouse NJ, Cotter TG, Green DR. Bax-induced caspase activation and apoptosis via cytochrome c release from mitochondria is inhibitable by Bcl-Xl. J Biol Chem 1999; 274: 2225–33.
25 Narita M, Shimizu S, Ito T, Chittenden T, Lutz RJ, Matsuda H, *et al*. Bax interacts with the permeability transition pore to induce permeability transition and cytochrome c release in isolated mitochondria. Proc Natl Acad Sci USA 1998; 95: 14681–6.
26 Szewczyk A, Wojtczak L. Mitochondria as a pharmacological target. Pharmacol Rev 2002; 5: 101–27.
27 Wu C, Fujihara H, Yao J, Qi S, Li H, Shimoji K, *et al*. Different expression patterns of Bcl-2, Bcl-xl, and Bax proteins after sublethal forebrain ischemia in C57Black/Crj6 mouse striatum. Stroke 2003; 34: 1803.
28 Plesnila N, Zinkel S, Le DA, Amin-Hanjani S, Wu Y, Qiu J, *et al*. BID mediates neuronal cell death after oxygen/glucose deprivation and focal cerebral ischemia. Proc Natl Acad Sci USA 2001; 98: 15318–23.

The First Scientific Meeting of the Asian Society for Vascular Biology

October 8–11, 2005 Shanghai, China

Info: YuHUANG
Department of Physiology
Chinese University of Hong Kong
Hong Kong SAR, China
Phn 852-2609-6787
Fax 852-2603-5022
E-mail yu-huang@cuhk.edu.hk
http://www.sbsonline.org/sbscon/2005/index.php

Acta Pharmacologica Sinica 2005 Jul; 26 (7): 821–827

Full-length article

Taurine inhibits ischemia/reperfusion-induced compartment syndrome in rabbits[1]

Ji-xian WANG[2,3], LI Yan[2], Li-ke Zhang[4], Jing ZHAO[5], Yong-zheng PANG[2,3], Chao-shu TANG[3,5], Jing ZHANG[2,3,6]

[2]Institute of Cardiovascular Disease Research, The First Hospital of Peking University, Beijing 100034, China; [3]Key Laboratory of Molecular Cardiovascular Science, Ministry of Education, Beijing 100083, China; [4]Department of Pathophysiology, Capital Institute of Medicine, Beijing 100054, China; [5]Department of Physiology, Health Center of Medical Sciences, Peking University, Beijing 100083, China

Key words

taurine; compartment syndromes; reperfusion injury

[1] Project supported by the State Major Basic Research Program of China (No G 200056905).
[6] Correspondence to Dr Jing ZHANG.
Phn 86-10-8280-2851.
E-mail exzhang@sina.com

Received 2005-01-31
Accepted 2005-03-15

doi: 10.1111/j.1745-7254.2005.00128.x

Abstract

Aim: To investigate effects of taurine on ischemia/reperfusion (I/R)-induced compartment syndrome in rabbit hind limbs. **Methods:** Rabbits underwent femoral artery occlusion after ligation of branches from terminal aorta to femoral artery. After a 7-h ischemia, reperfusion was established with the use of heparinized polyethylene shunts. Rabbits received taurine (1 g/kg) or normal saline (control) by iv infusion 10 min before shunt placement. During reperfusion, anterior compartment pressure (ACP) was monitored continuously in the left lower extremity. Gastrocnemius muscle triphenyltetrazolium chloride (TTC) level, taurine content and myeloperoxidase activity were assayed. Oxidative stress was induced in the *in vitro* gastrocnemius muscle slices by free radical generating systems (FRGS), and the malondialdehyde content was measured in presence or absence of taurine. **Results:** After 7 h of ischemia, none of the parameters that we measured were different from those before ischemia, except that TTC reduction decreased by 80%. In the control group, after 2 h of reperfusion, ACP increased 4.5-fold, and gastrocnemius muscle taurine content was reduced by 33%. In taurine-treated animals, at 2 h reperfusion, the mean arterial blood pressure and heart rate were increased, by 6% and 10%. ACP decreased by 39%, muscle edema decreased by 16%, TTC reduction increased by 150%, and lactate dehydrogenase decreased by 36% compared to control group. Plasma and muscle taurine content increased by 70% and 88%, respectively. In the taurine-treated group, at 2 h reperfusion, plasma malondialdehyde and conjugated diene content were decreased by 38% and 23%, respectively, and muscle malondialdehyde and conjugated diene content decreased by 22% and 30%, respectively compared to the control group. At 2 h reperfusion, myeloperoxidase activity was increased 3.5-fold in control animals. In the *in vitro* study, taurine decreased malondialdehyde content in muscle slices incubated with hypochlorous acid in a dose-dependent manner, but there was no change when incubated with hydrogen peroxide and xanthine oxidase. **Conclusion:** Treatment with taurine inhibited I/R-induced compartment syndrome by at least in part attenuating oxidative stress injury induced by I/R, suggesting clinical application of taurine might be a new strategy for the prevention and treatment of compartment syndrome.

Introduction

Compartment syndrome is characterized by increased tissue hydrostatic pressure within a closed fascial space and by secondary compromise of skeletal-muscle capillary perfusion, with resultant ischemia, tissue necrosis and po-

tential systemic toxicity[1]. The exact mechanisms of compartment syndrome are poorly understood; thus, effective treatments are deficient. The surgical management of compartment syndrome has changed little in the 70 years since fasciotomy was first described. Although effective, fasciotomy increases morbidity, length of hospitalization and patient suffering, and may require subsequent skin grafting. Prevention of compartment syndrome by pharmacological methods, therefore, is an attractive prospect.

Ischemia/reperfusion (I/R) injury is one of the main factors contributing to increased anterior compartment pressure (ACP) and tissue necrosis after trauma. I/R disturbs oxygen-derived free radical metabolism and induces lipid peroxidation injury, which is considered to be the most important mechanism of I/R injury pathogenesis[2]. Recently, more attention has been paid to the application of free radical scavengers and cytoprotective agents[3,4].

Taurine (2-aminoethane sulfonic acid), a sulfur-containing amino acid derived from the metabolism of methionine, is the most abundant intracellular amino acid in humans and is implicated in numerous biological and physiological functions. Taurine is not used in protein synthesis but rather is found free or in simple peptides. The diet of healthy individuals is the major source of taurine, although in the presence of vitamin B_6, taurine is also synthesized from methionine and cysteine. Taurine has been considered to be a strong endogenous cytoprotective agent. Its bioactions include inhibition of lipid peroxidation, detoxification, membrane stabilization, osmoregulation, modulation of cellular calcium levels, and it possibly acts physiologically as a trap for hypochlorous acid (HOCl). Exogenous administration of taurine has a preventive and therapeutic effect on tissue I/R injuries to the heart[5], liver[6], kidney[7] and hind limb muscles[8]. To explore the possibility of taurine therapy for compartment syndrome, we observed the alterations in muscular taurine content in the hind limbs of rabbits with I/R-induced compartment syndrome and the therapeutic effects of supplemental taurine on anterior compartment pressure and tissue damage.

Materials and methods

Reagents Taurine, triphenyltetrazolium chloride (TTC), sulphosalicylic acid, 3,3',5,5'-tetramethylbenzidine (TMB), thiobarbituric acid and 1,1,3,3-treaethyloxypropane were purchased from Sigma Company (St Louis, MO, USA). Other chemicals and reagents were of analytical purity.

Animals White rabbits weighing 1.5 kg to 2.0 kg were purchased from the Animal Center, Health Science Center, Peking University (Beijing, China). All animal experiments in this study were carried out with the approval of the Animal Care Committee of the First Hospital, Peking University, in accordance with the Chinese Council on Animal Care Guidelines. The rabbits were divided randomly into a taurine-treated group and a control group.

Preparation of ischemia-induced compartment syndrome model[9]. Briefly, white rabbits were anesthetized with intramuscular ketamine HCl (40 mg/kg) and acepromazine maleate (1 mg/kg) supplemented with 0.5% lidocaine HCl. A PE-50 tube filled with 0.9% NaCl and 10 kIU/L heparin was inserted into the right common carotid artery through a neck midline incision. The mean arterial blood pressure (MABP) and heart rate (HR) were recorded on a microcomputer-controlled physiological polygraph (PowerLab, 4s, Castle Hilllocation, Australia). A venous catheter was inserted into the right external jugular vein for collecting blood. A lower midline incision was made and extended across the groin. The dissection was carried caudally to the popliteal arteries. All arterial branches of the aorta, including the internal iliac arteries, were isolated, ligated with 4-0 silk sutures, and divided. The right hind limb was used for tibialis anterior muscle sampling for determination of TTC levels. The left hind limb was preserved for monitoring ACP. Ten minutes before ligation of both femoral arteries, animals given systemic infusions of heparin (100 IU/kg) to prevent aortic thrombosis. Just before femoral artery ligation, a full-thickness tibialis anterior muscle sample of the right hind limb was obtained to determine content of TTC, malondialdehyde and conjugated diene (CD), and venous blood was collected for assay of plasma malondialdehyde and CD content. After arterial ligation, the wounds were closed in a single layer with 3-0 silk sutures. The animals were allowed to recover and placed individually in a padded heated pen.

At the completion of the 7 h ischemic period, the animals were re-anesthetized and the lower midline incision and leg wounds were opened. Circulation between the proximal and the distal femoral arteries was restored by interposing a heparin-flushed polyethylene (PE 200) shunt. Five minutes before shunt placement, the animals received intravenous injections of heparin (100 IU/kg). Just before re-establishment of arterial flow, samples of tibialis anterior muscle were again obtained from the right hind limb. The pressure within the anterior muscle compartment of the left hind limb was measured with the use of the slit catheter technique, the catheter being connected to a saline-filled central venous pressure manometer[10]. Compartment pressure was monitored continuously and recorded at 1 h and 2 h of reperfusion. Beginning 10 min before shunt placement, experimental ani-

mals received 20 min intravenous infusions of taurine (1 g/kg in 8 mL normal saline) and the control group received 8 mL/kg normal saline only. Lactated Ringer's solution (10 mL·kg^{-1}·h^{-1}) was infused via an ear vein throughout each experiment. At the completion of each experiment, animals were humanely killed via lethal urethane injection.

Measurement of taurine content in plasma and gastrocnemius muscle Gastrocnemius muscle samples (0.2 g) were homogenized in 5 volumes of normal saline. The homogenate was mixed with 5 volumes of 10% sulphosalicylic acid and centrifuged at 1000×*g* for 10 min at 4 ºC. Plasma was obtained from collected blood by centrifugation at 2500×*g* for 10 min at 4 ºC. Taurine content in the tissue supernatant and plasma was determined by use of a high-performance amino acid analyzer (Hitachi Model 835, Hitachi, Japan).

Assay for TTC content and dry:wet ratios of tibialis anterior muscle The details of reduced TTC content as an estimate of oxidative metabolism have been reported by Belkin *et al*[11]. A spectrophotometric standard curve was constructed before each experiment. The TTC assay was repeated in duplicate at each of the experimental phases. In addition, at these intervals, minced samples of tibialis anterior muscle were weighed and allowed to dry at 90 ºC for 24 h. Samples were then re-weighed, and the dry weight : wet weight ratio value was calculated. These determinations were also carried out in duplicate.

Measurement of gastrocnemius muscle myeloperoxidase activity[12] Tissue myeloperoxidase activity was assessed by measuring the H_2O_2-dependent oxidation of TMB. The reactive mixture contained 2.1 mL of buffer-based (0.1 mol/L potassium phosphate buffer, pH 5.4) solution of H_2O_2 (0.1 mmol/L), 0.6 mL of the same buffer and 0.1 mL of TMB (1.6 mmol/L). The reaction was started by adding 200 μL of extract of tissue (at a protein concentration of 0.20 g/L), and the absorbance was measured every minute for 4 min. One unit of enzyme activity was defined as the amount of myeloperoxidase present that caused a change in absorbance of 1.0/min at 655 nm.

Assay of plasma lactate dehydrogenase (LDH) activity and content of malondialdehyde and CD in muscle and plasma Plasma LDH activity was measured by use of an automatic biochemistry analyzer. Malondialdehyde content was measured by use of the thiobarbituric acid reaction. Standard malondialdehyde was prepared by acid hydrolysis of 1,1,3, 3-treaethyloxypropane[13]. CD content was determined according to the method reported by Waller *et al*[14].

Incubation of muscle slices with oxidative stress *in vitro* The gastrocnemius were taken from another 6 normal anesthetized rabbits, and tissue slices (3 μm) were prepared. The 50 mg of prepared muscle slices was incubated in 1 mL of Krebs-Henseleit buffer at 37 ºC, equilibrated with 95% O_2 and 5% CO_2. The muscular oxidative stress was induced *in vitro* by adding three exogenous free radical-generating systems (FRGS): 400 μmol/L HOCL, 1.0 mmol/L hydrogen peroxide (H_2O_2), or an enzymatic system, composed of 20 IU/L of xanthine oxidase (XO) and its substrate xanthine (Xn, 0.5 mol/L). In each group, taurine (0, 5, 10, and 20 mmol/L)[15] was added. At the end of the incubation (10 min and 20 min, respectively), tissue slices were washed 3 times with ice-cold Krebs-Henseleit buffer, and homogenized for malondialdehyde determination.

Statistical analysis The data are expressed as mean±SD. Statistical analyses comparing multiple variables were carried out using ANOVA with the Student-Newman-Keuls test. For comparisons between 2 variables, the unpaired Student's *t*-test was used. $P<0.05$ was considered statistically significant.

Results

Ischemia/reperfusion-induced compartment syndrome in rabbits After 7 h of ischemia, the MABP, HR, ACP, muscular dry:wet ratio, taurine content and plasma LDH activity remained unchanged, but the TTC level was reduced by 80% ($P<0.01$). Compared with 7 h ischemia, 2 h reperfusion resulted in decreased MABP and HR ($P<0.01$); however, ACP increased 4.5-fold ($P<0.01$) (Figure 1) and plasma LDH activity increased 2.5-fold ($P<0.01$). Muscles showed edema, the dry:wet ratio decreased by 14%, and taurine content was reduced by 33% in gastrocnemius muscle, but increased by 37% in plasma. The muscular TTC level was not further altered from that after ischemia (Table 1).

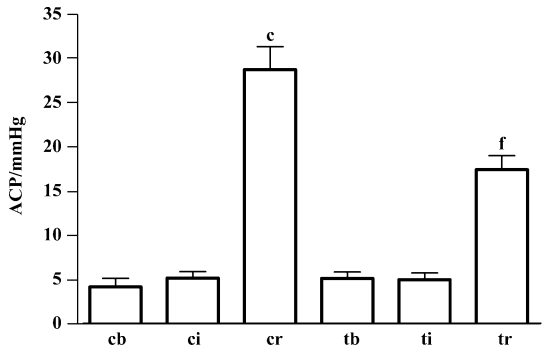

Figure 1. Changes in anterior compartment pressure (ACP). $^{c}P<0.01$ *vs* control at 7 h ischemia; $^{f}P<0.01$ *vs* control at 2 h reperfusion. n=8. Mean±SD. cb, control basal; ci, control ischemia; cr, control reperfusion; tb, taurine basal; ti, taurine ischemia; tr, taurine reperfusion.

Treatment with taurine inhibited skeletal muscle I/R injury After ischemia, the values of various parameters were not statistically different between the control and taurine groups. At 2 h reperfusion, the administration of taurine before reperfusion resulted in a stable MABP and HR, the values being higher than those in the control group ($P<0.01$). The ACP was lowered by 39% ($P<0.01$). The muscular dry:wet weight ratio increased by 16%. Tissue taurine content was elevated by 88%, but plasma LDH activity was decreased by 36% ($P<0.01$). Muscular TTC content was 1.5-fold higher than controls (Table 1).

Treatment with taurine inhibited muscular myeloperoxidase activity induced by I/R After 7 h of ischemia, the gastrocnemius muscle myeloperoxidase activity remained unchanged. However, 2 h reperfusion resulted in a significant 3.5-fold increase in gastrocnemius muscle myeloperoxidase activity ($P<0.01$). Administration of taurine before reperfusion inhibited the myeloperoxidase activity by 48% compared with the control group ($P<0.01$, Figure 2).

Supplementation of taurine attenuated lipid-peroxidation injury induced by I/R Ischemia (7 h) alone did not significantly change the levels of plasma and muscular lipid peroxidation products from those before ischemia (all $P>0.05$). After 2 h of reperfusion, the control group rabbits showed a significant increase in malondialdehyde and CD content in plasma and tibialis anterior muscle compared with before reperfusion (all $P<0.01$). The taurine group showed an inhibited formation of lipid peroxidation products: decreased plasma and muscle malondialdehyde content, by 38% and 22% ($P<0.01$), and decreased CD content, by 23% and 30% ($P<0.01$), respectively, compared with the control group (Table 2).

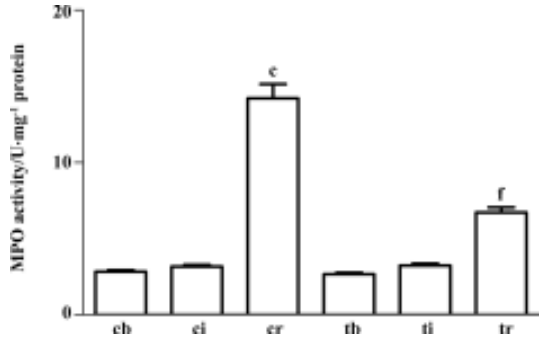

Figure 2. Changes of gastrocnemius muscle myeloperoxidase (MPO) activity. n=5. Mean±SD. $^{c}P<0.01$ *vs* control at 7 h ischemia. $^{f}P<0.01$ *vs* control at 2 h reperfusion. cb, control basal; ci, control ischemia; cr, control reperfusion; tb, taurine basal; ti, taurine ischemia; tr, taurine reperfusion.

Protective effects of taurine against *in vitro* FRGS-induced oxidative stress In our experiment the concentrations of three FRGS all induced lipid peroxidation, and malondialdehyde content increased to a resemble level ($P<0.01$). Taurine decreased malondialdehyde content in a concentration-dependent manner in tissue slices incubated with H_2O_2 for 20 min ($P<0.01$) and 20 mmol/L taurine slightly decreased malondialdehyde content in tissue slices incubated with H_2O_2 for 10 min ($P<0.05$). Taurine did not change malondialdehyde content when incubated with XO and Xn (produced O_2^-) ($P>0.05$). In muscle slices incubated with HOCl, taurine decreased malondialdehyde content in a concentration- and time-dependent manner ($P<0.01$). The effect was stronger than that against H_2O_2 and O_2^- (Figure 3, 4).

Table 1. Mean arterial blood pressure (MABP) (mmHg), heart rate (HR) (beat/min), anterior compartment pressure (ACP)(mmHg), dry weight : wet weight ratios, content of triphenyltetrazolium (TTC) (μg/mg protein) and taurine (μmol/L, μmol/g ww) and activity of lactate dehydrogenase (LDH)(IU/L) in plasma of rabbits with compartment syndrome. n=8. Mean±SD. $^{c}P<0.01$ *vs* control basal. $^{f}P<0.01$ *vs* control ischemia 7 h; $^{g}P<0.05$; $^{i}P<0.01$ *vs* control reperfusion 2 h.

	Control			Taurine		
	Basal	Ischemia	Reperfusion	Basal	Ischemia	Reperfusion
MABP	90±3	93±4	84±3^{f}	93±4	95±5	89±3^{h}
HR	262±14	280±16	228±20^{f}	277±12	288±19	251±17^{i}
Dry:wet weight ratio	0.23±0.01	0.22±0.02	0.19±0.02^{f}	0.23±0.01	0.22±0.01	0.22±0.02^{i}
Taurine content						
Plasma	204±17	211±14	288±23^{f}	218±15	222±14	488±31^{d}
Muscle	16.62±1.22	16.07±1.16	10.74±2.72^{f}	17.04±1.06	16.22±1.17	20.20±3.11^{i}
LDH in plasma	30.27±2.61	28.85±2.66	101.2±16.7^{f}	26.42±3.27	31.33±2.86	64.74±12.88^{i}
TTC in muscle	5.22±1.46	1.07±0.11^{c}	0.92±0.13	4.98±1.11	1.18±0.10	2.28±0.24^{i}

Table 2. Content of malondialdehyde (nmol/mg protein) and conjugated diene (CD) in plasma and muscle of rabbits with compartment syndrome. n=8. Mean±SD. ^{c}P<0.01 *vs* control ischemia 7 h. ^{f}P<0.01 *vs* control reperfusion 2 h.

	Control			Taurine		
	Basal	7-h Ischemia	2-h Reperfusion	Basal	7-h Ischemia	2-h Reperfusion
Malondialdehyde content						
Muscle	22.8±3.2	24.0±4.1	39.3±5.0^{c}	25.7±3.3	23.1±4.6	30.7±5.2^{f}
Plasma	2.78±0.26	2.46±0.24	5.79±1.12^{c}	2.51±0.31	2.97±0.27	3.58±0.41^{f}
CD content						
Muscle	1.17±0.21	1.33±0.31	2.02±0.48^{c}	0.93±0.31	1.18±0.41	1.48±0.38^{f}
Plasma	0.85±0.22	0.79±0.31	1.55±0.22^{c}	0.79±0.21	0.91±0.31	1.19±0.22^{f}

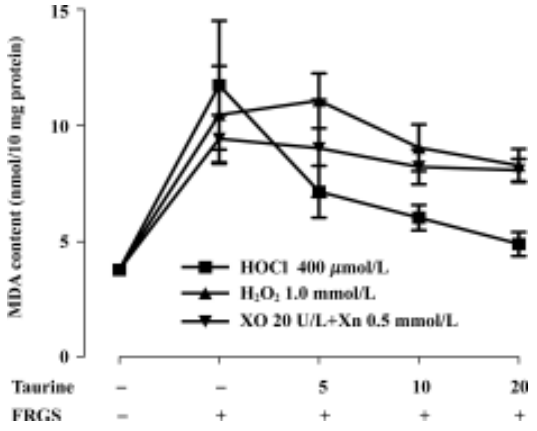

Figure 3. Protective effects of taurine (0, 5, 10, 20 mmol/L) against free radical-generating system (FRGS)-induced oxidative stress. Incubation continued for 10 min. n=6. Mean±SD.

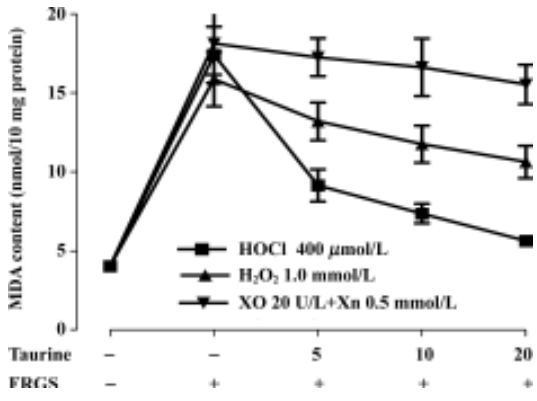

Figure 4. Protective effects of taurine (0, 5, 10, 20 mmol/L) against free radical generating system (FRGS)-induced oxidative stress. Incubation continued for 20 min. n=6. Mean±SD.

Discussion

A realistic, working definition of compartment syndrome is skeletal muscle injury that leads to partial or total destruction of the integrity of cell walls, with partial or total release of intracellular contents into the interstitial fluid space. Once in the interstitial fluid, these contents change the osmotic gradient of the tissues, with a subsequent shift of fluid from the circulation to the injured tissues, increasing the pressure within muscles encased in fascial sheaths. In compartment syndrome, swelling caused by the osmotic gradient increases the local pressure above the systolic pressure and hence suppresses blood flow within the muscular anatomic unit. This process leads to prolonged ischemia and further cell death with the additional release of intracellular contents.

The exact mechanism of compartment syndrome is not fully understood. Perler *et al*[16] reported that free radical-mediated reperfusion injury was the most important factor in compartment syndrome. Ablating free radicals by scavenging superoxide radicals at reperfusion with superoxide dismutase or by blocking secondary hydroxyl radical formation with deferoxamine significantly ameliorated the increased compartment pressure and improved muscle I/R injury. Oxidative stress can lead to compartment syndrome, as ischemia and hypoxia, reperfusion-induced alteration of intracellular osmostasis, induced cellular swelling, Ca^{2+} overload, decreased stability of cell membranes and leaking cytosolic enzymes.

Taurine is a strong endogenous cytoprotective agent and has multiple functions such as in membrane stabilization, detoxification, antioxidation, osmoregulation and calcium modulation[17]. Because taurine has protective effects in I/R injury in various organs[5–7], we investigated its possible effect in protecting skeletal muscle against I/R-induced com-

partment syndrome.

We chose the rabbit hind-limb model of compartment syndrome because the fascial compartments of rabbits are anatomically similar to those of humans. The elevation in ACP after 2 h of reperfusion was dramatic. The tissue showed edema, and the intracellular contents leaked into the extracellular space. TTC-level reduction, an indirect measure of oxidative metabolism, was decreased during ischemia and reperfusion and indicated that muscle viability was reduced. These observations have been reported in the literature[9]. During reperfusion, the taurine content of the gastrocnemius muscle was significantly reduced but that in plasma increased, which suggests increased release of taurine content out of the tissue. Administration of taurine before reestablishment of arterial flow increased tissue taurine content and resolved features of the compartment syndrome: MABP and HR were restored, ACP declined, and muscular edema and necrosis were relieved. Zhang *et al*[8] reported that taurine improved rat hind-limb I/R injury induced by a tourniquet through inhibiting lipid peroxidation. In this study, we found that malondialdehyde and CD levels, the final products of lipid peroxidation, were elevated during reperfusion, but pretreatment with taurine effectively inhibited the formation of lipid-peroxidation products, which suggests that taurine could be effective in ameliorating compartment syndrome. To illustrate the pathway by which taurine inhibited lipid peroxidation, we observed myelo-peroxidase activity in gastrocnemius muscle from rabbits with I/R injury. Muscular myeloperoxidase activity increased significantly showed that neutrophil infiltrated and HOCl induced oxidative stress injury during I/R. The results from these *in vitro* studies further confirmed that taurine could reduce the level of oxidative injury caused by HOCl specifically.

Taurine is a sulfur-containing amino acid, the most abundant free amino acid in excitable tissues and cells, including those in nerves and muscles. Experimental data reveals that many functions of taurine, such as membrane stabilization, osmoregulation and calcium modulation, could be considered to be beneficial for compartment syndrome. Transport of taurine across cell membranes is one of the major steps in its physiological roles. For example, the biophysical and biochemical properties of taurine make it an excellent candidate for osmoregulation. During hyper-osmolar conditions, the increase in cell taurine content appears to be achieved primarily by active transport of taurine into the cell, while under hypo-osmolar conditions, a decrease in intracellular taurine content is a consequence of a marked stimulation in taurine efflux, which protects cells from dehydration with edema[18]. Taurine regulates the metabolism of phospholipid, the main content of the cellular membrane, and directly affects the stability of the membrane. In addition, taurine maintains the homeostasis of calcium by regulating the interaction between Ca^{2+} and the membrane[19].

In addition, taurine is an antioxidative agent and prevents injury from lipid peroxidation. However, the mechanism by which it does this is unclear. In the present study, muscular myeloperoxidase activity was increased significantly in I/R-induced compartment syndrome, which suggested that HOCl-induced oxidative stress might play an important role in I/R-induced compartment syndrome. Aneja *et al*[20] reported that extensive I/R-induced tissue injury was associated with neutrophil infiltration and myeloperoxidase activity enhancement. Myeloperoxidase is a major neutrophil protein and is also present in monocytes. In neutrophils, it is stored in azurophilic granules and released during phagocytosis. It is a heme enzyme that uses the superoxide and hydrogen peroxide generated by the neutrophil oxidative burst to produce hypochlorous acid and other reactive oxidants. The role of HOCl is well established in tissue damage associated with reperfusion injury. HOCl is a major oxidant produced by neutrophils and monocytes, via the myeloperoxidase-catalyzed oxidation of chloride by hydrogen peroxide. HOCl is a potent oxidant capable of damaging host tissue during inflammation[21]. The strong oxidizing species HOCl plays a highly significant role in the bactericidal function of the neutrophil. However, inappropriate and/or excessive activation of neutrophils leads to oxidative stress and collateral damage to surrounding tissues.

As an antioxidant, taurine could effectively antagonize the toxic effect of HOCl. More recent information has revealed that taurine could interact with peroxide anions to form stable products such as taurine chloramine (TauCl). TauCl is formed through the sequestration of taurine with HOCl and has been found to be an exceptionally stable and long-lived compound with cytoprotective properties due to its ability to preserve cellular function in response to physiological stress[19]. In *in vitro* studies, taurine greatly inhibited lipid peroxidation induced by OCl^-, indicating the important protective role of taurine against OCl^- attack[22]. It is reasonable that taurine ameliorates ACP in compartment syndrome induced by I/R at least in part through scavenging HOCl and attenuating lipid peroxidation.

At present, the only approach to relieving compartment syndrome is surgical fasciotomy to allow decompression of the elevated intracompartmental pressure, thereby facilitating microvascular perfusion. Although highly effective, fasciotomy is an imperfect treatment, so effective pharmacological approaches to treat compartment syndrome are

required. Taurine is an endogenous substance in the body; it is therefore not associated with toxicity or drug dependence, and is well tolerated when used clinically[23]. It is reasonable to suggest that the clinical application of taurine could be a new strategy for the prevention and treatment of compartment syndrome.

References

1 Mubarek SJ, Hargens AR. Acute compartment syndromes. Surg Clin North Am 1983; 63: 539–65.

2 Timoshin AA, Lakomkin VL, Ruuge EK. Effect of a series of brief cycles of ischemia and reperfusion on free radical centers of isolated rat myocardial tissue. Biofizika 1998; 43: 134–8.

3 Van Haaften RI, Haenen GR, Evelo CT, Bast A. Effect of vitamin E on glutathione-dependent enzymes. Drug Metab Rev 2003; 35: 215–53.

4 Dogru Abbasoglu S, Kanbagli O, Balkan J, Cevikbas U, Aykac-Toker G, Uysal M. The protective effect of taurine against thioacetamide hepatotoxicity of rats. Hum Exp Toxicol 2001; 20: 23–7.

5 Oz E, Erbas D, Gelir E, Aricioglu A. Taurine and calcium interaction in protection of myocardium exposed to ischemic reperfusion injury. Gen-Pharmacol 1999; 33: 137–41.

6 Wettstein M, Haussinger D. Taurine attenuates cold ischemia-reoxygenation injury in rat liver. Transplantation 2000; 69: 2290–6.

7 Michalk DV, Hoffmann B, Minor T. Taurine reduces renal ischemia/reperfusion injury in the rat. Adv Exp Med Biol 2003; 526: 49–56.

8 Zhang LY, Dong SY, Xu J, Yu F, Pang YZ, Tang CS, *et al*. Effect of taurine on rats with tourniquet shock. China J Pathphysiol 1993; 9: 208.

9 Hakaim AG, Corsetti, R, Cho S. The pentafraction of hydroxyethyl starch inhibits ischemia-induced compartement syndrome. J Trauma 1994; 37: 18–21.

10 Rorabeck CH, Castle GSP, Hardie R, Logan J. Compartment pressure measurements: an experimental investigation using the slit catheter. J Trauma 1981; 21: 446–9.

11 Belkin M, Brown RD, Wright JC. A new quantitative spectrophotometric assay for ischemia-reperfusion injury in skeletal muscle. Am J Surg 1988; 156: 83–8.

12 Naito Y, Yoshikawa T, Matsuyama K, Yagi N, Arai M, Nakamura Y, *et al*. Neutrophils, lipid peroxidation, and nitric oxide in gastric reperfusion injury in rats. Free Radic Biol Med 1998; 24: 494–502.

13 Skawa T, Matashushita S. Thiobarbituric acid test for detecting lipid peroxide. Lipids 1979; 14: 401–6.

14 Waller RL, Recknagel RO. Determination of lipid conjugated dienes with tetracyanoethylene-^{14}C: significance for study of the pathology of lipid peroxidation. Lipids 1977; 12: 914–21.

15 Chang L, Xu JX, Zhao J, Pang YZ, Tang CS, Qi YF. Taurine antagonized oxidative stress injury induced by homocysteine in rat vascular smooth muscle cells. Acta Pharmacol Sin 2004; 25: 341–6.

16 Perler BA, Tohmeh AG, Buckley GB. Inhibition of the compartment syndrome by ablation of free radical mediated reperfusion injury. Surgery 1990; 108: 40–7.

17 Huxtable RJ. Physiological actions of taurine. Physiol Rev 1992; 72: 101–63.

18 Bitoum M, Levillain O, Tappaz M. Gene expression of the taurine transporter and taurine biosynthetic enzymes in rat kidney after antidiuresis and salt loading. Pflugers Arch Eur J Physiol 2001; 442: 87–95.

19 Lourenco R, Camilo ME. Taurine: a conditionally essential amino acid in humans? An overview in health and disease. Nutr Hosp 2002; 17: 262–70.

20 Aneja R, Hake PW, Burroughs TJ, Denenberg AG, Wong H, Zingarelli B. Epig allocatechin, a green tea polyphenol, attenuates myocardial ischemia reperfusion injury in rats. Mol Med 2004; 10: 55–62.

21 Winterbourn CC, Vissers MC, Kettle AJ. Myeloperoxidase. Curr Opin Hematol 2000; 7: 53–8.

22 Li JX, Pang YZ, Tang CS, Li ZQ. Protective effect of taurine on hypochlorous acid toxicity to nuclear nucleoside triphosphatase in isolated nuclei from rat liver. World J Gastroenterol 2004; 10: 694–8.

23 Chang L, Xu J, Yu F, Zhao J, Tang X, Tang CS. Taurine protected myocardial mitochondria injury induced by hyperhomocysteinemia in rats. Amino Acids 2004; 27: 37–48.

Acta Pharmacologica Sinica 2005 Jul; 26 (7): 828–834

Blackwell Publishing

Full-length article

Effect of hydrogen peroxide on persistent sodium current in guinea pig ventricular myocytes[1]

Ji-hua MA[2], An-tao LUO, Pei-hua ZHANG

Cardio-Electrophysiological Research Laboratory, Medical College, Wuhan University of Science and Technology, Wuhan 430080, China

Key words

hydrogen peroxide; myocardium; patch-clamp techniques; sodium channels

[1] Project supported by the Natural Science Foundation of Hubei Province (No 2003ABA189).
[2] Correspondence to Prof Ji-hua MA.
Phn/Fax 86-27-6886-2109.
E-mail mjhua@wust.edu.cn

Received 2005-01-11
Accepted 2005-04-11

doi: 10.1111/j.1745-7254.2005.00154.x

Abstract

Aim: To study the effect of hydrogen peroxide (H_2O_2) on persistent sodium current ($I_{Na.P}$) in guinea pig ventricular myocytes. **Methods:** The whole-cell, cell-attached, and inside-out patch-clamp techniques were applied on isolated ventricular myocytes from guinea pig. **Results:** H_2O_2 (0.1 mmol/L, 0.5 mmol/L and 1.0 mmol/L) increased the amplitude of whole-cell $I_{Na.P}$ in a concentration-dependent manner, and glutathione (GSH 1 mmol/L) reversed the increased $I_{Na.P}$. H_2O_2 (1 mmol/L) increased persistent sodium channel activity in cell-attached and inside-out patches. The mean open probability was increased from control values of 0.015±0.004 and 0.012±0.003 to 0.106±0.011 and 0.136±0.010, respectively ($P<0.01$ *vs* control). They were then decreased to 0.039±0.024 and 0.027±0.006, respectively, after the addition of 1 mmol/L GSH ($P<0.01$ *vs* H_2O_2). The time when open probability began to increase and reached a maximum was shorter in inside-out patches than that in cell-attached patches (4.8±1.0 min *vs* 11.5±3.9 min, $P<0.01$; 9.6±1.6 min *vs* 18.7±4.7 min, $P<0.01$). **Conclusion:** H_2O_2 increased the $I_{Na.P}$ of guinea pig ventricular myocytes in a concentration-dependent manner, possibly by directly oxidating the cell membrane.

Introduction

The persistent sodium current ($I_{Na.P}$) in ventricular myocytes results from inactivate-resistant sodium channels continuing to open for long periods during prolonged depolarization. It plays an important role in maintaining the plateau of the action potential (AP), determining AP duration and transmural dispersion of repolarization, and development of cardiac arrhythmias[1]. Some studies suggest that hypoxia can increase cardiomyocyte $I_{Na.P}$ and the potentiated $I_{Na.P}$ can induce intracellular calcium overload and ischemic arrhythmias[2,3]. Recently, we studied the mechanisms of $I_{Na.P}$ generation and augmentation in normoxic and hypoxic conditions. The results suggest that excess nitric oxide (NO) produced during hypoxia can increase ventricular myocyte $I_{Na.P}$ by oxidizing cell membrane sodium channel protein, and the reducing agent dithiothreitiol (DTT) can block the potentiated $I_{Na.P}$ completely. This implies that oxidants can increase cardiac $I_{Na.P}$, and that reducing and the antioxidation agents can reduce $I_{Na.P}$[4]. A burst of hydrogen peroxide (H_2O_2) is generated in the myocardium during ischemia. Its effects on cell damage and membrane lipid peroxidation have been reported widely. However, reports on the effect of H_2O_2 on $I_{Na.P}$ in ventricular myocytes are scarce and contradictory[5,6]. In the present study, we examined the effects of H_2O_2 on $I_{Na.P}$ in guinea pig ventricular myocytes and explored the possible mechanisms underlying them.

Materials and methods

Isolation of guinea pig ventricular myocytes Adult guinea pigs (250 g–300 g, of either sex, Grade II, Certificate No 19-023, the Experiment Animal Center of Wuhan University of Science and Technology, Wuhan, China) were anesthetized with pentobarbital sodium (30 mg/kg, ip) 20 min after an intraperitoneal injection of 2000 units of heparin. Hearts were excised rapidly and perfused retrogradely on a langendorff apparatus (with a Ca^{2+}-free Tyrode's solution for 5 min), before the perfusate was switched to an enzyme-

containing solution [0.1 g/L collagenase type I, 0.01 g/L protease E, 0.5 g/L bovine serum albumin (BSA) in the same solution] for 8 min–10 min. The perfusate was finally changed to KB solution containing: 70 mmol/L KOH, 20 mmol/L taurine,50 mmol/L glutamic acid, 40 mmol/L KCl, 20 mmol/L KH_2PO_4, 3 mmol/L $MgCl_2$, 0.5 mmol/L egtazic acid, 10 mmol/L HEPES, and 10 mmol/L glucose, pH 7.4, for a 5 min period. These perfusates were bubbled with 100% O_2 and maintained at 37 °C. The ventricles were cut into small chunks and gently agitated in KB solution. The cells were filtered through nylon mesh and stored in KB solution at 4 °C.

Electrical recordings Myocytes were transferred to a chamber mounted on the mechanical stage of an inverted microscope (XDS-1, Chongqing, China), and perfused with normal Tyrode's solution containing: 135 mmol/L NaCl, 5.4 mmol/L KCl, 1.8 mmol/L $CaCl_2$, 1 mmol/L $MgCl_2$, 0.33 mmol/L NaH_2PO_4, 10 mmol/L HEPES, 10 mmol/L glucose, pH7.4. Patch electrodes were pulled with a 2-stage puller (PP-830, Narishige Group, Tokyo, Japan). For whole-cell recordings, their resistances were in the range of 1.5 MΩ–3 MΩ when filled with a pipetted solution containing: 120 mmol/L CsCl, 1.0 mmol/L $CaCl_2$, 5 mmol/L $MgCl_2$, 5 mmol/L Na_2ATP, 10 mmol/L TEACl, 11 mmol/L egtazic acid, and 10 mmol/L HEPES, pH 7.3. The external solution was Tyrode's solution with $CdCl_2$ (200 μmol/L). For single-channel recordings, the shanks of pipettes with resistance of 6 MΩ–10 MΩ were coated with Sylgard and the tips were heat polished. The pipettes were filled with a solution composed of 180 mmol/L NaCl, 1.3 mmol/L KCl, 1.5 mmol/L $CaCl_2$, 0.5 mmol/L $MgCl_2$, 5 mmol/L Na_2ATP, 3.0 mmol/L $CoCl_2$, 10 mmol/L TEACl, 10 mmol/L 4-AP, 10 mmol/L CsCl, 5 mmol/L HEPES, and 5 mmol/L glucose, pH 7.4. For single-channel cell-attached recordings, the myocytes were perfused with normal Tyrode's solution. For single-channel inside-out recordings, the perfusate was composed of 120 mmol/L KCl, 0.1 mmol/L $CaCl_2$, 2.0 mmol/L $MgCl_2$, 0.1 mmol/L egtazic acid, and 10 mmol/L HEPES, pH 7.4. These perfusates were bubbled with 100% O_2. All experiments were carried out at room temperature (21±2 °C). Currents were obtained with a patch-clamp amplifier (EPC-9, Heka Electronic, Lambrecht, Pfalz, Germany), filtered at 2 kHz, digitized at 10 kHz, and stored on a computer hard disk for further analysis.

Drugs and reagents Collagenase type I and CsCl were obtained from Gibco (GIBCO TM, Invitrogen Co., Paisley, UK). Protease E, 4-AP, TEACl, Na_2ATP, and egtazic acid were purchased from Sigma Chemical Co (Saint Louis, Missouri, USA). Bovine serum albumin, HEPES, and taurine were obtained from Roche(Basel, Switzerland). Tetrodotoxin (TTX) was purchased from Hebei Fisheries Research Institute (Qinhuangdao, China). H_2O_2 was a production of Wuhan Zhongnan Chemical Reagent Co (Wuhan, China). Reduced GSH was a product of Shanghai Bio Life Science and Technology (Shanghai, China).

Data analysis Whole-cell recordings were analyzed using PulseFit (V8.65, HEKA). Current density was calculated by dividing the current amplitude by the cell capacitance. Single-channel recordings were analyzed using TAC+TACFit (X4.0.9, Bruxton, Seattle, Washington, USA). Capacitance transients and leakage currents were nullified by off-line subtracting fits of average blunt traces. The channel activity after a 50 ms depolarization pulse was calculated as persistent sodium channel. Open probability was calculated from the total open times of 50 sweeps divided by the total sweep duration. Histograms of channel open time distribution were fitted to single exponentials using TACFit. All data were expressed as mean±SD. Student's *t*-test was used for simple comparisons and ANOVA was used when appropriate. $P<0.05$ was considered to be statistically significant.

Results

H_2O_2 increases the amplitude of $I_{Na.P}$ in a concentration-dependent manner The experiments were carried out in the whole-cell configuration of the patch-clamp techniques. Currents were evoked by a 500 ms pulse to -30 mV from a holding potential of -120 mV. TTX (1.5 μmol/L) blocked completely the smaller persistent inward current, but had less effect on the transient sodium current ($I_{Na.T}$), (n=7 cells from 4 guinea pigs; Figure 1). The recorded current was proved to be $I_{Na.P}$.

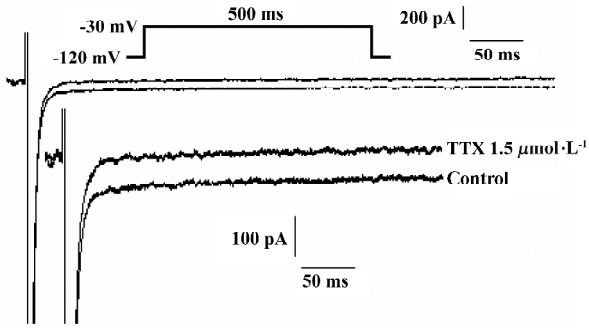

Figure 1. Effect of tetrodotoxin (TTX) on persistent sodium current ($I_{Na.P}$) in guinea pig ventricular myocytes. The figure shows the current curves before and after exposure to TTX (1.5 μmol/L).

Using the pulse protocol described above, 4 cells were perfused with H_2O_2 (0.5 mmol/L) after the $I_{Na.P}$ had stabilized. $I_{Na.P}$ began to increase at approximately 5 min and reached a

maximum at 10–12 min after perfusion with H_2O_2. The current is able to last for another 30 min at this level. In another 8 cells, H_2O_2 was added into solution in a cumulative manner after the control $I_{Na.P}$ values were recorded. Cells were perfused with H_2O_2 (0.1 mmol/L, 0.5 mmol/L and 1.0 mmol/L) and GSH (1.0 mmol/L) at 10 min intervals, and the currents were recorded in the same cell. H_2O_2 increased the amplitude of $I_{Na.P}$ in a concentration-dependent manner, while GSH reversed the increased $I_{Na.P}$ (Figure 2). The amplitude of $I_{Na.P}$ was recorded at 200 ms of the pulse to eliminate the effect of $I_{Na.T}$. H_2O_2 (0.1 mmol/L, 0.5 mmol/L, and 1.0 mmol/L) increased the mean current density of $I_{Na.P}$ from the control value 0.385±0.032 pA/pF to 0.578±0.080 pA/pF , 0.763±0.094 pA/pF, and 1.007±0.179 pA/pF, respectively (n=8, P<0.01 *vs* control). The mean current density was decreased to 0.329± 0.063 pA/pF after the application of 1.0 mmol/L GSH (n=8, P<0.05 *vs* control).

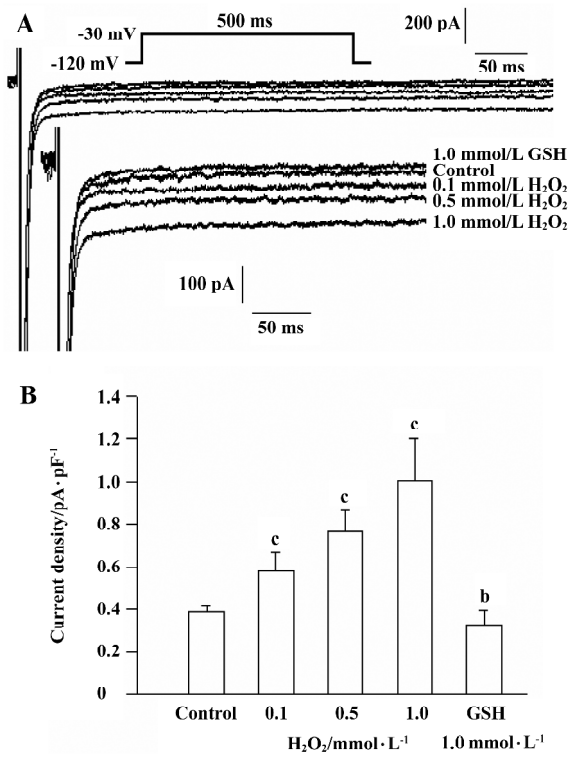

Figure 2. Effect of H_2O_2 on persistent sodium current ($I_{Na.P}$) in guinea pig ventricular myocytes. (A) H_2O_2 (0.1 mmol/L, 0.5 mmol/L and 1.0 mmol/L) increases $I_{Na.P}$ in a concentration-dependent manner, and glutathione (GSH; 1.0 mmol/L) reverses the increased $I_{Na.P}$ induced by H_2O_2. (B) The mean current densities of $I_{Na.P}$ under different conditions. n=8 cells. Mean±SD. ^bP<0.05; ^cP<0.01 *vs* control.

Effect of glutathione on persistent sodium channel activity induced by H_2O_2 The experiments were carried out in cell-attached and inside-out patches. Currents were activated by a 700 ms voltage pulse to -50 mV from a holding potential of -120 mV.

In cell-attached recording (the resting membrane potential was -74.6±7.7 mV, n=12, which was measured in current-clamp mode under identical conditions), bath solution with 1 mmol/L H_2O_2 was used to perfuse the cell. In 17 cell-attached patches, persistent sodium channel activity increased remarkably at 11.5±3.9 min. The current type was changed from background currents to burst currents (flaring up rapidly but subsiding over a very long period). At 18.7 ± 4.7 min the channel activity reached a maximum. In 6 of the 17 patches, the channel activity could maintain for another 30 min at this level (Figure 3).

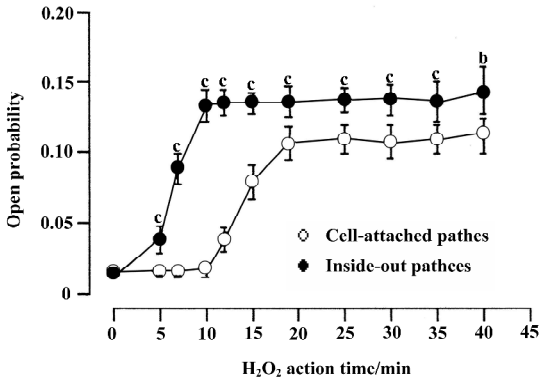

Figure 3. H_2O_2 increases persistent sodium channel activity in a time-dependent manner. The figure shows the mean open probability changing course with time in cell-attached (n=6) and inside-out (n=5) patches after the application of 1 mmol/L H_2O_2. The abscissa shows the action time of H_2O_2. The ordinate shows the mean open probability. n=5–6 patches. Mean±SD. ^bP<0.05; ^cP<0.01 *vs* cell-attached patches group.

In 5 of the 17 patches, lidocaine (100 μmol/L) was added to the bath solution and the increased $I_{Na.P}$ was blocked completely at approximately 5 min (Figure 4).

We applied 1 mmol/L GSH in 6 other patches. The presentation traces are shown in Figure 5. Before exposure to H_2O_2, channel activity was very low or often absent (Figure 5A). After 10-min treatment with H_2O_2, persistent sodium channel activity increased markedly (Figure 5B) and reached a maximum at 20 min (Figure 5C). GSH (1 mmol/L) reversed the increase in sodium channel activity caused by H_2O_2 (Figure 5D). H_2O_2 (1 mmol/L) increased the mean open probability and mean open time from control values of 0.015± 0.004 and 0.744±0.190 ms to 0.106±0.011 and 1.966±0.539 ms, respectively (n=6, both P<0.01 *vs* control). They were then decreased to 0.039± 0.024 and 1.137±0.153 ms, respectively,

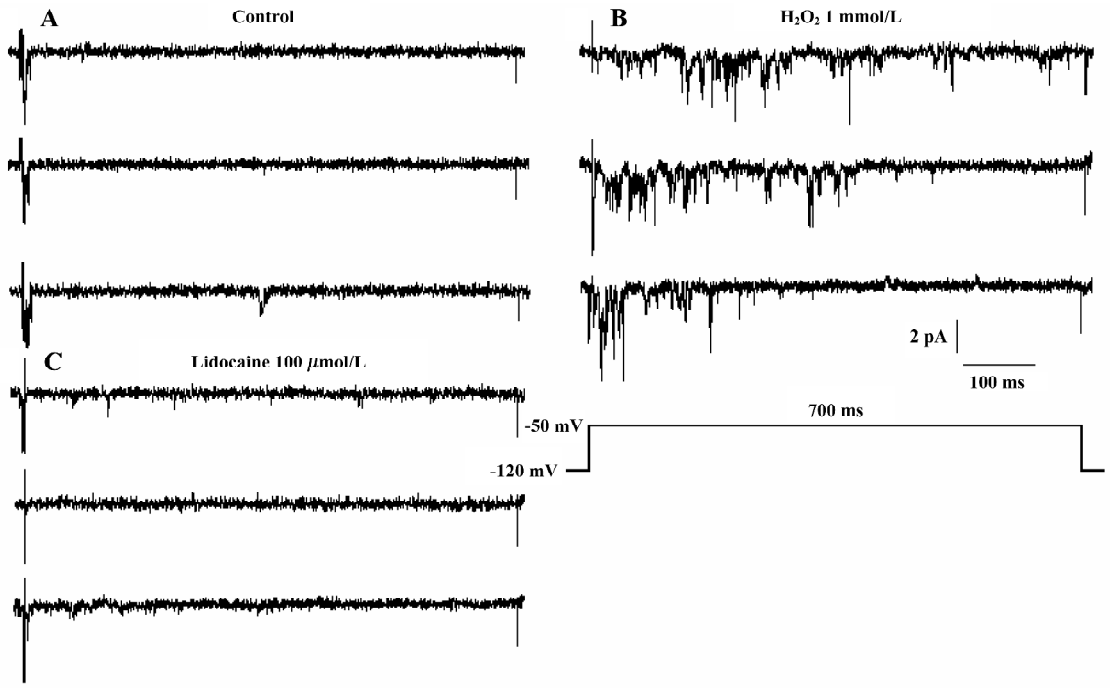

Figure 4. Lidocaine blocks persistent sodium channel activity induced by H_2O_2. The individual current traces were evoked by a voltage step to -50 mV from a holding potential of -120 mV in a cell-attached patch. (A) Control, (B) H_2O_2 (1 mmol/L) and (C) lidocaine (100 μmol/L).

after the application of 1 mmol/L GSH (n=6, both P<0.01 *vs* H_2O_2). Figure 6 gives an example of corresponding all-time histograms and mean open-time histograms from another cell-attached patch.

The results for inside-out recordings were similar to those for cell-attached recordings. In the 10 inside-out patches, persistent sodium channel activity increased markedly at 4.8±1.0 min and reached maximum at 9.6±1.6 min after the application of 1 mmol/L H_2O_2. Compared with the cell-attached recordings, the times when the sodium channel activity in inside-out recordings began to increase (4.8±1.0 min *vs* 11.5±3.9 min, P<0.01) and reached a maximum (9.6±1.6 min *vs* 18.7±4.7 min, P<0.01) were shorter. In 5 of the 10 patches, the channel activity could be maintained for another 30 min at this level (Figure 3). In the other 5 patches, 1 mmol/L GSH was applied. H_2O_2 (1 mmol/L) increased the mean open probability and mean open time from the control value 0.012±0.003 and 0.537±0.015 ms,respectively, to 0.136±0.010 and 0.966±0.130 ms, respectively (n=5, both P<0.01 *vs* control). They were decreased to 0.027±0.006 and 0.672±0.042 ms, respectively, after the application of 1 mmol/L GSH (n=5, both P<0.01 *vs* H_2O_2).

Discussion

A large number of studies have reported that H_2O_2 in cardiomyocytes is increased during ischemia. The excessive amount of H_2O_2 leads to intracellular Ca^{2+} overload and cell damage. Recent reports show that hypoxia can increase $I_{Na.P}$ in ventricular myocytes, induces intracellular sodium overload, which promotes Ca^{2+} overload via reverse Na^+-Ca^{2+} exchange, and prolongs the duration of action potential (AP) after-depolarization[2,3]. Thus, the present study on the effect of H_2O_2 on $I_{Na.P}$ is very important to further understand the mechanisms of cardiomyocytes injury induced by H_2O_2, and the nature of $I_{Na.P}$.

In whole-cell patch-clamp recordings, 1.5 μmol/L TTX blocked completely the smaller inactivation-resistant inward current (Figure 1). Similarly, in cell-attached recordings, 100 μmol/L lidocaine blocked the potentiated inward currents induced by H_2O_2 (Figure 4). These results affirm that the recorded currents are I_{NaP}. Barrington *et al* reported that there were no effects from a 30-min exposure to 1 mmol/L H_2O_2 on the slowly inactivating sodium currents of feline ventricular myocytes, so hydroperoxide could not induce an intracellular sodium overload[5]. However, our study shows that H_2O_2 increases the amplitude of whole-cell $I_{Na.P}$ of guinea pig ventricular myocytes in a concentration-dependent manner (Figure 2) and the activity of persistent sodium channel in both single-channel recordings (Figures 3–6). These results confirm that H_2O_2 can increase $I_{Na.P}$ of guinea pig

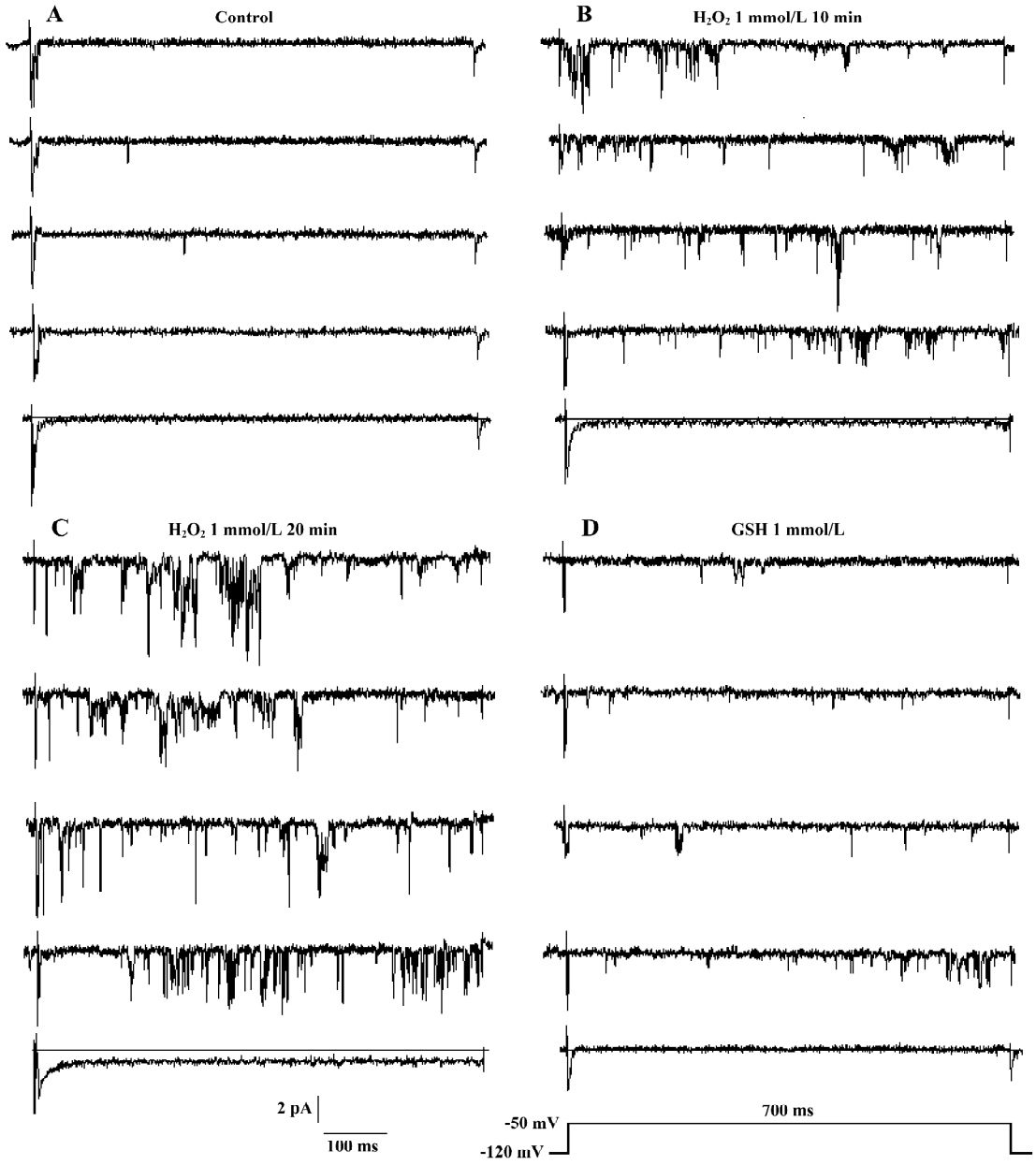

Figure 5. Effect of glutathione (GSH) on persistent sodium channel activity induced by H_2O_2. The individual current traces were evoked by a voltage step to -50 mV from a holding potential of -120 mV in a cell-attached patch. The upper four traces in each of parts (A–D) are original current records whereas the fifth trace in each panel shows the average of 50 sweeps. (A) Control, (B) 10 min after perfusion with 1 mmol/L H_2O_2, (C) 20 min after perfusion with 1 mmol/L H_2O_2 and (D) GSH (1 mmol/L).

ventricular myocytes, which is different from the report of Barrington *et al*. The disparity may be attributable to species differences. The result that H_2O_2 increases $I_{Na.P}$ in a concentration-dependent manner is similar to our previous report that hypoxia increases the $I_{Na.P}$ of guinea pig ventricular myocytes in a time-dependent manner[4], further suggesting that the increase in $I_{Na.P}$ is closely associated with reactive oxygen species. Ward and Giles observed that H_2O_2 produced a marked prolongation of the AP by slowing inactivation of the TTX-sensitive sodium current, which was verified by the single-channel cell-attached recording results that late opening events were enhanced when 200 μmol/L H_2O_2 was included in the recording pipette[6]. Bisindolylamaleimide, the protein kinase C (PKC) blocker, significantly

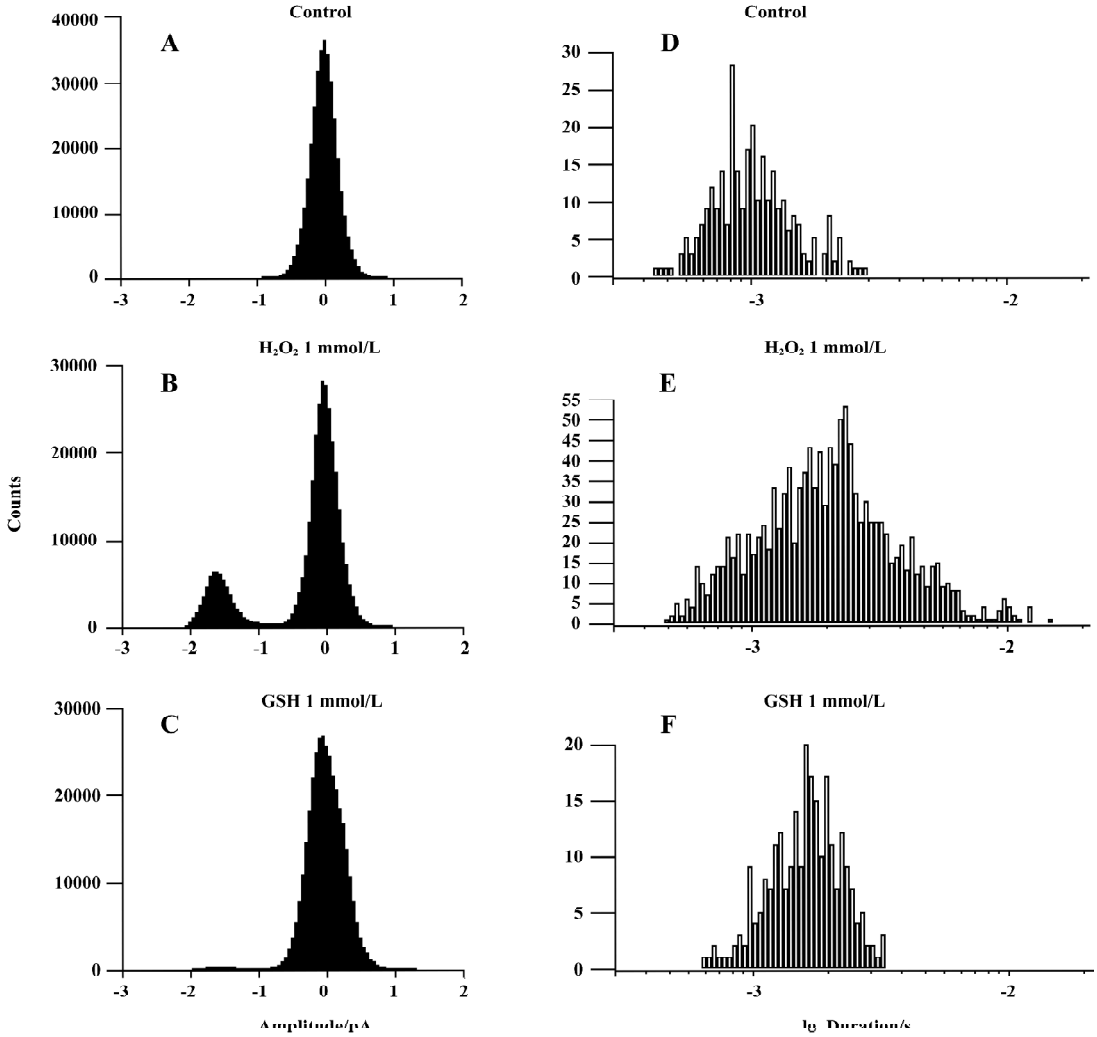

Figure 6. Effect of glutathione (GSH) on mean open probability and mean open time of persistent sodium channels enhanced by H_2O_2. Each figure comes from 50 individual current traces in a cell-attached patch. Parts (A–C) show the all-point histograms, and (D–F) show the mean open time histograms. (A,D) Control, (B,E) H_2O_2 (1 mmol/L) and (C,F) GSH (1 mmol/L). The fitted mean open times were 0.750 ms, 2.076 ms and 1.338 ms in (D–F), respectively.

delayed and attenuated the development of AP prolongation, which indicated involvement of an intracellular second messenger-PKC pathway[6]. In our study, H_2O_2 increased the persistent sodium channel activity in both the inside-out and cell-attached patches, which suggests that H_2O_2 may take effect by directly oxidizing the cell membrane in addition to its involvement as an intracellular second messenger. These results are consistent with the findings of Hammarström and Gage who reported that hypoxia, NO, and sodium cyanide could increase persistent sodium channel activity in rat hippocampal neurons in inside-out recordings, which could then be reversed by DTT[7,8].

H_2O_2 increased the persistent sodium channel activity in both cell-attached and inside-out patches (Figure 3). However, the time when the persistent sodium channel activity began to increase and reached a maximum was significantly shorter in inside-out patches compared with cell-attached patches. One possible explanation is that the inside-out patches, which were directly exposured to H_2O_2, lost the protection of intracellular antioxidant enzymes and antioxidants such as superoxide dismutase, catalase, glutathione peroxidase, ascorbic acid, α-tocopherol and glutathione.

Glutathione inhibited the H_2O_2-elicited persistent sodium channel activity (Figures 2,5,6), which suggested that H_2O_2 could take effect by oxidation. It is similar to our previous

report, which shows that excessive NO produced during hypoxia can increase the $I_{Na.P}$ of ventricular myocytes by oxidizing cell membrane sodium channel proteins and generating I_{NaP} under normoxic conditions, probably in association with the oxidation state of channel proteins[4]. H_2O_2 is a cysteine-specific oxidant[9] and GSH is an important antioxidant that can protect the protein's thiol group from oxidation[10]. The present study shows that GSH can reverse the persistent sodium channel activity caused by H_2O_2. Therefore, we think that persistent sodium channel activity may be associated with oxidation state, and oxidants can increase activity by oxidizing the channel protein. H_2O_2 as an oxidant may increase persistent sodium channel activity by oxidizing the thiol group of proteins in cell membranes.

References

1 Antzelevitch C. Electrical heterogeneity, cardiac arrhythmias, and the sodium channel. Circ Res 2000; 87: 910–4.

2 Ju YK, Saint DA, Gage PW. Hypoxia increases persistent sodium current in rat ventricular myocytes. J Physiol 1996; 497: 337–47.

3 Hammarström AKM, Gage PW. Hypoxia and persistent sodium current. Eur Biophys J 2002; 31: 323–30.

4 Ma JH, Wang XP, Zhang PH. Mechanisms on nitric oxide increasing persistent sodium current of ventricular myocytes in guinea pig during normoxia and hypoxia. Acta Physiol Sin 2004; 56: 603–8.

5 Barrington PL, Martin RL, Zhang K. Slowly inactivating sodium currents are reduced by exposure to oxidative stress. J Mol Cell Cardiol 1997; 29: 3251–65.

6 Ward CA, Giles WR. Ionic mechanism of the effects of hydrogen peroxide in rat ventricular myocytes. J Physiol 1997; 500: 631–42.

7 Hammarström AKM, Gage PW. Nitric oxide increases persistent sodium current in rat hippocampal neurons. J Physiol 1999; 520: 451–61.

8 Hammarström AKM, Gage PW. Oxygen-sensing persistent sodium channels in rat hippocampus. J Physiol 2000; 529: 107–18.

9 Prasad M, Goyal RK. Differential modulation of voltage-dependent K^+ currents in colonic smooth muscle by oxidants. Am J Physiol 2004; 286: C671–82.

10 Pastore A, Federici G, Bertini E, Piemonte F. Analysis of glutathione: implication in redox and detoxification. Clin Chim Acta 2003; 333: 19–39.

Acta Pharmacologica Sinica 2005 Jul; 26 (7): 835–839

Blackwell Publishing

Full-length article

Expression of pro-inflammatory and anti-inflammatory cytokines in brain of atherosclerotic rats and effects of *Ginkgo biloba* extract[1]

Ya-bin JIAO[2], Yao-cheng RUI[3], Tie-jun LI, Peng-yuan YANG, Yan QIU

Department of Pharmacology, School of Pharmacy, the Second Military Medical University, Shanghai 200433, China

Key words

atherosclerosis; cytokine; interleukin-1; tumor necrosis factor; interleukin-10; *Ginkgo biloba*; rats

[1] Project supported by the National Natural Science Foundation of China (No 30271509).
[2]Now in *Department of Pharmacology, School of Pharmacy, Shanghai University of Traditional Chinese Medicine, Shanghai 201203, China.*
[3]Correspondence to Prof Yao-cheng RUI. Phn/Fax 86-21-2507-4471.

Received 2004-10-09
Accepted 2005-01-23

doi: 10.1111/j.1745-7254.2005.00106.x

Abstract

Aim: To study the protein and mRNA expressions of pro-inflammatory and anti-inflammatory cytokines in the brain of rats with atherosclerosis (AS) and the effects of *Ginkgo biloba* extract (*Gb*E) on expressions of cytokines. **Methods:** The experimental model of AS in rats were established by intraperitioneal injection of vitamin D_3 with high fat/cholesterol diet. *Gb*E 100 mg/kg was administered to rats by ig. After 8 weeks, the expressions of IL-1β, TNF-α, IL-10, and IL-10R in the brain tissues of AS rats were detected by enzyme-linked immunosorbant assay, immunohistochemistry, Western blotting, and reverse transcriptase polymerase chain reaction. **Results:** The protein and mRNA expressions of IL-1β, TNF-α, and IL-10 in the brains were markedly higher in AS groups than that in control groups (6.11±0.15, 1.55±0.14, 0.54±0.04 ng/g wet weight *vs* 0.80±0.14, 0.33±0.09, and 0.33±0.02 ng/g wet weight, respectively). The protein and mRNA expressions of IL-1β and TNF-α in the brains were markedly lower in *Gb*E groups (3.82±0.54, 0.95±0.08 ng/g wet weight) than that in AS groups, the protein and mRNA expressions of IL-10 and IL-10R in the brains were markedly higher in *Gb*E groups (0.85±0.06 ng/g wet weight) than that in AS groups. **Conclusion:** *Gb*E inhibited production of pro-inflammatory cytokines IL-1β and TNF-α, but up-regulated the production of anti-inflammatory cytokines, IL-10 and IL-10R in brain, which might be related with its anti-AS actions.

Introduction

Atherosclerosis (AS) is not merely a disease in its own right, but a process that is the principal contributor to the pathogenesis of cardiovascular and cerebrovascular diseases. Despite the universal occurrence of atherosclerosis in the world, the pathogenesis of disease remains incompletely understood. In the injury theory of Ross, atherosclerosis can be considered to be a modified form of chronic inflammation. Uptake of oxidized low density lipoprotein (ox-LDL) by the macrophages through scavenger receptor (SR) will lead to foam cells formation and numerous cytokines; cell adhesion molecules, chemotactic factor and growth factors were excreted. All these factors induce the migration and proliferation of smooth muscle cells (SMC), this process repeats until the formation of atherosclerotic plaque. In recent years research results have indicated that an anti-inflammatory cytokine such as IL-10 is also concerned in the generation and development of AS, and can play an important protective role[1].

The rat was considered suitable for establishing cardiovascular disease model including cardiac hypertrophy, hypertension, and heart failure; but it is not such a good model in atherosclerosis due to its hyperlipidemia-resistant property. Recently, our task-group established the experimental model of AS in rats by combining the high fat/cholesterol diets containing sodium cholate and propyl-thyracil with injection of vitamin D_3[2].

Ginkgo biloba extract (*Gb*E) has beneficial effects on cardiovascular disease. Our previous study showed that the inhibitory effects of *Gb*E on vascular endothelial growth factor-induced permeability of bovine coronary endothelial cells

indicated that *Gb*E had the potential to protect against atherosclerosis[3].

Up to now, whether the expression of anti-inflammatory cytokines will have a change in the brain of rat with atherosclerosis remains unknown. The present study aims to investigate whether the anti-AS effect of *Gb*E was related with the expression of pro-inflammatory cytokines such as IL-1β and TNF-α, and anti-inflammatory cytokines such as IL-10 and IL-10R in the brain.

Materials and methods

Reagents *Gb*E (containing 24% flavone glycosides and 6% gingko lactone) was presented by Prof Wei-zhou CHEN (Shanghai Institute of Material Medica, Shanghai, China). Rat IL-1β, TNF-α, and IL-10 ELISA kit were purchased from Biosource (Camarillo, California, USA); Tissue/Cell Total RNA Isolation Kit was purchased from Watson Co (Shanghai, China); TaKaRa RNA PCR kit (AMV) Ver 2.1 was purchased from TaKaRa Biotechnology Co (Dalian, China). The antibodies for IL-1β, TNF-α, and IL-10 were purchased from Santa Cruz Biotechnology, Inc (Santa Cruze, CA, USA). Streptavidin/peroxidase (SP) kit and diaminobenzidine (DAB) kit were purchased from Zhongshan Biotechnology Co (Beijing, China).

Experimental protocol Thirty male Wistar rats were supplied by the Shanghai Experimental Animal Center of the Chinese Academy of Sciences. Qualification number is SCXK (hu) 2002-0010. The AS rat model was established by intraperitoneal injection with a single dose of vitamin D_3 600 kU/kg in addition to loading with high fat/cholesterol diet containing sodium cholate and propyl-thyracil as described previously[2]. The rats were divided into three groups: control, AS, and *Gb*E. The control group was fed with ordinary forage, while the AS and *Gb*E groups were fed with high fat/cholesterol diet after injection of vitamin D_3. At the same time, *Gb*E group rats were administered *Gb*E 100 mg/kg through intra-gastric method every day for 8 weeks.

Enzyme-linked immunosorbant assay (ELISA) The rat brains were homogenated with nomal saline at 2:1 ratio. The supernatant was used for the measurement of cytokine protein by ELISA as described in kit specification.

Immunohistochemistry The brain tissue was fixed in 4% paraformaldehyde and embedded in paraffin. Immunohistochemistry analysis was performed as specified by the kit protocol. Rabbit normal immune serum was used to replace primary antibody in the negative control group. PBS was used to replace immediate antibody in the control group.

Western blotting was performed to detect the cytokine protein expressions. Rat brain tissues were cut into small pieces. Protein extracts were prepared by homogenizing the 1 g brain tissues in cold 3 mL radioimmunoprecipitation (RIPA) buffer with a glass tissue homogenizer. The tissue homogenates were centrifuged at 10 000×*g* 4 °C for 10 min. The supernatants were collected and centrifuged at 10 000×*g* 4 °C for 10 min again. Protein concentration in the supernatant was determined by BCA method. Two times of loading buffer was then added to each supernatant with equal volume containing equal amounts of protein, which was subsequently boiled for 5 min and then electrophoresed on a 10% SDS-polyacrylamide gel. Proteins were transferred to nitrocellulose membrane and incubated sequentially with antibodies, and then with peroxidase-conjugated secondary antibodies in the second reaction. Detection was performed with enhanced chemiluminescence reagent.

RT-PCR for detection of the cytokine mRNA expressions Total RNA was isolated by Tissue/Cell Total RNA Isolation Kit. Total RNA was quantified with the ratio of absorption values of RNA samples at 260 nm and 280 nm. RT-PCR was performed by RNA PCR kit. Beta-actin was used as an internal positive control. Specific primer sequences of beta-actin, IL-1β[4], TNF-α, IL-10[5], and IL-10R[6] were as follows and the sizes of production were 587, 578, 315, 174, and 319 bp, respectively:

β-actin: sense 5'- AAGGCCAACCGTG AAAAGATGAC-3'; antisense 5'-GGGTACATGGTGGTGCCACCAGAC -3';

IL-1β: sense 5'-GACCTGTTCTTTGAGGCTGAC-3'; antisense 5'- TCCATCTTCTTCTTTGGGTATTGTT-3';

TNF-α: sense 5'-CATGATCCGAGATGTGGAACTGGC-3'; antisense 5' -CTGGCTCAGCCACTCCAGC -3';

IL-10: sense 5'- TAAGGGTTACTTGGGTTGCCAAGCC -3'; antisense 5'-AGGGGAGAAATCGATGACAGCG-3';

IL-10R: sense 5'- CCAACTGGACCATCACTGAAACTC -3'; antisense 5'- GCCTTGTTAATTCGGGATTCCAC- 3'.

The temperature profile of the amplification consisted of 45-s denaturation at 94 °C, 45-s annealing at 50 °C, and 2-min extension at 72 °C at 35 cycles. PCR products were sequenced to verify that desired product was amplified.

Statistical analysis Data were presented as mean±SD. Statistical significance was assessed by ANOVA test. $P<0.05$ was considered statistically significant.

Results

The experimental model of AS in rat was established (Figure 1).

IL-1β, TNF-α, and IL-10 protein levels in brain of AS rat by ELISA The protein levels of IL-1β, TNF-α, and IL-10 in the brains of the AS group were significantly increased compared with the control group. *Gb*E 100 mg/kg inhibited the

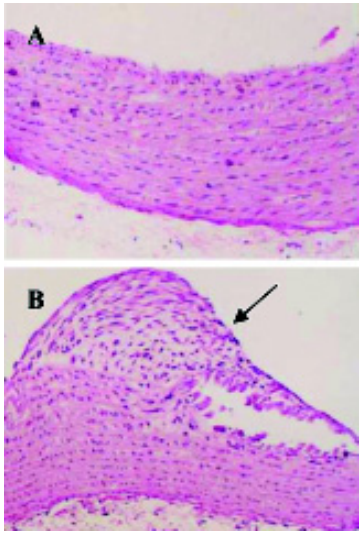

Figure 1. Typical plaques in aorta of AS rat. (A) Control; (B) Atherosclerosis. (×100).

protein levels of IL-1β and TNF-α, but up-regulated the protein levels of IL-10 (Table 1).

IL-1β, TNF-α, and IL-10 protein expressions in brain of AS rat Immunohistochemistry analysis showed that the expressions of IL-1β, TNF-α, and IL-10 were significantly increased in the cerebral cortex, hippocampus, and hypothalamus of AS rats compared with the control group. After the AS rats were given *Gb*E 100 mg/kg ig, the expressions of IL-1β and TNF-α in brain were decreased in the cerebral cortex, hippocampus, and hypothalamus but the expression of IL-10 was higher than pretreatment (Figure 2).

Table 1. Effects of *Gb*E 100 mg/kg on the level of IL-1β, TNF-α, and IL-10 in brain of atherosclerotic rat. n=6. Mean±SD. ^{c}P<0.01 *vs* control group. ^{f}P<0.01 *vs* AS group.

Group	IL-1β/ ng·g^{-1} wet weight	TNF-α/ ng·g^{-1} wet weight	IL-10/ ng·g^{-1} wet weight
Control	0.80±0.14	0.33±0.09	0.33±0.02
AS	6.11±0.15^{c}	1.55±0.14^{c}	0.54±0.04^{c}
AS+*Gb*E	3.82±0.54^{f}	0.95±0.08^{f}	0.85±0.06^{f}

IL-1β, TNF-α, and IL-10 protein expressions in brains of AS rats Western blotting analysis indicated that in the brains of the control group IL-1β and TNF-α were both expressed, and IL-10 had nearly no expression. The expressions of IL-1β, TNF-α, and IL-10 protein were all significantly increased in brain of AS rats compared with the control group.

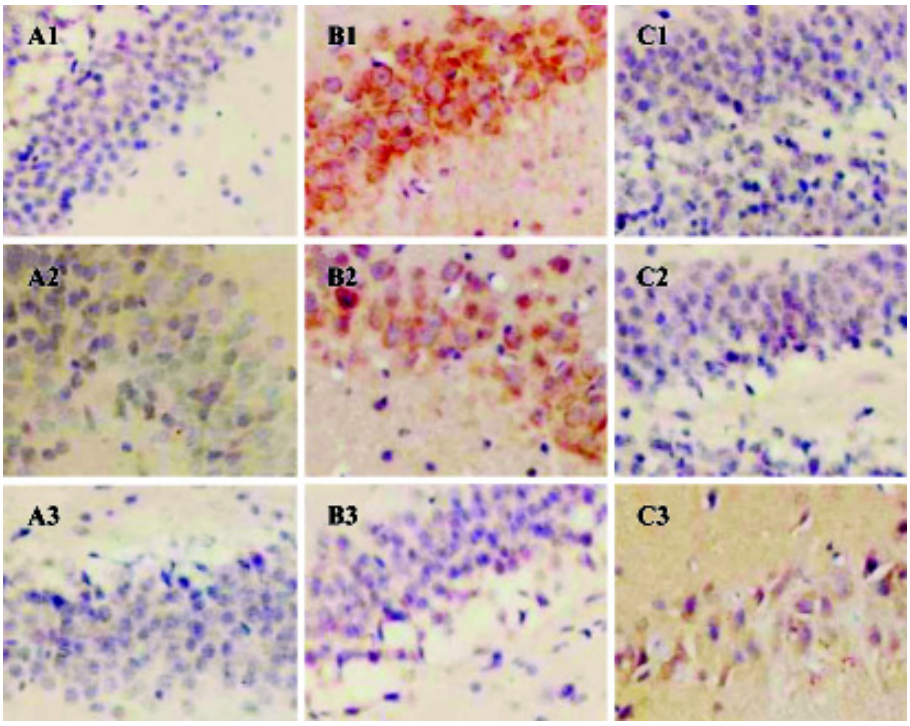

Figure 2. Effects of *Gb*E on expressions of IL-1β, TNF-α, and IL-10 in hippocampus of AS rat. (A) Control; (B) AS; (C) AS+*Gb*E. (1) IL-β; (2) TNF-α; (3) IL-10. (×200).

The expressions of IL-1β and TNF-α in brains were markedly lower in the *Gb*E group than that in AS group; but the expression of IL-10 in brains were markedly higher in the *Gb*E group than that in the AS group (Figure 3).

IL-1β, TNF-α, IL-10, and IL-10R mRNA expressions in the brains of AS rats RT-PCR analysis showed that IL-1β, TNF-α, IL-10, and IL-10R mRNA were all seldom expressed in the brains of the control group. The expressions of IL-1β, TNF-α, IL-10, and IL-10R mRNA were all markedly increased in the brains of AS rats compared with the control group. The expressions of IL-1β and TNF-α were lower, but the expressions of IL-10 and IL-10R mRNA were higher in the *Gb*E group than that in the AS group (Figure 4).

Discussion

We observed that the expressions of IL-1β, TNF-α, Il-10, and IL-10R in the brain were markedly higher in the AS rats than that in the control. The mRNA and protein expressions of IL-1β and TNF-α in the brains were markedly lower, but the mRNA and protein expressions of IL-10 and IL-10R in the brains were markedly higher in the *Gb*E 100 mg/kg group than that in the AS group. Our results were consistent with the recent findings that the serum levels of TNF-α and IL-1β in all patients with coronary heart diseases were higher than those in controls[7–9].

IL-10 was an anti-inflammatory cytokine with powerful immunoregulation potential[10]. It was excreted from mono-

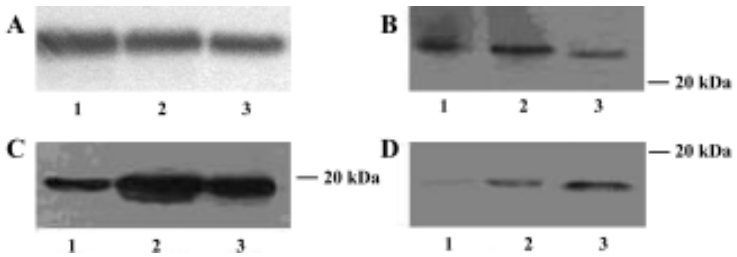

Figure 3. Effects of *Gb*E 100 mg/kg on expressions of IL-1β, TNF-α, and IL-10 in brain of atherosclerotic (AS) rat. (A) β-actin; (B) IL-1β; (C) TNF-α; (D) IL-10. Lane 1, Control; Lane 2, AS; Lane 3, AS+*Gb*E.

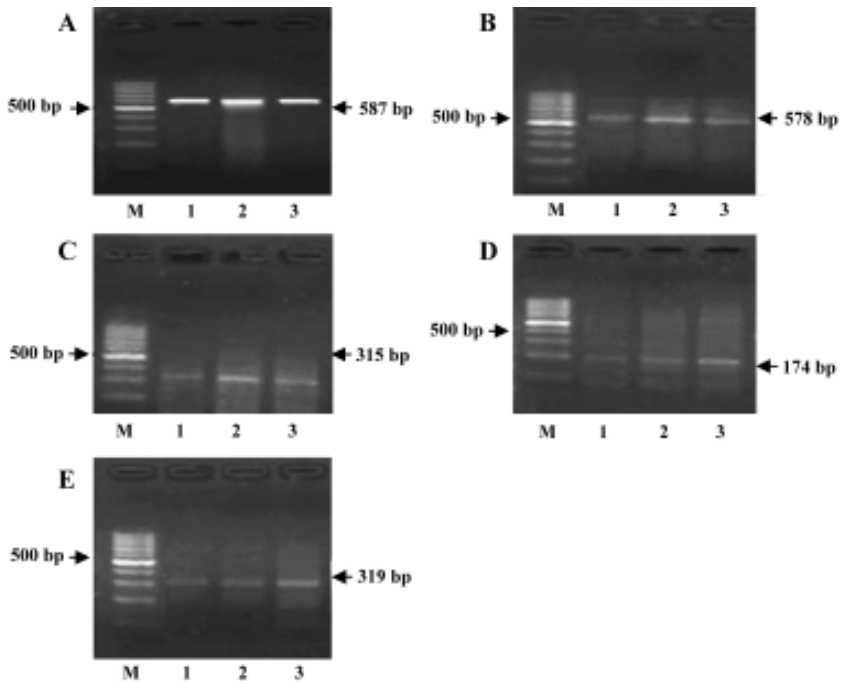

Figure 4. Effects of *Gb*E 100 mg/kg on expressions of IL-1β, TNF-α, IL-10, and IL-10R mRNA in brain of atherosclerotic (AS) rat. (A) β-actin; (B) IL-1β; (C) TNF-α; (D) IL-10; (E) IL-10R. Lane M, DNA marker; Lane 1, Control; Lane 2, AS; Lane 3, AS+*Gb*E.

cyte/macrophages and smooth muscle cells under certain conditions. Mallat *et al* found that IL-10-deficient mice fed with an atherogenic diet and raised under specific pathogen-free conditions exhibited a significant three-fold increase in lipid accumulation compared with wild-type mice[11]. Interestingly, the susceptibility of IL-10-deficient mice to atherosclerosis was more higher (30-fold increase) when the mice were housed under conventional conditions. Atherosclerotic lesions of IL-10-deficient mice showed increased T-cell infiltration, abundant interferon-γ expression, and decreased collagen content. *In vivo*, transfer of murine IL-10 achieved a 60% reduction in lesion size. These results indicated the critical roles of IL-10 in both atherosclerotic lesion formation and its stability. Serum levels of the anti-inflammatory cytokine, interleukin-10, are decreased in patients with unstable angina[12], this important finding also suggests that IL-10 has a protective role in atherosclerosis.

In other countries *Gb*E was used to treat cardiovascular and cerebrovascular diseases such as coronary heart diseases and stroke[13–18]. Our findings showed that *Gb*E inhibited the mRNA and protein expression of pro-inflammatory cytokines IL-1β and TNF-α, and up-regulated the mRNA and protein expression of anti-inflammatory cytokines, IL-10 and IL-10R in the brain of AS rats, which might be related with its anti-AS effects.

References

1 Mallat Z, Heymes C, Ohan J, Faggin E, Leseche G, Tedgui A. Expression of interleukin-10 in advanced human atherosclerotic plaques: relation to inducible nitric oxide synthase expression and cell death. Arterioscler Thromb Vasc Biol 1999; 19: 611–6.

2 Huang ZY, Yang PY, Almofti MR, Yu YL, Rui YC, Yang PY. Comparative analysis of the proteome of left ventricular heart of arteriosclerosis in rat. Life Sci 2004; 75: 3103–15.

3 Qiu Y, Rui YC, Li TJ, Zhang L, Yao PY. Inhibitory effect of extracts of *Ginkgo biloba* leaves on VEGF-induced hyperpermeability of bovine coronary endothelial cells *in vitro*. Acta Pharmacol Sin 2004; 25: 1306–11.

4 Hansen MK, Taishi P, Chen Z, Krueger JM. Cafeteria feeding induces interleukin-1β mRNA expression in rat liver and brain. Am J Physiol 1998: 274: R1734–9.

5 Adams JK , Tepperman BL. Colonic production and expression of IL-4, IL-6, and IL-10 in neonatal suckling rats after LPS challenge. Am J Physiol Gastrointest Liver Physiol 2001: 280: G755–62.

6 Mathurin P, Xiong S, Kharbanda KK, Veal N, Miyahara T, Motomura K, *et al*. IL-10 receptor and coreceptor expression in quiescent and activated hepatic stellate cells. Am J Physiol Gastrointest Liver Physiol 2002; 282: G981–90.

7 de Maat MP, Kluft C. The association between inflammation markers, coronary artery disease and smoking. Vascul Pharmacol 2002; 39: 137–9.

8 Wang YN, Che SM, Ma AQ. Clinical significance of serum cytokines IL-1β, sIL-2R, IL-6, TNF-α, and IFN-γ in acute coronary syndrome. Chin Med Sci J 2004; 19: 120–4.

9 Balbay Y, Tikiz H, Baptiste RJ, Ayaz S, Sasmaz H, Korkmaz S. Circulating interleukin-1 beta, interleukin-6, tumor necrosis factor-alpha, and soluble ICAM-1 in patients with chronic stable angina and myocardial infarction. Angiology 2001; 52: 109–14.

10 Opal SM, DePalo VA. Anti-inflammatory cytokines. Chest 2000; 117: 1162–72.

11 Mallat Z, Besnard S, Duriez M, Deleuze V, Emmanuel F, Bureau MF, *et al*. Protective role of interleukin-10 in atherosclerosis. Circ Res 1999; 85: 17–24.

12 Smith DA, Irving SD, Sheldon J, Cole D, Kaski JC. Serum levels of the antiinflammatory cytokine interleukin-10 are decreased in patients with unstable angina. Circulation 2001; 104: 746–9.

13 Kleijnen J, Knipschild P. *Ginkgo biloba*. Lancet 1992; 340: 1136–9.

14 Lin JY, Cheng FC, Chung SY, Lin MC. *Ginkgo biloba* extract (EGb761) and FK506 preserve energy metabolites in the striatum during focal cerebral ischemia and reperfusion in gerbils monitored by microdialysis. J Biomed Sci 2004; 11: 611–6.

15 Sun BL, Zhang J, Wang XC, Xia ZL, Yang MF, Zhang SM, *et al*. Effects of extract of *Ginkgo biloba* on spasms of the basilar artery and cerebral microcirculatory perfusion in rats with subarachnoid hemorrhage. Clin Hemorheol Microcirc 2003; 29: 231–8.

16 Chung SY, Wang MF, Lin JY, Lin MC, Liu HM, Cheng FC. Effect of one week treatment with *Ginkgo biloba* extract (EGb761) on ischemia-induced infarct volume in gerbils. Am J Chin Med 2003;31: 533–42.

17 Guillon JM, Rochette L, Baranes J. Effects of *Ginkgo biloba* extract on 2 models of experimental myocardial ischemia. Presse Med 1986; 15: 1516–9.

18 Chen J, Wang X, Zhu J, Shang Y, Guo X, Sun J. Effects of *Ginkgo biloba* extract on number and activity of endothelial progenitor cells from peripheral blood. J Cardiovasc Pharmacol 2004; 43: 347–52.

Acta Pharmacologica Sinica 2005 Jul; 26 (7): 840–844

Blackwell Publishing

Full-length article

Genistein inhibits carotid sinus baroreceptor activity in anesthetized male rats[1]

Hui-juan MA, Yi-xian LIU, Fu-wei WANG, Li-xuan WANG, Rui-rong HE, Yu-ming WU[2]

Department of Physiology, Institute of Basic Medicine, Hebei Medical University, Shijiazhuang 050017, China

Key words

genistein; carotid sinus; baroreflex; protein-tyrosine kinase; Bay K8644; *L*-NAME

[1] Project supported by a grant from Natural Science Foundation of Hebei Province of China (No 303467) and National Natural Science Foundation of China (No 304005).
[2] Correspondence to Prof Yu-ming WU.
Phn 86-311-626-5560.
Fax 86-311-538-3526.
E-mail wuym@hebmu.edu.cn

Received 2004-12-12
Accepted 2005-03-15

doi: 10.1111/j.1745-7254.2005.00127.x

Abstract

Aim: To study the effect of genistein (GST) on carotid baroreceptor activity (CBA). **Methods:** The functional curve of carotid baroreceptor (FCCB) was constructed and the functional parameters of carotid baroreceptor were measured by recording sinus nerve afferent discharge in anesthetized male rats with perfused isolated carotid sinus. **Results:** GST at 50, 100, and 200 μmol/L inhibited the CBA, which shifted FCCB to the right and downward, with a marked decrease in peak slope and peak integral value of carotid sinus nerve discharge in a concentration-dependent manner. Pretreatment with 100 μmol/L N^G-nitro-*L*-arginine methyl ester, an inhibitor of nitric oxide synthase, did not affect the effect of GST on CBA. Pretreatment with 500 nmol/L Bay K8644, an agonist of calcium channels, could completely abolish the effect of GST on CBA. A potent inhibitor of tyrosine phosphatase, sodium orthovanadate (1 mmol/L), could attenuate the inhibitory effect of GST. **Conclusion:** GST inhibits CBA, and the effect may be mediated by protein tyrosine kinase inhibition and a decrease in Ca^{2+} influx through the stretch-activated channels.

Introduction

Phytoestrogens are plant-derived diphenolic compounds that are structurally and functionally similar to estradiol. Accumulating evidence indicates that phytoestrogens may confer cardiovascular protection[1–3]. Genistein (GST), one of the most well-known phytoestrogens, is an isoflavone that is also a specific inhibitor of protein tyrosine kinase (PTK)[4]. It has been demonstrated that GST has a hypocholesterolemic effect in animals and humans, and is able to inhibit low density lipoprotein (LDL) oxidation, endothelial cell proliferation and angiogenesis[5], and to enhance the dilator response to acetylcholine of atherosclerotic arteries[6]. All of these effects may predict a favorable impact on the cardiovascular system. Li *et al* reported that GST decreased the contractile response of the aortic artery *in vitro*[7]. Furthermore, our previous studies showed that GST decreased the vascular tone in the femoral, renal and mesenteric vascular beds via protein tyrosine kinase (PTK) inhibition[8], reduced infarct size and apoptosis of myocytes in ischemia/reperfusion rabbit heart[9], and inhibited the voltage-dependent Ca^{2+} channel in isolated guinea pig ventricular myocytes[10]. Whether GST affects carotid baroreceptor activity (CBA) remains to be clarified. The aim of the present study was to observe the effects of GST on CBA in anesthetized male rats with perfusing isolated carotid sinus, and to elucidate the mechanism involved.

Materials and methods

Animals Sprague-Dawley rats (♂ , 350 ± 20 g, Grade II, Certificate No 04036), obtained from the Experimental Animal Center of Hebei Province, were anesthetized with urethane 1.0 g/kg, ip. The trachea was cannulated for ventilation.

Perfusion of left carotid sinus The method of isolating the carotid sinus was described in our previous study[11,12]. The left carotid sinus areas were fully exposed by turning the trachea and the esophagus rostrally. Sternohyoideus muscles and superior laryngeal nerves were sectioned. The bilateral aortic nerves, right carotid sinus nerves, cervical sympathetic nerves and recurrent laryngeal nerves were all sectioned. The common, external and internal carotid

arteries and smaller arteries originating from these vessels were exposed and ligated, while carefully leaving the left carotid sinus nerve undisturbed. Ligation of the occipital artery at its origin from the external carotid artery excluded chemoreceptors from the isolated carotid sinus, thereby preventing chemoreceptor activation secondary to decreased carotid sinus pressure. A plastic catheter introduced into the left common carotid artery in the anterograde way (serving as an inlet tube) was attached to a peristaltic pump that controlled the intrasinus pressure (ISP). ISP was monitored by a polygragh (RM-6240, Chengdu Instrument Factory, Chengdu, China) connected to the inlet tube. A plastic catheter inserted into the external carotid artery served as an outlet tube. The carotid sinus was then perfused with warm (37 °C) modified Krebs-Henseleit (K-H) solution (NaCl 118.0 mmol/L, $NaHCO_3$ 25.0 mmol/L, KCl 4.7 mmol/L, KH_2PO_4 1.2 mmol/L, $MgSO_4$ 1.2 mmol/L, $CaCl_2$ 2.5 mmol/L, glucose 5.6 mmol/L, pH 7.35–7.45) bubbled with 95% O_2 and 5% CO_2.

Recording of sinus nerve afferent discharge The left carotid sinus nerve was cut near the glossopharyngeal nerve and desheathed carefully. The isolated sinus nerve and surrounding structures were immersed in warm (37 °C) liquid paraffin to avoid drying of the tissues. The sinus nerve was placed on a bipolar platinum electrode and the bioelectrical signal was recorded on a polygragh (RM-6240, Chengdu Instrument Factory), with an integral time of 5 s. ISP and discharge of sinus nerve were recorded synchronously and at the end of the experiment, the integral of sinus nerve activity (ISNA) was obtained and measured.

Protocols With a computer-controlled program[13], ISP was altered in a stepwise manner by perfusing the left carotid sinus with K-H solution. After ISP was lowered from 100 mmHg to 0 mmHg, it began to increase slowly to 240 mmHg in a staircase manner, and then decreased to 0 mmHg in the same manner, and again stabilized at 100 mmHg. Each step of the staircase changed the ISP by 30 mmHg and lasted for 15 s. The functional curve for the ISP-ISNA relationship was constructed, and the functional parameters of carotid baroreceptor activity, such as peak slope (PS), peak integral value (PIV), threshold pressure (TP), saturation pressure (SP) and operation range (OR) were determined. TP was the ISP at which ISNA began to increase by 15% in response to an increase in ISP. SP was the ISP at which ISNA just showed no further increase with an increase in ISP. OR was calculated as the difference between SP and TP.

On perfusing the carotid sinus with K-H solution, the functional curve of carotid baroreceptor (FCCB) was drawn, obtaining the control parameters of TP, SP, OR, PS, and PIV. ISP was then fixed at 100 mmHg for 20 min, and K-H solution containing GST at 50, 100, and 200 μmol/L was then perfused to examine the changes in ISNA, followed by measurement of the parameters again. Finally, the carotid sinus was perfused with K-H solution as a postcontrol.

The effect of N^G-nitro-*L*-arginine methyl ester (*L*-NAME) on the response to GST was examined. After the control parameters of CBA were obtained, the isolated carotid sinus was perfused with K-H solution containing 100 μmol/L *L*-NAME for 20 min, and the above parameters were measured. Then GST 100 μmol/L was added to perfuse the sinus area. The parameters were measured within 15 min, and the drugs were then washed out with K-H solution. To determine whether Ca^{2+} was involved in the effect of GST, one experimental group was treated with 500 nmol/L Bay K8644 for 20 min before GST was added. To further determine the involvement of PTK, pretreatment with a potent inhibitor of tyrosine phosphatase, sodium orthovanadate (1 mmol/L), was carried out.

Drugs Genistein (purity 99%, Sigma, St Louis, MO, USA) was prepared with dimethyl sulphoxide. The final concentration of dimethyl sulphoxide in the perfusing solution was lower than 0.05%. *L*-NAME (Sigma) and sodium orthovanadate (Sigma) were dissolved in saline. Bay K8644 (Sigma) was dissolved in 99% ethyl alcohol. No changes in ISNA were observed during perfusion with ethyl alcohol (1:2000).

Statistical analysis All data are presented as mean±SD. The significance of group differences was determined by ANOVA and *t*-test. Differences were considered significant when $P<0.05$.

Results

Effect of GST on carotid baroreceptor activity By perfusing carotid sinus with K-H solution and elevating ISP from 0 mmHg to 240 mmHg in a stepwise manner, ISNA was increased. There was no difference in CBA parameters among the controls. As compared with control groups, treatment with GST decreased PIV and PS, and increased TP and SP, shifting FCCB to the right and downward (Table 1, Figure 1). The above effects occurred within 5 min of perfusing the carotid sinus with GST, and reached a peak during 8–12 min. Figure 2 is an original tracing showing the effects of GST on ISNA.

Effect of *L*-NAME on GST responses *L*-NAME (100 μmol/L) did not induce any change in the functional parameters of the carotid baroreceptor, and also did not influence the effect of 100 μmol/L GST (Table 2).

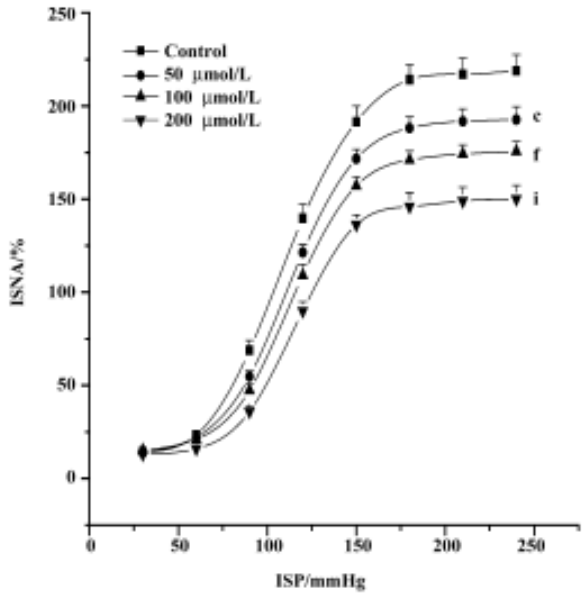

Figure 1. Effect of different concentrations of genistein (GST) on the functional curves of carotid baroreceptor in rats. n=6. Mean±SD. ^{c}P<0.01 *vs* control. ^{f}P<0.01 *vs* GST (50 μmol/L). ^{i}P<0.01 *vs* GST (100 μmol/L). ISP, intrasinus pressure; ISNA, integral of sinus nerve activity.

Effect of Bay K8644 on GST responses Bay K8644 (500 nmol/L) did not produce any change in the functional parameters of the carotid baroreceptor, but completely blocked the action of GST (Table 2).

Effect of sodium orthovanadate on GST responses Sodium orthovanadate (1 mmol/L) did not change CBA, but completely blocked the effect of GST (Table 2).

Discussion

The present study demonstrated that GST inhibited CBA in a concentration-dependent manner. By perfusing the left carotid sinus baroreceptor with GST, the FCCB were shifted to the right and downward, with a reduction in PS and PIV, indicating the inhibitory action of GST on CBA. It is well established that the arterial baroreceptors play an important role in the short-term control of cardiovascular activity. Inhibition of CBA is inclined to cause increased arterial blood pressure that can antagonize hypotensive effects caused by other ingredients.

As nitric oxide synthase (NOS) is present in afferent baroreceptor fibers innervating the carotid sinus[14], and increasing evidence has shown that nitric oxide (NO) may suppress the action potential of baroreceptors[15,16]. Furthermore, our previous study demonstrated that 17β-estradiol inhibited CBA via endothelial NO release. NO suppressed Na^{+} current in baroreceptor neurons and activated the cal-

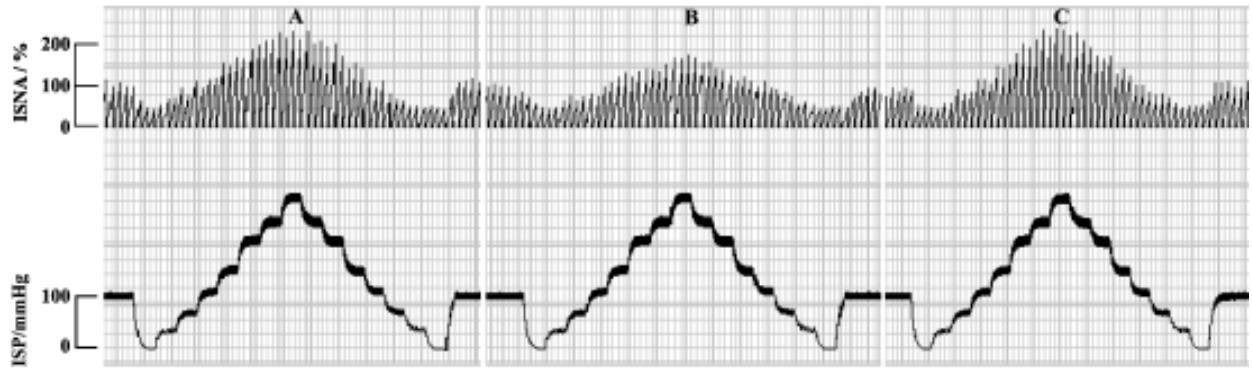

Figure 2. Original recording showing the responses of integral of sinus nerve activity to intrasinus perfusion with genistein (GST). (A) Control; (B) Perfusion with GST (100 μmol/L); (C) Washing out.

Table 1. Effect of genistein on the functional parameters of carotid baroreceptor in anesthetized male rats. n=6. Mean±SD. ^{b}P<0.05, ^{c}P<0.01 *vs* control. ^{e}P<0.05, ^{f}P<0.01 *vs* GST (50 μmol/L). ^{h}P<0.05, ^{i}P<0.01 *vs* GST (100 μmol/L).

Genistein (μmol/L)	TP (mmHg)	SP (mmHg)	OR (mmHg)	PS (%/mmHg)	PIV (%)
Control	63.0±3.2	164.7±3.7	101.7±0.5	2.52±0.07	215±8
50	68.9±4.0^{b}	175.7±6.6^{c}	102.3±1.4	2.39±0.03^{c}	191±7^{c}
100	74.7±2.8^{f}	179.3±2.8^{e}	103.0±0.5	2.29±0.04^{f}	177±5^{f}
200	81.9±2.6^{i}	185.0±3.7^{h}	103.9±1.2	2.16±0.03^{i}	155±7^{i}

Table 2. Effect of N^G-nitro-*L*-arginine methyl ester (*L*-NAME) 100 μmol/L, Bay K8644 500 nmol/L, and sodium orthovanadate 1 mmol/L on the responses of carotid baroreceptor to 100 μmol/L genistein (GST). n=6. Mean±SD. $^bP<0.05$, $^cP<0.01$ *vs* control. $^eP<0.05$, $^fP<0.01$ *vs* GST (100 μmol/L).

Drug	TP (mmHg)	SP (mmHg)	OR (mmHg)	PS (%/mmHg)	PIV (%)
Control	63.3±4.1	165.0±4.7	101.9±0.6	2.52±0.08	214±10
GST	74.9±3.5^c	178.5±3.5^c	103.8±0.5	2.29±0.05^c	177±6^c
L-NAME	64.2±3.3	166.2±4.3	101.7±0.6	2.50±0.08	212±9
L-NAME+GST	75.4±2.4	180.8±2.9	104.8±0.4	2.28±0.05	175±7
Control	64.5±2.6	166.2±3.4	101.8±0.4	2.49±0.05	211±8
GST	76.0±2.3^c	179.5±2.4^b	103.7±0.5	2.27±0.03^c	174±5^c
Bay K8644	61.8±3.2	163.1±3.0	101.7±0.6	2.50±0.06	217±7
Bay K8644+GST	65.4±2.1^f	167.5±2.8^e	102.0±0.7	2.47±0.07^f	210±6^f
Control	63.0±3.6	164.7±4.1	101.8±0.4	2.52±0.08	214±9
GST	75.5±4.2^c	179.0±3.2^b	103.2±0.9	2.28±0.09^b	176±6^c
Sodium orthovanadate	64.8±3.2	166.7±4.0	102.0±1.0	2.49±0.08	210±9
Sodium orthovanadate+GST	64.1±5.2^f	165.8±2.8^e	101.8±0.4	2.50±0.04^f	212±7^f

cium-dependent K^+ channels localized in vascular smooth muscle, then hyperpolarized baroreceptor neurons[17]. Both of these mechanisms may account for the inhibitory effect of 17β-estradiol on CBA. In the present study, pretreatment with *L*-NAME, a non-selective inhibitor of NOS, did not affect the action of GST, thus suggesting that locally released NO was not involved in the effect of GST on CBA. This result indicated that GST and 17β-estradiol inhibited CBA via different pathways.

It has been reported that a mechanosensitive ion channel is localized on the baroreceptor neurons, and that vascular distention is effectively translated to the deformation of the afferent nerve endings as arterial pressure rises. Deformation then depolarizes the nerve endings by opening non-selective cation channels to create a generator potential that triggers action potential discharge[18,19]. Moreover, it has been demonstrated that stretching of the walls of the carotid sinus may induce an increase in Ca^{2+} influx on baroreceptor neurons, which is mediated by stretch-activated channels[16]. Suppressing Ca^{2+} influx through the stretch-activated channels may be an important pathway in regulating CBA. Studies have shown that agmatine[20], cholecystokinin octapeptide[21] and aminoglycoside antibiotics (such as streptomycin)[22] can inhibit CBA in this way. We have observed that pretreatment with L-type calcium channel agonist Bay K8644 completely blocks the inhibitory effect of GST on CBA. Based on the above observations, it may be concluded that GST inhibits CBA through a decrease in Ca^{2+} influx by blocking the stretch-activated channels.

Genistein has also proved to be a specific inhibitor of PTK. Evidence has been presented to suggest that enhanced tyrosine phosphorylation participates in the mechanisms that regulate the contraction of smooth muscle[5]. Vanadate, an inhibitor of tyrosine phosphatase, can enhance protein tyrosine phosphorylation[6]. PTK has been described as an important modulator regulating the tone of vascular smooth muscle[23]. Our present study showed that the effect of GST on CBA was inhibited by pretreatment with sodium orthovanadate, suggesting that the PTK pathway is involved. From this data together with our previous findings, it may be inferred that GST inhibits PTK, relaxes the vascular smooth muscle, and then attenuates the stretch-activated Ca^{2+} channels on the baroreceptor neurons.

In summary, the present study has revealed that GST inhibits CBA, and the effect may be mediated by PTK inhibition and a decrease in Ca^{2+} influx through the stretch-activated channels.

References

1 Anthony MS, Clarkson TB, Williams JK. Effects of soy isoflavones on atherosclerosis: potential mechanisms. Am J Clin Nutr 1998; 68 (Suppl): S1390–3.

2 Anthony MS, Clarkson TB. Association between plasma isoflavone and plasma lipoprotein concentrations. J Med Food 1999; 2: 263–6.

3 Figtree GA, Griffiths H, Lu YQ, Webb CM, Macleod K, Collins P. Plant-derived estrogens relax coronary arteries *in vitro* by a calcium antagonistic mechanism. J Am Coll Cardiol 2000; 35: 1977–85.

4 Akiyame T, Ishida J, Nakagawa S, Ogawara H, Watanabe S, Itoh

N, *et al*. Genistein: a specific inhibitor of tyrosine-specific protein kinases. J Biol Chem 1987; 262: 5592–5.
5 Fotsis T, Pepper M, Adlercreuta H, Fleischmann G, Hase T, Montesano R, *et al*. Genistein, a dietary-derived inhibitor of *in vitro* angiogenesis. Proc Natl Acad Sci USA 1993; 90: 2690–4.
6 Honore EK, Williams JK, Anthony MS, Clarkson TB. Soy isoflavones enhance coronary vascular reactivity in atherosclerotic female macaques. Fertil Steril 1997; 67: 148–54.
7 Li HF, Wang LD, Qu SY. Phytoestrogen genistein decreases contractile response of aortic artery *in vitro* and arterial blood pressure *in vivo*. Acta Pharmacol Sin 2004; 25: 313–8.
8 Ji ES, Zhang LH, Wang YH, Yue H, He RR. Responses of regional vascular beds to local injection of genistein in rats. Acta Physiol Sin 2003; 55: 255–9.
9 Ji ES, Yue H, Wu YM, He RR. Effects of phytoestrogen genistein on myocardial ischemia/reperfusion injury and apoptosis in rabbits. Acta Pharmacol Sin 2004; 25: 306–12.
10 Ji ES, Wang C, He RR. Effects of genistein on intracellular free calcium concentration in guinea pig ventricular myocytes. Acta Physiol Sin 2004; 56: 204–9.
11 Zhao G, Ho SY. The facilitating effect of atrial natriuretic peptide in the carotid sinus baroreflex function. Acta Physiol Sin 1991; 43: 360–7.
12 Zhang H, Liu YX, Wu YM, Wang ZM, He RR. Capsaicin facilitates carotid sinus baroreceptor activity in anesthetized rats. Acta Pharmacol Sin 2004; 25: 1439–43.
13 Yi XL, Fan ZZ, He RR. An automatic system controlled by computer for carotid sinus perfusion. Chin J Appl Physiol 1993; 9: 156–9.
14 Hohler B, Mayer B, Kummer W. Nitric oxide synthase in the rat carotid body and carotid sinus. Cell Tissue Res 1994; 276: 559–64.
15 Li Z, Chapleau MW, Bates JN, Bielefeldt K, Lee HC, Abboud FM. Nitric oxide as an autocrine regulator of sodium currents in baroreceptor neurons. Neuron 1998; 20: 1039–49.
16 Chapleau MW, Hajduczok G, Sharma RV, Wachtel RE, Cunningham JT, Sullivan MJ, *et al.* Mechanisms of baroreceptor activation. Clin Exp Hypertens 1995; 17: 1–13.
17 Wang S, Fan ZZ, He RR. 17β-Estradiol inhibits carotid sinus baroreceptor activity in anesthetized male rats. Acta Pharmacol Sin 2001; 22: 440–4.
18 Grigg P. Biophysical studies of mechanoreceptors. J Appl Physiol 1986; 60: 1107–15.
19 Drummond HA, Welsh MJ, Abboud FM. EnaC subunits are molecular components of the arterial baroreceptor complex. Ann NY Acad Sci 2001; 940: 42–7.
20 Qin XM, Fan ZZ, He RR. Agmatine inhibits the afferent activity of carotid baroreceptor in rats. Acta Physiol Sin 2001; 53: 137–41.
21 Liu YX, Zhang H, Dong JH, Li Q, He RR. Cholecystopinin octapeptide inhibits carotid sinus baroreceptor activity in rats. Chin J Pharmacol Toxicol 2005; 19:18–23.
22 Qin XM, He RR. Role of calcium in the mechanism underlying the inhibitory effect of streptomycin on carotid sinus baroreflex in rats. Acta Physiol Sin 2000; 52: 463–7.
23 Hughes A, Wijetunge S. Role of tyrosine phosphorylation in excitation-contraction coupling in vascular smooth muscle. Acta Physiol Scand 1998; 164: 457–69.

Acta Pharmacologica Sinica 2005 Jul; 26 (7): 845–850

Full-length article

Similar effects on rat renal mesangial cells by expressing different fragments of adrenomedullin gene *in vitro*[1]

Shao-wei CHEN, Xiao-fang WANG, Ying SHAO, Hong XUE, Li ZHOU, Tai YAO, Li-min LU[2]

Department of Physiology and Pathophysiology, Shanghai Medical College, Fudan University, Shanghai 200032, China

Key words

adrenomedullin; transfection; glomerular mesangium; transforming growth factor-β1

[1] Project supported by the National Natural Science Foundation of China (No 30470627) and the Funds for Graduate Education sponsored by the Ministry of Education (No 20010246012).
[2] Correspondence to Prof Li-min LU.
Phn 86-21-5423-7716.
Fax 86-21-6417-1179
E-mail lulimin@shmu.edu.cn

Received 2005-02-21
Accepted 2005-03-24

doi: 10.1111/j.1745-7254.2005.00138.x

Abstract

Aim: To construct pEGFP-N3 recombinant vectors carrying adrenomedullin (*AM*) or fragments of the *AM* gene, and to express AM or fragments of AM from the pEGFP-N3 recombinant vectors (pEGFP-N3-AM1-2 and pEGFP-N3-AM1-3) and study their biological properties on cultured rat renal mesangial cells (RMC). **Methods:** Total RNA of rat kidney was obtained using TriZol reagent. The cDNA was synthesized by reverse transcriptase using oligo-deoxythymidine as primer. The fragments of *AM* gene were then amplified by polymerase chain reaction (PCR) with specific upstream and downstream oligonucleotides. The PCR products were digested with *Eco*RI and *Bam*HI and subcloned into the plasmid pEGFP-N3. Facilitated by cationic liposomes, RMC were transfected with pEGFP-N3-AM1-2 or pEGFP-N3-AM1-3. After 24 h, green fluorescent protein (GFP) fluorescent images were examined with a fluorescence microscope. After 48 h, the proliferation of RMC was detected using the MTT assay, and the mRNA expression of *transforming growth factor-β1* (*TGF-β1*) was measured by semiquantitative PCR. **Results:** DNA sequence reports verified that pEGFP-N3-AM1-2, which carried the full length *AM* gene translation fragment (preproadrenomedullin preproAM$_{1–185}$), and pEGFP-N3-AM1-3, which carried the translation fragment of preproAM [without adrenotensin (ADT, preproAM$_{150–185}$)], were constructed successfully. After 24 h, green fluorescence was observed in RMC into which either pEGFP-N3-AM1-2 or pEGFP-N3-AM1-3 was transfected, while in the control cells no fluorescence was observed. Either pEGFP-N3-AM1-2 or pEGFP-N3-AM1-3 delivery inhibited the proliferation of RMC ($P<0.01$) and decreased the mRNA transcription level of *TGF-β1* in RMC ($P<0.05$). However, no significant difference was observed between the effects of pEGFP-N3-AM1-2 and pEGFP-N3-AM1-3. **Conclusion:** pEGFP-N3-AM1-2 and pEGFP-N3-AM1-3 were constructed successfully and were functionally expressed in RMC. Expressing the fragment of *AM* without ADT has similar inhibitory biological effects on RMS proliferation and *TGF-β1* transcription with full length preproAM.

Introduction

Adrenomedullin (AM) was discovered in tissue extracts of human pheochromocytoma by Kitamura *et al* in 1993[1]. Subsequently identified as a potent vasodilator, AM was detected to be expressed in a wide range of tissues, such as the adrenal gland, kidney, heart, lung, spleen, and brain[2]. AM has since been suggested to play important roles in a great number of disease areas, "ranging widely from heart failure through to oncology", especially in cardiovascular and renal diseases[3,4]. Previous studies revealed that plasma AM levels were increased in hypertension and renal failure[5,6]. Researches have also shown that AM can improve cardiac function, renal function, and survival rate in hypertensive rat models[7,8].

The gene encoding preproadrenomedullin (preproAM),

a precursor molecule of *AM*, is termed as the *AM* gene. Sequence analysis of cloned rat *AM* showed that this precursor consisted of 185 amino acids, including a signal peptide[9]. After synthesis, the signal peptide is cleaved between Thr21 and Ala22. The remaining fragment of preproAM, which is termed as proadrenomedullin (proAM), is cleaved specifically by endopeptidase at Lys43–Arg44, Lys92–Arg93 and Arg145–Arg149, resulting in the production of four proAM-derived peptides: PAMP (proadrenomedullin N-terminal 20 peptide, preproAM$_{22–41}$), preproAM$_{45–91}$, AM (preproAM$_{94–143}$) and ADT (adrenotensin or preproAM$_{150–185}$)[9,10] (Figure 1).

Finding out the appropriate expression pattern is one of the major topics in gene delivery. It is well known that peptides derived from a common polypeptide precursor may have different, even opposite biological properties. Previous studies suggest that ADT may play a role that is opposite in effect to AM[11,12]. The present study was carried out in order to explore the different effects of expressing full length preproAM and a fragment of preproAM without ADT on renal mesangial cells (RMC).

Materials and methods

Materials pEGFP-N3 vector was obtained from BD Biosciences Clontech (Bedford, MA,USA). Top10 *Escherichia coli* was obtained from Invitrogen (Carlsbad, CA, USA) and primary rat RMC was a gift from the Department of Pathology, Shanghai Medical College (Shanghai, China).

Reagents Trizol, AMV reverse transcriptase, *Taq* DNA polymerase, Silver Beads DNA Gel Extraction Kit, kits for total RNA extraction, endonucleases *Eco*RI and *Bam*HI, and T4 DNA ligase were purchased from Sangon (Shanghai, China). Lipofectamine^{TM} 2000 was from Gibco (Grand Island, NY, USA), and MTT, dimethyl sulfoxide (Me_2SO) and Dulbecco's Modified Eagle's Medium (DMEM)/F-12 were from Sigma (St Louis, MO, USA).

Construction and confirmation of expression of vectors pEGFP-N3-AM1-2 and pEGFP-N3-AM1-3 Total RNA was isolated from rat kidney tissue samples using Trizol reagent. The full coding region of the *AM* gene was generated by reverse transcription-polymerase chain reaction (RT-PCR) using the following oligonucleotide primers: AM-1, 5'-TAC TGA ATT CGC CAC CAT GAA GC-3'; and AM-2, 5'-TTG CGG ATC CTA ACC TAG AGA C-3'. After an initial denaturation step at 94 °C for 3 min, PCR were carried out for 30 cycles at 94 °C for 30 s, 58 °C for 30 s, and 72 °C for 1 min, and then 72 °C for 10 min. The PCR products and pEGFP-N3 were digested with restriction endonucleases *Eco*RI and *Bam*HI (recognition sites in bold) and the purified digestion products were subcloned into the *Eco*RI and *Bam*HI sites of pEGFP-N3 with T4 DNA ligase. The recombinant plasmids were then transformed into competent Top10 *E coli* and amplified in the hosts. DNA sequencing was carried out to identify purified recombinant vectors. The recombinant vector carrying the full coding region of the rat *AM* gene was named pEGFP-N3-AM1-2. Using the same method (with oligonucleotide primers: AM-1, 5'-TAC TGA ATT CGC CAC CAT GAA GC-3'; and AM-3, 5'-TTG CGG ATC CAT AGC CTT GAG-3'), we developed another recombinant pEGFP-N3 vector (pEGFP-N3-AM1-3) with a fragment encoding a region of the rat *AM* gene in which the sequence encoding ADT was absent.

Cell culture and transfection Primary rat mesangial cells were cultured in DMEM/F-12 containing 10% heat-inactivated fetal calf serum (FCS) and incubated in a humidified 5% CO_2 incubator at 37 °C. Cells were growth-arrested in DMEM containing 1.0% FCS for 24 h prior to transfection. pEGFP-N3-AM1-2 or pEGFP-N3-AM1-3 was transfected into

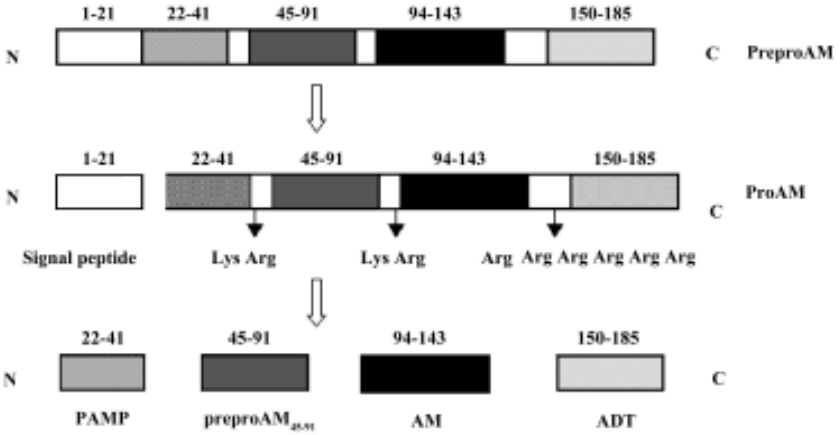

Figure 1. Schematic presentation of the biosynthesis of AM and ADT.

cultured RMC facilitated by cationic liposomes Lipofectamine™ 2000. At 24 h after transfection, phase contrast and fluorescence microscopy were carried out using a BX61olympus microscope (Melville, NY, USA)

Detection of cell proliferation by MTT assay Cellular proliferation was determined in triplicate with a colorimetric non-radioactive MTT proliferation assay. RMC were plated at 3×10^3 cells/well into 96-well plates and cultured in DMEM/F-12 medium supplemented with 10% FCS at 37 °C in a humidified atmosphere of 5% CO_2 for 24 h. The cultures were replaced with medium containing 1.0% FCS for another 24 h, and the cells were then transfected with pEGFP-N3-AM1-2 or pEGFP-N3-AM1-3 for 48 h. The effects of pEGFP-N3-AM1-2 and pEGFP-N3-AM1-3 on the proliferation of RMC were measured by MTT assay. Briefly, a 20 μL aliquot of 5 mg/mL MTT solution was added to each well. After 4 h of incubation, the absorbance of each well was measured at 490 nm.

Reverse transcription-polymerase chain reaction analysis of *transforming growth factor-β1* gene expression Expression of the *transforming growth factor-β1* (*TGF-β1*) gene was analyzed by semiquantitative PCR using glyceraldehyde-3-phosphate dehydrogenase (*GAPDH*) as an internal standard. Total RNA was isolated from cultured RMC following the protocol of RNA extraction kits. The amount of RNA isolated was determined by measuring the specific absorption at 260 nm. The integrity of the RNA isolated was confirmed by agarose gel electrophoresis, run under denaturing conditions. cDNA was synthesised in 40 μL reaction mixtures using 1 μg of total RNA; 2 μL of the cDNA solution was used for PCR amplification. The primers for the *TGF-β1* and *GAPDH* genes were as follows: *TGF-β1* sense, 5'-AAG TGG ATC CAC GAG CCC AA-3'; *TGF-β1* antisense, 5'-GTC GCA CTT GCA GGA GCG CA-3'; *GAPDH* sense, 5'-ACC ACA GTC CAT GCC ATC AC-3'; *GAPDH* antisense, 5'-CCA CCA CCC TGT CAT GCC ATC AC-3'. After an initial denaturation step at 94 °C for 3 min, PCR was carried out for 30 cycles and 94 °C for 30 s, 55 °C for 30 s, and 72 °C for 1 min, and then at 72 °C for 10 min.

Statistical analysis Statistical analysis was carried out using the statistical program SPSS 11.0 (Chicago, Illinois, USA). The data were expressed as mean±SD and the one-way analysis of variance (ANOVA) *t*-test was used for statistical analysis. $P<0.05$ was accepted as statistically significant.

Results

Construction and identification of pEGFP-N3-AM1-2 and pEGFP-N3-AM1-3 The full coding region of the rat *AM* gene and the fragment of coding region without ADT were subcloned separately into pEGFP-N3, producing pEGFP-N3-AM1-2 and pEGFP-N3-AM1-3, respectively. The construction of pEGFP-N3-AM1-2 and pEGFP-N3-AM1-3 was confirmed by DNA sequencing.

Expression of pEGFP-N3-AM1-2 and pEGFP-N3-AM1-3 in renal mesangial cells Cultured RMC were transfected with pEGFP-N3-AM1-2 or pEGFP-N3-AM1-3. After 24 h, green fluorescence was detected using a fluorescence microscope. Both pEGFP-N3-AM1-2 and pEGFP-N3-AM1-3 were expressed in RMC as bright green fluorescence was observed, indicating that the in-frame GFP-tagged *AM* sequences were expressed and translated successfully. The expression of GFP was observed in above 95% transfected RMC. No green fluorescence was detected in untransfected RMC (Figures 2–4).

Proliferation of renal mesangial cells in response to pEGFP-N3-AM1-2 and pEGFP-N3-AM1-3 To determine the

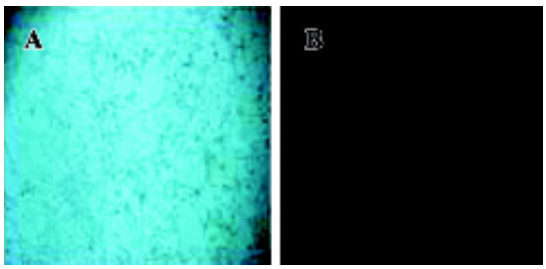

Figure 2. Phase contrast (A) and fluorescence (B) microscopy of normal cultured renal mesangial cells (×100).

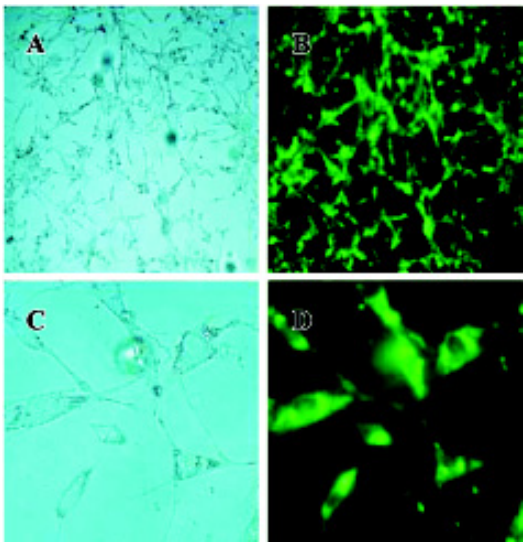

Figure 3. Phase contrast (A,C) and fluorescence (B,D) microscopy of renal mesangial cells transfected with pEGFP-N3-AM1-2. (A,B) ×100; (C,D) ×400.

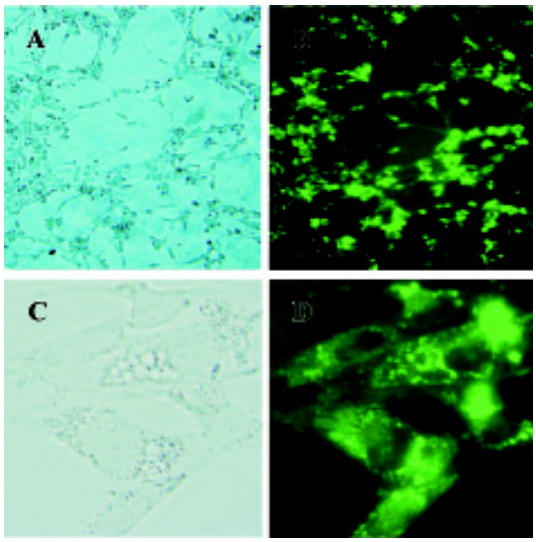

Figure 4. Phase contrast (A,C) and fluorescence (B,D) microscopy of renal mesangial cells transfected with pEGFP-N3-AM1-3. (A,B) ×100; (C,D) ×400.

biological activities of the recombinant vectors, proliferation of RMC was analyzed using the MTT assay 48 h after pEGFP-N3-AM1-2 or pEGFP-N3-AM1-3 delivery. Significant changes in optical density values at 24 h after transfection was observed with recombinant plasmids compared with the controls, indicating that pEGFP-N3-AM1-2 and pEGFP-N3-AM1-3 elicited a decrease in RMC proliferation (P<0.01) (Figure 5).

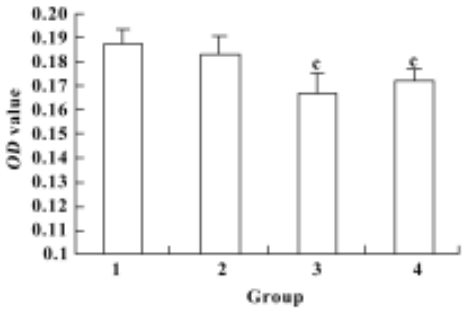

Figure 5. Effect of pEGFP-N3-AM1-2 or pEGFP-N3-AM1-3 on the proliferation of renal mesangial cells (RMC). (1) Normal cultured RMC (48 h); (2) RMC transfected with pEGFP-N3 (48 h); (3) RMC transfected with pEGFP-N3-AM1-2 (48 h); (4) RMC transfected with pEGFP-N3-AM1-3. n=12. Mean±SD. ^{c}P<0.01 *vs* group 2.

Analysis of the effects of pEGFP-N3-AM1-2 and pEGFP-N3-AM1-3 on *TGF-β1* gene expression Along with the control experiments, which indicated that product accumulation did not reach a plateau at 30 cycles under the assay conditions used, our results for semiquantitative PCR indicate that, compared with the control group, transfection of pEGFP-N3-AM1-2 and pEGFP-N3-AM1-3 suppressed *TGF-β1* mRNA expression in RMC (Figure 6).

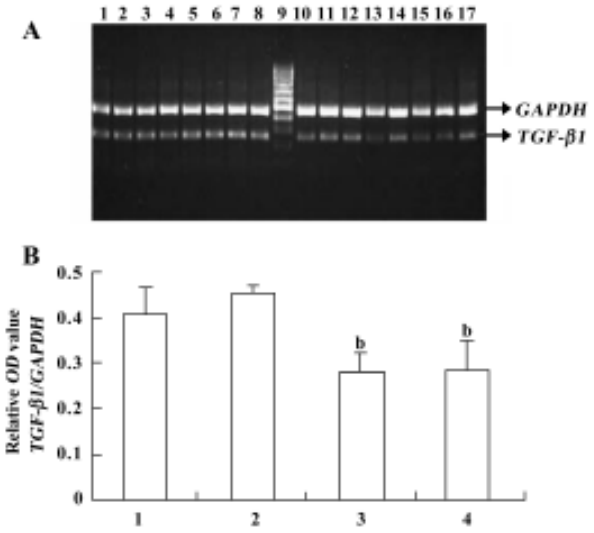

Figure 6. Semiquantitative analysis of the effect of pEGFP-N3-AM1-2 or pEGFP-N3-AM1-3 on *transforming growth factor-β1* (*TGF-β1*) mRNA expression in renal mesangial cells (RMC). (A) Electrophoresis of *TGF-β1* and glyceraldehyde-3-phosphate dehydrogenase (*GAPDH*): 1–4, normal cultured RMC; 5–8, RMC transfected with pEGFP-N3 (48 h); 9, DNA molecular weight marker; 10–13, RMC transfected with pEGFP-N3-AM1-2 (48 h); 14–17, RMC transfected with pEGFP-N3-AM1-3 (48 h). (B) Statistical results of *TGF-β1* mRNA expression in RMC. 1, normal cultured RMC (48 h); 2, RMC transfected with pEGFP-N3 (48 h); 3, RMC transfected with pEGFP-N3-AM1-2 (48 h); 4, RMC transfected with pEGFP-N3-AM1-3 (48 h). n=4. Mean±SD. ^{b}P<0.05 *vs* group 2.

Discussion

As an endogenous vasodilator and natriuretic peptide, AM is thought to have great potential in the treatment of cardiovascular and renal diseases[13,14]. However, there are still some impediments to understand AM's biological functions and the promising clinical uses of AM. One of the obstacles is the short half-life of AM. The plasma half-life of AM is estimated to be about only 22 min[15]. Gene transfer is a novel means of providing sustained and localized delivery of the required therapeutic protein. In order to achieve long-term expression of AM, *AM* gene delivery has been used in recent years. The studies show that *AM* gene delivery has multiple functions in protection against hypertension, renal damage, cardiac fibrosis and cardiac hypertrophy[16–20].

Currently, both non-viral and viral vectors are used to express the heterogeneous genes, each of them with their

own advantages and disadvantages. The advantages of non-viral vectors are: (i) non-vial vectors do not integrate the heterogeneous genes into recipient-cell genome, therefore it is considered safe for researchers and will have higher clinical acceptability; (ii) there are minimal or no immune effects, and none of the safety concerns regarding infection is found with viral vectors[21]; (iii) manipulate and delivery of plasmids into cells is much easier; and (iv) although plasmid-delivered DNA does not integrate into the recipient-cell genome, delivery of plasmids *in vivo* can maintain very prolonged effects[22]. In the present study, we chose plasmid pEGFP-N3 as the vector.

In our experiment, for the first time, the recombinant vector pEGFP-N3-AM1-3, which carries the DNA fragment encoding the AM protein without the ADT sequence, was designed and constructed successfully. It is well known that peptides derived from a common polypeptide precursor may have different, even opposite biological properties. As prior studies have demonstrated, ADT has some quite opposite vascular effects to those of AM[11,12]. We therefore hypothesized that the absence of ADT might have more effective effects in protecting heart and kidney.

The pEGFP-N3-AM1-2 and pEGFP-N3-AM1-3 plasmids were constructed successfully. As the fluorescent images showed, both of these vectors were expressed efficiently in RMC. Our data analysis showed that either pEGFP-N3-AM1-2 or pEGFP-N3-AM1-3 delivery inhibited the proliferation of RMC ($P<0.01$) and decreased the mRNA transcription of *TGF-β1* in RMC ($P<0.05$). However, no significant difference was observed between the effects of pEGFP-N3-AM1-2 and pEGFP-N3-AM1-3.

In kidney, mesangial cells have a central function in maintaining structural and functional integrity of the glomerulus, including "structural support of the capillary tuft, modulation of glomerular hemodynamics, and a phagocytic function allowing removal of macromolecules and immune complexes", and the proliferation of mesangial cells is a pivotal feature of glomerular disease[23]. Our results are in agreement with prior studies showing that AM can suppress RMC proliferation[24–26], and this may be one of the mechanisms by which *AM* gene delivery protects renal function. So far, no data about the effects of ADT on the proliferation of mesangial cells have been reported.

Transforming growth factor-β1 is a multifunctional peptide that regulates manifold cellular functions including cell proliferation, differentiation and apoptosis[27]. As a potent inducer of extracellular matrix synthesis leading to progressive glomerular fibrosis, TGF-β1 is also thought to be the major pathogenic factor in the development of renal fibrotic disorders[28]. A previous study showed that chronic AM infusion significantly reduced the *TGF-β/GAPDH* mRNA levels in the renal cortex[7]. In the present study, we demonstrated that either pEGFP-N3-AM1-2 or pEGFP-N3-AM1-3 delivery could decrease the mRNA transcription level of *TGF-β1* in RMC ($P<0.05$). This may contribute to the renal protective effects of *AM* gene delivery; the function of ADT in the regulation of *TGF-β1* mRNA expression requires further study.

In the present experiment, a very interesting phenomenon was observed in that there was no difference between pEGFP-N3-AM1-2 and pEGFP-N3-AM1-3 in their effects on the proliferation of RMC and the mRNA transcription level of *TGF-β1* in cultured RMC. Although ADT plays some opposite vascular effects to AM, previous studies indicate that there are complicated mutual regulation interactions between ADT and AM. In incubated blood vessels, AM could inhibit the synthesis and release of ADT, whereas ADT could enhance the synthesis and release of AM[29]. Therefore, in order to understand the mechanism of why pEGFP-N3-AM1-2 and pEGFP-N3-AM1-3 had similar effects on cultured RMC, further investigations are indispensable.

In conclusion, recombinant vectors pEGFP-N3-AM1-2, expressing preproAM, and pEGFP-N3-AM1-3, expressing a fragment of preproAM without ADT, were constructed successfully. The biological activity studies of pEGFP-N3-AM1-2 and pEGFP-N3-AM1-3 on cultured RMC showed that expressing the fragment of preproAM without ADT and the full-length preproAM had similar inhibitory effects on cell proliferation and *TGF-β1* gene transcription. As for the mechanism of why pEGFP-N3-AM1-2 and pEGFP-N3-AM1-3 had similar effects on cultured RMC, and what may be the effects of the 2 vectors on the kidney *in vivo*, further investigations are required.

References

1 Kitamura K, Kangawa K, Kawamoto M, Ichiki Y, Nakamura S, Matsuo H, *et al*. AM: a novel hypotensive peptide isolated from human pheochromocytoma. Biochem Biophys Res Commun 1993; 192: 553–60.

2 Ichiki Y, Kitamura K, Kangawa K, Kawamoto M, Matsuo H, Eto T. Distribution and characterization of immunoreactive AM in human tissue and plasma. FEBS Lett 1994; 338: 6–10.

3 Beltowski J, Jamroz A. Adrenomedullin–what do we know 10 years since its discovery? Pol J Pharmacol 2004; 56: 5–27.

4 Bunton DC, Petrie MC, Hillier C, Johnston F, McMurray JJ. The clinical relevance of adrenomedullin: a promising profile? Pharmacol Ther 2004; 103: 179–201.

5 Ishimitsu T, Nishikimi T, Saito Y, Kitamura K, Eto T, Kangawa K, *et al*. Plasma levels of adrenomedullin, a newly identified hypotensive peptide, in patients with hypertension and renal

failure. J Clin Invest 1994; 94: 2158–61.
6 Kato J, Kobayashi K, Etoh T, Tanaka M, Kitamura K, Imamura T, *et al*. Plasma adrenomedullin concentration in patients with heart failure. J Clin Endocrinol Metab 1996; 81: 180–3.
7 Mori Y, Nishikimi T, Kobayashi N, Ono H, Kangawa K, Matsuoka H. Long-term adrenomedullin infusion improves survival in malignant hypertensive rats. Hypertension 2002; 40: 107–13.
8 Chao J, Chao L. The role of adrenomedullin in cardiovascular and renal function. Drug News Perspect 2002; 15: 511–8.
9 Sakata J, Shimokubo T, Kitamura K, Nakamura S, Kangawa K, Matsuo H, *et al*. Molecular cloning and biological activities of rat adrenomedullin, a hypotensive peptide. Biochem Biophys Res Commun 1993; 195: 921–7.
10 Hinson JP, Kapas S, Smith DM. Adrenomedullin, a multifunctional regulatory peptide. Endocr Rev 2000; 21: 138–67.
11 Gumusel B, Chang JK, Hyman A, Lippton H. Adrenotensin: an ADM gene product with the opposite effects of ADM. Life Sci 1995; 57: PL87–90.
12 Gumusel B, Chang JK, Hao Q, Hyman A, Lippton H. Adrenotensin: an adrenomedullin gene product contracts pulmonary blood vessels. Peptides 1996; 17: 461–5.
13 Nakamura R, Kato J, Kitamura K, Imamura T, Eto T. Potential of adrenomedullin as a therapeutic tool for left ventricular remodeling after myocardial infarction. Nippon Rinsho 2004; 62: 302–6.
14 Savoia C, Schiffrin EL. Significance of recently identified peptides in hypertension: endothelin, natriuretic peptides, adrenomedullin, leptin. Med Clin North Am 2004; 88: 39–62.
15 Meeran K, O'Shea D, Upton PD, Small CJ, Ghatei MA, Byfield PH, *et al*. Circulating adrenomedullin does not regulate systemic blood pressure but increases plasma prolactin after intravenous infusion in humans: a pharmacokinetic study. J Clin Endocrinol Metab 1997; 82: 95–100.
16 Chao J, Jin L, Lin KF, Chao L. Adrenomedullin gene delivery reduces blood pressure in spontaneously hypertensive rats. [published erratum appears in Hypertens Res 2001; 24: 611]. Hypertens Res 1997; 20: 269–77.
17 Dobrzynski E, Montanari D, Agata J, Zhu J, Chao J, Chao L. Adrenomedullin improves cardiac function and prevents renal damage in streptozotocin-induced diabetic rats. Am J Physiol Endocrinol Metab 2002; 283: E1291–8.
18 Wang C, Dobrzynski E, Chao J, Chao L. Adrenomedullin gene delivery attenuates renal damage and cardiac hypertrophy in Goldblatt hypertensive rats. Am J Physiol Renal Physiol 2001; 280: F964–71.
19 Zhang JJ, Yoshida H, Chao L, Chao J. Human adrenomedullin gene delivery protects against cardiac hypertrophy, fibrosis, and renal damage in hypertensive dahl salt-sensitive rats. Hum Gene Ther 2000; 11: 1817–27.
20 Dobrzynski E, Wang C, Chao J, Chao L. Adrenomedullin gene delivery attenuates hypertension, cardiac remodeling, and renal injury in deoxycorticosterone acetate-salt hypertensive rats. Hypertension 2000; 36: 995–1001.
21 Pachori AS, Huentelman MJ, Francis SC, Gelband CH, Katovich MJ, Raizada MK. The future of hypertension therapy: sense, antisense, or nonsense? Hypertension 2001; 37: 357–64.
22 Lin KF, Chao L, Chao J. Prolonged reduction of high blood pressure with human nitric oxide synthase gene delivery. Hypertension 1997; 30: 307–13.
23 Kurogi Y. Mesangial cell proliferation inhibitors for the treatment of proliferative glomerular disease. Med Res Rev 2003; 23: 15–31.
24 Parameswaran N, Nambi P, Brooks DP, Spielman WS. Regulation of glomerular mesangial cell proliferation in culture by adrenomedullin. Eur J Pharmacol 1999; 372: 85–95.
25 Parameswaran N, Nowak W, Hall CS, Sparks HV, Spielman WS. Cellular and molecular actions of adrenomedullin in glomerular mesangial cells. Peptides 2001; 22: 1919–24.
26 Chini EN, Choi E, Grande JP, Burnett JC, Dousa TP. Adrenomedullin suppresses mitogenesis in rat mesangial cells via cAMP pathway. Biochem Biophys Res Commun 1995; 215: 868–73.
27 Sporn MB, Roberts AB. Transforming growth factor-beta: recent progress and new challenges. J Cell Biol 1992; 119: 1017–21.
28 Sharma K, Jin Y, Guo J, Ziyadeh FN. Neutralization of TGF-beta by anti-TGF-beta antibody attenuates kidney hypertrophy and the enhanced extracellular matrix gene expression in STZ-induced diabetic mice. Diabetes 1996; 45: 522–30.
29 Qi YF, Bu DF, Niu da D, Shi YR, Wang SH, Pang YZ, *et al*. Effects of different peptide fragments derived from proadrenomedullin on gene expression of adrenomedullin gene. Peptides 2002; 23: 1141–7.

Acta Pharmacologica Sinica 2005 Jul; 26 (7): 851–859

Full-length article

Ischemic preconditioning protects post-ischemic renal function in anesthetized dogs: role of adenosine and adenine nucleotides[1]

Fan-zhu LI[2,3], Shoji KIMURA[4], Akira NISHIYAMA[4], Matlubur RAHMAN[4], Guo-xing ZHANG[4], Youichi ABE[4]

[2]*Department of Pharmaceutics, Zhejiang College of Traditional Chinese Medicine, Hangzhou 310053, China;* [4]*Department of Pharmacology, Kagawa Medical University, 1750-1 Ikenobe, Kagawa 761-0793, Japan*

Key words

microdialysis; ischemia preconditioning; reperfusion injury; kidney; adenosine; adenosine A_1 receptor

[1] Project supported in part by the National Natural Science Foundation of China (No 30371781) and a grant-in-aid for Scientific Research from the Ministry of Education, Science and Culture of Japan.
[3] Correspondence to Prof Fan-zhu LI.
Phn 86-571-8661-3524.
Fax 86-571-8661-3606.
E-mail lifanzhu@zjtcm.net

Received 2004-11-12
Accepted 2005-02-05

doi: 10.1111/j.1745-7254.2005.00109.x

Abstract

Aim: To investigate the effects of renal ischemic preconditioning (IPC) on both renal hemodynamics and the renal interstitial concentrations of adenosine and adenine nucleotides induced by ischemia-reperfusion injury. **Methods:** Renal hemodynamics responses to ischemia-reperfusion injury in mongrel dog models were determined with or without multiple brief renal ischemic preconditioning treatments, as well as the adenosine A_1 receptor antagonist (KW-3902), respectively. The renal interstitial concentrations of adenosine and adenine nucleotides in response to ischemia-reperfusion injury, either following 1–3 cycles of IPC or not, were measured simultaneously using microdialysis sampling technology. **Results:** One 10-min IPC, adenosine A_1 receptor antagonist (KW-3902) also shortened the recovery time of renal blood flow (RBF) and urine flow (UF), as well as mean blood pressure (BP). Advanced renal IPC attenuated the increment of adenosine and adenine nucleotides, as well as recovery time during the 60-min reperfusion which followed the 60-min renal ischemia. All of these recovery times were dependent on the cycles of 10-min IPC. The renal interstitial concentrations of adenosine and adenine nucleotides increased and decreased during renal ischemia and reperfusion, respectively. **Conclusion**: A significant relativity in dog models exists between the cycles of 10-min renal IPC and the recovery time of BP, UF, and RBF during the 60-min renal reperfusion following 60-min renal ischemia, respectively. Renal IPC can protect against ischemia-reperfusion injury and the predominant effect of endogenous adenosine induced by prolonged renal ischemia; renal adenosine A_1 receptor activation during the renal ischemia-reperfusion injury is detrimental to renal function.

Introduction

Renal dysfunction is a serious and common complication of ischemia-reperfusion injury[1], and the onset of acute renal failure secondary to ischemia-reperfusion injury implies a poor prognosis and is frequently associated with a high mortality rate[2]. In animal and human models, it has been demonstrated that prolonged ischemia results in an immediate decrease in renal blood flow (RBF) and glomerular filtration rate (GRF)[3].

Recent developments in renal physiology have determined that rat kidneys can be ischemic preconditioned against ischemia-reperfusion injury[4]. A possible candidate mediator of ischemia-reperfusion injury is adenosine, which has been shown to be involved in ischemic-induced renal vasoconstriction via its effects on adenosine A_1 receptors. Its antagonist has a partial protective effect against renal vasoconstriction during ischemia[5]. Extensive evidence exists demonstrating the beneficial effects of ischemic preconditioning (IPC) in cardiac muscle[6,7]. However, evidence supporting a role for IPC in protecting against ischemia-reperfusion injury in kidney is minimal and controversial[4,8,9].

Recently, Lee and Emala[4] demonstrated that IPC (4 cycles of 8-min renal ischemia followed by 5-min reperfusion) protected renal function after ischemia and reperfusion (45 min of renal ischemia followed by 24-h reperfusion). However, Islam *et al*[8] failed to demonstrate protective effects of renal IPC in rats (4 cycles of 4-min renal ischemia followed by 11-min reperfusion periods).

Lee and Emala[4] reported that in the rat kidney, adenosine or A_1 receptor agonist infusions before ischemic insult protected renal function via A_1 adenosine receptor activation. However, Sugino *et al*[10] reported that the adenosine A_1 receptor antagonist failed to abolish the post-ischemic renal protective effects of IPC or exogenous adenosine in the rat kidney. The results of these experiments indicate that IPC appears to increase extracellular adenosine concentration, which in turn mimics post-ischemic renal function. Our previous study showed that renal interstitial adenosine[11] concentration significantly increased during ischemia. Adenosine has been demonstrated to elicit renal vasoconstriction[12–14]; it is suggested that extracellular adenosine could be involved in the mediation of post-occlusion renal ischemia[15–17]. However, findings in the above literature are indirect and do not provide any data supporting the renal interstitial concentrations of adenosine and adenine nucleotides during IPC followed by ischemia and reperfusion. In addition, it is not clear if IPC protects against post-ischemic renal functions in the dog kidney. The beneficial effects of using multiple cycles over single cycle IPC, that is, cycles of multiple brief IPC, is correlative to its protective effect and is poorly understood. As well as this, the influence of IPC on the intrarenal hemodynamics is unclear.

The aim of the present study is to confirm the protective role of IPC on ischemia-reperfusion injury in dogs, and to determine that a correlation exists between the cycles of IPC and its protective effects. This study was also undertaken to determine the relationship between multiple brief ischemic preconditioning and the intrarenal hemodynamics of adenosine and adenine necleotide, including the role of the adenosine A_1 receptor. In the present study, microdialysis sampling technology was introduced to measure the intrarenal hemodynamics as well as the dynamics of renal interstitial concentration of adenosine, adenine nucleotide during IPC and ischemia-reperfusion.

Materials and methods

General procedure All surgical and experimental procedures were performed according to the guidelines for the care and use of animals as established by the Kagawa Medical University. Adult mongrel dogs weighting 10–15 kg were used. They had been maintained on standard laboratory food for 1 week. The surgical preparation of the animals and basic experimental techniques are identical to those previously described[11,8]. The animals were anesthetized with sodium pentobarbital (0.03 g/kg, iv) and given additional doses as required. After tracheotomy, the animals were mechanically ventilated with Harvard apparatus ventilator (Harvard Apparatus, Millis, MA, USA). A polyethylene catheter was inserted into the right brachial vein for infusion of isotonic saline or drug solution. Isotonic saline or drug solution was infused at a rate of 0.2 $mL \cdot min^{-1} \cdot kg^{-1}$ throughout the experiment. Another catheter was placed in the abdominal aorta via the right femoral artery, and mean arterial pressure (MBP) was continuously measured and recorded with a pressure transducer (NEC-San-ei Model No 361, Tokyo, Japan) and a polygraph (NEC-San-ei Model No 361, Tokyo, Japan). An adjustable clamp was placed on the renal artery to be used later as an occlusion devise.

The left kidney was exposed through a retroperitoneal flank incision. The kidney was carefully denervated by dissecting all visible nerve fibers, as well as the tissue connecting the renal hilum cephalic, to the renal artery. An electromagnetic flowmeter (MFV-1200, Nihon Kohden, Tokyo, Japan) was positioned around the renal artery, and renal blood flow (RBF) was continuously monitored. A polyethylene catheter was inserted into the left ureter, and urine samples were continuously collected in tubes. The total of urine collected in every consecutive 10-min period was used to calculate urine flow (UF) rate (L/min). The renal capsule was carefully opened along the convexity, and the microdialysis probes were gently implanted into the renal cortex as shown by Nishiyama *et al*[11,19]. The probes were connected to a CMA/100 microinfusion pump (Carnergie Medicine, Stockholm, Sweden) and were perfused with isotonic saline solution with heparin (0.03 units/L) containing iodotubercidine (10 μmol), an inhibitor of adenosine kinase, and *erythro*-9-(2-hydroxy-3-nonyl)adenine (EHNA) (100 μmol), an inhibitor of adenosine deaminase, at a rate of 5 μL/min. The dialysate was collected in a chilled tube over a 5-min sample period and analyzed for adenosine concentration as well as inosine, hypoxanthine, xanthine, and uric acid concentrations. Samples were stored at -70 °C prior to analysis. After surgery, the dogs were left alone for 90 min for the tissue to recover from the trauma produced by insertion of the probes and to allow for the stabilization of mean arterial pressure, renal blood flow, and renal interstitial adenosine concentration. At the end of each experiment, the exact position of the probe was verified by inspection. If the probe was situated in the outer medulla at least in part, we omitted

the data of these dialysates.

Characteristics of microdialysis probe For the determination of renal interstitial concentrations of adenosine, inosine, hypoxanthine, xanthine, and uric acid, we used a microdialysis probe. The dialysis membrane is made from cuprophan fiber, measuring 15-mm in length with a 5500-Da transmembrane diffusion cut off (Toyobo, Otsu, Japan). Thin stainless steel tubes (outer diameter: 190 μm, inner diameter: 100 μm) were inserted into both sides of the cuprophan fiber. The inflow and outflow ends were inserted into the polyethylene tubes (PE-10) and sealed in place with glue. Preliminary results from *in vitro* experiments demonstrated that a negligible amount of adenosine, inosine, hypoxanthine, xanthine, and uric acid would stick to the polyethylene tubes.

The efficiency of the microdialysis probe was determined as follows. Briefly, the probes were soaked in beakers containing saline solution with different concentrations (0.1–5 μmol/L) of adenosine, inosine, hypoxanthine, xanthine, and uric acid (n=26). The probes were perfused with saline solution with heparin (0.03 units/L) containing iodotubercidine (10 μmol) and EHNA (100 μmol) at a rate of 5 μL/min. The dialysates were collected, and the equilibrium rates for adenosine, inosine, hypoxanthine, xanthine, and uric acid were calculated by dividing the concentrations in the dialysates at the concentrations in the medium. At a perfusion rate of 10 μL/min, the relative equilibrium rates of adenosine, inosine, hypoxanthine, xanthine, and uric acid were 36.9%±1.9%, 39.7%±3.2%, 50.3%±4.1%, 46.9%±2.5%, and 34.7%±4.2%, respectively.

Experimental protocols

Effects of ischemic-preconditioning on renal hemodynamics and renal interstitial concentration of adenosine and adenine nucleotides Dogs were randomized to 60-min renal ischemia and 60-min reperfusion (No IPC) group, which were treated with the adenosine A_1 receptor antagonist in advance, three ischemic preconditioning groups were treated with 1–3 cycles of 10-min renal ischemia and 10-min reperfusion, using an adjustable renal arterial clamp, respectively, followed by 60-min renal ischemia. During each ischemia-reperfusion interval, 5 min was allowed for stabilization before samples from all 5 probes used for measurements of adenosine, inosine, hypoxanthine, xanthine and uric acid were collected. After the initial stabilization period, the experimental protocols were started with renal interstitial adenosine and adenine nucleotides collections, and MBP, UF as well as RBF measurements for 2 consecutive 10-min periods. After collection or measurements of the second control sample, 60-min renal ischemia followed by 60-min reperfusion or IPC treatment were performed. At the same time, UF and RBF were also measured continuously.

Effects of ischemia-reperfusion on renal hemodynamics during treatment with KW3902 KW3902 (Kyowa Hakko Kogyo Co Ltd, Tokyo, Japan), a highly selective adenosine A_1 receptor antagonist, was dissolved in the lactated Ringer's solution containing 1% dimethylsulfoxide and 0.01 mol/L NaOH. After twice 10-min sampling periods, KW3902 (priming dose, 0.1 $mg \cdot kg^{-1} \cdot min^{-1}$; sustaining dose, 0.01 $mg \cdot kg^{-1} \cdot min^{-1}$) was administered in anesthetized dogs (n=11) during the following 60-min ischemia period simultaneously. At 60 min following KW3902 administration, the kidneys of the dogs were perfused again and urine flow and renal blood flow were measured continuously.

Analytical procedures

Adenosine Adenosine in the dialysate was measured according to the method developed by Miura *et al*[20]. The procedure is briefly described as follows: 100 μL of 1 mol/L acetate buffer (pH 4.5) and 4.5 μL of 40% cholroacetaldehyde were added. The preparation was incubated at 60 °C for 4 h to allow for the conversion of adenosine to a fluorescent 1, N^6-ethenoadenosine. After the incubation, the sample was mixed with a double volume of alaminefreon reagent and was centrifuged at 1000×g for 3 min, and the upper aqueous phase was collected. For high performance liquid chromatography, a reverse-phase column (Nucleosil 7C18, 4.6 m×25 cm, Nagel) was maintained at 30 °C with a column oven (655A-52, Hitachi Ltd, Tokyo, Japan). An isocratic elution with 7.5 % acetonitrile in 20 mmol/L potassium phosphate buffer (pH 5.7) at a flow rate of 1.32 mL/min was performed with a pump (L-600, Hitachi Ltd, Tokyo, Japan). Fifty microliters of the sample were injected with an autosampler (655A-40, Hitachi Ltd, Tokyo, Japan) and the elution was monitored using a fluorescence spectrometer (F-1000, Hitachi Ltd, Tokyo, Japan) at an excitation wavelength of 280 nm and an emission wavelength of 410 nm. A chromato integrator (D-2000, Hitachi Ltd, Tokyo, Japan) was used for recording.

Inosine, hypoxanthine, xanthine, and uric acid One hundred microliters of dialysate were directly applied onto the reverse-phase HPLC column (Nucleosil 7C18, 4.6 mm×25 cm, Nagel). The column was developed isocratically with 3.5% methanol in 10 mmol/L KH_2PO_4 at a flow rate of 1 mL/min. The effluent was monitored at a wavelength of 254 nm by an ultraviolet monitor. In every 10 samples, a standard sample was also injected.

Statistical analysis The values were presented as mean±SD. Statistical comparisons of mean values across multiple treatment groups were performed by a one-way ANOVA as appropriate, followed by Scheffe's *post hoc* test. A P-value below 0.05 was taken to indicate significant

difference.

Results

Effects of IPC on renal hemodynamics During 60-min renal ischemia, RBF and UF decreased from 78±18 mL/min to 0, and 260±80 μL/min to 0 respectively, whereas MBP increased slightly (Figure 1). After the release of the renal arterial clamp, RBF and UF increased to 59±27 mL/min, 170±150 μL/min, respectively (Table 1). In 1, 2, and 3 cycles of the preconditioning groups, RBF and UF descended to 0 during 60-min renal ischemia. During the reperfusion period, RBF increased to 76±11, 74±15, and 119±18 mL/min in 1, 2 and 3 cycles of the preconditioning of kidneys respectively (Table 1). UF gradually increased to 180±100, 110±70, and 260±170 μL/min in 1, 2, and 3 cycles of the preconditioning of ischemic kidneys, respectively. However, the recovery time of UF and RBF in the 3 cycles of the preconditioning of ischemic kidneys was markedly shorter compared to those of the 1 cycle or 2 cycles preconditioning of ischemic kidneys which were evaluated by percentage of changes in RBF and UF respectively (Figure 2, 3).

Table 1. Mean values of changes of renal hemodynamics in dogs during control, 60-min periods for ischemia reperfusion. Mean±SD. n=26. ^{b}P<0.05 *vs* control.

		RBF/ mL·min^{-1}	UF/ μL·min^{-1}
Ischemia reperfusion (Control group)	Control	78±18	260±80
	Ischemia 60 min	0	0
	Reperfusion 60 min	59±27	170±150
Preconditioning (1 cycle group)	Control	115±7	230±80
	Ischemia 60 min	0	0
	Reperfusion 60 min	76±11	180±100
Preconditioning (2 cycles group)	Control	90±13	160±40
	Ischemia 60 min	0	0
	Reperfusion 60 min	74±15	110±70
Preconditioning (3 cycles group)	Control	118±10	220±50
	Ischemia 60 min	0	0
	Reperfusion 60 min	119±18^{b}	260±170^{b}

Effects of IPC on the renal interstitial concentrations of adenosine and adenine nucleotides After clamping of the renal artery, adenosine, inosine, hypoxanthine, xanthine, and uric acid concentrations increased from 0.49 to 8.21 μmol/L,

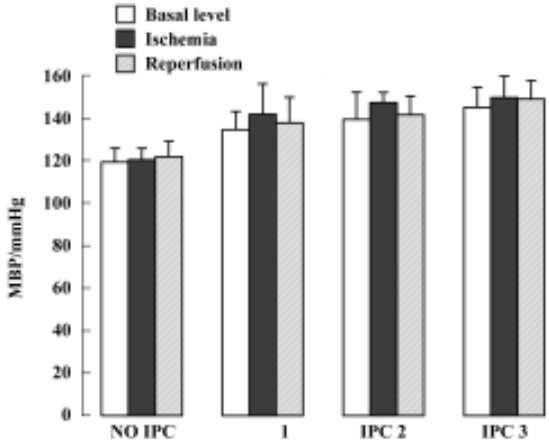

Figure 1. Changes in the mean blood pressure (MBP), measured without ischemic preconditioning-pretreatment (No IPC; n=6), with 1 cycle of ischemic preconditioning-pretreatment (IPC 1; n=6), 2 cycles of ischemic preconditioning-pretreatment (IPC 2; n=7), and 3 cycles of ischemic preconditioning-pretreatment (IPC 3; n=7) of 10-min ischemia with 10-min intervals, respectively. Not significantly different from each other. Mean±SD.

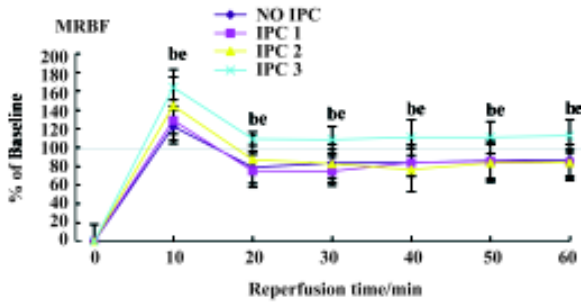

Figure 2. Percentage of changes in mean renal blood flow (MRBF) during reperfusion from no ischemic preconditioning (IPC) (n=6), IPC 1 (n=6), IPC 2 (n=7), and IPC 3 (n=7) groups, respectively. ^{b}P<0.05 *vs* IPC 1. ^{e}P<0.05 *vs* IPC 2. Mean±SD.

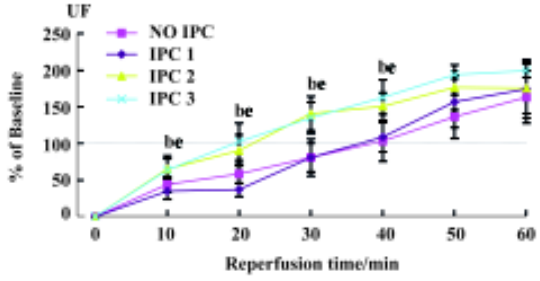

Figure 3. Percentage of change in urine flow (UF) during reperfusion from no ischemic preconditioning (IPC) (n=6), IPC 1 (n=6), IPC 2 (n=7), and IPC 3 (n=7) groups, respectively. ^{b}P<0.05 *vs* IPC 1. ^{e}P<0.05 *vs* IPC 2. Mean±SD.

0.16 to 0.85 μmol/L, 3.61 to 10.09 μmol/L, 0.72 to 7.50 μmol/L, and 1.89 to 3.20 μmol/L, respectively. After release of the clamp, adenosine, and other nucleotides concentrations, returned to their respective pre-ischemic levels in all cases. IPC1, IPC2, and IPC3 in Figure 4 show the renal interstitial concentrations of adenosine, inosine, hypoxanthine, xanthine and uric acid during 60-min ischemia and reperfusion in response to the 1, 2, and 3 cycles of IPC, respectively. In the single cycle of the preconditioning of kidneys during ischemia, adenosine, inosine, hypoxanthine, xanthine, and uric acid levels increased to 8.04, 0.42, 7.90, 7.50, and 1.84 μmol/L, respectively. The concentration of adenosine, inosine, hypoxanthine, xanthine, and uric acid was lower than that of the non-preconditioning ischemic kidneys (adenosine, inosine, and hypoxanthine, $P<0.05$). Similar patterns were also observed in the 2 and 3 cycles of the preconditioning ischemic kidney. However, the levels of adenosine, inosine, hypoxanthine, xanthine, and uric acid were markedly lower in 3 cycles of the preconditioning of ischemic kidneys than those in 1 and 2 cycles of preconditioning or non- preconditioning of ischemic kidneys (hypoxanthine and xanthine, $P<0.01$; adenosine, $P<0.05$; inosine and uric acid: $P>0.05$. Figure 4).

Effects of ischemia-reperfusion on renal hemodynamics during treatment with KW3902 An adenosine A_1 receptor antagonist, KW3902, shortened the recovery time of renal blood flow and urine flow, respectively, compared with the control groups during the reperfusion state following 60-min renal ischemia (Figure 5).

Discussion

The detrimental effects of renal ischemia-reperfusion injury, which are evident by increases in blood urea nitrogen (BUN) and creatinine (Cr)[4], reduction in the glomerular filtration rate (GFR) and renal blood flow (RBF), as well as morphological renal injury, have been well-studied *in vivo* or *in vitro* experiments. In the present study, we recognized mongrel dog renal hemodynamics parameters, urine flow (UF), RBF, mean blood pressure (BP), as well as renal interstitial adenosine and adenine nucleotide as experimental measurements using microdialysis sampling technology. Since the protective effects of ischemic preconditioning against ischemia-reperfusion injury are, at least in part, mediated by sympathetic nerves, as the protective effects were abolished by denervation[21], we denervated the dog kidneys before the experiments. Generally, during the renal 60-min ischemia followed by the 60-min reperfusion, the hemodynamic results were consistent with the data from previously published literature, returning to the respective control level quite slowly.

In 1986, it was first discovered by Murry *et al*[22] that multiple brief ischemia, which was defined as ischemic preconditioning (IPC) from then on, followed by the prolonged ischemia-reperfusion periods, could strengthen ischemia endurance of dog cardiac muscle and protect against post-ischemic myocardial injury and dysfunction. To date, a variety of studies have confirmed that IPC has species and organ generalization. However, evidence supporting a role for IPC in protecting against ischemia-reperfusion injury in kidneys is minimal and controversial[8,10,22-25]. In the present study, we proved that IPC with 1, 2, or 3 cycles of 10-min ischemia followed by 10-min reperfusion markedly increased 60-min post-ischemic UF and RBF, indicating the protective effects of IPC on dog renal ischemia-reperfusion injury. It is evident from our experimental results that IPC of 1 to 3 cycles with a 10-min interval shortened the recovery time of UF, RBF, and BP more significantly than that of without IPC in advance, which parallels the data reported in cardiac[6]. Previous studies[8,23] have suggested that IPC with brief cycles of ischemia and reperfusion is not effective in kidneys. However, recent studies[4,10,24,25], including the present one, have confirmed that there is an IPC effect in rat kidneys as well as dog kidneys. The discrepancies between the results of the earlier and recent studies might have arisen from the different preconditioning schedules.

A single cycle of brief ischemia is thought to be all that is needed to induce preconditioning, but most laboratories often use repetitive cycles of brief ischemia to the phenomenon. However, the beneficial effects of using multiple cycles over single cycle IPC is poorly understood. To clarify, we examined the effects of 1, 2, or 3 cycles of IPC on the renal function in ischemia-reperfusion kidney. As shown in our study, along with the increase of cycles of 10-min IPC, less recovery time during the 60-min reperfusion following 60-min ischemia is needed. To our knowledge, this is the first study that determines the cycles of 10-min renal IPC and the recovery time of BP, UF as well as RBF during 60-min renal reperfusion following 60-min renal ischemia, respectively, in dogs. The post-ischemic recovery of BP, UF as well as RBF occurred faster than that without IPC, and recovery time of BP, UF as well as RBF inversely related to the number of cycles, that is, more cycles of 10-min IPC (within 3 cycles), the shorter recovery time of BP, UF as well as RBF during the 60-min renal reperfusion following 60-min renal ischemia, respectively. Collectively, we can speculate that more cycles of renal IPC can protect against the renal ischemia-reperfusion injury better. In our present study, 10-min is-

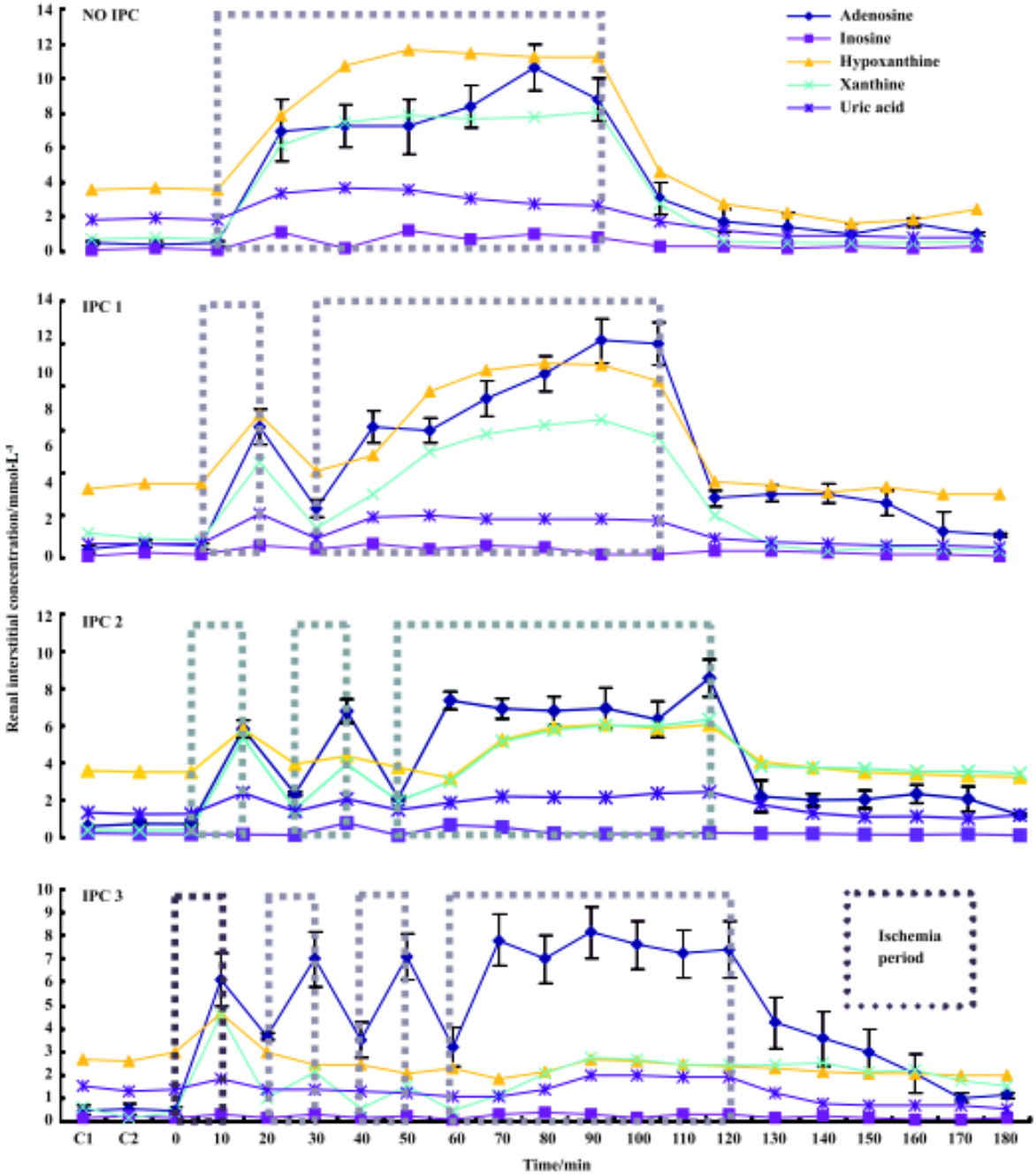

Figure 4. Changes in the renal interstitial concentration of adenosine, inosine, hypoxanthine, xanthine, and uric acid during ischemia-reperfusion, measured from no IPC (n=6), IPC 1 (n=6), IPC 2 (n=7), and IPC 3 (n=7) groups, respectively. C, control. Mean±SD.

chemia time intervals were chosen, which performed well during the experiment, even though it had been reported that 10-min renal ischemia produced some degree of cellular injury[8]. In our future experiments, we will increase the cycles of IPC and change the ischemia intervals. We will also prolong monitoring time after 60-min renal ischemia following different cycles of IPC in order to investigate the optimum duration of IPC and whether the "memory function" exists in the effect of IPC, that is, the protective effect of renal ischemic preconditioning under "optimum duration of IPC" can last very long time.

The precise mechanism of ischemic preconditioning, even

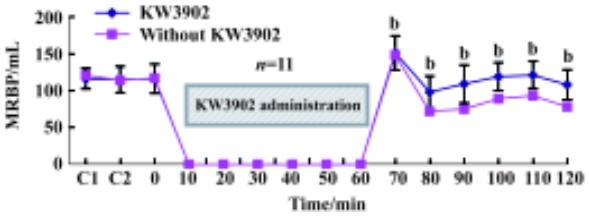

Figure 5. Comparison of changes in the mean renal blood flow (MRBF) during ischemia-reperfusion, with or without the treatment of KW3902, a highly selective adenosine A_1 receptor antagonist. C, control. $^bP<0.05$. n=11. Mean±SD. A similar pattern was observed for the comparison of urine flow.

in cardiac muscle, is not fully elucidated. However, numerous studies have been carried out to elucidate the mechanism of IPC, and special attention has been given to the finding that adenosine pretreatment mimics ischemic preconditioning in cardiac and renal tissue, and adenosine appears to be mediator of ischemic preconditioning[6,26,27]. Adenosine is released in large quantities within seconds after the onset of ischemia, including in the kidneys. The general concept is that a build-up of endogenous adenosine during the brief ischemia period (IPC period) can trigger protection via activation of adenosine receptors.

Previous studies suggest that renal ischemia increases the renal interstitial concentrations of adenosine and adenine nucleotide[11], and increased extracellular adenosine has been suggested as a regulator of renal hemodynamics in postischemia[15–17]. However, these findings are indirect and do not provide any data about the renal interstitial concentrations of adenosine and adenine nucleotides during IPC followed by ischemia and reperfusion. Therefore, the present study was performed to determine the levels of adenosine and adenine nucleotide in renal interstitial fluid during preconditioning followed by ischemia and reperfusion. Our results show that levels of adenosine and adenine nucleotides increase during IPC and the ischemic period. However, during ischemia, levels of adenosine and adenine nucleotides in renal interstitial fluid were lower than those of non-IPC kidney, and among the IPC groups, renal interstitial concentrations of adenosine and adenine nucleotides were markedly lower in ischemic kidney of 3 cycles IPC groups. The mechanism of IPC that decreased the levels of adenosine and adenine nucleotide during the ischemic period is not clear. Further research is necessary to evaluate how IPC lower renal interstitial concentrations of adenosine and adenine nucleotide during ischemic period.

Previous studies have shown that IPC improves the post-ischemic recovery of UF in rats[10]. In that study, the rats were subjected to 2 cycles of 3-min ischemia and 5-min reperfusion. The UF was examined at 90–120 min after ischemia. In the present experiment, dogs were subjected to 1, 2, or 3 cycles of 10-min ischemia and 10-min reperfusion. Our results also show that IPC improves the post-ischemic recovery of UF within 60 min. However, one important finding of our study is that IPC with 3 cycles is more protective compared to single or 2 cycles of IPC. The mechanism of more protective effects of IPC with multiple cycles is not clear. However, our results show that renal interstitial concentrations of adenosine and nucleotides are inversely related to the number of cycles. Therefore one possibility is that renal protective effect of IPC with 3 cycles is more effective because of lower renal interstitial concentrations of adenosine and adenosine nucleotides during ischemic insult.

At present, only 2 studies using the long duration of multiple cycles IPC have suggested the role of adenosine in IPC in the rat kidney[4,10]. In those studies, they have demonstrated that adenosine pretreatment or adenosine A_1 receptor activation by adenosine A_1 receptor agonist before ischemic insult protects post-ischemic renal function. However, Sugino *et al*[10] reported that adenosine A_1 receptor antagonist failed to abolish the post-ischemic renal protective effects of IPC or adenosine infusion in the rat kidney. In our study, the results using adenosine A_1 receptor antagonist consequently seem to indicate that the adenosine A_1 receptor activation deteriorates the renal function, supporting previously published studies[28], but is contradictory to the finding of Lee HT[4]. Agmon Y *et al*[29] found that interrenal adenosine reduced cortical blood flow and predominantly increased medullary flow via the A_1 and A_2 receptors, respectively. Also, it has been suggested[30] that vasoconstriction following brief renal artery occlusion is mediated by an increased accumulation of adenosine during the period of ischemia. Nishiyama *et al*[31], however, suggested that ischemia-induced accumulation of renal interstitial adenosine elicited renal vasoconstriction, at least in part, but might not have been the primary mediator of renal vasoconstriction in the maintenance phase of postischemia. At present, it is also suggested that renal IPC initiates the protective endocellular system and kidneys can release several kinds of interstitial mediators mediating the conduct of cell signals, including adenosine, which is recognized as an important factor in the protective effect of IPC. Collectively, we speculate that the conclusive effect of endogenous adenosine during ischemia-reperfusion is detrimental to the renal hemodynamics. This is because of the marked regional heterogeneity of the 3 adenosine receptor subtype distribution in dog kidneys which attenuate and prolong the recovery time of RBF and UF, respectively.

In summary, these results indicate that IPC protects post-ischemic renal function, and decreases the renal interstitial concentrations of adenosine and adenine nucleotides in ischemic kidneys. The present study showed that the shortened recovery time of BP, UF as well as RBF during the 60-min renal reperfusion following 60-min renal ischemia was progressively greater with multiple cycles of brief IPC. We have also confirmed that renal IPC can protect against ischemia-reperfusion injury. The predominant effect of endogenous adenosine induced by renal ischemia is detrimental to renal function because of the marked regional heterogeneity of the 3 adenosine receptor subtype distribution in dog kidneys.

Acknowledgements

We are grateful to Hidehiko SAKURAI and Motoki KYO (Toyobo, Otsu, Japan) for supplying the dialysis membrane and steel needles. Our thanks also to Kyowa Hakko Kogyo Co Ltd, for supplying KW-3902, and to Yumi IHARA for secretarial service.

References

1 Kerrigan CL, Stotland MA. Ischemia reperfusion injury: a review. Microsurgery 1993; 14: 165–75.
2 Aronson S, Blumenthal R. Perioperative renal dysfunction and cardiovascular anesthesia: concerns and controversies. J Cardiothorac Vasc Anesth 1998; 12: 567–86.
3 Huet F, Gouyou JB, Guignard JP. Prevention of hypoxemia-induced renal dysfunction by perindoprilat in the rabbit. Life Sci 1997; 61: 2157–65.
4 Lee HT, Emala CW. Protective effects of renal ischemic preconditioning and adenosine pretreatment: role of A_1 and A_3 receptors. Am J Physiol Renal Physiol 2000; 278: F380–7.
5 Nishiyama A, Miyatake A, Aki Y, Fukui T, Rahman M, Kimura S, *et al*. Adenosine A_1 receptor antagonist KW-3902 prevents hypoxia-induced renal vasoconstriction. J Pharmacol Exp Ther 1999; 291: 988–93.
6 Meldrum DR. Mechanisms of cardiac preconditioning: ten years after the discovery of ischemic preconditioning. J Surg Res 1997; 73: 1–13.
7 Reimer KA, Jennings RB. Ischemic preconditioning: a brief review. Basic Res Cardiol 1996; 91: 1–4.
8 Islam CF, Mathie RT, Dinneen MD, Kiely EA, Peters AM, Grace PA. Ischaemia-reperfusion injury in the rat kidney: the effect of preconditioning. Br J Urol 1997; 79: 842–7.
9 Turman MA, Bates CM. Susceptibility of human proximal tubular cells to hypoxia: effect of hypoxic preconditioning and comparison to glomerular cells. Ren Fail 1997; 19: 47–60.
10 Sugino H, Shimada H, Tsuchimoto K. Role of adenosine in renal protection induced by a brief episode of ischemic preconditioning in rats. Jpn J Pharmacol 2001; 87: 134–42.
11 Nishiyama A, Kimura S, He H, Miura K, Rahman M, Fujisawa Y, *et al*. Renal interstitial adenosine metabolism during ischemia in dogs. Am J Physiol Renal Physiol 2001; 280: F231–8.
12 Navar LG, Inscho EW, Majid SA, Imig JD, Harrison-Bernard LM, Mitchell KD. Paracrine regulation of the renal microcirculation. Physiol Rev 1996; 76: 425–536.
13 Spielman WS, Arend LJ. Adenosine receptors and signaling in the kidney. Hypertension 1991; 17: 117–30.
14 Spielman WS, Thompson CI. A proposed role for adenosine in the regulation of renal hemodynamics and renin release. Am J Physiol 1982; 242: F423–35.
15 Lin JJ, Churchill PC, Bidani AK. Effect of theophylline on the initiation phase of postischemic acute renal failure in rats. J Lab Clin Med 1986; 108: 150–4.
16 Lin JJ, Churchill PC, Bidani AK. The effect of dipyridamole on the initiation phase of postischemic acute renal failure in rats. Can J Physiol Pharmacol 1987; 65: 1491–5.
17 Lin JJ, Churchill PC, Bidani AK. Theophylline in rats during maintenance phase of post-ischemic acute renal failure. Kidney Int 1988; 33: 24–8.
18 Rahman M, Kimura S, Yoneyama H, Kasaka H, Nishiyama A, Fukui T, *et al*. Effects of furosemide on the tubular reabsorption of nitrates in anesthetized dogs. Eur J Pharmacol 2001; 428: 113–9.
19 Nishiyama A, Miyatake A, Kusudo K, Syokoji T, Yue W, Fukui T, *et al*. Effects of halothane on renal hemodynamics and interstitial nitric oxide in rabbits. Eur J Pharmacol 1999; 367: 299–306.
20 Miura K, Okumura M, Yukimura T, Yamamoto K. Fluorometric determination of plasma adenosine concentrations using high-performance liquid chromatography. Anal Biochem 1991; 196: 84–8.
21 Ogawa T, Mimura Y, Kaminishi M. Renal denervation abolishes the protective effects of ischaemic preconditioning on function and haemodynamics in ischaemia-reperfused rat kidneys. Acta Physiol Scand 2002; 174: 291–7.
22 Murry CE, Jennings RB, Reimer KA. Preconditioning with ischemia: A delay of lethal cell injury in ischemic myocardium. Circulation 1986; 74: 1124–36.
23 Zager RA, Jurkowitz MS, Merola AJ. Responses of the normal rat kidney to sequential ischemic events. Am J Physiol 1985; 249: F148–59.
24 Riera M, Herrero J, Torras J, Cruzado JM, Fatjo M, Lloberas N, *et al*. Ischemic preconditioning improves postischemic acute renal failure. Transplant Proc 1999; 31: 2346–7.
25 Cochrane J, Williams BT, Banerjee A, Harken AH, Burke TJ, Cairns CB, *et al*. Ischemic preconditioning attenuates functional, metabolic, and morphologic injury from ischemic acute renal failure in the rat. Ren Fail 1999; 21: 135–45.
26 Liu GS, Thornton J, Van Winkle DM, Stanley AW, Olsson RA, Downey JM. Protection against infarction afforded by preconditioning is mediated by A_1 adenosine receptors in rabbit heart. Circulation 1991; 84: 350–6.
27 Thornton JD, Liu GS, Olsson RA, Downey JM. Intravenous pretreatment with A_1-selective adenosine analogues protects the

heart against infarction. Circulation 1992; 85: 659–65.
28 Rossi N, Ellis V, Kontry T, Gunther S, Churchill P, Bidani A. The role of adenosine in $HgCl_2$-induced acute renal failure in rats. Am J Physiol 1990; 258: F1554–60.
29 Agmon Y, Dinour D, Brezis M. Disparate effects of adenosine A_1- and A_2-receptor agonists on intrarenal blood flow. Am J Physiol 1993; 265: F802–6.
30 Spielman WS, Osswald H. Blockade of postocclusive renal vasoconstriction by an angiotensin II antagonists: evidence for an angiotensin-adenosine interaction. Am J Physiol 1979; 237: F463–7.
31 Nishiyama A, Miura K, Miyatake A, Fujisawa Y, Yue W, Fukui T, *et al*. Renal interstitial concentration of adenosine during endotoxin shock. Eur J Pharmacol 1999; 385: 209–16.

Important Announcement: the Online Manuscript Submission and Review System was Launched!

Acta Pharmacologica Sinica is happy to announce that the online manuscript submission and review system, ScholarOne Manuscript Central (http://mc.manuscriptcentral.com/aphs), was launched on May 25, 2005.

As the leading web-based peer-review system, Manuscript Central is a complete, database-driven software for the online submission and review of full-text manuscripts and graphics. The system provides fully electronic workflow and will speed up the time from submission to decision.

We strongly recommend authors to submit manuscript via this system, which enables us to handle your manuscript quickly and efficiently. Please read the User Guide before submitting your manuscript online. For more detailed submission instruction, please consult the Manuscript Central Online User Guide (http://mcv3help.manuscriptcentral.com/tutorials/). You may also contact the Editorial Office who will be pleased to help you.

Acta Pharmacologica Sinica 2005 Jul; 26 (7): 860–864

Full-length article

Interaction effects between estrogen receptor α and vitamin D receptor genes on age at menarche in Chinese women

Hong XU[1,2], Ji-rong LONG[3], Miao-xin LI[1], Hong-wen DENG[1,3]

[1]Laboratory of Molecular and Statistical Genetics, College of Life Sciences, Hu-nan Normal University, Changsha 410081, China; [2]Department of Physiology, Jiangxi Medical College, Nanchang 330006, China; [3]Osteoporosis Research Center and Department of Biomedical Sciences, Creighton University Medical Center, 601 N 30th St, Suite 6787, Omaha, NE 68131, USA

Key words

menarche; association; haplotype; estrogen receptor α gene; vitamin D receptor gene

[2] Correspondence to Dr Hong-wen DENG.
Phn 86-731-887-2791.
Fax 86-731-887-2791
E-mail hwdeng@hunnu.edu.cn

Received 2004-11-22
Accepted 2005-02-28

doi: 10.1111/j.1745-7254.2005.00122.x

Abstract

Aim: To evaluate whether estrogen receptor α (ER-α) and vitamin D receptor (VDR) genes are associated with the age at menarche in Chinese women. **Methods**: A total of 390 pre-menopausal Chinese women were genotyped at the ER-α *Pvu*II, X*ba*I, and VDR *Apa*I loci using polymerase chain reaction (PCR)-restriction fragment length polymorphism (RFLP). **Results**: Neither the ER-α gene nor the VDR gene individually had significant effects on the age at menarche in our subjects (P>0.10). However, evidence of interaction effects between the two genes were observed: with the aa genotype at the VDR *Apa*I locus, subjects with haplotype PX at the ER-α gene had, on average, 6 months later onset of menarche than the non-carriers (P=0.01). **Conclusion:** We found that neither the ER-α gene or the VDR gene had a significant association with the age at menarche individually. However, potential interaction effects between the two genes were observed in Chinese women.

Introduction

Menarche, the first occurrence of menstruation, is a marked characteristic of a woman's sexual maturation and a biological signal for the onset of reproduction. Age at menarche is an important anthropological variable, which influences the total duration of women's estrogen exposure and thus has major implications for a woman's health later in life. Early menarche is associated with an increased risk of breast and endometrial cancer[1]. Delayed menarche increases the risk of Alzheimer's disease[1] and osteoporosis[2], but decreases the incidence of coronary heart disease[1]. Therefore, from a clinical point of view, it is of interest to identify factors that influence the variation of menarcheal age.

Age at menarche is known to be a complex trait that is determined by multiple genetic and environmental factors, including nutrition, exercise, socioeconomic conditions, childhood experience, and general health[1,3–5]. The importance of genetic factors in determining menarcheal age has recently been recognized. Twin studies have shown that genetic factors can explain more than 50% of the variation of menarcheal age[4]. There are highly significant correlations between age at menarche in mothers and daughters[3], and family history is a strong predictor for early menarche[5]. Recently, some candidate genes, such as the androgen receptor (AR) gene[6], the cytochrome P450 c17α (CYP17) gene[7,8] and the CYP3A4 gene[8], have been tested for association with age at menarche. The results so far have been inconsistent, and the specific gene responsible for age at menarche is still not clear.

The onset of menstruation is determined by the hypothalamic-pituitary-gonadal axis and is initiated by an increased amplitude of estrogen exposure of tissues[9]. Estrogen signal receptors including estrogen receptor α (ER-α) play an important role in mediating the specific effects of the estrogen on development, proliferation and differentiation of reproductive tissues[10]. In addition, mice deficient in ER-α are infertile and exhibit atrophy of the oviduct and uterus[11]. Thus, the ER-α gene may be a candidate gene for the onset of menstruation. An association has been observed between the ER-α gene and age at menarche in Greek adolescent females[12] but not in other populations[7,13,14].

The vitamin D receptor (VDR) gene may be another potential candidate gene for age at menarche. The expression of VDR is detected in reproductive organs[15]. In vitamin D-deficient mice, uterine hypoplasia with impaired folliculogenesis was found in the female reproductive organs[16]. The VDR gene has been associated with several diseases that may be related to total tissue estrogen exposure, including breast cancer[17], cardiovascular disease[18], and osteoporosis[19]. Recently, the VDR gene has been associated with the age of menarche in Japanese girls[20].

In the present study, we intended to investigate whether the ER-α and VDR genes, as well as interactions between the two, had effects on the age at menarche in the Chinese female population.

Materials and methods

Subjects The study subjects were selected from 401 nuclear families used in our previous epidemiological study[21], which was approved by the Research Administration Departments of the Shanghai Sixth People's Hospital and Hunan Normal University. All the subjects were recruited from the Shanghai urban area. They were all of the Han ethnic group, which accounts for more than 93% of the total Chinese population. Informed consent was obtained from each subject. For the study subjects, a detailed medical history, including menstrual history, was recorded by nurse-administered questionnaires. The sampling scheme and exclusion criteria have been detailed elsewhere[21].

For the present study, we randomly chose one pre-menopausal daughter from each nuclear family. Four hundred and one unrelated pre-menopausal women, who were all in good general health as defined by our exclusion criteria, were sampled. Among these women, 11 had no information of menarcheal age. Thus the 390 remaining pre-menopausal women were available for analysis. The women were unrelated and had regular menstrual cycles.

Genotyping Genomic DNA was isolated using the phenol-chloroform extraction method from whole blood. All subjects were genotyped by polymerase chain reaction followed by restriction fragment length polymorphism procedures (PCR-RFLP). For the ER-α gene, the forward primer (5'-CTG CCA CCC TAT CTG TAT CTT TTC CTA TTC TCC-3') and reverse primer (5'-TCT TTC TCT GCC ACC CTG GCG TCG ATT ATC TGA-3') were used to amplify a 1.3 kb DNA fragment in intron 1. For the *Apa*I inside the VDR gene, a 745 bp DNA fragment was produced using the forward primer in intron 8 (5'-CAG AGC ATG GAC AGG GAG CAA G-3') and the reverse primer in exon 9 (5'-GCA ACT CCT CAT GGC TGA GGT CTC A-3'). The PCR mix contained 50 ng genomic DNA, each of the four deoxyribonucleotides (dNTPs; 0.2 mmol/L), 0.6 U *Taq* polymerase (Sangon, Shanghai, China), $MgCl_2$ (1.5 mmol/L), each primer (0.4 μmol/L), and 1×PCR buffer in a total volume of 25 μL. PCR was performed in 38 cycles as follows: denaturation at 95 °C for 30 s, annealing at 50 °C for 30 s, and extension at 72 °C for 60 s on a PE9700 Thermal Cycler (Perkin-Elmer Cetus, Norwalk, CT, USA). After amplification, 8 μL of the PCR products was digested with the respectively restriction endonucleases *Pvu*II, *Xba*I, and *Apa*I (Promega, Madison, WI, USA) at 65 °C for 4 h and electrophoresed on 2% agarose gel, stained with ethidium bromide, and visualized under UV light. The genotypes were designated as PP, Pp, and pp for *Pvu*II, XX, Xx, and xx for *Xba*I, and AA, Aa, and aa for *Apa*I. Uppercase and lowercase letters represent the absence and presence of restriction sites, respectively.

Statistical analysis The χ^2 test was performed to test for the Hardy-Weinberg equilibrium (HWE) at the studied marker loci. The phenotypic values were verified for normal distribution by using the Shapiro-Wilks test. The Program SimWalk2 (available at http://www.genetics.ucla.edu/home/software.htm) was used to reconstruct the ER-α haplotypes according to the genotypes of all the subjects in the nuclear families, because the ER-α *Pvu*II and *Xba*I were in strong linkage disequilibrium (LD)[22]. Analysis of variance (ANOVA) was used to evaluate the effects of the ER-α and VDR gene polymorphisms on age at menarche. The frequency of genotype AA for the VDR gene (6.2%) was low in our subjects. If the subjects were divided into three groups, AA, Aa, and aa, the sample sizes for some groups were small, and it was not appropriate to analyze the interaction effect. Then the subjects were divided into two groups, those with and without the minor allele A. To analyze the effect of a special ER-α haplotype, the subjects with this haplotype were denoted as "1"; those without it were denoted as "0". The effect of a given ER-α gene haplotype was tested according to the special VDR genotypes. When a significant result appeared, it was regarded as indicative of an interaction between the ER-α and VDR genes. These statistical analyses were conducted using SAS version 6.12 (SAS Institute, Cary, NC, USA).

Results

Descriptive characteristics of the study subjects The basic characteristics of the 390 unrelated pre-menopausal women are summarized in Table 1. Allele frequencies at the three polymorphic sites in our subjects are summarized in Table 2. All three loci were in HWE (P>0.10). When the genotypes of the ER-α gene were defined according to the

Table 1. Descriptive characteristics of all the subjects. Values are expressed as mean±SD.

	Subjects
Sample size	390
Age/a	31.0±5.5
Height/cm	159.8±5.3
Weight/kg	55.0±8.1
Age at menarche/a	13.6±1.4

Table 2. Allele frequencies at the three polymorphic sites.

	Allele frequencies/%
ER-α *Pvu*II	P=37.1
	p=62.9
ER-α *Xba*I	X=22.4
	x=77.6
ER-α haplotype	PX=16.0
	px=56.6
	Px=21.0
	pX=6.4
VDR *Apa*I	A=27.4
	a=72.6

The *Pvu*II and *Xba*I polymorphisms of the ER-α and the *Apa*I polymorphism of the VDR were in Hardy-Weinberg equilibrium (P>0.10).

haplotypes, ten genotypes were found, with pxpx as the most common (frequency=0.331) and pXpX as the least common (frequency=0.002).

Association of the ER-α and VDR genes with the age at menarche We did not find a significant association between age at menarche and either the ER-α individual polymorphisms or the ER-α haplotypes, or the VDR *Apa*I locus (P> 0.10) (Table 3). Evidence of an interaction between the ER-α and VDR genes was observed. With the aa genotype at the VDR gene, subjects with haplotype PX at the ER-α gene had, on average, 6 months later onset of menarche than the non-carriers (P=0.01) (Table 4).

Discussion

Age at menarche is an important complex trait, which is controlled by both genetic and environmental factors. Some genetic studies have been performed in white and black women, and significant differences between different ethnic populations have been observed, that is, the average onset of menstruation in African-American girls is 9 months earlier than that in Caucasians[23]. However, few genetic studies

Table 3. Association analyses for the ER-α and VDR genes with age at menarche.

Polymorphisms		*n*	Age at menarche/ years
ER-α *Pvu*II	PP	50	13.4±1.5
	Pp	189	13.7±1.4
	pp	151	13.5±1.4
	P value		0.36
ER-α *Xba*I	XX	14	13.4±1.3
	Xx	147	13.7±1.4
	xx	229	13.5±1.4
	P value		0.57
ER-α haplotype	PX/px	73	13.7±1.2
	PX/Px	29	13.8±1.7
	px/px	129	13.5±1.4
	px/Px	89	13.7±1.5
	px/pX	21	13.6±1.2
	Px/pX	24	13.6±1.4
	P value		0.74
VDR *Apa*I	AA	24	13.4±1.3
	Aa	166	13.5±1.3
	aa	200	13.7±1.4
	P value		0.52

All data are presented as mean±SD of the age of menarche. Only 6 combinations of *Pvu*II and *Xba*I genotypes were included in the analysis, because the number of other possible genotypes is small. *P* values are the results of ANOVA.

Table 4. Interaction effects between the ER-α and VDR genes on the age at menarche.

		VDR gene	
		A	B
ER-α PX	0	13.6±1.4 (127)	13.5±1.4 (148)
	1	13.3±1.2 (63)	14.0±1.4 (52)
	P value	0.19	0.01
ER-α px	0	13.1±1.3 (33)	13.8±1.6 (45)
	1	13.6±1.4 (157)	13.6±1.4 (155)
	P value	0.10	0.45
ER-α Px	0	13.5±1.3 (118)	13.6±1.4 (119)
	1	13.5±1.4 (72)	13.8±1.6 (81)
	P value	1.00	0.23
ER-α pX	0	13.5±1.4 (167)	13.6±1.5 (174)
	1	13.7±1.3 (23)	13.6±1.4 (26)
	P value	0.56	1.00

All data are presented as mean±SD of the age of menarche. The sample size is listed in parentheses. "1" denotes carriers and "0" denotes non-carriers of the corresponding ER-α haplotype. "A" denotes the subjects with allele A (the AA and Aa genotypes) at the VDR *Apa*I locus and "B" denotes the subjects without allele A (the aa genotype) at the VDR *Apa*I locus.

have been conducted in Chinese. In this study, the potential interaction effects between the ER-α and VDR genes were observed, although neither of them was significantly associated with the age at menarche individually.

A preliminary study in Greek adolescent females has shown an association between ER-α *Xba*I and *Pvu*II and age at menarche[12]. Subjects with the genotype XX had later onset of menarche than those with genotypes Xx or xx. The study also found that haplotype PX homozygotes were correlated with later onset of age at menarche. However, such an association was not observed in Japanese women[7] or Dutch women[13,14]. Similar to these findings, we did not find any significant association between the ER-α *Xba*I or *Pvu*II polymorphisms and age at menarche in Chinese women.

For the VDR *Apa*I locus, no association was obtained in the present study. However, in a Japanese population, a significant association was found between the VDR gene and age at menarche[20].

Discrepancies between our study and the other studies may be due to differences in ethnic background, sample size, ascertainment schemes, and statistical methods. For example, if the sample sizes are limited, the power to detect the association will be very low. However, for a single candidate gene that can explain approximately 10% of the variation of menarcheal age, our study sample has about 70% power to detect its association with age at menarche. In addition, gene-by-gene or gene-by-environment interactions may also influence the results of association. For example, interaction between the ER-α and VDR genes was observed in our study. To our best knowledge, this is the first study to find an interaction effect between these two genes on age at menarche. This finding suggests that the magnitude and the direction of the effects of genotypes at one locus may be affected by the specific genotype at the other loci. It also implies that the combination of genotypes at several loci may be more important than a single one. The gene-by-gene interactions may be different in different populations, so the interaction effects observed here have yet to be confirmed by separate analyses in various populations or ethnic groups.

The mechanism by which these two genes interact with each other to affect the onset of menstruation is not clear; however, from a physiological point of view, interaction is possible. An estrogen-responsive promoter region has been characterized in the VDR gene. Transcription of the VDR promoter is dependent on the estrogen receptor[24]. On the other hand, vitamin D may influence the balance between androgens and estrogens, which in turn modulates the availability of steroid hormones for their receptors[25]. In addition, vitamin D may act at several points along the estrogen response pathway, affecting the levels of estrogen receptor as well as their ability to function as enhancers of transactivation[26].

Noticeably, there was a multiple-testing problem, because we tested multiple alleles in our analyses. If we use the *Bonferroni* correction to adjust for the multiple testing ($P \leq 0.006$ as the significant level), the interaction between the ER-α and VDR genes ($P=0.01$) will be close to, but not reach, statistical significance. In this situation, the *Bonferroni* correction is likely to be too conservative because it assumes that all variants are independent[27]. However, the statistical tests in the present study are expected to be highly correlated. For example, the *Xba*I and *Pvu*II polymorphisms are only 45 bp apart and in strong LD. Thus multiple testing corrections may lead to power loss and an increased rate of false-negative associations. To report some potentially important associations that are likely to be worthwhile pursuing further, we report the original statistical results.

For genetic investigations of complex traits, phenotype definition is a critical issue. In the present study, age at menarche was determined retrospectively based on self-report, and recall error may be inevitable. However, menarche is one of the most important milestones in a woman's life and retrospective recall is known to be reasonably accurate: recent studies have shown a high correlation between the recalled and actual ages at menarche[28]. Furthermore, it seems unlikely that this recall bias differs in different genotypes. Thus, our results based on the recalled age at menarche may be valid. Menarcheal age is affected by nutritional level and other living environmental factors. Such information was not recorded and was not used as covariates to adjust the raw data in the present study. In this study, we tried to limit the unrelated subjects to a similar age, so they would have a similar living environment. Such a method of subject ascertainment will have improved the accuracy of our association results.

In summary, the ER-α and VDR genes individually were not associated with the age of menarche in Chinese women. However, potential interaction effects between them were observed. Further studies in other populations with larger sample sizes and denser markers are required to confirm the findings reported here.

Acknowledgements

The study was partially supported by a key project grant (30230210), an Outstanding Young Scientist Award (30025025), a general grant (30470534) from the National Science Foundation of China, three projects from the Scientific

Research Fund of Hunan Provincial Education Department (02A027, 03C226, 04B039), and a grant from the Natural Science Foundation of Hunan Province (04JJ1004). Ji-rong LONG and Hong-wen DENG were partially supported by grants from the Health Future Foundation of the USA, grants from the National Institutes of Health (K01 AR02170-01, R01 GM60402-01 A1), and grants from the State of Nebraska Cancer and Smoking Related Disease Research Program (LB595), the State of Nebraska Tobacco Settlement Fund (LB692), and the US Department of Energy (DE-FG03-00ER63000/A00). We thank all of the study subjects for volunteering to participate in the study.

References

1 Rees M. The age of menarche. ORGYN 1995; 4: 2-4.
2 Ito M, Yamada M, Hayashi K, Ohki M, Uetani M, Nakamura T. Relation of early menarche to high bone mineral density. Calcif Tissue Int 1995; 57: 11–4.
3 Treloar SA, Martin NG. Age at menarche as a fitness trait: nonadditive genetic variance detected in a large twin sample. Am J Hum Genet 1990; 47: 137–48.
4 Kaprio J, Rimpela A, Winter T, Viken RJ, Rimpela M, Rose RJ. Common genetic influences on BMI and age at menarche. Hum Biol 1995; 67: 739–53.
5 Chie WC, Liu YH, Chi J, Wu V, Chen A. Predictive factors for early menarche in Taiwan. J Formos Med Assoc 1997; 96: 446–50.
6 Jorm AF, Christensen H, Rodgers B, Jacomb PA, Easteal S. Association of adverse childhood experiences, age of menarche, and adult reproductive behavior: does the androgen receptor gene play a role? Am J Med Genet 2004; 125B: 105–11.
7 Gorai I, Tanaka K, Inada M, Morinaga H, Uchiyama Y, Kikuchi R, *et al*. Estrogen-metabolizing gene polymorphisms, but not estrogen receptor-alpha gene polymorphisms, are associated with the onset of menarche in healthy postmenopausal Japanese women. J Clin Endocrinol Metab 2003; 88: 799–803.
8 Kadlubar FF, Berkowitz GS, Delongchamp RR, Wang C, Green BL, Tang G, *et al*. The CYP3A4*1B variant is related to the onset of puberty, a known risk factor for the development of breast cancer. Cancer Epidemiol Biomarkers Prev 2003; 12: 327–31.
9 Stoll BA. Western diet, early puberty, and breast cancer risk. Breast Cancer Res Treat 1998; 49: 187–93.
10 Pelletier G, El-Alfy M. Immunocytochemical localization of estrogen receptors alpha and beta in the human reproductive organs. J Clin Endocrinol Metab 2000; 85: 4835–40.
11 Rosenfeld CS, Roberts RM, Lubahn DB. Estrogen receptor- and aromatase-deficient mice provide insight into the roles of estrogen within the ovary and uterus. Mol Reprod Dev 2001; 59: 336–46.
12 Stavrou I, Zois C, Ioannidis JP, Tsatsoulis A. Association of polymorphisms of the oestrogen receptor alpha gene with the age of menarche. Hum Reprod 2002; 17: 1101–5.
13 Weel AE, Uitterlinden AG, Westendorp IC, Burger H, Schuit SC, Hofman A, *et al*. Estrogen receptor polymorphism predicts the onset of natural and surgical menopause. J Clin Endocrinol Metab 1999; 84: 3146–50.
14 Boot AM, van der Sluis IM, de Muinck Keizer-Schrama SM, van Meurs JB, Krenning EP, Pols HA, *et al*. Estrogen receptor alpha gene polymorphisms and bone mineral density in healthy children and young adults. Calcif Tissue Int 2004; 74: 495–500.
15 Walter MR. Newly identified actions of the vitamin D endocrine system. Endocr Rev 1992; 13: 719–64.
16 Yoshizawa T, Handa Y, Uematsu Y, Takeda S, Sekine K, Yoshihara Y, *et al*. Mice lacking the vitamin D receptor exhibit impaired bone formation, uterine hypoplasia and growth retardation after weaning. Nat Genet 1997; 16: 391–6.
17 Bretherton-Watt D, Given-Wilson R, Mansi JL, Thomas V, Carter N, Colston KW, *et al*. Vitamin D receptor gene polymorphisms are associated with breast cancer risk in a UK Caucasian population. Br J Cancer 2001; 85: 171–5.
18 Uitterlinden AG, Fang Y, Van Meurs JB, Van Leeuwen H, Pols HA. Vitamin D receptor gene polymorphisms in relation to vitamin D related disease states. J Steroid Biochem Mol Biol 2004; 89–90: 187–93.
19 Qin YJ, Zhang ZL, Huang QR, He JM, Hu YQ, Zhao Q, *et al*. Association of vitamin D receptor and estrogen receptor-alpha gene polymorphism with peak bone mass and bone size in Chinese women. Acta Pharmacol Sin 2004; 25: 462–8.
20 Kitagawa I, Kitagawa Y, Kawase Y, Nagaya T, Tokudome S. Advanced onset of menarche and higher bone mineral density depending on vitamin D receptor gene polymorphism. Eur J Endocrinol 1998; 139: 522–7.
21 Qin YJ, Shen H, Huang QR, Zhao LJ, Zhou Q, Li MX, *et al*. Estrogen receptor alpha gene polymorphisms and peak bone density in Chinese nuclear families. J Bone Miner Res 2003; 18: 1028–35.
22 Zhang YY, Long JR, Liu PY, Liu YJ, Shen H, Zhao LJ, *et al*. Estrogen receptor alpha and vitamin D receptor gene polymorphisms and bone mineral density: association study of healthy pre- and postmenopausal Chinese women. Biochem Biophys Res Commun 2003; 308: 777–83.
23 Anderson SE, Dallal GE, Must A. Relative weight and race influence average age at menarche: results from two nationally representative surveys of US girls studied 25 years apart. Pediatrics 2003; 111: 844–50.
24 Wietzke JA, Welsh J. Phytoestrogen regulation of a vitamin D3 receptor promoter and 1, 25-dihydroxyvitamin D3 actions in human breast cancer cells. J Steroid Biochem Mol Biol 2003; 84: 149–57.
25 Willing M, Sowers M, Aron D, Clark MK, Burns T, Bunten C, *et al*. Bone mineral density and its change in white women: estrogen and vitamin D receptor genotypes and their interaction. J Bone Miner Res 1998; 13: 695–705.
26 Swami S, Krishnan AV, Feldman D. 1alpha, 25-Dihydroxyvitamin D3 down-regulates estrogen receptor abundance and suppresses estrogen actions in MCF-7 human breast cancer cells. Clin Cancer Res 2000; 6: 3371–9.
27 Nyholt DR. Genetic case-control association studies: correcting for multiple testing. Hum Genet 2001; 109: 564–7.
28 Must A, Phillips SM, Naumova EN, Blum M, Harris S, Dawson-Hughes B, *et al*. Recall of early menstrual history and menarcheal body size: after 30 years, how well do women remember? Am J Epidemiol 2002; 155: 672–9.

Acta Pharmacologica Sinica 2005 Jul; 26 (7): 865–872

Full-length article

Design, synthesis, and anti-inflammatory evaluation of a series of novel amino acid-binding 1,5-diarylpyrazole derivatives

Ming-hui LI, Lin-lin YIN, Mao-jun CAI, Wei-yu ZHANG, Yue HUANG, Xin WANG, Xing-zu ZHU[1], Jing-kang SHEN[1]

State Key Laboratory of Drug Research, Shanghai Institute of Materia Medica, Shanghai Institutes for Biological Sciences, Chinese Academy of Sciences, Graduate School of the Chinese Academy of Sciences, Shanghai 201203, China

Key words

nonsteroidal anti-inflammatory agents; cyclo oxygenase inhibitors; celecoxib; pyrazole; sulfonamide; prodrugs

[1] Correspondence to Prof Jing-kang SHEN.
Phn 86-21-5080-6067.
Fax 86-21-5080-5901.
E-mail jkshen@ mail.shcnc.ac.cn
[1] Co-correspondence to Prof Xing-zu ZHU.
Phn/Fax 86-21-5080-6096.
E-mail xzzhu@mail.shcnc.ac.cn

Received 2005-04-14
Accepted 2005-05-16

doi: 10.1111/j.1745-7254.2005.00151.x

Abstract

Aim: To design and synthesize a series of novel amino acid-binding 1,5-diarylpyrazole derivatives, which are intended to act as prodrugs with better aqueous solubility than celecoxib, and which will exert potent anti-inflammatory activities after being converted to their parent compounds *in vivo*. **Methods:** To introduce an amino acid, celecoxib analogs containing amino or methylamino group were synthesized first through multi-step chemical reactions. All the synthesized compounds were screened in an intact cell-based assay *in vitro* and in carrageenan-induced mouse paw edema *in vivo*. Some active compounds were selected for further evaluation in a carrageenan-induced rat paw edema model. The preliminary pharmacokinetics experiments were conducted using high performance liquid chromatography/mass spectrometry (HPLC/MS). **Results:** Celecoxib, 6 of the 1,5-diarylpyrazole class of celecoxib analogs, and their amino acid derivatives (hydrochloride salts) were synthesized. *In vitro* screening, the hydrochloride salts showed decreased inhibitory effects on cyclooxygenase (COX)-1 and COX-2 compared with their parent compounds, but some exhibited potent anti-inflammatory activity *in vivo*. Compound 4a was selected for further evaluation, and its anti-inflammatory effect was equivalent to that of celecoxib after oral administration in the carrageenan-induced rat paw edema model. At three doses (25 mg/kg, 50 mg/kg, and 100 mg/kg) the percentage inhibition on edema was 20.7%, 52.6%, and 62.6% (for compound 4a) and 27.8%, 38.4%, and 40.1% (for celecoxib), respectively. Preliminary pharmacokinetic evaluations support the hypothesis that compound 4a was actually converted to its parent compound, compound 4. **Conclusion:** The compound bound with amino acid acts like prodrug, which can exert anti-inflammatory effect similar to celecoxib after being converted to its parent compound. This finding will be of great benefit in carrying out structural modifications of prodrug-like selective COX-2 inhibitors.

Introduction

Nonsteroidal anti-inflammatory drugs (NSAIDs) are widely used in the treatment of pain and inflammation. NSAIDs act by inhibiting the catalytic activity of cyclooxygenase (COX), which results in a blockage of the formation of prostaglandins (PGs). COX exists as two distant isoforms (COX-1 and COX-2)[1,2]. Inhibition of COX-2 accounts for the anti-inflammatory effects of NSAIDs, whereas interruption of COX-1 leads to gastrointestinal toxicity[2,3]. Therefore, it is proposed that a selective COX-2 inhibitor would have a superior safety profile[4] to traditional NSAID.

Since the discovery of COX-2, a large number of selective COX-2 inhibitors have been described[5–8], of which vicinal diaryl heterocycles represent the most important group[9–12]. These selective COX-2 inhibitors have pronounced anti-

inflammatory effects with reduced or no gastrointestinal side effects. Celecoxib, in the 1,5-diarylpyrazole class of compound[13], was the first launched selective COX-2 inhibitor, and has excellent selectivity and potent anti-inflammatory activity; however, its aqueous solubility is relatively low, which decreases its oral bioavailability[14]. One approach to address this problem is to convert the compound into a prodrug that is readily soluble in water. Researchers attempted to create a water-soluble form by *N*-acetylation of the sulfonamide group of celecoxib followed by preparation of its sodium salt[15], but the result was unsatisfactory. The acetylation product had a lower level of inhibitory effect on rat paw edema than that produced by celecoxib.

Recently, the cardiovascular safety of coxibs has raised serious concerns; Merck & Co even voluntarily withdrew a rofecoxib product from the market because of an increased risk of cardiovascular events. Although there has been concern about adverse cardiovascular events associated with the use of selective COX-2 inhibitors[16], there is still no evidence indicating that cardiac toxicity is linked with all COX-2 inhibitors[17,18]. Selective COX-2 inhibitors are still under development[5,19,20]. It has been proposed that drugs with higher selectivity for COX-2 tend to induce cardiovascular disease[18,21]. Therefore, we chose the moderately selective COX-2 inhibitor, celecoxib, as a target for modification (the COX-1/COX-2 IC_{50} ratios of etoricoxib, rofecoxib, valdecoxib and celecoxib are 106, 35, 30, and 7.6, respectively).

To improve the oral absorption of celecoxib, a prodrug strategy was used in this study. In our experiments, we were mindful of the following: (1) conserving the main structure of celecoxib, including the trifluoromethyl and benzenesulfonamide groups, which contribute to its inhibitive qualities and selectivity of COX-2[13]; (2) partially containing the methyl group in cycle C, because it can be metabolized to the corresponding hydroxymethyl and carboxylic acid analogs (glucuronide conjugation of the carboxylic acid metabolite is a major pathway of elimination in humans[22]); (3) introducing some polar groups, such as amino or methylamino groups, into cycle C; (4) binding with a natural amino acid followed by preparation of its hydrochloride acid salt. The amide bonds are inclined to be hydrolyzed *in vivo*, and the cleaved natural amino acid part is safe for humans.

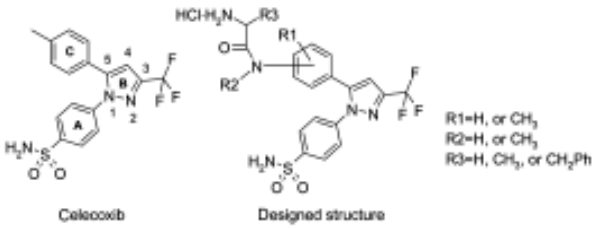

Structure of celecoxib and the designed compounds

Based on these considerations, in the present study, we designed and synthesized some 1,5-diarylpyrazole derivatives. These hydrochloride salts were expected to have good aqueous solubility and act like prodrugs, which can exhibit potent anti-inflammatory activity *in vivo* after being converted to their parent compounds.

Materials and methods

Animals Female Kun-ming mice (grade SPF II, certificate No SCXK 2003-0003) weighing 18–22 g and male Sprague-Dawley (SD) rats (grade SPF II, certificate No SCXK 2003-0003) weighing 180–200 g were provided by the Shanghai Experimental Animal Center, Chinese Academy of Sciences. These animals were fasted with free access to water for at least 12 h prior to the experiments. All the animal treatments were strictly in accordance with the Chinese National Institute of Health's Guide for the Care and Use of Laboratory Animals (National Research Council, 1996).

Chemicals and reagents Substituted acetophenone and ethyl trifluoracetate were purchased from Aldrich (St Louis, MO, USA) and Acros (Geel, Belgium). The tert-butoxycarbonyl (BOC)-protected amino acid was from GL Biochem (Shanghai, China). The other reagents were from the Shanghai Chemical Reagent Co (Shanghai, China). All the chemicals were analytical grade or above.

Chemistry To obtain the expected prodrugs, celecoxib (positive drug), and celecoxib analogs (parent compounds) containing amino or methylamino groups were synthesized first as follows.

4-[5-(4-Methylphenyl)-3-(trifluoromethyl)-1*H*-pyrazol-1-yl]benzenesulfonamide (celecoxib) Celecoxib (compound 2) was synthesized as described previously[13] with some modifications. In first step, sodium methanol was replaced with sodium ethanol, and the reaction time was reduced from 24 h to 4 h. In second step, dione 1 reacted with (4-sulfamoylphenyl)hydrazine hydrochloride (self-preparation) to produce celecoxib in the form of white crystals (Scheme 1, a-b). Purity as assessed by high performance liquid chromatography (HPLC) was 99.8%. The structure was identified by EI-MS, Mp, and H^1NMR.

Celecoxib analogs containing amino or methylamino groups (parent compounds) Three classes of 6 compounds were synthesized as followed.

1. 4-[5-(3-Amino-4-methylphenyl)-3-(trifluoromethyl)-1*H*-pyrazol-1-yl]benzenesulfonamide (compound 4) Celecoxib was treated with diluted HNO_3 2 mol/L and concentrated H_2SO_4 to give the nitration product 3. Then the nitro group was reduced to an amino group by 10% Pd/C

and H_2 to obtain compound 4. To introduce one methyl group on the N atom of the amino group, the N-formyl amine was obtained by the *N*-formylation of compound 4 with formic acid, then it was reduced by lithium aluminum hydride ($LiAlH_4$)[23] to give the desired *N*-monomethyl aromatic amine compound 5 (Scheme 1, c-e).

2. 4-[5-(3-Methyl-4-aminophenyl)-3-(trifluoromethyl)-1*H*-pyrazol-1-yl]benzenesulfonamide (compound 9) 3-Methyl-4-nitro acetophenone (compound 6) as a starting material was prepared as described previously[24] (Scheme 2, a–c). We tried the same method as used in the preparation of celecoxib, but did not obtain the desired compound 7. After different bases and solvents were experienced in step d, we found that the presence of benzene and tert-butanol potassium were suitable for dione (compound 6) synthesis, and that the temperature should be kept at less than 0 °C. Then compounds 9 and 10 were produced (Scheme 2, d-f). by similar method as Scheme 1.

3. 4-[5-(4-Aminophenyl)-3-(trifluoromethyl)-1*H*-pyrazol-1-yl]benzenesulfonamide (compound 11) 4-Nitro acetophenone was used as the starting material. Compounds 11 and 12 were synthesized in the same way as compounds 9 and 10.

All the 6 compounds were identified by EI-MS, Mp, and H^1NMR, and their purities as determined by HPLC were all above 99.3%.

Synthesis of prodrug derivatives The 3 classes of celecoxib analogs containing amino or methylamino groups reacted with several kinds of tert-BOC-protected amino acids in the presence of 1-(3-dimethylaminopropyl)-3-ethyl-

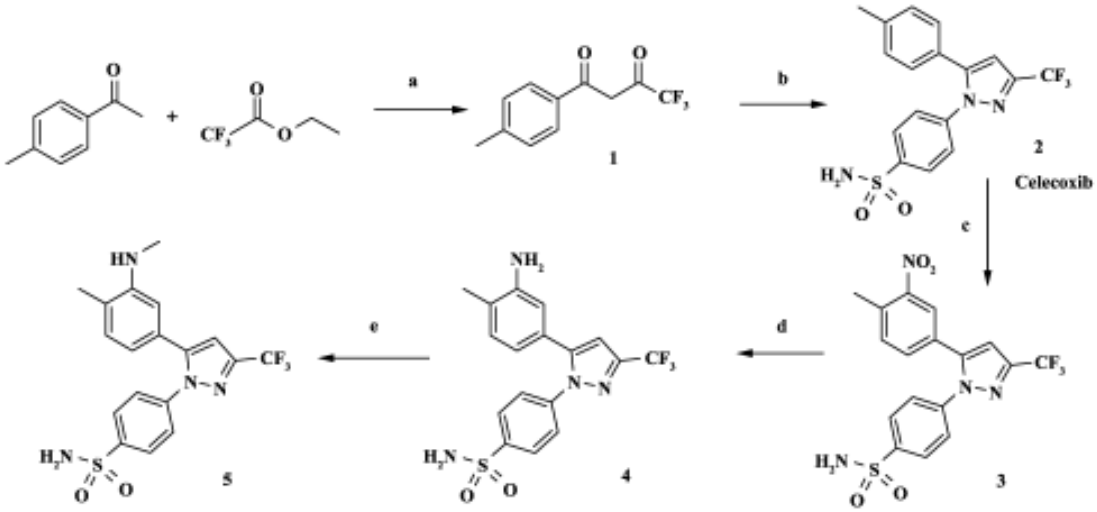

Scheme 1. (a) NaOEt/EtOH, N_2, refluxed for 4 h, yield 89%; (b) (4-sulfamoylphenyl)hydrazine hydrochloride, EtOH, refluxed for 6 h, yield 84%; (c) 2N HNO_3/H_2SO_4, -5–0 °C, 0.5 h, yield 79%; (d) 10% Pd/C, H_2, EtOH, rt, 5 h, yield 98%; (e) i. HCOOH, toluene, refluxed for 3 h, yield 98%; ii. $LiAlH_4$/THF, -5–0 °C, 2 h, yield 57%.

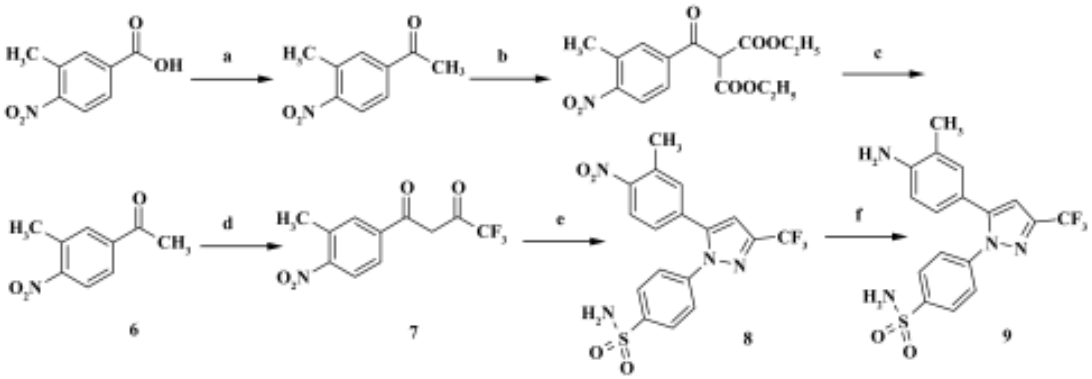

Scheme 2. (a) PCl_5, benzene, refluxed for 2 h; (b) $C_2H_5OMg{\cdot}CH$ $(COOC_2H_5)_2/Et_2O$/EtOH/benzene, refluxed for 0.5 h; (c) $HOAc/H_2SO_4/H_2O$, refluxed for 5 h. (a–c: overall yield 55%–65%); (d) $CF_3COOC_2H_5$, *t*-BuOK, benzene, ice-water bath, 3 h, yield 78%; (e) (4-sulfamoylphenyl) hydrazine hydrochloride, EtOH, refluxed for 5 h, yield 89%; (f) 10%Pd/C, H_2, EtOH, rt, 3 h, yield: 90%.

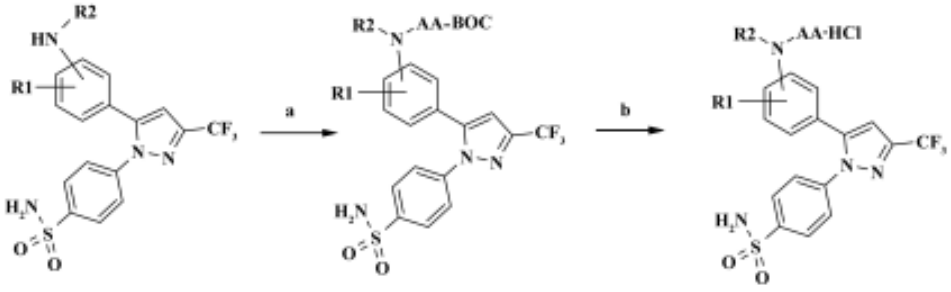

Scheme 3. (a) EDCI, BOC-AA-OH, THF, rt, overnight, yield 67%–92%; (b) saturated HCl-$CH_3COOC_2H_5$ solution, rt, overnight, yield 82%–93%. R_1= H or CH_3; R_2= H or CH_3; AA = amino acid.

carbodiimide hydrochloride (EDCI). Then the intermediates bound with the BOC group were deprotected with saturated hydrochloride-ethyl acetate solution to obtain the final amino acid hydrochloride salt (Scheme 3). All products were checked by EI-MS, Mp, H^1NMR, IR, and HRMS.

Biological assays

In vitro biochemical assays Cell-based assays were performed as described previously[25]. In brief, the drugs were pre-incubated with infected *Spodoptera frugiperda* (Sf9) cells for 15 min prior to a 10 min challenge with 10 μmol/L arachidonic acid. The concentration of prostaglandin E2 (PGE_2) was determined by interpolation from a standard curve and inhibition was calculated by comparison of PGE_2 production by drug-treated cells with that of Me_2SO-treated cells.

In vivo screening methods. Carrageenan-induced rat paw edema[26] Test compounds were suspended in 0.5% carboxymethylcellulose solution and intragastrically administered to rats at three doses (25 mg/kg, 50 mg/kg and 100 mg/kg) before carrageenan was injected. The control group rats received the same volume of vehicle (0.5% carboxymethylcellulose solution) according to their weight. Paw edema was then induced by subplantar injection of 50 μL 1% (w/v) sterile carrageenan in saline into the right hindpaw. Paw volume was measured before and 3 h after carrageenan injection with a plethysmometer (Shandong Academy of Medical Sciences, China). The extent of paw edema in the treatment group was compared to that of the vehicle control group and percentage inhibition was calculated in comparison to the vehicle group.

In the preliminary screening of mice *in vivo*, the inflammatory index was paw weight instead of volume, which was used for the rats.

Preliminary pharmacokinetic study of prodrugs As described previously[27], HPLC/MS was used to confirm the conversion of prodrug-like derivatives *in vivo* in rats. A single dose (100 mg/kg) of the selected compound (that showed potent inhibitory effects on rat paw edema), was orally administered to rats (n=6). Blood samples (50 μL) were taken before and 0.5 h, 2 h, 6 h, 12 h, 18 h, 24 h, 30 h, 36 h, 48 h, 60 h, and 72 h after intragastric administration, and immediately centrifuged at 10 000×g at 4 °C for 15 min. The plasma samples were stored at -20 °C.

Plasma concentration-time curves were evaluated by InnaPhase Kinetica (InnaPhase Corporation, Philadelphia, PA, USA)

Statistical analysis Data were expressed as mean±SEM (unless noted otherwise), and subjected to one-way analysis of variance (ANOVA) and Dunnett's test. P<0.05 was considered to be statistically significant.

Results

Chemistry Celecoxib, 6 of the 1,5-diarylpyrazole class of celecoxib analogs, and their amino acid derivatives (hydrochloride salts) were synthesized. Three kinds of BOC-protected natural amino acids were selected for introduction. They were glycine, *L*-alanine, and *L*-phenylalanine. The main analytical data, from ^{1}H NMR and HRMS, are summarized in Table 1.

The aqueous solubility of the hydrochloride salts was greatly improved compared with that of their parent compounds and celecoxib. Their aqueous solubilities were, respectively, 10–33 g/L, 0.1–1 g/L, and <0.05 g/L at 18 °C.

***In vitro* biochemical screening** All the compounds were evaluated using the intact cell assay. Parent compounds 4, 5, 9, and 10 exhibited potent and selective inhibition of COX-2 activity *in vitro* (Table 2), whereas the inhibitory activities of the hydrochloride salts were greatly decreased compared with their parent compounds.

***In vivo* biological evaluation** Although none of the hydrochloride salts had any anti-inflammatory activity *in vitro*, they could be expected to exert anti-inflammatory effects once they were converted into their parent compounds.

Table 1. Structure and analytical data (^{1}H NMR and HRMS) of synthesized compounds.

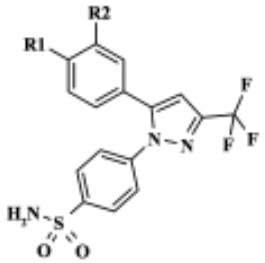

Compound	Substituted group R1	Substituted group R2	^{1}H NMR	HRMS (*m/z*) Found	HRMS (*m/z*) Calculated
Celecoxib	CH_3	H	($CDCl_3$): d 7.90 (dd, *J*=6.8,2.0 Hz, 2H), 7.6 (d, *J*=6.5 Hz, 2H), 7.46 (dd, *J*=6.8,2.0 Hz, 2H), 7.19 (d, *J*=6.5 Hz, 2H), 6.78 (s, 1H), 4.90 (s, 2H), 2.0 (s, 3H).	–	–
4	CH_3	NH_2	($CDCl_3$): δ 7.89 (ddd, *J*=8.8,2.3,2.3 Hz, 2H), 7.5 (ddd, *J*=8.8, 2.3,2.3 Hz, 2H), 7.02 (d, *J*=7.7 Hz, 1H), 6.70 (s, 1H), 6.54 (d, *J*=1.5 Hz, 1H), 6.49 (dd, *J*=7.7,1.5 Hz, 2H), 4.99 (s, 2H), 2.19 (s, 3H).	–	–
5	CH_3	NHMe	($CDCl_3$): δ 7.89 (ddd, *J*=8.93,2.2,2.2 Hz, 2H), 7.51 (ddd, *J*= 8.93,2.2,2.2 Hz, 2H), 7.0 (dd, *J*=7.56,0.42 Hz, 1H), 6.75 (s, 1H), 6.45 (dd, *J*=7.56, 1.70 Hz, 1H), 6.39 (d, *J*=1.70 Hz, 1H), 4.9 (s, -SO_2NH_2, 2H), 3.7 (s, -N<u>H</u>CH_3, 1H), 2.75 (s, -NHC<u>H$_3$</u>, 3H), 2.15 (s, C<u>H$_3$</u>-Ar, 3H).	–	–
11	NH_2	H	($CDCl_3$): δ 7.89 (dd, *J*=6.83,1.95Hz, 2H), 7.48 (dd, *J*=6.83,1.95 Hz, 2H), 6.94 (m, 2H), 6.64 (s, 1H), 6.61 (m, 2H), 4.84 (s, -SO_2NH_2, 2H), 3.84 (s, 2H).	–	–
12	NHMe	H	($CDCl_3$): δ 7.92 (d, *J*=8.8 Hz, 2H), 7.52 (d, *J*=8.8 Hz, 2H), 7.02 (m, 2H), 6.64 (s, 1H), 6.56 (m, 2H), 4.90 (s, -SO_2NH_2, 2H), 2.86 (s, 3H).		
9	NH_2	CH_3	(Me_2SO-d_6): δ 7.85 (ddd, *J*=8.80,2.20,2.20 Hz, 2H), 7.52 (ddd, *J*= 8.80, 2.20,2.20 Hz, 2H), 6.97 (s, 1H), 6.95 (d, *J*=1.4 Hz, 1H), 6.65 (dd, *J*=8.24, 2.2 Hz, 1H), 6.50 (d, *J*=8.24 Hz, 1H), 1.99 (s, 3H).	396.0861	396.0868
10	NHMe	CH_3	-	410.1026	410.1024
4a	CH_3	NH-Gly·HCl	(Me_2SO-d_6): δ 9.92 (s, 1H), 8.14 (s, 3H), 7.84 (m, 2H), 7.50–7.58 (m,5H), 7.26 (d, *J*=8.06 Hz, 1H), 7.14 (s, 1H), 7.01 (d, *J*=8.07 Hz, 1H), 3.80 (d, *J*=5.50 Hz, 2H), 2.22 (s, 3H).	453.1076	453.1083
4b	CH_3	NH-Ala·HCl	(Me_2SO-d_6): δ 10.08 (s, 1H), 8.23 (s, 3H), 7.84–7.87 (m, 2H), 7.52–7.55 (m, 2H), 7.51–7.52 (s, 2H), 7.42 (d, *J*=1.68 Hz, 1H), 7.25–7.28 (d, *J*=7.94 Hz, 1H), 7.15 (s, 1H), 7.0–7.03 (dd, *J*=7.94, 1.68 Hz, 1H), 4.10–4.13 (m, 1H), 2.01 (s, 3H), 1.42 –1.44 (d, *J*=6.87 Hz, 3H).	467.1241	467.1239
4c	CH_3	NH-Phe·HCl	(Me_2SO-d_6): δ 9.92 (s, 1H), 8.40 (s, 2H), 7.84–7.87 (d, *J*=8.78 Hz, 2H), 7.52–7.55 (d, *J*=8.80 Hz, 2H), 7.51 (s, -SO_2NH_2, 2H), 7.25–7.32 (m, 6H),7.21–7.23 (d, *J*=8.06 Hz, 1H), 7.10 (s, 1H), 6.99–7.01 (m, 1H), 4.30 (m, 1H), 3.06–3.08 (d, *J*=7.15 Hz, 1H), 2.01(s, 3H).	543.1535	543.1552
5a	CH_3	NMe-Gly·HCl	(Me_2SO-d_6): δ 7.88–7.91 (m, 2H), 7.52–7.56 (d, *J*=8.80 Hz, 2H), 7.42–7.44 (d, *J*=8.07 Hz, 1H), 7.29–7.32 (m, 2H), 7.18 (d, *J*=1.47 Hz, 1H), 3.0 (s, 3H), 2.2 (s, 3H).	467.1254	467.1239
11a	NH-Gly·HCl	H	(Me_2SO-d_6): δ 10.82 (s, 1H), 8.14–8.24(m, 2H), 7.82–7.84(d, *J*=8.79 Hz, 2H), 7.60(d, *J*=8.79 Hz, 2H), 7.50–7.54(m, 4H),	439.0924	439.0926

Compound	Substituted group R1	R2	^{1}H NMR	HRMS (*m*/*z*) Found	Calculated
11b	NH-Ala·HCl	H	7.26 (d, *J*=8.79 Hz, 2H), 7.18 (s, 1H), 3.74(s, 2H). (Me_2SO-d_6): δ 7.85–7.87 (d, *J*=8.61 Hz, 2H), 7.65–7.67(d, *J*= 8.80 Hz, 2H), 7.51–7.53 (m, 4H), 7.26–7.28 (d, *J*=8.80 Hz, 2H), 7.19 (s, 1H), 3.90–3.96 (d, *J*=6.97 Hz, 1H), 1.40 (d, *J*=6.78 Hz, 3H).	453.1086	453.1083
11c	NH-Phe·HCl	H	(Me_2SO-d_6): δ 10.99 (s, 1H), 8.37 (s, 1H), 7.85–7.88 (d, *J*=8.80 Hz, 2H), 7.56-7.59 (d, *J*=8.80 Hz, 2H), 7.51–7.54 (d, 4H), 7.26–7.30 (m, 7H), 7.20 (s, 1H), 4.22 (d, *J*=5.14 Hz, 1H), 3.14–3.20(m, 2H).	529.1380	529.1396
12a	NMe-Gly·HCl	H	(Me_2SO-d_6): δ 8.18 (s, 2H), 7.88–7.90 (d, *J*=8.8 Hz, 2H), 7.58–7.44 (m, 8H), 7.28 (s, 1H), 3.22(s, 3H).	453.1071	453.1083
9a	NH-Gly·HCl	CH_3	(Me_2SO-d_6): δ 9.96 (s, -NH_2), 8.23 (s, -NH-), 7.87–7.89 (d, *J*=8.40 Hz, 2H), 7.55–7.57(d, *J*=8.59 Hz, 2H), 7.53–7.55 (m, 1H), 7.33 (m, 1H), 7.20 (s, 1H), 7.02–7.05 (dd, *J*=8.27,1.57 Hz, 1H), 3.82 (s, 2H), 2.0 (s, 3H).	453.1088	453.1083
9b	NH-Ala·HCl	CH_3	(Me_2SO-d_6): δ 7.87–7.90 (ddd, *J*=8.61,2.20,2.20 Hz, 2H), 7.55–7.57 (m, 2H), 7.47–7.49 (d, *J*=8.41 Hz, 1H), 7.33 (d, *J*=1.76 Hz, 1H), 7.20 (s, 1H), 7.02–7.05 (dd, *J*=8.21,2.20 Hz, 1H), 4.10–4.13 (m, 1H), 2.0 (s, 3H), 1.43 (d, *J*=7.05 Hz, 3H).	467.1216	467.1239
9c	NH-Phe·HCl	CH_3	(Me_2SO-d6): δ 7.87–7.89 (m, 2H), 7.54–7.57 (m, 2H), 7.27–7.37 (m, 7H), 7.21 (s, 1H), 6.99–7.02 (m, 1H), 4.35 (m, 1H), 3.10–3.12 (d, *J*=7.22 Hz, 2H), 2.0 (s, 3H).	543.1537	543.1552

"-"= not determined.

Table 2. Inhibitory effect of test compounds on COX-1 and COX-2 *in vitro*.

Compound	IC_{50}/ μmol·L^{-1} COX-2	COX-1
Celecoxib	0.053	2.4
Compound 4	0.33	14.34
Compound 5	0.12	1.51
Compound 9	3.12	6.32
Compound 10	0.46	1.76

Average of at least three determinations, and the deviation from the mean is <10%.

Table 3. *In vivo* data for compounds celecoxib (positive drug), compound 4 (parent compound), and compound 4a (prodrug compoud) on carrageenan-induced rat paw edema. *n*=8. Mean±SEM. $^bP<0.05$, $^cP<0.01$ *vs* control vehicle groups.

Dose /mg·kg^{-1}	Inhibition/% Celecoxib	Compound 4	Compound 4a
25	27.76±4.35^b	26.63±6.47^b	20.68±5.44^b
50	38.4±3.87^b	57.41±2.83^b	52.55±3.26^b
100	40.12±4.45^b	67.29±3.69^b	62.55±3.48^c

Based on our preliminary biological evaluation in mice (data not shown), compound 4a was selected for further evaluation in carrageenan-induced rat paw edema because of its potent inhibitory effect on edema. Three doses (25 mg/kg, 50 mg/kg and 100 mg/kg) of each of celecoxib, compound 4, and compound 4a, respectively, were orally administered to rats. Compound 4a had a high level of efficiency, which was identical to that of the possible parent compound 4 and similar to that of celecoxib (Table 3). Furthermore, compound 4a dose-dependently inhibited the inflammatory response to carrageenan-induced edema.

Preliminary pharmacokinetic study A preliminary pharmacokinetic study of compound 4a in rats (*n*=6) was undertaken to prove that it was converted *in vivo* to compound 4. Figure 1 shows the representative chromatograms of blank plasma, plasma containing compound 4, compound 4a, and internal standard (IS), and plasma sample added with IS 6 h after intragastric administration. The retention times of compound 4a, compound 4, and IS were 5.71 min, 7.91 min, and 6.56 min in blank plasma, respectively. In a plasma sample 6

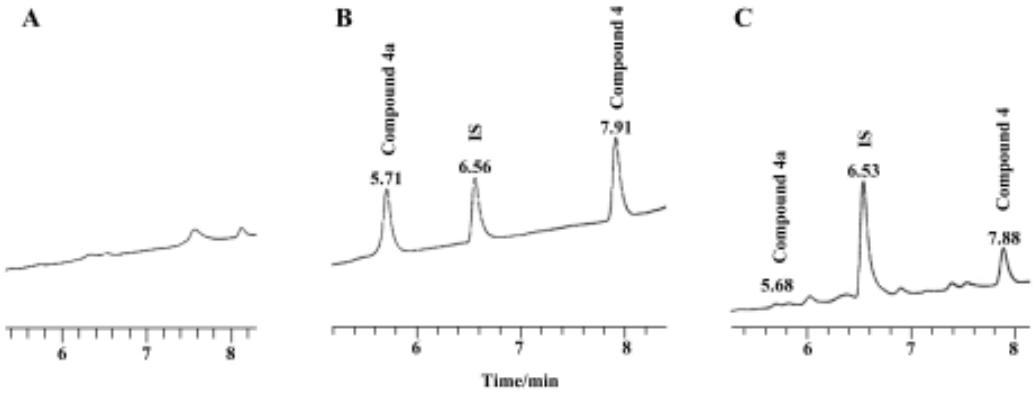

Figure 1. Representative chromatograms of (A) blank plasma; (B) plasma containing compound 4, compound 4a, and internal standard (IS); (C) plasma sample added with IS 6 h after intragastric administration.

h after intragastric administration, the retention times of compound 4a, compound 4 created from the conversion of compound 4a, and IS were 5.68 min, 7.88 min, and 6.53 min, respectively. The corresponding chromatography peak was identified by MS. We thus proved that compound 4a was actually converted to compound 4 after oral administration.

The pharmacokinetic parameters of compound 4 released from compound 4a were calculated by non-compartmental model analysis based on the drug concentration-time curve of 0–72 h sample dotting. Peak plasma concentration (C_{max}), the corresponding time (T_{max}), the area under the plasma concentration-time curve ($AUC_{0-\infty}$), and $T_{1/2}$ were 7.7±1.1 mg/L, 13.2±2.7 h, 165.3±21.8 mg·L^{-1}·h, and 6.4±1.3 h, respectively.

Discussion

In the present study, a series of amino acid-binding 1,5-diarylpyrazole derivatives were designed and synthesized as prodrugs. As expected, the aqueous solubility of these compounds was greatly improved compared with celecoxib. For example, the solubility of compound 4a in water at 18°C was 15–18 g/L, whereas that of celecoxib was <0.05 g/L. Good aqueous solubility should enhance the dissolution rate of a drug and thus improve its oral bioavailability[14].

In *in vitro* biological evaluations, it was found that the parent compounds 4, 5, 9, and 10 exhibited potent selectivity and inhibition of COX-2, although they all did not exceed celecoxib (Table 2). From the results, it was also found that the compounds containing the methylamino group had more potent inhibitory effects than those containing the amino group. In addition, all the hydrochloride salts showed extremely weak inhibition on COX activity.

Based on a previous hypothesis, the hydrochloride salt should bring about beneficial anti-inflammatory effects after delivering its parent compound *in vivo*. Therefore, anti-inflammatory evaluation *in vivo* was performed in carrageenan-induced mouse and rat paw edema models. Compound 4a brought about the expected potent inhibition of edema after intragastric administration. Furthermore, at doses of 50 mg/kg and 100 mg/kg, the anti-inflammatory effect of compound 4a was a little stronger than that of celecoxib, and identical to that of compound 4 (Table 3). Preliminary pharmacokinetic studies in rats also proved that compound 4a actually acted as a prodrug, which has an anti-inflammatory effect once it is converted into its active form, compound 4.

In the preliminary pharmacokinetic studies, the T_{max} of compound 4 (as derived from compound 4a) was found at 12 h after oral administration; however, the T_{max} of celecoxib was at 3 h after administration[28]. In our experiments, we only observed the inhibitory effects on edema at 3 h after oral administration. Therefore we predicted that when the concentration of compound 4 (as derived from compound 4a) reached a maximum, it should have stronger anti-inflammatory activity.

Although compound 4a did not exhibit more potency *in vivo* than its parent, compound 4, its potency was comparable with that of celecoxib (Table 3). We suppose that compound 4a was not completely converted to its parent compound, compound 4, or it produced other metabolisms *in vivo*. Similar prodrug conversion pharmacokinetics have been investigated by Mamidi *et al*[28]. Prodrugs derived from the same parent compound will have different activity *in vivo* when they are connected to different groups. Connecting more amino acids to the parent compound might offer a an exciting prospect for developing prodrug-like NSAIDs.

In summary, by introducing an amino or methylamino group, 6 celecoxib analogs were synthesized as parent compounds. The 6 compounds were combined with three

kinds of natural amino acids to obtain a series of novel hydrochloride salts. By biological evaluation *in vitro* and *in vivo*, and by further preliminary pharmacokinetic studies, compound 4a was discovered, which was confirmed to act as a prodrug, and exhibited marked anti-inflammatory activity *in vivo*. This finding will be of great benefit to the structural modifications of prodrug-like selective COX-2 inhibitors.

References

1 Xie WL, Chipman JG, Robertson DL, Erikson RL, Simmons DL. Expression of a mitogen-responsive gene encoding prostaglandin synthase is regulated by mRNA splicing. Proc Natl Acad Sci USA 1991; 88: 2692–6.

2 Vane JR, Bakhle YS, Botting RM. Cyclooxygenases 1 and 2. Annu Rev Pharmacol Toxicol 1998; 38: 97–120.

3 Smith WL, Garavito RM, DeWitt DL. Prostaglandin endoperoxide H synthases (cyclooxygenases)-1 and -2. J Biol Chem 1996; 271: 33157–60.

4 Masferrer JL, Zweifel BS, Manning PT, Hauser SD, Leahy KM, Smith WG, *et al*. Selective inhibition of inducible cyclooxygenase 2 *in vivo* is antiinflammatory and nonulcerogenic. Proc Natl Acad Sci USA 1994; 91: 3228–32.

5 Uddin MJ, Rao PN, McDonald R, Knaus EE. Design and synthesis of (E)-1,1,2-triarylethenes: novel inhibitors of the cyclooxygenase-2 (COX-2) isozyme. Bioorg Med Chem Lett 2005; 15: 439–42.

6 Ranatunge RR, Augustyniak M, Bandarage UK, Earl RA, Ellis JL, Garvey DS, *et al*. Synthesis and selective cyclooxygenase-2 inhibitory activity of a series of novel, nitric oxide donor-containing pyrazoles. J Med Chem 2004; 47: 2180–93.

7 Hinz B, Brune K. Cyclooxygenase-2: 10 years later. J Pharmacol Exp Ther 2002; 300: 367–75.

8 Dannhardt G, Kiefer W. Cyclooxygenase inhibitors: current status and future prospects. Eur J Med Chem 2001; 36: 109–26.

9 Chen XH, Bai JY, Shen F, Bai AP, Guo ZR, Cheng GF. Imrecoxib: a novel and selective cyclooxygenase 2 inhibitor with anti-inflammatory effect. Acta Pharmacol Sin 2004; 25: 927–31.

10 Singh SK, Vobbalareddy S, Shivaramakrishna S, Krishnamraju A, Rajjak SA, Casturi SR, *et al*. Methanesulfonamide group at position-4 of the C-5-phenyl ring of 1,5-diarylpyrazole affords a potent class of cyclooxygenase-2 (COX-2) inhibitors. Bioorg Med Chem Lett 2004; 14: 1683–8.

11 Ranatunge RR, Garvey DS, Janero DR, Letts LG, Martino AM, Murty MG, *et al*. Synthesis and selective cyclooxygenase-2 (COX-2) inhibitory activity of a series of novel bicyclic pyrazoles. Bioorg Med Chem 2004; 12: 1357–66.

12 Uddin MJ, Rao PN, Knaus EE. Design and synthesis of novel celecoxib analogues as selective cyclooxygenase-2 (COX-2) inhibitors: replacement of the sulfonamide pharmacophore by a sulfonylazide bioisostere. Bioorg Med Chem 2003; 11: 5273–80.

13 Penning TD, Talley JJ, Bertenshaw SR, Carter JS, Collins PW, Docter S, *et al*. Synthesis and biological evaluation of the 1,5-diarylpyrazole class of cyclooxygenase-2 inhibitors: identification of 4-[5-(4-methylphenyl)-3-(trifluoromethyl)-1*H*-pyrazol-1-yl]benzenesulfonamide (SC-58635, celecoxib). J Med Chem 1997; 40: 1347–65.

14 Chawla G, Gupta P, Thilagavathi R, Chakraborti AK, Bansal AK. Characterization of solid-state forms of celecoxib. Eur J Pharm Sci 2003; 20: 305–17.

15 Pal M, Madan M, Padakanti S, Pattabiraman VR, Kalleda S, Vanguri A, *et al*. Synthesis and cyclooxygenase-2 inhibiting property of 1,5-diarylpyrazoles with substituted benzenesulfonamide moiety as pharmacophore: preparation of sodium salt for injectable formulation. J Med Chem 2003; 46: 3975–84.

16 Bombardier C, Laine L, Reicin A, Shapiro D, Burgos-Vargas R, Davis B, *et al*. Comparison of upper gastrointestinal toxicity of rofecoxib and naproxen in patients with rheumatoid arthritis. VIGOR Study Group. N Engl J Med 2000; 343: 1520–8.

17 Couzin J. Drug safety. Withdrawal of Vioxx casts a shadow over COX-2 inhibitors. Science 2004; 306: 384–5.

18 Davies NM, Jamali F. COX-2 selective inhibitors cardiac toxicity: getting to the heart of the matter. J Pharm Pharm Sci 2004; 7: 332–6.

19 Velazquez C, Rao PN, McDonald R, Knaus EE. Synthesis and biological evaluation of 3,4-diphenyl-1,2,5-oxadiazole-2-oxides and 3,4-diphenyl-1,2,5-oxadiazoles as potential hybrid COX-2 inhibitor/nitric oxide donor agents. Bioorg Med Chem 2005; 13: 2749–57.

20 Chen QH, Rao PN, Knaus EE. Design, synthesis, and biological evaluation of *N*-acetyl-2-carboxybenzenesulfonamides: a novel class of cyclooxygenase-2 (COX-2) inhibitors. Bioorg Med Chem 2005; 13: 2459–68.

21 Dogne JM, Supuran CT, Pratico D. Adverse cardiovascular effects of the coxibs. J Med Chem 2005; 7: 2251-7.

22 Paulson SK, Vaughn MB, Jessen SM, Lawal Y, Gresk CJ, Yan B, *et al*. Pharmacokinetics of celecoxib after oral administration in dogs and humans: effect of food and site of absorption. J Pharmacol Exp Ther 2001; 297: 638–45.

23 Benington F, Morin RD, Leiand CC. Mescaline analogs, VIII. Substituted 5-methoxy- and 5,6,7-trimethoxyindoles. J Org Chem 1958; 23: 19–23.

24 Walker HG, Hauser CR. Synthesis of methyl ketones from diethyl acylmalonates. J Am Chem Soc 1946; 68: 1386-8.

25 Zhang WY, Yang XN, Jin DZ, Zhu XZ, Chen XH, Bai JY, *et al*. Expression and enzyme activity determination of human cyclooxygenase-1 and -2 in a baculovirus-insect cell system. Acta Pharmacol Sin 2004; 25: 1000–6.

26 Winter CA, Risley EA, Nuss GW. Carrageenin-induced edema in hind paw of the rat as an assay for antiiflammatory drugs. Proc Soc Exp Biol Med 1962; 111: 544–7.

27 Werner U, Werner D, Pahl A, Mundkowski R, Gillich M, Brune K. Investigation of the pharmacokinetics of celecoxib by liquid chromatography-mass spectrometry. Biomed Chromatogr 2002; 16: 56–60.

28 Mamidi RN, Mullangi R, Kota J, Bhamidipati R, Khan AA, Katneni K, *et al*. Pharmacological and pharmacokinetic evaluation of celecoxib prodrugs in rats. Biopharm Drug Dispos 2002; 23: 273–82.

Acta Pharmacologica Sinica 2005 Jul; 26 (7): 873–880

Full-length article

Regulating expressions of cyclin D1, pRb, and anti-cancer effects of deguelin on human Burkitt's lymphoma Daudi cells *in vitro*[1]

Hong-li LIU, Yan CHEN[2], Guo-hui CUI, Qiu-ling WU, Jing HE

Department of Hematology, Union Hospital, Tongji Medical College, Huazhong University of Science and Technology, Wuhan 430022, China

Key words

deguelin; Daudi cells; cyclin D1; pRb; apoptosis

[1] Project supported by the National Natural Science Foundation of China (No 30472267).
[2] Correspondence to Prof Yan CHEN.
Phn 86-27-6604-6609.
Fax 86-27-8572-6387.
E-mail liuhl60@tom.com

Received 2004-12-25
Accepted 2005-02-18

doi: 10.1111/j.1745-7254.2005.00104.x

Abstract

Aim: To investigate anticancer effects and molecular mechanism of deguelin on human Burkitt's lymphoma Daudi cells *in vitro* and compare the cytotoxicities of deguelin on Daudi cells and human peripheral blood monocular cells (PBMC). **Methods:** The effects of deguelin on the growth of Daudi cells were studied by 3-(4, 5-dimethyl-2-thiazolyl)-2,5-diphenyl-2*H*-tetrazolium (MTT) assay. Apoptosis were dectected through Hoechst 33258 staining and Annexin V/PI double-labeled cytometry. The effect of deguelin on the cell cycle of Daudi cells were studied by a propidium iodide method. The expressions of cyclin D1 and pRb were checked by Western blot. **Results:** The proliferation of Daudi cells were decreased in deguelin-treated group with a 24-h IC_{50} value of 51.55 nmol/L. Deguelin induced Daudi cells apoptosis was in a time- and dose-dependent manner. G_0/G_1 phase increased and S phase decreased in Daudi cells treated with deguelin. With deguelin 0, 5, 10, 20, and 40 nmol/L treatment for 24 h, G_0/G_1 phase increased from 37.34% to 56.56%, whereas S phase decreased from 37.72% to 21.36%. PBMC was less sensitive to the cytotoxic effect of deguelin than Daudi cells. The expression of cyclin D1 and pRb protein were decreased sharply in Daudi cells treated with deguelin. **Conclusion:** Deguelin is able to inhibit the proliferation of Daudi cells by regulating the cell cycle that arrested cells at G_0/G_1 phase and inducing the cell apoptosis. Moreover, deguelin selectively induced apoptosis of Daudi cells with low toxicity in PBMC. The antitumor effects of deguelin were related to down-regulating the expression of cyclin D1 and pRb protein.

Introduction

A large number of natural products have been evaluated as potential chemopreventive agents. Deguelin (Figure 1), a natural plant-derived rotenoid, most commonly used as an insecticide in Africa and South America, has been isolated from several plant species, including *Mundulea sericea* (*Leguminosae*). Its main active composition is rotenone, and it has very strong photodissociation[1]. The recent research has indicated that deguelin usually has a very strong antitumor function, and can suppress many kinds of tumors cell at nmol levels[1]. Notably, deguelin can suppress colon-cancer cell HT-29 growth[2], inhibit the growth of precancerous and cancerous lung cells, and induce premalignant and malignant human bronchial epithelial (HBE) cells apoptosis with no toxic effects on normal cells[3]. These recent experiments verified that deguelin could lead the cell cycle to block and induce apoptosis, however, its mechanism is not yet completely clear.

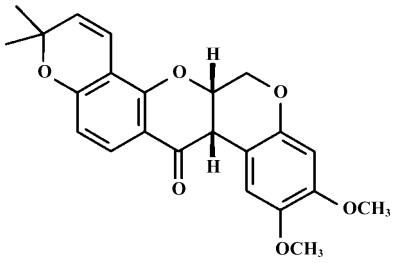

Figure 1. Structure of deguelin.

Burkitt's lymphoma (also called small noncleaved cell lymphoma) is a type of on-Hodgkin's lymphoma, a cancer in the lymphatic system. Despite recent advances in radiotherapy, chemotherapy, and stem cell transplant, the severe morbidity from lymphoma has not been improved[4]. Much effort has been focused on the discovery and development of new chemopreventive agents, especially agents targeted at mechanisms known to be involved in the process of carcinogenesis. Therefore, we have sought to identify novel agents that can prevent lymphoma carcinogenesis effectively but with minimal toxicity.

This study was designed to explore the mechanism of deguelin-induced apoptosis in Daudi cells. We studied deguelin on human Burkitt's lymphoma Daudi cells *in vitro* and compared the cytotoxicities of deguelin on Daudi cells with human peripheral blood monocular cell (PBMC), and focused on the changes in the expression of cyclin D1 and phosphor-Rb, and analyzed its underlying mechanism.

Materials and methods

Drugs and reagents Degulin was purchased from the Sigma Chemical Company (St Louis, MO, USA) and initially dissolved in dimethylsulfoxide(Me_2SO), and stoered at -20 °C, and thawed before use. MTT was purchased from Janssen Chimica Company (New Brunswick, NJ, USA). RPMI-1640 medium, Hoechst 33258, and Me_2SO were purchased from Sigma Co. Anti-cyclin D1 and anti-phosphor Rb antibodies were purchased from Santa Cruz (California, USA). Chemiluminescence (ECL) reagent kits were purchased from Pierce Biotechnology, Inc (Rockford, IL, USA). Daudi cells line was obtained from China Center for Typical Culture Collection (Wuhan,China). PBMC were obtained by Ficoll-Hypaque density gradient centrifugation. All kinds of cells were grown in RPMI-1640 culture medium containing 10% fetal calf serum (FCS) and 2 mmol/L *L*-glutamine at 37 ºC in a 5% CO_2 incubator.

MTT assay The antiproliferative effects of deguelin against different group cells were determined by the MTT dye uptake method. Briefly, the Daudi cells and PBMC (40 000 per well) were incubated in triplicate in a 96-well plate. Different concentrations of deguelin were added, and the final concentrations were 0, 5, 10, 20, 40, 80, and 160 nmol/L. The plates were in the presence or absence of the indicated test samples for 0, 24, 36, 48, 60, and 72 h. The group in maximal Me_2SO dissolution concentration acted as the control group. Thereafter, 20 μL MTT solution (5 mg/mL in phosphate-buffered saline [PBS]) was added to each well. After 4 h at 37 °C, the supernatant was removed and 150 μL Me_2SO was added. When the blue crystal was dissolved, the optical density (*OD*) was detected at 570 nm wavelength using a 96-well multiscanner autoreader (Biotech Instruments μQuant, New York, USA). The following formula was used: Cell proliferation(%)=[1–(*OD* of the experimental samples/ *OD* of the control)]×100%.

Hoechst 33258 staining Deguelin-induced apoptosis was monitored by the extent of nuclear fragmentation. Nuclear fragmentation was visualized by Hoechst 33258 staining of apoptotic nuclei. The apoptotic cells were collected by centrifugation, washed with PBS and fixed in 4% paraformaldehyde for 20 min at room temperature. Subsequently, the cells were washed and resuspended in 20 μL PBS before deposition on poly lysine-coated coverslips and were left to adhere on cover slips for 30 min at room temperature and then the coverslips were washed twice with PBS. The adhered cells were then incubated with 0.1% Triton X-100 for 5 min at room temperature and rinsed with PBS three times. The coverslips were treated with Hoechst 33258 for 30 min at 37 °C, rinsed with PBS and mounted on slides with glycerol- PBS. The cells were viewed with an Olympus BH-2 fluorescence microscope (Tokyo, Japan).

Annexin V-PI assay The cells were collected and washed with PBS, followed by being resuspended in binding buffer (HEPES-NaOH 10 mmol/L, pH 7.4, NaCl 140 mmol/L, $CaCl_2$ 2.5 mmol/L). The samples were incubated with 5 μL Annexin-V in dark for 15 min, washed with binding buffer and resuspended in 1% formaldehyde in the binding buffer at 4 ºC for 30 min. After being washed with binding buffer again, the cells were stained with 500 μL PI (1 μg/ml, Sigma) for 15 min then measured on flow cytometry (Stanford, Becton Dickinson, USA).

DNA content and cell cycle analysis Untreated and treated cells were collected, after cultured in the presence or absence of degulin for the indicated time, rinsed with PBS, and suspended in 75 % ethanol at –20 ºC overnight. Fixed cells were centrifuged at 1200×*g* and washed with PBS twice. To detect DNA content, cells were contained in the dark with PI 50 mg/L and 0.1 % RNAse A in 400 μL PBS at 25 ºC for 30 min. Stained cells were analyzed on FACSort (Becton Dickinson). The percentage of apoptotic cells was determined using the CellQuest software program.

Western blot analysis Lysates were prepared from 1×10^7 cells by dissolving cell pellets in 100 μL of lysis buffer (Na_2HPO_4 pH 7.4 20 mmol/L , 150 mmol/L NaCl, 1% Triton X-100, 1% aprotinin, 1 mmol/L phenylmethylsulfonyl fluoride, 10 g/L leupeptin, 100 mmol/L NaF, and 2 mmol/L Na_3VO_4). Lysates were centrifuged at 18 000×*g* for 15 min and the supernatant was collected. Protein content was determined

using a Bio-Rad protein assay (Bio-Rad Laboratories, Hercules, CA, USA). Sodium dodecylsulfate-polyacrylamide gel electrophoresis (SDS-PAGE) sample buffer (10 mmol/L Tris-HCl, pH 6.8, 2% SDS, 10% glycerol, 0.2 mol/L DTT) was added to the lysates. Lysates were heated to 100 ºC for 5 min, and 80 μg of protein was loaded into each well of a 10% SDS-PAGE gel. Resolved proteins were electrophoretically transferred to nitrocellulose and blocked with 5% non-fat milk, and the primary antibodies cyclin D1 and phosphor Rb (dilution 1:200), respectively. After overnight incubation at 4 °C the blots were washed, exposed to HRP-conjugated corresponding secondary antibodies for 1 h, and finally detected by ECL. Quantification of the bands was carried out using densitometric analysis software, Quantity One (Bio-Rad), and processed as described previously.

Statistical analysis All data were expressed as mean±SD using SPSS 10.0 for windows 98. Using linear *t*-tests for statistics analyses, *P* values of less than 0.01 or 0.05 were considered to be statistically significant.

Results

Effects of deguelin on proliferation of Daudi cells and PBMC Daudi cells and PBMC treated with deguelin for 0 h, 24 h, 36 h, 48 h, 60 h, and 72 h, respectively, resulted in the inhibition of cell proliferation in a dose- and time-dependent manner. The *OD* value of the deguelin-treated group decreased significantly compared with the untreated group and PBMC group. There are significant differences between the deguelin-treated and untreated group (Figure 2). It has also shown great difference between deguelin-treated and PBMC group (Figure 3). The IC_{50} value of 24 h on Daudi cell was 51.55 nmol/L, whereas the IC_{50} value of 24 h on PBMC was 1.63 μmol/L. The IC_{50} value of 24 h on PBMC was higher than Daudi cell group with great significance (P<0.01).

Hoechst 33258 staining We used Hoechest 33258 staining to investigate the changes in the nucleus of cells, and many apoptotic bodies containing nuclear fragments were found in deguelin-treated (40 nmol/L for 24 h) cells, but none in untreated cells. Arrows indicate apoptotic nuclear fragmentation (Figure 4). At the same time, cytoplasmic shrinkage was observed in cells cultured with deguelin.

Annexin V-PI assay All untreated cells were Annexin-V negative, which meant no apoptosis occured. In contrast, when Daudi was treated with deguelin, apoptotic cells became Annexin-V positive and PI negative almost all the apoptosis occured in cells undergoing the G1-phase. With the increasing dose of deguelin, early apoptotic cells increased from (15.46%±0.62%) to (18.48%±2.98%) with 20

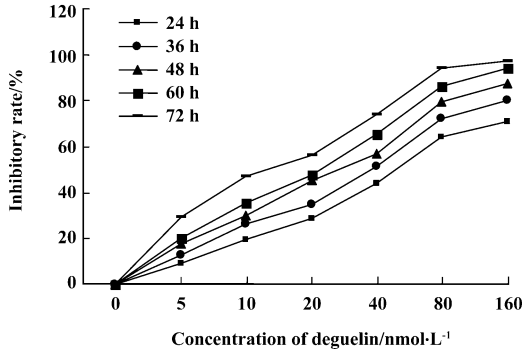

Figure 2. Antiproliferation effect of deguelin on Daudi cells. Daudi cells were treated with various concentrations of deguelin as indicated for 0, 24, 36, 48, 60, and 72 h. Growth inhibition was determined using a MTT assay and shown as an inhibitory rate. n=3.

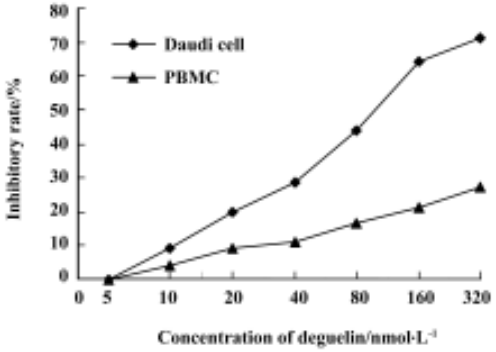

Figure 3. Comparison of the cytotoxicities of deguelin on Daudi cells and human peripheral blood monocular cell (PBMC). n=3.

nmol/L and 40 nmol/L deguelin, respectively (Figure 5). It meant that deguelin could induce G1-phase specific apoptosis.

Cell cycle analysis Figure 6 illustrates changes in DNA content distribution treated with deguelin 0, 5, 10, 20, 40, and 80 nmol/L for 24 h. As the treatment dose increased, the percentage of cells in G_1/G_0 phase increased and S phase decreased accordingly. Treated with 0, 5, 10, 20, 40, and 80 nmol/L deguelin for 24 h, the rate of G_1/G_0 phase cells were increased by 37.34%, 40.91%, 44.69%, 52.45%, and 56.56% in a dose-dependent manner. Meanwhile, the rate of S phase cells were decreased by 37.72%, 35.97%, 34.91, 24.11, and 21.36% in a dose-dependent manner. It showed few changes in G_2/M phase. These results illustrated that deguelin arrested the Daudi cells at G_1/G_0 phase *in vitro*.

Cyclin D and pRb analysis by Western blot After treated with 0, 50, 100, 200, and 400 nmol/L deguelin for 24 h, both the expression of cyclin D1 and pRb were down-regulated dramatically in a dose-dependent manner. The *OD* values of

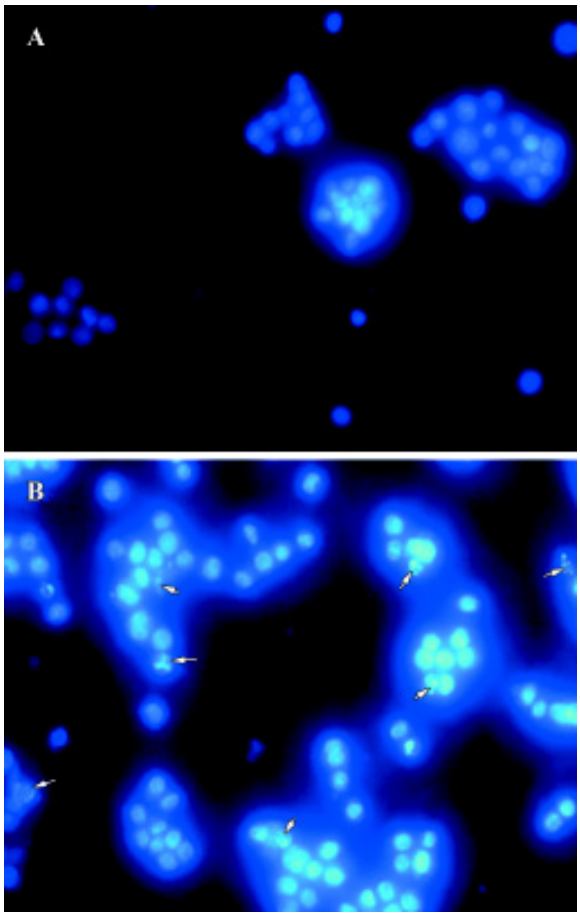

Figure 4. (A) Untreated Daudi cells; (B) Cells treated with 50 nmol/L deguelin for 24 h. Photographs were taken under an Olympus BH-2 fluorescence microscope (×40). Arrows indicate apoptotic nuclear fragmentation.

cyclin D1 and pRb on Daudi cells were greatly significant compared with the control cells, and *P* values were less than 0.05 or 0.01, respectively (Figure 7).

Discussion

Several natural compounds, especially plant products and dietary constituents, have been found to exhibit chemopreventive activities both *in vitro* and *in vivo* in model systems. Their mechanisms of action vary widely, with many suppressing cell growth or modulating cell differentiation and a few also inducing apoptosis. Rotenoids, which constitute a class of compounds from the flavonoid family, have chemopreventive activity, act by inhibiting NADH: ubiquinone oxidoreductase activity, and by suppressing steady-state mRNA levels and enzymatic activity of 12-*O*-tetradecanoylphorbol-13-acetate (TPA)-induced ornithine decarboxylase (ODC) activity[5]. One rotenoid, deguelin, has been

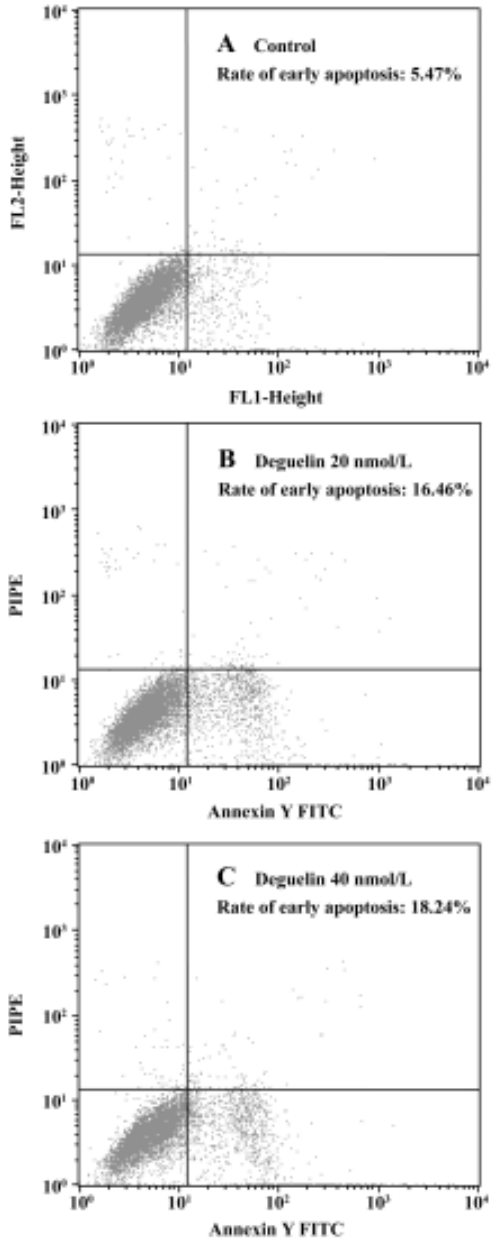

Figure 5. The rate of early apoptosis induced by deguelin with Annexin V-PI assay. A, B, and C show treatment with 0, 20, and 40 nmol/L deguelin for 24 h, respectively.

isolated from several plant species, including Mundulea sericea (Leguminosae)[6]. Deguelin has been shown to have cancer-chemopreventive effects in models of skin, mammary, and lung tumorigenesis. Deguelin has been widely used as an insecticide in Africa, South Africa, and China[7].

This experiment also founded that deguelin could suppress Daudi cell selectively, and it had low toxicity on human peripheral blood monocular cells (PBMC). Deguelin-

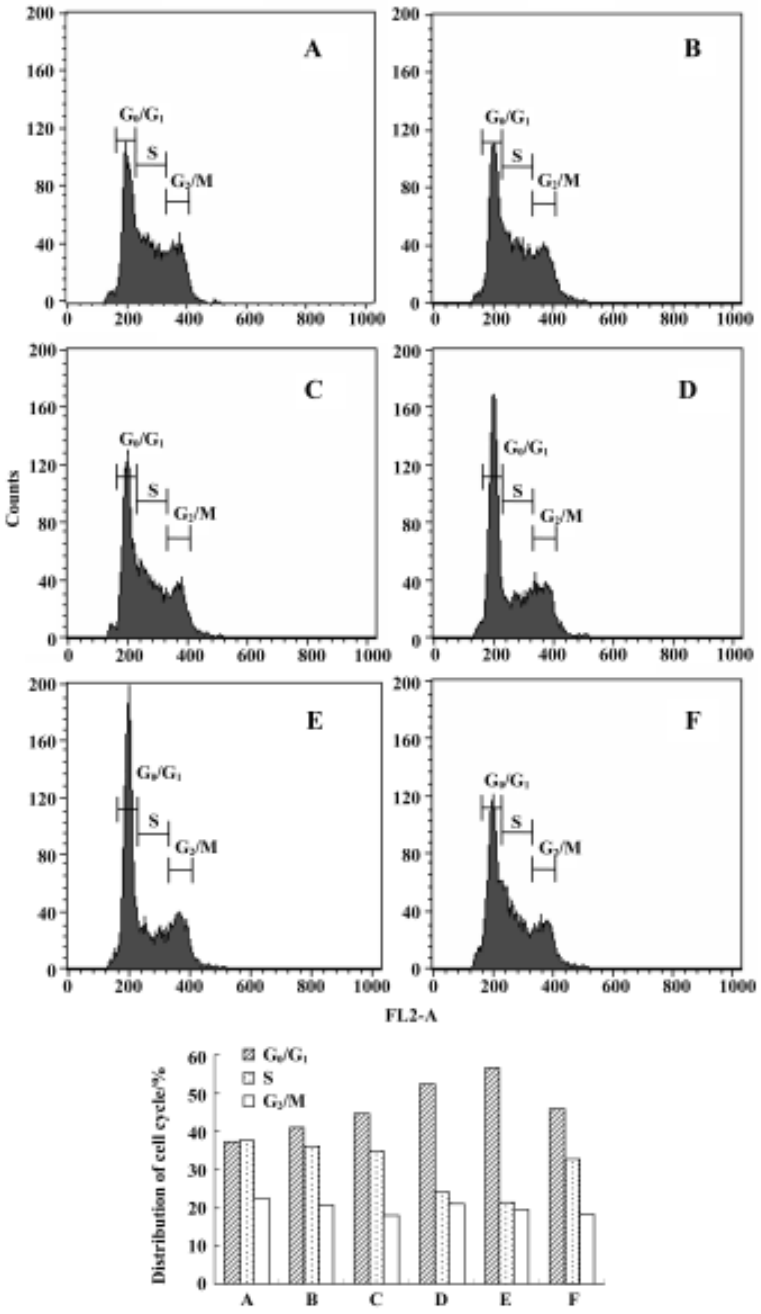

	Control	5 nmol/L	10 nmol/L	20 nmol/L	40 nmol/L	80 nmol/L
G_0/G_1	37.34	40.91	44.69	52.45	56.51	45.77
S	37.72	35.97	34.90	24.10	21.36	32.78
G_2/M	22.69	20.82	18.21	21.09	19.72	18.25

Figure 6. The distribution of cell cycle by deguelin with FACSort (Becton Dickinson, USA). A, B, C, D, E, and F are the control, and degulin 5, 10, 20, 40, and 80 nmol/L for 24 h, respectively.

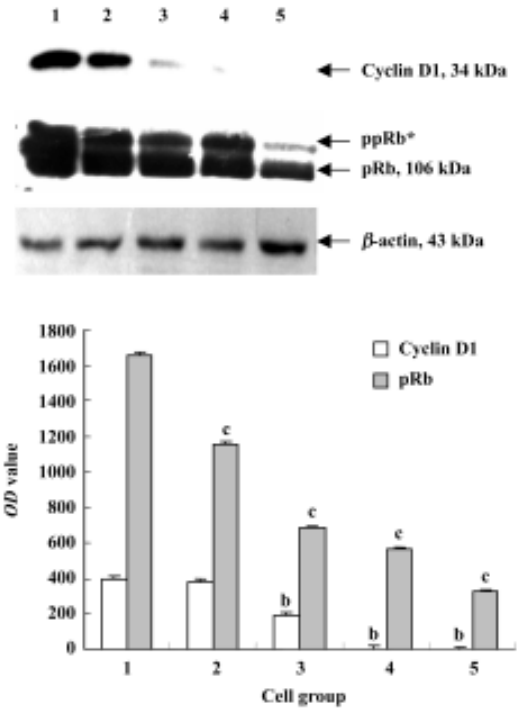

Figure 7. Effects of deguelin on the expression of cyclin D1 and pRb in Daudi cells. 1, 2, 3, 4, and 5 are control, and deguelin 50, 100, 200, and 400 nmol/L, respectively. n=3. Mean±SD. $^bP<0.05$, $^cP<0.01$, compared with control. ppRb* was inactive form. pRb was active form.

induced antiproliferative effects on Daudi cells, indicating that deguelin may have potential as they accumulated in the G_0/G_1 phase of the cell cycle and underwent apoptosis in a dose- and time-dependent manner. We found that deguelin decreased the expression of cyclin D1 and pRb in Daudi cells, suggesting that changes in the ratio of cyclin D1 and pRb might contribute to the apoptosis-promoting activity of deguelin in these cells. Cyclin D1 and pRb are important proteins for regulating cell cycle. Chun *et al*[4] found that deguelin could inhibit both premalignant and malignant HBE cells and these were more sensitive to deguelin than normal HBE cells. They also found deguelin increased the expression of Bax and decreased the expression of Bcl-2 in premalignant and malignant HBE cells, suggesting that changes in the ratio of Bax to Bcl-2 might contribute to the apoptosis-promoting activity of deguelin in these cells. This suggests that mechanisms of regulating cell cycle may contribute to the sensitivity of tumor cells to deguelin.

The results of Hoechest 33258 staining and Annexin V-PI assay showed that deguelin could induce Daudi cells apoptosis in a dose-dependent way. Arrows indicate apoptotic nuclear fragmentation. Apoptotic cells presented typical characteristics including the cell nuclear concentration, nucleus gathered by the core. With the increasing dose of deguelin, early apoptotic cells increased from 15.46%±0.62% to 18.48%±2.98% with 20 nmol/L and 40 nmol/L deguelin, respectively. The latest research materials indicate that deguelin can inhibit other tumor cell proliferation such as breast cancer, lung cancer, colon-cancer, and so on. Its underlying mechanism relates to inducing inhibition of cyclooxygenase-2 and extracellular signal-regulated kinase expression, participating in the phosphatidylinositol 3-kinase/Akt pathway[7–9].

The cell cycle is an ordered set of events, culminating in cell growth and division into two daughter cells. Non-dividing cells are not considered to be in the cell cycle. Severe defects in chromosomes block progression through the cell cycle, and can lead to cell suicide or apoptosis. In addition, cells have a finite lifespan, and at some point are no longer able to divide. Deguelin usually acts on different stages of the cell cycle of tumor cells and plays an antitumor role, and this may be one of its pharmacological mechanisms. In this report, Daudi cells were arrested in the G_0/G_1 phase mainly by deguelin, meanwhile the proportion of S phase was gradually reduced. After a different dose of deguelin for 24 h, cells in G_0/G_1 phase were most early influenced and increased gradually in a dose-dependent way with 40 nmol/L, and reached peak value. At the same time, cells in S phase were decreased gradually with 40 nmol/L resulting in the lowest value. The above data shows that deguelin usually regulates the G_1/S checkpoint. Deguelin regulating G_1/S check point was verified in other tumor cells. Chun *et al*[4] found that after treatment with 1×10^{-9}mol/L deguelin on premalignant and malignant HBE cell, the rate of G_0/G_1 cells increased from 76.1% to 91.2%. At the same time, deguelin arrested premalignant and malignant HBE cells in G_2/M phase that increased from 9.6% to 40.2%.

Rapidly developing technology in the field of molecular biology enables estimation of control mechanisms of cancer cells at the molecular level. Much interest has focused on the proteins participating in cell cycle control. The sequential transcriptional activation of cyclins, the regulatory subunits of cell-cycle-specific kinases, are thought to regulate progress through the cell cycle[10]. The orderly progression of dividing mammalian cells through the G_1, S, G_2, and M phases of the cell cycle is governed by a series of proteins called cyclins, which exert their effects by binding to and activating a series of specific cyclin-dependent kinases (CDK). Cyclins are therefore potential oncogenes. Cyclin D1 overexpression and/or amplification at its genomic locus, 11q13, are common features of several human cancers. The

cyclin D1 gene, which acts at the mid-portion of the G_1-S transition, is often overexpressed in human breast, colon, and squamous carcinomas, and several other types of cancer, and the cyclin E gene, which acts in late G_1 is also overexpressed and dysregulated in a variety of human cancers[11]. In mechanistic studies we demonstrated that overexpression of cyclin D1 played a critical role in Burkitt lymphorma carcinogenesis. Therefore, cyclin D1 may be a useful biomarker in molecular epidemiology studies, and inhibitors of its function may be useful in both cancer chemo-prevention and therapy.

Retinoblastoma (Rb) is a rare tumor of the retina, associated with mutations of chromosome 13q14. The protein encoded by the Rb gene, pRb, normally plays a key role as a negative regulator of the G_1/S transition in the cell cycle by binding the transcription factor E_2F and preventing it from activating the transcription of genes required for the S phase[12]. pRB gene product nuclear phosphoprotein undergoes differential phosphorylation during the cell cycle[13]. A number of cellular proteins interact with hypophosphorylated pRb including: E_2F transcription factor, several cyclins, RBP-1, RBP-2, c-myc, N-myc, and p46. During G1-phase, pRb is predominantly in a hypophosphorylated state and it becomes increasingly phosphorylated through the cell cycle until the end of mitosis when substantial dephosphorylation[14–16]. To further investigate the role of cyclin genes in mammary tumorigenesis, we analyzed the expression of cyclins D1 and pRb in Daudi cells by Western blot. In this study, deguelin was shown to down-regulate the expression of cyclin D1 and pRb on Daudi cells in a dose-dependent way. This incident was closely related to arrest in G_0/G_1. This shows that deguelin can regulate the function of molecule cyclin D1 and control cell cycle, reduce the expression of pRb, and realize its regulation and control function of G_1/S checkpoints.

B-NHL plays an important role in blood system tumor. Though traditional chemotherapy and radiotherapy can achieve progress, the long-term result of treatment is not obvious[17]. We chose Burkkit's lymphoma cell line Daudi cells as a research target. We found that deguelin could arrest Daudi cells in G_0/G_1 phase and induce apoptosis, and did not have any obvious poisonous function on the normal cell. As the source of deguelin is abundant and cheap, hopefully it will become a new-type of powerful antineoplastic medicine in treatment with B cells lymphoma.

Acknowledgements

Thanks to the Tumor Biology Laboratory, Center of Gynaecology, Tongji Hospital, Huazhong University of Science and Technology, China for offering relevant experimental facilities and technical support. We wish to particularly thank Prof Jian-feng ZHOU and Yun-ping LU for their guidance and help with the experiment.

References

1 Udeani GO, Gerhauser C, Thomas CF, Moon RC, Kosmeder JW, Kinghorn AD, *et al*. Cancer chemopreventive activity mediated by deguelin, a naturally occurring rotenoid. Cancer Res 1997; 57: 3424–8.

2 Lee HY, Suh YA, Kosmeder JW, Pezzuto JM, Hong WK, Kurie JM. Deguelin-induced inhibition of cyclooxygenase-2 expression in human bronchial epithelial cells. Clin Cancer Res 2004; 10: 1074–9.

3 Chun KH, Kosmeder JW 2nd, Sun S, Pezzuto JM, Lotan R, Hong WK, *et al*. Effects of deguelin on the phosphatidylinositol 3-kinase/Akt pathway and apoptosis in premalignant human bronchial epithelial cells. J Natl Cancer Inst 2003; 95: 291–302.

4 Weber AL, Rahemtullah A, Ferry JA. Hodgkin and non-Hodgkin lymphoma of the head and neck: clinical, pathologic, and imaging evaluation. Neuroimaging Clin N Am 2003; 13: 371–92.

5 Murillo G, Salti GI, Kosmeder JW 2nd, Pezzuto JM, Mehta RG. Deguelin inhibits the growth of colon cancer cells through the induction of apoptosis and cell cycle arrest. Eur J Cancer 2002; 38: 2446–54.

6 Evan GI, Vousden KH. Proliferation, cell cycle and apoptosis in cancer. Nature 2001; 411: 342–8.

7 Ormerod MG. Investigating the relationship between the cell cycle and apoptosis using flow cytometry. J Immunol Methods 2002; 265: 73–80.

8 Izevbigie EB, Bryant JL, Walker A. A novel natural inhibitor of extracellular signal-regulated kinases and human breast cancer cell growth. Exp Biol Med 2004; 229: 163–9.

9 Sun SY, Hail Jr N, Lotan R. Apoptosis as a novel target for cancer chemoprevention. J Natl Cancer Inst 2004; 96: 662–72.

10 Mitselou A, Ioachim E, Zagorianakou N, Kitsiou E, Vougiouklakis T, Agnantis NJ. Expression of the cell-cycle regulatory proteins (cyclins D1 and E) in endometrial carcinomas: correlations with hormone receptor status, proliferating indices, tumor suppressor gene products (p53, pRb), and clinicopathological parameters. Eur J Gynaecol Oncol 2004; 25: 719–24.

11 Feakins RM, Nickols CD, Bidd H, Walton SJ. Abnormal expression of pRb, p16, and cyclin D1 in gastric adenocarcinoma and its lymph node metastases: relationship with pathological features and survival. Hum Pathol 2003; 34: 1276–82.

12 Weinstein IB. Disorders in cell circuitry during multistage carcinogenesis: the role of homeostasis. Carcinogenesis 2000; 21: 857–64.

13 Solomon DA, Wang Y, Fox SR, Lambeck TC, Giesting S, Lan Z, *et al*. Cyclin D1 splice variants. Differential effects on localization, RB phosphorylation, and cellular transformation. J Biol Chem 2003; 278: 30339–47.

14 Shim MJ, Kim HJ, Yang SJ, Lee IS, Choi HI, Kim TU. Arsenic trioxide induces apoptosis in chronic myelogenous Leukemia K562 cells: possible involvement of p38 MAP kinase. J Biochem Mol Biol 2002; 35: 377–83.

15 Chen XC, Chen LM, Zhu YG, Fang F, Zhou YC, Zhao CH. Involvement of CDK4, pRB, and E2F1 in ginsenoside Rg1 protecting rat cortical neurons from β-amyloid-induced apoptosis. Acta Pharmacol Sin 2003; 24: 1259–64.
16 Pietenpol JA, Stewart ZA. Cell cycle checkpoint signaling: cell cycle arrest versus apoptosis. Toxicology 2002; 181–182: 475–81.
17 Liu HL, Chen Y, Cui GH, Zhou JF. Curcumin, a potent antitumor reagent, is a novel histone deacetylase inhibitor regulating B-NHL cell line Raji proliferation effect. Acta Pharmacol Sin 2005; 26: 603–9.

Notice of duplicate publication

Publication of the same research data in two or more journals (duplicate or redundant publication) is a practice that does not serve the interest of the medical community. Virtually most medical journals have policies against duplicate publication, and according to the recommendations of the International Committee of Medical Journal Editors (http://www.icmje.org), significant infractions should be reported to readers.

Now we regret to inform our readers of an article by Zhu *et al* published in Acta Pharmacol Sin 2004; 25 (8): 1045–1051 belongs to duplicate publication which shares the same data with another paper published in Zhongguo Zhong Yao Za Zhi (China J Mat Med 2004; 29(8): 777–781. in Chinese), just with different submission date and author sequence.

As our Information for Authors points out, prior and duplicate publication are not permitted. When submitting a paper, the authors must make a full statement to the editor about all submissions and previous reports that might be regarded as redundant or duplicate publications of their work. We wish the above case can help our authors learn how to avoid such scientific misconduct occur again in the future.

Acta Pharmacologica Sinica 2005 Jul; 26 (7): 881–886

Full-length article

GLB prevents tumor metastasis of Lewis lung carcinoma by inhibiting tumor adhesion actions[1]

Yan PAN[2], Qian-liu SONG[2], Yan-hua LIN[2], Ning LU[2], He-ming YU[3], Xue-jun LI[2,4]

[2]Department of Pharmacology, School of Basic Medical Sciences and State Key Laboratory of Natural Biomimetic Drugs, Peking University, Beijing 100083, China; [3]National Research Institute for Family Planning, Beijing 100081, China

Key words

neoplasm metastasis; adhesion; carcinoma, Lewis lung

[1] Project supported by the National Natural Science Foundation of China (No 39770286, 30171090) and 973 Program of the Ministry of Science and Technology (No 2004CB518902).
[4] Correspondence to Prof Xue-jun LI.
Phn 86-10-8280-2863
Fax 86-10-6217-9119.
E-mail xjli@bjmu.edu.cn

Received 2005-01-29
Accepted 2005-03-14

doi: 10.1111/j.1745-7254.2005.00125.x

Abstract

Aim: To investigate the inhibitory effect of a new compound of GLB on tumor metastasis *in vivo* and analyze its actions on tumor cell adhesion to clarify its mechanism. **Methods:** The effect of GLB on tumor metastasis was analyzed by Lewis lung carcinoma model. The pathological morphology of lung alveolar was evaluated by hematoxylin-eosin staining. The effect of GLB on the proliferation of human prostate cancer cell (PC-3M, with a high metastatic characteristic) was studied using the MTT method, and its actions on PC-3M cell adhesion to human umbilical vein endothelial cells (HUVEC) and laminin were analyzed *in vitro*. **Results:** GLB (100 $mg \cdot kg^{-1} \cdot d^{-1}$ for 28 d, ig) reduced the number of lung colonies of Lewis lung carcinoma metastasis significantly ($P<0.05$). Simultaneously, GLB could mitigate the damage of lung alveolar caused by metastasic tumor deposits. *In vitro*, GLB inhibited dramatically the adhesion of PC-3M cells to HUVEC ($P<0.01$) and laminin ($P<0.05$), without cytotoxic or anti-proliferative action on PC-3M cells. **Conclusion:** GLB has anti-tumor metastatic activity, which partly depends on its inhibition of tumor adhesion.

Introduction

The ability to metastasis is the most fearsome aspect of cancer and most cancer deaths are the sequel of metastatic diseases rather than primary tumor growth. In order to form overt metastases, a cell must complete the metastatic cascade, a series of well-defined steps including local invasiveness, intravasation, circulation, adhesion and extravasation, survival, proliferation and angiogenesis[1]. Within this multistep process, adhesive ability of metastatic tumor cells is a critical factor in extravasation and formation of new tumor foci[2–6].

Cancer continues to represent the largest cause of mortality in the world and claims over 6 million lives every year[7]. An extremely promising strategy for the management of cancer today is chemoprevention, which is defined as the use of synthetic or natural agents (alone or in combination) to block the development of cancer in humans[8,9]. Studies on the pharmacological mechanisms and the search for new anticancer and anti-metastasis drugs are necessary and hold great interest for scientists. The compound GLB, (2"*S*,3a*R*,6*S*,7a*R*)-3"-acetyl-3a,7a-dihydro-2,2,2',2'-tetramethyl-5"-(4–bromophenyl)-spiro{spiro[1,3-dioxolo(4,5-*D*)-pyrane-6(7*H*),5'(4'*H*)-1',3'-dioxolo]-7(6*H*),2"(3"*H*)-(1,3,4)-oxadiazole} (Figure 1), was synthesized by Prof Zhong-jun LI (School of Pharmacy, Peking University) in 2000 and was patented by National Patent of China (No 03119612.8). It is structurally based on fructose. Previous studies showed that the com-

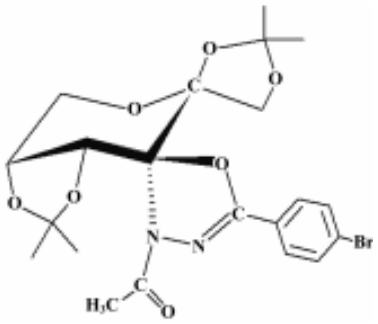

Figure 1. Chemical structure of GLB.

pound could inhibit the growth of S180 carcinoma in ICR and LACA mice. However, its precise function and mechanism of action on tumor and tumor metastasis have not been determined in full. In the present study, we investigated the effect of GLB on tumor metastasis in mice treated orally and examined its effect on the adhesion of tumor cells *in vitro* to clarify its possible mechanism of anti-metastasis.

Materials and methods

Cell culture Human umbilical vein endothelial cells (HUVEC) were isolated by collagenase I (1 g/L, Invitrogen, USA) digestion of umbilical veins from undamaged sections of fresh cords. HUVEC were grown in Medium 199 (Gibco, USA) supplemented with 20% heat-inactivated fetal bovine serum (FBS), 20 mg/L endothelial cell growth supplement (ECGS, Sigma, USA), 1×10^5 IU/L penicillin, 100 mg/L streptomycin and 2 mmol/L *L*-glutamine. Replicate cultures were obtained by trypsinization and cells of passages 3–6 were used in the experiments. The identification of HUVEC was confirmed by their polygonal morphology and by detecting their immunoreactivity for factor VIII-related antigens[10]. Human prostate carcinoma cells (PC-3M) were cultivated in RPMI-1640 containing 10% heat-inactivated FBS, 1×10^5 IU/L penicillin and 100 mg/L streptomycin in a humidified incubator with 5% CO_2 in air at 37 °C.

Assay of PC-3M cell adhesion to HUVEC PC-3M cells were labeled with CFDA (carboxyfluorescein diacetate, Sigma, 100 mg/L) for 30 min at 37 °C[11]. Cells were washed twice with phosphate-buffered saline (PBS) to remove residual fluorescent dye. The viability of the cells was not compromised by this labeling protocol, as indicated by Trypan blue exclusion.

HUVEC were cultured to confluence in 96-well dishes coated with 2% gelatin. Confluence was confirmed using microscopy and CFDA-labeled PC-3M cells were washed and resuspended in culture medium. One hundred microliters of the tumor-cell suspension (about 1×10^4 cells) was added to HUVEC monolayers in 96-well dishes and co-cultured for 30 min at 37 °C. At the end of the experiment, the wells were washed twice with PBS to remove non-adhering PC-3M cells. The adherent cells were counted under a fluorescence microscope using an excitation wavelength of 492 nm, using five fields in each well[10].

Assay of PC-3M cell adhesion to laminin The 96-well plates were coated with laminin (extracted by the Department of Cytobiology, Peking University) and incubated in RPMI-1640 containing 0.02% bovine serum albumin (BSA) for 15 min at 37 °C. In a total volume of 100 μL RPMI-1640, 8×10^4 PC-3M cells were added to each well and incubated for 4 h at 37 °C in the presence of GLB. After removing unattached cells with two washes with PBS, the attached cells were inccubated with 20 μL sterile MTT dye (Sigma) for a further 2 h at 37 °C. The medium was then removed, and 100 μL dimethyl sulfoxide (Me_2SO) was added and mixed thoroughly. Spectrometric absorbance at 540 nm (for formazan dye) and 690 nm (as background level) was measured using a microplate reader (Bio-Rad, USA)[12].

Proliferation assay PC-3M cells (1×10^4 cells/well) were cultured in 24-well plates and incubated for 1, 2, 3, 4, 5, and 6 d in the presence of GLB at various concentrations. The medium with GLB was changed every 48 h. After incubation the cells were harvested and washed with PBS. The number of viable cells in each well was then determined and counted using the Trypan blue exclusion assay[13].

Lewis lung carcinoma *in vivo* model Female C57BL/6 mice weighing 18 g–20 g were used and purchased from the Experimental Animal Center of Peking University (Grade II, Certificate No 11-00-0004). Lewis lung carcinoma (provided by the Chinese Medical Science Institute) was maintained in C57BL/6 mice by subcutaneous injection in the axillary's region of 0.2 mL of homogenized tumor tissue [tumor tissue (g): 0.9% sodium chloride (mL), 1:3] prepared from donors similarly inoculated for experimental tumor transplantation[14].

Metastasis *in vivo* GLB was suspended in 0.5% (w/v) sodium carboxyl methylcellulose (CMC-Na) in distilled water and administered orally for 27 d (25, 50, and 100 $mg\cdot kg^{-1}\cdot d^{-1}$) from the next day of tumor cell injection. After the d 6, the tumor volumes of mice were measured every 3 d. At the d 28, the mice were killed and the lungs and primary tumors were removed and weighed. The number of metastasized pulmonary colonies was counted and lung tissues were fixed in formalin for further analysis. The inhibitory rate of lung metastasis (%) was calculated using the equation $(W_{model}-W_{treatment})/(W_{model}-W_{control})\times100\%$, where W is lung wet weight[14–16].

Pathological evaluation of lung The fixed lung tissue samples were embedded in paraffin, sectioned at 5 μm and stained with hematoxylin and eosin to evaluate alveolar integrity by counting area percentage of alveolus in lung. A total of 5 fields from each lung sample were screened randomly; the mean value was accepted as representative of the sample[17].

Statistical analysis The experimental results were expressed as mean±standard deviation (SD). Statistical analysis was carried out using one-way analysis of variance (ANOVA) followed by Dunnett's test with SPSS version

10.0. $P<0.05$ was considered to be statistically significant.

Results

Inhibitory effects of GLB on spontaneous metastasis of Lewis lung carcinoma in mice We investigated the effect of oral administration of GLB on the spontaneous metastasis of Lewis lung carcinoma. GLB at the dose of 100 mg/kg significantly reduced the number of pulmonary metastatic colonies of Lewis lung carcinoma cells ($P<0.05$). The inhibitory rate of colony formation was approximately 31%. During the drug treatment, we found neither body weight loss nor toxic death in the GLB-treated mice. In addition to a reduction in the number of lung colonies by GLB, the survival rate of mice treated with GLB was significantly higher than that of untreated mice bearing Lewis lung carcinoma (Table 1). Although the mean weight and volume of the primary tumor in GLB-treated mice were less than those of vehicle-treated mice, there was no statistical difference ($P>0.05$, Table 1, Figure 2).

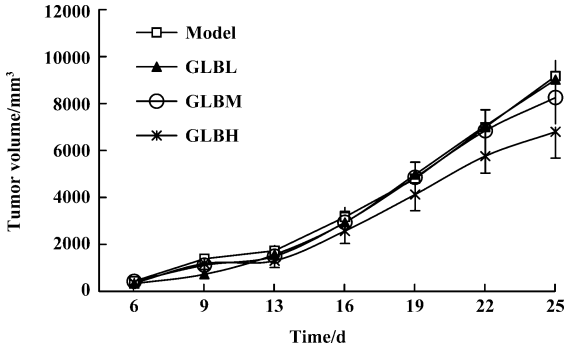

Figure 2. Effect of GLB on Lewis lung carcinoma primary tumor of C57BL/6 mice. C57BL/6 mice were implanted with Lewis lung carcinoma cells and systemic theated with vehicle (model) and doses of 25 mg/kg GLB (GLBL), 50 mg/kg GLB (GLBM) or 100 mg/kg GLB (GLBH) intragastrically once a day. After the 6 d, the mice tumor volume was measured every 3 d. $n>7$ mice. Mean±SD.

Effect of GLB on alveolar integrity in mice with Lewis lung carcinoma cells Alveolar integrity of lungs with metastatic tumor deposits in mice bearing Lewis lung carcinoma cells was significantly worse than that of normal lung tissue (area percentage of alveolus in lungs: 37.8%±7.44% *vs* 44.9%±7.6%, $P<0.05$). The lung tissue of mice treated with 100 mg/kg GLB was clearly better than that of tumor transplanted mice (area percentage of alveolus in lungs: 45.1%± 6.13% *vs* 37.8%±7.4%, $P<0.05$) (Figure 3).

Inhibitory effects of GLB on metastatic adhesion function of tumor cells We evaluated the effects of GLB on the metastatic adhesion functions of tumor cells by examining its effect on PC-3M cell adhesion to endothelial monolayers and laminin. GLB, at the concentrations of 1×10^{-5} mol/L and 10^{-6} mol/L, inhibited significantly the adhesion of PC-3M cells to HUVEC ($P<0.01$, Figure 4). GLB at these concentrations also inhibited the attachment of PC-3M cells to the laminin ($P<0.05$, Figure 5). To clarify whether the inhibitory action on adhesion function could be due to a cytotoxic effect, GLB was tested for its effect on PC-3M cell proliferation (Figure 6). GLB had no substantial effect on the growth of tumor cells after up to 5 d incubation. Until the latter period of cell growth (d 6 and 7), the proliferation of PC-3M cells treated with 1×10^{-5} mol/L and 1×10^{-6} mol/L GLB showed signs of a slight decrease.

Discussion

As has been demonstrated, the sequential process of micrometastasis formation by Lewis lung carcinoma includes single cells in the blood circulation escaping from the immune system, adhering to epithelial cells, migrating into the tissue, proliferating and making colonies in the lung[18]. Investigate the earliest events during micrometastasis formation is useful and could be simply applied for the estimation of anti-metastatic and anti-adhesive effects of various anticancer agents[12].

Table 1. Effect of GLB on lung colonization of Lewis lung carcinoma cells. Mean±SD. $^bP<0.05$ *vs* model.

Group	Dose (mg/kg, ig)	Body weight (g)	Survival (*n*)	Tumor weight (g)	Lung colonies (*n*)	Inhibitory rate of lung colonies (%)
Model	Vehicle	19.8±1.96	9/13	7.42±1.78	16±2.6	
GLBL	25	20.25±1.54	7/9	6.41±1.51	15±5.0	6
GLBM	50	19.08±2.67	7/9	6.18±1.11	12±5.2	26
GLBH	100	19.67±2.64	8/9	6.04±1.37	11±3.1^b	31

GLBL, GLB 25 mg·kg^{-1}·d^{-1}; GLBM, GLB 50 mg·kg^{-1}·d^{-1}; GLBH, GLB 100 mg·kg^{-1}·d^{-1}.

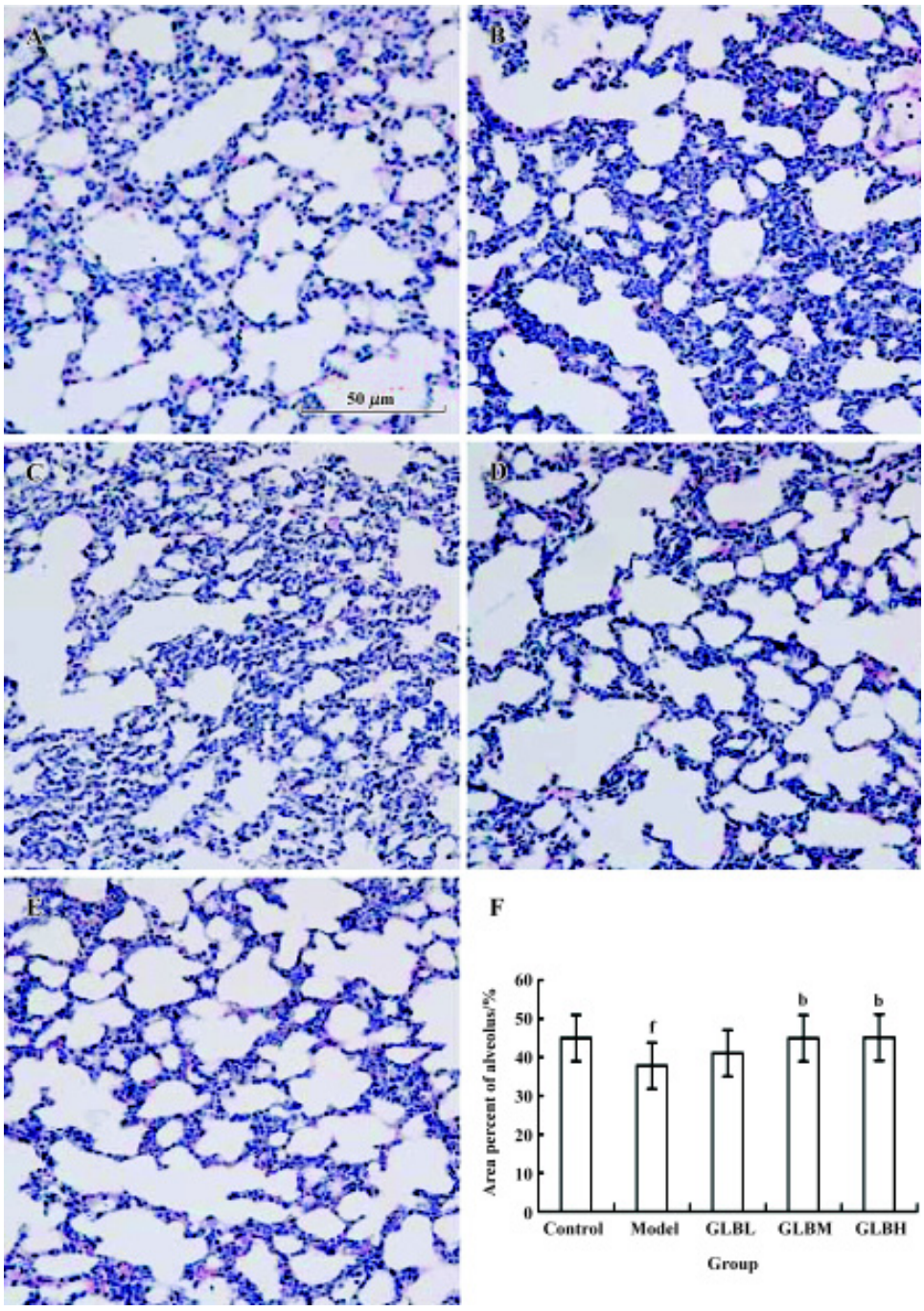

Figure 3. Effect of GLB on alveolar integrity in mice with Lewis lung carcinoma cells. The area percentage of alveolus in lung tissue of normal C57BL/6 mice was almost 50% (A), and that in lung of mice bearing Lewis lung carcinoma (model) was decreased (B). Lung tissues of C57BL/6 mice bearing Lewis lung carcinoma treated with (C) 25 mg/kg, (D) 50 mg/kg and (E) 100 mg/kg GLB were significantly better than the model. Hematoxylin-eosin stain, ×100. (F) The statistical result of alveolus area percentage. Control, normal; M, model; GLBL, GLB 25 mg·kg^{-1}·d^{-1}; GLBM, GLB 50 mg·kg^{-1}·d^{-1}; GLBH, GLB 100 mg·kg^{-1}·d^{-1}. n=5 mice. Mean±SD. ^{b}P<0.05 *vs* model. ^{f}P<0.05 *vs* control.

The antitumor activities of the derivatives of oxadiazoles, one-membered heterocycles, have been reported and are found to be related to their chelating abilities or non-polarity, which is essential to penetrate through intracellular sites[19]. These include the new 5-(2-amino-3-pyridyl)-2-thioxo-3*H*-1, 3,4-oxadiazole derivatives that have shown cytotoxic

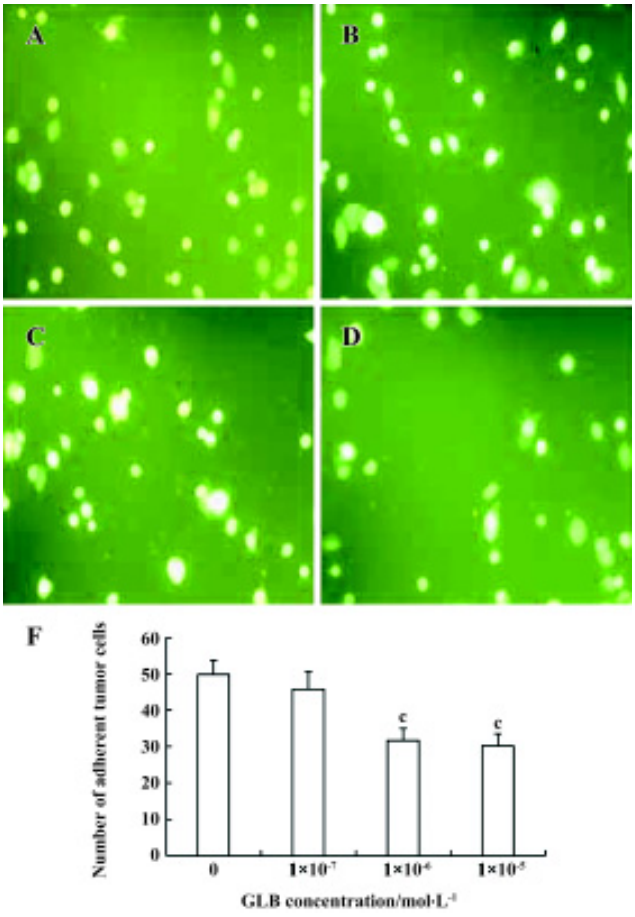

Figure 4. Inhibitory effect of GLB on adhesion of PC-3M to human umbilical vein endothelial cells (HUVEC). Carboxyfluorescein diacetate (CFDA)-labelled PC-3M cells were added to the HUVEC monolayer cultured at 37 °C for 30 min. The adherent tumor cells were counted in five fields in each plate, using a fluorescence microscope. (A) Control; (B) 1×10^{-7} mol/L GLB; (C) 1×10^{-6} mol/L GLB; (D) 1×10^{-5} mol/L GLB. Magnification ×400. (E) Inhibition of PC-3M adhesion to HUVEC by GLB. n=4 wells. Mean±SD. $^{c}P<0.01$ *vs* control.

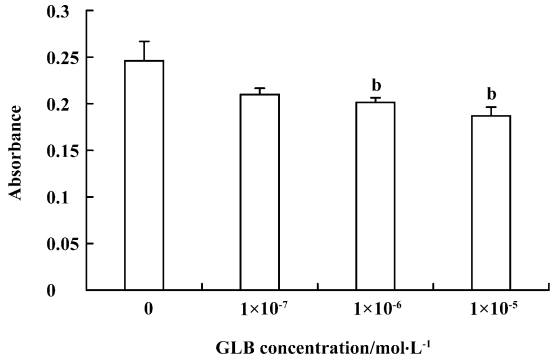

Figure 5. Inhibitory effect of GLB on adhesion of PC-3M to laminin. PC-3M cells were added to wells coated with laminin and incubated at 37 °C for 4 h in the presence of GLB. The number of adhesive cells per well was determined using the MTT assay and are shown as absorbance. n=6 wells. Mean±SD. $^{b}P<0.05$ *vs* control.

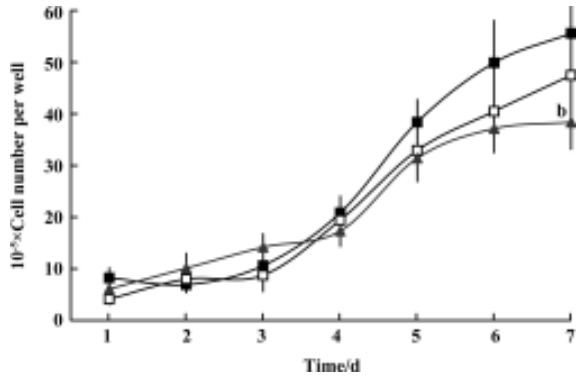

Figure 6. Effect of GLB on proliferation of PC-3M cells. PC-3M cells were cultured for 7 d in the absence (■) or presence of either 1×10^{-6} mol/L (□) or 1×10^{-5} mol/L (▲) GLB. n=4 wells. Mean±SD. $^{b}P<0.05$ *vs* control.

activity against the cells of 4 human tumor cell lines[20] and 2, 5-disubstituted-1,3,4-oxadiazole compounds, which are potential anticancer agents[21]. The present study demonstrated that oral administration of GLB inhibited the spontaneous pulmonary metastasis of tumor cells in C57BL/6 mice and increased the survival rate. GLB significantly inhibited the adhesion by PC-3M cells without affecting cell proliferation *in vitro*. The present data suggest that GLB prevents tumor metastasis partly by inhibiting the metastatic adhesion of tumor cells.

Tumor cell adhesion to endothelial monolayers is a critical step in tumor metastasis[22], as is laminin expression in endothelial cells, being one of the earliest extracellular matrix (ECM) proteins. Laminin interaction with the β-1 integrin has been shown to have an important role in the regulation of tumor-to-endothelial cell adhesion[10]. We demonstrated that GLB significantly inhibited the adhesion of tumor cells to laminin, using the same doses of GLB as had been found to inhibit adhesion of tumor cells to endothelial cells. This suggests that the anti-adhesion activity of GLB might be due to its effect on laminin, one of many other factors involved in adhesion.

β-1 Integrin is known to recognize many ECM proteins as ligands, such as laminin, collagen and fibronectin. Laminin has been identified as the most important of these ligands for β-1 integrin in the cell adhesion process[23,24]. Whether GLB exerts its function through β-1 integrin or not is yet to be determined.

In the present study, GLB showed no effect on the weight of the primary tumor site in C57BL/6 mice subcutaneously injected with a Lewis lung carcinoma tumor cell suspension (Table 1). In a preliminary experiment where S180 carcinomas were implanted subcutaneously into ICR and LACA mice, GLB-treated mice (50 mg·kg^{-1}·d^{-1} for 12 d, ip) showed a significant decrease in tumor weight, with inhibitory rates of 43% and 32% (tumor weight at d 12, mean±SD: 1.16±0.67 g *vs* 2.05 ± 0.64 g, $P<0.01$ for ICR mice; 1.81±0.68 g *vs* 2.65± 0.81 g, $P<0.05$ for LACA mice; $n=10$ mice). The different effects of GLB on these *in vivo* assay models may be dependent on the kind of tumor, the period of the experiment and route of administration. We speculate that there might be other mechanisms of action for GLB that require further study, including the relationship between its effects on tumor growth or metastasis and its inhibition of angiogenesis.

In conclusion, the compound GLB prevents tumor metastasis by inhibiting tumor adhesion. This suggests it has potential for future anti-metastatic development.

References

1 Gassmann P, Enns A, Haier J. Role of tumor cell adhesion and migration in organ-specific metastasis formation. Onkologie 2004; 27: 577–82.

2 Nicolson GL. Metastatic tumor cell interactions with endothelium, basement membrane and tissue. Curr Opin Cell Biol 1989; 1: 1009–19.

3 Lewalle JM, Cataldo D, Bajou K, Lambert CA, Foidart JM. Endothelial cell intracellular Ca^{2+} concentration is increased upon breast tumor cell contact and mediates tumor cell transendothelial migration. Clin Exp Metastasis 1998; 16: 21–9.

4 Honn KV, Tang DG. Adhesion molecules and tumor cell interaction with endothelium and subendothelial extracellular matrix. Cancer Metastasis Rev 1992; 11: 353–75.

5 Chambers AF, MacDonald IC, Schmidt EE, Koop S, Morris VL, Khokha R, *et al*. Steps in tumor metastasis: new concept for intravital videomicroscopy. Cancer Metastasis Rev 1995; 14: 279–301.

6 Tressler RJ, Yeatman T, Nicolson GL. Extracellular annexin VI expression is associated with divalent cation-dependent endothelial cell adhesion of metastatic RAW117 large-cell lymphoma cells. Exp Cell Res 1994; 215: 395–400.

7 Abdullaev FI, Luna RR, Roitenburd BV, Espinosa AJ. Pattern of childhood cancer mortility in Mexico. Arch Med Res 2000; 31: 526–31.

8 Gupta M, Mazumder UK, Kumar RS, Kumar TS. Antitumor activity and antioxidant role of *Bauhinia racemosa* against Ehrlich ascites carcinoma in Swiss albino mice. Acta Pharmacol Sin 2004; 25: 1070–6.

9 Rao KVK, Schwartz SA, Nair HK, Aalinkeel R, Mahajan S, Chawda R, *et al*. Plant derived products as a source of cellular growth inhibitory phytochemicals on PC-3M, DU-145 and LNCaP prostate cancer cell lines. Curr Sci 2004; 87: 1585–8.

10 Andrews EJ, Wang JH, Winter DC, Laug WE, Redmond HP. Tumor cell adhesion to endothelial cells is increased by endotoxin via an upregulation of β-1 integrin expression. J Surg Res 2001; 97: 14–9.

11 Woodward JK, Nichols CE, Rennie IG, Parsons MA, Murray AK, Sisley K. An *in vitro* assay to assess uveal melanoma invasion across endothelial and basement membrane barriers. Invest Ophthalmol Vis Sci 2002; 43: 1708–14.

12 Yoshitomi Y, Nakanishi H, Kusano Y, Munesue S, Oguri K, Tatematsu M, *et al*. Inhibition of experimental lung metastases of Lewis lung carcinoma cells by chemically modified heparin with reduced anticoagulant activity. Cancer Lett 2004; 207: 165–74.

13 Tozawa K, Kawai N, Hayashi Y, Sasaki S, Kohri K, Okamoto T. Gold compounds inhibit adhesion of human cancer cells to vascular endothelial cells. Cancer Lett 2003; 196: 93–100.

14 Xiang Y, Ma B, Li T, Yu HM, Li XJ. Acetazolamide suppresses tumor metastasis and related protein expression in mice bearing Lewis lung carcinoma. Acta Pharmacol Sin 2002; 23: 745–51.

15 Prontera C, Mariani B, Rossi C, Poggi A, Rotilio D. Inhibition of gelatinase A (MMP-2) by batimastat and captopril reduces tumor growth and lung metastases in mice bearing Lewis lung carcinoma. Int J Cancer 1999; 81: 761–6.

16 Ma B, Xiang Y, Li T, Yu HM, Li XJ. Inhibitory effect of topiramater on Lewis lung carcinoma metastasis and its relation with AQP1 water channel. Acta Pharmacol Sin 2004; 25: 54–60.

17 Ustundag N, Bozkurt AK, Demirkaya A, Koksal C, Mayda AS. Histopathological and immunohistochemical detection of protective effects of University of Wisconsin solution supplemented with iloprost on donor lung damage. Transplant Proc 2004; 36: 1271–4.

18 Hirano S. *In vitro* and *in vivo* cytotoxic effects of nitric oxide on metastatic cells. Cancer Lett 1997; 115: 57–62.

19 Mishra L, Said MK, Itokawa H, Takeya K. Antitumor and antimicrobial activities of Fe(II)/Fe(III) complexes derived from some heterocyclic compounds. Bioorg Med Chem 1995; 3: 1241–5.

20 Liszkiewicz H, Kowalska MW, Wietrzyk J, Opolski A. Synthesis and anti-proliferative activity *in vitro* of new 5-(2-amino-3-pyridyl)-2-thioxo-3*H*-1,3,4-oxadiazole derivatives. Indian J Chem, B 2003; 42B: 2846–52.

21 Shah HP, Shah BR, Bhatt JJ, Desai NC, Trivedi PB, Undavia NK. Synthesis of 2,5-disubstituted 1,3,4-oxadiazoles as potential antimicrobial, anticancer and anti-HIV agents. Indian J Chem, B 1998; 37B: 180–2.

22 Danen EH, Marcinkiewicz C, Cornelissen IM, van Kraats AA, Pachter JA, Ruiter DJ, *et al*. The disintegrin eristostatin interferes with integrin a4b1 function and with experimental metastasis of human melanoma cells. Exp Cell Res 1998; 238: 188–96.

23 Dejana, E. Endothelial cell adhesive receptors. J Cardiovasc Pharmacol 1993; 21: S18-21.

24 Kitayama J, Nagawa H, Tsuno N, Osada T, Hatano K, Sunami E, *et al*. Laminin mediates tethering and spreading of colon cancer cells in physiological shear flow. Br J Cancer 1999; 80: 1927–34.

Acta Pharmacologica Sinica 2005 Jul; 26 (7): 887–892

Full-length article

Tetramethylpyrazine protected photoreceptor cells of rats by modulating nuclear translocation of NF-κB[1]

Jin-nan YANG[2,3], Jin-mao CHEN[4], Lin LUO[4], Shao-chun LIN[4], Dai LI[4], Shi-xing HU[4,5,6]

[2]School of Pharmacy, Xinxiang Medical College, Xinxiang 453003, China; [4]Zhongshan Ophthalmic Centre, Sun Yat-sen University, Guangzhou 510060, China; [5]Eye Hospital of China, Academy of Traditional Chinese Medicine, Beijing 100040, China

Key words

tetramethylpyrazine; photoreceptors; methylnitrosourea; apoptosis; NF-kappa B; retinitis pigmentosa

[1] Project supported by the National Natural Science Foundation of China, No 30300467.
[3] Correspondence to Dr Jin-nan YANG.
Phn 86-373-3831-565.
Fax 86-373-3029-203.
E-mail jinnan1@126.com
[6] Co-correspondence to Prof Shi-xing HU.
Phn 86-10-6868-8877.

Received 2004-10-18
Accepted 2005-03-18

doi: 10.1111/j.1745-7254.2005.00141.x

Abstract

Aim: To evaluate the effect of tetramethylpyrazine (TMP) injection on retinal damage induced by *N*-methyl-*N*-nitrosourea (MNU) in rats and on nuclear factor-kappa B (NF-κB) family members. **Methods:** Female Sprague-Dawley (SD) rats were randomly divided into groups: (i), control group; (ii), model group; and (iii), TMP-injection groups, in which the rats were subdivided into 40 mg/kg, 80 mg/kg and 160 mg/kg groups. Drugs were injected ip into 47-day-old SD rats once a day. At 50 days of age, all rats in the model group and drug groups also received a single ip injection of 60 mg/kg MNU. Rats in group 1 received ip injection of physiological saline. All rats were killed at different times after MNU or physiological saline treatment. The apoptotic index of photoreceptor cells was calculated by TUNEL labeling; retinal damage was evaluated based on retinal thickness and the expression of NF-κB family members was detected by Western blot. **Results:** TMP injections, in a dose-dependent manner, suppressed photoreceptor cell apoptosis and decreased its loss in the peripheral retina. As compared with the MNU-treated group, TMP injection at a dose of 160 mg/kg also time-dependently upregulated the NF-κB/p65 protein level in the nucleus and downregulated the IκBα protein level in the cytoplasm. However, no protective effect of TMP injection on MNU-induced central retinal damage was found. **Conclusion:** TMP injection partially protects against MNU-induced retinal damage by upregulating the nuclear translocation of p65 to inhibit photoreceptor cells apoptosis.

Introduction

Apoptosis has been described as the final common pathway to photoreceptor cell death in many eye diseases, such as age-related macular degeneration (AMD), retinal detachment and retinal light damage[1]. It has also been found to occur in the hereditary retinal degeneration, retinitis pigmentosa (RP)[2]. However, it is not obvious how the initial insult to the retina, which could be genetic, environmental, or both, drives the photoreceptor cell toward cell death. Therefore, an understanding of mechanisms that control apoptosis is integral to the treatment and prevention of retinal diseases. Recent studies have shown that light-induced retinal damage is regulated by the transcriptional factor of nuclear factor-κB (NF-κB)[3,4].

NF-κB was identified in 1986 as a nuclear factor that bound to an enhancer element of the immunoglobulin (Ig)κ light-chain gene and was believed to be specifically expressed in B cells[5]. It has recently been implicated in cellular apoptosis. Subunits of NF-κB, p50, and p65 (RelA) form a heterodimer that exhibits DNA binding potential. NF-κB typically resides in the cytoplasm bound to an inhibitory subunit, IκBα or IκBβ, which prevents its translocation to the nucleus[6]. NF-κB is constitutively active in several cell lines including THP-1 cells[7], thymocytes[8], neurons[9], and photoreceptor cells[3] and thus may be universally important to cell survival.

RP is not only a progressively recessive disease, but

also a progressive dystrophia. Thus, we observed *in vivo* the retinoprotective effects of tetramethylpyrazine (TMP), which has the role of promoting blood circulation, on *N*-methyl-*N*-nitrosourea (MNU)-induced retinal damage and elucidated the involvement of NF-κB in the protection mechanism.

Materials and methods

Animals Six-week-old female Sprague-Dawley (SD) rats were purchased from Zhongshan Medical College, Sun Yat-sen University. Animals were maintained on a basal diet with free access to food and water and were housed in plastic cages in an air-conditioned room at 22±2 °C with a 12-h light/dark cycle.

Drugs and reagents MNU was purchased from Sigma (St Louis, MO, USA) and kept at -20 °C in the dark. The MNU solution was freshly prepared, dissolved in physiological saline, just before use. The *in situ* Cell Death Detection Kit was purchased from Roche Applied Science (Indianapolis, IN, USA). Mouse monoclonal Abs to rat NF-κB p65(sc-8008), IκBα (sc-1643), mouse β-actin (sc-8432) and HRP-conjugated antimouse IgG secondary Ab were purchased from Santa Cruz Biotechnology (Santa Cruz, CA, USA). The gel shift assay systems were purchased from Bio-Rad (Bio-Rad, CA, USA). The TMP injection was provided by Changzhou Pharmaceutical Factory (Changzhou, Jiangsu, China).

Morphometric analysis of retinal layers Animals were classified randomly into five groups as follows: (i), Control group (n=6); 47-day-old rats received a daily ip injection of physiological saline for 4 days. (ii), Model group (n=6); 47-day-old rats received a daily ip injection of physiological saline for 4 days. At 50 days of age, rats also received a single ip injection of 60 mg/kg body weight of MNU. (iii), TMP injection groups (n=18); rats were subdivided into 40 mg/kg, 80 mg/kg and 160 mg/kg groups. Drugs were injected ip into 47-day-old SD rats for 4 days, respectively. At 50 days of age, all rats received a single ip injection of 60 mg/kg MNU after TMP treatment for 12 h. All rats were killed 7 d after MNU or physiological saline treatment. Eyes were quickly removed and fixed overnight in 10% neutral buffered formalin. Tissues were processed routinely for paraffin embedding and stained with hematoxylin and eosin (HE). Each eye section was cut at the central part of the retina which was aligned parallel to the optic axis and nerve. Total retinal thickness (thickness from the internal limiting membrane to the pigment epithelium) as well as outer retinal thickness (thickness of the outer nuclear layer and photoreceptor layer) in the peripheral retina (average of approximately 400 mm from both sides of the ciliary body) and central retina (average of approximately 400 mm from both sides of the optic nerve) were measured. The HE specimens of the retina were prepared in a magnification of 40×10 and examined on an OLYMPUS BX 40 electron microscope (Carl Zeiss, Germany)[10].

***In situ* detection of apoptosis** The treatment schedule was the same as detailed in the above method. All rats were killed 24 h after MNU or physiological saline treatment and both eyes were quickly removed. The TUNEL method was performed in the formalin-fixed tissue samples by using an apoptosis detection kit according to the manufacturer's instructions[11]. The apoptotic index of the outer nuclear layer (number of fragmentation nuclei/number of whole photoreceptor cell nuclei×100) of retina was determined at twenty different fields in each section under ×400 magnification.

Preparation of cytoplasmic and nuclear extracts TMP injection at a dose of 160 mg/kg was injected ip into 47-day-old SD rats, once a day. At 50 days of age, rats were given a single ip injection of 60 mg/kg MNU. Control and model groups were the same as above. Each group had 4 rats. Rats were killed 12 and 24 h, and 3 and 7 d after MNU treatment, respectively. Nuclear and cytoplasmic extracts were prepared according to nuclear extract kits[7]. Whole retinas were isolated from the eyes of rats in each group, minced and homogenized. The pelleted cells were resuspended in 600 mL 1´Hypotonic buffer (10 mmol/L Hepes, pH 7.9, 1.5 mmol/L $MgCl_2$, 10 mmol/L KCl, 10% glycerol, 1 mmol/L DTT, 0.5 mmol/L PMSF) and incubated for 15 min on ice. Then 30 mL detergent was added and centrifuged for 30 s at 14 000×g at 4 °C. The supernatants (cytoplasmic fraction) were collected and stored at -80 °C. The nuclear pellets were resuspended in 200 mL complete lysis buffer (20 mmol/L Hepes, pH 7.9, 400 mmol/L NaCl, 1.5 mmol/L $MgCl_2$, 0.2 mmol/L EDTA, 20% glycerol, 1 mmol/L DTT, 0.5 mmol/L PMSF). Following a 30-min incubation on ice, the samples were centrifuged (14 000×g, 10 min, 4 °C), and the resulting supernatants (nuclear extracts) were transferred to a fresh microfuge tube and stored at -80 °C.

Western blot analysis Each protein sample (20 g) was denatured in boiling water for 10 min, loaded onto 10% SDS-PAGE and transferred to nitrocellulose membrane. Membranes were blocked overnight with a 5% (w/v) non-fat dry milk solution containing 10 mmol/L Tris-HCl, pH 8.0, 150 mmol/L NaCl and 0.1% Tween 20 (TBST) before incubation with primary antibodies (1 h for NF-κB p65, IκBα and β-actin antibodies). Primary antibodies were diluted in TBST (1:200 for NF-κB p65, IκBα and β-actin). After washing, the membranes were incubated for 1 h with horseradish peroxidase-labeled

secondary antibody diluted 1:1000 in TBST, and the labeled proteins were detected using enhanced chemiluminescence reagents as described by the manufacturer (Amersham Pharmacia Biotech, Piscataway, NJ, USA). The results were expressed as AU (D_{area}·$D_{density}$). The ratio of arbitrary unit (AU, D_{area}·$D_{density}$) of target protein over β-actin was used for expressing the relative level of target protein.

Statistical analysis Data were expressed as mean± standard deviation and analyzed by SPSS 10.0 software. One to one comparisons among multiple-samples were made using one-way analysis of variance (ANOVA). P<0.05 was considered significant.

Results

Effect of TMP injection on retinal thickness of MNU-treated retina in SD rats Compared with retinas from the age-matched control SD rats (Figures 1A, 2A), peripheral or central retinas from MNU-treated animals showed thinning with selective loss of the photoreceptor cells 7 days after MNU injection (Figures 1B, 2B). While in rats pretreated with TMP injections, the total as well as outer retinal thickness of the peripheral retina was significantly greater than that of model rats in a dose-dependent manner (Figure 1C, 1D, 1E). However, no protective effects of TMP injections on MNU-induced central retinal damage were found (Figure 2C,2D, 2E). The results are shown in Table 1.

Table 1. Effect of TMP injections on total retinal thickness and outer thickness of MNU-treated rats. Mean±SD. ^{c}P<0.01 *vs* group 1. ^{d}P>0.05, ^{e}P<0.05, ^{f}P<0.01 *vs* group 2. Each group consists of 12 eyes.

Group	MNU/ mg·kg^{-1}	TMP/ mg·kg^{-1}	Peripheral retina		Central retina	
			Total retina/mm	Outer retina/mm	Total retina/mm	Outer retina/mm
1	0	0	87±2	45±1	135±3	62±2
2	60	0	37±2^{c}	3±1^{c}	69±2^{c}	5±1^{c}
3	60	40	41±1^{e}	12±1^{f}	70±3^{d}	6±1^{d}
4	60	80	66±3^{f}	28±2^{f}	70±4^{d}	7±1^{d}
5	60	160	85±4^{f}	42±3^{f}	70±3^{d}	7±1^{d}

Effect of TMP injection on apoptotic index of photoreceptor cells induced by MNU in SD rats As TMP injection had no protective effect on damage to the central retina induced by MNU, we just detected the apoptotic index of photoreceptor cells in the peripheral retina. In MNU-treated rats, the 24 h post-MNU was (38.0±3.6)% in the peripheral retina.

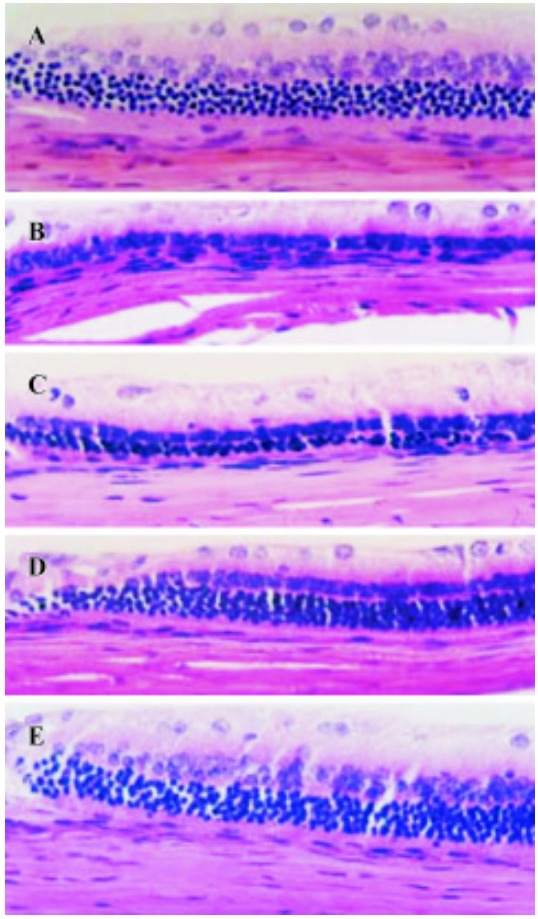

Figure 1. The protective effect of TMP injections on peripheral retina at the 7th day after MNU treatment. A: control group, the morphology of photoreceptor cells was uniform and the orientation of the photoreceptor segments was normal. B: model group, the photoreceptor cells disappeared. C, D, E: pretreatment with TMP injection 40, 80, and 160 mg/kg. HE×400.

When TMP at doses of 40, 80 and 160 mg/kg were injected ip into 47-day-old SD rats for 4 d, the apoptotic indexes were significantly decreased to (30.0±3.0)% (P<0.05), (15.6±1.7)% (P<0.01), and (8.4±2.6)% (P<0.01), respectively.

Effect of TMP injection on NF-κB p65 and IκBα protein levels in MNU-induced retinal damage of SD rats As compared with the untreated control, low levels of p65 protein were detected in the nuclear fraction only after MNU treatment for 12 h and 24 h (Figure 3A). While for pretreatment with TMP injection of 160 mg/kg, the nuclear levels of p65 protein were significantly increased after MNU treatment for 24 h and at the 3rd and 7th days (P<0.01) (Figure 3A). The relative level of p65 protein was at its peak at 24 h and was 2.3-fold than that of the MNU-treated group (Figure 3B).

After MNU treatment for 12 h, the IκBα protein levels in

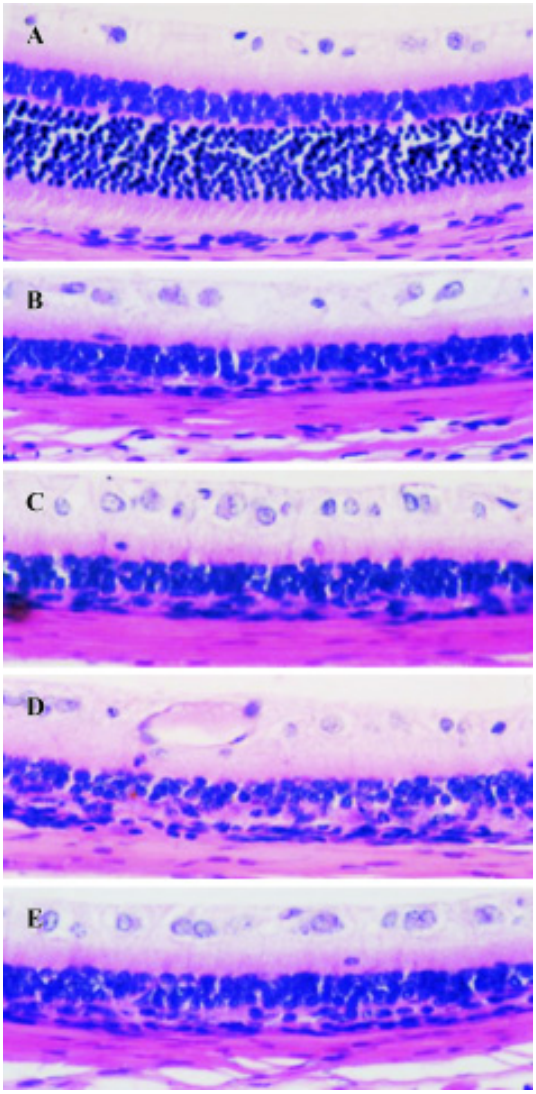

Figure 2. The protective effect of TMP injection on central retina after MNU treatment for 7 d. A: normal control. B: at the 7th day after MNU treatment, the photoreceptor cells were lost. C, D, E: pretreatment with TMP injection 40, 80 and 160 mg/kg. HE×400.

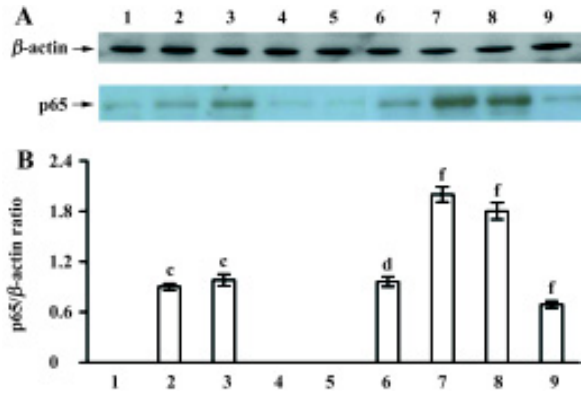

Figure 3. Effect of TMP 160 mg/kg injection on nuclear p65 protein level in MNU-induced retinal damage of SD rats. A, Western blotting analysis. B, relative level of nuclear p65 protein. Lane 1: control; Lane 2, 3, 4, 5: MNU treatment for 12 h, 24 h, 3 d, and 7 d. Lane 6, 7, 8, 9: pretreatment with TMP, then followed by MNU treatment for 12 h, 24 h, 3 d, and 7 d. Data were mean±SD from three independent experiments. $^{c}P<0.01$ *vs* control. $^{d}P>0.05$, $^{f}P<0.01$ *vs* MNU-treated group for corresponding time.

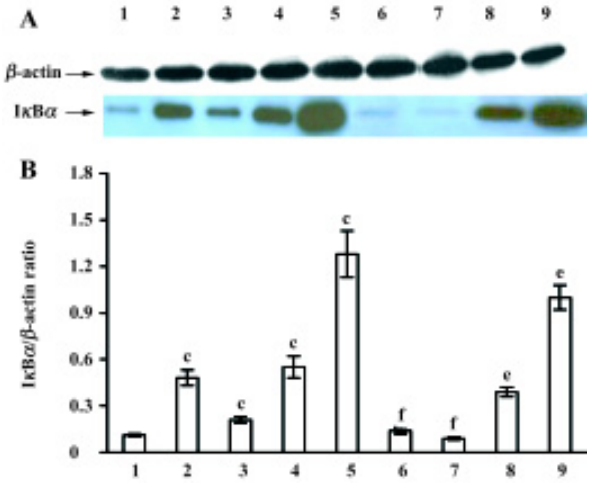

Figure 4. Effect of TMP injection at 160 mg/kg on cytoplasmic IκBα protein level in MNU-induced retinal damage of SD rats. A, Western blotting analysis. B, relative level of cytoplasmic IκBα protein. Lane 1: control; Lane 2, 3, 4, 5: MNU treatment for 12 h, 24 h, 3 d, and 7 d. Lane 6, 7, 8, 9: pretreatment with TMP, then followed by MNU treatment for 12 h, 24 h, 3 d, and 7 d. Data were mean±SD from three independent experiments. $^{c}P<0.01$ *vs* control. $^{e}P<0.05$, $^{f}P<0.01$ *vs* MNU-treated group for corresponding time.

the cytoplasm were markedly increased ($P<0.05$), and at a peak at 7 d (Figure 4A). In contrast to the MNU-treated group, TMP injection at 160 mg/kg time-dependently induced the down-regulation of cytoplasmic IκBα protein levels (Figure 4A). The relative level of IκBα protein in cytoplasm was 0.8-fold than that of the MNU-treated group at the 7th d of MNU treatment ($P<0.05$) (Figure 4B).

Discussion

The incidence of RP is approximately 1 in 4000, making it one of the major causes of blindness in humans. Although several genetic mutations have been implicated in RP, the final common pathway of the disease is apoptotic cell death of photoreceptor cells. Up to now, available treatments are of limited use in retarding this disease's progression. RP is not only a progressively recessive disease, but also pro-

gressive dystrophia. The change of retinal vessels associated with RP is also a prominent and common phenomenon. It has been reported that the blood volume of choroidal vessels became decreased and the choroidal capillaries became atrophic in RP[12].

According to above viewpoints, inhibition of apoptosis and promoting blood circulation will have common applicability and feasibility. The manipulation of factors that influence the apoptotic pathway and the blood supply of choroidal vessels may be of potential value for RP therapy. Thus, we observed *in vivo* the retinoprotective effect of Chinese medicines, which have the role of promoting blood circulation by removing blood stasis and activating the collaterals, on MNU-induced photoreceptor cell apoptosis in SD rats. TMP, one of the alkaloids in *Ligusticum wallichii* Franch (L. wallichii), an active ingredient in Chuanxiong, dilates arterioles, decreases blood and plasma viscosity and improves microcirculation of blood supply of important organs such as the eyes, brain, heart and so on[13,14]. It has been widely used, especially in the treatment of patients with cerebrovascular diseases in China were its therapeutic actions have been manifested. The present study indicates that MNU-induced retinal damage in rats was partially suppressed by the ip administration of TMP injection through the inhibition of photoreceptor cell apoptosis. However, TMP injection had no protective effect on central retina damage induced by MNU. As in MNU-induced retinal injury, photoreceptor cell apoptosis was evident at 12 h and peaked at 24 h, followed by extensive photoreceptor cell loss 7 days later. Moreover, the apoptotic index was higher in central than peripheral retina after MNU treatment[10,11]. It indicated that the damage preceded from the central to peripheral retina, the posterior portion of the retina around the optic nerve was more severely damaged than the peripheral retina. Therefore, the scheme of administration was different from clinical administration. We observed the preventive effect of TMP on MNU-induced retinal damage and found that the rapid and extensive cell loss in the central retina was beyond the rescue capacity of TMP. In contrast to the MNU-induced retinal damage, human disease starts in the equatorial area. The mean duration of visual loss in RP patients was 17 years. While, our study showed that TMP injection had a markedly protective effect on slow cell loss. So, it was possible that TMP could prevent the progress of disease and protect the central vision in RP patients. In order to best provide the clinical basis of TMP injection, we would investigate whether TMP injection could rescue photoreceptor cells in retinal degeneration slow (rds) mice in a similar way to human RP.

In 1999, Krishnamoorthy *et al* reported that the presence of NF-κB RelA subunit in the nucleus was essential for protection of photoreceptor cells against apoptosis[3]. Crawford *et al* also reported that bcl-2 overexpression protected photooxidative stress-induced apoptosis of photoreceptor cells through NF-κB preservation[4]. So, we investigated NF-κB family members in the present study to elucidate the molecular mechanisms of the protective effect of TMP injection on MNU-induced photoreceptor cell apoptosis in SD rats. In the classical model of NF-κB activation, NF-κB p65 exists in the cytoplasm of unstimulated cells in an inactive form associated with the inhibitory protein, IκBα. Following cell stimulation by extracellular stimuli, IκBα is phosphorylated through a cascade of inducible protein kinase, and selectively degraded in cytoplasm by the proteasome. Rapid degradation of IκBα allows for nuclear translocation of NF-κB where it binds specific DNA motifs in the promoter/enhancer regions of target genes and activates transcription[15,16].

Under our experimental conditions, the results showed that the amounts of IκBα in the cytoplasm were significantly accumulated in a time-dependent manner in the MNU-treated retina. It indicated that increases of IκBα would block the nuclear translocation of NF-κB. Very low levels of p65 protein in the nuclear extracts were only detectable post-MNU for 12 and 24 h, and no p65 protein was found on the 3rd and 7th days after MNU treatment. But using pretreatment with TMP injection, the cytoplasmic IκBα protein levels were time-dependently down-regulated. So, more cytoplasmic p65 protein was in a free condition and then moved to the nucleus to regulate the anti- and pro-apoptotic gene expression. It was in accordance with our results that the nuclear levels of p65 protein were significantly increased in the TMP-treated group, and TMP injection markedly increased photoreceptor cells compared with the MNU-treated group. It was further demonstrated that the p65 subunit of NF-κB may be important for photoreceptor cell survival. Meanwhile, the severe damage of central retina induced by MNU was beyond the protective effect of TMP injection, we also found that the cytoplasmic IκBα protein was increased and nuclear p65 protein was decreased at the 7th day after MNU treatment.

TMP exerts a variety of effects through antilipid peroxidation, inhibiting calcium overload, decreasing the activity of nitric oxide synthase and the expression of Fas protein, raising the ratio of Bcl-2/Fas protein and so on[17,18]. Therefore, TMP may also provide retinoprotection by multiple mechanisms. This needs to be further demonstrated. Although the factors that trigger or impede programmed cell death in photoreceptor cells have yet to be clarified, and the

apoptotic cascade may differ between rats and humans, the present findings indicate that TMP can prevent MNU-induced photoreceptor cell apoptosis and may provide a basis for the clinical use of TMP to protect or rescue human RP patients.

References

1 Abler AS, Chang CJ, Ful J, Tso MO, Lam TT. Photic injury triggers apoptosis of photoreceptor cells. Res Commun Mol Pathol Pharmacol 1996; 92: 177–89.

2 van-Soest S, Westerveld A, de-Jong PT, Bleeker-Wagemakers EM, Bergen AA. Retinitis pigmentosa: defined from a molecular point of view. Surv Ophthalmol 1999; 43: 321–34.

3 Krishnamoorthy RR, Crawford MJ, Chaturvedi MM, Jain SK, Aggarwal BB, Al-Ubaidi MR, *et al*. Photo-oxidative stress down-modulates the activity of nuclear factor-kappaB via involvement of caspase-1, leading to apoptosis of photoreceptor cells. J Biol Chem 1999; 274: 3734–43.

4 Crawford MJ, Krishnamoorthy RR, Rudick VL, Collier RJ, Kapin M, Aggarwal BB, *et al*. Bcl-2 overexpression protects photooxidative stress-induced apoptosis of photoreceptor cells via NF-kappa B preservation. Biochem Biophys Res Commun 2001; 281: 1304–12.

5 Sen R, Baltimore D. Inducibility of kappa immunoglobulin enhancer-binding protein NF-κB by a posttranslational mechanism. Cell 1986; 47: 921–8.

6 Legrand-Poels S, Schoonbroodt S, Matroule JY, Piette J. NF-kappa B: an important transcription factor in photobiology. J Photochem Photobiol B 1998; 45: 1–8.

7 Zhou JY, Tang FD, Mao GG, Bian RL. Effect of α-pinene on nuclear translocation of NF-κB in THP-1 cells. Acta Pharmacol Sin 2004; 25: 480–4.

8 Souabni A, Cobaleda C, Schebesta M, Busslinger M. Pax5 promotes B lymphopoiesis and blocks T cell development by repressing Notch1. Immunity 2002; 17: 781–93.

9 Bhakar AL, Tannis LL, Zeindler C, Russo MP, Jobin C, Park DS, *et al*. Constitutive nuclear factor-kappa B activity is required for central neuron survival. J Neurosci 2002; 22: 8466–75.

10 Yoshizawa K, Nambu H, Yang J, Oishi Y, Senzaki H, Shikata N, *et al*. Mechanisms of photoreceptor cell apoptosis induced by *N*-methyl-*N*-nitrosourea in Sprague-Dawley rats. Lab Invest 1999; 79: 1359–67.

11 Yang JN, Lin SC, Chen JM, Zhang Y, Hu SX. Photoreceptor cell apoptosis of rat's retina induced by *N*-methyl-*N*-nitrosourea. Chin J Ocul Fundus Dis 2004; 20: 33–6.

12 Zhao ZX, Guo XR, Li YS. Characteristics of retinitis pigmentosa in indocyanine green angiography. Chin J Ocul Fundus Dis 2001; 17: 26–9.

13 Li XY, Yang LZ, Kang FY, Zhang SS, Li GB, Huo YM, *et al*. The effect of ligustrazaine on the microcirculation of rabbit eyes with continuous elevated IOP. Chin J Microcirc 2001; 5: 119–20.

14 Feng GQ, Liu J, Fu RF, Feng GY, Weng SI. Protective effect of alprostadil combined with ligustrazine and *Astragalus membranaceus* on myocardial ischemia reperfusion injury in rats. Chin J New Drugs Clin Remedies 2001; 20: 3–6.

15 He JK, Gu ZL, Fan PS. Inhibitory effects of prostaglandin A1 on apoptosis of rat cardiac microvascular endothelial cells was mediated by NF-κB. Acta Pharmacol Sin 2002; 23: 331–5.

16 Karin M, Ben-Neriah Y. Phosphorylation meets ubiquitination: the control of NF-κB activity. Annu Rev Immunol 2000; 18: 621–63.

17 Zhang Z, Wei T, Hou J, Li G, Yu S, Xin W. Tetramethylpyrazine scavenges superoxide anion and decreases nitric oxide production in human polymorphonuclear leukocytes. Life Sci 2003; 72: 2465–72.

18 Lu YM, Wan FS, Tang SB. Effects of tetramethylpyrazine on expression of Bcl-2 and Fas proteins in myocardial injury induced by catecholamine in rats. Chin J Clin Pharmacol Ther 2004; 9: 197–200.

Acta Pharmacologica Sinica 2005 Jul; 26 (7): 893–896

Full-length article

Phase II metabolites of etofesalamide in filamentous fungi[1]

Hai-hua HUANG, Gui-lei MA, Yu-ming SUN[2], Qiang LI[2], Da-fang ZHONG[2,3]

Department of Pharmaceutical Microbiology; [2]Laboratory of Drug Metabolism and Pharmacokinetics, Shenyang Pharmaceutical University, Shenyang 110016, China

Key words

etofesalamide; *Cunninghamella;* metabolite; transformation; mass spectrum analysis

[1] Project supported by the National High Technology Research and Development Program of China (863 Program; No 2003AA2Z347C).
[3] Correspondence to Prof Da-fang ZHONG.
Phn 86-24-2390-2539.
Fax 86-24-2390-2539.
E-mail zhongdf@china.com

Received 2004-09-14
Accepted 2005-01-11

doi: 10.1111/j.1745-7254.2005.00091.x

Abstract

Aim: To study phase II metabolites of etofesalamide in filamentous fungi. **Methods:** Seven fungi were screened to transform etofesalamide. The metabolites of etofesalamide were assayed using liquid chromatography coupled to mass spectrometry. The major metabolite was subject to enzymatic hydrolysis to confirm its structure. **Results:** Etofesalamide was converted into two phase II metabolites: glucoside and riboside conjugates. Glucoside conjugate was the major product with a yield greater than 90%; no phase I metabolites were detected. **Conclusion:** Glucoside and riboside conjugations of etofesalamide in filamentous fungi differ from the phase II metabolism of glucuronidation in mammals.

Introduction

Etofesalamide [*N*-(4-ethoxyphenyl)-2-hydroxylbenzamide] is a new drug that has been developed by Shenyang Pharmaceutical University[1]. Etofesalamide is applied to acne, psoriasis, sensitization dermatitis, chronic eczema, and neurodermatitis in clinical use. The metabolism of etofesalamide in rabbits has been well studied[2, 3], and etofesalamide-2-glucuronide is the major metabolite.

Biotransformation of drugs by microbes has been examined extensively[4]. In recent years, a number of studies have shown that some fungi, particularly *Cunninghamella spp*, possess cytochrome P-450 monooxygenase systems analogous to those in mammals and phase II drug metabolism enzymes[5–7]. The present study uses etofesalamide as a substrate to explore the ability of fungi to convert etofesalamide into phase II metabolites, and compares these results with the results of etofesalamide metabolism in mammals to further investigate special characteristics of filamentous fungi in drug metabolism.

Materials and methods

Chemicals Etofesalamide was provided by the School of Pharmaceutical Engineering, Shenyang Pharmaceutical University (Shenyang, China) (purity >99%). β-*D*-glucosidase (EC 3.2.1.21) was purchased from Sigma (St Louis, MO, USA). All solvents used for assay were high performance liquid chromatography (HPLC) grade; the remaining chemicals were analytical grade or biochemical reagents.

Microorganisms *Aspergillus niger* and *Penicillium* were supplied by the Department of Microbiology, Shenyang Pharmaceutical University (Shenyang, China). *Mucor circinelloides* (AS 3.3421) was purchased from the Institute of Applied Ecology, Chinese Academy of Sciences (Shenyang, China). Other filamentous fungi, *Cunninghamella elegans* AS 3.156, *Cunninghamella elegans* AS 3.2028, *Cunninghamella echinulata* AS 3.2004, and *Cunninghamella blacksleana* AS 3.153, were purchased from the Institute of Microbiology, Chinese Academy of Sciences (Beijing, China).

Cultures Microbial cultures were maintained on potato dextrose agar slants at 4 °C and transferred every 6 months to maintain viability.

The broth consisted of glucose 20 g, peptone 5 g, yeast extract 5 g, K_2HPO_4 5 g, and NaCl 5 g. These ingredients were mixed in 1 000 mL of distilled water, and the pH was adjusted to 6.0 with HCl (6.0 mol/L). The broth was autoclaved in individual Erlenmeyer flasks at 115 °C for 30 min and cooled before incubation.

Microbial transformation Special strains kept at 4 °C were transferred to respective solid cultures and incubated at 28 °C for 7 d to obtain well-grown mycelium with spores. In first-stage fermentation, a loop of fresh spores was inoculated with a 250 mL Erlenmeyer flask containing 50 mL broth. The cultures were incubated at 28 °C for 24 h on a rotary shaker operating at 220 rpm to receive seed culture. A 1.0 mL portion from the first-stage flask was inoculated with a second-stage 100 mL flask containing 20 mL broth. After 24 h incubation, etofesalamide dissolved in acetone was added to yield a final concentration of 0.25 g/L and incubated for an additional 48 h. After microbial transformation, the flask contents were centrifuged at 1 500×g for 20 min, and the supernatant was transferred to tubes and kept at -20 °C until analysis.

Two types of controls were run synchronously with the fermentation and worked-up using the same method. One was a blank fungi control that was used to define and exclude the indigenous secondary metabolites generated by the fungi. The other was a blank substrate control (ie the culture with the etofesalamide but without the fungi) that was used to test whether etofesalamide would be chemically decomposed or spontaneously transformed under broth and microbial transformation conditions.

Enzymatic hydrolysis A 1.0 mL portion of each sample transformed by fungi was screened and incubated with β-*D*-glucosidase (100 kU/L) at 37 °C for 24 h after adjusting the pH to 5.0 using 50 mmol/L $NH_4H_2PO_4$ buffer (pH 3.0). Control experiments were carried out concurrently in the absence of α-*D*-glucosidase. Incubations were stopped by using solid-phase extraction (SPE) and analyzed using the liquid chromatography coupled to multistage mass spectrometry (LC/MS^n) method.

Extraction of metabolites and LC/MS^n assay After thawing, a 1.0 mL portion of each sample was applied to a Bond Elute C_{18} SPE column (Fuji Company, Tianjin, China) preconditioned with 2 mL methanol and 2 mL water. After loading the sample, the column was washed with 1 mL water and eluted with 2 mL methanol. The sample was evaporated to dryness at 35 °C under a gentle stream of nitrogen, and the residue was reconstituted with the addition of 100 μL of the mobile phase. A 20 μL aliquot of the solution was injected into the LC/MS^n system.

LC/MS^n analysis was carried out using a Finnigan LCQ ion trap mass spectrometer (San Jose, CA, USA) equipped with an electrospray ionization (ESI) source system, a Shimadzu LC-10AD pump (Kyoto, Japan) and a data system (Version 1.2, Finnigan). The interface was adjusted to the following conditions: ion mode, positive; spray voltage, 4.5 kV; capillary temperature, 200 °C; sheath gas (nitrogen), 0.75 L/min; auxiliary gas (nitrogen), 0.15 L/min. MS/MS spectra were obtained by collision-induced dissociation (CID) using helium (He) as the collision gas. The HPLC conditions were as follows: the column was a Diamonsil C_{18} column (particle size 5 μm, 4.6 mm × 200 mm ID, Dikma Company, Beijing, China). The mobile phase consisted of methanol-water (80:20, v/v) at a flow rate of 0.5 mL/min.

Results

Fungal metabolite profile of etofesalamide *C blacksleana* AS 3.153 supported significant metabolism and was chosen to illustrate the identification of metabolites. The microbial transformation and control samples were extracted and analyzed as described above. The chromatograms of the blank fungi controls showed no metabolites or etofesalamide and the blank substrate controls revealed only the presence of etofesalamide and no metabolites of etofesalamide. Authentic etofesalamide could generate a pseudomolecular ion $[M+H]^+$ at *m/z* 258. Compared with the standards, two $[M+H]^+$ ions correlated with the metabolism of etofesalamide were observed in the total ion current (TIC) of the sample transformed by *C blacksleana* AS 3.153, including ions at *m/z* 420 (M1) and *m/z* 390 (M2) (Figure 1). The LC/MS^n data of etofesalamide and its two metabolites are shown in Table 1.

Table 1. Multistage mass spectrometry characteristics of metabolites and etofesalamide.

Metabolite and substrate	$[M+H]^+$ (*m/z*)	MS^2 fragment (*m/z*)	MS^3 fragment (*m/z*)	t_R (min)
M1	420	258	121, 138	9.59
M2	390	258	121, 138	11.20
Etofesalamide	258	121, 138	–	20.25

t_R, retention time.

The pseudomolecular ion of M1 was at *m/z* 420, 162 higher than that of etofesalamide, which suggests that the corresponding metabolite might be a glucoside conjugate. The MS/MS spectrum of the ion at *m/z* 420 yielded a single ion at *m/z* 258 similar to the $[M + H]^+$ ion of etofesalamide. In addition, the MS^3 spectrum of the M1 ion at *m/z* 258 yielded the same fragment ions as the MS/MS spectrum of etofesalamide, indicating that M1 could be the glucoside conjugate of etofesalamide.

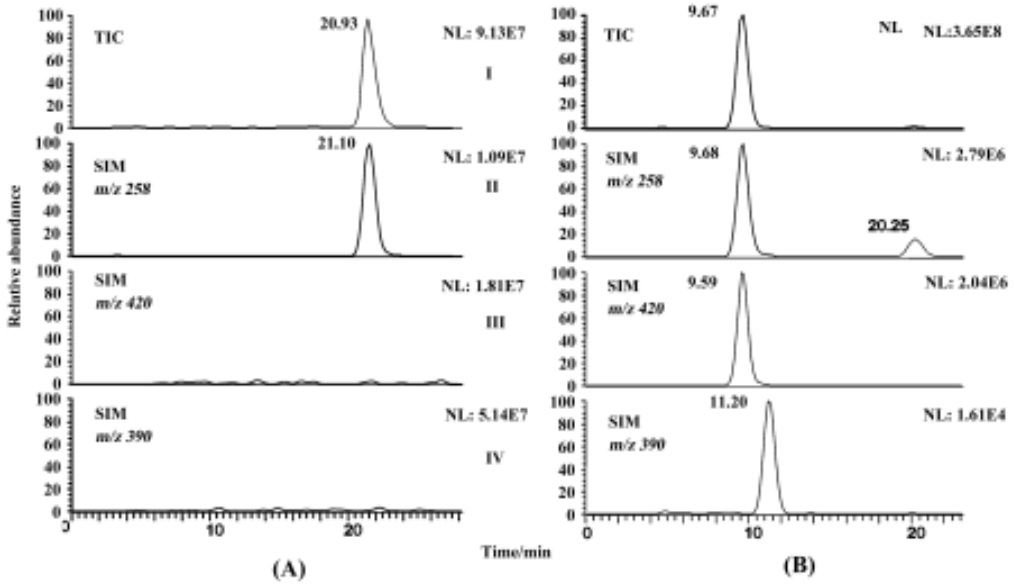

Figure 1. Chromatograms of total ion current (TIC, I) and selected ion monitoring (SIM, II, III, IV) scan modes in the LC/MS assay of authentic etofesalamide (A) and transformed etofesalamide (B).

According to the process described above, M2 could be a riboside conjugate of etofesalamide. Proposed metabolic pathways of etofesalamide in filamentous fungi are shown in Figure 2.

Enzymatic hydrolysis To further investigate the structure of M1, the sample of etofesalamide transformed by *C blacksleana* AS 3.153 was subjected to enzymatic hydrolysis. The results are expressed as the percentage of metabolite that was hydrolyzed with β-*D*-glucosidase compared to the control, which was hydrolyzed spontaneously. Treatment with β-*D*-glucosidase led to a greater than 50% reduction in M1. This result provides further evidence that M1 is the metabolite conjugated with glucoside because β-*D*-glucosidase is substrate selective.

Microbial transformation of etofesalamide by the screened fungi Table 2 shows the percentages of etofesalamide metabolized by different strains of fungi. In the seven fungi screened, *Aspergillus niger* and *Penicillium* had no ability to transform etofesalamide; four strains of *Cunninghamella spp* resulted in almost complete meta-bolism, particularly the *C blacksleana* AS 3.153 strain. *Mucor circinelloides* AS 3.3421 had a similar ability to *Cunninghamella spp* to transform etofesalamide. Etofesalamide was converted into two phase II metabolites by these fungi, glucoside and riboside conjugates, in which glucoside conjugate was the major product with the highest yield (94.5%). In addition, no phase I metabolites were detected, and *C blacksleana* AS 3.153 supported significant metabolism, which may be useful in the study of phase II metabolism of etofesalamide *in vitro*.

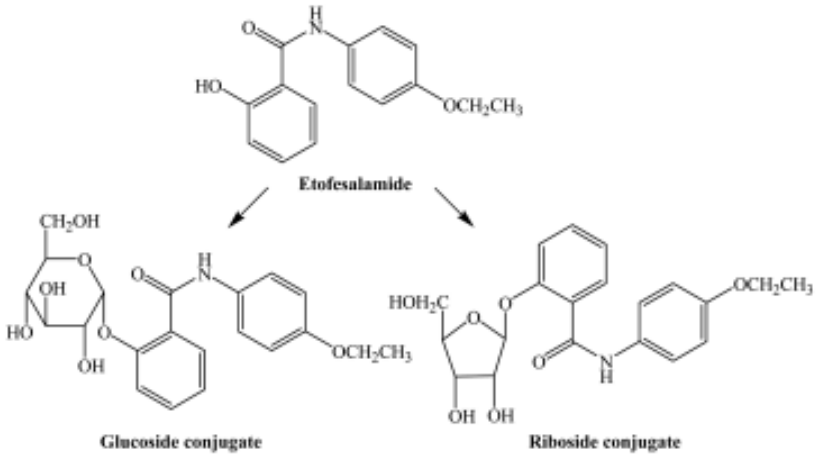

Figure 2. Proposed metabolic pathways of etofesalamide in filamentous fungi.

Discussion

In this study, seven filamentous fungi were screened for their abilities to metabolize etofesalamide. Four strains of *Cunninghamella* species showed a strong ability to convert etofesalamide into the phase II metabolites, glucoside and riboside

Table 2. Yields of transformation products and remaining etofesalamide by different fungal strains.

Strain	Total phase I metabolites* (%)	Glucoside* (%)	Riboside* (%)	Remaining etofesalamide (%)
C. blacksleana AS 3.153	0	94.5	1.5	4.0
C. echinulata AS 3.2004	0	90.8	2.1	7.1
C. elegans AS 3.2028	0	74.6	7.9	17.5
C. elegans AS 3.156	0	93.2	0	6.8
Mucor circinelloides AS 3.3421	0	38.8	9.2	52.0
Aspergillus niger	0	0	0	100
Penicillium	0	0	0	100

*The percentage of one metabolite compared to the total percentage of metabolites and remaining substrates. n=3.

conjugates. No phase I metabolites were observed. The high potential of certain fungal strains to produce phase II metabolites was illustrated by these results.

Our results show that a number of filamentous fungi transform etofesalamide by phase II reactions to excretable sugar conjugates. Glucoside and riboside conjugations differ from the phase II metabolism observed in mammals. In mammalian species, such as rabbits, glucuronide conjugation rather than glucoside conjugation is the major metabolic pathway for etofesalamide[2,3]. Conjugations with glucuronic acid are considered to be a dominant metabolic pathway in humans for detoxifying and eliminating lipophilic chemicals from the body[8]. In comparison with glucuronide conjugation, there is only limited information in the literature regarding the glucoside conjugation process in humans. At present, apart from N-linked glucoside drug metabolites, only two *O*-linked glucosides of mycophenolic acid and morphine have been identified in humans[9,10]. In addition, glucuronide conjugation, which is a characteristic conjugation in humans, is rarely found in microorganisms, and only two examples of glucuronide conjugation have been reported[11]. Compared with the phase II reactions in humans, glucoside conjugation is the major metabolic pathway in microorganisms, and it is used extensively to study the detoxification of cytotoxins and carcinogens[12-14]. Riboside conjugation is obviously another potential phase II reaction in biotransformation in filamentous fungi, but only one such conjugate has been reported recently[15].

References

1 Liu BL, Zhang XY, Wang SZ. Synthesis of etofesalamide. Acta Pharm Sin 1987; 22: 312–5.

2 Zhong DF, Chen XY, Chen RD, Luo X. The major metabolite of etofesalamide in rabbits. J Shenyang Pharm Univ 1996; 13: 240–4.

3 Chu DF, Gu JK, Zhong DF, Si DY, Zhou H. Isolation and identification of etofesalamide-2-glucuronide. Chem J Chin Univ 2002; 23: 376–8.

4 Srisilam K, Veeresham C. Biotransformation of drugs by microbial cultures for predicting mammalian drug metabolism. Biotechnol Adv 2003; 21: 3–39.

5 Zhang DL, Yang YF, Leakey JE, Cerniglia CE. Phase I and phase II enzymes produced by *Cunninghamella elegans* for the metabolism of xenobiotics. FEMS Microbiol Lett 1996; 138: 221–6.

6 Zhong DF, Sun L, Liu L, Huang HH. Microbial transformation of naproxen by *Cunninghamella* species. Acta Pharmacol Sin 2003; 24: 442–7.

7 Sun L, Huang HH, Liu L, Zhong DF. Transformation of verapamil by *Cunninghamella balkesleeama*. Appl Environ Microbiol 2004; 70: 2722–7.

8 Ritter JK. Roles of glucuronidation and UDP-glucuronosyl transferases in xenobiotic bioactivation reactions. Chem Biol Interact 2000; 129: 171–93.

9 Shipkova M, Strassburg CP, Braun F, Streit F, Grone HT, Armstrong VW. Glucuronide and glucoside conjugation of mycophenolic acid by human liver, kidney and intestinal microsomes. Br J Pharmacol 2001; 132: 1027–34.

10 Chen XY, Zhao LM, Zhong DF. A novel metabolic pathway of morphine: formation of morphine glucosides in cancer patients. Br J Clin Pharmacol 2003; 55: 570–8.

11 Azerad R. Microbial models for drug metabolism. Adv Biochem Eng Biotech 1999; 63: 169–218.

12 Kamimura H. Conversion of zearalenone to zearalenone glycoside by *Rhizopus sp*. Appl Environ Microbiol 1986; 52: 515–9.

13 Pothuluri JV, Evans FE, Heinze TM, Cerniglia CE. Formation of sulfate and glucoside conjugates of benzo[e]pyrene by *Cunninghamella elegans*. Appl Microbiol Biotechnol 1996; 45: 677–83.

14 Ye M, Qu G, Guo H, Guo D. Specific 12 beta-hydroxylation of cinobufagin by filamentous fungi. Appl Environ Microbiol 2004; 70: 3521–7.

15 Gesell M, Hammer E, Mikolasch A, Schauer F. Oxidation and ring cleavage of dibenzofuran by the filamentous fungus *Paecilomyces lilacinus*. Arch Microbiol 2004; 182: 51–9.

Acta Pharmacologica Sinica 2005 Aug; 26 (8): 897–907

Invited review

Molecular basis of ataxia telangiectasia and related diseases

Lindsay G BALL, Wei XIAO[1]

Department of Microbiology and Immunology, University of Saskatchewan, Saskatoon, SK Canada, S7N 5E5.

Key words

ataxia telangiectasia; DNA damage; DNA repair; cdc genes; phosphotransferases

[1] Correspondance to Dr Wei XIAO.
Phn 1-306-966-4308.
Fax 1-306-966-4311.
E-mail wei.xiao@usask.ca

Received 2005-04-08
Accepted 2005-05-05

doi: 10.1111/j.1745-7254.2005.00165.x

Abstract

Ataxia telangiectasia (AT) is a rare human disease characterized by extreme cellular sensitivity to radiation and a predisposition to cancer, with a hallmark of onset in early childhood. Several human diseases also share similar symptoms with AT albeit with different degrees of severity and different associated disorders. While all AT patients contain mutations in the AT-mutated gene (ATM), most other AT-like disorders are defective in genes encoding an MRN protein complex consisting of Mre11, Rad50 and Nbs1. Both ATM and MRN function as cellular sensors to DNA double-strand breaks, which lead to the recruitment and phosphorylation of an array of substrate proteins involved in DNA repair, apoptosis and cell-cycle checkpoints, as well as gene regulation, translation initiation and telomere maintenance. ATM is a member of the family of phosphatidylinositol 3-kinase-like protein kinases (PIKK), and the discovery of many ATM substrates provides the underlying mechanisms of heterologous symptoms among AT patients. This review article focuses on recent findings related to the initial recognition of double-strand breaks by ATM and MRN, as well as a DNA-dependent protein kinase complex consisting of the heterodimer Ku70/Ku80 and its catalytic subunit DNA-PKcs, another member of PIKK. This possible interaction suggests that a much greater complex is involved in sensing, transducing and co-ordinating cellular events in response to genome instability.

Ataxia telangiectasia clinical presentation

Ataxia telangiectasia (AT) is a rare human disease characterized by extreme sensitivity to radiation[1–5]. AT is a progressive neurodegenerative disorder causing a predisposition to cancer, with a hallmark of onset in early childhood[6–9]. AT is seen in approximately 1 in every 40 000 live births in the USA, although the frequency varies from country to country[10]. At birth, infants appear normal and begin walking at a normal age (approximately age 1 year); however, by age 2–3 ataxia (loss of muscle co-ordination) becomes visible and generally by age 10 patients are confined to a wheelchair[10]. Ataxia generally precedes telangiectasia, which is described as the chronic dilation of a group of capillaries causing elevated, dark red blotches on the skin or eyes[11]. This disease is additionally characterized by cerebellar degeneration, and immune system defects[12–14]. In younger children, diagnosis of AT is somewhat obscure as the cerebellum appears to be of normal size for several years although onset of ataxia is prevalent. However, by age 10 magnetic resonance imaging (MRI) generally shows an abnormal cerebellum that has decreased in volume[15]. Studies have shown a gradual decrease in granular and Purkinje cells, which are large branching cells of the nervous system and are located in the middle layer of the lower part of the brain, or the cerebellum[14–16]. Unfortunately, there is currently no treatment for AT except for supportive therapy of secondary symptoms[17].

In addition to an up to several hundredfold increase in developing certain types of cancers (eg lymphoma) in AT patients, epidemiological studies suggest that heterozygote AT mutation carriers are also at increased risk for cancer, particularly breast carcinoma[18,19]. This is of great significance as it is estimated that approximately 1% of the population are AT carriers. However, it is noted that a recent study showed that heterozygous AT mutations did not confer genetic predisposition to early onset of breast cancer[20].

Serum alphafetoprotein (AFP) levels are elevated in more than 95% of AT patients, which is therefore used to diagnose AT and to distinguish from AT variants[4,5,10,21]. When dealing with AFP it is important to note that AFP levels are normally higher at birth than those at age 2, thus diagnostics for AT using AFP cannot be conducted until after the age of 2. There are known malignancies associated with AFP[10,22]. For example, AFP is known to be elevated in case of spina bifida and anencephaly, and this elevation is the hallmark test for early detection of both conditions. Spina bifida is part of a group of birth defects called neural tube defects, which affect embryonic structures that eventually develop into the brain, spinal cord and tissues that enclose them. Anencephaly is a congenital condition in which portions of the brain fail to develop. Because AFP is such a diagnostic hallmark for AT, it is surprising that the mechanism of AFP upregulation in normal and AT cells has not been reported. Nevertheless, given the commonality of AFP elevation in all of the above 3 diseases, it is conceivable that the increased AFP level is responsible for the Purkinje cell degeneration in AT patients.

Ataxia telangiectasia-related diseases

There are several human deficiencies and diseases that are closely related to AT. For example, molecular cloning has now allowed for the distinction between AT and other autosomal recessive cerebellar ataxias (ARCA) such as Friedreich ataxia or A-T_{Fresno}, an old-fashioned term for an AT variant[23–25], oculomotor apraxias 1 (aprataxin deficiency), oculomotor apraxias 2 (senataxin deficiency), aicardi syndrome and AT-like disorder (ATLD)[26–29].

AT-like disorder is a very rare disorder with clinical features similar to those of AT, with the most prominent similarity being progressive cerebellar ataxia. However, ATLD patients that do not present with telangiectasia[30,31], have a later onset of neurological features, slower progression, and thus milder symptoms compared to AT patients[27].

Closely related to AT and ATLD is the Nijmegen breakage syndrome (NBS)[23–25]. NBS and ATLD have some overlapping features such as hypersensitivity to ionizing radiation and genome instability, and both are characterized by neurological deficits[32,33]. Thus, NBS was long considered as a clinical variant of AT. Clinical distinction has been made as NBS patients also present with a characteristic facial appearance and microcephaly as well as growth retardation[34]. Clearly the above AT-related human conditions suggest deficiency at common cellular function(s) and genetic pathway (s) with AT.

Laboratory findings in ataxia telangiectasia and ataxia telangiectasia-related patients

Laboratory findings in patients with AT show: immunodeficiencies emerging as decreased IgA, IgE and IgG2 levels[5,21,35–38], characteristic chromosomal aberrations and an increased rate of telomeric shortening[39], radiosensitivity[1–5], as well as sensitivity to other DNA damaging agents and non-DNA damaging agents[40]. Chromosome instability, cell-cycle checkpoint defects[3] and elevated serum levels of AFP[21,22] are prevalent in most AT patient cells. In addition, approximately one-third of AT patients develop cancer, which is usually lymphoid[10].

Both NBS and ATLD cells share a number of cellular phenotypes with AT cells, with the most prominent being the increased sensitivity to ionizing radiation, abnormal cell-cycle checkpoints, chromosome instability, immunodeficiency and accelerated shortening of telomeres[41,42]. In particular, all 3 disorders show an increased level of chromosome translocation in the peripheral blood between the loci of the immunoglobulin and T-cell receptor genes on chromosomes 7 and 14[43,44]. Hence, laboratory findings are most consistent with all 3 diseases belonging to a group of disorders referred to chromosome instability syndromes.

Molecular basis of ataxia telangiectasia and related diseases

AT is the result of mutations in the AT-mutated (*ATM*) gene, which was discovered in 1995[45,46]. AT patients suffer as a result of over 400 distinct *ATM* mutations, of which 85% are accounted for by null mutations in the *ATM* gene[21,47,48]. Thus, approximately 85% of AT sufferers have no detectable *ATM* protein[21,48]. There are a few reported genuine AT cases with normal ATM protein levels; however, in these cases the protein is defective in ATM enzyme activity[49,50]. The establishment of AT as a monogenetic disease assisted in efficient diagnosis and reevaluation of “AT variants”. The fact that some AT patients carry hypomorphic *ATM* mutations (ie mutations with partial functions) provides an underlying explanation for atypical AT patients with minimal signs of symptoms, such as very mild or late-onset of syndromes or a subset of disorders[51].

The ATM protein is a member of the phosphatidylinositol 3-kinase-like family of serine/threonine protein kinases (PIKK)[13,52]. It is thus grouped because all PIKK contain a conserved kinase domain initially reported in phosphatidylinositol 3-kinase. This family represents an atypical subclass of protein kinases responsible for phosphorylation of its substrates on serine or threonine followed by glutamine

(SQ or TQ)[53–55]. The mammalian PIKK known to be involved in the DNA damage response are: DNA-PKcs (the catalytic subunit of DNA-dependent protein kinase), ATM (ataxia telangiectasia gene product), ATR (ATM and Rad3-related), mTOR/FRAP (mammalian target of rapamycin/FKBP-rapamycin-associated protein) and ATX/SMG1[13].

The ATM protein is a fairly large (approximately 350 kDa) protein that can be divided into several structural and functional domains (Figure 1A). The first is an FAT domain, which is conserved among the PIKK family of proteins FRAP, ATR and TRRAP; the second is a phosphoinositide 3,4-kinase (PI3K) domain, which ATM has in common with DNA-PKcs; and the third is an FAT carboxy-terminal domain (FATC)[56]. In addition, the amino terminus of the ATM protein contains multiple HEAT (huntingtin, elongation factor 3, A subunit of protein phosphatase 2A and TOR1) repeats[57]. A recent solution structure analysis of the FATC domain[58] revealed an a-helix and a disulfide-bonded loop that undergoes conformational changes. Hence, the FATC domain may regulate protein activity and stability. The precise function of HEAT repeats is currently unknown, although it is speculated to be involved in the interaction with other proteins, as these repeats are anti-parallel α-helices linked by a flexible loop[40,57]. The overall shape of ATM is very similar to DNA-PKcs and is comprised of a head and a long arm that is thought to wrap around double-stranded DNA after a conformational change[59–63]. One of the hallmarks of the ATM protein is its rapid increase in kinase activity immediately following exposure to ionizing radiation (IR), or in the presence of double-strand breaks (DSB)[64,65].

The gene mutated in NBS was identified as *NBS1*[25,66,67] whereas ATLD is caused by mutations in the *MRE11* gene[29]. Unlike AT, which can result from complete inactivation of the coding gene, all NBS and ATLD patients carry hypomorphic mutations that express some level of corresponding protein, either truncated or full length with amino acid substitutions[27,68]. Indeed, attempts to create null *Mre11* mutations in mouse embryonic stem cells has failed and conditional knockout experiments demonstrated that this gene is required for normal cell proliferation[69], suggesting that *MRE11* is an essential gene in mammals. Similarly, complete *Nbs1* knockout mice are embryonic lethal[70,71]. This assertion is further confirmed by a report that disruption of mouse *Rad50*, encoding the third component of the MRN (MRX in yeast) complex consisting of Mre11, Rad50, and Nbs1 (aka nibrin and p95; Xrs2 in yeast), also causes embryonic stem

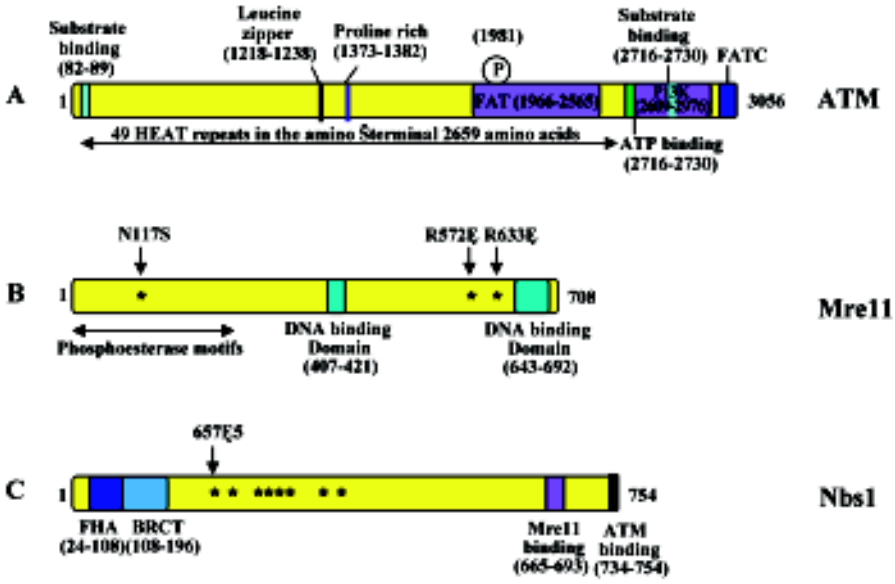

Figure 1. Schematic representation of the ATM, Mre11 and Nbs1 proteins. (A) ATM and its functional domains. Most domains have been discussed in the text. The letter "P" indicates the phosphorylation site required for its activation. (B) Mre11 and its functional domains. The asterisks represent the known mutations that cause ataxia telangiectasia-like disorder (ATLD). Note that only two families of ATLD with *MRE11* mutations were reported. One is homozygous for the mutation C1897T, resulting in R633Δ (stop codon), whereas the second family is heterozygous for A350G (N117S) and C1714T (R572Δ). (C) Nbs1 and its functional domains. The asterisks indicate the known *NBS1* mutations that cause Nijmegan breakage syndrome (NBS), among which the homozygous 657Δ5 mutation accounts for over 90% of NBS patients. 657Δ5 contains a 5-bp deletion, resulting in a truncated 26 kDa protein with only forkhead-associated (FHA) and BRCA1 C-terminus (BRCT) domains. Other *NBS1* mutations cause various degrees of symptoms.

cell lethality[72].

The human *MRE11* gene was initially isolated by its possible protein interaction with DNA ligase I[73] and was predicted to encode a 708-amino acid protein. However, subsequent reports appear to favor an Mre11B sequence (Figure 1B), which is different from Mre11 primarily at the C-terminal region and significantly strengthens its similarity with Mre11 from other species[74]. Mre11 contains a phosphoesterase motif at the N-terminal region that is highly conserved among all eukaryotic Mre11 and a similar motif is also found in *Escherichia coli* SbcD[75]. It also contains DNA-binding domains at the C-terminal region and region(s) for homodimerization[76,77]. Structural analyses[78–80] indicate that the MRN complex consists of two molecules of Mre11 and Rad50 (an E *coli* SbcC homolog) forming a rope-and-hook structure capable of bridging two DSB ends. *In vitro* characterization of the Rad50–Mre11 complex[76,81–84] demonstrates that it possesses 3´ to 5´ exonuclease and single-strand endonuclease activities, as well as ATP-dependent DNA binding and limited unwinding activity.

The phenotypic similarity between NBS and ATLD patients is attributed to the fact that both corresponding proteins are components of the MRN complex. Mre11 interacts with both Rad50 and Nbs1/Xrs2, and its homodimerization or self-interaction appears to be important for the Mre11–Rad50 and Mre11–Nbs1/Xrs2 interactions[76,77]. Interestingly, deficiency of the Mre11 protein results in decreased cellular levels of Nbs1 and Rad50, suggesting that the MRN complex is required for protein stability. The primary cellular function of MRN is a sensor for DNA strand breaks and to activate signaling pathways leading to cell-cycle checkpoint and recombination repair[32,85,86]. While Mre11 and Rad50 are highly conserved in eukaryotes, from unicellular yeasts to human cells[87,88], the third component, Nbs1, is less conserved structurally among eukaryotes, although the mammalian Nbs1 and yeast Xrs2 play similar roles within their respective MRN/MRX complex. Nbs1 has been suggested to be a regulatory subunit of MRN that is essential for Mre11 phosphorylation upon DNA damage[89] and its biochemical activities, such as ATP-dependent DNA unwinding and nuclease activity[90]. Although Nbs1 or Xrs2 is not required for the Mre11–Rad50 enzymatic activity *in vitro*, its activity appears to be absolutely required for MRX activity *in vivo*, as inactivation of any 1 of the 3 genes in yeast cells leads to complete loss of the MRX activity and indistinguishable cellular phenotypes[91–93]. This essential function of Nbs1/Xrs2 is probably due to its role in recruiting ATM/Tel1[94]. The Nbs1 protein has 4 known functional regions: the N-terminal forkhead-associated (FHA) domain followed by a BRCA1 C-terminus (BRCT) domain, a C-terminal Mre11-binding domain and an ATM-binding domain at the extreme C-terminus (Figure 1C). Interestingly, over 90% of all NBS patients analyzed to date contain a homozygous 5 bp truncating mutation, 657Δ5[25], resulting in the production of a 26-kDa protein with FHA and BRCT domains but lacking the Mre11-binding domain (Figure 1C). Knockout mice producing similar truncated Nbs1 proteins are viable and develop symptoms characteristic of the human disease[95,96], thus providing an animal model suitable for NBS research.

Phenotypic manifestation of genetic defects in ataxia telangiectasia and related diseases

One of the hallmarks of the ATM protein is its rapid increase in kinase activity immediately following DSB formation[64,65], and its kinase activity remains its only known function to date. The phenotypic manifestation of AT is due to the broad range of substrates for the ATM kinase, as compiled recently[40], involving DNA repair, apoptosis, G_1/S, intra-S checkpoint and G_2/M checkpoints, gene regulation, translation initiation, and telomere maintenance. Protein phosphorylation and de-phosphorylation is an important cellular regulatory mechanism that governs protein activity, stability, subcellular location and complex formation. We propose that although the primary ATM kinase substrates appear to be related to cellular response to DNA damage, novel ATM substrates and subsequent effects may explain all observed syndromes of AT patients, including elevated AFP level. We also propose that the multiple HEAT repeats in ATM may serve as a platform to interact with various regulatory and substrate proteins and to control its kinase activity in the aftermath of DNA damage. For example, the increased risk for breast cancer in AT patients has been implicated by the involvement of ATM in the interaction and phosphorylation of BRCA1 and its associated proteins following DNA damage[97,98].

The ATM protein also has the ability to interact with the ends of double-stranded DNA[99]. A recent model suggests that ATM is in an inactive dimeric or polymeric configuration, in which the kinase domain of each molecule is blocked by the FAT domain of the other[100]. Following DNA damage, each ATM molecule phosphorylates the other on a serine residue at position 1981 within the FAT domain and thus converts into fully active monomers. It was shown that protein serine-threonine phosphatase 5 (PP5) is required for the activation of ATM and its subsequent kinase activity[101].

The symptom similarity among AT, ATLD and NBS is apparently due to physical and genetic interactions between

ATM and MRN. Experimental results suggest that the ATM-MRN interaction in response to IR is complicated. First, the histone H2A isoform H2AX is rapidly phosphorylated (within 5 min) after irradiation in an ATM-dependent manner[102,103], and the phosphorylated gH2AX interacts with MRN via the FHA/BRCT region of Nbs1[103]. This interaction has been deemed indispensable for the recruitment of MRN[41]. Second, in response to IR, ATM phosphorylates Nbs1 *in vivo*[104], which is required for the subsequent phosphorylation of Mre11. Finally, phosphorylation and activation of the S-phase checkpoint effector Smc1 by ATM requires phosphorylated Nbs1[105,106]. The above observations suggest that ATM acts upstream of MRN and is required to recruit MRN to the damage sites observed as distinct nuclear foci. On the other hand, MRN/MRX is known to bind DSB ends and a careful choreographic analysis in yeast[107] indicates that MRX localization to nuclear DSB foci precedes and is required for that of Tel1, a yeast ATM ortholog[108,109]. In mammalian cells, Mre11 appears to be required for ATM activation as well[110], and this interaction was further reinforced very recently by an *in vitro* experiment showing that the MRN complex acts as a DSB sensor for ATM and recruits ATM to broken DNA molecules[111]. Interestingly, the unwinding of DNA ends by MRN appears to be essential for ATM stimulation[111], indicating that the MRN enzymatic activity plays a role in this process. In addition, a recent study[112] shows that NFBD/MDC1, which interacts with MRN, is required for ATM activation under certain conditions. Alternatively, NFBD1/MDC1 may help to recruit substrates, including Nbs1[113,114], to ATM[113–123]; suppression of NFBD1/MDC1 leads to decreased ATM activation and decreased phosphorylation of ATM substrates[112]. These observations support an assertion that MRN plays a crucial role in ATM phosphorylation of other substrates in response to DSB. The argument that MRN functions upstream of ATM is further strengthened by a very recent report that the extreme C-terminal 21 amino acid peptide of Nbs1 is required and sufficient for the interaction with ATM *in vivo* and *in vitro*, and that this interaction mediates ATM deposition to the sites of DNA damage and its checkpoint functions[94]. The above genetic and physical interactions between MRN and ATM underlie the molecular basis for the shared cellular functions in cell-cycle checkpoints and recombination repair of DSB, as well as common syndromes among AT, ATLD and NBS.

DNA-PK: a missing link?

Despite the great advances made in the past decade regarding AT research, many questions remain to be answered. One question that remains unsolved is the involvement of Ku70/Ku80 in ATM-mediated cellular events in response to DSB. Ku70 and Ku80 form a heterodimer as DNA end-binding subunits of DNA-PK[59–62]. It would be plausible to suggest that Ku70/Ku80 may also assist ATM's translocation to DSB, as Ku70/Ku80 is known to play such a role for DNA-PKcs, another member of PIKK with overall structural similarity to ATM[124]. Like ATM, DNA-PKcs recognizes the same consensus phosphorylation sequence SQ/TQ, and also undergoes DSB-induced autophosphorylation, which is required for DSB repair[125]. In addition, inactivation of either DNA-PK or ATM results in immunodeficiency; the former results in defective V(D)J recombination that leads to *scid* (severe combined immune deficiency) mutations[126,127], whereas the latter results in the disruption of immune gene rearrangement[128]. We propose that in the presence of Ku70/Ku80, DNA-PKcs and ATM may undergo conformational changes to be suitable for the suggested role of further wrapping around DNA[59–63]. Indeed, recent electron microscopy-based structural analyses of both DNA-PKcs[129–131] and ATM[63] suggest a similar architecture consisting of a "head" and a "palm" domain connected by an "arm". The palm domain binds DNA, which induces conformational changes and triggers an interaction between initially distant palm and head regions[130]. These DNA-induced conformational changes alter the catalytic core and regulate the kinase activity[131]. The difference between DNA-PKcs and ATM is that DNA-PKcs is activated in G_1 and is required for non-homologous end joining (NHEJ) and apoptosis if DNA damage is excessive[132], while ATM is activated in S and G_2 phases and is required for S-phase checkpoint and homologous recombination (HR)[40].

Another connection between ATM and Ku70/Ku80 is that yeast MRX is not only required for DSB signaling and HR, but also works with Ku70/Ku80 for NHEJ[133–136] and telomere maintenance[77,93,137,138]. The budding yeast *Saccaromyces cerevisiae* predominantly employs HR to repair DSB over NHEJ. On some occasions when DSB repair can be processed by either process, NHEJ was shown to precede HR[139]. A compiled model can be proposed in which the telomere acts as a repository for Ku proteins, which relocalize to DSB after DNA damage[140] and recruit MRX[141]. MRX can assist to recruit and activate Lif1 and Dnl4[142], resulting in ligation of the broken ends. However, in budding yeast, the MRX complex most likely initiates 5′ to 3′ end resection[76], hence committing to repair by HR. This commitment is probably due to the broken DSB ends that are unsuitable for direct ligation, or to the recruitment of Tel1 by MRX that

activates cell-cycle checkpoints and subsequent recruitment of other HR proteins[107]. A similar regulatory cascade may also exist in higher eukaryotes; however, because mammalian cells have an extended G_1 phase, the initial DSB binding by Ku70/Ku80 may stimulate NHEJ more frequently than in yeast. In addition, mammalian cells contain 3 major PIKK family proteins, namely ATM, ATR and DNA-PKcs, involved in different modes of DNA repair and overlapping signal transduction in response to DNA damage. The mechanism of their recruitment to sites of DNA damage is conserved via a newly discovered motif[94]. For example, ATR is recruited to a single-stranded DNA by ATRIP (ATR-interacting protein)[143,144], whereas DNA-PKcs and ATM are recruited to DSB by Ku70/K80 and MRN, respectively. Based on the above observations, we have proposed a working model of cellular response to DSB in mammals, as presented in Figure 2.

Finally, the physical and functional interactions among Ku, MRN/MRX and ATM/Tel1 can also be found in telomeres. Both yeast[145] and human[146] Ku is bound to telomeric DNA and protects its 3´ overhang. The MRX complex in budding yeast is also associated with telomeres, and mutants deficient in Ku or MRX activity exhibit telomere shortening[137,147]. Similar phenotypes are also observed in their homologous mutants in fission yeast and plants[148–150]. Tel1 works together with MRX by either regulating the access of telomerase to the DNA end[151], and/or preventing telomere end-to-end fusion[152]. Tel1 is activated by the MRX complex and in turn phosphorylates MRX[153], suggesting functional conservation between yeast and mammals. However, unlike Tel1, ATM has not been implicated in telomerase access to the telomere. Nevertheless, AT patient cells were shown to have shortened telomeres[39,154], as well as other telomere abnormalities[155,156]. Furthermore, transgenic mice defective in both ATM and telomerase dramatically increase telomere dysfunction compared to single mutants[157], suggesting roles of ATM in telomere maintenance. The telomeric functions of ATM may be related to some symptoms of AT patients.

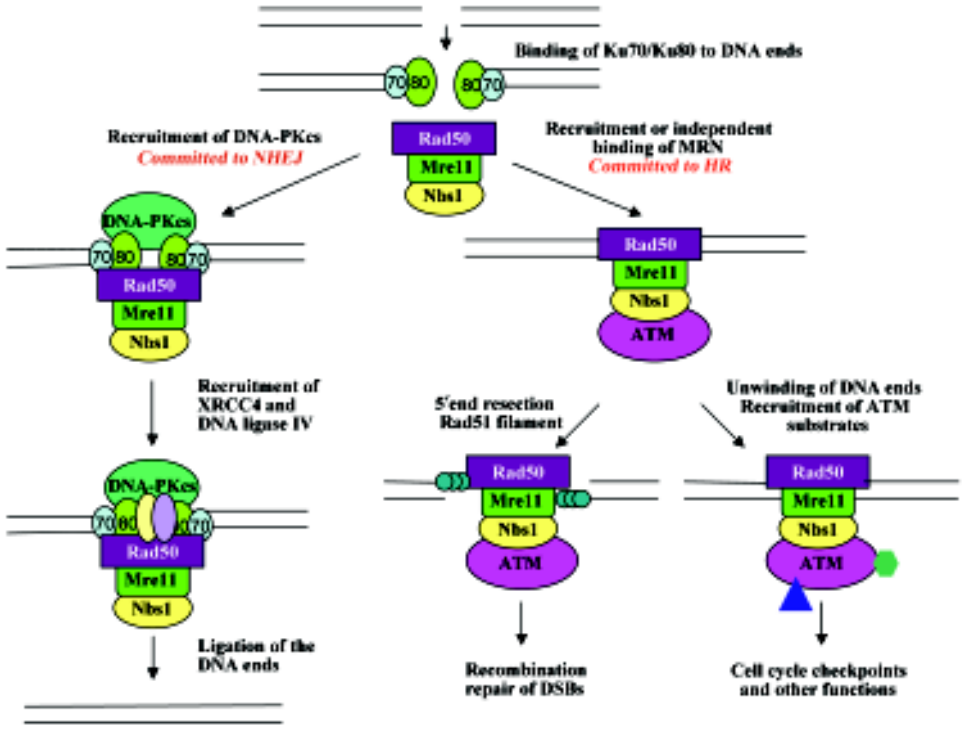

Figure 2. A proposed model for cellular response to DNA double-stranded breaks (DSB) in mammalian cells. The Ku70/Ku80 heterodimer binds to the broken DNA ends first, followed by the recruitment or the independent binding of the MRN complex (consisting of Mre11, Rad50 and Nbs1). If DNA-PKcs is recruited by interacting with the C-terminus of Ku80, cells are committed to non-homologous end joining. On the other hand, if ATM is recruited by interacting with the C-terminus of Nbs1, Ku70/Ku80 may be released and cells are probably committed to homologous recombination repair. Recruitment of ATM also leads to substrate phosphorylation and cell-cycle checkpoints. It should be noted that MRN may also bind to DNA ends without the assistance of Ku70/Ku80. Recent literature suggests that unwinding of DNA ends by MRN activates ATM and cell-cycle checkpoints, whereas DNA end resection by MRN initiates homologous recombination. The 2 processes may be co-regulated.

Conclusions

Since the initial discovery of the AT mutated gene 10 years ago, knowledge regarding the molecular mechanisms of AT and its related diseases has accumulated rapidly. It is now clear that the primary function of ATM and MRN, which is related to NBS and ATLD, is to respond to DNA damage, especially DSB. Two primary activities are cell-cycle checkpoint and DNA repair through HR, and these are achieved mainly via protein phosphorylation of various substrates, including ATM and MRN themselves. ATM and MRN are also involved in telomere maintenance and protection from chromosomal translocation, as well as efficient immune gene recombination. Although these cellular phenotypes are able to explain most phenotypes observed in AT and AT-related disease, some other associated symptoms may be due to diverse ATM substrates, unique MRN functions not shared by ATM, as well as the hypomorphic nature of the disease. Despite great advances in research, many questions remain to be answered especially with regard to treatment. Future efforts shall be directed to translational research for the cure and prevention of AT its and related diseases.

Acknowledgements

The authors wish to thank Michelle HANNA for proofreading the manuscript and other laboratory members for their helpful discussion. This work is supported by a Canadian Institutes of Health Research operating grant (MOP-53240) to WX.

References

1 Gotoff SP, Amirmokri E, Liebner EJ. Ataxia telangiectasia. Neoplasia, untoward response to x-irradiation, and tuberous sclerosis. Am J Dis Child 1967; 114: 617–25.
2 Taylor AM, Harnden DG, Arlett CF, Harcourt SA, Lehmann AR, Stevens S, *et al*. Ataxia telangiectasia: a human mutation with abnormal radiation sensitivity. Nature 1975; 258: 427–29.
3 Young BR, Painter RB. Radioresistant DNA synthesis and human genetic diseases. Hum Genet 1989; 82: 113–7.
4 Huo YK, Wang Z, Hong JH, Chessa L, McBride WH, Perlman SL, *et al*. Radiosensitivity of ataxia-telangiectasia, X-linked agammaglobulinemia, and related syndromes using a modified colony survival assay. Cancer Res 1994; 54: 2544–7.
5 Sun X, Becker-Catania SG, Chun HH, Hwang MJ, Huo Y, Wang Z, *et al*. Early diagnosis of ataxia-telangiectasia using radiosensitivity testing. J Pediatr 2002; 140: 724–31.
6 Boder E, Sedgwick RP. Ataxia-telangiectasia: a familial syndrome of progressive cerebellar ataxia, oculocutaneous telangiectasia and frequent pulmonary infection. Pediatrics 1958; 21: 526–54.
7 Boder E. Ataxia-telangiectasia: an overview. Kroc Found Ser 1985; 19: 1–63.
8 Gatti RA, Boder E, Vinters HV, Sparkes RS, Norman A, Lange K. Ataxia-telangiectasia: an interdisciplinary approach to pathogenesis. Medicine (Baltimore) 1991; 70: 99–117.
9 Gatti RA. Ataxia-telangiectasia. In: Vogelstein B, Kinzler KW, editors. The Genetic Basis of Human Cancer. New York: Mc Graw-Hill; 2002. p 239–65.
10 Chun HH, Gatti RA. Ataxia-telangiectasia, an evolving phenotype. DNA Repair (Amst) 2004; 3: 1187–96.
11 Cabana MD, Crawford TO, Winkelstein JA, Christensen JR, Lederman HM. Consequences of the delayed diagnosis of ataxia-telangiectasia. Pediatrics 1998; 102: 98–100.
12 Shiloh Y. ATM: ready, set, go. Cell Cycle 2003; 2: 116–7.
13 Shiloh Y. ATM and related protein kinases: safeguarding genome integrity. Nat Rev Cancer 2003; 3: 155–68.
14 Lavin MF, Shiloh Y. The genetic defect in ataxia-telangiectasia. Annu Rev Immunol 1997; 15: 177–202.
15 Tavani F, Zimmerman RA, Berry GT, Sullivan K, Gatti R, Bingham P. Ataxia-telangiectasia: the pattern of cerebellar atrophy on MRI. Neuroradiology 2003; 45: 315–9.
16 Nowak R. Discovery of AT gene sparks biomedical research bonanza. Science 1995; 268: 1700–1.
17 Perlman S, Becker-Catania S, Gatti RA. Ataxia-telangiectasia: diagnosis and treatment. Semin Pediatr Neurol 2003; 10: 173–82.
18 Swift M, Morrell D, Massey RB, Chase CL. Incidence of cancer in 161 families affected by ataxia-telangiectasia. N Engl J Med 1991; 325: 1831–6.
19 Swift M, Reitnauer PJ, Morrell D, Chase CL. Breast and other cancers in families with ataxia-telangiectasia. N Engl J Med 1987; 316: 1289–94.
20 FitzGerald MG, Bean JM, Hegde SR, Unsal H, MacDonald DJ, Harkin DP, *et al*. Heterozygous ATM mutations do not contribute to early onset of breast cancer. Nat Genet 1997; 15: 307–10.
21 Chun HH, Sun X, Nahas SA, Teraoka S, Lai CH, Concannon P, *et al*. Improved diagnostic testing for ataxia-telangiectasia by immunoblotting of nuclear lysates for ATM protein expression. Mol Genet Metab 2003; 80: 437–43.
22 McVey JH, Michaelides K, Hansen LP, Ferguson-Smith M, Tilghman S, Krumlauf R, *et al*. A G⟶A substitution in an HNF I binding site in the human alpha-fetoprotein gene is associated with hereditary persistence of alpha-fetoprotein (HPAFP). Hum Mol Genet 1993; 2: 379–84.
23 Weemaes CM, Hustinx TW, Scheres JM, van Munster PJ, Bakkeren JA, Taalman RD. A new chromosomal instability disorder: the Nijmegen breakage syndrome. Acta Paediatr Scand 1981; 70: 557–64.
24 Heil JA, Weemaes CM, van den Heuvel LP, van Engelen BG, Gabreels FJ, Smeets DF, *et al*. International Nijmegen Breakage Syndrome Study Group: Nijmegen breakage syndrome. Arch Dis Child 2000; 82: 400-406.
25 Varon R, Vissinga C, Platzer M, Cerosaletti KM, Chrzanowska KH, Saar K, *et al*. Nibrin, a novel DNA double-strand break repair protein, is mutated in Nijmegen breakage syndrome. Cell 1998; 93: 467–76.
26 Moreira MC, Klur S, Watanabe M, Nemeth AH, Le Ber I, Moniz JC, *et al*. Senataxin, the ortholog of a yeast RNA helicase, is mutant in ataxia-ocular apraxia 2. Nat Genet 2004; 36: 225–7.
27 Taylor AM, Groom A, Byrd PJ. Ataxia-telangiectasia-like disorder (ATLD) – its clinical presentation and molecular basis. DNA

Repair (Amst) 2004; 3: 1219–25.
28 Date H, Onodera O, Tanaka H, Iwabuchi K, Uekawa K, Igarashi S, *et al*. Early-onset ataxia with ocular motor apraxia and hypoalbuminemia is caused by mutations in a new HIT superfamily gene. Nat Genet 2001; 29: 184–8.
29 Stewart GS, Maser RS, Stankovic T, Bressan DA, Kaplan MI, Jaspers NG, *et al.* The DNA double-strand break repair gene hMRE11 is mutated in individuals with an ataxia-telangiectasia-like disorder. Cell 1999; 99: 577–87.
30 Klein C, Wenning GK, Quinn NP, Marsden CD. Ataxia without telangiectasia masquerading as benign hereditary chorea. Mov Disord 1996; 11: 217–20.
31 Hernandez D, McConville CM, Stacey M, Woods CG, Brown MM, Shutt P, *et al*. A family showing no evidence of linkage between the ataxia telangiectasia gene and chromosome 11q22-23. J Med Genet 1993; 30: 135–40.
32 D'Amours D, Jackson SP. The Mre11 complex: at the crossroads of DNA repair and checkpoint signalling. Nat Rev Mol Cell Biol 2002; 3: 317–27.
33 Petrini JH. The Mre11 complex and ATM: collaborating to navigate S phase. Curr Opin Cell Biol 2000; 12: 293–6.
34 Tauchi H, Kobayashi J, Morishima K, van Gent DC, Shiraishi T, Verkaik NS, *et al*. Nbs1 is essential for DNA repair by homologous recombination in higher vertebrate cells. Nature 2002; 420: 93–8.
35 Sanal O, Ersoy F, Yel L, Tezcan I, Metin A, Ozyurek H, *et al*. Impaired IgG antibody production to pneumococcal polysaccharides in patients with ataxia-telangiectasia. J Clin Immunol 1999; 19: 326–34.
36 Gatti RA. The inherited basis of human radiosensitivity. Acta Oncol 2001; 40: 702–11.
37 Riballo E, Critchlow SE, Teo SH, Doherty AJ, Priestley A, Broughton B, *et al.* Identification of a defect in DNA ligase IV in a radiosensitive leukaemia patient. Curr Biol 1999; 9: 699–702.
38 Bakhshi S, Cerosaletti KM, Concannon P, Bawle EV, Fontanesi J, Gatti RA, *et al*. Medulloblastoma with adverse reaction to radiation therapy in Nijmegen breakage syndrome. J Pediatr Hematol Oncol 2003; 25: 248–51.
39 Metcalfe JA, Parkhill J, Campbell L, Stacey M, Biggs P, Byrd PJ, *et al*. Accelerated telomere shortening in ataxia telangiectasia. Nat Genet 1996; 13: 350–3.
40 Kurz EU, Lees-Miller SP. DNA damage-induced activation of ATM and ATM-dependent signaling pathways. DNA Repair (Amst) 2004; 3: 889–900.
41 Kobayashi J, Antoccia A, Tauchi H, Matsuura S, Komatsu K. NBS1 and its functional role in the DNA damage response. DNA Repair (Amst) 2004; 3: 855–61.
42 Tauchi H, Matsuura S, Kobayashi J, Sakamoto S, Komatsu K. Nijmegen breakage syndrome gene, *NBS1*, and molecular links to factors for genome stability. Oncogene 2002; 21: 8967–80.
43 Chrzanowska KH, Kleijer WJ, Krajewska-Walasek M, Bialecka M, Gutkowska A, Goryluk-Kozakiewicz B, *et al*. Eleven Polish patients with microcephaly, immunodeficiency, and chromosomal instability: the Nijmegen breakage syndrome. Am J Med Genet 1995; 57: 462–71.
44 van der Burgt I, Chrzanowska KH, Smeets D, Weemaes C. Nijmegen breakage syndrome. J Med Genet 1996; 33: 153–6.
45 Savitsky K, Bar-Shira A, Gilad S, Rotman G, Ziv Y, Vanagaite L, *et al*. A single ataxia telangiectasia gene with a product similar to PI-3 kinase. Science 1995; 268: 1749–53.
46 Savitsky K, Sfez S, Tagle DA, Ziv Y, Sartiel A, Collins FS, *et al.* The complete sequence of the coding region of the ATM gene reveals similarity to cell cycle regulators in different species. Hum Mol Genet 1995; 4: 2025–32.
47 Gilad S, Chessa L, Khosravi R, Russell P, Galanty Y, Piane M, *et al*. Genotype–phenotype relationships in ataxia-telangiectasia and variants. Am J Hum Genet 1998; 62: 551–61.
48 Becker-Catania SG, Chen G, Hwang MJ, Wang Z, Sun X, Sanal O, *et al*. Ataxia-telangiectasia: phenotype/genotype studies of ATM protein expression, mutations, and radiosensitivity. Mol Genet Metab 2000; 70: 122–33.
49 Stankovic T, Kidd AM, Sutcliffe A, McGuire GM, Robinson P, Weber P, *et al*. ATM mutations and phenotypes in ataxia-telangiectasia families in the British Isles: expression of mutant ATM and the risk of leukemia, lymphoma, and breast cancer. Am J Hum Genet 1998; 62: 334–45.
50 Stewart GS, Last JI, Stankovic T, Haites N, Kidd AM, Byrd PJ, *et al.* Residual ataxia telangiectasia mutated protein function in cells from ataxia telangiectasia patients, with 5762ins137 and 7271T–>G mutations, showing a less severe phenotype. J Biol Chem 2001; 276: 30 133–41.
51 Lavin MF, Scott S, Gueven N, Kozlov S, Peng C, Chen P. Functional consequences of sequence alterations in the ATM gene. DNA Repair (Amst) 2004; 3: 1197–205.
52 Goodarzi AA, Block WD, Lees-Miller SP. The role of ATM and ATR in DNA damage-induced cell cycle control. Prog Cell Cycle Res 2003; 5: 393–411.
53 Manning G, Whyte DB, Martinez R, Hunter T, Sudarsanam S. The protein kinase complement of the human genome. Science 2002; 298: 1912–34.
54 Kim ST, Lim DS, Canman CE, Kastan MB. Substrate specificities and identification of putative substrates of ATM kinase family members. J Biol Chem 1999; 274: 37 538–43.
55 O'Neill T, Dwyer AJ, Ziv Y, Chan DW, Lees-Miller SP, Abraham RH, *et al*. Utilization of oriented peptide libraries to identify substrate motifs selected by ATM. J Biol Chem 2000; 275: 22 719–27.
56 Bosotti R, Isacchi A, Sonnhammer EL. FAT: a novel domain in PIK-related kinases. Trends Biochem Sci 2000; 25: 225–7.
57 Perry J, Kleckner N. The ATRs, ATMs, and TORs are giant HEAT repeat proteins. Cell 2003; 112: 151–5.
58 Dames SA, Mulet JM, Rathgeb-Szabo K, Hall MN, Grzesiek S. The solution structure of the FATC domain of the protein kinase TOR suggests a role for redox-dependent structural and cellular stability. J Biol Chem 2005; 280: 20558–64
59 Cary RB, Peterson SR, Wang J, Bear DG, Bradbury EM, Chen DJ. DNA looping by Ku and the DNA-dependent protein kinase. Proc Natl Acad Sci USA 1997; 94: 4267–72.
60 Smith GC, Jackson SP. The DNA-dependent protein kinase. Genes Dev 1999; 13: 916–34.
61 Merkle D, Douglas P, Moorhead GB, Leonenko Z, Yu Y, Cramb D, *et al.* The DNA-dependent protein kinase interacts with DNA to form a protein-DNA complex that is disrupted by phosphorylation. Biochemistry 2002; 41: 12 706–14.
62 Yaneva M, Kowalewski T, Lieber MR. Interaction of DNA-dependent protein kinase with DNA and with Ku: biochemical

and atomic-force microscopy studies. EMBO J 1997; 16: 5098–112.
63 Llorca O, Rivera-Calzada A, Grantham J, Willison KR. Electron microscopy and 3D reconstructions reveal that human ATM kinase uses an ATM-like domain to clamp around double-stranded DNA. Oncogene 2003; 22: 3867–74.
64 Canman CE, Lim DS, Cimprich KA, Taya Y, Tamai K, Sakaguchi K, *et al*. Activation of the ATM kinase by ionizing radiation and phosphorylation of p53. Science 1998; 281: 1677–9.
65 Banin S, Moyal L, Shieh S, Taya Y, Anderson CW, Chessa L, *et al*. Enhanced phosphorylation of p53 by ATM in response to DNA damage. Science 1998; 281: 1674–7.
66 Carney JP, Maser RS, Olivares H, Davis EM, Le Beau M, Yates JR, 3rd, *et al*. The hMre11/hRad50 protein complex and Nijmegen breakage syndrome: linkage of double-strand break repair to the cellular DNA damage response. Cell 1998; 93: 477–86.
67 Matsuura S, Tauchi H, Nakamura A, Kondo N, Sakamoto S, Endo S, *et al*. Positional cloning of the gene for Nijmegen breakage syndrome. Nat Genet 1998; 19: 179–81.
68 Digweed M, Sperling K. Nijmegen breakage syndrome: clinical manifestation of defective response to DNA double-strand breaks. DNA Repair (Amst) 2004; 3: 1207–17.
69 Xiao Y, Weaver DT. Conditional gene targeted deletion by Cre recombinase demonstrates the requirement for the double-strand break repair Mre11 protein in murine embryonic stem cells. Nucleic Acids Res 1997; 25: 2985–91.
70 Dumon-Jones V, Frappart PO, Tong WM, Sajithlal G, Hulla W, Schmid G, *et al*. Nbn heterozygosity renders mice susceptible to tumor formation and ionizing radiation-induced tumorigenesis. Cancer Res 2003; 63: 7263–9.
71 Zhu J, Petersen S, Tessarollo L, Nussenzweig A. Targeted disruption of the Nijmegen breakage syndrome gene *NBS1* leads to early embryonic lethality in mice. Curr Biol 2001; 11: 105–9.
72 Luo G, Yao MS, Bender CF, Mills M, Bladl AR, Bradley A, *et al*. Disruption of mRad50 causes embryonic stem cell lethality, abnormal embryonic development, and sensitivity to ionizing radiation. Proc Natl Acad Sci USA 1999; 96: 7376–81.
73 Petrini JH, Walsh ME, DiMare C, Chen XN, Korenberg JR, Weaver DT. Isolation and characterization of the human *MRE11* homologue. Genomics 1995; 29: 80–6.
74 Chamankhah M, Wei YF, Xiao W. Isolation of *hMRE11B*: failure to complement yeast mre11 defects due to species-specific protein interactions. Gene 1998; 225: 107–16.
75 Sharples GJ, Leach DR. Structural and functional similarities between the SbcCD proteins of *Escherichia coli* and the RAD50 and MRE11 (RAD32) recombination and repair proteins of yeast. Mol Microbiol 1995; 17: 1215–7.
76 Usui T, Ohta T, Oshiumi H, Tomizawa J, Ogawa H, Ogawa T. Complex formation and functional versatility of Mre11 of budding yeast in recombination. Cell 1998; 95: 705–16.
77 Chamankhah M, Xiao W. Formation of the yeast Mre11-Rad50-Xrs2 complex is correlated with DNA repair and telomere maintenance. Nucleic Acids Res 1999; 27: 2072–9.
78 Anderson DE, Trujillo KM, Sung P, Erickson HP. Structure of the Rad50 x Mre11 DNA repair complex from *Saccharomyces cerevisiae* by electron microscopy. J Biol Chem 2001; 276: 37 027–33.
79 Hopfner KP, Karcher A, Craig L, Woo TT, Carney JP, Tainer JA. Structural biochemistry and interaction architecture of the DNA double-strand break repair Mre11 nuclease and Rad50-ATPase. Cell 2001; 105: 473–85.
80 de Jager M, van Noort J, van Gent DC, Dekker C, Kanaar R, Wyman C. Human Rad50/Mre11 is a flexible complex that can tether DNA ends. Mol Cell 2001; 8: 1129–35.
81 Trujillo KM, Yuan SS, Lee EY, Sung P. Nuclease activities in a complex of human recombination and DNA repair factors Rad50, Mre11, and p95. J Biol Chem 1998; 273: 21447–50.
82 Paull TT, Gellert M. The 3' to 5' exonuclease activity of Mre11 facilitates repair of DNA double-strand breaks. Mol Cell 1998; 1: 969–79.
83 Paull TT, Gellert M. Nbs1 potentiates ATP-driven DNA unwinding and endonuclease cleavage by the Mre11/Rad50 complex. Genes Dev 1999; 13: 1276–88.
84 Moreau S, Ferguson JR, Symington LS. The nuclease activity of Mre11 is required for meiosis but not for mating type switching, end joining, or telomere maintenance. Mol Cell Biol 1999; 19: 556–66.
85 Haber JE. The many interfaces of Mre11. Cell 1998; 95: 583–6.
86 Symington LS. Role of *RAD52* epistasis group genes in homologous recombination and double-strand break repair. Microbiol Mol Biol Rev 2002; 66: 630–70.
87 Anderson RA, Boronenkov IV, Doughman SD, Kunz J, Loijens JC. Phosphatidylinositol phosphate kinases, a multifaceted family of signaling enzymes. J Biol Chem 1999; 274: 9907–10.
88 Kunz J, Wilson MP, Kisseleva M, Hurley JH, Majerus PW, Anderson RA. The activation loop of phosphatidylinositol phosphate kinases determines signaling specificity. Mol Cell 2000; 5: 1–11.
89 Dong Z, Zhong Q, Chen PL. The Nijmegen breakage syndrome protein is essential for Mre11 phosphorylation upon DNA damage. J Biol Chem 1999; 274: 19513–6.
90 Steimle PA, Hoffert JD, Adey NB, Craig SW. Polyphosphoinositides inhibit the interaction of vinculin with actin filaments. J Biol Chem 1999; 274: 18414–20.
91 Ivanov EL, Sugawara N, White CI, Fabre F, Haber JE. Mutations in *XRS2* and *RAD50* delay but do not prevent mating-type switching in *Saccharomyces cerevisiae*. Mol Cell Biol 1994; 14: 3414–25.
92 Johzuka K, Ogawa H. Interaction of Mre11 and Rad50: two proteins required for DNA repair and meiosis-specific double-strand break formation in *Saccharomyces cerevisiae*. Genetics 1995; 139: 1521–32.
93 Chamankhah M, Fontanie T, Xiao W. The *Saccharomyces cerevisiae mre11(ts)* allele confers a separation of DNA repair and telomere maintenance functions. Genetics 2000; 155: 569–76.
94 Falck J, Coates J, Jackson SP. Conserved modes of recruitment of ATM, ATR and DNA-PKcs to sites of DNA damage. Nature 2005; 434: 605–11.
95 Williams BR, Mirzoeva OK, Morgan WF, Lin J, Dunnick W, Petrini JH. A murine model of Nijmegen breakage syndrome. Curr Biol 2002; 12: 648–53.
96 Kang J, Bronson RT, Xu Y. Targeted disruption of NBS1 reveals its roles in mouse development and DNA repair. EMBO J 2002; 21: 1447–55.

97 Chen J. Ataxia telangiectasia-related protein is involved in the phosphorylation of BRCA1 following deoxyribonucleic acid damage. Cancer Res 2000; 60: 5037–9.
98 Li S, Ting NS, Zheng L, Chen PL, Ziv Y, Shiloh Y, *et al*. Functional link of BRCA1 and ataxia telangiectasia gene product in DNA damage response. Nature 2000; 406: 210–5.
99 Smith GC, Cary RB, Lakin ND, Hann BC, Teo SH, Chen DJ, *et al*. Purification and DNA binding properties of the ataxia-telangiectasia gene product ATM. Proc Natl Acad Sci USA 1999; 96: 11 134–9.
100 Bakkenist CJ, Kastan MB. DNA damage activates ATM through intermolecular autophosphorylation and dimer dissociation. Nature 2003; 421: 499–506.
101 Ali A, Zhang J, Bao S, Liu I, Otterness D, Dean NM, *et al*. Requirement of protein phosphatase 5 in DNA-damage-induced ATM activation. Genes Dev 2004; 18: 249–54.
102 Rogakou EP, Boon C, Redon C, Bonner WM. Megabase chromatin domains involved in DNA double-strand breaks *in vivo*. J Cell Biol 1999; 146: 905–16.
103 Kobayashi J, Tauchi H, Sakamoto S, Nakamura A, Morishima K, Matsuura S, *et al*. NBS1 localizes to gamma-H2AX foci through interaction with the FHA/BRCT domain. Curr Biol 2002; 12: 1846–51.
104 Zhao S, Weng YC, Yuan SS, Lin YT, Hsu HC, Lin SC, *et al*. Functional link between ataxia-telangiectasia and Nijmegen breakage syndrome gene products. Nature 2000; 405: 473–7.
105 Kim ST, Xu B, Kastan MB. Involvement of the cohesin protein, Smc1, in ATM-dependent and independent responses to DNA damage. Genes Dev 2002; 16: 560–70.
106 Yazdi PT, Wang Y, Zhao S, Patel N, Lee EY, Qin J. SMC1 is a downstream effector in the ATM/NBS1 branch of the human S-phase checkpoint. Genes Dev 2002; 16: 571–82.
107 Lisby M, Barlow JH, Burgess RC, Rothstein R. Choreography of the DNA damage response: spatiotemporal relationships among checkpoint and repair proteins. Cell 2004; 118: 699–713.
108 Greenwell PW, Kronmal SL, Porter SE, Gassenhuber J, Obermaier B, Petes TD. *TEL1*, a gene involved in controlling telomere length in *S. cerevisiae*, is homologous to the human ataxia telangiectasia gene. Cell 1995; 82: 823–9.
109 Morrow DM, Tagle DA, Shiloh Y, Collins FS, Hieter P. *TEL1*, an *S. cerevisiae* homolog of the human gene mutated in ataxia telangiectasia, is functionally related to the yeast checkpoint gene MEC1. Cell 1995; 82: 831–40.
110 Uziel T, Lerenthal Y, Moyal L, Andegeko Y, Mittelman L, Shiloh Y. Requirement of the MRN complex for ATM activation by DNA damage. EMBO J 2003; 22: 5612–21.
111 Lee JH, Paull TT. ATM activation by DNA double-strand breaks through the Mre11-Rad50-Nbs1 complex. Science 2005; 308: 551–4.
112 Mochan TA, Venere M, DiTullio RA, Jr, Halazonetis TD. 53BP1 and NFBD1/MDC1-Nbs1 function in parallel interacting pathways activating ataxia-telangiectasia mutated (ATM) in response to DNA damage. Cancer Res 2003; 63: 8586–91.
113 Goldberg M, Stucki M, Falck J, D'Amours D, Rahman D, Pappin D, *et al*. MDC1 is required for the intra-S-phase DNA damage checkpoint. Nature 2003; 421: 952–6.
114 Stewart GS, Wang B, Bignell CR, Taylor AM, Elledge SJ. MDC1 is a mediator of the mammalian DNA damage checkpoint. Nature 2003; 421: 961–6.
115 Wang B, Matsuoka S, Carpenter PB, Elledge SJ. 53BP1, a mediator of the DNA damage checkpoint. Science 2002; 298: 1435–8.
116 Lou Z, Minter-Dykhouse K, Wu X, Chen J. MDC1 is coupled to activated CHK2 in mammalian DNA damage response pathways. Nature 2003; 421: 957–61.
117 Shang YL, Bodero AJ, Chen PL. NFBD1, a novel nuclear protein with signature motifs of FHA and BRCT, and an internal 41-amino acid repeat sequence, is an early participant in DNA damage response. J Biol Chem 2003; 278: 6323–9.
118 Xu X, Stern DF. NFBD1/KIAA0170 is a chromatin-associated protein involved in DNA damage signaling pathways. J Biol Chem 2003; 278: 8795–803.
119 Peng A, Chen PL. NFBD1, like 53BP1, is an early and redundant transducer mediating Chk2 phosphorylation in response to DNA damage. J Biol Chem 2003; 278: 8873–6.
120 Fernandez-Capetillo O, Chen HT, Celeste A, Ward I, Romanienko PJ, Morales JC, *et al*. DNA damage-induced G2-M checkpoint activation by histone H2AX and 53BP1. Nat Cell Biol 2002; 4: 993–7.
121 DiTullio RA, Jr, Mochan TA, Venere M, Bartkova J, Sehested M, Bartek J, *et al*. 53BP1 functions in an ATM-dependent checkpoint pathway that is constitutively activated in human cancer. Nat Cell Biol 2002; 4: 998–1002.
122 Ward IM, Minn K, van Deursen J, Chen J. p53 Binding protein 53BP1 is required for DNA damage responses and tumor suppression in mice. Mol Cell Biol 2003; 23: 2556–63.
123 Morales JC, Xia Z, Lu T, Aldrich MB, Wang B, Rosales C, *et al*. Role for the BRCA1 C-terminal repeats (BRCT) protein 53BP1 in maintaining genomic stability. J Biol Chem 2003; 278: 14 971–7.
124. Hartley KO, Gell D, Smith GC, Zhang H, Divecha N, Connelly MA, *et al*. DNA-dependent protein kinase catalytic subunit: a relative of phosphatidylinositol 3-kinase and the ataxia telangiectasia gene product. Cell 1995; 82: 849–56.
125 Chan DW, Chen BP, Prithivirajsingh S, Kurimasa A, Story MD, Qin J, *et al*. Autophosphorylation of the DNA-dependent protein kinase catalytic subunit is required for rejoining of DNA double-strand breaks. Genes Dev 2002; 16: 2333–8.
126 Hendrickson EA, Qin XQ, Bump EA, Schatz DG, Oettinger M, Weaver DT. A link between double-strand break-related repair and V(D)J recombination: the scid mutation. Proc Natl Acad Sci USA 1991; 88: 4061–5.
127 Blunt T, Finnie NJ, Taccioli GE, Smith GC, Demengeot J, Gottlieb TM, *et al*. Defective DNA-dependent protein kinase activity is linked to V(D)J recombination and DNA repair defects associated with the murine scid mutation. Cell 1995; 80: 813–23.
128 Cohen MM, Levy HP. Chromosome instability syndromes. Adv Hum Genet 1989; 18: 43–149, 365-171.
129 Leuther KK, Hammarsten O, Kornberg RD, Chu G. Structure of DNA-dependent protein kinase: implications for its regulation by DNA. EMBO J 1999; 18: 1114–23.
130 Boskovic J, Rivera-Calzada A, Maman JD, Chacon P, Willison KR, Pearl LH, *et al*. Visualization of DNA-induced conformational changes in the DNA repair kinase DNA-PKcs. EMBO J 2003; 22: 5875–82.
131 Rivera-Calzada A, Maman JP, Spagnolo L, Pearl LH, Llorca O.

Three-dimensional structure and regulation of the DNA-dependent protein kinase catalytic subunit (DNA-PKcs). Structure (Camb) 2005; 13: 243–55.
132 Burma S, Chen DJ. Role of DNA-PK in the cellular response to DNA double-strand breaks. DNA Repair (Amst) 2004; 3: 909–18.
133 Yu J, Marshall K, Yamaguchi M, Haber JE, Weil CF. Microhomology-dependent end joining and repair of transposon-induced DNA hairpins by host factors in *Saccharomyces cerevisiae*. Mol Cell Biol 2004; 24: 1351–64.
134 Kramer KM, Brock JA, Bloom K, Moore JK, Haber JE. Two different types of double-strand breaks in *Saccharomyces cerevisiae* are repaired by similar RAD52-independent, nonhomologous recombination events. Mol Cell Biol 1994; 14: 1293–301.
135 Lewis LK, Resnick MA. Tying up loose ends: nonhomologous end-joining in *Saccharomyces cerevisiae*. Mutat Res 2000; 451: 71–89.
136 Moore JK, Haber JE. Cell cycle and genetic requirements of two pathways of nonhomologous end-joining repair of double-strand breaks in *Saccharomyces cerevisiae*. Mol Cell Biol 1996; 16: 2164–73.
137 Boulton SJ, Jackson SP. Components of the Ku-dependent non-homologous end-joining pathway are involved in telomeric length maintenance and telomeric silencing. EMBO J 1998; 17: 1819–28.
138 Nugent CI, Bosco G, Ross LO, Evans SK, Salinger AP, Moore JK, *et al*. Telomere maintenance is dependent on activities required for end repair of double-strand breaks. Curr Biol 1998; 8: 657–60.
139 Frank-Vaillant M, Marcand S. Transient stability of DNA ends allows nonhomologous end joining to precede homologous recombination. Mol Cell 2002; 10: 1189–99.
140 Martin SG, Laroche T, Suka N, Grunstein M, Gasser SM. Relocalization of telomeric Ku and SIR proteins in response to DNA strand breaks in yeast. Cell 1999; 97: 621–33.
141 Chen L, Trujillo K, Ramos W, Sung P, Tomkinson AE. Promotion of Dnl4-catalyzed DNA end-joining by the Rad50/Mre11/Xrs2 and Hdf1/Hdf2 complexes. Mol Cell 2001; 8: 1105–15.
142 Teo SH, Jackson SP. Lif1p targets the DNA ligase Lig4p to sites of DNA double-strand breaks. Curr Biol 2000; 10: 165–8.
143 Cortez D, Guntuku S, Qin J, Elledge SJ. ATR and ATRIP: partners in checkpoint signaling. Science 2001; 294: 1713–6.
144 Zou L, Elledge SJ. Sensing DNA damage through ATRIP recognition of RPA-ssDNA complexes. Science 2003; 300: 1542–8.
145 Gravel S, Larrivee M, Labrecque P, Wellinger RJ. Yeast Ku as a regulator of chromosomal DNA end structure. Science 1998; 280: 741–4.
146 Hsu HL, Gilley D, Blackburn EH, Chen DJ. Ku is associated with the telomere in mammals. Proc Natl Acad Sci USA 1999; 96: 12 454–8.
147 Kironmai KM, Muniyappa K. Alteration of telomeric sequences and senescence caused by mutations in *RAD50* of *Saccharomyces cerevisiae*. Genes Cells 1997; 2: 443–55.
148 Gallego ME, White CI. RAD50 function is essential for telomere maintenance in Arabidopsis. Proc Natl Acad Sci USA 2001; 98: 1711–6.
149 Wilson S, Warr N, Taylor DL, Watts FZ. The role of *Schizosaccharomyces pombe* Rad32, the Mre11 homologue, and other DNA damage response proteins in non-homologous end joining and telomere length maintenance. Nucleic Acids Res 1999; 27: 2655–61.
150 Ueno M, Nakazaki T, Akamatsu Y, Watanabe K, Tomita K, Lindsay HD, *et al*. Molecular characterization of the *Schizosaccharomyces pombe nbs1+* gene involved in DNA repair and telomere maintenance. Mol Cell Biol 2003; 23: 6553–63.
151 Ritchie KB, Petes TD. The Mre11p/Rad50p/Xrs2p complex and the Tel1p function in a single pathway for telomere maintenance in yeast. Genetics 2000; 155: 475–9.
152 Chan SW, Blackburn EH. Telomerase and ATM/Tel1p protect telomeres from nonhomologous end joining. Mol Cell 2003; 11: 1379–87.
153 Usui T, Ogawa H, Petrini JH. A DNA damage response pathway controlled by Tel1 and the Mre11 complex. Mol Cell 2001; 7: 1255–66.
154 Xia SJ, Shammas MA, Shmookler Reis RJ. Reduced telomere length in ataxia-telangiectasia fibroblasts. Mutat Res 1996; 364: 1–11.
155 Hande MP, Balajee AS, Tchirkov A, Wynshaw-Boris A, Lansdorp PM. Extra-chromosomal telomeric DNA in cells from Atm(-/-) mice and patients with ataxia-telangiectasia. Hum Mol Genet 2001; 10: 519–28.
156 Pandita TK, Dhar S. Influence of ATM function on interactions between telomeres and nuclear matrix. Radiat Res 2000; 154: 133–9.
157 Wong KK, Maser RS, Bachoo RM, Menon J, Carrasco DR, Gu Y, *et al*. Telomere dysfunction and Atm deficiency compromises organ homeostasis and accelerates ageing. Nature 2003; 421: 643–8.

Acta Pharmacologica Sinica 2005 Aug; 26 (8): 908–917

Blackwell Publishing

Invited review

Oxidative stress and stress signaling: menace of diabetic cardiomyopathy

Loren E WOLD[1], Asli F CEYLAN-ISIK[2], Jun REN[1,2,3]

[1]Department of Pharmacology, Physiology and Therapeutics, University of North Dakota, Grand Forks, ND 58203, USA; [2]Center for Cardiovascular Research and Alternative Medicine, University of Wyoming, Laramie, WY 82071, USA

Key words

diabetes; heart; cardiomyopathy; oxidative stress; signal transduction

[3]Correspondence to Dr Jun REN.
Phn 1-307-766-6131.
Fax 1-307-766-2953.
E-mail jren@uwyo.edu

Received 2005-03-02
Accepted 2005-04-13

doi: 10.1111/j.1745-7254.2005.00146.x

Abstract

Cardiovascular disease is the most common cause of death in the diabetic population and is currently one of the leading causes of death in the United States and other industrialized countries. The health care expenses associated with cardiovascular disease are staggering, reaching more than US$350 billion in 2003. The risk factors for cardiovascular disease include high fat/cholesterol levels, alcoholism, smoking, genetics, environmental factors and hypertension, which are commonly used to gauge an individual's risk of cardiovascular disease and to track their progress during therapy. Most recently, these factors have become important in the early prevention of cardiovascular diseases. Oxidative stress, the imbalance between reactive oxygen species production and breakdown by endogenous antioxidants, has been implicated in the onset and progression of cardiovascular diseases such as congestive heart failure and diabetes-associated heart dysfunction (diabetic cardiomyopathy). Antioxidant therapy has shown promise in preventing the development of diabetic heart complications. This review focuses on recent advances in oxidative stress theory and antioxidant therapy in diabetic cardiomyopathy, with an emphasis on the stress signaling pathways hypothesized to be involved. Many of these stress signaling pathways lead to activation of reactive oxygen species, major players in the development and progression of diabetic cardiomyopathy.

Introduction

Cardiovascular disease is the leading cause of death in Western societies, causing approximately one million deaths annually[1]. It is both a primary and a secondary disease, resulting from several other disorders, such as hypertension, diabetes, alcoholism, obesity and the metabolic syndrome. Cardiovascular disease is defined as any disorder that decreases normal heart and/or vascular function. One of the leading causes of cardiovascular disease is diabetes, of both type 1 and type 2 origins. The incidence of diabetes is predicted to double by the year 2030 because of people's sedentary lifestyles and an ever-growing cluster of pre-diabetic syndromes including metabolic syndrome, obesity, and insulin resistance[2]. Almost all of these metabolic disturbances are considered major risk factors in the development of heart dysfunction and congestive heart failure[3–7]. Nevertheless, the cellular mechanisms that relate to the development of cardiovascular complications in patients with diabetes have not been fully elucidated.

Diabetes mellitus is a group of metabolic disorders that are characterized by hyperglycemia resulting from defects in insulin secretion, action or both. Chronic hyperglycemia causes end-stage organ damage, dysfunction and failure of various organs, including the kidneys, nerves, eyes, blood vessels and hearts. Several pathological processes are involved in the development of diabetes, ranging from autoimmune destruction of the β-cells of the pancreas with resultant insulin deficiency (type 1 diabetes) to abnormalities that result in resistance to insulin (type 2 diabetes).

Impairment of insulin action and resistance to the action of insulin often coexist in the same patient, so it is unclear which abnormality is responsible for the hyperglycemia. Symptoms of chronic hyperglycemia include polyuria, polydipsia, weight loss and blurred vision. Long-term complications of diabetes include retinopathy[8] with potential loss of vision; peripheral neuropathy[9] with risk of amputation; autonomic neuropathy causing gastrointestinal, genitourinary and cardiovascular symptoms; and nephropathy[10] leading to kidney failure.

Functional alterations in diabetic cardiomyopathy

Sustained diabetes mellitus leads to a deterioration of heart function that is known as diabetic cardiomyopathy, which occurs independently of the macro- and micro-vascular diseases that are frequently seen in diabetic patients[11]. Diastolic dysfunction is the most prominent mechanical defect in diabetic cardiomyopathy and is characterized by decreased compliance and slower rates of myocardial relaxation[11–13]. Both systolic and diastolic dysfunctions have been characterized to include prolonged contraction and relaxation, reduced velocity of contraction and relaxation, and depressed myocardial contractility in whole heart, tissue, and isolated ventricular myocytes from both diabetic patients and experimental animals[11–13]. Functional changes have been observed by electrocardiogram and echocardiography, which are manifested by shorter left ventricular ejection time, increased pre-ejection period, increased wall stiffness, decreased fractional shortening, decreased rate of left ventricular filling and increased action potential duration in diabetes[14,15]. All of these findings suggest that diabetic cardiomyopathy is represented by left ventricular dysfunction.

The chronic alterations at the end stages of diabetes are believed to be due to increased glucose levels[16,17]. Although the pathogenesis of diabetic cardiomyopathy has not been precisely described, several mechanisms have been speculated, including reduced energy production because of decreases in mitochondrial respiration and pyruvate dehydrogenase activity, accumulation of free radical species, glucose toxicity-induced oxidative stress and malfunction of cardiac contractile and intracellular Ca^{2+} regulatory proteins such as myosin, sarco(endo)plasmic reticulum Ca^{2+}-ATPase (SERCA), and Na^{+}-Ca^{2+} exchanger[18–21]. The increased risk of diabetic cardiomyopathy and other heart complications warrants stringent and aggressive treatment against hyperglycemia, hyperinsulinemia, dyslipidemia and oxidative stress.

The most commonly used therapeutic regimes in diabetic patients with heart dysfunction include angiotensin-converting enzyme inhibitors, digoxin, diuretics, β-blockers, Ca^{2+} antagonists and spironolactone. Insulin-sensitizing agents such as thiazolidinediones are often prescribed in the treatment of diabetes more often than insulin-secretion-enhancing agents to avoid hyperinsulinemia and insulin resistance. In addition to pharmacological interventions, primary care for diabetic patients also includes lifestyle modifications such as smoking cessation, weight control, exercise and dietary restriction[7].

Diabetic cardiomyopathy type 1 diabetes

Type 1 diabetes mellitus leads to a cardiomyopathy in both human and animal models. The existence of a diabetic cardiomyopathy in humans is based on the presentation of ventricular dysfunction in patients without evidence of any other known cardiovascular disease (reviewed in Sowers *et al*[22] and Spector[23]). The clinical presentation of diabetic cardiomyopathy in type 1 diabetic patients was first presented by Rubler *et al*[24] based on four diabetic patients who suffered from congestive heart failure (CHF) in the absence of discernable coronary artery disease, valvular or congenital heart disease, hypertension or alcoholism. Numerous studies carried out since 1972 have supported the view that diabetic cardiomyopathy is a pervasive problem in type 1 diabetes and is first manifested by diastolic dysfunction[11,23]. Diabetic cardiomyopathy in experimental animal models of type 1 diabetes is characterized by phenotypic changes in the ventricular myocytes that occur in the presence or absence of coronary artery disease. This cardiomyopathy is well described in animal models with long-term type 1 diabetes and results in abnormal cardiomyocyte excitation-contraction (E-C) coupling [eg, prolonged action potentials, slowed cytosolic Ca^{2+} effluxes and slowed myocyte shortening and relengthening (reviewed by Pierce and Russell[25] and Chatham *et al*[26])]. The cellular mechanisms that contribute to myocyte dysfunction involve depressed expression and function of SERCA and Na^{+}/Ca^{2+} exchanger (NCX)[27]. Regulation of E-C coupling is also impaired in diabetic hearts, such that β-adrenergic receptor signaling is depressed, which may result from changes in β-adrenergic receptor density or redistribution of β-adrenergic receptor subtypes[28], or perhaps signaling downstream of the receptors[29]. Elevated protein kinase C (PKC) activity and changes in the expression of specific PKC isoforms are also found in type I diabetic hearts[30,31].

Diabetic cardiomyopathy in type 2 diabetes

The more prevalent type 2 diabetes is a combination of

resistance to insulin action and an inadequate compensatory insulin secretory response. Type 2 diabetic patients are able to survive with little or no insulin supplementation; however dietary modification and exercise are imperative for living with the disorder. Diabetic cardiomyopathy has also been determined clinically in the type 2 diabetic patients. Investigators in the Strong Heart Study (SHS) performed detailed echocardiographic analysis of a population of American Indians with a high rate of type 2 diabetes and reported that diabetes was associated with increased left ventricular (LV) mass, LV wall thickness, reduced systolic and particularly diastolic function, independent of hypertension[32,33]. Similar to diabetes, investigators from the Framingham Heart Study reported increased LV mass and wall thickness in individuals with glucose intolerance and insulin resistance[34]. There was also an association between left atrial (LA) size and insulin resistance. Since no relationship was found between systolic function and insulin resistance, one explanation for the relationship between LA size and insulin resistance offered was that the rising LA size might reflect the presence of diastolic dysfunction in insulin resistance (type 2 diabetes)[34]. Other studies in patients with diagnosed type 2 diabetes support the notion that the earliest cardiac abnormality is diastolic dysfunction[35]. Several investigators have experimentally shown that diabetes mellitus is associated with a specific cardiomyopathy[12,13] and depressed cardiac function independent of macro-/micro-vascular disease, suggesting the existence of a primary myocardial defect in both type 1 and type 2 diabetes mellitus[13,36].

Impaired insulin action (ie, insulin resistance) is characterized by a compensatory hyperinsulinemia and hyperlipidemia, which are major metabolic dysfunctions associated with the early stages of type 2 diabetes. Elevated plasma insulin and lipid levels can lead to numerous metabolic and pathophysiological derangements in various tissues, including the heart. Abnormal ventricular systolic and diastolic functions are reported in type 2 patients presenting without macrovascular disease or hypertension, providing indirect evidence that there is a diabetic cardiomyopathy in humans[37]. Furthermore, there is a considerable evidence that diastolic dysfunction occurs early in the disease process, which may contribute to high cardiac mortality among diabetic patients[38,39]. In clinical studies, detectable cardiac dysfunction has been reported to occur as early as the glucose intolerance phase (ie, hyperinsulinemmia and hyperglycemia) that follows insulin resistance[40].

The risk of congestive heart failure and other cardiovascular diseases is greatly increased in diabetic patients[41]. The Framingham Heart Study revealed that diabetic men had more than twice the frequency of congestive heart failure than did non-diabetic males, whereas diabetic women had a risk that was five times greater than non-diabetic women[34]. The development of diabetic cardiomyopathy is dependent on many factors; however, it is likely that all patients with diabetes will eventually develop some degree of diabetic cardiomyopathy.

Mechanisms of diabetic cardiomyopathy

Diabetic cardiomyopathy is a major reason for the high morbidity and mortality in diabetic populations[41], particularly among elderly people and postmenopausal women. In adult patients with diabetes, the risk of cardiovascular disease is three to five times greater than that in the general population. Several mechanisms for the development of cardiomyopathy have been postulated, including alterations in intracellular ion homeostasis, reduction in intracellular energy metabolism, alteration in glucose metabolism, disrupted polyol pathway and enhanced oxidative stress. Several mechanisms have been proposed to explain how all of the pathologies involved in the progression of diabetic cardiomyopathy can result from hyperglycemia. Four main hypotheses have been presented to describe how hyperglycemia can cause all of these diabetic complications[42]: increased polyol pathway flux, increased advanced glycation end-product (AGE) formation, increased protein kinase C isoform expression, and increased hexosamine pathway flux (Figure 1). We hope to show that all of these pathways, as well as several others, lead to hyperglycemia and increased reactive oxygen species (ROS) formation, causing diabetic cardiomyopathy.

Alterations in intracellular ions

Changes in intracellular cations are directly related to the altered electromechanical activities of diabetic hearts. Alterations in intracellular Na^+ are often accompanied by a decrease in K^+ and Ca^{2+} in diabetic heart, which may be related in part to a diabetes-induced conformational change in the Na^+-K^+-ATPase pump[43]. Decreases in Ca^{2+} uptake, Ca^{2+} binding to the sarcolemma and Ca^{2+} intake by the myofibrillar Ca^{2+}-ATPase activity have all been shown in diabetic rat hearts[43], which are partially reversible by insulin supplementation. Although the importance of these alterations in myocardial dysfunction seen in diabetes is not yet clear, the presence of abnormalities in Ca^{2+} handling and β-adrenergic stimulation is of paramount importance in understanding these myocardial dysfunctional changes[26]. Alterations in α_1-adrenergic signaling in streptozotocin (STZ)-induced dia-

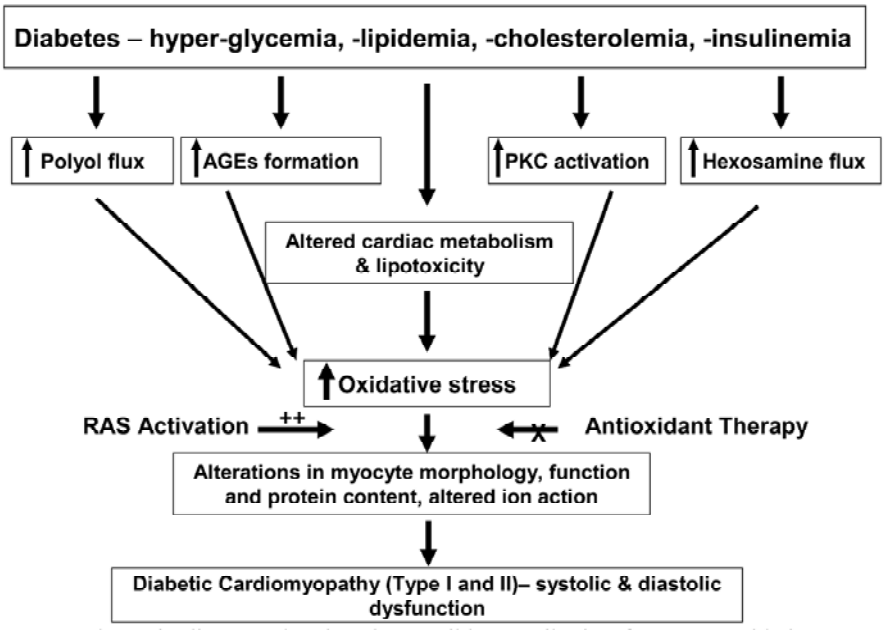

Figure 1. Schematic diagram showing the possible contributing factors to oxidative stress en route to the onset of diabetic cardiomyopathy in both type 1 and type 2 diabetes.

betic rat hearts have also been shown.

Increased polyol pathway flux

Increased glucose utilization by aldose reductase has been implicated in the development of diabetes complications. Aldose reductase is the first enzyme in the polyol pathway, which catalyses the NADPH-dependent reduction of carbonyl compounds, including glucose. In the polyol pathway, glucose is reduced to sorbitol by aldose reductase in the presence of NADPH, and sorbitol is then oxidized by sorbitol dehydrogenase (SDH) to fructose at the cost of NAD^+. Normally, aldose reductase has a low affinity for glucose in the non-diabetic, low-glucose state. However the affinity for glucose is dramatically increased in the diabetic, high-glucose state, which converts glucose to sorbitol, with resultant decreases in NADPH. It has been demonstrated that increased aldose reductase activity in diabetic animals is correlated with increased $NADH/NAD^+$[44]. There is further support from the facts that sorbitol and fructose levels in diabetic hearts are approximately nine-fold higher, and $NADH/NAD^+$ levels in diabetic hearts are approximately four-fold higher than in normal hearts[44]. Experiments have demonstrated that cytosolic $NADH/NAD^+$ was reduced by both SDH[45] and aldose reductase inhibition[44,46]. These data indicate that the polyol pathway is a target for cardioprotective interventions. This notion is supported by the observation that nitric oxide (NO) maintains aldose reductase in an inactive state and that this repression is relieved in diabetic tissues[47]. Thus, increasing NO availability may be a useful strategy for inhibiting the polyol pathway and preventing the development of diabetes complications. It is worth mentioning that contributions of the polyol pathway in diabetes are often tissue- and species-specific and may not fully explain the pathogenesis of all forms of diabetic complications[42].

One mechanism whereby increased polyol pathway flux leads to the complications of diabetes discussed earlier is that oxidation of sorbitol by NAD^+ increases the cytosolic $NADH:NAD^+$ ratio, leading to inhibition of the enzyme glyceraldehydes-3-phosphate dehydrogenase (GADPH) and increased concentrations of triose phosphate[42]. Increased triose phosphate could potentially increase the formation of AGEs and diacylglycerol (DAG), thus activating PKC isoforms[42].

Another mechanism whereby increased polyol pathway flux causes deleterious effects is that reduction of glucose to sorbitol by NADPH consumes NADPH, a cofactor in the generation of reduced glutathione (GSH), which could lead to increased oxidative stress. It has been shown that decreased levels of GSH are present in the lenses of transgenic mice overexpressing aldose reductase[48]. These observations have led many people to believe that this is the main mechanism whereby increased polyol pathway flux leads to

many of the complications seen in diabetes.

Increased advanced glycation end products formation

Advanced glycation endproducts are enhanced in the presence of hyperglycemia and oxidative stress[49,50]. They bind to their cell-surface receptors (RAGE) resulting in the activation of postreceptor signaling, generation of intracellular ROS and the activation of gene expression[51–58]. AGEs have also been shown to be mediators of late diabetic complications and chronic vascular disease[59].

The importance of AGEs in the development of diabetic complications is seen in the observation that two structurally similar AGE inhibitors partially prevented diabetic complications in the retina, kidney and nervous system[60–62]. One of the mechanisms how AGE precursors target cells is through the binding of AGE receptors to endothelial cells, mesangial cells and macrophages, inducing receptor-mediated production of ROS. This receptor ligation increases the production of the transcription factor NF-κB, also causing increased oxidative stress.

Some of the most striking data on the role of AGE and the development of diabetic complications has been obtained when looking at the receptor for AGE, RAGE. RAGE suppressed the formation of macrovascular disease in a type I diabetic mouse model in a glucose- and lipid-independent fashion[63]. It has also been shown that blockage of RAGE inhibited the formation of diabetic nephropathy and enhanced wound repair (known to be a problem in diabetics) in murine models. The mechanism involved in RAGE-associated development of diabetic complications appears to be related to increased production of ROS[42].

Activation of protein kinase C isoforms

Protein kinase C is also increased in the tissues of diabetic patients[64]. Activation of the PKC pathway by hyperglycemia can occur directly or indirectly (via ligation of AGE receptors[65] or increased activity of the polyol pathway[66]) and can synergize with other kinase pathways, that is, the MAPK pathway. Interactions between these pathways are likely to play a role in determining the long-term effects of hyperglycemia. As discussed earlier, sorbitol, whose formation from glucose is catalyzed by aldose reductase, is increased when intracellular glucose concentrations rise[67], and can accumulate intracellularly, which can cause cell damage. The p38 mitogen-activated protein kinase (MAPK) and c-Jun N-terminal kinase (JNK) pathways are also activated by sorbitol. The significance of the sorbitol pathway as a cause of diabetic complications was demonstrated in transgenic mice that overexpressed the aldose reductase gene[48,68–70] and by data showing that inhibitors of this enzyme prevent the development of long-term diabetic complications in these animals[71].

Increased hexosamine flux and glucose autooxidation

Hyperglycemia increases flux through the hexosamine pathway by providing more fructose-6-phosphate for glutamine: fructose-6-phosphate amidotransferase (GFAT), the rate-limiting enzyme of the pathway. The effect of hyperglycemia on flux of the hexoasamine pathway probably reflects increased fructose-6-phosphate levels, which result from inhibition of GAPDH by ROS[72].

Recently, ROS formation due to glucose autooxidation has been hypothesized to play a role in the pathogenesis of diabetic cardiomyopathy in diabetic populations; however, no unifying hypothesis exists as to how glucose autooxidation causes any of the complications seen in diabetes.

Alterations in stress signaling pathways

Hyperglycemia in diabetes causes changes in membrane function and metabolic and biochemical alterations within days, changes in contractile function within weeks, and morphological changes and heart dysfunction within months[26]. A significant increase in oxidative damage via lipid peroxidation was observed in the hearts of diabetic rats[73]. Production of hydroxyl radicals was also detected in diabetic rats induced by streptozotocin[74]. In the heart, hydroxyl radical production and elevated blood glucose concentration were directly correlated with the amount of STZ injected into rats, up to 60 mg/kg body weight[74]. With the use of fluorescent probes, myocytes isolated from STZ-induced diabetic mice were used to detect hydrogen peroxide and hydroxyl radicals, and increased ROS was observed compared with control mice[21]. Oxidative damage caused by ROS has been shown to lead to multiple complications of diabetes[75–78]. Blocking ROS and superoxide formation, however, has been shown to prevent hyperglycemia-induced organ damage in diabetes[79].

One major intracellular target of hyperglycemia and oxidative stress is NF-κB[80–84], which can be activated by a variety of exogenous and endogenous stimuli, including hyperglycemia, elevated free fatty acids, ROS, tumor necrosis factor-α (TNF-α) and other proinflammatory cytokines, p38 MAP kinase and ultraviolet irradiation[82]. NF-κB plays a crucial role in mediating immune and inflammatory responses and apoptosis. Alterations in NF-κB signaling are

associated with a number of chronic diseases, such as diabetes and atherosclerosis. The c-jun NH(2)-terminal kinases (JNK) and p38 MAPKs are members of the complex superfamily of MAP serine/threonine protein kinases and are known as stress-activated kinases. This is due to the fact that the activities of these enzymes are stimulated by a variety of exogenous and endogenous stress-inducing stimuli, including oxidative stress, ROS, hyperglycemia and proinflammatory cytokines[85]. JNK is activated by hyperglycemia-induced oxidative stress and is probably involved in apoptosis, which can be suppressed by the antioxidant vitamin C[86] and enhanced by angiotensin II[87]. p38 MAPK is also activated in response to hyperglycemia and in diabetes. In the glomeruli of STZ-induced diabetic rats, p38 MAPK activity was increased compared with control rats, followed by increased phosphorylation of heat shock protein (HSP) 25, a downstream substrate of p38 MAPK. These effects appeared to be the result of increased ROS production[88]. Taken together, these data suggest that NF-κB, JNK and p38 MAPK pathways are potential stress-signaling systems that can lead to late complications of diabetes.

Nitric oxide is an important regulator of cardiac function. However, NO may react with the surrounding O_2^- to form peroxynitrite ($ONOO^-$). Peroxynitrite, a very active radical similar to the hydroxyl radical, interacts with cytoplasmic proteins to form nitrotyrosine, which has been indicated as a marker for reactive nitrogen species-induced oxidative damage under *in vivo* conditions[21,89]. It has been suggested that excessive NO is pathophysiological because of its ability to form pro-oxidants. Cardiac NO production and NOS protein levels have been found to be elevated in the hearts of diabetic animals[90]. This is consistent with the observation of a significant increase in nitrotyrosine concentration in myocytes in the hearts of diabetic mice[21].

Role of antioxidants in diabetic cardiomyopathy

Mitochondrial damage is related to ROS formation and plays an important role in the development of diabetic cardiomyopathy[91,92]. Coenzyme Q (CoQ) is an important component in mitochondrial energy metabolism and is also a potent endogenous antioxidant *in vivo*. In heart mitochondrial preparations of diabetic rats, the concentration of α-tocopherol was increased; however, the concentration of both CoQ-9 and CoQ-10 was decreased[92]. Data from our group have shown that the reduction in coenzyme levels from diabetic animals is attenuated with the supplementation of insulin-like growth factor I (IGF-1)[19].

It is important to note that contractile function of the heart requires a high metabolic demand, and the mitochondrial respiratory chain is the primary energy-releasing system in the myocyte. Through the respiratory chain, a series of oxidation-reduction reactions continually take place in the myocyte. Therefore, an efficient antioxidant system, including superoxide dismutase (SOD), catalase, glutathione peroxidase (GPX), glutathione (GSH) and α-tocopherol are critical to effective functioning of the myocardium. However, in experimental animal models, the heart levels of these antioxidants are much lower than in other organ systems, even in non-diabetic normals[93,94]. In addition, hyperglycemia can impair and decrease the amount of antioxidants within the heart of a diabetic animal[95–97] making it more vulnerable to ROS-induced damage.

The increase in ROS serves to decrease the antioxidant capacity of the diabetic myocardium, contributing significantly to oxidative stress and resultant myocardial damage. This damage causes cardiac morphological and functional abnormalities. Epstein and colleagues[98,99] showed that type 1 diabetic cardiomyopathy could be prevented when the antioxidants metallothionein (MT) and catalase were overexpressed specifically in the heart. They also showed that ROS production was enhanced in genetically diabetic mice (OVE26), which could be prevented by genetically crossing the diabetic mice with those overexpressing the MT or catalase genes[98,99].

Cell death is an important determinant of cardiac remodeling because it causes a loss of contractile units, compensatory hypertrophy of myocardial cells and reparative fibrosis[17]. Apoptotic cell death associated with increased oxidative stress in multiple organ systems of diabetes mellitus has been well documented[100–102]. Recent *in vivo* experiments have demonstrated the induction of myocardial cell apoptosis in experimental diabetic rats[103], mice[21] and diabetic patients[89]. Heart specimens from diabetic patients (both hypertensive and non-hypertensive) showed an increase in myocyte, endothelial and fibroblast apoptosis[89]. The increased cell death was associated with an increase in ROS formation[21,89,103]. However, the precise mechanism(s) by which ROS accumulation leads to compromised heart function and the effect of antioxidant therapy in diabetic subjects is largely unknown. Therefore, it is important to study the signaling pathways and molecular mechanisms by which hyperglycemia-induced (or, presumably, STZ-induced) oxidative stress leads to cell death and myocardial pathogenesis.

Role of the renin-angiotensin system in the development of diabetic cardiomyopathy

The renin-angiotensin system (RAS) is known to play a major role in the regulation of blood pressure and other func-

tions of the cardiovascular system[104]. Enhanced RAS is implicated in the development of diabetic cardiomyopathy and other heart dysfunctions including coronary insufficiency, congestive heart failure and hypertensive cardiomyopathy[105]. The growth-promoting effects of angiotensin II are mediated primarily through its type 1 receptor (AT_1) and the action of RAS is speculated to contribute to diabetic cardiomyopathy[105]. It has been shown that stimulation of the AT_1 receptor generates oxygen-derived free radicals, having detrimental effects on the cardiovascular system[106,107]. The AT_1 receptor has been shown to be coupled to several postreceptor signaling pathways, including Janus kinase (JAK)/signal transducer and activator of transcription (STAT) and NADPH oxidase[104,108,109]. However, the precise role of RAS, in particular the AT_1 receptor, in the development of diabetic cardiomyopathy is still speculative and further study is warranted.

Future directions

Diabetic cardiomyopathy is a clinical problem that is present in both type 1 and type 2 diabetes, which potentially involves myocyte death and interstitial fibrosis. These myocyte and non-myocyte alterations may contribute to compromised ventricular function in diabetes, which is one of the leading causes of death in the world today. It is critical to investigate the underlying (myocyte) causes of diabetic cardiomyopathy and the synergistic impact of oxidative stress in combination with antioxidant therapy on the development of heart dysfunction associated with diabetes.

Acknowledgements

The work in our laboratory has been supported in part by the National Institutes of Health, American Diabetes Association, American Heart Association (Northland and Pacific Mountain Affiliates) and the Max Baer Heart Foundation.

References

1 Poulter N. Global risk of cardiovascular disease. Heart 2003; 89: 2–5.
2 Strandberg TE, Salomaa V. Factors related to the development of diabetes during a 20-year follow-up. A prospective study in a homogeneous group of middle-aged men. Nutr Metab Cardiovasc Dis 2000; 10: 239–46.
3 Garcia MJ, McNamara PM, Gordon T, Kannel WB. Morbidity and mortality in diabetics in the Framingham population. Sixteen year follow-up study. Diabetes 1974; 23: 105–11.
4 Sowers JR. Diabetes mellitus and cardiovascular disease in women. Arch Intern Med 1998; 158: 617–21.
5 Pradhan AD, Skerrett PJ, Manson JE. Obesity, diabetes, and coronary risk in women. J Cardiovasc Risk 2002; 9: 323–30.
6 Charpentier G, Genes N, Vaur L, Amar J, Clerson P, Cambou JP, *et al*. Control of diabetes and cardiovascular risk factors in patients with type 2 diabetes: a nationwide French survey. Diabetes Metab 2003; 29: 152–8.
7 Li S, Culver B, Ren J. Benefit and risk of exercise on myocardial function in diabetes. Pharmacol Res 2003; 48: 127–32.
8 Hammes HP, Du X, Edelstein D, Taguchi T, Matsumura T, Ju Q, *et al*. Benfotiamine blocks three major pathways of hyperglycemic damage and prevents experimental diabetic retinopathy. Nat Med 2003; 93: 294–9.
9 Feldman EL. Oxidative stress and diabetic neuropathy: a new understanding of an old problem. J Clin Invest 2003; 111: 431–3.
10 Gilbert RE, Tsalamandris C, Bach LA, Panagiotopoulos S, O'Brien RC, Allen TJ, *et al*. Long-term glycemic control and the rate of progression of early diabetic kidney disease. Kidney Int 1993; 44: 855–9.
11 Fein FS, Sonnenblick EH. Diabetic cardiomyopathy. Cardiovasc Drugs Ther 1994; 8: 65–73.
12 Ren J, Davidoff AJ. Diabetes rapidly induces contractile dysfunctions in isolated ventricular myocytes. Am J Physiol Heart Circ Physiol 1997; 272: H148–58.
13 Wold LW, Relling DP, Colligan PB, Scott GI, Hintz KK, Ren BH, *et al*. Characterization of contractile function in diabetic hypertensive cardiomyopathy in adult rat ventricular myocytes. J Mol Cell Cardiol 2001; 33: 1719–26.
14 Poirier P, Garneau C, Marois L, Bogaty P, Dumesnil JG. Diastolic dysfunction in normotensive men with well-controlled type 2 diabetes: importance of maneuvers in echocardiographic screening for preclinical diabetic cardiomyopathy. Diabetes Care 2001; 24: 5–10.
15 Buyukgebiz A, Saylam G, Dundar B, Bober E, Unal N, Akcoral A. Dilated cardiomyopathy as the first early complications in a 14 year-old girl with diabetes mellitus type 1. J Pediatr Endocrinol Metab 2000; 13: 1143–6.
16 Depre C, Young ME, Ying J, Ahuja HS, Han Q, Garza N, *et al*. Streptozotocin-induced changes in cardiac gene expression in the absence of severe contractile dysfunction. J Mol Cell Cardiol 2000; 32: 985–96.
17 Kang YJ. Molecular and cellular mechanisms of cardiotoxicity. Environ Health Perspect 2001; 109: 27–34.
18 Ren J, Bode AM. Altered cardiac excitation-contraction coupling in ventricular myocytes from spontaneously diabetic BB rats. Am J Physiol Heart Circ Physiol 2000; 279: H238–44.
19 Norby FL, Wold LE, Duan J, Hintz KK, Ren J. IGF-I attenuates diabetes-induced cardiac contractile dysfunction in ventricular myocytes. Am J Physiol Endocrinol Metab 2002; 283: E658–66.
20 Norby FL, Aberle NS, Kajstura J, Anversa P, Ren J. Transgenic overexpression of insulin-like growth factor I prevents streptozotocin-induced cardiac contractile dysfunction and beta-adrenergic response in ventricular myocytes. J Endocrinol 2004; 180: 175–82.
21 Kajstura J, Fiordaliso F, Andreoli AM, Li B, Chimenti S, Medow MS, *et al*. IGF-1 overexpression inhibits the development of diabetic cardiomyopathy and angiotensin II-mediated oxidative stress. Diabetes 2001; 50: 1414–24.
22 Sowers JR, Williams M, Epstein M, Bakris G. Hypertension in

patients with diabetes. Strategies for drug therapy to reduce complications. Postgrad Med 2000; 107: 47–54.
23 Spector KS. Diabetic cardiomyopathy. Clin Cardiol 1998; 21: 885–7.
24 Rubler S, Dlugash J, Yuceoglu YZ, Kumral T, Branwood AW, Grishman A. New type of cardiomyopathy associated with diabetic glomerulosclerosis. Am J Cardiol 1972; 30: 595–602.
25 Pierce GN, Russell JC. Regulation of intracellular Ca^{2+} in the heart during diabetes. Cardiovasc Res 1997; 34: 41–7.
26 Chatham JC, Forder JR, McNeill JH. The heart in diabetes. Norwell: MA Kluwer Academic Publishers; 1996.
27 Schaffer SW, Mozafferi M. Abnormal mechanical function in diabetes: relation to myocardial calcium handling. Coron Artery Dis 1996; 7: 109–15.
28 Dincer UD, Bidasee KR, Guner S, Tay A, Ozcelikay AT, Altan VM. The effect of diabetes on expression of beta1-, beta2-, and beta3-adrenoreceptors in rat hearts. Diabetes 2001; 50: 455–61.
29 Tamada A, Hattori Y, Houzen H, Yamada Y, Sakuma I, Kitabatake A, *et al*. Effects of beta-adrenoreceptor stimulation on contractility, $[Ca^{2+}]_i$, and Ca^{2+} current in diabetic rat cardiomyocytes. Am J Physiol Heart Circ Physiol 1998; 274: H1849–57.
30 Idris I, Gray S, Donnelly R. Protein kinase C activation: isozyme-specific effects on metabolism and cardiovascular complications in diabetes. Diabetologia 2001; 44: 659–73.
31 Given MB, Jie O, Zhao X, Giles TD, Greenberg SS. Protein kinase C isozymes in skeletal muscles during the early stage of genetic and streptozotocin diabetes. Proc Soc Exp Biol Med 1998; 218: 382–9.
32 Devereux RB, Roman MJ, Paranicas M, O'Grady MJ, Lee ET, Welty TK, *et al*. Impact of diabetes on cardiac structure and function: the strong heart study. Circulation 2000; 101: 2271–6.
33 Liu JE, Palmieri V, Roman MJ, Bella JN, Fabsitz R, Howard BV, *et al*. The impact of diabetes on left ventricular filling pattern in normotensive and hypertensive adults: the Strong Heart Study. J Am Coll Cardiol 2001; 37: 1943–9.
34 Rutter MK, Parise H, Benjamin EJ, Levy D, Larson MG, Meigs JB, *et al*. Impact of glucose intolerance and insulin resistance on cardiac structure and function: sex-related differences in the Framingham Heart Study. Circulation 2003; 107: 448–54.
35 Schannwell CM, Schneppenheim M, Perings SM, Zimmermann T, Plehn G, Strauer BE. Alterations of left ventricular function in women with insulin-dependent diabetes mellitus during pregnancy. Diabetologia 2003; 46: 267–75.
36 Dutta K, Podolin DA, Davidson MB, Davidoff AJ. Cardiomyocyte dysfunction in sucrose-fed rats is associated with insulin resistance. Diabetes 2001; 50: 1186–92.
37 Zarich SW, Nesto RW. Diabetic cardiomyopathy. Curriculum Cardiol 1989; 118: 1000–12.
38 Fraser GE, Luk R, Thompson S, Smith H, Carter S, Sharpe N. Comparison of echocardiography variables between Type 1 diabetics and normal control. Am J Cardiol 1995; 75: 141–5.
39 Raev DC. Which left ventricular function is impaired earlier in the evaluation of diabetic cardiomyopathy. Diabetes Care 1994; 17: 633–9.
40 Celentano A, Vaccaro O, Tammaro P, Galderisi M, Crivaro M, Oliviero M, *et al*. Early abnormalities of cardiac function in non-insulin-dependent diabetes mellitus and impaired glucose tolerance. Am J Cardiol 1995; 76: 1173–6.
41 Grundy SM, Benjamin IJ, Burke GL, Chait A, Eckel RH, Howard BV, *et al*. Diabetes and cardiovascular disease: a statement for healthcare professionals from the American Heart Association. Circulation 1999; 100: 1134–46.
42 Brownlee M. Biochemistry and molecular cell biology of diabetic complications. Nature 2001; 414: 813–20.
43 Cai L, Kang YJ. Oxidative stress and diabetic cardiomyopathy: a brief review. Cardiovasc Toxicol 2001; 1: 181–93.
44 Ramasamy R, Oates PJ, Schaefer S. Aldose reductase inhibition protects diabetic and nondiabetic rat hearts from ischemic injury. Diabetes 1997; 46: 292–300.
45 Hwang YC, Bakr S, Ellery CA, Oates PJ, Ramasamy R. Sorbitol dehydrogenase: a novel target for adjunctive protection of ischemic myocardium. FASEB J 2003; 17: 2331–3.
46 Ramasamy R. Aldose reductase: a novel target for cardioprotective interventions. Curr Drug Targets 2003; 4: 625–32.
47 Chandra D, Jackson EB, Ramana KV, Kelley R, Srivastava SK, Bhatnagar A. Nitric oxide prevents aldose reductase activation and sorbitol accumulation during diabetes. Diabetes 2002; 51: 3095–101.
48 Lee AY, Chung SS. Contributions of polyol pathway to oxidative stress in diabetic cataract. FASEB J 1999; 13: 23–30.
49 Makita Z, Vlassara H, Rayfield E, Cartwright K, Friedman E, Rodby R, *et al*. Hemoglobin-AGE: a circulating marker of advanced glycosylation. Science 1992; 258: 651–3.
50 Wolffenbuttel BH, Giordano D, Founds HW, Bucala R. Long-term assessment of glucose control by haemoglobin-AGE measurement. Lancet 1996; 347: 513–5.
51 Bierhaus A, Illmer T, Kasper M, Luther T, Quehenberger P, Tritschler H, *et al*. Advanced glycation end product (AGE)-mediated induction of tissue factor in cultured endothelial cells is dependent on RAGE. Circulation 1997; 96: 2262–71.
52 Bierhaus A, Hofmann MA, Ziegler R, Nawroth PP. AGEs and their interation with AGE-receptors in vascular disease and diabetes mellitus. I. The AGE concept. Cardiovasc Res 1998; 37: 586–600.
53 Schmidt AM, Stern DM. RAGE: a new target for the prevention and treatment of the vascular and inflammatory complications of diabetes. Trends Endocrinol Metab 2000; 11: 368–75.
54 Esposito C, Gerlach H, Brett J, Stern D, Vlassara H. Endothelial receptor-mediated binding of glucose-modified albumin is associated with increased monolayer permeability and modulation of cell surface coagulant properties. J Exp Med 1989; 170: 1387–407.
55 Li J, Schmidt AM. Characterization and functional analysis of the promoter of RAGE, the receptor for advanced glycation end products. J Biol Chem 1997; 272: 16 498–506.
56 Schmidt AM, Hori O, Brett J, Yan SD, Wautier JL, Stern D. Cellular receptors for advanced glycation end products. Implications for induction of oxidant stress and cellular dysfunction in the pathogenesis of vascular lesions. Arterioscler Thromb 1994; 14: 1521–8.
57 Ritthaler U, Deng Y, Zhang Y, Greten J, Abel M, Sido B, *et al*. Expression of receptors for advanced glycation end products in peripheral occlusive vascular disease. Am J Pathol 1995; 146: 688–94.
58 Yan SD, Stern D, Schmidt AM. What's the RAGE? The receptor

for advanced glycation end products (RAGE) and the dark side of glucose. Eur J Clin Invest 1997; 27: 179–81.
59 Lu M, Kuroki M, Amano S, Tolentino M, Keough K, Kim I, *et al*. Advanced glycation end products increase retinal vascular endothelial growth factor expression. J Clin Invest 1998; 101: 1219–24.
60 Soudis-Liparota T, Cooper M, Papazoglou D, Clarke B, Jerums G. Retardation by aminoguanidine of development of albuminura, mesangial expansion, and tissue fluorescence in streptozotocin-induced diabetic rat. Diabetes 1991; 40: 1328–34.
61 Nakamura S. Progression of nephropathy in spontaneous diabetic rats is prevented by OPB-9195, a novel inhibitor of advanced glycation. Diabetes 1997; 46: 895–9.
62 Hammes HP. Aminoguanidine treatment inhibits the development of experimental diabetic retinopathy. Proc Natl Acad Sci USA 1991; 88: 11555–9.
63 Park L. Suppression of accelerated diabetic atherosclerosis by the soluble receptor for advanced glycation endproducts. Nature Med 1998; 4: 1025–31.
64 Koya D, King GL. Protein kinase C activation and the development of diabetic complications. Diabetes 1998; 47: 859–66.
65 Portilla D. Etomoxir-induced PPARalpha-modulated enzymes protect during acute renal failure. Am J Physiol Renal Physiol 2000; 278: F667–75.
66 Keogh RJ, Dunlop ME, Larkins RG. Effect of inhibition of aldose reductase on glucose flux, diacylglycerol formation, protein kinase C, and phospholipase A2 activation. Metabolism 1997; 46: 41–7.
67 Stevens MJ, Obrosova I, Feldman EL, Greene DA. The sorbitol-osmotic and sorbitol-redox hypothesis. In: LeRoith D, Taylor SI, Olefsky JM, editors. Diabetes mellitus: a fundamental and clinical text. Philadelphia: Lippincott Williams & Wilkins; 2000. p 972–83.
68 Lee AY, Chung SK, Chung SS. Demonstration that polyol accumulation is responsible for diabetic cataract by the use of transgenic mice expressing the aldose reductase gene in the lens. Proc Natl Acad Sci USA 1995; 92: 2780–4.
69 Yamaoka T, Nishimura C, Yamashita K, Itakura M, Yamada T, Fujimoto J, *et al*. Acute onset of diabetic pathological changes in transgenic mice with human aldose reductase cDNA. Diabetologia 1995; 38: 255–61.
70 Yagihashi S, Yamagishi S, Wada R, Sugimoto K, Baba M, Wong HG, *et al*. Galactosemic neuropathy in transgenic mice for human aldose reductase. Diabetes 1996; 45: 56–9.
71 Singh SB, Malamas MS, Hohman TC, Nilakantan R, Carper DA, Kitchen D. Molecular modeling of the aldose reductase-inhibitor complex based on the X-ray crystal structure and studies with single-site-directed mutants. J Med Chem 2000; 43: 1062–70.
72 Du XL. Hyperglycemia-induced mitochondrial superoxide overproduction activates the hexosamine pathway and induces plasminogen activator inhibitor-1 expression by increasing Sp1 glycosylation. Proc Natl Acad Sci USA 2000; 97: 12222–6.
73 Kakkar R, Kalra J, Mantha SV, Prasad K. Lipid peroxidation and activity of antioxidant enzymes in diabetic rats. Mol Cell Biochem 1995; 151: 113–9.
74 Ohuwa T, Sato Y, Naoi M. Hydroxyl radical formation in diabetic rats induced by streptozotocin. Life Sci 1995; 56: 1789–98.
75 Bayes JW, Thorpe SR. Role of oxidative stress in diabetic complications: a new perspective on an old paradigm. Diabetes 1999; 48: 1–9.
76 Kowluru RA, Engerman RL, Kern TS. Diabetes-induced metabolic abnormalities in myocardium: effect of antioxidant therapy. Free Radical Res 2000; 32: 67–74.
77 Ustinova EE, Barrett CJ, Sun SY, Schultz HD. Oxidative stress impairs cardiac chemoreflexes in diabetic rats. Am J Physiol 2000; 279: 2176–87.
78 Rosen P, Du X, Sui GZ. Molecular mechanisms of endothelial dysfunction in the diabetic heart. Adv Exp Med Biol 2001; 498: 75–86.
79 Nishikawa T, Edelstein D, Du XL, Yamagishi S, Matsumura T, Kaneda Y, *et al*. Normalizing mitochondrial superoxide production blocks three pathways of hyperglycaemic damage. Nature 2000; 404: 787–90.
80 Mohamed AK, Bierhaus A, Schiekofer S, Tritschler H, Ziegler R, Nawroth PP. The role of oxidative stress and NF-κB activation in late diabetic complications. Biofactors 1999; 10: 157–67.
81 Mercurio F, Manning AM. NF-κB as a primary regulator of the stress response. Oncogene 1999; 18: 6163–71.
82 Barnes PJ, Karin M. Nuclear factor-κB: a pivotal transcription factor in chronic inflammatory disease. N Engl J Med 1997; 336: 1066–71.
83 Baldwin Jr AS. The transcription factor NF-κB and human disease. J Clin Invest 2001; 107: 3–6.
84 Tak PP, Firestein GS. NF-κB: a key role in inflammatory disease. J Clin Invest 2001; 107: 7-11.
85 Tibbles LA, Woodgett JR. The stress-activated protein kinase pathways. Cell Mol Life Sci 1999; 55: 1230–54.
86 Ho FM, Liu SH, Liau CS, Huang PJ, Lin-Shiau SY. High glucose-induced apoptosis in human endothelial cells is mediated by sequential activations of c-Jun NH(2)-terminal kinase and caspase-3. Circulation 2000; 101: 2618–24.
87 Natarajan R, Scott S, Bai W, Yerneni KKV, Nadler J. Angiotensin II signaling in vascular smooth muscle cells under high glucose conditions. Hypertension 1999; 33: 378–84.
88 Dunlop ME, Muggli EE. Small heat shock protein alteration provides a mechanism to reduce mesangial cell contractility in diabetes and oxidative stress. Kidney Intl 2000; 57: 464–75.
89 Frustaci A, Kajstura J, Chimenti C, Jakoniuk I, Leri A, Maseri A, *et al*. Myocardial cell death in human diabetes. Circ Res 2000; 87: 1123–32.
90 Stockklauser-Farber K, Ballhausen T, Laufer A, Rosen P. Influence of diabetes on cardiac nitric oxide synthase expression and activity. Biochim Biophys Acta 2000; 1535: 10–20.
91 Tomita M, Mukae S, Geshi E, Umetsu K, Nakatani M, Katagiri T. Mitochondrial respiratory impairment in streptozotocin-induced diabetic rat heart. Jpn Circ J 1996; 60: 673–82.
92 Kucharska J, Braunova Z, Ulicna O, Zlatos L, Gvozdjakova A. Deficit of coenzyme Q in heart and liver mitochondria of rats with streptozotocin-induced diabetes. Physiol Res 2000; 49: 411–8.
93 Doroshow JH, Locker GY, Myers CE. Enzymatic defenses of the mouse heart against reactive oxygen metabolites: alterations produced by doxorubicin. J Clin Invest 1980; 65: 128–35.
94 Chen Y, Saari JT, Kang YJ. Weak antioxidant defenses make the heart a target for damage in copper-deficient rats. Free Radical Biol Med 1994; 17: 529–36.

95 Kersten JR, Schmeling TJ, Orth KG, Pagel PS, Warltier DC. Acute hyperglycemia abolishes ischemic preconditioning *in vivo*. Am J Physiol 1998; 275: H721–5.

96 Joyeux M, Faure P, Godin-Ribuot D, Halimi S, Patel A, Yellon DM, *et al*. Heat stress fails to protect myocardium of streptozotocin-induced diabetic rats against infarction. Cardiovasc Res 1999; 43: 939–46.

97 Elangovan V, Shohami E, Gati I, Kohen R. Increased hepatic lipid soluble antioxidant capacity as compared to other organs of streptozotocin-induced diabetic rats: a cyclic voltametry study. Free Radical Res 2000; 32: 125–34.

98 Ye G, Metreveli NS, Ren J, Epstein PN. Metallothionein prevents diabetes-induced deficits in cardiomyocytes by inhibiting reactive oxygen species production. Diabetes 2003; 52: 777–83.

99 Ye G, Metreveli NS, Donthi RV, Xia S, Xu M, Carlson EC, *et al*. Catalase protects cardiomyocyte function in models of type 1 and type 2 diabetes. Diabetes 2004; 53: 1336–43.

100 Alici B, Gumustas MK, Ozkara H, Akkus E, Demirel G, Yencilek F, *et al*. Apoptosis in the erectile tissues of diabetic and healthy rats. BJU Int 2000; 85: 326–9.

101 Cai L, Chen S, Evans T, Deng DX, Mukherjee K, Chakrabarti S. Apoptotic germ-cell death and testicular damage in experimental diabetes: prevention by endothelin antagonism. Urol Res 2000; 28: 342–7.

102 Srinivasan S, Stevens M, Wiley JW. Diabetic peripheral neuropathy: evidence for apoptosis and associated mitochondrial dysfunction. Diabetes 2000; 49: 1932–8.

103 Fiordaliso F, Li B, Latini R, Sonnenblick EH, Anversa P, Leri A, *et al*. Myocyte death in streptozotocin-induced diabetes in rats is angiotensin II-dependent. Lab Invest 2000; 80: 531–7.

104 Privratsky JR, Wold LE, Sowers JR, Quinn MR, Ren J. AT_1 blockade prevents glucose-induced cardiac dysfunction in ventricular myocytes: role of the AT_1 receptor and NADPH oxidase. Hypertension 2003; 42: 206–12.

105 Dzau VJ. Theodore Cooper Lecture: tissue angiotensin and pathobiology of vascular disease: a unifying hypothesis. Hypertension 2001; 37: 1047–52.

106 Nickenig G, Harrison DG. The AT_1-type angiotensin receptor in oxidative stress and atherogenesis, part I: oxidative stress and atherogenesis. Circulation 2002; 105: 393–6.

107 Sowers JR. Hypertension, angiotensin II, and oxidative stress. N Engl J Med 2002; 346: 1999–2001.

108 Mascareno E, Siddiqui MA. The role of Jak/STAT signaling in heart tissue renin-angiotensin system. Mol Cell Biochem 2000; 212: 171–5.

109 Wang HD, Xu S, Johns DG, Du Y, Quinn MT, Cayatte AJ, *et al*. Role of NADPH oxidase in the vascular hypertrophic and oxidative stress response to angiotensin II in mice. Circ Res 2001; 88: 947–53.

Acta Pharmacologica Sinica 2005 Aug; 26 (8): 918–925

Invited review

Ion channelopathy and hyperphosphorylation contributing to cardiac arrhythmias[1]

De-zai DAI[2], Feng YU

Research Division of Pharmacology, China Pharmaceutical University, Nanjing 210009, China

Key words

ion channels; arrhythmia; ryanodine receptor calcium release channel; FKBP12.6; sarcoplasmic reticulum; phospholamban; phosphorylation

[1] Project supported by the National Natural Science Foundation of China (No 30230170).
[2] Correspondence to Prof De-zai DAI.
Phn 86-25-8327-1270.
Fax 86-25-8330-2827.
E-mail dezaidai@vip.sina.com

Received 2005-01-03
Accepted 2005-03-29

doi: 10.1111/j.1745-7254.2005.00134.x

Abstract

The occurrence of cardiac arrhythmias is related to the abnormality of ion channels not only in sarcolemma but also in the sarcoplasmic reticulum, which regulates the process of calcium release and up-take intracellularly. Patterns of ion channelopathy in the sarcolemma can be divided into single channel disorder from gene mutations and multiple channels disorder in a diseased hypertrophied heart. Abnormal RyR2, FKBP12.6, SERCA2a, and PLB are also involved in the initiation of cardiac arrhythmias. Maladjustment by hyperphosphorylation on the ion channels in the sarcolemma and RyR2-FKBP12.6 and SERCA2a-PLB is discussed. Hyperphosphorylation, which is the main abnormality upstream to ion channels, can be targeted for suppressing the deterioration of ion channelopathy in terms of new drug discovery in the treatment and prevention of malignant cardiac arrhythmias.

Introduction

Cardiac arrhythmias mostly occur in diseased hearts as a result of an abnormality in ion channels[1]. Diseased hearts with overt cardiac remodeling are at risk of developing severe and life-threatening arrhythmias. Patients suffering from sudden coronary death (SCD) were monitored with ECG to manifest ventricular tachyarrhythmias. Between 50% and 80% of deaths in patients suffering from congestive heart failure are caused by cardiac arrhythmias[2]. There have been significant advances in the molecular biological considerations of cardiac arrhythmias[3], however, there has been no success in suppressing ventricular tachyarrhythmias using antiarrhythmic agents[4,5]. Electronic devices and electrical defibrillators remain the first choice in controlling ventricular tachyarrhythmias.

Continuous effort has been made to search for new and effective antiarrhythmic agents for controlling life-threatening cardiac arrhythmias. The efficacy of antiarrhythmic agents to prevent cardiac sudden death was evaluated in patients with post-infarcted heart in clinical trials. Cardiac Arrhythmias Suppressing Trial (CAST, 1989) reported an increase in the mortality of the treated groups (flecainide and encainide) against the placebo[6]. A dramatic shift from Class I agents to Class III agents was made[[4]], and pure Class III drugs were considered as ideal agents (*d*-sotalol) in survival test with oral *d*-sotalol (SWORD, 1994). The *d*-sotalol, which is free from β-adrenergic blocking activity but can block the rapid component of delayed rectifier outward K^+ currents (I_{Kr}), only failed again with a higher mortality (3.9%) than that in the placebo (2.0%)[4,5]. The lack of success in the development of antiarrhythmic agents is likely because of the lack of awareness of the mechanisms of ion channelo-pathy in the diseased myocardium.

Effort to gain more insight into molecular aspects of ion channelopathy in cardiac arrhythmias in both the inherited long QT syndrom (LQTS) and cardiac remodeling of diseased hearts has been ongoing[7]. Cardiac remodeling resulting from infarction or cardiomyopathy has been targeted to investigate the mechanisms underlying cardiac arrhythmias. Aberrant molecular biology and ion channelopathy are focused on the affected myocardium. The responses to varying drug treatments are compared in amelioration and exacerbation of cardiac arrhythmias.

Different patterns of sarcolemmal ion channelopathy

Single channelopathy in LQTS Gene mutations which alters the peptide sequence of the K^+ and Na^+ ion channels in cardiomyocytes caused LQTS. There are three kinds of LQTS[1,7,8]: (i) downregulation of the slow component of delayed rectifier outward K^+ currents (I_{Ks}) by mutations in the *KvLQT1* (*KCNQ1*), and *HMINK* (*KCNE1*) gene; (ii) downregulation of the I_{Kr} channels by mutations in the *HERG* (*KCNH1*) gene; (iii) upregulation of the sodium currents (I_{Na}) by mutations in the SCN_5A gene. Ion channelopathy induced by mutations only involves an individual channel[9,10]. Two mutations in the *HERG* gene were found. An early appearance of STOP codon located at the nucleotide binding domain left one dysfunctional channel responsible for LQTS, but another in the minor region of the peptide chain as a result of polymorphism did not cause the change of QT interval[10].

Multi-channelopathy in cardiac remodeling In the hypertrophied ventricle following myocardial infarction or cardiomyopathy, the multiple ion channels involving the Na^+, K^+ and Ca^{2+} currents in the lipid membrane were downregulated in function or mRNA abundance[11–13], rather than being limited to a single one[14]. In the pulmonary hypertension the downregulation of the genes encoding the I_{to} channels (Kv 4.2 and Kv 4.3) was found in the hypertrophied right ventricle, but not the left ventricle[15]. The ion channelopathy in cardiac remodeling can be referred to as multiple and non-selective channelopathy, and is likely to be secondary to the pathological lesions upstream to the ion channels, including lesions in the affected lipid membrane and the altered transmembrane signaling system[9,10]. Ion channelopathy can be regressed when lesions upstream to the ion channels are relieved.

Upregulation of ion channels in cardiomyopathy by *L*-thyroxin A model of cardiomyopathy in rats was induced by repeated administration of *L*-thyroxin for 10 d which manifested exaggerated cardiac arrhythmias after ischemia/reperfusion[16]. The arrhythmogenesis in the model was associated with remarkable cardiac remodeling and an imbalance of transmembrane distribution of cation, shown by an augmented activity of Na^+/K^+ ATPase and Ca^{2+} ATPase in the sarcolemma and mitochondria[17,18].

The channels of slow component of delayed rectifier outward K^+ currents (I_{Ks}) and the rapid component of delayed rectifier outward K^+ currents (I_{Kr}) were upregulated accompanied with myocardium remodeling induced by *L*-thyroxin[19] which would cause a shortened action potential duration (APD). However, the $I_{Ca,L}$ was exacerbated in isolated myocytes in this model which had the potential to prolong APD[20]. The length of APD, in general, is not dependent on ions movement in a single channel, but is modulated by the balance of total currents in the repolarization of the membrane[9]. A simple mathematic equation denotes the balance between the influx and efflux of ions across the membrane: $APD=(I_{Ca,L}\cdot I_{Na})/(I_{Kr}\cdot I_{Ks})$. The final impact on the APD is dependent on the net influence summarized by the individual ion current. Varied repolarization, which contributes to cardiac arrhythmias in a diseased heart, shows retardation and dispersion of APD. The abnormality of repolarization can be measured by the length of either APD or the QT interval in ECG traces. Dispersion of APD between the right and left ventricle in association with arrhythmogenesis was developed in a hypertrophied canine heart by chronic destruction of the atrioventricular node[21]. More dispersed ion currents in repolarization create a higher risk of developing life-threatening arrhythmias. Arrhythmic models of the canine diseased heart and rat cardiomyopathy by *L*-thyroxin share important properties of dispersed repolarization and disturbed multiple ion channels[21,22].

The normal function of some ion channels is modulated by phosphorylation at the nucleotide binding domains of the channel peptide, mediated by cAMP and PKA[3,22]. Hyperphosphorylation under the pathological condition serves as an important etiological factor to develop severe cardiac arrhythmias in diseased status. The upregulation of I_{Ks}, I_{Kr}, and $I_{Ca,L}$ in cardiac remodeling by chronic administration of *L*-thyroxin was likely to cause overphosphorylation, so arrhythmias in this model were effectively suppressed by propranolol[16].

Ion channelopathy in sarcoplasmic reticulum

RyR2 and SERCA2a in the sarcoplasmic reticulum (SR) A rise of free calcium in the cytosol is initiated by an influx of Ca^{2+} through $I_{Ca,L}$ and is amplified up to 10-fold by calcium release from the RyR2/calcium release channels, which is mediated by the calcium-induced calcium release (CICR) that promotes a boost of free calcium in the systole. A rapid conversion into the diastolic phase is performed by SERCA2a/calcium-uptaking channels. The calcium-release channels (RyR2) and the uptake channels (SERCA2a) of the SR are modulated separately by two proteins, calstabin 2 protein (FKBP12.6, the stabilizing FK 506 binding protein) and phospholamban (PLB), which are under the control of the phosphorylation of PKA[23]. The association of FKBP 12.6 to the macromolecule RyR2 is essential in stabilizing the Ca^{2+} releasing function by tightly closing the channel against the low level of Ca^{2+} in the diastolic period. The movement

of the free calcium from cytosol into the SR by SERCA2a is slow as a result of suppression by PLB at the resting state. The efficacy of SERCA2a increases significantly when the PLB is phosphorylated. This is caused by the removal of the suppression through PLB phosphorylation. An abnormal boost of the free calcium in the diastolic phase is provided by the derangement of either RyR2-FKBP12.6 or PLB-SERCA2a systems that play active roles in exhibiting cardiac arrhythmias during stress-related conditions[3,24,25].

Inherited arrhythmogenetic disorders from mutations of RyR2 gene There are two inherited diseases that manifest cardiac arrhythmias stemming from RyR2 gene mutations. Arrhythmigenic right ventricular dysplasia/cardiomyopathy (ARVD/C) shows distinguished morphological changes in the right ventricle where myocytes are replaced by fibrosis and adipose tissue[26,27]. Catecholaminergic polymorphic ventricular tachyarrhythmias (CPVT)[28] is another inherited disease that puts patients at risk of developing arrhythmias during physical exercise, but not in a resting state[29]. More catecholamines are released in the process of physical exercise to initiate early after depolarization (EAD) and delayed after depolarization (DAD) in these patients through a mechanism of the triggering activity, as a consequence malignant ventricular arrhythmias are more likely to occur. Mutations in the RyR2 gene attenuated the affinity of RyR2 to FKBP12.6 which resulted in tachyarrhythmias.

Hyperphosphorylation of ion channels Both sarcolemmal ion channels and calcium-release and uptake channels in the sarcoplasmic reticulum can be hyperphosphorylated.

Hyperphosphorylation of ion channels in lipid membrane There is a nucleotide binding domain in the sequence of the channel peptide of I_{Kr}, I_{Kr}, and $I_{Ca,L}$. Hyperphosphorylation of the channel peptide promotes an upregulation that is likely to provide a molecular basis for the varying function of the ion channels in a diseased heart. The up-regulated I_{Kr} and I_{Ks} in *L*-thyroxin-induced cardiomyopathy[30] contributed to the retardation of APD. In contrast, an unregulated $I_{Ca,L}$[31], another consequence of hyperphosphorylation, offered the potential to shorten the APD by facilitating repolarization. The co-existence of two factors to prolong or shorten APD is responsible for the dispersion of repolarization in cardiac remodeling under the control of PKA phosphorylation. The existence of hyperphosphorylation has been evidenced by a significant increase in the PKA mRNA in the injured myocardium induced by *L*-thyroxin.

The post-infarcted rat heart with a hypertrophied ventricle presents a mild enhancement in cardiac arrhythmias that occur in the ischemia/reperfusion procedure using Langendorff apparatus. After a treatment with isoproterenol for 5 d, the severity of cardiac arrhythmias and cardiac remodeling are greatly exacerbated, which can be attributed to PKA-hyperphosphorylation. The impact of cardiac hypertrophy on the $I_{Ca,L}$ is uncertain, however, the intensity of the $I_{Ca,L}$ in the infarcted and isoproterenol treated rat model is augmented significantly in the left ventricle, but not in the right ventricle. A significant dispersion of the $I_{Ca.L}$ current by hyperphosphorylation has been found to be responsible for the exaggerated arrhythmias.

Hyperphosphorylation of RyR2-FKBP12.6 macromolecule complex Hyperphosphorylation of the RyR2 macromolecule complex that dissociates the FKBP12.6 from its binding site on the RyR2 can be developed by an overactivation of the β-adrenergic receptors[23]. This is presented in a failing heart with relevant cardiac arrhythmias[24,25]. Hyperphosphorylation converts the normal function of RyR2 into an oversensitive state towards the low diastolic low calcium levels. A substantial leakage of Ca^{2+} at the diastole, which is the main result of dissociation of FKBP12.6, contributes to a partial depolarization process by a boost in Ca^{2+} ion in repolarization. The delayed process of repolarization causes a prolonged APD that promotes EAD and DAD, and eventually induces cardiac tachyarrhythmias.

Hyperphosphorylation of PLB-SERCA2a system A maladaptive response to PLB by hyperphosphorylation[3,32] causes a depressed SERCA2a capacity, after which elevated Ca^{2+} levels at the diastole are initiated. Hyperphosphorylation of PLB could negatively modulate the maximal capacity of SERCA2a by means of transgenic procedure, possibly involving other phosphorylated proteins[3]. The mechanism of hyperphosphorylation might participate in arrhythmogenesis induced by *L*-thyroxin where the mRNA of SERCA is altered significantly.

The post-infarcted rat heart shows a mild-depressed SERCA2a mRNA and less severe cardiac arrhythmias, possibly reflecting hyperphosphorylation to a lesser extent[33]. After a 5-d treatment with isoproterenol, the infarcted heart was converted into a significantly augmented arrhythmia accompanied with more depressed mRNA of SERCA2a which was mediated by PKA-hyperphosphorylation.

Dispersion of the calcium-handling system by over-phosphorylation We demonstrated that the significant dispersion of depressed mRNA abundance of RyR2 and SERCA and upregulated mRNA abundance of sodium calcium exchanger (NCX) in infarcted heart was associated with an increase in arrhythmic score after an isoproterenol treatment. The mRNA abundance of RyR2 and SERCA2 were decreased by 83.6% and 77.6% in left ventricle and by 36.7% and 38.1% in right ventricle, respectively. The mRNA abundance of

NCX1 was increased by 63.8% in left ventricle and 40.4% in right ventricle. The difference between left and right ventricle was significant. This implies that the free calcium levels in the left ventricle could be relatively higher than in the right ventricle under hyperphosphorylation. An elevated diastolic calcium level is likely to be the result of an alternative route, which could be sourced by an increase in NCX under hyperphosphorylation. An up-regulated NCX mRNA in the left ventricle possibly indicates more calcium than that in the right ventricle[33]. A dispersion of the calcium-handling system under the control of PKA-overphosphorylation in an infarcted heart can be the basis for initiating cardiac arrhythmias under stress. The onset of severe cardiac arrhythmias based on not only the dispersion of the ion channels in the lipid membrane, but also the release, uptake, and exchange of the calcium-handling system.

The maladjustment in RyR2-FKBP12.6 and SERCA2a-PLB by hyperphosphorylation happened in various conditions (eg, in failing hearts and over-stimulation of the β-adrenergic receptors by activated sympathetic impulses). Sudden cardiac death results from the over-activation of PKA[34]. The aberrant RyR2-FKBP12.6 and SERCA2a-PLB are important to develop malignant arrhythmias in an affected heart and serve as new targets for drug intervention to suppress cardiac tachyarrhythmias. The severely exaggerated cardiac arrhythmias provoked by an ischemia/reperfusion episode in the hypertrophied ventricle are produced either by repeated administration of *L*-thyroxine or isoproterenol in chronic infarcted rat heart. These could be related to the dispersion of deranged activity of the intracellular calcium-handling system as a consequence of hyperphosphorylation of the SR.

Direct and indirect effects of drugs on ion channels

Direct effect on the ion channels The effects of antiarrhythmic agents on ion channels could be recognized as either, a direct action on ion channels or an indirect effect, with which an improvement can be achieved on the altered ion channels by relieving the upstream lesions. Using the regular micro-electrode and patch-clamp techniques we observed that CPU 86017 blocked sodium, potassium, and calcium channels. A biphasic effect on the APD is suggested to be the result of a multi-channel blockade[35]. So CPU 86017 could modulate APD in two directions, either prolonging the already shortened APD or shortening the already lengthened APD caused by lesions in a diseased myocardium. Therefore, reducing the dispersion of APD in a diseased heart to prevent cardiac arrhythmias is hopeful[36]. Prolonging APD by anti-arrhythmic agents is not beneficial for inhibiting ventricular tachyarrhythmias. In contrast, it always implies a potential of an adverse reaction by producing an increased incidence of *Torsades de pointes* (TdP)[37], a dangerous ventricular tachycardia with a greater tendency to ventricular fibrillation.

Most electrophysiological data of anti-arrhythmic agents on individual ion channels are collected from freshly isolated myocytes. However, cardiac arrhythmias appear frequently in diseased and remodeled rather than normal hearts, and the molecular biological properties of the myocardium are markedly different in many aspects between the normal and diseased hearts. Dispersed repolarization stems from disturbed channels in the diseased myocardium only. It is worthy of investigating drug effects on altered ion currents in isolated myocytes of diseased hearts.

Indirect effects on ion channelopathy Cardiac arrhythmias could be suppressed by chronic drug therapy for restoring the altered channels. The restoration of up-regulation of the I_{Kr}, I_{Ks} and $I_{Ca.L}$ current of isolated myocytes is confirmed by chronic medication of the propranolol, bepridil, and CPU 86017 in *L*-thyroxin-induced cardiomyopathy[30,31].

The ion channels in a chronically infarcted heart is mostly down-regulated. Therefore, it is confusing to face the fact that an anti-arrhythmic agent could stop tachyarrhythmias by overlapping its suppressive effect on a depressed channel in a remodeled myocardium. There should be some up-regulated ion channels in diseased hearts. The up-regulated channels, which are denoted clearly in the cardiomyopathy induced by *L*-thyroxin, are linked with the occurrence of cardiac arrhythmias and serve as the target for anti-arrhythmic therapy. The action of drugs on the ion channels can be described as direct and chronic rather than a direct effect alone (Figure 1). The ability of drugs to restore the diseased channels either mediated by an indirect action on the upstream lesion to the ion channels via chronic medication or an acute suppression on an individual current contributes to the correction of disordered channels and prevention from the sudden episode of cardiac death resultant from deterioration of ventricular fibrillation on stress-related events.

Phases of ion channelopathy

Two phases of ion channelopathy The pathological progression of ion channels in the myocardium either in the sarcolemmal membrane or in the SR could be subdivided into two different stages: the basal phase, in which no presentation of arrhythmias can be found; and the activated phase, in which arrhythmias appear when ion channelopathy

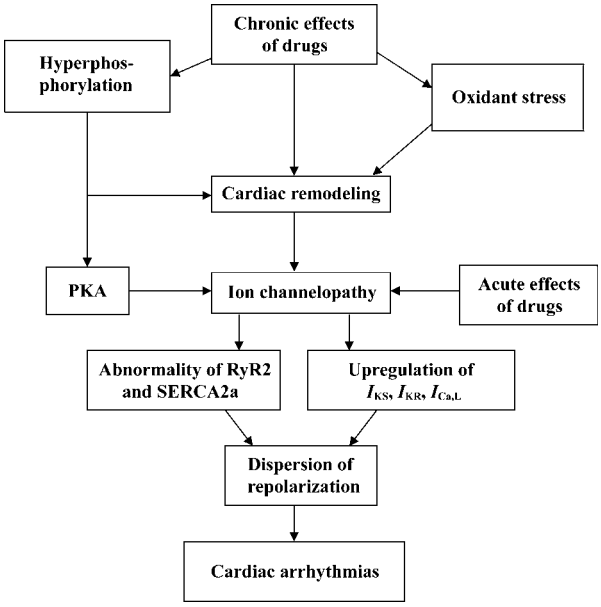

Figure 1. A diagram shows direct and indirect effect of drugs on ion channels and cardiac arrhythmias. The mechanisms underlying the arrhythmogenesis and ion channelopathies in relation to hyperphosphorylation are denoted in a diseased heart. Hyperphosphorylation, possibly including oxidative stress, is considered as crucial lesions at the upstream to ion channels and causes upregulation of ion channels and dispersion of repolarization.

is deteriorated.

Basal channelopathy with disturbed ion channels, which indicate an abnormal repolarization in the myocardium, manifests no arrhythmia. This is because of a reservoir of repolarization. The normal period of repolarization is less than 460 ms and an APD/QTc is referred as prolonged when beyond 460 ms. Malignant arrhythmias are most likely to occur when an APD/QTc is longer than 520 ms. A prolongation of APD/QTc in the range of 460 ms to 520 ms is considered as a repolarization reservoir at risk of developing TDP, however, there is no arrhythmia at the resting state. It is common that patients who either inherit mutation in genes of the *LQTS*, the *ARVD/C*, and *CPVT*, or possess predominant cardiac remodeling, exhibit no arrhythmia at the resting state, suggesting that prolonged APD/QTc is still within the repolarization reservoir. However, if an APD/QTc is prolonged over 520 ms, the incidence of malignant arrhythmias is very high and arrhythmias are more likely to occur sooner.

Ion channelopathy can be deteriorated. The occurrence of ventricular tachyarrhythmias needs an activation of the channelopathy accompanied with an over-activation of the β-adrenergic receptors induced by heavy physical or mental stress. The process involves a burst of oxidative stress and an imbalance of the oxygen supply and demand in the diseased myocardium. Hyperphosphorylation of RyR2 and PLB is involved in the exaggeration of the channelopathy by dissociating the FKBP12.6 and depressing the activity of SERCA2a, respectively. The process is not merely induced by the activation of β-adrenergic receptors, and the oxidative stress and activation of the ET-1 system and renninangiotension system are likely to mediate the activation pathological process.

Many kinds of drugs, such as ACEI, AT1 receptor blockers, endothelin receptor antagonists, the β-blockers, and anti-oxidative agents have antiarrhythmic effects by diminishing upstream lesions to relieve related channelopathy (ie, the cardiac remodeling and the abnormality of the transmembrane signaling system). Endothelins are biosynthesized and released in a substantial amount from the diseased myocardium and exert harmful effects on myocardium by stimulating cell proliferation, inducing apoptosis, and activating the production of free radicals. An excess of ET-1 promotes oxidative stress which is mediated by an increase in iNOS activity to form peroxynitrite $ONOO^{-}$. Peroxynitrite is cytotoxic to myocardium and is likely to take an active part in the progression of ion channelopathy and cardiac arrhythmias**.** The endothelin ET_A/ET_B receptor antagonists reduced cardiac remodeling and cardiac failure by blocking the overactivation of the ET system[37–39]. It is interesting to find that an endothelin receptor antagonist, Dajisentan (CPU 0213), is effective in suppressing cardiac arrhythmias after ischemia/reperfusion in *L*-thyroxin-induced cardiomyopathy, but has no effect on ischemia/reperfusion-induced arrhythmias in a normal rat heart.

Class III anti-arrhythmic agents

In controlling ventricular tachyarrhythmias the Class I agents (I_{Na} blocking agents) are not recommended to patients with a diseased ventricle because of their strong potency to induce arrhythmias by suppressing the propagation of impulse[40]. It is still questionable whether pure Class III antiarrhythmic agents would suppress ventricular tachyarrhythmias effectively and safely in a diseased heart. To date, the common opinion is that it is favorable to use the complex Class III agents, such as a low dose of amiodarone, rather than the pure Class III agents in treating ventricular tachyarrhythmias (Figure 2).

Pure Class III agents Dofetilide and ibutilide belong to pure Class III agents that prolong APD remarkably by inhibiting the I_{Kr} currents only[41,42]. The two agents are favorable in the treatment of atrial fibrillation and flutter, but not in the

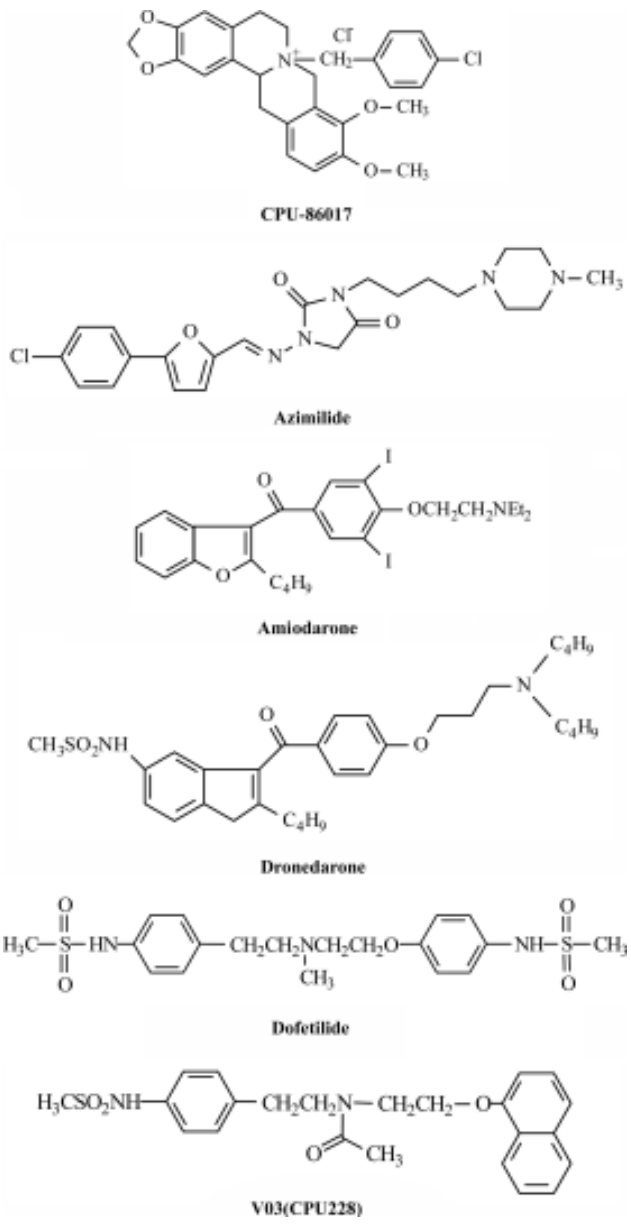

Figure 2. The Class III antiarrhythmic agents: CPU 86017, Azimilide, Amiodarone, Dronedarone, Dofetilide, and CPU 228.

control of ventricular tachyarrhythmias. Physicians should take care of monitoring the QTc in treatment of atrial flutter/fibrillation because of the high incidence of *Torsades de Pointes* when using the two agents. The outcome of clinical trials of dofetilide on mortality in the treatment of ventricular arrhythmias is neutral[40,42].

Complex Class III agents Complex Class III anti-arrhythmic agents block not only I_{Kr} currents but also other channels and receptors.

Complex Class III anti-arrhythmic agents block I_{Ks}. These include amiodarone, dronedarone, azimilide, CPU 86017, and so on. Blocking I_{Ks} is important to shorten the APD and control cardiac arrhythmias by reducing the interference of β-receptor stimulation that causes an exacerbated I_{Ks}.

Complex Class III anti-arrhythmic agents block $I_{Ca,L}$. These include amiodarone[43], dronedarone[44], azimilide[45], and CPU 86017[46]. An upregulation of the $I_{Ca,L}$ channels is associated with an enhancement of arrhythmogenesis in *L*-thyroxin-induced cardiac remodeling[20] and in an infarcted heart after isoproterenol treatment[31]. Blocking $I_{Ca,L}$ is beneficial to control arrhythmia by relieving calcium overload and restoring a disordered calcium-handling system in the diseased myocytes. In addition, an inhibition of the calcium current helps to prevent cardiac arrhythmias by restoring the imbalance of the altered ion currents during repolarization in diseased hearts.

Dofetilide has the potential to develop TdP by its tremendous effect in prolonging APD. A combination with an I_{Na} blocking agent was successful in attenuating the incidence of TdP induced by a pure Class III agent[47]. According to the mathematic equation to calculate the length of APD mentioned previously, we hypothesize that shortening in APD by blocking $I_{Ca,L}$ could reduce the incidence of TdP. Therefore, CPU 228 was created by modification on the moiety of dofetilide. Treatment with CPU 228 significantly decrease the incidence of TdP in the rabbit model[41]. CPU 228 can block both $I_{Ca,L}$ and I_{Kr}, so it is being converted from a pure Class III antiarrhythmic agent, dofetilide, into a complex Class III agent that has more potency to control arrhythmias in an animal model.

Conclusion

The concepts and targets for the development of antiarrhythmic drugs are evolving[48]. It is hopeful that more safe and effective agents will be obtained from continuous efforts based on regressing and relieving the basal ion channelopathy and preventing the deterioration of channelopathy in the view of biomolecular mechanisms. Propranolol and verapamil inhibit mRNA expression of RyR2 and SERCA in *L*-thyroxin-induced rat ventricular hypertrophyl[49]. β-Adrenergic stimulation increases current amplitude and activation of $I_{Ca\text{-}L}$[31] and I_{Ks}[50], causing dispersion of repolarization. More research at the molecular level will be needed on ion channelopathy. The safe and effective agents in controlling life-threatening arrhythmias can be obtained by relieving upstream lesions to ion channels, mainly through anti-hyperphosphorylation.

References

1 Roden DM, Balser JR, George Jr AL, Anderson ME. Cardiac ion channels. Ann Rev Physiol 2002; 64: 431–75.

2 Marban E. Cardiac channelopathies. Nature 2002; 415: 213–8.

3 Olson EN. A decade of discoveries in cardiac biology. Nat Med 2004; 10: 467–74.

4 Colastsky TJ. Antiarrhythmic drugs: where are we going? Pharm News 1995; 2: 17–23.

5 Guerra PG, Talajic M, Roy D, Dubuc M, Thibault B, Nattel S. Is there a future for antiarrhythmic drug therapy? Drugs 1998: 56: 767–81.

6 The Cardiac Arrhythmia Suppression Trial Investigations. Preliminary report: effect of encainide and flecainide on mortality in a randomized trial of arrhythmias suppression after myocardial infarction. N Engl J Med 1989; 321: 406–12.

7 Dumaine R, Antzelevitch C. Molecular mechanisms underlying the long QT syndrome. Curr Opin Cardiol 2002; 17: 36–42.

8 Roden DM, Lazzara R, Rosen M, Schwartz PJ, Towbin J, Vincent GM, *et al*. Multiple mechanisms in the long-QT syndrome current knowledge, gaps, and future directions. Circulation 1996; 94: 1996–2012.

9 Dai DZ. Vulnerable substrate and multiple ion channel disorder in a disease heart will be new targets for antiarrhythmic therapy. Acta Pharmacol Sin 2000; 21: 289–95.

10 Dai DZ. Disorder ion channels and antiarrhythmic agents. Pharm News 2001; 8: 1–6.

11 abauer M, Kaab S. Potassium channel down-regulation in heart failure. Cardiovasc Res 1998; 37: 324–34.

12 Qin DY, Zhang ZH, Caref EB, Boutjdir M, Jain P, Ei-Sherif N. Cellular and ionic basis of arrhythmias in post-infarction remodeled ventricular myocardium. Circ Res 1996; 79: 461–73.

13 Dai DZ. The ion channelopathy and reconsideration of antiarrhythmic drugs. In: Su DF, Miao ZY, Wang YM, editors. Advances in Pharmacology. Beijing: People's Medical Publishing House; 2002. p 202–11.

14 Dai DZ, Hu HQ, Yang P, Ma YP, Cao W, Wang H. The proarrhythmic activity and the ion channelopathy in remodeled myocardium. Chin J Pathophysiol 2000; 16: 945–8.

15 Zhang TT, Cui B, Dai DZ. Down-regulation of Kv4.2 and Kv4.3 channel gene expression in right ventricular hypertrophy induced by monocrotaline in rats. Acta Pharmacol Sin 2004; 25: 226-30.

16 Yu F, Dai DZ, An LF, Guo XF. Heart hypertrophy induced by levothyroxin aggravates ischemic lesions and reperfusion arrhythmias in rats. Acta Pharmacol Sin 1997; 18: 71–4.

17 Chen DD, Dai DZ, Wang CX. Effects of verapamil and captopril on cardiac hypertrophy and elevated left ventricular sarcolemmal Na^+,K^+-ATPase activity induced by *L*-thyroxin in rats. Chin J Pharmacol Toxicol 1995; 9: 228–30.

18 Chen DD, Dai DZ, Lu J, Zhang XK. Propranolol and bepridil attenuating levothyroxin-induced rat cardiac hypertrophy and mitochondrial Ca^{2+}-Mg^{2+}-ATPase activity elevation. Acta Pharmacol Sin 1996; 17: 516–8.

19 Ma YP, Hao XM, Zhang GQ, Zhou PA, Wu CH, Dai DZ. Blocking effect of CPU 86017 on slowly activated rectifier potassium current in single ventricular myocytes of guinea pigs. J Chin Pharm Univ 2000; 31: 121–5.

20 Dai DZ, Hu HJ, Yang DM, Hao XM, Zhang GQ, Zhou PA, *et al*. Chronic levothyroxin treatment in associated with ion channel abnormalities in cardiac and neuronal cells. Clin Exp Pharmacol Physiol 1999; 26: 819–21.

21 Volder PGA, Sipido KR, Vos MA. Downregulation of delayed rectifier K^+ current in dogs with chronic complete atrioventricular block and acquired *Torsades de Pointes*. Circulation 1999; 100: 2455-61.

23 Marx SO, Reiken S, Hisamatsu Y, Jayamana T, Burkhoff D, Rosemblit N, *et al*. PKA phosphorylation dissociated FKBP12.6 from the calcium release channel (ryanodine receptor) defective regulation in failing hearts. Cell 2000; 101: 365–76.

24 Wehrens XH, Lehnart SE, Huang F, Vest JA, Reiken SR, Mohler PJ, *et al*. FKBP12.6 deficiency and defective calcium release channel (ryanodine receptor) function linked to exercise-induced sudden cardiac death. Cell 2003; 113: 829–40.

25 Scoote M, Willians AJ. The cardiac ryanodine receptor (calcium release channel): emerging role in heart failure and arrhythmia pathogenesis. Cardiovasc Res 2002; 56: 359–72.

26 Paul M, Schulze-Bahr E, Breithardt G, Wichter T. Genetics of arrhythmogenic right ventricular cardiomyopathy−status quo and future perspectives. Z Kardiol 2003; 92; 3628–49.

27 Ahmad F. The molecular genetics of arrhythmogenic right ventricular dysplasia-cardiomyopathy. Clin Invest Med 2003; 26: 167–78.

28 Dulac Y, Acar P, Delay M. Diagnosis of adrenergic ventricular tachycardia in two homozygotic twins. Arch Mal Coeur Vaiss 2003; 96: 521–3.

29 Lahat H, Pras E, Eldar M. RYR2 and CASQ2 mutations in patients suffering from catecholaminergic polymorphic ventricular tachycardia. Circulation 2003; 107: e29.

30 Dai DZ, Zhang GQ, Yang P, Ma YP. Two patterns of ion channelopathies relating to arrhythmias and direct and indirect blockade of ion channels by antiarrhythmic agents. Drug Dev Res 2003; 58: 42–50.

31 Wang HL, Li SB, Dai DZ. Change of L-type calcium current in single guinea pig hypertrophic ventricular myocytes induced by levothyroxin. J Chin Pharm Univ 2000; 31: 130–4.

32 Hort BD, Tramuta DA, Kadambi VJ, Dash R, Ball N, Kranias EG, *et al*. Influence of transgenic overexpression of phospholamban on post-extrasystolic potentiation. J Mol Cell Cardiol 1999; 31: 2007–15.

33 Wang HL, Dai DZ, Gao F, Zhang YP, Lu F. Dispersion of ventricular mRNA of RyR2, and SERCA associated with arrhythmogenesis in rats. Acta Pharmacol Sin 2004; 25: 738–43.

34 Antos CL, Frey N, Marx SO, Reiken S, Gaburjakova M, Richardson JA, *et al*. Dilated cardiomyopathy and sudden death resulting from constitutive activation of protein kinase A. Circ Res 2001; 89: 997–1004.

35 Dai DZ, Yu F, Li HT, Tang YQ, An LF, Huang WL, *et al*. Blockade on sodium, potassium, and calcium channels by a new antiarrhythmic agent CPU 86017. Drug Dev Res 1996; 39: 138–46.

36 Lu HR, Yu F, Dai DZ, Remeysen P, De Clerck F. Reduction in QT dispersion and ventricular arrhythmias by ischaemic preconditioning in anaesthetized, normotensive and spontaneously hypertensive rats. Fundam Clin Pharmacol 1999; 13: 445–54.

37 Guillermo TA, Young JB, Durand JB, Bozkurt B, Mann DL, Kobrin I, *et al*. Hemodynamic effects of Tezosentan, an intravenous

dual endothelin receptor antagonist, in patients with class III to IV congestive heart failure. Circulation 2001; 103: 973–80.
38 Miyauchi T , Goto K. Heart failure and endothelin receptor antagonists. Trend Pharmacol Sci 1999; 20: 210-7.
39 Dai DZ, Huang M, Ji M, Liu LG. A novel endothelin receptor antagonist CPU 0213 and therapeutic effect on acute heart failure in rats. J China Pharm Univ 2005; 36: in press.
40 Van Gelder IC, Brugemann J, Crijns HJ. Current treatment recommendations in antiarrhythmic therapy. Drugs 1998; 55: 331–46.
41 Howard PA. Ibutilide: an antiarrhythmic agent for the treatment of atrial fibrillation or flutter. Ann Pharmacother 1999; 33: 38–47.
42 Brendorp B, Elming H, Jun L, Kober L, Torp-Pedersen C. Diamond Study Group. The prognostic value of QTc interval and QT dispersion following myocardial infarction in patients treated with or without dofetilide. Clin Cardiol 2003; 26: 219–25.
43 Yoshida H, Sugiyama A, Satoh Y, Ishida Y, Yoneyama M, Kugiyama K, *et al*. Comparison of the *in vivo* electrophysiological and proarrhyhmic effects of amiodarone with those of a selective class III drug, sematilide, using a canine chronic atrioventricular block model. Circ J 2002; 66: 75–62.
44 Doggrell SA, Hancox JC. Dronedarone: an amiodarone analogue. Expert Opin Investig Drugs 2004; 13: 415–26.
45 Fermini B, Jurkiewicz NK, Jow B, Guinosso PJ, Baskin EP, Lynch JJ, *et al*. Use-dependent effects of the class III antiarrhythmic agent NE-10064 (Azimilide) on cardiac repolarization: block of delayed rectifier potassium and L-type calcium currents. J Cardiovasc Pharmacol 1995; 26: 259–71.
46 Dai DZ. The anti-arrhythmic activity of protoberberines in relation to blockade of ion channels. Ion Channel Modulators 1997; 2: 383–90.
47 Hallman K, Carlsson L. Prevention of class III– induced proarrhythmias by flecainide in an animal model of the acquired long QT syndrome. Pharmacol Toxicol 1995; 77: 250–4.
48 Nemec J, Shen WK. Antiarrhythmic drugs: new agents and evolving concepts. Expert Opin Investig Drugs 2003; 12 :435–53.
49 Wu XD, Dai DZ, Zhang GQ, Gao F. Propranolol and verapamil inhibit mRNA expression of RyR2 and SERCA in *L*-thyroxin-induced rat ventricular hypertrophy. Acta Pharmacol Sin 2004; 25: 347–51.
50 Han W, Wang Z, Nattel S. Slow delayed rectifier current and repolarization in canine cardiac Purkinje cells. Am J Physiol Heart Circ Physiol 2001; 280: H1075–80.

Acta Pharmacologica Sinica 2005 Aug; 26 (8): 926–933

Review

Is COX-2 a perpetrator or a protector? Selective COX-2 inhibitors remain controversial[1]

Cheng LUO[2], Ming-liang HE[3], Lars BOHLIN[4]

[2]Institute of Molecular Biology, Faculty of Medicine, The University of Hong Kong, Hong Kong, China; [3]Center for Emerging and Infectious Diseases, Chinese University of Hong Kong, Hong Kong, China; [4]Department of Medicinal Chemistry, Biomedical Center, Uppsala University, Sweden

Key words

COX-2 inhibitor; nonsteroidal anti-inflammatory drug ; prostanoids; cardiovascular disease

[1] Disclaimer: the views expressed herein are those of the authors and are not intended to represent those of the institutions with which they are affiliated.

[2] Correspondence to Dr Cheng LUO.
Phn 852-2299-0759.
Fax 852-2817-1006.
E-mail luo58@yahoo.com

Received 2005-03-24
Accepted 2005-04-26

doi: 10.1111/j.1745-7254.2005.00150.x

Abstract

Aim: COX-2(cyclooxygenase-2) has sparked a surge in pharmaceutical interest since its discovery at the beginning of the 1990s. Several COX-2 selective inhibitors that avoid gastrointestinal side effects have been successfully launched into the market in recent years. The first selective COX-2 inhibitor, celecoxib, entered the market in December 1999. However, there are a few organs that physiologically and functionally express COX-2, particularly the glomeruli of the kidney and the cortex of the brain. Inhibition of COX-2 expression in these organs possibly causes heart attack and stroke in long-term COX-2 inhibitor users. Recently, a USA Food and Drug Agency (FDA) advisory panel re-evaluated COX-2 inhibitors and unanimously concluded that the entire class of COX-2 inhibitors increase the risk of cardiovascular problems. Thus the use of COX-2 inhibitors is still controversial, and there is a challenge for not only pharmacologists, but also the pharmaceutical industry, to develop improved painkilling and anti-inflammatory drugs. This may involve exploring a new generation of COX-2 inhibitors with different inhibitory mechanisms through computer-aided design, screening different sources of inhibitors with lower selectivity, or seeking completely new targets. Synthetic COX-2 inhibitors have high selectivity and the advantage of irreversible inhibition, whereas naturally derived COX-2 inhibitors have lower selectivity and fewer side effects, with the medical effects in general not being as striking as those achieved using synthetic inhibitors. This review discusses the mechanism of COX-2 inhibitor therapy and a possible new way of exploration in the development of anti-inflammatory, analgetic, and antipyretic drugs.

Introduction

Cyclooxygenase (COX) is a key enzyme in the conversion of polyunsaturated fatty acids and arachidonic acid to prostaglandin (PG) H_2, which is further converted into various prostanoids (PGs, prostacyclins and thromboxanes). Our knowledge about COX constantly changes, but basically COX-1 is constitutively expressed in most tissues, where it synthesizes physiological amounts of postaglandins. COX-2, on the other hand, is normally expressed in activated macrophages and becomes strongly upregulated after exposure to growth factors or inflammatory stimuli, and is elevated in malignant cells to promote angiogenesis in tumors[1–4]. It has been long believed that many of the side effects of nonsteroidal anti-inflammatory drugs (NSAIDs), for examples, gastrointestinal ulceration and bleeding, and platelet dysfunction, are due to the suppression of COX-1-derived prostanoids, whereas the inhibition of COX-2-dependent prostaglandin synthesis accounts for the anti-inflammatory, analgesic and antipyretic effects. Consequently, it has been hypothesized that specific inhibition of COX-2 might have therapeutic actions similar to those of NSAIDs, but without the unwanted side effects. This was the fundamental rationale for the development of selective inhibitors of the COX-2 enzyme as a new class of anti-inflammatory and analgesic agent with improved gastrointestinal tolerability. However,

the potential of this new class of drugs has not been realized, even though the rationale underpinning their use is likely to be correct.

COX-2 was discovered in the early 1990s, and a large amount of effort has been expended since then by the pharmaceutical industry in the search for COX-2 inhibitors. In 2000, COX-2 inhibitors were involved in clinical trials for the treatment of colon and rectal cancers because COX-2 overexpression had been found in malignant tumor samples. However, at this point, the risk of heart attack and stroke emerged, and this is possibly because COX-2 is physiologically expressed in the glomeruli and cortex, and COX-2 may also have an anti-inflammatory role[5]. Recently, a number of events regarding COX-2 inhibitors have attracted the attention of the media. Rofecoxib (Vioxx, Figure 1) was withdrawn by Merck & Co in September 2004 following the finding from the Vioxx Gastrointestinal Outcomes Research (VIGOR) trial for colon and rectal cancers that there were severe risks for the heart. Similar claims were made when a COX-2 inhibitor was used in the adenoma prevention with celecoxib (APC) trial, which was eventually suspended in December 2004 because analysis by an independent Data Safety and Monitoring Board showed that there was a risk of fatal and non-fatal major cardiovascular disease (CVD)[6]. On February 20, 2005, a US Food and Drug Agency (FDA) advisory panel unanimously concluded that all classes of COX-2 inhibitors increase a person's risk of heart attack and stroke, and recommended that, despite the risks, drugs including Vioxx should remain on the market but be accompanied by strong warnings. Following the FDA's decision, the European Union and countries in which COX-2 inhibitors were used imposed similar restrictions. Because the drugs are now "tainted", physicians are reluctant to prescribe them, and patients do not want to risk the health of their heart to ease pain, the sales of Celebrex, valdecoxib (Figure 1) and rofecoxib have dropped dramatically. As COX-2 inhibitors have become controversial, many pharmaceutical companies are having to renew their research efforts in the search for new effective anti-inflammatory drugs to treat arthritis and other inflammatory diseases[7].

Regulation of COX-2 expression during inflammation

One of the main reasons for COX-2 attracting pharmaceutical interest is its strikingly different method of gene regulation from COX-1. The genes of COX-1 and COX-2 are located in human chromosomes 9 and 1, respectively, with COX-1 lacking a TATA box[8]. The promoter of the immediate-early gene COX-2 contains a TATA box and binding sites for several transcription factors that are different from those of COX-1 (Table 1). The expression of COX-2 is regulated by a broad spectrum of mediators involved in inflammation. In general, lipopolysaccharides and proinflammatory cytokines, for example, interleukin- (IL)-1β, tumor necrosis factor (TNF), and growth factors, induce COX-2; whereas IL-4, IL-13 and the anti-inflammatory cytokine IL-10 inhibit the expression of the enzyme[9,10]. A recent study has shown that there is a positive feedback loop in COX-2-dependent prostaglandin production at the sites of inflammation. In particular, a COX-2 product, PGE_2, upregulates COX-2 expression by virtue of its cAMP-elevating capacity in human blood monocytes[11]. COX-2 is also regulated at the post-transcriptional level. Recently, a 3'-untranslated region of the COX-2 mRNA has been shown to contain multiple copies of adenylate- and

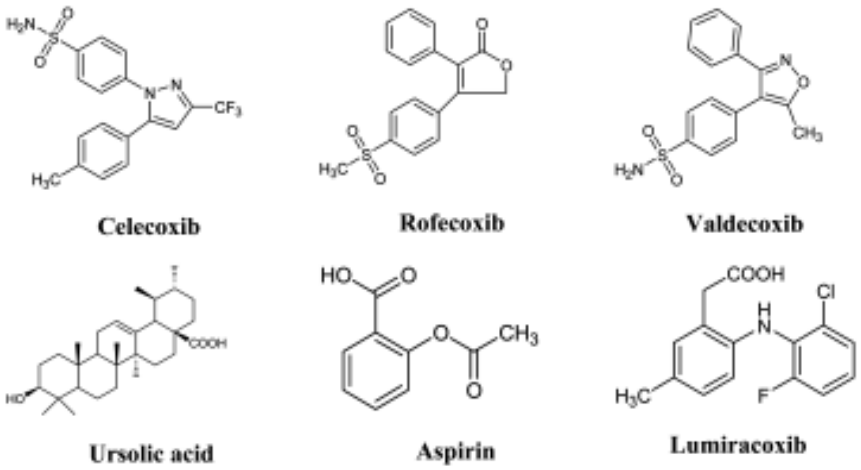

Figure 1. COX-2 inhibitors originating from nature and designed chemically using computer-aided design.

Table 1. Differences in the expression, regulation, and enzyme kinetics of COX-1 and COX-2.

Structural functional class	Isoforms of COX	
	COX-1	COX-2
Location on chromosome	9q32–q33.3	1q25
Amino acid homology	60% identity to COX-2 75% similarity to COX-2	60% identity to COX-1 75% similarity to COX-1
Enzyme location	Endoplasmic reticulum	Nuclear envelope
Size of gene	22 kb, 11 exons	9.4 kb, 10 exons
Size of mRNA	2.8 kb	4.5 kb
Length of 3' UTR	800 bp	2200 bp
3' UTR Shaw/Kamen sequence	Not present	17
Size of polypeptide	70 kDa, 604 amino acids	70 kDa, 604 amino acids
Regulation	Usually constitutive	Inducible
Range of induced gene expression	2–4 folds	10–80 folds
Rate of gene activation	24 h	0.5 h
Effect of glucorticods	Little or no effect	Inhibit expression
RNA instability elements, AUUUA in 3' UTR	Not present	Yes
TATA box	Not present	Yes

UTR=untranslated region.

uridylate-rich elements (AREs) that may confer post-transcriptional control of COX-2 expression by acting as mRNA instability determinants or as translation inhibitory elements. Loss of this post-transcriptional regulation of COX-2 through the mutation of proteins that specifically interact with the COX-2 ARE may lead to COX-2 overexpression, and this process has been proposed as a crucial factor in colon carcinogenesis[12,13]. The sustained increase of COX-2 expression is apparently due (at least in part) to IL-1A increasing the stability of COX-2 mRNA. This type of regulatory mechanism may play an important role in chronic inflammatory conditions.

Development of COX-2 inhibitors

Both COX-1 and COX-2 produce prostaglandin H2, which is further converted to different prostanoids, including PGD_2, PGE_2, PGF_2alpha, PGI_2 and thromboxane A2. COX-2-dependent prostaglandins have been implicated in various physiological events, including male fertility, menstruation, ovulation, pregnancy, implantation, and in the pathological action of different inflammatory and neoplastic diseases, notably arthritis and cancer. In the US, one-third of the adult population, or approximately 70 million people, are affected by arthritis or chronic joint symptoms, making arthritis one of the most prevalent diseases in that country. Onset of the disease starts at around the age of 30 years, and women have a higher incidence than men. Arthritis is the leading cause of disability in the US, accounting for 17.5% of all those on disability pensions. Thus there is an urgent need for the development of COX-2 inhibitors, and the development of suitable drugs would also be associated with large profits for pharmaceutical companies.

Inhibition of cyclooxygenases with aspirin can be traced back to ancient times. Chinese and Greek healers used willow bark that contained salicylic acid before AC aspirin, a modified form of acetylsalicylic acid developed by a German pharmacological chemist in 1898, was accepted as a safe and effective remedy for backache in 1903, for headache in 1923, and for arthritis in 1933 worldwidely. The mechanism by which aspirin exerts analgesic and antipyretic effects was found to be the inhibition of cyclooxygenase-dependent prostaglandins in 1971[14]. In the 1980s, aspirin was suggested to reduce the risk of heart attack by suppressing the production of prostacyclin in platelets[15]. Aspirin also slows the development of cataracts and reduces migraine attacks. However, gastrointestinal (GI) toxicity induced by aspirin and other NSAIDs is among the most common serious adverse drug events in the industrialized world[16]. Gastroduodenal ulcers can be found by endoscopy in 10% to 20% of patients who take NSAIDs on a regular basis. For decades, it has been a dream of pharmacologists to overcome this issue.

In the early 1990s, cyclooxygenase was found to exist in two distinct isoforms[1,2]. It was then very rapidly found that the COX-1 isoform is located in all tissues except red blood

cells, and is constitutively expressed in the stomach, kidneys, platelets, and endothelial cells under normal physiological conditions. In contrast, COX-2 is induced by proinflammatory substances, such as lipopolysaccharides, TNF-alpha, IL-1, platelet-derived growth factor (PDGF), and other growth factors. COX-2 is involved in inflammation, for example in macrophages, monocytes and synoviocytes that emerge in acute and chronic inflammatory states. COX-2 therefore became a very attractive pharmaceutical target, even though it was later found that COX-2 is constitutively expressed in pancreatic beta-cells[17], at the distal end of the vas deferens[18], and also functionally and physiologically expressed in the kidney glomeruli and cortex[19]. COX-2 was quickly crystallized and the structure was resolved by X-ray diffraction crystallography, which is a crucial step in drug design. The techniques of investigating the docking between small molecules and determining the structure of COX-2 were able to be carried out using different platforms. These approaches help to understand the mechanisms involved in protein–ligand binding in general, as well as helping to understand the details of the interactions in a specific protein or protein-ligand complex of interest[20]. Celecoxib was the first drug that was chemically designed by computer, and was exceptionally quickly approved for release by the FDA in December 1998. Rofecoxib and valdecoxib subsequently entered the market later. The makers of a new product containing lumiracoxib (Novartis) are now in the process of applying for a license. Lumiracoxib is claimed to reduce the from cancer. Prescriptions for COX-2-selective inhibitors represented up 61% of total prescriptions for NSAIDs in 2001 and 2002. In 2003, celecoxib was the ninth best-selling drug in the US, with sales of US$2.6 billion according to Forbes. Another impetus for COX-2 inhibitor development is for cancer chemotherapy. In one study, COX-2 knockout mice showed a reduced incidence of tumors[21], and COX-2 is overexpressed in many kinds of cancers, including colon, prostate and lung cancer. The function of COX-2 inhibitors that is relevant for cancer treatment is that they also induce apoptosis.

Mechanism of action of COX-2-dependent PGE_2 in pain perception

Inflammation causes an increased synthesis of COX-2-dependent PGs, which sensitize peripheral nociceptor terminals and produce localized pain hypersensitivity. A significant portion of these nociceptors are not activated by physiological stimuli such as gentle pressure or temperature. PGs regulate the sensitivity of so-called polymodal nociceptors that are present in nearly all tissues. PGE_2 and other inflammatory mediators facilitate the activation of tetrodotoxin (TTX)-resistant Na^+ channels in dorsal root ganglion neurons. These small dorsal root ganglion neurons are unmyelinated nerve fibers, conducting nociceptive stimuli. During inflammatory states, PGE_2 receptor E1 may significantly increase the excitability of nociceptive nerve fibers, thereby contributing to the activation of "sleeping" nociceptors, and also act in the central nervous system to produce hyperalgesia. COX-2 inhibitors act primarily in the dorsal horn to cause analgesia. The sensation of pain is assembled in the cortex. COX-2 is expressed constitutively in the dorsal horn of the spinal cord, and becomes upregulated briefly after a trauma, such as damage to a limb, in the corresponding sensory segments of the spinal cord. The induction of spinal cord COX-2-dependent PGs facilitates transmission of the nociceptive input[22]. Similar to *in vitro* IL-1-induced COX-2 expression, IL-1β was demonstrated to be the major inducer of COX-2 upregulation in the central nervous system. Accordingly, intraspinal administration of an interleukin-converting enzyme or COX-2 inhibitor is accompanied by decreases in both inflammation-induced central PGE_2 levels and mechanical hyperalgesia[23, 24]. For analgesia alone, opioid drugs are more effective in moderate-to-severe pain than NSAIDs, and possess other significant advantages including titratability, reversibility and lack of prostaglandin-associated side effects. Cocktails of weak opioids and other analgesic agents, such as tramadol plus acetaminophen, have been shown to have some merits[25].

After a debate lasting 30 years, the mechanism by which acetaminophen (commercial name Tylenol) exerts its analgesic and antipyretic action has also been elucidated by cyclooxygenase isoform studies. In contrast to the acidic antipyretic selective COX-2 inhibitors, due to the non-acidic chemistry of acetaminophen, the drug reaches higher concentrations within the central nervous system as compared with the acidic antipyretic analgesics (eg, aspirin and indomethacin) that accumulate in peripheral compartments with acidic extracellular pH (eg, inflamed tissue). Acetaminophen may inhibit nociception-induced spinal prostaglandin synthesis, and hydroperoxide may confer cellular selectivity on acetaminophen's inhibition of COX-2 activity[26]. In addition, acetaminophen has been suggested to inhibit a newly discovered COX isoform, derived from the same gene as COX-1 and referred to as COX-1b or COX-3. Acetaminophen's role in analgesia and hypothermia is due to the inhibition of COX-3, which is more dominantly involved in fever in children[27].

Synthetic COX-2 selective inhibitor with nephrotoxicity and cardiovascular disease

COX-2 immediately became a drug target after it was characterized as an inducible isoform in the early 1990s. Several crystal structures of COX-2 were quickly solved through the crystallization of the protein in different laboratories within a few years. In 1996, Searle improved the model and built up a structure with a high resolution of 2.15 Å. It was found that one of the enzymatic channels in COX-2 is wider than that of COX-1, and COX-2 has an open side pocket where the sulfonamide group of the selective inhibitors can bind. Human COX-2 has four amino acids that are different from COX-1 in the region corresponding to the side pocket. The most important difference is at position 523, where COX-1 has a bulky isoleucine and COX-2 has a valine that takes up less space[28]. The formation of five different hydrogen bonds between the selective inhibitors and the pocket of COX-2 is a strong and time dependent binding reaction, and site-directed mutations in the pocket region resulted in weaker binding and fewer hydrogen bonds[20,29]. The selectivity of COX-2 IC_{50}/COX-1 IC_{50} is 0.003 (or selective fold is 375:1) for celecoxib, 0.0026 for refecoxib, and 166 for aspirin. The high selectivity of celecoxib is due to the phenylsulfonamide moiety, which binds in a pocket that is more restricted in COX-1 and is unoccupied in complexes of COX-2 with non-selective inhibitors. This pocket branches off from the main channel that leads to the cyclooxygenase active site, and is more accessible in COX-2, primarily because of the previously mentioned substitution of isoleucine at position 523 in COX-2 to valine in COX-1. Aspirin mainly inhibits COX-1 irreversibly because it blocks the channel for accessing the substrate by permanently acetylating the serine of the cyclooxygenase enzymes. Celecoxib's reversibility and selectivity provided a new insight into drug design approaches for the pharmaceutical industry.

Nevertheless, the COX-2 inhibitors are associated with a number of potential pitfalls, which can be even more lethal than the side effects of other non-selective NSAIDs. These pitfalls arise from the fact that COX-2 induction is not exclusively associated with the onset of an inflammatory reaction. In fact, COX-2 can also be expressed chronically, and is seen during the resolution of inflammation and in areas of wound-healing[5]. Through studies of COX-2 knockout mice, COX-2 inhibition has been directly linked to several adverse outcomes, including reproductive failure, and reduced renin expression in the kidney. Renin is an active enzyme that converts angiotensinogen into angiotensin, which maintains or modulates the salt metabolism. It has been shown that renin expression is decisively regulated by COX-2 in kidney, especially in the abnormal intake of NaCl[30]. COX-2-deficient mice also develop lung fibrogenesis[31], which is a common attribute of lung cancer in humans. The application of COX-2-selective inhibitors during these periods has been shown to be deleterious, so that resolution of inflammation and gastric ulcer healing are actually delayed and, in some patients, ulcers have even been found to progress further to perforation. The suggestion has now been made that, in these situations, COX-2 may actually help resolve the pathology, perhaps by generating an alternative series of PGs, such as the cyclopentenone PGs. The finding that these PGs can affect proteins by direct chemical modifications as well as by having their own receptor families has rekindled debate on the deleterious and beneficial effects of COX-2-dependent prostanoids, and on the implications of inhibiting the production of these mediators in the body[32].

COX-2-synthesized PGs have important roles in the modulation of renal physiology. A number of pooled analyses have suggested the possibility of an increased risk of CVD, particularly acute myocardial infarction, because of a blunted PG response due to COX-2 inhibition in the kidney and blood vessels, which may depend on the individual to a certain extent. Many reports have stated that COX-2 inhibitors have the same nephrotoxicity as non-selective NSAIDs. PGs have a counterbalancing effect because they modulate the local actions of systemic and locally produced vasoconstrictor hormones. For this role, a variety of PGs with diverse biological effects are produced and metabolized by the kidney[33]. The major ones, synthesized at distinct anatomical locations within the renal parenchyma, include PGI_2, PGE_2, thromboxane A_2, and PGF_2. Of these, PGI_2 (produced most abundantly in the renal cortex by cortical glomeruli and arterioles) and PGE_2 (synthesized in the juxtamedullary glomeruli, medullary interstitial cells, and the medullary portion of the collecting duct) are physiologically predominant[34,35]. It used to be believed that the only side effects of COX-2 inhibitors were toxicity in the kidney. But now COX-2 has been found to be constitutively expressed in the endothelial cells of the arteries, arterioles, lung and brain, in addition to its highly constitutive expression in the vas deferens and beta-cells of the pancreas. COX-2 expression in the cortical thick ascending limb of the loop of Henle (medullary rays and macula densa) affects chloride ion pumps. In the medulla, COX-2 expression was detected in the endothelial lining of the vasa recta in 52 cases and in the collecting ducts in 5 cases. These data demonstrate significant constitutive expression of COX-2 in normal kidney and underscore the need for caution in the use of COX-2 selective inhibitors, especially on a long-

term basis. All in all, there is not much remaining of the original dogma that COX-1 is the housekeeping good guy and COX-2 is the perpetrator that mediates inflammation and damage. These finding are consistent with recent clinical data showing that COX-2 inhibitors are associated with CVD risk[36,37].

Naturally derived COX-2 inhibitors for anti-inflammation, and alternative targets for painkilling

Given that salicylic acid (later developed to aspirin) was originally extracted from the bark of the willow tree, there is a definite possibility of also finding COX-2 inhibitors in nature. In fact, there are some already known COX-2 favorable inhibitors of natural origin, and some of them have been used as natural modulators of inflammation in adjuvant chemotherapy. A recent review details a number of natural COX-2 inhibitors with different chemical structures and different modes of action[38]. It has been reported that ginger, curcumin, thunder god vine, plantago, and others contain COX-2 inhibitors. Some of these compounds not only inhibit COX-2, but are also antioxidants, for example resveratrol, which is found in the skin of grapes and inhibits the transcription or post-translation of the COX-2 gene[39]. Small synthetic COX-2 inhibitors can be inserted into loops that are different from COX-1. But there are many different methods of inhibition, and in general, there is no correlation between inhibition and the similarity of the chemical structures. Some characterized fatty acid COX-2 inhibitors, such as linoleic acid (LA), alpha-linolenic acid (alpha-LNA), myristic acid and palmitic acid have been isolated from different plant roots or leaves, and have IC_{50} values for cyclooxygenase ranging from 3.9 to180 μmol/L. The compound alpha-LNA is one of the most selective towards COX-2, with COX-2/COX-1 ratios of 0.1[40, 41].

In addition to fatty acids, steroid-like molecules are also attractive candidates for COX-2 inhibitors. A hexane structure of ursolic acid (Figure 1) has been investigated by bioactivity-directed fractionation. This triterpenoid had a COX-2 inhibitory effect, directly affecting the enzyme activity, with an IC_{50} value of 130 μmol/L and a COX-2/COX-1 selectivity ratio of 0.6. The structural isomer oleanolic acid is less active than ursolic acid, with an IC_{50} value of 295 μmol/L, but has a similar selectivity ratio (0.8). The direct inhibitory effect of ursolic acid and oleanolic acid on COX-2-catalyzed prostaglandin biosynthesis increased with preincubation, indicating a time-dependent inhibition. Interestingly, the effect on COX-1 was independent of preincubation time[42]. The problem with natural COX-2 inhibitors is the slower *onset* of relief *in vivo*. Effort needs to be directed towards screening natural anti-inflammatory/analgesic products that offer more effective inhibition, or stronger instantaneous relief of pain with no (or less) GI and cardiovascular risk. If this were to occur, then a natural COX-2 inhibitor, whether a single compound or a combination of multiple compounds, could be developed to provide gentle, effective and long-term relief.

Summary

Cyclooxygenases, particularly COX-2 inhibitors associated with CVD problems, have shown us that there are probably no absolute perpetrators and protectors in nature. However, selective COX-2 inhibitor studies and chemotherapy have extended our understanding of this system. All COX-2 inhibitors remain available for use in certain patients, such as those at risk of ulcers. COX-2 inhibitors can be explored further for cancer therapy, where because of their anti-angiogenic apoptosis-promoting properties, they might benefit those patients who are overexpressing COX-2. Rather than inhibitors, it is also possible to identify more COX-2 modulators, which could be found by screening small molecules from herbs or other natural sources. For simple painkilling, it is better to target end effectors. Screening for E1 receptor inhibitors is a new possibility because the analgesic actions of NSAIDs in inflammatory pain, especially visceral stimuli, are mediated to a significant degree by the inhibition of signaling through the E1 receptor. The absence of EP1 receptors results in structurally normal kidney, and does not result in a lowering of resting blood pressure[43].

Acknowledgments

We thank Dr Qing-yu HE (Department of Chemistry, The University of Hong Kong) for critical comments and discussion of the manuscript. LB is grateful for economic support from the Swedish Research Council for Environment, Agricultural Science and Spatial Planning.

References

1 Xie WL, Chipman JG, Robertson DL, Erikson RL, Simmons DL. Expression of a mitogen-responsive gene encoding prostaglandin synthase is regulated by mRNA splicing. Proc Natl Acad Sci USA 1991; 88: 692–6.

2 Fu JY, Masferr JL, Seibert K, Raz A, Needleman P. The induction and suppression of prostaglandin h_2 synthase (cyclooxygenase) in human monocytes. J Biol Chem 1990; 265: 16737–40.

3 Luo C, Laine JVO, Ylinen L, Teros T, Mäkinen M, Ristimäki A, *et al*. Expression of cyclooxygenase-2 in intestinal goblet cells of prediabetic non-obese diabetic mice. Acta Physiol Scand 2002;

174: 265–74.
4 Luo C, Trauss L, Treng T, Ristimäki A, Santti R. Constant exprkession of cyclooxygenase-2 gene in the lower urinary tract and prostate of the male rats treated with estrogen. Z Naturforsch 2001; 56C: 455–63.
5 Gilroy DW, Colville-Nash PR, Willis D, Chivers J, Paul-Clark MJ, Willoughby DA. Inducible cyclooxygenase may have anti-inflammatory properties. Nat Med 1999; 5: 621–2.
6 Topol EJ. Arthritis Medicines and Cardiovascular Events: "House of Coxibs". J Am Med Assoc 2005; 293: 366–8.
7 Warner TD, Mitchell JA. Cyclooxygenases: new forms, new inhibitors, and lessons from the clinic. FASEB J 2004; 18: 790–804.
8 Kraemer SA, Meade EA, DeWitt DL. Prostaglandin endoperoxide synthase gene structure: identification of the transcriptional start site and 5'-flanking regulatory sequences. Arch Biochem Biophys 1992; 293, 391–400.
9 Colville-Nash PR, Gilroy DW. Potential adverse effects of cyclooxygenase-2 inhibition: evidence from animal models of inflammation. BioDrugs 2001; 15: 1–9.
10 Onoe Y, Miyaura C, Kaminakayashiki T, Nagai Y, Noguchi K, Chen QR, *et al*. IL-13 and IL-4 inhibit bone resorption by suppressing cyclooxygenase-2-dependent prostaglandin synthesis in osteoblasts. J Immunol 1996; 156: 758–64.
11 Hinz B, Brune K, Pahl A. Cyclooxygenase-2 expression in lipopolysaccharide-stimulated human monocytes is modulated by cyclic AMP, prostaglandin E2 and non-steroidal anti-inflammatory drugs. Biochem Biophys Res Commun 2000; 278: 790–6.
12 Dixon DA, Kaplan CD, McIntyre TM, Zimmerman GA, Prescott SM. Post-transcriptional control of cyclooxygenase-2 gene expression. The role of the 3'- untranslated region. J Biol Chem 2000; 275: 11750–7.
13 Ristimäki A, Honkanen N, Jankala H, Sipponen P, Harkonen M. Expression of cyclooxygenase-2 in human gastric carcinoma. Cancer Res 1997; 57: 1276–80.
14 Vane JR. Inhibition of prostaglandin synthesis as a mechanism of action for the aspirin-like drugs. Nature 1971; 231: 232–5.
15 Michiels JJ. Aspirin and platelet-lowering agents for the prevention of vascular complications in essential thrombocythemia. Clin Appl Thromb Hemost. 1999; 5: 247–51.
16 Lichtenstein DR, Wolfe MM. COX-2 selective NSAID, new and improved? J Am Med Assoc 2000; 284: 1297–9.
17 Luo C, Kallajoki M, Mäkinen M, Teros T, Ylinen L, Simell O. Distribution and contribution of cyclooxygenase (COX)-2 for diabetogenesis in NOD mouse model. Cell Tissue Res 2002; 310: 169–75.
18 McKanna JA, Zhang MZ, Wang JL, Cheng H, Harris RC. Constitutive expression of cyclooxygenase-2 in rat vas deferens. Am J Physiol 1998; 275: R227–33.
19 Harris RC. Macula densa signaling, a potential role of cyclooxygenase-2 (COX-2)? Nephrol Dial Transplant 2000; 15: 1504–6.
20 Luo C, Laaja P. Inhibitors of JAKs/STATs and the kinases, a possible new cluster of drugs. Drug Discov Today 2004; 9: 268–75.
21 Tiano HF, Loftin CD, Akunda J, Lee CA, Spalding J, Sessoms A, *et al*. Deficiency of either cyclooxygenase (COX)-1 or COX-2 alters epidermal differentiation and reduces mouse skin tumorigenesis. Cancer Res 2002; 62: 3395–401.
22 Baba H, Kohno T, Moore KA and Woolf CJ. Direct activation of rat spinal dorsal horn neurons by prostaglandin E2. J Neurosci 2001; 21: 1750–6.
23 Samad TA, Moore KA, Sapirstein A, Billet S, Allchorne A, Poole S, *et al*. Interleukin-1b-mediated induction of Cox-2 in the CNS contributes to inflammatory pain hypersensitivity. Nature 2001; 410: 471–5.
24 Ma W, Eisenach JC. Morphological and pharmacological evidence for the role of peripheral prostaglandins in the pathogenesis of neuropathic pain. Eur J Neurosci 2002; 15: 1037–47.
25 Ellman MH, Curran J. Trial of tramadol/acetaminophen tablets for osteoarthritis pain in subjects receiving a COX-2 nonsteroidal antiinflammatory drug. J Rheumatol 2005; 32: 568–8.
26 Boutaud O, Aronoff DM, Richardson JH, Marnett LJ, Oates JA. Determinants of the cellular specificity of acetaminophen as an inhibitor of prostaglandin H2 synthases. Proc Natl Acad Sci USA 2002; 99: 7130–5.
27 Botting R, Ayoub SS. COX-3 and the mechanism of action of paracetamol/acetaminophen. Prostaglandins Leukot Essent Fatty Acids 2005; 72: 85–7.
28 van Ryn J, Trummlitz G, Pairet M. COX-2 selectivity and inflammatory processes. Curr Med Chem 2000; 7: 1145–61.
29 Kurumbail RG, Stevens AM, Gierse JK, McDonald JJ, Stegeman RA, Pak JY, *et al*. Structural basis for selective inhibition of cyclooxygenase-2 by anti-inflammatory agents. Nature 1997; 385: 555–62.
30 Yang T, Endo Y, Huang YG, Smart A, Briggs JP, Schnermann J. Renin expression in COX-2-knockout mice on normal or low-salt diets. Am J Physiol Renal Physiol 2000; 279: F819–25.
31 Bonner JC, Rice AB, Ingram JL, Moomaw CR, Nyska A, Bradbury A, *et al*. Susceptibility of cyclooxygenase-2-deficient mice to pulmonary fibrogenesis. Am J Pathol 2002; 161: 459–70.
32 Mukherjee D, Topol EJ. COX-2: where are we in 2003? Cardiovascular risk and COX-2 inhibitors. Arthritis Res Ther 2003; 5: 8–11.
33 Adegboyega PA, Ololade O. Immunohistochemical expression of cyclooxygenase-2 in normal kidneys. Appl Immunohistochem Mol Morphol 2004; 12: 71–4.
34 McAdam BF, Catella-Lawson F, Mardini IA, Kapoor S, Lawson JA, FitzGerald GA. Systemic biosynthesis of prostacyclin by cyclooxygenase (COX)-2: the human pharmacology of a selective inhibitor of COX-2. Proc Natl Acad Sci USA 1999; 96: 272–7.
35 Catella-Lawson F, McAdam B, Morrison BW, Kapoor S, Kujubu D, Antes L, et al. Effects of specific inhibition of cyclooxygenase-2 on sodium balance, hemodynamics, and vasoactive eicosanoids. J Pharmacol Exp Ther 1999; 289: 735–41.
36 Solomon SD, McMurray JJ, Pfeffer MA, Wittes J, Fowler R, Finn P, *et al*. Cardiovascular risk associated with celecoxib in a clinical trial for colorectal adenoma prevention. N Engl J Med 2005; 352: 1071–80.
37 Bresalier RS, Sandler RS, Quan H, Bolognese JA, Oxenius B, Horgan K, *et al*. Cardiovascular events associated with rofecoxib in a colorectal adenoma chemoprevention trial. N Engl J Med 2005; 352: 1092–102.
38 Perera P, Ringbom T, Huss U, Vasänge M., Bohlin L. Search for natural products with effect on cyclooxygenase-2. In: Tringali

C, editor. Bioactive Compounds from Natural Sources. London: Taylor & Francis; 2001. p433–72.
39 Subbaramaiah K, Michaluart P, Chung WJ, Tanabe T, Telang N, Dannenberg AJ. Resveratrol inhibits cyclooxygenase-2 transcription in human mammary epithelial cells. Ann NY Acad Sci 1999; 889: 214–23.
40 Ringbom T, Huss U, Stenholm A, Flock S, Skattebol L, Perera P, *et al*. COX-2 inhibitory effects of naturally occurring and modified fatty acids. J Nat Prod 2001; 64: 745–9.
41 Arita M, Bianchini F, Aliberti J, Sher A, Chiang N, Hong S, *et al*. Stereochemical assignment, antiinflammatory properties, and receptor for the omega-3 lipid mediator resolvin E1. J Exp Med 2005; 201: 713–22.
42 Ringbom T, Segura L, Noreen Y, Perera P, Bohlin L. Ursolic acid from *Plantago major*, a selective inhibitor of cyclooxygenase-2 catalyzed prostaglandin biosynthesis. J Nat Prod 1998; 61: 1212–5.
43 Stock JL, Shinjo K, Burkhardt J, Roach M, Taniguchi K, Ishikawa T, The prostaglandin E_2 EP1 receptor mediates pain perception and regulates blood pressure. J Clin Invest 2001; 107: 325–31.

SCI Impact Factor of Acta Pharmacologica Sinica increased to 1.125

According to the latest Journal Citation Report 2004 (JCR 2004) published by Institute for Scientific Information (ISI, USA), we are greatly pleased to announce that the Science Citation Index (SCI) Impact Factor of Acta Pharmacologica Sinica (APS) has risen from 0.884 to **1.125**, ranking the 132nd out of 187 journals in the category of PHARMACOLOGY & PHARMACY, and the 49th out of 125 journals in the category of CHEMISTRY, MULTIDISCIPLINARY. APS is continued to be the only journal listed in the SCI in Chinese Pharmacology and Pharmacy and ranked the 8th out of 71 Chinese journals listed in SCI.

Here we would like to share the good news with all our authors, reviewers and readers. Without your long-term contribution , APS cannot achieve such a progress! Hope to have your support continuosly!

Acta Pharmacologica Sinica 2005 Aug; 26 (8): 934–942

Full-length article

Interleukin-1 beta induction of neuron apoptosis depends on p38 mitogen-activated protein kinase activity after spinal cord injury[1]

Xin-jia WANG[2], Kang-mei KONG, Wei-li QI, Wei-lian YE, Pei-song SONG

Department of Spine Surgery, The Second Affiliated Hospital, Shantou University Medical College, Shantou 515041, China

Key words

apoptosis; interleukin-1; interleukin-1-receptor antagonist protein; p38 mitogen-activated protein kinase; spinal cord injury; TUNEL

[1] Project supported by grants from the Natural Science Foundation of Guangdong Province, China (No 013216), and the Foundation of Guangdong Health Bureau, China (No A2003521).
[2] Correspondence to Xin-jia WANG, PhD.
Phn 86-754-852-6948.
Fax 86-754-834-6543.
E-mail xj.wang2000@163.com

Received 2004-12-28
Accepted 2005-05-17

doi: 10.1111/j.1745-7254.2005.00152.x

Abstract

Aim: Interleukin–1 beta (IL-1β) has been implicated as an extracellular signal in the initiation of apoptosis in neurons and oligodendrocytes after spinal cord injury (SCI). To further characterize the apoptotic cascade initiated by IL-1β after SCI, we examined the expression of IL-1β, p38 mitogen-activated protein kinase (p38 MAPK) and caspase-3 after SCI, and further investigated whether p38 MAPK was involved in neuron apoptosis induced by IL-1β. **Methods:** Adult rats were given contusion SCI at the T-10 vertebrae level with a weight-drop impactor (10 g weight dropped 25.0 mm). The expression levels of IL-1β, p38 MAPK and caspase-3 after SCI were assessed with Western blots, immunohistochemistry staining, and real time reverse transcription polymerase chain reactions (RT-PCR). Neuron apoptosis was assessed with the terminal deoxynucleotidyl transferase-mediated deoxyuridine triphosphate-biotin nick end labeling (TUNEL) method. **Results:** Increased levels of IL-1β and p38 MAPK were observed soon after injury, with a peak in expression levels within 6 h of injury. By 24 h after injury, caspase-3 expression was markedly increased in the injured spinal cord. TUNEL-positive cells were first observed in the lesioned area 6 h after SCI. The largest number of TUNEL-positive cells was observed at 24 h post-SCI. Intrathecal injection of the IL-1 receptor antagonist IL-1Ra significantly reduced expression of p38 MAPK and caspase-3, and reduced the number of TUNEL-positive cells. Moreover, intrathecal injection of an inhibitor of p38 MAPK, SB203580, also significantly reduced the expression of caspase-3, and reduced the number of TUNEL-positive cells in the injured spinal cord. **Conclusion:** The p38MAPK signaling pathway plays an important role in IL-1β mediated induction of neuron apoptosis following SCI in rats.

Introduction

Traumatic spinal cord injury (SCI) often results in complete loss of voluntary motor and sensory function below the site of injury. Extensive evidence indicate that secondary injury of the cord involving widespread apoptosis of neurons and oligodendroglia after the trauma contributes significantly to long-term neurological deficits[1,2]. Interleukin-1 beta (IL-1β) induces apoptosis in neurons *in vitro*[3] and in cultured human astrocytes[4] and oligodendrocytes *in vivo*[5]. IL-1β expression is upregulated rapidly at the lesion site after SCI[6–8]. Furthermore, injection of an IL-1 receptor antagonist (IL-1Ra), a potent anti-inflammatory cytokine, reduces IL-1β production in the spinal cord and thereby may promote functional recovery following SCI[9]. Thus a rapid accumulation of IL-1β following SCI may initiate apoptosis in neurons and glial cells. The intracellular signaling events initiated by IL-1β that lead to apoptotic cell death *in vivo* however are not well understood.

Caspase-3 is a potential mediator of apoptosis after central nervous system (CNS) injury[10, 11] and its activation may be as a marker of apoptotic cell death. Several studies have provided evidence that cell death from moderate traumatic spinal cord injury is regulated, in part, by apoptosis that

involves the caspase family of cysteine proteases[9,11]. In the hippocampus of aged rats, the concentration of IL-1β is increased and this increase is accompanied by enhanced caspase-3 activity indicative of cell death[12]. These findings suggest that neuron apoptosis in the CNS is induced by increased IL-1β through activity of the caspase-3 apoptotic pathway.

p38 Mitogen-activated protein kinase (p38 MAPK) is a pivotal molecule in the signal pathway initiated by IL-1RI[13]. A subset of cyclin-dependent kinase/mitogen-activated protein kinase superfamily kinases has been implicated in neuron apoptosis[14,15]. In neurons of the hippocampus, inhibition of p38 MAPK activation induced by SB203580 blocks suppression of long term potentiation evoked by IL-1β[16] and cellular stress responses to IL-1β[17]. In addition, the cardiovascular and behavioral responses induced by intracerebral ventricular (icv) injection of IL-1β were abrogated by pretreatment with the p38 inhibitor SB203580 (icv) in awake rats[18]. These findings suggest that the effects of IL-1β are partially dependent upon p38 MAPK activation. In addition, IL-1β concentration was found to be increased and accompanied by enhanced caspase-3 activity in the hippocampus of aged rats[12]. Analysis of colocalization of activated caspase-3 with activated p38 MAPK (p-p38) in the hippocampus of aged rats, suggested that p-p38 was necessary for activation of caspase-3; while *in vitro* analysis indicated that the IL-1β-induced increase in caspase-3 activity was abrogated by the p38 MAPK inhibitor, SB203580[12]. Thus apoptosis activated by increased IL-1β after SCI may be dependent, at least in part, upon the activation of p38 MAPK.

In the present report, expression of IL-1β as well as expression of its potential downstream target molecules p38 MAPK and caspase-3 was examined in rats following SCI. If p38 MAPK signaling mediates IL-1β genetic induction of apoptosis, then p38 MAPK expression should be elevated after SCI together with IL-1β expression. Likewise, if the apoptotic program initiated by IL-1β involves caspase-3 as an effector of apoptosis, then a subsequent increase in caspase-3 levels should also be observed following SCI.

We further tested pharmacologically whether the apoptotic cascade initiated by IL-1β after SCI involved p38 MAPK signaling and caspase-3. If post-injury caspase-3 increases were induced by IL-1β signaling, then blocking IL-1 receptors should attenuate caspase-3 upregulation after injury. Moreover, if IL-1β induction of apoptosis after SCI was mediated by MAPK signaling, which then resulted in caspase-3 upregulation, then blocking MAPK activity should also attenuate caspase-3 upregulation as well as reduce the amount of apoptotic cells observed after SCI.

Materials and methods

Materials Rabbit antibodies directed against IL-1β, caspase-3 and normal rabbit serum were purchased from Sigma Biotechnologies (Sigma-Aldrich, Inc, Saint Louis, Missouri, USA). p38 MAP Kinase Assay Kits were purchased from Cell Signaling Technology™ (Cell Signaling, Beverly, USA). The p38 inhibitor 4-(4-fluorophenyl)-2-(4-methylsulfonylphenyl)-5-(4-pyridyl)-1*H*-imidazole(SB203580) was purchased from Calbiochem (Calbiochem, La Jolla, CA). Recombinant rat IL-1ra was purchased from R & D Systems (Minneapolis, MN, USA). Terminal Deoxynucleotidyl Transferase-Mediated Deoxyuridine Triphosphate-Biotin Nick End Labeling (TUNEL) detection kits were purchased from Sino-American Biotechnology Co (Sino-American Biotechnology Co, Luo Yang, China).

Spinal cord injury and pharmacological treatment Adult male Wistar rats, weighing about 250 g each (range from 220 g to 270 g), were used in this study (provided by the Experimental Animal Center of Shantou University Medical College). Rats were assigned randomly to either the SCI group, the sham-operated control group (n=54 for each group) or the drug-treated group (including SB203580; IL-1Ra; vehicle, n=18 for each group). Rats' spinal cords were contused extradurally with a 10-g weight-drop impactor dropped 25.0 mm onto the T9-T10 region of the cord exposed by laminectomy as described previously[19]. Drug treatments were given intrathecally immediately after the injury. Recombinant rat IL-1Ra (10 μg) was given to antagonize IL-1 receptors and SB203580 (4 kg in 10 μL) was given to inhibit p38 MAPK[9,20,21]. The animals in the sham-operated control group underwent a T9 laminectomy without injury and received intrathecal injections of only vehicle (10 μL saline). All animal care and surgical procedures were approved by the institutional animal care and use committee of Shantou University.

RNA purification and RT-PCR At several time points following impact, 4-mm thick tissue sections were collected by deep anesthesia and stored frozen at -80 °C. Total tissue RNA was purified by homogenization of 20 mg spinal cord using the RNeasy Mini kit (Qiagen, Valencia, CA) according to the manufacturer's instructions. RNA was washed, dried, resuspended in sterile nuclease-free water, and stored at -80 °C. After spectrophotometric quantification, the purified RNA was separated on a formaldehyde-agarose gel to assess the extent of degradation.

One microgram total RNA was reverse-transcribed into cDNA in each 50 μL reaction mixture, using one-step RT-PCR (QIAGEN One Step RT-PCR Kit, Qiagen, Valencia, CA)

according to the manufacturer's instructions. The sequences of forward and reverse primers for amplifying IL-1β cDNA were 5'-AGCTATGGCAACTGTCCCT-3' and 5'-AGCTATGGCAACTGTCCCT-3', respectively. After amplification, RT-PCR products were quantified with real time PCR.

Real time quantitative RT-PCR To compare the mRNA content of IL-1β in spinal cord after SCI with pharmacological treatment, reverse-transcribed cDNA standards and samples were amplified in parallel by PCR on a LightCycler using additional sequence-specific hybridization probes in combination with the LightCycler. PCR with *Taq* polymerase (Taqman; Applied Biosystems, Foster City, CA) on the cDNA samples was performed on a sequence detector (Prism 7700; Applied Biosystems, Foster City, CA). Equal amounts of cDNA were used in duplicate and amplified with the PCR mix (Taqman Master Mix; Applied Biosystems). Real time PCR protocols were performed as described previously[22]. Briefly, the PCR reaction mixture contained 2 mmol/L $MgCl_2$, 20 pmol of both PCR primers, 1 pmol of each hybridization probe, 2 μL of LightCycler. DNA master hybridization mix (Roche, Germany) and 2 μL of reverse-transcribed samples in a final volume of 25 μL. The PCR conditions were set at 50 °C for 2 min, 95 °C for 10 min followed by 40 cycles of 95 °C for 30 s and 60 °C for 1 min. Additional reactions were performed on known dilutions of rat IL-1β cDNA as a PCR template to construct a standard curve relating threshold cycle to template copy number.

The sample copy numbers were calculated using the LightCycler analysis software (Roche, Mannheim, Germany). The LightCycler software system analyzed the spectral data collected at the end of the annealing phase of each cycle and plotted fluorescence intensity versus cycle number. The cDNA standard curve was generated by the LightCycler. The Cts value against the logarithm of the calculated initial copy numbers was plotted by the Software system. The unknown initial sample copy numbers were then calculated automatically from their Cts, as compared to the cDNA standard curve.

Taq polymerase primer and probe sets for IL-1β were designed from sequences in the GenBank database of NCBI on DNAman. GenBank is provided in the public domain by the National Center for Biotechnology Information, Bethesda, MD (http://www.ncbi.nlm.nih.gov/Genbank). The primer and probe sequences used were as follows: IL-1β forward primer: 5'-CTGCACTGCAGGCTTCGA-3'; reverse primer: 5'-TGGAGAGCTTTCAGCTCACATG-3'; Taqman probe: 5'-FAM-ATGAACAACAAAAATGCCTCGTGCTGTCTGTAMRA-3'.

Western blot analysis At 30 min, 6 h, 24 h, 72 h after injury (n=3 per time point), an 8-mm spinal cord segment was dissected 4 mm rostral and 4 mm caudal from the lesion epicenter from each group. The cord tissues were resuspended in a lysis buffer (Cell Signaling, Beverly, USA) and homogenized in a dounce homogezenizer on ice. Tissue homogenate samples were centrifuged at 14 000 rpm for 10 min at 4 °C, and the supernatant samples were stored at -30 °C. Protein concentrations in the cell lysates were determined by Bio-Rad (Richmond, CA) protein assay, as recommended by the manufacturer. For analyses by Western blot, 20 μL of each suspension sample was separated in 12% SDS-PAGE, and the proteins were transferred to polyvivylidene difluorid membranes. Blots were blocked with 5% nonfat dry milk in tris-buffered saline (TBS) for 1 h at room temperature and then the membranes were incubated with 1:200 diluted monoclonal rabbit anti-rat antibodies against IL-1β (Sigma) or caspase-3 (Sigma) overnight at 4 °C. The membranes were then processed with HRP-conjugated goat anti-rabbit secondary antibody (1:500; Sigma). Immunoreactive bands were quantified using image analysis software.

p38 MAPK enzymatic activity was measured using a p38 MAP Kinase Assay Kit (Cell Signaling), and the protocol was performed according to the manufacturer's instructions. Briefly, 200 μL of protein content in clear supernatant was immunoprecipited using immobilized phospho-p38 MAP kinase (Thr180/Tyr182) monoclonal antibodies with gentle shaking overnight at 4 °C. The immunoprecipitate was washed twice with 500 μL ice-cold cell lysis buffer and twice with 500 μL ice-cold kinase buffer (25 mmol/L Tris (pH 7.5), 5 mmol/L β-glycerolphosphate, 2 mmol/L DTT, 0.1 mmol/L Na_3VO_4, and 10 mmol/L $MgCl_2$) at 4 °C. The kinase reactions were conducted in the presence of 200 μmol/L ATP and 2 μg activating transcription factor-2 (ATF-2) fusion protein at 30 °C for 30 min. After the reaction had been terminated by the addition of 3×SDS sample buffer, the mixture was boiled for 5 min, followed by brief centrifugation. Phospho-p38MAPK was selectively measured by Western immunoblotting as described previously[23], and then immunoreactive bands were quantified using image analysis software.

Immunohistochemistry At several time intervals after SCI (30 min, 6 h, 24 h, 72 h, 1 wk, 6 wk), animals were deeply anesthetized and perfused via cardiac puncture with 0.1 mol/L phosphate-buffered saline (PBS) 150 mL (pH 7.4) and subsequently with 4% paraformaldehyde in 0.1 mol/L PBS 250 mL. The spinal cord was carefully dissected, and an 8-mm segment containing the injured epicenter was dissected out and post-fixed by immersion in 4% paraformaldehyde for 3 h and then cryoprotected by immersion in 20% sucrose of PBS overnight. Tissue segments were embedded in OCT and frozen as described previously[24]. Free-floating transverse

sections (10 μm) were cut with a cryostat.

Immunohistochemical staining was performed by the avidin-biotin complex method as described previously[25]. The concentration for rabbit anti-IL-1β and rabbit anti-caspase-3 primary antibodies was 1:200. The concentration for biotinylated anti-rabbit antibodies was 1:200. Positive immunoreactive labeling was observed qualitatively.

Terminal deoxynucleotidyl transferase-mediated deoxyuridine triphosphate-biotin nick end labeling (TUNEL) Spinal cord specimens used for TUNEL staining were collected as described above for immunohistochemistry methods. The segment was embedded in paraffin as previously described[24] and 5 μm-thick serial transverse sections were collected. The sections were processed for TUNEL staining with an in site cell apoptosis detection kit, and the staining protocol was performed according to the manufacturer's instructions. The sections were counterstained with hematoxylin. The ratios of TUNEL positive cells to total cells were counted and analyzed by computer. All TUNEL analyses were carried out by investigators who were blind as to the experimental conditions.

Statistical analysis Data are expressed as mean±SD. Statistical significance was assessed with one-way ANOVA. The significant difference between pairs of groups was tested by *post hoc* analysis. $P<0.05$ was considered significant in all cases.

Results

Rapid expression of IL-1β in spinal cord after SCI The temporal expression of IL-1β mRNA and protein at pre-defined time intervals (30 min, 6 h, 24 h, 72 h after SCI; $n=3$ for each time point) was examined. Absolute quantification real-time reverse PCR (Q-RT-PCR) analysis revealed that by 30 min after the contusion injury, IL-1β mRNA levels (6.75± 0.42, log of the copy number of IL-1β cDNA) were significantly increased in the cords of injured rats relative to sham surgery control rats (4.98±0.49). IL-1β mRNA levels continued to rise, reaching peak levels at 6 h post-injury (6.97± 0.75) ($^cP<0.01$ *vs* control group), then falling by 24 h.

Western blot analysis also showed an increase in IL-1β levels following SCI (Figure 1). IL-1β protein was increased significantly by 30 min after the injury, reached peak levels by 6 h after the injury and declined thereafter. Both Western blot analysis (Figure 1) and immunohistochemistry examination (Figure 2A) revealed low levels of IL-1β protein in the sham controls. As early as 30 min after injury IL-1β immunoreactivity was observed in neurons within the gray matter in the lesion area, as well as in neurons located several microns, rostral and caudal of the lesion. The peak of immunoreactivity was observed 6 h after SCI (Figure 2B).

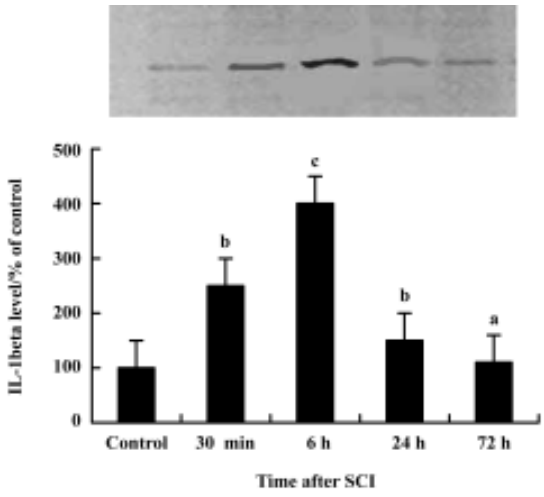

Figure 1. Western blot analysis of IL-1β protein level in the spinal cord afterframatic spinal cord injury (SCI). Each value was measured by densitometric analysis of the Western blots bands. Data were converted to percentages as compared to the sham-operated control as 100%. Mean±SD. $^aP>0.05$, $^bP<0.05$, $^cP<0.01$ *vs* control group.

p38 MAPK activation in the spinal cord after injury Immunoprecipitation and Western blot examinations revealed that 6 h after SCI total p38 MAPK levels in the spinal cord had not changed after contusion (Figure 3A). P-p38 MAPK levels however were significantly increased following the injury. This increase was detectable at 30 min after contusion and reached a peak at 6 h. P-p38 MAP returned to basal levels by 72 h post-injury (Figure 3B). These data indicate that increases in p-p38 after SCI are caused by increased phosphorylation rather than by elevated substrate.

Induction of caspase-3 after injury The post-injury temporal profile of caspase-3 expression was examined by immunohistochemistry and Western blot analysis. Both injured and sham-operated spinal cords were evaluated for caspase-3 expression at four pre-defined time points (30 min, 6 h, 24 h, and 72 h after SCI; $n=3$ for each time point). As expected, little caspase-3 immunoreactivity was observed in sham-operated spinal cords (Figure 2C). Weak caspase-3 immunoreactivity was first detected in a few neurons within the gray matter of the lesioned area 6 h after injury. Intense caspase-3 immunoreactivity was seen in gray matter neurons 24 h after injury and decreased thereafter (Figure 2D). Western blot analyses also showed that caspase-3 expression was up-regulated after SCI. Caspase-3 protein was detectable by 6 h, peaked 24 h post-injury and decreased thereafter (Figure 4).

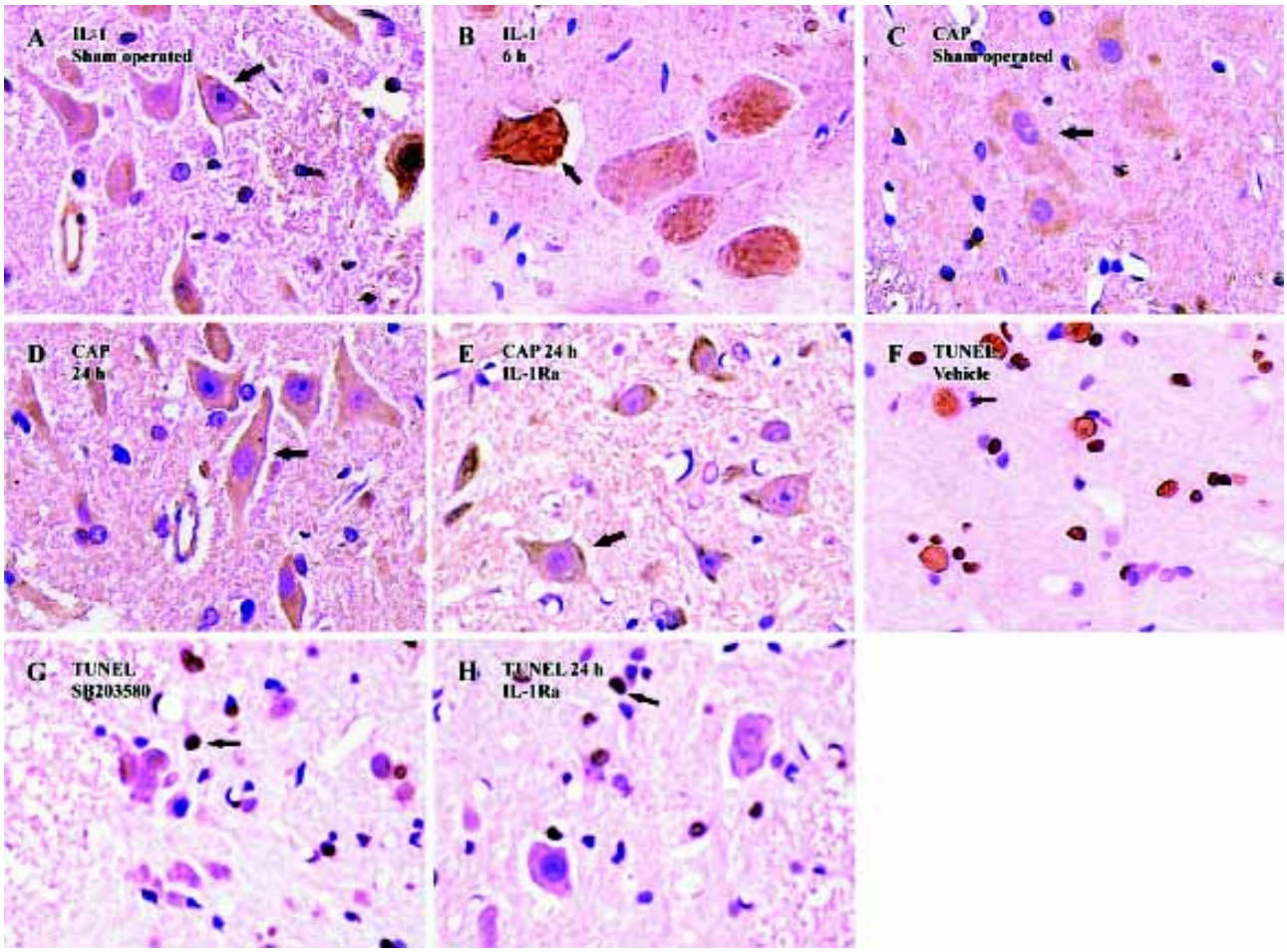

Figure 2. Immunocytochemical detection of IL-1, caspase-3 and TUNEL labeling after spinal cord injury. ×400. (A) IL-1β immunoreactivity in the sham-operated spinal cord, little IL-1β immunoreactivity (arrow) was detected. (B) IL-1β immunoreactivity (arrow) was intense in a section of the injured cord 6 h after SCI. (C) Little caspase-3 immunoreactivity (arrow) was observed in sham-operated spinal cords. (D) Intense caspase-3 immunoreactivity (arrow) in the gray matter neurons 24 h after injury. (E) Few caspase-3 positive immunoreactivity neurons (arrow) 24 h after SCI treated with IL-Ra. (F) TUNEL positive cells (arrow) in vehicle group. (G) IL-1Ra treatment significantly reduced the number of TUNEL-positive cells (arrow) in the cord relative to vehicle controls. (H) SB203580 treatment significantly reduced the number of TUNEL-positive cells (arrow) in the cord relative to vehicle controls.

SCI-induced p38 MAPK activation is mediated by IL-1β To test whether IL-1β plays a role in p38 MAPK activation after SCI, the IL-1 receptor antagonist, recombinant rat IL-1ra, was given after SCI. Western blot data showed an increase in p-p38 in spinal cord 6 h after SCI. Treatment with IL-1Ra markedly inhibited the injury-induced activation of p38 MAPK. These data suggest that p38 MAPK activation in spinal cord after SCI is mediated by IL-1β (Figure 5).

Inhibition of caspase-3 expression and reduction of apoptosis by IL-1Ra after injury To demonstrate whether the IL-1β induced expression of caspase-3 and the subsequent increased apoptosis of neurons after contusion injury, we compared both expression of caspase-3 and the number of apoptotic cells in the presence or absence of IL-1Ra after SCI. As shown in Figure 6, the induction of caspase-3 protein was inhibited significantly by IL-1Ra treatment. Few TUNEL-positive cells were initially present in the lesion area within 6 h of injury. The greatest numbers of TUNEL-positive cells were observed 24 h after injury. Treatment with IL-1Ra markedly reduced the number of TUNEL-positive cells in the cord relative to vehicle controls at 24 h after injury (Figure 2F, 2G).

p38 MAPK inhibition reduces neuron apoptosis and caspase-3 expression after SCI Treatment of the injured spinal cord with SB203580 resulted in a marked reduction in the number of TUNEL-positive cells as compared to that

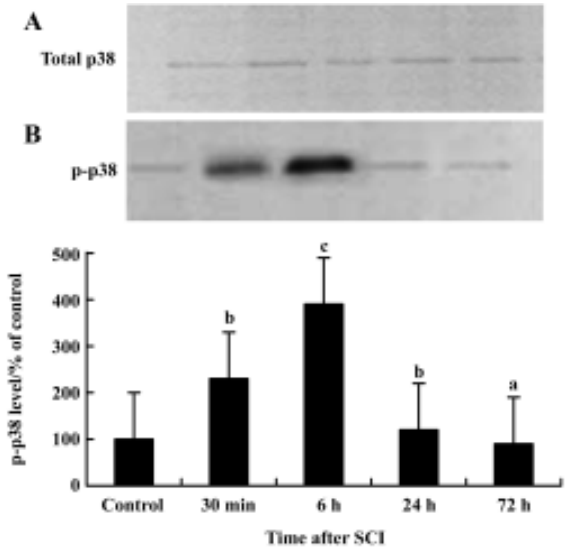

Figure 3. p38 MAPK activation in the spinal cord after injury. (A) Total nonphosphorylated p38 MAPK levels in the spinal cord did not change after contusion. (B) Phospho-p38 levels were significantly increased in the injured spinal cord, and peaked 6 h after SCI. [a]*P*>0.05, [b]*P*<0.05, [c]*P*<0.01 *vs* control group.

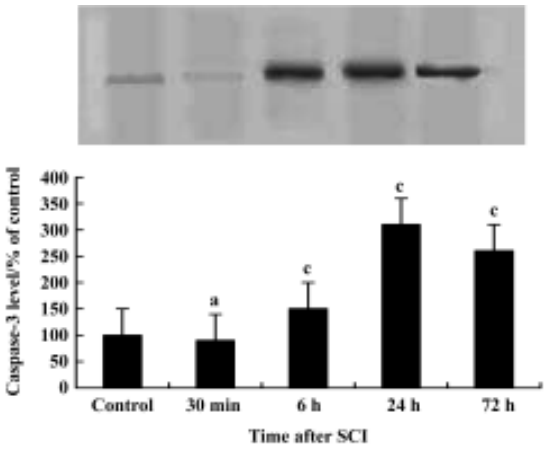

Figure 4. Western blot analysis showed time-dependent changes in caspase-3 protein levels in the spinal cord after injury. Sample from sham control and injured spinal cords were prepared for Western blotting at 30 min, 6 h, 24 h, 72 h after SCI. Caspase-3 protein levels peaked 24 h after injury and declined thereafter. [a]*P*>0.05, [c]*P*<0.01 *vs* sham-operated control group.

found in vehicle controls (Figure 2H). Notably, at 24 h post-injury the number of TUNEL-positive cells was reduced by 50% with the SB203580 treatment. The induction of caspase-3 protein was also inhibited significantly by treatment with SB203580 (Figure 7).

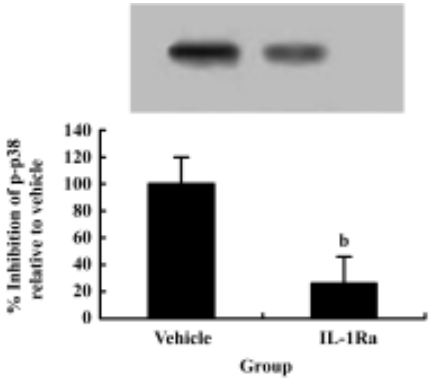

Figure 5. Treatment with IL-1Ra attenuated the injury-induced activation of p38 in the spinal cord. The phospho-p38 protein level in the IL-Ra-treated group was significantly less than that in the vehicle group at 6 h post-injury. Sham operated group was 100%. [b]*P*<0.05 *vs* vehicle group.

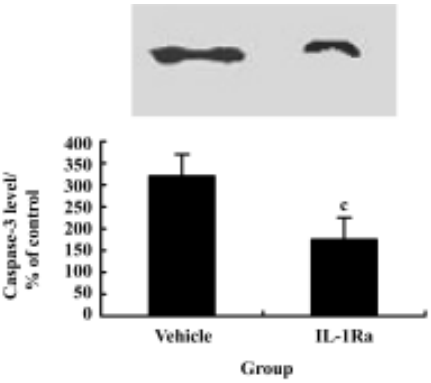

Figure 6. Treatment with IL-1Ra markedly inhibited the injury-induced activation of Caspase-3 in spinal cord. The caspase-3 protein level in the IL-1Ra treated group was significantly less than that in the vehicle group at 24 h. Sham operated group was 100%. [c]*P*<0.01 *vs* vehicle group.

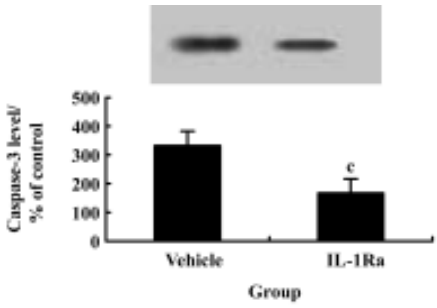

Figure 7. Caspase-3 protein level was significantly reduced in rats treated with SB203580 relative to the vehicle group at 24 h post-injury. Sham operated group was 100%. [c]*P*<0.01 *vs* vehicle group.

Discussion

Injury to the spinal cord induces a complex cascade of cellular reactions at the local lesion area that results in inflammation and secondary cell death[26]. IL-1β is a major mediator of inflammation and may play an important role in the consequences of traumatic spinal cord injury. Numerous studies have confirmed an increase in IL-1β expression after SCI[6–8]. In the present study, the expression of IL-1β and its mRNA was assessed in the rat spinal cord following a standardized contusion injury. IL-1β mRNA levels, as measured by quantitative RT-PCR, were significantly increased in the lesion area by 30 min after SCI, peaked at 6 h and returned to normal at 72 h post-injury. IL-1β protein levels, as measured by Western blot and immunohistochemical staining, were increased significantly in the lesion area by 30 min post-injury, peaked at 6 h and then remained significantly higher than normal through at least 3 d post-injury. These findings, along with the findings by others[6–8], suggest that the increased IL-1β mRNA and protein levels are an early and local response at the lesion site that could trigger other, later, responses to traumatic SCI.

The function of IL-1β remains unclear. Some evidence indicates that IL-1β may exert beneficial effects on the CNS after injury such that IL-1β and its type 1 receptor may be involved in the maintenance of cell survival rather than induction of neuronal death. Direct application of inflammatory cytokines with SCI has been shown to reduce tissue loss[27]. On the contrary, however, findings of several studies are consistent with the view that an increased level of IL-1β after injury is adverse. Namely, increased IL-1β in spinal cord has been associated with neuronal apoptosis[4,9]. Direct injection of IL-1β into the spinal cord enhances vascular permeability and produces lymphocyte recruitment[28]. As such, an early and rapid production of IL-1β after injury appears to be deleterious to the CNS by triggering apoptosis. It may be that whether one sees enhanced cell survival or augmented apoptosis depends of the dose of IL-1β present in the cord.

The IL-1β expression peak (6 h post-injury) occurred when few TUNEL-positive apoptotic cells were present in the lesion area. The number of observed apoptotic cells peaked much later, 24 h after the contusion injury. IL-1β receptor antagonism with IL-1Ra significantly reduced the number of apoptotic cells present after injury. These data suggest that IL-1β plays a causal role in neuronal apoptosis in the early phase of SCI. However, the intracellular signaling events initiated by IL-1β that lead to apoptotic cell death remain largely unknown.

A number of studies have provided evidence that cell death from moderate traumatic spinal cord injury is regulated, in part, by apoptosis that involves the caspase family of cysteine proteases. A recent study demonstrated that spinal cord injury rapidly increased activation of the effector caspase, caspase-3. The caspase-3 message was present and upregulated several fold after traumatic spinal cord injury[29]. Moreover, upstream and downstream components of the caspase-3 apoptotic pathway are activated after traumatic spinal cord injury in rats. These effects occur early in neurons in the injury site and hours to days later in oligodendrocytes adjacent to and distant from the injury site[11]. Nesic O *et al*[9] showed that downstream components of the caspase-3 apoptotic pathway were activated after SCI in the rat. Furthermore caspase inhibition reduced post-traumatic lesion size and improved motor performance[10], indicating that caspase-3 is a potential mediator of apoptosis following CNS injury[10,11]. However it has not been shown definitively whether IL-1β induces apoptosis after SCI by activating caspase-3. The present Western blot and immunohistochemistry analyses results showed that caspase-3 expression was up-regulated in a relatively small number of neurons within the gray matter of the lesioned area at 6 h after SCI. Intense caspase-3 immunoreactivity was seen in gray matter neurons by 24 h after injury. Furthermore, IL-1 receptor antagonist treatment after SCI attenuated injury-induced upregulation of caspase-3 gene expression and resulted in fewer TUNEL-positive cells. Thus, these results are consistent with the hypothesis that IL-1β-induced apoptosis is mediated via induction of caspase-3 expression following SCI.

The MAPKs are a family of signaling molecules that transduce extracellular stimuli into intracellular responses in a wide variety of circumstances[15,30]. p38 MAPK is a key component in stress-induced signal transduction pathways. To test whether p38 MAPK signaling is involved in IL-1β induction of apoptosis, we examined the expression of p38 MAPK after SCI with immunoprecipitation and Western blot techniques. Increased levels of phospho-p38 MAPK were observed following SCI. Intrathecal injection of IL-1Ra attenuated the expression of caspase-3, and reduced the number of TUNEL-positive cells. In addition, treating the injured spinal cord with the MAPK inhibitor SB203580 resulted in a marked reduction in the expression of caspase-3 and the number of TUNEL-positive cells in the cord as compared to that observed in vehicle controls. These results are consistent with the hypothesis that IL-1β-induced apoptosis is mediated in part by p38 MAPK activation following SCI, and further that the apoptotic signal may then subsequently be

mediated by caspase-3.

In conclusion, our study provides evidence that IL-1β serves as an external apoptosis triggering signal in the spinal cord after injury. Our results further suggest that the apoptotic cell death induced by IL-1β is mediated, in part, by phosphorylation of p38 MAPK and subsequent activation of the apoptotic gene caspase-3. These findings suggest that inhibition of p38 MAPK after SCI (ie by SB203580) may prevent neuronal cell death after SCI.

References

1 Beattie MS, Hermann GE, Rogers RC, Bresnahan JC. Cell death in models of spinal cord injury. Prog Brain Res 2002; 137: 37–47.

2 Emery E, Aldana P, Bunge MB, Puckett W, Srinivasan A, Keane RW, *et al*. Apoptosis after traumatic human spinal cord injury. J Neurosurg 1998; 89: 911–20.

3 Fankhauser C, Friedlander RM, Gagliardini V. Prevention of nuclear localization of activated caspases correlates with inhibition of apoptosis. Apoptosis 2000; 5: 117–32.

4 Ehrlich LC, Peterson PK, Hu S. Interleukin (IL)-1beta-mediated apoptosis of human astrocytes. Neuroreport 1999; 10: 1849–52.

5 Takahashi JL, Giuliani F, Power C, Imai Y, Yong VW. Interleukin-1beta promotes oligodendrocyte death through glutamate excitotoxicity. Ann Neurol 2003; 53: 588–95.

6 Hayashi M, Ueyama T, Nemoto K, Tamaki T, Senba E. Sequential mRNA expression for immediate early genes, cytokines, and neurotrophins in spinal cord injury. J Neurotrama 2000; 17: 203–18.

7 Pan JZ, Ni L, Sodhi A, Aguanno A, Young W, Hart RP. Cytokine activity contributes to induction of inflammatory cytokine mRNAs in spinal cord following contusion. J Neurosci Res 2002; 68: 315–22.

8 Wang CX, Olschowka JA, Wrathall JR. Increase of interleukin-1beta mRNA and protein in the spinal cord following experimental traumatic injury in the rat. Brain Res 1997; 759: 190–6.

9 Nesic O, Xu GY, McAdoo D, High KW, Hulsebosch C, Perez-Pol R. IL-1 receptor antagonist prevents apoptosis and caspase-3 activation after spinal cord injury. J Neurotrauma 2001; 18: 947–56.

10 Li M, Ona VO, Chen M, Kaul M, Tenneti L, Zhang X, *et al*. Functional role and therapeutic implications of neuronal caspase-1 and -3 in a mouse model of traumatic spinal cord injury. Neuroscience 2000; 99: 333–42.

11 Springer JE, Azbill RD, Knapp PE. Activation of the caspase-3 apoptotic cascade in traumatic spinal cord injury. Nat Med 1999; 5: 943–6.

12 Lynch AM, Lynch MA. The age-related increase in IL-1 type I receptor in rat hippocampus is coupled with an increase in caspase-3 activation. Eur J Neurosci 2002; 15: 1779–88.

13 Rothwell NJ, Luheshi GN. Interleukin 1 in the brain: biology, pathology and therapeutic target. Trends Neurosci 2000; 23: 618–25.

14 Maas JW Jr, Horstmann S, Borasio GD, Anneser JM, Shooter EM, Kahle PJ. Apoptosis of central and peripheral neurons can be prevented with cyclin-dependent kinase/mitogen-activated protein kinase inhibitors. J Neurochem 1998; 70: 1401–10.

15 Widmann C, Gibson S, Jarpe MB, Johnson GL. Mitogen-activated protein kinase: conservation of a three-kinase module from yeast to human. Physiol Rev 1999; 79: 143–80.

16 Aine K, Emily V, Yvonne N, Marcella B, Claire B, Christine EL, *et al*. Activation of p38 plays a pivotal role in the inhibitory effect of lipopolysaccharide and interleukin-1β on long term potentiation in rat dentate gyrus. J Biol Chem 2003; 278: 19453–62.

17 Cuenda A, Rouse J, Doza YN, Meier R, Cohen P, Gallagher TF, *et al*. SB 203580 is a specific inhibitor of a MAP kinase homologue which is stimulated by cellular stresses and interleukin-1. FEBS Lett 1995; 364: 229–33.

18 Zheng RM, Zou CJ, ZHU SG. p38 MAPK mediates cardiovascular and behavioral responses induced by central IL-1β and footshock in conscious rats. Acta Pharmacol Sin 2004; 25: 266–70.

19 Basso DM, Beattie MS, Bresnahan JC. Graded histological and locomotor outcomes after spinal cord contusion using the NYU weight-drop device versus transection. Exp Neurol 1996; 139: 244–56.

20 Mulcahy NJ, Ross J, Rothwell NJ, Loddick SA. Delayed administration of interleukin-1 receptor antagonist protects against transient cerebral ischaemia in the rat. Br J Pharmacol 2003; 140: 471–6.

21 Horiuchi H, Ogata T, Morino T, Chuai M, Yamamoto H. Continuous intrathecal infusion of SB203580, a selective inhibitor of p38 mitogen-activated protein kinase, reduces the damage of hind-limb function after thoracic spinal cord injury in rat. Neurosci Res 2003; 47: 209–17.

22 Hernandez-Rodriguez J, Segarra M, Vilardell C, Sanchez M, Garcia-Martinez A, Esteban MJ, *et al*. Tissue production of pro-inflammatory cytokines (IL-1beta, TNFalpha and IL-6) correlates with the intensity of the systemic inflammatory response and with corticosteroid requirements in giant-cell arteritis. Rheumatology (Oxford) 2004; 43: 294–301.

23 Jin SX, Zhuang ZY, Woolf CJ, Ji RR. p38 mitogen-activated protein kinase is activated after a spinal nerve ligation in spinal cord microglia and dorsal root ganglion neurons and contributes to the generation of neuropathic pain. J Neurosci 2003; 23: 4017–22.

24 Lee YB, Yune TY, Baik SY, Shin YH, Du S, Rhim H, *et al.* Role of tumor necrosis factor-α in neuronal and glial apoptosis after spinal cord injury. Exp Neurol 2000; 166: 190–5.

25 Tomlinson A, Appleton I, Moore AR, Gilroy DW, Willis D, Mitchell JA, *et al*. Cyclo-oxygenase and nitric oxide synthase isoforms in rat carrageenin-induced pleurisy. Br J Pharmacol 1994; 113: 693–8.

26 Bartholdi D, Schwab ME. Expression of pro-inflammatory cytokine and chemokine mRNA upon experimental spinal cord injury in mouse: an *in situ* hybridization study. Eur J Neurosci 1997; 9: 1422–38.

27 Klusman I, Schwab ME. Effect of pro-inflammatory cytokines in experimental spinal cord injury. Brain Res 1997; 762: 173–84.

28 Schnell L, Fearn S, Schwab ME, Perry VH, Anthony DC.

Cytokine-induced acute inflammation in the brain and spinal cord. J Neuropathol Exp Neurol 1999; 58: 245–54.
29 Citron BA, Arnold PM, Sebastian C, Qin F, Malladi S, Ameenuddin S, *et al*. Rapid upregulation of caspase-3 in rat spinal cord after injury: mRNA, protein, and cellular localization correlates with apoptotic cell death. Exp Neurol 2000; 166: 213–26.
30 Lee JC, Laydon JT, McDonnell PC, Gallagher TF, Kumar S, Green D, *et al*. A protein kinase involved in the regulation of inflammatory cytokine biosynthesis. Nature 1994; 372: 739.

Important Announcement: the Online Manuscript Submission and Review System was Launched!

Acta Pharmacologica Sinica announced that its online manuscript submission and review system based on ScholarOne Manuscript Central (http://mc.manuscriptcentral.com/aphs) was launched on May 25, 2005.

As the leading web-based peer-review system applied by many iournals, Manuscript Central is a complete, database-driven software for the online submission and review of full-text manuscripts and graphics. The system provides fully electronic workflow and will speed up the time from submission to decision.

Acta Pharmacologia Sinica strongly recommend its authors to submit manuscript via this system, which enables this journal to handle the manuscript quickly and efficiently. Please read the User Guide before submitting manuscript online. For more detailed submission instruction, please consult the Manuscript Central Online User Guide (http://mcv3help.manuscriptcentral.com/tutorials/). You may also contact the Editorial Office who will be pleased to help you.

Acta Pharmacologica Sinica 2005 Aug; 26 (8): 943–951

Full-length article

Sodium ferulate prevents amyloid-beta-induced neurotoxicity through suppression of p38 MAPK and upregulation of ERK-1/2 and Akt/protein kinase B in rat hippocampus[1]

Ying JIN[2], En-zhi YAN[3], Ying FAN[3], Zhi-hong ZONG[4], Zhi-min QI[3], Zhi LI[2,5]

[2]*Department of Ethnopharmacology, China Medical University, Shengyang 110001, China;* [3]*Department of Pharmacology, Jinzhou Medical College, Jinzhou 121001, China;* [4]*Department of Biochemistry, China Medical University, Shengyang 110001, China*

Key words

ferulic acid; amyloid; interleukin-1; p38 mitogen-activated protein kinases; extracellular signal-regulated kinases; proto-oncogene proteins c-akt; Alzheimer disease

[1] Project supported by Natural Science Foundation of Liaoning Province (No 20042171).
[5] Correspondence to Prof Zhi LI.
Phn 86-24-2325-6666, ext 5319.
Fax 86-24-8662-0932.
E-mail lizhijia@263.net

Received 2004-11-23
Accepted 2005-04-18

doi 10.1111/j.1745-7254.2005.00158.x

Abstract

Aim: To observe whether an amyloid β (Aβ)-induced increase in interleukin (IL)-1β was accompanied by an increase in the p38 mitogen-activated protein kinase (MAPK) pathway and a decrease in the cell survival pathway, and whether sodium ferulate (SF) treatment was effective in preventing these Aβ-induced changes. **Methods:** Rats were injected intracerebroventricularly with $A\beta_{25\text{-}35}$. Seven days after injection, immunohistochemical techniques for glial fibrillary acidic protein (GFAP) were used to determine the astrocyte infiltration and activation in hippocampal CA1 areas. The expression of IL-1β, extracellular signal-regulated kinase (ERK), p38 MAPK, Akt/protein kinase B (PKB), Fas ligand and caspase-3 were determined by Western blotting. The caspase-3 activity was measured by cleavage of the caspase-3 substrate (Ac-DEVD-pNA). Reverse transcription-polymerase chain reaction was used to analyze the changes in IL-1βmRNA levels. **Results:** Intracerebroventricular injection of $A\beta_{25\text{-}35}$ elicited astrocyte activation and infiltration and caused a strong inflammatory reaction characterized by increased IL-1β production and elevated levels of IL-1β mRNA. Increased IL-1β synthesis was accompanied by increased activation of p38 MAPK and downregulation of phospho-ERK and phospho-Akt/PKB in hippocampal CA regions prepared from Aβ-treated rats, leading to cell death as assessed by activation of caspase-3. SF significantly prevented Aβ-induced increases in IL-1β and p38 MAPK activation and also Aβ-induced changes in phospho-ERK and phospho-Akt/PKB expression levels. **Conclusion:** SF prevents Aβ-induced neurotoxicity through suppression of p38 MAPK activation and upregulation of phospho-ERK and phospho-Akt/PKB expression.

Introduction

Alzheimer disease (AD) is a neurodegenerative disorder characterized by progressive deposition of amyloid-β (Aβ) peptide in the brain to form senile plaques[1]. Neuronal cell loss is one feature of AD. Despite the ambiguity of the effectors of neuron loss in the AD brain, recent reports demonstrate that it is an apoptotic process. Cultured cortical neurons exposed to $A\beta_{1\text{–}40}$ exhibited increased expression of the proapoptotic protein Bax, increased activation of caspase-3 (a marker of apoptotic cell death), and increased terminal deoxynucleodityl transferase-mediated dUTP nick-end labeling reactivity[2]. Neuronal apoptosis is also seen in human AD brain[3]. Activation of the apoptotic cascade induced by Aβ could also explain many of the features of the disease and its progression. Furthermore, the proinflammatory cytokine, interleukin (IL)-1β, plays a significant role in mediating the effects of Aβ[2]. However, the underlying mechanisms of toxicity and activition of the neuronal cellular signaling cascades induced by Aβ are not fully understood.

It has become increasingly evident that there is a complex balance between survival and apoptotic signaling pathways in neurons that determines whether they will survive or die. For example, the serine/threonine kinase Akt/protein kinase B (PKB) is activated via a phosphoinositide 3-kinase (PI3K)-dependent signaling pathway when cells or tissues are exposed to growth factors, insulin, and certain cytokines[4]. Akt/PKB has received widespread attention as an important anti-apoptotic protein[5]. The extracellular signal-regulated kinase (ERK) pathway plays a major role in regulating cell growth and differentiation[6]. In contrast, the stress-activated protein kinases, including Jun N-terminal kinase (JNK) and p38 mitogen-activated protein kinase (MAPK), have been proposed to be important signaling components linking extracellular stimuli to cellular responses. JNK and p38 are highly activated in response to a variety of stress signals[7,8]. Their activation is most frequently associated with induction of apoptosis. However, the role of the MAPK and PI3K/Akt pathways in Aβ toxicity is unclear.

Sodium ferulate (SF), extracted from a traditional Chinese herbal medicine, has potent antioxidant[9] and anti-inflammatory activities[10]. It has recently been reported that long-term administration of ferulic acid protects mice against learning and memory deficits induced by centrally administered β-amyloid[11]. The primary site of action of ferulic acid could be microglia[12]. These previous reports prompted us to examine whether SF can suppress the Aβ-induced inflammatory response and neuronal apoptotic death in rat hippocampus. In addition, we considered that increased IL-1β concentration and upregulation of the IL-1β-induced cell signaling cascades might be accompanied by downregulation of survival signals. Therefore, in the present study, we investigated the MAPK and Akt/PKB signaling events in the inflammatory response and apoptosis evoked by preaggregated $A\beta_{25-35}$, and the protective effect caused by the oral administration of SF *in vivo*. $A\beta_{25-35}$, a short synthetic peptide possessing properties similar to $A\beta_{1-40}$ and $A\beta_{1-42}$[13,14], is suitable to be used in the study of Aβ toxicity.

Materials and methods

Materials Amyloid-β_{25-35} (Sigma Chemical Co, St Louis, MO, USA) was resuspended at a concentration of 1 mmol/L. To obtain the aggregated form of $A\beta_{25-35}$, the peptide solution was placed in an incubator at 37 °C for 48 h. SF, a colorless power with purity >99%, was obtained from Suzhou Changtong Chemical Co (Suzhou, China). Anti-phospho-ERK1/2 (Thr202/Tyr 204), anti-ERK1/2, anti-phospho-p38 MAPK (Thr180/Tyr182), anti-phospho-Akt/PKB (Thr-308), anti-Akt/PKB, and anti-Glial Fibrillary Acidic Protein (GFAP) antibodies were obtained from Santa Cruz Biotechnology (Santa Cruz, CA, USA). Anti-IL-1β, anti-Fas ligand (FasL) and anti-caspase-3 antibodies were purchased from BOSTER Biological Engineering Co (Wuhan, China). Goat anti-rabbit and goat anti-mouse secondary antibodies were obtained from Santa Cruz Biotechnology. RNA polymerase chain reaction (PCR) kit (AMV) was purchased from TaKaRa Biotechnology (Dalian, China). O-Dianisidine tetrazotited and β-naphthyl acid phosphate were purchased from Sigma Chemical Co. The caspase-3 colorimetric assay kit was obtained from BD Bioscience Clontech (1020 East Meadow Circle Palo Alto, CA).

Animals and drug treatment Groups of Sprague Dawley rats (Grade II, certificate No 2003-0009; Experimental Animal Center of China Medical University, Shengyang, China), maintained at an ambient temperature of 22–24 °C under a 12 h:12 h L:D cycle, were used in this experiment. The rats initially weighing 180–200 g were administrated with SF through an intragastric method (50 mg/kg, 100 mg/kg and 250 mg/kg, daily) for 3 weeks prior to $A\beta_{25-35}$ injection and 1 week after the injection. The rats were anesthetized with chloral hydrate (300 mg/kg) and placed in a stereotaxic apparatus. The rats were injected intracerebroventricularly with $A\beta_{25-35}$ (10 μL) or saline solution by means of a Hamilton microsyringe. The injection lasted 5 min and the needle with the syringe was left in place for 2 min after the injection for the completion of drug infusion. Control rats were injected with saline solution. The following studies were carried out 7 d after the injections.

Immunohistochemical staining for glial fibrillary acidic protein Seven days after injection of Aβ, the rats were perfused transcardially with 4% paraformaldehyde in phosphate-buffered saline (PBS). The brains were removed and post-fixed for 24 h and were embedded in paraffin wax. Serial coronal sections (5 μm thickness) were cut from various sections of the brain. After the coronal sections were rinsed in PBS 3 times, endogenous peroxidase activity was blocked by incubation with 3% H_2O_2 for 10 min. The sections were incubated with 10% normal goat serum. After the blocking serum was removed, sections were incubated with polyclonal antibody against GFAP (1:100 in Tris-buffered saline (TBS) containing 2.5% normal goat serum) overnight at 4 °C, then with biotinylated secondary antibody at 37 °C for 20 min. The GFAP-positive cells were detected using strept-avidin-biotin complex (SABC) and DAB kits.

Western blot analysis Western blotting was carried out for the analysis of IL-1β, p38 MAPK, ERK1/2, Akt/PKB, FasL and caspase-3. Hippocampal CA1 areas were stereotaxically

dissected free. The tissue was homogenized in RIPA buffer [1% Triton, 0.1% sodium dodecylsulfate (SDS), 0.5% deoxycholate, ethylenediaminetetracetic acid 1 mmol/L, Tris 20 mmol/L (pH 7.4), NaCl 150 mmol/L, NaF 10 mmol/L], and insoluble material was removed by centrifugation at 12 000×*g* for 20 min at 4 °C. Protein concentrations were quantified by the method of Lowry [15]. Tissue samples were equalized for protein concentration. Proteins were resolved by 9%–15% SDS-polyacrylamide gel electrophoresis (PAGE), and transferred to nitrocellulose membranes. The membranes were blocked with 5% milk powder in TBS (pH 7.6) for 1 h and incubated overnight at 4 °C with suitably diluted primary antibodies. After extensive washing with TBS, the membranes were incubated with anti-IgG-alkaline phosphatase conjugate. Finally, the blots were developed with the alkaline phosphatase substrate O-dianisidine tetrazotited along with β-naphthyl acid phosphate. Quantification of protein bands was achieved by densitometric analysis using Chem Image 5500 software (UVP, USA).

Analysis of caspase-3 activity The activity of caspase-3 proteases was measured using a caspase-3 colorimetric activity assay kit. Briefly, hippocampal CA1 areas were washed, homogenized in lysis buffer, incubated on ice for 20 min, analyzed for protein concentration, and diluted to equalize for protein concentration. All samples (95 μL) were added to 5 μL of 1 mmol/L caspase-3 substrate (Ac-DEVD-pNA, 50 μmol/L final concentration) and incubated for 1 h at 37 °C. Cleavage of Ac-DEVD-pNA by active caspase-3 resulted in the liberation of *p*-nitroanilide (pNA) into solution. The release of pNA was quantitated spectrophotometrically by measuring absorbance at 405 nm (Biocell 2010, Anthos Labtec Instruments, Austria), and enzyme activity was calculated with reference to a standard curve of pNA concentration versus absorbance. The data were represented as the nmol pNA·min^{-1}·mg of protein^{-1}.

Polymerase chain reaction analysis for interleukin-1β gene expression A semiquantitative reverse transcription-PCR (RT-PCR) assay was used to determine the mRNA levels of IL-1β in relation to β-actin message. Total RNA was extracted from hippocampal CA1 areas using TRIzol reagent (Invitrogen Life Technologies, Paisley, PA4 9RF, UK). cDNA synthesis was carried out on 1 mg total RNA using random 9mers by RT with 2.5 IU of Avian Myeloblastosis Virus (AMV) reverse transcriptase in RT buffer in the presence of 1 mmol/L each of dNTP and 10 IU of RNase inhibitor. The thermal cycler (Biometra, Germany) was programmed for 10 min at 30 °C, 30 min at 42 °C, 5 min at 99 °C, and 5 min at 5 °C. Equal amounts of cDNA were used for PCR amplification for 35 cycles, using a 3-step program (30 s at 94 °C, 30 s at 56 °C, and 1 min at 72 °C). After amplification, the products were separated by 7.5% SDS-PAGE (cast in the presence of ethidium bromide) and visualized under UV light. The following sequences of the primers were used: rat IL-1β (sense), 5'-TGA CTC GTG GGA TGA TGA CG-3'; rat IL-1β (antisense), 5'-CTG GAG ACT GCC CAT TCT CG-3'; β-actin (sense), 5'-GTG GGC CGC TCA AGG CAC CAA-3'; β-actin (antisense), 5'-CTT TAG CAC GCA CTG TAG TTT CTC-3'.

Statistical analysis All data were presented as mean±SD. Statistical analysis was carried out with one-way ANOVA, followed by LSD's *post hoc* test, which was provided by SPSS 11.5 statistical software. The level of significance was accepted as $P<0.05$.

Results

Sodium ferulate inhibited the amyloid-β$_{25-35}$-induced increase in interleukin-1β protein synthesis and mRNA expression Intracerebroventricular injection of preaggregated Aβ$_{25-35}$ increased protein expression of IL-1β, and densitometric analysis revealed that the mean value in samples prepared from Aβ-treated rats was significantly higher than that of control rats. SF (50, 100, and 250 mg/kg) significantly inhibited a Aβ$_{25-35}$-induced increase in protein expression of IL-1β in a dose-dependent manner (Figure 1). An Aβ-associated increase in IL-1β protein was mirrored by an Aβ-induced increase in IL-1β mRNA levels. SF induced a similar inhibition in IL-1β mRNA (Figure 2). On the other hand, the control results showed that only SF (100 mg/kg, daily for 4 weeks) had not effect on basal levels of IL-1β protein and mRNA expression in hippocampal CA1 areas (data not shown).

Sodium ferulate inhibited the amyloid-β$_{25-35}$-induced astrocyte activation The astrocyte reaction was visualized by means of the immunoreactivity for glial fibrillar acidic protein, a specific marker of astrocytes. Aβ$_{25-35}$ resulted in infiltration of astrocytes in hippocampal CA1, as well as transformation of astrocytes from a resting to an activated state, highlighted by phenotypic changes characterized by long, thick branching. SF at 50 mg/kg, 100 mg/kg, and 250 mg/kg significantly inhibited the Aβ$_{25-35}$-induced astrocytic reaction in hippocampal CA1 (Figure 3).

Sodium ferulate inhibited the amyloid-β$_{25-35}$-induced increase in phospho-p38 MAPK expression The p38 MAPK pathway, a major proinflammatory signal transduction pathway, is hyperactivated in the AD brain[16]. Therefore, p38 MAPK activation was examined by immunoblotting in rat hippocampal CA1 using anti-phospho-p38 MAPK, an antibody that specifically recognizes the activated, tyrosine-phosphorylated form of p38 MAPK. The results showed

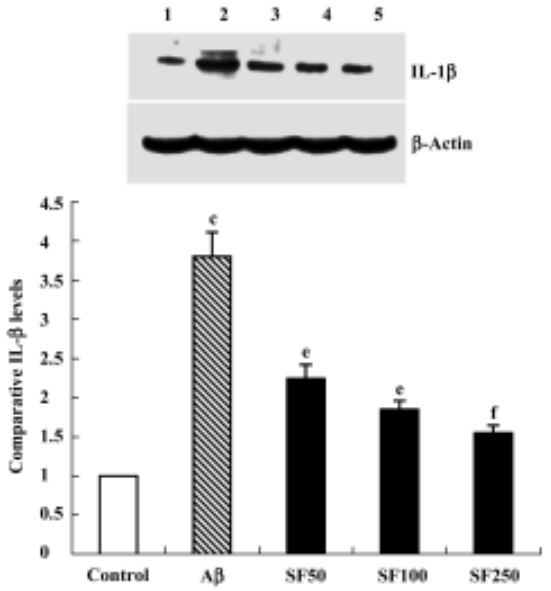

Figure 1. Inhibitory effect of sodium ferulate (SF) on the amyloid-β ($Aβ)_{25-35}$-induced increase in interleukin (IL)-1β protein expression in rat hippocampus. The immunoreactivities of IL-1β in hippocampal CA1 areas of $Aβ_{25-35}$ and $Aβ_{25-35}$+SF, as well as control animals, were determined by Western blotting. β-Actin was analyzed as a sample loading control. Lane 1, control; lane 2, Aβ-treated; lanes 3–5, Aβ+SF at 50 mg/kg, 100 mg/kg and 250 mg/kg, respectively. The bar chart shows the semiquantitative analysis of the expression of IL-1β. n=4. Mean±SD. $^cP<0.01$ *vs* control group. $^eP<0.05$, $^fP<0.01$ *vs* $Aβ_{25-35}$ group.

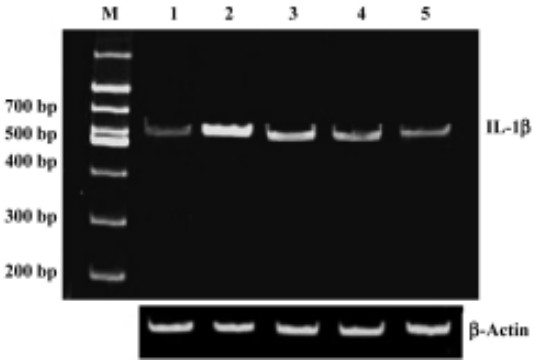

Figure 2. Reverse transcription-polymerase chain reaction analysis of the amyloid-β ($Aβ)_{25-35}$-induced increase in interleukin IL-1β mRNA expression, and the inhibitory effect of sodium ferulate (SF; 50 mg/kg, 100 mg/kg and 250 mg/kg). mRNA encoding IL-1β was expressed in the hippocampus of $Aβ_{25-35}$ and $Aβ_{25-35}$+SF, as well as control animals. mRNA encoding β-actin was used as a sample loading control. Lane M, DNA marker; lane 1, control; lane 2, Aβ-treated; lanes 3–5, Aβ+SF at 50 mg/kg, 100 mg/kg and 250 mg/kg, respectively.

that $Aβ_{25-35}$ led to a significant increase in phospho-p38 MAPK protein expression. The Aβ-induced increase in activation of p38 MAPK was paralleled by an Aβ-induced increase in IL-1β protein expression. The Aβ-induced increase in activation of p38 MAPK was prevented by SF (50, 100, and 250 mg/kg, daily for 4 weeks) in a dose-dependent manner (Figure 4). In addition, SF (100 mg/kg, daily) treatment alone for 4 weeks did not result in a significant reduction in the basal expression of phospho-p38 MAPK in rat hippocampus (data not shown).

Intracerebroventricular injection of amyloid-$β_{25-35}$ downregulated ERK-1/2, Akt/protein kinase B and the effects of sodium ferulate Although IL-1β-induced enhancement of p38 MAPK activation may lead to deterioration in cell function and even cell death, we considered that downregulation of cell survival signals may also contribute to Aβ-induced damages and, therefore, we analyzed the activity of ERK1/2 and Akt/PKB in the hippocampal CA1 region. The results showed that 7 d after injection, $Aβ_{25-35}$ elicited a significant decrease in the activated, tyrosine-phosphorylated form of ERK1 and ERK2, especially phospho-ERK1, compared to control rats. Aβ completely inhibited the expression of phospho-ERK1. SF (50 mg/kg, daily for 4 weeks) partly abolished the $Aβ_{25-35}$-induced decrease in ERK1 and ERK2 activation, but SF (100 mg/kg and 250 mg/kg, daily for 4 weeks) did not prevent the decrease in phosphorylated ERK1 and ERK2 induced by $Aβ_{25-35}$ (Figure 5A). SF treatment alone (100 mg/kg, daily for 4 weeks) exerted a decrease in phosphorylated ERK1 and ERK2 that did not reach statistical significance compared with control rats (data not shown). However, the underlying cause of this effect of SF (100 mg/kg and 250 mg/kg) on phosphorylated ERK1 and ERK2 remains to be identified. No significant difference in total ERK1/2 was apparent, as shown in the sample immunoblot (Figure 5B). Treatment with $Aβ_{25-35}$ also decreased the expression of phosphorylated Akt/PKB compared with control rats. SF (50 mg/kg, 100 mg/kg and 250 mg/kg, daily for 4 weeks) completely reversed the effect of $Aβ_{25-35}$ on phosphorylated Akt/PKB compared with control rats in a dose-dependent manner. The level of phospho-Akt/PKB expression in $Aβ_{25-35}$+ SF (100 mg/kg and 250 mg/kg) was significantly greater than in control rats (Figure 5C). However, no significant difference in the expression of total Akt/PKB was observed among treatment groups (Figure 5D). In addition, SF alone (100 mg/kg, daily for 4 weeks) had no obvious effect on the basal phosphorylation of Akt/PKB in the hippocampus (data not shown).

Sodium ferulate prevented the amyloid-$β_{25-35}$-induced increase in caspase-3 activity and caspase-3 protein expression in rat hippocampus Caspase-3 activity was measured

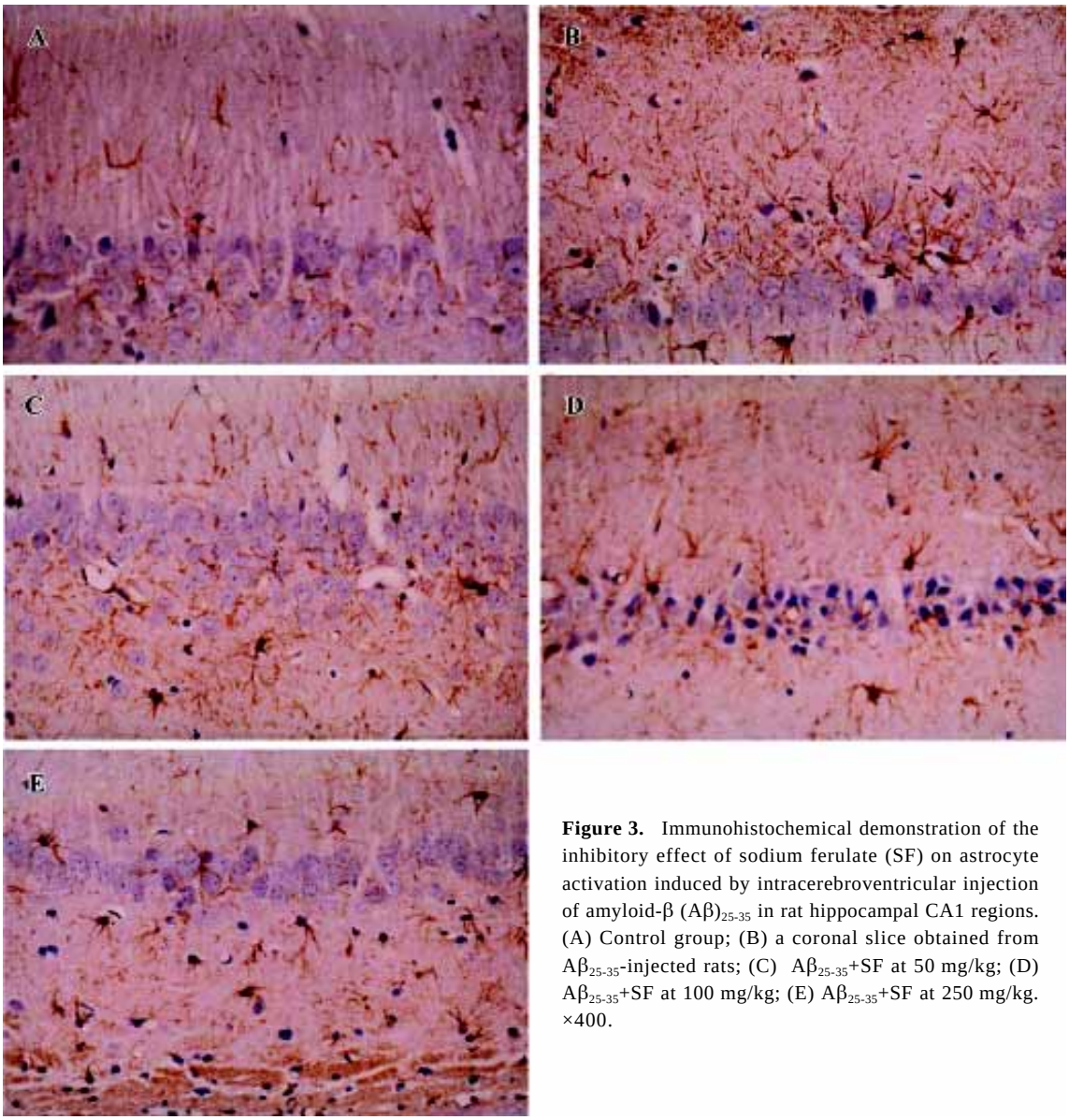

Figure 3. Immunohistochemical demonstration of the inhibitory effect of sodium ferulate (SF) on astrocyte activation induced by intracerebroventricular injection of amyloid-β $(Aβ)_{25-35}$ in rat hippocampal CA1 regions. (A) Control group; (B) a coronal slice obtained from $Aβ_{25-35}$-injected rats; (C) $Aβ_{25-35}$+SF at 50 mg/kg; (D) $Aβ_{25-35}$+SF at 100 mg/kg; (E) $Aβ_{25-35}$+SF at 250 mg/kg. ×400.

by cleavage of the caspase-3 substrate (Ac-DEVD-pNA). As shown in Figure 6A, caspase-3 activity was significantly enhanced in hippocampal CA1 prepared from Aβ-treated rats compared with control rats. This Aβ-induced increase in caspase-3 activity was inhibited by SF (50 mg/kg, 100 mg/kg and 250 mg/kg). Western blot analysis showed that $Aβ_{25-35}$ evoked a significant increase in caspase-3 protein expression. SF (50 mg/kg, 100 mg/kg and 250 mg/kg) prevented the increase in Aβ-induced caspase-3 protein expression (Figure 6B).

Sodium ferulate decreased the amyloid-$β_{25-35}$-induced expression level of Fas ligand protein Previous studies have shown that survival factor withdrawal leads to the induction of FasL protein and mRNA in cerebellar guanule neurons and PC 12 cells[17]. The binding of FasL to the Fas receptor is a prototypic signal for apoptosis, and therefore it was of interest to determine whether SF inhibits the Aβ-induced increase in FasL protein expression. As shown in Figure 7, $Aβ_{25-35}$ significantly enhanced the expression level of FasL protein in hippocampal CA1 regions. SF (50 mg/kg, 100 mg/kg and 250 mg/kg) demonstrated inhibition of the Aβ-induced increase in FasL protein expression level in a dose-dependent manner (Figure 7).

Discussion

Injection of aggregated Aβ into the brain of experimental animals may represent a valuable tool for studying the neu-

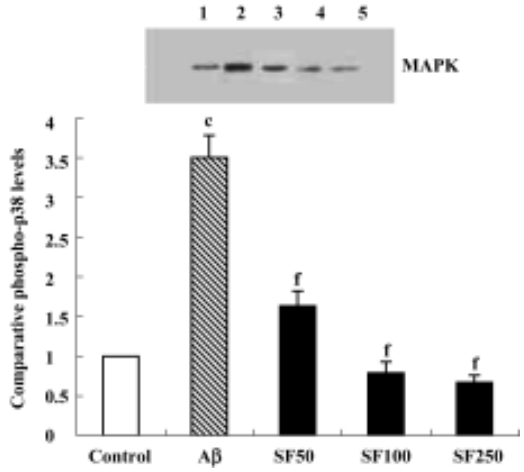

Figure 4. Inhibitory effects of sodium ferulate (SF) on the amyloid-β $(Aβ)_{25-35}$-induced increase in p38 mitogen-activated protein kinase (MAPK) activation in the rat hippocampus. The immunoreactivity of p38 MAPK in the hippocampus of $Aβ_{25-35}$ and $Aβ_{25-35}$+SF, as well as control animals, was determined by Western blotting. Lane 1, control; lane 2, Aβ-treated; lanes 3–5, Aβ+SF at 50 mg/kg, 100 mg/kg and 250 mg/kg, respectively. The bar chart shows the semiquantitative analysis of the expression of p38 MAPK. n=4. Mean±SD. $^cP<0.01$ *vs* control group. $^fP<0.01$ *vs* $Aβ_{25-35}$ group.

rotoxic effect of this peptide. We found that intracerebroventricular injection of $Aβ_{25-35}$ induced an increase in IL-1β protein and mRNA expression in hippocampal tissue, and this increase, in combination with enhanced activation of p38 MAPK and reduced activation of ERK1/2 and Akt/PKB, mediates the Aβ-induced activation of cell death events as assessed by activation of caspase-3. However, several of these changes, including Aβ-induced increase in caspase-3 activation, were prevented by treatment with SF. Indeed in AD brain, the increased levels of phosphorylated (active) p38 MAPK and diminished expression of Akt/PKB were detected[16,18]. Maher *et al* also found that increased IL-1β in the cortex of aged rats was accompanied by downregulation of ERK and PI3 kinase (an upstream kinase of Akt/PKB)[19]. These observations bear a marked similarity to our results. The Aβ-induced diminished expression of phospho-ERK1/2 and phospho-Akt/PKB in hippocampal tissue indicates that the neuron survival signal transduction pathway is impaired. The Aβ-induced increase in p38 MAPK phosphorylation and decrease in phosphorylated ERK1/2 and Akt/PKB parallel some changes that are hallmarks of cell death. For example, an increase in caspase-3 activity and FasL protein expression were observed in hippocampal tissue treated with Aβ, suggesting that sequential activation triggers apoptotic changes in the hippocampus.

Increased activation of p38 MAPK accompanied the Aβ-induced increase in IL-1β concentration, consistent with previous observations in hippocampal cells[20]. The evidence presented here pinpoints IL-1β-induced increased activation of p38 MAPK as a pivotal event in triggering changes that are characteristic of apoptotic cell death, for example, caspase-3 activation. Thus, inhibition of p38 MAPK by SB203580 has been shown to prevent the increase in IL-1β-induced caspase-3 activity[21]. A significant finding of this study is that SF treatment prevents the Aβ-induced increase in activation of p38 MAPK, caspase-3 and FasL expression, indicating a potential neuroprotective effect of SF. These findings suggest that the effects of SF on the activity of p38 MAPK and caspase-3 may be secondary to its ability to suppress the Aβ-induced increase in IL-1β synthesis.

It has also been shown that cell death is accompanied by a decrease in survival signals[22]. PI3K/Akt and ERK1/2 have been shown to be important for neuronal survival. Overexpressing active Akt/PKB rescues cells from apoptosis[23]. We report in this study that, in addition to increased p38 MAPK activation, the increase in casepase-3 activation may be associated with attenuated activity of ERK and Akt/PKB. SF treatment significantly prevented these Aβ-induced changes and, therefore, in Aβ-treated rats that were treated with SF, we found that caspase-3 activity was significantly decreased and paralleled the changes in activities of both ERK and Akt/PKB. These results are consistent with those described by Daniels *et al*[24] and Meng *et al*[18]. Therefore, downregulation of Akt/PKB may be another mechanism by which Aβ induces apoptosis. To our knowledge, this is the first indication that Akt/PKB activation in the hippocampus is decreased by Aβ *in vivo*. Thus, Aβ-induced increase in caspase-3 activity, which is considered to be a reliable indicator of apoptotic cell death, may arise from the coupled increase in p38 MAPK activation and decrease in ERK and Akt/PKB activation.

Several observations have contributed to the development of the idea that FasL expression and, consequently, Fas activation play a role in neurodegeneration[2,25], and we report that increased hippocampal expression of FasL accompanied the Aβ-induced increase in p38 MAPK phosphorylation and caspas-3 activation. The binding of Fas to FasL triggers activation of caspase-8 and, in turn, caspase-8 activates caspase-3[26]. SF markedly prevented the Aβ-induced increase in FasL protein expression.

In conclusion, our data suggest that Aβ-induced increased IL-1β, coupled with increased p38 MAPK activation, leads to cell death as assessed by activation of caspase-3. In addition, the data also show that downregulation of the

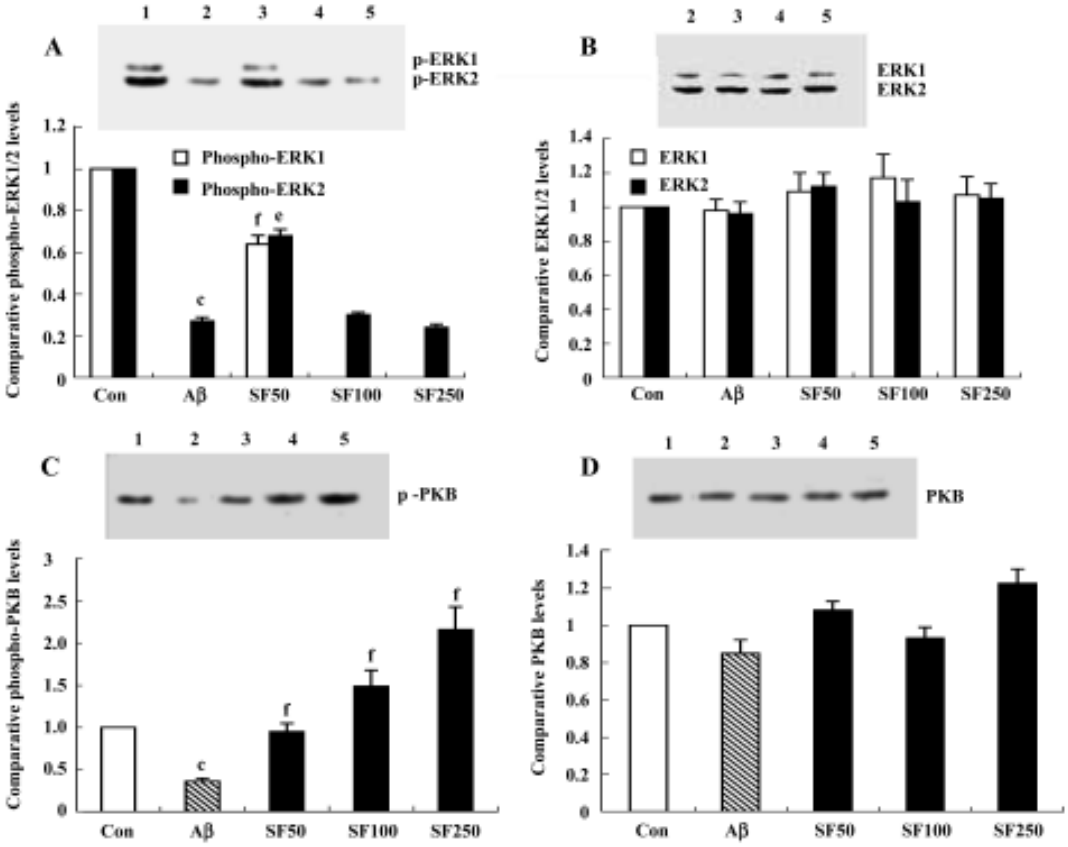

Figure 5. Sodium ferulate (SF) inhibited the amyloid-β $(Aβ)_{25-35}$-induced downregulation of phospho-extracellular signal-regulated kinase (ERK)1/2 and phospho-Akt/protein kinase B (PKB) expression. (A) Effect of SF on the $Aβ_{25-35}$-induced decrease in phosphorylated ERK1/2. (B) Total ERK1/2 showed no change. (C) Effect of SF on the $Aβ_{25-35}$-induced decrease in phosphorylated Akt/PKB. (D) Total Akt/PKB expression showed no change after stimulation with $Aβ_{25-35}$. The bar chart below each blot shows the semiquantitative analysis of the protein expression. Lane 1, control; lane 2, Aβ-treated; lanes 3–5, $Aβ_{25-35}$+SF at 50 mg/kg, 100 mg/kg and 250 mg/kg, respectively. Mean±SD. n=4. ^cP<0.01 *vs* control group. ^fP<0.01 *vs* $Aβ_{25-35}$ group.

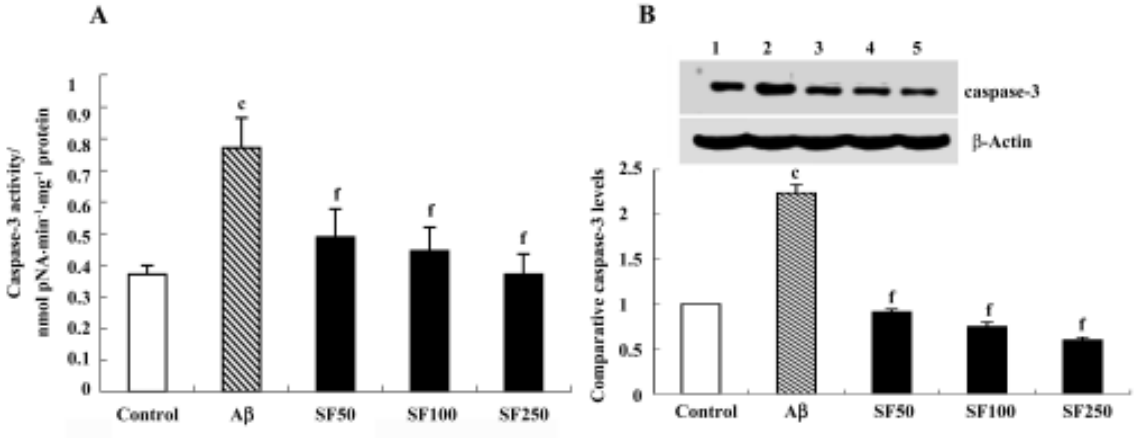

Figure 6. Inhibitory effects of sodium ferulate (SF) on the amyloid-β$(Aβ)_{25-35}$-induced increase in caspase-3 activity and caspase-3 protein expression in the rat hippocampus. (A) Caspase-3 activity was analyzed by caspase-3 colorimetric activity. (B) Caspase-3 protein expression was determined by Western blotting. β-Actin was analyzed as a sample loading control. The bar chart shows the semiquantitative analysis of the expression of caspase-3 protein. Lane 1, control; lane 2, Aβ-treated; lanes 3–5, $Aβ_{25-35}$+SF at 50 mg/kg, 100 mg/kg and 250 mg/kg, respectively. n=4. Mean±SD. ^cP<0.01 *vs* control group. ^fP<0.01 *vs* $Aβ_{25-35}$ group.

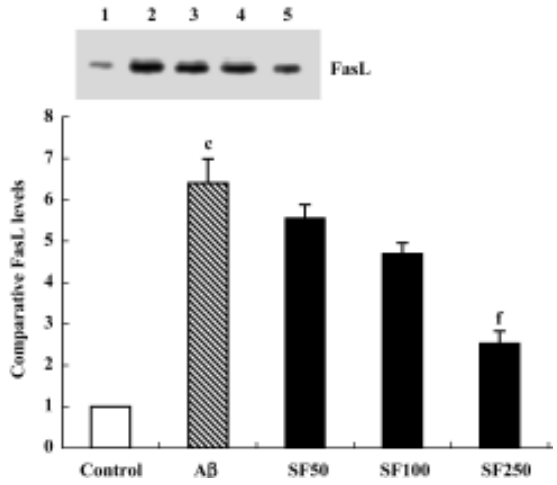

Figure 7. Inhibitory effects of sodium ferulate (SF) on the amyloid-β $(Aβ)_{25-35}$-induced increase in Fas ligand (FasL) expression in the rat hippocampus. FasL protein expression in control and experimental groups of animals was determined by Western blotting. The bar chart shows the comparative analysis of FasL expression. Lane 1, control; lane 2, Aβ-treated; lanes 3–5, $Aβ_{25-35}$+SF at 50 mg/kg, 100 mg/kg and 250 mg/kg, respectively. n= 4. Mean±SD. ^{c}P<0.01 *vs* control group. ^{f}P<0.01 *vs* $Aβ_{25-35}$ group.

survival signals ERK and Akt/PKB may contribute to the demise of the cells. These are significantly abrogated by SF treatment, which also attenuates Aβ-induced increase in caspase-3 activity and FasL expression.

References

1 Braak H, Braak E. Frequency of stages of Alzheimer-related lesions in different age categories. Neurobiol Aging 1997; 18: 351–7.

2 Minogue AM, Schmid AW, Fogarty MP, Moore AC, Campbell VA, Herron CE, *et al*. Activation of the c-Jun N-terminal kinase signaling cascade mediates the effect of amyloid-β on long term potentiation and cell death in hippocampus. A role for interleukin-1β? J Biol Chem 2003; 278: 27971–80.

3 Stadelmann C, Deckwerth TL, Srinivasan A, Bancher C, Bruck W, Jellnger K, *et al*. Activation of caspase-3 in single neurons and autophagic granules of granulovacuolar degeneration in Alzheimer's disease. Evidence for apoptotic cell death. Am J Pathol 1999, 155: 1459–66.

4 Dudek H, Datta SR, Franke TF, Birnbaum MJ, Yao R, Cooper GM, *et al*. Regulation of neuronal survival by the serine–threonine protein kinase Akt. Science 1997; 275: 628–30.

5 Zhou H, Li XM, Meinkoth J, Pittman RN. Akt regulates cell survival and apoptosis at a postmitochondrial level. J Cell Biol 2000; 151: 483–94.

6 Robinson MJ, Cobb MH. Mitogen-activated protein kinase pathways. Curr Opin Cell Biol 1997; 9: 180–6.

7 Wang X, Martindale JL, Liu Y, Holbrook NJ. The cellular response to oxidative stress: influences of mitogen-activated protein kinase signalling pathways on cell survival. Biochem J 1998; 333: 291–300.

8 Namgung U, Xia Z. Arsenite-induced apoptosis in cortical neurons is mediated by c-Jun N-terminal protein kinase 3 and p38 mitogen-activated protein kinase. J Neurosci 2000; 20: 6442–51.

9 Scott BC, Butler J, Halliwell B, Aruoma OI. Evaluation of the antioxidant action of ferulic acid and catechins. Free Radic Res Commun 1993; 19: 241–53.

10 Fernandez MA, Saenz MT, Garcia MD. Anti-inflammatory activity in rats and mice of phenolic acids isolated from Scrophularia frutescens. J Pharm Pharmacol 1998; 50: 1183–6.

11 Yan JJ, Cho JY, Kim HS, Kim KL, Jung JS, Huh SO, *et al*. Protection against beta-amyloid peptide toxicity *in vivo* with long-term administration of ferulic acid. Br J Pharmacol 2001; 133: 89–96.

12 Kim HS, Cho JY, Kim DH, Yan JJ, Lee HK, Suh HW, *et al*. Inhibitory effects of long-term administration of ferulic acid on microglial activation induced by intracerebroventricular injection of β-amyloid peptide (1–42) in mice. Biol Pharm Bull 2004; 27: 120–1.

13 Pike CJ, Walencewicz-Wasserman AJ, Kosmoski J, Cribbs DH, Glabe CG, Cotman CW. Structure-activity analyses of beta-amyloid peptides: contributions of the beta 25–35 region to aggregation and neurotoxicity. J Neurochem 1995; 64: 253–65.

14 Saito T, Kijima H, Kiuchi Y, Isobe Y, Fukushima K. β-Amyloid induces caspase-dependent early neurotoxic change in PC12 cells: correlation with H_2O_2 neurotoxicity. Neurosci Lett 2001; 305: 61–4.

15 Lowry OH, Rosebrough NJ, Farr AL, Randall RJ. Protein measurement with the folin phenol reagent. J Biol Chem 1951;193: 265–75.

16 Hensley K, Floyd RA, Zheng NY, Nael R, Robinson KA, Nguyen X, *et al*. p38 kinase is activated in the Alzheimer's disease brain. J Neurochem 1999; 72: 2053–8.

17 Le-Niculescu H, Bonfoco E, Easuya Y, Claret F-X, Green DR, Karin M. Withdrawal of survival factors results in activation of the JNK pathway in neuronal cells leading to Fas ligand induction and cell death. Mol Cell Biol 1999; 19: 751–63.

18 Meng Y, Xu H, Wang R, Ji Z, Yu S, Zhou J, *et al*. Impairment of signal transduction pathway on neuronal survival in brain of Alzheimer's disease. Chin J Pathol 2002; 31: 502–5.

19 Maher FO, Martin DS, Lynch MA. Increased IL-1β in cortex of aged rats is accompanied by downregulation of ERK and PI-3 kinase. Neurobiol Aging 2004; 25: 795–806.

20 O'Donnell E, Vereker E, Lynch MA. Age-related impairment in LTP is accompanied by enhanced activity of stress-activated protein kinases: analysis of underlying mechanisms. Eur J Neurosci 2000; 12: 345–52.

21 Martin DS, Lonergan PE, Boland B, Fogarty MP, Brady M, Horrobin DF, *et al*. Apoptotic changes in the aged brain are triggered by interleukin-1β-induced activation of p38 and reversed by treatment with eicosapentaenoic acid. J Biol Chem 2002; 277: 34 239–46.

22 Macdonald NJ, Decorti F, Pappas TC, Taglialatela G. Cytokine/neurotrophin interaction in the aged nervous system. J Anat 2000; 197: 543–51.

23 Liot G, Gabriel C, Cacquevel M, Ali C, MacKenzie ET, Buisson A, *et al*. Neurotrophin-3-induced PI-3 kinase/Akt signaling rescues cortical neurons from apoptosis. Exp Neurol 2004; 187: 38–46.
24 Daniels WM, Hendricks J, Salie R, Taljaard JJ. The role of the MAP-kinase superfamily in beta-amyloid toxicity. Metab Brain Dis 2001; 16: 175–85.
25 Su JH, Anderson AJ, Cribbs DH, Tu C, Tong L, Kesslack P, *et al* Fas and Fas ligand are associated with neuritic degeneration in the AD brain and participate in beta-amyloid-induced neuronal death. Neurobiol Dis 2003; 12: 182–93.
26 Suda T, Nagata S. Purification and characterization of the Fas-ligand that induces apoptosis. J Exp Med 1994; 179: 873–9.

Announcement

Acta Pharmacologica Sinica 2005 Aug; 26 (8): 952–958

Full-length article

Neuroprotective effects of cyclooxygenase-2 inhibitor celecoxib against toxicity of LPS-stimulated macrophages toward motor neurons

Yong HUANG, Jing LIU, Li-zhen WANG, Wei-yu ZHANG, Xing-zu ZHU[1]

Department of Pharmacology, Shanghai Institute of Materia Medica, Shanghai Institutes for Biological Sciences, Chinese Academy of Sciences, Graduate School of Chinese Academy of Sciences, Shanghai 201203, China

Key words

amyotrophic lateral sclerosis; celecoxib; macrophage; NSC34 cell; lipopolysaccharide; cyclooxygenase-2; prostaglandin E2; nitric oxide; reactive oxygen species

[1] Correspondence to Prof Xing-zu ZHU.
Phn/Fax 86-21-5080-6096.
E-mail xzzhu@mail.shcnc.ac.cn

Received 2005-03-01
Accepted 2005-05-16

doi: 10.1111/j.1745-7254.2005.00136.x

Abstract

Aim: To establish an *in vitro* injured motor neuronal model and investigate the neuroprotective effects and possible mechanism of celecoxib, a selective cyclooxygenase-2 (COX-2) inhibitor, on this model. **Methods:** After macrophages were stimulated with lipopolysaccharide (LPS)+interferon-γ (IFN-γ) in the presence or absence of celecoxib for 24 h, the cell-free supernatant of LPS-stimulated macrophages was transferred to the culture of NSC34 cells. Viability of NSC34 cells was assessed by MTT assay after a further 24 h and 72 h incubation. After macrophages were stimulated by LPS+IFN-γ for 12 h or 24 h, the release of prostaglandin E_2 (PGE_2), nitric oxide (NO), reactive oxygen species (ROS), tumor necrosis factor α (TNF-α) and interleukin-1β (IL-1β) from macrophages was measured by radioimmunoassay, Griess assay, fluorescence assay and enzyme-linked immunosorbent assay, respectively. The mRNA levels of COX-2, inducible nitric oxide synthase (iNOS), TNF-α and IL-1β in macrophages were determined by reverse transcription-polymerase chain reaction after macrophages were stimulated for 6 h and 12 h. **Results:** The supernatant of LPS-stimulated mouse macrophages induced the death of NSC34 cells and celecoxib protected the NSC34 cells against this toxicity. The LPS-induced increases in the release of PGE_2, NO, TNF-α and IL-1β from macrophages were attenuated by pre-treatment with celecoxib. However, celecoxib showed no effect on the ROS levels upregulated by LPS+IFN-γ in the macrophage supernatant. The mRNA levels of COX-2, iNOS, TNF-α and IL-1β were increased in LPS-activated macrophages and, except COX-2, reduced by pre-treatment with celecoxib. **Conclusion:** An *in vitro* injured motor neuronal model was established by using the toxicity of LPS-stimulated mouse macrophages toward motor neuronal NSC34 cells. In this model, celecoxib exerted neuroprotective effects on motor neurons via an inhibition of the neurotoxic secretions from activated macrophages.

Introduction

Amyotrophic lateral sclerosis (ALS) is a progressive fatal neurodegenerative disorder that primarily affects motor neurons in the cortex, brainstem and spinal cord. Evidence suggests that mutations in Cu/Zn superoxide dismutase (SOD-1), glutamate-mediated excitotoxicity, free radical-mediated damage, mitochondrial dysfunction and apoptosis may be involved in the pathogenesis of ALS[1]. However, the cause of ALS is not completely understood.

Accumulating evidence indicates that inflammatory processes, especially the activation of microglia, are involved in the pathogenesis of ALS[2]. Activated microglia are present before the onset of clinical symptoms and prior to significant motor neuron loss in transgenic mice with mutations of the SOD-1gene, an animal model of ALS[3]. Furthermore, some critical markers of microglia activation have also been found post-mortem in the cerebral cortex and spinal cord of pa-

tients with ALS[4,5]. Inflammatory processes would produce harmful effects on neuron survival in ALS tissues, include a prominent upregulation of inducible nitric oxide synthase (iNOS) activity with the subsequent generation of nitric oxide (NO)[6], the increased generation of reactive oxygen species (ROS) and glutamate[7], the enhanced secretions of inflammatory cytokines, such as tumor necrosis factor α (TNF-α), interleukin-1β (IL-1β), and interleukin-6 (IL-6)[8], as well as the enhanced expression of cyclooxygenase-2 (COX-2) with the subsequent production of prostaglandin E_2 (PGE_2)[9].

COX-2 was demonstrated to be crucial for prostaglandin synthesis in inflammation. COX-2 expression was shown to be dramatically increased in the spinal cord of both of ALS transgenic mice and ALS patients[10,11]. PGE_2 levels were also markedly increased in ALS cases compared to non-ALS specimens[12]. In addition, a selective COX-2 inhibitor, SC236, protected motor neurons in an organotypic cell culture model of ALS[13]. Furthermore, celecoxib, a highly selective COX-2 inhibitor clinically available for the treatment of rheumatoid arthritis[14], was proved to prolong survival in a transgenic mouse model of ALS[15]. These results support a potential role for COX-2 in the neurodegenerative processes of ALS and suggest that a selective COX-2 inhibitor may be effective in the treatment of ALS. However, research on the neuroprotective mechanism of COX-2 inhibition on a cellular level, and drug screens using an injured motor neuronal model are still lacking.

In order to investigate the possible neuroprotective mechanism of the COX-2 inhibitor on ALS and to screen candidate anti-inflammatory drugs for ALS, an injured motor neuronal model, which simulates *in vivo* human microglia activation and the neuronal damage observed during neurodegenerative disease processes, was developed in the present study. Microglia are the resident macrophages of the central nervous system (CNS) as microglia and macrophages, both being cells of the monocyte phagocytic system, have similar biochemical characteristics[16]. In addition, recent findings suggest that infectious agents may increase the risk of ALS and infected migratory mononuclear phagocytes may play an important role in the infection process[17]. Therefore mouse peritoneal macrophages as an accessible source of mononuclear phagocytes and neurotoxicity were used. NSC34 cells, a hybrid cell line obtained by fusion of motor neuron-enriched embryonic mouse spinal cord cells with mouse neuroblastoma N18TG cells, were used as the target motor neuronal cells[18]. Lipopolysaccharide (LPS), a cell wall component of gram-negative bacteria, can activate macrophages. Interferon (IFN)-γ is another important stimulant which can enhance cytokine production. A combination of LPS and IFN-γ was used to activate monocytes[19,20].

In the present study, we further verified the injured motor neuronal model by evaluating the neuroprotective effect of celecoxib, which prolongs the survival of ALS transgenic mice. In addition, the release of PGE_2, NO, ROS, inflammatory cytokines and the expression of relevant inflammatory genes in macrophages was studied to explore the possible mechanism of the neuroprotective effect of a COX-2 inhibitor against the toxicity of microglia activation on motor neuron viability.

Materials and methods

Drugs and reagents Celecoxib was kindly provided by Dr Yu-she YANG, Shanghai Institute of Materia Medica, Chinese Academy of Sciences, Shanghai, China. LPS (*Escherichia coli* 055:B5) was purchased from Sigma (St Louis, USA). IFN-γ was obtained from Clonbiotech (Shanghai, China). A radioimmunoassay (RIA) kit for PGE_2 was obtained from China PLA General Hospital (Beijing, China). Enzyme-linked immunosorbent assay (ELISA) kits for TNF-α and IL-1β were obtained from BD Biosciences (San Diego, CA, USA).

Cell culture Macrophages were obtained from the peritoneal exudates of female BALB/c mice (Grade II, Shanghai Experimental Animal Center, Shanghai, China; Certificate No 003) 4 d after intraperitoneal injection with 0.5 mL 3% thioglycollate (WAKO, Tokyo, Japan). The cells were harvested using cold peritoneal lavage with phosphate-buffered saline (PBS, pH 7.4) containing 1% fetal calf serum (FCS; PAA, Pasching, Austria), washed twice with PBS and resuspended in Dulbecco's modified eagle medium (DMEM)-F12 medium (Gibco, NY, USA) supplemented with 5% FCS, 0.1 g/L streptomycin, and 100 kU/L penicillin. The cells were seeded at a density of 1×10^6 cells/mL at 37 °C in a humidified atmosphere of 5% CO_2 and 95% air in an incubator. After adhering for 2 h, the cells were washed 3 times with warm PBS and incubated in DMEM-F12 medium supplemented with 5% FCS for the formal experiments. The viability of each cell preparation was more than 95%, as assessed by trypan blue staining (0.1% solution).

The mouse motor neuronal NSC-34 cell line was a gift from Dr Jin REN (Shanghai Institute of Materia Medica). NSC34 cells were maintained at 37 °C and 5% CO_2 in DMEM (Gibco) supplemented with 10% FCS, 0.1 g/L streptomycin and 100 kU/L penicillin.

Measurement of cell viability NSC34 cell viability was measured using the MTT assay as described by Hansen *et*

al[21]. Briefly, MTT (Sigma) was added to cell cultures to reach a final concentration of 0.2 g/L. Following a 4-h incubation at 37 °C, the dark crystals formed were collected and dissolved in 200 μL/well dimethylsulfoxide in 24-well plates. Subsequently, optical densities were measured at 570 nm by transferring 100 μL/well to 96-well plates and recording the values using a plate reader (POLARstar®; BMG, Victoria, Australia). The number of viable NSC34 cells was calculated as a percentage of the value obtained from the control NSC34 cells incubated with media only.

Measurement of nitric oxide Nitric oxide was determined by assaying for nitrite using Greiss reagent (1% sulfanilamide, 0.1% *N*-(1-naphthyl) ethylenediamine dihydrochloride in 5% H_3PO_4)[22]. Briefly, 100 μL of the supernatant from each well (24-well plates) was incubated for 5 min with 100 μL Griess reagent in 96-well plates. Optical densities of the samples were then obtained by reading absorbance at 540 nm.

Measurement of reactive oxygen species The ROS assay was modified from the fluorescence assay described by Gunasekar *et al*[23]. Briefly, 90 μL of supernatant from each well (24-well plates) was transferred to 96-well fluorescence assay plates, incubated to 37 °C, and then added 10 μL Krab's Ringer buffer (127 mmol/L NaCl, 5.5 mmol/L KCl, 2 mmol/L $MgSO_4$, 1 mmol/L $CaCl_2$, 20 mmol/L HEPES, 10 mmol/L dextrose, pH 7.4) with 50 μmol/L 2',7'-dichlorofluorescein diacetate (DCFH-DA; Sigma) and 20 IU/mL horseradish peroxide(SABC, Shanghai, China). The fluorescence value of each well was read at 30 s intervals for 5 min at 485 nm excitation wavelength and 520 nm emission wavelength. The ROS value of each sample was calculated as the slope of its time-fluorescence value curve.

Measurement of PGE_2, TNF-α and IL-1β The concentrations of PGE_2, TNF-α and IL-1β were determined by RIA and ELISA according to the manufacturer's instructions.

Measurement of mRNA The mRNA levels of COX-2, iNOS, TNF-α and IL-1β were detected by real-time quantitative reverse transcription-polymerase chain reaction (RT-PCR) using β-actin mRNA as an internal control. Briefly, macrophages from various treatments in 6-well plates were washed twice with ice-cold PBS. Total RNA was extracted from the cells in each well with RNAzol (Dingguo Biotechnology, Beijing, China) according to the manufacturer's instructions. First-strand cDNA synthesis was carried out using 2 μg total RNA and M-MLV reverse transcriptase (Promega, Madison, USA). The reaction mix was incubated at 42 °C for 60 min, and then heated at 70 °C for 10 min. Each reaction mixture was diluted 4 times with 0.1% diethyl pyrocarbonate (DEPC)-treated H_2O. A 2-μL aliquot from each diluted reaction mixture was used for real-time PCR amplification. The primer sequences and PCR cycle parameters for β-actin[24], COX-2[24], iNOS[25], TNF-α[26],and IL-1β[27] are listed in Table 1.

Real-time quantitative RT-PCR was carried out as described by Livak[28]. Each reaction contained 2 μL of the cDNA sample with 1 IU *Taq* DNA polymerase (Dingguo Biotechnology) and 0.5 μL Sybr Green (OPE, Shanghai, China) in a total volume of 20 μL in a real-time quantitative PCR cycler (DNA Engine Opticon® Continuous Fluorescence Detection System; MJ Research, USA). The mRNA level was estimated as a relative value by normalizing with β-actin mRNA. Reaction products were also separated on a 1.5% agarose gel, stained with ethidium bromide, and photographed to validate the reliability of the objective genes.

Statistical analysis Data were presented as mean±SD of the values from 3 independent experiments and the

Table 1. Primer sequence and polymerase chain reaction (PCR) cycle parameters for β-actin, cyclooxygenase-2 (COX-2), inducible nitric oxide synthase (iNOS), tumor necrosis factor-α (TNF-α) and interleukin-1β (IL-1β) genes.

Gene	Primer sequence (sense, antisense)	PCR cycle parameters
β-Actin (300 bp)	5′-GTGGGCCGCTCTAGGCACCAA-3′, 5′-CTCTTTGATGTCACGCACGAT TTC-3′	94 °C 30/45 s, 63 °C 45 s, 72 °C 60/90 s (35 cycles)
COX-2 (300 bp)	5′-TTCAAAAGAAGTGCTGGAAAAGGT-3′, 5′-GATCATCTCTACCTGAGTGTCTTT-3′	94 °C 30 s, 63 °C 45 s, 72 °C 60 s (35 cycles)
iNOS (947 bp)	5′-TTTGGAGCAGAAGTGCAAAGTCTC-3′, 5′-GATCAGGAGGGATTTCAAAGACCT-3′	94 °C 45 s, 55 °C 45 s, 72 °C 90 s (35 cycles)
TNF-α (200 bp)	5′-TCTCATCAGTTCTATGGCCC-3′, 5′-GGGAGTAGACAAGGTACAAC-3′	94 °C 45 s, 55 °C 45 s, 72 °C 90 s (35 cycles)
IL-1β (563 bp)	5′-ATGGCAACTGTTCCTGAACTCAAC-3′, 5′-CAGGACAGGTATAGATTCTTTCCTTT-3′	94 °C 45 s, 60 °C 45 s, 72 °C 90 s (35 cycles)

Student's *t*-test was used for the comparison. Values of P <0.05 were considered statistically significant.

Results

Toxicity of LPS+IFN-γ-stimulated macrophages toward NSC34 cells and inhibitory effect of celecoxib on cytotoxicity The supernatant of the macrophages stimulated with a combination of LPS and IFN-γ significantly inhibited the viability of motor neuron NSC34 cells (Figure 1). Adding celecoxib enhanced the survival of these NSC34 cells (Figure 1). The neuroprotective effect of celecoxib was due to an effect on macrophage neurotoxic secretions because celecoxib showed no neuroprotective effect on NSC34 cells if it was added to the supernatant of NSC34 cells directly (data not shown).

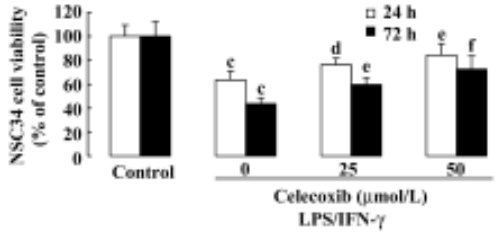

Figure 1. Inhibitory effect of celecoxib on the cytotoxicity of lipopolysaccharide (LPS)/interferon (IFN)-γ-stimulated macrophages toward NSC34 cells (MTT assay). Data (mean±SD) from 3 independent experiments (each done in 2 wells, n=6) are expressed as a percentage of each control. ^{c}P<0.01 *vs* control. ^{d}P<0.05, ^{e}P<0.05, ^{f}P<0.01 *vs* celecoxib 0 μmol/L.

Effect of celecoxib on the production of PGE_2, NO, ROS, TNF-α and IL-1β on LPS+IFN-γ-stimulated macrophages To confirm that the production of PGE_2, NO, ROS, TNF-α and IL-1β was increased in LPS+IFN-γ-stimulated macrophages, their concentrations were measured in the macrophage supernatants. Compared with resting macrophages, LPS+IFN-γ-stimulated macrophages significantly increased the release of PGE_2, NO, ROS, TNF-α, and IL-1β (Figure 2A–2E). To determine whether celecoxib regulates PGE_2, NO, ROS, TNF-α, and IL-1β release from activated macrophages, macrophages were preincubated with celecoxib for 30 min prior to the addition of LPS+ IFN-γ. After the macrophages were stimulated for 12 h or 24 h, the concentrations of PGE_2, NO, ROS, TNF-α, and IL-1β in the macrphage supernatants were measured. The increased productions of PGE_2, NO, TNF-α, and IL-1β were attenuated by preincubation with celecoxib (Figure 2A–2E). However, pretreatment with celecoxib had no effect on the level of ROS in macrophage supernatants (Figure 2C).

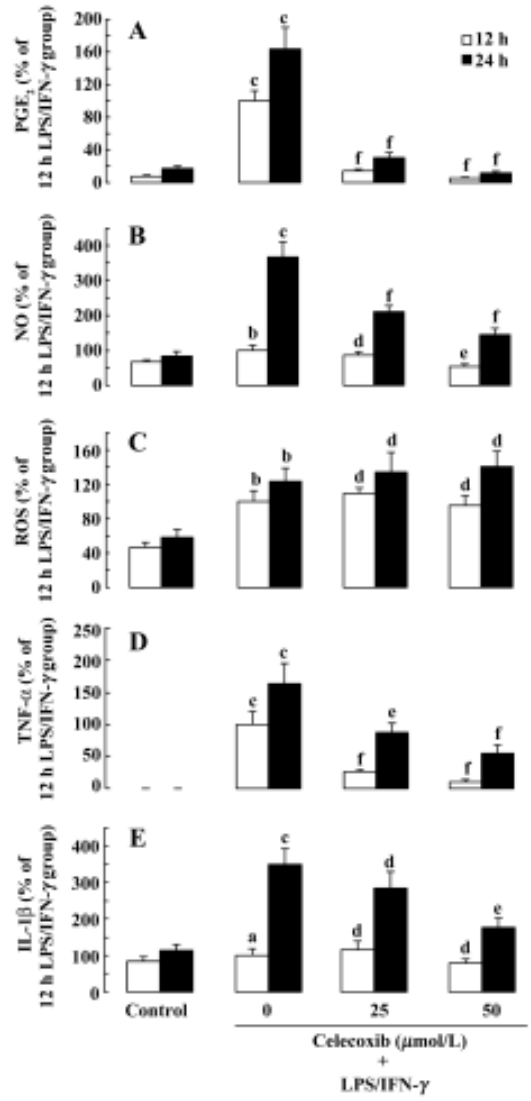

Figure 2. Effect of celecoxib on the release of prostaglandin E_2 (PGE_2), nitric oxide (NO), reactive oxygen species (ROS), tumor necrosis factor-α (TNF-α) and interleukin-1β (IL-1β) in lipopolysaccharide (LPS)/interferon (IFN)-γ-stimulated macrophages. Data (mean±SD) from 3 independent experiments (each done in 2 wells, n=6) are expressed as a percentage of the values from the 12 h LPS/IFN-γ treatment. ^{a}P>0.05, ^{b}P<0.05, ^{c}P<0.01 *vs* control. ^{d}P>0.05, ^{e}P<0.05, ^{f}P <0.01 *vs* celecoxib 0 μmol/L.

Effect of celecoxib on mRNA levels of COX-2, iNOS, TNF-α and IL-1β in LPS+IFN-γ-stimulated macrophages To determine whether LPS stimulation increases the mRNA levels of COX-2, iNOS, TNF-α, and IL-1β in macrophages, the mRNA levels of these genes were determined by real time RT-PCR. Stimulated macrophages strongly expressed mRNA of COX-2, iNOS, TNF-α and IL-1β following treatment with LPS+IFN-γ (Figure 3A–3D), whereas resting macrophages expressed these mRNA very weakly. Furthermore,

preincubation with celecoxib inhibited the increases of the mRNA levels of iNOS, TNF-α and IL-1β, which were induced by LPS+IFN-γ in macrophages and had no effect on the mRNA level of COX-2 (Figure 3).

Discussion

In the present study, we demonstrated that the supernatant of macrophages stimulated with LPS 0.5 mg/L plus IFN-γ 1.5×10^5 IU/L caused a loss of NSC34 cells following either a 24-h or 72-h exposure. In consisten with the previous results[19,20,29], no neurotoxicity was observed when the supernatant from unstimulated macrophages was transferred to NSC34 cells, and LPS (0.0005−5.0 mg/L) increased the neurotoxity of the supernatant of macrophages on NSC34 cells dose-dependently. LPS did not show toxic effects on NSC34 cells when it was added to the supernatant of NSC34 cells directly (data not shown). These results indicate that NSC34 cells injured by the supernatant of LPS-stimulated macrophages can be used to develop an injured motor neuronal model, whose neurotoxicity was due mainly to inflammatory secretions of macrophages. In the present invastigation, Celecoxib was used to verify the model because of its beneficial effects on ALS transgenic mice. It was shown that celecoxib significantly enhanced the survival of NSC34 cells . These results indicate that this model may have valuable applications for drug screening and further research the mechanisms involved. No improvement in NSC34 cell viability was observed when celecoxib was added directly to NSC34 cells (data not shown). This suggests that the target cells of celecoxib are macrophages rather than motor neurons and that the action of celecoxib on macrophages is likely a reduction of neurotoxic macrophage secretions. Another COX-2 selective inhibitor, NS398, has been reported to have neuroprotective effects on neuronal-like SH-SY5Y cells by suppressing the toxic actions of human monocytic THP-1 cells[20,29].

PGE_2 is an important mediator involved in a variety of inflammatory processes and COX-2 has been shown to be primarily responsible for the synthesis of PGE_2. COX-2 is rapidly induced by various proinflammatory agents, including LPS, cytokines and mitogens[30]. In the present study, exposure of LPS to macrophages resulted in an increase in the level of PGE_2 released and an induction of COX-2 expression at the mRNA level (Figure 3). Results from previous studies have also shown that proinflammatory stimuli induce PGE_2 release and COX-2 expression[30]. Our results showed that PGE_2 release was inhibited by the addition of celecoxib in LPS-stimulated macrophages (Figure 2), suggesting that celecoxib exerts neuroprotective effects on motor neuron NSC34 cells by inhibiting COX-2 activity and the subsequent production of PGE_2 in LPS-stimulated macrophages.

The expression and activity of iNOS plays a pivotal role in sustained and elevated NO release[31]. It has previously been reported that microglial cells are the main source of LPS-induced iNOS/NO both in neuron-glial culture and *in vivo*[32]. In addition, there is "cross-talk" between iNOS/NO

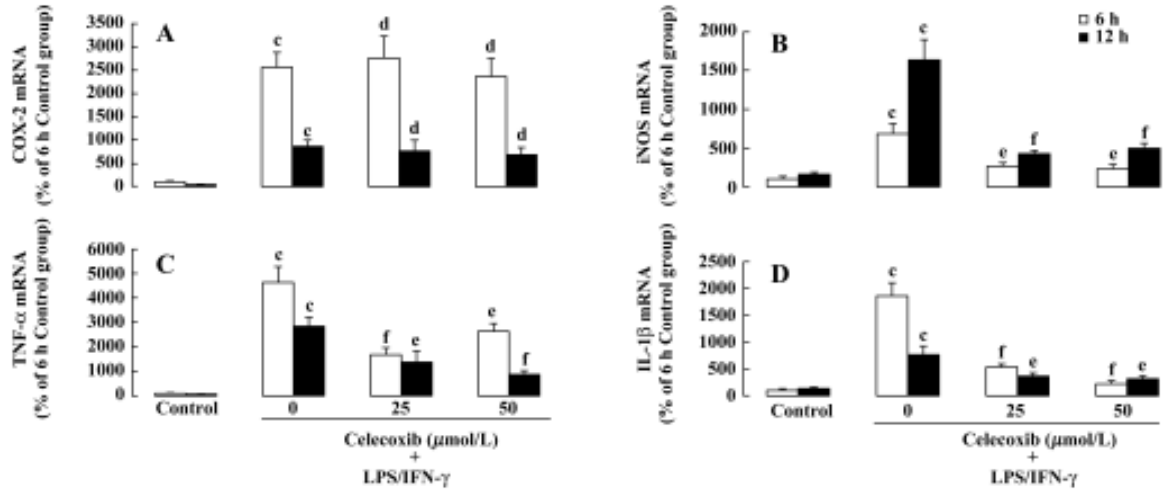

Figure 3. Effect of celecoxib on the mRNA levels of cyclooxygenase-2 (COX-2), inducible nitric oxide synthase (iNOS), tumor necrosis factor-α (TNF-α) and interleukin-1β (IL-1β) in lipopolysaccharide (LPS)/interferon (IFN)-γ-stimulated macrophages. Data (mean±SD) are from 3 independent experiments and are expressed as a percentage of the 6 h control. $^cP<0.01$ *vs* control . $^dP>0.05$, $^eP<0.05$, $^fP<0.01$*vs* celecoxib 0 μmol/L.

and COX-2/PGE_2[33]. In the present study, we demonstrated that celecoxib significantly inhibits LPS-stimulated iNOS expression and NO release in macrophages. These results suggest that downregulation of iNOS/NO by celecoxib might be involved in the neuroprotective effect of celecoxib against LPS-induced motor neuronal death[32].

Although one previous study found that LPS-induced ROS was increased in neurons, not microglial cells, in neuron-glial coculture[33], the most abundant source of oxygen free radicals in the CNS is the respiratory burst system of activated microglia[2]. A recent study reported that LPS treatment increased intracellular ROS in rat microglia in a dose-dependent manner and ROS played a regulatory role in the expression of COX-2 and the subsequent production of PGE_2 during the process of microglial activation[34]. On the other hand, Gunasekar *et al* reported that pretreatment with NS398 significantly decreased potassium cyanide (KCN)-induced ROS generation in cerebellar granule cells. The results indicated the involvement of COX-2 in KCN-induced oxidant generation[23], which further suggests a level of "cross-talk" between ROS and COX-2 in activated microglia. The present studies showed that extracellular ROS levels from LPS-stimulated macrophages were upregulated. However, celecoxib showed no effect on the extracellular ROS level in our study. The results suggest that celecoxib exerts its neuroprotective effect against the toxicity of LPS-stimulated macrophages probably not by the regulation of extracellular ROS.

TNF-α is a potent proinflammatory cytokine that plays an important role in immunity and inflammation. The present study showed that LPS-stimulation increases TNF-α secretion from macrophages. A previous study found that LPS-stimulation increases TNF-α secretion in microgila such as BV-2 cells[19]. We further demonstrated that celecoxib significantly downregulates TNF-α mRNA level and TNF-α secretion induced by LPS in macrophages. The results suggest that inhibition of TNF-α secretion from the LPS-activated macrophages probably participates in the neuroprotective effect of celecoxib on motor neurons.

Interleukin-1β is an important cytokine in the inflammation process, and microglia are an important source of IL-1 in the human CNS[35]. The release of IL-1 plays a critical role in the effect of microglial activation on motor neuron viability and IL-1 is amongst a wide range of factors that upregulate the expression of COX-2 and the subsequent production of proinflammatory cytokines and PGE_2[9]. Previous studies reported that LPS increases the secretions of IL-1β in monocytic THP-1 cells[35]. In addition, another study indicated that celecoxib decreases the secretion of IL-1β in rats[36]. The data from the present study show that celecoxib inhibits the level of IL-1β, which is increased in LPS-stimulated macrophages. Therefore, the inhibitory effect of celecoxib on the level of IL-1β may be involved in the mechanism of its neuroprotective effect.

In summary, an injured motor neuronal model was established. The selective COX-2 inhibitor celecoxib showed beneficial effects against motor neuronal death induced by inflammatory reaction. The neuroprotective effect of celecoxib might be associated with downregulation of the levels of PGE_2, NO, TNF-α and IL-1β as well as gene expression of iNOS, TNF-α and IL-1β. Since PGE_2[12], NO[37–39] and TNF-α[19,40] have been reported to be upregulated in ALS, indicating COX-2 inhibitors would be promising candidates for the treatment of ALS.

References

1 Dib M. Amyotrophic lateral sclerosis progress and prospects for treatment. Drugs 2003; 63: 289–310.

2 McGeer PL, McGeer EG. Inflammatory processes in amyotrophic lateral sclerosis. Muscle Nerve 2002; 26: 459–70.

3 Alexianu ME, Kozovska ME, Appel SH. Immune reactivity in a mouse model of familial ALS correlates with disease progression. Neurology 2001; 57: 1282–9.

4 Kawamata T, Akiyama H, Yamada T, McGeer PL. Immunologic reactions in amyotrophic lateral sclerosis brain and spinal cord tissue. Am J Pathol 1992; 140: 691–707.

5 Troost D, Van den Oord JJ, Vianney de Jong JM. Immunohistochemical characterization of the inflammatory infiltrate in amyotrophic lateral sclerosis. Neuropathol Appl Neurobiol 1990; 16: 401–10.

6 Abe K, Abe Y, Saito H. Agmatine suppresses nitric oxide production in microglia. Brain Res 2000; 872: 141–8.

7 Piani D, Frei K, Do KQ, Cuenod M, Fontana A. Murine brain macrophages induce NMDA receptor mediated neurotoxicity *in vitro* by secreting glutamate. Neurosci Lett 1991; 133: 159–62.

8 Chao CC, Hu S, Peterson PK. Glia, cytokines, and neurotoxicity. Crit Rev Neurobiol 1995; 9: 189–205.

9 Levi G, Minghetti L, Aloisi F. Regulation of prostanoid synthesis in microglial cells and effects of prostacyclin E2 on microglial functions. Biochimie 1998; 80: 899–904.

10 Almer G, Guegan C, Teismann P, Naini A, Rosoklija G, Hays AP, *et al*. Increased expression of the pro-inflammatory enzyme cyclooxygenase-2 in amyotrophic lateral sclerosis. Ann Neurol 2001; 49: 176–85.

11 Yasojima K, Tourtellotte WW, McGeer EG, McGeer PL. Marked increase in cyclooxygenase-2 in ALS spinal cord: implications for therapy. Neurology 2001; 576: 952–6.

12 Maihofner C, Probst-Cousin S, Bergmann M, Neuhuber W, Neundorfer B, Heuss D. Expression and localization of cyclooxygenase-1 and -2 in human sporadic amyotrophic lateral sclerosis. Eur J Neurosci 2003; 18: 1527–34.

13 Drachman DB, Rothstein JD. Inhibition of cyclooxygenase-2 protects motor neurons in an organotypic model of amyotrophic lateral sclerosis. Ann Neurol 2000; 48: 792–5.

14 Seibert K, Zhang Y, Leahy K, Hauser S, Masferrer J, Perkins W, *et al*. Pharmacological and biochemical demonstration of the role of cyclooxygenase-2 in inflammation and pain. Proc Natl Acad Sci USA 1994; 91: 12013–7.
15 Drachman DB, Frank K, Dykes-Hoberg M, Teismann P, Almer G, Przedborski S, *et al*. Cyclooxygenase 2 inhibition protects motor neurons and prolongs survival in a transgenic mouse model of ALS. Ann Neurol 2002; 52: 771–8.
16 Thomas WE. Brain marcrophages: evaluation of microglia and their functions. Brain Res Brain Res Rev 1992; 17: 61–74.
17 Portegies P, Cohen ES. Possible etiological role retroviruses and enteroviruses in the development ofamyotrophic lateral sclerosis. Ned Tijdschr Geneeskd 2002; 146: 1398–400.
18 Cashman NR, Durham HD, Blusztajn JK, Oda K, Tabira T, Shaw IT, *et al*. Neuroblastoma X spinal cord (NSC) hybrid cell lines resemble developing motor neurons. Dev Dyn 1992; 194: 209–21.
19 He BP, Wen WY, Strong MJ. Activated microglia (BV-2) facilitation of TNF-α-mediated motor neuron death *in vitro*. J Neuroimmunol 2002; 128: 31–8.
20 Klegeris A, McGeer PL. Cyclooxygenase and 5-lipoxygenase inhibitors protect against mononuclear phagocyte neurotoxicity. Neurobiol Aging 2002; 237: 787–94.
21 Hansen MB, Nielsen SE, Berg K. Re-examination and further development of a precise and rapid dye method for measuring cell growth/cell kill. J Immunol Meth 1989; 119: 203–10.
22 Eigler A, Moeller J, Endres S. Exogenous and endogenous nitric oxide attenuates tumor necrosis factor synthesis in ht murine macrophage cell line RAW 264.7. J Immunol 1995; 154: 4048–54.
23 Gunasekar PG, Borowitz JL, Isom GE. Cyanide-induced generation of oxidative species: involvement of nitric oxide synthase and cyclooxygenase-2. J Pharmacol Exp Ther 1998; 285: 236–41.
24 Hewett SJ, Uliasz TF, Vidwans AS, Hewett JA. Cyclooxygenase-2 contributes to *N*-methyl-*D*-aspartate-mediated neuronal cell death in primary cortical cell culture. J Pharmacol Exp Ther 2000; 293: 417–25.
25 Jeon HK, Jung NP, Choi IH, Oh YK, Shin HC, Gwag BJ. Substance P augments nitric oxide production and gene expression in murine macrophages. Immunopharmacology 1999; 41: 219–26.
26 Suzuki T, Ogata A, Tashiro K, Nagashima K, Tamura M, Yasui K, *et al*. Japanese encephalitis virus up-regulates expression of macrophage migration inhibitory factor (MIF) mRNA in the mouse brain. Biochim Biophys Acta 2000; 1517: 100–6.
27 Choi CY, Kim JY, Kim YS, Chung YC, Hahm KS, Jeong HG. Augmentation of macrophage functions by an aqueous extract isolated from *Platycodon grandiflorum*. Can Lett 2001; 166: 17–25.
28 Livak KJ, Schmittgen TD. Analysis of relative gene expression data using real-time quantitative PCR and the $2^{-\Delta\Delta C}{}_{T}$ method. Methods 2001; 25: 402–8.
29 Klegeris A, Walker DG, McGeer PL. Toxicity of human THP-1 monocytic cells towards neuron-like cells is reduced by non-steroidal anti-inflammatory drugs (NSAIDS). Neuropharmacology 1999; 38: 1017–25.
30 Callejas NA, Castrillo A, Bosca L, Marin-Sanz P. Inhibition of prostaglandin synthesis up-regulates cyclooxygenase-2 induced by lipopolysaccharide and peroxisomal proliferators. J Pharmacol Exp Ther 1999; 288: 1235–41.
31 Nathan C. Nitric oxide as a secretory product of mammalian cells. FASEB J 1992; 6: 3051–64.
32 Heneka MT, Feinstein DL. Expression and function of inducible nitric oxide synthase in neurons. J Neuroimmunol 2001; 114: 8–18.
33 Kim EJ, Kwon KJ, Park JY, Lee SH, Moon CH, Baik EJ. Neuroprotective effects of prostaglandin E2 or cAMP against microglia and neuronal free radical mediated toxicity associated with inflammation. J Neurosci Res 2002: 70: 97–107.
34 Wang T, Qin L, Liu B, Liu Y, Wilson B, Eling TE, *et al*. Role of reactive oxygen species in LPS-induced production of prostaglandin E2 in microglia. J Neurochem 2004; 88: 939–47.
35 Klegeris A, McGeer PL. Inflammatory cytokine levels are influenced by interactions between THP-1 monocytic, U-373 MG astrocytic, and SH-SY5Y neuronal cell lines of human origin. Neurosci Lett 2001; 31: 341–4.
36 Casolini P, Catalani A, Zuena AR, Angelucci L. Inhibition of COX-2 reduces the age-dependent increase of hippocampal inflammatory markers, corticosterone secretion, and behavioral impairments in the rat. J Neurosci Res 2002; 68: 337–43.
37 Chou SM, Wang HS, Komai K. Colocalization of NOS and SOD1 in neurofilament accumulation within motor neurons of amyotrophic lateral sclerosis: an immunohistochemical study. J Chem Neuroanat 1996; 10: 249.
38 Sasaki S, Shibata N, Komori T, Iwata M. iNOS and nitro tyrosine immunoreactivity in amyotrophic lateral sclerosis. Neurosci Lett 2000; 291: 44.
39 Almer G, Vukosavic S, Romero N, Przedborski S. Inducible nitric oxide synthase upregulation in a transgenic mouse model of familial amyotrophic lateral sclerosis. J Neurochem 1999; 72: 2415–25.
40 Poloni M, Facchetti D, Mai R, Micheli A, Agnoletti L, Francolini G, *et al*. Circulating levels of tumour necrosis factor-alpha and its soluble receptors are increased in the blood of patients with amyotrophic lateral sclerosis. Neurosci Lett 2000; 287: 211–4.

Acta Pharmacologica Sinica 2005 Aug; 26 (8): 959–962

Blackwell Publishing

Full-length article

Blood pressure variability and baroreflex sensitivity are not different in spontaneously hypertensive rats and stroke-prone spontaneously hypertensive rats[1]

Lin-shu ZHAN, Yun-feng GUAN, Ding-feng SU, Chao-yu MIAO[2]

Department of Pharmacology, Second Military Medical University, Shanghai 200433, China

Key words

blood pressure variability; baroreflex; hypertension; genetics

[1] Project supported by the National Natural Science Foundation of China (No 30371649) and "Shu Guang" project supported by the Shanghai Municipal Education Commission and Shanghai Education Development Foundation (No 04SG37).

[2] Correspondence to Prof Chao-yu MIAO.
Phn 86-21-2507-4374.
Fax 86-21-6549-3951.
E-mail cymiao@citiz.net

Received 2005-01-17
Accepted 2005-03-28

doi: 10.1111/j.1745-7254.2005.00144.x

Abstract

Aim: To demonstrate and compare hemodynamic phenotypes of blood pressure (BP), blood pressure variability (BPV) and baroreflex sensitivity (BRS) in genetic hypertensive rats. **Methods:** BP was recorded continuously in conscious, freely moving rats using a computerized technique. BPV was expressed as the standard deviation of beat-to-beat BP values during a 1-h period. BRS was determined by measuring the heart period prolongation in response to the elevation in BP produced by an intravenous injection of phenylephrine. **Results:** Body weight and heart period were not different between spontaneously hypertensive rats (SHR) and stroke-prone spontaneously hypertensive rats (SHR-SP) at the age of 15 weeks. The BP level was markedly higher in SHR-SP than SHR, whereas there were no significant differences in BPV and BRS. Quantitatively, systolic, diastolic and mean BP were significantly elevated by 36.9%, 42.9% and 39.5%, respectively, in SHR-SP compared with SHR ($P<0.01$). However, their variabilities were elevated only by 14.0%, 0.4% and 10.1%, respectively, without statistical significance ($P>0.05$). **Conclusion:** BPV and BRS were not changed in parallel with the BP alterations in SHR and SHR-SP.

Introduction

Blood pressure (BP) is not constant. Spontaneous variations exist in BP. The extent of the variation in BP is defined as the blood pressure variability (BPV). This new parameter of cardiovascular function can be determined through continuous ambulatory BP monitoring using a computerized technique[1,2], which can provide beat-to-beat BP tracings. It is understood that BPV is independent of BP[2,3], and high BPV is a novel risk factor for cardiovascular damage, such as aortic hypertrophy and renal lesions[2,4,5]. In the post-genome era, attaching physiology and pharmacology to the genome has become more and more important, as the combined physiological, pharmacological and genomic information should facilitate the development of new therapeutics[6]. To obtain genomic information on BPV, one of the strategies is to use linkage analysis in segregating populations produced by crossbreeding of inbred strains[7]. The first step of this strategy is to select two parental strains for crossbreeding. It is generally realized that the greater the difference in phenotype between two parental strains, the better for the linkage study.

Spontaneously hypertensive rat (SHR), an inbred strain for genetic hypertension, has a higher BPV compared with normotensive controls, such as Wistar-Kyoto rats and Sprague-Dawley rats[1,5]. Stroke-prone spontaneously hypertensive rat (SHR-SP), a sub-strain of SHR, has a much higher BP level than SHR[8,9]. However, little is known about the BPV of SHR-SP. We hypothesized that SHR-SP had a higher BPV than SHR in parallel with their BP changes, and thus would be more appropriate as a parental strain crossbred with another parental strain of normal rats. To test this hypothesis, hemodynamics were compared between SHR and SHR-SP in the present study.

Materials and methods

Animals Male SHR and SHR-SP were provided by the

Animal Center of the Second Military Medical University, Shanghai, China. Animals were housed at controlled temperature (23 °C–25 °C) and lighting (8:00–20:00) and with free access to tap water and rat chow. At the age of 15 weeks, hemodynamic parameters, including BP, BPV, and baroreflex sensitivity (BRS), were measured in conscious, freely moving rats. All procedures were in accordance with the guidelines for animal care of the Second Military Medical University.

Measurement of blood pressure and its variability Rats were anesthetized with an injection of ketamine (50 mg/kg, ip) and diazepam (5 mg/kg, ip). A catheter was placed into the lower abdominal aorta via the left femoral artery for measurement of BP and heart period (HP), and another catheter was inserted into the left femoral vein for drug administration. Both catheters were tunneled subcutaneously and exteriorized between the scapulae. After a 2-d recovery, animals were placed in individual cylindrical cages. The aortic catheter was connected to a BP transducer (PT14M2, Fudan University, Shanghai, China) via a rotating swivel that allowed the animal to move freely in the cage. After approximately 14 h habituation, the BP signals were digitized and processed by a microcomputer, which calculated systolic BP (SBP), diastolic BP (DBP), mean BP (MBP), and HP values on-line for 2 h–3 h. These values were sampled beat-to-beat at 1000 Hz. In off-line analysis, the mean values of SBP, DBP, MBP, and HP over a 1-h period (10:00–11:00) were calculated and served as SBP, DBP, MBP, and HP, respectively. The standard deviation values of SBP, DBP, and MBP over the 1-h period were calculated and defined as systolic BPV (SBPV), diastolic BPV (DBPV), and mean BPV (MBPV), respectively[1,3–5].

Measurement of baroreflex sensitivity After BP and BPV measurement, BRS was determined using a method described previously[10]. The principle of this method is to measure the HP prolongation in response to an elevation in blood pressure. A bolus intravenous injection of phenylephrine was used to raise SBP to between 30 mmHg and 40 mmHg. HP was plotted against SBP for linear regression analysis; the slope of the linear regression equation was expressed as BRS (ms/mmHg).

Statistical analysis Data are expressed as mean±SEM. The differences between 2 groups were evaluated using the two-tailed Student's unpaired *t*-test. Statistical significance was judged at $P<0.05$.

Results

Blood pressure and its variability Body weight and heart period were not significantly different between SHR and SHR-SP at the age of 15 weeks (Table 1). BP was markedly higher in SHR-SP than SHR, whereas there was no significant difference in BPV. To show clearly that BPV was not changed in parallel with the BP changes in SHR and SHR-SP, BP and BPV were compared quantitatively using percentage difference (Table 1). Systolic, diastolic and mean BP were elevated significantly by 36.9%, 42.9%, and 39.5%, respectively, in SHR-SP compared with SHR ($P<0.01$). However, their variabilities were elevated only by 14.0%, 0.4%, and 10.1%, respectively, without statistical significance ($P>0.05$). Figure 1 shows the representative values of systolic blood pressure tracings during a 1-h period in SHR and SHR-SP.

Baroreflex sensitivity There was no significant differ-

Table 1. Blood pressure and its variability in spontaneously hypertensive rats (SHR) and stroke-prone spontaneously hypertensive rats (SHR-SP) aged 15 weeks. $^cP<0.01$ *vs* SHR.

	SHR (n=7)	SHR-SP (n=7)	Difference (%)
Body weight/g	227±5	213±5	–6.2
SBP/mmHg	179±7	245±4^c	36.9
DBP/mmHg	119±2	170±5^c	42.9
MBP/mmHg	147±4	205±5^c	39.5
SBPV/mmHg	9.0±0.3	10.3±0.5	14.0
DBPV/mmHg	8.2±0.4	8.2±0.5	0.4
MBPV/mmHg	8.4±0.4	9.3±0.6	10.1
HP/ms	137±4	141±2	2.9

DBP, diastolic blood pressure; DBPV, diastolic blood pressure variability; HP, heart period; MBP, mean blood pressure; MBPV, mean blood pressure variability; SBP, systolic blood pressure; SBPV, systolic blood pressure variability.

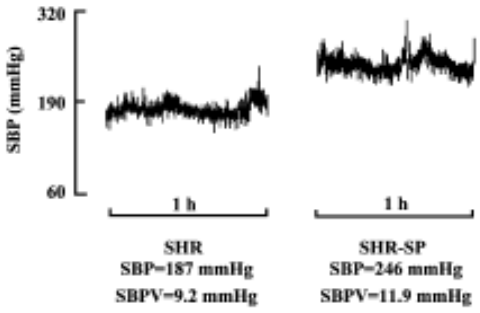

Figure 1. Representative values of systolic blood pressure tracings during a 1-h period in spontaneously hypertensive rats (SHR) and stroke-prone spontaneously hypertensive rats (SHR-SP) aged 15 weeks. SBP, systolic blood pressure; SBPV, systolic blood pressure variability.

ence in BRS between SHR and SHR-SP (Figure 2, upper part, $P>0.05$). The representative valuess of BRS in SHR and SHR-SP are shown in the lower part of Figure 2.

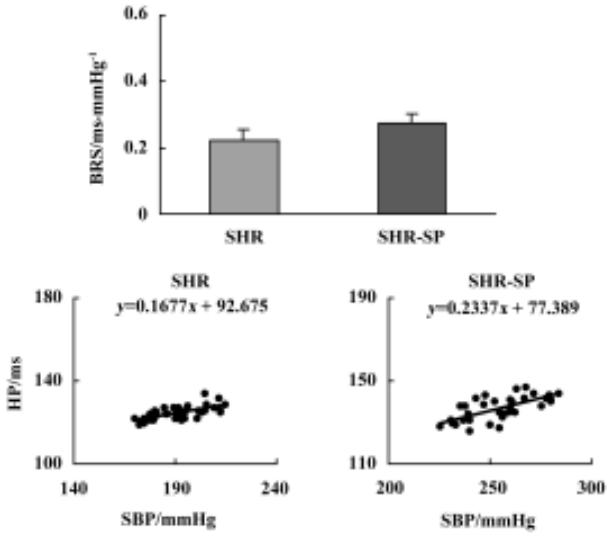

Figure 2. Baroreflex sensitivity (BRS) in spontaneously hypertensive rats (SHR) and stroke-prone spontaneously hypertensive rats (SHR-SP) aged 15 weeks. Upper: $n=7$ in each group. Mean±SEM. Lower: Representative values of BRS. BRS is the slope of the line. HP, heart period; SBP, systolic blood pressure.

Discussion

In the present study, 15-week-old rats were used for comparisons of hemodynamic phenotypes, including BP, BPV, and BRS. This is because BP levels reach a plateau at this adult age[9,11]. It is well known that BP level is markedly higher in SHR-SP than SHR in both conscious and anesthetized states[8,9,12]. Our present data are in accordance with previous results[8,9].

In contrast to our hypothesis, there was no significant difference in BPV between SHR-SP and SHR. In other words, BPV was not elevated in parallel with the remarkable elevations in BP in SHR-SP compared with SHR. The BPV data combined with the shorter life span of SHR-SP (about 45 weeks)[9] compared with SHR (about 75 weeks)[13] lead us to the unequivocal conclusion that SHR is more appropriate as a parental strain than SHR-SP for crossbreeding in BPV linkage studies.

Blood pressure variability is increased in almost all hypertensive patients and animals[1,14]. This often leads to the deduction that alterations in BP and BPV occur in parallel. The present study showed that SHR-SP, a sub-strain of SHR, had a markedly higher BP level without a significant increase in BPV, when compared with SHR. These provide a good example to delineate that BPV is not necessarily dependent on BP level. The facts were also demonstrated in other previous studies. Under physiological conditions, rabbits are known for their unstable BP, and when compared with rats, rabbits exhibit a higher BPV and a lower BP level[15]. In pathophysiological states of baroreflex interruption, BPV is increased markedly with no change in the average BP level after sinoaortic denervation or nucleus tractus solitarii lesions[2,4,5,16]. Frequent ventricular premature beats in myocardial infarction rats cause high BPV with unchanged BP level[3]. Finally, in pharmacological studies, BPV is reduced significantly by simultaneous infusion of phenylephrine and adenosine when the BP level maintains unchanged[17]. All of the above results confirm that BPV may not be associated with BP level.

Two reports have analyzed the BRS data of SHR and SHR-SP within the same study. In these previous studies, BRS was estimated either in an anesthetized state using intravenous infusion of phenylephrine for 30 min[12] or in a conscious state using cross-spectral analysis[9]. In the present study, BRS was determined in conscious, freely moving rats using a bolus intravenous injection of phenylephrine. These three studies provide similar evidence showing that the impairment of baroreflex function, expressed as decreased BRS, is not significantly different between SHR and SHR-SP.

In summary, the current study demonstrated and compared the hemodynamic phenotypes of BP, BPV and BRS in SHR and SHR-SP. For the first time, we have provided evidence that in addition to BRS, BPV is not changed in parallel with BP changes in SHR-SP and SHR. Together with the short life span of SHR-SP, these findings indicate that SHR is more appropriate than SHR-SP for crossbreeding in future linkage studies on BPV and BRS. The data are meaningful in attaching the physiological variables of BPV and BRS to the genome, especially as the rat has become researchers' favorite laboratory animal due to the recent availability of its genome sequence[6,18,19].

References

1 Miao CY, Shen FM, Su DF. Blood pressure variability is increased in genetic hypertension and *L*-NAME-induced hypertension. Acta Pharmacol Sin 2001; 22: 137–40.

2 Su DF, Miao CY. Blood pressure variability and organ damage. Clin Exp Pharmacol Physiol 2001; 28: 709–15.

3 Miao CY, Xu LP, Liu JG, Xie HH, Yuan WJ, Su DF. Frequent ventricular premature beats increase blood pressure variability in rats. Acta Pharmacol Sin 2004; 25: 545–53.

4 Miao CY, Su DF. The importance of blood pressure variability in

rat aortic and left ventricular hypertrophy produced by sinoaortic denervation. J Hypertens 2002; 20: 1865–72.
5 Miao CY, Yuan WJ, Su DF. Comparative study of sinoaortic-denervated rats and spontaneously hypertensive rats. Am J Hypertens 2003; 16: 585–91.
6 Jacob HJ, Kwitek AE. Rat genetics: attaching physiology and pharmacology to the genome. Nat Rev Genet 2002; 3: 33–42.
7 Rapp JP. Genetic analysis of inherited hypertension in the rat. Physiol Rev 2000; 80: 135–72.
8 Griffin KA, Churchill PC, Picken M, Webb RC, Kurtz TW, Bidani AK. Differential salt-sensitivity in the pathogenesis of renal damage in SHR and stroke prone SHR. Am J Hypertens 2001; 14: 311–20.
9 Nagai R, Nagata S, Fukuya F, Higaki J, Rakugi H, Ogihara T. Changes in autonomic activity and baroreflex sensitivity with the hypertension process and age in rats. Clin Exp Pharmacol Physiol 2003; 30: 419–25.
10 Xie HH, Miao CY, Liu JG, Su DF. Effects of long-term treatment with candesartan on organ damages in sinoaortic denervated rats. J Cardiovasc Pharmacol 2003; 41: 325–31.
11 Miao CY, Liu KL, Benzoni D, Sassard J. Acute pressure-natriuresis function curve shows early impairment in Lyon hypertensive rats. J Hypertens 2005; 23: 1225–31.
12 Chan JY, Chen WC, Lee HY, Chan SH. Elevated Fos expression in the nucleus tractus solitarii is associated with reduced baroreflex response in spontaneously hypertensive rats. Hypertension 1998; 32: 939–44.
13 Wang X, Ajikobi DO, Salevsky FC, Cupples WA. Impaired myogenic autoregulation in kidneys of Brown Norway rats. Am J Physiol Renal Physiol 2000; 278: F962–9.
14 Parati G, Pomidossi G, Albini F, Malaspina D, Mancia G. Relationship of 24-hour blood pressure mean and variability to severity of target organ damage in hypertension. J Hypertens 1987; 5: 93–8.
15 Sato K, Chatani F, Sato S. Circadian and short-term variabilities in blood pressure and heart rate measured by telemetry in rabbits and rats. J Auton Nerv Syst 1995; 54: 235–46.
16 Buchholtz RA, Nathan NA. Chronic lability of the arterial pressure produced by electrolytic lesions of the nucleus tractus solitarii in the rat. Circ Res 1984; 54: 227–38.
17 Jacob HJ, Alper RH, Brody MJ. Lability of arterial pressure after baroreceptor denervation is not pressure dependent. Hypertension 1989; 14: 501–10.
18 Gibbs RA, Weinstock GM, Metzker ML, Muzny DM, Sodergren EJ, Scherer S, *et al*. Genome sequence of the Brown Norway rat yields insights into mammalian evolution. Nature 2004; 428: 493–521.
19 Abbott A. Laboratory animals: the renaissance rat. Nature 2004; 428: 464–6.

Acta Pharmacologica Sinica 2005 Aug; 26 (8): 963–968

Full-length article

Adeno-associated virus-mediated bone morphogenetic protein-7 gene transfer induces C2C12 cell differentiation into osteoblast lineage cells[1]

Min YANG[2], Qing-jun MA[2,4], Geng-ting DANG[2], Kang-tao MA[3], Ping CHEN[3], Chun-yan ZHOU[3,4]

[2]Department of Orthopedics, Peking University Third Hospital, Beijing 100083, China;[3]Department of Biochemistry and Molecular Biology, School of Basic Medical Sciences, Peking University Health Science Center, Beijing 100083, China

Key words

C2C12; adeno-associated virus; bone morphogenetic protein-7; gene therapy

[1] Project supported by the National Natural Science Foundation of China (No 30170947), 211 Project of the Ministry of Education and 985 Project Foundation of Peking University.
[4] Correspondence to Prof Chun-yan ZHOU.
Phn/Fax 86-10-8280-2417.
E-mail chunyanzhou@bjmu.edu.cn
Prof Qing-jun MA.
Phn/Fax 86-10-8232-9564.
E-mail qingjun_ma@sohu.com

Received 2005-01-17
Accepted 2005-04-26

doi:10.1111/j.1745-7254.2005.00159.x

Abstract

Aim: To investigate the effects of bone morphogenetic protein-7 (BMP7)-expressing recombinant adeno-associated virus (AAV) vector on the differentiation of C2C12 cells. **Methods:** AAV-BMP7 was packaged by infecting the stable cell clone BHK-21 (integrated with recombinant AAV vector plasmid pSNAV-BMP7) with recombinant herpes simplex virus type 1, which expresses AAV-2 Rep and Cap and possesses AAV packaging functions. Following infection with AAV-BMP7 at multiplicities of infection of 1×10^5 vector genomes per cell and subsequent culture, C2C12 cells were assessed qualitatively for BMP7 production, alkaline phosphatase activity, osteocalcin production and Cbfal and MyoD expression. **Results:** C2C12 cells transduced with AAV-BMP7 could produce BMP7 protein until d 28. Alkaline phosphatase in the cultured C2C12 cell lysate was elevated. Secreted osteocalcin in the culture medium was detectable at d 12 and Cbfal mRNA expression level was upregulated, coinciding with downregulation of MyoD in a temporal manner. **Conclusion:** The present *in vitro* study demonstrated that AAV-BMP7 could infect and efficiently convert C2C12 cells from myoblasts into osteoblast lineage cells.

Introduction

Currently, the repair of massive segmental bone defects and non-healing fractures remains a challenging problem in orthopedic surgery. Bone morphogenetic proteins (BMP) are known to possess strong osteoinductive properties and BMP gene therapy plays an important role in modulating bone regeneration[1]. However, more efficient and safe delivery vectors must be obtained before clinical trials can be carried out successfully. Previous work with recombinant adeno-associated virus (AAV) vector for gene therapy has shown some outstanding advantages and has made it an attractive candidate for clinical trials in recent years[2]. However, there have only been a small number of experiments using AAV vectors carrying BMP to induce bone healing[3–5]. Previous studies have indicated that the C2C12 myoblast cell line may be a useful model to investigate osteoblast differentiation during bone formation in muscular tissues[6–8]. Although it has been reported that continuous exposure of C2C12 cells to BMP7 protein could inhibit myotube formation and induce osteoblastic differentiation[6], it is not known whether transfer of the *BMP7* gene into C2C12 cells using a BMP7-harboring AAV could also produce consistent results. This committed osteoblastic differentiation would be important for AAV-BMP7 *in vivo* gene therapy for bone healing. In addition, because recombinant AAV does not cause disease in humans and does not contain coding sequences necessary to trigger inflammatory or immune responses[2–4], we speculate that the AAV-BMP7 vectors could be injected into the fracture sites or segmental bone defects to induce bone formation by direct local gene therapy. To investigate the feasibility of *BMP7* gene transfer into C2C12 cells using the AAV vector, we constructed an AAV vector carrying the *BMP7* gene, designated AAV-BMP7. C2C12 cells were infected with AAV-BMP7 and their committed differentiation was examined *in vitro*. This study provides fundamental understanding and a platform for future applications of AAV-BMP7 local gene therapy.

Materials and methods

Cells HEK293, BHK-21 and C2C12 cells (all from ATCC, Manassas, VA, USA) were cultured in Dulbecco's modified Eagle's medium (DMEM) (Gibco BRL, Grand Island, NY, USA) containing 10% fetal bovine serum (FBS) (Hyclone, Logan, UT, USA) and penicillin/streptomycin at 37 °C in humidified 5% CO_2 atmosphere.

Plasmids The recombinant AAV2 packaging plasmid pSNAV[9] was constructed by deleting all viral open reading frames and introducing the sequences for human cytomegalovirus promoter/enhancer, a multiple-cloning site, a neomycin-resistant gene, a simian virus 40 promoter and a polyadenylation signal, retaining the 2 inverted terminal repeats (ITR), which contain the palindromic sequences necessary in cis for replication of the intact viral genome. The AAV plasmid pSNAV-BMP7 (Figure 1) was constructed by inserting full-length human BMP7 (*hBMP7*) cDNA (1.3 kb) into the restriction sites between *Kpn*I and *Bgl*II of the multiple-cloning site. The *BMP7* cDNA was cloned by reverse transcription-polymerase chain reaction from HEK293 cells using the following set of primers: forward, 5´-GTG GTA CCG ATG CAC GTG CGC TCA CTG-3´; reverse, 5´-AGA AGA TCT CTC GGA GGA GCT AGT GGC AG-3´ (introduced *Kpn*I and *Bgl*II restriction sites are underlined).

Figure 1. Schematic representation of the adeno-associated virus (AAV) vector used in this study. CMV, human cytomegalovirus promoter; ITR, inverted terminal repeat; MCS, multiple cloning site; PolA, polyadenylation signal.

Adeno-associated virus vector packaging, purification and titration BHK-21 cells were transfected with the purified pSNAV-BMP7 plasmid according to a standard calcium phosphate precipitation method. The cells were then cultured in selection media containing 500 μg/mL G418 (Gibco/BRL). G418-resistant BHK-21 cell clones were isolated and the integrity of *hBMP7* gene was determined by polymerase chain reaction (PCR) using the above PCR primers. To package the virus, stably transfected BHK-21 cells were subsequently infected with recombinant herpes simplex virus type 1 (rHSV-1)[10], which can express the AAV-2 Rep and Cap genes of wild-type AAV and possesses packaging functions for recombinant AAV. For large-scale recombinant AAV production and purification, BHK-21 cells were incubated in 6 roller bottles (Ø 110 mm×480 mm; Wheaton, Millville, NJ, USA) at 37 °C at 1 roll/min. Confluent cells in a volume of 10 mL medium were infected with helper virus rHSV-1 at multiplicities of infection (MOI) of 0.1 for 2 h. The collected cells were processed by chloroform treatment, PEG8000/NaCl precipitation and chloroform extraction for purification[11]. The titer was determined using quantitative DNA dot blots[12] and the purity was examined by sodium dodecyl sulphate-polyacrylamide gel electrophoresis[11]. Titers averaged approximately 2×10^{12} vector genomes (v g) per mL and purity was >97%. Recombinant AAV-enhanced green fluorescence protein (EGFP) was also constructed using the same procedure.

Adeno-associated virus vector transduction C2C12 cells were placed in monolayer culture in 6-well plates at a density of 2×10^5 cells per well in DMEM containing 10% FBS. Subconfluent cells were incubated with either AAV-BMP7 or AAV-EGFP at an MOI of 1×10^5 v.g. per cell, or as a control, left alone in a total volume of 500 μL serum-free medium for 1 h at 37 °C. The medium was then aspirated and 1 mL growth medium (DMEM supplemented with 5% FBS, 50 mmol/L sodium butyrate) was added. An MOI of 1×10^5 was chosen as a result of pilot studies demonstrating that an MOI of 1×10^5 produced the highest level of EGFP transgene expression. Morphological changes were monitored with a phase contrast microscope. All experiments were carried out in triplicate.

Determination of bone morphogenetic protein-7 production To quantify BMP7 levels, culture medium of C2C12 cells was collected for enzyme-linked immunosorbent assay (ELISA) every 2 d up to 28 d after transduction. ELISA was carried out according to the manufacturer's recommendations (ADL, San Antonio, TX, USA). Briefly, standards and culture media were incubated at room temperature with sample buffer in 96-well plates for 90 min and then with biotin-labeled anti-human BMP7 detection antibody for 60 min. Finally, a streptavidin-horseradish peroxidase conjugate was added at room temperature for 30 min. Bound BMP7 was detected by adding tetramethylbenzidine substrate solution for 15 min and the plates were read at 450 nm.

Gene expression of *Cbfal* and *MyoD* A total of 2 μg cellular RNA from C2C12 cells was reverse transcribed using Mouse Moloney murine leukemia virus reverse transcriptase and oligo(dT) 15 primer (both from Promega, Madison, Wisconsin, USA). PCR were carried out for 25 cycles (94 °C for 1 min, 55 °C for 1 min, 72 °C for 1 min) for *MyoD* and glyseraldehyde-3-phosphate dehydrogenase (*GAPDH*), and 30 cycles for *Cbfal* (annealing temperature 62 °C). Primers were: *MyoD* (expected product size 275 bp): upstream, 5´-TCCAACTGCTCTGATGGCA-3´; downstream, 5´-GTTCCC-TGTTCTGTGTCGCT-3´; *Cbfal* (expected product size 330 bp)[13]: upstream, 5´-CTTCATTCGCCTCACAAAC-3´; downstream, 5´-CACGTCGCTCATCTTGCCGG-3´. *GAPDH*

was used as an internal control (expected product size 413 bp): upstream, 5´-GGAAAGCTGTGGCGTGATGG-3´; downstream, 5´-GTAGGCCATGAGGTCCACCA-3´. The PCR products were subjected to electrophoresis on 1.5% agarose gels, scanned, and semiquantitated using Image-Quant software (Kodak I D V3.53; Kodak, Tokyo, Japan).

Alkaline phosphatase activity assay and osteocalcin production C2C12 cells were rinsed twice with phosphate-buffered saline, then collected into 50 mmol/L Tris-HCl, 0.1% Triton X-100, pH 7.5, and sonicated for 10 s at 4 °C. The samples were centrifuged for 5 min at 13400×*g*. Alkaline phosphatase (ALP) activity was measured using an ALP assay kit (Zhongsheng Biochemical, Beijing China) at 37 °C. The enzyme activity was normalized against the protein concentration and expressed as $U \cdot g^{-1} \cdot L^{-1}$ [14]. Protein concentration was measured using the bicinchoninic acid protein assay kit (Pierce Biotechnology, Rockford, IL, USA) using bovine serum albumin as a standard. The amount of osteocalcin secreted into the culture medium was determined by radioimmunoassay using a mouse osteocalcin assay kit following the manufacturer's recommendations (Biomedical Technologies, Stoughton, MA, USA).

Statistical analysis Data (mean±SD) were analyzed using two-tailed Student's *t*-test with a level of significance of 0.05.

Results

Bone morphogenetic protein-7 expression in C2C12 cells The *in vitro* release kinetics of BMP7 from AAV-BMP7-infected C2C12 cells was evaluated over the course of 28 d using ELISA. No detectable BMP7 was produced by the uninfected and AAV-EGFP-treated C2C12 cells. However, cells transduced with AAV-BMP7 produced low levels of BMP7 by 48 h (12±8 ng/10^6 cells per 48 h), followed by an increase in production with a mean of 165±10 ng/10^6 cells per 48 h from d 6 to d 28 (Figure 2).

Effect of bone morphogenetic protein-7 on C2C12 cell morphology After cultured in DMEM with 5% FBS for 6 d, the phenotype of C2C12 cells displayed obvious changes. Elongated and multinucleated thin myotubes formed by cells fusing with each other were observed in uninfected C2C12 cells and cells infected with AAV-EGFP. In contrast, most cells infected with AAV-BMP7 revealed an unfused, mononuclear round-cell morphology, resembling that of osteoblastic cells (Figure 3).

Differentiation of C2C12 cells treated with AAV-BMP7 In order to further investigate the function of BMP7 expression, we examined the gene expression changes for osteoblast-specific genes, and also measured ALP activity

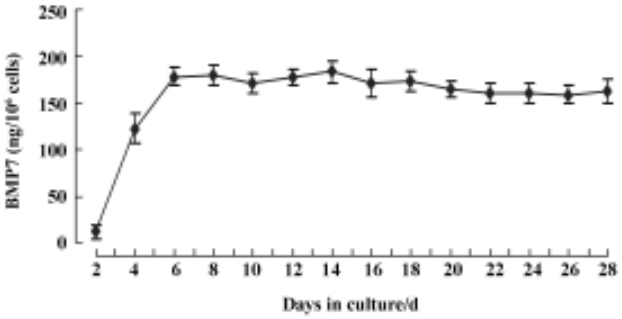

Figure 2. The time course of bone morphogenetic protein-7 (BMP7) production in C2C12 cells in 48 h after infected with adeno-associated virus (AAV)-BMP7 by enzyme-linked immunosorbent assay quantitative analysis. *n*=3. Mean±SD.

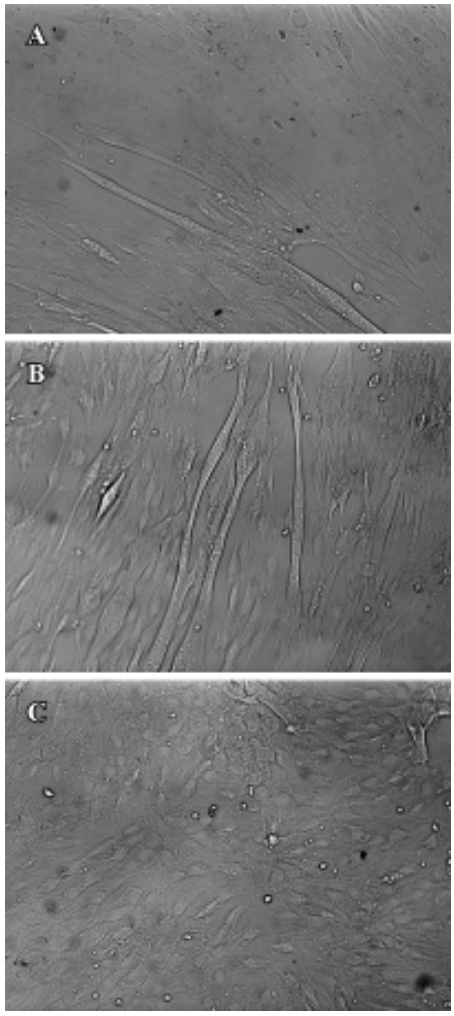

Figure 3. Morphological changes in C2C12 cells on d 6. (A) Uninfected C2C12 cells. (B) C2C12 cells transduced with adeno-associated virus (AAV)-enhanced green fluorescence protein (EGFP). (C) C2C12 cells transduced with AAV-bone morphogenetic protein-7 (BMP7). ×100.

and osteocalcin production, in C2C12 cells infected with AAV-BMP7. In AAV-BMP7-treated C2C12 cells the mRNA expression level of *Cbfa*1 (an osteoblast specific transcription regulatory factor[15]) was upregulated after 4 d of treatment, a significant increase was detected at d 6 and its level continued to increase until d 12 (Figure 4). In contrast, the expression level of muscle-specific regulatory factor *MyoD* was reduced dramatically after 8 d of treatment and became undetectable by d 12.

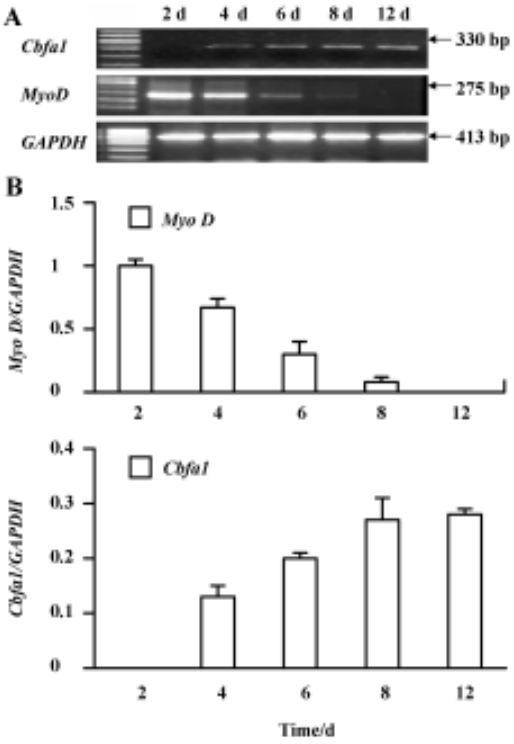

Figure 4. The expression changes of osteoblastic and myoblastic markers in adeno-associated virus (AAV)-bone morphogenetic protein-7 (BMP7)-treated C2C12 cells. The expression of glyseraldehyde-3-phosphate dehydrogenase (GAPDH) was used as an internal control. Results of the (A) electrophoretic and (B) semiquantitative analyses are shown. n=3. Mean±SD.

The uninfected and AAV-EGFP-infected C2C12 cells were found to have low levels of ALP activity with no significant change at all time points (Figure 5). A significant upregulation of ALP activity was observed in AAV-BMP7-treated cells, starting from d 2 and peaking at d 8. Osteocalcin production was detected at d 12 as 35±6 ng/mL (Figure 6); no detectable osteocalcin was found in non-treated and AAV-EGFP-treated cells.

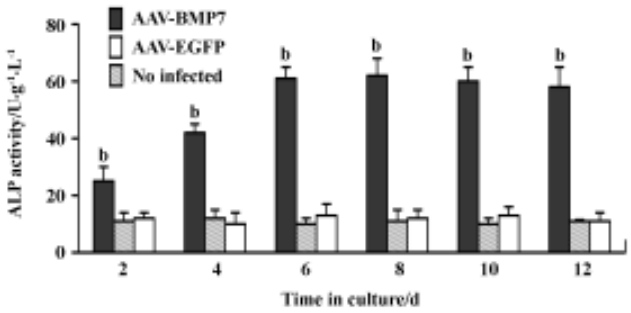

Figure 5. Time course of alkaline phosphatase (ALP) activity in the lysates of C2C12 cells. n=3. Mean±SD. $^bP<0.05$ *vs* the uninfected and adeno-associated virus (AAV)-enhanced green fluorescence protein (EGFP)-treated groups.

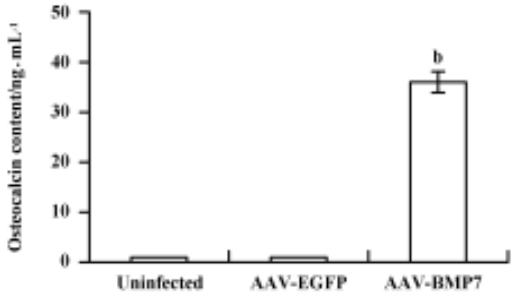

Figure 6. Comparison of osteocalcin production in C2C12 cells treated with adeno-associated virus (AAV)-enhanced green fluorescence protein (EGFP) or AAV-bone morphogenetic protein-7 (BMP7) at d 12. n=3. Mean±SD. $^bP<0.05$ *vs* the uninfected and AAV-EGFP-treated groups.

Discussion

Our *in vitro* experiments demonstrated that C2C12 cells infected with AAV-BMP7 were able to generate BMP7 protein and showed a concomitant shift from myoblastic to osteoblastic differentiation. In addition, the highly efficient recombinant adeno-associated viral vector packaging system, rHSV-1/AAV hybrid helper viral system[10], provided us with high-titer purified AAV-BMP7 for further experiments. Our subsequent AAV-BMP7 transduction analysis suggested that recombinant AAV vector could mediate efficient transduction in C2C12 cells. At the same time, the amount of secreted BMP7 protein could reach the level of protein needed for cellular responses. The elevated ALP activity and osteocalcin production, together with osteoblast-like morphology, confirmed that the AAV-BMP7-infected C2C12 cells displayed differentiation to an osteoblastic phenotype.

Previous studies have shown that BMP7 at 200 ng/mL can completely inhibit myogenic differentiation of C2C12 cells

and successfully induce expression of both important early and late osteoblastic differentiation markers (ALP and osteocalcin, respectively)[6]. Although BMP7 protein could satisfactorily induce C2C12 cell differentiation into osteoblastic cells *in vitro*, it requires supra-physiological amounts of BMP7 to overcome rapid clearance due to its short life span, in order to accelerate fracture healing, bridge segmental bone defects and generate spine fusion in animal models[16]. Hence, protein therapies are hampered by high manufacturing costs, unpredictable side effects and the lack of an ideal matrix to deliver protein in a continuous manner over times[16]. Local BMP7 gene therapy provides an alternative method for the delivery of BMP7 protein to stimulate bone regeneration[17–20]. Recent studies have demonstrated that recombinant AAV vector is an ideal vector to deliver therapeutic factors. Recombinant AAV vector is non-pathogenic and elicits no inflammatory response. It is also an advantage that recombinant AAV vector often leads to efficient long-term expression of secreted proteins *in vivo* and *in vitro*[21]. However, whether AAV-BMP7 could induce bone formation *in vitro* and *in vivo* remains unclear. In this study, a recombinant AAV-BMP7 vector was constructed successfully. The sustained secretion of BMP7 protein was detected in culture medium up to d 28 by C2C12 cells infected with AAV-BMP7. Mouse myoblast C2C12 cells displayed an osteoblastic phenotype. It has been reported that C2C12 cells are pluripotent mesenchymal precursor cells, capable of differentiating into myoblasts, adipocytes and osteoblasts under appropriate stimulation conditions[22,23]. Further studies demonstrated that BMP7 protein was a potent inducer of osteoblastic differentiation of C2C12 cells by upregulating *Runx2/Cbfa1* gene transcription[24]. The core binding factor *Runx2/Cbfa1* is a specific transcriptional activator and a molecular switch of osteoblast differentiation[25]. Thus, C2C12 cells infected with AAV-BMP7 could be finally restricted to give rise to one terminally differentiated cell type expressing the markers of osteoblasts (eg ALP and osteocalcin). This osteogenic committed differentiation mediated by genetic modification is safe as it gives the desired cell type and avoids the possibility of giving rise to unlimited cell growth or unwanted cell types. The committed differentiation could also be controlled by using tissue-specific promoters or the “tet switch system”.

In this study, we found an interesting feature of the AAV vector, namely delayed transgene expression. The production of BMP7 protein reached a peak as late as 6 d after infection, compared with adenovirus-mediated gene delivery in C2C12 cells in which the desired BMP2 protein could be produced as early as 24 h after infection[7]. This difference may be due to the fact that AAV is a single-stranded DNA virus; there is, therefore, a rate-limiting step of second-strand DNA synthesis in the nucleus of infected cells[21]. However, the delayed BMP7 protein expression using the AAV vector did not affect the osteogenic biological function of BMP7 in our study. Some *in vivo* examinations have also demonstrated the same delayed transgene expression[26,27]. From a clinical standpoint, it seems that the short period of delayed osteoinductive protein production does not hamper the treatment of relative longer-term and non-emergency cases of fracture healing or spinal fusion. Furthermore, delayed transgene expression might protect secreted therapeutic proteins from immunologic attack induced by destruction of the vascular barrier at the time of virus injection[28].

We first report that AAV-based BMP7 gene transfer could represent a new and feasible way to induce a committed osteoblast differentiation in an *in vitro* culture system using C2C12 cells. This approach would be preferred in a great range of applications for some orthopedic disorders in which it is necessary to increase the formation of bone. Unlike the adenoviral-based vectors that are limited by their non-specific immune response[1], the AAV-BMP7 vectors could be injected directly into the segmental bone defect that does not heal spontaneously to promote bone formation by recruiting locally responsive cells to differentiate into osteoblasts. In addition, the AAV-BMP7 vectors could be added to autologous bone grafts to serve as an osteoinductive agent to augment bone regeneration at the fusion site and decrease the need for extensive harvesting of autograft from the iliac crest. Furthermore, direct injection of these vectors into the spine could generate spine fusion in a less invasive way. For some systemic and metabolic bone diseases such as osteoporosis, the efficient long-term secretion of BMP7 proteins mediated by AAV is another outstanding advantage. The advantages of direct gene therapy strategy also include relatively simple technique requirements, minimized invasion and the potential for lower costs.

Although the detailed mechanisms of C2C12 cells differentiating into osteoblasts remains unclear, our current study suggests that AAV-BMP7 may be a valuable viral vector in the treatment of orthopedic disorders. Further *in vivo* studies are under consideration.

Acknowledgements

The authors thank AGTC Gene Technology Company (Beijing, China) for their technical assistance in packaging the AAV vector. We also thank Dr Jason WONG from Cambridge University (Cambridge, UK) for his help in the prepa-

ration of this manuscript.

References

1 Hannallah D, Peterson B, Lieberman JR, Fu FH, Huard J. Gene therapy in orthopaedic surgery. J Bone Joint Surg Am 2002; 84A: 1046–61.

2 Monahan PE, Samulski RJ. AAV vectors: is clinical success on the horizon? Gene Ther 2000; 7: 24–30.

3 Luk KD, Chen Y, Cheung KM, Kung HF, Lu WW, Leong JC. Adeno-associated virus-mediated bone morphogenetic protein-4 gene therapy for *in vivo* bone formation. Biochem Biophys Res Commun 2003; 308: 636–45.

4 Chen Y, Luk KD, Cheung KM, Xu R, Lin MC, Lu WW, *et al*. Gene therapy for new bone formation using adeno-associated viral bone morphogenetic protein-2 vectors. Gene Ther 2003; 10: 1345–53.

5 Gafni Y, Pelled G, Zilberman Y, Turgeman G, Apparailly F, Yotvat H, *et al*. Gene therapy platform for bone regeneration using an exogenously regulated, AAV-2-based gene expression system. Mol Ther 2004; 9: 587–95.

6 Yeh LC, Tsai AD, Lee JC. Osteogenic protein-1 (OP-1, BMP-7) induces osteoblastic cell differentiation of the pluripotent mesenchymal cell line C2C12. J Cell Biochem 2002; 87: 292–304.

7 Okubo Y, Bessho K, Fujimura K, Iizuka T, Miyatake S. Expression of bone morphogenetic protein-2 via adenoviral vector in C2C12 myoblasts induces differentiation into the osteoblast lineage. Biochem Biophys Res Commun 1999; 262: 739–43.

8 Kim YJ, Lee MH, Wozney JM, Cho JY, Ryoo HM. Bone morphogenetic protein-2-induced alkaline phosphatase expression is stimulated by Dlx5 and repressed by Msx2. J Biol Chem 2004; 279: 50773–80.

9 Wu ZJ, Wu XB, Hou YD. Construction of a series of adeno-associated virus vectors and their expression of β-galactosidase gene. Chin J Virol 2000; 16: 1–6.

10 Wu ZJ, Wu XB, Hou YD. Generation of a recombinant herpes simplex virus which can provide packaging function for recombinant adeno-associated virus. Chin Sci Bull 1999; 44: 715–9.

11 Wu XB, Dong XY, Wu ZJ, Cao H, Niu DB, Qu JG, *et al*. A novel method for purification of recombinant adeno-associated virus vectors on a large scale. Chin Sci Bull 2000; 45: 2071–5.

12 Ponnazhagan S, Yoder MC, Srivastava A. Adeno-associated virus type 2-mediated transduction of murine hematopoietic cells with long-term repopulating ability and sustained expression of a human globin gene *in vivo*. J Virol 1997; 71: 3098–104.

13 Bonnelye E, Merdad L, Kung V, Aubin JE. The orphan nuclear estrogen receptor-related receptor α (ERRα) is expressed throughout osteoblast differentiation and regulates bone formation *in vitro*. J Cell Biol 2001; 153: 971–84.

14 Song CL, Guo ZQ, Ma QJ, Chen ZQ, Liu ZJ, Jia HT, *et al*. Simvastatin induces osteoblastic differentiation and inhibits adipocytic differentiation in mouse bone marrow stromal cells. Biochem Biophys Res Commun 2003; 308: 458–62.

15 Xiao ZS, Liu SG, Hinson TK, Quarles LD. Characterization of the upstream mouse Cbfa1/Runx2 promoter. J Cell Biochem 2001; 82: 647–59.

16 Li R, Wozney J. Delivering on the promise of bone morphogenetic proteins. Trends Biotechnol 2001; 19: 255–65.

17 Krebsbach PH, Gu K, Franceschi RT, Rutherford RB. Gene therapy-directed osteogenesis: BMP-7-transduced human fibroblasts form bone *in vivo*. Hum Gene Ther 2000; 11: 1201–10.

18 Franceschi RT, Wang D, Krebsbach PH, Rutherford RB. Gene therapy for bone formation: *in vitro* and *in vivo* osteogenic activity of an adenovirus expressing BMP7. J Cell Biochem 2000; 78: 476–86.

19. Breitbart AS, Grande DA, Mason JM, Barcia M, James T, Grant RT. Gene-enhanced tissue engineering: applications for bone healing using cultured periosteal cells transduced retrovirally with the BMP-7 gene. Ann Plast Surg 1999; 42: 488–95.

20 Mason JM, Grande DA, Barcia M, Grant R, Pergolizzi RG, Breitbart AS. Expression of human bone morphogenic protein 7 in primary rabbit periosteal cells: potential utility in gene therapy for osteochondrial repair. Gene Ther 1998; 5: 1098–104.

21 Schwarz EM. The adeno-associated virus vector for orthopaedic gene therapy. Clin Orthop 2000; 379 Suppl: S31–9.

22 Fux C, Langer D, Fussenegger M. Dual-regulated myoD- and msx1-based interventions in C2C12-derived cells enable precise myogenic/osteogenic/adipogenic lineage control. J Gene Med 2004; 6: 1159–69.

23 Fux C, Mitta B, Kramer BP, Fussenegger M. Dual-regulated expression of C/EBP-α and BMP-2 enables differential differentiation of C2C12 cells into adipocytes and osteoblasts. Nucleic Acids Res 2004; 32: e1.

24. Tou L, Quibria N, Alexander JM. Transcriptional regulation of the human Runx2/Cbfa1 gene promoter by bone morphogenetic protein-7. Mol Cell Endocrinol 2003; 205: 121–9.

25 Zheng H, Guo Z, Ma Q, Jia H, Dang G. Cbfa1/osf2 transduced bone marrow stromal cells facilitate bone formation *in vitro* and *in vivo*. Calcif Tissue Int 2004; 74: 194–203.

26 Kay MA, Manno CS, Ragni MV, Larson PJ, Couto LB, McClelland A, *et al*. Evidence for gene transfer and expression of factor IX in haemophilia B patients treated with an AAV vector. Nat Genet 2000; 24: 257–61.

27 Song S, Morgan M, Ellis T, Poirier A, Chesnut K, Wang J, *et al*. Sustained secretion of human α-1-antitrypsin from murine muscle transduced with adeno-associated virus vectors. Proc Natl Acad Sci USA 1998; 95: 14384–8.

28 Aubert D, Pichard V, Durand S, Moullier P, Ferry N. Cytotoxic immune response after retroviral-mediated hepatic gene transfer in rat does not preclude expression from adeno-associated virus 1 transduced muscles. Hum Gene Ther 2003; 14: 473–81.

Acta Pharmacologica Sinica 2005 Aug; 26 (8): 969–975

Full-length article

Apoptosis initiated by carbon tetrachloride in mitochondria of rat primary cultured hepatocytes

Yan CAI[1,2], Li-kun GONG[1,2], Xin-ming QI[1,2], Xiang-hong LI[1], Jin REN[1,3]

[1]State Key Laboratory of Drug Research, Shanghai Institute of Materia Medica, Shanghai Institutes for Biological Sciences, Chinese Academy of Sciences, Shanghai 201203, China; [2]Graduate School of the Chinese Academy of Sciences, Shanghai 201203, China

Key words

carbon tetrachloride; hepatocytes; mitochondria; caspase 3; cytochrome c

[3] Correspondence to Prof Jin REN.
Phn/Fax 86-21-5080-6031.
E-mail jren@mail.shcnc.ac.cn

Received 2005-01-11
Accepted 2005-04-18

doi: 10.1111/j.1745-7254.2005.00143.x

Abstract

Aim: To investigate the mitochondria-initiated apoptosis pathway involved in Carbon tetrachloride (CCl_4) hepatotoxicity *in vitro*. **Methods:** Several cytotoxicity endpoints, including WST-8 metabolism, lactate dehydrogenase leakage and morphological changes, were examined. The 5,5'-dithio-bis(2-nitrobenzoic acid) reaction was used to measure reduced glutathione level, and the malondialdehyde level was determined using the thiobarbituric acid assay. The release of cytochrome c and Bcl-X_L was detected by Western blot. Caspase-3 activity was measured using the fluorogenic substrate Ac-DEVD-AMC. DNA fragmentation was used to evaluate cell apoptosis. **Results:** A time- and dose-dependent decrease in cellular glutathione content was observed, along with a concomitant increase in malondialdehyde levels following the application of CCl_4. Caspase 3 activity was stimulated at all doses of CCl_4, with the most significant activation at 3 mmol/L. Cytochrome c was released obviously after CCl_4 treatment. A time-dependent decrease in Bcl-X_L expression was observed. DNA fragmentation results revealed apoptosis and necrosis following CCl_4 treatment. **Conclusion:** Oxidative damage is one of the essential mechanisms of CCl_4 hepatotoxicity, which triggers apoptosis via the mitochondria-initiated pathway.

Introduction

Apoptosis is a genetically encoded form of cell suicide central to the development and homeostasis of multicellular organisms[1–3]. Once researchers assumed that the activation of endonucleases and specific proteases (such as caspases) reflect the key mechanism of apoptosis[4,5]. However, a number of studies disclose that mitochondria play a key role in apoptosis[1,4,6]. The mitochondrial pathway is partly dependent on the release of cytochrome c. After release from mitochondria to the cytosol, cytochrome c binds to apoptosis-activating factor-1 (Apaf-1), ATP (or dATP), and possibly a cytosolic protein (Apaf-3), and activates caspase 9, which in turn stimulates caspase 3 activity. Caspase 3 cleaves and activates DNA fragmentation factor (DFF), resulting in DNA degradation[2,4,7].

Bcl-2 proteins act on mitochondria to regulate apoptosis. The Bcl-2 family consists of both cell death promoters and preventers, including the anti-apoptotic proteins Bcl-2, Bcl-X_L, Mcl-1, A1/Bfl-1 and Bcl-W, and the pro-apoptotic members Bax, Bcl-X_S, Bak, Bad, Bik, Bim, Bid, Hrk and Bok[8]. Bcl-2 and Bcl-X_L prevent cytochrome c from entering the cytosol, either by blocking release or binding to the cytochrome in a direct or indirect fashion, and consequently inhibiting activation of the downstream caspase cascade[4].

Reactive oxygen species (ROS), which induce the onset of the mitochondrial permeability transition (MPT), play an important role in mitochondrial apoptosis. Activation of MPT is a major controlling mechanism in some apoptotic systems, and also contributes to the release of cytochrome c and other apoptogenic proteins[4,9]. However, the mechanisms of ROS generation and its relationship with the well-documented caspase activation remain to be elucidated. In the present investigation, the levels of reduced glutathione (GSH) and malondialdehyde (MDA) are measured as reliable markers of oxidative stress.

Carbon tetrachloride (CCl_4) is a typical poison that induces severe oxidative stress followed by activation of caspase 3 in rat liver[10]. Moreover, GSH depletion and MDA induction by CCl_4 are evident in rat primary hepatocytes and HepG2, a human hepatoma cell line[11]. However, it is currently unclear whether both oxidative stress and apoptosis occur in rat primary hepatocytes induced by CCl_4.

Mitochondrial damage by CCl_4 is involved in the apoptotic process *in vivo*, during which caspase 3 is activated[10]. A histological study suggests that apoptosis is additionally induced by CCl_4 in liver[12]. However, the pathway by which CCl_4 mediates apoptosis in rat primary hepatocytes is currently unknown.

In the present report, CCl_4 mediation of the expression and activation of different proteins involved in apoptotic cell death is investigated. Moreover, the relationship between peroxidative damage and apoptosis induced by CCl_4 in rat primary hepatocytes is explored.

Materials and methods

Materials and culture of hepatocytes CCl_4 and Me_2SO were purchased from Shanghai Chemical Reagent Company (Shanghai, China). CCl_4 was dissolved in 10% Me_2SO HBS solution (in mmol/L: HEPES 33, NaCl 160.8 mmol/L, KCl 3.15 mmol/L, $Na_2HPO_4 \cdot 12H_2O$ 0.7 mmol/L) and diluted to final concentration of 0.1 mmol/L, 0.3 mmol/L, 1 mmol/L, 3 mmol/L, and 9 mmol/L, respectively.

Hepatocytes were isolated from Sprague-Dawley male rats (180 g–220 g) by 2-step collagenase perfusion, as described previously[13–15], with some modifications. Collagenase IV was purchased from Sigma Chemical Company (St Louis, USA). Hepatocytes were seeded on collagen-coated plastic dishes at a density of 3×10^5 viable cells/mL, and cultured in Ham's F-12/Dulbecco's modified Eagle's medium (DMEM) (Invitrogen, Carlsbad, CA, USA) (1:1) medium supplemented with 15% fetal bovine serum (PAA Laboratories, Linz, Austria), 0.1 g/L penicillin (Shanghai Fourth Pharmaceuticals, Shanghai, China), 0.07 g/L streptomycin (Shanghai Fourth Pharmaceuticals, Shanghai, China) and 0.2% bovine serum albumin (Roche, NJ, USA). After 3 h, the medium was altered. Cells were incubated in medium containing different concentrations of CCl_4 solution.

Cell viability and lactate dehydrogenase leakage assay Rat primary hepatocytes were treated with CCl_4 for 20 h, and the general viability of cultured cells was assayed at 450 nm with the Cell Counting Kit-8 (Dojindo Laboratories, Tokyo, Japan).

Hepatocytes were seeded on collagen-coated 96-well microtiter plates at a density of 3×10^4 cells/well. After treatment with increasing concentrations of CCl_4 for 20 h, lactate dehydrognase (LDH) released into the culture supernatants was measured in a 3-min coupled enzymatic assay that results in the conversion of a tetrazolium salt (NBT) into a formazan product[16]. The amount of color formed is proportional to the number of lysed cells. Visible wavelength absorbance data at 490 nm were collected using a standard 96-well plate reader (SOFTmax® PRO, Molecular Devices, Sunnyvale, CA, USA).

General morphology of cultured cells Hepatocytes were cultured with CCl_4 for 20 h, and cell morphology was examined using inverted microscopy.

Intracellular glutathione content assay Hepatocytes were treated separately with CCl_4 for 4 h, 8 h, 12 h, 16 h, or 24 h. Cells in monolayers were gently washed 3 times with phosphate-buffered saline (PBS) (pH 7.4), scraped in ice-cold PBS, and sonicated intermittently 3 times. Cell homogenates were added to solution containing 10% trichloroacetic acid and 20 mmol/L EDTA-Na_2. The mixture was centrifuged for 5 min at $3000\times g$. The suspension was mixed with buffer (0.4 mmol/L Tris-HCl, 20 mmol/L EDTA-Na_2) and 5,5'-dithiobis(2-nitrobenzoic acid) (DTNB), and measured at a wavelength of 412 nm within 5 min. Reduced pure GSH was used to obtain a standard curve.

Lipid peroxidation assay for malondialdehyde Malondialdehyde levels were measured spectrophotometrically using a thiobarbituric acid (TBA) fluorescence assay. Cell homogenates were mixed with solution (20 mmol/L TBA/glacial acetic acid, 1:1), and heated for 60 min at 100 ºC in a water bath. After cooling down, the mixture was extracted in methanol and centrifuged for 10 min at $5000\times g$. The suspension was measured in a fluorimeter with excitation at 515 nm and emission at 550 nm.

Western blot analysis Hepatocytes were scraped in ice-cold PBS obtained by centrifugation at $300\times g$ for 5 min. Cells were gently lysed for 30 s in 75 μL ice-cold buffer containing 250 mmol/L sucrose, 1 mmol/L edetic acid, 0.05% digitonin, 25 mmol/L Tris, pH 6.8, 1 mmol/L dithiothreitol, and protease inhibitor (10^{-3} g/L leupeptin and aprotinin, and 0.1 mmol/L phenylmethylsulfonyl fluoride). Lysates were then homogenized through a 26-gauge needle for 30 passages and centrifuged twice at $800\times g$ for 20 min at 4 ºC. The pooled supernatant was centrifuged at 10 000$\times g$ for 10 min at 4 ºC to collect the mitochondria fractions. This supernatant was then transferred to fresh tubes and centrifuged at 16 000$\times g$ for 20 min at 4 ºC to remove any residual mitochondria. The supernatant was stored as the cytosolic fraction of hepatocytes. Cytosolic and mitochondria fractions were

subjected to 15% sodium dodecyl sulphate-polyacrylamide gel electrophoresis. The gel was transferred to a PVDF membrane. Monoclonal rat anti-cytochrome c antibody was purchased from Neomarkers (Lab Vision & NEOMARKERS, UK) and polyclonal rat anti-bcl-X_L antibody was from Cell Signaling Technology (Beverly, MA, USA). Following incubation with horseradish peroxidase-conjugated secondary antibody (Rockland, Gilbertsville, PA, USA), the blot was developed using the enhancing chemiluminescence detection system.

Caspase 3 activity assay Following incubation of hepatocytes in the absence of CCl_4 for the indicated times, caspase 3 activation was measured with the Caspase 3 assay kit (BD Biosciences Pharmingen, San Diego, CA, USA). In brief, culture cells were washed with ice-cold PBS (pH 7.4), and lysed in buffer provided by the kit for 30 min on ice. Reaction mixtures containing Ac-DEVD-AMC and cell lysates in buffer were incubated for 1 h at 37 ºC. AMC liberated from Ac-DEVD-AMC was measured in a fluorimeter with excitation at 380 nm and emission at 460 nm.

DNA gel electrophoresis assay Cultured cells were washed 3 times with ice-cold PBS, scraped in the same PBS, and collected by centrifugation for 5 min at 600×*g*. Cells were resuspended in 10 mmol/L EDTA and 50 mmol/L Tris-HCl (pH 8.0) containing 0.5% sodium lauryl sarcosinate and 0.5 g/L proteinase K, and incubated for 60 min at 50 ºC. Next, 10 mmol/L EDTA containing 0.25% bromophenol blue and 40% sucrose was mixed with each DNA extract. Individual extracts were loaded into the wells of a 2% agarose gel containing 3×10^{-3} g/L ethidium bromide. Electrophoresis was carried out in 40 mmol/L Tris-HCl containing 40 mmol/L acetic acid and 1 mmol/L EDTA.

Statistical analysis Data were entered into a database and analyzed using SPSS software. Group mean values and standard deviations were calculated. After homogenetic analysis, homogeneous data were analyzed with one-way analysis of variance and a *post hoc* test of least significant difference. Heterogeneous data were analyzed using the *t*-test. $P<0.05$ was considered statistically significant.

Results

Cytotoxicity induction by CCl_4 in rat primary hepatocytes Cells were exposed to 0.1–9 mmol/L CCl_4 for 20 h, and viability was measured. Cell viability decreased in a dose-dependent manner (Table 1).

Intracellular LDH release as a result of plasma membrane breakdown and alteration of permeability was evaluated. A dose-dependent increase in LDH release in rat primary hepatocytes was observed in the presence of CCl_4 (Table 2).

Table 1. Cytotoxicity of CCl_4 in the rat primary hepatocytes. n=4. Mean±SD. $^cP<0.01$ *vs* control group.

CCl_4/mmol·L^{-1}	Cell viability of control group/%
0	100
0.1	82.5±6.0^c
0.3	72.4±5.3^c
1	68.2±4.4^c
3	61.8±4.4^c
9	47.3±2.9^c

Table 2. Intracellular lactate dehydrogenase release induced by CCl_4 after 20 h. n=5. Mean±SD. $^cP<0.01$ *vs* control group.

CCl_4 /mmol·L^{-1}	A_{490}	Fold change in absorbance compared with control group
0	0.0047±0.0044	1
0.1	0.0025±0.0023	0.54±0.04
0.3	0.0098±0.0095	2.05±0.15^c
1	0.0321±0.0035	6.73±0.49^c
3	0.0869±0.0051	18.23±1.17^c
9	0.1499±0.0063	31.43±2.28^c

Hepatocyte morphology Cultured cell morphology examination revealed that 9 mmol/L CCl_4 significantly inhibited the confluence of cultured hepatocytes (Figure 1).

Glutathione depletion CCl_4 induced a dose- and time-dependent depletion of GSH in rat primary hepatocytes. The GSH level was significantly reduced after cell incubation with 1 mmol/L CCl_4 for 8 h, 12 h, 16 h, and 24 h, but not at 4 h. The exhaustion of GSH was observed initially with 3 mmol/L CCl_4 after a 16-h incubation (Figure 2).

Malondialdehyde formation We observed dose- and time-dependent induction of MDA formation in the presence of CCl_4 in rat primary hepatocytes. CCl_4 induced significant amounts of MDA at concentrations of 3 mmol/L and 9 mmol/L after a 12-h incubation and at 0.3–9 mmol/L after 20 h. There was no evident MDA induction after 4 h of CCl_4 treatment at all the doses tested (Table 3).

Cytochrome c release Cytochrome c was detected in the cytosolic fractions of hepatocytes. Hepatocytes were treated with 0.3, 1, 3 and 9 mmol/L CCl_4 up to 16 h. CCl_4 induced time-dependent cytochrome c release in rat primary hepatocytes. Evident dose-dependent release of cytochrome c was observed at 4 h and 8 h (Figure 3A). In contrast, a dose- and time-dependent decrease in mitochondria cyto-

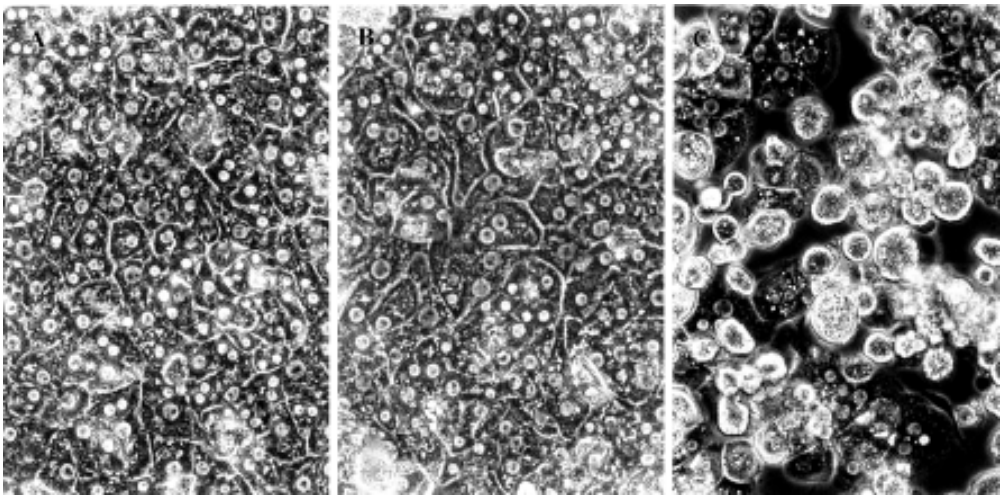

Figure 1. Light micrographs of rat primary hepatocytes at 20 h after treatment with CCl_4. (A) Control cells; (B) CCl_4 3 mmol/L; (C)CCl_4 9 mmol/L. ×20.

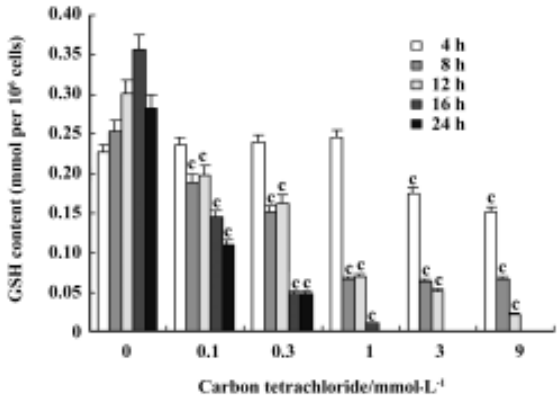

Figure 2. Levels of glutathione (GSH) measured in rat primary hepatocytes with increasing concentrations of CCl_4. Results are expressed as GSH content (mmol) per 10^6 cells. n=4. Mean±SD. ^cP<0.01 *vs* control (CCl_4 0 mmol/L).

Table 3. Time and dose course of malondialdehyde (MDA) content in rat primary hepatocytes treated with CCl_4. n=4. Mean±SD. ^bP< 0.05 *vs* 12 h control. ^eP<0.05 *vs* 20 h control.

CCl_4/mmol·L^{-1}	MDA/μmol·g^{-1} protein		
	4 h	12 h	20 h
0	0.041±0.004	0.038±0.006	0.022±0.003
0.1	0.043±0.001	0.046±0.002	0.021±0.013
0.3	0.038±0.004	0.038±0.004	0.026±0.006^e
1	0.048±0.018	0.042±0.004	0.026±0.006^e
3	0.036±0.003	0.054±0.001^b	0.029±0.001^e
9	0.042±0.002	0.053±0.003^b	0.040±0.007^e

chrome c was observed (Figure 3B).

Caspase 3 activation by carbon tetrachloride Caspase 3 activity was examined in cultured hepatocytes treated with

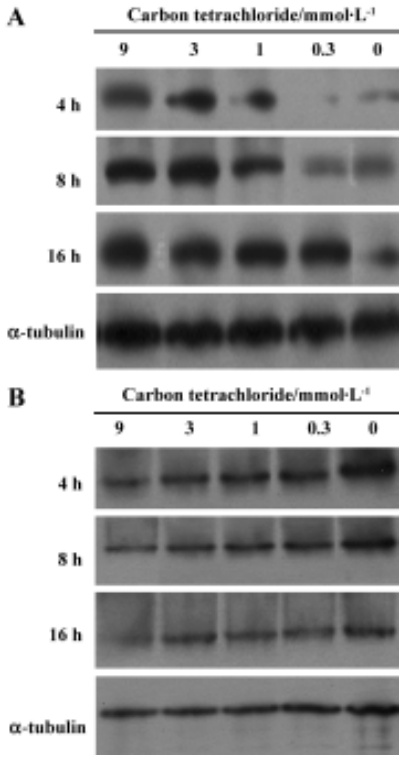

Figure 3. Effect of CCl_4 on cytochrome c release from mitochondria into the cytosol in rat primary hepatocytes. Cytochrome c was analyzed in the cytosolic (A) and mitochondrial (B) fractions of hepatocytes treated with increasing concentrations of CCl_4 for up to16 h.

increasing concentrations of CCl_4 for 8 h. A dose-dependent increase in caspase 3 activity was observed in the presence of 0.3–3 mmol/L CCl_4, which decreased slightly at 9 mmol/L CCl_4 (Table 4).

Table 4. Dose-course analysis of caspase 3 activation after 8 h treatment of CCl_4. n=4. Mean±SD. ^cP<0.01 *vs* control group.

CCl_4/mmol·L	Caspase 3 activity/fluorescence·h^{-1}·g^{-1} protein
0	685±85
0.3	1040±44^c
1	1227±55^c
3	1442±30^c
9	1062±55^c

Bcl-X_L analysis Bcl-X_L protein levels were analyzed in cultured hepatocytes treated with different concentrations of CCl_4. Hepatocytes were exposed to CCl_4 for 4 h, 8 h and 16 h (Figure 4). No significant dose-dependent change was observed, but a time-dependent decrease in Bcl-X_L expression was observed.

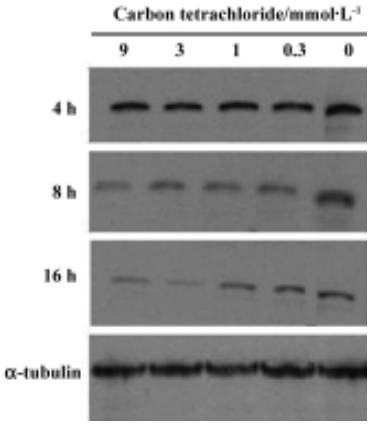

Figure 4. Effect of CCl_4 on Bcl-X_L expression in rat primary hepatocytes treated with 0.3 mmol/L, 1 mmol/L, 3 mmol/L, and 9 mmol/L CCl_4 for up to 16 h.

DNA fragmentation To confirm whether CCl_4 induces DNA fragmentation in rat primary hepatocytes, DNA was extracted from treated cells. No ladder was observed in control cells at 0 h, 8 h, or 20 h of CCl_4 treatment. Apoptosis was initially observed in the presence of 9 mmol/L CCl_4 after 8 h treatment, followed by 3 mmol/L and 1 mmol/L CCl_4 after 20 h treatment (Figure 5).

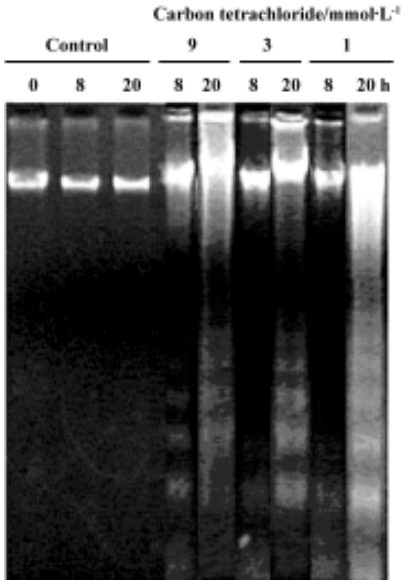

Figure 5. DNA fragmentation in rat primary hepatocytes treated with CCl_4 1 mmol/L, 3 mmol/L and 9 mmol/L CCl_4 for 8 h and 20 h.

Discussion

Carbon tetrachloride is a typical hepatotoxin used in liver injury research. Early studies showed that the damage induced by CCl_4 in liver is partly involved in the apoptosis pathway *in vivo*. At least 2 different apoptosis pathways – the mitochondrial pathway and the death-receptor pathway – lead to caspase activation[17]. Although past reports have disclosed caspase 3 activation and other histopathological changes in CCl_4-induced apoptotic hepatocytes[10,12], little is known about the precise molecular mechanisms of apoptosis induction. In this study, we investigated the molecular mechanism of CCl_4-induced apoptosis in rat primary hepatocytes. Release of cytochrome c first occurred at 4 h and then up to 16 h (Figure 3A). On the other hand, cytochrome c remaining in the mitochondria was found to decrease in a dose- and time-dependent manner (Figure 3B). In addition, it was found that caspase 3 was significantly activated after 8 h at all doses (Table 4). As a result of caspases cascade activation, DNA fragmentation first appeared at 9 mmol/L after 8 h and formed at all concentrations after 20 h (Figure 5). It is well known that cytochrome c released from mitochondria into the cytosol triggers the activation of caspase 9 and caspase 3 in the mitochondrial pathway. In view of this, we propose the involvement of the mitochondrial pathway via cytochrome c release in CCl_4-induced apoptosis.

In the present study, we investigted the level of Bcl-X_L, an anti-apoptotic protein, in CCl_4-induced apoptosis in rat

primary hepatocytes. Bcl-X_L, the only member of the Bcl-2 family present in hepatocytes, is one of the markers used to identify apoptosis in rat primary hepatocytes[18]. Bcl-X_L exerts an anti-apoptosis function by interacting with cytochrome c, either directly or indirectly via Apaf-1, which binds to both Bcl-X_L and cytochrome c[2,4,19,20]. Therefore, decreased Bcl-X_L levels and increased cytochrome c release are specific biomarkers for the mitochondrial pathway of apoptosis[18]. In our experiments, cytochrome c levels increased markedly after a 8-h CCl_4 treatment with a concomitant decrease in Bcl-X_L protein expression. Bcl-X_L may not execute its anti-apoptotic function once large amounts of cytochrome c are released from the mitochondria when the cell is over-exposed to stimuli, for example, lipid peroxidation induced by CCl_4 in this system. These findings strongly suggest the involvement of cytochrome c release from mitochondria accompanied by Bcl-X_L regulation in CCl_4-induced apoptosis in rat primary hepatocytes.

Hepatic injury through CCl_4-induced lipid peroxidation is used extensively in experimental models to elucidate the cellular mechanisms behind oxidative damage[11,21–23]. In the present study, we confirm time- and dose-dependent depletion in the intracellular GSH content after CCl_4 treatment. MDA, an important lipid peroxidation product, increased in a time- and dose-dependent manner in our system. The data suggest that oxidative damage is one of the essential mechanisms of hepatotoxicity induced by CCl_4 *in vitro*.

The relationship between ROS and apoptosis has been under investigation for a number of years[4,9]. ROS play important roles in apoptosis initiated in mitochondria[24,25]. It has been documented that GSH depletion and MDA increase, events observed frequently during oxidative damage, are inducers of mitochondrial permeability transition (MPT)[11,26]. Triggering of MPT leads to the release of several different factors relevant to apoptosis, such as cytochrome c, Apoptosis-inducing factor (AIF), and endonuclease G[2,8,9,27]. In this study, we demonstrated GSH depletion, MDA increase and apoptosis initiated from mitochondria of CCl_4-treated rat primary hepatocytes. Our results collectively indicate that CCl_4 induces apoptosis partly via a mitochondria-dependent pathway, dependent on ROS production in rat primary hepatocytes.

To elucidate other possible mechanisms of CCl_4-induced apoptosis, we analyzed the expression of endonuclease G, a caspase-independent apoptotic protein released from mitochondria that translocates to the nucleus during apoptosis[28,29]. Western blot analysis of endonuclease G revealed no evident release in rat primary hepatocytes treated with CCl_4 (data not shown). The finding implies that endonuclease G does not participate in apoptosis induced by CCl_4.

In summary, our results confirm that oxidative damage is one of the essential mechanisms of hepatotoxicity induced by CCl_4. Moreover, mitochondria-initiated apoptosis triggered by ROS plays an important role in this hepatotoxicity in rat primary hepatocytes.

References

1 Ravagnan L, Roumier T, Kroemer G. Mitochondria, the killer organelles and their weapons. J Cell Physiol 2002; 192: 131–7.
2 Van Gurp M, Festjens N, Van Loo G, Saelens X, Vandenabeele P. Mitochondrial intermembrane proteins in cell death. Biochem Biophys Res Commun 2003; 304: 487–97.
3 Zhang J, Dong M, Li L, Fan Y, Pathre P, Dong J, *et al*. Endonuclease G is required for early embryogenesis and normal apoptosis in mice. Proc Natl Acad Sci USA 2003; 100: 15782–7.
4 Susin SA, Zamzami N, Kroemer G. Mitochondria as regulators of apoptosis: doubt no more. Biochim Biophys Acta 1998; 1366: 151–65.
5 Lorenzo HK, Susin SA. Mitochondrial effectors in caspase-independent cell death. FEBS Lett 2004; 557: 14–20.
6 Wang X. The expanding role of mitochondria in apoptosis. Genes Dev 2001; 15: 2922–33.
7 Li P, Nijhawan D, Budihardjo I, Srinivasula SM, Ahmad M, Alnemri ES, *et al*. Cytochrome c and dATP-dependent formation of Apaf-1/caspase-9 complex initiates an apoptotic protease cascade. Cell 1997; 91: 479–89.
8 Reed JC, Jurgensmeier JM, Matsuyama S. Bcl-2 family proteins and mitochondria. Biochim Biophys Acta 1998; 1366: 127–37.
9 Cai J, Jones DP. Superoxide in apoptosis. Mitochondrial generation triggered by cytochrome c loss. J Biol Chem 1998; 273: 11 401–4.
10 Sun F, Hamagawa E, Tsutsui C, Ono Y, Ogiri Y, Kojo S. Evaluation of oxidative stress during apoptosis and necrosis caused by carbon tetrachloride in rat liver. Biochim Biophys Acta 2001; 1535: 186–91.
11 Beddowes EJ, Faux SP, Chipman JK. Chloroform, carbon tetrachloride and glutathione depletion induce secondary genotoxicity in liver cells via oxidative stress. Toxicology 2003; 187: 101–15.
12 Shi J, Aisaki K, Ikawa Y, Wake K. Evidence of hepatocyte apoptosis in rat liver after the administration of carbon tetrachloride. Am J Pathol 1998; 153: 515–25.
13 Berry MN, Friend DS. High-yield preparation of isolated parenchymal cells: a biochemical and fine structural study. J Cell Biol 1969; 43: 506–20.
14 Orrenius S, Thor H, Rajs J, Berggren M. Isolated rat hepatocytes as an experimental tool in the study of cell injury. Effect of anoxia. Forensic Sci 1976; 8: 255–63.
15 Seglen PO. Preparation of isolated rat liver cells. Methods Cell Biol 1976; 13: 29–83.
16 Decker T, Lohmann-Matthes ML. A quick and simple method for the quantitation of lactate dehydrogenase release in measurements of cellular cytotoxicity and tumor necrosis factor (TNF) activity. J Immunol Methods 1988; 15: 61–9.
17 Araragi S, Kondoh M, Kawase M, Saito S, Higashimoto M, Sato

M. Mercuric chloride induces apoptosis via a mitochondrial-dependent pathway in human leukemia cells. Toxicology 2003; 184: 1–9.
18 Gómez-Lechón MJ, O'Connor E, Castell JV, Jover R. Sensitive markers used to identify compounds that trigger apoptosis in cultured hepatocytes. Toxicol Sci 2002; 65: 299–308.
19 Skulachev VP. Cytochrome c in the apoptotic and antioxidant cascades. FEBS Lett 1998; 423: 275–80.
20 Finucane DM, Bossy-Wetzel E, Waterhouse NJ, Cotter TG, Green DR. Bax-induced caspase activation and apoptosis via cytochrome c release from mitochondria is inhibitable by Bcl-X_L. J Biol Chem 1999; 274: 2225–33.
21 Recknagel RO, Glende EA Jr, Dolak JA, Waller RL. Mechanisms of carbon tetrachloride toxicity. Pharmacol Ther 1989; 43: 139–45.
22 Zimmerman HJ. Hepatotoxicity: The adverse effects of drugs and other chemicals on the liver. 2nd ed. Indirect cytotoxic hepatotoxins. New York: Appleton-Century-Crofts; 1978. p 255–95.
23 Basu S. Carbon tetrachloride-induced lipid peroxidation: eicosanoid formation and their regulation by antioxidant nutrients. Toxicology 2003; 189: 113–27.
24 Pereira CF, Oliveira CR. Oxidative glutamate toxicity involves mitochondrial dysfunction and perturbation of intracellular Ca^{2+} homeostasis. Neurosci Res 2000; 37: 227–36.
25 Ding WX, Nam Ong C. Role of oxidative stress and mitochondrial changes in cyanobacteria-induced apoptosis and hepatotoxicity. FEMS Microbiol Lett 2003; 220: 1–7.
26 Herrera B, Alvarez AM, Sanchez A, Fernandez M, Roncero C, Benito M, *et al*. Reactive oxygen species (ROS) mediates the mitochondrial-dependent apoptosis induced by transforming growth factor (beta) in fetal hepatocytes. FASEB J 2001; 15: 741–51.
27 Hengartner MO. Apoptosis. DNA destroyers. Nature 2001; 412: 27–9.
28 Li LY, Luo X, Wang X. Endonuclease G is an apoptotic DNase when released from mitochondria. Nature 2001; 412: 95–9.
29 Van Loo G, Schotte P, Van Gurp M, Demol H, Hoorelbeke B, Gevaert K, *et al*. Endonuclease G: a mitochondrial protein released in apoptosis and involved in caspase-independent DNA degradation. Cell Death Diff 2001; 8: 1136–42.

Acta Pharmacologica Sinica 2005 Aug; 26 (8): 976–981

Full-length article

Expression of feeding-related peptide receptors mRNA in GT1-7 cell line and roles of leptin and orexins in control of GnRH secretion[1]

Ying YANG, Li-bin ZHOU, Shang-quan LIU, Jing-feng TANG, Feng-yin LI, Rong-ying LI, Huai-dong SONG, Ming-dao CHEN[2]

Rui-jin Hospital Affiliated to Shanghai Second Medical University, Shanghai Institute of Endocrine and Metabolic Diseases, Shanghai 200025, China

Key words

GT1-7 cell line; bombesin; cholecystokinin; neuropeptide Y; neurotensin; orexin; leptin; gonadorelin

[1] Project supported by the National Natural Science Foundation of China (No 39970927 and 30270626) and the Rockefeller Foundation of the USA.
[2] Correspondence to Prof Ming-dao CHEN.
Phn 86-21-6431-5587.
Fax 86-21-6467-3639.
E-mail mingdaochensh@yahoo.com

Received 2004-12-15
Accepted 2005-02-28

doi: 10.1111/j.1745-7254.2005.00113.x

Abstract

Aim: To investigate the expression of feeding-related peptide receptors mRNA in GT1-7 cell line and roles of leptin and orexins in the control of GnRH secretion. **Methods:** Receptors of bombesin3, cholecystokinin (CCK)-A, CCK-B, glucagon-like peptide (GLP)1, melanin-concentrating hormone (MCH)1, orexin1, orexin2, neuromedin-B, neuropeptide Y (NPY)1 and NPY5, neurotensin (NT)1, NT2, NT3, and leptin receptor long form mRNA in GT1-7 cells were detected by reversed transcriptase-polymerase chain reaction. GT1-7 cells were treated with leptin, orexin A and orexin B at a cohort of concentrations for different lengths of time, and GnRH in medium was determined by radioimmunoassay (RIA). **Results:** Receptors of bombesin 3, CCK-B, GLP1, MCH1, orexin1, neuromedin-B, NPY1, NPY5, NT1, NT3, and leptin receptor long form mRNA were expressed in GT1-7 cells, of which, receptors of GLP1, neuromedin-B, NPY1, and NT3 were highly expressed. No amplified fragments of orexin2, NT2, and CCK-A receptor cDNA were generated with GT1-7 RNA, indicating that the GT1-7 cells did not express mRNA of them. Leptin induced a significant stimulation of GnRH release, the results being most significant at 0.1 nmol/L for 15 min. In contrast to other studies in hypothalamic explants, neither orexin A nor orexin B affected basal GnRH secretion over a wide range of concentrations ranging from 1 nmol/L to 500 nmol/Lat 15, 30, and 60 min. **Conclusion:** Feeding and reproductive function are closely linked. Many orexigenic and anorexigenic signals may control feeding behavior as well as alter GnRH secretion through their receptors on GnRH neurons.

Introduction

Reproduction including mating, pregnancy, and lactation is an energy-demanding process. In normal circumstances, energy intake and expenditure from food is used for essential life activities such as maintenance of basal body temperature, cellular metabolism, fertility and storage of energy in fat tissue. When the food intake is limited or when an inordinate fraction of the available energy is diverted to other uses such as exercise or fattening, reproductive attempts are sacrificed in favor of more critical life activities[1,2]. The negative energy balance, as typified by fasting, anorexia nervosa or exercise-induced amenorrhea, is associated with a suppression of reproductive function and ovarian cyclicity. Appropriate regulation of reproduction, energy intake and energy expenditure, and thus maintenance of body weight and fertility, relies on complex hypothalamic neuro-circuitry, which serve as key signals to integrate and/or coordinate the status of energy balance and the neuroendocrine reproductive axis. Many neuropeptides that have been shown to play a role in the regulation of food intake have overlapping functions in the regulation of reproductive function[3].

Successful reproduction and thus survival of the species in mammals is dependent on the GnRH pacemaker. The network of neurons that controls GnRH secretion is not yet defined, but it is thought to be the final common pathway

through which many factors influence gonadal activity, including metabolic status[4]. GT1-7 cells, a subclone of the GT1 cell line, were developed by targeting expression of the potent oncogene, SV40 T-antigen, with the regulatory region of GnRH gene, has been shown to faithfully exhibit many of the known characteristics of GnRH neurons. To date, the GT1 cells have proven to be the best characterized cell model available to study biology of the hypothalamic GnRH neurons[5].

In the last few years, the receptors for several families of neurotransmitters known to modify GnRH secretion have been identified on GT1 cells, and the stimulatory or inhibitory activity of the corresponding ligands on GnRH secretion has been documented[6–8]. Here we used the GT1-7 cells to investigate the expression of some feeding-related peptide receptors mRNA and the effects of leptin and orexins on GnRH secretion.

Materials and methods

Cell culture and reagents GT1-7 cells kindly provided by Dr KNOBIL (University of Texas-Houston Medical School, Houston, Texas, USA), were maintained in high-glucose Dulbecco's modified Eagle's medium (DMEM) supplemented with 10% fetal calf serum at 37 °C in an atmosphere of 5% CO_2+95% air. GnRH antiserum was the generous gift of Dr KNOBIL. GnRH, chloramine T, sodium pyrosulfite, leptin, bacitracin, orexin A, and orexin B were purchased from Sigma-Aldrich (St Louis, MO, USA). TRIZOL Reagent was purchased from GIBCO-BRL (Gaithersburg, Maryland, USA). SuperScript II reverse transcriptase was obtained from Life Technologies (Rockville, USA). All oligodeoxynucleotides were synthesized from Biosia Co Ltd (China).

RT-PCR analysis Total RNA was isolated from GT1-7 cells and rats hypothalamus by the TRIZOL extraction method. The first-strand cDNA was synthesized from 1–10 μg deoxyribonuclease treated RNA using SuperScript II reverse transcriptase. The RT reaction was primed with oligo. The specificity of each amplification reaction was monitored by control reactions with RT omission reaction. Because all these receptors have previously been reported in the hypothalamus, we used the rat hypothalamic tissue as a positive control. Polymerase chain reaction (PCR) amplifications were performed with 1.25 U *Taq* polymerase from Sangon in a 50-μL reaction for 35 cycles (1 min at 94 °C, 45 s at 55–60 °C, 1 min at 72 °C). The primers selected were shown in Table 1. PCR products were electrophoresed in 1.5% agarose and visualized by ethidium bromide staining.

Static incubation For GnRH secretion studies, GT1-7 cells were plated in 24-well multiwell plates at a density of 2×10^5 cells/well and grown in culture for 3–4 d, the medium was replaced by DMEM with 0.2% BSA 16 h before the experiments. Confluent cells were washed three times with Locke's mediums (NaCl 154 mmol/L, KCl 5.6 mmol/L, $CaCl_2$ 2.2 mmol/L, $MgCl_2$ 1 mmol/L, $NaHCO_3$ 6 mmol/L, glucose 10 mmol/L, HEPES 2 mmol/L) containing 0.2% bovine serum albumine (BSA), 20 μmol/L bacitracin and then were treated with or without leptin, orexin A and B at a cohort of concentrations for 15, 30, and 60 min in Locke's medium. At the end of incubation period, media were stored at -80 ºC until radioimmunoassay (RIA) for GnRH.

RIA The concentration of GnRH released into the me-

Table 1. Primers used for PCR amplification.

PCR products	Sense primer (5'–3')	Antisense primer (5'–3')	bp
Bombesin3 receptor	agacctgtgcaaaagctggt	gtcaccaagaggaggctcag	590
Cholecystokinin-A receptor	tcagtgacctcatgctttgc	tctgcaagtaacagccatcg	585
Cholecystokinin-B receptor	aaggccgtttcctacctcat	ccatcactgtcttccccagt	512
Glucagon-like peptide 1 receptor	ctggtggaaggcgtgtatct	cagcatttccgaaactccat	518
Melanin-concentrating hormone 1 receptor	ctccgatggccaggataat	gccacacaggagtgatgcta	488
Orexin 1 receptor	tgctgatggtagtcctgctg	gcttaggggacacaacctca	511
Orexin 2 receptor	cagagcaaggctcggattag	gggcctcttctctcagacct	555
Neuromedin-B receptor	tcagaagtagcacgcattgg	agcaaagggattgacacagg	426
Neuropeptide 1 receptor	ctgatggaccactgggtctt	tgattcgcttggtctcactg	481
Neuropeptide 5 receptor	cgcttccatctcaagcaga	gccaggttgcctatgagaaa	405
Neurotensin 2 receptor	gttctccccttgggaactc	gtcactgccgagctgacata	418
Neurotensin 3 receptor	ggctgcattttgggctataa	tcctcatctgagtcgtcgtg	575
Neurotensin 1 receptor	tgtctgacctgctcatcctg	catgacggtcagtttgttgg	470
Leptin long form receptor	caaaccccaagaattgttcctg	ttccactgttttcacgttgctg	368

dium (1 mL/well) was measured by RIA in duplicate. GnRH was iodinated by chloramine T technique as described[9]. Purification was achieved on a sephadex G25 column, using 0.1 mol/L acetic acid with 0.25% BSA as eluant. Aliquots of medium (150 μL) were cultured with 50 μL polyclonal antiserum (1: 24 000) for 24 h at 4 °C. The antigen-antibody complex was precipitated with a goat anti-rabbit g-globulin and ethanol. The limit of detection was 0.5 pg/tube, and the intra-assay coefficient of variation was 6.7%.

Statistical analysis For assessment of statistical significance, data were analyzed using analysis of variance. Comparisons between individual pairs were determined using Student's *t*-test. Statistical significance was defined as $P<0.05$.

Results

RT-PCR analysis of the feeding-related peptide receptors transcript in GT1-7 cells Feeding-related peptide is known to have a profound effect on the regulation of reproductive function through the GnRH neuron, however, it is not yet known whether the GnRH neuron itself contains receptors for them. The expression of orexin, neurotensin, neuropeptide Y (NPY), glucagon-like peptide 1 (GLP-1), melanin-concentrating hormone (MCH), cholecystokinin (CCK), leptin, neuromedin B and bombesin receptor mRNA were analyzed. Our results confirmed that bombesin3, CCK-B, GLP1, MCH1, orexin1, neuromedin-B, NPY1, NPY5, NT1, NT3 and leptin long form receptor mRNA were expressed in GT1-7 cells, the amplified fragments were identical in size to those amplified by total RNA derived from the rat hypothalamus, which was used as the positive control. No amplification fragment was obtained from RNA samples when the incubation with RT was omitted, a fact that excludes contamination of the samples with genomic DNA and the pseudo-positive bands, in which, GLP1, neuromedin-B, NPY1, and NT3 receptor were highly expressed in GT1-7 cell line. Additionally, though the primers designed for orexin2, NT2, CCK-A receptor cDNA amplified the fragments of the expected size with rat hypothalamic RNA (data not shown), no amplified fragment was generated with GT1-7 RNA, indicating that the GT1-7 cells did not express mRNA for them (Figure 1).

Dose-response effect of leptin on GnRH release from GT1-7 cells In experiments conducted under static conditions, GT1-7 cells were treated with leptin for 15, 30, and 60 min, and GnRH peptide levels in the medium were measured by RIA (Figure 2). Exposure of GT1-7 cells to leptin resulted in dose-dependent stimulation of GnRH release at concentrations of 0.1, 1, 10, and 100 nmol/L with rapid effect. The most profound changes of GnRH release were induced at the dose of 0.1 nmol/L after 15 min, with an increased extension of 1.5 fold (*vs* basal release, 2.69±0.49 pg/tube *vs* 1.87±0.33 pg/tube). However, as mentioned above, the release of GnRH was routinely measured after 30 and 60 min, extending leptin treatment in GT1-7 cells did not further increase the stimulation of GnRH secretion.

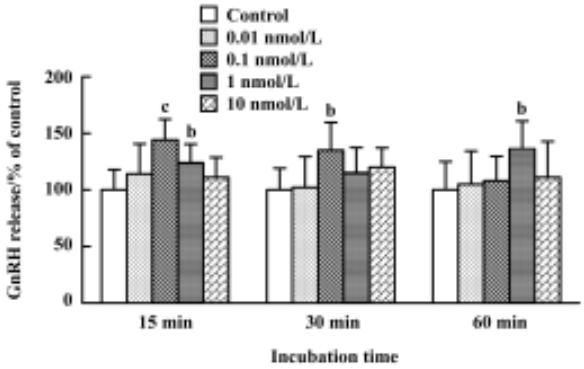

Figure 2. Effect of leptin on the release of GnRH by GT1-7 cells (static incubation). GT1-7 cells were treated with leptin (0.01–100 nmol/L) for 15, 30, or 60 min. GnRH released into the medium was assayed by RIA. n=8–10. Mean±SEM. $^bP<0.05$, $^cP<0.01$ *vs* control (Tukey test).

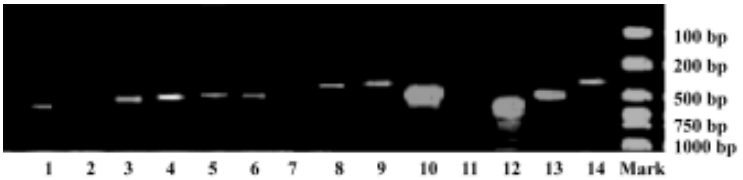

Figure 1. Expression of the feeding-related peptide receptors mRNA in GT1-7 cells. 1: bombesin3 receptor; 2: CCK-A receptor; 3: CCK-B receptor; 4: GLP1 receptor; 5: MCH1 receptor; 6: orexin1 receptor; 7: orexin2 receptor; 8: neuromedin-B receptor; 9: NPY5 receptor; 10: NPY1 receptor; 11: NT2 receptor; 12: NT3 receptor; 13: NT1 receptor; 14: leptin long form receptor. Note the presence of the receptor of bombesin3, CCK-B, GLP1, MCH1, orexin1, neuromedin-B, NPY 1 and 5, NT1 and 3, leptin long form PCR products of the appropriate size in GT1-7 cells, and no amplified fragments of receptor of orexin 2, NT2, and CCK-A cDNA were generated.

Effect of orexin A and B on release of GnRH from GT1-7 cells Using RT-PCR, we observed readily detectable orexin 1 receptor mRNA in GT1-7 cells. To verify whether orexin receptors play a physiological role in these cells, the effects of orexin A and B on the release of GnRH were subsequently investigated. GnRH secretion has previously been shown to be stimulated by orexin A from hypothalamic explants in male rats and females at proestrus. However, in GT1-7 cells, we were unable to detect a similar stimulated effect, neither orexin A nor orexin B affected basal GnRH secretion over a wide range of concentrations ranging from 1 nmol/L to 500 nmol/L for 15, 30, and 60 min. The positive control (56 mmol/L KCl) significantly increased GnRH release in this study.

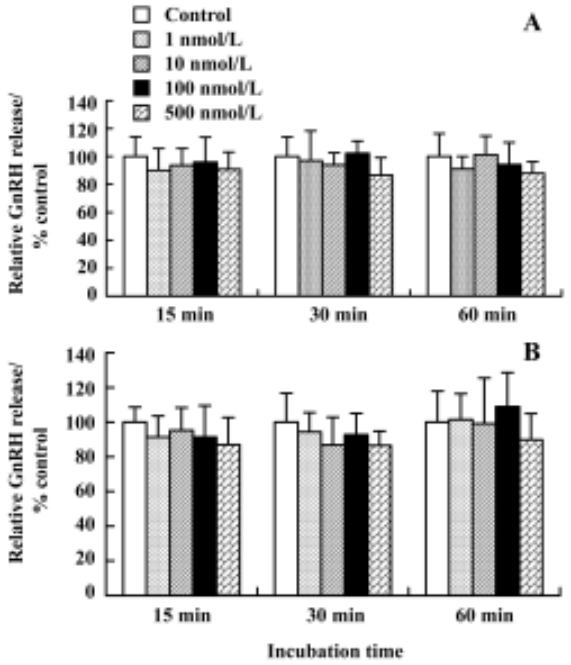

Figure 3. Neither orexin A nor orexin B cause a significant change in GnRH release levels in GT1-7 cells. GT1-7 cells were incubated for 15, 30, and 60 min in 1 mL Locke's medium with increasing concentrations of either orexin A (A) or orexin B (B). None of the values analyzed reached statistical significance (P>0.05).

Discussion

In mammals, hypothalamic control of food intake involves counter-regulation of appetite by orexigenic peptides and anorexigenic peptides, which are produced in the central nervous system and periphery. Several major orexigenic signals have been identified including NPY, the orexins, MCH, endorphins, galanin, growth hormone-releasing hormone, γ-aminobutyric acid, and agouti-related protein, similarly, a few major anorexigenic signals of recent interest include bombesin, glucagon-like peptide-1 (GLP-1), corticotropin-releasing hormone, CCK, cocaine and amphetamine-regulated transcript, serotonin, neurotensin, neuromedin α-melanocyte-stimulating hormone, leptin, ciliary neurotrophic factor, urocortin and dopamine[2], these essential messenger molecules serve as a communication bridge between neural processes that regulate reproduction and energy homeostasis.

The expression of feeding stimulant receptors mRNA of MCH, NPY, the orexins were detected first. Previous studies have shown that the GnRH-releasing effect of MCH is estrous-cycle stage dependent and it takes place only in proestrous rats[10]. MCH has been shown to bind and activate two G-protein-coupled receptors, called MCH receptor 1 and MCH receptor 2, expressed in the human brain and other tissues, but several non-human species (ie, rat, mouse, hamster, guinea pig, and rabbit) did not have functional MCH receptor 2 receptors, or encode a nonfunctional MCH receptor 2 pseudogene while retaining MCH receptor 1 expression[11]. We detected MCH receptor 1 mRNA in the GT1-7 cell line by RT-PCR, suggesting that MCH released from the median eminence might act directly on GnRH nerve terminals through MCH receptor 1. The NPY1 and NPY5 receptor subtypes are believed to play a role in appetite control[12,13]. There was evidence that NPY stimulated GnRH release from GT1-7 cells through a direct, Y1-like receptor-mediated action on the GnRH neuron itself[14], further research is needed to verify whether the NPY5 receptor exerts its effects at the hypothalamic level by regulating the release of GnRH.

Orexin A and B were first discovered in rats and found to increase feed intake in these animals when administered directly into the brain. Orexins orchestrate their actions by orexin-1 receptor and orexin-2 receptor. Orexin-2 receptor is a nonselective receptor that binds both orexin A and B, and orexin-R1 is highly selective for orexin A[15]. It was found that about 75%–85% of GnRH neurons contacted by orexin fibers and approximately 85% of GnRH neurons were colocalized with the orexin receptor 1, which provided the basis for a functional neuroanatomical pathway[16]. In whole hypothalamic tissue, orexin A stimulated GnRH release harvested from male rats and from females at proestrus, with no effect at estrus or metestrus[17]. To further investigate the mechanism underlying the orexins stimulating the release of GnRH, we used the GnRH immortalized cell line GT1-7 cells. However, we were unable to detect a similar stimulating effect of orexin A and B. the different effects observed in hypothalamic explants and GT1-7 cells could be explained by differences between GnRH neurons from animal tissue and cultured GnRH neurons.

The receptors of feeding suppressant including CCK,

bombesin, GLP-1, neuromedin, neurotensin and leptin were also observed. CCK is involved in the modulation/control of multiple central functions, these actions are mediated by at least two distinct receptors (CCK-A and CCK-B). The CCK-B receptor antagonist L-365,260, but not the CCK-A receptor antagonist L-364,718 infused into the medial preoptic area of recently mated females blocked pregnancy. These findings implicated CCK acting on CCK-B receptors in the medial preoptic area as a mediator of olfactory influenced on reproductive physiology[18], and was further supported by our findings that provided the first evidence of the presence of CCK-B receptor but not CCK-A receptor mRNA in total RNA isolated from GT1-7 cells.

The central GLP-1 system has been implicated in the control of feeding behavior. GLP-1 receptor has been identified in the medial and lateral preoptic areas, regions rich in GnRH neurons. The GLP-1 receptor knock-out mouse had delayed puberty[19]. We showed that GLP-1 receptor was highly expressed in GT1-7 cells, suggesting that GLP-1 may have a permissive role in the regulation of the reproductive axis.

Bombesin, neuromedin, and neurotensin are known to be essential to the regulation of feeding behavior. Neurotensin exerts its effects through at least three receptors that have been cloned and designated NT1 (high affinity), NT2 and NT3[20]. Dual-label in situ hybridization revealed that NT1 mRNA was expressed in some GnRH neurons in the OVLT/rPOA region, the percentage of dual-labeled neurons varied significantly depending on the stage of the cycle surge[21]. We demonstrated that NT1 and NT3 but not NT2 receptor sub-types were in fact expressed in GT1-7 cells. Bombesin and its structurally related peptide neuromedin-B belonged to negative regulators of appetite[22,23], the present study provided the first evidence of the presence of bombesin receptor 3 and neuromedin-B receptor mRNA in GT1-7 cells, strongly supporting the possibility that hypothalamic LHRH neurons in situ might also express these receptors. Studies are continuing to determine whether the receptors encoded by these mRNA mediate the actions of their neuropeptides on GnRH release from GT1-7 cells.

Leptin, a fat-derived anorexigenic hormone, has been described to be an important peripheral signal that indicates body fat stores to the hypothalamus and thus links nutrition and reproductive processes. Leptin treatment corrected infertility, hyperinsulinemia, and hyperglycemia of ob/ob mice, however, diet restriction alone is ineffective in restoring fertility to either female or male ob/ob mice, suggesting that obesity is not the sole cause of infertility and that leptin may be essential for normal reproductive function[24]. Our results seem to agree with others studies, reporting that treatment of GT1-7 cells with leptin stimulated the release of GnRH. Moreover, we found a rapid stimulation of leptin after 15 min of incubation, at concentrations of 0.1–100 nmol/L with moderate, but significant increments, which suggested a more direct and immediate modulation of GnRH release.

In summary, our results suggested that feeding-related peptide receptors of bombesin3, CCK-B, GLP1, MCH1, orexin1, neuromedin-B, NPY1, NPY5, NT1, NT3 and leptin long form mRNA were expressed in GT1-7 cells, in which, receptor of GLP1, neuromedin-B, NPY1 and NT3 were highly expressed. Additionally, no amplified fragments of orexin2, NT2 or CCK-A receptor cDNA were generated, indicating that the GT1-7 cells did not express mRNA for them. Leptin showed a rapid stimulating effect on GnRH release after 15 min incubation, and neither orexin A nor orexin B affected basal GnRH secretion from GT1-7 cells. The different effects of orexin A observed in hypothalamic explants and GT1-7 cells could be explained by differences between GnRH neurons from animal tissue and cultured GnRH neurons. These results, in accordance with previous findings, suggest that in addition to any indirect actions, feeding-related peptides may also exert their effects directly on hypothalamic GnRH neurons as a results of expression of their receptors mRNA. Feeding and reproductive function are closely linked.

References

1 Judd SJ. Disturbance of the reproductive axis induced by negative energy balance. Reprod Fertil Dev 1998; 10: 65–72.

2 Ordog T, Chen MD, O'Byrne KT, Goldsmith JR, Connaughton MA, Hotchkiss J, *et al*. On the mechanism of lactational anovulation in the rhesus monkey. Am J Physiol 1998; 274: E665–76.

3 Smith MS, Grove KL. Integration of the regulation of reproductive function and energy balance: lactation as a model. Front Neuroendocrinol 2002; 23: 225–56.

4 Blache D, Chagas LM, Blackberry MA, Vercoe PE, Martin GB. Metabolic factors affecting the reproductive axis in male sheep. J Reprod Fertil 2000; 120: 1–11.

5 Mellon PL, Windle JJ, Goldsmith PC, Padula CA, Roberts JL, Weiner RI. Immortalization of hypothalamic GnRH neurons by genetically targeted tumorigenesis. Neuron 1990; 5: 5–10.

6 Wetsel W. Immortalized hypothalamic luteinizing hormone-releasing hormone (LHRH) neurons: a new tool for dissecting the molecular and cellular basis of LHRH physiology. Cell Mol Neurobiol 1995; 15: 43–78.

7 Cui H, Lin SY, Belsham DD. Evidence that dehydroepiandrosterone, DHEA, directly inhibits GnRH gene expression in GT1-7 hypothalamic neurons. Mol Cell Endocrinol 2003; 203: 13–23.

8 Beltran-Parrazal L, Noris G, Clapp C, Martinez de la Escalera G. GABA inhibition of immortalized gonadotropin-releasing hormone neuronal excitability involves GABA(A) receptors negatively coupled to cyclic adenosine monophosphate formation.

Endocrine 2001; 14: 189–95.
9 Clemens LE, Kelch RP, Markovs M, Westhoff MH, Dermody WC. Analysis of the radioimmunoassay for gonadotropin-releasing hormone (GnRH): studies on the effect of radioiodinated GnRH. J Clin Endocrinol Metab 1975; 41: 1058–64.
10 Chiocchio SR, Gallardo MG, Louzan P, Gutnisky V, Tramezzani JH. Melanin-concentrating hormone stimulates the release of luteinizing hormone-releasing hormone and gonadotropins in the female rat acting at both median eminence and pituitary levels. Biol Reprod 2001; 64: 1466–72.
11 Tan CP, Sano H, Iwaasa H. Melanin-concentrating hormone receptor subtypes 1 and 2: species-specific gene expression. Genomics 2002; 79: 785–92.
12 Kanatani A, Mashiko S, Murai N, Sugimoto N, Ito J, Fukuroda T, *et al*. Role of the Y1 receptor in the regulation of neuropeptide Y-mediated feeding: comparison of wild-type, Y1 receptor-deficient, and Y5 receptor-deficient mice. Endocrinology 2000; 141: 1011–6.
13 Criscione L, Rigollier P, Batzl-Hartmann C, Rueger H, Stricker-Krongrad A, Wyss P, *et al*. Food intake in free-feeding and energy-deprived lean rats is mediated by the neuropeptide Y5 receptor. J Clin Invest 1998; 102: 2136–45.
14 Besecke LM, Wolfe AM, Pierce ME, Takahashi JS, Levine JE. Neuropeptide Y stimulates luteinizing hormone-releasing hormone release from superfused hypothalamic GT1-7 cells. Endocrinology 1994; 135: 1621–7.
15 Sakurai T, Amemiya A, Ishii M, Matsuzaki I, Chemelli RM, Tanaka H, *et al*. Orexins and orexin receptors: a family of hypothalamic neuropeptides and G protein-coupled receptors that regulate feeding behavior. Cell 1998; 92: 573–85.
16 Campbell RE, Grove KL, Smith MS. Gonadotropin-releasing hormone neurons coexpress orexin 1 receptor immunoreactivity and receive direct contacts by orexin fibers. Endocrinology 2003; 144: 1542–8.
17 Russell SH, Small CJ, Kennedy AR, Stanley SA, Seth A, Murphy KG, *et al*. Orexin A interactions in the hypothalamo-pituitary gonadal axis. Endocrinology 2001; 142: 5294–302.
18 Li CS, Kaba H, Saito H, Seto K. Cholecystokinin: critical role in mediating olfactory influences on reproduction. Neuroscience 1992; 48: 707–13.
19 MacLusky NJ, Cook S, Scrocchi L, Shin J, Kim J, Vaccarino F, *et al*. Neuroendocrine function and response to stress in mice with complete disruption of glucagon-like peptide-1 receptor signaling. Endocrinology 2000; 141: 752–62.
20 Rostene WH, Alexander MJ. Neurotensin and neuroendocrine regulation. Front Neuroendocrinol 1997; 18: 115–73.
21 Smith MJ, Wise PM. Neurotensin gene expression increases during proestrus in the rostral medial preoptic nucleus: potential for direct communication with gonadotropin-releasing hormone neurons. Endocrinology 2001; 142: 3006–13.
22 Maekawa F, Quah HM, Tanaka K, Ohki-Hamazaki H. Leptin resistance and enhancement of feeding facilitation by melanin-concentrating hormone in mice lacking bombesin receptor subtype-3. Diabetes 2004; 53: 570–6.
23 Williams G, Cardoso HM, Lee YC, Ball JM, Ghatei MA, Stock MJ, *et al*. Hypothalamic regulatory peptides in obese and lean Zucker rats. Clin Sci (Lond) 1991; 80: 419–26.
24 Mounzih K, Lu R, Chehab FF. Leptin treatment rescues the sterility of genetically obese ob/ob males. Endocrinology 1997; 138: 1190–3.

Acta Pharmacologica Sinica 2005 Aug; 26 (8): 982–986

Blackwell Publishing

Full-length article

Puerarin reduces increased c-fos, c-jun, and type IV collagen expression caused by high glucose in glomerular mesangial cells

Cai-ping MAO, Zhen-lun GU[1]

Department of Pharmacology, Suzhou Institute of Chinese Materia Medica,Medical College of Soochow University, Suzhou 215007, China

Key words

puerarin; glomerular mesangial cells; extracellular matrix; diabetic nephropathy

[1] Correspondence to Prof Zhen-lun GU
Phn/Fax 86-512-519-0599.
E-mail zhenlungu.2003@163.com

Received 2004-12-07
Accepted 2005-04-04

doi: 10.1111/j.1745-7254.2005.00133.x

Abstract

Aim: Increased expression of c-fos, c-jun and type IV collagen (CoIV) in glomerular mesangial cells (GMC) are important characteristics of diabetic nephropathy. Both c-fos and c-jun regulate the gene expression of extracellular matrix components, and CoIV is the main component of the extracellular matrix. It has been reported that puerarin inhibits aggregation of the extracellular matrix in diabetic rats by an as yet unknown mechanism. The aim of this study is to investigate the effect of puerarin on c-fos, c-jun and CoIV expression in GMC cultured in medium containing 5.6 or 27.8 mmol/L glucose. **Methods:** The expressions of c-fos and c-jun were measured at the protein level using flow cytometry. CoIV content was detected using radioimmunoassay. Protein kinase C (PKC) activity was measured using liquid scintillation counting. **Results:** Puerarin (10^{-5} mmol/L) significantly ameliorated the high-glucose effect on c-fos, c-jun and CoIV expression. This effect is accompanied by a reduced PKC activity in these cells. **Conclusion:** Our results suggest that reduced PKC activity and expression of c-fos and c-jun in GMC might participate in the mechanisms underlying the therapeutic effect of puerarin on diabetic nephropathy.

Introduction

Glomerular mesangial cells (GMC), the major cell type synthesizing and excreting extracellular matrix (ECM) components and various cellular factors, are one of the major indispensable glomerular cells. GMC proliferation can lead to the excess production and accumulation of ECM, whose progressive accumulation is an important character of diabetic nephropathy in its early stages, which can lead to glomerulosclerosis[1]. Recent data suggest that progressive ECM accumulation can be detected by increasing levels of *c-fos* and *c-jun* oncogene mRNA in the early stages of diabetic rats. The expression products of *c-fos* and *c-jun* form a steady dimer (activated protein-1, AP-1), which translocates from the cytosol to the cell membrane and binds to specific sequences of certain ECM gene promoters, regulating the transcription and expression of ECM components[2]. AP-1 activity can be regulated by various protein kinases as well as protein modulation after its synthesis and translocation. Protein kinase C (PKC) is an important molecule in cellular signaling transcription pathways, where it is located upstream of c-fos and c-jun. Diabetes-induced PKC activation can induce diabetic nephropathy, for example, by modifying cytoskeleton proteins, regulating ECM gene expression and promoting growth factor transcription[3,4].

Puerarin is one of the major effective extract from the radix of *Puerarin Lobata (wild) ohwi* and *P thomsonii Benth.* Modern pharmacology has demonstrated that puerarin can activate blood and eliminate stasis, improve micro-circulation, inhibit aldose reductase activity and decrease blood glucose. Furthermore, it has been shown to have clinical applications in the treatment of coronary heart disease, angina, myocardial infarction and diabetic nephropathy[5]. In the diabetic nephropathy rat model where the kidney is unilaterally removed, hypertrophy of the glomerular basement membrane and increased PKC activity of the glomerular membrane have been reported[3]. Puerarin can inhibit aggregation of the ECM and improve translocation of PKC to the cell membrane. However, it is not known whether high glucose regulates protein expressions of c-fos and c-jun by activating PKC,

nor has the underlying mechanism by which puerarin preventing against diabetic nephropathy been fully demonstrated. In the present study, we investigate changes in protein expressions of c-fos and c-jun, CoIV synthesis and PKC activity of GMC cultured under high glucose conditions. We also investigated puerarin's effect on these changes in order to explain the underlying mechanism by which diabetic nephropathy occurs and develops.

Materials and methods

Chemicals and reagents Puerarin was purchased from Guangdong Yantang Biochemistry (2 mL/100 mg, No 040310; Guangdong, China). Cell culture medium RPMI-1640 (containing 5.6 mmol/L or 27.8 mmol/L glucose) was purchased from Gibco (USA). Ethidium bromide and bromophenol blue were the products of Sigma (USA). CoIV radioimmunoassay analysis kit was the product of Shanghai Haiyan Medical Bio-tech Institute (No 20040328; Shanghai, China). Breaking membrane reagent, and c-fos and c-jun rabbit anti-rat monoclonal antibodies and goat anti-rabbit IgG-fluorescein-isothiocyanate (FITC) were purchased from Santa Cruz Inc (USA). PKC protein kinase assay kit was purchased from Gibco (No 20040220; USA).

Cell culture The rat GMC cell line[6] purchased from the Nephropathy Laboratory of the Second Military Medical University Changzheng Hospital (Shanghai, China) was plated in 10% RPMI-1640 containing 10% fetal bovine serum (FBS, Gibco), averaged into 2 culture containers (5 mL in each container), and cultured in a humidified atmosphere of 95% air and 5% CO_2 at 37 ºC. Before the experiment, cells were pre-incubated with RPMI-1640 culture medium without FBS. After 48 h, GMC were cultured and divided into five groups: (i) RPMI-1640 containing 5.6 mmol/L glucose; (ii) RPMI-1640 containing 27.8 mmol/L glucose; (iii) RPMI-1640 containing 27.8 mmol/L glucose+puerarin (10^{-5} mol/L); (iv) RPMI-1640 containing 27.8 mmol/L glucose+puerarin (1×10^{-6} mol/L); (v) RPMI-1640 containing 27.8 mmol/L glucose+puerarin (1×10^{-7} mol/L). Each group was incubated in 5% CO_2 at 37 ºC.

Detection of c-fos and c-jun protein expression in GMC using flow cytometry Glomerular mesangial cells (2×10^6) were collected after they were cultured for 24 h, 48 h, or 96 h. Breaking membrane reagent 1 (Santa Cruz Inc, USA) was added to cell pellets, which were homogenized, fixed at 25 ºC for 15 min, washed with phosphate-buffered saline (PBS) and centrifuged at 300×*g* for 5 min, and the supernatant was removed. Breaking membrane reagent 2 was then added to the remaining pellet, which was homogenized, dissolved at 25 ºC for 5 min and incubated with rabbit anti-rat c-fos or c-jun protein polyclonal antibodies for 30 min at 25 ºC. The first antibody was then washed out using PBS, and cells were incubated at 25 ºC for 20 min with goat anti-rabbit IgG-FITC. After the second PBS washes, cells were suspended in 0.5% formaldehyde and detected using a flow cytometer (Becton Dickinson Co, USA). The Cell Quest™ analysis system was used to detect c-fos and c-jun positive cells

Type IV collagen content in the supernatant of GMC After GMC (1×10^6) were cultured for 24 h, 48 h or 96 h, the supernatants from the cell cultures were collected to measure CoIV content using a competitive radioimmunoassay. Samples were homogenized with type-IV-collagen labeled by ^{125}I, incubated at 4 ºC overnight. The secondary antibody was then added to the assay system and incubated at 4 ºC for 60 min. The supernatant was removed by centrifugation at 10 000×*g* for 10 min and the radioactivity in the pellet was counted.

Protein kinase C activity After GMC (2×10^6) had been treated for 24 h, the homogenate was prepared with 2 mL PBS, and centrifuged at 100 000×*g* (4 ºC) for 1 h. The supernatant containing PKC from the cytosol, was collected and stored separately. PBS containing 0.1% Triton X-100 was added to the pellet. The mixture was bathed in ice, extracted for 30 min, centrifugated at 100 000×*g* (4 ºC) for 30 min, and the remaining particles are PKC. The protein content was measured using a coomassie brilliant blue assay (to quantify PKC activity), and PKC activity was measured using a liquid scintillation counter (LS2000; Beckman Coulter, USA). The units are presented as $pmol\cdot min^{-1}\cdot mg^{-1}$ protein.

Statistical methods Differences between groups were analyed by one-way ANOVA with SPSS 10.0 software, and the results were expressed as mean±SD. $P<0.05$ was considered to be statistically significant.

Results

Protein expressions of c-fos and c-jun in different GMC groups Of the GMC cultured in RPMI-1640 for 24 h, 48 h and 96 h, protein expression of c-fos and c-jun was higher in the 27.8 mmol/L glucose group than in the 5.6 mmol/L glucose group ($P<0.01$). At 24 h and 48 h, protein expression of c-fos and c-jun in cells cultured in RPMI-1640 containing 27.8 mmol/L glucose+puerarin (1×10^{-5} mol/L) decreased significantly compared with those cultured in 27.8 mmol/L glucose alone ($P<0.05$). At 96 h, protein expression of c-jun was still increased, but protein expression of c-fos decreased. At 48 h, protein expression of c-fos and c-jun in the 27.8 mmol/L glucose+puerarin (10^{-6} mol/L) group decreased markedly compared with cells cultured in RPMI-1640 containing 27.8 mmol/L glucose alone ($P<0.05$). These results suggest that

protein expression of c-fos and c-jun in GMC may be increased at an early stage after treatment with high concentrations of glucose (27.8 mmol/L), but the increase in c-jun expression was sustained for longer than that of c-fos, Puerarin can inhibit GMC protein expression of c-fos and c-jun under high concentrations of glucose (27.8 mmol/L) (Tables 1, 2)

Type IV collagen synthesis in different GMC groups At 24 h, 48 h and 96 h of the investigation, CoIV synthesis in the 27.8 mmol/L glucose group was higher than in the 5.6 mmol/L glucose group ($P<0.05$). CoIV synthesis in the 27.8 mmol/L group was also higher than in the 27.8 mmol/L glucose+ puerarin (10^{-5} and 10^{-6} mol/L) groups ($P<0.05$). These results indicate that high glucose concentrations (27.8 mmol/L) can increase CoIV synthesis in GMC, which can be partly inhibited by puerarin (Table 3).

Protein kinase activity in different GMC groups At 24 h and 48 h of the investigation, the PKC activity in the cytosol decreased. However, in the granule (which included membrane and nucleolus) of the high glucose concentration group (containing 27.8 mmol/L glucose), PKC activity was increased significantly compared with the low glucose concentration group (containing 5.6 mol/L glucose) ($P<0.01$). PKC activity in the membrane fraction from the high glucose

Table 3. Effect of puerarin on type IV collagen in glomerular mesangial cells. n=6. Mean±SD. $^bP<0.05$, $^cP<0.01$ *vs* 5.6 mmol/L glucose. $^eP<0.05$, $^fP<0.01$ *vs* 27.8 mmol/L glucose.

Group	Type IV collagen/μg·L^{-1}		
	24 h	48 h	96 h
Glucose (5.6 mmol/L)	38.26±5.13	57.67±7.28	68.21±9.04
Glucose (27.8 mmol/L)	45.18±6.15^b	67.55±6.45^b	90.45±10.32^c
Glucose (27.8 mmol/L) +puerarin (10^{-5} mol/L)	39.03±5.24^e	58.02±6.33^e	70.33±8.29^e
Glucose (27.8 mmol/L) +puerarin (10^{-6} mol/L)	40.12±5.46	59.39±7.51^f	77.96±9.21^f
Glucose (27.8 mmol/L) +puerarin (10^{-7} mol/L)	43.76±6.19	65.17±7.38	85.68±8.63

Table 1. Effect of puerarin on protein expression of c-fos in glomerular mesangial cells. n=5. Mean±SD. $^bP<0.05$, $^cP<0.01$ *vs* Glucose (5.6 mmol/L). $^eP<0.05$, $^fP<0.01$ *vs* Glucose (27.8 mmol/L). FI, fluorecence intensity; PPC, percentage of positive cells.

Group	24 h		48 h		96 h	
	FI	PPC	FI	PPC	FI	PPC
Glucose (5.6 mmol/L)	10.54±0.87	9.06±0.84	12.62±1.56	10.41±0.81	10.86±1.33	8.96±1.25
Glucose (27.8 mmol/L)	13.16±1.29^c	10.97±1.04^c	14.96±1.44^b	11.53±0.96^b	12.18±1.07	10.11±1.63
Glucose (27.8 mmol/L) +puerarin (10^{-5} mol/L)	10.62±0.91^f	9.51±0.87^f	13.12±0.95^e	10.28±0.71^e	11.38±1.43	9.56±1.39
Glucose (27.8 mmol/L) +puerarin (10^{-6} mol/L)	11.84±1.21	9.94±0.65	13.31±1.29^e	10.39±1.02^e	11.90±1.02	9.77±1.26
Glucose (27.8 mmol/L) +puerarin (10^{-7} mol/L)	12.81±1.35	10.42±0.92	14.51±0.82	10.81±0.82	11.88±0.95	10.03±1.04

Table 2. Effect of puerarin on protein expression of c-jun in glomerular mesangial cells. n=5. Mean±SD. $^bP<0.05$, $^cP<0.01$ *vs* Glucose (5.6 mmol/L). $^eP<0.05$, $^fP<0.01$ *vs* Glucose (27.8 mmol/L). FI, fluorescence intensity; PPC, percentage of positive cells.

Group	24 h		48 h		96 h	
	FI	PPC	FI	PPC	FI	PPC
Glucose (5.6 mmol/L)	14.98±0.72	10.65±0.92	15.04±0.76	10.40±0.68	15.82±0.67	10.91±1.37
Glucose (27.8 mmol/L)	19.06±0.88^c	10.97±1.18^c	19.13±1.02^c	14.32±0.94^c	17.36±1.42^b	12.73±0.89^b
Glucose (27.8 mmol/L) +puerarin (10^{-5} mol/L)	16.23±0.75^f	12.61±1.34^f	16.09±1.23^e	11.96±0.72^e	15.51±0.88^f	11.64±0.73^f
Glucose (27.8 mmol/L) +puerarin (10^{-6} mol/L)	17.79±0.91	13.67±0.85^e	17.43±0.81^f	12.99±0.82^f	15.96±1.21	11.76±0.81
Glucose (27.8 mmol/L) +puerarin (10^{-7} mol/L)	18.24±0.69	14.22±0.69	18.75±0.94	13.83±1.09	16.35±1.36	12.58±0.48

(containing 27.8 mmol/L glucose)+puerarin (10^{-5} mol/L) group decreased significantly compared with the high glucose concentration group (containing 27.8 mmol/L glucose). These results suggest that PKC can translocate from the cytosol of GMC to the membrane under conditions of high glucose concentrations, resulting in a sustained increase in PKC activity in the membrane. Puerarin can apparently inhibit such membrane translocation (Table 4).

Table 4. Effect of puerarin on protein kinase C (PKC) activity in glomerular mesangial cells. n=6. Mean±SD. $^{b}P<0.05$, $^{c}P<0.01$ *vs* 5.6 mmol/L glucose. $^{e}P<0.05$, $^{f}P<0.01$ *vs* 27.8 mmol/L glucose.

Group	PKC activity/pmol·min^{-1}·mg^{-1} protein		
	Cytosol	Membrane	Total
Glucose (5.6 mmol/L)	112.3±10.6	39.7±9.6	151.3±10.2
Glucose (27.8 mmol/L)	95.6±8.2^{c}	198.2±17.3^{c}	294.7±14.9^{c}
Glucose (27.8 mmol/L) +puerarin (10^{-5} mol/L)	108.2±6.3^{f}	59.1±8.9^{e}	168.5±8.1^{e}
Glucose (27.8 mmol/L) +puerarin (10^{-6} mol/L)	105.4±7.5^{e}	76.5±10.3^{e}	174.9±8.7^{e}
Glucose (27.8 mmol/L) +puerarin (10^{-7} mol/L)	97.2±6.4	91.7±7.2^{e}	189.2±6.7^{e}

Discussion

Recent studies demonstrate that abnormalities in GMC protein metabolism in various cells play a key role in the occurrence and development of diabetic nephropathy. GMC, the major cell type synthesizing and excreting ECM components and various cell factors, are a key factor in the occurrence and development of many diseases. The present study focused on GMC and discussed the excretion of CoIV, a main component of the ECM, on a cellular level when cells are exposed to high glucose concentrations. The results demonstrated that high glucose concentrations significantly increased CoIV content in GMC, which could be effectively inhibited by puerarin. These results are also supported by previous animal experiments[7].

We investigated the effect of high glucose on the protein expressions of c-fos and c-jun in mesangial cells. The results suggest that when GMC are treated with a high concentration of glucose (27.8 mmol/L) for 24 h and 48 h, nuclear protein expression levels are higher than following treatment with a low concentration of glucose (5.6 mmol/L). However, when treated with a high concentration of glucose (27.8 mmol/L) for 96 h, c-fos nuclear protein level is approximately the same as that in the low glucose concentration (5.6 mmol/L) group, while c-jun nuclear protein content continues to increase, which is the same result as in other studies[8]. This suggests that high concentrations of glucose can induce increases in c-fos and c-jun nuclear protein translocation.

In the condition of diabetes mellitus, hyperglycemia results in a series of metabolic disorders and plays a key role in the degeneration of nephrosis. There are many mechanisms by which high glucose concentrations exert pathological and physiological effects, one of which is the PKC signaling pathway. PKC normally exists in an inactive form in cytosol, and in an active form in the cell membrane and nucleus. An increase in PKC activity therefore suggests that PKC is translocated and activated. Various middle products, not involved in the progression of high blood glucose metabolism, can synthesize diacylglycerol (DAG), the main activator of PKC. Through a series of intracellular signaling pathways, such PKC activation can upregulate gene expression of ECM components, and further promote its protein expression[3,9,10]. When signals are translocated to the nucleolus, the transcription of certain genes is upregulated immediately. Most of these genes are protooncogenes whose expression products exert effects within the nucleolus. They can also encode certain key regulatory proteins and be distributed in various tissues and cells. The most important protooncogenes are the c-fos and c-jun gene expression products, all of which are phosphorylated proteins of middle molecular weight[4,11]. In cellular signaling pathways, PKC is an important molecule located upstream of c-fos and c-jun, both of which can participate in regulating gene expression of ECM components, such as CoIV, Fibronectin and laminin. In the promoter regions of the CoIV, FN and LN genes there are similar sites that can combine with c-fos and c-jun heterodimers. We chose GMC to investigate the effect of high glucose on c-fos and c-jun protein expression, and examine PKC activity in the membrane and cytosol of GMC under high glucose concentrations. The results indicate that at the early stage of high glucose treatment, protein expression products of c-fos and c-jun increase at the same time. However the duration of increased c-jun protein expression was longer than that of c-fos, as shown in the study of Shankland and Scholey[8]. At 24 h and 48 h of investigation, protein expression of c-fos and c-jun in GMC in the high concentration glucose+puerarin group was less than that of the high concentration glucose group, indicating that puerarin may inhibit the increase in c-fos and c-jun protein expression in GMC under the influence of high glucose concentrations. At 48 h, PKC activity in the cytosol of the high concentration glucose group was lower than that of the low concentration glucose group, but in the membrane fraction of the high concentration glucose group, PKC

activity was higher than that of the low concentration glucose group. As PKC activation involves translocation from the cytosol to the membrane, the total PKC activity increase indicated that high glucose concentrations could not only promote PKC activation, but also up-regulate PKC protein expression. Our results demonstrate that after the addition of high concentration glucose+puerarin into GMC culture, puerarin inhibits PKC activity increases in GMC membranes at high glucose concentrations, consistent with diabetic nephropathy rats PKC membrane translocation in animal experiments[7]. All of these results further suggest that protein expression of c-fos and c-jun is up-regulated in GMC at high glucose concentrations, and CoIV synthesis is increased, both of which could be induced by PKC activation. Puerarin effectively inhibits this upregulation.

In summary, high glucose concentrations could induce PKC membrane translocation in GMC leading to the up-regulation of c-fos and c-jun gene products, an increase in CoIV synthesis and aggravating the occurrence and development of diabetic nephropathy, all of which could be inhibited by puerarin. Undoubtedly, these results will provide a molecular and pharmacological basis for puerarin's development as a new drug against diabetic nephropathy.

References

1 Gao YJ, Yue ZJ, Yan LJ, Nan CH, Li DM. Effects of high glucose condition on expression of extracellular matrix of glomerular mesangial cells in rats. Sect Clin Biochem & Lab Med Foreign Med Sci 2004; 25: 99–101.

2 Kikkawa R, Koya D, Haneda M. Progression of diabetic nephropathy. Am J Kidney Dis 2003; 41: S19–21.

3 Haneda M, Koya D, Kikkawa R. Cellular mechanisms in the development and progression of diabetic nephropathy: activation of the DAG-PKC-ERK pathway. Am J Kidney Dis 2001; 38: 178–81.

4 Zhang L, Zhang L, Zhao GS. The regulation of AP-1 on mitosin activating protein kinase signaling pathway. Pathophysiol Clin Med 2002; 20: 32–5.

5 Mao CP, Gu ZL. Researches of puerarin on pharmacological effect and clinical application. Chin J Hemorh 2004; 14: 138–42.

6 Mei CL, Zhang LM, Chen L. Establish and identify rat mesangial cells. J Nephro Dial Transplant 1996; 5: 90–2.

7 Mao CP, Gu ZL, Cao L. Experimental studies on the effects and mechanisms of puerarin in diabetic uninephrectomized rats. Jiangsu Med J 2005; 31: 223–5.

8 Shankland SJ, Scholey JW. Expression of growth-related protooncogenes during diabetic renal hypertrophy. Kidney Int 1995; 47: 782–8.

9 Murphy M, McGinty A, Godson C. Protein kinase C: potential targets for intervention in diabetic nephropathy. Curr Opin Nephrol Hypertens 1998; 7: 563–70.

10 Koya D, King GL. Protein kinase C activation and the development of diabetic complications. Diabetes 1998; 47: 859–66.

11 Pariat M, Salvat C, Bebien M, Brockly F, Altieri E, Carillo S, *et al*. The sensitivity of c-Jun and c-Fos proteins to calpains depends on conformational determinants of the monomers and not on formation of dimers. Biochem J 2000; 345: 129–38.

Acta Pharmacologica Sinica 2005 Aug; 26 (8): 987–991

Full-length article

Protective effect of membrane cofactor protein against complement-dependent injury

Dong XU, Shou-jian HUANG[1], Jin-qun WANG, Chu-kun WU

Department of Pharmacology, Sun Yat-Sen Medical College of Sun Yat-Sen University, Guangzhou 510080, China

Key words

CD46 antigen; complement; heart; reverse Arthus reaction

[1]Correspondence to Prof Shou-jian HUANG.
Phn 86-20-8733-0553.
Fax 86-20-8733-0561.
E-mail hsjian@gzsums.edu.cn

Received 2005-03-21
Accepted 2005-04-11

doi: 10.1111/j.1745-7254.2005.00147.x

Abstract

Aim: To evaluate the protective role of membrane cofactor protein (MCP, CD46) on complement-dependent injury. **Methods:** MCP was separated by ion exchange chromatography on a DEAE sephadex A-50 column from pig erythrocyte ghosts. Its protective effect was tested in models such as cobra venom factor (CVF)-induced platelet metamorphosis and aggregation, human serum-induced injury in isolated working guinea pig heart and reverse passive Arthus reaction. **Results:** MCP inhibited CVF-induced platelet metamorphosis with an IC_{50} of 56.7 mg/L±2.6 mg/L, and prevented injury induced by activated complement in isolated working guinea pig hearts. In the rat model of reverse Arthus reaction, MCP relieved the skin lesions induced by immune complexes. **Conclusion:** MCP has a protective effect against complement-dependent injury.

Introduction

The first barrier to a successful xenograft is the hyperacute rejection (HAR), that is initiated by the activation of complement on the graft' vessel walls. The fragments of activated complement, such as C3a, C5a and membrane attack complex (MAC), promote blood coagulation and induce endothelial cell injury. Although drugs with anti-complement activity, such as heparin and FUT-175, have been used to prevent thrombosis, their clinical application is limited because they interfere with host blood coagulation or have other toxic effects. If the activation of complement is blocked, intravascular coagulation can be prevented effectively.

Membrane cofactor protein (MCP, CD46) belongs to the complement regulator protein family. It is located on the cellular membrane of all nucleated cells. MCP inhibits the activation of complement by combining with C3b/C4b and serves as a cofactor in their proteolytic cleavage by complement serine protease factor I. Generally, MCP function downregulates complement activation. Therefore, it is possible to prevent lesions caused by abnormal activated complement[1].

In this study, cobra venom factor (CVF), zymosan A and the ovalbumin (OVA)–anti-OVA complex were used as complement activators to observe the protective effect of MCP on complement-dependent lesions.

Materials and methods

Reagents and animals Cobra venom factor (CVF) was isolated and purified by successive column chromatography from the venom of *Naja naja* atra, as described previously[2]. DEAE-sephadex A-50 was purchased from Pharmacia, USA; β-mercaptoethanol, Coomassie brilliant blue R-250 and Nonidet P-40 were from Fluka, USA; acrylamide and *N*,*N*-methylene bisacrylamide was from Bio-Rad, USA; sodium azide, Evans blue dye, zymosan A and OVA were from Sigma, USA; rabbit anti-OVA from Chemicon; and benzanidine and phenylmethyl sulfonyl fluoride (PMSF) were from Amresco, USA. All chemicals were of analytical grade.

Blood was freshly obtained from pigs or sheep. O-type human plasma was purchased from the blood bank of the First Affiliated Hospital of Sun Yat-Sen University. Sprague-Dawley rats (Grade II, Certificate No 99A005), and New Zealand rabbits and guinea pigs (Certificate No 99A016, 99A015 conferred by the Medical Animal Management Committee, Guangdong Province) were provided by the Experimental Animal Center of Sun Yat-Sen University.

Isolation of membrane proteins from pig erythrocyte ghosts Pig erythrocytes were washed 3 times with phosphate buffered solution (PBS, in mmol: Na_2HPO_4 10.1, KH_2PO_4 1.7, NaCl 137, KCl 2.7; pH 7.4) and resuspended (1/10) in lysis buffer [in mmol: Na_2HPO_4 5, edetic acid (EDTA) 2,

benzanidine 1, Phenylmethylsulfonyl Fluoride (PMSF) 1, sodium azide 0.05%; pH 7.4]. After being stirred overnight at 4 ºC, the erythrocyte ghosts were concentrated (12 000×*g*, 4 ºC, 45 min), and washed again with lysis buffer (1:1) and centrifuged (12 000×*g*, 4 ºC, 45 min). The erythrocyte ghosts were then diluted 1/5 in PBS and extracted with 0.1% Nonidet P-40 at 4 ºC for 1 h. After centrifugation (12 000×*g*, 4 ºC, 30 min), the erythrocyte ghost extract was added to the top of a DEAE sephadex A-50 column (∅: 2.6 cm; L: 25 cm) and washed with PBS containing a NaCl concentration gradient from 0 to 1 mol/L. The flow-rate was 24 mL/h. The fraction corresponding to the second ultraviolet absorbance peak, which possessed anti-complement activity, was collected and stored.

Identification of MCP The molecular weight of MCP was determined according to R_f on reduced SDS-PAGE, stained with Coomassie brilliant blue R-250. CH_{50} was determined according to the absorbance of sensitized sheep erythrocytes incubated with fresh guinea pig plasma, to which a series of concentrations of MCP were added. Protein concentrations were determined by using the Coomassie brilliant blue R-250 method.

Platelet metamorphosis and aggregation The metamorphosis and aggregation of male guinea pig platelets in platelet rich plasma (PRP) were recorded by an aggrometer (Chrono-Log, USA) linked to a computer with an A/D converter. Platelet poor plasma (PPP) was used for a control. After the baseline was steady, MCP (0, 20, 40, 80, and 160 mg/L) was added to PRP 3 min before CVF (80 mg/L) to observe the aggregation line changes.

Isolated working guinea pig heart Male guinea pigs weighing 380 g±35 g (*n*=15) were divided randomly into three groups. The guinea pig hearts were removed quickly and then perfused in a retrograde manner with modified Krebs-Henseleit buffer (in mmol: NaCl 11.2, KCl 5.7, $MgCl_2$ 1.2, $CaCl_2$ 2.5, $NaHCO_3$ 26.2, Na_2-EDTA 0.5, glucose 11.0; pH 7.2) at 37 ºC, saturated by a mixture of 95% O_2 and 5% CO_2. After the heart began to beat again, a plastic cannula was inserted into the left atrium, and retrograde perfusion was changed to anterograde. Left ventricular pressure (LVP) was detected by a pressure transducer connected to the canal, which was inserted into the left ventricular cave. LVP, d*p*/d*t*, and heart rate (HR) were recorded by a polygraph (LMS-2A, Shanghai, China). Aortic flow (AF) was measured by an electromagnetic flowmeter (MFV-1200, Nihon Kohden, Japan), and coronary flow (CF) was measured manually. Cardiac output (CO) was defined as the sum of AF and CF.

After the CF became steady at 8 to 9 mL per min, we carried out the following treatment: 56 ºC preheated human plasma was added into perfusate in the negative control group. Human plasma pre-incubated with zymosan A was used for the positive control group. In group 3, human plasma was incubated with both MCP and zymosan A before being added.

Reverse passive Arthus reaction Anesthetized female rats (140 g–170 g, *n*=10) were given 0.6 mL of 0.9% NaCl solution iv, which contained 5 mg OVA and 2% Evans blue dye. Five minutes later, 0.1 mL PBS containing 0.5 mg rabbit-anti-OVA IgG with or without 0.4 mg MCP was injected sc on both sides of the back. Six hours later, rats were killed, and the area of dye leakage was measured. Skin samples were dissected, fixed with formalin, and then stained with hematoxylin and eosin.

Statistical analysis Statistical tests were performed using the *t*-test of SigmaPlot software. $P<0.05$ was considered to be statistically significant.

Results

Isolation of MCP A total of 2.1 mg MCP was gained from 100 mL pig erythrocytes. The molecular weight of MCP was determined to be 51 kDa according to the R_f value from SDS-PAGE. One anti-complement activity unit (CH_{50}) of MCP was 39.8±0.7 μg

Inhibition of CVF-induced platelet metamorphosis and aggregation MCP, at concentrations from 20 mg/L to 160 mg/L, dose-dependently inhibited the rat platelet metamorphosis induced by CVF (Figure 1). The linear regression equation was $Y=89.3\lg X-106.6$ (where Y is the inhibitory ratio percentage, and X is the concentration of MCP; $r=0.98$, $n=20$, $P<0.05$). The IC_{50} was 56.7±2.6 mg/L. MCP had little effect on CVF-induced platelet aggregation.

Protection of human complement-induced lesions on isolated working hearts Cardiac function parameters, namely LVP, d*p*/d*t*, CO, CF, AF, and HR, remained relatively stable for about 2 h in 56 ºC inactivated complement treatment (negative control group). In positive control group, hearts quickly became non-functional after zymosan A (16.7 mg/L) activated complement was added. CF, CO, LVP and d*p*/d*t* decreased markedly after 5 min (Figure 2; $P<0.05$ *vs* negative control group, $n=5$), and declined to their lowest levels at 30 min. Yet when 1.3 mg/L MCP was co-incubated with zymosan A and complement, no change was seen in the first 20 min ($P<0.05$ *vs* negative control group, $n=5$).

Reverse passive Arthus reaction In our study, vigorous infiltration of polymorphonuclear cells, perivascular cuffing and mini clots were seen in the skin lesions under light microscopy (Figure 3A,3B), and the skin lesion area (dye

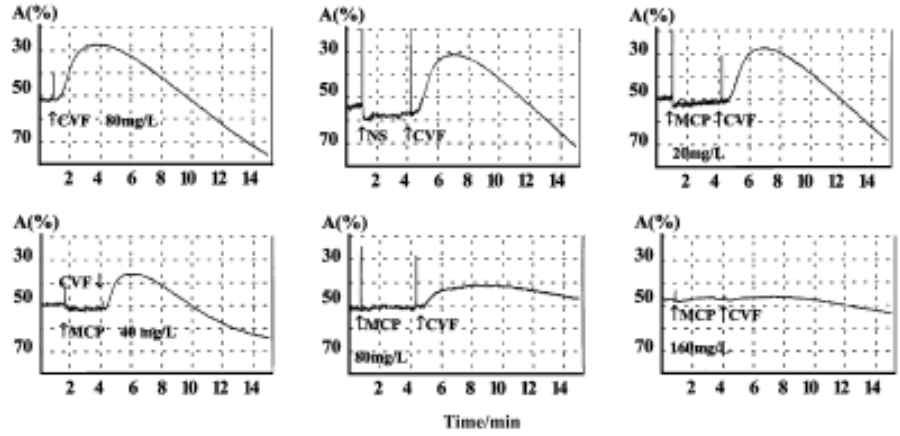

Fig 1. MCP dose-dependently inhibited rat platelet metamorphosis induced by CVF. CVF: cobra venom factor; NS: 0.9% NaCl solution; MCP: membrane cofactor protein; Y axis: A (absorbance) of PRP. The A raise means the increase of platelet metamorphosis. And its drop is the platelet aggregation; X axis: the duration of observation.

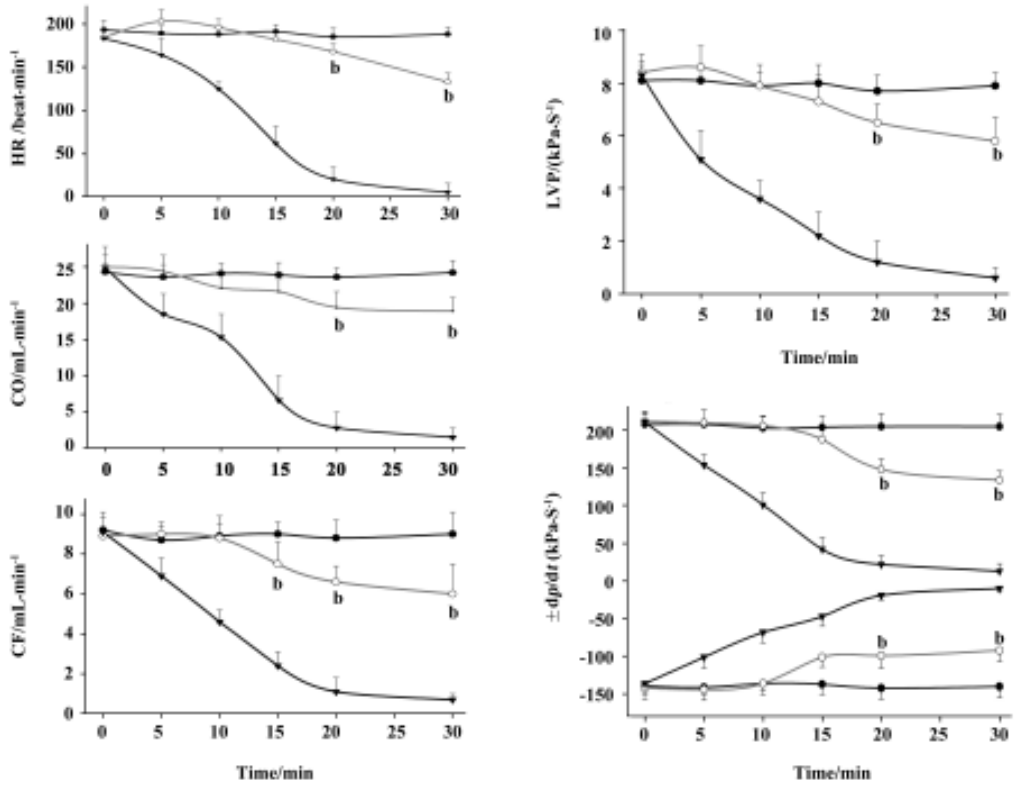

Fig 2. Changes of cardiac function parameters of isolated working hearts. ●: Negative control group: perfused with 56 ℃ inactivated human plasma. ▼: Positive control group: perfused with Zymosan A pre-incubated human plasma. ○: MCP treated group: perfused with MCP (1.3 mg/L) with Zymosan A pre-incubated human plasma. n=5. Mean±SD. ^bP<0.05 *vs* negative control group.

leakage indicating edema) was 330 mm^2±15 mm^2 in size (n=5). The skin lesion area in the MCP-treated group, 149 mm^2±10 mm^2 in size, was smaller (P<0.05 *vs* control, n=5). The inflammatory reaction (cellular infiltrate) was less than that in the control group and no clotting or perivascular cuffing was found (Figure 3C, 3D), which suggests that MCP signifi-

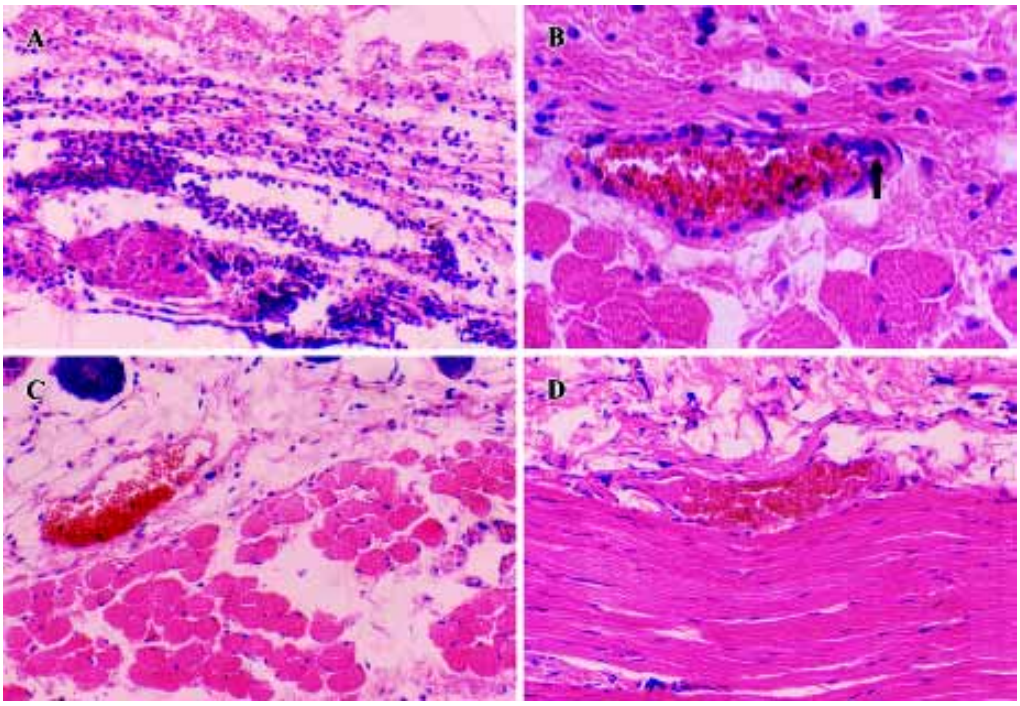

Figure 3. MCP (0.4 mg) prevented inflammatory cellular infiltrate in reverse passive arthus reaction; Control group (A, B): polymorphonuclear cells, perivascular cuffing and mini clot was seen; MCP-treated group (C, D): inflammatory cellular infiltrate was obviously lightened. HE Stain, ×100.

cantly reduced the extent of inflammatory injury.

Discussion

MCP is widely distributed on epithelial and endothelial cells, cells originating from fibroblasts, and all animal blood cells except human erythrocytes[3]. Because it is more abundantly expressed on erythrocytes from pigs than on those from other animals, the MCP used in this study was derived from pig erythrocytes. Structurally, pig-derived MCP amino acid sequence has 43% homology with human-derived MCP[4], and it has no *N*-glycosylation site in the second repeated motif (short consensus repeat, SCR), which serves as a measles receptor. Because it is a safer complement inhibiting factor than human-derived MCP, pig-derived MCP was worth testing for its protective action in complement-dependent injury. The DEAE sephadex A-50 anion exchange column is able to separate proteins by both their charge and molecular weight. Although one-step anion exchange separation can result in only impure proteins, in our study, the pig-derived MCP did shown the complement regulation ability, more importantly, the high yield made continuation of our experiment possible.

CVF can activate complement through an alternative pathway: its terminal product MAC can induce platelet metamorphosis and express binding sites for the coagulation factors Va and Xa on platelet membranes, triggering coagulation[5]. In the present study, MCP inhibited the platelet metamorphosis induced by MAC. Thus, MCP can be used to prevent the intravascular coagulation initiated by activated complement. Decay-accelerating factor (DAF, CD59), another complement-regulating protein, has been reported to have a similar effect[2].

We further investigated the anti-complement effect of MCP *in vivo* and *in vitro*. The isolated working heart was an *in vitro* model of HAR. When zymosan A-treated serum reached the coronary vessel wall, the complement was activated and then cascade responses initiated the HAR, causing the hearts to fail quickly. However, when MCP was preincubated, it inhibited the complement activation by zymosan A. Thus, hemodynamic indexes such as LVP, d*p*/d*t*, HR , CO and CF, were well maintained. This observation shows that MCP protects the isolated working heart from complement injury. DAF has also been found to have a similar protective effect[6]. The above facts show that downregulating complement activation is an effective way to alleviate the HAR.

The reverse passive Arthus reaction is an *in vivo* model

of HAR, and it refers a type III immune complex mediated hypersensitivity reaction that occurs following the intradermal injection of antigen in the presence of a high level of circulating antibody. In that process, antigen-antibody complex also activated complement. The histological lesions in the MCP-treated group were smaller than those in the control group, suggesting that MCP blocks the classical pathway of complement activation. This finding corresponds with that of an earlier report about blockades preventing monocyte activation and anaphylatoxin damage[7].

Because of its antigenicity, MCP is not completely safe for clinical uses. To improve its safety, further research and chemical modifications are required. Recently, a human transgenic pig model has been established, and it has been shown that HAR in xenotransplantation is suppressed to a large degree[8,9,].

In summary, we showed that MCP alleviated complement-mediated injury. Preventing the activation of complement is an effective method to ameliorate such complement-mediated injury.

References

1 Song WC. Membrane complement regulatory proteins in autoimmune and inflammatory tissue injury. Curr Dir Autoimmun 2004; 7: 181–99.

2 Gu YJ, Huang SJ, Sun JJ. Fractionation of CD59 from human erythrocyte membrane and protection on complement-dependent platelet injury. Chin Pharma Bull 1998; 14: 512–15.

3 Liszewski MK, Post TW, Atkinson JP. Membrane cofactor protein (MCP or CD46): newest member of the regulators of complement activation gene cluster. Annu Rev Immunol 1991; 9: 431–55.

4 Toyomura K, Fujimura T, Murakami H, Natsume T, Shigehisa T, Inoue N, *et al*. Molecular cloning of a pig homologue of membrane cofactor protein (CD46). Int Immunol 1997; 9: 869–76.

5 Gorbet MB, Sefton MV. Biomaterial-associated thrombosis: roles of coagulation factors, complement, platelets and leukocytes. Biomaterials 2004; 25: 5681–703.

6 Wu SH, Ma H, Huang SJ, Dong YG, Wu CK, Sun JJ. CD59 prevents human complement-mediated injuries in isolated guinea pig hearts. Chin Med J (Engl) 2002; 115: 175–8.

7 Rinder CS, Rinder HM, Johnson K, Smith M, Lee DL, Tracey J, *et al*. Role of C3 cleavage in monocyte activation during extracorporeal circulation. Circulation 1999; 100: 553–8.

8 Diamond LE, Quinn CM, Martin MJ, Lawson J, Platt JL, Logan JS. A human CD46 transgenic pig model system for the study of discordant xenotransplantation. Transplantation 2001; 71: 132–42.

9 Loveland BE, Milland J, Kyriakou P, Thorley BR, Christiansen D, Lanteri MB, *et al*. Characterization of a CD46 transgenic pig and protection of transgenic kidneys against hyperacute rejection in non-immunosuppressed baboons. Xenotransplantation 2004; 11: 171–83.

Acta Pharmacologica Sinica 2005 Aug; 26 (8): 992–999

Full-length article

Protective effects of *L*-arginine on pulmonary oxidative stress and antioxidant defenses during exhaustive exercise in rats[1]

Wan-teng LIN[2,5], Suh-ching YANG[3], Kung-tung CHEN[4], Chi-chang HUANG[3], Ning-yuean LEE[2,6]

[2]Department of Nutrition and Food Sciences, Fu-Jen Catholic University, Taipei, China; [3]School of Nutrition and Health Sciences, Taipei Medical University, Taipei, China; [4]Department of General Education, Ming Hsin University of Science and Technology, Hsinchu, China; [5]De Lin Institute of Technology, Taipei, China

Key words

L-arginine; oxidative stress; xanthine oxidase; myeloperoxidase; exhaustive exercise; lung

[1] Project supported by grants from the National Science Council of Taiwan (No NSC 92-2413-H-030-009).
[6] Correspondence to Prof Ning-yuean LEE.
Phn 886-2-2905-2503.
Fax 886-2-2904-3234.
E-mail als2046@mails.fju.edu.tw

Received 2005-01-26
Accepted 2005-05-02

doi: 10.1111/j.1745-7254.2005.00155.x

Abstract

Aim: To assess the effects of *L*-arginine (*L*-Arg) supplementation on pulmonary oxidative stress and antioxidant defenses in rats after exhaustive exercise. **Methods:** Rats were randomly divided into four groups: sedentary control (SC), sedentary control with *L*-Arg treatment (SC+Arg), exhaustive exercise with control diet (E) and exhaustive exercise with *L*-Arg treatment (E+Arg). Rats in groups SC+Arg and E+Arg received a 2% *L*-Arg diet. Rats in groups E and E+Arg underwent an exhaustive running test on a motorized treadmill. Pulmonary oxidative stress indices [xanthine oxidase (XO), myeloperoxidase (MPO), and malondialdehyde (MDA)] and antioxidant defense systems [superoxide dismutase (SOD), catalase (CAT), glutathione peroxidase (GPX), glutathione reductase (GR), and glutathione (GSH)] were investigated in this study. **Results:** *L*-Arg supplementation significantly reduced exercise-induced elevations of XO and MPO activities in lung. *L*-Arg reversed the exercise-induced increase in SOD and GR activities, but increased CAT and GPX activities. *L*-Arg administration also significantly increased the GSH levels in plasma. **Conclusion:** *L*-Arg supplementation can prevent elevations of XO and MPO activities in the lung and favorably influence pulmonary antioxidant defense systems after exhaustive exercise.

Introduction

In recent years, it has been shown that *L*-arginine (*L*-Arg) serves as a precursor to the synthesis of NO and may participate in amino acid metabolism[1]. Most pharmacological actions of *L*-Arg are attributed to nitric oxide (NO), and NO has various physiological properties including vasodilatation, inhibition of platelet aggregation and neutrophil adhesion, scavenging superoxide ($O_2^{\cdot-}$) formation and suppression xanthine oxidase (XO)[2,3]. More recently, *L*-Arg has shown protective role against reactive oxygen radical (ROS) attack as a result of its interaction with $O_2^{\cdot-}$ *in vitro*[4]. There is evidence that *L*-Arg is closely linked to protective properties against oxidative stress[5,6]. Furthermore, *L*-Arg administration to rats prevented pulmonary neutrophil accumulation and preserved pulmonary endothelial function after endotoxin[7]. The XO activity of pulmonary artery endothelial cells decreased using *L*-Arg, suggesting that NO generated in the endothelial cells negatively regulates this enzyme[8].

Strenuous physical exercise may be associated with a 10- to 20-fold increase in whole body oxygen consumption and oxidative stress shown in both human and experimental animal studies[9,10]. The mitochondrial electron transport chain, XO and neutrophils of inflammatory response have been identified as major sources of intracellular free radical generation during exercise[11]. XO, a metalloflavoprotein, is an important source of ROS. The enzyme catalyzed the reduction of O_2, leading to the formation of $O_2^{\cdot-}$ and H_2O_2 , and it has been proposed as a major mechanism of oxidative injury[12]. Reddy *et al* reported that XO activity and lipid peroxides increased in the lung tissue after exhaustive swimming exercise[13]. In addition, the activity of glutamine synthetase and reactive carbonyl derivatives enhanced in the

rat lung during exhaustive running[14]. Similarly, activated neutrophils are known as a major source of ROS[15]. Neutrophils are capable of further generation of ROS through NADPH oxidase and producing hypochlorous acid from H_2O_2 through MPO reaction[16]. The NADPH oxidase system has been shown to be activated in response to various stimuli that can be provoked by strenuous exercise[17]. However, the lung tissue presents a significant first target of free radical species and gas exchange function of the respiratory system during exercise. Thus, the lung may be more vulnerable to oxidative damage as a result of exercise. Nevertheless, the pulmonary system has a series of defense mechanisms including SOD, CAT, GPX, GR, and GSH to protect the cell against these toxic oxygen metabolites, such as $O_2^{\cdot-}$, H_2O_2 and hydroxyl radicals ($OH^{\cdot}$). Strenuous exercise generated ROS seems to increase the activity of antioxidant enzymes and decrease GSH levels in the muscle and heart[18], possibly as a compensatory mechanism to cope with oxidative stress induced by exhaustive running.

However, the roles of *L*-Arg administration in exhaustive exercise-induced oxidative damage and inflammatory response in lung tissues are still not clear. Therefore, we studied whether *L*-Arg administration can protect lung tissue and have beneficial effects on ameliorating exercise-induced oxidative stress and reserve antioxidant defense capability in the lung of rats.

Materials and methods

Animals and treatment Adult male Sprague-Dawley rats (n=32), weighing 280–300 g and aged 8 weeks old, were purchased from the National Laboratory Animal Breeding and Research Center (Taipei). All rats were given standard rat chows and tap water *ad libitum* and housed at 23±2 °C on a 12:12-h dark-light cycle in the first week. This experiment was approved by the Fu-Jen Catholic University Animal Care and Usage Committee and followed the guidelines established by the National Laboratory Animal Breeding and Research Center in Taiwan. In the second week, in order to adapt to the experimental standard diet, all rats were fed AIN-93 purified diet[19]. Rats were then randomly divided into four groups: sedentary group with control AIN-93 diet (SC, n=8); sedentary group with AIN-93 containing 2% *L*-Arg diet (SC+Arg, n=8); exhaustive exercise with control AIN-93 diet (E, n=8); and exhaustive exercise with AIN-93 containing 2% *L*-Arg diet (E+Arg, n=8). Rats were fed diets for 30 d beginning from the third week. Both diets were identical in calorie content (Table 1)[19,20].

Exercise protocol All rats in the two exercise groups were introduced to treadmill running with 15–20 min exercise bouts at 15–30 m/min for 6 d to accustom them to running. In the formal run, the rats were warmed up for 15 min running at a speed of 15 m/min. They then progressed to running for 15 min at 20 m/min and 30 min at 25 m/min. They were then made to run to exhaustion at a final speed of 30 m/min, 10% grade, approximately 70%–75% VO_{2max}[21]. The treadmill was equipped with an electric shock grid on the rear barrier to provide the animal with exercise motivation (using a T510E treadmill device; DR Instrument, Taipei). The point of exhaustion was determined by the loss of righting reflex when turned on its back. To eliminate diurnal effects, the experiments were performed at the same time (09:00–12:00 h). It is also well known that exercise performance is limited by the increase of body temperature during exercise. In order to eliminate this complicating factor, all running tests were conducted in an environmental chamber at 10–12 °C to reduce undue rise in body temperature caused by sustained exercise. All animals were anesthetized with ethyl ether and killed immediately after exhaustive exercise. Blood was collected through the abdominal aorta, and lung tissues were stored at -80 °C for further analysis. All chemicals used in this study were purchased from Sigma Chemical (St Louis, MO, USA) unless otherwise stated.

Table 1. Composition of diets[1].

Ingredient/g·kg^{-1}	Sedentary control		Exhaustive exercise	
	SC	SC+Arg	E	E+Arg
Casein	200	200	200	200
L-Cystine	3	3	3	3
L-Arginine	0	16	0	16
Corn starch	397.5	381	397.5	381
Maltodextrin	132	132	132	132
Sucrose	100	100	100	100
Soybean oil	70	70	70	70
Cellulose	50	50	50	50
AIN-93 mineral mix	35	35	35	35
AIN-93 vitamin mix	10	10	10	10
Choline bitartrate	2.5	2.5	2.5	2.5
Tert-Butylhydroquinone	0.014	0.014	0.014	0.014

[1] Components for the diets were purchased from ICN Biochemicals (Costa Mesa, CA, USA) with the exception of *L*-arginine, sucrose and soybean oil which were obtained from Sigma (St Louis, MO, USA). American Institute of Nutrition (AIN).

Plasma parameters Blood samples were centrifuged at 1400×g at 4 °C for 10 min. The supernatants (plasma) were used for determination of uric acid (UA) with an automatic analyzer (Hitachi 7170; Hitachi, Tokyo, Japan). In addition,

nitrate/nitrite (NOx) levels in plasma were quantified by using the Griess reagent to measure nitrite ion concentration[22]. NOx concentrations in plasma were measured spectrophotometrically at 550 nm according to a previous study[23].

Total protein concentration of lung tissues In order to express the antioxidant enzyme activities per gram of protein, total protein concentration of tissue samples was spectrophotometrically estimated using a Bio-Rad DC protein assay kit (Cat No 500-0116; Bio-Rad Laboratories, Hercules, CA, USA).

Assay of xanthine oxidase activity in lung tissues XO (EC.1.2.3.2) activities of tissue samples were determined using the method outlined by Westerfeld *et al*[24]. A diluted sample was added to 0.1 mmol/L xanthine (dissolved in 50 mmol/L sodium phosphate buffer, pH 7.5). XO activity was measured at 25 °C on a Hitachi U-2000 Spectrophotometer at 290 nm for 3 minutes. A unit of XO activity was to form one mmmol of urate per minute at 25 °C. XO activity was expressed as U·g protein^{-1} for specific activity.

Assay of myeloperoxidase activity in lung tissues MPO (EC.1.11.1.7) activities of tissue samples were determined as a marker enzyme for measuring neutrophil accumulated in tissue samples, because correlates closely with the number of neutrophils present in the tissue[25]. MPO activity was determined using the method described by Schierwagen *et al*[26]. Fifty microlitre of diluted sample was added to 1 mL of mixed substrate containing 3 mmol/L hydrogen peroxide dissolved in 3,3',3,5'-tetramethylbenzidine (R&D Systems, Minneapolis, MN, USA). MPO activity was measured at 37 °C on a Hitachi U-2000 Spectrophotometer at 655 nm for 3 min. One unit of MPO activity was defined arbitrarily as the amount of enzyme necessary to catalyze an increase in absorbance of 1.0 at 655 nm per minute at 37 °C. MPO activity was expressed as U·mg protein^{-1} for specific activity.

Lipid peroxidation in plasma and lung tissues The malondialdehyde (MDA) concentrations of plasma and tissue samples were assessed colorimetrically at 586 nm using a commercial kit (Calbiochem 437634; Calbiochem-Novabiochem, La Jolla, CA, USA). The concentration was expressed in μmol/L in plasma and in μmol·mg protein^{-1} in lung tissues.

Assay of superoxide dismutase activity in lung tissues SOD (E.C.1.15.1.1) activities of tissue samples were measured with a commercial kit (SD 125; Randox Laboratories, Antrim, UK). Fifty microlitre of diluted sample was added to 1.7 mL of mixed substrate (50 μmol/L xanthine and 25 μmol/L 2-(4-iodophenyl)-3-(4- nitrophenol)-5-phenyltetrazolium chloride, INT). Two hundred and fifty microlitre of XO were added to the mixture and SOD was measured at 37 °C on a Hitachi U-2000 Spectrophotometer at 505 nm for 3 min. Activity was expressed as U·mg protein^{-1} for specific activity.

Assay of catalase activity in lung tissues CAT (EC.1.11.1.6) activities of tissue samples were determined at 25 °C with Hitachi U-2000 Spectrophotometer UV-VIS spectrophotometer using the method described by Beers and Sizer[27]. A diluted sample was added to 59 mmol/L hydrogen peroxide (dissolved in 50 mmol/L potassium phosphate buffer, pH 7.0) and CAT was measured at 240 nm for 3 min. One unit of CAT activity was defined as the H_2O_2 degraded (mmol·min^{-1}·mg protein^{-1}). Activity was expressed as U·mg protein^{-1} for specific activity.

Assay of glutathione peroxidase activity in lung tissues GPX (EC.1.11.1.9) activities of tissue samples were determined with a commercial kit (RS 504; Randox Laboratories, Antrim, UK). Twenty microlitre of diluted sample was added to 1 mL of mixed substrate. Forty microlitre of cumene hydroperoxide (diluted in deionized water) was added to the mixture and GPX was measured at 37 °C with a Hitachi U-2000 Spectrophotometer at 340 nm for 3 min. Activity was expressed as U·mg protein^{-1} for specific activity.

Assay of glutathione reductase activity of lung tissues GR (E.C.1.6.4.2) activity of tissue samples was measured with a commercial kit (Calbiochem 359962; Calbiochem-Novabiochem). Two hundred mmL of diluted sample was added to 400 μL of 2.4 mmol/L GSSG buffer (dissolved in 125 mmol/L potassium phosphate buffer, pH 7.5, 2.5 mmol/L EDTA). Four hundred mmL of 0.55 mmol/L NADPH (dissolved in deionized water) was added to the mixture and GR activity was measured at 340 nm for 5 min on a Hitachi U-2000 Spectrophotometer. The activity was expressed in mU·g protein^{-1} in tissue samples.

Assay of glutathione levels in plasma and lung tissues The concentrations of GSH in plasma and tissue samples were measured spectrophotometrically at 400 nm using a commercial kit (Calbiochem 354102; Calbiochem-Novabiochem, La Jolla, CA, USA). The concentration was expressed in μmol/L in plasma and in μmol·mg protein^{-1} in tissue samples.

Statistical analysis Values were expressed as mean± SEM. To evaluate differences between the groups, two-way analysis of variance (ANOVA) with Fisher's *post hoc* test was used. The SAS software (version 8.2, SAS Institute, NC, USA) was used to analyze all data. Differences were considered statistically significant when $P<0.05$.

Results

Bodyweight and endurance time On d 30, bodyweight in the groups SC, SC+Arg, E and E+Arg were 446±7, 446±10,

447±6, and 451±8 g, respectively. There was no significant difference in bodyweight between the 4 groups. The mean endurance time of treadmill running to exhaustion was 81±4 min for the group E and 87±5 min for the group E+Arg, which showed no significant difference between the 2 groups.

XO and MPO activities of lung tissues The XO and MPO activities of lungs in group E were significantly elevated by 113% and 55%, respectively, compared to those in the SC group (P<0.05). In contrast, the XO and MPO activities of lungs in the E+Arg group were significantly reduced by 65% and 24%, respectively, compared with those in the E group (P<0.05). Furthermore, there was no difference between the SC+Arg and E+Arg groups (Figure 1).

Uric acid and nitrite/nitrate concentrations of plasma The UA concentration of plasma in the E and E+Arg groups were significantly increased by 268% and 41%, respectively, compared with those in the SC and SC+Arg groups (P<0.05). Although, the UA concentration of plasma in the SC+Arg group was significantly increased compared with the SC group. This indicated that exogenous *L*-Arg may elevate UA in the plasma, and reduce UA excretion. However, *L*-Arg supplement might ameliorate UA concentration in plasma after exercise (Table 2). The NOx concentrations of plasma in the E and E+Arg groups were significantly increased by 93% and 82%, respectively, compared with those in the SC and SC+Arg groups (P<0.05). However, there was no difference between the SC and SC+Arg or E and E+Arg groups (Table 2).

MDA levels of plasma and lung tissues The MDA levels of the plasma and lung showed no changes between SC+Arg and E+Arg groups. In contrast, the MDA levels of plasma and lung in the E group were significantly increased by 81% and 32%, respectively, compared to those in the SC group (P <0.05). There was a slight but not significant decrease in the MDA level of plasma in the E+Arg group compared to that in the E group (P>0.05) (Table 3).

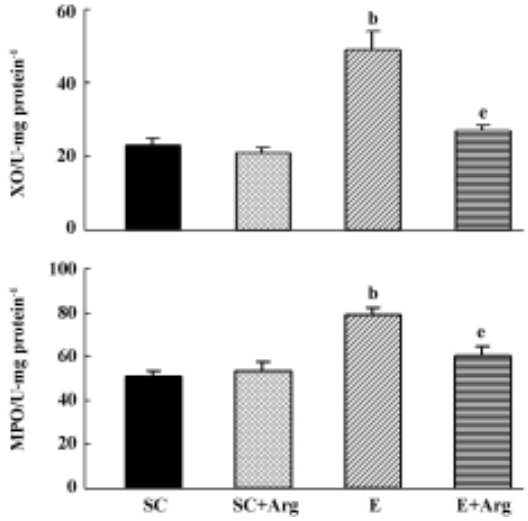

Figure 1. Effects of *L*-arginine supplementation on xanthine oxidase (XO) and myeloperoxidase (MPO) activities of lung tissue after exhaustive exercise. Mean±SEM. n=8. ^bP<0.05 *vs* group SC. ^eP<0.05 *vs* group E.

Antioxidant enzymes activities of lung tissues Table 4 shows the antioxidant enzyme activities. The E+Arg group had significantly higher GPX and CAT activities by 19% and 25%, respectively, than the group E (P<0.05), but showed no difference when compared with the SC+Arg group. Furthermore, the GRD and SOD activities of the E group were significantly elevated by 44% and 96%, respectively, compared with those of the SC group (P<0.05), but they were significantly reduced by 35% and 58%, respectively, in the E+Arg group compared with the E group (P<0.05).

GSH concentrations of plasma and lung tissues The GSH concentration of plasma showed no change between

Table 2. Effects of *L*-arginine supplementation on uric acid (UA) and nitrate/nitrite (NOx) levels of plasma after exhaustive exercise. Mean±SEM. n=8. ^bP<0.05 *vs* group SC. ^eP<0.05 *vs* group SC+Arg.

	Sedentary control		Exhaustive exercise	
	SC	SC+Arg	E	E+Arg
UA/mg·dL^{-1}	0.94±0.1	1.99±0.28	3.5±0.3^b	2.8±0.2
NOx/μmol·L^{-1}	1.38±0.14	1.48±0.20	2.7±0.2^b	2.7±0.5^c

Table 3. Effects of *L*-arginine supplementation on malondialdehyde (MDA) concentrations of plasma and lung tissues after exhaustive exercise. n=8. Mean±SEM. ^bP<0.05 *vs* group SC. ^eP<0.05 *vs* group E.

	Sedentary control		Exhaustive exercise	
	SC	SC+Arg	E	E+Arg
Plasma MDA/μmol·L^{-1}	3.9±0.3	4.9±0.6	7.0±0.7^b	5.16±0.62^e
Lung MDA/μmol·mg protein^{-1}	22±1	24±2	29±2^b	26±2

Table 4. Effects of *L*-arginine supplementation on antioxidant enzymes superoxide dismutase (SOD), catalase (CAT), glutathione peroxidase (GPX), and glutathione reductase (GR) activities of lung tissues after exhaustive exercise. Mean±SEM. $^{b}P<0.05$ *vs* group SC. $^{e}P<0.05$ *vs* group E.

	Sedentary control		Exhaustive exercise	
	SC	SC+Arg	E	E+Arg
SOD/U·mg protein^{-1}	3.2±0.6	2.2±0.8	6.3±1.6^{b}	2.6±0.7^{e}
CAT/U·mg protein^{-1}	23±1	25±1	20±2	25±1^{e}
GPX/U·mg protein^{-1}	87±4	98±5	95±5	113±8^{e}
GR/mU·g protein^{-1}	16±1	13±1	23±1^{b}	15±1^{e}

SC+Arg and E+Arg groups. In contrast, the GSH concentration of plasma in the E group was significantly decreased by 25% compared with the SC group ($P<0.05$). Moreover, the GSH concentration of plasma in the E+Arg group was significantly increased by 31% compared with the E group ($P<0.05$). However, there was no difference in the GSH concentration of lungs in any group (Table 5).

Discussion

The lung represents the front line of defense against a number of airborne toxicant and oxidant stress because it is directly exposed to higher oxygen tensions. In this study, we investigated whether *P*-Arg supplementation attenuates exhaustive exercise-induced pulmonary oxidative stress. More recently, there has been some evidence to show that strenuous exercise simulates the condition of heart I/R and may activate the XO pathway[28,29]. Hypoxanthine and UA are known to elevate in plasma during high intensity exercise[30]. Our results indicate that in exhaustive exercise with higher anaerobic components, the lactate concentrates in the plasma of the E group (E: 76±6 mg/dL *vs* SC: 55±4 mg/dL, $P<0.05$), but not in the E+Arg group. XO activity in the lung and plasma UA levels was also significantly increased in group E ($P<0.05$). Our data are consistent with previously published reports[30,31].

According to Yokoyama *et al*[32], the XO that is formed by the inadequate supply of oxygen to exercising muscles might have generated oxidative damage in other organs including the lung by causing an increase in the circulating level of XO, which binds in the lung to provide a pulmonary source of $O_2^{\cdot-}$. This is a possible mechanism that could explain increased XO activity in the lung under the current study. Lipid peroxidation causing tissue damage has been estimated by an extensively used indicator, such as MDA. The present study showed that after exhaustive running MDA levels ($P<0.05$) were significantly increased in the lung and plasma of the E group, compared to the SC group. However, the extent of the increase in pulmonary and plasma MDA levels in the E+Arg group was comparatively low as compared to the non-Arg group with exercise. This may suggest that the XO derived ROS exert some toxicant effect on lung tissue. In contrast, a smaller increase in XO and MDA concentration activity was observed in *L*-Arg fed rats in response to exhaustive exercise. This result in *L*-Arg fed rats could be responsible for protecting oxidative damage in the E+Arg group.

Numerous studies have shown that *L*-Arg is a precursor of NO, which can increase coronary vasodilation, scavenge various free radicals, inactivate Fe-S centers of XO and suppress XO activity as well as inhibit platelet and neutrophil adhesion to the endothelium[33,34]. Hence, the protective role of NO is probably a result of its ability to scavenge free radicals, reduce lipid peroxidation, and inhibit XO, which are in accordance with our results for the E+Arg group.

The current study showed that MPO activity in lungs from E group significantly increased after exhaustive exercise ($P<0.05$). However, there was no significant difference between E+Arg and SC groups. Hence, *L*-Arg supplementation to rats is successful in reducing post-exercise lung MPO activity and oxidative damage in lungs. These results are in accordance with previous studies about protecting the role of NO[12].

In the present study, our results indicate that both the E and E+Arg groups significantly increase plasma NOx after exhaustive exercise compared to the control. NO, however,

Table 5. Effects of *L*-arginine supplementation on glutathione (GSH) concentrations of plasma and lung tissues after exhaustive exercise. Mean±SEM. $^{b}P<0.05$ *vs* group SC. $^{e}P<0.05$ *vs* group E.

	Sedentary control		Exhaustive exercise	
	SC	SC+Arg	E	E+Arg
Plasma GSH/μmol·L^{-1}	551±63	553±39	415±42^{b}	542±44^{e}
Lung GSH/μmol·mg protein^{-1}	764±55	751±61	742±45	874±167

is also a free radical and hence the toxicity of NO (excess product of NO) is markedly enhanced by its reaction with $O_2^{\cdot-}$ from peroxynitrite ($ONOO^-$), which is extremely cytotoxic[35]. However, Rubbo *et al*[36] recently reported that NO actually inhibits peroxynitrite-induced lipid peroxidation. This report demonstrated that NO will significantly enhance lipid peroxidation only when rates of NO production approach or are equivalent to rates of $O_2^{\cdot-}$ production by XO. In the current study, we measure the effect of exhaustive exercise on the rate of NOx synthesis in plasma in both exercised groups. Although *L*-Arg supplementation effects animals subjected to exhaustive exercise on levels of NOx production, so the results cannot be distinctly different between both exercise groups in our study. This is likely to be related to the following two mechanisms. First, *L*-Arg serves as a precursor to the synthesis of NO that may act as an indirect antioxidant role by scavenging $O_2^{\cdot-}$ and inhibiting XO activity from exercise-induced stress[37]. Our results suggest that *L*-Arg protection is generated through NO. NO has the capacity to inhibit reactive oxygen metabolites, including $O_2^{\cdot-}$ and XO to prevent cellular damage, but in presence of the NO synthase inhibitor *L*-NAME, this protection was abolished, which suggests that the protection *L*-Arg is through the generation of NO[38]. Second, *L*-Arg has some protective roles against ROS attack possibly because of its direct chemical property interaction with $O_2^{\cdot-}$, thus suggesting a protective effect for *L*-Arg involving antioxidant mechanisms[4]. Obviously, the E group does cause a significant increase in XO and MPO activities, as well as MDA levels that are a result of oxidative stress in lung tissues. This means that the enhanced production of $O_2^{\cdot-}$ by XO, may possibly be the combined work of higher level NO and $O_2^{\cdot-}$ to form cytotoxic $ONOO^-$ after exhaustive exercise. In contrast with the E+Arg group, when NO concentrations are increased the protective role of NO is probably be a result of its ability to scavenge free radicals and possibly inhibit XO and inflame neutrophils. Therefore, this study suggests that the E+Arg group has higher levels of NO to inhibit $ONOO^-$ formation leading to lipid peroxidation and it is unlikely that $ONOO^-$ may have a role in this process.

In this study, SOD activity in the lung was significantly increased in response to exercise in the E group. As SOD is known to be an enzyme induced by its $O_2^{\cdot-}$ substrate, the increase in the E group indicates an increased production of $O_2^{\cdot-}$. This finding was in agreement with Reddy *et al*[13], that SOD activity in the lung tissue significantly increased after strenuous swimming exercise. However, the SOD activity in the lung tissue of *L*-Arg-fed animals after exhaustive exercise was well below the control level, suggesting reduced generation of $O_2^{\cdot-}$ and protection offered by *L*-Arg.

Furthermore, the CAT enzyme works on cooperating with GPX to scavenge excess H_2O_2 as well as lipid peroxides in response to oxidative stress. Under this situation, when $O_2^{\cdot-}$ production through XO and neutrophils becomes an overwhelming compensatory mechanism, inadequate consequences take place. Possible mechanisms that could explain excess $O_2^{\cdot-}$ are the inhibition of the activity of CAT by reduction of the Fe III center and inactivated GPX activity by oxidation of the selenium active site[39,40]. This interaction suggests SOD, CAT and GPX constitute a mutually supportive team of enzymes that provide a defense against the intermediaries of ROS. This study confirms Kono *et al*'s and Blum *et al*'s hypothesis, because overproducing $O_2^{\cdot-}$ may speculate an inactive CAT and GPX activities and reciprocally influence these enzymes[39,40]. In contrast with the E+Arg group, the increased CAT and GPX activities seem to be an adaptive response of the lung to oxidative stress generated by exercise. An increase in activity of those enzymes is possibly a result of exposure to various oxygen toxicants. GR catalyzes the reduction of oxidized gluthione (GSSG) to GSH at the expense of NADPH and maintains high GSH/GSSG ratios in the cell. In the present study, GR activity of lung tissue was significantly increased after exhaustive running ($P<0.05$). The increase in GR activity of the lung suggested that the pulmonary antioxidant defense system of exercised rats reacted positively to combat ROS toxicity giving the tissue an adaptive response to oxidative stress. However, our data showed that GR maintains the same levels in the *L*-Arg-fed animals at rest and after exercise, indicating that *L*-Arg supplementation has beneficial effects on attenuating the oxidative stress and maintaining GSH levels. GSH is the first line of defense against various types of chemicals[41]. As described, the GSH levels decreased in the liver and muscles after exhaustive exercise in rats[11]. In the current study, our data showed a depletion in pulmonary GSH and a significant decrease in plasma GSH in the E group compared with the SC group. However, in the E+Arg group the levels of GSH were restored, suggesting that the mechanism of protective action by *L*-Arg may involve maintenance of the thiol group of GSH. Our data correspond with previous reports that exhaustive exercise causes GSH oxidation in blood in both animals and in human beings[42,43].

Other possible mechanisms for an increase in GSH in lung tissue are that GSH synthesized primarily in the liver and was then transported to different organs of the body through the blood during prolonged exercise in order to maintain GSH homeostasis to cope with oxidative stress[44].

In conclusion, an acute bout of exhaustive exercise causes

oxidative stress, tissue damage and antioxidant responses in the lungs. This study suggests that *L*-Arg supplementation can prevent elevations of XO and MPO activities in the lungs and can favorably influence pulmonary antioxidant defense systems after exhaustive exercise.

References

1 Wu G, Morris SM Jr. Arginine metabolism: nitric oxide and beyond. Biochem J 1998; 336: 1–17.
2 Kelly RA, Balligand JL, Smith TW. Nitric oxide and cardiac function. Circ Res 1996; 79: 363–80.
3 Fukahori M, Ichimori K, Ishida H, Nakagawa H, Okino H. Nitric oxide reversibly suppresses xanthine oxidase activity. Free Radical Res 1994; 21: 203–12.
4 Lass A, Suessenbacher A, Wolkart G, Mayer B, Brunner F. Functional and analytical evidence for scavenging of oxygen radicals by *L*-arginine. Mol Pharmacol 2002; 61: 1081–8.
5 Lubec B, Hayn M, Kitzmuller E, Vierhapper H, Lubec G. *L*-Arginine reduces lipid peroxidation in patients with diabetes mellitus. Free Radic Biol Med 1997; 22: 355–7.
6 Adawi D, Kasravi FB, Molin G, Jeppsson B. Oral arginine supplementation in acute liver injury. Nutrition 1996; 12: 529–33.
7 Sheridan BC, Mcityre RC, Meldrum DR, Fullerton DA. *L*-Arginine prevents lung neutrophil accumulation and preserves pulmonary endothelial function after endotoxin. Am J Physiol Lung Cell Mol Physiol 1998; 274: 337–42.
8 Cote CG, Yu FS, Zulueta JJ, Vosatka RJ, Hassoun PM. Regulation of intracellular xanthine oxidase by endothelial-derived nitric oxide. Am J Physiol Lung Cell Mol Physiol 1996; 271: 869–74.
9 Sen CK. Oxidants and antioxidants in exercise. J Appl Physiol 1995; 79: 675–86.
10 Ji LL. Oxidative stress during exercise: implication of antioxidant nutrients. Free Radic Biol Med 1995; 18: 1078–86.
11 Ji LL. Antioxidants and oxidative stress in exercise. Proc Soc Exp Biol Med 1999; 222: 283–92.
12 McCord JM. Oxygen-derived free radicals in postischemic tissue injury. N Eng J Med 1985; 312: 159–63.
13 Reddy KV, Kumar TC, Prasad M, Reddanna P. Pulmonary lipid peroxidation and antioxidant defenses during exhaustive physical exercise: the role of vitamin E and selenium. Nutrition 1998; 14: 448–51.
14 Radak Z, Nakamura A, Nakamoto H, Asano K, Ohno H, Goto S. A period of anaerobic exercise increases the accumulation of reactive carbonyl derivatives in the lungs of rats. Pflugers Arch 1998; 435: 439–41.
15 Zhang SH, Wang SY, Yao SL. Antioxidative effect of propofol during cardiopulmonary bypass in adults. Acta Pharmacol Sin 2004; 25: 334–40.
16 Tiidus PM. Radical species in inflammation and overtraining. Can J Physiol Pharmacol 1998; 76: 533–8.
17 Suzuki K, Sato H, Kikuchi T, Abe T, Nakaji S, Sugawara K, *et al*. Capacity of circulating neutrophils to produce reactive oxygen species after exhaustive exercise. J Appl Physiol 1996; 81: 1213–22.
18 Ji LL. Exercise and oxidative stress: role of cellular antioxidant systems. Exerc Sport Sci Rev 1995; 23: 135–66.
19 Reeves PG, Nielsen FH, Fahey GC Jr. AIN-93 purified diets for aboratory rodents: final report of the American Institute of Nutrition ad hoc writing committee on the reformulation of the AIN-76A rodent diet. J Nutr 1993; 123: 1939–51.
20 Lewis B, Langkamp-Henken B. Arginine enhances in vivo immune responses in young, adult and aged mice. J Nutr 2000; 130: 1827–30.
21 Brooks GA, White TP. Determination of metabolic and heart rate responses of rats to treadmill exercise. J Appl Physiol 1978; 45: 1009–15.
22 Green LC, Wagner DA, Glogowski J, Skipper PL, Wishnok JS, Tannenbaum SR. Analysis of nitrate, nitrite and [I5N] nitrate in biological fluids. Anal Biochem 1982; 126: 131–8.
23 Schmidt HH, Warner TD, Nakane M, Forstermann U, Murad F. Regulation and subcellular location of nitrogen oxide synthases in RAW264.7 macrophages. Mol Pharmacol 1992; 41: 615–24.
24 Westerfeld WW, Richert DA, Higgins ES. Further studies with xanthine oxidase inhibitors. J Biol Chem 1959; 234: 1897–900.
25 Mullane KM, Kraemer R, Smith B. Myeloperoxidase activity as a quantitative assessment of neutrophil infiltration into ischemic myocardium. J Pharmacol Methods 1985; 14: 157–67.
26 Schierwagen C, Bylund-Fellenius AC, Lundberg C. Improved method for quantification of tissue PMN accumulation measured by myeloperoxidase activity. J Pharmacol Methods 1990; 23: 179–86.
27 Beers RF Jr, Sizer IW. A spectrophotometric method for measuring the breakdown of hydrogen peroxide by catalase. J Biol Chem 1952; 195: 133–40.
28 Westing YH, Ekblom B, Sjodin B. The metabolic relation between hypoxanthine and uric acid in man following maximal short-distance running. Acta Physiol Scand 1989; 137: 341–5.
29 Vina J, Gimeno A, Sastre J, Desco C, Asensi M, Pallardo FV, *et al*. Mechanism of free radical production in exhaustive exercise in humans and rats; role of xanthine oxidase and protection by allopurinol. IUBMB Life 2000; 49: 539–44.
30 Hellsten-Westing Y, Sollevi A, Sjodin B. Plasma accumulation of hypoxanthine, uric acid and creatine kinase following exhausting runs of differing durations in man. Eur J Appl Physiol Occup Physiol 1991; 62: 380–4.
31 Yamanaka H, Kawagoe Y, Taniguchi A, Kaneko N, Kimata S, Hosoda S, *et al*. Accelerated purine nucleotide degradation by anaerobic but not by aerobic ergometer muscle exercise. Metabolism 1992; 41: 364–9.
32 Yokoyama Y, Beckman JS, Beckman TK, Wheat JK, Cash TG, Freeman BA, *et al*. Circulating xanthine oxidase: potential mediator of ischemic injury. Am J Physiol 1990; 258: G564–70.
33 Hassoun PM, Yn FS, Zulueta JJ, White AC, Lanzilla JJ. Effect of nitric oxide and cell redox status on the regulation of endothelial cell xanthine dehydrogenase. Am J Physiol Lung Cell Mol Physiol 1995; 268: 809–17.
34 Nonami Y. The role of nitric oxide in cardiac ischemia-reperfusion injury. Jpn Circ J 1997; 61: 119–32.
35 Beckman JS, Koppenol WH. Nitric oxide, superoxide, and peroxynitrite: the good, the bad and ugly. Am J Physiol Cell Physiol 1996; 271: C1424–37.
36 Rubbo H, Radi R, Trujillo M, Telleri R, Kalyanaraman B, Barnes S, *et al*. Nitric oxide regulation of superoxide and peroxynitrite-dependent lipid peroxidation. Formation of novel nitrogen-containing oxidized lipid derivatives. J Biol Chem 1994; 269:

26066–75.
37 Pabla R, Buda AJ, Flynn DM, Blesse SA, Shin AM, Curtis MJ, *et al*. Nitric oxide attenuates neutrophil-mediated myocardial contractile dysfunction after ischemia and reperfusion. Circ Res 1996; 78: 65 –72.
38 Souza-Costa DC, Zerbini T, Metzger IF, Rocha JB, Gerlach RF, Tanus-Santos JE. *L*-Arginine attenuates acute pulmonary embolism-induced oxidative stress and pulmonary hypertension. Nitric Oxide 2005; 12: 9–14.
39 Kono Y, Fridovich I. Superoxide radical inhibits catalase. J Biol Chem 1982; 257: 5751–4.
40 Blum J, Fridovich I. Inactivation of glutathione peroxidase by superoxide radical. Arch Biochem Biophys 1985; 240: 500–8.
41 Meister A, Anderson ME. Glutathione. Annu Rev Biochem 1983; 52: 711–60.
42 Gohil K, Viguie C, Stanley WC, Brooks GA, Packer L. Blood glutathione oxidation during human exercise. J Appl Physiol 1988; 64: 115–9.
43 Sastre J, Asensi M, Gasco E, Pallardo FV, Ferrero JA, Furukawa T, *et al*. Exhaustive physical exercise causes oxidation of glutathione status in blood: prevention by antioxidant administration. Am J Physiol Regulatory Integrative Comp Physiol 1992; 263: 992–5.
44 Ji LL, Fu R, Mitchell EW. Glutathione and antioxidant enzymes in skeletal muscle: effects of fiber type and exercise intensity. J Appl Physiol 1992; 73: 1854–9.

SBS 11th Annual Conference and Exhibition Drug Discovery: From Targets to Candidates

September 11–15, 2005 Geneva, Switzerland

Info: The Society for Biomolecular Screening
36 Tmarack Avenue, #348
Danbury, CT06811, USA
Phn 1(203) 743-1336
Fax 1(203) 748-7557
E-mail email@sbsonline.org
Http://www.sbsonline.org/sbscon/2005/index.php

Acta Pharmacologica Sinica 2005 Aug; 26 (8):1000 –1008

Full-length article

Cytotoxicity, apoptosis induction, and mitotic arrest by a novel podophyllotoxin glucoside, 4DPG, in tumor cells[1]

Yi-lin QI[2,4], Fan LIAO[2,4], Chang-qi ZHAO[2], Yong-da LIN[2], Ming-xue ZUO[2,3,5]

[2]College of Life Sciences, Beijing Normal University, Beijing 100875, China; [3]Key Laboratory for Molecular Biology and Gene Engineering Drugs of Beijing, Beijing 100875, China

Key words

4-demethyl-picropodophyllotoxin 7'-*O*-β-*D*-glucopyranoside; podophyllotoxin; flow cytometry; microtubulin; apoptosis

[1] Project supported by the National Natural Science Foundation of China (No 30270449; No 30370196) and Beijing Natural Science Foundation (No 5052016).
[4] The two authors contributed equally to this work
[5] Correspondence to Prof Ming-xue ZUO.
Phn 86-10-5880-8558
E-mail mxzuo@bnu.edu.cn

Received 2005-04-01
Accepted 2005-04-11

doi: 10.1111/j.1745-7254.2005.00148.x

Abstract

Aim: To define the *in vitro* cytotoxic activities of 4-demethyl-picropodophyllotoxin 7'-*O*-β-*D*-glucopyranoside (4DPG), a new podophyllotoxin glucoside. **Methods:** Antiproliferation activity was measured in several tumor cell lines by using the microculture tetrazolium MTT assays. Cell cycle distribution was analyzed using flow cytometry and mitosis index assays. Furthermore, transmission electron microscopy, TUNEL, DNA agarose electrophoresis, and activated caspase-3 were used to analyze the induction of apoptotic cell death. Moreover, intracellular changes in the cytoskeleton were detected using immunocytochemistry. **Results:** 4DPG effectively inhibited the proliferation of cancer cells (HeLa, CNE, SH-SY5Y, and K562 cell lines). For the K562 cell line, the antiproliferation effect of 4DPG was much more potent than that of etoposide (IC_{50} value: 7.79×10^{-9} mol/L for 4DPG *vs* 2.23×10^{-5} mol/L for etoposide). Further, 4DPG blocked the cell cycle in the mitotic phase. The induction of apoptosis and elevated levels of activated caspase-3 were confirmed in cells treated with 4DPG. The microtubule skeleton of HeLa cells was disrupted immediately after treatment with 4DPG. **Conclusion:** The cytotoxicity of 4DPG is due to its inhibition of the microtubule assembly of cancer cells at a low concentration, thus inducing apoptosis. These properties qualify 4DPG to be a potential antitumor drug.

Introduction

Natural products have long been an important source of treatments for cancer. At present, there are more than one thousand plants that have been found to possess significant anticancer properties. Although many molecules obtained from plants have been shown to have antineoplastic activity, a huge number of molecules still remain to be isolated or studied in detail. Recently, traditional Chinese medicines have attracted much interest, and evaluations of potential antineoplastic herbal ingredients are currently being carried out in laboratories[1–3].

Of the natural compounds with anticancer properties, podophyllotoxin occupies a very important position[4]. Podophyllotoxin is a naturally occurring lignan, which is isolated from the dried roots and rhizomes of *Podophyllum* plants, and has been proven to possess antineoplastic properties. Although its unacceptable levels of cytotoxicity precluded the use of podophyllotoxin as an anticancer drug, subsequent research aimed to abstract and synthesize new analogues of podophyllotoxin, and analyzed podophyllotoxin's structure-function relationship and its mechanism of action. Several decades' efforts have proven that the cytotoxicity of podophyllotoxin is due to its interaction with β-tubulin, because it disrupts microtubule organization and leads to mitotic arrest, in a manner that is similar to the action of colchicines[5–8]. Meanwhile, many analogues of podophyllotoxin have been determined, and most exhibit pronounced biological activity as strong antiviral or antineoplastic agents[4,9–11]. Among these molecules, etoposide is a notably successful derivative of podophyllotoxin[12,13], with demonstrated efficacy against a broad spectrum of human

malignancies, including testicular, germ cell, lung, and other cancers[14–17]. Etoposide arrests cancer cell growth prior to mitosis as a DNA topoisomerase II inhibitor[18–21], whereas podophyllotoxin has no inhibitory effect on this enzyme[22]. Conversely, an isomer of podophyllotoxin, picropodophyllotoxin, has no inhibitory effect on microtubules and apparently lacks cytotoxicity[4,22–26]. After these observations were made, little or no attention was paid to picropodophyllotoxin. However, some recent studies on picropodophyllotoxin produced different and exciting results. Some derivatives of picropodophyllotoxin have high levels of antiproliferation activity against the L1210 cell line because they inhibit microtubule assembly[27]. The cyclolignan podophyllotoxin and picropodophyllotoxin inhibit tyrosine phosphorylation of the insulin-like growth factor-1 receptor (IGF-1R), but have no effect on the highly homologous insulin receptor (IR) or tyrosine kinases that are related to other major cancer-relevant growth factor receptors, so they specifically inhibit malignant cells[28,29]. These results could cause more research interest to be focused on the analogues of podophyllotoxin, in order to identify the derivatives with the most potent and specific antitumor activity (ie, to optimize the structure), or to develop an alternative and renewable source of podophyllotoxin.

Sinopodophyllum emodi (Wall) Ying, mainly distributed over the Western region of the Qinling mountains of China, is a type of *Podophyllum*. In the area in which it is grows, *S emodi* has been used as a folk medicine to treat cancer and various types of verrucosis, but the pharmacology of its constituent ingredients has not been investigated. Our previous study revealed that 4-demethyl-picropodophyllotoxin 7'-*O*-β-*D*-glucopyranoside (4DPG) (Figure 1) is a novel podophyllotoxin glucoside isolated from *S emodi*[30]. A significant structural characteristic of 4DPG is that it belongs to the picropodophyllin family. Therefore, as a herbal medicine ingredient and a podophyllotoxin analogue with a quite different structure, we wondered what the biological activity of this molecule would be.

In this study, we demonstrate that 4DPG is a highly potent inhibitor of microtubule assembly, leading to mitotic arrest, induction of apoptosis, and inhibition of the proliferation of malignant cells.

Materials and methods

Chemicals 4DPG was isolated from *Sinopodophillum emodi* (Wall) Ying (Berberidaceae) by our group[30]. The extracted 4DPG was dissolved in methanol (0.01 mol/L) and stored at room temperature.

Cell lines and cell culture A human cervical carcinoma cell line (HeLa), a human nasopharyngeal carcinoma cell line (CNE) and a human neuroblastoma cell line (SH-SY5Y) were grown in Dulbecco's MEM (Hyclone, Logan, USA) and a human chronic myelogenous leukemia cell line (K562) was maintained in RPMI-1640, supplemented with 10% heat-inactivated fetal calf serum (FCS), 100 U/mL penicillin and 100 μg/mL streptomycin in a humidified atmosphere (37 ºC, 5% CO_2).

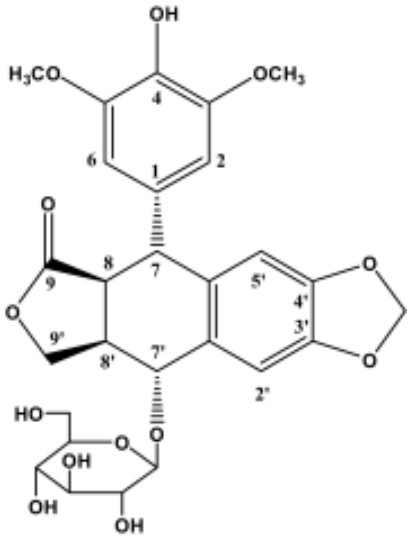

Figure 1. Chemical structure of 4DPG.

Cytotoxicity assay The MTT assay to determine the cytotoxicity of 4DPG was performed as described previously[31]. Briefly, cells were plated onto 96-well plates at 2×10^3 cells per well for the HeLa, CNE, and SH-SY5Y cell lines or at 5×10^3 cells/well for the K562 cell line. After incubation with medium containing 0.1% methanol, 2×10^{-5} mol/L 4DPG and etoposide (VP-16) for 48 h, MTT (Sigma Chemical Co, St Louis, USA) was added to cell cultures to a final concentration of 0.5 mg/mL and incubated at 37 ºC for 4 h. Then, the adherent cells were solubilized with 200 mL dimethyl sulfoxide (Me_2SO, Sigma), and K562 cells were exposed to 100 mL 0.04 N 2-propanolic hydrochloric acid. Absorbance at 570 nm was measured on a multiplate reader (Bio-Rad 550, Hercules, USA).

In the same way, K562 cells treated with gradient concentrations of 4DPG and etoposide for 48 h were tested. The drug concentration required to inhibit cell growth by 50% (IC_{50}) was determined by interpolation from dose-response curves. All assays were carried out in quadruplicate. The inhibition rate of cell proliferation was calculated by:

$$\text{Inhibition rate (\%)} = \frac{OD_{\text{control}} - OD_{\text{treated}}}{OD_{\text{control}}} \times 100\%$$

Cell cycle analysis K562 cells were treated with 1×10^{-9} mol/L, 1×10^{-8} mol/L,1×10^{-7} mol/L, and 1×10^{-6} mol/L 4DPG, respectively. After incubation for 48 h, cells were collected and fixed with 70% ethanol at 4 ºC for 24 h, then stained with 50 μg/mL propidium iodide (Sigma). The cell cycle distribution from 10 000 cells was collected by using the Epics flow cytometer (Coulter Electronics, Fullerton, USA). Cell cycle analysis was performed by using Multicycle software (Phoenix Flow Systems, San Diego, USA).

The mitotic index was determined by Giemsa staining. K562 cells were incubated with or without 1×10^{-6} mol/L 4DPG for 48 h. Then, fixed cells were stained with Giemsa solution and mitotic cells were counted per visual field. Quadruplicate fields were measured.

DNA fragmentation assay K562 cells were exposed to 0.01% methanol, 1×10^{-6} mol/L 4DPG and 1×10^{-6} mol/L etoposide for 48 h, and then cells were collected by centrifugation. Total DNA was purified with a DNA isolation kit (R&D Systems, Minneapolis, USA) according to the manufacturer's protocol. The DNA was separated in 1.5% agarose gel and visualized by ultraviolet illumination after staining with ethidium bromide.

TUNEL assay After incubation with 1×10^{-6} mol/L 4DPG for 12 h, 24 h, and 48 h, cells were rinsed three times with phosphate-buffered saline (PBS) and fixed with methanol. Based on the TUNEL protocol (Roche, Basel, Switzerland), cells were permeabilized with 0.1% Triton X-100 in 0.1% sodium citrate and then rinsed twice with PBS. The DNA nick-labeling reaction was performed using 50 μL TUNEL reaction mixture, including 45 μL enzyme solution and 5 μL nucleotide mix at 37 ºC for 60 min. Then the samples were rinsed three times with PBS and analyzed under a fluorescence microscope.

Morphology analysis by transmission electron microscopy K562 cells treated with 1×10^{-6} mol/L 4DPG were washed with PBS, centrifuged, and pre-fixed with 2.5% glutaraldehyde in 0.1 mol/L phosphate buffer at 4 ºC for 2 h. The cells were then rinsed thoroughly in phosphate buffer and post-fixed in 1% OsO_4 at 4 ºC for 30 min. After being fixed, the cells were pelleted in 2% agar, then cell blocks were prepared, dehydrated through a graded ethanol series, and embedded in Epon 812 (Spi supplies, West chester, USA). The ultrastructure of cells was analyzed in ultrathin sections in a transmission electron microscope (Hitachi H-600, Tokyo, Japan) after the sections were stained with uranyl acetate and lead citrate.

Caspase-3 cleavage assay After the K562 cells were treated with 10^{-6} mol/L 4DPG as described above, the cells were fixed and incubated with cleaved caspase-3 (Asp175) antibody (Cell Signaling, Beverly, USA) as a primary antibody, which specifically recognizes activated caspase-3 resulting from cleavage adjacent to Asp175, and then with biotinylated goat antirabbit IgG as a secondary antibody. Finally, the cells were incubated with the ABC kit (Vector, Peterborough, England) and visualized by incubation with the colorigenic substrates (DAB, Promega, Madison, USA).

Indirect immunofluorescence staining Exponentially growing HeLa cells were seeded into 96-well plates, then after 12 h, the medium was replaced with complete medium containing 10^{-6} mol/L 4DPG. After treatment with 4DPG for 1 h, 2 h, 3 h, 12 h, 24 h, or 48 h, immunofluorescence staining was performed. The cells were incubated with anti-α-tubulin antibody (ZSBiO, Beijing, China) as a primary antibody, which was followed by a secondary antibody, TRITC-conjugated rabbit antimouse IgG. After being washed three times with PBS, the labeled cells were observed and photographed with a fluorescence microscope (Olympus IX70, Tokyo, Japan).

HeLa cells plated onto cover slips were treated with the 10^{-6} mol/L 4DPG for 24 h. As per the procedure described earlier, the cytoskeletons of the adherent and suspension cells were photographed on a confocal laser scanning biological microscope (Olympus Fluoview FV300).

Statistics Data were expressed as mean±SD and analyzed using two-way analysis of variance (ANOVA). The differences between two groups were determined by using the *t*-test, and statistical significance was set at $P<0.05$.

Results

Chemical structure of 4DPG 4DPG, as a congener of podophyllotoxin, has the same multiple ring structure; however, it differs with respect to the composition and minor modifications of the podophyllotoxin rings, including the steric orientation of a carbon-carbon bond and substitution on the ring. 4DPG has a hydroxy group in the 4-carbon position, but podophyllotoxin has a methoxy group at this position. Another site that differs is the 7'-carbon position, which is substituted in podophyllotoxin with an unmodified glucoside. Among the analogues of podophyllotoxin reported previously, 4DPG is the isomer of the 4'-demethylpodophyllotoxin glucoside DMPG[22].

Effect of 4DPG on proliferation of tumor cells As shown in Figure 2, 4DPG induced a significant inhibition of proliferation in the tested cell lines (SH-SY5Y, CNE, HeLa and K562). Compared with etoposide, 4DPG had much more potent cytotoxic effect on CNE and K562 cells.

After a 48 h-treatment, 4DPG had maximal cytotoxic effect on K562 cells at a concentration of 1×10^{-8} mol/L. The

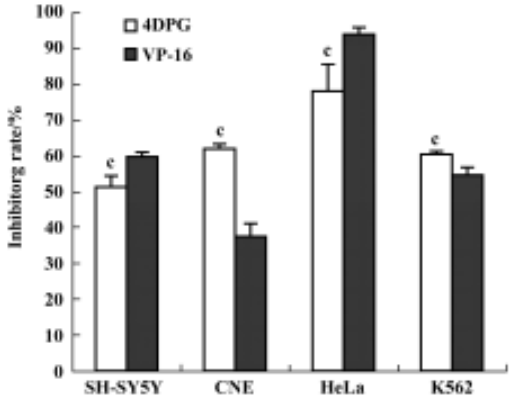

Figure 2. The inhibitory effect of 4DPG on the proliferation of four tumor cell lines (SH-SY5Y, CNE, HeLa, K562) was measured by MTT assays after treatment with 4DPG for 48 h. n=4. Mean±SD. ^cP<0.01 *vs* VP-16.

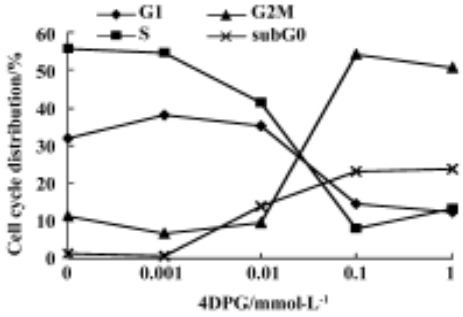

Figure 4. The effect of 4DPG on G2/M phase arrest and induction of apoptosis in K562 cells was dose-dependent. K562 cells were treated with 1×10^{-9} mol/L, 1×10^{-8} mol/L, 1×10^{-7} mol/L or 1×10^{-6} mol/L 4DPG for 48 h. The negative control was the vehicle-treated sample.

maximal inhibition rate was 72.82%, and the IC_{50} value was 7.79×10^{-9} mol/L (Figure 3). Under the same conditions, the maximal effect on cell proliferation inhibition was observed with etoposide at a concentration of 2.5×10^{-4} mol/L , which inhibited 95.25% of cells, with an IC_{50} value of 2.23×10^{-5} mol/L (data not shown).

Mitotic arrest was induced by 4DPG treatment As shown in Figure 4, 4DPG caused a significant dose-dependent accumulation of K562 cells in the G2/M and sub-G0 phases, and a decrease in the G0/G1 and S phases from 1×10^{-9} mol/L to 1×10^{-6} mol/L at 48 h. The differences in cell cycle distribution between vehicle-treated K562 cells and 1×10^{-8} mol/L, 1×10^{-7} mol/L, 1×10^{-6} mol/L treatment are statistically significant (P<0.01).

To further characterize the cell cycle distribution, mitotic index detection was performed. We found that approximately 50% of cells treated with 10^{-6} mol/L 4DPG for 48 h were blocked in mitosis, which was consistent with the result from flow cytometry, but for vehicle-treated cells, only 6.8% were in mitosis (P<0.01).

4DPG induced apoptosis in K562 cells 4DPG treatment resulted in the formation of a DNA ladder in K562 cells at 48 h (Figure 5), but etoposide did not produce the same result. Additionally, as shown in Figure 6, the longer K562 cells were exposed to 1×10^{-6} mol/L 4DPG, the more cells that had DNA strand breaks were labeled by TUNEL.

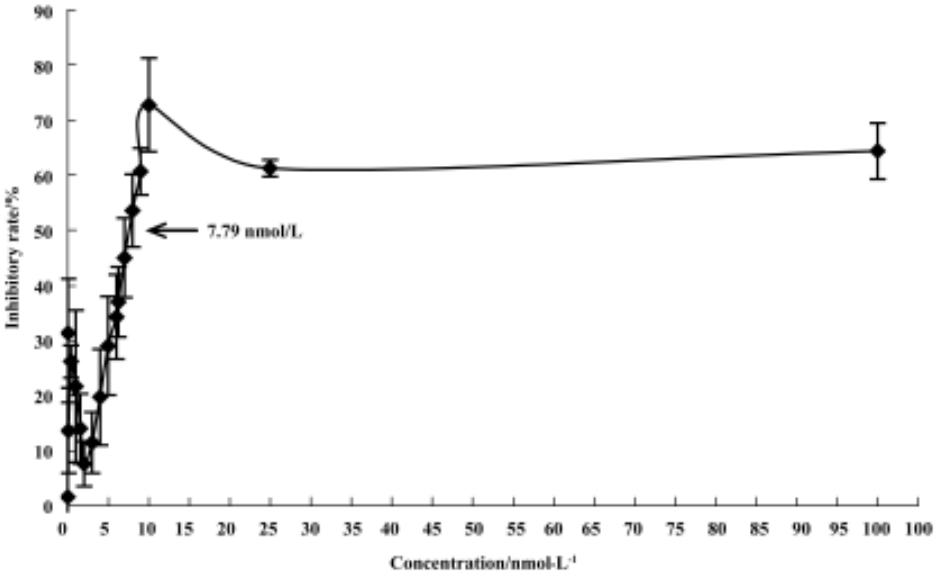

Figure 3. Dose-response curve for the inhibition of cell proliferation. K562 cells were incubated with gradient concentrations of 4DPG for 48 h. n=4. Mean±SD. The inhibition value was calculated using the means of $OD_{control}$ and $OD_{treated}$.

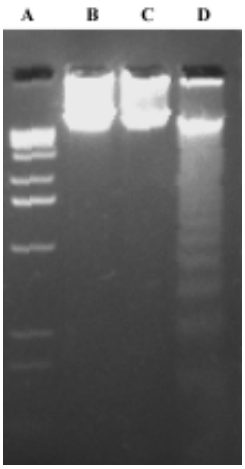

Figure 5. DNA fragmentation in K562 cells treated with 4DPG for 48 h. Lane A: 1 kb marker; lane B: normal control; lane C: treated with 1×10^{-6} mol/L etoposide for 48 h; lane D: treated with 1×10^{-6} mol/L 4DPG for 48 h.

Observations of ultrastructure showed that K562 cells displayed the characteristics of apoptosis after the incubation of 1×10^{-6} mol/L 4DPG for 24 h and 48 h, respectively. That is, some slim protuberances packed with the unit membrane and numerous substances were released around the cell; this was followed by increases of the structure of the membrane in the cytoplasm, and the cytoplasm was separated into several units in which a few vacuoles could be seen; then, the nuclear membrane became unclear, and the chromatin condensed and turned into single chromosome spots (Figure 7).

4DPG induced the activation of caspase-3 As shown in Figure 8, after incubation with 1×10^{-6} mol/L 4DPG for 12 h, the number of activated caspase-3-positive cells had changed little; however, the number had increased greatly after 24 h, and further increased after 48 h.

4DPG inhibited microtubule polymerization At 1 h after 1×10^{-6} mol/L 4DPG treatment, a marked inhibition of microtubule assembly in HeLa cells was observed. Compared with the vehicle-treated cells, the most significant change was the disappearance of the bipolar mitotic spindles in the cell division phase (Figure 9). Additionally, the results from confocal fluorescent microscopy further confirmed that 4DPG

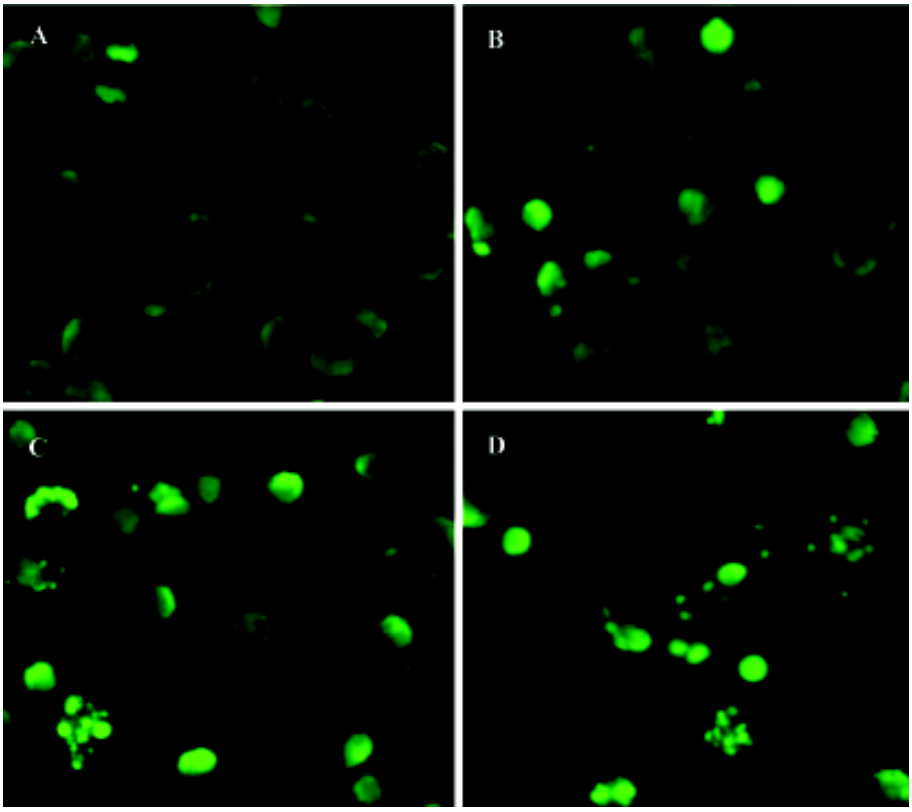

Figure 6. DNA breaks induced by 1×10^{-6} mol/L 4DPG were detected by TUNEL. (A) Vehicle-treated K562 cells (only cells involved in mitosis were positively labeled); (B) after 12 h exposure, the chromatin in a few cells condensed and broke; (C) after 24 h exposure, many more cells were positively labeled; (D) after 48 h exposure, condensed and separated chromatins were dispersed in the cytoplasm (×400).

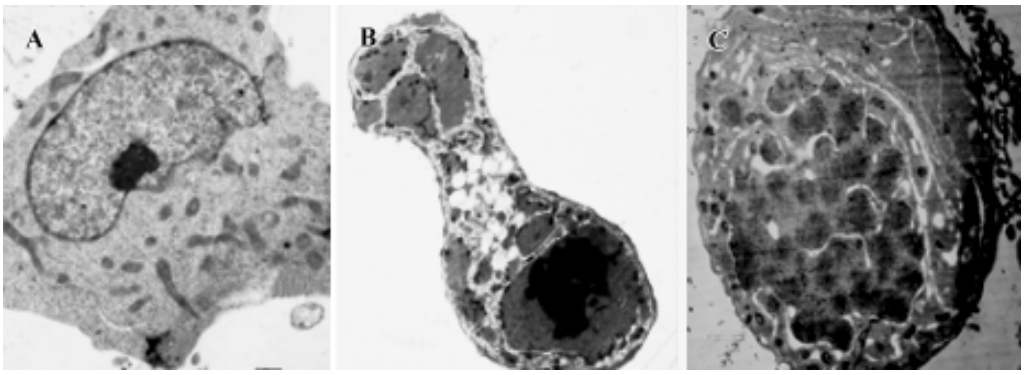

Figure 7. Ultrastructural photomicrographs of K652 cells after treatment with 1×10^{-6} mol/L 4DPG, visualized by transmission electron microscopy. (A) Normal control, the nucleolus and nuclear membrane were clear, chromatin was dispersed and uncondensed (×5000); (B) after 4DPG treatment for 24 h, the nucleolus disappeared and the nuclear chromatin was condensed (×3500); (C) after treatment with 4DPG for 48 h, the nuclear membrane was becoming unclear, and the chromatin was condensed and separated. Cells displayed the characteristics of apoptosis and mitosis (×5 000).

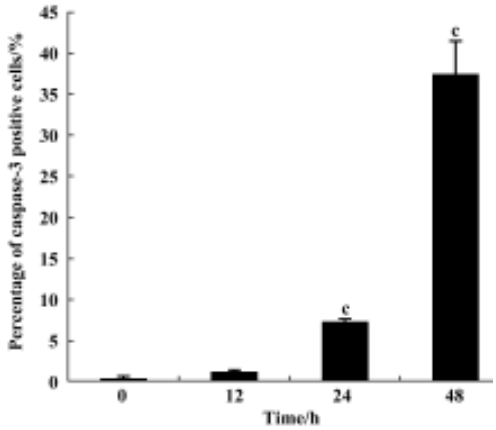

Figure 8. The percentage of activated caspase-3 in K562 cells increased greatly with increased exposure to 1×10^{-6} mol/L 4DPG. n=4. Mean±SD. ^cP<0.01 *vs* 0 h.

disrupted normal microtubule polymerization (Figure 10).

Discussion

By screening new potential antitumor agents using a cytotoxicity assay, we identified 4DPG as an agent that possessed antiproliferative properties. 4DPG has been found to have an extensive and significant inhibitory effect on the proliferation of various carcinoma cell lines. In this study, we found that compared with etoposide, 4DPG is much more potent in some cell lines, such as HeLa and K562. The IC_{50} value of 4DPG on K562 cells was 2–3 orders of magnitude lower than that of etoposide. The cytotoxic effect of 4DPG on K562 cells is dose-dependent. Furthermore, regarding the effect of 4DPG on the cell cycle distribution, 4DPG was found to cause significant mitotic arrest in K562 cells. These findings regarding the picro derivatives are different from those reported previously, which considered that these compounds lacked biological activity and that the C-8α, C-8'βtrans configuration is of crucial importance for biological activity[4]. However, recent studies on a new derivative of picropodophyllotoxin, 4-amino-4 deoxypicropodophyllotoxin, have proven that it exerts antitumor activity through inhibiting microtubule assembly[27]. These results suggest that the modification of picropodophyllotoxin with a free hydroxy group in the 4-position or substitution at the 7'-position can also produce molecules with high levels of biological activity. Moreover, the specific inhibitive effect of tyrosine phosphorylation of IGF-1R and malignant cell growth by picropodophyllotoxin that was observed by Girnita and coworkers provide another perspective on this molecule[28,29]. These new discoveries suggest that picro derivatives retain a high biological activity and could become an important family of anticancer agents.

In the podophyllotoxin family, there are two well-investigated mechanisms that cause cytotoxicity[4]. The first is the inhibition of microtubule polymerization (eg, podophyllotoxin[5,6]) and the second is the inhibition of topoisomerase II (eg, etoposide[18]). As shown in Figure 8, after just 1 h exposure to 4DPG, the fibroid microtubule skeleton in normal HeLa cells was broken and the tubulin-α tagged by TRITC was distributed in the cytoplasm homogeneously. These observations indicate that the cytotoxicity of 4DPG is caused by disrupting the microtubule assembly, which interferes with mitosis at low concentrations. This property is similar to that of podophyllotoxin, indicating that 4DPG is a new antimicrotubule agent. However, reports regarding the effectiveness of podophyllotoxin and picropodophyllotoxin

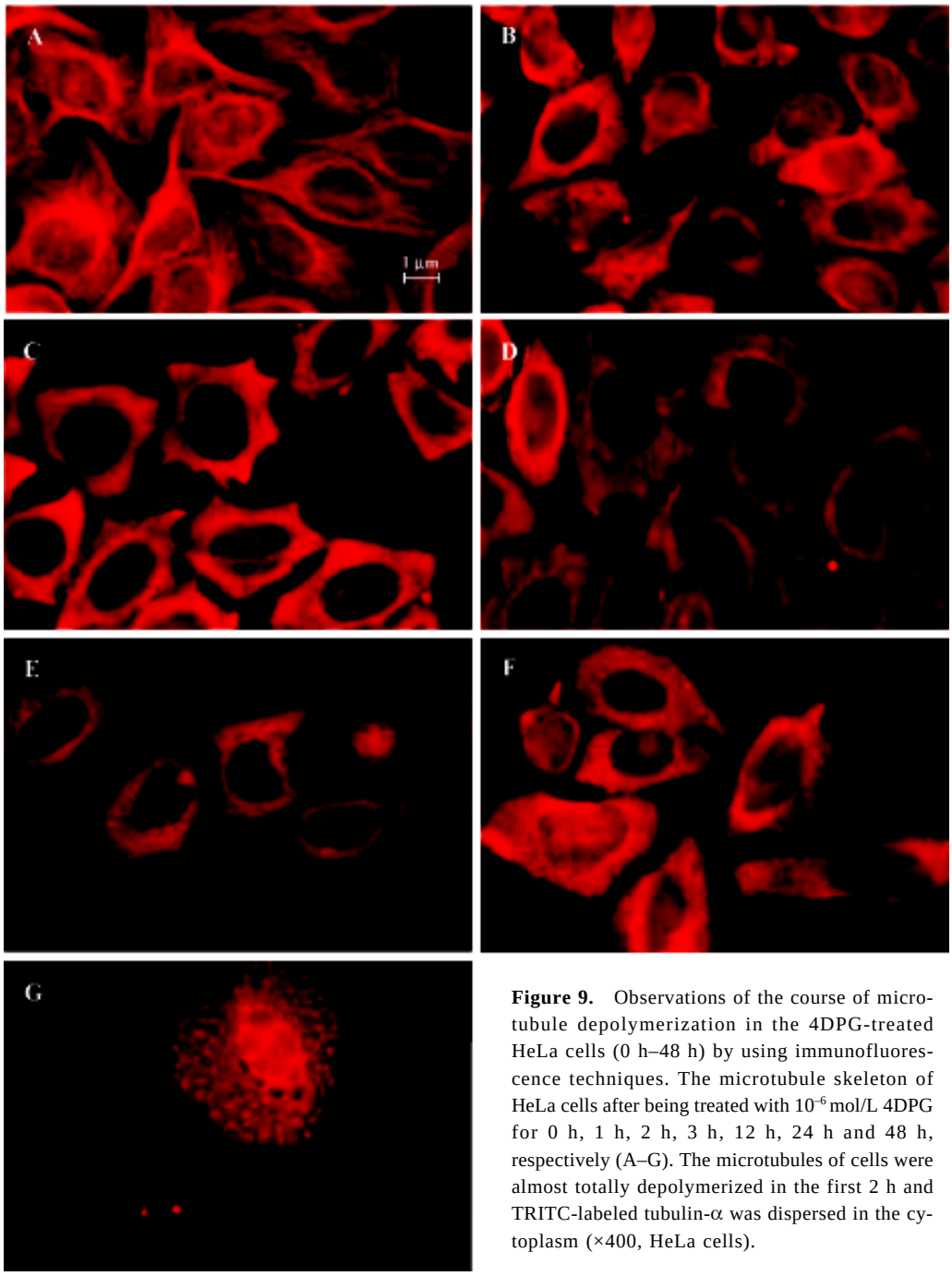

Figure 9. Observations of the course of microtubule depolymerization in the 4DPG-treated HeLa cells (0 h–48 h) by using immunofluorescence techniques. The microtubule skeleton of HeLa cells after being treated with 10^{-6} mol/L 4DPG for 0 h, 1 h, 2 h, 3 h, 12 h, 24 h and 48 h, respectively (A–G). The microtubules of cells were almost totally depolymerized in the first 2 h and TRITC-labeled tubulin-α was dispersed in the cytoplasm (×400, HeLa cells).

as inhibitors of IGF-1R suggest that there is another possible mechanism by which podophyllotoxin inhibits malignant cell proliferation at the same time as it interferes with microtubule assembly[28]. It could be necessary to carry out a study to determine whether 4DPG also possesses this activity.

Microtubules are important cytoskeletal components involved in the regulation of cell proliferation, differentiation, and apoptosis[32]. Microtubule-targeted agents, in particular taxanes[33], have been shown clinically to exert a high level of anticancer activity, and they have also been shown to be promoters of apoptosis in cancer cells[34]. In the present study, the apoptosis-inducing effects of 4DPG were also proven by several observations, including ultrastructure changes, DNA strand breaking and fragmentation, and a subdiploid peak. Apoptosis induced by antimicrotubule

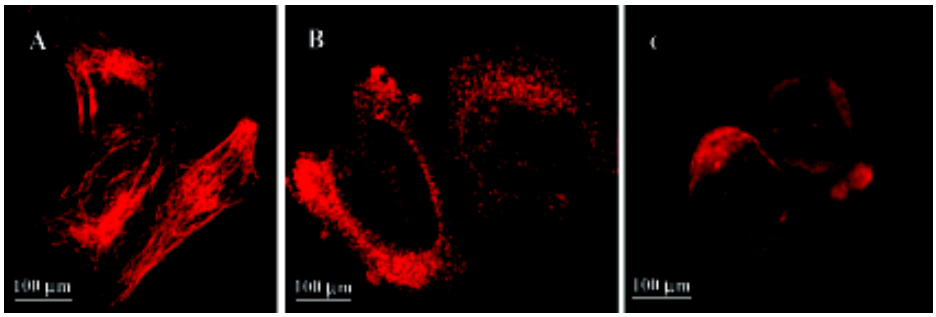

Figure 10. Comparison of the changes in the microtubules of HeLa cells in the control and the 4DPG-treated groups by using confocal immunofluorescence microscopy. (A) The microtubules of normal cells were fibroid and interweaved. (B) When treated with 1×10^{-6} mol/L 4DPG for 24 h, the microtubules of the adherent cells were depolymerized. (C) When treated with 1×10^{-6} mol/L 4DPG for 24 h, most of the suspension cells also disappeared(HeLa cells).

agents is a very complex progress. Many proteins involved in these signal pathways have yet to be identified, and many questions about the process remain unanswered[35,36–38]. It is conceivable that different microtubule binding sites and different disruptions caused by antimicrotubule agents trigger different protein kinase signal pathways. The present study demonstrated clearly that activated caspase-3 increased greatly after treatment with 4DPG for 24 h. This result is quite consistent with the observations gained from TUNEL, suggesting that 4DPG causes the induction of apoptosis through a caspase-3-dependent signaling pathway. The other proteins involved in this apoptotic signaling pathway also need to be determined.

In summary, our results demonstrate that 4DPG has a powerful cytotoxic activity at very low concentrations (<0.01 μmol/L), through interrupting microtubule assembly. It is worth noting that 4DPG is a natural podophyllotoxin glucoside with a unique structure. These findings about the biological activity and mechanism of 4DPG are not only valuable additions to the body of information regarding the structure-activity relationships in the podophyllotoxin family, but also suggest a way forward for exploring natural antitumor products.

References

1 Mukherjee AK, Basu S, Sarkar N, Ghosh AC. Advances in cancer therapy with plant based natural products. Curr Med Chem 2001; 8: 1467–86.
2 Tsai TH. Analytical approaches for traditional Chinese medicines exhibiting antineoplastic activity. J Chromatogr B Biomed Sci Appl 2001; 764: 27–48.
3 Lee KH. Novel antitumor agents from higher plants. Med Res Rev 1999; 19: 569–96.
4 Imbert F. Discovery of podophyllotoxins. Biochimie 1998; 80: 207–22.
5 Cortese F, Bhattacharyya B, Wolf J. Podophyllotoxin as a probe for the colchicine binding site of tubulin. J Biol Chem 1977; 252: 1134–40.
6 Sackett DL. Podophyllotoxin, steganacin and combretastatin: natural products that bind at the colchicine site of tubulin. Pharmacol Ther 1993; 59: 163–228.
7 ter Haar E, Rosenkranz HS, Hamel E, Day BW. Computational and molecular modeling evaluation of the structural basis for tubulin polymerization inhibition by colchicine site agents. Bioorg Med Chem 1996; 4: 1659–71.
8 Desbene S, Giorgi-Renault S. Drugs that inhibit tubulin polymerization: the particular case of podophyllotoxin and analogues. Curr Med Chem Anti-Canc Agents 2002; 2: 71–90.
9 Gordaliza M, Castro MA, del Corral JM, Feliciano AS. Antitumor properties of podophyllotoxin and related compounds. Curr Pharm Des 2000; 6: 1811–39.
10 Gordaliza M, Garcia PA, del Corral JM, Castro MA, Gomez-Zurita MA. Podophyllotoxin: distribution, sources, applications and new cytotoxic derivatives. Toxicon 2004; 44: 441–59.
11 Kelleher JK. Correlation of tubulin-binding and antitumor activities of podophyllotoxin analogs. Cancer Treat Rep 1978; 62: 1443–7.
12 Hainsworth JD, Greco FA. Etoposide: twenty years later. Ann Oncol 1995; 6: 325–41.
13 Schacter L. Etoposide phosphate: what, why, where, and how? Semin Oncol 1996; 23 (Suppl 13): 1–7.
14 Evans WK, Eisenhauer E, Hughes P, Maroun JA, Ayoub J, Shepherd FA, *et al*. VP-16 and carboplatin in previously untreated patients with extensive small cell lung cancer: a study of the National Cancer Institute of Canada Clinical Trials Group. Br J Cancer 1988; 58: 464–8.
15 Splinter T, Kok T, Kho S, Lameris H, ten Kate F, Dalesio O, *et al*. A multicenter phase II trial of cisplatin and oral etoposide (VP-16) in inoperable non-small-cell lung cancer. Semin Oncol 1986; 13 (Suppl 3): 97–103.
16 Aisner J, Lee EJ. Etoposide. Current and future status. Cancer 1991; 67 (Suppl 1): 215–9.
17 Hande KR. Etoposide pharmacology. Semin Oncol 1992; 19 (Suppl 13): 3–9.
18 Minocha A, Long BH. Inhibition of the DNA catenation activity of type II topoisomerase by VP16–213 and VM26. Biochem

Biophys Res Commun 1984; 122: 165–70.
19 Tewey KM, Chen GL, Nelson EM, Liu LF. Intercalative antitumor drugs interfere with the breakage-reunion reaction of mammalian DNA topoisomerase II. J Biol Chem 1984; 259: 9182–7.
20 Long BH and Stringfellow DA. Inhibitors of topoisomerase II: structure-activity relationships and mechanism of action of podophyllin congeners. Adv Enzyme Regul 1988; 27: 223–56.
21 Long BH. Mechanisms of action of teniposide (VM-26) and comparison with etoposide (VP-16). Semin Oncol 1992; 19 (Suppl 6): 3–19.
22 Long BH, Musial ST, Brattain MG. Comparison of cytotoxicity and DNA breakage activity of congeners of podophyllotoxin including VP16-213 and VM26: a quantitative structure-activity relationship. Biochemistry 1984; 23: 1188–94.
23 Paulson JC, McClure WO. Microtubules and axoplasmic transport. Inhibition of transport by podophyllotoxin: an interaction with microtubule protein. J Cell Biol 1975; 67: 461–7.
24 Loike JD, Brewer CF, Sternlicht H, Gensler WJ, Horwitz SB. Structure-activity study of the inhibition of microtubule assembly in vitro by podophyllotoxin and its congeners. Cancer Res 1978; 38: 2688–93.
25 Bedows E, Hatfield GM. An investigation of the antiviral activity of *Podophyllum peltatum*. J Nat Prod 1982; 45: 725–9.
26 Davis RE, Schlumpf BE, Klinger PD. Comparative neurotoxicity of tubulin-binding drugs: inhibition of goldfish optic nerve regeneration. Toxicol Appl Pharmacol 1985; 80: 308–15.
27 Roulland E, Magiatis P, Arimondo P, Bertounesque E, Monneret C. Hemi-synthesis and biological activity of new analogues of podophyllotoxin. Bioorg Med Chem 2002; 10: 3463–71.
28 Girnita A, Girnita L, del Prete F, Bartolazzi A, Larsson O, Axelson M. Cyclolignans as inhibitors of the insulin-like growth factor-1 receptor and malignant cell growth. Cancer Res 2004; 64: 236–42.
29 Vasilcanu D, Girnita A, Girnita L, Vasilcanu R, Axelson M, Larsson O. The cyclolignan PPP induces activation loop-specific inhibition of tyrosine phosphorylation of the insulin-like growth factor-1 receptor. Link to the phosphatidyl inositol-3 kinase/Akt apoptotic pathway. Oncogene 2004; 23: 7854–62.
30 Zhao C, Huang J, Hagatsu A, Ogihara Y. Two new podophyllotoxin glucosides from *Sinopodophyllum emodi* (Wall) Ying. Chem Pharm Bull 2001; 49: 773–5.
31 Mosmann T. Rapid colorimetric assay for cellular growth and survival: application to proliferation and cytotoxicity assays. J Immunol Methods 1983; 65: 55–63.
32 Gundersen GG, Cook TA. Microtubules and signal transduction. Curr Opin Cell Biol 1999; 11: 81–94.
33 Miller KD, Sledge GW Jr. Taxanes in the treatment of breast cancer: a prodigy comes of age. Cancer Invest 1999; 17: 121–36.
34 Mollinedo F, Gajate C. Microtubules, microtubule-interfering agents and apoptosis. Apoptosis 2003; 8: 413–50.
35 Jordan MA, Wendell K, Gardiner S, Derry WB, Copp H, Wilson L. Mitotic block induced in HeLa cells by low concentrations of paclitaxel (Taxol) results in abnormal mitotic exit and apoptotic cell death. Cancer Res 1996; 56: 816–25.
36 Tseng CJ, Wang YJ, Liang YC, Jeng JH, Lee WS, Lin JK, *et al*. Microtubule damaging agents induce apoptosis in HL60 cells and G2/M cell cycle arrest in HT29 cells. Toxicology 2002; 175: 123–42.
37 Wang LG, Liu XM, Kreis W, Budman DR. The effect of antimicrotubule agents on signal transduction pathways of apoptosis: a review. Cancer Chemother Pharmacol 1999; 44: 355–61.
38 Bhalla KN. Microtubule-targeted anticancer agents and apoptosis. Oncogene 2003; 22: 9075–86.

Acta Pharmacologica Sinica 2005 Aug; 26 (8): 1009–1016

Full-length article

Effect of curcumin on multidrug resistance in resistant human gastric carcinoma cell line SGC7901/VCR

Xiao-qing TANG[1], Hu BI[1], Jian-qiang FENG[2], Jian-guo CAO[3]

[1]Department of Physiology, Nanhua University, Hengyang 421001, China; [2]Department of Physiology, Zhongshan Medical College, Sun Yat-sen University, Guangzhou 510080, China; [3]Institute of Oncology, Nanhua University, Hengyang 421001, China

Key words

curcumin; multidrug resistance; apoptosis; P-glycoprotein; caspase-3

[3] Correspondence to Prof Jian-guo CAO.
Phn/Fax 86-73-4828-1673.
E-mail txq01001@163.com

Received 2005-01-27
Accepted 2005-03-31

doi: 10.1111/j.1745-7254.2005.00149.x

Abstract

Aim: To investigate the reversal effects of curcumin on multidrug resistance (MDR) in a resistant human gastric carcinoma cell line. **Methods:** The cytotoxic effect of vincristine (VCR) was evaluated by MTT assay. The cell apoptosis induced by VCR was determined by propidium iodide (PI)-stained flow cytometry (FCM) and a morphological assay using acridine orange (AO)/ethidium bromide (EB) dual staining. P-glycoprotein (P-gp) function was demonstrated by the accumulation and efflux of rhodamine123 (Rh123) using FCM. The expression of P-gp and the activation of caspase-3 were measured by FCM using fluorescein isothiocyanate (FITC)-conjugated anti-P-gp and anti-cleaved caspase-3 antibodies, respectively. **Results:** Curcumin, at concentrations of 5 μmol/L, 10 μmol/L, or 20 μmol/L, had no cytotoxic effect on a parent human gastric carcinoma cell line (SGC7901) or its VCR-resistant variant cell line (SGC7901/VCR). The VCR-IC_{50} value of the SGC7901/VCR cells was 45 times more than that of the SGC7901cells and the SGC7901/VCR cells showed apoptotic resistance to VCR. SGC7901/VCR cells treated with 5 μmol/L, 10 μmol/L, or 20 μmol/L curcumin decreased the IC_{50} value of VCR and promoted VCR-mediated apoptosis in a dose-dependent manner. Curcumin (10 μmol/L) increased Rh123 accumulation and inhibited the efflux of Rh123 in SGC7901/VCR cells, but did not change the accumulation and efflux of Rh123 in SGC7901 cells. P-gp was overexpressed in SGC7901/VCR cells, whereas it was downregulated after a 24-h treatment with curcumin (10 μmol/L). Resistant cells treated with 1 μmol/L VCR alone showed 77% lower levels of caspase-3 activation relative to SGC7901 cells, but the activation of caspase-3 in the resistant cell line increased by 44% when cells were treated with VCR in combination with curcumin. **Conclusion**: Curcumin can reverse the MDR of the human gastric carcinoma SGC7901/VCR cell line. This might be associated with decreased P-gp function and expression, and the promotion of caspase-3 activation in MDR cells.

Introduction

Although progress has been made in the treatment of patients with gastric cancer over the last two decades, a significant percentage of these patients fail to achieve complete remission or they relapse due to the phenomenon of multidrug resistance (MDR). In tumor cell lines, MDR is often associated with the overexpression of ATP-dependent drug efflux proteins belonging to the superfamily of ATP-binding cassette (ABC) transporters: the 170 kDa P-glycoprotein (P-gp) encoded by the MDR1 gene and the 190 kDa multidrug resistance-associated protein-1 encoded by the MRP-1 gene[1,2]. These proteins bind to and transport various structurally unrelated compounds to maintain their intracellular concentrations below cytotoxic levels.

Over the last two decades, considerable efforts have been

made to circumvent the problem with multidrug resistance. One approach is to use various resistance modulators to reverse MDR mechanisms and thus sensitize MDR tumor cells to anticancer drugs. Several compounds can reverse MDR, such as calcium channel blockers, CsA, MK571, buthionine sulfoximine (BSO) and genistein. However, the use of effective doses of these agents for systemic chemotherapy has been difficult because of their side effects and dose-limiting toxicity. Therefore, it is necessary to find new reversing agents that do not have the undesirable toxicological effects[3].

Curcumin is a natural phenolic coloring compound that is found in the rhizomes of *Curcuma longa* L, commonly called turmeric. It has been widely used as a spice, to color cheese and butter, as a cosmetic[4], and in some medicinal preparations[5]. Curcumin has a wide range of biological and pharmacological activities, including antioxidant properties[6], anti-inflammatory properties[5], anti-mutagenic activity[7], and anti-carcinogenic[8], hypocholesterolemic[9] and hypoglycemic effects[10]. The safety of *C longa* and its derivatives has been studied in various animal models[11], and it is clear that turmeric is not toxic even at high doses in laboratory animals. A single feeding of a 30% turmeric diet to rats did not produce any toxic effects. In a 24-h acute toxicity study, mice were fed doses of 0.5 g/kg, 1.0 g/kg, and 3.0 g/kg of turmeric extract daily. There was no increase in the mortality rate when compared with the controls in either study.

Because of its wide range of biological and pharmacological effects, and a lack of toxicity in animal models, curcumin has been examined to determine whether it interacts with MDR. *In vitro* studies have demonstrated that curcumin is able to modulate both the expression and function of P-gp in multidrug-resistant KB cells[12,13] and primary cultures of rat hepatocytes[14]. It is not clear whether curcumin can reverse the P-gp-mediated MDR of resistant gastric cancer cells. This led us to evaluate the effect of curcumin on the MDR of a vincristine (VCR)-resistant gastric cancer cell line (SGC7901/VCR). We found that treatment of drug-resistant SGC7901/VCR cells with curcumin increased their sensitivity to vincristine, which was consistent with decreased P-gp function and expression. In addition, curcumin was able to promote VCR-stimulated caspase-3 activation in SGC7901/VCR cells. It is possible that curcumin could be useful in the treatment of drug resistant gastric cancer cells as a MDR modulator.

Materials and methods

Reagents Curcumin, MTT, ethidium bromide (EB), acridine orange (AO) and rhodamine123 (Rh123) were obtained from Sigma (St Louis, MO, USA); vincristine (VCR) was obtained from Farmitalia Carlo Erba (Milan, Italy); the anti-cleaved caspase-3 antibody was purchased from Cell Signaling Technology (Beverly MA); the anti-P-gp antibody and FITC-conjugated goat antimouse IgG were bought from Beijing Zhongshan Biological Technology Co (Peking, China).

Cells and cell cultures Gastric cancer cell line SGC7901 and VCR-resistant gastric cancer SGC7901/VCR cells were kindly provided by the Department of Gastroenterology, Xijing Hospital, the Fourth Military Medical University (Xi'an China). The MDR subline SGC7901/VCR was developed by exposing the parental SGC7901 cells to increasing concentrations of the anticancer drug VCR. All cells were cultivated in RMPI-1640 supplemented with 10% heat-inactivated fetal bovine serum at 37 °C in a 5% CO_2 atmosphere. The medium for SGC7901/VCR cells was further supplemented with VCR (0.25 μmol/L). Before their use in experiments, the SGC7901/VCR cells were cultured in a drug-free medium for 2 weeks.

Cytotoxicity assay by MTT Cells were seeded into 96-well plates at densities of 1×10^4 SGC7901/VCR cells per well and 0.5×10^4 SGC7901 cells per well, and incubated in a humidified atmosphere of 5% CO_2+95% air overnight, then normal cell medium containing either test compounds or solvents at the desired concentration were added. After 72 h incubation, 20 μL MTT (5 g/L in phosphate buffered saline, PBS) were added. The plates were incubated for 4 h and the blue dye formed was dissolved in 100 μL dimethyl sulfoxide (DMSO or Me_2SO). The absorbance at 570 nm was recorded using an ELISA reader. The survival rate was calculated as follows:

$$\text{Survival rate}\,(\%)=(T-B)/(U-B)\times100\%$$

where T is the absorbance of treated tumor cells when exposed to drugs, U is the absorbance of untreated cells, B is the absorbance when neither the drug nor MTT was added (blank).

The 50% inhibitory concentration (IC_{50}) of 3 d exposure for a particular agent was defined as the drug concentration that causes in a 50% reduction in the number of cells compared with the untreated control. The IC_{50} values were determined by Bliss software.

Apoptosis assay by flow cytometer using propidium iodide staining Cells were treated with various concentrations of VCR and curcumin for 24 h, and then harvested with 0.25% trypsin and washed with PBS. Cells (2×10^5) were fixed in 70% ice-cold EtOH/PBS for 20 min on ice, and then washed with PBS and incubated in propidium iodide (PI) solution (69 mmol/L PI, 388 mmol/L sodium citrate, 100 μg/mL RNase A)

for 15 min at 37 °C. Cells were immediately analyzed with FAC scan flow cytometry (Becton Dickinson, San Jose, CA).

Apoptosis detection by morphological observation after AO/EB staining Cells were treated with various concentrations of VCR and curcumin for 24 h, and then harvested with 0.25% trypsin and resuspended in RPMI-1640 medium. After staining for 10 min with 4 mL of an AO (100 mg/mL)/EB (100 mg/mL) dye mixture, cells were visualized immediately under a fluorescence microscope.

Accumulation and efflux of Rh123 as measured by flow cytometry The measurement of Rh123 accumulation was performed as previously described[15]. Briefly, cells (5×10^5 per sample) were incubated with 1 μg/mL of Rh123 in the dark at 37 °C in 5% CO_2 for 120 min. Curcumin (dissolved in 0.1% DMSO) was added to cultures at the same time as Rh123. A final concentration of 0.1% Me_2SO (v/v) was used for all experiments and controls. Following Rh123 accumulation, cells were washed twice with ice-cold Hanks' Balanced Salt (HBSS) (without phenol red), placed in HBSS with 10% fetal bovine serum on wet ice. The green fluorescence of Rh123 was measured by using a FAC scan flow cytometer (Becton Dickinson).

For determination of Rh123 efflux, cells were loaded for 60 min with Rh123 in the absence of curcumin, and then the medium was replaced with Rh123-free medium containing curcumin, or the vehicle (Me_2SO). Following efflux intervals of 60 min, the medium was removed, and the cells were washed twice with ice-cold HBSS and prepared for flow cytometry as described earlier. As measured by Trypan blue exclusion, the cells remained viable during the Rh123 accumulation and efflux studies with curcumin.

Flow-cytometric analysis of the expression of P-gp and the activation of caspase-3 The cells were collected and adjusted to a concentration of 1×10^6 cells per mL and centrifuged at 1500×*g* for 5 min at 20 °C. The cell pellet was resuspended in 20 mL anti-P-gp or anti-active caspase-3 antibody (1:400), and then incubated at 4 °C for 30 min while being protected from light. After three washes with cold PBS containing l % fetal calf serum (FCS), cells were incubated while being protected from light at 4 °C for 30 min with FITC-conjugated goat antimouse IgG (l:1000). Then cells were centrifuged at 1500×*g* for 5 min at 20 °C and were resuspended with PBS. The fluorescence intensity of cells was then analyzed by using a flow cytometer (Becton Dic-kinson).

Statistical analysis Data were expressed as mean±SD. Student's *t*-test was used to assess the statistical significance of differences. $P<0.05$ was considered to be statistically significant.

Results

Cytotoxic effect of curcumin on SGC7901 and SGC7901/VCR cells We found that 1–20 μmol/L curcumin was not obviously cytotoxic to gastric cancer cell line SGC7901 or VCR-resistant gastric cancer SGC7901/VCR cells (survival rate >85%). However, 40–160 μmol/L curcumin caused significant cytotoxicity in SGC7901 and SGC7901/VCR cells (Figure 1). Because treatment of the cells with 5 μmol/L, 10 μmol/L, and 20 μmol/L curcumin had no significant effect on cell viability, we used these concentrations for further analysis.

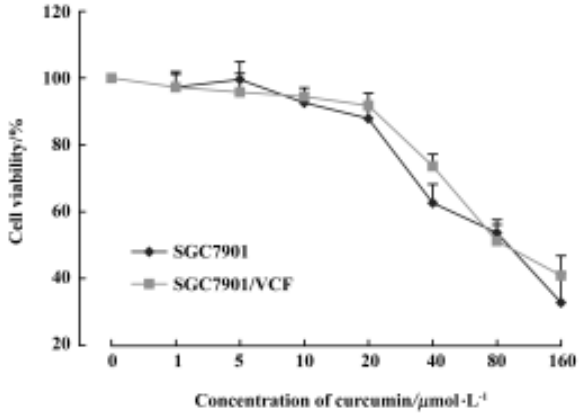

Figure 1. Effects of curcumin on SGC7901 and SGC7901/VCR cells growth. Cells were treated with various curcumin concentrations for 3 d. *n*=3 independent experiments. Mean±SD.

Effect of curcumin on VCR resistance in SGC7901/VCR cells The IC_{50} values of VCR were 0.49 μmol/L and 22.27 μmol/L in the sensitive and resistant lines, respectively, which indicated that the SGC7901/VCR cell line was 45 times more resistant to VCR than the parent SGC7901 cell line. As shown in Figure 2, when 5 μmol/L, 10 μmol/L, or 20 μmol/L curcumin was added, the IC_{50} value of VCR in the SGC7901/VCR cell line significantly decreased from 22.27 μmol/L to 11.60 μmol/L, 3.28 μmol/L, and 1.53 μmol/L, respectively, in a dose-dependent manner. After treatment with 20 μmol/L verapamil (positive control), the IC_{50} value of VCR in the SGC7901/VCR cell line only decreased from 22.27 μmol/L to 3.13 μmol/L.

Effect of curcumin on the apoptotic resistance of SGC7901/VCR cells Apoptotic cells were quantified as the proportion of cells that had a DNA content of less than 2N (sub-G_1 DNA content)[16]. As shown in Figure 3, after treatment with 1 μmol/L VCR for 24 h, the apoptosis of SGC7901/VCR cells was only 12.5%, but significant apoptosis was observed in the parental cells (61.4%, $P<0.01$) at the same

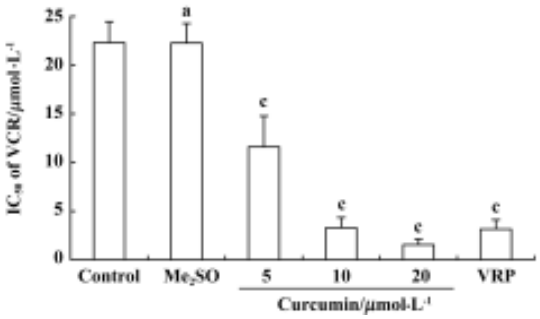

Figure 2. Effect of curcumin on VCR resistance in SGC7901/VCR cells. The SGC7901/VCR cells were grown in medium with 0.1% Me_2SO (vehicle control), 5 μmol/L, 10 μmol/L, 20 μmol/L curcumin or 20 μmol/L verapamil (positive control) in the presence of different concentration of VCR. The cell viability was determined by MTT assay and the IC_{50} of VCR was analyzed by Bliss software. n=3 independent experiments. Means±SD ^aP>0.05, ^cP<0.01 *vs* control group.

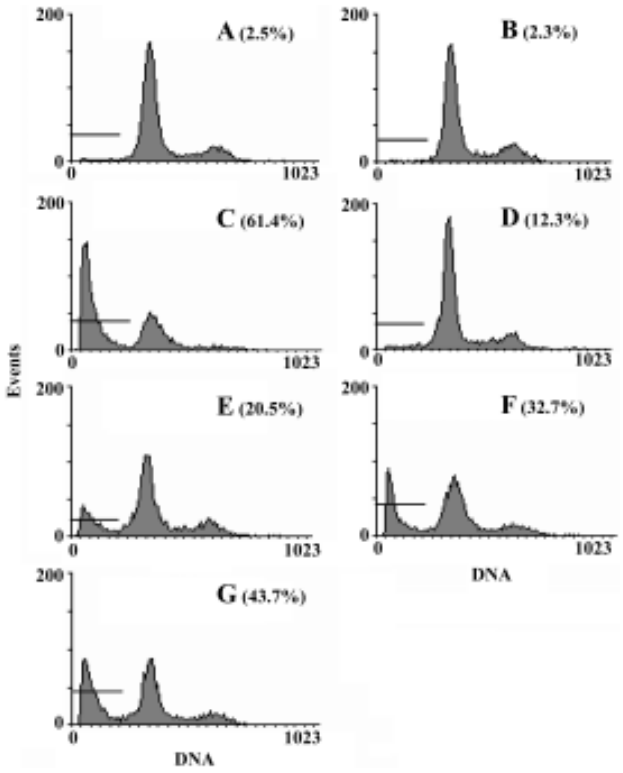

Figure 3. Effect of curcumin on the apoptosis of SGC7901/VCR cells. A, B: SGC7901/VCR cells were treated by 0.1% Me_2SO and 10 μmol/L of curcumin for 24 h, respectively; C, D: SGC7901 and SGC7901/VCR cells were treated by 1 μmol/L of VCR for 24 h, respectively; E, F, G: SGC7901/VCR cells were treated with 1 μmol/L of VCR combination with 5, 10, 20 μmol/L of curcumin for 24 h, respectively. The percentage of apoptotic cells was assayed by flow cytometer using propidum iodide staining.

drug concentration, indicating that SGC7901/VCR cells had apoptotic resistance to VCR. Curcu-min, at concentrations of 5 μmol/L, 10 μmol/L, and 20 μmol/L for 24 h, promoted the VCR-mediated apoptosis of SGC7901/VCR cells from 12.3% to 20.5%, 32.7%, and 43.7%, respectively, in a dose-dependent manner. Moreover, AO/EB staining also revealed that curcumin promoted VCR-induced apoptosis in SGC7901/VCR cells (Figure 4). These results demonstrate that curcumin is able to overcome the apoptotic resistance of SGC7901/VCR cells to VCR.

Effect of curcumin on P-gp functions To examine the function of P-gp on the surface of viable cells, Rh123 accumulation and efflux studies were chosen because they appear to be sensitive indicators of P-gp activity when assayed by FAC scans[17,18]. As shown in Figure 5A, Rh123 accumulation in SGC7901/VCR cells was obviously less than that in SGC7901 cells after being incubated with Rh123 for 120 min (P<0.01). After treatment with curcumin (10 μmol/L), Rh123 accumulation in SGC7901/VCR cells was increased by 40%; however, there was no change in SGC7901 cells. The effect of curcumin on the P-gp-mediated efflux of Rh123 in SGC7901 and SGC7901/VCR cells was also examined. As shown in Figure 5B, Rh123 retention in SGC7901/VCR cells was obviously less than that in SGC7901 cells. When SGC7901/VCR cells were treated with curcumin (10 μmol/L) for 60 min, Rh123 retention increased by 80% compared with the vehicle control (0.1% Me_2SO), indicating that curcumin could cause a significant decrease in Rh123 efflux. However, in SGC7901 cells, there was no change in Rh123 retention in the presence of curcumin.

Effect of curcumin on P-gp expression Cells were plated at a concentration of 6×10^4 cells per mL in supplemented RPMI-1640. At 24 h after plating, the medium was replaced with fresh medium containing 0.1% Me_2SO (vehicle control) or 10 μmol/L curcumin. After 24 h, cells were collected to examine the expression of P-gp by flow cytometry. The expression rate of P-gp was 42.73% in SGC7901/VCR cells and 2.03% in SGC7901 cells. Treatment with curcumin (10 μmol/L) for 24 h led to downregulation of P-gp expression in MDR cells. The expression rates of P-gp in SGC7901/VCR cells decreased from 42.73% to 17.69% after curcumin treatment (Figure 6).

Effect of curcumin on the activation of caspase-3 in SGC7901/VCR cells The activation of caspase-3 was assessed by examining the expression of cleaved caspase-3 by flow cytometry. SGC7901/VCR cells treated with VCR (1 μmol/L) alone for 24 h showed 77% lower levels of caspase-3 activation than did SGC7901 cells (Figure 7). When cells were treated with VCR (1 μmol/L) in combination with

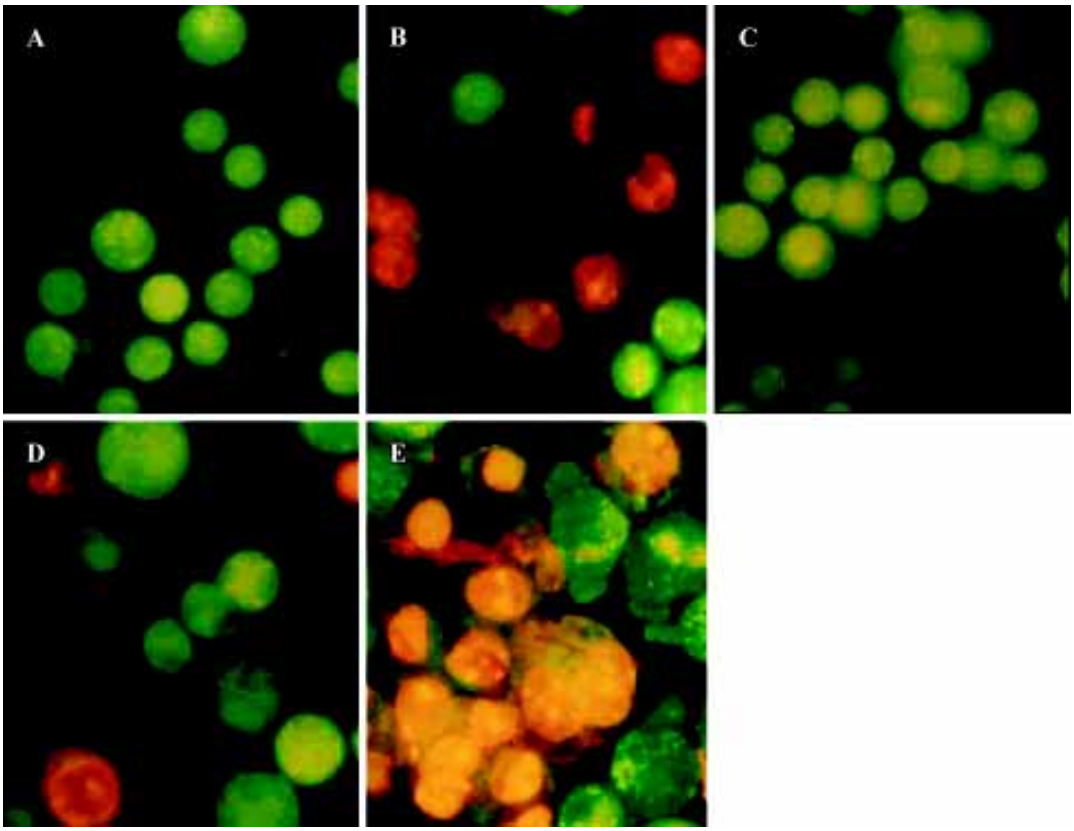

Figure 4. Apoptosis of SGC7901 and SGC7901/VCR cells detected by AO/EB staining. A, SGC7901 cells; B, SGC7901 cells treated by 1 μmol/L of VCR for 24 h; C, SGC7901 /VCR cells; D, SGC7901 /VCR cells treated by 1 μmol/L of VCR for 24 h; E, SGC7901/VCR cells treated by 1 μmol/L of VCR combination with 20 μmol/L of curcumin for 24 h. Apoptotic cells detected by morphological observation after AO/EB staining.

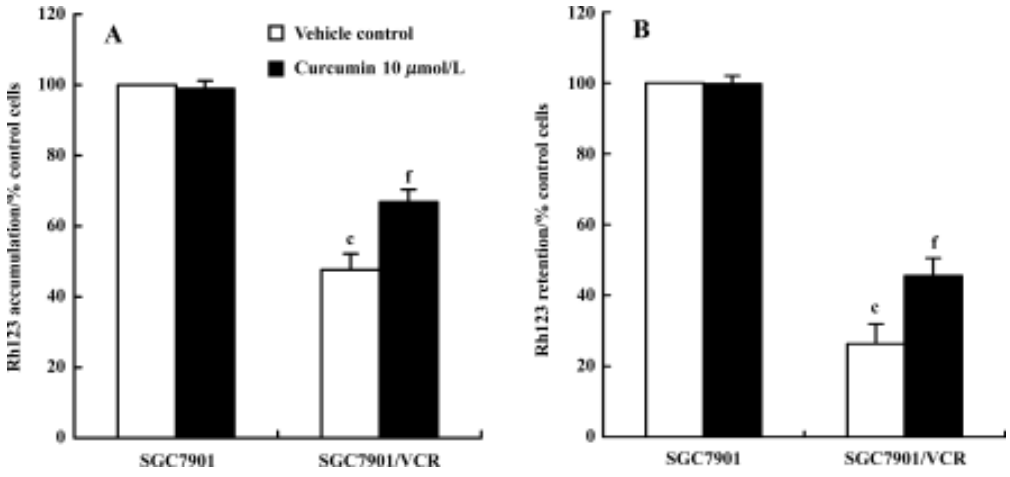

Figure 5. Effects of curcumin on Rh123 accumulation (A) and retention (B) in SGC7901 and SGC7901/VCR cells. (A) Cells treated with 10 μmol/L curcumin or vehicle control (0.1% Me_2SO). Rh123 (1 μg/mL) was added, and the cells were incubated for 120 min. (B) Cells were incubated with Rh123 for 60 min, washed, and resuspended in medium with 10 μmol/L curcumin or vehicle control (0.1% Me_2SO) for 60 min. Rh123 fluorescence was measured using FAC scan. Means±SD from three independent experiments. $^{c}P<0.01$ *vs* SGC7901 cells. $^{f}P<0.01$ *vs* vehicle control.

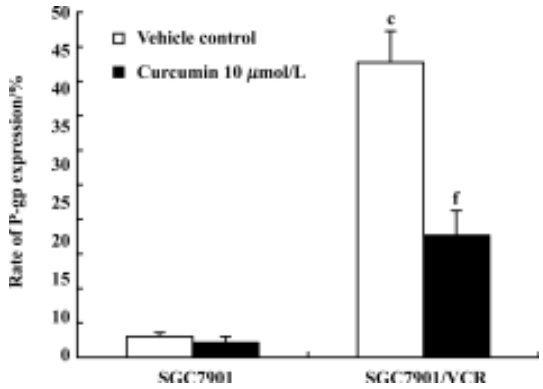

Figure 6. Effect of curcumin on the expression of P-gp in SGC7901/VCR cells. The level of P-gp expression, following treatment with 0.1% Me_2SO (vehicle control) or curcumin (10 μmol/L) for 24 h, was determined in cells by flow cytometer. Means±SD from three independent experiments. $^cP<0.01$ *vs* SGC7901 cells. $^fP<0.01$ *vs* vehicle control.

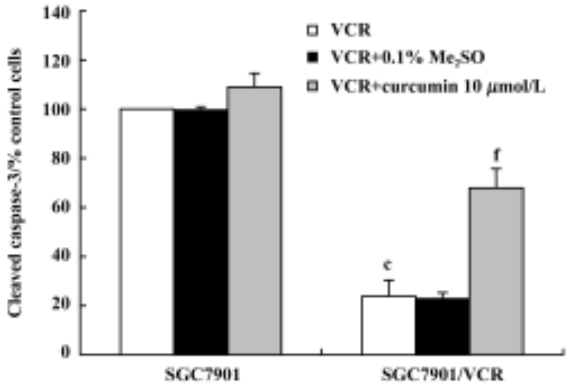

Figure 7. Effect of curcumin on the activation of caspase-3 in cells. The level of caspase-3 activation, following treatment with VCR (1 μmol/L) in the presence or absence of 0.1% Me_2SO (vehicle control) and curcumin (10 μmol/L) for 24 h, was determined by flow cytometer. Means±SD from three independent experiments. $^cP<0.01$ *vs* SGC7901 cells. $^fP<0.01$ *vs* VCR treatment alone.

curcumin (10 μmol/L) for 24 h, the activation of caspase-3 was increased by 44% ($P<0.01$) in the SGC7901/VCR cell line.

Discussion

The development of P-gp-dependent multidrug resistance in tumors is a major obstacle for successful chemotherapy[19]. For this reason, there is an increasing search for new reagents that inhibit the expression and/or function of P-gp to overcome MDR. Recent studies have shown that curcumin is able to modulate the expression and function of P-gp, and therefore it might be an possible new agent for the chemosensitization of cancer cells[12–14]. VCR-resistant gastric cancer SGC7901/VCR cells have been shown to express P-gp at a high level, but P-gp was not expressed in the drug-sensitive cells (SGC7901)[20]. Thus, in the present study, we wanted to demonstrate the possibility of using curcumin in gastric cancer as an MDR modulator.

We showed that curcumin enhanced the toxicity of VCR in the MDR cell line SGC7901/VCR. The SGC7901/VCR cell line was 45 times more resistant than the parental SGC7901 cell line. Curcumin, at concentrations of 5.0 μmol/L, 10.0 μmol/L and 20.0 μmol/L, is able to decrease the IC_{50} of VCR to SGC7901/VCR cells in a dose-dependent manner. These data indicate that curcumin is able to reverse MDR in the SGC7901/VCR cell line.

The potent MDR-reversing capacity of curcumin in tumor cells was further confirmed by its ability to enhance VCR-induced apoptosis in MDR SGC7901/VCR cells. Apoptotic and anti-apoptotic character are also strongly related to drug sensitivity and resistance. A number of tumor cells have been reported to undergo apoptotic cell death when treated with such chemotherapeutic agents as etoposide, camptothecin, cisplatin, Ara-C, mitomycin C, adriamycin, and vincristine. These findings indicate that apoptosis in tumor cells plays a critical role in chemotherapy-induced tumor cell killing, and also suggest that blockade of the apoptosis-inducing pathway could be another mechanism for MDR to chemotherapy[21]. VCR, at a concentration of 1 μmol/L, did not induce apoptosis in SGC7901/VCR cells, but significantly induced apoptosis in the parental cells, which indicated that the MDR SGC7901/VCR cell line was also apoptosis-resistant. In our study, we found that curcumin could promote the VCR-mediated apoptosis of MDR SGC7901/VCR cells, which suggests that curcumin could overcome the apoptosis-resistance of MDR cells.

The experiment for evaluating the effect of curcumin treatment on P-gp expression determined that curcumin clearly inhibited P-gp expression in SGC7901/VCR cells. The uptake and/or efflux of Rh123 is frequently used for assays of P-gp in tumor cells[22,23]. In the present study, we also investigated the effects of curcumin on the P-gp function of SGC7901/VCR cells. Curcumin caused a substantial increase in the accumulation of Rh123 in SGC7901/VCR cells, and inhibited the efflux of Rh123, but had no effect on drug-sensitive cells (SGC7901), which do not overexpress P-gp. Because Rh123 is known to be a good substrate for P-gp, we suppose that curcumin modulates intracellular Rh123 level by inhibiting P-gp. It is unlikely that curcumin acts by downregulating P-gp expression because the time of exposure of cells to curcumin in these experiments was short (1–2 h). Taken together, our data indicate that treatment of

drug-resistant SGC7901/VCR cells with curcumin increased their sensitivity to VCR, which is consistent with an increase in intracellular drug concentration by decreasing P-gp function and expression.

Although P-gp is best known for its ability to efflux a variety of amphiphilic substances across plasma membranes, new functions are emerging. Transfected MDR1 in Chinese hamster ovary fibroblasts results in a decrease in growth factor withdrawal-induced apoptosis[24]. P-gp has been shown to inhibit apoptosis induced by anti-fas, ultraviolet radiation, and tumor necrosis factor in both lymphoid and myeloid cell lines[25,26], to resist spontaneous apoptosis in acute myeloid leukemia (AML) blasts[27,28], and is implicated in the inhibition of ceramide-induced apoptosis in TF-1 cells[29]. P-gp has also been shown to protect kidney proximal tubule cells from cadmium- and oxygen species-induced apoptosis[30]. Therefore we suggest that, besides exporting a wide range of xenobiotics from cells, the multidrug transporter P-gp may also confer resistance to apoptosis from different stimuli. Our results suggest that the ability of curcumin to promote VCR-induced apoptosis in drug-resistant SGC7901/VCR cells might be associated with a decrease in P-gp function and expression.

Recent studies have shown that functional P-gp plays a role in regulating cell death not only by removing drugs from the cell, but also by inhibiting the activation of proteases involved in apoptotic signaling (caspase-8)[25] and execution (caspase-3)[25,26]. In agreement with this, our data indicate that SGC7901/VCR cells inhibited VCR-induced caspase-3 activation. However, treatment of drug-resistant SGC7901/VCR cells with curcumin promoted VCR-induced caspase-3 activation. The results of a previous study have demonstrated that curcumin overcomes P-gp-mediated multidrug resistance through induction of caspase-3 activation[31]. Our results indicate that the MDR reverse function of curcumin may be associated with promoting anticancer agent-induced caspase-3 activation.

Summing up, our results suggest that curcumin could be considered a promising chemosensitizer of MDR in gastric cancer.

References

1 Lehne G. P-glycoprotein as a drug target in the treatment of multidrug resistant cancer. Curr Drug Targets 2000; 1: 85–99.

2 Hamilton KO, Topp E, Makagiansar I, Siahaan T, Yazdanian M, Audus KL. Multidrug resistance-associated protein-1 functional activity in Calu-3 cells. J Pharmacol Exp Ther 2001; 298: 1199–205.

3 Silva KL, Vasconcelos FC, Marques-Santos LF, Kwee JK, Maia RC. CPT-11-induced cell death in leukemic cells is not affected by the MDR phenotype. Leukemia Res 2003; 27: 243–51.

4 Suhaimi H, Ahmad FB, Friberg SE. Curcumin in a model skin lotion formulation. J Pharm Sci 1995; 84: 376–80.

5 Ammon HPT, Wahl MA. Pharmacology of *Curcuma longa*. Planta Med 1991; 57: 1–7.

6 Mishra B, Priyadarsini KI, Bhide MK, Kadam RM, Mohan H. Reactions of superoxide radicals with curcumin: probable mechanisms by optical spectroscopy and EPR. Free Radic Res 2004; 38: 355–62.

7 Nagabhushan M, Bhide SV. Nonmutagenicity of curcumin and its antimutagenic action versus chili and capsaicin. Nutr Cancer 1986; 8: 201–10.

8 Limtrakul P, Anuchapreeda S, Lipigorngoson S, Dunn FW. Inhibition of carcinogen induced c-Ha-ras and c-fos proto-oncogenes expression by dietary curcumin. BMC Cancer 2001; 1: 1–7.

9 Asai A, Miyazawa T. Dietary curcuminoids prevent high-fat diet-induced lipid accumulation in rat liver and epididymal adipose tissue. J Nutr 2001; 131: 2932–5.

10 Suryanarayana P, Krishnaswamy K, Reddy GB. Effect of curcumin on galactose-induced cataractogenesis in rats. Mol Vis 2003; 9: 223–30.

11 Qureshi S, Shah AH, Ageel AM. Toxicity studies on Alpinia galanga and *Curcuma longa*. Planta Med 1992; 58: 124–7.

12 Anuchapreeda S, Leechanachai P, Smith MM, Ambudkar SV, Limtrakul PN. Modulation of P-glycoprotein expression and function by curcumin in multidrug-resistant human KB cells. Biochem Pharmacol 2002; 64: 573–82.

13 Limtrakul P, Anuchapreeda S, Buddhasukh D. Modulation of human multidrug-resistance MDR-1 gene by natural curcuminoids. BMC Cancer 2004; 4: 13.

14 Romiti N, Tongiani R, Cervelli F, Chieli E. Effects of curcumin on P-glycoprotein in primary cultures of rat hepatocytes. Life Sci 1998; 62: 2349–58.

15 Chaudhary PM, Roninson IB. Expression and activity of P-glycoprotein, a multidrug efflux pump, in human hematopoietic stem cells. Cell 1991; 66: 85–94.

16 Maxwell SA, Davis GE. Biological and molecular characterization of an ECV-304-derived cell line resistant to p53-mediated apoptosis. Apoptosis 2000; 5: 277–90.

17 Efferth T, Lohrke H, Volm M. Reciprocal correlation between expression of P-glycoprotein and accumulation of rhodamine 123 in human tumors. Anticancer Res 1989; 9: 1633–7.

18 Chaudhary PM, Roninson IB. Expression and activity of P-glycoprotein, a multidrug efflux pump, in human hematopoietic stem cells. Cell 1991; 66: 85–94.

19 Arceci RJ. Tumor cell survival and resistance to therapy. Curr Opin Hematol 1996; 3: 279–287.

20 Cao JG, Tang XQ, Shi SH. Multidrug resistance reversal in human gastric carcinoma cells by neferine. World J Gastroenterol 2004; 10: 3062–4.

21 Tsuruo T, Naito M, Tomida A, Fujita N, Mashima T, Sakamoto H *et al*. Molecular targeting therapy of cancer: drug resistance, apoptosis and survival signal. Cancer Sci 2003; 94: 15–21.

22 Chen LM, Liang YJ, Ruan JW, Ding Y, Wang XW, Shi Z, *et al*. Reversal of P-gp mediated multidrug resistance *in-vitro* and *in-vivo* by FG020318. J Pharm Pharmacol 2004; 56: 1061–6.

23 Liu ZL, Hirano T, Tanaka S, Onda K, Oka K. Persistent reversal of P-glycoprotein-mediated daunorubicin resistance by tetrandrine

in multidrug-resistant human T lymphoblastoid leukemia MOLT-4 cells. J Pharm Pharmacol 2003; 55: 1531–7.

24 Robinson LJ, Roberts WK, Ling TT, Lamming D, Sternberg SS, Roepe PD. Human MDR1 protein overexpression delays the apoptotic cascade in Chinese hamster ovary fibroblasts. Biochemistry 1997; 36: 11169–78 .

25 Johnstone RW, Cretney E, Smyth MJ. P-glycoprotein protects leukemia cells against caspase-dependent, but not caspase-independent, cell death. Blood 1999; 93: 1075–85.

26 Smyth MJ, Krasovskis E, Sutton VR, Johnstone RW. The drug efflux protein, P-glycoprotein, additionally protects drug-resistant tumor cells from multiple forms of caspase-dependent apoptosis. Proc Natl Acad Sci USA 1998; 95: 7024–9.

27 Pallis M, Russell N. P-glycoprotein plays a drug-efflux-independent role in augmenting cell survival in acute myeloblastic leukemia and is associated with modulation of a sphingomyelin-ceramide apoptotic pathway. Blood 2000; 95: 2897–904.

28 Pallis M, Turzanski J, Grundy M, Seedhouse C, Russell N. Resistance to spontaneous apoptosis in AML blasts is associated with P-glycoprotein exression and function, but not with the presence of FLT3 internal tandem duplications. Br J Haematol 2003; 120: 1009–16.

29 Turzanski J, Grundy M, Shang S, Russell N, Pallis M. P-glycoprotein is implicated in the inhibition of ceramide-induced apoptosis in TF-1 acute myeloid leukemia cells by modulation of the glucosylceramide synthase pathway. Exp Hematol 2005; 33: 62–72.

30 Thevenod F, Friedmann JM, Katsen AD, Hauser IA. Up-regulation of multidrug resistance P-glycoprotein via nuclear factor-kappaB activation protects kidney proximal tubule cells from cadmium- and reactive oxygen species-induced apoptosis. J Biol Chem 2000; 275: 1887–96.

31 Bielak-Mijewska A, Piwocka K, Magalska A, Sikora E. P-glycoprotein expression does not change the apoptotic pathway induced by curcumin in HL-60 cells. Cancer Chemother Pharmacol 2004; 53: 179–85.

The First Scientific Meeting of the Asian Society for Vascular Biology

October 8–11, 2005 Shanghai, China

Info: Yu HUANG
Department of Physiology
Chinese University of Hong Kong
Hong Kong SAR, China
Phn 852-2609-6787
Fax 852-2603-5022
E-mail yu-huang@cuhk.edu.hk
http://www.sbsonline.org/sbscon/2005/index.php

Acta Pharmacologica Sinica 2005 Aug; 26 (8): 1017–1024

Full-length article

Effects of navelbine and docetaxel on gene expression in lung cancer cell strains[1]

Li CAI[2], Hai-ying DONG, Guang-jie SUI

Internal Medicine of Oncology, the Third Affiliated Hospital of Harbin Medical University, Harbin 150040, China

Key words

cDNA macroarray; lung neoplasms; navelbine; docetaxel

[1] Project supported by a Repatriation Grant from the Foundation of Science Bureau of Harbin, China (2003AFLXJ009), also funded by Overseas Scholar Grant from the Department of Education of HeiLongJiang Province,China (1055HZ020).
[2] Correspondence to Dr Li CAI.
Phn 86-451-8878-1355.
Fax 86-451-8866-9005.
E-mail caiwenxin76@yahoo.com.cn

Received 2005-01-21
Accepted 2005-05-19

doi: 10.1111/j.1745-7254.2005.00142.x

Abstract

Aim: To search genes sensitivity to the anti-cancer drugs navelbine (NVB) and docetaxel (DOC) in small-cell lung cancer (SCLC) and non-small-cell lung cancer (NSCLC) cell strains. **Methods:** The sensitivity of 4 strains of SCLC and 6 strains of NSCLC to NVB and DOC was evaluated using the MTT assay. The expression of 1291 sensitive-related genes to the anti-cancer drugs in 10 lung cancer cell strains was measured using cDNA macroarrays and the relationship was analyzed. **Results:** In total, there were 56 ($r \geq 0.4$) genes sensitive to NVB and DOC. For NVB: 36 genes were sensitive to NVB, 20 co-expressed genes between the SCLC+NSCLC set and the NSCLC set; 27 expressed genes and 7 specially expressed genes in the SCLC+NSCLC set; and 29 expressed genes and 9 specially expressed genes in the NSCLC set. For DOC, 50 genes were sensitive to DOC, 12 co-expressed genes between the SCLC+NSCLC set and the NSCLC set; 24 expressed genes and 12 specially expressed genes in the SCLC+NSCLC set; and 38 expressed genes and 26 specially expressed genes in the NSCLC set. The genes sensitive to NVB and DOC in lung-cancer cell stains were mainly divided into the following 4 categories: signal transduction molecules, cell factors, transcription factors and metabolism-related enzymes and inhibitors. **Conclusions:** There were obvious differences in genes related to NVB and DOC between SCLC and NSCLC cell strains, but the same as categories of function.

Introduction

Chemotherapy failure in lung cancer is usually caused by multidrug resistance. Discovering ways to overcome resistance to chemotherapeutic drugs is the main problem to be resolved. There are different mechanisms of resistance to different drugs, while various mechanisms can produce resistance to the same drug. Many of these mechanisms, such as drug transition protein (CABC and lung cancer resistant protein), change the molecular target, the state of detoxifying enzymes, the obstruction of apoptosis, the repairing ability of DNA or the activity of oncogenes. Much work has been reported on the function of drug resistant genes in lung cancer using calcium antagonists and the MTT assay, as well as other methods, but there are few reports about the relationship between anticancer drug sensitivity and related genes.

Gene chip technology has provided a powerful tool to study the expression profile of genes and their related genes, providing much better data than the previous gene-monitoring techniques. The cDNA gene chip techniques can be divided into 2 types according to the different density of hybridized genes: (i) macroarrays[1]; and (ii) microarrays[2]. Macroarrays are better than microarrays in that they are economical, have a high level of repeatability and therefore accuracy, and they do not require special instruments. We therefore used macroarrays to measure the gene expression profiles of 10 lung cancer cell strains. We also measured drug sensitivity to navelbine (NVB) and docetaxel (DOC) in 10 lung cancer cell strains using the MTT assay, and analyzed the relationship between them. The precision of our results was then confirmed by reverse transcription–polymerase chain reaction (RT-PCR). This outcome has significance for clinical therapy.

Materials and methods

Cell strains There were 11 cell strains used in the experiments, of which 6 were NSCLC strains (LK-2, PC-7, PC-9, PC-14, A549 and Lu65) and 4 were SCLC strains (H69, N231, Lu135 and SBC-3); BET2A was used as a control. All cell strains were cultured in RPMI 1640 supplemented with 5% fetal bovine serum at 37 ºC in humidified air containing 5% CO_2.

Concentration adjustment of anticancer drugs The concentration of NVB was adjusted to within the range 0.005 μg/mL–10 μg/mL using RPMI 1640, and DOC was adjusted to within the range 0.005 μg/mL–50 μg/mL using dimethylsulphoxide (DMSO).

Measurement of cell sensitivity to anticancer drugs Sensitivity to the anticancer drugs was assessed using the MTT assay[3]. The IC_{50} was calculated using the Reed-Muench method[4], while the index of sensitivity was calculated as: IC_{50}/peak plasma concentration (PPC).

Anticancer drug sensitivity-related genes Genes related to anticancer drug sensitivity were assessed using cDNA macroarray.

Isolation of mRNA from total RNA Total RNA was isolated from 1×10^8 cells, which were grown in suspension, at A_{260}/A_{280} ratio$\in$[1.8, 2.0]. mRNA was isolated by incubation with oligo-dT-magentic beads (Toyobo Co, Osaka, Japan), followed by washing to remove non-specific binding.

Reverse transcription-polymerase chain reaction and labeling of the mRNA polyA$^+$RNA 0.8 μg was picked and RT-PCR was carried out using the RT, Rever TraAce (Toyobo Co, Osaka, Japan). The probes were labeled with biotin by incorporation of biotin-16-dUTP during the synthesis of cDNA.

Making the filters Gene Navigator cDNA Array System-Cancer Selected (Geneticlab, Sapporo Co, Osaka, Japan) was used. Anti-cancer drug-sensitivity genes (1291 species) were spotted onto the filter in duplicate. There were 280 non-mammalian genes and 49 housekeeping genes as negative controls[5]. A list of the set of genes on the filter is shown on the web site(http: //www.toyobo.co.jp/seihin/xr/product/genenavi/genenavigator.html).

cDNA array hybridization Filters were preincubated in 30 mL Perfect Hyb (Toyobo Co, Osaka,Japan) at 68 ºC for 30 min. Biotin-labeled probes (100 μL) were denatured at 100 ºC for 5 min before being added to the prehybridization solution. The filters were incubated in the hybridization mixture at 68 ºC for 20 h, then the filters were washed 3 times at 68 ºC for 10 min using 30 mL 2×SSC/0.1% sodium dodecylsulfate (SDS) and 0.1×SSC/0.1% SDS.

Signal measuring After washing the filters, specific signals on the filters were detected using the Imaging High Chemifluorescence Detection Kit (Toyobo Co, Osaka,Japan). Vistra ECF substrate (AttoPhos) (Amersham Pharmacia Biotech,Uppsala,Sweden)was used as the chemifluorescence substrate. Substrate images were acquired by Fluorimager (Amersham Pharmacia Biotech,Uppsala, Sweden).

Measuring gene expression The drugs were clustered on the basis of Pearson correlation coefficients relating their patterns across the 10 cell strains to the expression patterns of genes. These correlation coefficients were calculated for each combination of gene and drug by taking the level of expression of the gene in each cell line, enhancing it by the corresponding sensitivity of the cell to the drug, summing the results over all of the cell strains and renormalizing. This produced 1291 correlation coefficients (1 for each gene and target) for each of the 2 drugs. We then clustered the 2 drugs on the basis of these correlation coefficients.

Computer soft analysis "A" was designed as a drug active model (the drug sensitivity of 10 lung cancer cell strains to NVB and DOC-IC_{50}), Tr was the related data model of the level of mRNA expression (the expression of 1291 genes from 10 lung cell strains), and gene expression data included the rate of expression intensity of measuring gene and BET2A cells.

Statistical analysis The AT-clustered image map (CIM; Figure 1 and Figure 2) summarizes the relationship between drug activity and gene expression by means of the clustering method. In this CIM, drugs were together with related genes, and genes were also together with related drugs. Each color reflects the connection of one gene and one drug. For example, a red point (high positive Pearson correlation coefficient) indicates that cell strains with more expressed genes tend to be more sensitive to the agent; a blue point (high negative Pearson correlation coefficient) indicates the opposite; a yellow point and a green point indicate a lower correlation.

Expression of clusterin, galectin-1 mRNA Following RT-PCR, Generunner software was used to design specific primers (Table 1), and the specificity of the primer was proved through the BLAST(Basic Local Alignment Search Tool) internet database. Total RNA was extracted from LK-2 and A549 cell lines according to methods described previously and the first chain was finished through RT-PCR. b-Actin was used as an internal control.

The PCR amplification products were visualized by bromide-ethyl pastille following sodium dodecyl sulphate-polyacrylamide gel electrophoresis with the DL-2000 molecular weight standard (Generunner).

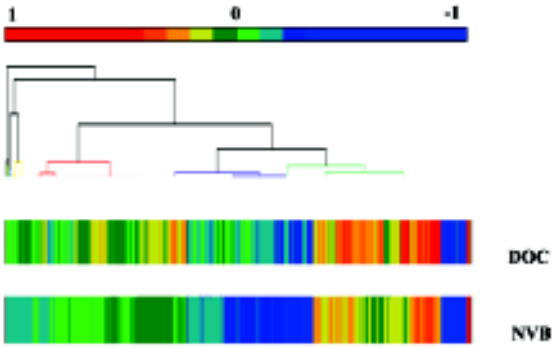

Figure 1. Comparison of the effects of docetaxel (DOC) and navelbine (NVB) on the clustered image map in 10 lung cancer cell strains.

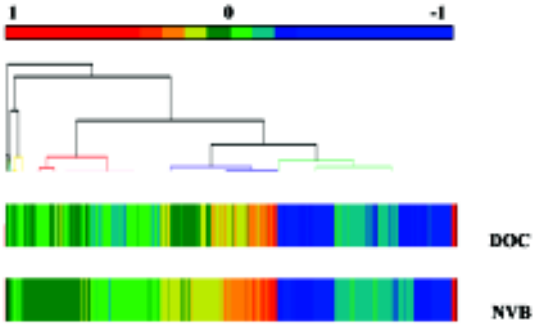

Figure 2. Comparison of the effects of docetaxel (DOC) and navelbine (NVB) on the clustered image map in NSCLC. Gene expression analysis for genes sensitive to DOC and NVB in lung cancer cell strains is detailed in Table 3 and Table 4.

Table 1. Length of reverse transcription-polymerase chain reaction primers and products.

Sample	Sequence of primer (5'-3')	Product size (bp)
Clusterin		469
Forward	GGAGTGTGCAATGAGACCATGATGG	
Reverse	GCTGAGCCTCGTGTATCATCTCAAGG	
Galectin		422
Forward	AATCATGGCTTGTGGTCTGGTC	
Reverse	CTGGCTGATTTCAGTCAAAGGC	
β-Actin		501
Forward	AGCGCAAGTACTCCGTGTG	
Reverse	AAGCAATGCTATCACCTCC	

Results

Comparison of the sensitivity of the lung cancer cell strains to navelbine and docetaxel The anti-cancer drug sensitivity of the lung cancer cell strains to NVB was greater than that to DOC (Table 2).

Comparing the clustered image map of the drugs with the clustered image map of genes The study related the 1291 gene expression profiles from the CIM of the lung cancer cell strains to NVB and DOC (Figure 1 and Figure 2). In the 10 lung cancer cell strains, there were more genes positively correlated to DOC than to NVB, but there were more genes negatively related to NVB than to DOC. Of the 6 NSCLC cell strains, there were more genes that expressed either positive or negative correlations to DOC than to NVB.

Table 2. Comparison of the anticancer sensitivity of lung cancer cell strains to navelbine (NVB) and docetaxel (DOC)*.

Cell stains	IC_{50}/μg·mL^{-1}		IC_{50}/PPC	
	NVB	Doc	NVB	Doc
N231	0.006±0.004	6.035±2.685	0.057±0.038	3.018±1.342
Lu135	0.022±0.016	0.529±0.189	0.223±0.116	0.265±0.095
H69	0.020±0.016	4.716±1.801	0.200±0.165	2.342±0.875
SBC-3	0.508±0.104	>50	5.080±1.044	>25.00
Lu65	0.064±0.030	3.606±1.388	0.637±0.301	1.803±0.694
LK-2	0.025±0.014	26.312±3.329	0.247±0.142	13.140±1.679
PC-9	1.430±0.436	21.336±5.380	14.303±4.365	13.970±8.235
PC-7	2.642±0.960	2.456±1.223	26.423±9.599	1.229±0.612
PC14	>10	20.381±1.816	>100	10.019±0.181
A549	>10	21.308±2.114	>100	9.989±0.509

*The peak plasma concentration (PPC) of NVB is 0.1 μg/mL; the PPC of DOC is 2 μg/mL.

In total, there were 51 genes sensitive to NVB and DOC in the 10 lung cancer cell strains, 3.95% of all the genes in the experiment. There were 24 genes sensitive to DOC (11 positive Pearson correlation coefficients, 13 negative Pearson correlation coefficients), and 27 genes sensitive to NVB (3 positive Pearson correlation coefficients, 24 negative Pearson correlation coefficients, Table 3).

Table 3. Analysis of drug sensitivity-related genes in lung cancer cell strains to docetaxel (DOC) and navelbine (NVB).

Pearson correlation coefficient	DOC			NVB		
	Negative	Positive	Total	Negativ	Positive	Total
≥0.4	8	10	18	13	2	15
≥0.5	4	1	5	4	1	5
≥0.6	1	0	1	5	0	5
≥0.7	0	0	0	2	0	2
Total	13	11	24	24	3	27

In total, there were 67 genes sensitive to DOC and NVB in 6 NSCLC cell strains. They made up 5.19% of all the experimental genes. Thirty-eight genes were sensitive to DOC and 29 genes were sensitive to NVB. There were more genes negatively related to NVB and DOC than positively related (Table 4).

Table 4. Analysis of drug sensitivity-related genes in NSCLC cell strains to docetaxel (DOC) and navelbine (NVB)

Pearson correlation coefficient	DOC			NVB		
	Negative	Positive	Total	Negative	Positive	Total
≥0.4	20	4	24	10	4	14
≥0.5	9	0	9	10	0	10
≥0.6	4	0	4	3	0	3
≥0.7	1	0	1	2	0	2
Total	34	4	38	25	4	29

* NSCLC (PC7, PC14, PC9, A549, LK-2, LU65)

Analysis of gene sensitivity to navelbine and docetaxel In total, there were 56 genes related significantly to NVB and DOC ($r \geq \pm 0.4$; Table 5 and Table 6). They can be divided into 11 types:

1 11 genes negatively related to DOC and NVB in the SCLC and NSCLC. They were *metallothinein, cathepsin B, TNF-R1, cathepsin L, TGFb-induced* 68 kDa, TIMP1, PAI-1, IGFBP4, UPAR, CD13 and Jagged.

2 7 genes negatively related to NVB in the SCLC and NSCLC. Genes negatively related to DOC were only in the NSCLC. They were *Galectin-1, Annexin 11, aA-AR, EphA2, Rho C, GATA-6 and Fibromodulin.*

3 6 genes negatively related to DOC and NVB in the NSCLC. They were *APC, Clusterin, FGFR-2, thrombospondin 1, HSC70*, and *HSP32*, but the *TPA* gene was a positively related gene.

4 The procoagulant gene was positively related to NVB in the SCLC and NSCLC. The *midkine* gene was positively related to DOC.

Table 5. Drug sensitivity-related genes co-expressed in SCLC and NSCLC.

Entering serial number	Gene name	NVB		DOC	
		SCLC + NSCLC	NSCLCS	CLC + NSCLC	NSCLC
X64177	Metallothinein	-0.715	-0.721	-0.683	-0.713
L16510	Cathepsin B	-0.712	-0.707	-0.552	-0.682
X55313	TNF-R1	-0.668	-0.605	-0.521	-0.608
X12451	Cathepsin L	-0.617	-0.540	-0.544	-0.511
*	TGFβ-induced, 68 kDa	-0.648	-0.572	-0.573	-0.543
X03124	TIMP1	-0.684	-0.688	-0.481	-0.689
M16006	PAI-1	-0.541	-0.478	-0.454	-0.509
M63403	IGFBP4	-0.521	-0.558	-0.435	-0.561
X51675	UPAR	-0.510	-0.477	-0.462	-0.476
X13276	CD13	-0.482	-0.426	-0.435	-0.477
U61276	Jagged	-0.491	-0.408	-0.421	-0.409

*Non-entering serial number;
serial number of function (see Table 7); DOC, docetaxel; NVB, navelbine.
NSCLC (PC7, PC14, PC9, A549, LK-2, LU65)

Table 6. Specific expression of the drug sensitivity-related genes in SCLC and NSCLC.

Entering serial number	Gene name	NVB		DOC	
		SCLC + NSCLC	NSCLC	SCLC + NSCLC	NSCLC
J04456	Galectin-1	-0.621	-0.687	—	-0.654
*	Annexin ll	-0.569	-0.521	—	-0.422
U03864	Alphal A-AR	-0.483	-0.569	—	-0.580
M59371	Eph A2 (Eck)	-0.468	-0.501	—	-0.545
L25081	Rho C	-0.413	-0.468	—	-0.426
U66075	GATA-6	-0.456	-0.419	—	-0.440
*	Fibromodulin	-0.425	-0.418	—	-0.414
M64722	Clusterin	—	-0.599	—	-0.586
M87770	FGRF-2	—	-0.528	—	-0.547
X14787	Thrombospondin 1	—	-0.505	—	-0.513
Y00371	HSC70	—	-0.528	—	-0.481
M74088	APC	—	-0.411	—	-0.404
X06985	HSP32	—	-0.432	—	-0.434
M15518	TPA	—	0.431	—	0.408
M14113	Procoagulant	0.516	0.484	—	—
Z12020	MDM2	0.423	0.484	0.475	—
AF101264	CaMKK	—	0.432	0.526	—
L33801	GSK-3 beta	-0.424	—	-0.401	—
L15409	VHL	-0.471	—	-0.494	—
AB002409	SLC	-0.416	—	—	-0.400
Z11887	MMP-7	-0.459	—	—	—
L47345	Elongin A	-0.437	—	—	—
AB006780	Galectin-3	-0.419	—	—	—
U16957	AT2	0.429	—	—	—
*	Lactate	—	-0.416	—	—
M69148	Midkine	—	—	0.430	0.455
X13247	IFNg	—	—	0.402	—
*	Phospholipase D	—	—	0.403	—
X78686	ENA-78	—	—	0.416	—
X79389	GSTT1	—	—	0.430	—
*	Id4	—	—	0.430	—
M12828	CD8a	—	—	0.445	—
U81234	GCP-2	—	—	0.450	—
U10990	TAK1	—	—	0.418	—
U22322	Rak	—	—	—	-0.452
U39487	XO	—	—	—	-0.428
U01877	P300	—	—	—	-0.427
X61615	LIFR	—	—	—	-0.425
U20240	C/EBPγ	—	—	—	-0.418
J03817	GSTM1B	—	—	—	-0.408
U44378	Smad4	—	—	—	-0.407
*	Thymosin b	—	—	—	-0.404
X07979	CD29	—	—	—	-0.411
X15606	ICAM-2	—	—	—	0.403
*	Ataxia Telangiectasia Group D-Associated Protein	—	—	—	0.427

*Non-entering serial number;
serial number of function (see Table 7); DOC, docetaxel; NVB, navelbine.
NSCLC (PC7, PC14, PC9, A549, LK-2, LU65)

Table 7. Classification of gene sensitivity to navelbine (NVB) and docetaxel (DOC) in lung cancer cell strains.

Serial number of function	Classification	NVB				DOC			
		SCLC	NSCLC	Co-expressed	Total	SCLC	NSCLC	Co-expressed	Total
1	Signal transduction molecule	7	9	7	9	7	13	4	16
2	Growth factor receptor	0	1	0	1	0	1	0	1
3	Growth factor	0	0	0	0	1	1	1	1
4	Apoptosis related	1	1	1	1	0	1	0	1
5	Cell factor	5	1	1	5	5	3	1	7
6	Cyclin protein	1	1	1	1	1	0	0	1
7	Transcription factor	2	1	1	2	2	2	0	4
8	Metabolism-related enzymes and inhibitors	5	6	4	7	4	8	4	8
9	Proteolysis	1	1	1	1	2	2	2	2
10	Molecular chaperone	0	1	0	1	0	1	0	1
11	Other*	4	6	2	8	3	6	1	8
Total		26	28	19	36	25	38	13	50

*Refers to non-classified genes.
NSCLC (PC7, PC14, PC9, A549, LK-2, LU65)
SCLC (Lu135, N231, H69, SBC-3)

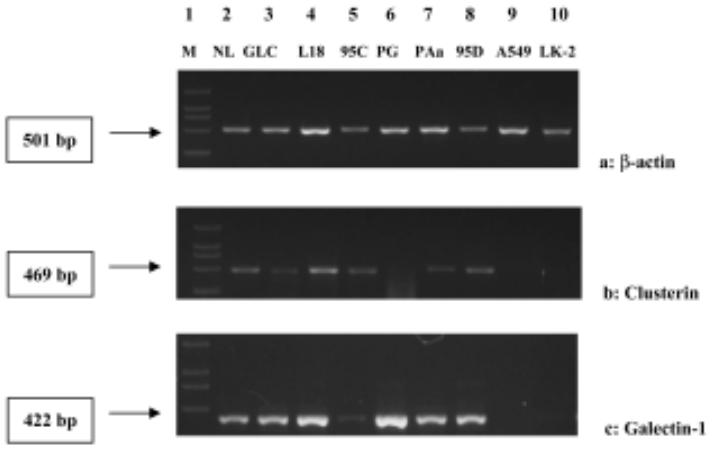

Figure 3. Gene expression of *Clusterin, Galectin-1, TIMP-1* and *metallothionein* in NSCLC (PC7, PC14, PC9, A549, LK-2, LU65) cell lines were verified by reverse transcription polymerase chain reaction. 1, PCR marker, M; 2, normal lung, NL; 3–10, NSCLC. (A) PCR product of β-actin. Reaction conditions: 94 °C, 3 min; 94 °C, 20 s; 56 °C, 30 s; 72 °C, 50 s; 72 °C, 10 min for extension. After 23 cycles, expression could be seen in NL and 8 NSCLC. (B–E) PCR products of *TIMP-1, Clusterin, Galectin-1* and *metallothionein*, with β-actin as an internal control. Reaction conditions: 94 °C, 3 min; 94 °C, 40 s; 60 °C, 40 s; 72 °C, 40 s, 72 °C, 10 min for extension. 22, 26, 26 and 32 cycles, respectively. (B) *Clusterin* was not expressed in the A549 and LK-2 cell lines, but was expressed weakly in the GLC and PG cell lines. (C) *Galectin-1* was not expressed in the A549 and LK-2 cell lines, but was expressed weakly in the 95C cell line.

5 The *MDM2* gene was positively related to NVB in the NSCLC and SCLC. The *CaMKK* gene was positively related to NVB only in the NSCLC, *MDM2* and *CaMKK* were both positively related to DOC in the SCLC.

6 GSK-*3β* and *VHL2* were both negatively related to NVB and DOC in the SCLC.

7 *Elongin A*, *MMP-7* and *Galectin-3* were negatively related to NVB in the SCLC. *Elongin A*, *MMP-7*, *Galectin-3* were negatively related to DOC in the NSCLC, but the *AT2* gene was positively related to NVB in the SCLC.

8 8 genes positively related to DOC in the SCLC. They were *TAK1*, *IFN-γ*, *Phospholipase D* ,*ENA-78*, *GSTT1*, *Id4*, *CD8α* and *GCP-2*.

9 9 genes negatively related to DOC in the NSCLC. They were *Rak*, *XO*, *P300*, *LIFR*, *C/EBPγ*, *GSTMIB*, *Smad4*, *Thymosin b* and *CD29*.

10 *ICAM-2* and *Ataxia Telangiectasia Group D-Associated Protein* were positively related to DOC in the NSCLC.

11 *ICAM-2* and *Ataxia Telangiectasia Group D Associated Protein* and NSCLC were positively related to DOC.

The classification of gene sensitivity to NVB and DOC in lung cancer cell strains is shown in Table 7. They were divided into 4 types: signal transduction molecules, cell factors, transcription factors, and metabolism-related enzymes and inhibitors.

Verification In order to verify the reliability of hybridization, GLC, L18, 95C, PG, PAa, 95D, A549 and LK-2 cell lines were chosen. cDNA of *Galectin-1*,and *Clusterin*, which were downregulated in expression and selected with cDNA macroarray, was used in semi-quantitative RT-PCR. The results are shown in Figure 3A–3C.

Discussion

The morbidity of lung cancer is higher now than in the past, and lung cancer therapy is less sensitive to chemotherapy than other kinds of cancer. Because most patients are in the middle or late stages when cancer is found, the rate of surgical success is low. Therefore, chemotherapy is a commonly integrated treatment for lung cancer patients. NVB and Doc are both new anticancer drugs act on microtubules[6–9]. NVB can inhibit the assembly of tubulin and act on the mid-stage of mitosis, leading to stasis of cancer cell growth. Because of its special anticancer function, in December 1994 the FDA (Food and Drug Administration) approved NVB in combination with CDDP for use as a first-line therapy for advanced NSCLC patients[10]. As for DOC, its mechanism is to promote the aggregation of tubulin and to inhibit its disassembly, preventing cells from entering into the growth phase. It is widely used in cancer treatments, mainly for lung cancer and breast cancer in advanced stages[11].

In clinical cases there are usually different sensitivities to anticancer drugs. The same chemotherapeutic medicine is often used for patients with different types of cancer cells, even for different individuals with the same type of cancer cells. This is due to such factors as the different biological characters of tumors, different patients and different drug responses.

There are many methods to determine sensitivity to anticancer drugs by analyzing gene expression. Only 1 gene at a time can be tested through northern blotting, which has an obvious disadvantage in automation. Other methods include differential display, cDNA sequence analysis and SAGE, but they also have many disadvantages. For any organism, we can analyze many different drug responses by means of DNA gene chip technology, and obtain more reliable results than with other methods. We conclude that other single element methods are less advantageous than the DNA gene chip technique[12–15].

A recent study showed that drug sensitivity to DOC is concerned with P-GP(P Glucose protein), and changes in target molecules, changes in signal transduction system, cell-control factors and apoptosis-related factors. In addition, the metabolism of DOC in the body is primarily through the sub-family of CYP3A proteins. The activity of enzyme in this family varies greatly among individuals, and the factors sensitive to NVB have not yet been reported.

We have examined the genes sensitive to DOC and NVB in 10 lung cancer cell strains using cDNA macroarrays. The results showed that there were 56 genes significantly related to NVB and DOC ($r \geq \pm 0.4$). Among them, 36 were related to NVB, 20 were co-expressed in the NSCLC set and the NSCLC+SCLC set; 27 were related in the NSCLC+SCLC set and 7 were specifically related genes; 29 were related genes in the NSCLC set, and 9 were specifically related genes. There was a total of 50 genes related to DOC and 12 co-expressed genes related in the NSCLC and NSCLC+SCLC sets; 24 related genes in the NSCLC+SCLC set and 12 specifically related genes. In the NSCLC set there were 38 related genes and 26 specifically related genes.

The genes described above are mainly signal transduction molecules, metabolism-related enzymes and inhibitors, cell factors and transcription factors. At the same time, *Clusterin* and *Galectin-1* genes, which were downregulated in expression in LK-2, were tested using RT-PCR. The results were in agreement with those obtained through cDNA macroarray. However, with the A549 cell line, the cDNA macroarray did not show the same downregulated expression as with RT-PCR. Genes screened by cDNA macroarray therefore need to be further tested using other methods.

In this study, we identified the relationship among the gene expression profiles of 10 lung cancer cell strains, which focused on 1291 genes and drug sensitivity to DOC and NVB. This study may help to explain the mechanisms of action of NVB and DOC, provide theoretical evidence in the search for new ways to overcome drug resistance, discover new anticancer drugs by providing new targets, and facilitate individualized therapy regimens and increased response

rates. The aim of our future work is to identify and analyze these new genes screened for drug sensitivity, especially those not known to us previously.

References

1 Ohira T, Akutagawa S, Usuda J, Nakamura T, Hirano T, Tsuboi M. Up-regulated gene expression of angiogenesis factors in post-chemotherapeutic lung cancer tissues determined by cDNA macroarray. Oncol Rep 2002; 9: 723–8.

2 Califano A, Stolovitzky G, Tu Y. Analysis of gene expression microarrays for phenotype classification. Proc Int Conf Intell Syst Mol Biol 2000; 8: 75–85.

3 Shimoyama Y, Kubota T, Watanabe M, Ishibiki K, Abe O. Predictability of *in vivo* chemosensitivity by *in vitro* MTT assay with reference to the clonogenicassay. J Surg Oncol 1989; 41: 12–8.

4 Reed LJ, Muench HA. Simple method of estimating fifty percent end points. Am J Hyg 1938; 27: 493.

5 A.Gemma K, Takenaka Y, Hosoya K, Matuda M, Seike F, Kurimoto Y. Altered expression of several genes in highly metastatic subpopulations of a human pulmonary adenocarcinoma cell line. Eur J Cancer 2001; 37: 1554–61.

6 Le Chevalier T, Brisgand D, Douillard JY, Pujol JL, Alberola V, Monnier A, *et al*. Randomized study of vinorelbine and cisplatin versus vindesine and cisplatin versus vinorelbine alone in advanced non-small-cell lung cancer: results of a European multicenter trial including 612 patients. J Clin Oncol 1994; 12: 360–7.

7 Wozniak AJ, Crowley JJ, Balcerzak SP, Weiss GR, Spiridonidis CH, Baker LH, *et al*. Randomized trial comparing cisplatin with cisplatin plus vinorelbine in the treatment of advanced non-small-cell lung cancer: a Southwest Oncology Group study. J Clin Oncol 1998; 16: 2459–65.

8 Adjei AA, Argiris A. Murren JR. Docetaxel and irinotecan, alone and in combination, in the treatment of non-small cell lung cancer. Semin Oncol 1999; 26: s32–40.

9 Robinet G, Thomas P, Perol M, Vergnenegre A, Lena H, Taytard A, *et al*. Phase II study of docetaxel in inoperable advanced non small cell lung cancer. Bull Cancer 2000; 87: 253–8.

10 Dong M, Feng FY, Shi YK. Studying progress about the anticancer drug Vinorelbine. Foreign Med Sci Cancer Sec 1998; 25: 145.

11 Sun Y, Li WL, Guan ZH, Li LQ, Zhang XR, Wu HY, *et al*. Clinical Validation of Doc- etaxel in treatment of advanced breast cancer and NSCLC. J Chin New Med 1998; 7: 165 –7.

12 Khan J, Bittner ML, Chen Y, Meltzer PS, Trent JM. DNA microarray technology: the anticipated impact on the study of human disease. Biochim Biophys Acta 1999; 1423: M17–28.

13 Wildsmith SE, Elcock FJ. Microarrays under the microscope. Mol Pathol 2001; 54: 8–16.

14 Scherf U, Ross DT, Waltham M, Smith LH, Lee JK, Tanabe L, *et al*. A gene expression database for the molecular pharmacology of cancer. Nat Genet 2000; 24: 236–44.

15 Dan S, Tsunoda T, Kitahara O, Yanagawa R, Zembutsu H, Katagiri T, *et al*. An integrated database of chemosensitivity to 55 anticancer drugs and gene expression profiles of 39 human cancer cell lines. Cancer Res 2002; 62: 1139–47.

Acta Pharmacologica Sinica 2005 Sep; 26 (9): 1025–1033

Invited review

Histone deacetylase inhibitors for treatment of hepatocellular carcinoma

Danila CORADINI[1], Annalisa SPERANZA

UO Tumor Biology and Experimental Therapy, Department of Experimental Oncology, Istituto Nazionale per lo Studio e la Cura dei Tumori, 20133 Milan, Italy

Key words

hepatocellular carcinoma; histone deacetylase inhibitors; cancer therapy

Abbreviations: HCC, hepatocellular carcinoma; HBV, hepatitis B virus; HCV, hepatitis C virus; HAT, histone acetyltransferase; HDAC, histone deacetylase; NB, sodium butyrate; TSA, trichostatin A; SAHA, suberoylanilide hydroxamic acid; PBA, phenylbutyrate; HA-But, hyaluronic butyric ester; HA, hyaluronic acid.

[1] Correspondence to Dr Danila CORADINI.
Phn 39-2-2390-3053.
Fax 39-2-2390-3052.
E-mail danila.coradini@istitutotumori.mi.it

Received 2005-06-03
Accepted 2005-06-30

doi: 10.1111/j.1745-7254.2005.00195.x

Abstract

Hepatocellular carcinoma (HCC) is one of the most common cancers in the world. Surgical resection has been considered the optimal treatment approach, but only a small proportion of patients are suitable candidates for surgery, and the relapse rate is high. Approaches to prevent recurrence, including chemoemboliza-tion before and adjuvant therapy after surgery, have proven to have a limited benefit; liver transplantation is successful in treating limited-stage HCC because only a minority of patients qualify for transplantation. Therefore, new therapeutic strategies are urgently needed. Because in addition to the classical genetic mechanisms of deletion or inactivating point mutations, epigenetic alterations, such as hyperacetylation of the chromatin-associated histones (responsible for gene silencing), are believed to be involved in the development and progression of HCC, novel compounds endowed with a histone deacetylase (HDAC) inhibitory activity are an attractive therapeutic approach. In particular, pre-clinical results obtained using HA-But, an HDAC inhibitor in which butyric acid residues are esterified to a hyaluronic acid backbone and characterized by a high affinity for the membrane receptor CD44, indicated that this class of compounds may represent a promising approach for hepatocellular carcinoma treatment.

Introduction

Hepatocellular carcinoma (HCC) is currently the fifth most common solid tumor worldwide and the fourth most common cause of cancer-related death[1]. The incidence of HCC is approximately 1 000 000 cases worldwide; and although in Europe and the USA the incidence of HCC is 4/100 000, it is 120/100 000 in Asia and Sub-Saharan Africa[2]. In particular, statistical data from the last decade show that HCC is the second most prevalent cause of cancer deaths in men and the third most prevalent cause in women in mainland China, with more than 500 000 new cases every year[3,4]. Moreover, a rise in the incidence of disease and mortality from HCC, most likely reflecting the increased prevalence of hepatitis C virus (HCV), has recently been observed also in Japan, Western Europe and the USA[5,6].

The major etiologies of HCC are well defined, and some of the steps in its molecular pathogenesis have been elucidated. HCC arises commonly, but not exclusively, in the context of liver injury, which leads to inflammation, hepatocyte regeneration, liver matrix remodeling, fibrosis and, ultimately, cirrhosis. In fact, cirrhosis represents the most important risk factor for HCC (70%–90% of cases of HCC develop in cirrhotic liver) and it is principally imputable to chronic viral hepatitis B and/or C (HBV, HCV), although other risk factors are alcohol abuse, metabolic liver disease (such as hemochromatosis, α_1-antitrypsin deficiency and steatosis), androgenic steroid use and aflatoxin exposure[7]. In particular, chronic HBV infection is strongly associated with hepatocellular cancer in China[8], while HCV infection and subsequently cirrhosis is the leading cause of chronic hepatitis and HCC in Japan and Western countries[9].

Current trends in the management of HCC

The rates of early detection, treatment and prevention of HCC are poor, and a majority of patients (70%–85%) are affected by advanced or unresectable disease. Despite the

many treatment options, the prognosis of HCC remains dismal. In fact, even for those patients who undergo resection, the recurrence rate can be as high as 50% at 2 years[10,11] and a meta-analysis that evaluated the results of 37 randomized clinical trials of systemic and regional chemotherapy in more than 2000 HCC patients concluded that non-surgical therapies were ineffective or minimally effective[12]. In addition, most published studies of systemic chemotherapy report a response rate ranging from 0% to 25%; treatment failure is most likely due to the particular resistance to cytostatic agents displayed by HCC cells[12,13], which are known to express the multidrug-resistant gene MDR-1[14]. Liver-directed therapies, such as transarterial chemoembolization or percutaneous ethanol injection, are palliative treatments, with encouraging results only for patients with small HCC[15,16].

Alternative therapeutic approaches have been investigated, but with disappointing results. The effectiveness of hormone therapy with anti-estrogens, anti-androgens or somatostatin analogues has been studied in several trials[17,18], but these treatments were found to be generally ineffective or to not produce reproducible results[19].

At present, orthotopic liver transplantation is considered the only curative treatment option for HCC, bringing about an increase in the 5-year survival rate from the historical 20%–36% to the recent 61%, which is likely related to adoption of the Milan criteria at US transplantation centers[23,24]. However, most patients with cirrhosis are not generally considered good candidates for liver transplantation, or they remain on the waiting list until they die from tumor progression or cirrhosis-related complications.

An understanding of tumor biology and the key molecular events leading to HCC development is therefore fundamental for identifying new therapeutic strategies that are effective against HCC but not toxic to normal cells, and are well-tolerated by the typical patient with underlying cirrhosis.

HCC biology and targeted therapies

In most types of cancer, hepatocarcinogenesis is a multistep process involving different genetic alterations, including cellular oncogene activation, tumor suppressor gene inactivation (possibly in cooperation with genomic instability), DNA repair defects, overexpression of growth and angiogenic factors, and telomerase activation, which ultimately lead to malignant transformation of the hepatocyte[20]. For a more comprehensive review of the complex molecular pathogenesis of HCC the reader may refer to some excellent papers including those by Ozturk[21], Moradpour and Wands[22], Thorgeirsson and Grisham[7] and Suriawinata and Xu[23].

On the basis of knowledge of the molecular pathways that are associated with the malignant phenotype, new and promising agents, which are specifically targeted to tumor cell receptors or signaling events, are emerging. This is the case for the selective growth factor receptors, tyrosine kinase inhibitors, the fundamental role of which is to block signal transduction[24,25], or farnesyltransferase inhibitors, which counteract oncogene *ras*-mediated signaling[26]. Moreover, to stimulate an immunological response against liver tumors, other agents have been tested, for example interferon-α, which can significantly prolong the survival of HCC patients when given at high doses[27], interleukin-2, which can produce objective remission when given alone[28] or in combination with melatonin[29], or tumor necrosis factor-α-related apoptosis-inducing ligand (TRAIL), which has not yet been tested in humans, but has been found to be effective in pre-clinical experiments[30].

Gene therapy is a new and promising therapeutic strategy that is based on the introduction of genetic material, for example natural genes, chimeric genes or subgenomic molecules, into cells in order to generate a beneficial effect against disease[31]. So far, a variety of gene therapy approaches have been designed to treat liver cancer, including the replacement of functional tumor suppressor genes[32], inhibition of oncogenes[33], selective prodrug activation within the tumor[34], stimulation of antitumor immunity[35] and inhibition of tumor vascularization[36], although encouraging results have been mostly only obtained in pre-clinical models.

Histone acetylation status and HCC development

In addition to the classical genetic alterations (chromosomal deletions and rearrangements, and gene amplifications and mutations) first recognized as being responsible for hepatocarcinogenesis, molecular approaches have recently been used to identify alterations in the epigenetic control of gene transcription that positively mediate cellular proliferation or inactivate tumor suppressor genes[37]. In particular, acetylation, methylation and phosphorylation of the N-terminal lysine tails of the chromatine core histones have been found to play a critical role in post-translational modifications, suggesting the hypothesis of a histone "code"[38]. Among these modifications, the acetylation status of the histones constitutes the major epigenetic alteration, and is fundamentally involved in transcriptional regulation[39].

The acetylation level of histones is determined by the equilibrium between the activities of two groups of enzymes, histone acetyltransferases (HAT) and histone deacetylases

(HDAC), which respectively add or remove acetyl groups from the lysine tails[40]. Hypoacetylated histones are associated with a more packaged chromatin structure and with suppression of gene transcription, whereas highly acetylated histones activate gene transcription by releasing the chromatin structure[41]. At present, eleven mammalian HDAC have been identified, and these have been ordered into 3 classes[42]. Class I deacetylases (HDAC 1, 2, 3, and 8) share homology in the catalytic sites; class II includes HDAC 4, 5, 6, 7, 9, 10, and 11, of which HDAC 4, 5, 7, and 9 share homology in the C-terminal catalytic domain and N-terminal regulatory domain, whereas HDAC11 contains conserved residues in the catalytic core regions shared by both classes I and II, and HDAC6 and HDAC10 have two regions that are homologous with the class II catalytic site. The third class of HDAC is the conserved nicotinamide adenine dinucleotide-dependent Sir2 family. Increasing evidence indicates that HDAC are not redundant in function and distribution: class I HDAC are found exclusively in the nucleus, whereas class II HDAC shuttle between the nucleus and cytoplasm in response to certain cellular signals[43]. HDAC do not bind directly to DNA, but are recruited by protein complexes that can differ in their subunit composition.

The balance between HAT and HDAC activity in regulating DNA folding and gene transcription can be disrupted by HDAC inhibitors, which act by blocking HDAC enzymes; HDAC inhibition leads to lysine residue hyperacetylation and to DNA conformation changes (Figure 1). Inaccessible promoter regions thus become available targets for transcription factors, which activate the re-expression of several genes, including those involved in cell growth arrest, differentiation and apoptosis[44,45].

HDAC inhibitors and cancer treatment

Several lines of evidence suggest that inappropriate transcriptional activation commonly occurs in the formation of many types of cancer and that an imbalance between HAT and HDAC activity may be responsible for the alteration. Because HDAC dysregulation has been demonstrated in many solid cancers, including hepatocellular carcinoma, HDAC inhibitors have been investigated for their therapeutic potential to reprogram transcription and inhibit tumor cell growth and progression[46]. Historically, sodium butyrate (NB), which is normally present in the human colon as a product of the metabolic degradation of complex carbohydrates by colonic bacteria, was the first compound found to cause an increase in histone acetylation[47] and to regulate the physiological differentiation of colonocytes[48], suggesting its possible use in the prevention of colorectal cancer

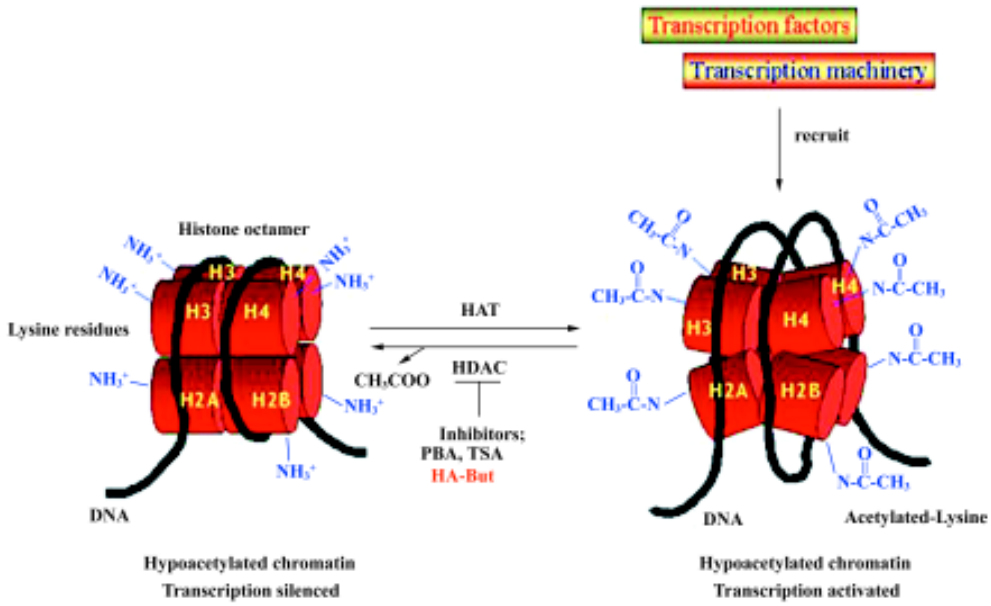

Figure 1. Schematic diagram of the activity of the histone acetyltransferase (HAT) and histone deacetylase (HDAC) enzyme inhibitors, which lead to chromatin hyperacetylation or hypoacetylation, respectively. HDAC inhibitors such as phenylbutyrate (BPA), trichostatin A (TSA) and HA-But act by restoring the re-expression of several genes, including those involved in cell growth arrest, differentiation and apoptosis.

and the treatment of premalignant and neoplastic lesions. Many other HDAC inhibitors have since been identified, which belong to several chemical structure classes: 1) short-chain fatty acids, of which NB represents the prototype; 2) hydroxamic acids, including trichostatin A (TSA)[49] and a series of hydroxamic acid-based hybrid polar compounds, such as suberoylanilide hydroxamic acid (SAHA)[50]; 3) cyclic tetrapeptides, which may or may not contain the 2-amino-8-oxo-9,10 epoxy-decanoyl moiety (trapoxins A and B[51], FK228/depsipeptide[52] and apicidin[53]); and 4) benzamides (MS-275)[54] and others, such as valproic acid[55] and oxamflatin[56].

Several of these compounds, including SAHA, MS-275 and FK228/depsipeptide, are undergoing phase I and II clinical trials to examine their potential use as anticancer drugs for solid and hematological tumor treatment either as monotherapies or in combination with other cytotoxic and differentiation agents. For example, in a phase I clinical trial, SAHA was well tolerated when administered either intravenously or orally, and it was found to have antitumor activity in heavily pre-treated patients with advanced solid and hematological tumors. Furthermore, SAHA has good bioavailability when administered orally and it induces objective responses in patients with prior therapy-resistant cutaneous T cell lymphomas[57]. Similarly, a phase II trial demonstrated that FK228/depsipepide was active against refractory neoplasms[58] and chronic lymphocytic and acute myeloid leukemia[59]. MS-275 is also well-tolerated when orally administered in patients with refractory or relapsed hematological malignancies, and it is biologically active in terms of histone acetylation[60]. However, none of these studies have been specifically focused on hepatocellular carcinoma, and in addition, despite the encouraging results obtained for several types of tumors, these drugs do not achieve the major goal in cancer therapy: to selectively target anti-cancer molecules to organs or compartments that harbor tumor cells.

HA-But as an HDAC inhibitor target delivery

As mentioned earlier in this paper, NB was the first compound found to cause an increase in histone acetylation[50], so given its antiproliferative and differentiation activities, together with a relative absence of systemic toxicity, it was a candidate for the prevention of colorectal cancer and a therapeutic agent for the treatment of pre-neoplastic and neoplastic lesions. Unfortunately, the first clinical study undertaken using high doses of NB resulted in only a partial and temporary remission, principally due to the relatively low potency of the drug and a low plasma concentration that was not sufficient to inhibit cell growth, but high enough to induce side-effects[61]. Both to overcome chemical constraints that restrict the clinical application of NB, and to specifically target the compound to cancer cells, a bioconjugate (HA-But), in which a hyaluronic acid backbone was used as a suitable carrier for butyric residues, was developed[62].

Hyaluronic acid (HA), also referred to as hyaluronan, is a polysaccharide molecule whose repeated disaccharide motif comprises *D*-glucuronic acid and *D*-*N*-acetylglucosamine linked together through alternating β-1,4 and β-1,3 glycosidic bonds. HA is present in all vertebrates and is a major constituent of the extracellular matrix, where it is organized, by specific interactions, with other matrix macromolecules[63]. HA has a high rate of turnover (in the bloodstream its half-life is 2–5 min) because it is rapidly captured by receptors on hepatic sinusoidal endothelial cells, which internalize it, and subsequently catabolize it in lysosomes. Sinusoidal endothelial cells actively remove almost 90% of the circulating HA, even though the spleen is also involved in its degradation[64]. The chemical properties of HA determine its physiological role as an essential structural element in the extracellular matrix, where it regulates the retention of water molecules in the interstitial space. In addition, HA provides support for cell orientation through some specific cell surface receptors, including CD44[65]. CD44 is a single-pass transmembrane glycoprotein consisting of 4 functional domains: the distal extracellular domain (responsible for the binding of HA), the membrane-proximal extracellular domain (whose sequence depends on the alternative CD44 mRNA splicing), the transmembrane domain (similar to that of many other single-pass proteins), and the cytoplasmic domain (which has protein motifs that either interact with the cytoskeletal proteins or are responsible for intracellular signaling)[68]. Although physiologically expressed by some normal human epithelial and mesenchymal cells, where it plays an important role in immune recognition, cell-cell aggregation and cell-matrix-cell signaling, CD44 is overexpressed in most human cancers, including hepatic carcinoma, and is associated with tumor progression[66,67]. In fact, clinical evidence indicates that in comparison with normal hepatocytes, HCC is frequently associated with an increased expression of CD44 receptors[73,74], an overexpression that provides them with an essential migration-promoting advantage as demonstrated by Lara-Pezzi *et al*[68]. In their interesting pre-clinical study, these authors demonstrated a link between CD44 expression and HBV infection. In fact, a CD44-dependent migratory phenotype was induced by the stable transfection of Chang liver cells with the gene coding for the hepatitis B virus X protein (HBx), which was able to

enhance cell motility by altering the cellular morphology and inducing the formation of pseudopodal protrusions and cytoskeletal rearrangements together with the polarization of cell-surface adhesion molecule CD44. This finding is particularly relevant because it supports the relationship between HBV infection and hepatocarcinogenesis, underlining the role of HBx protein in the transformed phenotype.

In developing HA-But synthesis, we took advantage of some molecular properties of HA that satisfy some important biochemical concerns. In fact, HA can make stable bonds with butyric residues, increasing their *in vivo* half-life without affecting their pharmacological activity. In addition, we exploited its high affinity with the CD44 receptor, which is generally overexpressed on tumor cell membranes, to selectively target the butyric residues directly to neoplastic lesions, with minimal effects on normal cells. In fact, in agreement with data in the literature[69], we found that in normal cells such as fibroblasts, which express a percentage of CD44-positive cells (as evaluated by flow cytometry) similar to that of tumor cells, HA-But had no effect, suggesting that it is only really effective in actively proliferating cells, such as tumor cells (Figure 2).

HA-But: pre-clinical *in vitro* results

When we analyzed the antiproliferative effect of HA-But on two hepatocellular carcinoma cell lines, namely Hep3B and HepG2, which both expressed CD44 receptors (although to different extents), we found that after 6 days of treatment it exerted a dose-dependent effect, almost completely inhibiting the CD44-rich Hep3B (90%) cells, and moderately (but significantly) inhibiting (60%) the CD44-poor HepG2 cells; furthermore, this growth arrest corresponded to a block in the G_0/G_1 phase of the cell cycle[70]. As shown in Figure 3, the progression of the cell cycle is regulated by cyclin/cyclin-dependent kinase (cdk) complexes and cdk inhibitors, such as $p16^{ink4}$, $p21^{waf1}$, and $p27^{kip1}$ proteins. Because it is known that overexpression of cdk inhibitors leads to cell-cycle arrest and apoptosis, we investigated the effect of HA-But on the expression of some of the molecules responsible for

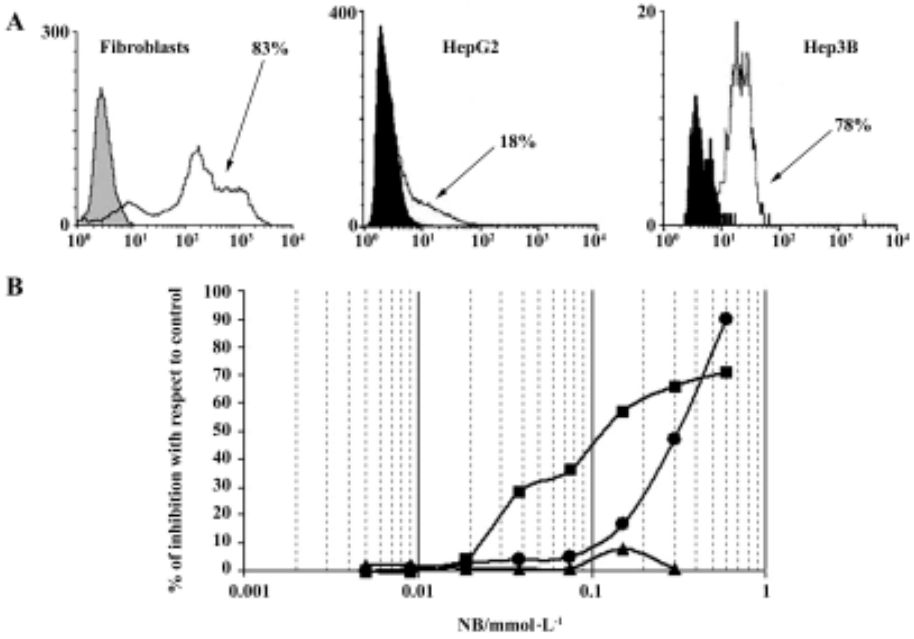

Figure 2. A: Cell surface CD44 expression on fibroblasts, and HepG2 and Hep3B cell lines as evaluated by flow cytometry. Cells (1×10^6) were first incubated with mouse antihuman CD44 antibody, and then with goat FITC-labeled antimouse secondary antibody. Negative controls (gray or black) and stained samples (white) are shown. B: Antiproliferative effect of scalar doses of HA-But on the growth of fibroblasts (▲), and HepG2 (■) and Hep3B (●) cell lines, after 6 d of treatment. Briefly, cells (1000 cells per well) were seeded in 96-well plates in RPMI-1640 medium supplemented with 10% fetal calf serum and allowed to adhere for 24 h. The seeding medium was removed and replaced with experimental medium supplemented with increasing concentrations of HA-But. At the end of the experiments the antiproliferative effect was evaluated by using the 3-(4,5-dimethyl-2-thiazoyl)-2,5-diphenyl-2*H*-tetrazolium bromide (MTT) method. Results are expressed as percentage of inhibition with respect to control (cells maintained in the presence of culture medium alone). Each point represents the mean value from 3 independent experiments. The variation coefficient was <5% and therefore error bars are not shown.

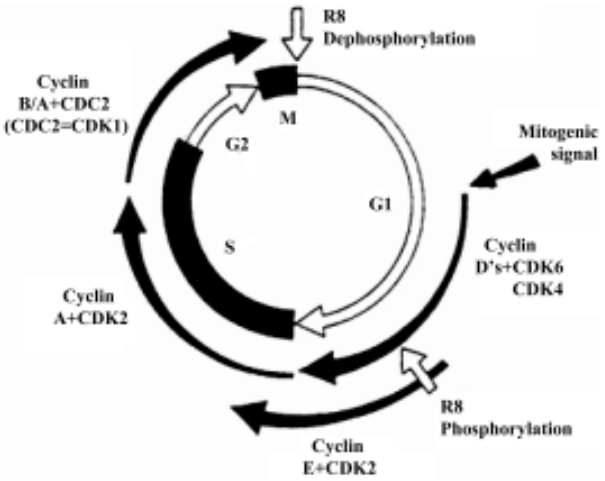

Figure 3. Schematic representation of cell cycle phases. In proliferating cells, the cell cycle consists of 4 phases. Gap1 (G1) is the interval between mitosis and DNA replication, which occurs during the synthesis (S) phase. The S phase is followed by a second gap phase (G2), during which growth and preparation for cell division occurs. Mitosis and the production of 2 daughter cells occur in M phase. Passage through the 4 phases of the cell cycle is regulated by a family of cyclins that act as regulatory subunits for cyclin-dependent kinases (cdks). The activity of the various cyclin/cdk complexes that regulate the progression through the G1-S-G2 phases of the cell cycle is controlled by the synthesis of the appropriate cyclins during a specific phase of the cell cycle. In addition, there are several proteins, including $p16^{ink4}$, $p21^{waf1}$, and $p27^{kip1}$ (termed cdk inhibitors) that can inhibit the cell cycle in G1 when an adverse event, such as DNA damage, has occurred.

growth arrest, including cyclin D1, which is involved in the regulation of the G_1 phase of the cell cycle, and whose gene is found amplified in 10%–20% of HCC,[71] but leads, when combined for example with $p16^{ink4}$ amplification, to a loss of growth control in more than 30% of HCC. Experimental findings indicated that as in other types of tumors, such as lung cancer[65], and in agreement with the effect of other HDAC inhibitors on hepatoma cells[72,73], HA-But increased cdk-inhibitor expression (ie, the protein level of $p27^{kip1}$ and $p21^{waf1}$), while decreasing cyclin D1 protein levels, suggesting that the HA backbone does not interfere with the activity of butyric residues, which maintain their biological properties. In fact, as previously demonstrated in lung cancer[65], and similarly to NB, HA-But induces a hyperacetylation of histone H4, a dose-dependent overexpression of $p27^{kip1}$ and $p21^{waf1}$, and a block of cell growth in the G_0/G_1 phase of the cell cycle. In addition, cytometric analysis showed that CD44 receptor turnover was not affected by treatment with HA-But, which is a finding of great pharmacological relevance, because the stable presence of the receptors on plasma membranes guarantees a continuous internalization of the drug.

cDNA microarray analysis is a technical approach that enables investigators to measure the expression of thousands of mRNAs simultaneously in a biological specimen, providing comprehensive information that is useful for diagnosis and therapeutic intervention. Data gathered using this technique have further confirmed the previous experimental findings regarding the mechanism of action of HDAC inhibitors, and demonstrated that almost all HDAC inhibitors exerted their antiproliferative effects by modulating a small set of genes that regulate key cellular activities such as proliferation and differentiation. In particular, it has been shown that TSA, SAHA, depsipeptide are able to modulate genes involved in apoptosis and cell cycle pathways, among which are cdk inhibitors such as $p16^{ink4}$, $p21^{waf1}$, and bcl-2[74,75]. In addition, gene expression profiling of hepatocellular carcinomas has provided qualitative and quantitative evidence that the genes involved in the development and progression of a HCC correlate with the dysregulation of pathways associated with cell cycle regulation[76], apoptosis[77], signal transduction[78], cellular adhesion and angiogenesis[79,80]. Thus, the finding that HDAC inhibitors, including HA-But, can restore growth control and induce differentiation is particularly exciting.

HA-But: pre-clinical *in vivo* results

There are very few studies that have aimed to investigate the *in vivo* effect of HDAC inhibitors on tumor growth or the metastatic spread of liver tumors. Among the studies that have been conducted, a study using 4-phenylbutyrate, a derivative of the short-chain fatty acid butyrate, found that when administered via intratumor catheter, the compound reduced the growth of xenograft tumors derived from hepatocarcinoma cell lines, most likely by the induction of $p21^{waf1}$ expression and the activation of apoptosis[78].

The *in vivo* capability of HA-But to inhibit primary tumor growth and metastatic spread has been investigated in several animal models[65,75], and evaluation of the drug biodistribution, by using the compound labeled with ^{99m}Technetium, found that a few minutes after iv administration, there was a substantial accumulation of the compound in the liver, uniformly distributed in both lobes[75]. These results have been confirmed by the evaluation of the *ex vivo* distribution of HA-But, which showed that the liver was the organ of preferential accumulation, in agreement both with the finding obtained by using native HA[81] and with the observation that circulating hyaluronan is physiologically degraded by hepatic sinusoidal endothelial cells

via CD44 receptors[82]. All these findings clearly suggest that iv injection can be appropriately exploited to treat intrahepatic lesions. In fact, when we explored the therapeutic potential of HA-But for the treatment of intrahepatic lesions induced in the mouse by intrasplenically inoculated Lewis lung carcinoma cells (LL3) and B16/F10 melanoma cells (two cell lines known for their particular aggressiveness[83,84], and which express high percentages of CD44-positive cells), we found that a prolonged iv administration of HA-But affected the survival time of tumor-bearing animals, reducing the number of intrahepatic metastatic lesions. In addition, prolonged treatment with low doses of HA-But significantly increased the survival time of treated mice relative to untreated controls. It is noteworthy that 90 d after tumor implantation, 80% of HA-But treated animals were still alive versus approximately one-third in the untreated group[75].

Conclusions and future perspectives

Experimental evidence and preliminary clinical phase I and II trials indicate that HDAC inhibitors acting on a pivotal mechanism of gene transcription such as histone acetylation may represent an innovative therapeutic approach for solid and hematological cancer. In particular, recent findings indicate that in pre-clinical studies HA-But is able to inhibit hepatocellular carcinoma cell growth, and that this antiproliferative activity is due to an increase in some cell-cycle related proteins, such as $p21^{waf1}$ and $p27^{kip1}$, and a decrease in some others, including cyclin D1. Furthermore, the results provide experimental evidence for the clinical use of HA-But as a promising agent for the treatment of hepatocellular carcinoma, a tumor that is otherwise particularly resistant to chemotherapy. The treatment exploits the overexpression of CD44 receptors on tumor cell membranes, which allows selective targeting of the compound to the neoplastic lesion.

In addition to DNA acetylation, which hampers gene transcription, aberrant DNA hypermethylation of cytosine residues in the promoter region can cause growth-controlling gene silencing, a frequently observed phenomenon for several genes in HCC[7]. Therefore, the additional inhibition of DNA methyltransferase (DNMT), the enzyme responsible for such hypermethylation (the activity of which can be reversed using specific DNMT inhibitors, such as 5-aza-2-deoxycytidine, 5-AZA) could be an interesting candidate for further study. Therefore, a promising development for HA-But could be a new chemical compound in which HA-But is simultaneously esterified with 5-AZA. Such a molecule should be able to reactivate silenced genes and enhance the re-expression of specific genes involved in cell growth arrest, terminal differentiation and apoptosis in aggressive tumors such as hepatocellular carcinoma.

Acknowledgements

The authors wish to thank Drs I Scarlata, C Pellizzaro, and S Zorzet, who contributed to the HA-But synthesis, *in vitro*, and *in vivo* experiments, respectively.

References

1 Parkin DM, Pisani P, Ferlay J. Estimates of the worldwide incidence of 25 major cancers in 1990. Int J Cancer 1999; 80: 827–41.
2 Yu MC, Yuan JM, Govindarajan S, Ross RK. Epidemiology of hepatocellular carcinoma. Can J Gastroenterol 2000; 14: 703–9.
3 Tang ZY. Hepatocellular carcinoma: cause, treatment and metastasis. World J Gastroenterol 2001; 7: 445–54.
4 Parkin DM, Bray FI, Devesa SS. Cancer burden in the year 2000: The global picture. Eur J Cancer 2001; 37: S4–66.
5 Deuffic S, Poynard T, Buffat L, Valleron AJ. Trends in primary liver cancer. Lancet 1998; 351: 214–5.
6 El-Serag HB, Devila JA, Petersen NJ, McGlynn KA. The continuing increase in the incidence of hepatocellular carcinoma in the United States: an update. Ann Intern Med 2003; 139: 817–23.
7 Thorgeisson SS, Grisham JW. Molecular pathogenesis of human hepatocellular carcinoma. Nat Genet 2002; 31: 339–46.
8 Ding X, Park YN, Taltavull TC, Thung SN, Jin XM, Jin Y, *et al*. Geographic characterization of hepatitis virus infections, genotyping of hepatitis B virus, and p53 mutation in hepatocellular carcinoma analyzed by *in situ* detection of viral genomes from carcinoma tissues: a comparison among six different countries. Jpn J Infect Dis 2003; 56: 12–8.
9 National Institutes of Health Consensus Development Conference Statement: Management of Hepatitis C: 2002. Hepatology 2002; 36: S1–20.
10 Yamamoto J, Kosuge T, Takayama T, Shimada K, Yamasaki S, Ozaki H, *et al*. Recurrence of hepatocellular carcinoma after surgery. Br J Surg 1996; 83: 1219–22.
11 Figueras J, Jaurrieta E, Valls C, Ramos E. Resection or transplantation for hepatocellular carcinoma in cirrhotic patients: outcomes based on indicated treatment strategy. J Am Coll Surg 2000; 190: 580–7.
12 Lai EC, Lo CM, Fan ST, Liu CL, Wong J. Postoperative adjuvant chemotherapy after curative resection of hepatocellular carcinoma: a randomized controlled trial. Arch Surg 1998; 133: 183–8.
13 Yamamoto M, Arii S, Sugahara K, Tobe T. Adjuvant oral chemotherapy to prevent recurrence after curative resection for hepatocellular carcinoma. Br J Surg 1996; 83: 336–40.
14 Kato A, Miyazaki M, Ambiru S, Yoshitomi H, Ito H, Nakagawa K, *et al*. Multidrug resistance gene (MDR-1) expression as a useful prognostic factor in patients with human hepatocellular carcinoma after surgical resection. J Surg Oncol 2001; 78: 110–5.
15 Camma C, Schepis F, Orlando A, Albanese M, Shahied L, Trevisani F, *et al.* Transarterial chemoembolization for unresectable hepatocellular carcinoma: Meta-analysis of randomized controlled trials. Radiology 2002; 224: 109–14.

16 Vilana R, Bruix J, Bru C, Ayuso C, Sole M, Rodes J. Tumor size determines the efficacy of percutaneous ethanol injection for the treatment of small hepatocellular carcinoma. Hepatology 1992; 16: 353–7.
17 CLIP Group (Cancer of the Liver Italian Programme). Tamoxifen in treatment of hepatocellular carcinoma: a randomized controlled trial. Lancet 1998; 352: 17–20.
18 Kouroumalis E, Skordilis P, Thermos K, Vasilaki A, Moschandrea J, Manousos ON. Treatment of hepatocellular carcinoma with octreotide: a randomized controlled study. Gut 1998; 42: 442–7.
19 Pignata S, Daniele B, Gallo C, De Vivo R, Monfardini S, Perrone F. Endocrine treatment of hepatocellular carcinoma: Any evidence of benefit? Eur J Cancer 1998; 34: 25–32.
20 Hanahan D, Weinberg RA. The hallmarks of cancer. Cell 2000; 100: 50–70.
21 Ozturk M. Genetic aspects of hepatocellular carcinogenesis. Semin Liver Dis 1999; 19: 235–42.
22 Moradpour D, Wands JR. Molecular pathogenesis of hepatocellular carcinoma. In: Zakim D, Boyer TD (eds), Hepatology. A Textbook of liver disease. Philadelphia: WB Sauders; 2002. p 1333–54.
23 Suriawinata A, Xu R. An update on the molecular genetics of hepatocellular carcinoma. Semin Liver Dis 2004; 24: 77–88.
24 Matsuo M, Sakurai H, Saiki I. ZD1839, a selective epidermal growth factor receptor tyrosine kinase inhibitor, shows antimetastatic activity using hepatocellular carcinoma model. Mol Cancer Ther 2003; 2: 557–61.
25 Midgley R, Kerr D. Bevacizumab: current status and future directions. Ann Oncol 2005; 16: 999–1004.
26 Sebti SM, Adjei AA. Farnesyltransferase inhibitors. Semin Oncol 2004; 31: 28–39.
27 Lai CL, Lau JY, Wu PC, Ngan H, Chung HT, Mitchell SJ, *et al.* Recombinant interferon-alpha in inoperable hepatocellular carcinoma: a randomized controlled trial. Hepatology 1993; 17: 389–94.
28 Palmieri G, Montella L, Milo M, Fiore R, Biondi E, Bianco AR, *et al.* Ultra-low-dose interleukin-2 in unresectable hepatocellular carcinoma. Am J Clin Oncol 2002; 25: 224–6.
29 Alleghi R, Dissoni P, Barni S, Ardizzola A, Tanchini G, Piperno A, *et al.* Low-dose interleukin-2 subcutaneous immunotherapy in association with the pineal hormone melatonin as a first-line therapy in locally advanced or metastatic hepatocellular carcinoma. Eur J Cancer 1994; 30A: 167–70.
30 Pei Z, Chu L, Zou W, Zhang Z, Qiu S, Qi R, *et al.* An oncolytic adenoviral vector of Smac increases antitumor activity of TRAIL against HCC in human cells and in mice. Hepatology 2004; 39: 1371–81.
31 Sangro B, Herraiz M, Prieto J. Gene therapy of neoplastic liver diseases. Int J Biochem Cell Biol 2003; 35: 135–48.
32 Anderson SC, Johnson DE, Harris MP, Engler H, Hancock W, Huang WM, *et al.* p53 gene therapy in a rat model of hepatocellular carcinoma: intra-arterial delivery of a recombinant adenovirus. Clin Cancer Res 1998; 4: 1649–59.
33 Nguyen TH, Loux N, Dagher I, Vons C, Carey K, Briand P, *et al.* Improved gene transfer selectivity to hepatocarcinoma cells by retrovirus vector displaying single-chain variable fragment antibody against c-Met. Cancer Gene Ther 2003; 10: 840–9.
34 Bilbao R, Gerolami R, Bralet MP, Qian C, Tran PL, Tennant B, *et al.* Transduction efficacy, antitumoral effect, and toxicity of adenovirus-mediated herpes simplex virus thymidine kinase/ganciclovir therapy of hepatocellular carcinoma: the woodchuck animal model. Cancer Gene Ther 2000; 7: 657–62.
35 Sangro B, Mazzolini G, Ruiz J, Herraiz M, Quiroga J, Herrero I, *et al.* Phase I trial of intratumoral injection of an adenovirus encoding interleukin 12 for advanced digestive tumors. J Clin Oncol 2004; 22: 1389–97.
36 Schmitz V, Wang L, Barajas M, Peng D, Prieto J, Qian C. A novel strategy for the generation of angiostatic kringle regions from a precursor derived from plasminogen. Gene Ther 2002; 9: 1600–6.
37 Kondoh N, Wakatsuki T, Hada A, Shuda M, Tanaka K, Arai M, *et al.* Genetic and epigenetic events in human hepatocarcinogenesis. Int J Oncol 2001; 18: 1271–8.
38 Jenuwein T, Allis CD. Translating the histone code. Science 2001; 293: 1074–80.
39 Grunstein M. Histone acetylation in chromatin structure and transcription. Nature 1997; 389: 349–52.
40 Wade PA, Pruss D, Wolffe AP. Histone acetylation: chromatin in action. Trends Biochem Sci 1997; 22: 128–32.
41 Hebbes TR, Thorne AW, Crane-Robinson C. A direct link between core histone acetylation and transcriptionally active chromatin. EMBO J 1988; 7: 1395–402.
42 de Ruijter Aj, van Gennip AH, Caron HN, Kemp S, van Kuilenburg AB. Histone deacetylases: characterisation of the classical HDAC family. Biochem J 2003; 3707: 37–49.
43 Khochbin S, Verdel A, Lemercier C, Seigneurin-Berny D. Functional significance of histone deacetylase diversity. Curr Opin Genet 2001; 11: 162–6.
44 Marks PA, Rifkind RA, Richon VM, Breslow R, Miller T, Kelley WK. Histone deacetylases and cancer: causes and therapies. Nat Rev Cancer 2001; 1: 194–202.
45 Csordas A. The biological role of histone acetylation. Biochemistry 1990; 332: 353–7.
46 Marks PA, Richon VM, Breslow R, Rifkind RA. Histone deacetylase inhibitors as new cancer drugs. Curr Opin Oncol 2001; 13: 477–83.
47 Vidali G, Boffa LC, Bradbury EM, Allfrey VG. Butyrate suppression of histone deacetylation leads to accumulation of multiacetylated forms of histones H3 and H4 and increased DNase I sensitivity of the associated DNA sequences. Proc Natl Acad Sci USA 1978; 75: 2239–43.
48 McIntyre A, Gibson PR, Young GP. Butyrate production from dietary fibre and protection against large bowel cancer in a rat model. Gut 1993; 34: 386–91.
49 Yoshida M, Kijima M, Akita M, Beppu T. Potent and specific inhibition of mammalian histone deacetylase both *in vivo* and *in vitro* by trichostatin A. J Biol Chem 1990; 265: 17174–9.
50 Richon VM, Zhou X, Rifkind RA, Marks PA. Histone deacetylase inhibitors: development of suberoylanilide hydroxamic acid (SAHA) for the treatment of cancers. Blood Cells Mol Dis 2001; 27: 260–4.
51 Kijima M, Yoshida M, Sugita K, Horinouchi S, Beppu T. Trapoxin, an antitumor cyclic tetrapeptide, is an irreversible inhibitor of mammalian histone deacetylase. J Biol Chem 1993; 268: 22 429–35.
52 Nakajima H, Kim YB, Erano H, Yoshida M, Horinouchi S. FR901228 a potent antitumor antibiotic is a novel histone

deacetylase inhibitor. Exp Cell Res 1998; 241: 126–33.
53 Darkin-Rattray SJ, Gurnett AM, Myers RW, Dulski PM, Crumley TM, Allocco JJ, *et al.* Apicidin: a novel antiprotozoal agent that inhibits parasite histone deacetylase. Proc Natl Acad Sci USA 1996; 93: 13143–7.
54 Saito A, Yamashita T, Mariko Y, Nosaka Y, Tsuchiya K, Ando T, *et al.* A synthetic inhibitor of histone deacetylase, MS-275, with marked *in vivo* antitumor activity against human tumors. Proc Natl Acad Sci USA 1999; 96: 4592–7.
55 Gottlicher M, Minucci S, Zhu P, Kramer OH, Schimpf A, Giavara S, *et al.* Valproic acid defines a novel class of HDAC inhibitors inducing differentiation of transformed cells. EMBO J 2001; 20: 6969–78.
56 Kim YB, Lee KH, Sugita K, Yoshida M, Horinouchi S. Oxamflatin is a novel antitumor compound that inhibits mammalian histone deacetylase. Oncogene 1999; 18: 2461–70.
57 Kelly WK, Richon VM, O'Connor O, Curley T, MacGregor-Curtelli B, Tong W, *et al.* Phase I clinical trial of histone deacetylase inhibitor: suberoylanilide hydroxamic acid (SAHA) administered intravenously. Clin Cancer Res 2003; 9: 3578–88.
58 Vigushin DM. FR-901228 Fujisawa/National Cancer Institute. Curr Opin Investig Drugs 2002; 3: 1396–402.
59 Byrd JC, Marcucci G, Parthun MR, Xiao JJ, Klisovic RB, Moran M, *et al.* A phase 1 and pharmacodynamic study of depsipeptide (FK228) in chronic lymphocytic leukemia and acute myeloid leukemia. Blood 2005; 105: 959–67.
60 Gojo I, Karp JE, Mann D. Phase I study of histone deacetylase inhibitor (HDI)MS-275 in adults with refractory or relapsed haematologic malignancies. Proc Am Soc Hem 2002; abstract no 2198.
61 Miller AA, Kurschel E, Osieka R, Schmidt CG. Clinical pharmacology of sodium butyrate in patients with acute leukemia. Eur J Cancer Clin Oncol 1987; 23: 1283–7.
62 Coradini D, Pellizzaro C, Abolafio G, Bosco M, Scarlata I, Stucchi L, *et al.* Hyaluronic acid butyric esters as promising antineoplastic agents in human lung carcinoma: a preclinical study. Invest New Drugs 2004; 22: 207–17.
63 Tammi MI, Day AJ, Turley EA. Hyaluronan and homeostasis: a balancing act. J Biol Chem 2001; 277: 4581–4.
64 Fraser JR, Alcorn D, Laurent TC, Robinson AD, Ryan GB. Uptake of circulating hyaluronic acid by the rat liver. Cell Tissue Res 1985; 242: 505–10.
65 Isacke CM, Yarwood H. The hyaluronan receptor CD44. J Biochem Cell Biol 2002; 34: 718–21.
66 Seiter S, Arch R, Reber S, Komitowski D, Hofmann M, Ponta H, *et al.* Prevention of tumor metastasis formation by anti-variant CD44. J Exp Med 1993; 177: 443–55.
67 Gunthert U, Hofmann M, Rudy W, Reber S, Zoller M, Haussmann I, *et al.* A new variant of glycoprotein CD44 confers metastatic potential to rat carcinoma cells. Cell 1991; 65: 13–24.
68 Lara-Pezzi E, Serrador JM, Montoya MC, Zamora D, Yanez-Mo M, Carretero M, *et al.* The hepatitis B virus protein (HBx) induces a migratory phenotype in a CD44-dependent manner: possible role of HBx in invasion and metastasis. Hepatology 2001; 33: 1270–81.
69 Byrd JC, Shinn C, Ravi R, Willis CR, Waselenko JK, Flinn IW, *et al.* Depsipeptide (FR901228): a novel therapeutic agent with selective *in vitro* activity against human B-cell chronic lymphocytic leukaemia cells. Blood 1999; 94: 1401–8.
70 Coradini D, Zorzet S, Rossin R, Scarlata I, Pellizzaro C, Turrin C, *et al.* Inhibition of hepatocellular carcinomas *in vitro* and hepatic metastases *in vivo* in mice by the histone deacetylase inhibitor HA-But. Clin Cancer Res 2004; 10: 4822–30.
71 Nishida N, Fukuda Y, Komeda T, Kita R, Sando T, Furukawa M, *et al.* Amplification and overexpression of the cyclin D1 gene in aggressive human hepatocellular carcinoma. Cancer Res 1994; 54: 3107–10.
72 Herold C, Ganslmayer M, Ocker M, Hermann M, Geerts A, Hahn EG, *et al.* The histone-deacetylase inhibitor Trichostatin A blocks proliferation and triggers apoptotic programs in hepatoma cells. J Hepatol 2002; 36: 233–40.
73 Svechnikova I, Gray SG, Kundrotiene J, Ponthan F, Kogner P, Ekstrom TJ. Apoptosis and tumor remission in liver tumor xenografts by 4-phenylbutyrate. Int J Oncol 2003; 22: 579–88.
74 Chiba T, Yokosuka O, Arai M, Tada M, Fukai K, Imazeki F, *et al.* Identification of genes up-regulated by histone deacetylase inhibition with cDNA microarray and exploration of epigenetic alterations on hepatoma cells. J Hepatol 2004; 41: 436–45.
75 Peart MJ, Smyth GK, van Laar RK, Bowtell DD, Richon VM, Marks PA, *et al.* Identification and functional significance of genes regulated by structurally different histone deacetylase inhibitors. Proc Natl Acad Sci USA 2005; 102: 3697–702.
76 Xu XR, Huang J, Xu ZG, Qian BZ, Zhu ZD, Yan Q, *et al.* Insight into hepatocellular carcinogenesis at transcriptome level by comparing gene expression profiles of hepatocellular carcinoma with those of corresponding noncancerous liver. Proc Natl Acad Sci USA 2001; 98: 15089–94.
77 Tannapfel A, Wittekind C. Genes involved in hepatocellular carcinoma: deregulation in cell cycling and apoptosis. Virchows Arch 2002; 440: 345–52.
86 McGary CT, Yannariello-Brown J, Kim DW, Stinson TC, Weigel PH. Degradation and intracellular accumulation of a residualizing hyaluronan derivative by liver endothelial cells. Hepatology 1993; 18: 1465–76.
79 Chen X, Cheung ST, So S, Fan ST, Barry C, Higgins J, *et al.* Gene expression patterns in human liver cancers. Mol Biol Cell 2002; 13: 1929–39.
80 Delpuech O, Trabut JB, Carnot F, Feuillard J, Brechot C, Kremsdorf D. Identification, using cDNA microarray analysis, of distinct gene expression profiles associated with pathological and virological features of hepatocellular carcinoma. Oncogene 2002; 21: 2926–37.
81 Gustafsson S, Bjorknan T, Westlin JE. Labelling of high molecular weight hyaluronan with ^{125}-I-tyrosine. Studies *in vitro* and *in vivo* in the rat. Glyco Conj J 1994; 11: 608–13.
82 Saegusa S, Shuji I, Kawarada Y. Changes in serum hyaluronic acid levels and expression of CD44 and CD44 mRNA in hepatic sinusoidal endothelial hepatectomy in cirrhotic rats. World J Surg 2002; 26: 694–9.
83 Barbara-Guillem E, Alonso-Varona A, Vidal-Vanaclocha F. Selective implantation and growth in rats and mice of experimental liver metastasis in acinar zone one. Cancer Res 1989; 49: 4003–10.
84 Carrascal MT, Mendoza L, Valcarcel M, Salado C, Egilegor E. Interleukin-18 binding protein reduces B16 melanoma hepatic metastasis in neutralizing adhesiveness and growth factors of sinusoidal endothelium. Cancer Res 2003; 63: 491–7.

Acta Pharmacologica Sinica 2005 Sep; 26 (9): 1034–1038

Short communication

Chronic morphine exposure induces degradation of receptive field properties of LGN cells in cats[1]

Li-hua HE[2], Guang-xing LI[2], Xiang-rui LI[2], Yi-feng ZHOU[2,3,4]

[2]Hefei National Laboratory for Physical Sciences at Microscale and School of Life Science, University of Science and Technology of China, Hefei 230027, China; [3]Laboratory of Visual Information Processing, Institute of Biophysics, Chinese Academy of Sciences, Beijing 100101, China

Key words

direction sensitivity; orientation sensitivity; signal-to-noise ratio; spontaneous response; evoked response

[1] Project supported by the National Natural Science Foundation of China (No 30470561).
[4] Correspondence to Dr Yi-feng ZHOU.
Phn 86-551-360-1436.
Fax 86-551-360-7014.
E-mail zhouy@ustc.edu.cn

Received 2005-05-16
Accepted 2005-06-20

doi: 10.1111/j.1745-7254.2005.00190.x

Abstract

Aim: To investigate the effect of chronic morphine exposure on the receptive field properties of lateral geniculate nucleus (LGN) neurons in cats. **Methods:** Cats were injected with morphine (10 mg/kg) or saline twice daily, for 10 d. Subsequently, extracellular single-unit recording techniques were used to examine the sensitivity of LGN neurons to visual stimuli in chronic morphine-treated and saline-treated cats. **Results:** Compared with saline-treated cats (as controls), LGN neurons in morphine-treated cats had decreased signal-to-noise ratios (1.9 *vs* 3.1), and orientation and direction sensitivity (0.103 *vs* 0.135 and 0.074 *vs* 0.10, respectively), accompanied by significant increases in spontaneous (27.4 *vs* 17.5) and evoked activity (preferred: 42.2 *vs* 38.1; average: 28.1 *vs* 22.3). **Conclusion:** Chronic morphine exposure can lead to the functional degradation of LGN neurons in cats, which might result from the effects of chronic morphine exposure on inhibitory neurotransmission.

Introduction

The brain is rich in opiate receptors, and significant concentrations of opiate receptors are observed in the visual systems of cats[1], macaques[2], and rats[3]. It has been suggested that the visual system is subject to opiate modulation. Previous studies have shown that morphine-like drugs decrease visual sensitivity in humans[4], affect visual discrimination performance in rats[5], and evoke cortical potentials by stimulating the optic chiasm in cats[6].

Repeated use of addictive drugs leads to multiple adaptive neuronal responses[7,8]. Increasingly, research suggests that chronic exposure to opiates significantly changes glutamatergic synaptic transmission and neuronal plasticity in many brain regions[9,10]. Similarly, GABAergic synaptic transmission is also influenced by opiates[11–13]. However, normal excitatory and inhibitory synaptic transmission is crucial for the development and maintenance of visual function. These findings indicate that opiates might influence the performance of neurons in the lateral geniculate nucleus (LGN). In the present study, we tested this possibility by using extracellular single-unit recording techniques to examine the stimulus sensitivity of LGN neurons in chronic morphine-treated cats.

Materials and methods

Subjects and drug exposure The experiments were performed on 8 healthy adult male cats (2–3 kg), 4 of which were allocated to the morphine treatment group and 4 of which were used as controls. All animals were treated strictly in accordance with the Chinese National Institutes of Health's Guide for the Care and Use of Laboratory Animals. The method of morphine treatment was similar to that used by other researchers[9]. Morphine HCl (10 mg/kg) was administered by cervical subcutaneous injection twice per day at 9:00 and 21:00 for 10 d before the electrophysiological experiments. Control cats were treated similarly with saline instead of morphine.

All cats were examined ophthalmoscopically before the experiment to confirm that they had no optical problems or obvious retinal problems that would impair the visual function.

Preparation for extracellular recording On the 11th

day of morphine administration, animals were prepared for extracellular single-unit recording as described previously[14,15]. A typical recording session lasted for 3 d. During recording, morphine or saline was injected in the same way as described in the previous section.

Visual stimulation The receptive fields of cells were first plotted by using manually controlled stimuli displayed on the tangent screen. Computer-controlled visual stimuli consisting of drifting sinusoidal gratings were presented on a CRT (cathode-ray tube) monitor (1024×768, 85 Hz), placed 57 cm away from the animals' eyes. The program to generate the stimulus was written in MATLAB, using the extensions provided by the high-level Psychophysics Toolbox[16] and the low-level Video Toolbox[17]. The time frequency of drifting gratings was set at 3 Hz. At first, a tuning curve of spatial frequency was plotted. We selected a high spatial frequency where cells' responses were approximately half of that at peak frequency to compile the orientation and direction tuning curves. Before each stimulus presentation, 5 s spontaneous activities were obtained while the mean luminance was shown on the display. Additional stimuli were used to identify a cell as X- or Y-type, and on- or off-center. The contrast of the stimulus was set at 80%. The mean luminance of the display was 19 cd/m^2, and the environment luminance on the cornea was 0.1 lux.

Data collection and analysis After the neuronal signal was amplified with a microelectrode amplifier (Nihon Kohden, Tokyo, Japan) and a differential amplifier (FHC, Bowdoinham, USA), action potentials were fed into a window discriminator with an audio monitor. The original voltage traces were digitized using an acquisition board (National Instruments, Austin, USA) controlled by IGOR software (WaveMetrics, Portland, USA). The original data were saved for online and offline analysis. The post-stimulus time histograms (PSTH) of neuronal responses with a bin width of 10 ms were obtained for further analysis. The responses of cells to the sinusoidal gratings were treated using a fast Fourier transform and the amplitude was defined as the resultant fundamental Fourier component (FFT1) of the PSTH. The FFT1 value of each stimulus orientation (direction) was used to draw the spatial frequency and orientation (direction) tuning curves. The method for calculation of orientation bias (OB) and direction bias (DB) has been described elsewhere[18,19]. A cell with bias=0.1 was considered significantly biased for orientation or direction. A cell with bias=0.2 was considered strongly biased for orientation or direction. A cell's signal-to-noise ratio (STN) was defined as the ratio of the cell's visual evoked response (FFT1 value in preferred orientation and direction) to spontaneous response. To avoid data skewing or overestimation, all spontaneous activities below 1 spike per second were set equal to 1 spike per s for signal-to-noise analysis.

Statistical comparisons between morphine-treated and saline-treated cat data were carried out using *t*-test. All mean values were presented as mean±SEM.

Results

The results described here were obtained from 168 cells in 4 morphine-treated cats (abbreviated to MCs) and 173 cells in 4 saline-treated cats (abbreviated to control) in LGN. Our chief findings were that chronic morphine exposure led to a decrease in the signal-to-noise ratio and a degradation in the orientation and direction sensitivity of LGN cells, which was accompanied by an increase in spontaneous and evoked response. Our analysis revealed that there was a consistent effect of chronic morphine exposure on different types of LGN cells (X or Y; on or off), so comparisons of data between two groups ignore the type of cell.

Orientation and direction sensitivity As an example, we show here the response of an LGN cell to a drifting sinusoidal grating (Figure 1A) and its PSTH (Figure 1B). Figure 1C and 1D illustrate the tuning curve of a cell from controls (OB=0.2, DB=0.01) and MCs (OB=0.1, DB=0.08), respectively. MCs have a decrease in orientation and direction sensitivity relative to controls. The average OB and DB values varied individually in both MCs and controls. The OB were significantly smaller in MCs (0.103±0.068) than in control cats (0.135±0.084, $P<0.01$; Figure 1E). Sixty-three percent of LGN cells in controls and 50% of cells in MCs had significant orientation sensitivity (OB=0.1). In MCs, the percentage of cells (10%) with strong orientation sensitivity (OB=0.2) was half of that in controls (20%). Similarly, the direction sensitivity of LGN cells was also affected by chronic morphine exposure. The DB of LGN cells were significantly less for MCs (0.074±0.059) than for controls (0.100±0.064, $P<0.01$; Figure 1F). As with the orientation bias, the percentages of cells having significant and strong direction bias in MCs (30% and 6%, respectively) were less than those in controls (47% and 10%, respectively).

Visually evoked activity To explore whether the sensitivity decrease of cells in MCs resulted from an increase of responsiveness to previously non-preferred orientations and directions or from a reduction of responsiveness to the previously preferred orientations and directions, or both, we compared the average response (AR) to all stimulating grating orientations of LGN cells in MCs and controls. Cells in MCs showed a tendency for an increase in the AR compared

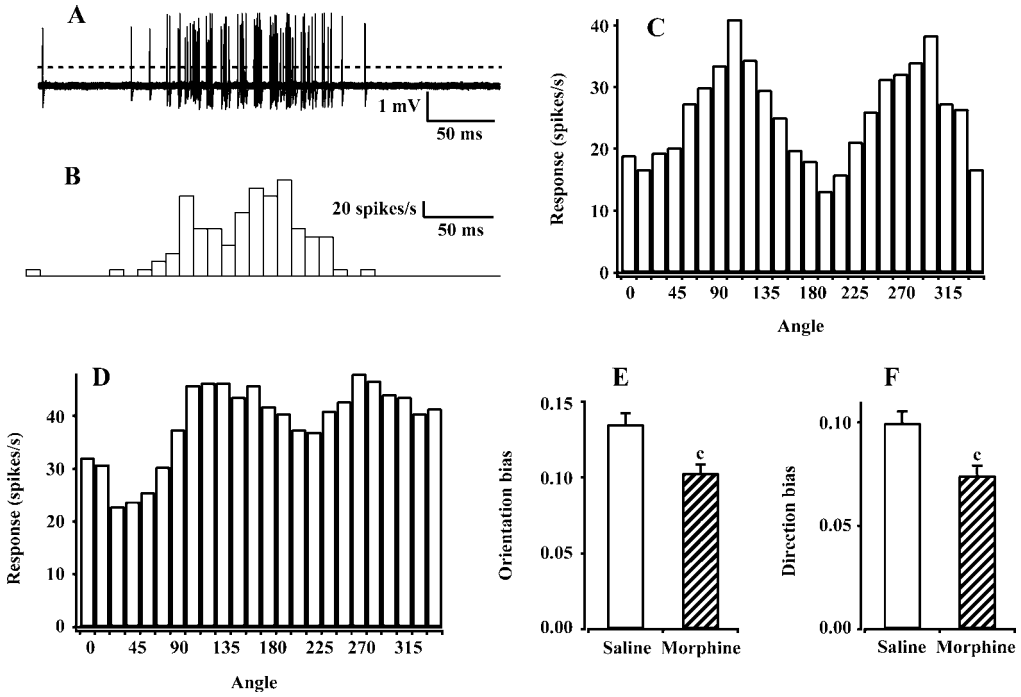

Figure 1. (A) An example of the responses of a neuron to the drifting sinusoidal grating. Ten cycles of the neuron's original response are superimposed in one stimulus period. A spike above the broken horizontal line is counted as an action potential. (B) The PSTH derived from (A) for further analysis. Bin width was 10 ms. (C, D) The neuron's orientation tuning curve from saline-treated (C) and morphine-treated cats (D). The responses were defined as the fundamental Fourier components (FFT1). The FFT1 at each stimulus direction was computed from the PSTH such as the one shown in (B). (E, F) Comparison of orientation (E) and direction (F) biases of LGN cells between morphine-treated (n=4) and saline-treated (n=4) cats. The data were expressed as mean±SEM. ^cP<0.01 *vs* saline.

with controls (Figure 2A). Half of the cells (50.3%) in MCs had an AR value of more than 25 spikes per second. In contrast, most cells (63.2%) in controls had an AR value of less than 25 spikes per second. A statistical analysis showed that the mean AR value in MCs (28.1±16.1) was significantly larger than that in controls (22.3±11.3, P<0.01). Moreover, we also compared the response of LGN cells to their preferred orientation and direction in MCs and controls. For convenience, we call this the preferred response (PR). Similar to the AR, the PR value in MCs was also increased relative to that in controls (Figure 2B). The t-test indicated that the mean PR value (42.2±19.1) for MCs was significantly higher compared with that for controls (38.1±16.2, P<0.05). Therefore, LGN cells in MCs have increased responsiveness to both preferred and non-preferred stimuli.

Spontaneous activity and signal-to-noise ratio LGN cells

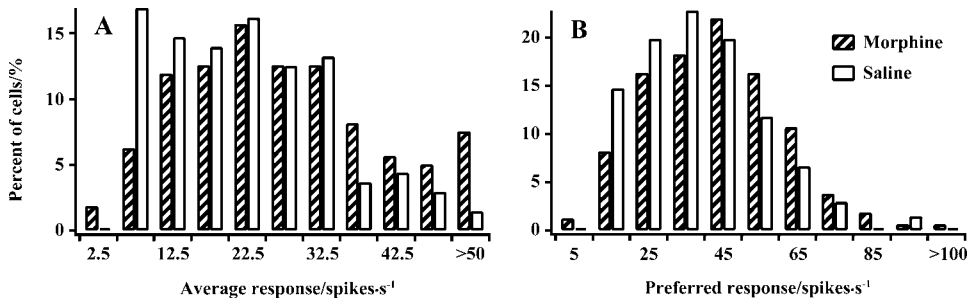

Figure 2. Percentage of cells with different average response (AR) and preferred response (PR) values for morphine-treated and saline-treated cats. (A) Percentage of cells with different AR values for all stimulus orientations. (B) Percentage of cells with different PR values. The mean AR and PR values are significantly different between the two groups.

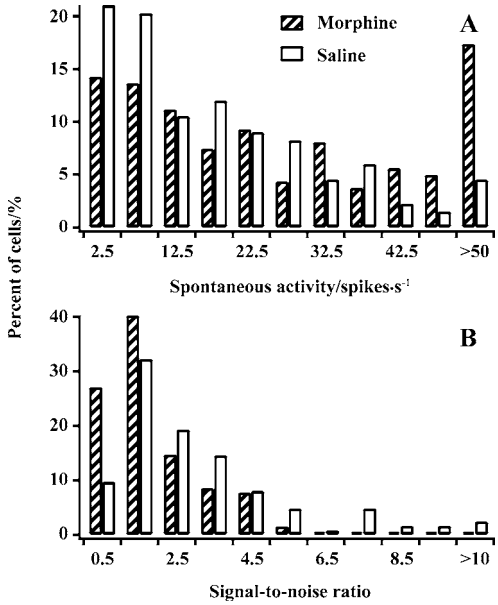

Figure 3. Comparison of spontaneous activity (A) and signal-to-noise ratio (B) between morphine-treated and saline-treated cats. Neurons in morphine-treated cats had decreased signal-to-noise ratio, which is mainly attributable to increased spontaneous activity.

in controls trended to have a small spontaneous response (SR) value, whereas cells in MCs had a more extensive distribution. Most cells (63.9%) in controls had an SR value of less than 20 spikes per second. In contrast, approximately half of the cells (53.4%) in MCs had an SR value of more than 20 spikes per second. The average SR value (27.4±22.5) in MCs was significantly higher than that in controls (17.5± 14.3, $P<0.01$; Figure 3A).

Figure 3B presents the distribution of various signal-to-noise ratios (STN=PR/SR) for cells in MCs and controls. The number of cells with lower STN was much more for MCs than for controls. Almost all cells (98.4%) in MCs had an STN value of less than 5. However, quite a number of cells (16.1%) had an STN value of more than 5 in controls. A comparison of the averaged STN for controls (3.1±2.3) versus MCs (1.9±1.2) showed that the difference was statistically significant ($P<0.01$). Taken together, these data suggest that chronic morphine exposure results in an increase in spontaneous activity and a decrease in signal-to-noise ratio in LGN cells in MCs.

Discussion

We found significant degradation in the receptive field properties of LGN neurons in MCs. The morphine-derived degradation in orientation and direction sensitivity in LGN neurons was accompanied by an unspecific increase in responsiveness. The average response across all orientations of stimulus gratings for MCs increased by 26.0% compared with controls, whereas the response to preferred stimuli increased by only 11.2%. Thus, the increased responsiveness to non-preferred orientations and directions appears to be an important mechanism mediating the reduction in cells' sensitivity to stimuli in MCs. On the other hand, the spontaneous activity of LGN neurons in MCs increased by 56.6% compared with controls. This increase was much higher than the increase in preferred response. As a result, the ratio of preferred response to spontaneous activity (signal-to-noise ratio) in MCs was much lower than in controls. The decrease in signal-to-noise ratio in MCs thus appears to mainly reflect the large increase in spontaneous activity.

Orientation and direction sensitivity is a well-known receptive field property of neurons in the mammalian visual cortex[20]. However, it is quite controversial whether orientation and direction sensitivity exists in LGN neurons. Many tests beyond the peak spatial frequency have shown that a lot of LGN cells are sensitive to stimulus orientation or direction[14,21]. The results of the present study also show this. It has been proposed that an elliptical shape of the receptive-field center and asymmetry in the inhibitory surrounds contribute to the orientation and direction sensitivity of LGN cells. Previous investigations suggest that microiontophoresis of bicuculline (an antagonist of the $GABA_A$ receptor) affects the orientation and direction sensitivity of neurons in LGN of cats[22,23]. Moreover, LGN cells also have increased spontaneous and evoked activity when GABAergic inhibition is blocked[22,24]. In the present study, LGN cells in MCs had decreased orientation and direction sensitivity accompanied by increased spontaneous and evoked activity. Furthermore, research on drug abuse suggests that the decline of inhibitory neurotransmission actually happens in many brain regions[11–13]. In view of the extensive expression of opiate receptors throughout the visual system, reduced GABAergic inhibition might be a reasonable explanation for the degradation of receptive field properties of LGN cells in MCs. Nevertheless, some studies have shown that drug abuse also affects glutamatergic and other transmitter systems, indicating that these transmitter systems might affect the sensitivity of LGN cells to visual stimuli following chronic morphine exposure. Additionally, LGN neurons reflect the properties of the center-surround organized retinal receptive fields and convey them to the cortex in a way that does not significantly alter their spatial structure[24]. Therefore, the action of chronic morphine exposure on the

retina might be one factor resulting in the degradation of the receptive field properties of LGN cells in MCs.

In summary, our results suggest that chronic morphine exposure can lead to the degradation of the receptive field properties of LGN cells in cats. Morphine-derived decreases of GABAergic inhibition together with other factors might contribute to the functional degradation of LGN cells in MCs. All in all, much remains to be learned about the role of opiate receptors in the visual system and the morphine-derived decay of receptive field properties of LGN neurons.

References

1 Walker JM, Bowen WD, Thompson LA, Frascella J, Lehmkuhle S, Hughes HC. Distribution of opiate receptors within visual structures of the cat brain. Exp Brain Res 1988; 73: 523–32.

2 Wise SP, Herkenham M. Opiate receptor distribution in the cerebral cortex of the Rhesus monkey. Science 1982; 218: 387–9.

3 Lewis ME, Pert A, Pert CB, Herkenham M. Opiate receptor localization in rat cerebral cortex. J Comp Neurol 1983; 216: 339–58.

4 Rothenberg S, Peck EA, Schottenfeld S, Betley GE, Altman JL. Methadone depression of visual signal detection performance. Pharmacol Biochem Behav 1979; 11: 521–7.

5 Grilly DM, Genovese RF, Nowak MJ. Effects of morphine, *xd*-amphetamine, and pentobarbital on shock and light discrimination performance in rats. Psychopharmacology (Berl) 1980; 70: 213–7.

6 Wilkison DM, Hosko MJ. Selective augmentation of visual pathways by morphine in alpha-chloralose-anesthetized cats. Exp Neurol 1982; 77: 519–33.

7 Robinson TE, Kolb B. Persistent structural modifications in nucleus accumbens and prefrontal cortex neurons produced by previous experience with amphetamine. J Neurosci 1997; 17: 8491–7.

8 Robinson TE, Kolb B. Morphine alters the structure of neurons in the nucleus accumbens and neocortex of rats. Synapse 1999; 33: 160–2.

9 Pu L, Bao GB, Xu NJ, Ma L, Pei G. Hippocampal long-term potentiation is reduced by chronic opiate treatment and can be restored by re-exposure to opiates. J Neurosci 2002; 22: 1914–21.

10 Martin G, Ahmed SH, Blank T, Spiess J, Koob GF, Siggins GR. Chronic morphine treatment alters NMDA receptor-mediated synaptic transmission in the nucleus accumbens. J Neurosci 1999; 19: 9081–9.

11 Vaughan CW, Ingram SL, Connor MA, Christie MJ. How opioids inhibit GABA-mediated neurotransmission. Nature 1997; 390: 611–4.

12 Laviolette SR, Gallegos RA, Henriksen SJ, van der Kooy D. Opiate state controls bi-directional reward signaling via $GABA_A$ receptors in the ventral tegmental area. Nat Neurosci 2004; 7: 160–9.

13 Cruz HG, Ivanova T, Lunn ML, Stoffel M, Slesinger PA, Luscher C. Bi-directional effects of GABA(B) receptor agonists on the mesolimbic dopamine system. Nat Neurosci 2004; 7: 153–9.

14 Zhou Y, Leventhal AG, Thompson KG. Visual deprivation does not affect the orientation and direction sensitivity of relay cells in the lateral geniculate nucleus of the cat. J Neurosci 1995; 15: 689–98.

15 Shou T, Li X, Zhou Y, Hu B. Adaptation of visually evoked responses of relay cells in the dorsal lateral geniculate nucleus of the cat following prolonged exposure to drifting gratings. Vis Neurosci 1996; 13: 605–13.

16 Brainard DH. The psychophysics toolbox. Spat Vis 1997; 10: 433–6.

17 Pelli DG. The VideoToolbox software for visual psychophysics: transforming numbers into movies. Spat Vis 1997; 10: 437–42.

18 Levick WR, Thibos LN. Analysis of orientation bias in cat retina. J Physiol 1982; 329: 243–61.

19 Schmolesky MT, Wang Y, Pu M, Leventhal AG. Degradation of stimulus selectivity of visual cortical cells in senescent Rhesus monkeys. Nat Neurosci 2000; 3: 384–90.

20 Hubel DH, Wiesel TN. Receptive fields and functional architecture of monkey striate cortex. J Physiol 1968; 195: 215–43.

21 Thompson KG, Leventhal AG, Zhou Y, Liu D. Stimulus dependence of orientation and direction sensitivity of cat LGNd relay cells without cortical inputs: a comparison with area 17 cells. Vis Neurosci 1994; 11: 939–51.

22 Hu B, Li X, Zhou Y, Shou T. Effects of GABA antagonist bicuculline on the orientation tuning character of relay cells in dorsal geniculate nucleus (dLGN). Acta Biophys Sin 1994; 10: 121–7.

23 Hu B, Li X, Zhou Y, Shou T. Effects of bicuculline on direction-sensitive relay cells in the dorsal lateral geniculate nucleus (LGNd) of cats. Brain Res 2000; 885: 87–93.

24 Holdefer RN, Norton TT, Godwin DW. Effects of bicuculline on signal detectability in lateral geniculate nucleus relay cells. Brain Res 1989; 488: 341–7.

Acta Pharmacologica Sinica 2005 Sep; 26 (9): 1039-1044

Full-length article

Involvement of nociceptin/orphanin FQ in release of hypothalamic GnRH mediated by ORL1 receptor in ovariectomized rats

Xiao-fei AN, Hai-ping CHEN, Shu-lan MA, Yi FENG, Jun-wei HAO, Bo-ying CHEN[1]

Department of Neurobiology and Integrative Medicine, Shanghai Medical College, Fudan University, Shanghai 200032, China

Key words

nociceptin; ORL1 receptor; gonadorelin; hypothalamus

[1] Correspondence to Prof Bo-ying CHEN.
Phn 86-21-5423-7693.
Fax 86-21-5423-7023.
E-mail bychen@shmu.edu.cn

Received 2005-02-03
Accepted 2005-05-23

doi: 10.1111/j.1745-7254.2005.00172.x

Abstract

Aim: To investigate effect of the nociceptin/orphanin FQ (OFQ) on hypothalamus gonadotropin-releasing hormone (GnRH) release in ovariectomized (OVX) rats. **Methods:** GnRH radioimmunoassay (RIA) was used to study the effect of OFQ on GnRH release in hypothalamus slices *in vitro*. Push-pull perfusion and intracerebroventicular (icv) injection were used to examine the effect of OFQ on GnRH release in the hypothalamus medial preoptic area (POA) *in vivo*. Ovariectomies were performed on female Sprague-Dawley rats, and their plasma luteinizing hormone (LH) levels were measured after icv injection of OFQ with or without [Nphe^1]NC(1-13)NH_2, a competitive antagonist of opioid receptor-like1 receptor (ORL1 receptor). Reverse transcription-polymerase chain reaction (RT-PCR) was used to investigate the expression of the ORL1 receptor in rat pituitary. **Results:** GnRH release from hypothalamus slices was inhibited 90 min after the administration of 2 mmol/L and 20 mmol/L OFQ (P<0.05). Accordingly, GnRH release from hypothalamus POA was also significantly reduced by the injection of 0.2 mmol/L and 2 mmol/L OFQ. Plasma LH levels were also decreased significantly 2 h after icv injection of 20 nmol OFQ in OVX rats (P<0.05) and this effect could be abolished by pretreatment with 20 nmol [Nphe^1]NC(1-13)NH_2, that is, NC13. More interestingly, plasma LH levels in OVX rats increased markedly 2 h after icv injection of 100 nmol and 200 nmol NC13. RT-PCR analysis further revealed that the ORL1 receptor was not expressed in the pituitary of OVX rats. **Conclusion:** Central administration of nociceptin/orphanin FQ might inhibit the release of hypothalamic GnRH and decrease the plasma LH levels through ORL1 receptors in OVX rats.

Introduction

Nociceptin/orphanin FQ (OFQ) is a heptadecapeptide that has high amino acid sequence homology to the endogenous opioid peptides, especially dynorphin A[1,2]. OFQ is the putative endogenous ligand for the opioid receptor-like1 receptor (ORL1 receptor)[2,3]. The ORL1 receptor has structural and functional homology with the δ,κ, and μ classic opioid receptors. Despite its close similarity to opioid receptors, the ORL1 receptor does not selectively bind opioids and opioids antagonists[3]. A number of physiological effects of OFQ have been reported, including nociceptive modulation, and cardiovascular and renal physiological functions[2,4,5].

The classic opiates are involved in the regulation of anterior pituitary hormone secretion. Opiate administration increases prolactin and growth hormone[6], while decreasing the release of luteinizing hormone in a naloxone-reversible manner[7]. The homology between the opiate peptides and OFQ as well as between their receptors, coupled with the localization of OFQ in the hypothalamus suggest a neuroendocrine role for OFQ[8,9].

GnRH, as an important hypothalamic decapeptide, plays a key role in the functions of the hypothalamic-pituitary-ovary axis (HPOA) by modulating the secretion of luteinizing hormone (LH) and follicle-stimulating hormone (FSH)

from the anterior pituitary[10]. Endogenous opioid peptides, particularly β-endorphin, constitute an important inhibitory component of the neural circuitry that regulates GnRH secretion and a significant decrease in the inhibitory opioid tone is critical for the generation of a LH surge during the estrous cycle[11].

OFQ and the ORL1 receptor are densely localized in the preoptic area (POA), ventralmedial hypothalamus (VMH) and arcuate nucleus (ARC), all of which have been identified as the chief hypothalamic nuclei regulating GnRH release[8]. It has been demonstrated that OFQ activates the G protein-coupled inwardly rectifying K^+ channel (GIRK) and hyperpolarizes many hypothalamic neurosecretion cells, especially in the ARC[12]. Recent studies have revealed that OFQ potently and dose-dependently inhibits forskolin-induced GnRH release from rat hypothalamic fragments[13]. We postulated that OFQ might play a role in the regulation of GnRH release in rat hypothalamus. To test the hypothesis, the effects of the central administration of OFQ on rat hypothalamus GnRH release and plasma LH levels were observed in the present study.

Materials and methods

Animals and drugs Female Sprague-Dawley rats weighing 200–220 g obtained from the Animal Center of Shanghai Medical School of Fudan University had both ovaries surgically removed under aseptic conditions. They were kept in an air-conditioned room with controlled lighting (light 12 h: dark 12 h) and given free access to laboratory chow and tap water. Experiments were carried out 4–6 weeks after the ovariec-tomies. Nociceptin/orphanin FQ (MW 1810) and [$Nphe^1$]NC(1-13)NH_2 (NC13; MW=1382) were purchased from Phoenix Pharmaceutical Company (St Joseph, MD, USA). The compounds were dissolved in artificial cerebrospinal fluid (ACSF; 128 mmol/L NaCl, 2.5 mmol/L KCl, 1.4 mmol/L $CaCl_2$, 1.0 mmol/L $MgCl_2$ and 1.2 mmol/L Na_2HPO_4; pH 7.4)[14]. All other reagents and solvents were of analytical grade.

Incubation of hypothalamus slices Animals were killed by decapitation in a period of less than 30 min and medial basal hypothalamus slices were quickly dissected at 4 ºC as described by Lamar *et al*[15]. The slices were placed into 2 mL ice-cold ACSF in a chamber made from a 5 mL plastic syringe specially modified for incubation. The slices were maintained at 37 ºC in an atmosphere of 5% CO_2 and 95% O_2 with gentle agitation for 30 min preincubation. The slices then were treated with ACSF or 0.2, 2, and 20 mmol/L OFQ and incubated for 2 h. Every 30 min, 200 μL medium was extracted, then 200 μL fresh ACSF was added to the system. The incubation medium was collected in tubes and stored at -20 ºC for GnRH radioimmunoassay.

Push-pull perfusion Animals were anesthetized with sodium pentobarbital (40 mg/kg, ip) and placed on a stereotaxic instrument. A push-pull cannula with a removable inner stylette constructed in our laboratory was implanted towards the hypothalamus POA (Bregma AP: 0.4 mm; L: 0.8 mm; H: 8.5 mm)[16]. The device was fixed onto the rat skull with an anchor screw and dental cement, and the animals were given a minimum recovery period of 7 d. On the day of perfusion, the inner stylette was removed and replaced with the inner cannula perfusion assembly. ACSF was infused through the push cannula and collected from the pull cannula at a flow rate of 10 μL/min. After a 30 min equilibration period, 0.02, 0.2, or 2 mmol/L OFQ solution was perfused. The perfusate was collected every 20 min over a total period of 2 h and stored at -80 ºC for GnRH radioimmunoassay.

Intracerebroventicular injection Implantation of the cannula was performed stereotaxically under anesthesia with sodium pentobarbital (40 mg/kg, ip). Stereotaxic surgical procedures were used to implant one 22 gauge stainless steel guide cannula with a removable 28 gauge inner stylette to the left lateral ventricle (Bregma AP: 1.0 mm; L: 1.5 mm; H: 3.0 mm)[16]. Experiments with icv injection were performed at least 7 d after operation. The OFQ solution was added with protease inhibitor (1 g/L) for preventing proteolysis after injection. Two, 20 or 200 nmol OFQ dissolved in 10 μL ACSF was infused through a 28 gauge cannula extended 0.5 mm beyond the guide cannula. The needle was connected to a 10-μL syringe by a polyethylene tube and the drug solutions were delivered by infusion pump at a flow rate of 5 μL/min. The injection needle was maintained in place for an extensive period of 10 min after the injection. Under anesthesia conditions, OVX rats were injected with ACSF, OFQ (2, 20, or 200 nmol OFQ in 10 μL ACSF) or NC13 (20, 50, 100, and 200 nmol NC13 in 10 μL ACSF). Blood samples of 400 μL were withdrawn from the rat tail vein every hour over a total period of 4 h after icv injection. Blood plasma (200 μL) was separated from each blood sample by centrifugation and stored at -20 °C until LH radioimmunoassay.

RT-PCR analysis Total cytoplasmic RNA was isolated from the medial basal hypothalamus, hippocampus and pituitary of ovariectomized rats using the Trizol reagent (Life Technologies, Rockville, MD, USA). Total RNA (4 μg) was digested with DNase RNase-free enzyme to eliminate genomic DNA, and then converted to complementary DNA (cDNA) using 200 U Moloney murine leukemia virus reverse transcriptase (Promega, Madison, WI, USA) in 20 μL of buffer containing 0.4 mmol/L deoxynucleotide triphosphates, 20 U

RNase inhibitor and 0.8 μg oligo (deoxythymidine)$_{15}$ (Sino-American Biotechnology Company, Shanghai, China). Specific primers were 5'-CAGGCTGTTAATGTGGCCATATG-3' and 5'-GAGCCTGAAAGCAGACGGACACC-3' (synthesized in Shanghai Sangon Biological Engineering Technology and Service Company), which annealed to bases 493–515 and 743–721 of the ORL1 receptor[17]. Twenty-eight cycles under the following PCR conditions were carried out: denaturation at 94 °C for 45 s, annealing at 60 °C for 45 s and elongation at 72 °C for 60 s with Thermus aquaticus DNA polymerase (Promega, Medison, WI, USA). The RT-PCR products (5 μL) were electrophoresed in a 1.6% agarose ethidium bromide gel and visualized using the SYNGENE imaging system (GeneSnape Software, London, UK).

GnRH and LH radioimmunoassay GnRH in perfusate was assayed by using a commercial RIA kit (Sigma) and measurements were performed according to the manufacturer's instructions. Plasma LH was measured by using an LH RIA kit (Shanghai Institute of Biologic Products, Shanghai, China), and the sensitivity of the assay was 0.4 pg/mL. The intra-assay coefficient of variation was 3.5% and the intro-assay variation was 4.8%.

Statistical analysis All results are expressed as mean±SD and were analyzed by the Statistical Package for the Social Sciences (SPSS) statistical software. The data in Figures 1–3 were analyzed by using a two-way repeated measures analysis of variance (ANOVA) with time as the repeated measure. The other results were analyzed by one-way ANOVA and the significance of difference was determined by the Newman-Keuls test. When only two treatment groups were being compared, Student's *t*-test was used. A probability of $P<0.05$ was considered to be statistically significant.

Results

Effect of OFQ on GnRH release from hypothalamus slices It was apparent that GnRH release began to decrease 60 min after OFQ administration. In the 2 mmol/L and 20 mmol/L OFQ groups, GnRH concentrations in the medium were significantly decreased ($P<0.05$) at 90 min (21.01±3.77 pg/mL and 15.78±3.02 pg/mL) after OFQ administration compared with the control group at the same time (31.49±3.34 pg/mL). OFQ at a concentration of 0.2 mmol/L did not affect GnRH release during the 120 min incubation time (Figure 1).

Effect of OFQ on GnRH release from POA OFQ evoked a dose-dependent inhibitory effect on POA GnRH release in ovariectomized rats ($P<0.05$). GnRH release stayed at approximately the same level over 120 min in the control group. The administration of 0.2 mmol/L and 2.0 mmol/L

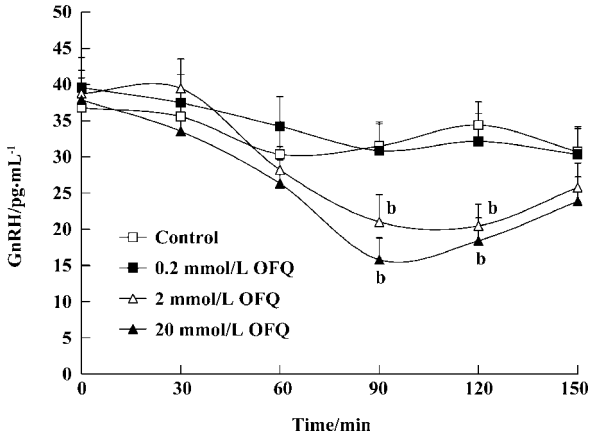

Figure 1. Dose-response curves for the effect of OFQ on GnRH release from medial basal hypothalamic slices from OVX rats. OFQ and ACSF were administered at $t=0$. $n=5$. Mean±SD. $^bP<0.05$ *vs* control.

OFQ caused a significant decrease in GnRH release at 40 min (19.83±2.35 pg/mL and 14.77±2.31 pg/mL, respectively), which lasted approximately 20 min, as compared with the control group (31.79±6.19 pg/mL). OFQ at a concentration of 0.02 mmol/L had no significant effect on GnRH release over 120 min (Figure 2).

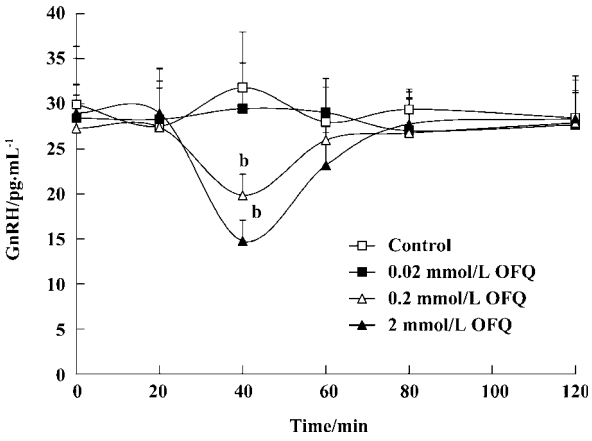

Figure 2. Dose-response curves for the effect of OFQ on GnRH release in the medial preoptic area of the hypothalamus. OFQ or ACSF was administered at $t=0$. The concentrations of GNRH in perfusates were measured every 20 min for 2 h. $n=5$–6. Mean±SD. $^bP<0.05$ *vs* control.

Effect of icv injection of OFQ and NC13 on plasma LH levels A dose-dependent decreasing effect on plasma LH levels was observed 2 h after icv injection of OFQ. The plasma LH levels in the control group ranged from 3.08±0.33 ng/mL to 3.27±0.37 ng/mL and were not significantly

different from those of the 2 nmol OFQ group at any time point over 4 h. Administration of 20 nmol and 200 nmol OFQ significantly decreased pituitary LH secretion (P<0.05). The strongest effect was achieved at 2 h after injection in the 20 nmol and 200 nmol OFQ groups (2.47±0.30 ng/mL and 2.12±0.32 ng/mL), as compared with the control group (3.11± 0.31 ng/mL). The LH decrease occurred at 2 h after injection for both doses and persisted until 3 h (Figure 3).

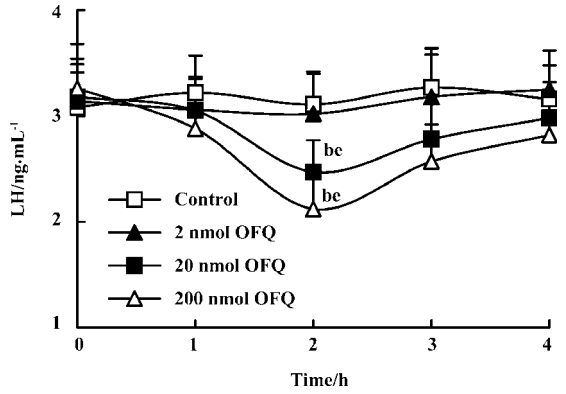

Figure 3. Time course study for the effect of OFQ on plasma LH levels of OVX rats. OFQ or ACSF was administered at t=0. The plasma LH levels were measured every hour for 4 h. n=8. Mean±SD. ^bP<0.05 *vs* control. ^eP<0.05 *vs* before administration.

A significant decrease in plasma LH level (2.47± 0.30 ng/mL) induced by 20 nmol OFQ was abolished by pretreatment with 20 nmol NC13, a competitive antagonist of the ORL1 receptor (3.02±0.39 ng/mL). No change in plasma LH level was observed with a single icv injection of 20 nmol NC13 (Figure 4).

Effect of icv injection of NC13 at different doses on plasma LH levels The plasma LH levels in the 20 nmol and 50 nmol NC13 groups (3.18±0.36 ng/mL and 3.78±0.46 ng/mL) were not significantly different from those of the control group (3.13±0.34 ng/mL) 2 h after administration. Interestingly, 100 nmol and 200 nmol NC13 stimulated a significant increase in plasma LH levels (4.27±0.51 ng/mL, 4.95± 0.53 ng/mL) 2 h after icv infusion (P<0.05) and the effect was dose-dependent. This reveals that a single high-dose icv injection of NC13 produces a significant increase in plasma LH levels in OVX rats (Figure 5).

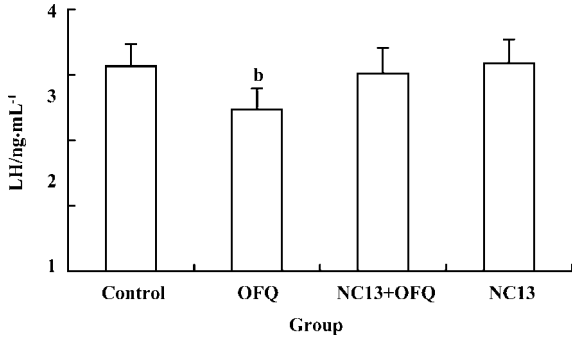

Figure 4. Effect of pretreatment with NC13 on the decrease of plasma LH levels induced by OFQ. The plasma LH levels were measured 2 h after icv injection. n=8. Mean±SD. ^bP<0.05 *vs* control.

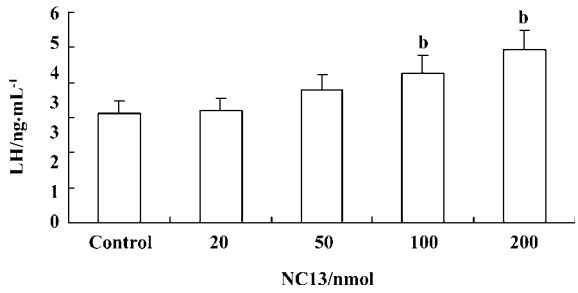

Figure 5. Dose-dependent study for the effect of NC13 on plasma LH levels in OVX rats. The plasma LH levels were measured 2 h after icv injection. n=8. Mean±SD. ^bP<0.05 *vs* control.

RT-PCR analysis RT-PCR analysis to check for ORL1 receptor expression revealed that the ORL1 receptor transcript was expressed in the hypothalamus and hippocampus of OVX rats, but not in the pituitary (Figure 6).

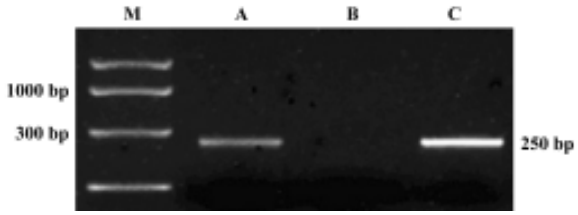

Figure 6. RT-PCR analysis for the expression of the ORL1 receptor in rat hippocampus, pituitary, and hypothalamus. The RT-PCR product of 250 bp, corresponding to the ORL1 receptor, was detected in rat hippocampus and hypothalamus but not in the pituitary. Lane M: marker; A: hippocampus; B: pituitary; C: hypothalamus.

Discussion

OFQ and its receptor are densely distributed in several nuclei in the hypothalamus, suggesting that OFQ might mediate and modulate hypothalamic functions[2,8]. There is evidence that OFQ is involved in the regulation of some important hypothalamic functions, such as feeding behavior, temperature control and sexual behavior[18–20]. OFQ has been

shown to stimulate prolactin and growth hormone secretion in male and female rats as an endogenous opioid peptide[21]. Our results show that central administration of OFQ can inhibit the release of GnRH in the hypothalamus *in vitro* and *in vivo* and decrease the plasma LH level, suggesting that OFQ might play a role in the modulation of hypothalamic GnRH secretion and pituitary LH release. Recent data from our laboratory and from other investigators indicate a neuroendocrine role for OFQ in mechanisms of the hypothalamus governing reproduction[13,21].

It is known that GnRH is the key central regulator in the estrous cycle. Despite intensive investigation, the mechanism underlying GnRH secretion remains poorly understood[10]. GnRH cell bodies form a loose continuum from the medial septum to the ventral anterior hypothalamus. GnRH is released from nerve terminals in the median eminence, where it is transported to the anterior pituitary to act on gonadotropes to stimulate LH and FSH secretion to the blood[22]. The ovariectomy performed in our experiments was intended to remove the effects of the estrous cycle on the hypothalamus GnRH and plasma LH secretion in female rats. Our results show that 2 mmol/L and 20 mmol/L OFQ inhibits GnRH release from rat medial basal hypothalamus slices in a dose-dependent manner, which is in agreement with previous reports[13]. Moreover, by using push-pull perfusion, we demonstrated that OFQ could also inhibit GnRH release from rat hypothalamus POA *in vivo*, further indicating the pharmacological effect of OFQ on hypothalamic GnRH release.

It was observed in our study that central injection of 20 nmol OFQ significantly decreased plasma LH levels, and the strongest effects occurred 2 h after administration. Pretreatment with 20 nmol selective ORL1 receptor antagonist NC13 can reverse the inhibitory effect that is induced by icv injection of 20 nmol OFQ. These results further confirm that the decrease of pituitary LH secretion induced by OFQ administration is mediated by the ORL1 receptor in the brain. We found that the ORL1 receptor was not expressed in rat pituitary by using RT-PCR analysis, indicating that OFQ might have no direct effect on pituitary hormone secretion. There has been no evidence of OFQ receptors on the anterior pituitary gland until now. These results strongly suggest that by interacting with its own receptor, the ORL1 receptor, OFQ elicits its inhibitory effect on hypothalamus GnRH release, thus decreasing the plasma LH level.

Time course studies reveal that the strongest effect of OFQ on GnRH release occurred at 40 min after OFQ administration *in vivo*, but it takes 2 h before any significant effects are seen on LH levels. The apparent discrepancy is probably due to the interval required by neuroendocrine transduction. The neural signal of GnRH decrease evoked by OFQ is transduced from the medial basal hypothalamus to the median eminence and then to the anterior pituitary, resulting in a decrease of LH secretion. Likewise, the time discrepancy in these results could also offer support for this postulation.

The effect of OFQ on GnRH secretion is likely to be due to an indirect mechanism of action, because OFQ has no such inhibitory effect when applied directly to immortalized GnRH (GT-1) neurons *in vitro*[13]. There is accumulating evidence that OFQ is able to inhibit the K^+-evoked release of glutamate and suppress glutamate transmission in the central nervous system of various species[23–25]. There is a general agreement that the glutamatergic pathway is a major excitory element in the regulation of GnRH release [26]. We speculate that hypothalamic glutamate might mediate the inhibitory effects of OFQ on GnRH secretion. Therefore, we are currently investigating the effects of NMDA or non-NMDA antagonists on the decrease of GnRH and LH secretions induced by OFQ. Undoubtedly, our hypothesis needs to be supported by more experimental evidence, and at this stage we could not exclude the possibility that OFQ has a direct effect on GnRH neurons *in vivo*.

Several studies have indicated that OFQ has an anti-opioid effect in nociceptive modulation because OFQ can induce hyperalgesia and antagonize opioid analgesia mediated by the μ and δ receptors in the brain[27,28]. Morphine and endogenous opioid peptides such as β-endorphin decrease the release of GnRH and LH in a naloxone-reversible manner[7,29]. Our data suggest that OFQ also plays a negative neuroendocrine role in the modulation of GnRH and LH release as classic opioids.

As the first identified selective ORL1 receptor antagonist, NC13 has allowed us to characterize some biological effects that are clearly mediated through the ORL1 receptor *in vitro* and *in vivo*[4]. It is shown in our work that NC13 can antagonize the inhibitory effect of OFQ on LH secretion. Nevertheless, we also observed that icv injection of 100 nmol and 200 nmol NC13 alone enhanced the plasma LH levels of ovariectomized rats. The present study reveals an unexpected function of NC13, that is, it can also act as a potent stimulator of LH release at a higher concentration. This suggests that OFQ has a tonic physiological role in the control of pituitary LH secretion. Our next study will focus on elucidating the mechanism for the involvement of the endogenous OFQ/ORL1 receptor system in regulating GnRH and LH release in male and female rats.

In summary, these results demonstrate that central administration of OFQ might inhibit the release of hypotha-

lamic GnRH and decrease the level of plasma LH via the ORL1 receptor in OVX rats. In addition, our work implies that hypothalamic OFQ might participate in the neuroendocrine regulation of GnRH and LH secretion in female rats. Although the neuroendocrine role of OFQ remains to be explored more directly, our results provide evidence for novel mechanisms for hypothalamic OFQ regulation of GnRH and LH secretion.

References

1 Reinscheid RK, Nothacker HP, Bourson A, Ardati A, Henningsem RA, Bunzow JR, *et al*. Orphanin FQ: a neuropeptide that activates an opioid-like G protein-coupled receptor. Science 1995; 270: 792–4.

2 Meunier JC, Mollereau C, Toll L, Suaudeau C, Moisand C, Alvinerie P, *et al*. Isolation and structure of the endogenous agonist of opioid receptor-like ORL1 receptor. Nature 1995; 377: 532–5.

3 Mollereau C, Parmentier M, Mailleux P, Butour JL, Moisand C, Chalon P, *et al*. ORL1, a novel member of the opioid receptor family: cloning, functional expression and localization. FEBS Lett 1994; 341: 33–8.

4 Calo G, Guerrini R, Rizzi A, Salvadori S, Regoli D. Pharmacology of nociceptin and its receptor: a novel therapeutic target. Br J Pharmacol 2000; 129: 1261–83.

5 Kapusta DR. Neurohumoral effects of orphanin FQ/nociceptin: relevance to cardiovascular and renal function. Peptides 2000; 21: 1081–99.

6 Janik J, Callahan P, Rabii J. The role of μ_1 opiate receptor subtype in the regulation of prolactin and growth hormone secretion by β-endorphin in female rats: Studies with naloxonazine. J Neuroendocrinol 1992; 4: 701–8.

7 Meites J, Bruni JF, Vanvugt D, Smith AF. Regulation of endogenous opioid peptides and morphine to neuroendocrine function. Life Sci 1977; 24: 1325–30.

8 Neal CR, Mansour A, Reinscheid R, Nothacker HP, Civelli O, Watson SJ. Localization of orphanin FQ (nociceptin) peptide and messenger RNA in the central nervous system. J Comp Neurol 1999; 406: 503–47.

9 Henderson G, McKnight AT. The orphan opioid receptor and its endogenous ligand nociceptin/orphanin FQ. Trends Pharm Sci 1997; 18: 293–300.

10 Herbison AE. Multimodal influence of estrogen upon gonadotropin releasing hormone. Endocr Rev 1998; 19: 302–30.

11 Kalra SP. Mandatory neuropeptide-steroid signaling for the preovulatory luteinizing hormone-releasing hormone discharge. Endocr Rev 1993; 14: 507–37.

12 Wanger EJ, Ronnekleiv OK, Grandy DK, Kelly MJ. The peptide orphanin FQ inhibits beta-endorphin neurons and neurosecretory cells in the hypothalamic arcuate nucleus by activating an inwardly-rectifying K^+ conductance. Neuroendocrinology 1998; 67: 73–82.

13 Dhandapani KM, Brann DW. Orphanin FQ inhibits GnRH secretion from rat hypothalamic fragments but not GT1-7 neurons. Neuroreport 2002; 13: 1247–9.

14 Watanobe H, Sasaki S, Takebe K. Evidence that intravenous administration of interleukin-1 stimulates corticotropin releasing hormone secretion in the median eminence of freely moving rats: estimation by push-pull perfusion. Neurosci Lett 1991; 133: 7–10.

15 Lamar CA, Bhat GK, Mahesh VB, Brann DW. Evidence that neuronal oxide synthase but not heme oxygenase increases in the hypothalamus on proestrous afternoon. Neuroendocrinology 1999; 70: 360–7.

16 Paxinos G, Watson C. The rat brain in stereotaxic coordinates. 4th ed. New York: Academic Press; 1998.

17 Briscini L, Corradini L, Ongini E, Bertorelli R. Up-regulation of ORL1 receptors in spinal tissue of allodynic rats after sciatic nerve injury. Eur J Pharmacol 2002; 447: 59–65.

18 Olszewski PK, Levine AS. Characterization of influence of central nociceptin/orphanin FQ on consummatory behavior. Endocrinology 2004; 145: 2627–32.

19 Chen XH, McClatchy DB, Geller EB, Liuchen LY, Tallarida RJ, Adler MW. Possible mechanism of hypothermia induced by intracerebroventricular injection of orphanin FQ/nociceptin. Brain Res 2001; 904: 252–8.

20 Sinchak K, Hendricks DG, Baroudi R, Micevych PE. Orphanin FQ/nociceptin in the ventromedial nucleus facilitates lordosis in female rats. Neuroreport 1997; 22: 3857–60.

21 Bryant W, Janik J, Baumann M, Callahan P. Orphanin FQ stimulates prolactin and growth hormone secretion in male and female rats. Brain Res 1998; 802: 228–33.

22 Smith MJ, Jennes L. Neural signals that regulate GnRH neurones directly during the oestrous cycle. Reproduction 2001; 122: 1–10.

23 Nicol B, Rowbotham DJ, Lambert DG. Nociceptin/orphanin FQ inhibits glutamate release from rat cerebellar and brain stem slices. Neurosci Lett 2002; 326: 85–8.

24 Meis S, Pape HC. Control of glutamate and GABA release by nociceptin/orphanin FQ in the rat lateral amygdala. J Physiol 2001; 532: 701–12.

25 Schlicker E, Morari M. Nociceptin/orphanin FQ and neurotransmitter release in the central nervous system. Peptides 2000; 21: 1023–9.

26 Jennes L, Lin W, Lakhlani S. Glutamatergic regulation of gonadotropin-releasing hormone neurons. Prog Brain Res 2002; 141: 183–92.

27 Mogil JS, Grisel JE, Reinscheid RK, Civelli O, Belknap JK, Grandy DK. Orphanin FQ is a functional anti-opioid peptide. Neuroscience 1996; 75: 333–7.

28 Zhu CB, Zhang XL, Xu SF, Cao XD, Wu GC, Li MY, *et al*. Antagonistic effect of orphanin FQ on opioid analgesia in rat. Acta Pharmacol Sin 1998: 19: 10–4.

29 Ching M. Morphine suppresses the proestrous surge of GnRH in pituitary portal plasma of rats. Endocrinology 1983; 112: 2209–21.

Acta Pharmacologica Sinica 2005 Sep; 26 (9): 1045–1048

Full-length article

Involvement of GABA and opioid peptide receptors in sevoflurane-induced antinociception in rat spinal cord

Ying-wei WANG[1], Xiao-ming DENG[2], Xin-min YOU[1], Shu-xiao LIU[2], Zhi-qi ZHAO[3]

[1]Department of Anesthesiology, Xinhua Hospital, Shanghai Second Medical University, Shanghai 200092, China; [2]Department of Anesthesiology, Changhai Hospital, Second Military Medical University, Shanghai 200433, China; [3]Institute of Neurobiology, Fudan University, Shanghai 200433, China

Key words

sevoflurane; spinal cord; pain measurement; GABA receptors; opioid receptors

[1] Correspondence to Dr Ying-wei WANG.
Phn 86-21-6579-0000.
Fax 86-21-5522-7368.
E-mail wangyingwei@yahoo.com

Received 2005-03-17
Accepted 2005-06-13

doi: 10.1111/j.1745-7254.2005.00175.x

Abstract

Aim: The spinal cord is pivotal in immobility induced by volatile anesthetics because the anesthetics depress the activity of motor neurons in the spinal cord. The aim of this study was to observe the effects of sevoflurane on pain processing at the spinal level. **Methods:** The firing of the gastrocnemius muscle was evoked by electrical stimulation to the ipsilateral hindpaw in rats. The nociceptive C response of electromyography (EMG) was selected to study. The $GABA_A$ receptor antagonist bicuculline (0.1 mg/kg) and opioid receptor antagonist naloxone (0.4 mg/kg) were administered intravenously, either in the presence or in the absence of 1.0% sevoflurane. **Results:** In rats with transected spinal cord, sevoflurane produced a profound reduction in the C response in a dose- and time-dependent manner. In the presence of 1.0% sevoflurane, the C responses were increased after injections of bicuculline and naloxone. **Conclusion:** Sevoflurane is a volatile anesthetic that acts directly on the spinal cord to suppress the nociceptive reflex. The sevoflurane-induced suppression of the C response is antagonized by either bicuculline or naloxone. The results suggest that spinal $GABA_A$ receptors and opioid peptide receptors are involved in the sevoflurane-induced suppression of spinal nociception.

Introduction

Gamma-aminobutyric acid (GABA) and opioid peptides are the major inhibitory transmitters in the central nervous system, and both transmitter systems are likely to play important roles in anesthetic mechanisms. For example, a common property of a wide spectrum of general anesthetics, including barbiturates and propofol, is enhancement of the action of $GABA_A$ receptors[1–4].

Increasing evidence have indicated that the spinal cord is pivotal in the immobility induced by volatile anesthetics because the anesthetics depress the activity of α-motoneurons in the spinal cord[5,6], in which process spinal GABA receptors and opioid peptide receptors may be involved[7–10]. However, there has been few study on the effects of sevoflurane on pain processing in the spinal cord. Given the high density of GABA receptors and opioid peptide receptors located in the dorsal horn of the spinal cord, in the present study we examine whether the suppression of nociceptive effects by sevoflurane is mediated by actions at $GABA_A$ and opioid receptors in the spinal cord.

Materials and methods

Animals and surgical preparation This study was approved by animal experimentation committee of Xinhua hospital. The experiments were performed on 37 male Sprague-Dawley rats weighing 215–345 g (provided by the Animal Center of the Chinese Academy of Sciences). Animals were divided into 5 groups according to the different tests. Group I (n=6) animals were used to test the effects of sevoflurane after transection of the spinal cord. Anesthesia for surgical preparation was induced by 2.5% sevoflurane in

95% O_2–5% N_2 and maintained by 0.8%–1.5% sevoflurane through a tightly fitting mask. Group II (*n*=11) animals were used to test the time course of sevoflurane in the spinally transected rats; Group III (*n*=9), group IV (*n*=6) and group V (*n*=5) animals were used to test the effect of bicuculline ($GABA_A$ receptor antagonist), phaclofen ($GABA_B$ receptor antagonist) and naloxone (opioid receptor antagonist), respectively. Animals in groups II–V were anesthetized with urethane (1.0 g/kg, ip). The trachea, left internal jugular vein and carotid artery were cannulated for artificial ventilation, drug administration and blood pressure monitoring, respectively.

Following laminectomy, the spinal cord was transected at T_9–T_{10} with 2.0% lidocaine surface anesthesia. The experiments were started at least 2 h after transection. During experiments, core body temperature was maintained at 37–39 ºC by a warm blanket and a heat lamp. In order to maintain effective circulation, 0.5–1 mL 5% glucose was injected into the internal jugular vein every 1–2 h.

Electrophysiological recording Electromyographic measurements were taken in the gastrocnemius muscles. Two stainless steel needles were separately inserted into the two toes of the ipsilateral hindpaw for electrical stimulation. The intensity of electrical stimulation (1 ms, 50 V, 3 pulses, 1 Hz) was sufficient to excite the C-fiber nociceptors. Two components of the electromyographic response, the A- and C-responses, were evoked by the electrical stimulation. The C response was an indication of nociceptive reflex. An averaged C response was analyzed by a signal processing system (SMUP-PC, Fudan University).

Drug administration In group I, sevoflurane was delivered at concentrations of 0.8%, 1.0%, 1.5%, 2.0%, and 2.5%. Electromyographic measurements were taken 25 min after inhalation of sevoflurane. In group II, 1.0% sevoflurane was given, and electromyographic measurements were taken every 3 min. In groups III, IV, and V, as a control, bicuculline (0.1 mg/kg), phaclofen (0.6 mg/kg) or naloxone (0.4 mg/kg) were first intravenously administered without inhalation of sevoflurane. Two hours later, bicuculline, phaclofen, or naloxone at the same doses was administered, respectively, 15 min after inhalation of 1.0% sevoflurane.

Data analysis The effects of drugs, dose dependence, and time course were analyzed by using the paired *t*-test. Differences between groups were determined to be statistically significant if $P<0.05$. All data are shown as mean±SD.

Results

Consistent with our previous study[11], the strong current-induced electromyographic responses from the gastrocnemius muscle consisted of two components: first, a primary myelinated afferent fiber-mediated A response with a latency of 5–10 ms, and second, the unmyelinated fiber-mediated C response with latency of >100 ms. Given that primary afferent C fibers conduct nociceptive information, this study focused on the change in C responses.

Effect of sevoflurane on the spinal cord To examine whether inhalation of sevoflurane affects the spinal cord neurons, the spinal cord was transected at the $T_{9–10}$ segment. Following inhalation of sevoflurane at concentrations of 1.0%, 1.5%, 2.0%, and 2.5%, C responses were reduced to 36.1%±17.4%, 11.7%±8.6%, 2.2%±5.2% and 0% of control ($P<0.01$), respectively (Figure 1). The inhibition occurred in a time-dependent manner. When 1.0% sevoflurane was inhaled, C responses were 60.0%±18.1%, 50.4%±13.5%, 42.0%±14.5%, 33.2%±13.5%, and 31.5%±13.8% at 1 min, 4 min, 7 min, 10 min, and 13 min after inhalation, respectively, compared with the group without sevoflurane (Figure 2). C responses recovered almost completely within 9 min of ceasing inhalation.

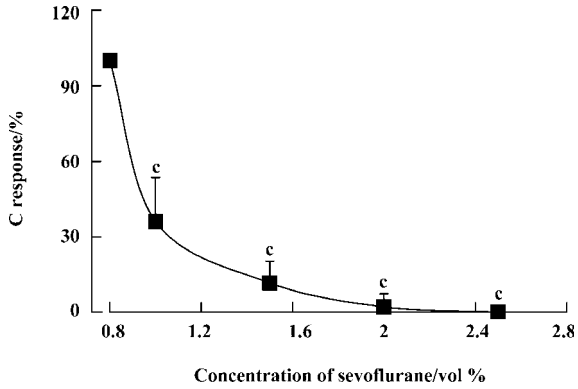

Figure 1. Inhalation of sevoflurane dose-dependently reduces the C response in rats with transected spinal cords. Before inhalation of sevoflurane, the baseline area of the C response is considered to be 100%. *n*=6. Mean±SD. $^cP<0.01$ *vs* baseline.

Reversal of sevoflurane-induced inhibition by bicuculline and naloxone As shown in Figure 3, bicuculline (0.1 mg/kg, iv) failed to alter the C response in the absence of sevoflurane. Following 20 min of inhalation of 1.0% sevoflurane, bicuculline at the same dose significantly increased the C responses at the time points of 1 min, 4 min, 7 min, 10 min, and 13 min ($P<0.05$). However, phaclofen (0.6 mg/kg) failed to alter the C response in the absence or presence of sevoflurane.

Although the C responses appeared to be slightly

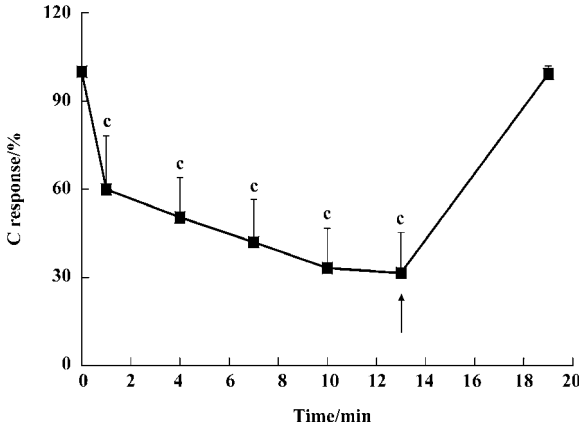

Figure 2. Time course of 1.0% sevoflurane-induced depression of C responses in rats with transected spinal cords. Before inhalation of sevoflurane, the baseline area of the C response is considered to be 100%. ↑ indicates the time point at which inhalation of sevoflurane was terminated. n=11. Mean±SD. ^{c}P<0.01 *vs* baseline.

enhanced by naloxone alone (0.4 mg/kg, iv) in the absence of sevoflurane, this effect was not statistically different from the control (Figure 4). After the rats inhaled 1% sevoflurane, naloxone significantly increased their C responses at time points of 1 min, 4 min, 7 min, 10 min, 13 min, and 16 min (P< 0.05).

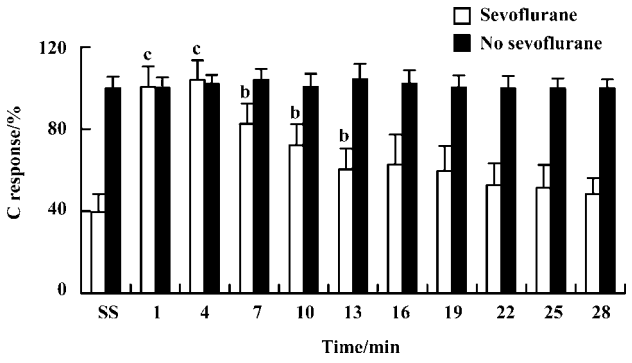

Figure 3. Effects of bicuculline on C responses evoked in spinally transected rats in the presence or absence of 1.0% sevoflurane. SS indicates the steady-state area of the C response before administration of bicuculline (0.1 mg/kg, iv). Before SS, the baseline area of the C response is considered to be 100%. All rats were given bicuculline at the steady-state time point. n=9. Mean±SD. ^{b}P<0.05, ^{c}P<0.01 *vs* steady-state.

Discussion

Several studies have shown that the mechanisms underlying the suppression of noxious stimuli-induced motor reactions by volatile anesthetics, including sevoflurane, are likely to be spinal in nature rather than involving superspinal structures[5,6,12]. Apart from immobility mediated by reducing the activity of spinal α-motoneurons, studies on the effects of sevoflurane on nociceptive sensory neurons in the spinal cord are generally lacking. The C-fiber-induced response recorded in the peripheral nerve or muscle is commonly used to characterize spinal processing and is considered to be an acute pain model[11]. By means of this model, the present work for the first time shows that inhalation of sevoflurane produces a dose-dependent reduction of primary sensory afferent C-fiber-mediated nociceptive responses in the rat after transection of the spinal cord at T_{9-10}. This indicates that sevoflurane not only suppresses excitation in α-motor neurons but also inhibits the activity of pain-sensitive neurons in the dorsal horn of the spinal cord, in the absence of supraspinal input.

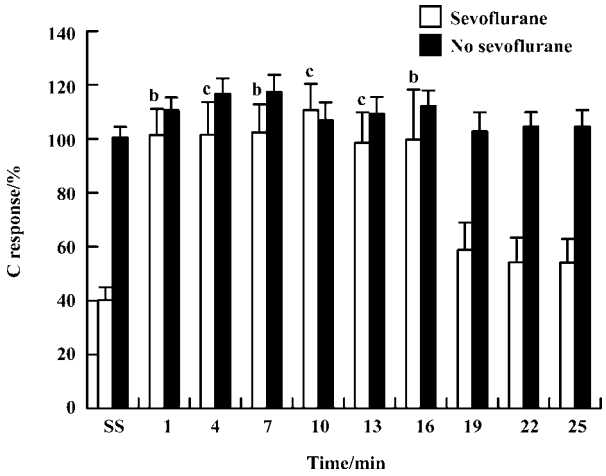

Figure 4. Effect of naloxone on the C response evoked in spinally transected rats in the presence or absence of 1.0% sevoflurane. SS indicates the steady-state area of the C response before the administration of naloxone (0.4 mg/kg, iv). Before SS, the baseline area of the C response is considered to be 100%. All rats were given bicuculline at the steady-state time point. n=5. Mean±SD. ^{b}P<0.05, ^{c}P<0.01 *vs* steady-state.

It is well-known that GABA receptors exist in the spinal cord and, when activated, cause decreased excitability of the neurons in which they exist[13]. A recent report showed that the intrathecal administration of $GABA_A$ or glycine receptor antagonists increased the MAC (minimum alveolus concentration) value of isoflurane by approximately 40% in rats[14]. Yamauchi *et al* also observed an approximately 50% reversal of halothane depression[15]. Similarly, in the present study, the sevoflurane-induced inhibition of nociceptive C responses was reversed by the intravenous administration of 0.1 mg/kg bicuculline, a $GABA_A$ receptor antagonist. This

reversal effect by bicuculline seems unlikely to be involved in a release of a GABA-mediated tonic inhibition, given that 0.1 mg/kg bicuculline in the absence of sevoflurane did not increase nociceptive C responses significantly. Previous studies have revealed that the sevoflurane-induced inhibition of field potentials evoked from CA1 of the hippocampus is partially antagonized by phaclofen, a competitive antagonist of the $GABA_B$ receptor[16]. However, the antinocifensive effect of halothane was not affected by the intrathecal administration of $GABA_B$ receptor antagonist CGP 35348[7]. Similarly, our preliminary results show that intravenous administration of 0.6 mg/kg phaclofen failed to affect nociceptive C responses (data not shown). Taken together, these results suggest that the antinociceptive effect of sevoflurane might be mainly mediated by $GABA_A$ receptors in the spinal cord rather than $GABA_B$ receptors.

Opioid receptors are densely localized presynaptically and postsynaptically on pain-sensitive neurons in the spinal cord, which play a critical role in spinal antinociception. It has been reported that intravenous or intrathecal morphine is able to reduce the minimum alveolar concentration of halothane[8–10]. In the present study, the fact that naloxone blocked the sevoflurane-induced inhibition of nociceptive C responses provides further support for the involvement of spinal opioid receptors in antinociception mediated by sevoflurane.

In conclusion, the volatile anesthetic sevoflurane can directly depress spinal transmission of nociceptive information in the spinal cord, by a mechanism that may involve GABA receptors and opioid receptors.

Acknowledgement

We thank Christopher J LINGLE (Washington University, Saint Louis, Missouri, USA) for helpful discussions and editing this paper.

References

1 Jones MU, Brooks PA, Harrison NL. Enhancement of gamma-aminobutyric acid-activated Cl^- currents in cultured rat hippocampal neurons by three volatile anaesthetics. J Physiol (Lond) 1992; 449: 279–93.

2 Krasowski MD, Harrison NL. General anaesthetic actions on ligand-gated ion channels. Cell Mol Life Sci 1999; 55: 1278–303.

3 Franks NP, Lieb WR. Which molecular targets are most relevant to general anaesthesia? Toxicol Lett 1998; 100-101: 1–8.

4 Bernd A. Different actions of general anaesthetics on the firing patterns of neocortical neurons mediated by the $GABA_A$ receptor. Anaesthesiology 1999; 91: 500–11.

5 Rampil IJ, King BS. Volatile anaesthetics depress spinal motor neurons. Anaesthesiology 1996; 85: 129–34.

6 Kammer T, Rehberg B, Menne D, Wartenberg HC, Wenningmann I, Urban BW. Propofol and sevoflurane in subanaesthetic concentrations act preferentially on the spinal cord. Anaesthesiology 2002; 97: 1416–25.

7 Mason P, Owens CA, Hammond DL. Antagonism of the antinocifensive action of halothane by intrathecal administration of $GABA_A$ receptor antagonists. Anaesthesiology 1996; 84: 1205–14.

8 Schwieger IM, Klopfenstein CE, Forster A. Epidural morphine reduces halothane MAC in humans. Can J Anaesth 1992; 39: 911–4.

9 Drasner K, Bernards CM, Ozanne GM. Intrathecal morphine reduces the minimum alveolar concentration of halothane in humans. Anaesthesiology 1988; 69: 310–2.

10 Criado AB, Gomez de Segura IA, Tendillo FJ, Marsico F. Reduction of isoflurane MAC with buprenorphine and morphine in rats. Lab Anim 2000; 34: 252–9.

11 Bai L, Zhao ZQ. Ketamine-induced peripheral analgesia in rats. Acta Pharmacol Sin 1997; 18: 377–9.

12 Antognini JF, Carstens E, Buzin V. Isoflurane depresses motoneuron excitability by a direct spinal action: an F-wave study. Anaesth Analg 1999; 88: 681–5.

13 Sivilotti L, Nistri A. GABA receptor mechanisms in the central nervous system. Prog Neurobiol 1991; 36: 35–92.

14 Zhang Y, Wu S, Eger I II, Sonner JM. Neither $GABA_A$ nor strychnine-sensitive glycine receptors are the sole mediators of MAC for isoflurane. Anaesth Analg 2001; 92: 123–7.

15 Yamauchi M, Sekiyama H, Shimada SG, Collins JG. Halothane suppression of spinal sensory neuronal responses to noxious peripheral stimuli is mediated, in part, by both $GABA_A$ and glycine receptor systems. Anaesthesiology 2002; 97: 412–7.

16 Hirota K, Roth SH. Sevoflurane modulates both $GABA_A$ and $GABA_B$ receptors in area CA1 of rat hippocampus. Br J Anaesth 1997; 78: 60–5.

Acta Pharmacologica Sinica 2005 Sep; 26 (9): 1049–1056

Full-length article

Blood pressure, baroreflex sensitivity, and end organ damage in hybrid offspring of spontaneously hypertensive rats and Sprague-Dawley rats[1]

He-hui XIE[2], Fu-ming SHEN[2], Chao-yu MIAO, Ding-feng SU[3]

Department of Pharmacology, Second Military Medical University, Shanghai 200433, China

Key words

baroreflex; blood pressure; end organ damage; hypertension; genetic hybridization

[1] Project supported by grants from the National Natural Science Foundation of China (No 30170385, 30330650, 30371649) and the Shanghai Foundation for Science and Technology Development (No 014909004).
[2] The two authors contributed equally to this work.
[3] Correspondence to Prof Ding-feng SU.
Phn 86-21-2507-0323.
Fax 86-21-6549-3951.
E-mail dfsu@citiz.net

Received 2004-12-20
Accepted 2005-04-22

doi: 10.1111/j.1745-7254.2005.00162.x

Abstract

Aim: To investigate the blood pressure (BP), baroreflex sensitivity (BRS), and organ damage in hybrids of spontaneously hypertensive rats and Sprague-Dawley rats. **Methods:** Spontaneously hypertensive rats and Sprague-Dawley rats were crossbred, and the F_1 hybrids were inbred randomly to produce an F_2 generation. At the age of 52 weeks, the F_1 and F_2 hybrids were tested to determine BP and BRS in a conscious state. Histopathological examinations were carried out after BP recording and BRS studies. **Results:** BP and BRS were not different in F_1 and F_2 hybrids. BRS was inversely related to systolic BP (SBP) in male, female, or whole populations of hybrids. Quantitatively, BRS values were one-third determined by SBP level (the determinant coefficient was 0.326). The indexes for left ventricular hypertrophy, aortic hypertrophy, and renal damage were all positively related to BP, and negatively related to BRS. In multiple-regression analysis, left ventricular and aortic hypertrophy and glomerulosclerosis score were all most significantly associated with lower BRS and higher systolic BP. The contribution of BRS to left ventricular and aortic hypertrophy and glomerulosclerosis was greater than that of SBP. **Conclusion:** The present work with hybrid rats demonstrated quantitatively that the BRS value was one-third determined by SBP level. Both BP level and BRS value contributed greatly to the hypertensive organ damage. However, the contribution of BRS to the hypertensive organ damage was greater than that of BP level in these rats.

Introduction

Arterial baroreflex (ABR) plays a crucial role in cardiovascular regulation. It was found that ABR function, expressed by baroreflex sensitivity (BRS), was impaired in hypertensive patients and animals[1–4]. This impairment of BRS is attributed mainly to the high blood pressure (BP) level based on the following observations. (i) In renovascular hypertensive rats, BRS decreased significantly 1 d and 7 d after renal artery clipping[5,6]. One day after removal of a left renal artery clip, BRS was inversely related to the BP level. BRS was restored as early as renovascular hypertension was reversed[7]. (ii) In spontaneously hypertensive rats (SHR), many antihypertensive drugs lower BP and restore BRS at the same time[8,9]. On the other hand, it was found that BRS might be lower in normotensive children with hypertensive parents or in young spontaneously hypertensive rats (SHR) before hypertension[10,11]. Therefore, it is not yet clear how important BP level is in influencing BRS. To answer quantitatively this question was the first aim of the present work.

It is well known that BP level is an important determinant for end-organ damage (EOD) in hypertensive patients and hypertensive animals. However, it is certainly not the only determinant for EOD. In our previous work, it was found that BRS was related to the severity of EOD in SHR[12]. The second aim of the present work was to ascertain whether BRS was as important as BP level in determining the severity of EOD.

Hybrid offspring of SHR and normotensive rats are used widely to analyze the relationship between BP level and other

parameters. The present work was designed to study the features of BP, BRS, and EOD, and the relationships between these parameters in hybrid offspring of SHR and Sprague-Dawley (SD) rats.

Materials and methods

Animals Sprague-Dawley rats were purchased from the Sino-British SIPPR/BK Lab Animal Ltd (Shanghai, China). SHR were provided by the Animal Center of the Second Military Medical University (Shanghai, China). SHR and SD rats were crossbred, and the F_1 hybrids were inbred randomly to produce F_2 hybrids. All rats were housed at controlled temperature (23 °C–25 °C) and lighting (8:00–20:00 light: dark cycle) with free access to food and tap water. All animals used in this work received humane care in compliance with institutional animal care guidelines.

Blood pressure measurement At the age of 52 weeks, the F_1 and F_2 hybrids were tested to determine BP in a conscious state. Systolic BP (SBP), diastolic BP (DBP), and heart period (HP) were recorded continuously using techniques described previously[13,14]. The BP signal was digitized by a microcomputer. SBP, DBP, and HP values from every heartbeat were determined on line. The mean values of these parameters during a period of 24 h were calculated, and served as SBP, DBP, and HP.

Baroreflex sensitivity measurement To determine the function of ABR in conscious rats, the methods widely used are derived from that of Smyth, which was first applied to humans[15]. The principle of this method is to measure the prolongation of HP in response to an elevation of BP. With some modifications, this method has been used in conscious rats[16,17]. A bolus injection of phenylephrine was used to induce an elevation of BP. The dose of phenylephrine was adjusted to raise SBP to between 20 mmHg and 40 mmHg. HP was plotted against SBP for linear regression analysis and the slope of SBP-HP was expressed as BRS (ms/mmHg). As there exists a delay between the stimulus and response (approximately 1 s), the slopes were calculated by computer with 1–10 beats of shift for linear regression analysis, and the slope with the highest correlation coefficient was used as BRS. A correlation analysis with 5 beats of shift, for example, means that values of HP_6/SBP_1, HP_7/SBP_2, and HP_8/SBP_3 were used.

Morphological examination Morphological examinations were carried out after BP recording and BRS studies. The animals were weighed and killed by decapitation. The thoracic and peritoneal cavities were opened immediately. The right kidney, aorta, and heart were excised and rinsed in cold physiological saline. The right kidney was blotted and weighed. The left ventricle was isolated, blotted, and weighed. At the same time, the aorta was cleaned of adhering fat and connective tissue. Just below the branch of the left subclavicular artery, a 30 mm-long segment of thoracic aorta was harvested, blotted, and weighed. Ratios of left ventricular weight to body weight (LVW/BW), right ventricular weight to body weight (RVW/BW), ventricular weight to body weight (VW/BW), left ventricular weight to right ventricular weight (LVW/RVW), and aortic weight to the length of aorta (AW/length) were calculated[18,19]. Histopathological observation was also carried out using our conventional method[20]. Briefly, immediately after gross detection, all samples of left ventricles in 2 mm-thick to 3 mm-thick slices, aortae, and kidney were immersed in formalin solution for more than 1 week, dehydrated in ethanol, cleared in dimethylbenzene and embedded in paraffin. The 5 μm-thick sections were then prepared and stained with hematoxylin and eosin for light microscopic evaluation.

Glomerulosclerosis score For the semiquantitative evaluation of glomerular damage, the glomerulosclerosis score (GSS) was defined as described previously[21]. From the light microscopic specimens, approximately 50 glomeruli from the outer cortex and the same number of glomeruli from the inner cortex of each kidney were graded according to the degree of sclerosis: 0, no mesangial expansion; 1, mild mesangial expansion (less than 30% of a glomerular area); 2, moderate mesangial expansion (30%–60% of a glomerular area); 3, marked mesangial expansion (more than 60% of a glomerular area); and 4, global sclerosis. This was carried out by one observer in a blind fashion using coded slides. A weighted composite sclerosis score was then calculated for each kidney according to the following formula: glomerulosclerosis score=[1×(number of grade 1 glomeruli)+2×(number of grade 2 glomeruli)+3×(number of grade 3 glomeruli)+4×(number of grade 4 glomeruli)]×100/(number of glomeruli observed).

Statistical analysis Data were expressed as mean±SEM. Comparisons between 2 groups were made by Student's *t*-test. The relationships between hemodynamic parameters and organ damage parameters were analyzed by classic univariate correlation analysis. Stepwise multiple-regression analysis was used to study the independent effect of hemodynamic parameters on organ damage. F to enter and F to remove were set to $P<0.05$ and $P>0.10$, respectively. $P<0.05$ was considered statistically significant. Statistical analysis was carried out using software SPSS 11.0.0 (SPSS, Chicago, Illinois, USA).

Results

Blood pressure and baroreflex sensitivity in the F_1 hybrids with different parenthood Blood pressure, HP, and BRS values in the F_1 hybrids are shown in Figure 1. BP was slightly higher in H×S offspring rats (hybrids derived from male SHR and female SD rats) than in S×H offspring rats (hybrids derived from male SD and female SHR rats). This difference reached a significant level only for DBP in males and in the whole F_1 hybrid group. Male H×S rats possess significantly higher DBP than female H×S rats, but this sex difference in DBP of S×H rats was not significant. A similar sex-difference tendency was found in SBP but never reached statistical significance. No obvious sex or strain differences in HP or BRS were found in F_1 hybrids.

Blood pressure and baroreflex sensitivity in the F_1 and F_2 hybrids As shown in Figure 2, no obvious difference was found between F_1 (including H×S and S×H offspring rats) and F_2 hybrids with respect to BP, HP, and BRS. In F_1 and F_2 hybrids, male rats tended to have slightly higher BP than female rats. However, these sex differences in SBP and DBP did not reach statistical significance. The distribution of SBP and BRS in F_1 and F_2 hybrids is shown in Figure 3. No obvious difference between F_1 and F_2 was noted.

Relationship between systolic blood pressure and baroreflex sensitivity in the F_1 and F_2 hybrids It was found that BRS was significantly and inversely related to SBP in both F_1 (r=-0.599, n=96, P<0.01) and F_2 offspring (r=-0.510, n=36, P<0.01) (Figure 4A,4B). When the whole population (F_1+ F_2) were analyzed, the correlation coefficient (r) was -0.571 (n=132, P<0.01) (Figure 4C) and the determinant coefficient (r^2) was 0.326. This value means that the BRS value is 33% determined by SBP level. In accordance with this result, it was found that lower BRS was not always linked to higher BP in the hybrid offspring rats. In the hybrids studied (Figure 4), we found some normotensive animals with a lower BRS (SBP<140 mmHg, BRS<0.4 ms/mmHg; n=5) and hypertensive animals with a higher BRS (SBP>150 mmHg, BRS>0.7 ms/mmHg; n=22). Two examples for BRS obtained from the hybrids are shown in Figure 5A, a normotensive animal with a lower BRS; and Figure 5B, a hypertensive animal with a higher BRS.

Organ damage in the F_1 and F_2 hybrids The average values of LVW/BW, AW/length, and GSS are presented in Figure 6. No obvious difference between F_1 and F_2 hybrids was found.

Relationships between blood pressure, baroreflex sensitivity, and organ damage in hybrids The relationships between BP, HP, BRS, and organ damage in the hybrids were shown in Table 1. It was found that LVW/BW, an index for left ventricular hypertrophy, AW/length, an index for aortic hypertrophy, and GSS, an index for renal damage, were all

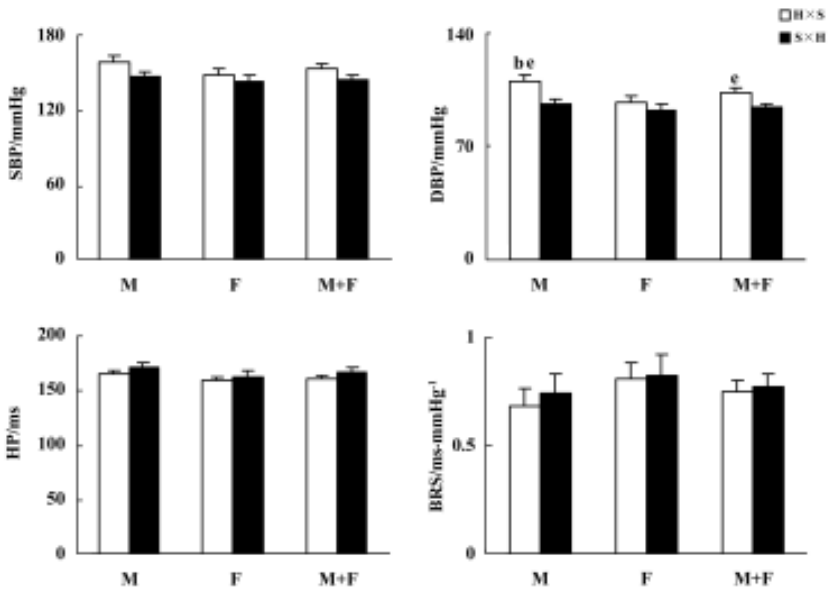

Figure 1. Blood pressure (BP), heart period (HP) and baroreflex sensitivity (BRS) in the F_1 hybrids with different parenthood. BRS, baroreflex sensitivity; DBP, diastolic blood pressure; H×S, hybrids derived from male spontaneously hypertensive rats (SHR) and female Sprague-Dawley (SD) rats; SBP, systolic blood pressure; S×H, hybrids derived from male SD rats and female SHR. The numbers of rats used were 24 and 25 in male (M), 29 and 18 in female (F), and 53 and 43 in total (M+F) H×S and S×H rats, respectively. ^bP<0.05 *vs* female H×S. ^eP< 0.05 *vs* corresponding S×H strain.

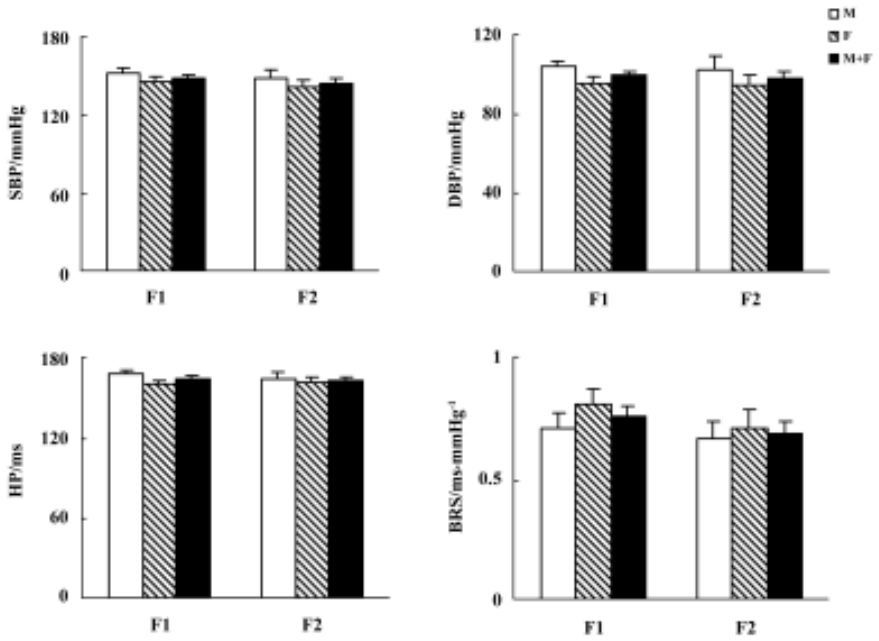

Figure 2. Blood pressure (BP), heart period (HP), and baroreflex sensitivity (BRS) in the F_1 and F_2 hybrids. See Figure 1 for abbreviations. The numbers of rats used were 49 and 16 in male (M), 47 and 20 in female (F), and 96 and 36 in total (M+F) F_1 and F_2 hybrids, respectively.

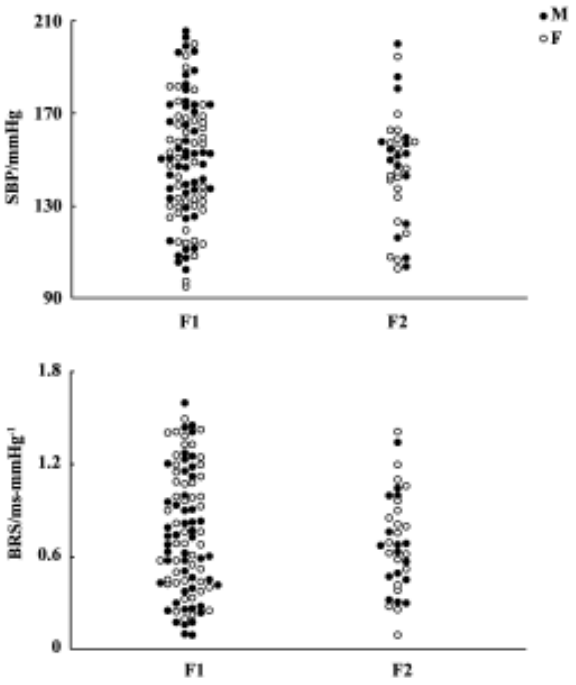

Figure 3. The distribution of systolic blood pressure (SBP) and baroreflex sensitivity (BRS) in the F_1 and F_2 hybrids. See Figure 1 for abbreviations. The numbers of rats used were 49 and 16 in male (M), and 47 and 20 in female (F) F_1 and F_2 hybrids, respectively.

related positively to BP, and related negatively to BRS. There was no significant relationship between HP and organ damage parameters (Table 1). Some examples for important correlations were shown in Figure 7.

Table 1. Linear regression coefficient (*r*) between blood pressure (BP), heart period (HP) and baroreflex sensitivity (BRS) values and organ damage in hybrids. n=132. ^cP<0.01.

	LVW/BW	AW/length	GSS
SBP	0.492^c	0.464^c	0.465^c
DBP	0.416^c	0.303^c	0.411^c
HP	-0.162	-0.074	-0.164
BRS	-0.646^c	-0.559^c	-0.590^c

AW, aortic weight; BW, body weight; DBP, diastolic blood pressure; GSS, glomerulosclerosis score; LVW, left ventricular weight; SBP, systolic blood pressure.

The relative dependencies of organ damage on hemodynamic parameters were assessed by stepwise multiple-regression analysis. LVW/BW, AW/length, and glomerulosclerosis score were all most significantly associated with lower BRS (β=-0.542, P<0.01; β=-0.436, P<0.01; and β=-0.482, P<0.01, respectively) and higher SBP (β=0.183, P<0.01; β=0.216, P<0.01; and β=0.191, P<0.01, respectively). After comparing the standardized partial regressive coefficients, it was found that the contribution of BRS to left ventricular, aortic hypertrophy, and glomerulosclerosis was greater than

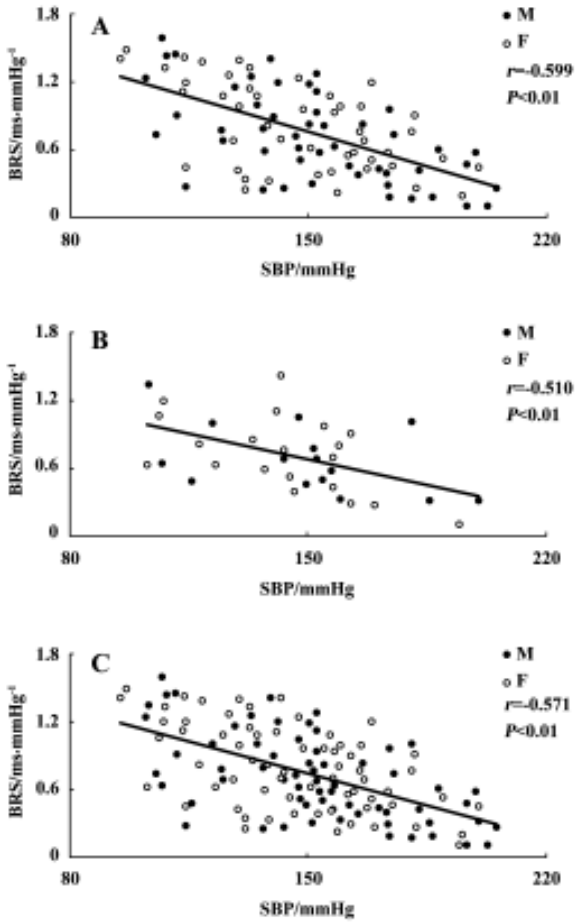

Figure 4. Correlation between blood pressure (SBP) and baroreflex sensitivity (BRS) in the F_1, F_2, and F_1+F_2 hybrids. See Figure 1 for abbreviations. The numbers of male (M) and female (F) rats used were 49 and 47, 16 and 20, and 65 and 67 in F_1 (A), F_2 (B), and F_1 + F_2 (C) hybrids, respectively.

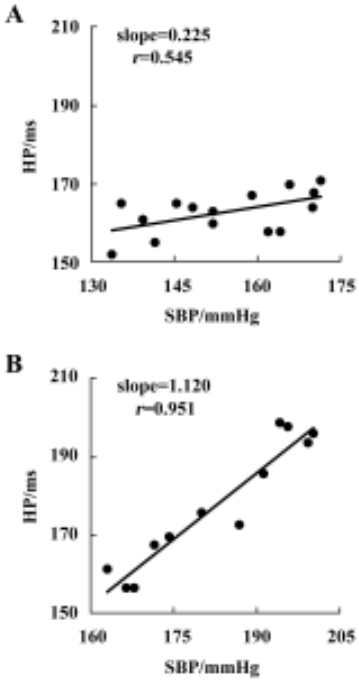

Figure 5. Schematic presentation of baroreflex sensitivity obtained from the hybrids. See Figure 1 for abbreviations. (A) A normotensive rat with lower baroreflex sensitivity. (B) A hypertensive rat with normal baroreflex sensitivity. Slope of the regression is expressed as baroreflex sensitivity.

that of SBP.

Discussion

The main contributions of the present work may be summarized as follows:

(i) It is well known that the BRS value is closely related to and importantly determined by BP level. The present work is the first to demonstrate quantitatively that BRS value is one-third determined by SBP level (the determinant coefficient was 0.326).

(ii) Both BRS and SBP level contributed to organ damage. This report is the first to show that the contribution of BRS to organ damage is greater than that of SBP.

(iii) F_1 hybrid offspring are suitable for studying the relationships between BP level and other parameters.

Many abnormalities or changes have been reported to relate to high BP level in hypertension. Among these abnormalities or changes, some are intrinsically related to hypertension and some are only accompanying phenomena in hypertension. Hybrid offspring of hypertensive and normotensive rats are often used to distinguish these 2 sorts of changes found in hypertension. Using these hybrid offspring, it was found that the genes responsible for the hypertensive trait and those responsible for the hyperactivity trait are not tightly linked[22,23]. The relationships between BP and other parameters, such as salt appetite[24], temperature[25], and sensitivity to stress[26], have also been studied in the hybrids rats derived from hypertensive and normotensive rats. Recently, hybrid rats derived from a hypertensive and normotensive strain were produced to study genetic markers for blood pressure using statistical techniques for quantitative trait loci analysis[27]. It has been noted that BRS is lower in hypertensive patients and hypertensive animals. However, no study has been carried out using hybrid rats to analyze the relationship between BP and BRS. This may be due to the large quantity of work that it entails; the measurement of BRS in conscious and unrestrained rats requires a computerized BP monitoring system and more than 100 rats are

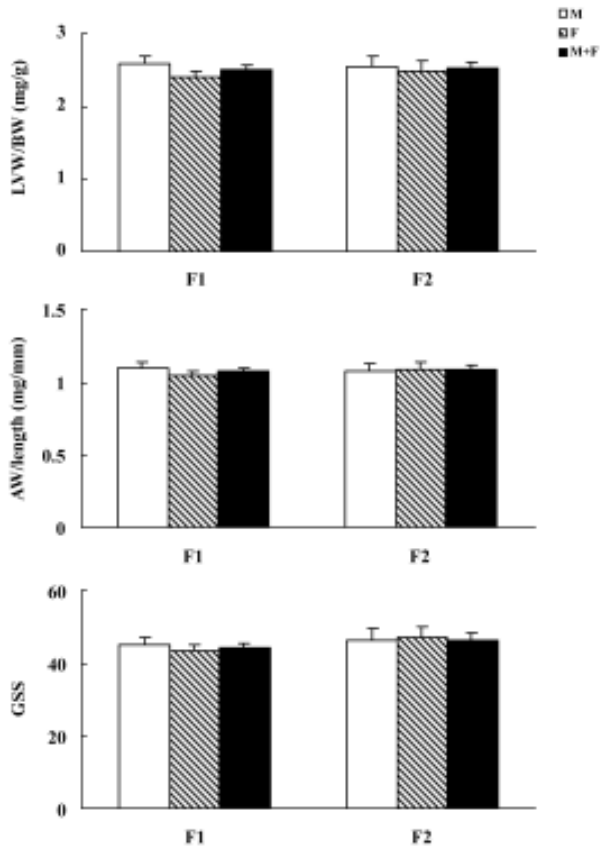

Figure 6. Organ damage in the F_1 and F_2 hybrids. AW, aortic weight; BW, body weight; GSS, glomerulosclerosis score; LVW, left ventricular weight. The numbers of rats used were 49 and 16 in male (M), 47 and 20 in female (F), and 96 and 36 in total (M+F) F_1 and F_2 rats, respectively.

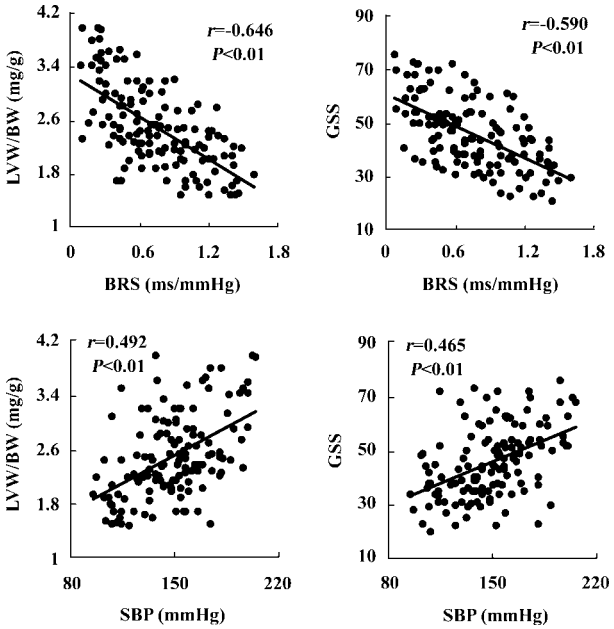

Figure 7. Examples of the correlation between hemodynamic parameters and organ damage parameters in hybrids. n=132. See Table 1 for abbreviations.

needed for such a study. Investigating the relationship between BP and BRS using hybrid offspring rats was the first aim of the present work.

To analyze the links between BP and other parameters previous studies have used hybrid rats derived from a cross between SHR and Wistar-Kyoto (WKY) rats[22–26], stroke-prone SHR (SHRSP) and WKY rats[28], Dahl/Iwai salt-sensitive rats and WKY rats[29], New Zealand genetically hypertensive rats and Wistar rats[23], and SHR and Donryu rats[30]. In the present study, SHR were crossbred with SD rats, but not with WKY rats. This is based on the following considerations: (i) WKY rats possess a relatively higher BP level than SD rats; and (ii) compared with WKY rats, the genetic background of SD rats is more different from that of SHR. Therefore, using SD rats may help to produce hybrid rats exhibiting wider range of BP levels or BRS values, which would be expected for the correlation analysis.

It was found in previous studies that the BP of hybrid offspring derived from SHR and WKY rats depended on the strain of the male progenitor of the cross; male offspring with an SHR male progenitor had significantly higher BP (SBP, +20 mmHg) than male offspring with a WKY male progenitor[31]. The same results were also found in hybrids of SHRSP and WKY rats (SBP/DBP, +20/15 mmHg)[28]. These observations showed strong evidence for a locus or loci on the SHR or SHRSP Y chromosome that contributed to hypertension in these models. Some subsequent studies confirmed the Y-chromosome effect on BP[27,32]. In accordance with previous reports, the current work showed that the male F_1 hybrids with hypertensive fathers had higher BP levels than those with normotensive fathers (SBP/DBP, +12/14 mmHg). The difference reached a significant level only for DBP. These differences found in the present work were slightly lower than those in previous studies. This might be due to the difference in BP measurement: we measured BP continuously for 24 h while others measured BP either once by tail sphygmomanometry[31] or by using average values sampled every 5 min for 10 s over a 4 d period using the radiotelemetry system[28]. However, in our study, the F_1 hybrids with different parenthood had similar HP and BRS values.

In previous studies concerning hybrid offspring rats, F_1, F_2 or the whole population of F_1 and F_2 were used[22–26,30]. The use of F_2 hybrids is based on the expectation of obtaining a wider distribution range in the parameters studied. In the present work, no obvious differences in the average val-

ues of SBP and BRS were found between F_1 and F_2 hybrids. In addition, the distribution of SBP and BRS values was similar in F_1 and F_2 hybrids. It is known that BP and BRS phenotypes are not controlled by only one gene, but rather by many genes[27]. This may explain the wide distribution range of SBP and BRS values. Accordingly, we propose that F_1 hybrids may be suitable for these kinds of studies.

Abnormalities in baroreflex have been demonstrated in numerous studies in both experimental and human hypertension[15,33], and the impairment in baroreflex is thought to be the result of elevated BP or reduced arterial distensibility[6,7]. In agreement with previous studies, we found that BRS was significantly and inversely related to SBP in the hybrid offspring rats. However, in the hybrids studied, we also found some normotensive animals with a lower BRS and hypertensive animals with a higher BRS. These results indicate that lower BRS is not always linked to higher blood pressure in the hybrid offspring rats. Previous studies have shown that impairment of BRS may be present early in the course of, or may precede the development of, hypertension. BRS has been shown to be diminished in the early phase of hypertension in SHR as well as in borderline essential hypertension in humans; impairment of BRS is thought to be genetically determined in part[10,34]. In addition, it was found that other factors, such as alterations in endothelial prostaglandins and opioid peptides, might also contribute to the impairment of BRS[35,36]. Therefore, BP is not the only determinant of BRS. However, it is not clear how important BP level is in influencing BRS. Our study, for the first time, demonstrated quantitatively that BRS was one-third determined by SBP level (the determinant coefficient was 0.326).

It is well known that high BP level induces organ damage, while decreasing BP level can prevent EOD. Our present study showed that both SBP and DBP were significantly and positively related to LVW/BW, AW/length, and GSS. These results indicate that elevated BP has a major effect on EOD in hybrid offspring rats. However, BP level is not the only determinant for EOD. Our previous study proposed that BRS was one of the independent variables related to EOD score [12]. In the present work, BRS was significantly and negatively related to LVW/BW, AW/length, and GSS. Multiple-regression analysis showed that the contribution of BRS to left ventricular, aortic hypertrophy, and glomerulosclerosis was greater than that of SBP. The present study is the first to show that BRS makes a greater contribution to hypertensive organ damage than does BP level.

In conclusion, the present work with hybrid rats demonstrated quantitatively that BRS value was one-third determined by SBP level. Both BP level and BRS value contributed to the hypertensive organ damage. However, the contribution of BRS to the hypertensive organ damage was greater than that of BP level in these rats.

References

1 Parati G, Saul JP, Castigliooni P. Assessing arterial baroreflex control of heart rate: new perspectives. J Hypertens 2004; 22: 1259–63.

2 Mancia G, Grassi G, Ferrari AU. Reflex control of the circulation in experimental and human hypertension. In: Zanchetti A, Mancia G, editors. Handbook of hypertension. Amsterdam: Elsevier Science BV; 1997; p568–601.

3 Bristow JD, Honour AJ, Pickering GW, Sleight P, Smyth HS. Diminished baroreflex sensitivity in high blood pressure. Circulation 1969; 39: 48–54.

4 Su DF, Cerutti C, Barres C, Vincent M, Sassard J. Blood pressure and baroreflex sensitivity in conscious hypertensive rats of Lyon strain. Am J Physiol 1986; 251: H1111–7.

5 Jones JV, Floras JS. Baroreflex sensitivity changes during the development of Goldblatt two-kidney one-clip hypertension in rats. Clin Sci 1980; 59: 347–52.

6 Moyes MR, Carbral AM, Marcal D, Vasquez EC. Sigmoidal curve-fitting of baroreceptor sensitivity in renovascular 2K1C hypertensive rats. Braz J Med Biol Res 1994; 27: 1419–24.

7 Jones JV, Floras JS. Baroreflex sensitivity changes during the reversal of Goldblatt two-kidney one-clip hypertension in rats. Clin Exp Hypertens A 1982; 4: 903–14.

8 Lu ZA, Xie HH, Xu LP, Yin AF, Miao CY, Su DF. Restoration of arterial baroreflex function contributes to organ protection in spontaneously hypertensive rats treated with long-term hydrochlorothiazide mixture. Clin Exp Pharmacol Physiol 2003; 30: 49–54.

9 Du WM, Miao CY, Liu JG, Shen FM, Yang XQ, Su DF. Effects of long-term treatment with ketanserin on blood pressure variability and end-organ damage in spontaneously hypertensive rats. J Cardiovasc Pharmacol 2003; 41: 233–9.

10 Parmer RJ, Cervenka JH, Stone RA. Baroreflex sensitivity and heredity in essential hypertension. Circulation 1992; 85: 497–503.

11 Yamada Y, Miyajima E, Tochikubo O, Matsukawa T, Shionoiri H, Ishii M, *et al*. Impaired baroreflex changes in muscle sympathetic nerve activity in adolescents who have a family history of essential hypertension. J Hypertens Suppl 1988; 6: S525–8.

12 Shan ZZ, Dai SM, Su DF. Relationship between baroreceptor reflex function and end-organ damage in spontaneously hypertensive rats. Am J Physiol 1999; 277: H1200–6.

13 Miao CY, Su DF. The importance of blood pressure variability in rat aortic and left ventricular hypertrophy by sinoaortic denervation. J Hypertens 2002; 20: 1865–72.

14 Su DF, Xu LP, Miao CY, Xie HH, Shen FM, Jiang YY. Two useful methods for evaluating antihypertensive drugs in conscious freely moving rats. Acta Pharmacol Sin 2004; 25: 148–51.

15 Smyth HS, Sleight P, Pickering GW. Reflex regulation of arterial pressure during sleep in man: a quantitative method of assessing baroreflex sensitivity. Circ Res 1969; 24: 109-21.

16 Su DF, Chen L, Kong XB, Cheng Y. Determination of arterial

baroreflex-blood pressure control in conscious rats. Acta Pharmacol Sin 2002; 23: 103–9.
17 Su DF, Cerutti C, Barres C, Julien C, Vincent M, Paultre C, *et al*. Arterial baroreflex control of heart period is not related to blood pressure variability in conscious hypertensive and normotensive rats. Clin Exp Pharmacol Physiol 1992; 19: 767–75.
18 Hayakawa H, Raij L. The link among nitric oxide synthase activity, endothelial function, and aortic and ventricular hypertrophy in hypertension. Hypertension 1997; 29: 235–41.
19 Miao CY, Xie HH, Wang JJ, Su DF. Candesartan inhibits sinoaortic denervation-induced cardiovascular hypertrophy in rats. Acta Pharmacol Sin 2002; 23: 713–20.
20 Miao CY, Tao X, Gong K, Zhang SH, Chu ZX, Su DF. Arterial remodeling in chronic sinoaortic-denervated rats. J Cardiovasc Pharmacol 2001; 37: 6–15.
21 Kimula K, Tojo A, Matsuoka H, Sugimoto T. Renal arteriolar diameters in spontaneously hypertensive rats: Vascular cast study. Hypertension 1991; 18: 101–10.
22 Hendley ED, Atwater DG, Myers MM, Whitehorn D. Dissociation of genetic hyperactivity and hypertension in SHR. Hypertension 1983; 5: 211–7.
23 Wickens JR, Macfarlane J, Booker C, McNaughton N. Dissociation of hypertension and fixed interval responding in two separate strains of genetically hypertensive rat. Behav Brain Res 2004; 152: 393–401.
24 Yongue BG, Myers MM. Further evidence for genetic independence of blood pressure and salt appetite in spontaneously hypertensive and Wistar-Kyoto rats. Clin Exp Hypertens A 1989; 11: 25–33.
25 Myers MM. Blood pressure development in F_2 rats derived from SHR and WKY progenitors. Clin Exp Hypertens A 1991; 13: 573–86.
26 Bachmanov AA. The characteristics of the F_1 hybrids of spontaneously hypertensive and normotensive rats. Fiziol Zh SSSR Im I M Sechenova 1989; 75: 1714–7.
27 Rapp JP. Genetic analysis of inherited hypertension in the rat. Physiol Rev 2000; 80: 135–72.
28 Davidson AO, Schork N, Jaques BC, Kelman AW, Sutcliffe RG, Reid JL, *et al*. Blood pressure in genetically hypertensive rats. Influence of the Y chromosome. Hypertension 1995; 26: 452–9.
29 Takami S, Higaki J, Miki T, Katsuya T, Nakata Y, Rakugi H, *et al*. Analysis and comparison of new candidate loci for hypertension between genetic hypertensive rat strains. Hypertens Res 1996; 19: 51–6.
30 Harrap SB, Jones EF. Cardiovascular hypertrophy does not predispose to genetic hypertension. Clin Exp Hypertens 1997; 19: 531–41.
31 Ely DL, Turner ME. Hypertension in the spontaneously hypertensive rat is linked to the Y chromosome. Hypertension 1990; 16: 277–81.
32 Ely DL, Daneshvar H, Turner ME, Johnson ML, Salisbury RL. The hypertensive Y chromosome elevates blood pressure in F_{11} normotensive rats. Hypertension 1993; 21: 1071–5.
33 Parmer RJ, Cervenka JH, Stone RA, O'Connor DT. Autonomic function in hypertension: Are there racial difference? Circulation 1990; 81: 1305–11.
34 Eckberg DL. Carotid baroreflex function in young men with borderline blood pressure elevation. Circulation 1979; 59: 632–6.
35 Xie P, Chapleau MW, McDowell TS, Hajduczok G, Abboud FM. Mechanism of decreased baroreceptor activity in chronic hypertensive rabbits. J Clin Invest 1990; 86: 625–30.
36 Weinstock M, Korner PI, Head GA, Dorward PK. Differentiation of cardiac baroreflex properties by cuff and drug methods in two rabbit strains. Am J Physiol 1988; 255: R654–64.

Acta Pharmacologica Sinica 2005 Sep; 26 (9): 1057–1062

Full-length article

Relationship between leukocyte count and angiographical characteristics of coronary atherosclerosis[1]

En-zhi JIA[2,5], Zhi-jian YANG[2], Biao YUAN[3], Xiao-ling ZANG[4], Rong-hu WANG[4], Tie-bing ZHU[2], Lian-sheng WANG[2], Bo CHEN[2], Wen-zhu MA[2]

[2]Departments of Cardiovascular Medicine, [3]Chest Surgery, and [4]Clinical Laboratory, the First Affiliated Hospital of Nanjing Medical University, Nanjing 210029, China

Key words

leukocyte count; lymphocyte count; monocyte count; neutrophils; coronary atherosclerosis; Gensini's score

[1] Project supported by the National Natural Science Foundation of China (No 30400173).
[5] Correspondence to Dr En-zhi JIA.
Phn 86-139-5162-3205.
E-mail enzhijia@yahoo.com.cn

Received 2005-02-05
Accepted 2005-04-27

doi: 10.1111/j.1745-7254.2005.00169.x

Abstract

Aim: To explore the relationship between differential leucocyte count and coronary atherosclerosis. **Methods:** The study population consisted of 507 consecutive patients (376 male and 131 female) who underwent coronary angiography for suspected or known coronary atherosclerosis. The patients' smoking and drinking habits were investigated, and anthropometric measurements, serum measurements, and hematological measurements were conducted for every patient. The severity of coronary atherosclerosis was defined by using Gensini's score system. One-way ANOVA, Spearman's correlation analysis, and multivariate stepwise linear regression analysis were employed to explore the relationship between differential leucocyte count and coronary atherosclerosis. **Results:** One-way ANOVA indicated that the diastolic blood pressure, glucose, urea, creatinine, leukocyte count, neutrophil count, monocyte count, hemoglobin, and platelet count differed among the groups according to Gensini's score, the tertile values of which were used as cutoff points. Spearman's correlation analysis suggested that Gensini's score was significantly correlated with age, diastolic blood pressure, glucose, urea, creatinine, leukocyte count, neutrophil count, monocyte count, hemoglobin, and erythrocyte count, respectively. Multivariate stepwise linear regression analysis show that neutrophil count (β=0.247, P=0.000), age (β=0.141, P=0.001), glucose (β=0.173, P=0.000), creatinine (β=0.088, P=0.063), hemoglobin (β=-0.168, P=0.013) and sex (men were coded as 1 and women were coded as 2; β=-0.121, P=0.012) were significantly independently associated with the Gensini's score. **Conclusion:** The independent association of neutrophil count with the angiographical characteristics of coronary atherosclerosis, as estimated by Gensini's score, strongly suggests that granulocytosis may play a role in the development of coronary atherosclerosis.

Introduction

Inflammation is a key feature of atherosclerosis, and leukocyte count is a marker of inflammation that is widely available in clinical practice. Numerous epidemiological and clinical studies have shown leukocytosis to be an independent predictor of future cardiovascular events, both in healthy individuals free of coronary heart disease, and in patients with stable angina, unstable angina, or a history of myocardial infarction. This relationship has been observed in prospective and retrospective cohort studies, as well as in case-control studies[1]. The relationship is strong, consistent, temporal, dose-dependent, and biologically plausible. Elevated differential cell counts, including eosinophil, neutrophil, and monocyte counts, also predict the future incidence of coronary heart disease[2]. Clinical studies suggest that neutrophil infiltration is actively associated with acute coronary events. The high number of neutral endopeptidase-positive neutrophils in ruptured plaques, compared

with eroded plaques, may reflect differences in the underlying pathophysiological mechanisms[3]. However, there is little information available about the association between the angiographical characteristics of coronary atherosclerosis as estimated by conventional coronary angiography and circulating leukocyte count.

Gensini's scoring system assigns a severity score for a stenosed vessel depending on the degree of luminal narrowing and the importance of its location[4]. Therefore, we evaluated the association between the angiographical characteristics of coronary atherosclerosis and circulating leukocyte count.

Materials and methods

Study subjects The study population consisted of 507 consecutive patients who underwent coronary angiography for suspected or known coronary atherosclerosis at the First Affiliated Hospital of Nanjing Medical University, Nanjing, China, from 2004 to 2005. Patients with spastic angina pectoris (ie, acetylcholine-positive) were excluded. Patients with 2-week infectious processes before catheterization, heart failure (Killip class =2 after acute myocardial infarction), hepatic dysfunction, vascular disease (aortitis treated with prednisolone), familial hypercholesterolemia, thyroid dysfunction, or adrenal dysfunction were also excluded. This study was approved by the Ethics Committee of the First Affiliated Hospital of Nanjing Medical University and informed consent was obtained from all patients.

Coronary angiography Coronary arteries were cannulated by using the Judkins technique[5] with 5F catheters, and recorded on Kodak, 35 mm Cinefilm at a rate of 30 frames per second. When stenotic coronary arteries were found, the presence of stenosis was determined by using a computer-assisted coronary angiography analysis system (Mipron 1; Kontron) after the direct intracoronary injection of isosorbide dinitrate (ISDN; 2.5 mg in 5 mL solution over 20 s). One minute after the injection of ISDN through the Judkins catheter, coronary angiography was performed from several projections. The severity of coronary atherosclerosis was measured by using Gensini's scoring system, based on the hypothesis that the severity of coronary heart disease is a consequence of the functional significance of vascular narrowing and the extent of the area perfused by the involved vessel or vessels. In this scoring system, a greater reduction of the lumen diameter is assigned a higher score than a distal lesion[4].

Cigarette smoking and alcohol intake The subjects' cigarette smoking and alcohol intake habbits were assessed by means of a standardized questionnaire. Past or current smokers were asked about the number of cigarettes smoked per day, and those who reported smoking at least 1 cigarette per day during the preceding year were classified as current smokers. With regard to smoking status, subjects were classified as "never a smoker" and "smoker" (including "formerly a smoker" and "currently a smoker"). Subjects who reported consuming at least 50 g alcohol/week were regarded as "current drinkers". Subjects were classified as "never a drinker" and "drinker" (including "formerly a drinker" and "currently a drinker").

Anthropometric measurements Anthropometric measurements were taken after the patients had removed their shoes and upper garments and had donned an examining gown. Each measurement was performed twice and the average was used in the analysis. Height was measured to the nearest 0.1 cm using a wall-mounted stadiometer. Weight was measured to the nearest 0.1 kg using a hospital balance beam scale. Body mass index (BMI) was calculated as weight (kg) divided by the square of height (m^2). Blood pressure was measured in the right arm with the participant seated and the arm bared. Three readings were recorded for each individual, and the average was recorded.

Hematological measurements Blood samples from every patient were taken at admission to the coronary unit and measurements including total leukocyte count, neutrophil count, eosinophil count, lymphocyte count, monocyte count, basophil count, hemoglobin, erythrocyte count, and platelet count were carried out by an automated blood analyzer.

Laboratory measurements The 12-h fasting blood samples were taken in the morning and the sera were stored at -70 ^{o}C immediately after centrifugation until being assayed. All laboratory measurements were conducted at the Central Clinical Laboratory at the First Affiliated Hospital of Nanjing Medical University. Total cholesterol, triglyceride, fasting blood glucose, urea, creatinine, and uric acid were determined by enzymatic procedures on an automated autoanalyzer (AU 2700 Olympus, 1st Chemical Ltd, Japan). The laboratory was monitored for the precision and accuracy of glucose and lipid measurements by the surveillance program. Measurements of agency-assigned quality control samples showed no consistent bias over time within or between surveys.

Statistical analysis Data analysis was performed using the Statistical Package for the Social Sciences (SPSS for Windows, version 10.0; SPSS, Chicago, IL, USA). Patients were classified into 3 groups with low, intermediate, and high Gensini's scores using the tertile values as cutoff points, so that each group had an approximately equal number of pa-

tients to minimize any bias that may have been produced in the statistical analysis. Results for continuous variables are expressed as mean±SD and comparisons of continuous variables were analyzed by the one-way analysis of variance (ANOVA). Categorical variables were compared among the groups of patients by a chi-squared analysis. The Spearman two-way test was used to assess the relationship between 2 quantitative variables. We assessed independent predictors of Gensini's score with multiple regression analysis. Differences were considered to be significant if the null hypothesis could be rejected with >95% confidence. All *P* values are 2-tailed.

Results

Clinical and biochemical characteristics in patients grouped according to Gensini's score Table 1 show the clinical and biochemical characteristics in patients grouped according to Gensini's score, tertile values of which were used as cutoff points. Patients in tertiles I, II, and III had an increasingly higher Gensini's score. The frequency distribution of sex (P=0.009) and smoking status (P=0.000) were different among the 3 groups, and drinking status was similar among the 3 groups. The distribution levels of BMI, systolic blood pressure, total cholesterol, triglyceride, uric acid, eosinophil count, basophil count, and lymphocyte count were similar among the 3 groups (P>0.05), whereas those of age (P=0.000), diastolic blood pressure (P=0.011), fasting blood glucose (P=0.000), urea (P=0.012), creatinine (P=0.005), leukocyte count (P=0.000), neutrophil count (P=0.000), monocyte count (P=0.000), hemoglobin (P=0.000), erythrocyte count (P=0.008) and platelet count (P=0.019) differed among the groups.

Spearman correlations between Gensini's score and leukocyte count, anthropometric measurements, and biochemical characteristics in patients Table 2 shows the results of Spearman correlations between Gensini's score and leukocyte count, anthropometric measurements, and biochemical characteristics in patients. The Spearman correlation analysis indicated that the level of Gensini's score was significantly correlated with age (r=0.225, P=0.000), DBP (r=-0.106, P=0.017), fasting blood glucose (r=0.195, P=0.000), urea (r=0.137, P=0.002), creatinine (r=0.165, P=0.000), leukocyte count (r=0.303, P=0.000), neutrophil count (r=0.326, P=0.000), monocyte count (r=0.253, P=0.000), hemoglobin (r=-0.133, P=0.003), and erythrocyte count (r=-0.094, P=

Table 1. Clinical and biochemical characteristics in patients grouped according to Gensini's score (the tertile values of which were used as cutoff points).

Variables	Gensini's score			Parameter	
	0–4.0 (n=169)	4.1–34 (n=166)	>34.1 (n=172)	F value or χ^2 value	P value
Age/a	59.07±10.48	61.77±11.76	64.46±10.07	10.669	0.000
Sex/M·F^{-1}	111/58	130/36	135/37	9.517	0.009
BMI/kg·m^{-2}	24.79±3.41	24.87±3.2	24.61±3.15	0.277	0.758
Smoker/Y·N^{-1}	109/60	67/99	80/92	21.370	0.000
Drinker/Y·N^{-1}	134/35	123/43	134/38	1.277	0.528
SBP/mmHg	133.63±20.40	131.96±21.80	130.67±20.91	0.850	0.428
DBP/mmHg	80.09±11.74	79.17±11.92	76.40±11.58	4.572	0.011
Cholesterol/mmol·L^{-1}	4.10±0.93	4.12±0.97	4.04±1.05	0.278	0.757
Triglyceride/mmol·L^{-1}	1.66±1.08	1.64±1.04	1.70±1.14	0.133	0.857
Glucose/mmol·L^{-1}	4.81±1.06	5.11±1.32	5.92±2.81	14.949	0.000
Urea/mmol·L^{-1}	5.25±1.78	5.71±2.02	6.06±3.28	4.468	0.012
Creatinine/μmol·L^{-1}	71.57±18.55	73.79±20.21	79.30±26.79	5.324	0.005
Uric acid/μmol·L^{-1}	351.84±88.83	355.03±95.74	364.05±102.99	0.715	0.490
10^{-9}×Leukocyte/L^{-1}	6.02±1.61	6.89±2.31	8.22±3.54	30.174	0.000
10^{-9}×Neutrophil/L^{-1}	3.61±1.31	4.45±2.08	5.61±3.18	31.558	0.000
10^{-9}×Eosinophil/L^{-1}	0.13±0.10	0.15±0.11	0.17±0.17	2.943	0.054
10^{-9}×Lymphocyte/L^{-1}	1.79±0.55	1.74±0.59	1.76±0.75	0.262	0.770
10^{-9}×Monocyte/L^{-1}	0.47±0.25	0.53±0.22	0.65±0.42	14.718	0.000
10^{-9}×Basophil/L^{-1}	0.029±0.047	0.029±0.039	0.036±0.044	1.757	0.174
Hemoglobin/g·L^{-1}	134.90±15.56	132.73±17.98	127.59±18.64	7.838	0.000
10^{-12}×Erythrocyte/L^{-1}	4.43±0.61	4.42±0.63	4.24±0.68	4.859	0.008
10^{-9}×Platelet/L^{-1}	170.89±55.88	188.75±63.52	187.32±71.88	4.019	0.019

Table 2. Spearman correlations between Gensini's score and leukocyte count, anthropometric measurements, and biochemical characteristics in patients.

Variables	Gensini's score	
	Correlation coefficient	*P* value
Age/a	0.225	0.000
Body mass index/kg·m^{-2}	-0.021	0.636
Systolic blood pressure/mmHg	-0.041	0.359
Diastolic blood pressure/mmHg	-0.106	0.017
Cholesterol/mmol·L^{-1}	-0.007	0.885
Triglyceride/mmol·L^{-1}	-0.014	0.763
Glucose/mmol·L^{-1}	0.195	0.000
Urea/mmol·L^{-1}	0.137	0.002
Creatinine/μmol·L^{-1}	0.165	0.000
Uric acid/μmol·L^{-1}	0.071	0.117
10^{-9}×Leukocyte/L^{-1}	0.303	0.000
10^{-9}×Neutrophil/L^{-1}	0.326	0.000
10^{-9}×Eosinophil/L^{-1}	0.040	0.372
10^{-9}×Lymphocyte/L^{-1}	-0.063	0.161
10^{-9}×Monocyte/L^{-1}	0.253	0.000
10^{-9}×Basophil/L^{-1}	0.079	0.076
Hemoglobin/g·L^{-1}	-0.133	0.003
10^{-12}×Erythrocyte/L^{-1}	-0.094	0.035
10^{-9}×Platelet/L^{-1}	0.077	0.084

0.035), whereas a significant correlation was not found between Gensini's score and Body Mass Index, SBP, total cholesterol, triglyceride, uric acid, eosinophil count, basophil count, lymphocyte count, or platelet count.

Multiple linear regression analysis with Gensini's score as dependent variable To examine the independent associations between Gensini's score and leukocyte count, multiple linear regression analysis was performed. In this model, Gensini's score was used as the dependent variable and the independent variables included age, sex, smoking status, drinking status, body mass index , SBP, DBP, total cholesterol, triglyceride, fasting blood glucose, urea, creatinine, uric acid, leukocyte count, neutrophil count, eosinophil count, basophil count, lymphocyte count, hemoglobin, erythrocyte count, and platelet count. In the final model (Table 3), neutrophil count (β=0.247, *P*=0.000), age (β=0.141, *P*=0.001), glucose (β=0.173, *P*=0.000), creatinine (β=0.088, *P*=0.063), hemoglobin (β=-0.168, *P*=0.013) and sex (men were coded as 1 and women were coded as 2; β=-0.121, *P*=0.012) were significantly independently associated with Gensini's score.

Discussion

Cardiovascular disease is the leading cause of death in the world[6]. One of its most insidious forms is coronary heart disease due to atherosclerosis[7]. Although many risk factors for coronary heart disease have been identified, they do not fully account for all cases of the disease. Thus, searches are underway for additional biological markers and especially inflammatory markers for the disease. Numerous epidemiological and clinical studies have shown leukocyte count to be an independent risk factor for coronary heart disease, a risk factor for future cardiovascular events in individuals apparently without cardiovascular disease, and a prognostic marker of future events in patients who already have cardiovascular disease[1]. Although leukocyte count appears to be an independent predictor of cardiovascular events, some of its predictive ability can be explained by its interdependence with smoking. Therefore, further studies are needed to clarify just how prominent a role leukocytes play in the pathogenesis of coronary heart disease, as well as the clinical implications. Obviously, there is a need to determine the degree to which leukocyte count is independent of smoking and other risk factors [2].

The present study was conducted to evaluate the association between the angiographical characteristics of coronary atherosclerosis and leukocyte count in patients with suspected coronary heart disease. The main finding of the present study is that the neutrophil count is significantly associated with Gensini's score according to one-way ANOVA, the Spearman correlation, and multiple linear stepwise regression analysis in these 507 Chinese subjects. This finding is consistent with results from previous studies, in which leukocytosis has been consistently shown to be an independent risk factor for coronary heart disease regardless of disease status[2]. Furthermore, this study suggests a link between inflammatory and coronary atherosclerosis.

Our study is the first to document the independent association of neutrophil count with the angiographical characteristics of coronary atherosclerosis, which were approximated by using Gensini's score in Chinese subjects, and which is in agreement with the results of previous studies. In a meta-analysis of 1764 cases of coronary heart disease from 7 long-term prospective studies, involving a total of 30 374 participants, the association of coronary heart disease with neutrophil count was somewhat stronger than that with other specific leucocyte components[8]. In a prospective cohort study of 55 patients with non-ST segment elevation acute coronary syndromes and angiographically documented coronary disease, acute inflammatory markers such as neutrophil count were higher among patients with multiple angiographically complex plaques than among those without[9]. The results from an immunohistochemical study

Table 3. Predictors of Gensini's score from multiple linear regression among patients.

Variable	Unstandardized coefficient		Standardized coefficients	*t*	*P*
	B	SE	(β)		
Constant	5.230	19.782	—	0.264	0.792
10^{-9}×Neutrophil/L^{-1}	3.635	0.636	0.247	5.718	0.000
Age/a	0.456	0.142	0.141	3.210	0.001
Glucose/mmol·L^{-1}	3.309	0.822	0.173	4.027	0.000
Creatinine/μmol·L^{-1}	0.141	0.076	0.088	1.866	0.063
Hemoglobin/g·L^{-1}	-0.362	0.145	-0.168	-2.493	0.013
Sex	-9.777	3.880	-0.121	-2.520	0.012

on coronary artery segments suggest that neutrophil infiltration is actively associated with acute coronary events[3]. Granulocytosis affects the development of coronary atherosclerosis through multiple pathological mechanisms that mediate inflammation, cause proteolytic and oxidative damage to the endothelial cells, plug the microvasculature, induce hypercoagulability, and promote infarct expansion[2].

Moreover, another finding of this study is that age (β=0.141, *P*=0.001), creatinine (μmol/L; β=0.088, *P*=0.063), glucose (mmol/L; β=0.173, *P*=0.000), hemoglobin (g/L; β=-0.168, *P*=0.013), and sex (men were coded as 1 and women were coded as 2, β=-0.121, *P*=0.012) were significantly associated with Gensini's score after adjusting for the other cardiovascular risk factors. The results of the Atherosclerosis Risk in Communities study, a community-based study of risk factors for coronary heart disease (CHD) in middle-aged people indicated that high serum creatinine was associated with almost a 3-fold risk of coronary heart disease among middle-aged people with anemia (anemia was defined as hemoglobin <130 g/L in men and <120 g/L in women), whereas no increased risk was found in people with high serum creatinine in the absence of anemia[10]. Another study found a relationship between low hemoglobin level and adverse cardiovascular outcomes in women with suspected ischemia[11]. Several investigations as well as prospective studies have shown a significant correlation between glucose metabolism and atherosclerosis in patients without diabetes, and have shown that the glycemic milieu correlates with the cardiovascular risk according to a linear model[12]. In addition, the present study demonstrated that age and being male were independent risk factors for coronary atherosclerosis, which was consistent with results from other studies[13].

A limitation of the present study is that the subjects were from one center rather than multiple centers, which may result in selective bias; however, given the large size sample of this study, it may minimize the bias. In fact, the present study is only a cross-sectional study rather than a retrospective study. And the other limitation of the study is that it provides no information regarding the cause and effect relationship between neutrophil count and coronary atherosclerosis. Although the correlation between neutrophil count and coronary atherosclerosis is significant in the present study, the clinical significance of this finding requires further investigation.

In conclusion, the independent association of neutrophil count with the angiographical characteristics of coronary atherosclerosis as approximated by Gensini's score strongly suggests that granulocytosis may play a role in the development of coronary atherosclerosis. Thus, it may prove to be an equally informative, but less expensive and more readily available risk marker than other currently available risk factors. Further studies are required, however, to determine the implications of using the leukocyte count to predict clinical risk and outcome.

References

1 Danesh J, Collins R, Appleby P, Peto R. Association of fibrinogen, C-reactive protein, albumin, or leukocyte count with coronary heart disease: meta-analyses of prospective studies. JAMA 1998; 279: 1477–82.

2 Madjid M, Awan I, Willerson JT, Casscells SW. Leukocyte count and coronary heart disease: implications for risk assessment. J Am Coll Cardiol 2004; 44: 1945–56.

3 Naruko T, Ueda M, Haze K, van der Wal AC, van der Loos CM, Akira Itoh A, *et al*. Neutrophil infiltration of culprit lesions in acute coronary syndromes. Circulation 2002; 106: 2894–900.

4 Gensini GG. A more meaningful scoring system for determining the severity of coronary heart disease. Am J Cardiol 1983; 51: 606.

5 Judkins MP. A percutaneous transfemoral technique. Radiology 1967; 89: 815–21.

6 American Heart Association. Heart Disease and Stroke Statistics: 2003 Update. Dallas, Texas: American Heart Association; 2002.

7 Ross R. Atherosclerosis: an inflammatory disease. N Engl J Med

1999; 340: 115–26.
8 Wheeler JG, Mussolino ME, Gillum RF, Danesh J. Associations between differential leucocyte count and incident coronary heart disease: 1764 incident cases from seven prospective studies of 30,374 individuals. Eur Heart J 2004; 25: 1287–92.
9 Avanzas P, Arroyo-Espliguero R, Cosin-Sales J, Aldama G, Pizzi C, Quiles J, *et al*. Markers of inflammation and multiple complex stenoses (pancoronary plaque vulnerability) in patients with non-ST segment elevation acute coronary syndromes. Heart 2004; 90: 847–52.
10 Jurkovitz CT, Abramson JL, Vaccarino LV, Weintraub WS, McClellan WM. Association of high serum creatinine and anemia increases the risk of coronary events: results from the prospective community-based atherosclerosis risk in communities (ARIC) study. J Am Soc Nephrol 2003; 14: 2919–25.
11 Arant CB, Wessel TR, Olson MB, CN BM, Sopko G, Rogers WJ, *et al*. Hemoglobin level is an independent predictor for adverse cardiovascular outcomes in women undergoing evaluation for chest pain: results from the National Heart, Lung, and Blood Institute Women's Ischemia Syndrome Evaluation Study. J Am Coll Cardiol 2004; 43: 2009–14.
12 Sasso FC, Carbonara O, Nasti R, Campana B, Marfella R, Torella M, *et al*. Glucose metabolism and coronary heart disease in patients with normal glucose tolerance. JAMA 2004; 291: 1857–63.
13 Faxon DP, Creager MA, Smith SC Jr, Pasternak RC, Olin JW, Bettmann MA, *et al*. Atherosclerotic vascular disease conference. Executive summary: atherosclerotic vascular disease conference proceeding for healthcare professionals from a Special Writing Group of the American Heart Association. Circulation 2004; 109: 2595–604.

SCI Impact Factor of Acta Pharmacologica Sinica increased to 1.125

According to the latest Journal Citation Report 2004 (JCR 2004) published by Institute for Scientific Information (ISI, USA), we are greatly pleased to announce that the Science Citation Index (SCI) Impact Factor of Acta Pharmacologica Sinica (APS) has risen from 0.884 to **1.125**, ranking the 132nd out of 187 journals in the category of PHARMACOLOGY & PHARMACY, and the 49th out of 125 journals in the category of CHEMISTRY, MULTIDISCIPLINARY. APS is continued to be the only journal listed in the SCI in Chinese Pharmacology and Pharmacy and the latest impact factor is ranking the 8th out of 71 Chinese journals listed in SCI.

Here we would like to share the good news with all our authors, reviewers, and readers. Without your long-term contribution, APS cannot achieve such a progress! Hope to have your support continuously!

Acta Pharmacologica Sinica 2005 Sep; 26 (9): 1063–1068

Full-length article

Honokiol inhibits arterial thrombosis through endothelial cell protection and stimulation of prostacyclin

He HU[1], Xiao-xue ZHANG[1], Yin-ye WANG[1,2], Shi-zhong CHEN[3]

[1]Department of Molecular and Cellular Pharmacology, Beijing University, Beijing 100083, China; [3]Department of Natural Medicinal Chemistry, School of Pharmaceutical Sciences, Peking University, Beijing 100083, China

Key words

honokiol; platelet aggregation; thrombosis; cultured cells; endothelium; prostacyclin; nitric oxide

[2]Correspondence to Prof Yin-ye WANG.
Phn 86-10-8280-2652.
Fax 86-10-6201-5584.
E-mail wangyinye@bjmu.edu.cn

Received 2005-03-12
Accepted 2005-04-29

doi: 10.1111/j.1745-7254.2005.00164.x

Abstract

Aim: To study the effect of honokiol on arterial thrombosis and endothelial cells. **Methods:** Rabbit platelet aggregation was performed with Born's turbid method. Thrombosis was produced by the endothelial injury stimulated with electric current. Rat aortic endothelial cells (RAEC) were cultured and cell viability was assessed using the MTT assay. Nitric oxide (NO) concentrations in serum-free media of RAEC were determined using the kinetic cadmium-reduction method. The stable metabolite prostacyclin was measured in serum-free media of RAEC by radioimmunoassay. **Results:** Honokiol (37.6–376 μmol/L) decreased rabbit platelet aggregation *in vitro* in a concentration-dependent manner, while intravenously injection of honokiol (0.12–12 μg/kg) significantly inhibited rabbit platelet aggregation induced by collagen *ex vivo*. In the electrical current-stimulated carotid thrombosis model in rats, honokiol (5–50 μg/kg, iv) prolonged the thrombus occlusion time in a does-dependent manner. *In vitro* honokiol (0.376–37.6 μmol/L) effectively protected cultured RAEC against oxidized low density lipoprotein (ox-LDL) injury, and significantly increased 6-keto-$PGF_{1\alpha}$ (the stable metabolite of prostacyclin) in serum-free media of RAEC. Honokiol also increased NO level in RAEC serum-free medium at a lower concentration range (0.0376–0.376 μmol/L), but honokiol 3.76 μmol/L decreased NO level. **Conclusion:** Honokiol is a potent arterial thrombosis inhibitor. Endothelial cell protection and the stimulation of prostacyclin release may be its main anti-thrombosis mechanism. Stimulation of NO release in endothelial cells may play a role, but it is not a key factor.

Introduction

Platelet activation and aggregation play essential roles in thromboembolic disorders[1]. When platelets are activated they adhere to the injured blood vessel walls. This results in the formation of an occlusive thrombus in the lumen of the vessel[2,3]. These thrombi are the source of many thromboembolic cerebral vascular diseases, including strokes[4].

Honokiol is the main biphenyl neolignan isolated from Hou pu, the cortex of *Magnolia officinalis* (Magnoliaceae), which has been used for treatment of acute enteritis, bacterial or amebic diarrhea, chronic gastritis, *etc*, in traditional Chinese medicine. The pharmacological effects of honokiol included inhibition of platelet aggregation by blocking thromboxane A_2 (TXA_2) generation and intracellular calcium mobilization[5], protection of the myocardium against ischemic injury[6], and suppression of ventricular arrhythmia[7]. Recently honokiol was found to protect rat brain from focal cerebral ischemia–reperfusion injury by inhibiting neutrophil infiltration and reactive oxygen species production[8]. However, the effects of honokiol on thrombosis and its influence on endothelial cells have not yet been reported. The aim of this study was to investigate the effects of honokiol on arterial thrombosis and endothelial cells to explore its potential mechanism of action.

Materials and methods

Chemicals and reagents Honokiol injection was prepared by the Department of Natural Medicinal Chemistry, School of Pharmaceutical Sciences, Peking University (Beijing, China). This water-soluble preparation of honokiol contains polyvinyl and other auxiliary materials. Before use it was diluted with normal saline to different concentrations for intravenous injection (0.5 μg/mL, 5 μg/mL, 50 μg/mL for rats; 0.12 μg/mL, 1.2 μg/mL, 12 μg/mL for rabbits; concentrations vary with surface area of the animals). Acetylsalicylic acid (ASA) was the product of Astra (Wuxi, China) and was dissolved in normal saline by sonication before use. Collagen was purchased from Sigma (St Louis, MO, USA) and dissolved in normal saline before use. Oxidized low density lipoprotein (ox-LDL) was the product of Beijing Union Sanyou Science and Technology Development Co (Beijing, China). 6-keto-$PGF_{1\alpha}$ [the stable metabolite of prostacyclin (PGI_2)] immunoassay kits and nitric oxide (NO)/nitrate assay commercial kits were products of the Radioimmunology Institute of People Liberation Army General Hospital (Beijing, China). α-Tocopherol (VE) was the product of Beijing Double-Crane Pharmaceutical Co (Beijing, China). MTT was the product of Sigma. The control was normal saline plus defined proportion of auxiliary materials.

Experimental animals Male Sprague-Dawley rats and male New Zealand rabbits were obtained from the Experimental Animal Center of Peking University. The experimental procedures were approved by the Local Committee on Animal Care and Use.

Platelet aggregation study *in vitro* Blood samples were obtained from the auditive arteries of Male New Zealand rabbits weighing 3.0–4.0 kg into a syringe containing a 1:10 volume of 3.8% sodium citrate. Platelet-rich plasma (PRP) and platelet-poor plasma (PPP) were prepared by centrifugation of blood samples at 120×*g* and 850× *g*, respectively, for 15 min. The platelet count was adjusted to 1.8×10^9 platelets/mL with PPP. Platelet aggregation was measured using the 490 optical aggregometer (Chrono-log Co. Harvertown, PA USA) as described by Born[9]. Collagen was used as an inducer with a final concentration of 40–50 μg/mL.

Platelet aggregation study *ex vivo* Male rabbits weighing 3.0–3.5 kg were used after overnight fasting. The rabbits were administered intravenously with either control, honokiol 0.12, 1.2, and 12 μg/kg or ASA 1.2 mg/kg. Blood samples were then collected from the auditive arteries of the rabbits into a syringe containing a 1:10 volume of 3.8% sodium citrate at 10 min after administration. PRP and PPP were prepared as above. The platelet count was adjusted to 1.8×10^9 platelets/mL with PPP and platelet aggregation was measured with the Chrono-log mode 490 optical aggregometer. Collagen was used as an inducer with a final concentration of 40–50 μg/mL.

Carotid thrombosis model in rats induced by electric current Male Sprague-Dawley rats (280–320 g) were anesthetized with urethane (1.5 g/kg, ip) after overnight fasting. The left carotid arteries were then isolated carefully and treated intravenously with either control, honokiol 0.5, 5, 50 μg/kg or ASA 5 mg/kg. Carotid thrombus formation was induced using the modified Hladovec method[10] on an Electric Thrombosis Stimulator (BT87-3, Baotou Medical College, Baotou, China) by delivering a current of 3 mA for 3 min at 10 min after treatment. Occlusion time (OT) of the arteries was measured through a timer linked to the temperature sensor on the Thrombosis Stimulator.

Culture of rat aortic endothelial cells Endothelial cells were isolated from rat aorta by gentle scraping with vertical ophthalmic forceps. The rat aortic endothelial cells (RAEC) were then grown in T75 polystyrene flasks in the presence of antibiotics (100 U/mL penicillin G and 100 mg/mL streptomycin) and subcultured as described by Centra *et al*[11]. The endothelial cells were allowed to grow undisturbed for several days and thereafter the media were changed every 2 d for a total culturing period of 8–10 d. Cell culture purity (99%) was assessed by staining for factor VIII antigen, as described by Jaffe *et al*[12] and by visual inspection of their typical morphology. After mechanical disruption of cell monolayers by gente scraping and triturating, the cells were subcultured. Experiments were carried out using confluent cultures between passages 5 and 7.

Cultured rat aortic endothelial cell injury induced by ox-LDL Rat aortic endothelial cells of passage 5 were seeded at 1×10^5 cells/mL in 96-well plates and grown to confluence. The cells were treated with control or honokiol (final concentration 0.0376 μmol/L, 0.376 μmol/L or 3.76 μmol/L) or Vitamin E for 30 min in serum-free medium, and then incubated with ox-LDL (final concentration 50 μg/mL) for 24 h as described previously[13]. The viability of cells was assayed using the MTT assay.

Measurement of 6-keto-$PGF_{1\alpha}$ levels in serum-free medium of injured rat aortic endothelial cells by ox-LDL The culture medium was removed after RAEC were grown to confluence, and cells were washed twice with phosphate-buffered saline and pre-incubated with the serum-free medium for 30 min. After the cells were treated with control, honokiol 0.376, 3.76, 37.6 μmol/L, or VE 100 mg/L at 37 ºC for 30 min, the cultures were incubated with ox-LDL (final concentration 50 μg/mL) for 24 h to induce injury. Incubations were terminated by placing them in an ice bath. Culture

fluids were saved for the determination of 6-keto-$PGF_{1\alpha}$, and cells were collected for protein content measurement. 6-keto-$PGF_{1\alpha}$ was determined using immunoassay kits, and protein content was measured using the Bradford method[14].

Determination of nitric oxide levels in serum-free medium of injured rat aortic endothelial cells by ox-LDL Cells were cultured and treated as described above. The level of NO in culture fluid was determined using a kinetic cadmium-reduction method[15] with NO/nitrate assay commercial kits.

Statistical analysis The data were expressed as mean±SD and represent data from 5 repeated assays. Statistical evaluation was carried out using the Dunnet *t*-test to compare the differences between treated groups and control groups. $P<0.05$ was considered to be statistically significant.

Results

Effects of honokiol on rabbit platelet aggregation *in vitro* and *ex vivo* As shown in Figure 1, honokiol displayed a concentration-dependent inhibitory effect on platelet aggregation *in vitro*. Honokiol at 0.376 μmol/L did not influence platelet aggregation, but honokiol 37.6 μmol/L decreased the platelet aggregation from 78.0%±5.7% to 13.5%±5.9%, and an almost complete inhibition was observed when 376 μmol/L honokiol was used (from 78.0%±5.7% to 0.6%±1.1%). At 15 min after bolus intravenous administration, honokiol significantly inhibited platelet aggregation induced by collagen. The maximum aggregation rates were 70.0%±7.4% for the control group, 22.9%±17.0 % for the 0.12 μg/kg group, 18.4%± 19.8% for the 1.2 μg/kg group and 14.5%±19.0% for the 12 μg/kg group. It was evident that honokiol inhibited collagen-induced platelet aggregation in a dose-dependent manner. ASA, a typical anti-platelet agent, also inhibited collagen-induced platelet aggregation at 1.2 mg/kg under the same conditions (Figure 2). It is evident that honokiol has a potent inhibitory effect on collagen-induced platelet aggregation *ex vivo*; its effective dose is lower than that of ASA.

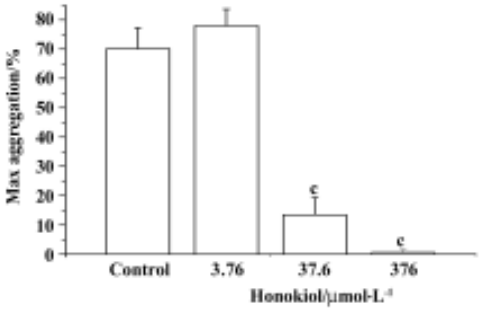

Figure 1. Inhibitory effects of honokiol on collagen-induced platelet aggregation *in vitro*. Platelet aggregation of rabbits was induced by collagen as described by Born. n=4 from 4 rabbits. Mean±SD. $^cP<0.01$ *vs* control.

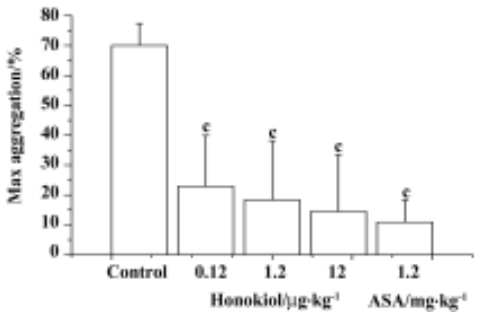

Figure 2. Inhibitory effects of honokiol on collagen-induced rabbit platelet aggregation *ex vivo*. PRP and PPP were prepared from blood samples of rabbits at 15 min after the intravenous administration and platelet aggregation was induced by collagen as described by Born. n=6 samples from 6 rabbits. Mean±SD. $^cP<0.01$ *vs* control.

Effect of honokiol on electrical current-stimulated carotid thrombosis in rats The effects of honokiol on the carotid thrombus model in rats were measured at 10 min after bolus intravenous injection. The OT for the control group was 534 s±66 s, and for the 0.5 μg/kg, 5 μg/kg and 50 μg/kg of honokiol groups the OT were 654 s±204 s, 684 s±186 s and 954 s±282 s, respectively, while the OT for the 5 mg/kg ASA group was 804 s±318 s (Figure 3). It indicated that honokiol dose-dependently inhibited thrombosis induced by endothelium injury *in vivo*. ASA at 5 mg/kg also significantly inhibited thrombosis.

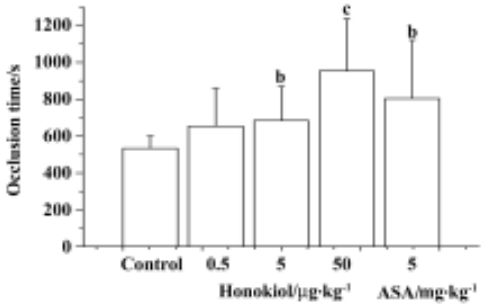

Figure 3. Effects of honokiol on carotid thrombosis. Endothelial injured-thrombus formation in SD rats was stimulated by electric current at 10 min after treatment with control vehicle, honokiol or ASA intravenously. n=10 samples from 10 rats. Mean±SD. $^bP<0.05$, $^cP<0.01$ *vs* control.

Effect of honokiol on viability of normal cultured rat aortic endothelial cells Honokiol 0.376–3.76 μmol/L significantly increased cell viability. However, honokiol 37.6 μmol/L and VE 100 mg/L did not influence cell viability. This

suggested that low concentrations of honokiol could stimulate normal endothelial cell proliferation (Figure 4).

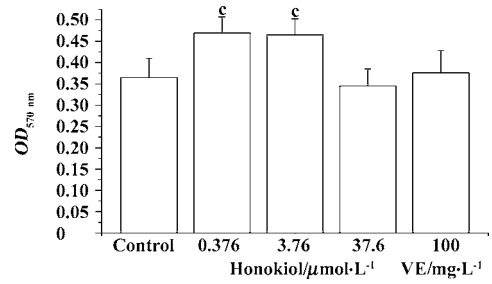

Figure 4. Effect of honokiol on normal rat aortic endothelial cells. The viability of cells was measured using MTT reduction assay. n=4 tests. Mean±SD. ^cP<0.01 *vs* normal control cells.

Protective effect of honokiol against cultured rat aortic endothelial cell injury induced by ox-LDL The ox-LDL-injured cells showed an obvious decrease in *OD* values compared with control-treated uninjured cells. Treatment of injured cells with honokiol 0.376–3.76 μmol/L significantly enhanced *OD* values in a concentration-dependent manner. Honokiol 37.6 μmol/L also increased *OD* value but no further increase was obtained compared with honokiol 3.76 μmol/L. It indicated that honokiol could protect endothelial cells against ox-LDL injury and increase cell viability. VE 100 mg/L also significantly increased cell viability (Figure 5).

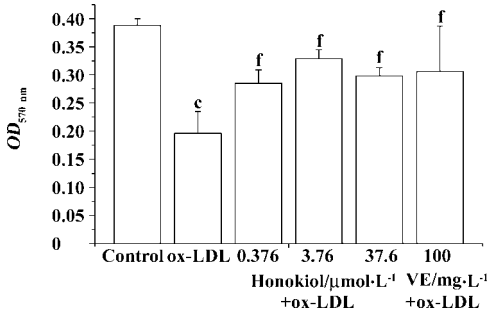

Figure 5. Effect of honokiol on ox-LDL-induced rat aortic endothelial cell injury. The viability of cells was measured using MTT assay. n=4 tests. Mean±SD. ^cP<0.01 *vs* control cells. ^fP<0.01 *vs* ox-LDL injured cells.

Influence of honokiol on 6-keto-PGF$_{1\alpha}$ concentration in serum-free medium of rat aortic endothelial cells ox-LDL injury significantly decreased the PGI_2 level in serum-free medium. Honokiol 0.376–36.7 μmol/L concentration-dependently increased 6-keto-PGF$_{1\alpha}$ concentration in medium of injured rat aortic endothelial cells, which was significantly higher than that of injured cells and normal cells. VE 100 mg/L showed a similar result (Figure 6). These results demonstrated that both honokiol and VE were potent PGI_2-release enhancers.

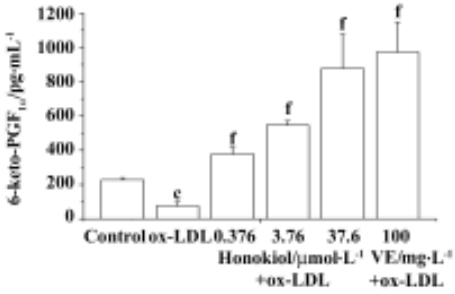

Figure 6. Effect of honokiol on the level of 6-keto-PGF$_{1\alpha}$ in cultured fluid of rat aortic endothelial cells. 6-keto-PGF$_{1\alpha}$ was determined with immunoassay kits. n=4 tests. Mean±SD. ^cP<0.01 *vs* control. ^fP<0.01 *vs* ox-LDL.

Effect of honokiol on nitric oxide concentration in serum-free medium of rat aortic endothelial cells Honokiol 0.0376–0.376 μmol/L significantly increased NO levels in serum-free medium of rat aortic endothelial cells. However honokiol 3.76 μmol/L did not increase NO level but slightly decreased its level. This result showed that appropriate concentrations of honokiol could promote NO release from rat aortic endothelial cells (Figure 7).

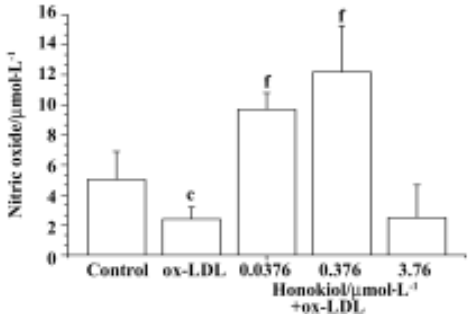

Figure 7. Effect of honokiol on the level of NO in cultured fluid of ox-LDL-injured rat aortic endothelial cells. NO was measured using a kinetic cadmium-reduction method with NO/nitrate assay commercial kits. n=4 tests. Mean±SD. ^cP<0.01 *vs* control. ^fP<0.01 *vs* ox-LDL.

Discussion

Other authors have demonstrated that honokiol inhibits platelet aggregation in rabbits[5]. It has protective effects against myocardial ischemia[6,7] and cerebral infarction[8]. We

have also found that honokiol can prevent cerebral injury caused by middle cerebral artery occlusion and cerebral ischemia reperfusion injury[16]. This study demonstrated that honokiol significantly inhibited arterial thrombosis induced by endothelium injury in rats, and the results on platelet aggregation *in vivo* and *in vitro* were basically consistent with those described previously[5]. We observed that the effective dose of honokiol was much lower than ASA, suggesting that honokiol is a potent platelet aggregation and thrombosis inhibitor. A previous study indicated that the anti-platelet aggregation activity of honokiol was due to its inhibitory effect on TXA_2 formation and intracellular calcium mobilization[5]. In our preliminary study, honokiol significantly inhibited endothelium-injured thrombosis in rats, and its concentration for inhibiting platelet aggregation *in vitro* was 10 times higher than that for anti-thrombosis. We hypothesize that there is another mechanism mediating its anti-thrombotic effects.

Endothelial cell structure and functional integrity are important in the maintenance of blood vessel walls and circulatory function. They produce and release a variety of vasoactive substances, such as PGI_2 and NO[17]. PGI_2 is a potent endogenous platelet aggregation inhibitor and produces vasodilatation of all vascular beds studied[18,19]. We found that honokiol protected cultured RAEC from ox-LDL injury, and it potently increased PGI_2 concentration in cell media in a concentration-dependant manner. The PGI_2 level in cell media treated with honokiol and VE were much higher than that in normal cells, suggesting that both honokiol and VE not only protect cells from injury but also stimulate PGI_2 release from normal RACE. This increase in PGI_2 release may play a crucial role in the anti-thrombotic effect of honokiol. Simultaneously, we have observed that lower concentrations of honokiol 0.376–3.76 μmol/L stimulate normal RACE proliferation, and this effect may be important for maintaining vascular normal state and integrity as well as the concrescence of injured vessels. However, this effect of honokiol needs to be studied further.

At honokiol 37.6 μmol/L, the cell viability is not maximum but PGI_2 level is highest. The reason for this phenomenon is not clear but it is indeed a fact that we confirmed with three separate experiments. We observed that cell shape had a little change at this concentration. Maybe honokiol at this concentration slightly inhibits cell growth or damages cell function. Under this condition the increase of PGI_2 may be a response of cell to injurious stimulation[20]. This fact suggested that ideal effective concentration of honokiol should be less than 37.6 μmol/L.

According to Teng *et al*, honokiol inhibited TXA_2 formation in platelets[5]. This may be due to inhibition of enzymes involved in TXA_2 synthesis, including cyclooxygenase (COX) and TXA_2 synthase in platelets. But our findings suggested that honokiol stimulated PGI_2 release from endothelial cells. A possible explanation for this is that honokiol inhibits TXA_2 synthase in platelets but activates PGI_2 synthase in endothelial cells. However, definitive evidence needs to be provided.

The continuous release of NO from the endothelium has an important role in blood flow modulation. NO may also modulate interactions between inflammatory cells and the endothelium. It reduces platelet, monocyte, macrophages, and neutrophils adhesion to endothelial cells and inhibits platelet aggregation[21–25]. This study showed that honokiol 0.0376–0.376 μmol/L stimulated NO release, but honokiol 3.76 μmol/L did not and caused a slight decrease in NO level. The effective concentration range of honokiol in stimulating NO release is 10 times lower than that in increasing cell viability. Thereby NO release may not play an important role in the anti-thrombotic effect of honokiol. Accordingly, protection of endothelial cells and stimulation of PGI_2 release from endothelial cells may be the main mechanism by which honokiol inhibited thrombosis, apart from its inhibitory effect on platelet arachidonic acid pathway as described by Teng *et al*[5]. However, honokiol and VE showed similar effects in cell protection and PGI_2 release under present condition. Whether these effects are the results of their anti-oxidative properties or they themselves have a stimulatory effect on PGI_2 release is not clear yet. In addition, the results of this study cannot explain whether honokiol stimulates PGI_2 generation in endothelial cells. The limitation of this study is that it did not supply direct evidence of the importance of PGI_2 on anti-thrombosis caused by honokiol.

In conclusion, this study showed that honokiol is a potent arterial thrombosis inhibitor. Protection of endothelial cells and stimulation of PGI_2 release may be the main mechanism. NO release from endothelial cells may play some roles but is not a key factor. The detailed mechanism by which honokiol stimulates PGI_2 release and promotes endothelial cell proliferation requires further study.

References

1 Fitzgerald DJ, Roy L, Catella F, Fitzgerald GA. Platelet activation in unstable coronary disease. New Engl J Med 1986; 315: 983–9.

2 Fuster V, Chesebro JH. Mechanisms of unstable angina. New Engl J Med 1986; 315: 1023–5.

3 Willerson JT, Hillis LD, Winniford M, Buja LM. Speculation regarding mechanisms responsible for acute ischemic heart dis-

ease syndromes. J Am Coll Cardiol 1986; 8: 245–51.
4 Pachham MA. Role of platelets in thrombosis and homeostasis. Can J Physiol Pharmacol 1994; 72: 278–84.
5 Teng CM, Chen CC, Ko FN, Lee LG, Huang TF, Chen YP, *et al*. Two anti-platelet agents from *Magnolia officinalis*. Thromb Res 1988; 50: 757–65.
6 Tsai SK, Huang SS, Hong CY. Myocardial protective effect of honokiol: an active component in *Magolia officinalis*. Planta Med 1996; 62: 503–06.
7 Tsai SK, Huang CH, Huang SS, Hung LM, Hong CY. Antiarrhythmic effect of magnolol and honokiol during acute phase of coronary occlusion in anesthetized rats: influence of *L*-NAME and aspirin. Pharmacology 1999; 59: 227–33.
8 Liou KT, Shen YC, Chen CF, Tsao CM, Tsai SK. Honokiol protects rat brain from focal cerebral ischemia–reperfusion injury by inhibiting neutrophil infiltration and reactive oxygen species production. Brain Res 2003; 992: 159–66.
9 Born GVR. Aggregation of blood platelet by adenosine diphosphate and its reversal. Nature 1962; 194: 927–9.
10 Hladovec J. Experimental arterial thrombosis in rats with continuous registration. Thromb Diath Haemorrh 1974; 26: 407–10.
11 Centra M, Ratych RE, Cao GL, Li J, Williams E, Taylor RM, *et al*. Culture of bovine pulmonary artery endothelial cells on Gelfoam blocks. FASEB J 1992; 6: 3117–21.
12 Jaffe EA, Hoyer LW, Nachman RL. Synthesis of antihemophilic factor antigen by cultured human endothelial cells. J Clin Invest 1973; 52: 2757–64.
13 Yan JC, Liu NF, Chen RX. Effects of oxidized low density lipoprotein and vitamin E on nitric oxide production and nitric oxide synthase activity in cultured human umbilical vein endothelial cells. Chin J Arterioscler 1999; 7: 145–8.
14 Bradford M. A rapid and sensitive method for the quantitation of microgram quantities of protein utilizing the principle of protein-dyebinding. Anal Biochem 1976; 72: 248–54.
15 Cortas NK, Wakid NW. Determination of inorganic nitrate in serum and urine by a kinetic cadmium-reduction method. Clin Chem 1990; 36: 1440–4.
16 Chen SZ, Wang H, Wang YY, Hu YH, inventors; Beijing Kelong Huanyu Patent Office, assignee. Application of honokiol, magnolol and their preparation in cardiovascular and cerebral vascular diseases. Chinese patent: 200310121303.0. 2005 Jun 15.
17 Sumpio BE, Riley JT, Dardik A. Molecules in focus, cells in focus: endothelial cell. Int J Biochem Cell Biol 2002; 34: 1508–12.
18 Weksler BB, Marcus AJ, Jaffe EA. Synthesis of prostaglandin I_2 (prostacyclin) by cultured human and bovine endothelial cells. Proc Natl Acad Sci USA 1977; 74: 3922–7.
19 Moncada S, Vane JR. Pharmacology and endogenous roles of prostaglandin endoperoxides thromboxane A_2 and prostacyclin. Pharmacol Rev 1978; 30: 293–31.
20 Miceli F, Tringali G, Tropea A, Minici F, Orlando MT, Lanzonec A, *et al*. The effects of nitric oxide on prostanoid production and release by human umbilical vein endothelial cells. Life Sci 2003; 73: 2533–42.
21 Bath PM, Hassall DG, Gladwin AM, Palmer RM, Martin JF. Nitric oxide and prostacyclin. Divergence of inhibitory effects on monocyte chemotaxis and adhesion to endothelium *in vitro*. Arterioscler Thromb 1991; 11: 254–60.
22 Kubes P, Suzuki M, Granger DN. Nitric oxide: an endogenous modulator of leukocyte adhesion. Proc Natl Acad Sci USA 1991; 88: 4651–5.
23 Radomski MW, Vallance P, Whitley G, Foxwell N, Moncada S. Platelet adhesion to human vascular endothelium is modulated by constitutive and cytokine induced nitric oxide. Cardiovasc Res 1993; 27: 1380–2.
24 De Caterina R, Libby P, Peng HB, Thannickal VJ, Raja-vashisth TB, Gimbrone MA, *et al*. Nitric oxide decreases cytokine-induced endothelial activation. Nitric oxide selectively reduces endothelial expression of adhesion molecules and proinflammatory cytokines. J Clin Invest 1995; 96: 60–8.
25 Cartwright JE, Johnstone AP, Whitley GJ. Inhibition of nitric oxide synthase by antisense techniques: investigations of the roles of NO produced by murine macrophages. Br J Pharmacol 1997; 120: 146–52.

Acta Pharmacologica Sinica 2005 Sep; 26 (9): 1069–1075

Full-length article

Therapeutic neovascularization by autologous transplantation with expanded endothelial progenitor cells from peripheral blood into ischemic hind limbs[1]

Chun-ling FAN, Ping-jin GAO, Zai-qian CHE, Jian-jun LIU, Jian WEI, Ding-liang ZHU[2]

Shanghai Key Laboratory of Vascular Biology, Shanghai Institute of Hypertension, Ruijin Hospital, Shanghai Second Medical University and National Key Laboratory for Medical Genomics, Health Science Center, Shanghai Institute for Biological Sciences, Chinese Academy of Sciences, Shanghai 200025, China

Key words

vascular endothelium; hindlimb; ischemia; physiologic neovascularization; stem cell transplantation

[1] Project supported by grants from the National Key Program of Basic Research (No G2000056904), from the Shanghai Science and Technology Committee (No 1DJ14005), and from the Shanghai Higher Education Bureau (No 02BQ22).
[2] Correspondence to Prof Ding-liang ZHU.
Phn 86-21-6437-0045, ext 610901.
Fax 86-21-5465-4498.
E-mail zhudingliang@sibs.ac.cn

Received 2005-01-27
Accepted 2005-04-27

doi: 10.1111/j.1745-7254.2005.00168.x

Abstract

Aim: To investigate the hypothesis that transplantation with expanded autologous endothelial progenitor cells (EPC) could enhance neovascularization. **Methods:** Peripheral blood mononuclear cells (PB-MNC) isolated from New Zealand White rabbits were cultured *in vitro*. At d 7, the adherent cells were collected for autologous transplantation. Rabbits with severe unilateral hind limb ischemia were randomly assigned to receive phosphate-buffered saline or expanded EPC in phosphate-buffered saline, administered by intramuscular injection in 6 sites of the ischemic thigh at postoperative d 7. Neovascularization was monitored by using the calf blood pressure ratio to indicate tissue perfusion, digital subtraction angiography to identify collateral vessel development and histological analysis of capillary density in the ischemic limb at d 35 after surgery. **Results:** Autologous EPC transplantation produced significant amelioration in ischemic hind limbs, as indicated by a greater calf blood pressure ratio (0.52±0.04 *vs* 0.42±0.05, $P<0.01$), angiographic score (1.44±0.06 *vs* 0.98±0.08, $P<0.01$) and capillary density in muscle (195.2±5.4/mm^2 *vs* 169.4±6.4/mm^2, $P<0.05$), than controls. **Conclusion:** Transplantation of autologous expanded EPC can promote neovascularization in ischemic hindlimbs.

Introduction

The maintenance of constant tissue perfusion is necessary for physiological organ function. Under certain pathological conditions, however, vascular supply can be reduced to such an extent that tissue necrosis results. Various angiogenic approaches have already been widely explored to revascularize ischemic tissue in animal models of ischemia and in clinical trials[1–5]. Most interventions involve the delivery of angiogenic growth factors such as vascular endothelial growth factor, basic fibroblast growth factor genes encoding these proteins to the ischemic tissue to stimulate the growth of new vessels. In recent years, ample evidence has established that bone marrow-derived endothelial progenitor cells (EPC) are present in the systemic circulation, are augmented in response to certain cytokines and/or tissue ischemia, and home to as well as incorporate into sites of neovascularization (which is defined as postnatal vasculogenesis)[6–9]. Experimental studies have shown that bone marrow-derived or blood-derived EPC may contribute to the regeneration of ischemic tissues and enhance the neovascularization of ischemic hind limbs or myocardium[10–14]. Therapeutic vasculogenesis in which EPC are actively involved is a new strategy for ischemic disease. Allogenetic or heterogenetic transplantation of EPC into ischemic animals has produced promising results, and thus brought attention to the possibility of using such treatments clinically.

To use EPC safely in a clinical setting for ischemic disease, autologous EPC are the first choice. Circulating EPC are at a very low level in adults, and the number is insufficient for

transplantation unless they are enriched in some way[15,16]. The use of expanded EPC is one solution to the problem. Therefore, we investigated the feasibility of using intramuscular injections of autologous expanded endothelial progenitor cells to treat rabbits with hind limb ischemia.

Materials and methods

Hind limb ischemia model Twelve male New Zealand white rabbits (weighing 2.8–3.2 kg) were used for this study. The initial surgery to induce hind limb ischemia has been described by others[17]. Briefly, the rabbits were first anesthetized with sodium pentobarbital (30 mg/kg, iv), then under sterile surgical conditions, a longitudinal incision was made on the medial thigh of one hind limb, extending from the inguinal ligament to a point just proximal to the patella. After the skin incision, the entire femoral artery and all its major branches including the inferior epigastria, deep femoral, lateral circumflex and superficial epigastria arteries were dissected free. The external iliac artery and all of the arteries listed were ligated. Finally, the femoral artery was excised from its proximal origin as a branch of the external iliac artery, to the point distally where it bifurcates into the saphenous and popliteal arteries. As a consequence, blood flow to the ischemic limb became completely dependent upon collateral vessels issuing from the internal iliac artery. The incision was closed in three layers with 3.0 silk. All rabbits were closely monitored by veterinary staff and received an antibiotic (20 mg/kg gentamycin sulfate, im) for 3 d. The experimental protocols were approved by the Institutional Animal Care and Use Committee of Shanghai Second Medical University, Shanghai.

Mononuclear cell isolation and culture Samples of peripheral blood (12–15 mL) from the central auricular artery of rabbits were harvested 1 h before surgery and anticoagulated with heparin. The isolation and culture of mononuclear cells has been described previously[18]. In brief, peripheral blood mononuclear cells (PB-MNC) were isolated by density-gradient centrifugation and resuspended in Iscove's Modified Dulbecco's Medium (IMDM, Gibco Invitrogen, Shanghai, China) supplemented with 20% fetal calf serum (FCS; CCT, Cansera Internationa, Ontario, Canada). The cells were then seeded into 48-well plates (Sumilon, Sumitomo Bakelite, Osaka City, Japan) at a density of 1×10^6 cells per well and cultured at 37 °C and 5% CO_2. The medium was replaced completely at d 3 or d 4.

To confirm EPC phenotype, the adherent cells were incubated with 1,1'-dioctadecyl-3,3,3',3'-tetramethyl-indocarbocyanine perchlorate-labeled acetylated low density lipoprotein (LDL) (DiI-Ac-LDL, 10 mg/mL; Biomedical Technologies, Stoughton, USA) at 37 °C for 2 h at d 7 in culture. Then the cells were fixed with 2% paraformaldehyde for 10 min and incubated with fluorescein isothiocyanate-labeled *Ulex europeus* agglutinin (UEA-1 lectin, 10 mg/mL; Sigma, St Louis, USA) for 1 h. The lectin binding is a marker of endothelial cell (EC) lineage and the incorporation of acLDL is a characteristic function of EC[13]. Nearly all adherent cells (>97%) were DiI-acLDL(+) UEA 1-lectin(+) as analyzed by a fluorescence-activated cell sorter (FACS).

Experimental groups and EPC transplantation After femoral artery excision, the rabbits were randomly assigned to one of 2 groups: (a) control group (n=6, receiving vehicle PBS); (b) EPC group (receiving expanded EPC, n=6).

At d 7, EPC in culture were trypsinized and collected for transplantation. EPC in 0.6 mL of phosphate-buffered saline (PBS) were injected im into 6 different sites of the ischemic thigh skeletal muscles (100 mL to each site) with a 22-gauge needle. The control group received 0.6 mL PBS. Overall, a mean of $2.11\times10^6\pm0.51\times10^6$ EPC were injected per rabbit.

To elucidate *in vivo* differentiation to endothelial lineage, 2×10^6 EPC from autologous PB-MNC were labeled with fluorescent carbocyanine 1,1'-dioctadecyl-3,3,3',3'-tetramethyl-indocarbocyanine perchlorate (DiI, Molecular Probes (Eugene, Oregon, USA) and were injected via a 22-gauge needle to the ischemic thigh muscles 7 d after surgery. Four weeks after cell transplantation, 5 mg of UEA-1 lectin (Sigma) was infused intravenously before the rabbits were killed by an overdose of pentobarbital. Ischemic hind limb thigh muscles were embedded in OCT compound and snap-frozen for fluorescence microscopy to examine the incorporation of transplanted cells into foci of neovascularization.

Calf blood pressure ratio Calf blood pressure was measured at the posterior tibial artery before surgery and at 7, 14, 21, 28, and 35 d in both hind limbs using a Doppler Flowmeter (Model ALF 2100, Advance Advance Co, Tokyo, Japan) and a cuff (PC 2.5 cm×12 cm, Hokanson, Bellevue, USA) connected to a pressure manometer as described by others[2]. The calf blood pressure ratio (BPR) was defined for each rabbit as the ratio of systolic pressure of the ischemic hind limb to that of the normal hind limb.

Intra-iliac arterial angiography The collateral arteries in the medial thigh region of the ischemic limb originate from the internal iliac artery[19,20]. Digital subtraction angiography (DSA; Model Advantx-LC-DLX, General Electronic) of the hind limb was performed on postoperative d 35 to obtain an anatomical measurement of the growth and development of the larger conduit vessels in the medial portion of the upper limb. Each animal was anesthetized, and the right

common carotid artery was exposed. A 4-F polyethylene catheter (Cordis, Corporation, Miami Lakes, USA) was introduced into the right common carotid artery through a small cutdown and the tip of the catheter was positioned just proximal to the point where it bifurcates into the right and left common iliac arteries under fluoroscopic guidance. Immediately following an intra-arterial bolus injection of the vasodilator sodium nitroprusside (300 μg in 1 mL saline), iodinated contrast media (Huaihai Pharmaceutical Company, Shanghai, China) was infused intra-arterially at a rate of 1 mL/s for 5 s using an automated angiographic injector (LF, Liebel-Flarsheim Co, Cincinnati, OH, USA). Perfusion of the hind limb was observed on a monitor in real time and a series of angiographic images were taken after the start of contrast media infusion.

The angiograms at 4 s were quantified by image analysis using Qwin software (Leica, Bensheim, Germany). In brief, the area occupied by all small visible arteries in the medial thigh, including the branches of the femoral artery and collateral vessels from the intra-iliac artery (excluding the intra- and extra-iliac, femoral, saphenous and popliteal arteries) was calculated. The angiographic score was calculated by a single observer who was blinded to the treatment regimen, and the score was defined for each rabbit as the ratio of the area occupied by vessels of the ischemic thigh to that of the normal thigh.

Histological determination of capillary density Immediately after angiography, the rabbits were killed, then the hind limbs were dissected, and samples of the adductor muscle and the semimembranous muscle were removed for histological evaluation. The tissues were placed in plastic cassettes and covered with OCT compound (Tissue-Tek, Sakura Finetechnical Co, Tokyo, Japan) before being snap frozen in liquid nitrogen. Multiple frozen sections were cut (10 mm thickness) on a cryostat (CM 3050, Leica) and placed on glass slides. Tissue sections were stained for alkaline phosphatase using the indoxyl-tetrazolium method[21] to detect capillary endothelial cells, and were counterstained with eosin. The number of capillaries was counted under a 20×objective lens using an image analysis system (Qwin, Leica) by a single observer blinded to the treatment regimen. Capillaries in 15 randomly selected fields were analyzed. Capillary density was calculated as the number of capillaries per mm^2 of muscle.

Clinical assessment All rabbits were clinically evaluated for the incidence of distal limb ulcers and necrosis by macroscopic examination during the study; this was considered significant if a skin ulcer or necrosis was observed at the leg, foot or ankle.

Statistical analysis All data are reported as mean±SEM. Differences between control and EPC groups were analyzed by using the paired Student's *t*-test. A value of $P<0.05$ was considered statistically significant.

Results

Characterization of EPC expanded *ex vivo* Freshly isolated PB-MNC were round and small, but became larger with more cytoplasm on the second day. Large round adherent cells appeared from d 2–d 3, then they assumed a spindle-shaped, endothelial cell-like morphology. Significant proliferation was observed from d 3, and the adherent cells were almost convergent at d 6–d 7. The morphology of the adherent cells is shown in Figure 1A,1B; >97% of the adherent cells had taken up acetylated LDL (red fluorescence) and had bound the lectin (green fluorescence) (Figure 1C, 1D). The percentage of EPC in freshly isolated PB-MNC was much less than that in the adherent cells in culture (data not shown).

The incubation of PB-MNC *in vitro* resulted in a 100- to 200-fold increase in differentiating EPC which were DiI-acLDL (+) UEA 1-lectin (+). This calculation is based on our findings that freshly isolated PB-MNC had much fewer (about 0.06%) EPC (data not shown). We were able to obtain $1.07\times10^5\pm0.33\times10^5$ EPC/1×10^6 MNC after 7 d of the *ex vivo* culture, thus yielding a 100- to 200-fold increase in EPC number.

Effect of transplanted autologous EPC on neovascularization

Calf blood pressure ratio The systolic blood pressure of the ischemic hind limb showed a tendency to increase after surgery in both the EPC and control groups. EPC transplantation promoted the recovery of blood perfusion to the ischemic hind limb, as by the greater ischemic/normal calf blood pressure ratio than that observed in the control group. The ischemic/normal calf blood pressure ratio measured at d 28 and d 35 was 0.47±0.02 and 0.52±0.02, respectively, for the EPC group, which are significantly higher than those of the control animals (0.38±0.01 and 0.42±0.03; Figure 2). Thus, EPC transplantation significantly increased the ischemic/normal calf blood pressure ratio, suggesting augmented perfusion in the EPC-treated group compared to control rabbits.

Angiographic analysis Collateral vessel development in the medial thigh was assessed by digital subtraction angiography as described earlier. There were more collateral vessels in the EPC group compared with the control. The angiographic score at d 35 in the EPC group was significantly higher than that of the control group (control=0.98±0.08; EPC=1.44±0.06; $P<0.01$; Figure 3).

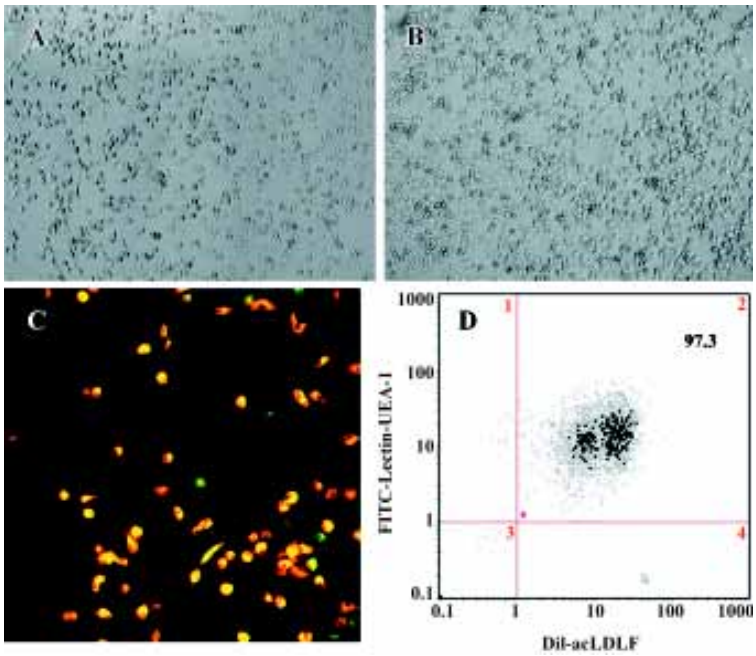

Figure 1. Characteristics of peripheral blood EPC in culture at (A) d 4 and (B) d7 (×10). Cultivated EPC were incubated with DiI-acLDL (red fluorescence) and stained with lectin (green fluorescence), viewed by (C) confocal microscopy and (D) analyzed by FACS.

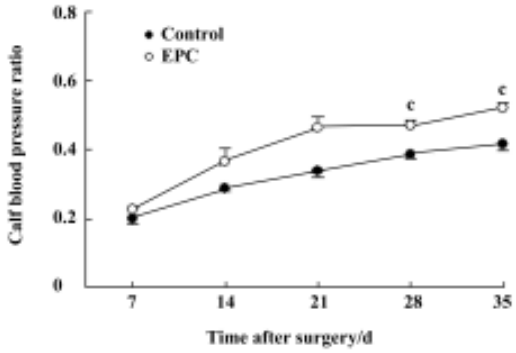

Figure 2. Time-course of the calf blood pressure ratio in the hind limbs of rabbits treated with transplanted EPC. Results are presented for animals receiving PBS (control) or transplanted EPC at d 7, 14, 21, 28, and 35 post-surgery. n=6. Mean±SEM. $^cP<0.01$ *vs* control.

Histological evaluation of capillary density Histological staining of alkaline phosphatase was performed to identify capillaries in ischemic muscles on d 35 after surgery. Tissue sections retrieved from the medial thigh muscles of the ischemic hind limbs showed a marked increase in capillary number in EPC-treated animals. Capillary density in the EPC group was significantly greater than that in the controls (control=169.4±6.4/mm^2; EPC=195.2±5.4/mm^2; $P<0.05$; Figure 4).

Transplanted autologous EPC incorporate into foci of neovascularization Four weeks after autologous EPC transplantation, tissue sections from the ischemic thigh muscles were examined under fluorescence. Transplanted autologous EPC marked with DiI fluorescenced red, whereas

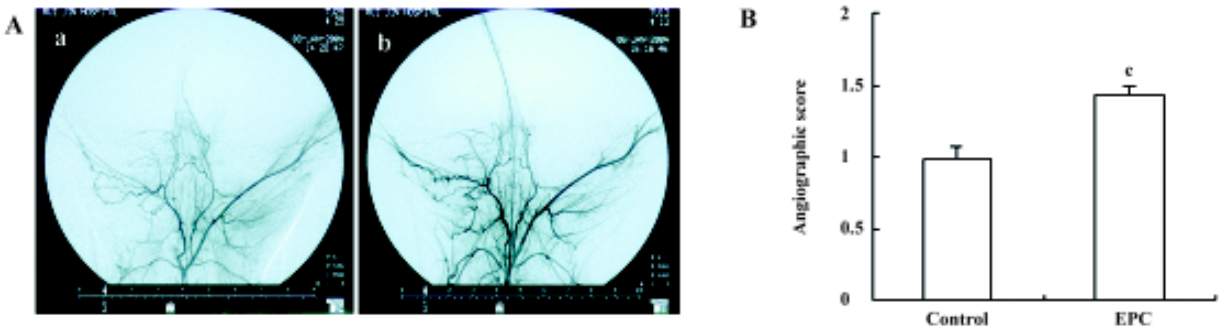

Figure 3. Effect of transplanted endothelial progenitor cells (EPC) on collateral vessel development in ischemic hind limbs of rabbits at d 35 post-surgery. (A) Representative angiograms of ischemic hind limbs. (a) Control rabbits receiving PBS; (b) Rabbits receiving EPC transplantation. (B) Effect of EPC transplantation on angiographic score compared with control (angiographic score is defined in the text). n=3. Mean±SEM. $^cP<0.01$ *vs* control.

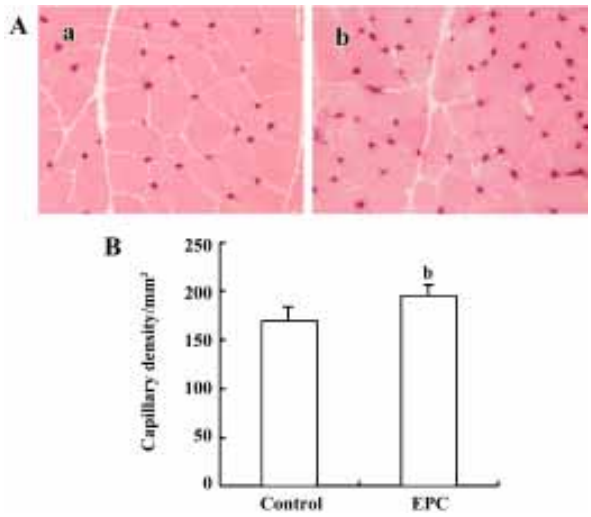

Figure 4. Histological evaluation of capillary density in ischemic hind-limb muscle on d 35 post-surgery. (A) Representative images of alkaline phosphatase-stained capillaries (×20). (a) Control rabbits receiving PBS; (b) Rabbits receiving transplanted EPC. (B) Quantitative analysis of capillary density. n=6. Mean±SEM. $^bP<0.05$ *vs* control.

the rabbit vasculature, stained by a premortem administration of UEA-1 lectin, were identified by green fluorescence in the same tissue section. DiI-labeled EPC were distributed principally in the ischemic area of the hind limb neovascularization and incorporated into tubular structures and capillaries, which is consistent with neovasculature (Figure 5). Thus, locally transplanted EPC were incorporated into the foci of neovascularization and differentiated into mature endothelial cells in the ischemic hind limbs.

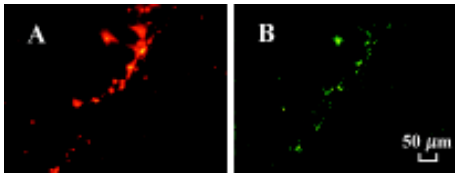

Figure 5. Histological identification of epithelial progenitor cells (EPC) incorporation *in vivo*. Tissue sections were retrieved from ischemic muscles. (A) Red fluorescence marks autologously transplanted DiI-labeled EPC. (B) Green fluorescence indicates UEA-1 lectin binding identifying endothelial cells (×10).

Clinical assessment All animals were conscious within 1 h of the surgery, and they developed a limp in their hind limbs. Two animals from the control group developed skin ulcers at the knees of the ischemic limb. Animals from the EPC group did not have any skin ulcers or necrosis.

Discussion

The present study describes for the first time autologous transplantation with expanded EPC from peripheral blood in hind limb ischemia. We found that the transplantation of EPC was associated with a significant increase in the calf blood pressure ratio, collateral vessel development, and muscle capillary density, suggesting a beneficial effect on neovascularization.

Postnatal EPC have been implicated in the neovascularization associated with postnatal vasculogenesis. In animal experiments, allogenetic or heterogenetic transplantation of blood-derived cells containing EPC into ischemic animals have been shown to regenerate infarcted myocardium and coronary capillaries, thus limiting functional impairment after myocardial ischemia. Enhanced neovascularization by EPC was also observed in animals with hind limb ischemia.

After favorable results were found in studies of allogenetic and heterogenetic transplantations of EPC, studies were carried out to investigate the efficiency of autologous transplantation of EPC in animals and humans[15,16,22–28] to overcome the limitations of immunorejection, but these studies did not answer the crucial questions such as cell populations for transplantation, delivery method, and therapy time for cell transplantation, which are important for efficient transplantation.

In the present study, we used expanded EPC for transplantation based on the following considerations. First, the number of EPC after expansion greatly exceeds the number of EPC in freshly isolated cells, which need mononuclear cell apheresis to enrich the EPC-containing cell population. Second, expanded EPC are pure and uncontaminated, and are exempt from the potential inflammatory response induced by other cells from a hematopoietic lineage. In the present study, EPC expanded 100- to 200-fold in number after 7 d of culture *in vitro*. Kalka *et al* reported a 80- to 90-fold expansion of EPC when cultured in a fibronectin-coated dish in a commercial medium (EBM-2) supplemented with a cocktail of growth factors including VEGF, bFGF, insulin-like growth factor (IGF), and epidermal growth factor (EGF) [13]. Our study used a simple medium supplemented with FCS, but which did not compromise the expansion potential. The culture conditions used in the present study are much more economical and accessible than those used by Kalka *et al*. Our findings regarding autologous expanded EPC transplantation are consistent with those of Shintani *et al*, in which autologous expanded EPC from bone marrow promoted neovascularization in hind limb ischemia[22]. However, expanding EPC from peripheral blood is clearly less invasive than aspirating bone marrow. The culture-expanded EPC

may consist of EPC at different stages of differentiation depending on the culture conditions or duration. Recently, Hur *et al* sequentially cultured total mononuclear cells from a source of adult peripheral blood and found 2 types of EPC: early and late EPC. However, there was no difference in the contributions of the 2 types to neovascularization in ischemic limbs[29].

The incorporation rate of transplanted cells is greatly influenced by the delivery method. When infused intravenously, the number of infused cells incorporated in ischemic vasculature was much less than that being injected near the ischemic zone. To deliver the EPC efficiently, we directly injected the cells into the ischemic thigh muscle to ensure a maximum available concentration of EPC at the site of the ischemic hind limb. The optimal time for cell transplantation is also a primary concern; to mimic ischemic events in a clinical setting, and using the course of events after myocardial ischemia for reference, we set the time point for EPC injection at d 7 after ischemia.

A limitation of the present study is that no control cells were used to demonstrate the advantage of expanded EPC. In a heterogenetic transplantation study with human EPC, Murasawa and Aahara used either human microvascular EC (HMVEC) or medium as a control in a nude mouse model of hind limb ischemia. They found that the outcomes in the mice receiving control cells (HMVEC) and those receiving the medium were similar[30]. The appropriate control cells for the present study would have been mature vascular EC. However, preparation of vascular EC for autologous transplantation is not feasible, so we had to use saline for the control.

In conclusion, we found that neovascularization was enhanced by autologous expanded EPC from peripheral blood when injected intramuscularly at the site of ischemia at d 7 after hind limb ischemia in rabbits. Our data indicate that autologous expanded EPC from peripheral blood may be an important and novel therapeutic approach for ischemic disease via enhancing neovascularization.

Acknowledgements

The authors are very grateful to Prof Ke-min CHEN, Dr Jin-qing HU, and Dr Xian-wei ZENG from Ruijin Hospital, Shanghai, for their assistance in performing the angiography.

References

1 Risau W. Mechanisms of angiogenesis. Nature 1997; 386: 671–4.
2 Takeshita S, Zheng LP, Brogi E, Kearney M, Pu LQ, Bunting S, *et al*. Therapeutic angiogenesis. A single intraarterial bolus of vascular endothelial growth factor augments revascularization in a rabbit ischemic hind limb model. J Clin Invest 1994; 93: 662–70.
3 Harada K, Grossman W, Friedman M, Edelman ER, Prasad PV, Keighley CS, *et al*. Basic fibroblast growth factor improves myocardial function in chronically ischemic porcine hearts. J Clin Invest 1994; 94: 623–30.
4 Ylä-Herttuala S, Alitalo K. Gene transfer as a tool to induce therapeutic vascular growth. Nat Med 2003; 9: 694–701.
5 Baumgartner I, Pieczek A, Manor O, Blair R, Kearney M, Walsh K, *et al*. Constitutive expression of phVEGF165 after intramuscular gene transfer promotes collateral vessel development in patients with critical limb ischemia. Circulation 1998; 97: 1114–23.
6 Shi Q, Rafii S, Wu MH, Wijelath ES, Yu C, Ihida A, *et al*. Evidence for circulating bone marrow-derived endothelial cells. Blood 1998; 92: 362–7.
7 Aahara T, Masuda H, Takahashi T, Kalka C, Pastore C, Silver M, *et al*. Bone marrow origin of endothelial progenitor cells responsible for postnatal vasculogenesis in physiological and pathological neovascularization. Circ Res 1999; 85: 221–8.
8 Iner JM, Aahara T. Angiogenesis and vasculogenesis as therapeutic strategies for postnatal neovascularization. J Clin Invest 1999; 103: 1231–6.
9 Takahashi T, Kalka C, Masuda H, Chen D, Silver M, Kearney M, *et al*. Ischemia- and cytokine-induced mobilization of bone marrow-derived endothelial progenitor cells for neovascularization. Nat Med 1999; 5: 434–8.
10 Aahara T, Murohara T, Sullivan A, Silver M, van der Zee R, Li T, *et al*. Isolation of putative progenitor endothelial cells for angiogenesis. Science 1997; 275: 964–7.
11 Kocher AA, Schuster MD, Szabolcs MJ, Takuma S, Burkhoff D, Wang J, *et al*. Neovascularization of ischemic myocardium by human bone marrow-derived angioblasts prevents cardiomyocyte apoptosis, reduces remodeling and improves cardiac function. Nat Med 2001; 7: 430–6.
12 Kawamoto A, Gwon HC, Iwaguro H, Yamaguchi JI, Uchida S, Masuda H, *et al*. Therapeutic potential of *ex vivo* expanded endothelial progenitor cells for myocardial ischemia. Circulation 2001; 103: 634–7.
13 Kalka C, Masuda H, Takahashi T, Kalka-Moll WM, Silver M, Kearney M, *et al*. Transplantation of *ex vivo* expanded endothelial progenitor cells for therapeutic neovascularization. Proc Natl Acad Sci USA 2000; 97: 3422–7.
14 Kawamoto A, Tkebuchava T, Yamaguchi J, Nishimura H, Yoon YS, Milliken C, *et al*. Intramyocardial transplantation of autologous endothelial progenitor cells for therapeutic neovascularization of myocardial ischemia. Circulation 2003; 107: 461–8.
15 Tateishi-Yuyama E, Matsubara H, Murohara T, Ikeda U, Shintani S, Masaki H, *et al*. Therapeutic angiogenesis using cell transplantation (TACT) study investigators. Therapeutic angiogenesis for patients with limb ischemia by autologous transplantation of bone-marrow cells: a pilot study and a randomized controlled trial. Lancet 2002; 360: 427–35.
16 Asmus B, Schachinger V, Teupe C, Britten M, Lehmann R, Dobert N, *et al*. Transplantation of progenitor cells and regeneration enhancement in acute myocardial infarction (TOPCARE-AMI).

Circulation 2002; 106: 3009–17.
17 Pu LQ, Jackson S, Lachapelle KJ, Arekat Z, Graham AM, Lisbona R, *et al*. A persistent hindlimb ischemia model in the rabbit. J Invest Surg 1994; 7: 49–60.
18 Fan CL, Li Y, Gao PJ, Liu JJ, Zhang XJ, Zhu DL. Differentiation of endothelial progenitor cells from human umbilical cord blood CD 34^+ cells *in vitro*. Acta Pharmacol Sin 2003; 24: 212–8.
19 Ito WD, Arras M, Scholz D, Winkler B, Htun P, Schaper W. Angiogenesis but not collateral growth is associated with ischemia after femoral artery occlusion. Am J Physiol 1997; 273: H1255–65.
20 Takeshita S, Rossow ST, Kearney M, Zheng LP, Bauters C, Bunting S, *et al*. Time course of increased cellular proliferation in collateral arteries after administration of vascular endothelial growth factor in a rabbit model of lower limb vascular insufficiency. Am J Pathol 1995; 147: 1649–60.
21 Flanagan MF, Fujii AM, Colan SD, Flanagan RG, Lock JE. Myocardial angiogenesis and coronary perfusion in left ventricular pressure-overload hypertrophy in the young lamb. Circ Res 1991; 68: 1458–70.
22 Shintani S, Murohara T, Ikeda H, Ueno T, Sasaki K, Duan J, *et al*. Augmentation of postnatal neovascularization with autologous bone marrow transplantation. Circulation 2001; 103: 897–903.
23 Fuchs S, Baffour R, Zhou YF, Shou M, Pierre A, Tio FO, *et al*. Transendocardial delivery of autologous bone marrow enhances collateral perfusion and regional function in pigs with chronic experimental myocardial ischemia. J Am Coll Cardiol 2001; 37: 1726–32.
24 Strauer BE, Brehm M, Zeus T, Kostering M, Hernandez A, Sorg RV, *et al*. Repair of infarcted myocardium by autologous intracoronary mononuclear bone marrow cell transplantation in humans. Circulation 2002; 106: 1913–8.
25 Perin EC, Dohmann HF, Borojevic R, Silva SA, Sousa AL, Mesquita CT, *et al*. Transendocardial, autologous bone marrow cell transplantation for severe, chronic ischemic heart failure. Circulation 2003; 107: 2294–302.
26 Te HF, Kwong YL, Chan JK, Lo G, Ho CL, Lau CP. Angiogenesis in ischemic myocardium by intramyocardial autologous bone marrow mononuclear cell implantation. Lancet 2003; 361: 47–9.
27 Stamm C, Westphal B, Kleine HD, Petzsch M, Kittner C, Klinge H, *et al*. Autologous bone-marrow stem-cell transplantation for myocardial regeneration. Lancet 2003; 361: 45–6.
28 Kang HJ, Kim HS, Zhang SY, Park KW, Cho HJ, Koo BK, *et al*. Effects of intracoronary infusion of peripheral blood stem-cells mobilized with granulocyte-colony stimulating factor on left ventricular systolic function and restenosis after coronary stenting in myocardial infarction: the MAGIC cell randomized clinical trial. Lancet 2004; 363: 751–6.
29 Hur J, Yoon CH, Kim HS, Choi JH, Kang HJ, Hwang KK, *et al*. Characterization of two types of endothelial progenitor cells and their different contribution to neovasculogenesis. Arterioscler Thromb Vasc Biol 2004; 24: 288–93.
30 Murasawa S, Aahara T. Endothelial progenitor cells for vasculogenesis. Physiology 2005; 20: 36–42.

Acta Pharmacologica Sinica 2005 Sep; 26 (9): 1076–1080

Blackwell Publishing

Full-length article

Overexpression of heat-shock protein 20 in rat heart myogenic cells confers protection against simulated ischemia/reperfusion injury[1]

Yan-hui ZHU, Xian WANG[2]

Department of Physiology and Pathophysiology, Basic Medical College, Key Laboratory of Molecular Cardiovascular Biology, Ministry of Education, Peking University, Beijing 100083, China

Key words

reperfusion injury; adenovirus; apoptosis; necrosis; heat-shock proteins

[1] Project supported by the National Basic Research Program of China (No G2000056908) awarded to Xian WANG.
[2] Correspondence to Prof Xian WANG.
Phn/Fax 86-10-8280-1443.
E-mail xwang@bjmu.edu.cn

Received 2004-11-08
Accepted 2005-03-29

doi: 10.1111/j.1745-7254.2005.00137.x

Abstract

Aim: To explore whether overexpression of the small heat shock protein HSP20 in rat cardiomyocytes protects against simulated ischemia/reperfusion (SI/R) injury. **Methods:** Recombinant adenovirus expressing HSP20 was used to infect rat H9c2 cardiomyocytes at high efficiency, as assessed by green fluorescent protein. H9c2 cells were subjected to SI/R stress; survival was estimated through assessment of lactate dehydrogenase and cell apoptosis through caspase-3 activity. **Results:** Overexpression of HSP20 decreased lactate dehydrogenase release by 21.5% and caspase-3 activity by 58.8%. Pretreatment with the protein kinase C inhibitor Ro-31-8220 (0.1 μmol/L) for 30 min before SI/R canceled the protective effect of HSP20. The selective mitochondrial K^+_{ATP} channel inhibitor 5-hydroxydecanoate (100 μmol/L) had a similar effect. However, the non-selective K^+_{ATP} channel inhibitor glibenclamide (100 μmol/L) had no significant effect. **Conclusion:** These data indicate that the protective effect of HSP20 *in vitro* is primarily due to reduced necrotic and apoptotic death of cardiomyocytes, possibly via the protein kinase C/mitochondrial K^+ATP pathway.

Introduction

Heat shock proteins (HSP) are highly conserved molecules that fulfill a range of functions, including cytoprotection and the intracellular assembly, folding, and translocation of oligomeric proteins[1]. Expression of these proteins can be induced by a range of cellular insults, which include high temperature, oxidative stress, viral infection, and nutritional deprivation[2].

Previous studies have demonstrated that increased expression of various HSP, such as HSP70, HSP60, HSP10, and HSP90, protected against stress insult. Recently, the cytoprotective properties of small HSP have drawn increased attention. Small HSP, including HSP20, HSP25, HSP27, αB-crystallin, and myotonic dystrophy kinase binding protein, are a group of proteins expressed in muscle tissues and share sequence homology of approximately 80–100 amino acids at the C terminus, known as the α crystallin domain[3,4]. It was reported that overexpression of HSP27 by transfection into rodent and Chinese hamster cell lines directly correlated with survival from hyperthermia[5–7]. Overexpression of αB-crystallin has a similar effect[8–10]. It was also reported that overexpression of both HSP27 and αB-crystallin protected against ischemic injury in cardiac myocytes[11].

HSP20 is a newly discovered small HSP that was co-purified with αB-crystallin and HSP27 from skeletal muscle by affinity chromatography[12]. Previous reports demonstrated that HSP20 redistributed from the cytosol to insoluble fractions and dissociated from the aggregated form to the small form when rat diaphragm was exposed to heat stress *in vitro*[13]. Stable overexpression of HSP20 in Chinese hamster ovary cells results in enhanced survival after heat shock, which is similar to the results for αB-crystallin[14]. However, the effect of HSP20 on ischemia-mediated injury in cardiac myocytes has not been explored.

In our previous study, we showed that overexpression of HSP20 in rat heart *in vivo* protected against simulated ischemia/reperfusion (SI/R) injury, the mechanism of which related to the reduction of necrosis and apoptosis of ventricular cardiomyocytes (unpublished data). In the present

study, our aim was to determine whether increased expression of HSP20 exerted a protective effect against SI/R injury in cardiac myocytes. We demonstrated, for the first time, that overexpression of HSP20 protected against ischemic damage in rat H9c2 cardiomyocytes, the protective effect of HSP20 *in vitro* being due primarily to reduced necrotic and apoptotic cell death, possibly via the protein kinase C (PKC)/ mitochondrial K^+_{ATP} channel (mito K^+_{ATP}) pathway.

Materials and methods

Construction of recombinant adenovirus The recombinant adenovirus encoding HSP20 (Ad.HSP20) and adenovirus encoding GFP (Ad.GFP) were prepared as described previously[15]. Adenovirus was propagated in 293 cells and purified by 2 rounds of CsCl density ultracentrifugation (4 ºC, 13000×*g* for 105 min and 16 h, respectively). Viral stocks were desalted through a PD-10 desalting column (Amersham Biosciences UK, Buckinghamshire, UK) into a Tris-buffered solution (10 mmol/L Tris, pH 8.0, 2 mmol/L $MgCl_2$ and 4% sucrose)[16], plaque-titered, aliquoted, and stored at -80 ºC with 4% sucrose until use.

Cell culture and simulated ischemia/reperfusion H9c2 cells were purchased from ATCC, the Global Bioresource Center (No CRl-1446; Hong Kong, China) and were cultured in Dulbecco's modified Eagle's medium (DMEM) supplemented with 10% fetal bovine serum (FBS). Cells were infected with Ad.HSP20 or Ad.GFP at a multiplicity of infection of 50 in no-serum DMEM when the confluence was 60%. After 2 h, the medium was removed and supplemented with DMEM containing 1% FBS for 24 h. Infected cells and the efficiency of infection were monitored by GFP expression with the use of fluorescent microscopy. After 24 h of infection, cells underwent 8 h of simulated ischemia and 24 h of reperfusion. Simulated ischemia was achieved by placing cells in a hypotonic balanced salt solution consisting of 1.3 mmol/L $CaCl_2$, 5 mmol/L KCl, 0.3 mmol/L KH_2PO_4, 0.5 mmol/L $MgCl_2$, 0.4 mmol/L $MgSO_4$, 69 mmol/L NaCl, 4 mmol/L $NaHCO_3$, and 0.3 mmol/L Na_2HPO_4 without glucose or serum, and hypoxia was induced for 8 h at 37 ºC[17]. Hypoxia was attained with an airtight jar from which the oxygen was exhausted through the oxygen-consuming GasPak System from BBL Microbiology Systems (Cockeysville, MD)[17]. At the end of the experiment, the dishes were removed from the chamber with the medium, and cells were reperfused in no-serum DMEM for 24 h. The control H9c2 cells were cultured in DMEM supplemented with 10% FBS, and cells were cultured in no-serum DMEM when the confluence was 60%. After 2 h, the medium was removed and cells were supplemented with DMEM containing 1% FBS. After 24 h, the medium was removed and cells were supplemented with a balanced salt solution at 37 ºC for 8 h. The medium was then removed and the cells were cultured in no-serum DMEM for 24 h at 37 ºC. The supernatant and cells were assayed separately for both lactate dehydrogenase (LDH) or caspase-3 activity.

Evaluation of necrosis and apoptosis by flow cytometry After SI/R, cells were harvested, washed, and double-stained using an annexin V-fluorescein-isothiocyanate (FITC) apoptosis detection kit. This kit is based on the observation that soon after initiating apoptosis most cell types translocate the membrane phospholipid phosphatidylserine from the inner face of the plasma membrane to the cell surface. Annexin V has a strong affinity for phosphatidylserine and therefore serves as a probe for detecting apoptosis. Cells that have lost membrane integrity will show red staining (propidium iodide) throughout the nucleus and therefore will be easily distinguishable from apoptotic cells. Samples were incubated for 15 min in the dark with annexin V and propidium iodide, and flow cytometry was carried out using a FACScan (Becton Dickinson, Heidelberg, Germany). Annexin V-FITC and propidium iodide-related fluorescence were recorded using FL1-H (525 nm) and FL2-H (575 nm) filters, respectively.

Lactate dehydrogenase (LDH) release assay Lactate dehydrogenase activity released into the medium or remaining in the cells was determined with the use of an LDH assay kit (Roche Diagnostics, Basel, Switzerland). The LDH activity is determined in an enzymatic test. In the first step, NAD^+ is reduced to $NADH/H^+$ by the LDH-catalyzed conversion of lactate to pyruvate. In the second step the catalyst transfers H/H^+ from $NADH/H^+$ to the tetrazolium salt INT, which is reduced to formazan, and the absorbance of the samples is measured at 490 nm using an enzyme-linked immunosorbent assay reader. Necrosis of cardiomyocytes was evaluated by the percentage of LDH release, which was calculated by the LDH activity in the medium divided by the total enzyme activity (medium and remaining activity in the cells) after reperfusion for 24 h.

Measurement of caspase-3 activity Cardiomyocytes were examined for apoptosis after simulated reperfusion for 24 h. Caspase-3 activity was determined by use of the caspase-3 Colorimetric Assay (R&D Systems, Minneapolis, MN, USA). Cells that were suspected to be or had been induced to undergo apoptosis were first lysed to collect their intracellular contents. The cell lysate was then tested for protease activity by the addition of a caspase-specific peptide that was conjugated to the color reporter molecule *p*-nitroanilide (*p*-NA). Cleavage of the peptide by caspase released the

chromophore *p*-NA, which was quantitated spectrophotometrically at a wavelength of 405 nm.

Statistical analysis Data are expressed as mean±SD. Difference was analyzed for significance by one-way repeated-measures ANOVA and further analyzed with the use of the Newman-Keuls test for multiple comparisons between treatment groups. The results were considered significant at $P<0.05$.

Results

Gene transfer of Hsp20 inhibits necrosis and apoptosis of H9c2 cells We infected H9c2 cells with Ad.HSP20 or Ad.GFP. The infection efficiency was 94.7% ± 2.1% (n=5) with Ad.HSP20 and 95.2%±2.6% (n=5) with Ad.GFP, as indicated by GFP fluorescence (Figure 1). Importantly, there was no apparent morphological alteration or difference in the number of adherent cells between control cells, Ad.HSP20-infected cells, and Ad.GFP-infected cells. We determined the levels of necrosis and apoptosis of H9c2 cells double-stained by annexin V-FITC and propidium iodide after SI/R by flow cytometry. The lower-left quadrants of the cytograms showed the viable cells, which excluded propidium iodide-stained cells and cells that were negative for annexin V-FITC binding. The lower-right quadrants represented the apoptotic cells, annexin V-FITC-positive cells, and propidium iodide-negative cells. The upper-right quadrants contained necrotic and late-apoptotic cells, positive for annexin V binding and for propidium iodide uptake. The upper-left quadrants represented cells damaged during the procedure. For each treatment group, 10 000 cells were analyzed. In the control group, most of the cells were healthy (93.0%) (Figure 2A). Of the H9c2 cells exposed to SI/R, 22.3% were propidium iodide negative (lower-right quadrant) while 23.7% were propidium iodide positive (upper-right quadrant), which indicated early apoptosis and late apoptosis/necrosis, respectively (Figure 2B). Overexpression of HSP20 significantly reduced the number of cells labeled with annexin-V. The percentage of early apoptotic and late apoptotic/necrotic cells was significantly decreased to 5.1% and 1.0%, respectively (Figure 2C). H9c2 cells infected with control virus had no such result (Figure 2D).

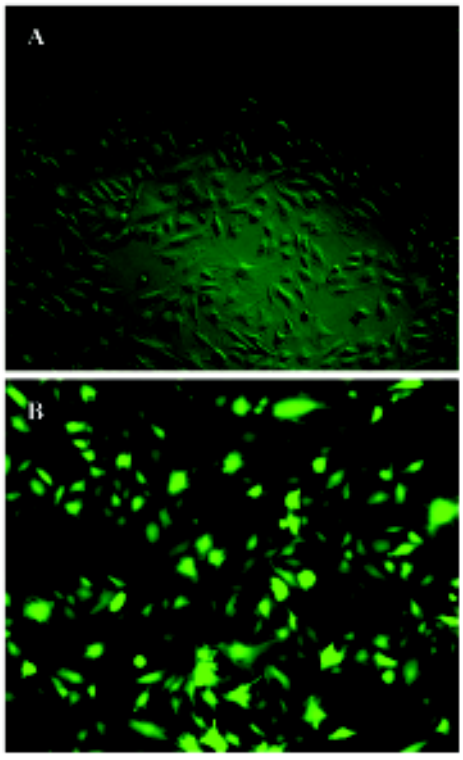

Figure 1. Typical light microscope (A) and fluorescence (B) images of H9c2 cells infected with Ad.HSP20 for 24 h were observed in a high-power field (×40).

We also detected necrosis and apoptosis by LDH release and caspase-3 activity, respectively. Cellular damage was measured by the amount of cytosolic LDH release after SI/R. Cell apoptosis was quantitated by caspase-3 activity. Overexpression of HSP20 in cardiomyocytes resulted in a 21.5% reduction in the proportion of cytosolic LDH release and a 58.8% reduction in caspase-3 activity, compared with Ad.GFP-treated cells (Figure 3B).

Protein kinase C inhibitor and mitochondrial K^+_{ATP} channel inhibitor reversed the protective effect of HSP20 Pretreatment with the PKC inhibitor Ro-31-8220 (0.1 μmol/L) for 30 min prior to SI/R reversed the protective effect of HSP20 on LDH release and caspase-3 activity (Figure 3). Pretreatment with the selective mitochondrial K^+_{ATP} channel inhibitor 5-hydroxydecanoate (5-HD, 100 μmol/L) for 30 min prior to SI/R also canceled the protective effect of HSP20, whereas pretreatment with the non-selective K^+_{ATP} channel inhibitor glibenclamide (100 μmol/L) had no significant effect (Figure 3). These data suggest that the protective effect of HSP20 *in vitro* is due to reduced necrotic and apoptotic death of cardiomyocytes, possibly via the PKC/mito K^+_{ATP} pathway.

Discussion

Our previous study demonstrated that overexpression of HSP20 in rat heart protected against ischemia/reperfusion, the protective effect relating to the reduction of necrosis and apoptosis of ventricular cardiomyocytes. In the present study, we used H9c2 cardiomyocytes, which originated from rat embryonic cardiac tissue and retained certain features of

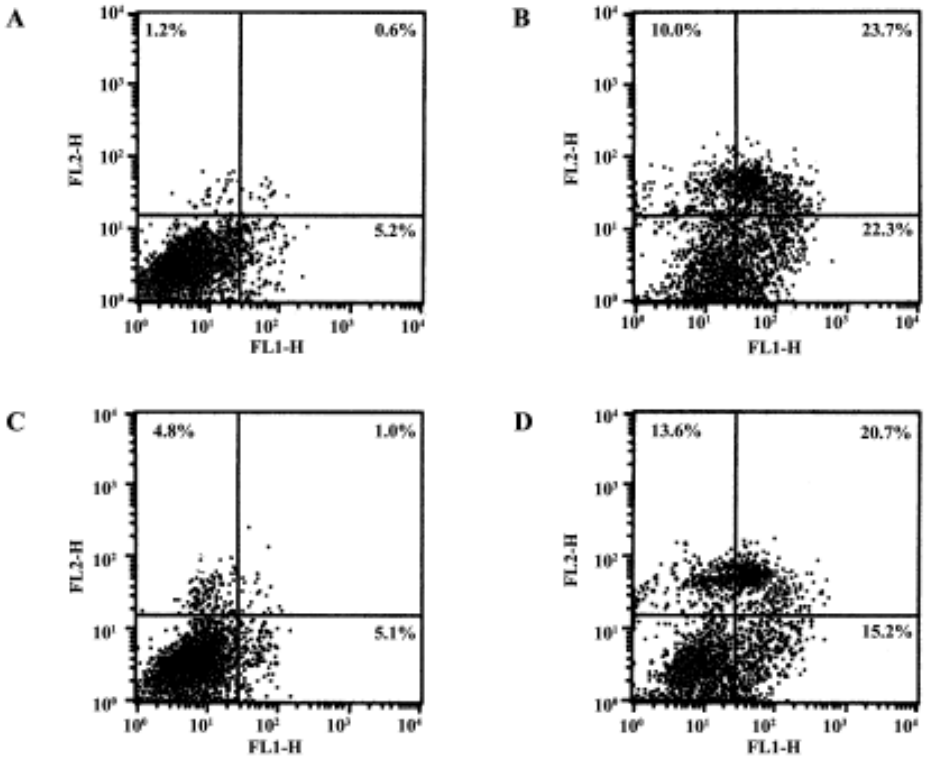

Figure 2. Flow cytometric histograms of H9c2 cells induced by simulated ischemia/reperfusion (SI/R). Cells were infected with Ad.HSP20 or Ad.GFP 24 h before the SI/R. Control cells were not infected with adenovirus or exposed to SI/R. After SI/R, cells were harvested and labeled with a combination of annexin V-fluorescein-isothiocyanate and propidium iodide. (A) Control; (B) SI/R; (C) SI/R+Ad.HSP20; (D) SI/R+Ad.GFP. FL1-H, 525 nm filter; FL2-H, 575 nm filter.

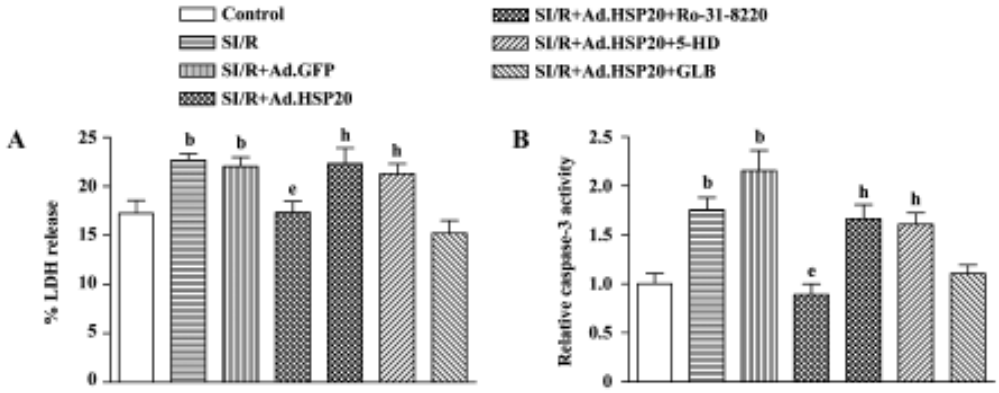

Figure 3. Effect of HSP20, protein kinase C inhibitor Ro-31-8220 and K^+_{ATP} channel inhibitors on (A) lactate dehydrogenase (LDH) release and (B) caspase-3 activity induced by SI/R. Cells were infected with Ad.HSP20 or Ad.GFP 24 h before the simulated ischemia/reperfusion (SI/R). Control cells were not infected with adenovirus or exposed to SI/R. n=5 independent experiments. Mean±SD. $^bP<0.05$ *vs* control. $^eP<0.05$ *vs* SI/R. $^hP<0.05$ *vs* SI/R+Ad.HSP20. 5-HD, 5-hydroxydecanoate; GLB, glibenclamide.

cardiac specificity[18,19], to investigate the mechanism of the protective effect of HSP20.

By detecting annexin V-FITC and propodium iodide double-stained H9c2 cells after SI/R by flow cytometry, we detected the necrosis and apoptosis of cells. We also detected the necrosis and apoptosis of H9c2 cells by LDH release and caspase-3 activity. Similar to the *in vivo* experiments, our results *in vitro* suggest that the protective effect of HSP20 also relates to the reduction of necrosis and apoptosis, which is indicated by flow cytometry, LDH re-

lease and caspase-3 activity (unpublished data).

Myocardial ischemia is frequently followed by reperfusion. Reperfusion and the resultant reoxygenation lead to the generation of oxygen radicals that can cause reperfusion injury. In the present study, we used H9c2 to mimic *in vivo* ischemia/reperfusion injury. We used LDH to evaluate the cell damage *in vitro*. The overexpression of HSP20 protected H9c2 cells against SI/R injury by reducing the LDH level. These data indicate that HSP20 reduces necrosis of cardiomyocytes. Our *in vitro* results also showed that H9c2 cells with overexpressed HSP20 had reduced caspase-3 activity. These data indicate that the anti-apoptotic effect of HSP20 in cardiomyocytes is mediated through reduced caspase-3 activity. In addition, Fan *et al*[15] showed that the protective effects of HSP20 were further increased by the constitutively phosphorylated HSP20 mutant (S16D). In our study, the PKC inhibitor Ro-31-8220 (0.1 μmol/L) and selective mitochondrial K^+_{ATP} channel inhibitor 5-HD (100 μmol/L) blocked the HSP20-induced protective effect. Our results are similar to those of previous reports showing that the PKC inhibitor blocks the cardioprotective effect of the mitochondrial K^+_{ATP} channel[20,21], which indicates that PKC lies upstream of the mitochondrial K^+_{ATP} channel.

Our results suggest that the protective effect of HSP20 is attributed to a reduction of necrosis and apoptosis in cardiomyocytes. Therefore, the cardioprotective effect of HSP20 *in vitro* might be mediated mainly by inhibiting cardiomyocyte necrotic and apoptotic cell death, possibly via the PKC/mito K^+_{ATP} pathway.

Acknowledgements

We are grateful to Prof Rui-ping XIAO (Laboratory of Cardiovascular Science, Gerontology Research Center, National Institutes of Health, Bethesda, MD, USA) for her advice during this research.

References

1 Hightower LE. Heat shock, stress proteins, chaperones and proteotoxicity. Cell 1991; 66: 191–7.
2 Welch WJ. How cells respond to stress. Sci Am 1993; 268: 56–64.
3 Boelens WC, Croes Y, de Ruwe M, de Reu L, de Jong WW. Negative charges in the C-terminal domain stabilize the αB-crystallin complex. J Biol Chem 1998; 273: 28085–90.
4 Suzuki A, Sugiyama Y, Hayashi Y, Nyu IN, Yoshida M, Nonaka I, *et al*. A novel member of the small heat shock protein family, binds and activates the myotonic dystrophy protein kinase. J Cell Biol 1998; 140: 1113–24.
5 Landry J, Chretien P, Lambert H, Hickey E, Weber LA. Heat shock resistance conferred by expression of the human hsp27 gene in rodent cells. J Cell Biol 1989; 109: 7–15.
6 Chretien P, Landry J. Enhanced constitutive expression of the 27-kDa heat shock proteins in heat-resistant variants from Chinese hamster cells. J Cell Physiol 1988; 137: 157–66.
7 Lavoie JN, Gingras-Breton G, Tanguay RM, Landry J. Induction of Chinese hamster hsp27 gene expression in mouse cells confers resistance to heat shock. J Biol Chem 1993; 268: 3420–9.
8 Aoyama A, Frohli E, Schafer R, Klemenz R. αB Crystallin expression in mouse NIH 3T3 fibroblasts: glucocorticoid responsiveness and involvement in thermal protection. Mol Cell Biol 1993; 13: 1824–35.
9 Blackburn R, Galoforo S, Berns CM, Ireland M, Cho JM, Corry PM, *et al*. Thermal response in murine L929 cells lacking αB crystallin expression and αB crystallin expressing L929 transfectants. Mol Cell Biochem 1996; 55: 51–60.
10 Iwaki A, Iwaki T, Tateishi J, Goldman JE. Sense and antisense modification of glial alpha B-crystallin production results in alterations of stress fiber formation and thermoresistance. J Cell Biol 1994; 125: 1385–93.
11 Martin JL, Mestril R, Hilal-Dandan R, Brunton LL, Dillmann WH. Small heat shock proteins and protection against ischemic injury in cardiac myocytes. Circulation 1997; 96: 4343–8.
12 Kato K, Shinohara H, Goto S, Inaguma Y, Morishita R, Asan T. Copurification of small heat shock protein with alpha B crystallin from human skeletal muscle. J Biol Chem 1992; 267: 7718–25.
13 Kato K, Goto S, Inaguma Y, Hasegawa K, Morishita R, Asano T. Purification and characterization of a 20-kDa protein that is highly homologous to αB crystallin. J Biol Chem 1994; 269: 15302–9.
14 van de Klundert FAJM, van den Issel PRLA, Stege GJ, de Jong WW. Rat Hsp20 confers thermoresistance in a clonal survival assay, but fails to protect coexpressed luciferase in Chinese hamster ovary cells. Biochem Biophys Res Commun 1999; 254: 164–8.
15 Fan GC, Chu G, Mitton B, Song Q, Yuan Q, Kranias EG. Small heat-shock protein Hsp20 phosphorylation inhibits β-agonist-induced cardiac apoptosis. Circ Res 2004; 94: 1474–82.
16 Nyberg-Hoffman C, Aguilar-Cordova E. Instability of adenoviral vectors during transport and its implication for clinical studies. Nat Med 1999; 5: 955–7.
17 Mestril R, Chi SH, Sayen MR, O'Reilly K, Dillmann WH. Expression of inducible stress protein 70 in rat heart myogenic cells confers protection against simulated ischemia-induced injury. J Clin Invest 1994; 93: 759–67.
18 Heshscheler J, Meyer R, Plant S, Krautwurst D, Rosenthal W, Schultz G. Morphological, biochemical and electrophysiological characterization of a clonal cell (H9c2) line from rat heart. Circ Res 1991; 69: 1476–86.
19 Kimes BW, Brandt BL. Properties of a clonal muscle cell line from rat heart. Exp Cell Res 1976; 98: 367–81.
20 Wang Y, Ashraf M. Role of protein kinase C in mitochondrial K_{ATP} channel-mediated protection against Ca^{2+} overload injury in rat myocardium. Circ Res 1999; 84: 1156–65.
21 Sato T, O'Rourke B, Marban E. Modulation of mitochondrial ATP dependent K^+ channels by protein kinase C. Circ Res 1998; 83: 110–4.

Acta Pharmacologica Sinica 2005 Sep; 26 (9): 1081–1086

Full-length article

Effect of daidzin, genistin, and glycitin on osteogenic and adipogenic differentiation of bone marrow stromal cells and adipocytic transdifferentiation of osteoblasts

Xiang-hui LI[1], Jin-chao ZHANG[2,3], Sen-fang SUI[1,4], Meng-su YANG[3,4]

[1]*State Key Laboratory of Biomembrane, Department of Biological Sciences and Biotechnology, Tsinghua University, Beijing 100084, China;* [2]*Department of Chemistry, College of Chemistry and Environmental Science, Hebei University, Baoding 071002, China;* [3]*Department of Biology and Chemistry, City University of Hong Kong, Hong Kong, China*

Key words

daidzin; genistin; glycitin; bone marrow stromal cells; osteogenic differentiation; adipogenic differentiation; osteoblasts; adipocytic transdifferentiation

[4] Correspondence to Prof Sen-fang SUI and Phn 86-10-6278-4768.
E-mail suisf@mail.tsinghua.edu.cn
Prof Meng-su YANG
Phn 86-852-2788-7797.
E-mail bhmyang@cityu.edu.hk

Received 2005-03-25
Accepted 2005-05-09

doi: 10.1111/j.1745-7254.2005.00161.x

Abstract

Aim: To examine the effect of daidzin, genistin, and glycitin on the osteogenic and adipogenic differentiation of bone marrow stromal cells (MSC) and the adipogenic transdifferentiation of osteoblasts. **Methods:** MTT test, alkaline phosphatase (ALP) activity measurement, Oil Red O stain and measurement were employed. **Results:** Daidzin, genistin, and glycitin 1×10^{-8}, 5×10^{-7}, 1×10^{-6}, 5×10^{-6}, and 1×10^{-5} mol/L all promoted the proliferation of primary mouse bone MSC and osteoblasts. Daidzin 5×10^{-7} mol/L and genistin 1×10^{-6} mol/L promoted the osteogenesis of MSC. Genistin 1×10^{-8}, 5×10^{-7}, 1×10^{-6}, 5×10^{-6}, and 1×10^{-5} mol/L and glycitin 1×10^{-8}, 1×10^{-6}, and 1×10^{-5} mol/L inhibited the adipogenesis of MSC. Daidzin, genistin, and glycitin 1×10^{-8}, 5×10^{-7}, 1×10^{-6}, 5×10^{-6}, and 1×10^{-5} mol/L all inhibited the adipocytic transdifferentiation of osteoblasts. **Conclusions:** Daidzin, genistin, and glycitin may modulate differentiation of MSC to cause a lineage shift toward the osteoblast and away from the adipocytes, and could inhibit adipocytic transdifferentiation of osteoblasts. They could also be helpful in preventing the development of osteonecrosis.

Introduction

Bone metabolism is regulated by functions of osteoblasts and osteoclasts, which are localized in bone tissues. Osteoblasts stimulate bone formation and calcification while osteoclasts promote bone resorption. Many experimental results on the action of isoflavones on the differentiation and/or function of osteoblasts and/or osteoclasts have been reported[1].

Bone marrow stromal cells (MSC) are pluripotent cells that have the capacity to differentiate into osteoblasts, adipocytes, chondrocytes, myoblasts, or fibroblasts[2,3]. Thus, lineage determination between osteoblasts and adipocytes could be a critical component in the regulatory pathways of osteoblastogenesis[4]. Consistently, an increased lipid accumulation in the bone marrow has been reported in association with age-related bone loss implying an inverse relationship between osteoblastogenesis and adipogenesis. Indeed, it is now hypothesized that an increase in the number of adipocytes occurs at the expense of osteoblasts in osteopenic disorders. Furthermore, there is more and more evidence that suggest a large degree of plasticity exists between osteoblasts and adipocytes and that this transdifferentiation is reciprocal[5]. It was reported that there was a therapeutic opportunity to either prevent or treat osteopenic disorders by inhibiting marrow adipogenesis[6]. Therefore, it is possible that the inhibition of marrow adipogenesis with a concomitant increase in osteoblastogenesis could provide a therapeutic target with which to either prevent further increases in adipocyte formation or divert existing adipocytes to become more osteoblasts with a resulting increase in functional bone cells[7]. Moreover, recent studies *in vitro* have demonstrated that 17β-estradiol suppresses

the expression of lipoprotein lipase (LPL), a marker of adipocyte differentiation in an extramedullary preadipocytic cell line, 3T3L1[8]. Okazaki *et al* reported that 17β-estradiol directly modulated differentiation of bipotential stromal cells into the osteoblast and adipocyte lineages, promoting osteoblast differentiation and inhibiting adipocyte differentiation, causing a lineage shift toward the osteoblast[9]. Such effects will lead to direct stimulation of bone formation and thereby contribute to the protective effects of 17β-estradiol on bone.

So far, the effect of daidzin, genistin, and glycitin on the osteogenic and adipogenic differentiation of MSC and the adipogenic transdifferentiation of osteoblasts was not reported. The aim of the present investigation was to address the question of whether daidzin, genistin and glycitin had effects on osteogenic and adipogenic differentiation of primary mouse MSC and to investigate the adipogenic transdifferentiation of primary mouse osteoblasts compared with 17β-estradiol.

Materials and methods

Materials Kunming (KM) mice were purchased from the Guangming Weiwu Biological Product Factory (Shenzhen, China). Dulbecco's modified Eagle's medium (DMEM) and fetal bovine serum were purchased from Gibco (Carlsbad, CA, USA). The 17β-estradiol, benzylpenicillin, streptomycin, MTT, β-glycerophosphate, dexamethasone, ascorbic acid, insulin, oil red O stain were obtained from Sigma Chemical Co (St Louis, MO, USA). Demethyl sulfoxide (Me_2SO) was purchased from Sangon (Shanghai, China). Genistin, daidzin, and glycitin were from Shanghai TAUTO Biotech Co (Shanghai, China). An alkaline phosphatase (ALP) activity kit was obtained from Nanjing Jiancheng Biological Engineering Institute (Nanjing, China), micro-protein assay kit was purchased from Beyotime Biotechnology (Haimen, China).

Isolation and culture of primary bone MSC The mouse bone MSC were obtained from adult KM mice (4–6 weeks) using the method previously reported[10] with minor modification. Mice were killed by decapitation. Femora and tibiae were aseptically harvested, and the whole bone marrow was flushed using DMEM in a 1 mL syringe and a 25-gauge needle. The cells were collected and cultured in a culture flask. After a 3-d incubation in a 37 ℃, 5% CO_2 humidified incubator, the nonadherent cells were removed from the cultures by gentle aspiration and the medium replaced with fresh DMEM. The medium was changed every 3 d in all the experiments.

Isolation and culture of primary osteoblasts The mice osteoblasts were isolated mechanically from newborn mice skull using a modification of the method previously reported[11]. Briefly, the skull (frontal and parietal bones) was dissected from KM mice, the endosteum and periosteum were stripped off, and the bone was cut into approximately 1–2 mm^2 pieces and digested with trypsin (2.5 g/L) for 30 min, and the digestion was discarded. The bone was then digested twice with collagenase A (2.0 g/L) for an 1 h each time. The cells were collected and cultured in a culture flask. After being placed overnight in a 5% CO_2 humidified incubator at 37 ℃, the DMEM was removed. The medium was then changed every 3 d in all the experiments.

Assessment of primary mouse bone MSC and osteoblast growth The protocol described by Mosmann was followed with some modifications[12]. Briefly, MSC (3×10^6 cells per well) and osteoblasts (1×10^4 cells per well) were plated in 96-well culture plates and cultured overnight at 37 ℃ in a 5% CO_2 humidified incubator. Daidzin, genistin, glycitin, and 17β-estradiol were then added to the wells at final concentrations of 1×10^{-8}, 5×10^{-7}, 1×10^{-6}, 5×10^{-6}, and 1×10^{-5} mol/L. Control wells were prepared with the addition of DMEM. Wells containing DMEM without cells were used as blanks. The plates were incubated at 37 ℃ in a 5% CO_2 incubator for 48 h. Upon completion of the incubation, stock MTT dye solution (20 μL, 5 g/L) was added to each well. After 4-h incubation, the supernatant was removed and Me_2SO (100 μL) was added to solubilize the MTT. The optical density of each well was measured on a microplate spectrophotometer (Bio-Rad Model 680, Hercules, CA, USA) at a wavelength of 570 nm. The proliferation rate/% of control was calculated according to the formula: $OD_{treated}/OD_{control}\times100\%$.

Measurement of ALP activity The bone MSC were isolated as above. MSC (3×10^6 cells per well) were plated in 48-well culture plates, after being induced by an osteogenic supplement (1×10^{-7}mol/L dexamethasone, 5.0 mmol/L β-glycerophosphate, 50 mg/L ascorbic acid) and treated with daidzin, genistin, glycitin and 17β-estradiol at final concentrations of 1×10^{-8}, 5×10^{-7}, 1×10^{-6}, 5×10^{-6}, 1×10^{-5} mol/L for 7 d. The plates were washed thrice with ice-cold PBS and lysed by two cycles of freezing and thaw. Aliquots of supernatants were subjected to alkaline phosphatase activity and protein content measurement using an alkaline phosphatase kit and a micro-Bradford assay kit, respectively. The osteogenic differentiation rate was calculated according to the formula: ALP $activity_{treated}$/ALP $activity_{control}\times100\%$.

Oil red O stain and measurement The bone MSC and osteoblasts were isolated as above. MSC (3×10^6 cells per well) and osteoblasts (1×10^4 cells per well) were plated in 48-

well culture plates, after being induced by adipogenic supplement (10 mg/L insulin, 1×10^{-7} mol/L dexamethasone and treated with daidzin, genistin, glycitin, and 17β-estradiol at final concentrations of 1×10^{-8} , 5×10^{-7}, 1×10^{-6}, 5×10^{-6}, 1×10^{-5} mol/L for 14 d and 9 d, respectively. Fat droplets within differentiated adipocytes from MSC and transdifferentiated adipocytes from osteoblasts were observed using the oil red O staining method described by Ichiro *et al.* with some modification[13]. Cell monolayers were fixed in 4% formaldehyde, washed in water and stained with a 0.6% (*w/v*) oil red O solution (60% isopropanol, 40% water) for 15 min at room temperature. For quantification, cell monolayers were then washed extensively with water to remove unbound dye, then 1 mL of isopropyl alcohol was added to the stained culture dish. After 5 min, the absorbance of the extract was assayed by a spectrophotometer at 510 nm. The adipogenic differentiation rate and adipocytic transdifferentiation rate were calculated according to the formula: $OD_{treated}/OD_{control}\times100\%$.

Statistical analysis Data were expressed as mean±SD of at least three separate experiments. The statistical differences were analyzed using Student *t*-test.

Results

Effect of daidzin, genistin and glycitin on the MSC proliferation MTT tests showed that daidzin, genistin, and glycitin significantly promoted MSC proliferation and all the promotion rates were less than that of 17β-estradiol at the same concentrations (Figure 1).

Effect of daidzin, genistin, and glycitin on osteoblast proliferation The daidzin, genistin, and glycitin significantly promoted osteoblast proliferation and the promotion rate of daidzin was greater than those of genistin and glycitin at the same concentrations (Figure 2).

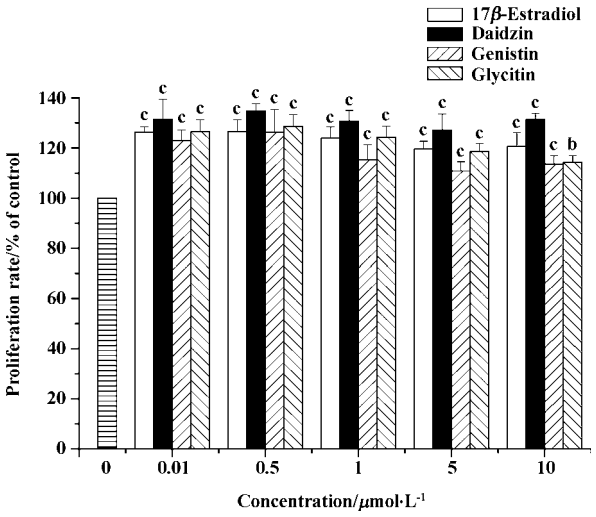

Figure 2. Effect of daidzin, genistin, and glycitin on the proliferation of osteoblasts. n=5. Mean±SD. $^bP<0.05$, $^cP<0.01$ *vs* control.

Effect of daidzin, genistin, and glycitin on the osteogenic differentiation of MSC ALP activity measurements at d 7 showed that neither daidzin, genistin, and glycitin inhibited the osteogenic differentiation of MSC. Daidzin at concentration of 5×10^{-7}mol/L and genistin at concentrations of 1×10^{-6}, 5×10^{-6}, and 1×10^{-5} mol/L promoted the osteogenic differentiation and all the promotion rates were less than those of 17β-estradiol at the same concentrations (Figure 3).

Effects of daidzin, genistin, and glycitin on the adipogenic differentiation of MSC Oil red O stain and measurement on

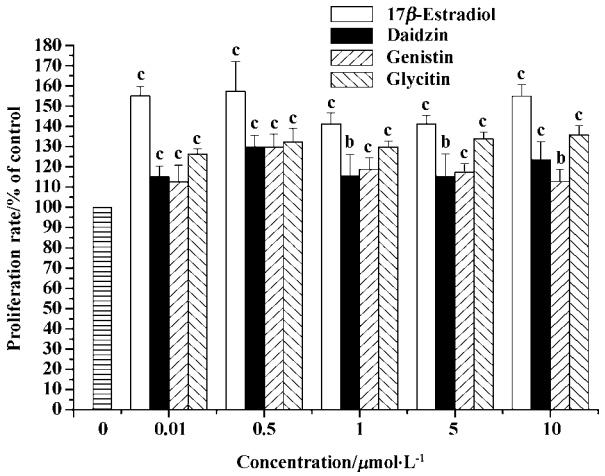

Figure 1. Effect of daidzin, genistin, and glycitin on the proliferation of bone MSC. n=5. Mean±SD. $^bP<0.05$, $^cP<0.01$ *vs* control.

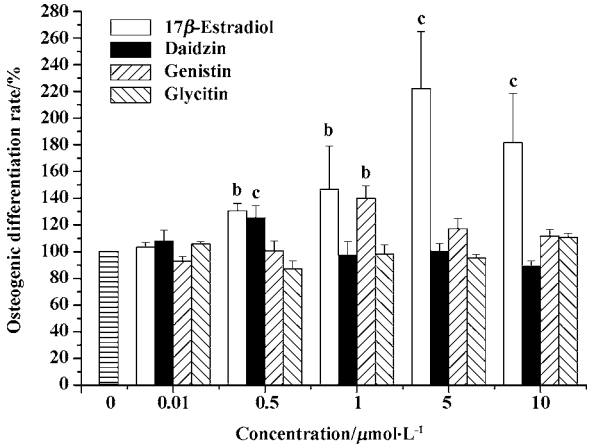

Figure 3. Effect of daidzin, genistin, and glycitin on the osteogenic differentiation of MSC. n=5. Mean±SD. $^bP<0.05$, $^cP<0.01$ *vs* control.

d 14 showed that the effect of daidzin, genistin and glycitin on adipogenic differentiation depended on concentrations. Genistin inhibits adipogenic differentiation at concentrations of 1×10^{-8}–1×10^{-5}mol/L, and the effect was stronger than that of 17β-estradiol (Figure 4). The morphologic observation was in accordance with this result (Figure 5).

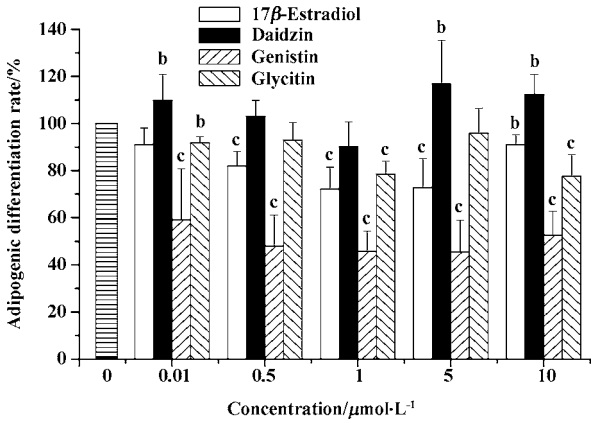

Figure 4. Effect of daidzin, genistin, and glycitin on the adipogenic differentiation of MSC. n=5. Mean±SD. $^bP<0.05$, $^cP<0.01$ *vs* control.

Effect of daidzin, genistin, and glycitin on adipocytic transdifferentiation of osteoblasts Oil red O stain and measurement showed that daidzin, genistin and glycitin inhibited adipocytic transdifferentiation of osteoblasts at all concentrations in a dose-independent manner. The effects of these were stronger than that of 17β-estradiol (Figure 6). The morphologic observation was in accordance with the results (Figure 7).

Discussion

Adipocytic and osteogenic cells are believed to be derived from multipotential stromal cells in the marrow, and *in vitro* studies have shown an inverse relationship between the differentiation of adipocytic and osteogenic cells[5].

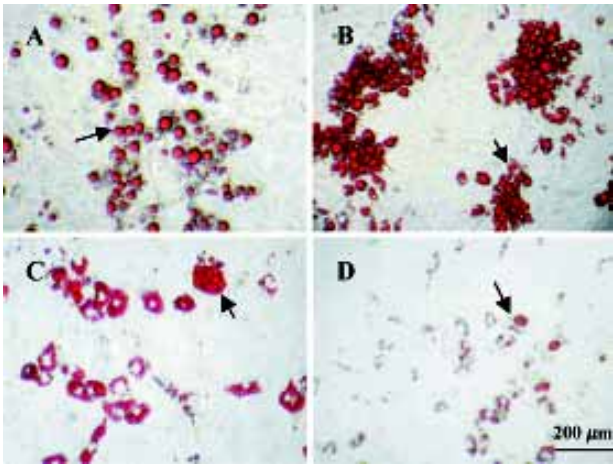

Figure 5. Effect of daidzin, genistin, and glycitin on adipogenic differentiation of MSC. (A) Adipogenic supplement; (B) Adipogenic supplement+5×10^{-7}mol/L daidzin; (C) Adipogenic supplement+5×10^{-7} mol/L glycitin; (D) Adipogenic supplement+5×10^{-7}mol/L genistin. ×100.

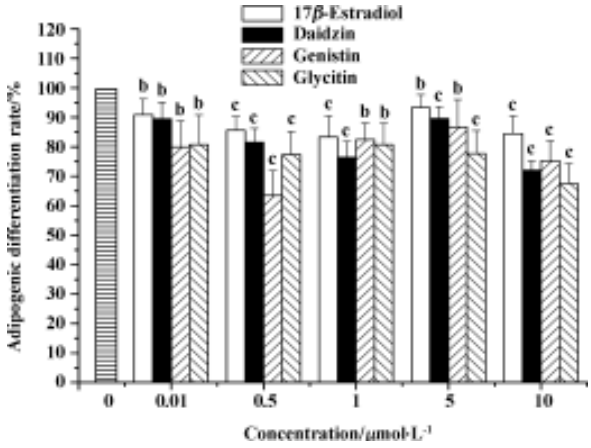

Figure 6. Effect of daidzin, genistin, and glycitin on the adipocytic transdifferentiation of osteoblasts. n=5. Mean±SD. $^bP<0.05$, $^cP<0.01$ *vs* control.

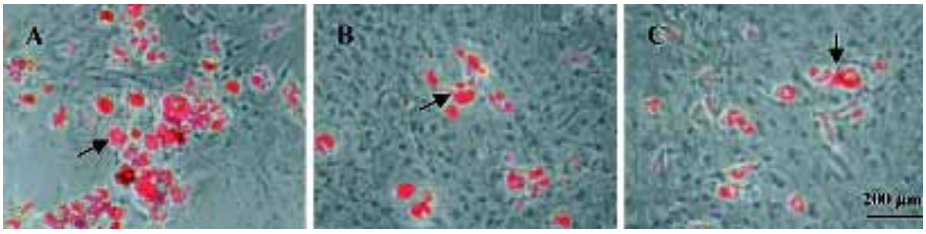

Figure 7. Effect of daidzin, genistin and glycitin on adipocytic transdifferentiation of osteoblasts. (A) Adipogenic supplement; (B) Adipogenic supplement+5×10^{-7} mol/L genistin; (C) Adipogenic supplement+1×10^{-5}mol/L glycitin. ×100.

Besides having a passive role of space-filling in bone marrow cavity, recent data suggest that medullary adipocytes are secretory cells that may influence hematopoiesis and osteogenesis[14]. A variety of peptide and nonpeptide compounds are synthesized and released by adipocytes[15]. Adipocytes also secrete cytokines such as tumor necrosis factor-α (TNF-α) and interleukin (IL-6), and the main effect of these cytokines is a stimulation of bone resorption[16]. In addition, Benayahu *et al* reported that preadipocytes had the potential to stimulate osteoclast differentiation[17]. On the relationship between adipogenesis and the ability to support osteoclast formation, Sakaguchi *et al* have demonstrated that adipocyte-enriched stromal cells also support osteoclast formation[18]. It has been reported that preadipocytes isolated from mouse marrow may regulate the activity and final differentiation of marrow precursors of osteoblasts. The condition medium harvested from mouse stromal preadipocytes decreased the alkaline phosphatase activity of a mouse stromal osteoblastic cell line[19]. So a reversal of adipogenesis will also be important as a therapeutic approach to treat age-related osteoporosis.

Osteonecrosis is a disabling condition that can be defined as the death of the cell components of the bone (including osteocytes and bone marrow cells). Possible pathogenesis of osteonecrosis is an increased size of marrow fat cells, a high intraosseous pressure, an accumulation of lipids within the osteocytes, and fat embolisms. Cui *et al* reported that steroid-induced adipogenesis by bone progenitor cells in the marrow might influence the development of osteonecrosis[20]. Lipid clearing agents, such as lovastatin, which promote osteogenic differentiation and inhibit adipogenic differentiation of MSC, might be helpful in preventing the development of steroid induced osteonecrosis.

In the present study we have examined the effects of daidzin, genistin, and glycitin on osteogenic and adipogenic differentiation of MSC and the adipogenic transdifferentiation of osteoblasts in an *in vitro* assay employing isolated mouse primary bone marrow stromal cells and osteoblasts. The results indicate that daidzin, genistin, and glycitin promoted osteogenic differentiation and inhibited adipogenic differentiation of MSC. It also inhibited adipocytic transdifferentiation of osteoblasts at appropriate concentrations similar to 17β-estradiol. These results were further supported by the fact that daidzin, genistin and glycitin did not inhibit proliferation of the MSC and osteoblasts. This suggests that daidzin, genistin and glycitin regulate a dual differentiational process of bone MSC into the osteogenic and adipogenic lineages, and transdifferentiational process of primary osteoblasts into the adipocyte lineages, causing a lineage shift toward osteoblasts. So, we deduced that the protective effects of daidzin, genistin, and glycitin on bone might be mediated by decreasing adipocytic cell formation from MSC. This may promote osteoblast proliferation, differentiation and mineralization, and secrete less cytokines, which may inhibit osteoclast formation and activation. In addition, the results also indicate that daidzin, genistin, and glycitin may be helpful in preventing the development of steroid induced osteonecrosis. The mechanisms of the effects of daidzin, genistin, and glycitin on the osteogenic and adipogenic differentiation of bone MSC, and the adipogenic transdifferentiation of osteoblasts, need to be studied further.

References

1 Masayoshi Y. Isoflavone and bone metabolism: its cellular mechanism and preventive role in bone loss. J Health Sci 2002; 48: 209–22.

2 Ahdjoudj S, Fromigue O, Marie PJ. Plasticity and regulation of human bone marrow stromal osteoprogenitor cells: potential implication in the treatment of age-related bone loss. Histol Histopathol 2004; 19: 151–7.

3 Dominici M, Hofmann TJ, Horwitz EM. Bone marrow mesenchymal cells: biological properties and clinical applications. J Biol Regul Homeost Agents 2001; 15: 28–37.

4 Li X, Cui Q, Kao C, Wang GJ, Balian G. Lovastatin inhibits adipogenic and stimulates osteogenic differentiation by suppressing PPARα2 and increasing Cbfa1/Runx2 expression in bone marrow mesenchymal cell cultures. Bone 2003; 33: 652–9.

5 Beresford JN, Bennett JH, Devlin C, Leboy P, Owen ME. Evidence for an inverse relationship between the differentiation of adipocytic and osteogenic cells in rat marrow stromal cell cultures. J Cell Sci 1992; 102: 341–51.

6 Nuttall ME, Gimble JM. Is there a therapeutic opportunity to either prevent or treat osteopenic disorders by inhibiting marrow adipogenesis? Bone 2000; 27: 177–84.

7 Song CL, Dan GT. Adipocytes in marrow space and osteoporosis. Chin J Osteoporos 2002; 8: 266–9.

8 Homma H, Kurachi H, Nishio Y, Takeda T, Yamamoto T, Adachi K, *et al*. Estrogen suppresses transcription of lipoprotein lipase gene. Existence of a unique estrogen response element on the lipoprotein lipase promoter. J Bio Chem 2000; 275: 11404–11.

9 Okazaki R, Inoue D, Shibata M, Saika M, Kido S, Ooka H, *et al*. Estrogen promotes early osteoblast differentiation and inhibits adipocyte differentiation in mouse bone marrow stromal cell lines that express estrogen receptor(ER) α or β. Endocrinology 2002; 143: 2349–56.

10 Verma S, Rajaratnam JH, Denton J, Hoyland JA, Byer RJ. Adipocytic proportion of bone marrow is inversely related to bone formation in osteoporosis. J Clin Pathol 2002; 55: 693–8.

11 Thomas OC, Kathleen CM, Bruce E, Monica A, Thomas LM, Michael C, *et al*. Osteocalcin production in primary osteoblast cultures derived from normal and *Hyp* mice. Endocrinology 1998, 139: 35–43.

12 Mosmann T. Rapid colorimetric assay for cellular growth and survival: application to proliferation and cytotoxicity assays.

J Immunol Methods 1983; 65: 55–63.
13 Katherine AK, Jeffrey MG. 1,25-Dihydroxy vitamin D3 inhibits adipocyte differentiation and gene expression in murine bone marrow stromal cell clones and primary cultures. Endocrinology 1998; 139: 2622–8.
14 Gimble, JM. The function of adipocytes in the bone marrow stroma. New Biol 1990; 2: 304–12.
15 Ailhaud G, Grimaldi P, Negrel R. Cellular and molecular aspects of adipose tissue development. Annu Rev Nutr 1992; 12: 207–33.
16 Mundy GR. Cytokines and bone remodeling. In: Marcus R, Feldman D, Kelsey J, editors. Osteoporosis. San Diego: Academic Press; 1996. p301.
17 Benayahu D, Peled A, Zipori D. Myeloblastic cell line expresses osteoclastic properties following coculture with marrow stromal adipocytes. J Cell Biochem 1994; 56: 374–84.
18 Sakaguchi K, Morita I, Murota S. Relationship between the ability to support differentiation of osteoclast-like cells and adipogenesis in murine stromal cells derived from bone marrow. Prostag Leukotr Ess 2000; 62: 319–27.
19 Benayahu D, Zipori D, Wientroub S. Marrow adipocytes regulate growth and differentiation of osteoblasts. Biochem Biophys Res Commun 1993; 197: 1245–52.
20 Cui Q, Wang GJ, Balian G. Steroid-induced adipogenesis in a pluripotential cell line from bone marrow. J Bone Joint Surg Am 1997; 79: 1054–63.

Important Announcement: the Online Manuscript Submission and Review System was Launched!

Acta Pharmacologica Sinica announced that its online manuscript submission and review system based on ScholarOne Manuscript Central (http://mc.manuscriptcentral.com/aphs) was launched on May 25, 2005.

As the leading web-based peer-review system applied by many journals, Manuscript Central is a complete, database-driven software for the online submission and review of full-text manuscripts and graphics. The system provides fully electronic workflow and will speed up the time from submission to decision.

Acta Pharmacologica Sinica strongly recommend its authors to submit manuscript via this system, which enables this journal to handle the manuscript quickly and efficiently. Please read the User Guide before submitting manuscript online. For more detailed submission instruction, please consult the Manuscript Central Online User Guide (http://mcv3help.manuscriptcentral.com/tutorials/). You may also contact the Editorial Office who will be pleased to help you.

Acta Pharmacologica Sinica 2005 Sep; 26 (9): 1087–1092

Full-length article

α-Helical domain is essential for antimicrobial activity of high mobility group nucleosomal binding domain 2 (HMGN2)[1]

Yun FENG[2], Ning HUANG, Qi WU, Lang BAO, Bo-yao WANG

Research Unit of Infection and Immunity, West China School of Preclinical and Forensic Medicine, Sichuan University, Chengdu 610041, China

Key words

HMGN2; antimicrobial activity; antimicrobial domain

[1] Project supported by the National Natural Science Foundation of China (No 30300127 to YF) and China Medical Board of New York Inc (No 98-681 to BW).
[2] Correspondence to Dr Yun FENG.
Phn 86-28-8550-3159.
E-mail fengyunxixi@yahoo.com.cn

Received 2004-12-23
Accepted 2005-03-09

doi: 10.1111/j.1745-7254.2005.00132.x

Abstract

Aim: To examine the antimicrobial spectrum and functional structure of high mobility group nucleosomal binding domain 2 (HMGN2). **Methods:** OMIGA protein structure software was used to analyze the two-dimensional structure of HMGN2. Synthetic short peptides were generated for studying the relationship between function and structure. Prokaryotic expression vectors were constructed for the holo-HMGN2 and its helical domain. Their *E coli*-based products were also prepared for antimicrobial testing. The antimicrobial assay included minimal effective concentration, minimal inhibitory concentration, and minimal bactericidal concentration. **Results:** OMIGA protein structure software analysis revealed a transmembrane α-helical structure (the putative antimicrobial domain) located from position 18 to 48 of the HMGN2 protein sequence. The antimicrobial assay showed that the MIC of the recombinant holo-HMGN2 against *E coli* ML-35p (an ampicillin-resistance strain), *Pseudomonas aeruginosa* ATCC 27853 and *Candida albicans* ATCC 10231 were 12.5, 25, and 100 mg/L, respectively. Against the same microorganisms, the MIC of the synthetic HMGN2 α-helical domain were 12.5, 25, and 100 mg/L, respectively, that is, the same as with the recombinant form of HMGN2. In contrast, recombinant holo-HMGN2 was inactive against *Staphylococcus aureus* ATCC 25923. The synthetic N-terminal and C-terminal fragments of HMGN2 had no antimicrobial activity against *E coli* ML-35p, *P aeruginosa* ATCC 27853 or *C albicans* ATCC 10231. **Conclusion:** HMGN2 showed potent antimicrobial activity against *E coli* ML-35p, *P aeruginosa* ATCC 27853 and, to some extent, against *C albicans* ATCC 10231, but was inactive against *S aureus* ATCC 25923 in these assay systems. Its α-helical structure may be essential for the antimicrobial activity of HMGN2.

Introduction

Cationic antimicrobial peptides play a crucial role in the host defense against infections[1]. It has been shown that the antimicrobial activity of human mononuclear leukocytes originates from natural killer (NK) cells[2], T cells[3] and monocytes[4]. Several antimicrobial peptides or proteins have been described in NK and T cells. Granulysin is a recently characterized antimicrobial polypeptide from T and NK cells[5]. The porcine counterpart of granulysin (NK-lysin) was characterized as an antimicrobial and cytotoxic polypeptide expressed by NK and T cells[6]. The antimicrobial peptides LL-37 and human neutrophil defensins (HNP1-HNP3) were found in the supernatant of enriched T and NK cells[7]. We isolated and characterized an antimicrobial polypeptide from human circulatory mononuclear leukocytes. Its N-terminal sequence was identical to high mobility group nucleosomal binding domain 2 (HMGN2)[8]. HMGN2 was identified as a non-histone chromosomal protein in invertebrates and vertebrates and may play a role in gene transcription and organogenesis[9–12]. However, the biological role of this protein has not

been fully defined. In this study, we prepared recombinant holo-molecule, recombinant or synthetic helical domain, N-terminal and C-terminal fragments to further determine the antimicrobial spectrum and functional structure of HMGN2.

Materials and methods

Synthetic peptide Synthetic N- and C-terminal fragments, and the α-helical domain of HMGN2, were prepared by Shanghai Genebase Gen-Tech (Shanghai, China). Their amino acid sequences are as follows:

Fragment 1: MPKRKAEGDA KGDKAKV (position 1-17 of the HMG 2 amino acid sequence)

Fragment 2 : KDEPQRRSAR LSAKPAPPKP EPKPKKAPAK K (position 18–48 of the HMGN2 amino acid sequence)

Fragment3:GEKVPKGKKGKADAGKEGNNPAENGDA-KTD QAQKAEGAGD AK (position 49–90 of the HMGN2 amino acid sequence)

High-performance liquid chromatography (HPLC) and mass spectroscopy analysis of these peptides revealed a purity of >95%. The peptides were dissolved in 10 mmol/L potassium phosphate buffer (PPB, pH 7.0) to a final concentration of 10 g/L.

Antimicrobial activity assay Rabbit neutrophil defensin (NP-1) and HNP1–3 were used as the control antimicrobial peptides, and were prepared as described elsewhere[13,14].

Evaluation of minimal effective concentration The minimal effective concentrations (MEC) were tested using a radial diffusion assay. Briefly, soy broth (*E coli* ML-35p, *Pseudomonas aeruginosa* ATCC 27853, S*taphylococcus aureus* ATCC 25923) or sabouraud dextrose broth (*Candida albicans* ATCC 10231) underlay gel mixture containing 1×10^6 colony-forming units (CFU)/mL of organisms was decanted into a dish. Sample wells of 3-mm diameter were punched and 5 μL of serial dilutions of the peptides (200, 100, 50, 25, 12.5, 6.25, and 3.125 mg/L) were added to the wells. After 3 h of incubation, overlay soy broth (for growing *E coli* ML-35p, *P aeruginosa* ATCC 27853, *S aureus* ATCC 25923) or sabouraud dextrose broth (for growing *C albicans* ATCC 10231) gels were poured and incubated continuously at 37 °C overnight, the resulting clear zones were measured and expressed in units (1 mm=10 U) after subtracting the well diameter. A linear regression analysis of peptide concentration (*x*-axis) against the zone diameter (*y*-axis) was carried pit to determine the x-intercept, whose value represented the MEC.

Evaluation of minimal inhibitory concentration and minimal bactericidal concentration The minimal inhibitory concentration (MIC) and minimal bactericidal concentration (MBC) of the peptides were examined using bacteria at 1×10^6 CFU/mL in the soy broth and serial dilutions of the peptides (500, 250, 200, 150, 100, 50, 25, 12.5, and 6.25 mg/L). Inhibition of growth was determined by measuring optical density (OD) at 492 nm on a UV/VIS spectrometer after incubation at 37 °C for 12–16 h. Antimicrobial activity was expressed as the MIC, the concentration at which 100% inhibition of growth was observed, and the MBC, the concentration at which no CFU were observed after incubation for 12–16 h on soy broth (for growing *E coli* ML-35p, *P aeruginosa* ATCC 27853, and *S aureus* ATCC 25923) or sabouraud dextrose broth (for growing *C albicans* ATCC 10231) solid media.

***E coli*-based production of recombinant human holo-HMGN2 and its α-helical domain** Total RNA was isolated with Trizol Reagent (Gibco BRL, Washington, USA) from the stimulated mononuclear leukocytes. The full-length HMGN2 cDNA was amplified by reverse transcription–polymerase chain reaction (RT-PCR) and ligated to pMD-18T vector (TakaRa,Tokyo, Japan) for DNA sequencing. Generation of DNA of holo-HMGN2 and the HMGN2 α-helical domain was carried out by PCR amplification. Primers containing *Bam*H I and *Eco*R I restriction sites were designed as follows:P1(5'-ACGGATCCCCCAAGAGAAAGGCTG-3')and P2(5'-TAGAATTCCTTGGCATCCTCCAGCAC-3') for amplifying holo-HMGN2 cDNA; P3 (5'-CAGGATCC AAGGACGAACCACAG-3') and P4 (5'-GCGAATTC CTTCTTTGCAGGGGCCT-3') for synthesizing DNA encoding HMGN2 α-helical domain. *Bam*HI and *Eco*RI restriction sites are underlined. After digestion with *Bam*HI and *Eco*RI, the PCR products were inserted into the pGEX-1λT vector (Amersham Biosciences, Uppsala, Sweden). DNA sequencing of the recombinant prokaryotic expression vectors pGEX-1λT-HMGN2 and pGEX-1λT-HMGN2α was carried out to confirm the insert sequences.

The transformed *E coli* JM109 carrying pGEX-1λT-HMGN2 and pGEX-1λT-HMGN2α were cultured in Luria-Bertani (LB) medium for 12 h in the presence of isopropylthio-β-*D*-galactoside (IPTG) to induce protein expression. The induced cultures were washed with phosphate-buffered saline and cell lysates were obtained by freezing/thawing in the presence of lysozyme. After centrifugation (10000 r/min, 4 ºC, 5 min), the fusion proteins were purified from the supernatants using Bulk Glutathione Sepharose 4B columns (Amersham Biosciences). The purified fusion proteins were cleaved by thrombin digestion. Holo-HMGN2 and its α-helical domain were obtained by acid-urea polyacrylamide gel electrtophoresis (AU-PAGE) elution and HPLC purification.

Results

Analysis of the HMGN2 two-dimensional structure OMIGA protein structure software analysis revealed a transmembrane α-helical structure, the putative antimicrobial domain, located from position 18 to 48 of the HMGN2 protein sequence (Figure 1).

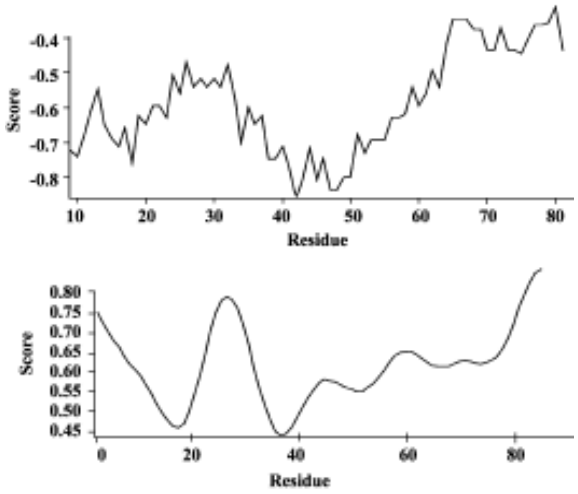

Figure 1. OMIGA protein structure software analysis of high mobility group nucleosomal binding domain 2 (HMGN2). (A) Hydrophobicity analysis using the Janin method. (B) Transmembrane helices analysis using the Argos Method.

Antimicrobial activity of the synthetic peptide fragments Sodium dodecyl sulphate-polyacrylamide gel electrophoresis of the synthetic fragments of HMGN2 is shown in Figure 2. The agar radial diffusion assay indicated that the α-helical domain of HMGN2 had strong antimicrobial activity against an antibiotic-resistant strain of *E coli*. In contrast, no antimicrobial activity was observed for its N-terminal or C-terminal fragments using this assay system (Figure 3).

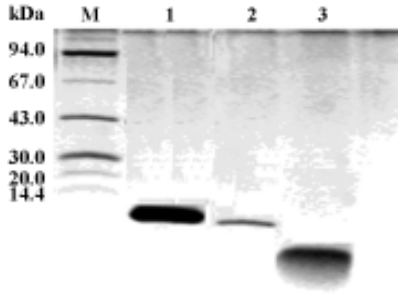

Figure 2. Tricine sodium dodecyl sulphate-polyacrylamide gel electrophoresis of synthetic N-and C-terminal fragments and the α-helical domain of high mobility group nucleosomal binding domain 2 (HMGN2). M, protein marker; 1, C-terminal fragment; 2, α-helical domain; 3, N-terminal fragment.

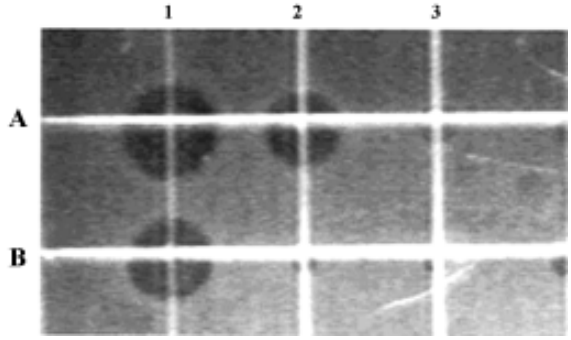

Figure 3. Antimicrobial activity against *E coli* of the synthetic peptide fragments of high mobility group nucleosomal binding domain 2 (HMGN2). A1, Lysozyme (10 g/L); A2, lysozyme (5 g/L); B1, α-helical domain (1 g/L); B2, N-terminal fragment (1 g/L); B3, C-terminal fragment (1 g/L).

Construction of holo-HMGN2 and HMGN2 α-helical domain prokaryotic expression vectors The cDNA encoding mature holo-HMGN2 and its α-helical domain were obtained by PCR (Figure 4), and their corresponding prokaryotic expression vectors were constructed. Sequence analysis indicated that the insert sequences and their orientation were correct in the recombinant vectors.

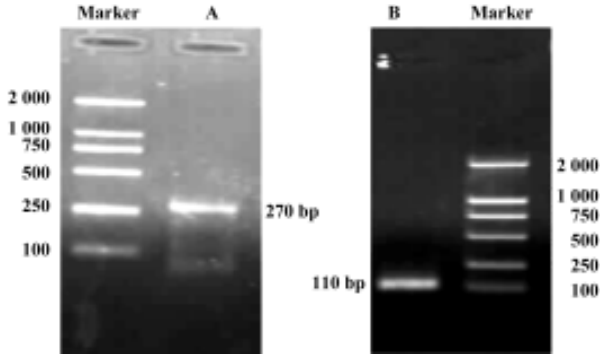

Figure 4. The cDNA fragments of high mobility group nucleosomal binding domain 2 (HMGN2) and its α-helical domain. A, Full length of HMGN2 cDNA; B, HMGN2 α-helical domain cDNA fragment.

***E coli*-based production of human holo-HMGN2 and its α-helical domain** pGEX-1λT-HMGN2 or pGEX-1λT-HMGN2α-transformed *E coli* produced bulk amounts of the HMGN2 and HMGN2α fusion proteins. The fusion proteins

were purified by glutathione *S*-transferase (GST) affinity chromatography. The purified recombinant holo-HMGN2 and its α-helical domain were obtained using AU-PAGE elution from thrombin-digested fusion proteins and reverse-phase HPLC (Figure 5).

Antimicrobial properties of human holo-HMGN2 and its α-helical domain As shown in Table 1, the MIC, MEC, and MBC assays indicated that the recombinant human HMGN2 and its transmembrane α-helical domain (synthetic and recombinant) had potent antimicrobial activity against *E coli*, *P aeruginosa* and, to some extent, against *C albicans*. However, human HMGN2 was inactive against *S aureus* in this assay system (data not shown). All experiments were repeated 3 times.

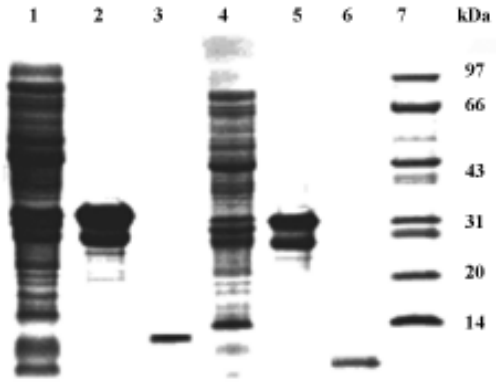

Figure 5. Tricine sodium dodecyl sulphate–polyacrylamide gel electrophoresis of recombinant high mobility group nucleosomal binding domain 2 (HMGN2) and HMGN2 α-helical domain. 1, Total protein of recombinant *Escherichia coli* (HMGN2); 2, GST–HMGN2 fusion protein; 3, Purified HMGN2; 4, Total protein of recombinant *E coli*; 5, GST–HMGN2 α–helical domain fusion protein; 6, Purified HMGN2 α-helical domain; 7, Protein marker.

Discussion

High mobility group (HMG) proteins have been described as an abundant family of non-histone proteins in the cell nucleus of vertebrate and invertebrate organisms[15]. In the narrowest traditional sense, this HMG protein family consists of 6 proteins and is subdivided into 3 subfamilies: the HMG-box (HMGB) (formerly HMG-1/-2), the HMG AT-hook (HMGA) (formerly HMG-I/Y/C), and the HMG nucleosomal binding domain (HMGN) (formerly HMG-14/-17) subfamilies. Each of these classes seems to have a distinct function in the nucleus[16]. HMGN has a cell cycle-related cellular location[17]. The functional gene is located on chromosome 1p36.1[9], and it contains 6 exons, with an extremely high GC content and a "HTF" island, indicative of a housekeeping gene that could be crucial for regulating the function of cells[9]. However, up to now, the biological role of this protein has not been clear. A variety of experiments have shown that HMGN2 is preferentially associated with chromatin subunits contain-

Table 1. Antimicrobial activities of several peptides.

Peptide	Assay	*Escherichia coli* Ml-35p	*Pseudomonas* aeruginosa ATCC27853	*Candida albicans* ATCC10231
HMGN2 α-helical domain	MIC	12.5	25	100
(synthetic)	MBC	25	50	150
/mg·L^{-1}	MEC	NT	NT	NT
HMGN2 α-helical domain	MIC	12.5	25	100
(*E coli*-based prod uction)	MBC	25	50	150
/mg·L^{-1}	MEC	6.25	NT	NT
HMGN2	MIC	12.5	25	100
(*E coli*-based production)	MBC	25	50	150
/mg·L^{-1}	MEC	3.125	NT	NT
HNP1-3	MIC	12.5	NT	NT
/mg·L^{-1}	MBC	25	NT	NT
	MEC	6.25	NT	NT
NP-1	MIC	6.25	12.5	25
/mg·L^{-1}	MBC	12.5	25	50
	MEC	3.125	NT	NT

HMGN2, high mobility group nucleosomal binding domain 2; HNP-1, human neutrophil defensin 1; MBC, minimal bactericidal concentration; MEC, minimal effective concentration; MIC, minimal inhibitory concentration; NP-1, rabbit neutrophil defensin 1; NT, not tested.

ing transcribed genes and enhances the transcriptional potential of corresponding genes[10,11]. Other experiments indicate that HMGN2 maintains the timing of early embryonic development in the mouse, and shows developmental regulation during organogenesis[12]. Furthermore, abnormal gene or protein expression of HMGN2 is related to some diseases such as neoplasms and autoimmune diseases[18,19]. The significance of HMGN2 in the host defense against infection is unclear. Frohm and colleagues attempted to identify antimicrobial polypeptides from human wound and blister fluid. Several known antimicrobial peptides or proteins, eg defensins HNP1–3, lysozyme, FALL-39 and histone H2B fragments, were found. Although HMGN2 was isolated, its antimicrobial property was not determined[20]. More recently, Fernandes *et al* have described a potent antimicrobial peptide isolated from the skin mucus secretions of fish[21], that is a member of the HMG protein family. In our experiment we observed the antimicrobial activity of the HMGN2 protein.

Many cationic antibiotic peptides are suggested to be membrane-active, assembling to form channels[22]. Alternatively, certain peptides cluster at the membrane surface cause a cooperative permeabilization by the carpet effect[23–25]. On the other hand, apidaecins function through a receptor-activated non-pore-forming mechanism involving stereospecificity[25]. PR-39 kills bacteria by interrupting both DNA and protein synthesis and the DNA binding property of tachyplesin I has also been implicated in antimicrobial activity[26]. By protein structure analysis of HMGN2, a transmembrane α-helical structure located at residues 18–48 was found, and this location is related to the DNA binding domain of this protein. As such, we prepared a recombinant α-helical domain and confirmed its antimicrobial activity. Thus, the transmembrane α-helical domain may be essential for the antimicrobial activity of HMGN2. The antimicrobial mechanisms of HMGN2 should be further studied.

References

1 Boman HG. Peptide antibiotics and their role in innate immunity. Annu Rev Immunol 1995; 13: 61–92.

2 Garcia-Penarrubia P, Koster FT, Kelley RO, McDowell TD, Bankhurst AD. Antimicrobial activity of human natural killer cells. J Exp Med 1989; 169: 99–113.

3 Levitz SM, Mathews HL, Murphy JW. Direct antimicrobial activity of T cell. Immunol Today 1995; 16: 387–90.

4 Prokesova L, Dung DH, Trebichavsky I, Formankova E, Stepankova V, John C. Antimicrobial activity of human mononuclear leukocytes against *Staphylococcus aureus*. Folia Microbiol (Praha) 1994; 39: 428–34.

5 Kumar J, Okada S, Clayberger C, Krensky AM. Granulysin: a novel antimicrobial. Expert Opin Investig Drugs 2001; 10: 321–9.

6 Andersson M, Gunne H, Agerberth B, Boman A, Bergman T, Sillard R, *et al*. NK-lysin, a novel effector peptide of cytotoxic T and NK cells. Structure and cDNA cloning of the porcine form, induction by interleukin 2, antimicrobial and antitumor activity. EMBO J 1995; 14: 1615–25.

7 Agerberth B, Charo J, Werr J, Olsson B, Idali F, Lindbom L, *et al*. The human antimicrobial and chemotactic peptides LL-37 and alpha-defensins are expressed by specific lymphocyte and monocyte populations. Blood 2000; 96: 3086–93.

8 Yang H, Huang N, Wu Q, Wang B. Isolation and characterization of an antimicrobial polypeptide from human LAK cells. Chin J Microbial Immunol 2003; 23: 241–3.

9 Landsman DO, McBride W, Bustin M. Chromosomal protein HMGN2. Complete human cDNA sequence and evidence for a multigene family. Nucleic Acids Res 1986; 17: 2301–14.

10 Tremethick DJ, Hyman L. High mobility group protein 14 and 17 can prevent the close packing of nucleosomes by increasing the strength of protein contacts in the linker DNA. J Biol Chem 1996; 271: 12009–16.

11 Vestner B, Bustin M, Gruss C. Stimulation of replication efficiency of a chromatin template by chromosomal protein HMGN2. J Biol Chem 1998; 273: 9409–14.

12 Lehtonen S, Lehtonen E. HMGN2 is an early marker of inductive interactions in the developing mouse kidney. Differentiation 2001; 67: 1541–63.

13 Selsted ME, Szklarek D, Lehrer RI. Purification and antimicrobial activity of antimicrobial peptides of rabbit granulocytes. Infect Immun 1984; 45: 150–4.

14 Ganz T, Selsted ME, Szklarek D, Harwig SSL, Daher K, Bainton DF, *et al*. Defensins, natural peptide antibiotics of human neotrophils. J Clin Invest 1985; 76: 1427–35.

15 Postnikov YV, Herrera JE, Hock R, Scheer U, Bustin M. Cluster of nucleosomes containing chromosomal protein HMGN2 in chromatin. J Mol Biol 1997; 274: 454–65.

16 Bustin M. Regulation of DNA-dependent activities by the functional motifs of the high-mobility group chromosomal proteins. Mol Cell Biol 1999; 19: 5237–46.

17 Hock R, Scheer U, Bustin M. Chromosomal protein HMG-14 and HMGN2 are released from mitotic chromosomes and imported into the nucleus by active transport. J Cell Biol 1998; 143: 1427–36.

18 Spieker N, Beitsma M, Sluis PV, Roobeek I, Dunnen JTD, Speleman F, *et al*. An integrated 5-Mb physical, genetic, and radiation hybrid map of a 1p36.1 region implicated in neuroblastoma pathogenesis. Genes Chromosomes Cancer 2000; 27: 143–52.

19 Ayer LM, Rubin RL, Dixon GH, Fritzler MJ. Antibodies to HMG proteins in patients with drug-induced autoimmunity. Arthritis Rheum 1994; 37: 98–103.

20 Frohm M, Gunne H, Bergman AC, Agerberth B, Bergman T, Boman A, *et al*. Biochemical and antimicrobial analysis of human wound and blister fluid. Eur J Biochem 1996; 237: 86–92.

21 Fernandes JMO, Saint N, Kemp GD, Smith VJ. Oncoryncin III: a potent antimicrobial peptide derived from the nonhistone chromosomal protein H6 of rainbow trout, *Oncorhynchus mykiss*. Biochem J 2003; 373: 621–8.

22 Tiozzo E, Rocco G, Tossi A, Romeo D. Wide-spectrum antibiotic activity of synthetic amphipathic peptides. Biochem Biophys Res Commun 1998; 249: 202–6.

23 Gennaro R, Zanetti M. Structural features and biological activities of the cathelicidin-derived antimicrobial peptides. Biopolymers 2000; 55: 31–49.
24 Yang YX, Feng Y, Wang BY. PCR-based site-specific mutagenesis of peptide antibiotic FALL-39 and its biologic activities. Acta Pharmacol Sin 2004; 25: 239–45.
25 Cabiaux V, Agerberth B, Johansson J, Homble F, Goormaghtigh E, Ruysschaert JM. Secondary structure and membrane interaction of PR-39, a Pro+Arg-rich antibacterial peptide. Eur J Biochem 1994; 224: 1019–27.
26 Agerberth B, Lee JY, Bergman T, Carlquist M, Boman HG, Mutt V, *et al*. Amino acid sequence of PR-39. Isolation from pig intestine of a new member of the family of proline–arginine-rich antimicrobial peptides. Eur J Biochem 1991; 202: 849–54.

The First Scientific Meeting of the Asian Society for Vascular Biology

October 8–11, 2005 Shanghai, China

Info: YuHUANG
Department of Physiology
Chinese University of Hong Kong
Hong Kong SAR, China
Phn 852-2609-6787
Fax 852-2603-5022
E-mail yu-huang@cuhk.edu.hk
http://www.sbsonline.org/sbscon/2005/index.php

Acta Pharmacologica Sinica 2005 Sep; 26 (9): 1093–1103

Full-length article

Preparation of recombinant human bone morphogenetic protein-2 loaded dextran-based microspheres and their characteristics[1]

Fa-ming CHEN[2,3], Zhi-fen WU[3], Qin-tao WANG[3], Hong WU[4], Yong-jie ZHANG[2], Xin NIE[2], Yan JIN[2,5]

[2]Center for Tissue Engineering, College of Stomatology; [3]Department of Periodontology and Mucosal Diseases, College of Stomatology; [4]Department of Chemistry, Faculty of Preclinical Medicine, the Fourth Military Medical University, Xi-an 710032, China

Key words

bone morphogenetic proteins; drug delivery system; sustained-release; tissue regeneration

[1] Project supported by Hi-Tech Research and Development Program (863 Program) of China (No 2002AA205041).
[5] Correspondence to Prof Yan JIN.
Phn 86-29-8337-6147.
Fax 86-29-8321-8039.
E-mail yanjin@fmmu.edu.cn

Received 2005-04-06
Accepted 2005-05-23

doi: 10.1111/j.1745-7254.2005.00180.x

Abstract

Aim: To prepare new pharmaceutical forms with sustained delivery properties of recombinant human bone morphogenetic protein-2 ($rhBMP_2$) for tissue engineering and guided tissue regeneration (GTR) use. **Methods:** $rhBMP_2$-loaded dextran-based hydrogel microspheres ($rhBMP_2$-MPs), which aimed to keep $rhBMP_2$ bioactivity and to achieve long-term sustained release of $rhBMP_2$, were prepared by double-phase emulsified condensation polymerization. The physical, chemical performances and biological characteristics of those microspheres were studied both *in vitro* and *in vivo*. **Results:** The microspheres' average diameter was 30.33±4.32 μm with 75.4% ranging from 20 μm to 40 μm and the drug loading and encapsulation efficiency were 7.82% and 82.25%, respectively. The $rhBMP_2$-releasing profiles *in vitro* showed that $rhBMP_2$ release could be maintained more than 10 d. The $rhBMP_2$-MPs, with good swelling and biodegradation behavior, could be kept for 6 months at below 4 ºC without significant characteristic change or bioactivity loss. Cytology studies showed that $rhBMP_2$-MPs could promote the proliferation of periodontal ligament cells (PDLCs) approximately 10 d, while the bioactivity of concentrated $rhBMP_2$ solution could keep no more than 3 d. Scanning electron microscope showed that $rhBMP_2$-MPs could be enchased into the porous structure of calcium phosphate ceremic (CPC) and the eugonic growth of PDLCs in CPC/$rhBMP_2$-MPs scaffolds. Animal experiments indicated that using CPC/$rhBMP_2$-MPs scaffolds could gain more periodontal tissue regeneration than using $rhBMP_2$ compound firsthand with CPC (CPC/$rhBMP_2$). **Conclusion:** By encapsulating $rhBMP_2$ into dextran-based microspheres, a small quantity of $rhBMP_2$ could achieve equivalent effects to the concentrated $rhBMP_2$ solution and at the same time, could prolong $rhBMP_2$ retention both *in vitro* and *in vivo*.

Introduction

Tissue engineering is one of the biomedical technologies used to induce tissue regeneration or repair body defects. The goal is to isolate adult stem cells in the tissue, then grow them in experimental devices into types of tissue that can be placed into injured regions to promote regeneration of tissue in and around injured areas of the body[1,2]. Drug delivery is an area in which chemical engineers have had a major impact, particularly for controlled delivery of pharmaceuticals to specific target sites such as tumors. Gene therapy is really metabolic engineering combined with drug delivery. It is a quantitative problem requiring a systems analysis. The right genes need to be delivered to the desired tissues, and proteins from that gene need to be made at the right time in the right amount. The lack of success with gene therapy is, at least in part, due to the inability of medical scientists to deal with these issues of well-controlled gene delivery and gene expression. This is a broad area that includes materials that are produced using biological processes

and biologically compatible materials that are used for drug delivery and other medical applications. However, questions pertaining to the scarce resources and the potential risk of seed cells, the biomaterials of scaffold and the methods used to design the cell and scaffold complex remain unresolved, which have resulted in their limited clinical application [3–5]. So far, several research approaches – both in animal experiments and in clinical treatment – have been attempted to promote tissue regeneration by bioactive agents, including members of the bone morphogenic protein, transforming growth factor, and insulin-like growth factor families, which are important to the maintenance and repair of most tissue defects[6–8]. Since periodontal tissue defects typically remain unhealed and often lead to further tissue degeneration and the loss of teeth, understanding the physiological role of these proteins in the wound-healing cascade and tissue regeneration is of critical importance in advancing the treatment of periodontal tissue loss and in enhancing periodontal tissue regeneration. Most of the research in this field has centered on examining the therapeutic effects that these molecules have on hard or soft tissues with the presence of 1 or more growth factors[9–16]. However, as the fields of tissue engineering and biomaterials merge with molecular and cellular biology, new drug delivery vehicles can be utilized to study the *in vivo* effect of these molecules on periodontal tissue regeneration or periodontal defect repair. Accordingly, this paper details the design and development of a genus of new composite scaffolds with the sustained delivery property of recombinant human bone morphogenetic protein-2 ($rhBMP_2$).

Bone morphogenetic proteins (BMPs) have been shown to modulate the wound-healing response in both hard and soft tissues. During the past decade, many investigators have demonstrated the anabolic effects of these wound-healing molecules on the promotion of periodontal attachment structures, namely alveolar bone, periodontal ligament and tooth root cementum[6–8,10–13]. However, because of their drawbacks such as short-term BMP retention and losable BMP biological activity *in vivo*, using agents for BMPs sustained release is of great importance . Although many agents such as calcium phosphate cement (CPC), collagen, bioactive glass ceramic (BGC), hydroxyapaite (HA) and more recently, some hydrogels have been used to enhance tissue regeneration and have gained good results. The actual effect is still uncertain considering the time BMP bioactivity might keep *in vivo*, as those materials themselves could not preserve BMPs from humoral dilution, metabolized and degraded action. There is evidence that the continuous presence of some growth factors at the periodontal tissue interface to provide a tangible effect is essential, which can accelerate the soft and hard tissue regeneration[6–8,17]. Therefore, it is rather inviting to search for new pharmaceutical forms that can sustain elevated growth factor levels and increase or improve tissue regeneration in periodontal diseases treatment or periodontal defect repair[18–20].

Microspheres as drug carriers have the advantage of sustained or controlled release, passive or active drug targeting to specific tissues, which notably reduce the side effects of drugs and improve their bioavailability. Therefore, microspheres as a drug delivery system have drawn much attention in the pharmaceutical field and have been successfully used in tumor chemotherapeutics and in the treatment of diabetes. Dextran-based hydrogels are widely used polymers in pharmaceutical products. The good biocompatibility, the degradation to non-toxic and readily excreted products were the main attractive characteristics of dextran-based hydrogels, which suggest its use in the drug delivery field[21]. In addition, dextran is relatively cheap and dextran-co-gelatin hydrogels have putative bioadhesive properties that allow the drug delivery systems, designed in different forms, to meet the need of periodontal tissues and mucosal tissues, as well as other especial tissues, such as the eye, nasal, gastrointestinal and urinary epithelial tissues[22–24]. In order to improve the therapeutic efficiency and to prolong BMP retention in periodontal bone defects , and to explore the possibility of preparing targeted $rhBMP_2$ delivery devices, this study was aimed at developing a new kind of $rhBMP_2$ delivery system: $rhBMP_2$-loaded dextran-based microspheres ($rhBMP_2$-MPs). The results indicated that using this delivery system could result in a long-term release of $rhBMP_2$ and could enhance periodontal tissue regeneration continually when compounded with tissue engineering scaffold materials.

Materials and methods

Materials Dextran (M_r 69 800 with 5% branches) was purchased from Xia-si Biomaterial Inc (Beijing, China), Gelatin G-6650 was obtained from Sigma (Sigma Chemicals, Saint-Louis, MO, USA) and dried at 60 ºC in a vacuum oven for 2 d. Span-80 and Dextranase (400–800 U/mg protein) was also purchased from Sigma. Triethylamine, 2,20-dimethoxy-2-phenyl acetophenone (DMAP), dimethyl formamide (DMF), *N*-methyl pyrrolidone (NMP) and *N*,*N*,*N*′,*N*′- tetramethylethylene diamine (TEMED) were obtained from E Merk (Mumbai, India). Glycidyl methacrylate (GMA) was purchased from Bioengineering Inc (Boston, MA, USA). All these materials were dried overnight at 70 ºC in a vacuum oven. $RhBMP_2$ were obtained from the Academy of Military

Medical Science (Beijing, China), acrylic acid (AA, Merck) was used after vacuum distillation. Water was double distilled. All other chemicals and solvents were used without further purification.

Preparation of $rhBMP_2$-MPs Using dextran and GMA, we synthesized the dex-GMA precursor as the method we reported recently with some modifications[25]. The synthesized procedure was as follows: Dextran was dissolved in a dimethyl sulphoxide(Me_2SO) solvent system (60 mL with Span-80 0.4 mL and TEMED 0.2 mL, DMAP 1.5 g, DMF 0.2 g and NMP 0.2 g) at 60 ºC under N_2 gas and stirred for 15 min. After dissolving, the solution was cooled down to 35 ºC and GMA was then slowly added to the dextran solution. The reaction was conducted at 35 ºC for 72 h under N_2 gas. The reaction product was precipitated with cold isopropyl alcohol, filtered, washed several times with isopropyl alcohol, and then freeze-dried in a vacuum oven. The degree of substitution (DS) of the dex-GMA precursor was estimated by the ^{1}H-NMR method. There is an anomeric proton attached to the C1 position of the dextran glucose ring that appears at 4.5–5.5 ppm in the NMR spectrum, where the protons of the hydroxyl groups appear. This proton does not react during the GMA substitution reaction, while some of the other protons of other hydroxyl groups are substituted by GMA. So, we can use the ratio of the normalized, integrated intensities of the sum of the hydroxyl group peaks to the normalized, integrated intensities of the anomeric proton peak to estimate the DS. For unsubstituted pure dextran, the ratio should be 3; while for GMA-substituted dextran, this ratio should be less than 3, and the magnitude would depend on the number of substitution. Thus, the DS could be calculated from the ratio: 3×(difference of the NMR proton intensity between dextran and dextran derivatives)/dextran. The dex-GMA precursor synthesized in this study had a DS of 2.6, that is, 2.6 hydroxyl groups per dextran glucose ring were substituted by GMA. Using dex-GMA, we synthesized a species of biodegradable poly (dex-GMA-co-gelatin) hydrogel microspheres, which were used as the carrier of $rhBMP_2$. The $rhBMP_2$-MPs were prepared by double-phase emulsified condensation polymerization method and optimal preparation parameters were obtained by the orthogonal design. The technique was as follows: 3 cuvettes of equivalent homogeneous aqueous dex-GMA and gelatin solution (10%, w/v) of 6 mL, each containing 0.6 g dex-GMA and 0.15 g gelatin, were preheated to 30 ºC and dropped into 3 different reactor systems comprising of 30 mL paraffin liquid, 0.2 mL Span-80 and 0.01 mL, 0.02 mL, or 0.03 mL TEMED. The 3 reactor systems were at 30 ºC in a water bath, forming a water-in-oil emulsion by stirring with a two-paddle stirrer. Ten minutes later, as the emulsion was obtained, concentrated $rhBMP_2$ solution (containing 0.08 g $rhBMP_2$) was dropped into the reactor systems. The resulting microspheres were washed 3 times with cool isopropanol, ethyl ether to remove the residual paraffin, washed with $rhBMP_2$ saturation water and then lyophilized, sized by passing through sieves of different apertures. The collected loaded microspheres were preserved in a desiccator. Unloaded microspheres were synthesized by the same procedure, with the exception of the concentrated $rhBMP_2$ solution added and $rhBMP_2$ saturation water washing.

Morphology, size, and swelling analysis Freeze-dried microspheres were sprinkled onto a piece of electric-glue paper, gold-sprinkled in a vacuum and then examined by scanning electron microscopes (SEM,S-520, Hitachi, Japan). Size and size distribution were calculated by 500 microparticles during SEM and the roundness of the microspheres were determined by a particle size analyzer (BI-90, Brookhaven Co, California, USA). At the same time, freeze-dried microspheres (5 mg) were suspended in aqueous solution (4 mL) for 5 min using an ultrasonic bath and then dropped onto a sheet glass. The morphology of swelling microspheres was observed by photomicroscope (XI 70, Olympus, Tokyo, Japan). Another solidified $rhBMP_2$-MPs powder (weight W_o of 5 mg) was dipped in aqueous solution for approximately 30 min, then using filtered paper absorbed the water and weighed the weight of the swollen microspheres (W_s). The swelling ratio (Rs) of the microspheres was calculated by the following formula:

$$Rs\,(\%) = (W_s - W_o)/W_o \times 100\%$$

Determination of drug loading and drug encapsulation efficiencies Drug encapsulation efficiencies(DE) and drug loading (DL) are 2 main indexes of pharmaceutical forms. DE reflects the pharmaceutical form's ability to encapsulating drugs and high DE means little drug wasted during preparation, while DL reflects the effectual drug component in a pharmaceutical form and high DL means high therapeutic component available. They are all of great importance. The determination methods included an exact weighed amount of $rhBMP_2$-MPs (100 mg); unloaded microspheres (100 mg) were treated with 50 mL NaOH (10%, *w*/*v*) water solution at 80 ºC for 20 min. Fully degraded dex-GMA/gelatin solution were adjusted to neutral solution with 3 $mol \cdot L^{-1}$ HCl and centrifugated for 5 min. The supernatants were mixed with total-ionic-strength adjusting buffer (TISAB II)and made into 50 mL of solution. Drug content in the solution were conducted by means of High Performance Liquid Chromatography (HPLC) (94-09SC, Orion Research Inc, Boston, MA, USA). The actual weight of $rhBMP_2$ found loaded should be

equal to the remainder of the $rhBMP_2$ contents between $rhBMP_2$-loaded and unloaded microspheres.

DE (%)=(Weight of $rhBMP_2$ found loaded)/(Weight of $rhBMP_2$ input)×100%

DL (%)=(Weight of $rhBMP_2$ found loaded)/(Weight of $rhBMP_2$-loaded microspheres)×100%

Biodegradation of $rhBMP_2$-MPs Reports have been found to show that dextran-based biomaterials could be biodegraded in any liquid with presence a very tiny quantity of dextranase. Thirty-six exact weighed amounts of $rhBMP_2$-MPs (100 mg) were dipped in 0.9% physiological saline (containing 0.05 μg/mL,0.1 μg/mL and 0.2 μg/mL dextranase, respectively) and divided into 4 groups at certain time intervals of 10 d, 20 d, 30 d, and 40 d; three of each group were collected and freeze-dried. The morphology of the biodegraded microspheres was observed by SEM and weight loss was also studied.

Stability and biological activities of $rhBMP_2$-MPs Dry $rhBMP_2$-MPs were sealed and deposited in a 4 ºC refrigerator or at room temperature for 6 months respectively. Their appearance, morphology, DE and DL were checked as routine procedure. The bioactivity of the microspheres were evaluated by the biological effects they had on the cultured cells *in vitro*, and at the same time, we investigated the biological effects of loaded microspheres compared to the equivalent concentrated $rhBMP_2$ solution. Human periodontal ligament cells (PDLCs) were obtained from premolars extracted for orthodontic reasons from a 14-year-old patient, using cultured methods as previously described by Somerman *et al*[26]. The protocol was approved by the Ethical Committee in Research from the Fourth Military Medical University. The cell growth assay was performed by MTT (purchased from Sigma, Saint-Louis, MO, USA) methods[27]. Generally, PDLCs were placed in a 96-well culture plate (Nunc A/S, Roskilde, Denmark) at a density of 30,000 cells/well in 2 μL of DMEM containing 10% FBS and antibiotics. After 16 h, the cells were washed with PBS and cultured in serum-free (CT)-FBS/DMEM supplemented with 100 μg/mL $rhBMP_2$ (group I) or 782 μg/mL $rhBMP_2$-MPs synthesized within 3 d (equal to 100 μg/mL $rhBMP_2$; group II), or 782 μg/mL $rhBMP_2$-MPs deposited in a 4 ºC refrigerator for 6 months (group III), or at room temperature for 6 months (group IV), the control group (group IV) served as the control supplemented with nothing. After 1, 2, 3, 5, 7, 10, 12 d, absorbance was read at 570 nm according to routine MTT methods. The cellular proliferation was calculated as the amount of MTT uptake.

Drug release study *in vitro* *In vitro* drug release profiles were obtained by a dynamic dialysis method simulating the temperature *in vivo*. Briefly, 3 groups of $rhBMP_2$-MPs (50 mg), according to different quantity of TEMED (0.01 mL, 0.02 mL and 0.03 mL) when prepared, were poured into a dialysis tube (IL61105, Rockford, USA), then placed at 37.0±0.5 ºC into phosphate buffer solution (PBS) of 150 mL (pH=7.0), respectively, and continuously stirred with a magnetic stirrer at 200 r/min. At specific time intervals of 5 h, 20 h, 30 h, 60 h, 90 h, 120 h, 150 h, 190 h, and 250 h, 10 mL of samples were removed from the release medium and the same volume and temperature of PBS was added back to the release medium. The samples were then assayed for drug content according to intraday standard curve. Results of triplicate test data were used to calculate accumulated drug release. Cumulative release profiles of different $rhBMP_2$-MPs were studied respectively.

CPC/$rhBMP_2$-MPs scaffolds preparation The calcium phosphate ceremic (CPC) was purchased from Rui Bang Biomaterial Inc (Shanghai, China) and CPC/$rhBMP_2$-MPs was obtained by a physical concoction mechanism using CPC, PBS, and $rhBMP_2$-MPs with the inverse proportion being 1:3:0.01, and then solidified in a vacuum desiccator. Human PDLCs cultured *in vitro* were collected and seeded on the concreting compound, the cell growth in the scaffolds and CPC/$rhBMP_2$-MPs framework were observed by SEM.

Animal experiment After receiving approval from the Committee of Research Facilities for Laboratory Animal Science, Fourth Military Medical University, 12 female beagle dogs weighing 10 to 14 kg and aged 12 to 20 months were used in this study. Good oral health was established by scaling and mechanical tooth-brushing. All surgical procedures were performed under general anesthesia with sodium pentobarbital (40 mg/kg), and local infiltrated anesthesia with 2% lidocaine with 1:80 000 noradrenaline. Experimental Class III furcation defects prepared in this study were based on the model described by Lindhe *et al*[28]. The second, third, and fourth premolars (P2, P3, and P4) in each dog were selected for experimentation (Figure 1A). Following sulcular incisions, mucoperiosteal flaps were raised, and Class III furcation defects were created surgically at P2, P3, and P4. The Class III defect height from the cemento-enamel junction to the reduced alveolar crest was 5.00±0.20 mm. Denuded root surfaces were prepared to remove all periodontal ligament and cementum. The roots were denuded only in the area within the furcation and extending to the mesial line angle for the mesial root and to the distal line for the distal root. Reference notches were placed around the circumference of the mesial and distal roots at the bottom of the bone level. All teeth were divided into 4 sub areas: maxillary left and right, submaxilla left and right, and then divided into 2 groups stochastically (to avoid the interaction of defects in

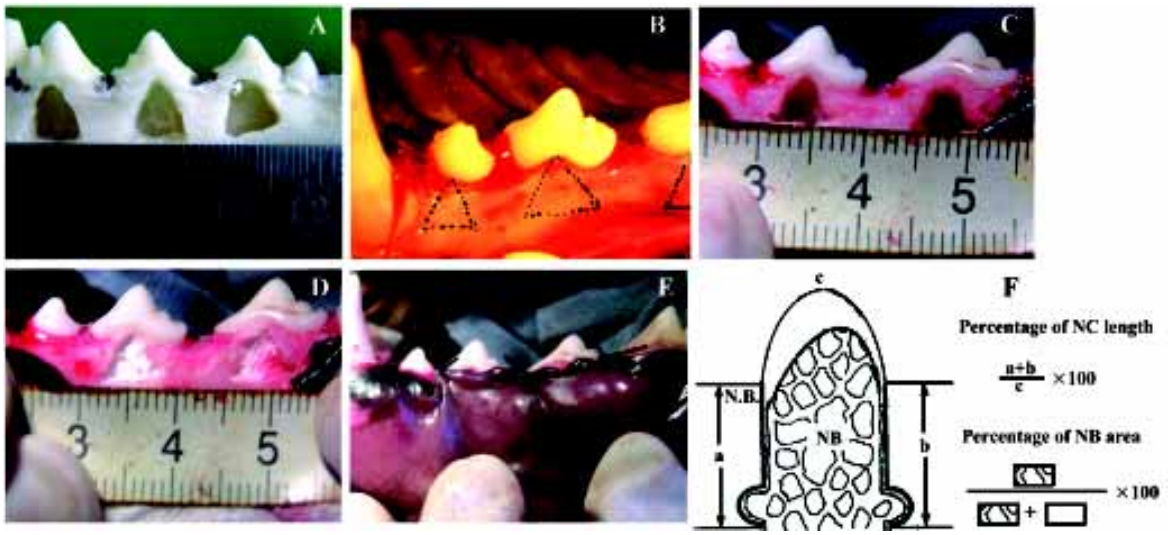

Figure 1. Animal experiment (A) Lindhe's model of Class III furcation defects; (B) Presurgical view of the mandibular premolar area and Class III furcation defects circumscription demarcation; (C) After defect preparation; (D) After transplantation of CPC/rhBMP$_2$-MPs scaffolds; (E) After repositioning of gingival flaps and suturing; (F) Schematic drawing of percentage of new cementum length and percentage of new bone.

one subarea): the experimental group and the control group. The experimental group was transplanted with CPC/rhBMP$_2$-MPs scaffolds while the control group was transplanted with CPC concreting compound soaked with the commensurate quantity of concentrated rhBMP$_2$ compared with rhBMP$_2$-MPs. In another words, the actual rhBMP$_2$ quantity transplanted into each Class III furcation defects was exactly same (Figure 1B, 1C, 1D, 1E). One or 2 months after transplantation, anesthetized animals were perfused with 1% glutaraldehyde in a sodium cacodylate buffer containing 0.05% calcium chloride (pH 7.3). The periodontal tissue regeneration was evaluated by unaided eye and X-ray. After that, the mandibles and maxillas were dissected and immersed in the same fixative. After decalcification with hydrochloride for 3 to 5 d, the mandibles and maxillas were dehydrated in paraffin. Serial section (5 μm) were cut in the mesial-distal plane throughout the buccal-lingal extension of the tooth. The sections were stained with hematoxylin and eosin (HE) or the Azan method, and observed using a light microscope. The center-most section and the immediate section on either side were subjected to morphometric analysis. The percentage of new cementum (NC) length and percentage of new bone (NB) area were measured on digitized photomicrographs captured in a computer. The lengths of NC formed along the denuded root surface on each specimen were added, and the percentage of the lengths to the total root surface length from one notch to the next notch was calculated. The area of NB on each specimen was calculated as a percentage of the area surrounded with reference notches at mesial and distal root surfaces space is present in normal periodontal tissue (Figure 1F). All data were statistically analyzed using the Mann-Whitney U test.

Results

Morphology and particle size The SEM photomicrographs of dried rhBMP$_2$-MPs showed a smooth and uniform surface (Figure 2A). The roundness of microspheres was 1.020±0.005. The average diameter was (30.33±4.32) μm with 75.4% ranging from 20 μm to 40 μm, The swelling ratio for solidified and dried microspheres was 4.18±0.06, and the size of the soggy microspheres size was approximately 5–10 times larger (Figure 2B). The morphology and particle size analysis showed no difference between loaded and unloaded freeze-dried or swelling microspheres, but when the swelling microspheres were sprinkled onto a piece of glass, half freeze-dried and then observed through a photomicroscope (XI 70, Olympus), the loaded microspheres were found to be a little fuscous. The unloaded microspheres were briefly translucent (Figure 2C, 2D), which was perhaps caused by the increase of the microspheres' density when drugs were encapsulated into the microspheres. Thus, we could presume that drug encapsulation was the primary drug association mechanism of dex-GMA-co-gelatin microspheres.

DL and DE The calculated results of DL and DE were 7.82% and 82.25%, respectively. In the present study, we achieved optimal preparation parameters using the orthogonal design, which was rhBMP$_2$ (0.5 mmol·L^{-1}), dex-GMA/gelatin solution (20%, *m*/*v*), emulsifying agent (1%, *m*/*v*), and 1:5

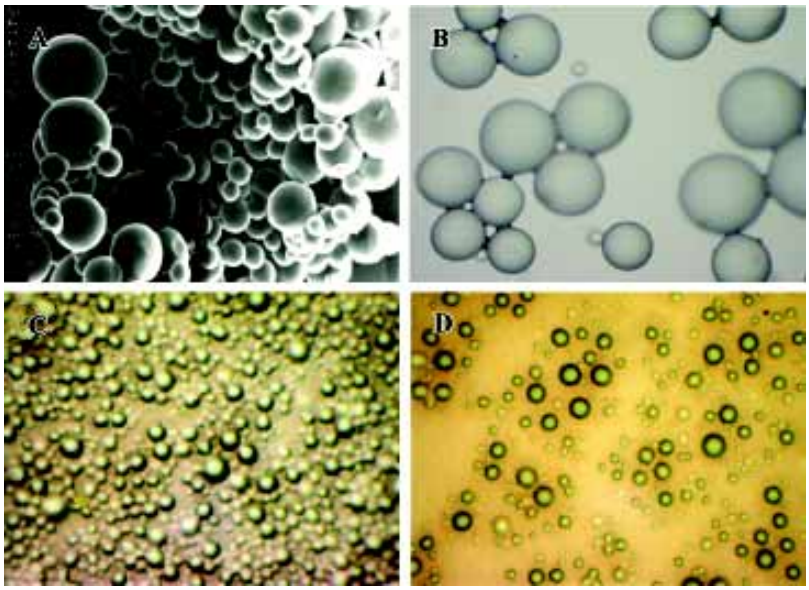

Figure 2. Micrographs of rhBMP$_2$-MPs. (A) SEM micrographs of dried rhBMP$_2$-MPs (×400); (B) Optical micrographs of soggy rhBMP$_2$-MPs(×100); (C) Loaded microspheres (×100); (D) Unloaded microspheres (×100).

(*v*/*v*) of water phase to oil phase. During the experiment we discovered that the concentration of rhBMP$_2$ affected the quality of the microspheres. When the content of rhBMP$_2$ exceeded 1 mmol/L, the microspheres' morphology was not uniform, and was prone to sticking. When the concentration was lower than 0.1 mmol/L, the drug content was also too low and thus, unfit for practical application. In order to reduce the loss of rhBMP$_2$ during the process of preparation, and improve the encapsulation efficiencies, presolidification was introduced and microspheres were washed with concentrated rhBMP$_2$ solution. Glutaraldehyde (25%, *v*/*v*) was used to solidify; the solidification time was over 24 h. The encapsulation efficiencies of rhBMP$_2$-MPs reached 86.73%, which was much higher than other biomaterials that have been reported[29].

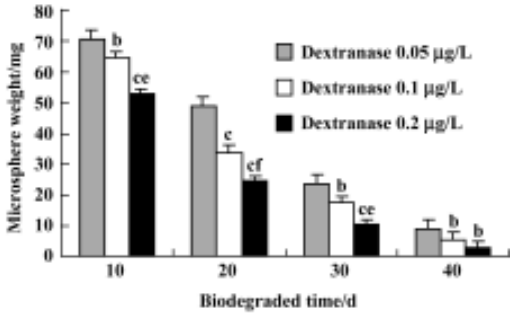

Figure 4. Weight of rhBMP$_2$-MPs at certain time intervals when degraded under conditions with different quantities of dextranase which showed significant difference. n=4. Mean±SEM. ^bP<0.05, ^cP<0.05 *vs* dextranase 0.05 μg/L. ^eP<0.05, ^fP<0.05 *vs* dextranase 0.1 μg/L.

Biodegradation of rhBMP$_2$-MPs rhBMP$_2$-MPs could completely degrade within 30–40 d by dextranase action (Figure 3) . The weight at specific time intervals was shown in Figure 4, and the microspheres eventually dissolved. However, Figure 4 also shows that the degraded speed interrelated closely to the consistence of dextranase. This might have important clinical meanings. In periodontal diseases such as periodontitis, especially rapidly progressive periodontitis, when the prolific nosogenetic bacteria and organisms in local environment (which cause excessive dex-

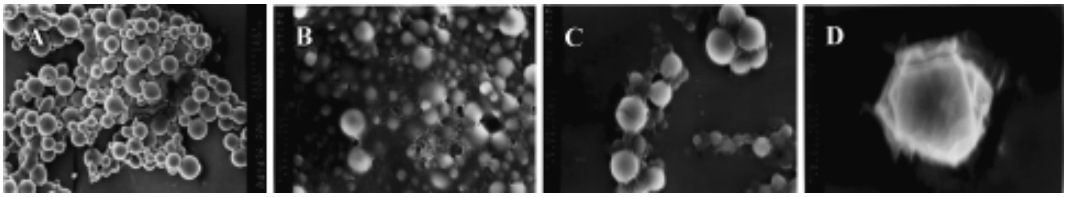

Figure 3. SEM of rhBMP$_2$-MPs biodegradation in certain time intervals. (A) After 10 d, rhBMP$_2$-MPs begin to be felted and dissolution can be seen (×200); (B) After 20 d rhBMP$_2$-MPs were felted diffusely and many rhBMP$_2$-MPs degraded (×100); (C) After 30 d most of rhBMP$_2$-MPs degraded (×1500); (D) After 40 d most of rhBMP$_2$-MPs disappeared and the surface of residuary rhBMP$_2$-MPs became scraggly (×4000).

tranase biosynthesis and the biodegradation of rhBMP$_2$-MPs more rapidly), rapid releasing rhBMP$_2$ from microspheres is beneficial for tissue repair and at the same time, can prevent tissue loss. It could be hypothesized that when rhBMP$_2$-MPs are topically applied, their presence in the periodontal environment, even at low concentrations, can prevent demineralization as well as promote remineralization of incipient lesions through rhBMP$_2$ release which are quickened under more dextranase conditions.

Stability of rhBMP$_2$-MPs The rhBMP$_2$-MPs were stable when sealed and stored below 4 ºC for 6 months without obvious physical and chemical characteristics change. However, when stored at room temperature, rhBMP$_2$-MPs biomorphic characteristic could not keep unchangeable and with a configuration of conglutination and abnormity (Figure 5). The proliferation curves of PDLCs in different groups are shown in Figure 6. Cytology studies showed that there was no significant differences between groups II and III (P> 0.05), indicating no significant bioactivity loss of rhBMP$_2$-MPs when stored below 4 ºC for 6 months. On the other hand, after 6 months of being stored at room temperature, rhBMP$_2$-MPs would no longer have any biological activity (P<0.01). In addition, the rhBMP$_2$-MPs could enhance the proliferation of PDLCs for more than 12 d continuously, while the pute rhBMP$_2$ bioactivity could function only in 3 d, which also showed the sustained delivery property of rhBMP$_2$-MPs (Figure 6).

***In vitro* release studies** The release profiles of rhBMP$_2$ from microspheres as a function of time showed that rhBMP$_2$-

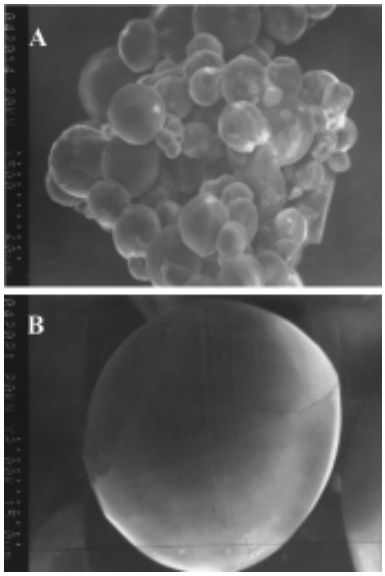

Figure 5. SEM of rhBMP$_2$-MPs stored at room temperature after 6 months. (A) ×500; (B) ×2000.

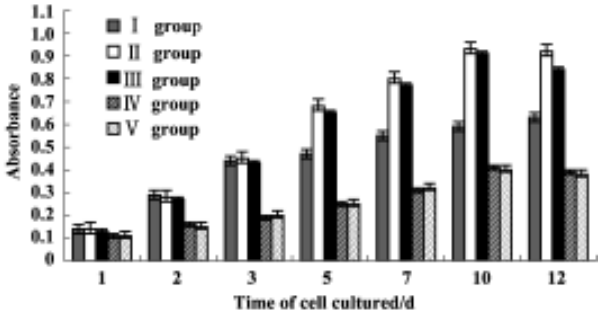

Figure 6. Enhancement effect on the proliferation responses of PDLCs by different cultured medium.

releasing kinetics *in vitro* fitted to first-order and Higuchi equations. From Figure 7 we could see that the drug release from rhBMP$_2$-MPs mainly consisted of 2 components with an initial rapid release followed by a slower exponential stage. The release profile *in vitro* was in accord with 2-phase kinetics law and more than 80% of the drugs were released during the first 10 d. Furthermore, changing the quantity of TEMED could influence drug release; rhBMP$_2$ release from rhBMP$_2$-MPs was slower when the quantity of TEMED was increased during preparation, which could be caused by the DS of microspheres increase followed with TEMED increased. During the initial stages, the microspheres were absorbed and the sphere enlarged rapidly; the drugs were rapidly released from the microspheres through the exoteric microaperture; When swelling was counterpoise, the drug release slowed down and was determined by drug pervasion and microsphere biodegradation. Thus, we can speculate that rhBMP$_2$ release from rhBMP$_2$-MPs might be controlled by some preparation technique change.

Cells growth on CPC/rhBMP$_2$-MPs scaffolds A scanning electron microscope showed that the porous structure

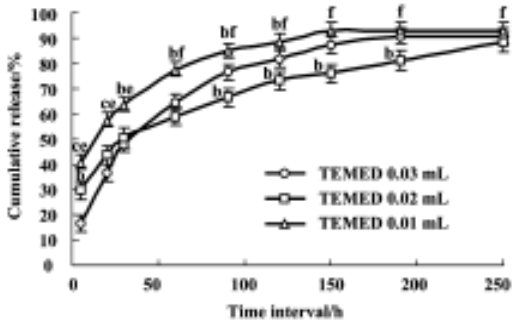

Figure 7. Cumulative release profiles of different rhBMP$_2$-MPs prepared with different quantities of TEMED. n=4. Mean±SEM. ^bP<0.05, ^cP<0.05 *vs* TEMED 0.03 mL. ^eP<0.05, ^fP<0.05 *vs* TEMED 0.02 mL.

of CPC/rhBMP$_2$-MPs compound and rhBMP$_2$-MPs could be adhered in the porous structure (Figure 8A). After 3 d, human PDLCs could grow on CPC/rhBMP$_2$-MPs compound both in the porous structure (Figure 8B) and on the material's surface (Figure 8C).

Animal experiment When observed with unaided eye in the experimental group, the defect was well regenerated after 1 month (Figure 9A) and was almost completely regenerated after 2 months (Figure 9B). The control group gained less tissue regeneration than the experimental group even after 2 months (Figure 9C). The X-ray observation results were shown in Figure 10. In the experimental group, a significant amount of new bone and an adequate width of periodontal ligament were observed (Figure 11A). The denuded root surface was almost completely covered with NC, and regenerated periodontal ligament separated the NB from the cementum. On the denuded root surfaces of the furcation area, newly formed cementum covered the surface, and the Sharpey's fibers inserted into the cementum were frequently observed (Figure 11B). In the control group, no cementum regeneration was observed (Figure 11C) and epithelial cells invaded into the top of the furcation in the area (Figure11D). Less bone regeneration was observed in this group compared to the experimental group. The percentages of NC length in the experimental group after 1 and 2 months were 93.9%±14.2% and 96.7%±5.29%, respectively, compared to 70.4%±12.1% and 72.8%±9.2% in the control group. The results showed significant difference (P<0.01). Accordingly,

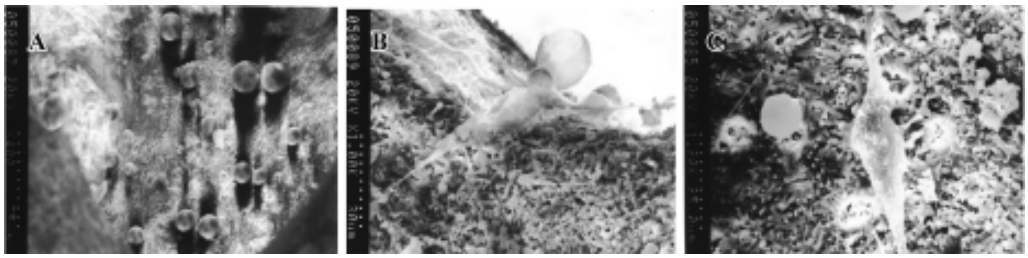

Figure 8. SEM of CPC/rhBMP$_2$-MPs scaffolds and cell growth. (A) CPC/rhBMP$_2$-MPs scaffolds (×400); (B, C) Cell growth on CPC/rhBMP$_2$-MPs scaffolds (×1000).

Figure 9. Tissue regeneration observed with unaided eye. (A) After 1 month experimental group; (B) After 2 months experimental group; (C) After 2 months control group.

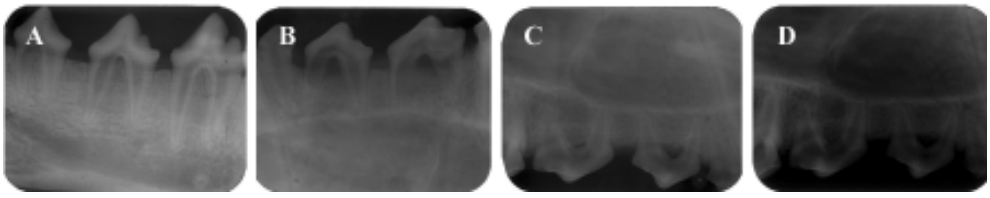

Figure 10. Tissue regeneration observed with X-ray after 2 months. (A) Tooth in mandible experimental group, well-regeneration in the Class III furcation defect area could be seen and the radiograph was on the verge of normal dental film; (B) Tooth in mandible control group, shadow in the furcation area was still obvious; (C) Tooth in maxilla experimental group, bone image in the furcation defect area showed well bone regeneration; (D) Tooth in maxilla control group, compared to experimental group, little new bone could be observed.

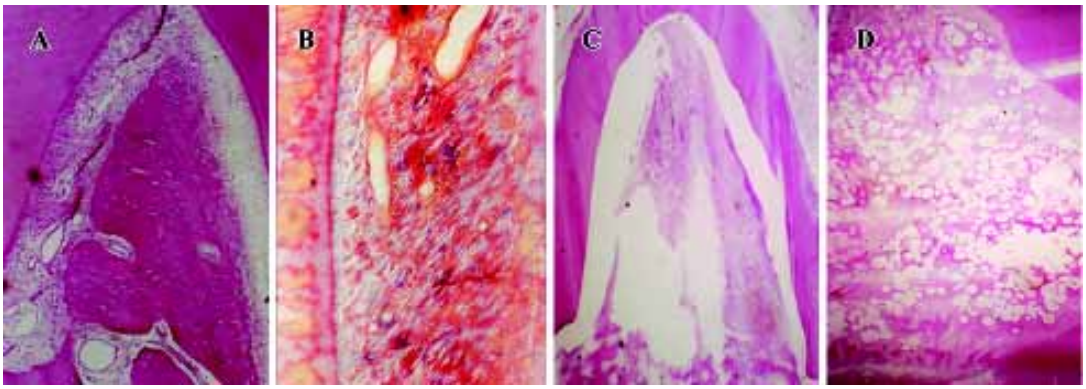

Figure 11. Histological analysis of periodontal tissue regeneration after 2 months. (A) HE×13 experimental group. After 2 months, there was a significant amount of NB and NC; (B) Azan method ×100 experimental group. An adequate width of periodontal ligament can be observed; (C) HE×13 control group. Less NB and NC can be observed; (D) HE×100 control group. Epithelial cells invaded the top of the furcation.

the percentages of NB were 62.6%±13.5% and 68.7%±9.73% in the experimental group and 54.7%±10.73% and 57.3%± 11.2% in the control group also showed significant difference (P<0.01).

Discussion

Biodegradable hydrogel microspheres are attractive devices for drug release because they combine good tissue biocompatibility with the possibility of manipulating the permeability for solutes. In particular, their use in pharmaceutics shows promise since recent advancements in biotechnology have led to a great variety of pharmacologically active peptides and proteins that are not adequately released from systems that are not biodegradable. Degradation of the hydrogel microspheres not only allows a tailored release of entrapped molecules, but also circumvents the removal of the empty device from the body[30–32]. Although the use of biodegradable hydrogel microspheres related to prolonged and/or controlled drug delivery has been widely investigated, the need for the development of hydrogels using simpler and more feasible methods still exists. Among the starting materials, polysaccharides and polyaminoacids represent good candidates to prepare biodegradable hydrogels by photocrosslinking reactions. Besides their biocompatibility and biodegradability, these polymers can also have functional groups incorporated into their structures. These functional groups include acrylic or methacrylic ones, which can easily lead to the formation of inter- and intra-chain bonds by UV irradiation. In this context, the synthesis and characterization of dextran-co-gelatin hydrogel microspheres show good biocompatibility and biodegradability. Dextran is a natural polysaccharide that is widely used in the pharmaceutical field[33–37]. It is water soluble, inert in biological systems and does not affect cell viability. The characteristic α-1,6-glucosidic linkage is hydrolyzed by dextranases, enzymes produced by various molds and certain bacteria as well as by mammalian cells. It has also been found that dextranases are produced by anaerobic Gram-negative intestinal bacteria[38]. The use of hydrogels based on dextran represents a strategy to release drug molecules in the colon after hydrolysis of the polysaccharide microspheres[39]. After sucking and swelling *in vivo*, $rhBMP_2$-MPs can keep $rhBMP_2$ concentrations over prolonged periods of time, which might be explained by the sustained-release of $rhBMP_2$ from $rhBMP_2$-MPs and dextran-based microspheres' bioadhesive properties to mouth parenchyma. Experiments conducted using $rhBMP_2$-MPs and $rhBMP_2$ solution as control revealed that $rhBMP_2$-MPs maintained $rhBMP_2$ elevation above baseline for about 10 d, but $rhBMP_2$ maintained for less than 3 d. This indicated the possibility that $rhBMP_2$-MPs could meet clinical intermittent administration by prolonging $rhBMP_2$ retention time significantly.

Many biomaterials such as Chitosan, polylacticacid (PLA), polyglycolicacid (PGA), PGA-co-PLA polymers (PLGA), poly (ethylene glycol) (PEG), gelatin, and polybutylcyanoacrylate (PBCA) were all reported to prepare growth factor-sustained release systems recently, but a lot of questions remain unanswered. The outstanding obstacle in the clinical application of growth factor carriers to promote tissue regeneration and control release of growth factors is still unrealized, which results in the growth factors not being able to maintain enough time or concentration during the tissue regenerated period. To meet the need of periodontal regeneration, new biomaterials used to prepare controlled release system of growth factors have become increasingly

important. From this study, we prepared a new carrier for the sustained release of $rhBMP_2$, which can be used to synthesize guided tissue regeneration biomembranes and build functional scaffolds in tissue engineering. In summary, for the first step in developing a new type of $rhBMP_2$ agent, we chose dextran-based micropspheres as sustained release carriers for topical $rhBMP_2$ applications. We proved the ability of $rhBMP_2$-MPs in prolonging $rhBMP_2$ release and their potential in prohibiting demineralization and enhancing the $rhBMP_2$ retention both *in vitro* and *in vivo*. This work offered a new method in contributing growth factors, not only BMPs, but also other growth factors for clinical use, which can be popularized with further evaluation both in animal experiment and in clinical cases. However, some limitations of using the microsphere-carrier combination, including the potential difficulty in manufacturing the carrier, and the expensive price considering the costly price of growth factors themselves. Moreover, the manufacture procedure and the application of this pharmaceutical form still require further study both experimentally and clincally.

References

1 Yu TT, Shoichet MS. Guided cell adhesion and outgrowth in peptide-modified channels for neural tissue engineering. Biomaterials 2005; 26: 1507–14.

2 Cheng MH, Brey EM, Allori A, Satterfield WC, Chang DW, Patrick CW Jr, *et al*. Ovine model for engineering bone segments. Tissue Eng 2005; 11: 214–25.

3 Choo AB, Padmanabhan J, Chin AC, Oh SK. Expansion of pluripotent human embryonic stem cells on human feeders. Biotechnol Bioeng 2004; 88: 321–31.

4 Hsu SH, Tsai CL, Tang CM. Evaluation of cellular affinity and compatibility to biodegradable polyesters and type-II collagen-modified scaffolds using immortalized rat chondrocytes. Artif Organs 2002; 26: 647–58.

5 Kim SS, Vacanti JP. The current status of tissue engineering as potential therapy. Semin Pediatr Surg 1999; 8: 119–23.

6 Sorensen RG, Wikesjo UM, Kinoshita A, Wozney JM. Periodontal repair in dogs: evaluation of a bioresorbable calcium phosphate cement (Ceredex) as a carrier for rhBMP-2. J Clin Periodontol 2004; 31: 796–804.

7 Wikesjo UM, Sorensen RG, Kinoshita A, Jian Li X, Wozney JM. Periodontal repair in dogs: effect of recombinant human bone morphogenetic protein-12 (rhBMP-12) on regeneration of alveolar bone and periodontal attachment. J Clin Periodontol 2004; 31: 662–70.

8 Hanisch O, Sorensen RG, Kinoshita A, Spiekermann H, Wozney JM, Wikesjo UM. Effect of recombinant human bone morphogenetic protein-2 in dehiscence defects with non-submerged immediate implants: an experimental study in Cynomolgus monkeys. J Periodontol 2003; 74: 648–57.

9 Camargo PM, Lekovic V, Weinlaender M, Vasilic N, Madzarevic M, Kenney EB. A reentry study on the use of bovine porous bone mineral, GTR, and platelet-rich plasma in the regenerative treatment of intrabony defects in humans. Int J Periodontics Restorative Dent 2005; 25: 49–59.

10 Wikesjo UM, Qahash M, Thomson RC, Cook AD, Rohrer MD, Wozney JM, *et al*. rhBMP-2 significantly enhances guided bone regeneration. Clin Oral Implants Res 2004; 15: 194–204.

11 Wikesjo UM, Xiropaidis AV, Thomson RC, Cook AD, Selvig KA, Hardwick WR. Periodontal repair in dogs: space-providing ePTFE devices increase rhBMP-2/ACS-induced bone formation. J Clin Periodontol 2003; 30: 715–25.

12 Wikesjo UM, Xiropaidis AV, Thomson RC, Cook AD, Selvig KA, Hardwick WR. Periodontal repair in dogs: rhBMP-2 significantly enhances bone formation under provisions for guided tissue regeneration. J Clin Periodontol 2003; 30: 705–14.

13 Ripamonti U, Reddi AH. Tissue engineering, morphogenesis, and regeneration of the periodontal tissues by bone morphogenetic proteins. Crit Rev Oral Biol Med 1997; 8: 154–63.

14 Nevins M, Camelo M, Nevins ML, Schenk RK, Lynch SE. Periodontal regeneration in humans using recombinant human platelet-derived growth factor-BB (rhPDGF-BB) and allogenic bone. J Periodontol 2003; 74: 1282–92.

15 Park YJ, Ku Y, Chung CP, Lee SJ. Control release of platelet-derived growth factor from porous poly (*L*-lactide) membranes for guided tissue regeneration. J Control Release 1998 12; 51: 201–11.

16 Wikesjo UM, Razi SS, Sigurdsson TJ, Tatakis DN, Lee MB, Ongpipattanakul B, *et al*. Periodontal repair in dogs: effect of recombinant human transforming growth factor-beta1 on guided tissue regeneration. J Clin Periodontol 1998; 25: 475–81.

17 Rimondini L, Nicoli-Aldini N, Fini M, Guzzardella G, Tschon M, Giardino R. *In vivo* experimental study on bone regeneration in critical bone defects using an injectable biodegradable PLA/PGA copolymer. Oral Surg Oral Med Oral Pathol Oral Radiol Endod 2005; 99: 148–54.

18 Hench LL, Xynos ID, Polak JM. Bioactive glasses for *in situ* tissue regeneration. J Biomater Sci Polym Ed 2004; 15: 543–62.

19 Schmokel HG, Weber FE, Seiler G, von Rechenberg B, Schense JC, Schawalder P, *et al*. Treatment of nonunions with nonglycosylated recombinant human bone morphogenetic protein-2 delivered from a fibrin matrix. Vet Surg 2004; 33: 112–8.

20 Holland TA, Tessmar JK, Tabata Y, Mikos AG. Transforming growth factor-beta 1 release from oligo (poly(ethylene glycol) fumarate) hydrogels in conditions that model the cartilage wound healing environment. J Control Release 2004; 94: 101–14.

21 Vandelli MA, Rivasi F, Guerra P, Forni F, Arletti R. Gelatin microspheres crosslinked with *D,L*-glyceraldehyde as a potential drug delivery system: preparation, characterisation, *in vitr*o and *in vivo* studies. Int J Pharm 2001; 215: 175–84.

22 Brime B, Ballesteros MP, Frutos P. Preparation and *in vitro* characterization of gelatin microspheres containing levodopa for nasal administration. J Microencapsul 2000; 17: 777–84.

23 Morimoto K, Katsumata H, Yabuta T, Iwanaga K, Kakemi M, Tabata Y, *et al*. Evaluation of gelatin microspheres for nasal and intramuscular administrations of salmon calcitonin. Eur J Pharmacol Sci 2001; 13: 179–85.

24 Nakase H, Okazaki K, Tabata Y, Uose S, Ohana M, Uchida K, *et al*. Development of an oral drug delivery system targeting immune-regulating cells in experimental inflammatory bowel disease:

a new therapeutic strategy. J Pharmacol Exp Ther 2000; 292: 15–21.
25 Chen FM, Wu ZF, Jin Y, Wang QT, Wu H, Wang GF, *et al*. Development of a hydrogel microsphere delivery system for rhBMP$_2$. J Pract Stomatol 2005; 21: 174–7. Chinese.
26 Someman MJ, Foster RA, Vorsteg GM, Progebin K, Wynn RL. Effects of minocycline on fibroblast attachment and spreading. J Periodontal Res 1988; 23: 154–9.
27 Coletta RD, Almeida OP, Graner E, Page RC, Bozzo L. Differential proliferation of fibroblast cultured from hereditary gingival fibromatosis and normal gingival. J Periodontal Res 1998; 33: 469–75.
28 Lindhe J, Pontoriero R, Berglundh T, Araujo M. The effect of flap management and bioresorbable occlusive devices in GTR treatment of degree III furcation defects. An experimental study in dogs. J Clin Periodontol 1995; 22: 276–83.
29 Ko JA, Park HJ, Hwang SJ, Park JB, Lee JS. Preparation and characterization of chitosan microparticles intended for controlled drug delivery. Int J Pharm 2002; 249: 165–74.
30 Stenekes RJ, Franssen O, van Bommel EM, Crommelin DJ, Hennink WE. The preparation of dextran microspheres in an all-aqueous system: effect of the formulation parameters on particle characteristics. Pharm Res 1998; 15: 557–61.
31 Kamath KR, Park K. Biodegradable hydrogels in drug delivery. Adv Drug Delivery Rev 1993; 11: 59–84.
32 Kuijpers AJ, van Wachem PB, van Luyn MJ, Brouwer LA, Engbers GH, Krijgsveld J, *et al*. *In vitro* and *in vivo* evaluation of gelatin-chondroitin sulphate hydrogels for controlled release of antibacterial proteins. Biomaterials 2000; 21: 1763–72.
33 Chourasia MK, Jain SK. Polysaccharides for colon targeted drug delivery. Drug Deliv 2004; 11: 129–48.
34 Harada M, Murata JI, Sakamura Y, Sakakibara H, Okuno S, Suzuki T. Carrier and dose effects on the pharmacokinetics of T-0128, a camptothecin analogue-carboxymethyl dextran conjugate, in non-tumor- and tumor-bearing rats. J Control Release 2001; 71: 71–86.
35 Kojima T, Hashida M, Muranishi S, Sezaki HJ. Mitomyc in C dextran conjugate: a novel high molecular weight pro-drug of mitomycin C. J Pharm Pharmacol 1980; 32: 30–4.
36 Williams AS, Taylor G. Synthesis, characterization and release of cromoglycate from dextran conjugates. Int J Pharm 1992; 83: 233–9.
37 Kim IS, Jeong YI, Kim DH, Lee YH, Kim SH. Albumin release from biodegradable hydrogels composed of dextran and poly (ethylene glycol) macromer. Arch Pharm Res 2001; 24: 69–73.
38 Sery TW, Herhe EJ. Degradation of dextrans by enzymes of intestinal bacteria. J Bacteriol 1956; 71: 373–80.
39 Brondsted H, Andersen C, Hovgaard L. Crosslinked dextran—a new capsule material for colon targeting of drugs. J Control Release 1998; 53: 7–13.

Acta Pharmacologica Sinica 2005 Sep; 26 (9): 1104–1110

Full-length article

Antihyperglycemic effects of total ginsenosides from leaves and stem of *Panax ginseng*

Jing-tian XIE[1,3], Chong-zhi WANG[1,3], An-bao WANG[1,3], Jian WU[1,3], Daniel BASILA[1,3], Chun-su YUAN[1,2,3,4]

[1]*Tang Center for Herbal Medicine Research*; [2]*Committee on Clinical Pharmacology*; [3]*Departments of Anesthesia and Critical Care, the Pritzker School of Medicine, University of Chicago, Chicago, Illinois 60637, USA*

Key words

Panax ginseng; total ginsenosides; diabetes mellitus; hyperglycemia; obesity; *ob/ob* mice

[4] Correspondence to Prof Chun-su YUAN, MD, PhD.
Phn 1-773-702-1916.
Fax 1-773-834-0601.
E-mail cyuan@midway.uchicago.edu

Received 2005-03-09
Accepted 2005-04-19

doi: 10.1111/j.1745-7254.2005.00156.x

Abstract

Aim: The antihyperglycemic effects of the total ginsenosides in Chinese ginseng (TGCG), extracted from leaves and the stem, were evaluated in diabetic C57BL/6J *ob/ob* mice. **Methods**: Animals received daily intraperitoneal injections of TGCG (100 and 200 mg/kg) or oral administration (150 and 300 mg/kg) for 12 d. Fasting blood glucose levels and body weight were measured after fasting the animals for 4 h. Peripheral glucose use was also measured using an intraperitoneal glucose tolerance test. **Results**: In the injection group, a high dose of TGCG (200 mg/kg) significantly lowered the fasting blood glucose levels in *ob/ob* mice on d 12 (153±16 mg/dL *vs* 203±9.8 mg/dL, $P<0.01$, compared to vehicle-treated group). In the oral group, blood glucose decreased notably with a dose of TGCG (300 mg/kg) on d 12 (169.1±12.6 mg/dL *vs* 211.6±13.8 mg/dL, $P<0.05$, compared to the vehicle-treated group). Glucose tolerance was also improved markedly in *ob/ob* mice. Furthermore, a significant reduction in bodyweight ($P<0.05$) was observed after 12 d of TGCG (300 mg/kg) treatment in mice from the oral group. **Conclusion**: The results indicated that in a diabetic *ob/ob* mouse model TGCG was endowed with significant anti-hyperglycemic and anti-obesity properties. Therefore, the total ginsenosides extracted from Chinese ginseng leaves and the stem may have some potential for treating diabetes.

Introduction

Diabetes mellitus is a devastating disease affecting approximately 8% of the total population in the USA and 3% of the population world wide, 90% of which suffer from type 2 diabetes[1]. Diabetes is a chronic metabolic disease that has a significant impact on the patients' quality of life as well as on the health care system. The incidence of diabetes is increasing rapidly, which will lead to a worldwide increase in the cost of management of the disease and its complications. Generally, diabetes is classified into two major categories: type 1 diabetes (formerly known as insulin-dependent diabetes mellitus, or IDDM), and type 2 diabetes (formerly known as non-insulin dependent diabetes mellitus, or NIDDM)[1,2]. Although the two types of diabetes have distinct pathogeneses, hyperglycemia and various life-threatening complications resulting from long-term hyperglycemia are common to both[3–7].

The drugs currently available for type 2 diabetes have a number of limitations, such as significant side effects and high rates of secondary failure. As the knowledge of the heterogeneity of this disorder increases, there is a need to look for more effective agents with fewer side effects[8]. This has led to the search for alternative therapies that may have a similar degree of efficacy without the troublesome side effects associated with conventional drug treatment. The identification of compounds with antihyperglycemic activity from medicinal plants may provide an opportunity to develop a new class of antidiabetic agents. According to previous reports, ginseng is one of the most important and valuable plants with antidiabetic properties[9].

Ginseng is a perennial herb of the *Araliaceae* family, cultivated in China, Japan, Korea, and Russia, as well as in the

USA and Canada. Ginseng has been used as a tonic remedy in traditional Chinese medicine for several thousands of years[10]. The pharmacological properties of ginseng are mainly attributed to ginsenosides, the active constituents that are found in the extracts of different species of ginseng[11,12]. Over 80 years ago, Japanese scientists observed that ginseng root extracts had antidiabetic properties[13,14]. Sub-sequently, the blood glucose-lowering effect of ginseng root was investigated by other researchers[15-19]. It has been reported that both Chinese ginseng (*Panax ginseng* C A Meyer) and American ginseng (*Panax quinquefolium* L) roots possess antihyperglycemic properties[18,20,21]. A limitation of using ginseng root, however, is its high cost. Other parts of the ginseng plant, namely; berries, leaves, and the stem, can also be harvested and could yield additional herbal material and improve the cost-efficiency of ginseng cultivation. Recently, we have demonstrated the antihyperglycemic properties of Chinese ginseng berry and root extract, American ginseng berry and leaf extract, polysaccharide fractions from American ginseng berry, and ginsenoside Re in diabetic *ob*/*ob* mice[22–28]. Moreover, our past data indicated that American ginseng leaf extract, with its high ginsenoside yield, could be an inexpensive alternative to the root in the treatment of diabetes[27]. In the present study, the total ginsenosides in Chinese ginseng (TGCG) were evaluated for antihyperglycemic and antiobesity properties in order to further examine the antidiabetic properties of the Chinese ginseng plant.

Materials and methods

Animals Adult male, diabetic C57BL/6J *ob*/*ob* mice were used in the present study, and were purchased from Jackson Laboratory (Bar Harbor, ME, USA). The study protocol was approved by the Institutional Animal Care and Use Committee of the University of Chicago. Animals were housed under controlled conditions with a 12-h light/dark cycle. Animals had free access to standard rodent pellet food (Zeigler Bros, Gardners, PA, USA) and water *ad libitum*, except when fasted before experiments. After 2–3 weeks of acclimation under these conditions, animals were grouped for the experiment.

Thirty-four diabetic *ob*/*ob* mice, 10–16 weeks old, weighing 58.2±0.6 g, were randomly divided into two groups used for the experiments: Group 1, Injection Group (*ip*) including high-dose TGCG group (200 mg/kg, n=7), low-dose TGCG group (100 mg/kg, n=6), and vehicle group (n=6); and Group 2, Oral Group (ig) including high-dose TGCG group (300 mg/kg, n=5), low-dose TGCG group (150 mg/kg, n=5), and vehicle group (n=5). Dose selection was based on previous reports[22]. The TGCG solution was injected intraperitoneally or orally administered once a day. Vehicle group animals received an equivalent volume of saline. No irritation or restlessness was observed following administration of the test solutions. All mice were housed in the same conditions during all experiments.

TGCG preparation The dried TGCG extracts were a gift from Mr Qing-hua ZHANG at Nankai University in Tianjin, China. Leaves and stems of *Panax ginseng* were purchased from Jilin Province in China. TGCG was analyzed using HPLC in our laboratory. The dried TGCG were dissolved in saline and vortexed for 2 min at room temperature before use.

Blood glucose levels As in our previous studies[22, 23, 27], fasting blood glucose levels (measured by Glucose Analyzer, Hemocue, Angelholm, Sweden) and bodyweight were measured after fasting the animals for 4 h (starting from 09:00) on d 0 (before treatment), d 5, and d 12. Blood glucose levels were determined from tail vein blood samples at 13:00 using the Glucose Analyzer.

Glucose tolerance test To evaluate the peripheral glucose use, an intraperitoneal glucose tolerance test (IPGTT) was performed on d 0 and d 12. On the test days, animals were fasted for 4 h starting from 09:00 followed by an ip administration of glucose (2 g/kg). Blood glucose levels were determined in blood samples from the tail vein at 0 (prior to glucose administration), 30, 60 and 120 min after glucose administration.

Statistical analysis Data are expressed as mean±SEM. Statistical significance between vehicle-treated versus drug-treated mice, and between before treatment versus after treatment were determined by a paired Student's t-test. A value of $P<0.05$ was considered statistically significant.

Results

HPLC assay Figure 1 shows the HPLC-UV (202 nm) chromatogram of TGCG. The analyzed results were Rb1 (0.32%), Rb2 (1.45%), Rc (1.68%), Rd (2.60%), Re (20.42%), Rg1 (14.60%), and Rg2 (4.64%). The rank order of the quantity of ginsenoside was Re>Rg1>Rg2>Rd>Rc>Rb2>Rb1. The results show that ginsenosides Re and Rg1 in TGCG are much higher than other ginsenosides.

Effect of TGCG on blood glucose levels in injection group Blood glucose levels in C57BL/6J *ob/ob* mice after 4 h fasting were measured on d 0, d 5, and d 12 after daily ip administration of TGCG or vehicle. As shown in Figure 2, diabetic *ob*/*ob* mice had remarkably high baseline fasting blood glucose levels (>200 mg/dL), which decreased significantly after administration of high-dose of TGCG. For example, on d 5 blood glucose levels were 179.0±12.7 mg/dL

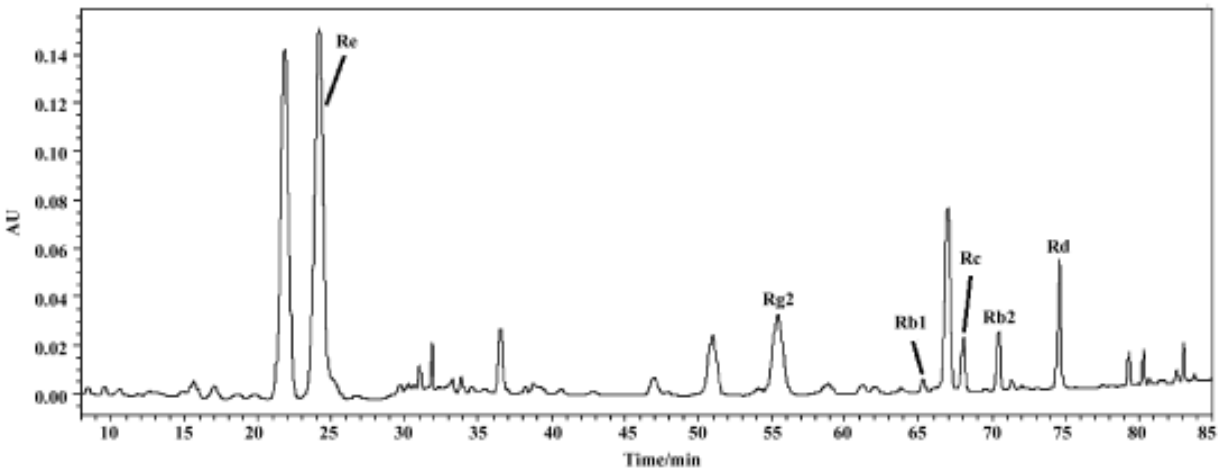

Figure 1. Chromatogram of total ginsenosides of Chinese ginseng (TGCG) extracted from leaves and stem.

(P<0.05) compared to the vehicle group, 192.0±10.7 mg/dL. On d 12, the high-dose group were normoglycemic (153.0± 16.8 mg/dL) compared to the vehicle group (203.0±9.8 mg/dL, P<0.01). At the low-dose (100 mg/kg), however, the blood glucose decreased from 203.0±15.0 mg/dL to 189.0±20.0 mg/dL on d 5 and 170.0±9.0 mg/dL on d 12 (P<0.05). Figure 2 also indicates that mice in the vehicle group did not show any remarkable changes in blood glucose levels. In contrast, TGCG inhibited blood glucose level in a dosage-dependent manner. The blood glucose lowering effect of TGCG was comparable to Chinese and American ginseng berry extracts and ginseng leaf extracts[22–28].

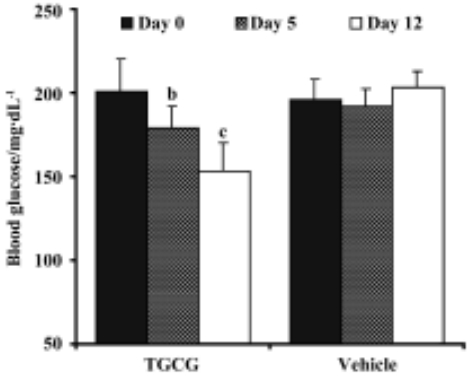

Figure 2. Effect of total ginsenosides of Chinese ginseng (TGCG; 200 mg/kg, ip, n=7) and vehicle (n=6) on fasting blood glucose in *ob*/*ob* mice. ^bP<0.05, ^cP<0.01 *vs* vehicle group.

Effects of TGCG on glucose tolerance test in injection group Glucose tolerance was evaluated by IPGTT, prior to and 12 d after treatment with TGCG. As shown in Figure 3A (high-dose group, 200 mg/kg) and Figure 3B (vehicle group), on d 0, *ob*/*ob* mice demonstrated basal hyperglycemia. This hyperglycemia was exacerbated by the ip glucose load and failed to return to baseline after 120 min, indicating glucose intolerance. After 12-d treatment with TGCG 200 mg/kg the overall glucose tolerance was improved remarkably. Figure 3A also shows that the area under the curve (AUC) decreased by 42% (from 830.4 mg·mL^{-1}·min^{-1} on d 0 to 486.3 mg·mL^{-1}·min^{-1} on d 12, P<0.01) after treatment. In the vehicle group (Figure 3B), however, the AUC decreased less than 10% (from 590.6 mg·mL^{-1}·min^{-1} on d 0 to 533.9 mg·mL^{-1}·min^{-1} on d 12, P>0.05).

Effect of TGCG on blood glucose levels in oral group We also evaluated the effects of orally administered (oral gavage) TGCG (150 and 300 mg/kg) on blood glucose in *ob/ob* mice. As shown in Table 1, after the TGCG high-dose treatment (300 mg/kg), fasting blood glucose levels significantly decreased from 209.8±16.7 mg/dL (d 0) to 186.2±11.0 mg/dL (d 5, P<0.05), and 169.1±12.6 mg/dL (d 12, both P<0.05, compared to vehicle group). In the low-dose group (150 mg/kg), blood glucose was lowered significantly on d 12 (183.5±10.9 mg/dL, P<0.05 *vs* vehicle group). The results showed that TGCG (150 and 300 mg/kg) caused anti-hyperglycemic effects after oral administration.

Effect of TGCG on body weight in oral group The aver-

Table 1. Effects of oral administration of total ginsenosides in Chinese ginseng (TGCG) on fasting blood glucose in *ob/ob* mice. ^bP<0.05 *vs* vehicle group.

		Blood glucose/mg·dL^{-1}		
	n	d 0	d 5	d 12
TGCG 150 mg/kg	5	214.0±21.1	201.7±16.1	183.5±10.9^b
TGCG 300 mg/kg	5	209.8±16.7	186.2±11.0^b	169.1±12.6^b
Vehicle	5	210.3±14.6	212.5±10.8	211.6±13.8

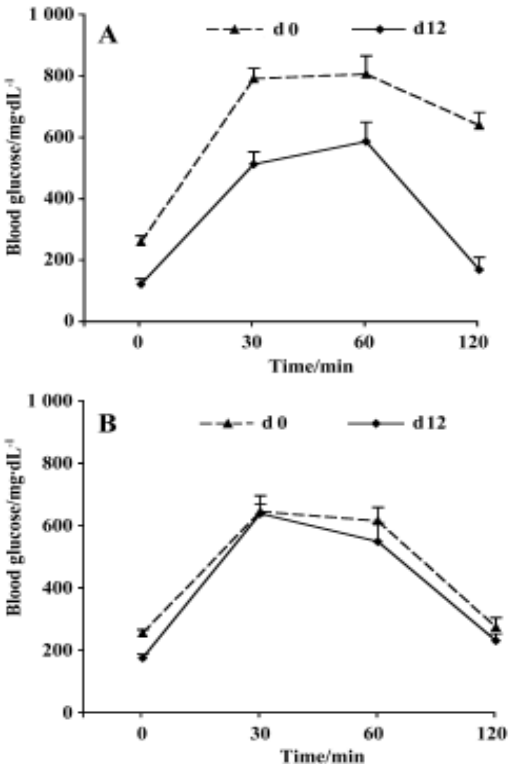

Figure 3. Effect of total ginsenosides in Chinese ginseng (TGCG) and vehicle on intraperitoneal glucose tolerance test in *ob*/*ob* mice before (d 0) and after a 12-d treatment (d 12). (A) TGCG (200 mg/kg, ip, n=7); (B) vehicle (n=6).

age bodyweight of adult *ob/ob* mice is almost twice as great as their lean littermates. As shown in Figure 4, the body weight of *ob/ob* mice in the oral vehicle group had a tendency to increase from d 0 (57.9±2.3 g) to d 12 (59.1±1.1 g). In contrast, in the oral administration of TGCG high-dose group (300 mg/kg), the body weight decreased from 60.8±0.5 g (d 0) to 57.2±1.0 g (P<0.05 compared to d 0) after 12-d TGCG

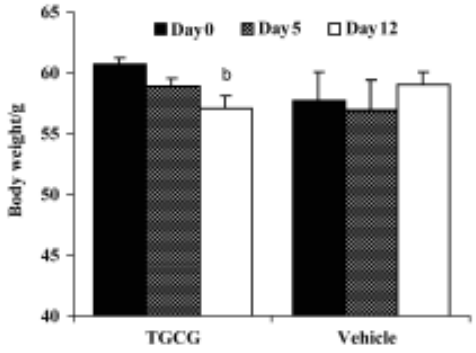

Figure 4. Effect of total ginsenosides of Chinese ginseng (TGCG; 300 mg/kg, ig, n=5) and vehicle (n=5) on body weight by oral administration in *ob/ob* mice. ^{b}P<0.05 *vs* d 0.

treatment. On d 5, however, the bodyweight was not significantly reduced (P>0.05 compared to d 0). The data indicated that TGCG (300 mg/kg, ig) possessed the effect of lowering the bodyweight in *ob*/*ob* mice. The body weight reduction activity of TGCG by oral administration was similar with Chinese and American ginseng berry extracts and ginseng leaf extracts by ip administration[22–28].

Discussion

Diabetes mellitus is a serious and chronic disease. Although oral antihyperglycemic agents and insulin are often successful in diabetes treatment, they have prominent side effects and fail to significantly alter the course of diabetic complications[8,29]. Therefore, there is an urgent need to look for more effective agents with fewer side effects, especially in medicinal plants. Previous records reveal that ginseng possesses anti-hyperglycemic properties[9]. The blood glucose-lowering effect of ginseng root has been studied[15–20,30]. According to our recent results, Chinese ginseng and American ginseng root, berry, and leaf extract, American ginseng berry polysaccharide fractions and their major active constituent ginsenoside Re, show anti-hyperglycemic properties in diabetic animals[22–28]. For a thorough study of the ginseng plant, other parts of ginseng should be analyzed for chemical composition, studied for biological activity and compared with ginseng root[31]. Recently in our laboratory, a comparison of constituent analyses among American ginseng root, berry, and leaf extract, using HPLC indicated that total ginsenosides (%) were different in ginseng berries, roots, and leaves. The total ginsenosides (%) in leaves are much higher than those in roots, and the content of ginsenoside Re in leaves is much higher than that in roots. The rank order of the quantity of total ginsenoside Re was leaves, berries, then roots[22–28]. Therefore, the ginseng leaf extract, with its high ginsenoside yield, has a promising potential to be an inexpensive alternative to the root in the treatment of diabetes. The major findings in the present study are as follows: (1) TGCG (200 and 100 mg/kg by ip and 300 and 150 mg/kg by ig) decreased fasting blood glucose levels significantly; (2) TGCG (200 mg/kg by ip) improved glucose tolerance; and (3) TGCG (300 mg/kg by ig) lowered the body weight in our experimental conditions.

As previous studies have shown the blood glucose lowering effects of ginseng root, berry, and leaf extracts individually[22–28]; the results from the present study indicate that TGCG also possesses an anti-hyperglycemic property. Both injection and oral administration of TGCG can decrease blood glucose. The results of IPGTT indicated that TGCG increased the peripheral glucose use and lowered blood glu-

cose levels. There are considerable amounts of data indicating that the chronic elevation of blood glucose causes many of the major complications of diabetes, including nephropathy, retinopathy, neuropathy, and macro- and microvascular damage[32]. Effective control of the blood glucose level, therefore, is a key step in preventing or reversing diabetic complications and improving the quality of life in both type 1 and type 2 diabetic patients[3–6]. Sustained reductions in hyperglycemia will decrease the risk of developing microvascular complications, and most likely reduce the risk of macrovascular complications[7]. The present data show TGCG not only lowers blood glucose in diabetic *ob/ob* mice, but also improves glucose tolerance. The anti-hyperglycemic effect and body weight reduction activity of TGCG may prove to be of clinical importance in improving the management of type 2 diabetes.

The mechanisms for improved blood glucose levels associated with ginseng part extract, including TGCG, and its major active components, ginsenosides, may be multifaceted and remain unclear so far. According to previous studies, there are several plausible hypotheses that may work independently or concurrently.

First, inhibition digestion and increase of energy expenditure may be involved. Our results have demonstrated that ginseng berry extract significantly decreased food intake activity, which reduced the source of carbohydrates[22]. Energy expenditure values were obtained in *ob/ob* mice treated with vehicle or Chinese ginseng berry extract. After the 12-d treatment, there was a significant increase in energy expenditure in *ob/ob* mice ($P<0.01$). However, we also showed that ginseng berry extract increased body temperature significantly in *ob/ob* mice. Increases in body temperature suggested that the carbohydrate metabolism in mice was enhanced, consistent with the increased basal metabolic rate.

Second, there can be improvement in sensitivity to insulin and changes in blood insulin levels. Prospective studies of populations at high risk for type 2 diabetes suggest that in most patients, the initial inherited damage is insulin resistance[33,34]. The *ob/ob* mice mimic these characteristics of type 2 diabetes and demonstrate insulin resistance and hyperinsulinemia by 6 weeks of age[35]. Our study confirmed these characteristics, and showed reduced glucose disposal rates during the glucose clamp study in vehicle-treated *ob/ob* mice, which suggested insulin resistance was partly caused by reduced insulin receptor sensitivity. Treatment with ginseng extract improved peripheral insulin action as suggested by the significantly improved insulin-stimulated glucose disposal. Improvement in peripheral insulin sensitivity should increase tissue glucose uptake, lower blood glucose levels towards normal[23], and should also result in reduced insulin requirements. This is consistent with our present data, which demonstrate a significant reduction in serum insulin levels following treatment with ginseng extract, accompanied by improved peripheral insulin action.

While we have indicated a decreased serum insulin level with ginseng treatment, there are reports in the published literature that ginseng treatment increases serum insulin. Kimura *et al* indicated that administration of ginseng to alloxan-treated rats resulted in increased serum insulin levels[36,37]. Obviously, the effect of ginseng on the serum insulin level is dependent on the animal model used. The *ob/ob* mice show typical characteristics similar to type 2 diabetes mellitus, where impaired glucose tolerance is caused by decreased peripheral insulin sensitivity and a compensatory excess insulin release, which is corrected by ginseng treatment. However, alloxan-treated diabetic animal models are characterized by chemical destruction of pancreatic islets and a decreased insulin level. Ginseng treatment in this model caused stimulation of the residual islets and increased serum insulin and glucose-stimulated insulin secretion[38].

Because ginsenosides were shown to release nitric oxide (NO) from vascular tissues[39], and NO is known to stimulate glucose-dependent secretion of insulin in rat islet cells[40], ginseng extract may affect glucose transport, which is mediated by NO and thus modulates NO-mediated insulin secretion[41,42]. Ginseng may act through both mechanisms in exerting its antidiabetic effect; however, the more relevant mechanism in the type 2 diabetic model would be improved insulin sensitivity, thereby reducing insulin requirements and decreasing serum insulin.

The last hypothesis addresses the importance of antioxidants. It is clear that antioxidants are important in diabetes and circulating levels of radical scavengers were impaired throughout the progression of diabetes[43]. Therefore, the antioxidant character of ginseng extract may be a significant mechanism of antidiabetic properties. Recently, we used a cardiomyocyte culture model to measure the antioxidant effect of American ginseng berry extract[44] and ginsenoside Re (unpublished data). The results demonstrated that American ginseng berry extract and Re attenuated oxidant stress and protected cells from lethal oxidant damage. Therefore, American ginseng berry extract and ginsenoside Re have antioxidant properties. The antioxidant character of ginseng extract may be an important mechanism in the antidiabetic action.

In summary, our results have demonstrated that TGCG possesses anti-hyperglycemic and anti-obesity properties in diabetic *ob/ob* mice *in vivo*. We conclude that the total ginsenoside fraction of the leaf and stem extract could po-

tentially be developed into newer anti-diabetic agents subject to confirmation of its efficacy in clinical trials.

Acknowledgement

This work was supported in part by the Tang Foundation for the Research of Traditional Chinese Medicine, NIH/NCCAM grants AT00381, AT00563, and AT002176.

References

1 Skyler JS. Diabetes mellitus: pathogenesis and treatment strategies. J Med Chem 2004; 47: 4113–7.
2 American Diabetes Association and National Institutes of Diabetes Digestive and Kidney Diseases. The prevention or delay of type 2 diabetes. Diabetes Care 2002; 25: 742–9.
3 Abraira C, Colwell JA, Nuttall FQ, Sawin CT, Nagel NJ, Comstock JP, *et al*. Veterans Affairs Cooperative Study on glycemic control and complications in type II diabetes (VA CSDM). Results of the feasibility trial. Veterans Affairs Cooperative Study in Type II Diabetes. Diabetes Care 1995; 18: 1113–23.
4 Ohkubo Y, Kishikawa H, Araki E, Miyata T, Isami S, Motoyoshi S, *et al*. Intensive insulin therapy prevents the progression of diabetic microvascular complications in Japanese patients with non-insulin-dependent diabetes mellitus: a randomized prospective 6-year study. Diabetes Res Clin Pract 1995; 28: 103–17.
5 Diabetes Control and Complications Trial Research Group. The effect of intensive treatment of diabetes on the development and progression of long-term complications in insulin-dependent diabetes mellitus. N Engl J Med 1993; 329: 977–86.
6 DeFronzo RA. Pharmacologic therapy for type 2 diabetes mellitus. Ann Intern Med 1999; 131: 281–303.
7 Gaster B, Hirsch IB. The effects of improved glycemic control on complications in type 2 diabetes. Arch Intern Med 1998; 158: 134–40.
8 Rang HP, Dale MM. The endocrine system pharmacology, UK: Longman Group; 1991. p504–8.
9 Xie JT, Mehendale S, Yuan CS. Ginseng and diabetes. Am J Chin Med 2005; 33: 397–404
10 Chevallier A. Encyclopedia of herbal medicine, New York: DK Publishing; 2000. p 40–3.
11 Attele AS, Wu JA, Yuan CS. Ginseng pharmacology: multiple constituents and multiple actions. Biochem Pharmacol 1999; 58: 1685–93.
12 Attele AS, Xie JT. Evidence based herbal pharmacology: an example using ginseng. In: Yuan CS, Beiber E, editors. A textbook of complementary and alternative therapies. New York: CRC Press Company; 2002. p202–18.
13 Wang C. Advances in study of pharmacology of ginseng. Acta Pharm Sin 1965; 12: 477–586.
14 Wang C. Recent advances in study of pharmacology of ginseng. Acta Pharm Sin 1980; 15: 312–20.
15 Ackerknecht EH. A short history of medicine, Baltimore: Johns Hopkins University Press; 1982. p35–46.
16 Bensky D, Gamble A. Chinese Herbal Medicine, Materia Medica. In: Ginseng. Seattle (WA): Eastland Press; 1993. p314–7.
17 Sotaniemi EA, Haapakoski E, Rautio A. Ginseng therapy in non-insulin-dependent diabetic patients. Diabetes Care 1995; 18: 1373–5.
18 Vuksan V, Sievenpiper JL, Koo VY, Francis T, Beljan-Zdravkovic U, Xu Z, *et al*. American ginseng (*Panax quinquefolius* L) reduces postprandial glycemia in nondiabetic subjects and subjects with type 2 diabetes mellitus. Arch Intern Med 2000; 160: 1009–13.
19 Chung SH, Choi CG, Park SH. Comparisons between white ginseng radix and rootlet for antidiabetic activity and mechanism in KKAy mice. Arch Pharm Res 2001; 24: 214–8.
20 Vuksan V, Stavro MP, Sievenpiper JL, Beljan-Zdravkovic U, Leiter LA, Josse RG, *et al*. Similar postprandial glycemic reductions with escalation of dose and administration time of American ginseng in type 2 diabetes. Diabetes Care 2000; 23: 1221–6.
21 Kimura M, Waki I, Tanaka O, Nagai Y, Shibata S. Pharmacological sequential trials for the fractionation of components with hypoglycemic activity in alloxan diabetic mice from ginseng radix. J Pharmacobiodyn 1981; 4: 402–9.
22 Attele AS, Zhou YP, Xie JT, Wu JA, Zhang L, Dey L, *et al*. Antidiabetic effects of *Panax ginseng* berry extract and the identification of an effective component. Diabetes 2002; 51: 1851–8.
23 Xie JT, Aung HH, Wu JA, Attele AS, Yuan CS. Effects of American ginseng berry extract on blood glucose levels in *ob/ob* mice. Am J Chin Med 2002; 30: 187–94.
24 Xie JT, Zhou YP, Dey L, Attele A, Wu J, Gu M, *et al*. Ginseng berry reduces blood glucose and body weight in db/db mice. Phytomedicine 2002; 9: 254–8.
25 Dey L, Xie JT, Wang A, Wu J, Maleckar SA, Yuan CS. Anti-hyperglycemic effects of ginseng: comparison between root and berry. Phytomedicine 2003; 10: 600–5.
26 Xie JT, Wu JA, Mehendale S, Aung HH, Yuan CS. Anti-hyperglycemic effect of the polysaccharides fraction from American ginseng berry extract in *ob/ob* mice. Phytomedicine 2004; 11: 182–7.
27 Xie JT, Mehendale A, Wang A, Aung H, Wu J, Osinski J, *et al*. American ginseng leaf: Ginsenoside analysis and hypoglycemic activity. Pharmacol Res 2004; 49: 113–7.
28 Yuan CS. Anti-diabetic and anti-obese effects of ginseng: from root to berry. In: Baek IN, editor. Advances in ginseng research. Seoul, Korea: The Korean Society of Ginseng; 2002. p 129–44.
29 Grover JK, Yadav S, Vats V. Medicinal plants of India with antidiabetic potential. J Ethnopharmacol 2002; 81: 81–100.
30 Zhonghua Bencao Editors. Zhonghua Bencao (Chinese Herbal Medicine). Shanghai: Shanghai Science and Technology Publishing House; 1996. p 268–81.
31 Jung CH, Chio IW, Cho HY. Antioxidant activities of cultivated and wild Korean ginseng leaves. Food Chem 2004; 92: 535–40
32 Evans JL, Goldfine ID, Maddux BA, Grodsky GM. Are oxidative stress-activated signaling pathways mediators of insulin resistance and beta-cell dysfunction? Diabetes 2003; 52: 1–8.
33 Lillioja S, Mott DM, Spraul M, Ferraro R, Foley JE, Ravussin E, *et al*. Insulin resistance and insulin secretory dysfunction as precursors of non-insulin-dependent diabetes mellitus. Prospective studies of Pima Indians. N Engl J Med 1993; 329: 1988–92.
34 Taylor SI, Accili D, Imai Y. Insulin resistance or insulin deficiency. Which is the primary cause of NIDDM? Diabetes 1994; 43: 735–40.
35 Genuth SM, Przybylski RJ, Rosenberg DM. Insulin resistance in

genetically obese, hyperglycemic mice. Endocrinology 1971; 88: 1230–8.
36 Kimura M, Suzuki J. The pattern of action of blended Chinese traditional medicines to glucose tolerance curves in genetically diabetic KK-CAy mice. J Pharmacobiodyn 1981; 4: 907–15.
37 Kimura M, Suzuki J, Koizumi T. Glucose tolerance curves in genetically diabetic KK-CAy mice: the pharmacokinetic analysis for humping effect. J Pharmacobiodyn 1981; 4: 149–61.
38 Kimura M, Waki I, Chujo T, Kikuchi T, Hiyama C, Yamazaki K, *et al*. Effects of hypoglycemic components in ginseng radix on blood insulin level in alloxan diabetic mice and on insulin release from perfused rat pancreas. J Pharmacobiodyn 1981; 4: 410–7.
39 Chen X. Cardiovascular protection by ginsenosides and their nitric oxide releasing action. Clin Exp Pharmacol Physiol 1996; 23: 728–32.
40 Spinas GA, Laffranchi R, Francoys I, David I, Richter C, Reinecke M. The early phase of glucose-stimulated insulin secretion requires nitric oxide. Diabetologia 1998; 41: 292–9.
41 Hasegawa H, Matsumiya S, Murakami C, *et al*. Interactions of ginseng extract, ginseng separated fractions, and some triterpenoid saponins with glucose transporters in sheep erythrocytes. Planta Med 1994; 60: 153–7.
42 Roy D, Perreault M, Marette A. Insulin stimulation of glucose uptake in skeletal muscles and adipose tissues *in vivo* is NO dependent. Am J Physiol 1998; 274: E692–9.
43 McCune LM, Johns T. Antioxidant activity in medicinal plants associated with the symptoms of diabetes mellitus used by the indigenous peoples of the North American boreal forest. J Ethnopharmacol 2002; 82: 197–205.
44 Shao ZH, Xie JT, Vanden Hoek TL, Mehendale S, Aung H, Li CQ, *et al*. Antioxidant effects of American ginseng berry extract in cardiomyocytes exposed to acute oxidant stress. Biochim Biophys Acta 2004; 1670: 165–71.

Acta Pharmacologica Sinica 2005 Sep; 26 (9): 1111–1116

Full-length article

Association of polymorphisms in low-density lipoprotein receptor-related protein 5 gene with bone mineral density in postmenopausal Chinese women[1]

Zhen-lin ZHANG[2], Yue-juan QIN, Jin-wei HE, Qi-ren HUANG, Miao LI, Yun-qiu HU, Yu-juan LIU

Center for Preventing and Treating Osteoporosis, Osteoporosis Research Unit, the Sixth People's Hospital, Shanghai Jiaotong University, Shanghai 200233, China

Key words

bone density; low-density lipoprotein receptor-related protein 5; polymorphism

[1]Project supported by the grant from the Natural Science Foundation of Shanghai (No 03ZR 14056).
[2]Correspondence to Dr Zhen-lin ZHANG. Phn/Fax 86-21-6408-1474. E-mail ZZL2002@medmail.com.cn

Received 2005-01-07
Accepted 2005-05-27

doi: 10.1111/j.1745-7254.2005.00173.x

Abstract

Aim: To investigate the possible association of Q89R, N740N and A1330V polymorphisms in low-density lipoprotein receptor-related protein 5 (LRP5) gene with bone mineral density (BMD) in postmenopausal Chinese women. **Methods:** Q89R, N740N and A1330V genotypes were determined by polymerase chain reaction-restriction fragment length polymorphism (PCR-RFLP) in 647 unrelated healthy postmenopausal Han Chinese women aged 43–76 years in Shanghai. BMD at lumbar spine 1–4 and the left proximal femur including the femoral neck, trochanter and Ward's triangle were measured by dual-energy X-ray absorptionmetry in all subjects. **Results:** The distribution of the Q89R, N740N and A1330V genotypes in this population was as follows: QQ 80.5%, QR 18.7%, and RR 0.8%; TT 66.9%, TC 31.1%, and CC 2.0%; AA 68.0%, AV 29.7%, and VV 2.3%. The frequencies of the Q89R, N740N and A1330V genotypes and alleles did not deviate from the Hardy-Weinberg equilibrium. We found that the Q89R and A1330V polymorphisms were in linkage disequilibrium in our population (χ^2=13.50, P<0.01). Both before and after adjusting for age, years since menopause, height, and weight, the Q89R or N740N genotypes were significantly associated with BMD at the femoral neck (P<0.05). Subjects with the Q89R QQ genotype or the N740N TT genotype had a significantly higher BMD at the femoral neck, compared with those with the QR/RR or TC/CC genotypes, respectively. No significant association was found between A1330V polymorphism and BMD at any site. **Conclusion:** Our findings suggest that the LRP5 gene is a candidate for the genetic determination of BMD in postmenopausal Chinese women.

Introduction

Osteoporosis is characterized by a decrease in bone mass as well as a deterioration of the bone architecture, resulting in an increased risk of fracture. The disease is multifactorial, and it depends on environmental and genetic factors. Twin studies have shown that genetic factors account for 60%–80% of the variance in bone mineral density (BMD)[1–3], which is the best predictor of the risk of osteoporosis. Several candidate genes that may contribute to BMD have been identified. Vitamin D receptor (VDR), estrogen receptor-alpha (ER-alpha), and collagen type I alpha 1 (COL1A1) genes are three important candidate genes that could potentially regulate BMD. Association and linkage studies have been performed in order to identify these candidate genes in the pathogenesis of osteoporosis[4–8]. However, their effect on the variation of BMD in the general population is controversial[9–11].

Recently, osteoporosis-pseudoglioma (OPPG), an autosomal recessive disease characterized by low bone mass, childhood fractures and abnormal eye development, has been shown to be due to an inherited loss of function of the gene for low-density lipoprotein receptor related protein 5 (LRP5)[12]. Moreover, two independent studies have sug-

gested that a mutation (G171V) in the LRP5 gene is associated with high bone mass (HBM)[13,14]. In addition to the above mentioned G171V mutation in the LRP5 gene, Gong *et al*[12] identified three potential disease-associated missense mutations in regions encoding the LRP5 extracellular domain: R494Q, R570W and V667M. More recently, mutation analysis have identified seven novel sequence variants in the human LRP5 gene[15]. Two of them are missense mutations (c.314A>G: Q89R and c.4037C>T: A1330V). Although Koller *et al*[16] found the evidence that a quantitative trait locus (QTL) contributed to normal variation in BMD on chromosome 11q12–13 (the chromosome region where LRP5 is located), only a few studies have investigated the association between LRP5 gene polymorphisms and variation in BMD in the general population[17–20]. However, these studies yielded inconsistent reports of the association between candidate loci and BMD, and only small groups of subjects were studied in the Japanese and Korean studies. In the present study, we investigated the association between BMD and Q89R, A1330V, and N740N polymorphisms in the LRP5 gene in 647 postmenopausal Chinese women.

Materials and methods

Study population The study population comprised of 647 unrelated, postmenopausal, healthy volunteers aged 43–76 years (mean±SD, 60.1±6.3 years) living in Shanghai, China. All participants were of the Han ethnic group. The clinical data taken included questions on medical history, including medication, and a survey of the incidence of disease. A physical checkup was carried out on all subjects, and all were found to be in good health. No participant had medical complications or was undergoing treatment for conditions known to affect bone metabolism, such as hyperthyroidism, diabetes mellitus, primary hyperparathyroidism, renal failure, pituitary and adrenal disease, or rheumatic disease. Postmenopausal women who had experienced early menopause (before 40 years of age) and those who had undergone ovariectomy or who were receiving estrogen replacement therapy were excluded. The study protocol was approved by the Committee on the Ethics of Human Research of Shanghai Jiaotong University Affiliated Sixth People's Hospital.

BMD measurements A total of 647 subjects were measured for BMD. The BMD of the lumbar spine 1–4 (L1–4) and the left proximal femur including femoral neck, trochanter, and Ward's triangle was measured by dual-energy X-ray aborptionmetry (DXA) on a Hologic QDR 2000 (Hologic, Bedford, MA, USA). The machine was calibrated daily, and the coefficient of variation (CV) values of the DXA measurements (which were obtained from 7 individuals repeatedly measured 5 times) at L1–4, the femoral neck, trochanter, and Ward's triangle were 0.9%, 1.93%, 1.48% and 2.85%, respectively[6,21]. The long-term reproducibility of our DXA data during the trial based on weekly repeated phantom measurements was 0.45%.

Genotyping DNA was isolated from peripheral blood leukocytes using conventional methods. Using the methods described by Okubo *et al*[15], we genotyped subjects with the LRP5 Q89R, N780N and A1330V polymorphisms. Genomic DNA (0.1 μg) was carried out in 30 μL buffer solution (10 mmol/L Tris-HCL, 50 mmol/L KCl, 1.5 mmol/L $MgCl_2$, 200 μmol/L of each of the four deoxyribonucleotides [dNTPs], 2.5 U of *Tag* polymerase, and 0.25 μmol/L of each primer).

Table 1. Three LRP5 gene polymorphisms were identified in this study.

Location	Sequence alteration	Amino acid change	PCR primer for RFLP detection	Restriction enzyme	Fragment size /bp
Exon 2	c.314 A>G	Q89R	Forward: 5'-TCTGGGCATAGTGCTCCATC-3' Reverse: 5'-TTCCGGGATGTGCCATTGAG-3'	*Ava*II	Wild (Q): 436 Variant (R): 274+162
Exon 10	c.2268 T>C	N740N	Forward: 5'-CTACTGGGCCGACACTGGGATTAA-3' Reverse: 5'-ACAGCTCTAATCACTGAGGG-3'	*Ase*I	Wild (t): 216+21 Variant (c): 237
Exon 18	c.4037 C>T	A1330V	Forward: 5'-GACTGTCAGGACCGCTCACACG-3' Reverse: 5'-AAGGTTTTCAGAGCCCCTAC-3'	*Dra*III	Wild (A): 143 Variant (V): 119+24

The polymerase chain reaction (PCR) was performed by using the following steps: 94 ºC for 5 min and then 94 ºC for 1 min, 56 ºC for 1 min, 72 ºC for 1 min, for 30 cycles, and 72 ºC for 7 min. The PCR primers and restriction endonucleases used for genotyping are summarized in Table 1. The PCR products were digested with *AvaI* I, *Ase* I, and *Dra*III restriction endonucleases, respectively. The Q89R genotypes were separated by electrophoresis in 1.5% agarose gel. The QQ genotype produces a 436 bp fragment, the RR genotype produces 274 bp and 162 bp fragments, and the heterozygous QR genotype produces 436 bp, 274 bp and 162 bp fragments. The N740N and A1330V genotypes were separated by electrophoresis on 8.0% polyacrylamide gel electrophoresis gels. The N740N CC genotype produces a 237 bp fragment, the TT genotype produces 216 bp and 21 bp fragments, and heterozygous TC genotypes produce 237 bp, 216 bp and 21 bp fragments. The A1330V AA genotype produces a 143 bp fragment, the VV genotype produces 119 bp and 24 bp fragments, and the heterozygous AV genotype produces 143 bp, 119 bp and 24 bp fragments.

Statistical analysis Allele frequencies were estimated by using the gene counting method, and the chi-squared test was used to identify significant departures from the Hardy-Weinberg equilibrium and linkage disequilibrium between genotypes. The relationship between various LRP5 genotypes and BMD was analyzed by using the unpaired Student's *t*-test. All associations were further evaluated using multiple linear regression analysis to adjust for risk factor. BMD was a dependent variable and the independent variables included age, height, weight, years since menopause, and LRP5 Q89R genotype (0=QQ, 1=QR+RR), N740N genotype (0=TT, 1=TC+CC), and A1330V genotype (0=AA, 1=AV+VV). $P<0.05$ was considered to be statistically significant. All statistical calculations were performed using the SPSS 9.0 program (SPSS, Chicago, IL, USA).

Results

Frequency distribution of LRP5 gene polymorphisms The genotype distribution and allele frequencies of polymorphisms of the LRP5 gene are shown in Table 2. Frequencies of the Q89R, N740N, and A1330V genotypes and alleles did not deviate from Hardy-Weinberg equilibrium. Strong linkage disequilibrium was found between Q89R and A1330V polymorphisms in our population ($\chi^2=13.50$, $P<0.01$; Table 3). However, no linkage disequilibrium was found between Q89R and N740N or between A1330V and N740N polymorphisms in these subjects.

Association between BMD and LRP5 genotype Because the frequencies of the Q89R RR, N780N CC and A1330V VV genotypes were all very low, we compared the background parameters and BMD in the QQ and QR/RR, TT and TC/CC, and AA and AV/VV groups for further analysis. The association between BMD and LRP5 genotype was analyzed us-

Table 2. Genotype distribution and allele frequencies of polymorphisms of the LRP5 gene in 647 postmenopausal Chinese women.

Polymorphism	Genotype frequencies			Allele frequencies	
Q89R	QQ	QR	RR	Q	R
	521 (80.5%)	121 (18.7%)	5 (0.8%)	0.899	0.101
N740N	T T	TC	CC	T	C
	433 (66.9%)	201 (31.1%)	13 (2.0%)	0.825	0.175
A1330V	AA	AV	VV	A	V
	440 (68.0%)	192 (29.7%)	15 (2.3%)	0.828	0.172

Table 3. Frequency of LRP5 genotypes by combination of Q89R and A1330V polymorphisms. Values represent the observed number of subjects with the combined genotypes of Q89R and A1330V; in parentheses are the expected numbers under linkage equilibrium. $\chi^2=13.50$; $P<0.01$ for linkage disequilibrium.

		A1330V polymorphic site		
		AA	AV	VV
Q89R	QQ	389 (355.61)	124 (155.17)	8 (12.13)
polymorphic	QR	48 (79.90)	66 (34.87)	7 (2.72)
site	RR	3 (4.49)	2 (1.96)	0 (0.15)

ing the unpaired Student's *t*-test (Table 4). BMD at the femoral neck was significantly higher in subjects with the Q89R QQ genotype than in the combined group with QR/RR genotypes ($P<0.05$). A similar finding was observed for the N740N genotype; that is, that subjects with the N740N TT genotype had significantly higher BMD at the femoral neck compared with those with TC/CC genotypes ($P<0.05$). Moreover, we further used multiple linear analysis to adjust for age, years since menopause, height, and weight. We found that BMD at the femoral neck was significantly associated with the Q89R polymorphism and the N740N polymorphism ($P<0.05$; Tables 5, 6). However, no significant association was found between the A1330V genotype and BMD at any site according to the unpaired Student's *t*-test or multiple linear analysis (Tables 4, 7).

Discussion

In this cross-sectional study of postmenopausal Chinese women, we found that differences existed in the frequencies of the Q89R, N740N and A1330V LRP5 polymorphisms compared with frequencies in Caucasian people; in particular,

Table 4. BMD and other characteristics according to Q89R, N740N and A1330V polymorphisms in the LRP5 gene in postmenopausal Chinese women. Mean±SD. $^cP<0.05$ *vs* QR/RR genotypes. $^eP<0.05$ *vs* TC/CC genotypes.

	Q89R genotype		N740N genotype		A1330V genotype	
	QQ	QR/RR	TT	TC/CC	AA	AV/VV
Number	521	121/5	433	201/13	440	192/15
Age (years)	59.8±6.2	60.2±6.8	59.9±6.3	59.8±6.2	60.0±6.3	59.5±6.2
Years since menopause (years)	11.3±8.5	11.7±8.1	11.3±8.9	11.4±7.4	11.7±9.0	10.4±6.5
Height (cm)	154.5±5.4	154.3±5.9	154.8±5.3	153.7±5.8	154.7±5.2	153.8±5.9
Weight (kg)	58.5±8.3	59.0±9.4	58.9±8.6	57.9±8.3	59.2±8.6	57.4±8.1
L1–4 BMD (g/cm^2)	0.798±0.140	0.795±0.146	0.805±0.142	0.782±0.138	0.803±0.140	0.786±0.143
Femoral neck BMD (g/cm^2)	0.662±0.114^c	0.644±0.108	0.665±0.117^e	0.645±0.103	0.664±0.115	0.646±0.109
Trochanter BMD (g/cm^2)	0.534±0.100	0.523±0.099	0.535±0.103	0.525±0.092	0.535±0.101	0.525±0.096
Ward's triangle BMD (g/cm^2)	0.493±0.144	0.469±0.135	0.494±0.149	0.477±0.128	0.494±0.144	0.476±0.143

Table 5. Multiple linear analysis with BMD as the dependent variable, and age, years since menopause, height, weight and Q89R genotype as the independent variables.

BMD site	Age	Years since menopause	Height	Weight	Q89R	
	β(*P*)	β(*P*)	β(*P*)	β(*P*)	β(*P*)	R^2
L1–4	-0.285 (0.000)	0.028 (0.640)	0.012 (0.819)	0.463 (0.000)	-0.017 (0.689)	0.291
Femoral neck	-0.436 (0.000)	0.069 (0.163)	-0.054 (0.151)	0.502 (0.000)	-0.065 (0.039)	0.379
Trochanter	-0.335 (0.000)	-0.029 (0.977)	-0.033 (0.397)	0.482 (0.000)	-0.042 (0.194)	0.334
Ward's triangle	-0.438 (0.000)	0.015 (0.774)	-0.025 (0.525)	0.334 (0.000)	-0.064 (0.056)	0.289

Table 6. Multiple linear analysis with BMD as the dependent variable, and age, years since menopause, height, weight and N740N genotype as the independent variables.

BMD site	Age	Years since menopause	Height	Weight	N740N	
	β(*P*)	β(*P*)	β(*P*)	β(*P*)	β(*P*)	R^2
L1–4	-0.283 (0.000)	0.026 (0.672)	0.008 (0.874)	0.462 (0.000)	-0.032 (0.462)	0.291
Femoral neck	-0.436 (0.000)	0.063 (0.197)	-0.058 (0.118)	0.499 (0.000)	-0.067 (0.033)	0.379
Trochanter	-0.335 (0.000)	-0.004 (0.938)	-0.034 (0.374)	0.481 (0.000)	-0.028 (0.384)	0.333
Ward's triangle	-0.438 (0.000)	0.011 (0.831)	-0.028 (0.483)	0.331 (0.000)	-0.044 (0.190)	0.287

Table 7. Multiple linear analysis with BMD as the dependent variable, and age, years since menopause, height, weight and A1330V genotype as the independent variables.

BMD site	Age	Years since menopause	Height	Weight	A1330V	
	β(*P*)	β(*P*)	β(*P*)	β(*P*)	β(*P*)	R^2
L1–4	-0.286 (0.000)	0.027 (0.658)	0.010 (0.851)	0.462 (0.000)	-0.017 (0.695)	0.291
Femoral neck	-0.437 (0.000)	0.064 (0.193)	-0.055 (0.142)	0.497 (0.000)	-0.044 (0.166)	0.376
Trochanter	-0.335 (0.000)	-0.003 (0.949)	-0.033 (0.401)	0.480 (0.000)	-0.013 (0.702)	0.332
Ward's triangle	-0.439 (0.000)	0.011 (0.841)	-0.027 (0.502)	0.329 (0.000)	-0.045 (0.186)	0.287

the Q89R polymorphism is very rare in Caucasian people[22,23]. However, the frequencies of genotypes and alleles of Q89R, N740N and A1330V LRP5 polymorphisms in Chinese women are similar to those found in Japanese and Korean subjects[15,17]. We found that the prevalent frequencies of the Q, T and A alleles in Chinese women were 89.9%, 82.5%, and 82.8%, respectively, as compared with 92%, 81%, and 82%, respectively, in Japanese subjects; furthermore, the frequencies of the Q89R Q and A1330V A alleles were 92% and 85% in Korean subjects. Therefore, LRP5, similar to other candidate genes (eg, VDR and COL1A1) had significantly different frequencies of genotypes and alleles in various ethnic groups[9,24].

In the present study, a significant association was observed between the Q89R genotype or the N740N genotype and BMD at the femoral neck both before and after adjusting for confounding factors, and subjects with the QQ genotype or the TT genotype had significantly higher BMD. Our findings are consistant with those of Koh *et al*[17], who recently reported that the Q89R polymorphism was significantly associated with BMD at the femoral neck and Ward's triangle in 219 young Korean men. After adjusting for age, weight, and height, a marginal association was observed at the femoral neck (P=0.098). However, the N740N polymorphism was not investigated in Korean men. The Q89R and A1330V polymorphisms are located in exon 2 and exon 18 in the LRP5 gene, respectively. The Q89R and A1330V polymorphisms were in linkage disequilibrium in our study population. This finding is similar to that for a Korean population[17], but differs from that for a European population[22]. Although the A1330V polymorphism is a functional mutation, no significant association was observed between the A1330V polymorphism and BMD either in postmenopausal Chinese women or in young Korean men. Similarly, Ferrari *et al*[18] failed to find a significant association between c.4037C>T (A1330V) polymorphism and lumbar bone mineral content and bone area in 889 healthy Caucasian people of both sexes.

LRP5 is a single pass membrane receptor whose extracellular domain contains four modules consisting of six YWTD repeats followed by an epidermal growth factor (EGF)-like motif and an LDLR-like ligand-binding domain[25,26]. Recent studies have shown that LRP5 and its closely related LRP family member, LRP6, are Wnt co-receptors that are capable of interacting with several key components of the Wnt pathway, and research regarding the signaling mechanisms involved in bone regulation by LRP5 has focused on this pathway[27–29]. The LRP5 gene has 23 exons. In addition to the G171V substitution in HBM, nine disease-causing mutations in exons encoding the LRP5 extracellular domain have been identified in patients with OPPG[12,13]. We found that the Q89R and N740N polymorphisms were only associated with BMD at the femoral neck, and were not associated with BMD at the lumbar spine in this large group of postmenopausal Chinese women, which suggests that the Q89R and N740N polymorphisms can influence the attainment of peak bone mass. Although the molecular mechanisms that underlie the association of the Q89R and N740N polymorphisms of the LRP5 gene with BMD remain unclear, we consider that the Q89R and N740N or related linked polymorphisms in the region might alter LRP5 protein function and might be associated with BMD.

In conclusion, we found a significant association between the Q89R and N740N polymorphisms in the LRP5 gene and BMD at the femoral neck in postmenopausal Chinese women, but we failed to observe a significant association between the A1330V polymorphism and BMD at any site. Our findings suggest that the LRP5 gene is a candidate for the genetic determination of BMD in postmenopausal Chinese women. Further studies will be needed to determine an association between the LRP5 gene polymorphisms and the risk of osteoporosis in the general population.

References

1 Nguyen TV, Howard GM, Kelly PJ, Eisman JA. Bone mass, lean mass and fat mass: same genes or same environments. Am J Epidemiol 1998; 147: 3–16.

2 Pocock NA, Eisman JA, Hopper JL, Yeates MG, Sambrook PN, Eberl S. Genetic determinants of bone mass in adults: a twin study. J Clin Invest 1987; 80: 706–10.
3 Hopper JL, Green RM, Nowson CA, Young D, Sherwin AJ, Kaymakci B, *et al*. Genetic, common environment, and individual specific components of variance for bone mineral density in 10- to 26-year-old females: a twin study. Am J Epidemiol 1998; 147: 17–29.
4 Morrison NA, Qi JC, Tokita A, Kelly PJ, Crofts L, Nguyen TV, *et al*. Prediction of bone density by vitamin D receptor alleles. Nature 1997; 367: 284–7.
5 Grant SF, Reid DM, Blake G, Herd R, Fogelman I, Ralston SH. Reduced bone density and osteoporotic fracture associated with a polymorphism Sp1 binding site in the collagen type I 1 gene. Nat Genet 1996; 14: 203–5.
6 Zhang ZL, Qin YJ, Huang QR, He JW, Li M, Hu YQ, *et al*. Association of estrogen receptor-alpha and vitamin D receptor genotypes with therapeutic response to calcium in postmenopausal Chinese women. Acta Pharmacol Sin 2004; 25: 1690–7.
7 Qin YJ, Zhang ZL, Huang QR, He JW, Hu YQ, Zhou Q, *et al*. Association of vitamin D receptor and estrogen receptor- gene polymorphism and peak bone mass and bone size in Chinese women. Acta Pharmacol Sin 2004; 25: 462–8.
8 Kobayashi S, Inoue S, Hosoi T, Ouchi Y, Shiraki M, Orimo H. Association of bone mineral density with polymorphism of the estrogen gene. J Bone Mineral Res 1996; 11: 306–11.
9 Gong G, Haynatzki G. Association between bone mineral density and candidate genes in different ethnic populations and its implications. Calcif Tissue Int 2003; 72: 113–23.
10 Han KO, Moon IG, Kang YS, Chung HY, Min HK, Han IK. Nonassociation of estrogen receptor genotypes with bone mineral density and estrogen responsiveness to hormone replacement therapy in Korean postmenopausal women. J Clin Endocrinol Metab 1997; 82: 991–5.
11 Ioannidis JP, Stavrou I, Trikalinos TA, Zois C, Brandi ML, Gennari L, *et al*. Association of polymorphism of the estrogen receptor gene with bone mineral density and fracture risk in women: A meta-analysis. J Bone Miner Res 2002; 17: 2048–60.
12 Gong Y, Slee RB, Fukai N, Rawadi G, Roman-Roman S, Reginato AM, *et al*. LDL receptor-related protein 5 (LRP5) affects bone accrual and eye development. Cell 2001; 107: 513–23.
13 Little RD, Carulli JP, Del Mastro RG, Dupuis J, Osborne M, Folz C, *et al*. A mutation in the LDL receptor related protein 5 gene results in the autosomal dominant high-bone-mass trait. Am J Hum Genet 2002; 70: 11–9.
14 Boyden LM, Mao J, Belsky J, Mitzner L, Farhi A, Mitnick MA, *et al*. High bone density due to a mutation in LDL-receptor-related protein 5. N Engl J Med 2002; 346: 1513–21.
15 Okubo M, Horinishi A, Kim DH, Yamamoto TT, Murase T. Seven novel sequence variants in the human low density lipoprotein receptor related protein 5 (LRP5) gene. Hum Mutat 2002; 19: 186.
16 Koller DL, Rodriguez LA, Christian JC, Slemenda CW, Econs MJ, Hui SL, *et al*. Linkage of a QTL contribution to normal variation in bone mineral density to chromosome 11q12–13. J Bone Mineral Res 1998; 13: 1903–8.
17 Koh JM, Jung MH, Hong JS, Park HJ, Chang JS, Shin HD, *et al*. Association between bone mineral density and LDL receptor-related protein 5 gene polymorphism in young Korean men. J Korean Med Sci 2004; 19: 407–12.
18 Ferrari SL, Deutsch S, Choudhury U, Chevalley T, Bonjour JP, Dermitzakis ET, *et al*. Polymorphisms in the low-density lipoprotein receptor-related protein 5 (LRP5) gene are associated with variation in vertebral bone mass, vertebral bone size, and stature in Whites. Am J Hum Genet 2004; 74: 866–75.
19 Urano T, Shiraki M, Ezura Y, Fujita M, Sekine E, Hoshino S, *et al*. Association of a single-nucleotide polymorphism in low-density lipoprotein receptor protein 5 gene with bone mineral density. J Bone Miner Metab 2004; 22: 341–5.
20 Koay MA, Woon PY, Zhang Y, Miles LJ, Duncan EL, Ralston SH, *et al*. Influence of LRP5 polymorphisms on normal variation in BMD. J Bone Miner Res 2004; 19: 1619–27.
21 Qin YJ, Shen H, Huang QR, Zhao LJ, Zhou Q, Li MX, *et al*. Estrogen receptor α gene polymorphism and peak bone density in Chinese nuclear families. J Bone Miner Res 2003; 18: 1028–35.
22 Twells RC, Mein CA, Phillips MS, Hess JF, Veijola R, Gilbey M, *et al*. Haplotype structure, LD blocks, and uneven recombination within the LRP5 gene. Genome Res 2003; 13: 845–55.
23 Van Wesenbeeck L, Cleiren E, Gram J, Beals RK, Benichou O, Scopelliti D, *et al*. Six novel missense mutations in the LDL receptor-related protein 5 (LRP5) gene in different conditions with an increased bone density. Am J Hum Genet 2003; 72: 763–71.
24 Lau EM, Young RP, Ho SC, Woo J, Kwok JL, Birjandi Z, *et al*. Vitamin D receptor gene polymorphisms and bone mineral density in elderly Chinese men and women in Hong Kong. Osteoporos Int 1999; 10: 226–30.
25 Brown MS, Herz J, Goldstein JL. LDL-receptor structure: Calcium cages, acid baths and recycling receptors. Nature 1997; 388: 629–30.
26 Wehrli M, Dougan ST, Caldwell K, O'Keefe L, Schwartz S, Vaizel-Ohayon D, *et al*. Arrow encodes and LDL-receptor-related protein essential for Wingless signalling. Nature 2000; 407: 527–30.
27 Tamai K, Semenov M, Kato Y, Spokony R, Liu C, Katsuyama Y, *et al*. LDL-receptor-related proteins in Win signal transduction. Nature 2000; 407: 530–5.
28 Mao J, Wang J, Liu B, Pan W, Farr GH 3rd, Flynn C, *et al*. Low-density lipoprotein receptor-related protein-5 binds to axin and regulates the canonical Win signaling pathway. Mol Cell 2001; 7: 801–9.
29 Kato M, Patel MS, Levasseur R, Lobov I, Chang BH, Glass DA 2nd, *et al*. Cbfa1-inderpendent decrease in osteoblast proliferation, osteopenia, and persistent embryonic eye vascularization in mice deficient in LRP5, a Wnt coreceptor. J Cell Biol 2002; 157: 303–14.

Acta Pharmacologica Sinica 2005 Sep; 26 (9): 1117–1122

Full-length article

Effects of CpG oligodeoxynucleotide on transcription factors GATA-3 and T-bet mRNA expression in asthmatic mice

Zu-qun WU[1,2], Yi-ping XU[3], Hua XIANG[4], Hua-hao SHEN[1]

[1]Department of Respiratory Medicine, the Second Affiliated Hospital, [4]Department of Pathology, the First Affiliated Hospital, School of Medicine, Zhejiang University, Hangzhou 310009, China; [3]Department of Respiratory Medicine, Renji Hospital, Shanghai Second Medical University, Shanghai 200001, China

Key words

asthma; inflammation; CpG oligodeoxynucleotide; GATA-3; T-bet; mice

[2] Correspondence to Dr Zu-qun WU.
Phn/Fax 86-571-8778-4553.
E-mail wuzuqun522@sohu.com

Received 2004-11-03
Accepted 2005-04-10

doi: 10.1111/j.1745-7254.2005.00157.x

Abstract

Aim: To investigate effects of CpG oligodeoxynucleotide (CpG ODN) on the mRNA expression of transcription factors GATA binding protein 3 (GATA-3) and T-box expressed in T cells (T-bet) in asthmatic mice. **Methods:** An asthmatic mouse model was established and treated with CpG ODN. Total inflammatory cells and eosinophils in bronchoalveolar lavage fluid (BALF) were counted and inflammatory cell infiltration in lung tissue was evaluated. Interferon-γ and interleukin-4 concentrations in BALF and splenocyte culture supernatants were detected using an enzyme-linked immunosorbent assay. Transcription factor GATA-3 and T-bet mRNA expression in splenocytes and lung tissue were detected by reverse transcription-polymerase chain reaction. **Results:** Total inflammatory cells and eosinophils in BALF were reduced in the CpG ODN-treated group compared with the asthma group, and inflammatory cell infiltration in lung tissue was also significantly alleviated. CpG ODN treatment increased the interferon-γ concentration but decreased the interleukin-4 concentration in both BALF and splenocyte culture supernatants. GATA-3 mRNA expression was reduced in both lung tissue and splenocytes in the CpG ODN-treated group, while the mRNA ratio of T-bet to GATA-3 in splenocytes was increased. **Conclusion:** CpG ODN treatment inhibits airway inflammatory cell infiltration and regulates interferon-γ/interleukin-4 synthesis in asthmatic mice, possibly through a mechanism of downregulation of GATA-3 mRNA expression in both lung tissue and splenocytes.

Introduction

Asthma is a chronic airway inflammatory disease involving multiple inflammatory cells and cytokines. T-helper type 2 cells (Th2) are considered to play central role in the pathogenesis of asthma by producing a variety of cytokines such as interleukin (IL)-4, IL-5, IL-9, and IL-13[1,2]. These cytokines promote IgE synthesis and mediate airway inflammatory cells (such as eosinophil, mast cell, T lymphocyte and neutrophil) infiltration. On the other hand, T-helper type 1 cells (Th1) inhibit Th2 function by producing interferon (IFN)-γ. Recent studies show that bacterial DNA containing unmethylated CpG motifs, or immunostimulatory sequences (ISS), can induce strong Th1-polarized immune responses both *in vivo*[3] and *in vitro*[4,5]. The induction of Th1 responses is thought to result from the ability of ISS (containing CpG) to induce activation and secretion of IL-12 and IL-18 by macrophages and dendritic cells[6,7], which promote IFN-γ production and polarize T-helper type 0 cells (Th0) to Th1. Studies also show that T-box expressed in T cells (T-bet) and GATA binding protein 3 (GATA-3) are 2 T cell-specific transcription factors. T-bet promotes Th1 polarization while GATA-3 enhances Th2 polarization. In the present study, we investigated the effects of the CpG oligodeoxynucleotide (ODN) on the mRNA expression of transcription factors GATA-3 and T-bet in splenocytes and lung tissue in a mouse model of asthma.

Materials and methods

Mice and reagents Thirty-six male BALB/c mice (approximately 6–10 weeks old, purchased from the Shanghai Experimental Animal Center of the Chinese Academy of Sciences, Shanghai, China) were maintained in specific pathogen free (SPF) animal facility at Renji Hospital, Shanghai Second Medical University (Shanghai, China). The CpG ODN consisted of 20 bases containing 2 CpG motifs: TCCATGACGTTCCTGACGTT was synthesized and purified by Sangon Biological Engineering and Technology (Shanghai, China), and ovalbumin (OVA) was purchased from Sigma (St Louis, MO, USA). IL-4 and IFN-γ enzyme-linked immunosorbent assay (ELISA) kits were purchased from JingMei Biotech (Shenzhen, China). Trizol reagent was purchased from Invitrogen (Carlsbad, CA, USA). Oligo$(dT)_{18}$ primer and 2×Master Mix were purchased from MBI Fermentas (Hanover, MD, USA).

OVA sensitization and challenge Mice were divided into 3 groups: (i) group A, control group; (ii) group B, OVA-sensitized and -challenged; and (iii) group C, OVA-sensitized and challenged, CpG ODN-treated. Mice were sensitized and challenged with chicken OVA as described previously[8]. Briefly, on d 0, d 7, d 14, and d 21, all animals were injected with 0.2 mL phosphate-buffered saline (PBS) containing 100 μg OVA and 2 mg aluminum hydroxide (alum). On d 26, d 30, d 36, and d 37, animals were challenged with 2% OVA aerosol for 30 mins. Control mice (group A) received a saline-only aerosol.

Administration of CpG oligodeoxynucleotide On d 24, d 28, and d 32, mice in group C were injected with 0.1 mL PBS containing 50 μg CpG ODN. Mice were assessed for pulmonary cellular infiltration histopathology on d 38.

Cellular count in branchoalveolar lavage fluid and lung histology Bronchoalveolar lavage (BAL) was carried out as in Kline *et al*[9]. After euthanasia, the trachea was cannulated and the lungs underwent lavage 3 times with 0.5 mL PBS. The lavage samples were processed immediately for total and differential cell counts. BAL fluid (BALF; 10 μL) was used for counting total inflammatory cells. The residual BALF was centrifuged (10 min, 2000×*g*) and the supernatant was stored at -30 °C for cytokine detection. The precipitated cells were used to prepare cell slides, which were stained with hematoxylin and eosin (HE), and 200 cells were counted for differential cell counting. The right lung was preserved in liquid nitrogen for mRNA extraction, while the left lung was fixed with 10% formalin and embedded in paraffin. Sections 4-μm thick were used to prepare slides, which were stained with HE.

Measurement of cytokines Approximately 5×10^6 single suspended splenocytes were stimulated with 20 μg/mL OVA for 72 h, centrifuged (10 min, 2000×*g*) and the supernatant was preserved for cytokine detection. The concentrations of IL-4 and IFN-γ in BALF and splenocyte culture supernatants were determined by using ELISA kits according to the manufacturer's recommendations.

Reverse transcription-polymerase chain reaction Total RNA was extracted from lung tissue and splenocytes using Trizol reagent, according to the manufacturer's instructions. Reverse transcription (RT) was carried out with 2 μg of total RNA using an oligo $(dT)_{18}$ primer, and polymerase chain reaction (PCR) was carried out using 2×Master Mix. The T-bet primer was designed according to Chakir *et al*[10], while the GATA-3 primer was designed according to Ise *et al*[11]. The primer sequences were as follows: β-actin, sense 5'-GTGGGCCGCTCTAGGCACCA-3', antisense 5'-CGGTTGGCCTTAGGGTTCAGGGGG-3'; GATA-3, sense 5'-GAAGGCATCCAGACCCGAAAC-3', antisense 5'-ACCCATGGCGGTGACCATGC-3'; T-bet, sense 5'-AACCAGTATC CTGGTCCCAGC-3', antisense 5'-TGTC GCCACTGGAA GGATAG-3'. PCR were run for 35 cycles and the annealing temperatures were as follows: GATA-3 and β-actin, 55 °C; T-bet, 57 °C. Semiquantitative RT-PCR was carried out using β-actin as an internal control to normalize gene expression for the PCR templates. The PCR product sizes were as follows: T-bet, 436 bp; GATA-3, 255 bp; β-actin, 245 bp. PCR products were electrophoresed in 2% agrose gel and the net intensity of the corresponding bands was analysed using Tian-Neng gel image software (Shanghai Tian-neng Technology Corporation, Shanghai, China).

Statistical analysis All data were expressed as mean± SD. Using Prism software, one-way ANOVA analysis was used to assess statistical significance between the different groups. $P<0.05$ was considered to be significant.

Results

CpG oligodeoxynucleotide reduced the total number of inflammatory cells and the percentage of eosinophils in branchoalveolar lavage fluid The total number of inflammatory cells and the percentage of eosinophils were $(100.4\pm7.1)\times10^5$/mL and 43.3%±2.5%, respectively, in BALF from the asthma group of mice (group B). CpG ODN treatment reduced the total number of inflammatory cells and the percentage of eosinophils to $(40.5\pm2.9)\times10^5$/mL and 10.2%± 0.5%, respectively (Table 1).

CpG oligodeoxynucleotide inhibited infiltration of airway inflammatory cells In asthma-group mice, lung pathological slides showed significant bronchial epithelial proliferation and shedding, bronchoconstriction and mucus production, as well as abundant inflammatory cell infiltra-

Table 1. Effect of CpG oligodeoxynucleotide on the number of inflammatory cells in branchoalveolar lavage fluid. n=12. Mean±SD. ^{c}P<0.01 *vs* A; ^{f}P<0.01 *vs* B.

Group	Total cell count ($\times10^5$/mL)	Differential cell count ($\times10^5$/mL)			
		Monocyte	Eosinophil	Lymphocyte	Other
A	9.4±0.4	85.8±1.4	0±0	7.1±1.0	6.8±0.9
B	100.4±7.1^{c}	16.1±1.6	43.3±2.5^{c}	15.1±1.3	25.5±2.0
C	40.5±2.9^{f}	67.4±1.3	10.2±0.5^{f}	11.2±1.6	11.2±2.2

A, control group; B, asthma group; C, CpG oligodeoxynucleotide-treated group.

tion in the airway wall. In CpG ODN-treated mice, lung pathological slides showed that bronchoconstriction, airway inflammatory cell infiltration and mucus production were alleviated significantly, compared with asthma-group mice (Figure 1).

Effects of CpG oligodeoxynucleotide on the interferon-γ concentration and the interleukin-4 concentration Compared with the asthma group, IFN-γ was increased in the CpG ODN-treated group in both BALF and splenocyte culture supernatants, but IL-4 was reduced in both BALF and splenocyte culture supernatants (Table 2).

Effects of CpG oligodeoxynucleotide on GATA-3 and T-bet mRNA expression Compared with the asthma group, GATA-3 mRNA expression was reduced in splenocytes in

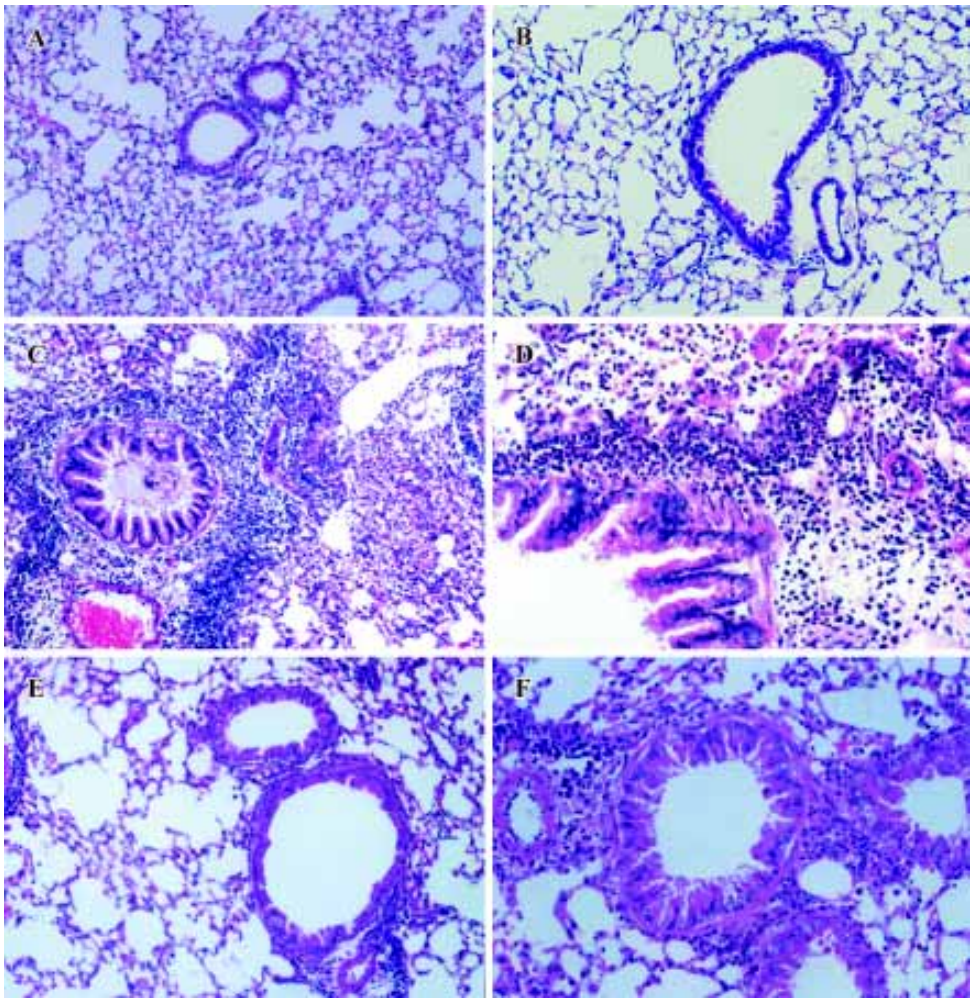

Figure 1. Lung tissue sections. (A, B) Control-group mice had smooth airway walls and no inflammatory cell infiltration. (C, D) In asthma-group mice, there was obvious bronchoconstriction, mucus secretion, epithelial proliferation and shedding, and inflammatory cell infiltration. (E, F) In the CpG oligodeoxynucleotide-treated group of mice, airway inflammatory cell infiltration was alleviated significantly compared with the asthma group (HE stain. A, C, E, ×100; B, D, F, ×200).

Table 2. Interleukin (IL)-4 and interferon (IFN)-γ concentrations in branchoalveolar lavage fluid (BALF) and splenocyte culture supernatant. n=12. Mean±SD. ^cP<0.01 *vs* B.

Group	IL-4 /μg·L^{-1}		IFN-γ /μg·L^{-1}	
	BALF	Supernatant	BALF	Supernatant
A	0.034±0.005	0.019±0.002	0.022±0.001	0.021±0.003
B	0.095±0.002	0.065±0.011	0.019±0.001	0.029±0.005
C	0.040±0.004^c	0.025±0.001^c	0.030±0.003^c	0.114±0.010^c

A, control group; B, asthma group; C, CpG oligodeoxynucleotide-treated group.

the CpG ODN-treated group, although no difference was found in T-bet mRNA expression between the 2 groups. However, the mRNA ratio of T-bet to GATA-3 was increased in the CpG ODN-treated group compared with the asthma group (Figure 2). In lung tissue, CpG ODN treatment also decreased mRNA ratio of GATA-3 to β-actin compared with the asthma group (0.19±0.04 *vs* 0.35±0.04 , P<0.02). T-bet mRNA was not detected under the same conditions.

Discussion

Airway eosinophil infiltration is one of the most prominent characteristics of asthma[12–14]. In the present study, a typical asthmatic mouse model was established, as evidenced by increased total inflammatory cells, increased percentage of eosinophils in BALF, and obvious bronchoconstriction, mucus secretion, epithelial proliferation and shedding, and inflammatory cell infiltration in the lungs in the asthma group compared with the control group.

Prior studies have demonstrated that CpG ODN treatment inhibits asthmatic airway inflammation and increases Th1 cytokine IFN-γ while decreasing Th2 cytokine, IL-4 and IL-5 levels in asthmatic mouse models[15–17]. In the present study, our data showed that CpG ODN treatment reduced total inflammatory cells and the percentage of eosinophils in BALF when CpG ODN was administered (ip) after allergen sensitization. Lung tissue pathological slides showed that inflammatory cell infiltration were significantly alleviated in CpG ODN treated group compared with asthma group. The inhibitory effect of CpG ODN on lung inflammation was accompanied by increased IFN-γ levels but decreased IL-4 levels in both BALF and splenocyte culture supernatants. IL-4-producing Th2 cells are considered to play an important role in the immune reaction of local tissue inflammation[18]. Xie *et al* demonstrated that in a rat asthma model, the decrease in IFN-γ level was accompanied by an increase in IL-4 level, which resulted in a decreased IFN-γ/IL-4 ratio in the BALF after the sensitized rats were challenged with aerosol anti-

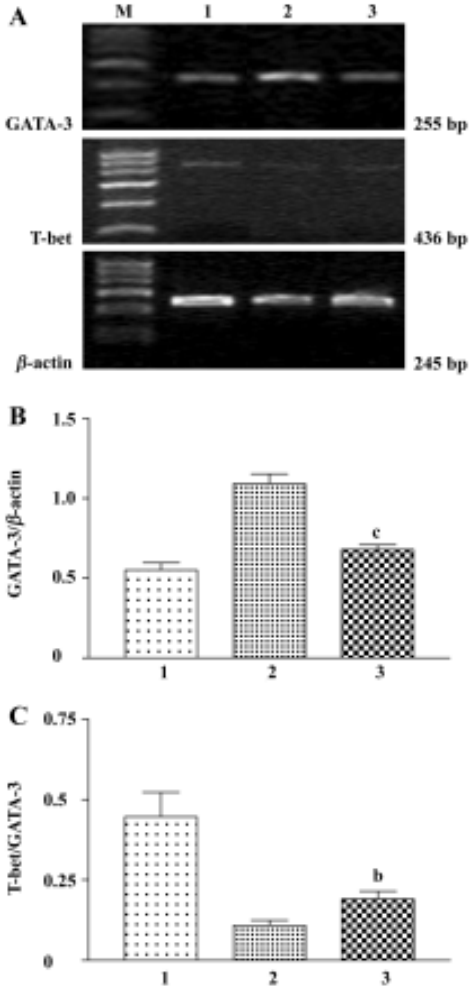

Figure 2. Effect of CpG oligodeoxynucleotide (ODN) on T-box expressed in T cell (T-bet) and GATA binding protein 3 (GATA-3) mRNA expression following ovalbumin (OVA) sensitization and challenge in splenocytes. (A) Reverse transcription polymerase chain reaction results. β-Actin was used as an internal standard. (B) GATA-3 mRNA densitometric scanning for DNA bands of each group. (C) mRNA expression ratio of T-bet to GATA-3 for each group. M, marker; 1, control group; 2, asthma group; 3, CpG ODN-treated group. ^bP<0.05, ^cP<0.01 *vs* asthma group.

gen[19]. These results suggest that the inhibitory effect of CpG ODN on airway inflammatory cell infiltration maybe the result of a downregulation of Th2 cytokine synthesis with an upregulation of Th1 cytokine synthesis.

Recent studies have shown that T-bet and GATA-3 are 2 major T helper-specific transcription factors that regulate the expression of Th1 and Th2 cytokine genes, and play a crucial role in T-helper cell differentiation. T-bet is thought to initiate Th1 development while inhibiting Th2 cell differentiation[20]. GATA-3 plays a pivotal role in the development of the Th2 phenotype while inhibiting Th1 cell differentiation[21]. Because asthma is a Th2-mediated airway inflammatory disease, both T-bet and GATA-3 may play an important role in the pathogenesis of asthma by directing Th0 differentiation. Finotto *et al* demonstrated that expression of T-bet in T cells from airways of patients with asthma was reduced compared with that in T cells from airways of non-asthmatic patients, suggesting that loss of T-bet might be associated with asthma[22]. Nakamura *et al* demonstrated that GATA-3 mRNA expression was increased significantly in the airways of asthmatic subjects and the number of cells expressing GATA-3 mRNA correlated significantly with reduced airway caliber and airway hyperresponsiveness[23]. Furthermore, GATA-3 mRNA-positive cells correlate significantly with the number of cells expressing IL-5 mRNA, and double *in situ* hybridization demonstrates that approximately 76% of GATA-3 mRNA-positive cells coexpress IL-5 mRNA and 91% of IL-5 mRNA-positive cells coexpress GATA-3 mRNA[23]. Blockade of GATA-3 mRNA expression by GATA-3 antisense oligonucleotides in lung tissue significantly inhibits Th2 cytokine production and airway inflammatory cells infiltration in an asthmatic mouse model[24].

Most studies have focused on the effect of CpG ODN on the Th1/Th2 cytokine balance in a murine model, but data regarding the effect of CpG ODN on the mRNA expression of transcription factors GATA-3 and T-bet have not been reported. In the present study, we first investigated the effects of CpG ODN on GATA-3 and T-bet mRNA expression in a mouse model of asthma. Our data showed that, compared with the asthma group, CpG ODN treatment reduced GATA-3 mRNA expression and increased the mRNA ratio of T-bet to GATA-3 in splenocytes, although no difference was found in T-bet mRNA expression between the 2 groups. In lung tissue, GATA-3 mRNA expression was also decreased in the CpG ODN-treated group compared with the asthma group. Chakir *et al* demonstrated that T-bet and GATA-3 gene expression reflected changes in Th1-specific cytokine IFN-γ and Th2-specific cytokine IL-4 in DO11.10 $CD4^+$ T cells as well as in a mixed population of BBc rat splenocytes, and the T-bet/GATA-3 ratio reflects the Th1/Th2 differentiation status[10].

Our data demonstrated that CpG ODN downregulated GATA-3 mRNA expression both in lung tissue and in splenocytes, which may be an important mechanism for reducing Th2 cytokine synthesis in asthmatic mouse model. Moreover, as the mRNA ratio of T-bet to GATA-3 in splenocytes was increased in the CpG ODN-treated group compared with the asthma group, CpG ODN may also regulate T cell differential status by promoting Th0 differentiation to Th1. In summary, our data have shown that reducing GATA-3 mRNA expression both in lung tissue and in splenocytes may be an important mechanism for CpG ODN to regulate Th1/Th2 cytokine synthesis, thereby alleviating airway eosinophilia in an asthmatic mouse model.

Acknowledgement

We thank Dr Yi-hong HU's help in experimental work from the Institute of Biochemistry and Cell Biology, Shanghai Institutes for Biological Sciences, Chinese Academy of Sciences, Shanghai, China.

References

1 Tournoy KG, Kips JC, Pauwels RA. The allergen-induced airway hyperresponsiveness in a human-mouse chimera model of asthma is T cell and IL-4 and IL-5 dependent. J Immunol 2001; 166: 6982–91.

2 Temann UA, Geba GP, Rankin JA, Flavell RA. Expression of interleukin 9 in the lungs of transgenic mice causes airway inflammation, mast cell hyperplasia, and bronchial hyperresponsiveness. J Exp Med 1998; 188: 1307–20.

3 Shirota H, Sano K, Kikuchi T, Tamura G, Shirato K. Regulation of T-helper type 2 cell and airway eosinophilia by transmucosal coadministration of antigen and oligodeoxynucleotides containing CpG motifs. Am J Respir Cell Mol Biol 2000; 22: 176–82.

4 Sun S, Zhang X, Tough DF, Sprent J. Type I interferon-mediated stimulation of T cells by CpG DNA. J Exp Med 1998; 188: 2335–42.

5 Sun S, Kishimoto H, Sprent J. DNA as an adjuvant: capacity of insect DNA and synthetic oligodeoxynucleotides to augment T cell responses to specific antigen. J Exp Med 1998; 187: 1145–50.

6 Hartmann G, Weiner GJ, Krieg AM. CpG DNA: a potent signal for growth, activation, and maturation of human dendritic cells. Proc Natl Acad Sci USA 1999; 96: 9305–10.

7 Wagner H. Bacterial CpG DNA activates immune cells to signal infectious danger. Adv Immunol 1999; 73: 329–68.

8 Broide D, Schwarze J, Tighe H, Gifford T, Nguyen MD, Malek S, *et al*. Immunostimulatory DNA sequences inhibit IL-5, eosinophilic inflammation, and airway hyperresponsiveness in mice. J Immunol 1998; 161: 7054–62.

9 Kline JN, Krieg AM, Waldschmidt TJ, Ballas ZK, Jain V, Businga TR. CpG oligodeoxynucleotides do not require TH1 cytokines

to prevent eosinophilic airway inflammation in a murine model of asthma. J Allergy Clin Immunol 1999; 104: 1258–64.

10 Chakir H, Wang H, Lefebvre DE, Webb J, Scott FW. T-bet/GATA-3 ratio as a measure of the Th1/Th2 cytokine profile in mixed cell populations: predominant role of GATA-3. J Immunol Methods 2003; 278: 157–69.

11 Ise W, Totsuka M, Sogawa Y, Ametani A, Hachimura S, Sato T, *et al*. Naive $CD4^+$ T cells exhibit distinct expression patterns of cytokines and cell surface molecules on their primary responses to varying doses of antigen. J Immunol 2002; 168: 3242–50.

12 Kang H, Wei EQ, Yang XH, Zhang WP, Shen JZ. VCAM-1 expression, eosinophil infiltration, and pharmacological modulation in rat allergic airway inflammation. Acta Pharmacol Sin 2002; 23: 157–61.

13 Lee JJ, Dimina D, Macias MP, Ochkur SI, McGarry MP, O'Neill KR, *et al*. Defining a link with asthma in mice congenitally deficient in eosinophils. Science 2004; 305: 1773–6.

14 Zhang YJ, Zhang L, Wang SB, Shen HH, Wei EQ. Montelukast modulates lung CysLT(1) receptor expression and eosinophilic inflammation in asthmatic mice. Acta Pharmacol Sin 2004; 25: 1341–6.

15 Broide DH, Stachnick G, Castaneda D, Nayar J, Miller M, Cho JY, *et al*. Systemic administration of immunostimulatory DNA sequences mediates reversible inhibition of Th2 responses in a mouse model of asthma. J Clin Immunol 2001; 21: 175–82.

16 Serebrisky D, Teper AA, Huang CK, Lee SY, Zhang TF, Schofield BH, *et al*. CpG oligodeoxynucleotides can reverse Th2-associated allergic airway responses and alter the B7.1/B7.2 expression in a murine model of asthma. J Immunol 2000; 165: 5906–12.

17 Santeliz JV, Van Nest G, Traquina P, Larsen E, Wills-Karp M. Amb a 1-linked CpG oligodeoxynucleotides reverse established airway hyperresponsiveness in a murine model of asthma. J Allergy Clin Immunol 2002; 109: 455–62.

18 Muller KM, Jaunin F, Masouye I, Saurat JH, Hauser C. Th2 cells mediate IL-4-dependent local tissue inflammation. J Immunol 1993; 150: 5576–84.

19 Xie QM, Chen JQ, Shen WH, Bian RL. Correlative changes of interferon-gamma and interleukin-4 between cortical layer and pulmonary airway of sensitized rats. Acta Pharmacol Sin 2002; 23: 248–52.

20 Szabo SJ, Kim ST, Costa GL, Zhang X, Fathman CG, Glimcher LH. A novel transcription factor, T-bet, directs Th1 lineage commitment. Cell 2000; 100: 655–69.

21 Zhang DH, Cohn L, Ray P, Bottomly K, Ray A. Transcription factor GATA-3 is differentially expressed in murine Th1 and Th2 cells and controls Th2-specific expression of the interleukin-5 gene. J Biol Chem 1997; 272: 21597–603.

22 Finotto S, Neurath MF, Glickman JN, Qin S, Lehr HA, Green FH, *et al*. Development of spontaneous airway changes consistent with human asthma in mice lacking T-bet. Science 2002; 295: 336–8.

23 Nakamura Y, Ghaffar O, Olivenstein R, Taha RA, Soussi-Gounni A, Zhang DH, *et al*. Gene expression of the GATA-3 transcription factor is increased in atopic asthma. J Allergy Clin Immunol 1999; 103: 215–22.

24 Finotto S, De Sanctis GT, Lehr HA, Herz U, Buerke M, Schipp M, *et al*. Treatment of allergic airway inflammation and hyperresponsiveness by antisense-induced local blockade of GATA-3 expression. J Exp Med 2001; 193: 1247–60.

Acta Pharmacologica Sinica 2005 Sep; 26 (9): 1123–1129

Full-length article

Nitric oxide inhalation inhibits inducible nitric oxide synthase but not nitrotyrosine formation and cell apoptosis in rat lungs with meconium-induced injury[1]

Mei-ping LU, Li-zhong DU[2], Wei-zhong GU, Xiang-xiang CHEN

Neonatal Intensive Care Unit, Department of Pediatrics, Children's Hospital, Zhejiang University School of Medicine, Hangzhou 310003, China

Key words

inhaled nitric oxide; meconium; acute lung injury; nitrotyrosine; apoptosis

[1] Project supported by the National Natural Science Foundation of China (No 30371498), the Commission of Science and Technology of Zhejiang Province (No 2004C33019) and the Bureau of Education of Zhejiang Province (No 20030304), partly supported by E-Institute of Shanghai Municipal Education Commission (Project No E-04010, China)
[2] Correspondence to Dr Li-zhong DU.
Phn 86-138-0572-2352.
Fax 86-571-8703-3296.
E-mail dulizhong@yahoo.com.cn

Received 2005-01-10
Accepted 2005-06-03

doi: 10.1111/j.1745-7254.2005.00153.x

Abstract

Aim: To investigate the effects of inhaled nitric oxide (NO) on pulmonary inflammation, apoptosis, peroxidation and protein nitration in a rat model of acute lung injury (ALI) induced by meconium. **Methods:** Twenty-four healthy male Sprague-Dawley rats were randomly devided into 3 groups (n=8): meconium-induced ALI with intratracheal instillation of 1 mL/kg saline (Mec/saline group), continuous inhalation of NO at 20 μL/L. (Mec/iNO), and the control group (control). Electromicroscopic examination was used to determine the extent of epithelial apoptosis. TUNEL was used to detect DNA fragmentation in pulmonary apoptotic cells, expressed as the apoptosis index (AI). Western blotting was used to detect pulmonary inducible NO synthase (iNOS) expression. RT-PCR was used to detect interleukin (IL)-1β mRNA expression. Cell count in bronchoalveolar lavage (BAL), myeloperoxidase (MPO) activity, as well as malondialdehyde (MDA) and nitrotyrosine formation, the markers of toxic NO-superoxide pathway in rat lung parenchyma specimens, were also examined. **Results:** Expression of iNOS protein and IL-1β mRNA were increased significantly in the Mec/saline group (both P<0.01) compared with the control group. BAL cell count, MPO activity, lung injury score, pulmonary AI, MDA level and nitrotyrosine formation were also increased significantly (all P<0.01). The meconium-induced iNOS protein and IL-1β mRNA expression were inhibited significantly by NO inhalation when compared with the Mec/saline group (both P<0.01). BAL cell count, MPO activity and lung injury score were also decreased significantly (P<0.01 or P<0.05). However, there were no statistical differences in MDA level, nitrotyrosine formation or pulmonary AI between the Mec/saline and Mec/iNO groups. Electromicroscopic examination revealed a significant degree of epithelial apoptosis in both the Mec/saline and Mec/iNO groups. **Conclusions:** Early continuous inhalation of NO 20 μL/L may protect the lungs from inflammatory injury, but does not decrease epithelial apoptosis or lung nitrotyrosine formation. Inhalation of NO alone is not associated with a detectable increase in oxidant stress.

Introduction

Meconium aspiration syndrome (MAS) remains a significant cause of morbidity and mortality in term newborn infants with intrauterine hyperoxia, despite improvements in obstetric care. The pathophysiology of lung injury in MAS is very complicated. The complex nature of MAS contributes to its poor response to many therapeutic interventions[1–4]. Clinical and experimental evidence suggest that inhaled nitric oxide (NO) reduces pulmonary hypertension, improves systemic oxygenation and inhibits the transendothelial migration of activated neutrophils in a variety of patho-

logical conditions of the lungs, including meconium aspiration[3,5,6].

As a free radical, however, NO inhalation is potentially toxic. NO induces apoptosis in various cell lines[7]. NO inhalation can cause damage to the lung tissue through its reaction with superoxide anions, resulting in the production of peroxynitrite anion ($ONOO^-$). Nitrotyrosine is a marker of $ONOO^-$ production, which provides evidence for therapy-induced iNO toxicity[8]. A previous study showed that NO inhalation during the early phase of inflammation did not increase, but rather decreased nitrotyrosine formation[8,9]. However, nitrotyrosine formation in meconium-induced acute lung injury (ALI) with or without inhalation of NO has not been investigated. The anti-inflammatory effect of iNO in meconium-induced ALI is still controversial[3].

The aims of our present study were to explore the mechanism of anti-inflammatory effects and to investigate the possible toxic role of iNO in meconium-induced ALI. A rat model of ALI following meconium aspiration was established. The pulmonary inducible NO synthase (iNOS) protein and interleukin (IL)-1β mRNA expression, nitrotyrosine formation, pulmonary apoptosis, as well as lung injury score, bronchoalveolar lavage (BAL) cell count, myeloperoxidase (MPO) activity and malondialdehyde (MDA) level were measured.

Materials and methods

Meconium preparation First-passed meconium was taken from urine-free diapers of healthy term neonates. The meconium was placed in a sterile jar and frozen for less than 7 d and then lyophilized, pooled and diluted with sterile saline to a final concentration of 20% suspension[10]. This meconium slurry was frozen at -70 °C until use.

Animal management Twenty-four 30–45 d old Sprague-Dawley rats weighing 130 –170 g were studied. A rat model of meconium-induced ALI was established as previously described[10,11]. Briefly, rats were anesthetized with sodium pentobarbital (40 mg/kg, ip). After tracheotomy, an endotracheal tube was placed through the incision, and then stabilized. Prior to meconium instillation, rats were given vecuronium bromide (2 mg/kg, ip). After 15 min, the rats were randomized into 3 groups (n=8 each). Sixteen of the rats were instilled intratracheally with meconium (1 mL/kg) followed by a 3 mL bolus of air to disperse the meconium into the lung to establish the model of ALI. Half of the dose was given with the rat lying on one side and the other half with the rat lying on the other side and then randomized into the Mec/saline group, with intratracheal instillation of 1 mL/kg saline, or the Mec/iNO group, with continuous inhalation of NO at 20 μL/L. The remaining 8 rats were given 1 mL/kg sterile saline intratracheally followed by a 3 mL bolus of air as control. At 60 min after surgery, skin and tracheal incisions were closed with a 4–0 nylon suture. The rats in the Mec/saline group and in the control group were allowed to breath spontaneously in room air.

Nitric oxide exposure Immediately after the skin and tracheal incisions were closed, the rats in the Mec/iNO group were housed for 24 h in a sealed Plexiglas chamber that was flushed continuously with a precise dilution of NO gas (800 μL/L) and medical air (4 mL/kg) to achieve a final NO concentration of 20 μL/L NO concentration in the chamber was continuously monitored by a NO/NO_2 monitor confirming that the NO concentration was maintained at 20±1 μL/L and that the NO_2 concentration was consistently <2 μL/L.

Sample collection and storage The animals were killed 24 h after treatment. The chest was opened by a midline incision. The lungs were isolated and left lung lavage was carried out. Tissue samples from the right lung were obtained. Apoptosis of lung tissue cells was evaluated using electron microscopy and a terminal deoxynucleodityl transferase-mediated dUTP nick-end labeling (TUNEL) assay was carried out.

Bronchoalveolar lavage total cell count The left lung was lavaged using 31 mL aliquots of cold sterile saline following tracheotomy. Each lung was instilled and cleared 3 times. The recovered amount was always more than 90%. A total BAL cell count was obtained within 4 h.

Pulmonary myeloperoxidase activity and malondialdehyde assay Myeloperoxidase (MPO) activity was assessed as a measure of pulmonary neutrophil influx and activity. Pulmonary MPO activity and malondialdehyde (MDA) levels were assayed in duplicate on homogenized lung samples, according to the manufacturer's manual. One unit of MPO activity was expressed as units per gram of wet lung tissue. MDA levels were standardized for tissue protein concentration determined by the Bradford protein assay[12].

Reverse transcription-polymerase chain reaction (PCR) analysis of pulmonary IL-1β mRNA expression Total RNA was isolated with Trizol Reagent (Sangon, Shanghai, China) in accordance with the manufacturer's instructions. Complementary DNA (cDNA) was prepared by reverse transcription (RT) of 10 μg total RNA using oligo dT18 and 200 u MmuLV reverse transcriptase (Sangon) at 37 °C for 90 min according to the manufacturer's manual. cDNA was used as a template in the PCR, which was run in *Tag*-polymerase buffer, supplemented with 1.5 mmol/L $MgCl_2$, 5 μg/mL of each primer, 4 μL of 10 mmol/L dNTPs, and 1 U of *Tag*-polymerase (TaKaRa, Dalian, China). The total reaction volume

was 50 μL. The primers used for IL-1β in RT-PCR were coding, 5'-GAA GCT GTG GCA GCT ACC TAT GTC T-3' and uncoding, 5'-CTC TGC TTG AGA GGT GCT GAT GTA C-3', which yielded a PCR product of 520 bp. The primers for β-actin (200 bp) were coding, 5'-ATG CCA ACA CAG TGC TGT CT-3' and uncoding, 5'-CTG CTT GCT GAT CCA CAT CT-3'. Amplification was carried out for 30 cycles at 94 ºC for 1 min, 65 ºC for 45 s, 72 ºC for 45 s, followed by a 7 min extension at 72 ºC. Gene expression was determined by the size of the PCR product in 1.6% agorose gels (in Tris-buffer, pH 8.0), stained with 0.1% μg/mL ethidium bromide and observed under ultraviolet light. The data of the IL-1β mRNA levels was normalized against the housekeeping gene β-actin. Molecular weight markers were run in parallel.

Western blot analysis of pulmonary nitrotyrosine formation and inducible nitric oxide synthase expression Frozen lung tissues were homogenized in protein extraction buffer. The homogenate was left on ice for 30 min before centrifugation at 10 000×*g*. Protein content was estimated[12], and aliquots of 50 μg homogenate protein were run on 10% (w/v) sodium dodecylsulfate (SDS)-polyacrylamide gel electrophoresis (PAGE) gels. Proteins were subsequently transferred to nitrocellulose membranes and stained with Coomassie blue to verify the equivalent transfer of samples. Membranes were blocked by incubation with 3% (w/v) fat dry milk in PBS for 1 h at room temperature, with shaking. Thereafter, the membranes were incubated overnight at 4 ºC with either mouse monoclonal anti-nitrotyrosine (Calbiochem-Novabiochem, San Diego, CA, USA) or rabbit polyclonal anti-iNOS or rabbit polyclonal anti-actin (Santa Cruz, Califonia, USA). The primary antibody was used at dilutions from 1:500 to 1:1000. The blots were washed 4 times (10 min each time) with Tris-buffered saline Tween-20 (TBST), comprising 50 mmol/L Tris-HCl (pH 7.6), 150 mmol/L NaCl and 0.1% Triton X-100, and subsequently incubated for 2 h at room temperature in Tris-buffered saline with horseradish peroxidase-conjugated anti-rabbit or anti-mouse IgG antibody (1:5000; Pierce, Rockford, IL, USA). Immunoreactive bands were visualized using the enhanced chemiluminescence system (Pierce) and quantified by densitometric analysis using Scion image software (Kodak, EDAS290 Imager Analysis). Results were calculated as the relative ratio of the specific band compared with actin.

Histological examination Pulmonary tissue samples from the right lower lobe were fixed in 10% buffered formalin, embedded in paraffin, and stained with hematoxylin and eosin for determination of the severity of lung injury. Samples were assessed by a blinded pathologist who was unaware of the group of the rats. A score from 0 to 4 represented the percentage of affected area on the lung section (0=0%, 1=1%–25%, 2=26%–50%, 3=51%–75%, and 4=76%–100%) and was assigned for 3 different characteristics: (i) extension of pulmonary leukocyte infiltration; (ii) amount of intra-alveolar leukocytes; and (iii) amount of exudative debris and edema fluid. The calculated total injury score represents the sum of these scores[3].

Quantification of apoptosis in lung tissues by TUNEL The semiquantification of apoptotic cells in lung tissue was carried out by in situ TUNEL using the Apop Tag Peroxidase *In Situ* Cell Death Detection Kit (Roche Diagnostic GmbH Mannheim, Germany) according to the manufacturer's protocol. The number of positive signals in each section was evaluated by 3 independent pathologists using light microscopy. The apoptosis index (AI) was calculated. AI is a measure of the number of positive cells in each 100 cells counted in 5 different blocks in the same section[13].

Electron microscopy Small pieces of lung tissue (1 mm^3) from the left lower lobe were obtained for ultrastructural analysis of apoptotic pulmonary cell death by electron microscopy.

Statistical analysis Data are expressed as mean±SD. Statistical significance among sample groups was analyzed with ANOVA. The Mann-Whitney test was used to analyze the data from lung injury score. A level of $P<0.05$ was considered statistically significant.

Results

The meconium-instilled group showed increased BAL cell count, pulmonary MPO activity and lung injury score when compared with the control group (all $P<0.01$; Table 1). The expression of IL-β mRNA and iNOS protein was also increased significantly (both $P<0.01$; Figures 1,2). Pulmonary nitrotyrosine, a marker of $ONOO^-$ formation as an index of pulmonary peroxidation, and MDA, a marker of lipid peroxidation, were increased significantly as well (both $P<0.01$; Table 1; Figure 3). Pulmonary AI, demonstrated by TUNEL staining, was significantly elevated at 24 h after the treatment ($P<0.01$; Figure 4). This was confirmed by the electron microscopic finding that apoptotic change occurred in pulmonary epithelium in the meconium-instilled rat lungs (Figure 5).

Inhalation of NO (20 μL/L) significantly inhibited meconium-induced iNOS protein and IL-1β mRNA expression when compared with the Mec/saline group (both $P<0.01$; Figures 1, 2). BAL cell count, MPO activity, and lung injury score were also decreased ($P<0.01$, $P<0.01$, and $P<0.05$, respectively; Table 1). However, there were no statistical

Table 1. Bronchoalveolar lavage (BAL) cell count, pulmonary myeloperoxidase (MPO) activity, malondialdehyde (MDA) and lung injury score in rats with intratracheal saline (control) or meconium instillation followed by saline instillation (Mec/saline) or nitric oxide (NO) inhalation (Mec/iNO). n=8. Mean±SD. ^{c}P<0.01 *vs* control; ^{e}P<0.05, ^{f}P<0.01 *vs* Mec/saline.

Group	10^6×Cell count (cells/mL)	MPO (U/g wet lung tissue)	MDA (nmol/mg protein)	Lung injury score
Control	0.53±0.19	0.62±0.16	1.40±0.35	2.25±1.04
Mec/saline	4.68±1.40^{c}	1.54±0.24^{c}	3.50±0.82^{c}	10.00±1.07^{c}
Mec/iNO	3.38±0.58^{cf}	1.24±0.14^{cf}	3.25±1.20^{c}	8.50±1.14^{ce}

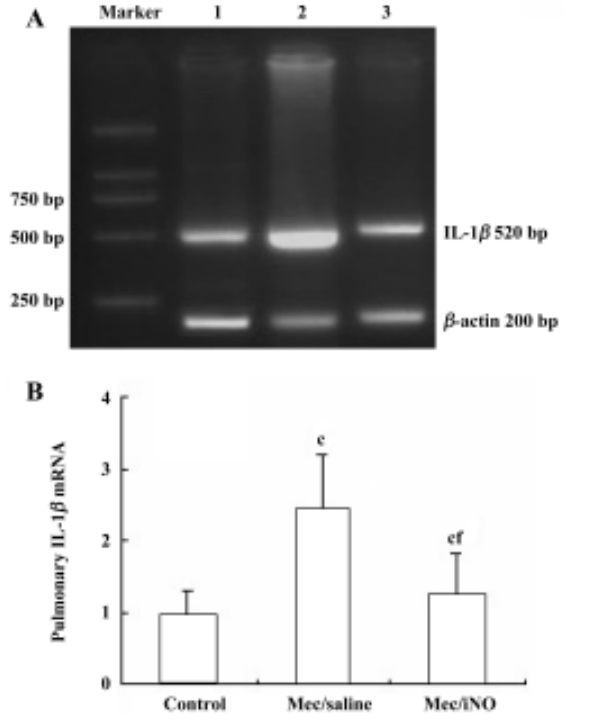

Figure 1. (A) Representative reverse transcription-polymerase chain reaction analysis of pulmonary interleukin (IL)-1β mRNA (520 bp) from control (1, control), acute lung injury with intratracheal-instilled saline (2, Mec/saline) or with 20 μL/L. nitric oxide (NO) inhalation (3, Mec/iNO). (B) NO inhalation inhibits the expression of pulmonary IL-1β mRNA (n=8 in each group), and the intensity of the bands is greater in the Mec/saline and Mec/iNO lanes compared with the control. ^{c}P<0.01 *vs* control. ^{f}P<0.01 *vs* Mec/saline.

differences in MDA level, nitrotyrosine formation or pulmonary AI between the Mec/saline and Mec/iNO groups (Table 1; Figures 3, 4). Electron microscopy revealed a significant amount of epithelial apoptosis in rat lung from both

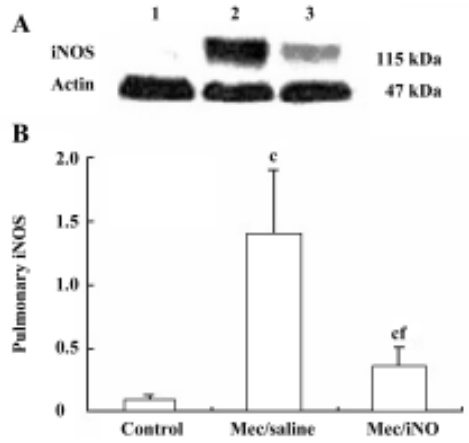

Figure 2. (A) Representative Western blot analysis of inducible nitric oxide synthase (iNOS) (~115 kDa) from control (1, control), acute lung injury with intratracheal instilled saline (2, Mec/saline) or with 20 μL/L . nitric oxide (NO) inhalation (3, Mec/iNO). (B) The intensity of the bands is greater in the Mec/saline and Mec/iNO lanes compared with the control. NO inhalation inhibits the expression of pulmonary iNOS protein (n=8 in each group). ^{c}P<0.01 *vs* control. ^{f}P<0.01 *vs* Mec/saline.

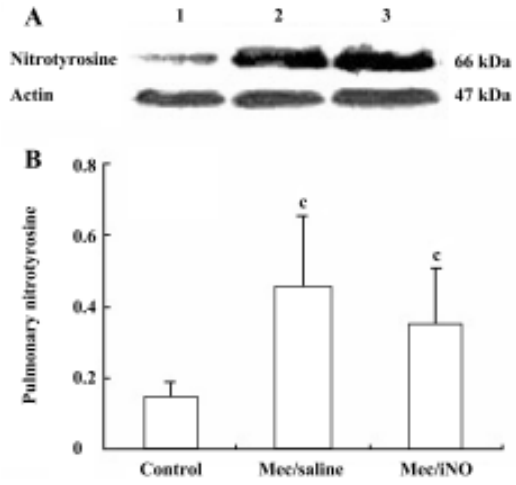

Figure 3. (A) Representative Western blot analysis of nitrotyrosine (~66 kDa) formation from control (1, control), acute lung injury with intratracheal instilled saline (2, Mec/saline) or with 20 μL/L. nitric oxide (NO) inhalation (3, Mec/iNO). (B) The intensity of the bands is greater in the Mec/saline and Mec/iNO lanes compared with the control (n=8 in each group). ^{c}P<0.01 *vs* control.

the Mec/saline and the Mec/iNO group (Figure 5).

Discussion

The present study shows that meconium aspiration in meconium-induced ALI, compared with NO inhalation, is associated with increased MPO activity, lung injury score,

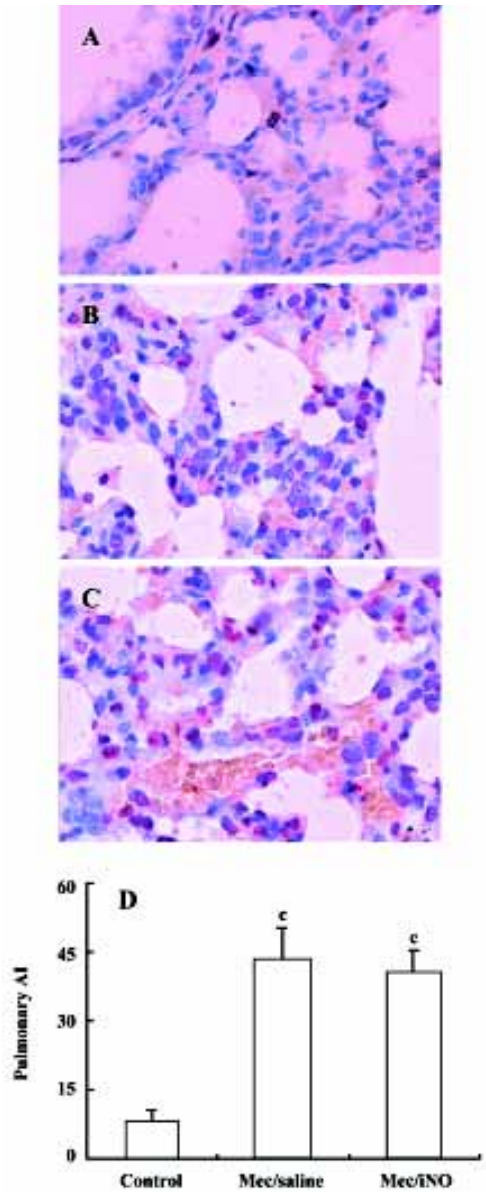

Figure 4. Representative lung sections from (A) control, (B) acute lung injury with intratracheal instilled saline (Mec/saline) or (C) with 20 μL/L. nitric oxide (NO) inhalation (Mec/iNO), showing stained brown nuclei of apoptotic cells with terminal deoxynucleodityl transferase-mediated dUTP nick-end labeling. (D) Pulmonary apoptotic cells are more numerous and the pulmonary apoptosis index is significantly increased in the Mec/saline and Mec/iNO groups compared with the control (n=8). $^cP<0.01$ *vs* control.

high numbers of neutrophils in BAL, and increased iNOS protein and IL-1β mRNA expression. It demonstrates that early NO inhalation at a dose of 20 μL/L. inhibits the pulmonary inflammatory injury, but does not increase pulmonary MDA and nitrotyrosine formation in meconium induced-ALI. These findings indicate that NO inhalation may protect the

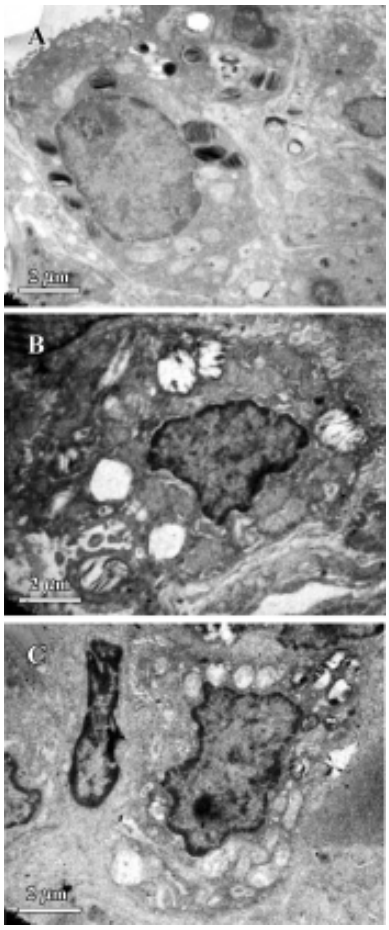

Figure 5. Representative electron microscopic figures from (A) a control lung (control), (B) a lung with acute lung injury with intratracheal instilled saline (Mec/saline) or (C) 20 μL/L. nitric oxide (NO) inhalation (Mec/iNO). Apoptotic change occurred in type II pneumocytes in both (B) and (C). The condensed chromatin represents apoptotic change.

lung tissue against the meconium-induced pulmonary inflammatory response and that at the present dosage, the oxidative effects of iNO are not clinically significant.

Meconium contains variable amounts of proinflammatory substances, such as IL-1β, IL-6, IL-8, TNF-α, and heme, which may activate lung inflammatory cells to produce cytokines and elicit inflammatory reactions[11,14]. This is also demonstrated in the rat lungs in our study by induction of pulmonary IL-1β mRNA expression. As previously reported, high expression of iNOS might lead to overproduction of NO[15,16]. NO is an important mediator in inflammation and high levels of NO produced by iNOS can mediate lung injury[8]. During inflammatory conditions, meconium is able to activate macrophages to produce oxygen radicals, including superoxide anions[4]. Reaction of NO with superoxide anions produces

peroxynitrite, which is a highly oxidative species and is capable of nitrating tyrosine residues of numerous proteins, leading to the formation of nitrotyrosine that may result in protein inactivation and lipid and DNA degradation. Nitrotyrosine is a product of the peroxynitrite pathway that has been used as a probe to detect NO-mediated oxidative reactions[8]. Our findings show that meconium aspiration results in the expression of iNOS and the production of MDA and nitrotyrosine, indicating that meconium-induced ALI is associated with pulmonary inflammatory and oxidative/nitrosative injury.

Findings from earlier studies suggest that inhaled NO can decrease inflammatory reactions in neonatal and adult lungs[6,17]. In the present study, we showed an attenuation in pulmonary inflammatory injury after NO treatment, similar to earlier findings. Evidence from our study shows that the mechanism of the anti-inflammatory effects of NO inhalation may be associated with inhibited expression of pulmonary iNOS protein and IL-1β mRNA. On the other hand, during inflammatory conditions, inhaled NO might increase the reaction between superoxide and NO to enhance tissue nitration and exacerbate injury. Nitrotyrosine has been found in the lungs of patients with acute respiratory distress syndrome who have received inhaled nitric oxide[18,19]. In newborn piglets the formation of peroxynitrite may be enhanced in lungs exposed to high doses of inhaled NO or hyperoxia[20]. However, inhaled NO might have contradictory effects on lung tissue: first, an increase in nitration as a result of increased amounts of NO and nitrite, thereby enhancing the production of peroxynitrite and the reaction via peroxidase as a source of nitrite[19]; and second, a decrease in nitration by inhibiting leukocyte accumulation in the lungs, thereby reducing the production of NO and superoxide[9,21]. In the present study, inhaled NO at 20 μL/L. does not further increase pulmonary nitrotyrosine formation. Some studies have also shown that early inhalation of NO in severe respiratory failure is not associated with increased NO toxicity. In the rat model of lipopolysaccharide-induced ALI, NO inhalation during the early phase of inflammation did not increase, but rather decreased tyrosine nitration and chlorination, possibly by reducing neutrophil sequestration[9]. Inhaled NO at 100 μL/L was shown to increase the survival of rats with hyperoxia[22]. Inhaled NO at 20 μL/L with concurrent hyperoxia did not increase intracellular or intercellular nitrotyrosine in a mouse model[23]. According to evidence from this and from previous studies, the oxidative effects of iNO are not clinically significant.

There is some indirect evidence suggesting that apoptosis may play an important role in ALI. Aspirated meconium may cause apoptotic cell death of the airway epithelium, supposedly through the action of bile salt or pulmonary inflammatory cells. Increased release of reactive oxygen and nitrogen species by pulmonary inflammatory cells may be associated with apoptotic cell death in the lung. Previous studies indicate that NO may function as an inhibitor of the apoptotic death program. An earlier study showed that NO inhalation inhibited pulmonary apoptosis in porcine meconium aspiration[3]. However, there was a bulk of evidence indicating that NO induced apoptosis in different cell lines[7]. In this study we found that NO inhalation did not protect the lung from meconium-induced apoptosis, despite the positive effect on pulmonary inflammatory injury.

In summary, meconium-induced ALI is associated with inflammatory oxidant injury and epithelial apoptosis. Early inhalation of NO at a dose of 20 μL/L. does not seem to prevent epithelial apoptosis caused by meconium aspiration. Inhalation of NO at the present dose is not associated with any detectable increase in oxidative or nitrosative damage. The results presented here suggest a lack of toxicity of inhaled NO due to oxidant injury and further justify therapeutic trials on inhaled NO in clinical respiratory failure. Caution with regard to pulmonary toxicity is still required.

Acknowledgement

We thank Mr Zhong-sheng YU and Mr Yao-sheng DONG for excellent technical assistance.

References

1 Cleary GM, Wiswell TE. Meconium-stained amniotic fluid and the meconium aspiration syndrome: an update. Pediatr Clin North Am 1998; 45: 511–29.

2 MH, Bae CW. Inhibitory effect of meconium on pulmonary surfactant function tested *in vitro* using the stable microbubble test. Eur J Pediatr 2000; 159: 770–4.

3 Holopainen R, Aho H, Laine J, Halkola L, Kaapa P. Nitric oxide inhalation inhibits apoptosis but not inflammatory injury in porcine meconium aspiration. Acta Pediatr 1999; 8: 1147–55.

4 Soukka HR, Ahotupa M, Ruutu M, Kaapa PO. Meconium stimulates neutrophil oxidative burst. Am J Perinatol 2002; 19: 279–84.

5 Miao CH, Sun B, Jiang H, Xue ZG, Lindwall R. Pharmacodynamics and pharmacokinetics of inhaled nitric oxide in dogs with septic acute respiratory distress syndrome. Acta Pharmacol Sin 2002; 23: 278–84.

6 Kinsella JP, Parker TA, Galan H, Sheridan BC, Halbower AC, Abman SH. Effects of inhaled nitric oxide on pulmonary edema and lung neutrophil accumulation in severe experimental hyaline membrane disease. Pediatr Res 1997; 41 Suppl: 457–63.

7 Brune B, von Knethen A, Sandau KB. Nitric oxide and its role in apoptosis. Eur J Pharmacol 1998; 351: 261–72.

8 Lang JD, McArdle PJ, O'Reilly PJ, Matalon S. Oxidant-antioxidant balance in acute lung injury. Chest 2002; 122 Suppl: S314–20.
9 Hataishi R, Kobayashi H, Takahashi Y, Hirano S, Zapol WM, Jones RC. Myeloperoxidase-associated tyrosine nitration after intratracheal administration of lipopolysaccharide in rats. Anesthesiology 2002; 97: 887–95.
10 Lu MP, Du LZ, Yu ZZ, Chen XX. Protective effects and mechanisms of recombinant human superoxide dismutase in acute lung injury of rats following meconium aspiration. Chin J Pediatr 2004; 42: 777–81.
11 Zagariya A, Bhat R, Uhal B, Navale S, Freidine M, Vidyasagar D. Cell death and lung cell histology in meconium aspirated newborn rabbit lung. Eur J Pediatr 2000; 159: 819–26.
12 Bradford, M. A rapid and sensitive method for the quantitation of microgram quantities of protein utilizing the principle of dye-binding. Anal Biochem 1976; 72: 248–54.
13 Li HP, Li X, He GJ, Yi XH, Kaplan AP. The influence of dexamethasone on the proliferation and apoptosis of pulmonary inflammatory cells in bleomycin-induced pulmonary fibrosis in rats. Respirology 2004; 9: 25–32.
14 de Beaufort AJ, Bakker AC, van Tol MJ, Poorthuis BJ, Schrama AJ, Berger HM. Meconium is a source of pro-inflammatory substances and can induce cytokine production in cultured A549 epithelial cells. Pediatr Res 2003; 54: 491–5.
15 Ding HL, Zhu HF, Dong JW, Zhu WZ, Yang WW, Yang HT, *et al*. Inducible nitric oxide synthase contributes to intermittent hypoxia against ischemia/reperfusion injury. Acta Pharmacol Sin 2005; 26: 315–22.
16 Li YH, Yan ZQ, Braune A, Tullus K. Meconium induces expression of inducible NO synthase and activation of NF-kappaB in rat alveolar macrophages. Pediatr Res 2001; 49: 820–5.
17 Du LZ, Long XY. Effects of inhaled nitric oxide on lung injury and neutrophil accumulation in rabbits with meconium aspiration. Acta Pharmacol Sin 2002; 23 (Suppl): 165–6.
18 Lamb NJ, Quinlan GJ, Westerman ST, Gutteridge JM, Evans TW. Nitration of proteins in bronchoalveolar lavage fluid from patients with acute respiratory distress syndrome receiving inhaled nitric oxide. Am J Respir Crit Care Med 1999; 160: 1031–4.
19 Weinberger B, Laskin DL, Heck DE, Laskin JD. The toxicology of inhaled nitric oxide. Toxicol Sci 2001; 59: 5–16.
20 Youssef JA, Thibeault DW, Rezaiekhaligh MH, Mabry SM, Norberg MI, Truog WE. Influence of inhaled nitric oxide and hyperoxia on Na, K-ATPase expression and lung edema in newborn piglets. Biol Neonate 1999; 75: 199–209.
21 Honda K, Kobayashi H, Hataishi R, Hirano S, Fukuyama N, Nakazawa H, *et al*. Inhaled nitric oxide reduces tyrosine nitration after lipopolysaccharide instillation into lungs of rats. Am J Respir Crit Care Med 1999; 160: 678–88.
22 Sato Y, Walley KR, Klut ME, English D, D'yachkova Y, Hogg JC, *et al*. Nitric oxide reduces the sequestration of polymorphonuclear leukocytes in lung by changing deformability and CD18 expression. Am J Respir Crit Care Med 1999; 159: 1469–76.
23 Lorch SA, Foust R 3rd, Gow A, Arkovitz M, Salzman AL, Szabo C, *et al*. Immunohistochemical localization of protein 3-nitrotyrosine and *S*-nitrosocysteine in a murine model of inhaled nitric oxide therapy. Pediatr Res 2000; 47: 798–805.

Acta Pharmacologica Sinica 2005 Sep; 26 (9): 1130–1137

Full-length article

Effects of *Ganoderma lucidum* polysaccharides on proliferation and cytotoxicity of cytokine-induced killer cells

Xiao-ling ZHU, Zhi-bin LIN[1]

Department of Pharmacology, School of Basic Medical Science, Peking University Health Science Center, Beijing 100083, China

Key words

Ganoderma lucidum; polysaccharides; cell proliferation; cytotoxicity; immunomodulation

[1] Correspondence to Prof Zhi-bin LIN.
Phn/Fax 86-10-8280-1686.
E-mail linzb@public3.bta.net.cn

Received 2004-11-23
Accepted 2005-03-14

doi: 10.1111/j.1745-7254.2005.00171.x

Abstract

Aim: To study the effects (and the mechanisms thereof) of *Ganoderma lucidum* polysaccharides (*Gl*-PS) on the proliferation and the anti-tumor activity of cytokine-induced killer (CIK) cells, and to make use of CIK cells as a means to investigate the interactions between *Gl*-PS and cytokines. **Methods:** CIK cells were prepared by using the standard protocol as a positive control. Experimental groups also underwent the standard protocol, except that *Gl*-PS (400 mg/L or 100 mg/L) was added and the dose of anti-CD3 and interleukin-2 they received was reduced by 50% and 75%, respectively. For negative controls, *Gl*-PS in the experimental protocol was replaced with soluble starch or methylcellulose (400 mg/L or 100 mg/L). CIK cell proliferation, cytotoxicity, and phenotype were determined by using the Trypan blue exclusion method, MTT assay, and flow cytometry. **Results:** By synergizing cytokines, *Gl*-PS (400 mg/L or 100 mg/L) could decrease the amount of cytokine in lymphokine activated killer (LAK) cells and CIK cells culture, but had no significant effect on the proliferation, cytotoxicity, or phenotype of LAK cells, or CIK cells induced by cytokines at higher doses alone, in which CIK cells expanded about 80-fold and the main effectors, $CD3^+NK1.1^+$ cells, expanded by more than 15%. The cytotoxicity of CIK cells in experimental groups was 79.3%±4.7%, 76.9%±6.8% versus the positive control 80.7%±6.8% against P815 ($P>0.05$) and 88.9%±5.5%, 84.7%±7.9% versus the positive control 89.8%±4.5% against YAC-1 ($P>0.05$). The activity of *Gl*-PS could mostly be blocked by anti-CR3. **Conclusion:** *Gl*-PS was shown to be a promising biological response modifier and immune potentiator. The effect of *Gl*-PS on CIK cells is possibly mediated primarily through complement receptor type 3.

Introduction

The fungus *Ganoderma lucidum* (Leyss, ex Fr) Karst (known in China as "lingzhi" and in Japan as "reishi") has a long history of use in traditional Chinese medicine. Polysaccharides from *Ganoderma lucidum* have been reported to have promising immune modulating effects; for example, they have been shown to promote the function of the mononuclear phagocyte system, antigen-presenting cells and cytotoxic T lymphocytes (CTL) induced by dendritic cells[1–3], to enhance lymphocyte proliferation and antibody production[4–6], to potentiate cytokine production by splenocytes and macrophages[7], and to inhibit spontaneous and Fas-mediated apoptosis in neutrophils[8]. The antitumor effect of *Gl*-PS is reportedly due to its effects on the immune system, and there is reportedly no associated toxicity in humans[9].

Over the past 20 years or so, investigators have attempted to develop adoptive cellular immunotherapy for cancer treatment. Cytokine-induced killer (CIK) cells have been shown to generate effector cells with higher proliferative capacity, increased cytotoxicity and fewer side effects than lymphokine activated killer (LAK) cells[10,11]. Some reports have demonstrated that *Gl*-PS can enhance the cytotoxicity of CTL and natural killer (NK) cells[1], but little is known about the effects of *Gl*-PS on the development and cytotoxic

activity of CIK cells. The present study was undertaken to elucidate the effects (and mechanisms thereof) of *Gl*-PS on LAK cells and CIK cells induction and anti-tumor activity.

Materials and methods

Animals and drugs Male C57BL/6j mice 6–8-week-old were purchased from the Department of Experimental Animals, Health Science Center, Peking University, Beijing, China. *Gl*-PS were isolated from *Ganoderma lucidum* (Leyss, ex Fr) Karst by placing the fungus in boiling water, followed by ethanol precipitation, dialysis, and protein depletion using the Sevag method. The isolated molecule was a polysaccharide peptide with a molecular weight of 584 900, and a ratio of polysaccharides to peptides of 93.61%:6.49%. The polysaccharides included *D*-rhamnose, *D*-xylose, *D*-fructose, *D*-galactose, *D*-mannose and *D*-glucose with a molar ratio of 0.793:0.964: 2.944:0.167:0.389:7.94, linked together with β-glycosidic linkages. The peptides contained 16 kinds of amino acids[2]. *Gl*-PS was isolated as a water-soluble powder that was dissolved in serum-free RPMI-1640 medium (Gibco BRL, NY, USA), then filtered through a 0.22 μm filter and stored at 4 °C. This solution was further diluted to the required concentrations before assay.

Isolation and culture of LAK cells LAK cells were generated as previously described[9]. Briefly, mice were killed by cervical dislocation. Suspensions of spleen single cells were pooled in serum-free RPMI-1640 medium by filtering the suspension through mesh with the aid of a glass homogenizer to exert gentle pressure on the spleen fragments. Erythrocytes were lysed with an ammonium chloride solution [0.15 mol/L NH_4Cl, 10 mmol/L $KHCO_3$, 0.1 mmol/L edetic acid (EDTA), pH 7.2]. Obtained cells were washed twice with phosphate-buffered saline (PBS) and resuspended in the complete RPMI-1640 medium [RPMI-1640 medium supplemented with 10% inactivated fetal calf serum (FCS), 2 mmol/L *L*-glutamine, 25 mmol/L $NaHCO_3$, 1 mmol/L sodium pyruvate, 25 mmol/L *N*-2-hydroxyethylpiperazine-*N'*-2-ethanesulfonic acid (HEPES), 100 kU/L penicillin G, and 100 mg/L streptomycin]. Adherent cells were removed via adherence to glass surfaces. Nonadherent mononuclear cells were obtained and the percentage of viable cells was >95%. Murine recombinant interleukin-2 (rIL-2) (300 kU/L) was added on d 0. Cells were incubated at 37 °C in a humidified atmosphere of 5% CO_2 at a concentration of 1×10^9 cells/L. Cell density was determined every 4 d, and cells were subcultured in fresh complete medium containing 150 kU/L IL-2. LAK cells were cultured in complete medium with 300 kU/L IL-2 for the positive control, with 75 kU/L IL-2 plus 400 mg/L or 100 mg/L *Gl*-PS for experimental groups 1 and 2, respectively, and with 75 kU/L IL-2 plus 400 or 100 mg/L soluble starch (SS) or methylcellulose (MC) as negative controls 1–4, respectively.

Isolation and culture of CIK cells CIK cells were generated as previously described[10]. Nonadherent splenocytes were suspended in complete RPMI-1640 medium at a concentration of 1×10^9 cells/L. Murine γ-interferon (IFN-γ; 1000 kU/L) was added on d 0. After 24 h of incubation, 50 mg/L monoclonal antibodies (mAb) against CD3 (dilution of supernatant from hybridoma 145-2C11), 300 kU/L IL-2, and 100 kU/L murine rIL-1 were added. Fresh IL-2 (150 kU/L) and fresh medium were added every 3 d to maintain a cell density of 1.5×10^9–2.0×10^9 cells/L for 14–21 d. All the cytokines were purchased from PeproTech EC, London, UK. CIK cells were prepared by using the standard protocol described earlier for the positive control. Experimental groups 1 and 2 were prepared according to the standard protocol except that *Gl-PS* (400 or 100 mg/L) was added, and the dose of anti-CD3 and IL-2 was decreased by 50% and 75%, respectively. For negative control groups 1–4, *Gl*-PS in the experimental protocol was replaced with SS or MC (400 or 100 mg/L).

LAK and CIK cell proliferation assay Cell density was assessed every 3 d, and cells were subcultured in fresh complete medium containing IL-2 as described previously[10]. Viable cell numbers were determined by the Trypan blue dye exclusion method at each time point. LAK and CIK cell proliferation was analyzed by cell growth curves.

Preparation of target cells P815 (NK-resistant) and YAC-1 (NK-sensitive) cells proliferating in a logarithmic manner were used as target cells for the cytotoxicity assay. Cells (2×10^8 cells/L) were maintained in complete RPMI-1640 medium as described earlier. On the day of testing, cells were washed once with PBS and re-suspended in a complete medium at a concentration of 2×10^8 cells/L.

Cytotoxicity assay The MTT colorimetric assay was used for testing cytotoxic activity *in vitro*[12]. LAK cells or CIK cells were used as effectors, and were coincubated with P815 or YAC-1 cells as targets for 4 h at effector:target ratios of 20:1. Cells were plated in triplicate in 96-well microculture plates (Corning Costar, MA, USA). MTT (Sigma, St Louis, MO, USA) was dissolved at 5 g/L in PBS and filtered through a 0.22 μm filter. MTT solution (20 μL) was added to each well, and the microplates were further incubated at 37 °C for 4 h. The 96-well microplates were centrifuged at 200×*g* for 15 min, then supernatants were discarded, and 150 μL of Me_2SO was added into each well. The tray was gently shaken thoroughly for 10 min to dissolve the dark blue crystals of formazan that could be measured spectrophotometrically. Data are expressed as mean absorbance value (optical density, *OD*) of samples±SD. Percentage-specific cytotox-

icity (% C) was calculated as follows: % C={1–[(*OD* of effectors+targets)–*OD* of effectors]/*OD* of targets}×100%.

Flow cytometric assays Effector cells were harvested and washed twice with ice cold FACScan buffer (PBS containing 2% FCS and 0.1% sodium azide). To block nonspecific antibody binding, 20% mixed mouse and rat serum was used and then cells were stained with mAb against CD3 coupled to fluorescein isothiocyanate (FITC) and/or mAb against NK1.1 coupled to phycoerythrin (PE) (antibodies from Santa Cruz, CA, USA or Pharmingen, CA, USA) for 45 min at 4 °C in the dark. The stained cells were washed twice and fixed with 1% paraformaldehyde in FACScan buffer and then analyzed by using a FACScan flow cytometer (Becton Dickinson, NJ, USA). Dead cells and debris were gated out.

Antibody block experiment CIK cells were induced by using the standard protocol described earlier for the positive control, except that *Gl*-PS (400 or 100 mg/L) was added and the dose of anti-CD3 and IL-2 was decreased by 50% and 75% (experimental groups 1 and 2, respectively) or *Gl*-PS in the experimental group protocol was replaced by SS (400 mg/L or 100 mg/L) or MC (400 mg/L or 100 mg/L) as negative controls 1–4, respectively. Anti-CR3 (eBioscience, San Diego, CA, USA) or its isotype immunoglobulin G (IgG) was added 30 min prior to *Gl*-PS in the experimental group protocol, in anti-CR3 groups 1 or 2 and isotype antibody groups 1 or 2. Cells were harvested on d 7. The proliferation and cytotoxicity of different groups were determined by MTT colorimetric assay.

Statistical analysis Data were analyzed using general linear models (2-way ANOVA) in SPSS statistical software (version 10.0) with a significance level of α=0.05. Comparisons between means were made using the least significant difference multiple comparisons *t*- test of Dunnett's *t*-test. Results are presented as the mean±SD. Values of $P<0.05$ were considered to be statistically significant.

Results

Effects of *Gl*-PS on LAK cell proliferation Nonadherent splenocytes were incubated at 1×10^9 cells/L in complete medium with IL-2 alone or IL-2 at different concentrations plus *Gl*-PS at different concentrations. Cells were harvested after 4 d to generate LAK cells. Statistical tests of the between-subject effects showed that there were significant differences according to univariate analyses of variance (two-way ANOVA). The interaction between IL-2 and *Gl*-PS was significant, which suggests a synergy between IL-2 and *Gl*-PS. The effect of IL-2 was bigger than that of *Gl*-PS. For the factor "IL-2", there was no statistically significant difference between neither the 150 kU/L nor the 75 kU/L level when compared with the 300 kU/L level ($P>0.05$). For the factor "*Gl*-PS ", the 400 mg/L and 100 mg/L levels were significantly different from the 0 mg/L level ($P<0.01$). The combination of 75 kU/L IL-2 and 400 mg/L or 100 mg/L *Gl*-PS was optimal for the least usage of IL-2 (75 kU/L), and LAK cell proliferation induced by the combination was not less than that of the positive control, in which only IL-2 (300 kU/L) was added (Table 1). Compared with only 75 kU/L IL-2 in the LAK cell culture, the effects of SS or MC in different concentrations plus 75 kU/L IL-2 were not significant, therefore SS and MC were chosen as negative controls (data not shown).

Cells in different groups were harvested and viable cell numbers were determined on d 1, 4, 8, and 12. The difference in cell numbers across groups was not significant on d 1. Following 4 d of culture, the number of viable cells of the positive control and experimental groups increased 2-fold in comparison to the negative controls, but the difference between experimental groups and the positive control was not significant at that time. The number of viable cells in the positive control and experimental groups increased markedly compared with negative controls on d 8. However, at that time, there was no significant difference between the

Table 1. Influences of *Gl*-PS and IL-2 at different concentrations on LAK cells proliferation (1×10^9 cells/L). n=6. Mean±SD. [a]$P>0.05$, [c]$P<0.01$ *vs* positive control.

Group	*Gl*-PS concentration/mg·L^{-1}					
	1000.00	400.00	100.00	25.00	6.25	0.00
IL-2 /kU·L^{-1}						
300.0	1.62±0.12	2.25±0.12	2.26±0.12	2.05±0.14	1.85±0.16	1.79±0.19
150.0	1.86±0.18	2.25±0.14	2.04±0.12	1.88±0.16	1.78±0.12	1.30±0.18
75.0	1.50±0.15	2.22±0.13[a]	2.23±0.11[a]	1.81±0.14	1.65±0.13	1.11±0.16
37.5	0.81±0.12	0.81±0.14	0.71±0.12	0.74±0.11	0.74±0.13	0.76±0.12
0.0	0.94±0.17	0.82±0.11	0.77±0.12	0.63±0.11	0.62±0.13	0.56±0.10[c]

IL-2 (300 kU/L) was added alone in complete medium as a positive control.

positive control and experimental groups. After 8 d of culture, cells in all groups no longer proliferated, died gradually, and decreased on d 12 relative to the number present on d 1 (Figure 1).

Effects of *Gl*-PS on CIK cell proliferation With respect to the synergistic interaction of *Gl*-PS (400 mg/L or 100 mg/L) and IL-2 (75 kU/L), experimental groups 1 and 2 were the same as the positive control except for the addition of 400 or 100 mg/L *Gl*-PS and a reduction in the doses of anti-CD3 and IL-2 by 50% and 75%, respectively. For negative controls 1–4, *Gl*-PS was replaced with SS or MC (400 mg/L or 100 mg/L) in the protocol used in the experimental groups. We observed that the proliferation of CIK cells in the experimental groups was also similar to that of the positive control. The reduction of cell numbers in the negative controls was significant compared with the positive control on d 6 to d 21. The number of CIK cells in the positive control and experimental groups peaked at d 21 and was expanded about 80-fold relative to the beginning culture. Their increase in activity was much larger than that observed in LAK cells (LAK proliferation peaked at d 4–8 and the cell number increased 2-fold relative to the initial culture). This suggests that 400 mg/L or 100 mg/L *Gl*-PS decreased the usage of IL-2 and anti-CD3 by 75% and 50%, respectively, and that the influence on CIK cell proliferation was almost equal to that of cytokines alone at higher doses (Figure 2).

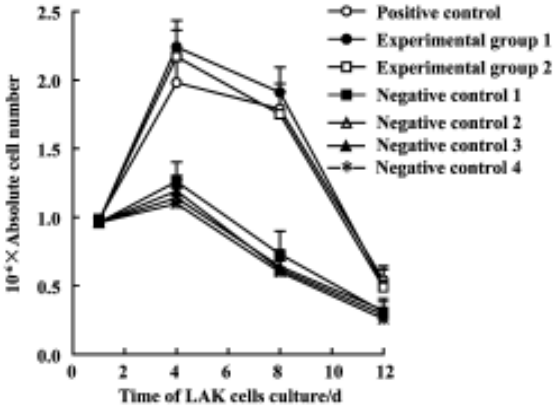

Figure 1. Effects of *Gl*-PS on the expansion of LAK cells. LAK cells were cultured in complete medium with 300 kU/L IL-2 as a positive control, with 75 kU/L IL-2 plus 400 mg/L or 100 mg/L *Gl*-PS for experimental groups 1 and 2, respectively, and with 75 kU/L IL-2 plus 400 or 100 mg/L SS or MC for negative controls 1–4, respectively. n=9. Mean±SD.

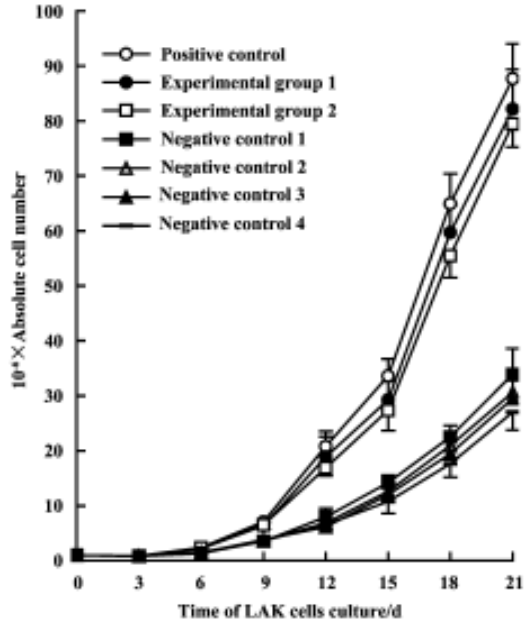

Figure 2. Effect of *Gl*-PS on CIK cell proliferation. CIK cells were induced by using a standard protocol as described in the text (positive control). Experimental groups 1 and 2 were treated in the same way as the standard protocol except that *Gl*-PS (400 mg/L or 100 mg/L) was added, and the dose of anti-CD3 and IL-2 was reduced by 50% and 75%, respectively. For the negative control groups 1–4, *Gl*-PS was replaced with SS or MC (400 mg/L or 100 mg/L) using the same protocol as the experimental group. n=9. Mean±SD.

Effects of *Gl*-PS on cytotoxicity of LAK Compared with induction by 300 kU/L IL-2 alone, no significant difference in the cytotoxicity of LAK cells induced by 75 kU/L IL-2 plus 400 mg/L or 100 mg/L *Gl*-PS was observed, but cytotoxicity induced by 75 kU/L IL-2 plus SS or MC instead of *Gl*-PS in the negative controls was reduced. This suggests that a certain concentration of *Gl*-PS increases the cytotoxicity of LAK cells (Figure 3).

Effects of *Gl*-PS on cytotoxicity of CIK cells Compared with the standard protocol for preparing CIK cells, the cytotoxicity of CIK cells in the experimental groups was not significantly different, but was higher than that in the negative control groups. We found that CIK cells in every group achieved higher cytotoxicity than LAK cells. This suggests that 400 mg/L or 100 mg/L *Gl*-PS decreases the usage of IL-2 and anti-CD3 by 75% and 50%, respectively, but has no influence on CIK cell cytotoxicity induced by cytokines alone at higher doses (Figure 4).

Immunophenotype of effector cells in the presence of *Gl*-PS Flow cytometric assays showed that LAK cells represented a heterogeneous population, in which the major effector cells generally had an $NK1.1^+$ cell surface phenotype. Compared with LAK cells in the positive control groups, the phenotype of LAK cells in the experimental groups was not significantly different. Most CIK cells expressed CD3, a sur-

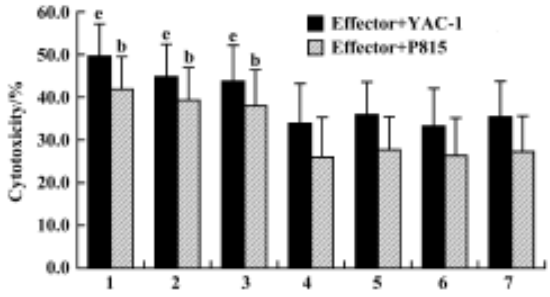

Figure 3. Effect of *Gl*-PS on the cytotoxicity of LAK cells. LAK cells were induced by different protocols and tested for cytotoxicity at an effector:target ratio of 20:1. 1: Positive control, 300 kU/L IL-2; 2,3: experimental groups 1 and 2, 75 kU/L IL-2 plus 400 or 100 mg/L *Gl*-PS, respectively; 4–7: negative controls 1–4, 75 kU/L IL-2 plus 400 or 100 mg/L SS or MC, respectively. n=9. Mean±SD. $^bP<0.05$ *vs* negative controls against P815. $^eP<0.05$ *vs* negative controls against YAC-1.

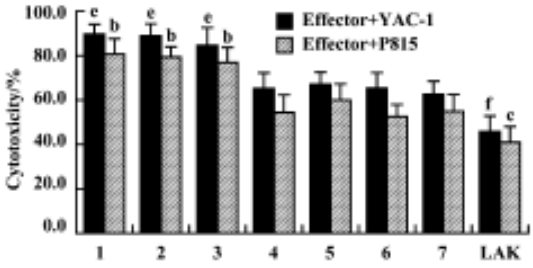

Figure 4. Evaluation of effects of *Gl*-PS on the cytotoxicity of CIK cells. CIK cells induced by different protocols were harvested on d 15 and tested for cytotoxicity. Effector:target ratio is 20:1. 1: Positive control, standard protocol described in text; 2,3: experimental groups 1 and 2 received the standard protocol except that *Gl*-PS (400 mg/L or 100 mg/L) was added and the doses of anti-CD3 and IL-2 were reduced by 50% and 75%, respectively; 4–7: negative controls 1–4, *Gl*-PS in the experimental protocol was replaced with SS or MC (400 mg/L or 100 mg/L), respectively; LAK, LAK cells. n=9. Mean±SD. $^bP<0.05$, $^cP<0.01$ *vs* every group of CIK cells against P815 . $^eP<0.05$, $^fP<0.01$ *vs* every group of CIK cells against YAC-1.

face marker of T cells. Treatment with 400 mg/L or 100 mg/L *Gl*-PS in the experimental groups did not alter the phenotype of CIK cells (Table 2).

Effect of anti-CR3 on proliferation and cytotoxicity of CIK cells induced by stimuli containing *Gl-PS* CIK cell proliferation and cytotoxicity were reduced to <40% of that in the experimental groups by the addition of anti-CR3 30 min prior to the addition of *Gl*-PS in CIK cell culture, but not by nonspecific isotype IgG (Figures 5, 6).

Discussion

Polysaccharides isolated from *Ganoderma* are high-molecular-weight polysaccharides linked together by β-glycosidic linkages. These polysaccharides exhibit immunological activity, for example promoting cellular immunity and humoral immunity[1–8,13–15]. Biological and immunopharmacological activities depend on the conformation of polysaccharides, molecular mass, solubility in water and triple-helical structure. Soluble starch is an α-(1,4)-bonding glucose polymer, and methylcellulose links by uniform β-(1,4) glycosidic linkages[16]. Because they lack a helical structure, neither of these compounds have the immunological activity, so they served as negative controls. Flow cytometry indicated that LAK and CIK cells populations were heterogeneous. Effector cells in LAK cell culture generally have the $CD3^-NK1.1^+$ cell surface phenotype[17]; however, most CIK cells express T-cell markers. Earlier studies have shown that cytotoxicity correlates with the expansion of $CD3^+NK1.1^+$ lymphocytes, which are the main effector cells in CIK cell cultures[18]. The present study demonstrated that the optimal combination of *Gl*-PS (400 mg/L or 100 mg/L) and certain cytokines did not alter the phenotype of LAK cells or CIK cells, and had no effect on the percentage of effector cells. For this reason, the cytotoxicity of LAK cells and CIK cells in the experimental groups was similar to that of the positive control, which contained cytokines alone at higher doses.

CIK cells with enhanced cytotoxicity and a higher proliferative capacity relative to LAK cells were described first by Schmidt-Wolf and colleagues in 1991. They reported that treatment of tumor cells from bone marrow with CIK cells effectively reduced the tumor cell burden, allowing animals to survive[10]. As demonstrated here, LAK and CIK cells

Table 2. Influences of *Gl*-PS on the immunophenotype of murine LAK cells and CIK cells. n=6. Mean±SD.

Group	$CD3^+$/%	$NK1.1^+$/%	$CD3+NK1.1^+$/%
LAK cells			
Group 1	62.2±7.3	11.3±4.3	3.8±0.9
Group 2	58.6±9.3	10.8±4.5	3.7±1.0
Group 3	57.5±7.2	10.4±5.0	3.4±1.1
CIK cells			
Group 4	96.8±4.5	20.3±6.3	18.3±5.4
Group 5	95.4±4.6	19.1±5.8	16.9±5.1
Group 6	95.1±3.2	18.2±6.4	15.7±4.5

LAK and CIK cells were induced by different protocols as described in the text. Group 1: LAK cells in the positive control group; groups 2 and 3: LAK cells in experimental groups 1 and 2; group 4: CIK cells in the positive control group; groups 5 and 6: CIK cells in experimental groups 1 and 2.

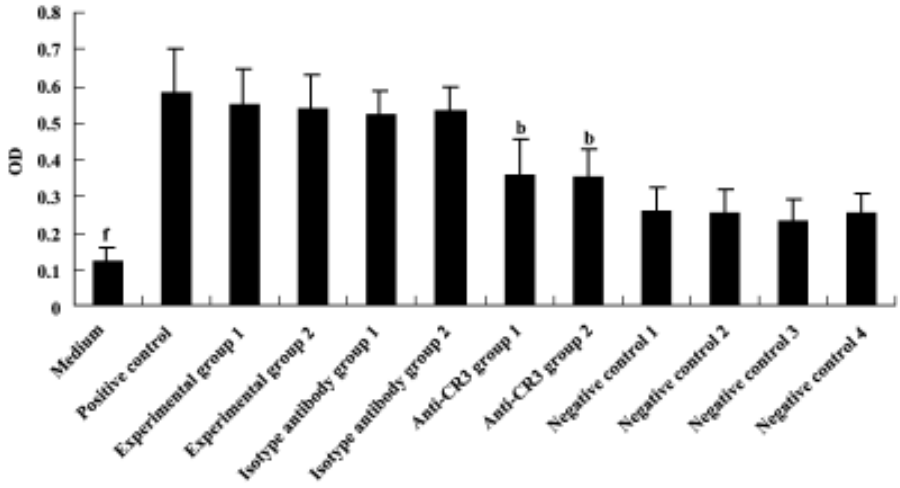

Figure 5. Effect of anti-CR3 on the proliferation of CIK cells induced by *Gl*-PS and cytokines. CIK cells were induced by using the standard protocol for the positive control group, by using the standard protocol plus the addition of *Gl*-PS (400 mg/L or 100 mg/L) and a decreased dose of anti-CD3 and IL-2 by 50 % and 75 %, respectively, for experimental groups 1 and 2, and by replacing *Gl*-PS in the experimental group protocol with SS or MC (400 mg/L or 100 mg/L) for negative controls 1–4, respectively. Anti-CR3 (10 mg/L) or its isotype IgG were added 30 min prior to *Gl*-PS in the experimental group protocol for anti-CR3 groups 1 and 2 and isotype antibody groups 1 and 2, respectively. Cells were incubated only in complete medium without any stimuli for medium group. n=9. Mean±SD. ^{b}P<0.05 *vs* positive control, experimental groups and isotype antibody groups. ^{f}P<0.01 *vs* the every other group.

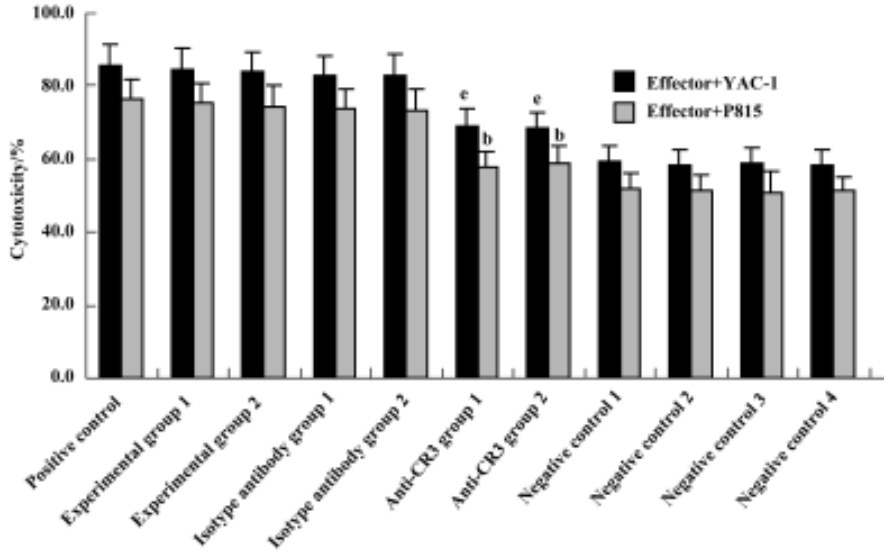

Figure 6. Effect of anti-CR3 on cytotoxicity of CIK cells induced by *Gl*-PS and cytokines. CIK cells were induced by using the standard protocol for the positive control group, by using the standard protocol plus the addition of *Gl*-PS (400 mg/L or 100 mg/L) and a decreased dose of anti-CD3 and IL-2 by 50 % and 75 %, respectively, for experimental groups 1 and 2, and by replacing *Gl*-PS in the experimental group protocol with SS or MC (400 mg/L or 100 mg/L) for negative controls 1–4, respectively. Anti-CR3 (10 mg/L) or its isotype IgG were added 30 min prior to Gl-PS in the experimental group protocol for anti-CR3 groups 1 and 2 and isotype antibody groups 1 and 2, respectively. Effector:target ratio is 20:1. n=6. Mean±SD. ^{b}P<0.05 *vs* positive control, experimental groups and isotype antibody groups against P815. ^{e}P<0.05 *vs* standard group, experimental groups and isotype antibody groups against YAC-1.

possess cytotoxic effects against both NK-sensitive and NK-resistant tumor cells, and CIK cells are more cytotoxic than LAK cells. Previous studies have shown that CIK cells express both the Fas receptor and FasL. Fas-sensitive and previously activated T cells are eliminated in the early stages of CIK cell culture through either IFN-γ, activation-induced

cell death or both. To generate CIK cells, splenocytes are stimulated with IFN-γ 24 h prior to anti-CD3 and IL-2 treatment. This combination of cytokines might select for a population of Fas-resistant cells[19]. In the present study, the CIK cell growth curve decreased in the initial stages, then increased. The initial decrease might be related to the downregulation of cell proliferation caused by IFN-γ. In the present study, a synergistic interaction between IL-2 (75–300 kU/L) and *Gl*-PS (400 mg/L or 100 mg/L) enhanced LAK cell development and cytotoxicity. In combination with 1000 kU/L IFN-γ, 75 kU/L IL-2, 25 mg/L anti-CD3 and 100 kU/L IL-1, *Gl*-PS (400 mg/L or 100 mg/L) decreased the dose of IL-2 and anti-CD3 by 75% and 50% respectively, but did not influence CIK cell proliferation and cytotoxicity. These results show that only intermediate concentrations (not too high or too low) of *Gl*-PS enhance immunocyte development; and the results also suggest that a certain concentration of *Gl*-PS could be an immune potentiator to reduce the dose of cytokine inducing LAK and CIK cells. Previous studies have shown that *Gl*-PS can stimulate splenocytes and macrophages to produce cytokines, including IL-1, IL-2, IFN-γ and tumor necrosis factor[5,20–23]. Whether *Gl*-PS exerts its activity by promoting the release of cytokines by the precursors of CIK cells is currently under investigation.

β-Glucans are known to bind to receptors, for example CR3. The binding site of CR3 has a broad specificity for certain polysaccharides containing glucose and mannose, as well as *N*-acetyl-*D*-glucosamine[24]. *Gl*-PS is a heteroglycan that contains primarily glucose[2], and CR3 is expressed mostly by activated lymphocytes, NK cells, macrophages and granulocytes[25]. Our results demonstrated that the activity of CIK cells mediated by *Gl*-PS was drastically inhibited (60%–70%) by prior treatment of murine splenocytes with anti-CR3. These results correspond with those of Xia *et al*, who found that β-Glucans bound to CR3 on macrophages, neutrophils, and NK cells in humans and mice, and cytotoxicity mediated by β-glucans can be blocked by anti-CR3 added before or after β-glucan treatment[25]. It has been confirmed that anti-CR3 had no effect on the cytotoxic activity of CIK cells[26]. These results suggest that the immune-modulating effect of *Gl*-PS on CIK cells is mediated primarily through CR3. Our study provides useful data for the use of *Gl*-PS in combination with other immunoactivators.

Acknowledgements

This research was supported by the Research Fund of Shanghai Green Valley Holdings Co. The *Gl*-PS was kindly provided by Prof Shu-qian LIN and Associate Prof Sai-zhen WANG from the Fuzhou Institute of Green Valley Bio-Pharm Technology.

References

1 Lin ZB, Zhang HN. Anti-tumor and immunoregulatory activities of *Ganoderma lucidum* and its possible mechanisms. Acta Pharmacol Sin 2004; 25: 1387–95.
2 Cao LZ, Lin ZB. Regulation on maturation and function of dendritic cells by *Ganoderma lucidum* polysaccharides. Immunol Lett 2002; 83: 163–9.
3 Cao LZ, Lin ZB. Regulatory effect of *Ganoderma lucidum* polysaccharides on cytotoxic T-lymphocytes induced by dendritic cells *in vitro*. Acta Pharmacol Sin 2003; 24: 321–6.
4 Zhang J, Tang Q, Zimmerman-Kordmann M, Reutter W, Fan H. Activation of B lymphocytes by GLIS, a bioactive proteoglycan from *Ganoderma lucidum*. Life Sci 2002; 71: 623–38.
5 Bao XF, Zhen Y, Ruan L, Fang JN. Purification, characterization, and modification of T lymphocyte-stimulating polysaccharide from spores of *Ganoderma lucidum*. Chem Pharm Bull (Tokyo) 2002; 50: 623–9.
6 Wasser SP, Weis AL. Therapeutic effects of substances occurring in higher Basidiomycetes mushrooms: a modern perspective. Crit Rev Immunol 1999; 19: 65–96.
7 Lin ZB, Zhang QH. Effect of *Ganoderma lucidum* polysaccharide B on TNF-α and IFN-γ production and their mRNA expression. J Beijing Med Univ 1999; 31: 179–83.
8 Hsu MJ, Lee SS, Lin WW. Polysaccharide purified from *Ganoderma lucidum* inhibits spontaneous and Fas-mediated apoptosis in human neutrophils through activation of the phosphatidylinositol 3 kinase/Akt signaling pathway. J Leukoc Biol 2002; 72: 207–16.
9 Lin ZB. Progress of studies on the anti-tumor activity and immunomodulating effect of *Ganoderma*. J Beijing Med Univ 2002; 34: 493–8.
10 Schmidt-Wolf IG, Negrin RS, Kiem HP, Blume KG, Weissman IL. Use of a SCID mouse/human lymphoma model to evaluate cytokine-induced killer cells with potent anti-tumor cell activity. J Exp Med 1991; 174: 139–49.
11 Lu PH, Negrin RS. A novel population of expended human $CD3^+CD56^+$ cells derived from T cells with potent *in vivo* antitumor activity in mice with severe combined immunodeficiency. J Immunol 1994; 153: 1687–96.
12 Ferrari M, Fornasiero MC, Isetta AM. MTT colorimetric assay for testing macrophage cytotoxic activity *in vitro*. J Immunol Methods 1990; 131: 165–72.
13 Zákány J, Chihara G, Fachet J. Effect of Lentinan on tumor growth in murine allogeneic and syngeneic host. Int J Cancer 1980; 25: 371–6.
14 Zákány J, Chihara G, Fachet J. Effect of Lentinan on the production of migration inhibitory factor induced by syngeneic tumor in mice. Int J Cancer 1980; 26: 783–8.
15 Bao XF, Wang XS, Dong Q, Fang JN, Li XY. Structural features of immunologically active polysaccharides from *Ganoderma lucidum*. Phytochemistry 2002; 59: 175–81.
16 Chen HL. Studies of the conformation and activity of

polysaccharides. Shanghai: Shanghai Medical University Press; 1997.

17 Schmidt-Wolf IG, Lefterova P, Johnston V, Scheffold C, Csipai M, Mehta BA, *et al*. Sensitivity of multidrug-resistant tumor cell lines to immunologic effector cells. Cell Immunol 1996; 169: 85–90.

18 Schmidt-Wolf IG, Lefterova P, Mehta BA, Fernandez LP, Huhn D, Blume KG, *et al*. Phenotypic characterization and identification of effector cells involved in tumor recognition of cytokine-induced killer cells. Exp Hematol 1993; 21: 1673–9.

19 Verneris MR, Kornacker M, Mailänder V, Negrin RS. Resistance of *ex vivo* expanded $CD3^+CD56^+$ T cells to Fas-mediated apoptosis. Cancer Immunol Immunother 2000; 49: 335–45.

20 Wang YY, Khoo KH, Chen ST, Lin CC, Wong CH, Lin CH. Studies on the immuno-modulating and antitumor activities of *Ganoderma lucidum* (Reishi) polysaccharides: functional and proteomic analyses of a fucose-containing glycoprotein fraction responsible for the activities. Bioorg Med Chem 2002; 10: 1057–62.

21 Ma L, Lin ZB, Li RZ, He YQ. Effects of *Ganoderma* polysaccharides on IL-2 production by mouse splenocytes *in vitro*. J Beijing Med Univ 1991; 23: 412–6.

22 Lei LS, Lin ZB. Effects of *Ganoderma* polysaccharides on T cell subpopulations and production of interleukin 2 in mixed lymphocyte response. Acta Pharmacol Sin 1992; 27: 331–5.

23 Zhang QH, Lin ZB. The antitumor activity of *Ganoderma lucidum* (Curt Fr) P Karst (Ling Zhi) (Aphyllophoromycetideae) polysaccharides is related to tumor necrosis factor-α and interferon-γ. Int J Med Mushroom 1999; 1: 207–15.

24 Thornton BP, Vetvicka V, Pitman M, Goldman RC, Ross GD. Analysis of the sugar specificity and molecular location of the beta-glucan-binding lectin site of complement receptor type 3 (CD11b/CD18). J Immunol 1996; 156: 1235–46.

25 Xia Y, Vetvicka V, Yan J, Hanikyrova M, Mayadas T, Ross GD. The beta-glucan-binding lectin site of mouse CR3 (CD11b/CD18) and its function in generating a primed state of the receptor that mediates cytotoxic activation in response to iC3b-opsonized target cells. J Immunol 1999; 162: 2281–90.

26 Schmidt-Wolf IG, Lefterova P, Johnston V, Huhn D, Blume KG, Negrin RS. Propagation of large numbers of T cells with natural killer cell markers. Br J Haematol 1994; 87: 453–8.

Acta Pharmacologica Sinica 2005 Sep; 26 (9): 1138–1144

Full-length article

Mitochondria-dependent apoptosis induced by a novel amphipathic photochemotherapeutic agent $ZnPcS_2P_2$ in HL60 cells[1]

Hui-fang HUANG, Yuan-zhong CHEN[2], Yong WU

Fujian Institute of Hematology, Union Hospital, Fujian Medical University, Fuzhou 350001, China

Key words

photodynamic therapy; zinc phthalocyanine; apoptosis; cytochrome c; caspases; HL60 cells

[1] Project supported by a grant from the Fujian Provincial Science Foundation (No 2003D10, No 2004Y020).
[2] Correspondence to Dr Yuan-zhong CHEN.
Phn 86-591-8335-1966.
Fax 86-591-8332-4116.
E-mail chenyz@pub3.fz.fj.cn

Received 2005-03-05
Accepted 2005-04-29

doi: 10.1111/j.1745-7254.2005.00160.x

Abstract

Aim: To investigate the mechanism underlying the killing effects of a novel amphipathic photosensitizer, disulfonated diphthalimidomethyl phthalocyanine zinc ($ZnPcS_2P_2$), mediated photodynamic therapy (ZnPc-PDT) in human myelogenous leukemia HL60 cells. **Methods:** After incubation for 5 h with 0.5 μmol/L $ZnPcS_2P_2$, the HL60 cells were exposed to a light source of 670 nm wavelength. Thereafter, the cells were detected at different time intervals after PDT. The characteristics of apoptosis were detected by observation of ultrastructure assay, DNA fragmentation assay and terminal deoxynucleotidyl transferase deoxyuridine nick-end labeling method (TUNEL). Mitochondria-dependent apoptosis was determined by the detection of mitochondrial membrane potential ($\Delta\psi m$), activities of caspase family protease and of caspase-3, cytosol cytochrome c. Proteins Bcl-2 and Bax were detected by immunoblot analysis. **Results:** Evident characteristics of apoptosis were observed post-ZnPc-PDT with ultrastructure assay, DNA fragmentation assay and TUNEL staining. TUNEL assay showed that apoptotic rates in the cells collected from 6 h, 12 h and 24 h after PDT were 9.6%, 24.4%, and 33.0%, respectively. HL60 cells underwent mitochondria-dependent apoptosis as a result of cytochrome c release from mitochondria into cytosol accompanied by a reduction of $\Delta\psi m$. The activities of caspase family protease and of caspase-3 were elevated. Furthermore, ZnPc-PDT could remarkably down-regulate the Bcl-2 pro-apoptotic protein and up-regulate the anti-apoptotic Bax protein. **Conclusion:** ZnPc-PDT could induce mitochondria-dependent apoptosis in HL60 cells.

Introduction

Photodynamic therapy (PDT), a promising cancer therapeutic approach, utilizes a photosensitizing agent followed by illumination at a specific "activating" wavelength of light. PDT produces singlet oxygen and other reactive oxygen species (ROS), leading to lipid peroxidation and damage to membranes, DNA, cytoskeleton, and other sites, and eventual cell death[1–3]. Individually, photosensitizers and light are nontoxic, but tumoricidal when combined. Electron microscopy, histological and biochemical studies have shown that PDT with different photosensitizers induces apoptotic or necrotic cell death in different cell types[4–8]. Photosensitizers are key factors for PDT. According to previous studies[9,10], $ZnPcS_2P_2$ presents 4 advantages over conventional photosensitizers such as hematoporphyrin derivatives (HpD) or other porphyrin derivatives. The first advantage is that the wavelength of suitable exicited light for $ZnPcS_2P_2$ is 670 nm, which is good for penetrating into tissues. The second advantage is that $ZnPcS_2P_2$ has no obvious absorption in the visible part as with HpD with the result of decreased skin phototoxicity from natural light to a larger extent. The third advantage is that the exicited triplet state of $ZnPcS_2P_2$ has a larger quantum yield and longer lifetime. The fourth advantage is that the amphipathic structure of $ZnPcS_2P_2$ results in the increase of selective uptake of sensitizers by tumor cells. Our previous investigation manifested that leukemic cell lines exhibited higher susceptibility to ZnPc-PDT than normal hematopoietic cells and ZnPc-PDT could eliminate the residual leukemia cells in normal bone marrow mononuclear cells[11]. However, the mechanism underlying the killing ef-

fects of ZnPc-PDT on leukemic cells is still unknown. In the present paper, we studied the death pathway of HL60 cells induced by ZnPc-PDT and the mechanism of its action.

The mitochondrion plays a central role in the control of apoptosis by releasing the apoptogenic proteins apoptosis-inducing factor (AIF) and cytochrome c into the cytosol. The released proteins activate pathways essential for carrying out the morphological and biochemical changes. For example, cytochrome c, normally residing between the mitochondrial outer and inner membranes and serving as a diffusible electon carrier in the intermembrane space, has been demonstrated to be a co-activator of caspase-9, which in turn activates caspase-3. The active caspase-3 then activates caspase-activated DNA (CAD). Active CAD initiates chromatin and DNA fragmentation[12–22]. Therefore, in the present study, we investigate the relationship between the death mechanism induced by ZnPc-PDT and the mitochondria-dependent apoptosis. Furthermore, it is well known that Bcl-2 serves to inhibit apoptosis by antagonizing the release of mitochondrial cytochrome c, whereas Bax promotes apoptosis[24,25]. The Bcl-2 protein was reported to be a damage target of PDT and contributes to PDT-efficient induction of apoptosis[25]. Therefore, we also detect the kinetic change of Bcl-2 and Bax expression following ZnPc-PDT.

Materials and methods

Cell line Human myelogenous leukemia HL60 cells provided by the Shanghai Institute of Cytobiology (Institute of Chinese Academy of Sciences, China) were maintained in continuous culture in RPMI-1640 (GIBCO BRL), supplemented with 10% (*v*/*v*) heat-inactivated fetal calf serum (FCS), penicillin 100 U/mL, 100 μg/mL streptomycin, and 0.25 mmol/L *L*-glutamine at 37 °C under 5% CO_2 humidified air. The viability of cells was determined by Trypan blue dye exclusion. Cells were maintained in log phase with viability greater than 95%.

Photosensitizer $ZnPcS_2P_2$ was a gift from the Department of Chemistry, Institute of Research on Functional Materials, Fuzhou University, China. It was dissolved in a solution comprised of Cremophor EL 2%(*v*/*v*), propylene glycol 20% (*v*/*v*), NaCl 0.9%(*w*/*w*) and stored in the dark at 4 °C.

Photodynamic treatment HL60 cell suspensions (5×10^6/mL in RPMI-1640) were incubated with 0.5 μmol/L of $ZnPcS_2P_2$ for 5 h. The cell suspensions were then photoirradiated using a LD-670 semi-conductor laser (Laboratory of Laser Medicine, Tianjin Medical University, China) emitting red light at a 670 nm wavelength. The power density at the illumination area was 53 mW/cm^2 and total light dose was 2.1 J/ cm^2. A control group (cells incubated with same volume of saline for 5 h) was established. Thereafter, cells were harvested at 6 h, 12 h, and 24 h, respectively.

Apoptosis assays Ultrastructure was analyzed under a HU-12A electron microscope. DNA fragmentation assay was followed as described[26]. TUNEL stains were carried out according to the manufacture's instructions (Promega) and the apoptotic cells characterized with brown nuclei were counted under microscope and photographed.

Assays for mitochondrial membrane potential (Δψm), caspase-family protease activity and caspase-3 activity The procedure was carried out according to the manufacture's instructions (Biovision). The results were then analyzed by flow cytometry (BD). The Δψm detection kit utilized MitoCapture™ (BioVision), a cationic dye that fluoresces differently in healthy cells and apoptotic cells. In healthy cells, MitoCapture accumulated and aggregated in the mitochondria, giving off a bright red fluorescence. In apoptotic cells, MitoCapture could not aggregate in the mitochondria due to the altered Δψm, and thus it remained in the cytoplasm in its monomer form, emitting green fluorescence. The fluorescent signal could be analyzed by flow cytometry FITC channel for green monomers and PI channel for red aggregates. The assay for caspase activity was based on the cleavage of $(aspartyl)_2$-Rhodamine 110 (D_2R), a reported substrate for members of caspase family proteases. D_2R was non-fluorescent, however, upon cleavage of the substrate by cellular caspases, the released rhodamine 110 resulted in a green fluorescence. The caspase-3 activity detection kit utilized the caspase-3 inhibitor DEVD-FMK, conjugated to FITC as the fluorescent *in situ* marker. FITC-DEVD-FMK was cell-permeable, nontoxic, and irreversibly binds to activated caspase-3 in apoptotic cells.

Assay for cytochrome c Western blotting was performed according to previously published methods[27], with minor modification. In brief, cell pellets were washed once with ice-cold phosphate-buffered saline (PBS) and lysed in lysis buffer (in mmol/L: 20 Hepes-KOH, 250 sucrose, pH 7.5, 10 KCl, 1.5 $MgCl_2$, 1 sodium ethylene diaminetetraacetic acid (EDTA), 1 dithiothreitol, and 0.1 phenylmethylsulfonyl fluoride). The cells were homogenized on ice for 15 min and the homogenates were centrifuged twice at 1000×*g* for 10 min. The supernatants were centrifuged at 12000×*g* for 15 min at 4 °C, and the supernatants were cytosol without mitochondria. Protein concentration of cell extracts was determined with Bradford protein assay (Coomassie Brilliant Blue G-250 obtained from BBI). Cytosol protein was loaded and separated on 12% sodium dodecyl sulfate (SDS) polyacrylamide gel and transferred to a nitrocellulose membrane

by standard electric transfer protocol. The chemiluminescent detection of membrane-bound proteins was performed according to the manufacture's instructions (KPL, Kirkegaard & Perry Laboratories). In brief, the membranes were blocked in blocking buffer for 1 h at room temperature and then incubated with anti-human cytochrome c mouse monoclonal antibody (Neomarkers) in blocking buffer overnight at 4 °C. After washing, the membranes were incubated with anti-mouse secondary antibody horseradish peroxidase conjugate and then detected by enhanced chemiluminescent detection system. Finally, the bands were visualized by autoradiography using X-ray film and scanned and quantified by Imager Quant (Alpha Innotech Corporation, San Leandro, USA). The relative levels of cytochrome c were obtained after normalization with β-actin values in the same lane. At the same time, the distribution of cytochrome c was detected by immunohistochemistry staining and the signals were visualized with an alkaline phosphatase-linked assay system (DAKO LSAB labeled streptavidin-biotin, DakoCytomation Inc). The proteins were detected under microscope and photographed.

Assay for Bcl-2 protein and Bax protein To prepare lysates, cells were initially washed once with ice-cold PBS. Cell pellets were treated with lysis buffer [1% Nonidet P-40 detergent (NP-40), 50 mmol/L Tris-HCl buffer, pH 8, 0.1% SDS, 0.1 mmol/L phenylmethylsulphonyl fluoride (PMSF), 0.02% sodium azide] for 15 min on ice. Lysates were centrifuged at 12 000×*g* 4 °C for 15 min. Protein concentration of cell extracts was determined with Bradford protein assay. The detergent-soluble proteins were detected using the same procedure as cytochrome c. The intensities of the bands were determined with the utilization of the ratios of Bax (21 kDa) to Bcl-2 (26 kDa). The anti-human monoclonal antibodies were purchased from NeoMarkers.

Statistical analysis All data were presented as mean±SD of 3 independent experiments. Statistical significance was determined with Student's unpaired two-tailed *t*-test (SPSS 10.0 software, SPSS Inc, Chicago, USA). $P<0.05$ was considered statistically significant.

Results

Characteristics of apoptosis in HL60 cells after ZnPc-PDT Electron microscopy studies showed that in ZnPc-PDT group, the features of HL60 cells appeared obviously as following: the cell size decreasing, cell membrane blebbing,

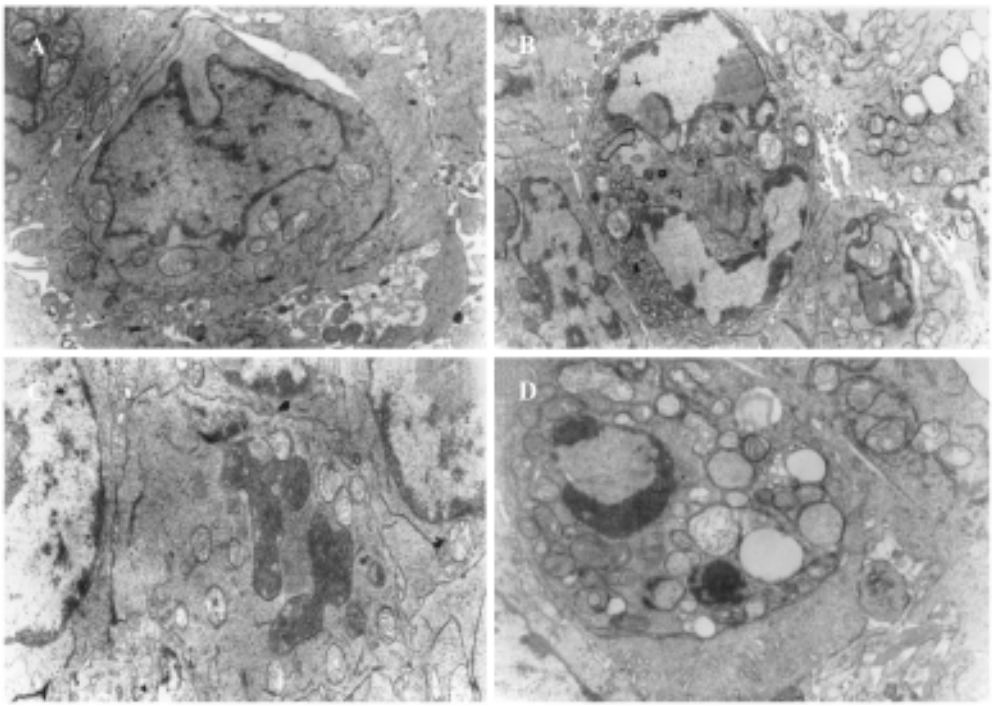

Figure 1. ZnPc-PDT induced apoptosis in HL60 cells. Electron micrographs of HL60 cells in control group (A, ×6000) or in ZnPc-PDT group(B–D, incubated with 0.5 μmol/L of $ZnPcS_2P_2$ for 5 h and then exposed to 670 nm light source of total light dose of 2.1 J/cm^2). B: nuclear chromatin condensation (×4800, 6 h post-PDT); C: nuclear chromatin cleavage (×7000, 24 h post-PDT); D: formation of apoptotic bodies (×7000, 24 h post-PDT).

cytoplasm shrinkage, nuclear chromatin condensation or cleavage and formation of apoptotic bodies (Figure 1). And characteristic chromosomal DNA fragmentation appeared in the cells after ZnPc-PDT. By contrast, no DNA ladder existed in the control groups (Figure 2). TUNEL staining analysis showed many apoptotic cells which nuclei stained brown existed in ZnPc-PDT groups and the average apoptosis rates significantly increased in a time-dependent manner. At the 3 different time points after PDT, the mean TUNEL-positive rates were 9.6%, 24.4%, and 33.0%, respectively (Figure 3). However, few apoptotic cell was detected in the control group. The results indicated that ZnPc-PDT could induce evident apoptosis in HL60 cells.

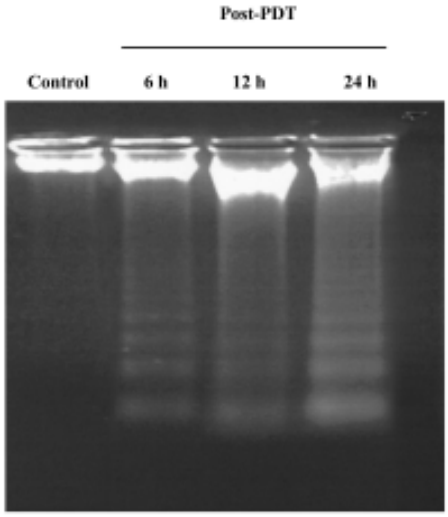

Figure 2. DNA electrophoresis of HL60 cell extracts. Control group: No DNA ladder existed. Post-PDT: HL60 cells were incubated with 0.5 μmol/L of $ZnPcS_2P_2$ for 5 h and then exposed to 670 nm light source of total light dose of 2.1 J/cm^2. The cells were harvested at 6 h, 12 h and 24 h post-PDT. Characteristic DNA ladder appeared. (Original magnification×1.5)

Characteristics of mitochondria-dependent apoptosis in HL60 cells after ZnPc-PDT In the control group, the positive rates of assays for Δψm, activities of caspase family proteases and caspase-3 were all less than 1%. In the ZnPc-PDT groups, compared with the control group, the positive rates of the 3 indexes increased remarkably (P<0.01) as shown in Figure 4. In the ZnPc-PDT groups, Δψm altered significantly and the positive rates increased in a time-dependent manner. When detecting caspase-3 activity, approximately 75.4% cells presented proteases activities at 6 h post-PDT. Caspase family proteases were activated comparatively slightly and slowly after PDT.

Compared with the control groups, in the ZnPc-PDT

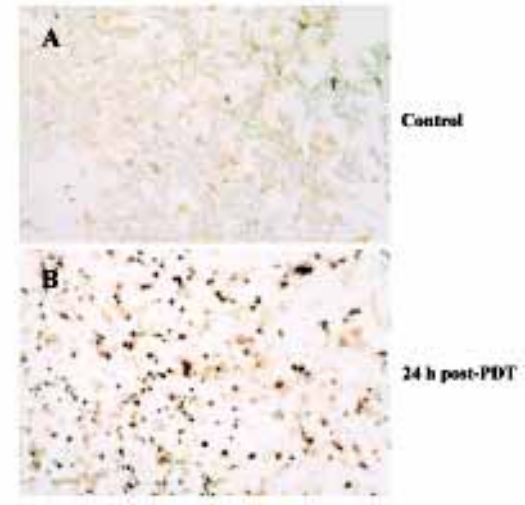

Figure 3. TUNEL staining analysis. A: Control group. B: 24 h post-PDT (HL60 cells were incubated with 0.5 μmol/L of $ZnPcS_2P_2$ for 5 h and then exposed to 670 nm light source of total light dose of 2.1 J/cm^2). (Original magnification×400.)

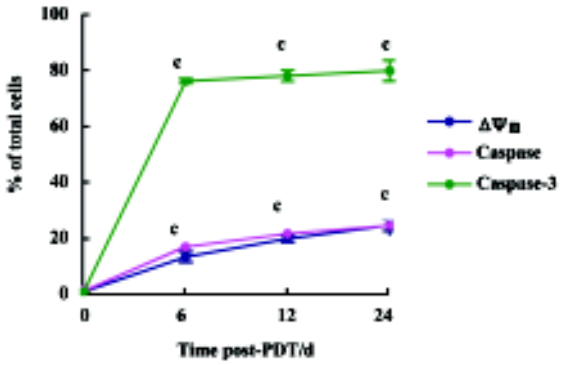

Figure 4. Time course of changes in Δψm, activities of caspase and caspase-3 post-PDT (HL60 cells were incubated with 0.5 μmol/L of $ZnPcS_2P_2$ for 5 h and then exposed to 670 nm light source of total light dose of 2.1 J/cm^2). n=3. Mean±SD. ^cP<0.01 *vs* control.

groups the ratio of cytosol cytochrome c (15 kDa) to β-actin (43 kDa) assessed by Western blot analysis increased significantly (P<0.01). Significant difference existed between 6 h and 12 h post-PDT (P<0.01). However the difference between 12 h and 24 h points was minor (P>0.05) (Figure 5A). Immunochemistry assay showed that after ZnPc-PDT, cytochrome c translocated from its original location adjacent to nucleus and dispersed into cytosol and the positive particles were stained obviously darker (Figure 5B). The 2 indexes showed that ZnPc-PDT induced evident release of cytochrome c from the mitochondria into the cytosol.

Summing up the results from different observations as

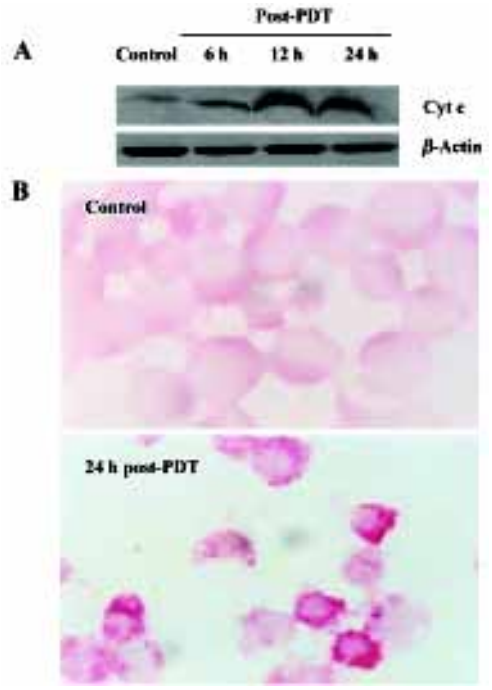

Figure 5. Results of the detection of cytosol cytochrome c. A: Western blotting showed that the intensity of cytochrome c bands strengthen remarkably after ZnPc-PDT (HL60 cells were incubated with 0.5 μmol/L of $ZnPcS_2P_2$ for 5 h and then exposed to 670 nm light source of total light dose of 2.1 J/cm^2). (Original magnification ×2) B: Immunohistochemistry assay showed that after PDT, cytochrome c translocated from its original location adjacent to nucleus to cytosol (×1000).

previously discussed, we concluded that ZnPc-PDT could induce HL60 cells apoptosis through mitochondria-dependent ways.

Effects of ZnPc-PDT on the expression of Bcl-2 and Bax

Western blot assays showed that ZnPc-PDT could down-regulate Bcl-2 expression and up-regulate Bax expression. After PDT, the ratio of Bax to Bcl-2 increased significantly in a time-dependent manner (Figure 6).

Discussion

PDT has emerged as a promising therapeutic procedure for the treatment of many tumors. The cytotoxic efficacy relies on a bimodal protocol comprised of chemical-photosensitizer and light-irradiation. Separately, neither the photosensitizer nor the light is toxic[1,11]. The mechanism of the PDT-mediated cytotoxic effects is not well defined. However it is generally believed that the apoptotic response of PDT is critical for its therapeutic efficacy and the generation of ROS is essential for PDT effects[2,3,25]. Some results have demonstrated that PDT could induce the permeability transition pore open and the opening leads to the loss of integrity of the outer mitochondrial membrane, thus releasing the inter-membrane proteins, such as cytochrome c, into the cytosol[12–16]. When released from the mitochondria, cytochrome c combines with an inactive protease precursor, procaspase-9, to form the “apoptosome”. The apoptosome attacks procaspase-3 and cleaves it to form active caspase-3, which can lead to DNA breakage, nuclear chromatin condensation, then cause cell death[20,21].

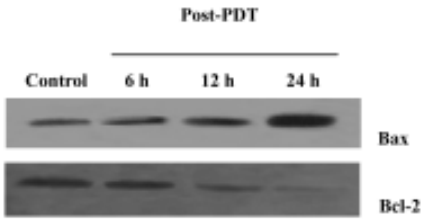

Figure 6. Western blot analysis of Bax and Bcl-2. Bcl-2 expression decreased and Bax expression increased after ZnPc-PDT (HL60 cells were incubated with 0.5 μmol/L of $ZnPcS_2P_2$ for 5 h and then exposed to 670 nm light source of total light dose of 2.1 J/cm^2). (Original magnification ×2)

A number of studies have documented that cell death response to PDT varies due to the physical properties of the photosensitizer employed, PDT dose and the cell type[4–8]. Different subcellular localization of the photosensitizer results in different responses[6,7]. Even the same photosensitizer-mediated PDT could lead to different outcomes. At low doses, the cellular machinery for apoptosis is activated, however, higher doses lead to the inhibition of apoptosis with cell death via a necrotic process[4,8]. In the present study, a novel photosensitizer agent, $ZnPcS_2P_2$, developed in China, was employed. Our previous studies have demonstrated that ZnPc-PDT could exert significant photodamage to HL60 cells[11]. In the present study, 0.5 μmol/L drug level was selected as the experimental condition. Under the condition, ZnPc-PDT could inhibit the proliferation of HL60 cells at 51%.

It is well known that there are two major pathways that are involved in the initiation of apoptosis: the “extrinsic” death receptor pathway and the “intrinsic” mitochondrial pathway. The present study provides direct evidence for the role of mitochondria in HL60 cells apoptosis induced by ZnPc-PDT. Cytochrome c appeared in the cytosol 6 h following light activation of $ZnPcS_2P_2$. The main cytochrome c release occurred later, between 6 h and 12 h after PDT. However, caspase-3 could be quickly activated by ZnPc-PDT. Remarkable activity of caspase-3 was observed 6 h post-PDT in almost all cells. According to recent studies[28],

during genotoxic stress-induced apoptosis, the release of cytochrome c from mitochondria occurrs in 2 distinct stages. The early release of low levels of cytochrome c into the cytosol precedes the activation of caspase 9 and 3. The late stage cytochrome c release results in a drastic loss of mitochondrial cytochrome c and the activities of caspases contribute to the late cytochrome c release mentioned earlier. In the present study, PDT induced the early release of low levels of cytochrome c into the cytosol in the first 6 h. The cytochrome c then combined with procaspase-9 to form the "apoptosome". The apoptosome activated caspase-3 that induced the late cytochrome c release. Therefore, between 6 h and 12 h post-PDT, the main cytochrome c release occurred. At the time of cytochrome c release and remarkable caspase-3 activation (6 h after PDT), only a 12.6% fraction of the cells detected disruption of $\Delta\psi m$. The data are in agreement with the previous conclusion[19] that the dissipation of $\Delta\psi m$ is not required for the release of cytochrome c from the mitochondria. Also, the up-regulation of pro-apoptotic protein Bax, and the down-regulation of anti-apoptotic protein Bcl-2 by ZnPc-PDT appeared significantly and could result in activating mitochondria-mediated apoptosis. The results coincide with those of other previously published studies[25,29]. It is also reported that in many cell types, there is delicate coordination and cross talk between the extrinsic and intrinsic pathways that leads to the activation of the executioner caspase cascade[30,31]. Therefore, the study of the role of the death receptor pathway in the apoptosis induced by ZnPc-PDT should be pursued.

Thus, we conclude that the main mechanism for the apoptosis in HL60 cells induced by ZnPc-PDT appeared to be mitochondria-mediated pathway accompanied with cytochrome c release from the mitochondria into the cytosol followed by the activation of caspase-3. Our findings would provide a fundamental basis for the clinical application of ZnPc-PDT.

Acknowledgments

We wish to thank Prof Jin-ling HUANG and Prof Naisheng CHEN for the gift of $ZnPcS_2P_2$, Prof Shu-sen XIE and Prof Rong CHEN for instructions in semi-conductor laser operation.

References

1 Moan J, Berg K. Photochemotherapy of cancer: experimental research. Photochem Photobiol 1992; 55: 931–48.
2 Henderson B, Dougherty TJ. How does photodynamic therapy work? Photochem Photobiol 1992; 55: 145–57.
3 Niedre M, Patterson MS, Wilson BC. Direct near-infrared luminescence detection of singlet oxygen generated by photodynamic therapy in cells *in vitro* and tissues *in vivo*. Photochem Photobiol 2002; 75: 382–91.
4 Wyld L, Reed MW, Brown NJ. Differential cell death response to photodynamic therapy is dependent on dose and cell type. Br J Cancer 2001; 84: 1384–6.
5 Luo Y, Kessel D. Initiation of apoptosis versus necrosis by photodynamic therapy with chloroaluminum phthalocyanine. Photochem Photobiol 1997; 66: 479–83.
6 Kessel D, Luo Y, Deng Y. The role of subcellular localization in initiation of apoptosis by photodynamic therapy. Photochem Photobiol 1997; 65: 422–6.
7 Noodt BB, Berg K, Stokke T, Pen Q, Nosland JM. Different apoptotic pathways are induced from various intra cellular sites by tetraphenylporphyrins and light. Br J Cancer 1999; 79: 72–81.
8 Kessel D, Poretz RD. Sites of photodamage induced by photodynamic therapy with a chlorine 6 triacetoxymethyl ester (CAME). Photochem Photobiol 2000; 71: 94–6.
9 Huang JL, Chen NS, Huang JD, Liu ES, Xue JP, Yang SL, *et al*. Synthesis, peculiarity and anti-tumor potency of the double affinity photosensitizer-zinc phthalocyanine. Sci China (Series B) (Chin) 2000; 30: 481–8.
10 Huang JL, Chen NS, Huang JD, Liu ES, Xue JP, Yang SL, *et al*. Metal phthalocyanine as photosensitizer for photodynamic therapy (PDT). Sci China (Series B) 2001; 44: 113–22.
11 Huang HF, Chen YZ, Wu Y. Experimental studies of the effects of $ZnPcS_2P_2$-based-photodynamic therapy on bone marrow purging. Natl Chin Med J 2005; 118: 105–10.
12 Vantieghem A, Xu Y, Declercq W, Vandenabeele P, Denecker G, Vandenheede JR, *et al*. Different pathways mediate cytochrome C release after photodynamic therapy with hypericin. Photochem Photobiol 2001; 74: 1333–42.
13 Matroule JY, Carthy CM, Granville DJ, Jolois O, Hunt DW, Piette J. Mechanism of colon cancer cell apoptosis mediated by pyropheophorbide-a methylester photosensitization. Oncogene 2001; 20: 4070–84.
14 Casas A, Fukuda H, Di Venosa G, Batle A. Photosensitization and mechanism of cytotoxicity induced by the use of ALA derivatives in photodynamic therapy. Br J Cancer 2001; 85: 279–84.
15 Chiu SM, Evans H, Lam M, Nieminen A, Oleinick NL. Phthalocyanine 4 photodynamic therapy-induced apoptosis of mouse L5178Y-R cells results from a delayed but extensive release of cytochrome C from mitochondria. Cancer Lett 2001; 165: 51–8.
16 Kessel D, Luo Y. Mitochondrial photodamage and PDT-induced apoptosis. J Photochem Photobiol B 1998; 42: 89–95.
17 Morgan J, Oseroff AR. Mitochondria-based photodynamic anticancer therapy. Adv Drug Deliv Rev 2001; 49: 71–86.
18 Belichenko I, Morishima N, Separovic D. Caspase-resistant Vimentin suppresses apoptosis after photodynamic treatment with a silicon phthalocyanine in Jurkat cells. Arch Biochem Biophys 2001; 390: 57–63.
19 Chiu SM, Oleinick NL. Dissociation of mitochondrial depolarization from cytochrome C release during apoptosis induced by photodynamic therapy. Br J Cancer 2001; 84: 1099–106.
20 Gad F, Viau G, Boushira M, Bertrand R, Bissonnette R. Photodynamic therapy with 5-aminolevulinic acid induces apoptosis and caspase activation in malignant T cells. J Cutan Med Surg 2001; 5: 8–13.

21 Xue LY, Chiu SM, Oleonick NL. Photodynamic therapy-induced death of MCF-7 human breast cancer cells: a role for caspase-3 in the late steps of apoptosis but not for the clinical lethal event. Exp Cell Res 2001; 263: 145–55.
22 He J, Whitacre CM, Xue LY, Berger NA, Oleinick NL. Protease activation and cleavage of poly (ADP-ribose) polymerase: an integral part of apoptosis in response to photodynamic treatment. Cancer Res 1998; 58: 940–6.
23 Reed JC. Double identity for proteins of Bcl-2 family. Nature 1997; 387: 773–6.
24 Reed JC, Miyashita T, Takayama S, Wang HG, Sato T, Krajewski S, *et al*. Bcl-2 family proteins: regulators of cell death involved in the pathogenesis of cancer and resistance to therapy. J Cell Biochem 1996; 60: 23–32.
25 Xue LY, Chiu SM, Oleinick NL. Photochemical destruction of the Bcl-2 oncoprotein during photodynamic therapy with the phthalocyanine photosensitizer Pc4. Oncogene 2001; 20: 3420–7.
26 Wu Y, Chen YZ, Huang HF, Chen P. Recombinant fibronectin polypeptide antagonizes hepatic failure induced by endotixin in mice. Acta Pharmacol Sin 2004; 25: 283–8.
27 Yang J, Liu XS, Kapil B, Caryn NK, Ana MI, Cai JY, *et al*. Prevention of apoptosis by Bcl-2: release of cytochrome c from mitochondria blocked. Science 1997; 275: 1129–32.
28 Chen Q, Gong B, Almasan A. Distinct stages of cytochrome c release from mitochondria: evidence for a feedback amplification loop linking caspase activation to mitochondrial dysfunction in genotoxic stress induced apoptosis. Cell Death Differ 2000; 7: 227–33.
29 Srivastava M, Ahmad N, Gupta S, Mukhtar H. Involvement of Bcl-2 and Bax in photodynamic therapy-mediated apoptosis. Antisense Bcl-2 oligonucleotide sensitizes RIF 1 cells to photodynamic therapy apoptosis. J Biol Chem 2001; 276: 15481–8.
30 Jung JY, Kim WJ. Involvement of mitochondrial- and Fas-mediated dual mechanism in $CoCl_2$-induced apoptosis of rat PC12 cells. Neurosci Lett 2004; 371: 85–90.
31 Khosravi-Far R, Esposti MD. Death receptor signals to mitochondria. Cancer Biol Ther 2004; 3: 1051–7.

Acta Pharmacologica Sinica 2005 Sep; 26 (9): 1145 –1152

Full-length article

Influence of dosage forms on pharmacokinetics of daidzein and its main metabolite daidzein-7-*O*-glucuronide in rats[1]

Feng QIU[2], Xiao-yan CHEN[2], Bo SONG[2], Da-fang ZHONG[3], Chang-xiao LIU[4]

[2]*Laboratory of Drug Metabolism and Pharmacokinetics, Shenyang Pharmaceutical University, Shenyang 110016, China*

Key words

daidzein; daidzein-7-*O*-glucuronide; influence; dosage forms; pharmacokinetics; rats

[1] Project supported by the National Natural Science Foundation of China (No 30271525).
[3] Correspondence to Prof Da-fang ZHONG. Phn/Fax 86-24-2390-2539.
E-mail zhongdf@china.com
[4] Now in *Tianjin Key Laboratory of Drug Metabolism and Pharmacokinetics, Tianjin Institute of Pharmaceutical Research, Tianjin 300193, China*.

Received 2005-03-25
Accepted 2005-07-11

doi: 10.1111/j.1745-7254.2005.00187.x

Abstract

Aim: To investigate the influence of dosage forms on the pharmacokinetics of daidzein and its main metabolite daidzein-7-*O*-glucuronide in Wistar rats. **Methods:** After administration of two typical dosage forms (daidzein solution and suspension), the concentrations of daidzein and daidzein-7-*O*-glucuronide were determined by an LC-MS-MS method. The pharmacokinetic parameters were calculated and analyzed statistically using the Student's *t*-test. **Results:** Absorption of daidzein after administration of daidzein solution (t_{max}=0.46 h) was more rapid than that of the suspension (t_{max}=5.00 h). The peak plasma concentrations of daidzein after administration of daidzein solution and suspension were 601.1 μg/L and 127.3 μg/L, respectively, and those of daidzein-7-*O*-glucuronide were 3000 μg/L and 192.6 μg/L, respectively. The absolute bioavailabilities of free daidzein in rats after administration of daidzein solution and suspension were 12.8% and 6.1%, respectively, which were calculated to be 47.0% and 12.2%, respectively, in the form of total daidzein (free plus conjugated daidzein). **Conclusion:** Absorption of daidzein solution was better than absorption of suspension (P<0.05).

Introduction

Daidzein [7-hydroxy-3-(4-hydroxyphenyl)-4*H*-1-benzopyran-4-one, CAS 486-66-8, Figure 1] is one of the naturally occurring isoflavones present mainly in leguminous plants, especially in soybeans, soy foods and *Pueraria lobata* Ohwi (Leguminosae). Several epidemiological studies in humans have suggested that daidzein intake is inversely associated with the incidence of hormone-dependent diseases, especially breast and prostate cancer[1]. In addition to its putative anticarcinogenic effects, daidzein has also been investigated as an antihyperlipidemic agent and a therapeutic substance to combat osteoporosis[2,3].

After oral administration, daidzein is subject to glucuronidation at the 7-hydroxyl position, and daidzein-7-*O*-glucuronide is its main metabolite in human[4] and rat[5] plasma and urine. The pharmacokinetics of daidzein in humans has been the subject of several studies[6–10], but there have been no reports about the pharmacokinetics of its main metabolite daidzein-7-*O*-glucuronide. Due to its poor hydrophilicity and lipophilicity, the pharmacokinetics of daidzein may be influenced by the dosage form. However, the influence of dosage forms on the pharmacokinetics of daidzein

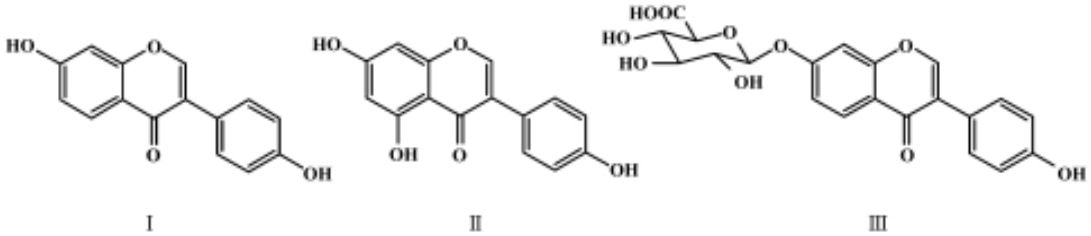

Figure 1. Chemical structures of daidzein (I), genistein (II, internal standard) and daidzein-7-*O*-glucuronide (III).

and its main metabolite daidzein-7-*O*-glucuronide have not been investigated previously. Furthermore, the extent of the influence of dosage forms remains unknown.

In the present study, the influence of two typical dosage forms (solution and suspension) on the pharmacokinetics of daidzein and its main metabolite daidzein-7-*O*-glucuronide was investigated after oral administration of 20 mg/kg purified daidzein to rats.

Materials and methods

Chemicals and reagents Daidzein and genistein (internal standard) were purchased from Huike Botanical (Xi'an, Shaanxi, China). The purities of these 2 compounds were 99.3% and 98.9%, respectively, which was verified using high-performance liquid chromatography (HPLC) methods. β-Glucuronidase (EC 3.2.2.21, 542 200 units/g of solid) was purchased from Sigma (St Louis, MO, USA). CMC-Na was purchased from Shenyang Chemical Factory (Shenyang, Liaoning, China). Acetonitrile and methanol (Yuwang Chemical Factory, Shandong, China) were of HPLC grade. Other chemicals were of analytical grade. Distilled water, prepared from demineralized water, was used throughout the study.

Preparations of dosage forms A transparent solution of daidzein was prepared by dissolving an appropriate amount of daidzein in 0.9% NaCl solution (water was used as solvent) and adjusting the pH to 7.0 by the addition of 1 mol/L NaOH. A daidzein suspension with good physical stability was achieved by dispersing grinded daidzein in 0.5% CMC-Na solution (water was used as solvent and CMC-Na was used as co-suspension reagent). The concentrations of daidzein in both dosage forms were determined to be 2.0 g/L by a validated HPLC-UV method. The 2 dosage forms were prepared freshly for animal administration.

Instrumentation A Finnigan TSQ API II tandem mass spectrometer equipped with an atmospheric pressure chemical ionization (APCI) source (San Jose, CA, USA), an Agilent 1100 autosampler (Agilent, Wilminton, DE, USA) and a Shimadzu LC-10AD pump (Kyoto, Japan) were used for LC-MS-MS analyses. Analytical data were acquired using Xcalibur 1.1 software (Finnigan) and quantitative processing was carried out using LCQuan software (Finnigan).

LC-MS-MS conditions The LC-MS-MS method used for the determination of daidzein and daidzein-7-*O*-glucuronide was a slightly modified version of one described previously[11]. The LC separation was carried out using a Diamonsil C_{18} column (200 mm×4.6 mm ID, 5 mm; Dikma, Beijing, China) and a SecurityGuard C_{18} guard column (4 mm×3.0 mm ID; Phenomenex, Torrance, CA, USA). The isocratic mobile phase consisted of acetonitrile-water-formic acid (80:20:1, *v*:*v*:*v*) at a flow rate of 0.75 mL/min. The column temperature was maintained at 20 ºC.

The mass spectrometer was operated in positive APCI mode with the corona discharge current set at 4.00 μA. Nitrogen was used as the sheath gas (0.6 MPa) and auxiliary gas (3 L/min) for nebulization. The heated capillary and vaporizer temperatures were set to 280 ºC and 450 ºC, respectively. For collision-induced dissociation (CID), argon was used as the collision gas at a pressure of 0.19 Pa. Quantification was carried out using selected reaction monitoring (SRM) of the transitions *m/z* 255→199 for daidzein and *m/z* 271→153 for genistein, with a scan time of 0.3 s/transition. The optimized collision energies of 30 eV and 35 eV were chosen for daidzein and genistein, respectively.

Sample preparation To determine free (unconjugated) daidzein, 50 μL internal standard solution (genistein, 50 mg/L in methanol) and 50 μL water were added to 50 μL of each rat plasma sample. $NH_4H_2PO_4$ buffer (pH 5.0; 200 μL of 0.05 mol/L) was added. The mixture was vortexed for 10 s and extracted with 2 mL *n*-hexane-diethyl ether (1 : 4, *v*/*v*) by shaking for 10 min. After centrifugation at 2000×*g* for 10 min, the organic phase was transferred into another tube and evaporated to dryness at 40 ºC under a stream of nitrogen. The residue was reconstituted in 100 μL of the mobile phase and vortexed for 1 min. A 20-μL aliquot of the solution was injected onto the LC-MS-MS system.

To determine total daidzein (free plus conjugated daidzein), 100 μL β-glucuronidase enzyme solution (1084 U/mL in 0.05 mol/L $NH_4H_2PO_4$ buffer, pH 5.0) was added to a 50 μL aliquot of rat plasma. The mixture was incubated in a water bath at 37 ºC for 16 h. After enzymatic hydrolysis, 50 μL internal standard and 50 μL water were added. The mixture was treated as described above.

Those plasma samples whose concentrations were higher than the highest calibration point were diluted appropriately with blank rat plasma in order to make the concentration within the range of the standard curve before sample preparation.

The concentration of daidzein-7-*O*-glucuronide was calculated using the following formula:

$$C_{DG} = (C_t - C_f) \times 430/254,$$

where C_{DG} was the mass concentration of daidzein-7-*O*-glucuronide (conjugated daidzein), C_t was the total mass concentration of daidzein, C_f was the mass concentration of free (unconjugated) daidzein, and 254 and 430 were the molecular weights of daidzein and daidzein-7-*O*-glucuronide, respectively.

Study design Eighteen Wistar rats (Grade II, Certificate

No 042; 9 males and 9 females; Laboratory Animal Center of Shenyang Pharmaceutical University, Shenyang, China) weighing 200 g–250 g were divided into 3 groups at random in the studies. Each group contained 3 male and 3 female rats. All experimental procedures were carried out in accordance with the guidelines of the Experimental Animal Care and Use Committee of Shenyang Pharmaceutical University. The rats were housed under standard conditions and had *ad libitum* access to water and a standard laboratory diet (isoflavone free). All rats were dosed following an overnight fast; food was returned 0.5 h after dosing. Water was available *ad libitum* throughout the experiments.

Polyethylene cannulas were implanted in the femoral vein 2 d before the experiment while the rats were anesthetized with pentobarbital (50 mg/kg, ip). The cannulas were externalized at the back of the neck and filled with heparinized saline (20 000 U/L). One group of 6 rats weighing 224±13 g were dosed orally with daidzein solution at 20 mg/kg (10 mL/kg, 2 g/L), the second group of 6 rats weighing 230±16 g were dosed orally with daidzein suspension at 20 mg/kg (10 mL/kg, 2 g/L), and the third group of 6 rats weighing 227±10 g were dosed intravenously with daidzein solution at 20 mg/kg (10 mL/kg, 2 g/L). Serial blood samples (0.25 mL) were collected at 0 h, 5 min, 10 min, 30 min, 1 h, 3 h, 5 h, 8 h, 12 h, 24 h and 48 h post dose. Plasma was separated by centrifugation at 2 000×*g* for 10 min and stored frozen at -20 ºC until analysis.

Data analysis Plasma concentrations were subjected to an appropriate pharmacokinetic analysis on mean data points. Values below the quantification limit were considered to be zero. The peak concentration (C_{max}) and the corresponding peak times (t_{max}) were determined by visual inspection of the mean data. The elimination half-life ($t_{1/2}$) was calculated using the non-compartmental model of the TOPFIT program on a personal computer. The area under the plasma concentration-time curve (AUC) from time zero to the last measurable plasma concentration point (t=48 h) ($AUC_{0-48\,h}$) was calculated using the linear trapezoidal rule. Extrapolation to time infinity ($AUC_{0-\infty}$) was calculated as follows:

$$AUC_{0-\infty}=AUC_{0-48\,h}+C_{48\,h}/k_e,$$

where $C_{48\,h}$ was the last measurable plasma concentration and k_e was the elimination rate constant. The bioavailability (F) of free daidzein was calculated as follows:

$$F=AUC_{0-\infty,\,po}/AUC_{0-\infty,\,iv},$$

where $AUC_{0-\infty,\,po}$ and $AUC_{0-\infty,\,iv}$ were the AUC values of free daidzein after oral and intravenous administration of daidzein. The bioavailability (F) of total daidzein (free plus conjugated daidzein) was calculated as follows:

$$F= AUC_{0-\infty,\,po}/AUC_{0-\infty,\,iv},$$

where $AUC_{0-\infty,\,po}$ and $AUC_{0-\infty,\,iv}$ were the AUC values of total daidzein after oral and intravenous administration of daidzein.

The main pharmacokinetic parameters, including $t_{1/2}$, k_e, t_{max}, C_{max}, $AUC_{0\text{-}48\,h}$, $AUC_{0-\infty}$, and F, were analyzed using the Student's t-test. A probability level of $P<0.05$ was defined as being statistically significant.

Results

Mass spectrometry Using the positive APCI mode, the analyte and internal standard formed predominately protonated molecules $[M+H]^+$ in full-scan spectra. To determine daidzein using the SRM mode, full-scan and product-ion spectra of daidzein and internal standard were investigated under the present HPLC conditions. Figure 2 shows the product ion spectra of $[M+H]^+$ ions of daidzein and genistein. Several fragment ions were observed in the product-ion spectra. The major fragment ions at *m/z* 199 and 153 were chosen in the SRM acquisition for daidzein and genistein, respectively.

Method validation Selectivity was assessed by comparing the chromatograms of 6 different batches of blank rat plasma with the corresponding spiked plasma. Figure 3

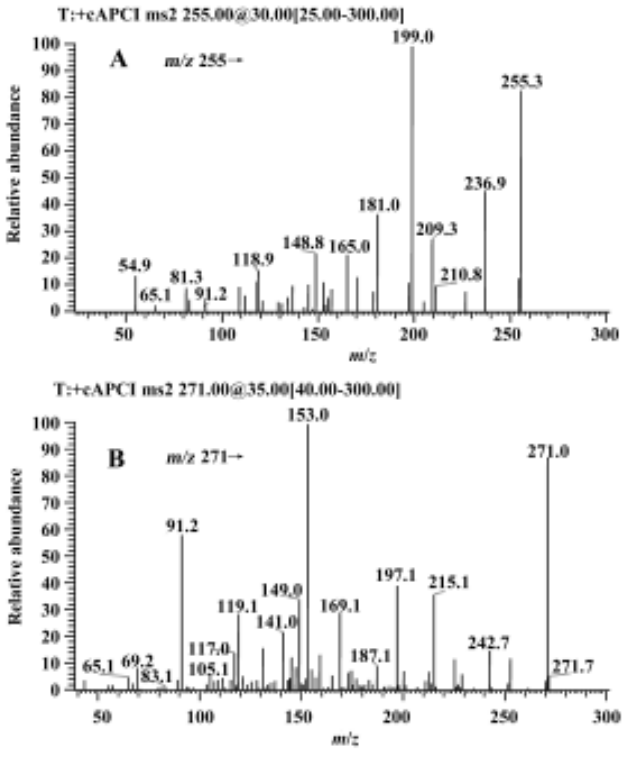

Figure 2. Full-scan product-ion spectra of $[M + H]^+$ of (A) daidzein and (B) genistein.

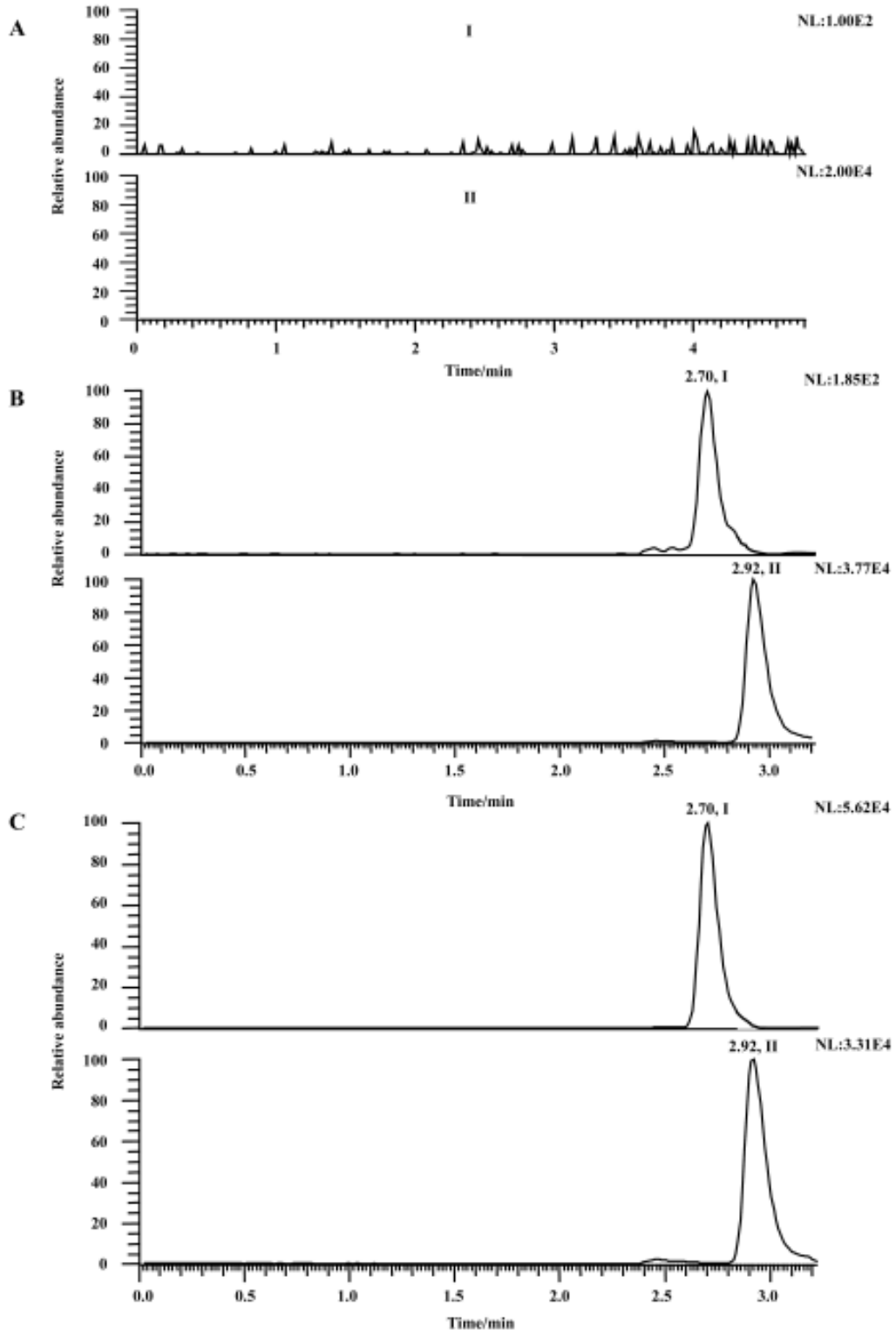

Figure 3. Representative selected reaction monitoring chromatograms of daidzein plasma samples determined using the LC-MS-MS method. (A) Blank plasma sample; (B) Blank plasma sample spiked with daidzein at the LLOQ of 0.24 μg/L and genistein (IS, 50 mg/L); (C) Rat plasma sample collected at 30 min after oral administration of daidzein (20 mg/kg). Peak I, daidzein; peak II, genistein.

shows the typical chromatograms of a blank plasma sample, a blank plasma sample spiked with daidzein at the LLOQ and genistein, and a plasma sample from a Wistar rat 30 min after oral administration. No significant interference from endogenous substances with analyte or genistein were detected. The typical retention times for daidzein and genistein were 2.7 min and 2.9 min, respectively.

Calibration standards were prepared by spiking 50 μL of the appropriate standard solutions of daidzein to 50 μL of blank rat plasma. Plasma concentrations were 0.24 μg/L, 0.50 μg/L, 1.5 μg/L, 20 μg/L, 100 μg/L, 500 μg/L and 1000 μg/L for daidzein. The linear regression of the peak area ratios versus concentrations was fitted over the concentration range of 0.24 μg/L-1000 μg/L in rat plasma. A typical equation of the calibration curve was as follows:

$$y=3.888\times10^{-4}+6.030\times10^{-4}\ x\ (r=0.9981),$$

where y is the peak area ratio of daidzein to genistein, and x is the concentration of daidzein. The present assay method had an LLOQ of 0.24 μg/L with an accuracy of 14.3% and a precision of 12.7% (n=5), which was sufficient for monitoring daidzein plasma levels over a period of 48 h after a single oral administration.

Table 1 summarizes the intra-day and inter-day precision and accuracy for daidzein from QC samples. In this assay, the intra-day and inter-day precisions ranged from 3.4% to 7.1% and from 6.3% to 13.2% for each QC level. The accuracy ranged from -0.5% to 2.4%. The results, calculated using a one-way ANOVA, indicated that the values were within the acceptable range and that the method was accurate and precise[12].

Table 1. Precision and accuracy of the LC-MS-MS method in determining daidzein concentrations in rat plasma.

Concentration/μg·L^{-1}		RSD/%		RE/%
Added	Found	Intra-day	Inter-day	
0.50	0.51	7.1	10.7	2.0
50.0	51.2	6.5	13.2	2.4
800.0	796.0	3.4	6.3	-0.5

RE, relative error. RSD, relative standard deviation.

The extraction recovery of daidzein, determined at 3 concentrations (0.50 μg/L, 50 μg/L, 800 μg/L), were 73.8%, 75.1% and 76.3% (n=6), respectively. The extraction recovery of genistein was also investigated as 64.2% (n=6).

Daidzein in the plasma was shown to be stable for at least 30 d stored at -20 ºC. The relative error (RE%) of daidzein between the initial concentrations and the concentrations of the following 3 freeze–thaw cycles ranged from -6.7% to 2.4%, which indicated the stability of daidzein during freeze–thaw. Processed samples were also found to be stable in the reconstituted solution of acetonitrile-water-formic acid (80:20:1, *v*:*v*:*v*) for at least 24 h at room temperature. These data are summarized in Table 2.

Table 2. Stability of daidzein in rat plasma (n=6).

Stability	Daidzein concentration/μg·L^{-1}		
	0.50	50.0	800.0
Storage (≤–20 ºC, relative error, %)			
0 d	2.6	-1.1	2.9
30 d	-4.7	-5.8	3.5
Freeze-thaw (relative error, %)			
0 cycles	-0.4	2.4	-2.1
3 cycles	-2.7	-5.6	-6.7
Processed plasma samples at room temperature (relative error, %)			
0 h	0.7	-3.2	0.3
24 h	-2.6	1.9	-3.8

Pharmacokinetics The mean plasma concentration versus time curves of daidzein and daidzein-7-*O*-glucuronide after oral administration of 2 different dosage forms (daidzein solution and suspension) are given in Figure 4. The mean plasma concentration versus time curves of daidzein and daidzein-7-*O*-glucuronide after intravenous administration of daidzein solution are given in Figure 5. Table 3 summarizes the pharmacokinetic parameters of daidzein and daidzein-7-*O*-glucuronide after administration of 2 different dosage forms. The pharmacokinetic parameters of daidzein and daidzein-7-*O*-glucuronide after intravenous administration of daidzein solution are given in Table 4.

Pharmacokinetics of daidzein After oral administration of 2 different dosage forms, the absorption of daidzein after administration of daidzein solution (t_{max}=0.46 h) was more rapid than that of suspension (t_{max}=5.00 h). The peak plasma concentration after administration of daidzein solution was 601.1 μg/L, which was approximately 4 times higher than that of suspension (127.3 μg/L). The absolute bioavailability of daidzein in rats after administration of daidzein solution was 12.8%, but the absolute bioavailability of daidzein after administration of daidzein suspension was only 6.1%.

There are significant differences of daidzein parameters in the values of t_{max} and C_{max} (P<0.05) between daidzein solution and suspension.

Pharmacokinetics of daidzein-7-*O*-glucuronide After

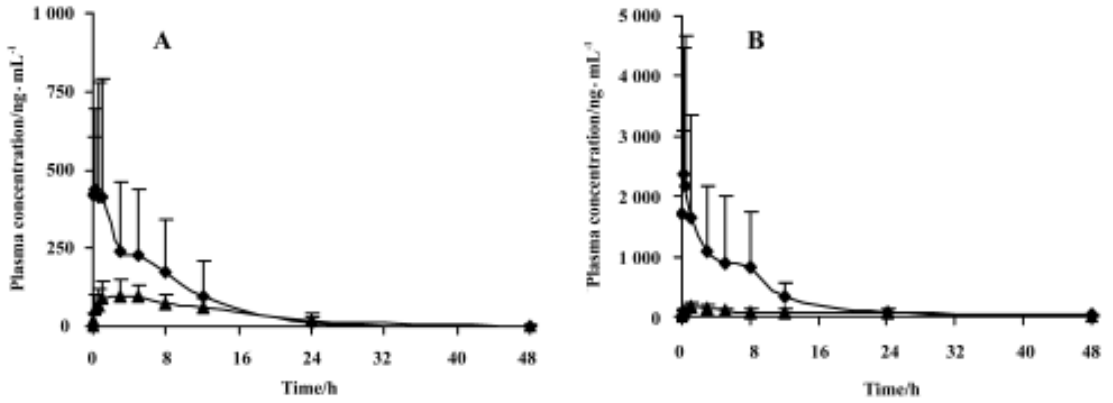

Figure 4. Mean plasma concentration–time curves of (A) daidzein and (B) daidzein-7-*O*-glucuronide following oral administration of 20 mg/kg daidzein solution (◆) and suspension (▲) to Wistar rats. *n*=6. Mean±SD.

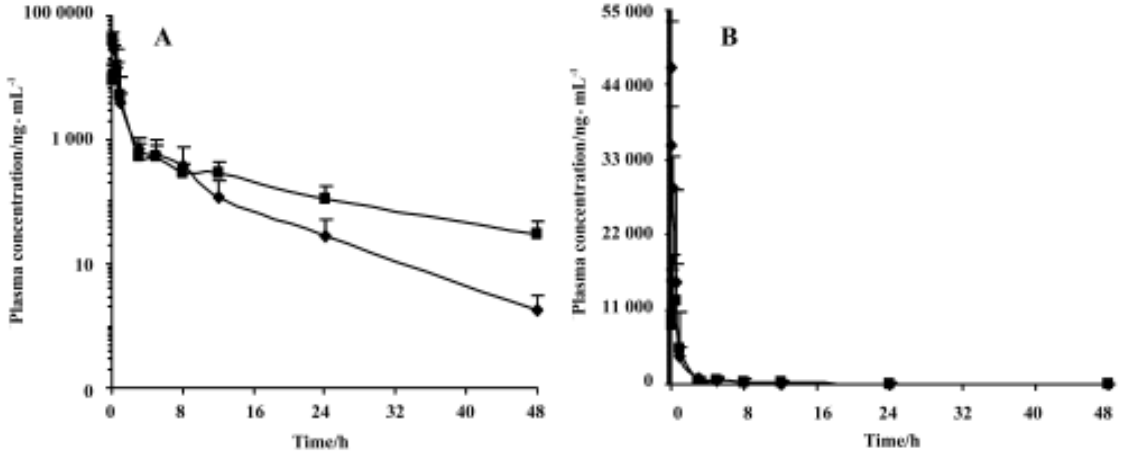

Figure 5. Mean plasma concentration–time curves of daidzein (◆) and daidzein-7-*O*-glucuronide (■) following intravenous administration of 20 mg/kg daidzein solution to Wistar rats. A: Semi-logarithmic coordinate profiles; B: Normal coordinate profiles. *n*=6. Mean±SD.

Table 3. Pharmacokinetic parameters of daidzein and daidzein-7-*O*-glucuronide after oral administration of 2 different dosage forms to rats (20 mg/kg, *n*=6). Each value represents the mean±SD for 6 individual values. [b]*P*<0.05 *vs* solution.

Parameter	Unit	Daidzein		Daidzein-7-*O*-glucuronide	
		Solution	Suspension	Solution	Suspension
$t_{1/2}$	h	3.38±1.88	4.61±1.69	10.8±4.97	10.3±2.56
k_e	h^{-1}	0.26±0.12	0.17±0.06	0.07±0.02	0.07±0.02
t_{max}	h	0.46±0.45	5.00±4.10[b]	0.40±0.34	3.67±4.18
C_{max}	$\mu g \cdot L^{-1}$	601.1±301.3	127.3±49.0[b]	3 000±2 476	192.6±54.6[b]
$AUC_{0-48\,h}$	$\mu g \cdot h \cdot L^{-1}$	3 379±2 982	1 610±819.2	15 154±13 434	2 653±1 624[b]
$AUC_{0-\infty}$	$\mu g \cdot h \cdot L^{-1}$	3 380±2981	1 615±827.7	15 343±13 318	2 734±1 719[b]
F	%	12.8±11.3	6.1±3.1	47.0±42.4[1)]	12.2±9.9[b,1)]

[1)] Calculated with total daidzein (free plus conjugated daidzein).

oral administration of 2 different dosage forms, absorption of daidzein after administration of daidzein solution (t_{max}= 0.40 h) was more rapid than that of suspension (t_{max}=3.67 h). The peak plasma concentration after administration of

Table 4. Pharmacokinetic parameters of daidzein and daidzein-7-*O*-glucuronide after intravenous administration of daidzein solution to rats (20 mg/kg, n=6). Each value represents the mean±SD for 6 individual values.

Parameter	Unit	Daidzein	Daidzein-7-*O*-glucuronide
$t_{1/2}$	h	6.40±2.45	11.4±3.93
k_e	h^{-1}	0.13±0.07	0.07±0.02
$AUC_{0-48\,h}$	$mg \cdot h \cdot L^{-1}$	26.5±7.20	20.8±12.8
$AUC_{0-\infty}$	$mg \cdot h \cdot L^{-1}$	26.5±7.20	21.4±13.2
CL_{TOT}	$mL \cdot min^{-1} \cdot kg^{-1}$	13.4±3.63	18.8±6.46
V_Z	$L \cdot kg^{-1}$	7.65±4.64	17.5±6.37
MRT	h	2.00±1.00	8.09±3.41
V_{ss}	$L \cdot kg^{-1}$	1.45±0.47	9.58±5.66

daidzein solution was 3000 μg/L, which was approximately 14 times higher than that of suspension (192.6 μg/L). The absolute bioavailability of total daidzein (free plus conjugated daidzein) in rats after administration of daidzein solution was 47.0%, but the absolute bioavailability of total daidzein (free plus conjugated daidzein) after administration of daidzein suspension was only 12.2%.

In general, there are significant differences between the main pharmacokinetic parameters of daidzein and daidzein-7-*O*-glucuronide after administration of 2 different dosage forms (P<0.05). There is better absorption following administration of daidzein solution than after administration of suspension.

Discussion

Daidzein shows poor hydrophilicity and lipophilicity due to the typical plane structure of the isoflavones. However, it can be dissolved in weak alkaline solution and form a sodium salt at the hydroxyl groups; as a result its water solubility is greatly increased to 2 g/L. Daidzein solution was found to be stable during a period of at least 24 h (data not shown).

In present study, we choose solution and suspension as the 2 representative dosage forms. Daidzein suspension has similar *in vivo* processes to solid preparations, while daidzein solution is a typical liquid preparation. As a compound with poor solubility, the form of administration may have a great influence on its absorption and pharmacokinetics.

After oral administration, daidzein is subject to glucuronidation at its 7-hydroxyl group, and glucuronide conjugate is its main metabolite and the form in which it mainly exists *in vivo*. The pharmacological effects of daidzein-7-*O*-glucuronide have not been reported in the literature. Daidzein can transform into daidzein-7-*O*-glucuronide as a substrate of glucurotransferases, and daidzein-7-*O*-glucuronide can transform back into daidzein by the action of a hydrolase. As a result, it is necessary to determine the concentrations of free daidzein and daidzein-7-*O*-glucuronide in order to study its absorption and pharmaco-kinetics.

Previous studies, which focused on the pharmacokinetics after consumption of known amounts of soy foods or limited purified isoflavones (solid preparations), found that daidzein was absorbed poorly[6–10]. In our investigations, there are significant differences in pharmacokinetic parameters of daidzein and daidzein-7-*O*-glucuronide between solution and suspension. After administration of daidzein solution, daidzein is absorbed well and is mostly metabolized into daidzein-7-*O*-glucuronide. The reason for the significant differences was the poor solubility of daidzein.

Wojcicki *et al*[13] reported that there were no statistically significant differences in the pharmacokinetics and bioavailability of flavonoid glycosides of *Ginkgo biloba* (quercetin, kaempferol and isorhamnetin) after a single oral administration of 3 formulations to healthy volunteers, which seems to contradict the results of the present study. However, the 3 formulations adopted in that report were capsules, drops and tablets, which were all solid formula-tions, while in present study, solution and suspension (solid) formulations were prepared to investigate their pharma-cokinetics. In fact, there does exist significant differences in the pharmacokinetic parameters of solid and liquid formula-tions.

Pharmacokinetic parameters varied a great deal among individuals, indicating great inter-individual variability of daidzein disposition *in vivo*, which is in accordance with the results found in the literature[9]. There were more factors to affect the pharmacokinetic behavior of daidzein and daidzein-7-*O*-glucuronide after oral administration compared with using an intravenous dose, and this may be the reason that larger RSD values of $AUC_{0-48\,h}$ were achieved after oral administration (88.2% for oral solution and 50.9% for oral suspension; 27.3% for intravenous solution). Furthermore, different distribution amounts of β-glucuronidase *in vivo* and strong hepatic–intestinal cycles may also account for the large differences in the amounts of daidzein and its main metabolite daidzein-7-*O*-glucuronide *in vivo*.

In conclusion, dosage forms have a great influence on the bioavailability of daidzein. Solution preparations are more bioavailable than solid preparations. As a result, the solution preparations of daidzein are recommended for development in order to improve its oral bioavailability.

References

1 Pereira MA, Barnes LH, Rassman VL, Kelloff GV, Steele VE. Use of azoxymethane-induced foci of aberrant crypts in rat colon to identify potential cancer chemopreventive agents. Carcinogenesis 1994; 15: 1049–54.

2 Anderson JJ, Anthony MS, Cline JM, Washburn SA, Garner SC. Health potential of soy isoflavones for menopausal women. Public Health Nutr 1999; 2: 489–504.

3 Cassidy A, Bingham S, Setchell KD. Biological effects of a diet of soy protein rich in isoflavones on the menstrual cycle of premenopausal women. J Clin Nutr 1994; 60: 333–40.

4 Thomas BF, Zeisel SH, Busby MG, Hill JM, Mitchell RA, Scheffler NM, *et al*. Quantitative analysis of the principle soy isoflavones genistein, daidzein and glycitein, and their primary conjugated metabolites in human plasma and urine using reversed-phase high-performance liquid chromatography with ultraviolet detection. J Chromatogr B 2001; 760: 191–205.

5 Yasuda T, Kano Y, Saito K, Ohsawa K. Urinary and bilary metabolites of daidzin and daidzein in rats. Biol Pharm Bull 1994; 17: 1369–74.

6 Bloedon LT, Jeffcoat AR, Lopaczynski W, Schell MJ, Black TM, Dix KJ, *et al*. Safety and pharmacokinetics of purified soy isoflavones: single-dose administration to postmenopausal women. Am J Clin Nutr 2002; 76: 1126–37.

7 Busby MG, Jeffcoat AR, Bloedon LT, Koch MA, Black T, Dix KJ, *et al*. Clinical characteristics and pharmacokinetics of purified soy isoflavones: single-dose administration to healthy men. Am J Clin Nutr. 2002; 75: 126–36.

8 Fischer L, Mahoney C, Jeffcoat AR, Koch MA, Thomas BF, Valentine JL, *et al*. Clinical characteristics and pharmacokinetics of purified soy isoflavones: multiple-dose administration to men with prostate neoplasia. Nutr Cancer 2004; 48: 160–70.

9 Setchell KD, Faughnan MS, Avades T, Zimmer-Nechemias L, Brown NM, Wolfe BE, *et al*. Comparing the pharmacokinetics of daidzein and genistein with the use of ^{13}C-labeled tracers in premenopausal women. Am J Clin Nutr 2003; 77: 411–9.

10 Watanabe S, Yamaguchi M, Sobue T, Takahashi T, Miura T, Arai Y, *et al*. Pharmacokinetics of soybean isoflavones in plasma, urine and feces of men after ingestion of 60 g baked soybean powder (kinako). J Nutr 1998; 128: 1710–5.

11 Chen XY, Qiu F, Zhong DF, Duan XT, Liu CX. Validated liquid chromatography-tandem mass spectrometric method for the quantitative determination of daidzein and its main metabolite daidzein-7-*O*-glucuronide in rat plasma. Pharmazie 2005; 60: 334–8.

12 Shah VP, Midha KK, Findlay JW, Hill HM, Hulse JD, McGilveray IJ, *et al*. Bioanalytical method validation: A revisit with a decade of progress. Pharm Res 2000; 17: 1551–7.

13 Wojcicki J, Gawronska-Szklarz B, Bieganowski W, Patalan M, Smulski HK, Samochowiec L, *et al*. Comparative pharmacokinetics and bioavailability of flavonoid glycosides of *Ginkgo biloba* after a single oral administration of three formulations to healthy volunteers. Mater Med Pol 1995; 27: 141–6.

Acta Pharmacologica Sinica 2005 Oct; 26 (10): 1153–1164

Invited review

Introduction to 3D reconstruction of macromolecules using single particle electron microscopy[1]

Oscar LLORCA[2]

Centro de Investigaciones Biológicas, Consejo Superior de Investigaciones Científicas, Ramiro de Maeztu, 9 Campus Universidad Complutense, 28040 Madrid, Spain

Key words

single particle electron microscopy; 3D reconstruction; cryoelectron microscopy; image processing; DNA-PK

[1]Project supported by projects SAF2002-01715 and GEN2003-20239-C06-06 from the Spanish Ministry of Education to OL.
[2]Correspondence to Dr Oscar LLORCA.
Phn 34-91-837-3112, ext 4446.
Fax 34-91-536-0432.
E-mail ollorca@cib.csic.es

Received 2005-06-21
Accepted 2005-08-01

doi: 10.1111/j.1745-7254.2005.00203.x

Abstract

Single-particle electron microscopy has now reached maturity, becoming a commonly used method in the examination of macromolecular structure. Using a small amount of purified protein, isolated molecules are observed under the electron microscope and the data collected can be averaged into a 3D reconstruction. Single-particle electron microscopy is an appropriate tool for the analysis of proteins that can only be obtained in modest quantities, like many of the large complexes currently of interest in biomedicine. Whilst the use of electron microscopy expands, new methods are being developed and improved to deal with further challenges, such as reaching higher resolutions and the combination of information at different levels of structural detail. More importantly, present methodology is still not robust enough when studying certain "tricky" proteins like those displaying extensive conformational flexibility and a great deal of user expertise is required, posing a threat to the consistency of the final structure. This mini review describes a brief outline of the methods currently used in the 3D analysis of macromolecules using single-particle electron microscopy, intended for those first approaching this field. A summary of methods, techniques, software, and some recent work is presented. The spectacular improvements to the technique in recent years, its advantages and limitations compared to other structural methods, and its future developments are discussed.

Introduction

Transmission electron microscopy (TEM) is a structural technique that has existed for many years in biology to study the ultra-structure of cells. However, it has only been more recently that outstanding technical advances have consolidated the prospect of observing single protein molecules at the electron microscope level with such sufficient structural details to use these data to reconstruct the molecule in three dimensions (3D). These methodological improvements lie at the level of the instrument itself, that is, better microscopes, but most significantly, more powerful algorithms and software platforms, and, importantly, dramatically increased speed of computers to deal with the noisy images of proteins obtained with the microscope. As a result of these advances, analysis of macromolecules using single-particle electron microscopy (EM) can be widely noticed in a fast-increasing number of publications. Hence, the need rapidly emerged to store and make accessible all of this 3D information to the scientific community, and the Macromolecular Structure Data Base (at the European Bioinformatics Institute, Cambridge, UK) has been created to this end (http://www.ebi.ac.uk/msd/). Most scientific journals now make mandatory the deposition of any 3D structure obtained by EM into this data base, importantly using standard formats to guarantee the interchange of the data. This will certainly stimulate both the flow of EM structures among scientists (as already happens with atomic coordinates) as well as the quality of the EM work deposited.

As EM spreads out, its interaction and dependence on other structural techniques has deepened. A modern ap-

proach to the exploration of macromolecular structures requires a wise combination of molecular biology, biochemistry, biocomputing, X-ray crystallography, nuclear magnetic resonance (NMR), EM and any other structural technique (ultracentrifugation, small-angle neutron scattering, *etc*). An important challenge will therefore be to develop methods to combine all of this multi-resolution information in a comprehensive way.

In the following sections, I will describe the major methods that EM employs today, how relevant structural information is extracted, and the present limitations of these approaches. Supplementary and more in-depth information can be found elsewhere[1–9] and on the web (eg the 3D-electron microscopy data base at http://3dem.ucsd.edu/index.html, the Electron Microscopy Yellow Pages at http://cimewww.epfl.ch/EMYP/comp.html, or the SPIDER web site at http://www.wadsworth.org/spider_doc/spider/docs/spider.html).

Basics of single-particle electron microscopy

The protein of interest must be purified to homogeneity prior to any EM analysis, as image processing is most generally based on the assumption that every single image we take derives from the same specimen (Figure 1A). The sample is then applied to EM grids covered by a thin carbon support film (which can contain small holes in the case of cryo-EM, where specimens are vitrified) and visualized under the electron microscope (Figure 1B). Molecules of the protein adsorb to the carbon film in orientations determined by the charges on their surface and their overall shape. Ideally, a random distribution of orientations is desirable, because this will allow recording images of the protein from many different angles, a requirement to obtain a correct 3D reconstruction. Before insertion into the microscope, the sample must be prepared to withstand the incident radiation (electrons). For this purpose, the protein on the EM grid can be either stained with heavy-atom salts, known as negative staining (uranyl acetate, uranyl formiate and ammonium molibdate, as the most widely used staining agents), or quickly vitrified into liquid ethane and kept under liquid nitrogen temperatures (cryo-EM). Each method has its own advantages and limitations widely discussed before and beyond the scope of this review[5,7,10]. Briefly, negative staining provides a higher contrast at the expense of resolution and only the surface or topography of the molecule is actually defined. Performing cryo-EM experiments is technically more demanding for the microscopist, but perfectly preserves the structure of the protein at high resolution within the vitrified buffer. Nevertheless, contrast is strongly reduced, thus small proteins might only be analyzed with the help of staining agents[10–12].

Images obtained with the electron microscope are projections of the molecules along the direction of the electron beam. In a very simplified view, we can state that as the beam encounters more atoms along its path within the protein, the fewer electrons get into the detector, either photographic film or CCD, therefore integrating the 3D information of the molecule along the beam direction. Large collections of images from single molecules are selected and boxed out from each micrograph (after digitalization) or CCD frames (Figure 1C), which become the starting data set for image processing. These single particle images are always noisy, because low levels of electrons are used during imaging to reduce radiation damage and so minimize the destruction of the structural information. Furthermore, single particle images are intentionally under focus to secure sufficient contrast of the protein over the background, so molecules can be identified within the micrographs. Both the high noise levels and the under focus of the micrographs are responsible for the experimental limitations to reach high resolution in 3D reconstructions using EM. Consequently, the aims of image processing (Figure 1D) are 2-fold: first, to reduce the noise present in the images by averaging similar projections in 2 dimensions and, later on, into a 3D volume; second, to correct the consequences of under focus and other optical effects during the generation of images in the microscope (globally known as contrast transfer function, CTF). This second aspect of image processing will not be discussed in this review, but it has been nicely introduced elsewhere[7,13,14]. Generally speaking, image processing in 2D is required at some stage in order to classify those images corresponding to similar projections of the molecules (therefore, similar "shape") and to align them in 2D, this is, to place them into register, so that they can be averaged pixel-by-pixel to improve their signal-to-noise ratio. How is a 3D structure then reconstructed from the 2D data recorded? It is demonstrated that 2D projections along a 3D object contain sufficient information to restore the original object if the orientation angles of each projection are known, and several algorithms and approximations can easily perform this task. For instance, in medical tomography a radiation source is used to acquire projections of the patient along a set of established directions and then a 3D reconstruction is generated. Just a word of caution to point out that several algorithms exist to reconstruct a 3D structure from its projections at known orientations and the mathematics behind them and its relevance to the correctness of the resulting structure is

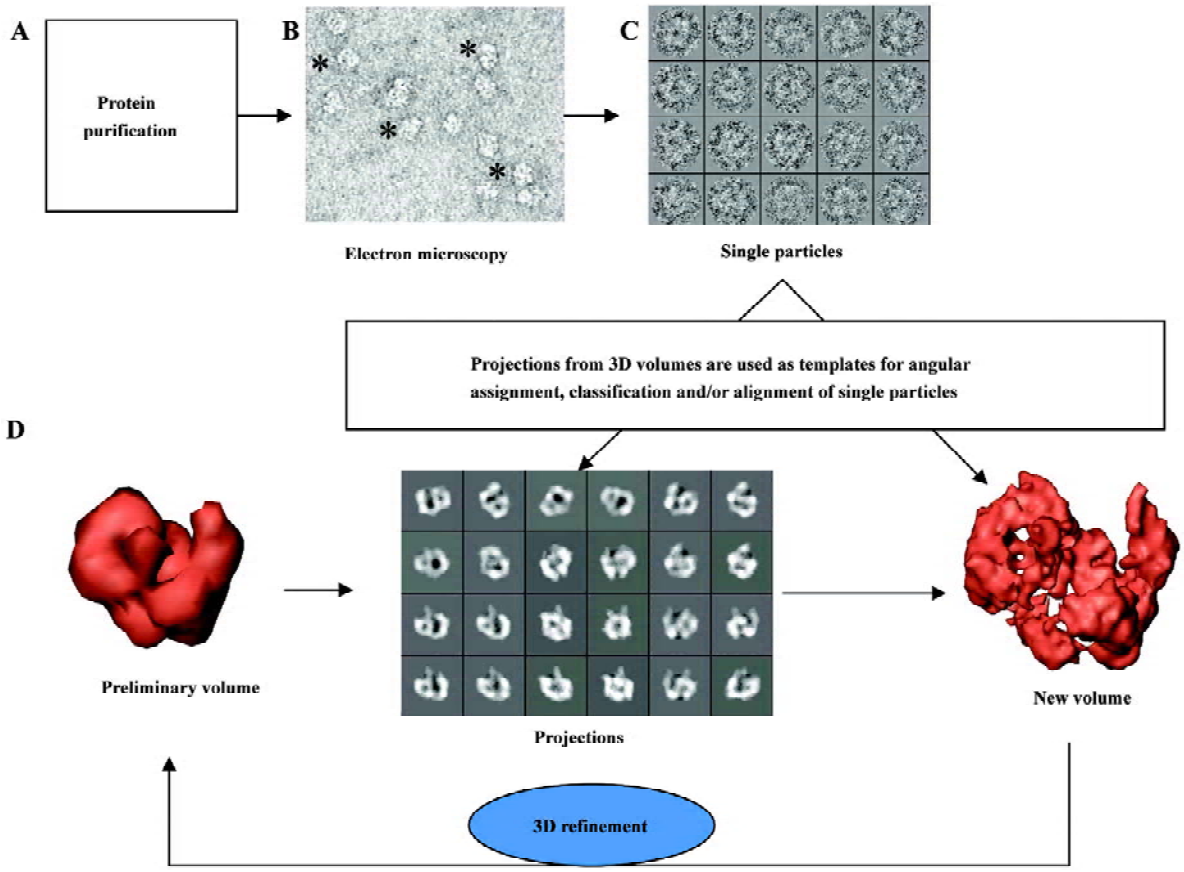

Figure 1. Basic procedures used in single-particle electron microscopy (EM) and 3D reconstruction. The work carried out by our group on DNA-PKcs, a kinase implicated in DNA repair, is shown as an example throughout the whole set of figures[33,76]. (A) Proteins must be purified to homogeneity before attempting an EM experiment because most methods are based on the assumption that the majority of collected images originate from the same specimen. (B) Proteins are adsorbed onto EM grids and observed under the electron microscope. Images from single molecules are detected over the noisy background (asterisks). (C) Micrographs are scanned and thousands of single images extracted (only a small gallery shown) and they constitute the starting data set. (D) To generate a 3D reconstruction of the target protein, the input raw images must be subjected to 2D and 3D image processing. The main purpose of image processing is the assignment to each input particle of its orientation angles, so all particles can be merged and averaged in 3D. Angular assignment is performed by a process known as "angular refinement" where projections of preliminary volumes are used as templates for alignment, classification or angular assignment. Preliminary assignments permit reconstruction of an improved 3D volume that functions as the source of more accurate template projections for the next round of refinement. As this process is repeated iteratively, angular assignment is improved and the correct 3D structure can be calculated.

not insignificant[15–17]. In single-particle EM, different views of the same protein are contained within each micrograph as, frequently, molecules interact with the support film or are enclosed within the vitrified ice (in cryo-EM) at many different orientations. In order to generate a "correct" 3D structure, all these projections of the molecule must evenly fill Fourier space, meaning we are merging in 3D images from all possible angles. Nevertheless, there are cases where the shape of the molecule can make it mathematically redundant to collect all possible views. For instance, GroEL, a molecular chaperon made up of 2 back-to-back stacked rings can be reconstructed just from its side views because the protein rotates along its longitudinal axis filling all Fourier space without the need to incorporate top views during image processing[18,19]. Therefore, once a sufficient data set is collected, the only requirement to resolve the 3D structure of the protein is to establish the orientation of each projection image with respect to a common set of reference coordinates. The problem of reconstructing a volume from projections is mostly reduced to that of angular assignment. This is actually the most time- and effort-consuming task during single particle EM and the heart of the image processing itself (Figure 1D). Several software platforms are commonly used, each one with a specific vision on how to approach the problem of

angular assignment and 3D reconstruction, which in all cases incorporates some type of iterative refinement of the data (Figure 1D).

These procedures described above require images from the same molecule at the same conformation taken in several orientations. In some cases, such data cannot be collected either because the protein binds to the grid in a preferred view, or because conformational flexibility exists in the protein, and therefore different views cannot be unambiguously assigned to a specific conformation. In such situations, the random conical tilt method can deliver a 3D structure for each type of view and generate a volume without a template[20–22].

Several commonly used software packages can do the job

Along the already relatively extended history of electron microscopy and image processing, several groups have deposited a lot of effort into the development of theory, methodological approaches, algorithms and complete platforms for the analysis of single-molecule images taken under the electron microscope. It is an outstanding effort that all microscopists should thank because they provide us with the tools we need in our everyday work. Original work by Crowther and colleagues developed the first methods to combine images of the same specimen lying at different orientations and applied them to icosahedral viruses[23,24]. Moreover, works performed on the structural determination of viral capsids have led the way in the possibilities of 3D EM. Accordingly, in 1997 2 groups, led by Crowther at Cambridge (UK) and Steven at the National Institutes of Health in Bethesda (USA), managed to visualize secondary structural elements in the 3D structure of hepatitis B viral cores at 7.4 Å and 9 Å[25,26], a major breakthrough at the time and the beginning of today's improvements in the EM field.

At present, some kind of implicit standard has been reached and most EM work is performed using 1 of 3 distinct software platforms: SPIDER[27], IMAGIC[28] and EMAN[16]. As a note of prudence, other popular platforms and programs exist, many of them dedicated to the processing of particles with icosahedral symmetry[29], which will not be discussed in this review. SPIDER was developed by the group of Joachim Frank in Albany (NY, USA), IMAGIC by Marin van Heel's group in London (UK) and EMAN by Steve Ludtke and Wah Chiu in Houston (TX, USA). EMAN is the most recent platform and it is available completely free of charge. More information about each package is found on their respective web sites: SPIDER (http://www.wadsworth.org/spider_doc/spider/docs/spider.html), IMAGIC (http://www.imagescience.de/imagic/) and EMAN (http://ncmi.bcm.tmc.edu/ncmi/).

Other research groups are also intensively contributing to software development and implementation for EM analysis, whose strength lies in that they mostly attend to aspects or approaches in image processing not sufficiently looked after by the previous platforms. This software can therefore add force to the potential of the most commonly used packages. This is the case with XMIPP, which includes a good repertoire of classification and alignment algorithms[30–32] (http://www.cnb.uam.es/~bioinfo/), FREALIGN (http://emlab.rose2.brandeis.edu/grigorieff/downloads.html) designed for extracting high-resolution features at the final stages of refinement, and BSOFT (http://www.niams.nih.gov/labbranch/lsbr/software/bsoft) containing, among other tools, a good algorithm to estimate and correct the CTF of the micrographs. To this day, the most common way for EM groups to make use of all of these computational possibilities is to choose 1 or 2 of the above main platforms while using other software to complement them for specific tasks.

It is as well worth mentioning that these efforts in software development for EM processing have been matched by spectacular improvements in the programs needed to render and visualize the 3D data. Many different programs are now available, all of them very good, each displaying advantages in specific features. Just a few of the most typically used by the EM community are AMIRA (http://www.amiravis.com/), CHIMERA (http://www.cgl.ucsf.edu/chimera/), VMD (visual molecular dynamics; REF; http://www.ks.uiuc.edu/Research/vmd/) or PYMOL (http://pymol.sourceforge.net/).

In the following paragraphs I will summarize the basic features of each one of the main platforms (SPIDER, IMAGIC and EMAN)[16,27,28], pointing out those aspects that make each software package exceptional (Figure 2). Globally, the main differences among them center on (i) the use of either single particles or their 2D averages to build the volumes; and (ii) the means for angular assignment, either "angular reconstitution" or "projection matching"[7]. With respect to the first point, all 3 platforms use the images from single particles as input data, but only SPIDER directly utilizes these to reconstruct the volume, because both IMAGIC and EMAN classify and average single images from similar views of the protein in order to produce a 2D average with improved signal-to-noise ratio. These averages then constitute the input to reconstruct the 3D structure. With respect to the second point, and as mentioned earlier, the fundamental aspect of image processing corresponds to the determination of the orientation angle of each image (or average) with respect to

a common set of coordinates. SPIDER and EMAN define these angles by comparison with projections of preliminary volumes that act as templates of known angles. Within each cycle of refinement the reconstructed volumes and their projections are improved, so that angular assignment is also iteratively improved. This strategy is known as "projection matching". Alternatively, IMAGIC defines orientation angles using "common lines", an algorithm that can potentially find the angular relation between projections without additional input. I will not get into the principles that underlie common lines but this requires a high signal-to-noise ratio to diminish false solutions and, consequently, IMAGIC spends much of its efforts in particle classification, alignment and averaging. Its great conceptual advantage is that angles come directly from the data, thus the name "angular reconstitution"[7]. Model bias in the assignment of angles is therefore greatly reduced, though some bias still exists because projections from iteratively improved 3D models are used to increase the accuracy in particle alignment and classification. It is imperative to point out that, besides these differences in the general approaches among several platforms, each of these contains the tools required to perform almost any operation with the images from the electron microscope, and are consequently intrinsically very flexible. Therefore, for instance, a "projection matching" strategy can be perfectly carried out using tools provided by IMAGIC.

Figure 2 outlines a generalised flow-through during image processing with each platform. SPIDER[27] initiates from a rough starting model to generate projections of defined angular spacing (Figure 2A). Each single particle is compared with all projections so that it receives those angles of that template with which it better fits. This preliminary angular assignment is used to build a new 3D model that acts as a new source for projections. As this process is repeated iteratively ("angular refinement"), projections better match the real data and, at the end, the angles assigned to the particles allow reconstruction of the structure. Refinement in IMAGIC[28] (Figure 2B), on the other hand, makes use of the projection templates just to align the particles, so classification and averaging can be iteratively improved, but angles are defined using the 2D averages and common lines. Finally, EMAN[16] (Figure 2C) has adopted a scheme somehow in between those of SPIDER and IMAGIC. Angular assignment for each particle in EMAN is defined based in their correlation with projection templates, as with SPIDER. But instead of using particles directly to build the volumes, all particles with a similar orientation constitute a group or class to be averaged, and only these averages are then used to reconstruct a volume. The process of averaging in EMAN incorporates a very good set of parameters that can be tuned to improve averaging and discard "bad" particles. An especially interesting feature of EMAN is that particles within a class are actually "refined" during averaging so that model bias is strongly minimised and single images with a standard deviation above a certain threshold are not incorporated into the final average. Common to all 3 systems is that either mechanism of angular assignment is repeated iteratively (angular refinement) until the angles assigned to the particles and the resulting 3D structure are stabilised. At the end, if correctly used, any of these 3 software platforms can construct an accurate structure. Nevertheless, it is extremely important to note that image processing is far from a fully automated method that does not require user intervention. On the contrary, each processing platform just provides a large number of computing tools to deal with the data from the microscope, but evaluation of the output results and decisions during processing are completely user dependent. Consequently, an inexperienced user could end up with a wrong structure.

The resolution problem or how to solve the resolution gap

Once we have the final 3D reconstruction of our macromolecule, the last stage of the research involves the in-depth inspection and description of the structure. This is a crucial step because interpretation of the 3D data is the source for the extraction of biologically relevant information, and therefore the source of our conclusions about the processes we are studying. In single-particle EM this task is problematic because the structures are solved to resolutions above those required to trace the polypeptide chain, due to the difficulties still present during averaging and alignment of the noisy images obtained with the microscope. Typically, EM analysis provides structures ranging from 8 Å–10 Å to 30 Å–40 Å resolution, and the consequences of these resolutions for the way in which a macromolecule is visualized can be perceived in Figure 3C, where I have used as an example the recent atomic model of DNA-PKcs, a kinase implicated in DNA repair[33]. While at a resolution of 9 Å secondary structural elements, such as alpha helices, can still be distinguished in favorable cases[19,34], at poorer resolutions (>15 Å), rarely anything more than the overall shape of the protein is apparent (Figure 3C).

To bridge the gap between the atomic information we would wish to have in our structure and the medium or low resolution of the actual EM reconstructions, 3 "multi-resolution" methods have been proposed[35–39]. These suggest

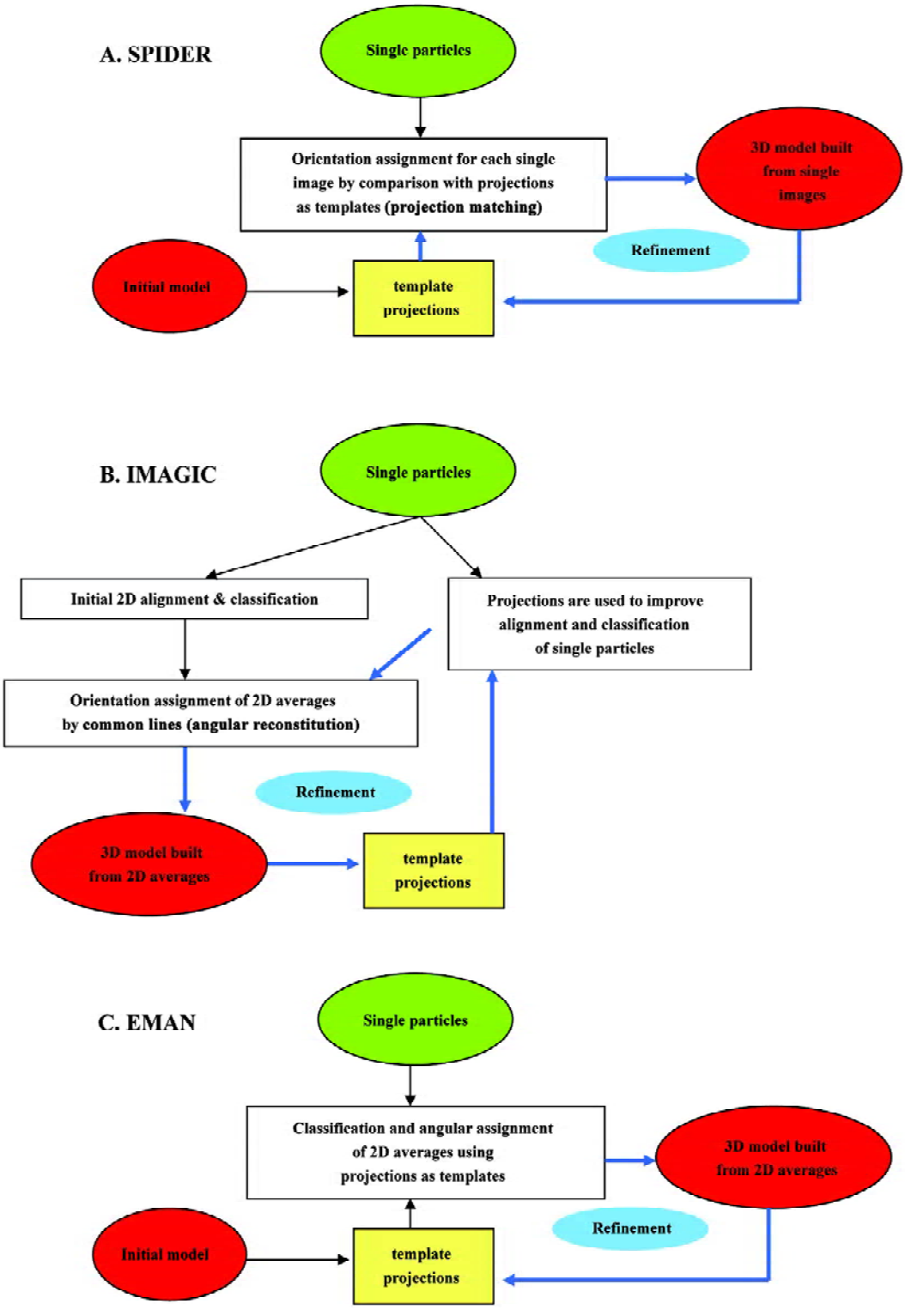

Figure 2. Several software packages exist for single-particle image processing, the 3 most widely used being: (A) SPIDER, (B) IMAGIC and (C) EMAN. Each platform deals with input images from electron micrographs as the source to build the 3D structures, but each one uses slightly different approaches to reach that goal, which have been summarized in this figure (and the text).

combining information at different levels of resolution in order to investigate complex systems.

Rigid-body fitting A medium-resolution EM structure can be depicted as a convolution of its atomic features; hence a pseudo-atomic model can be obtained by computationally placing ("fitting") atomic coordinates into the EM map[36]. The atomic structure is considered to be a rigid body with no conformational changes, whose density has to be located and placed within the 3D reconstruction. Rigid-body fitting is a very appropriate mode to map domains into a larger complex that contains several domains or proteins, and it has been extensively used already to propose pseudo-atomic models of macromolecular complexes. However, it is important to bear in mind that the accuracy of this computational approach can be seriously hampered by a lack of resolution of the target 3D model and by the size, shape and conformational flexibility of the fitted atomic structure. Figure 3 shows a recent example from our group where the 3D structure of the DNA-PKcs kinase[33] was fitted with atomic structures of individual domains (Figure 3A) to produce a pseudo-atomic model for some portions of the molecule (Figure 3B). This atomic model, when filtered to the resolution experimentally obtained by EM, very much resembles the corresponding segments of the 3D structure (Figure 3C). Many other examples can be found in the recent literature where these methods have been applied[40–42].

Several algorithms have been developed that consider different sides of the problem[35,36], but this is still a very active field where a consensus about the best approaches has not yet been reached. Some of the most commonly used tools are those implemented in SITUS[43] (http://situs.biomachina.org/), EMAN[16] (http://ncmi.bcm.tmc.edu/ncmi/)

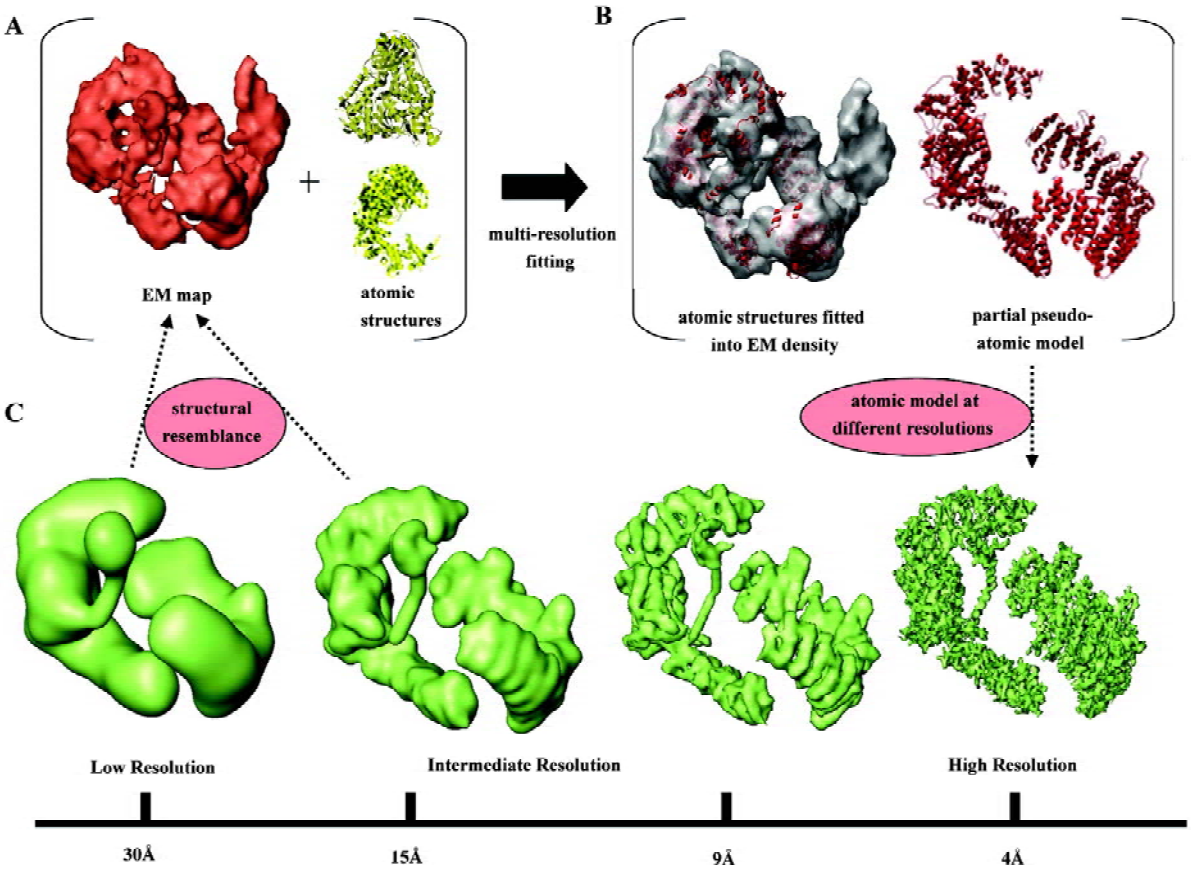

Figure 3. Multi-resolution fitting. (A) Medium- or low-resolution maps obtained by electron microscopy (EM) do not provide atomic information of macromolecules, but (B) atomic structures of parts of the proteins can be fitted into the EM density to generate a likely model at atomic resolution for parts of the macromolecule (usually referred to as "pseudo-atomic models"). (C) The consequences of the loss of resolution on the structural details that are observed in 3D EM can be shown after low-pass filtering of the atomic model in (B) at different resolutions. When the pseudo-atomic model is rendered at resolutions compatible to those of the experimentally obtained EM maps, structural resemblance between the model and the 3D reconstruction should be evident.

and EM fit[44]. Nevertheless, other algorithms are also frequently used[45–47]. At low resolution, several solutions could comply with our fitting criteria, so one must be cautious with the results, which, if much uncertainty persists, should ideally be supported or validated with external information.

Flexible fitting It is very likely that an atomic structure will not perfectly match one solved by EM, especially when the portion represented by the atomic structure is part of a larger complex solved by EM or it is at a different stage of its functional cycle. In such cases, and if sufficiently good resolution is present, the atomic coordinates can be modified so that they better fit into the EM density. By doing so, we can not only place a domain within a larger structure (as in rigid-body fitting), but we can also actually identify a new conformation of the protein. A nice example has been shown recently in the 6 Å structure of GroEL, where some displacement of helices were found compared to its atomic coordinates[19]. Both SITUS[48] and EMAN[16] contain algorithms to perform flexible fitting.

Prediction of secondary structure elements and protein folds In those cases where the resolution of an EM map is very good (usually anything below 8 Å), instead of fitting known atomic structures, a more powerful approach can be carried out, and the actual recognition of secondary structure elements within the map can be achieved. The AIRS platform in EMAN has several commands (helixhunter, ssehunter) to look for sheets and helices in the maps. A score is supplied to help discriminate real from spurious findings. In favorable cases, a whole fold type can be defined and consequently a sufficiently realistic atomic model. A brilliant example has been recently published describing a pseudo-atomic model for the capsid of phi29 phage[34]. Other groups are also currently working on fold predictions from EM reconstructions[49]. Importantly, results in the area of secondary structure prediction need to be handled with great care due to the still innovative nature of this field.

Some notable recent electron microscopy studies

The last 2–3 years have been characterized by a rapid increase in EM publications. I wish to point out some significant works recently published, which have been dealing with some challenging applications of single-particle EM. These works shed light on where the field is going in the very near future. I strongly apologize to all whose work has not been reflected in this review.

Small, asymmetric and flexible proteins Certainly, EM has clear limitations with respect to the smallest size of the molecules it can analyze. Proteins must be visualized above a noisy background to be extracted and processed, and only large macromolecules can therefore fit this criterion. There are also deeper conceptual reasons that do not allow reconstruction of very small molecules[50]. As a result, proteins targeted by EM studies are usually above 200 kDa–300 kDa. Having said that, some recent outstanding works have challenged these difficulties and studied small proteins, many with molecular weights around, or even below, 100 kDa, and these have been reconstructed at decent resolutions (around 20 Å–30 Å): geminin[51], separase[11], the Arp2/3 complex[52] and the mammalian fatty acid synthase[53], to name a few.

A common feature of many of these proteins is that they participate in very relevant pathways in the biology of the cell (eg signaling pathways, DNA repair, oncogenes and tumor suppressors), and though they are not extremely large, they are still difficult to purify in large quantities for X-ray studies. This is the case, for instance, with Vav, an activator of Rho/Rac GTPases, whose 3D structure has been solved in the inactive and active conformations, plus a ~85 kDa truncated mutant with oncogenic potential[12], providing insights into its regulatory mechanisms. Another remarkable example is the structure of the tetrameric KvAP voltage-dependent K^+ channel[54] with a mass of 100 kDa, which the authors deliberately increased up to 300 kDa by addition of 4 Fab fragments.

Generally speaking, all of these works have the challenging difficulty of collecting good microscopy data and being able to correctly align images of small molecules, which, on top of that, frequently display no symmetry at all. But an even further twist to these already difficult experiments comes when the protein under study is flexible; several conformations are present in the same micrographs whose identification is not always straightforward. In some of these cases, the method called "random conical tilt"[20,22] (developed some time ago to obtain 3D structures from proteins bound to the EM grids with preferential views) might be the only tactic available to solve these structures without mixing several conformations. In this regard, it is worth taking a look at some recent excellent works by Tomas Waltz's group[55,56]

Structures of the ribosome The complex structure of the ribosome and the process of mRNA translation have been extensively studied by several groups in the last decade. These authors regularly provide structures at resolutions better than 12 Å and the wealth of biological information obtained by combining EM and X-ray crystallography of the ribosome is unprecedented. Two groups have been leading this research: Joachim Frank at Albany (NY, USA)[57–61] and Marin van Heel at London (UK)[62–64].

Multi-protein macromolecular complexes or "molecular machines" The natural targets of EM are those complexes that contain several proteins, are very large in size, are heterogeneous in their composition, have complex functional cycles and are difficult to purify; all of these qualities making complicated a traditional analysis by crystallography or NMR. Interestingly, these large and transient complexes, sometimes named "molecular machines", have been admitted by modern biology to comprise the basics for a major number of cellular processes, and are therefore a subject of great interest. Some EM works have started to obtain 3D information on some of these complexes, such us the spliceosome (implicated in mRNA splicing)[65–68], the SAGA complex from *Saccharomyces cerevisiae*[69], the apoptosome involved in procaspase-9 binding and activation during apoptosis[70], and several complexes between chaperonins with their substrates and co-chaperons[71–74].

DNA-bound protein complexes Determination of the 3D structure of complexes between proteins and DNA substrates has been accomplished, for instance, the large T antigen bound to the simian virus 40 origin of replication[75], the DNA-PKcs kinase bound to a double-stranded DNA fragment that simulates a DNA repair signal[33,76], and the clamp-loading complex for DNA replication[77].

High resolution structures Averaging of the noise images from single-particle EM has the potential to deliver 3D structures with a resolution sufficient to trace the polypeptide chain[50]. A Nature paper published in 2003 on the flagellar structure[78] demonstrated that if good single images can be accurately aligned, they are able to deliver atomic information. The authors made use of a trick to align the images according to their regular arrangement within the flagella. Nevertheless, the outstanding merit of the work was that no diffraction information was used during their processing. It seems clear that reaching very high resolution will only be possible for adequate specimens of large size, high symmetry and by means of high-quality (ie high signal-to-noise ratio) images, derived probably from helium-cooled microscopes. However, the race is on to increase the resolution of single-particle reconstructions both with improved equipment and better algorithms. Some recent examples are the GroEL structure at 6 Å[19] using EMAN, the *Escherichia coli* large ribosomal subunit at 7.5 Å[79], and the 8 Å resolution structure of microtubules[41] using SPIDER.

Other noteworthy works Other recent studies of special interest have been the definition of the structural basis of pore formation by the bacterial toxin pneumolysin, by the group of Helen Saibil[80], and the pseudo-atomic model of the capsid of phage phi29[34].

Future prospects and limitations of single-particle electron microscopy

Single-particle EM analysis has become a trendy structural tool in biology despite not providing atomic resolution information. This is due to some of the great advantages of this method in comparison to more established atomic resolution techniques: (i) small amounts of purified protein are required, compatible with those ordinarily obtained for large macromolecules or multi-subunit protein complexes, possibly its key advantage when compared to crystallography and NMR as EM can deliver biological information from modest quantities of material; (ii) macromolecules are trapped in their native conformation in physiological buffers; and (iii) preparations containing mixed populations or contaminated samples could be potentially analyzed whenever the distinct populations can be separated, either visually or computationally. Consequently, single-particle EM is a technique very suitable for determining the 3D structure of large macromolecule complexes ("molecular machines"), which are now known to be implicated in many cellular processes. This is so because macromolecular complexes can be very large and challenging to crystallize; they can frequently be purified only in modest quantities, while at the same time being very flexible and of variable composition.

Future developments of the technique are being directed toward improved resolution and a more profound examination of the volumetric data by either the fitting of atomic structures or the identification of folds. All of these advances will require new methods now under development[7,13,81]. Automation of data collection and analysis is also becoming an important goal for EM. The long learning process needed to properly operate a modern electron microscope, to collect good-quality data and to perform a flawless image processing means that only those with extended experience in EM can really do the job. Hence, making as many of those processes as automatic as possible is a great need for the future development of EM, especially when collecting the many thousands of single images needed when high resolutions are the goal. Some interesting approximations are already under development[82–87], and there are no serious conceptual reasons why automation of the most repetitive microscope tasks should not be achieved in the near future. However, one of the more important challenges for the future will be to deal with conformational flexibility and the heterogeneity of large protein complexes. As resolution increases, more data on identical conformations must be averaged, but the better the resolution, the more likely it is that molecules will differ in their exact conformation.

Suggested solutions implicate the refinement of the data into more than one possible 3D volume and the exploration of the conformational space of a protein using normal-mode analysis[88–91].

Still, EM analysis presents some important limitations that are essential to keep in mind. To begin with, the methods we use today are still very much dependent on the expertise of the user to deliver the correct structure, especially when dealing with small and low-symmetry molecules or heterogeneous samples. Things can be done wrong, and an inexperienced user can end up in local minima not representing the real 3D structure. Consequently, a great challenge for the near future should be to standardize methods and controls as is done in modern X-ray crystallography. A further limitation to the method is that, in some cases, structures of macromolecular complexes are solved only to moderate resolutions, which might provide few or no biologically relevant information, especially when no atomic data of any part of a complex is known. Nevertheless, in these cases, EM structures can still be interpreted by calculating difference maps among several reconstructions to then determine the position of components in the complex. Besides these limitations, single-particle EM will certainly cope with its future challenges to become a widespread method to study the 3D structures of macromolecules in conjunction with other structural techniques.

Acknowledgement

I greatly acknowledge the constant support by Laurence H Pearl at the Institute of Cancer Research (London, UK) in the DNA-PK work presented in the figures of this review. I am also very thankful for the work of Angel Rivera-Calzada and Ernesto Arias-Palomo in my lab. I apologize to all those groups working in the EM field whose studies have not been reflected in this mini review, which was just intended as an initiation for those outside of our discipline.

References

1 Baumeister W, Steven AC. Macromolecular electron microscopy in the era of structural genomics. Trends Biochem Sci 2000; 25: 624–31.
2 Saibil HR. Macromolecular structure determination by cryo-electron microscopy. Acta Crystallogr D Biol Crystallogr 2000; 56: 1215–22.
3 Saibil HR. Conformational changes studied by cryo-electron microscopy. Nat Struct Biol 2000; 7: 711–4.
4 Orlova EV, Saibil HR. Structure determination of macromolecular assemblies by single-particle analysis of cryo-electron micrographs. Curr Opin Struct Biol 2004; 14: 584–90.
5 Frank J. Single-particle imaging of macromolecules by cryo-electron microscopy. Annu Rev Biophys Biomol Struct 2002; 31: 303–19.
6 Frank J, Schlichting I. Time-resolved imaging of macromolecular processes and interactions. J Struct Biol 2004;147: 209–10.
7 van Heel M, Gowen B, Matadeen R, Orlova EV, Finn R, Pape T, *et al*. Single-particle electron cryo-microscopy: towards atomic resolution. Q Rev Biophys 2000; 33: 307–69.
8 van Heel M. Angular reconstitution: a posteriori assignment of projection directions for 3D reconstruction. Ultramicroscopy 1987; 21: 111–23.
9 Nogales E, Grigorieff N. Molecular machines: putting the pieces together. J Cell Biol 2001; 152: F1–10.
10 Ohi M, Li Y, Cheng Y, Walz T. Negative staining and image classification–powerful tools in modern electron microscopy. Biol Proced Online 2004; 6: 23–34.
11 Viadiu H, Stemmann O, Kirschner MW, Walz T. Domain structure of separase and its binding to securin as determined by EM. Nat Struct Mol Biol 2005; 12: 552–3.
12 Llorca O, Arias-Palomo E, Zugaza JL, Bustelo XR. Global conformational rearrangements during the activation of the GDP/GTP exchange factor Vav3. Embo J 2005; 24: 1330–40.
13 Mindell JA, Grigorieff N. Accurate determination of local defocus and specimen tilt in electron microscopy. J Struct Biol 2003; 142: 334–47.
14 Velazquez-Muriel JA, Sorzano CO, Fernandez JJ, Carazo JM. A method for estimating the CTF in electron microscopy based on ARMA models and parameter adjustment. Ultramicroscopy 2003; 96: 17–35.
15 Penczek PA, Zhu J, Frank J. A common-lines based method for determining orientations for N>3 particle projections simultaneously. Ultramicroscopy 1996; 63: 205–18.
16 Ludtke SJ, Baldwin PR, Chiu W. EMAN: semiautomated software for high-resolution single-particle reconstructions. J Struct Biol 1999; 128: 82–97.
17 Sorzano CO, Marabini R, Boisset N, Rietzel E, Schroder R, Herman GT, *et al*. The effect of overabundant projection directions on 3D reconstruction algorithms. J Struct Biol 2001; 133: 108–18.
18 Sewell BT, Best RB, Chen S, Roseman AM, Farr GW, Horwich AL, *et al*. A mutant chaperonin with rearranged inter-ring electrostatic contacts and temperature-sensitive dissociation. Nat Struct Mol Biol 2004; 11: 1128–33.
19 Ludtke SJ, Chen DH, Song JL, Chuang DT, Chiu W. Seeing GroEL at 6 A resolution by single particle electron cryomicroscopy. Structure (Camb) 2004; 12: 1129–36.
20 Radermacher M. Three-dimensional reconstruction of single particles from random and nonrandom tilt series. J Electron Microsc Tech 1988; 9: 359–94.
21 Golas MM, Sander B, Will CL, Luhrmann R, Stark H. Major conformational change in the complex SF3b upon integration into the spliceosomal U11/U12 di-snRNP as revealed by electron cryomicroscopy. Mol Cell 2005; 17: 869–83.
22 Carazo JM, Wagenknecht T, Frank J. Variations of the three-dimensional structure of the Escherichia coli ribosome in the range of overlap views. An application of the methods of multicone and local single-cone three-dimensional reconstruction. Biophys J 1989; 55: 465–77.
23 Crowther RA, Amos LA, Finch JT, De Rosier DJ, Klug A. Three

dimensional reconstructions of spherical viruses by Fourier synthesis from electron micrographs. Nature 1970; 226: 421–5.
24 Crowther RA, Klug A. Structural analysis of macromolecular assemblies by image reconstruction from electron micrographs. Annu Rev Biochem 1975; 44: 161–82.
25 Bottcher B, Wynne SA, Crowther RA. Determination of the fold of the core protein of hepatitis B virus by electron cryomicroscopy. Nature 1997; 386: 88–91.
26 Conway JF, Cheng N, Zlotnick A, Wingfield PT, Stahl SJ, Steven AC. Visualization of a 4-helix bundle in the hepatitis B virus capsid by cryo-electron microscopy. Nature 1997; 386: 91–4.
27 Frank J, Radermacher M, Penczek P, Zhu J, Li Y, Ladjadj M, *et al*. SPIDER and WEB: processing and visualization of images in 3D electron microscopy and related fields. J Struct Biol 1996; 116: 190–9.
28 van Heel M, Harauz G, Orlova EV, Schmidt R, Schatz M. A new generation of the IMAGIC image processing system. J Struct Biol 1996; 116: 17–24.
29 Conway JF, Steven AC. Methods for reconstructing density maps of "single" particles from cryoelectron micrographs to subnanometer resolution. J Struct Biol 1999; 128: 106-18.
30 Sorzano CO, Marabini R, Velazquez-Muriel J, Bilbao-Castro JR, Scheres SH, Carazo JM, *et al*. XMIPP: a new generation of an open-source image processing package for electron microscopy. J Struct Biol 2004; 148: 194–204.
31 Scheres SH, Valle M, Nunez R, Sorzano CO, Marabini R, Herman GT, *et al*. Maximum-likelihood multi-reference refinement for electron microscopy images. J Mol Biol 2005; 348: 139–49.
32 Scheres SH, Marabini R, Lanzavecchia S, Cantele F, Rutten T, Fuller SD, *et al*. Classification of single-projection reconstructions for cryo-electron microscopy data of icosahedral viruses. J Struct Biol 2005; 151: 79–91.
33 Rivera-Calzada A, Maman JD, Spagnolo L, Pearl LH, Llorca O. Three-dimensional structure and regulation of the DNA-dependent protein kinase catalytic subunit (DNA-PKcs). Structure (Camb) 2005; 13: 243–55.
34 Morais MC, Choi KH, Koti JS, Chipman PR, Anderson DL, Rossmann MG. Conservation of the capsid structure in tailed dsDNA bacteriophages: the pseudoatomic structure of phi29. Mol Cell 2005; 18: 149–59.
35 Wriggers W, Chacon P. Modeling tricks and fitting techniques for multiresolution structures. Structure (Camb) 2001; 9: 779–88.
36 Chacon P, Wriggers W. Multi-resolution contour-based fitting of macromolecular structures. J Mol Biol 2002; 317: 375–84.
37 Jiang W, Baker ML, Ludtke SJ, Chiu W. Bridging the information gap: computational tools for intermediate resolution structure interpretation. J Mol Biol 2001; 308: 1033–44.
38 Rossmann MG, Morais MC, Leiman PG, Zhang W. Combining x-ray crystallography and electron microscopy. Structure (Camb) 2005; 13: 355–62.
39 Chiu W, Baker ML, Jiang W, Dougherty M, Schmid MF. Electron cryomicroscopy of biological machines at subnanometer resolution. Structure (Camb) 2005; 13: 363–72.
40 Rossmann MG, Mesyanzhinov VV, Arisaka F, Leiman PG. The bacteriophage T4 DNA injection machine. Curr Opin Struct Biol 2004; 14: 171–80.
41 Li H, DeRosier DJ, Nicholson WV, Nogales E, Downing KH. Microtubule structure at 8 A resolution. Structure (Camb) 2002; 10: 1317–28.
42 Fotin A, Cheng Y, Sliz P, Grigorieff N, Harrison SC, Kirchhausen T, *et al*. Molecular model for a complete clathrin lattice from electron cryomicroscopy. Nature 2004; 432: 573–9.
43 Wriggers W, Milligan RA, McCammon JA. Situs: a package for docking crystal structures into low-resolution maps from electron microscopy. J Struct Biol 1999; 125: 185–95.
44 Rossmann MG, Bernal R, Pletnev SV. Combining electron microscopy with X-ray crystallographic structures. J Struct Biol 2001; 136: 190–200.
45 Hinsen K, Reuter N, Navaza J, Stokes DL, Lacapere JJ. Normal mode-based fitting of atomic structure into electron density maps: application to sarcoplasmic reticulum Ca-ATPase. Biophys J 2005; 88: 818–27.
46 Navaza J, Lepault J, Rey FA, Alvarez-Rua C, Borge J. On the fitting of model electron densities into EM reconstructions: a reciprocal-space formulation. Acta Crystallogr D Biol Crystallogr 2002; 58: 1820–5.
47 Roseman AM. Docking structures of domains into maps from cryo-electron microscopy using local correlation. Acta Crystallogr D Biol Crystallogr 2000; 56: 1332–40.
48 Wriggers W, Birmanns S. Using situs for flexible and rigid-body fitting of multiresolution single-molecule data. J Struct Biol 2001; 133: 193–202.
49 Velazquez-Muriel JA, Sorzano CO, Scheres SH, Carazo JM. SPI-EM: towards a tool for predicting CATH superfamilies in 3D-EM maps. J Mol Biol 2005; 345: 759–71.
50 Henderson R. The potential and limitations of neutrons, electrons and x-rays for atomic resolution microscopy of unstained biological molecules. Q Rev Biophys 1995; 28: 171–93.
51 Okorokov AL, Orlova EV, Kingsbury SR, Bagneris C, Gohlke U, Williams GH, *et al*. Molecular structure of human geminin. Nat Struct Mol Biol 2004; 11: 1021–2.
52 Rodal AA, Sokolova O, Robins DB, Daugherty KM, Hippenmeyer S, Riezman H, *et al*. Conformational changes in the Arp2/3 complex leading to actin nucleation. Nat Struct Mol Biol 2005; 12: 26–31.
53 Rodal AA, Sokolova O, Robins DB, Daugherty KM, Hippenmeyer S, Riezman H, *et al*. Structure and molecular organization of mammalian fatty acid synthase. Nat Struct Mol Biol 2005; 12: 225–32.
54 Jiang QX, Wang DN, MacKinnon R. Electron microscopic analysis of KvAP voltage-dependent K^+ channels in an open conformation. Nature 2004; 430: 806–10.
55 Skiniotis G, Boulanger MJ, Garcia KC, Walz T. Signaling conformations of the tall cytokine receptor gp130 when in complex with IL-6 and IL-6 receptor. Nat Struct Mol Biol 2005; 12: 545–51.
56 Nakagawa T, Cheng Y, Ramm E, Sheng M, Walz T. Structure and different conformational states of native AMPA receptor complexes. Nature 2005; 433: 545–9.
57 Valle M, Zavialov A, Sengupta J, Rawat U, Ehrenberg M, Frank J. Locking and unlocking of ribosomal motions. Cell 2003; 114: 123–34.
58 Valle M, Gillet R, Kaur S, Henne A, Ramakrishnan V, Frank J. Visualizing tmRNA entry into a stalled ribosome. Science 2003; 300: 127–30.
59 Frank J. Electron microscopy of functional ribosome complexes.

Biopolymers 2003; 68: 223–33.
60 Rawat UB, Zavialov AV, Sengupta J, Valle M, Grassucci RA, Linde J, *et al*. A cryo-electron microscopic study of ribosome-bound termination factor RF2. Nature 2003; 421: 87–90.
61 Halic M, Becker T, Pool MR, Spahn CM, Grassucci RA, Frank J, *et al*. Structure of the signal recognition particle interacting with the elongation-arrested ribosome. Nature 2004; 427: 808–14.
62 Klaholz BP, Myasnikov AG, van Heel M. Visualization of release factor 3 on the ribosome during termination of protein synthesis. Nature 2004; 427: 862–5.
63 Klaholz BP, Pape T, Zavialov AV, Myasnikov AG, Orlova EV, Vestergaard B, *et al*. Structure of the *Escherichia coli* ribosomal termination complex with release factor 2. Nature 2003; 421: 90–4.
64 Stark H, Rodnina MV, Wieden HJ, Zemlin F, Wintermeyer W, van Heel M. Ribosome interactions of aminoacyl-tRNA and elongation factor Tu in the codon-recognition complex. Nat Struct Biol 2002; 9: 849–54.
65 Jurica MS, Sousa D, Moore MJ, Grigorieff N. Three-dimensional structure of C complex spliceosomes by electron microscopy. Nat Struct Mol Biol 2004; 11: 265–9.
66 Jurica MS, Licklider LJ, Gygi SR, Grigorieff N, Moore MJ. Purification and characterization of native spliceosomes suitable for three-dimensional structural analysis. RNA 2002; 8: 426–39.
67 Boehringer D, Makarov EM, Sander B, Makarova OV, Kastner B, Luhrmann R, *et al*. Three-dimensional structure of a precatalytic human spliceosomal complex B. Nat Struct Mol Biol 2004; 11: 463–8.
68 Golas MM, Sander B, Will CL, Luhrmann R, Stark H. Molecular architecture of the multiprotein splicing factor SF3b. Science 2003; 300: 980–4.
69 Wu PY, Ruhlmann C, Winston F, Schultz P. Molecular architecture of the *S cerevisiae* SAGA complex. Mol Cell 2004; 5: 199–208.
70 Acehan D, Jiang X, Morgan DG, Heuser JE, Wang X, Akey CW. Three-dimensional structure of the apoptosome: implications for assembly, procaspase-9 binding, and activation. Mol Cell 2002; 9: 423–32.
71 Llorca O, McCormack EA, Hynes G, Grantham J, Cordell J, Carrascosa JL, *et al*. Eukaryotic type II chaperonin CCT interacts with actin through specific subunits. Nature 1999; 402: 693–6.
72 Llorca O, Martin-Benito J, Ritco-Vonsovici M, Grantham J, Hynes GM, Willison KR, *et al*. Eukaryotic chaperonin CCT stabilizes actin and tubulin folding intermediates in open quasi-native conformations. EMBO J 2000; 19: 5971–9.
73 Martin-Benito J, Boskovic J, Gomez-Puertas P, Carrascosa JL, Simons CT, Lewis SA, *et al*. Structure of eukaryotic prefoldin and of its complexes with unfolded actin and the cytosolic chaperonin CCT. EMBO J 2002; 21: 6377–86.
74 Martin-Benito J, Boskovic J, Gomez-Puertas P, Carrascosa JL, Simons CT, Lewis SA, *et al*. Structure of the complex between the cytosolic chaperonin CCT and phosducin-like protein. Proc Natl Acad Sci USA 2004; 101: 17 410–5.
75 Gomez-Lorenzo MG, Valle M, Frank J, Gruss C, Sorzano CO, Chen XS, *et al*. Large T antigen on the simian virus 40 origin of replication: a 3D snapshot prior to DNA replication. EMBO J 2003; 22: 6205–13.
76 Boskovic J, Rivera-Calzada A, Maman JD, Chacon P, Willison KR, Pearl LH, *et al*. Visualization of DNA-induced conformational changes in the DNA repair kinase DNA-PKcs. EMBO J 2003; 22: 5875–82.
77 Miyata T, Oyama T, Mayanagi K, Ishino S, Ishino Y, Morikawa K. The clamp-loading complex for processive DNA replication. Nat Struct Mol Biol 2004; 11: 632–6.
78 Yonekura K, Maki-Yonekura S, Namba K. Complete atomic model of the bacterial flagellar filament by electron cryomicroscopy. Nature 2003; 424: 643–50.
79 Matadeen R, Patwardhan A, Gowen B, Orlova EV, Pape T, Cuff M, *et al*. The *Escherichia coli* large ribosomal subunit at 7.5 A resolution. Structure Fold Des 1999; 7: 1575–83.
80 Tilley SJ, Orlova EV, Gilbert RJ, Andrew PW, Saibil HR. Structural basis of pore formation by the bacterial toxin pneumolysin. Cell 2005; 121: 247–56.
81 Rosenthal PB, Henderson R. Optimal determination of particle orientation, absolute hand, and contrast loss in single-particle electron cryomicroscopy. J Mol Biol 2003; 333: 721–45.
82 Rath BK, Frank J. Fast automatic particle picking from cryo-electron micrographs using a locally normalized cross-correlation function: a case study. J Struct Biol 2004; 145: 84–90.
83 Plaisier JR, Koning RI, Koerten HK, van Heel M, Abrahams JP. TYSON: robust searching, sorting, and selecting of single particles in electron micrographs. J Struct Biol 2004; 145: 76–83.
84 Booth CR, Jiang W, Baker ML, Zhou ZH, Ludtke SJ, Chiu W. A 9 angstroms single particle reconstruction from CCD captured images on a 200 kV electron cryomicroscope. J Struct Biol 2004; 147: 116–27.
85 Nickell S, Forster F, Linaroudis A, Net WD, Beck F, Hegerl R, *et al*. TOM software toolbox: acquisition and analysis for electron tomography. J Struct Biol 2005; 149: 227–34.
86 Lei J, Frank J. Automated acquisition of cryo-electron micrographs for single particle reconstruction on an FEI Tecnai electron microscope. J Struct Biol 2005; 150: 69–80.
87 Suloway C, Pulokas J, Fellmann D, Cheng A, Guerra F, Quispe J, *et al*. Automated molecular microscopy: the new Leginon system. J Struct Biol 2005; 151: 41–60.
88 Tama F, Wriggers W, Brooks CL. Exploring global distortions of biological macromolecules and assemblies from low-resolution structural information and elastic network theory. J Mol Biol 2002; 321: 297–305.
89 Chacon P, Tama F, Wriggers W. Mega-Dalton biomolecular motion captured from electron microscopy reconstructions. J Mol Biol 2003; 326: 485–92.
90 Wriggers W, Chakravarty S, Jennings PA. Control of protein functional dynamics by peptide linkers. Biopolymers 2005; in press.
91 Carazo JM. Accessing information on the conformational flexibility of molecular machines. Structure (Camb) 2004; 12: 170–1.

Acta Pharmacologica Sinica 2005 Oct; 26 (10): 1165–1173

Blackwell Publishing

Invited review

HIV entry inhibitors: a new generation of antiretroviral drugs

Elias KRAMBOVITIS[1,3], Filippos PORICHIS[1,2], Demetrios A SPANDIDOS[2]

[1]*Department of Applied Biochemistry and Immunology, Institute of Molecular Biology and Biotechnology, Vassilika Vouton, Heraklion, Crete, Greece*; [2]*Greece Department of Virology, Medical School, University of Crete, Heraklion, Crete, Greece*

Key words

highly active antiretroviral therapy; HIV receptors; HIV fusion inhibitors; HIV

[3]Correspondence to Prof Elias KRAMBOVITIS.
Phn 30-81-39-1020.
Fax 30-81-39-1101.
E-mail krambo@imbb.forth.gr

Received 2005-05-15
Accepted 2005-06-27

doi: 10.1111/j.1745-7254.2005.00193.x

Abstract

AIDS is presently treatable, and patients can have a good prognosis due to the success of highly active antiretroviral therapy (HAART), but it is still not curable or preventable. High toxicity of HAART, and the emergence of drug resistance add to the imperative to continue research into new strategies and interventions. Considerable progress in the understanding of HIV attachment and entry into host cells has suggested new possibilities for rationally designing agents that interfere with this process. The approval and introduction of the fusion inhibitor enfuvirtide (Fuzeon) for clinical use signals a new era in AIDS therapeutics. Here we review the crucial steps the virus uses to achieve cell entry, which merit attention as potential targets, and the compounds at pre-clinical and clinical development stages, reported to effectively inhibit cell entry.

Introduction

Acquired immunodeficiency syndrome (AIDS) was recognized in 1981, and the first human immunodeficiency virus (HIV) was isolated 2 years later, heralding a new era in the fight against pathogenic viruses[1,2]. Since then, HIV infection has become a major public health problem worldwide, with an estimated 39.4 million infected people as at the end of 2004 (Table 1)[3]. According to the Joint United Nations Programme on HIV/AIDS (UNAIDS) epidemic update, in 2004 there were more than 3.1 million AIDS deaths, including 500 000 children under 15 years of age[4]. The prevalence of HIV-1 is greater in developing countries, and especially in Sub-Saharan Africa, where the infrastructure to prevent and treat the infection is limited[5]. These "hotspots" absorb most of the attention of international committees and organizations, and a significant part of the funding for AIDS prevention and treatment goes towards attempting to scale up antiretroviral (ARV) therapy in developing and transitional countries[6].

HIV is a lentinovirus that is predominantly transmitted by sexual contact, as virus particles can cross the mucosal epithelium and infect specific cells[7,8] expressing the CD4 receptor. Cells bearing CD4 receptors on their membrane belong to the macrophage/monocyte lineage and to a subset of T-cells[9,10]. Initial indications were that HIV-1 used only CD4 to identify and enter the target cells. Soon, however, it became apparent that additional co-receptors were probably required in order for the virus to complete cell entry. Subsequently, several such potential co-receptors were proposed[11,12], but the CCR5 and CXCR4 chemokine receptors are today considered to be the major co-receptors for HIV-1 entry[13–15]. T-cell tropic HIV strains use mainly CXCR4 as a co-receptor and are called X4 strains, whereas macrophage-

Table 1. Worldwide distribution of estimated number of people living with HIV[4].

Region	Estimated number[1)]
North America	1.0 million (540 000–1.6 million)
Caribbean	440 00 (270 000–780 000)
Latin America	1.7 million (1.3–2.2 million)
Western and Central Europe	610 000 (480 000–760 000)
Eastern Europe and Central Asia	1.4 million (920 000–2.1 million)
North Africa and Middle East	540 000 (230 000–1.5 million)
Sub-Saharan Africa	25.4 million (23.4–28.4 million)
East Asia	1.1 million (560 000–1.8 million)
South and South-East Asia	7.1 million (4.4–10.6 million)
Oceania	35 000 (25 000–48 000)

[1)]The ranges around the estimates define the boundaries within which the actual numbers lie based on the best available information[4].

tropic strains, responsible for host-to-host transmission, use CCR5 as a co-receptor, and are referred to as R5 strains. Thus, macrophages are the principal targets for the establishment of the infection in new individuals[16]. Although it is not always the case[17,18], the transition from viral isolates that use the CCR5 receptor to isolates that use the CXCR4 receptor has been linked with the transition from the latent asymptomatic phase to the clinical manifestations associated with AIDS[19,20].

The most striking feature of HIV-1 infection is the gradual depletion of circulating $CD4^+$ T cells, which leads to increased sensitivity of the patient to opportunistic and chronic infections and to oncogenesis. The cause of the $CD4^+$ T cell depletion is still under debate[21–23]. It is generally accepted, however, that during the asymptomatic phase the daily replenishment rate of $CD4^+$ T cells is much higher than the turnover of infective virus particles for the cytopathicity model to explain the progressive depletion of $CD4^+$ T cells from circulation[24]. An alternative hypothesis proposes that certain viral components contribute to dysfunction of a vital immune mechanism[25].

Over the past 23 years, the main objective in the field of HIV research has been the discovery of drugs that will combat the disease. Satisfactory progress has already been made and there are now more than 20 anti-HIV drugs approved by the American Food and Drug Administration (FDA)[26]. ARV drugs are categorized according to their mode of action into three main groups: 1) the nucleoside reverse transcriptase inhibitors (NRTI); 2) the non-nucleoside reverse transcriptase inhibitors (NNRTI)[27,28]; and 3) the protease inhibitors (PI)[29]. ARV drugs from these categories are now administered in combination (as cocktails) to produce more efficient treatment[30]. This type of therapy, termed "highly active antiretroviral therapy" or HAART, has markedly decreased mortality and morbidity in the developed world. Efforts have been made by the World Health Organization (WHO) and UNAIDS to substantially increase the number of people on HAART in developing and transitional countries[6].

Despite the fact that current antiviral treatments have improved prognosis, drug resistance and high toxicity are serious limitations to current treatments that justify the continuation of research efforts for new strategies and interventions[31,32]. Today, AIDS is treatable, and patients can have a good prognosis, but it is still not curable. A new generation of drugs was recently introduced that inhibit viral cell entry (to be discussed later). HIV entry inhibitors appear to be a rational step forward in ARV therapy, because they prevent the virus from infecting new host cells, and may potentially stop or significantly limit HIV transmission[33–35]. In order to rationally design effective drugs, the pathophysiology of HIV must be better understood for ARV therapy research to target specific events in the biology of the virus within the host cell[36,37].

HIV entry

HIV-1 predominately infects cells that have the CD4 receptor on their surface membrane, although this is not always the case[38,39]. Achievement of infection of these cells involves three discrete steps: viral attachment, then co-receptor binding, and finally fusion (see Figure 1). Recognition of the "correct" target cell and attachment to it is primarily achieved through envelope glycoprotein gp120, which binds to CD4 molecules. Gp120 is generated within the infected host cell after cleavage of gp160 by cellular proteases into two functional proteins: gp120 and gp41. It consists of 5 variable (V1-V5) and 5 conserved (C1-C5) regions[40]. Gp120 and gp41 are glycosylated in the Golgi apparatus, and then transported to the membrane that is later incorporated in the viral envelope during the budding of the viral particles to form mature viruses[41]. The envelope membrane is studded with trimers of gp120-gp41 heterodimers, where gp41 forms

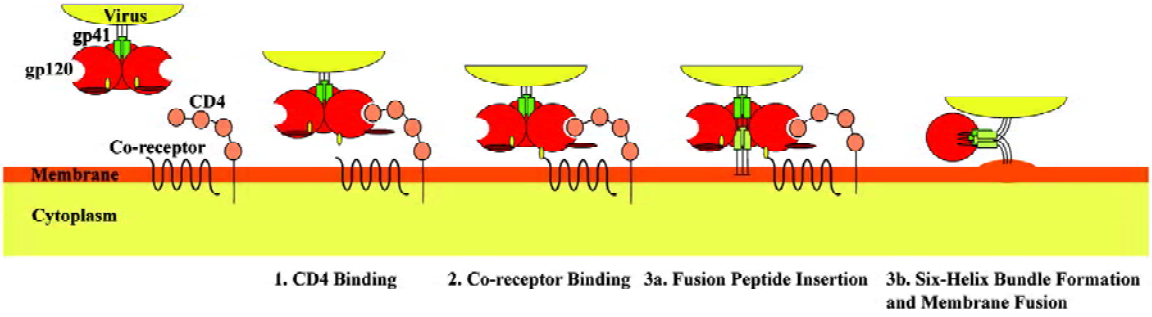

Figure 1. Schematic representation of the mechanism for HIV-1 cell entry.

the cytosolic part and gp120 the extracellular part[42].

Binding of viral gp120 to host cell CD4 is achieved through interactions of several conserved gp120 residues with the second complementarity-determining region (CDR2) of CD4[43,44]. This interaction alone is not sufficient to achieve cell entry, but it is necessary in order to identify the target cell and also to increase the affinity of other viral components for the co-receptor molecules. Indeed, binding of gp120 to CD4 causes conformational changes to the variable loop regions V1/V2 and V3 of gp120, causing the V3 loop to evaginate, thus becoming exposed to the co-receptors[45] (Figure 1). The major co-receptors that HIV-1 uses are the CCR5 and CXCR4 chemokine receptors. The exact mechanism of interaction between the variable loop regions V1/V2 and V3 and the chemokine receptors is not well understood and it merits a more detailed investigation. It has been suggested, however, that the interaction between V3 and CCR5 is ionic in nature, and results in enhancement of the process of activation-induced cell death of responding effector $CD4^+$ T cells during antigen presentation[22,46,47].

The final step for viral entry requires fusion of the viral envelope components with the target surface membrane; this is achieved with the use of gp41, which is a glycoprotein consisting of 3 main domains: an intracellular domain (endodomain), a transmembrane anchor and an extracellular domain (ectodomain). The ectodomain is the key structure responsible for fusion and consists of a hydrophobic fusion peptide sequence at the N-terminal, two hydrophobic heptad repeats (HR1 and HR2) at the C-terminal, and a hinge region, where a disulfide-bond loop is formed between the two heptad repeats during fusion[48,49]. On binding of gp120 to CD4 and subsequently to the co-receptor, further conformational changes occur that lead to gp41 dissociation from gp120. The gp41 unfolds and the hydrophobic fusion peptide sequence extends out of the viral membrane towards the host cell membrane. Insertion of the fusion peptide into the host cell membrane leads gp41 to fold into a hairpin-like structure where the two hydrophobic heptad repeats (HR1 and HR2) lie antiparallel, forming a 6-helix bundle[50,51]. This hairpin structure is believed to be responsible for the fusion of the HIV envelope to the host cell membrane.

Enfuvirtide: the first FDA-approved fusion inhibitor

Enfuvirtide (formerly known as T-20) is the first fusion inhibitor approved by the FDA and the European Commission for the Treatment of AIDS, and is available under the trade name Fuzeon (Trimeris and Roche). It is a 36 amino acid synthetic peptide homologous to the HR2 region of gp41 (residues 127-162)[52,53], that has the ability to interfere with the fusion pathway by mimicking the HR2 domain[54]. The accepted mode of action proposes that enfuvirtide targets conformational changes during fusion by binding to the HR1 domain. Recent evidence indicates that enfuvirtide interacts with multiple sites in gp41 and gp120[55]. This binding prevents the formation of the 6-helix bundle by preventing HR2 from refolding antiparallel to HR1[56,57]. Thus, inhibition of fusion of the viral envelope to cell membranes is achieved by blocking a critical step in the fusion pathway (Figure 2).

In the initial stages of discovery, enfuvirtide appeared to inhibit HIV-1 replication very effectively in various cell types and clinical trials proved to be very promising. Phase I/II trials provided proof that HIV entry was inhibited after treating patients with 100 mg enfuvirtide twice daily for 14 d. The levels of plasma HIV RNA after 14 d of treatment demonstrated a 1.96 lg median decline[58]. Phase II clinical trials were performed on 71 HIV-infected individuals who were treated with 50 mg enfuvirtide together with other ARV drugs for 48 weeks. There was a 1.0 $\log_{10}$ decline from baseline in HIV RNA and a median gain of CD4 cell counts of 84.9 cells/μL, with no significant toxicity[59].

Furthermore, two TORO (T-20 *vs* Optimized Regimens Only) Phase III clinical trials were performed in America (TORO 1) and in Europe and Australia (TORO 2). The trials had similar protocols: they compared the efficacy and safety of enfuvirtide plus an optimized antiretroviral regimen with the efficacy and safety of an optimized antiretroviral regimen alone[60,61]. In both studies the least-squares mean change from baseline in the plasma viral load indicated a significant difference in the decrease in the enfuvirtide group compared with the control ($P<0.01$). In the same way, the mean count of CD4 cells/mL was significantly greater in the enfuvirtide group compared with the controls ($P<0.01$).

Further studies are currently being performed on the exact metabolic pathway of enfuvirtide, potential drug resistance problems, and identification of synergistic interactions with other drugs. Several reports concluded that enfuvirtide does not appear to interfere with the activities of cytochrome P450, probably because it is a peptide and is easily hydrolyzed in the body[62,63]. Enfuvirtide was found to act synergistically with other potential entry inhibitors *in vitro*, such as AMD3100 and PRO542, producing results that encouraged the use of combinations of entry inhibitors as part of a new generation of ARV strategies[64,65]. However, HIV resistance has been reported in patients treated with enfuvirtide, indicating a hotspot from codons 36 to 38 of the HR1 domain[66],

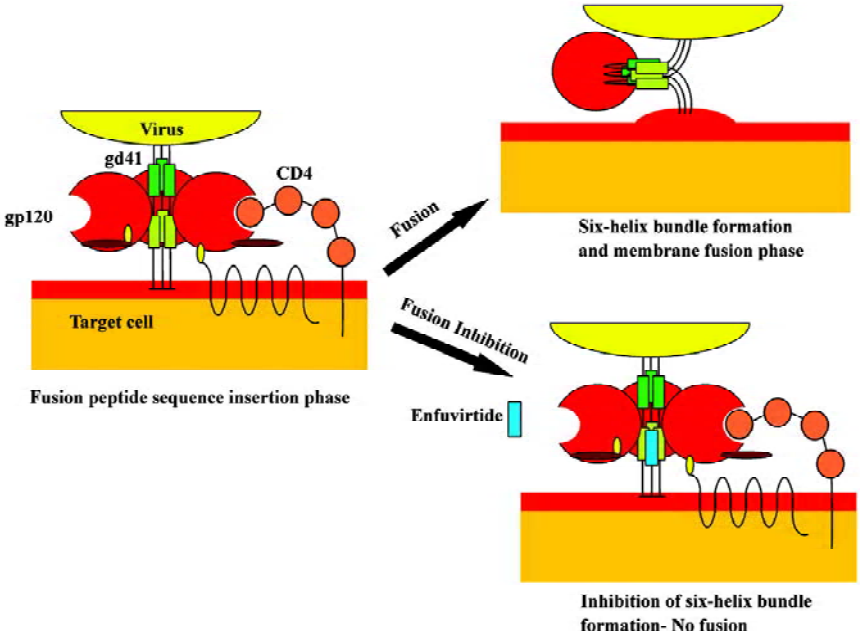

Figure 2. Mechanism of inhibition of HIV fusion to the cell membrane by enfuvirtide.

as well as other sites in gp41[67–69]. Additionally, primary resistance has been reported, which appears to be more frequent than predicted[70], indicating that more research is needed in this field.

Enfuvirtide obtained accelerated approval by the FDA in 2003 and became the 17th licensed ARV drug and the first to inhibit HIV entry. The drug is supplied as a lyophilized powder in single-dose vials containing 108 mg of the drug. Reconstitution of the powder in 1.1 mL sterile water for injection produces a single dose of 90 mg/mL[71] that is injected subcutaneously. Enfuvirtide has two currently known major drawbacks. First, being a peptide, it can only be administered by injection and not orally. This makes usage more difficult, because patients must be educated for self-administration. Second, the cost of enfuvirtide is high, because it is a synthetic peptide that is manufactured by a highly complicated process involving large amounts of raw materials[72,73]. It is estimated that the annual cost of enfuvirtide therapy is approximately US$20 000 per patient, and if taken in combination with other ARV drugs then the cost of therapy could approach US$30 000.

Potential drugs targeting entry and fusion

Attachment inhibitors Current novel antiretroviral drugs aim to interfere with the crucial HIV entry steps: viral attachment, co-receptor binding and fusion. One approach for interfering with viral attachment involves the use of a tetravalent fusion protein construct, consisting of a human IgG2 in which the Fv portions of both the heavy and light chains have been replaced with the D1 and D2 domains of human CD4[74,75]. This CD4-immunoglobulin fusion construct, called PRO 542, is suggested to bind to the viral gp120 and thus prevent the virus from interacting with CD4-bearing host cells. Phase I clinical trials indicated that PRO 542 has a half-life of 3–4 d when a relatively high dose was used (10 mg/kg), and no dose-limiting toxicities were observed[76]. In addition, in phase II clinical trials, 12 HIV-infected patients were treated with 25 mg/kg single-dose PRO 542. The drug was well tolerated and the acute reduction caused in the HIV-1 RNA was statistically significant, even in patients with advanced AIDS[77].

In the same way, several other compounds target either the gp120 or the CD4 receptor and interfere with HIV attachment. FP-21399 is a bis(disulfonapthelene) derivative that binds to gp120, most probably near the third variable domain, because interactions with antibodies against the V3 loop region were blocked[78]. A phase I study showed that it caused an increase in CD4 cell counts, and a significant decrease in viral load and minor side effects[79]. BMS-378806, a 4-methoxy-7-azaindole derivative, is a compound that can be administered orally, and was developed by Bristol Myers Squibb[80,81]. Despite the fact that phase I and II studies showed promising results, Bristol Myers Squibb decided to investigate similar drugs such as BMS-488043, an analogue of BMS-378806, in order to optimize its effectiveness[82]. A series of polyanionic compounds, for example dextrin-2-sulfate, Carraguard and PRO 2000 are in clinical trials, and

are designed to be topically administered[83–85]. Finally, TNX-355, a humanized anti-CD4 mAB that binds to CD4 without interfering with its biological function, significantly decreased viral load and increased CD4 cell counts in a phase I trial[86].

Co-receptor binding inhibitors The most interesting target in HIV entry is the co-receptor binding phase. Current drug research is focused on designing compounds that prevent the virus interacting with the chemokine receptors. The CCR5 receptor is the principal target, and a number of potential drugs are currently being studied. SCH-C is a small molecule that inhibits the binding of gp120 to CCR5, and initial *in vitro* experiments have indicated good inhibitory activity against R5 viruses as well as synergistic effects with several ARV drugs, including enfuvirtide[87,88]. Although it can be administered orally and clinical studies showed decreased viral loads, electrocardiographic anomalies due to arrhythmias were reported at high dosages[89]. Another compound, SCH-D, has been found to have greater *in vitro* and *in vivo* antiviral properties, with no apparent side effects. Clinical studies for this drug are still ongoing[90]. Interestingly, it was recently reported that V3-like peptides from X4 strains with more electropositive V3 domains were effective antagonists and potential infectivity blockers of R5 variants[91].

TAK-779 was the first non-peptidic molecule found to inhibit co-receptor attachment by binding to CCR5 at transmembrane helices 1, 2, 3, and 7[92,93]. It has the disadvantage of intravenous administration and because of irritations observed at the injection site, its development was discontinued. It was replaced by another compound, T-220, which can be administered orally, and shows promising anti-R5 HIV activity[94]. Similarly, UK-427,857 is a novel CCR5 inhibitor that has acceptable pharmacokinetic and metabolic rates in mice, rats, dogs and humans, and can be administered orally[95]. Finally, PRO 140 is one of the few monoclonal antibodies that has been used as an entry inhibitor and has been reported to block co-receptor attachment without down-modulating or inducing signaling of the CCR5 chemokine receptor[96,97].

CXCR4, the second major HIV co-receptor, is also a target for current drug research. AMD-3100, one of the first entry inhibitors, was found to inhibit viral entry well before the discovery of co-receptor usage by HIV[98]. It is a bicyclam compound of low molecular weight that inhibits the electrostatic interaction between CXCR4 and gp120 by ionic binding to the second extracellular loop (ECL2) and the adjacent membrane-spanning domain (TM4) of the CXCR4 receptor[99]. Despite the fact that in phase I and II clinical trials, intravenous administration of AMD-3100 significantly reduced the viral load[100], it was later replaced by an orally available compound, AMD-070. A non-peptidic compound, KRH-1636, which is absorbed through the duodenum, had similar efficacies to AMD-3100[101]. Finally, T-22 and ALX40-4C are positively charged peptides that occupy the V3 region and competitively inhibit binding of gp120 to the negatively charged amino acid residues on CXCR4[102–104].

In conclusion, the role of the V3 region in the mechanism of cell attachment and entry in relation to the major co-receptors is being actively pursued. In addition to biological studies, physicochemical studies on the interacting protein domains are being carried out in an attempt to decipher the interface conformations between the virus and the cell[105].

Fusion inhibitors Understanding the mechanism of fusion of the viral envelope with the host membrane played a crucial role in the development of new generation ARV drugs. This became apparent when enfuvirtide was licensed as the first viral entry inhibitor, and it is currently used in HAART. Resistance to enfuvirtide has been reported, which has led to the design of a second generation HR2 mimetic peptide. T-1249 is a 39-L-amino acid synthetic peptide that contains a pocket-binding sequence that makes the HR1 and HR2 interaction more stable. Studies on T-1249 showed that it has greater efficacy and longer half-life than enfuvirtide. Additionally, efficacy against enfuvirtide-resistant viruses has been reported, indicating that this second generation fusion inhibitor is a step forward[106,107]. However, Roche and Trimeris decided to halt clinical development due to formulation concerns[108].

5-Helix is a newly designed recombinant C-peptide that consists of 5 of the 6 helices that are formed during the fusion phase. A CHR domain is missing for the 6-helix bundle formation, and thus there is one exposed groove. This groove binds to a CHR domain in gp41 and inhibits fusion of the viral membrane to the host membrane[109]. Because it is a recombinant peptide, it has a much lower cost of production compared with the synthetic enfuvirtide. Initial studies demonstrated potent antiretroviral activity, with IC_{50} values in the low nanomolar range[110].

Finally, N-peptides represent another group of peptides with potential inhibitory effects against HIV entry. Initial studies have indicated that they are weaker inhibitors than the C-peptides, with IC_{50} values in the micromolar range. However, chimeric molecules composed of soluble trimeric coiled coils have shown promising results. IQN17 is one of the first such peptides with potent inhibitory effects, and the current most potent chimeric N-peptide, IQN23, is reported to have an IC_{50} value of 15 nmol/L[111].

Conclusion

Antiretroviral chemotherapy has recently acquired a new "weapon" in the fight against AIDS. Enfuvirtide is the first HIV entry inhibitor that was approved by FDA, and it is currently used in combination with other ARV drugs. Results from clinical trials indicated that it had potent activity against HIV strains that are resistant to other ARV drugs, although some resistance to enfuvirtide has been reported. The design of other entry inhibitors has moved forward, and every phase of HIV entry is actively pursued as a target for potential inhibitors. Probably the most exciting prospect is potential interference with co-receptor usage, particularly that of CCR5.

ARV drug development aims to produce drugs with potent antiretroviral activity, with IC_{50} values in the nanomolar range, with no or limited toxicity and that can be administered orally. Several compounds are currently in clinical trials, and we are optimistic that new, more effective drugs will be added to the ARV armory.

References

1 Barre-Sinoussi F, Chermann JC, Rey F, Nugeyre MT, Chamaret S, Gruest J, *et al*. Isolation of a T-lymphotropic retrovirus from a patient at risk for acquired immune deficiency syndrome (AIDS). Science 1983; 220: 868–71.

2 Gallo RC, Sarin PS, Gelmann EP, Robert-Guroff M, Richardson E, Kalyanaraman VS, *et al*. Isolation of human T-cell leukemia virus in acquired immune deficiency syndrome (AIDS). Science 1983; 220: 865–7.

3 HIV/AIDS Facts and figures [database on the internet]. New Delhi: WHO Reginal Office for South-East Asia . [cited 2005 Apr 20]. Available from: http://w3.whosea.org/EN/Section10/Section18/Section348.htm#Global

4 UNAIDS/WHO. AIDS Epidemic Update. Geneva: UNAIDS; 2004.

5 Gayle HD, Hill GL. Global impact of human immunodeficiency virus and AIDS. Clin Microbiol Rev 2001; 14: 327–35.

6 UNAIDS/WHO. '3 by 5' Progress Report. France: WHO; 2005.

7 Bomsel M. Transcytosis of infectious human immunodeficiency virus across a tight human epithelial cell line barrier. Nat Med 1997; 3: 42–7.

8 Ullrich R, Schmidt W, Zippel T, Schneider T, Zeitz M, Riecken EO. Mucosal HIV infection. Pathobiology 1998; 66: 145–50.

9 Dalgleish AG, Beverley PC, Clapham PR, Crawford DH, Greaves MF, Weiss RA. The CD4 (T4) antigen is an essential component of the receptor for the AIDS retrovirus. Nature 1984; 312: 763–7.

10 Klatzmann D, Champagne E, Chamaret S, Gruest J, Guetard D, Hercend T, *et al*. T-lymphocyte T4 molecule behaves as the receptor for human retrovirus LAV. Nature 1984; 312: 767–8.

11 Rucker J, Samson M, Doranz BJ, Libert F, Berson JF, Yi Y, *et al*. Regions in beta-chemokine receptors CCR5 and CCR2b that determine HIV-1 cofactor specificity. Cell 1996; 87: 437–46.

12 Roderiquez G, Oravecz T, Yanagishita M, Bou-Habib DC, Mostowski H, Norcross MA. Mediation of human immunodeficiency virus type 1 binding by interaction of cell surface heparan sulfate proteoglycans with the V3 region of envelope gp120-gp41. J Virol 1995; 69: 2233–9.

13 Berson JF, Long D, Doranz BJ, Rucker J, Jirik FR, Doms RW. A seven-transmembrane domain receptor involved in fusion and entry of T-cell-tropic human immunodeficiency virus type 1 strains. J Virol 1996; 70: 6288–95.

14 Deng H, Liu R, Ellmeier W, Choe S, Unutmaz D, Burkhart M, *et al*. Identification of a major co-receptor for primary isolates of HIV-1. Nature 1996; 381: 661–6.

15 Dragic T, Litwin V, Allaway GP, Martin SR, Huang Y, Nagashima KA, *et al*. HIV-1 entry into CD4+ cells is mediated by the chemokine receptor CC-CKR-5. Nature 1996; 381: 667–73.

16 van't Wout AB, Kootstra NA, Mulder-Kampinga GA, Albrecht-van Lent N, Scherpbier HJ, Veenstra J, *et al*. Macrophage-tropic variants initiate human immunodeficiency virus type 1 infection after sexual, parenteral, and vertical transmission. J Clin Invest 1994; 94: 2060–7.

17 de Roda Husman AM, van Rij RP, Blaak H, Broersen S, Schuitemaker H. Adaptation to promiscuous usage of chemokine receptors is not a prerequisite for human immunodeficiency virus type 1 disease progression. J Infect Dis 1999; 180: 1106–15.

18 Schuitemaker H, Koot M, Kootstra NA, Dercksen MW, de Goede RE, van Steenwijk RP, *et al*. Biological phenotype of human immunodeficiency virus type 1 clones at different stages of infection: progression of disease is associated with a shift from monocytotropic to T-cell-tropic virus population. J Virol 1992; 66: 1354–60.

19 Bjorndal A, Sonnerborg A, Tscherning C, Albert J, Fenyo EM. Phenotypic characteristics of human immunodeficiency virus type 1 subtype C isolates of Ethiopian AIDS patients. AIDS Res Hum Retroviruses 1999; 15: 647–53.

20 Richman DD, Bozzette SA. The impact of the syncytium-inducing phenotype of human immunodeficiency virus on disease progression. J Infect Dis 1994; 169: 968–74.

21 Roumier T, Castedo M, Perfettini JL, Andreau K, Metivier D, Zamzami N, *et al*. Mitochondrion-dependent caspase activation by the HIV-1 envelope. Biochem Pharmacol 2003; 66: 1321–9.

22 Zafiropoulos A, Baritaki S, Sioumpara M, Spandidos DA, Krambovitis E. V3 induces in human normal cell populations an accelerated macrophage-mediated proliferation: apoptosis phenomenon of effector T cells when they respond to their cognate antigen. Biochem Biophys Res Commun 2001; 281: 63–70.

23 Dockrell DH, Badley AD, Algeciras-Schimnich A, Simpson M, Schut R, Lynch DH, *et al*. Activation-induced CD4+ T cell death in HIV-positive individuals correlates with Fas susceptibility, CD4+ T cell count, and HIV plasma viral copy number. AIDS Res Hum Retroviruses 1999; 15: 1509–18.

24 Graziosi C, Pantaleo G, Butini L, Demarest JF, Saag MS, Shaw GM, *et al*. Kinetics of human immunodeficiency virus type 1 (HIV-1) DNA and RNA synthesis during primary HIV-1 infection. Proc Natl Acad Sci USA 1993; 90: 6405–9.

25 Krambovitis E, Zafiropoulos A, Baritaki S, Spandidos DA. Simple electrostatic interaction mechanisms in the service of HIV-1 pathogenesis. Scand J Immunol 2004; 59: 231–4.
26 De Clercq E. Antiviral drugs in current clinical use. J Clin Virol 2004; 30: 115–33.
27 Imamichi T. Action of anti-HIV drugs and resistance: reverse transcriptase inhibitors and protease inhibitors. Curr Pharm Des 2004; 10: 4039–53.
28 Zapor MJ, Cozza KL, Wynn GH, Wortmann GW, Armstrong SC. Antiretrovirals, Part II: focus on non-protease inhibitor antiretrovirals (NRTIs, NNRTIs, and fusion inhibitors). Psychosomatics 2004; 45: 524–35.
29 Dunn BM, Goodenow MM, Gustchina A, Wlodawer A. Retroviral proteases. Genome Biol 2002; 3: REVIEWS 3006.
30 Pereira CF, Paridaen JT. Anti-HIV drug development: an overview. Curr Pharm Des 2004; 10: 4005–37.
31 Johnson VA, Brun-Vezinet F, Clotet B, Conway B, D'Aquila RT, Demeter LM, *et al*. Update of the drug resistance mutations in HIV-1: 2004. Top HIV Med 2004; 12: 119–24.
32 van Heeswijk RP. Optimized antiretroviral therapy: the role of therapeutic drug monitoring and pharmacogenomics. Expert Rev Anti Infect Ther 2003; 1: 75–81.
33 Stone A. Microbicides: a new approach to preventing HIV and other sexually transmitted infections. Nat Rev Drug Discov 2002; 1: 977–85.
34 Moore JP, Shattock RJ. Preventing HIV-1 sexual transmission: not sexy enough science, or no benefit to the bottom line? J Antimicrob Chemother 2003; 52: 890–2.
35 Shattock RJ, Moore JP. Inhibiting sexual transmission of HIV-1 infection. Nat Rev Microbiol 2003; 1: 25–34.
36 Sleasman JW, Goodenow MM. 13. HIV-1 infection. J Allergy Clin Immunol 2003; 111: S582–92.
37 De Clercq E. HIV-chemotherapy and -prophylaxis: new drugs, leads and approaches. Int J Biochem Cell Biol 2004; 36: 1800–2.
38 Zerhouni B, Nelson JA, Saha K. CXCR4-dependent infection of CD8+, but not CD4+, lymphocytes by a primary human immunodeficiency virus type 1 isolate. J Virol 2004; 78: 12288–96.
39 Zerhouni B, Nelson JA, Saha K. Isolation of CD4-independent primary human immunodeficiency virus type 1 isolates that are syncytium inducing and acutely cytopathic for CD8+ lymphocytes. J Virol 2004; 78: 1243–55.
40 Farzan M, Choe H, Desjardins E, Sun Y, Kuhn J, Cao J, *et al*. Stabilization of human immunodeficiency virus type 1 envelope glycoprotein trimers by disulfide bonds introduced into the gp41 glycoprotein ectodomain. J Virol 1998; 72: 7620–5.
41 Leonard CK, Spellman MW, Riddle L, Harris RJ, Thomas JN, Gregory TJ. Assignment of intrachain disulfide bonds and characterization of potential glycosylation sites of the type 1 recombinant human immunodeficiency virus envelope glycoprotein (gp120) expressed in Chinese hamster ovary cells. J Biol Chem 1990; 265: 10373–82.
42 Yang X, Farzan M, Wyatt R, Sodroski J. Characterization of stable, soluble trimers containing complete ectodomains of human immunodeficiency virus type 1 envelope glycoproteins. J Virol 2000; 74: 5716–25.
43 Olshevsky U, Helseth E, Furman C, Li J, Haseltine W, Sodroski J. Identification of individual human immunodeficiency virus type 1 gp120 amino acids important for CD4 receptor binding. J Virol 1990; 64: 5701–7.
44 Kwong PD, Wyatt R, Robinson J, Sweet RW, Sodroski J, Hendrickson WA. Structure of an HIV gp120 envelope glycoprotein in complex with the CD4 receptor and a neutralizing human antibody. Nature 1998; 393: 648–59.
45 Sullivan N, Sun Y, Sattentau Q, Thali M, Wu D, Denisova G, *et al*. CD4-Induced conformational changes in the human immunodeficiency virus type 1 gp120 glycoprotein: consequences for virus entry and neutralization. J Virol 1998; 72: 4694–703.
46 Zafiropoulos A, Baritaki S, Vlata Z, Spandidos DA, Krambovitis E. Dys-regulation of effector CD4+ T cell function by the V3 domain of the HIV-1 gp120 during antigen presentation. Biochem Biophys Res Commun 2001; 284: 875–9.
47 Baritaki S, Zafiropoulos A, Sioumpara M, Politis M, Spandidos DA, Krambovitis E. Ionic interaction of the HIV-1 V3 domain with CCR5 and deregulation of T lymphocyte function. Biochem Biophys Res Commun 2002; 298: 574–80.
48 Bernstein HB, Tucker SP, Kar SR, McPherson SA, McPherson DT, Dubay JW, *et al*. Oligomerization of the hydrophobic heptad repeat of gp41. J Virol 1995; 69: 2745–50.
49 Chambers P, Pringle CR, Easton AJ. Heptad repeat sequences are located adjacent to hydrophobic regions in several types of virus fusion glycoproteins. J Gen Virol 1990; 71: 3075–80.
50 Lu M, Blacklow SC, Kim PS. A trimeric structural domain of the HIV-1 transmembrane glycoprotein. Nat Struct Biol 1995; 2: 1075–82.
51 Weissenhorn W, Dessen A, Harrison SC, Skehel JJ, Wiley DC. Atomic structure of the ectodomain from HIV-1 gp41. Nature 1997; 387: 426–30.
52 Wild C, Oas T, McDanal C, Bolognesi D, Matthews T. A synthetic peptide inhibitor of human immunodeficiency virus replication: correlation between solution structure and viral inhibition. Proc Natl Acad Sci USA 1992; 89: 10537–41.
53 Wild CT, Shugars DC, Greenwell TK, McDanal CB, Matthews TJ. Peptides corresponding to a predictive alpha-helical domain of human immunodeficiency virus type 1 gp41 are potent inhibitors of virus infection. Proc Natl Acad Sci USA 1994; 91: 9770–4.
54 Chen CH, Matthews TJ, McDanal CB, Bolognesi DP, Greenberg ML. A molecular clasp in the human immunodeficiency virus (HIV) type 1 TM protein determines the anti-HIV activity of gp41 derivatives: implication for viral fusion. J Virol 1995; 69: 3771–7.
55 Liu S, Lu H, Niu J, Xu Y, Wu S, Jiang S. Different from the HIV fusion inhibitor C34, the anti-HIV drug Fuzeon (T-20) inhibits HIV-1 entry by targeting multiple sites in gp41 and gp120. J Biol Chem 2005; 280: 11259–73.
56 Lawless MK, Barney S, Guthrie KI, Bucy TB, Petteway SR Jr., Merutka G. HIV-1 membrane fusion mechanism: structural studies of the interactions between biologically-active peptides from gp41. Biochemistry 1996; 35: 13697–708.
57 Furuta RA, Wild CT, Weng Y, Weiss CD. Capture of an early fusion-active conformation of HIV-1 gp41. Nat Struct Biol 1998; 5: 276–9.
58 Kilby JM, Hopkins S, Venetta TM, DiMassimo B, Cloud GA, Lee JY, *et al*. Potent suppression of HIV-1 replication in humans by T-20, a peptide inhibitor of gp41-mediated virus entry.

Nat Med 1998; 4: 1302–7.
59 Lalezari JP, Eron JJ, Carlson M, Cohen C, DeJesus E, Arduino RC, *et al*. A phase II clinical study of the long-term safety and antiviral activity of enfuvirtide-based antiretroviral therapy. Aids 2003; 17: 691–8.
60 Lalezari JP, Henry K, O'Hearn M, Montaner JS, Piliero PJ, Trottier B, *et al*. Enfuvirtide, an HIV-1 fusion inhibitor, for drug-resistant HIV infection in North and South America. N Engl J Med 2003; 348: 2175–85.
61 Lazzarin A, Clotet B, Cooper D, Reynes J, Arasteh K, Nelson M, *et al*. Efficacy of enfuvirtide in patients infected with drug-resistant HIV-1 in Europe and Australia. N Engl J Med 2003; 348: 2186–95.
62 Zhang X, Lalezari JP, Badley AD, Dorr A, Kolis SJ, Kinchelow T, *et al*. Assessment of drug-drug interaction potential of enfuvirtide in human immunodeficiency virus type 1-infected patients. Clin Pharmacol Ther 2004; 75: 558–68.
63 Ruxrungtham K, Boyd M, Bellibas SE, Zhang X, Dorr A, Kolis S, *et al*. Lack of interaction between enfuvirtide and ritonavir or ritonavir-boosted saquinavir in HIV-1-infected patients. J Clin Pharmacol 2004; 44: 793–803.
64 Tremblay CL, Kollmann C, Giguel F, Chou TC, Hirsch MS. Strong *in vitro* synergy between the fusion inhibitor T-20 and the CXCR4 blocker AMD-3100. J Acquir Immune Defic Syndr 2000; 25: 99–102.
65 Nagashima KA, Thompson DA, Rosenfield SI, Maddon PJ, Dragic T, Olson WC. Human immunodeficiency virus type 1 entry inhibitors PRO 542 and T-20 are potently synergistic in blocking virus-cell and cell-cell fusion. J Infect Dis 2001; 183: 1121–5.
66 Rimsky LT, Shugars DC, Matthews TJ. Determinants of human immunodeficiency virus type 1 resistance to gp41-derived inhibitory peptides. J Virol 1998; 72: 986–93.
67 Wei X, Decker JM, Liu H, Zhang Z, Arani RB, Kilby JM, *et al*. Emergence of resistant human immunodeficiency virus type 1 in patients receiving fusion inhibitor (T-20) monotherapy. Antimicrob Agents Chemother 2002; 46: 1896–905.
68 Poveda E, Rodes B, Toro C, Martin-Carbonero L, Gonzalez-Lahoz J, Soriano V. Evolution of the gp41 env region in HIV-infected patients receiving T-20, a fusion inhibitor. Aids 2002; 16: 1959–61.
69 Xu L, Pozniak A, Wildfire A, Stanfield-Oakley SA, Mosier SM, Ratcliffe D, *et al*. Emergence and evolution of enfuvirtide resistance following long-term therapy involves heptad repeat 2 mutations within gp41. Antimicrob Agents Chemother 2005; 49: 1113–9.
70 Carmona R, Perez-Alvarez L, Munoz M, Casado G, Delgado E, Sierra M, *et al*. Natural resistance-associated mutations to Enfuvirtide (T20) and polymorphisms in the gp41 region of different HIV-1 genetic forms from T20 naive patients. J Clin Virol 2005; 32: 248–53.
71 Fuzeon [package insert]. Injection Instructions. Durham, NC, and Nutley, NJ: Trimeris Inc and Roche Laboratories Inc; 2003.
72 Steinbrook R. HIV infection: a new drug and new costs. N Engl J Med 2003; 348: 2171–2.
73 Tashima KT, Carpenter CC. Fusion inhibition: a major but costly step forward in the treatment of HIV-1. N Engl J Med 2003; 348: 2249–50.
74 Allaway GP, Davis-Bruno KL, Beaudry GA, Garcia EB, Wong EL, Ryder AM, *et al*. Expression and characterization of CD4-IgG2, a novel heterotetramer that neutralizes primary HIV type 1 isolates. AIDS Res Hum Retroviruses 1995; 11: 533–9.
75 Trkola A, Pomales AB, Yuan H, Korber B, Maddon PJ, Allaway GP, *et al*. Cross-clade neutralization of primary isolates of human immunodeficiency virus type 1 by human monoclonal antibodies and tetrameric CD4-IgG. J Virol 1995; 69: 6609–17.
76 Jacobson JM, Lowy I, Fletcher CV, O'Neill TJ, Tran DN, Ketas TJ, Trkola A, *et al*. Single-dose safety, pharmacology, and antiviral activity of the human immunodeficiency virus (HIV) type 1 entry inhibitor PRO 542 in HIV-infected adults. J Infect Dis 2000; 182: 326–9.
77 Jacobson JM, Israel RJ, Lowy I, Ostrow NA, Vassilatos LS, Barish M, *et al*. Treatment of advanced human immunodeficiency virus type 1 disease with the viral entry inhibitor PRO 542. Antimicrob Agents Chemother 2004; 48: 423–9.
78 Ono M, Wada Y, Wu Y, Nemori R, Jinbo Y, Wang H, *et al*. FP-21399 blocks HIV envelope protein-mediated membrane fusion and concentrates in lymph nodes. Nat Biotechnol 1997; 15: 343–8.
79 Dezube BJ, Dahl TA, Wong TK, Chapman B, Ono M, Yamaguchi N, *et al*. A fusion inhibitor (FP-21399) for the treatment of human immunodeficiency virus infection: a phase I study. J Infect Dis 2000; 182: 607–10.
80 Lin PF, Blair W, Wang T, Spicer T, Guo Q, Zhou N, *et al*. A small molecule HIV-1 inhibitor that targets the HIV-1 envelope and inhibits CD4 receptor binding. Proc Natl Acad Sci USA 2003; 100: 11013–8.
81 Si Z, Madani N, Cox JM, Chruma JJ, Klein JC, Schon A, *et al*. Small-molecule inhibitors of HIV-1 entry block receptor-induced conformational changes in the viral envelope glycoproteins. Proc Natl Acad Sci USA 2004; 101: 5036–41.
82 Hanna G, Lalezari J, Hellinger J, Wohl D, Masterson T, Fiske W, *et al*. Antiviral activity, safety, and tolerability of a novel, oral small-molecule HIV-1 attachment inhibitor, BMS-488043, in HIV-1-infected subjects. In: Proceedings of the 11th conference on retroviruses and opportunistic infections; 2004 Feb 8-11, San Francisco. 2004.
83 Shaunak S, Thornton M, John S, Teo I, Peers E, Mason P, *et al*. Reduction of the viral load of HIV-1 after the intraperitoneal administration of dextrin 2-sulphate in patients with AIDS. Aids 1998; 12: 399–409.
84 Dezzutti CS, James VN, Ramos A, Sullivan ST, Siddig A, Bush TJ, *et al*. In vitro comparison of topical microbicides for prevention of human immunodeficiency virus type 1 transmission. Antimicrob Agents Chemother 2004; 48: 3834–44.
85 Morrow K, Rosen R, Richter L, Emans A, Forbes A, Day J, *et al*. The acceptability of an investigational vaginal microbicide, PRO 2000 Gel, among women in a phase I clinical trial. J Womens Health (Larchmt) 2003; 12: 655–66.
86 Kuritzkes DR, Jacobson J, Powderly WG, Godofsky E, DeJesus E, Haas F, *et al*. Antiretroviral activity of the anti-CD4 monoclonal antibody TNX-355 in patients infected with HIV type 1. J Infect Dis 2004; 189: 286–91.
87 Tremblay CL, Giguel F, Kollmann C, Guan Y, Chou TC, Baroudy BM, *et al*. Anti-human immunodeficiency virus interactions of SCH-C (SCH 351125), a CCR5 antagonist, with other antiret-

roviral agents *in vitro*. Antimicrob Agents Chemother 2002; 46: 1336–9.
88 Tsamis F, Gavrilov S, Kajumo F, Seibert C, Kuhmann S, Ketas T, *et al*. Analysis of the mechanism by which the small-molecule CCR5 antagonists SCH-351125 and SCH-350581 inhibit human immunodeficiency virus type 1 entry. J Virol 2003; 77: 5201–8.
89 Reynes J, Rouzier R, Kanouni T, Baillat V, Baroudy B, Keung A. SCH C: Safety and antiviral effects of a CCR5 receptor antagonist in HIV-1-infected subjects. In: Proceedings of the 9th conference on retroviruses and opportunistic infections; 2002 Feb 24-28, San Francisco. 2002
90 Schurmann D, Rouzier R, Nougarede R, Reynes J, Fatkenheuer G, Raffi F, *et al*. SCH D: Antiviral activity of a CCR5 receptor antagonist. In: Proceedings of the 11th conference on retroviruses and opportunistic infections, 2004 Feb 8-11, San Francisco. 2004.
91 Baritaki S, Dittmar MT, Spandidos DA, Krambovitis E. *In vitro* inhibition of R5 HIV-1 infectivity by X4 V3-derived synthetic peptides. Int J Mol Med 2005; 16: 333–6.
92 Baba M, Nishimura O, Kanzaki N, Okamoto M, Sawada H, Iizawa Y, *et al*. A small-molecule, nonpeptide CCR5 antagonist with highly potent and selective anti-HIV-1 activity. Proc Natl Acad Sci USA 1999; 96: 5698–703.
93 Dragic T, Trkola A, Thompson DA, Cormier EG, Kajumo FA, Maxwell E, *et al*. A binding pocket for a small molecule inhibitor of HIV-1 entry within the transmembrane helices of CCR5. Proc Natl Acad Sci USA 2000; 97: 5639–44.
94 Iizawa Y, Kanzaki N, Takashima K, Miyake H, Tagawa Y, Sugihara Y, *et al*. Anti-HIV-1 Activity of TAK-220, a Small Molecule CCR5 Antagonist. In: Proceedings of the 10th conference on retroviruses and opportunistic infections, 2003 Feb 10-14, San Francisco. 2003.
95 Walker DK, Abel S, Comby P, Muirhead GJ, Nedderman AN, Smith DA. Species differences in the disposition of the CCR5 antagonist, UK-427,857, a new potential treatment for HIV. Drug Metab Dispos 2005; 33: 587–95.
96 Olson WC, Rabut GE, Nagashima KA, Tran DN, Anselma DJ, Monard SP, *et al*. Differential inhibition of human immunodeficiency virus type 1 fusion, gp120 binding, and CC-chemokine activity by monoclonal antibodies to CCR5. J Virol 1999; 73: 4145–55.
97 Trkola A, Ketas TJ, Nagashima KA, Zhao L, Cilliers T, Morris L, *et al*. Potent, broad-spectrum inhibition of human immunodeficiency virus type 1 by the CCR5 monoclonal antibody PRO 140. J Virol 2001; 75: 579–88.
98 de Clercq E, Yamamoto N, Pauwels R, Balzarini J, Witvrouw M, De Vreese K, *et al*. Highly potent and selective inhibition of human immunodeficiency virus by the bicyclam derivative JM3100. Antimicrob Agents Chemother 1994; 38: 668–74.
99 Labrosse B, Brelot A, Heveker N, Sol N, Schols D, De Clercq E, *et al*. Determinants for sensitivity of human immunodeficiency virus coreceptor CXCR4 to the bicyclam AMD3100. J Virol 1998; 72: 6381–8.
100 Hendrix CW, Flexner C, MacFarland RT, Giandomenico C, Fuchs EJ, Redpath E, *et al*. Pharmacokinetics and safety of AMD-3100, a novel antagonist of the CXCR-4 chemokine receptor, in human volunteers. Antimicrob Agents Chemother 2000; 44: 1667–73.
101 Ichiyama K, Yokoyama-Kumakura S, Tanaka Y, Tanaka R, Hirose K, *et al*. A duodenally absorbable CXC chemokine receptor 4 antagonist, KRH-1636, exhibits a potent and selective anti-HIV-1 activity. Proc Natl Acad Sci USA 2003; 100: 4185–90.
102 Doranz BJ, Grovit-Ferbas K, Sharron MP, Mao SH, Goetz MB, Daar ES, *et al*. A small-molecule inhibitor directed against the chemokine receptor CXCR4 prevents its use as an HIV-1 coreceptor. J Exp Med 1997; 186: 1395–400.
103 Murakami T, Nakajima T, Koyanagi Y, Tachibana K, Fujii N, Tamamura H, *et al*. A small molecule CXCR4 inhibitor that blocks T cell line-tropic HIV-1 infection. J Exp Med 1997; 186: 1389–93.
104 Murakami T, Zhang TY, Koyanagi Y, Tanaka Y, Kim J, Suzuki Y, *et al*. Inhibitory mechanism of the CXCR4 antagonist T22 against human immunodeficiency virus type 1 infection. J Virol 1999; 73: 7489–96.
105 Galanakis PA, Spyroulias GA, Rizos A, Samolis P, Krambovitis E. Conformational properties of HIV-1 gp120/V3 immunogenic domains. Curr Med Chem 2005; 12: 551–68.
106 Eron JJ, Gulick RM, Bartlett JA, Merigan T, Arduino R, Kilby JM, *et al*. Short-term safety and antiretroviral activity of T-1249, a second-generation fusion inhibitor of HIV. J Infect Dis 2004; 189: 1075–83.
107 Lalezari JP, Bellos NC, Sathasivam K, Richmond GJ, Cohen CJ, Myers RA, *et al*. T-1249 retains potent antiretroviral activity in patients who had experienced virological failure while on an enfuvirtide-containing treatment regimen. J Infect Dis 2005; 191: 1155–63.
108 Martin-Carbonero L. Discontinuation of the clinical development of fusion inhibitor T-1249. AIDS Rev 2004; 6: 61–3.
109 Root MJ, Kay MS, Kim PS. Protein design of an HIV-1 entry inhibitor. Science 2001; 291: 884–8.
110 Root MJ, Hamer DH. Targeting therapeutics to an exposed and conserved binding element of the HIV-1 fusion protein. Proc Natl Acad Sci USA 2003; 100: 5016–21.
111 Eckert DM, Kim PS. Design of potent inhibitors of HIV-1 entry from the gp41 N-peptide region. Proc Natl Acad Sci USA 2001; 98: 11187–92.

Acta Pharmacologica Sinica 2005 Oct; 26 (10): 1174

Comment

Perfect high throughput screening assay: a crucial technique for drug discovery

Guan-hua DU[1]

Institute of Materia Medica, Peking Union Medical College & Chinese Academy of Medical Sciences, Beijing 100050, China

[1] Correspondence to Prof Guan-hua DU. Phn 86-10-6316-5184. Fax 86-10-6301-7757. E-mail dugh@imm.ac.cn

Received 2005-08-14
Accepted 2005-08-24

doi: 10.1111/j.1745-7254.2005.00215.x

Since being developed approximately 20 years ago, high throughput screening (HTS) has become one of the key techniques used in drug discovery[1]. However, three main problems are recognized with the use of HTS; namely, with the compound library, drug targets, and assay methods. Until now, the compound library has evolved based on the techniques of combinatorial chemistry and modern phytochemistry. Several functional proteins have emerged following the advance of genomics and proteomics. However, although many functional proteins have been discovered recently, they are not, as sometimes claimed, real drug targets; at best, they might be potential drug targets. The ideal targets selected for drug screening should qualify as drug targets[2]. The selection of targets for drug screening is a crucial procedure in drug screening.

However, the main problem for drug discovery is in finding drugs or candidates based on the targets and compounds[3]. There are many different techniques used in drug discovery, such as virtual screening, and computer aid molecular design. However, all of the active compounds should be evaluated using biological methods. Therefore, establishing a novel biological assay is very important for drug screening in HTS. The assays used in HTS require high sensitivity and high stability, and must be performed automatically. The homogeneous assay is a simple and useful method for drug screening. It is suitable for automatic performance and can enhance the efficiency of screening, especially in HTS. Therefore, the homogenous system has become the favored technique in HTS.

The basic goal of small-molecule screening is to identify chemically "interesting" starting points for elaboration towards a drug[4]. The establishment of new screening assays will promote the discovery of lead compounds or candidates[5]. The HTS has been used in China since 1998 and, since then, experts have attempted to resolve some key problems with HTS, such as with target validation, compound collection, and assay establishment[6]. In the current issue of *Acta Pharmacologica Sinica*, Dr Ming-wei WANG *et al.* introduced a homogeneous high throughput drug screening assay based on scintillation proximity assay technology for the identification of ligands of subunit acetylcholine receptors[7]. This assay is not only in a homogeneous system, but has a new target, a subunit of the acetylcholine receptor. The assay of homogeneous binding for $\alpha4\beta2$ nicotinic acetylcholine receptor is a new assay for HTS to screen for ligands of $\alpha4\beta2$ nicotinic acetylcholine receptors. This assay, with state-of-the-art design and interesting targets can be performed easily and automatically. The lead compound is valuable for new drug development and might also be used for validating the functions of the $\alpha4\beta2$ nicotinic acetylcholine receptor. Screening with this assay might help us find new drugs with new mechanisms.

References

1 Bleicher KH, Bohm HJ, Muller K, Alanine AI. Hit and lead generation: beyond high-throughput screening. Nat Rev Drug Discov 2003; 2: 369–78.
2 Du GH, Liu AL. Application of bioinformatics in the high throughput screening. In: Zhen YS, editor. Anticancer drug research and development. Beijing: Chemical Industrial Press; 2004. p199–216.
3 Archer JR. History, evolution, and trends in compound management for high throughput screening. Assay Drug Dev Technol 2004; 2: 675–81.
4 Walters WP, Namchuk M. Designing screens: how to make your hits a hit. Nat Rev Drug Discov 2003; 2: 259–66.
5 Comess KM, Schurdak ME. Affinity-based screening techniques for enhancing lead discovery. Curr Opin Drug Discov Devel 2004; 7: 411–6.
6 Du GH. High throughput pharmaceutical screening in China. Acta Pharm Sin 2000; 35 (Suppl): 14–7.
7 Hui X, Gao J, Xie X, Suto N, Ogiku T, Wang MW. A robust homogeneous binding assay for $\alpha4\beta2$ nicotinic acetylcholine receptor. Acta Pharmacol Sin 2005: 26: 1175–80.

Acta Pharmacologica Sinica 2005 Oct; 26 (10): 1175–1180

Full-length article

A robust homogeneous binding assay for α4β2 nicotinic acetylcholine receptor[1]

Xin HUI[2], Jie GAO[2], Xin XIE[2], Naoki SUTO[3], Tsuyoshi OGIKU[3], Ming-Wei WANG[2,4]

[2]*The National Center for Drug Screening, Shanghai Institute of Materia Medica, Shanghai Institutes for Biological Sciences, Chinese Academy of Sciences, Graduate School of Chinese Academy of Sciences, Shanghai 201203, China;* [3]*Discovery and Pharmacology Research Laboratories, Tanabe Seiyaku Co, 2-50, Kawagishi 2-Chome, Toda, Saitama 335-8505, Japan*

Key words

nicotinic acetylcholine receptor; scintillation proximity assay; high-throughput screening

[1] Project supported in part by grants from the Ministry of Science and Technology of China (2002AA2Z343A and 2004CB518902), Chinese Academy of Sciences (KSCX1-SW-11-2) and Shanghai Pharmaceutical (Group) Co.
[4] Correspondence to Dr Ming-wei WANG.
Phn 86-21-5080-0598.
Fax 86-21-5080-0721.
E-mail mwwang@siniwest.com

Received 2005-04-26
Accepted 2005-08-02

doi: 10.1111/j.1745-7254.2005.00202.x

Abstract

Aim: To develop a homogeneous high-throughput screening (HTS) assay based on scintillation proximity assay (SPA) technology for identification of novel α4β2 nicotinic acetylcholine receptor (nAChR) modulators. **Methods:** Membrane preparation of HEK293 cells expressing α4β2 nAChR, [^{3}H]cytisine and wheat germ agglutinin (WGA)-coupled microbeads were used to develop an HTS assay based on SPA technology. This method was validated against a conventional filter binding approach and applied to large-scale screening of a library containing 32 000 synthetic compounds. Intracellular calcium measurement was carried out to verify the bioactivities of the hits found by the SPA assay. **Results:** IC_{50} values of 2 reference compounds (epibatidine and RJR 2403) determined by SPA and filter binding methods were comparable and consistent with those reported elsewhere. A total of 54 compounds, showing more than 60% competitive inhibition on [^{3}H]cytisine binding to α4β2 nAChR, were identified initially following an HTS campaign. Secondary screening confirmed that 17 compounds with novel chemical structures possessed relatively high binding affinity to α4β2 nAChR (K_i<2 μmol/L). Eight compounds displayed antagonistic effects with >50% inhibition on ABT-594-induced calcium mobilization while none showed any agonist activity. **Conclusions:** This homogeneous binding assay is a highly efficient, amenable to automation and robust tool to screen potential α4β2 nAChR modulators in an HTS setting. Its application may be expanded to other membrane receptors and ion channels.

Introduction

Nicotinic acetylcholine receptors (nAChR) are excitatory ligand-gated ion channels mainly distributed in the central and peripheral nervous systems, neuromuscular junctions and adrenal glands[1]. The nAChR channel complex is composed of 5 protein subunits, which form a pore that is permeable to Na^+, K^+, and Ca^{2+}. To date, α, β, γ, δ, and ε subunits have been cloned, with 9 different α and 4 varieties of β subunits identified[2]. The α4β2 is the predominant nAChR subtype in the mammalian brain and has a high affinity for nicotine. nAChR consisting of α4 and β2 subunits modulates neurotransmitter release and plays a direct role in nicotine addiction. This group of nAChR was implicated in the pathological pathways of Alzheimer disease, Parkinson disease, schizophrenia, epilepsy and pain[3].

The anti-nociceptive effects of (–)-nicotine have been known for over 60 years. This non-selective nAChR agonist could not be applied as an analgesic agent due to serious adverse events. Although (–)-epibatidine is a highly selective α4β2 nAChR agonist that displays a more potent analgesic activity than morphine in nociceptive tests[4], toxicities in the cardiovascular and central nervous systems rendered it unsuitable for therapeutic use[5]. Therefore, a primary goal in the development of novel analgesic agents based on α4β2 nAChR is to discover subtype-specific ago-

nists with less liability.

An accurate and robust receptor-binding assay is highly desirable to screen a large collection of chemical entities. Associated techniques are generally based on absorbance, fluorescence and radiometric assays. Scintillation proximity assay (SPA), because of its simplicity and high-throughput nature, has broad applications in measuring receptor-ligand interactions and enzyme reactions. Conventional filter binding assays involve 1 or more separation steps and, thus, are laborious, non-homogeneous and not suitable for automation. SPA technology[6], on the other hand, provides a homogeneous screening approach that does not require post-reaction liquid handling steps and is well suited to automation and high-throughput screening (HTS). Briefly, the receptor is anchored to a scintillant-impregnated microbead. When an isotope (eg, [^{3}H]) is brought very close to the microbead by binding to its surface, it activates the scintillant leading to light emission. Because the emitted β particles or augur electrons can only travel short distances in the bulk solution, the microbead preferentially captures electrons from the bound radiolabeled ligand. Therefore, the amount of light emitted from the scintillant in the microbead is directly proportional to the amount of bound radiolabeled ligand. In the present paper, we describe a simple SPA method to assess specific binding properties of various known ligands to α4β2 nAChR. It was further validated and optimized in the context of HTS for a library containing 32 000 synthetic compounds. More than a dozen compounds with novel chemical structures were found to have relatively high binding affinity to α4β2 nAChR and 8 of them showed significant antagonist activities in a functional assay.

Materials and methods

Reagents Potassium chloride, sodium phosphate monobasic anhydrous, and magnesium chloride haxahydrate were purchased from Shanghai Chemical Co (Shanghai, China). Aprotinin and leupeptin were purchased from Merck KGaA (Darmstadt, Germany). RJR 2403 and epibatidine were purchased from Sigma-Aldrich (St Louis, MO, USA). [^{3}H] Cytisine (37 Ci/mmol) was obtained from Amersham Biosciences UK (Buckinghamshire, UK). FlashBlue™ GPCR beads, Isoplate™ and Filtermat B made of glass fiber were bought from PerkinElmer Life and Analytical Sciences (Boston, MA, USA).

Cell culture and membrane preparation The full-length cDNA of the α4 (GenBank Accession No L35901) and β2 (GenBank Accession No U62437) subunits of nAChR were cloned into pcDNA3.1 (Invitrogen, Carlsbad, CA, USA) and pIRESpuro2 (BD Clontech, Mountain View, CA, USA), respectively. They were subsequently cotransfected into HEK293 cells and clones stably expressing α4β2 nAChR were selected and characterized by calcium mobilization assay[7]. The cells were maintained in Dulbecco's modified Eagle's medium (DMEM) (Sigma) containing 10% fetal calf serum (FCS) in the presence of penicillin (100 mg/L), streptomycin (100 mg/L), G418 (400 mg/L) and puromycin (5 mg/L) at 37 °C in a humidified atmosphere of 5% CO_2. For membrane preparation, cells were treated with 0.25% trypsin (Sigma) for 5 min and centrifuged at 1000×*g* for 10 min. The pellets were resuspended in hypotonic buffer [50 mmol/L Tris-HCl, pH 7.5, 5 mmol/L ethylenediaminetetracetic acid (EDTA)] and homogenized with a BioNeb® cell disruption system (Glas-Col, Terre Haute, IN, USA) followed by centrifugation at 1200×*g*, 4 °C for 20 min to precipitate nuclear debris. The supernatant was then centrifuged at 20 000×*g* for 30 min to pellet the membrane. The latter was resuspended in 50 mmol/L Tris-HCl, pH 7.5, 5 mmol/L EDTA with 30% (w/v) sucrose. The protein content was determined using a spectrophotometer (Thermo Electron, Waltham, MA, USA).

Filter binding assay Various amounts of the above membrane receptor preparation, 3 nmol/L [^{3}H]cytisine and different concentrations of known ligands to α4β2 nAChR were added to the binding buffer (50 mmol/L Tris HCl, 120 mmol/L NaCl, 5 mmol/L KCl, 1 mmol/L $MgCl_2$, 2.5 mmol/L $CaCl_2$, pH 7.4) to give a final volume of 0.1 mL. After incubation at 4 °C for 8 h, the membrane fraction was harvested on the Filtermat B presoaked with a solution consisting of the washing buffer (50 mmol/L Tris HCl, pH 7.4) and 0.5% (v/v) polyethyleneimine. The Filtermat B was washed 3 times with the washing buffer and dried at 55 °C for 45 min before counting on a Microbeta scintillation counter (PerkinElmer). Nonspecific binding activity was determined in the presence of 2 μmol/L epibatadine.

SPA binding assay Various amounts of the above membrane receptor preparation, 3 nmol/L [^{3}H]cytisine, FlashBlue™ GPCR beads (62.5 μg/well) and different concentrations of known ligands to α4β2 nAChR were added to the binding buffer to give a final volume of 0.1 mL. The plates were incubated at 4 °C for 12 h and centrifuged for 3 min at 2500×*g* before counting on the Microbeta scintillation counter.

Calcium mobilization assay The above cells expressing α4β2 nAChR were detached and loaded with 5 μmol/L Fluo-4 (Molecular Probes, Eugene, OR, USA) in culture medium supplemented with 2.5 mmol/L probenecid (Sigma) for 45 min. They were then washed twice with solB buffer containing: 10 mmol/L HEPES, 5 mmol/L NaCl, 5 mmol/L KCl, 2 mmol/L

$CaCl_2$, 140 mmol/L *N*-methyl-D-glucamine and 10 mmol/L glucose (pH 7.4). The cells were resuspended in solB buffer, plated onto 96-well plates at a density of 60 000 cells in 80 μL per well, and reattached by centrifugation. Effects of the hit compounds on calcium influx were analyzed by FlexStation™ (Molecular Devices, Sunnyvale, CA, USA) with excitation wavelength 485 nm and emission wavelength 525 nm. An α4β2 nAChR agonist, ABT-594[8], was used as a positive control.

HTS campaign The compound library used for screening consisted of 32 000 pure synthetic compounds. A 10-compound pool per well mix was applied to the primary screening, with an average concentration of 7 μmol/L for each compound dissolved in 100% dimethylsulphoxide (Me_2SO) solution. This matrix system maximizes the advantage of HTS and allows duplicate screening of each compound[9]. In each 96-well Isoplate™, 16 wells were used as positive controls (epibitadine) and samples showing greater than 60% inhibition were considered as "hits".

Data analysis Data were analyzed using GraphPad Prism software (GraphPad, San Diego, CA, USA). Non-linear regression analyses were performed to generate dose-response curves. K_i values were calculated from IC_{50} using the equation of Cheng and Prusoff[10].

$$K_i = \frac{IC_{50}}{1 + \frac{[\text{radioligand}]}{K_d}}$$

Results

Assay optimization For HTS purposes, 96-well microtiter plates were used and reaction volume was adjusted to 100 μL/well. At a concentration equivalent to the previously reported K_d value (~0.5 nmol/L)[11], more than 25% of [^{3}H] cytisine added was bound to the receptor (data not shown). To avoid excessive ligand depletion, the concentration was increased to 3 nmol/L, in which the bound form accounted for less than 10%. The best signal-to-background (S/B) ratio was observed in a matrix experiment when 62.5 μg/well microbeads and 10 μg/well membrane preparation were used. However, 5 μg/well was selected for the HTS campaign to conserve the membrane preparation. Under these assay conditions, a sound S/B ratio (~30) was achieved (Figure 1). Me_2SO, at concentrations below 3%, did not affect the assay performance (data not shown).

Binding saturation A serial titration of [^{3}H]cytisine was prepared to study binding characteristics of the SPA assay (Figure 2). The B_{max} and K_d values calculated from the SPA and filter binding assays were strikingly similar: 2.26 pmol/mg *vs* 2.31 pmol/mg and 0.65 nmol/L *vs* 0.70 nmol/L, respectively.

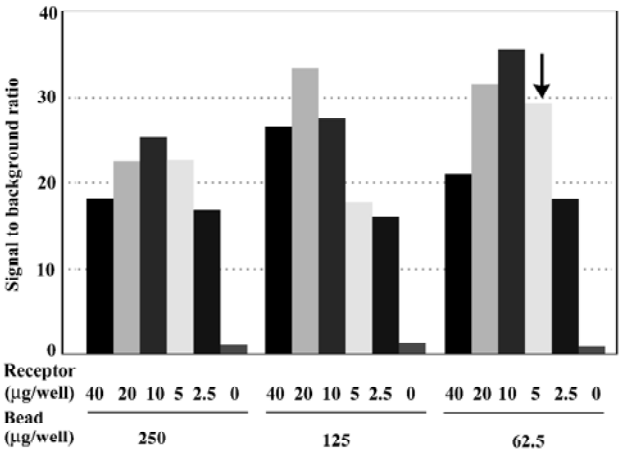

Figure 1. Assay optimization. Different concentrations of FlashBlue™ GPCR beads and membrane preparation were mixed in the presence of 3 nmol/L of [^{3}H]cytisine. Unlabeled epibatidine was included at a concentration of 2 μmol/L to determine non-specific binding. The signal was measured after 12 h incubation using a MicroBeta scintillation counter. The arrow indicates the conditions to be optimised.

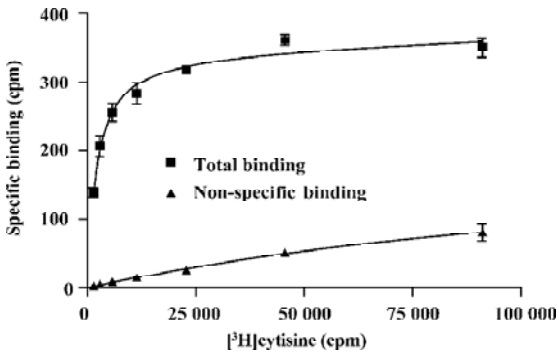

Figure 2. Saturation study in the scintillation proximity assay. A series titration of [^{3}H]cytisine was made to determine receptor binding characteristics in the presence and absence of 2 μmol epibatidine. *n*=3. Mean±SD.

Assay performance As shown in Figure 3, the average Z' value for the SPA binding assay was 0.78 with a S/B ratio of 29, indicating that the system was adequately optimized for HTS. Assay stability was evaluated by incubating the plates overnight at 4 °C and both the Z' factor and the S/B ratio remained unchanged. Two known α4β2 nAChR ligands, namely, epibatidine and RJR2403, were used to compare the 2 assay methods and the binding affinities measured were within the same range (Figure 4).

HTS campaign Of the 32 000 samples initially screened, 54 hits (0.17%) showing greater than 60% competitive inhibition on [^{3}H]cytisine binding to α4β2 nAChR were discov-

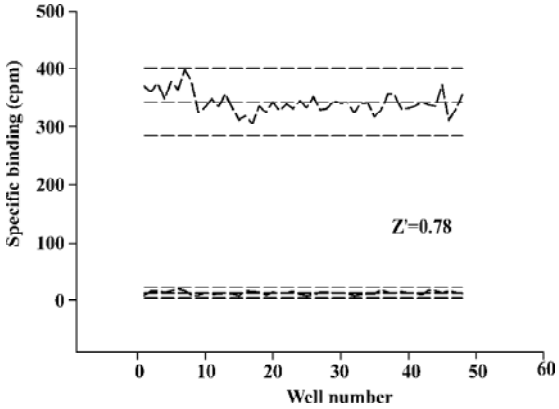

Figure 3. Z' factor determination. Assays were performed at optimized conditions (62.5 μg beads+5 μg membrane preparation). Forty-eight replicates of total and non-specific signals were studied. Dashed lines indicate means and mean±3SD of 48 data points.

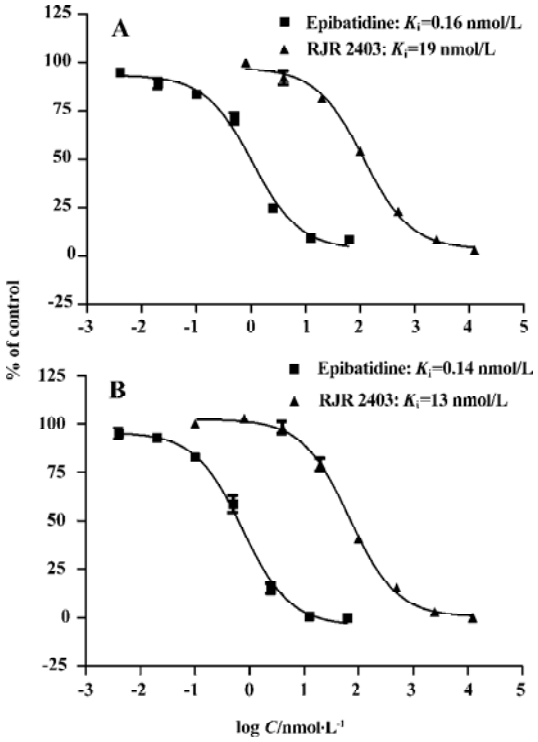

Figure 4. Dose-response curves of epibatidine and RJR 2403 measured by the (A) scintillation proximity assay or (B) filter binding method from which respective K_d values were calculated. n=3. Mean±SD.

ered (Figure 5). Secondary (single compound per well) screening confirmed that 17 of the above hits displayed consistent inhibitory effects with K_i values below 2 μmol/L. These active compounds are of different chemical structures including thiophene, piperidine, azole and other types of heterocyclic derivatives. The HTS campaign was high quality in nature with a Z' factor and S/B ratio equaling 0.73 and 29, respectively. The bioactivities of the confirmed hits were further evaluated with a functional assay. Eight compounds displayed antagonistic effects with >50% inhibition at 6.7 mg/L on ABT-594-induced calcium mobilization while none showed any agonist activity (Figure 6).

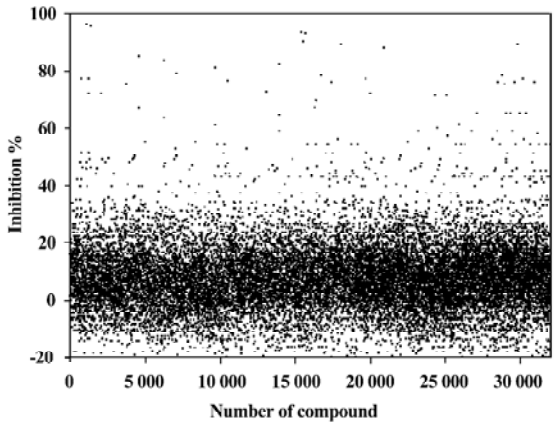

Figure 5. High-throughput screening of 32 000 compounds using the scintillation proximity assay. Results are expressed as percentage inhibition of [^{3}H]cytisine binding to α4β2 nicotinic acetylcholine receptor.

Discussion

Taking advantage of our prior experience in the development of a SPA-based nuclear receptor binding HTS method[12], efforts were made to expand the knowledge to membrane receptors such as α4β2 nAChR described in this paper. Although similar SPA approaches have been employed to study ligand-binding characteristics of a variety of G protein-coupled receptors[6,13–15], its application in α4β2 nAChR is novel and may be expandable to other ligand-gated ion channels.

When developing a SPA-based receptor-binding assay, many factors have to be considered in order to maximize the S/B ratio. The optimization procedure may include scintillant-impregnated microbead selection, assay buffer and volume determination, or protein/bead ratio verification. While the assay buffer could be readily transferred from a conventional filter binding assay, the amount of receptor protein and its relative ratio to the quantity of beads used are critical to assay performance. An adequate amount of beads is required to saturate the protein in order to achieve a maximal binding signal. However, excessive beads will lead to undesired exposure of bead surface to non-specific ligand binding. Therefore, the amount of beads applied should be kept to a minimum where protein saturation is still achievable.

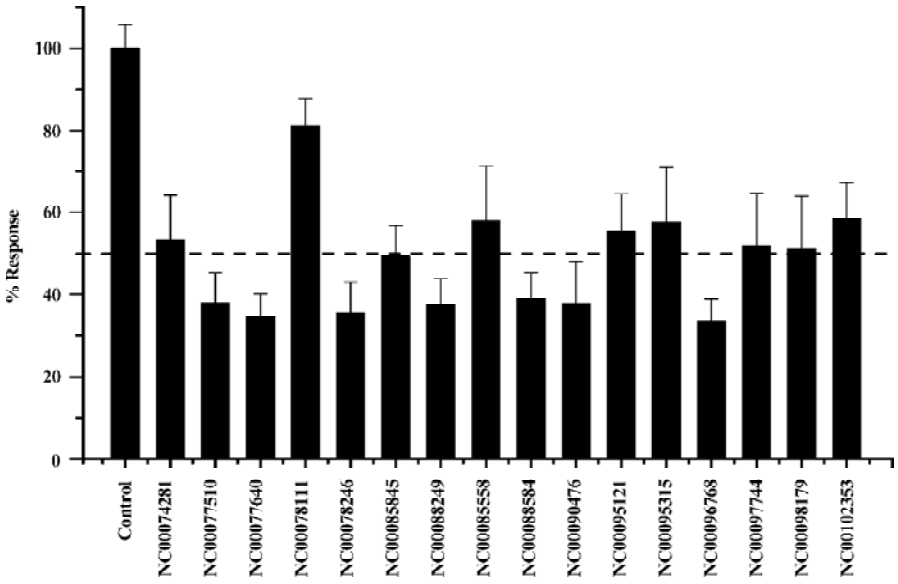

Figure 6. Inhibition of α4β2 nicotinic acetylcholine receptor agonist ABT-594-induced calcium mobilization by 16 hit compounds (6.7 mg/L). One compound was not included due to auto-fluorescence. Cells were pretreated with test compounds or dimethylsulphoxide (control) for 2 min and calcium influx was stimulated by ABT-594 (166 nmol/L). n=3. Mean±SEM.

On the other hand, stable signal is highly dependent on protein stability and its coating ability on the beads. In the assay system reported here, no signal shift was observed for more than 48 h, indicating a very stable interaction among various reagents.

It was learned from other membrane receptor screening settings that assay sensitivity can be improved by choosing a radiolabeled ligand concentration at or below its K_d to permit effective competition by an unlabeled ligand[14]. In the present study, we selected a relatively higher concentration of [^{3}H]cytisine (ie, 3 nmol/L) as opposed to the K_d value (0.6 nmol/L) of unlabeled ligand. This arrangement allowed us to accurately measure K_i values of the 2 reference compounds as well as to confirm hits identified from the HTS campaign, while keeping [^{3}H]cytisine bound to the receptor to a minimum (<10%). Conceivably, such a practice would compromise assay sensitivity thereby reducing the hit rate. Considering our initial intention of finding hits with K_i values below 2 μmol/L from primary screening, this purpose was well served as evidenced by a confirmed hit rate of 0.05% and the identification of 1 highly active compound (23 nmol/L; data not shown). In addition, the bioactivities of the hits discovered by the SPA method were confirmed with a cell-based functional assay where 8 compounds were found to demonstrate significant antagonistic effects on ABT-594-induced calcium mobilization.

In comparison with conventional filter binding techniques, the SPA method omits steps such as pre-coating, pre-incubation, separation and excessive washing, and thus, simplifies the assay protocol, mitigating labor intensity and reducing systemic error. It is also readily adaptable to HTS and automation, as demonstrated in this study. When deduced to practice, both approaches yielded similar K_i values for 2 known α4β2 nAChR ligands (epibatidine and RJR2403), which are not only consistent with those reported elsewhere[16] but also exhibited the same affinity rank order and pK_i features (in agreement within 1/2 log unit). In addition, the cost and amount of wastage are significantly less if SPA technology is employed. This advantage could be further explored by utilizing high-density plate formats (eg, 384-well plate) where filtering assays clearly show their limitations.

The Z' factor is a useful tool for evaluating bioassay qualities[17]. In general, a Z' value above 0.5 suggests that an assay is robust enough for HTS. The SPA system described herein consistently displayed a Z' value between 0.73 and 0.78. This, and in conjunction with other parameters such as S/B ratio, B_{max} and K_d values, indicate that the assay is high quality in nature.

In summary, a simple and SPA-based HTS binding assay was developed and validated for identification of compounds with specificity and functionality for α4β2 nAChR. Receptor coating onto the beads and ligand binding are achieved in 1 mixing step and the procedure is homogeneous. Its application may be expanded to other membrane receptors and ion channels.

Acknowledgements

We are indebted to Mr Bin WU and Ms Juan MA for their technical assistance, and to Dr DE MAIS for his valuable comments and critical review of this manuscript.

References

1 Lukas RJ, Changeux JP, Novere N, Albuquerque EX, Balfour DJ, Berg DK, *et al*. International Union of Pharmacology. XX. Current status of the nomenclature for nicotinic acetylcholine receptors and their subunits. Pharmacol Rev 1999; 51: 397–401.

2 Albuquerque EX, Alkondon M, Pereira EF, Castro NG, Schrattenholz A, Barbosa CT, *et al*. Properties of neuronal nicotinic acetylcholine receptors: pharmacological characterization and modulation of synaptic function. J Pharmacol Exp Ther 1997; 280: 1117–36.

3 Cordero-Erausquin M, Marubio LM, Klink R, Changeux JP. Nicotinic receptor function: new perspectives from knockout mice. Trends Pharmacol Sci 2000; 21: 211–7.

4 Kesingland AC, Gentry CT, Panesar MS, Bowes MA, Vernier JM, Cube R, *et al*. Analgesic profile of the nicotinic acetylcholine receptor agonists, (+)-epibatidine and ABT-594 in models of persistent inflammatory and neuropathic pain. Pain 2000; 86: 113–8.

5 Boyce S, Webb JK, Shepheard SL, Russell MG, Hill RG, Rupniak NM. Analgesic and toxic effects of ABT-594 resemble epibatidine and nicotine in rats. Pain 2000; 85: 443–50.

6 Carpenter JW, Laethem C, Hubbard FR, Eckols TK, Baez M, McClure D, *et al*. Configuring radioligand receptor binding assays for HTS using scintillation proximity assay technology. Methods Mol Biol 2002; 190: 31–49.

7 Chavez-Noriega LE, Gillespie A, Stauderman KA, Crona JH, Claeps BO, Elliott KJ, *et al*. Characterization of the recombinant human neuronal nicotinic acetylcholine receptors $\alpha 3\beta 2$ and $\alpha 4\beta 2$ stably expressed in HEK293 cells. Neuropharmacology 2000; 39: 2543–60.

8 Donnelly-Roberts DL, Puttfarcken PS, Kuntzweiler TA, Briggs CA, Anderson DJ, Campbell JE, *et al*. ABT-594 [(R)-5-(2-azetidinylmethoxy)-2-chloropyridine]: a novel, orally effective analgesic acting via neuronal nicotinic acetylcholine receptors: In vitro characterization. J Pharmacol Exp Ther 1998; 285: 777–86.

9 Qian J, Voorbach MJ, Huth JR, Coen ML, Zhang HC, Ng SC, *et al*. Discovery of novel inhibitors of Bcl-xL using multiple high-throughput screening platforms. Anal Biochem 2004; 328: 131–8.

10 Cheng Y, Prusoff WH. Relationship between the inhibition constant (K_i) and the concentration of inhibitor which causes 50 percent inhibition (IC_{50}) of an enzymatic reaction. Biochem Pharmacol 1973; 22: 3099–108.

11 Khan IM, Yaksh TL, Taylor P. Ligand specificity of nicotinic acetylcholine receptors in rat spinal cord: studies with nicotine and cytisine. J Pharmacol Exp Ther 1994; 270: 159–66.

12 Wu B, Gao J, Wang M-W. Development of a complex scintillation proximity assay for high-throughput screening of PPARγ modulators. Acta Pharmacol Sin 2005; 26: 339–44.

13 Crane K, Shih DT. Development of a homogeneous binding assay for histamine receptors. Anal Biochem 2004; 335: 42–9.

14 Gobel J, Saussy DL, Goetz AS. Development of scintillation-proximity assays for alpha adrenoceptors. J Pharmacol Toxicol Methods 1999; 42: 237–44.

15 Rodgers G, Hubert C, McKinzie J, Suter T, Statnick M, Emmerson P, *et al*. Development of displacement binding and GTPγS scintillation proximity assays for the identification of antagonists of the micro-opioid receptor. Assay Drug Dev Technol 2003; 1: 627–36.

16 Xiao Y, Baydyuk M, Wang HP, Davis HE, Kellar KJ. Pharmacology of the agonist binding sites of rat neuronal nicotinic receptor subtypes expressed in HEK 293 cells. Bioorg Med Chem Lett 2004; 14: 1845–8.

17 Zhang JH, Chung TD, Oldenburg KR. A simple statistical parameter for use in evaluation and validation of high throughput screening assays. J Biomol Screen 1999; 4: 67–73.

Acta Pharmacologica Sinica 2005 Oct; 26 (10): 1181–1186

Full-length article

Identification of human dopamine D1-like receptor agonist using a cell-based functional assay[1]

Nan JIANG[2], Ke-qing OU-YANG[3], Shao-xi CAI[3], Ying-he HU[2], Zhi-liang XU[2,4]

[2]Shanghai Institute of Brain Functional Genomics and Key Lab of Brain Functional Genomics, Ministry of Education, Science and Technology Commission of Shanghai Municipality, East China Normal University, Shanghai 200062; [3]College of Bioengineering, Chongqing University, Chongqing 400044, China

Key words

dopamine D1 receptors; drug screening; Chinese herbal drugs

[1] Project supported by grants from the Shanghai Commission for Education, Shanghai Commission for Science and Technology, and the Ministry of Science and Technology of China (No 010231006, 2003CB716600).
[4] Correspondence to Dr Zhi-liang XU.
Phn/Fax 86-21-6223-3953.
E-mail zlxu@brain.ecnu.edu.cn

Received 2005-03-27
Accepted 2005-06-28

doi: 10.1111/j.1745-7254.2005.00199.x

Abstract

Aim: To establish a cell-based assay to screen human dopamine D1 and D5 receptor agonists against compounds from a natural product compound library. **Methods:** Synthetic responsive elements 6×cAMP response elements (CRE) and a mini promoter containing a TATA box were inserted into the pGL3 basic vector to generate the reporter gene construct pCRE/TA/Luci. CHO cells were co-transfected with the reporter gene construct and human D1 or D5 receptor cDNA in mammalian expression vectors. Stable cell lines were established for agonist screening. A natural product compound library from over 300 herbs has been established. The extracts from these herbs were used for human D1 and D5 receptor agonist screenings. **Results:** A number of extracts were identified that activated both D1 and D5 receptors. One of the herb extracts, SBG492, demonstrated distinct pharmacological characteristics with human D1 and D5 receptors. The EC_{50} values of SBG492 were 342.7 μg/mL for the D1 receptor and 31.7 μg/mL for the D5 receptor. **Conclusion:** We have established a cell-based assay for high-throughput drug screening to identify D1-like receptor agonists from natural products. Several extracts that can active D1-like receptors were discovered. These compounds could be useful tools for studies on the functions of these receptors in the brain and could potentially be developed into therapeutic drugs for the treatment of central nervous system diseases.

Introduction

The dopamine receptors fall into two families called D1-like and D2-like receptors, based on their structural and pharmacological features[1]. The D1 family includes D1- and D5-receptor subtypes, and the D2 family consists of D2-, D3- and D4-receptor subtypes. Dopamine receptors are mainly expressed in the central nervous system and control motor function, emotional state and endocrine physiology[2,3].

Many central nervous system (CNS), cardiovascular and renal diseases have been shown to be associated with alterations in dopamine receptors. These diseases include Parkinson disease, schizophrenia, migraine, drug dependence, depression and Gilles de la Tourette syndrome[4]. Dopamine is one of the principal neurotransmitters in the basal ganglia, and plays a critical role in motor control and cognitive function through interactions with dopamine receptors. The possible role of dopamine D1-like receptors in brain function, especially in learning and memory, has recently been studied extensively[5–7]. Indeed, D1-like receptors play essential roles in working memory[8] and other forms of cognition activity[9]. The abnormality of these receptors also contribute to Parkinson disease[10,11]. In addition, the D5 receptor subtype is involved in modulating the release of hippocampal acetylcholine, a neurotransmitter implicated in a variety of cognitive processes[12].

Much evidence has been accumulated to indicate that dopamine receptor agonists or antagonists can be developed into therapeutic drugs for the treatment of CNS diseases. It has been reported that D1-like receptor agonists improve learning and memory in different animal models[13,14]. Furthermore, D1-like receptor agonists or antagonists are

potential therapeutic drugs for addiction and Parkinson disease[15–18]. Receptor agonists and antagonists also provide essential tools for pharmacological and functional characterization of the receptors.

Several high throughput screening methods to screen agonists and antagonists of G-protein coupled receptors (GPCR) have been developed[19–22]. Recently, we developed a universal functional assay for GPCR[23]. In the present report, we further modified this functional assay for human D1-like agonist screening. A number of natural compounds were identified that can specifically activate both human D1 and D5 receptors. Detailed pharmacological analysis demonstrated that one of the agonists had distinct pharmacological properties for these 2 receptors.

Materials and methods

Plasmid construction Human D1 and D5 receptors were cloned by polymerase chain reaction (PCR). The primers used for the PCR were: D1R5', 5'-GCT GGA TCC GTG CCC AAG ACA GTG ACC T-3'; D1R3', 5'-GGG AGC TCC GAG GGG TAC AAA ACA TCA-3'; D5R5', 5'-GGC GAA TTC GCG TGT GTG TGC GTG CTT GTC AGT GT-3'; and D5R3', 5'-GGG AAG CTT CTG AAG TTG GGA CCG CGC ACA GAC CG-3'. PCR products were digested with *Eco*RI and *Hind*III and subcloned into the *Eco*RI/*Hind*III-digested mammalian expression vector pCDNA3.1 (Invitrogen) to generate pCDNA3.1/D1 and pCDNA3.1/D5. The 6×CRE and a mini promoter with 49 bps, containing a TATA box, were synthesized and inserted into the pGL3 basic vector (Promega) to produce pCRE/TA/Luci as a reporter gene. All plasmids were confirmed by DNA sequencing.

Cell culture, transfection and stable cell line generation CHO cells were maintained in RPMI-1640 medium containing 10% fetal calf serum at 37 °C. Cells were transfected with dopamine D1 and D5 receptors and the reporter construct using Lipofectin (Invitrogen). Stably transfected cells were generated in the presence of 0.8 mg/mL G418.

Natural product extracts Traditional Chinese Medicines (TCM) were purchased from a local pharmacy in Chongqing, China. Fifty grams of each TCM were extracted twice with 500 mL water at 80 °C for 2 h. The extracts were concentrated to 100 mL by evaporation under low pressure at 80 °C. Using this method, we prepared more than 300 samples for human dopamine receptor agonist screening.

Luciferase assay Aliquots of 90 μL cells (3×10^5 cells/mL) were seeded into each well of 96-well plates and incubated overnight at 37 °C. A natural product sample (10 μL) was added to each well and incubated at 37 °C for 6 h–10 h. Bright-Glo™ Lucifease assay reagent (100 μL; Promega) was then added to each well, and the luciferase activity was measured using Analyst™ HT (Molecular Device).

Results

Characterization of the CRE/TA/Luci reporter gene in CHO cells We generated a reporter gene construct for human dopamine D1 and D5 agonist screening. The construct contained 6 copies of CRE and a TATA box linked to the luciferase gene. The reporter gene construct was stably transfected into CHO cells to generate the CRE/TA/Luci/CHO cell line. This cell line was treated with forskolin (an adenyl cyclase activator) at different concentrations, and luciferase activity was measured. Our results showed that forskolin stimulated reporter gene luciferase expression in a dose-dependent manner (Figure 1). This result indicated that increasing intracellular cAMP levels led to the activation of CRE and TATA promoter and suggested that this assay could be used for Gs-coupled receptor agonist screening. To examine whether there was any endogenous dopamine receptor in the CHO cells, we tested several dopamine receptor agonists in the stable reporter gene cell line. Our results demonstrated that none of the dopamine receptor agonists had any effect on the cell line, indicating that no dopamine receptor was expressed in CHO cells.

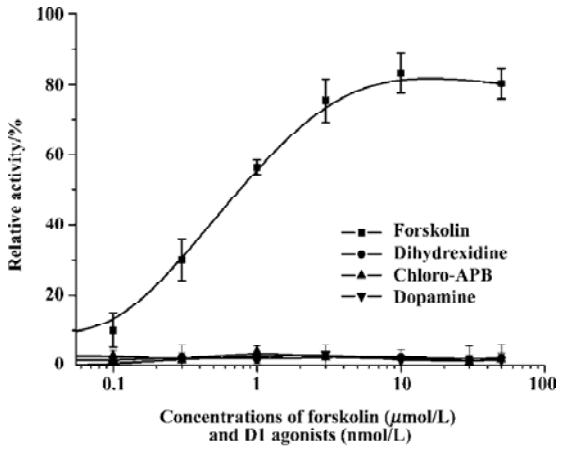

Figure 1. The activity of forskolin and D1-like receptor agonists in CRE/TA/Luci/CHO cells. The cells were incubated with different concentrations of D1 agonists and forskolin for 6 h, and luciferase activity was measured.

Development of reporter gene assay for D1-like receptor agonist screening Mammalian expression vectors containing human dopamine D1 or D5 receptors were transfected into the reporter gene cell line. Activation of the receptors

leads to the elevation of cAMP and activates the cAMP response element, and therefore induces the expression of the reporter gene luciferase. We tested the natural ligand dopamine and two other D1-like receptor agonists, dihydrexidine and chloro-APB, in the stable cell lines expressing both dopamine receptors and the reporter gene. The results are shown in Figure 2. The rank order of potency, dopamine>dihydrexidine>chloro-APB, agreed with the ligand-receptor binding analysis[24,25].

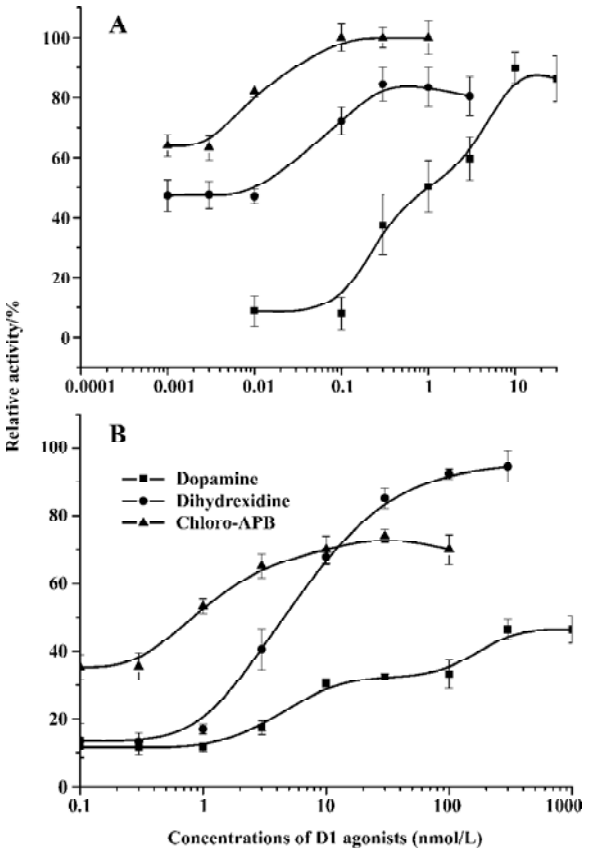

Figure 2. The activities of D1-like receptor agonists in cell lines expressing human D1 or D5 receptors. (A) D1/CRE /TA/CHO cells were incubated with D1-like receptor agonists for 6 h; (B) D5/CRE/TA/CHO cells were incubated with D1-like receptor agonists for 6 h.

Optimization of the reporter gene assay conditions We carried out a series of experiments to optimize the reporter gene assay for drug screening. First, we examined the incubation time for the D1-like receptor agonist in the assay. Different concentrations of dihydrexidine were used for the experiment. Our results showed that approximately 8 h incubation with the agonist gave the highest response at all concentrations (Figure 3). Therefore, we used an 8-h incubation time for all of our experiments, unless otherwise indicated.

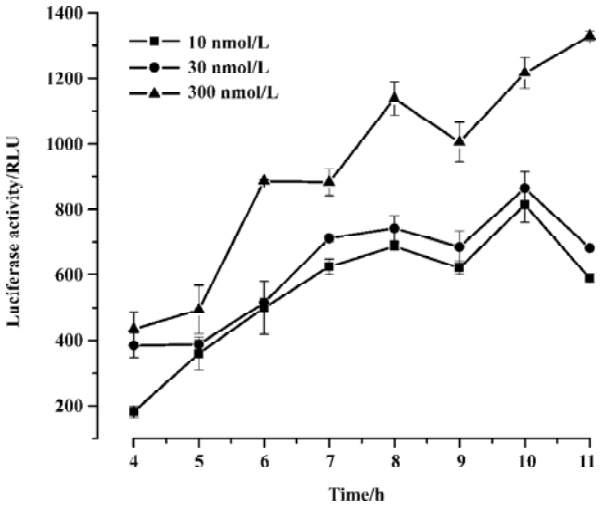

Figure 3. The effects of dihydrexidine on the activity of luciferase in the D5/CRE/TA/Luci/CHO cells at different incubation times. The concentrations of dihydrexidine were 10 nmol/L, 30 nmol/L and 300 nmol/L. Cells were incubated with D1-like receptor agonist dihydrexicine for 6 h and luciferase activity was measured.

Second, because the compounds were in dimethylsulphoxide (Me_2SO) solution, we tested the effects of Me_2SO at different concentrations in the assay. Me_2SO concentrations of 1% or less had no effect on the signal (data not shown). In our compound screen assays, the final concentration of Me_2SO was adjusted at 1% or less. Finally, we found that the number of cells in each well may influence the reporter gene assay. Figure 4 shows that although increasing cell number gave a better signal after agonist stimulation, the background was also higher. The best number of cells to use was

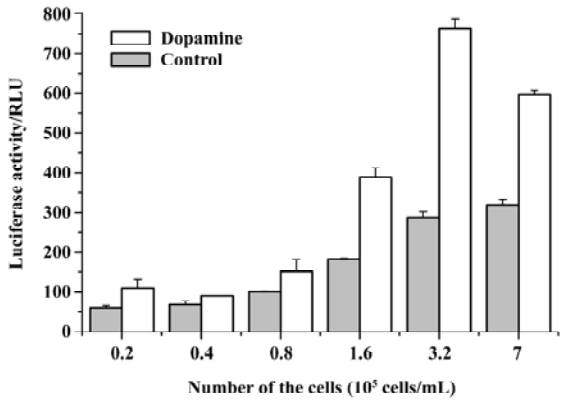

Figure 4. The effects of cell number on the luciferase activity in D5/CRE/TA/Luci/CHO cells in the presence of dopamine. D5/CRE/TA/Luci/CHO cells were treated with either saline or 100 nmol/L dopamine for 6 h, and luciferase activity was measured.

between 2×10^5 cells/mL and 4×10^5 cells/mL. Therefore, we used 3×10^5 cells/mL in all compound screens using the reporter gene assay. In addition, we calculated the coefficient of variation (CV) for the assay in a standard 96-well plate. The CV values were 6.5% for non-activated cells and 5.8% for dopamine-stimulated cells. The Z' factor[26] was 0.58. These results suggest that the reporter gene assay system was suitable for dopamine receptor agonist screening.

Identification of extracts active for the D1-like receptor More than 300 herb extract samples were used for the D1-like receptor agonist screening. From our previous experiences for other G-protein coupled receptor agonist or antagonist screens, we found that it was necessary to use different concentrations of the raw extracts for the screen. Therefore, in the D1-like receptor agonist screen, the extract samples were screened twice at different concentrations. One was at the original concentration and the other was a 5-fold dilution of the sample. The samples that gave signals larger than the mean value +3SD were selected as agonist candidates (Figure 5). To eliminate the possibility that the agonist candidates activated the reporter gene expression through intracellular pathways other than the D1-like receptor, we tested the samples in a cell line expressing the reporter gene alone, without the D1-like receptor. We found that some of the agonist candidates, such as Chinese ester pillar fungus, could stimulate the reporter gene luciferase expression in the reporter gene cell line (Figure 6). In contrast, sample SBG492 activated the expression of the reporter gene in the D1-like receptor expressing cell line, but had no effect in the reporter gene cell line. This result suggested that SBG492 activated the reporter gene expression through human D1-like receptor (Figure 6). Furthermore, we tested the sample in more than 20 different GPCR using the same reporter gene assay system (data not shown). Our results demonstrated SBG492 could not activate other GPCR, suggesting that the sample contained specific human D1-like receptor agonist. We further analyzed the pharmacological properties of SBG492 for human D1 and D5 receptors. The EC_{50} values of SBG492 were 342.7 μg/mL for the D1 receptor and 31.7 μg/mL for the D5 receptor (Figure 7).

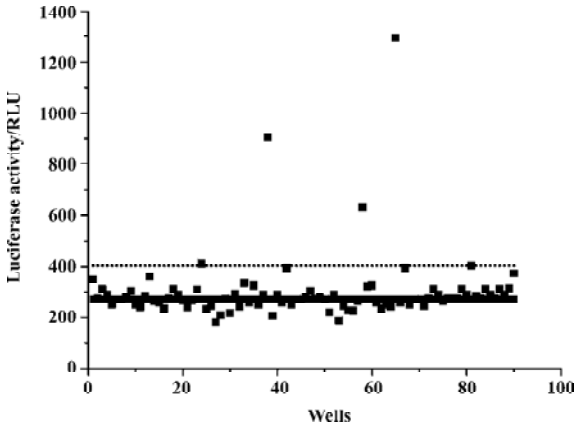

Figure 5. D1-like receptor agonist screening. Reporter gene cell line expressing human D1-like receptor was treated with herb extracts and luciferase activity was measured. The solid line indicates basal activity of luciferase without treatment. The dotted line represents mean±SD.

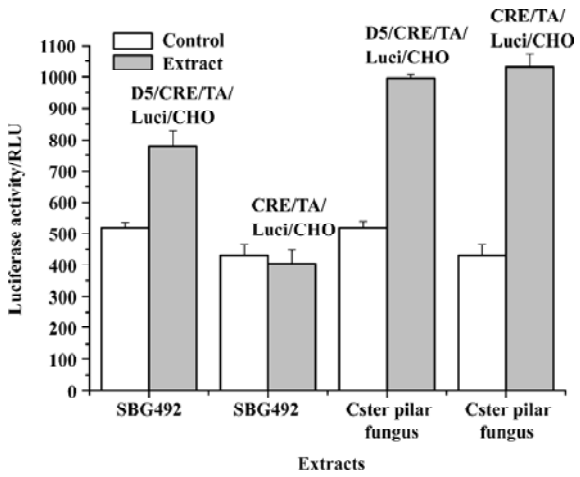

Figure 6. The activity of SBG492 and Chinese ester pillar fungus in D5/CRE/TA/Luci/CHO and TA/Luci/Luci/CHO cell lines. The cells were treated with 100 μg/mL extracts for 8 h and luciferase activity was measured.

Discussion

Dopamine receptors are a subclass of the superfamily of GPCR. Within the dopamine receptor family, both D1 and D5 are Gs-coupled receptors. Interaction of the receptors with the natural ligand dopamine or other agonists leads to the activation of adenyl cyclase and increases the intracellular concentration of cAMP. The cAMP second messenger system ultimately activates CRE and induces gene expression. This is the basis of our reporter gene assay, which contains 6×CRE linked to the reporter gene luciferase.

The D1 and D5 dopamine receptors are genetically distinct, sharing over 80% sequence homology within the highly conserved 7 transmembrane-spanning domains, but display only 50% overall homology at the amino acid level[27]. The D1-like dopamine receptors, including D1 and D5, have similar pharmacological properties[28]. Indeed, it is often difficult to pharmacologically distinguish between dopamine D1 and D5 receptors using the same ligands. Therefore, identification of agonists that have distinct pharmacological

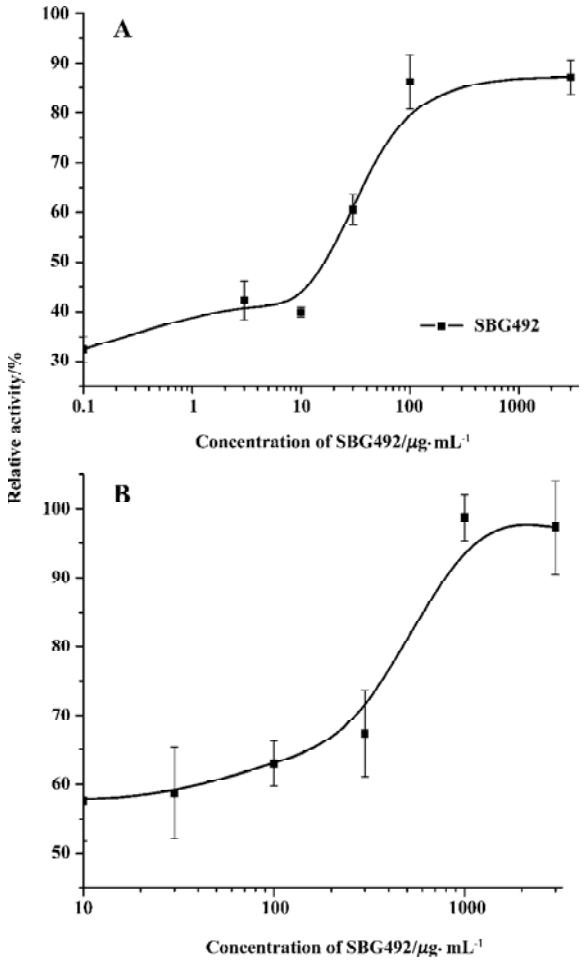

Figure 7. Pharmacological characterization of SBG492 on luciferase activity of D5/CRE/TA/Luci/CHO and D1/CRE/TA/Luci/CHO cells. (A) D5/CRE/TA/Luci/CHO cells were treated with different concentrations of SBG492 for 8 h and luciferase activity was measured. (B) D1/CRE/TA/Luci/CHO cells were incubated with SBG492 for 8 h and luciferase activity was measured.

properties for these 2 receptors should provide a useful tool for their functional studies.

In our previous agonist or antagonist screening for GPCR and other targets, we have successfully isolated active components from crude extracts of herbs[29–31]. Subsequent purification of the active components lead to the identification of a single effective compound. The advantage of using the crude extract is that the samples are easy to prepare and a large amount of herbs can be screened in a short period of time. On the other hand, since the crude extracts contain hundreds of different compounds, some of them may have negative effects on the targets or may even be harmful to cells. Indeed, we found that in some cases, high concentrations of the extracts in our cell-based assay had no effects, while after dilution the samples showed agonist or antagonist activity. Therefore, we used 2 concentrations of each extract for the screening to increase the chances of identifying D1-like receptor agonists. A number of extracts were isolated as potential receptor agonists using the reporter gene assay.

There are several other possible ways in which that the extracts can activate the reporter gene expression other than as human D1-like receptor agonists. For example, the extracts may activate or inhibit other components in the cAMP signal pathway, such as adenyl cyclase, protein kinase A, cAMP-dependent phosphodiesterase or CRE binding protein, and eventually lead to the activation of the reporter gene. It is also possible that the extracts may activate other endogenous GPCR in the cell and lead to the induction of reporter gene expression. To examine these possibilities, we tested the activity of the herb extracts in a reporter gene cell line that did not express human D1-like receptors. We found that SBG492 did not induce the expression of the reporter gene in the cell line, indicating that the extract activated the reporter gene through the receptor. It is interesting to note that SBG492 is approximately 10 times more potent for human D1 receptor than for D5 receptor. Further characterization of the agonist could provide important information for pharmacological and functional studies on human D1-like receptors.

Acknowledgements

We thank Hong GAO, Lu WANG, and Li-ping WANG for their excellent technical assistance.

References

1 Braun AR, Laruelle M, Mouradian MM. Interactions between D1 and D2 dopamine receptor family agonists and antagonists: the effects of chronic exposure on behavior and receptor binding in rats and their clinical implications. J Neural Transm 1997; 104: 341–62.

2 Vallone D, Picetti R, Borrelli E. Structure and function of dopamine receptors. Neurosci Biobehav Rev 2000; 24: 125–32.

3 Meyer ME, Cottrell GA, Van Hartesveldt C, Potter TJ. Effects of dopamine D1 antagonists SCH23390 and SK&F83566 on locomotor activities in rats. Pharmacol Biochem Behav 1993; 44: 429–32.

4 Emilien G, Maloteaux JM, Geurts M, Hoogenberg K, Cragg S. Dopamine receptors-physiological understanding to therapeutic intervention potential. Pharmacol Ther 1999; 84: 133–56.

5 Xu M, Moratalla R, Gold LH, Hiroi N, Koob GF, Graybiel AM, *et al*. Dopamine D1 receptor mutant mice are deficient in striatal expression of dynorphin and in dopamine-mediated behavioral responses. Cell 1994; 79: 729–42.

6 El-Ghundi M, Fletcher PJ, Drago J, Sibley DR, O'Dowd BF, George

SR. Spatial learning deficit in dopamine D(1) receptor knockout mice. Eur J Pharmacol 1999; 383: 95–106.
7 Centonze D, Grande C, Saulle E, Martin AB, Gubellini P, Pavon N, *et al*. Distinct roles of D1 and D5 dopamine receptors in motor activity and striatal synaptic plasticity. J Neurosci 2003; 23: 8506–12.
8 Lidow MS, Koh PO, Arnsten AF. D1 dopamine receptors in the mouse prefrontal cortex: immunocytochemical and cognitive neuropharmacological analyses. Synapse 2003; 47: 101–8.
9 Williams GV, Goldman-Rakic PS. Modulation of memory fields by dopamine D1 receptors in prefrontal cortex. Nature 1995; 376: 572–5.
10 Hurley MJ, Mash DC, Jenner P. Dopamine D(1) receptor expression in human basal ganglia and changes in Parkinson's disease. Brain Res Mol Brain Res 2001; 87: 271–9.
11 Mailman R, Huang X, Nichols DE. Parkinson's disease and D1 dopamine receptors. Curr Opin Invest Drugs 2001; 2: 1582–91.
12 Hersi AI, Kitaichi K, Srivastava LK, Gaudreau P, Quirion R. Dopamine D-5 receptor modulates hippocampal acetylcholine release. Brain Res Mol Brain Res 2000; 76: 336–40.
13 Castellano C, Cestari V, Cabib S, Puglisi-Allegra S. Post-training dopamine receptor agonists and antagonists affect memory storage in mice irrespective of their selectivity for D1 or D2 receptors. Behav Neural Biol 1991; 56: 283–91.
14 Castner SA, Goldman-Rakic PS. Enhancement of working memory in aged monkeys by a sensitizing regimen of dopamine D1 receptor stimulation. J Neurosci 2004; 24: 1446–50.
15 Linazasoro G. Conversion from dopamine agonists to pramipexole. An open-label trial in 227 patients with advanced Parkinson's disease. J Neurol 2004; 251: 335–9.
16 Jenner P. Dopamine agonists, receptor selectivity and dyskinesia induction in Parkinson's disease. Curr Opin Neurol 2003; 16 Suppl 1: 3–7.
17 Ruggieri S, Stocchi F, Baronti F, Viselli F, Horowski R, Lucarelli C, *et al*. Antagonist effect of terguride in Parkinson's disease. Clin Neuropharmacol 1991; 14: 450–6.
18 Meyer ME, Van Hartesveldt C, Potter TJ. Locomotor activity following intra-accumbens microinjections of dopamine D1 agonist SK&F 38393 in rats. Synapse 1993; 13: 310–4.
19 Kariv II, Stevens ME, Behrens DL, Oldenburg KR. High throughput quantitation of camp production mediated by activation of seven transmembrane domain receptors. J Biomol Screen 1999; 4: 27–32.
20 Fitzgerald LR, Mannan IJ, Dytko GM, Wu HL, Nambi P. Measurement of responses from Gi-, Gs-, or Gq-coupled receptors by a multiple response element/cAMP response element-directed reporter assay. Anal Biochem 1999; 275: 54–61.
21 George SE, Bungay PJ, Naylor LH. Functional analysis of the D2L dopamine receptor expressed in a cAMP-responsive luciferase reporter cell line. Biochem Pharmacol 1998; 56: 25–30.
22 Hertzberg RP, Pope AJ. High-throughput screening: new technology for the 21st century. Curr Opin Chem Biol 2000; 4: 445–51.
23 Jiang C, Chen G, Zeng X, Ouyang K, Hu Y. Generation of a bioactive neuropeptide in a cell-free system. Anal Biochem 2003; 316: 34–40.
24 Gilmore JH, Watts VJ, Lawler CP, Noll EP, Nichols DE, Mailman RB. "Full" dopamine D1 agonists in human caudate: biochemical properties and therapeutic implications. Neuropharmacology 1995; 34: 481–8.
25 Grandy DK, Zhang YA, Bouvier C, Zhou QY, Johnson RA, Allen L, et al. Multiple human D5 dopamine receptor genes: a functional receptor and two pseudogenes. Proc Natl Acad Sci USA 1991; 88: 9175–9.
26 Zhang JH, Chung TD, Oldenburg KR. A simple statistical parameter for use in evaluation and validation of high throughput screening assays. J Biomol Screen 1999; 4: 67–73.
27 Sidhu A. Coupling of D1 and D5 dopamine receptors to multiple G proteins: Implications for understanding the diversity in receptor-G protein coupling. Mol Neurobiol 1998; 16: 125–34.
28 Seeman P, van Tol HH. Dopamine receptor pharmacology. Curr Opin Neurol Neurosurg 1993; 6: 602–8.
29 Xu ZL, Gao H, Ou-Yang KQ, Cai SX, Hu YH. Establishment of a cell-based assay to screen regulators for Klotho gene promoter. Acta Pharmacol Sin 2004; 25: 1165–70.
30 Zheng XX, Ou-Yang KQ, Gao H, Xu ZL, Hu YH, Cai SX. Study on high throughput screening method of identifying agonist for neuromedin U2 receptor. Chin Pharm J 2004; 9: 185–8. Chinese.
31 Gao H, Ou-Yang KQ, Zheng XX, Xu ZL, Hu YH, Cai SX. High throughput screening method of identifying agonist for muscarinic receptor. Chin Pharmacol Bull 2003; 19: 776–9. Chinese.

Acta Pharmacologica Sinica 2005 Oct; 26 (10): 1187–1192

Blackwell Publishing

Full-length article

Comparative study on pharmacological effects of DM-phencynonate hydrochloride and its optical isomers[1]

Li-yun WANG, Jian-quan ZHENG[2], Yun WANG, Bo-hua ZHONG, Jin-xiu RUAN, Ke-liang LIU

Beijing Institute of Pharmacology and Toxicology, Beijing 100850, China

Key words

optical isomers; muscarinic acetylcholinic receptors; pharmacological profiles; radioligand binding assay

[1] Project supported by the Major Programs Project, National Natural Science Foundation of China (No 203900508).
[2] Correspondence to Prof Jian-quan ZHENG.
Phn 86-10-6693-1635.
Fax 86-10-6821-1656.
E-mail jqzh@yahoo.com

Received 2005-03-20
Accepted 2005-05-20

doi: 10.1111/j.1745-7254.2005.00183.x

Abstract

Aim: The 3-azabicyclo(3,3,1)nonanyl-9-α-yl-α-cyclopentyl-α-phenyl-α-glycolate (DM-phencynonate hydrochloride, DMCPG) is a demethylated metabolite of 3-methyl-3-azabicyclo(3,3,1)nonanyl-9-α-yl-α-cyclopentyl-α-phenyl-α-glycolate (phencynonate hydrochloride, CPG). (±)DMCPG had one chiral center and two enantiomers [R(–) and S(+)DMCPG]. Here we carried out a comparative study of the pharmacological profiles of these optical isomers. **Methods:** Affinity and relative efficacy were tested using a radioligand-binding assay with muscarinic acetylcholine receptors from the rat cerebral cortex. Pharmacological activity was assessed in three individual experiments: (1) potentiating the effect of a sub-threshold hypnotic dose of sodium pentobarbital; (2) inhibiting oxotremorine-induced salivation; and (3) inhibiting the contractile response to carbachol. **Results:** In the competitive binding assay, R(–)DMCPG (K_i=763.75 nmol/L) was 4- and 2-fold more potent than (±)DMCPG (K_i=3186 nmol/L) and S(+)DMCPG (K_i=1699 nmol/L) in inhibiting the binding of [^{3}H]QNB. The R(–) and S (+) configurations showed positive cooperation (n_H>1) with the muscarinic receptor, whereas (±)DMCPG had a negative cooperation (n_H<1) relationship with the muscarinic receptor in a radio-binding assay. Both the R(–) and S(+) configurations could potentiate the effect of sub-threshold hypnotic dose of sodium pentobarbital in a dose-dependent manner (the ED_{50} values were 2.53 and 18.65 mg/kg, respectively), but (±)DMCPG did not display significant central depressant effects at doses from 10 to 29.15 mg/kg (P>0.05). (±)DMCPG and its optical isomers suppressed the guinea pig ileum contractile response to carbachol. The IC_{50} values were 7.78×10^{-9}, 1.88×10^{-7}, and 1.03×10^{-7} nmol/L, respectively. In the anti-salivation study, (±)DMCPG and its enantiomers depressed oxotremorine- induced salivation in a dose-dependent manner, and the order of potency was R(–)DMCPG (ED_{50}=0.44 mg/kg)>(±)DMCPG (ED_{50}=2.88 mg/kg)>S(+)DMCPG (ED_{50}=5.05 mg/kg). **Conclusion:** (±)DMCPG and its optical isomers have differences in their pharmacological potencies as anticholinergic agents, and the R(–) configuration is more active than the S(+) configuration.

Introduction

In order to develop more potent drugs for muscarinic intervention in disorders of the central and peripheral nervous system, a series of heterocyclic compounds including esters, alkanes, and ether derivatives were designed and synthesized in our institute. One of the compounds, CPG, has been developed as a novel anti-motion-sickness drug with higher efficacy and lower central inhibitory side effects than diphenidol HCl and scopolamine HBr, and is used clinically[1–3]. (±)DMCPG, which has one chiral center and two enantiomers [R(–) and S(+)DMCPG] was the active dominant N-demethyl metabolite of CPG. We believe that this is an important way of looking for active compounds from the

metabolites to discover new medicines. We synthesized (±)DMCPG and its two enantiomers (Figure 1). To avoid adverse effects and to optimize the therapeutic value of enantiomeric drugs, it is necessary to establish the effectiveness of isomers of the chiral drug, and to detect the presence of the enantiomer with lower therapeutic activity and undesirable adverse effects. For this purpose, we investigated the binding characteristics of these new chiral compounds by using a radioligand receptor-binding assay with muscarinic receptors from rat brain, and compared its pharmacological effects on muscarinic receptors by means of *in vitro* and *in vivo* assays.

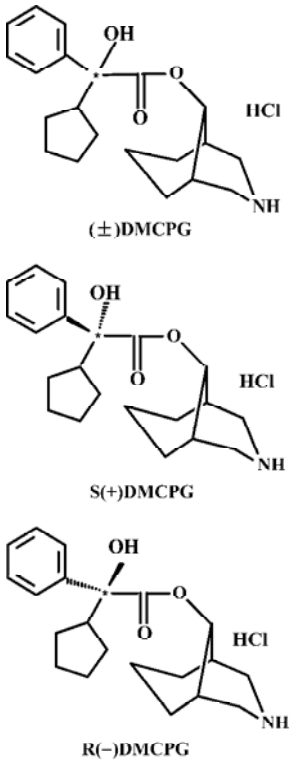

Figure 1. Chemical structures of (±)DMCPG and its optical isomers.

Materials and methods

Animals The experiments were carried out in accordance with the Guide for the Care and Use of Laboratory Animals, from the National Research Council (1996), under the approved protocols. Animals used in the present study were as follows: Kunming species mice weighing 18–22 g [grade II, certificate No scxk (Army) 2002-001], provided by our animal center; male and female Wistar rats weighing 180–220 g [grade II, certificate No scxk (Jing) 2002-0003], and male guinea pigs weighing 200–300 g [grade II, certificate No scxk (Jing) 2002-0003] purchased from Weitonglihua Co (Beijing, China).

Compounds ^{3}H-quinuclindinyl benzilate ([^{3}H]QNB; 43.3 Ci/mmol) was purchased from Amersham (Uppsala, Sweden; TRK604). (±)DMCPG and its isomers were synthesized at our institute. The (±)DMCPG comprised equal proportions of R(–) and S(+)DMCPG. Atropine, pentobarbital, oxotremorine and carbachol were purchased from Sigma (St Louis, MO, USA).

Binding assays on rat cerebral cortex homogenate Male or female Wistar rats were killed by decapitation. The cerebral cortex was immediately removed and processed as described by Yamamura and Snyder[4].The protein concentration was determined by using the method of Lowry *et al*[5]. The samples of homogenate (each containing 50 mg of protein) were incubated for 30 min at 37 ºC in 0.5 mL of assay buffer containing 6 nmol/L [^{3}H]QNB and various concentrations of drugs. In saturation binding assays, the homogenate was incubated as indicated above, in the presence of [^{3}H]QNB (0.25–20 nmol/L). Non-specific binding was defined as binding in presence of atropine (1 μmol/L). Each sample was filtered through GF/C glass fibers with vacuum. The filters were rinsed 3 times with 3 mL cold buffer, and placed in scintillation vials containing 3 mL of scintillation fluid. Radioactivity trapped on the filters was determined by liquid scintillation spectrometry at approximately 40%–50% efficiency.

Carbachol-induced contraction Male guinea pigs were killed by cervical dislocation. The organs required were set up rapidly under 1 g of tension in 20 mL organ baths containing physiological salt solution (PSS), which was kept at 37 ºC and aerated with 5% CO_2 and 95% O_2. Two-centimeter-long portions of terminal ileum were taken at about 5 cm from the ileum–cecum junction and mounted in PSS at 37 ºC. The composition of PSS was as follows (mmol/L): NaCl 118, $NaHCO_3$ 23.8, KCl 4.7, $MgSO_4 \cdot 7H_2O$ 1.18, KH_2PO_4 1.18, $CaCl_2$ 2.52, glucose 11.7. Tension changes were recorded isotonically. Tissues were equilibrated for 90 min before the experiments were conducted.

The carbachol-induced ileum contraction was obtained by incubation with carbachol (10^{-5} mol/L) until the concentration had reached a plateau. Then, the ileum strips were washed several times with PSS until the tension of the strips relaxed to the baseline level. Following washing, the strips were incubated with different concentrations of R(–), S(+), or (±)DMCPG for 10–15 min. After incubation, the maximum contraction induced by carbachol (10^{-5} mol/L) was observed again in the presence of increased concentrations of different antagonists. The IC_{50} values for the carbachol-induced contractions in the presence of the antagonists were ob-

tained to assess the pharmacological potency of (±)DMCPG and its optical isomers.

Effect on sub-threshold hypnotic dose of sodium pentobarbital induced-sleep Four dosage groups were used for each drug and each group consisted of 10 mice of each sex. Mice were pretreated with (±)DMCPG and its optical isomers intraperitoneally (ip), then after 15 min, a sub-threshold hypnotic dose of sodium pentobarbital (30 mg/kg) was given ip. The loss of righting reflex was used as a measure of the central inhibitory effect of drugs. The ED_{50} values of these three drugs were estimated to compare the central inhibitory effect of the indicated agents.

Inhibition of oxotremorine-induced salivation Kunming mice were assigned randomly into 4 groups for each drug. Each group consisted of 10 mice of each sex. (±)DMCPG and its optical isomers were administered ip 15 min prior to oxotremorine (3 mg/kg) being injected subcutaneously (sc). ED_{50} values were calculated to evaluate the anti-secretive potencies of the compounds used.

Data analysis and statistics

Binding assays The IC_{50} values were obtained from at least three separate experiments performed in triplicate with 6-8 concentrations of drugs. Data were analyzed by curvilinear regression using the program ORIGIN 6.0. The inhibition constants (K_i) were calculated using the Cheng-Prusoff equation[6], $K_i=IC_{50}/(1+L/K_d)$, where L and K_d are the concentration and the equilibrium dissociation constant of [^{3}H]QNB, respectively.

Functional assays In the carbachol-induced contraction experiments, the maximum contractile response (E_{max}) was obtained from the maximum stress, and the IC_{50} value was calculated from a semi-logarithmic plot of the percentage of the maximum response versus drug concentration. Data were computer analyzed by curvilinear regression using the program ORIGIN 6.0. Statistical analyses for comparisons among groups were performed using analysis of variance (ANOVA). $P<0.05$ was considered statistically significant. To evaluate the effect of (±)DMCPG and its optical isomers on anti-salivation induced by oxotremorine and sleeping induced by a sub-threshold hypnotic dose of sodium pentobarbital, ED_{50}±95% CL (confidence limit) values were calculated and compared by weighted probit analysis. Data are shown as mean±SD.

Results

Competitive binding of (±)DMCPG and its optical isomers to rat central muscarinic acetylcholine receptors The K_d value for [^{3}H]QNB binding to receptors was 6.66±0.95 nmol/L. The B_{max} was 760±92 fmol/mg. The competitive binding potency of R(–)DMCPG for [^{3}H]QNB corresponded to a K_i value of 763.75±7.31 nmol/L (n=4). An average Hill coefficient (n_H) was 1.17±0.15. The affinity of R(–)DMCPG at central muscarinic acetylcholine receptors was higher than that of (±)DMCPG (K_i=3180±263 nmol/L, n_H=0.42) and S(+)DMCPG (K_i=1699±260 nmol/L, n_H=1.26). The isomer with R(–) configuration was more potent than the isomer with S(+) configuration and (±)DMCPG. The competition profiles of R(–)DMCPG and S(+)DMCPG to rat cortex muscarinic receptors were steep and adequately described by a one-site model, $n_H>1$, which exhibited positive cooperative effects at muscarinic receptors. However, for (±)DMCPG, $n_H<1$, which exhibited negative cooperative effects at muscarinic receptors, which is not consistent with a one-site binding model (Figure 2).

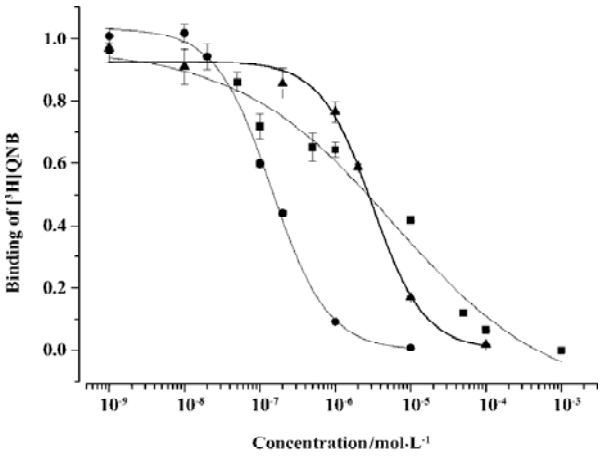

Figure 2. Effects of (±)DMCPG and its optical isomers on the binding of [^{3}H]QNB to rat central muscarinic acetylcholine receptors [●, R(–)DMCPG; ▲, S(+)DMCPG; ■, (±)DMCPG]. Rat cerebral cortex homogenate was incubated with 6 nmol/L [^{3}H]QNB for 30 min at 37 ºC in the absence and presence of increasing concentrations of different drugs. Data are the means of four independent experiments performed in duplicate.

Effect of (±) DMCPG and its optical isomers on carbachol-induced contraction Carbachol (10^{-5} nmol/L) caused contractions in guinea pig ileum. The E_{max} values for the carbachol-induced contractions were 2.90±0.17 g (n=30). (±)DMCPG and its optical isomers (10^{-9}–10^{-4} mol/L) significantly suppressed the carbachol-induced contractions ($P<0.05$; Figure 3). The IC_{50} values of (±) DMCPG , R(–) DMCPG and S(+)DMCPG were 7.78×10^{-9}, 1.88×10^{-7}, and 1.03×10^{-7} mol/L, respectively. The results revealed that (±)DMCPG was more potent in the anti-contraction of smooth

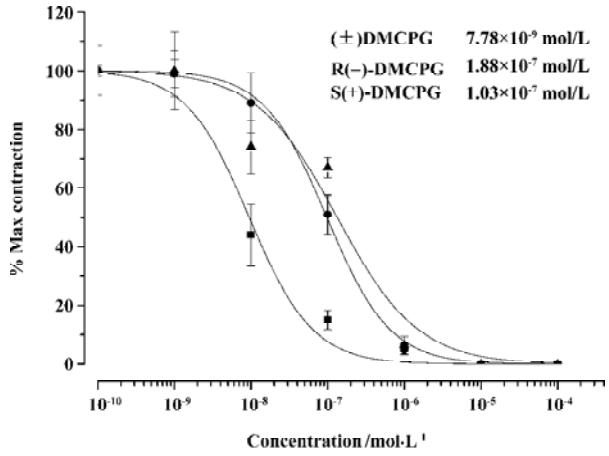

Figure 3. Concentration-response curves for (±)DMCPG and its optical isomers (10^{-9}–10^{-5} mol/L) on the maximum contractile response induced by carbachol (10^{-5} mol/L) in guinea pig ileum (●, R(–)DMCPG; ▲, S(+)DMCPG; ■, (±)DMCPG). For each experiment, contractile responses are expressed as percentages of the maximum contractile response in the absence of any antagonist. Each point represents the mean±SD of the results from 6–8 separate experiments. If not shown, SD bars fall within the boundaries of the symbol.

muscle induced by carbachol than the other two configurations (P<0.05).

Potentiation of the effect of a sub-threshold hypnotic dose of sodium pentobarbital Pentobarbital (ip, 30 mg/kg) alone did not cause sleep in mice (n=50). However, after pretreatment with R(–)DMCPG (1.68–4.89 mg/kg) and S(+)DMCPG (10–29.15 mg/kg) at 15 min intervals, sedation effects induced by a sub-threshold hypnotic dose of sodium pentobarbital were enhanced in a dose-dependent manner (Table 1). The ED_{50} values ±95% confidence limits of R(–) and S(+)DMCPG were 2.53±0.37 and 18.65±4.03 mg/kg. Of the 10 mice pre-administered with (±)DMCPG at the highest dose (29.15 mg/kg), only 2 mice lost their righting reflex, which indicates that (±)DMCPG has a weak central depressant action. The order of central inhibition effects was R(–)DMCPG> S(+)DMCPG>(±)DMCPG.

Inhibition of oxotremorine-induced salivation Oxotremorine (sc, 3 mg/kg) induced obvious salivation in mice (n=50), whereas (±)DMCPG and its optical isomers produced anti-salivation effects in a dose-dependent manner when mice were pretreated with these compounds. The ED_{50}±95% CL values for (±)DMCPG and the R(–), S (+) configurations were 2.88±0.35, 0.44±0.03, and 5.05±0.33 mg/kg, respectively, which indicates that the order of potency for inhibiting glandular secretion is R(–)DMCPG>(±)DMCPG>S(+)DMCPG (Table 2).

Table 1. Effect of (±)DMCPG and its optical isomers on sleep induced by sub-threshold hypnotic doses of sodium pentobarbital. For each experiment, the rate of loss in righting reflex is expressed as the proportion of mice that lost their righting reflex per 10 mice. n=10. Mean±SD.

Chiral compound	Dose (mg/kg)	Rate of loss in righting reflex	ED_{50}±95% CL (mg/kg)
(±)DMCPG			–
R(–)DMCPG	10.00	0.00	
	14.28	0.00	
	20.41	0.00	
	29.15	0.20	
S (+)DMCPG	1.68	0.10	2.53±0.37
	2.40	0.50	
	3.43	0.70	
	4.90	1.00	
	10.00	0.10	18.64±4.03
	14.28	0.30	
	20.41	0.60	
	29.15	0.80	

Table 2. Effect of (±)DMCPG and its optical isomers on oxotremorine-induced salivation. For each experiment, the rate of anti-salivation is expressed as the proportion of mice without salivation per 10 mice. n=10. Mean±SD.

Chiral compound	Dose (mg/kg)	Rate of loss in righting reflex	ED_{50}±95% CL (mg/kg)
(±)DMCPG			–
R(–)DMCPG	1.68	0.80	2.88±0.35
	2.40	0.60	
	3.43	0.40	
	4.90	0.20	
S (+) DMCPG	0.28	0.90	0.44±0.03
	0.40	0.70	
	0.58	0.50	
	0.82	0.20	
	2.40	0.80	5.05±0.33
	3.43	0.50	
	4.90	0.20	
	7.00	0.00	

Discussion

(±)DMCPG is a derivative of its parent compound CPG, and there is one chiral carbonic atom in the molecular struc-

ture of (±)DMCPG, causing the R(–) and S(+) enantiomers. In this study, we compared the pharmacological activities of these enantiomers, to further investigate the relationships between anti-muscarinic activity and muscarinic receptors. Interestingly, for muscarinic acetylcholinic receptors, (±)DMCPG and its optical isomers did not have the same potency trends in the tests.

In the present investigation, the pharmacological activities of (±)DMCPG and its isomers were subjected to comparative radiobinding and functional assays. In the competitive binding assay, R(–)DMCPG was 4- and 2-fold more potent than its racemate and the S(+) configuration in inhibiting the binding of [^{3}H]QNB. These results demonstrate that there was receptor stereo selective action between the muscarinic receptor and R (–)DMCPG. In this case of receptor binding, R(–)DMCPG is the eutomer. The R(–) and S(+) configurations showed positive cooperation (n_H>1) but (±)DMCPG had a negatively cooperative (n_H=0.42) relationship with the muscarinic receptor. Low Hill numbers are most often attributed to recognition by the antagonist of more than one receptor site or receptor conformation, or to an interaction of the antagonist with a second binding site on the receptor molecule causing a negative cooperative effect for the first site[7–9]. There is a second ligand-binding site on muscarinic receptors. A wide array of compounds is capable of modulating the binding of classical ligands to all five muscarinic subtypes[10–12]. Allosteric modulation of muscarinic receptors has been much investigated[13,14]. Proška and Tuèek (1994) proposed that the binding site for modulators such as alcuronium, gallamine, and related compounds is located near the binding site for classical ligands, but more superficially[15]. Our results imply that (±)DMCPG may act at the second binding site with an allosteric mechanism to muscarinic receptors. (±)DMCPG is composed of the R(–) and S(+) configurations, and R(–) and S(+)DMCPG showed marked central inhibitory effects, but (±)DMCPG had only a weak effect, even at a higher dose. Inversely, the ability of (±)DMCPG to inhibit the contraction of guinea pig ileum induced by carbachol was approximately 10 and 100 times more potent than that of R(–) and S(+)DMCPG. (±)DMCPG was the lowest one bound to the muscarinic receptor, and we can also deduce that the enantiomers must interact with each other to affect its binding characteristics and bioactivities. The allosteric mechanism of these chiral drugs needs to be further explored in subsequent experiments. However, our experiments showed that pharmacological differences exist between the optical isomers. The R(–) configuration was more potent at binding receptors and inhibiting glandular secretion, but had moderate effects on the contraction of smooth muscle. The pharmacological differences may be due to the distribution of different subtypes in different tissues. Muscarinic acetylcholine receptors (mAChR) include five subtypes of receptors (M_1–M_5). The selective action on the salivary gland of R(–)DMCPG may be related to its subtype-selective effects. Individual members of the mAChR are expressed in a complex overlapping fashion in most tissues and cell types[16]. The M_1, M_2, and M_4 subtypes of the mAchR are the predominant receptors in the central nervous system[17]. The M_1 and M_3 subtypes are the major muscarinic acetylcholine receptors in the salivary glands and M_3 is thought to be more abundant[18,19]. Guinea pig ileum smooth muscle is enriched with muscarinic receptors, the majority of which are of the M_2 subtype, and the remaining minority are of the M_3 subtype[20,21]. In our experiments, we comparatively studied the anti-muscarinic pharmacological profiles of these compounds to see whether there is any correlation between pharmacological activity and muscarinic subtype selectivity. Fulfilling our expectations, of these three chiral drugs, (±)DMCPG had the greatest ability to inhibit smooth muscle contraction as a muscarinic receptor antagonist, whereas R(–)DMCPG had a moderate effect on smooth muscle contraction, but had the greatest anti-salivary effect and enhancement of sedation effects caused by sub-threshold hypnotic doses of sodium pentobarbital. S(+)DMCPG was less potent in all experimental models. Our results imply that there are subtype-selective mechanisms that correspond to the different pharmacological actions of the compounds. Therefore, further studies are necessary to resolve the underlying actions of (±)DMCPG and its enantiomers with respect to muscarinic subtype receptors.

In conclusion, the present work demonstrated that that there are receptor stereo selective actions between muscarinic receptors and the R(–) configuration of DMCPG. R(–) DMCPG acted as a eutomer relative to its S(+) configuration in the racemate. These differences must be related to subtype selectivity and allosteric mechanisms.

References

1 Dai JG, Liu CG, Yu LS, Yang AZ, Jia HB, Wang, KN. Antimotion sickness effect of phencynonate hydrochloride in man. Chin J Aerospace Med 1997; 8: 10–4.

2 Deng YJ, Zhang YM. Study on the efficacy of phencynonate hydrochloride tablets in prevention of motion sickness. Chin J New Drugs 2001; 10: 453–4.

3 Wang LY, Zheng JQ, Zhong BH, Ruan JX, Liu KL. Pharmacological profiles of anticholinergic agents, phencynonate hydrochloride and its optical isomers. Acta Pharmacol Sin 2005; 26: 613–40.

4 Yamamura HI, Snyder SH. Muscarinic cholinergic binding in rat brain. Proc Natl Acad Sci USA 1974; 71: 1725–9.
5 Lowry OH, Rosebrough NJ, Farr AL, Randall RJ. Protein measurement with the Folinphenol reagent. J Biol Chem 1951; 193: 265–75.
6 Cheng Y, Prusoff WH. Relationship between the inhibition constant (Ki) and the concentration of inhibitor which causes 50 percent inhibition (IC_{50}) of an enzymatic reaction. Biochem Pharmacol 1973; 22: 3099–108.
7 Nathanson NM. Molecular properties of the muscarinic acetylcholine receptor. Annu Rev Neurosci 1987; 10: 195–236.
8 Hulme EC, Berrie CP, Birdsall NJM, Burgen ASV. Two populations of binding sites for muscarinic receptor antagonists in the rat heart. Eur J Pharmacol 1981; 73: 137–42.
9 Stockton J, Birdsall NJM, Burgen ASV, Hulme EC. Modification of the binding properties of muscarinic receptors by gallamine. Mol Pharmacol 1983; 23: 551–7.
10 Ellis J. Allosteric binding sites on muscarinic receptors. Drug Dev Res 1997; 40: 193–204.
11 Christopoulos A, Lanzafame A, Mitchelson F. Allosteric interactions at muscarinic cholinoceptors. Clin Exp Pharmacol Physiol 1998; 25: 185–94.
12 Lee NH, El-Fakahany EE. Allosteric antagonists of the muscarinic acetylcholine receptor. Biochem Pharmacol 1991; 42: 199–205.
13 Holzgrabe U, Mohr K. Allosteric modulators of ligand binding to muscarinic acetylcholine receptors. Drug Res Today 1998; 3: 214–22.
14 Christopoulos A, Lanzafame A, Mitchelson F. Allosteric interactions at muscarinic cholinoceptors. Clin Exp Pharmacol Physiol 1998; 25: 185–94.
15 Proška J, Tuèek S. Mechanisms of steric and cooperative actions of alcuronium on cardiac muscarinic acetylcholine receptors. Mol Pharmacol 1994; 45: 709–17.
16 Wess J. Novel insights into muscarinic acetylcholine receptor function using gene targeting technology. Trends Pharmacol Sci 2003; 24: 414–20.
17 Volpicelli LA, Levey AI. Muscarinic acetylcholine receptor subtypes in cerebral cortex and hippocampus. Prog Brain Res 2004; 145: 59–66.
18 Nakamura T, Matsui M, Uchida K, Futatsugi A, Kusakawa S, Matsumoto N, *et al*. M (3) muscarinic acetylcholine receptor plays a critical role in parasympathetic control of salivation in mice. J Physiol 2004; 558: 561–75.
19 Gautam D, Heard TS, Cui Y, Miller G, Bloodworth L, Wess J. Cholinergic stimulation of salivary secretion studied with M1 and M3 muscarinic receptor single- and double-knockout mice. Mol Pharmacol 2004; 66: 260–7.
20 Ehlert FJ, Thomas EA. Functional role of M2 muscarinic receptors in the guinea pig ileum. Life Sci 1995; 56: 965–71.
21 Honda K, Takano Y, Kamiya H. Pharmacological profiles of muscarinic receptors in the longitudinal smooth muscle of guinea pig ileum. Jpn J Pharmacol 1993; 62: 43–7.

Acta Pharmacologica Sinica 2005 Oct; 26 (10): 1193–1200

Full-length article

Gene transfer of heat-shock protein 20 protects against ischemia/reperfusion injury in rat hearts[1]

Yan-hui ZHU, Tie-min MA, Xian WANG[2]

Department of Physiology and Pathophysiology, Basic Medical College, Key Laboratory of Molecular Cardiovascular Biology, Ministry of Education, Peking University, Beijing 100083, China

Key words

reperfusion injury; adenovirus; apoptosis; myocardial infarction; heat-shock proteins

[1] Project supported by the National Basic Research Program of China (No G2000056908) awarded to Xian WANG.
[2] Correspondence to Prof Xian WANG. Phn/Fax 86-10-8280-1443. E-mail xwang@bjmu.edu.cn

Received 2004-12-08
Accepted 2005-03-30

doi: 10.1111/j.1745-7254.2005.00139.x

Abstract

Aim: To explore whether overexpression of HSP20 in the myocardium could protect against ischemia/reperfusion injury in rats. **Methods:** Rat hearts were injected with vector, recombinant adenovirus encoding green fluorescent protein (Ad.GFP) or recombinant adenovirus encoding wild-type HSP20 (Ad.HSP20) in the left ventricle. Four days later, hearts were removed and expression of HSP20 was measured in the left ventricle. Subsets of animals in the vector-, Ad.GFP- , and Ad.HSP20-treated groups were subjected to 20-min ischemia and 120-min reperfusion. Myocardial injury was evaluated by infarct size and level of serum cardiac troponin T and creatine phosphokinase. Apoptosis of cardiomyocytes was determined by TUNEL staining. Cardiac function was evaluated by hemodynamic indexes. **Results:** Infarct size and serum cardiac troponin T and creatine phosphokinase levels were significantly reduced in Ad.HSP20-treated hearts compared with vector- and Ad.GFP-treated hearts. The ratio of TUNEL-positive cardiomyocytes to total number of cardiomyocytes in the Ad.HSP20 group was significantly reduced as compared with the vector and Ad.GFP groups. Left ventricular end systolic pressure, and maximal rate of pressure increase ($+dp/dt_{max}$) and decrease ($-dp/dt_{min}$) values were increased significantly, while left ventricular end diastolic pressure was decreased significantly in Ad.HSP20-treated hearts compared with vector- and Ad.GFP-treated hearts. **Conclusion:** These data indicate that the cardioprotective effects of HSP20 may contribute to the reduction of myocardial necrosis and apoptosis in ischemia/reperfusion injury in rats.

Introduction

Members of the small heat shock protein (sHSP) family, including HSP20, HSP25, HSP27, αB-crystallin, and myotonic dystrophy kinase binding protein, are expressed in muscle tissues and share a homologous sequence of approximately 80–100 amino acids at the C-terminus, known as the α crystallin domain[1,2]. The past decade has witnessed the discovery of new mammalian sHSP, of which HSP20 is the best characterized. HSP20 was co-purified from skeletal muscle with αB-crystallin and HSP27 by affinity chromatography on a column of immobilized antibodies against αB-crystallin[3]. Exposure of rat diaphragm tissue to heat stress *in vitro* results in the redistribution of HSP20, as well as αB-crystallin and HSP27, from the cytosol into insoluble fractions, and enhanced dissociation of the aggregated form to the small form, which is characteristic of stress proteins[4]. Stable overexpression of HSP20 in Chinese hamster ovary cells results in enhanced survival after heat shock, which is similar to results obtained with αB-crystallin[5]. Chu *et al*[6] were the first to identify the *de novo* phosphorylation of cardiac HSP20 in mouse cardiomyocytes after prolonged activation of the β-adrenergic signaling pathway. The adenovirus-mediated overexpression of HSP20 in adult rat cardiomyocytes increases cell contractility, which indicates that HSP20 is involved in the regulation of myocardial contractility[6,7].

Heat shock proteins have been implicated in modulating the cellular response to many stressors, and as molecular

chaperones in suppressing the aggregation or assisting in the refolding of partially denatured proteins. They usually protect against ischemic/reperfusion (I/R) injury *in vitro*[8–11] and *in vivo*[12–14]. However, whether gene transfer of the HSP20 gene into the beating heart produces a myocardial protective effect has not been shown. In the present study, we transferred the HSP20 gene through a recombinant adenovirus encoding HSP20 into the myocardium, and showed that HSP20 protected against I/R injury, probably by reducing myocardial apoptosis and necrosis in rats.

Materials and methods

Animals and experimental protocols Male adult Sprague-Dawley rats (230 g–280 g) received a standard diet and free water. The treatment of the animals and experimental protocols adhered to the guidelines of the Health Sciences Center of Peking University (Beijing, China). The animals were allowed to readjust to the new housing environment for 1 week before the experiments.

Rats were assigned randomly to 4 groups. In the no-vector control group, the chest was opened and injected with saline. The I/R control group was also injected with saline. The third group received the recombinant adenovirus encoding wild-type HSP20 (Ad.HSP20), and the fourth group received the recombinant adenovirus encoding green fluorescent protein (Ad.GFP).

Construction of recombinant adenoviruses The recombinant Ad.HSP20 and Ad.GFP were prepared as described previously[15]. Adenovirus was propagated in 293 cells and purified by 2 rounds of CsCl density ultracentrifugation (4 °C, 13 000×*g* for 105 min and 16 h, respectively). Viral stocks were then desalted through a PD-10 desalting column (Amersham Biosciences, Buckinghamshire, UK) into a Tris-buffered solution (10 mmol/L Tris, pH 8.0, 2 mmol/L $MgCl_2$ and 4% sucrose)[16], plaque-titered, aliquoted, and stored at -80 °C with 4% sucrose until use.

***In vivo* intracoronary delivery of adenoviruses** The surgical procedures were carried out as described previously[17]. Donor rats were anesthetized with sodium pentobarbital (50 mg/kg, ip). Further injections were given as needed throughout the surgical procedure. Animals were placed supine on a thermoregulated table (37 °C) . The surgery was carried out under sterile conditions. The animals were intubated and ventilated on a positive-pressure ventilator. The tidal volume was set at 1.5 mL–2.5 mL, and the respiratory rate was adjusted to within the range of 80 cycles/min to 90 cycles/min to maintain normal arterial p_{aO2}, p_{aCO2}, and pH. The chest was entered through a left intercostal approach. Before virus infusion, adenosine (0.15 mg), lidocaine (0.03 mg), and heparin (50 U) were administered via the jugular vein. With the use of a 26 gauge needle, 200 μL diluted replication-deficient adenovirus (2.2×10^{10} pfu) or 200 μL sterile saline were injected from the apex of the left ventricle into the left ventricular cavity while the aorta and pulmonary arteries were clamped just above the aorta root. The clamp was maintained for 15 s when the heart pumped against a closed system. After injection, the exposed heart was monitored for 5 min for resumption of normal sinus rhythm. Hemodynamic indices were measured and electrocardiography was carried out throughout the experimental period.

Myocardial infarction protocol Four days after the injection of saline or virus, the animals were re-anesthetized and ventilated artificially with room air. The thorax was reopened and the heart were exposed to identify the left anterior descending coronary artery (LAD). A 7-0 silk suture was passed around the LAD with an atraumatic needle just 4 mm inferior to the left auricle, and the artery was occluded by snaring with a vinyl tube through which the ligature had been passed. The coronary artery was occluded by pulling the snare tight and securing it with a hemostat. Ischemia was confirmed by myocardial blanching and electrocardiography evidence of injury. After 20-min ischemia, the ligature was released and the heart was reperfused for 2 h. Reperfusion was identified by an obvious ST segment change.

Measurement of infarction At the end of the infarction protocol, the ligature around the LAD was retightened and 0.1 mL of 10% Evans blue dye was injected as a bolus into the left ventricle (LV) cavity with a 26-gauge needle positioned in the apex of the heart. When the eyes turned blue, the animals were euthanized immediately, the heart was excised and rinsed in water to remove excess dye, the atria and right ventricular free wall were removed, and the remaining LV was frozen. The LV was then cut from apex to base into 4–6 transverse slices of 2 mm thick. Each slice was weighed and then incubated in 4% triphenyltetrazolium chloride solution (TTC) in isotonic pH 7.4 phosphate buffer at 37 °C for 30 min. The slices were subsequently fixed in 10% formalin solution for 24 h. Viable tissue (red-stained by the TTC) was distinguished easily from the infarcted regions (pale or unstained by the TTC) and the risk area (unstained by Evans blue). The total slice area, the infarcted area, and the risk area of each slice were determined by computer-assisted planimetry (Leica Qwin image analysis software; Leica, Cambridge, UK). During planimetry, the operator was blinded as to the type of animal. The ratios of risk area to total slice area, infarct area to total slice area, and infarct area to risk

area were calculated and multiplied by the weight of the slice to determine risk and infarct weight per slice. Infarct size was expressed as a proportion of LV mass or risk area mass.

Hemodynamic studies Hemodynamic measurements were taken at 0 min, 10 min and 20 min ischemia and 30 min, 60 min and 120 min reperfusion. A 1.5 F micronanometer-tipped catheter was advanced into the LV through the right carotid artery. The heart rate, blood pressure, left ventricular end diastolic pressure (LVEDP), left ventricular end systolic pressure (LVESP) and maximal rates of pressure increase ($+dp/dt_{max}$) and decrease ($-dp/dt_{max}$) were recorded on a polygraph (NEC San-ei Instruments, Japan).

Measurement of serum cardiac troponin T (cTnT) and creatine phosphokinase (CK) levels At the end of the myocardial I/R experiment, a 1-mL blood sample was obtained from the carotid cannula, stored at 4 °C for 30 min, and centrifuged at 3000×*g* for 10 min. The serum was stored at -40 °C prior to analysis. The concentration of serum cTnT was determined by the short-turn-around-time (STAT) assay (Roche Diagnostics, Basel, Switzerland), with use of the Roche Elecsys 2010 immunoassay analyzer (Roche Diagnostics). The serum was also analyzed spectrophotometrically for CK activity (Roche Diagnostics).

Western blot analysis Three hearts from each of the experimental groups were used separately for measurement of HSP20 by Western blot analysis. After 4 d of injection of saline or virus, the hearts were removed quickly, and the LV was separated and frozen in liquid nitrogen. The frozen LV tissue was homogenized in protein extraction buffer containing 20 mmol/L Tris-HCl, pH 7.4, 1% Trion X-100, 150 mmol/L NaCl, 1 mmol/L ethylenediaminetetracetic acid, 2.5 mmol/L sodium pyrophosphate, 1 mmol/L NaF, 1 mmol/L Na_3VO_4 and 0.1 mmol/L phenylmethylsulfonyl fluoride. Aliquots were resolved on sodium dodecyl sulphate-polyacrylamide gel electrophoresis. Proteins were transferred to polyvinylidene difluoride membranes (Schleicher & Schuell, Keene, NH, USA) and incubated with primary polyclonal anti-HSP20 antibodies (1:1000) (presented by Prof Rui-ping XIAO, NIH, USA), which recognized HSP20, at 4 °C overnight. Bound antibodies were detected using a secondary antibody conjugated to horseradish peroxidase (Santa Cruz Biotechnology, Inc, CA,USA) and visualized by use of an enhanced chemiluminescence kit (SuperSignal® West Pico Trial Kit, Pierce Biotechnology, Inc, IL, USA) and exposed to X-ray film for the appropriate time.

Terminal dUTP nick-end labelling staining Hearts were isolated from each group after I/R for analysis using the terminal dUTP nick-end labeling (TUNEL) assay. Tissue samples were fixed in a 4% paraformaldehyde solution, paraffin embedded, and cut transversely into 6-μm sections. The assay was operated according to the manufacturer's instructions (DeadEnd™ Fluorometric TUNEL System; Promega, WI, USA). Stained samples were analyzed using a confocal microscope; at least 500 cells were counted in randomly selected views.

Statistical analysis Data were expressed as mean±SD. Differences were analyzed for significance by one-way repeated-measures ANOVA and further analyzed with the use of the Newman-Keuls test for multiple comparisons between treatment groups. The results were considered significant at $P<0.05$.

Results

Expression of HSP20 Intraventricular injection of Ad.HSP20 *in vivo* resulted in increased HSP20 expression in the LV as compared with vector and Ad.GFP treatments (Figure 1A). The hearts treated with Ad.GFP showed only low-level of HSP20 expression, which indicates that treatment with viral vectors has no significant effect on HSP20 expression in the rat myocardium. LV treated with Ad.HSP20 showed homogenous expression of GFP, whereas those treated with vector showed no background fluorescence (Figure 1B).

Myocardial infarction Ad.HSP20-treated hearts showed a significant reduction in infarct size (39.2%±4.3% risk area) compared with vector- and Ad.GFP-treated hearts (56.3%±2.9% and 54.9%±8.1%, respectively; $P<0.01$; Figure 2A). Infarct size did not differ between vector- and Ad.GFP-treated hearts ($P>0.05$). A similar result was observed when infarct size was expressed as a proportion of LV (Figure 2B). Both results suggest that the reduced infarct size observed in Ad.HSP20-injected hearts is entirely due to the overexpression of HSP20. However, the risk areas (% of LV) were not significantly different among the groups (ie 53.2%±6.5%, 57.9%±7.3%, and 56.4%±7.5% in the vector-, Ad.GFP-, and Ad.HSP20-treated groups, respectively; $P>0.05$; Figure 2C).

HSP20 gene delivery reduced serum cTnT and CK levels Ad.HSP20-treated hearts showed a significant reduction in cTnT release (2.2 μg/L±1.7 μg/L) compared with vector- and Ad.GFP-treated hearts (12.9 μg/L±3.2 μg/L, and 11.8 μg/L±3.1 μg/L, respectively; $P<0.01$; Figure 3A). Similar results were observed for CK release (Figure 3B).

HSP20 gene delivery attenuated apoptosis in the acute ischemia/reperfusion rat model Figure 4A shows representative apoptotic cardiomyocytes identified by TUNEL staining in the I/R-injured region. The ratio of TUNEL-positive

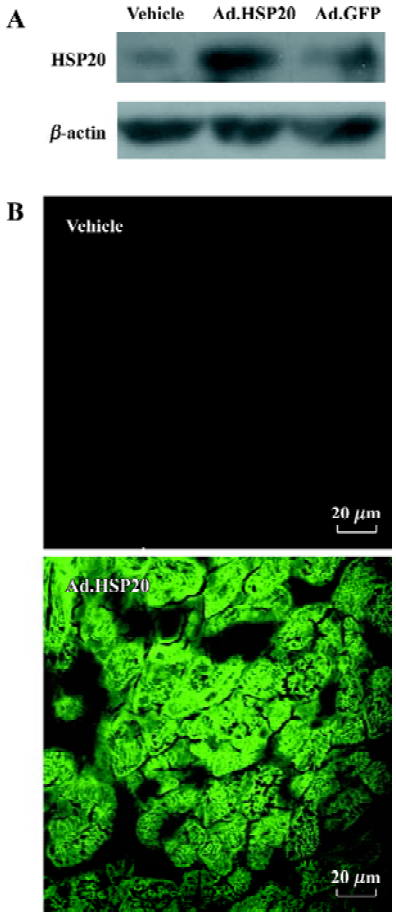

Figure 1. Expression of adenovirus-mediated gene delivery 4 d after intracoronary gene delivery. (A) Western blot showing expression of HSP20 proteins and β-actin after intracoronary delivery of vector, recombinant adenovirus encoding wild-type HSP20 (Ad.HSP20) or recombinant adenovirus encoding green fluorescent protein (Ad.GFP). (B) Representative image of high efficiency of GFP expression in hearts compared with vector after injection of Ad.HSP20.

cardiomyocytes to total number of cardiomyocytes in the Ad.HSP20 group was significantly reduced as compared with the vector and Ad.GFP groups (15.4%±3.2% *vs* 25.7%±4.5% and 27.6%±2.2%, $P<0.01$; Figure 4B).

HSP20 gene delivery improved cardiac function *in vivo* LVEDP, LVESP, $+dp/dt_{max}$ and $-dp/dt_{max}$ values are shown in Figure 5. All parameters were comparable among the 3 groups before and during ischemia and during reperfusion. All parameters, except LVEDP, declined in value after ischemia. LVEDP in HSP20-treated rats was significantly decreased after 60-min reperfusion compared with that in vector- and Ad.GFP-treated rats ($P<0.05$, Figure 5A). LVESP, $+dp/dt_{max}$, and $-dp/dt_{max}$ values in HSP20-treated rats were significantly increased after 60-min reperfusion compared with those in vector- and Ad.GFP-treated rats ($P<0.05$, Figure 5B, 5C, 5D).

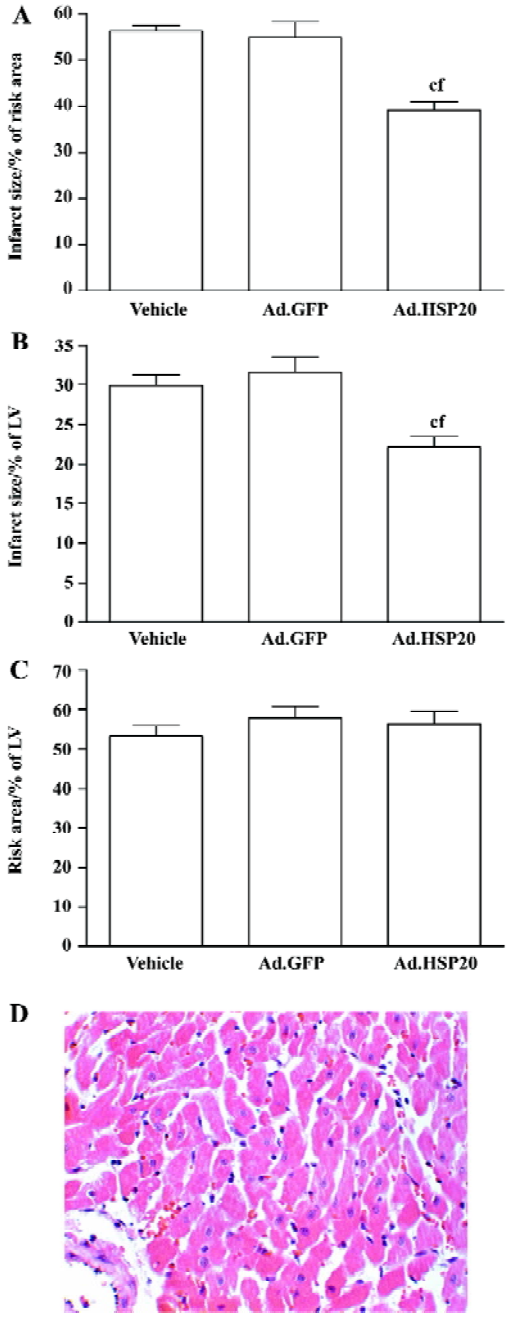

Figure 2. Effect of HSP20 gene delivery on infarct size. (A) Ratio of infarct sizes to risk areas. (B) Ratio of infarct sizes to left ventricle. (C) Ratio of risk areas to left ventricle. $n=6$. Mean±SD. $^cP<0.01$ *vs* Ad.GFP. (D) Typical reperfusion injury was observed in all groups by high-power microscopy (×40).

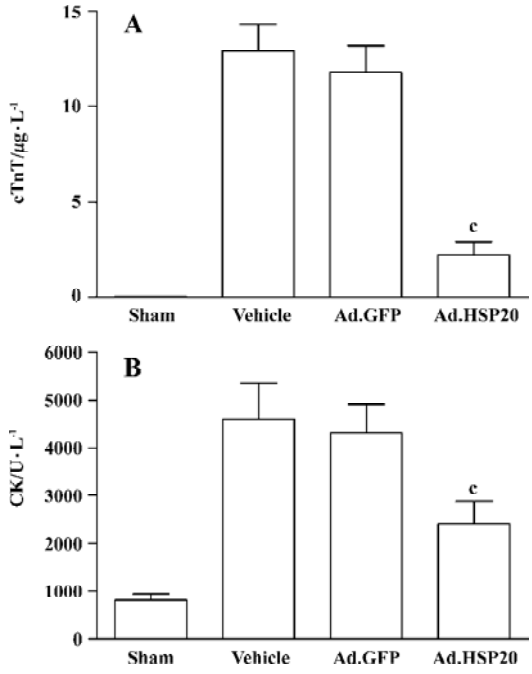

Figure 3. (A) Alterations in the serum levels of cardiac troponin T (cTnT). (B)Alterations in the serum levels of creatine phosphokinase (CK). n=6. Mean±SD. ^cP<0.01 *vs* Ad.GFP.

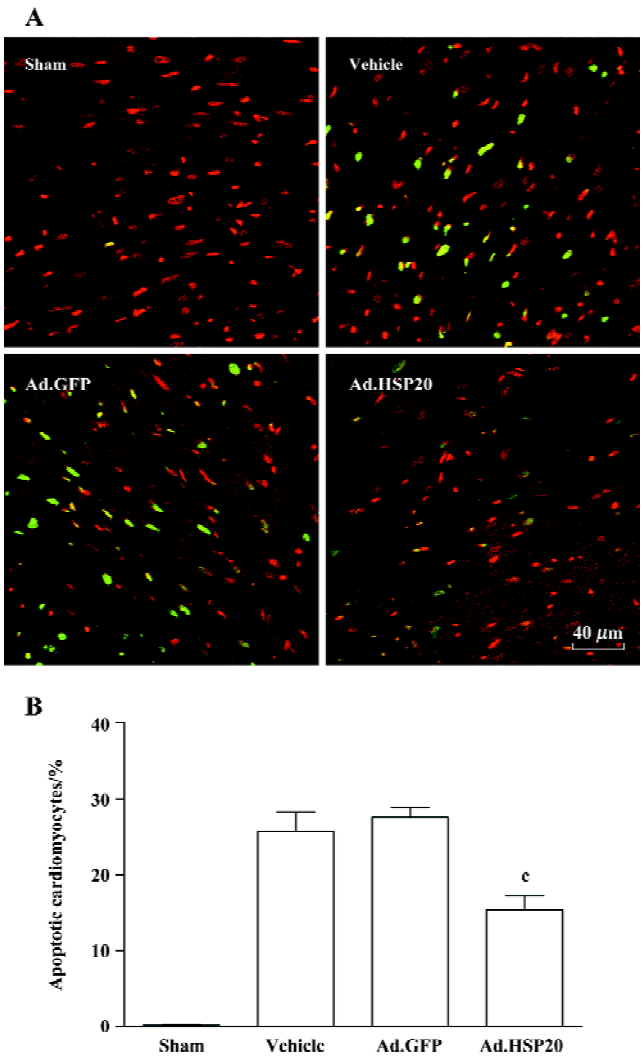

Figure 4. Terminal dUTP nick-end labelling staining showed *in vivo* cardiomyocyte apoptosis after 20-min ischemia and 120-min reperfusion. (A) Cardiomyocytes are depicted by red fluorescence from propidium iodide. Yellow fluorescence showed TUNEL-positive nuclei. (B) Proportion of positive TUNEL-stained nuclei in tissue sections from the no-vector control group or rat hearts exposed to ischemia/reperfusion under different treatments. n=3–4. Mean±SD. ^cP<0.01 *vs* Ad.GFP.

Discussion

Gene therapy has emerged as a genuine alternative therapy in coronary artery disease, including ischemic heart disease. One of the commonly used intramyocardial gene transfer methods is direct intramyocardial injection. There have been a few promising trials involving the use of direct intramyocardial injection in this area[18,19]. However, the technical problems with this method are that only a small volume of the myocardium is accessible for transfection and the distribution of transgenes in the myocardium is not homogeneous. To overcome these problems, we used an *in vivo* intracoronary gene delivery method that modified the approach of Hajjar *et al*[17] to transduce the HSP20 gene into the ventricular muscle with the use of recombinant adenoviral vectors. The adenoviral vectors are delivered into the myocardium via the coronary circulation. Using this delivery method, we sought to elucidate a direct cause and effect relationship between HSP20 and cardioprotective effects in the intact rat heart.

The present study demonstrates, for the first time, that gene transfer of Ad.HSP20 into the LV muscle causes robust expression of HSP20 as compared with vector or Ad.GFP transfer. Ad.GFP-treated LV showed no significant increase in HSP20 expression compared with vector-treated LV. These results suggest that the increased expression in the Ad.HSP20-treated hearts is not due to virus-related stress.

Infarct size was reduced significantly in the I/R hearts injected with Ad.HSP20. We also examined serum cTnT and CK levels independently. cTnT originating exclusively from the myocardium clearly differs from skeletal muscle troponin T. As a result of its high tissue specificity, cTnT is a cardio-specific, highly sensitive marker for myocardial damage[20]. Our results showed that the cTnT level in Ad.HSP20-treated

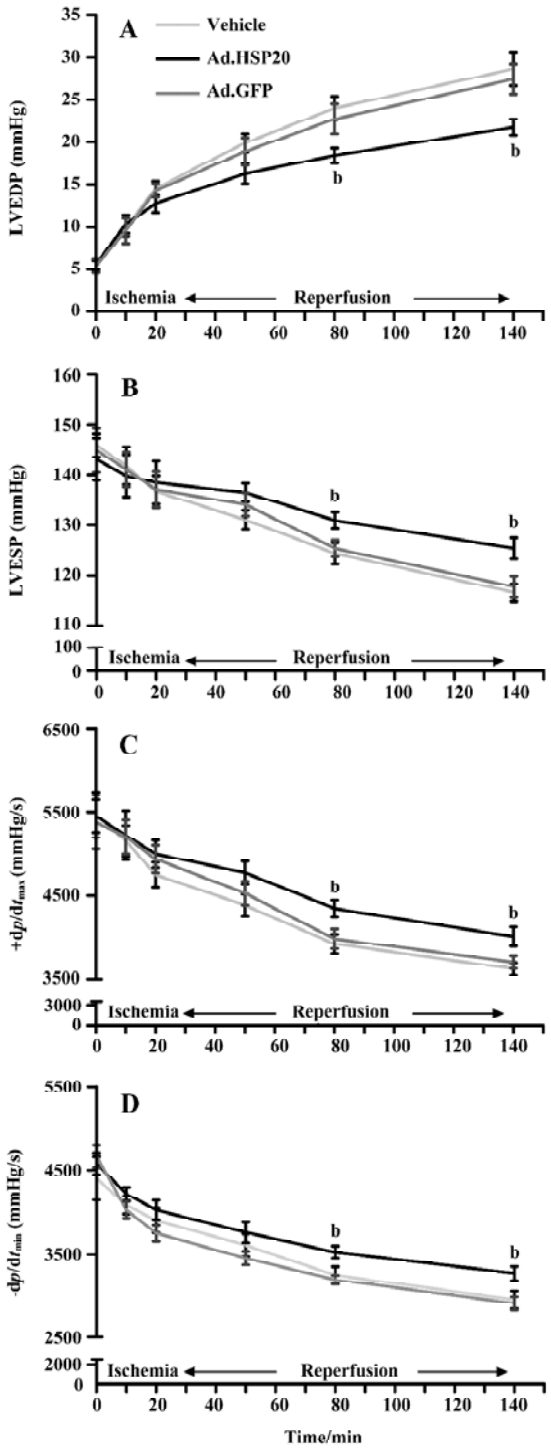

Figure 5. Cardiac function *in vivo*. Left ventricular end diastolic pressure (LVEDP) (A), left ventricular end systolic pressure (LVESP) (B), maximal rate of pressure increase ($+dp/dt_{max}$) (C), and decrease ($-dp/dt_{min}$) (D) were measured in the left ventricle at different time points in vector-, Ad.HSP20-, or Ad.GFP-treated hearts. n=6−8. Mean±SD. $^bP<0.05$ *vs* Ad.GFP.

hearts was reduced significantly as compared with that in vector- and Ad.GFP-treated hearts. Similar results were shown with CK. TUNEL staining showed that apoptosis of cardiomyocytes was reduced in Ad.HSP20-treated hearts.

The decrease of LVEDP and increase of LVESP, $+dp/dt_{max}$ and $-dp/dt_{max}$ in HSP20-treated hearts may be explained by HSP20 being an actin-associated protein. It is biochemically associated with αB-crystallin and localized to distinct transverse bands in a pattern similar to αB-crystallin and sarcomeric actin[21,22]. Phosphorylated HSP20 increases the contractility rate of cardiac myocytes, which indicates that HSP20 is involved in the regulation of myocardial contractility[6,7].

Heat shock proteins are a family of endogenous protective proteins. Various HSP have protective effects against stress injury. HSP70 prevents cell death by inhibiting apoptosis via associating with apoptosis protease activating factor-1 (Apaf-1) and blocking the assembly of a functional apoptosome[23]. Combined and individual mitochondrial HSP60 and HSP10 expression in cardiomyocytes protects mitochondrial function and decreases apoptotic cell death induced by simulated I/R accompanied by decreased mitochondrial cytochrome c release and caspase-3 activity[11]. HSP60 interacts with Bax and Bak to regulate apoptosis[24]. Overexpression of αB-crystallin in transgenic mice hearts provides resistance to I/R injury by negatively regulating myocyte and non-myocyte apoptosis[25]. HSP27 binds to cytochrome c released from the mitochondria into the cytosol and prevents cytochrome c-mediated interaction of Apaf-1 with procaspase-9[26]. These results highlight the notion that the protective effects of HSP are closely related to mitochondrial function. Thus, HSP are anti-apoptotic proteins in cardiomyocytes.

Myocardial ischemia is followed frequently by reperfusion. Reperfusion and the resultant re-oxygenation lead to the generation of oxygen radicals that can cause reperfusion injury. Our results *in vivo* are consistent with those of Fan *et al*[15], who showed that HSP20 and its phosphorylation at Ser16 might provide protective effects against β-agonist-induced apoptosis *in vitro*.

Death of cardiomyocytes due to I/R injury is caused by 2 distinct mechanisms, necrosis, and apoptosis, which contribute independently to myocardial infarction[25,27]. The infarct area represents cell death, including necrotic cell death and apoptotic cell death. cTnT and CK are indicators of myocardial necrosis, whereas TUNEL staining can reveal apoptosis. Thus, our results suggest that the protective effect of HSP20 is attributed to a reduction of necrosis and apoptosis in cardiomyocytes. In addition, our recent data shows that lactate dehydrogenase release and caspase-3

activity in H9c2 cells infected with Ad.HSP20 are also decreased. Therefore, the cardioprotective effect of HSP20 *in vivo* might be mediated mainly by inhibiting both cardiomyocyte necrosis and apoptosis.

In conclusion, our results show that overexpression of HSP20 protects against I/R injury *in vivo*, not only by inhibiting cardiomyocyte necrosis and apoptosis but also by increasing myocardial contractility. Our data suggest that HSP20 is a potential therapeutic protein for ischemic diseases and additional experiments should be carried out.

Acknowledgements

We are grateful to Prof Rui-ping XIAO (Laboratory of Cardiovascular Science, Gerontology Research Center, National Institutes of Health, Bethesda, MD, USA) for her advice during this research.

References

1 Boelens WC, Croes Y, de Ruwe M, de Reu L, de Jong WW. Negative charges in the C-terminal domain stabilize the αB-crystallin complex. J Biol Chem 1998; 273: 28085–90.

2 Suzuki A, Sugiyama Y, Hayashi Y, Nyu IN, Yoshida M, Nonaka I, *et al*. A novel member of the small heat shock protein family, binds and activates the myotonic dystrophy protein kinase. J Cell Biol 1998; 140: 1113–24.

3 Kato K, Shinohara H, Goto S, Inaguma Y, Morishita R, Asan T. Copurification of small heat shock protein with alpha B crystallin from human skeletal muscle. J Biol Chem 1992; 267: 7718–25.

4 Kato K, Goto S, Inaguma Y, Hasegawa K, Morishita R, Asano T. Purification and characterization of a 20-kDa protein that is highly homologous to αB crystallin. J Biol Chem 1994; 269: 15302–9.

5 van de Klundert FAJM, van den IJssel PRLA, Stege GJ, de Jong WW. Rat Hsp20 confers thermoresistance in a clonal survival assay, but fails to protect coexpressed luciferase in Chinese hamster ovary cells. Biochem Biophys Res Commun 1999; 254: 164–8.

6 Chu G, Egnaczyk GF, Zhao W, Jo SH, Fan GC, Maggio JE, *et al*. Phosphoproteome analysis of cardiomyocytes subjected to β-adrenergic stimulation: identification and characterization of a cardiac heat shock protein p20. Circ Res 2004; 94: 184–93.

7 Pipkin W, Johnson JA, Creazzo TL, Burch J, Komalavilas P, Brophy C. Localization, macromolecular associations, and function of the small heat shock-related protein HSP20 in rat heart. Circulation 2003; 107: 469–76.

8 Mestril R, Chi SH, Sayen MR, O'Reilly K, Dillmann WH. Expression of inducible stress protein 70 in rat heart myogenic cells confers protection against simulated ischemia-induced injury. J Clin Invest 1994; 93: 759–67.

9 Lau S, Patnaik N, Sayen MR, Mestril R. Simultaneous overexpression of two stress proteins in rat cardiomyocytes and myogenic cells confers protection against ischemia-induced injury. Circulation 1997; 96: 2287–94.

10 Martin JL, Mestril R, Hilal-Dandan R, Brunton LL, Dillmann WH. Small heat shock proteins and protection against ischemic injury in cardiac myocytes. Circulation 1997; 96: 4343–8.

11 Lin KM, Lin B, Lian IY, Mestril R, Scheffler IE, Dillmann WH. Combined and individual mitochondrial HSP60 and HSP10 expression in cardiac myocytes protects mitochondrial function and prevents apoptotic cell deaths induced by simulated ischemia-reoxygenation. Circulation 2001; 103: 1787–92.

12 Okubo S, Wildner O, Shah MR, Chelliah JC, Hess ML, Kukreja RC. Gene transfer of heat-shock protein 70 reduces infarct size *in vivo* after ischemia/reperfusion in the rabbit heart. Circulation 2001; 103: 877–81.

13 Hutter JJ, Mestril R, Tam EK, Sievers RE, Dillmann WH, Wolfe CL. Overexpression of heat shock protein 72 in transgenic mice decreases infarct size *in vivo*. Circulation 1996; 94: 1408–11.

14 Zhong N, Zhang Y, Fang QZ, Zhou ZN. Intermittent hypoxia exposure-induced heat-shock protein 70 expression increases resistance of rat heart to ischemic injury. Acta Pharmacol Sin 2000; 21: 467–72.

15 Fan GC, Chu G, Mitton B, Song Q, Yuan Q, Kranias EG. Small heat-shock protein Hsp20 phosphorylation inhibits β-agonist-induced cardiac apoptosis. Circ Res 2004; 94: 1474–82.

16 Nyberg-Hoffman C, Aguilar-Cordova E. Instability of adenoviral vectors during transport and its implication for clinical studies. Nat Med 1999; 5: 955–7.

17 Hajjar RJ, Schmidt U, Matsui T, Guerrero JL, Lee KH, Gwathmey JK, *et al*. Modulation of ventricular function through gene transfer *in vivo*. Proc Natl Acad Sci USA 1998; 95: 5251–6.

18 Losordo DW, Vale PR, Symes JF, Dunnington CH, Esakof DD, Maysky M, *et al*. Gene therapy for myocardial angiogenesis. Initial clinical results with direct myocardial injection of phVEGF165 as sole therapy for myocardial ischemia. Circulation 1998; 98: 2800–4.

19 Rosengart TK, Lee LY, Patel SR, Sanborn TA, Parikh M, Bergman GW, *et al*. Angiogenesis gene therapy: phase I assessment of direct intramyocardial administration of an adenovirus vector expression VEGF121 cDNA to individuals with clinically significant severe coronary artery disease. Circulation 1999; 100: 468–74.

20 Zacharowski K, Otto M, Hafner G, Chatterjee PK, Thiemermann C. Endotoxin induces a second window of protection in the rat heart as determined by using *p*-nitro-blue tetrazolium staining, cardiac troponin T release, and histology, Arterioscler Thromb Vasc Biol 1999; 19: 2276–80.

21 Brophy CM, Lamb S, Graham A. The small heat shock-related protein-20 is an actin-associated protein. J Vasc Surg 1999; 29: 326–33.

22 Rembold CM, Zhang E. Localization of heat shock protein 20 in swine carotid artery. BMC Physiol 2001; 1: 10.

23 Beere HM, Wolf BB, Cain K, Mosser DD, Mahboubi A, Kuwana T, *et al*. Heat-shock protein 70 inhibits apoptosis by preventing recruitment of procaspase-9 to the Apaf-1 apoptosome. Nat Cell Biol 2000; 2: 469–75.

24 Kirchhoff SR, Gupta S, Knowlton AA. Cytosolic heat shock protein 60, apoptosis, and myocardial injury. Circulation 2002; 105: 2899–904.

25 Ray PS, Martin JL, Swanson EA, Otani H, Dillman WH, Das DK. Transgene overexpression of αB crystallin confers simultaneous protection against cardiomyocyte apoptosis and necrosis during

myocardial ischemia and reperfusion. FASEB J 2001; 15: 393–402.
26 Bruey JM, Ducasse C, Bonniaud P, Ravagnan L, Susin SA, Diaz-Latoud C, *et al*. Hsp27 negatively regulates cell death by interacting with cytochrome C. Nat Cell Biol 2000; 2: 645–52.
27 Kajstura J, Cheng W, Reiss K, Clark WA, Sonnenblick EH, Krajewski S, *et al*. Apoptotic and necrotic myocyte cell deaths are independent contributing variables of infarct size in rats. Lab Invest 1996; 74: 86–107.
28 Zhu YH, Wang X. Overexpression of heat-shock protein 20 in rat heart myogenic cells confers protection against simulated ischemia/reperfusion injury. Acta Pharmacol Sin 2005; 26: 1076–80.

Acta Pharmacologica Sinica 2005 Oct; 26 (10): 1201–1211

Full-length article

Novel cyclophilin D inhibitors derived from quinoxaline exhibit highly inhibitory activity against rat mitochondrial swelling and Ca^{2+} uptake/release

Hong-xia GUO[2,3], Feng WANG[2,3], Kun-qian YU[3], Jing CHEN[3], Dong-lu BAI[3], Kai-xian CHEN[3], Xu SHEN[3,4,5], Hua-liang JIANG[3,4,5]

[3]*Drug Discovery and Design Center, State Key Laboratory of Drug Research, Shanghai Institute of Materia Medica, Shanghai Institutes for Biological Sciences, Graduate School of the Chinese Academy of Sciences, Chinese Academy of Sciences, Shanghai 201203, China;* [4]*School of Pharmacy, East China University of Science and Technology, Shanghai 200237, China*

Key words

cyclophilin; quinoxalines; surface plasmon resonance; mitochondrial permeability transition; fluorescence titration; inhibitor

[1] Project supported by the State Key Program for Basic Research of China (No 2004CB-518905), the National High Technology Research and Development Program of China (No 2002AA33011 and 2005AA235030), the National Natural Science Foundation of China (No 20372069 and 20472095), and the Shanghai Basic Research Project from the Shanghai Science and Technology Commission (No 03DZ19212 and 03DZ19228).
[2] These authors contributed equally.
[5] Correspondence to Dr Hua-liang JIANG.
Phn 86-21-5080-6600, ext 1210.
Fax 86-21-5080-7088.
E-mail hljiang@mail.shcnc.ac.cn
Dr Xu SHEN, Phn/Fax 86-21-5080-6918.
E-mail xshen@mail.shcnc.ac.cn

Received 2005-04-27
Accepted 2005-06-10

doi: 10.1111/j.1745-7254.2005.00189.x

Abstract

Aim: To investigate methods for identifying specific cyclophilin D (CypD) inhibitors derived from quinoxaline, thus developing possible lead compounds to inhibit mitochondrial permeability transition (MPT) pore opening. **Methods:** Kinetic analysis of the CypD/inhibitor interaction was quantitatively performed by using surface plasmon resonance (SPR) and fluorescence titration (FT) techniques. IC_{50} values of these inhibitors were determined by PPIase inhibition activity assays. **Results:** All the equilibrium dissociation constants (K_D) of the seven compounds binding to CypD were below 10 μmol/L. The IC_{50} values were all consistent with the SPR and FT results. Compounds GW2, 5, 6, and 7 had high inhibition activities against Ca^{2+}-dependent rat liver mitochondrial swelling and Ca^{2+} uptake/release. Compound GW5 had binding selectivity for CypD over CypA. **Conclusion:** The agreement between the measured IC_{50} values and the results of SPR and FT suggests that these methods are appropriate and powerful methods for identifying CypD inhibitors. The compounds we screened using these methods (GW1–7) are reasonable CypD inhibitors. Its potent ability to inhibit mitochondrial swelling and the binding selectivity of GW5 indicates that GW5 could potentially be used for inhibiting MPT pore opening.

Introduction

Apoptosis is essential for normal development and aging in multicellular organisms, and abnormal regulation of apoptosis can result in multiple human diseases. Mitochondria release apoptogenic proteins such as cytochrome C and apoptosis-inducing factor (AIF) into the cytosol, which are involved in the signaling pathway of caspases and induce cell apoptosis[1–3]. One major pathway of the release of the apoptogenic factors to the cytosol is via the rupture of the outer mitochondrial membrane due to mitochondrial permeability transition (MPT) pore opening[3]. It is suggested that MPT pores play a potent role in cell aging[4,5], and opening of the MPT pores may cause changes in mitochondrial shape and function, such as the massive swelling of mitochondria, rupture of the outer membrane and release of inter-membrane components that induce apoptosis. It has been reported that the agents that inhibit MPT may have therapeutic potential for the treatment of human diseases such as ischemia-reperfusion injury in peripheral organs, trauma and neurodegenerative diseases[5–7].

Recent studies have shown that the MPT pore is composed of three major proteins: the voltage-dependent anion channel (VDAC) in the outer membrane that forms a large H_2O-filled pore with a diameter of 2.5–3.0 nm, the adenine nucleotide translocator (ANT) that mediates the ADP-ATP

exchange in the inner membrane, and cyclophilin D (CypD)[8]. CypD belongs to the family of highly homologous peptidyl prolyl *cis-trans* isomerases (PPIases) that are thought to be important for protein folding, and can bind to the immunosuppressor cyclosporin A (CSA)[9,10]. It is known that CypD is a mitochondrial-targeted PPIase, even though its specific physiological role is largely obscure[11,12]. CypD has been confirmed to play a decisive role in MPT pore regulation, and PPIase activity of CypD might be a necessary step in MPT pore opening[8,13]. A model was recently proposed concerning the mechanism of permeability transition-related cytochrome c release, whereby the Ca^{2+} requirement for the induction of the MPT pore opening might be due to the Ca^{2+}-dependent interaction between CypD and ANT[14–16]. It has been reported that CypD inhibitor CSA and its analogues may block MPT pore opening[17,18], which thereby makes discovering the CypD inhibitor an appealing project. However, to our knowledge, investigating the small molecular CypD-specific inhibitor for allowing brain penetration is still a challenge.

In this paper, we report 7 novel quinoxaline derivatives (Scheme 1 and Figure 1) that inhibit the PPIase activity of CypD. By using surface plasmon resonance (SPR) and fluorescence titration techniques, the kinetics of the CypD-inhibitor interaction was investigated. The compounds' inhibition effects against rat liver Ca^{2+}-depedent mitochondrial swelling and Ca^{2+} uptake/release were also determined. The binding selectivity of CypD over CypA for the tested compounds was analyzed, and explained based on the molecular docking technique. We hope that this research will provide a useful approach for the discovery of cyclophilin D inhibitors, and thus help to develop promising compounds using CypD as a drug target for the inhibition of MPT pore opening.

Materials and methods

All solvents and reagents were purchased commercially and were used without further purification. ^{1}H nuclear mag-

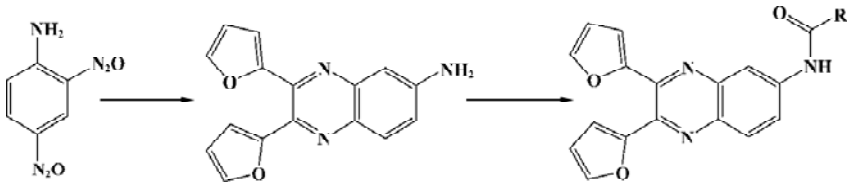

Scheme 1. General synthetic procedure for the seven tested compounds (GW1–7).

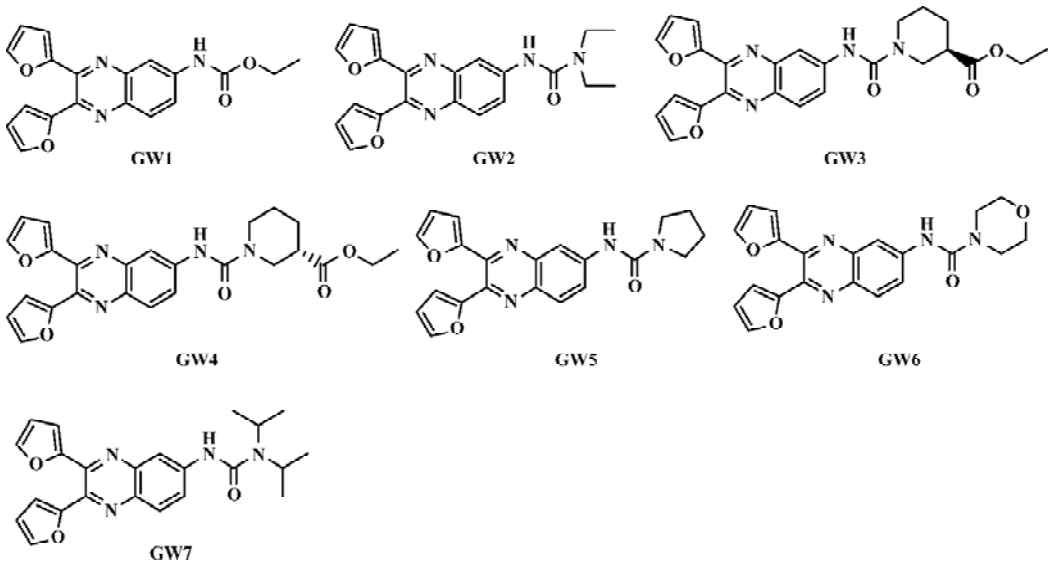

Figure 1. Chemical structures of GW1–7. GW1: R=ethoxy; GW2: R=diethylamino; GW3: R=3-((R)-ethoxycarbonyl) piperidino; GW4: R=3-((S)-ethoxycarbonyl) piperidino; GW5: R=pyrrolidin-1-yl; GW6: R=morpholino; GW7: R=*N*,*N*-diisopropylamino.

netic resonance (NMR) spectra (400 MHz) were recorded on a Varian (Palo Alto, California, USA) Mercury-400 spectrometer. Plasmid extraction was performed using the GenElute Plasmid Miniprep Kit (Sigma-Aldrich, St Louis, Missouri, USA).

The compound 6-amino-2,3-di(furan-2-yl)quinoxaline was synthesized according to the patented method[19]. (*R*)-ethyl nipecotate and (*S*)-ethyl nipecotate were prepared according to a previously published method[20].

General preparation procedure of compounds GW1–7 The chemical structures of the seven tested compounds are shown in Figure 1, and the general synthetic procedure is shown in Scheme 1. Briefly, the compounds were prepared from 2,4-dinitroaniline in five steps.

2,3-di(furan-2-yl)-6-ethoxycarbonylamino quinoxaline (GW1) To a solution of 6-amino-2,3-di(furan-2-yl)quinoxaline (83.1 mg, 0.30 mmol) and triethylamine (100 μL, 0.72 mmol) in dichloromethane (10 mL) we added triphosgene (30 mg, 0.10 mmol) while stirring. The mixture was stirred at room temperature for 1 h, then ethanol (100 μL, 1.7 mmol) was added. After another 1 h of stirring, the solvent was evaporated in a vacuum to give the crude product, which was further purified by flash column chromatography on a silica gel using petro-ether/ethyl acetate (3:1) as the eluent. The obtained compound GW1 (45.2 mg, 43% yield) was a yellowish amorphous solid. ^{1}HNMR ($CDCl_3$, 400 MHz). d: 8.10 (d, 1H, J=2.4 Hz), 8.05 (d, 1H, J=9.1Hz), 7.87 (dd, 1H, J=2.2 Hz, 9.1 Hz), 7.60 (m, 2H), 7.17 (s, 1H), 6.62 (m, 2H), 5.54 (m, 2H), 4.28 (q, 2H, J=7.0 Hz), 1.32 (t, 3H, J=7.0 Hz); IR (KBr): 3419, 3246, 2982, 2928, 1732, 1622, 1572, 1539, 1495, 1261, 1226 per cm; High-resolution mass spectra(electron impact) calculated value [HRMS(EI) Calcd] for $C_{19}H_{15}N_3O_4$ 349.1063; Found 349.1068.

2,3-di(furan-2-yl)-6-*N*-(*N*′,*N*′-diethylcarbamoyl)amino quinoxaline (GW2) GW2 was synthesized by using a method similar to that described for the preparation of GW1, except that diethylamine was used instead of ethanol. GW2 is a brown amorphous solid (63.0 mg, 56% yield). ^{1}H NMR ($CDCl_3$, 400 MHz). δ: 8.03 (d, 2H, J=1.8 Hz), 7.96 (d, 1H, J=1.0 Hz), 7.59 (dd, 2H, J=0.7 Hz, 1.0 Hz), 6.78 (s, 1H), 6.61 (ddd, 2H, J= 0.7 Hz, 3.5 Hz, 12.2 Hz), 6.54 (m, 2H), 3.42 (q, 4H, J=7.2 Hz), 1.25 (t, 6H, J=7.2 Hz); IR (KBr): 3440, 3114, 2972, 2929, 1649, 1524, 1491, 1429, 1265 per cm; HRMS (EI) Calcd for $C_{21}H_{20}N_4O_3$ 376.1535; Found 376.1528.

2,3-di(furan-2-yl)-6-((*R*)-3-ethoxycarbonyl-piperidino) carbonylamino quinoxaline (GW3) GW3 was prepared by using a method similar to that described for the preparation of GW1, except that (*R*)-ethyl nipecotate was used instead of ethanol. GW3 is a yellow amorphous solid (66.4 mg, 48% yield). ^{1}H NMR ($CDCl_3$, 400 MHz). δ: 8.13 (s, 1H), 8.02 (m, 1H), 7.95 (m, 2H), 7.59 (m, 2H), 6.59 (m, 2H), 6.53 (m, 2H), 4.22 (m, 2H), 3.99 (m, 2H), 3.48 (dd, 1H, J=3.3, 14.2 Hz), 3.10 (m, 1H), 2.70 (m, 1H), 2.20 (m, 1H), 1.45–1.95 (m, 3H), 1.29 (t, 3H, J=6.1 Hz); IR (KBr): 3404, 2937, 2860, 1728, 1649, 1570, 1527, 1473, 1431, 1256 cm^{-1}; HRMS(EI) Calcd for $C_{25}H_{24}N_4O_5$ 460.1747; Found 460.1725. $[\alpha]_D^{20}$ = -52° (c=0.83, CH_3OH).

2,3-di(furan-2-yl)-6-((*S*)-3-ethoxycarbonyl-piperidino) carbonylamino quinoxaline (GW4) GW4 was prepared by using a method similar to that described for GW1 except that (*S*)-ethyl nipecotate was used instead of ethanol. GW4 was a yellow amorphous solid (68.7 mg, 50% yield). ^{1}H NMR ($CDCl_3$, 400 MHz). δ: 8.13(s, 1H), 8.02 (m, 1H), 7.95 (m, 2H), 7.59 (m, 2H), 6.59 (m, 2H), 6.53 (m, 2H), 4.22 (m, 2H), 3.99 (m, 2H), 3.48 (dd, 1H, J=3.3, 14.2 Hz), 3.10 (m, 1H), 2.70 (m, 1H), 2.20 (m, 1H), 1.45–1.95 (m, 3H), 1.29 (t, 3H, J=6.1 Hz); IR (KBr): 3404, 2937, 2860, 1728, 1649, 1570, 1529, 1475, 1431, 1254 cm^{-1}; HRMS(EI) Calcd for $C_{25}H_{24}N_4O_5$ 460.1747; Found 460.1738. $[\alpha]_D^{20}$ = +55° (c=1.78, CH_3OH).

2,3-di(furan-2-yl) -6-(pyrrolidin-1-yl)carbonylamino quinoxaline (GW5) GW5 was prepared by using a method similar to that described for the preparation of GW1 except that pyrrolidine was used instead of ethanol. GW5 is a brown amorphous solid (106.9 mg, 95% yield). ^{1}H NMR ($CDCl_3$, 400 MHz). δ: 8.18 (dd, 1H, J=2.3, 9.2 Hz), 8.02 (m, 2H), 7.60 (m, 2H), 6.68 (s, 1H), 6.65 (d, 1H, J=3.4 Hz), 6.60 (dd, 1H, J=0.7, 3.4 Hz), 6.55 (m, 2H), 3.53 (t, 4H, J=6.6 Hz), 2.00 (t, 4H, J=6.6 Hz); IR (KBr): 3404, 2970, 2877, 1672, 1568, 1525, 1502, 1429, 1382, 1340, 1203 per cm; HRMS(EI) Calcd for $C_{21}H_{18}N_4O_3$ 374.1379; Found 374.1360.

2,3-di(furan-2-yl)-6-morpholinocarbonylaminoquinoxaline (GW6) GW6 was prepared by using a method similar to that described for the preparation of GW1 except that morpholine was used instead of ethanol. GW6 was a yellow amorphous solid (101.4 mg, 87% yield). ^{1}H NMR ($CDCl_3$, 400 MHz). δ: 7.96–8.06 (m, 3H), 7.60 (m, 2H), 6.99 (s, 1H), 6.66 (dd, 1H, J=0.8, 3.5 Hz), 6.63 (dd, 1H, J=0.8, 3.5 Hz), 6.56 (m, 2H), 3.77 (t, 2H, J=4.9 Hz), 3.56 (t, 2H, J=4.9 Hz), 1.80 (b, 4H); IR (KBr): 3423, 2920, 2852, 1653, 1529, 1475, 1429, 1333, 1254 per cm; HRMS(EI) Calcd for $C_{21}H_{18}N_4O_4$ 390.1328; Found 390.1309.

2,3-di(furan-2-yl) -6-*N*-(*N*′,*N*′-diisopropylcarbamoyl) amino quinoxaline (GW7) GW7 was prepared by using a method similar to that described for the preparation of GW1 except that diisopropylamine was used instead of ethanol. GW7 is a brown amorphous solid (43.9 mg, 36% yield). ^{1}H NMR ($CDCl_3$, 400 MHz). δ: 7.99–8.06 (m, 2H), 7.90 (d, 1H, J= 2.3 Hz), 7.57 (m, 2H), 6.76 (s, 1H), 6.59 (m, 2H), 6.51 (m, 2H), 3.99 (m, 2H), 1.32 (d, 12H, J=6.9 Hz); IR (KBr): 3427, 2968, 2928, 1647, 1566, 1520, 1495, 1433, 1375, 1205 per cm; HRMS

(EI) Calcd for $C_{23}H_{24}N_4O_3$ 404.1848; Found 404.1857.

Preparation of His-tagged human CypA protein All cloning techniques including polymerase chain reaction (PCR), restriction, ligation, *E coli* transformation, and plasmid DNA preparation were carried out according to standard methods[21]. The His-tagged CypA protein was expressed and purified from the plasmid pQE30-CypA according to the published procedure[22].

Preparation of rat CypD protein The plasmid pcDNA3.1(+)/Zeo-CypD was kindly provided by Dr James D LECHLEITER (University of Texas Health Science Center, U3SA). By using the forward primer 5'-ATAGAATTCATGCTAGCTCTGCGCTGCG-3' (containing an *Eco*RI site) and the reverse primer 5'-ATATCTCGAGGCTCAACTGGCCACAGTC-3' (containing an *Xho*I site), the PCR product was subcloned into the vector pGEX-4T-1 between the *Eco*RI and *Xho*I sites to obtain the expression plasmid pGEX-4T-1-CypD. Sequencing was carried out to confirm the insertion.

E coli strains were prepared in Luria-Bertani medium containing 100 mg/mL ampicillin. BL21 (DE3) bacteria transformed with pGEX-4T-1-CypD were grown until the OD_{600} reached 0.8, and isopropylthio-β-*D*-galactoside (IPTG) was added to a final concentration of 0.2 mmol/L to induce GST-CypD expression at 25 C overnight.

Bacteria were harvested and lysed by sonication in a sonication buffer [1×phosphate-buffered saline (PBS), 1 mmol/L phenylmethylsulfonyl fluoride (PMSF), pH 7.3, 1 mmol/L ethylenediamine tetraacetic acid (EDTA), 1% Triton X-100]. The bacterial lysate was centrifuged and the supernatant was collected. GST-CypD protein was purified by using a glutathione Sepharose 4B column (Amersham Biosciences, Uppsala, Sweden), and the purified CypD protein was obtained by the on-column cleavage of GST-CypD using thrombin according to the instructions given by the manufacturers of the glutathione Sepharose 4B column (Amersham Biosciences). The purity of the obtained CypD protein was verified by sodium dodecyl sulfate-polyacrylamide gel electrophoresis as a single band.

Surface plasmon resonance technology-based Biacore 3000 analyses The interactions between compounds GW1–7 and CypD (A) were performed using the dual flow cell Biacore 3000 instrument (Biacore AB, Uppsala, Sweden). All the experiments were carried out using HBS-EP (10 mmol/L *N*-2-hydroxyethylpiperazine-*N'*-2-ethanesulfonic acid [HEPES], 150 mmol/L NaCl, 3.4 mmol/L EDTA and 0.005% surfactant P20 at pH 7.4) as a running buffer at a constant flow rate of 20 μL/min at 25 °C. The protein was immobilized directly and covalently on the hydrophilic carboxymethylated dextran matrix of the CM5 sensor chip (BIAcore) by using the standard primary amine coupling reaction. The protein to be bound to the sensor chip was diluted in 10 mmol/L sodium acetate buffer (pH 6.5) to a concentration of 17 μmol/L. The concentrations of the compounds dissolved in the running buffer varied from 1.18 to 10 μmol/L. All the data analyses were carried out using BIAevaluation software, and the sensorgrams were processed by automatic correction for nonspecific bulk refractive index effects. The kinetic analyses of the ligand binding to the protein were performed based on the 1:1 Langmuir binding fit model according to the procedures described in the software manual.

Fluorescence titration assay Fluorescence measurements were performed on a Hitachi(Tokyo, Japan) F-2500 fluorescence spectrophotometer equipped with a thermal controller. The change in the intrinsic tryptophan fluorescence when the compound bound to the protein (CypA or CypD) was monitored using a procedure similar to that described in the literature[23,24]. The experiments were carried out at 25 °C in PBS (pH 7.3) with the protein concentration set at 13 μmol/L and the compound concentrations varied from 0 to 40 μmol/L. The compounds were prepared in dimethylsulfoxide as a stock solution of 10 mmol/L. The fluorescent absorption was recorded with excitation at 280 nm and emission at 340 nm.

PPIase inhibition activity assay The PPIase activity assay for the proteins CypA and CypD was performed based on a published method[25] with some modifications. The substrate *N*-succinyl-Ala-Ala-Pro-Phe-p-nitroanlilide (Suc-AAPF-pNA, S-7388) and α-chymotrypsin (C-7762) were purchased from Sigma (St Louis, Missouri, USA). Suc-AAPF-pNA was dissolved in tetrahydrofuran containing 400 mmol/L of LiCl, and the stock solution concentration was 10 mmol/L. α-chymotrypsin was dissolved in 1 mmol/L HCl containing 2 mmol/L $CaCl_2$, and the stock solution concentration was 80 mmol/L. The assay buffer (173 μL of 50 mmol/L HEPES, 100 mmol/L NaCl; pH 8.0 at 0 °C; final concentration 43 mmol/L HEPES, 86 mmol/L NaCl), 15 μL of de-ionized water and CypD (2 μL of a 2700 nmol/L stock solution) and the compounds (final concentration ranging from 100 nmol/L to 50 μmol/L) were pre-equilibrated for 3 h on ice. Immediately before the assay was started, 7.5 μL of chymotrypsin solution was added. Absorbance readings at 390 nm were recorded when 2.5 μL of the peptide substrate was added into the 1 cm path length cuvette and the solution was mixed rapidly. The data were collected on a Hitachi U2010 spectrophotometer.

Rat liver mitochondrial swelling and Ca^{2+} uptake/release inhibition assays The mitochondrial swelling and Ca^{2+} uptake/release inhibition assays were carried out according to published methods[26]. The mitochondria were isolated

by differential centrifugation from the livers of adult Wistar rats (180–200 g) after overnight starvation treatment. The rat livers were excised and washed with 0.25 mol/L sucrose. The fat and connective tissue were removed, and the livers were homogenized (1/10, w/v) using buffer A (250 mmol/L mannitol, 0.5 mmol/L EDTA, 5 mmol/L HEPES, 0.1% bovine serum albumin; pH 7.4) on ice. The homogenate was centrifuged at 1000×*g* for 10 min in a Biofuge Stratos centrifuge (Hereus Company, Hanau, Germany). The sediment was discarded and the supernatant was centrifuged at 1000×*g* for 10 min twice. The collected supernatant was then further centrifuged at 10 000×*g* for 15 min. The pellet (mitochondrial fraction) was resuspended in the test buffer (250 mmol/L mannitol, 70 mmol/L sucrose, 5 mmol/L HEPES; pH 7.4). The total mitochondrial protein was determined by using the Lowry assay using bovine serum albumin as a standard. Rat mitochondria were added to the test buffer to yield a final concentration of 0.5 mg protein per mL[27]. The tested compounds (100 μmol/L) were mixed with mitochondria for 1 h before $CaCl_2$ (200 μmol/L) was added. Mitochondrial swelling was determined by monitoring absorbance at 540 nm using a Hitachi U2010 spectrophotometer and the mitochondrial Ca^{2+} uptake/release assay was monitored using a Hitachi F-2500 fluorescence spectrophotometer as described previously[26].

Molecular modeling and docking The CypD sequence from *Rattus norvegicus* was retrieved from GenBank (GenBank protein ID U68544; http://www.ncbi.nlm.nih.gov). The CLUSTAL W program was used to carry out sequence alignment between the sequences of CypD from *Rattus norvegicus* and human CypA[28]. The sequence similarity identity between CypD and CypA was 63%, and positives were 81%, making the Protein Data Bank (PDB) of human CypA an ideal template for CypD 3-D model building. The 3-D model of the TrpRS was generated based on PDB templates 1AK4[29], 1AWT[30], and 1NMK[31] retrieved from the Protein DataBase by using the MODELLER program[32] encoded in Insight II[33]. MODELLER uses a spatial restraint method to build up 3-D protein models. The structure of each template protein was used to derive spatial restraints expressed as probability density functions for each of the restrained features of the models. The structure with the lowest violation score and lowest energy score was chosen as the candidate. Refinements of the routine in the Homology module of Insight II were used to adjust the positions of the side chains. Finally, the structural models were optimized using Amber force field[34] with the following parameters: a distance-dependent dielectric constant of 4.0, nonbonded cut-off 10 Å, and Kollman-all-atom charges[34]. The structures were first minimized by steepest descent, then by conjugating the gradient method to the energy gradient root-mean-square <0.05 kcal·(mol·Å)$^{-1}$. Several structural analysis software packages were used to check the structure quality. The Prostat module of Insight II was used to analyze the bonds, angles and torsions. The Profile-3D program[35] was used for checking the structure and sequence compatibility. The 3-D structures of the compounds GW1–7 were constructed from scratch by Sybyl 6.8[36], and optimized to energy convergence with the Tripos force field and MMFF94 charges.

The major residues possibly comprising the binding site of CypD were identified by sequence alignment with human CypA, and the SiteID program encoded in Sybyl 6.8[36]. The surface structure of the binding pocket was constructed by using the MOLCAD module of Sybyl 6.8.

The DOCK suite of programs is designed to find possible orientations of a ligand in a "receptor" site[37]. The orientation of a ligand is evaluated with a shape-scoring function and/or a function approximating the ligand-receptor binding energy. The shape-scoring function is an empirical function resembling the van der Waals' attractive energy. The ligand-receptor binding energy is taken to be approximately the sum of the van der Waals' and electrostatic interaction energies. After the initial orientation and scoring evaluation, a grid-based rigid body minimization is carried out for the ligand to locate the nearest local energy minimum within the receptor binding site. The position and conformation of each docked molecule were optimized using the single anchor search and torsion minimization method of DOCK 4.0. Thirty conformations per ligand building a cycle and 50 maximum anchor orientations were used in the anchor-first docking algorithm. All docked configurations were energy minimized using 100 maximum iterations and one minimization cycle.

Results and Discussion

Synthesis of the compounds Generally, the compounds GW1–7 were synthesized as outlined in Scheme 1.

Kinetic analysis of CypD (A) binding to GW1–7 by surface plasmon resonance In order to perform kinetic analyses of the binding of GW1–7 to CypD and CypA, the Biacore 3000 instrument (based on surface plasmon resonance [SPR] technology) was used. As a typical example, the Biacore sensorgrams for the binding of GW2 to the immobilized CypD are shown in Figure 2. The 1:1 Langmuir binding fit model was used for determining the equilibrium dissociation constant (K_D), and the association (k_{on}) and dissociation (k_{off}) rate constants by using Equations (1) and (2).

$$\frac{dR}{dt} = k_{on} \times C \times (R_{max} - R) - k_{off} \times R \quad (1)$$

where R represents the response unit, C is the concentration of the analyte, and

$$K_D = k_{off}/k_{on} \quad (2)$$

The obtained results were evaluated by χ^2 analysis. All the kinetic parameters are listed in Table 1.

The Biacore results show that all the 7 tested compounds exhibited strong binding affinities with CypD, with K_D values approximately 3–6 μmol/L. Due to the high structural homology of CypD and CypA, the tested compounds had high binding affinities with CypA, as indicated in Table 1. However, compound GW5 exhibited higher binding specificity with CypD than with CypA. This was further verified by the intrinsic fluorescence titration analysis and cyclophilin PPIase activity inhibition assay as shown in Tables 2 and 3. Structurally, the R group of the compound (Scheme 1) might play an important role in the ligand binding selectivity for CypD over CypA.

In addition, the K_D values obtained from the Biacore assay agreed with the apparent equilibrium dissociation constants (K_D') from the intrinsic fluorescence titration analysis and the IC_{50} values in the cyclophilin PPIase activity inhibition determination as shown in Tables 2 and 3. In agreement with Huber *et al*[38], we suggest that Biacore is a powerful and useful method for screening cyclophilin inhibitors.

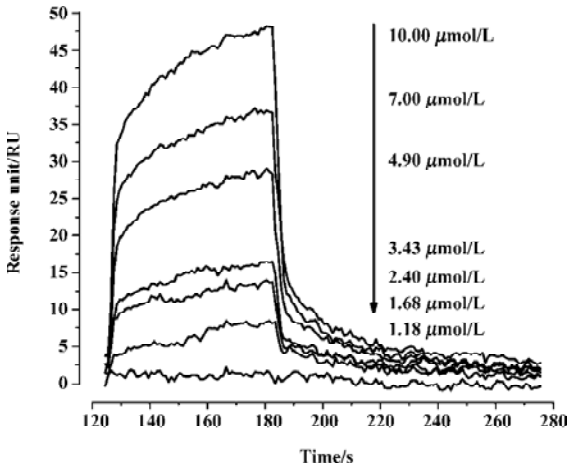

Figure 2. Sensorgrams of the binding of GW2 to CypD measured by the Biacore assay. Representative sensorgrams obtained from the injection of GW2 at concentrations of 1.18, 1.68, 2.40, 3.43, 4.90, 7.00, and 10.00 μmol/L over CypD immobilized on the CM5 chip.

Table 1. Kinetic parameters of GW1–7 binding to CypD and CypA (in parentheses) as analyzed using Biacore 3000.

Compound	R_{max}	k_{on}/mol·L^{-1}·s^{-1}	k_{off}/s^{-1}	K_D/μmol·L^{-1}	χ^2
GW1	50.9	$3.57\pm0.25\times10^3$	$2.16\pm0.05\times10^{-2}$	6.05±0.21	0.52
	(49.3)	($3.82\pm0.17\times10^2$)	($9.28\pm0.21\times10^{-3}$)	(24.3±0.91)	(0.552)
GW2	48.7	$3.14\pm0.17\times10^3$	$2.13\pm0.04\times10^{-2}$	6.77±0.22	0.626
	(47.6)	($4.73\pm0.19\times10^2$)	($1.25\pm0.02\times10^{-2}$)	(26.4±0.87)	(0.841)
GW3	52.7	$1.99\pm0.12\times10^3$	$6.39\pm0.04\times10^{-3}$	3.20±0.11	0.337
	(54.6)	($1.28\pm0.09\times10^3$)	($4.79\pm0.17\times10^{-3}$)	(3.74±0.12)	(0.862)
GW4	54.7	$3.69\pm0.21\times10^3$	$1.81\pm0.03\times10^{-2}$	4.89±0.12	0.467
	(57.2)	($2.09\pm0.13\times10^3$)	($7.96\pm0.16\times10^{-3}$)	(3.81±0.22)	(1.34)
GW5	56.3	$1.11\pm0.09\times10^3$	$2.36\pm0.06\times10^{-3}$	2.13±0.17	0.675
	(51.3)	($2.59\pm0.12\times10^2$)	($6.22\pm0.07\times10^{-2}$)	(24.0±0.78)	(1.02)
GW6	58.6	$3.49\pm0.13\times10^3$	$1.24\pm0.03\times10^{-2}$	3.55±0.18	0.569
	(58.7)	($6.81\pm0.22\times10^3$)	($4.66\pm0.09\times10^{-2}$)	(6.84±0.11)	(0.903)
GW7	57.8	$2.79\pm0.15\times10^3$	$8.06\pm0.04\times10^{-3}$	2.89±0.20	0.574
	(50.7)	($3.78\pm0.08\times10^3$)	($1.68\pm0.04\times10^{-2}$)	(4.44±0.21)	(0.697)

R_{max}, maximum analyte binding capacity; k_{on}, association rate constant; k_{off}, dissociation rate constant; K_D, equilibrium dissociation constant. $K_D=k_{off}/k_{on}$; χ^2, statistical value in Biacore.

Table 2. Apparent equilibrium dissociation constants (K_D') of the binding of GW1–7 to CypD and CypA evaluated by using the tryptophan fluorescence quenching method.

Cyclophilin	Compound (K_D' in μmol/L)						
	GW1	GW2	GW3	GW4	GW5	GW6	GW7
CypD	5.60±0.19	6.49±0.20	3.00±0.13	5.51±0.17	2.02±0.09	3.23±0.12	2.52±0.11
CypA	11.32±0.13	11.64±0.16	4.02±0.08	4.76±0.08	20.9±0.18	7.18±0.12	4.22±0.09

K_D', apparent equilibrium dissociation constant.

Table 3. IC_{50} values of compounds GW1–7 in the inhibition of the PPIase activities of CypA and CypD.

Cyclophilin	Compound (K_D' in μmol/L)						
	GW1	GW2	GW3	GW4	GW5	GW6	GW7
CypD	6.17±0.11	7.18±0.13	3.24±0.09	4.09±0.10	1.34±0.07	3.78±0.10	2.15±0.09
CypA	13.66±0.22	14.62±0.26	2.74±0.09	3.16±0.10	21.39±0.31	6.34±0.13	4.80±0.12

Intrinsic fluorescence titration analysis of compounds binding to CypD(A) Because both of the binding sites of CypD and CypA have a tryptophan residue (Trp 124 for CypD and Trp 121 for CypA), we investigated the binding affinities of the tested compounds for CypD and CypA by using an intrinsic fluorescence titration technique[23]. During the assay, a 1:1 ratio of CypD(A) to binding compound was used based on published information about CypA/CSA interactions[39,40] and the results of our molecular docking analyses. The apparent equilibrium dissociation constant (K_D') used for evaluating CypD(A) binding affinity to the tested compound was calculated according to the method in the literature[23]. We assumed that a 50% occupancy of CypD (or CypA) is set at a fractional fluorescence change of 0.5 ($FC_{0.5}$), and at this point the concentration of the bound ligand is equal to that of the bound protein, which is half of the total concentration of protein. Accordingly, K_D' is equal to the total ligand concentration minus the concentration of the bound protein at $FC_{0.5}$[23].

Figure 3 shows the typical tryptophan fluorescence quenching of CypD induced by titration of the tested compounds with an increase in their concentration. Since none of the compounds showed any intrinsic fluorescence absorption, their possible effects on the experiments could be discounted (data not shown). The K_D' values of GW1–7 are summarized in Table 2. Obviously, the binding selectivity of GW5 for CypD over CypA could also be determined, and the K_D' values are very comparable to the K_D values determined by the Biacore assay.

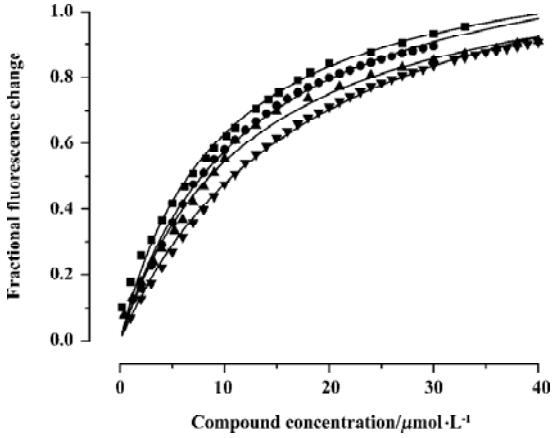

Figure 3. Tryptophan fluorescence quenching by compounds binding to CypD. CypD (13 mmol/L) was incubated with increasing amounts of GW1–7, respectively. ▲, GW1, 0–30 μmol/L; ▼, GW2, 0–30 μmol/L; ■, GW3, 0–40 μmol/L; ●, GW4, 0–40 μmol/L. The data for GW5–7 are not shown here for clarity. The resulting fluorescence change is plotted as a fraction of the maximal change.

CypD (A) PPIase activity inhibition assay Both CypD and CypA belong to the PPIase family, and classic spectrophotometric methods[41] can be used to determine the PPIase inhibition activity of GW1–7 against CypD and CypA. During the assay, the rate constants for the *cis-trans* interconversion were evaluated by fitting the data to the integrated first-order rate equation by nonlinear least-square analysis[25,41].

As a typical example, Figure 4 shows the CypD PPIase inhibition results with increases in the concentrations of the

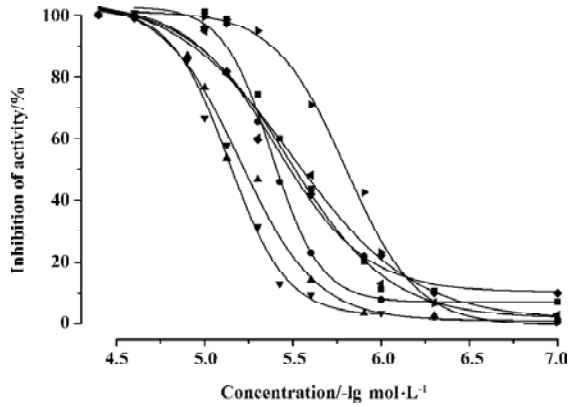

Figure 4. CypD PPIase activity inhibition assay for GW1–7. PPIase (26 nmol/L) was pre-incubated with the tested compound at a number of concentrations, and the PPIase activity change was plotted as a fraction of the maximal change. ▲, GW1 (1.0, 1.25, 2.5, 5.0, 7.5, 10.0, 12.5, 25.0, 50.0 μmol/L); ▼, GW2 (1.0, 2.5, 3.75, 5.0, 7.5, 10.0, 12.5, 25.0, 50.0 μmol/L); ■, GW3 (0.1, 0.5, 1.0, 1.25, 2.5, 3.75, 5.0, 7.5, 10.0, 25.0 μmol/L); ●, GW4 (0.1, 0.5, 1.0, 1.25, 2.5, 3.75, 5.0, 7.5, 10.0, 25.0 μmol/L); ▶, GW5 (0.1, 0.5, 1.0, 2.5, 5, 7.5, 10.0, 25.0, 50.0 μmol/L); ◆, GW6 (0.1, 0.5, 1.0, 2.5, 5, 7.5, 10.0, 25.0, 50.0 μmol/L); ◀, GW7 (0.1, 0.5, 1.0, 2.5, 5, 7.5, 10.0, 25.0, 50.0 μmol/L).

compounds, and Table 3 shows the IC_{50} values of GW1–7 against CypD and CypA. The fact that the IC_{50} values accord well with the Biacore and fluorescence titration results (Tables 1, 2) confirms the reliability of these three detection approaches.

Rat Ca^{2+}-dependent mitochondrial swelling and Ca^{2+} uptake/release inhibition assays In general, MPT pores are open when mitochondria encounter abnormally high concentrations of exogenous Ca^{2+} ions. These pores allow solutes of <1500 Da in size across the inner mitochondrial membrane, leading to mitochondrial swelling. Such swelling can be detected by time scans of absorbance at 540 nm (A_{540}) and the extent of swelling is proportional to A_{540}[26].

Fluo-5N fluorescence is quite low without binding to Ca^{2+} in controls, because the high mitochondrial membrane potential prevents the release of endogenous mitochondrial Ca^{2+}. When exogenous Ca^{2+} was added, Fluo-5N fluorescence increased immediately and decreased rapidly as Ca^{2+} ions were taken up into the mitochondria. Subsequently, the accumulation of cations in the mitochondria led to mitochondrial swelling and depolarization. Ca^{2+} ions were then released from mitochondria as a consequence of the onset of MPT, as indicated by an increase in Fluo-5N fluorescence. Ca^{2+} release was completely blocked by 1 μmol/L CSA. Fluo-5N fluorescence also revealed that compounds GW1–7 inhibited the uptake/release of exogenously added Ca^{2+} to a certain extent.

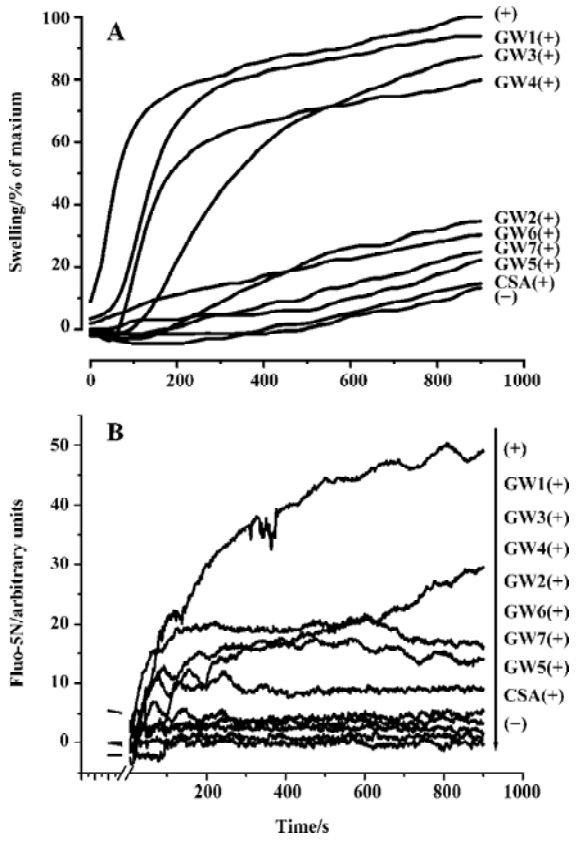

Figure 5. Ca^{2+}-dependent mitochondrial swelling and Fluo-5N fluorescence after induction of MPT with $CaCl_2$. Mitochondria (0.5 mg/mL) were mixed with CSA (1 μmol/L) (as a control) or the compounds GW1–7 (100 μmol/L for each). The symbols (+) and (–) represent the solution with or without 200 μmol/L of $CaCl_2$, respectively. Absorbance changes at 540 nm (A) and Fluo-5N fluorescence excited at 485 nm (B) were monitored soon after $CaCl_2$ (200 μmol/L) was added, as described in the text.

Figure 5A shows the results of the rat mitochondrial swelling inhibition assay for GW1–7 (100 μmol/L) with CSA (1 μmol/L) as a control. Figure 5B gives the results of the mitochondrial Ca^{2+} uptake/release inhibition assay for GW1–7 (100 μmol/L). The results show that the inhibition abilities of compounds GW1–7 against Ca^{2+} uptake/release are in good agreement with their inhibition abilities against mitochondrial swelling. We found that compounds GW2, 5, 6, and 7 had a strong ability, whereas GW1, 3, and 4 did not have any inhibition activity, which could be because of the R group. Compared with GW2, 5, 6, and 7, the tails of GW1, 3, and 4 were ethoxycarbonyl, which might prevent them from transferring into mitochondria through the membranes or cause the loss of inhibition ability for other (unclear) reasons. The behavior of CypD in mitochondria is much more complicated

than that of the purified CypD protein, so the different R groups might cause different results. CSA had the highest inhibition activity, and the relative general inhibition abilities of the other compounds were: GW5>GW7>GW6>GW2. Such a sequence seems to be consistent with the CypD PPIase inhibition ability of the compounds (Table 3). This result thus confirms the fact that CypD inhibitors may possess possible inhibition activity against Ca^{2+}-dependent MPT pore opening.

Molecular docking analyses To gain further insight into the CypD(A)/inhibitor interaction model at the atomic level, docking analysis based on molecular modeling was carried out without the published rat CypD crystal data. Our rat CypD model tallies very well with the human CypD crystal [PDB ID: 2bit] structure shown in Figure 6A. The weighted root mean square distance is 0.6040 and the identity score is 95.7%. Because of the similar structures of the compounds, they share the same precursor, with some overlapping structural elements in common (Figure 6B). Similar to CypA, the binding pocket of CypD is also fairly large and shallow, and is composed of residues Arg58, Ile60, Phe63, Met64, Glu66, Gly75, Thr76, Gly77, Ala104, Asn105, Ala106, Gln114, Phe116, Thr122, Trp124, Leu125, Lys128, and His129. GW1–7 and CSA bind to the same binding site of CypD. Unlike the case of full occupation by CSA, GW1–7 occupied only part of the binding pocket and might swing in the pocket. Helekar and Patrick even demonstrated that Arg55 of CypA was a key determinant against PPIase activity[42]. Compounds GW1–7 showed their hydrophobic contact with Arg58 of CypD (Arg55 of CypA). Therefore, the PPIase activity of CypD could be inhibited by hydrophobic interactions with the inhibitors. In addition, GW1–7 formed stacking interactions with Trp124 of CypD (Trp121 of CypA) and the only tryptophan residues of CypD and CypA that contribute to the change in fluorescence intensity (data not shown).

Conclusion In this work, we reported on 7 small quinoxaline derivatives as novel CypD inhibitors. *In vitro* assays indicated that compounds GW2, 5, 6, and 7 inhibit Ca^{2+}-dependent rat liver mitochondrial swelling and Ca^{2+} uptake/release. By using SPR and fluorescence titration techniques, kinetic analysis of CypD/inhibitor interactions were quantitatively performed. The measured IC_{50} values for the tested compounds are all in good agreement with the SPR and fluorescence titration results, which suggests that these are powerful methods for identifying CypD inhibitors[38]. Further studies indicated that GW5 has binding selectivity for CypD over CypA.

In summary, in this present work we used an appropriate and powerful approach for identifying CypD inhibitors, and developed a small compound that shows specific ligand-binding ability for CypD, which could be used in the inhibition of MPT pore opening.

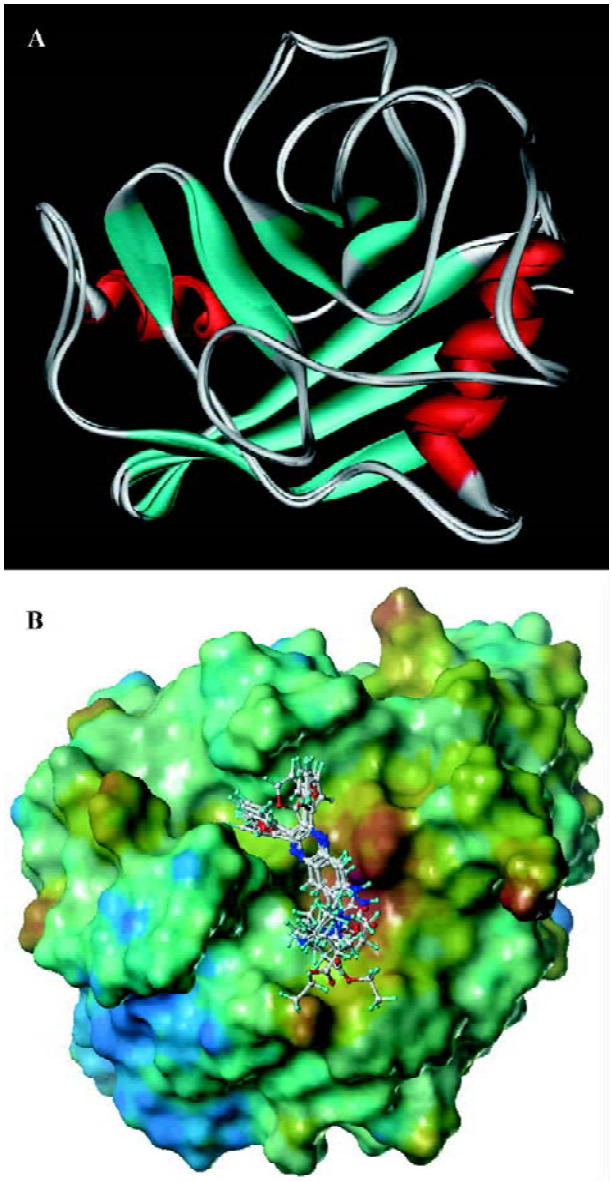

Figure 6. Overlapping of the rat CypD model/human CypD crystal data (A) and GW1–7 in the binding pocket of rat CypD (B).

Acknowledgements

We thank Dr James D LECHLEITER for providing the rat CypD gene and Research Collaboratory for Structural Bioinformatics Protein Data Bank (RCSB PDB) for providing human cyclophilin D structure information.

References

1 Liu X, Kim CN, Yang J, Jemmerson R, Wang X. Induction of apoptotic program in cell-free extracts: requirement for dATP and cytochrome c. Cell 1996; 86: 147–57.

2 Susin SA, Lorenzon HK, Zamzami N, Marzo I, Snow BE, Brothers GM, *et al*. Molecular characterization of mitochondrial apoptosis-inducing factor. Nature 1999; 397: 441–6.

3 Olson M, Kornbluth S. Mitochondria in apoptosis and human disease. Curr Mol Med 2001; 1: 91–122.

4 Crompton M. Mitochondria and aging: a role for the permeability transition? Aging Cell 2004; 3: 3–6.

5 Waldmeier PC, Zimmermann K, Qian T, Tintelnot-Blomley M, Lemasters JJ. Cyclophilin D as a drug target. Curr Med Chem 2003; 10: 1485–506.

6 Mattson MP, Kroemer G. Mitochondria in cell death: novel targets for neuroprotection and cardioprotection. Trends Mol Med 2003; 9: 196–205.

7 Sullivan PG, Rabchevsky AG, Waldmeier PC, Springer JE. Mitochondrial permeability transition in CNS trauma: cause or effect of neuronal cell death? J Neurosci Res 2005; 79: 231–9.

8 Crompton M. On the involvement of mitochondrial intermembrane junctional complexes in apoptosis. Curr Med Chem 2003; 10: 1473–84.

9 Connern CP, Halestrap AP. Purification and N-terminal sequencing of peptidyl-prolyl cis-trans-isomerase from rat liver mitochondrial matrix reveals the existence of a distinct mitochondrial cyclophilin. Biochem J 1992; 284: 381–5.

10 Fischer G, Wittmann-Liebold B, Lang K, Kiefhaber T, Schmid FX. Cyclophilin and peptidyl-prolyl *cis-trans* isomerase are probably identical proteins. Nature 1989; 337: 476–8.

11 Lin DT, Lechleiter JD. Mitochondrial targeted cyclophilin D protects cells from cell death by peptidyl prolyl isomerization. J Biol Chem 2002; 277: 31134–41.

12 Li Y, Johnson N, Capano M, Edwards M, Crompton M. Cyclophilin-D promotes the mitochondrial permeability transition but has opposite effects on apoptosis and necrosis. Biochem J 2004; 383: 101–9.

13 Schubert A, Grimm S. Cyclophilin D, a component of the permeability transition-pore, is an apoptosis repressor. Cancer Res 2004; 64: 85–93.

14 Machida K, Osada H. Molecular interaction between cyclophilin D and adenine nucleotide translocase in cytochrome c release: does it determine whether cytochrome c release is dependent on permeability transition or not? Ann NY Acad Sci 2003; 1010: 182–5.

15 Crompton M. The mitochondrial permeability transition pore and its role in cell death. Biochem J 1999; 341: 233–49.

16 Halestrap AP, McStay GP, Clarke SJ. The permeability transition pore complex: another view. Biochimie 2002; 84: 153–66.

17 Crompton M, Costi A. Kinetic evidence for a heart mitochondrial pore activated by Ca^{2+}, inorganic phosphate and oxidative stress. A potential mechanism for mitochondrial dysfunction during cellular Ca^{2+} overload. Eur J Biochem 1988; 178: 489–501.

18 Crompton M, Barksby E, Johnson N, Capono M. Mitochondrial intermembrane junctional complexes and their involvement in cell death. Biochimie 2002; 84: 143–52.

19 Alaimo RJ [inventor]. Norwich Eaton Pharmaceuticals [assignee]. Thiocyanatoquinoxaline compounds with immunomodulating activity. US patent 4540693. September 10, 1985.

20 Magnus P, Thurston LS. Synthesis of the vinblastine-like antitumor bis-indole alkaloid navelbine analogue desethyldihydronavelbine. J Org Chem 1991; 56: 1166–70.

21 Sambrook J, Fritsch EF, Maniatis T. Molecular Cloning: A Laboratory Manual. 2nd ed. New York: Cold Spring Harbor Laboratory Press; 1989.

22 Luo C, Luo H, Zheng S, Gui C, Yue L, Yu C, *et al*. Nucleocapsid protein of SARS coronavirus tightly binds to human cyclophilin A. Biochem Biophys Res Commun 2004; 321: 557–65.

23 Husi H, Zurini MGM. Comparative binding studies of cyclophilins to cyclosporin A and derivatives by fluorescence measurement. Anal Biochem 1994; 222: 251–5.

24 Handschumacher RE, Harding MW, Rice J, Drugge RJ. Cyclophilin A: a specific cytosolic binding protein for cyclosporin A. Science 1984; 226: 544–7.

25 Kofron JL, Kuzmic P, Kishore V, Colon-Bonilla E, Rich DH. Determination of kinetic constants for peptidyl prolyl cis-trans isomerases by an improved spectrophotometric assay. Biochemistry 1991; 30: 6127–34.

26 Blattner JR, He L, Lemasters JJ. Screening assays for the mitochondrial permeability transition using a fluorescence multiwell plate reader. Anal Biochem 2001; 295: 220–6.

27 Lowry OH, Rosenbrough NH, Farr AL, Randall JR. Protein measurement with the folin phenol reagent. J Biol Chem 1951; 193: 265–75.

28 Thompson J, Higgins D, Gibson T. CLUSTAL_W: improving the sensitivity of progressive multiple sequence alignment through sequence weighting, position-specific gap penalties and weight matrix choice. Nucleic Acids Res 1994; 22: 4673–80.

29 Gamble T, Vajdos F, Yoo S, Worthylake D, Houseweart M, Sundquist WI, *et al*. Crystal structure of human cyclophilin a bound to the amino-terminal domain of HIV-1 capsid. Cell 1996; 87: 1285–94.

30 Vajdos F, Yoo S, Houseweart M, Sundquist W, Hill C. Crystal structure of cyclophilin a complexed with a binding site peptide from the HIV-1 capsid protein. Protein Sci 1997; 6: 2297–307.

31 Sedrani R, Kallen J, Martin Cabrejas L, Papageorious C, Senia F, Rohrbach S, *et al*. Sanglifehrin-cyclophilin interaction: degradation work, synthetic macrocyclic analogues, x-ray crystal structure and binding data. J Am Chem Soc 2003; 125: 3849–59.

32 Sali A, Blundell T. Comparative protein modelling by satisfaction of spatial restraints. J Mol Biol 1993; 234: 779–815.

33 Insight II [molecular modeling package]. San Diego, California, the United States: Molecular Simulations; 2000.

34 Cornell WD, Cieplak P, Bayly CI, Gould IR, Merz KM, Ferguson DM, *et al*. A Second generation force field for the simulation of proteins, nucleic acids, and organic molecules. J Am Chem Soc 1995; 117: 5179–97.

35 Bowie JU, Luthy R, Eisenberg D. A method to identify protein sequences that fold into a known three-dimensional structure. Science 1991; 253: 164–70.

36 Sybyl [molecular modeling package]. St Louis, MO: Tripos Associates; 2000.

37 Ewing T, Kuntz ID. Critical evaluation of search algorithms for automated molecular docking and database screening. J Comput

Chem 1997; 18: 1175–89.
38 Huber W, Persicace S, Kohler J, Muller F, Schlatter D. SPR-based interaction studies with small molecular weight ligands using hAGT fusion proteins. Anal Biochem 2004; 333: 280–8.
39 Kallen J, Spitzfaden C, Zurini MGM, Wider G, Widmer H, Wuthrich K, *et al*. Structure of human cyclophilin and its binding site for cyclosporin A determined by X-ray crystallography and NMR spectroscopy. Nature 1991; 353: 276–9.
40 Pfluefel G, Kallen J, Schirmer T, Jansonius JN, Zurini MGM, Walkinshaw MD, *et al*. X-ray structure of a decameric cyclophilin-cyclosporin crystal complex. Nature 1993; 361: 9–4.
41 Fischer G, Berger E, Bang H. Kinetic β-deuterium isotope effects suggest a covalent mechanism for the protein folding enzyme peptidylprolyl *cis/trans*-isomerase. FEBS Lett 1989; 250: 267–70.
42 Helekar S, Patrick J. Peptidyl prolyl *cis-trans* isomerase activity of cyclophilin A in functional homo-oligomeric receptor expression. Proc Natl Acad Sci USA 1997; 94: 5432–7.

Important Announcement: the Online Manuscript Submission and Review System was Launched!

Acta Pharmacologica Sinica is happy to announce that the online manuscript submission and review system, ScholarOne Manuscript Central (http://mc.manuscriptcentral.com/aphs), was launched on May 25, 2005.

As the leading web-based peer-review system, Manuscript Central is a complete, database-driven software for the online submission and review of full-text manuscripts and graphics. The system provides fully electronic workflow and will speed up the time from submission to decision.

We strongly recommend authors to submit manuscript via this system, which enables us to handle your manuscript quickly and efficiently. Please read the User Guide before submitting your manuscript online. For more detailed submission instruction, please consult the Manuscript Central Online User Guide (http://mcv3help.manuscriptcentral.com/tutorials/). You may also contact the Editorial Office who will be pleased to help you.

Acta Pharmacologica Sinica 2005 Oct; 26 (10): 1212–1216

Blackwell Publishing

Full-length article

Effects of propyl gallate on interaction between TNF-α and sTNFR-I using an affinity biosensor[1]

Jing LI, Jia-dong HUANG, Bao-yan WU, Qiang CHEN[2]

Laboratory of Biosensors, College of Life Science, Nankai University, Tianjin 300071, China

Key words

propyl gallate; tumor necrosis factor-α; soluble tumor necrosis factor receptor; affinity biosensor

[1]Project supported by the National Natural Science Foundation of China (No 90209054).
[2] Correspondence to Prof Qiang CHEN.
Phn 86-22-2350-6182.
Fax 86-22-2350-6122.
E-mail qiangchen@nankai.edu.cn

Received 2005-05-21
Accepted 2005-06-29

doi: 10.1111/j.1745-7254.2005.00198.x

Abstract

Aim: To study the effects of propyl gallate on the interaction of tumor necrosis factor-α (TNF-α) with its soluble receptor, sTNFR-I. **Methods:** Interactions between TNF-α and sTNFR-I were analyzed using an IAsys biosensor. sTNFR-I was immobilized on the carboxymethyl dextran (CMD) surface of the IAsys biosensor cuvettes, and TNF-α preincubated with different concentrations of propyl gallate was added to the cuvettes. The resonant angle shift caused by the binding between TNF-α and sTNFR-I was then recorded. **Results:** sTNFR-I was immobilized on the CMD surface at a density of 2.76 ng/mm^2. TNF-α then bound the immobilized sTNFR-I specifically, and propyl gallate was able to enhance the binding between TNF-α and sTNFR-I in a dose-dependent manner. **Conclusion:** The binding between TNF-α and sTNFR-I is one of the targets that propyl gallate can act on *in vivo*. The IAsys biosensor offers a new clue as to the study on the mechanisms of action of propyl gallate.

Introduction

Propyl gallate (PG) is a well-known synthetic antioxidant on the US Food and Drug Administration list (Figure 1). It is a derivative of gallic acid, which is one of the active ingredients of *Paeoniae Radix*, a commonly used traditional Chinese medicine (TCM). Besides its antioxidant activity, PG has many pharmacological effects such as free radical elimination[1,2], inhibiting platelet aggregation[3,4], anti-inflammatory effects[5] and anti-tumor activities[6]. It is used widely to nourish blood, activate circulation, alleviate pain, regulate menstruation and treat liver disease and cancer. However, until now the research on PG has been focused on its curative effects at the holistic level. There are no detailed studies on the mechanism and dynamics of action at the molecular level, which limits the further clinical use of PG.

Tumor necrosis factor-α (TNF-α) is produced mainly by activated macrophages and monocytes. Mature TNF-α molecules are released as 17 kDa monomers, under physiological conditions, and the monomers associate non-covalently to form a homotrimer that is biologically active[7,8]. TNF-α is one of the most pleiotropic cytokines; besides its antitumor activity *in vitro* and *in vivo*, it plays an important role in many physiological and pathophysiological responses, such as inflammatory reactions, thrombosis, cardiac failure, infection, immune regulation, antiviral responses and endotoxic shock, as well as in the pathogenesis of certain autoimmune diseases[9–13].

The biological activities of TNF-α are mediated by binding to 2 distinct membrane TNF receptors (TNFR), TNFR-I (p55, ~55 kDa) and TNFR-II (p75, ~75 kDa). Although both TNFR-I and TNFR-II bind TNF-α with high affinity, it has been generally believed that most of the cellular TNF responses are dominated by TNFR-I. Membrane TNFR (mTNFR) can be cleaved proteolytically to release soluble forms of the receptors (sTNFR). Though sTNFR lacks an intracellular domain, it binds free TNF-α with high affinity, competing with mTNFR[14,15].

Though their physiological roles are not fully understood, sTNFR might regulate the function of TNF *in vivo* through 2 different mechanisms: (i) by eliminating mTNFR and thereby reducing cellular reactivity to TNF, sTNFR may protect the cell from TNF pathological injury; and (ii) whereas sTNFR inhibits the activity of TNF by binding and neutralizing the cytokines at high concentrations, it may also enhance TNF

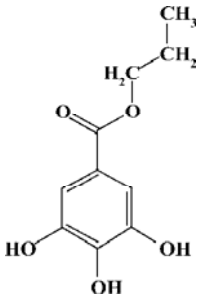

Figure 1. Chemical structure of propyl gallate, M_r 213.

activity at low concentrations by stabilizing TNF trimer molecules and prolonging their availability for binding mTNFR, thereby acting as an immunoregulator[16,17].

Because sTNFR is present constitutively in serum derived from receptor shedding after cellular activation by stimuli such as TNF-α production[18], sTNFR serum level is considered a reliable indicator of TNF-α system activation[19]. Moreover, TNF-α and sTNFR are considered to be key disease molecules and therapeutic targets[9,20]. Because the pharmacological functions of PG and the biological activity of TNF-α are probably correlative, the TNF-α–mTNFR–sTNFR system may be a potential target of PG *in vivo*. In order to find out if this is the case, in the present paper, an affinity biosensor, the cuvette-based IAsys biosensor, was used to study the effects of PG on the interaction of TNF-α with sTNFR-I.

Materials and methods

Chemicals *N*-hydroxysuccinimide (NHS), 1-ethyl-3-(3-dimethylaminopropyl) carbodiimide (EDC), ethanolamine and PG were purchased from Sigma-Aldrich (St Louis, MO, USA). TNF-α and sTNFR-I were purchased from PeproTech EC (London, UK). Carboxymethyl dextran (CMD) dual-well cuvettes were purchased from Labsystems Affinity Sensors (Cambridge, UK). Phosphate-buffered saline Tween-20 (PBST, pH 7.4) was composed of 10 mmol/L Na_2HPO_4/NaH_2PO_4, 138 mmol/L NaCl, 2.7 mmol/L KCl and 0.05% Tween-20. All solutions were made by using deionized water. All reagents were of analytical grade and were used without further purification.

Apparatus All analyses were carried out using an IAsys Plus optical biosensor (Labsystems Affinity Sensors, Cambridge, UK), which is based on resonant mirror technology. This instrument employs a dual-well stirred cuvette (pre-derivatized with CMD) and monitors the interaction between a pair of biomolecules inside the reaction cuvette[21–23]. One of the biomolecules, the ligand, is immobilized to the sensing surface of the cuvette. Its binding partner, the ligate, is then injected into the cuvette. Changes in refractive index and thickness on the sensing surface occur upon binding (association) of ligate to the immobilized ligand. The IAsys biosensor detects these changes continuously, producing a plot of responses that are measured in arc seconds[24–27]. Following each interaction, the surface of the cuvette is regenerated to remove bound ligate, and another ligate can then be introduced to the sensing surface. The IAsys biosensor has been applied to many kinds of studies on molecular recognition, affinity, kinetics, solute concentrations and multi-molecular interactions. It is especially useful for capturing measurements quickly and in real time, and can eliminate the need for radiolabels or other chemical tags. Compared to traditional methods, numerous additional steps are saved.

sTNFR-I immobilization To examine the binding of TNF-α to sTNFR-I, the receptor protein was immobilized onto the cuvette surface through its residual amine groups via amide with CMD. The IAsys instrument parameters were set at 100% for stirring, and 0.3 s for the sampling interval. The running buffer was PBST. Data acquisition then began and baseline data was gathered for several minutes. The surface of the cuvette was activated with 40 μL of a 1:1 (v/v) EDC/NHS mixture (0.4 mol/L EDC and 0.1 mol/L NHS) for 7 min. The function of EDC/NHS is to activate and promote the formation of covalent linkages by forming the N-hydroxysuccinimide ester. The carboxyl on the CMD bound NHS under the action of EDC and created active ester intermediates that bound the primary amines of sTNFR-I to make the amide bonds. Thus, sTNFR-I can be covalently immobilized on the CMD. The cuvette was subsequently washed with PBST and 10 mmol/L acetate (pH 5.5). After gathering baseline data in the acetate buffer, 10 μL diluted sTNFR-I was added to the cuvette to begin the electrostatic uptake of protein and covalent coupling. After a sufficient reaction time, 15 min or so, unreacted NHS esters were blocked by 40 μL 1 mol/L ethanolamine (pH 8.5) and the baseline was stabilized by washing with PBST.

At the same time, another cuvette channel was used as the blank control, without anchoring of sTNFR-I. The acetate buffer was injected instead of the sTNFR-I solution.

Binding detection The sTNFR-I modified and unmodified cuvettes were both rinsed 3 times with 40 μL PBST, and 10 μL TNF-α (0.01 mg/mL) was then added into each of the cuvettes to equilibrate for 15 min, before they were washed with PBST. The resonant angle response was recorded. The chip surface was then regenerated by adding 10 mmol/L HCl, until the response signal returned to baseline to proceed with another binding cycle. To evaluate the affinity binding

of TNF-α and sTNFR-I, a wide range of TNF-α concentrations (from 0.625 μg/mL to 20 μg/mL) were used.

Effects of PG on binding of TNF-α and sTNFR-I After 3 times of washes with 40 μL PBST, 10 μL TNF-α (0.01 mg/mL), preincubated with different concentrations of PG, was added into the sTNFR-I-modified cuvette. Binding between TNF-α and sTNFR-I was detected as described above.

Results

sTNFR-I immobilization on the surface of cuvettes As described in the "sTNFR-I immobilization" section, the sTNFR-I molecules were immobilized onto the surface of the IAsys cuvette by the ester exchange reaction of NHS to COOH groups on CMD. Figure 2 shows the response sensorgram of the IAsys biosensor to EDC/NHS activation as well as to the consequent sTNFR-I immobilization (solid line). Phase (1) is the initial baseline obtained when the surface of the cuvette was exposed to the PBST; phase (2) is the addition of EDC/NHS mixture to the sensor chip; phase (3) is the buffer washing to remove unreacted EDC/NHS mixture; phase (4) is the washing with acetate buffer; phase (5) is the addition of sTNFR-I; phase (6) is the dissociation course by washing with PBST; phase (7) is the blocking of non-coupled activated CMD sites with ethanolamine; phase (8) is the baseline stabilization. Arrow (9) is the resonant angle shift caused by the immobilization of sTNFR-I onto the cuvette surface. The broken line indicates the reference channel signal in order to follow non-specific binding on the biosensor surface.

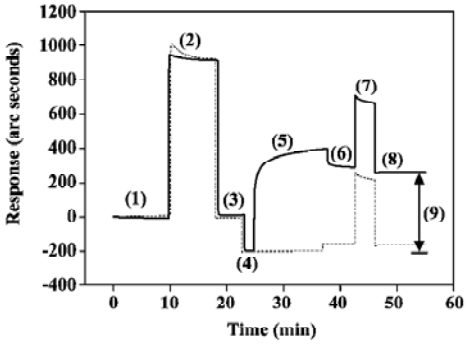

Figure 2. Sensorgram of EDC/NHS activation and soluble tumor necrosis factor receptor-I (sTNFR-I) immobilization. (1) Initial baseline obtained when the surface of the cuvette was exposed to the phosphate-buffered saline Tween-20 (PBST); (2) addition of the EDC/NHS mixture to the sensor chip (7 min reaction time); (3) PBST washing to remove unreacted EDC/NHS mixture; (4) acetate buffer re-equilibration; (5) addition of sTNFR-I; (6) PBST washing to allow dissociation; (7) blocking of non-coupled activated carboxymethyl dextran sites with ethanolamine; and (8) baseline stabilization. Arrow (9) is the resonant angle shift caused by the sTNFR-I immobilization.

The amount of immobilized sTNFR-I was calculated by subtracting the baseline level after phase (4) from that after phase (8), described in Figure 2 as arrow (9), which is approximately 450.61 arc seconds. The sensitivity of the CMD cuvette is 163 arc seconds/ng per mm^2. Thus the density of immobilized sTNFR-I is 2.76 ng/mm^2. Dual-well IAsys cuvettes have a sensor area of 4 mm^2, so the total amount of sTNFR-I immobilized was 11.04 ng.

Detection of interaction between sTNFR-I and TNF-α Figure 3 shows the comparison of TNF-α binding to the sTNFR-I modified cuvette surface (solid line) and the unmodified surface (broken line). The results showed that there was no specific binding on the unmodified cuvette surface except for non-specific absorption, which was easily washed away. This indicates that TNF-α bound sTNFR-I on the cuvette surface specifically.

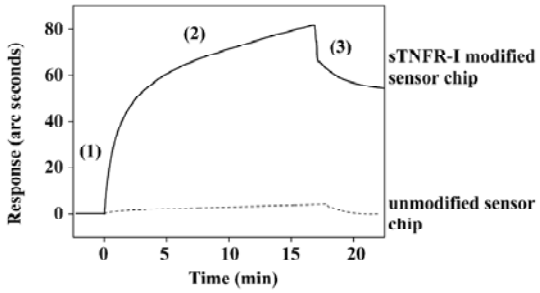

Figure 3. Sensorgram of the interaction between soluble tumor necrosis factor receptor-I (sTNFR-I) and tumor necrosis factor-α (TNF-α) on the cuvette surface. (1) phosphate-buffered saline Tween-20 (PBST) re-equilibration and baseline stabilization; (2) TNF-α addition with increase in irreversible response; (3) PBST washing to remove non-specific absorption.

The dissociation equilibrium constant (K_D) of binding of TNF-α and sTNFR-I were determined by using the FASTfit program, which is specifically designed for biomolecular interaction analysis using the IAsys biosensor. The K_D value was 5.05×10^{-7} mol/L, while the K_D of TNF-α/mTNFR-I binding has been reported as about 1×10^{-9} mol/L[28]. It can be inferred that though sTNFR-I can bind TNF-α with high affinity, its binding ability is lower than mTNFR-I. The results indicate that sTNFR-I binding affinity for TNF-α is decreased, which is probably attributable to the denaturation that occurred when sTNFR-I was produced.

Effects of PG on the interaction between TNF-α with sTNFR-I Figure 4 shows the experimental results obtained at a PG concentration of 500 nmol/L. With the presence of PG, the initial velocity of TNF-α/sTNFR-I binding increased

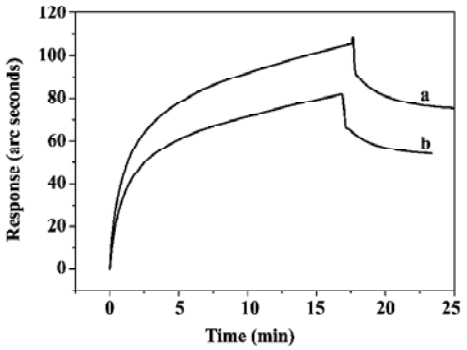

Figure 4. Comparison between the binding reactions of tumor necrosis factor-α (TNF-α) (b) and TNF-α–propyl gallate mixture (a) on the soluble tumor necrosis factor receptor-I-modified surface.

and the time taken to approach equilibrium decreased, which indicated that PG was able to enhance the binding of TNF-α to sTNFR-I.

The concentration-dependent effects of PG on the binding of sTNFR-I and TNF-α were studied. The PG concentrations varied from 5 nmol/L to 500 nmol/L, and the results are summarized in Figure 5. The increase in amplitude of the initial velocity of TNF-α/sTNFR-I binding, as well as the decrease in amplitude of the time taken to approach equilibrium, both increased as PG concentration increased, which indicated that PG enhanced TNF-α/sTNFR-I binding in a dose-dependent manner.

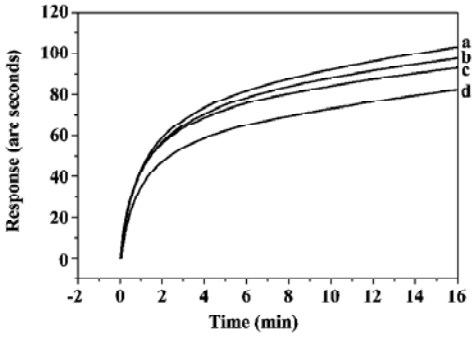

Figure 5. Binding reactions on a CMD surface of immobilized sTNFR-I and TNF-α with 500 nmol/L PG (a), 50 nmol/L PG (b), 5 nmol/L PG (c) and without sTNFR-I (d).

Discussion

Recent researches showed that the pathogenesis of the traditional Chinese medicine syndromes is the result of perturbation of cytokine networks, and the mechanism of TCM is to regulate and correct the perturbation of cytokine networks. It has been observed for many years that Chinese prescriptions can regulate the gene expression level of cytokines or their receptors. But for the initial step of the cytokine action, the binding to the corresponding receptor, there is few reports mainly due to the lack of appropriate methods. In the present study, an affinity biosensor, the IAsys biosensor, was used to explore the interaction of the cytokine and its receptor. The involvement of TNF-α in the pathogenesis of various diseases makes it an obvious and attractive therapeutical target. The effects of PG on the interaction between TNF-α and sTNFR-I were examined by using the IAsys biosensor in an *in vitro* assay. The experimental results showed that PG enhanced TNF-α/sTNFR-I binding in a dose-dependent manner. Though the mechanisms of PG are not clear and the roles of TNF-α and sTNFR-I are debated, it can be concluded that the binding between TNF-α and sTNFR-I is another target that PG can act on *in vivo*. Researches showed that serum level of sTNFR-I are often increased in a variety of conditions which are characterized by an antecedent increase in TNF-α, such as sepsis, inflammatory responses, autoimmune diseases, human immuno-deficiency virus infection, transplant rejection and malignant tumor[29–32], which indicated that sTNFR-I production seems to neutralize and reduce the toxicity associated with the elevated serum TNF-α level. PG can enhance the cellular protection of sTNFR-I through increasing neutralization to TNF-α, which is in agreement with the experimental and clinical results reported[33]. Thus it may sound theoretically that PG is helpful for therapy or assistant therapy in TNF-α corresponding diseases, which may leads to the new therapeutic application of PG. These are the first results obtained using affinity biosensors for studying the interactions of these molecules. This finding offers a new clue to the study of the mechanism of action of PG. The IAsys biosensor could be used widely as a reliable tool for similar studies. With respect to most of the other available methodologies to study biomolecular interactions, there are many advantages of this new method, such as real time measurement, high sensitivity, high selectivity and high veracity, as well as being easy to handle and eliminating the need for labeled compounds. It has tremendous application prospects in studies on the mechanisms of TCM *in vitro*. It will be more compellent when data on bioactivity, such as from cell experiments, were acquired to support the results from those from biosensor technology. Further studies in this area are in progress.

References

1 Reddan JR, Giblin FJ, Sevilla M, Vanita P, Dorothy CD, Victor RL, *et al*. Propyl gallate is a superoxide dismutase mimic and protects cultured lens epithelial cells from H_2O_2 insult. Exp Eye Res 2003; 76: 49–59.

2 Shanker G, Aschner M. Methylmercury-induced reactive oxygen species formation in neonatal cerebral astrocytic cultures is attenuated by antioxidants. Brain Res Mol Brain Res 2003; 110: 85–91.

3 Panganamala RV, Miller JS, Gwebu ET, Sharma HM, Cornwell DG. Differential inhibitory effects of vitamin E and other antioxidants on prostaglandin synthetase, platelet aggregation and lipoxidase. Prostaglandins 1977; 14: 261–71.

4 Chen KJ. Antithrombosis of propyl gallate. Chin Prescrip Drug 2003; 9: 38–9.

5 Franzone JS, Natale T, Cirillo R. Influence of propyl gallate and 2-mercapto-propionyl glycine on the development of acute inflammatory reactions and on biosynthesis of PGE_2. Bull Soc Ital Biol Sper 1980; 56: 2539–45.

6 Lee SMY, Li MLY, Tse YC, Leung SCL, Lee MMS, Tsui SKW, *et al*. Paeoniae Radix, a Chinese herbal extract, inhibits hepatoma cells growth by inducing apoptosis in a p53 independent pathway. Life Sci 2002; 71: 2267–77.

7 Carswell EA, Old LJ, Kassel RL, Green S, Fiore N, Williamson B. An endotoxin-induced serum factor that causes necrosis of tumors. Proc Natl Acad Sci USA 1975; 72: 3666–70.

8 Smith RA, Baglioni C. The active form of tumor necrosis factor is a trimer. J Biol Chem 1987; 262: 6951–4.

9 Taylor PC, Williams RO, Feldmann M. Tumour necrosis factor α as a therapeutic target for immune-mediated inflammatory diseases. Curr Opin Biotechnol 2004, 15: 557–63.

10 Piguet PF, Vesin C, Chen DK. Activation of platelet caspases by TNF and its consequences for kinetics. Cytokine 2002; 18: 222–30.

11 Guarntz D, Cowling RT, Vaiki N, Frikovsky E, Moore CD, Greenberg BH. IL-1β and TNF-α upregulate angiotensin II type 1 (AT_1) receptors on cardiac fibroblasts and are associated with increased AT_1 density in the post-MI heart. J Mol Cell Cardiol 2005; 38: 505–15.

12 Zimmermann VS, Bondanza A, Rovere-Querini P, Colombo B, Sacchi A, Fascio U, *et al*. Characterisation of functional biotinylated TNF-á targeted to the membrane of apoptotic melanoma cells. J Immunol Methods 2003; 276: 79–87.

13 Mocellin S, Rossi CR, Pilati P, Nitti D. Tumor necrosis factor, cancer and anticancer therapy. Cytokine Growth Factor Rev 2005; 16: 35–53.

14 Mwangi SM, Stabel J, Lee EK, Kehrli ME, Taylor MJ. Expression and characterization of a recombinant soluble form of bovine tumor necrosis factor receptor type I. Vet Immunol Immunopathol 2000; 77: 233–41.

15 Bao L, Lindgren JU, Zhu Y, Ljunggren HG, Zhu J. Exogenous soluble tumor necrosis factor receptor type I ameliorates murine experimental autoimmune neuritis. Neurobiol Dis 2003; 12: 73–81.

16 Pennica D, Kohr WJ, Fendly BM, Shire SJ, Raab HE, Borchardt PE, *et al*. Characterization of a recombinant extracellular domain of the type 1 tumor necrosis factor receptor: evidence for tumor necrosis factor a induced receptor aggregation. Biochemistry 1992; 31: 1134–41.

17 Aderka D, Engelmann H, Maor Y, Brakebusch C, Wallach D. Stabilization of the bioactivity of tumor necrosis factor by its soluble receptors. J Exp Med 1992; 175: 323–9.

18 Beutler B, van Huffel C. Unraveling function in the TNF ligand and receptor families. Science 1994; 264: 667–8.

19 Leist M, Gantner F, Jilg S, Wendel A. Activation of the 55 kDa TNF receptor is necessary and sufficient for TNF-induced liver failure, hepatocyte apoptosis, and nitrite release. J Immunol 1995; 154: 1307–16.

20 Punzon C, Alcaide A, Fresno M. *In vitro* anti-inflammatory activity of *Phlebodium decumanum*. Modulation of tumor necrosis factor and soluble TNF receptors. Int Immunopharmacol 2003; 3: 1293–9.

21 Gambari R. Biospecific interaction analysis (BIA) as a tool for the design and development of gene transcription modifiers. Curr Med Chem 2001; 1: 277–91.

22 Baker KN, Rendall MH, Patel A, Boyd P, Hoare M, Freedman RB, *et al*. Rapid monitoring of recombinant protein products: a comparison of different technologies. Trends Biotechnol 2002; 20: 149–56.

23 Wilson WD. Analyzing biomolecular interactions. Science 2002; 295: 2103–5.

24 Buckle PE, Davies RJ, Kinning T, Yeung D, Edwards PR, Pollard KD. The resonant mirror: a novel optical sensor for direct sensing of biomolecular interactions: Part II. Applications. Biosens Bioelectron 1993; 8: 355–68.

25 Karlsson R, Michaelsson A, Mattsson L. Kinetic analysis of monoclonal antibody–antigen interactions with a new biosensor based analytical system. J Immunol Methods 1991; 145: 229–40.

26 Dmitriev DA, Massino YS, Segal OL. Kinetic analysis of interactions between bispecific monoclonal antibodies and immobilized antigens using a resonant mirror biosensor. J Immunol Methods 2003; 280: 183–202.

27 Bertucci C, Cimitan S, Menotti L. Optical biosensor analysis in studying herpes simplex virus glycoprotein D binding to target nectin1 receptor. J Pharm Biomed Anal 2003; 32: 697–706.

28 Fang J, Wang DB, Chen CQ. Expression in BHK cells of two human TNF receptors and their interaction with hTNF-α. Acta Biochim Biophys Sin 1999; 31: 25–30.

29 Carmen P, Antonio A, Manuel F. In vitro anti-inflammatory activity of Phlebodium decumanum. Modulation of tumor necrosis factor and soluble TNF receptors. Inter Immunopharm 2003; 3: 1293–9.

30 Le Y. Clinical implication of soluble tumor necrosis factor receptors of infection diseases. Clin Med J Chin 2004; 11(2): 184–5.

31 Klaus P. Biological functions of tumor necrosis factor cytokines and their receptors. Cytokine Growth Factor Rev 2003; 14: 185–91.

32 Monika H, Thomas P, Janet MM. Diurnal and sleep-wake dependent variations of soluble TNF- and IL-2 receptors in healthy volunteers. Brain Behavior Immunity 2004; 18: 361–7.

33 Jiang YR, Yin HJ, Chen KJ. Current status of research on paeoniae radix 801. Chin J Integ Tradit West Med 2004; 24: 760–3.

Acta Pharmacologica Sinica 2005 Otc; 26 (10): 1217–1224

Full-length article

Assessing phylogenetic relationships of *Lycium* samples using RAPD and entropy theory[1]

Xiao-lin YIN[2,3], Kai-tai FANG[4], Yi-zeng LIANG[5], Ricky NS WONG[6], Amber WY HA[6]

[2]School of Mathematics and Statistics, Northeast Normal University, Changchun 130024, China; [4]Department of Mathematics, Hong Kong Baptist University, Hong Kong, China; [5]College of Chemistry and Chemical Engineering, Central South University, Changsha 410083, China; [6]Department of Biology, Hong Kong Baptist University, Hong Kong, China

Key words

DNA fingerprinting; RAPD technique; lab-on-a-chip; entropy; UPGMA

[1] Project supported by the National Natural Science Foundation of China (No 10371015 and 10329102) and a grant from the Hong Kong Baptist University (No FRG/02-03/II-62).
[3] Correspondence to Dr Xiao-lin YIN.
Phn 86-431-509-8576.
E-mail yinxl805@nenu.edu.cn

Received 2005-05-17
Accepted 2005-06-23

doi: 10.1111/j.1745-7254.2005.00197.x

Abstract

Aim: To evaluate the phylogenetic relationships among related species of *Lycium* samples. **Methods:** Random amplified polymorphic DNA (RAPD) fingerprinting and lab-on-a-chip electrophoresis techniques were used to analyze the characteristics of *Lycium* species. Seven species and 3 varieties of *Lycium* were studied. Based on RAPD fingerprint data obtained from 11 primers, we proposed a new index, called dispersivity, using entropy theory and projection methods to depict the diversity of the DNA fingerprints. **Results:** Using the proposed dispersivity, primers were sorted and the dendrograms of the 7 species and 3 varieties of *Lycium* were constructed synthetically by merging primer information. **Conclusion:** Phylogenetic relationships among *Lycium* samples were constructed synthetically based on RAPD fingerprint data generated from 11 primers.

Introduction

Traditional Chinese medicine (TCM) has been used for thousands of years in China. It represents the collective wisdom of the Chinese people to utilize nature for survival[1]. With the advantages of multi-target effects, low toxicity and the current appeal for more 'natural' remedies, TCM has become widely used as an alternative to treat various complex and chronic diseases. Authentication of Chinese medicinal materials is an old but important issue. With the unprecedented development of modern biological methods, identification of species relationships using traditional anatomical and physiochemical methods is being supplemented by DNA fingerprinting techniques, such as random amplified polymorphic DNA (RAPD) analysis.

The fruit of *Lycium* species, especially *Lycium barbarum*, has been used in TCM to improve eyesight, protect liver and kidney, and to replenish vital essence. The fruit of the *Lycium* species are all red in color with very similar physical appearance and anatomical structure. Chemical analysis methods, such as high-performance liquid chromatography, have been used for different species of *Lycium*, but have failed to differentiate the *Lycium* species.

Recently, a Fourier-transform infrared spectroscopy method was used to identify 7 species and 3 varieties of *Lycium*[2]. The method provides a novel approach for the identification and differentiation of plants used in TCM. Such a technique can serve as a rapid, simple, reliable and non-destructive analytical method for differentiating *Lycium* species. Alternatively, with the development of modern biotechnology, a polymerase chain reaction (PCR)-based method using random primers (10-mers), known as RAPD[3,4], has become another method for the study of TCM[5,6]. RAPD analysis is simple and effective. It has many advantages, such as it only requires a minute quantity of DNA; no prior sequence data are needed, many primers can be used; and the method is relatively simple. However, RAPD suffers the drawback of low reproducibility, which has severely hampered the popularity of this method. Usually, PCR products are analyzed by agarose gel electrophoresis followed by densitometric analysis of the DNA banding pattern. In the present study, the lab-on-a-chip (Agilent 2100 Bioanalyzer DNA 7500 assays, Agilent Technologies, Palo Alto,

California, USA) was used to analyze the PCR products of *Lycium* samples, including 7 species and 3 varieties. After preprocessing using the Agilent 2100 Bioanalyzer, including baseline adjustment and alignment, data were exported as XML files, which were imported into the Matlab software. All further analyses were performed using Matlab. We will clarify these analyses in detail in the following sections.

Materials and methods

Sample preparation Twelve *Lycium* samples were used in this study. Dried fruits of *Lycium* were rinsed with 70% ethanol and distilled water for surface sterilization. They were then ground in liquid nitrogen with a mortar and pestle. Information for the samples is summarized in Table 1. Samples of *Lycium barbarum*, LB and LBB, were treated as positive controls in the RAPD analysis. The remaining 10 samples, which represent 7 species and 3 varieties, were used in our data analysis.

Table 1. List of Lycium species analyzed in this study.

Scientific name	Abbreviation	Chinese name
Lycium barbarum	LB	Ningxiagouqi
Lycium barbarum	LBA	Ningxiagouqi
Lycium barbarum	LBB	Ningxiagouqi
Lycium barbarum var Auranticarpum	LBV	Huangguogouqi
Lycium chinense	LC	Gouqi
Lycium chinense var potaninii	LCV	Beifanggouqi
Lycium dasystemum	LD	Xinjianggouqi
Lycium dasystemum var rubricaulium	LDV	Hongzhigouqi
Lycium cylindricum	LE	Zhutonggouqi
Lycium ruthenicum	LR	Heiguogouqi
Lycium truncatum	LT	Jieegouqi
Lycium yunnanense	LY	Yunnangouqi

Genomic DNA extraction The cetyl triethylammonium bromide (CTAB) extraction method, a modified protocol of Draper and Scott[7], was used for the extraction of DNA. *Lycium* powder was mixed with 600 μL of 1×CTAB extraction buffer [50 mmol/L Tris-HCl (pH 8.0), 0.7 mol/L NaCl, 10 mmol/L ethylenediaminetetracetic acid (EDTA), 1% CTAB], which was preheated at 60 °C. The mixture was then incubated for 30 min with occasional shaking. After cooling to room temperature, the mixture was extracted with an equal volume of chloroform/isoamyl alcohol (24:1, v/v). After centrifugation at 13 000×*g* for 15 min at room temperature, the supernatant was collected and a 0.1 mol/L volume of 10% CTAB solution (10% CTAB, 0.7 mol/L NaCl) and an equal volume of chloroform/isoamyl alcohol were added for another extraction. After centrifugation at 13 000×*g* for 15 min at room temperature, the supernatant was collected and extracted with an equal volume of CTAB precipitation buffer [50 mmol/L Tris-HCl (pH 8.0), 10 mmol/L EDTA, 1% CTAB]. It was then allowed to stand at room temperature for at least 1 h, before being centrifuged again at 13 000×*g* for 15 min at room temperature. The pellet was resuspended in 400 μL of 1 mol/L NaCl, which was pre-heated at 60 °C. For further purification, it was extracted again with an equal volume of chloroform/isoamyl alcohol. After centrifugation at 13 000×*g* for 15 min at room temperature, the supernatant was collected and 800 μL of cold absolute ethanol was added. The solution was allowed to stand at -20 °C overnight for precipitation of DNA. To recover the DNA, the suspension was centrifuged at 13 000×*g* for 20 min at 4 °C. The pellet was collected and washed twice with 75% ethanol. After that, the pellet was air-dried and resuspended in 30 μL distilled water.

Estimation of DNA concentration and purity The concentration and purity of DNA was checked by UV spectroscopy at wavelengths 230 nm, 260 nm, and 280 nm. The quality of DNA (5 μL) was also checked by electrophoresis on a 1% agarose gel in 1×TBE (Total Binding Energy) buffer.

RAPD and optimization of PCR conditions The RAPD reactions were carried out as described by Nadeau *et al*[8] in a 25 μL reaction mixture containing DNA (10 ng–100 ng), 0.1 mmol/L dNTP, 25 pmol primer, 1×*Taq* buffer [20 mmol/L $(NH_4)_2SO_4$, 75 mmol/L Tris-HCl (pH 8.8), 0.01% Tween-20, 2.5 mmol/L $MgCl_2$, 0.001% gelatin (w/v)] and 0.5 U *Taq* DNA polymerase. The tubes were placed in the thermocycler (PTC-100™, MJ Research Inc Waltham, Massachusetts, USA) and subjected to the following profiles: denaturation for 5 min at 94 °C, then 45 cycles at 94 °C for 1 min, 35 °C for 1 min, 72 °C for 2 min, final extension at 72 °C for 5 min. In order to optimize the RAPD conditions, the PCR conditions were varied using 100-fold, 500-fold, 1000-fold and 5000-fold dilutions of genomic DNA, 2 mmol/L or 2.5 mmol/L $MgCl_2$, 1 U or 1.25 U *Taq* polymerase in the presence or absence of the final extension step. The PCR products were monitored by 1.5% agarose gel electrophoresis and the DNA fragments were visualized by staining with ethidium bromide. The amplification products (1 μL) were also analyzed with the lab-on-a-chip system, the Agilent 2100 Bioanalyzer, using the DNA 7500 assays kit according to the manufacturer's instructions.

Results

Preprocessing of raw data Raw lab-on-a-chip DNA fingerprints can be treated as multi-dimensional vectors or functional curves. Because they are usually observed and stored discretely, in the present study, the vector form was adopted to represent the DNA fingerprint. We let (t_i, x_i), i=1, ..., T denote the discrete observations for a DNA fingerprint, where x_i is the fluorescence intensity measured at migration time t_i and T is the number of migration time points. Customarily, fluorescence intensity is referred while ommitting migration time in representing DNA fingerprint, namely, $(x_1, ..., x_T)$ represents a fingerprint, where a is the transpose of a vector for a.

A complete preprocessing for raw fingerprint data includes baseline adjustment, alignment, linear interpolation match and normalization issues. In order to eliminate the background and peak drift effect for DNA fingerprints, we used the up-to-date Agilent 2100 Bioanalyzer[9] software to adjust baseline and handle alignment based on the ladder, lower marker and upper marker. Figure 1 shows the alignment process.

After baseline adjustment and alignment, we exported the data into an XML format, which could be opened by Microsoft Excel. The XML files were then imported by the

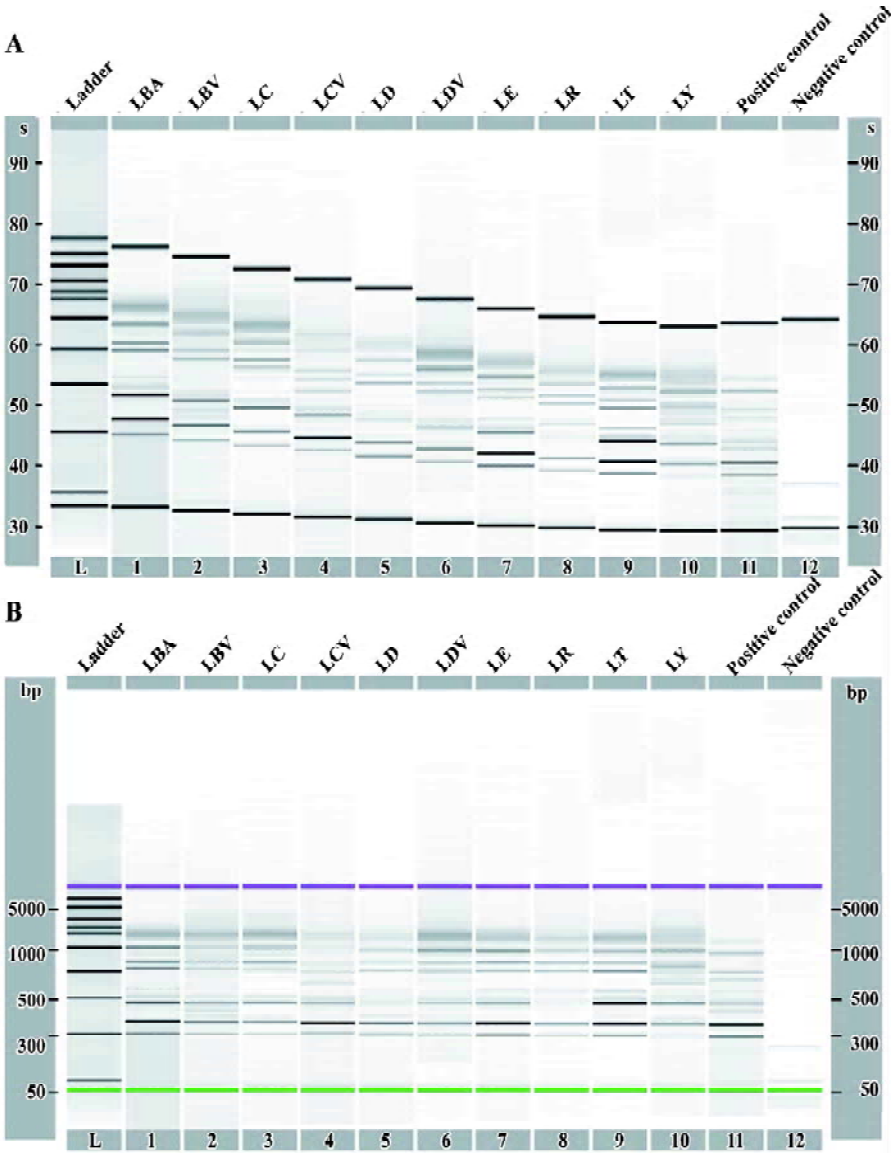

Figure 1. RAPD fingerprints of 10 *Lycium* samples (1–10), two control samples (11, 12) and ladder sample (L) obtained from primer opam2 performed by Agilent 2001 Expert software. (A) Fingerprints without alignment; (B) aligned fingerprints.

software Matlab, which was our main tool for further analysis. It was easy to detect the lower marker and upper marker that define the informative region for each fingerprint. Therefore, we could concentrate on the observations between the lower and upper markers. However, fingerprint data after baseline adjustment and alignment was shown with relative migration time, which was different from the unaligned data, that is, fingerprint data with the same length of interval between the lower marker and upper marker but with different number of migration time points. Here linear interpolation was used to match all of the fingerprints such that they had the same number of migration time points between the lower marker and upper marker. This method is called linear interpolation match (LIM). Our main purpose for using LIM was to render the fingerprints directly comparable. Another reason was to make the data format suitable for our statistical analysis. Details about the LIM method are described using *Lycium* samples as follows.

After exporting *Lycium* sample data from Agilent 2100 Expert software, the total 110 fingerprints produced by 11 primers and the corresponding number of migration time points were denoted by $x_i(k)$ and $n_{k,j}$,k=1, ..., 11; i=1, ..., 10. Because these fingerprints shared the common interval between the lower marker and the upper marker, we first chose the minimum number $\{n_{k,j}\}$, denoted as m, and then made the migration time points the same for all of the other fingerprints in the following way. We uniformly partitioned m–1 cells on interval [0,1]. Similarly, for any fingerprint that had s migration time points, we uniformly partitioned s–1 cells on interval [0,1]. The total migration time points corresponded to 0, 1/(s-1), 2/(s-1), ..., 1. For any i/(s-1), 0<i<s-1, we found j such that i/(s-1) located on an exclusive interval [j/(m-1), (j+1)/(m-1)]. Liner interpolation of the fluorescence intensity value at corresponding retention time j/(m-1) and (j+1)/(m-1) was changed to the i-th fluorescence intensity value for the newly matched fingerprint. Following the above rule, all of the fingerprints were matched with the same number of migration time points. After performing LIM, the common peaks of both ends, which were parts of the lower and upper markers, were removed as these peaks were of no concern. For simplicity, the number of migration time points of these fingerprints was still noted as T.

Because the outcomes of most statistical methods are strongly influenced by the scale and range of the fingerprint data, it was necessary to normalize all of the fingerprint data before analysis. To accomplish this goal, the sample mean and variance of the fingerprint x=(x_1, ..., x_T)' were calculated as follows:

$$m(x) = \frac{1}{T}\sum_{t=1}^{T} x_t \tag{1}$$

$$s^2(x) = \frac{1}{T}\sum_{t=1}^{T} (x_t - m(x))^2 \tag{2}$$

All of the fingerprints were normalized by subtracting the sample mean and then dividing by the standard deviation, namely the following form:

$$x \leftarrow \frac{x - m(x)}{s(x)} \tag{3}$$

The effect of this normalization is shown in Figure 2. From then on, fingerprint i referred to the registered fingerprint after normalization.

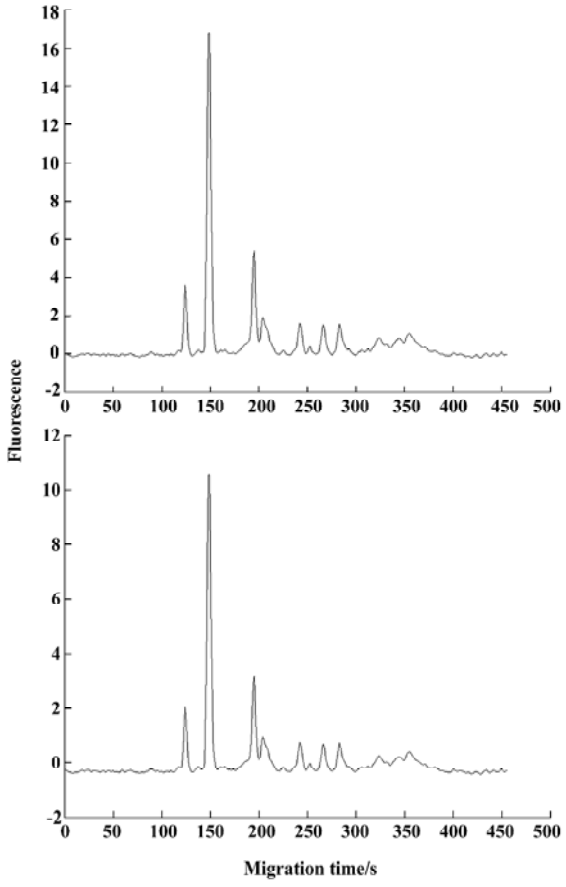

Figure 2. Normalization effect on fingerprints. (A) Fingerprint before normalization; (B) fingerprint after normalization.

Primer sorting by the revealed fingerprint diversity DNA fingerprinting performed by RAPD using different primers may have had different detected diversities. The diversity of fingerprints obtained from a primer, what we call

dispersivity, can be regarded as an index to indicate whether this primer is effective or not. As an example, for our tested DNA fingerprints of *Lycium* samples representing 7 species and 3 varieties, all DNA fingerprint data were denoted by:

$$X=(X^{(1)}, ..., X^{(11)}),$$

where $X^{(k)}=(X_1^{(k)}, ..., X_{10}^{(k)})$, k=1, ..., 11, k denotes k-th primer, and the total primer number 11, 10 denotes the total number of *Lycium* samples, namely, 7 species and 3 varieties. $X_i^{(k)}$ is a T-dimensional column vector that denotes the fingerprint of *Lycium* sample from species i obtained from primer k. T is the number of migration time points. Initially, the information about dispersivity revealed by primer k was contained in the data set $X^{(k)}$. Usually the more peaks in the data set $X^{(k)}$ obtained form primer k, the higher the dispersivity. However, that is not always true because the difference in peak location and the variation in peak height and peak shape among fingerprints obtained from primer k can also affect the corresponding dispersivity. It is necessary and important to integrate all of the factors in the evaluation of the dispersivity for each fingerprint set $X^{(k)}$.

In the present study, we used the concept of entropy, introduced by Shannon and Weaver[10], to quantify the dispersivity revealed by primer k. For a discrete probability distribution p, the motivated definition of entropy by statistical mechanics is:

$$h(p)=-\sum_{i=1}^{n} p_i \times \ln(p_i) \quad (4)$$

were $\sum_{i=1}^{n} p_i = 1$.. In the context of probability, $h(p)$ is regarded as a measure of the information carried by p, with high entropy corresponding to much uncertainty. This uncertainty score reflects the property of dispersiity. Intuitively, it manifests itself as the way we describe dispersivity.

The dispersivity revealed by primer k is defined as the following way:

Step 1. Compute the sample covariance matrix $S^{(k)}=(s(x_i^{(k)}, x_j^{(k)}))_{(10\times10)}, 1\le i, j\le 10,$ where

$$s(x_i^{(k)}, x_j^{(k)})=\frac{1}{T}\sum_{t=1}^{T}(x_{it}^{(k)}-m(x_i^{(k)}))(x_{jt}^{(k)}-m(x_j^{(k)})) \quad (5)$$

Step 2. Calculate the eigenvalues of $S^{(k)}$ and note them as $\lambda^{(k)}=(\lambda_1^{(k)}, ..., \lambda_{10}^{(k)})'$

Step 3. Make the sum of eigenvalues equal to 1, namely,

$$\lambda_j^{(k)} \leftarrow \frac{\lambda_j^{(k)}}{\sum_{j=1}^{10}\lambda_j^{(k)}}, j=1,...,10$$

Setp 4. Compute entropy of $\lambda^{(k)}$, namely,

$$h(\lambda^{(k)})=-\sum_{j=1}^{10}\lambda_j^{(k)}\times\ln(\lambda_j^{(k)}).$$

$h(\lambda^{(k)})$ is defined as the dispersivity revealed by the primer k. The definition of dispersivity is very intuitive. In the first step, we used the covariance matrix $S^{(k)}$ to describe all of the variant information for the fingerprints obtained from primer k. The variant information was then extracted by computing the eigenvalues of $S^{(k)}$. These eigenvalues, $\lambda^{(k)}$, can be regarded as the information reconstructed from $X^{(k)}$ and can be interpreted by the principal component analysis (PCA). Sort λ_1^k, ..., λ_{10}^k as $\lambda_{(1)}^{(k)}\ge ...\ge\lambda_{(10)}^{(k)}$, for the fixed primer k, the closer to 1 for

$$\lambda_{(1)}^k / \sum_{j=1}^{10}\lambda_{(j)}^k,$$

which can be considered as the contribution rate for the first principal component, the stronger for the first principal component to synthesize the information of $X^{(k)}$. For example, if fingerprints $l_1^{(k)}$, ..., $l_{10}^{(k)}$ are very similar, it will result in the contribution rate for the first component being close to 1 and the sum of the remaining 9 being near to 0, which means that the first component can synthesize almost all of the information. This case is not expected, because it reflects little diversity for $X^{(k)}$. We desired that the contribution rates for all of the components were scattered, not concentrated, and allowed for the entropy, which has the property that the more dispersive it is for the probability distribution, the larger the corresponding entropy value. Finally, we defined the dispersivity revealed by primer k as

$$h(\lambda^{(k)})=-\sum_{j=1}^{10}\lambda_j^{(k)}\times\ln(\lambda_j^{(k)})$$

Here all the $\lambda_j^{(k)}$ denote the contribution rates subject to the sum being equal to 1. From the definition of dispersivity, some eigenvalues may be equal to 0, which will result in no meaning due to the function. In such cases, we defined $0\times\ln(0)=0$, which is reasonable because $\lambda\times\ln(\lambda)$ will approach 0 if λ approaches 0 from the positive direction.

For our *Lycium* data, 11 primers were used to perform the analysis. A direct question is which primer is the best one as far as dispersivity is concerned? To some extent, the best primer would be able to differentiate the *Lycium* samples to the maximum degree. The dispersivity revealed by primer k was given by $h(\lambda^{(k)})$, simply noted as $D(X^{(k)})=h(\lambda^{(k)})$, where $\lambda^{(k)}$ is dependent on $X^{(k)}$. The best primer was chosen as the one that maximized the value of $D(X^{(k)})$. Memory the best primer and the corresponding dispersivity value as $S1$ and D_{S1}, respectively.

After choosing the primer $S1$, we then wanted to chose a second primer from the remaining 10, such that the fingerprints obtained from these 2 primers had the maximum

diversity. In order to do this, we had to define the dispersivity of the 2 primers. For a striking example, if fingerprints $X^{(i)}$ and $X^{(j)}$ obtained from primers *i* and *j*, respectively, were very similar, that would mean that primers *i* and *j* almost revealed the same dispersivity. Furthermore, if primer *i* revealed the maximum dispersivity and primer *j* revealed the second maximum dispersivity, then primer *i* would be picked as the best primer, while in most cases, primer *j* would not be selected as the primer that reveals the maximum diversity combined with primer *i*, because $X^{(i)}$ and $X^{(j)}$ have much mutual information. This indicated to us that we should remove overlapping information before choosing primers from the remaining 10. The method of space projection was utilized to solve the information overlap.

The dispersivity revealted by primers *i* and *j*, on condition that primer *i* was chosen, was defined as $D(X^{(i)},(1-X^{(i)}(X^{(i)})^{+})X^{(j)})$, where A^{+} denotes the pseudoinverse of matrix A[11] and can be numerically calculated by Matlab. The computation of $D(A,B)$ was similar to $D(A)$ except for substituting *A* union *B* for *A*. For simplicity, we define $CP(X^{(i)}|X^{j})=(1-X^{(i)}(X^{(i)+})X^{j}$. Matrix $CP(X^{(i)}|X^{j})$ was corthogonal to the space expanded by $X^{(i)}$. That means that it contained extra information relative to $X^{(i)}$. The eigenvalues of covariance matrix for $X^{(i)}$ union $CP(X^{(i)}|X^{j})$ were the union of eigenvalues of covariance matrix for $X^{(i)}$ and $CP(X^{(i)}|X^{j})$. For our *Lycium* data, on the condition that primer *S*1 was chosen, the second primer cosen was he one that corresponded to the maximum value of $D(X^{(S1)},CP(X^{(S1)}|X^{(k)})$, $k\in\{1,2,...,11\}/\{S1\}$, were *A*/*B* denotes the set that includes the elements belonging to *A* but not to *B*. Without loss of generality, the second primer chlosen is recorded as *S*2, the corresponding dispersivity value is denoted by $D_{S1,S2}$.

We could then obtain the order of primers, denoted *S*1, ..., *S*11. The corresponding dispersivities for the primers were denoted D_{S1}, ..., $D_{S1,\ ...,\ S11}$. For illustrating our space projection method, in Figure 3, we plot the original fingerprint for primer *S*9, namely, *X*(*S*9), extra information relative to primer *S*1, namely, $CP(X^{(S1)}|X^{S9})$, and extra information relative to primers *S*1, ..., *S*8, namely, $CP\{X^{(S1)}, CP(X^{(S1)}|X^{(S2)}), ..., CP[X^{(S1)}, CP(X^{(S1)}|X^{(S2)}, ..., CP(X^{(S1)}|X^{(S8)})]\}|X^{(S9)}$. Comparing the plots in Figure 3, the information provided by primer *S*9 gradually decreased as the mutual parts relative to primers chosen earlier *S*1, ..., *S*8 were removed one by one. This property can be interpreted by the projection theory and Figure 3 is an intuitive manifestation.

Construction of the dendrogram for *Lycium* samples From

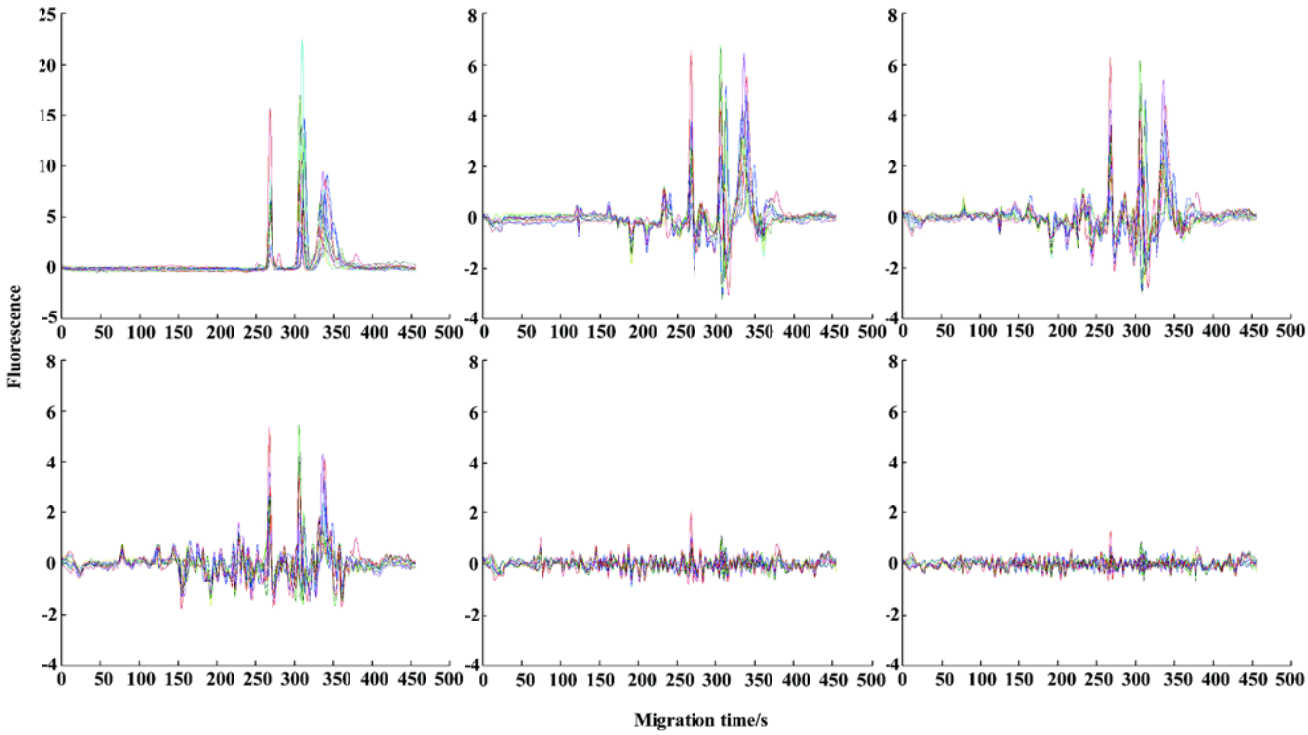

Figure 3. Fingerprints obtained from primer *S*9 and extra information relative to the earlier-picked primers. (A) Original fingerprints for primer *S*9; (B) extra information relative to primer *S*1; (C) extra information relative to primers *S*1,*S*2; (D) extra information relative to primers *S*1,*S*2,*S*3; (E) extra information relative to primers *S*1, ..., *S*7; (F) extra information relative to primers *S*1, ..., *S*8.

Figure 4, the x coordinate denotes the primers according to the order in which they were chosen and the y coordinate denotes the corresponding dispersivity. For example, 2 denotes primers *S*1 and *S*2, and the corresponding y-value is $D_{S1,S2}$, which shows that the dispersivity increases as the newly chosen primer is added. Furthermore, the extent of the increase becomes smaller and smaller. That means that adding a primer can increase the amount of information available while the last primer chosen provides less information than the previous primer. Generally, the more primers chosen, the better the conclusion drawn, such as in distinguishing and constructing the dendrogram for our *Lycium* samples of 7 species and 3 varieties. However, because the last primers chosen provided relatively little information, it was not necessary to pick all 11 of the primers to construct the dendrogram. In the present study, we decided on the primer number that contained almost all of the information to distinguish and construct the dendrogram for *Lycium* samples using $\text{argmin}(D_{S1,\ldots,Si})/(D_{S1,\ldots,S11})>95\%$. For our *Lycium* samples, $(D_{S1,\ldots,S11})'$=(1.9476, 2.3398, 2.6624, 2.8600, 3.0690, 3.2071, 3.3133, 3.3998, 3.4380, 3.4611, 3.4772)'. The number of primers to use can be obtained by simple computation according our proposed rule. Because, (3.2072/7.3772)=0.9223<0.95, (3.3133/3.4772)=0.9529>0.95, 7 primers, *S*1, ..., *S*7, were chosen for final analysis. We used the 95% rule to decide the number of primers. Generally, in most data analyses (such as PCA) it is possible to use other rules, for example, the 80% rule, to decide the number of principal components. However, we used the larger number 95% because our proposed dispersivity is a sensitive index. This means that the dispersivity changes only a small amount, while the fingerprint changes much. It is therefore better to widen the boundaries for choosing in case some important primers are lost.

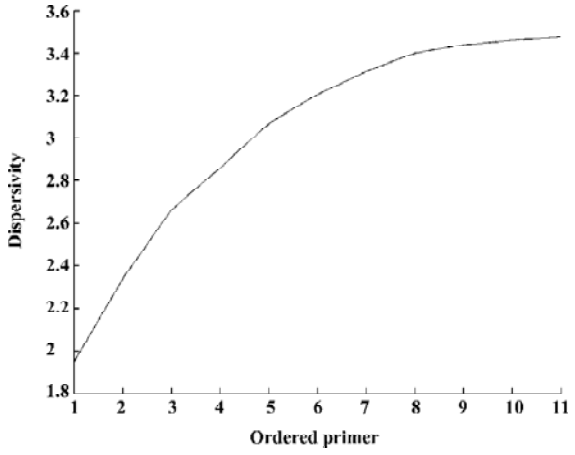

Figure 4. Plot of $\{(i, D_{S1,\ldots,Si})\}$ for *Lycium* samples.

In the present study, we used the hierarchical cluster method to construct a dendrogram of *Lycium* species. Because each *Lycium* sample was analyzed using 7 primers, the primer information was merged by weighting. The weights were assigned by $\omega_1=D_{S1}/D_{S1,\ldots,S7}$, $\omega_k=(D_{S1,\ldots,Sk}-D_{S1,\ldots,S(k-1)})/D_{S1,\ldots,S7}$, k=2, ..., 7. Using the obtained weights of primers, the distance of each *Lycium* sample from species *i* and *j* was defined by:

$$d(x_i, x_j) = \sum_{k=1}^{7} \omega_k d(x_i^{(k)}, x_j^{(k)}), \qquad (6)$$

were

$d(x_i^{(k)}, x_j^{(k)})=1-\rho^2(x_i^{(k)}, x_j^{(k)})$, $\rho(x_i^{(k)}, x_j^{(k)}) = \dfrac{s(x_i^{(k)}, x_j^{(k)})}{s(x_i^{(k)})s(x_j^{(k)})}$,

$s(x_i^{(k)}, x_j^{(k)})$ and $s(x_i^{(k)})$ are defined by (5) and (2). $\rho(x_i^{(k)}, x_j^{(k)})$ is the correlation coefficient between $x_i^{(k)}$ and $x_j^{(k)}$, which is often used to measure the similarity of fingerprint. In order to use distance matrices to onstruct the dendrogram, we transformed the data by $1-\rho(x_i^{(k)}, x_j^{(k)})^2$.

Unweighted pair-group method using arithmetic average (UPGMA) linkage, which defines the cluster distance, is advocated for constructing a dendrogram. Details about the UPGMA clustering method can be found in Sokal and Michener[12]. Using the above distance measure between fingerprints and the UPGMA cluster method, we visualized the cluster results using the dendrogram shown in Figure 5.

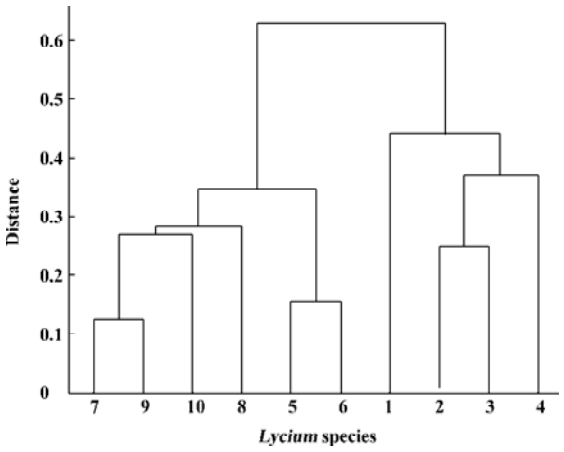

Figure 5. Dendrogram of 10 *Lycium* samples using the first 7 primers ordered.

For evaluating our procedure to decide the number of primers, we used primers *S*1, ..., *S*8 to construct the dendrogram as above, further more, we use the first ordered 9, 10, and 11 primers to construct dendrogram, respectively. All of these were similar to Figure 5. This indicated that the first 7 primers contained almost all of the information provided by

the total 11 primers. Furthermore, when using primers *S*1, ..., *S*6, the outcome shows little difference relative to Figure 5 (Figure 6). It manifests our picking procedure for primer number is so delicate.

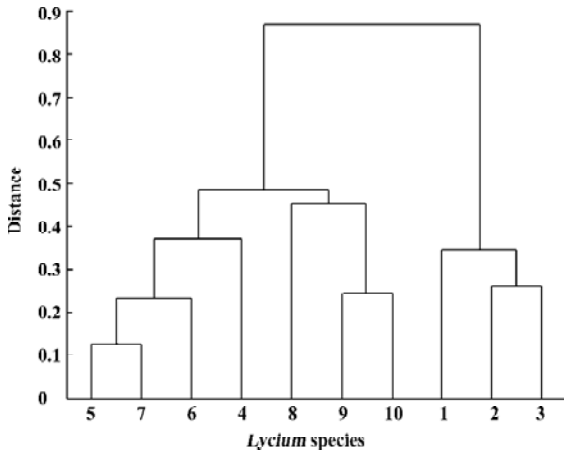

Figure 6. Dendrogram of 10 *Lycium* samples using the first 6 primers ordered.

Discussion

Phylogenetic relationship construction based on RAPD fingerprint data generated from a number of primers was investigated in this study. We proposed an index called dispersivity using entropy theory to describe the diversity of RAPD fingerprints obtained by several primers. Generally, this index can be applied to other DNA fingerprint data, such as arbitrarily primered PCR and DNA amplification fingerprinting, and to chromatographic fingerprints, such as chromatogram, spectrum and mass spectrum. Based on this index, the order for choosing primers is obtained using the orthogonal projection method and entropy theory. Our proposed method provides the guidelines for primer picking in the consequent experiments. An on-line analysis program on RAPD primer selection is provided on the web site: http://math.nenu.edu.cn/shiz/yinxiaolin.files/program.htm, which can be downloaded easily if required.

Acknowledgements

We are grateful to Dr Daniel KWONG (the Chemistry Department of Hong Kong Baptist University) for his valuable comments on the manuscript.

References

1 Chan K, Lee H. The way forward for Chinese medicine. London: Taylor and Francis; 2002.
2 Peng Y, Sun SQ, Zhao ZZ, Leung HW. A rapid method for identification of genus *Lycium* by FTIR spectroscopy. Spectrosc Spect Anal 2004; 24: 679–81.
3 Welsh J, McCelland M. Fingerprinting genomes using PCR with arbitrary primers. Nucleic Acids Res 1990; 18: 7213–8.
4 Williams CE, Ronald PC. PCR template-DNA isolated quickly from monocot and dicot leaves without tissue homogenisation. Nucleic Acids Res 1994; 22: 1917–8.
5 Shaw PC, Wang J, But PPH. Authentication of Chinese medicinal materials by DNA technology. London: Word Scientific Publishing; 2002.
6 Zhang AJ, Wong NS, Ha WY, Hu YH, Fang KT. Authentication of traditional Chinese medicines using RAPD and functional polymorphism analysis. In: Fang KT, Liang YZ, Yu RQ, editors. Proceedings of the 1st Conference on Data Mining and Bioinformatics in Chemistry and Chinese Medicines; 2003 Apr 6–16; Shenzhen, China; 2003. p 81–98.
7 Draper J, Scott R. Plant genetic transformation and gene expression. London: Blackwell Scientific Publishing; 1988.
8 Nadeau JH, Bedigian HG, Bouchard G, Denial T, Kosowsky M, Norberg R, *et al*. Multilocus markers for mouse genome analysis: PCR amplification based on single primers of arbitrary nucleotide sequence. Mamm Genome 1992; 3: 55–64.
9 Agilent [http://www.home.agilent.com]: Agilent Technologies. 2100 Bioanalyzer Expert User's Guide; c2000-2005 [updated 2004 Mar 1; cited 2005 May 10]. Available from: http://www.chem.agilent.com/scripts/LiteraturePDF.asp?iWHID=36738
10 Shannon CE, Weaver W. The mathematical theory of communication. Urbana, IL: University of Illinois Press; 1949.
11 Rao CR, Mitra SK. Generalized inverse of matrices and its applications. New York: Wiley; 1971.
12 Sokal RR, Michener CD. A statistical method for evaluating systematic relationship. Univ Kans Sci Bull 1958; 28: 1409–38.

Acta Pharmacologica Sinica 2005 Oct; 26 (10): 1225–1232

Blackwell Publishing

Full-length article

Cloning, expression, and characterization of pollen allergens from *Humulus scandens* (Lour) Merr and *Ambrosia artemisiifolia* L[1]

Ai-lin TAO[2,3], Shao-heng HE[2,4]

[2]*Allergy and Inflammation Research Institute, Shantou University Medical College, Shantou 515031, China;* [3]*The Second Affiliated Hospital of Guangzhou Medical College, Guangzhou 510260, China*

Key words

pollen; allergen; profilin; gene expression

[1] Project supported by the National Natural Science Foundation of China (No 30470996), the Natural Science Foundation of Guangdong Province (No 034617) and the Li Ka Shing Foundation, Hong Kong, China (No C0200001).
[4]Correspondence to Dr Shao-heng HE.
Phn 86-754-890-0405.
Fax 86-754-890-0192.
E-mail shoahenghe@hotmail.com

Received 2005-05-16
Accepted 2005-06-24

doi: 10.1111/j.1745-7254.2005.00194.x

Abstract

Aim: To clone the pollen allergen genes in *Humulus scandens* (Lour) Merr (LüCao in Chinese) and short ragweed (*Ambrosia artemisiifolia* L) for recombinant allergen production and immunotherapy. **Methods:** The allergen genes were selectively amplified in the weed pollen cDNA pool by using a special PCR profile, with the primers designed by a modeling procedure. Following truncated gene cloning and confirmation of the pollen source, unknown 3'cDNA ends were identified by using the 3'-RACE method. The gene function conferred by the full-length coding region was evaluated by a homologue search in the GenBank database. Recombinant proteins expressed in *Escherichia coli* pET-44 RosettaBlue cells were subsequently characterized by N-terminal end sequencing, IgE binding, and cross-reactivity. **Results:** Three full-length cDNAs were obtained in each weed. Multiple alignment analysis revealed that the deduced amino acid sequences were 83% identical to each other and 56%–90% identical to panallergen profilins from other species. Five recombinant proteins were abundantly expressed in non-fusion forms and were confirmed by using the N-terminal end sequence identity. Sera from patients who were allergic to *A artemisiifolia* reacted not only with rAmb a 8(D03) derived from *A artemisiifolia*, but also with recombinant protein rHum s 1(LCM9) derived from *H scandens*, which confirmed the allergenicity and cross-reactivity of the recombinant proteins from the 2 sources. Comparison of the degenerate primers used for truncated gene cloning with the full-length cDNA demonstrated that alternative nucleotide degeneracy occurred. **Conclusion:** This study demonstrates a useful method for cloning homologous allergen genes across different species, particularly for little-studied species. The recombinant allergens obtained might be useful for the immunotherapeutic treatment of *H scandens* and/or *A artemisiifolia* pollen allergies.

Introduction

Accurate allergy diagnosis and efficient immunotherapy protocols are strongly dependent on the use of standardized extracts or well-characterized allergen mixtures[1–3]. However, standardization of specific allergens from natural allergen extracts is a huge task[4] and it is almost impossible to carry out standardization on a large scale for day-to-day clinical practice. Recombinant allergens that have similar structures, functions and immunoreactivity to their native counterparts could be used to overcome this problem, given that they can be produced in large quantities, leading to more specific, effective and safer immunotherapy treatment[5].

Currently, gene cloning for novel allergens is mainly based on the construction of a cDNA library, which is time-consuming and expensive[6–9]. Other methods for isolating unknown allergens involve using the polymerase chain reaction (PCR) with either degenerate primers consisting of a

pool of primers containing most or all of the possible nucleotide sequences encoding a conserved amino acid motif[10], or consensus primers consisting of a single primer containing the most common nucleotide at each codon position within the motif[11]. Although these strategies have been successful in isolating closely related sequences, they have generally failed when sequences are more distantly related[11]. Many programs and algorithms have been developed for sequence comparisons of multiple members of protein families[12–15]. By using alignment techniques, the first amino acid sequence that emerges, that is, the sequence aligned uppermost in each large and dense cluster in the output tree produced, has provided the most information about amino acid diversity in the cluster. In the current study, we refer to these sequences as "core sequences", and we designed the degenerate primers based on the core sequences and their cognates. Under special PCR conditions, we expected that the degenerate primers could match all associated sequences in the abovementioned cluster, and thus could be used for cloning new allergen gene members in a distantly related species. We will hereafter refer to these primers as "pan-degenerate primers". We expected that the process involving the pan-degenerate primers would be more efficient and less expensive than the cDNA library technique, and would have a higher success rate than an ordinary PCR method.

Humulus scandens (Lour) Merr (Moraceae: Cannaboideae; Lücao in Chinese) is a weed that grows in most provinces of China. The plant blossoms in summer and bears a large quantity of pollen. Short ragweed (*Ambrosia artemisiifolia* L; Compositae) is one of the most invasive weeds in the world. It was introduced to China in 1930s, and is now distributed from the Yantze River to the 3 northeastern provinces of China. Nanning, Wuhan, Nanchang-Jiujiang and Shenyang-Tieling-Dandong are the 4 areas in which the weed is most pervasive in China. Pollen from *H scandens* and *A artemisiifolia* have become the main source of pollen allergens in this country. However, little is known of the actual allergens in the pollen of the weeds. In this study, we report on the cloning, expression and characterization of 6 pollen allergen genes from the 2 weeds. Following the non-fusion expression and purification of the 5 encoded proteins, 2 representative proteins of the 5, provisionally named rAmb a 8 (D03) and rHum s 1(LCM9), were immunologically characterized in detail.

Materials and methods

Sample preparations Wild plants of *H scandens* and *A artemisiifolia* were harvested in Wuhan. Flowers were bagged, and the pollen collected from each plant was mixed with other pollen collected from the same plant. All pollen collected was immediately submerged in liquid nitrogen until use. Twenty-five patients with *A artemisiifolia* pollen allergy and 10 patients with *H scandens* pollen allergy (as assessed by a positive skin prick test reaction to *A artemisiifolia* and a serum level of *A artemisiifolia/H scandens* specific IgE higher than 3.5 kU_A/L) and 13 healthy volunteers were recruited. Blood samples were taken from all participants in the Allergy Clinic, Shenyang North Hospital. All the samples were tested by using the UniCAP Specific IgE Fluoroenzymeimmunoassay (Pharmacia Diagnostics AB, Uppsala, Sweden). After centrifugation at 500×*g*, 4 °C, for 10 min, serum from each individual was collected and stored at -70 °C until use. The study was approved by the Ethics Committee of Shenyang North Hospital, Shenyang, China, and written informed consent was obtained from all participants.

Primer design The 478 pollen allergens and their related sequences were retrieved by keyword searches in the SWISS-PROT and TrEMBL websites (http://www.expasy.org) and were multiple-aligned online by using Clustal W software[16]. For alignment, the default values were used to obtain the output tree in a phylogram pattern, with the absolute distances labeled. The uppermost allergen sequence in each large and dense cluster in the output tree was taken as the core sequence. There were several of these core sequences found in the output phylogenetic trees. Based on the core sequences, allergen sequences with high homology (with BLAST E values $\leq 10^{-10}$) were selected for further analysis to acquire conservative gene domains. Pan-degenerate primers, which we expected to be successful in all species, were thus designed according to cDNA sequences of the conservative domains chosen.

RT-PCR analysis Frozen pollen samples were ground in a mortar filled with liquid nitrogen, and the total RNA was extracted by using an RNeasy Maxi Kit (Qiagen Valencia, CA, USA) according to the manufacturer's instructions. After quality and concentration assessments, the RNA was either immediately used for RT-PCR analysis or stored at -80 ºC until use.

After reverse transcription (2 μg total RNA per sample) was performed by using the ProtoScript First Strand cDNA Synthesis Kit (New England Biolabs, Beverly, MA, USA) according to the manufacturer's instructions, PCR was carried out by using 50 ng of the reverse transcription product in 25 μL of the reaction mixture containing 1.25 U HotstarTaq DNA polymerase (Qiagen), 1× PCR buffer (Qiagen), 0.2 mmol/L dNTP, and 0.4 μmol/L of each primer. Thermal cycling was

performed in a PTC-200 Peltier Thermal Cycler (MJ Research, Watertown, MA, USA) as follows: after an initial step at 95 °C for 15 min to activate the DNA polymerase, 9 touchdown cycles were carried out at 94 °C for 45 s, 68 °C for 30 s and 72 °C for 30 s, with the annealing temperature decreasing by 1 ºC per cycle. This was followed by 26 gradient cycles at 94 ºC (45 s)→55 ºC→61 ºC (30 s)→72 ºC (30 s). After purification with a QIAquick PCR Purification Kit (Qiagen), the PCR products were cloned into the pGEM-T easy vector (Promega, Madison, WI, USA). The inserted plasmids were transformed into JM109 (Promega). Positive clones were confirmed first by colony PCR with the former PCR primers, and then by sequencing. DNA sequencing was carried out by the BioAsia Biotechnology Co (Shanghai, China) by using the dideoxy chain-terminating method.

Full-length cDNA synthesis and sequencing The clones derived from the degenerate primers did not cover the full-length coding region. Gene-specific primers were therefore synthesized (Table 1), and combined using the RACE process[17] with RA3, a 3' reverse primer from the GeneRacer Kit (Invitrogen Corporation, Carlsbad, CA, USA). The PCR conditions were similar to those for RT-PCR, with a slight modification in the denaturing temperature and extension time. PCR products were also cloned into the pGEM-T easy vector, and positive clones were confirmed by colony PCR and sequencing. Full-length cDNAs, acquired by deduction of the truncated gene and its 3' end, were translated into amino acid sequences, with their isoelectric point and molecular weight calculated (http://www.expasy.org). cDNA and protein homologues, retrieved by using the BLAST program in the NCBI website (http://www.ncbi.nlm.nih.gov/), were aligned by using the CLUSTAL W (1.82) program[16]. Phylogenetic trees were subsequently generated using MEGA2 software[18].

Northern blot Northern blots were performed according to the membrane manufacturer's instructions. Briefly, a total of 20 μg RNA was loaded on to a formaldehyde-containing gel. After running the gels at 40 V for 3 h, the RNA bands were electrically transferred onto Nytran SuPerCharge nylon transfer membrane (Schleicher & Schull BioScience, New Hampshire, USA). After UV cross-linking treatment, the membrane was stained with methylene blue [0.02% [w/v] methylene blue in 0.3 mol/L sodium acetate(pH 5.5)] to investigate the transferring efficiency. Following destaining, BrightStar Psoralen-Biotin (Ambion Inc, Autin, TX, USA)-labeled probe D03 was applied for hybridization in ULTRhyb hybridization buffer (Ambion Inc). The membrane was washed twice with a buffer containing 2× SSC (0.3 mol/L NaCl, 0.03 mol/L sodium citrate) and 0.1% sodium dodecylsulfate before the probes were detected by using the Phototope Star Detection Kit (New England Biolabs). Finally, the filter was exposed to Fuji Medical X-ray film at room temperature for 5–8min.

Protein expression and immunoblotting To enable non-fusion protein expression, the S-protein tag and His-tag were removed from the pET-44 vector and the allergen-coding regions were decorated by introducing restriction sites (5' *Nde*I and 3' *Pst*I) by PCR using the corresponding primers (Table 1). Subsequent to double restriction digestion and purification, the PCR products were ligated with the pET-44 EK/LIC vector (Novagen, Madison, WI, USA). After transformation of the ligation products into NovaBlue Singles

Table 1. Sequences of primers used in this study. The underlined sequences denote the restriction sites of *Nde*I and *Pst*I, respectively. Bracketed alternative nucleotides in primer Sg1P3 represent the degenerate loci.

Primer	Sequence (5' → 3')	Length (base)	Use
Sg1p5	ATGTCGTGGCAGGCGTACGT	20	Degenerate PCR
Sg1p3	CCTCTCAACAA(T/G)CA(C/T)GTTGCATTGTCC	32	Degenerate PCR
PC11	GACCATCTGATGTGCGAAATCGATGG	26	Specific PCR
PA04	GGGAACCAGGTGCTGTTATCAGAGG	25	Specific PCR
PD10	GGAGCTGTGATTCGAGGGAAAAAGG	25	Specific PCR
PD03	CTGCATCAAGAAAACAGGCCAAGC	24	Specific PCR
RA3	CTGCATCAAGAAAACAGGCCAAGC	24	Specific PCR
A5RA4	GGTCATATGTCGTGGCAGGCGTACGT	26	For construct
B3LA4	AGTCTGCAGTCATTAGAAACCCTGTTCGAGGAG	33	For construct
B3LD3	ATCTGCAGTCATTACATGCCCTGATCGATGAGAT	34	For construct
B3CM9	AGTCTGCAGTCATTAGAGACCCTGATCAATGAGATAATC	39	For construct
B3CS13	AGTCTGCAGTCATTAGAGGTTCTGATCAATAAGGTAATCTC	41	For construct
SProt	CACGATGCGTCCGGCGTAGAG	21	Colony PCR

cells (Novagen), positive clones and in-frame insertions were confirmed, initially by colony PCR with the primer SProt and 3' primers related to each clone, and then by sequencing with the S-Tag 18-mer primer or ColiDown primer (Novagen). Plasmid DNA was extracted with the QIAprep Miniprep Kit (Qiagen), and transformed into *E coli* RosettaBlue (DE3) cells (Novagen) for expression, following the manufacturer's instructions. Cells were grown in 1 L Luria-Bertani (LB)-medium until the OD_{600} value reached 0.6. Target protein expression was induced by the addition of isopropyl-D-thio-galactopyranoside (IPTG) to 1 mmol/L for 4 h at 30 °C before harvest. Finally, the recombinant proteins were purified by affinity chromatography using poly-(L)-proline as the solid phase. The bacterium lysate was applied to the column, followed by washing with 1 mol/L urea and elution with 6 mol/L urea. The elution product was dialyzed stepwise against decreasing amounts of urea (6, 4, 2 mol/L, no urea) in phosphate-buffered saline (PBS; 1.8 mmol/L potassium phosphate, pH 7.4, 0.137 mol/L NaCl) and then dialyzed against double-distilled water, followed by freeze-drying.

Purified rAmb a 8(D03) and rHum s(LCM9) were selected as representatives for immunoblotting. Fifteen micrograms of protein were loaded onto the 15% SDS-PAGE gel, and were then electrically transferred to a polyvinylidene difluoride (PVDF) membrane (Amersco, Solon, OH, USA). Following blocking the membrane overnight with a 4% bovine serum albumin solution at 4 ºC, allergic sera (diluted 1:7) were added to each membrane strip for 2 h before the addition of peroxidase conjugated goat anti-human IgE (Sigma-Aldrich, Saint Louis, MO, USA). The blotted band was finally visualized with a diaminobenzidine (DAB) chromogenic substrate solution (Amersco).

N-terminal end sequencing Sequencing of the N-terminal end of recombinant proteins was performed by using the Applied Biosystems Procise 491 Sequencer from Applied Biosystems, according to the manufacturer's instructions.

Results

Homology between different allergen genes The 478 pollen allergens obtained from the SWISS-PROT and TrEMBL websites were clustered into 8 large groups, which consisted of a number of subgroups. Further searching with the core sequences from each subgroup demonstrated that these core sequences matched a large quantity of closely related homologues. For instance, Q9XF40, the first core sequence in group 8, was an apple pollen allergen with extensive homology with other pollen allergens from different species (Figure 1), such as *Poa pratensis, Lolium perenne, Dactylis glomerata, Hordeum vulgare, Holcus lanatus* (e values $<2e^{-25}$). The conservative domains in the Q9XF40 cDNA sequence (1–20 bp, 343–369 bp) as resolved by multiple sequence alignment of Q9XF40 and its cognates were taken as the Sg1p5/Sg1p3 primer sequence (Table 1). Other degenerate primers were designed following the same principle.

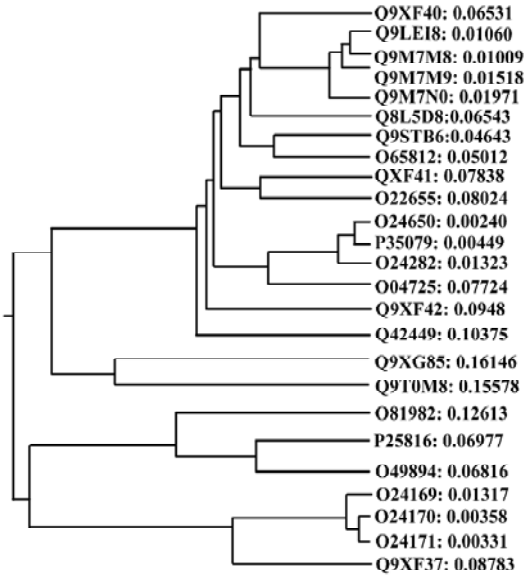

Figure 1. The core subgroup cut off from the large group VIII clustered from 478 allergens obtained from SWISS-PROT. The conserved regions in Q9XF40, O81982 and Q9XF37 were used for pan-degenerate primer (Sg1P5/P3) design. Q9XF40 and O81982 were selected for their clustering priority, whereas Q9XF37 was selected for its amino acid length of 133 aa. All allergens shown were from SWISS-PROT. The numbers on the right-hand sides of each allergen denote absolute distance.

Full-length cDNA generation By combining the gradient PCR with touchdown PCR, 3 gene fragments were obtained from each weed species, and were subsequently inserted into the pGEM-T vector. Sequence analysis showed that the inserts, 5 of 363 bp and 1 of 369 bp, were homologous to the known allergen gene profilin from different species with up to 90% (5 clones except for D03) and 79% (for D03) identity, but with ~30 bp truncated at the 3' ends, suggesting a further requirement of the RACE process for the full-length cDNA. After cloning of the amplificants from the specific PCR with primer pairs PC11/RA3, PM9/RA3, PD10/RA3 and PD03/RA3, a total of 29 positive RACE clones were detected. Subsequent sequencing reactions demonstrated that they all contained the initiation and stop codons, primer sequences and poly (A) tails, reflecting the mRNA source of the clones. Northern blotting with a clone D03 probe further confirmed that the cDNA cloned was derived from the pollen

mRNA (Figure 2). Bridging the 3' end and the corresponding fragment genes produced 6 novel full-length coding genes, among which LCS13, LCM20 and LCM9 were from *H scandens*, whereas A0418, D106 and D03 were from *A artemisiifolia*. They are all available in GenBank under accession Nos AY268422-AY268427.

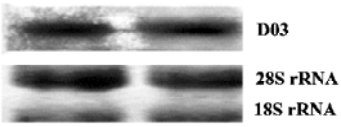

Figure 2. Northern blot results of the total RNA extracted from the *A artemisiifolia* pollen at different times. Total RNA of 20 μg was electrophoresed, blotted onto Nytran SuPerCharge nylon transfer membranes (Schleicher & Schull BioScience) and stained with methylene blue to confirm the transferred RNA quality. After destaining, Psoralen-Biotin labeled probes for D03 were applied for hybridization.

Sequence analysis Sequence analysis revealed that there were several altered nucleotides in the cDNA sequences compared with the degenerate primers used in the fragment-gene cloning process (data not shown), which means that the degeneracy was effectively expanded. The predicted amino acid sequences of the 6 genes were acidic proteins (pI of approximately 5.0) with molecular weights of approximately 14 kDa. Multiple sequence alignment demonstrated that these 6 novel sequences shared a high homology, up to 83%. Moreover, cDNA and protein sequence searches with Blastn and Blastx programs in GenBank showed that the new genes were homologous to profilin genes from more than 10 plant families including Rosaceae, Euphorbiaceae, Phaseoleae, Liliaceae, Poaceae, Urticaceae, Apiaceae, Oleaceae, Solanaceae, Brassicaceae, and Compositae. Alignment of the cognates derived from this search produced a phylogenetic tree, which showed that the 6 novel genes cloned were clearly separated into 3 subgroups, but with high homology (Figure 3).

Of the 6 clones, A0418, D106 and LCM9, 3 closely related clones that encoded 131-amino acid residues, exhibited high homology with apple pollen allergen Q9XF41 (Mal d 4; GenBank accession number: AF129427). LCS13 and LCM20, 2 clones from *H scandens*, had only differences in the cDNA non-coding regions and therefore encoded the same protein, which had 80% and 85% identity with Q8L5D8 from date palm pollen and Q9XF40 from apple pollen, respectively. Clone D03 encoded 133 amino acid residues, and had an identity of 79% and 72% with O81982 (Hela 2)[19] and CAD12862[20], 2 profilin proteins from common sunflower and mugwort. Hel a 2 and D03, along with the timothy grass profilins O24282, P35079, O24650, were clustered into one

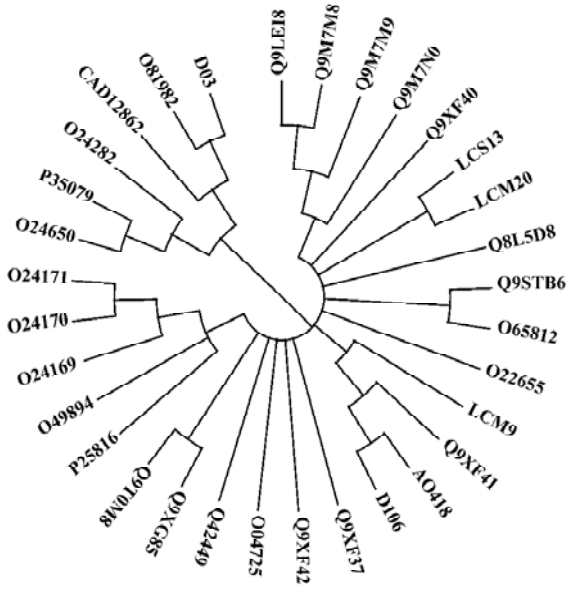

Figure 3. Phylogenetic relationship between the profilin cognates and the 6 novel allergens cloned in the current study as analyzed by using the Mega2 software with amino acid sequences. The amino acid sequences of the 6 new allergens (LCS13, LCM20, LCM9, A0418, D106, D03) are available from GenBank (accession numbers: AAP15198, AAP15199, AAP15200) and SWISS-PROT (accession numbers Q64LH2, Q64LH1, Q64LH0).

subgroup (Figure 3). Furthermore, D03 was quite different from the other 5 clones in 4 regions of its amino acid sequence, which represents an approximately 90% difference between D03 and other profilins (Figure 4).

Protein expression and purification, and immunoblotting After detecting the correct reading frame of the target protein gene in the expression vector, the in-frame plasmids were then successfully transformed into *E coli* RosettaBlue (DE3) cells. Following induction and further incubation at 30 ℃ for 6 h, the recombinant non-fusion proteins were visualized using SDS-PAGE, and had an apparent molecular mass of ~14 kDa (Figure 5A). The N-terminal sequence of 10 amino acids of rAmb a 8(D03) confirmed that the recombinant protein was the same as that deduced from the cDNA sequence. The yield of purified protein was approximately 8 mg per L of cultured bacteria.

IgE antibodies from 6 of 8 sera (75%) from the *A artemisiifolia* allergic patients reacted with recombinant protein rAmb a 8(D03) in the immunoblot experiments. The bands occurred at approximately 14 kDa (Figure 5B). Other recombinant proteins were also very efficiently expressed and purified in non-fusion form (Figure 5C, 5D). As a representative from *H scandens*, the immunoblotting profile of rHum s 1(LCM9) is shown in Figure 5E. Interestingly, rHum s 1(LCM9) not only

```
LCS13  MSWQAYVDDHLMCEIDG--QHLTAAAIIGHDGSVWAQSSTFPQFKPEEIAAIMKDFEEPGSLAPTGLHLG 68
LCM20  MSWQAYVDDHLMCEIDG--QHLTAAAIIGHDGSVWAQSSTFPQFKPEEIAAIMKDFEEPGSLAPTGLHLG 68
A0418  MSWQAYVDDHLMCEIEG--NHLSAAAIIGHDGVVWAQSATFPQVKPEEITGIMNDFNEPGSLAPTGLYLG 68
D106   MSWQAYVDDHLMCEIEG--NHLSAAAIIGHDGVVWAQSATFPQVKPEEITGIMNDFNEPGSLAPTGLYLG 68
LCM9   MSWQAYVDDHLMCEIDG--NHLSAAAIIGHDGSVWAQSAAFPQLKPEEVTGIMNDFNEPGTLAPTGLYLG 68
D03    MSWQAYVDEHLMCDIEGTGHHLTSAAILGHDGTVWAQSSNFPQFKPEEMKGIITEFDQAGTLAPTGMFIA 70
       ********:****:*:*  :**::***:**** *****: ***.****: .*:.:*::.*:*****:.:.

LCS13  GIKYMVIMGEQGAVIRGKKGAGGITVKKTGAAMIIGIYDEPLTPGQCNMIVERLGDYLIDQNL 131
LCM20  GIKYMVIMGEQGAVIRGKKGAGGITVKKTGAAMIIGIYDEPLTPGQCNMIVERLGDYLIDQNL 131
A0418  GTKYMVIQGEPGAVIRGKKGPGGVTIKKTTMALIIGIYDEPMAPGQCNMIVERLGDYLLEQGF 131
D106   GTKYMVIQGEPGAVIRGKKGPGGVTIKKTTMSLIIGIYDEPMTPGQCNMLVERPGDYLLEQGF 131
LCM9   GTKYMVIQGEPGAVIRGKKGAGGVTIKKTSQALIIGVYDEPMTPGQCNMIVERLGDYLIDQGL 131
D03    GAKYMVLQGEQGAVIRGKKGAGGICIKKTGQALVMGIYDEPVAPGQCNMVVERLGDYLIDQGM 133
       * ****: ** *********.**: :***  ::::*:****::******:*** ****::*.:
```

Figure 4. ClustalX (1.8) alignment of the deduced amino acid sequences of the 6 clones obtained from the pollen of *H. scandens* and *A. artemisiifolia*. The amino acid residues shown represent the specific region in clone D03 that was markedly different from the profilin proteins of other species. The conservative domains in each clone are shown in bold, and the different amino acid residues are in gray.

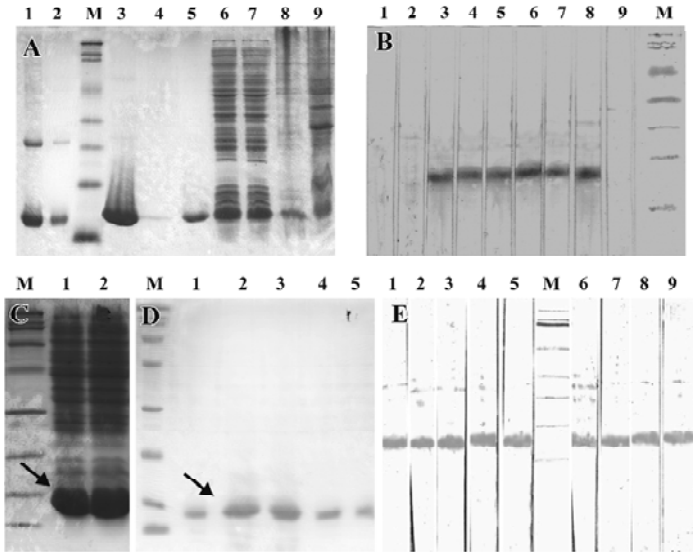

Figure 5. Non-fusion expression, purification and immunological characterization of recombinant proteins. A: 15% SDS-PAGE analysis of the no-fusion expression profile of rAmb a 8 (D03). Lanes 1 and 2, purified target protein in non-reducing loading buffer; Lane M, broad range prestained SDS-PAGE standards (Bio-Rad, catalog No 161-0318), similar to Lane M in all other panels; Lanes 4 and 5, re-purified target protein in non-reducing loading buffer; Lane 6, re-purified target protein in reducing loading buffer; Lanes 7 and 8, cell lysate in loading buffer; Lanes 9 and 10, supernatant and sediment of the cell lysate. B: Western blot of rAmb a 8(D03). Fifteen micrograms of the purified rAmb a 8(D03) was loaded into each lane and blotted. Lanes 3–8, sera from patients with allergy to *A artemisiifolia*; Lanes 1, 2 and 9, healthy control sera. C: Representative presentation of non-fusion protein expression of rHum s 1(LCS13) (Lane 1) and rHum s 1(LCM9) (Lane 2) (arrowhead). D: Recombinant proteins purified by affinity chromatography. Lanes 1–5 represent rAmb a 8(D03), rHum s 1(LCS13), rHum s 1(LCM9), rAmb a 8(D106) and rAmb a 8 (A0418), respectively. E: Western blot of rHum s 1(LCM9), which was detected in sera from both patients with *H scandens allergies* (lanes 1–5) and patients with *A artemisiifolia* allergies (lanes 6–9).

reacted with the sera from 5 patients with *H scandens* allergy, but also reacted with sera from patients with *A artemisiifolia* allergy, which suggests that cross-reactivity occurred for rAmb a 8(D03) and rHum s 1(LCM9).

Discussion

In the past, most allergen genes have been cloned by cDNA library screening[7–9], and hundreds of pollen allergen genes from more than 170 species are available in online databases, which can be sorted into several groups. This means that homologous genes exist in many related or unrelated species, which provided support for the current method. In this study, we designed pan-degenerate primers and succeeded in cloning pollen allergen cDNAs from different weeds, thus showing that there is a way to clone homologous genes from distantly related species or little-studied species. Furthermore, by using a combination of the gradient PCR process and touchdown steps, the genes with some divergence in their primer regions could be obtained in the weed genome; that is, the degeneracy of the primers was expanded. The method could therefore be used to clone the same allergens in other species or to clone other kinds of allergen genes.

It has been argued that allergenicity cannot be rationalized on the basis of either overall folding pattern or biological function, and thus any protein should be regarded as a potential allergen[19]. According to alignment studies, the proteins coded by our new clones had more than 60% identity over the full-length peptide with the known allergens, suggesting that the proteins would be allergenic. Thus, D03 and LCM9, the most different variants of the 6 clones obtained, were expressed as recombinant proteins. Through efficient expression in a pET-44 system, ideal solubility of all the recombinant proteins was obtained, which facilitated protein purification through affinity chromatography, and would ensure efficiency in commercial production.

The molecular basis of cross-reactivity has been of primary concern in numerous publications[19–21]. The relationship between sequence similarity, as obtained by pair-wise alignment, and structural or functional properties has been the goal of much research[22–24]. Recent studies have confirmed a widely accepted rule-of-thumb that 30% or 35% identity over aligned regions suffices for structural or functional deduction[25,26]. A remote homologue study[27] demonstrated that allergens from diverse sources have a common structural motif, namely a groove located inside an α-β motif, which could potentially serve as a ligand-binding site, thus leading to the stimulation of the T cell helper type 2 (Th2) response and a subsequent bias towards the synthesis of IgE. This result expanded cross-reactivity to between microbes and higher plants. In the present study, the clones were different from each other in their cDNA or protein sequence, suggesting open pollination and/or large genetic variation in the weeds. This was also consistent with other studies on ragweed and timothy grass sequence polymorphism[28,29]. However, multiple sequence analysis demonstrated that the newly cloned genes had up to 83% homology with each other and 60%–90% identity with previously described allergen profilins from latex, food, and pollens from various organisms, which can produce extensive cross-reactivity[30,31]. This result demonstrated that proteins from *H scandens* and *A artemisiifolia* would have cross-reactivity. In a previous study we also inferred that the proteins coded by clone D106 would have cross-reactive properties for food- and/or pollen-sensitive allergic individuals[32,33]. All of these results imply that the newly cloned genes would function the same way as pan-allergen profilins. Based on the issues described herein and the results obtained in the current study, we assume that cross-reactivity would occur so widely that atopic individuals would be surrounded by a dynamic network of allergens, and would be predisposed towards allergic diseases.

References

1 van Ree R. Analytic aspects of the standardization of allergenic extracts. Allergy 1997; 52: 795–805.

2 Durham SR, Walker SM, Eva-Maria V, Ikilar J, O'Brien F, Noble W, *et al*. Long-term clinical efficacy of grass-pollen immunotherapy. N Engl J Med 1999; 341: 468–75.

3 van Hage-Hamsten M, Johansson E, Roquet A, Peterson C, Andersson M, Greiff L, *et al*. Nasal challenges with recombinant derivatives of the major birch pollen allergen. Clin Exp Allergy 2002; 32: 1448–53.

4 Valenta R, Kraft D. Recombinant allergen molecules: tools to study effector cell activation. Immunol Rev 2001; 179: 119–27.

5 Villalba M, Batanero E, Monsalve RI, Gonzalez de la Pena MA, Lahoz C, Rodriguez R. Cloning and expression of Ole e I, the major allergen from olive tree pollen. Polymorphism analysis and tissue specificity. J Biol Chem 1994; 269: 15 217–22.

6 Schramm G, Bufe A, Petersen A, Schlaak M, Becker WM. Molecular and immunological characterization of group V allergen isoforms from velvet grass pollen (*Holcus lanatus*). Eur J Biochem 1998; 52: 200–6.

7 Kawamoto S, Fujimura T, Nishida M, Tanaka T, Aki T, Masubuchi M, *et al*. Molecular cloning and characterization of a new Japanese cedar pollen allergen homologous to plant isoflavone reductase family. Clin Exp Allergy 2002; 32: 1064–70.

8 Scholl I, Wiedermann U, Forster-Waldl E, Ganglberger E, Baier K, Boltz-Nitulescu G, *et al*. Phage-displayed Bet mim 1, a mimotope of the major birch pollen allergen Bet v 1, induces B cell responses to the natural antigen using bystander T cell help. Clin Exp Allergy 2002; 32: 1583–8.

9 Yu CJ, Lin YF, Chiang BL, Chow LP. Proteomics and immunological analysis of a novel shrimp allergen, Pen m 2. J Immunol 2003; 170: 445–53.

10 Lüttkopf D, Müller U, Skov PS, Ballmer-Weber BK, Wüthrich B, Skamstrup Hansen K, *et al*. Comparison of four variants of a major allergen in hazelnut (*Corylus avellana*) Cor a 1.04 with the major hazel pollen allergen Cor a 1.01. Mol Immunol 2001; 38: 515–25.

11 Rose TM, Schultz ER, Henikoff JG, Pietrokovski S, McCallum CM, Henikoff S. Consensus-degenerate hybrid oligonucleotide primers for amplification of distantly related sequences. Nucleic Acids Res 1998; 26: 1628–35.

12 Corpet F. Multiple sequence alignment with hierarchical clustering. Nucleic Acids Res 1988; 16: 10881–90.

13 Heger A, Holm L. Sensitive pattern discovery with 'fuzzy' alignments of distantly related proteins. Bioinformatics 2003; 19: I130–7.

14 Plewniak F, Bianchetti L, Brelivet Y, Carles A, Chalmel F, Lecompte O, *et al*. PipeAlign: a new toolkit for protein family analysis. Nucleic Acids Res 2003; 31: 3829–32.

15 Bennett SP, Lu L, Brutlag DL. 3MATRIX and 3MOTIF: a protein structure visualization system for conserved sequence motifs. Nucleic Acids Res 2003; 31: 3328–32.

16 Higgins D, Thompson JD, Higgins DG, Gibson TJ. CLUSTAL W: Improving the sensitivity of progressive multiple sequence alignment through sequence weighting, position-specific gap penalties and weight matrix choice. Nucleic Acids Res 1994; 22: 4673–80.

17 Frohman MA, Dush MK, Martin GR. Rapid production of full-length cDNAs from rare transcripts: amplification using a single gene-specific oligonucleotide primer. Proc Natl Acad Sci USA 1988; 85: 8998–9002.
18 Kumar S, Tamura K, Jakobsen IB, Nei M. MEGA2: molecular evolutionary genetics analysis software. Bioinformatics 2001; 17: 1244–5.
19 Mirza O, Henriksen A, Ipsen H, Larsen JN, Wissenbach M, Spangfort MD, *et al*. Dominant epitopes and allergic cross-reactivity: complex formation between a Fab fragment of a monoclonal murine IgG antibody and the major allergen from birch pollen Bet v 1. J Immunol 2000; 165: 331–8.
20 Vieths S, Scheurer S, Ballmer-Weber B. Current understanding of cross-reactivity of food allergens and pollen. Ann NY Acad Sci 2002; 964: 47–68.
21 Fluckiger S, Fijten H, Whitley P, Blaser K, Crameri R. Cyclophilins, a new family of cross-reactive allergens. Eur J Immunol 2002; 32: 10–7.
22 Bolten E, Schliep A, Schneckener S, Schomburg D, Schrader R. Clustering protein sequences: structure prediction by transitive homology. Bioinformatics 2001; 17: 935–41.
23 Pearson WR. Identifying distantly related protein sequences. Comput Appl Biosci 1997; 13: 325–32.
24 Brenner SE, Chothia C, Hubbard TJ. Assessing sequence comparison methods with reliable structurally identified distant evolutionary relationships. Proc Natl Acad Sci USA 1998; 95: 6073–8.
25 Rost B. Twilight zone of protein sequence alignments. Protein Eng 1999; 12: 85–94.
26 Hileman RE, Silvanovich A, Goodman RE, Rice EA, Holleschak G, Astwood JD, *et al*. Bioinformatic methods for allergenicity assessment using a comprehensive allergen database. Int Arch Allergy Immunol 2002; 128: 280–91.
27 Furmonaviciene R, Shakib F. The molecular basis of allergenicity: comparative analysis of the three dimensional structures of diverse allergens reveals a common structural motif. J Clin Pathol Mol Pathol 2001; 54: 155–9.
28 Rafnar T, Griffith IJ, Kuo MC, Bond JF, Rogers BL, Klapper DG. Cloning of Amb a I (Antigen E), the major allergen family of short ragweed pollen. J Biol Chem 1991; 266: 1229–36.
29 Asturias JA, Arilla MC, Bartolome B, Martinez J, Martinez A, Palacios R. Sequence polymorphism and structural analysis of timothy grass pollen profilin allergen (Phl p1l). Biochim Biophys Acta 1997; 1352: 253–7.
30 Federov AA, Ball T, Mahoney NM, Valenta R, Almo SC. The molecular basis for allergen cross-reactivity: crystal structure and IgE-epitope mapping of birch pollen profilin. Structure 1997; 5: 33–45.
31 Yagami T. Allergies to cross-reactive plant proteins. Latex-fruit syndrome is comparable with pollen-food allergy syndrome. Int Arch Allergy Immunol 2002; 128: 271–9.
32 Tao AL, He SH. Bridging PCR and partially overlapping primers for novel allergen gene cloning and expression insert decoration. World J Gastroenterol 2004, 10: 2103–8.

Acta Pharmacologica Sinica 2005 Oct; 26 (10): 1233–1242

Blackwell Publishing

Full-length article

Role of arachidonic acid in hyposmotic membrane stretch-induced increase in calcium-activated potassium currents in gastric myocytes[1]

Meng YANG[2], Xing-lan LI[3], Hui-ying XU[3], Jia-bin SUN[3], Bin MEI[4], Hai-feng ZHENG[3], Lian-hua PIAO[3], De-gang XING[3], Zhai-liu LI[3], Wen-xie XU[2,5]

[2]Department of Physiology, Shanghai Jiaotong University School of Medicine, Shanghai 200030; [3]Department of Physiology, Yanbian University College of Medicine, Yanji 133000; [4]East China Normal University School of Life Science, Shanghai 200062, China

Key words

gastric myocyte; arachidonic acid; hyposmotic membrane stretch; calcium-activated potassium current.

[1]Project supported by the National Natural Science Foundation of China (No 30160028).
[5] Correspondence to Prof Wen-xie XU.
Phn 86-21-5474-7639.
Fax 86-21-6283-2528.
E-mail wenxiexu@sjtu.edu.cn

Received 2005-05-22
Accepted 2005-07-06

doi: 10.1111/j.1745-7254.2005.00201.x

Abstract

Aim: To study effects of arachidonic acid (AA) and its metabolites on the hyposmotic membrane stretch-induced increase in calcium-activated potassium currents (I_{KCa}) in gastric myocytes. **Methods:** Membrane currents were recorded by using a conventional whole cell patch-clamp technique in gastric myocytes isolated with collagenase. **Results:** Hyposmotic membrane stretch and AA increased both $I_{K(Ca)}$ and spontaneous transient outward currents significantly. Exogenous AA could potentiate the hyposmotic membrane stretch-induced increase in $I_{K(Ca)}$. The hyposmotic membrane stretch-induced increase in $I_{K(Ca)}$ was significantly suppressed by dimethyleicosadienoic acid (100 μmol/L in pipette solution), an inhibitor of phospholipase A_2. Nordihydroguaiaretic acid, a lipoxygenase inhibitor, significantly suppressed AA and hyposmotic membrane stretch-induced increases in $I_{K(Ca)}$. External calcium-free or gadolinium chloride, a blocker of stretch-activated channels, blocked the AA-induced increase in $I_{K(Ca)}$ significantly, but it was not blocked by nicardipine, an L-type calcium channel blocker. Ryanodine, a calcium-induced calcium release agonist, completely blocked the AA-induced increase in $I_{K(Ca)}$; however, heparin, a potent inhibitor of inositol triphosphate receptor, did not block the AA-induced increase in $I_{K(Ca)}$. **Conclusion:** Hyposmotic membrane stretch may activate phospholipase A_2, which hydrolyzes membrane phospholipids to ultimately produce AA; AA as a second messenger mediates Ca^{2+} influx, which triggers Ca^{2+}-induced Ca^{2+} release and elicits activation of $I_{K(Ca)}$ in gastric antral circular myocytes of the guinea pig.

Introduction

Mechanical stretch is an important physiological stimulus in gut smooth muscles. It is well known that mechanical stretch induces myogenous contraction of gut smooth muscle, but the mechanism underlying this ionic channel process remains unknown. Mechanical stretch regulates the activities of ionic channels, which exist widely in the membranes of various cells and activate many signal transduction pathways. A hypothesis was proposed that membrane stretch induces alterations in the lipid bilayer, which transmits membrane tension to channel proteins or generates lipid-soluble second messengers, such as arachidonic acid (AA) and other endogenous fatty acids, by membrane-bound phospholipases[1,2]. Unsaturated fatty acids are major components of membrane lipids and they are mainly released by phospholipase A_2 (PLA_2) activation. AA in the cell membrane is esterified in phospholipids and can be released by PLA_2 in response to various extracellular stimuli[3,4]. AA and other unsaturated fatty acids modulate the activities of various ion channels and enzymes through direct or indirect pathways. For example: AA potentiates hKir2.3 in part by decreasing inward rectification of the channel[5]; AA induces membrane depolarization by inhibiting K_{ATP} currents in murine colonic smooth muscle cells[6]; and AA increases choline acetyltransferase activity in spinal cord neurons, and

this effect is mediated by protein kinase C (PKC)[7]. In addition, it was shown that AA induces endothelium-dependent hyperpolarization and relaxation of rabbit aorta through activation of apamin-sensitive K^+ currents[8]. Abundant evidence has revealed that AA is an important mediator in hyposmotic stress. It was observed that swelling induces AA release via the 85 kDa cell phospholipase A_2 ($cPLA_2$) in human neuroblastoma cells[9], and that cell swelling activates PLA_2 in ehrlich ascites tumor cells[10]. Tinel *et al*[11] also reported that AA acts as a second messenger for hypotonic-induced calcium transients in rat inner medullary collecting duct (IMCD) cells.

The calcium-activated potassium current ($I_{K(Ca)}$) has been considered to play an important role in excitability and functional regulation in excitable cells. In our previous study, AA and other unsaturated fatty acids directly inhibited calcium currents[12] and muscarinic currents[13]. For both AA and hyposmotic membrane stretch-activated $I_{K(Ca)}$[14,15], activation by hyposmotic membrane stretch is associated with calcium-induced calcium release (CICR)[16], which is triggered by extracellular calcium influx through the stretch-activated channels (SAC) in gastric antral circular myocytes of the guinea pig. However, the roles of AA and other unsaturated fatty acids in the process of $I_{K(Ca)}$ activation by membrane stretch in gastric myocytes remains unclear. In the present study, we therefore investigated the effects of AA and its metabolites on hyposmotic membrane stretch-induced increases in $I_{K(Ca)}$ in gastric antral circular myocytes of guinea pig.

Materials and methods

Preparation of cells EWG/B guinea pigs (obtained from the Experimental Animal Department of Norman Bethune University, Changchun, China; Certificate No 10-6004) of either sex, weighing 250–350 g, were killed by lethal dose of pentobarbital sodium (50 mg/kg, iv). The antral part of the stomach was cut rapidly, and the muscosal layer was separated from the muscle layer. Circular muscle was dissected from the longitudinal layer using fine scissors, and cut into small segments (1 mm×4 mm). These segments were kept in a modified Kraft-Bruhe (K-B) medium at 4 ºC for 15 min. The muscle segments were incubated at 36 ºC in 4 mL of digestion medium [calcium-free physiological salt solution (Ca^{2+}-free PSS)] containing 0.1% collagenase (II), 0.1% dithioerythreitol, 0.15% trypsin inhibitor and 0.2% bovine serum albumin for 25–35 min. The softened muscle segments were then transferred into the modified K-B medium, and cells were dispersed individually by gentle agitation with a wide-pore fire-polished glass pipette. Isolated gastric myocytes were kept in modified K-B medium at 4 ºC until use.

Electrophysiological recording Isolated cells were transferred to a small chamber (0.1 mL) on the stage of an inverted microscope (IX-70 Olympus, Tokyo, Japan) for 10–15 min to settle down. The cells were superfused continuously with isosmotic PSS by gravity (0.9–1.0 mL/min). An 8-channel perfusion system (L/M-sps-8, List Electronics, Darmstadt, Germany) was used to change solution. Experiments were carried out at 20–25 ºC and the whole-cell configuration of the patch-clamp technique was used. Patch-clamp pipettes were manufactured from borosilicate glass capillaries (GC 150T-7.5, Clark Electromedical Instruments, Kent, UK) using a 2-stage puller (PP-83, Narishige, Japan). The resistance of the patch pipette was 3–5 MΩ when filled with pipette solution. Liquid junction potentials were canceled before seal formation. Whole-cell currents were recorded with an EPC-10 patch-clamp amplifier (HEKA Instrument, Darmstadt, Germany) and command pulses were applied by using the Pentium IV-grade computer and pCLAMP software (Version 6.02; Axon Instruments, USA).

Drugs and solutions All drugs were purchased from Sigma (Sigma-Aldrich Corp St Louis, MO, USA). Tyrode's solution contained 147 mmol/L NaCl, 4 mmol/L KCl, 1.05 mmol/L $MgCl_2 \cdot 6H_2O$, 2 mmol/L $CaCl_2 \cdot 2H_2O$, 0.42 mmol/L NaH_2PO_4, 1.81 mmol/L $Na_2HPO_4 \cdot 2H_2O$ and 5.5 mmol/L glucose, and the pH was adjusted to 7.35 with NaOH. Ca^{2+}-free solution contained 134.8 mmol/L NaCl, 4.5 mmol/L KCl, 10 mmol/L HEPES, 1 mmol/L $MgCl_2$ and 5 mmol/L glucose, and the pH was adjusted to 7.4 with TRIZMA BASE (Tris). The isosmotic solution (290 Osmmol/kg) contained 80 mmol/L NaCl, 4.5 mmol/L KCl, 1 mmol/L $MgCl_2 \cdot 6H_2O$, 2 mmol/L $CaCl_2 \cdot 2H_2O$, 5 mmol/L glucose, 10 mmol/L HEPES and 110 mmol/L sucrose, and the pH was adjusted to 7.4 with Tris. Hypoosmotic solution (200 Osmmol/kg) contained 30 mmol/L sucrose, with the other ingredients at the same concentrations as in the isosmotic solution. Modified K-B solution contained 50 mmol/L *L*-glutamate, 50 mmol/L KCl, 20 mmol/L taurine, 20 mmol/L KH_2PO_4, 3 mmol/L $MgCl_2 \cdot 6H_2O$, 10 mmol/L glucose, 10 mmol/L HEPES, and 0.5 mmol/L egtazic acid, and the pH was adjusted to 7.4 with KOH. The pipette solution contained 110 mmol/L K-aspartic acid, 5 mmol/L Mg-ATP, 1 mmol/L $MgCl_2 \cdot 6H_2O$, 20 mmol/L KCl, 0.1 mmol/L or 10 mmol/L egtazic acid, 2.5 mmol/L di-tris-creatine phosphate and 2.5 mmol/L disodium-creatine phosphate, and the pH was adjusted to 7.3 with KOH. AA, nordihydroguaiaretic acid (NDGA) and dimethyleicosadienoic acid (DEDA) were all prepared as aqueous stock solutions (1 mmol/L).

Data analysis Data were expressed as mean±SD. Statistical significance was evaluated using the Student's *t*-test.

Differences were considered to be statistically significant when $P<0.05$.

Results

Effects of hyposmotic membrane stretch and AA on $I_{K(Ca)}$ and STOC Under whole-cell configuration, membrane potential was clamped at -60 mV, and $I_{K(Ca)}$ was elicited by a single-step command pulse from -60 mV to +60 mV for 400 ms at 15 s intervals. $I_{K(Ca)}$ started increasing at 139.3 s±11.3 s after cells were exposed to hyposmotic solution (200 mOsm), and at 165.0 s±25.1 s after cells were exposed to 10 μmol/L AA (Figure 1A,1B). There was no significant difference between the 2 latent periods. Hyposmotic membrane stretch and 10 μmol/L AA increased markedly in peak current of $I_{K(Ca)}$ to 168.3%±16.1% and 158.5%±20.5%, respectively (n=6, Figure 1B.).

The calcium-activated potassium current is activated by intracellular Ca^{2+} and can be monitored by spontaneous transient outward currents (STOC)[17]. We therefore observed STOC to investigate effects of hyposmotic membrane stretch and AA on $I_{K(Ca)}$. In whole cell configurations, the holding

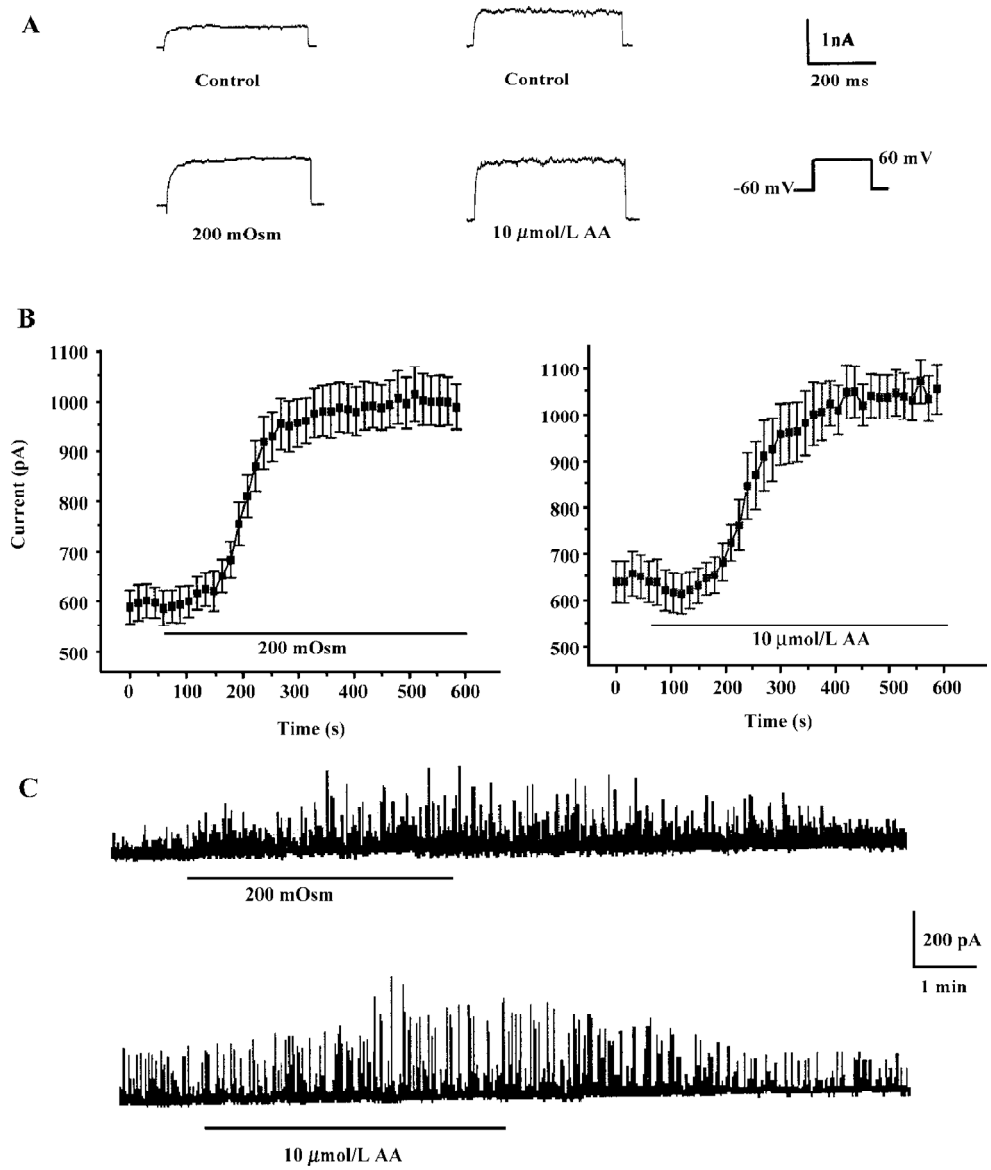

Figure 1. Effects of hyposmotic membrane stretch and arachidonic acid (AA) on calcium-activated potassium currents (I_{KCa}). (A) Raw traces of hyposmotic membrane stretch and AA-induced increase in $I_{K(Ca)}$. (B) The time courses of $I_{K(Ca)}$ increased by hyposmotic membrane stretch and arachidonic acid. Membrane potential was depolarized from -60 mV to +60 mV at 15 s intervals to elicit $I_{K(Ca)}$. (C) Effects of hyposmotic membrane stretch and AA on spontaneous transient outward currents.

potential was clamped at -20 mV, and STOC were elicited and enhanced by hyposmotic membrane stretch and 10 μmol/L AA, respectively (Figure 1C).

Effects of exogenous AA on hyposmotic membrane stretch-induced increase in $I_{K(Ca)}$ Under whole-cell configuration, membrane potential was clamped at -60 mV, and $I_{K(Ca)}$ was elicited by a step voltage command pulse from -40 mV to +100 mV for 400 ms with a 20-mV increment at 10-s intervals. Exogenous AA significantly increased $I_{K(Ca)}$ elicited by the command step pulse when membrane potential was depolarized from -40 mV to+100 mV, and hyposmotic membrane stretch potentiated the AA-induced increase in $I_{K(Ca)}$ when the membrane potential was depolarized from -40 mV to+100 mV (Figure 2A, 2B). Hyposmotic membrane stretch also increased $I_{K(Ca)}$ elicited by the command step pulse when the membrane potential was depolarized from

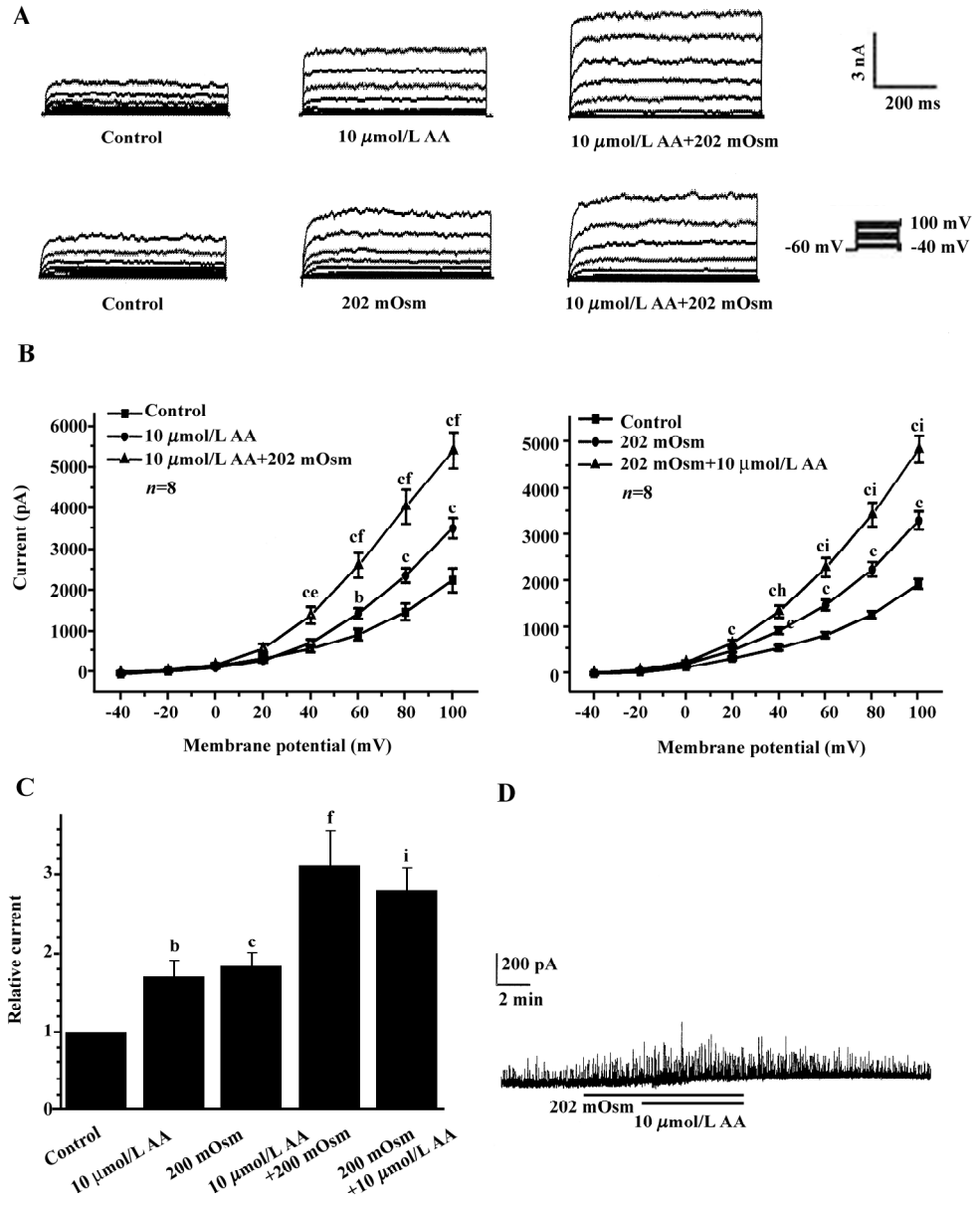

Figure 2. The effect of exogenous arachidonic acid (AA) on the hyposmotic membrane stretch-induced increase in calcium-activated potassium currents (I_{KCa}). (A) Raw traces of exogenous AA on the hyposmotic membrane stretch-induced increase in $I_{K(Ca)}$. (B) *I/V* relation curves. (C) Summary of the effects of exogenous AA on the hyposmotic membrane stretch-induced increase in $I_{K(Ca)}$ and those of hyposmotic membrane stretch on the exogenous AA-induced increase in $I_{K(Ca)}$ at +60 mV. (D) The effect of exogenous AA on the hyposmotic membrane stretch-induced increase in spontaneous transient outward currents. $^{b}P<0.05$, $^{c}P<0.01$ *vs* control. $^{e}P<0.05$, $^{f}P<0.01$ *vs* 10 μmol/L AA. $^{h}P<0.05$, $^{i}P<0.01$ *vs* 202 mOsm.

-40 mV to +100 mV, and AA potentiated hyposmotic membrane stretch-induced increase in $I_{K(Ca)}$ when membrane potential was depolarized from -40 mV to +100 mV (Figure 2A, 2B). The peak current of $I_{K(Ca)}$ was increased to 184.2%±17.7% by hyposmotic membrane stretch and then the hyposmotic membrane stretch-induced increase in $I_{K(Ca)}$ was potentiated by 10 μmol/L AA, and the peak current increased to 281.3%±28.3% at +60 mV (n=8, Figure 2C). In another way, the peak current of $I_{K(Ca)}$ was increased to 171.8%±20.3 % by 10 μmol/L AA, and the AA-induced increase in $I_{K(Ca)}$ was potentiated by hyposmotic membrane stretch, with the peak current increasing to 311.5%±44.4% at +60 mV (n=8; Figure 2C). However, there was no significant difference between the potentiated effects of AA on the hyposmotic membrane stretch-induced increase in $I_{K(Ca)}$ and hyposmotic membrane stretch on the AA-induced increase in $I_{K(Ca)}$ (P>0.05, Figure 2C). As with the protocol above, the effects of hyposmotic membrane stretch and AA on STOC were investigated. Hyposmotic membrane stretch markedly increased STOC, and 10 μmol/L AA potentiated this effect (n=2, Figure 2D).

Effects of endogenous AA and its metabolites on hyposmotic membrane stretch-induced increase in $I_{K(Ca)}$ Intracellular free AA are metabolized by 3 enzymes: cycooxygenase, lipoxygenase and epoxygenase. To determine the effects of endogenous AA and its metabolites on the hyposmotic membrane stretch-induced increase in $I_{K(Ca)}$, DEDA, a non-selective inhibitor of PLA_2, and NDGA, a lipoxygenase inhibitor, were used to inhibit the hydrolyzation of AA from membranes and to decrease the production of AA metabolites. DEDA (100 μmol/L in pipette) significantly suppressed the hyposmotic membrane stretch-induced increase in $I_{K(Ca)}$ (Figure 3A,3B), and the increased percentage was reduced from 164.3%±9.8 % of the control to 113.4%±3.6% at +60 mV (n=15, Figure 3C). When cells were pretreated for 15 min with 10 μmol/L NDGA, AA (Figure 4A,4B) and hyposmotic stretch-induced increases in $I_{K(Ca)}$ could be significantly suppressed (Figure 5A,

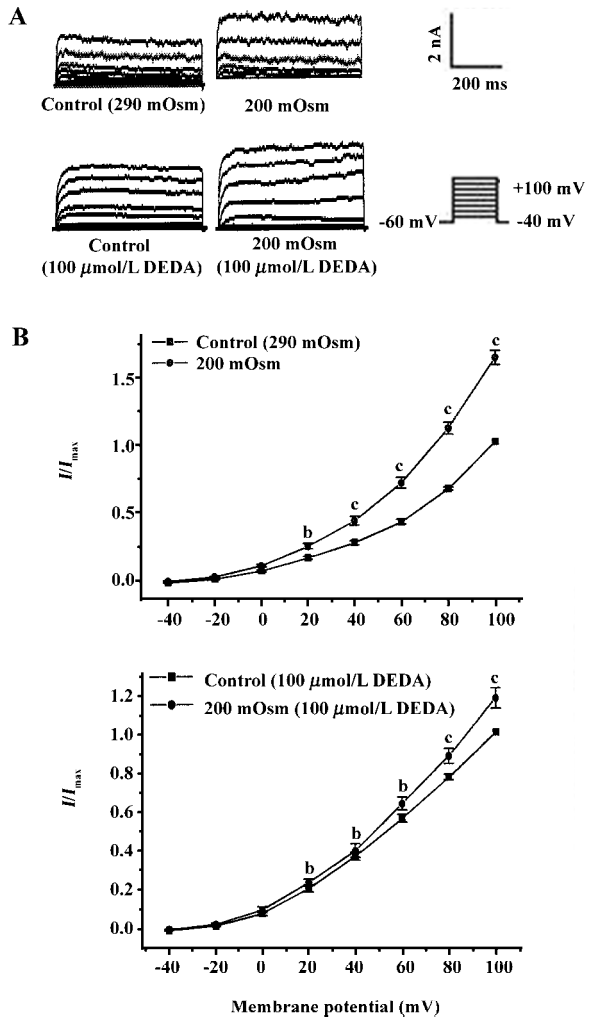

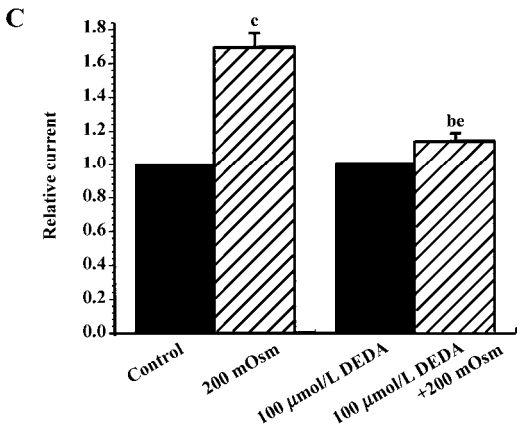

Figure 3. The inhibitory effect of dimethyleicosadienoic acid (DEDA), an inhibitor of phospholipase A_2 (PLA_2), on calcium-activated potassium currents (I_{KCa}) increased by hyposmotic membrane stretch. (A) Raw traces of the hyposmotic membrane stretch-induced increase in $I_{K(Ca)}$ in the presence of DEDA. (B) I/V relation curves of the hyposmotic membrane stretch-induced increase in $I_{K(Ca)}$ in the presence of DEDA and control. Peak values of the currents were normalized to the values at +100 mV under control conditions. (C) The inhibitory effect of DEDA on $I_{K(Ca)}$ increased by hyposmotic membrane stretch at +60 mV. ^bP<0.05, ^cP<0.01 *vs* control. ^eP<0.05 *vs* 200 mOsm.

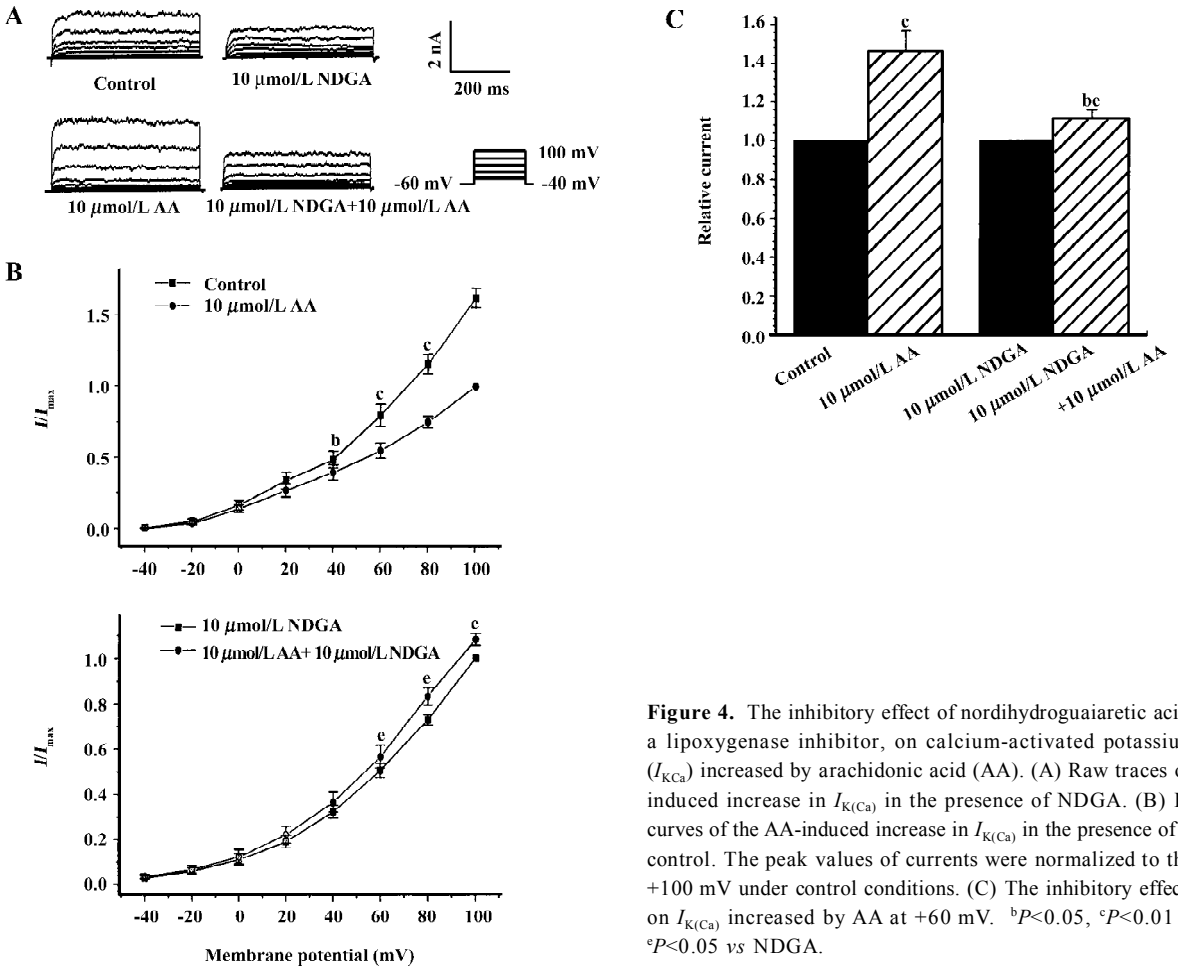

Figure 4. The inhibitory effect of nordihydroguaiaretic acid (NDGA), a lipoxygenase inhibitor, on calcium-activated potassium currents (I_{KCa}) increased by arachidonic acid (AA). (A) Raw traces of tThe AA-induced increase in $I_{K(Ca)}$ in the presence of NDGA. (B) I/V relation curves of the AA-induced increase in $I_{K(Ca)}$ in the presence of NDGA and control. The peak values of currents were normalized to the values at +100 mV under control conditions. (C) The inhibitory effect of NDGA on $I_{K(Ca)}$ increased by AA at +60 mV. $^bP<0.05$, $^cP<0.01$ *vs* control. $^eP<0.05$ *vs* NDGA.

5B). The AA-induced increase in $I_{K(Ca)}$ was decreased from 145%±10% to 110%±4% by NDGA (n=8, Figure 4C). NDGA also suppressed the hyposmotic membrane stretch-induced increase in $I_{K(Ca)}$ (Figure 5A,5B) and the increased percentage was reduced from 170%±10% to 142%±3% at +60 mV (Figure 5C). These results showed that endogenous AA and its metabolites were involved in the hyposmotic membrane stretch-induced increase in $I_{K(Ca)}$.

Effect of calcium mobilization on AA-induced increase in $I_{K(Ca)}$ It is well known that $I_{K(Ca)}$ is activated by intracellular free calcium, while extracellular calcium is necessary for efficiently controlling calcium homeostasis. To determine whether the AA-induced increase in $I_{K(Ca)}$ was mediated by calcium influx, the effect of AA on $I_{K(Ca)}$ was observed following the removal of extracellular calcium and the addition of 10 μmol/L EGTA in bath solution. The AA-induced increase in $I_{K(Ca)}$ was completely blocked by the removal of extracellular calcium, and the changes in the percentage of $I_{K(Ca)}$ were 146.30%±10.4% and 95.64%±11.7% in the presence or absence of extracellular calcium, respectively (n=6, Figure 6A). Our previous study indicated that hyposmotic membrane stretch activated L-type calcium currents[12] and calcium-activated potassium currents via extracellular calcium influx through SAC in gastric myocytes of guinea pig[15,16]. We therefore examined the relationship between the AA-induced increase in $I_{K(Ca)}$ and L-type calcium channels or SAC. However, 5 mmol/L nicardipine, an L-type calcium channel blocker, did not block the AA-induced increase in $I_{K(Ca)}$, but gadolinium (Gd^{3+}), a blocker of SAC, completely suppressed the AA-induced increase in $I_{K(Ca)}$. The changes in the percentage of $I_{K(Ca)}$ were 146.3%±10.4%, 151.1%±14.4% and 102.5%±2.2% in the control, nicardipine and Gd^{3+} groups, respectively (n=6, Figure 6A).

Intracellular free calcium has 2 sources: extracellular calcium influx and intracellular calcium release from calcium stores. Intracellular calcium is released through 2 pathways, one is CICR and the other is inositol-triphosphate-induced calcium release (IICR). We therefore investigated the role of intracellular calcium release in the AA-induced increase in $I_{K(Ca)}$. Heparin (3 mg/mL), a potent inhibitor of IICR, could

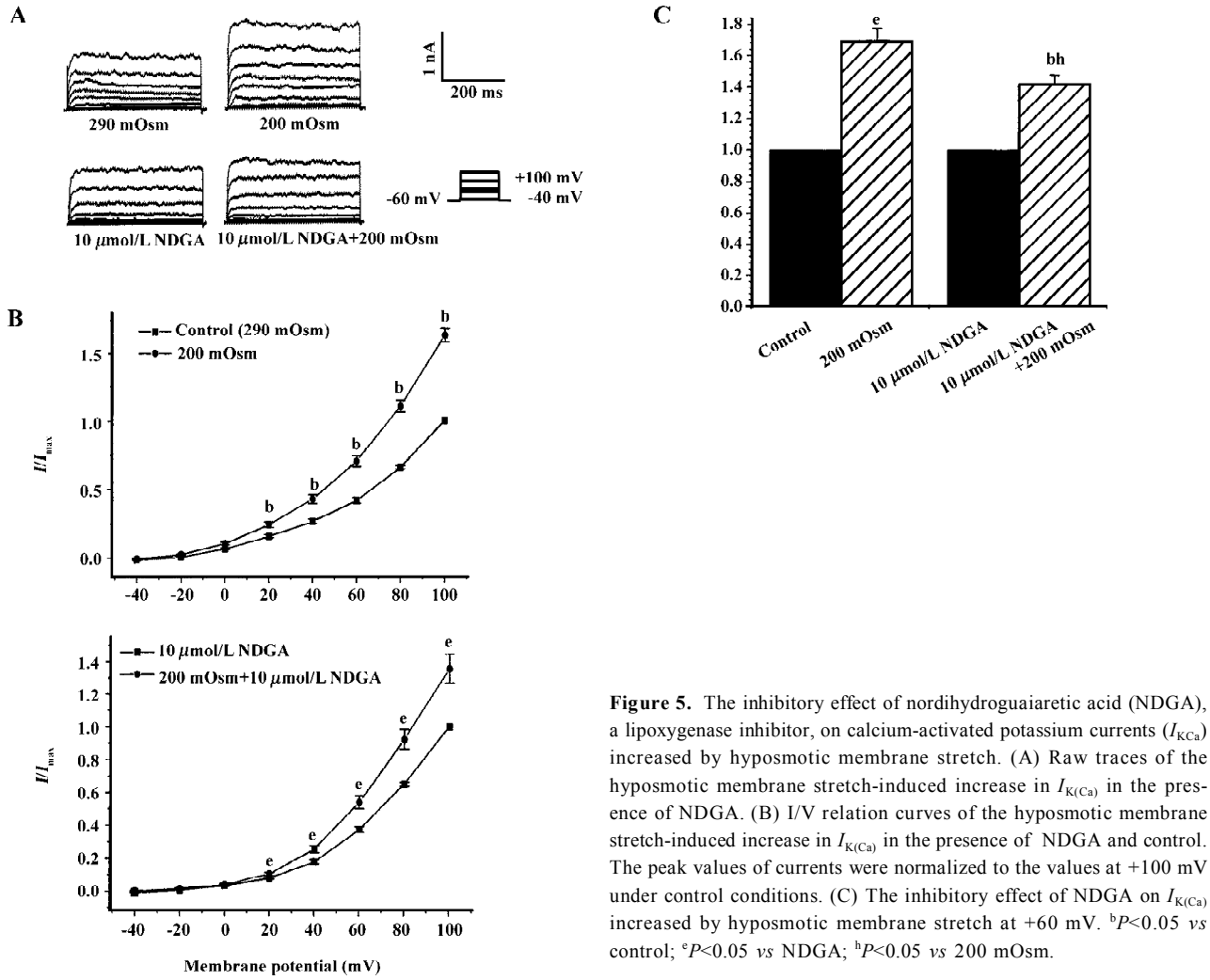

Figure 5. The inhibitory effect of nordihydroguaiaretic acid (NDGA), a lipoxygenase inhibitor, on calcium-activated potassium currents ($I_{K(Ca)}$) increased by hyposmotic membrane stretch. (A) Raw traces of the hyposmotic membrane stretch-induced increase in $I_{K(Ca)}$ in the presence of NDGA. (B) I/V relation curves of the hyposmotic membrane stretch-induced increase in $I_{K(Ca)}$ in the presence of NDGA and control. The peak values of currents were normalized to the values at +100 mV under control conditions. (C) The inhibitory effect of NDGA on $I_{K(Ca)}$ increased by hyposmotic membrane stretch at +60 mV. $^bP<0.05$ *vs* control; $^eP<0.05$ *vs* NDGA; $^hP<0.05$ *vs* 200 mOsm.

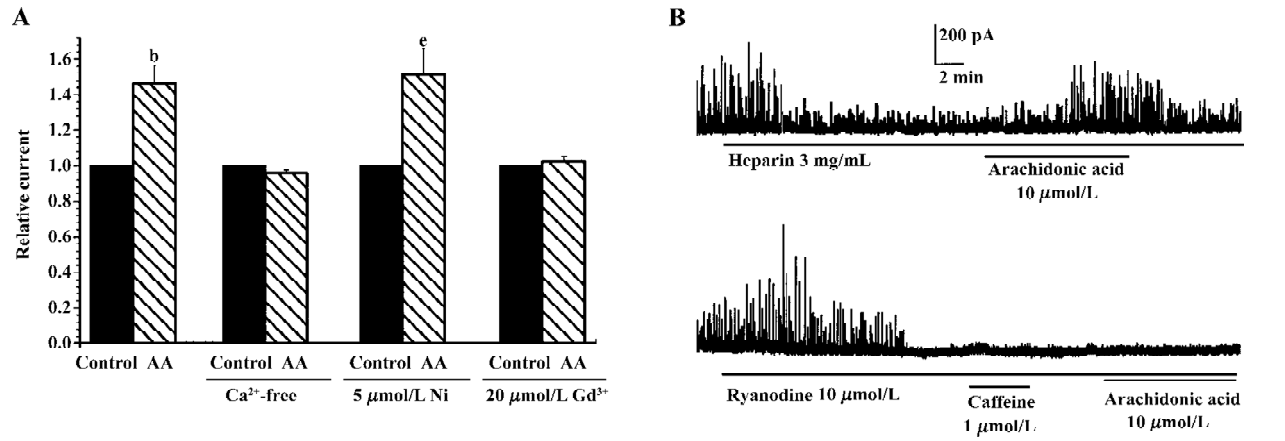

Figure 6. The effect of calcium mobilization on $I_{K(Ca)}$ increased by arachidonic acid (AA) 10 μmol/L. (A) Summary of $I_{K(Ca)}$ increased by AA at +60 mV under conditions of no external Ca^{2+}, administration of nicardipine (Ni) and gadolinium (Gd^{3+}). (B) Effect of inositol triphosphate-induced calcium release on the AA-induced increase in spontaneous transient outward currents (STOC) and effect of calcium-induced calcium release on the AA-induced increase in STOC. $^bP<0.05$ *vs* control. $^eP<0.05$ *vs* Ni.

inhibit STOC significantly, but did not block the AA-induced increase in STOC (Figure 6B). Ryanodine (10 μmol/L), a specific CICR inhibitor, binds to CICR channels and locks them in a subconductance state, thereby functionally depleting calcium stores[18]. In the present study, ryanodine increased STOC, and STOC were then almost abolished by ryanodine after approximately 8 min with caffeine, a CICR activator; AA could not then enhance them again (Figure 6B). These results indicated that CICR, but not IICR, was involved in the AA-induced increase in $I_{K(Ca)}$.

Discussion

Our previous study demonstrated that $I_{K(Ca)}$ was activated by hyposmotic membrane stretch and Ca^{2+} signaling played an important role in the process in gastric antral circular myocytes of guinea pig[15,16]. Under hyposmotic conditions, extracellular calcium influx through SAC triggered CICR, and intracellular free calcium then activated $I_{K(Ca)}$. However, it remains obscure how the membrane stretch is turned into the signal for Ca^{2+} entry from the extracellular space. We therefore investigated whether AA is involved in the hyposmotic membrane stretch-induced increase in $I_{K(Ca)}$.

In the present study, both hyposmotic membrane stretch and AA significantly increased $I_{K(Ca)}$ with a similar latent period. Moreover, exogenous AA potentiated the hyposmotic membrane stretch-induced increase in $I_{K(Ca)}$ (Figure 1). The results indicated that there may be a similar mechanism for the $I_{K(Ca)}$ activated by hyposmotic membrane stretch and AA. Activation of various signaling pathways may induce an increase in the production of AA, for example, phospholipase C, phospholipase D and PLA_2. In mammalian tissues AA is mainly liberated directly from phospholipids by PLA_2, which is a ubiquitous enzyme[4]. We have observed that when cells are exposed to DEDA, a non-selective inhibitor of PLA_2, the hyposmotic membrane stretch-induced increase in $I_{K(Ca)}$ is significantly blocked by DEDA (Figure 3). The results suggest that hyposmotic membrane stretch activates PLA_2, which hydrolyzes membrane phospholipids to produce AA, and AA as a second messenger mediates the hyposmotic membrane stretch-induced increase in $I_{K(Ca)}$ in gastric myocytes of guinea pig. Many experiments also support our results. It was observed that hyposmotic cell swelling induced AA release from cell membranes in human neuroblastoma cells[9] and Ehrilich ascites tumor cells[10]. In rat inner medullary collecting duct cells, AA acted as a second messenger in hypotonicity-induced calcium transients[11]. AA was also a second messenger in cultured rabbit principal cells[19] and ciliary epithelial cells under hyposmotic conditions[20]. Meanwhile, many reports have described that AA is able to affect cell functions, via its metabolites, under hyposmotic conditions in several cell systems. Leucotrienes, for example, appeared to mediate the inositol efflux in glial cells[21], and to activate chloride and potassium conductances as well as taurine transport in Ehrlich ascites cells[22]. In the present study, we also examined the possibility that AA metabolites could be involved in activating potassium currents under hyposmotic conditions by using NDGA, a lipoxygenase inhibitor. NDGA significantly inhibited AA and the hyposmotic membrane stretch-induced increase in $I_{K(Ca)}$ (Figure 4). These results suggest that AA metabolites generated by lipoxygenase mediate the hyposmotic membrane stretch-induced increase in $I_{K(Ca)}$ in gastric myocytes.

In various cell types, AA was found to induce Ca^{2+} flux and to mobilize intracellular calcium to trigger different Ca^{2+}-dependent physiological functions in cells. For example, AA or its metabolites mobilized Ca^{2+} from intracellular stores, and intracellular Ca^{2+} then activated ion transport[19]. In several cell types, for example, in rat IMCD cells[11], human embryonic kidney (HEK293) cells[23] and *Dictyostelium discoideum*[24], AA released Ca^{2+} from the stores to trigger extracellular Ca^{2+} entry, and Ca^{2+} released from calcium stores was a prerequisite for extracellular Ca^{2+} entry. However, Murthy *et al*[20] found that AA induces Ca^{2+} influx, which triggers CICR in longitudinal smooth muscle of the intestine. Our previous study also demonstrated that hyposmotic membrane stretch activates $I_{K(Ca)}$ via CICR in gastric myocytes[15]. In the present study, the roles of AA and its metabolites in the relationships among hyposmotic membrane stretch-induced increase in $I_{K(Ca)}$, extracellular Ca^{2+} and intracellular calcium mobilization were investigated. Under extracellular calcium-free conditions, $I_{K(Ca)}$ was not increased by AA or hyposmotic membrane stretch (Figure 6). It was elucidated that extracellular calcium is necessary for AA and the hyposmotic membrane stretch-induced increase in $I_{K(Ca)}$, and some ionic channels participate in extracellular calcium influx. McCarty and O'Neil indicated that there are 2 alternative kinds of channel activated by hyposmotic swelling: voltage-activated Ca^{2+} channels and stretch-activated channels[25]. We observed previously that hyposmotic membrane stretch increases L-type current in gastric myocytes of guinea pig[12], and Yamamoto and Suzuki[26] also observed that there are 2 kinds of SAC in gastric myocytes of guinea pig. In the present study we examined whether these 2 channels are associated with extracellular calcium influx. Nicardipine, an L-type calcium channel blocker, could not block the AA-induced increase in $I_{K(Ca)}$. However, it was completely blocked by Gd^{3+}, which blocks not only SAC but also store-operated

Ca^{2+} channels (Figure 6). A similar effect of Gd^{3+} in blocking AA-induced Ca^{2+} entry has also been observed in other cell types, such as IMCD[11] and HEK293 cells[23].

Intracellular Ca^{2+} release from Ca^{2+} stores is the primary source of the increase in intracellular calcium. It was found that the entry of extracellular calcium via activating stretch-sensitive channels is amplified by calcium release from internal stores in toad gastric myocytes[26]. Sutko and Airey[27] suggested that ryanodine-sensitive calcium stores were positioned near the surface membrane in some smooth muscle cells, Ca^{2+} release from which was found to influence the activity of $I_{K(Ca)}$. Our previous study also indicated that hyposmotic membrane stretch activates $I_{K(Ca)}$[15,16] and carbachol currents[13], and the activations are associated with CICR, which is triggered by extracellular calcium influx[15,28]. In the present study, heparin, a potent inhibitor of inositol triphosphate receptor, did not block the AA-induced increase in $I_{K(Ca)}$; however, ryanodine, a CICR agonist, completely blocked the AA-induced increase in $I_{K(Ca)}$ (Figure 6B). The results suggest that AA mobilizes intracellular calcium via triggering CICR and activates $I_{K(Ca)}$ in gastric antral circular myocytes of guinea pig. The potassium efflux through $I_{K(Ca)}$ hyperpolarized the membrane potential of smooth muscle cells, thereby limiting depolarization-dependent calcium and promoting relaxation. CICR can thus participate in both the contraction and relaxation of smooth muscle cells. Therefore, AA may be involved in both the contraction via activating extracellular Ca^{2+} influx and relaxation via activating $I_{K(Ca)}$ in gastric antral circular myocytes of the guinea pig.

In summary, hyposmotic membrane stretch may act on cell membranes to activate PLA_2 and then generate AA. AA may then act as a second messenger to mediate extracellular calcium entry and trigger CICR to activate $I_{K(Ca)}$ in gastric myocytes of the guinea pig. AA and its metabolites may play an important role in regulating many cell functions under the hyposmotic conditions in gastric antral circular myocytes of the guinea pig.

References

1 Morris CE. Are stretch-sensitive channels in molluscan cells and elsewhere physiological mechanotransducers? Experientia 1992; 48: 852–8.

2 Ordway RW, Petrou S, Kirber MT, Walsh JV Jr, Singer JJ. Stretch activation of a toad smooth muscle K^+ channel may be mediated by fatty acid. J Physiol 1995; 484: 331–7.

3 Dennis EA, Rhee SG, Billah MM, Hannun YA. Role of phospholipase in generating lipid second messengers in signal transduction. FASEB J 1991; 5: 2068–77.

4 Graber R, Sumida C, Nunez EA. Fatty acids and cell signal transduction. J Lipid Mediat 1994; 9: 91–116.

5 Liu Y, Liu D, Krafte DS. Decrease of inward rectification as a mechanism for arachidonic acid-induced potentiation of hKir2.3. Eur Biophys J 2002; 31: 497–503.

6 Jun JY, Yeum CH, Park YW, Jang IY, Kong ID, Sim JH, *et al*. Effects of arachidonic acid on ATP-sensitive K^+ current in murine colonic smooth muscle cells. Jpn J Pharmacol 2002; 90: 81–7.

7 Chalimoniuk M, King-Pospisil K, Pedersen WA, Malecki A, Wylegala E, Mattson MP, *et al*. Arachidonic acid increases choline acetyltransferase activity in spinal cord neurons through a protein kinase C-mediated mechanism. J Neurochem 2004; 90: 629–36.

8 Gauthier KM, Spitzbarth N, Edwards EM, Campbell WB. Apamin-sensitive K^+ currents mediate arachidonic acid-induced relaxations of rabbit aorta. Hypertension 2004; 43: 413–9.

9 Basavappa S, Pedersen SF, Jorgensen NK, Ellory JC, Hoffmann EK. Swelling-induced AA release via the 85-kDa $cPLA_2$ in human neuroblastoma cells. J Neurophysiol 1998; 79: 1441–9.

10 Thoroed SM, Lauritzen L, Lambert IH, Hansen HS, Hoffmann EK. Cell swelling activates phospholipase A_2 in Ehrlich ascites tumor cells. J Membr Biol 1997;160: 47–58.

11 Tinel H, Wehner F, Kinne RKH. Arachidonic acid as a second messenger for hypotonicity-induced calcium transients in rat IMCD cells. Pflügers Arch 1997; 433: 245–53.

12 Xu WX, Kim SJ, Kim SJ, So I, Kang TM, Rhee JC, *et al*. Effect of stretch on calcium channel currents recorded from the antral circular myocytes of guinea-pig stomach. Pfluegers Arch 1996; 432: 159–64.

13 Cui YF, Li L, Yu YC, Jin ZY, Li ZL, Xu WX. Role of unsaturated fatty acids in the enhancement of muscarinic current by hyposmotic membrane stretch in guinea pig smooth muscle cells. Acta Physiol Sin 2003; 55: 96–100.

14 Zheng HF, Li XL, Jin ZY, Sun JB, Li ZL, Xu WX. Effect of unsaturated fatty acid on calcium-activated potassium current in guinea pig gastric myocytes. World J Gastroenterol 2005; 11: 672–5.

15 Piao L, Li Y, Li L, Xu WX. Increment of calcium-activated and delayed rectifier potassium current by hyposmotic swelling in gastric antral circular myocytes of guinea pig. Acta Pharmacol Sin 2001; 22: 566–72.

16 Piao L, Li Y, Li L, Ng J, Li ZL, Xu WX. The involvement of calcium mobilization in the calcium-activated potassium currents activated by hyposmotic swelling in gastric antral circular myocytes of the guinea-pig. Jpn J Physiol 2001; 51: 223–30.

17 Bolton TB, Lim SP. Properties of calcium stores and transient outward currents in single smooth muscle cells of rabbit. J Physiol (Lond) 1988; 409: 385–400.

18 Sutko JL, Airey J. Ryanodine receptor Ca^{2+} release channels. Physiol Rev 1996; 76: 1027–71.

19 Ling BN, Webster CL, Eaton DC. Eicosanoids modulate apical Ca^{2+}-dependent K^+ channels in cultured rabbit principal cells. Am J Physiol 1992; 63: F116–26.

20 Civan MM, Coca-Prados M, Peterson-Yantorno K. Pathways signaling the regulatory volume decrease of cultured nonpigmented ciliary epithelial cells. Invest Ophthalmol Vis Sci 1994; 5: 2876–86.

21 Strange K, Morrison R, Shrode L, Putnam R. Mechanism and regulation of swelling-activated inositol efflux in brain glial cells. Am J Physiol 1993, 265: C244–56.

22 Hoffmann EK, Dunham PB. Membrane mechanisms and intracellular signalling in cell volume regulation. Int Rev Cytol 1995; 161: 173–262.
23 Luo D, Broad LM, Bird GSJ, Putney Jr WJ. Signaling pathways underlying muscarinic receptor-induced $[Ca^{2+}]_i$ oscillations in HEK293 cells. J Biol Chem 2001; 276: 5613–21.
24 Schaloske R, Sonnemann J, Malchow D, Schlatterer C. Fatty acids induce release of Ca^{2+} from acidosomal stores and activate capacitative Ca^{2+} entry in *Dictyostelium discoideum*. Biochem J 1998; 332: 541–8.
25 McCarty NA, O'Neil RG. Calcium signaling in cell volume regulation. Physiol Rev 1992; 2: 1037–61.
26 Yamamoto Y, Suzuki H. Two types of stretch-activated channel activities in guinea-pig gastric smooth muscle cells. Jpn J Physiol 1996; 6: 337–45.
27 Sutko JL, Airey J. Ryanodine receptor Ca^{2+} release channels. Physiol Rev 1996; 6: 1027–71.
28 Yu YC, Guo HS, Piao L, Li L, Lee ZL, Xu WX. Intracellular calcium involved in muscarinic currents increased by hyposmotic membrane stretch in gastric myocytes of guinea-pig. Acta Pharmacol Sin 2002; 23: 961–1056.

Acta Pharmacologica Sinica 2005 Oct; 26 (10): 1243–1247

Blackwell Publishing

Full-length article

Anti-implantation effect of droloxifene in rats and its relationship with anti-estrogenic activity[1]

Yong HUANG, Yu SHEN, Ying FENG, Lin CAO, Ying LENG[2]

Shanghai Institute of Materia Media, Shanghai Institute for Biological Sciences, Chinese Academy of Sciences, Graduate School of the Chinese Academy of Sciences, Shanghai 201203, China

Key words

3-hydroxytamoxifen; implantation; estrogen; progesterone; rats

[1]Project supported by the National Natural Science Foundation of China (No 30000210).
[2]Correspondence to Dr Ying LENG.
Phn/Fax 86-21-5080-6059.
E-mail yleng@mail.shcnc.ac.cn

Received 2005-06-17
Accepted 2005-06-24

doi: 10.1111/j.1745-7254.2005.00191.x

Abstract

Aim: To investigate the anti-implantation effect of droloxifene and study the possible relationship between the anti-estrogenic activity of droloxifene and its anti-implantation effect. **Methods:** Pregnant rats were treated orally with droloxifene at 10:00 AM on d 2 at doses of 1.25–20 mg/kg to observe anti-implantation effects, and then doses of 14 mg/kg or 2.5 mg/kg were given at different time on d 2 to d 5 to determine the optimal administration time for anti-implantation effects. Pregnant rats were treated with a combination of droloxifene (2.5 mg/kg, ig) and E2 (0.5–8.0 μg/kg, sc) on the optimal administration time to observe the antagonistic effect of external estrogen on the anti-implantation effect of droloxifene. Serum estrogen and progesterone levels were measured by carrying out radioimmunoassays on d 1 to d 6 in droloxifene-treated and control rats to determine the surge time for nidatory estrogen and the effect of droloxifene on ovary function. **Results:** Droloxifene has anti-implantation effects in rats. The optimal oral administration time was at 22:00 PM on d 4, which was after the surge time for nidatory estrogen (on d 4 at 10:00 AM). This suggests that the anti-implantation effect of droloxifene is not attributable to antagonism of the surge in secretion of nidatory estrogen. External estrogen did not antagonize the anti-implantation effect of droloxifene. Droloxifene had no effect on the serum levels of estrogen and progesterone on d 5 or d 6 when administered on d 4 at 22:00 PM. **Conclusion:** Droloxifene has an anti-implantation effect in rats, and the effect appears to be not completely due to its anti-estrogenic activity.

Introduction

Droloxifene, a derivative of the triphenylethylene drug tamoxifen, is a novel selective estrogen receptor modulator (SERM)[1]. Its higher affinity to the estrogen receptor, higher anti-estrogenic to estrogenic ratio, more effective inhibition of cell growth and division in estrogen receptor-positive cell lines, and lower toxicity give it theoretical advantages over tamoxifen in the treatment of human breast cancer[2]. Droloxifene may also be a potentially useful agent for the treatment of postmenopausal osteoporosis because it can prevent estrogen deficiency-induced bone loss without causing uterine hypertrophy[3]. Droloxifene may have an effect on bone and breast tissue because it induces apoptosis[4]. The corpus luteum is an ovarian tissue that synthesizes and secretes progesterone, which plays a key role in the establishment and maintenance of pregnancy in mammals. Abnormal regression of the corpus luteum will disturb or even terminate both the implantation process and early pregnancy. Apoptosis is involved in the regression of the corpus luteum in many species[5]. Therefore, better understanding the compounds that induce the apoptosis of luteal cells may contribute to the development of new anti-implantation agents. Our laboratory was the first to report that droloxifene induceed the apoptosis of rat luteal cells *in vitro* and the pre-implantation luteal cells in pregnant rats[6–8]. Moreover, droloxifene facilitates the apoptosis of luteal cells and short-

ens the period of pseudopregnancy in pseudopregnant rats[9]. These results suggest that droloxifene induces the regression of the corpus luteum and has potential anti-implantation effects. Exact equilibrium of estrogen and progesterone is essential for implantation, and any disturbance in the effects of these hormones can cause infertility[10]. As a novel selective estrogen receptor modulator with greater anti-estrogenic effects, droloxifene seems to interfere with the effect of estrogen and cause anti-implantation effects. However, the anti-implantation effect of droloxifene has not been evaluated and reported on. Therefore, in the present study, the anti-implantation effect of droloxifene was evaluated and the relationship between the anti-estrogenic activity of droloxifene and its anti-implantation effect was analyzed in rats.

Materials and methods

Drugs and reagents The droloxifene was synthesized by Prof Peng XIA (Department of Organic Chemistry, College of Pharmacy, Fudan University, Shanghai) and was suspended in 1% sodium carboxymethylcellulose (CMC). Estradiol (E_2) was purchased from the Shanghai 9th Pharmaceutical Factory (Shanghai, China) and was suspended in corn oil. Serum estrogen and progesterone radioimmunoassay (RIA) kits were obtained from DEPU Ltd (Tianjin, China).

Animals and treatment Sprague-Dawley rats (body weight: female, 220–250 g an male 300–350 g, SIPPR/BK LtdShanghai) were kept in a temperature-controlled (24–26 °C) and light-regulated (12 h light, 12 h dark) room, and were given *ad libitum* access to standard chow and water. The female animals were cohabited with male animals at a ratio of 2:1. The day that sperm were found in the vaginal smear was designated as d 1 of pregnancy.

Evaluation of anti-implantation efficacy Confirmed pregnant female rats were randomly assigned into different groups and were treated with droloxifene (ig), estradiol (E_2, sc), or 1% CMC (as a control, ig). The doses and treatment times of the different experiments are shown in the results section. At autopsy on d 9, the number of animals with implantation sites in each group was recorded. The Bliss method was used to calculate the ED_{95}, ED_{90}, and ED_{50} of the anti-implantation effect of droloxifene.

Assay of the serum levels of estrogen and progesterone The pregnant rats were treated orally with 2.5 mg/kg droloxifene or 1% CMC at 22:00 PM on d 4. Blood samples of 0.5 mL were obtained from the tail veins of pregnant rats at 10:00 AM on d 1, d 2, d 3, d 4, d 5 and d 6, and at 22:00 PM on d 4. The serum levels of estrogen and progesterone were measured by RIA according to the manufacturer's instructions.

Statistical analysis Differences in pregnancy rates between the groups were tested by using the χ^2 test. Serum levels of estrogen and progesterone are expressed as mean±SD and Student's *t*-test was used to calculate significance.

Results

Optimal administration time for the anti-implantation effect of droloxifene Pregnant rats were treated orally with droloxifene with doses ranging from 1.25 to 20.0 mg/kg at 10:00 AM on d 2. Within the treatment time, droloxifene had an anti-implantation effect in rats (ED_{95}=17.62 mg/kg and ED_{50}=5.34 mg/kg; Table 1). To determine the optimal administration time for the anti-implantation effect of droloxifene, pregnant rats were treated orally with droloxifene at either a high dose (14 mg/kg) or a low dose (2.5 mg/kg) at 10:00 AM on d 2, d 3, d 4, or d 5, or at 22:00 PM on d 4. Although the differences in the anti-implantation rates in different groups were not significant for the 14 mg/kg groups, the anti-implantation rates of rats treated with droloxifene at 22:00 PM on d 4 were the highest in the two dose groups (Table 2). These results suggest that droloxifene has anti-implantation effects in rats, and that the optimal administration time is at 22:00 PM on d 4.

Table 1. Anti-implantation effects of droloxifene in rats treated in at 10:00 AM on d 2. n=10. Mean±SD. $^bP<0.05$, $^cP<0.01$ *vs* control.

Droloxifene (mg/kg)	Pregnant rats	Rate of anti-implantation (%)	ED_{50} (mg/kg)	ED_{95} (mg/kg)
20	0^c	100		
10	3^c	70		
5	5^b	50	5.34	17.62
2.5	8	20		
1.25	10	0		
0	10	0		

ED_{95}, ED_{90}, and ED_{50} for the anti-implantation effect of droloxifene Pregnant rats were treated orally with droloxifene at various doses (10, 5.0, 2.5, 1.25, 0.62, 0.31, or 0.15 mg/kg) at 22:00 PM on d 4. The anti-implantation rates of the droloxifene groups (0.62–10 mg/kg) were higher than that observed in the control group ($P<0.01$; Table 3). There was a dose-dependent relationship between the anti-implantation rates and droloxifene doses from 0.15 mg/kg to 5.0 mg/kg. The values of ED_{95}, ED_{90} and ED_{50} were 3.70 mg/kg, 2.63

Table 2. Anti-implantation effects of droloxifene on rats treated at various times. [b]*P*<0.05, [c]*P*<0.01 *vs* control. [f]*P*<0.01 *vs* droloxifene (at 22:00 PM, on d 4).

Droloxifene (mg/kg)	*n*	Time of treatment	Pregnant rats	Anti-implantation rates (%)
14	12	10:00 AM, d 2	3[c]	75.0
14	12	10:00 AM, d 3	3[c]	75.0
14	12	10:00 AM, d 4	2[c]	83.3
14	12	22:00 PM, d 4	1[c]	91.7
14	12	10:00 AM, d 5	10	16.7
2.5	10	10:00 AM, d 2	10[f]	0
2.5	10	10:00 AM, d 3	8[b,f]	20
2.5	10	10:00 AM, d 4	4[b]	60
2.5	10	22:00 PM, d 4	1[b]	90
2.5	10	10:00 AM, d 5	10[f]	0
0	12	22:00 PM, d 4	12	0

Table 3. Anti-implantation effects of various doses of droloxifene in rats treated at 22:00 PM on d 4. *n*=10. [b]*P*<0.05, [c]*P*<0.01 *vs* control.

Droloxifene (mg/kg)	Number of pregnant rats	Rates of anti-implantation (%)	ED_{50} mg/kg	ED_{90} mg/kg	ED_{95} mg/kg
10	0[c]	100			
5	0[c]	100			
2.5	1[c]	90	0.79	2.63	3.70
1.25	4[c]	60			
0.625	6[b]	40			
0.312	8	20			
0.15	10	0			
0	10	0			

mg/kg and 0.79 mg/kg, respectively.

Antagonistic effect of external E_2 on the anti-implantation effect of droloxifene To investigate the antagonistic effect of external E_2 on the anti-implantation effect of droloxifene, the anti-implantation effect of external E_2 only was first evaluated. When rats were treated at 22:00 PM on d 4 with external E_2 at doses of 2.0 μg/kg or 8.0 μg/kg (sc), significant anti-implantation effects were observed (P<0.05), whereas at doses of 0.5 μg/kg or 1.0 μg/kg, there was no anti-implantation effect. For rats treated at 22:00 PM on d 4 with 2.5 mg/kg droloxifene alone or 2.5 mg/kg droloxifene combined with various doses of E_2, there was no difference in implantation rates, although E_2 at higher doses (2.0 or 8.0 μg/kg) reduced the anti-implantation rates (Table 4).

Table 4. Antagonistic effects of E_2 on the anti-implantation effect of droloxifene (2.5 mg/kg) in rats. Pregnant rats were treated with only E_2 (sc) or with a combination of droloxifene (ig) and E_2 (sc) at 22:00 PM on d 4. [b]*P*<0.05, [c]*P*<0.01 *vs* vehicle control group. [d]*P*>0.05 *vs* droloxifene (2.5 mg/kg) group.

Droloxifene (mg/kg)	E_2 (μg/kg)	Number of treated rats	Number of pregnant rats	Rate of anti-implantation (%)
0.0	0.5	8	8	0
0.0	1.0	8	7	12.5
0.0	2.0	7	4[b]	42.9
0.0	4.0	8	2[c]	75.0
0.0	8.0	7	1[c]	85.7
2.5	0.5	8	0[b,d]	100.0
2.5	1.0	8	1[c,d]	87.5
2.5	2.0	8	0[c,d]	100.0
2.5	4.0	10	4[c,d]	60.0
2.5	8.0	9	4[c,d]	55.6
2.5	0.0	9	1[c]	88.9
0.0	0.0	9	9	0

Effect of droloxifene on the serum level of estrogen during early pregnancy Pregnant rats were treated orally with 2.5 mg/kg droloxifene or 1% CMC at 22:00 PM on d 4. The rate of implantation was 100% and 0% in the control and droloxifene groups, respectively. In the control group, the serum level of estrogen remained at low levels from d 1 to d 3, began to rise on d 3, reached the maximum at 10:00 AM on d 4, then declined sharply, such that the levels on d 5 and d 6 were similar to those on d 3. The serum estrogen levels in the droloxifene group between d 1 and d 6 were not significantly different from those in the control group (Figure 1). These results indicate that there was a surge of estrogen in the pregnant rats at 10:00 AM on d 4, and that treatment with droloxifene at 22:00 AM on d 4 had no effect on the level of estrogen; however, a significant anti-implantation effect was induced. Therefore, the anti-implantation effect of droloxifene in rats appears not to be due to antagonism of a surge in the secretion of nidatory estrogen.

Effect of droloxifene on serum levels of progesterone during early pregnancy in rats Pregnant rats were treated orally with 2.5 mg/kg droloxifene or 1% CMC at 22:00 PM on d 4. The rates of implantation were 100% and 0% in the control and droloxifene groups, respectively. In the control

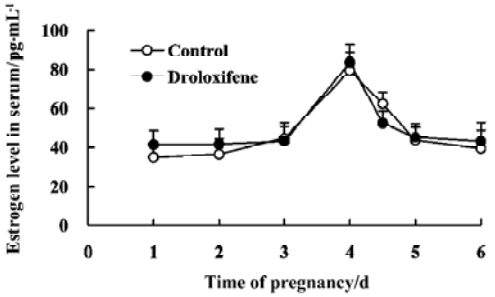

Figure 1. Nidatory estrogen surge and effect of droloxifene on serum levels of estrogen during early pregnancy in rats. *n*=4. Mean±SD.

groups, the serum levels of progesterone rose from 10:00 AM on d1 to 22:00 PM on d 4 and remained at high levels until d 6. In groups treated with droloxifene at 22:00 PM on d 4, the levels of progesterone were similar to that of controls (Figure 2). These results indicate that treatment with droloxifene at 22:00 PM on d 4 had no effect on the level of progesterone in early pregnancy.

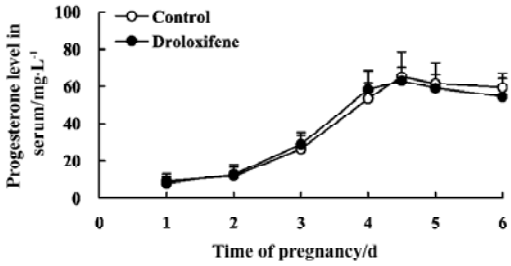

Figure 2. Effect of droloxifene on the serum levels of progesterone during early pregnancy in rats. *n*=4. Mean±SD.

Discussion

It is well established that an exact equilibrium of estrogen and progesterone is indispensable for implantation in rats[10]. A nidatory c surge that occurs on d 4 is essential for the sensitization of the uterus to induce decidual cell reaction, the most specific function of the progestational endometrium[11,12]. As a novel selective estrogen receptor modulator with considerable anti-estrogenic effects, droloxifene might disturb the hormonal effects and cause an anti-implantation effect. The present study found that droloxifene had anti-implantation effects in rats (Tables 1–3) and that 22:00 PM on d 4 was the optimal oral administration time. At this time there was a good dose-effect relationship between the anti-implantation rates and droloxifene doses from 0.31 mg/kg to 5.0 mg/kg. The ED_{95}, ED_{90} and ED_{50} of droloxifene were 3.70 mg/kg, 2.63 mg/kg, and 0.79 mg/kg, respectively.

We found that the serum levels of estrogen in pregnant rats reached a peak at 10:00 AM on d 4, which indicates that the nidatory estrogen surge before implantation occurs at approximately this time. However, the optimal oral administration time of droloxifene for anti-implantation effects was at 22:00 PM on d 4, 12 h later than the nidatory estrogen surge. Therefore, we propose that the anti-implantation effect of droloxifene is not caused by its interfering with the nidatory estrogen surge via its anti-estrogenic effect. The effects of droloxifene are different from those of tamoxifen, a triphenylethyl compound, which antagonizes the nidatory estrogen surge[13,14].

In order to further clarify the relationship between the anti-implantation effect and the anti-estrogenic activity of droloxifene, the antagonistic effect of external E_2 on the anti-implantation effect of droloxifene was observed in rats. At first, the anti-implantation effect of external estrogen (0.5–8.0 μg/kg, sc) was examined after administration at 22:00 PM on d 4. We found that E_2 at doses of 0.5–1.0 μg/kg produced no anti-implantation effect (Table 4), and had no antagonistic effect on the anti-implantation effect of droloxifene ($P>0.05$; Table 4). When droloxifene was combined with E_2 at higher doses (4.0 or 8.0 μg/kg), the anti-implantation effect of droloxifene was reduced, but the difference was not significant according to the χ^2 test. Therefore, it seems that the anti-implantation effect of droloxifene may be not related to its anti-estrogenic activity, especially at physiological doses.

Because an exact equilibrium of estrogen and progesterone is essential for implantation, and any disturbance in the effects of these hormones can cause infertility, we investigated whether droloxifene inhibited implantation by affecting the serum levels of estrogen and progesterone. We found that droloxifene had no effect on the serum estrogen and progesterone levels in early pregnancy when treated at 22:00 PM on d 4. However, in our previous study, we found that apoptosis of luteal cells and decreases in serum progesterone levels were induced by treatment with droloxifene at a dose of 20 mg/kg on d 2 in pregnant rats[8]. The differences between the two experiments can be explained by the different doses and administration times. In addition, the period of observation was too short in the present study.

In conclusion, droloxifene can inhibit implantation in rats and the optimal oral administration time is 22:00 PM on d 4. ED_{90} was 2.63 mg/kg. The anti-implantation effect of droloxifene is not related to its antiestrogenic activity, or an antagonistic effect on the nidatory estrogen surge. The direct inhibition of endometrial receptivity to blastocyst signal (s) and the apoptosis of luteal cells might be involved in the anti-implantation mechanism of droloxifene. This characteristic may make droloxifene useful in developing new

contraceptives.

Acknowledgment

We are grateful to Prof Zhi-ping GU for valuable discussions throughout this study and helpful comments on the manuscript.

References

1 Eppenberger U, Wosikowski K, Kung W. Pharmacologic and biologic properties of droloxifene, a new antiestrogen. Am J Clin Oncol 1991; 14: S5–14.
2 Hasmann M, Rattel B, Loser R. Preclinical data for droloxifene. Cancer Lett 1994; 84: 101–6.
3 Ke HZ, Chen HK, Qi H, Pirie CM, Simmons HA, Ma YF, *et al*. Effects of droloxifene on prevention of cancellous bone loss and bone turnover in the axial skeleton of aged, ovariectomized rats. Bone 1995; 17: 491–6.
4 Grasser WA, Pan LC, Thompson DD, Paralkar VM. Common mechanism for the estrogen agonist and antagonist activities of droloxifene. J Cell Biochem 1997; 65: 159–71.
5 Palumbo A, Yeh J. Apoptosis as a basic mechanism in the ovarian cycle: follicular atresia and luteal regression. J Soc Gynecol Investig 1995; 2: 565-73.
6 Leng Y, Yang B, Cao L, Gu ZP. Effects of anordrin, droloxifene, nomegestrol, and mifepristone on cultured rat luteal cell apoptosis. Acta Pharmacol Sin 1999; 20: 400–4.
7 Leng Y, Gu ZP, Cao L. Apoptosis induced by droloxifene and c-myc, bax and bcl-2 mRNA expression in cultured luteal cells of rats. Eur J Pharmacol 2000; 409: 123–31.
8 Leng Y, Gu ZP, Cao L. Apoptosis induced by droloxifene and C-myc, Bax, Bcl-2 protein expression in corpus luteum of pregnant rats. Acta Pharmacol Sin 2001; 22: 327–34.
9 Leng Y, Feng Y, Cao L, Gu ZP. Effects of droloxifene on apoptosis and Bax, Bcl-2 protein expression of luteal cells in pseudopregnant rats. Acta Pharmacol Sin 2001; 22: 155–62.
10 Kodaman PH, Taylor HS. Hormonal regulation of implantation. Obstet Gynecol Clin North Am 2004; 31:745–66.
11 Finn CA. Oestrogen and decidual cell reaction of implantation in mice. J Endocrinol 1965; 32: 223–9.
12 Liu Y, Jia XC. Changes of oestrogen and its receptor levels during implantation period in pregnant rats. Acta Physiol Sin 1981; 33: 44–50.
13 Watson J, Anderson FB, Alam M, O'Grady JE, Heald PJ. Plasma hormones and pituitary luteinizing hormone in the rat during the early stages of pregnancy and after post-coital treatment with tamoxifen (ICI 46,474). J Endocrinol 1975; 65: 7–17.
14 Bloxham PA, Pugh DM, Sharma SC. Abolition of the pre-implantation surge of plasma oestrogens in mice with tamoxifen. Irc Med Sci Reprod Obstet Gynecol 1977; 5: 432.

Acta Pharmacologica Sinica 2005 Oct; 26 (10): 1248–1252

Blackwell Publishing

Full-length article

Anticancer activity of sodium caffeate and its mechanism[1]

Feng XU[2,3,4], Sheng-hua ZHANG[3], Rong-guang SHAO[3], Yong-su ZHEN[3]

[2]Department of Pharmacology, Zhujiang Hospital, Southern Medical University, Guangzhou 510280; [3]Department of Oncology, Institute of Medicinal Biotechnology, Chinese Academy of Medical Sciences and Peking Union Medical College, Beijing 100050, China

Key words

caffeic acid; anticancer activity; cell division; cell apoptosis; cell cycle; phytogenic antineoplastic agent; flow cytometry; Western blotting

[1]Project supported by the National Key Basic Research Development Program of China (No 2002CB513108).
[4]Correspondence to Dr Feng XU.
Phn 86-20-6164-3555.
Fax 86-20-6164-3020.
E-mail andrewfxu@sina.com.cn

Received 2005-03-16
Accepted 2005-06-24

doi: 10.1111/j.1745-7254.2005.00196.x

Abstract

Aim: To study the anticancer activity of sodium caffeate (SC). **Methods:** A nucleoside transport assay was used to analyze the inhibitory effects of SC on nucleoside rescue. The MTT assay was used to measure cell proliferation. Flow cytometry was used to measure the apoptosis of BEC-7402 induced by SC and the cell cycle distribution change . Western blotting analysis was employed to investigate Bcl-2, caspase and Bax expression. Intracellular Ca^{2+} and mitochondrial membrane potential were determined by flow cytometry. *In vivo* anti-tumor activity was measured using a tumor transplantation model in mice. **Results:** SC inhibited the nucleoside transport of BEL-7402 cells with an IC_{50} of 1.02 mg/mL. SC inhibited tumor cell proliferation with an IC_{50} between 100 μg/mL and 200 μg/mL. SC induced BEL-7402 cell apoptosis in a time- and dose-dependent manner, which was induced by arresting cells in S phase. The *in vivo* study showed that tumor growth was inhibited in a dose-dependent manner. Activated caspase-3 and Bax expression were up-regulated after treatment with SC, while Bcl-2 expression was down-regulated. Intracellular Ca^{2+} was increased while mitochondrial membrane potential was decreased by SC. **Conclusion:** SC is a new anticancer agent with promising potential.

Introduction

There have been an increasing number of anticancer phytochemicals identified in our daily diet. Some of the most promising and extensively investigated are those present in the cruciferous family of vegetables, alliums and tea. Phytochemicals should be considered as an inexpensive and readily applicable, acceptable and accessible approach to cancer control and management for general populations. This is particularly important considering the sluggish progress made in cancer treatment. It is still an urgent task to seek new anticancer drugs from natural resources in oncology pharmacology.

Cinnamic acid is one of the phytochemicals with potential chemopreventive effects in preventing carcinogenesis[1,2]. Cinnamamide, a natural compound containing the cinnamic acid structure, is a new antitumor agent that acts on matrix metalloproteinase, which has been demonstrated by previous work in our laboratory[3]. Caffeic acid (3,4-dihydroxycinnamic acid) is a polyphenol that is found in coffee, fruits, vegetables, grains and many others plants[4–7]. It is also particularly abundant in propolis beehives with 20%–25% content and has various pharmacological activities, such as antioxidant and antiviral effects[8]. The anticancer effect of caffeic acid, however, has not been reported up to now. Because caffeic acid is prone to air oxidation and is only slightly soluble in water, its stable sodium salt (sodium caffeate, SC) was prepared in our laboratory and used in the present study. Here we report the antitumor effect of SC both *in vitro* and *in vivo*.

Materials and methods

Reagents RPMI-1640 medium was purchased from Gibco BRL (Gaithersburg, Maryland, USA). Fetal calf serum (FCS) was purchased from Hyclone (Logan, Utah, USA). MTT, nonidet P-40(NP-40), phenylmethylsulfonyl fluoride (PMSF), aprotinin, ponceau S, Triton X-100, propidium

iodide, Fluo-3, rhodamine 123, RNase A, proteinase K, Hoechst 33342 and other reagents were purchased from Sigma (StLouis , Missouri, USA). [H^3]TdR was purchased from Chinese Atomic Energy Institutes (Beijing, China). Annexin V-FITC/PI apoptosis detection kit was purchased from BioVision company (Hannover, Germany). Mouse anti-Bcl-2 monoclonal antibody, mouse anti-caspase-3 monoclonal antibody and rabbit anti-bax polyclonal antibody were products of Calbiochem (San Diego, California, USA). Horseradish peroxidase-conjugated secondary anti-mouse antibody and anti-rabbit antibody were products of Santa Cruz Biotechnology, Inc(Santa Cruz, California,USA). Enhanced luminol reagent and oxidizing reagent were products of NEN Life Science Products (Boston, Massachusetts, USA). Dr Dan-qing SONG in Department of Chemistry, Institute of Medicinal Biotechnology (Beijing, China) synthesized the SC.

Cells and carcinoma Human oral cavity epidermis squamocellular carcinoma cell line (KB), human hepatocarcinoma cell line (BEL-7402) and human acute promyelocytic cell line (HL-60) were purchased from the Shanghai Institute of Cell Biology, Chinese Academy of Sciences (Shanghai, China), and were grown routinely in RPMI-1640 supplemented with 10% heat-inactivated FCS. The medium was supplemented with 100 U/mL penicillin, 100 μg/mL streptomycin and 2 mmol/L glutamine, and the cells were incubated in a humidified atmosphere, with 5% CO_2 in air at 37 °C.

Mouse-transplanted hepatocarcinoma H22 and mouse colorectal cancer C26 cell lines were maintained by serial transplantation into mice in our laboratory. Kunming species mice were supplied by the Experimental Animal Center, Chinese Academy of Medical Sciences (Beijing, China).

Nucleoside transport assay[9] Briefly, cells in the logarithmic growth phase were harvested. The cell suspension was prepared with RPMI-1640 medium at 5×10^6 in 0.9 mL in each test tube. Different concentrations of SC in 0.1 mL RPMI-1640 were added and the tube was kept in a water bath at 37 °C for 5 min. Phosphate-buffered solution (PBS) was used as a control. RPMI-1640 0.1 mL (containing 3.7×10^4 Bq of [^{3}H]TdR in medium free of serum) was added for 30 s and 5 mL ice-cold normal saline was added to terminate the reaction. The reaction was filtrated through a GF/B glass fiber filter (Whatman International, Maidstone, UK) under vacuum. The filters were washed with 0.2 mL of 1 mol/L NaOH and 0.5 mL ethanol, dried under vacuum and placed in scintillation vials containing 2 mL of dimethylbenzene with 0.4% PPO/0.01% POPOP. The cpm (counts per minute) were measured using an LS-9800 scintillometer (Beckman Instruments, Fullerton, California, USA).

MTT assay Briefly, cells in the logarithmic growth phase were harvested and seeded in 96-well plates (Costar, Cambridge, Massachusetts, USA) overnight. The test compound was added and cells were further incubated for 72 h. The viability of cells was determined using the MTT assay according to the method described by Carmichael *et al* [10].

Long-term clonogenicity Cell survival was tested using a clonogenic assay, as described by Valduga *et al*[11]. Briefly, cells in the logarithmic growth phase were harvested and 250 cells/mL of a single-cell suspension was prepared with medium. The cell suspension 200 μL was seeded in 96-well plates (50 cells/well) overnight, and the test compound was added. After 1 week of incubation at 37 °C in air with 5% CO_2, colonies were counted.

Flow cytometry After appropriate treatment, cells were harvested by centrifugation and washed with PBS. The cells were fixed with ice-cold 75% ethanol for 18 h at 4 °C. The cell apoptosis was measured according to the protocol of Annexin V-FITC/PI apoptosis detection kit. Cell cycles change was measured by treatment of the fixed cell suspensions which were washed with PBS and stained with 80 μL of 50 μg/mL propidium iodide and 50 μg/mL RNase A for 30 min in the dark. Samples were run through an EPICS XL flow cytometer (Coulter, Miami, Florida, USA). Results are presented as the number of cells versus the amount of DNA as indicated by the intensity of fluorescence[12]. The results on flow cytometry represented the average of 3 individual experiments.

Western blotting assay The cells were lysed in lysis buffer at 4 °C with sonication. The lysates were centrifuged at 15 000×*g* for 15 min and the concentration of protein in each lysate was determined using Coomassie Brilliant Blue G-250. Loading buffer was added to each lysate, which was subsequently boiled for 3 min and then electrophoresed by sodium dodecyl sulfate-polyacrylamide gel electrophoresis. Proteins were transferred to nitrocellulose and incubated with anti-Bcl-2, anti-caspase-3 or anti-Bax antibodies and then with peroxidase-conjugated secondary antibodies. Detection was carried out using an enhanced chemiluminescence agent[13,14]. The results on Western blot analysis represented the average of 3 individual experiments.

Intracellular Ca^{2+} and mitochondrial membrane potential ($\Delta\Psi$) Following appropriate treatment, cells were collected by centrifugation and incubated at 37 °C with Fluo-3 for 40 min and then with rhodamine 123 for 20 min. Cells were then washed 3 times with cold PBS, and the intracellular Ca^{2+} concentration and $\Delta\psi$ were measured by flow cytometry[15–17].

Tumor transplantation and drug administration H22 as-

cites were diluted to 7.5×10^5/mL suspension and 0.2 mL of the cell suspension was inoculated subcutaneously into the right axilla of each mouse of the Kunming species (weighing 20±2 g). A C26 tumor-cell suspension was prepared by gently suspending tumor tissue in normal saline (1 g of tumor tissue with 3 mL of normal saline) in a cold water bath and inoculated as above. After 24 h of tumor cell inoculation, SC was administered intraperitoneally for 10 d. Normal saline was used as a control. On the d 11 the mice were killed, and body weight and tumor tissue were weighed.

Statistical analysis The data are the mean values of at least 3 experiments and are expressed as mean±SD. The Student's *t*-test was used to compare data. $P<0.05$ was considered to be statistically significant.

Results

Inhibition of nucleoside transport by SC SC inhibited nucleoside transport in the hepatocarcinoma BEL-7402 cell line with an IC_{50} of 1.02 mg/mL. However, the inhibiting effect on nucleoside transport was not very strong.

Inhibition of proliferation and induction of apoptosis by SC SC inhibited tumor-cell proliferation with an IC_{50} of between 100 μg/mL and 200 μg/mL (Table 1). Inhibition of BEL-7402 cells proliferaction by SC was dose-dependent and time-dependent (Figure 1).

Table 1. Inhibition of proliferation by sodium caffeate treatment for 72 h in different cell lines. *n*=3. Mean±SD.

Cell line	IC_{50} /μg·mL^{-1}
HL-60	135±19
KB	157±22
BEL-7402	192±28

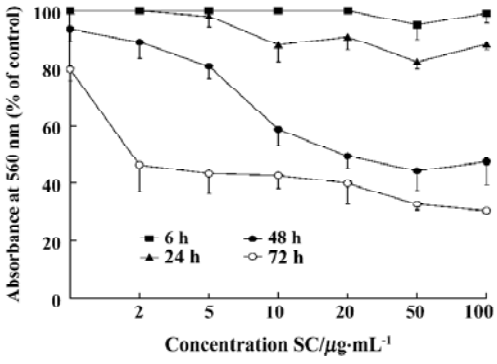

Figure 1. Inhibition of proliferation by SC in BEL-7402 cells. n=3. Mean±SD.

Flow cytometry showed that SC induced BEL-7402 cell apoptosis in a time- and dose-dependent manner (Table 2). After 24 h of treatment with SC, the cell cycle changed. The percentages of cells in S phase increased markedly while percentages of cells in G_2/M phase decreased, which suggested the apoptosis was induced by arresting the cells in S phase (Table 3).

Table 2. SC-induced apoptosis (%) in BEL-7402 cells. *n*=3. Mean±SD.

SC /μg·mL^{-1}	24 h	48 h	72 h
0	2.3±1.2	2.4±1.1	7.8±5.2
25	13.2±4.5	15.0±2.8	42.7±15.5
100	27.4±3.9	44.4±10.1	55.9±16.3
400	41.1±10.1	62.4±12.5	77.7±18.5

Table 3. Effect of sodium caffeate on cell cycle of BEL-7402 cells. *n*=3. Mean±SD.

SC /μg·mL^{-1}	G_1	S	G_2/M
0	55.0±7.2	22.3±2.3	22.7±2.3
10	64.4±10.0	26.7±5.6	8.9±2.2
25	65.1±11.1	28.8±6.9	6.1±1.7
100	65.7±8.9	34.3±7.5	0.0±0.0
400	66.5±7.1	33.5±5.6	0.0±0.0

Inhibition of clonogenicity by SC SC inhibited cell clonogenicity with an IC_{50} between 0.5 μg/mL and 3 μg/mL (Table 4). SC was capable of inhibiting the different cell lines to different extents.

Table 4. Clonogenicity inhibition by sodium caffeate. *n*=3. Mean±SD.

Cell line	IC_{50} /μg·mL^{-1}
KB	0.45±0.04
BEL-7402	2.89±0.07

Effect of SC on transplanted tumor growth H22 and C26 were inoculated subcutaneously into mice. After SC administration for 10 d, tumor growth was inhibited in a dose-dependent manner. No significant difference in body weight was found between the groups, suggesting that SC does not show toxicity *in vivo* (Table 5 and 6).

Table 5. Anti-tumor activity of sodium caffeate treatment for 10 d on Kunming mice with transplanted H22 cells . $^cP<0.01$ *vs* control. n=10. Mean±SD. No mouse died during the experimental period.

Group	Dose /g· kg^{-1}	Body weight change/g	Tumor weight/g	Inhibition/%
Control	0.00	+4.9	4.13±0.19	0
SC	0.15	+4.3	3.00±0.69	27.4^c
SC	0.50	+5.1	2.90±0.58	29.9^c
SC	1.00	+4.0	2.40±0.64	41.9^c
SC	2.00	+5.5	1.19±0.59	71.2^c

Table 6. Anti-tumor activity of sodium caffeate treatment for 10 d on Kunming mice with on transplanted C26 cells. $^cP<0.01$ *vs* control. n=10. Mean±SD. No mouse died during the experimental period.

Group	Dose /g· kg^{-1}	Body weight change/g	Tumor weight/g	Inhibition/%
Control		+2.5	2.66±0.54	
SC	0.5	+3.8	1.85±0.65	30.5^c
SC	1.0	+5.8	1.22±0.36	54.1^c
SC	2.0	+5.6	1.13±0.42	57.5^c

Effect of SC on expression of apoptosis-associated proteins The bands were scanned with light density. Activated caspase-3 and Bax expression were up-regulated after SC treatment, while Bcl-2 expression was down-regulated (Figure 2).

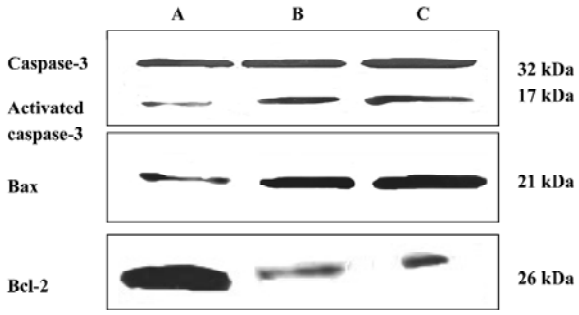

Figure 2. Caspase-3, Bax and Bcl-2 expression in BEL-7402 cells treated with sodium caffeate (SC). (A) Control; (B) 10 μg/mL SC; and (C) 25 μg/mL SC.

Effect of SC on intracellular Ca^{2+} and mitochondrial membrane potential After treatment with 10 μg/mL SC for 24 h, intracellular Ca^{2+} was increased 1.78-fold compared to the control. Δψ was decreased by 22.7% compared to the control. The results showed that SC increased intracellular Ca^{2+} levels and decreased Δψ.

Discussion

Most anti-metabolites in tumor chemotherapy inhibit nucleoside *de novo* synthesis but can not block nucleoside rescue in cancer cells. It is therefore important to control nucleoside rescue by inhibiting nucleoside transport. Previous work found that dipyridamole enhanced the anticancer effect of acivicin by inhibiting nucleoside transport[9].The present study demonstrated that SC was a new member of the nucleoside transport inhibitor family.

Caffeic acid is an active phytophenol that has been found to inhibit rat glutathione-*S*-transferase isoenzymes both *in vitro* and *in vivo*[18]. A large number of population-based studies have found that consumption of wholegrains, vegetables and fruits abundant in caffeic acid reduces the risk of cancer[19–21]. The aqueous extract of *Salvia miltiorrhiza*, a traditional Chinese herb containing caffeic acid was found to strongly inhibit the proliferation of human hepatoma $HepG_2$ cells. It was also observed that its crude extract caused apoptotic cell death[22]. Salvianolic acid A, a caffeic acid trimer, showed synergistic effects in combination with other antitumor agents. Further, salvianolic acid A could increase the antitumor effects of 5-flurouracil without increasing its toxicity in an animal study [2]. However, no report has been published on the anticancer effects of caffeic acid either *in vitro* or *in vivo*. We are the first to report that the sodium salt of caffeic acid inhibits proliferation of cancer cells, with IC_{50} between 100 μg/mL and 200 μg/mL. Further, we showed that it induced the apoptotic cell death and changed cell-cycle distribution by arresting cells in S phase. The *in vivo* study showed that SC inhibited the tumor growth of transplanted H22 and C26 cells in mice with an inhibition rate of 42%–54% when treated with 1 g/kg SC for 10 d.

Preliminary studies on the anticancer mechanism of SC demonstrated that after treatment with SC, Bcl-2 expression was down-regulated and mitochondrial membrane permeability was changed. The mitochondrial permeability transition pore was opened and the mitochondrial membrane potential was broken up. The mitochondrion was swelled and in α state of hyperosmosis before apoptosis was induced. Meanwhile cytochrome c was released, caspase-3 was activated in the presence of Apaf-1 and caspase-9, and apoptosis was induced[23–27].

References

1 Liu L, Hudgins WR, Shack S, Yin MQ, Samid D. Cinnamic acid:

a natural product with potential use in cancer intervention. Int J Cancer 1995; 62: 245–50.
2 Jiang RW, Lau KM, Hon PM, Mak TC, Woo KS, Fung KP. Chemistry and biological activities of caffeic acid derivatives from *Salvia miltiorrhiza*. Curr Med Chem 2005; 12: 237–46.
3 Jiang XF, Zhen YS. Cinnamamide, an antitumor agent with low cytotoxicity acting on matrix metalloproteina Anticancer Drugs 2000; 11: 49–54.
4 Radtke J, Linseisen J, Wolfram G. Phenolic acid intake of adults in a Bavarian subgroup of the national food consumption survey. Ernahrungswiss 1998; 37: 190–7.
5 Eberhardt MV, Lee CY, Liu RH. Antioxidant activity of fresh apples. Nature 2000; 405: 903–4.
6 Mattila P, Kumpulainen J. Determination of free and total phenolic acids in plant-derived foods by HPLC with diode-array detection. J Agric Food Chem 2002; 50: 3660–7.
7 Bryngelsson S, Dimberg LH, Kamal-Eldin A. Effects of commercial processing on levels of antioxidants in oats (*Avena sativa L*). J Agric Food Chem 2002; 50: 1890–6.
8 Greenaway W, Scaysbrook T, Whatley FR. The analysis of bud exudate of *Populus x euramericana* and of propolis by gas chromatography-mass spectrometry. Proc R Scot Lond 1987; B232: 249–72.
9 Zhen YS, Liu MS, Weber G. Effects of acivicin and dipyridamole on hepatoma 3924A cells. Cancer Res 1983; 43: 1616–9.
10 Carmichael J, Degraff WG, Gazdar AF, Minna JD, Mitchell JB. Evaluation of a tetrazolium-based semiautomated colorimetric assay: assessment of chemosensitivity testing. Cancer Res 1987; 47: 936–42.
11 Valduga G, Reddi E, Garbisa S, Jori G. Photosensitization of cells with different metastatic potentials by liposome-delivered Zn-(II)-pathalocyanine. Int J Cancer 1998; 75: 412–7.
12 Chiao C, Carothers AM, Grunbergers D, Solomon G, Preston GA, Barrett JC. Apoptosis and altered redox state induced by caffeic acid phenethyl ester (CAPE) in transformed rat fibroblast cells. Cancer Res 1995; 55: 3576–83.
13 Hu ZB, Minden MD, McCulloch EA. Post-transcriptional regulation of bcl-2 in acute myleoblastic leukemia: significance for response to chemotherapy. Leukemia 1996; 10: 410–6.
14 Xu F, Zhen YS. (-)-Epigallocatechin-3-gallate enhances antitumor effects of cytosine arabinoside on HL-60 cells. Acta Pharmacol Sin 2003; 24: 163–8.
15 Kluck RM, McDougall CA, Harmon BV, Halliday JW. Calcium chelators induce apoptosis: evidence that raised intracellular ionized calcium is not essential for apoptosis. Biochim Biophys Acta 1994; 1223: 247–54.
16 Tatton WG, Olanow CW. Apoptosis in neurodegenerative diseases: the role of mitochondria. Biochim Biophys Acta 1999; 1410: 195–213.
17 Ichas F, Mazat JP. From calcium signaling to cell death: two conformations for the mitochondrial permeability transition pore. Switching from low to high conductance state. Biochim Biophys Acta 1998; 1366: 33–50.
18 Ploemen JH, van Ommen B, de Haan A, Schefferlie JG, van Bladeren PJ. *In vitro* and *in vivo* reversible and irreversible inhibition of rat glutathione-*S*-transferase isoenzymes by caffeic acid and its 2-*S*-glutathionyl conjugate. Food Chem Toxicol 1993; 31: 475–82.
19 Shahrzad S, Bitsch I. Determination of some pharmacologically active phenolic acids in juices by high-performance liquid chromatography. J Chromatogr A 1996; 741: 223–31.
20 Slavin J, Jacobs D, Marquart L. Whole-grain consumption and chronic disease: protective mechanisms. Nutr Cancer 1997; 27: 14–21.
21 Surh YJ. Transcription factors in the cellular signaling network as prime targets of chemopreventive phytochemicals. Cancer Treat Res 2004; 36: 275–86.
22 Liu J, Shen HM, Ong CN. *Salvia miltiorrhiza* inhibits cell growth and induces apoptosis in human hepatoma $HepG_2$ cells. Cancer Lett 2000; 153: 85–93.
23 Yang J, Liu X, Bhalla K, Kim CN, Ibrado AM, Cai J, *et al*. Prevention of apoptosis by Bcl-2: release of cytochrome c from mitochondria blocked. Science 1997; 275: 1129–32.
24 Adams JM, Cory S. The Bcl-2 protein family: arbiters of cell survival. Science 1998; 281: 1322–6.
25 Thornberry NA, Lazebnik Y. Caspase: enemies within. Science 1998; 281: 1312–6.
26 Green DR, Reed JC. Mitochondria and apoptosis. Science 1998; 281: 1309–12.
27 Wallace DC. Mitochondrial disease in man and mouse. Science 1999; 283: 1482–8.

Acta Pharmacologica Sinica 2005 Oct; 26 (10): 1253–1258

Full-length article

Expression of proline-rich Akt-substrate PRAS40 in cell survival pathway and carcinogenesis[1]

Bei HUANG[2,4], Gavin PORTER[3]

[2]Department of Biological Science, Anhui University School of Life Science, Hefei, Anhui 230039, China; [3]Department of Pharmacology, Emory University School of Medicine, Atlanta, GA 30032, USA

Key words

PRAS40; PI3K-Akt pathway; kinase inhibitors; 14-3-3 protein;

[1]Project supported in part by Anhui Key Laboratory of Eco-engineering and Biotechnique Fund and National Institutes of Health Grants GM60033-03.
[4]Correspondence to Prof Bei HUANG.
Phn 86-551-510-7354.
Fax 86-551-510-7341.
E-mail beihuang@163.com

Received 2005-04-18
Accepted 2005-06-10

doi: 10.1111/j.1745-7254.2005.00184.x

Abstract

Aim: To study the expression of proline-rich Akt-substrate PRAS40 in the cell survival pathway and tumor progression. **Methods:** The effects of three key kinase inhibitors on PRAS40 activity in the cell survival pathway, serum withdrawal, H_2O_2 and overexpression of Akt were tested. The expression of PRAS40, Akt, Raf and 14-3-3 in normal cells and cancer cell lines was determined by Western blot. **Results:** The PI3K inhibitors worthmannin and Ly294002, but not rapamycin, completely inhibited the phosphorylation of Akt and PRAS40. The phosphorylation level of Akt decreased after serum withdrawal and treatment with the MEK inhibitor Uo126, but increased after treatment with H_2O_2 at low concentration, whereas none of these treatments changed PRAS40 activity. 14-3-3 is a PRAS40 binding protein, and the expression of 14-3-3, like that of PRAS40, was higher in HeLa cells than in HEK293 cells; PRAS40 had a stronger phosphorylation activity in A549 and HeLa cancer cells than in HEK293 normal cells. In the breast cancer model (MCF10A/MCF7) and lung cancer model (BEAS/H1198/H1170) we also found the same result: PRAS40 was constitutively active in H1198/H1170 and MCF7 premalignant and malignant cancer cells, but weakly expressed in MCF10A and BEAS normal cell. We also discussed PRAS40 activity in other NSCLC cell lines. **Conclusion:** The PI3K-Akt survival pathway is the main pathway that PRAS40 is involved in; PRAS40 is a substrate for Akt, but can also be activated by an Akt-independent mechanisms. PRAS40 activation is an early event during breast and lung carcinogenesis.

Introduction

Chemoprevention is a logical and obvious strategy to help alleviate the effects of cancer[1,2]. Much effort has been focused on the discovery and development of new chemopreventive agents, especially agents targeted at mechanisms known to be involved in the process of carcinogenesis[3,4].

The PI3K-Akt signaling pathway regulates many normal cellular processes including cell proliferation, survival, growth and motility, which are critical for tumorigenesis. The role of the PI3K-Akt signaling pathway in oncogenesis has been extensively investigated and altered expression or mutation of many components of this pathway have been implicated in human cancer[5]. Akt functions as a major downstream target of phosphatilylinositol-3-kinase (PI3K), carrying out functions including stimulation of glucose uptake and cell growth as well as inhibition of apoptosis[6,7].

Kovacina *et al* used a combination of the 14-3-3 protein and anti-pAkt substrate antibodies to screen and isolate a substrate of Akt, the major 14-3-3 binding protein observed in cells after insulin treatment (a 40 kDa molecule)[8]. This protein contains a consensus Akt phosphorylation site (Thr-246) but not other recognizable motif. It is highly proline-rich, with 15% of its amino acids being proline (versus 5% for a typical protein), and these proline-rich regions are potential SH3 and/or WW domain binding partners. The protein has therefore been named PRAS40, which stands for the "proline-rich Akt substrate of 40 kDa". Activation of induc-

ible Akt alone was sufficient to stimulate PRAS40 phosphorylation, and phosphorylation of this protein was reduced in cells lacking Akt1 and Akt2. Thus PRAS40 is a novel substrate of Akt, the phosphorylation of which leads to binding of this protein to 14-3-3[8]. Saito *et al* demonstrated that the expression of PRAS40, PRAS40/Akt and PRAS40/14-3-3 increased in Nerve Growth Factor (NGF) treated mice but decreased with inhibition of PI3K and the NGF receptor after transient focal cerebral ischemia (tFCI)[9].

However, the critical role of PRAS40 in the biological processes of cell proliferation and carcinogenesis remains unknown. The aim of our study was to examine the expression of PRAS40 in the cell survival signaling pathway, tumor progression and its relationship with Akt and 14-3-3. Information from this study will be helpful for further functional studies of PRAS40.

Materials and methods

Plasmids and expression The constitutively active Akt plasmid HA-Akt-ΔpH and kinase mutation Akt plasmid HA-Akt-Km were the gift of Prof Dr Haian FU (Emory university, USA). After transfection into human embryonic kidney cell HEK293, the supernatant was boiled for 5 min in sodium dodecylsulfate (SDS) sample buffer and resolved using SDS-polyacrylamide gel electrophoresis (SDS-PAGE, 12.5%), The proteins were transferred to polyvinylidene difluoride (PVDF) membranes (BIO-RAD, CA, USA). The primary antibodies were 1:2000 dilution of mouse monoclonal antibody against HA-Prob, Western blots were performed with horseradish peroxidase-conjugate anti-mouse IgG. Cross-reacting materials were visualized using ECL Detection Reagents (Amersham Biosciences, UK).

Source of antibody Rabbit polyclonal antibody against phosphorylated PRAS40(T246), and mouse monoclonal antibody against PRAS40 were purchased from BioSource International (Camarillo, CA, USA); Rabbit polyclonal antibodies against phosphorylated Akt (S473), Akt, phosphorylated-Raf (S338) and Raf were purchased from Cell Signaling Technology (Beverly, MA, USA); Rabbit polyclonal antibody against 14-3-3 (Pan-14-3-3), mouse monoclonal antibody against tubulin and HA-Prob, goat anti-mouse IgG-HRP and goat anti-rabbit IgG-HRP were purchased from Santa Gruz Biotechnology (CA, USA).

Reagents Ly294002/worthmannin (PI3K inhibitor) were purchased from Cell Signaling Technology; rapamycin (mTOR inhibitor) was purchased from Calbiochemistry (USA); hydrogen peroxide and U0126 (MEK inhibitor) were obtained from Sigma-Aldrich (St Louis, MO, USA).

Cell culture and DNA transfection HEK293, A549, HeLa and other cancer cells were provided by the Winship Cancer Institute (Atlanta, GA, USA) and maintained in Dulbecco's modified Eagle's medium (DMEM) or RPMI1640 (GIBCO Invitrogen, CA, USA) with 10% heat inactivated fetal bovine serum (FBS) and 5% CO_2 at 37 ^oC. The confluent cells were separated and trypsinized with 0.05% trypsin-ethylenediamine tetraacetic acid (EDTA) to produce single cells. They were then seeded at 1×10^5 per cm^2 and allowed to form subcultures. Cells were transfected with plasmids using the FuGENE6 reagent (Roche Applied Science, USA) according to the manufacturer's instructions.

Western blot After the cells were transfected, harvested and lysed by in 1% NP-40 lysis buffer [0.15 mol/L NaCl, 0.01 mol/L N-2-hydroxyethylpiperazine-N'-2-ethanesulfonic acid (HEPES), 1% NP-40, 5 mmol/L sodium pyrophosphate, 5 mmol/L sodium fluoride, 2 mmol/L sodium orthovanadate, 10 mg/L aprotinin, 10 mg/L leupetin, 1 mmol/L phenylmethlsulfonyl fluoride (PMSF)] at 4 ^oC for 20 min, cell extracts were clarified by centrifugation, prepared in SDS sample buffer, boiled for 5 min, and resolved using SDS-PAGE (12.5%) for Western blot. The enzyme-linked immunoblotting procedures were performed essentially as described previously[10]. Corresponding secondary antibodies were used against each primary antibody: horseradish peroxidase-conjugated goat anti-mouse IgG was used for monoclonal antibodies and horseradish peroxidase-conjugated goat anti-rabbit IgG was used for polyclonal antibodies. Cross-reacting materials were visualized using ECL detection reagents.

Saito *et al* suggested that PRAS40 might play a critical role in the neuronal cell survival pathways mediated by NGF after cerebral ischemia[9]. In order to test which cell survival signal cascade PRAS40 is involved in, we used three key kinase inhibitors (Worthmannin/Ly294002, Uo126, rapamycin) and cell death or apoptosis induction factors (serum withdrawal, H_2O_2) to treat normal cell line HEK293 and cancer cell line A549 and HeLa. The expression of PRAS40, Akt, Raf and 14-3-3 were analyzed by Western blot.

Results

PRAS40 was mainly involved in the PI3K-Akt survival pathway After treatment with the PI3K inhibitor Worthmannin (2 μmol/L) or Ly294002 (25 μmol/L) in HEK293 for 2 h, Worthmannin and Ly294002 almost completely blocked phospho-PRAS40 and phospho-Akt activity, compared with total expression of PRAS40 and Akt. However, inhibition of Akt phosphorylation was also induced by serum withdrawal. Overexpression of constitutively active Akt (Akt-ΔpH) promoted the expression of phopho-PRAS40 in HEK293, compared with negative control Kinase mutation Akt (Akt-Km)

(Figure 1). Therefore, the main pathway that PRAS40 is involved in is the PI3K-Akt pathway, and Akt is the upstream kinase of PRAS40 .

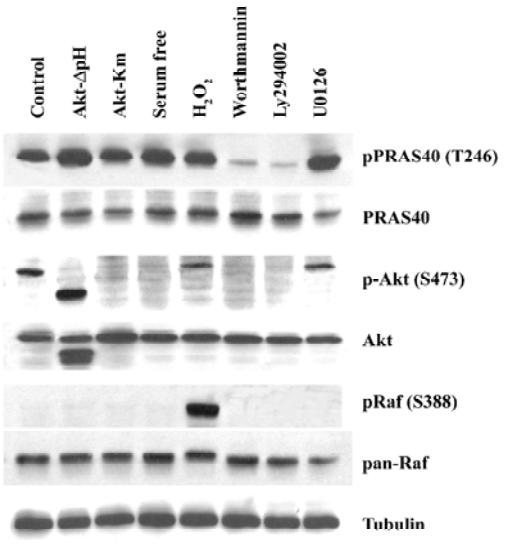

Figure 1. Western blot analysis for endogenous expression of PRAS40, Akt and Raf activity in HEK293, which were treated with different drugs or overexpression of Akt (n=3). Overexpression of constitutively active Akt (Akt-ΔpH) and kinase mutation Akt (Akt-Km). HEK293 were treated with serum withdrawal for 24 h, 1 mmol/L H_2O_2 for 20 min, 2 μmol/L Worthmannin for 2h, 25 μmol/L Ly294002 for 2 h, or 25 μmol/L U0126 for 20 min. Tubulin analysis is shown as an internal control.

MEK-ERK pathway is not necessary for PRAS40 activity The Raf-dependent activity of the MEK-ERK pathway promotes cell survival by targeting various death pathways[11]. To test whether MEK-ERK is involved in the regulation of PRAS40/Akt activity, we used the MEK antagonist U0126 to treat HEK293, A549 and HeLa cell lines. Western blot analysis revealed that U0126 had no effect on PRAS40 activity (Figure 1, 2), which implies that PRAS40 does not contribute to the MEK-ERK pathway.

ROS induced phosphorylation of Raf/Akt activity but not PRAS40 at low concentration ASK1 is known to play an important role in the apoptotic response induced by ROS, in particular H_2O_2. Goldmann *et al* showed that phosphorylation of ASK1 at Ser-976 by H_2O_2 stimulation was dose-dependent, and that treatment with 1 mmol/L H_2O_2 for 30 min could completely dephosphorylate ASK1 at Ser-967[12]. In our experiment, the increase in phospho-Akt and phospho-Raf expression was induced by treatment with 1 mmol/L H_2O_2 for 20 min in HEK293 and A549, but there was no change on PRAS40 activity (Figure 1, 2).

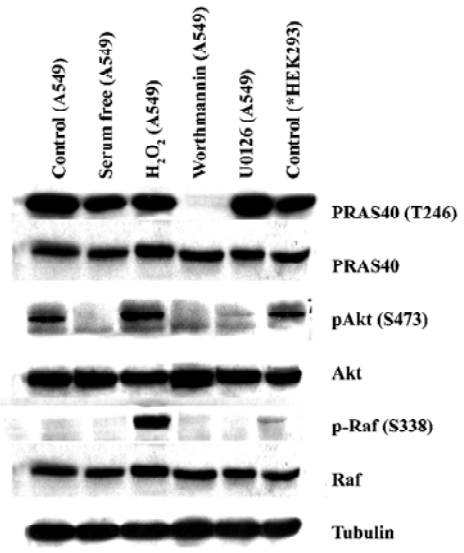

Figure 2. Western blot analysis for PRAS40, Akt and Raf expression in the A549 cell line. A549 cells were treated with serum withdrawal, 1 mmol/L H_2O_2 for 20 min, 2 μmol/L worthmannin for 2 h, 25 μmol/L Ly294002 for 2 h, 25 μmol/L U0126 for 20 min, or untreated HEK293 as a control, the cells were than lysed, followed by Western blot. Tubulin analysis is also shown as an internal control.

Akt was not the only upstream kinase of PRAS40 Akt phosphorylation could be blocked by worthmannin, U0126 and serum withdrawal in A549 and HEK293 cells; however, only worthmannin and Ly294002 inhibited phospho-PRAS40 activity (Figure 1, 2), Therefore, Akt was not the only upstream kinase of PRAS40. PRAS40 could also be activated by an Akt-independent mechanism. Western blot analysis showed that the phospho-PRAS40 and phospho-Akt activity in A549 cancer cells were stronger than in HEK293 normal cell line (Figure 2).

Expression of PRAS40 and 14-3-3 was higher in HeLa than in HEK293 cells The 14-3-3 protein is an anchor protein for some Akt substrates, and it is also a PRAS40 binding protein. Therefore, we investigated the relationship between PRAS40 and 14-3-3 expression in normal and cancer cells. HEK293 and HeLa cells were treated with serum withdrawal, H_2O_2, rapamycin (mTOR inhibitor), worthmannin and U0126. Western blot demonstrated that, except for worthmannin, these treatments produced no significant difference with regard to PRAS40 activity in HEK293 and HeLa cells. We found that HEK293 was more sensitive: treatment with worthmannin only decreased the phosphorylation of PRAS40 in HeLa cells, but completely blocked PRAS40 phosphorylation in HEK293 cells. We also found that phospho-PRAS40 and 14-3-3 were expressed more strongly in HeLa cells than in HEK293 cells, and the total expression of PRAS40

was almost the same in the two cell lines (Figure 3).

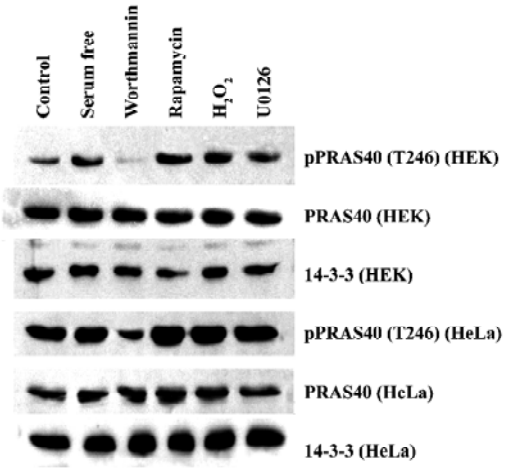

Figure 3. Western blot analysis for endogenous expression of PRAS40 and 14-3-3 in HEK293 and HeLa cell lines. Cells were treated with serum withdrawal for 24 h, 1 mmol/L H_2O_2 for 20 min, 2 μmol/L worthmannin for 2 h, 25 μmol/L Ly29004 for 2 h, or 25 μmol/L U0126 for 20 min, followed by Western blot.

We also noticed that there was a difference in sensitivity to worthmannin between normal cells and cancer cells (HEK293 and HeLa) and among cancer cells (A549 and HeLa).

PRAS40 phosphorylation activity was stronger in cancer cells than in normal cells In order to determine if PRAS40 activity is different in normal cells, different types and different development phases of cancer cells, we used Western blot analysis to determine the expression of phospho-PRAS40, PRSA40, Akt and Raf *in vitro*. Because Akt and Raf are the key control factors in the cell survival pathway (PI3K-Akt pathway and Raf-MEK pathway), we used them to find a expression relationship between PRSA40, Akt and Raf.

For a breast cancer model, we used the MCF10A/MCF7 cell lines. MCF10A is a normal breast cell line and MCF7 is a breast carcinoma line. For a lung cancer model, we used the BEAS/H1190/H1170 cell lines. BEAS cells are Human bronchial epithelial cells, immortalized with the hybrid adenovirus/simian virus 40. H1198 and H1170 are both derived from BEAS cells; H1198 is pre-malignant, because 1) it is sensitive to serum in that it was growth inhibited and terminally differentiates into squamous cells similar to normal HBE and BEAS-2B cells; 2) *in vitro* invasiveness was detected after exposure of BEAS cells to either phorbol myristate acetate or cigarette smoke condensate (CSC). H1170 is defined as a malignant cell line because it exhibits several features that are typical of invasive adenocarcinomas, including increased expression of epidermal growth factor receptor (EGFR) and transforming growth factor-α (TGFα)[13]. We also investigated other non-small cell lung cancer (NSCLC) cell lines: H460, H1299, H596, H157, H552, H1944, H1792. The details of each cancer cell lines are given in Table 1.

We found that the expression levels of phospho-PRAS40 were higher in pre-maligment and maligmant cells than in normal cell lines (eg MCF10A); Later phase cancer cells, such as H1198/H1170, showed stronger PRAS40 activity than pre-cancer cell lines (eg BEAS) except H460, H1299, H1944, in which there were no p53 mutations. We also noticed that there was no difference in the total expression of PRAS40 and Akt, whereas the total expression of Raf was different in different types of cancer cell lines, for example, there was no expression in BEAS and H1944, and weak expression in H460

Table 1. Cancer cell lines.

Name	Tumor histology	p53 mutation	Ras mutation	Reference
MCF10A	Normal breast cell line			
MCF7	Breast carcinoma cell line			
BEAS	Human bronchial epithelial cell + adenoriuns			Kyung-Hee,Chun,2003
H1198	Pre-malignant BEAS			Kyung-Hee,Chun,2003
H1170	Malignant BEAS			Kyung-Hee,Chun,2003
H460	Large cell carcinoma	No	Yes	Mitsudomi *et al* 1991
H1299	Large cell carcinoma	No	Yes	Mitsudomi *et al* 1992
H596	Adenosquamous carcinoma	Yes	No	Mitsudomi *et al* 1992
H157	Squaqmous cell carcinoma	Yes	Yes	Mitsudomi *et al* 1992
A549	Adenocarcinoma	No	Yes	Crespo NC *et al* 2002
H552	Adenocarcinoma	Yes	Yes	Mitsudomi *et al* 1992
H1944	Adenocarcinoma	No		Mitsudomi *et al* 1992
H1792	Adenocarcinoma	Yes	Yes	Mitsudomi *et al* 1992

and H157 (Figure 4).

Discussion

The PI3K-Akt pathway has been implicated in the development of multiple human cancers[14,15]. PI3K has an active role in oncogenic transformation. Akt, an important and probably essential downstream component of PI3K-mediated oncogenic signaling[16], provides a critical cell survival signal for tumor progression by phosphorylating a number of proteins involved in cell cycle regulation and proapoptotic factors[17]. Because only a subset of the cellular processes regulated by the PI3K-Akt pathway, are involved in tumorigenesis, the choice of drug targets must take into account the adverse effects resulting from the inhibition of other PI3K-Akt-dependent cellular processes. For example, the effects of insulin on metabolism are mediated through the PI3K-Akt pathway, so inhibitors of PI3K or Akt are therefore likely to perturb glucose homeostasis. It would be desirable, therefore, to target components of branches further downstream in the PI3K-Akt pathway[18].

Our data provided evidence that the proline-rich Akt-substrate PRAS40 showed higher expression levels in cancer cells (eg A549 and HeLa) than in normal cells (eg HEK293). In our breast cancer model (MCF10A/MCF7) and lung cancer model (BEAS/H1198/H1170) we also found the same result: PRAS40 was constitutively active in pre-malignant and malignant cancer cells (H1198/H1170 and MCF7), but only weakly expressed in normal cells (MCF10A and BEAS). In the NSCLC cell line, we found some interesting results: a higher expression level of phospho-PRAS40 was found in lung cancer cells with p53 mutations (eg H596, H157, H522 and H1792) than in other lung cancer cells. PRAS40 activity in lung cancer cells with only Ras mutations was almost the same as in the MCF10A normal cells (eg H460, H1299 and H1944). The strongest activity of PRAS40 was in H157, which had both the p53 mutation and the Ras mutation. The p53 mutation could be related to PRAS40 activity, but further studies are needed to clarify this relationship. These results suggested that PRAS40 activation is an early event during breast and lung carcinogenesis, PRAS40 could be used as a early detection marker in carcinogenesis.

We tested the effect of key kinase inhibitors on PRAS40 activity: PI3K inhibitors Worthmannin or Ly294002, MEK inhibitor Uo126 and mTOR inhibitor rapamycin. Only the PI3K inhibitors inhibited or decreased PRAS40 activity, therefore the PI3K-Akt survival pathway is the main pathway that PRAS40 is involved in; The Raf-MEK pathway probably doesn't contribute to PRAS40 activity. Also, PRAS40 is the substrate of Akt, but it can be activated by an Akt- independent mechanism, for example, serum withdrawal decreases Akt activity, but has no effect on PRAS40.

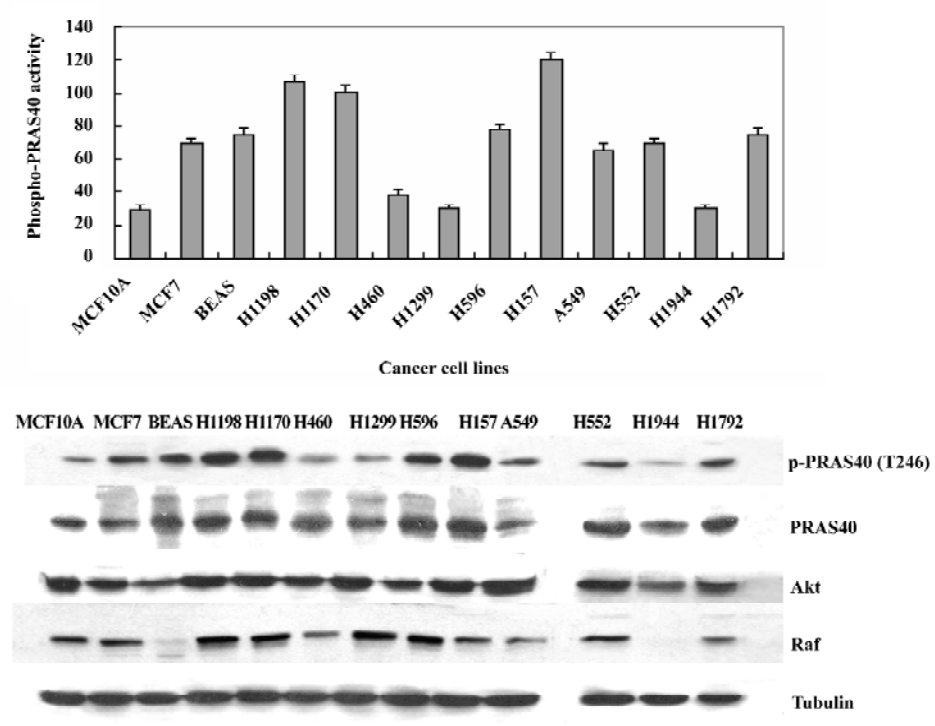

Figure 4. Western blot analysis for PRAS40, Akt and Raf in the cytosolic fraction in different types and different development phases of cancer cell lines. Tubulin was used as an internal control for the cytosolic fraction. n=3. Mean±SD.

14-3-3 is also a PRAS40 binding protein. A striking feature of the 14-3-3 proteins is their ability to bind a multitude of functionally diverse signaling proteins. This plethora of interacting proteins allows 14-3-3 to play important roles in a wide range of vital regulatory processes, such as mitogenic signal transduction, apoptotic cell death and cell cycle control[19]. Our data show that the expression level of 14-3-3, like that of PRAS40, is higher in the HeLa cell line than in HEK293, but exactly how 14-3-3 helps PRAS40 in the PI3K-Akt pathway is unknown and warrants further investigation.

To our knowledge, our results provide the first evidence that PRAS40 is constitutively active in pre-malignant and malignant breast and lung cancer cell lines, and that PRAS40 is mainly involved in the PI3K-Akt survival pathway. However, PRAS40 can also be activated by Akt- independent mechanisms. We suggest that PRAS40 could be chosen as an early detection marker in carcinogenesis, but it is also a protein that can be targeted by anti-tumor drugs, that is a "druggable" protein.

Acknowledgements

We thank Prof Hai-an FU for the generous gift of plasmids. We also thank the members of Prof Fu's laboratory at Emory University for helpful discussions.

References

1 Khuri FR, Herbst RS, Fossella FV. Emerging therapies in non-small-cell lung cancer. Ann Oncol 2001; 12: 739–44.
2 Mc Williams A, Lam S. New approaches to lung cancer prevention. Curr Oncol Rep 2002; 4: 489–94.
3 Goodman GE. Lung cancer 1: prevention of lung cancer. Thorax 2002; 57: 994–9.
4 Hong WK, Sporn MB. Recent advances in chemoprevention of cancer. Science 1997; 278: 1073–7.
5 Vivanco I, Sawyers Cl. The phosphatidylinositol 3-kinase Akt pathway in human cancer. Nat Rev Cancer 2002; 2: 489–501.
6 Cantley LC. The phosphoinositide 3-kinase pathway. Science 2002; 296: 1655–7.
7 Manning BD, Cantley LC. United at last: the tuberous sclerosis complex gene products connect the phosphoinositide 3-kinase/Akt pathway to mammalian target of rapmycin (mTOR) signaling. Biochem Soc Trans 2003; 31: 573–8.
8 Kovacina KS, Park GY, Bea SK, Gruzzetta AW, Schaefer E, Birnbaum MJ. Identification of a proline-rich Akt substrate as a 14-3-3 binding partner. J Biol Chem 2003; 12: 10189–94.
9 Saito A, Narasimhan P, Hayashi T, Okuno S, Ferrand-Drake M, Chan PH. Neuroprotective role of a proline-rich Akt substrate in apoptotic neuronal cell death after Stroke: relationships with nerve growth factor. J Neurosci 2004; 24: 1584–93.
10 Zhang L, Chen J, Fu H. Suppression of apoptosis signal-regulating kinase 1 induced cell death by 14-3-3 protein. Proc Natl Acad Sci USA 1999; 96: 8511–5.
11 Chen J, Fujii K, Zhang L, Roberts T, Fu H. Raf-1 promotes cell survival by antagonizing apoptosis signal-regulating kinase 1 through a MEK-ERK independent mechanism. Proc Natl Acad Sci USA 2001; 14: 7783–8.
12 Goldman EH, Chen J, Fu H. Activation of apoptosis signal-regulating kinase 1 by reactive oxygen species through dephosphorylation at Ser967 and 14-3-3 dissociation. J Biol Chem 2004; 279: 10442–9.
13 Chun KH, Kosmeder JW, Sun S, Pezzuto JM, Lotan R, Hong WK. Effect of deguelin on the phosphatidylinositol 3-Kinase/Akt pathway and apoptosis in premalignant human bronchial epithelial cells. J Nat Cancer Inst 2003; 4: 292–302.
14 Chang HW, Aoki M, Fruman D, Auger KR, Bellacosa A, Tsichlis PN, et al. Transformation of chicken cells by the gene encoding the catalytic subunit of PI3K-Kinase. Science 1997; 276: 1848–50.
15 Klippel A, Escobedo MA, Wachowicz MS, Apell G, Brown TW, Giedlin MA, et al. Activation of phosphatidylinositol 3-kinase is sufficient for cell cycle entry and promotes cellular changes characteristic of oncogenic transformation. Mol Cell Biol 1998; 18: 5699–711.
16 Toker A, Cantley L. Signaling through the lipid products of phosphoinositide-3-OH kinase. Nature 1997; 387: 673–6.
17 Kobayashi M, Nagata S, Iwasaki T. Dedifferentiation of adenocarcinomas by activation of phosphatidylinositol 3-kinase. Proc Natl Acad Sci USA 1999; 96: 4874–9.
18 Luo J, Manning BD, Cantley LC. Targeting the PI3K-akt pathway in human cancer: Rationale and promise. Cancer Cell 2003; 4: 257–62.
19 Fu H, Subramanian HRS, Masters SC. 14-3-3 Proteins: structure, function, and regulation. Ann Rev Pharmacol Toxicol 2000; 40: 619–49.

Acta Pharmacologica Sinica 2005 Oct; 26 (10): 1259–1264

Blackwell Publishing

Full-length article

Radioimmunotherapy of carcinoma of colon with [^{131}I]-labeled recombinant chimeric monoclonal antibodies to carcinoembryonic antigen

Qiu-jun LU[1], Guang-xing BIAN, Yuan-yuan CHEN, Min ZHANG, Shao-ming GUO, Li-qing WEN

Institute of Radiation Medicine, Beijing 100850, China

Key words

humanized chimeric recombinant monoclonal antibody; radioimmunotherapy; colonic cancer; nude mice

[1] Correspondence to Prof Qiu-jun LU.
Phn 86-10-6693-2201.
Fax 86-10-6821-4653.
E-mail luqj66@yahoo.com.cn

Received 2005-03-20
Accepted 2005-05-30

doi: 10.1111/j.1745-7254.2005.00177.x

Abstract

Aim: To study the distribution of [^{131}I]-labeled anti-CEA MoAbs and its therapeutic effect on the human colonic cancer model in nude mice. **Methods:** A nude mice model of human colonic cancer was established. [^{131}I]-labeled anti-CEA MoAbs were injected intravenously into mice. The distribution of the MoAbs was then determined and the effect of RIT on human colonic cancer was observed. **Results:** The [^{131}I]-labeled anti-CEA MoAbs had a specific distribution after injection. Tumor/non-tumor ratios for [^{131}I]-labeled anti-CEA MoAbs were 10–20 times higher than [^{131}I]-labeled IgG 96 h after injection. Thirty days after injection, significant inhibition of the volume and weight of tumor was observed in the treated mice compared with the control. The tumor growth inhibition rate of 3.1 mCi/kg CEA MoAbs group (LS180, LS174T, SW1116) was 47.8%–64.0%. This was 69.6%–78.6% in the 6.25 mCi/kg CEA MoAbs group, and 81.8%–86.2% in the 12.5 mCi/kg [^{131}I]-labeled anti-CEA MoAbs group. The plasma CEA level was also lower in treated mice. **Conclusion:** The results indicate that [^{131}I]-labeled anti-CEA MoAbs can be effective in RIT on colonic cancers.

Introduction

Human colonic carcinoma is one of the most common cancers. The 5-year survival rate of patients with chemotherapy is zero. More than half of the patients with this tumor experience metastasis or reoccurrence after treatment. The liver is the most common metastasis foci[1]. Radiolabeled MoAbs offer the prospect of a localized, highly targeted radiation treatment for these cancers. The range of action for radionuclides is defined predominantly by the nature of the particle and energy of the emission. One of the earliest radioisotopes to be coupled to antibodies for therapeutic purposes was Iodine 131 (^{131}I). Its high-energy α particles can penetrate approximately three tumor cells, so it can be effective even when only deposited near the tumor cells and has minor toxicology to normal cells[2]. There are several antibodies for a variety of human tumors that have been used to localize human tumors in xenograft models as well as in patients. Several of these antigens have served as targets for testing whether MoAbs as conjugates with radionuclides can act as selective therapeutic agents. For example, antibodies directed against CEA, α-fetoprotein, ferritin, melanoma, and epithelial-specific antibody have been radiolabeled with ^{131}I and used in the treatment of human cancers[3,4].

In histological classifications, colon cancers are over 90% adenocarcinoma. CEA can be observed in either the cancer cell surface or patients blood serum in this type of tumor[5]. Until recently, three products have been approved worldwide for the treatment of tumors in patients: Bexxar, Zevalin and ChTNT. The antibody used in this experiment is a new product awaiting permission for clinical trial, provided by Beijing Second Pharmaceutical Co, Ltd (Beijing). We undertook this study to determine the antitumor effect of the [^{131}I]-labeled anti-CEA MoAbs and its distribution in nude mice bearing xenografts.

Materials and methods

Mice Athymic nude female BABL/c nu/nu mice, 4–6 weeks old, were obtained from the Institute of Laboratory Animals, Chinese Medical Science Academy. Mice were kept under

SPF conditions and were fed with a diet of sterile mice chow and water. Animals were given 10% Lugol's (5% Iodine and 10% KI) water from 2 d before the start of the experiment beginning until the experiment was completed.

Cell lines Three colonic carcinoma derivative cell lines were used: LS180 (ATCC No: CL-187) with a cell surface CEA expression rate of 81%; LS174T (ATCC No: CL-188) with a cell surface CEA expression rate of 66%; SW1116 (ATCC No: CCL-233) with a cell surface CEA expression rate of 2654 ng/10^6 cells[6]. LS180 was grown in DMEM/F-12 (Hyclone) medium, LS174T and SW1116 in MEM (Invitrogen Technologies, Inc, Carlsbad) essential medium, supplemented with 10% FBS, 2 mmol/L *L*-glutamine, 100 U/mL penicillin and 100 U/mL streptomycin.

[^{131}I]-labeled anti-CEA MoAbs [^{131}I]-labeled anti-CEA humanized chimeric recombinant MoAbs ([^{131}I]-labeled-rch24) were supplied by Beijing SaiKe Pharmaceutical. Radioactivity was 5 mCi/mg. Radiochemical purity was more than 98.5%.

Establishing colon tumors in nude mice The three tumor cells were harvested and suspended in sterile PBS at a concentration of 25×10^6 cells/mL. Cell viability was determined by trypan blue dye exclusion. Cells (5×10^6) in sterile PBS were inoculated subcutaneously into the flank of nude mice[7]. Tumors became apparent in 8–10 d.

Radiolabeled antibody treatment of tumors Mice bearing tumors were randomly divided into groups outlined in Table 1. Mice were administered i.v. in the tail vein. Antibodies were given 2 times with the interval of 10 d. The positive chemotherapy drug (5-FU) was given 2 weeks, 6 times a week.

Radiolabeled antibody effect The tumor growth rate was determined by measuring the length (a) and width (b) (mm) of each tumor using a caliper. Tumor volume=$a\times b^2/2$. The relative tumor volume (RTV), RTV=V_t/V_o. V_o is the tumor volume when the experiment started. V_t is the measured tumor volume at different experiment time. The relative tumor growth rate was calculated by % of T/C=T_{RTV} (treated group)/ C_{RTV} (control group)×100%. The effective criterion is T/C (%) above or equal to 60%. Tumor growth inhibition rate was calculated by S%=(mean weight of treated group-mean weight of control group)/(mean weight of control group) ×100%[8].

To evaluate peripheral plasma CEA levels, mice in each group were bled from the eye using heparinized capillary tubes. The plasma CEA level was determined by ELISA (Hoffmann-La Roche Ltd).

Radiolabeled antibody biodistribution Two animals from each group were bled, killed, and dissected at 24 h, 48 h, or 96 h after treatment, respectively. Tissues and organs were immediately dissected, rinsed with saline, blotted dry, and placed in plastic tubes and weighed. The radioactivity of each sample of blood, liver, heart, lung, kidney, and tumor tissue was measured using a well-type gamma counter. From the data, [^{131}I]-labeled anti-CEA MoAbs biodistributions (%ID/g) were calculated: %ID/g=(tissue or organ cpm)/(total injected cpm)/ (tissue or organ weight).

Statistical analysis Differences among the groups were tested using a one-way ANOVA. Results are given as mean±SD unless indicated otherwise.

Results

Distribution studies Tables 2, 3 and 4 summarize the tumor/non-tumor ratios found with either [^{131}I]-labeled anti-CEA MoAbs or [^{131}I]-labeled-IgG in mice with tumors. The results confirmed the tumor-specific targeting and retention of [^{131}I]-labeled anti-CEA MoAbs in tumor tissues in contrast to [^{131}I]-labeled-IgG. While the percentage of injected dose per gram (%ID/g) in the normal tissues continued to

Table 1. Animal group and treatment.

	Group name	Drug and dosage
A	Model control	Saline
B	Low dosage "nude" anti-CEA MoAbs control	156.2 μg/kg
C	High dosage "nude" anti-CEA MoAbs control	625.0 μg/kg
D	Low dosage human IgG control	3.1 mCi/kg ^{131}I labeled-IgG
E	High dosage human IgG control	12.5 mCi/kg ^{131}I labeled-IgG
F	Low dosage ^{131}I labeled anti-CEA MoAbs	3.1 mCi/kg ^{131}I labeled-rch24
G	Middle dosage ^{131}I labeled anti-CEA MoAbs	6.25 mCi/kg ^{131}I labeled-rch24
H	Low dosage "nude" anti-CEA MoAbs	12.5 mCi/kg ^{131}I labeled-rch24
F	Positive chemotherapy control	5-fluorouracil (5-FU) 10 mg/kg

Table 2. Distribution of [^{131}I]-labeled anti-CEA MoAbs (LS180). $^{c}P<0.01$ *vs* IgG-low. $^{f}P<0.01$ *vs* IgG-high. $^{i}P<0.05$ *vs* 3.1 mCi/kg. $^{l}P<0.01$ *vs* 6.25 mCi/kg. n=7. Mean±SD.

Group	Time	Distribution of radioisotope in tumor and non-tumor (% ID/g)				
		IgG-low	IgG-high	3.1 mCi/kg	6.25 mCi/kg	12.5 mCi/kg
Blood	24 h	0.299±0.038	0.496±0.022	0.439±0.037^{cf}	0.656±0.075^{cf}	0.474±0.089^{cf}
	48 h	0.538±0.166	0.584±0.037	0.694±0.036^{cf}	0.834±0.037^{cf}	0.568±0.042^{cf}
	96 h	0.694±0.222	0.759±0.062	1.874±0.160^{cf}	1.325±0.179^{cf}	2.337±0.224^{cfi}
Heart	24 h	0.881±0.019	1.079±0.019^{c}	0.663±0.008^{cf}	1.255±0.007^{cfi}	1.210±0.001^{cfi}
	48 h	2.147±0.105	1.550±0.011	1.129±0.003^{cf}	1.828±0.114^{cf}	1.867±0.066^{cfil}
	96 h	2.934±0.033	3.336±0.294	3.095±0.027^{cf}	2.729±0.079^{cf}	2.839±0.004^{cfl}
Liver	24 h	0.772±0.090	1.050±0.036	0.670±0.036^{cf}	0.678±0.002^{cfi}	1.217±0.057^{cfi}
	48 h	1.324±0.035	1.203±0.093	0.946±0.042^{cf}	1.439±0.086^{cf}	1.764±0.131^{cfi}
	96 h	3.245±0.124	5.717±0.383	4.646±0.132^{cf}	3.763±0.064^{cf}	3.905±0.212^{cf}
Lung	24 h	0.528±0.024	0.688±0.016^{c}	0.426±0.016^{cf}	0.676±0.013^{cf}	0.604±0.019^{cfi}
	48 h	0.754±0.007	0.767±0.053	0.586±0.020^{cf}	0.857±0.028^{cfi}	0.829±0.059^{cf}
	96 h	1.506±0.136	2.377±0.241	2.080±0.086^{cf}	1.509±0.158^{cfi}	1.580±0.004^{cfi}
Kidney	24 h	0.972±0.089	1.256±0.047	0.935±0.144^{cf}	1.148±0.071^{cf}	1.110±0.115^{cfi}
	48 h	1.536±0.003	1.736±0.049	1.434±0.015^{cf}	2.121±0.010^{cf}	2.214±0.107^{cfi}
	96 h	2.734±0.394	5.424±0.051	5.391±0.107^{cf}	2.997±0.121^{cfi}	4.078±0.124^{cfl}

Table 3. Distribution of [^{131}I]-labeled anti-CEA MoAbs (LS174T). $^{c}P<0.01$ *vs* IgG-low. $^{f}P<0.01$ *vs* IgG-high. $^{i}P<0.05$ *vs* 3.1 mCi/kg. $^{l}P<0.01$ *vs* 6.25 mCi/kg. n=7. Mean±SD.

Group	Time	Distribution of radioisotope in tumor and non-tumor (% ID/g)				
		IgG-low	IgG-high	3.1 mCi/kg	6.25 mCi/kg	12.5 mCi/kg
Blood	24 h	0.320±0.008	0.503±0.016	0.403±0.028^{cf}	0.623±0.089^{cf}	0.530±0.038^{cf}
	48 h	0.583±0.014	0.679±0.042	0.824±0.070^{cf}	1.010±0.131^{cf}	0.619±0.023^{cfil}
	96 h	0.686±0.003	0.766±0.118^{c}	1.738±0.103^{cf}	1.196±0.049^{cf}	2.038±0.138^{cfi}
Heart	24 h	0.913±0.033	1.048±0.043^{c}	0.693±0.014^{cf}	1.277±0.015^{cfi}	1.259±0.005^{cfi}
	48 h	2.471±0.172	1.706±0.082	1.188±0.034^{cf}	1.946±0.030^{cf}	2.103±0.038^{cfi}
	96 h	3.153±0.014	3.385±0.012	3.097±0.064^{cf}	2.920±0.151^{cf}	2.915±0.096^{cfil}
Liver	24 h	0.786±0.024	1.026±0.008	0.656±0.016^{cf}	0.686±0.014^{cfi}	1.210±0.021^{cf}
	48 h	1.433±0.017	1.331±0.091	1.033±0.028^{cf}	1.577±0.049^{cf}	1.869±0.004^{cf}
	96 h	3.379±0.143	5.734±0.081^{c}	4.802±0.104^{cf}	3.766±0.079^{cf}	4.019±0.112^{cfi}
Lung	24 h	0.546±0.010	0.707±0.035^{c}	0.436±0.001^{cf}	0.686±0.001^{cf}	0.623±0.010^{cf}
	48 h	0.853±0.061	0.905±0.002	0.664±0.027^{cf}	0.923±0.120^{cf}	0.952±0.020^{cfi}
	96 h	1.433±0.019	2.441±0.209	2.153±0.058^{cf}	1.562±0.016^{cf}	1.636±0.020^{cfi}
Kidney	24 h	0.920±0.099	1.275±0.032	0.888±0.012^{cf}	1.111±0.045^{cf}	1.085±0.028^{cfi}
	48 h	1.789±0.046	1.904±0.018	1.616±0.096^{cf}	2.335±0.155^{cf}	2.575±0.049^{cfil}
	96 h	2.827±0.553	5.594±0.072^{c}	5.561±0.025^{cf}	3.073±0.017^{cfi}	4.229±0.085^{cfi}

decrease over time for both [^{131}I]-labeled anti-CEA MoAbs and [^{131}I]-labeled-IgG, the percentage of [^{131}I]-labeled anti-CEA MoAbs increased in the tumor between d 1 and 4. This caused the T/NT ratios continue to increase in this period. T/NT ratios for [^{131}I]-labeled anti-CEA MoAbs were 2–2.5 times higher than [^{131}I]-labeled-IgG on d 1 and continued to increase so that T/NT ratios were 10–20 times higher than [^{131}I]-labeled-IgG by day 4.

Inhibition of tumor growth The biological effect of [^{131}I]-labeled anti-CEA MoAbs in mice bearing three tumor types was assessed. The tumor growth curves are summarized in Figures 1, 2 and 3. The volume of both [^{131}I]-labeled anti-CEA MoAbs groups was less than the control group. As the administrative dosage increased, the tumor volume increment rate became slow or was not obvious.

The relative tumor growth rate of three tumor types was

Table 4. Distribution of [^{131}I]-labeled anti-CEA MoAbs (SW1116). $^{c}P<0.01$ *vs* IgG-low. $^{f}P<0.01$ *vs* IgG-high. $^{i}P<0.05$ *vs* 3.1 mCi/kg. $^{l}P<0.01$ *vs* 6.25 mCi/kg. n=7. Mean±SD.

Group	Time	Distribution of radioisotope in tumor and non-tumor (% ID/g)				
		IgG-low	IgG-high	3.1 mCi/kg	6.25 mCi/kg	12.5 mCi/kg
Blood	24 h	0.640±0.035	0.514±0.005*	0.437±0.068^{cf}	0.684±0.086	0.447±0.031^{cfi}
	48 h	0.641±0.026	0.735±0.096	0.561±0.022^{cf}	0.942±0.135	0.630±0.041^{cfi}
	96 h	0.831±0.048	0.760±0.169	1.865±0.111^{cf}	1.357±0.262^{cf}	0.860±0.075^{cfi}
Heart	24 h	1.886±0.022	2.314±0.035	1.420±0.003^{cf}	2.707±0.068^{cfi}	2.647±0.003^{cfi}
	48 h	2.986±0.115	2.733±0.089	1.569±0.019^{cf}	2.910±0.084^{cf}	2.795±0.089^{cfi}
	96 h	3.386±0.198	2.801±0.067	2.820±0.211^{cf}	3.278±0.049^{cfi}	2.829±0.021^{cfi}
Liver	24 h	1.644±0.137	2.250±0.101	1.438±0.059^{cf}	1.470±0.011^{cf}	2.559±0.028^{cf}
	48 h	1.831±0.034	2.300±0.111	1.529±0.096^{cf}	1.951±0.019^{cf}	2.702±0.125^{cfi}
	96 h	3.413±0.007	4.154±0.243^{c}	3.268±0.104^{cf}	3.725±0.025^{cf}	3.915±0.227^{cfil}
Lung	24 h	1.146±0.065	1.669±0.064	0.816±0.004^{cf}	1.112±0.004^{cf}	1.141±0.026^{cf}
	48 h	1.175±0.024	1.707±0.003^{c}	1.202±0.061^{cf}	1.130±0.037^{cfi}	1.145±0.043^{cfi}
	96 h	1.517±0.053	2.471±0.021^{c}	2.059±0.034^{cf}	1.539±0.064^{cfi}	1.561±0.023^{cfi}
Kidney	24 h	2.100±0.041	2.716±0.072	1.858±0.055^{cf}	2.506±0.019^{cfi}	2.417±0.114^{cfi}
	48 h	2.119±0.012	2.771±0.048^{c}	1.998±0.008^{cf}	2.819±0.101^{cfi}	3.081±0.148^{cfi}
	96 h	2.707±0.389	5.371±0.049^{c}	5.339±0.105^{cf}	2.968±0.120^{cf}	4.039±0.123^{cfil}

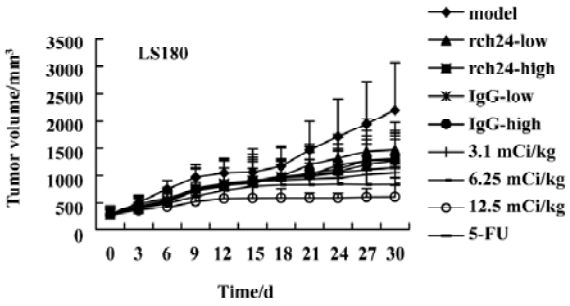

Figure 1. The effect of [^{131}I]-labeled anti-CEA MoAbs on tumor growth curve of LS180. n=7. Mean±SD.

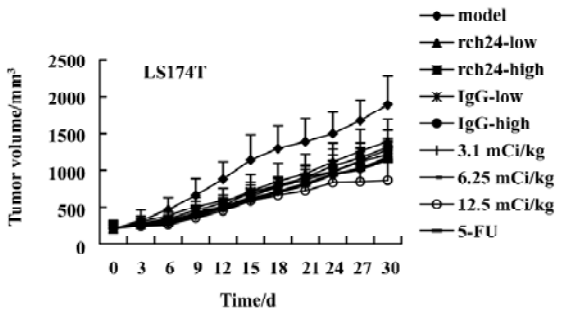

Figure 2. The effect of [^{131}I]-labeled anti-CEA MoAbs on tumor growth curve of LS174T. n=7. Mean±SD.

calculated. The growth of tumors were inhibited significantly at the dosage groups of 3.1 mCi/kg, 6.25 mCi/kg, and 12.5 mCi/kg in nude mice bearing LS180 or LS174T (T/C%<60%).

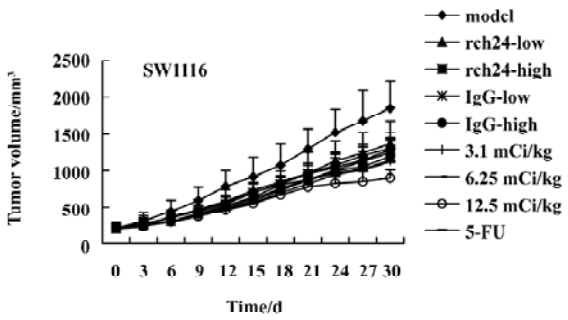

Figure 3. The effect of [^{131}I]-labeled anti-CEA MoAbs on tumor growth curve of SW1116. n=7. Mean±SD.

For SW1116, only the 6.25 mCi/kg and 12.5 mCi/kg dosages were effective. With the increasing dosage, more obvious inhibition of the tumor growth was observed.

Tumor weight and tumor growth inhibition rate (TIR) were calculated. The data is shown in Table 5. The tumor weights of three dosage [^{131}I]-labeled anti-CEA MoAbs groups were all less than that of the control. With the increase in dosage, the tumor growth inhibition rate was more obvious. The tumor growth inhibition rate of the 3.1 mCi/kg CEA MoAbs group (LS180, LS174T, SW1116) was 47.8%–64.0%. This was 69.6%–78.6% in the 6.25 mCi/kg CEA MoAbs group, and 81.8%–86.2% in the 12.5 mCi/kg [^{131}I]-labeled anti-CEA MoAbs group.

Plasma CEA level The plasma CEA level is shown in Table 6. Three groups' CEA levels were lower than the control group. This shows a relationship between the CEA level

Table 5. Tumor weight and tumor inhibition rate (TIR) of [^{131}I]-labeled anti-CEA MoAbs on mice bearing tumor. $^{c}P<0.01$ *vs* model. $^{f}P<0.01$ *vs* rch24-low. $^{i}P<0.01$ *vs* rch24-high. $^{l}P<0.01$ *vs* IgG-low. $^{o}P<0.01$ *vs* IgG-high. $^{r}P<0.05$ *vs* 3.1 mCi/kg. n=7. Mean±SD.

Group	LS180		LS174T		SW1116	
	Tumor Weight (g)	TIR (%)	Tumor Weight (g)	TIR (%)	Tumor Weight (g)	TIR (%)
Model	2.8±0.8	–	2.5±0.2	–	2.2±0.1	–
rch24-low	1.7±0.5	39.3	1.6±0.3	36.0	1.6±0.2	27.3
rch24-high	1.4±0.3	50.0	1.3±0.2	48.0	1.4±0.2	36.4
IgG-low	1.1±0.2	60.7	1.1±0.2	56.0	1.2±0.2	45.5
IgG-high	0.9±0.2	67.9	1.0±0.2	60.0	1.0±0.1	54.5
3.1mCi/kg	0.8±0.2^{cfl}	71.4	0.9±0.1^{cfl}	64.0	0.9±0.2^{cfl}	59.1
6.25mCi/kg	0.7±0.2^{cr}	75.0	0.7±0.1^{cr}	72.0	0.8±0.2^{cr}	63.6
12.5mCi/kg	0.4±0.1^{cior}	85.7	0.5±0.1^{cior}	80.0	0.7±0.1^{cior}	68.2
5-FU	1.6±0.3^{c}	42.9	1.4±0.2^{c}	44.0	1.5±0.2^{c}	31.8

Table 6. Plasma CEA levels of mice bearing different types of tumor. $^{c}P<0.01$ *vs* model. $^{f}P<0.01$ *vs* rch24-low. $^{i}P<0.01$ *vs* rch24-high. $^{l}P<0.01$ *vs* IgG-low. $^{o}P<0.01$ *vs* IgG-high. $^{r}P<0.05$ *vs* 3.1 mCi/kg. n=7. Mean±SD.

Group	CEA level (ng/mL)		
	LS180	LS174T	SW1116
Model	39.2±4.5	36.1±1.7	36.7±3.7
rch24-low	33.0±5.9	33.3±1.2	34.1±4.4
rch24-high	28.5±4.3	28.9±1.9	29.1±1.5
IgG-low	28.8±5.0	27.1±1.6	27.7±1.8
IgG-high	25.1±5.7	24.0±1.6	27.1±1.2
3.1 mCi/kg	23.4±4.1^{cf}	22.8±2.9^{cf}	24.2±2.6^{cf}
6.25 mCi/kg	21.0±4.7^{c}	20.8±1.5^{c}	21.0±1.7^{c}
12.5 mCi/kg	17.4±3.7^{cil}	17.3±1.2^{cil}	18.8±1.0^{cil}
5-FU	25.4±1.2^{c}	21.1±1.5^{c}	26.6±1.0^{c}

and dosage. Compared with the "nude" antibody and [^{131}I]-labeled-IgG, [^{131}I]-labeled anti-CEA MoAbs was more effective in lowering the CEA level.

Discussion

A new approach in radiation therapy for cancer involves the use of radiolabeled MoAbs raised against tumor-associated antigens[9]. The approach adopted in this study was the use of [^{131}I]-labeled anti-CEA MoAbs at different doses to produce tumor growth inhibition in groups of athymic nude mice bearing human colon adenocarcinoma xenografts. The two principal objectives of this study were to examine the biodistribution and antitumor activity of the [^{131}I]-labeled anti-CEA MoAbs.

Our data show that [^{131}I]-labeled anti-CEA MoAbs at different dosages can significantly inhibit the growth rate of tumors (LS180, LS174T, SW1116) in a dose-dependent manner. We are encouraged by the finding that the destruction of tumors was apparent in approximately 50% of tumors in the animals given 3.1 mCi/kg of radiolabeled rch24 antibody. This suggests that we may be able to use a low dosage to produce slight toxicity.

With one exception, most therapeutic studies with [^{131}I]-labeled antibodies in experimental animals have failed to inhibit completely the growth of well-established tumors[10–12]. However, Cheung *et al* were able to ablate 0.5–2.0 cm^3 neuroblastoma xenografts in nude mice with a single injection of 1 mCi of [^{131}I]-labeled 3F8 MoAbs[13]. Whether these results are a result of a property of the antibody, radiosensitivity of the tumor or some other factor, is unclear, but all current experimental evidence indicates that radiolabeled antibodies can be effectively used to inhibit tumor growth.

In this report we examined the distribution of [^{131}I]-labeled anti-CEA MoAbs. Targeting was observed 24 h after the drug was administered. It was more obvious 96 h after administration. The blood and liver have the main uptake and the kidney has a low uptake. Toxicity was measured by the change in bodyweight and by determination of the total peripheral white blood cells (WBC). There was no significant difference in the bodyweight and peripheral WBC counts between the treated groups and model control (data not shown).

Because [^{131}I] is not an as effective radionuclide as other isotopes, other radioconjugates are being pursued[14,15]. One of the best candidates for convenient coupling to antibodies is Yttrium-90 [^{90}Y]. But there are difficulties in the application. These include high uptake in normal tissue,

especially the liver, and problems associated with obtaining high specific activity [^{90}Y]. In addition, [^{90}Y] are known to concentrate in the bone[16]. This may cause severe problems. Each radionuclide antibody tumor system has advantages and disadvantages, but [^{131}I] label is the most promising method at present.

Overall, the results of the present study indicate that tumor growth inhibition using radiolabeled antibodies can be confirmed. Using selectively localizing antitumor antibodies conjugated with suitably cytotoxic radionuclides may provide a useful new approach to the treatment of disseminated cancers.

References

1 Debinski W, Karlsson B, Lindholm L, Siegall CB, Willingham MC, FitzGerald D, *et al*. Monoclonal antibody C242-Pseudomonas exotoxin A. A specific and potent immunotoxin with antitumor activity on a human colon cancer xenograft in nude mice. J Clin Invest 1992; 90: 405–11.

2 Ditzel HJ, Garrigues U, Andersen CB, Larsen MK, Garrigues HJ, Svejgaard A, *et al*. Modified cytokeratins expressed on the surface of carcinoma cells undergo endocytosis upon binding of human monoclonal antibody and its recombinant Fab fragment. Proc Natl Acad Sci USA 1997; 94: 8110–5.

3 Philben VJ, Jakowatz JG, Beatty BG, Vlahos WG, Paxton RJ, Williams LE, *et al*. The effect of tumor CEA content and tumor size on tissue uptake of indium 111-labeled anti-CEA monoclonal antibody. Cancer 1986; 57: 571–6.

4 Buchegger F, Pfister C, Fournier K, Prevel F, Schreyer M, Carrel S, *et al*. Ablation of human colon carcinoma in nude mice by 131I-labeled monoclonal anti-carcinoembryonic antigen antibody F(ab')2 fragments. J Clin Invest 1989; 83: 1449–56.

5 Dohlsten M, Hedlund G, Akerblom E, Lando PA, Kalland T. Monoclonal antibody-targeted superantigens: a different class of anti-tumor agents. Proc Natl Acad Sci USA 1991; 88: 9287–91.

6 Han JS, Nair PP. Flow cytometric identification of cell surface markers on cultured human colonic cell lines using monoclonal antibodies. Cancer 1995; 76: 195–200.

7 Xu X, Clarke P, Szalai G, Shively JE, Williams LE, Shyr Y, *et al*. Targeting and therapy of carcinoembryonic antigen-expressing tumors in transgenic mice with an antibody-interleukin 2 fusion protein. Cancer Res 2000; 60: 4475–84.

8 Buchegger F, Mach JP, Pèlegrin A, Gillet M, Vogel CA, Buclin T, *et al*. Radiolabeled chimeric anti-CEA monoclonal antibody compared with the original mouse monoclonal antibody for surgically treated colorectal carcinoma. J Nucl Med 1995; 36: 420–9.

9 Hajjar G, Sharkey RM, Burton J, Zhang CH, Yeldell D, Matthies A, *et al*. Phase I radioimmunotherapy trial with iodine-131-labeled humanized MN-14 anti-carcinoembryonic antigen monoclonal antibody in patients with metastatic gastrointestinal and colorectal cancer. Clin Colorectal Cancer 2002; 2: 31–42.

10 Zhu H, Baxter LT, Jain RK. Potential and limitations of radioimmunodetection and radioimmunotherapy with monoclonal antibodies. J Nucl Med 1997; 38: 731–41.

12 Ychou M, Pèlegrin A, Faurous P, Robert B, Saccavini JC, Guerreau D, *et al*. Phase I/II radio-immunotherapy study with iodine-131-labeled anti-CEA monoclonal antibody F6 F(ab')2 in patients with non-resectable liver metastases from colorectal cancer. Int J Cancer 1998; 75: 615–9.

13 Cheung NK, Landmeier B, Neely J, Nelson AD, Abramowsky C, Ellery S, *et al*. Complete tumor ablation with iodine 131-radiolabeled disialoganglioside GD2-specific monoclonal antibody against human neuroblastoma xenografted in nude mice. J Natl Cancer Inst 1986; 77: 739–45.

14 Denardo SJ, O'Grady LF, Richman CM, Goldstein DS, O'Donnell RT, Denardo DA, *et al*. Radioimmunotherapy for advanced breast cancer using I-131-ChL6 antibody. Anticancer Res 1997; 17: 1745–51.

15 Sharkey RM, Brenner A, Burton J, Hajjar G, Toder SP, Alavi A, *et al*. Radioimmunotherapy of non-Hodgkin's lymphoma with 90Y-DOTA humanized anti-CD22 IgG (90Y-Epratuzumab): do tumor targeting and dosimetry predict therapeutic response? J Nucl Med 2003; 44: 2000–18.

16 Wong JY, Shibata S, Williams LE, Kwok CS, Liu A, Chu DZ, *et al*. A Phase I trial of 90Y-anti-carcinoembryonic antigen chimeric T84.66 radioimmunotherapy with 5-fluorouracil in patients with metastatic colorectal cancer. Clin Cancer Res 2003; 9: 5842–52.

Acta Pharmacologica Sinica 2005 Oct; 26 (10): 1265–1273

Full-length article

Deguelin regulates nuclear pore complex proteins Nup98 and Nup88 in U937 cells *in vitro*[1]

Hong-li LIU[2], Yan CHEN[2,3], Guo-hui CUI[2], Qiu-ling WU[2], Jing HE[2], Wei-hua CHEN[2], Jian-feng ZHOU[4]

[2]*Department of Hematology, Union Hospital, Tongji Medical College, Huazhong University of Science and Technology, Wuhan 430022;* [4]*Department of Hematology, Tongji Hospital, Tongji Medical College, Huazhong University of Science and Technology, Wuhan 430030, China*

Key words

deguelin; U937 cells; nucleoporin; Nup98; Nup88

[1] Project supported by the National Natural Science Foundation of China (No 30472267).
[3] Correspondence to Prof Yan CHEN.
Phn 86-27-6604-6609.
Fax 86-27-8572-6916.
E-mail liuhl60@tom.com

Received 2005-04-25
Accepted 2005-06-25

doi: 10.1111/j.1745-7254.2005.00192.x

Abstract

Aim: To investigate the anticancer effects and the molecular mechanisms of deguelin on human U937 leukemia cells, and to explore the underlying mechanism regulating nucleoporin 98 (Nup98) and nucleoporin 88 (Nup88) *in vitro*. **Methods:** The effects of deguelin on the growth of U937 cells were studied by MTT assay. The effect of deguelin on the cell cycle of U937 cells was studied by using a propidium iodide method. The localization of the nuclear pore complex proteins Nup98 and Nup88 was investigated by using immunofluorescence and immunoelectron microscopy. The expression of Nup98 and Nup88 in U937 cells was investigated by using flow cytometry and Western blot. **Results:** The proliferation of U937 cells was inhibited in the deguelin-treated group, with a 24-h IC_{50} value of 21.61 nmol/L and a 36-h IC_{50} value of 17.07 nmol/L. U937 cells treated with deguelin had reduced percentages of cells in the G_0/G_1 phase, whereas cells accumulated in the S and G_2/M phases. Nup88 and Nup98 were found on both the nuclear and cytoplasmic sides of the U937 cells by using immunofluorescence and immunoelectron microscopy. The expression of Nup98 was upregulated and that of the Nup88 protein was downregulated in U937 cells treated with deguelin. **Conclusion:** Deguelin is able to inhibit the proliferation of U937 cells by regulating the cell cycle such that cells are arrested at the S and G_2/M phases, so that the proportion of cells in the G_0/G_1 phase decreases. The antitumor effects of deguelin are related to upregulating the expression of Nup98 and downregulating the expression of Nup88 protein in U937 cells.

Introduction

The nuclear pore complex (NPC) comprises a central eightfold symmetrical ring and spoke assembly, cytoplasmic fibers, and a filamentous nuclear basket[1]. Molecular trafficking between the nucleus and the cytoplasm of interphase cells occurs via the NPC, which are large molecular assemblies that are embedded in the double-membraned nuclear envelope (NE)[2]. The NPC provide peripheral channels of approximately 9 nm in diameter, which allow the diffusion of ions and small molecules, and mediate the selective transport of nuclear proteins, RNA, and ribonucleoprotein (RNP) particles by energy-dependent mechanisms. Several interactions between individual FG (Phe-Gly) repeat-containing nucleoporins and transport factors have been reported, leading to the idea that such interactions may play a pivotal role in the docking, translocation, and/or termination steps of the transport process[3]. Recent research has shown that Nup98 can dynamically associate with the nuclear pore and shuttle between the NPC and intranuclear bodies, and additionally between the nucleus and the cytoplasm in a transcription-dependent manner. The most common oncogenic fusions involve a segment of the gene encoding the FG-repeat domain of Nup98, which, in turn, becomes linked to genes of the homeobox family of transcription factors[4]. Nucleoporins are involved in several types of acute myeloid

leukemia and a few other hematological malignancies, as well as rare cases of other tumors. Overexpression of nucleoporin 88 (Nup88) is associated with malignant tumors, whereas in most other cases the role of the Nup proteins in tumorigenesis stems from chromosomal rearrangements that results in oncogenic fusion proteins[5]. Nup98 and Nup88 play important roles in nucleocytoplasmic shuttling activity in carcinoma cells.

Several natural compounds, in particular plant products and dietary constituents, have been found to have chemopreventive activities both *in vitro* and *in vivo*[6]. Deguelin has been isolated from several plant species, including *Mundulea sericea* (Leguminosae). Recent experiments have verified that deguelin can lead the cell cycle to block and induce apoptosis; however, the mechanism by which it acts is not yet completely clear[7–9]. In our previous studies, we found that deguelin was able to inhibit the proliferation of Burkitt's lymphoma cell line Daudi cells by regulating the cell cycle such that cells were arrested at the G_0/G_1 phase, and apoptosis was induced. Moreover, deguelin has low toxicity in human peripheral blood monocular cells (PBMC), but selectively induces the apoptosis of Daudi cells. Deguelin has antitumor effects because it downregulates the expression of cyclin D1 and the pRb protein[10]. In the present study, we chose human myeloid precursor cell line U937 cells as the target. This study was designed to explore the mechanism by which deguelin regulates Nup98 and Nup88 in U937 cells. We focused on changes in the expression of Nup98 and Nup88, and analyzed the underlying mechanism by which molecular trafficking between the nucleus and the cytoplasm is carried out.

Materials and methods

Drugs and reagents Deguelin was purchased from the Sigma (St Louis, MO, USA) and was initially dissolved in dimethylsulfoxide (Me_2SO), and stored at -20 °C, and was then thawed before use. 3-(4,5-dimethyl-2 thiazolyl)-2,5-diphenyl-2H-tetrazolium bromide (MTT) was purchased from Janssen Chimica Company (New Brunswick, NJ, USA). RPMI-1640 medium, propidium iodide (PI), Hoechst 33258, and Me_2SO were purchased from Sigma. Fetal calf serum (FCS), anti-Nup88 and anti-Nup98 antibodies were purchased from Santa Cruz (California, USA). Fluorescein isothiocyanate (FITC)-labeled secondary antibodies were purchased from Zhongshan Company (Beijing, China). Chemiluminescence (ECL) reagent kits were purchased from Pierce Biotechnology (Rockford, IL, USA). The U937 cell line was obtained from the China Center for Typical Culture Collection (Wuhan, China). All cell groups were grown in an RPMI-1640 culture medium containing 10% FCS and 2 mmol/L *L*-glutamine at 37 ºC in a 5% CO_2 incubator.

MTT assay The antiproliferative effect of deguelin against different group cells was determined by using the MTT dye uptake method as described previously[11]. Briefly, the final concentrations of deguelin were 0, 5, 10, 20, 40, 80, and 160 nmol/L. Each concentration of deguelin was added to 6 wells, respectively. The plates were in the presence or absence of the indicated test samples for 0 h, 12 h, 24 h, 36 h, 48 h, 60 h, and 72 h. Thereafter, 20 μL MTT solution [5 mg/mL in phosphate-buffered saline (PBS)]was added to each well. After incubation for 4 h at 37 °C, the supernatant was removed and 150 μL Me_2SO was added. When the blue crystals were dissolved, the optical density (*OD*) was detected in a microplate reader at a wavelength of 570 nm using a 96-well multiscanner autoreader (Biotech Instruments μQuant, NY, USA). The following formula was used: cell proliferation inhibited (%)=[1–(*OD* of the experimental samples/*OD* of the control)]×100% (n=6. Mean±SD).

DNA content and cell cycle analysis Untreated and treated cells were collected, after being cultured in the presence or absence of deguelin for the indicated time, rinsed with PBS, and suspended in 75% ethanol at -20 ºC overnight. Fixed cells were centrifuged at 1200×*g* and washed twice with PBS. For detecting DNA content, cells were incubated in the dark with 50 mg/L PI and 0.1% RNase A in 400 μL PBS at room temperature for 30 min. Stained cells were analyzed using FACSort (Becton Dickinson, New Jersey, USA). The percentage of cells was determined using the CellQuest software program (Becton Dickinson, New Jersey, USA). Cells were grouped as follows: the control group; and those treated with deguelin at concentrations of 5, 10, 20, 40, and 80 nmol/L for 24 h, respectively (n=3).

Immunofluorescence with confocal microscopy For the immunofluorescence experiments, cells were fixed in 4% paraformaldehyde for 10 min and permeabilized with 0.2% Triton X-100 on ice for 10 min. Samples were blocked with 3% bovine serum albumin plus 0.02% Triton X-100 in PBS for 30 min, incubated with anti-Nup88 (1:200) and anti-Nup98 (1:100) antibodies overnight at 4 ºC, and washed 4 times with 1.5 % bovine serum albumin plus 0.02% Triton X-100 in PBS. FITC-labeled secondary antibodies diluted in PBS were applied for 30 min, and cells were washed 3 times every 15 min. Hoechst 33258 (1 μg/mL) and PI (50 mg/L) were included in the penultimate wash step to visualize the DNA. Coverslips were mounted with 3-amino propyltriethoxy silane (APES). Images were captured using a FV500 confocal microscope (Olympus, Tokyo, Japan).

Nup98 and Nup88 protein analysis using flow cytometry Flow cytometry was performed to determine the expression of Nup98 and Nup88 in cells by using primary antibodies to the peptide-binding domain. A total of 1×10^6 cells were collected, washed with PBS, and anti-Nup88 antibody (1:50) and anti-Nup98 antibody (1:50) were added, then the mixture was kept at 4 ºC overnight. Mouse IgG1 (1:50) antibody was the isotype control group. FITC-labeled secondary antibody diluted in PBS (1:100) was applied for 30 min at room temperature. Stained cells were analyzed by using FACSort. A total of 10 000 cells were analyzed from each cell group. The percentage of cells was determined using the CellQuest software program. Cells were grouped as follows: the negative group; the blank group; those treated with 10 nmol/L deguelin for 24 h; those treated with 20 nmol/L deguelin for 24 h.

Immunoelectron microscopy U937 cells on coverslips were fixed in 4% paraformaldehyde and 0.2% glutaraldehyde and washed with 0.1 mol/L phosphate buffer (PB; pH 7.4), followed with PB containing 0.1% sodium borohydride to inactivate residual aldehyde groups. The cells were permeabilized with PB containing 0.05% Triton X-100 for 20 min at room temperature and washed with PB. The blocking solution was PBS (pH 7.4) containing 4% normal goat serum (NGS). After blocking, cells were incubated with affinity-purified goat anti-Nup98 antibody (1:100) and affinity-purified mouse anti-Nup88 antibody (1:100) in PBS containing 1% NGS at 4 ºC overnight. After 6 washes with PBS, cells were incubated with a biotinylated respondent secondary antibody (1:200) in PBS and 1% NGS. Immunoreactivity was visualized by incubation with 0.05% diamino-benzidine (DAB; Sigma) and 0.003% hydrogen peroxide in 0.05 mol/L Tris (pH 7) for 2 min. Cells were washed, postfixed with 2.5% glutaraldehyde in PB, washed again, fixed with 0.5% osmium tetroxide for 15 min, dehydrated, and embedded in Leica ultracut UCT (Wetzlar, Germany) for sectioning. Sections were observed on an electron microscope (Tecnai F12; FEI, Eindhoven, the Netherlands).

Western blot analysis Lysates were prepared from 1×10^7 cells by dissolving cell pellets in 100 μL of lysis buffer [20 mmol/L Na_2PO_4 (pH 7.4), 150 mmol/L NaCl, 1% Triton X-100, 1% aprotinin, 1 mmol/L phenylmethylsulfonyl fluoride, 10 g/L leupeptin, 100 mmol/L NaF, and 2 mmol/L Na_3VO_4]. Lysates were centrifuged at 18 000×*g* for 15 min and the supernatant was collected. Protein content was determined using a Bio-Rad protein assay (Bio-Rad laboratories, Hercules, CA, USA). Sodium dodecylsulfate-polyacrylamide gel electrophoresis (SDS-PAGE) sample buffer [10 mmol/L Tris-HCl (pH 6.8) 2% SDS, 10% glycerol, 0.2 mol/L 1,4-Dithiothreitol, (DTT)] was added to the lysates. Lysates were heated to 100 ºC for 5 min, and 100 μg of protein was loaded into each well of a 10% SDS-PAGE gel. Resolved proteins were electrophoretically transferred to nitrocellulose and blocked with 5% nonfat milk. After incubation with the Nup88 antibody (at a 1:2500 dilution) and the Nup98 antibody (dilution 1:1000) at 4 °C overnight, the blots were washed 3 times with TBS/Tween [TBST; 25 mmol/L Tris-HCl (pH 8.0), 125 mmol/L NaCl, 0.1% Tween 20], and exposed to horseradish peroxidase (HRP)-conjugated corresponding secondary antibodies for 1 h, and finally detected by using ECL. Quantification of the bands was carried out using the Quantity One densitometric analysis software (Bio-Rad).

Statistical analysis All data are expressed as mean±SD, and analyzed using SPSS 10.0 for Windows 98. Linear *t*-test were used for statistical analyses, and $P<0.05$ was considered to be statistically significant.

Results

Effects of deguelin on proliferation of U937 cells U937 cells treated with different concentrations of deguelin (0, 5, 10, 20, 40, 80, or 160 nmol/L) for 0 h, 12 h, 24 h, 36 h, 48 h, 60 h, and 72 h, respectively, resulted in the inhibition of cell proliferation in a dose- and time-dependent manner. The *OD* value of the deguelin-treated group was significantly lower than that of the untreated group (Figure 1). The IC_{50} value for 24 h for the U937 cells was 21.61 nmol/L, whereas the IC_{50} value for 36 h was 17.07 nmol/L.

Effects of deguelin on the cell cycle of human leukemia U937 cells Figure 2 illustrates the changes in DNA content

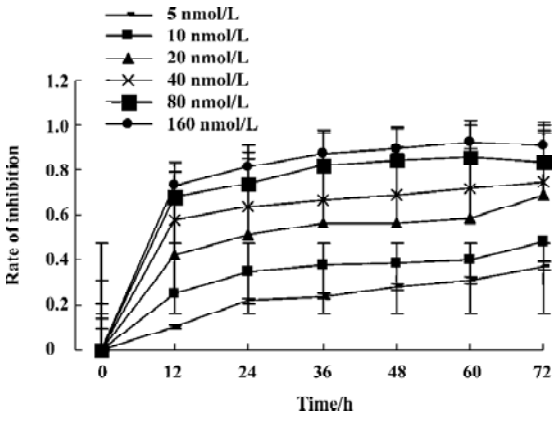

Figure 1. Antiproliferation effect of deguelin on U937 cells. U937 cells were treated with various concentrations of deguelin as indicated for 0, 12, 24, 36, 48, 60, or 72 h. Growth inhibition was determined using an MTT assay and is shown as an inhibitory rate. *n*=6. Mean±SD.

distribution in cells treated with 0, 5, 10, 20, 40, or 80 nmol/L deguelin for 24 h. As the treatment dose increased, the percentage of cells in S phase and G_2/M phase increased, whereas the number in the G_1/G_0 phase decreased accordingly. After treatment with 0, 5, 10, 20, 40, or 80 nmol/L deguelin for 24 h, the proportion of cells in the G_1/G_0 phase were 73.01%, 71.15%, 68.42%, 53.83%, 43.99%, and 22.82%, respectively; the proportion decreased in a dose-dependent manner. The proportion of S phase cells were 17.18%, 16.30%, 18.09%, 27.56%, 31.21%, and 46.85%, respectively; the proportion increased in a dose-dependent manner. The proportion in the G_2/M phase was 9.75%, 12.31%, 13.99%, 18.99%, 24.83%, and 27.79%, respectively. These results show that deguelin arrested the U937 cells at the S phase and the G_2/M phase, and decreased the number of cells in the G_1/G_0 phase *in vitro*.

Effects of deguelin on Nup98 and Nup88 in U937 cells

In this study, FITC-labeled secondary antibodies marked Nup98 and Nup88 with green fluorescence, and Hoechst 33258 and PI labeled the DNA of U937 cells with blue and red fluorescence, respectively. In Figure 3, part Ad is merged parts Ab and Ac, and part Bd is merged parts Bb and Bc using confocal microscopy. We found that Nup98 had low fluorescence intensity, with an *OD* value of 50.23 in U937 cells, and the fluorescence was located both within the nucleoplasm and nucleus in intensely fluorescent dots. After treatment with 20 nmol/L deguelin for 24 h, Nup98 had greater fluorescence intensity, with an *OD* value of 252.28, and its distribution was mainly within the nucleus. In U937 cells, Nup88 had high fluorescence intensity, with an *OD* value of 215.16. After treatment with 20 nmol/L deguelin for 24 h, Nup88 had lower fluorescence intensity, with an *OD* value of 63.24. Compared with the control group, expression of Nup98 and Nup88 after treatment with 20 nmol/L deguelin for 24 h was significantly different ($P<0.05$). When these

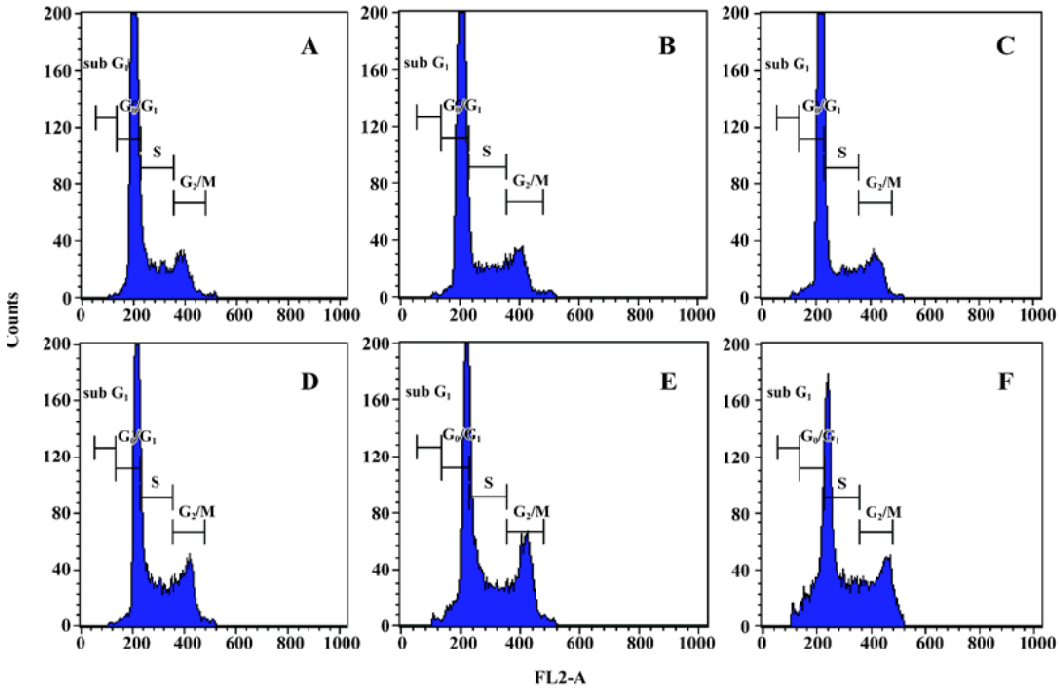

	Concentration/nmol·L^{-1}					
	Control	5	10	20	40	80
G_0/G_1 (%)	73.01	71.15	68.42	53.83	43.99	22.82
S (%)	17.18	16.30	18.09	27.56	31.21	46.85
G_2/M (%)	9.75	12.31	13.99	18.99	24.83	27.79

Figure 2. Distribution of cells in phases of the cell cycle caused by deguelin. Data were obtained using FACSort (Becton Dickinson). A is the control; B, C, D, E, F are cells treated with 5, 10, 20, 40, or 80 nmol/L deguelin for 24 h, respectively (n=3).

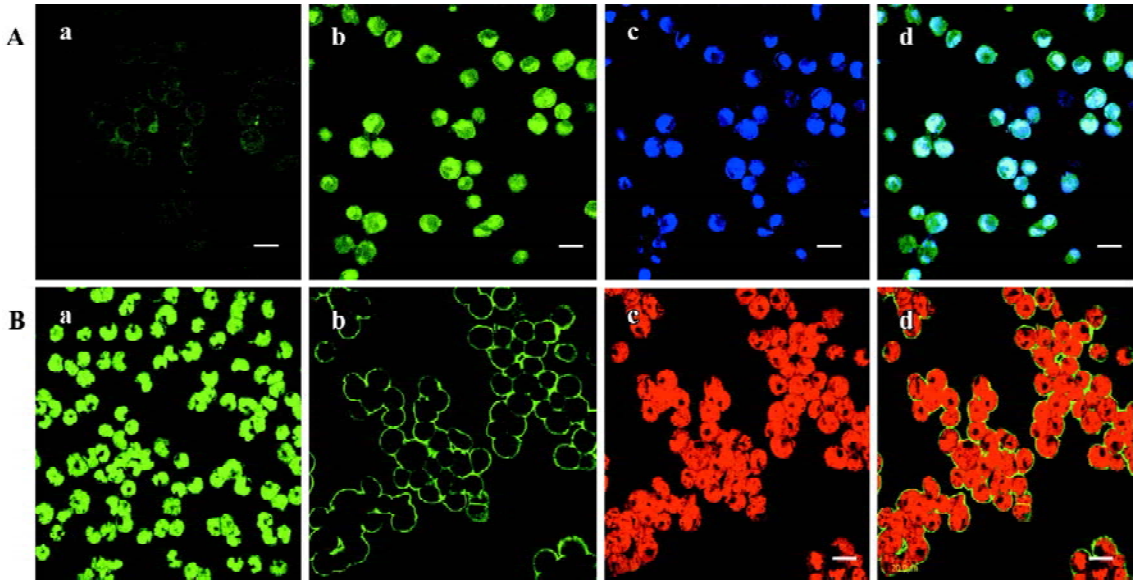

Figure 3. Deguelin regulates the expression of Nup98 and Nup88 proteins in U937 cells. Images were obtained using an FV500 confocal microscope. In part A, a, b, c, and d correspond to the expression of Nup98 in control U937 cells, treatment with 20 nmol/L deguelin for 24 h, DNA staining with Hoechst 33258, and merged parts Ac and Ad, respectively. In part B, a, b, c, and d correspond to the expression of Nup88 in control U937 cells, treatment with 20 nmol/L deguelin for 24 h, DNA staining with PI, and merged parts Bc and Bd, respectively. Scale bars=20 μm.

data are considered together, we conclude that Nup98 and Nup88 are regulated by deguelin, but the mechanism by which this occurs is not completely clear.

Nup98 and Nup88 protein analysis in U937 cells We used flow cytometry to measure the expression of Nup98 and Nup88 in untreated U937 cells, and in U937 cells treated with deguelin. In untreated cells, the average fluorescence intensity of Nup98 in the blank controls was 23.55. In cells treated with 10 nmol/L and 20 nmol/L deguelin for 24 h, the average fluorescence intensity of Nup98 was 189.58 and 249.32, respectively. The average fluorescence intensity of Nup88 in the blank controls was 53.92. When cells were treated with 10 nmol/L and 20 nmol/L deguelin for 24 h, the average fluorescence intensity of Nup88 was 11.12 and 10.03, respectively (Figure 4; n=3).

Location of Nup98 and Nup88 in U937 cells To visualize the subcellular location of Nup98 and Nup88, untreated and treated U937 cells were detected by using immunoelectron microscopy. In Figure 5, the nuclear pore proteins are indicated by arrowheads and are mainly located within the nuclear membrane. The density of the nuclear pore protein is based on DAB staining. In Figure 5, the electronic density of Nup98 in untreated cells is lower than that in deguelin-treated U937 cells. The electronic density of Nup88 in untreated cells was higher than that in deguelin-treated U937 cells.

Expression of Nup98 and Nup88 in U937 cells Our results reveal that deguelin can induce antiproliferation and apoptosis in U937 cells. However, it is unclear how U937 induces these effects. U937 cells treated with 10 nmol/L and 20 nmol/L of deguelin for 24 h were lysed and resolved using 10% SDS-PAGE, and then Western blot analysis was carried out using anti-Nup98 and anti-Nup88. Figure 6 shows the marked change in Nup98 and Nup88 expression following deguelin treatment. Deguelin is related to upregulating the expression of Nup98 and downregulating the expression of the Nup88 protein. This indicates that Nup98 and Nup88 are related to the deguelin-mediated nucleocytoplasm shuttling activity, which is related to cell proliferation and apoptosis.

Discussion

Deguelin, a natural plant extract, is commonly used as an insecticide in Africa, South America and China. Deguelin belongs to a class of compounds called rotenoids, which have chemopreventive activity[6]. In fact, deguelin has already been shown to prevent skin and breast tumors in experimental models[7]. It has chemopreventive activity, and acts by inhibiting NADH:ubiquinone oxidoreductase activity, and by regulating the cell cycle and inducing apoptosis[7]. Chun *et al* found that deguelin inhibited the growth of and promoted apoptosis of premalignant and malignant cells[8].

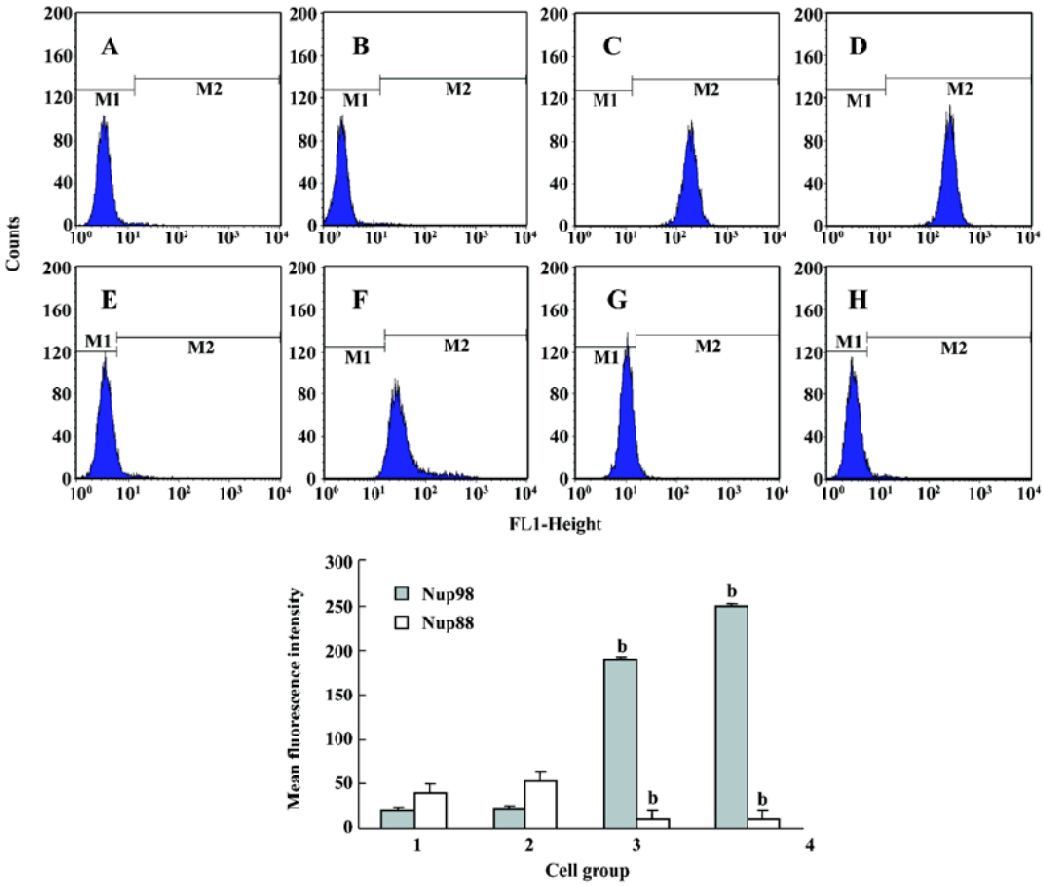

Figure 4. Deguelin regulates the expression of Nup98 and Nup88 protein in U937 cells. Data were obtained using FACSort (Becton Dickinson). A and E are the negative controls (1); B and F are the Nup98 blank control and the Nup88 blank control (2); C and G are cells treated with 10 nmol/L deguelin for 24 h (3); D, H are cells treated with 20 nmol/L deguelin for 24 h (4). n=3. Mean±SD. ^{b}P<0.05 *vs* blank control.

In contrast, the compound had little effect on normal HBE cells. The drug's antineoplastic effects and specificity appeared to be due to its ability to inhibit phosphatidylinositol 3-kinase (PI3K)/Akt-mediated signaling pathways[9,10]. Bortul *et al* found that deguelin enhanced the sensitivity of U937 leukemia cells and acute myeloid leukaemia (AML) blasts to chemotherapeutic drugs with an activated PI3K/Akt network[10]. In the present experiment we found that deguelin suppressed the proliferation of U937 cells, and that deguelin may have potential as an anti-tumor medicine. After treatment with different doses of deguelin, U937 cells accumulated in the S and G_2/M phases, whereas the number of cells in the G_0/G_1 phase decreased in a dose-dependent manner. We also found that deguelin upregulated the expression of Nup98 and downregulated the expression of Nup88 in U937 cells. This suggests that changes in the ratio of Nup98 and Nup88 might contribute to the apoptosis-promoting activity of deguelin in these cells. The changes effected in nucleoporin in U937 cells by deguelin offer new possibilities for exploring the underlying anti-tumor mechanism of deguelin.

The various events of nuclear division, cytoplasmic division, cell growth, and cell maturation are repeated in each generation of cells[12]. The periods of time and the sequence of events from one cell division to the next are collectively referred to as the cell cycle. Severe defects in chromosomes block progression through the cell cycle, and can lead to cell suicide or apoptosis[13]. Deguelin plays an important pharmacological role by acting on different stages of the cell cycle in tumor cells. In this study, U937 cells were arrested mainly in the S and G_2/M phases by deguelin, whereas the proportion of cells in the G_0/G_1 phase gradually declined. After treatment with different doses of deguelin for 24 h, cells in the G_0/G_1 phase were earliest influenced, and the proportion of cells in this phase decreased gradually in a dose-dependent manner. At the same time, the proportion of cells in the S phase increased gradually, with treatment

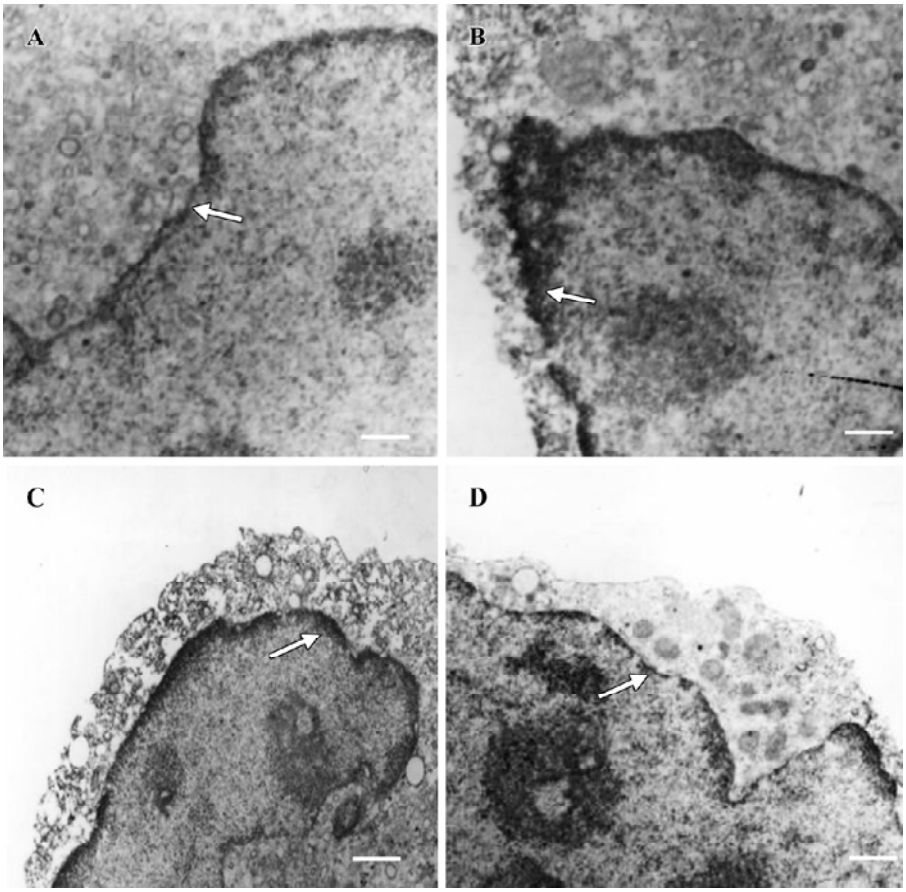

Figure 5. Regulation of Nup98 and Nup88 in U937 cells by deguelin. Images were obtained by immunoelectron microscopy. Nuclear pore proteins are indicated by arrowheads and are mainly located within the nuclear membrane. A and B show the localization of Nup98 in the untreated and deguelin-treated U937 cells. C and D show the localization of Nup88 in the untreated and deguelin-treated U937 cells. B and C show images with higher electronic density than A and D. In all panels, orientation is with cytoplasm up, nucleus down. Bars=800 nm.

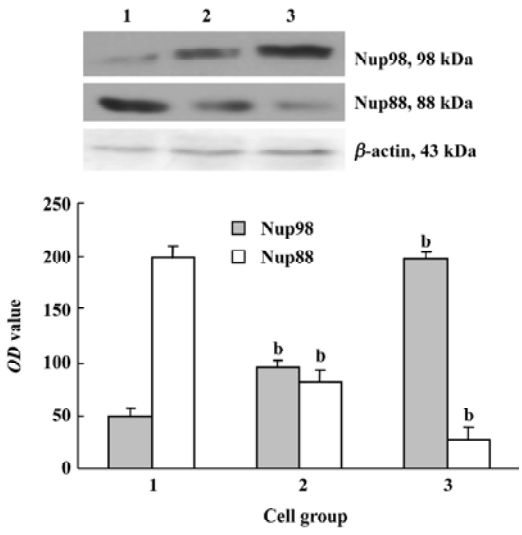

Figure 6. Effect of deguelin regulating the expression of Nup98 and Nup88 in U937 cells. Cells were treated with different concentrations of deguelin for 24 h, and Nup98 and Nup88 expression was evaluated by using Western blot analysis. 1, 2, and 3 are the control, 10 nmol/L deguelin and 20 nmol/L deguelin, respectively. n=3. Mean±SD. $^bP<0.05$ compared with the control.

with 80 nmol/L deguelin resulting in the highest value. The proportion of cells in the G_2/M phase increased in a dose-dependent manner. These data show that deguelin usually regulates the G_1/S and G_2/M checkpoints in U937 cells. Cell cycle checkpoint controls at the G_1 to S transition and the G2 to M transition prevent the cell cycle from progressing when DNA is damaged[14]. That deguelin regulates the cell cycle checkpoints has been verified in other tumor cells. Chun *et al* found that after treatment with deguelin, the proportion of premalignant cells in the G_0/G_1 phase increased and the proportion of malignant HBE cells in the G_2/M phase increased from 9.6% to 40.2%[8]. Bortul *et al* found that deguelin (10 nmol/L) induced S phase arrest by interrfering with the progression to G_2/M[10]. In our previous studies[11], we found that deguelin was able to inhibit the proliferation of Daudi cells by regulating the cell cycle that arrests cells at the G_0/G_1 phase, and had no effect on the G_2/M phase. The mechanism by which deguelin causes these different cell cycle changes is not yet completely clear, but it is mainly related to the sensitivity of tumor cells to deguelin.

Transport between the nucleus and the cytoplasm occurs through NPC embedded in the nuclear envelope.

Nucleoporins are involved in several types of acute myeloid leukemia and a few other hematological malignancies, as well as rare cases of other tumors[15]. An expanding subgroup of chromosomal translocation-generated oncoproteins in human acute myeloid leukemias (AML) involve the FG repeat-containing NPC proteins Nup98 and CAN/Nup214[16]. The *Nup98* gene is found at the breakpoints of two distinct chromosomal rearrangements: t (7;11)(p15;p15) and inv(11)(p15; q22), which link Nup98 to the class I homeotic transcription factor HOXA9 and the putative RNA helicase DDX10, respectively. The most common oncogenic fusions involve a segment of the gene encoding the FG-repeat domain of Nup98, which, in turn, becomes linked to genes of the homeobox family of transcription factors. The Nup98-derived FG-repeat segments of the resulting oncogene interact with the transcriptional coactivators CBP (CREB binding protein) and P300, thereby leading to increased gene transcription[17]. FG-repeat segments of two other nucleoporins, Nup153 and CAN/Nup214, can substitute for the Nup98 segment in the oncogenic fusion protein. When Nup98 is disrupted, it selectively impairs discrete protein import pathways, which supports the idea that transport of distinct import complexes through the NCP is mediated by specific subsets of nucleoporins. Because Nup98 plays a role in RNA export, its mobility suggests that Nup98 might associate with RNA close to its transcription site and then further accompany the processed RNA through the NPC into the cytoplasm[18]. Using confocal microscopy, we found that Nup98 was present on both sides of the NPC in U937 cells, and was localized inside the nucleus. When cells were treated with 10 nmol/L and 20 nmol/L deguelin for 24 h, the average fluorescence intensity of Nup98 was 189.58 and 249.32. Deguelin can regulate the expression of Nup98, and this shows that deguelin participates in Nup98 leading nucleocytoplasmic traffic.

Nup88 is a NCP protein; the *Nup88* gene is localized at 17p13 and the Nup88 protein is involved in nuclear–cytoplasmic transport and cell growth[19]. Overexpression of Nup88 has been found in human tumors of the stomach, colon, liver, pancreas, breast, lung, ovary, uterus, prostate and kidney[20]. The Nup88 protein is also overexpressed in malignant tumor tissue relative to normal surrounding tissue. Recent studies have found that the Nup88 protein is enhanced in most metastatic melanomas relative to their corresponding primary tumors[21]. Both RNA transcription and protein expression levels are higher in malignant tumor cell lines compared with non-transformed cells. The Nup88 protein is strongly expressed in the invasive margins of both primary and metastatic breast, endometrial and colorectal carcinomas[22]. Overexpression of Nup88 in malignant tumors is probably due to the enhanced nucleocytoplasmic transport required to meet the increased demand for proteins in the tumor cells. Nup88 is considered to be a tumor growth factor, and is a positive regulator in the cell cycle. For this reason, we devised the present study on Nup88 expression in U937 cells and studied the regulative effects of deguelin on Nup88. Our data support the idea that Nup88 might be involved in the tumor progression of U937 cells, and these findings show that deguelin participates in Nup88 leading nucleocytoplasmic traffic.

In summary, our results show that deguelin can inhibit U937 cell proliferation in a dose- and time-dependent manner, with an IC_{50} value for 24 h of 21.61 nmol/L and an IC_{50} value for 36 h of 17.07 nmol/L. Deguelin usually regulates the G_1/S and G_2/M checkpoints. In addition, deguelin causes upregulation of the expression of Nup98, and downregulation of the Nup88 protein in U937 cells. The reasons for this effect, and the mechanisms for this regulation of Nup98 and Nup88, and whether these mechanisms are linked to inhibited cell proliferation, are unknown, but our findings suggest that Nup98 and Nup88 may be involved in nucleocytoplasmic shuttling in carcinoma cells.

Acknowledgements

We thank the Tumour Biology Laboratory, Center of Gynaecology, Tongji Hospital, Huazhong University of Science and Technology, China, for offering relevant experimental facilities and technical support. We wish to particularly thank Prof Yun-ping LU for guidance and help with the experiment.

References

1 Frosst P, Guan T, Subauste C, Hahn K, Gerace L. Tpr is localized within the nuclear basket of the pore complex and has a role in nuclear protein export. J Cell Biol 2002; 156: 617–30.

2 Enninga J, Levy DE, Blobel G, Fontoura BM. Role of nucleoporin induction in releasing an mRNA nuclear export block. Science 2002; 295: 1523–5.

3 Griffis ER, Xu SL, Powers MA. Nup98 localizes to both nuclear and cytoplasmic sides of the nuclear pore and binds to two distinct nucleoporin subcomplexes. Mol Biol Cell 2003; 14: 600–10.

4 Griffis ER, Altan N, Lippincott-Schwartz J, Powers MA. Nup98 is a mobile nucleoporin with transcription-dependent dynamics. Mol Biol Cell 2002; 13: 1282–97.

5 Nerea M, Angel A, Moragues MD, Jose P, Jose S. The nuclear pore complex protein Nup88 is overexpressed in tumor cells. Cancer Res 1999; 59: 5408–11.

6 Udeani GO, Gerhauser C, Thomas CF, Moon RC, Kosmeder JW, Kinghorn AD, *et al*. Cancer chemopreventive activity mediated

by deguelin, a naturally occurring rotenoid. Cancer Res 1997; 57: 3424–8.
7 Lee HY, Suh YA, Kosmeder JW, Pezzuto JM, Hong WK, Kurie JM. Deguelin-induced inhibition of cyclooxygenase-2 expression in human bronchial epithelial cells. Clin Cancer Res 2004; 10: 1074–9.
8 Chun KH, Kosmeder JW 2nd, Sun S, Pezzuto JM, Lotan R, Hong WK, *et al*. Effects of deguelin on the phosphatidylinositol 3-kinase/Akt pathway and apoptosis in premalignant human bronchial epithelial cells. J Natl Cancer Inst 2003; 95: 291–302.
9 Murillo G, Salti GI, Kosmeder JW, Pezzuto JM, Mehta RG. Deguelin inhibits the growth of colon cancer cells through the induction of apoptosis and cell cycle arrest. Eur J Cancer 2002; 38: 2446–54.
10 Bortul R, Tazzari PL, Billi AM, Tabellini G, Mantovanil l, Cappellini A, *et al*. Deguelin, a PI3K/AKT inhibitor, enhances chemosensitivity of leukaemia cells with an active PI3K/AKT pathway. Br J Haematol 2005; 129: 677–86.
11 Liu HL, Chen Y, Cui GH, Wu QL, He J. Experimental study on regulating expressions of cyclin D1, pRb, and anticancer effects of deguelin on human Burkitt's lymphoma Daudi cells *in vitro*. Acta Pharmacol Sin 2005; 26: 873–80.
12 Liu HL, Chen Y, Cui GH, Zhou JF. Curcumin, a potent anti-tumor reagent, is a novel histone deacetylase inhibitor regulating B-NHL cell line Raji proliferation effect. Acta Pharmacol Sin 2005; 26: 603–9.
13 Evan GI, Vousden KH. Proliferation, cell cycle and apoptosis in cancer. Nature 2001; 411: 342–8.
14 Sun SY, Hail N Jr, Lotan R. Apoptosis as a novel target for cancer chemoprevention. J Natl Cancer Inst 2004; 96: 662–72.
15 Pietenpol JA, Stewart ZA. Cell cycle checkpoint signaling: cell cycle arrest versus apoptosis. Toxicology 2002; 181: 475–81.
16 Hodel AE, Hodel MR, Griffis ER, Hennig KA, Ratner GA, Xu S, *et al*. The three-dimensional structure of the autoproteolytic, nuclear pore-targeting domain of the human nucleoporin Nup98. Mol Cell 2002; 10: 347–58.
17 Gould VE, Martinez N, Orucevic A, Schneider J, Alonso A. A novel, nuclear pore-associated, widely distributed molecule overexpressed in oncogenesis and development. Am J Pathol 2000; 157: 1605–13.
18 Kobzev YN, Martinez-Climent J, Lee S, Chen J, Rowley JD. Analysis of translocations that involve the NUP98 gene in patients with 11p15 chromosomal rearrangements. Genes Chromosomes Cancer 2004; 41: 339–52.
19 Slape C, Aplan PD. The role of NUP98 gene fusions in hematologic malignancy. Leuk Lymphoma 2004; 45: 1341–50.
20 Zhang H, Schneider J, Rosdahl I. Expression of p16, p27, p53, p73 and Nup88 proteins in matched primary and metastatic melanoma cells. Int J Oncol 2002; 21: 43–8.
21 Agudo D, Gomez EF, Martinez AF, Nunez MJ, Pollan M, Schneider J. Nup88 mRNA overexpression is associated with high aggressiveness of breast cancer. Int J Cancer 2004; 109: 717–20.
22 Gould VE, Orucevic A, Zentgraf H, Gattuso P, Martinez N, Alonso A. Nup88 (karyoporin) in human malignant neoplasms and dysplasias: correlations of immunostaining of tissue sections, cytologic smears, and immunoblot analysis. Hum Pathol 2002; 33: 536–44.
23 Boer J, Bonten-Surtel J, Grosveld G. Overexpression of the nucleoporin CAN/NUP214 induces growth arrest, nucleocytoplasmic transport defects, and apoptosis. Mol Cell Biol 1998; 18: 1236–47.

Acta Pharmacologica Sinica 2005 Oct; 26 (10): 1274–1280

Full-length article

Pharmacokinetics of sifuvirtide, a novel anti-HIV-1 peptide, in monkeys and its inhibitory concentration *in vitro*[1]

Shu-jia DAI[2], Gui-fang DOU[3], Xiao-hong QIAN[4,5], Hai-feng SONG[4], Zhong-ming TANG[2], De-sheng LIU[2], Xiu-wen LIU[2], Liu-meng YANG[6], Yong-tang ZHENG[6], Qing LIANG[7]

[2]Laboratory of Metabolism of Biotechnology Derived Drugs, Beijing Institute of Radiation Medicine, Beijing 100850; [3]Laboratory of Drug Metabolism and Pharmacokinetics, Beijing Institute of Transfusion Medicine, Beijing 100850; [5]Laboratories of Genomics and Proteomics, Beijing Institute of Radiation Medicine, Beijing 100850; [6]Laboratory of Molecular Immunopharmacology, Kunming Institute of Zoology, Chinese Academy of Sciences, Kunming 650223; [7]FusoGen Pharmaceuticals Inc, Tianjin 300051, China

Key words

sifuvirtide; pharmacokinetics; HIV; HIV fusion inhibitors; enfuvirtide; on-line solid-phase extraction; macaque

[1] Project supported by the National Natural Science Foundation of China (No 39930180, 20275046, 30321003, 30371669), the National High Technology Research and Development Program (No 2003AA2Z347B, 2002BA711A11, 2004BA711A18, 2004-BA719A14), and Key Scientific and Technological Projects of Yunnan (No 2004NG12).
[4] Correspondence to Assoc Prof Hai-feng SONG.
Phn/Fax 86-10-6693-1230.
E-mail songhf@nic.bmi.ac.cn
Prof Xiao-hong QIAN.
Phn/Fax 86-10-6827-9585.
E-mail qianxh@nic.bmi.ac.cn

Received 2005-03-07
Accepted 2005-04-30

doi: 10.1111/j.1745-7254.2005.00163.x

Abstract

Aim: To study the pharmacokinetics of sifuvirtide, a novel anti-human immunodeficiency virus (HIV) peptide, in monkeys and to compare the inhibitory concentrations of sifuvirtide and enfuvirtide on HIV-1-infected-cell fusion. **Methods:** Monkeys received 1.2 mg/kg iv or sc of sifuvirtide. An on-line solid-phase extraction procedure combined with liquid chromatography tandem mass spectrometry (SPE-LC/MS/MS) was established and applied to determine the concentration of sifuvirtide in monkey plasma. A four-^{127}I iodinated peptide was used as an internal standard. Fifty percent inhibitory concentration (IC_{50}) of sifuvirtide on cell fusion was determined by co-cultivation assay. **Results:** The assay was validated with good precision and accuracy. The calibration curve for sifuvirtide in plasma was linear over a range of 4.88–5000 μg/L, with correlation coefficients above 0.9923. After iv or sc administration, the observed peak concentrations of sifuvirtide were 10 626±2 886 μg/L and 528±191 μg/L, and the terminal elimination half-lives ($T_{1/2}$) were 6.3±0.9 h and 5.5±1.0 h, respectively. After sc, T_{max} was 0.25–2 h, and the absolute bioavailability was 49%±13%. Sifuvirtide inhibited the syncytium formation between HIV-1 chronically infected cells and uninfected cells with an IC_{50} of 0.33 μg/L. **Conclusion:** An on-line SPE-LC/MS/MS approach was established for peptide pharmacokinetic studies. Sifuvirtide was rapidly absorbed subcutaneously into the blood circulation. The $T_{1/2}$ of sifuvirtide was remarkably longer than that of its analog, enfuvirtide, reported in healthy monkeys and it conferred a long-term plasma concentration level which was higher than its IC_{50} *in vitro*.

Introduction

Human immunodeficiency virus (HIV) infection is now a major public health problem for both developing and developed countries as it has dramatically increased the global burden of disease[1–5]. Many efforts have been made on research and discovery of anti-HIV drugs; however, it still remains difficult to develop more effective, affordable, and less toxic anti-HIV drugs for the increasing number of HIV-infected patients[6].

In recent years, more and more researchers have fixed their eyes on preventing the entry of HIV into a host cell at the step of gp41-mediated viral and cellular membrane fusion, which was denoted as fusion inhibitors[7]. The Food and Drug Administration of the United States announced, in 2003, the accelerated approval of enfuvirtide, the first fusion inhibitor, for use in combination with other anti-HIV medications to treat advanced HIV-1 infection in adults and children aged 6 years and older[8]. Enfuvirtide is administered twice daily by subcutaneous injection into the abdomen, the upper arm, or the anterior thigh for clinical therapeutics[9].

Sifuvirtide is a linear 36-amino acid peptide with an amino

acid sequence of Acetyl-SWETWEREIENYTRQIYRILEE-SQEQQDRNERDLLE. It is a novel antiviral peptide that has been classified as a fusion inhibitor. The profiles of absorption, distribution, metabolism and excretion of sifuvirtide have been characterized in rats and monkeys by using radioactive ^{125}I-sifuvirtide combined with radioactivity detection of samples derived from trichloroacetic acid precipitation or size-exclusion chromatography. For the requirement of clinical pharmacokinetic (PK) study, we have developed an advanced and validated on-line solid-phase extraction procedure combined with liquid chromatography tandem mass spectrometry (SPE-LC/MS/MS) approach for determination of non-labeled sifuvirtide in monkey plasma[10].

In the present study, an *in vitro* fusion inhibitory experiment was used to determine the 50% inhibitory concentration (IC_{50}) of sifuvirtide. According to the results of 50 times lower IC_{50} value than enfuvirtide and the pharmacological experiments in monkeys, a relatively low clinical dosage was set at about 10 mg per adult, per day (while that of enfuvirtide was 180 mg[9]). The PK profiles and bioavailability of sifuvirtide following single sc or iv dosage of 1.2 mg/kg in rhesus monkeys were investigated. The preliminary results indicated that sifuvirtide made a difference in antiviral activity *in vitro* and PK behaviors *in vivo* compared with enfuvirtide.

Materials and methods

Drugs and reagents The sifuvirtide standard was provided by FusoGen Pharmaceuticals (Tianjin, China). Enfuvirtide was obtained from Hoffmann-La Roche (Nutley, NJ, USA). RPMI-1640 complete culture medium containing 10% heat-inactivated newborn calf serum (NCS), *L*-glutamine 2 mmol/L, 4-(2-hydroxyethyl)-1-piperazineethanesulfonic acid (HEPES) 10 mmol/L, 2-mercaptoethanol 50 μmol/L, benzylpenicillin 100 kIU, and streptomycin sulfate 100 mg/mL were purchased from Gibco BRL (Gaithersburg, Maryland, USA) . C8166 and HIV-1_{IIIB} chronically infected H9 cell lines (HIV-1_{IIIB}/H9) were kindly donated by the Medical Research Council of United Kingdoms (AIDS Reagent Project) (London, UK). Drug-free monkey plasma was collected from 6 healthy rhesus monkeys of both sexes. Acetonitrile (ACN) and other solvents were of HPLC-grade and purchased from Fisher Scientific (Pittsburgh, PA, USA). A protease inhibitor cocktail tablet, Complete Mini (Roche Diagnostics, Mannheim, Germany), without ethylene diamine tetraacetic acid, was used to prevent peptide degradation in biological matrixes. Formic acid (FA), trifluoroacetic acid (TFA) and sodium iodine were obtained from Aldrich Chemical Co (Milwaukee, WI, USA). Highly purified water was produced by a Millipore Simplicity 185 Unit (Millipore, Bedford, MA, USA). Mobile phase A (MP_A) was 0.1% (v/v) FA in water. Mobile phase B (MP_B) was 0.1% (v/v) FA in ACN.

Synthesis of the internal standard In this study, a novel strategy, non-radioactive iodination of peptides, was used to acquire an internal standard (IS) for the quantitative assay. Reaction of iodination was carried out mainly as described previously[11]. To acquire the highest productivity of peptide iodide, the molar ratio of iodine-127 to peptide standard was at least 20:1. The reaction was carried out at room temperature for 10 min. The reaction mixture was then desalted and purified by a RP-HPLC method utilizing a Vydac analytical C18 column (5 μm, 300 Å, 4.6 mm×150 mm; Vydac, Hesperia, CA, USA) with a gradient of MP_B increasing from 25% to 75% in 20 min, coupled with fraction collection equipment (Pharmacia, Uppsala, Sweden). The purified product was stored at 4 °C and identified using LC/MS/MS to be the goal peptide (purity >97%) with the 4-^{127}I modifications ($^{127}I_4$-sifuvirtide) on tyrosine (Y) residues [SWETWEREIENY(I_2) TRQIY(I_2)RILEESQEQQDRNERDLLE].

Cell fusion assay The inhibition of sifuvirtide on cell-to-cell transmission of HIV-1 was determined by co-cultivation of uninfected normal cells and HIV-1_{IIIB} chronically infected cells, as described previously[12]. Briefly, 3×10^4 C8166 cells were mixed with 1×10^4 HIV-1_{IIIB} chronically infected H9 cells in 96-well plates in the presence or absence of sifuvirtide at various concentrations. Enfuvirtide was used as the control. After co-culture for 24 h at 37 ºC in 5% CO_2, the number of syncytia was counted using an inverted microscope. The percentage inhibition of cell fusion was calculated by dividing the number of syncytial cells in compound-treated cultures by those in untreated cultures. The IC_{50} was determined from a dose-response curve.

On-line sample preparation The on-line extraction column was prepared using an empty stainless steel column (size of 50 mm length×2.1 mm ID, 2 μm frit; GEA Co, Beijing, China) packed with reversed-phase materials. The packing materials used for SPE were obtained from Agilent (Zorbax C18; spherical; average particle size 50 μm; pore size 80 Å; Agilent; Waldbronn, Germany). Aliquots of calibrators or unknown samples (100 μL) were introduced onto the extraction column for on-line preparation and LC/MS/MS analysis. The plasma samples were diluted 5 times on-line, based on the design of an on-line splitter, between the sample loop and bypassing branch at a ratio of approximately 1:4. The whole process, including sample loading, extraction, separation and analysis, was carried out based on the column-switching program. Programmed events corresponding to valve switching were set up using the ChemStation (version

9.02) for Agilent 1100 series HPLC system and Xcalibur™ (version 1.4) for LTQ-MS system.

LC/MS/MS system The separation and detection section, the LC/MS/MS system used for the assay, was made up of the Agilent 1100 series HPLC system (including an online degasser), a 100-vial autosampler, a temperature control compartment equipped with a 6-port/2-position switching valve, and a binary solvent delivery pump, coupled to a novel linear ion trap mass spectrometer, LTQ-MS (Thermo Finnigan, San Jose, CA, USA), equipped with a new atmospheric pressure ionization interface, Ion MAX™. MS/MS detection was operated in electrospray ionization positive ion mode. The representative parameters of MS were as shown below. The spray voltage was 4.5 kV and the temperature of the heated capillary was set at 200 °C. The flow rates of sheath gas, auxiliary gas and sweep gas were set (in arbitrary units/min) to 20, 5, and 4, respectively. Other parameters were optimized automatically by infusing the analyte in water: ACN:formic acid (49.9:50:0.1, v:v:v) at a flow rate of 200 μL/min. Quantitation was carried out using selected reaction monitoring (SRM) of the transitions *m/z* 946.5→ *m/z* 871.8 for sifuvirtide and *m/z* 1047.2→*m/z* 972.3 for the IS ($^{127}I_4$-sifuvirtide).

Preparation of stock solutions and calibration standard samples Stock solutions of sifuvirtide were prepared at concentrations of 1.0 g/L in a MP_A:MP_B (90:10, v/v) solvent system. The drug-free monkey blood was deactivated by spiking with protease inhibitor cocktail tablets (2 tablets/5 mL whole blood). All blood samples collected from monkey sources were transferred immediately into tubes coated with calculated heparin and an inhibitor mixture of protease and peptidase on the tube surface. After incubation on ice for 30 min, they were centrifuged at 1000×*g* for 10 min. The supernatant of each was then harvested and stored at -80 °C until analysis. The deactivated drug-free plasma from monkey sources was used as the standard dilution for the calibration samples. Each calibration curve consisted of blank samples, zero samples (plasma sample processed with IS), and 6 non-zero samples, ranging from 4.88 μg/L to 5000 μg/L. Before the assay, the frozen samples were thawed at ambient temperature, vortex-mixed and centrifuged at 1000×*g* for 5 min. For each of the calibrators or unknown samples, 100 μL aliquots of supernatant were added to vials containing 10 μL $^{127}I_4$-sifuvirtide working solution (5 mg/L) and 10 μL 2.5% ammonia solution ($NH_3 \cdot H_2O$, w/v). The vials were vortex-mixed for 30 s, placed immediately in the autosampler tray and kept at room temperature for assay.

Method validation The calibration curve and the concentration of unknown sample were acquired using LCQuan software (version 2.0) from Thermo Finnigan. A weighting of $1/x^2$ (where x is the concentration of a given standard) was used for curve fit. The intra-day and inter-day accuracy and precision of the method presented here was investigated by analyzing plasma samples at the whole calibration concentration levels. The regression equation for the calibration curve was used to back-calculate the measured concentration for each standard, and the results were compared to the theoretical concentration to calculate the accuracy, expressed as a percentage of the theoretical value, for each standard measured.

Animal experiments Three rhesus monkeys (2 ♀ and 1 ♂, body weight of 4.1±0.4 kg) were provided by the Animal Center of the Academy of Military Medical Sciences, with certificate number 97083. The monkeys were fasted overnight prior to dosing and given free access to food and water 48 h post dosage. A dosing solution (1.0 g/L) was formulated in saline. Sifuvirtide was administered iv to monkeys at 1.2 mg/kg via a side femoral venous catheter. Blood samples (0.5 mL) were collected from a femoral venous catheter on the opposite side at 0 min, 1 min, 5 min, 15 min, 30 min, 1 h, 2 h, 4 h, 6 h, 8 h, 12 h, 24 h, and 48 h after dosing. After a 7-d washout period, the monkeys were administered the same dosage and blood samples were harvested at 0 min, 10 min, 15 min, 30 min, 1 h, 2 h, 4 h, 5 h, 6 h, 8 h, 10 h, 12 h, 24 h, 36 h, and 48 h following dosing. All samples were harvested and treated in the same way as calibrators. A 200 μL aliquot from each time point was used for the assay. The plasma samples from 1 min, 5 min, and 15 min after iv were diluted 5 times because their concentrations were suspected to be higher than detectable levels. The curve according to plasma sifuvirtide concentration versus time after dosing was obtained using Origin software (Version 5.0; Microcal, Northampton, MA, USA).

Estimation of pharmacokinetic parameters Pharmacokinetic modeling and estimation of PK parameters were carried out using Excel XP software (Microsoft, Redmond, WA, USA). C_{max} and T_{max} were observed values. Other PK parameters, including area under the concentration-time curve (AUC), apparent plasma terminal elimination $T_{1/2}$, mean residence time (MRT), volume of distribution (V_d) and systematic clearance (CL), were calculated according to a previous description of the non-compartmental approach[13]. In addition, the absolute bioavailability (F_{abs}, %) was calculated by the following equation: [(subcutaneous AUC_{0-t}/intravenous AUC_{0-t})×100%].

Results

Effects of sifuvirtide on HIV-1 entry Sifuvirtide inhib-

ited syncytium formation between HIV-1_{IIIB}/H9 cells and C8166 cells with an IC_{50} value of 0.33 μg/L. The IC_{50} of sifuvirtide was approximately 50-fold lower than that of enfuvirtide (16.8 μg/L). The results suggested that sifuvirtide was more effective than enfuvirtide in blocking HIV-1 entry into cells.

Mass spectrometry detection of sifuvirtide and $^{127}I_4$-sifuvirtide The mass spectrum obtained by infusing 10 mg/L solution of sifuvirtide and $^{127}I_4$-sifuvirtide in water:ACN (50:50, *v*/*v*) at a flow rate of 5 μL/min is shown in Figure 1A. A series of multiply charged ions, $[M+5H]^{5+}$ at *m/z* 946.5, $[M+4H]^{4+}$ at *m/z* 1182.9 and $[M+3H]^{3+}$ at *m/z* 1576.6 for sifuvirtide, and $[M+5H]^{5+}$ at *m/z* 1047.2, $[M+4H]^{4+}$ at *m/z* 1308.7 and $[M+3H]^{3+}$ at *m/z* 1744.6 for $^{127}I_4$-sifuvirtide, were observed in positive ion mode. Deconvoluted mass obtained automatically utilizing the Bioworks software (Ver 3.1 SR1, Thermo-Electron, San Jose, CA, USA) showed a difference of 503.3 u (theoretical value was 503.6 u) between sifuvirtide and $^{127}I_4$-sifuvirtide, which demonstrated that a complete iodination had been performed and reached the goal product. The most abundant ions of sifuvirtide and $^{127}I_4$-sifuvirtide, $[M+5H]^{5+}$ at *m/z* 946.5 and *m/z* 1047.2, respectively, were selected as parent ions for a collision-induced dissociation experiment. The most intensive product ions for sifuvirtide and IS were observed at *m/z*=871.87 ($b33^{5+}$) and *m/z*=972.6 ($b33^{5+}$), respectively, both with optimized normalized collision energy of 28%[10].

Method validation Under the established SPE-LC/MS/MS conditions, the typical retention times for sifuvirtide and IS were 7.68 min and 7.91 min, respectively, without interference from endogenous plasma components. The limit of detection was 1.22 μg/L, which represented 122 pg on-column injected analyte (approximately 26 fmol in drug-free monkey plasma, absolute recovery was seen as 100%), with a signal to noise (S/N) ratio above 10. The typical chromatograms of sifuvirtide in monkey plasma are illustrated in Figure 2. Calibration curves exhibited excellent linearity over a range of 4.88 μg/L to 5000 μg/L, and the typical regression equation for sifuvirtide was y=0.01736–0.003759x, with a r^2 of 0.9929. The intra-assay and inter-assay precision and accuracy values of the method were assessed using spiked plasma samples at whole calibration concentration levels for sifuvirtide, shown in Table 1. The mean accuracy of back-calculated concentrations of the standards compared with theoretical ones ranged from -5.36% to 4.61%. The inter-batch CV ranged from 2.9% to 8.8%, and the intra-batch CV

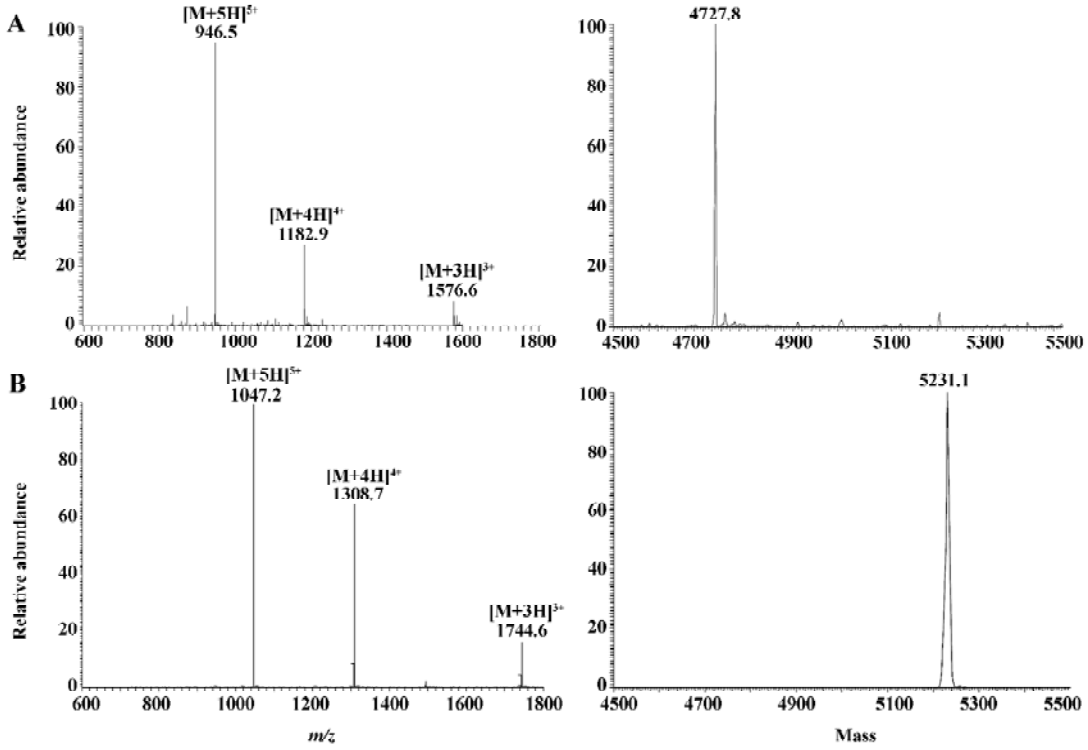

Figure 1. Electrospray ionization mass spectra (left) and deconvoluted spectra (right) of (A) sifuvirtide and (B) the internal standard $^{127}I_4$-sifuvirtide in positive ion mode. The observed masses (*m/z*) of multiply charged ions are given in this figure.

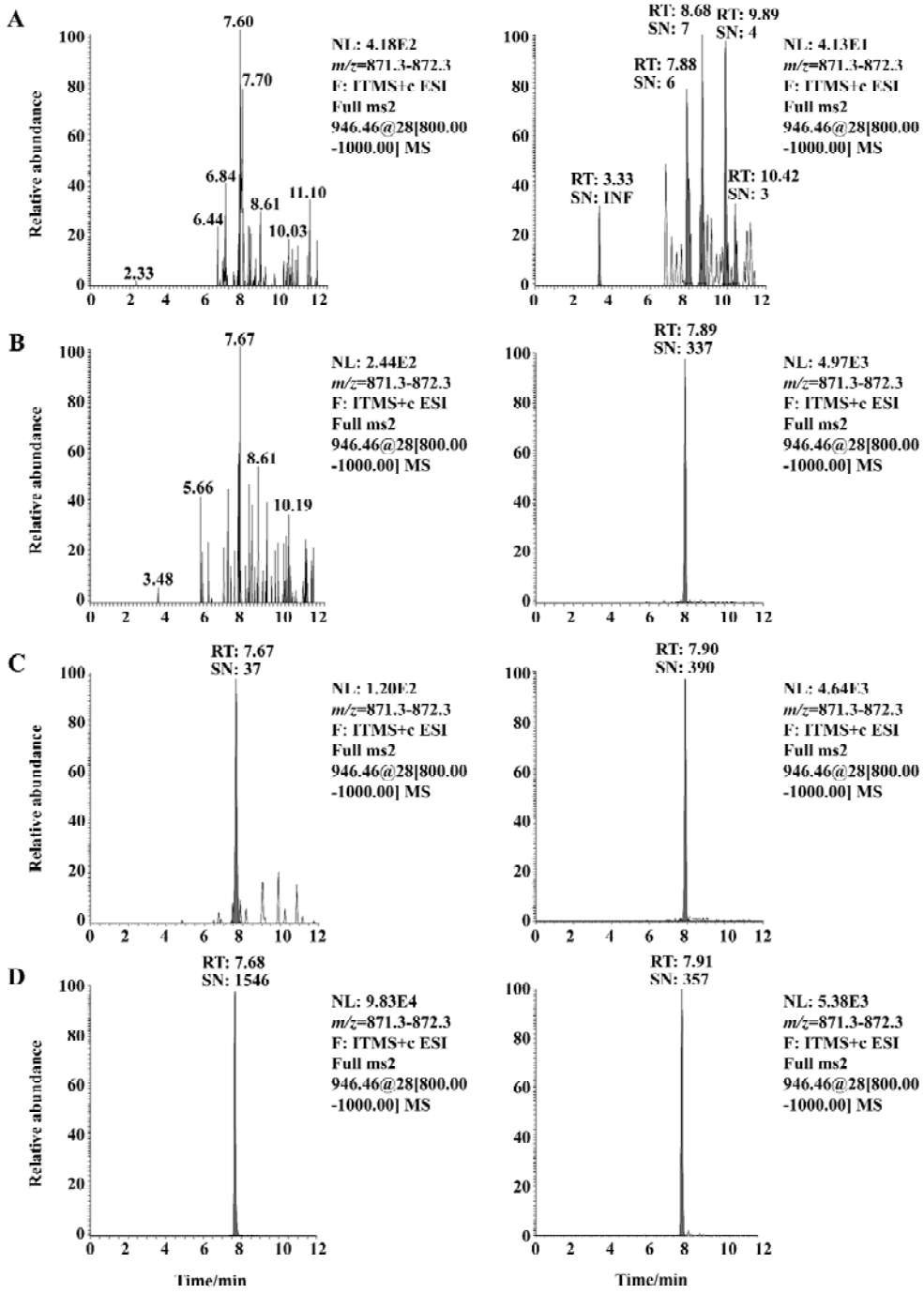

Figure 2. Selected reaction monitoring of sifuvirtide (left) and the internal standard (IS) $^{127}I_4$-sifuvirtide (right) in (A) blank drug-free monkey plasma and (B) plasma samples at zero concentration (with IS), (C) lower limit of quantitation (4.88 μg/L sifuvirtide) and (D) upper limit of quantitation (5000 μg/L sifuvirtide).

did not exceed 10.5%. The stability of sifuvirtide in solution and in plasma samples was also evaluated[10]. The areas ratios of SRM chromatography spectra of sifuvirtide versus IS were investigated in stock solution kept in 4 °C for approximately 15 d and in plasma samples left at 15 °C overnight (12 h–14 h). No real change in the area ratio of sifuvirtide to IS was observed.

Phamacokinetics of sifuvirtide in rhesus monkeys The individual concentration-time profiles of sifuvirtide after iv or sc administration are shown in Figure 3. Plasma concen-

Table 1. Accuracy and precision of a solid-phase extraction procedure combined with liquid chromatography tandem mass spectrometry method to determine sifuvirtide concentrations in monkey plasma.

Calibration level	1	2	3	4	5	6
Nominal concentration/μg·L^{-1}	4.88	19.5	78.1	312.5	1250	5000
	Back-calculated concentration in pooled monkey plasma/μg·L^{-1}					
Intra-batch number						
1	4.76	18.3	83	289	1179	5022
2	5.44	17.5	74	310	1223	4872
3	4.21	21.6	83	323	1334	5521
4	4.92	18.2	68	332	1386	4915
Mean	4.83	18.9	77.1	314	1281	5083
SD	0.51	1.8	7.0	18	96	299
CV/%	10.5	9.6	9.1	5.9	7.5	5.9
Accuracy/%	-1.04	-3.33	-1.34	0.36	2.46	1.65
Inter-batch number						
1	4.76	18.3	83	289	1179	5022
2	5.47	17.4	71	323	1275	5078
3	5.09	20.9	84	275	1218	4832
Mean	5.1	18.9	79	296	1224	4978
SD	0.4	1.2	5.7	23	70	144
CV/%	8.8	6.1	7.2	7.8	5.7	2.9
Accuracy/%	4.61	-3.40	1.63	-5.36	-2.09	-0.45

tration versus time data was analyzed and the PK parameters are shown in Table 2. After administration of sifuvirtide at doses of 1.2 mg/kg, the observed peak concentration was 10 626±2886 μg/L for iv at 1 min, and 528±191 μg/L for sc at 0.25 h–2 h, respectively. The terminal elimination plasma half-lives ($T_{1/2}$) after iv or sc were 6.3±0.9 h and 5.5±1.0 h, respectively. Following sc administration, sifuvirtide was absorbed and distributed rapidly, and meanwhile was eliminated quickly in plasma. The bioavailability after sc injection was 49%±13%. In the present study, a remarkable inter-individual variability of the PK parameters, such as AUC, C_{max}, T_{max}, and F_{abs}, of sifuvirtide was observed in both iv and sc administration groups.

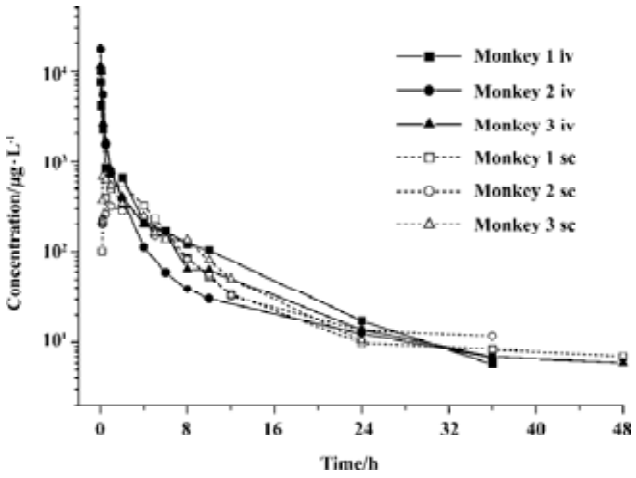

Figure 3. Concentration-time profiles of sifuvirtide in 3 monkeys after intravenous or subcutaneous administration at 1.2 mg/kg.

Table 2. Pharmacokinetic parameters of sifuvirtide after iv or sc administration at 1.2 mg/kg weight in rhesus monkeys. *n*=3. Mean±SD.

Parameter	Intravenous	Subcutaneous
T_{max}/h	–	1.1± 0.9 (0.25–2.0)
Observed peak concentration/μg·L^{-1}	10626±2886 (7503–11180)	528±191 (318–692)
AUC_{0-t}/μg·h·L^{-1}	4703±413 (4230–4987)	2263±452 (1758–2632)
$AUC_{0-\infty}$/μg·h·L^{-1}	4763±425 (4276–5059)	2355±421 (1889–2709)
MRT/h	2.2±0.5 (1.6–2.7)	4.7±0.9 (4.1–5.8)
CL_S/L·h^{-1}·kg^{-1}	0.253±0.024 (0.237–0.281)	0.52±0.10 (0.44–0.64)
V_d/L·kg^{-1}	0.55±0.19 (0.39–0.76)	2.5±1.0 (1.8–3.7)
Terminal $T_{1/2}$/h	6.3±0.9 (5.5–7.2)	5.5±1.0 (4.6–6.6)
F_{abs}/%	–	49±13 (35–62)

AUC, area under the concentration-time curve; CL, systematic clearance; F_{abs}, absolute bioavailability; MRT, mean residence time; V_d, volume of distribution.

Discussion

In the present study, the advanced on-line SPE-LC/MS/MS system was validated as being reliable, reproducible, and highly sensitive for the quantitative determination of sifuvirtide in monkey plasma. The programmable column-switching technique was the core of this fully automatic system. Based on the design of on-line splitting injection mode (OSIM), this novel on-line SPE system showed a powerful performance and capability for sample preparation of more than 300 raw plasma samples. The addition of pH adjusting solvent is very important for increasing the extraction efficiency of sifuvirtide. Coupled with LTQ-MS, a novel quadrupole ion trap mass spectrometer, a satisfactory sensi-

tive and good calibration curves yielding a wide linearity range over 3 orders of magnitude with correlation coefficients higher than 0.9923 were obtained.

Due to the lack of effective vaccines for the prevention of HIV infection, development of potent and affordable anti-HIV drugs is an international priority. As the first fusion inhibitor, enfuvirtide has been considered to have the disadvantages of short elimination half-life (2.5 h–3.5 h in the monkey via sc route[14]), which is administered twice at a high cost. A lower IC_{50} value of sifuvirtide for cell-to-cell transmission inhibition of HIV-1 *in vitro* was determined at around 0.33 μg/L, which is lower than that of enfuvirtide (16.8 μg/L). Therefore, a relatively lower dosage of sifuvirtide is recommended for future clinical treatments. In addition, the PK parameters of sifuvirtide after sc or iv dosing at 1.2 mg/kg weight in rhesus monkeys were below those of enfuvirtide (0.8 mg/kg in cynomolgus monkey[14]). Although the average observed concentration of sifuvirtide at 10 min after dosing was lower than that of enfuvirtide, the plasma concentration profiles of sifuvirtide after iv or sc were sustained at a relatively higher ratio to the *in vitro* IC_{50}, even at 36 h after dosing. The terminal half-life of sifuvirtide was estimated as 5.5 h–7.2 h after iv and 4.6 h–6.6 h after sc administration, which is longer than that of enfuvirtide. A lower average $AUC_{0-\infty}$ and higher mean V_d and CL (normalized by animal weight) was found for sifuvirtide compared with enfuvirtide, which indicated that sifuvirtide was widely distributed to tissues or organs via circulation of blood and showed the benefit of antiviral action *in vivo*. These results were in accordance with those derived from tissue distribution experiments by radioactive determination (data not shown). The comparative MRT and F_{abs} (%) of two peptides were estimated in monkeys by the non-compartmental approach. All of these results derived from inhibitory activity *in vitro* and PK characteristics provide an important reference for future clinical studies.

Acknowledgements

We thank Dr Zhi-yun MENG and Mr Jun LI for their helpful discussions and excellent technical support.

References

1 Locatelli GA, Cancio R, Spadari S, Maga G. HIV-1 reverse transcriptase inhibitors: current issues and future perspectives. Curr Drug Metab 2004; 5: 283–90.

2 Imamichi T. Action of anti-HIV drugs and resistance: reverse transcriptase inhibitors and protease inhibitors. Curr Pharm Des 2004; 10: 4039–53.

3 Mocroft A, Katlama C, Johnson AM, Pradier C, Antunes F, Mulcahy F, *et al*. AIDS across Europe, 1994–98: the EuroSIDA study. Lancet 2000; 356: 291–6.

4 Li Y, McDonald AM, Dore GJ, Kaldor JM. Improving survival following AIDS in Australia, 1991–1996. National HIV Surveillance Committee. AIDS 2000; 14: 2349–54.

5 Stolk LM, Luers JF. Increasing number of anti-HIV drugs but no definite cure. Review of anti-HIV drugs. Pharm World Sci 2004; 26: 133–6.

6 Ruprecht RM, Ferrantelli F, Kitabwalla M, Xu W, McClure HM. Antibody protection: passive immunization of neonates against oral AIDS virus challenge. Vaccine 2003; 21: 3370–3.

7 Wild CT, Shugars DC, Greenwell TK, McDanal CB, Matthews TJ. Peptides corresponding to a predictive alpha-helical domain of human immunodeficiency virus type 1 gp41 are potent inhibitors of virus infection. Proc Natl Acad Sci USA 1994; 91: 9770–4.

8 Williams IG. Enfuvirtide (Fuzeon): the first fusion inhibitor. Int J Clin Pract 2003; 57: 890–7.

9 Steinbrook R. HIV infection–a new drug and new costs. N Engl J Med 2003; 348: 2171–2.

10 Dai SJ, Song HF, Dou GF, Qian XH, Zhang YJ, Cai Y, *et al*. Quantification of sifuvirtide in monkey plasma by an on-line solid-phase extraction procedure combined with liquid chromatography/electrospray ionization tandem mass spectrometry. Rapid Commun Mass Spectrom 2005; 19: 1273–82.

11 Tejedor F, Ballesta JP. Iodination of biological samples without loss of functional activity. Anal Biochem 1982; 127: 143–9.

12 Wang Q, Wang YT, Pu SP, Zheng YT. Zinc coupling potentiate anti-HIV-1 activity of baicalin. Biochem Biophys Res Commun 2004; 324: 605–10.

13 Dunne A. Statistical moments in pharmacokinetics: models and assumptions. J Pharm Pharmacol 1993; 45: 871–5.

14 US Food and Drug Administration [homepage on the internet]. Rockville MD: Food and Drug Administration; 2003 [date created 2003 Jul 23; cited 2005 Feb, 19]. Available from: http://www.fda.gov/cder/foi/nda/2003/021481_fuzeon_review.htm

Acta Pharmacologica Sinica 2005 Nov; 26 (11): 1281–1287

Blackwell Publishing

Invited review

Recent progress in α_1-adrenergic receptor research

Zhong-jian CHEN, Kenneth P MINNEMAN[1]

Department of Pharmacology, School of Medicine, Emory University, Atlanta, GA 30322, USA

Key words

alpha1-adrenergic receptor; noncompetitive drug; protein-protein interaction; dimerization; cell surface expression

[1] Correspondence to Dr Kenneth P MINNEMAN.
Phn 1-404-727-5985.
Fax 1-404-727-0365.
E-mail kminneman@pharm.emory.edu

Received 2005-04-18
Accepted 2005-08-28

doi: 10.1111/j.1745-7254.2005.00224.x

Abstract

α_1-Adrenergic receptors (AR) play an important role in the regulation of physiological responses mediated by norepinephrine and epinephrine, particularly in the cardiovascular system. The three cloned α_1-AR subtypes (α_{1A}, α_{1B}, and α_{1D}) are G protein-coupled receptors that signal through the $G_{q/11}$ signaling pathway, each showing distinct pharmacological properties and tissue distributions. However, due to the lack of highly subtype-selective drugs, the functional roles of individual subtypes are still not clear. Development of new subtype-specific drugs will greatly facilitate the identification of the functions of each subtype. Conopeptide ρ-TIA has been found to be a new α_{1B}-AR selective antagonist with different modes of inhibition at α_1-AR subtypes. In addition, recent studies using genetically engineered mice have shed some light on α_1-AR functions *in vivo*, especially in the cardiovascular system and brain. Several proteins have been shown to interact directly with particular α_1-AR, and may be important in regulating receptor function. Receptor heterodimerization has been shown to be important for cell surface expression, signaling and internalization. These new observations are likely to help elucidate the functional roles of individual α_1-AR subtypes.

Introduction

α_1-Adrenergic receptors (AR) are members of the G protein-coupled receptor (GPCR) superfamily that mediate physiological responses to norepinephrine (NE) and epinephrine (EPI). Pharmacological analysis and molecular cloning have shown that this receptor family has three subtypes (α_{1A}, α_{1B}, α_{1D}), which have different pharmacological properties and amino acid sequences[1]. Four C-terminal splice variants of the α_{1A}-AR have been found[2,3]. Stimulation of all three subtypes results in activation of the $G_{q/11}$ signaling pathway, involving activation of phospholipase C, generation of the second messengers inositol (1,4,5) triphosphate and diacylglycerol, and mobilization of intracellular calcium. Because of their clinical importance, research on α_1-AR has been very active for many years. Several recent reviews have summarized this research from different perspectives[4–9]. In this review, we mainly focus on recent developments in subtype-selective drugs, genetically engineered mouse models, interacting proteins, receptor dimerization, and factors controlling receptor cell surface expression.

α_1-AR subtype selective drugs

Although all three α_1-AR subtypes activate the same $G_{q/11}$ protein signaling pathway, their different tissue distributions suggest that they play distinct functional roles. For example, the α_{1A}-AR subtype has been considered to be the dominant receptor subtype controlling benign prostatic hypertrophy, and is an important therapeutic target for treatment of this disease[10]. Therefore, identifying the specific functions of individual α_1-AR subtypes is of considerable therapeutic interest. Unfortunately, this has proved difficult because of difficulties in identifying highly subtype-selective drugs. Despite extensive efforts to address this difficulty, only a few subtype-selective compounds have been characterized[11,12]. WB 4101[13], (+)-niguldipine[14], and 5-methylurapidil[15] have been used extensively as α_{1A}-AR selective antagonists, and BMY7378[16] is widely used to characterize α_{1D}-AR. However, there has been little progress in identifying α_{1B}-AR selective antagonists. Chlorethyclonidine was originally characterized as an α_{1B}-AR selective site-directed alkylating agent[17]; however, it has limited selectivity in alkylating the cloned

subtypes, and is no longer widely used. Recently, a conopeptide isolated from a sea snail, known as ρ-TIA, was identified as a non-competitive α_{1B}-AR antagonist[18,19] that may serve as an allosteric modulator, but acts as a competitive inhibitor at the other two subtypes[20,21]. This suggests that ρ-TIA may interact with a novel antagonist binding site specific to the α_{1B}-AR and serve as a template for development of highly selective α_{1B}-AR drugs.

Genetically engineered mouse models

Since attempts to elucidate the function of individual receptor subtypes has been limited by a lack of agonists, antagonists, and antibodies with adequate subtype selectivity, recent studies using genetically engineered mice have shed some light on the contributions of each subtype to physiological responses to NE and EPI. In general, α_1-AR knockout mice do not show overt physical abnormalities (Table 1). Studies in knockout mice lacking a single α_1-AR subtype have shown that all three subtypes seem to be involved in the regulation of blood pressure. Consistent with previous pharmacological characterization *in vitro*, studies in α_{1D}-AR knockout mice have shown that the α_{1D}-AR subtype plays a dominant role in aortic contraction[22]. Not only do genetically engineered mouse models help clear up some of the confusing cardiovascular effects mediated by individual subtypes, they also provide clues as to the functional roles of each subtype in the central nervous system, where these receptors are expressed in high concentrations, but their functions have been difficult to determine. The involvement of α_{1B}-AR in the regulation of locomotion has been suggested by pharmacological manipulation[23]. Interestingly, knockout mice lacking α_{1B}-AR also showed decreased locomotor hyperactivity in response to psychostimulants and opiates, suggesting that targeting the α_{1B}-AR might be a useful therapeutic strategy in the treatment of drug abuse[24]. In addition to the altered phenotypes being examined in the knockout or transgenic models, the underlying molecular mechanisms have been investigated using olignucleotide microarrays. Alteration in the expression of NMDA receptors, $GABA_A$ receptors, and apoptotic and calcium regulatory genes shown in transgenic murine brains may provide a potential molecular basis for neurodegeneration induced by overexpressed constitutively active α_{1B}-AR[25]. Despite the new insights provided by the genetically engineered studies, some discrepancies have been noticed from different studies, such as the contribution of α_{1B}-AR in the aortic contractile response[26,27]. In addition, some of the altered phenotypes observed in the α_{1B}-AR knockout model may result from compensatory effects of other receptor subtypes[28]. Further investigation using classic pharmacological approaches with highly subtype-selective drugs would be useful to facilitate future interpretations of those data.

Receptor interacting proteins

Recent studies have revealed that GPCR can interact with various cellular proteins in addition to the cognate G proteins, thereby expanding the receptor signaling network and establishing the distinct functional roles of closely-related receptor subtypes within the same family[29,30]. Those interacting proteins include cytoplasmic and membrane proteins that may play regulatory roles in receptor pharmacology, trafficking and signaling[31]. Although all three α_1-AR subtypes couple to $G_{q/11}$ signaling pathways, previous studies have shown that the three subtypes can activate distinct downstream signaling components in the $G_{q/11}$ signaling pathway or couple to different signaling pathways[1]. Because of their relatively long C-termini, which have the least sequence homology among the three subtypes, most attention has been focused on finding binding partners interacting with this region. In addition, the sequence diversity in the third intracellular loop (I3 loop) is also attractive due to its importance in coupling to $G_{q/11}$. In a similar manner, it has been shown that the three β-AR subtypes differentially associate with a variety of proteins other than G proteins[32]. However, only a handful of interacting proteins have been identified for α_1-AR subtypes (Table 2). A few of these interactions have been shown to have functional consequences, but most of them require further evaluation. For example, gC1qR and the mu2 subunit of the AP2 clathrin adaptor complex are involved in α_{1B}-AR trafficking or internalization. Although transglutaminase II (Gh) is the first non-$G_{q/11}$ binding partner found to specifically associate with the α_{1B}- and α_{1D}-AR[33,34], the α_1-AR signaling pathways seem to remain intact in Gh knockout mice[35]. Nevertheless, the search for novel binding partners should be considered as an alternative approach to study the molecular differences among the three α_1-AR subtypes.

Receptor dimerization

Unlike the conventional view that GPCR are monomers, a growing body of evidence indicates that GPCR are able to form dimers or oligomers that are required for their pharmacology, function and/or cell surface expression. This concept has gained great appreciation for the class III GPCR subfamily, including the $GABA_B$ receptors[36,37] and taste receptors[38]. However, the significance of class I GPCR dimerization has been under debate, due to difficulties in identify-

Table 1. Characteristics of α_1-AR knockout or overexpression models.

	No alteration	Altered phenotype	Reference
Knockout			
α_{1A}	Cardiac output and renal function	Decreased basal blood pressure; reduced blood pressure response to α_1 agonist (PE)	[55]
α_{1B}	Basal blood pressure	Reduced blood pressure and aorta contractile responses to α_1 agonists (NE, PE)	[26]
	General physical mobility (motor activity)	Impaired modulation of memory consolidation and fear-motivated exploratory activity	[56]
		Increased exploratory response to novelty	[57]
		Attenuated hypertrophic growth after vascular injury	[58]
	Blood glucose, insulin and free fatty acid levels in the fed state	Elevated leptin concentration in the fed state; impaired glucose homeostasis and free fatty acid levels in the fasted state; increased parasympathetic activity	[59]
	Basal dopaminergic activity and basal locomotor behavior	Reduced locomotor responses induced by psychostimulants and opiates	[24]
α_{1D}	Cardiac function	Decreased basal blood pressure; decreased aorta contractile response to α_1 agonists (NE, PE)	[22]
	Renal function	Attenuated increase in blood pressure in salt-induced hypertension	[60]
	Mechanical and chemical nociception	Impaired thermal nociception	[61]
	Basal locomotor activity	Better motor coordination; impaired working memory or attention	[62]
	Hypertrophic growth after vascular injury		[58]
α_{1A}/α_{1B}	Heart sizes for female mice; basal blood pressure	Smaller heart sizes for male mice; decreased heart rate	[63]
		Increased myocardial contraction; decreased responsiveness to β-AR stimulation	[64]
Overexpression			
α_{1A}	Basal blood pressure	Enhanced cardiac contractility	[65]
α_{1B}	Basal blood pressure	Cardiac hypertrophy	[66]
		Granulovascular neurodegeneration; locomotor impairment and seizure	[67]
		Myocardial hypertrophy and hypertension	[68]
	Basal cardiac parameters (heart rate, blood pressure)	Decreased inotropic response to PE	[69]

NE, norepinephrine; PE, phenylephrine.

ing unique functional responses or pharmacological properties. Our group has shown that the three α_1-AR subtypes can form homodimers and subtype-specific heterodimers with other AR[39,40], which has been confirmed by data from other groups[41,42]. Because truncation of either the amino or the carboxyl terminus of the receptor does not affect receptor dimerization[40], the transmembrane domains or associated loops have been proposed to be involved in this interaction. Because the pharmacological analyses of the three cloned α_1-AR subtypes in heterologous expression systems have not yet recapitulated all the receptor subtypes previously defined by pharmacological criteria in tissues, such as the α_{1L}-AR[43], the newly found receptor dimers have been hypothesized to perform atypical α_1-AR pharmacology, which has been seen in the opioid receptor family[44]. Although the homo- or heterodimers formed by α_{1A}-AR C-terminal splice variants have failed to show any novel pharmacology when studied with existing selective drugs[45], it is still hard to conclude that the dimerization does not have effects on receptor pharmacology, because the available drugs are limited and the particular receptor dimers may yet be identified. On the other hand, the α_1-AR sub-

Table 2. Receptor interacting proteins other than $G_{q/11}$ with potential functional roles.

Subtypes	Interacting proteins	Interacting domains	Roles	Reference
α_{1A}	Regulator of G protein signaling 2 (RGS2)	I3 loop	Signaling	[70]
	Bone morphogenetic protein-1 (BMP-1)	C-terminus	Unknown	[71]
	nNOS	Unknown	Unknown	[72]
	Active Bcr-related protein			[73]
	Filamin C	C-terminus	Unknown	[73]
	Tissue transglutaminase (Gh)	I3 loop	Signaling	[33,34]
α_{1B}	Spinophilin	I3 loop	Signaling	[74]
	gC1qR	C-terminus	Cellular localization	[75]
	AP2 clathrin adaptor complex, μ_2 subunit	C-terminus	Internalization	[76]
	nNOS	Unknown	Unknown	[72]
	Filamin C	C-terminus	Unknown	[73]
	Tissue transglutaminase (Gh)	I3 loop	Signaling	[34]
α_{1D}	gC1qR	C-terminus	Unknown	[77]
	nNOS	Unknown	Unknown	[72]
	Filamin C	C-terminus	Unknown	[73]

type-specific dimerization has been found to be important for receptor trafficking and signaling (summarized in the next section).

α_{1D}-AR cell surface expression

Theoretically, all three α_1-AR subtypes should be present at the cell surface to be recognized by their highly hydrophilic natural ligands that are unlikely to cross cell membranes. However, when expressed in recombinant systems, the α_{1D}-AR subtype has been noted to show almost exclusively intracellular expression[46,47], which makes them difficult to characterize. We recently reported that cell surface expression of the α_{1D}-AR could be specifically rescued by coexpression with the α_{1B}-AR but not the α_{1A}-AR[48]. The coexpressed receptors seem to form a new receptor entity, and then modulate signaling and internalization of each receptor subtype in the complex. Recently, the β_2-AR was also reported to be able to translocate α_{1D}-AR[49]. Besides receptor dimerization, removal of the long amino-terminus of the α_{1D}-AR has also been shown to facilitate translocation of intracellular receptors to the cell surface[50]. Subsequent studies using receptor N-terminal chimeras showed that this N-terminal domain might convey a retention signal to prevent receptor cell surface expression[51]. Moreover, the density of α_{1D}-AR cell surface expression was shown to increase upon sequential truncation[52].

Future directions

In the past few years, our knowledge of the functional roles of the α_1-AR family has been dramatically expanded using many different approaches. These findings generate several interesting directions that may be worth pursuing.

1 Further development of highly subtype-selective drugs, especially non-competitive antagonists: most of the specific α_1-AR drugs available are competitive antagonists with moderate subtype-selectivity, which also target other cell surface proteins. Since the three α_1-AR subtypes have relatively high homologies among the transmembrane domains that are believed to form the ligand binding pocket, designing new subtype-selective drugs that compete for this site has not been easy. However, development of noncompetitive drugs may be a good strategy because those drugs normally recognize a different site with less homology. This strategy has been successfully applied in designing highly subtype-selective drugs for other GPCR[53].

2 Investigate the physiological relevance of receptor oligomers: the success of this direction requires the advance of two other research fields, characterization of subtype-specific antibodies and development of new α_1-AR drugs. Although receptor dimerization and protein–protein interactions have been identified in recombinant systems, and their importance in advancing our knowledge of the α_1-AR family has been recognized, their physiological relevance *in vivo* cannot be confirmed and exploited without subtype-specific antibodies. On the other hand, new subtype-selective drugs may recognize the discrete pharmacology of receptor dimers, therefore expanding the existing cloned α_1-AR family and providing new therapeutic targets.

3 Characterize subtype-specific interacting proteins: the

growing list of GPCR interacting proteins has elucidated the molecular mechanisms of the differences among subtypes, which could lead to the development of drugs specifically targeting to such interactions. Because previous evidence suggests that the three α_1-AR subtypes might couple to different signaling pathways, it is likely that more interacting proteins would be identified through the approaches that have been successfully used, such as yeast two-hybrid screenings and pull-down assays with fusion proteins.

4 Study the functional role of α_1-AR in the central nervous system[5]. In fact, almost all typical and atypical antipsychotics are α_1-AR antagonists, although they show little, if any, subtype selectivity[54]. In addition, tricyclic antidepressants are also α_1-AR antagonists, and it is possible that this property may contribute to their therapeutic efficacy. We believe that studies focusing on those directions would further improve our understanding of the functional roles of each α_1-AR subtype.

References

1 Zhong H, Minneman KP. Alpha1-adrenoceptor subtypes. Eur J Pharmacol 1999; 375: 261–76.

2 Hirasawa A, Shibata K, Horie K, Takei Y, Obika K, Tanaka T, *et al.* Cloning, functional expression and tissue distribution of human alpha 1c-adrenoceptor splice variants. FEBS Lett 1995; 363: 256–60.

3 Chang DJ, Chang TK, Yamanishi SS, Salazar FH, Kosaka AH, Khare R, *et al.* Molecular cloning, genomic characterization and expression of novel human alpha1A-adrenoceptor isoforms. FEBS Lett 1998; 422: 279–83.

4 Piascik MT, Perez DM. Alpha1-adrenergic receptors: new insights and directions. J Pharmacol Exp Ther 2001; 298: 403–10.

5 Pupo AS, Minneman KP. Adrenergic pharmacology: focus on the central nervous system. CNS Spectrums 2001; 6: 656–62.

6 Tanoue A, Koshimizu TA, Tsujimoto G. Transgenic studies of alpha(1)-adrenergic receptor subtype function. Life Sci 2002; 71: 2207–15.

7 Hague C, Chen Z, Uberti M, Minneman KP. alpha(1)-Adrenergic receptor subtypes: non-identical triplets with different dancing partners? Life Sci 2003; 74: 411–8.

8 Koshimizu TA, Tanoue A, Hirasawa A, Yamauchi J, Tsujimoto G. Recent advances in alpha1-adrenoceptor pharmacology. Pharmacol Ther 2003; 98: 235–44.

9 Hawrylyshyn KA, Michelotti GA, Coge F, Guenin SP, Schwinn DA. Update on human alpha1-adrenoceptor subtype signaling and genomic organization. Trends Pharmacol Sci 2004; 25: 449–55.

10 Nagarathnam D, Wetzel JM, Miao SW, Marzabadi MR, Chiu G, Wong WC, *et al.* Design and synthesis of novel alpha1a adrenoceptor-selective dihydropyridine antagonists for the treatment of benign prostatic hyperplasia. J Med Chem 1998; 41: 5320–33.

11 Hancock AA. alpha1-adrenoceptor subtypes: a synopsis of their pharmacology and molecular biology. Drug Dev Res 1996; 39: 54–107.

12 Romeo G, Materia L, Salerno L, Russo F, Minneman KP. Novel antagonists for alpha1-adrenoceptor subtypes. Expert Opin Ther Patents 2004; 14: 619–37.

13 Morrow AL, Creese I. Characterization of alpha 1-adrenergic receptor subtypes in rat brain: a reevaluation of [^{3}H]WB4104 and [^{3}H]prazosin binding. Mol Pharmacol 1986; 29: 321–30.

14 Boer R, Grassegger A, Schudt C, Glossmann H. (+)-Niguldipine binds with very high affinity to Ca^{2+} channels and to a subtype of alpha 1-adrenoceptors. Eur J Pharmacol 1989; 172: 131–45.

15 Gross G, Hanft G, Rugevics C. 5-Methyl-urapidil discriminates between subtypes of the alpha 1-adrenoceptor. Eur J Pharmacol 1988; 151: 333–5.

16 Goetz AS, King HK, Ward SD, True TA, Rimele TJ, Saussy DL. BMY 7378 is a selective antagonist of the D subtype of alpha 1-adrenoceptors. Eur J Pharmacol 1995; 272: R5–6.

17 Han C, Abel PW, Minneman KP. Heterogeneity of alpha 1-adrenergic receptors revealed by chlorethylclonidine. Mol Pharmacol 1987; 32: 505–10.

18 Sharpe IA, Gehrmann J, Loughnan ML, Thomas L, Adams DA, Atkins A, *et al.* Two new classes of conopeptides inhibit the alpha1-adrenoceptor and noradrenaline transporter. Nat Neurosci 2001; 4: 902–7.

19 Sharpe IA, Thomas L, Loughnan M, Motin L, Palant E, Croker DE, *et al.* Allosteric alpha 1-adrenoreceptor antagonism by the conopeptide rho-TIA. J Biol Chem 2003; 278: 34451–7.

20 Chen Z, Rogge G, Hague C, Alewood D, Colless B, Lewis RJ, *et al.* Subtype-selective noncompetitive or competitive inhibition of human alpha1-adrenergic receptors by rho-TIA. J Biol Chem 2004; 279: 35326–33.

21 Lima V, Mueller A, Kamikihara SY, Raymundi V, Alewood D, Lewis RJ, *et al.* Differential antagonism by conotoxin rho-TIA of contractions mediated by distinct alpha1-adrenoceptor subtypes in rat vas deferens, spleen and aorta. Eur J Pharmacol 2005; 508: 183–92.

22 Tanoue A, Nasa Y, Koshimizu T, Shinoura H, Oshikawa S, Kawai T, *et al.* The alpha(1D)-adrenergic receptor directly regulates arterial blood pressure via vasoconstriction. J Clin Invest 2002; 109: 765–75.

23 Stone EA, Lin Y, Itteera A, Quartermain D. Pharmacological evidence for the role of central alpha 1B-adrenoceptors in the motor activity and spontaneous movement of mice. Neuropharmacology 2001; 40: 254–61.

24 Drouin C, Darracq L, Trovero F, Blanc G, Glowinski J, Cotecchia S, *et al.* Alpha1b-adrenergic receptors control locomotor and rewarding effects of psychostimulants and opiates. J Neurosci 2002; 22: 2873–84.

25 Yun J, Gaivin RJ, McCune DF, Boongird A, Papay RS, Ying Z, *et al.* Gene expression profile of neurodegeneration induced by alpha1B-adrenergic receptor overactivity: NMDA/$GABA_A$ dysregulation and apoptosis. Brain 2003; 126: 2667–81.

26 Cavalli A, Lattion AL, Hummler E, Nenniger M, Pedrazzini T, Aubert JF, *et al.* Decreased blood pressure response in mice deficient of the alpha1b-adrenergic receptor. Proc Natl Acad Sci USA 1997; 94: 11589–94.

27 Cavalli A, Lattion AL, Hummler E, Nenniger M, Pedrazzini T, Aubert JF, *et al.* A knockout approach indicates a minor vasoconstrictor role for vascular alpha1B-adrenoceptors in mouse.

Physiol Genomics 2002; 9: 85–91.
28 Deighan C, Woollhead AM, Colston JF, McGrath JC. Hepatocytes from alpha1B-adrenoceptor knockout mice reveal compensatory adrenoceptor subtype substitution. Br J Pharmacol 2004; 142: 1031–7.
29 Hall RA, Premont RT, Lefkowitz RJ. Heptahelical receptor signaling: beyond the G protein paradigm. J Cell Biol 1999; 145: 927–32.
30 Hall RA, Lefkowitz RJ. Regulation of G protein-coupled receptor signaling by scaffold proteins. Circ Res 2002; 91: 672–80.
31 Bockaert J, Fagni L, Dumuis A, Marin P. GPCR interacting proteins (GIP). Pharmacol Ther 2004; 103: 203–21.
32 Hall RA. Beta-adrenergic receptors and their interacting proteins. Semin Cell Dev Biol 2004; 15: 281–8.
33 Nakaoka H, Perez DM, Baek KJ, Das T, Husain A, Misono K, *et al*. Gh: a GTP-binding protein with transglutaminase activity and receptor signaling function. Science 1994; 264: 1593–6.
34 Chen S, Lin F, Iismaa S, Lee KN, Birckbichler PJ, Graham RM. Alpha1-adrenergic receptor signaling via Gh is subtype specific and independent of its transglutaminase activity. J Biol Chem 1996; 271: 32385–91.
35 Nanda N, Iismaa SE, Owens WA, Husain A, Mackay F, Graham RM. Targeted inactivation of Gh/tissue transglutaminase II. J Biol Chem 2001; 276: 20673–8.
36 White JH, Wise A, Main MJ, Green A, Fraser NJ, Disney GH, *et al*. Heterodimerization is required for the formation of a functional GABA(B) receptor. Nature 1998; 396: 679–82.
37 Kuner R, Kohr G, Grunewald S, Eisenhardt G, Bach A, Kornau HC. Role of heteromer formation in $GABA_B$ receptor function. Science 1999; 283: 74–7.
38 Nelson G, Hoon MA, Chandrashekar J, Zhang Y, Ryba NJ, Zuker CS. Mammalian sweet taste receptors. Cell 2001; 106: 381–90.
39 Vicentic A, Robeva A, Rogge G, Uberti M, Minneman KP. Biochemistry and pharmacology of epitope-tagged alpha(1)-adrenergic receptor subtypes. J Pharmacol Exp Ther 2002; 302: 58–65.
40 Uberti MA, Hall RA, Minneman KP. Subtype-specific dimerization of alpha 1-adrenoceptors: effects on receptor expression and pharmacological properties. Mol Pharmacol 2003; 64: 1379–90.
41 Stanasila L, Perez JB, Vogel H, Cotecchia S. Oligomerization of the alpha 1a- and alpha 1b-adrenergic receptor subtypes. Potential implications in receptor internalization. J Biol Chem 2003; 278: 40239–51.
42 Carrillo JJ, Pediani J, Milligan G. Dimers of class A G protein-coupled receptors function via agonist-mediated trans-activation of associated G proteins. J Biol Chem 2003; 278: 42578–87.
43 Ohmura T, Sakamoto S, Hayashi H, Kigoshi S, Muramatsu I. Identification of alpha 1-adrenoceptor subtypes in the dog prostate. Urol Res 1993; 21: 211–5.
44 Jordan BA, Devi LA. G-protein-coupled receptor heterodimerization modulates receptor function. Nature 1999; 399: 697–700.
45 Ramsay D, Carr IC, Pediani J, Lopez-Gimenez JF, Thurlow R, Fidock M, *et al*. High-affinity interactions between human alpha1A-adrenoceptor C-terminal splice variants produce homo- and heterodimers but do not generate the alpha1L-adrenoceptor. Mol Pharmacol 2004; 66: 228–39.
46 McCune DF, Edelmann SE, Olges JR, Post GR, Waldrop BA, Waugh DJ, *et al*. Regulation of the cellular localization and signaling properties of the alpha(1B)- and alpha(1D)-adrenoceptors by agonists and inverse agonists. Mol Pharmacol 2000; 57: 659–66.
47 Chalothorn D, McCune DF, Edelmann SE, Garcia-Cazarin ML, Tsujimoto G, Piascik MT. Differences in the cellular localization and agonist-mediated internalization properties of the alpha(1)-adrenoceptor subtypes. Mol Pharmacol 2002; 61: 1008–16.
48 Hague C, Uberti MA, Chen Z, Hall RA, Minneman KP. Cell surface expression of alpha 1D-adrenergic receptors is controlled by heterodimerization with alpha 1B-adrenergic receptors. J Biol Chem 2004; 279: 15541–9.
49 Uberti MA, Hague C, Oller H, Minneman KP, Hall RA. Heterodimerization with {beta}2-adrenergic receptors promotes surface expression and functional activity of {alpha}1D-adrenergic receptors. J Pharmacol Exp Ther 2005; 313: 16–23.
50 Pupo AS, Uberti MA, Minneman KP. N-terminal truncation of human alpha(1D)-adrenoceptors increases expression of binding sites but not protein. Eur J Pharmacol 2003; 462: 1–8.
51 Hague C, Chen Z, Pupo AS, Schulte N, Toews ML, Minneman KP. The N-terminus of the human alpha-1D-adrenergic receptor prevents cell surface expression. J Pharmacol Exp Ther 2004; 309: 388–97.
52 Petrovska R, Kapa I, Klovins J, Schioth HB, Uhlen S. Addition of a signal peptide sequence to the alpha(1D)-adrenoceptor gene increases the density of receptors, as determined by [(3)H]-prazosin binding in the membranes. Br J Pharmacol 2005; 144: 651–9.
53 Christopoulos A, Kenakin T. G protein-coupled receptor allosterism and complexing. Pharmacol Rev 2002; 54: 323–74.
54 Stone EA, Lin Y, Rosengarten H, Kramer HK, Quartermain D. Emerging evidence for a central epinephrine-innervated alpha 1-adrenergic system that regulates behavioral activation and is impaired in depression. Neuropsychopharmacology 2003; 28: 1387–99.
55 Rokosh DG, Simpson PC. Knockout of the alpha 1A/C-adrenergic receptor subtype: the alpha 1A/C is expressed in resistance arteries and is required to maintain arterial blood pressure. Proc Natl Acad Sci USA 2002; 99: 9474–9.
56 Knauber J, Muller WE. Decreased exploratory activity and impaired passive avoidance behaviour in mice deficient for the alpha (1b)-adrenoceptor. Eur Neuropsychopharmacol 2000; 10: 423–7.
57 Spreng M, Cotecchia S, Schenk F. A behavioral study of alpha-1b adrenergic receptor knockout mice: increased reaction to novelty and selectively reduced learning capacities. Neurobiol Learn Mem 2001; 75: 214–29.
58 Zhang H, Cotecchia S, Thomas SA, Tanoue A, Tsujimoto G, Faber JE. Gene deletion of dopamine beta-hydroxylase and alpha1-adrenoceptors demonstrates involvement of catecholamines in vascular remodeling. Am J Physiol Heart Circ Physiol 2004; 287: H2106–14.
59 Burcelin R, Uldry M, Foretz M, Perrin C, Dacosta A, Nenniger-Tosato M, *et al*. Impaired glucose homeostasis in mice lacking the alpha1b-adrenergic receptor subtype. J Biol Chem 2004; 279: 1108–15.

60 Tanoue A, Koba M, Miyawaki S, Koshimizu TA, Hosoda C, Oshikawa S, *et al*. Role of the alpha1D-adrenergic receptor in the development of salt-induced hypertension. Hypertension 2002; 40: 101–6.
61 Harasawa I, Honda K, Tanoue A, Shinoura H, Ishida Y, Okamura H, *et al*. Responses to noxious stimuli in mice lacking alpha(1d)-adrenergic receptors. Neuroreport 2003; 14: 1857–60.
62 Mishima K, Tanoue A, Tsuda M, Hasebe N, Fukue Y, Egashira N, *et al*. Characteristics of behavioral abnormalities in alpha1d-adrenoceptors deficient mice. Behav Brain Res 2004; 152: 365–73.
63 O'Connell TD, Ishizaka S, Nakamura A, Swigart PM, Rodrigo MC, Simpson GL, *et al*. The alpha(1A/C)- and alpha(1B)-adrenergic receptors are required for physiological cardiac hypertrophy in the double-knockout mouse. J Clin Invest 2003; 111: 1783–91.
64 McCloskey DT, Turnbull L, Swigart P, O'Connell TD, Simpson PC, Baker AJ. Abnormal myocardial contraction in alpha(1A)- and alpha(1B)-adrenoceptor double-knockout mice. J Mol Cell Cardiol 2003; 35: 1207–16.
65 Lin F, Owens WA, Chen S, Stevens ME, Kesteven S, Arthur JF, *et al*. Targeted alpha(1A)-adrenergic receptor overexpression induces enhanced cardiac contractility but not hypertrophy. Circ Res 2001; 89: 343–50.
66 Milano CA, Dolber PC, Rockman HA, Bond RA, Venable ME, Allen LF, *et al*. Myocardial expression of a constitutively active alpha 1B-adrenergic receptor in transgenic mice induces cardiac hypertrophy. Proc Natl Acad Sci USA 1994; 91: 10109–13.
67 Zuscik MJ, Sands S, Ross SA, Waugh DJ, Gaivin RJ, Morilak D, *et al*. Overexpression of the alpha1B-adrenergic receptor causes apoptotic neurodegeneration: multiple system atrophy. Nat Med 2000; 6: 1388–94.
68 Zuscik MJ, Chalothorn D, Hellard D, Deighan C, McGee A, Daly CJ, *et al*. Hypotension, autonomic failure, and cardiac hypertrophy in transgenic mice overexpressing the alpha 1B-adrenergic receptor. J Biol Chem 2001; 276: 13738–43.
69 Ross SA, Rorabaugh BR, Chalothorn D, Yun J, Gonzalez-Cabrera PJ, McCune DF, *et al*. The alpha(1B)-adrenergic receptor decreases the inotropic response in the mouse Langendorff heart model. Cardiovasc Res 2003; 60: 598–607.
70 Hague C, Bernstein LS, Ramineni S, Chen Z, Minneman KP, Hepler JR. Selective inhibition of alpha1A-adrenergic receptor signaling by RGS2 association with the receptor third intracellular loop. J Biol Chem 2005; 280: 27289–95.
71 Xu Q, Zhang T, Han QD, Zhang YY. Binding between alpha 1A-adrenergic receptor and segment of bone morphogenetic protein-1 in human embryonic cell 293. Acta Physiol Sin 2003; 55: 692–8. Chinese.
72 Pupo AS, Minneman KP. Interaction of neuronal nitric oxide synthase with alpha1-adrenergic receptor subtypes in transfected HEK-293 cells. BMC Pharmacol 2002; 2: 17.
73 Zhang T, Xu Q, Chen FR, Han QD, Zhang YY. Yeast two-hybrid screening for proteins that interact with alpha1-adrenergic receptors. Acta Pharmacol Sin 2004; 25: 1471–8.
74 Wang X, Zeng W, Soyombo AA, Tang W, Ross EM, Barnes AP, *et al*. Spinophilin regulates Ca(2+) signalling by binding the N-terminal domain of RGS2 and the third intracellular loop of G-protein-coupled receptors. Nat Cell Biol 2005; 7: 405–11.
75 Xu Z, Hirasawa A, Shinoura H, Tsujimoto G. Interaction of the alpha(1B)-adrenergic receptor with gC1q-R, a multifunctional protein. J Biol Chem 1999; 274: 21149–54.
76 Diviani D, Lattion AL, Abuin L, Staub O, Cotecchia S. The AP2 complex directly interacts with the alpha-1b-adrenergic receptor and plays a role in receptor endocytosis. J Biol Chem 2003; 278: 19331–40.
77 Pupo AS, Minneman KP. Specific interactions between gC1qR and alpha1-adrenoceptor subtypes. J Recept Signal Transduct Res 2003; 23: 185–95.

Acta Pharmacologica Sinica 2005 Nov; 26 (11): 1288–1289

Blackwell Publishing

Comment

Pharmacological attenuation of blood pressure variability

Claude JULIEN[1]

Laboratoire de Physiologie, Faculté de Pharmacie, Université Claude Bernard Lyon 1, Lyon 69373, France

[1] Correspondence to Dr Claude JULIEN.
Phn 33-478-777072.
Fax 33-478-777118.
E-mail julien@univ-lyon1.fr

Received 2005-08-01
Accepted 2005-09-07

doi: 10.1111/j.1745-7254.2005.00221.x

Over the past few years, the research team of Professor Ding-feng SU has reported an impressive quantity of experimental data about the relationships between blood pressure variability (BPV) and end-organ damage, a topic of obvious clinical interest. This research work has been summarized in a paper that appeared in the August issue of the renowned journal *Trends in Pharmacological Sciences*[1]. The studies by Su *et al* provide convincing evidence that BPV is an independent cardiovascular risk factor that should be considered as such and, therefore, might become an important target for therapeutic interventions. Besides these exciting perspectives in the prevention and treatment of cardiovascular diseases, the work by Su *et al* raises a series of physiological questions.

In most, if not all, studies by Su *et al*, BPV is expressed as the standard deviation of beat-to-beat blood pressure data[2,3]. The standard deviation provides an index of overall BPV that incorporates all kinds of blood pressure (BP) variations, from those resulting from the respiratory cycle to the slow trends occurring over the whole recording period. However, when studied in the frequency domain, it becomes apparent that the bulk of BPV is concentrated at low frequencies (<0.15 Hz in rats)[4]. In other words, the standard deviation of BP essentially corresponds to the low-frequency component of the BP spectra. In the low frequency band, BPV is mainly the result of opposing interactions between hemodynamic perturbations and the corrective feedback provided by the arterial baroreceptor reflex. Hemodynamic studies in conscious rats with neonatal chemical sympathectomy[5], chronic sinoaortic baroreceptor denervation[6], and acute neurohumoral blockade[7] have revealed that one major source of slow (or low frequency) hemodynamic perturbations is the myogenic response of vascular smooth muscle cells that promotes vasoconstriction in regional circulations when BP increases and vasodilatation when BP decreases (Figure 1)[8].

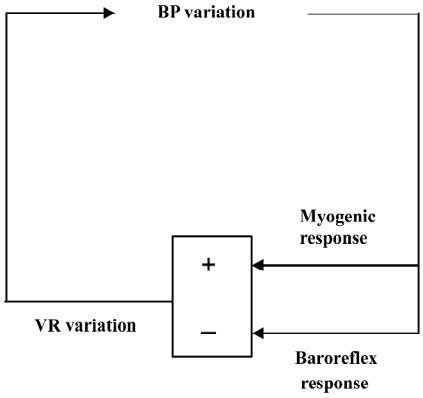

Figure 1. Schematic diagram of opposing interactions between myogenic and baroreflex responses. The relative importance of these responses determines the net change in vascular resistance (VR) in regional vascular beds as well as in the systemic circulation.

Taking into consideration this fundamental underlying physiology of BPV, the soundest pharmacological approach to reducing BPV is twofold. First, it would be beneficial to enhance baroreflex function. Chronic treatment with a non-antihypertensive dose of ketanserin increases baroreflex sensitivity while reducing BPV in spontaneously hypertensive rats[3]. This effect was observed for the cardiac component of the baroreceptor reflex. It is not known whether this also applies to the sympathetic component. The second

approach would be to attenuate myogenic responses of regional circulations (Figure 1). This can be achieved with dihydropyridine L-type calcium channel blockers. Su *et al* have demonstrated that nitrendipine can selectively reduce BPV[2]. However, this strategy is more problematic than the first because although the reduction of BPV afforded by calcium channel blockers would be beneficial in terms of arterial stiffness and left ventricular workload, this would probably be achieved at the cost of a reduced protection of capillary vascular beds (eg in the brain and kidney)[9]. Further investigations including regional hemodynamic measurements are required to clarify this issue. Finally, it should be noted that the research team of Professor Su will soon make available a rat strain with a spontaneous deficiency in baroreflex function[10], which will undoubtedly facilitate the study of pharmacological modulation of BPV.

References

1 Su DF, Miao CY. Reduction of blood pressure variability: a new strategy for the treatment of hypertension. Trends Pharmacol Sci 2005; 26: 388–90.

2 Liu JG, Xu LP, Chu ZX, Miao CY, Su DF. Contribution of blood pressure variability to the effect of nitrendipine on end-organ damage in spontaneously hypertensive rats. J Hypertens 2003; 21: 1961–7.

3 Xie HH, Shen FM, Cao YB, Li HL, Su DF. Effects of low-dose ketanserin on blood pressure variability, baroreflex sensitivity and end-organ damage in spontaneously hypertensive rats. Clin Sci (Lond) 2005; 108: 547–52.

4 Chapuis B, Vidal-Petiot E, Oréa V, Barrès C, Julien C. Linear modelling analysis of baroreflex control of arterial pressure variability in rats. J Physiol 2004; 559: 639–49.

5 Zhang ZQ, Julien C, Gustin MP, Cerutti C, Barrès C. Hemodynamic analysis of arterial pressure lability in sympathectomized rat. Am J Physiol 1994; 267: H48–56.

6 Zhang ZQ, Barrès C, Julien C. Involvement of vasodilator mechanisms in arterial pressure lability after sino-aortic baroreceptor denervation in rat. J Physiol 1995; 482: 435–48.

7 Létienne R, Barrès C, Cerutti C, Julien C. Short-term haemodynamic variability in the conscious areflexic rat. J Physiol 1998; 506: 263–74.

8 Burattini R, Borgdorff P, Westerhof N. The baroreflex is counteracted by autoregulation, thereby preventing circulatory instability. Exp Physiol 2004; 89: 397–405.

9 Griffin KA, Hacioglu R, Abu-Amarah I, Loutzenhiser R, Williamson GA, Bidani AK. Effects of calcium channel blockers on “dynamic” and “steady-state step” renal autoregulation. Am J Physiol Renal Physiol 2004; 286: F1136–43.

10 Su DF, Miao CY. Arterial baroreflex function in conscious rats. Acta Pharmacol Sin 2002; 23: 673–9.

Acta Pharmacologica Sinica 2005 Nov; 26 (11): 1290–1296

Blackwell Publishing

Full-length article

Changes of brain neuropeptide Y and its receptors in rats with flurazepam tolerance and dependence[1]

Li-ping ZHANG, Li WANG[2]

Department of Pediatrics, Peking University First Hospital, Beijing 100034, China

Key words

benzodiazepines; neuropeptide Y; flurazepam

[1] Project supported by the National Natural Science Foundation of China (No 30170994).
[2] Correspondence to Prof Li WANG.
Phn 86-10-6655-1122, ext 5303.
Fax 86-10-6613-4261.
E-mail wangli5000@126.com

Received 2005-04-04
Accepted 2005-05-27

doi: 10.1111/j.1745-7254.2005.00179.x

Abstract

Aim: Anticonvulsant tolerance and dependence are two obstacles that restrict the clinical use of benzodiazepines (BDZ). In order to explore the mechanism of these two adverse reactions, changes of neuropeptide Y (NPY) and its receptors in the hippocampus of rat models, in relation to flurazepam (FZP, a member of BDZ) tolerance and dependence, were investigated. **Methods:** The mRNA of preproNPY and its receptors (Y_1, Y_2, and Y_5) in the hippocampus were determined by competitive RT-PCR, and the distribution of NPY in the hippocampus was examined by immunohistochemistry. **Results:** A decrease of preproNPY mRNA in the hippocampus was found in tolerant and dependent rats. The level of preproNPY mRNA in the hippocampus was reversely correlated with the degree of tolerance and dependence, measured by the threshold of pentylenetetrazol-induced seizures. Immunohistochemistry indicated a decrease of NPY-immunoreactive material in neurons of the CA1, CA3, and dentate gyrus regions of both tolerant and dependent rats. The mRNA of NPY receptors Y_1 and Y_5 decreased in tolerant rats but did not change in dependent rats. The mRNA of NPY receptor Y_2 increased in tolerant rats but decreased in dependent rats. **Conclusion:** A decrease of NPY in the hippocampus might be involved in anticonvulsant tolerance and dependence following long-term treatment with FZP. Y_1, Y_2, and Y_5 mRNA were also altered in FZP tolerance and dependence.

Introduction

Benzodiazepines (BDZ) have been widely used as anxiolytics, sedatives, hypnotics and anticonvulsants. BDZ produce therapeutic effects through the major fast inhibitory neurotransmitter receptors, $GABA_A$ receptors, in the central nervous system (CNS). BDZ positively modulate $GABA_A$ receptors by increasing their affinity for GABA and thus reduce the excitability of the post-synaptic neurons.

However, long-term treatment with BDZ often leads to drug tolerance, which means the therapeutic efficacy of the drug decreases after a period of continuous administration. Another consequence of chronic administration of BDZ is the dependence manifested by the aggravation of primary symptoms and/or appearance of abstinence syndrome, which includes anxiety, discomfort, diarrhea, loss of bodyweight and salivating when the drug is withdrawn abruptly. Tolerance and dependence are frequently encountered in the clinical use of BDZ as an antiepileptic medicine. The usefulness of BDZ is therefore limited, although most have primarily satisfactory antiepileptic efficacies.

Many studies have focused on the mechanisms of tolerance and dependence. Changes of binding capacity, gene expression and metabolism in neural receptors, including $GABA_A$ receptors[1], glutamatergic receptors[2] and peripheral BDZ receptors[3], were studied in the presence of tolerance and/or dependence. Other factors, such as nitric oxide[4], calcium-channel blockers[5], protein kinases[6] and bicarbonate radicals[7] were also studied. However, the exact mechanism underlying the tolerance and dependence is still unknown.

Neuropeptide Y (NPY) is a polypeptide of 36 amino acid residues widely distributed in the nervous system. This neuropeptide regulates various functions such as food

uptake, blood pressure, circadian rhythm and anxiety. It induces the central and peripheral activities through at least six receptor subtypes called Y_1–Y_6 that belong to the G-protein coupled receptor superfamily[8].

After a period of BDZ treatment, the glutamatergic system was modified, which was thought to be one of the reasons underlying tolerance to BDZ. For example, an increase of 206% in *in vitro* glutamate release was found in the hippocampus of animals chronically treated with lorazepam[2]. Based on the facts that the NPYergic system inhibited the release of glutamate from presynaptic membranes[9] and that NPY was reduced in the CNS in alcohol dependence[10], the changes of NPYergic system in rat models with BDZ tolerance and dependence attracted our attention.

In this study, rat models of anticonvulsant tolerance and dependence to flurazepam (FZP, a BDZ) were established and the changes of NPY and its receptors (Y_1, Y_2, and Y_5) in the hippocampus of these rat models were investigated.

Materials and methods

The establishment of rat models and the experiments on rats in this study were approved by the Ethics Committee of Animal Experiments of Peking University First Hospital.

Rat model of FZP tolerance The rat model of FZP tolerance used was produced by following the method developed by Rosenberg[11]. Male Sprague-Dawley rats (initial weight 180–200 g) were housed in a climate-controlled room with free access to standard rat food. FZP dissolved in a 0.02% saccharin solution was given as drinking water for 1 week (FZP-tolerant group, n=10). The concentration of FZP was adjusted to provide a daily dose of up to 100 mg/kg for the first 3 d and 150 mg/kg for the next 4 d. All rats consumed an average concentration of more than 100 mg/kg FZP daily. Control rats (n=10) were handled identically, but received 0.02% saccharin solution without the drug. After one week of treatment, rats were given saccharin solution as drinking water. Withdrawal signs such as overt ataxia, anxiety and hyperactivity were not found with this treatment[12].

Tolerance to FZP was evaluated 12 h after discontinuation of FZP intake. Because of the very rapid biotransformation of FZP and its metabolites in rats, and the corresponding plasma half-life ($T_{1/2}$) of less than 2 h, the residual drug should not interfere with the anticonvulsant test at this time[13]. FZP dissolved in distilled water (100 mg/mL) was diluted to 20 mg/mL with normal saline for injection. This solution was injected intraperitoneally to deliver a dose of 20 mg/kg. After 30 min, 20 mg/mL pentylenetetrazol (PTZ, freshly prepared in normal saline) was infused at a constant rate of 0.5 mL/min into a tail vein, and clonus of the front legs was monitored to determine the threshold of PTZ-induced seizures. The onset time of clonus was recorded, and the PTZ threshold (mg/kg) was then derived. Rats in the control group were tested along with those in the FZP-tolerant group using the same procedure. FZP tolerance was determined by the decrease of PTZ threshold as compared with that of the control group. After the PTZ threshold test, the brain was removed and stored at -70 ºC immediately.

Rat model of FZP dependence We integrated the methods reported by Rosenberg[11] and Izzo *et al*[14] to establish a rat model of FZP dependence. The animals used, drug dosage, method of drug intake and PTZ threshold test were from the method reported by Rosenberg[11], but the days of drug administration and the dependence test were from the method reported by Izzo *et al*[14]. To obtain a more stable blood concentration, male Sprague-Dawley rats were given FZP dissolved in 0.02% saccharin solution as drinking water instead of an oral gavage of diazepam three times daily[14]. For rats in the FZP-dependent group (n=10), FZP was given at increasing doses for 14 d: d 1–3, 100 $mg \cdot kg^{-1} \cdot d^{-1}$; d 4–7, 150 $mg \cdot kg^{-1} \cdot d^{-1}$; d 8–10, 200 $mg \cdot kg^{-1} \cdot d^{-1}$; and d 11–14, 250 $mg \cdot kg^{-1} \cdot d^{-1}$. Control rats ($n$=10) were handled identically, but received 0.02% saccharin solution without the drug as drinking water. The emergence of dependence was determined by the susceptibility to PTZ-induced seizures 96 h after termination of the 14-day FZP administration. PTZ (20 mg/mL) was infused at a constant rate of 0.5 mL/min into a tail vein and the infusion was discontinued at the first sign of tonic-clonic seizures. The PTZ threshold (mg/kg) was derived from the amount of PTZ used to induce tonic-clonic seizures. Rats in the control group were treated identically. FZP dependence was determined by the decrease of the PTZ threshold as compared with that of the control group. After the PTZ threshold test, the brain was removed and stored at -70 ºC immediately.

PTZ-induced seizures themselves may also cause changes in the brain. To minimize these interferences, we killed rats immediately after the PTZ threshold test and compared the changes in the hippocampus with those from the respective control rats.

Reagents FZP was purchased from DaZhong Pharmaceutical (Shanghai, China).

Rats were from the Animal Department of Peking University Health Sciences Center. PTZ and anti-NPY antibody were from Sigma-Aldrich (Saint Louis, MO, USA). RNase-free DNase I was obtained from Promega (Madison, WI, USA), Trizol reagent and M-MuLV reverse transcriptase were from Gibco (Rockville, MD, USA). The sequences of oligonucle-

otide primers for the amplification of preproNPY (386 bp), Y_1 (426 bp), Y_2 (393 bp), and Y_5 (391 bp) cDNA are: NPY-F, 5'-TATCCCTGCTCGTGTGTTTG-3'; NPY-R, 5'-AACGACAA-CAAGGGAAATGG-3'; Y_1-F, 5'-ACTCTCACAGGCTGTC-TTAC-3'; Y_1-R, 5'-ATAGTCTCGTAGTCGTCGTC-3'; Y_2-F, 5'-AGCCTTTCCACCCTGCTAAT-3'; Y_2-R, 5'-GTGAATGGCA-TCCAACCTCT-3'; Y_5-F, 5'-CACCTAGCCGTTCCAGAA-AA-3'; Y_5-R, 5'-GGGCTCTCAAGTCTGCTTTG-3'.

Measurement of preproNPY and NPY receptor cDNA in hippocampus by competitive RT-PCR Animals were decapitated immediately after the PTZ threshold test. The hippocampus was quickly removed and stored at -70 ºC until use. Brain tissue was homogenized in Trizol reagent in a precooled mortar following manufacturer's protocol[15]. Total RNA samples were treated with RNase-free DNase I to eliminate genomic DNA contamination before reverse transcription. Total RNA of 3 μg was reversely transcribed into cDNA using oligo d $(T)_{15}$ as the primer and M-MuLV reverse transcriptase.

The internal competitive standards for the measurement of preproNPY, Y_1, Y_2, and Y_5 cDNA were made using PCR. These DNA fragments had the same sequences as their respective PCR products, except that approximately 80 bp at the downstream site of the forward primers were deleted. Quantitative PCR was performed in a 0.2 mL tube containing brain cDNA 1 μL, internal competitive standard 1 μL, 5 μmol/L each primer mixture 1μL, 2.5 mmol/L each dNTP mixture 1 μL, 1.5 mmol/L $MgCl_2$, 10×PCR buffer 2.5 μL, and 1.25 unit *Taq* DNA polymerase, in a total volume of 25 μL. PCR was run at 94 ºC 30 s, 62 ºC 30 s, and 72 ºC 40 s (93 ºC 1 min, 65 ºC 2 min and 72 ºC 2 min for the amplification of Y_1 cDNA) for 35 cycles. PCR products were separated in a 1.5% agarose gel and stained using ethidium bromide. The ratio of the optical density of the two DNA bands under UV light was measured by a gel image analysis system. A standard curve of the ratio was drawn using the same conditions as described above, except that brain cDNA was changed to a serial dilution of the purified PCR product. The relative amount of the cDNA in a sample was then obtained from the standard curve.

Immunohistochemistry of NPY in hippocampus After anesthesia, rats were perfused through the left ventricle with 0.9% sodium chloride followed by 4% paraformaldehyde in phosphate buffer solution for approximately 30 min. The removed brain was sequentially soaked in 4% paraformaldehyde in phosphate buffer solution for 24 h and 30% sucrose at 4 ºC for 72 h. Frozen sections of 8-mm thickness in a coronal plane were used for immunohistochemistry. One brain section from the treated rat and one from the respective control rat were placed on one slide and processed together. After treatment with 0.3% H_2O_2 to block the endogenous peroxidase, sections were incubated with 1:50 polyclonal anti-NPY antibody overnight at 4 ºC. The secondary antibody was biotinylated anti-rabbit IgG antibody (Vector, Burlingame, CA, USA). Signals were visualized by horseradish peroxidase conjugated avidin and diaminobenzidine. The relative density of NPY-immunoreactive material in neurons in the pyramidal cell layer of CA1, CA3 region and granular cell layer of the dentate gyrus region was measured in a defined area by a densitometer.

Statistical analysis Data were expressed as mean±SD. Paired *t*-tests were used to evaluate the significance of intergroup differences. $P<0.05$ was considered as significant.

Results

Rat models of FZP tolerance and dependence

FZP-tolerant model The rat model of FZP tolerance was evaluated by studying the FZP anticonvulsant efficacy after discontinuing the 7-d FZP treatment for 12 h when the brain FZP should have been metabolized[13]. Anticonvulsive efficacy of a single dose of 20 mg/kg FZP was measured by studying the threshold of PTZ-induced seizures after 30 min. In comparison with the control group, the average PTZ threshold decreased by more than 3 times in the FZP-tolerant group, indicating the successful establishment of an FZP-tolerant model in rats (Table 1).

FZP-dependent model In contrast to the evaluation of FZP tolerance, FZP dependence was estimated by studying the PTZ threshold after discontinuing the 14-d FZP treatment for 96 h when maximum withdrawal signs were expected to occur[14]. As shown in Table 1, the average PTZ threshold in the FZP-dependent model was lower than that in its control group by more than 2 times, indicating that the FZP-dependent model is acceptable for further study (Table 1).

Changes of preproNPY cDNA in hippocampus of FZP-tolerant and -dependent rats In the hippocampus, preproNPY

Table 1. Extent of FZP tolerance and dependence evaluated by the threshold of PTZ-induced seizures. $n=10$. $^bP<0.05$ *vs* the respective control groups.

Group	Threshold of PTZ-induced seizures/mg·kg^{-1}
FZP-tolerant	22.47±10.24^b
Control	71.74±23.68
FZP-dependent	5.69±1.77^b
Control	15.91±2.45

cDNA was dramatically reduced both in FZP-tolerant and -dependent groups, as compared with that of the respective control groups (Table 2, Figure 1).

Table 2. Relative amount of preproNPY, Y_1, Y_2, and Y_5 cDNA in hippocampus of rats with anticonvulsant tolerance and dependence to FZP. n=8. Mean±SD. $^bP<0.05$ *vs* those of the respective control groups.

Group	PreproNPY	Y_1	Y_2	Y_5
FZP-tolerant	0.09±0.01^b	0.99±0.13^b	16.32±6.26^b	0.64±0.16^b
Control	5.37±1.06	3.67±1.10	3.11±1.13	3.75±1.33
FZP-dependent	0.78±1.56^b	2.89±1.31	0.54±1.59^b	3.41±1.66
Control	5.16±1.70	3.61±1.79	3.33±1.37	3.51±0.86

NPY-immunoreactive cells were found in many brain regions, with the hippocampus showing the most remarkable changes in FZP tolerant and dependent rats. In the hippocampus of control animals, NPY-immunoreactive cells were mostly located in CA1, CA3, and dentate gyrus regions. NPY-immunoreactive cells were large multipolar or fusiform neurons, and NPY positive material was found in their cytoplasm and processes (Figure 2A, 2B). In the hippocampus from FZP-tolerant and FZP-dependent rats, NPY-immunoreactive material in the cytoplasm and processes was significantly reduced as compared with that in the same regions of the respective control rats (Figure 2C, 2D, Table 3).

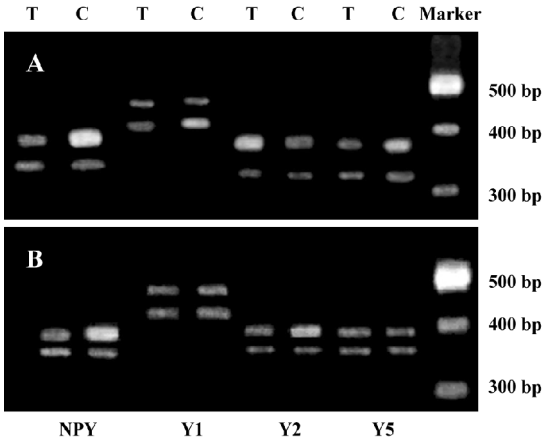

Figure 1. Representative electrophoresis profiles of competitive PCR for the quantification of preproNPY, Y_1, Y_2, and Y_5 cDNA in the hippocampus of FZP-tolerant model (A) and FZP-dependent model (B). The density ratio of the upper/lower bands in a lane is positively proportional to the amount of the cDNA in the hippocampus. Lane T, samples from FZP-treated rats; lane C, samples from control rats.

Changes of NPY receptor cDNA in hippocampus of FZP-tolerant and -dependent rats Y_1 and Y_5 cDNA were decreased in the tolerant group as compared with those of the respective control group. However, no quantitative changes of these two cDNA were found in the FZP-dependent group. In contrast, Y_2 cDNA was increased significantly in the FZP-tolerant group, but was decreased in the FZP-dependent

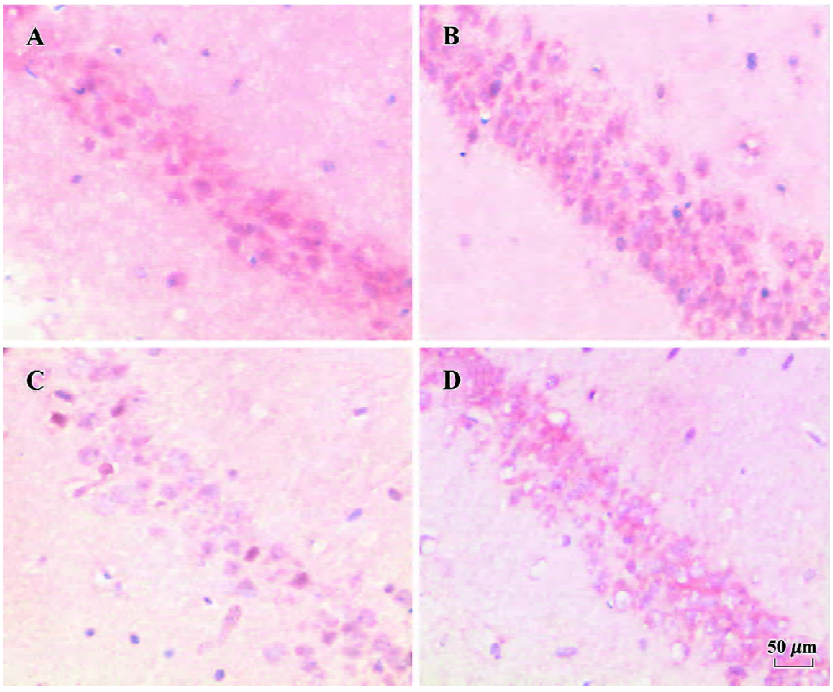

Figure 2. NPY-immunoreactive cells in pyramidal cell layers of CA1 region detected by immunohistochemistry (counterstained by hematoxylin ×400). (A), A sample from a control rat for FZP-tolerant group and (B), a sample from a control rat for FZP-dependent group show plenty of NPY-immunoreactive material (brown-red colour) in the cytoplasm of most neurons as well as neurofibers in white matter. (C), A sample from an FZP-tolerant rat and (D), a sample from an FZP-dependent rat show reduced NPY-immunoreactive material in the neuronal cytoplasm and neurofibers.

Table 3. Relative density of NPY-immunoreactive material in neurons of the hippocampus (area of 0.05 mm^2). n=6. ^bP<0.05 *vs* control groups.

Group	CA1	CA3	Dentate gyrus
FZP-tolerant	31.12±5.43^b	33.04±7.13^b	30.58±5.99^b
Control	209.47±11.18	221.84±14.05	218.58±13.94
FZP-dependent	75.33±9.86^b	71.65±7.25^b	72.97±6.34^b
Control	202.51±10.09	214.59±13.28	227.76±11.62

group, as compared with that of the respective controls (Table 2, Figure 1).

Correlations between the threshold of PTZ-induced seizures and the levels of preproNPY, Y_1, Y_2, and Y_5 cDNA in hippocampus of FZP-tolerant and -dependent rats The correlations were examined to show whether changes of NPY and its receptors in the hippocampus were related to the pathogenesis of FZP tolerance and dependence. The PTZ threshold was positively correlated with the level of preproNPY cDNA in the hippocampus both in FZP-tolerant and -dependent groups (Figure 3A, 3B). In other words, the lower the expression of NPY in the hippocampus, the higher degree of tolerance and dependence the rat showed. The PTZ threshold was negatively correlated with the level of hippocampal Y_2 cDNA in the FZP-tolerant group and was positively correlated with the level of hippocampal Y_2 cDNA in the FZP-dependent group (Figure 3C, 3D). No correlation between the PTZ threshold and the changes of Y_1 and Y_5 cDNA were found (data not shown).

Discussion

Pharmacologically, BDZ produce their sedative, anxiolytic and antiepileptic activities through a modulation action on $GABA_A$ receptors. However, tolerance to BDZ and dependence on BDZ are the two major adverse reactions in clinical practice. Neuronal hyperexcitability may be the common basis for the tolerance and dependence, although they may have different manifestations.

Hippocampus is implicated in the generation and modulation of seizure activities, and plays a central role in controlling excitability of the CNS[16]. In the present study, the hippocampus was separated to investigate the changes of NPY and its receptors (Y_1, Y_2, and Y_5) in rat models with

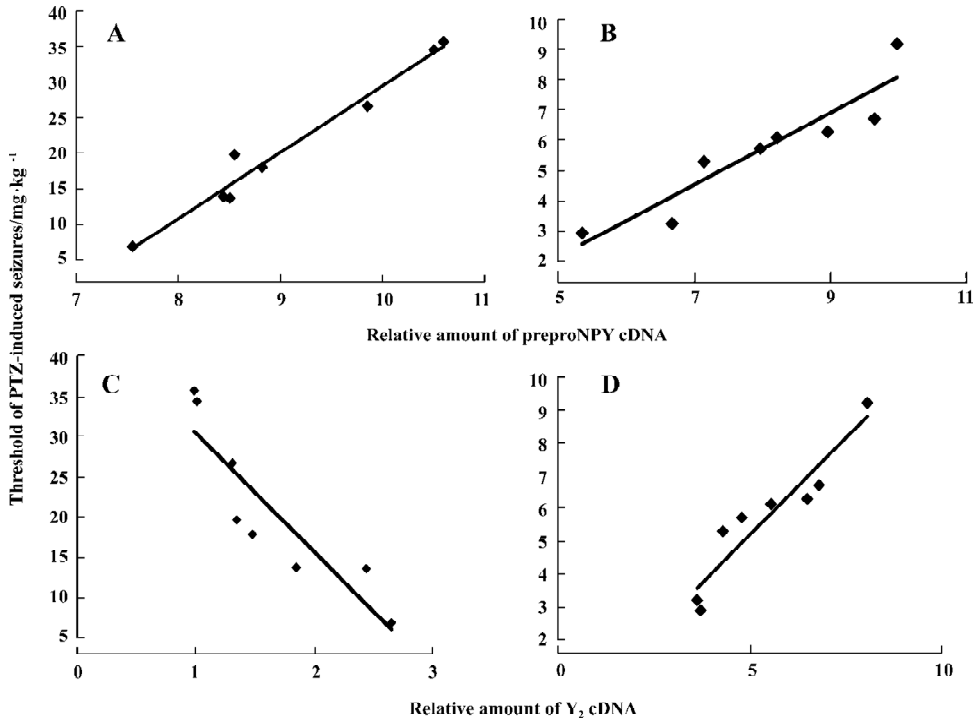

Figure 3. Correlations between the PTZ threshold and the level of hippocampal preproNPY cDNA: (A), in the FZP-tolerant group (r=0.9855, P<0.01) and (B), in the FZP-dependent group (r=0.9295, P<0.01). Correlation between the PTZ threshold and the level of hippocampal Y_2 cDNA: (C), in FZP-tolerant group (r=-0.8986, P<0.01) and (D), in FZP-dependent group (r=0.9414, P<0.01).

anticonvulsant tolerance and dependence to FZP.

We found that preproNPY cDNA in the hippocampus was significantly decreased in both the FZP-tolerant and FZP-dependent groups. Immunohistochemistry also showed the reduction of NPY-immunoreactive material in the neuronal cytoplasm and neurofibers of CA1, CA3, and dentate gyrus regions. Y_1 and Y_5 receptor cDNA were decreased in the tolerant group but were not changed in the dependent group. Y_2 receptor cDNA was increased in the tolerant group but was decreased in the dependent group.

To date, only one paper has been published on the relationship between the NPYergic system and drug tolerance and/or dependence[17]: contingent tolerance to carbamazepine after repeatedly giving the drug may be associated with the down-regulation of NPY. However, no data about the changes of the NPYergic system following long-term treatment of BDZ have been found in the published literature.

The level of preproNPY cDNA in the hippocampus reversely relating to the degree of tolerance and dependence may suggest that the changes of preproNPY cDNA are involved in the pathogenesis of FZP tolerance and dependence. NPY, one of the most abundant and widely distributed neuropeptides in the central and peripheral nervous systems, acts as an endogenous modulator to reduce seizure activities. In the hippocampus, the inhibition of epileptiform discharges after NPY treatment was attributed to the decrease of glutamate released from the presynaptic nerve terminals through blocking of the G-protein dependent calcium channel[18]. Therefore, the decrease of cellular NPY we found may result in neuronal hyperexcitability that is the fundamental pathological state of BDZ tolerance and dependence.

Six subtypes of NPY receptors, Y_1–Y_6, have been identified. Their pharmacological characteristics are very similar, although the identity of amino acid sequences is as low as 30% among these receptor subtypes[19]. Of the six receptor subtypes, Y_1, Y_2, and Y_5 are the major functional receptors and are expressed abundantly. In rodents, changes in the Y_1 receptor and its mRNA in the CNS can be induced by various stimuli, suggesting the multiple functions of the Y_1 receptor[20]. The Y_2 receptor demonstrates a predominant role in modulation of seizure activity[21]. The Y_5 receptor may also be involved in the modulation of anticonvulsant activity in rodents[22,23]. Theoretically, drug tolerance and dependence are caused by the imbalance of excitation over inhibition in the brain, and NPY receptors would decrease in association with the decrease of NPY. The different changes to NPY receptors between the FZP-tolerant and FZP-dependent group and the increase of Y_2 in FZP-tolerant rats in this study can not be satisfactorily explained because of the insufficient and conflicting data regarding Y_1, Y_2, and Y_5 receptors in the regulation of neuronal excitability at the present time. More experiments should be performed on the distribution and ligand binding capacity of the three subtype receptors in FZP tolerance and dependence.

Our preliminary results suggest that the decrease of NPY in the hippocampus plays an important role in the generation of anticonvulsant tolerance and dependence following long-term FZP treatment. The NPYergic system may be a new target for the comprehension of these adverse effects of BDZ.

References

1 Brown MJ, Wood MD, Coldwell MC, Bristow DR. Gamma-aminobutyric acid A receptor function is desensitised in rat cultured cerebellar granule cells following chronic flunitrazepam treatment. J Neurochem 1998; 71: 1232–40.

2 Bonavita C, Ferrero A, Cereseto M, Velardez M, Rubio M, Wikinski S. Adaptive changes in the rat hippocampal glutamatergic neurotransmission are observed during long-term treatment with lorazepam. Psychopharmacology (Berl) 2003; 166: 163–7.

3 Byrnes JJ, Miller LG, Perkins K, Greenblatt DJ, Shader RI. Chronic benzodiazepine administration. XI. Concurrent administration of PK11195 attenuates lorazepam discontinuation effects. Neuropsychopharmacology 1993; 8: 267–73.

4 Gupta N, Bhargava VK, Pandhi P. Tolerance and withdrawal to anticonvulsant action of clonazepam: role of nitric oxide. Methods Find Exp Clin Pharmacol 2000; 22: 229–35.

5 Mizoguchi H, Yoshiike M, Suzuki T, Misawa M. Effects of Ca^{2+} channel blockers on physical dependence on diazepam in mice. Life Sci 1993; 53: PL365–70.

6 Lilly SM, Zeng XJ, Tietz EI. Role of protein kinase A in $GABA_A$ receptor dysfunction in CA1 pyramidal cells following chronic benzodiazepine treatment. J Neurochem 2003; 85: 988–98.

7 Zeng XJ, Tietz EI. Role of bicarbonate ion in mediating decreased synaptic conductance in benzodiazepine tolerant hippocampal CA1 pyramidal neurons. Brain Res 2000; 868: 202–14.

8 Blomqvist AG, Herzog H. Y-receptor subtypes — how many more? Trends Neurosci 1997; 20: 294–8.

9 Colmers WF, Lukowiak K, Pittman QJ. Neuropeptide Y action in the rat hippocampal slice: site and mechanism of presynaptic inhibition. J Neurosci 1988; 8: 3827–37.

10 Bison S, Crews F. Alcohol withdrawal increases neuropeptide Y immunoreactivity in rat brain. Alcohol Clin Exp Res 2003; 27: 1173–83.

11 Rosenberg HC. Differential expression of benzodiazepine anticonvulsant cross-tolerance according to time following flurazepam or diazepam treatment. Pharmacol Biochem Behav 1995; 51: 363–8.

12 Rosenberg HC, Chiu TH. Tolerance during chronic benzodiazepine treatment associated with decreased receptor binding. Eur J Pharmacol 1981; 70: 453–60.

13 Lau CE, Falk JL, Dolan S, Tang M. Simultaneous determination of flurazepam and five metabolites in serum by high-perfor-

mance liquid chromatography and its application to pharmacokinetic studies in rats. J Chromatogr 1987; 423: 251–9.
14 Izzo E, Auta J, Impagnatiello F, Pesold C, Guidotti A, Costa E. Glutamic acid decarboxylase and glutamate receptor changes during tolerance and dependence to benzodiazepines. Proc Natl Acad Sci USA 2001; 98: 3483–8.
15 Sammbrook J, Fritsch EF, Maniatis T. Molecular cloning, a laboratory manual, 3rd Ed. Cold Spring Harbor (NY): Cold Spring Harbor Laboratory Press; 2001. p 8.86–9.
16 Loscher W, Ebert U. The role of the piriform cortex in kindling. Prog Neurobiol 1996; 50: 427–81.
17 Weiss SR, Clark M, Rosen JB, Smith MA, Post RM. Contingent tolerance to the anticonvulsant effects of carbamazepine: relationship to loss of endogenous adaptive mechanisms. Brain Res Brain Res Rev 1995; 20: 305–25.
18 Qian J, Colmers WF, Saggau P. Inhibition of synaptic transmission by neuropeptide Y in rat hippocampal area CA1: modulation of presynaptic Ca^{2+} entry. J Neurosci 1997; 17: 8169–77.
19 Parker RM, Herzog H. Regional distribution of Y-receptor subtype mRNAs in rat brain. Eur J Neurosci 1999; 11: 1431–48.
20 Gariboldi M, Conti M, Cavaleri D, Samanin R, Vezzani A. Anticonvulsant properties of BIBP3226, a non-peptide selective antagonist at neuropeptide Y Y1 receptors. Eur J Neurosci 1998; 10: 757–9.
21 Kaga T, Fujimiya M, Inui A. Emerging functions of neuropeptide Y Y(2) receptors in the brain. Peptides 2001; 22: 501–6.
22 Woldbye DP, Larsen PJ, Mikkelsen JD, Klemp K, Madsen TM, Bolwig TG. Powerful inhibition of kainic acid seizures by neuropeptide Y via Y5-like receptors. Nat Med 1997; 3: 761–4.
23 Wu YF, Li SB. Neuropeptide Y expression in mouse hippocampus and its role in neuronal excitotoxicity. Acta Pharmacol Sin 2005; 26: 63–8.

Acta Pharmacologica Sinica 2005 Nov; 26 (11): 1297–1302

Blackwell Publishing

Full-length article

Histidine enhances carbamazepine action against seizures and improves spatial memory deficits induced by chronic transauricular kindling in rats[1]

Qing LI[2,3], Chun-lei JIN[2], Li-sha XU[2], Zheng-bin ZHU-GE[2], Li-xia YANG[2], Lu-ying LIU[2], Zhong CHEN[2,4]

[2]Department of Pharmacology, Zhejiang University, Hangzhou 310031, China; [3]Department of Physiology, Zhejiang Medical College, Hangzhou 310053, China

Key words

histidine; carbamazepine; memory disorders; transauricular kindled seizures; epilepsy

[1] Project supported by the National Natural Science Foundation of China (No 30371638, 30472013), Natural Science Foundation of Zhejiang Province (No R303779), Scientific Research Foundations of Zhejiang Province (No 2004C34002) and the Scientific Foundation of the Department of Education of Zhejiang Province (No 20040284).
[4] Correspondence to Prof Zhong CHEN.
Phn/Fax 86-571-8721-7446.
E-mail chenzhong@zju.edu.cn

Received 2005-07-05
Accepted 2005-08-22

doi: 10.1111/j.1745-7254.2005.00220

Abstract

Aim: To investigate whether histidine can enhance the anticonvulsant efficacy of carbamazepine (CBZ) and simultaneously improve the spatial memory impairment induced by transauricular kindled seizures in Sprague-Dawley rats. **Methods:** Chronic transauricular kindling was induced by repeated application of initially subconvulsive electrical stimulation through ear-clip electrodes once every 24 h until the occurrence of 3 consecutive clonic-tonic seizures. An 8-arm radial maze (4 arms baited) was used to measure spatial memory, and histamine and γ-aminobutyric acid levels were measured by high performance liquid chromatography (HPLC). **Results:** Chronic transauricular kindling produced a significant impairment of spatial memory and a marked decrease in histamine content in the hypothalamus, the brainstem, and the hippocampus. Injection of histidine (1000 mg/kg or 1500 mg/kg, ip) significantly inhibited transauricular kindled seizures. Injection of histidine at lower doses (200 mg/kg or 500 mg/kg, ip) had no appreciable anticonvulsant effect when administered alone, whereas it significantly potentiated the protective effects of CBZ against kindled seizures. CBZ had no ameliorative effect on memory deficit, but, in contrast, histidine (200 mg/kg or 500 mg/kg, ip) alone or co-administered with CBZ significantly ameliorated the memory deficits induced by the seizures. **Conclusion:** Chronic transauricular kindling is a very useful animal model for evaluating memory deficits associated with epilepsy, and histidine has both a potentiate effect on the anticonvulsant efficacy of CBZ and an ameliorative effect on the spatial memory deficits induced in this model. Histidine at a specific dosage range might serve as a beneficial adjuvant for the clinical treatment of epilepsy, especially when accompanied by impaired spatial memory.

Introduction

Epilepsy is frequently accompanied by impairments in various cognitive functions. More than 45% of epileptics have psychological or social problems with behavioral manifestations and are completely or partly disabled[1]. Although the causes of cognitive impairment in patients with epilepsy have not yet been completely elucidated, 3 factors are proposed: the underlying etiology of the epilepsy, the effects of seizures themselves, and the side-effects of antiepileptic drugs (AEDs) at therapeutic doses[2]. There is a need for drugs or adjuvants that can simultaneously suppress seizures and ameliorate the concomitant cognitive impairment.

Brain histamine levels might play an important role in the regulation of seizure susceptibility. Injection of histidine ip, a precursor of histamine, and metoprine, a histamine N-methyltransferase inhibitor, or icv injection of histamine, inhibited seizures induced by pentylenetetrazol, maximal electroshock (MES) or amygdaloid kindling in mice or rats[3–6], whereas α-fluoromethylhistidine, a selective and irreversible histidine decarboxylase inhibitor, increases the duration of clonic convulsions induced by MES in mice[3] and causes severe seizure development in pentylenetetrazol-induced

kindling[7]. In contrast, the involvement of histamine in learning and memory processes has also been well documented. Histamine significantly ameliorates memory deficits induced by aging, dorsal hippocampal lesions, scopolamine and MK-801, as determined in rats using passive and active avoidance tasks and the 8-arm radial maze[8–12]. It is proposed that histamine and histaminergic compounds might be useful adjuncts for conventional AEDs, with dual advantages: one for enhancement of the anticonvulsant efficacy of AEDs, and the other for improvement of the memory deficits occurring with epilepsy.

The objectives of the present study were to further clarify whether histidine can both enhance the anticonvulsant efficacy of AEDs and ameliorate the spatial memory impairment induced by seizures. The chronic transauricular kindling procedure was used in rats as a new animal model of epilepsy, and an 8-arm (4 arms baited) radial maze paradigm was used to evaluate spatial memory and differentiate between short-term and long-term memory.

Materials and methods

Animals All experiments were carried out in accordance with the National Institutes of Health Guide for the Care and Use of Laboratory Animals. Male Sprague-Dawley rats (220–270 g, Grade II, Certificate No 22-9601018, Experimental Animal Center, Zhejiang University) were maintained in an air-conditioned room at 22–26 °C and 40%–70% humidity, and housed in individual cages with a 12-h light-dark cycle (lights on from 8:00 to 20:00). Animals were given free access to water and kept at 80%–85% of their free feeding body weight throughout the radial-arm maze experiments. Experiments were carried out each day between 10:00 and 17:00.

Radial-arm maze training The apparatus used is described in our previous reports[9,10,13]. The rats were familiarized with the radial maze once per day for 2 d prior to training. Food pellets (45 mg each, Bio-Serv) were scattered over the entire maze surface, and 3 or 4 rats were simultaneously placed in the maze and allowed to explore and take food freely for 10 min. After adaptation, all rats were trained with 1 trial per day. In each trial, only 4 arms (3, 5, 6, and 8) were baited, and the sequence was never changed throughout the experiment. One rat was placed on the center platform that was closed off by a door. After 15 s, the door was opened and the rat was allowed to make an arm choice to obtain food pellets until all 4 pellets had been eaten or 5 min had elapsed. The number of entries into unbaited arms was regarded as the total error (TE). The number of entries into never-baited arm was taken as reference memory error (RME), whereas re-entry into arms where the pellet had already been eaten was considered as a working memory error (WME). Rats continued training until reaching a criterion of less than 1 error per trial for 5 consecutive trials. Memory retrieval was tested in the same maze.

Chronic transauricular kindling After successful training in the radial maze, each rat in the experimental group was given 1 subconvulsive electrical stimulation daily via ear-clip electrodes (40 mA, 0.2 s, Hugo Saches type 221) until fully kindled. Animals in the sham group had the electrodes applied, but no current was delivered. Each rat was placed separately under a glass funnel, and the appearance of clonic-tonic seizures was recorded. When rats exhibited clonic-tonic seizures after each of 3 consecutive stimulations, they were regarded as fully kindled and used for the drug study. The endpoint of efficacy was taken as the inhibition of tonic hindlimb extension (HLE). The number of animals showing complete abolition of tonic HLE was expressed as percent protection.

Measurements of brain histamine and γ-aminobutyric acid (GABA) content

Sample preparation Rats were sacrificed by decapitation. The brain was quickly removed, placed on an ice-cold stainless steel plate, and dissected into the cortex, hippocampus, brainstem and hypothalamus according to the methods of Glowinski and Iversen[14]. The brain tissues were stored at -80 ℃ until assayed. The tissue was homogenized in 3% perchloric acid containing 5 mmol/L disodium EDTA and 5-hydro-N^{ω}-methyltryptamine in a Polytron homogenizer (Kinematica) at the maximum setting for 20 s in an ice bath. The homogenate was centrifuged at 15 000×*g* at 4 ℃ for 20 min. Then, the supernatant was removed and filtered with a 0.22 μm polyvinylidene difluoride membrane.

Chromatographic conditions Tissue samples were analyzed by high performance liquid chromatography (HPLC) combined with electrochemical detection using a technique developed in our laboratory for the simultaneous and sensitive analysis of histamine and GABA. The system consisted of a model 582 pump, a model 540 autosampler and a 4-channel CoulArray electrochemical detector. The HPLC was controlled and the data acquired and analyzed using CoulArray software. All of the above equipment was obtained from ESA. After reacting with the derivate *o*-phthalaldehyde, analytes were separated on a 3 μm, 3 mm×50 mm Capcell Pak MG C18 column from Shiseido. A 2-component gradient elution system was used, with component A of the mobile phase being 100 mmol/L Na_2HPO_4, 13% acetonitrile, and 22% methanol, pH 6.8, and component B being similar to A except with 5.6% acetonitrile and 9.4% methanol. The gradient elu-

tion profile was as follows: 0–3.5 min, isocratic 100% B; 3.5–20 min, linear ramp to 0% B; 20–22 min, isocratic 0% B; 22–23 min, linear ramp to 100% B; 23–30 min, isocratic 100% B. Flow rate was set to 0.75 mL/min. The first cell was set at +250 mV, whereas the second cell was set at +350 mV. All standards were obtained from Sigma. The retention times of GABA and histamine were 15.16 min and 18.36 min, respectively.

Drugs Histidine monohydrochloride and carbamazepine (CBZ) were obtained from Sigma. Histidine was dissolved in saline, and CBZ was suspended in a 1% solution of Tween 80. All drugs were injected ip in a volume of 1 mL/kg of body weight. Histidine was injected 1 h before and CBZ was injected 0.5 h before transauricular electrical stimulation or before the radial maze test. Drugs were given once a week. The same animals were used repeatedly, and they experienced all doses of each drug given in ascending order.

Statistical analysis Results were expressed as mean± standard error of the mean and analyzed by one-way analysis of variance followed by Dunnett's *t*-test. For percentage incidence, the χ^2-test with Fisher's exact test was used. All statistical analyses were carried out using SPSS 11.5 for Windows. $P<0.05$ was considered as statistically significant.

Results

Effects of histidine and CBZ on transauricular kindled seizures in rats Both histidine and CBZ inhibited transauricular kindled seizures in a dose-dependent manner, as reflected by the increase in percentage protection against tonic HLE. Histidine at doses of 200 mg/kg and 500 mg/kg slightly inhibited tonic HLE, but had no significant effect, whereas at doses of 1000 mg/kg and 1500 mg/kg, it significantly inhibited tonic HLE ($P<0.05$). CBZ at doses of 1 mg/kg and 2 mg/kg showed a tendency to inhibit tonic HLE, but no significant effect was observed, whereas at doses of 5 mg/kg and 10 mg/kg, it provided significant protection against tonic HLE ($P<0.01$). In addition, histidine at a low dose of 200 mg/kg showed a tendency to potentiate the anticonvulsant effects of 1 mg/kg CBZ and it significantly potentiated the anticonvulsant effects of 2 mg/kg CBZ ($P<0.05$). At a dose of 500 mg/kg histidine significantly potentiated the anticonvulsant effects of CBZ (1 mg/kg or 2 mg/kg) ($P<0.05$ and $P<0.01$, respectively) (Figure 1).

Effects of histidine and CBZ on radial maze performance in rats with spatial memory deficits induced by chronic transauricular kindled seizures The chronic transauricular kindling resulted in a significant increase in the number of TE, WME, and RME in the spatial memory retrieval process ($P<0.01$). Histidine at doses of 200 mg/kg and 500 mg/kg

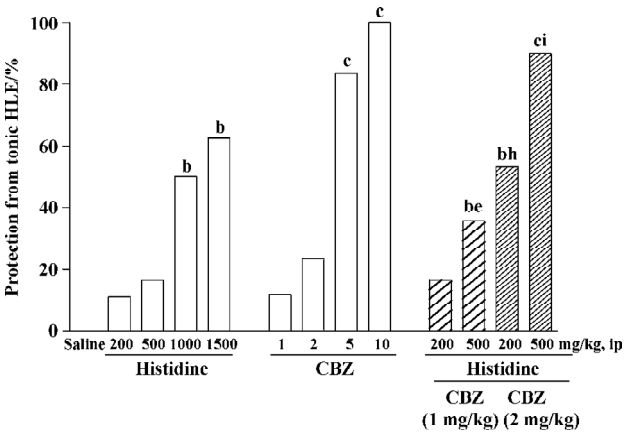

Figure 1. Effects of histidine and carbamazepine (CBZ) on transauricular kindled seizures in rats. Histidine was injected ip at 1 h and CBZ 0.5 h before chronic transauricular electrical stimulation. n=14–18 rats. Mean±SEM. $^bP<0.05$, $^cP<0.01$ *vs* saline group. $^eP<0.05$ *vs* CBZ (1 mg/kg) group. $^hP<0.05$, $^iP<0.01$ *vs* CBZ (2 mg/kg) group. HLE: hindlimb extension.

significantly decreased the number of TE and WME ($P<0.05$), but not the number of RME. However, histidine at doses of 1000 mg/kg and 1500 mg/kg had no ameliorative effect on the spatial memory deficits induced by transauricular kindled seizures. In contrast, CBZ (2, 5, 10, and 20 mg/kg) had no effect on memory impairment. The co-administration of CBZ also did not influence the improvement of spatial memory deficits induced by 500 mg/kg histidine (Table 1).

Effects of histidine and CBZ on brain histamine content Compared with control rats, chronic transauricular kindling produced a significant decrease in the histamine content of the hypothalamus (41.8%), hippocampus (43.6%), and brainstem (57.3%) ($P<0.05$). Histidine (500 mg/kg, ip) significantly increased the histamine content of the hypothalamus (157.9%) ($P<0.05$) and slightly increased that of the cortex (114.7%), hippocampus (112.7%) and brainstem (122.7%). CBZ (2 mg/kg) had no effect on the increased histamine content induced by histidine treatment (Table 2).

Effect of histidine and CBZ on brain GABA content Neither treatment with histidine (500 mg/kg) or CBZ (2 mg/kg) alone, nor co-administration of the 2 drugs had any effect on brain GABA levels (Table 3).

Discussion

In the present study, we provide evidence for the first time that chronic transauricular kindling can induce not only generalized tonic-clonic seizures but also spatial memory deficits in rats. So far, few animal models are suitable for studing the memory deficits associated with epilepsy, espe-

Table 1. Effects of histidine and carbamazepine (CBZ) on radial maze performance in rats with spatial memory deficits induced by chronic transauricular kindled seizures. CBZ and histidine were injected ip 0.5 h and 1 h before the radial maze test, respectively. Saline was injected 1 mL/kg ip 0.5 h before the radial maze test. n=10−15 rats. Mean±SEM. $^{c}P<0.01$ *vs* pre-kindled group. $^{e}P<0.05$, $^{f}P<0.01$ *vs* kindled group. TE: total errors; WME: working memory errors; RME: reference memory errors.

Group	Dose/mg·kg^{-1}, ip	TE	RME	WME
Pre-kindled+saline	–	0.4±0.1	0.3±0.1	0.1±0.1
Kindled+saline	–	5.1±0.4^{c}	2.8±0.2^{c}	1.4±0.2^{c}
Kindled+CBZ	2	5.3±1.4	2.7±0.4	1.5±0.6
	5	5.5±0.8	3.0±0.4	1.5±0.4
	10	5.2±1.0	2.8±0.4	1.4±0.3
	20	5.2±0.9	3.1±0.4	1.2±0.5
Kindled+histidine	200	3.1±0.8^{e}	2.1±0.6	0.9±0.2^{e}
	500	2.8±0.3^{e}	2.0±0.3	0.7±0.3^{e}
	1000	5.2±0.6	3.1±0.3	1.2±0.3
	1500	4.8±0.7	2.9±0.3	1.8±0.5
Kindled+histidine 500 mg/kg+CBZ	2	2.2±0.6^{f}	1.8±0.5	0.4±0.1^{f}
	5	2.5±0.5^{f}	2.1±0.3	0.4±0.2^{f}

Table 2. Effects of histidine and carbamazepine (CBZ) on brain histamine content. Histamine levels were measured at 1 h and 0.5 h after ip injection of histidine and CBZ, respectively. Saline was injected 1 mL/kg ip at 0.5 h before decapitation. n=6–8 rats. Mean±SEM. $^{b}P<0.05$ *vs* control group. $^{e}P<0.05$ *vs* kindled group.

Group	Dose/ mg·kg^{-1}, ip	Concentration/ng·g^{-1} tissue Cortex	Hypothalamus	Brainstem	Hippocampus
Control+saline	–	123.1±8.8	446.6±30.3	115.6±8.4	138.7±14.3
Kindled+saline	–	112.6±12.5	259.8±30.9^{b}	49.4±8.4^{b}	78.2±3.0^{b}
Kindled+CBZ	2	118.1±11.4	285.1±29.3	53.8±5.8	81.8±14.6
Kindled+histidine	500	129.2±29.1	410.1±29.2^{e}	60.6±5.5	88.1±8.5
Kindled+histidine 500 mg/kg+CBZ	2	146.5±12.1	429.2±40.1^{e}	65.3±6.0	87.9±4.5

Table 3. Effects of histidine and carbamazepine (CBZ) on brain γ-aminobutyric acid (GABA) content. GABA levels were measured at 1 h and 0.5 h after ip injection of histidine and CBZ, respectively. Saline was injected 1 mL/kg ip 0.5 h before decapitation. n=6–8 rats. Mean±SEM.

Group	Dose/ mg·kg^{-1}, ip	Concentration/μg·g^{-1} tissue Cortex	Hypothalamus	Brainstem	Hippocampus
Kindled+saline	–	207.1±11.9	956.3±42.8	197.6±13.3	264.6±15.4
Kindled+CBZ	2	204.2±10.4	979.0±134.1	201.3±9.5	286.5±42.2
Kindled+histidine	500	185.0±7.2	846.2±32.3	157.2±7.9	206.8±10.8
Kindled+histidine 500 mg/kg+CBZ	2	216.2±13.9	864.8±55.0	197.7±14.9	280.8±43.3

cially for the form with generalized tonic-clonic seizures[15]. MES is a representative animal model of generalized tonic-clonic seizures[16]; however, it has no appreciable effect on cognitive behaviors, such as in passive avoidance learning[17,18]. This might be because MES is a model of acute seizures (reactive or provoked), rather than a model of epilepsy[19]. In the present study, we developed a chronic transauricular kindling model that was relatively simple and required neither expensive equipment nor highly skilled personnel. We found that chronic transauricular kindled

seizures produced spatial memory deficits, which remained in a steady state for approximately 3 weeks after fully kindled (data not shown). Therefore, it is likely that the chronic transauricular kindling model is a very useful animal model for evaluating memory deficits associated with epilepsy, and in drug screening for both anticonvulsant and memory-improving actions.

In the present study, high doses of histidine (1000 mg/kg and 1500 mg/kg), a precursor of histamine, significantly inhibited chronic transauricular kindled seizures, but had no ameliorative effect on the spatial memory deficits induced by these seizures in rats. However, at doses of 200 mg/kg and 500 mg/kg, although it had no appreciable anticonvulsant effect, histidine significantly ameliorated spatial memory deficits. Therefore, it is proposed that at a lower dose, histidine combined with CBZ can simultaneously enhance the anticonvulsant effects and ameliorate spatial memory impairment in rats. Interestingly, we found that the lower doses of histidine significantly potentiated the protective effects of CBZ against transauricular kindled seizures and the cognitive improvement was not affected by co-administration of CBZ. Therefore, our results indicate that histidine, at a specific dosage range, potentiates both the anticonvulsant efficacy of CBZ and ameliorates the spatial memory deficits induced by chronic transauricular kindled seizures in rats. This indicates that histidine might serve as a beneficial adjuvant for the clinical treatment of epilepsy.

In addition, we found that chronic transauricular kindling resulted in a marked decrease of histamine content in the hypothalamus (41.8%), hippocampus (43.6%) and brainstem (57.3%). Consistent with our findings, decreased histamine content of the amygdala and hypothalamus has been reported to follow amygdaloid kindling[20]. The observed decrease in histamine levels following chronic transauricular kindled seizures further supports the concept of histamine as an endogenous anticonvulsant[21]. However, in contrast to our data, Vohora *et al* reported that acute MES significantly increased histamine concentration in the brainstem[22]. We have no data to explain this difference, which might be a result of different mechanisms underlying the seizures (acute *vs* chronic). Therefore, our results might at least partly elucidate why acute MES has no appreciable effect on cognitive behavior, whereas chronic transauricular kindling induces significant spatial memory deficits in rats[17,18].

It remains unclear why and how histidine potentiates the anticonvulsant effect of CBZ. A possible pharmacokinetic interaction is unlikely, because the plasma levels of CBZ remain unchanged in the presence of histidine[17]. Furthermore, we found the GABA levels in the brain after treatment with histidine and/or CBZ were not significantly different from the values in the control group, which suggests that the enhancement of the anticonvulsant effect of CBZ at the doses used is independent of GABA levels. However, treatment with histidine (200 mg/kg or 500 mg/kg) significantly increased brain histamine content in the hypothalamus. The significant increase of brain histamine content induced by injection of histidine might at least partly contribute to the observed enhanced anticonvulsant efficacy of CBZ.

It is interesting that the effects of histidine on performance in the radial maze showed a bell-shaped inhibition. These results are in accordance with the reports by Sakai *et al*[23] and Ghi *et al*[24], who found dose-dependent biphasic effects of histamine on locomotor activity. Alvarez *et al* also reported that treatment with a lower dose of histamine (45 nmol) in the hippocampus improved memory retrieval in contrast to the effect of a higher dose (90 mg/kg)[25]. These findings suggest that the biphasic effects of histamine in the brain might be mediated through different mechanisms, and the memory improvement induced by histidine only occurs within a specific lower range of dosage.

We were further interested to find that histidine significantly decreased both the number of TE and WME, but not the number of RME induced by transauricular kindled seizures in rats. Our data suggests that histidine can only ameliorate the short-term memory deficit induced by the kindled seizures. Similar findings show that histidine, at doses that cause a significant increase of brain histamine content, improves the working memory deficit induced by 8-OH-DPAT and 7-chlorokynurenic acid in rats[26,27]. Our previous work also shows that the H_3-antagonist clobenpropit facilitates deficits of working memory induced by intrahippocampal application of MK-801, and we demonstrate that the effects on working memory are a result of an increase in endogenous histamine, whereas the effects on reference memory are most likely a result of neurotransmitters other than histamine[28]. From the above evidence, it is likely that different mechanisms underlie working memory and reference memory, and brain histamine mainly participates in the former. Because short-term memory complaints are frequent in patients with epilepsy[29], the improvement in working memory induced by co-treatment with CBZ and histidine appears potentially useful.

In conclusion, we found that chronic transauricular kindling in rats was a very useful animal model for evaluating memory deficits associated with epilepsy. Histidine at relatively low doses significantly enhanced the anticonvulsant efficacy of CBZ against the kindled seizures and also had a significant ameliorative effect on the spatial memory impair-

ment induced by these seizures. It is proposed that histidine, at a specific range of dosages, might serve as a beneficial adjuvant for the clinical treatment of epilepsy, especially when it is accompanied by impairment of spatial memory.

Acknowledgement

We are very grateful to Dr Iain C BRUCE (University of Hong Kong) for reading the manuscript.

References

1 Genkova-Papazova MG, Petkova B, Shishkova N, Lazarova-Bakarova M. Effect of the calcium channel blockers nifedipine and diltiazem on pentylenetetrazole kindling-provoked amnesia in rats. Eur Neuropsychopharmacol 2001; 11: 91–6.

2 Kwan P, Brodie MJ. Neuropsychological effects of epilepsy and antiepileptic drugs. Lancet 2001; 357: 216–22.

3 Yokoyama H, Onodera K, Maeyama K, Yanai K, Iinuma K, Tuomisto L, *et al*. Histamine levels and clonic convulsions of electrically-induced seizure in mice: the effects of alpha-fluoromethylhistidine and metoprine. Naunyn-Schmiedeberg's Arch Pharmacol 1992; 346: 40–5.

4 Chen Z, Li WD, Zhu LJ, Shen YJ, Wei EQ. Effects of histidine, a precursor of histamine, on pentylenetetrazole-induced seizures in rats. Acta Pharmacol Sin 2002; 23: 361–6.

5 Zhang LS, Chen Z, Ren KM, Leurs R, Chen JC, Zhang WB, *et al*. Effects of clobenpropit on pentylenetetrazole-kindled seizures in rats. Eur J Pharmacol 2003; 482: 169–75.

6 Chen Z, Sakurai E, Hu WW, Jin CL, Kiso Y, Kato M, *et al*. Pharmacological effects of carcinine on histaminergic neurons in the brain. Br J Pharmacol 2004; 143: 573–80.

7 Zhang LS, Chen Z, Huang YW, Hu WW, Wei EQ, Yanai K. Effects of endogenous histamine on seizure development of pentylenetetrazole-induced kindling in rats. Pharmacology 2003; 69: 27–32.

8 Kamei C, Chen Z, Nakamura S, Sugimoto Y. Effects of intracerebroventricular injection of histamine on memory deficits induced by hippocampal lesions in rats. Methods Find Exp Clin Pharmacol 1997; 19: 253–9.

9 Chen Z, Kamei C. Facilitating effects of histamine on spatial memory deficit induced by scopolamine in rats. Acta Pharmacol Sin 2000; 21: 814–8.

10 Chen Z. Effect of histamine H_3-receptor antagonist clobenpropit on spatial memory of radial maze performance in rats. Acta Pharmacol Sin 2000; 21: 905–10.

11 Chen Z, Sugimoto Y, Kamei C. Effects of intracerebroventricular injection of α-fluoromethylhistidine on radial maze performance in rats. Pharmacol Biochem Behav 1999; 64: 513–8.

12 Huang YW, Chen Z, Hu WW, Zhang LS. Facilitating effect of histamine on spatial memory deficits induced by dizocilpine as evaluated by 8-arm radial maze in SD rats. Acta Pharmacol Sin 2003; 24: 1270–6.

13 Chen Z, Zhao Q, Sugimoto Y, Fujii Y, Kamei C. Effects of histamine on MK-801-induced memory deficits in radial maze performance in rats. Brain Res 1999; 839: 186–9.

14 Glowinski J, Iversen LL. Regional studies of catecholamines in the rat brain. I. The disposition of [^{3}H]norepinephrine, [^{3}H] dopamine and [^{3}H]dopa in various regions of the brain. J Neurochem 1966; 13: 655–69.

15 Majak K, Pitkanen A. Do seizures cause irreversible cognitive damage? Evidence from animal studies. Epilepsy Behav 2004; 5 Suppl 11: 35–44.

16 Loscher W, Fassbender CP, Nolting B. The role of technical, biological and pharmacological factors in the laboratory evaluation of anticonvulsant drugs. II. Maximal electroshock seizure models. Epilepsy Res 1991; 8: 79–94.

17 Kaminski RM, Zolkowska D, Kozicka M, Kleinrok Z, Czuczwar SJ. L-histidine is a beneficial adjuvant for antiepileptic drugs against maximal electroshock-induced seizures in mice. Amino Acids 2004; 26: 85–9.

18 Swiader M, Wielosz M, Czuczwar SJ. Interaction of astemizole, an H_1 receptor antagonist, with conventional antiepileptic drugs in mice. Pharmacol Biochem Behav 2003; 76: 169–78.

19 Loscher W. Animal models of epilepsy for the development of antiepileptogenic and disease-modifying drugs. A comparison of the pharmacology of kindling and post-status epilepticus models of temporal lobe epilepsy. Epilepsy Res 2002; 50: 105–23.

20 Kamei C, Ishizawa K, Kakinoki H, Fakunaga M. Histaminergic mechanisms in amygdaloid-kindled seizures in rats. Epilepsy Res 1998; 30: 187–94.

21 Leurs, R, Blandina P, Tedford C, Timmerman H. Therapeutic potential of histamine H_3 receptor agonists and antagonists. Trends Pharmacol Sci 1998; 19: 177–83.

22 Vohora D, Pal SN, Pillai KK. Histamine and selective H_3-receptor ligands: a possible role in the mechanism and management of epilepsy. Pharmacol Biochem Behav 2001; 68: 735–41.

23 Sakai N, Sakurai E, Onodera K, Sakurai E, Asada H, Miura Y, *et al*. Long-term depletion of brain histamine induced by alpha-fluoromethylhistidine increases feeding-associated locomotor activity in mice with a modulation of brain amino acid levels. Behav Brain Res 1995; 72: 83–8.

24 Ghi P, di Carlo G, Molinengo L. Effects of thioperamide on locomotor activity and on memory processes. Prog Neuropsychopharmacol Biol Psychiatry 1998; 22: 387–95.

25 Alvarez EO, Banzan AM. Effects of localized histamine microinjections into the hippocampal formation on the retrieval of a one-way active avoidance response in rats. J Neural Transm Gen Sect 1995; 101: 201–11.

26 Isayama S, Sugimoto Y, Nishiga M, Kamei C. Effects of histidine on working memory deficits induced by the 5-HT_{1A}-receptor agonist 8-OH-DPAT. Jpn J Pharmacol 2001; 86: 451–3.

27 Nishiga M, Kamei C. Ameliorative effects of histamine on 7-chlorokynurenic acid-induced spatial memory deficits in rats. Psychopharmacology (Berl) 2003; 166: 360–5.

28 Huang YW, Hu WW, Chen Z, Zhang LS, Shen HQ, Timmerman H, *et al*. Effect of the histamine H_3-antagonist clobenpropit on spatial memory deficits induced by MK-801 as evaluated by radial maze in Sprague-Dawley rats. Behav Brain Res 2004; 151: 287–93.

29 Shannon HE, Love PL. Effects of antiepileptic drugs on working memory as assessed by spatial alternation performance in rats. Epilepsy Behav 2004; 5: 857–65.

Acta Pharmacologica Sinica 2005 Nov; 26 (11): 1303–1308

Blackwell Publishing

Full-length article

Synergistic effects of atenolol and amlodipine for lowering and stabilizing blood pressure in 2K1C renovascular hypertensive rats[1]

Fu-ming SHEN[2], He-hui XIE[2], Gang LING, Li-ping XU, Ding-feng SU[3]

Department of Pharmacology, Second Military Medical University, Shanghai 200433, China

Key words

atenolol; amlodipine; blood pressure; blood pressure variability; hypertension

[1] Project supported by the Foundation for the Science and Technology Development of Shanghai (No 04JC14001) and the High Tech Research and Development (863) Program of China (No 2002 AA2Z346C).
[2] These authors contributed equally to this work.
[3] Correspondence to Prof Ding-feng SU.
Phn 86-21-2507-0323.
Fax 86-21-6549-3951.
E-mail dfsu@citiz.net

Received 2005-05-28
Accepted 2005-06-11

doi: 10.1111/j.1745-7254.2005.00185.x

Abstract

Aim: To test the synergistic effects of atenolol and amlodipine on lowering blood pressure (BP) and reducing blood pressure variability (BPV) in 2-kidney, one-clip (2K1C) renovascular hypertensive rats. **Methods:** Forty-eight 2K1C renovascular hypertensive rats were randomly divided into 6 groups. They were respectively given 0.8% carboxymethylcellulose sodium (control), atenolol (10.0 mg/kg), amlodipine (1.0 mg/kg), and combined atenolol and amlodipine (low dose: 5.0+0.5 mg/kg; intermediate dose: 10.0+1.0 mg/kg; high dose: 20.0+2.0 mg/kg). The drugs were given via a catheter in a gastric fistula. BP was recorded for 25 h from 1 h before drug administration to 24 h after administration. **Results:** Compared with BP before medication, all 3 doses of combined atenolol and amlodipine significantly decreased the BP at 24 h after administration, except for the low dose on diastolic BP. Compared with the control group, all 3 doses of combined atenolol and amlodipine significantly reduced the average BP levels for the 24 h period after administration; furthermore, the high and intermediate doses also significantly decreased the BPV levels for the same period. The *q* values calculated by probability sum analysis for systolic and diastolic BP for the 24 h period after administration were 2.29 and 1.45, respectively, and for systolic and diastolic BPV for the same period they were 1.41 and 1.60, respectively. **Conclusion:** There is significant synergism between atenolol and amlodipine in lowering and stabilizing BP in 2K1C renovascular hypertensive rats.

Introduction

Blood pressure (BP) is not constant, and can vary spontaneously. This variation is defined as blood pressure variability (BPV). BPV is increased in hypertensive humans and animals[1-3]. Furthermore, BPV is positively related to the severity of organ damage in hypertensive humans and rats[4–6]. In other words, increased BPV can produce organ damage. Therefore, it has been proposed that antihypertensive drugs with a BP-stabilizing effect would act to protect organs in the treatment of hypertension. We have demonstrated that long-term treatment with ketanserin, candesartan, nitrendipine , a combination of nitrendipine and atenolol, and a hydrochlorothiazide mixture not only decrease BP, but also decrease BPV, and have obvious effects on organ protection in spontaneously hypertensive rats as well. Importantly, organ protection was attributed to the decrease in BPV[7–10].

Clinically, combination therapy against hypertension using 2 or more drugs from different classes can produce better drug efficacy[11]. Furthermore, the use of such synergistic therapy is also recommended for the initial treatment of hypertension[12]. Both β-blockers and dihydropyridine calcium antagonists are widely used in the treatment of hypertension. Atenolol and amlodipine are examples of long-acting drugs from these 2 classes. We hypothesized that these 2 drugs combined would produce a synergistic effect in the treatment of hypertension. Therefore, this study was designed to investigate the synergistic effects of atenolol and amlodipine on both lowing and stabilizing BP in 2K1C renovascular hypertensive rats (RVHR).

Materials and methods

Drugs and drug administration Amlodipine (Nanjing Pharmaceutical Co, Nanjing, China), atenolol (Shanghai Second Pharmaceutical Co, Shanghai, China) and a combination of these 2 drugs were dissolved in 0.8% carboxymethylcellulose sodium (CMC). The doses used were as follows: atenolol 10.0 mg/kg , amlodipine 1.0 mg/kg and 5.0+0.5 mg/kg, 10.0+1.0 mg/kg, and 20.0+2.0 mg/kg combinations of the 2 drugs. Five groups of rats received antihypertensive drugs and one group of rats received 0.8% CMC as control. Drugs were administered by a catheter in a gastric fistula implanted 3 days before treatment.

Animals and RVHR preparation Male Sprague–Dawley rats (160–180 g), purchased from the Sino-British SIPPR/BK Lab Animal Ltd (Shanghai, China), were anesthetized with a combination of ketamine (40 mg/kg) and diazepam (6 mg/kg). The right renal artery of each animal was isolated through a flank incision as described previously[13], and a silver clip (0.2 mm internal gap) was placed on the renal artery. Five weeks after placement of the clip, the systolic blood pressure (SBP) of rats was measured by using the tail-cuff method (CB10; Alcott Biotech Co, Shanghai, China). In total, 48 RVHR whose SBP was greater than 160 mmHg were used in this study. Rats were kept in a controlled temperature (23 °C–25 °C) and lighting (light 08:00–20:00, dark 20:00–08:00) environment, and had free access to food and tap water. All the animals used in this work received humane care in compliance with institutional animal care guidelines.

BP and BPV measurement SBP, diastolic blood pressure (DBP) and heart period (HP) were continuously recorded using a previously described technique[10]. Briefly, rats were anesthetized by injection (ip) with a combination of ketamine (40 mg/kg) and diazepam (6 mg/kg). A floating polyethylene catheter was inserted into the lower abdominal aorta via the left femoral artery for BP measurement, and another catheter was placed into the stomach via a mid-abdominal incision for drug administration. The catheters were exteriorized through the interscapular skin. After a 2-d recovery period, the animals were placed for BP recording in individual cylindrical cages containing food and water. The aortic catheter was connected to a BP transducer via a rotating swivel that allowed the animals to move freely in the cage. After approximately 14-h habituation, at 9:00 o'clock the BP signal was begun to be digitized by a microcomputer. One hour later, at 10:00 o'clock the drug was given via the catheter in the gastric fistula. SBP, DBP, and HP values were recorded beat-to-beat for 25 h, up to 10:00 o'clock on the second day. The mean values of these parameters during a designated period were calculated and served as SBP, DBP and HP values. The standard deviation of all values obtained over 24 h was denoted as the quantitative parameter of variability; that is, SBP variability (SBPV), DBP variability (DBPV), and HP variability (HPV) for each rat.

Probability sum test To determine whether the drugs were acting synergistically, we used the probability sum test. This test comes from classic probability analysis and is useful for evaluating the synergistic interactions between 2 drugs (q test)[10,14,15].

In the present work, we used the following criteria. Compared with the mean values from control rats, treated rats with a decrease in BP (SBP or DBP) >20 mmHg were defined as responders and rats with a decrease in BP≤20 mmHg were defined as non-responders. For BPV (SBPV or DBPV), the criterion was 2 mmHg. The formula used is as follows: $q=P_{A+B}/(P_A+P_B-P_A\times P_B)$. Here, A and B indicate drug A and drug B; P (probability) is the percentage of responders in each group. P_{A+B} is the real percentage of responders and $(P_A+P_B-P_A\times P_B)$ is the expected response rate. P_A+P_B is the sum of the probabilities when drug A and drug B are used alone. $P_A\times P_B$ is the probability of rats responding to both drugs when they were used alone. When $q<0.85$, the combination is antagonistic, when $q>1.15$, the combination is synergistic, and when q is between 0.85 and 1.15, the combination is additive.

Statistical analysis Data were expressed as mean±SEM. Comparisons between values obtained in the same group before and after drug administration were made using the paired t-test. Comparisons among groups were carried out using ANOVA followed by Duncan's test. $P<0.05$ was considered statistically significant.

Results

Effects of atenolol and amlodipine on BP and HP at 24 h after treatment The effects of atenolol and amlodipine alone and in combination on BP and HP at 24 h after administration in 2K1C RVHR are shown in Table 1. The mean values of these variables 1 h before administration serve as the control values and are defined as "before"; the mean values at 24 h after administration are defined as "after". We found that SBP was significantly decreased in all 3 groups treated with both atenolol and amlodipine when compared with "before". A significantly lower DBP was also found in 2 groups of rats treated with both atenolol and amlodipine (10.0+1.0 mg/kg and 20.0+2.0 mg/kg) when compared with "before". Relative to "before" , the mean HP value at 24 h after administration was higher only in rats treated with atenolol (10.0

Table 1. Effects of atenolol (Ate) and amlodipine (Aml) alone and in combination on 1-h blood pressure and heart period (HP) in 2K1C renovascular hypertensive rats. n=8. Mean±SEM. ^{b}P<0.05, ^{c}P<0.01 *vs* before administration. ^{e}P<0.05, ^{f}P<0.01 *vs* Ate+Aml (5+0.5 mg/kg).

Groups	Dose/mg·kg^{-1}	SBP/mmHg		DBP/mmHg		HP/ms	
		Before	After	Before	After	Before	After
Control	0	170.0±3.2	172.0±4.2	99.0±2.8	100.0±3.9	172.0±5.7	178.0±4.2
Ate	10	172.0±3.9	161.0±4.2	101.0±3.5	94.0±3.5	167.0±3.9	207.0±6.7^{c}
Aml	1	172.0±3.9	162.0±3.5	102.0±3.2	92.0±3.9	168.0±7.1	172.0±4.9
Ate+Aml	5+0.5	174.0±4.2	159.0±3.9^{b}	102.0±3.9	89.0±4.6	175.0±6.0	180.0±7.0
Ate+Aml	10+1	171.0±3.2	146.0±4.2^{ce}	98.0±2.8	83.0±5.0^{b}	178.0±3.2	179.0±4.2
Ate+Aml	20+2	172.0±3.2	141.0±2.5^{cf}	104.0±3.2	82.0±4.2^{c}	176.0±5.3	170.0±5.7

SBP, systolic blood pressure; DBP, diastolic blood pressure; Before, the mean value of 1-h blood pressure and HP before administration; After, the mean blood pressure and HP value at 24 h after administration.

mg/kg) alone. Of the 3 groups treated with both atenolol and amlodipine, we found that both the intermediate and the high doses reduced SBP at 24 h after administration more effectively than the low dose.

Effects of atenolol and amlodipine on BP and HP for the 24-h period after administration We found that the average SBP in control rats during the 24 h after administration was 171.0±3.5 mmHg. The average SBP over this time was significantly lower in all 5 groups treated with either atenolol, or amlodipine, or both when compared with the control group (Figure 1). The minimal decrease (-13.0 mmHg) was found in rats treated with amlodipine alone and the maximal decrease (-39.0 mmHg) was found in rats treated with both atenolol and amlodipine at a high dose (20.0+2.0 mg/kg). Compared with control, the decrease in average DBP in the experimental groups during the 24 h after administration was also significant but not so profound. The mean value of HP during this time was only increased in the group treated with atenolol (10.0 mg/kg) alone. Of the 3 groups treated with both atenolol and amlodipine, both the intermediate and the high doses reduced SBP more obviously than the low dose (Figure 1).

Effects of atenolol and amlodipine on BPV and HPV for the 24-h period after administration Compared with the control group (13.00±0.53 mmHg for SBPV and 9.40±0.64 mmHg for DBPV), a significant decrease in BPV was found in groups treated with both atenolol and amlodipine at an intermediate (8.80±0.85 mmHg for SBPV and 7.60±0.53 mmHg for DBPV) and high dose (8.50±0.71 mmHg for SBPV and 7.30±0.53 mmHg for DBPV) (Figure 2).

Synergistic interaction of atenolol and amlodipine on BP and BPV for the 24-h period after administration Based on the results presented in Figure 1, the effectiveness of the decrease in BP was calculated for rats individually. Rats with a decrease in BP >20 mmHg (relative to controls) were defined as responders and those with a decrease in BP ≤20 mmHg as non-responders. The results of probability testing are presented in Table 2. We arrived at q values of 2.29 for SBP and 1.45 for DBP for the combination of both atenolol and amlodipine (10.0+1.0 mg/kg). Compared with the mean values for control rats, rats with a decrease in SBPV or DBPV >2 mmHg were defined as responders. According to this criterion, the q values were 1.41 for SBPV and 1.60 for DBPV for the combination of both atenolol and amlodipine (10.0+1.0 mg/kg).

Table 2. Results of probability sum tests for the combination of atenolol (Ate; 10.0 mg/kg) and amlodipine (Aml; 1.0 mg/kg) on blood pressure and blood pressure variability for the 24-h period after administration in 2K1C renovascular hypertensive rats. n=8.

Groups	Dose/ mg·kg^{-1}	SBP P	DBP P	SBPV P	DBPV P
Ate	10	2/8	1/8	2/8	1/8
Aml	1	2/8	2/8	3/8	1/8
Ate+Aml	10+1	8/8	4/8	6/8	3/8
q values		2.29	1.45	1.41	1.60

SBP P, percentage of responders for systolic blood pressure; DBP P, percentage of responders for diastolic blood pressure; SBPV P, percentage of responders for systolic blood pressure variability; DBPV P, percentage of responders for diastolic blood pressure variability. $q=P_{Ate+Aml}/(P_{Ate}+P_{Aml}-P_{Ate}\times P_{Aml})$. If q<0.85, the combination is antagonistic, if q>1.15, the combination is synergistic, if q is between 0.85 and 1.15, the combination is additive.

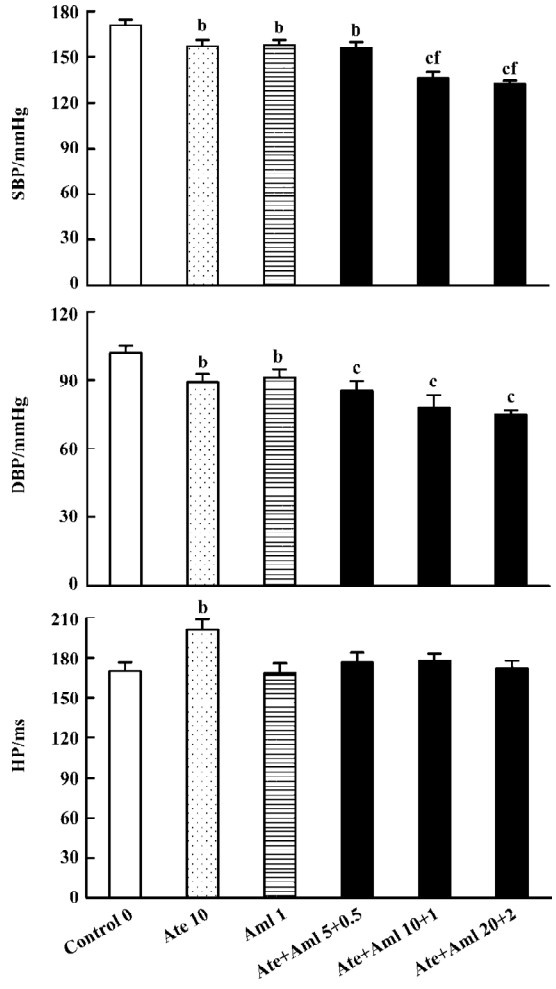

Figure 1. Effects of atenolol (Ate) and amlodipine (Aml) alone and in combination on blood pressure and heart period (HP) in 2K1C renovascular hypertensive rats for the 24-h period after administration. SBP, DBP, and HP are the mean values of systolic blood pressure, diastolic blood pressure, and heart period, respectively, and were calculated from each beat during the 24-h test period. The numbers shown after the compounds are dosages (mg/kg). n=8 rats. Mean±SEM. $^{b}P<0.05$, $^{c}P<0.01$ *vs* control. $^{f}P<0.01$ *vs* Ate+Aml (5+0.5 mg/kg).

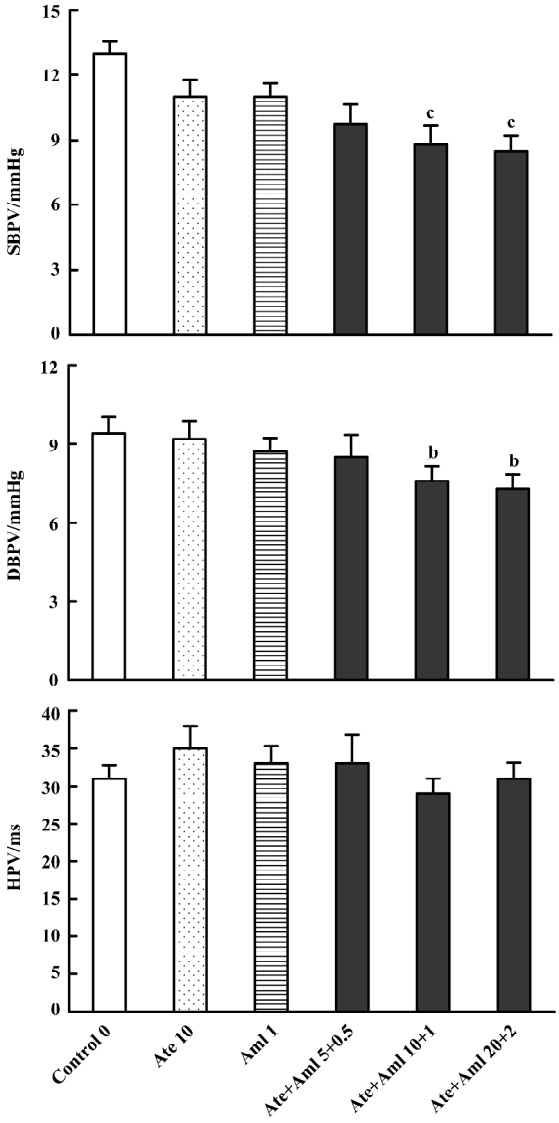

Figure 2. Effects of atenolol (Ate) and amlodipine (Aml) alone and in combination on blood pressure variability and heart period variability (HPV) in 2K1C renovascular hypertensive rats for the 24-h period after administration. SBPV, DBPV, and HPV are the standard deviations of systolic blood pressure, diastolic blood pressure, and heart period, respectively, and were calculated from each beat during the 24-h test period. The numbers shown after the compounds are dosages (mg/kg). n=8 rats. Mean±SEM. $^{b}P<0.05$, $^{c}P<0.01$ *vs* control.

Discussion

The purpose of using fixed-dose combinations of 2 different kinds of antihypertensive drugs in the treatment of hypertension is to obtain increased BP control and to enhance compliance by using a single tablet that is taken once or twice daily[16]. Furthermore, by combining 2 different agents at lower doses, the clinical and metabolic side effects that would be produced by either drug at higher doses can be minimized[17]. Therefore, fixed-dose combinations of antihypertensive drugs could potentially increase BP control, simplify dosage regimens, improve compliance, decrease dose-dependent side effects, and reduce costs as the first-line treatment for hypertension[18]. These advantages make combination antihypertensive therapy the recommended initial treatment, particularly in patients with end-organ damage (EOD) or more severe initial hypertension[19,20]. However, high BP is not a unique factor determining hypertensive EOD. Parati *et al* found that for patients with similar mean hypertension levels for the 24 h after treatment, those whose BPV

levels were lower had less severe organ damage than those with higher BPV levels[4]. Our previous study found that in 60-week-old spontaneously hypertensive rats , the severity of organ damage was positively related to BP (r=0.31–0.32, n=50, P<0.05) and BPV levels (r=0.63–0.65, n=50, P<0.01), and BPV was positively related to the extent of organ damage, so BPV might be a new determinant of EOD[6,21,22].

Therefore, it seems very important to emphasize the role of BPV in antihypertensive therapy. However, it is not clear how BPV can be controlled in the treatment of hypertension. We have previously proposed 2 ways to reduce BPV in antihypertensive therapy[6]: (1) find antihypertensive drugs that decrease BPV even at a dose that does not affect BP, for example ketanserin; and (2) treat patients with long-acting antihypertensive drugs, for example candesartan or amlodipine. In the present work, we investigated a third way to control BPV in the treatment of hypertension, that is, combination therapy.

Both β-blockers and dihydropyridine calcium antagonists are widely used in antihypertensive therapy. The combination of a β-blocker and a dihydropyridine calcium antagonist is a logical choice[23], and is effective for treating hypertensive patients with chronic renal insufficiency and left ventricular hypertrophy[24]. Theoretically, calcium antagonists are vasodilators and tend to increase plasma renin, therefore combining them with β-blockers is a good idea[25]. A combination of these compounds can also neutralize the side effects of both, for example the initial heart rate increases induced by dihydropyridine calcium antagonists, and the rise in peripheral resistance elicited by some β-blockers[26].

In terms of the synergistic effects of atenolol (10.0 mg/kg) and amlodipine (1.0 mg/kg) on BP reduction, the findings of the present work are: (1) the combination of atenolol and amlodipine significantly decreases BP 24 h after administration, whereas neither drug alone had an obvious influence; (2) both atenolol or amlodipine alone reduced the average BP for the 24 h period after administration by less than 15 mmHg, but in combination they decreased SBP by up to 35 mmHg and DBP by approximately 25 mmHg. The q values for SBP and DBP for the 24 h period after administration were 2.29 and 1.45, respectively, which are higher than 1.15, the threshold value for synergistic effects. Concerning the synergism of combined atenolol and amlodipine on the reduction in BPV for the 24 h period after administration, we found that BPV was not influenced by treatment with atenolol or amlodipine alone, but was markedly reduced when they were used in combination. The q values for SBPV and DBPV for the 24 h period after administration were 1.41 and 1.60, respectively. These findings demonstrate that the combination of atenolol and amlodipine has a significant synergistic effect on lowing BP and stabilizing BPV in RVHR.

Our previous studies have demonstrated that long-term (4 months) treatment with a hydrochlorothiazide mixture, which consisted of 5 drugs at low doses, markedly reduced BP and BPV in spontaneously hypertensive rats[9]. Long-term (3 months) treatment with atenolol and nitrendipine had a significant protective effect on organs in spontaneously hypertensive rats[8].

We conclude that atenolol and amlodipine in combination have a synergistic effect in lowering and stabilizing BP in RVHR. Combination therapy is likely to be the optimal way to control BP and reduce BPV in the treatment of hypertension.

References

1 Mancia G, Ferrari A, Gregorini L, Parati G, Pomidossi G, Bertinieri G, *et al*. Blood pressure and heart rate variabilities in normotensive and hypertensive human beings. Circ Res 1983; 53: 96–104.

2 Su DF, Cerutti C, Barres C, Vincent M, Sassard J. Blood pressure and baroreflex sensitivity in conscious hypertensive rats of Lyon strain. Am J Physiol 1986; 251: H1111–7.

3 Miao CY, Shen FM, Su DF. Blood pressure variability is increased in genetic hypertension and *L*-NAME-induced hypertension. Acta Pharmacol Sin 2001; 22: 137–40.

4 Parati G, Pomidossi G, Albini F, Malaspina D, Mancia G. Relationship of 24-hour blood pressure mean and variability to severity of target-organ damage in hypertension. J Hypertens 1987; 5: 93–8.

5 Mancia G, Frattola A, Parati G, Santucciu C, Ulian L. Blood pressure variability and organ damage. J Cardiovasc Pharmacol 1994; 24: S6–11.

6 Su DF, Miao CY. Blood pressure variability and organ damage. Clin Exp Pharmacol Physiol 2001; 28: 709–15.

7 Du WM, Miao CY, Liu JG, Shen FM, Yang XQ, Su DF. Effects of long-term treatment with ketanserin on blood pressure variability and end-organ damage in spontaneously hypertensive rats. J Cardiovasc Pharmacol 2003; 41: 233–9.

8 Xie HH, Miao CY, Liu JG, Su DF. Importance of blood pressure variability in organ protection in spontaneously hypertensive rats treated with combination of nitrendipine and atenolol. Acta Pharmacol Sin 2002; 23: 1199–204.

9 Lu ZA, Xie HH, Xu LP, Yin AF, Miao CY, Su DF. Restoration of arterial baroreflex function contributes to organ protection in spontaneously hypertensive rats treated with long-term hydrochlorothiazide mixture. Clin Exp Pharmacol Physiol 2003; 30: 49–54.

10 Xie HH, Miao CY, Jiang YY, Su DF. Synergism of atenolol and nitrendipine on hemodynamic amelioration and organ protection in hypertensive rats. J Hypertens 2005; 23: 193–201.

11 Materson BJ, Reda DJ, Cushman WC, Massie BM, Freis ED, Kochar MS, *et al*. Single-drug therapy for hypertension in men: a comparison of six antihypertensive agents with placebo: the

Department of Veterans Affairs Cooperative Study Group on Antihypertensive Agents. N Engl J Med 1993; 328: 914–21.
12 The sixth report of the Joint National Committee on prevention, detection, evaluation, and treatment of high blood pressure. [published erratum appears in Arch Intern Med 1998; 158: 573] Arch Intern Med 1997; 157: 2413–46.
13 Guan S, Fox J, Mitchell KD, Navar LG. Angiotensin and angiotensin-converting enzyme tissue levels in two-kidney, one clip hypertensive rats. Hypertension 1992; 20: 763–7.
14 Jin ZJ. About the evaluation of drug combination. Acta Pharmacol Sin 2004; 25: 146–7.
15 Su DF, Xu LP, Miao CY, Xie HH, Shen FM, Jiang YY. Two useful methods for evaluating antihypertensive drugs in conscious freely moving rats. Acta Pharmacol Sin 2004; 25: 148–51.
16 Eisen SA, Miller DK, Woodward RS, Spitznagel E, Przybeck TR. The effect of prescribed daily dose frequency on patient medication compliance. Arch Intern Med 1990; 150: 1881–4.
17 Sica DA. Fixed-dose combination antihypertensive drugs. Do they have a role in rational therapy? Drugs 1994; 48: 16–24.
18 Prisant LM. Fixed low-dose combination in first-line treatment of hypertension. J Hypertens 2002; 20: S11–9.
19 Moser M. Current recommendations for initial therapy in hypertension: are they still valid? Introduction. Am J Hypertens 1998; 11: 69S–72S.
20 Moser M, Black HR. The role of combination therapy in the treatment of hypertension. Am J Hypertens 1998; 11: 73S–78S.
21 Shan ZZ, Dai SM, Su DF. Relationship between baroreceptor reflex function and end-organ damage in spontaneously hypertensive rats. Am J Physiol 1999; 277: H1200–6.
22 Su DF, Miao CY. Reduction of blood pressure variability: a new strategy for treatment of arterial hypertension. Trends Pharmacol Sci 2005; 26: 388–90.
23 Weir MR. The rationale for combination versus single-entity therapy in hypertension. Am J Hypertens 1998; 11: 163S–169S.
24 Suzuki H, Moriwaki K, Kanno Y, Nakamoto H, Okada H, Chen XM. Comparison of the effects of an ACE inhibitor and alphabeta blocker on the progression of renal failure with left ventricular hypertrophy: preliminary report. Hypertens Res 2001; 24: 153–8.
25 Waeber B, Detry JM, Dahlof B, Puig JG, Gundersen T, Hosie J, *et al*. Felodipine-metoprolol combination tablet: a valuable option to initiate antihypertensive therapy? Am J Hypertens 1999; 12: 915–20.
26 Menard J. Critical assessment of combination therapy development. Blood Press 1993; 1 Suppl: 5–9.

Acta Pharmacologica Sinica 2005 Nov; 26 (11): 1309–1316

Blackwell Publishing

Full-length article

CPU 86017, *p*-chlorobenzyltetrahydroberberine chloride, attenuates monocrotaline-induced pulmonary hypertension by suppressing endothelin pathway[1]

Tian-tai ZHANG, Bing CUI, De-zai DAI[2], Wei SU

Research Division of Pharmacology, China Pharmaceutical University, Nanjing 210009, China

Key words

pulmonary artery; hypertension; endothelin-1; nitric-oxide synthase; reactive oxygen species; monocrotaline; CPU 86017

[1] Project supported by the National Natural Science Foundation of China (No 30230170).
[2] Correspondence to Prof De-zai DAI.
Phn 86-25-8327-1270.
Fax 86-25-8330-2827.
E-mail dezaidai@vip.sina.com

Received 2005-07-08
Accepted 2005-08-02

doi: 10.1111/j.1745-7254.2005.00214.x

Abstract

Aim: To elucidate the involvement of the endothelin (ET) pathway in the pathogenesis of monocrotaline (MCT)-induced pulmonary arterial hypertension (PAH) and the therapeutic effect of CPU 86017 (*p*-chlorobenzyltetrahydroberberine chloride) in rats. **Methods:** Rats were injected with a single dose (60 mg/kg, sc) of MCT and given CPU 86017 (20, 40, and 80 $mg \cdot kg^{-1} \cdot d^{-1}$, *po*) or saline for 28 d. The hemodynamics, mRNA expression, and vascular activity were evaluated. **Results:** Right ventricular systolic pressure and central venous pressures were elevated markedly in the PAH model and decreased by CPU 86017. In the PAH group, the endothelin-1 (ET-1) in serum and lungs was dramatically increased by 54% (79.9 pg/mL, $P<0.01$) and 93% (166.2 pg/mL, $P<0.01$), and mRNA levels of preproET-1, eNOS, and iNOS also increased dramatically compared with control. Compared with PAH group, CPU 86017 decreased the content of ET-1 to the normal level in lung tissue, but was less effective in serum. The level of NO was significantly increased in CPU 86017 at 80 and 40 $mg \cdot kg^{-1} \cdot d^{-1}$ groups in tissue, whereas the difference in serum was not significant. A significant reduction in MDA production and an increase in the SOD activity in the serum and lungs was observed in all three CPU 86017 groups. CPU 86017 80 $mg \cdot kg^{-1} \cdot d^{-1}$ *po* increased the activity of cNOS by 33% ($P<0.01$). The up-regulation of eNOS and iNOS mRNA levels induced by MCT was significantly reversed in 3 CPU 86017 groups, and preproET-1 mRNA abundance was also reduced notably in CPU 86017 80 $mg \cdot kg^{-1} \cdot d^{-1}$ group *vs* the PAH group. The KCl-induced vasoconstrictions in the calcium-free medium decreased markedly in PAH group but recovered partially after CPU 86017 intervention. The constrictions in the presence of Ca^{2+} was not improved by CPU 86017. The phenylephrine-induced vasoconstrictions in the calcium-free medium decreased markedly in PAH group but not recovered after CPU 86017 intervention. The constrictions in the presence of Ca^{2+} completely returned to the normal after CPU 86017 intervention. **Conclusion:** CPU 86017 suppressed MCT-induced PAH mainly through an indirect suppression of the ET-1 system, which was involved in the pathogenesis of the disease.

Introduction

Pulmonary arterial hypertension (PAH) is a common disease induced by many etiological factors. Pulmonary vascular remodeling by monocrotaline (MCT) affects both vascular smooth muscle and vascular wall connective tissue at the molecular level[1]. Endothelium plays an important role in controlling vascular tone as well as vascular remodeling by releasing endothelium-derived relaxing factors [EDRF, nitric oxide (NO)] and contracting factors mainly endothelin-1

(ET-1)[2]. ET-1 is a potent endothelium-derived vasoconstrictor peptide, which possesses mitogenic effects to proliferate the vascular smooth muscle cells (VSMC) in the development of PAH[3]. NO, which is released from the endothelium, attenuates proliferation of VSMC[4] and is opposed functionally to ET-1[5].

Monocrotaline (MCT), a pyrrole alkaloid, causes substantial and sustained inflammatory damage to the pulmonary arterial system and, therefore, causes PAH in rats[5]. CPU 86017, *p*-chlorobenzyltetrahydroberberine (Figure 1), a new compound derived from berberine, possesses a calcium channel blocking effect[6], combined with an antioxidative effect[7]. CPU 86017 ameliorates the progression of chronic congestive heart failure in relation to suppression of the ET-1 system[8]. Therefore, it is hypothesized that CPU 86017 might relieve the pulmonary hypertension, with an indirect effect on the overactive ET pathway underlying the pulmonary hypertension induced by MCT. We intend to explore the pathogenesis of PAH induced by MCT in relation to an activated ET pathway, and its downstream events (iNOS and ROS activity) in response to the medication of CPU 86017.

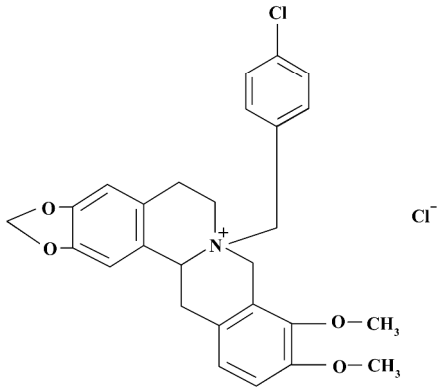

Figure 1. The chemical structure of CPU 86017.

Materials and methods

Experimental protocol Sixty-five male Sprague-Dawley rats (weighing 250 g-300 g, from the Experimental Animal Center of Nanjing Medical University) were randomized into 5 groups (n =13). Animals (apart from the normal group) were injected with a single dose 60 mg/kg, sc) of MCT (Promega). *p*-Chloro-benzyl-tetrahydro-berberine chloride (CPU 86017) was first synthesized by the New Drug Center of China Pharmaceutical University and provided by Shandong Xinhua Pharmaceutical Industry Co. The 5 groups were the normal group (Ctl), PAH untreated group (PAH), and the 3 treatment groups (CPU 86017 20, 40, and 80 mg·kg^{-1}·d^{-1}, *po,* daily for 28 d from the day of MCT, sc). CPU 86017 was suspended freshly in 0.5% CMC-Na of 0.4%, 0.8%, and 1.6% (20, 40, and 80 mg·kg^{-1}·d^{-1}, sc). The normal and PAH groups were given an equal volume of CMC-Na.

The investigation was performed in accordance with the Guide for the Care and Use of Laboratory Animals in Jiangsu Province.

Hemodynamic analysis and heart weight index After 4 weeks of MCT medication and interventions with CPU 86017, rats were killed with urethane (1.5 mg/kg, ip). RVSP (right ventricular systolic pressure), CVP (central venous pressure), and blood pressure were measured using 2 catheters separately, as described previously[9]. Animals were then exsanguinated, and the hearts and lungs were dissected and weighed. The right ventricular remodeling was assessed by measuring the RVWI (right ventricle weight index): the RV weight to body weight ratio (RVW/BW, mg/g) and the RV-to-left ventricular (LV) plus septal (S) weight ratio [RVW/(LVW+SW), mg/g]. The improvement after drug intervention was calculated as follows: improvement % = (PAH-Treated)/(PAH-Normal)×100%.

ET-1, NO, NOS, superoxide dismutase (SOD), and malondialdehyde (MDA) assays Blood samples were col-

Table 1. Primer sequences used for determination of prepro endothelin-1 (ET-1), iNOS, eNOS, and β-actin expression.

Name	GenBank Number	Primers nucleotide sequence	Location, nt	Size/bp
PreproET-1	NM_010104	Sense: 5'-AGCAATAGCATCAAGGCATC-3'	550–569	465
		Antisense: 5'-TCAGACACGAACACTCCCTA-3'	995–1014	
iNOS	D12520	Sense: 5'-ATCCCGAAACGCTACACTT-3'	2261–2279	314
		Antisense: 5'-TCTGGCGAAGAACAAATCC-3'	2557–2574	
eNOS	NM_008713	Sense: 5'-TGGCAAGACAGACTACACGA-3'	3077–3096	422
		Antisense: 5'-CGCAATGTGAGTCCGAAA-3'	3481–3498	
β-actin	AF421789	Sense: 5'-GAAGATCCTGACCGAGCGTG-3'	632–651	518
		Antisense: 5'-CGTATTCCTGCTTGCTGATCC-3'	1129–1149	

lected in chilled vials containing 30 mL EDTA2Na and 20 mL Aprotinin. ET-1, NOS activity, SOD, and MDA in serum and lung tissue were measured using radioimmunoassay or the kits supplied by Nanjing Jiancheng Biotechnological Co, following the practice described previously[9].

Assessment of pulmonary artery remodeling Transverse sections of lungs, 4 μm in thickness, were cut at the right middle zones and stained with hematoxylin-eosin, then the wall thickness of small pulmonary arteries (diameter<150 μm) was analyzed using a colorful picture analysis system (Quantment 500), as described in a previous report[9]. The thickness (μm) and WT (wall thickness ratio) percentage value were determined as the average data of 10 fields per slice and the WT was calculated as below: WT%= ($diameter_{ext}$-$diameter_{int}$)/$diameter_{ext}$×100.

mRNA expressions of preproET-1, iNOS, and eNOS in lung tissue Lung tissue was homogenized in TRIZOL, and then extracted with hydroxybenzene-chloroform. Reverse transcription-polymerase chain reaction (RT-PCR) was performed in 25 μL final volume under the following conditions: initial denaturalization at 94 ºC for 5 min, denaturalization at 94 ºC for 40 s, annealing for 40 s at 64 ºC for preproET-1, at 58 ºC for eNOS, at 58 ºC for iNOS, and at 60 ºC for β-actin, all extension at 72 ºC for 1 min. The circular numbers of β-actin, preproET-1, eNOS, and iNOS were 25, 28, 26 and 28, respectively. The sequences of primers are shown in Table 1 and the procedures were the same as described previously[9]. The PCR products were electrophoresed and determined semi-quantitatively.

Functional assessment of isolated pulmonary arterial rings The pulmonary arteries were carefully isolated and cleaned of outer connective tissue in cold K-H solution saturated with 100% oxygen. The rings from each pulmonary artery (approximately 3 mm in length) were mounted vertically between 2 hooks in organ chamber myographs, which were filled with K-H solution and kept at 37 ºC. Isometric tension was measured with force transducers (MPA-V). Constrictions of the isolated pulmonary arterial rings by KCl 100 mmol/L or phenylnephrine 1 μmol/L were performed in calcium free KH solution and after adding up to 2.5 mmol/L Ca^{2+} in the presence of either KCl or phenylephrine, separately[10–12].

Statistical analysis Data are presented as mean±SEM. For statistical evaluation one-way analysis of variance was used, following Dennett's test. The Student Newman Keuls test was performed when the variance was equal, and the Games-Howell test was performed when variance was not equal. Pearson correlation analysis was also carried out on some indices. A value of $P<0.05$ was considered statistically significant.

Results

Hemodynamic changes The RVSP and CVP in MCT PAH group were elevated markedly by 79% ($P<0.01$) and 2400% ($P<0.01$) compared with normal, respectively. CPU 86017 20, 40, and 80 mg·kg^{-1}·d^{-1} *po* decreased the RVSP by -18.5%, -37.2%, and -15.1%, compared to the PAH ($P<0.01$), respectively, and the reduction in CVP was by -66.7%, -73.3%, and -80.0%, respectively ($P<0.01$, Table 2).

Regression in RVWI The RVWI in the control group was increased by 50.0 % in RVW/BW and 53.3 % in RVW/(RVW+SW) ($P<0.01$), respectively. Reduction in RVW/BW by CPU 86017 20, 40, and 80 mg·kg^{-1}·d^{-1}, *po* was -30.5%, -33.3%, and -25.9%, respectively, compared to the untreated group and in RVW/(RVW+SW) was -28.2%, -30.4%, and -28.2% ($P<0.01$), respectively. The remodeling of the right ventricle was regressed remarkably in each intervention group (Table 3).

Regression in the vasculature of the pulmonary arteriole In PAH group, the thickness (μm) and the relative value of

Table 2. Effect of CPU 86017 on pulmonary hemodynamics in monocrotaline-induced pulmonary arterial hypertension (PAH). Mean±SEM. $^{c}P<0.01$ *vs* control. $^{f}P<0.01$ *vs* PAH.

Dose/mg·kg^{-1}·d^{-1}	*n*	RVSP/kPa	CVP/kPa	BP/kPa	HR/min^{-1}
Control	10	2.92±0.16	0.03±0.01	15.44±0.44	350±11
PAH	10	5.24±0.19^{c}	0.75±0.05^{c}	15.01±0.51	360±12
PAH+CPU 20	10	4.27±0.18^{f}	0.25±0.07^{f}	15.90±0.69	378±11
PAH+CPU 40	9	3.29±0.14^{f}	0.20±0.03^{f}	15.69±0.28	362±15
PAH+CPU 80	10	4.45±0.18^{f}	0.15±0.04^{f}	16.13±0.72	367±12

CPU: CPU 86017. RVSP: right ventricular systolic pressure. CVP: central venous pressure. BP: blood pressure. HR: heart rate.

Table 3. Effect of CPU 86017 on right ventricular hypertrophy in monocrotaline-induced pulmonary arterial hypertension (PAH). $^{c}P<0.01$ *vs* control. $^{f}P<0.01$ *vs* PAH.

Dose/mg·kg^{-1}·d^{-1}	*n*	BW (g)	RVW/BW (mg/g)	RVW/(LVW +SW) (mg/g)
Control	10	305±8	0.72±0.03	0.30±0.01
PAH	12	252±8	1.08±0.05^{c}	0.46±0.02^{c}
PAH+CPU 20	11	267±6	0.75±0.03^{f}	0.33±0.01^{f}
PAH+CPU 40	11	281±9	0.72±0.03^{f}	0.32±0.02^{f}
PAH+CPU 80	11	272.0±0.9	0.80±0.03^{f}	0.33±0.01^{f}

CPU: CPU 86017. BW: body weight. RV: right ventricle. LV: left ventricle. S: septum.

WT% (wall thickness percentage) of small pulmonary arteries (<150 μm in diameter) were increased by 106.0% and 80.7% ($P<0.01$) compared with the control group. In CPU 86017 80, 40, and 20 mg·kg^{-1}·d^{-1} groups, thickness (μm) and the relative value of WT percentage of small pulmonary arteries decreased significantly compared with the untreated group (Table 4, Figure 2).

Table 4. Effect of CPU 86017 on wall thickness in small pulmonary artery in rats with monocrotaline-induced pulmonary arterial hypertension (PAH). $n=60$ vessels. Mean±SEM. $^{c}P<0.01$ *vs* control. $^{d}P>0.05$, $^{e}P<0.05$, $^{f}P<0.01$ *vs* PAH.

Dose/mg·kg^{-1}·d^{-1}	Thickness/μm	WT/%
Control	11.20±0.27	31.6±2.5
PAH	23.14±0.39^{c}	57.1±4.1^{c}
PAH+CPU 20	20.03±0.27^{d}	48.2±3.6^{d}
PAH+CPU 40	17.69±0.27^{e}	41.5±4.7^{e}
PAH+CPU 80	11.64±0.19^{f}	29.5±2.9^{f}

WT, wall thickness (%) of the total area of the vascular transactions.

NO, ET-1, cNOS, SOD, and MDA in serum and lung tissue In the PAH group, the ET-1 in the serum and lungs was dramatically increased by 53.9% ($P<0.01$) and 93.7% ($P<0.01$), respectively. CPU 86017 decreased the content of ET-1 to the normal level in lung tissue, but was less effective in serum. The NO content was increased by 60.0% ($P<0.01$) in serum, but decreased by -52.5% ($P<0.01$) in pulmonary tissue, compared to that of the normal group. The level of NO was significantly increased in CPU 86017 80 and 40 mg·kg^{-1}·d^{-1} groups in tissue, whereas the difference was not significant in serum. Activity of cNOS in tissue decreased by -38.5%

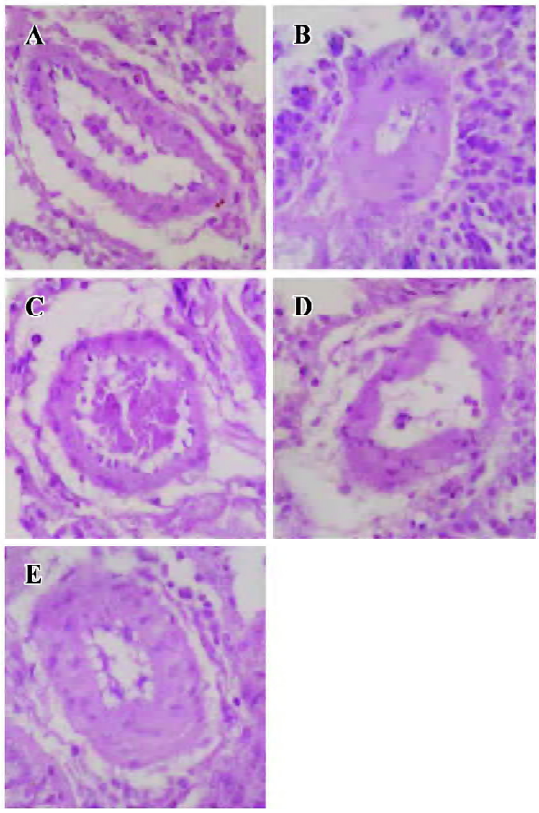

Figure 2. Morphological analysis of the wall thickness of pulmonary arteriole transactions in monocrotaline-induced pulmonary artery hypertension (PAH) in rats. (A) Normal; (B) PAH; (C) CPU 86017 80 mg·kg^{-1}·d^{-1} for 28 d; (D) CPU 86017 40 mg·kg^{-1}·d^{-1} for 28 d; (E) CPU 86017 20 mg·kg^{-1}·d^{-1} for 28 d. HE stain. ×900.

($P<0.01$) in the PAH group compared to the normal. The activity of cNOS was increased by 33.0% ($P<0.01$) in CPU 86017 80 mg·kg^{-1}·d^{-1} *po* group compared to the PAH (Table 5, 6). The MDA was significantly increased in both the serum and lungs, whereas the activity of SOD decreased markedly. A significant reduction in MDA production was observed in all three CPU 86017 groups, which was associated with an increase in the SOD activity in the serum and lungs.

PreproET-1, iNOS, and eNOS mRNA expression Twenty-eight days after MCT injection, the mRNA expression of preproET-1, eNOS, and iNOS in the PAH group was upregulated by approximately 4, 6.5, and 2.7 times, respectively, against the normal lung tissue. The upregulation of eNOS and iNOS mRNA levels was significantly reversed in three CPU 86017 groups, and preproET-1 mRNA abundance was also reduced notably in CPU 86017 80 mg·kg^{-1}·d^{-1} group versus the PAH group (Figure 3).

Isolated pulmonary artery activity Two sorts of pulmonary vascular activities were assessed using high KCl and

Table 5. Effect of CPU 86017 on the contents of SOD, MDA, and NO in serum and pulmonary tissue in monocrotaline-induced pulmonary arterial hypertension (PAH) in rats. Mean±SEM. $^{c}P<0.01$ *vs* control. $^{d}P>0.05$, $^{e}P<0.05$, $^{f}P<0.01$ *vs* PAH.

Dose/mg·kg^{-1}·d^{-1}	*n*	SOD		MDA		NO	
		Serum /U·mL^{-1}	Pulmonary tissue/U·mg^{-1} protein	Serum /nmol·L^{-1}	Pulmonary tissue/nmol·g^{-1} protein	Serum /μmol·L^{-1}	Pulmonary tissue/μmol·g^{-1} protein
Control	10	117±12	150.0±3.1	5.40±0.23	1.40±0.07	35.0±2.6	0.40±0.01
PAH	10	61±13^{c}	105.0±2.3^{c}	6.90±0.34^{c}	2.60±0.18^{c}	56.0±6.8^{c}	0.19±0.01^{c}
PAH+CPU20	10	67±17^{d}	116.0±3.9^{e}	5.90±0.52^{d}	1.70±0.18^{f}	57.0±5.2^{d}	0.20±0.02^{d}
PAH+CPU40	9	78±23^{e}	145.0±8.7^{f}	5.00±0.49^{f}	1.60±0.06^{f}	58.0±6.1^{d}	0.29±0.04^{f}
PAH+CPU80	10	80±12^{f}	153.0±4.1^{f}	4.80±0.28^{f}	1.50±0.08^{f}	52.0±4.8^{d}	0.31±0.02^{f}

SOD, superoxide dismutase. MDA, malondialdehyde. NO, nitric oxide.

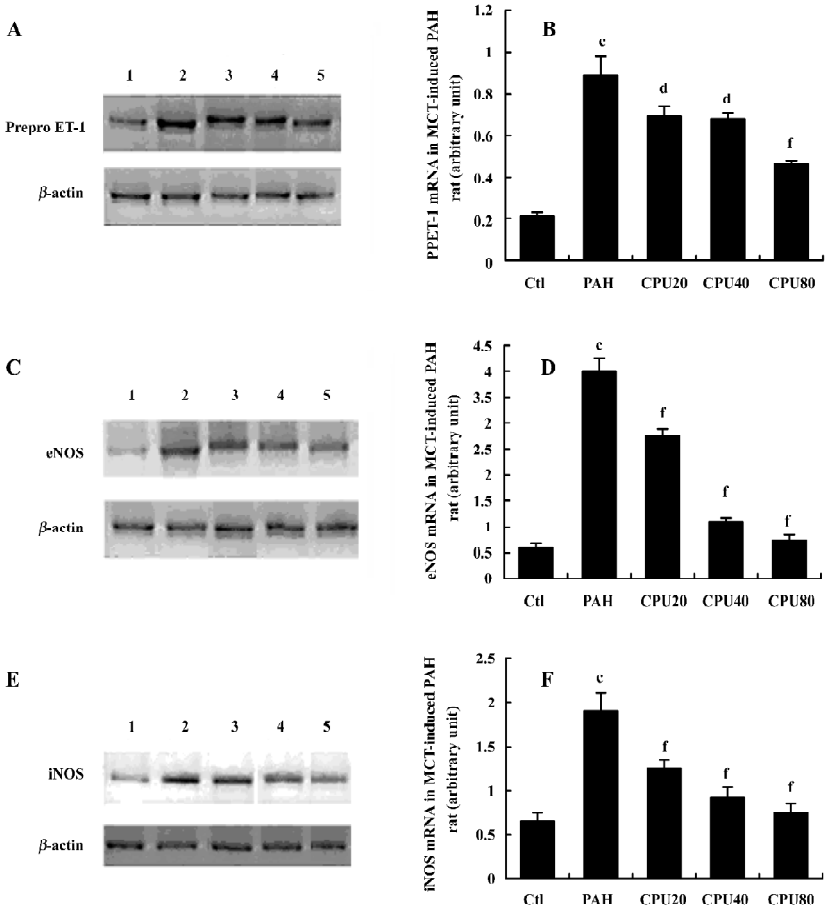

Figure 3. The RT-PCR analysis of the mRNA expression of preproET-1, eNOS, and iNOS in lung tissue, respectively. (A, B) mRNA of preproET-1; (C, D), mRNA of eNOS; (E, F): mRNA of iNOS. Lane 1, 2, 3, 4, 5 represents control, pulmonary artery hypertension, CPU 86017 20, 40, 80 mg·kg^{-1}·d^{-1} for 28 d *po*, respectively. (B, D, F) showed the densitometry readings normalized to β-actin for preproET-1, eNOS, and iNOS transcripts in lung tissue. n=10. Mean±SEM. $^{c}P<0.01$ *vs* control. $^{d}P>0.05$, $^{f}P<0.01$ *vs* PAH.

phenylephrine in separate experiments. Each was evaluated in 2 phases of constriction of the isolated pulmonary artery rings in calcium-free medium, and up to 2.5 mmol/L calcium was added to the calcium-free medium in the presence of

Table 6. Effect of CPU 86017 on the activity of cNOS in pulmonary tissue and content of ET-1 in plasma and pulmonary tissue of monocrotaline-induced pulmonary artery hypertension (PAH) rats. n=8 for ET-1. n=10 for cNOS. Mean±SEM. $^{c}P<0.01$ *vs* control. $^{d}P>0.05$, $^{f}P<0.01$ *vs* PAH.

Dose/mg·kg^{-1}·d^{-1}	ET-1		cNOS
	Plasma /pg·mL^{-1}	Tissue /pg·mL^{-1}	Tissue /U·mg^{-1} protein
Control	51.9±3.6	85.8±8.9	1.87±0.06
PAH	79.9±5.3^{c}	166.2±6.8^{c}	1.15±0.05^{c}
PAH+CPU 20	75.9±6.4^{d}	98.7±12.7^{f}	1.21±0.10^{d}
PAH+CPU 40	74.1±3.9^{d}	102.2±6.8^{f}	1.39±0.05^{f}
PAH+CPU 80	64.7±2.8^{e}	90.6±14.8^{f}	1.53±0.06^{f}

ET-1, endothelin-1; cNOS, constructive nitric oxide synthase.

either high KCl or phenylephrine. The KCl induced vasoconstrictions in the calcium-free medium decreased markedly in the PAH group and recovered partially after CPU 86017 intervention. The constrictions by the calcium influx on adding calcium into calcium-free medium in the presence of KCl 100 mmol/L were impaired markedly in the untreated group, whereas there was no improvement in the CPU 86017-treated groups (Figure 4). The contractions by phenylephrine in the calcium-free medium were notable in the untreated group, and no improvement could be found after CPU 86017 treatments. A markedly impaired vascular tone of contractions by calcium influx resulting from an addition of

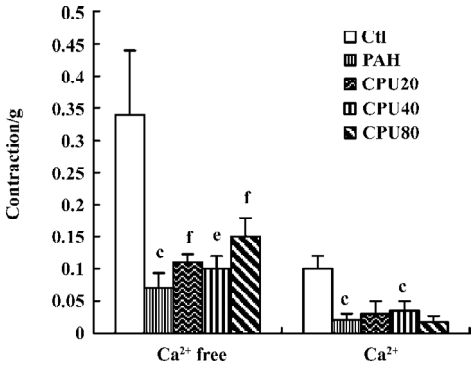

Figure 4. Contraction of pulmonary artery ring induced by KCl isolated from the rats with monocrotaline-induced pulmonary artery hypertension (PAH). Left: Contractions is induced by KCl in Ca^{2+} free K-H solution. Right: Contraction is induced by adding Ca^{2+} 2.5 mmol/L in the Ca^{2+}-free K-H solusion in the presence of the KCl. Ctl: control; CHU 20, CPU 40, CPU 80: CPU 86017 20, 40, and 80 mg·kg^{-1}·d^{-1}, *po*, for 28 d. $^{c}P<0.01$ *vs* control. $^{e}P<0.05$, $^{f}P<0.01$ *vs* PAH.

Ca^{2+} into the medium in the presence of phenylephrine 1 μmol/L was found and vascular tension completely returned to normal in the CPU 86017 groups of 80 and 40 mg·kg^{-1}·d^{-1}, *po* (Figure 5).

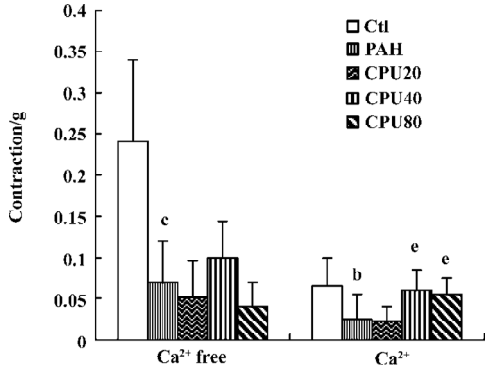

Figure 5. Contraction of pulmonary artery ring induced by phenylephrine 1 μmol/L isolated from rats with monocrotaline-induced pulmonary artery hypertension (PAH). Left: contractions by phenylephrine in Ca^{2+} free K-H solution. Right: contraction is induced by adding Ca^{2+} up to 2.5 mmol/L in the Ca^{2+}-free K-H solusion in the presence of phenylephrine. Phe, phenylephrine; Ctl, control; CPU20, CPU40, CPU80: CPU 86017 20, 40, and 80 mg·kg^{-1}·d^{-1}, *po*, for 28 d. $^{b}P<0.05$, $^{c}P<0.01$ *vs* control. $^{e}P<0.05$ *vs* PAH.

Discussion

CPU 86017 is derived from chemical modification of the moiety of berberine and possesses a blocking effect on the K^{+} and Ca^{2+} channels[13], together with an improvement in the water solubility and availability in pharmacokinetics. The chemical reformation leads to a reinforcement of calcium antagonism, providing a potential beneficial use in the treatment of cardiovascular disorders[12].

The chronic inflammation of the lung tissue by MCT contributes to an insult to vascular endothelium and myocardium, consequently resulting in a substantial increase in ET-1 release, which promotes the pathological progression of PAH. The voltage-dependent calcium channels are coupled to ET_A receptors by G proteins; therefore, an enhancement of the calcium influx is anticipated to follow an excess ET-1 release, as we found in the PAH. The activation of the L-type Ca^{2+} channels caused by an excess ET-1 in the myocardium and vasculature is an important etiological factor resulting in maladjustment and remodeling changes in the pulmonary vessels and the right ventricle.

The ET-1 closely linked with the ROS system is an important pathway involved in cardiovascular derangement[14]. One of the up-stream events in the pathway to the tissue ET-1 is

the mRNA of preproET-1, which is also elevated significantly. An excess of ET-1 binding to the ET_A receptors stimulates the protein kinase C (PKC), mitogen-activated protein kinase (MAPK) pathway, finally leading to an abnormality of phenotype of genes encoding the preproET-1, iNOS, and cNOS, matrix formation, as well as to pulmonary VSMC proliferation[15–17].

A low level of NO and elevated ET-1 in the pulmonary tissue is a result of endothelial damage and dysfunction by MCT. MCT selectively damages pulmonary endothelium, reducing NO production and secretion. The vascular NO is biosynthesized and released in a constant manner, which is necessary to maintain the normal vascular vasodilatation response. The bioavailability of NO (ie basal release) is compromised significantly, resulting in impaired vascular activity in the PAH group. An abnormally low NO exerts a suppressive effect on the proliferation of smooth muscle cells, because of an excess of ET-1, which mediates an activation of MAPK pathway. An increased serum NO in the PAH group is a result of activated activity of the iNOS resulting from the stimulation of chronic inflammation by MCT, which accelerates both pulmonary artery hypertension and portal hypertension[18].

The ROS play an important role in remodeling of the small pulmonary artery, as they proliferate smooth muscle cells by activating the phosphorylation of ERK/MAPK. The ET-1 stimulates the downstream events in the pathway; that is, activation of iNOS and ROS. It is likely that a circulated activation mechanism takes place between the upstream and the downstream to exacerbate an activation of the ET pathway involved in the pathological process. An increment of ROS causes an increase in the abundance of mRNA of preproET-1, eNOS, and iNOS, attributable to the enhancement of the transcription process in the nucleus[19,20]. This is easily reversed by suppression of the ET–ROS pathway after treatment with CPU 86017.

An intervention to interrupt the targets located at either the upstream or the downstream of the ET pathway is capable of relieving the disturbance in the PAH by MCT. The insult to the pulmonary endothelium and the later developed myocardial insufficiency of the right ventricle are the main factors contributing to excess ET-1 and the over-stimulation of the ET pathway. The overactivated ET pathway can be reversed indirectly by the calcium antagonism and antioxidative effects of CPU 86017. Actually an attenuation of the activated ET pathway by CPU 86017 in the MCT PAH in rats can not be ascribed to a direct blocking action on ET receptors, but ascribed to a calcium antagonism relieving an injury of the pulmonary endothelium and the myocardium and rebalancing an interruption of the ROS formation. A reduced formation of the ET-1 and an indirect blockade of endothelin receptors to alleviate its downstream events are achieved using CPU 86017 chronic medication.

Plasma ET-1 was less responsive than the pulmonary origin ET-1to CPU 86017 treatment. The ET can be sourced from the two: physiological and pathological conditionas, sush as the ET in the affected lung is totally from the insult from MCT. In the blood stream the majority of ET is released from the organ under normal conditions such as the central nervous system, the kidney, endometrium, and normal tissue[21], but ET from the affected lung contributes to a small portion of plasma ET-1. So only a heavy inhibition of the release from the pathological lung by the high dose of CPU 86017 could provide a reduction in the seral total ET, but not the middle and small doses. In contrast, paracrine and autocrine ET-1 is effective in the local region. The pulmonary origin of ET-1 was the main pathological factor and responded well to the CPU 86017 treatment.

We found that eNOS mRNA expression was significantly increased in MCT-induced PAH, and was up to 6.5 times higher than that in normal group, whereas both NOS activity and NO content decreased in the same way as reported by Resta *et al*[22]. Such a contradiction might be contributed to damage to endothelium by MCT with which the eNOS can not be converted into a normally active form. The maladjustment resulted from phosphorylation of threonine[23], which causes defective activity of the eNOS, contributing to PAH progression[24].

In conclusion, an activated ET-ROS pathway damages the endothelium system which results in consequent pulmonary vasculature derangement in PAH by MCT in rats. By suppressing the ET pathway, CPU 86017 relieves MCT PAH.

References

1 Jeffery TK, Morrell NW. Molecular and cellular basis of pulmonary vascular remodeling in pulmonary hypertension. Prog Cardiovasc Dis 2002; 45: 173–202.

2 Tuder RM, Cool CD, Yeager M, Taraseviciene-Stewart L, Bull TM, Voelkel NF. The pathobiology of pulmonary hypertension. Endothelium. Clin Chest Med 2001; 22: 405–18.

3 Wort SJ, Woods M, Warner TD, Evans TW, Mitchell JA. Endogenously released endothelin-1 from human pulmonary artery smooth muscle promotes cellular proliferation: relevance to pathogenesis of pulmonary hypertension and vascular remodeling. Am J Resp Cell Mol Biol 2001; 25: 104–10.

4 Michelakis ED. The role of the NO axis and its therapeutic implications in pulmonary arterial hypertension. Heart Fail Rev 2003; 8: 5–21.

5 Alexandru B, Bogdan MA. Monocrotaline induces pulmonary hypertension in animal models. Pneumologia 2001; 50: 85–9.

6 Wang HL, Li SB, Dai DZ. Effects of CPU 86017 on L-type calcium current in single guinea pig hypertrophic ventricular myocytes. J China Pharm Univ 2004; 35: 259–62.
7 Hao JM, Dai DZ, Yu F. The oxidative stress is enhanced after *L*-thyroxin medication and suppressed by CPU 86017. Prog Pharm Sci 2005; 29: 417–21.
8 Wang YQ, Shi YP, Dai DZ. The therapeutic effects of CPU 86017 on acute and chronic congestive cardiac failure mediated by reducing ET-1, NOS and oxidative stress in rats. Drug Dev Res 2004; 63: 22–32.
9 Zhang TT, Dai DZ. Therapeutic effects of nifedipine on pulmonary hypertension and mechanism involved. Prog Pharm Sci 2003, 27: 227–9.
10 Dai DZ, Feng Y, Li HT. Blockade on sodium, potassium, and calcium channels by a new antiarrhythmic agent CPU 86017. Drug Dev Res 1996; 39: 138–46.
11 Dai DZ, Jiang JM. *p*-Chlorobenzyltetrahydroberberine inhibits vascular smooth muscle contractions caused by Ca^{2+}. Acta Pharmacol Sin 1998; 19: 543–7.
12 Dai DZ, He Y, Huang FH. Comparison of inhibitory activity of berberine derivate CPU 86017 and berberine on vascular contraction. J China Pharm Univ 2000; 31: 447–50.
13 Dai DZ, Hu HJ, Zhao J, Hao XM, Yang DM, Zhou PA, *et al*. Blockade of L-type calcium channel in myocardium and calcium-induced contractions of vascular smooth muscle by CPU 86017. Acta Pharmacol Sin 2004; 25: 416–23.
14 Xu FP, Chen MS, Wang YZ, Yi Q, Lin SB, Chen AF, *et al*. Leptin induces hypertrophy via endothelin-1-reactive oxygen species pathway in cultured neonatal rat cardiomyocytes. Circulation 2004; 110: 1269–75.
15 Mazzocchi G, Rossi GP, Malendowicz LK, Champion HC, Nussdorfer GG. Endothelin-1 [1-31], acting as an ETA-receptor selective agonist, stimulates proliferation of cultured rat zona glomerulosa cells. FEBS Lett 2000; 487: 194–8.
16 Piacentini L, Gray M, Honbo NY, Chentoufi J, Bergman M, Karliner JS. Endothelin-1 stimulates cardiac fibroblast proliferation through activation of protein kinase C. J Mol Cell Cardiol 2000; 32: 565–76.
17 Herman WH, Simonson MS. Nuclear signaling by endothelin-1: a Ras pathway for the activation of the c-fos serum response element. J Biol Chem 1995; 270: 654–61.
18 Perazzo J, Eizayaga F, Romay S, Bengochea L, Pavese A, Lemberg A. An experimental model of liver damage and portal hypertension induced by a single dose of monocrotaline. Hepatogastroenterology 1999; 46: 432–5.
19 Bai XC, Lu D, Liu AL, Zhang ZM, Li XM, Zou ZP, *et al*. Reactive oxygen species stimulates receptor activator of NF-kappaB ligand expression in osteoblast. J Biol Chem 2005; 280: 17497–506.
20 Rodriguez JA, Nespereira B, Perez-Ilzarbe M, Eguinoa E, Paramo JA. Vitamins C and E prevent endothelial VEGF and VEGFR-2 overexpression induced by porcine hypercholesterolemic LDL. Cardiovasc Res 2005; 65: 665–73.
21 Hsu YH, Huang SC. Immunohistochemical localization of endothelin-converting enzyme-1 in neuroendocrine tumors and normal human tissue. Kaohsiung J Med Sci 2003; 19: 555–62.
22 Resta TC, Chicoine LG, Omdahl JL, Walker BR. Maintained upregulation of pulmonary eNOS gene and protein expression during recovery from chronic hypoxia. Am J Physiol 1999; 276: H699–H708.
23 Fleming I, Fisslthaler B, Dimmeler S, Kemp BE, Busse R. Phosphorylation of Thr^{495} regulates Ca^{2+}/calmodulin-dependent endothelial nitric oxide synthase activity. Circ Res 2001; 88: E68–E75.
24 Murata T, Sato K, Hori M, Ozaki H, Karaki H. Decreased endothelial nitric-oxide synthase (eNOS) activity resulting from abnormal interaction between eNOS and its regulatory proteins in hypoxia-induced pulmonary hypertension. J Biol Chem 2002; 277: 44085–92.

Acta Pharmacologica Sinica 2005 Nov; 26 (11): 1317–1321

Blackwell Publishing

Full-length article

Chemokine RANTES is upregulated in monocytes from patients with hyperhomocysteinemia[1]

Wei SUN[2,5], Guang WANG[3,5], Zhen-min ZHANG[4], Xiao-kun ZENG[2], Xian WANG[2,4,6]

[2]Institute of Vascular Medicine; [3]Department of Gerontology, Peking University Third Hospital; [4]Department of Physiology and Pathophysiology, Key Laboratory of Molecular Cardiovascular Science, Ministry of Education, Basic Medical College, Peking University, Beijing 100083, China

Key words

homocysteine; monocytes; RANTES; folic acid; atherosclerosis; humans

[1] Project supported by the Major National Basic Research Program of China (No G2000056908), Program for Changjiang Scholars and Innovative Research Team in University (PCSIRT), and a grant from the National Natural Science Foundation of China (No 30330250) to Prof Xian WANG.
[5] These authors contributed equally to this work.
[6] Correspondence to Dr Xian WANG.
Phn/Fax 86-10-8280-1443.
E-mail xwang@bjmu.edu.cn

Received 2005-04-07
Accepted 2005-06-06

doi: 10.1111/j.1745-7254.2005.00178.x

Abstract

Aim: To investigate the changes in plasma level of the chemokine RANTES (regulated upon activation, normal T cells expressed and secreted) and the responsiveness of lipopolysaccharide (LPS)-induced RANTES secretion from monocytes in patients with hyperhomocysteinemia (HHcy). **Methods:** The plasma levels of homocysteine (Hcy), folate, and RANTES were measured in 38 control patients with normal Hcy levels and 40 patients with HHcy and the mRNA synthesis of RANTES in isolated human monocytes was determined by RNase protection assays. **Results:** The plasma level of RANTES was elevated in HHcy patients compared with controls (median 5.3 *vs* 3.5 ng/mL, $P<0.01$). LPS-induced RANTES production from monocytes of HHcy patients was also increased significantly. In addition, Hcy directly increased the mRNA level of RANTES in isolated normal human monocytes in a time- and dose-dependent manner. **Conclusion:** Upregulated RANTES from monocytes in HHcy patients may be involved in the atherogenesis of HHcy-induced atherosclerosis.

Introduction

Elevated plasma homocysteine (Hcy) concentration is an independent risk factor for cardiovascular disease[1,2]. Although the exact mechanism by which hyperhomocysteinemia (HHcy) induces cardiovascular disease is still uncertain, recent evidence suggests that HHcy may induce the process of atherogenesis by initiating inflammation. Hcy may affect inflammatory cells, such as mononuclear leukocytes, monocytes, and T cells, as well as multiple cytokines, to alter the inflammatory status of endothelial cells, smooth muscle cells (SMC) and intimal macrophages during the formation of lesions[3,4]. Hcy induces the expression and secretion of monocyte chemoattractant protein -1 (MCP-1) and interleukin-8 (IL-8)in human aortic endothelial cells, SMC lines, and monocyte cells[5–8]. Furthermore, we have shown that Hcy not only promotes the secretion of MCP-1 and IL-8 but also enhances their gene expression in primary cultured human monocytes[7]. Holven *et al*[9] also reported that the plasma level of the chemokine epithelial neutrophil-activating peptide-78 (ENA-78) and growth-regulated oncogene (GROα) was elevated in patients with HHcy. This evidence suggests a role of pro-inflammatory chemokines in HHcy-initiated atherogenesis.

RANTES (regulated upon activation, normal T cells expressed and secreted) is a CC chemokine, normally derived by T lymphocytes. It is also produced by mono/macrophages. It plays an important role in the inflammatory process. It has been found to play an important role in autoimmune disorders such as asthma or systemic lupus erythematosus and is nearly as potent a chemoattractant for monocytes as MCP-1[10,11]. To date, no evidence exists on the relation between HHcy and RANTES. In the present study, we determined the plasma level of RANTES and the responsiveness of monocytes to low-dose lipopolysaccharide (LPS)-induced RANTES secretion in patients with HHcy and elucidated the direct effect of Hcy on RANTES mRNA level in human monocytes.

Materials and methods

Subjects Two groups of subjects were studied: 40 patients with HHcy (plasma Hcy level more than 15 μmol/L) and 38 control patients with normal blood Hcy level (NHcy). All subjects had no infectious diseases, malignancies or immunologic or hematological diseases; were not being treated with anti-inflammatory drugs other than low-dose aspirin; did not use any vitamins including folic acid during the study period; had no depressed cardiac function (ejection fraction <40%); were younger than 75 years; had no renal failure; and had not had acute myocardial infarction in the previous 3 months.

Venous blood samples were obtained from fasting subjects to assay the chemokines from plasma and isolated monocytes stimulated by low-dose LPS. All subjects gave their written, informed consent. This study was approved by the Ethics Committee of the Health Science Center, Peking University.

Measurement of RANTES The supernatant of cultured monocytes and plasma stored at -70 °C were used to measure the chemokines. The concentration of RANTES was determined by ELISA according to the manufacturer's protocols (R&D Systems, Minneapolis, MN, USA).

Measurement of plasma level of Hcy and folate A plasmid-encoding human placental AdoHcy hydrolase (pPROK-1) kindly provided by the University of Kansas (USA) was overexpressed in *E coli* JM109 cells transformed with pPROK-1 and purified as described in a previous study[12]. Total Hcy level in plasma was determined with the use of an assay based on the conversion of Hcy to *S*-adenosyl-homocysteine (SAH) in the presence of adenosine and SAH hydrolase as described from our previous study[8]. Briefly, plasma samples from fasting subjects were collected. Protein-bound circulating Hcy was reduced to free Hcy with the use of dithioerythreitol as a reductant. The free Hcy was then converted to SAH by using SAH hydrolase and excess adenosine. Samples were quantified by HPLC. The range of measurement was 1–100 μmol/L, with a sensitivity of less than 0.5 μmol/L. The within-assay and between-assay coefficients of variation were 3.5% and 4.9%, respectively.

Plasma folate was measured by radioisotope dilution assay with use of a kit from Nanjing Jiangcheng Bioengineering Institute (Nanjing, China).

Responsiveness of human monocytes to LPS Blood of HHcy and NHcy patients was drawn into heparinized syringes. The whole blood was separated into peripheral blood mononuclear cells and neutrophils by use of the density gradient from Nycoprep 1.077 (Life Technologies, Grand Island, NY, USA). Monocytes were then isolated from the peripheral blood mononuclear cells by their adherence to a serum-coated culture flask for 2 h. Adherent cells were then detached and resuspended in RPMI-1640 medium containing 5% autologous plasma. Freshly isolated monocytes (5×10^5) were incubated at 37 ºC and treated with or without LPS (final concentration 0.01–0.1 μg/mL) for 24 h. The cell-free supernatant was harvested and stored at -70 ºC for chemokine analysis. Cellular viability was determined with Trypan blue exclusion. Only cell preparations with 95% viability or greater were used.

RNase protection assays Total RNA was isolated from healthy human monocytes with Trizol Reagent (Life Technologies). Assays involved use of a nuclease protection assay kit (Riboquant, Pharmingen, San Diego, CA, USA) as used in our previous published report[7]. In summary, the isolated RNA (2 mg) was hybridized with ^{32}P end-labeled RANTES oligonucleotide probes overnight at 30 °C, followed by nuclease digestion. A GAPDH and L-32 rRNA oligonucleotide probe was used as an internal control. After digestion, the protected fragments were resolved on a denatured 12% polyacrylamide gel containing 8 mol/L urea, then transferred to filter paper, which was later exposed to X-ray film. The bands corresponding to RANTES, L-32 or GAPDH mRNA were analyzed by use of a gel documentation system (Cold-Spring Eletro Doc and Analyst Edas 290, New York, USA).

Statistical analysis Because chemokine and Hcy values do not follow a normal distribution in patients, comparisons between groups involved the use of the Mann-Whitney test. Values are expressed as median, 25th and 75th percentile, and 10th and 90th percentile. Patients' age, body-mass index and plasma level of cholesterol, triglycerides and creatinine were analyzed with use of the Student's *t*-test and expressed as mean±SD. Proportions were analyzed by use of the Chi-squared test. $P<0.05$ (two-tailed) was considered statistically significant.

Results

Clinical characteristics of the study participants The NHcy control and HHcy groups did not differ significantly with respect to age, sex, and body-mass index. The prevalence of smoking, coronary artery disease, hypertension and diabetes, as well as base-line demographic characteristics and laboratory values, were also similar in the two groups (Table 1).

Plasma level of Hcy, folate, and RANTES The Hcy level was significantly higher in HHcy subjects than that in NHcy controls, while the folate level was lower in HHcy subjects than that in NHcy controls. In the HHcy group, the plasma

Table 1. Clinical characteristics of the study participants. Mean±SD.

	NHcy Control *n*=38	HHcy Group *n*=40
Age	53±9	57±8
Body-mass index (BMI)	24.0±3.0	25.0±3.1
Sex (M/F)	25/13	27/13
Risk factors	4 (10)	5 (12)
No patients with family history of CAD/%	4.9±0.9	5.0±1.0
Cholesterol level/mmol·L^{-1}	1.2±0.2	1.2±0.2
HDL level/mmol·L^{-1}	2.9±0.8	3.1±1.1
LDL level/mmol·L^{-1}	1.5±0.6	1.4±0.6
Triglyceride level/mmol·L^{-1}	95±12	99±15
Creatinine level/μmol·L^{-1}	16 (42)	20 (50)
No patients with CAD/%	6 (15)	7 (17)
No patients with diabetes/%	12 (31)	15 (37)
No of patients with hypertension/%	20 (52)	23 (57)
No patients smoking/%	10 (26)	9 (22)
No patients on medication/%	10 (26)	8 (23)
Nitrates	13 (34)	15 (37)
Calcium antagonists	14 (36)	17 (42)
β-Blockers	6 (15)	8 (20)
Aspirin	8 (21)	7 (18)

The diagnosis of diseases is guided by definitions from the World Health Organization or authorized textbooks. Especially, the diagnosis of coronary artery disease (CAD) determined by coronary angiography; at least 50% stenosis in at least 1 main coronary vessel. The continuous variables were compared by Student's *t*-test. Proportions were compared by chi-squared test. HDL, high density lipoprotein; LDL, low density lipoprotein.

level of RANTES was significantly elevated (median 5.3 ng/mL) compared with NHcy controls (3.5 ng/mL) (Table 2).

Chemokine secretion from isolated monocytes in response to LPS To test whether monocytes isolated from patients with HHcy exhibited enhanced inflammatory response of RANTES production, monocytes were incubated with low-dose LPS (0.01 μg/mL) for 24 h. As shown in Figure 1, RANTES production was not significantly increased in HHcy patients without LPS stimulation, but LPS treatment (0.01 μg/mL) significantly increased the level of RANTES secretion of monocytes from HHcy patients compared with that of NHcy controls. Thus, monocytes from patients with HHcy may show an enhanced RANTES secretion response in a pro-inflammatory condition.

Effect of Hcy on RANTES mRNA expression To determine whether Hcy modulates the expression of RANTES mRNA, total RNA was isolated from normal human monocytes treated with Hcy at various times and at different concentrations. As shown in Figure 2, RNase protection

Table 2. Plasma level of Hcy, folate, and chemokine RANTES in NHcy controls and HHcy subjects. Values are expressed as medians and ranges. The comparison was made by Wilcoxon's matched-pairs signed ranks test or Kruskal-Wallis one-way ANOVA test. $^{b}P<0.05$ *vs* NHcy control group.

	NHcy control *n*=38	HHcy *n*=40	*P* value
Hcy/μmol·L^{-1}	9.5 (5.8–11.3)	20.6^{b} (18.0–57.1)	<0.01
Folate/ng·mL^{-1}	5.6 (3.8–7.2)	4.2^{b} (3.6–5.6)	<0.05
RANTES/ng·mL^{-1}	3.5 (0.5–6.4)	5.3^{b} (2.1–8.4)	<0.01

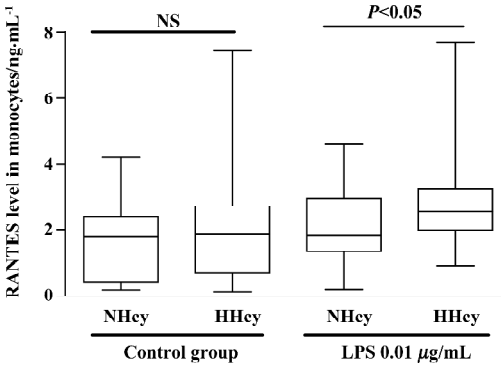

Figure 1. LPS-induced RANTES production in isolated monocytes from NHcy controls and HHcy human subjects. Cells were incubated with LPS (0.01 μg/mL) for 24 h, and the production of RANTES from monocytes was assessed by ELISA. Data are presented as median and ranges (Kruskal-Wallis one-way ANOVA test). *n*=38 in NHcy control group. *n*=40 in HHcy group. Mean±SD.

assays revealed that the expression of RANTES mRNA was significantly enhanced after Hcy treatment. Cultured monocytes incubated with Hcy (10–1000 μmol/L) for 8 h showed significantly increased RANTES expression as compared with untreated cells (Figure 2A), beginning as low as Hcy 10 μmol/L. The increased level of RANTES mRNA after incubation with Hcy 100 μmol/L peaked at 4–8 h after incubation (Figure 2B).

Discussion

The results from the present study demonstrated that the plasma RANTES level was elevated in HHcy individuals and RANTES secretion from monocytes was increased. We also provided evidence that Hcy directly induced RANTES mRNA synthesis from isolated human monocytes.

Atherosclerosis is a chronic inflammatory disease char-

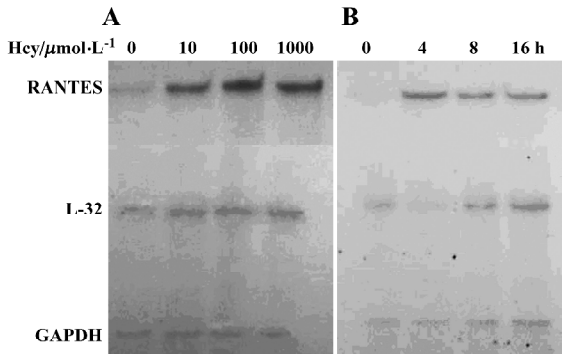

Figure 2. Effect of Hcy on RANTES mRNA expression. A, Representative autoradiogram of RNase protection assay for RANTES, L-32, and GAPDH mRNA in cultured human monocytes treated with Hcy 10–1000 μmol/L for 8 h. B, Representative autoradiogram of RNase protection assay for RANTES, L-32, and GAPDH mRNA in human monocytes treated with Hcy 100 μmol/L for the indicated times. Data are representative of at least three independent experiments (the monocytes were isolated from different subjects).

acterized by the recruitment of monocytes and lymphocytes to the artery wall. Increasing evidence supports the involvement of inflammation in the early phases of atherogenesis. Recruitment of leukocytes within the vascular wall is an essential process in the development of this common disease, which is mainly regulated by adhesion to molecules and chemokines[3,4]. In the classic inflammatory response, adhesion is followed by transmigration of the leukocytes through the endothelial layer into the intima. This process is also mediated by chemotactic factors.

A number of studies have determined the important role of chemokines such as MCP-1 and IL-8 in the initial stages of atherosclerotic plaque formation[5,6]. RANTES, a CC chemokine, has been found to play an important role in autoimmune injury to several tissues. RANTES is generated by circulatory lymphocytes and some kinds of tissue cell monocytes. RANTES is nearly as potent a chemoattractant for monocytes as MCP-1. RANTES induces leukocyte transendothelial migration, implicated in the initial stages of the inflammatory part of the atherosclerotic process[13]. Furthermore, evidence implies the important role RANTES plays in atherosclerosis. Simeoni *et al*[14] reported that a mutant RANTES genotype was associated with the increased coronary heart disease death rate, independent of conventional risk factors. A causal role for RANTES in atherosclerosis was also shown by a protective effect of the blockage of RANTES receptors with the CC chemokine antagonist Met-RANTES in an ApoE-deficient hypercholesterolemic mouse model[15]. These data suggest that the alteration of the level of the chemokine RANTES may affect the progress of atherogenesis through the inflammatory pathway.

Hyperhomocysteinemia is found in 30% of patients with premature atherosclerosis of carotid and peripheral arteries. Elevated plasma Hcy levels have been implicated as an independent risk factor for coronary heart disease[16,17]. Therefore, intensive studies have focused on whether HHcy is the cause or merely a marker for cardiovascular disease. Hcy significantly enhances MCP-1 and IL-8 levels in healthy human monocytes, which can increase leukocyte chemotaxis[7]. However, compared with studies of MCP-1 and IL-8, little study has focused on RANTES secretion in HHcy. Economou *et al*[17] reported the negative association of circulating Hcy and RANTES in prepubescent lean children. Until now, no direct evidence of the relation between HHcy and RANTES in human monocytes exists.

In the present study, we found that both the plasma level of RANTES and low-dose LPS-induced RANTES production in isolated monocytes from patients with HHcy were significantly elevated. Hcy not only increased the RANTES level in HHcy patients but also increased RANTES gene expression in primary human monocytes. Thus, our results support our hypothesis that HHcy may play an important role in the pathogenesis of atherosclerosis through a mechanism involving an increase in RANTES secretion in human monocytes.

Our recent published data show that folate acid treatment in HHcy patients can reverse the hyper-responsiveness of MCP-1 and IL-8 secretion from monocytes[8]. On the basis of the current results, further study should focus on whether the intervention of HHcy influences monocyte-derived RANTES secretion and also the exact mechanism underlying the Hcy-upregulated RANTES production.

References

1 Wald NJ, Watt HC, Law MR, Weir DG, Mcpartlin J, Scott JM. Homocysteine and ischemic heart disease: results of a prospective study with implications regarding prevention. Arch Int Med 1998; 158: 862–7.

2 Tsai JC, Perrella MA, Yoshizumi M, Hsieh CM, Haber E, Schlegel R, *et al*. Promotion of vascular smooth muscle cell growth by homocysteine: a link to atherosclerosis. Proc Natl Acad Sci USA 1994; 91: 6369–73.

3 Sheikine Y, Hansson GK. Chemokines and atherosclerosis. Ann Med 2004; 36: 98–118.

4 Bursill CA, Channon KM, Greaves DR. The role of chemokines in atherosclerosis: recent evidence from experimental models and population genetics. Curr Opin Lipidol 2004; 15: 145–9.

5 Poddar R, Sivasubramanian N, Dibello PM, Robinson K, Jacobsen DW. Homocysteine induces expression and secretion of monocyte chemoattractant protein-1 and interleukin-8 in human aortic endothelial cells: implications for vascular disease. Circula-

tion 2001; 103: 2717–23.
6 van Aken BE, Jansen J, van Deventer SJ, Reitsma PH. Elevated levels of homocysteine increase IL-6 production in monocytic Mono Mac 6 cells. Blood Coagul Fibrinolysis 2000; 11: 159–64.
7 Zeng X, Dai J, Remick DG, Wang X. Homocysteine mediated expression and secretion of monocyte chemoattractant protein-1 and interleukin-8 in human monocytes. Circ Res 2003; 93: 311–20.
8 Wang G, Dai J, Mao J, Zeng X, Yang X, Wang X. Folic acid reverses hyper-responsiveness of LPS-induced chemokine secretion from monocytes in patients with hyperhomocysteinemia. Atherosclerosis 2005; 179: 395–402.
9 Holven KB, Aukrust P, Holm T, Ose L, Nenseter MS. Folic acid treatment reduces chemokine release from peripheral blood mononuclear cells in hyperhomocysteinemic subjects. Arterioscler Thromb Vasc Biol 2002; 22: 699–703.
10 Schall TJ, Bacon K, Toy KJ, Goeddel DV. Selective attraction of monocytes and T lymphocytes of the memory phenotype by cytokine RANTES. Nature 1990; 347: 669–71.
11 Rollins BJ. Chemokines. Blood 1997; 90: 909–28.
12 Chen J, Liu Q, Yang X, Wang K. Copper ions inactivate *S*-adenosyl-*L*-homocysteine hydrolase. Chin Sci Bull 2002; 47: 1176–9.
13 Simeoni E, Winkelmann BR, Hoffmann MM, Fleury S, Ruiz J, Kappenberger L, *et al*. Association of RANTES G-403A gene polymorphism with increased risk of coronary arteriosclerosis. Eur Heart J 2004; 25: 1378–81.
14 Veillard NR, Kwak B, Pelli G, Mulhaupt F, James RW, Proudfoot AE, *et al*. Antagonism of RANTES receptors reduces atherosclerotic plaque formation in mice. Circ Res 2004; 94: 253–61.
15 Malinow MR, Nieto FJ, Szklo M, Chambless LE, Bond G. Carotid artery intimal-medial wall thickening and plasma homocyst(e)ine in asymptomatic adults. The Atherosclerosis Risk in Communities Study. Circulation 1993; 87: 1107–13.
16 Clarke R, Daly L, Robinson K, Naughten E, Cahalane S, Fowler B, *et al*. Hyperhomocysteinemia: an independent risk factor for vascular disease. N Engl Med 1999; 324: 1149–55.
17 Economou EV, Malamitsi-Puchner AV, Pitsavos CP, Kouskouni EE, Magaziotou-Elefsinioti I, Damianaki-Uranou D, *et al*. Negative association between circulating total homocysteine and proinflammatory chemokines MCP-1 and RANTES in prepubertal lean, but not in obese, children. J Cardiovasc Pharmacol 2004; 44: 310–5.

Important Announcement: the Online Manuscript Submission and Review System was Launched!

Acta Pharmacologica Sinica is happy to announce that the online manuscript submission and review system, ScholarOne Manuscript Central (http://mc.manuscriptcentral.com/aphs), was launched on May 25, 2005.

As the leading web-based peer-review system, Manuscript Central is a complete, database-driven software for the online submission and review of full-text manuscripts and graphics. The system provides fully electronic workflow and will speed up the time from submission to decision.

We strongly recommend authors to submit manuscript via this system, which enables us to handle your manuscript quickly and efficiently. Please read the User Guide before submitting your manuscript online. For more detailed submission instruction, please consult the Manuscript Central Online User Guide (http://mcv3help.manuscriptcentral.com/tutorials/). You may also contact the Editorial Office who will be pleased to help you.

Acta Pharmacologica Sinica 2005 Nov; 26 (11): 1322–1333

Blackwell Publishing

Full-length article

Predicting MDCK cell permeation coefficients of organic molecules using membrane-interaction QSAR analysis[1]

Li-li CHEN, Jia YAO, Jian-bo YANG, Jie YANG[2]

State Key Laboratory of Pharmaceutical Biotechnology, College of Life Sciences, Nanjing University, Nanjing 210093, China

Key words

quantitative structure-activity relationship; molecular models; organic chemicals; artificial membranes; cell membrane permeability; MDCK cells

[1] Project supported by the National Natural Science Foundation of China (No 30171094 and No 30271497).
[2] Correspondence to Dr Jie YANG.
Phn 86-25-8359-4060.
Fax 86-25-8332-4605.
E-mail luckyjyj@sina.com.cn

Received 2005-05-10
Accepted 2005-07-20

doi: 10.1111/j.1745-7254.2005.00166.x

Abstract

Aim: To use membrane-interaction quantitative structure-activity relationship analysis (MI-QSAR) to develop predictive models of partitioning of organic compounds in gastrointestinal cells. **Methods:** A training set of 22 structurally diverse compounds, whose apparent permeability accross cellular membranes of Madin-Darby canine kidney (MDCK) cells were measured, were used to construct MI-QSAR models. Molecular dynamic simulations were used to determine the explicit interaction of each test compound (solute) with a dimyristoyl-phosphatidyl-choline monolayer membrane model. An additional set of intramolecular solute descriptors were computed and considered in the trial pool of descriptors for building MI-QSAR models. The QSAR models were optimized using multidimensional linear regression fitting and the stepwise method. A test set of 8 compounds were evaluated using the MI-QSAR models as part of a validation process. **Results:** MI-QSAR models of the gastrointestinal absorption process were constructed. The descriptors found in the best MI-QSAR models are as follows: 1) Clog*P* (the logarithm of the 1-octanol/water partition coefficient); 2) E_{HOMO} (the highest occupied molecular orbital energy); 3) E_s (stretch energy); 4) PM_Y (the principal moment of inertia *Y*, the inertia along the *y* axis in the rectangular coordinates; 5) C_t (total connectivity); and 6) E_{nb} (the energy of interactions between all of the nonbonded atoms). The most important descriptor in the models is Clog*P*. **Conclusion:** Permeability is not only determined by the properties of drug molecules, but is also very much influenced by the molecule-membrane interaction process.

Introduction

A majority of drugs used today are taken orally, so the drugs must traverse several semipermeable cell membranes before reaching the systemic circulation[1]. These membranes are biological barriers that selectively inhibit the passage of drug molecules and are composed primarily of a bimolecular lipid matrix, containing mostly cholesterol and phospholipids. The lipids provide stability to the membrane and determine its permeability characteristics. Drugs can cross a biological barrier by passive diffusion, facilitate passive diffusion, active transport, and pinocytosis, but passive diffusion is the most common method[1]. In the small intestine, in which the major part of oral drug absorption occurs, the barrier to drug absorption is a membrane comprising intestinal columnar epithelial cells. For any novel drug that is developed, it is necessary to examine how it is absorbed in the small intestine. In the absorption process, transport across a cell membrane depends on the concentration gradient of the solute. Most drug molecules are transported across a membrane by simple diffusion from a region of high concentration (eg gastrointestinal fluids) to one of low concentration (eg blood)[2]. Because drug molecules are rapidly removed by the systemic circulation and distributed into a large volume of body fluids and tissues, drug concentration in the blood is initially low compared with that at the administration site, producing a large gradient. The diffusion rate is directly proportional to the gradient, but also depends on the molecule's lipid solubility, degree of ionization, and the size and the area of the absorptive surface[3]; that is, the diffusion rate depends

on the characteristics and area of the intestinal membrane and the drug's properties, as well as the drug concentration gradient on both sides of the membrane.

Given the limitations of biomembranes, artificial membranes are usually used instead of biomembranes to study the absorption of drugs in the intestine. *In vitro* studies show that artificial membranes have some properties that are similar to those of biomembranes *in vivo*; that is, artificial membranes can be good mimics of biomembranes[3–5]. The Caco-2 cell monolayer is commonly used as an artificial membrane. When cultured on semipermeable membranes, Caco-2 cells, which are derived from a human colon adenocarcinoma, differentiate into a highly functionalized epithelial barrier with remarkable morphological and biochemical similarity to small intestinal columnar epithelium. The P_{app} values obtained from Caco-2 transport studies have been proven to correlate with those of human intestinal absorption, and the Caco-2 monolayer model has been proven to be extremely useful as a tool for mechanistic studies of drug absorption[3]. However, although the Caco-2 model is well characterized and has been proven to be useful, assays using the system are not perfect. The system requires a 3-week growth period and regular maintenance feeding, so it remains a relatively low throughput method. Irvine and co-workers tried another system using Madin-Darby canine kidney (MDCK) cells and found that it was possibly a useful tool for testing rapid membrane permeability[3]. MDCK cells are commonly used for studying cell growth regulation, metabolism, and transport mechanisms in distal renal epithelia. They can also differentiate into columnar epithelia and form tight junctions when cultured on semipermeable membranes. Irvine and co-workers studied a large number of compounds using both MDCK and Caco-2 assays to evaluate the suitability of MDCK cells as a possible tool for assessing membrane permeability and found that they were well suited. Others have also pointed out that MDCK cells are good candidates for modeling simple epithelia[6].

Based on the study carried out by Irvine and coworkers, we built membrane-interaction quantitative structure-activity relationship analysis (MI-QSAR) models to predict drug permeability through MDCK cells. The QSAR approach involves statistical analysis of various molecular descriptors for a series of biologically active molecules. The result of a QSAR study provides useful clues regarding the type of substituents that should be tested to improve the activity further. QSAR can play a vital role in lead exploitation. One successful example is the transformation of nalidixic acid with the help of QSAR into an important family of drugs: the quinolone carboxylates[7]. Since the method was established in the 1960s, QSAR equations have been used to describe the biological activities of thousands of different drugs and drug candidates[8,9]. Some new approaches have been used in QSAR since its initial development, for example, principal component analysis (PCA), partial least squares (PLS), artificial neural network (ANN)[10]. MI-QSAR is an advanced form of QSAR, in which membrane-interaction properties are added to the descriptor pool. MI-QSAR models predicting drug permeability through Caco-2 cells have been built by Kulkarni and co-workers[11]. In the present study, we built MDCK cell models for MI-QSAR analysis.

Materials and methods

MDCK cell permeation coefficients The dependent variable used in MI-QSAR analysis is the MDCK cell permeability coefficient, P_{app}. Irvine and co-workers performed permeability experiments on a data set of 55 structurally and chemically diverse drugs ranging in molecular weight from 130 to 470 and varying in net charge at pH 7.4[3]. MDCK cells were obtained from the American Type Culture Collection (ATCC; Rockville, MD, USA). MDCK cells were maintained in minimal essential medium containing 10% fetal bovine serum and fresh *L*-glutamine 2 mmol/L. Culture inserts were preincubated with culture medium at 37 °C for 1 h and then seeded with 6.64×10^5 cells per cm^2. MDCK monolayers were washed and fed with fresh medium 1 h post-seeding and again 24 h post-seeding. After 3 d of culturing, MDCK monolayers could be used to test the permeability of compounds. All compounds were tested in 6 replicate monolayers. Monolayers were incubated with donor and acceptor solutions for 60 min at 37 °C, 95% humidity, with 30 r/min reciprocal shaking[3,12]. The permeability coefficient was calculated according to the following equation[3]:

$$P_{app} = \left(\frac{dQ}{dt}\right) \times \frac{1}{C_0} \times \frac{1}{A} \quad (1)$$

In this equation dQ/dt is the permeability rate, C_0 is the initial concentration in the donor compartment, and A is the surface area of the filter.

Table 1 contains the P_{app} values for 22 structurally diverse drugs used as a training set of compounds and 8 drug compounds as a test set. The 22 training set compounds and 8 test compounds were selected according to the criterion that members of the test set were to be representative of all members of the training set in terms of the range of P_{app} values, molecular weights, and structural and chemical diversities, to achieve a composite representative subset. Table 1 also contains a composite summary of the human

Table 1. Molecular weight, MDCK permeability coefficient, and corresponding percentage of drug absorbed (as available) for the drugs of the training set and test set.

ID	Drug	Molecular weight	Permeability (μm/s)	Percentage absorbed
Training Set				
1	Acetaminophen	151.16	0.35	80
2	Acetylsalicylic acid	180.16	0.074	100
3	Acyclovir	225.21	0.0021	16
4	Alprenolol hydrochloride	285.81	1.6	93
5	Amoxicillin	365.4	0.0024	94
6	Atenolol	266.34	0.18	50
7	Bupropion hydrochloride	276.20	1.3	87
8	Cefatrizine propylene glycol	462.5	0.025	76
9	Corticosterone	346.47	1.4	100
10	Lamotrigine	256.09	0.88	70
11	Methylprednisolone	374.48	0.16	82
12	Nadolol	309.4	0.014	34
13	Ondansetron	293.37	1.1	100
14	Penicillin V	350.39	0.0015	45
15	Phenytoin	252.27	1.2	90
16	Pindolol	248.32	0.59	90
17	Practolol	266.34	0.013	100
18	Progesterone	314.46	1.6	91
19	Propranolol hydrochloride	295.80	1.7	90
20	Salicylic acid	138.12	0.1	100
21	Testosterone	288.43	1.4	100
22	Trimethoprim	290.32	0.52	97
Test set				
23	Antipyrine	188.22	1.5	100
24	Dexamethasone	392.46	0.2	100
25	Guanabenz	231.08	1.9	75
26	Hydrocortisone	362.46	0.31	91
27	Propylthiouracil	170.22	0.41	75
28	AZT	267.24	0.06	100
29	Cephalexin	347.39	0.0048	98
30	Gabapentin	171.24	0.0036	50

percentage absorption values of many of the drugs in the table. These data were obtained from published values. Compared with the P_{app} value and the human percentage absorption value, it is obvious that the P_{app} values are indicative of *in vivo* drug uptake. Figure 1 shows the structures of these thirty molecules.

Building solute molecules and a dimyristoyl-phosphatidyl-choline (DMPC) monolayer All the solute molecules of the training set and test set were built using HyperChem software[13]. A single DMPC molecule was built using HyperChem from the published crystal structure data[14]. The DMPC molecule was selected as the model phospholipid in this study. The structure of the DMPC molecule is shown in Figure 2. An assembly of 25 DMPC molecules, 5×5×1 in x, y, and z directions, respectively, was used as the model membrane monolayer. The size of the monolayer simulation system was selected based on the work done by van der Ploeg and Berendsen[15]. These workers built 2 decanoate bilayers, with 2×8×2 and 2×16×2 phospholipid molecules, respectively, and performed a molecular dynamic simulation for each of them. It was found that the estimated order parameters for these 2 model bilayers agreed with one another, which suggests that the smaller assembly is adequate for modeling short-range properties. Other researchers have obtained similar geometric and energetic equilibrium property values with regard to the size of the simulation system that permits a minimum effective size (phospholipids) of the monolayer to be defined[16].

To prevent unfavorable van der Waals' interactions between solute molecules and the membrane DMPC molecules, the single DMPC molecule in the center of the monolayer, which was located at position x, y=3,3 of the 5×5 DMPC monolayer model, was taken out[11], creating a space for the test solute molecules to insert into. Each of the test solute molecules of the permeation data set was inserted at 3 different positions or depths in the DMPC monolayer, with the most polar group of the solute facing toward the head group region of the monolayer. Three corresponding MDS (molecular dynamic simulation) models were generated for each solute molecule with regard to the trial positions of the solute molecules in the monolayer. The 3 trial positions were as follows[4,5,17]: solute molecule in the head group region, solute molecule between the head group region and the aliphatic chains, and solute molecule in the tail region of the aliphatic chains.

The energetically favorable geometry of the solute molecule in the monolayer was sought after using each of these trial positions. The 3 different positions of AZT, one of the training set solute molecules, are shown in Figure 3A to illustrate this modeling procedure. The most energetically favorable geometry of this solute molecule in the model DMPC monolayer is shown in Figure 3B.

Molecular dynamic simulations MDS were carried out using the Discover module in Material Studio[18] with compass force field and NVT ensemble(an ensemble in which the dynamics are modified to allow the system to exchange heat with the environment at a controlled temperature). The selection of the simulation temperature was based on the phase transition temperature for DMPC, which was 297 K[11]. A simulation temperature of 311 K was selected because it is

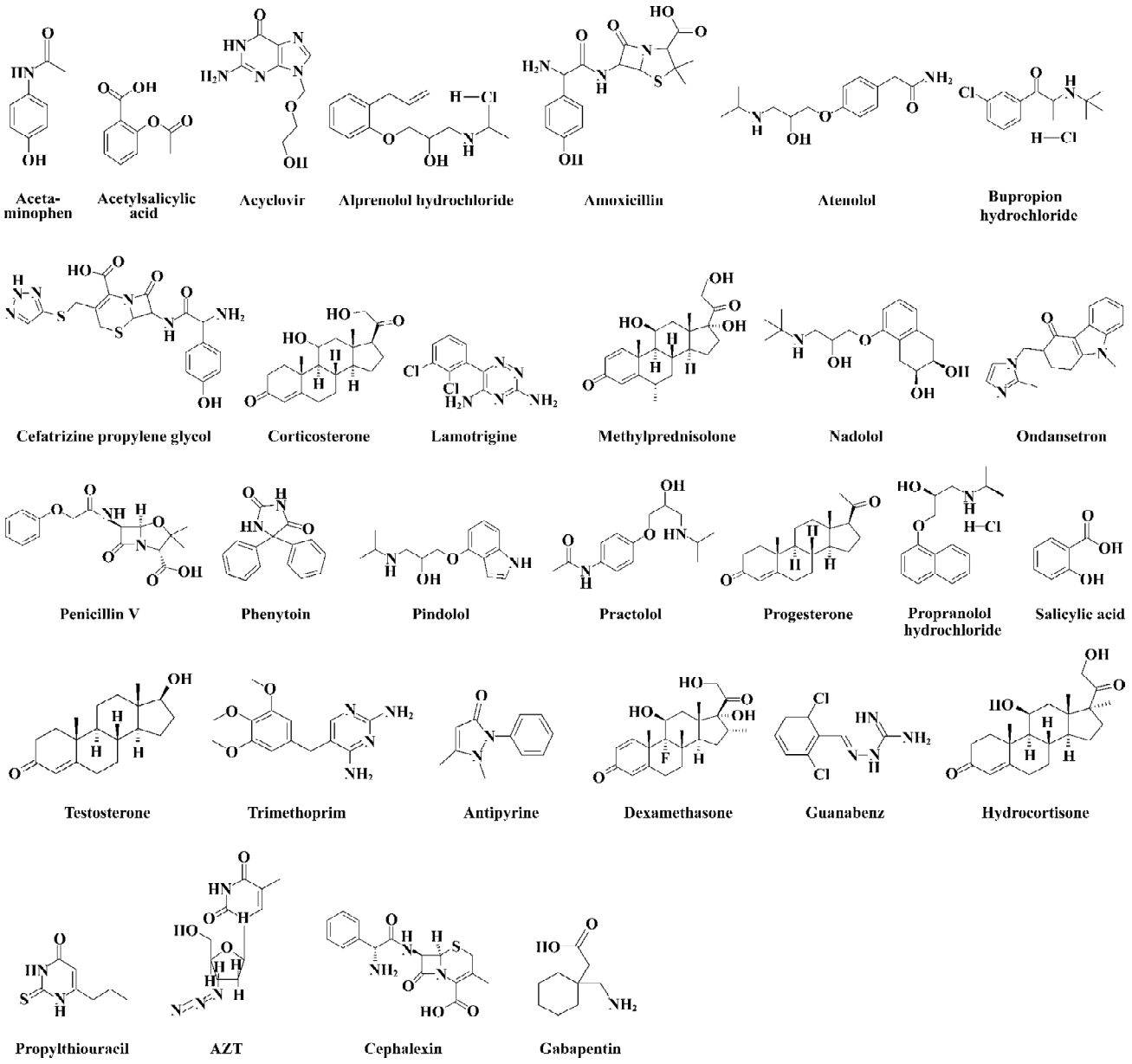

Figure 1. Structures of training set compounds and test set compounds.

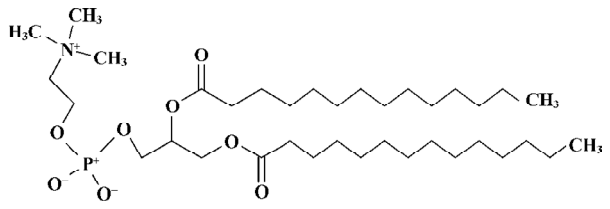

Figure 2. Chemical structure of a DMPC molecule.

body temperature, and it is also above the DMPC phase transition temperature. Temperature was held constant in the MDS by coupling the system to an external fixed temperature bath. The trajectory step size was 0.001 ps over a total simulation time of 10 ps for each solute of the training set and test set. After 10 ps of simulation, molecule-membrane interactions arrived at an energetically stable phase (Figure 4). Two-dimensional periodic boundary conditions were used (a=32 Å, b=32 Å, c=80 Å, and γ=96.0º) for the

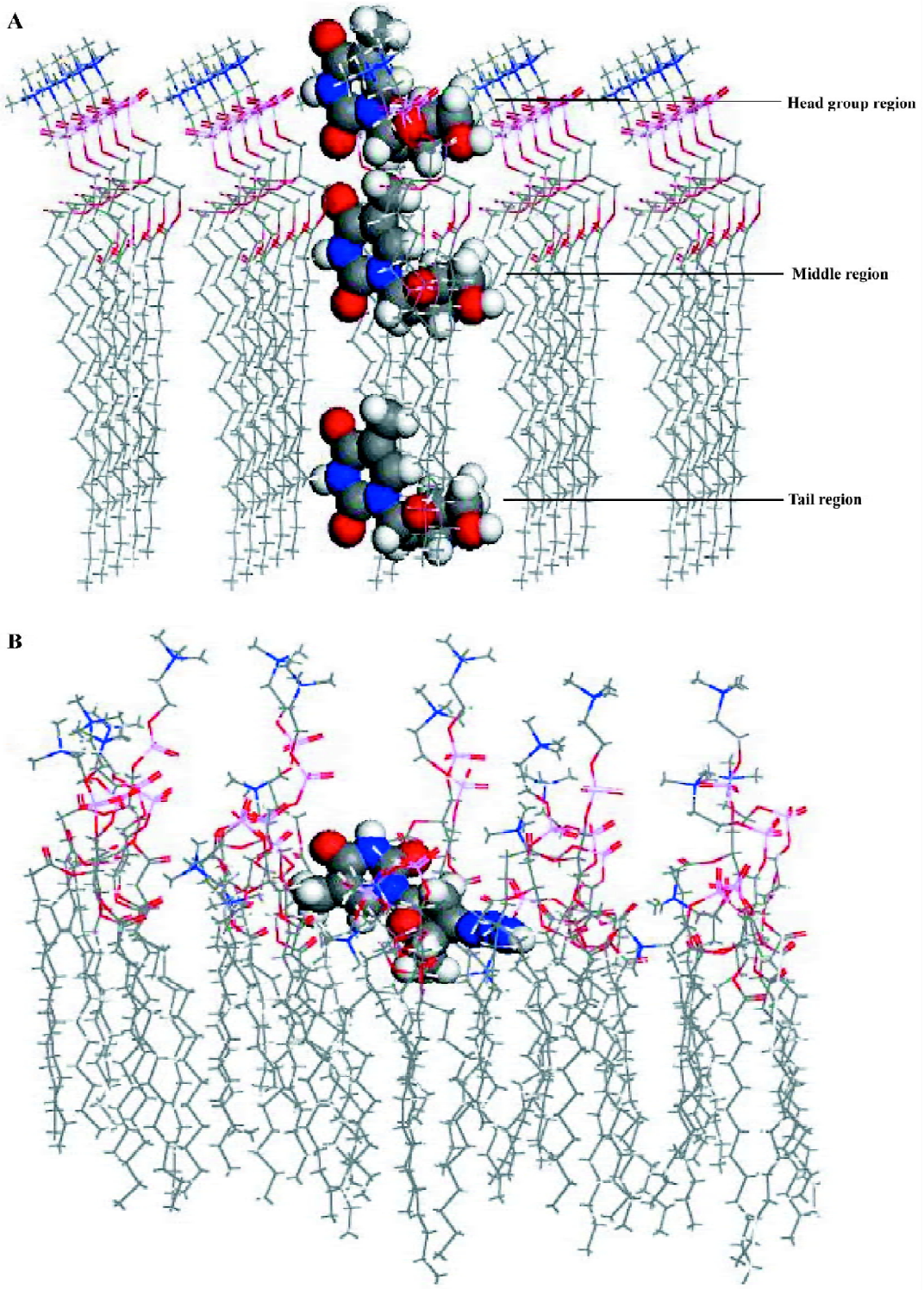

Figure 3. (A) "Side" view of an AZT molecule inserted at 3 different positions in the DMPC model monolayer, prior to the start of each simulation; (B) "Side" view of the most energetically favorable geometry of AZT in the DMPC model monolayer.

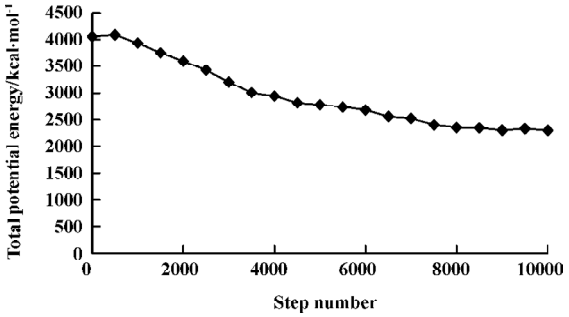

Figure 4. Total potential energy vs trajectory step number for acyclovir embedded in the model DMPC monolayer.

DMPC molecules of the monolayer model, but not the test solute molecule. Only a single solute molecule was explicitly considered in each MDS. The angle γ is the angle that an extended DMPC molecule makes with the "planar surface" of the monolayer. Each of the solute molecules was placed at each of the 3 different positions in the monolayer, as described earlier, with the most polar portion of the solute "facing" toward the head group region. A snapshot of molecule AZT and the membrane around it was taken after MDS, as shown in Figure 3b.

Calculation of descriptors Both intramolecular physicochemical properties and features of the solute molecules and intermolecular solute-membrane interaction properties were calculated. These properties and features will both be referred to as descriptors from this point forward because they constitute the trial pool of independent variables used to build the QSAR models. The descriptors used in the MI-QSAR analysis can also be divided into the following 3 kinds: 1) solute aqueous dissolution and solvation descriptors; 2) solute-membrane interaction descriptors; and 3) general intramolecular solute descriptors. Table 2 and Table 3 reporting the trial pool of descriptors used in the MDCK cell permeation MI-QSAR modeling use both classifications of the descriptors.

The general intramolecular solute descriptors included as part of the trial descriptor pool are defined in Table 2. The term "general" is used because solute descriptors in this class may be useful in describing different aspects of the bioavailability (in this case the MDCK cell permeation process) of a solute. There are other intermolecular properties computed using intramolecular computational methods, which are not included in Table 2, for example Clog*P* (the logarithm of 1-octanol/water partition coefficient), MP (melting point), Tc (critical tempeture), Sol (water solubility). All of these descriptors are intermolecular properties. They

Table 2. General intramolecular solute descriptors used in the MI-QSAR descriptor pool.

Descriptors	Explanation of descriptors
HOMO	Highest occupied molecular orbital energy
LUMO	Lowest occupied molecular orbital energy
Dp	Dipole moment
V_m	Molecular volume
SA	Molecular surface area
MW	Molecular weight
MR	Molecular refractivity
PM(x,y,z)	Principal moment of inertia along the x,y,z axis in the rectangular coordinate
HF	Heat of formation (Δh_f) for the structure at 298.15 K and 1 atm
H	The logarithm of Henry's law constant
G	Standard Gibbs free energy
Ovality	The ratio of the molecular surface area to the minimum surface area, which is the surface area of a sphere having a volume equal to the solvent-excluded volume of the molecule
E_b	Sum of the angle bending terms of the force-field equation
E_c	Sum of the electrostatic energy representing the pairwise interaction of charged atoms
E_v	Sum of pairwise van der Waals' interaction energy terms for atoms separated by more than 3 chemical bonds
E_s	Stretch energy, the energy contribution associated with the deformation of a bond from its equilibrium bond length
E_{sb}	Sum of the stretch-bend coupling terms of the force-field equation
E_t	Sum of the dihedral bond rotational energy term of the force-field equation
E14	Sum of pairwise van der Waals' interaction energy terms for atoms separated by exactly 3 chemical bonds
NRE	Repulsion energy
C_t	A kind of index defined according to the number of atoms and bonds and how they connect together

are classified as solvation and dissolution intermolecular descriptors and are reported in Table 3b. In Table 3a, there are solute-membrane interaction descriptors extracted directly from the MDS trajectories. These intermolecular descriptors were calculated using the most stable (lowest total potential energy) solute-membrane geometry from the 3 positions sampled for each of the solutes. For example, Figure 3b shows the lowest potential energy state of AZT in the membrane monolayer, which was used to estimate the solute-membrane interaction descriptors. Other solute-membrane interaction descriptors used in the QSAR descriptor trial set were determined using data from the MDS trajectories.

Construction and testing of MI-QSAR models Independent and useful descriptors can be extracted from all descriptors calculated earlier. The methods in common use are forward regression, backward regression and stepwise regression. Stepwise regression is the method used most frequently. The resulting regression equation from the stepwise regression method is not the best, rather it is an optimized result. SPSS was used to obtain the regression equation; it selected proper variables according to the partial sum of squares of regression in every step. The partial sum of squares for regression means that the sum of squares for regression increased or decreased after one variable was added to or deducted from the present regression equation. A parameter, F, is defined to check whether to introduce a variable or reject it when partial sum of squares for regression is of some value.

The stepwise regression method was used in this study, which was the combination of forward regression and backward regression methods. The single worst variable was picked out after each new variable was added. Two threshold constants, F_{entry} and $F_{removal}$ ($F_{entry}<F_{removal}$), were given before the regression. If the F value of one variable, which had the largest partial sum of squares for regression of all the variables not included in the regression equation, was larger than or equal to F_{entry}, the variable could be introduced into the equation. Conversely, if the F value of one variable, which had the smallest partial sum of squares for regression among all the variables included in the regression equation, was less than or equal to $F_{removal}$, the variable should be removed from the regression equation. These steps were carried out alternately until there was no variable to be introduced into the regression equation and none to be removed from it. The adjustment of the threshold values F_{entry} and $F_{removal}$ could affect the result of the selection of variables. If the prepared variables were few, it was appropriate to increase F_{entry} in order to introduce variables to the regression

Table 3. Intermolecular interaction descriptors in the trial MI-QSAR descriptor pool.

Part a

Membrane-solute descriptors	Description of the membrane-solute descriptors
Potential	The energy of a particle or system of particles derived from position, or condition, rather than motion
Electrostatic	The energy created by the interaction of charges between the molecule and the membrane
E_{nb}	The energy of interactions between non-bonded atoms
Angle	Valence angle bending
Bond	Bond stretching
Torsion	Dihedral angle torsion
Out-of-plane	Part of nearly all force fields for a covalent system

Part b

Dissolution and solvation-solute descriptors	Description of the dissolution and solvation–solute descriptors
Clog*P*	The logarithm of l-octanol/water partition coefficient
MP	The melting point for the structure at 1 atm
Tc	The temperature above which the gaseous form of the structure cannot be liquefied, no matter what pressure is applied
Sol	Solubility of the structure in water at 25 °C

Note: Part a includes the membrane-solute interaction descriptors and Part b lists the intermolecular dissolution and solvation descriptors of the solute.

equation as much as possible. If the prepared variables were too many, $F_{removal}$ could be decreased to cut down the number of variables introduced into the regression equation.

SPSS was used to carry out the regressions and construct the models[19].

Results and Discussion

The best MI-QSAR models for MDCK cell permeability were realized by considering the combination of general intramolecular solute, intermolecular dissolution/solvation solute, and intermolecular membrane-solute descriptors presented as a function of the number of terms, that is, descriptors, included in a given MI-QSAR model:

$$P_{app}=115.657+319.687\text{Clog}P$$
$$n=22 \quad R^2=0.646 \quad S=0.396 \qquad (2)$$

$$P_{app}=3113.84+374.691\text{Clog}P+338.881E_{HOMO}$$
$$n=22 \quad R^2=0.719 \quad S=0.362 \qquad (3)$$

$$P_{app}=3115.743+399.894\text{Clog}P+374.586E_{HOMO}+35.07E_s$$
$$n=22 \quad R^2=0.764 \quad S=0.341 \qquad (4)$$

$$P_{app}=3453.482+409.333\text{Clog}P+391.596E_{HOMO}+48.403E_s-0.0971PM_Y$$
$$n=22 \quad R^2=0.813 \quad S=0.312 \qquad (5)$$

$$P_{app}=3609.933+387.817\text{Clog}P+356.922E_{HOMO}+32.256E_s-0.163PM_Y-16594C_t$$
$$n=22 \quad R^2=0.866 \quad S=0.272 \qquad (6)$$

$$P_{app}=1029.094+398.972\text{Clog}P+459.781E_{HOMO}+24.048E_s-0.174PM_Y-18164.4C_t+2.594E_{nb}$$
$$n=22 \quad R^2=0.896 \quad S=0.248 \qquad (7)$$

where n is the number of compounds, R^2 is the coefficient of determination, and S is the standard error of the estimate (and its value could be different if the unit of the variables changed). The descriptors found in the best MI-QSAR models are as follows: 1) Clog P is the logarithm of the l-octanol/water partition coefficient; 2) E_{HOMO} is the highest occupied molecular orbital energy; 3) E_s is stretch energy, the energy contribution associated with the deformation of a bond from its equilibrium bond length; 4) PM_Y is principal moment of inertia Y, the inertia along the y axis in the rectangular coordinates; 5) C_t is total connectivity, which is a kind of index defined according to the number of atoms and bonds and their connecting sequence (C_t is a structural parameter; molecules with different structures have different connectivity indices according to a given definition); and 6) E_{nb} is the energy of interactions between all of the non-bonded atoms.

The values of the 6 descriptors found in the 1–6 term MI-QSAR models for each compound in the training set and test set are given in Table 4.

The observed and predicted (using the 3–6 term MI-QSAR models) MDCK cell permeation coefficients of the training and test set compounds are listed in Table 5 and plotted in Figure 5. Corticosterone, ondansetron, phenytoin, progesterone, propranolol hydrochloride, and testosterone are observed to permeate better than predicted by each of the MI-QSAR models, whereas acetylsalicylic acid, bupropion hydrochloride, methylprednisolone, and nadolol have a lower permeation coefficient than the one predicted by any of the models. Nevertheless, none of the compounds in either the training or test sets are outliers for the 3–6 term MI-QSAR models. Figure 6 contains plots of R^2 and S for the training set. R^2 increases with increasing numbers of descriptor terms, whereas the value of S decreases when the number of descriptor terms increases.

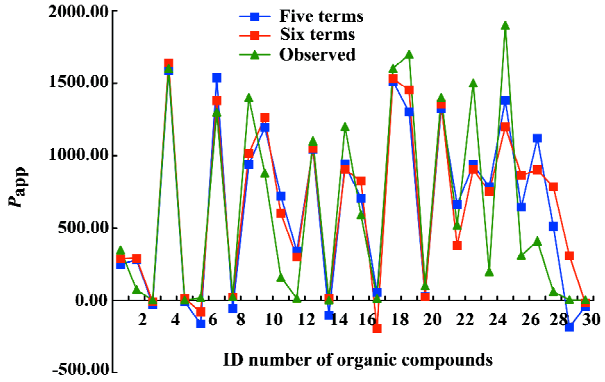

Figure 5. Observed versus predicted MDCK cell permeability coefficients for all the compounds of the training and test sets in the corresponding MI-QSAR model.

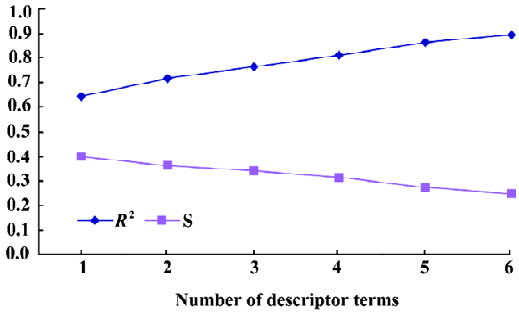

Figure 6. Diagnostic plot of the MI-QSAR. R^2 is the correlation coefficient and S is standard error of the estimate in the regression progress.

Analyzing Equations 2–7, it appears that Clog$P$ in the 1-term model accounts for much of the variance of P_{app} across the training set. Both principal moment of inertia Y and total

Table 4. Values of the 6 descriptors found to be the significant MI-QSAR terms in Equations 2–7.

ID	Structure name	Clog*P*	E_{HOMO}/eV	E_s/kcal·mol^{-1}	PM_Y[1)]	C_t	E_{nb}/kcal·mol^{-1}
Training set							
1	Acetaminophen	0.61	−8.62	6.10	942.88	3.40E−02	1393.32
2	Acetylsalicylic acid	1.24	−9.72	3.38	765.36	1.96E−02	1404.13
3	Acyclovir	−1.45	−8.74	9.80	1663.84	4.01E−05	1392.69
4	Alprenolol hydrochloride	3.81	−8.85	6.50	3020.37	3.47E−03	1384.42
5	Amoxicillin	−0.15	−9.27	7.61	3030.93	2.57E−04	1408.59
6	Atenolol	0.56	−9.11	7.08	5650.81	2.84E−03	1432.93
7	Bupropion hydrochloride	4.05	−8.95	5.19	2792.27	9.82E−03	1305.57
8	Cefatrizine propylene glycol	−0.89	−8.75	18.43	4873.42	1.52E−05	1456.15
9	Corticosterone	3.08	−10.15	12.51	3983.53	1.36E−04	1471.39
10	Lamotrigine	2.39	−8.84	6.15	1897.16	4.63E−03	1391.16
11	Methylprednisolone	2.78	−10.03	13.56	5053.62	9.65E−05	1398.77
12	Nadolol	1.27	−9.07	5.81	4280.39	8.18E−04	1370.14
13	Ondansetron	0.97	−8.66	16.00	2238.49	2.23E−04	1396.91
14	Penicillin V	0.57	−9.13	6.36	5382.44	2.73E−04	1442.01
15	Phenytoin	2.26	−9.59	3.77	1432.63	8.68E−04	1371.56
16	Pindolol	1.01	−8.24	7.22	3405.34	2.00E−03	1401.22
17	Practolol	0.64	−8.53	5.08	5380.10	2.84E−03	1274.31
18	Progesterone	4.63	−9.99	8.68	3716.02	2.36E−04	1423.14
19	Propranolol hydrochloride	2.80	−8.23	5.60	3766.75	1.42E−03	1401.56
20	Salicylic acid	1.46	−9.45	2.64	412.02	4.81E−02	1401.56
21	Testosterone	3.84	−9.95	7.98	2910.24	4.09E−04	1423.14
22	Trimethoprim	0.51	−8.63	11.61	2604.18	9.45E−04	1274.31
Test set							
23	Antipyrine	0.79	−8.27	8.62	1063.6	8.02E−03	1344.44
24	Dexamethasone	2.65	−10.25	16.84	4504.26	8.35E−05	1449.02
25	Guanabenz	2.95	−8.71	6.82	1547.79	1.39E−02	1293.76
26	Hydrocortisone	2.37	−10.02	12.88	4435.55	1.18E−04	1527.47
27	Propylthiouracil	3.25	−9.10	6.19	860.4	3.40E−02	1301.05
28	AZT	−1.54	−6.22	3.52	2232	1.89E−03	1376.28
29	Cephalexin	−0.54	−8.86	5.33	3630.21	2.57E−04	1571.03
30	Gabapentin	0.96	−10.08	3.96	807.524	2.55E−02	1431.10

connectivity have a negative effect on the permeation coefficient. In 1-term to 5-term models, the descriptors are all intramolecular descriptors, but in the 6-term model, one membrane-solute interaction descriptor, E_{nb}, is added in.

Eight compounds from the parent MDCK cell permeation coefficient data were selected to construct a test set to validate the MI-QSAR models. The molecules of the test set were selected so as to span the entire range of MDCK cell permeability for the composite training set. At the bottom of Table 5 are the observed and predicted P_{app} values for this test set. Figure 5 plots the test set as the last 8 compounds. There are no outliers, but antipyrine and guanabenz, compounds 1 and 3 of the test set, are predicted to have lower permeability coefficients than observed. Conversely, dexamethasone, hydrocortisone, propylthiouracil and AZT have higher predicted P_{app} values in all the models than the observed value.

The most important descriptor in the models is Clog*P*. Clog*P* is the computed logarithm of the l-octanol/water partition coefficient, and it has been ubiquitously used as a quantitative measure of hydrophobicity/lipophilicity since the 1960s[20,21]. A high Clog*P* value of a molecule implies that the molecule dissolves easily in hydrophobic materials and dissolves poorly in water. In the MI-QSAR models we built, Clog*P* had a positive effect on P_{app}, which implies that chemicals with high lipophilicity have better permeability through membranes than hydrophilic structures. It is easy to see why this is the case, because biomembranes are mainly composed

Table 5. Observed and predicted MDCK permeability coefficients for the 3–6 term MI-QSAR models.

	Structure name	Observed P_{app}	3-term	4-term	5-term	6-term
Training set						
1	Acetaminophen	350.0	343.16	529.78	246.92	286.17
2	Acetylsalicylic acid	74.0	89.80	244.65	280.48	289.21
3	Acyclovir	2.1	–393.51	–248.96	–26.92	–8.91
4	Alprenolol hydrochloride	1600.0	1550.53	1566.97	1586.89	1636.99
5	Amoxicillin	2.4	–150.74	–165.04	–10.67	10.81
6	Atenolol	18.0	177.07	–89.12	–162.70	–81.56
7	Bupropion hydrochloride	1300.0	1566.62	1588.50	1537.19	1379.35
8	Cefatrizine propylene glycol	25.0	127.43	80.46	–59.50	21.67
9	Corticosterone	1400.0	985.72	959.89	935.15	1015.25
10	Lamotrigine	880.0	977.29	1085.06	1195.33	1262.35
11	Methylprednisolone	160.0	946.65	830.13	720.90	600.99
12	Nadolol	14.0	428.39	285.60	339.90	297.99
13	Ondansetron	1100.0	821.84	1017.46	1043.64	1050.40
14	Penicillin V	1.5	147.21	–102.81	–104.00	11.30
15	Phenytoin	1200.0	559.43	666.59	937.19	904.82
16	Pindolol	590.0	686.72	659.43	705.59	823.54
17	Practolol	13.0	356.30	100.34	55.06	–195.28
18	Progesterone	1600.0	1528.22	1494.60	1508.96	1530.93
19	Propranolol hydrochloride	1700.0	1348.61	1281.68	1301.12	1450.92
20	Salicylic acid	100.0	253.68	439.76	24.13	21.74
21	Testosterone	1400.0	1204.89	1233.46	1324.80	1357.07
22	Trimethoprim	520.0	494.62	592.32	662.24	379.69
Test set						
23	Antipyrine	1500.0	635.25	851.38	935.33	904.85
24	Dexamethasone	200.0	924.92	900.40	785.27	750.10
25	Guanabenz	1900.0	1271.01	1428.98	1381.52	1198.71
26	Hydrocortisone	310.0	760.79	691.49	642.19	864.34
27	Propylthiouracil	410.0	1225.72	1438.47	1119.10	900.19
28	AZT	60.0	292.54	340.14	510.15	785.71
29	Cephalexin	4.8	–230.65	–330.13	–184.49	308.96
30	Gabapentin	3.6	–137.18	12.50	–42.70	–18.71

of double phospholipid layers, so small hydrophobic molecules can pass through the layer with little obstruction. Commonly, lipophilic drugs permeate the small intestinal columnar epithelium quicker and easier than hydrophilic drugs.

In Equation 3, another descriptor, E_{HOMO} appears, which represents HOMO energy. HOMO energy is the energy of the highest occupied molecular orbit, which is the opposite of LUMO energy, the energy of the lowest unoccupied molecular orbit[22]. The greater E_{HOMO} is, the greater the electron-donating capability; conversely, the smaller E_{LUMO} is, the smaller the resistance to accept electrons. Compounds that present larger values of E_{HOMO} are more electron donor and the compounds that present smaller values of E_{LUMO} are more electron acceptor. These variables are interpreted as measures of molecular reactivity and stability. As E_{HOMO} increases (relative to other molecules), the molecule is less stable and more reactive. For E_{LUMO}, the situation is the opposite. HOMO energy is relevant because Equation 3 measures the electron-donating character of the drug molecules. P_{app} has a positive relationship with HOMO energy, which means that drug molecules with higher electron-donating capacities can permeate membranes better.

As seen in the literature, energy is often discussed in many research programs. There is another energy descriptor, stretch energy, which influences P_{app} as E_{HOMO} does in our models. Stretch energy is the energy contribution associated with the deformation of a bond from its equilibrium bond

length. It is a kind of vibration energy, which is composed of bend energy and stretch energy. From Models 3–6, we can see that stretch energy is positively correlated with the value of P_{app}. Increasingly positive stretch energy values correspond to increasing P_{app}. Drug molecules with higher stretch energies metamorphose better and can permeate membranes more easily.

PM_Y is the principal moment of inertia along the *y* axis. It gives information about how the product of force and distance influence the value of P_{app}. P_{app} decreases as the value of PM_Y increases. The coefficients of PM_Y in Models 4–6 are very small when contrasted with the coefficients of other variables. This indicates that a change in PM_Y value has comparatively little effect on the value of P_{app} and the permeability of the drug molecules.

Compared with the descriptors discussed earlier, connectivity is an element that rarely appeared in QSAR models constructed by other researchers. Connectivity is a parameter defined according to the conformation of a molecule, and presumes that there is some functional relationship between molecule properties and connectivity. One standard definition of connectivity is as follows[23,24]:

Figure 7 is the structure of isopentanol without hydrogens. The figures are the bond numbers of each carbon connected with other carbons.

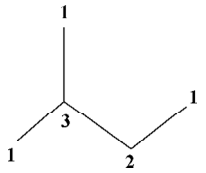

Figure 7. Structure of isopentanol without hydrogens.

$$Connectivity = \frac{1}{\sqrt{1\times3\times2\times1\times1}}$$ [24]

From the foregoing equation, we can see that connectivity reflects the connection and ramification conditions of the molecules. Connectivity is the quantitative description of the molecular structure. Molecules with different structures have different connectivity values. The connectivity method has been widely used in structure-activity analyses. In the models we constructed, connectivity is included in Model 5 and Model 6 and it has a negative effect on the P_{app} value. The larger the connectivity value, the more complicated the structure will be, and there will be more branch chains. Therefore an increase in connectivity will decrease the permeability of a molecule.

E_{nb} is the energy of interactions between non-bonded atoms. It includes van der Waals' energy, electrostatic energy and hydrogen bond terms in some older forcefields, as the following equation describes[25],

$$E_{non\text{-}bond}=E_{vdW}+E_{coulomb}+E_{hbond} \quad (8)$$

The non-bond energy terms in Equations 6 and 7 suggest that permeability increases with increasing binding of the solute to the phospholipid regions of the membranes.

Kulkarni and coworkers carried out MI-QSAR analysis using the permeability coefficients of some drug molecules tested by Caco-2 cells. Thirty molecules were included in their training set, and significant MI-QSAR models were built. Twenty-three intramolecular descriptors, and 11 membrane-solute interaction descriptors were calculated. In our study, we calculated more than 70 descriptors for every drug molecule in the training set, including electronic, steric, and thermodynamic properties. MI-QSAR models were built based on the analysis of these descriptors. In addition, the present study confirmed the conclusion of Irvine and coworkers, that MDCK cells are suitable for studying drug permeability through biomembranes.

Acknowledgements

We are very grateful to the administrators in the Computer Laboratory of College of life, Nanjing University, for their support in carrying out this study.

References

1 Moo JC, David PT, Clay TC, Thomas JV, Jeffrey FS. The Madin Darby Canine Kidney (MDCK) epithelial cell monolayer as a model cellular transport barrier. Pharm Res 1989; 6: 71–7.

2 Magali T, Peter R, Daniel HS. Pharmacology. Churehill Livingstone: Harcourt Asia; 1998.

3 Irvine JD, Takahashi L, Lockhart K, Cheong J, Tolan JW, Selick HE, *et al*. MDCK (Madin-Darby Canine Kidney) cells: a tool for membrane permeability screening. J Pharm Sci 1999; 88: 28–33.

4 Kulkarni A, Hopfinger AJ, Osbrone R, Bruner LH, Thompson ED. Prediction of eye irritation from organic chemicals using membrane-interaction QSAR analysis. Toxicol Sci 2001; 59: 335–45.

5 Kulkarni A, Hopfinger AJ. Membrane-interaction QSAR analysis: application to the estimation of eye irritation by organic compounds. Pharm Res 1999; 16: 1244–52.

6 Rothen-Rutishauser B, Kraemer SD, Braun A, Guenthert M, Wunderli-Allenspach H. MDCK cell cultures as an epithelial *in vitro* model: cytoskeleton and tight junctions as indicators for the definition of age-related stages by confocal microscopy. Pharm Res 1998; 15: 964–71.

7 Alka K. C-QSAR: a database of 18000 QSARs and associated biological and physical data. J Comput Aided Mol Des 2003; 17: 187–96.

8 Hugo K. QSAR and 3D-QSAR in drug design. Part 1: methodology.

Drug Discov Today 1997; 2: 457–67.
9 Hugo K. QSAR and 3D-QSAR in drug design. Part 2: applications and problems. Drug Discov Today 1997; 2: 538–46.
10 Lennart E, Erik J. Multivariate design and modeling in QSAR. Chemometrics Intell Lab Syst 1996; 34: 1–19.
11 Kulkarni A, Han Y, Hopfinger AJ. Predicting Caco-2 cell permeation coefficients of organic molecules using membrane-interaction QSAR analysis. J Chem Inf Comput Sci 2002; 42: 331–42.
12 Braun A, Hammerle S, Suda K, Rothen-Rutishauser B, Gunthert M, Kramer SD, *et al*. Cell cultures as tools in biopharmacy. Eur J Pharm Sci 2000; 11 Suppl 2: S51–60.
13 HyperChem. HyperChem, Release 6.0 for MS Windows. Waterloo (Ontario, Canada): Hypercube; 2001.
14 Hauser H, Pascher I, Pearson RH, Sundell S. Preferred conformation and molecular packing of phosphatidylethanolamine and phosphatidylcholine. Biochim Biophys Acta 1981; 650: 21–51.
15 van der Ploeg P, Berendsen HJC. Molecular dynamic simulation of a bilayer membrane. J Chem Phys 1982; 76: 3271–6.
16 Stouch TR. Lipid membrane structure and dynamics studied by all atom molecular dynamics simulations of hydrated phosphatidylcholine vesicles. Mol Simulation 1993; 1: 335–62.
17 Gurtovenko AA, Patra M, Karttunen M, Vattulainen I. Cationic DMPC/DMTAP lipid bilayers: molecular dynamics study. Biophys J 2004; 86: 3461–72.
18 Accelrys: Materials Studios. San Diego (USA): Accelrys; 2001.
19 SPSS. SPSS for Windows. Chicago (USA): SPSS Inc; 2001.
20 Butina D, Segall MD, Frankcombe K. Predicting ADME properties in silico: methods and models. Drug Discov Today 2002; 7 Suppl 11: S83–8.
21 Albert PL. Screening for human ADME/Tox drug properties in drug discovery. Drug Discov Today 2001; 6: 357–66.
22 Honorio KM, Da Siliva ABF. An AM1 study on the electron-donating and electron-accepting character of biomolecules. Int J Quant Chem 2003; 95: 126–32.
23 Kier LB, Hall LH. Molecular connectivity in chemistry and drug research. New York: Academic Press; 1976.
24 Kier LB, Hall LH. Molecular connectivity in structure-activity analysis. London: John Wiley; 1986.
25 Iyer M, Mishra R, Han Y, Hopfinger AJ. Predicting blood-brain barrier partitioning of organic molecules using membrane-interaction QSAR analysis. Pharm Res 2002; 19: 1611–21.
26 Deretey E, Feher M, Schmidt JM. Rapid prediction of human intestinal absorption. Quant Struct-Act Relat 2002; 21: 493–506.
27 Levet-Trafit B, Gruyer MS, Marjanovic M, Chou RC. Estimation of oral drug absorption in man based on intestine permeability in rats. Life Sci 1996; 58: 359–63.
28 Zhao YH, Abraham MH, Hersey A, Luscombe CN. Quantitative relationship between rat intestinal absorption and Abraham descriptors. Eur J Med Chem 2003; 38: 939–47.
29 Peter B. Modeling liquid properties, solvation, and hydrophobicity: A molecular size-based perspective. Perspect Drug Discov Des 2000; 19: 19–45.

Acta Pharmacologica Sinica 2005 Nov; 26 (11): 1334–1338

Blackwell Publishing

Full-length article

Roles of nitric oxide in protective effect of berberine in ethanol-induced gastric ulcer mice[1]

Long-rui PAN[2,3], Qiang TANG[2], Qin FU[2], Ben-rong HU[2], Ji-zhou XIANG[2,4], Jia-qing QIAN[2]

[2]Department of Pharmacology, Tongji Medical College of Huazhong University of Science and Technology, Wuhan 430030, China; [3]Department of Pharmacology, Yunyang Medical College, Shiyan 442000, China

Key words

berberine; nitric oxide; protective agents; ethanol-induced disorders; stomach ulcer

[1] Project supported by the National Natural Science Foundation of China, No 30171151.
[4] Correspondence to Prof Ji-zhou XIANG.
Phn 86-27-8369-2802.
Fax 86-27-8369-2608.
E-mail jzxiang@mails.tjmu.edu.cn

Received 2005-05-06
Accepted 2005-07-21

doi: 10.1111/j.1745-7254.2005.00186.x

Abstract

Aim: To investigate the protective effects of berberine on ethanol-induced gastric ulcer in mice. **Methods:** Gastric ulcers were induced by oral ingestion of ethanol. Nitric oxide (NO) content was measured, and mRNA expression of endothelial nitric oxide synthase (eNOS) and inducible nitric oxide synthase (iNOS) were analyzed by reverse transcription-polymerase chain reaction (RT-PCR). **Results:** The ulcer index (UI) at 1 h, 2 h, 3 h and 6 h after oral administration of ethanol was 23.8±1.4, 23.3±2.2, 22.3±1.2 and 20.8±1.1, respectively. The UI in the berberine-treated groups (5 mg/kg and 50 mg/kg) was less than the control group. The content of NO in the control group was 73.3±7.3 μL/L, 94.0±9.2 μL/L, 109.6±6.4 μL/L and 138.2±10.2 μL/L in gastric juice and 5.8±1.1 μmol/g protein, 8.3±1.1 μmol/g protein, 9.8±1.1 μmol/g protein and 11.9±1.2 μmol/g protein in gastric tissue at 1 h, 2 h, 3 h and 6 h, respectively, after the oral administration of ethanol. The content of NO in the berberine-treated groups (5 mg/kg and 50 mg/kg) was higher than the control group at 1 h after the oral administration of ethanol ($P<0.05$), and was lower at 6 h ($P<0.05$). Analysis by RT-PCR showed that expression of eNOS was inhibited but iNOS expression was enhanced by ethanol. However, the expression of eNOS could be enhanced and iNOS expression could be inhibited by berberine ($P<0.01$). **Conclusion:** Berberine could significantly protect gastric mucosa from damage by ethanol. This effect may be related to the increased expression of eNOS mRNA and inhibited expression of iNOS mRNA.

Introduction

Berberine, also known as huangliansu, is an isoquinoline alkaloid derived from the Chinese herb Huanglian, Huangbai and other plants. It has multiple pharmacological actions, such as antibacterial activity and anti-inflammatory effects, and is used in the treatment of diarrhea and other digestive disorders[1]. Berberine has been found to protect the gastric mucosa and inhibit gastric ulcers[2], but the pharmacological mechanisms for the protective effect of berberine are not clear. Accumulating evidence from both animal and human studies indicates that nitric oxide (NO) plays a key role in normal wound repair. The beneficial effects of NO on wound repair may be attributed to its functional influences on angiogenesis and inflammation[3]. A recent study demonstrated that NO generated from endothelial nitric oxide synthase (eNOS) played an important role in gastric ulcer formation and gastric healing[4]. However, NO generated from inducible nitric oxide synthase (iNOS) participates in ulcer formation through the production of peroxide free radicals and their cytotoxic action[5]. At the same time, it was reported that berberine could induce the thoracic aorta of rats to release endothelial NO[6], and 13-methylberberine and 13-ethylberberine reduced the production of NO and the expression of iNOS protein in a concentration-dependent manner in lipopolysaccharide (LPS)-stimulated macrophages[7]. We therefore inferred that it was possible for berberine to protect the gastric mucosa and accelerate the healing of peptic ulcers through the NO pathway. In the present study, we

attempted to investigate whether the protective effect of berberine on gastric mucosa was related to NO and nitric oxide synthase (NOS).

Materials and methods

Drugs and reagents Berberine was supplied by Prof Jialin WANG (Department of Pharmacology, Tongji Medical College, Huazhong University of Science and Technology, Wuhan, China). The NO kit was supplied by Nanjing Jian Cheng Bioengineering Company (Nanjing, China).

Animals The present study was carried out using 72 Kunming mice (Certificate No SYXK 2004-0028) weighing 18 g–22 g from the Experimental Animal Center of Tongji Medical College. Both sexes were used. They were kept in separate cages at room temperature and deprived of food 24 h before oral administration of ethanol but were allowed free access to water.

Induction of gastric ulcer Gastric ulcers were produced by oral administration of ethanol 24 h after starvation. Each of the mice was given 0.1 mL ethanol (100%, anhydrous alcohol).

Drugs treatments and measurement of ulcer size Animals were divided into 3 groups of 24 mice each. Group I received saline at a dose of 0.1 mL/kg (ip) and served as the control group. Group II received berberine at a dose of 5 mg/kg (ip) while group III received berberine at a dose of 50 mg/kg (ip).

Drugs were given 30 min before the oral administration of ethanol. The mice were killed by cervical dislocation 1 h, 2 h, 3 h and 6 h after oral administration of ethanol, and the gastric juice was sucked from the stomach before the stomach was removed. It was then opened along the greater curvature and the mucosa of the glandular portion of the stomach was rinsed gently with saline. Macroscopic damage was assessed and the number of ulcers, ulcer severity and ulcer index (UI) were recorded. Because each mouse had many lesions or ulcers and most gastric mucosal lesions were punctate or linear, each ulcer was graded according to severity using a scale of 1–4, as follows: 1, punctate ulcer; 2, linear ulcer of length ≤2 mm; 3, linear ulcer of length 2 mm–4 mm; and 4, linear ulcer of length ≥4 mm. The UI was calculated by summing the total number of ulcers, as described previously[8,9]. The gastric tissues were stored at -70 °C until biochemical analysis.

Measurement of nitric oxide The content of nitric oxide in the gastric juice and gastric tissue was measured through the method of nitric acid reductase, and the operational processes were carried out strictly in accordance with the NO kit instructions.

Reverse-transcription polymerase chain reaction for the detection of eNOS and iNOS mRNA The stomachs were removed from the saline-treated (0.1 mL/kg) and berberine-treated (50 mg/kg) groups both before and after ulcer induction (1 h, 3 h and 6 h) for the determination of eNOS and iNOS mRNA expression by reverse transcription-polymerase chain reaction (RT-PCR) using specific primers. Total RNA was isolated from gastric tissues using Trizol reagent (Gibco BRL, Gathersburg, MD, USA). First-strand cDNA was synthesized from 5 μg of total cellular RNA using oligo-$(dt)_{20}$ primers with the thermoscript RT-PCR system (Gibco BRL). PCR cycles were carried out for amplification of eNOS, iNOS and β-actin cDNA using a thermal cycler (Perkin-Elmer Corporation 850 Lincoln Centre Drive, Foster City, California, USA) and oligonucleotides (Boya, Shanghai, China). The primers for eNOS were 5'-TTC CGG CTG CCA CCT GAT CCT AA-3' (sense) and 5'-AAC ATA TGT CCT TGC TCA AGG CA-3' (antisense)[10]. The β-actin primer sequences for iNOS were 5'-CGG GCA TTG CTC CCT TCC GAA AT-3'(sense) and 5'-CTT CAT GAT AAC GTT TCT GGC TCT-3' (antisense)[11]. The oligonucleotide primer sequences for β-actin were 5'-TCA CCC ACA CTG TGC CCA TCT ACG A-3' (sense) and 5'-GGA TGC CAC AGG ATT CCA TAC CCA-3' (antisense). The number of PCR cycles was adjusted carefully to avoid saturation of the amplification system. In the RT step, the cellular mRNAs were reverse-transcribed into a "library" of cDNAs. This cDNA library was then used for the analysis of various genes in the PCR step. Briefly, total RNA (2.5 μg) from each of the tissues was reverse transcribed into single-stranded cDNA in a 20-μL reaction mixture containing: 4 μL 5' buffer, 20 IU ribonuclease inhibitor, 10 mmol/L dNTP, 0.5 μg oligo-$(dt)_{20}$ primer, 20 IU RNasin and 200 IU M-MLV reverse transcriptase. After incubation for 1 h at 42 °C, the RT mixture was incubated at 70 °C for 10 min to inactivate the reverse transcriptase. PCR was then carried out using 5 μL cDNA in a final reaction volume of 50 μL. The assay mix contained 50 mmol/L KCl, 10 mmol/L Tris-HCl (pH 8.3), 1.5 mmol/L $MgCl_2$, 0.2 mmol/L dNTP, 1 mmol/L of the respective primers and 1.5 IU of *Taq* DNA polymerase. The PCR cycling program was set for 1 cycle of pre-denaturation at 94 °C for 1 min, and then 35 cycles at 94 °C for 30 s, 55 °C for 30 s, 72 °C for 1 min, followed by 1 cycle at 72 °C for 5 min. PCR products were visualized by UV illumination after electrophoresis on a 2% agarose gel containing 0.5 μL ethidium bromide. The location of a predicted product was confirmed using a 100 bp DNA ladder (Gibco BRL) as a standard size marker. The gel photographs were scanned with a computerized densitometer (SYNGENE, London, Britain). The signals for eNOS and iNOS mRNA were standardized against

the β-actin signal for each sample and the results are expressed as eNOS and iNOS mRNA/β-actin mRNA ratio.

Statistical analysis All of the data were expressed as mean±SD and the analysis was carried out using the *t*-test. Values of $P < 0.05$ were considered statistically significant.

Results

Effects of berberine on ethanol-induced gastric lesions The UI of ethanol-induced gastric lesions are shown in Figures 1 and 2. In the control group, the UI at 1 h, 2 h, 3 h and 6 h after oral administration of ethanol averaged 23.8±1.4, 23.3±2.2, 22.3±1.2 and 20.8±1.1, respectively. The UI in the berberine-treated groups (5 mg/kg and 50 mg/kg) were less than the control group and this effect was time-dependent

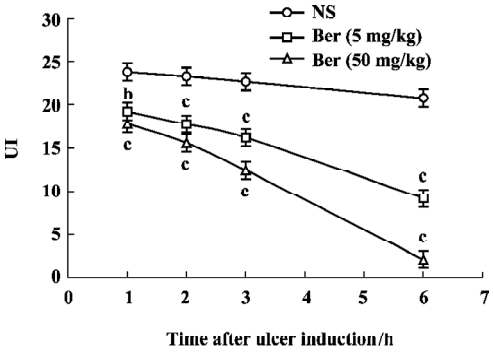

Figure 2. The ulcer index (UI) of ethanol-induced gastric lesions in the different treatment groups. n=6. Mean±SD. $^bP<0.05$, $^cP<0.01$ *vs* NS group.

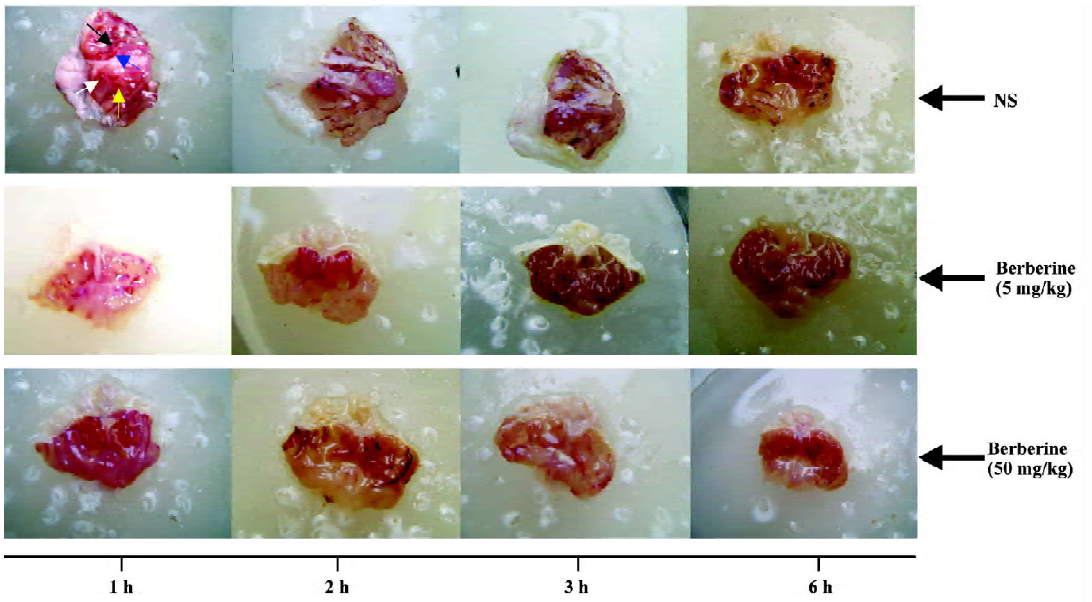

Figure 1. The appearance of gastric mucosa in mice 1 h, 2 h, 3 h and 6 h after being given 0.1 mL ethanol. After oral administration of ethanol, the gastric mucosa had many lesions, which were punctate or linear. Ulcer severity was graded using a score of 1 to 4. 1, punctate ulcer (white arrow); 2, linear ulcer of length =2 mm (yellow arrow); 3, linear ulcer of length 2–4 mm (blue arrow); and 4, linear ulcer of length =4 mm (black arrow).

Table 1. The content of nitric oxide in gastric juice and gastric tissue. n=6. Mean±SD. $^bP<0.05$, $^cP<0.01$ *vs* NS group. $^fP<0.01$ *vs* 1 h.

Group	NO in gastric juice/μmol·L^{-1}				NO in gastric tissue/μmol·g^{-1} protein			
	1 h	2 h	3 h	6 h	1 h	2 h	3 h	6 h
NS	73.3±7.3	94.0±9.2^f	109.6±6.4^f	138.2±10.2^f	5.8±1.1	8.3±1.1^f	9.8±1.1^f	11.9±1.2^f
Berberine (5 mg/kg)	88.2±11.0^b	95.0±6.2	100.8±8.9	99.3±8.8^c	6.8±1.6^b	7.8±0.8	8.3±1.0^b	8.3±2.2^c
Berberine (50 mg/kg)	91.9±8.4^c	101.1±9.8	109.3±12.3	110.9±7.8^b	7.9±2.1^c	9.2±0.8	9.4±1.3	9.3±1.5^b

NO, nitric oxide; NS, normal saline.

($P< 0.05$ and $P<0.01$, respectively).

Change in nitric oxide content with the time The content of NO in gastric tissue and gastric juice is shown in Table 1. In the control group, the content of NO in gastric juice at 1 h, 2 h, 3 h and 6 h after oral administration of ethanol was 73.3 ±7.3 μL/L, 94.0±9.2 μL/L, 109.6±6.4 μL/L and 138.2±10.2 μL/L, respectively, while the NO content in gastric tissue averaged 5.8±1.1 μmol/g protein, 8.3±1.1 μmol/g protein, 9.8±1.1 μmol/g protein and 11.9±1.2 μmol/g protein, respectively. However, in both gastric tissue and gastric juice the content of NO in the berberine-treated groups (5 mg/kg and 50 mg/kg) was higher than that in the control group at 1 h after oral administration of ethanol ($P<0.05$, $P<0.01$), but lower at 6 h after oral administration of ethanol ($P<0.05$,$P<0.01$).

Expression of eNOS and iNOS mRNA Expression of iNOS and eNOS mRNA is shown in Figures 3 and 4. In the base statement the mRNA of eNOS could be expressed while that of iNOS could almost not be expressed. In the control group the expression of eNOS was inhibited and iNOS was enhanced by ethanol, while in the berberine-treated groups the expression of eNOS could be enhanced and iNOS could be inhibited.

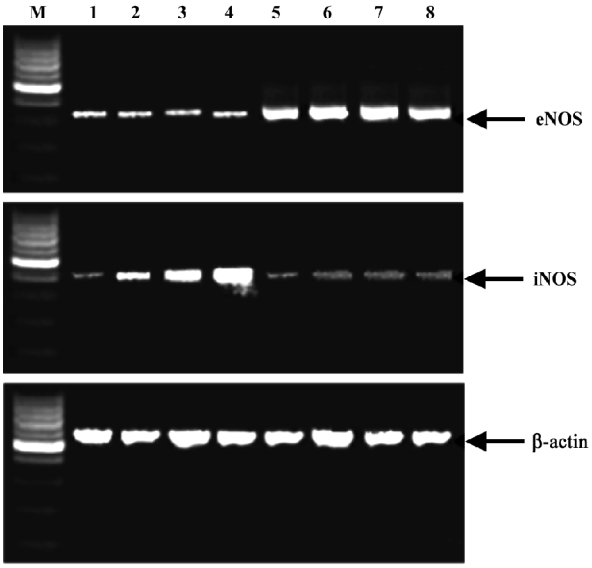

Figure 3. Determination of endothelial nitric oxide synthase (eNOS) and inducible nitric oxide synthase (iNOS) mRNA by reverse transcription-polymerase chain reaction in mouse gastric mucosa treated with saline before ulcer induction (lane 1), 1 h (lane 2), 3 h (lane 3) and 6 h after ulcer induction (lane 4), treated with berberine (50 mg/kg) before ulcer induction (lane 5), and 1 h (lane 6), 3 h (lane 7) and 6 h after ulcer induction (lane 8). M=100 bp ladder molecular weight DNA marker.

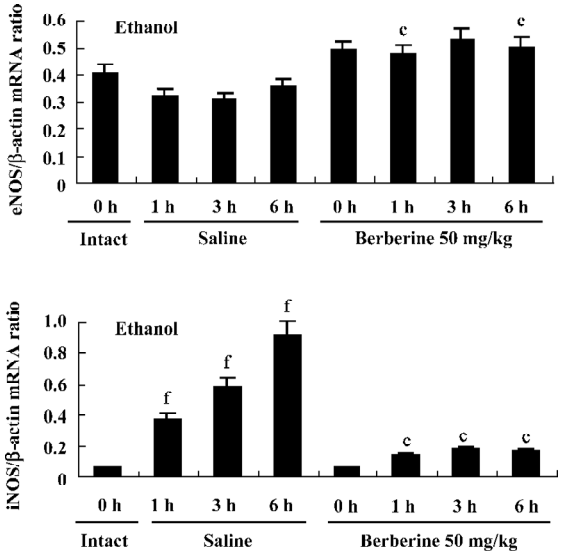

Figure 4. Determination of endothelial nitric oxide synthase (eNOS) and inducible nitric oxide synthase (iNOS) mRNA expression by the ratio of eNOS and iNOS mRNA over β-actin mRNA, as in experiments presented in Figure 2. n=6. Mean±SD. $^cP<0.01$ *vs* saline-treated group. $^fP<0.01$ *vs* before ulcer induction.

Discussion

Nitric oxide plays an important role in the host defense and inflammatory response[12,13]. It also plays an important role in the mechanism of gastric mucosal protection and injury induced by pressure, ethanol, stress and endo toxins[14–17]. Endogenous NO has a dual action in the gastrointestinal tract: protective effects by constitutive nitric oxide synthase (cNOS)/NO and proulcerogenic effects by iNOS/NO[8].

cNOS lies in gastric endotheliocytes in the gastric tissue, also called eNOS[18]. NO derived from eNOS is a pivotal mediator to accelerate gastric ulcer healing; it maintains the integrity of the gastric epithelium, regulates gastric mucosal blood flow, and stimulates gastric mucus secretion and synthesis[19]. On the other hand, NO stimulates the release of vasoactive intestinal peptide (VIP) in gastric tissue and increases the concentration of cGMP[20]. NO/cGMP plays a central role in producing relaxation of mouse gastric fundus smooth muscle, and cGMP protects gastric parietal cells from ethanol-induced cytotoxicity, implicating a basolateral Cl^- channel in the plasma membrane or that pepsinogen secretion stimulated by a Ca^{2+}-mediated agonist is modulated by a NO/cGMP pathway[8]. The results of the present study have shown that the content of NO in tissue from the berberine-treated group was higher than control group at 1 h after oral administration of ethanol, and further study has shown that expression of eNOS is higher. Therefore, we might conclude

that berberine can increase NO production through improving eNOS mRNA expression. The effect of berberine on NO formation in the vascular system was also demonstrated[6,21].

High expression of iNOS was found in ulcer tissue of the control group at 3 h and 6 h after ulcer induction. A similar phenomenon was also found by Peng *et al*[22]. Large amounts of NO synthesized from the inducible isoform have been implicated in tissue injury in the gut during inflammatory reactions[23]. Guo *et al*[24] also reported that high expression and activity of iNOS were found to coincide with severe inflammation in ulcer tissue. It is known that induction of high-output iNOS usually occurs in an oxidative environment, and thus high levels of NO have the opportunity to react with superoxide anion (O_2^-) leading to peroxynitrite ($ONOO^-$) formation and cell toxicity, protein tyrosine nitration, hydroxyl radical production and tissue damage[24,25]. The results of the present study have shown that iNOS is under low-expression conditions at all times in the berberine-treated groups, as the content of NO had no peak and it was kept at a relatively steady level. This demonstrated that berberine might decrease NO production through inhibition of iNOS expression in the gastric ulcer tissue, prevent the abundant release of NO that aggravates gastric mucosal injury and, ultimately, improve the healing of ulcers. The study of Lee *et al*[7] also showed that 13-methyberine and 13-ethyberberine both inhibited iNOS expression in LPS-stimulated macrophages. In conclusion, the protective effect of berberine results in an increase in eNOS mRNA expression, which inhibits the iNOS mRNA expression process.

References

1 Pan JF, Yu C, Zhu DY, Zhang H, Zeng JF, Jiang SH, *et al*. Identification of three sulfate-conjugated metabolites of berberine chloride in healthy volunteers' urine after oral administration. Acta Pharmacol Sin 2002; 23: 77–82.

2 Hicano H. Protective effects of Huanglian on gastric mucosa. Foreign Med Sci 1998; 20: 31.

3 Luo JD, Chen AF. Nitric oxide: a newly discovered function on wound healing. Acta Pharmacol Sin 2005; 26: 259–64.

4 Ma L, Wallace JL. Endothelial nitric oxide synthase modulates gastric ulcer healing in rats. Am J Physiol Gastrointest Liver Physiol 2000; 279: 341–6.

5 Cho CH. Current roles of nitric oxide in gastrointenstinal disorders. J Physiol Paris 2001; 95: 253–6.

6 Kang DG, Sohn EJ, Kwon EK, Han JH, Oh H, Lee HS. Effects of berberine on angiotensin-converting enzyme and NO/cGMP system in vessels. Vascul Pharmacol 2002; 39: 281–6.

7 Lee DU, Kang YJ, Park MK, Lee YS, Seo HG, Kim TS, *et al*. Effects of 13-alkyl-substituted berberine alkaloids on the expression of COX-II, TNF-α, iNOS, and IL-12 production in LPS-stimulated macrophages. Life Sci 2003; 73: 1401–12.

8 Jimenez D, Martin MJ, Pozo D, Alarcon C, Md JE, Bruseghini L, *et al*. Mechanisms involved in protection afforded by *L*-arginine in ibuprofen-induced gastric damage: role of nitric oxide and prostaglandins. Dig Dis Sci 2002; 47: 44–53.

9 Qureshi MA, Darzi A, Leahy AL, Bouchier-Hayes DJ. Transient reduction in gastric acid secretion following gastric mucosal laser irradiation. Surg Laparosc Endosc 1998; 8: 356–9.

10 Laufs U, Gertz K, Dirnagl U, Bohm M, Nickenig G, Endres M. Rosuvastatin, a new HMG-CoA reductase inhibitor, upregulates endothelial nitric oxide synthase and protects from ischemic stroke in mice. Brain Res 2002; 942: 23–30.

11 Garhart CA, Heinzel FP, Czinn SJ, Nedrud JG. Vaccine-induced reduction of *Helicobacter pylori* colonization in mice is interleukin-12 dependent but gamma interferon and inducible nitric oxide synthase independent. Infect Immun 2003; 71: 910–21.

12 Ma L, Wallace JL. Endothelial nitric oxide synthase modulates gastric ulcer healing in rats. Am J Physiol Gastrointest Liver Physiol 2000; 279: 341–6.

13 Ma JJ, Li SA. Nitric oxide and gastric ulcer. Prog Physiol Sci 1998; 29: 260–1.

14 Nishida K, Ohta Y, Ishiguro I. Role of gastric mucosal constitutive and inducible nitric oxide synthases in the development of stress-induced gastric mucosal lesions in rats. Biochem Biophys Res Commun 1997; 236: 275–9.

15 Qiu BS, Pfeiffer CJ, Cho CH. Effects of chronic nitric oxide synthase inhibition in cold-restraint and ethanol-induced gastric mucosal damage in rats. Digestion 1996; 57: 60–6.

16 Tepperman BL, Soper BD. Nitric oxide synthase induction and cytoprotection of rat gastric mucosa from injury by ethanol. Can J Physiol Pharmacol 1994; 72: 1308–12.

17 Zhang GF, Zhang MA, Chen YR, Wang L. The roles of endothelin and nitric oxide in gastric mucosa injuries in rats with endotoxemia. World Chin J Digestol 2000; 8 Suppl 8: 24.

18 Fischer H, Becker JC, Boknik P, Huber V, Lüss H, Neumann J, *et al*. Expression of constitutive nitric oxide synthase in rat and human gastrointestinal tract. Biochim Biophys Acta 1999; 1450: 414–22.

19 Li Y, Wang WP, Wang HY, Cho CH. Intragastric administration of heparin enhances gastric ulcer healing through a nitric oxide-dependent mechanism in rats. Eur J Pharmacol 2000; 399: 205–14.

20 Yu XE, Luo QN. Protective effects of exogenous nitric oxide on acid-ethanol induced gastric ulcer in guinea-pig. World Chin J Digestol 2000; 8: 224.

21 Ko WH, Yao XQ, Lau CW, Law WI, Chen ZY, Kwok W, *et al*. Vasorelaxant and antiproliferative effects of berberine. Eur J Pharmacol 2000; 399: 187–96.

22 Peng X, Feng JB, Wang SL, You ZY, Li A. Alterations of nitric oxide synthase and nitric oxide in gastric tissues of burned rats. World Chin J Digestol 1997; 5: 765–6.

23 Barrachina MD, Panes J, Esplugues JV. Role of nitric oxide in gastrointestinal inflammatory and ulcerative diseases: perspective for drugs development. Curr Pharm Des 2001; 7: 31–48.

24 Guo JS, Cho CH, Wang WH, Shen XZ, Cheng CL, Koo MW. Expression and activity patterns of three inducible enzymes in the healing of gastric ulcers in rats. Word J Gastroenterol 2003; 9: 1767–71.

25 Ding HL, Zhu HF, Dong JW, Zhu WZ, Yang WW, Yang HT, *et al*. Inducible nitric oxide synthase contributes to intermittent hypoxia against ischemia/reperfusion injury. Acta Pharmacol Sin 2005; 26: 315–22.

Acta Pharmacologica Sinica 2005 Nov; 26 (11): 1339–1344

Blackwell Publishing

Full-length article

Chemopreventive effect of dimethyl dicarboxylate biphenyl on malignant transformation of WB-F344 rat liver epithelial cells[1]

Hua SUN, Geng-tao LIU[2]

[2]*Department of Pharmacology, Institute of Materia Medica, Peking Union Medical College & Chinese Academy of Medical Sciences, Beijing 100050, China*

Key words

dimethyl dicarboxylate biphenyl; liver neoplasm; cell transformation; chemoprevention; epithelial cell; gap junctions

[1] This work was supported by grant 2004AA2Z3814 from the Chinese Ministry of Sciences and Technology.
[2] Correspondence to Prof Geng-tao LIU.
Phn 86-10-6316-5178.
Fax 86-10-6301-7757.
E-mail liugt@imm.ac.cn

Received 2005-04-14
Accepted 2005-07-25

doi: 10.1111/j.1745-7254.2005.00208.x

Abstract

Aim: To study the potential chemopreventive effect of dimethyl dicarboxylate biphenyl (DDB), an anti-hepatitis drug, on hepatocarcinogenesis *in vitro*. **Methods:** The anti-carcinogenesis effect of DDB was assessed on a two-stage chemical oncogenesis model induced by 3-methylcholanthrene and 12-*O*-tetradecanoyl phorbol 13-acetate (TPA) with WB-F344 rat liver epithelial cells (WB-F344 cells) *in vitro*. A soft-agar colony formation assay was used to determine the tumorigenic potential of the transformed WB-F344 cells. The gap junctional intercellular communication (GJIC) was detected using the scrape loading/dye transfer technique. **Results:** DDB at 1 μmol/L, 2 μmol/L, and 4 μmol/L significantly prevented the malignant transformation of WB-F344 cells induced by 3-methylcholanthrene and TPA. The average number of transformed foci decreased dramatically by 10.0%, 37.2%, and 47.4%, respectively. In soft agar, a remarkable decrease in colony numbers was observed in transformed cells treated with 2 μmol/L and 4 μmol/L DDB. DDB at 1 μmol/L, 2 μmol/L, and 4 μmol/L inhibited the downregulation of GJIC induced by TPA in a dose-dependent manner. The GJIC recovered to 25.6%, 34.6%, and 44.9%, respectively, of the control WB-F344 cells by DDB. **Conclusion:** DDB has a potential chemopreventive effect on hepatocarcinogenesis induced by carcinogens *in vitro*.

Introduction

Human hepatocellular carcinoma (HCC) is one of the most frequent malignant cancers. The carcinogenesis of HCC is a multifactorial event. Chronic hepatitis B virus (HBV) and hepatitis C virus (HCV) infections are the most frequent causes of HCC[1]. Approximately 80% of human HCC are attributable to HBV infection[2]. Chronic HBV carriers are 100–400 times more likely to develop HCC than non-carriers[3]. HCV is the second most common cause of HCC after HBV[4]. Currently, HCC represents more than 4% of all cancer cases worldwide and causes at least 315 000 deaths every year[5]. Although early HCC can be cured by surgical resection, many HCC are asymptomatic, so most HCC patients are not diagnosed in time.

An effective approach to cancer control is chemoprevention. It is known that the therapy of both chronic HBV and HCV generally involves a long-term course. An anti-hepatitis drug with an inhibiting or a suppressing effect on the development of hepatocarcinogenesis, besides its improvement of abnormal liver function, would be of great clinical value.

Dimethyl dicarboxylate biphenyl (DDB) is a synthetic analogue of Schizandrin C, which was isolated from Fructus Schizandrae chinensis[6]. Since 1983, DDB has been widely used to treat hepatitis B patients in China and is exported to Korea, Egypt, Vietnam, Indonesia, Pakistan, and Burma for the treatment of HBV and HCV. The results of the clinical application indicated that DDB markedly improved impaired liver functions, such as the elevated serum transaminase, bilirubin, α-fetal protein, and symptoms of the patients. Pharmacologically, DDB has a protective action against

experimental liver injury in mice and rats[7,8,9]. DDB also had anticancer activity and differentiation-inducing effect on cancer cells[10]. In the present paper, the chemoprevention effect of DDB on hepatocellular carcinogenesis *in vitro* is studied.

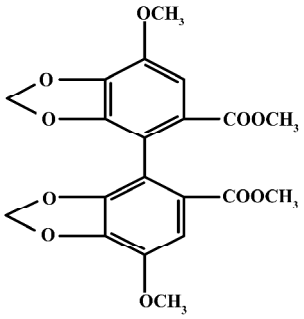

Materials and methods

Chemicals DDB with 99% purity was provided by the Beijing Union Pharmaceutical Plant. As DDB is not water-soluble, it was dissolved in dimethyl sulfoxide (Me_2SO) for *in vitro* use. 3-Methylcholanthrene (3MC), 12-*O*-tetradecanoyl phorbol 13-acetate (TPA), MTT, and Lucifer yellow CH were obtained from Sigma Chemical Company. Other chemicals were of analytical grade and purchased from Beijing Chemical Company.

Cell culture WB-F344 cells were grown in DMEM (GIBCO) media containing 10% newborn calf serum, 100 kU/L penicillin, and 100 mg/L streptomycin in a 37 °C humidified incubator containing 5% CO_2 and 95% air, and passaged using 0.25% trypsin plus 0.02% EDTA treatment. The culture medium was changed every other day.

MTT assay Cytotoxicity was determined by MTT assay according to the method of Mosmann[11]. WB-F344 cells (3×10^3cells per well) were plated on 96-well plates, and 24 h later various concentrations of DDB were added (0.5 μmol/L–100 μmol/L). The cells were incubated at 37 °C in a CO_2 incubator for 72 h. The culture supernatant was sucked out and MTT 0.5 g/L stock solution was added to each well. After 4 h of incubation, Me_2SO was added. The optical density of each well was determined by a microplate reader at a wavelength of 570 nm. The values of absorbance were expressed as relative viable cell number.

***In vitro* transformation of WB-F344 cells** WB-F344 cells were seeded on 25-cm^2 tissue culture flasks containing the complete medium at a density of 4×10^3cells per flask. The medium was replaced with the complete medium containing 3MC (2 mg/L) or 0.1% Me_2SO 24 h after seeding, and the cells were incubated for another 72 h. After the removal of the medium, the cells were washed twice with sterile phosphate-buffered saline (PBS) and incubated in fresh medium for 4 d. The cells were then incubated with medium containing 100 μg/L TPA. The TPA-containing medium was changed every 2–3 d for 14 d. After sucking out the TPA-containing medium, the cells were washed twice with sterile PBS and then incubated in fresh medium containing 10% newborn calf serum. The fresh medium was changed every 2 d until d 30. DDB was added to the medium from 24 h after cell seeding until the end of the experiment. At d 30, three of these flasks from each group were stained with Wright-Giemsa, and scored for transformed colonies. The remainders were used for soft-agar assay.

Soft-agar colony formation assay Cells derived from each group were seeded separately. Agar (0.6%) in the complete medium was kept at 44 °C and poured into 6-well plates (2 mL per well) as to form the lower layer. After the agar medium had set, 1×10^4cells per well in 2 mL of 0.3% agar (44 °C) were layered onto the gelled agar as the form of the upper layer. The cells were incubated in a humidified atmosphere of 95% air and 5% CO_2 at 37 °C. On d 9 and d 18, 1 mL of 0.3% agar in the complete medium was added. After 28 d, colonies of more than 20 cells were counted under contra-phase microscope.

Cell-cell communication assay The scrape loading/dye transfer (SL/DT) technique was used to detect GJIC according to the method of E1-Fouly *et al*[12]. WB-F344 cells were pretreated with various concentrations of DDB for 1 h at 24 h prior to the addition of TPA (100 μg/L) for 1 h. The other cells were pretreated with 4 μmol/L DDB for 24 h, 48 h, and 72 h before treatment with TPA. Following incubation, the cells were washed twice with PBS. Then Lucifer yellow CH (a fluorescent dye permeating gap-junctional channels) was added and several scrapes were made with a surgical steel-bladed scalpel at low light intensities. These scrapes were performed to ensure that the scrape traversed a large group of confluent cells. After 3 min incubation, the cells were washed with PBS again. Dye migration was observed and photographed with an inverted fluorescent microscope (Olympus, Japan) at ×200 magnification. The number of dyed cells represents the ability of cells to communicate via GJIC. GJIC data are reported as a percentage of the corresponding mean control value. The data are obtained from 3 views per plate, pooled 4 separate plates for each point.

Statistical analysis Results are expressed as mean±SD. To compare mean values between 2 groups, the Student's *t*-test was used. $P<0.05$ was considered statistically significant.

Results

Cytotoxicity of DDB to WB-F344 cells To select the appropriate doses of DDB for the present study, the cytotoxicity of DDB to WB-F344 cells was assessed using the MTT assay. No significant cytotoxic effect on the cells was observed when the concentrations of DDB were below 4 μmol/L (Table 1). Therefore, 1 μmol/L, 2 μmol/L, and 4 μmol/L of DDB were used in the subsequent experiments.

Table 1. Cytotoxicity of dimethyl dicarboxylate biphenyl (DDB) to WB-F344 rat liver epithelial cells. n=9. Mean±SD. $^bP<0.05$ *vs* control group.

Group	Dose/μmol·L^{-1}	Survival rate/%
Control	0	100.0±0.0
DDB	0.5	97.9±13.6
	1	105.1±9.3
	2	104.9±12.4
	4	90.2±4.7
	5	79.4±6.9^b
	10	78.4±17.6^b
	50	79.2±5.1^b
	100	61.8±5.4^b

Effect of DDB on two-stage transformation of WB-F344 cells A two-stage (initiation and promotion) chemical induction oncogenesis model with WB-F344 cells was established. The WB-F344 cells became transformed after 3-MC (2 mg/L) initiation for 72 h and then TPA (100 μg/L) promotion for 14 d. The transformed cells were grown in a disorganized multilayer instead of in a monolayer (Figure 1). DDB at concentrations of 1 μmol/L, 2 μmol/L, and 4 μmol/L markedly inhibited transformation of WB-F344 cells in a dose-dependent manner. The average number of transformed foci decreased dramatically by 10.0%, 37.2%, and 47.4%, respectively, after DDB treatment (Table 2).

Table 2. The inhibitory effect of dimethyl dicarboxylate biphenyl (DDB) on transformed foci in WB-F344 rat liver epithelial cells undergoing initiation with 3-methylcholanthrene (3-MC) followed by promotion with 12-*O*-tetradecanoyl phorbol 13-acetate (TPA). n=3. Mean±SD. $^bP<0.05$, $^cP<0.01$ *vs* the model group. Transformed foci/flask: colonies containing >~100 cells were scored positive.

Group	3-MC+TPA	Transformed foci/plate	Inhibitory rate/%
Control	–	4.5±1.3	–
Model	+	53.8±8.2	–
DDB 1 μmol/L	+	48.4±13.4^b	10.0
2 μmol/L	+	33.8±5.1^c	37.2
4 μmol/L	+	28.3±3.3^c	47.4

Effect of DDB on colony of transformed WB-F344 cells in soft agar To evaluate the tumorigenic potential of the treated WB-F344 cells, the efficiency of their soft-agar colony formation was determined. As shown in Table 3, no colony formed in soft agar in untreated WB-F344 cells, whereas the cells initiated with 3-MC and promoted with TPA developed the transformed phenotype of colony formation in soft agar. A remarkable increase in colony numbers was observed. The cells treated with 2 μmol/L and 4 μmol/L DDB also developed the transformed phenotype of colony formation, but the colony numbers significantly decreased compared with

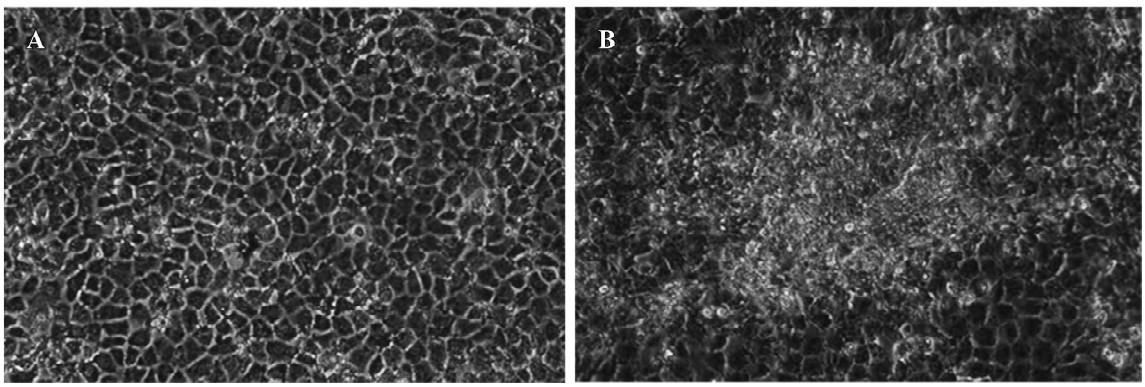

Figure 1. Morphology of WB-F344 cells treated with 3-methylcholanthrene (3-MC)/12-*O*-tetradecanoyl phorbol 13-acetate (TPA) or the vehicle dimethyl sulfoxide. (A) control cells, (B) cells treated with TPA 100 μg/L plus 3-MC 2 mg/L. At d 30 of incubation, cell morphology was examined under a microscope (×200). Cells treated with 3-MC and TPA were highly transformed in appearance with the formation of foci.

Table 3. Effect of dimethyl dicarboxylate biphenyl (DDB) on tumorigenicity of transformed WB-F344 rat liver epithelial cells using the soft agar culture assay. n=3. Mean±SD. ^cP<0.01 *vs* the model group. Colony forming rate/1×10^{4}cells: colonies containing >~20 cells were scored positive. 3-MC, 3-methylcholanthrene; TPA, 12-*O*-tetradecanoyl phorbol 13-acetate.

Group	3-MC+TPA	Colony forming rate/1×10^{4}cells	Inhibitory rate/%
Control	–	0.0±0.0	–
Model	+	231.0±17.1	–
DDB 2 μmol/L	+	136.0±19.1^c	41.1
4 μmol/L	+	85.0±7.9^c	63.2

the model group.

Effect of DDB on GJIC The GJIC of normal WB-F344 cells was well- characterized and did not decrease during the experimental incubation period (Figure 2Aa). After exposing the cells to TPA (100 μg/L) for 1 h, over 85% inhibition of GJIC was detected. The Lucifer yellow CH only stayed at the incision sites or artificially damaged cells (Figure 2Ab). When the cells were pretreated with DDB 1 μmol/L, 2 μmol/L, and 4 μmol/L, respectively, for 24 h, a dose-dependent inhibition of TPA-induced downregulation of GJIC was observed. The GJIC recovered to 25.6%, 34.6%, and 44.9% of the control group, respectively (Figure 2B). The time-dependent inhibitory effect of 4 μmol/L DDB on TPA-induced downregulation of GJIC is shown in Figure 3. By the addition of 4 μmol/L DDB for 24 h, 48 h, and 72 h, TPA-induced downregulation of GJIC was markedly reversed in a time-dependent manner.

Discussion

WB-F344 cells have often been used in the study of hepatocarcinogenesis[13]. In the present study, we found that the anti-hepatitis drug DDB at non-toxic doses markedly prevented the transformation of WB-F344 cells induced by 3-MC and TPA *in vitro*, which expressed as significant decrease of the number of transformed foci and the malignant degree of transformed cells.

It is well known that carcinogenesis is a multistage and multimechanism process, involving the irreversible alteration of a stem cell (the initiation phase), followed by the clonal

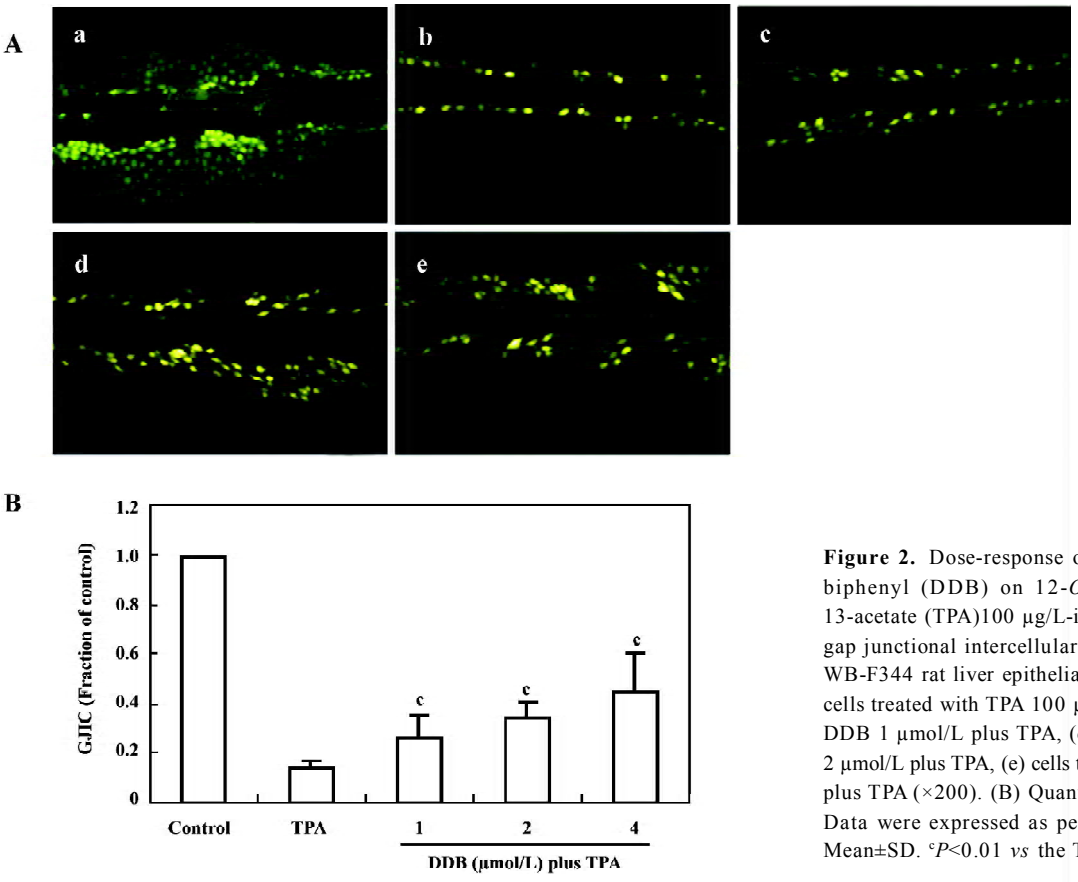

Figure 2. Dose-response of dimethyl dicarboxylate biphenyl (DDB) on 12-*O*-tetradecanoyl phorbol 13-acetate (TPA)100 μg/L-induced downregulation of gap junctional intercellular communication(GJIC) in WB-F344 rat liver epithelial cells. (A)(a) control, (b) cells treated with TPA 100 μg/L, (c) cells treated with DDB 1 μmol/L plus TPA, (d) cells treated with DDB 2 μmol/L plus TPA, (e) cells treated with DDB 4 μmol/L plus TPA (×200). (B) Quantification of recovery rate. Data were expressed as percentage of control. n=4. Mean±SD. ^cP<0.01 *vs* the TPA model group.

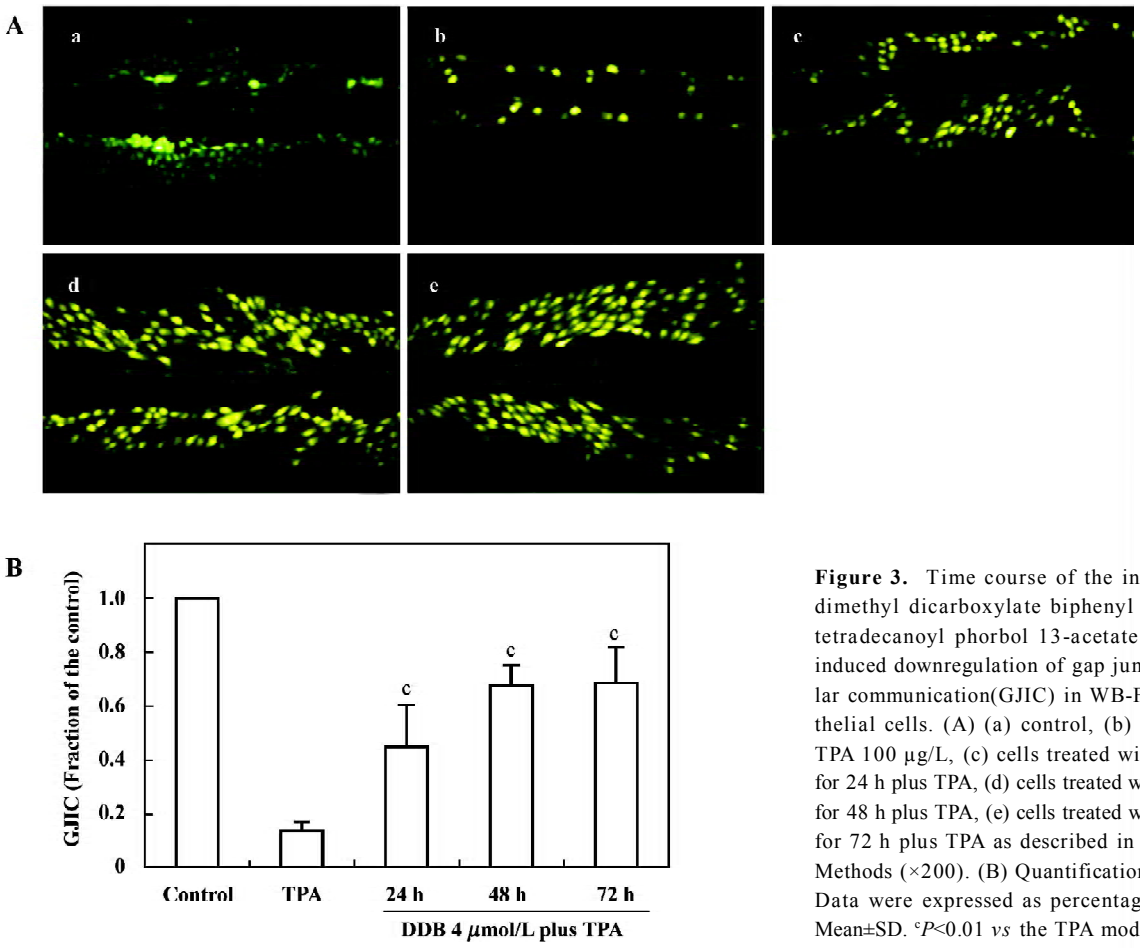

Figure 3. Time course of the inhibitory effect of dimethyl dicarboxylate biphenyl (DDB) on 12-*O*-tetradecanoyl phorbol 13-acetate (TPA)100 μg/L-induced downregulation of gap junctional intercellular communication(GJIC) in WB-F344 rat liver epithelial cells. (A) (a) control, (b) cells treated with TPA 100 μg/L, (c) cells treated with DDB 4 μmol/L for 24 h plus TPA, (d) cells treated with DDB 4 μmol/L for 48 h plus TPA, (e) cells treated with DDB 4 μmol/L for 72 h plus TPA as described in the Materials and Methods (×200). (B) Quantification of recovery rate. Data were expressed as percentage of control. n=4. Mean±SD. ^cP<0.01 *vs* the TPA model group.

proliferation of the initiated stem cell (the promotion phase), from which the acquisition of the invasive and metastasis phenotypes are generated (the progression phase). Intervention to prevent cancer can occur at each step. For chemoprevention of carcinogenesis, the development of anti-tumor promoting agent has been regarded as the most effective pathway.

Intercellular communication is necessary in multicellular organisms to maintain tissue homeostasis and to control cell growth and differentiation. Gap junction channels play an important role in intercellular communication by providing a direct pathway for the movement of molecular information, including ions, polarized and non-polarized molecules up to a molecular mass of 1 kDa between adjacent cells[14,15]. Much evidence has been documented to support the hypothesis that the downregulation of GJIC is a cellular event underlying the tumor promotion process, and that any treatment to prevent downregulation of GJIC is important in prevention of tumor promotion[16,17]. Many tumor promoters have been shown to inhibit gap junctional communication *in vitro*[18,19]. TPA is a well-known classical inhibitor of cell communication in most cells, including the WB-F344 cell[20]. In the present study, the underlying mechanisms of DDB against hepatocarcinogenesis were investigated during the promotional phase using TPA to inhibit GJIC. The WB-F344 cells are known to have high GJIC. The treatment with TPA significantly inhibited GJIC, as was determined using the SL/DT assay. The counteracting effect of DDB on GJIC inhibition caused by TPA suggests that DDB has a significant action in maintaining GJIC function, and that it might be beneficial in preventing tumor promotion.

In summary, the results of the present study suggest that DDB can prevent the malignant transforming of WB-F344 cells induced by 3-MC and TPA *in vitro*. The restoration of GJIC in the promotion phase should contribute, at least in part, to the anti-hepatocarcinogenic property of DDB. We conducted other experiments and found that DDB significantly inhibited liver carcinogenesis induced by DEN/PB in mice; the data from these experiments will be published in another paper soon. Both *in vitro* and *in vivo* experiments

demonstrated that DDB had a chemopreventive effect on hepatocarcinogenesis. It is worthy to pay attention to whether DDB potentially prevents liver carcinogenesis in patients with chronic viral hepatitis.

References

1 Feitelson MA, Pan J, Lian Z. Early molecular and gentic determinants of primary liver malignancy. Surg Clin N Am 2004; 84: 339–54.

2 Yerian LM, Anders RA, Tretiakova M, Hart J. Caveolin and thrombospondin expression during hepatocellular carcinogenesis. Am J Surg Pathol 2004; 28: 357–63.

3 Birrer RB, Birrer D, Klavins JV. Review: Hepatocellular carcinoma and hepatitis virus. Ann Clin Lab Sci 2003; 33: 39-54.

4 Robert S, Brown J, Paul JG. Scope of worldwide hepatitis C problem. Liver Transpl 2003; 9: s10–s13.

5 Glinghammar B, Skogsberg J, Hamsten A, Ehrenborg E. PPARä activation induces COX-2 gene expression and cell proliferation in human hepatocellular carcinoma cells. Biochem Biophys Res Commun 2003; 308: 361–8.

6 Liu GT. From the study of Fructus Schizandrae to the discovery of biphenyl dimethyl-dicarboxylate. Acta Pharm Sin 1983; 18: 714–20.

7 Liu GT, Wang GF, Wei HL, Bao TT, Song ZY. A comparison of the protective actions of biphenyl dimethyl-dicarboxylate, transstilbene, alcoholic extracts of Fructus Schizandrae and ganoderma against expeimental liver injury in mice. Acta Pharm Sin 1979; 14: 598–604.

8 Liu GT, Wei HL, Song ZY. Further studies on the protective action of biphenyl dimethyl-dicarboxylate (BDD) against experimental liver injury in mice. Acta Pharm Sin 1982; 17: 101–6.

9 Wang GX, Ben CE, Ye BK, Yang M, Gao JL. Reparative effects of biphenyl dimethyl dicarboxylate on experimental liver injury in rats with histochemical and electronmicroscopy study. Chin J Integrat Tradit Western Med 1988; 8: 158–60.

10 Liu ZY, Cui Q, Fu T, Liu GT. Inducing effect of dimethy-4,4'-dimethoxy-5,6,5',6-dimethylenedioxybipheny-2,2'-dicarboxylate (DDB) on differentiation of leukemia HL-60 cells. Natl Med J China 1996; 76: 214–7.

11 Mosmann T. Rapid colorimetric assay for cellular growth and survival: application to proliferation and cytotoxicity assays. J Immunol Methods 1983; 65: 55–63.

12 El-Fouly MH, Trosko JE, Chang CC. Scrape-loading and dye transfer: A rapid and simple technique to study gap junctional intercellular communication. Exp Cell Res 1987; 168: 422–30.

13 Tsao MS, Smith JD, Nelson KG, Grisham JW. A diploid epithelial cell line from normal adult rat liver with phenotypic properties of “oval” cells. Exp Cell Res 1984; 154: 38–52.

14 Cho JH, Cho SD, Hu H, Kim SH, Lee SK, Lee YS, *et al*. The role of ERK1/2 and p38 MAP kinase in the preventive mechanisms of mushroom phellinus linteus against the inhibition of gap junctional communication by hydrogen peroxide. Carcinogenesis 2002; 23: 1163–9.

15 Simon AM, Goodenough DA. Diverse functions of vertrbrate gap junction. Trends Cell Biol 1998; 8: 477–83.

16 Niloofar A-A, Wilhelm S, Helmut S. (-)-Epicatechin effects in rat liver epithelial cells: stimulation of gap junctional communication and counteraction of its loss due to the tumor promoter 12-O-tetradecanoylthorbol-13-acetate. Biochem Pharm 2002; 63: 2145–9.

17 Hu J, Engman L, Cotgreave IA. Redox-actine chalcogen-containing glutathione peroxidase minetics and antioxidants inhibit tumour promoter-induced downregulation of gap junctional intercellular communication between WB-F344 liver epithelial cells. Carcinogenesis 1995; 16: 1815–24.

18 Guan X, Randall GR. Gap junction endocytosis and lysosomal degradation of connexin43-P2 in WB-F344 rat liver epithelial cells treated with DDT and lindane. Carcinogenesis 1996; 17: 1791–8.

19 Ping R, Parmender PM, Randall JR. Inhibition of gap junctional intercellular communication by tumor promoters in connexin43 and connexin32-expressing liver cells: Cell specificity and role of protein kinase C. Carcinogenesis 1998; 19: 169–75.

20 Kang KS, Kang BC, Lee BJ, Che JH, Li GX, Trosko JE, *et al*. Preventive effent of epicatechin and ginsenoside Rb2 on the inhibition of gap junctionsl intercellular communication by TPA and H_2O_2. Cancer Lett 2000; 152: 97–106.

Acta Pharmacologica Sinica 2005 Nov; 26 (11): 1345–1351

Blackwell Publishing

Full-length article

Effects of specific interleukin-1β-converting enzyme inhibitor on ischemic acute renal failure in murine models[1]

Hua-feng LIU[2], Dong LIANG, Li-ming WANG, Nan ZHOU, Cui-wei YAO, Tao HONG, De-shen TANG, Xiao-wen CHEN

Institute of Nephrology, Affiliated Hospital of Guangdong Medical College, Zhanjiang 524001, China

Key words

kidney failure; ischemia; caspase-1; interleukin-1β-converting enzyme inhibitor; interleukin-1; interleukin-18; interferon type II

[1] Project supported by the Fatal Diseases Prevention and Cure Program of Zhanjiang (2003).
[2] Correspondence to Prof Hua-feng LIU.
Phn 86-759-238-7164.
E-mail hf-liu@263.net

Received 2005-05-19
Accepted 2005-07-01

doi: 10.1111/j.1745-7254.2005.00200.x

Abstract

Aim: To study the effect of selective interleukin-1β-converting enzyme (ICE, caspase-1) inhibitor on ischemic acute renal failure (ARF). **Methods:** Mouse models of ischemic ARF were treated with the specific ICE inhibitor AC-YVAD-CMK. A renal function assay and renal morphological studies were employed to estimate the renal protective effect of AC-YVAD-CMK. The survival rate of mouse models was also analyzed by a time series test. Furthermore, renal ICE activity, mature interleukin-18 (IL-18) protein expression and interferon-γ (IFN-γ) mRNA expression were also detected by fluorescent enzyme-linked immunosorbent assay (ELISA), ELISA, and semi-quantitative reverse transcription-polymerase chain reaction, respectively. **Results:** The levels of blood urea nitrogen (BUN) and serum creatinine (Scr) increased remarkably in the model controls compared with the sham-operated groups ($P<0.01$). Typical renal tubular necrosis was found in the model controls. Renal ICE activity, mature IL-18 protein expression, and IFN-γ mRNA expression were also increased significantly in the model controls compared with the sham-operated groups. The levels of BUN and Scr in the AC-YVAD-CMK therapy group were decreased significantly compared with the untreated model controls ($P<0.01$). Renal tubulointerstitial lesion was also attenuated significantly ($P<0.05$). AC-YVAD-CMK therapy alleviated the clinical features of ARF, and increased the survival rate ($P<0.01$). Furthermore, AC-YVAD-CMK therapy also decreased ICE activity, mature IL-18 protein expression, and IFN-γ mRNA expression in renal tissue ($P<0.05$). **Conclusion:** The selective ICE inhibitor AC-YVAD-CMK can effectively protect the kidney from acute ischemic lesions. This protective effect is associated with decreased renal ICE activity and suppressed IL-18 maturation and IFN-γ mRNA transcription.

Introduction

Acute renal failure (ARF) is a clinical syndrome with high morbidity and mortality. The incidence of ischemic ARF has been rising rapidly, especially with the rapid development of various difficult surgical operations and kidney transplantation[1,2]. Unfortunately, up to now, there was no really effective medicine available to treat this disease.

Several recent studies have reported that, aside from tubular injury directly caused by renal abnormal hemodynamic states, the recruitment and activation of numerous inflammatory cells after ischemia, and immune inflammatory responses mediated by the expression and secretion of inflammatory cytokines are the main causes of ischemic acute renal injury[3–5]. Among the various cytokines produced during renal ischemia, interleukin-18 (IL-18), interleukin-1β (IL-1β) and interferon-gamma (IFN-γ), a group of proinflammatory cytokines with closely related function, play an important role in the inflammatory reaction and renal tubulointerstitial impairment[6–9]. Other studies have reported that applying antibodies or soluble receptors to block the roles of these cytokines can alleviate ischemic ARF[10,11]. It has been demonstrated that both IL-1β and IL-18 are members of the IL-1 family, which can be activated by interleukin-1β-

converting enzyme (ICE) via cleaved precursor peptide, and furthermore, that IL-18 is the strongest inducing factor of IFN-γ[12,13]. We therefore postulated that it would be more effective to protect the kidney from acute ischemic injury by regulating the whole cytokine network, including IL-1β, IL-18, and IFN-γ, with selective ICE inhibitors, instead of only blocking any one of the cytokines using antibodies or soluble receptors. More significantly, several kinds of ICE inhibitors with simple structure and low antigenicity have been synthesized by chemical methods. The inhibitors are superior to cytokine antibodies and soluble receptors, which are difficult to produce, expensive, hypersensitive and require injection.

The present study aimed at exploring the role of selective ICE inhibitors in preventing the kidney from ischemic ARF by the combined inhibition of IL-1β, IL-18, and IFN-γ in mouse models of ischemic ARF.

Materials and methods

Materials All reagents were obtained from Sigma (St Louis, MO, USA), unless otherwise indicated.

Ischemic ARF model induction Male Kunming mice (SPF grade, Experimental Animal Center of Guangdong Medical College, Zhanjiang, China) weighing 22.1±1.3 g (20 g–25 g) were used. After being anesthetized with an injection of 0.3% sodium pentobarbital (5 mL/kg–10 mL/kg, ip), an abdominal mid-line incision was made and the renal pedicles were clamped bilaterally for 45 min with non-traumatic microaneurysm clamps. Restoration of blood flow was confirmed when the kidneys returned to their original color after the clamps were removed. Afterward, the abdomen was closed and the mice were allowed to recover. The mice were observed for 2 h after the operation was finished. A model was considered to be developed successfully if the animal's behavior returned to normal. Those that failed to return to normal behavior after operation or those in which any 1 of the kidneys failed to return to normal color after the clamps were removed were regarded as unsuccessful models and were removed from the experiment. The sham-operated group consisted of the same surgical procedure except that clamps were not applied.

Experimental groups Animals were kept in a clean environment at 24 °C–29 °C with free access to standard food and water after model induction. The study was composed of 3 parts as follows. **Experiment I:** Thirty-nine mice were distributed randomly into the sham-operated group, the model control group or the therapy group. After post-operative elimination, these groups contained 13, 13, and 11 mice, respectively. The therapy group was administered AC-YVAD-CMK (6.25 mg/kg, ip; Calbiochem, Darmstadt, Germany), which was dissolved in 2% Me_2SO saline, at 2 h, 8 h, and 16 h after surgery. The other 2 groups received the vehicle; an equal volume of 2% Me_2SO saline at the same times as the therapy group. All of the mice were killed at 24 h after surgery. **Experiment II:** Forty-five mice were enrolled in this part of the experiment and were also distributed randomly into 3 groups as in Experiment I. Each group contained 13 mice after model construction and elimination. The mice underwent similar procedures as those in Experiment I, except that either AC-YVAD-CMK or the vehicle were administered to the mice at 2 h, 8 h, 14 h, 20 h, 28 h, and 36 h, and the mice were killed at 48 h after surgery. **Experiment III:** Thirty-nine mice were distributed randomly into the 3 groups as in Experiment I and Experiment II, and each group contained 12 mice. AC-YVAD-CMK or the vehicle was administered in the same way as in Experiment II, but the animals were not killed. Their clinical features were observed and recorded twice per day for 14 d after surgery.

Sample collection and pretreatment Blood samples were obtained via orbital cavity after removing eyeballs. The blood samples were then centrifuged to separate the serum. The kidneys were collected, each of which was divided into 4 equal sections. One section was fixed in 10% neutral formalin solution while the others were frozen immediately in liquid nitrogen and preserved at -72 °C until use.

Blood biochemical parameters assay The levels of blood urea nitrogen (BUN) and serum creatinine (Scr) were measured using an automatic biochemical analyzer (Beckman Instruments, Fullerton, CA, USA).

Renal histological examination The 4% paraformaldehyde-fixed and paraffin-embedded kidney samples were sectioned at 3 μm and stained with hematoxylin-eosin (HE) and periodic acid-Schiff (PAS) using standard methods. Histological examinations were carried out in a single blinded fashion. Histological changes due to acute renal tubulointerstitial injury were quantitated using the method of Paller *et al*[14]. Five fields (×200) were reviewed for each slide. The scores included: diffuse tubular epithelial cell flattening and tubular lumen dilatation (1 point), lesion of brush border (1 point), loss of brush border (2 points), cell membrane bleb formation (1 point), cytoplasmic vacuolization (1 point), interstitial edema (1 point), necrotic cells in tubular lumen but no cast formation (1 point), and casts or cell pieces formation (2 points). Higher scores represented more severe damage.

Renal ICE activity assay Renal ICE activity was measured using a ICE fluorescent assay kit (Calbiochem),

according to the manufacture's protocols. Briefly, 1 mL of tissue lytic buffer (containing 1×phosphate-buffered saline, 1% Nonidet P-40, 0.5% sodium deoxycholate, 0.1% sodium dodecylsulfate, 10 μg/mL phenylmethylsulfonylfluoride and 10 μL/mL Aprotinin) was added to approximately 100 mg renal tissue. The renal tissues were then homogenized artificially and incubated on ice for 1 h. The tissue lysate was then centrifuged at 4 °C at 12 000×*g* for 5 min. The supernatant was collected in a separate microfuge tube and stored immediately at -72 °C until use. The protein concentration of each tissue lysate was measured by spectrophotometry after being dyed with Coomassie brilliant blue G250. Supernatants were adjusted to a final protein concentration of 150 μg/μL–200 μg/μL. The enzymatic activity was measured as follows: 50 μL of 2×ICE assay buffer, 5 μL of substrate (1 mmol/L YVAD-AFC) and 50 μL protein solution were added to a 96-well polyvinyl plate. The reaction system, kept in darkness, was incubated at 37 °C for 90 min. The absorbance of each well was then read by a DA620 fluorescence microplate reader (Bio-Tek, Winooski, Vermont, USA) at an excitation wavelength of 380 nm and an emission wavelength of 460 nm. Tissue lytic buffer was replaced with tissue lysate as a negative control. A ICE standard curve was determined for the experiment at the same time. ICE activity was expressed as units per mg protein.

Assay for expression of mature renal IL-18 protein The level of mature IL-18 protein expressed in renal tissue was measured using a mouse IL-18 enzyme-linked immunosorbent assay kit (MBL, Nagoga, Japan), which was only specific for mature IL-18. Renal tissue total protein was extracted as described above. The assay procedures strictly followed the manufacturer's instructions. Every sample was measured by double parallel wells, and was remeasured when the intra-error was over 10%.

Assay for renal IFN-γ mRNA expression Approximately 100 mg of frozen kidney sample was homogenized in a muller by adding liquid nitrogen to crisp the tissue. Total RNA was extracted from kidney tissue using TRIzol reagent (Invitrogen, Carlsbad, CA, USA). cDNA was synthesized with the SuperScription™ First-Strand Synthesis System (Invitrogen) according to the manufacturer's protocol. The primers used for the IFN-γ polymerase chain reaction (PCR) were as follows: 5'-AGG AAC TGG CAA AAG GAT GGTG-3' (sense), and 5'-GTG CTG GCA GAA TTA TTC TTA TTG-3' (anti-sense), and the product was 353 bp. The primers used for the glyceraldehyde-3-phosphate dehydrogenase (GAPDH) PCR were as follows: 5'-AAC GAC CCC TTC ATT GAC-3' (sense), and 5'-TCC ACG ACA TAC TCA GCAC-3' (anti-sense), and the product was 191 bp. Primers were synthesized and purified by Shanghai Biological Engineering (Shanghai, China). The PCR-amplified system included 1.2 μL of 25 mmol/L $MgCl_2$, 0.4 μL of 10 mmol/L dNTP mix, 0.8 μL of 5 μmol/L sense and anti-sense primers, 2 U of *Taq* DNA polymerase, 1 μL of cDNA and sterile purified water to 20 μL. The IFN-γ PCR was carried out in a thermal cycler (Eppendorf, New York city, New York, USA) at 95 °C for 60 s, 58 °C for 60 s, and 72 °C for 60 s. The GAPDH PCR was carried out at 94 °C for 60 s, 58 °C for 60 s, and 72 °C for 60 s. IFN-γ was amplified for 35 cycles and GAPDH for 28 cycles. Equal volumes of each PCR product were loaded into gels and electrophoresis was carried out. The ethidium bromide-stained gels were analyzed semiquantitatively using a gel imaging system (UVP, Cambridge, UK). The quantity of IFN-γ expression in every renal tissue was the integral absorbency of the IFN-γ amplification band divided into GAPDH amplification band.

Statistical analysis SPSS version 11.0 software was used to obtain data statistics. Measurement data were expressed as mean±SD. One-way ANOVA was used for statistical analysis among multiple groups. Kaplan-Meier was used for statistical analysis of survival rates among multiple groups.

Results

Effect of AC-YVAD-CMK on renal function in ischemic ARF mice The levels of Scr and BUN in model controls were increased significantly compared with sham-operated groups both in experiment I and experiment II. The levels of Scr decreased significantly but that of BUN did not decrease significantly in the AC-YVAD-CMK therapy group compared with the vehicle-treated group in experiment I; the levels of both Scr and BUN decreased significantly in the therapy group in experiment II (Table 1).

Effect of AC-YVAD-CMK on renal tubulointerstitial injury in ischemic ARF mice Kidneys from sham-operated groups were normal in form and rubicund color while those from model control groups were swollen with pale cortex and congested medulla. These anatomical changes were also observed but were significantly less in kidneys from AC-YVAD-CMK therapy groups. Renal tissues from sham-operated groups had a basically normal microcosmic structure except for focal vacuolation of tubular epithelial cells (TECs). Renal tissues from model control groups showed severe damage in microcosmic structure, including extensive TECs vacuolation, scattered TECs brush border flatting, shrinkage and loss as well as focal TECs nucleus nakedness and necrosis. Dilated lumens and cast formation were also found in parts of the tubules. Interstitial inflammatory cell

Table 1. Effect of AC-YVAD-CMK on renal function in an ischemic acute renal failure model. Mean±SD. $^{b}P<0.05$, $^{c}P<0.01$ *vs* sham-operated group. $^{e}P<0.05$, $^{f}P<0.01$ *vs* model control group.

Group	Experiment I			Experiment II		
	n	Scr/μmol·L^{-1}	BUN/mmol·L^{-1}	*n*	Scr/μmol·L^{-1}	BUN/mmol·L^{-1}
Sham	13	27.8±5.3	8.9±1.3	13	13.5±2.4	7.4±1.6
Model	13	53.5±18.8^{b}	13.9±3.0^{b}	13	41.7±5.9^{c}	21.0±4.1^{c}
AC-YVAD-CMK	11	35.1±8.2^{e}	11.5±2.2	13	34.8±5.1^{f}	14.2±2.9^{f}

infiltration was also found, especially with neutrophil cells. Renal tissue damage was relieved significantly in AC-YVAD-CMK therapy groups. The main histological changes included extensive TECs vacuolation, focal TECs nucleus nakedness and very rare TECs necrosis. The basement membranes were basically integrated; casts were seldom. Inflammatory infiltration in interstitial areas was slight. The mean histological score for the kidney tissue of model control groups was significantly higher than that of the sham-operated groups, both in experiment I and experiment II. The mean score for the AC-YVAD-CMK therapy groups was much lower than that for the vehicle-treated groups, again in both experiment I and experiment II (Figure 1, Table 2).

Effect of AC-YVAD-CMK on survival rate in ischemic ARF mice In Experiment III, Sham-operated groups had no apparent abnormal appearance, activity or ingestion during the whole observation period, and all of them had survived at the end of observation. Model controls were cachexia in different extents, with reduced activity and ingestion. Anasarca and dyspnea occurred gradually. The survival rate was 83.3% on d 7, 58.3% on d 10, and only 8.3% on d 14. However, the clinical features were relatively improved in the AC-YVAD-CMK therapy group during the period of observation compared with model controls. The survival rate was 100.0% on d 7, 91.6% on d 10, and 25.0% on d 14.

Table 2. Effect of AC-YVAD-CMK on renal tubulointerstitial injuries in an ischemic acute renal failure model. Mean±SD. $^{b}P<0.05$, $^{c}P<0.01$ *vs* sham-operated group. $^{e}P<0.05$ *vs* model control group.

Group	Experiment I		Experiment II	
	n	Score for renal tubulointerstitial damage	*n*	Score for renal tubulointerstitial damage
Sham	13	13.5±5.4	13	5.6±1.4
Model	13	22.6±4.6^{b}	13	20.9±4.9^{c}
AC-YVAD-CMK	11	17.0±5.3^{e}	13	16.6±2.2^{e}

All together, the 2-week accumulated survival rate in the AC-YVAD-CMK therapy group was higher than that of the vehicle-treated group by survival analysis for time ($P<0.01$, Figure 2).

Effect of AC-YVAD-CMK on renal ICE activity in ischemia ARF mice ICE activity in renal tissue from model controls was 347.0±97.5 U/mg protein in experiment I and 536.1±43.0 U/mg protein in experiment II, both much higher than that for the sham-operated groups, which was 239.5±56.5 U/mg protein in experiment I and 237.2±27.4 U/mg protein in experiment II. The ICE activity for the therapy group was 314.0±56.0 U/mg protein in experiment I and 412.2±

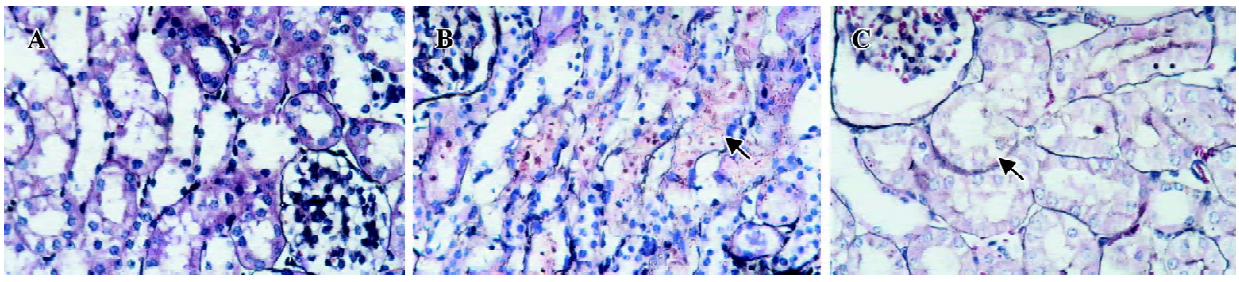

Figure 1. Effect of AC-YVAD-CMK on renal tubulointerstitial injuries in an ischemic acute renal failure model (experiment II). Periodic acid-Schiff stain, ×400. (A) Sham-operated group, basically normal structure of renal tissues. (B) Model control group, tubular epithelial cell (TEC) necrosis and detachment (arrow). (C) AC-YVAD-CMK therapy group, TEC vacuolation (arrow).

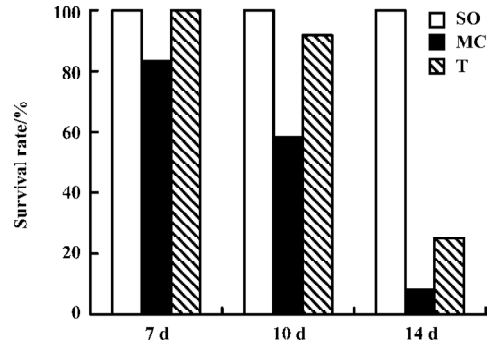

Figure 2. Effect of AC-YVAD-CMK on survival rate in an ischemic acute renal failure model. SO, sham-operated groups; MC, model control groups; T, AC-YVAD-CMK therapy groups. n=12. Mean±SD. ^{c}P<0.01 *vs* MC.

12.5 U/mg protein in experiment II. ICE activity was decreased significantly compared with the model control group in experiment II, but not in experiment I (Figure 3).

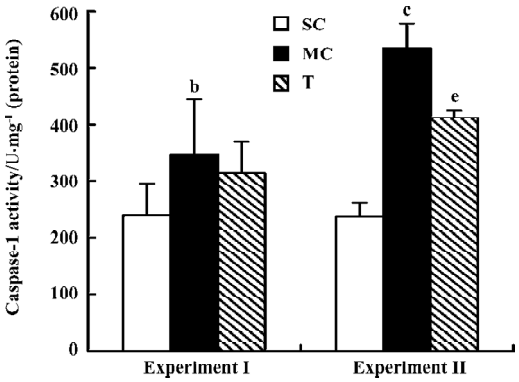

Figure 3. Effect of AC-YVAD-CMK on renal ICE (caspase-1) activity in ischemic acute renal failure mice. SO, sham-operated groups; MC, model control groups; T, AC-YVAD-CMK therapy groups. n=11–13. Mean±SD. ^{b}P<0.05, ^{c}P<0.01 *vs* SO. ^{e}P<0.05 *vs* MC.

Effect of AC-YVAD-CMK on expression of renal mature IL-18 protein in ischemia ARF mice Interleukin-18 expression in renal tissue from model controls was 28.9±11.6 pg/mg protein in experiment I and 15.2±9.4 pg/mg protein in experiment II, both much higher than for the sham-operated groups, which was 13.1±3.5 pg/mg protein in experiment I and 7.3±3.5 pg/mg protein in experiment II. Mature IL-18 protein expression was 16.7±4.8 pg/mg protein in experiment I and 6.9±3.5 pg/mg protein in experiment II in AC-YVAD-CMK therapy groups; both were decreased significantly compared with model control groups (Figure 4).

Effect of AC-YVAD-CMK on renal IFN-γ mRNA expression in ischemia ARF mice Model controls had a significantly higher expression of IFN-γ mRNA in renal tissues than

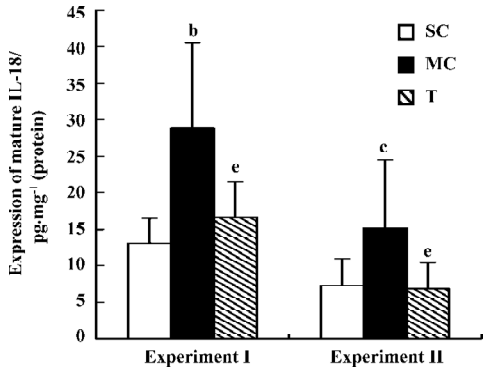

Figure 4. Effect of AC-YVAD-CMK on renal mature interleukin-18 (IL-18) expression in ischemic acute renal failure mice. SO, sham-operated groups; MC, model control groups; T, AC-YVAD-CMK therapy groups. n=11–13. Mean±SD. ^{b}P<0.05, ^{c}P<0.01 *vs* SO. ^{e}P<0.05, ^{f}P<0.01 *vs* MC.

sham-operated groups. The expression level in the AC-YVAD-CMK therapy group was decreased significantly compared with the vehicle-treated group (Table 3, Figure 5).

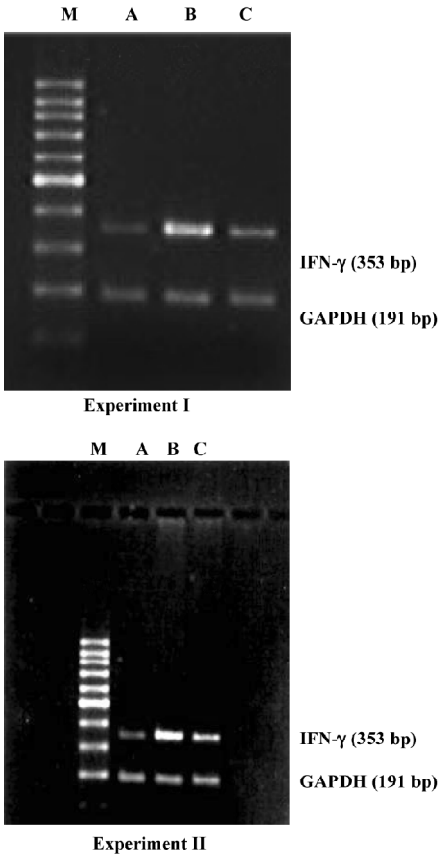

Figure 5. Effect of AC-YVAD-CMK on renal interferon-γ (IFN-γ) mRNA expression in ischemic acute renal failure mice. M, marker; A, sham-operated groups; B, model control groups; C, AC-YVAD-CMK therapy groups. GAPDH, glyceraldehyde-3-phosphate dehydrogenase.

Table 3. Effect of AC-YVAD-CMK on renal interferon-γ (IFN-γ) mRNA expression in ischemic acute renal failure mice. Mean±SD. $^{b}P<0.05$ *vs* sham-operated group. $^{e}P<0.05$ *vs* model control groups.

Group	Experiment I		Experiment II	
	n	IFN-γ mRNA/ GAPDH mRNA	*n*	IFN-γ mRNA/ GAPDH mRNA
Sham	13	0.53±0.17	13	0.44±0.12
Model	13	1.15±0.28^{b}	13	1.06±0.24^{b}
AC-YVAD-CMK	11	0.65±0.21^{e}	13	0.74±0.18^{e}

Discussion

The present study developed a successful ischemic ARF model according to the dynamic changes of the kidneys color during operation and the changes in renal function and morphological structure after operation. However, we also found that renal function parameters, especially the level of Scr, and renal histological scores in experiment I were higher than those in experiment II in the sham-operated group. This phenomenon may be caused by muscle lesion during peritoneotomy and incomple recovery from stress after anesthesia and surgical operation. The difference might also result from the variation between experiments at different times.

Based on a successful mouse model of ischemic ARF, we first studied the renal protective effects of AC-YVAD-CMK dynamically using a renal function assay and renal morphological study at different times. The results showed that renal function and morphological impairment were significantly improved in the ischemic ARF mouse model after being treated with specific ICE inhibitor. The findings demonstrate that a specific ICE inhibitor can exert remarkable renal-protective effects against acute ischemic lesion.

However, the ultimate objective of ischemic ARF therapy is to increase patient survival from the disease. In the past decade, different kinds of medicines, such as prostaglandins, "renal-dose" dopamine and atrial natriuretic factor, have been tried to treat patients with ischemic ARF and these animal models. Although some of these agents have improved renal function, urine output and even renal histological impairment in patients and animal models, few studies have demonstrated that these medicines can reduced the mortality of the disease[15–18]. In the present study, we found that applying this specific ICE inhibitor in the initial term of the disease remarkably increased the survival rate in this animal model. If it were applied continually for a longer period of time, the model's survival rate might be further improved. Thus, we speculate that this medicine might be superior in some way to traditional medicines with regard to protection against ischemic ARF.

Caspases are a group of protein-cleaving enzymes, and play an important role in cell apoptosis and inflammatory responses. ICE, also known as interleukin-1β-converting enzyme, is a member of the inflammatory group in the caspase family. It is a key initiative factor and an important inducer of inflammatory chain responses secondary to an organ's ischemic impairment[19]. Kaushal *et al*[20] reported that expression of the ICE gene and protein were up-regulated in an ischemic ARF rat model. In the present study, ICE activity was also increased in renal tissue of an ischemic ARF mouse model. All of the evidence above strongly revealed that gene transcription, protein synthesis and enzyme activation of ICE were up-regulated during the progression of ischemic ARF. Melnikov *et al*[11] reported that renal tubular impairment and renal interstitial inflammatory infiltration were much slighter in ICE gene knock-out mice than in wild-type mice after renal ischemia reperfusion. The present study also found that ICE inhibitor alleviated the impairment of renal tissue and down-regulated the activity of renal ICE. We conclude that excessive ICE activity prompts the development of ischemic ARF, and selectively inhibiting sham-operated groups ICE activity can exert renal-protective effects on the disease. ICE activity was not suppressed to normal levels by the dose of inhibitor used in the present study. We presume that a better protective effect would be achieved if a larger dose were administered.

Precursors of IL-18 and IL-1β are the main substrates of ICE[12,13], and many reports have proved these 2 cytokines can prompt acute ischemic organ impairment[21–23]. Recent reports seem to emphasize the role of IL-18. Mice with ischemic ARF have increased renal mature IL-18 expression, and IL-18 antiserum can significantly improve the state of the illness[11,22]. It was reported recently by Parikh *et al*[7] that urinary IL-18 level was increased almost 50-fold in patients with ARF, and the urinary IL-18 level in patients transplanted with corpse kidney was 10-fold that in patients transplanted with living kidney. These studies prove that IL-18 plays an important role in prompting renal impairment during acute ischemia. Does ICE mediate the acute renal impairment through prompting activation of IL-18 and IL-1β? In the present study we detected the expression of mature IL-18 in renal tissue. The results showed that expression of activated IL-18 increased remarkably in model controls and decreased significantly after the models were treated with ICE inhibitor, which demonstrates that the excessive activation of IL-18 resulting from ICE hyperactivity is one of the

main mechanisms causing renal tissue impairment. We infer that IL-1β was also over-activated by ICE in this model. Specific ICE inhibitor indirectly inhibits activation of IL-18 and IL-1β through inhibiting the activity of ICE, and thereby protects against acute ischemic ARF.

Because IL-18 is the strongest IFN-γ inducer[13], we then detected the expression of the IFN-γ gene in renal tissue. We found that renal IFN-γ mRNA expression was up-regulated significantly in model controls, and decreased after the mice were treated with specific ICE inhibitor. The results again demonstrate that IFN-γ plays an important role in ischemic ARF, and ICE inhibitor suppresses the expression of IFN-γ mRNA through inhibiting activation of IL-18, thus further protecting against ischemic ARF.

In summary, the present study demonstrates that specific ICE inhibitors are promising agents in the treatment of ischemic ARF. It exerts renal-protective effects by inhibiting strong ICE activity, thereby regulating the activation of IL-18 and IL-1β, and further regulating abnormal expression of IFN-γ.

References

1 Carmichael P, Carmichael AR. Acute renal failure in the surgical setting. ANZ J Surg 2003; 73: 144–53.

2 Wiecek A, Nowicki M, Kokot F, Ritz E. Acute failure of the transplanted kidney – pathophysiology, diagnosis and prevention. Ann Transplant 1996; 1: 5–9.

3 Ysebaert DK, De Greef KE, De Beuf A, Van Rompay AR, Vercauteren S, Persy VP, *et al*. T cells as mediators in renal ischemia/reperfusion injury. Kidney Int 2004; 66: 491–6.

4 Bonventre JV, Zuk A. Ischemic acute renal failure: an inflammatory disease? Kidney Int 2004; 66: 480–5.

5 Friedewald JJ, Rabb H. Inflammatory cells in ischemic acute renal failure. Kidney Int 2004; 66: 486–91.

6 Burne-Taney MJ, Kofler J, Yokota N, Weisfeldt M, Traystman RJ, Rabb H, *et al*. Acute renal failure after whole body ischemia is characterized by inflammation and T cell-mediated injury. Am J Physiol Renal Physiol 2003; 285: F87–94.

7 Parikh CR, Jani A, Melnikov VY, Faubel S, Edelstein CL. Urinary interleukin-18 is a marker of human acute tubular necrosis. Am J Kidney Dis 2004; 43: 405–14.

8 Burne MJ, Daniels F, El Ghandour A, Mauiyyedi S, Colvin RB, O'Donnell MP, *et al*. Identification of the CD4(+) T cell as a major pathogenic factor in ischemic acute renal failure. J Clin Invest 2001; 108: 1283–90.

9 Daemen MA, van't Veer C, Wolfs TG, Buurman WA. Ischemia/reperfusion-induced IFN-gamma up-regulation: involvement of IL-12 and IL-18. J Immunol 1999; 162: 5506–10.

10 Kitada H, Suitani A, Yamamoto H, Otomo N, Okabe Y, Inoue S, *et al*. Attenuation of renal ischemia-reperfusion injury by FR167653 in dogs. Surgery 2002; 131: 654–9.

11 Melnikov VY, Faubel S, Siegmund B, Lucia MS, Ljubanovic D, Edelstein CL, *et al*. Neutrophil-independent mechanisms of caspase-1 and IL-18-mediated ischemic acute tubular necrosis in mice. J Clin Invest 2002; 110: 1083–91.

12 Dinarello CA. Interleukin-1 beta, interleukin-18, and the interleukin-1 beta converting enzyme. Ann NY Acad Sci 1998; 856: 1–11.

13 Okamura H, Tsutsi H, Komatsu T, Yutsudo M, Hakura A, Tanimoto T, *et al*. Cloning of a new cytokine that induces IFN-gamma production by T cells. Nature 1995; 378: 88–91.

14 Paller MS, Hoidal JR, Ferris TF. Oxygen free radicals in ischemic acute renal failure in the rat. J Clin Invest 1984; 74: 1156–64.

15 Denton MD, Chertow GM, Brady HR. 'Renal-dose' dopamine for the treatment of acute renal failure: scientific rationale, experimental studies and clinical trials. Kidney Int 1996; 50: 4–14.

16 Alkhunaizi AM, Schrier RW. Management of acute renal failure: new perspectives. Am J Kidney Dis 1996; 28: 315–28.

17 Mitaka C, Hirata Y, Habuka K, Narumi Y, Yokoyama K, Makita K, *et al*. Atrial natriuretic peptide infusion improves ischemic renal failure after suprarenal abdominal aortic cross-clamping in dogs. Crit Care Med 2003; 31: 2205–10.

18 Chatterjee PK, Patel NS, Cuzzocrea S, Brown PA, Stewart KN, Mota-Filipe H, *et al*. The cyclopentenone prostaglandin 15-deoxy-Delta(12,14)-prostaglandin J2 ameliorates ischemic acute renal failure. Cardiovasc Res 2004; 61: 630–43.

19 Tilney NL, Guttmann RD. Effects of initial ischemia/reperfusion injury on the transplant kidney. J Transplant 1997; 64: 945–7.

20 Kaushal GP, Singh AB, Shah SV. Identification of gene family of caspases in rat kidney and altered expression in ischemia–reperfusion injury. Am J Physiol 1998; 274: 587–95.

21 Haq M, Norman J, Saba SR, Ramirez G, Rabb H. Role of IL-1 in renal ischemic reperfusion injury. J Am Soc Nephrol 1998; 9: 614–9.

22 Melnikov VY, Ecder T, Fantuzzi G, Siegmund B, Lucia MS, Dinarello CA, *et al*. Impaired IL-18 processing protects caspase-1 deficient mice from ischemic acute renal failure. J Clin Invest 2001; 107: 1145–52.

23 Hedtjarn M, Leverin AL, Eriksson K, Blomgren K, Mallard C, Hagberg H, *et al*. Interleukin-18 involvement in hypoxic-ischemic brain injury. J Neurosci 2002; 22: 5910–9.

Acta Pharmacologica Sinica 2005 Nov; 26 (11): 1352–1358

Blackwell Publishing

Full-length article

A novel artemisinin derivative, 3-(12-β-artemisininoxy) phenoxyl succinic acid (SM735), mediates immunosuppressive effects *in vitro* and *in vivo*[1]

Wen-liang ZHOU[2], Jin-ming WU[3], Qing-li WU[2], Jun-xia WANG[2], Yu ZHOU[2], Ru ZHOU[2], Pei-lan HE[2], Xiao-yu LI[2], Yi-fu YANG[2], Yu ZHANG[3], Ying LI[3], Jian-ping ZUO[2,4]

Laboratories of [2]Immunopharmacology and [3]Synthetic Chemistry, Graduate School of the Chinese Academy of Sciences, State Key Laboratory of Drug Research, Shanghai Institute of Materia Medica, Shanghai Institutes for Biological Sciences, Chinese Academy of Sciences, Shanghai 201203, China

Key words

artemisinin; non-steroidal anti-inflammatory agents; SM735; immuno-suppressive activity

[1] Project supported by the Knowledge Innovation Program of the Chinese Academy of Sciences (No KSCX2-SW-202).
[4] Correspondence to Dr Jian-ping ZUO.
Phn/Fax 86-21-5080-6701.
E-mail jpzuo@mail.shcnc.ac.cn

Received 2005-08-01
Accepted 2005-08-28

doi: 10.1111/j.1745-7254.2005.00232.x

Abstract

Aim: To study the immunosuppressive activity of SM735 {[3-(12-β-artemisininoxy)] phenoxyl succinic acid}, a synthetic artemisinin derivative with nonsteroidal anti-inflammatory drug structure, with the aim of finding potential immunosuppressive agents. **Methods:** Concanavalin A (ConA), lipopolysaccharide (LPS), and mixed lymphocyte reaction (MLR), were used to induce the proliferation of splenocytes, and [^{3}H]-thymidine incorporation was used to evaluate the proliferation of splenocytes. Cytokine production was promoted with ConA, LPS, or PMA plus ionomycin, and was detected with the enzyme-linked immunosorbent assay. Dinitrofluorobenzene (DNFB) and sheep red blood cells (SRBC) were used to induce delayed-type hypersensitivity and quantitative hemolysis of SRBC (QHS) mouse models, as criteria for the evaluation of *in vivo* immune activity. **Results:** SM735 strongly inhibited the proliferation of splenocytes induced by ConA, LPS, or MLR, with IC_{50} values of 0.33 μmol/L, 0.27 μmol/L, and 0.51 μmol/L, respectively. When compared with a CC_{50} value of 53.1 μmol/L, SM735 had a favorable safety range. SM735 dose-dependently inhibited proinflammatory cytokine production [including interleukins (IL)-12, interferon (IFN)-γ and IL-6] induced by LPS or PMA plus ionomycin. Upon ConA stimulation, SM735 suppressed IFN-γ in a dose-dependent manner, but did not affect IL-2 secretion. SM735 also strongly suppressed both T-cell-mediated delayed-type hypersensitivity (DTH) and B-cell-mediated QHS reactions. **Conclusion:** SM735 had strong immunosuppressive activity *in vitro* and *in vivo*, suggesting a potential role for SM735 as an immunosuppressive agent, and established the groundwork for further research on SM735.

Introduction

Artemisinin is extracted from the herb *Artemisia annua* L, and various forms of the drug are used as anti-malarial agents[1,2]. Artemisinin is a potent anti-malarial agent with low toxicity, and its derivatives have improved efficacy in malaria treatment relative to artemisinin itself. In addition to anti-malarial effects, anti-lymphocytic effects have also been reported for artemisinin derivatives[3,4]. Since the 1980s, the immunosuppressive actions of artemisinin and its derivatives have been studied in China. Artemisinin derivatives have also been tested for the treatment of dermatoses such as photoallergic skin diseases and systemic lupus erythematosus, and promising results have been reported[5–7].

Researchers have demonstrated that the anti-malarial activity of artemisinin and its derivatives is associated with their endoperoxides[8,9]. When catalyzed by the ferrous ion in heme, cleavage of peroxy bonds produces free radicals and thus causes damage to malarial DNA and proteins. However, the underlying mechanism of the anti-lymphocytic

action of artemisinin and its derivatives is poorly understood.

Despite their anti-lymphocytic mechanisms being poorly understood, we hypothesized that artemisinin derivatives might be promising immunosuppressive agents, because some clinical studies have shown that they are effective in the treatment of immune dysfunction diseases. When considering an optimal molecular structure (higher efficacy and lower toxicity) for artemisinin derivatives for use as immunosuppressants, we noticed that nonsteroidal anti-inflammatory drugs (NSAIDs) remained the first-line therapy for most people with arthritis and other inflammatory diseases. Compared with other anti-inflammatory or immunosuppressive drugs such as steroids and cyclosporine, the molecular structures of NSAIDs are relatively simple and easy to synthesize. In addition, NSAIDs have few side effects, and a low level of toxicity, which are clinically desirable features. Given the relevance of the structure of NSAIDs to their immunosuppressive activity, we became interested in combining artemisinin and NSAIDs to develop a new class of immunosuppressive agents. Therefore, we synthesized and studied more than 100 different artemisinin derivatives. As a result of this screening program and subsequent medicinal chemistry studies, we obtained some derivatives that have significant immunosuppressive activity. Previous studies indicated that SM735 ([3-(12-β-artemisininoxy)]phenoxyl succinic acid, $C_{25}H_{32}O_9 \cdot 1/2H_2O$, MW: 485.5, Figure 1) is a representative compound, with markedly lower toxicity and higher immunosuppressive activity than artemisinin[10]. Here, we further investigate its immunological characteristics both *in vitro* and *in vivo*.

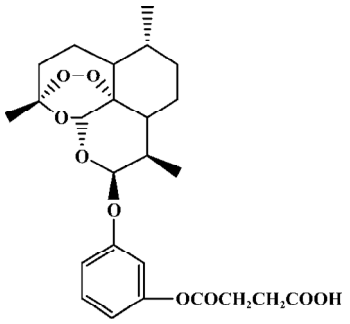

Figure 1. Chemical structure of 3-(12-β-artemisininoxy) phenoxyl succinic acid (SM735).

The discovery of cyclosporine (cyclosporin A; CsA) and its successful utilization in organ transplantation was a milestone in clinical transplantation. CsA has produced a new era in transplantation in terms of both efficiency and quality of life for patients. In addition, research into the mechanisms by which CsA acts has been rewarding in that we now have a better understanding of the mechanisms leading to T lymphocyte activation[11,12]. Recently, Noori *et al* reported that the immunosuppressive activity of artemisinin was even greater than that of CsA, as indicated by both *in vivo* and *in vitro* studies[13]. Therefore, in the present study, we demonstrate that SM735 has strong immunosuppressive effects *in vitro* and *in vivo*, and explore its possible mechanism of action.

Materials and methods

Reagents Concanavalin A, lipopolysaccharide (*Escherichia coli* 055:B5), ionomycin, phorbol 12-myristate 13-acetate (PMA), 3-[4,5-dimethylthylthiazol-2-yl]-2,5-diphenyl-tetrazolium bromide (MTT), and 3,3',5,5'-tetramethylbenzidine were purchased from Sigma (St Louis, MO, USA). Mitomycin-C was purchased from Kyowa Hakko (Tokyo, Japan). RPMI-1640 and fetal bovine serum (FBS) was purchased from Gibco (Life Technology, NY, USA). 1-Fluoro-2, 4-dinitrobenzene (DNFB) was purchased from Merck (Hong Kong, China). Mouse enzyme-linked immunosorbent assay (ELISA) kits of interleukin (IL)-2, IL-12p40, interferon (IFN)-γ and IL-6 were purchased from Pharmingen (San Diego, CA, USA).

Cyclosporine (Sandimmun) was purchased from Novartis Pharma AG, Switzerland. Cyclophosphamide was purchased from Hualian Pharma (Shanghai, China). SM735 [3-(12-β-artemisininoxy)phenoxyl succinic acid] was synthesized by us. Before use, SM735 was dissolved in pure dimethyl sulfoxide (Me_2SO; 100 g/L) as a stock solution, and stored at 4 °C. The stock solution was diluted to the needed concentrations with RPMI-1640 supplemented with 10% FBS. The final concentration of Me_2SO in the culture medium was less than 0.01%, which had no influence on the assays[10,14]. For *in vivo* experiments, both SM735 and the reference drugs were dissolved in 0.5% Tween-80, 0.33% Me_2SO in saline.

Animals and housing conditions Inbred 7–9-week-old BALB/c, C57BL/6 mice were obtained from the Shanghai Experimental Animal Center of the Chinese Academy of Sciences (Certificate No 99-003). The mice were housed in specific pathogen-free conditions with a room temperature of 24±2 °C, a 12-h light/dark cycle, and provided with sterile food and water *ad libitum*. All mice were allowed to acclimatize in our facility for 1 week before any experiments were started. All experiments were carried out according to the National Institutes of Health Guide for the Care and Use of Laboratory Animals, and were approved by the Bioethics Committee of the Shanghai Institute of Materia Medica.

Preparation of splenocytes Splenocytes were prepared

aseptically from inbred 7–9-week-old BALB/c, C57BL/6 mice, and cultured in RPMI-1640 supplemented with 10% endotoxin-free, heat-inactivated FBS, 100 kU/L penicillin, 100 mg/L streptomycin, 10 mmol/L *N*-2-hydroxyethylpiperazine-*N*′-2-ethanesulfonic acid (HEPES), and 50 μmol/L 2-mercaptoethanol (2-ME).

Lymphocyte proliferation and cytotoxicity assay Lymphocyte proliferation was carried out as described elsewhere[15]. Briefly, 7–8-week-old male BALB/c mice were killed and splenocytes were prepared aseptically to a single-cell suspension. Splenic lymphocytes were stimulated with ConA (5 mg/L) or lipopolysaccharide (LPS 10 mg/L), plus the required concentrations of drugs. The cell cultures were then incubated for 48 h at 37 ºC in a humidified 5% CO_2 incubator. Cells were pulsed with 0.5 μCi/well [^{3}H]-thymidine 8 h prior to the end of the culture. After 48 h, cells were harvested onto a glass fiber filter using a HARVESTER96® (TOMTEC , USA) 96-well cell harvester and incorporated radioactivity was counted with a Beta Scintillation counter (1450 MicroBeta Trilux, PerkinElmer Life Sciences, Boston, MA, USA).

Cytotoxicity was assessed by using the MTT assay. Briefly, 15 μL of 5 g/L MTT was pulsed 4 h prior to the end of the culture (in a total volume of 160 μL), and then 80 μL solvent [10% sodium dodecylsulfate (SDS), 50% N,N-dimethyl formamide, pH 7.2] was added to dissolve the precipitate. The solution was incubated for another 7 h and $OD_{570\,nm}$ was read by using a microplate reader (Bio-Rad, Model 550, Tokyo, Japan).

Mixed lymphocyte reaction proliferation assay The mixed lymphocyte reaction (MLR) was carried out as previously described, with some modifications[16]. Briefly, spleen cells from 7–9-week-old BALB/c mice were prepared in a 1×10^{10} cells/L suspension, which was inactivated for 2 h with 50 mg/L of mitomycin C. Cells were washed and co-cultured with freshly prepared splenocytes from C57/BL6 mice (the ratio of stimulator to responder was 1.0) in a final concentration of 1.5×10^9 cells/L for 96 h. The desired concentrations of each compound were added in cultures for immunological activity assays. [^{3}H]Thymidine (0.5 μCi/well) was pulsed 24 h prior to the end of the culture and then cells were harvested onto a glass fiber filter for measurement of incorporated radioactivity.

Cytokine production and analysis Splenocytes (5×10^6) were prepared from 7–9-week-old BALB/c mice, added to 1 mL of RPMI-1640 media, and then were incubated with 5 mg/L of ConA, 10 mg/L of LPS, or 10 μg/L of PMA plus 1 μmol/L of ionomycin, for 24 h of culture in 48-well microculture plates. The supernatants were harvested and stored at –80 ºC before the assay was carried out. Cytokine levels in supernatants were measured by ELISA, according to the manufacturer's instructions (Pharmingen, San Diego, CA, USA). 3,3',5,5'-Tetramethylbenzidine was used to develop the color reaction. The absorbance was read at 450 nm by a microplate reader (Bio-Rad, model 550, Tokyo, Japan). Cytokine concentrations were calculated based on a standard curve created using standard murine cytokines.

DNFB-induced delayed-type hypersensitivity response Female BALB/c mice were randomized into 6 groups and sensitized with 20 μL of 0.5% DNFB dissolved in acetone-olive oil (4:1) on each hind foot on d 0 and d 1. Me_2SO vehicle, CsA and SM735 were administered to each group (n=10) by intraperitoneal injection on 4 consecutive days (d 7–d 10). On d 9 mice were challenged with 10 μL of 0.2% DNFB on both sides of the right ear, using the method described by Phanuphak *et al*, with some modifications[17]. The extent of ear swelling was expressed as the difference between the weight of punches taken from the left and right ears by using an 8-mm punch 48 h after the second challenge.

Quantitative hemolysis of sheep red blood cells Female BALB/c mice were immunized by ip injection with 0.2 mL of 16.7% sheep red blood cells (SRBC) on d 0. Me_2SO vehicle, 25 mg/kg of cyclophosphamide and SM735 were administered to each group (n=6) by ip injection on 4 consecutive days (d 1–d 4). On d 5, mice were killed, and mixed suspensions of 2×10^9 spleen cells/L were made. A total of 1 mL of cell suspension was incubated with 1 mL of 0.5% SRBC and 1 mL of 1:10 dilution of guinea pig complement for 0.5 h at 37 ºC. The suspension was then centrifuged (3 min at 3000×g) and the extent of hemolysis in the supernatant was determined at 520 nm, according to the method used by Simpson and Gozzo with some modifications[18].

Statistical analysis Three independent experiments were performed with similar results. We counted the 50% cytotoxic concentration (CC_{50}) and the 50% inhibitory concentration (IC_{50}) values using the Origin software package (Microcal Software). Student's t-test and one-way analysis of variance (ANOVA) with Newman-Keuls multiple comparisons on post-tests were used to analyze data and compare groups. P<0.05 was considered significant.

Results

Cytotoxicity of SM735 for murine splenocytes To determine the safe dose range of SM735, we first examined the cytotoxic effect of the compound. As Figure 2A shows, in a 48-h culture, SM735 had a typical S-shaped concentration-toxicity relationship for murine splenocytes. SM735 at

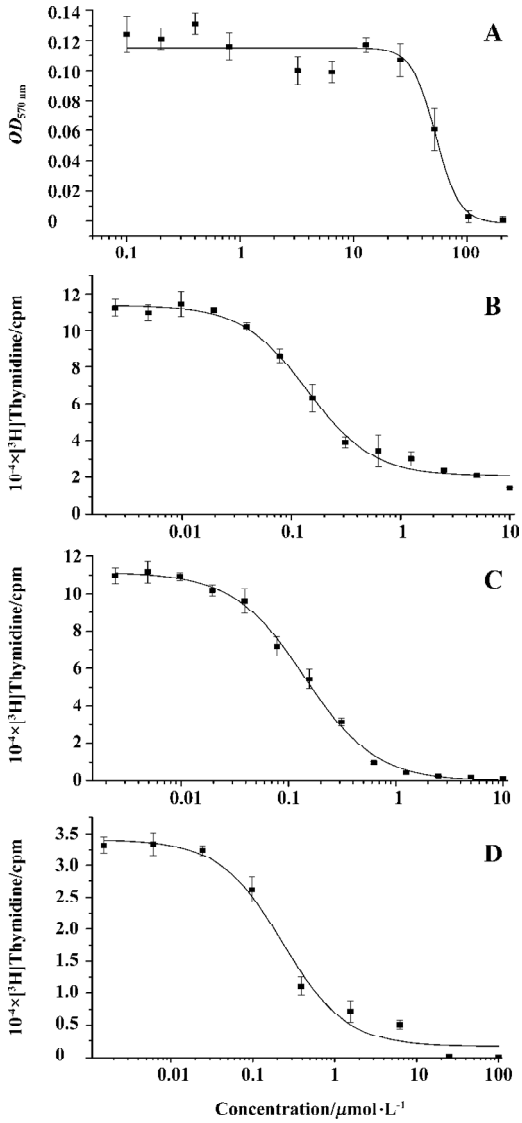

Figure 2. (A) Cytotoxicity of SM735 was tested in BALB/c mice splenocytes using the MTT assay on a 48-h culture, with a CC_{50} value of 53.1±7.8 μmol/L. (B) SM735 inhibited ConA-induced splenocyte proliferation in a 48-h culture, with an IC_{50} value of 0.33±0.06 μmol/L. (C) SM735 inhibited LPS-induced splenocyte proliferation in a 48-h culture, with an IC_{50} value of 0.27±0.02 μmol/L. (D) SM735 suppressed the mixed lymphocyte reaction, with an IC_{50} value of 0.86± 0.18 μmol/L. Mitomycin C-inactivated splenocytes from BALB/c mice were co-cultured with splenocytes from C57BL/6 mice for 96 h in the presence of SM735. Three independent experiments were performed with similar results. Mean±SEM. The data were fitted with sigmoidal functions and the IC_{50} values were counted by using the Origin software package. Correlation indices: (A) R^2=0.960; (B) R^2=0.993; (C) R^2=0.997; (D) R^2=0.984.

a dose of 25 μmol/L showed no cytotoxicity (inhibitive rate <10%, P>0.05). The 50% cytotoxic concentration (CC_{50}) value of SM735 was 53.1±7.8 μmol/L for a 48-h culture.

SM735 inhibits mitogen-induced murine splenocyte proliferation Concentration-dependent suppression of murine splenocyte proliferation in response to ConA and LPS was observed when SM735 was added to cell cultures. Figure 2B, 2C shows that proliferation induced by ConA or LPS was significantly inhibited by SM735 exposure. Both concentration-dependencies fitted typical S-shaped curves. Comparisons with a vehicle control showed that this effect was statistically significant (P<0.05) when concentrations of SM735 were above 0.04 μmol/L in response to ConA and above 0.02 μmol/L in response to LPS. In response to ConA, the IC_{50} value of SM735 inhibition of lymphocyte proliferation was 0.33±0.06 μmol/L, and in response to LPS, the IC_{50} value was 0.27±0.02 μmol/L.

SM735 inhibits splenocyte proliferation in MLR Mitomycin C-inactivated splenocytes from BALB/c mice (H-2^d) were applied as allogeneic stimuli to proliferating splenocytes of C57BL/6 mice (H-2^b). As shown in Figure 2D, SM735 strongly suppressed T cell proliferation in MLR in a dose-dependent manner, with an IC_{50} value of 0.86±0.18 μmol/L for a 96-h co-culture. When concentrations of SM735 were above 0.08 μmol/L, comparisons with the vehicle control showed that this effect was statistically significant (P<0.05). The IC_{50} values were comparable to those when ConA-stimulated T cell proliferation was suppressed.

Effects of SM735 on cytokine production We used ConA alone, LPS alone, or PMA plus ionomycin as stimuli to promote cytokine secretion in mouse splenocytes. Then the effects of SM735 on the production of proinflammatory cytokine IL-6, and Th1-type cytokines IL-2, IL-12, and IFN-γ, were examined. The results are summarized in Table 1. The production of IL-12, IFN-γ, and IL-6 was significantly decreased in a concentration-dependent manner when the splenocyte cultures were exposed to SM735, upon stimulation with LPS or PMA plus ionomycin. We also detected a strong inhibitive effect of SM735 on IFN-γ production induced by ConA. Unexpectedly but interestingly, we did not observe a significant effect of SM735 on IL-2 production.

SM735 suppresses DNFB-induced delayed-type hypersensitivity reaction Figure 3 illustrates the dose-dependent inhibitory effect of SM735 on DNFB-induced DTH ear swelling. When SM735 was administered for 4 consecutive days, at doses of 7.5, 15, and 30 mg/kg, SM735 significantly suppressed ear swelling by 19.6%, 35.5%, and 55.4%, respectively. The inhibition was comparable to that of CsA, which exerted 55.2% suppression at a dose of 50 mg/kg.

SM735 suppresses anti-SRBC specific immunoglobulin production Quantitative hemolysis of SRBC (QHS) is a model of primary antibody production in response to anti-

Table 1. Effects of SM735 on cytokine production by stimulated splenocytes. Splenocytes from BALB/c mice were stimulated for 24 h. Cytokine production was measured in cell-free supernatants using ELISA. n=3. Data are mean±SEM. $^bP<0.05$, $^cP<0.01$ *vs* stimulated-cells without SM735.

SM735/ mol·L^{-1}	Stimulus	Cytokine production/μg·L^{-1} IL-2	IFN-γ	
–	–	27±2	83±7	
–	ConA	2321±33	1523±22	
1×10^{-7}	ConA	2250±77	1219±33^c	
1×10^{-6}	ConA	2343±154	976±18^c	
1×10^{-5}	ConA	2053±162	322±18^c	
		IL-12	IFN-γ	IL-6
–	–	145±17	97±21	397±27
–	LPS	707±8	240±13	1013±43
1×10^{-7}	LPS	592±33^b	207±13^b	840±10^c
1×10^{-6}	LPS	565±18^c	172±2^c	792±42^c
1×10^{-5}	LPS	292±26^c	103±7^c	522±1^c
–	PMA+Ion	699±29	844±36	3256±176
1×10^{-7}	PMA+Ion	586±52^b	768±6^c	2886±26^b
1×10^{-6}	PMA+Ion	487±37^c	557±31^c	2663±52^c
1×10^{-5}	PMA+Ion	198±35^c	144±21^c	1465±35^c

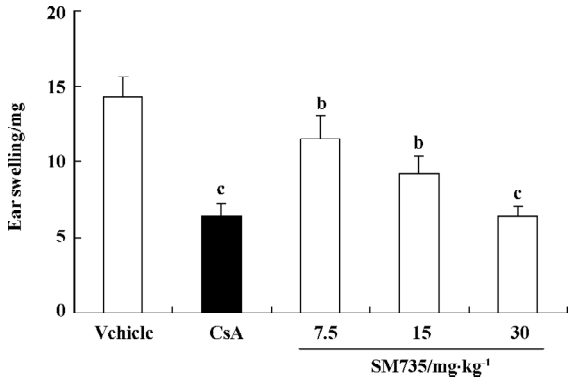

Figure 3. BALB/c mice were initially sensitized with DNFB on d 0 and d 1, and then challenged with DNFB on d 9. Vehicle, CsA or SM735 was administered on d 7–d 10. Ear punches were taken 48 h post challenge, and ear swelling was calculated as the difference between the weights of the punches taken from the left ear (DNFB treated) and the right ear (untreated). n=10. Mean±SD. $^bP<0.05$, $^cP<0.01$ *vs* vehicle group. Three independent experiments were performed with similar results.

genic stimulation. Because CsA specifically blocks T cell activation by suppressing IL-2 production, with little effect on B cells, we chose cyclophosphamide (CTX) as a reference drug in the present study[19]. As Figure 4 shows, administration of 15 and 30 mg/kg SM735 for 4 consecutive days significantly suppressed QHS in a dose-dependent manner. The inhibitive rates were 15.3% ($P<0.05$) and 25.4% ($P<0.01$), respectively, slightly less potent than the 31.8% inhibition effected by CTX ($P<0.01$).

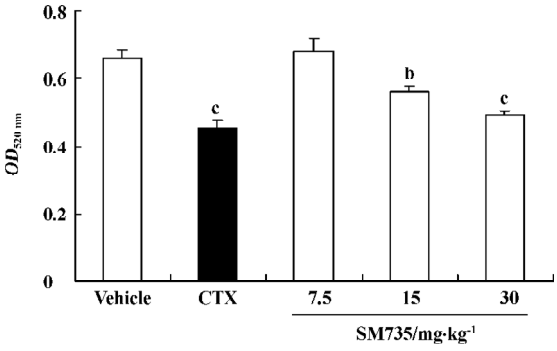

Figure 4. BALB/c mice were immunized with SRBC for testing immunoglobulin secretion. Vehicle, 25 mg/kg CTX and SM735 were administered to each group for 4 consecutive days. Supernatant hemolysis at 520 nm was read to assess the immunoglobulin-secreting activity of B cells. n=6. Mean±SD. $^bP<0.05$, $^cP<0.01$ *vs* vehicle group.

Discussion

Patients who receive organ grafts are principally treated with immunosuppressive agents. In addition, there are a number of other autoimmune chronic inflammatory disorders that might be able to be treated with immunosuppressive drugs. In the 1970s and 1980s, the discovery and clinical use of CsA and tacrolimus (FK506) enabled the successful transplantation of major organs in human patients. However, it seems now that neither are able to be tolerated in the long term[20,21]. These drugs cause systemic immunosuppression that greatly increases the risks of tumors arising and lethal fungal infections occurring. Therefore, new immunosuppressants are required that possess better therapeutic effects or can be combined with currently used drugs to reduce long-term tolerance and side effects.

Previous studies have indicated that artemisinin possesses anti-lymphocytic activities. There are numerous reports of clinical cases in which autoimmune diseases have been treated with artemisinin and artesunate; therapeutic

effects were achieved in these cases, thus encouraging us to study artemisinin and its derivatives. To improve the efficacy of the drug, we optimized artemisinin by linking it with various NSAID structures. Here, we report that a newly synthesized artemisinin derivative, SM735, possesses potent immunosuppressive activity both *in vitro* and *in vivo*.

Lymphocyte proliferation is a crucial event in the activation cascade of both cellular and humoral immune responses. Treatment with SM735 can dose-dependently reduce both the T and B cell proliferation promoted by mitogens. Because it has a relatively high CC_{50} value, SM735 has a favorably large safety range.

A mixed lymphocyte reaction is induced by allogeneic stimuli, and T lymphocytes are the main responders, indicating an immune response very similar to that which occurs in post-transplantation graft-versus-host diseases[22,23]. MLR is often used clinically for tissue typing to identify the compatibility of donor organs and recipients. Furthermore, the suppression of MLR by immunosuppressants also helps improve the success of transplantation[24,25]. Here we show that SM735 also potently inhibited MLR, with an IC_{50} value comparable to that for the inhibition of T cell proliferation. At concentrations above 10 μmol/L, SM735 almost completely abrogated MLR. This suggests that SM735 would probably act as an immunosuppressant in physiological conditions.

Cytokines are important modulators and effectors in the immune system. In particular, multiple proinflammatory cytokines have been proved to be closely associated with many autoimmune diseases. It is critical to silence proinflammatory cytokines to maintain successful immunosuppression[26–28]. In the present study, we used mitogen ConA, bacterial LPS, and PMA plus ionomycin, which agitated the whole cell population by activating protein kinase C, to promote cytokine production in splenocytes. The results showed that SM735 significantly inhibited IL-12, IFN-γ and IL-6 production with LPS or PMA plus ionomycin stimulation. When using ConA as a stimulant, we also observed a dose-dependent inhibition of IFN-γ production. Unexpectedly, the IL-2 level was not obviously altered. Although the two cornerstone immunosuppressants, CsA and FK506, are putatively regarded as IL-2 inhibitors, it seems that SM735 acts totally differently, on some event(s) downstream of IL-2-mediated naive T cell activation. IL-2 is widely considered to be a key cytokine in T-cell-dependent immune responses. However, the main non-redundant activity of this cytokine centers on the regulation of T cell tolerance, and recent studies have indicated that a failure in the production of $CD4^+CD25^+$ regulatory T cells is the underlying cause of autoimmunity in the absence of IL-2[29]. Thus, the fact that SM735 does not inhibit IL-2 indicates that further research is necessary on the induction of long-term immune tolerance by SM735.

To examine the immunoregulatory effects of SM735 *in vivo*, we used a mouse DTH model and the QHS model. Ear swelling in DTH is primarily the result of antigen-specific $CD4^+$ T cell activation[30]. Administration of SM735 for 4 consecutive days significantly suppressed ear swelling, indicating that SM735 is capable of inhibiting the T-cell-dependent immune response *in vivo*. In our experiments, the effect of SM735 was comparable to that of cyclosporine at a curative dose. The QHS model reflects the antibody-producing capacity of plasma cells in response to SRBC[18,19]. The suppressive effect of SM735 in QHS indicated that it also suppressed antibody-secreting B cells *in vivo*.

In conclusion, our results demonstrate that SM735, a newly synthesized artemisinin derivative, has strong immunosuppressive effects *in vitro* and *in vivo*. Because artemisinin and its derivatives potentially have low toxicity and few side effects[4,31], our study suggests the possibility of developing SM735 and other artemisinin derivatives as novel safe immunosuppressants, probably with a different mechanism from that of CsA or FK506. However, further studies are necessary to elucidate the details of the mechanism.

References

1 Luo XD, Shen CC. The chemistry, pharmacology, and clinical applications of qinghaosu (artemisinin) and its derivatives. Med Res Rev 1987; 7: 29–52.

2 Klayman DL. Qinghaosu (artemisinin): an antimalarial drug from China. Science 1985; 228: 1049–55.

3 Li Y, Wu YL. An over four millennium story behind qinghaosu (artemisinin): a fantastic antimalarial drug from a traditional Chinese herb. Curr Med Chem 2003; 10: 2197–230.

4 Tawfik AF, Bishop SJ, Ayalp A, el-Feraly FS. Effects of artemisinin, dihydroartemisinin and arteether on immune responses of normal mice. Int J Immunopharmacol 1990; 12: 385–9.

5 Yu Q, Jin H. Artesunate in treatment of dermatosis. Bengbu Yixueyuan Xuebao 1997; 22: 309–10. Chinese.

6 Yu Q, Gao Y. Systemic lupus erythematosus treated with artesunate. Chin J Dermatol 1997; 30: 51–2. Chinese.

7 Zhang J, Zhong J, Shi Z, Dai X. Effects of lingdan and artesunate on T cell populations in human SLE. Chin Interg Tradit West Med 2002; 7: 489. Chinese.

8 Meshnick SR, Taylor TE, Kamchonwongpaisan S. Artemisinin and the antimalarial endoperoxides: from herbal remedy to targeted chemotherapy. Microbiol Rev 1996; 60: 301–15.

9 Yang YZ, Little B, Meshnick SR. Alkylation of proteins by artemisinin. Effects of heme, pH, and drug structure. Biochem Pharmacol 1994; 48: 569–73.

10 Yang ZS, Zhou WL, Sui Y, Wang JX, Wu JM, Zhou Y, *et al*. Synthesis and immunosuppressive activity of new artemisinin

derivatives. Part I. [12(β or α)-dihydroartemisininoxy] phen (ox)yl aliphatic acids/esters. J Med Chem 2005; 48: 4608–17.
11 Allison AC. Immunosuppressive drugs: the first 50 years and a glance forward. Immunopharmacology 2000; 47: 63–83.
12 Liu J. FK506 and cyclosporin, molecular probes for studying intracellular signal transduction. Immunol Today 1993; 14: 290–5.
13 Noori S, Naderi GA, Hassan ZM, Bathaie SZ, Hashemi SM. Immunosuppressive activity of a molecule isolated from *Artemisia annu*a on DTH responses compared with cyclosporin A. Int Immunopharmacol 2004; 4: 1301–6.
14 Rowland TL, McHugh SM, Deighton J, Dearman RJ, Ewan PW, Kimber I. Differential regulation by thalidomide and dexamethasone of cytokine expression in human peripheral blood mononuclear cells. Immunopharmacology 1998; 40: 11–20.
15 Feng YH, Zhou WL, Wu QL, Li XY, Zhao WM, Zou JP. Low dose of resveratrol enhanced immune response of mice. Acta Pharmacol Sin 2002; 23: 893–7.
16 Wu QL, Fu YF, Zhou WL, Wang TX, Feng YH, Liu J, *et al*. Inhibition of *S*-adenosyl-*L*-homocysteine hydrolase induces immunosuppression. J Pharmacol Exp Ther 2005; 313: 705–11.
17 Phanuphak P, Moorhead JW, Claman HN. Tolerance and contact sensitivity to DNFB in mice. I. *In vivo* detection by ear swelling and correlation with *in vitro* cell stimulation. J Immunol 1974; 112: 115–23.
18 Simpson MA, Gozzo JJ. Spectrophotometric determination of lymphocyte mediated sheep red blood cell hemolysis *in vitro*. J Immunol Methods 1978; 21: 159–65.
19 Bin-Hafeez B, Ahmad I, Haque R, Raisuddin S. Protective effect of *Cassia occidentalis* L on cyclophosphamide-induced suppression of humoral immunity in mice. J Ethnopharmacol 2001; 75: 13–8.
20 Toungouz M, Donckier V, Goldman M. Tolerance induction in clinical transplantation: the pending questions. Transplantation 2003; 75 Suppl 9: 58S–60S.
21 Offermann G. Immunosuppression for long-term maintenance of renal allograft function. Drugs 2004; 64: 1325–38.
22 Tourkova IL, Yurkovetsky ZR, Shurin MR, Shurin GV. Mechanisms of dendritic cell-induced T cell proliferation in the primary MLR assay. Immunol Lett 2001; 78: 75–82.
23 Amrolia PJ, Muccioli-Casadei G, Yvon E, Huls H, Sili U, Wieder ED, *et al*. Selective depletion of donor allo-reactive T-cells without loss of anti-viral or anti-leukemic responses. Blood 2003; 102: 2292–9.
24 Tiercy JM, Villard J, Roosnek E. Selection of unrelated bone marrow donors by serology, molecular typing and cellular assays. Transpl Immunol 2002; 10: 215–21.
25 Goes N, Chandraker A. Human leukocyte antigen matching in renal transplantation: an update. Curr Opin Nephrol Hypertens 2000; 9: 683–7.
26 Firestein GS. The T cell cometh: interplay between adaptive immunity and cytokine networks in rheumatoid arthritis. J Clin Invest 2004; 114: 471–4.
27 Matei I, Matei L. Cytokine patterns and pathogenicity in autoimmune diseases. Rom J Intern Med 2002; 40: 27–41.
28 Semenkov VF, Artemjeva OV, Shishina RN, Golubeva VL, Serova LD. Influence of clinical immunosuppression on proinflammatory cytokines and acute-phase proteins. Transplant Proc 1998; 30: 4195.
29 Malek TR, Bayer AL. Tolerance, not immunity, crucially depends on IL-2. Nat Rev Immunol 2004; 4: 665–74.
30 Frew AJ, Varney VA, Gaga M, Kay AB. Immunohistology of human allergic late-phase skin reactions. Skin Pharmacol 1991; 4 Suppl 1: 71–8.
31 Yamachika E, Habte T, Oda D. Artemisinin: an alternative treatment for oral squamous cell carcinoma. Anticancer Res 2004; 24: 2153–60.

Acta Pharmacologica Sinica 2005 Nov; 26 (11): 1359–1364

Blackwell Publishing

Full-length article

Effects of CpG-ODN on gene expression in formation of foam cells[1]

Kai LI, Bin WAN, Zhen-lin HU, Ying HE, Xiao-wen HE, Lei JIANG, Shu-han SUN[2]

Department of Medical Genetics, College of Basic Medical Sciences, the Second Military Medical University, Shanghai 200433, China

Key words

CpG islands; oligodeoxyribonucleotides; foam cells; macrophages; LDL lipoprotein; gene expression; cholesterol; CD 36 antigens; lipoprotein lipase; Fc gamma receptor IIb

[1] Project supported by the National Natural Science Foundation of China (No 30370741).
[2] Correspondence to Prof Shu-han SUN.
Phn 86-21-2507-0331.
Fax 86-21-2507-0331.
E-mail shsun888@hotmail.com

Received 2005-04-20
Accepted 2005-08-02

doi: 10.1111/j.1745-7254.2005.00167.x

Abstract

Aim: To investigate the effects of CpG-oligodeoxynucleotide (CpG-ODN) on the formation of macrophage foam cells and related gene expression. **Methods:** A gene expression profile was examined by microarray techniques, and mRNA expression was detected by reverse transcriptase polymerase chain reaction (RT-PCR). The cholesterol and cholesteryl ester contents of cells were determined by high performance liquid chromatography. **Results:** CD36, LPL, and Fcγ2b, which were related to lipid metabolism and the formation of macrophage foam cells, were upregulated after CpG-ODN stimulation. The mRNA expression related to the formation of foam cells was confirmed by semiquantitative RT-PCR. Moreover, histochemical analysis confirmed that lipid deposits inside cells increased after CpG-ODN treatment. However, using flow cytometry, we found that CpG-ODN had no effect on the expression of membrane receptors. **Conclusion:** CpG-ODN up-regulated the expression of genes in macrophage foam cell formation.

Introduction

CpG-oligodeoxynucleotides (CpG-ODN), the synthetic oligodeoxynucleotides containing unmethylated CpG dinucleotides in specific sequence contexts, are novel immune enhancers for systemic and mucosal immunization[1]. Animal studies suggest that CpG-ODN could be used as vaccine adjuvants, or antiallergenic, chemotherapeutic, or immunoprotective agents[2–5]. Although the immunological effects of CpG-ODN have been widely studied[6–9], including the mechanism by which CpG-ODN binds to the cell surface and the way in which its immunostimulatory activity is modulated by extracellular pH[10], its biological activities are not comprehensively understood. To improve our knowledge of the biological activities of CpG-ODN, we used a DNA microarray to profile the gene expression in an immune cell line after CpG-ODN treatment, and found that some genes related to the formation of macrophage foam cells were upregulated. We therefore reasoned that CpG-ODN might affect the lipid metabolism and the formation of foam cells. Foam cells are characteristic pathological cells in atherosclerotic lesion. An excess lipid loading in macrophages results in the formation of foam cells, and this is a key process in the early stages of atherosclerotic lesions[11]. Therefore, it is very important to investigate how CpG-ODN affects the formation of foam cells. In the present study, we investigated the effects of CpG-ODN on the gene expression of the related receptors or enzymes involved in atherosclerosis, and further confirmed the results by using semiquantitative RT-PCR. Furthermore, by histochemical and high performance liquid chromatography (HPLC) analysis, we demonstrated that CpG-ODN could affect the formation of foam cells.

Materials and methods

CpG-ODN ODN-1826 (5'-TCCATGACGTTCCTGACGTT-3') and ODN-2006 (5'-TCGTCGTTTTGTCGTTTGTCGTT-3') were synthesized by Sangon Biotechnology Co in Shanghai, China.

Cell culture The mouse macrophage line RAW264.7 and the human monocyte line U937 were obtained from the Cell Bank in the Shanghai Institutes of Biochemistry and Cell Biology, Chinese Academy of Sciences, and were cultured in RPMI-1640 medium (Gibco/BRL, Rockville, USA), supplemented with 10% fetal bovine serum, 2 mmol/L glutamine, and 50 mg/mL gentamycin in 5% CO_2 at 37 ºC. The culture medium was changed every 48 h.

Analysis of gene expression profile of immune cells by

using a cDNA microarray The MGEC-80s microarray obtained from Biostar Genechip (Shanghai) was used. RAW264.7 cells were stimulated with ODN-1826 6 μmol/L for 6 h, and total RNA was isolated from cultured cells using TRIzol reagent (Gibco). mRNA was purified using the Oligotex mRNA midi Kit (Qiagen, Germany). The fluorescent cDNA probes were synthesized from total RNA by reverse transcription and then purified, referring to the protocol of Schena *et al* and Shalon D *et al*[12,13]. The probes from the control were labeled with Cy3-dUTP; those from the stimulated cells by ODN-1826 were labeled with Cy5-dUTP. The probes were mixed and precipitated with ethanol, and resolved in 20 μL hybridization solution [5×SSC+0.4% sodium dodecylsulfate (SDS)+50% formamide+5× Denhardt's solution]. Chips were prehybridized with the hybridization solution+3 μL denatured salmon sperm DNA at 42 ºC for 6 h. After denaturing at 95 ºC for 5 min, the probe mixture was added to the prehybridized chip and covered with glass. Hybridization was performed at 60 ºC for 16 h. After hybridization of a sample to the microarray, the sample was removed, and arrays were washed in solutions of 2×SSC + 0.2% SDS, 0.1% SSC + 0.2% SDS, and 0.1×SSC at 60 ºC, respectively, for 10 min each, then dried at room temperature. Arrays were scanned with a laser scanner (ScanArray4000, General Scanning Inc, Watertown, Massachusetts) at 2 wavelengths. The acquired images were processed using a modification of GenePix Pro 3.0 software. The intensity of each spot at the 2 wavelengths represented the quantity of Cy3-dUTP and Cy5-dUTP, respectively. Each ratio of Cy3 to Cy5 was computed. The overall intensity was normalized by a coefficient according to the ratios of the 40 housekeeping genes that were also located.

Semiquantitative RT-PCR Total RNA of the U937 cells was extracted, purified using the Tissue/Cell Total RNA Isolation Kit (Watson, Shanghai), and quantified spectrophotometrically. A total of 200 ng RNA was reverse transcribed to cDNA in a volume of 20 μL using oligo(dT) primers and a commercially available kit (Reverse Transcription System, Promega, USA) according to the manufacturer's instructions. For transcription, the RNA was denatured at 70 ºC and then transcribed for 1 h at 42 ºC. After inactivation of the avian myeloblastosis virus (AMV), (1 min at 99 ºC), the transcript was cooled down to 4 ºC. Four microliters of the reaction mixture was subjected to a final PCR reaction in a total volume of 20 μL, containing 0.5 μL of *Taq* polymerase (Takara Biotechnology, Dalian, China), 2 μL of 10×PCR Buffer (Mg^{2+} Plus, Takara, Dalian), 2 μL dNTP mix (2.5 mmol/L), 0.5 μL of each of the 5' and 3' primers, and 10.5 μL of H_2O. All gene-specific PCR primers were designed based on the DNA sequences in GenBank (National Center for Biotechnology Information, Bethesda, MD, USA). The sequence of the primers and the annealing temperatures are shown in Table 1. The amplification was carried out over 35 cycles of the following: denaturation, 1 min at 94 ºC; annealing, 30 s, at temperature see Table 1; elongation, 1 min at 72 ºC. PCR products were separated by agarose gel electrophoresis. β-actin was used as a control. The intensities of the gene-specific PCR products were quantified from scanned images using the AlphaEase FC software (Alpha).

Preparation of ox-LDL Low-density lipoprotein (LDL) (d=1.019 to 1.063 kg/L; Sigma) was sterilized by filtration through 0.45 μm Millipore membranes, and stored at 4 ºC as described previously[14]. After edetic acid was removed by dialysis, LDL were oxidized by incubation in $CuSO_4$ 10 μmol/L at 37 ºC for 12 h, and then dialyzed in phosphate buffered saline (PBS) containing edetic acid 0.1 mmol/L at 4 ºC for 24 h.

***In vitro* induction of foam cell formation** Confluent U937 cells were pretreated in serum-free RPMI-1640 for 24 h and then incubated with ox-LDL 80 mg/L for 48 h. The foam cell model was thus established. In the experiments, U937 cells were cultured with ODN-2006 6 μmol/L and ox-LDL 80 mg/L for 48 h, which were added to the medium simultaneously. The control group was the U937 cells without ODN-2006 treatment. The morphological form of the foam cells was

Table 1. Primers used for RT-PCR.

	5 Primer (5'–3')	3 Primer (5'–3')	Length/bp	Annealing temperature/ºC
CD36	cctttgcctctccagttgaa	tgtttgccttctcatcacca	390	64
FcγR	aaggacaagcctctggtcaa	ctgaaatccgctttttcctg	295	64
LPL	gaggacacttgccacctcat	ggaccctctggtgaatgtgt	498	56
β-actin	tcaccctgaagtaccccatc	aggaaggaaggctggaagag	607	64

LPL, lipoprotein lipase.

analyzed by histochemical methods.

Histochemical analysis of foam cells The foam cells were collected and fixed with 4% paraformaldehyde for 12 h on the slides as described previously[15]. The slides were rinsed in water and placed in fresh 0.3% oil red O (Amresco, Solon, USA) solution for 20 min. The slides were rinsed in 50% isopropyl alcohol and examined.

Lipid extraction Lipids were extracted by using the method of Hara and Radin[16] with modifications. The cells were collected from the culture flasks into 0.9% NaCl (2 mL per 75 cm^2 flask) and homogenized on ice by sonication for 10 s with a Sonifier 450 sonicator (Branson Ultrasonics, Danbury, USA) set to maximum power. The protein concentration of the cell lysate was determined by the method of Lowry *et al*[17]. To a volume of cell suspension known to contain 1 mg of protein was added 100 μg of cholesteryl heptadecanoate in chloroform as an internal standard. An equal volume of freshly prepared cold (-20 °C) KOH in ethanol (150 g/L) was then added and the cell lysate was repeatedly vortexed until clear with 6% trichloroacetic acid. An equal volume of 4:1 hexane-isopropanol (*v*/*v*) was added and the mixture was vortexed for 5 min followed by centrifugation at 800×*g* and 15 °C for a further 5 min. The extraction procedure was repeated twice (a total of three extraction procedures). The combined organic phase was transferred to clean tapered glass tubes and thoroughly dried in a vacuum freeze dryer at 65 °C. The tubes were allowed to cool to room temperature, 100 μL of the mixture of isopropyl alcohol-*n*-heptane-acetonitrile at 35:12:52 (*v*:*v*:*v*) was added, and the sample was solubilized by placing it in an ultrasound water bath for 5 min at room temperature. After centrifugation at 800×*g* for 5 min, 20 μL of the sample was introduced into the HPLC device.

Determination of cholesterol and cholesteryl ester content of U937 cells by HPLC The cholesterol and cholesteryl ester content of cells were analyzed by HPLC as described previously[18]. HPLC was performed using a Waters device (Milford, USA) equipped with a model 1525 binary pump, a model 717 plus autosampler, a model 2487 dual λ absorbance detector, and a 4.6 mm×100 mm Gen-Pak FAX column (Waters). Waters' Breeze software was used to control the HPLC system. Cholesterol and cholesteryl esters were eluted isocratically at a flow rate of 0.5 mL/min and at a temperature of 4 °C using an eluent consisting of isopropanol-*n*-heptane-acetonitrile at the ratio of 35:12:52 (*v*:*v*:*v*) and detected by ultraviolet absorption at 206 nm.

Statistics Every experiment was repeated at least 3 times. All values are expressed as mean±SD. Differences were considered statistically significant when $P<0.05$ as determined by the paired *t*-test.

Results

Gene expression profile in immune cells By using the cDNA microarray, 119 genes related to cell cycle, immune modulation, and signal transduction were found to be differentially expressed, of which 3 genes related to the formation of macrophage foam cells had increased expression after ODN-1826 6 μmol/L stimulation (Table 2).

Table 2. Genes upregulated in RAW264.7 cells after ODN-1826 6 μmol/L stimulation.

GenBank ID	Definition
NM_007643	*Mus musculus* CD36 antigen (Cd36)
NM_008509	*Mus musculus* lipoprotein lipase (Lpl)
NM_010187	*Mus musculus* Fc receptor, IgG, low affinity IIb (Fcγ2b)

Confirmation of foam cell-related gene expression by RT-PCR According to the 3 genes in Table 2, we designed primers and performed semiquantitative RT-PCR. The expression of these genes in the ODN-2006 treated group was markedly increased, compared with the control group (Figure 1).

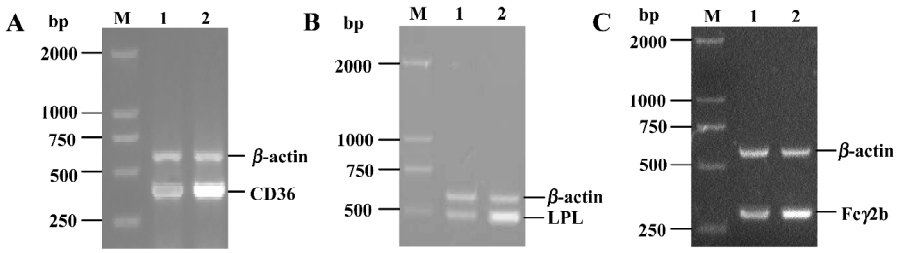

Figure 1. Confirmation of foam cell-related gene expression in U937 cell line by RT-PCR. M: DL2000 marker; 1: Control; 2: ODN-2006 6 μmol/L. (A) CD36; (B) LPL; (C) Fcγ2b

Effect of CpG-ODN on lipid deposition in cells Lipid drops inside the foam cells were stained with oil red O, and some of the red pellets were found in the plasma of the U937 cells after being incubated with ox-LDL, indicating that the foam cell model was formed. After ODN-2006 6 μmol/L was added to the medium, lipid deposition in U937 foam cells was enhanced (Figure 2).

Effect of CpG-ODN on cholesterol and cholesteryl ester in foam cells After incubation with ODN-2006 6 μmol/L and ox-LDL 80 mg/L for 48 h, the level of cholesteryl ester in foam cells increased markedly compared with the controls (Figure 3). This suggests that CpG-ODN can also increase lipid accumulation (based on the assay of the concentrations of cholesteryl ester and the ratio of cholesteryl ester to total cholesterol; Table 3). Cholesterol concentration has a strong linear relationship with its peak area within 0.05–1.0 mg/L (r^2 in each case was >0.998).

Discussion

Previous reports have suggested that CpG-ODN is mainly involved in immunomodulation[19,20]. Nevertheless, in the study presented here, we investigated immune cells treated with CpG-ODN using cDNA microarray technology and, surprisingly, found that the expression of 3 genes (CD36 [NM_007643], LPL [NM_008509], and Fcγ2b [NM_010187]) increased markedly. These results were further confirmed by semiquantitative RT-PCR. CD36, LPL, and Fcγ2b are thought to be closely related to lipid metabolism and the formation of macrophage foam cells, therefore CpG-ODN is able to modulate gene expression in foam cells, and increase lipid accumulation in foam cells. Our findings suggest that CpG-ODN has a novel biological activity.

Atherosclerosis, and the resulting coronary heart disease and cerebral stroke, is the most common cause of death

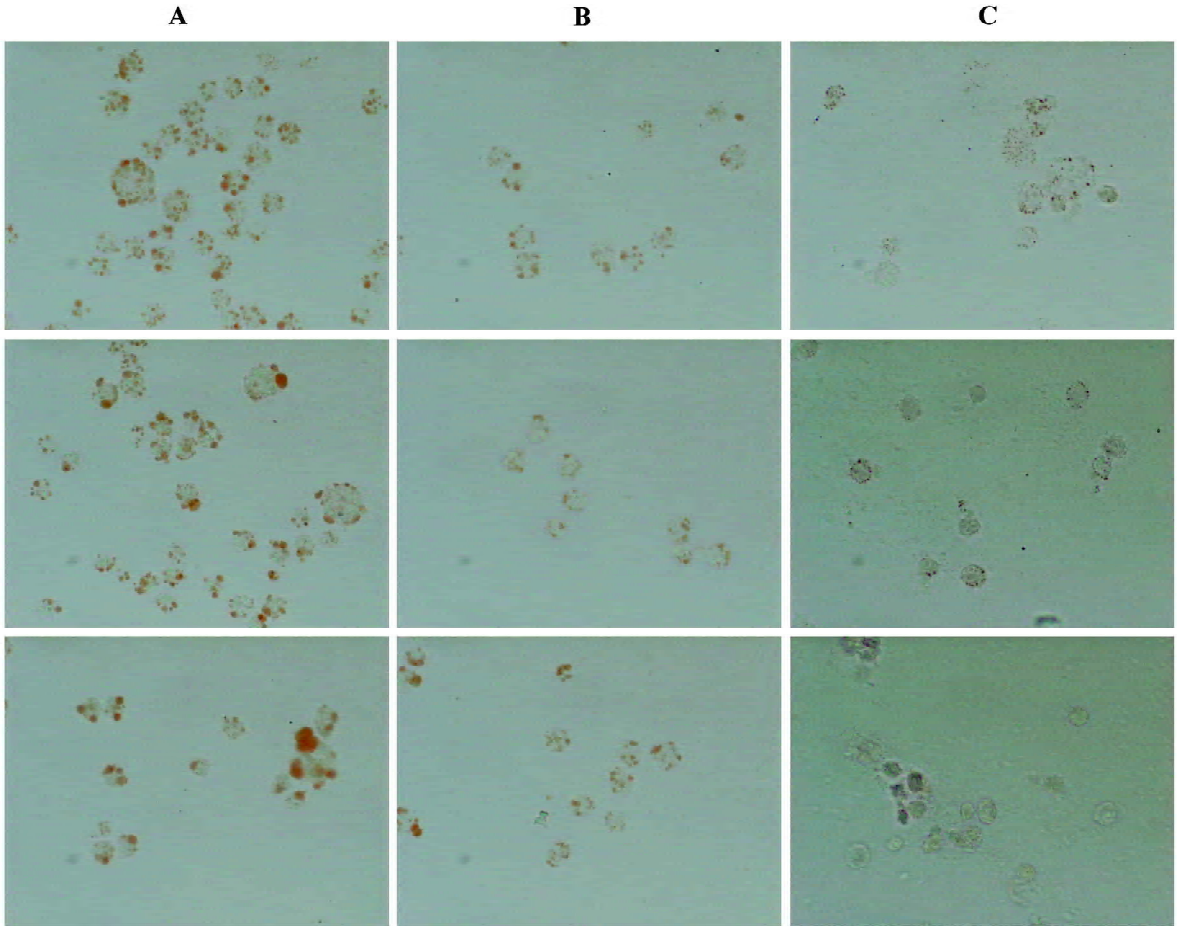

Figure 2. Effect of ODN-2006 on lipid deposition in U937 cells. Lipid drops (red pellets in the plasma of the cells) were stained by oil red O (×400). (A) CpG-ODN 6 μmol/L and ox-LDL 80 mg/L treated group. (B) ox-LDL 80 mg/L treated group. (C) Normal U937 cells. The three photos from the top to the bottom in each group represented different fields at the same treatment.

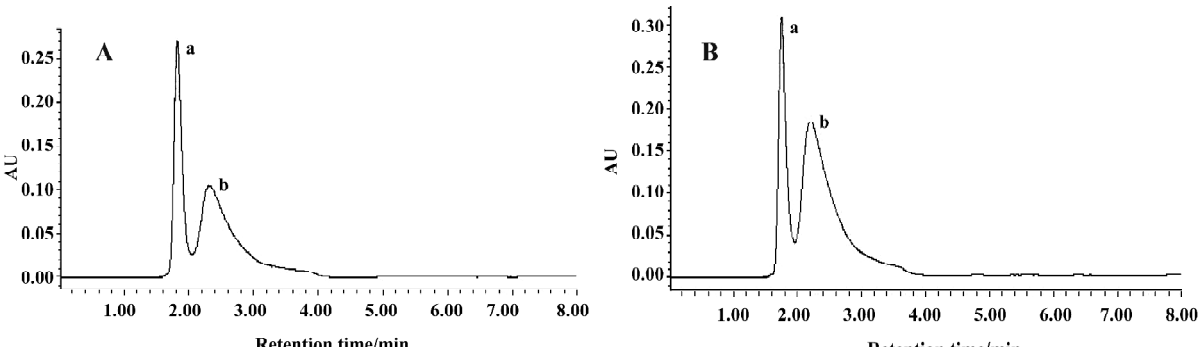

Figure 3. Effect of ODN-2006 on cholesterol and cholesteryl ester inside foam cells detected by HPLC. (A) The ox-LDL 80 mg/L loaded U937 cell; (B) The ODN-2006 6 μmol/L and ox-LDL 80 mg/L stimulated U937 cell. (a) The peak of cholesterol; (b) The peak of cholesteryl ester.

Table 3. Effect of ODN-2006 on lipid deposits (mg/g) in U937 monocytes. n=9. Mean±SD. ^cP<0.01 *vs* control group.

Group	Total cholesteryl	Free cholesterol	Cholesteryl ester	Cholesterol ester/ total cholesterol (%)
Control group	374±21	181±14	191±17	51.6±3.1
CpG group	357±42	128±18	228±35	63.8±3.8^c

in industrialized nations. Mammalian cells have evolved complex feedback mechanisms to ensure a sufficient supply of cholesterol and to prevent its excessive accumulation. During the process of atherosclerosis, these homeostatic mechanisms fail in macrophages. Uncontrolled cholesterol deposition is promoted by scavenger functions of the macrophages and the adaptive mechanisms elicited are not sufficient to process the lipid load. Consequently, a lipid-laden "foam cell" is formed. The active stages of atherosclerotic lesions are characterized by the extensive infiltration of blood-derived monocyte/macrophages through the endothelium into the arterial intima. The monocytes migrate into the arterial intima where they internalize ox-LDL through scavenger receptors and become macrophage-derived foam cells results in the formation of fatty streaks, which are believed to represent the earliest type of atherosclerotic plaque. CpG-ODN can upregulate the related gene expression in foam cells, which implies that CpG-ODN might function as a facilitative atherosclerotic factor. This suggests that the clinical application of CpG-ODN might be risky in cases of atherosclerosis.

Macrophage-derived foam cells in atherosclerotic lesions are generally thought to play a major role in the pathology of the disease. The uptake of ox-LDL by macrophages is a key event implicated in the initiation and development of atherosclerotic lesions. Two macrophage surface receptors, CD36 (a class B scavenger receptor) and the macrophage scavenger receptor (a class A scavenger receptor), have been identified as the major receptors that bind and internalize ox-LDL. CD36 is an 88 kDa transmembrane glycoprotein that is expressed on monocytes, platelets, and microvascular endothelium. The expression of CD36 in monocytes/macrophages in tissue culture is dependent both on their differentiation state and exposure to soluble mediators (cytokines and growth factors). Modified lipoproteins such as LDL immune complexes can also enter the macrophage through the Fcγ receptor, which is a classic inhibitory receptor that is widely expressed on B cells, macrophages, neutrophils, and mast cells. Once LDL immune complexes combine with the Fcγ receptor, it may enhance LDL oxidation and expression of the scavenger receptor[21]. Lipoprotein lipase (LPL) is the enzyme primarily responsible for the hydrolysis of core triglycerides in circulating chylomicrons and very low density lipoproteins (VLDL) to generate cholesterol-enriched remnants[22]. LPL is synthesized by many cell types, including vascular smooth muscle cells (VSMC) and macrophages, and associates with the vascular endothelium. Increased LPL activity in the arterial wall correlates with increased areas of lipid deposition and increased atherosclerotic lesion forma-

tion[23]. The activity of LPL in promoting atherosclerosis may depend on its dual role as an enzyme and as a bridging protein that increases the binding of lipoproteins to the cell surface[22].

Our data suggest that CpG-ODN upregulates the expression of CD36, Fcγ2b, and LPL in foam cells, which indicates that CpG-ODN might have some influence on the formation of foam cells and related gene expression.

References

1 McCluskie MJ, Davis HL. CpG DNA is a potent enhancer of systemic and mucosal immune responses against hepatitis B surface antigen with intranasal administration to mice. J Immunol 1998; 161: 4463–6.

2 Sommer F, Wilken H, Faller G, Lohoff M. Systemic Th1 immunization of mice against *Helicobacter pylori* infection with CpG oligodeoxynucleotides as adjuvants does not protect from infection but enhances gastritis. Infect Immun 2004; 72: 1029–35.

3 Weigel BJ, Rodeberg DA, Krieg AM, Blazar BR. CpG oligodeoxynucleotides potentiate the antitumor effects of chemotherapy or tumor resection in an orthotopic murine model of rhabdomyosarcoma. Clin Cancer Res 2003; 9: 3105–14.

4 Jorgensen JB, Johansen LH, Steiro K, Johansen A. CpG DNA induces protective antiviral immune responses in Atlantic salmon (*Salmo salar* L). J Virol 2003; 77: 11 471–9.

5 Sur S, Wild JS, Choudhury BK, Sur N, Alam R, Klinman DM. Long term prevention of allergic lung inflammation in a mouse model of asthma by CpG oligodeoxynucleotides. J Immunol 1999; 162: 6284–93.

6 Yi AK, Klinman DM, Martin TL, Matson S, Krieg AM. Rapid immune activation by CpG motifs in bacterial DNA. Systemic induction of IL-6 transcription through an antioxidant-sensitive pathway. J Immunol 1996; 157: 5394–402.

7 Ballas ZK, Rasmussen WL, Krieg AM. Induction of NK activity in murine and human cells by CpG motifs in oligodeoxynucleotides and bacterial DNA. J Immunol 1996; 157: 1840–5.

8 Verthelyi D, Ishii KJ, Gursel M, Takeshita F, Klinman DM. Human peripheral blood cells differentially recognize and respond to two distinct CpG motifs. J Immunol 2001; 166: 2372–7.

9 Sparwasser T, Koch ES, Vabulas RM, Heeg K, Lipford GB, Ellwart JW, *et al*. Bacterial DNA and immunostimulatory CpG oligonucleotides trigger maturation and activation of murine dendritic cells. Eur J Immunol 1998; 28: 2045–54.

10 Hu ZL, Sun SH, Zhou FJ. The binding of CpG-oligodeoxynucleotides to cell-surface and its immunostimulatory activity are modulated by extracellular acidic pH. Vaccine 2003; 21: 485–90.

11 Vainio S, Ikonen E. Macrophage cholesterol transport: a critical player in foam cell formation. Ann Med 2003; 35: 146–55.

12 Schena M, Salon D, Heller R. Parallel human genome analysis: microarray-based expression monitoring of 1000 genes. Proc Natl Acad Sci USA 1996; 93: 10 614–9.

13 Shalon D, Smith SJ, Brown PO. A DNA microarray system for analyzing complex DNA samples using two-color fluorescent probe hybridization. Genome Res 1996; 6: 639–45.

14 Kuzuya M, Naito M, Funaki C, Hayashi T, Asai K, Kuzuya F. Lipid peroxide and transition metals are required for the toxicity of oxidized low density lipoprotein to cultured endothelial cells. Biochim Biophys Acta 1991; 1096: 155–61.

15 Yang PY, Rui YC, Li K, Huang XH, Jiang JM, Yu L. Expression of intercellular adhesion molecule-1 in U937 foam cells and inhibitory effect of imperatorin. Acta Pharmacol Sin 2002; 23: 327–30.

16 Hara A, Radin NS. Lipid extraction of tissues with a low-toxicity solvent. Anal Biochem 1978; 90: 420–6.

17 Lowry OH, Rosebrough NJ, Farr AL, Randall RJ. Protein measurement with the Folin phenol reagent. J Biol Chem 1951; 193: 265–75.

18 Wang Z, Liu YL, Jiang ZS. A new method to measure the level of *L*-arginine of aortic wall in rabbits. Chin J Arterioscler 1996; 4: 72–4.

19 Klinman DM, Yi AK, Beaucage SL, Conover J, Krieg AM. CpG motifs present in bacteria DNA rapidly induce lymphocytes to secrete interleukin 6, interleukin 12, and interferon gamma. Proc Natl Acad Sci USA 1996; 93: 2879–83.

20 Horner AA, Raz E. Immunostimulatory sequence oligodeoxynucleotide-based vaccination and immunomodulation: two unique but complementary strategies for the treatment of allergic diseases. J Allergy Clin Immunol 2002; 110: 706–12.

21 Kiener PA, Rankin BM, Davis PM, Yocum SA, Warr GA, Grove RI. Immune complexes of LDL induce atherogenic responses in human monocytic cells. Arterioscler Thromb Vasc Biol 1995; 15: 990–9.

22 Goldberg IJ. Lipoprotein lipase and lipolysis: central roles in lipoprotein metabolism and atherogenesis. J Lipid Res 1996; 37: 693–707.

23 Stein Y, Stein O. Lipoprotein lipase and atherosclerosis. Atherosclerosis 2003; 170: 1–9.

Acta Pharmacologica Sinica 2005 Nov; 26 (11): 1365–1372

Blackwell Publishing

Full-length article

Effect of protein kinase C alpha, caspase-3, and survivin on apoptosis of oral cancer cells induced by staurosporine[1]

Yu-xia ZHANG[2,4], Shi-bin YU[3,4], Jing-ping OU-YANG[2,5], Dong XIA[2], Min WANG[2], Jin-rong LI[3]

[2]Department of Pathology and Pathophysiology, School of Medicine; [3]The First Department of Oral and Maxillofacial Surgery, School of Stomatology, Wuhan University, Wuhan 430071, China

Key words

protein kinase C alpha; caspase-3; survivin protein; apoptosis; staurosporine; carcinoma, squamous cell; mouth

[1] Project supported in part by Natural Science Foundation of Hubei Province (No 304130550).
[4] Who contributed equally to this article.
[5] Correspondence to Prof Jing-ping OU-YANG.
Phn 86-27-8733-1241.
Fax 86-27-8733-1077.
E-mail zhangyuxiacn@hotmail.com

Received 2005-03-11
Accepted 2005-07-22

doi: 10.1111/j.1745-7254.2005.00205.x

Abstract

Aim: To elucidate inhibition of protein kinase C α (PKC α) activity by staurosporine on apoptosis of oral cancer cell line tongue squamous cell carcinoma (TSCCa) cells and to clarify the role of survivin and caspase-3 in mediating apoptosis. **Methods:** TSCCa cell viability was measured by MTT assay after 100 nmol/L staurosporine treatment. Apoptotic cells were identified by using phase contrast microscopy, acridine orange/ethidium bromide staining, and flow cytometry. Level of PKC α and its subcellular location were investigated using Western blot analysis. Expression of survivin and caspase-3 were evaluated using immunocytochemistry. **Results:** Staurosporine significantly inhibited the cell viability of TSCCa cells in a dose- and time-dependent manner. Marked cell accumulation in G_2/M phase was observed after 100 nmol/L staurosporine exposure for 6 h and 12 h. In addition, the percentage of apoptosis increased in a time-dependent manner, from 2.9% in control cultures to approximately 27.4% at 100 nmol/L staurosporine treatment for 24 h. Staurosporine displayed difference in inhibitory efficacy between cytosolic and membrance-derived PKC α. The content of PKCα in membrane versus cytosol decreased quickly, from 0.45 in ethanol-treated control cultures to 0.18 after staurosporine exposure for 24 h (P<0.01). After treatment with staurosporine, a time-dependent reduction of survivin and an activation of caspase-3 were observed in TSCCa cells. **Conclusion:** Staurosporine inhibited cell viability and promoted apoptosis in TSCCa cells. Inhibition of PKCα activity might be a potential mechanism for staurosporine to induce apoptosis in this cell line. The cleavage of survivin and activation of caspase-3 signaling pathway might contribute to PKC α inhibition-induced apoptosis.

Introduction

Cell proliferation, differentiation and apoptosis are central features of tissue homeostasis, and inhibition of apoptosis might be involved in the pathogenesis of cancer by prolonging cell life and sustaining growth of malignant tissues[1,2]. Protein kinase C (PKC) is a family of phospholipid-dependent serine/threonine kinases and participates in many cellular responses, including cell apoptosis, which can be inhibited by staurosporine[3–5]. The family contains at least 12 isoforms, and specific roles in cell cycle progression and in apoptosis have been hypothesized for the different PKC isoenzymes. Of these PKC isoforms, PKCα is distributed in almost all tissues and is involved in various signal transductions. Considerable evidence suggests that PKCα plays an important role in the apoptosis of some tumor cells and that the inhibition of PKCα might induce apoptosis[5,6]. In contrast, one recent study reported that elevated expression of PKCα might promote the apoptosis of gastric cancer cells[7]. However, little is known about the protein level and subcellular distribution of PKC α in the apoptosis of oral cancer cells. Elucidating the patterns of PKCα action will lead to a better understanding of the molecular mechanism of the PKCα signal pathway involved in the apoptosis of

oral cancer cells.

The activation of caspases, particularly caspase-3, appears to be a central part in most apoptotic pathways and most types of cells[8,9]. Caspases have been shown to be cleaved and possibly activated by PKCs suggesting that they act downstream of PKCs as effectors in the apoptotic machinery[6]. Survivin, a recently characterized inhibitor of apoptosis protein (IAP), is abundantly expressed in oral squamous cell carcinoma (OSCC), but undetectable in normal oral tissues[10,11], suggesting a potential role in oral carcinogenesis. However, no direct molecular interaction has been described so far between PKCα, survivin and caspase-3 in mediating apoptosis of oral cancer cells.

In the present study, we investigated the functional and molecular interactions among PKCα, survivin and caspase-3 in apoptosis induced by staurosporine with the aim of further highlighting their relevance in OSCC biology.

Materials and methods

Reagents Fetal bovine serum (FBS) and Dulbecco's modified Eagle's medium (DMEM) were obtained from Gibco Laboratories (Gibro/BRL, Grand Island, NY). MTT, acridine orange (AO), ethidium bromide (EB), propidium iodide (PI) and staurosporine were obtained from Sigma Biotechnologies (Sigma-Aldrich, Inc, Saint Louis, Missouri, USA). Staurosporine was dissolved in ethanol to make a stock solution of 1 mmol/L and diluted to their final concentrations in the culture medium. The final concentration of ethanol never exceeded 0.01%, a concentration at which there is no discernible effect on tongue squamous cell carcinoma (TSCCa) cells in comparison with the control. Primary antibodies including mouse monoclonal antibodies to PKCα (H-7, sc-8393), β-actin (C-2, sc-8432), caspase-3 (E-8, sc-7272) and rabbit polyclonal antibody against survivin (FL-142, sc-1081) were obtained from Santa Cruz Biotechnology (Santa Cruz, California, USA). An enhanced chemiluminescent detection system (ECL kit) from Amersham international Plc (Amersham Biosciences, Buckinghamshire, UK) was used for Western blot analysis. All other reagents were analytical reagents.

Cell culture TSCCa cell line was established by Dr Huixi JIN from a patient with OSCC of the tongue[12]. TSCCa cells were cultured in DMEM, supplemented with 10% heat-inactivated FBS, 100 kU/L penicillin, and 0.1 g/L streptomycin. The cells were maintained at 37 °C in a humidified atmosphere of 5% CO_2. TSCCa cells were cultured and treated with either 0.01% ethanol (vehicle) or 1–100 nmol/L staurosporine. The treated cells were examined by phase contrast microscope (Nikon Instech Co Ltd, Kanagawa, Japan) for evidence of morphological changes induced by staurosporine treatment.

MTT assay Cell viability and activity were detected using MTT dye assay, in which the dye was converted into formazan granules in the presence of reactive oxygen. TSCCa cells were plated at a density of 5×10^3 cells per well on a 96-well plate. At 24 h after seeding, straurosporine (1–100 nmol/L) was added to the culture medium. At 6 h, 12 h, and 24 h after drug treatment, MTT was added to each well at a concentration of 500 mg/L and incubated for 4 h at 37 °C. After that, media were aspirated and cells were solubilized in 400 μL Me_2SO. Cells were incubated for 10 min at 37 °C with gentle shaking. Absorbance was measured at 540 nm using a computerized microplate analyzer.

AO/EB staining To assess apoptosis, cells were stained with AO/EB. In brief, after TSCCa cells were treated with 100 nmol/L straurosporine for 24 h, nonadherent cells in the medium and trypsinized adherent cells were centrifuged at 200×*g* for 10 min at 4 °C and all but 50 μL media was removed. The pellet was resuspended with 2 μL for each 0.1 g/L AO and EB. Cells were immediately viewed using a fluorescence microscope (Leica Microsystems AG, Wetzlar, Germany). Morphology was defined according to descriptions from Kern and Kehrer for general apoptotic characteristics[13].

Flow cytometry For flow cytometric assessment of apoptosis and cell cycle phases, TSCCa cells were fixed with ice-cold 75% ethanol following 100 nmol/L staurosporine treatment for 6 h, 12 h or 24 h, and washed twice with phosphate-buffered saline (PBS). Cells were incubated at 37 °C for 30 min in PBS containing 1 g/L RNase, then stained with 100 mg/L PI. Cellular DNA content was measured by Beckman Coulter Epics Altra II cytometer (Beckman Coulter, California, USA).

PKCα subcellular fractionation and Western blot analysis TSCCa cells treated with 100 nmol/L staurosporine for 12 h and 24 h were washed twice with PBS and were then scraped from the culture vessels and collected. Harvested cells were suspended in 0.5 mL of hypotonic buffer [10 mmol/L *N*-2-hydroxyethylpiperazine-*N*′-2-ethanesulfonic acid (HEPES, pH 7.4), 1.5 mmol/L $MgCl_2$, 10 mmol/L KCl, 0.2 mmol/L phenylmethylsulfonyl fluoride (PMSF), 0.5 mmol/L DTT] and homogenized with a Dounce homogenizer at 4°C. Unlysed cells, nuclei and cell debris were pelleted by centrifugation at 1000×*g* at 4 °C for 5 min . The supernatant was centrifuged at 100 000×*g* at 4 °C for 1 h . The 100 000×*g* supernatant was designated as a cytosol fraction. The 100 000×*g* pellet was suspended in hypotonic buffer containing 1% Triton X-100 and centrifuged at 10 000×*g* for 10 min, and the resulting supernatant is referred to as the membrane fraction. Protein

samples were mixed with an equal volume of 2×sodium dodecyl sulfate polyacrylamide gel electrophoresis (SDS-PAGE) sample buffer, boiled for 5 min, and then separated using 10% SDS-PAGE gels with 20 μg of protein loaded per lane. After electrophoresis, proteins were transferred to PVDF membranes by semi-dry electrophoretic transfer. The membranes were blocked in 5% dry milk (1 h), rinsed and then incubated with primary antibody of PKCα (1:1000 dilution) overnight at 4 °C. The primary antibody was removed, membranes were washed 4 times, and 0.1 mg/L peroxidase-labeled goat secondary antibody was added for 1 h. Bands were then visualized by ECL kit and exposed to X-ray film. Percentage of membrane or cytosol band was calculated by a Bio-Rad (Richmond, CA) model GS-670 Imaging Densitometer.

Immunocytochemistry TSCCa cells were seeded on 8-chamberred glass slides and treated with 100 nmol/L staurosporine for 12 h and 24 h as described above. Cells were fixed for 10 min in 100% methanol at room temperature. Then, cells were washed with PBS, treated with 3% hydrogen peroxide to block endogenous peroxidase activity and incubated with normal serum. After a 2-h incubation with primary antibodies, cells were washed 3 times with PBS and incubated with biotin-labeled anti-mouse or anti-rabbit immunoglobin G for 20 min. After washing 3 times with PBS, cells were stained using the UltraSensitive streptavidin-peroxidase detection system (Maixin Biotechnology, Fuzhou, China). Positive reaction was seen as brown staining. One hundred cells were counted to determine the intensities of protein expression of caspase-3 and survivin by using HPLAS-2000 analysis software (Qianping Biotechnology, Wuhan, China).

Statistical analysis Data were expressed as mean±SD. Statistical significance was assessed with one-way ANOVA followed by Duncan's multiple-range test. $P<0.05$ was considered statistically significant.

Results

Effect of staurosporine on cell viability in TSCCa cells In the present study, the effect of staurosporine on TSCCa cell viability was evaluated using a MTT assay. Staurosporine exerted a marked dose- and time-dependent inhibitory effect on the viability of TSCCa cells. The effect was observed at 12 h after treatment, and increased with time, so that after 24 h with 100 nmol/L staurosporine cell viability was reduced to only 24% of the control (Figure 1).

Morphological changes in TSCCa cells induced by staurosporine To address the ability of staurosporine to induce cell death, we first investigated the effect of staurosporine on cell morphological changes using a phase contrast microscope. Numerous TSCCa cells exhibited a flat appearance in the absence of staurosporine (Figure 2A). After incubation with 100 nmol/L staurosporine, TSCCa cells presented remarkable morphological changes. TSCCa displayed a long spindle shape 6 h after stimulation (Figure 2B). Then the number of TSCCa cells decreased, with an increased, large amount of intracellular vesicles (Figure 2C). After 24 h of staurosporine stimulation, we observed that treatment resulted in cells exhibiting evidence of apoptosis, including cell detachment, loss of cell processes and membrane shrinkage, as evidenced by curling up of cells (Figure 2D).

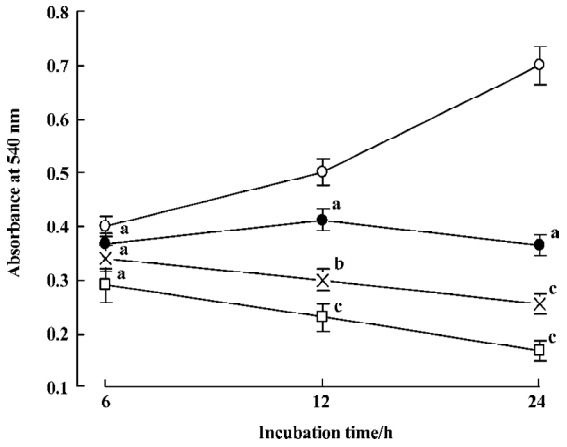

Figure 1. Effect of staurosporine on cell viability of tongue squamous cell carcinoma cells by colorimetric methylthiazol tetrazolium (MTT) assay. n=4. Mean±SD. [a]$P>0.05$, [b]$P<0.05$, [c]$P<0.01$ *vs* control. (○) control; (●) staurosporine 1 nmol/L; (×) staurosporine 10 nmol/L; (□)staurosporine 100 nmol/L.

Morphological changes of TSCCa cells were also investigated by AO/EB staining using fluorescence microscopy. Live cells stain only with AO, which shows up green inside the cell. Apoptotic cells induce fragmentation of the yellow organelle. Necrotic cells stain with EB, and are detected by their red color. The images in Figure 3 show that with a dose of 100 nmol/L staurosporine treatment for 24 h, there were increasing amounts of swollen and distorted cells coupled with organelle disintegration and a rise in necrotic cells.

DNA content analysis of TSCCa cells treated with staurosporine To determine the effects of staurosporine on cell cycle progression and apoptosis, TSCCa cells were stained with PI and subjected to flow cytometric analysis. A representative cell cycle profile of control cells is shown in Figure 4A. Treatment with 100 nmol/L staurosporine for various periods of time resulted in changed DNA content profiles. Staurosporine treatment for 6 h and 12 h caused an

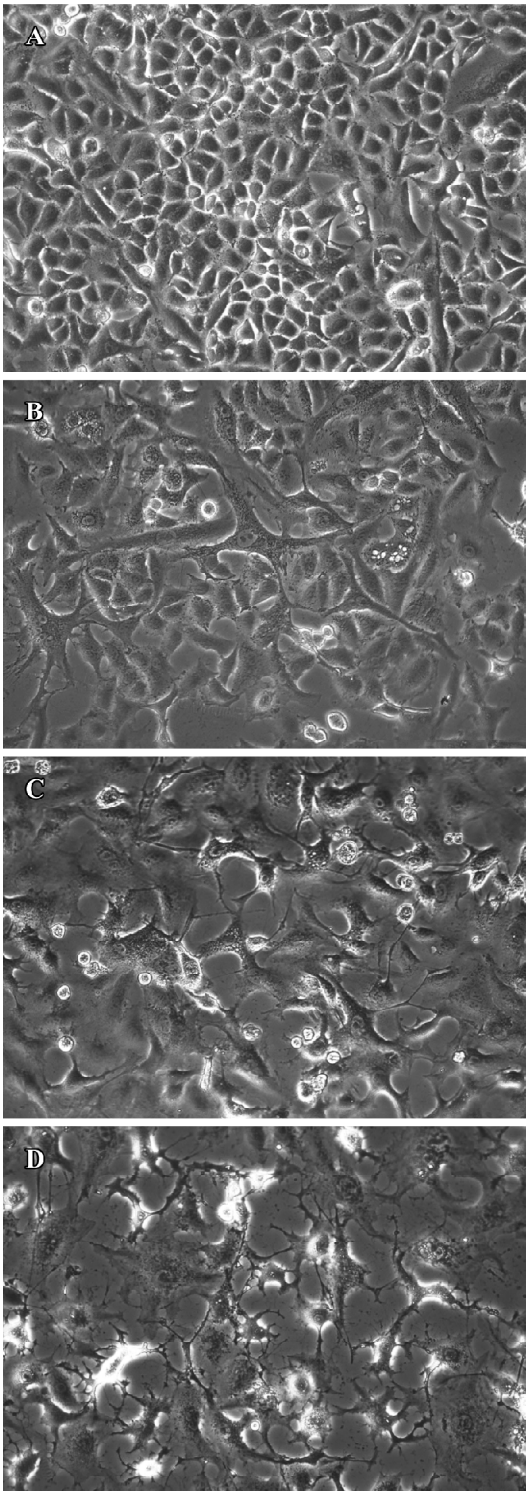

Figure 2. Morphological changes of TSCCa cells caused by 100 nmol/L staurosporine incubation and photographed with a phase-contrast microscope. (A) control ; (B) staurosporine exposure for 6 h; (C) staurosporine exposure for 12 h; (D) staurosporine exposure for 24 h. ×200.

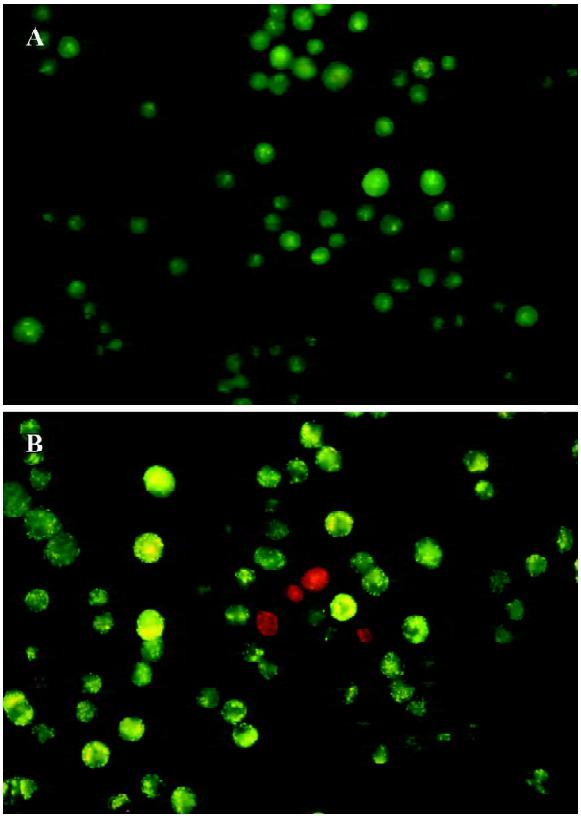

Figure 3. Fluorescence micrographs of TSCCa cells stained with acridine orange/ethidium bromide treated with or without 100 nmol/L staurosporine. (A) control TSCCa cells; (B) staurosporine exposure for 24 h. ×400.

accumulation of the cells in G_2/M phase of approximately 26.6% and 34.0%, respectively; and that of the control was approximately 9.9% (Table 1). This indicates that the appearance of a G_2/M arrest of staurosporine in TSCCa cells is time-dependent. With the time prolonged, the G_2/M arrest caused by staurosporine released and cells returned to G_0/G_1 phase and S phase. After 24 h of staurosporine treatment, the percentage of cells in G_2/M decreased to 19.8%;

Table 1. Effect of staurosporine on cell cycle distribution and apoptosis of tongue squamous cell carcinoma cells. n=3. Mean±SD. [a]P>0.05, [c]P<0.01 *vs* control.

Groups	Cell cycle/%			Apoptosis/%
	G_0/G_1	S	G_2/M	
Control	58.9±1.0	31.2±2.1	9.9±1.2	2.9±0.3
Staurosporine 6 h	58.4±1.9[a]	15.0±0.4[c]	26.6±1.8[c]	7.3±0.4[c]
Staurosporine 12 h	56.0±0.7[a]	9.9±0.4[c]	34.0±1.0[c]	10.6±1.5[c]
Staurosporine 24 h	59.5±1.0[a]	20.7±0.1[c]	19.8±0.9[c]	27.4±0.7[c]

however, this was still higher than that of the control (Figure 4).

The percentage of cells or cell fragments with DNA content less than 2 *N* (hypodiploid or apoptotic shift) increased in a time-dependent manner, from 2.9% in control cultures to approximately 27.4% at 100 nmol/L staurosporine exposure for 24 h (Table 1, Figure 4).

Changes in PKC α content and subcellular distribution in TSCCa cells Because the translocation of PKC α from cytosol to the membrane is a hallmark of PKC α activation, Western blot experiments were performed to detect the protein level of PKC α in cytosol and membrane of TSCCa cells treated with 100 nmol/L staurosporine for different periods of time. We found that PKC α is expressed in both cytosol and membrane in ethanol-treated control TSCCa cells. After treatment with staurosporine for various periods of time, PKC α content in cytosol and membrane decreased in a time-dependent manner (Figure 5). In addition, the percentage of PKC α content in membrane versus cytosol decreased quickly in staurosporine treated cells, from 0.45 in ethanol-treated control cultures to 0.18 at staurosporine exposure for 24 h (Table 2).

Effect of staurosporine on the activation of caspase-3 and the protein level of survivin To further characterize the mechanisms that control apoptosis in TSCCa cells, protein levels of caspase-3 and survivin in TSCCa cells treated with 100 nmol/L staurosporine for 12 h and 24 h was measured by immunocytochemical staining. In untreated TSCCa cells, there was a faint brown cytoplasmic staining for caspase-3 (Figure 6Aa). After incubation with staurosporine for 12 h and 24 h, cytoplasmic caspase-3 staining was substantially

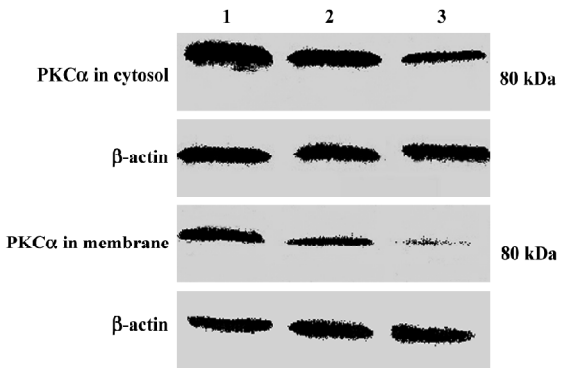

Figure 5. Subcellular localization of protein kinase Cα in tongue squamous cell carcinoma cells treated with or without 100 nmol/L staurosporine examined by Western blot. Cell lysates were fractionated into cytosol and membrane fractions, and 20 μg of protein was loaded in each lane. An antibody against β-actin was used as a loading control. Lane 1, control; Lane 2, staurosporine exposure for 12 h; Lane 3, staurosporine exposure for 24 h.

Table 2. Effect of staurosporine treatment on subcellular localization of PKCα in tongue squamous cell carcinoma cells detected by Western blot. n=3. Mean±SD. $^aP>0.05$, $^cP<0.01$ *vs* control.

Groups	Protein level of PKCα		
	Cytosol	Membrane	Membrane/ Cytosol
Control	1.00±0.10	0.45±0.03	0.45±0.01
Staurosporine 12 h	0.72±0.01^c	0.31±0.02^c	0.43±0.02^a
Staurosporine 24 h	0.55±0.02^c	0.09±0.01^c	0.18±0.01^c

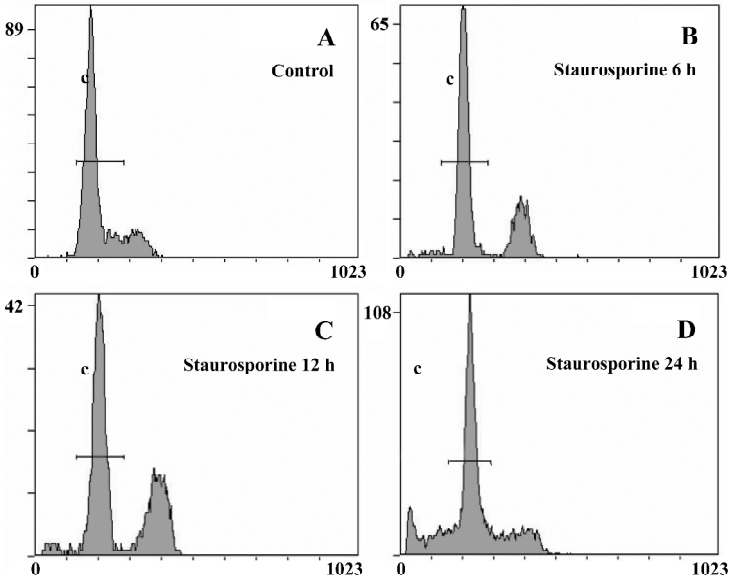

Figure 4. Effect of staurosporine on cell cycle and apoptosis of tongue squamous cell carcinoma cells measured by flow cytometry. (A) control; (B) 100 nmol/L staurosporine exposure for 6 h; (C) 100 nmol/L staurosporine exposure for 12 h; (D) 100 nmol/L staurosporine exposure for 24 h.

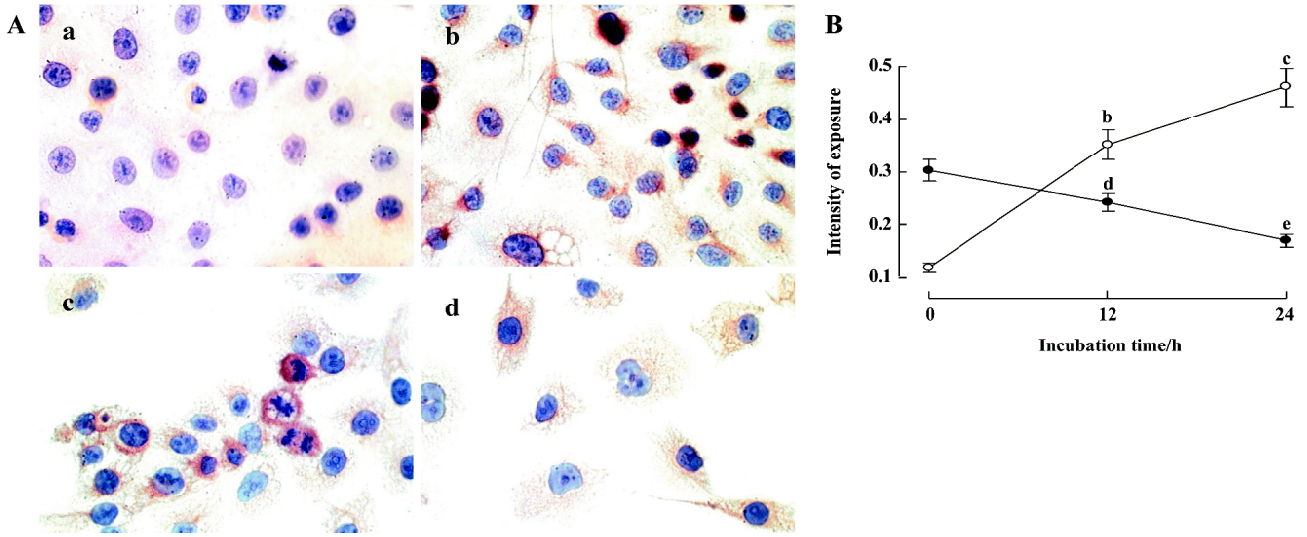

Figure 6. Protein levels of caspase-3 and survivin in tongue squamous cell carcinoma cells cultured for 12–24 h following 100 nmol/L staurosporine exposure were examined by immunocytochemical staining. (Aa) staining for caspase-3 in control cells; (Ab) staining for caspase-3 with staurosporine exposure for 24 h; (Ac) staining for survivin in control cells; (Ad) staining for survivin in staurosporine exposure for 24 h. (B) Time-dependent changes of caspase-3 and survivin in TSCCa cells after staurosporine exposure. Original magnification, ×400. n=100. Mean±SD. $^{b}P<0.05$, $^{c}P<0.01$ *vs* intensity of caspase-3 in control cells. $^{d}P>0.05$, $^{e}P<0.05$ *vs* intensity of survivin in control cells. (○) intensity of caspase-3; (●) intensity of survivin.

increased in a time-dependent manner (Figure 6B). TSCCa cells with fusiform shape, numerous intracellular vesicles and shrinking cells showed deep brown cytoplasmic granules of caspase-3 staining (Figure 6Ab).

Furthermore, a strong cytoplasmic staining of survivin was observed in control cells, especially in nuclear division cells (Figure 6Ac). After incubation with staurosporine for 24 h, survivin expression was diminished (Figure 6Ad, 6B).

Discussion

The molecular mechanisms associated with apoptosis have been widely explored, but are not yet precisely understood[14]. Staurosporine has been shown to induce apoptosis in a wide variety of cell types, such as rat cardiomyocytes, human dermal papilla fibroblasts and luteinized granulose cells. Therefore, staurosporine-induced apoptosis has been recognized as a useful model for investigating the mechanism of apoptosis in mammalian cells[15]. To assess whether staurosporine induces apoptosis in oral cancer cells, 3 specific methods were used in the present study to evaluate apoptosis. The presented data demonstrate that apoptotic changes induced by staurosporine were confirmed by morphological changes observed under phase contrast microscopy, AO/EB staining and flow cytometric analyses of cellular DNA content. A significant proportion of cells at G_2/M phase were also observed after 6 h treatment with staurosporine, and appeared at peak after 12 h of treatment. With the time prolonged, the G_2/M arrest caused by staurosporine released and cells returned to G_0/G_1 phase and S phase after 24 h of treatment, whereas a significant proportion of cells appeared at sub-G_0/G_1 apoptotic peak. Another report showed that staurosporine induced apoptosis in Chang liver cells by a mitochondria-caspase-dependent pathway, which can be suppressed by z-VAD-fmk, a general inhibitor of caspases; whereas the arrest of cells in G_2/M phase of cell cycle was not modified by z-VAD-fmk, suggesting that apoptosis and G_2/M arrest caused by staurosporine might be controlled in different independent pathways[16]. Although cells with typical apoptotic morphology were observed after the treatment, we cannot exclude the possibility that some necrosis occurred with the high staurosporine dose. However, our findings were consistent with other reports showing that staurosporine at 100 nmol/L concentration can trigger apoptosis regardless of the cell cycle status[15].

To explore more precisely the mechanisms of staurosporine-induced TSCCa cells apoptosis, we investigated whether the PKCα signal pathway was involved, as it has been shown that perturbation of PKCα activity can induce or repress apoptosis[5–7]. We determined, using Western blot analysis, that cultured TSCCa cells expressed PKC α both in cytosol and membrane under 10% serum concentration.

When TSCCa cells were treated with staurosporine, content of PKC α in cytosol and membrane decreased dramatically, especially in membrane. One important factor in determining specific functions of PKC isoforms is their intracellular localization. PKC isoforms show different patterns of subcellular localization, which can vary for the various isoforms according to tissue and cell type. PKC α typically reside in the cytosol in an inactive state. After cell stimulation, they are often translocated to other compartments. Our results suggest that inhibition of PKC α translocated from cytosol to membrane might mediate staurosporine-induced TSCCa cells apoptosis. It is not clear, however, how the complex isoform-specific subcellular distribution and stimulus-induced redistribution can be achieved. As staurosporine was a wide inhibitor of PKC, we could not exclude the possibility that other PKC isoenzymes could also mediate staurosporine-induced TSCCa cells' apoptosis.

Caspase-3 has been reported to play a key role in apoptosis[8,9]. Caspase-3 normally exists in the cytosolic fraction of cells as an inactive precursor, activating proteolytically when cells are signaled to undergo apoptosis. Multiple apoptotic signals, including serum withdrawal and treatment with a variety of pharmacological agents, activate caspase-3. The role of caspase-3 in apoptosis of oral cancer cells has not yet been reported. Lewis *et al* report that PKC inhibition induces DNA fragmentation in the colon cancer cell line, COLO 205 cells, which is blocked by cysteine protease inhibition but not mediated through caspase-3[17]. However, we have examined the caspase-3 content changes in TSCCa cells after staurosporine exposure for various periods of time, and have shown that staurosporine activates caspase-3 in a time-dependent manner. These results suggest that caspase-3 was activated by staurosporine in TSCCa cells, and might mediate staurosporine-induced TSCCa cells apoptosis.

Survivin is associated with the microtubules of the mitotic spindle. Disruption of the survivin-microtubule interaction leads to loss of survivin function and increased proapoptotic caspase-3 activity[18]. In the present study, the majority of ethanol-treated control TSCCa cells overexpressed survivin, but this was not enough to protect TSCCa cells from staurosporine-induced apoptosis. Furthermore, a dose-related decrease of survivin content in TSCCa cells was associated with the induction of apoptosis by staurosporine; these results suggest that survivin in TSCCa cells could not protect TSCCa cells from the lethal effects of staurosporine.

In conclusion, the present study demonstrates that staurosporine induces apoptosis in TSCCa cells. Our results document, for the first time, the potential roles of the inhibition of PKC α in TSCCa cells' apoptosis. This property of PKC α appears to be linked to the cleavage of survivin and activation of caspase-3. Previous studies have reported that PKC activation could cause stimulation of the transcription factor NF-κB, which in turn induced expression of the IAP[19–22]. As discussed in the present study, the IAPs are known to block caspase-3 activity and apoptosis. Therefore, it is possible that PKC α inhibition-mediated staurosporine causes reduction of survivin and results in the activation of the caspase-3 signaling pathway. Further study is needed to understand the role of other caspases in staurosporine-induced TSCCa cells apoptosis, which might be a potential target in the treatment of oral cancer diseases.

References

1 Meier P, Finch A, Evan G. Apoptosis in development. Nature 2000; 407: 796–801.

2 Thompson CB. Apoptosis in the pathogenesis and treatment of disease. Science 1995; 267: 1456–62.

3 Newton AC. Protein kinase C: structure, function, and regulation. J Biol Chem 1995; 270: 28495–8.

4 Newton AC. Protein kinase C: structural and spatial regulation by phosphorylation, cofactors, and macromolecular interactions. Chem Rev 2001; 101: 2353–64.

5 Chae HJ, Kang JS, Byun JO, Han KS, Kim DU, Oh SM, *et al*. Molecular mechanism of staurosporine-induced apoptosis in osteoblasts. Pharmacol Res 2000; 42: 373–81.

6 Adayev T, Ray I, Sondhi R, Sobocki T, Banerjee P. The G protein-coupled 5-HT_{1A} receptor causes suppression of caspase-3 through MAPK and protein kinase Cα. Biochim Biophys Acta 2003; 1640: 85–96.

7 Zhang B, Wu Q, Ye XF, Liu S, Lin XF, Chen MC. Roles of PLC-γ2 and PKCα in TPA-induced apoptosis of gastric cancer cells. World J Gastroenterol 2003; 9: 2413–8.

8 Nicholson DW, Ali A, Thornberry NA, Vaillancourt JP, Ding CK, Gallant M, *et al*. Identification and inhibition of the ICE/CED-3 protease necessary for mammalian apoptosis. Nature 1995; 376: 37–43.

9 Khan SM, Dauffenbach LM, Yeh J. Mitochondria and caspases in induced apoptosis in human luteinized granulosa cells. Biochem Biophys Res Commun 2000; 269: 542–5.

10 Lo Muzio L, Pannone G, Staibano S, Mignogna MD, Rubini C, Mariggio MA, *et al*. Survivin expression in oral squamous cell carcinoma. Br J Cancer 2003; 89: 2244–8.

11 Tanaka C, Uzawa K, Shibahara T, Yokoe H, Noma H, Tanzawa H. Expression of an inhibitor of apoptosis, survivin, in oral carcinogenesis. J Dent Res 2003; 82: 607–11.

12 Shang ZJ, Li JR, Li ZB. Effect of exogenous nitric oxide on oral squamous cell carcinoma: an *in vitro* study. J Oral Maxillofac Surg 2002; 60: 905–10.

13 Kern JC, Kehrer JP. Acrolein-induced cell death: a caspase-influenced decision between apoptosis and oncosis/necrosis. Chem Biol Interact 2002; 139: 79–95.

14 Yang LC, Yang SH, Tai KW, Chou MY, Yang JJ. MEK inhibition

enhances bleomycin A5-induced apoptosis in an oral cancer cell line: signaling mechanisms and therapeutic opportunities. J Oral Pathol Med 2004; 33: 37–45.
15 Zhang BF, Peng FF, Zhang W, Shen H, Wu SB, Wu DC. Involvement of cyclin dependent kinase 5 and its activator p35 in staurosporine-induced apoptosis of cortical neurons. Acta Pharmacol Sin 2004; 25: 1105–11.
16 Giuliano M, Bellavia G, Lauricella M, D'Anneo A, Vassallo B, Vento R, *et al*. Staurosporine-induced apoptosis in Chang liver cells is associated with down-regulation of Bcl-2 and Bcl-X_L. Int J Mol Med 2004; 13: 565–71.
17 Lewis AE, Wong BCY, Langman MJS, Eggo MC. Protein kinase C inhibition induces DNA fragmentation in COLO 205 cells which is blocked by cysteine protease inhibition but not mediated through caspase-3. Exp Cell Res 2003; 289: 1–10.
18 Shin S, Sung BJ, Cho YS, Kim HJ, Ha NC, Hwang JI, *et al*. An antiapoptotic protein human survivin is a direct inhibitor of caspase-3 and -7. Biochemistry 2001; 40: 1117–23.
19 Joshi SG, Francis CW, Silverman DJ, Sahni SK. NF-kappaB activation suppresses host cell apoptosis during Rickettsia rickettsii infection via regulatory effects on intracellular localization or levels of apoptogenic and anti-apoptotic proteins. FEMS Microbiol Lett 2004; 234: 333–41.
20 Zou T, Rao JN, Guo X, Liu L, Zhang HM, Strauch ED, *et al*. NF-kappaB-mediated IAP expression induces resistance of intestinal epithelial cells to apoptosis after polyamine depletion. Am J Physiol Cell Physiol 2004; 286: C1009–18.
21 Luschen S, Scherer G, Ussat S, Ungefroren H, Adam-Klages S. Inhibition of p38 mitogen-activated protein kinase reduces TNF-induced activation of NF-kappaB, elicits caspase activity, and enhances cytotoxicity. Exp Cell Res 2004; 293: 196–206.
22 Yang LQ, Fang DC, Wang RQ, Yang SM. Effect of NF-kappaB, survivin, bcl-2 and caspase 3 on apoptosis of gastric cancer cells induced by tumor necrosis factor related apoptosis inducing ligand. World J Gastroenterol 2004; 10: 22–5.

Acta Pharmacologica Sinica 2005 Nov; 26 (11): 1373–1381

Blackwell Publishing

Full-length article

Antitumor activity of a novel recombinant mutant human tumor necrosis factor-related apoptosis-inducing ligand[1]

Fang FANG[2], Ai-ping WANG[2], Shi-fang YANG[3]

[2]*Institute of Materia Medica, Chinese Academy of Medical Sciences and Peking Union Medical College, Beijing 100050;* [3]*Beijing Sunbio Biotech LTD, Beijing 100081, China*

Key words

antineoplastic agents; tumor necrosis factor-related apoptosis-inducing ligand; apoptosis; flow cytometry; NCI-H460 cells

[1] Project supported by the Innovation Fund for Small Technology-based Firms (No 04C26211100286) and High Technology Research and Development Program of China (863 Program) (No 2005AA2Z3H50)
[3] Correspondence to Prof Shi-fang YANG.
Phn 86-10-6891-8579.
Fax 86-10-6891-8595.
Email ysf2k@263.net

Received 2005-04-19
Accepted 2005-07-23

doi: 10.1111/j.1745-7254.2005.00206.x

Abstract

Aim: To investigate the antitumor activity and safety of a novel recombinant mutant human tumor necrosis factor-related apoptosis-inducing ligand (rmh TRAIL). **Methods:** Antitumor activity of rmh TRAIL was evaluated by using several tumor cell lines by MTT assay *in vitro*, and by using a mouse xenograft model *in vivo*. rmh TRAIL-induced apoptosis in tumor cells was detected by cell death enzyme-linked immunosorbent assay (ELISA), TdT-mediated dUTP nick-end labeling (TUNEL) assay and flow cytometry. The safety of rmh TRAIL was also evaluated in several normal human cell lines. **Results**: At the concentration of 0.32–1 000 ng/mL, rmh TRAIL remarkably inhibited the proliferation of 5 tumor cell lines from lung, colon, and breast cancer compared with wild type (wt TRAIL) *in vitro*, whereas at the concentration of 1 ng/mL–10 μg/mL, rmh TRAIL showed no or mild cytotoxicity in the normal cell lines. rmh TRAIL (3, 15 mg/kg, ip, once daily for 10 d) exerted a significant inhibition on the growth of xenograft tumor NCI-H460 in nude mice compared with the saline group ($P<0.01$), and was more potent than wt TRAIL, a positive control. The apoptosis of NCI-H460 cells was markedly induced in a concentration-dependent and time-dependent manner after rmh TRAIL treatment. The percentage of apoptotic cells induced by rmh TRAIL in NCI-H460 cells was significantly higher than that by wt TRAIL. **Conclusion**: rmh TRAIL provided potent antitumor activity *in vivo* and *in vitro*, whereas most normal human cells were resisitant to rmh TRAIL. The results suggested that rmh TRAIL might be a useful anticancer agent in future.

Introduction

Apoptosis, or programmed cell death, is a regulated process that is essential to metazoan development and tissue homeostasis[1]. Instructive apoptosis plays a physiological role in deletion of activated lymphocytes at the end of an immune response and in elimination of virus-infected cells and oncogenically transformed cells. Deregulation of programmed cell death leads to several human diseases, including cancer, neurodegenerative disorders, and acquired immunodeficiency syndrome[2]. Since the 1980s, biotherapy has become an important modality for treating cancer[3]. Biotherapy is achieved by inducing apoptosis of tumor cells, which is the ultimate objective of tumor therapy. The members of the tumor necrosis factor (TNF) family became the focus of biotherapy of cancer[4]. Despite the potential of TNF and Fas ligand (FasL; also called CD95L) to induce apoptosis in many types of tumor cells, severe toxic side-effects preclude both of these ligand from use in systemic anticancer therapy[5,6]. TNF infusion causes a lethal inflammatory response that resembles septic shock mediated by activation of the proinflammatory transcription factor NF-kappaB in vascular endothelial cells and macrophages. Infusion of agonistic anti-Fas antibody causes lethal liver damage as a result of the induction of Fas-dependent apoptosis in hepatocytes. Tumor necrosis factor-related apoptosis-inducing ligand (TRAIL, also called Apo2 ligand) is a newly discovered TNF superfamily member initially cloned

from human heart and lymphocyte cDNA libraries because of its sequence homology to TNF and FasL[7,8]. The TRAIL mRNA is constructively expressed at significant levels in many tissues in humans (eg lung, liver, spleen, kidney, thymus, prostate, ovary, intestine, periphero-lymphoid nodes, heart, placenta, and skeletal muscle). Recent studies have shown that TRAIL could induce apoptosis in numerous transformed cell lines of different lineage, but showed nontoxicity systemically unlike TNF and FasL, ionizing radiation and chemotherapy[9–11]. The combination of TRAIL and ionizing radiation or chemotherapy appears to have an enhancing effect on cancer therapy, and consequently reduces the dose and side-effects of chemotherapeutants[12–16]. Therefore, TRAIL is considered to be the most promising among antitumor agents at present.

TRAIL is expressed as a type II transmembrane protein, as are other members TNF and FasL[8], and its extracellular region forms a soluble molecule upon cleavage[17]. There are several forms of recombinant TRAIL: soluble TRAIL fusion protein (termed LZ-TRAIL) in which the extracellular region of the ligand (amino acids 95-281) is linked to an exogenous, modified leucine zipper that drives trimerization[11]; soluble TRAIL containing just the extracellular region (amino acids 114–281); polyhistidine-tagged soluble form (his-TRAIL, amino acids 114–281)[8,18]; glutathione *S*-transferase-TRAIL (GST-TRAIL, amino acids 95–281); and flag epitope-tagged form (amino acids 95–281)[8,18]. However, these other forms have deficiencies in solubility, antitumor activity and security. Therefore, Beijing Sunbio Biotech developed recombinant mutant human TRAIL (rmh TRAIL). The aim of the present work was to evaluate the antitumor activity of rmh TRAIL *in vitro* and *in vivo*, and to explore its antitumor mechanism.

Materials and methods

Expression and purification of protein *Escherichia coli* BL21 (DE3) strain was used for the expression of rmh TRAIL. After transformed the plasmid of rmh TRAIL [with a circular permuted extracellular sequence of native human Apo2L/TRAIL (amino acid 121-281)], which was built by Beijing Sunbio Biotech, into the expression vector, expression was induced by isopropyl-beta-*D*-thiogalactopyranoside (IPTG) at 37 °C for 4 h . Optimized IPTG concentration was 1 mmol/L for the protein. Bacteria were harvested and resuspended in phosphate-buffered saline (PBS, containing 137 mmol/L NaCl, 2.7 mmol/L KCl, 4.3 mmol/L Na_2HPO_4, 1.4 mmol/L KH_2PO_4, pH 7.3), sonicated on an ice bath, and centrifuged before further analysis. Purification of rmh TRAIL was performed with Ni^{2+}-loaded chelating (Amersham Pharmacia Biotech, Piscataway, USA) and purified protein was subjected to desalting with S-200 (Amersham Pharmacia Biotech). rmh TRAIL molecular weight is 19 kDa, and purity is >98%.

Reagents The wild type TRAIL (wt TRAIL) (amino acids 114–281) used in our experiments was produced by Beijing Sunbio Biotech, or purchased from Merck (Whitehouse Station, USA) (used only *in vitro*). An Annexin V-FITC apoptosis detection kit was obtained from Oncogene (Cambridge, USA). *In situ* cell death detection kit (peroxidase, POD) and cell death detection enzyme-linked immunosorbent assay (ELISA)^{PLUS} kit were from Roche (Nutley, USA). DAB kit was purchased from Beijing Zhongshan Golden Bridge Biotech. MTT was from Sigma (St Louis, USA). DTT and proteinase K was from Merck. All the reagents, including dimethyl sulfoxide (Me_2SO) (Tianjin Fuchen Chemicals Reagent Factory), ethanol, methanol, saturated phenol, paraformaldehyde (Beijing Chemical Reagents Company) were of analytical grade.

Animals BALB/c nude mice (female), 6–8 weeks old, weighing 23–27 g, were supplied by National Institute for the control of Pharmaceutical and Biological Products. Animals were kept at room temperature of 18–22 °C, with a relative humidity of 70%.

Cell culture Tumor cell lines: NCI-H460 human non-small cell lung cancer cells and COLO205 human colon cancer cells were obtained from American Type Culture Collection (ATCC); QG-56 human lung squamous cells were obtained from the cell bank of the Chinese Academy of Sciences; MDA-MB-231 and MCF-7 human breast cancer cells were obtained from the Institute of Materia Medica, Chinese Academy of Medical Sciences and Peking Union Medical College.

Normal cell lines: EC-304 human blood vessel endothelial cells were purchased from Nanjing KeyGen Biotech. Human embryonic lung fibroblasts (HELF) were obtained from the Institute of Materia Medica, Chinese Academy of Medical Sciences and Peking Union Medical College. HL-7702 normal human hepatocytes were obtained from the cell bank of the Chinese Academy of Sciences. CCC-HEH-1 human primary embryo myocardium-derived cells, CCC-HEL-1 human primary embryo liver-derived cells, CCC-HBE-2 human primary embryo trachea-derived cells, MRC-5 human embryonic lung fibroblasts, CCC-ESF-1 human primary embryo skin fibroblast cells, and HK-2 human primary nephritic tubular epithelium cells, were all obtained from cell center of the Chinese Academy of Medical Sciences and Peking Union Medical College.

NCI-H460, COLO205, QG-56, EC-304, HELF and HL-7702 were cultured in RPMI-1640 medium (GIBCO, Carlsbad, USA) supplemented with 10% fetal bovine serum (FBS) (Lanzhou

National HyClone Bio-engineering, Lanzhou, China). MCF-7 and MRC-5 were cultured in Minimum Essential Medium (MEM, GIBCO) supplemented with 10% FBS. MDA-MB-231 cells were cultured in Leibovitz's L-15 medium (GIBCO) supplemented with 15% FBS. CCC-HEH-1, CCC-HEL-1, CCC-HBE-2, and CCC-ESF-1 were cultured in Dulbecco's Modified Eagle's Medium (DMEM) medium (GIBCO) supplemented with 20% FBS. Insulin 0.2 IU/mL and hydrocortisone 1 μg/mL were added to CCC-HBE-2 cells. HK-2 cells were cultured in DF-12 medium (GIBCO) supplemented with 10% FBS.

Cell growth inhibition assay The cytotoxicity of the rmh TRAIL and wt TRAIL was determined using a colorimetric MTT assay. Cells in the logarithmic growth phase were dispersed to prepare a suspension of cell density of 6×10^4–20×10^4 mL^{-1}. Then cell suspension was seeded in a 96-well plate in total volume of 100 μL per well and incubated in a 5% CO_2 atmosphere at 37 °C for 24 h. Then, the supernatant was removed and the cells were added with 100 μL of different concentrations of the drugs followed by incubation at 37 °C for another 24 or 72 h. For controls, cells were placed in medium only. After removal of the supernatant, the cells were treated with 5.0 g/L MTT for 4 h, the purple blue sediment was dissolved in 150 μL Me_2SO, and the absorbance at 490 nm was measured using a microplate reader (BIO-RAD, Hercules, USA, model 550). The survival rate of cell growth was calculated using the following formula:

Survival rate (%)=A_{490}(drug)/A_{490}(control)×100%. Triplicate wells were analyzed for each concentration.

The 50% inhibitory concentration (IC_{50}) is the concentration required for 50% inhibition, which is calculated from the linear equation, which was educed by concentration versus survival rate regression curve. The experiments were performed in triplicates.

Mouse xenograft tumor model According to the protocol of transplantation tumor research[19], NCI-H460 tumor tissues were chopped into 2 mm^3, and then transplanted sc into the right flank of nude mice. The diameter of transplantion tumor was measured with a vernier caliper. When the tumor size grew to 280 mm^3, the 32 tumor-grafted mice were randomly divided into 4 groups (n=8); that is, negative control group (treated with normal saline), positive control group (wt TRAIL, 15 mg/kg) and rmh TRAIL treated groups (3 and 15 mg/kg). All drugs or saline were injected ip once daily for 10 d followed by another 14 d observation.

The tumor volume (TV) was calculated using the following formula:

$TV=1/2\times a\times b^2$ (in which a is the length and b is the width of tumor).

The evaluation index of anti-tumor activity was relative tumor weight inhibition ratio (%), which was calculated by the following formula:

Tumor weight inhibition ratio (%)=(1–T/C)×100% (T: test group's or positive control group's mean tumor weight; C: negative control group's mean tumor weight).

The data were then subjected to a statistical analysis (t-test) for actual efficiency of the material tested.

Assessment of apoptosis Various methods, described below, were used to evaluate NCI-H460 apoptosis.

(a) DNA fragmentation detection by ELISA A cell death detection ELISA kit was used according to the manufacturer's instructions for DNA fragment detection[20]. The DNA fragments are discrete multiples of a 180–200 bp subunit, which can be detected as a DNA ladder on agarose gel. The enrichment of mono- and oligonucleosomes in the cytoplasm of the apoptotic cells is a result of DNA degradation that occurs several hours before plasma membrane breakdown. The principle on which this test is based is the detection of mono- and oligonucleosomes in the cytoplasmic fractions of cell lysates by using biotinylated antihistone- and peroxidase-coupled anti-DNA antibodies. The enrichment of mono- and oligonucleosomes released into the cytoplasm is calculated as the ratio of absorbance of sample cells to absorbance of control cells. The enrichment factor was used as a parameter of apoptosis and is shown on the Y axis as mean±SD of triplicate experiments performed in triplicates. An enrichment factor of 1 represents spontaneous apoptosis. NCI-H460 were grown in 96-well plates and exposed to rmhTRAIL 10 ng/mL for 0.5 to 4 h or 0.0128 ng/mL to 40 ng/mL for 2 h.

(b) TdT-mediated dUTP nick-end labeling (TUNEL) assay After incubated with 15 ng/mL rmh TRAIL for 1, 2, and 4 h, NCI-H460 cells were smeared on slides, fixed by 4% paraformaldehyde in PBS (pH 7.2) for 30 min at room temperature, washed 3 times with PBS, and blocked by 0.3% H_2O_2. Then, cells were permeabilized on ice using 0.3% Triton X-100 in PBS for 2 min. Subsequent operations were refered to the manufacturer's instruction of *In situ* cell death detection kit and DAB kit. The samples were dehydrated by ethanol and cleared in dimethylbenzene, analyzed by microscopy and photos were taken using a Nikon 4 500 digital camera.

(c) Flow cytometry For apoptotic cell detection analysis, NCI-H460 cells were treated with rmh TRAIL or wt TRAIL (1, 10, and 100 ng/mL) for 12 h. All of the attached and the detached cells were harvested. Detection of the apoptotic cells was referred to the manufacturer's instruction of Annexin V-FITC apoptosis detection kit.

Results evaluation:

Non-apoptotic cells: Annexin V negative and PI negative;

Early apoptotic cells: Annexin V positive and PI negative;

Necrotic cells or late apoptotic cells: Annexin V positive and PI positive.

Statistical analysis Data were expressed as mean±SD. Data of the representatives were analyzed for statistical significance using a *t*-test. $P<0.05$ was considered statistically significant.

Results

Various tumor cell lines are sensitive to rmh TRAIL-induced death *in vitro* To explore the antitumor activity of rmh TRAIL against a spectrum of cancer cell lines, we tested its effect *in vitro* on the inhibition of 5 different cell lines derived from cancers of the lung, colon, and breast (2 lung cancer cell lines, 2 breast cancer cell lines, and 1 colon cancer cell line) by MTT assay. rmh TRAIL exerted a cytotoxic effect on these cell lines and inhibited cell growth after cells being treated for 24 h or 72 h. Furthermore, the antitumor activity of rmh TRAIL was notably higher than that of wt TRAIL, and IC_{50} for rmh TRAIL against all cell lines were significantly lower than wt TRAIL (Table 1, $P<0.01$). Treatment with rmh TRAIL at the dose of 200 ng/mL caused substantial cell death. The morphology of the cells treated by rmh TRAIL was characteristic of apoptotic cells: blebbing and shrinkage of cytoplasm (Figure 1).

Antitumor activity of rmh TRAIL in a mouse xenograft study To determine whether the tumoricidal activity of rmh TRAIL observed *in vitro* could be demonstrated *in vivo*, BALB/c nude mice were transplanted sc with NCI-H460 tumor tissue, which showed intermediate sensitivity to rmh TRAIL *in vitro* (Table 1), and allowed tumors to establish. The tumors in the control group grew steadily in an exponential manner. wt TRAIL treatment gave a 25.7% reduction in mean tumor volume, which was lower than that of rmh TRAIL. In contrast, the rmh TRAIL treated groups showed a marked reduction in tumor size, especially during the treatment period (Figure 2, Table 2). The tumors in some

Table 1. Antitumor activity of rmh TRAIL and wt TRAIL on human tumor cell lines *in vitro* represented by IC_{50}. n=3. Mean±SD. $^cP<0.01$ *vs* wt TRAIL.

Tumor cell lines	IC_{50} /μg·mL^{-1}	
	rmh TRAIL	wt TRAIL
COLO205	0.007±0.003^c	0.260±0.051
MDA-MB-231	0.006±0.004^c	0.121±0.038
NCI-H460	0.006±0.003^c	0.238±0.052
QG-56	0.012±0.003^c	0.804±0.082
MCF-7	0.086±0.038^c	>1 μg/mL

rmh TRAIL, recombinant mutant human TRAIL; wt TRAIL, wild type TRAIL.

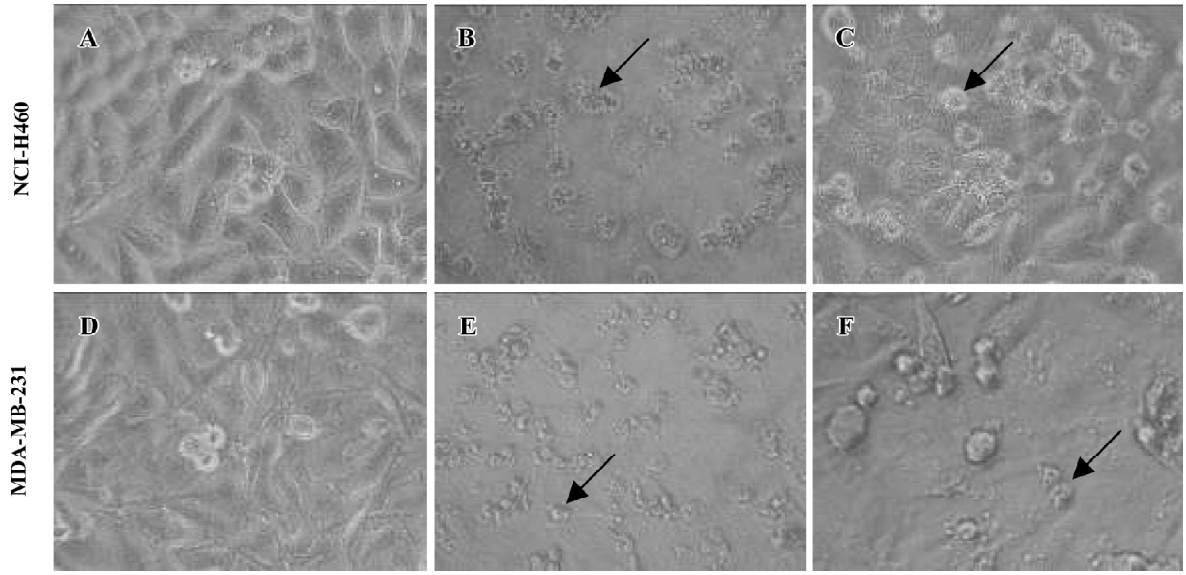

Figure 1. Morphological changes of NCI-H460 cells (A–C) and MDA-MB-231 cells (D–F), A and D: control, untreated. B and E: treated with recombinant mutant human (rmh) TRAIL 200 ng/mL for 24 h. C and F: treated with wild type (wt) TRAIL 200 ng/mL for 24 h. The photographs were taken using an Olympus CK40 inverted laboratory system microscope (×20). Arrow indicates dead cells.

Table 2. The experimental therapeutic efficacy of ip injection of rmh TRAIL and wt TRAIL on xenograft tumor NCI-H460 in nude mice. n=8. Mean±SD. ^{c}P<0.01 *vs* control. ^{f}P<0.01 *vs* rmh TRAIL 15 mg/kg. ^{i}P<0.01 *vs* rmh TRAIL 3 mg/kg.

Group	Dose/mg·kg^{-1}	Animal number		Body weight/g		Tumor weight/g	Inhibition ratio/%
		D_0	D_n	D_0	D_n		
Control	0	8	8	24.1±1.4	29.4±1.9	3.15±0.50	
rmh TRAIL	15	8	8	26.2±1.0	27.1±1.7	0.42±0.18^{c}	86.7
rmh TRAIL	3	8	8	24.5±1.6	27.4±1.0	1.12±0.36^{cf}	64.4
wt TRAIL	15	8	8	24.6±1.4	29.3±1.3	2.34±0.42^{ci}	25.7

D_0, the day of the start of treatment; D_n, the day of the end of the experiments, which was after a 10 day treatment and a 14 day withdrawal. rmh TRAIL, recombinant mutant human TRAIL; wt TRAIL, wild type TRAIL.

mice in the high-dose rmh TRAIL group became invisible during the treatment period and shortly after withdrawal. The suppressed tumors recommenced growing 5 d after withdrawal, but still more slowly than the control group. The inhibitory effect of rmh TRAIL on transplantation of tumor NCI-H460 was in a dose-dependent manner. Tumor suppression in 3 mg/kg rmh TRAIL-treated group was less than 15 mg/kg group, but greater than 15 mg/kg in the wt TRAIL-treated group (Figure 2, Table 2).

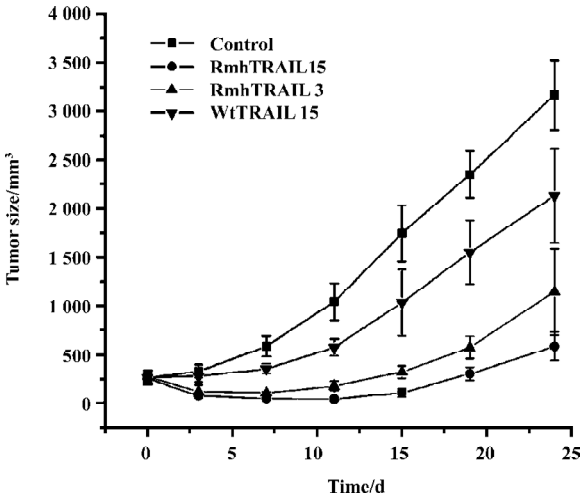

Figure 2. Inhibitory effects of rmh TRAIL and wt TRAIL on the volumes of xenograft tumor NCI-H460 in nude mice. n=8. Mean±SD. Control: normal saline group; recombinant mutant human (rmh) TRAIL-15: 15 mg/kg rmh TRAIL-treated group; rmh TRAIL-3: 3 mg/kg rmh TRAIL-treated group; wild type (wt) TRAIL-15: 15 mg/kg wt TRAIL-treated group. All drugs or saline was injected ip once daily for 10 d followed by 14-d observation.

Apoptosis induced by rmh TRAIL

a.rmh TRAIL-induced cell death of NCI-H460 cells detected by ELISA rmh TRAIL 10 ng/mL was chosen for DNA fragmentation experiment by ELISA at different time points. This concentration of rmh TRAIL-induced apoptosis showed a time-dependent manner. At 2 and 4 h after treatment, rmh TRAIL induced a significant increase of cytoplasmic nucleosomes (Figure 3A). The result accords with agarose gel electrophoesis result (data not shown). More-over, we examined different concentrations (from 0.0128 ng/mL to 40 ng/mL) of rmh TRAIL-induced apoptosis for 2 h. The result showed a dose-dependent manner (Figure 3B).

b. TUNEL assay The pictures displayed in the Figure 4 were taken after incubation with rmh TRAIL 15 ng/mL for 1, 2, and 4 h. The nucleus condensation and segmentation were observed by microscope. Lots of apoptotic bodies were found in rmh TRAIL-treated cells but none in untreated cells.

c. Flow cytometry To confirm that the percentage of apoptosis induced by various concentration of rmh TRAIL in NCI-H460 cells, Annexin V and PI double staining and flow cytometry were performed. The percentages of apoptosis induced by rmh TRAIL and wt TRAIL (1 ng/mL, 10 ng/mL, 100 ng/mL) for 12 h were 8.11%, 32.80%, 59.68% and 4.96%, 7.08%, 14.11%, respectively (Figure 5).

Effect of rmh TRAIL on normal cell types To test whether rmh TRAIL initiates apoptosis in normal cells, 9 lines of normal cells, were exposed to rmh TRAIL (1 ng/mL–10 μg/mL) or wt TRAIL (1 ng/mL–10 μg/mL) for 24 h. No morphological evidence of apoptosis was observed as induced by rmh TRAIL (except for HL-7702); in addition, there was no decreased cell viability in staining of the cells by MTT (Figure 6), which indicated that rmh TRAIL was not cytotoxic toward these normal cell types. There was mild injury on HL-7702 hepatocytes elicited by both rmh TRAIL and wt TRAIL, and no cytotoxicity on CCC-HEL-1, human primary embryo liver-derived cells (Figure 6). The IC_{50} of rmh TRAIL and wt

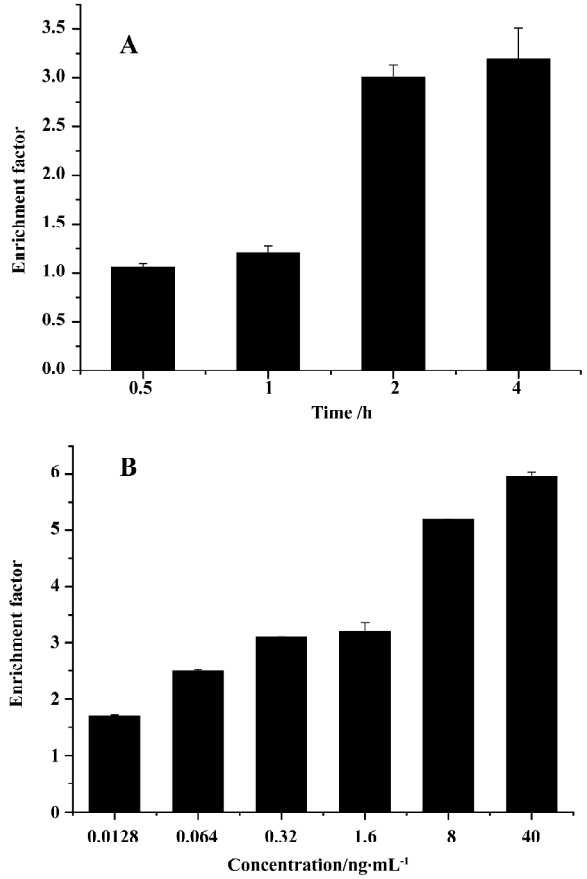

Figure 3. Quantification of nucleosomal DNA fragmentation. The cell death detection ELISA^{PLUS} was used to quantify DNA fragmentation in NCI-H460 cells undergoing apoptosis in the presence of recombinant mutant human (rmh) TRAIL; A) rmh TRAIL 10 ng/mL treated for different time (0.5, 1, 2 and 4 h); B) treatment with different concentrations of rmh TRAIL (0.0128 ng/mL–40 ng/mL) for 2 h. The rate of apoptosis is reflected by the enrichment factor of nucleosomes in the cytoplasm shown on the *Y* axis. An enrichment factor of 1 is equivalent to background apoptosis. Experiments were performed in triplicate and repeated 3 times. n=3. Mean±SD.

TRAIL on HL-7702 exceeded 10 μg/mL.

Discussion

Although TNF and FasL have potent cytotoxic activity against many types of tumor cells, the application of these death ligands to cancer therapy has been restricted by their severe toxicity to normal tissues. The discovery of TRAIL as a death ligand, with its wide tissue-mRNA distribution and its unique receptor system, suggests that this ligand might be more suitable than TNF or FasL for systemic cancer therapy.

rmh TRAIL, developed by Beijing Sunbio Biotech, is a mutant form of human native TRAIL, but the functional sequences are conservative. Native TRAIL is expressed as a type II transmembrane protein that can be cleaved proteolytically to form a soluble homotrimer[7,8]. The therapeutic potential of a recombinant soluble version of human TRAIL that can be produced in *E coli* and purified as a 60-kDa homotrimer has been evaluated[9,11]. An optimized antineoplastic agent can selectively induce apoptosis of cancer cells while sparing normal cells. Some scientists have oppugned the safety of TRAIL on hepatocytes[22,23]. To obtain a form of TRAIL that has higher antitumor activity and safety, Beijing Sunbio Biotech produced rmh TRAIL with a circular permuted extracellular sequence of native human Apo2L/TRAIL. Our previous work revealed that rmh TRAIL had a high affinity for its death receptors and water-solubility (data not shown). This molecule forms more stable homotrimers. The pharmacokinetics research of rmh TRAIL indicates that the concentration in tumor tissue was higher than that in plasma. Furthermore, rmh TRAIL was more resistant to trypsin proteolysis *in vitro* than wt TRAIL (data not shown). All of the above suggests that rmh TRAIL could contribute to long-standing antitumor activity.

The present study first assesses the antitumor activity of rmh TRAIL *in vitro*. A spectrum of cancer cell lines exhibited sensitivity *in vitro* to rmh TRAIL. This finding is consistent with previous reports that native TRAIL is cytotoxic toward cell lines from cancers of the lung, colon, and breast[9-11]. rmh TRAIL triggers more cell death *in vitro* than wt TRAIL. The study of NCI-H460 xenograft models indicates that rmh TRAIL can cause tumor regression or suppress tumor growth, and can initiate tumor cell apoptosis, which is consistent with its apoptosis-inducing activity *in vitro*. The antitumor activity of TRAIL after ip administration has been demonstrated in several mouse xenograft models of human cancers, including colorectal[9], breast[11], and glioma[24]. rmh TRAIL caused a dose-dependent suppression of tumor growth, and 15 mg/kg rmh TRAIL resulted in a 86.7% reduction in mean tumor volume, whereas wt TRAIL only caused a 25.7% reduction using the same dose. Therefore, in the present study, the antitumor activity of rmh TRAIL is higher than that of wt TRAIL in the experiments both *in vivo* and *in vitro*. Compared with wt TRAL, rmh TRAIL can achieve same antitumor activity under lower dosages.

Second, rmh TRAIL induced apoptosis in NCI-H460 was confirmed by cell death ELISA assay, TUNEL assay, and flow cytometry. Nucleus condensation, apoptotic body appearance, and DNA fragmentation are universal characteristics in the cells undergoing apoptosis. Furthermore, cell

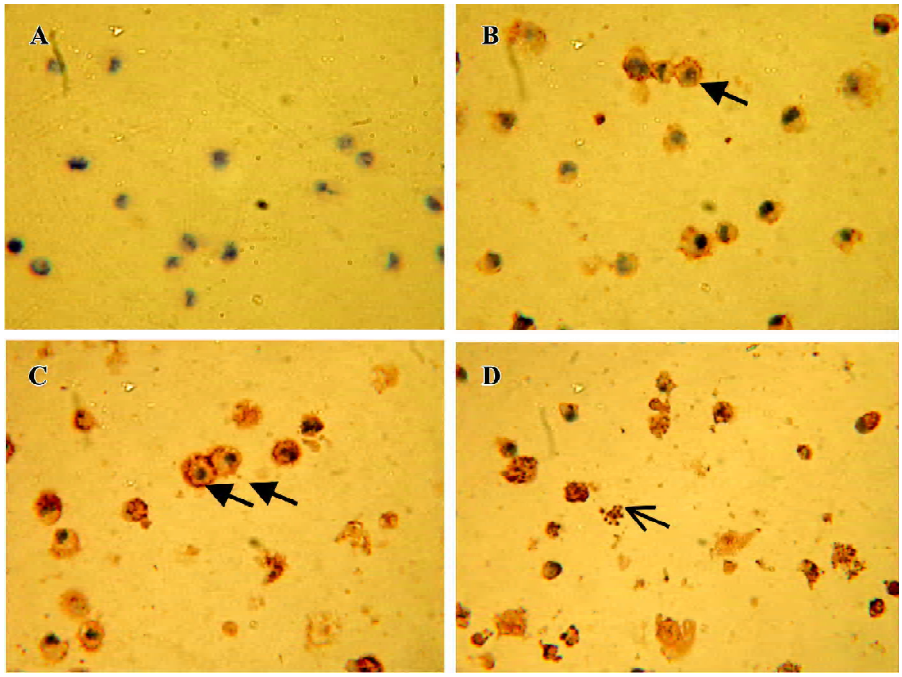

Figure 4. *In situ* detection of DNA fragmentation by TdT-mediated dUTP nick-end labeling (TUNEL) method: showing condensation and segmentation of nucleus in NCI-H460 cells at different times after treatment with 15 ng/mL recombinant mutant human (rmh) TRAIL. (A) Control (no TdT); (B) rmh TRAIL 1 h; (C) rmh TRAIL 2 h; (D) rmh TRAIL 4 h; (×20).
↑ Apoptotic cells: chromatin condensation and present circularity
↑ Apoptotic cells: small vesicles called apoptotic bodies

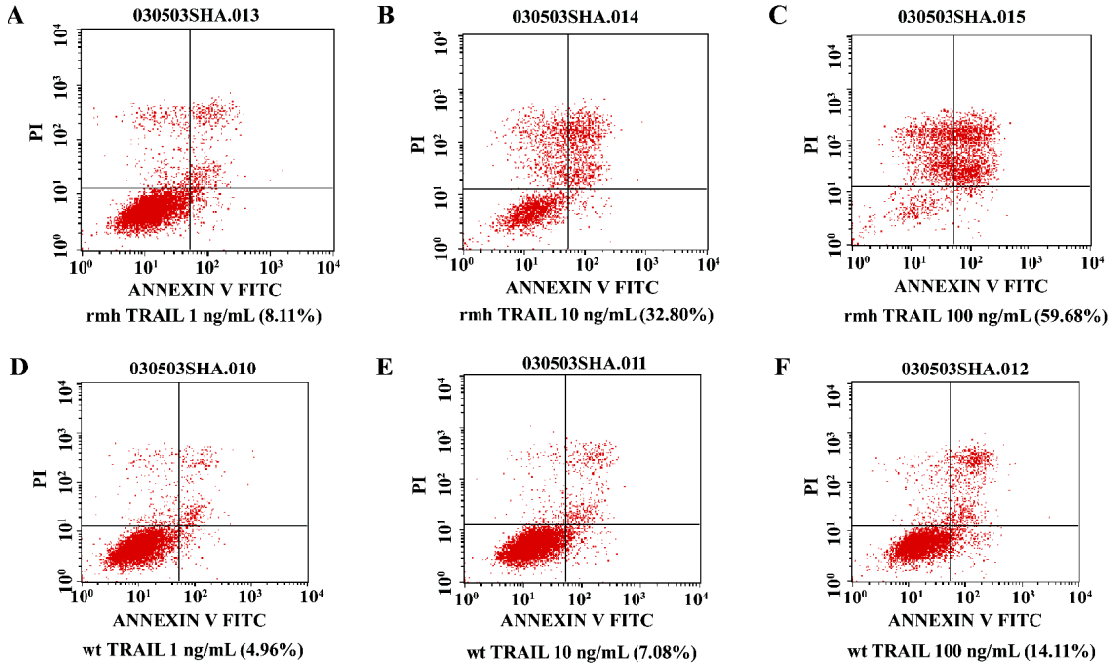

Figure 5. The flow cytometry using Annexin-V/PI double staining was performed on NCI-H460 cells. Representative dot plots of recombinant mutant human (rmh) TRAIL 1, 10, 100 ng/mL (A–C) and wild type (wt) TRAIL 1, 10, 100 ng/mL (D–F) treated for 12 h. The numbers in brackets denote percentage of apoptotic cells. The upper right quadrant represents apoptotic or necrotic cells positive for both Annexin and PI. Data from 1×10^4 cell per sample were collected.

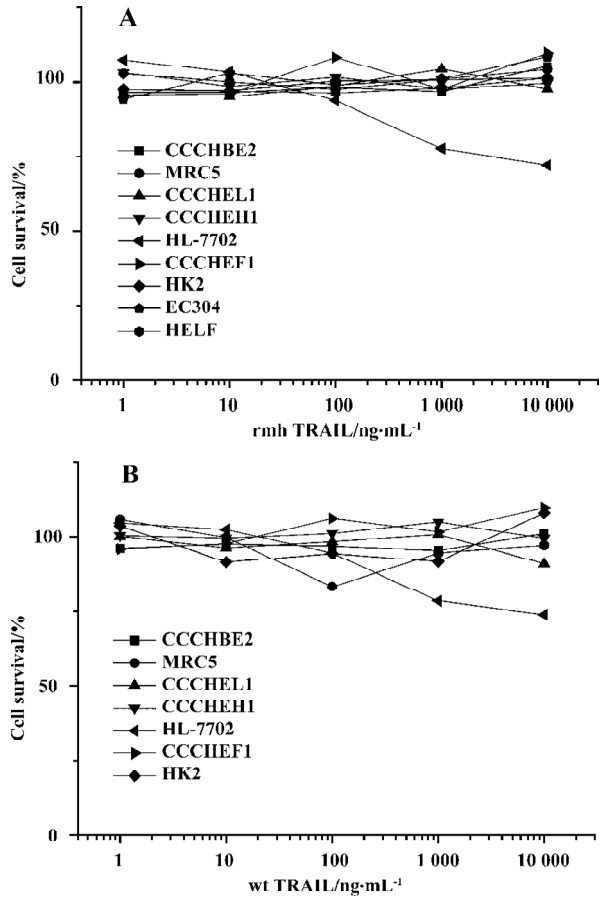

Figure 6. Effect of rmh TRAIL or wt TRAIL on proliferation in normal cell lines. Cells were incubated with serial dilutions of recombinant mutant human (rmh) TRAIL (1 ng/mL–10 μg/mL) or wild type (wt) TRAIL (1 ng/mL–10 μg/mL) for 24 h, and cell growth relative to medium controls was determined by MTT assay.

death ELISA assay and flow cytometry showed the quantity of apoptotic cells. From the evidence in the present study, it is elicited that rmh TRAIL could induce NCI-H460 apoptosis, that and it is time- and concentration-dependent.

Third, MTT assay was used to examine the cytotoxicity effect of rmh TRAIL on normal cells. Although rmh TRAIL was cytotoxic toward many tumor cell lines *in vitro*, rmh TRAIL showed no inhibition on normal cells tested in the experiment from endothelial, fibroblastic, myocardial, cutaneous, lung, renal, and tracheal origin, supporting the notion that rmh TRAIL dose did not increase cytotoxicity to generally nontransformed cells. The results are consistent with Ashkenazi *et al*[9,10,25,26]. rmh TRAIL and wt TRAIL showed mild cytotoxicity to HL-7702 cells, which are separated from adult liver. The IC_{50} of rmh TRAIL exceeded 10 μg/mL. The IC_{50} for non-small cell lung cancer and colonic cancer, the main clinical indications, are all 0.01 μg/mL, which is at least 1000 times lower than the IC_{50} for HL-7702. Furthermore, the pharmacokinetics research on nonhuman primates (cynomolgus monkeys) indicated that the maximal plasma concentration (C_{max}) of rmh TRAIL (iv, 5 mg/kg) was 25 μg/mL (data not shown). The dose used in humans would be no more than 5 mg/kg. Therefore, the C_{max} will be no more than 25 μg/mL, which is less than the IC_{50} of HL-7702. The results suggest that the clinical effective dose of rmh TRAIL might be safety for human.

In conclusion, rmh TRAIL provided potent antitumor activity *in vitro* and *in vivo*, although it did not exert obvious cytotoxicity on a wide variety of normal cells. Therefore, rmh TRAIL might prove to be a useful new agent in fighting cancer cells, leaving normal cells unharmed.

References

1 Jacobson MD, Weil M, Raff MC. Programmed cell death in animal development. Cell 1997; 88: 347–54.
2 Steller H. Mechanisms and genes of cellular suicide. Science 1995; 267: 1445–9.
3 Wyllie AH. Apoptosis: cell death in tissue regulation. J Pathol 1987; 153: 313–6.
4 Moriya N, Miwa H, Orita K. Antitumor effects of bacterial lipopolysaccharide and tumor necrosis factor in mice. Jpn J Surg 1984; 14: 163–6.
5 Ishida Y, Kondo T, Tsuneyama K, Lu P, Takayasu T, Mukaida N. The pathogenic roles of tumor necrosis factor receptor p55 in acetaminophen-induced liver injury in mice. J Leukoc Biol 2004; 75: 59–67.
6 Lombard C, McKallip RJ, Hylemon PB, Nagarkatti PS, Nagarkatti M. Fas ligand-dependent and -independent mechanisms of toxicity induced by T cell lymphomas in lymphoid organs and in the liver. Clin Immunol 2003; 109: 144–53.
7 Wiley SR, Schooley K, Smolak PJ, Din WS, Huang CP, Jillian K, *et al*. Identification and characterization of a new member of the TNF family that induces apoptosis. Immunity 1995; 3: 673–82.
8 Pitti RM, Marsters SA, Ruppert S, Donahue CJ, Moore A, Ashkenzai A. Induction of apoptosis by Apo-2 ligand, a new member of the tumor necrosis factor cytokine family. J Biol Chem 1996; 271: 12687–90.
9 Ashkenazi A, Pai RC, Fong S, Leung S, Lawrence DA, Marsters SA, *et al*. Safety and antitumor activity of recombinant soluble Apo2 ligand. J Clin Invest 1999; 104: 155–62.
10 Kelley SK, Harris LA, Xie D, DeForge L, Totpal K, Bussiere J, *et al*. Preclinical studies to predict the disposition of Apo2L/tumor necrosis factor-related apoptosis-inducing ligand in humans: characterization of *in vivo* efficacy, pharmacokinetics, and safety. J Pharmacol Exp Ther 2001; 299: 31–8.
11 Walczak H, Miller RE, Ariail K, Gliniak B, Griffith TS, Kubin M, *et al*. Tumoricidal activity of tumor necrosis factor-related apoptosis-inducing ligand *in vivo*. Nat Med 1999; 5: 157–63.
12 Voelkel-Johnson C, King DL, Norris JS. Resistance of prostate cancer cells to soluble TNF-related apoptosis-inducing ligand

(TRAIL/Apo2L) can be overcome by doxorubicin adenoviral delivery of full-length TRAIL. Cancer Gene Ther 2002; 9: 164–72.

13 Yoshida S, Narita T, Koshida S, Ohta S, Takeuchi Y. TRAIL/Apo2L ligands induce apoptosis in malignant rhabdoid tumor cell lines. Pediatr Res 2003; 54: 709–17.

14 Bouralexis S, Findlay DM, Atkins GJ, Labrinidis A, Hay S, Evdokiou A. Progressive resistance of BTK-143 osteosarcoma cells to Apo2L/TRAIL-induced apoptosis is mediated by acquisition of DcR2/TRAIL-R4 expression: resensitisation with chemotherapy. Br J Cancer 2003; 89: 206–14.

15 Frese S, Brunner T, Gugger M, Uduehi A, Schmid RA. Enhancement of Apo2L/TRAIL(tumor necrosis factor-related apoptosis-inducing ligand)-induced apoptosis in non-small cell lung cancer cell lines by chemotherapeutic agents without correlation to the expression level of cellular protease caspase-8 inhibitory protein. J Thorac Cardiovasc Surg 2002; 123: 168–74,

16 Evdokiou A, Bouralexis S, Atkins GJ, Chai F, Hay S, Clayer M, *et al*. Chemotherapeutic agents sensitize osteogenic sarcoma cells, but not normal human bone cells, to Apo2L/TRAIL-inducing apoptosis. Int J Cancer 2002; 99: 491–504.

17 Mariani SM, Matiba B, Armandola EA, Krammer PH. Interleukin 1 beta-converting enzyme related proteases/caspases are involved in TRAIL-induced apoptosis of myeloma and leukemia cells. J Cell Biol 1997; 137: 221–9.

18 Marsters SA, Pitti RM, Donahue CJ, Ruppert S, Bauer KD, Ashkenazi A, *et al*. Activation of apoptosis by Apo-2 ligand is independent of FADD but blocked by CrmA. Curr Biol 1996; 6: 750–2.

19 Wand WR. *In vivo* methods. In: Teicher BA, editor. Anticancer drug development guide, preclinical screening, clinical trials, and approval. Humana Press: Totowa NJ; 1997. p59–213.

20 Aragane YD, Kulms D, Metza D, Wilkes G, Poppelman B, Luger TA, *et al*. Ultraviolet light induces apoptosis via direct activation of CD95 (Fas/Apo-1) independently of its ligand CD95L. J Cell Biol 1998; 140: 171–82

21 Hymowitz SG, O'Connell MP, Ultsch MA, Hurst A, Totpal K, Ashkenzai A, *et al*. A unique zinc-binding site revealed by a high-resolution x-ray structure of homotrimeric Apo2L/TRAIL. Biochemistry 2000; 39: 633–40.

22 Armeanu S, Lauer UM, Smirnow I, Schenk M, Weiss TS, Gregor M, *et al*. Adenoviral gene transfer of tumor necrosis factor-related apoptosis-inducing ligand overcomes an impaired response of hepatoma cells but causes severe apoptosis in primary human hepatocytes. Cancer Res 2003; 63: 2369–72.

23 Mundt B, Kuhnel F, Zender L, Paul Y, Tillmann H, Trautwein C, *et al*. Involvement of TRAIL and its receptors in viral hepatitis. FASEB J 2003; 17: 94–6.

24 Roth W, Isenman S, Naumann U, Kugler S, Bahr M, Dichgans JA, *et al*. Locoregional Apo2L/TRAIL eradicates intracranial human malignant glioma xenografts in athymic mice in the absence of neurotoxicity. Biochem Biophys Res Commun 1999; 265: 479–83.

25 Lawrence D, Shahrokh Z, Marsters S, Achilles K, Shih D, Mounho B, *et al*. Differential hepatocyte toxicity of recombinant Apo2L/TRAIL versions. Nat Med 2001; 7: 383–5.

26 Srivastava RK. TRAIL/Apo-2L: mechanisms and clinical applications in cancer. Neoplasia 2001; 3: 535–46.

Acta Pharmacologica Sinica 2005 Nov; 26 (11): 1382–1386

Blackwell Publishing

Full-length article

Induction of liver cytochrome P450 1A2 expression by flutamide in rats[1]

Hai-xue WANG, Xiao LIU, Chang-jiang XU, Xiao-chao MA[3], Jian-er LONG[4], Duan LI[4,5]

[2]Department of Pharmacology, School of Pharmacy, Fudan University, Shanghai 200032, China; [3]State Key Laboratory of Drug Research, Shanghai Institute of Biological Sciences, Shanghai Institute of Materia Medica, Chinese Academy of Sciences, Shanghai 200031, China; [4]Institute of Molecular Virus, School of Basic Medical Science, Fudan University, Shanghai 200031, China

Key words

flutamide; cytochrome P450 1A2; induction

[1] Project supported by Fudan University Innovation Foundation (No CQF303801).
[5] Correspondence to Prof Duan LI.
Phn 86-21-5423-7465.
E-mail dli@shmu.edu.cn

Received 2005-06-24
Accepted 2005-08-15

doi: 10.1111/j.1745-7254.2005.00211.x

Abstract

Aim: To investigate the modulation of liver cytochrome P450 1A2 (CYP1A2) expression by giving flutamide to adult rats. **Methods:** Rats were given 50, 100, and 200 mg/kg *po* of flutamide for 2 weeks. Liver CYP1A2 mRNA was measured using reverse transcription-polymerase chain reaction. CYP1A2 protein was detected using immunoblotting. CYP1A2 activity was assayed using high performance liquid chromatography, with caffeine as the CYP1A2 substrate. **Results:** *CYP1A2* mRNA levels after flutamide treatment at 100 mg/kg and 200 mg/kg were, respectively, 1.86 and 3.11-fold higher than those of the control. Correspondingly, CYP1A2 protein increased 1.78 and 2.89-fold and CYP1A2 activity increased approximately 1.65 and 2.83-fold, respectively, relative to controls. Flutamide treatment at 50 mg/kg had no significant effect on CYP1A2 mRNA, protein, or enzyme activity. **Conclusion:** Giving rats flutamide induced liver CYP1A2 expression in a dose-dependent manner.

Introduction

Flutamide, 3'-trifluoromethyl-4'-nitro-2-methylpropinoylanilide, is a nonsteroidal antiandrogen[1,2] devoid of other hormonal activity and is recognized worldwide as the most beneficial drug for the treatment of patients with advanced prostate cancer[3–5] when used in combination with various luteinizing hormone-releasing factor agonists. This antiandrogen is also used in combination with oral contraceptives for the treatment of hirsutism[6] and benign prostatic hyperplasia[7, 8].

However, flutamide therapy is associated with hepatitis in a few subjects. The incidence of liver toxicity (as defined by an increase in serum transaminase activity of fourfold greater than upper normal limits) was found to be 0.36% in 1091 consecutively treated prostate cancer patients[9–11]. Flutamide-induced hepatitis was decreased using piperonyl butoxide [cytochrome P450 (CYP450) inhibitor] and increased using β-naphthoflavone (CYP450 1A inducer)[12].

Previous results show that CYP1A2 is involved in flutamide bioactivation[12,13]. CYP1A2 is a cytochrome P-450 enzyme constitutively expressed in the liver, which catalyzes the metabolism of many drugs, such as caffeine, phenacetin, and propranolol[14]. The enzyme also participates in the metabolic activation of chemical mutagens in cooked food such as 2-amino-3-methylimidazo[4,5-f]quinoline and 2-amino-3,8-dimethylimidazo[4,5-f]quinoxaline and 2-amino-1-methyl-6-phenylimidazo[4,5-b]pyridine[15]. Previous studies have reported flutamide bioactivation using the P450 enzyme system generated a nitro anion free radical after treatment[16]. These radicals can bind covalently to proteins and lipids, or remove hydrogen atoms from polyunsaturated fatty acids in lipids, thereby initiating lipid peroxidation and liver cell injury[17]. Therefore, CYP1A2 increase might be a risk factor for flutamide-associated hepatotoxicity or carcinogenicity. In the present study, we investigate the modulation of CYP1A2 expression in adult male rats given flutamide for 2 weeks.

Materials and methods

Chemicals Flutamide was provided by the Shanghai Hongqi Pharmaceutics Factory. Trizol reagent was obtained from Life Technologies and reverse transcription-polymerase chain reaction kits were obtained from Sangon Biological Technique. Caffeine and its metabolite, and β-hydroxyethyl-

theophyline (HT) were obtained from Sigma Chemical Company. Rabbit anti-rat CYP1A2 monoclonal antibody was obtained from Santa Cruz Biotechnology (kindly provided by Dr XC MA).

Animals and treatment Adult male Sprague-Dawley rats weighing between 200 g and 250 g (Experimental Animal Center of Fudan University, grade II, certification No 01212) were housed at a temperature of 20 °C–25 °C under a 12 h light/dark cycle with 50% relative humidity in filtered and pathogen-free air. The animals were acclimatized for 1 week prior to use. For CYP1A2 induction studies, rats were divided into five groups of 10 animals each. The first group was given 0.5% carboxymethylcellulose sodium (CMC) as a control, and the second group of rats received 3-methylcholanthrene (3-MC, 30 mg/kg, ip, for 5 d) as a positive control for CYP1A2 induction. Flutamide and 3-MC were also suspended in 0.5% CMC. The rats were treated once daily, ig, for 14 consecutive days. All rats were killed on d 16. Livers were excised and immediately frozen on ice and stored at -80 °C for total RNA and liver microsomal preparation.

RNA extraction and cDNA synthesis Total RNA was obtained from frozen rat livers (0.5 g–1 g) using Trizol reagent. The RNA concentration was determined spectroscopically at 260 nm, and 5 μg of total RNA was taken for reverse transcription. Random primer (300 ng) was added and primer annealing was performed using incubation for 10 min at 65 °C and 10-min progressive cooling on ice. Deoxynucleotides (dNTP) (4 mmol/L each), 5 μL of 10×reaction buffer, 50 U of block ribonuclease inhibitor, and 200 U of SuperScript II RNase reverse transcriptase were added to a final volume of 50 μL, and samples were incubated at 42 °C for 30 min. The reaction was stopped by heating to 90 °C for 5 min. Control samples contained distilled water instead of RNA. The synthesized cDNA was stored at -20 °C until use.

Polymerase chain reaction Reverse transcription sample of 2.5 mL was added to the corresponding polymerase chain reaction mixture containing 0.5 μmol/L sense and antisense primer, 2 mmol/L $MgCl_2$, 10 mmol/L Tris-HCl (pH 9), 50 mmol/L KCl, 0.1% Triton X-100, and 80 μmol/L dNTP. After heating at 95 °C for 5 min and cooling to the primer-annealing temperature for 5 min (60 °C), 2 U of *Taq* DNA polymerase was added. The following primers were used: CYP1A2 forward (+127to+147), 5'-GGACCCTGGGGCTTGCCCTTC-3'; reverse (+484 to +504), 5'-AGCCTCTTTGCTCACGTGCTC-3'; β-actin forward (+59to+69), 5'-CCCAAGTCGCCTCC-GTCCCGC-3'; reverse (+894 to +914), 5′-CCCTCCAGGAGCCCCATGAGC-3'. The specificity of *CYP1A2* primers was confirmed through alignment with the CYP subfamily DNAs. Amplification conditions for all primer pairs were used as follows: 94 °C 30 s, 60 °C 30 s, and 72 °C 30 s for 30 cycles. β-actin segment was amplified separately and used as an external standard, because interaction of primer pairs caused a decrease in signal intensity. A total 12 μL of each preparation was subjected to agarose gel electrophoresis in the presence of ethidium bromide. The gel was photographed using Polaroid 665 film and the intensity of each band was quantified using the software provided with the ABI 7700 system. Each assay was performed in triplicate. Results were expressed as a ratio of the optical intensity of the *CYP1A2* to that of the β-actin. This approach allows for the semiquantita-tion of the expression of the *CYP1A2* gene.

Immunoblot analysis Liver microsomes were prepared as described by Kamataki and Kitagawa[18]. The protein concentration was determined using Bradford's method[19], using a protein assay with bovine serum albumin as a standard. Three micrograms of microsomal protein were resolved separately by electrophoresis on 10% SDS-polyacrylamide gel and then transferred onto a nitrocellulose membrane. The membrane was incubated with a rabbit anti-rat CYP1A2 monoclonal antibody, and further incubated with goat anti-rabbit secondary antibody conjugated with horseradish peroxidase, followed by detection with 3,3'-diaminobenzidine and hydrogen peroxide. The membrane was scanned with an image scanner, and the signal intensity was quantified using the software provided with the ABI 7700 system. In the present study, the levels of CYP1A2 proteins were in the linear range for densitometric readings.

CYP1A2 activity Caffeine was used as a probe for CYP1A2 activity and plasma caffeine (137X) and its metabolite (17X) were assayed using high performance liquid chromatography[20]. After the last dose of flutamide and overnight fast, each rat received 20 mg/kg (ip) of caffeine. Blood samples (2 mL) were drawn after caffeine administration. Plasma was separated and frozen at -20°C for later analysis. The mixtures of plasma containing 17X and 137X was extracted with chloroform/isopropanol (9:1). The residue remaining after evaporation was dissolved in 0.1 mL elution and 20 μL was injected into the chromatographic system. HT was chosen as an internal standard (IS). All components were separated isocratically on a reversed-phase column using 0.05% acetic acid:acetonitrile:methanol (82:8:10) as a mobile phase at a flow rate of 1 mL/min. Ultraviolet detection wavelength was 282 nm. The retention times for 17X, 137X, and IS were 4.50 min, 5.03 min, and 8.13 min, respectively. The CYP1A2 activity was expressed as a ratio of the concentration of 17X to that of 137X observed 6 h after giving caffeine.

Statistical analysis The statistical significance of the difference between the means of the two groups was assessed using the independent *t* test (SPSS software package, 1997). $P<0.05$ was considered statistically significant.

Results

***CYP1A2* mRNA levels** The levels of *CYP1A2* mRNA were normalized using a comparison with β-actin, constitutively expressed in the rat liver. The increase in *CYP1A2* mRNA was expressed as a percentage of the control. After flutamide treatment (50 mg/kg) of rats for 14 d, liver *CYP1A2* mRNA levels were similar to control levels, but *CYP1A2* mRNA levels were increased 1.86 and 3.11-fold relative to controls in rats in flutamide 100 mg/kg and 200 mg/kg group, respectively. *CYP1A2* mRNA levels were increased 15.6-fold by 3-MC treatment (Figure 1).

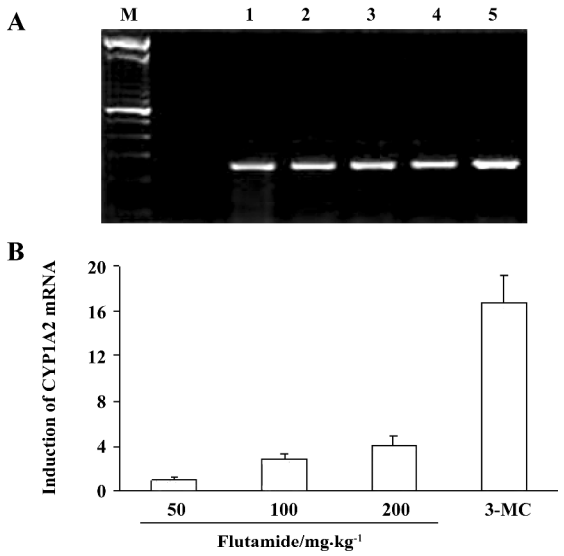

Figure 1. Effects of flutamide on cytochrome P450 1A2 (CYP1A2) mRNA levels in rats. (A) Total RNA was extracted from liver tissues, CYP1A2 and β-actin mRNA levels were detected using reverse transcription-polymerase chain reaction. Each lane contains 1 μg total of RNA from the liver of the control rats, flutamide and 3-MC treated rats. Lane 1 corresponds to the control liver, whereas lanes 2, 3, and 4 correspond to liver RNA from rats treated with flutamide at 50 mg/kg, 100 mg/kg, and 200 mg/kg, respectively. Lane 5 corresponds to liver RNA from the 3-MC treated rats. (B)Signal intensity was quantified by a bioimage analyzer (n=10). The signals were normalized using β-actin. The columns represent the induction (fold) of *CYP1A2* mRNA relative to the control.

CYP1A2 protein Similar results were obtained for the analysis of the P450 protein. After 50 mg/kg flutamide treatment, CYP1A2 protein in rat liver microsomes was similar to that in the control group. However, CYP1A2 protein levels increased 1.78 and 2.89-fold respectively, after 100 mg/kg and 200 mg/kg flutamide treatment as compared to those in controls. In contrast, 3-MC treatment increased the CYP1A2 protein content 13.8-fold (Figure 2).

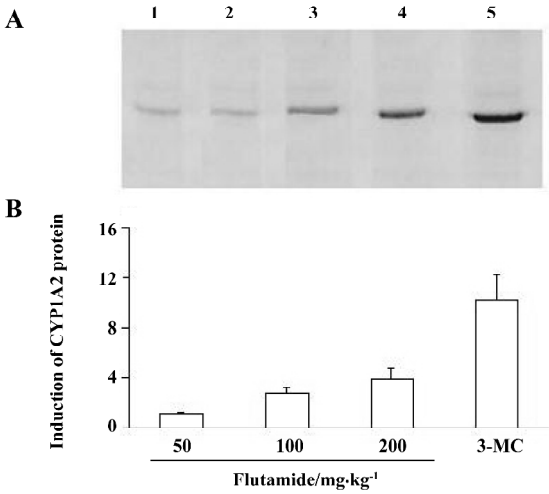

Figure 2. Induction of cytochrome P450 1A2 (CYP1A2) protein in the rat liver after flutamide treatment. (A) Liver microsomes (3 g) were separated using SDS-polyacrylamide gel electrophoresis, blotted onto a nitrocellulose membrane, and then probed with antibodies against rat CYP1A2. Liver microsomes prepared from 3-MC-treated rats were used as positive control in these analyses (lane 5). Lanes 2, 3, 4 correspond to liver microsomes from rats treated with flutamide (50 mg/kg, 100 mg/kg, and 200 mg/kg), respectively. Lane 1 corresponds to liver microsomes from control rats. (B) Immunoblots were scanned with an image scanner and then analyzed using software provided with the ABI 7700 system (n=10). The columns represent the induction (fold) of CYP1A2 protein as compared to the control.

CYP1A2 enzyme activity Caffeine is hydroxylated to form paraxanthine (17X) using CYP1A2. Concentration ratio of caffeine metabolite paraxanthine to caffeine (17X/137X) was used to express the activity of CYP1A2. After giving caffeine for 6 h, CYP1A2 activity in rats treated with flutamide (50 mg/kg) was similar to that in the control group. In rats given 100 mg/kg and 200 mg/kg of flutamide, CYP1A2 enzyme activity increased 1.65 and 2.83-fold, respectively, as compared to that in the control group. 3-MC increased CYP1A2 activity 8.50-fold more than those in the control group (Figure 3).

Discussion

In the present study, *CYP1A2* mRNA, protein, and enzyme activity were induced by flutamide treatment in rats.

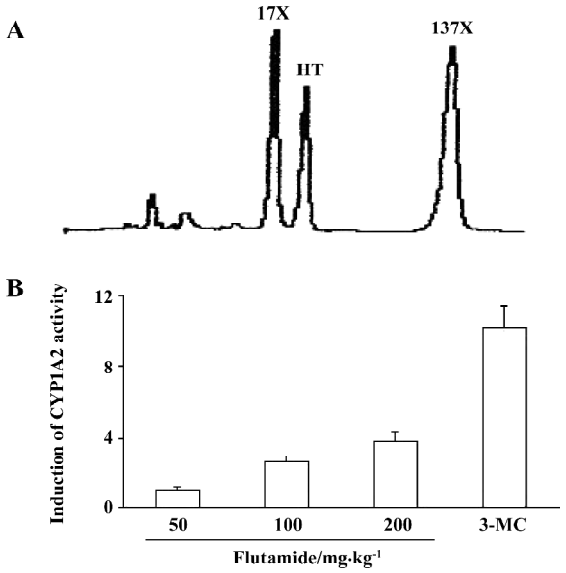

Figure 3. Increase of cytochrome P450 1A2 (CYP1A2)enzyme activity using flutamide treatment. (A) Chromatograms of caffeine (137X), its metabolite paraxanthine (17X) and β-hydroxyethyl-theophylline (HT) in serum sample, the retension time for 17X, HT, and 137X were 4.50 min, 5.03 min, and 8.13 min, respectively. (B) CYP1A2 activity (fold) in flutamide (50, 100, 200 mg/kg) and 3-MC treated-rats as compared to the controls, which is expressed as ratio of caffeine metabolite (paraxanthine) concentration to that of caffeine.

It is reasonable to speculate that flutamide is a CYP1A2 inducer in rats. This P450 induction is dose-dependent as it increases with increasing amounts of flutamide in the liver. The magnitude of CYP1A2 induction assessed using three different parameters, that is, mRNA, protein, and enzyme activity, was found to be comparable. The differences between the mRNA and protein induction and between protein and enzyme activity in rats were less than 2-fold; therefore, it is highly probable that the CYP1A2 induction occurs mainly at a pretranslational level, and we speculate that flutamide-mediated CYP1A2 induction is a result of increased rate of transcription.

CYP1A2 is one of the major constitutively expressed P-450 in the liver tissue. It catalyzes steroid hydroxylations, such as 17β-estradiol 2-hydroxylation[21,22]. Of considerable interest is the ability of P4501A2 to catalyze the *N*-hydroxylation of carcinogenic aryl amines and heterocyclic amines[23–25]. The oxidized products can modify DNA, either directly or following conjugation with acryl or sulfate groups[26,27]. The heterocyclic amines are of considerable interest in that they are found in charbroiled food and cigarette smoke. There is some epidemiological evidence that elevated levels of CYP1A2 can be a predisposing factor to colon cancer, although the risk is marginal unless high levels of N-acetyltransferase are present along with high charbroiled meat consumption.

Flutamide can be metabolized by CYP1A2 to form the reactive metabolites. Nitro radical and one-electron reduction products have toxic effects on the liver cells[16]. Induction of CYP1A2 can increase the formation of toxic metabolites, and increase the incidence of liver toxicity. This might explain why flutamide had no significant liver toxicity after low doses (50 mg/kg), although it caused liver toxicity at higher doses (100 mg/kg and 200 mg/kg) in previous studies[28]. Therefore, the induction of CYP1A2 might have a large influence on the therapeutic efficacy and liver toxicity associated with flutamide treatment. Induction of CYP1A2 using flutamide treatment and its possible effects on the metabolism of other drugs and the carcinogenesis of heterocyclic amines in human beings would be useful topics of further study.

Acknowledgments

We thank Yi WANG for kindly supplying β-actin primer. The supports from PhD Xin WU and Hong-Xin ZHU from our university are also acknowledged.

References

1 Neri RO, Florance K, Koziol P. A biological profile of a nonsteroidal antiandrogen, SCH13521(4'-nitro-3'trifluoromethylisobutyranilide). Endocrinology 1972; 91: 427–37.
2 Neri RO, Monahan M. Effects of novel nonsteroidal antiandrogen on canine prostatic hyperplasia. Invest Urol 1972; 10: 123–30.
3 Labrie F, Dupont A, Cusan L, Manhes G, Bergeron N, Lacourciere Y. Combination therapy with castration and flutamide: today's treatment of choice for prostate cancer. J Steroid Biochem 1989; 33: 817–21.
4 Chen DH, Kaung HL, Miller CM, Resnick MI, Marengo SR. Microarray analysis of changes in renal phenotype in the ethylene glycol rat model of urolithiasis: potential and pitfalls. BJU Int 2004; 93: 637–50.
5 Pitts WR Jr. The use of flutamide as a single antiandrogen treatment for hormone-refractory prostate cancer. BJU Int 2004; 93: 1119–20.
6 Andrade RJ, Lucena MI, Fernandez MC, Suarez F, Montero JL, Fraga E. Fulminant liver failure associated with flutamide therapy for hirsutism. Lancet 1999; 353: 983–6.
7 Caine M, Perlberg S, Gordon R. The treatment of benign prostatic hypertrophy with flutamide: a placebo controlled study. J Urol 1975; 114: 564–6.
8 Bonard M, Almeida S. Placebo-controlled double-blind study in human benign obstructive prostatic hypertrophy with flutamide. Eur Urol 1975; 2: 24–8.
9 Lubbert C, Wiese M, Haupt R, Ruf BR. Toxic hepatitis and liver failure under therapy with flutamide. Internist (Berl) 2004; 45: 333–40.
10 Ometz JL, Dupont A, Cusan L, Tremblay M, Suburu R, Lrmay M.

Incidence of liver toxicity associated with the use of flutamide in prostate cancer patients. Am J Med 1992; 92: 465–70.
11 Anjumath S, Michael M, Charles W. Metabolism of the antiandrogenic drugs (flutamide) by human CYP1A2. Drug Metab Dispos 1997; 25: 1298–304.
12 Wang HX, Li D, Xu CJ, Liu X. Flutamide-associated acute liver failure. Ann Ital Med Int 2003; 18: 250–3.
13 Aizawa Y, Ikemoto I, Kishimoto K. Flutamide-induced hepatic dysfunction in relation to steady-state plasma concentrations of flutamide and its metabolites. Mol Cell Biochem 2003; 252: 149–56.
14 Gonzales FJ, Liu SY, Yano M. Regulation of cytochrome P450 genes: molecular mechanism. Pharmacogenetics 1993; 3: 51–7.
15 Boobis AR, Gooderham NJ, Rich KJ, Zhao K, Edwards RJ, Murray BP, *et al*. Enzymatic studies of the activation of heterocyclic food mutagens in man. Princess Takamatsu Symp 1995; 23: 134–44.
16 Vazquez RM, Gil GL, Lopez SP, Aleman VS, Garcia PA. Liver toxicity associated with flutamide. An Med Intern 2004; 21: 307–8.
17 Williams AT, Burke RF. Carbon tetrachloride hepatotoxicity: an example of free radical-mediated injury. Semin Liver Dis 2000; 10: 279–84.
18 Kamataki T, Kitagawa H. Effects of lyophilization and storage of rat liver microsomes on activity of aniline hydroxylase, contents of cytochrome b5 and cytochrome P-450 and aniline-induced P-450 difference spectrum. Jpn J Pharmacol 1974; 24: 195–203.
19 Bradford MM. A rapid and sensitive method for the quantitation of microgram quantities of protein utilizing the principle of protein-dye binding. Anal Biochem 1976; 72: 248–54.
20 Casler WL, Menzies JA, Whitehouse LW, Moon TW. Detection of quantitative trait loci affecting caffeine metabolism by interval mapping in a genome-wide scan of C3H/HEJ×APNF$_2$ mice. Drug Metab Dispos 1999; 27: 1375–80.
21 Sandhu P, Guo Z, Baba T, Martin MV, Turkey RH, Guengerich FP. Expression of modified human cytochrome P450 1A2 in *Escherichia coli* stabilization, purification, characterization, and catalytic activities of the enzyme. Arch Biochem Biophys 1994; 309: 168–77.
22 Zacharova LY, Gulyaeva LF, Lyakhovich VV. Rat hepatic CYP1A1 and CYP1A2 induction by menadione. Toxicol Lett 2005; 155: 253–8.
23 McManus ME, Burgess WE, Weronese ME, Huggett A, Quattrochi LC, Tukey RH. Metabolism of 2-acetylaminofluorene and benzopyrene and activation of food-derived heterocyclic amine mutagens by human cytochromes P-450. Cancer Res 1990; 50: 3367–76.
24 Toyoshiba H, Walker NJ, Bailer AJ, Portier CJ. Evaluation of toxic equivalency factors for induction of cytochromes P450 CYP1A1 and CYP1A2 enzyme activity by dioxin-like compounds. Toxicol Appl Pharmacol 2004; 194: 156–68.
25 Butler MA, Iwasaki M, Guengerich FP, Kadlubar FF. Human cytochrome P450, the phenacetin *O*-deethylase, is primarily responsible for the hepatic 3-demethylation of caffeine and *N*-oxidation of carcinogenic arylamines. Proc Natl Acad Sci USA 1989; 86: 7696–700.
26 Kadlubar PF, Hammons GK. The role of cytochrome P-450 in the metabolism of chemical carcinogens, in mammalian cytochromes P-450. Boca Raton (FL): CRC Press; 1987.
27 Walubo A, Barr S, Abraham AM, Coetsee C. The role of cytochrome-P450 inhibitors in the prevention of hepatotoxicity after paracetamol overdose in rats. Hum Exp Toxicol 2004; 23: 49–54.
28 Wang HX, Xu CJ, Li D. Influence of flutamide on liver biotransformation enzymes and antioxidation in rats. J Fudan Univ (Med Sci) 2001; 28: 299–302.

Acta Pharmacologica Sinica 2005 Nov; 26 (11): 1387–1394

Blackwell Publishing

Full-length article

Alterations of placental cytochrome P450 1A1 and P-glycoprotein in tobacco-induced intrauterine growth retardation in rats[1]

You-e YAN[2], Hui WANG[2,3], Ying-hong FENG[2]

[2]*Department of Pharmacology, Medical College of Wuhan University, Wuhan 430071, China*

Key words

intrauterine growth retardation; tobacco; placenta; cytochrome P450 1A1; P-glycoprotein; rats

[1] Project supported by the Youth Foundation, Family Planning Commission of Hubei, China (No 30114).
[3] Correspondence to Prof Hui WANG.
Phn 86-27-6875-8665.
Fax 86-27-8733-1670.
E-mail clbwhcbd@yahoo.com

Received 2005-05-24
Accepted 2005-08-12

doi: 10.1111/j.1745-7254.2005.00209.x

Abstract

Aim: To investigate the alterations of placental P-glycoprotein (P-gp) and cytochrome P450 1A1 (*CYP1A1*) at different gestational days (GD), and to explore the possible significance of placental P-gp and *CYP1A1* in tobacco smoke-induced intrauterine growth retardation (IUGR) in rats. **Methods:** An IUGR model was produced by passive tobacco smoking from GD 7 to parturition (GD 21) and predicted using fetal development parameters. Placental structure and function were monitored by observing pathological alteration and antioxidative function, including the content of malondialdehyde and the activities of superoxide dismutase and catalase (CAT). The expressions of *CYP1A1* and P-gp (*mdr* 1a and *mdr* 1b) were detected using a reverse transcription polymerase chain reaction and immunohistochemistry. **Results:** Placental pathological changes occurred and the malondialdehyde content increased, whereas the activities of superoxide dismutase and CAT lowered, when compared to their controls. In the rat placenta of the tobacco group, the level of *CYP1A1* mRNA increased significantly; the level of *mdr*1a mRNA increased significantly at GD 21 but not at GD 14, whereas the level of *mdr*1b mRNA in different term remained stable; the expression of P-gp increased significantly only in full-term placenta. **Conclusion:** The expression of placental *CYP1A1* and P-gp increased in tobacco-induced IUGR. Overexpression of placental *CYP1A1* can attribute to the metabolism of tobacco and the generation of reactive metabolites, which can trigger IUGR. As a compulsory mechanism, upregulation of P-gp might decrease tobacco exposure to a developing fetus with IUGR.

Introduction

There is ample epidemiological evidence that individuals with intrauterine growth retardation (IUGR) carry an increased risk of prenatal morbidity and mortality[1] and that those born with IUGR are at a much greater risk of a wide range of medical problems, such as mental handicaps and neurobehavioral disorders[2,3]. There are various possible causes of pathologically induced IUGR, and it is reported that some xenobiotic exposure during pregnancy, including to tobacco and drugs, could be attributable to IUGR[4,5]. Clinically, there is no generally accepted effective treatment at present and, therefore, the understanding of the mechanisms for controlling fetal growth and the causes for IUGR induced by xenobiotics is extremely important in the development of therapeutic options.

The placenta is the organ responsible for the transfer of nutrients and waste products between the fetal and maternal circulations, and plays a pivotal role in fetal growth[6]. The placenta receives oxygen from the maternal circulation and is positioned in an oxygen gradient between the mother and fetus. The placenta provides a link between the circulations of 2 distinct individuals, but also acts as a barrier to protect the fetus from xenobiotics in the maternal blood. Animal studies, such as embryo transplant and cross breeding experiments, have shown that, unlike postnatal growth, the

growth of the fetus is controlled predominately by the uterine environment, and not by fetal or maternal genetic factors[7]. Therefore, placental dysfunction can have an important effect on fetal intrauterine development and can lead to fetal diseases such as IUGR.

The placenta can perform xenobiotic transportation and biotransformation. The transfer of foreign chemicals across the placenta can be modified by metabolism in the placenta itself. The extent to which drugs cross the placenta is also modulated by the actions of placental phase I and II drug-metabolizing enzymes. Cytochrome P450 enzymes in particular have been well characterized in the placenta at the level of mRNA, protein, and enzyme activity[8]. In some cases, however, the enzymes can activate exogenous compounds, making them toxic to the fetus[6]. Cytochrome P450 1A1 (*CYP1A1*) exists mainly in extra-hepatic tissue, and can activate some xenobiotics with possible deleterious effects. The alteration in *CYP1A1* expression, for example, as a result of inducers/inhibitors or maternal diseases, could potentially adversely affect placental function and pregnancy outcome[9]. Studies show that *CYP1A1* expresses in the placentas of women who are exposed to cigarettes[6]. However, little is known about the possible changes of placental *CYP1A1* expression over the course of pregnancy and its roles in IUGR formation.

Some drugs are pumped across the placenta by various active transporters located on both the fetal and maternal side of the trophoblast layer, and instances of drug-induced birth defects have been in part blamed on the placenta's apparent 'leakiness' to maternal blood-borne agents[8]. The impact of active transporters such as P-glycoprotein (P-gp) on the disposition of drugs has been demonstrated in some studies[10–12]. P-gp, which is encoded by the *mdr* gene, is a membrane transport protein that functions as an efflux pump for various cytotoxic compounds and, therefore, reduces the intracellular concentrations of these compounds[10]. Studies suggest that P-gp of the trophoblast cells is involved in the function of the blood–placental barrier and is necessary in reducing fetal drug exposure[11,12], although little is known about the expression of placental P-gp in different gestational time and its significance to IUGR.

It is difficult to correlate toxic chemicals and their transportation and metabolism in the human placenta with IUGR. The rat placenta is morphologically and histologically similar to the human one; both of them are of the same hemochorial type. Therefore, a rat model of IUGR established by tobacco smoking is useful in providing us with information about the relationships among xenobiotics, placental transportations/metabolisms, and IUGR. To understand the toxic mechanism of tobacco in IUGR formation, in the present study, the alterations of placental *CYP1A1* and P-gp expressions were investigated in IUGR rats, so as to explore the possible significance of placental *CYP1A1* and P-gp in tobacco-induced IUGR.

Materials and methods

Chemicals Thiobarbituric acid (TBA) and 5, 5'-dithio-2, 2'-dinitrobenzoic acid were obtained from Sigma. Trizol reagent was obtained from Molecular Research Center and One Step RNA PCR Kit was obtained from TaKaRa Biotechnology. Oligonucleotide primers were custom synthesized by Sangon Biological Engineering Technology. Rabbit anti-rat mdr1 and streptavidin-peroxidase (SP) reagent were obtained from BOSTER Biotechnology. All other chemicals and reagents were of analytical grade.

Animals Specific pathogen free(SPF) Wistar rats with the weights of 190±18 g (female)/280±23 g (male) were obtained from the Experimental Center of Medical Scientific Academy of Hubei (China, No 2003-0005). Virgin female and male rats were left undisturbed for 5 d and then subjected to experimental conditions. Overnight, every 2 females was mated up with 1 male rat and the occurrence date of a vaginal plug was considered as gestational d 0 (GD 0). Pregnant rats were then housed 1 per cage in an environment of constant temperature (21±2 °C) and relative humidity (50%±10%) with a 12 h L:D cycle. *Ad libitum* access to a standard diet and water was permitted. The study protocol was in accordance with the guidelines for animal research and was approved by the Ethical and Research Committee of Wuhan University.

Tobacco smoke exposure On GD 7, pregnant rats were allocated to either a control group or a tobacco group. A rat IUGR model was processed, with modification, according to the procedure of Younoszai and Li[13,14]. From GD 7 till parturition (GD 21), at 8:00, 11:00, 14:00, and 17:00, four pregnant rats from the tobacco group were subjected to cigarette smoke in a chamber measuring 40 cm×28 cm×18.5 cm for 15 min, with the gross smoke concentration set at 9 $g \cdot m^{-3}$. The tar and nicotine yields of commercial cigarettes were 15 and 1.1 mg per cigarette, respectively. The control group was sham-treated; that is, a group of 4 pregnant rats were in the same chamber without cigarette smoke for 15 min. The pregnant rats were weighed at GD 0, GD 7, GD 14, and GD 21. Animals were killed at 8:00 on GD 14 and GD 21, corresponding to mid and late gestational time[15]. Each feto-placental unit was removed quickly from the uterus and placenta specimens were excised, rinsed with cold saline, immediately fro-

zen in liquid nitrogen and stored at -80°C until used. Placenta weight and fetal development parameters (fetal body and organ weights, and fetal body and tail lengths) were recorded.

Placental pathomorphological observations and immunohistochemistry Fresh placentas were put into 4% paraformaldehyde in phosphate buffered saline (PBS) for 24 h. The fixed placental samples were processed using standard histological techniques and stained with hematoxylin and eosin. The slides were observed using light microscopy (Axiopstar PLUS).

Routine immunohistochemistry SP method was carried out. The paraffin slides were deparaffinized with xylene and rehydrated in a graded series of ethanol. To quench endogenous peroxidase activity 0.3% H_2O_2 was added for 10 min, and preimmune goat serum was used to block non-specific binding sites. Sections were then incubated at 37 °C for 20 min with a rabbit polyclonal anti-mdr1 antibody diluted in PBS (1:100). The slides were then incubated at 37°C for 15 min with an anti-rabbit secondary antibody and visualized with a DAB chromatogen system. PBS substituted for anti-mdr1 antibody for negative staining control. The slides were observed under light microscopy (Axiopstar PLUS) and the average gray level was measured using Photo Imaging System (HMIAS-2000). The quantitative stereology was performed in triplicates with 5 fields in each slide.

Tissue biochemical analysis Placentas at GD 21 were homogenized with saline to be 10% (*w*/*v*) homogenates. After the homogenates were centrifuged at 200×*g* for 10 min, the supernatants were centrifuged at 9 000×*g* for 20 min and, finally, collected and stored at -30 °C for the further assays. Placental protein concentrations were determined using the Lowry method[16], with the bovine serum albumin (BSA) as standard. The extent of lipid peroxidation was detected by measuring malondialdehyde (MDA) content using TBA according to a modified procedure described by Ondrejickova *et al*[17]. The activities of superoxide dismutase (SOD) and catalase (CAT) were measured as described above[18, 19].

Preparation of placental total RNA Total RNA was isolated from the frozen placentas according Trizol reagent instructions. The protocol involved disruption of cells, denaturation of nucleoprotein complexes, inactivation of endogenous ribonuclease (RNase) activity and, finally, removal of proteins and degradation of residual DNA by nuclease digestion. The concentration and purity of RNA were determined using a spectrophotometer (UV-1601, Shimadzu) and adjusted to 1 μg/μL. Total RNA was stored in DEPC-H_2O at -80 °C until used.

Semiquantitative reverse transcriptase-polymerase chain reaction The cDNA synthesis and polymerase chain reaction (PCR) amplification were produced in 1 step using Promega's reverse transcriptase-polymerase chain reaction (RT-PCR) System. Different primers and PCR products are shown in Table 1. The final concentrations of reagents in the RT-PCR reaction system were as follows: 1×One Step RNA PCR buffer, 5 mmol/L $MgCl_2$, 1 mmol/L of each dNTP, 0.8 U/μL RNase inhibitor, 0.1 U/μL avian myeloblastosis virus (AMV) RTase XL, 0.1 U/μL AMV-optimized *Taq*, 0.4 μmol/L of each primer, and 0.02 U/μL placenta RNA in each 50 μL reaction volume. For quantitative analysis of mRNA expression, the housekeeping gene cyclophilin, an internal loading control[22], was used to amplify together with the specific target gene in 1 tube. RT-PCR reactions were carried out in a thermal cycler: 50 °C for 30 min for reverse transcription, then 94 °C, 2 min for RT inactivation; finally 72 °C, 5 min for a terminal elongation step following the amplification cycles. PCR cycling conditions were as follows: 94 °C, 30 s; 62 °C, 45 s; 72 °C, 30 s, 45 cycles for *CYP1A1*. 94 °C, 30 s; 54 °C, 60 s; 72 °C, 30 s, 30 cycles for *mdr*1a. 94 °C, 30 s; 56 °C, 20 s; 72 °C, 30 s, 25 cycles for *mdr*1b. DEPC-H_2O substituted for placental RNA for negative control. An aliquot (4 μL) of the RT-PCR reactions was separated on a 1.5% agarose gel containing ethidium bromide, visualized under UV light, photographed, and analyzed by densitometry using Photo Documentation and Imaging System (Bio-1D). The expression level of target gene mRNA was shown as the ratio of the intensities of the target-specific band and the CYC band individually.

Statistical analysis The experimental results were expressed as mean±SD. Statistical Packages for Social Sci-

Table 1. Gene-specific oligonucleotide polymerase chain reaction (PCR) primers. *CYP1A1*, cytochrome P450 1A1; CYC, cyclophilin .

Gene	Forward primer	Reverse primer	PCR product/bp	Reference
CYP1A1	CTGGTTCTGGATACCCAGCTG	CCTAGGGTTGGTTACCAGG	331	[20]
*mdr*1a	GATGGAATTGATAATGTGGAC	AAGGATCAGGAACAATAAA	351	[21]
*mdr*1b	GAAATAATGCTTATGAATCCCAAAG	GGTTTCATGGTCGTCGTCTCTTGA	326	[21]
CYC	CTTCGACATCACGGCTGATGG	CAGGACCTGTATGCTTCAGG	265	[20]

ences (SPSS) was used for data analysis. Analysis of variance (ANOVA) was used for comparison of means of several groups and χ-square analysis was performed to test for differences in proportions of categorical variables between 2 groups. The level of significance was set at $P< 0.05$.

Results

Maternal body weights The change in pregnant rat body weight is a useful, indirect indicator of physical development. During the period of GD 7 to GD 21, there was a significant decline in the body weight and percentage weight gain after tobacco exposure (Figure 1).

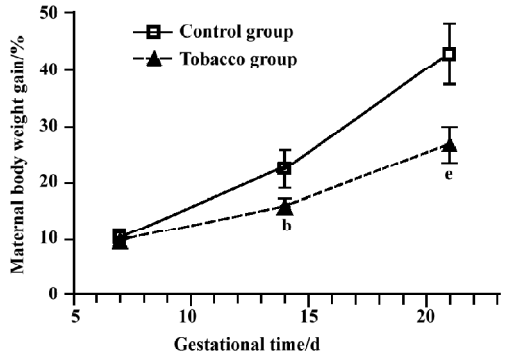

Figure 1. Effects of prenatal tobacco exposure on the percentage of maternal body weight gain. n=8. Mean±SD. $^bP<0.05$ *vs* control group at gestational d 14 (GD 14). $^eP<0.05$ *vs* control group at GD 21.

Neonatal body weights and physical development indexes Body weight was an important index for diagnosing IUGR (IUGR was diagnosed by the standard that the mean body weight in the treated group was less 2 standard deviations than that in the control group)[23]. The offspring in the tobacco group showed a lower average body weight (3.20 g) than the control group (4.30 g) at GD 21, indicating fetal IUGR. The ratio of IUGR increased to 44.74% (34/76) in the tobacco group, whereas it was only 5.06% (4/79) in the control group. In addition, the body and tail lengths, and liver and brain weights of the tobacco group significantly lagged behind those of control group at GD 21, with a suppression of 14.2 %, 8.9 %, 22.9 %, and 10.5 %, respectively ($P<0.01$) (Table 2).

Table 2. Effects of prenatal tobacco exposure on the body weights and physical development indexes of rats' offspring on gestational d 21. n=8. Mean±SD. $^cP<0.01$ *vs* control group. IUGR, intrauterine growth retardation.

Indexes	Control	Tobacco
Body weight/g	4.30±0.68	3.20±0.85^c
Ratio of IUGR	5.06% (4/79)	44.74% (34/76)^c
Body length/cm	3.87±0.26	3.32±0.32^c
Tail length/cm	1.35±0.15	1.23±0.13^c
Liver weight/mg	0.35±0.07	0.27±0.08^c
Brain weight/mg	0.19±0.02	0.17±0.02^c

Placental pathomorphology The rat placenta is composed of 3 distinct zones: labyrinth, basal, and maternal deciduas; where the labyrinth zone represents the main area of maternal-fetal exchange. According to our results, compared to those in the control group (Figure 2A), the obvious changes occurred in the labyrinth and basal deciduas of the full-term placenta in IUGR rats, such as through interstitial and endovascular hemorrhage in the labyrinth zone, and trophoblast cells necrosis in the basal zone (Figure 2B). Full-term placental weight (0.39±0.08 g) of tobacco-induced IUGR

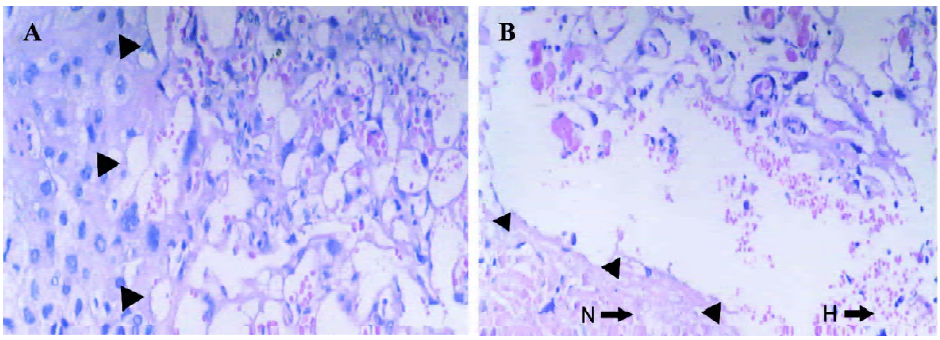

Figure 2. Effects of prenatal tobacco exposure on placental pathomorphological changes at gestational d 21. A: control group; B: tobacco exposure group. Black arrowheads indicate between labyrinth and basal zone. Hemorrhage in labyrinth zone and necrosis in basal zone are represented by H and N, respectively. ×200.

rats decreased by more than that of the normal placentas (0.49±0.06 g).

Placental antioxidative system In the tobacco exposure group, placental MDA content was significantly increased by 50.0% ($P<0.05$), and the activities of SOD and CAT were notably decreased by 58.2% and 30.6% ($P<0.05$, $P<0.01$), respectively (Table 3).

Table 3. Effects of prenatal tobacco exposure on full-term placental antioxidative function in rats. n=8. Mean±SD. $^bP<0.05$, $^cP<0.01$ *vs* control group.

Groups	Malondialdehyde /mmol·mg^{-1} protein	Superoxide dismutase /U·mg^{-1} protein	Catalase /k·mg^{-1} protein
Control	30±6	3.9±1.2	0.62±0.16
Tobacco	60±14^c	1.6±0.5^c	0.43±0.07^b

Placental *CYP1A1* mRNA expression No PCR product for *CYP1A1* mRNA was detected in normal placentas. However, expression was detected in the placentas of the tobacco exposure group; furthermore, the level at GD 21 was approximately 1.39-fold higher than that at GD 14, with a faint band (Figure 3).

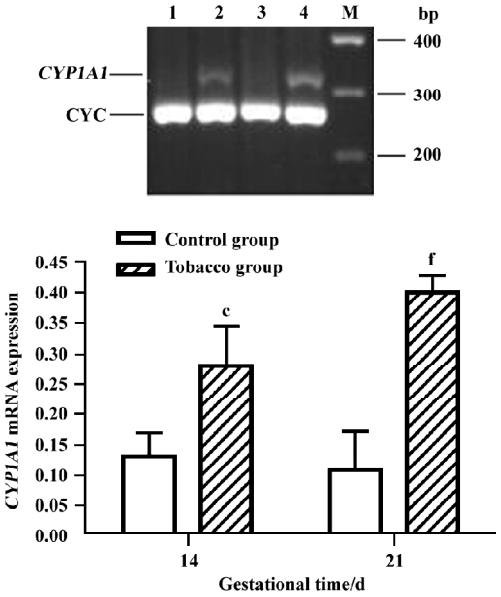

Figure 3. Effects of prenatal tobacco exposure on expression of placental *CYP1A1* mRNA at different times by the quantitative reverse transcriptase-polymerase chain reaction using cyclophilin as internal control (n=4 per treatment). Lane 1: control group at gestational d 14 (GD 14); lane 2: tobacco group at GD 14; lane 3: control group at GD 21; lane 4: tobacco group at GD 21. $^cP<0.01$ *vs* control at GD 14. $^fP<0.01$ *vs* control at GD 21.

Placental P-gp and *mdr*1 mRNA expression Immunohistochemical analysis with anti-mdr specific antibody showed strong positive staining in placenta trophoblasts (Figure 4A–D). The P-gp level at GD 14 in the tobacco group (Figure 4B) was similar to that of the normal placenta

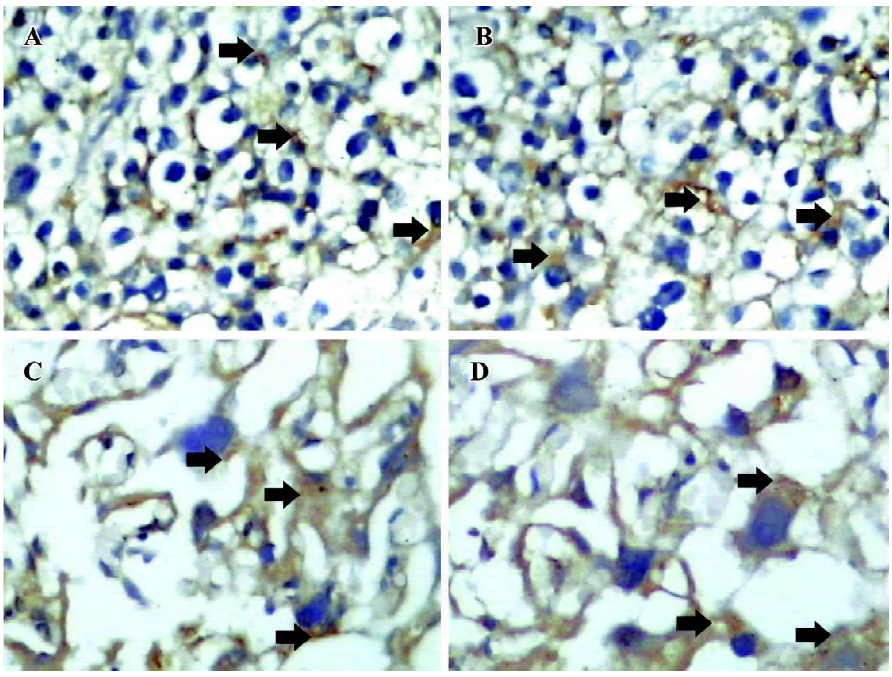

Figure 4. Effects of prenatal tobacco exposure on the expression of P-glycoprotein (P-gp) at different times by immuno-histochemistry. A: control group at gestational d 14 (GD 14); B: tobacco group at GD 14; C: control group at GD 21; D: tobacco group at GD 21. P-gp (arrow) was detected in the developing labyrinth zone of the rat placenta. ×400.

(Figure 4A). However, the level at GD 21 in the tobacco group (Figure 4D) was higher than that of normal placenta (Figure 4C), almost 1.24-fold higher (P<0.05).

The levels of *mdr*1a mRNA at GD 14 and GD 21 in the placentas of tobacco groups were approximately 1.10-fold and 1.32-fold higher than those in the normal placentas (Figure 5). *mdr*1b mRNA level, however, was not significantly different between the 2 groups (Figure 6).

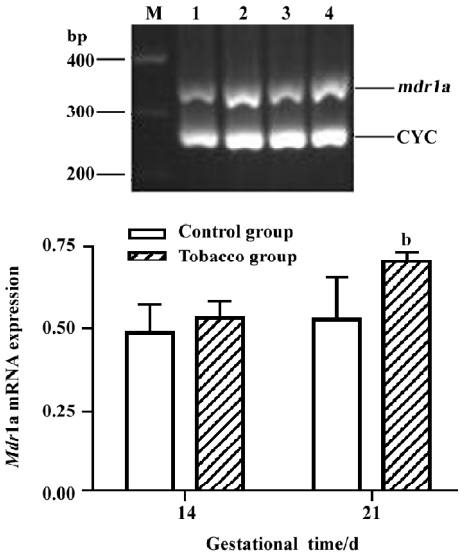

Figure 5. Effects of prenatal tobacco exposure on expressions of placental *mdr*1a mRNA at different times by the quantitative reverse transcriptase-polymerase chain reaction using cyclophilin as internal control (n=4 per treatment). Lane 1: control group at gestational d 14 (GD 14); lane 2: tobacco group at GD 14; lane 3: control group at GD 21; lane 4: tobacco group at GD 21. ^{b}P<0.05 *vs* control at GD 21.

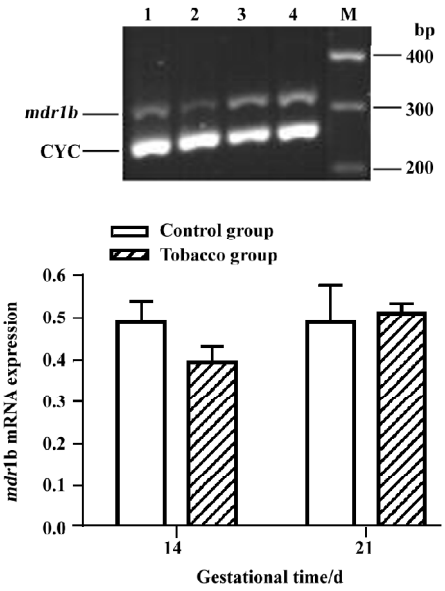

Figure 6. Effects of prenatal tobacco exposure on expressions of placental *mdr*1b mRNA at different times by the quantitative reverse transcriptase-polymerase chain reaction using cyclophilin as internal control (n=4 per treatment). Lane 1: control group at gestational d 14 (GD 14); lane 2: tobacco group at GD 14; lane 3: control group at GD 21; lane 4: tobacco group at GD 21.

Discussion

The placenta, which is derived from both fetal and maternal tissues, is considered the first fetal organ to be exposed to exogenous substances and plays an important role in fetal intrauterine development. In the present study, gestational tobacco smoking resulted in significantly delayed fetal growth, as indicated by the fetal development parameters, especially fetal body weight. Meanwhile, placental weight decreased and obvious pathomorphological changes were observed. Our result showed that the content of MDA was higher and the activities of SOD and CAT were lower in IUGR placentas, suggesting a decreased ability of placental antioxidative defense. Therefore, these results suggest that prenatal tobacco exposure has a specific and deleterious effect on the placenta that secondarily limits fetal growth.

The placenta is now viewed as a metabolic barrier rather than a physical barrier[24]. The placenta can perform biotransformation that occurs in the liver. Numerous foreign compounds reach the placenta through the maternal circulation and placental tissue is capable of oxidizing several of them. In present study, the expression of *CYP1A1* mRNA was detected in the placentas of the tobacco group, but not in the normal placentas; furthermore, the expression of *CYP1A1* mRNA was higher in full-term placentas than that in mid-term placentas. These results demonstrate that an increase of *CYP1A1* with environmental tobacco exposure is obvious and that a time-response relationship exists during tobacco consumption. There are many well-known *CYP1A1* inducers in tobacco, and smoking is one important source of exposure to them. Increased *CYP1A1* level might explain the toxic mechanism because polyarylhydrocarbons can be bioactivated by *CYP1A1* and can generate reactive metabolites[25]. Wu *et al* found that placental and fetal tissues were capable of metabolizing benzo(a)pyrene [B(a)P], albeit to a lower extent, and that *CYP1A1* was involved in metabolism of inhaled B(a)P[26]. In addition, *CYP1A1* can result in free radical formation and lipid peroxidation, and then affect uterine redox environment and fetal growth. Oxidative stress has been increasingly postulated as a major contributor to

dysfunction in IUGR[27], and our data indicates a decreased ability of placental antioxidative defense. The present finding of significant upregulation of placental *CYP1A1* mRNA subsequent to prenatal tobacco exposure supports a hypothesis that an elevated placental *CYP1A1* level can be a trigger for IUGR.

In P-gp, generally, mdr1a appeared to be the pharmacologically most relevant isotype. Schinkel *et al* also indicated that mdr1a was the critical placental P-gp in mice[28]. In a study by Lin, *Mdr*1b was highly induced in the secretary epithelium endometrium of the uterus in mice during pregnancy and might protect steroid secreting cells from potentially damage[29]. In the present study, we analyzed P-gp expression in the rat placenta during its maturation, using the methods of immunohistochemistry. Intensive immunoreactivity for P-gp was found in the developing labyrinth zone of normal placentas. Furthermore, tobacco smoking induced P-gp expression of the trophoblast cells only in full-term placentas. We examined the changes of *mdr*1 levels in different stages, using the RT-PCR method. We found different P-gp members displayed distinct inductive patterns. Our PCR data indicates that the expression of *mdr*1a gene tends to increase from GD 14 to GD 21 in the normal placenta, which correlates well with the results of Novotna *et al*[30]. During tobacco smoke exposure, a significant increase in the amount of *mdr*1a mRNA has been observed at GD 21, although it remained steady at GD 14. The level of *mdr*1b almost remained steady at GD 14 and GD 21 between control and tobacco groups. These results suggest that tobacco smoke induced P-gp, especially *mdr*1a. The different expressional patterns of *mdr*1a and *mdr*1b genes show that they were not co-regulated during pregnancy and signified that the expression of both genes probably underlied different regulation pathways, which is supported by the recent data of Lee[31,32]. P-gp was able to extrude a wide variety of structurally and chemically unrelated compounds out of cells[33]. Researches have selected B(a)P as a potential P-gp substrate[34]. Therefore, we suspect that the higher expression of P-gp in rat IUGR placenta might be caused by the pumping out of part of the tobacco toxins, to decrease toxicity and, thus, to protect the fetus from potentially harmful xenobiotics during tobacco exposure, which might be a compulsory mechanism of IUGR. However, we cannot exclude the possibility that there exist some P-gp inducers in tobacco. Further experiments are needed to examine this possibility.

In summary, the present study has discussed the abnormal alterations of placental morphology and function in tobacco-induced IUGR. The expression of placental *CYP1A1* and P-gp increased in tobacco-induced IUGR. Overexpression of placental *CYP1A1* can contribute to the metabolism of tobacco and can generate reactive metabolites, which can be a trigger for IUGR. However, upregulation of P-gp might pump out part of the tobacco toxins, as a compulsory mechanism of IUGR, to decrease tobacco exposure to the developing fetus.

References

1 Genbacev O, McMaster MT, Zdravkovic T, Fisher SJ. Disruption of oxygen-regulated responses underlies pathological changes in the placentas of women who smoke or who are passively exposed to smoke during pregnancy. Reprod Toxicol 2003; 17: 509–18.

2 Amin H, Singhal N, Sauve RS. Impact of intrauterine growth restriction on neurodevelopmental and growth outcomes in very low birth weight infants. Acta Paediatr 1997; 86: 306–14.

3 Spinillo A, Stronati M, Ometto A, Fazzi E, Lanzi G, Guaschino S. Infant neurodevelopmental outcome in pregnancies complicated by gestational hypertension and intra-uterine growth retardation. J Perinat Med 1993; 21: 195–203.

4 Peacock JL, Cook DG, Carey IM, Jarvis MJ, Bryant AE, Anderson HR, *et al*. Maternal cotinine level during pregnancy and birth weight for gestational age. Int J Epidemiol 1998; 27: 647–56.

5 Chiaffarino F, Parazzini F, Paladini D, Acaia B, Ossola W, Marozio L, *et al*. A small randomised trial of low-dose aspirin in women at high risk of pre-eclampsia. Eur J Obstet Gynecol Reprod Biol 2004; 112: 142–4.

6 Pasanen M, Pelkonen O. The expression and environmental regulation of P450 enzymes in human placenta. Crit Rev Toxicol 1994; 24: 211–29.

7 Holmes R, Montemagno R, Jones J, Rodeck C, Soothill P. Fetal and maternal plasma insulin-like growth factors and binding proteins in pregnancies with appropriate or retarded fetal growth. Early Hum Dev 1997; 49: 7–17.

8 Syme MR, Paxton JW, Keelan JA. Drug transfer and metabolism by the human placenta. Clin Pharmacokinet 2004; 43: 487–514.

9 Pasanen M. The expression and regulation of drug metabolism in human placenta. Adv Drug Deliv Rev 1999; 38: 81–97.

10 Islam OM, Hara M, Miyake J. Induction of P-glycoprotein, glutathione-*S*-transferase and cytochrome P450 in rat liver by atrazine. Environ Toxicol Pharmacol 2002; 12: 1–6.

11 Lankas GR, Wise LD, Cartwright ME, Pippert T, Umbenhauer DR. Placental P-glycoprotein deficiency enhances susceptibility to chemically induced birth defects in mice. Reprod Toxicol 1998; 12: 457–63.

12 Smit JW, Huisman MT, Tellingen O, Wiltshire HR, Schinkel AH. Absence or pharmacological blocking of placental P-glycoprotein profoundly increases fetal drug exposure. J Clin Invest 1999; 104: 1441–7.

13 Younoszai MK, Peloso J, Haworth JC. Fetal growth retardation in rat exposed to cigarette tobacco during pregnancy. Am J Obstet Gynecol 1969; 104: 1027.

14 Li Y, Wang H, Li JF. In utero exposure to tobacco and alcohol modifies neurobehavioral development in mice offspring: Con-

sideration a role of oxidative stress. Pharmacol Res 2004; 49: 467–73.
15 Kenagy J, Liu F, Soares M, Audus KL. Gestational and tobacco effects on peptidase activity in the placenta. Peptides 1998; 19: 1659–66.
16 Lowry OH, Rosebrough NJ, Farr AL, Randall RJ. Protein measurement with the Folin phenol reagent. J Biol Chem 1951; 193: 265–75.
17 Ondrejickova O, Horakova L, Juranek I, Ziegelhoeffer A, Stolc S. Effect of stobadine on lipid peroxidation in brain and heart after ischemia and reperfusion of the brain. Life Sci 1999; 65: 1959–61.
18 Wang H, Peng RX, Kong R, Zeng HG. Effect of allicin on ethanol-induced hepatotoxicity in mice. Wei Sheng Yan Jiu 1998; 27: 415–7.
19 Wang H, Peng RX, Wang RK, Kong R. Antagonizing effect of sodium ferulate on the changes of hepatic antioxidative function induced by ethanol in mice. Acta Pharm Sin 1997; 32: 511–4.
20 Morris DL, Davila JC. Analysis of rat cytochrome P450 isoenzyme expression using semi- quantitative reverse transcriptase-polymerase chain reaction (RT-PCR). Biochem Pharmacol 1996; 52: 781–92.
21 Kwan P, Sills GJ, Butler E, Gant TW, Brodie MJ. Differential expression of multidrug resistance genes in naive rat brain. Neurosci Lett 2003; 339: 33–6.
22 Cavicchioli L, Flanigan TP, Dickson JG, Vantini G, Dal Toso R, Fusco M, *et al*. Choline acetyltransferase messenger RNA expression in developing and adult rat brain: Regulation by nerve growth factor. Brain Res Mol Brain Res 1991; 9: 319–25.
23 Chatelain P. Children born with intra-uterone growth retardation (IUGR) or small for gestational age (SGA): Long term growth and metabolic consequences. Endocr Regul 2000; 34: 33–6.
24 Gupta RC, Sastry BV. Toxicology of the placenta. In: Ballantyne B, Marrs TC, Syversen T, editors. General and applied toxicology. London: MacMillan; 2000. p 1233–63.
25 Whitlock JP. Induction of cytochrome P4501A1. Annu Rev Pharmacol Toxicol 1999; 39: 103–25.
26 Wu J, Ramesh A, Nayyar T, Hood DB. Assessment of metabolites and AhR and CYP1A1 mRNA expression subsequent to prenatal exposure to inhaled benzo(a)pyrene. Int J Dev Neurosci 2003; 21: 333–46.
27 Takagi Y, Nikaido T, Toki T, Kita N, Kanai M, Ashida T, *et al*. Levels of oxidative stress and redox-related molecules in the placenta in preeclampsia and fetal growth restriction. Virchows Arch 2004; 444: 49–55.
28 Schinkel AH, Mayer U, Wagenaar E, Mol CA, van Deemter L, Smit JJ, *et al*. Normal viability and altered pharmacokinetics in mice lacking mdr1-type (drug-transporting) P-glycoproteins. Proc Natl Acad Sci USA 1997; 94: 4028–33.
29 Lin JH. Drug–drug interaction mediated by inhibition and induction of P-glycoprotein. Adv Drug Deliv Rev 2003; 55: 53–81.
30 Novotna M, Libra A, Kopecky M, Pavek P, Fendrich Z, Semecky V, *et al*. P-glycoprotein expression and distribution in the rat placenta during pregnancy. Reprod Toxicol 2004; 18: 785–92.
31 Lee CH. Induction of P-glycoprotein mRNA transcripts by cycloheximide in animal tissues: Evidence that class I Pgp is transcriptionally regulated whereas class II Pgp is posttranscriptionally regulated. Mol Cell Biochem 2001; 216: 103–10.
32 Lee CH. Differential regulation of P-glycoprotein genes in primary rat hepatocytes by collagen sandwich and drugs. J Cell Biochem 2002; 86:12–20.
33 Gottesman MM. How cancer cells evade chemotherapy: sixteenth Richard and Hinda Rosenthal Foundation Award Lecture. Cancer Res 1993; 53: 747–54.
34 Doi AM, Holmes E, Kleinow KM. P-glycoprotein in the catfish intestine: inducibility by xenobiotic and functional properties. Aquat Toxicol 2001; 55: 157–70.

Acta Pharmacologica Sinica 2005 Nov; 26 (11): 1395–1401

Blackwell Publishing

Full-length article

Multivesicular liposome formulations for the sustained delivery of interferon α-2b[1]

Jian QIU[1], Xiao-hui WEI[1], Fang GENG[1], Rui LIU[1], Jing-wu ZHANG[2], Yu-hong XU[1,3]

[1]School of Pharmacy, Shanghai Jiao Tong University, Shanghai 200030, China; [2]Joint Immunology Laboratory of Institute of Health Science and Shanghai Institute of Immunology, Shanghai Institutes for Biological Sciences, Chinese Academy of Sciences and Shanghai Second Medical University, Shanghai 200025, China

Key words

interferon α-2b; liposomes; delayed-action preparations

[1] Project supported by Science and Technology Commission of Shanghai Municipality (No 024319120 and No 04DZ14902).
[3] Correspondence to Dr Yu-hong XU.
Phn 86-21-6293-3466
Fax 86-21-6293-3466
E-mail yhxu@sjtu.edu.cn

Received 2005-06-17
Accepted 2005-07-15

doi: 10.1111/j.1745-7254.2005.00188.x

Abstract

Aim: To develop and optimize a sustained release multivesicular liposome (MVL) formulation of interferon (IFN) α-2b. **Methods:** IFN α-2b MVL were prepared using a typical double-emulsion procedure. The sustained release effects of IFN α-2b MVL were investigated by monitoring the blood IFN α-2b concentration using an enzyme-linked immunosorbent assay test after subcutaneous administration to healthy mice. **Results:** IFN α-2b was successfully encapsulated in MVL with high efficiency, and the integrity of encapsulated protein was maintained. After subcutaneous injection, the MVL slowly released IFN α-2b into systemic circulation in a sustained manner. The estimated serum half-life of IFN α-2b was approximately 30 h. In addition, varying the size of the MVL preparations could further modify the *in vivo* release profile. **Conclusion:** IFN α-2b MVL may be a useful sustained release formulation in the clinical treatment of viral diseases.

Introduction

Interferon (IFN) α-2b is an important cytokine and has been used widely as a therapeutic agent to treat patients with viral and oncological diseases. It is an essential component of the treatment of chronic hepatitis B infection[1]. However, in the recommended dosing regimen, the protein needs to be administered every other day for 3 months, which brings about much inconvenience to the patients. The $t_{1/2}$ of IFN α-2b, when administered subcutaneously, is only about 4 h[2].The protein was shown to be cleared quickly, therefore frequent repeated administrations are necessary.

Much effort has been devoted to the development of IFN α-2b-based products with persistent effects. One approach, covalent attachment of polyethylene glycol (PEG) to the protein surface (PEGylation), has been the most successful. Several PEGylated IFNα products are already on the market. The half-life of the PEGylated protein is 40 h, thus it only needs to be administered once a week for similar therapeutic effects[3]. However, the chemical conjugation process of PEGylation is rather complex and the PEGylated products are usually mixtures with different PEG conjugation sites. In addition, a few studies have suggested that the chemical modifications can sometimes affect the structure as well as the bioactivity of the protein[4].

An alternative approach is to develop sustained-release depot formulations of IFN α-2b. Liposome formulations of IFNγ have been developed and have been reported to have prolonged release profiles of up to 160 h. Even so, using conventional liposome formulations, the drug loading capacity and encapsulation efficiency are still rather low and variable[5].

Multivesicular liposomes (MVL), on the other hand, have a different structure and possess some distinctive properties. They usually contain a larger internal space, which would allow more drug to be loaded. Their larger size would also deter rapid clearance by tissue macrophages so that they may act as drug depots to enable sustained release of drugs[6]. The MVL formulation of the anticancer drug cytarabine (Depocyt™) has been developed successfully and is now being used widely for the treatment of leukemia[7].

We took a similar approach in the present study and evalu-

ated the MVL formulation of IFN α-2b and its biopharmaceutical properties. Some of the parameters that affected the MVL *in vivo* pharmacokinetic behaviors were further investigated. Our data suggest that MVL formulation of IFN α-2b can be developed with satisfactory sustained release properties *in vivo*, which may have useful clinical applications.

Materials and methods

Materials 1,2-dioleoyl-sn-glycero-3-phosphocholine (DOPC), cholesterol, triolein and 1,2-dipalmitoyl-sn-3-phosphoglycerol (DPPG) were all purchased from Sigma (St Louis, MO, USA). *L*-lysine was purchased from Sangon Biological Engineering Technology and Service Co (Shanghai, China). IFN α-2b (recombinant human interferon α-2b) was kindly provided by Pan Asia Bio (Shanghai, China), and all other reagents were of analytical grade and purchased from Shanghai Chemical Reagent Co (Shanghai, China).

Multivesicular liposome preparation The MVL formulations of IFN α-2b were prepared based on the typical double-emulsion procedure developed by Kim *et al*[8–12]. Briefly, 1 mL chloroform containing the lipids (molar ratio DOPC:cholesterol:DPPG: triolein, 7:11:1:1; two other molar ratios were also used: 7:11:1:4 and 7:11:1: 8) was emulsified at 10 000 r/min for 10 min with 1 mL aqueous solution containing IFN α-2b in phosphate-buffered solution (PBS) and various sucrose concentrations to produce a water-in-oil emulsion. This water-in-oil emulsion was subsequently emulsified with 4 mL of an aqueous solution containing 4% glucose (*w*/*v*) and 20 mmol/L lysine at 2500 r/min for 10 s, and then poured into another 4 mL of the same aqueous solution. Chloroform was removed by flushing nitrogen over the surface of the double emulsion at 37 °C for approximately 15 min. The resultant MVL were pelleted at 600 ×*g* and washed twice with PBS to remove unencapsulated IFN α-2b. The IFN α-2b concentration in MVL was determined by HPLC quantification and adjusted accordingly.

For preparing MVL samples with narrower size distributions, the procedures were further modified. For large-sized MVL, a smaller emulsification force (1000 r/min) was applied during the second emulsification and the chloroform was removed slowly (over 30 min). The large MVL were purified and harvested by centrifugation at 100×*g* and only the pellet was collected. For small-sized MVL, the second emulsification step was carried out at 10 000 r/min. Chloroform was removed over approximately 15 min. The resultant MVL were then centrifuged twice at 100×*g* for 10 min, and the precipitants were discarded. Small-sized MVL were then harvested in the pellet after centrifugation at 600×*g* for 10 min. The size distributions were quite reproducible because of the purification-by-centrifugation step. The IFN α-2b concentration was determined by HPLC quantification and adjusted accordingly.

Multivesicular liposome size measurements The MVL suspensions were diluted in saline. The particle size distribution was measured using a CIS100 particle size analyzer (Ankersmid, the Netherlands).

Encapsulation efficiency determination IFN α-2b encapsulation efficiency was determined by measuring the amount of encapsulated protein as compared to the total amount added[13]. Briefly, the MVL were pelleted by centrifugation at 600×*g* for 10 min. The pellet was then treated with extraction solution (0.2% Triton X-100, 28% ethanol, 71.2% water, *v*/*v*) and quantified using the HPLC assay described below.

IFN α-2b characterization IFN α-2b was characterized using reverse phase (RP)-HPLC, sodium dodecyl sulphate-polyacrylamide gel electrophoresis (SDS-PAGE) and enzyme-linked immunosorbent assays (ELISA). RP-HPLC was carried out on a Agilent 1100 liquid chromatography system at 45 °C using a linear gradient of 45%–70% solvent B [CH_3CN, 0.1% Trifluoroacetic Acid (TFA)] over 11 min, and then a sharp linear gradient of 70%–100% solvent B over 9 min at a flow rate of 1.0 mL/min. Solvent A was water (0.1% TFA). IFN α-2b was detected by UV absorbance at 280 nm. The standard curve showed a linear correlation within the range of 2.0 μg/mL–100 μg/mL. The intra-day and inter-day assay precisions were determined to be less than 3% and 2%, respectively. SDS-PAGE analyses of encapsulated IFN α-2b were carried out using 12% acrylamide gels under reducing conditions and stained with silver stain. ELISA were carried out using the human interferon α ELISA Kit (sandwich method) from PBL Biomedical Laboratories (Piscataway,NJ, USA). The protein control and the MVL samples were both treated with extraction solution (0.2% Triton X-100, 28% ethanol, 71.2% water) for 30 min and then applied to the ELISA plate. IFN α-2b concentrations were determined according to the standard curve supplied with the kit.

***In vitro* drug release study** Aliquots of IFN α-2b MVL (500 μL) were pipetted into a 50 mL beaker containing 25 mL of saline solution. The beaker was incubated at 37 °C under constant rotation at 12 r/min. Three samples were collected at each time point (0 h, 24 h, 48 h, 72 h, 96 h, 120 h, 144 h, and 168 h) and were centrifuged at 600×*g* for 10 min. The protein concentrations in the pellets were determined using the RP-HPLC assay[14].

***In vivo* pharmacokinetic studies** Free IFN α-2b and IFN α-2b MVL suspensions were injected subcutaneously

in a single dose in female SD rats. Three rats were included in each group. Blood samples (0.3 mL) were collected at specific time points (5 min, 30 min, 2 h, 8 h, 12 h, 24 h, 48 h, 72 h, 96 h, and 120 h after injection) and were placed aside for 30 min at room temperature. The supernatant (serum) was collected by centrifugation at 700×*g* for 10 min. IFN α-2b concentrations were determined using ELISA, which has a detection limit of 30 pg/mL. Any values lower than 30 pg/mL were considered undetectable.

Results

Interferon α-2b encapsulation in multivesicular liposomes Multivesicular liposomes containing IFN α-2b were prepared according to the standard double-emulsion method. The preparations were highly reproducible, usually yielding MVL with similar size distributions and encapsulation efficiencies. A representative light microscope image of the resultant MVL is shown in Figure 1A. The particle size distribution analysis is shown in Figure 1B. The MVL had a rather broad size distribution ranging from 2 μm to 50 μm in diameter. The median size was approximately 18 μm.

The encapsulated proteins were characterized using SDS-PAGE, ELISA, and HPLC. There was no chemical degradation in the peptide chain after the preparation. The structural integrity of the protein is considered crucial to its activity. We used an ELISA to partially characterize the 3-dimensional conformational change in the protein. Our data showed that the antibody binding affinity to the protein was only slightly reduced, indicating that there was a substantial amount of native structure remaining in the protein sample after preparation (Figure 2).

Interferon α-2b encapsulation efficiencies Several parameters were evaluated for their effects in optimizing IFN α-2b encapsulation efficiencies. Table 1 lists some of the representative scenarios. Using the standard lipid MVL formulation (48.3 mmol/L DOPC, 70.7 mmol/L cholesterol, 6.7 mmol/L DPPG and 6.7 mmol/L triolein), the encapsulation efficiency was approximately 30%. It can be further increased by adding more lipids. At a protein-to-lipid ratio of 0.031 (*w*/*w*), the encapsulation efficiency was more than 60%. In contrast to the reported development of MVL formulation of progenipoietin, we did not find any evident correlation between the sucrose concentration in the first aqueous phase and IFN α-2b encapsulation efficiency[15]. Furthermore, the encapsulation capacity only seemed to vary slightly with different triolein contents.

Interferon α-2b release from multivesicular liposomes *in vitro* The MVL were stable when stored in saline in small volumes at 4 °C, with less than 2% protein leaked after 3 months (data not shown). When the MVL were diluted

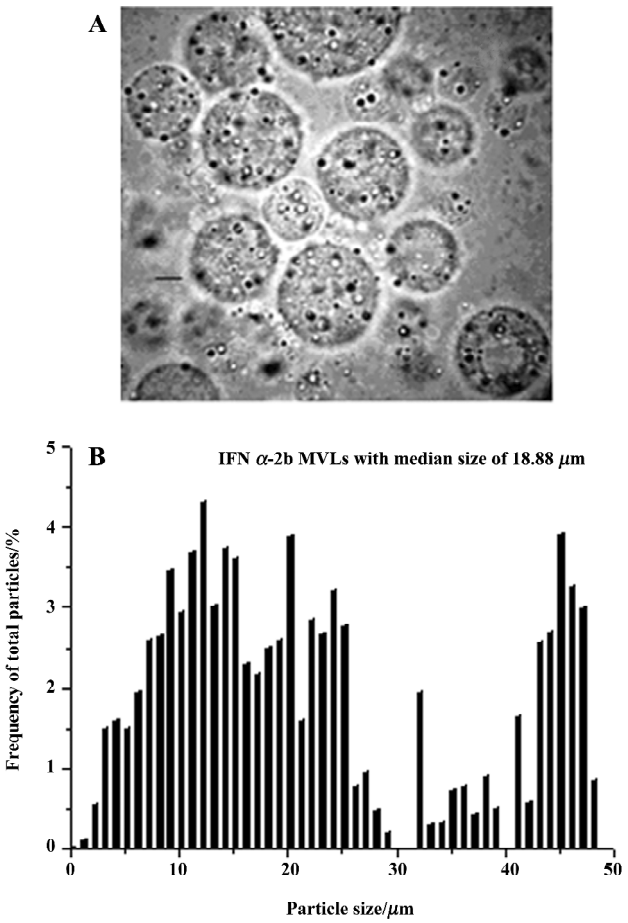

Figure 1. (A) Light micrograph of interferon (IFN) α-2b multivesicular liposomes (MVL) at 400×magnification. Scale bar=5 μm. (B) Particles size distribution of IFN α-2b MVL.

Table 1. Interferon α-2b encapsulation efficiencies in various multivesicular liposome formulations. *n*=3. Mean±SD.

Sucrose concentration (%, *w*/*v*)	Protein-to-lipid ratio (mg/mg)	Triolein-to-DOPC ratio (molar)	Encapsulation efficiency (%)
2.5	0.063	0.139	34.10±0.70
4.0	0.063	0.139	23.60±0.50
5.0	0.063	0.139	36.25±2.15
5.0	0.031	0.139	66.70±1.30
5.0	0.042	0.139	53.0±0.60
5.0	0.126	0.139	21.85±0.55
7.0	0.063	0.139	39.0±1.15
5.0	0.063	0.596	29.60±1.20
5.0	0.063	1.190	27.25±0.85

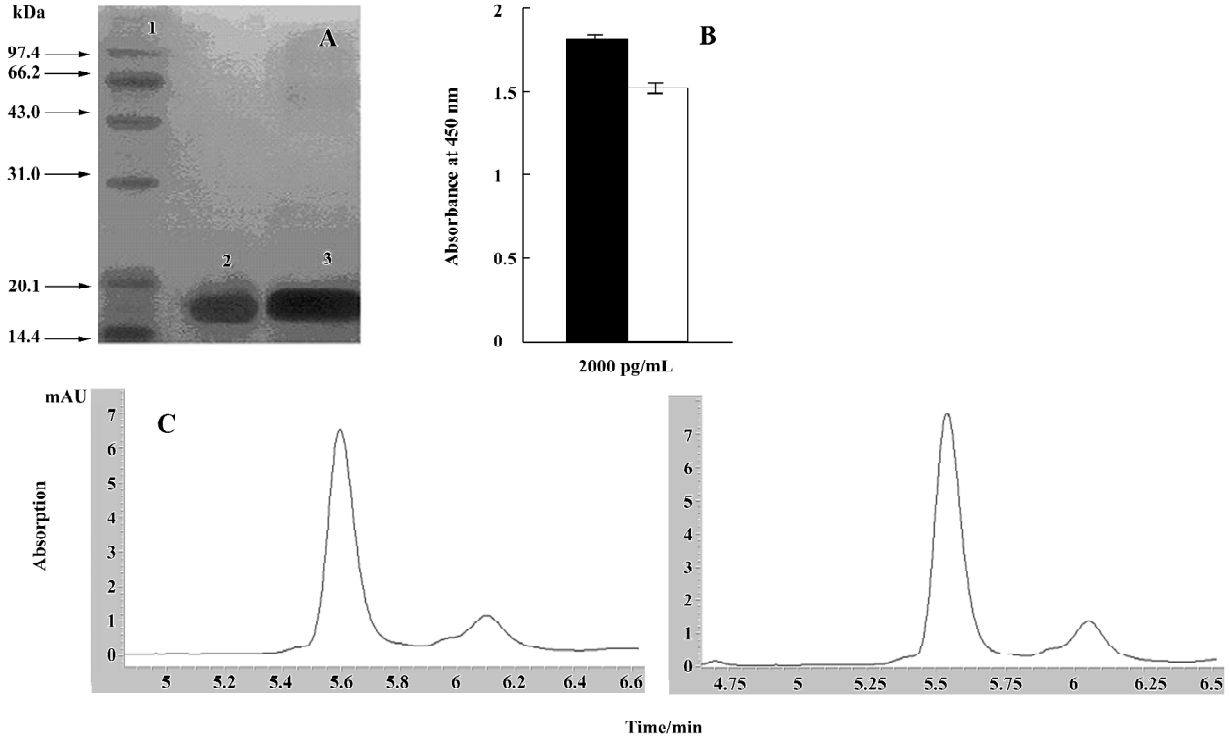

Figure 2. (A) Sodium dodecyl sulphate-polyacrylamide gel electrophoresis of interferon (IFN) α-2b before and after multivesicular liposome (MVL) encapsulation. Lane 1, low molecular weight standard; lane 2, IFN α-2b extracted from MVL; lane 3, native IFN α-2b. (B) Enzyme-linked immunosorbent assay binding activities of unencapsulated IFN α-2b and IFN α-2b extracted from MVL (2000 pg/mL). □: Unencapsulated IFN α-2b; ■: IFN α-2b from MVL. The data represent the mean±SD (n=3). (C) Comparison of the reverse phase high performance liquid chromatography profile of unencapsulated (free form) IFN α-2b to that of IFN α-2b extracted from DepoFoam particles. Above: unencapsulated IFN α-2b; below: IFN α-2b encapsulated in MVL.

into a large amount of saline (1:50 dilution) under well-mixed conditions, the encapsulated protein would gradually leak out (Figure 3). Approximately 90% of the content was shown to have been released after 7 d.

***In vivo* pharmacokinetic profiles** After subcutaneous injection of a dose of 2.5 mg/kg, free IFN α-2b proteins were cleared quickly within 1 d (the detection limit of the ELISA kit was at 30 pg/mL). The MVL sustained release formulations, however, would provide a continuous supply of IFN α-2b to the systemic circulation, which lasted more than 2 d. The detailed pharmacokinetic behavior was found to be related to the triolein content in the MVL formulation (Figure 4). Increases in triolein content resulted in longer release times.

Effect of multivesicular liposome size on *in vivo* protein release profiles To further optimize the sustained release profile of IFN α-2b MVL formulations, we specifically compared the *in vivo* release properties of MVL with different sizes. As the typical MVL preparation procedure yielded MVL with rather broad size distributions (Figure 1B), we modified some emulsification parameters and added a final fractionation step to obtain MVL samples in much narrower size distributions. The lipid formulation remained the same.

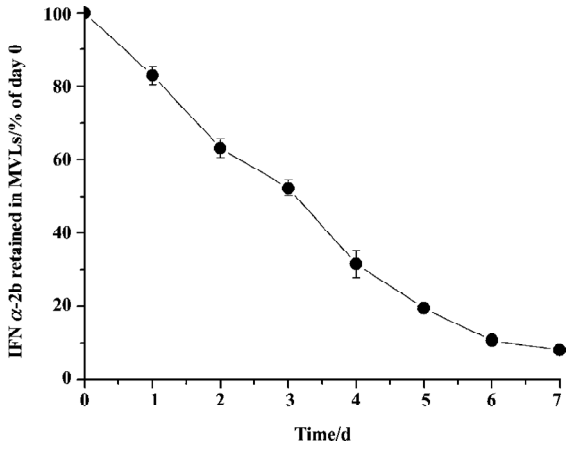

Figure 3. Interferon (IFN) α-2b *in vitro* release profile from multivesicular liposomes (MVL) in saline. The data represent the percentage of total IFN α-2b retained in MVL at various incubation time points. n=3. Mean±SD.

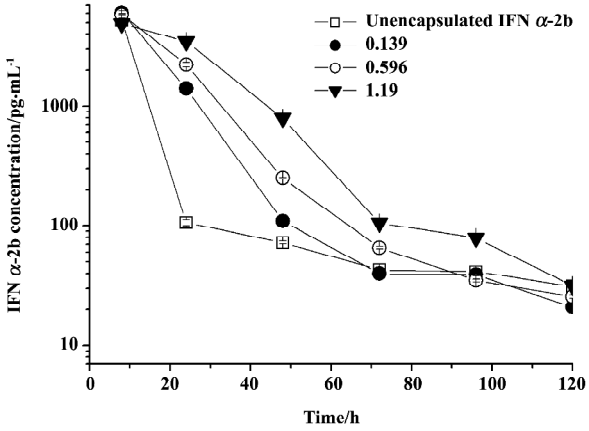

Figure 4. Serum interferon (IFN) α-2b concentrations after subcutaneous injection of IFN α-2b multivesicular liposomes (MVL) prepared using various molar ratios of triolein to DOPC (0.139, 0.596 or 1.19). The dosage is 1.6 mg/kg. □: Unencapsulated IFN α-2b; ●: triolein/DOPC=0.139; ○: triolein/DOPC=0.596; ▼: triolein/DOPC=1.19. Blood samples were collected at 8 h, 24 h, 48 h, 72 h, 96 h, 120 h after administration. *n*=3. Mean±SD.

Two different-sized populations were obtained and their size profiles are shown in Figure 5A. The large MVL had sizes of approximately 40 μm–60 μm diameter, and the small MVL were approximately 10 μm–25 μm in diameter. The samples were administered subcutaneously at a dose of 1.2 mg/kg and the IFN α-2b serum concentrations were determined and plotted in Figure 5B. It shows that small MVL released the encapsulated protein content over a longer time compared with large MVL.

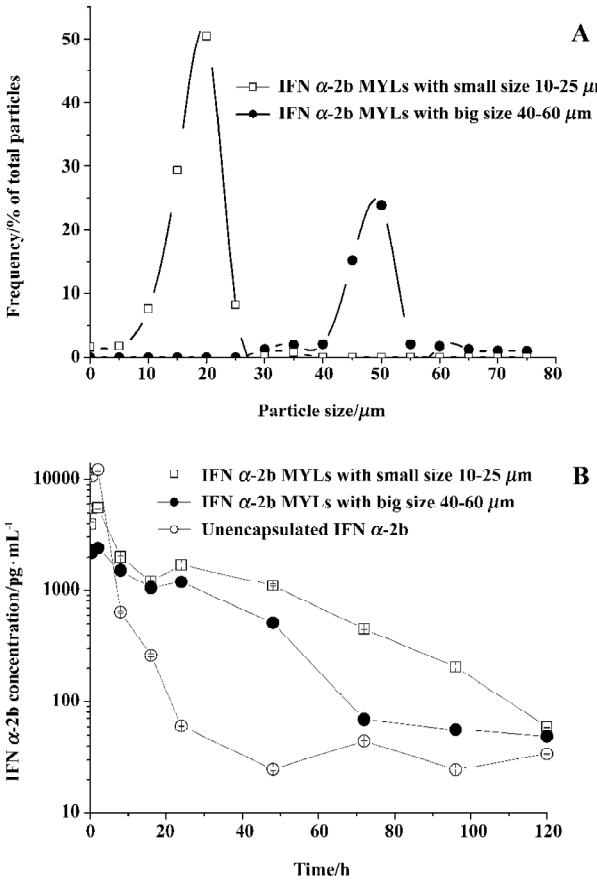

Figure 5. (A) Particle size distribution of 2 different preparations of interferon (IFN) α-2b multivesicular liposomes (MVL). (B) Serum IFN α-2b concentrations after subcutaneous injection of IFN α-2b MVL with different sizes. ○: Free IFN α-2b; ●: IFN α-2b MVL with larger sizes (40 μm–60 μm); □: IFN α-2b MVL with smaller sizes (10 μm–25 μm). The dosage was 800 μg/kg. Blood samples were collected at 5 min, 30 min, 2 h, 8 h, 16 h, 24 h, 48 h, 72 h, 96 h, and 120 h after administration. *n*=3. Mean±SD.

Discussion

Multivesicular liposome formulations have been developed successfully for the prolonged release of cytarabine, morphine and other drugs[16,17]. The long-lasting sustained release properties were most evident when the formulations were administered in a small confined space, such as the epidural. We showed here that MVL could also be used to achieve reasonable prolonged release properties after subcutaneous administration, and MVL IFN α-2b formulations may be developed for the treatment of viral infections requiring less frequent dosing. Our data indicate that MVL can maintain their structure in the subcutaneous interstitial space for a few days and slowly release the encapsulated proteins into the systemic circulation. There was considerable protein detected in the circulation for more than 5 d, and the serum half-life was estimated to be approximately 30 h.

The prolonged serum half-life that we achieved is actually comparable to what has been reported for the PEGylated IFN α-2b product currently in clinical use, even though their mechanisms for sustained serum concentration are quite different. PEGylated IFN α-2b requires chemical modification of the protein structure, which might affect its bioactivity. The PEGylated proteins are absorbed into the systemic circulation quickly after administration but remain there for a long time by avoiding various clearance mechanisms. In contrast, the proteins in MVL formulations are unmodified, which wait inside the subcutaneous MVL depot, slowly leak out, and enter the circulation. They should maintain their original structure, and most likely their full bioactivities. Their distribution and clearance mechanisms should also follow the same pathway as natural IFN α-2b. Therefore, compared to the PEGylated product, MVL formulations would have a more defined safety profile, established manufacture proce-

dures and drug efficacy, and side effects that are easier to evaluate. We therefore believe that MVL formulation may be an attractive candidate for the sustained delivery of IFN α-2b for the treatment of viral infections.

Another significant advantage of the MVL formulations is its high drug loading capacity. Compared with conventional liposomes, which often have limited encapsulation for hydrophilic proteins, the MVL offer a much larger internal space and therefore usually have higher encapsulation efficiencies. For IFN α-2b, the encapsulation efficiency was usually more than 30%. However, the double-emulsion preparation method has been shown to cause protein degradation and denaturation[18]. Also, there might exist protein-liposomal bilayer interactions that may affect protein conformation and activity[19,20]. We used three methods to test protein chemical and structural changes after encapsulation. Both the SDS-PAGE and HPLC analyses showed that the proteins were chemically intact. For protein conformational changes, some studies have used biophysical methods such as circular dichroism and fluorescence spectroscopy to detect the secondary structure or local amino acid environment changes[19]. We adopted a biochemical approach using an ELISA to probe possible 3-dimensional conformational changes. The ELISA may have its limitations because it can only detect changes of structure near binding sites. However, antibody binding has been shown to be very sensitive to protein denaturing effects, and ELISA are commonly used in protein formulation studies to assay protein structure integrity[21]. Our data showed that the antibody binding affinity for the protein after encapsulation was only slightly reduced, indicating that substantial native structure remained after preparation. Further studies are needed to confirm the detailed bioactivity of the encapsulated IFN α-2b.

We also tested several parameters that might affect the release profile of MVL. Triolein is used as a hydrophobic space filler at lipid membrane intersection points and can stabilize the junctions[11]. The amount of triolein in the MVL formulation was suggested to be important for MVL morphology and stability[11,22]. We showed that it had a significant impact on the *in vivo* release profiles of IFN α-2b (Figure 4). It is possible that when more triolein is present, the lipid walls are more stable and therefore the protein is released more slowly.

With a similar argument, we hypothesized that the size of the MVL would also be important for the drug release profile, because the inter-compartmental fusion and diffusion of the proteins in larger MVL would add another rate-limiting step and would eventually result in faster protein release into the environment. However, when we used the typical preparation procedure, the resultant MVL size distribution was rather broad, ranging from 2 μm to 50 μm (Figure 1). It is difficult to differentiate the release profile of different-sized MVL. Therefore, we developed a modified procedure to make MVL with much narrower size distributions (Figure 5). Based on our data, the protein release from MVL with smaller sizes (10 μm–25 μm) was indeed slower than that from larger MVL (40 μm–60 μm), which is an important observation. We therefore suggest that, in further development of control-released formulations, MVL sizes will need to be optimized and well controlled.

In summary, we have demonstrated that IFN α-2b MVL formulation can achieve high encapsulation efficiency, good stability and sustained release effects. The sustained release effect can be affected by the triolein content and particle sizes. Further optimization is needed in order to develop a clinically valuable sustained release formulation of IFN α-2b.

Acknowledgement

We would like to thank Pan Asia Bio (Shanghai, China) for providing IFN α-2b.

References

1 Wai CT, Lok AS. Treatment of hepatitis B. J Gastroenterol 2002; 37: 771–8.

2 Bukowski RM, Tendler C, Cutler D, Rose E, Laughlin MM, Statkevich P. Treating cancer with PEG intron. Cancer 2002; 95: 389–96.

3 Glue P, Fang JW, Rouzier PR, Raffanel C, Sabo R, Gupta SK, *et al*. Pegylated interferon-α2b: pharmacokinetics, pharmacodynamics, safety, and preliminary efficacy data. Clin Pharmacol Ther 2000; 68: 556–7.

4 Foser S, Schacher A, Weyer KA, Brugger D, Dietel E, Marti S, *et al*. Isolation, structural characterization, and antiviral activity of positional isomers of monopegylated interferon α-2a (PEGASYS). Protein Expr Purif 2003; 30: 78–87.

5 Vanslooten ML, Boerman O, Romoren K, Kedar E, Crommelin DJ, Storm G. Liposomes as a sustained release system for human interferon-γ: Biopharmaceutical aspects. Biochim Biophys Acta 2001; 1530: 134–45.

6 Howell SB. Clinical application of a novel sustained-release injectable drug delivery system: DepoFoam™ Technology. Cancer J 2001; 7: 219–25.

7 Kim S, Khatibi S, Howell SB, McCully C, Balis FM, Poplack DG. Prolongation of drug exposure in cerebrospinal fluid by encapsulation into DepoFoam. Cancer Res 1993; 53: 1596–8.

8 Kim S, Turker MS, Chi EY, Sela S, Martin GM. Preparation of multivesicular liposomes. Biochim Biophys Acta 1983; 728: 339–48.

9 Katre NV, Asherman J, Schaefer H, Hora M. Multivesicular Liposome (DepoFoam) technology for the sustained delivery of

insulin-like growth factor-1 (IGF-1). J Pharm Sci 1997; 87: 1341–6.
10 Ye Q, Asherman J, Stevenson M, Brownson E, Katre NV. DepoFoam™ technology: a vehicle for controlled delivery of protein and peptide drugs. J Control Release 2000; 64: 155–66.
11 Mantripragada S. A lipid-based depot (DepoFoam technology) for sustained release drug delivery. Prog Lipid Res 2002; 41: 392–406.
12 Bilati U, Allemann E, Doelker E. Strategic approaches for overcoming peptide and protein instability within biodegradable nano- and microparticles. Eur J Pharm Biopharm 2005; 59: 375–88.
13 Ramprasad MP, Anantharamaiah GM, Garber DW, Katre NV. Sustained-delivery of an apolipoprotein E peptidomimetic using multivesicular liposomes lowers serum cholesterol levels. J Control Release 2002; 79: 207–18.
14 Xiao CJ, Qi XR, Maitani Y, Nagai T. Sustained release of cisplatin from multivesicular liposomes: potentiation of antitumor efficacy against S180 murine carcinoma. J Pharm Sci 2004; 93: 1718–24.
15 Ramprasad MP, Amini A, Kararli T, Katre NV. The sustained granulopoietic effect of progenipoietin encapsulated in multivesicular liposomes. Int J Pharm 2003; 261: 93–103.
16 Chamberlain MC, Khatibi S, Kim JC, Howell SB, Chatelut E, Kim S. Treatment of leptomeningeal metastasis with intraventricular administration of Depot Cytarabine (DTC101). Arch Neurol 1993; 50: 261–4.
17 Yaksh TL, Provencher JC, Rathbun ML, Myers RR, Powell H, Richter P, *et al*. Safety assessment of encapsulated morphine delivered epidurally in a sustained-release multivesicular liposome preparation in dogs. Drug Deliv 2000; 7: 27–36.
18 Van de Weert M, Hennink WE, Jiskoot W. Protein instability in poly(lactic-co-glycolic acid) microparticles. Pharm Res 2000; 17: 1159–67.
19 Van Slooten ML, Visser AJWG, Van Hoek A, Storm G, Crommelin DJA, Jiskoot W. Conformational stability of human interferon-gamma on association with and dissociation from liposomes. J Pharm Sci 2000; 89: 1605–19.
20 Koppenhagen FJ, Visser AJWG, Herron JN, Storm G, Crommelin DJA. Interaction of recombinant interleukin-2 with liposomal bilayers. J Pharm Sci 1998; 87: 707–14.
21 Braun A, Alsenz J. Development and use of enzyme-linked immunosorbent assays (ELISA) for the detection of protein aggregates in interferon-alpha (IFN-α) formulations. Pharm Res 1997; 14: 1394–400.
22 Langston MV, Ramprasad MP, Kararli TT, Galluppi GR, Katre NV. Modulation of the sustained delivery of myelopoietin (Leridistim) encapsulated in multivesicular liposomes (DepoFoam). J Control Release 2003; 89: 87–99.

Acta Pharmacologica Sinica 2005 Nov; 26 (11): 1402–1408

Blackwell Publishing

Full-length article

Permeation-enhancing effects of chitosan formulations on recombinant hirudin-2 by nasal delivery *in vitro* and *in vivo*

Yu-jie ZHANG[1,2], Chang-hua MA, Wan-liang LU, Xuan ZHANG, Xiao-liang WANG, Jian-ning SUN, Qiang ZHANG[1,3]

[1]*School of Pharmaceutical Sciences, Peking University Health Science Center, Beijing 100083, China;* [2]*Department of Chinese Pharmacy, Beijing University of Traditional Chinese Medicine, Beijing 100102, China*

Key words

nasal absorption; hirudin; chitosan formulation; permeability; bioavailability; enhancer; ciliotoxicity

[3] Correspondence to Prof Qiang ZHANG.
Phn 86-10-8280-2791.
Fax 86-10-8280-2791.

E-mail zqdodo@bjmu.edu.cn
Received 2005-03-20
Accepted 2005-05-08

doi: 10.1111/j.1745-7254.2005.00174.x

Abstract

Aim: To investigate the enhancing effects of chitosan with or without enhancers on nasal recombinant hirudin-2 (rHV2) delivery *in vitro* and *in vivo*, and to evaluate the ciliotoxicity of these formulations. **Methods:** The permeation-enhancing effect of various chitosan formulations was estimated by using the permeation coefficient of fluorescein isothiocyanate recombinant hirudin-2 (FITC-rHV2) across the excited rabbit nasal epithelium *in vitro*. The effect was further evaluated by measuring the blood concentration level after nasal absorption of FITC-rHV2 in rats. The mucosal ciliotoxicity of different formulations was evaluated with an *in situ* toad palate model. **Results:** Chitosan at a concentration of 0.5% with or without various enhancers significantly increased the permeability coefficient (P) and relative bioavailability (Fr) of FITC-rHV2 compared with the blank control. The addition of 1% sodium dodecylsulfate, 5% Brij35, 5% Tween 80, 1.5% menthol, 1% glycyrrhizic acid monoammonium salt (GAM) or 4% Azone into the 0.5% chitosan solution resulted in a further increase in absorption ($P<0.05$) compared with 0.5% chitosan alone. But co-administration of chitosan with 5% hydroxylpropyl-beta-cyclodextrin (HP-β-CD), 5% lecithin or 0.1% ethylenediamine tetraacetic acid (EDTA) was not more effective than using the 0.5% chitosan solution alone. Chitosan alone and with 5% HP-β-CD, 0.1% EDTA, 1% GAM or 5%Tween80 was relatively less ciliotoxic. **Conclusion:** Chitosan with or without some enhancers was able to effectively promote the nasal absorption of recombinant hirudin, while not resulting in severe mucosal ciliotoxicity. A chitosan formulation system would be a useful approach for the nasal delivery of recombinant hirudin.

Introduction

Hirudin, a 65–66 amino acid polypeptide (7 kDa), is one of the most potent inhibitors of thrombin and has proven to have outstanding anticoagulant and antithrombotic activities[1]. Recombinant hirudin (rHV), which can now be produced through DNA techniques, has a similar anticoagulative effect to natural hirudin[2]. Compared with other anticoagulants, including heparin, rHV possesses many advantages with respect to safety, antigenicity, and toxicity[3]. Currently, rHV has been used for the prophylaxis and treatment of heparin-induced thrombocytopenia (HIT), venous and arterial thrombosis, and shunt thrombosis, and the treatment of disseminated intravascular coagulation (DIC)[4,5].

However, because of its susceptibility to protease degradation and low mucosal permeability, only parenteral injection (iv or sc) is available for the delivery of rHV. Frequent injections, especially when rHV is indicated by chronic symptoms (and during prophylactic usage) would cause considerable discomfort to patients. Therefore, considerable effort has been directed towards developing alternative administration routes other than injection. Although recombinant hirudin-1 (rHV1) and rHV2 can be absorbed in the gastrointestinal tracts of rats after duodenal and oral administration, the absorption was limited or it varied depending on the analytical methods used, which indicated

that the results were unreliable[6,7]. As a convenient method of administration, nasal delivery has many benefits relative to oral administration, including the avoidance of the liver first-pass effect and a higher bioavailability. Additionally, for polypeptides, nasal delivery is one of a few non-parenteral administrative routes that have gained regulatory approval so far. Nasal delivery formats for polypeptide drugs such as calcitonin, insulin, desmopressin and growth hormone are already commercially available or in clinical trials. However, there is limited information about intranasal delivery of rHV.

The main barriers to the nasal administration of hydrophilic peptides are mucosal penetration and mucociliary clearance. Chitosan, a positively charged bioadhesive polysaccharide, has been found to be able to improve the nasal absorption of peptides and reduce the clearance of liquid formulations from the nasal cavity through its bioadhesive characteristics, while causing negligible damage to the nasal mucosal membrane[8,9].

The present study was therefore intended to investigate the nasal administration of rHV using chitosan. To further improve the enhancing activity of chitosan, we studied the effects of chitosan with some enhancers on the permeation of rHV across excised rabbit nasal epithelium *in vitro* and the absorption of rHV by nasal delivery in rats. Furthermore, the mucosal ciliotoxicity of different formulations was also evaluated by using an *in situ* toad palate model[10]. In the present study, we chose rHV2 as the model drug. For the assays, the rHV2 was labeled with fluorescein isothiocyanate (FITC), which formed a stable covalent conjugate (FITC-rHV2) that could be assayed by fluorometry.

Materials and methods

Materials Recombinant hirudin-2 (rHV2, rHV-Lys47) was obtained from the College of Life Science (Peking University, Beijing, China), and chitosan (M_r 250 kDa, degree of deacetylation >85%) was from Yuhuan Ocean Biochemical Co (Zhejiang, China). FITC, Brij35, ethylenediamine tetraacetic acid (EDTA), lecithin and Sephadex G-25 were purchased from Sigma (St Louis, MO, USA), and sodium dodecylsulfate (SDS), hydroxyl-propyl-beta-cyclodextrin (HP-β-CD), menthol, l-dodecylazacycloheptan-2-one (Azone) and Tween 80 were from Beijing Chemical Co (Beijing, China). Glycyrrhizic acid monoammonium salt (GAM) was the product of Xinjiang Tianshan Pharmaceutical Industry Co (Wulumuqi, Xinjiang, China). All other chemicals were in analytical grade.

Animals Male rats (Sprague–Dawley, weighing 280–300 g) and male rabbits (Japanese White, weighing 2.5–3.0 kg) were obtained from the Experimental Animal Center of Weitonglihua (Beijing, China); toads (weighing 30–40 g) were from the Experimental Animal Center of the Health Science Center of Peking University (Beijing, China).

The care and handling of animals was performed with the approval of the Institutional Authority for Laboratory Animal Care.

Preparation and purification of FITC-rHV2 The synthesis of FITC-labeled rHV2 was based on the reaction between the isothiocyanate group of FITC and the tyrosine in rHV2[11]. FITC in 0.5 mol/L carbonate buffer (pH 9.5) was added into a 1/10 volume of rHV2 solution (20 g/L in 0.01 mol/L phosphate buffered saline [PBS]; pH 7.1); the molar rate of the two compounds was 3:1. After 4 h of reaction with magnetic mixture in the dark at 0–9 °C, FITC-labeled rHV2 was separated from unreacted FITC in a Sephadex G-25 column (2.0 cm ID×30 cm L) pre-washed with PBS (pH 7.4). A sample of approximately 1 mL was put on the top of the column and then washed with PBS as an elution solvent. The first yellow band was collected. After the collections were mixed, FITC-rHV2 was obtained by freeze-drying. All experiments were carried out under light exclusion conditions. The molecular weight of FITC-rHV2 was determined to be 7388.99 by mass spectrometry (data not shown). This result indicated that one rHV2 molecule had combined with one molecule of FITC. FITC-rHV2 and rHV2 were found to have similar activities when measured using the chromogenic thrombin substrate assay[12].

Preparation of FITC–rHV2 formulations For the *in vitro* studies, FITC-rHV2 was dissolved in 0.5% chitosan (pH 5.0, *w/v*) at a concentration of 400 mg/L for transport. In the *in vivo* studies, FITC-rHV2 was dissolved in 0.5% chitosan solution at a concentration of 36 g/L for intranasal administra-tion. When required, the enhancers were added into these formulations (menthol, Azone and lecithin were initially dissolved in propylene glycol). The concentration of FITC-rHV2 for transport control was 400 mg/L in Ringer's solution and for subcutaneous administration was 0.5 g/L in 0.9% NaCl. All the formulations were prepared on the day of the experiments.

FITC-rHV2 assay The concentration of FITC-rHV2 was determined in a fluorescence spectrofluorometer (650–60; Hitachi, Japan) at an excitation wavelength of 495 nm and an emission wavelength of 515 nm. A standard curve was prepared using FITC-rHV2 at concentrations between 4 μg/L and 200 μg/L. The FITC-rHV2 concentrations of the test samples were estimated using the standard curve.

Nasal epithelium preparation Rabbit nasal epithelium was prepared as described by previous reports[13]. After

each rabbit was killed, its nasal septum was surgically removed with a scalpel immediately, and then the epithelium was carefully excised from the septum and stored in ice-cold Ringer's solution (pH 7.4; 125 mmol/L NaCl, 5 mmol/L KCl, 10 mmol/L $NaHCO_3$, 1.2 mmol/L NaH_2PO_4, 1.4 mmol/L $CaCl_2$ and 11 mmol/L *D*-glucose). The epithelium was used within 0.5 h of removal.

***In vitro* permeability experiments** Prior to the experiment, Ringer's solution was added to both sides of the horizontal diffusion chamber with a 4 mL volume in each side, and the excised rabbit nasal epithelium was mounted in the diffusion chamber at 37 °C. After an equilibration period of approximately 0.5 h, the buffer was replaced with the FITC-rHV2 solution on the donor side (mucosal), and fresh buffer on the receiver side (serosal). A 200 μL aliquot of sample was taken from the receiver side at particular times (0, 0.5, 1, 1.5, 2, 3, 4 and 6 h), and at the same time an equal volume of Ringer's solution was added to the receiver side. The FITC-rHV2 concentration in the receiver side (*C*r) was determined by FITC-rHV2 assay. All experiments were carried out under light exclusion conditions.

Calculation of the permeability coefficient The *C*r values were plotted as a function of time (*t*) from 0 h to 6 h. The permeability coefficient (*P*) was calculated according to the following equation:

$$P = (dq/dt) / (C_0 A)$$

where dq/dt (μg/s) represents the permeability rate, C_0 (μg/mL) was the initial concentration in the donor chamber, and A (cm^2) is the effective cross-sectional area available for diffusion (0.126 cm^2). The transport enhancement ratios (ER) were calculated using the following equation:

$$ER = P_{enh} / P_{ctrl}$$

where P_{enh} and P_{ctrl} refer to the *P* values with added and no added enhancers, respectively. Student's *t*-test was used to determine statistical significance.

***In vivo* studies** The *in vivo* studies were performed as previously described[14]. The rats were fasted overnight before the study. Anesthesia was induced by intraperitoneal injection of 40 mg/kg sodium pentobarbital and maintained by additional 15 mg/kg doses as required. The rats were fixed on their backs on boards and were surgically prepared by cannulation of the trachea to enable breathing, cannulation of the carotid artery to facilitate blood sample collection, and ligation of the esophagus to prevent samples being swallowed. A 50 μL dose of the formulations was administered into the left nares via a flexible polyethylene tube attached to a microsyringe. In addition, 0.9% NaCl was administered as a control to ensure that there was no interference with FITC-rHV2. For the calculation of Fr, FITC-rHV2 solution (0.5 mg/kg) was subcutaneously administered by bolus injection. Blood samples (400 μL) were withdrawn from the carotid artery into the plastic microfuge tubes at particular times (0, 0.5, 1, 1.5, 2, 3, 4 and 6 h). The blood samples were anticoagulated with 3.8% (*w*/*v*) trisodium citrate solution at a ratio of 8.25:1.75 (*v*/*v*), and plasma was separated after centrifugation at 1 300×*g* for 5 min .

The fluorescence intensity in the plasma before and after trichloroacetic acid (TCA) precipitation was determined, and the intensity of the insoluble portion was used to calculate the intact FITC-rHV2 concentration[15].

Data analysis The area under the FITC-rHV2 concentration time curves (AUC) was calculated by using the trapezoidal method. The relative bioavailability (Fr) was calculated by comparing the area under the curve obtained after intranasal administration with that obtained after subcutaneous injection. Statistical analysis was performed using Student's *t*-test. Differences were considered to be significant for values of $P<0.05$.

Ciliotoxicity evaluation An *in situ* toad palate model[10] was used. SDS (1%), Brij35 (5%), HP-β-CD (5%), Tween 80 (5%), EDTA (0.1%), and GAM (1%) were directly dissolved in a chitosan solution, and menthol (1.5%), Azone (4%), and lecithin (5%) were initially dissolved in propylene glycol and then in chitosan solution. The toads were fixed on their backs and their mouths were opened with pincers. The test formulations (0.5 mL) were applied to the upper palate of the toads for 30 min, and then the palates were rinsed twice with 0.9% NaCl. The palates were dissected out, and the mucocilia were examined with an optical microscope (Olympus, Japan). The duration of ciliary movement in different formulations was recorded and then the relative durations compared with 0.9% NaCl were calculated. Each group was duplicated 3 times and Student's *t*-test was used to determine statistical significance.

Results

The time versus the amount of FITC-rHV2 that had permeated across the excised rabbit nasal epithelium after application of the chitosan solution with or without enhancers to the mucosal side is shown in Figure 1. The corresponding permeability coefficients and the transport enhancement ratios (ER) are listed in Table 1. When chitosan or chitosan with various enhancers was added into the FITC-rHV2 formulation, the amount of FITC-rHV2 moving across the epithelium increased, and there were significant increases in the permeability coefficient. We found that the permeability coefficient of FITC-rHV2 in various chitosan formulations

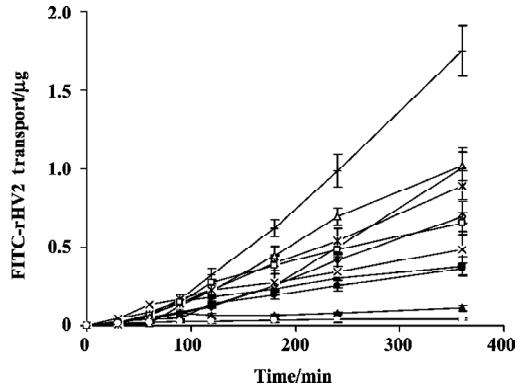

Figure 1. Effect of chitosan with or without enhancers on the transport of FITC-rHV2 across excised rabbit nasal epithelium. n=5–6. Mean±SD. (■) 0.5% chitosan; (●) +0.1% EDTA; (□) +1% GAM; (△) +5% Tween 80; (▲) +5% lecithin; (*) +5% Brij35; (◇) +1.5% menthol; (–) +4% Azone; (×) +5% HP-β-CD; (+) +1% SDS; (○) Ringer's solution.

Table 1. Permeability coefficients (P) and transport enhancement ratio(ER)values across excised rabbit nasal epithelium with different FITC-rHV2 formulations *in vitro*. Values for P were calculated from the results of *in vitro* experiments and data are expressed as the Mean±SD. n=5–6. $^{b}P<0.05$, $^{c}P<0.01$ *vs* control (Ringer's solution); $^{d}P>0.05$, $^{e}P<0.05$, $^{f}P<0.01$ *vs* 0.5% chitosan.

Formulation	$10^{-7}\times P$/cm·s^{-1}	ER
Chitosan (0.5%)	3.49±0.91	6.98^{cd}
+SDS (1%)	16.59±1.75	33.18^{cf}
+Brij35 (5%)	8.49±1.62	16.98^{cf}
+Menthol (1.5%)	6.55±2.01	13.10^{ce}
+GAM (1%)	6.45±1.93	12.90^{ce}
+Azone (4%)	9.11±1.14	18.22^{cf}
+Lecithin (5%)	0.87±0.31	1.74^{bf}
+HP-β-CD (5%)	4.34±1.03	8.68^{cd}
+Tween 80 (5%)	10.18±3.90	20.36^{ce}
+EDTA (0.1%)	3.53±1.47	7.06^{cd}
Ringer's solution	0.49±0.08	1.0

was 1.7-fold to 33-fold higher than that without chitosan. In addition, there was a marked increase in the permeability coefficient of FITC-rHV2 in chitosan formulations with 1% SDS, 5% Brij35, 5% Tween 80, 1.5% menthol, 1% GAM or 4% Azone (P<0.05) compared with chitosan alone. No significant difference (P>0.05) in the permeability coefficient was observed between the chitosan formulations containing 5% HP-β-CD or 0.1% EDTA and chitosan alone, although there was a significant decrease in the permeability coefficient in the formulation containing 5% lecithin.

The mean plasma concentration of FITC-rHV2 versus time after nasal administration to rats using various formulations is shown in Figure 2, and the Fr values are given in Table 2. When administered intranasally, in a formulation containing neither chitosan nor enhancer (as a control), FITC-rHV2 was only poorly absorbed, with an Fr value of 1.86% compared with subcutaneous injection (Figure 2, Table 2). The addition of chitosan at a concentration of 0.5% resulted in a significant improvement, with an Fr value of 8.26%, which is 4-fold that of the control. After enhancers were

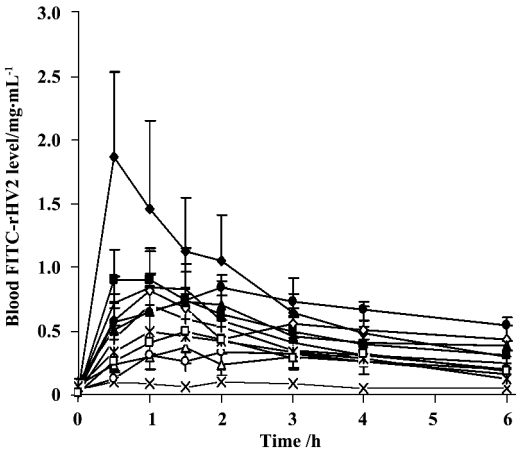

Figure 2. Plasma concentration profiles after intranasal administration of FITC-rHV2 formulations (6 mg/kg) to rats. n=5–6. Mean±SD. (*) 0.5% chitosan; (○) +0.1% EDTA; (▲) +1% GAM; (●) +5% Tween 80; (△) +5% Lecithin; (–) +5% Brij35; (◇) +1.5% Menthol; (■) +4% Azone; (+) +5% HP-β-CD; (◆) +1% SDS; (×) 0.9% NaCl; (□) sc injection.

Table 2. AUC and relative bioavailability (Fr) of FITC-rHV2 after intranasal administration of various chitosan formulations in rats. sc refers subcutaneous administration; n=5–6. Mean±SD. $^{c}P<0.01$ *vs* control (0.9% NaCl); $^{d}P>0.05$, $^{e}P<0.05$, $^{f}P<0.01$ *vs* 0.5% chitosan.

Formulations	Dose /mg·kg^{-1}	$AUC_{0-6\,h}$ /ng·h·mL^{-1}	Fr/%
Chitosan (0.5%)	6.0	1854.00±966.7	8.26^{c}
+Brij35 (5%)	6.0	2705.95±704.72	12.06^{ce}
+SDS (1%)	6.0	4672.40±1204.39	20.83^{cf}
+Lecithin (5%)	6.0	1493.73±422.6	6.66^{cd}
+HP-β-CD (5%)	6.0	2315.68±759.54	10.32^{cd}
+Menthol (1.5%)	6.0	3113.19±854.7	13.50^{ce}
+Tween 80 (5%)	6.0	3869.06±1126.92	17.25^{ce}
+GAM (1%)	6.0	2956.23±634.2	13.18^{ck}
+EDTA (0.1%)	6.0	1504.20±452.8	6.70^{cd}
+Azone (4%)	6.0	3147.18±832.96	14.03^{ce}
NaCl (0.9%)	6.0	417.02±185.45	1.86
sc injection	0.5	1869.45±517.97	100.0

added to the 0.5% chitosan solution, the Fr values of FITC-rHV2 changed markedly in some formulations. Compared with chitosan alone, the addition of 1% SDS, 5% Tween 80, 4% Azone, 1.5% menthol, 1% GAM or 5% Brij35 significantly increased the Fr of FITC-rHV2 ($P<0.05$), whereas the addition of 5% HP-β-CD, 5% lecithin or 0.1% EDTA did not increase Fr to any significant extent.

Regarding the permeability or absorption of FITC-rHV2 in chitosan formulations with or without enhancers, the results of the *in vitro* experiment (ER values) were in agreement with the *in vivo* results (Fr values), as shown in Figure 3 (R^2=0.9059).

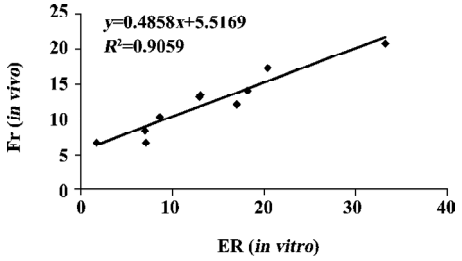

Figure 3. Correlation of the absorption-enhancing effects between ER (*in vitro*) and Fr (*in vivo*) of different formulations.

The effects of chitosan with or without enhancers on the ciliary movement duration in toad palate are shown in Figure 4. Ciliary movements were significantly inhibited by co-administration of chitosan with 1% SDS, 5% Brij35, 4% Azone, 5% lecithin, 0.1% EDTA or 1.5% menthol compared with the 0.9% NaCl control, but not significantly inhibited by 0.5% chitosan alone or 0.5% chitosan with 5% HP-β-CD, 5% tween80 or 1% GAM. Based on these data, the rank order of ciliotoxicity for different chitosan formulations based on the relative ciliary movement durations was as follows: no enhancer<0.5% chitosan<+5% HP-β-CD<+1% GAM<+5% Tween80<+5% lecithin<+0.1% EDTA<+5% Brij35<+4% Azone<+1.5% menthol<+1% SDS.

Discussion

For a nasal solution formulation, 0.5%–1.0% chitosan and a molecular weight greater than 100 kDa are preferred[16,17]. In the present study, we used 0.5% chitosan and found that at this concentration, the chitosan solution could significantly enhance the efflux as well as the nasal absorption of FITC-rHV2 both *in vitro* and *in vivo*. This result can be attributed to a combination of bioadhesion and a transient opening of the tight junctions in the cell membrane to allow hydrophilic macromolecules to pass through[8,9].

SDS, Brij35, Tween 80 and Azone are all percutaneous enhancers[18-20]. In our experiments, the addition of any of these agents into the chitosan solution significantly increased nasal absorption of FITC-rHV2 compared with chitosan alone. This result may be due to the fact that these compounds can all change the arrangement of the epithelial cell membrane phospholipids and increase the fluidity of the membrane lipid bilayers or interact with the membrane protein, therefore resulting in a transcellular pathway transport of FITC-rHV2. Chitosan was able to affect the paracellular pathway transport of FITC-rHV2 by its mucoadhesive properties and opening of the tight junction effect[8,9]. The combined effect of the two agents consequently increased the absorption of FITC-rHV2 compared with chitosan alone.

When EDTA was added to the FITC-rHV2 solution containing chitosan, EDTA activated protein kinase C by depletion of extracellular calcium via chelation, resulting in an expansion of the paracellular route[21], and chitosan interacted with the membrane protein, also causing the tight junctions

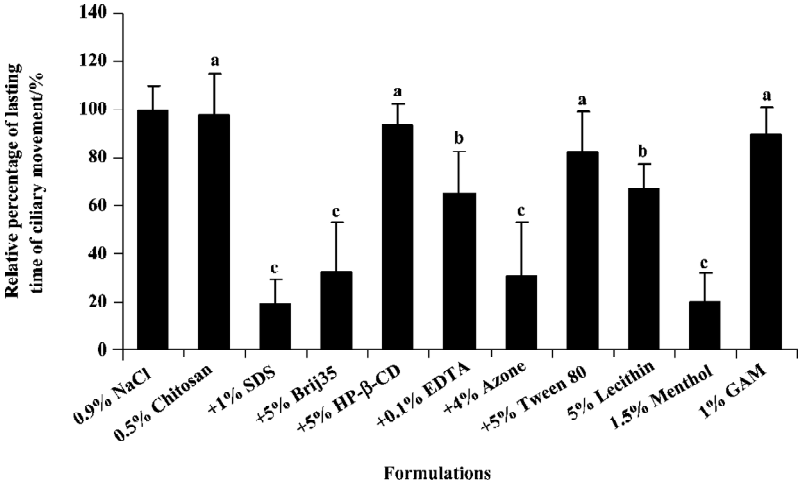

Figure 4. Mucosal ciliotoxicity of various chitosan formulations. n=5 experiments. Mean±SD. $^aP>0.05$, $^bP<0.05$, $^cP<0.01$ *vs* 0.9% NaCl.

to open. The combination of these two effects could potentially result in a marked enhancement of FITC-rHV2 absorption. However, the negatively charged carboxyl groups of EDTA interact with the positively charged amino groups of chitosan, which may inhibit the enhancing action of both agents. Therefore, in the present study we did not observe any absorption enhancement of FITC-rHV2 with EDTA added to chitosan compared with chitosan alone.

There exists a controversial explanation for the enhancing mechanism of cyclodextrins; that is, that the enhancing effects include the disaggregation of protein aggregates (insulin), an interaction with lipids and divalent cations on the membrane surface, and a direct effect on the paracellular pathway by a transient effect on tight junctions[22,23]. However, in most cases, cyclodextrin systems are used as a means of enhancing drug solubilisation[24]. In our experiment, when HP-β-CD was co-administered with chitosan, we did not observe the reported synergistic effect for FITC-rHV2 absorption[25]. The most likely reason is that FITC-rHV2 is not like insulin, which usually aggregates in hexamers in solution, and is more unstable in the presence of proteolytic enzymes in the nasal mucosa, so addition of HP-β-CD may lead to insulin deaggregation from hexamers to dimers and protect insulin from degradation by proteolytic enzymes in the nasal mucosa.

Phospholipids can bring about enhanced delivery of polar compounds administered nasally by inhibiting the apical membrane sodium channels and causing structural changes in tight junctions[26]. However, in our experiment a significant decrease in FITC-rHV2 absorption was observed when lecithin was added to the chitosan solution. This was probably because lecithin is a negatively charged compound, whereas chitosan has positively charged amino groups, so the two oppositely charged molecules might interact and produce no increase in FITC-rHV2 absorption.

Menthol is a monocyclic terpene. The mechanism of its enhancing effect is mainly due to it forming a eutectic with the penetrating compound, thereby increasing its solubility, and also enhancing the fluidity of the local lipid bilayers[27]. In the present study, the co-administration of menthol with chitosan markedly increased FITC-rHV2 absorption compared with chitosan solution alone, suggesting that the co-administration of the two agents cause the FITC-rHV2 molecule to more easily penetrate the cell membrane.

Sakai *et al* found that dipotassium glycyrrhizinate decreased intracellular calcium ion levels and did not induce any significant histomorphological changes in the actin filaments[28]. In addition, dipotassium glycyrrhizinate enhanced the cellular permeability of sodium fluorescein and fluorescein isothiocyanate dextran by enhancing the activation of a protein kinase C via sodium deoxycholate (an enhancer)[29]. Also, the combined use of the two enhancers had fewer toxic effects. In the present experiment we found that chitosan with GAM exerted an obvious enhancing effect on FITC-rHV2 absorption compared with chitosan alone, but it was not clear whether this effect was related to the mechanism described.

Because rat nasal epithelium covers an area that is too small to fit the device used in the *in vitro* experiment, we chose to use rabbit nasal epithelium instead. As shown in Figure 3, there is considerable correlation (R^2=0.9059) between ER and Fr, suggesting a relationship between the *in vitro* and *in vivo* studies. Therefore, in the present study, it appears that using nasal mucosa from different animal species in the *in vitro* and *in vivo* experiments did not influence the correlation between the absorption-enhancing effects of formulations *in vitro* and *in vivo*.

For most absorption enhancers, a direct relationship may exist between the absorption-promoting effect and local toxicity, hence it is important to evaluate the local toxic effect for a prospective novel enhancer system. An *in situ* toad palate model was used in the present study to evaluate the ciliotoxicity of different formulations. Although recording the duration of ciliary movement may be less objective and less accurate than the ciliary beating frequency method, using a microscope it is possible to directly examine the quantity of fallen cilia, as well as the integrity of the mucosa at the same time. This method is especially suitable for the initial screening of drugs or formulations. Among the tested enhancers, chitosan alone and chitosan with HP-β-CD, GAM or Tween 80 were least ciliotoxic.

In conclusion, chitosan is an effective enhancer for increasing the nasal absorption of FITC-rHV2, and co-administration of chitosan with other enhancers can improve absorption further. Some chitosan formulations were less ciliotoxic than others. The chitosan formulation system could be a useful approach for improving nasal absorption.

Acknowledgement

The authors are very grateful to Prof Sheng-geng ZHU for kindly providing the rHV2.

References

1 Walenga JM, Pifarre R, Fareed J. Recombinant hirudin as an antithrombotic agent. Drugs Future 1990; 15: 267–80.

2 Markwardt F, Fink G, Kaiser B, Klocking HP, Nowak G, Richter M, *et al*. Pharmacological survey of recombinant hirudin.

Pharmazie 1988; 43: 202–7.
3 Doutremepuich C, Deharo E, Guyot M, Lalanne MC, Walenga JM, Fareed J. Antithrombotic activity of recombinant hirudin in rat: a comparative study with heparin. Thrombos Res 1989; 54: 435–45.
4 Markwardt F. The development of hirudin as an antithrombotic drug. Thromb Res 1994; 74: 1–23.
5 Markwardt F. Prospective clinical use of hirudin as an anticoagulant. Biomed Prog 1990; 3: 19–23.
6 Han YM, Lu YF, Wang ZH. Studies on the effects of anticoagulant and anti-thrombin after duodenal administration of recombinant hirudin in rats. Chin J Hematol 1999; 20: 483–4.
7 Yang XY, Wang XT, Zhang XN, Zhang Q. Gastrointestinal absorption of recombinant hirudin-2 in rats. J Pharmacol Exp Ther 2004; 308: 774–9.
8 Schipper NG, Olsson S, Hoogstraate JA, deBoer AG, Varum KM, Artursson P. Chitosan as absorption enhancers for poorly absorbable drugs. 2: Mechanism of absorption enhancement. Pharm Res 1997; 14: 923–9.
9 Aspden TJ, Mason JD, Jones NS, Lowe J, Skaugrud O, Illum L. Chitosan as a nasal delivery system: the effect of chitosan solutions on *in vitro* and *in vivo* mucociliary transport rates in human turbinates and volunteers. J Pharm Sci 1997; 86: 509–13.
10 Jiang XG, Cui JB, Fang XL, Wei Y, Xi NZ. Toxicity of drugs on nasal mucocilia and method of its evaluation. Acta Pharm Sin 1995; 30: 848–53.
11 Wang HD, Zhou SH. Marking techniques of biomedicine. Beijing: People's Medical Publishing House; 1995.
12 Griessbach U, Stürzebecher J, Markwardt F. Assay of hirudin in plasma using a chromogenic thrombin substrate. Thromb Res 1985; 37: 347–50.
13 Hosoya K, Kubo H, Natsume H, Sugibayashi K, Morimoto Y. Evaluation of enhancers to increase nasal absorption using chamber technique. Biol Pharm Bull 1994; 17: 316–22.
14 Chandler SG, Illum L, Tomas NM. Nasal absorption in rats. II Effect of enhancers on insulin absorption and nasal histology. Int J Pharm 1991; 76: 61–70.
15 Temesvari LA, Bush JM, Peterson MD, Novak KD, Titus MA, Cardelli JA. Examination of the endosomal and lysosomal pathways in *Dictyostelium discoideum* myosin I mutants. J Cell Sci 1996; 109: 663–73.
16 Illum L. Chitosan and its use as a pharmaceutical excipient. Pharm Res 1998; 15: 1326–31.
17 Illum L, Farraj NF, Davis SD. Chitosan as a novel basal delivery system for peptide drugs. Pharm Res 1994; 11: 1186–9.
18 Shojaei AH. Buccal mucosa as a route for systemic drug delivery: a review. J Pharm Pharm Sci 1998; 1:15–30.
19 Rege BD, Kao JP, Polli JE. Effects of nonionic surfactants on membrane transporters in Caco-2 cell monolayers. Eur J Pharm Sci 2002; 16: 237–46.
20 Sugibayashi K, Nakayama S, Seki T, Hosoya K, Morimoto YJ. Mechanism of skin penetration-enhancing effect by laurocapram. Pharm Sci 1992; 81: 58–64.
21 Wang GS, Zabner J, Deering C, Launspach J, Shao JQ, Bodner M. Increasing epithelial junction permeability enhances gene transfer to airway epithelia *in vivo*. Am J Respir Cell Mol Biol 2000; 22: 129–38.
22 Marttin E, Verhoef JC, Cullander C, Romeijn SG, Nagelkerke JF, Merkus FW. Confocal laser scanning microscopic visualization of the transport of dextrans after nasal administration to rats: effects of absorption enhancer. Pharm Res 1997; 14: 631–7.
23 Yang T, Hussain A, Paulson J, Abbruscato TJ, Ahsan F. Cyclodextrins in nasal delivery of low-molecular-weight heparins: *in vivo* and *in vitro* studies. Pharm Res 2004; 21: 1127–36.
24 Merkus FW, Verhoef JC, Marttin E, Romeijn SG, van der Kuy PH, Hermens WA, *et al*. Cyclodextrins in nasal drug delivery. Adv Drug Deliv Rev 1999; 36: 41–57.
25 Yu SY, Zhao Y, Wu FL, Zang X, Lü WL, Zhang H. Nasal insulin delivery in the chitosan solution: *in vitro* and *in vivo* studies. Int J Pharm 2004; 281: 11–23.
26 Maitani Y, Nakamura K, Suenaga H, Kamata K, Takayama K, Nagai T. The effect of soybean-derived sterylglucoside and β-sitosterol β-*D*-glucoside on nasal absorption in rabbits. Int J Pharm 2000; 200: 17–26.
27 Kaplun-Frischoff Y, Touitou E. Testosterone skin permeation enhancement by menthol through formation of eutectic with drug and interaction with skin lipids. J Pharm Sci 1997; 86: 1394–9.
28 Sakai M, Imai T, Ohtake H, Azuma H, Otagiri M. Effects of absorption enhancers on cytoskeletal actin filaments in Caco-2 cell monolayers. Life Sci 1998; 63: 45–54.
29 Sakai M, Imai T, Ohtake H, Azuma H, Otagiri M. Simultaneous use of sodium deoxycholate and dipotassium glycyrrhizinate enhances the cellular transport of poorly absorbed compounds across Caco-2 cell monolayers. J Pharm Biomed Anal 2004; 36: 915–9.

Acta Pharmacologica Sinica 2005 Dec; 26 (12): 1409–1420

Invited review

Molecular mechanisms regulating expression and function of transcription regulator "inhibitor of differentiation 3"

Robert Wai-sui LIM[1,3], Jin-mei WU[2]

[1]Department of Medical Pharmacology and Physiology, University of Missouri-Columbia, Columbia, Missouri, 65212 USA; [2]College of Biotechnology, Jiangsu University of Science and Technology, Zhenjiang 212018, China

Key words

gene expression regulation; inhibitor of differentiation 3 protein; transcription factors; neoplasm

[3] Correspondence to Prof Robert Wai-sui LIM.
Phn 1-573-882-1560.
Fax 1-573-884-4558.
E-mail limr@health.missouri.edu

Received 2005-05-16
Accepted 2005-06-24

doi: 10.1111/j.1745-7254.2005.00207.x

Abstract

The transcription factor antagonist inhibitor of differentiation 3 (Id3) has been implicated in many diverse developmental, physiological and pathophysiological processes. Its expression and function is subjected to many levels of complex regulation. This review summarizes the current understanding of these mechanisms and describes how they might be related to the diverse functions that have been attributed to the Id3 protein. Detailed understanding of these mechanisms should provide insights towards the development of therapeutic approaches to various diseases, including cancer and atherogenesis.

Introduction

Inhibitor of differentiation (Id) proteins are a family of transcriptional regulators that have been implicated in several developmental, physiological and pathological processes. Their name relates to their ability to inhibit the differentiation of a variety of cells by inhibiting the DNA binding activity of many transcription factors that regulate expression of cell-type specific genes. Id genes are widely expressed in the animal kingdom from humans to zebra fish[1]. Four Id genes, Id1–Id4 have been found in humans and in rodents. A homologous Id-like gene, extramacrochaetae has been identified in drosophila[2].

The Id proteins are small proteins of approximately 13 kDa–20 kDa. All 4 Id proteins contain a relatively conserved helix-loop-helix (HLH) structural motif in the middle of the protein, but are otherwise quite divergent in sequences. The 4 Id proteins constitute 1 subclass (Class V) of the large family of HLH transcriptional regulators. Unlike other HLH proteins that can bind to DNA as either homodimers or heterodimers, the Id proteins lack the basic amino acid domain needed for DNA binding. Instead, they are believed to function primarily by forming heterodimers with the "ubiquitous" Class I HLH proteins known as E-proteins. This prevents the E-proteins from interacting with each other and with the cell-type specific Class II HLH proteins, inhibiting their binding to DNA and blocks their ability to modulate gene expression (Figure 1).

The first Id gene, Id1, was identified by virtue of the ability of its encoded protein to inhibit muscle differentiation and the activation of muscle-specific gene promoters[3]. However, the Id proteins are now known to be important in other physiological systems and pathophysiological situations. In addition to the E-protein partners, Id proteins regulate other transcription factors such as ternary complex factor (TCF)/ETS[4,5], Pax 5 and sterol regulatory element binding protein-1[6]. Individual Id proteins might also interact selectively with proteins not recognized by other Id family members. For example, Id1 is the only Id protein shown to bind the proteasomal protein S5a[7]. Similarly, only Id2 binds to the tumor suppressor retinoblastoma protein Rb and interferes with the ability of hypophosphorylated Rb to suppress cell proliferation when both are ectopically expressed (Figure 1)[8].

Evidence to date indicates that the Id proteins are likely to carry out both common and distinct biological functions,

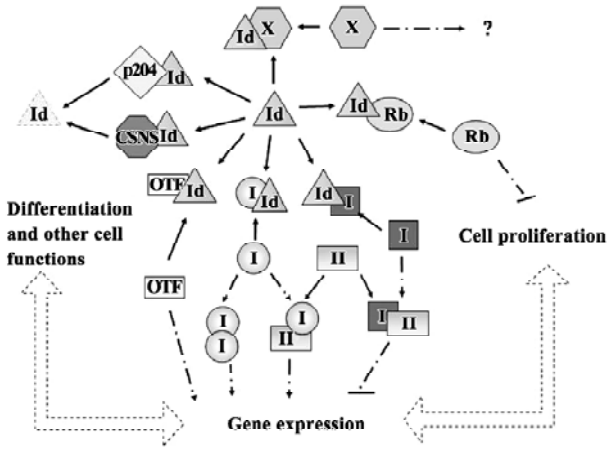

Figure 1. Inhibitor of differentiation (Id) proteins function by interacting with various protein partners. Binding of Id proteins to the class I basic-helix-loop-helix (bHLH) proteins (I) prevents them from forming homodimers or heterodimers with the class II bHLH proteins (II). This leads to the inhibition of gene expression (broken arrows). Alternatively, because some class I bHLH proteins repress transcription, sequestration of these repressor proteins could ameliorate their inhibitory effects. More recent data suggests that Id proteins also interact with and inhibit other transcription factors (OTF) such as ETS, SREBP-1 and Pax5. Individual members of the Id family proteins might interact selectively with specific proteins. For example, Id2 protein binds to the retinoblastoma protein (Rb) and prevents it from blocking cell cycle entry, thus stimulating cell proliferation. Id proteins also affect cell proliferation, as well as differentiation and other cell functions indirectly by modulating the expression of specific genes. Interaction with other proteins (p204, GSN5) accelerates Id3 degradation. Additional protein partners (X) could exist that might explain the many biological effects of the Id proteins.

depending in part on when and where the proteins are expressed. Consistent with this idea, mice engineered to be deficient in a single Id gene are viable, albeit with developmental defects in certain specific cell lineages depending on the particular gene that has been inactivated[9–15]. For example, Id3-deficient mice have defects in both B cell[14] and T cell[15] maturation and develop salivary gland defects reminiscent of the autoimmune Sjogren's syndrome, but are otherwise generally normal[16]. In contrast, mice with both copies of Id1 and Id3 genes inactivated die *in utero* (embryonic d 13.5) with severe vascular defects in the forebrain, aberrant neuronal differentiation[17] and multiple cardiac abnormalities[18]. In fact, mice with both copies of any 2 of the 3 Id genes (Id1–Id3) inactivated exhibit similar cardiac defect and are embryonic lethal. Mice with loss of 1–3 copies of the Id1/1d3 genes are viable but exhibit increasing degrees of resistance to tumor-induced angiogenesis[17]. The lethality of the double knockout mice and the dosage-dependent tumor angiogenesis phenotype clearly indicates that the Id genes mediate overlapping function in some developmental lineage. However, the developmental defects in specific cell lineages manifested in single knockouts suggest that Id genes are unable to compensate in some cells, perhaps because they are not co-expressed or, as in the case of Id2, because of specific dimerization with different protein partners such as Rb.

Many excellent and extensive reviews covering the Id family proteins have been published in recent years[19–26]. Most of these reviews have dealt with the Id proteins as a group and concentrated primarily on the potential biological functions of the Id proteins. Relatively less attention has been devoted to reviewing the molecular mechanisms that regulate the expression and function of individual Id genes and proteins.

The present review will focus on the third member of the Id gene family, Id3, particularly on the mechanisms involved in its regulation. The Id3 gene was first identified as a serum-inducible immediate early gene in an established murine fibroblastic cell line[27]. Subsequent studies have documented its involvement in various biological processes, including T and B cell development[15,14], skeletal muscle differentiation[28,29], vascular smooth muscle cell proliferation[30,31], embryonic neurogenesis[17], osteogenesis[32] and tumor-induced angiogenesis[17].

Expression and function of the protein is under many complex layers of regulation (Figure 2) and, therefore, could provide rich targets for therapeutic interventions.

Developmental and cell-type specific expression pattern of Id3

The most direct way to regulate the function of a particular protein is to control when and where the gene encoding the particular protein is expressed. Several studies have characterized the expression of Id3 at either the mRNA or the protein level. A wide range of techniques have been utilized, including Northern, in situ hybridization, reverse transcription with polymerase chain reaction, various genome expression profiling assays, Western immunoblots and immunocytochemical staining procedures.

Like other Id genes, the expression of Id3 is dynamically regulated during embryonic development. The general expression level is high at the early embryonic ages, but progressively declines as the embryo develops[27,33]. Id3 is widely expressed throughout the embryo proper. Its expression is readily detectable within regions that are undergoing active

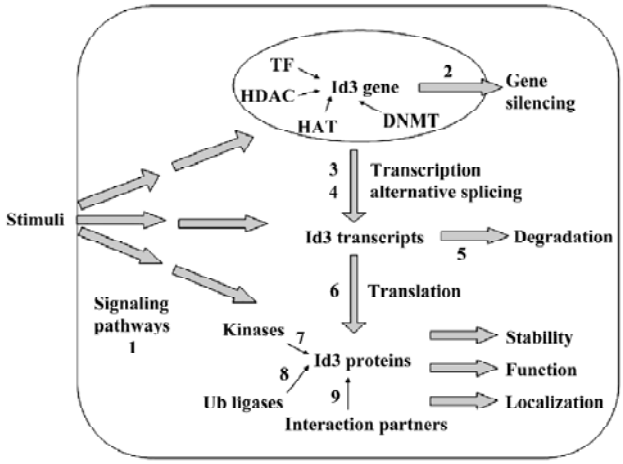

Figure 2. Multiple mechanisms regulating inhibitor of differentiation 3 (Id3) expression and function. A variety of stimuli and physiological states activate diverse signal transduction pathways (1) to regulate the expression and function of Id3 at multiple levels. For example, DNA methyltransferases (DNMT), histone acetyl transferases (HAT) and histone deacetylases (HDAC) might work together to control the silencing of the Id3 gene under certain conditions (2), whereas a variety of different transcription factors (TF) act in conjunction with each other to regulate transcription (3). The Id3 transcripts are also subjected to alternative splicing (4) that results in protein isoforms with distinct biological properties. Interaction of the Id3 transcript with additional factors likely affects its stability (5) and translation (6). The protein products undergo phosphorylation (7) and ubiquitination (8) mediated by specific kinases and ubiquitin ligases that modulate its function and stability. Finally, the subcellular localization and the ultimate biological effect of Id3 might be dependent on the availability, relative abundance and physiological significance of its various protein partners (9).

morphogenesis[34], but can also be detected in some undifferentiated tissues[33].

The expression pattern of Id3 during embryonic development overlaps with, but is not identical to that of, the other Id genes. At an early embryonic age, Id1 and Id3 are expressed in the tissues derived from the inner cell mass; Id2 is expressed in tissues derived from trophoblasts; but no Id4 expression is evident. In the primitive gut, Id1 and Id3 signals are expressed in the mesenchyme, whereas Id2 expression occurs within the epithelium[34]. During early spinal cord development, expression of Id1 and Id2 are restricted to the roof plate, whereas Id3 is expressed both in the roof and the floor plate. At later stages, Id1 and Id3 expression is detected in the dividing neuroblasts, whereas Id2 and 4 are expressed in presumptive neurons undergoing maturation[35]. Generally speaking, the pattern of Id3 expression most closely resembles that of Id1, but the coincidence is not absolute[33].

Expression of Id3 in adult tissues is widely spread but not universal and the level of expression varies substantially among different tissues. Id3 is expressed in many cell types *in vivo* and in both primary cultures and established cell lines (Table 1). Depending on the cell and tissue type, the expression might be constitutive or detectable only after exposure to appropriate stimulus. The level of Id3 expression is generally high in proliferating, undifferentiated cells, but downregulated when cells undergo terminal differentiation[28,29,36–39]. Expression of Id3 also tends to be higher in immortalized cell lines, consistent with the putative involvement of Id proteins in combating cellular senescence[40,41] and maintaining the capacity for self-renewal in embryonic stem cells[42].

Knowing what tissues and cell types express Id3 is, however, probably akin to just seeing the tip of the iceberg. The level of Id3 expression is not static, but varies dramati-

Table 1. Summary of the expression and regulation of Id3 in selected cell types.

Cell types	Comments	References
Cultured fibroblasts	Inducible by many agents as immediate early gene	[27]
Myogenic and osteogenic precursor cells	Downregulated with terminal differentiation	[93,47]
Preadipocytes	Downregulated following adipogenesis and no longer inducible by serum	[38]
Sertoli cells	Induced by serum but not follicle stimulatory hormone	[98]
Lymphoid and monoblastic cell lines	Downregulated in mature differentiated cells	[73,39,99,100]
Astrocytes	Upregulated in astrocytoma	[101,54]
Prostate epithelial cells	Detectable only following serum stimulation	[102]
Human dermal microvascular cells	Downregulated by treatment with statins	[103]
Ovarian surface epithelial cells	Downregulated in ovarian adenocarcinoma	[47,104]
Schwann cells	Downregulated during nerve maturation	[86]
Human keratinocytes	Protein localized to nucleus, downregulated with differentiation	[45]

cally with the growth and physiological state of the cells and is modulated in response to diverse extracellular stimuli. There are other layers of regulation superimposed upon the regulation at the expression level (Figure 2). Additional caveats should also be kept in mind when interpreting the results from the aforementioned studies. Results using immortalized cell lines need to be viewed with caution because the process of immortalization might involve alterations in Id3 expression not seen *in vivo*. Direct examinations of tissue sections *in vivo* or with primary cell cultures eliminate such concerns. However, the sensitivity of the assays used for detecting Id3 expression in various studies are not precisely known and might not always be comparable. The specificity of the antibodies used for immunodetection might not have always been adequately scrutinized. Therefore, care should be taken in making a firm conclusion as to whether Id3 is or is not expressed in a certain tissue or cell type. Nevertheless, because Id3 is expressed at many, but not all, cells indicates that its regulation is likely to involve both ubiquitous as well as cell-type specific regulatory mechanisms.

Altered patterns of Id3 expression in diseases and pathophysiological situations

Perturbation of Id3 expression has been correlated with a variety of disease states and pathological situations, including cancer, aging, atherosclerosis, muscle atrophy, and inflammation. Conversely, altered expression of Id3 has been detected during the regenerative process following tissue injury.

It is generally believed that members of the Id gene family behave like oncogenes. Overexpression of one or more Id genes has been detected in various cancers. The situation with Id3 is consistent in most part with this generalization[43–45], but there are some exceptions. In certain neurological tumors, Id3 upregulation is observed not only in the tumors themselves but also in the vascular tissues surrounding the tumors[44]. In contrast, expression is reduced in papillary thyroid carcinoma[46] and ovarian carcinomas[47], and either increased[48] or absent[49] in seminoma. The expression pattern is even more complex during the development of liver diseases and liver cancer. Id3 expression is low in normal liver, increases with the progression of liver diseases from chronic hepatitis to liver cirrhosis and is expressed at high levels in well-differentiated hepatocarcinomas, but not in the more advanced de-differentiated tumors[50].

Variations in Id gene expression have also been correlated with aging in animals. Expression of Id1, Id2, and Id3 increases in hind limb muscles of aging rats[51]. Because increased levels of Id proteins are associated with muscle disuse atrophy[52], the upregulated Id expression in aging muscle might contribute to the loss of muscle mass that commonly accompanies aging. In contrast, Id3 expression appears to be reduced in the pituitary gland in aged rats[53]. Taken together, the results suggest that some other aging-related physiological perturbations rather than aging per se might be responsible for the altered Id expression in different tissues.

Id3 expression level also changes in inflammatory and atherogenic processes. Id gene expression is upregulated in reactive astrocytes activated as part of the inflammatory process following spinal cord injury[54]. Id3 expression is also altered in vascular smooth muscle cells (VSMC) during atherogenesis. It is expressed at low level in normal vessels of the carotid artery, but is increased within 3 d of balloon injury and remains high through 14 d postinjury[30]. This is accompanied by the appearance of a novel differentially spliced Id3 transcript.

Changes in Id3 expression are not limited to pathological situations: increased Id3 expression has been implicated in tissue regeneration. In the African clawed frog, *Xenopus laevis*, which does not completely regenerate the missing limb following amputation, Id3 expression is upregulated transiently but returns to basal level when terminal differentiation of the limb stump tissues is initiated. In the Japanese newt, *Cynops pyrrhogaster*, which is capable of regenerating a complete limb, expression of Id3 persists until the stage of digit formation[55]. The earlier downregulation of Id3 in the *Xenopus* might have contributed to premature differentiation and the aborted regeneration program. Similarly, Id3 upregulation might also contribute to the liver regeneration following partial hepatomy in mice[56].

The mechanisms accounting for the perturbation of expression of Id3 under different conditions are largely unknown. The presumption is that it involves changes in transcription, but the hypothesis is as yet unproven. No evidence has been found so far that would implicate either gene amplification or deletion in the altered pattern of Id3 expression found in different cancers; therefore, the change is probably epigenetic. There is some evidence that DNA methylation or histone acetylation might contribute to Id3 regulation but exactly how such processes affect Id3 expression is not known (see below). In most cases, the change in Id3 expression is likely to be either secondary to changes in the cell physiology and/or in response to environmental signals.

Stimulus and signaling pathways regulating Id3 expression

Id3 was originally identified as a serum-inducible gene in Balb/c3T3 fibroblasts and found to be induced in these cells, to a varying degree, by a variety of other agents[27]. The Id3 transcript was induced rapidly and transiently, with peak accumulation occurring at about 1 h after stimulation. In this system, Id3 appears to behave as "immediate-early" or "primary response" genes, and can be induced in the absence of ongoing protein synthesis.

Id3 expression has been shown to be responsive to even more diverse stimuli in a variety of cell types (Table 2). Several conclusions can be drawn from this plethora of information. First, although the ability to regulate Id3 expression is wide spread, not all agents regulate Id3 expression in the same manner in all cell types. For example, the phorbol ester, phorbol 12-myristate 13-acetate (PMA), stimulates Id3 expression in thyrocytes[46] but downregulates Id3 levels in the SH-SY5Y neuroblastoma cells[57]. This suggests that the regulatory pathways might be different among

Table 2. Stimuli and signaling pathways implicated in Id3 regulation.

Stimuli	Cell types	Signaling pathways	Responses	References
Thyroid stimulating hormone	Dog thyrocytes	cAMP-dependent	Rapid increase	[46]
PMA, insulin	Dog thyrocytes	ND	Rapid increase	[46]
PMA	SH-SY5Y neuroblastoma	ND	Downregulation after 24 h	[57]
Insulin, methylisoxanthine, dexamethasone	3T3L1 preadipocytes	MEK-, PKC- and PI3K-independent	Rapid increase	[105]
TGF-β	B-lymphocyte progenitor	Smad	Transient increase, returned to basal within 24 h	[13]
TGF-β	Epithelial	ND	Biphasic, transient increase followed by long term suppression	[58,59]
BMP	Mesenchymal stem cells	ND	Transient increase, returned to basal within 3 d	[60]
BMP	Embryonic stem cells	ND	Increase	[42]
BMP	Epithelial	Smad 4	Sustained induction	[59]
TNF-β	Astrocytes, microglias	ND	Rapid and transient increase	[54]
B-cell receptor engagement	Mature B-cells	ND	Increase	[14]
PMA	Mature B-cells	ND	Biphasic, transient increase with a secondary peak	[61]
B-cell receptor engagement	WEHI-231 immature B-cells	ND	Persistent increase	[62]
T-cell receptor (TCR) ligation	T lymphocytes	RAS, ERK, Egr-1	Increase	[63]
Endostatin	Endothelial	ND	Increase	[106]
Estrogen	VSMC	ND	Decrease	[107]
Angiotensin II, Superoxide free radical	VSMC	ERK, p38MAPK, calcium	Rapid increase	[64]
Hydroxyl free radicals	VSMC	ND	Down increase	[69]

ND, not determined; PMA, phorbol 12-myristate 13-acetate; TGF-β, transforming growth factor-β;VSCM, vascular smooth muscle cells.

different cell types. Second, the temporal pattern of Id3 expression is very complex, and differs depending on the cell type and stimuli. In many cases, the induction is transient but biphasic, with an early peak of expression followed either by a later second peak or conversely by long-term suppression. In other cases, the change appears to be more persistent. For example, Id3 is induced transiently by transforming growth factor-β (TGF-β) in B-lymphocyte progenitors, but returns to basal level within 20 h[13]; whereas in epithelial cells, the transient increase is followed by long-term suppression[58,59]. Id3 is also transiently induced by bone morphogenetic proteins (BMP) in mesenchymal stem cells[60], but a sustained induction is observed following BMP treatment of epithelial cells[59]. Finally, and perhaps most importantly, the differences in the patterns of expression have immense biological significance. For example, insulin, which is an adipogenic agent, induces Id3 transiently in 3T3L1 preadipocytes, but adipogenic differentiation itself is accompanied by long-term downregulation of Id3 in 3T3F24A cells[38]. Similarly, B cell receptor (BCR) engagement in mature B cells results in transient Id3 induction and stimulation of cell proliferation[14]. PMA, which is also mitogenic, results in a biphasic response with a transient peak at 4 h and a secondary peak at 24 h, around the time when the stimulated cells are entering S[61]. In contrast, a more persistent Id3 expression is induced by BCR engagement in immature B cells and results in the inhibition of cell proliferation[62].

Because Id3 expression is regulated by many cytokines, hormones and other environmental signals, several different signal transduction pathways presumably contribute to its regulation. Pathways that have been implicated include the Ras, the ERK1/2 pathway following TCR engagement[63], the Smad-dependent pathway in response to TGF-β and BMP[59,13] and the p38, ERK and calcium-dependent pathways following superoxide free radical-induced oxidative stress[64]. In the case of TGF-β, the biphasic response could reflect the differential actions of 2 classes of TGF-β receptors (Activin receptor-like kinase 1 and Activin receptor-like kinase 2) that are preferentially coupled to different Smad proteins[65]. In most cases, the precise signaling pathway(s) responsible for regulating Id3 expression has not been completely defined. In addition, it has not been conclusively demonstrated that the change in transcript level reflects authentic transcriptional regulation.

Regulatory elements and transcription factors involved in Id3 promoter regulation

A systematic analysis of the Id3 promoter and the mechanisms involved in its regulation has yet to be carried out. Yeh and Lim reported in 2000 the cloning and initial characterization of the promoter region of the mouse Id3 gene extending approximately 1 kb upstream of the transcription start site[66] and found that a 180 bp proximal Id3 promoter fragment was sufficient for substantial transcriptional activity in the proliferating myogenic cell line C2C12[66]. Recently, a 254 bp Id3 promoter fragment (-200/+54) has been shown also to be transcriptionally active and responsive to BCR engagement in the WEHI-231 immature lymphoid cells[67]. Several putative transcription factor binding sites have been identified by computer-based analysis, but whether they are bona fide regulatory motifs has not been determined (Figure 3). Using *in vitro* DNase protection assay, we have identified 2–3 protected footprints within this region, at least 1 of which (site 1) seems to be responsible for much of the Id3 promoter activity seen in proliferating C2C12 cells[67a]. Moreover, electrophoretic mobility shift assays detected proteins in the nuclear extracts of proliferating C2C12 cells that bind to the 180 bp Id3 promoter frag-ment[66]. A mutation that eliminates the DNA binding to site 1 reduced the transcriptional activity of the Id3 promoter, indicating that the site is likely to be functional. Consistent with this idea, protein binding to the site declined substantially when incubated *in vitro* with nuclear extracts isolated from differentiated muscle cells that no longer express Id3[68]. It is yet to be determined whether the site in the endogenous Id3 promoter is occupied by transcription factor *in vivo*.

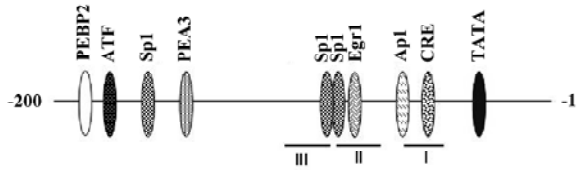

Figure 3. Locations of putative transcription factor binding sites and footprints identified by computer analysis and DNase protection assay. The locations of putative transcription factor binding sites in the proximal 200 bp region of the mouse Id3 gene is determined by computer-based search of the TRASFAC database and indicated in the figure. Three regions (footprints) that are protected from DNase digestion following incubation with nuclear extracts of proliferating C2C12 cells are also indicated (numbered I-III) below the DNA fragment[68].

The second DNase footprint (site 2) encompasses a previously identified early growth response factor 1 (egr-1) site that has been shown to bind recombinant egr-1 *in vitro*[27]; whether the site binds egr-1 *in vivo* has not been established. Others have reported that the upregulation of Id3 upon TCR

engagement involves egr-1, but direct egr-1 binding to the promoter has not been demonstrated and the egr-1 binding site responsible for the upregulation of Id3 promoter activity has not been localized[63]. We have found, however, that mutating the egr-1 site in footprint 2 does not affect the promoter activity of the proximal promoter in proliferating C2C12 cell[68]. Either other sites are involved in mediating egr-1 dependent activation of the Id3 promoter or the mechanism of promoter regulation differs between the muscle and T-cell systems.

Several other transcription factors have been reported to either directly or indirectly regulate Id3 expression. The zinc finger transcription factor, gut-enriched kruppel-like factor (GKLF), downregulates the expression of Id3 in response to hydroxyl free radicals in VSMC, apparently by binding to a GKLF site in the Id3 promoter[69]. Likewise, the transcriptional repressor, B lymphocyte induced maturation protein-1, also appears to act directly on the Id3 promoter region as demonstrated by the chromatin immunoprecipitation assay in mature B-lymphoblast cells[70].

Exactly how the other transcription factors affect Id3 expression is not known. For example, ectopic expression of myoD in proliferating muscle cells upregulates Id3[71], but it is not known whether this involves direct binding of myoD to the Id3 promoter. We did not find any E-box motif corresponding to myoD binding sites within the 1 kb region that we have analyzed, but interactions at more distal sites have not been ruled out. Other transcription factors, such as the homeodomain protein AT binding factor 1A (ATBF1A), the lymphocyte specific transcription coactivator BOB.1/OBF.1, and the forkhead transcription factor FOXM1B, have all been shown to either up or downregulate Id3 expression when overexpressed, but in no case has direct interaction between these factors and the Id3 promoter been establish-ed[72,73,56]. Cells that are deficient in Smad4 fail to alter their Id3 level in response to either TGF-β or BMP, suggesting that the Smad proteins are involved in mediating the regulatory effect of these cytokines[59,60]. However, direct binding of Smad on the Id3 promoter has not been demonstrated.

Several lines of evidence suggest that DNA methylation and histone acetylation might either directly or indirectly regulate Id3 expression. In some non-lymphoid hematopoietic cell lines, the lack of Id3 expression has been correlated with hypermethylation of DNA upstream of the Id3 transcription start site[74]. Whether similar methylation events take place in other cases where Id3 expression is silenced is not known. Treatment with 5 azacytidine, an inhibitor of DNA methyl transferase, blocks the neuronal differentiation of PC12 cells induced by NGF and inhibits NGF-induced Id3 downregulation that occurs during differentiation[36]. Conversely, Id3 expression is downregulated in lymphoblastic cells from patients with immunodeficiency, centromere instability and facial anomalies syndrome, a disease syndrome caused by a defective DNA methyltransferase (DNMT3B)[75]. It is not yet known whether the methylation state of the Id3 promoter itself is directly affected in either case. Similarly, addition of histone deacetylase inhibitors to lung adnocarcinoma cells and the K562 hematoprogenitor cells upregulates Id3 expression, but whether this represents a direct effect on the histones associated with the Id3 promoter is not clear[76–78].

Regulation of Id3 isoform expression by differential splicing

The Id3 gene is composed of three exons and two introns. The first exon includes the 5' untranslated region (UTR) and the coding region corresponding to the first 100 amino acid residues. The coding region is interrupted by a 105 bp intron at the +357 position of the mouse Id3 gene. The second exon contains the last 19 amino acid coding region and 26 bp of the 3' UTR of the mouse Id3 transcript. In the mouse gene, this is followed by a 506 bp second intron and the third exon coding for the rest of the UTR[66]. Both the human and rat Id3 genes appear to be similarly organized, although the length and exact nucleotide sequence of the introns vary substantially among species.

It has been shown in both rats and human that an alternative transcript can be generated under certain conditions by the retention of the first intron[79,31], resulting in the production of a novel Id3 protein isoform with an altered C-terminus. However, because of the divergent nucleotide sequences in the intron, the novel Id3 C-terminal peptides vary substantially in both length and sequences across species. In humans, the novel terminus is 60 amino acids in length; whereas in mice and rats it is only 29 amino acids long, with 7 out of the 29 amino acids differing between the two species. In contrast, the original protein isoform from the mouse and rat differs by only 1 amino acid substitution out of 119.

With such divergence in sequence among closely related species, one might have predicted that the novel isoforms (referred to as Id3L in humans and Id3a in rats) would have dubious biological significance. Contrary to this expectation, *in situ* hybridization and immunolocalization using isoform-specific antibody indicates that the novel variant is not produced in normal vasculature, but is dramatically upregulated during the later stages of vascular lesion formation, whereas

the original Id3 variant is upregulated earlier in the neointima[30]. Furthermore, the 2 Id3 protein variants appear to be functionally distinct. The human Id3L protein is a weaker inhibitor of the binding of E-proteins to DNA *in vitro* than the original shorter Id3 isoform[31]. Overexpression of the original shorter rat Id3 protein in VSMC promotes proliferation and S-phase entry and inhibits transcription of the cyclin dependent kinase (cdk) inhibitor $p21^{Cip1}$, whereas overproduction of the novel Id3a does not inhibit p21 transcription, and causes a decrease in cell number, presumably by promoting apoptosis[30].

What accounts for the unique biological functions of the novel Id3 isoform is perplexing, because the C-termini encoded by the non-spliced Id3 variants would be very different between humans and rats and differ substantially even between the more closely related rodent species. One possible explanation of this conundrum is that the altered C-termini might lead to a protein that acts essentially like a "dominant negative" mutant. In support of this possibility, we have shown that truncation of the Id3 C-terminal to a site roughly corresponding to the spliced junction resulted in a protein that was incapable of blocking E-protein binding, and the inhibition of E-box dependent transcription was compromised[80]. Swapping the Id3 C-terminal with the corresponding region of the Id2 C-terminal likewise reduced the ability of the fusion protein to block E-protein activity. Why the C-terminus of the Id3 protein is so critical for its activity is presently unknown. Much remains to be learned about how the alternative splicing is regulated and when and where else the novel Id3 variant might be expressed. Because most of the earlier studies did not take into account the existence of the novel isoform, some of the expression data might need to be revisited.

Regulation of Id3 transcript and protein stability

Like many other immediate early genes, the Id3 transcript has a rather short half-life[81]. Examination of the cDNA sequence revealed the presence of instability elements in the 3' UTR that bind to RNA-binding protein[82,83]; sequence elements that regulate cytoplasmic polyadenylation are also present[84]. These sequence motifs are likely to contribute to the regulation of the stability and/or translation of the Id3 transcripts, but detailed studies have yet to be reported.

The Id3 protein is also rather short lived, with a half-life of approximately 20 min when overexpressed in 293 cells. As with other short-lived proteins, Id3 appears to be degraded by proteasomes in an ubiquitination dependent manner[85]. Treatment with proteasome inhibitors stabilizes Id3, allowing it to accumulate. Cells with mutations in the E1 ubiquitin activating enzyme show increased Id3 stability. Co-expression of the bHLH protein E47 with Id3 significantly reduces the rate of degradation of Id3[86]. In contrast, interaction with the interferon-inducible protein p204, which is upregulated during terminal muscle differentiation, enhances Id3 degradation[87], suggesting that the stability of the Id3 protein might be affected by its dimerization partner.

Whether and how ubiquitination of Id3 is regulated by the cellular environment is not known. Id3 has been shown to interact physically with CSN5, a subunit of the COP9 signalsome complex that has been implicated in the regulation of the ubiquitination of a large number of cellular proteins. Inhibitors of the COP9-associated kinases increase the ubiquitination of Id3 and accelerate its degradation, whereas overexpression of another COP9 subunit CSN2 stabilizes the Id3 protein. Given these data, it has been speculated that CSN-mediated phosphorylation inhibits ubiquitination of Id3[88].

Although the role of ubiquitination in Id3 degradation is now well-documented, we found that replacing all 4 lysine found in the mouse Id3 protein with arginine failed to stabilize the protein. This suggests that Id3 might be added to an increasing list of proteins like myoD[89], Id2[90], and $p21^{cip1}$[91], that gets ubiquitinated at the α-amino group of the N-terminal residue instead of an internal lysine residue.

How much the regulation at the level of protein stability contributes to the overall regulation of Id3 expression level is not presently known. In one study, experimental denervation to the muscle of young rats results in an increase in Id3 protein levels in both the soleus (900%) and gastrocnemius (80%) without apparently affecting the mRNA level[51]. Similar regulation might occur under other conditions.

Regulation of protein localization and function

Although Id3 preferentially interacts with the class I HLH proteins (E proteins) and exhibits little or no affinity towards the class II bHLH proteins[92], it also binds to other transcription factors such as TCF[4] and the homeodomain protein Pax5[6] through the HLH domain. Co-expression of E-proteins competes with Pax5 for binding to Id3. Other protein partners might also compete with each other for binding. The relative abundance of the various protein components could, therefore, affect the precise compositions of the protein complexes that are formed. This might in turn determine the biological effects of Id3 under conditions where Id3 level is limiting. In addition, because some E-protein isoforms can act as transcriptional inhibitors[93], Id3 might even be expected to activate gene expression under certain circumstances.

Dimerization between Id3 and its target proteins might also affect its subcellular localization. When expressed alone in COS cells, Id3 is predominantly cytoplasmic/perinuclear. Co-expression with E-proteins causes it to accumulate in the nucleus[94]. Whether other proteins or mechanisms might control the subcellular distribution of Id3 is presently unknown. Interestingly, the Id3 protein has been reported to be localized to specific subcellular locations in some cell types[48,95], but the mechanism responsible remains unknown.

The Id3 protein contains several potential phosphorylation sites for various protein kinases[96], including a conserved putative cdk2 site around Ser5 in the N-terminus, which is phosphorylated in a cell cycle-dependent manner (during late G1 to S). Id3 proteins with a mutation of Ser5 to Asp5 to mimic phosphorylation are better able to block the formation of heterodimers between E-protein and myoD but are less able to block E-protein homodimerization. Phosphorylation by cdk2 also interferes with the ability of Id3 to bind to TCF proteins[5], suggesting that Ser5 phosphorylation might alter the dimerization specificity of Id3. In fibroblasts, the Id3 Asp5 mutant (mimicking phosphorylation) is unable to promote S-phase transition, whereas the non-phosphorylatable Ala5 mutant is more effective than the wild type[61]. In contrast, in VSMC, the non-phosphorylatable Id3 Ala 5 mutant activates the cdk inhibitor $p21^{cip1}$ promoter and is unable to promote an increase in cell number when overexpressed[97]. Why the behavior is different between the two cell types is unknown.

Conclusions

It is clear from this brief review that the expression and function of the Id3 protein are regulated in a very complex manner. Much remains to be learned about how the Id3 gene is regulated transcriptionally. Almost nothing is known about how the alternative splicing event that generates a potentially dominant negative protein is controlled. Post-translational modifications might impact the stability, dimerization specificity and/or subcellular localization of the protein, which might then affect the function of the protein. In view of the many physiological and pathophysiological situations where Id protein function is involved or perturbed, understanding these issues will, no doubt, provide a fertile ground for the development of potential therapeutic interventions.

References

1 Dickmeis T, Rastegar S, Lam CS, Aanstad P, Clark M, Fischer N, *et al*. Expression of the helix-loop-helix gene Id3 in the zebrafish embryo. Mech Dev 2002; 113: 99–102.

2 Campuzano S. Emc, a negative HLH regulator with multiple functions in Drosophila development. Oncogene 2001; 20: 8299–307.

3 Benezra R, Davis RL, Lassar A, Tapscott S, Thayer M, Lockshon D, *et al*. Id: a negative regulator of helix-loop-helix DNA binding proteins. Control of terminal myogenic differentiation. Ann NY Acad Sci 1990; 599: 1–11.

4 Yates PR, Atherton GT, Deed RW, Norton JD, Sharrocks AD. Id helix-loop-helix proteins inhibit nucleoprotein complex formation by the TCF ETS-domain transcription factors. EMBO J 1999; 18: 968–76.

5 Stinson J, Inoue T, Yates P, Clancy A, Norton JD, Sharrocks AD. Regulation of TCF ETS-domain transcription factors by helix-loop-helix motifs. Nucleic Acids Res 2003; 31: 4717–28.

6 Roberts EC, Deed RW, Inoue T, Norton JD, Sharrocks AD. Id helix-loop-helix proteins antagonize pax transcription factor activity by inhibiting DNA binding. Mol Cell Biol 2001; 21: 524–33.

7 Anand G, Yin X, Shahidi AK, Grove L, Prochownik EV. Novel regulation of the helix-loop-helix protein Id1 by S5a, a subunit of the 26 S proteasome. J Biol Chem 1997; 272: 19140–51.

8 Lasorella A, Iavarone A, Israel MA. Id2 specifically alters regulation of the cell cycle by tumor suppressor proteins. Mol Cell Biol 1996; 16: 2570–8.

9 Volpert OV, Pili R, Sikder HA, Nelius T, Zaichuk T, Morris C, *et al*. Id1 regulates angiogenesis through transcriptional repression of thrombospondin-1. Cancer Cell 2002; 2: 473–83.

10 Yan W, Young AZ, Soares VC, Kelley R, Benezra R, Zhuang Y. High incidence of T-cell tumors in E2A-null mice and E2A/Id1 double-knockout mice. Mol Cell Biol 1997; 17: 7317–27.

11 Yokota Y, Mansouri A, Mori S, Sugawara S, Adachi S, Nishikawa S, *et al*. Development of peripheral lymphoid organs and natural killer cells depends on the helix-loop-helix inhibitor Id2. Nature 1999; 397: 702–6.

12 Hacker C, Kirsch RD, Ju XS, Hieronymus T, Gust TC, Kuhl C, *et al*. Transcriptional profiling identifies Id2 function in dendritic cell development. Nat Immunol 2003; 4: 380–6.

13 Kee BL, Rivera RR, Murre C. Id3 inhibits B lymphocyte progenitor growth and survival in response to TGF-beta. Nat Immunol 2001; 2: 242–7.

14 Pan L, Sato S, Frederick JP, Sun XH, Zhuang Y. Impaired immune responses and B-cell proliferation in mice lacking the Id3 gene. Mol Cell Biol 1999; 19: 5969–80.

15 Rivera RR, Johns CP, Quan J, Johnson RS, Murre C. Thymocyte selection is regulated by the helix-loop-helix inhibitor protein, Id3. Immunity 2000; 12: 17–26.

16 Li H, Dai M, Zhuang Y. A T cell intrinsic role of Id3 in a mouse model for primary Sjogren's syndrome. Immunity 2004; 21: 551–60.

17 Lyden D, Young AZ, Zagzag D, Yan W, Gerald W, O'Reilly R, *et al*. Id1 and Id3 are required for neurogenesis, angiogenesis and vascularization of tumour xenografts. Nature 1999; 401: 670–7.

18 Fraidenraich D, Stillwell E, Romero E, Wilkes D, Manova K, Basson CT, *et al*. Rescue of cardiac defects in id knockout embryos by injection of embryonic stem cells. Science 2004; 306: 247–52.

19 Sikder HA, Devlin MK, Dunlap S, Ryu B, Alani RM. Id proteins in cell growth and tumorigenesis. Cancer Cell 2003; 3: 525–30.

20 Benezra R, Rafii S, Lyden D. The Id proteins and angiogenesis. Oncogene 2001; 20: 8334–41.
21 Lasorella A, Uo T, Iavarone A. Id proteins at the cross-road of development and cancer. Oncogene 2001; 20: 8326–33.
22 Zebedee Z, Hara E. Id proteins in cell cycle control and cellular senescence. Oncogene 2001; 20: 8317–25.
23 Yokota Y, Mori S. Role of Id family proteins in growth control. J Cell Physiol 2002; 190: 21–8.
24 Ruzinova MB, Benezra R. Id proteins in development, cell cycle and cancer. Trends Cell Biol 2003; 13: 410–8.
25 Alani RM, Silverthorn CF, Orosz K. Tumor angiogenesis in mice and men. Cancer Biol Ther 2004; 3: 498–500.
26 Norton JD. ID helix-loop-helix proteins in cell growth, differentiation and tumorigenesis. J Cell Sci 2000; 113 (Pt 22): 3897–905.
27 Christy BA, Sanders LK, Lau LF, Copeland NG, Jenkins NA, Nathans D. An Id-related helix-loop-helix protein encoded by a growth factor-inducible gene. Proc Natl Acad Sci USA 1991; 88: 1815–9.
28 Atherton GT, Travers H, Deed R, Norton JD. Regulation of cell differentiation in C2C12 myoblasts by the Id3 helix-loop-helix protein. Cell Growth Differ 1996; 7: 1059–66.
29 Melnikova IN, Christy BA. Muscle cell differentiation is inhibited by the helix-loop-helix protein Id3. Cell Growth Differ 1996; 7: 1067–79.
30 Forrest ST, Barringhaus KG, Perlegas D, Hammarskjold ML, McNamara CA. Intron retention generates a novel Id3 isoform that inhibits vascular lesion formation. J Biol Chem 2004; 279: 32897–903.
31 Deed RW, Jasiok M, Norton JD. Attenuated function of a variant form of the helix-loop-helix protein, Id-3, generated by an alternative splicing mechanism. FEBS Lett 1996; 393: 113–6.
32 Maeda Y, Tsuji K, Nifuji A, Noda M. Inhibitory helix-loop-helix transcription factors Id1/Id3 promote bone formation *in vivo*. J Cell Biochem 2004; 93: 337–44.
33 Ellmeier W, Weith A. Expression of the helix-loop-helix gene Id3 during murine embryonic development. Dev Dyn 1995; 203: 163–73.
34 Jen Y, Manova K, Benezra R. Expression patterns of Id1, Id2, and Id3 are highly related but distinct from that of Id4 during mouse embryogenesis. Dev Dyn 1996; 207: 235–52.
35 Jen Y, Manova K, Benezra R. Each member of the Id gene family exhibits a unique expression pattern in mouse gastrulation and neurogenesis. Dev Dyn 1997; 208: 92–106.
36 Persengiev SP, Kilpatrick DL. The DNA methyltransferase inhibitor 5-azacytidine specifically alters the expression of helix-loop-helix proteins Id1, Id2 and Id3 during neuronal differentiation. Neuroreport 1997; 8: 2091–5.
37 Moldes M, Boizard M, Liepvre XL, Feve B, Dugail I, Pairault J. Functional antagonism between inhibitor of DNA binding (Id) and adipocyte determination and differentiation factor 1/sterol regulatory element-binding protein-1c (ADD1/SREBP-1c) transfactors for the regulation of fatty acid synthase promoter in adipocytes. Biochem J 1999; 344: 873–80.
38 Moldes M, Lasnier F, Feve B, Pairault J, Djian P. Id3 prevents differentiation of preadipose cells. Mol Cell Biol 1997; 17: 1796–804.
39 Meyer KB, Skogberg M, Margenfeld C, Ireland J, Pettersson S. Repression of the immunoglobulin heavy chain 3' enhancer by helix-loop-helix protein Id3 via a functionally important E47/E12 binding site: implications for developmental control of enhancer function. Eur J Immunol 1995; 25: 1770–7.
40 Alani RM, Young AZ, Shifflett CB. Id1 regulation of cellular senescence through transcriptional repression of p16/Ink4a. Proc Natl Acad Sci USA 2001; 98: 7812–6.
41 Nickoloff BJ, Chaturvedi V, Bacon P, Qin JZ, Denning MF, Diaz MO. Id-1 delays senescence but does not immortalize keratinocytes. J Biol Chem 2000; 275: 27501–4.
42 Ying QL, Nichols J, Chambers I, Smith A. BMP induction of Id proteins suppresses differentiation and sustains embryonic stem cell self-renewal in collaboration with STAT3. Cell 2003; 115: 281–92.
43 Wilson JW, Deed RW, Inoue T, Balzi M, Becciolini A, Faraoni P, *et al*. Expression of Id helix-loop-helix proteins in colorectal adenocarcinoma correlates with p53 expression and mitotic index. Cancer Res 2001; 61: 8803–10.
44 Vandeputte DA, Troost D, Leenstra S, Ijlst-Keizers H, Ramkema M, Bosch DA , *et al*. Expression and distribution of Id helix-loop-helix proteins in human astrocytic tumors. Glia 2002; 38: 329–38.
45 Langlands K, Down GA, Kealey T. Id proteins are dynamically expressed in normal epidermis and dysregulated in squamous cell carcinoma. Cancer Res 2000; 60: 5929–33.
46 Deleu S, Savonet V, Behrends J, Dumont JE, Maenhaut C. Study of gene expression in thyrotropin-stimulated thyroid cells by cDNA expression array: ID3 transcription modulating factor as an early response protein and tumor marker in thyroid carcinomas. Exp Cell Res 2002; 279: 62–70.
47 Arnold JM, Mok SC, Purdie D, Chenevix-Trench G. Decreased expression of the Id3 gene at 1p36.1 in ovarian adenocarcinomas. Br J Cancer 2001; 84: 352–9.
48 Sablitzky F, Moore A, Bromley M, Deed RW, Newton JS, Norton JD. Stage- and subcellular-specific expression of Id proteins in male germ and Sertoli cells implicates distinctive regulatory roles for Id proteins during meiosis, spermatogenesis, and Sertoli cell function. Cell Growth Differ 1998; 9: 1015–24.
49 Albanese JM, Reuter VE, Bosl GJ, Houldsworth J, Chaganti RS. Expression of ID genes in differentiated elements of human male germ cell tumors. Diagn Mol Pathol 2001; 10: 248–54.
50 Damdinsuren B, Nagano H, Kondo M, Yamamoto H, Hiraoka N, Yamamoto T, *et al*. Expression of Id proteins in human hepatocellular carcinoma: relevance to tumor dedifferentiation. Int J Oncol 2005; 26: 319–27.
51 Alway SE, Degens H, Krishnamurthy G, Chaudhrai A. Denervation stimulates apoptosis but not Id2 expression in hindlimb muscles of aged rats. J Gerontol A Biol Sci Med Sci 2003; 58: 687–97.
52 Gundersen K, Merlie JP. Id-1 as a possible transcriptional mediator of muscle disuse atrophy. Proc Natl Acad Sci USA 1994; 91: 3647–51.
53 Chen H. Gene expression by the anterior pituitary gland: effects of age and caloric restriction. Mol Cell Endocrinol 2004; 222: 21–31.
54 Tzeng SF, Kahn M, Liva S, de VJ. Tumor necrosis factor-alpha regulation of the Id gene family in astrocytes and microglia during CNS inflammatory injury. Glia 1999; 26: 139–52.

55 Shimizu-Nishikawa K, Tazawa I, Uchiyama K, Yoshizato K. Expression of helix-loop-helix type negative regulators of differentiation during limb regeneration in urodeles and anurans. Dev Growth Differ 1999; 41: 731–43.
56 Wang X, Bhattacharyya D, Dennewitz MB, Kalinichenko VV, Zhou Y, Lepe R, *et al*. Rapid hepatocyte nuclear translocation of the Forkhead Box M1B (FoxM1B) transcription factor caused a transient increase in size of regenerating transgenic hepatocytes. Gene Expr 2003; 11: 149–62.
57 Lopez-Carballo G, Moreno L, Masia S, Perez P, Barettino D. Activation of the phosphatidylinositol 3-kinase/Akt signaling pathway by retinoic acid is required for neural differentiation of SH-SY5Y human neuroblastoma cells. J Biol Chem 2002; 277: 25297–304.
58 Kang Y, Chen CR, Massague J. A self-enabling TGFbeta response coupled to stress signaling: Smad engages stress response factor ATF3 for Id1 repression in epithelial cells. Mol Cell 2003; 11: 915–26.
59 Kowanetz M, Valcourt U, Bergstrom R, Heldin CH, Moustakas A. Id2 and Id3 define the potency of cell proliferation and differentiation responses to transforming growth factor beta and bone morphogenetic protein. Mol Cell Biol 2004; 24: 4241–54.
60 Peng Y, Kang Q, Luo Q, Jiang W, Si W, Liu BA, *et al*. Inhibitor of DNA binding/differentiation helix-loop-helix proteins mediate bone morphogenetic protein-induced osteoblast differentiation of mesenchymal stem cells. J Biol Chem 2004; 279: 32941–9.
61 Deed RW, Hara E, Atherton GT, Peters G, Norton JD. Regulation of Id3 cell cycle function by Cdk-2-dependent phosphorylation. Mol Cell Biol 1997; 17: 6815–21.
62 Hata K, Yoshimoto T, Mizuguchi J. CD40 ligand rescues inhibitor of differentiation 3-mediated G1 arrest induced by anti-IgM in WEHI-231 B lymphoma cells. J Immunol 2004; 173: 2453–61.
63 Bain G, Cravatt CB, Loomans C, Alberola-Ila J, Hedrick SM, Murre C. Regulation of the helix-loop-helix proteins, E2A and Id3, by the Ras-ERK MAPK cascade. Nat Immunol 2001; 2: 165–71.
64 Mueller C, Baudler S, Welzel H, Bohm M, Nickenig G. Identification of a novel redox-sensitive gene, Id3, which mediates angiotensin II-induced cell growth. Circulation 2002; 105: 2423–8.
65 Miyazono K, Miyazawa K. Id: a target of BMP signaling. Science STKE 2002; available from http://stke.sciencemag.org/cgi/content/full/sigtrans;2002/151/pe40.
66 Yeh K, Lim RW. Genomic organization and promoter analysis of the murine Id3 gene. Gene 2000; 254: 163–71.
67 Li XJ, Hata K, Mizuguchi J. Engagement of membrane immunoglobulin enhances Id3 promoter activity in WEHI-231 B lymphoma cells. Acta Pharmacol Sin 2005; 26: 486–91.
68 Wu J, Lim RW. Regulation of inhibitor of differentiation gene 3 (Id3) expression by Sp2-motif binding factor in myogenic C2C12 cells: Down regulation of DNA binding activity following muscle differentiation. Biochim Biophy Acta 2005;1731:13–22.
69 Nickenig G, Baudler S, Muller C, Werner C, Werner N, Welzel H, et al. Redox-sensitive vascular smooth muscle cell proliferation is mediated by GKLF and Id3 *in vitro* and *in vivo.* FASEB J 2002; 16: 1077–86.
70 Shaffer AL, Lin KI, Kuo TC, Yu X, Hurt EM, Rosenwald A, et al. Blimp-1 orchestrates plasma cell differentiation by extinguishing the mature B cell gene expression program. Immunity 2002; 17: 51–62.
71 Wyzykowski JC, Winata TI, Mitin N, Taparowsky EJ, Konieczny SF. Identification of novel MyoD gene targets in proliferating myogenic stem cells. Mol Cell Biol 2002; 22: 6199–208.
72 Berry FB, Miura Y, Mihara K, Kaspar P, Sakata N, Hashimoto-Tamaoki T, *et al*. Positive and negative regulation of myogenic differentiation of C2C12 cells by isoforms of the multiple homeodomain zinc finger transcription factor ATBF1. J Biol Chem 2001; 276: 25057–65.
73 Brunner C, Laumen H, Nielsen PJ, Kraut N, Wirth T. Expression of the aldehyde dehydrogenase 2-like gene is controlled by BOB.1/OBF.1 in B lymphocytes. J Biol Chem 2003; 278: 45231–9.
74 Deed RW, Jasiok M, Norton JD. Lymphoid-specific expression of the Id3 gene in hematopoietic cells. Selective antagonism of E2A basic helix-loop-helix protein associated with Id3-induced differentiation of erythroleukemia cells. J Biol Chem 1998; 273: 8278–86.
75 Ehrlich M, Buchanan KL, Tsien F, Jiang G, Sun B, Uicker W, *et al*. DNA methyltransferase 3B mutations linked to the ICF syndrome cause dysregulation of lymphogenesis genes. Hum Mol Genet 2001; 10: 2917–31.
76 Eickhoff B, Ruller S, Laue T, Kohler G, Stahl C, Schlaak M, *et al*. Trichostatin A modulates expression of p21waf1/cip1, Bcl-xL, ID1, ID2, ID3, CRAB2, GATA-2, hsp86 and TFIID/TAFII31 mRNA in human lung adenocarcinoma cells. Biol Chem 2000; 381: 107–12.
77 Eickhoff B, Germeroth L, Stahl C, Kohler G, Ruller S, Schlaak M, *et al*. Trichostatin A-mediated regulation of gene expression and protein kinase activities: reprogramming tumor cells for ribotoxic stress-induced apoptosis. Biol Chem 2000; 381: 1127–32.
78 Plonczynski M, Hardy CL, Safaya S, Harrell A, McCoy L, Brinson A, *et al*. Induction of globin synthesis in K562 cells is associated with differential expression of transcription factor genes. Blood Cells Mol Dis 1999; 25: 156–65.
79 Matsumura ME, Li F, Berthoux L, Wei B, Lobe DR, Jeon C, *et al*. Vascular injury induces posttranscriptional regulation of the Id3 gene: cloning of a novel Id3 isoform expressed during vascular lesion formation in rat and human atherosclerosis. Arterioscler Thromb Vasc Biol 2001; 21: 752–8.
80 Chen B, Han BH, Sun XH, Lim RW. Inhibition of muscle-specific gene expression by Id3: requirement of the C-terminal region of the protein for stable expression and function. Nucleic Acids Res 1997; 25: 423–30.
81 Barone MV, Pepperkok R, Peverali FA, Philipson L. Id proteins control growth induction in mammalian cells. Proc Natl Acad Sci USA 1994; 91: 4985–8.
82 King PH, Levine TD, Fremeau RT Jr, Keene JD. Mammalian homologs of Drosophila ELAV localized to a neuronal subset can bind *in vitro* to the 3' UTR of mRNA encoding the Id transcriptional repressor. J Neurosci 1994; 14: 1943–52.
83 Keene JD. Ribonucleoprotein infrastructure regulating the flow of genetic information between the genome and the proteome. Proc Natl Acad Sci USA 2001; 98: 7018–24.
84 Afouda AB, Reynaud-Deonauth S, Mohun T, Spohr G. Localized XId3 mRNA activation in *Xenopus* embryos by cytoplasmic polyadenylation. Mech Dev 1999; 88: 15–31.

85 Bounpheng MA, Dimas JJ, Dodds SG, Christy BA. Degradation of Id proteins by the ubiquitin-proteasome pathway. FASEB J 1999; 13: 2257–64.
86 Thatikunta P, Qin W, Christy BA, Tennekoon GI, Rutkowski JL. Reciprocal Id expression and myelin gene regulation in Schwann cells. Mol Cell Neurosci 1999; 14: 519–28.
87 Liu CJ, Ding B, Wang H, Lengyel P. The MyoD-inducible p204 protein overcomes the inhibition of myoblast differentiation by Id proteins. Mol Cell Biol 2002; 22: 2893–5.
88 Berse M, Bounpheng M, Huang X, Christy B, Pollmann C, Dubiel W. Ubiquitin-dependent degradation of Id1 and Id3 is mediated by the COP9 signalosome. J Mol Biol 2004; 343: 361–70.
89 Breitschopf K, Bengal E, Ziv T, Admon A, Ciechanover A. A novel site for ubiquitination: the N-terminal residue, and not internal lysines of MyoD, is essential for conjugation and degradation of the protein. EMBO J 1998; 17: 5964–73.
90 Fajerman I, Schwartz AL, Ciechanover A. Degradation of the Id2 developmental regulator: targeting via N-terminal ubiquitination. Biochem Biophys Res Commun 2004; 314: 505–12.
91 Coulombe P, Rodier G, Bonneil E, Thibault P, Meloche S. N-Terminal ubiquitination of extracellular signal-regulated kinase 3 and p21 directs their degradation by the proteasome. Mol Cell Biol 2004; 24: 6140–50.
92 Langlands K, Yin X, Anand G, Prochownik EV. Differential interactions of Id proteins with basic-helix-loop-helix transcription factors. J Biol Chem 1997; 272: 19785–93.
93 Chen B, Lim RW. Physical and functional interactions between the transcriptional inhibitors Id3 and ITF-2b. Evidence toward a novel mechanism regulating muscle-specific gene expression. J Biol Chem 1997; 272: 2459–63.
94 Deed RW, Armitage S, Norton JD. Nuclear localization and regulation of Id protein through an E protein-mediated chaperone mechanism. J Biol Chem 1996; 271: 23603–6.
95 Stewart HJ, Zoidl G, Rossner M, Brennan A, Zoidl C, Nave KA, *et al*. Helix-loop-helix proteins in Schwann cells: a study of regulation and subcellular localization of Ids, REB, and E12/47 during embryonic and postnatal development. J Neurosci Res 1997; 50: 684–701.
96 Nagata Y, Shoji W, Obinata M, Todokoro K. Phosphorylation of helix-loop-helix proteins ID1, ID2 and ID3. Biochem Biophys Res Commun 1995; 207: 916–26.
97 Forrest ST, Taylor AM, Sarembock IJ, Perlegas D, McNamara CA. Phosphorylation regulates Id3 function in vascular smooth muscle cells. Circ Res 2004; 95: 557–9.
98 Chaudhary J, Johnson J, Kim G, Skinner MK. Hormonal regulation and differential actions of the helix-loop-helix transcriptional inhibitors of differentiation (Id1, Id2, Id3, and Id4) in Sertoli cells. Endocrinology 2001; 142: 1727–36.
99 Ishiguro A, Spirin KS, Shiohara M, Tobler A, Gombart AF, Israel MA, *et al*. Id2 expression increases with differentiation of human myeloid cells. Blood 1996; 87: 5225–31.
100 Cooper CL, Brady G, Bilia F, Iscove NN, Quesenberry PJ. Expression of the Id family helix-loop-helix regulators during growth and development in the hematopoietic system. Blood 1997; 89: 3155–65.
101 Tzeng SF, de VJ. Expression and functional role of the Id HLH family in cultured astrocytes. Brain Res Mol Brain Res 1997; 46: 136–42.
102 Chaudhary J, Schmidt M, Sadler-Riggleman I. Negative acting HLH proteins Id1, Id2, Id3, and Id4 are expressed in prostate epithelial cells. Prostate 2005; 64: 353–64.
103 Pammer J, Reinisch C, Kaun C, Tschachler E, Wojta J. Inhibitors of differentiation/DNA binding proteins Id1 and Id3 are regulated by statins in endothelial cells. Endothelium 2004; 11: 175–80.
104 Shepherd TG, Nachtigal MW. Identification of a putative autocrine bone morphogenetic protein-signaling pathway in human ovarian surface epithelium and ovarian cancer cells. Endocrinology 2003; 144: 3306–14.
105 Inuzuka H, Nanbu-Wakao R, Masuho Y, Muramatsu M, Tojo H, Wakao H. Differential regulation of immediate early gene expression in preadipocyte cells through multiple signaling pathways. Biochem Biophys Res Commun 1999; 265: 664–8.
106 Abdollahi A, Hahnfeldt P, Maercker C, Grone HJ, Debus J, Ansorge W, *et al*. Endostatin's antiangiogenic signaling network. Mol Cell 2004; 13: 649–63.
107 Watanabe T, Akishita M, Nakaoka T, He H, Miyahara Y, Yamashita N, *et al*. Caveolin-1, Id3a and two LIM protein genes are upregulated by estrogen in vascular smooth muscle cells. Life Sci 2004; 75: 1219–29.

Acta Pharmacologica Sinica 2005 Dec; 26 (12): 1421–1434

Blackwell Publishing

Invited review

Molecular mechanism and regulation of autophagy[1]

Ya-ping YANG[2], Zhong-qin LIANG[2], Zhen-lun GU[2], Zheng-hong QIN[2,3]

[2]*Department of Pharmacology, Soochow University School of Medicine, Suzhou 215007, China*

Key words

autophagy; phosphatidylinositol 3-kinase; Atg protein; mTOR protein; protein degradation

[1] Supported by the National Natural Science Foundation of China (No 3037506).
[2] Correspondence to Prof Zheng-hong QIN.
Phn 86-512-6512-2087.
Fax 86-512-6519-0599.
E-mail zhqin5@hotmail.com

Received 2005-06-30
Accepted 2005-08-26

doi: 10.1111/j.1745-7254.2005.00235.x

Abstract

Autophagy is a major cellular pathway for the degradation of long-lived proteins and cytoplasmic organelles in eukaryotic cells. A large number of intracellular/extracellular stimuli, including amino acid starvation and invasion of microorganisms, are able to induce the autophagic response in cells. The discovery of the *ATG* genes in yeast has greatly advanced our understanding of the molecular mechanisms participating in autophagy and the genes involved in regulating the autophagic pathway. Many yeast genes have mammalian homologs, suggesting that the basic machinery for autophagy has been evolutionarily conserved along the eukaryotic phylum. The regulation of autophagy is a very complex process. Many signaling pathways, including target of rapamycin (TOR) or mammalian target of rapamycin (mTOR), phosphatidylinositol 3-kinase-I (PI3K-I)/ PKB, GTPases, calcium and protein synthesis all play important roles in regulating autophagy. The molecular mechanisms and regulation of autophagy are discussed in this review.

Introduction

Cell homeostasis is maintained by a precisely regulated balance between synthesis and degradation of cellular components. There are 2 powerful hydrolytic mechanisms in eukaryotic cells: the proteasome and the lysosome/ vacuole. More than 90% of cellular proteins are long-lived. These proteins and some cytoplasmic organelles are believed to be degraded within a specific compartment, the lysosome/ vacuole[1]. There are at least 3 different pathways for lysosomal protein degradation: Cvt (cytosol to vacuole targeting pathway)[2], Vid (vacuolar import and degradation pathway)[3] and autophagy[4]. Autophagy plays important roles in physiology and pathophysiology in all cell types. In addition to its role in protein and organelle degradation, autophagy may induce a type of programmed cell death that is different from apoptosis, namely type II programmed cell death[5]. Recently it has been found that autophagy may be a transitory tactical response, and that it affects a range of normal developmental processes, such as sporulation in yeast and pupa formation in *Drosophila melanogaster*[6,7]. Furthermore, autophagy may contribute to the extension of lifespan induced by caloric restriction[8]. Autophagy might also act as a means of defense against invasion by various bacteria and viruses. There is a potential link between autophagy and a number of diseases in humans. For example, cancer, cardiomyopathy and neurodegenerative disorders such as Alzheimer's, Parkinson's and Huntington's diseases, amyotrophic lateral sclerosis and prion diseases are all associated with increased autophagy activity[9]. Consequently, study of the molecular basis of autophagy would result in a better understanding of the role of autophagy in cell death and ageing, and would also result in proposals for new therapeutic approaches for neurodegenerative diseases.

The morphology of autophagy was first characterized in studies of mammalian cells. With a few exceptions, however, the molecular components of autophagy were initially elucidated in yeast because of the convenience of gene analysis. Recent studies in various eukaryotic systems have revealed a conservation of the autophagic mechanism[10]. In the past, the many terms used in the autophagy field have been highly confusing: Aut (autophagocytosis), Apg (autophagy), Vps (vacuolar protein-sorting) all have been used. Recently, the autophagy-related genes and the products of these genes were named *ATG* and Atg, respectively[11].

Classification of autophagy

Autophagy is a ubiquitous physiological process that occurs in all eukaryotic cells. There are three primary forms of autophagy: macroautophagy, microautophagy and chaperone-mediated autophagy (CMA). Macroautophagy is the most prevalent form of autophagy. It comprises the following processes: initially, a "C" shape double-membrane structure appears in the cytoplasm, and then at both ends of this membrane a structure grows, and finally closes to form a vacuole. The bulk of the cytoplasm and some organelles are wrapped into the vacuole (autophagosome). Then the autophagosome targets the lysosome/vacuole, where its outer membrane fuses with the lysosomal membrane and the inter sac (autophagic body) enters the lysosome/vacuole. The autophagic body is degraded in the lysosome/vacuole so the carrying constituent components can be recycled[12]. Microautophagy is a form with few features. In this pathway, the membrane of the lysosome/vacuole invaginates, and then finally pinches off to form an internal vacuolar vesicle that contains material derived from the cytoplasm, akin to the autophagic bodies formed in macroautophagy. The notable difference between macroautophagy and microautophagy is that in the latter the cytoplasm is directly up taken into the lysosome/vacuole[13]. CMA differs from the other lysosomal degradation pathways in that vesicular traffic is not involved. Cytosolic proteins with particular peptide sequence motifs are recognized by a complex of molecular chaperones, then bind to a receptor in the lysosomal membrane, the lysosome-associated membrane protein (Lamp) type 2a. Proteins are delivered to lysosomes with the help of molecular chaperones and Lamp 2a[14].

Autophagy is basically a non-selective process, in which bulk cytoplasm is randomly sequestered into the cytosolic autophagosome. However, in some cases it may select its target. For example, autophagy can selectively eliminate some organelles, such as injured or excrescent peroxisomes, endoplasmic reticulum (ER) and mitochondria[15]. A recent report shows that in yeast, *Saccharomyces cerevisiae*, the cytosolic protein acetaldehyde dehydrogenase (Ald6) is delivered to the vacuole and degraded by means of specific autophagy[16].

Molecular mechanisms of macroautophagy

Macroautophagy, a major form of autophagy, is relatively well characterized at present. Autophagy and the related processes are dynamic, and many molecules involved in the autophagic process have been identified. At least 25 specific yeast genes are exclusively involved in autophagy, and there are more than 40 additional yeast genes required for autophagy, but they also play roles in other pathways[11]. However, the physiological functions of many of these genes need to be further clarified.

Origin of the autophagosomal membrane There is still debate on the origin of autophagosome membranes. Initially, the ribosome-free region of the rough ER and Golgi were proposed as the source of autophagosomal membranes[17,18]. Now, it is generally accepted that the phagophore, a poorly characterized organelle, may be the major source of the autophagosomal membrane and related structures[19].

Autophagosome formation

Two ubiquitin-like conjugation systems In yeast, autophagy almost completely shuts off under growing conditions, although every *ATG* gene is expressed. Molecular biological and biochemical analyses of these gene products uncovered the genetic and biophysical interactions among the Atg proteins. One of the most remarkable findings regarding the Atg proteins is the discovery of two ubiquitin-like conjugation systems, Atg12-Atg5 and Atg8-phosphatidylethanolamine (PE) (Figure 1). In fact, half of the *APG* genes essential for autophagy are involved in these conjugation systems, and these two conjugation systems are well conserved among eukaryotes. Furthermore, Atg12-Atg5 and Atg8 conjugation systems are somehow related to each other[20–22]: if the former is defective, the latter can not target to the pre-autophagosomal structure (PAS); the levels of Atg8-PE also play an important role in the conjugation of Atg12-Atg5.

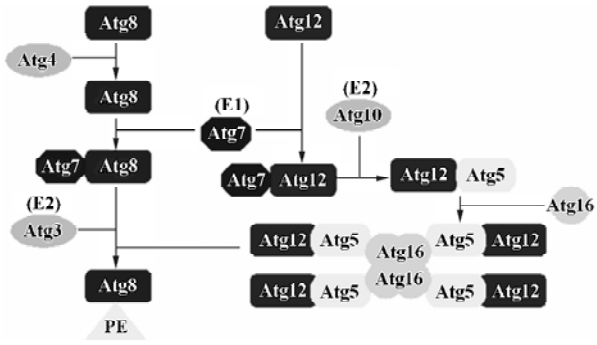

Figure 1. Two ubiquitin-like conjugation systems are involved in autophagosome formation.

Atg12-Atg5 conjugation system Atg12, a small hydrophilic protein of 186 amino acids with no apparent homology to ubiquitin, can covalently link to a unique target protein, Atg5[23]. The mode of conjugation of Atg12 and Atg5 is quite similar to that of ubiquitination. Atg12 is first

activated in an ATP-dependent manner by Atg7 (it functions as an ubiquitin-activating enzyme, E1), leading to the formation of a thioester bond between the C-terminal glycine in Atg12 and a cysteine residue in Atg7[24]. The C-terminal glycine in Atg12 is then transferred to the cysteine in Atg10 (it functions as a ubiquitin-conjugating enzyme, E2), forming a new thioester bond, and Atg7 is released[25]. Finally, the C-terminal glycine in Atg12 forms an isopeptide bond with the ε-amino group of lysine 149 in Atg5, and Atg10 is in its free state again. The formation of the Atg12-Atg5 conjugate is indispensable to autophagosome formation. It seems that this ubiquitin-like system is a constitutive process, because the formation of the Atg12-Atg5 conjugate is not dependent upon starvation or other autophagy-inducing conditions[26]. Atg12 and Atg5 form a conjugate immediately after their synthesis, and free forms of these are hardly detectable. The conjugation reaction between Atg5 and Atg12 is irreversible, and so far no protease has been found to deconjugate this conjugate. Atg16 also binds preferentially to the Atg12-Atg5 conjugate. Atg16 links with Atg12-Atg5 through self-oligomerization, and its C-terminal coiled-coil region may be responsible for this oligomerization. Therefore, Atg16 forms a 350 kDa multimeric complex with the Atg12-Atg5 conjugates. It should be pointed out that Atg16 only binds to Atg5, and not to Atg12[27,28]. This new complex is necessary for the elongation of the isolation membranes (used for formation of the autophagosomal membrane). A small fraction of the Atg12-Atg5·Atg16 complex initially associates with a small crescent-shaped vesicle evenly. As the membrane elongates, Atg12-Atg5 shows asymmetric localization and most of these proteins associate with the convex surface of the isolation membrane. This complex will dissociate from the membrane upon completion of autophago-some formation; thus, it is not present in the mature autophagosome[29]. The molecular basis of this transient association of Atp12-Atg5 conjugates with the autophago-some membrane is not yet known.

In mammalian cells, Atg5 and Atg12 are conjugated to each other in the same way as they are in yeast, but the complex interacts with Atg16L, forming an ~800 kDa structure instead of a 350 kDa complex in yeast[27]. Atg16L is a 63 to 74 kDa protein, which has a binding region and coiled-coil region similar to that of Atg16. However, Atg16L has a long C-terminal extension containing 7 WD repeats, but the role of the WD repeats in autophagy has not yet been elucidated.

Atg8 conjugation system The second ubiquitin-like protein essential for autophagy is Atg8 (Aut7/Apg8). Atg8 is a 117-amino acid protein and is present in the early isolation membranes, autophagosomes and autophagic bodies[30]. This feature makes Atg8 a good marker for studying membrane dynamics during autophagy. Cell fractionation studies have shown that Atg8 is mostly membrane-bound; approximately half of it is peripherally bound to the membrane and the other half behaves like an intrinsic membrane protein. Atg4, a novel cysteine protease, is responsible for processing Atg8 by cleaving a single Arg residue from it, consequently exposing Gly in the C-terminus of Atg8[31]. Atg8 can be activated by Atg7 (E1) in an ATP-dependent manner and transferred to a conjugating E2 enzyme, Atg3[32]. Atg7 is a unique enzyme that activates two different ubiquitin-like proteins, Atg12 and Atg8, and assigns them to their proper E2 enzymes, Atg10 and Atg3, respectively. Interestingly, in the final step, Atg8 does not form a conjugate with other proteins, but interacts with PE, an abundant membrane phospholipid[32]. This lipidation reaction leads to a conformational change of Atg8 that is necessary for the membrane dynamics of autophagy[33]. In addition, Atg8-PE is deconjugated by Atg4, which cleaves the lipid-protein linkage and provides a new source of cytoplasmic Atg8. The cycle of conjugation and deconjugation is important for the normal progression of autophagy.

Microtubule-associated protein 1 light chain 3 (LC3), the mammalian orthologue of Atg8, targets to the autophagosomal membranes in an Atg5-dependent manner and remains there even after Atg12-Atg5 dissociates. Thus LC3 is the only credible marker of the autophagosome in mammalian cells[12]. In wild-type cells, LC3 is detected in 2 forms: LC3-I (18 kDa) and LC3-II (16 kDa)[34]. Twenty-two amino acids in the C-terminus of the newly synthesized LC3 are cleaved immediately by the mammalian orthologue of the yeast cysteine proteinase Atg4, autophagin, to produce an active cytosolic form, LC3-I[35]. Then with the catalysis of Atg7 and Atg3, LC3-I undergoes a series of ubiquitination-like reactions, and is modified to LC3-II. LC3-I is located in the cytoplasm, while LC3-II is a tightly membrane bound protein and is attached to PAS and autophagosomes. The relative amount of membrane-bound LC3-II reflects the abundance of autophagosomes, so the induction and inhibition of autophagy can be monitored through measuring total and free LC3-II levels by means of immunoassay[34]. In addition, studies have shown that the Atg12 and LC3 systems have a functional relationship. In *ATG5*$^{-/-}$ cells, LC3-II is not generated at all[21]. As a result, LC3 cannot target the autophagosomal membranes. The recent generation of transgenic mice expressing green fluorescent protein (GFP) fused to LC3 provides a useful tool to investigate autophagy in various mammalian organs *in vivo*[36].

In addition to LC3, at least another two mammalian

orthologs of yeast Atg8 have been identified[37,38]: γ-aminobutyric acid type A receptor-associated protein (GABARAP) and Golgi-associated ATPase enhancer of 16 kDa (GATE-16). The 2 proteins also covert to membrane bound forms (form II), which are recovered in membrane fractions[39]. These results suggest that all mammalian Atg8 homologues receive common modifications to associate with autophagosomal membranes, but the functions of these orthologs and their modified form II need to be further studied.

Two kinase complexes

Atg 1 protein kinase Atg1 is a serine/threonine protein kinase, which forms a protein complex with different regulatory proteins such as Atg13, Vac8, Atg17 and Cvt9. The complex controls the switch between Cvt and autophagy pathways (Figure 2). The composition of this complex is dynamic and it may vary depending on nutrient conditions[40]. Under nutrient-rich conditions, Atg13 is hyperphosphorylated so that its association with Atg1 is blocked. On the other hand, under nutrient starvation conditions or after treatment with rapamycin, Atg13 becomes partially dephosphorylated. This dephosphorylation leads to an Atg1-Atg13 interaction and subsequent generation of autophagosomes instead of Cvt vesicles and, thus, activates autophagy. Vac8, the vacuolar inheritance protein that acts in the Cvt pathway is not essential for starvation-induced autophagy[41]. Vac8 is also a phosphoprotein and may help to facilitate the phosphorylation of Atg13. Atg1 also interacts with 2 other proteins. One of these is Cvt9, which is only required for the Cvt pathway[42]. Cvt9 is a large coiled-coil protein, and it interacts with itself, possibly through the coiled-coil domain. This could potentially crosslink the Atg1 complex into a higher-order structure required early in the sequestration process of autophagy. The other protein, Atg17, is only required for the autophagic import and has been proposed to play a role in Atg1-Atg13 interactions[43]. Recently, Atg17 has been found to interact with 2 Cvt pathway-specific components, Atg24/Cvt13/Snx4 and Atg20/Cvt20, proteins that contain PI3P-binding PX domains[44,45]. But it remains a challenge to evaluate the meaning of interactions between the autophagic-specific Atg17 protein and Cvt pathway-specific Atg24 and Atg20 proteins. Genetic analysis suggests that the Atg1 complex functions at a rather late stage of autophagosome formation[22]. The Atg1 complex may control membrane dynamics, rather than act as a signal transducer. The kinase activity of Atg1 is upregulated during induction of autophagy, thus the levels of kinase activity seem to be important for the regulation of autophagosome formation[43]. A recent report has shown that Atg1 may only have a non-kinase structural role in autophagy induction, although the kinase activity of Atg1 is involved in autophagy; however, it plays more important roles in the Cvt pathway[46].

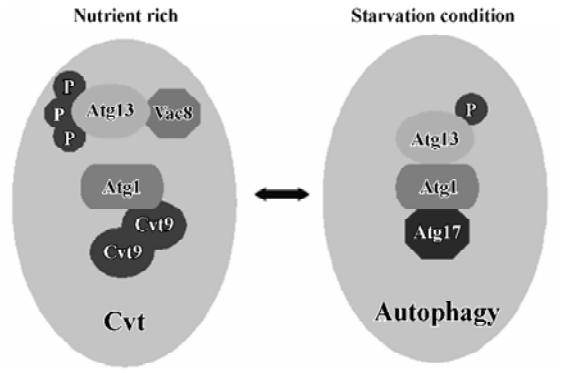

Figure 2. The Atg1 kinase complex includes components that are specific for the Cvt pathway or autophagy.

Two putative human homologs of Atg1 have been identified[47]: the UNC-51-like kinases ULK1 and ULK2. ULK1 has been shown by yeast two-hybrid screening to interact with GATE-16 and GABARAP, two homologs of the yeast autophagy protein Atg8.

Vps34/PI3K Early in 1982, it was found that 3-MA (3-methyladenine) inhibits the formation of autophagosomes[48]. 3-MA is a PI3K inhibitor[49]. Several studies have demonstrated that PI3K inhibitors interfere with the formation of autophagosomes in rat hepatocytes[50]. Yeast is known to contain only one PI3K, Vps34[51]. Vps34 function is regulated by the protein kinase activity of Vps15, with which it forms a stable, membrane-associated complex under normal conditions. This complex links the Vps34 kinase to cytoplasmic membranes. Vps34-Vps15 is present in 2 complexes, which are involved in a variety of membrane transport events (Figure 3)[52]: complex I, which is composed of Vps34-Vps15, Atg6 and Atg14, controls autophagy, whereas complex II, which is composed of Vps34-Vps15, Atg6 and Vps38, is essential for sorting of carboxypeptidase Y (CPY) into the vacuole. Atg6 is a possible coiled-coil protein and is associated with the membrane through Vps15 and Vps34. Atg14 is a specific factor in the autophagy-specific PI3K complex. Complex I functions primarily, but not exclusively, at the PAS, whereas complex II functions at the endosome. The lipid kinase activity associated with Vps34 is thought to create lipid patches of PI3-P, the reaction product of class III PI3K, at specific trans-Golgi locations, and these patches then function in protein sorting into vesicles that travel from the Golgi to the endosome.

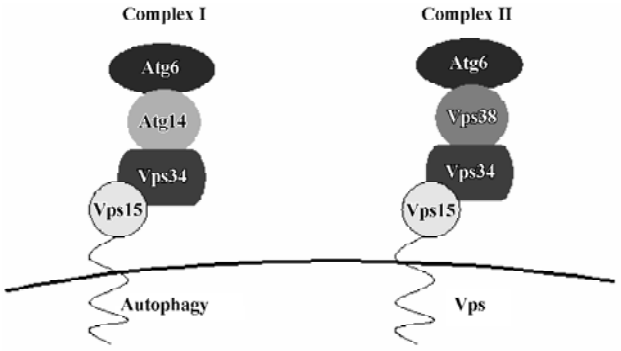

Figure 3. Two different PI3-kinase complexes participate in vacuolar protein targeting.

In mammalian cells, there are 3 classes of PI3K. Class I PI3K is an inhibitor of autophagy[53]. Class II PI3K activity is thought to have no relevance to autophagy control. Class III PI3K, a functional orthologue of yeast Vps34, is an activator of autophagy and plays a crucial role at an early step of autophagosome formation in mammalian cells[54], and it is required for increasing the size of the sequestering membrane, presumably through fusion events. PI3-P interacts with proteins containing FYVE or PX motifs, thus recruiting such proteins from the cytosol for autophagosome biogenesis[55]. The activation of a population of PI3K located in a determined membrane domain may be responsible for autophagosome biogenesis. In addition, the presence of PI3-P in a specific membrane location may generate significant asymmetries and drive membrane curvature of PAS[54]. Finally, PI3-P may be converted to higher-order polyphosphoinositides (PI), which are involved in diverse signaling functions. The mammalian cell orthologue of Vps15 is p150. It is associated with class III PI3K, and interacts with beclin-1, a functional orthologue of yeast Atg6 in mammalian cells[56]. Beclin1, which is the first autophagy-related tumor suppressor gene reported so far, is required for both autophagy and Cvt pathways. The characterization of the tumor suppressor activity of beclin-1 could establish an important relationship between cancer and the autophagic pathway. Beclin-1 was originally isolated as a bcl-2-interacting protein that can downregulate bcl-2, but it is still unclear whether this interaction is instrumental in autophagy[57].

Atg 9 complex Atg9 is an integral membrane protein, containing several potential transmembrane domains[58]. A fraction of Atg9 is located in the PAS together with other autophagy proteins, but it is absent in the membranes of mature autophagosomes[59,60]. If cells lack Atg9, neither the Cvt pathway nor autophagy can take place. However, Cvt and autophagy can still accumulate protease-sensitive prApe1 (the precursor to aminopeptidase I), indicating that Atg9 has an effect prior to closure of the double-bilayer vesicle[61]. A soluble protein, Atg2 physically interacts with Apg9, and this interaction is indispensable to autophagosome formation[62]. The localization of Atg2 to the PAS requires the activity of several proteins, such as Atg1 and Atg9, but the kinase activity of Atg1 seems to be of questionable importance to this function. Atg18 is also indispensable to correct Atg2 localization, suggesting that there is a potential link between this protein and the Atg9 system[63].

Mammalian orthologs of Atg2 and Atg9 are present in the genome sequence databases, but they have not been studied in detail.

PAS All the abovementioned Atg proteins have a function before or during the formation of autophagosomes. Thus, it is important to find out the distribution of these Atg proteins in cytoplasm. By using fluorescent protein fused with Atg proteins, it has been shown that Atg8 stains autophagosomes, autophagic bodies in the vacuoles, and also the intermediate isolation membrane. However, Atg5 shows a single bright dot structure next to the vacuole. This structure has been named the PAS, and Atg8 also co-localizes with it[64,22]. In addition, no Golgi, ER or late-endosomal markers has been found in the PAS, suggesting that this is a novel structure that has not been described so far[59]. However, little is known about the existence of a PAS-like structure in mammalian cells. Almost all Atg proteins are co-localized in the PAS, suggesting that it is an organizing center of the autophagosome. The autophagy-specific PI3K complex, PI3-P, may recruit different proteins such as Atg18, Atg20, Atg21, Atg24, and Atg27 to the PAS[54,65,66]. The interaction between PI3-P and these proteins is a requisite for the re-recruitment of Atg proteins to the PAS. None of these proteins contains PX or FYVE motifs, so the domain of the lipdation has not been identified. Atg9 also has a strong effect on organization of the PAS, whereas defects in the Atg1 kinase complex show little effect on the PAS structure. Indeed, a recent study suggests that, in nutrient-rich conditions, the PAS does not form in the absence of prApe1, Atg19 or Atg11[67].

Autophagosome fusion with the vacuole/lysosome In yeast, the fusion of autophagosomes with the vacuole requires several factors that are involved in other types of vesicular transport. Molecular genetic studies have indicated that the machinery required for homotypic vacuole fusion is also required for the fusion of autophagosomes with the vacuole. This machinery includes: the SNARE proteins Vam3, Vam7, Vti1, and Ykt6; the NSF, SNAP, and GDI

homologs Sec17, Sec18, and Sec19; the Rab protein Ypt7; members of the class C Vps/HOPS complex; and Ccz1 and Mon1[68]. However, it remains to be determined whether different SNARE and/or other fusion components operate during autophagy. If the fusion process begins prior to completion of the double-membrane vesicle, the cargo will remain in the cytosol, so the timing of vesicle fusion with the lysosome/vacuole must be precisely regulated. Atg8-PE, which is located on the outer surface of the autophagosome, is removed prior to fusion as a result of a second cleavage by Atg4. Removal of Atg8-PE from autophagosomes can prevent premature fusion with lysosomes. Atg12-Atg5•Atg16 may have the same function. The expression of Atg8ΔR is a mutated form of Atg8 lacking the ultimate arginine residue, bypassing the need for the initial Atg4-dependent cleavage step. However, the mutation causes a loss of ability of Atg to carry out the second cleavage event that releases Atg8 from PE and results in a partial defect in autophagy[31].

In mammalian cells, autophagosome fusion with lysosomes is a more complex process in which the autophagosome requires a series of maturation steps prior to its fusion with the lysosome. Similar to yeast, the activity of monomeric GTPases (Rab22, Rab24) and mammalian orthologs of SNARE protein family members and the NSF protein are needed for correct autophagosome maturation[69,70]. Prior to their fusion with lysosomes, autophagosomes have to fuse with endosomes or endosome-derived vesicles. Overexpression of a mutant form of the regulator of endosome sorting, SKD1 ATPase, which is unable to hydrolyze ATP, hampers endosome function and causes a massive accumulation of nascent autophagosomes[71]. Rab7, which is associated with autophagic vacuoles, is involved in maturation of autophagosomes. Overexpression of a Rab7 dominant negative mutant hampers fusion between autophagosomes and the late endosome/lysosomal compartment, leading to the accumulation of autophagosomes with a concomitant decrease in the degradation of long-lived proteins[72]. In addition, the cytoskeletal elements are also involved in either autophagosome maturation or autophagosome-lysosome fusion. The microtubule is another important factor for this event, because treatment of cells with microtubule-destabilizing drugs blocks autophagosome maturation. For example, cells treated with cytochalasin D, an agent that disrupts actin filaments, display a significant reduction in autophagosome formation[73], whereas the microtubule stabilization mediated by a new antitumor drug, taxol, increases the fusion of amphisomes with lysosomes[74].

Degradation of autophagic body The main purpose of autophagy in yeast is to degrade cytoplasm and recycle the resulting macromolecules for use in the synthesis of essential components during nutrient stress. Degradation of autophagy bodies requires a low pH, proteinase B (Prb1) and Atg15/Cvt17[75,76]. Prb1 is a hydrolase that is involved in the activation of many other vacuolar zymogens, which indirectly affects the vesicle breakdown. Atg15/Cvt17 has sequence similarity to a family of lipases, and seems to function directly in vesicle breakdown. It is the only putative lipase that has been identified that has a role in the degradation of autophagic bodies[76]. So far, we know that the expression of Atg15 is low in the vesicle, but the mechanism or site of action of Atg15 is unknown. Another protein, Atg22, has also been implicated in this last step. Atg22 is an integral membrane protein, and is needed only for the degradation of autophagic bodies[77].

Molecular mechanisms of CMA

CMA is one of several lysosomal pathways of proteolysis. CMA is activated by physiological stressors such as prolonged starvation. During starvation, macroautophagy is activated first, but this process quickly declines and CMA is then activated. The mechanisms by which these 2 lysosomal protein degradation pathways interact, if any, are unknown. We now know that cytosolic proteins can be degraded by CMA in rat liver, kidney, heart, and other tissues. However, to date, there are no physiological phenomena similar to CMA found in yeast. Only the cytosolic proteins with exposed pentapeptide sequence motifs related to KFERQ can act as substrate proteins, and be recognized by a complex of molecular chaperones whose major constitutive form is the heat shock 70 kDa protein (hsc70)[78]. The substrate protein and molecular chaperone complex bind to the lysosomal membrane and interact with lamp2a. The protein is unfolded by the molecular chaperone complex prior to importation into the lysosome. The protein is pulled into the lysosomal lumen with the help of lysosomal hsc70 (ly-hsc70)[14,79]. The level of lamp2a can be a rate-limiting step in CMA. A lamp2 knockout mouse without any of the lamp2 isoforms showed a reduction in rate of protein degradation and an increase in accumulation of autophagic vacuoles in heart, skeletal muscle, and other tissues[80]. The amount of lamp2a in the lysosomal membrane is regulated, in part, by changes in its degradation rate. For example, during starvation lamp2a levels increase due to a decrease in lamp2a degradation. The mechanisms of lamp2a degradation include an initial cleavage by the lysosomal protease cathepsin A. In fact, cathepsin A knockout mice had elevated levels of lamp2a in the lysosomal membrane and showed higher activity of CMA[81]. A metalloprotease yet to be identified also

contributes to lamp2a degradation and works in cooperation with cathepsin A. A more rapid adjustment of lamp2a in the lysosomal membrane occurs through changing the proportions of lamp2a sequestered in the lysosomal matrix.

Regulation of autophagy

Autophagy is probably the main mechanism for degradation of long-lived proteins and cytoplasmic organelles. A great number of extracellular stimuli (starvation, hormone or therapeutic treatment) as well as intracellular stimuli (accumulation of misfolded proteins, invasion of microorganisms) are able to modulate the autophagic response. In yeast and mammalian cells, autophagy is a fundamental biological event that occurs under normal growth conditions. Thus, there must be an array of mechanisms by which extracellular and/or intracellular signals can be accepted and transmitted to the regulatory factors to promote or inhibit autophagy when it is needed.

TOR/mTOR There are a number of signaling complexes and pathways involved in the initiation and maturation of autophagy. The central player in these signaling pathways is TOR, the target of rapamycin. TOR is a serine/threonine kinase involved in most regulatory pathways that control the response to changes in nutrient conditions and energy metabolism. TOR acts as a good gate-keeper in autophagy and exerts an inhibitory effect on autophagy (Figure 4). TOR kinase may inhibit autophagy through two general mechanisms. First, TOR acts in a signal transduction cascade through various downstream effectors to control both translation and transcription[82]. Second, TOR appears to directly or indirectly affect the Atg proteins, resulting in interference with the formation of autophagosomes[83]. In mammalian cells, there is a TOR orthologue, mTOR, which appears to modulate autophagy in a manner similar to that observed in yeast.

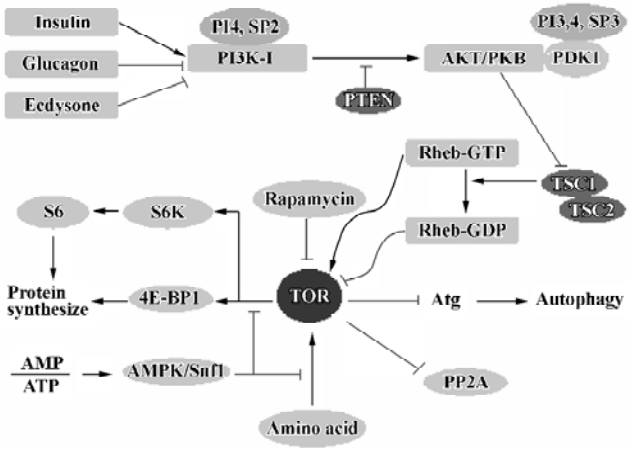

Figure 4. TOR/mTOR and PI3K-I/PKB signaling in the regulation of autophagy.

Protein phosphatase 2A (PP2A) In yeast, TOR phosphorylates the protein Tap42, causing its association with PP2A[84]. This interaction significantly reduces the enzyme activity of PP2A. Inhibition of TOR by nutrient stress or rapamycin results in the dephosphorylation and dissociation of Tap42 from PP2A. PP2A may then dephosphorylate its targets, which eventually leads to a variety of antiproliferative responses and induction of autophagy. PP2A is a phosphatase that acts on several TOR substrates, including glutaminase (Gln3). Dephosphorylation of Gln3 by PP2A promotes its dissociation from urease 2 (Ure2) and its successive translocation into the nucleus, where it activates the transcription of several genes[85,86]. Some of those genes are parts of the autophagy machinery such as Atg8 and Atg14[87,88].

4E-BP1 mTOR has a serine/threonine kinase activity, and eukaryotic initiation factor 4E binding protein-1 (4E-BP1) is one of its substrates[89]. 4E-BP1 is an inhibitor of translation and can be directly phosphorylated by mTOR. After phosphorylation, 4E-BP1 will dissociate from eukaryotic initiation factor 4E (eIF4E). Free eIF4E binds to the 5' terminal cap structure of RNAs and promotes the progress of translation.

p70S6 kinase p70S6 kinase (p70S6) is also a candidate of the substrates of mTOR, which can be called S6K for short. S6K is a protein kinase of ribosomal 40S subunit S6. Phosphorylation of S6 upregulates the translation of mRNAs containing 5' terminal oligopyrimidine tract (5' Top). The 5' Top mRNAs account for approximately 20% of all cell mRNAs and are foundations of protein biological synthesis. The major products of 5' Top mRNAs include ribosomal protein, elongation factor (EFla, EF2), and polyA binding protein. When nutrition is sufficient, TOR is turned on and the activity of the enzyme S6K increases. Recently, it has been found that S6K is needed for the entire process of autophagy activation, and it must be activated first for maximal activation of autophagy[90]. However, there is a contradictory phenomenon, in that TOR, an activator of S6K, is an inhibitor of autophagy. The possible explanation is that S6K needs to be active under starvation conditions in which its activator, TOR, is turned off. Perhaps, after TOR is switched off, any active S6K remains active for some time, ensuring maximal autophagy induction can be achieved, but other mechanisms might then gradually deactivate the p70S6 kinase, thereby preventing excessive autophagy, which

could be harmful.

Hormones The hormones glucagon and ecdysone in *Drosophila larvae* inhibit TOR by downregulating PI3K-I, resulting in an increase in autophagy. Conversely, the hormone insulin appears to have an inhibitory effect on the autophagic pathway[91,92]. In response to food, insulin is produced; insulin binds a receptor on the surface of cells and triggers a signaling cascade. Insulin first activates its tyrosine kinase receptors, causing these receptors to phosphorylate themselves. P85 as a regulatory subunit of PI3K activates PI3K by association with these phosphorylated insulin receptors. The active PI3K transfers to the inter surface of the cell membrane and phosphorylates the lipid phosphatidylinositol, leading to the activation of protein kinase B (AKT/PKB) and other enzymes. This is followed by the activation of TOR. The latter then negatively regulates Atg proteins to prevent autophagy activation.

Amino acids Amino acids, which are the final products of autophagic protein degradation, act as negative feedback regulators for the process. In almost all cell types, especially in hepatocytes, a combination of leucine and a few other amino acids is very effective in inhibiting autophagy[93–95]. It was discovered that the addition of amino acids (leucine in particular) in the absence of insulin or other growth factors resulted in a strong and fairly rapid stimulation of the phosphorylation of ribosomal protein S6K[96,97]. Phosphorylation of 4E-BP1, similar to that of S6K, requires the presence of amino acids, and amino acids alone, but not insulin alone, stimulate phosphorylation of this protein in a rapamycin-sensitive manner[98,99]. Furthermore, leucine activates glutamate dehydrogenase, which contributes to the ability of leucine to potentiate insulin production in β-cells[100]. Amino acids and insulin act synergistically on both processes to inhibit autophagy[96,97]. The amino acid/TOR signaling pathway can be confronted by the AMP-dependent protein kinase (AMPK). However, this effect can be blocked by rapamycin and two inhibitors of PI3K, wortmannin and LY294002[101]. Recently, it has been found that amino acids can modulate activation of the kinase Raf-1. Raf-1 acts upstream of the mitogen-activated protein kinase (MAPK) and extracellular signal-regulated kinase (Erk1/2) cascades[102]. However, the mechanism by which amino acids regulate the activation of Raf-1 remains to be elucidated.

ATP Autophagic sequestration is ATP-dependent, and the depletion of ATP inhibits autophagic sequestration[103]. Because of adenylate kinase equilibrium in the cell, a fall in ATP is often associated with an increase in AMP. AMPK, which serves as a general integrator of metabolic responses to changes in energy availability, is activated in response to elevations of the AMP/ATP ratio. Thus, autophagy can be suppressed by AMP through activation of AMPK. In addition, high levels of AMP can be reached under hypoxia and other conditions of energy depletion, which also suppress autophagy[104,105]. Different studies suggest that in liver and muscle cells AMPK negatively modulates protein synthesis by impairing the mTOR-dependent signals to p70S6 kinase and 4E-BP1[106], interfering with the occurrence of autophagy. Although AMPK is involved in the control of mTOR signaling, its role in autophagy needs to be clarified. However, Snf1, the yeast homologue of AMPK, has been identified as a positive regulator of autophagy[107].

Atg proteins TOR signaling negatively regulates the association between Atg1 and Atg13. Under nutrient-rich conditions, active TOR causes hyperphosphorylation of Atg13, preventing or modulating its association with Atg1[43]. It is not clear whether TOR directly phosphorylates Atg13. TOR inactivation by starvation or rapamycin treatment promotes the rapid dephosphorylation of Atg13, a process that seems to be independent of PP2A. Dephosphorylated Atg13 binds to Atg1. This association promotes autophosphorylation and activation of Atg1, leading to the induction of autophagy. The inhibition of TOR signaling also promotes the assembling of other regulatory proteins in the membrane of PAS due to increased Atg1 kinase activity. In other words, inactivation of TOR is necessary for the prolongation of pre-autophagosomal membranes and enhancement of the expression of autophagic specific genes such as Atg8.

PI3K-I/PKB The PI3K-I/PKB pathway is involved in the negative modulation of autophagy (Figure 4). If PI3K-I is activated, it will phosphorylate PI4P and PI(4,5)P_2 to produce PI(3,4)P_2 and PI(3,4,5)P_3[108]. These lipids have a role in the PAS structure to recruit proteins necessary for the biogenesis of autophagosomes. These lipids bind to protein kinase B (Akt/PKB) and its activator phosphoinositide-dependent kinase-1 (PDK1) via its pleckstrin homology (PH) domains. Upon lipid binding, Akt/PKB is then activated[108]. Furthermore, PDK1 phosphorylates other kinases, including p70S6 kinase, making them acquire kinase activity[109]. Activation of this pathway by expression of a constitutive active form of PDK1 and PKB has an inhibitory effect on autophagy. The phosphatase PTEN, which selectively hydrolyzes PI(3,4,5)P3, has a stimulatory effect on autophagy by relieving class I PI3K/PKB inhibition[55]. Rapamycin can reverse most of the inhibition of autophagy because of activation of the class I PI3K pathway, which suggests that mTOR is a downstream target. The activation of PI3K/PKB has been shown to relieve the inhibitory effects of the tuberous sclerosis complex (TSC1/TSC2, hamartin/tuberin) on

mTOR/p70S6 kinase signaling[110]. TSC2 has a GTPase-activating activity towards monomeric Rheb, which controls mTOR/p70S6 kinase signaling[111], so TSC2 can promote the conversion of Rheb from the GTP-bound state (inhibitor of TOR) to the GDP-bound state (activator of TOR).

Beclin1/PI3K- III The beclin 1/PI3K-III complex is involved in the formation of autophagosomes and initiation of autophagy. 3-MA, wortmannin, and LY294002, three PI3K-III inhibitors, interfere with this pathway[50]. Recently, it has been shown that in muscle cells, amino acids can negatively regulate autophagy by interference with the activity of class III PI3K[55]. Further studies showed that all beclin forms a complex with PI3K, whereas ~50% of PI3K remains free from beclin. Indirect immunofluorescence microscopy demonstrated that the majority of beclin and PI3K localized to the trans-Golgi network (TGN). Some PI3K also distributed in the late endosome[112]. This suggests that beclin and PI3K control autophagy by functioning in PI3-P sorting into vesicles that travel from the Golgi to the endosome as a complex at the TGN. In addition, an increase in the class III PI3K product, PI3-P, can also stimulate autophagy[49]. Beclin-1, as an important element of mammalian autophagy, is consistently mono-allellically deleted in 40–75% of human sporadic breast, prostate and ovarian cancers. In *in vitro* cultured MCF-7 cells, overexpression of beclin-1 induces autophagy and is associated with inhibition of MCF-7 cell proliferation[56]. The protein beclin-1 is able to shuttle between the nucleus and the cytoplasm[113]. Its role in the nucleus is unknown, but nuclear beclin-1 does not control autophagy and does not inhibit tumorigenicity of breast carcinoma cells. Beclin-1 contains a leucine-rich nuclear export signal that is required for its autophagy and tumor suppressor functions[113]. This nuclear export traffic is modulated by nuclear export protein chromosome region maintenance 1(CRM1)[113]. The CRM1-dependent nuclear export traffic plays an important role in the regulation of autophagy. However, when the traffic is inhibited by daunomycin B or a mutation of the nuclear export signal, beclin-1 exists almost exclusively in the nucleus. Thus, autophagy induction by starvation cannot be initiated and its anti-tumor effect is also blunted.

GTPases

Heterotrimeric G proteins and partners In the human colon cancer cell line HT-29, it was found that the trimeric G_{i3} ($\alpha_{i3}\beta\gamma$) control the autophagic pathway at the sequestration step[114]. The activity of autophagy was low when the $G_{\alpha i3}$ protein was in the GTP-bound form, and it was stimulated when GDP was bound to the $G_{\alpha i3}$ protein[115]. The localization of the G_{ai3} protein is also essential in controlling autophagy. It must first associate with the ER or Golgi in order to control autophagy. The guanine nucleotide cycle of the $G_{\alpha i3}$ protein is dependent upon the activity of the G alpha interacting protein (GAIP). GAIP belongs to the regulators of the G-protein signaling (RGS) family and is a GTPase-activating protein towards the $G_{\alpha i3}$ protein. The phosphorylation of a conserved serine residue in the RGS domain of GAIP stimulates its GAP activity, and consequently the autophagic pathway[116]. In addition, GAIP is a cytoplasmic substrate for the MAP kinase Erk1/2 and its phosphorylation is reduced in the presence of amino acids. The different domains of the activator of G-protein signaling 3 (AGS3) are all involved in the regulation of autophagy[117]: its N-terminal part containing 7 tetratricopeptide regulatory (TPR) repeats can decrease the occurrence of autophagy; its C-terminal part containing G-protein regulatory (GPR or GoLoco) motifs can interact and stabilize the $G_{\alpha i3}$ protein in its GDP-bound conformation. Recently, investigators showed that AGS3 had a stimulatory effect on autophagy in human colon cancer cells[118], but this stimulatory effect could be counteracted by GoLoco motifs. The $G_{\alpha i3}$ protein and its partners (GAIP and AGS3) act prior to the formation of the autophagosome. They may be involved in the control of membrane flux to the autophagic pathway. What is noticeable is that the $G_{\alpha i3}$ protein and its partner proteins can control the balance between the flow of membranes in the exocytic pathway and the delivery of membrane constituents to the macroautophagic pathway.

Monomeric G proteins Rab proteins are monomeric GTPases necessary for vesicular transport in the exo/endocytic pathway, in which Rab22a is associated with early and late endosomes. However, Rab22aQ64L, a mutant with low GTPase activity of Rab22a co-localizes with the autophagic vacuoles[69]. In addition, another monomeric GTPase, Rab24, existing preferentially in a GTP-bound state when expressed in cultured cells, is redistributed and co-localized with MAP1-LC3 during starvation. It has been shown that Rab24 has a role in autophagy. The GTP membrane-bound forms of Rab proteins are able to recruit cytosolic proteins, which target vesicles to appropriate sites on the acceptor membrane[119]. Whether or not this function of Rab proteins is essential for membrane fusion, transport, and the maturation of autophagic vesicles is still to be investigated.

Calcium Autophagy is dependent on the presence of sequestered Ca^{2+} in some intracellular storage compartments that are sensitive to interference by a number of Ca^{2+}-perturbing agents[120]. ER is the major reservoir for intracellular calcium, thus thapsigargin, which inhibits the ER calcium/ATPase promotes the release of intracellular calcium from ER and thereby lowers ER calcium levels leading to notable

inhibition of autophagy. This implies that depletion of sequestered, rather than of cytosolic, intracellular Ca^{2+} should be responsible for the common mechanism of autophagy inhibition. Inhibitors of Ca^{2+}-activated protein kinases (KN-62, H-7, W-7) had little or no effect on autophagy, indicating that the Ca^{2+} requirement of autophagy was not mediated by these kinases. Recent studies have shown that elements that modify the lysosomal calcium levels, such as phorbol myristate acetate, ionophore A23187, and phentolamine, may modulate the total volume of autophagic vacuoles[121].

Protein synthesis pathway In rat hepatocytes, the phosphorylation of the ribosomal S6 protein, a p70S6 kinase substrate, is also related to the inhibition of autophagy. The degree of S6 phosphorylation determines the degree of occupancy of the endoplasmic reticulum by ribosomes, and thus determines the rate of autophagic sequestration and the rate of ER-linked protein synthesis[97]. So it is possible that there is a relationship between the control of protein synthesis and of autophagy. Furthermore, the finding of the involvement of eukaryotic initiation factor-2 alpha (eIF2α) kinases in autophagy strengthens this view. The eIF2a kinases are members of a family of evolutionarily conserved serine/threonine kinases that regulate stress-induced translational arrest. Recently, it was demonstrated that two eIF2α kinases (GCN2 and PKR) positively controled autophagic sequestration in yeast and mammalian cells in response to nutrient deprivation by phosphorylating the translation factor eIF2α[122]. However, a general inhibition of protein synthesis does not trigger autophagy. For example, when translation is inhibited by cycloheximide, autophagy is not induced, but the formation of smaller autophagosomes is observed. These results indicate that protein synthesis is required for the expansion of the preautophagosome vesicle[123]. In addition, the *de novo* synthesis of proteins is also required after the sequestration step during the maturation of autophagosomes.

Other regulatory factors The regulation of autophagy is very complex. In addition to the above mentioned molecular mechanisms, microtubule-associated protein, integrin, and some other kinases such as tyrosine protein kinase II, naringin-sensitive protein kinase, death-associated related protein kinase-1 (DRP-1), death-associated protein kinase (DAPK) all have a role[124]. However, the molecular mechanisms by which these regulatory factors contribute to the control of autophagy are still largely unknown and their downstream targets also remain to be identified.

Autophagy and diseases

Autophagy is an important gate-keeping mechanism for the stabilization of cell homeostasis, which is required for eliminating discarded or damaged organelles and/or cytoplasmic components and remodeling cytoplasm. Autophagy has been studied for more than 40 years, but it is only in the last 10 years that the molecular basis of autophagy has been gradually understood through the utilization of yeast genes. The discovery of the *ATG* genes and the dissection of the signaling pathways involved in the regulation of autophagy have greatly increased our knowledge of the occurrence and development of this lysosomal degradation pathway. In yeast, many questions about the molecular mechanisms of autophagy have already been investigated, but there are a great number of tasks ahead, such as clarification of the putative links between the different signaling complexes and elucidation of the specific mechanisms mediating autophagosome biogenesis, transport, fusion and autophagic degradation. Although the molecular machinery of the autophagic pathway is well conserved during evolution in multicellular organisms, especially in mammals, this process is much more complex in mammals than it is in yeast. At present, many autophagic genes in mammals still remain unknown and their functions in autophagy also remain undiscovered. The creation and analysis of transgenic and knockout animal models will help to understand the evolutionarily-acquired complexity of autophagy-mediated processes in mammals. Some gene (*beclin-1*, *ATG5*, and *ATG7*) knockout mice have already been used in experiments to explore the functions of these genes and the relationships between autophagy and some diseases[21,125,126]. For example, with a targeted *beclin-1* mutant mouse model, it has been shown that heterozygous disruption of *beclin-1* increases the frequency of spontaneous malignancies and accelerates the development of hepatitis B virus-induced premalignant lesions. In addition, it has also been demonstrated that *beclin-1* is a haplo-insufficient tumor-suppressor gene, and therefore it is possible that the genetic disruption of autophagy, either by mutations of downstream autophagy-execution genes or by mutations in upstream autophagy-regulatory signaling pathways, may be an important mechanism of oncogenesis[126]. Thus, mutation of *beclin-1* or other autophagy genes might contribute to the pathogenesis of human cancers. A growing number of pathological conditions, including cancer and neurodegenerative disorders, are associated with autophagy, so it is very important to reveal the molecular relationships between autophagy and diverse diseases. In our laboratory, we found that autophagy may have dual functions in cultured tumor cells. On the one hand, it may delay the apoptotic process in one cell type; but on the other hand, it may promote cell

death in other cell types (Yan *et al*, unpublished observations). Autophagy plays important roles in the degradation of misfolded or aggregated proteins and, therefore, may play a role in certain neurodegenerative diseases that feature the misfolding and aggregation of disease proteins, such as Huntington's disease and Parkinson's disease. We have studied the degradation of mutant huntingtin by autophagy. We found that autophagy upregulated cathepsins and enhanced the clearance of huntingtin fragments, but mutant huntingtin was relatively resistant to degradation by cathepsin D[127]. Over-stimulation of autophagy by mutant huntingtin resulted in mislocalization and dysfunction of mitochondria (Qin *et al*, unpublished observations). In our recent studies, we also found that an autophagic mechanism was involved in excitotoxicity. Activation of the NMDA (*N*-methyl-*D*-aspartate)- and KA (kainic acid)-type glutamate receptors stimulated autophagy and lysosomal enzymes. The apoptotic death of striatal neurons was blocked by 3-MA and a cathepsin B inhibitor, suggesting that the activation of autophagy probably contributes to excitotoxicity[128]. These studies have opened a new field for investigating the pathogenic mechanisms in neurodegenerative diseases related to protein misfolding, aggregation and excitotoxicity.

References

1 Gronostajski RM, Pardee AB, Goldberg AL. The ATP dependence of the degradation of short- and long-lived proteins in growing fibroblasts. J Biol Chem 1985; 260: 3344–9.

2 Scott SV, Hefner-Gravink A, Morano KA, Noda T, Ohsumi Y, Klionsky DJ. Cytoplasm-to-vacuole targeting and autophagy employ the same machinery to deliver proteins to the yeast vacuole. Proc Natl Acad Sci USA 1996; 93: 12304–8.

3 Shieh HL, Chiang HL. *In vitro* reconstitution of glucose-induced targeting of fructose-1,6-bisphosphatase into the vacuole of semi-intact yeast cells. J Biol Chem 1998; 273: 3381–7.

4 Lockshin RA, Zakeri Z. Apoptosis, autophagy and more. Int J Biochem Cell Biol 2004; 36: 2405–19.

5 Bursch W, Ellinger A, Gerner C, Schulte-Hermann R. Autophagocytosis and programmed cell death. In: Klionsky DJ, editor. Autophagy. Georgetown, TX: Landes Bioscience; 2004. p 287–303.

6 Bergamini E, Cavallini G, Donati A, Gori Z. The anti-ageing effects of caloric restriction may involve stimulation of macroautophagy and lysosomal degradation, and can be intensified pharmacologically. Biomed Pharmacother 2003; 57: 203–8.

7 Melendez A, Talloczy Z, Seaman M, Eskelinen EL, Hall DH, Levine B. Autophagy genes are essential for dauer development and life-span extension in C elegans. Science 2003; 301: 1387–91.

8 Bergamini E, Cavallini G, Donati A, Gori Z. The role of macroautophagy in the ageing process, anti-ageing intervention and age-associated diseases. Int J Biochem Cell Biol 2004; 36: 2392–404.

9 Shintani T, Klionsky DJ. Autophagy in health and disease: a double-edged sword. Science 2004; 306: 990–5.

10 Mizushima N, Ohsumi Y, Yoshimori T. Autophagosome formation in mammalian cells. Cell Struct Funct 2002; 27: 421–9.

11 Klionsky DJ, Cregg JM, Dunn WA Jr, Emr SD, Sakai Y, Sandoval IV, *et al*. A unified nomenclature for yeast autophagy-related genes. Dev Cell 2003; 5: 539–45.

12 Yoshimori T. Autophagy: a regulated bulk degradation process inside cells. Biochem Biophys Res Commun 2004; 313: 453-8.

13 Wang CW, Klionsky DJ. Microautophagy. In: Klionsky DJ, editor. Autophagy. Georgetown, TX: Landes Bioscience; 2004. p 107–14.

14 Majeski AE, Dice JF. Mechanisms of chaperone-mediated autophagy. Int J Biochem Cell Biol 2004; 36: 2435–44.

15 Elmore SP, Qian T, Grissom SF, Lemasters JJ. The mitochondrial permeability transition initiates autophagy in rat hepatocytes. FASEB J 2001; 15: 2286–7.

16 Onodera J, Ohsumi YJ. Ald6p is a preferred target for autophagy in yeast, *Saccharomyces cerevisiae*. J Biol Chem 2004; 279: 16071–6.

17 Dunn WA Jr. Studies on the mechanisms of autophagy: formation of the autophagic vacuole. J Cell Biol 1990; 110: 1923–33.

18 Yamamoto A, Masaki R, Tashiro Y. Characterization of the isolation membranes and the limiting membranes of autophagosomes in rat hepatocytes by lectin cytochemistry. J Histochem Cytochem 1990; 38: 573–80.

19 Fengsrud M, Roos N, Berg T, Liou W, Slot JW, Seglen PO. Ultrastructural and immunocytochemical characterization of autophagic vacuoles in isolated hepatocytes: effects of vinblastine and asparagine on vacuole distributions. Exp Cell Res 1995; 221: 504–19.

20 Kim J, Huang WP, Klionsky DJ. Membrane recruitment of Aut7p in the autophagy and cytoplasm to vacuole targeting pathways requires Aut1p, Aut2p, and the autophagy conjugation complex. J Cell Biol 2001; 152: 51–64.

21 Mizushima N, Yamamoto A, Hatano M, Kobayashi Y, Kabeya Y, Suzuki K, *et al*. Dissection of autophagosome formation using Apg5-deficient mouse embryonic stem cells. J Cell Biol 2001; 152: 657–67.

22 Suzuki K, Kirisako T, Kamada Y, Mizushima N, Noda T, Ohsumi Y. The pre-autophagosomal structure organized by concerted functions of APG genes is essential for autophagosome formation. EMBO J 2001; 20: 5971–81.

23 Mizushima N, Noda T, Yoshimori T, Tanaka Y, Ishii T, George MD, *et al*. A protein conjugation system essential for autophagy. Nature 1998; 395: 395–8.

24 Tanida I, Tanida-Miyake E, Ueno T, Kominami E. The human homolog of *Saccharomyces cerevisiae* Apg7p is a protein-activating enzyme for multiple substrates including human Apg12p, GATE-16, GABARAP, and MAP-LC3. J Biol Chem 2001; 276: 1701–6.

25 Shintani T, Mizushima N, Ogawa Y, Matsuura A, Noda T, Ohsumi Y. Apg10p, a novel protein-conjugating enzyme essential for autophagy in yeast. EMBO J 1999; 18: 5234–41.

26 Mizushima N, Noda T, Ohsumi Y. Apg16p is required for the function of the Apg12p-Apg5p conjugate in the yeast autophagy pathway. EMBO J 1999; 18: 3888–96.

27 Mizushima N, Kuma A, Kobayashi Y, Yamamoto A, Matsubae M, Takao T, *et al*. Mouse Apg16L, a novel WD-repeat protein, targets to the autophagic isolation membrane with the Apg12-

Apg5 conjugate. J Cell Sci 2003; 116: 1679–88.
28 Kuma A, Mizushima N, Ishihara N, Ohsumi Y. Formation of the approximately 350-kDa Apg12-Apg5Apg16 multimeric complex, mediated by Apg16 oligomerization, is essential for autophagy in yeast. J Biol Chem 2002; 277: 18619–25.
29 George MD, Baba M, Scott SV, Mizushima N, Garrison BS, Ohsumi Y, *et al*. Apg5p functions in the sequestration step in the cytoplasm-to-vacuole targeting and macroautophagy pathways. Mol Biol Cell 2000; 11: 969–82.
30 Kirisako T, Baba M, Ishihara N, Miyazawa K, Ohsumi M, Yoshimori T, *et al*. Formation process of autophagosome is traced with Apg8/Aut7p in yeast. J Cell Biol 1999; 147: 435–46.
31 Kirisako T, Ichimura Y, Okada H, Kabeya Y, Mizushima N, Yoshimori T, *et al*. The reversible modification regulates the membrane-binding state of Apg8/Aut7 essential for autophagy and the cytoplasm to vacuole targeting pathway. J Cell Biol 2000; 151: 263–76.
32 Ichimura Y, Kirisako T, Takao T, Satomi Y, Shimonishi Y, Ishihara N, *et al*. A ubiquitin-like system mediates protein lipidation. Nature 2000; 408: 488–92.
33 Ichimura Y, Imamura Y, Emoto K, Umeda M, Noda T, Ohsumi Y. *In vivo* and *in vitro* reconstitution of Atg8 conjugation essential for autophagy. J Biol Chem 2004; 279: 40584–92.
34 Kabeya Y, Mizushima N, Ueno T, Yamamoto A, Kirisako T, Noda T, *et al*. LC3, a mammalian homologue of yeast Apg8p, is localized in autophagosome membranes after processing. EMBO J 2000; 19: 5720–8.
35 Kabeya Y, Mizushima N, Yamamoto A, Ohsumi Y, Yoshimori T. LC3, GABARAP and GATE16 localize to autophagosomal membrane depending on form-II formation. J Cell Sci 2004; 117: 2805–12.
36 Mizushima N, Yamamoto A, Matsui M, Yoshimori T, Ohsumi Y. *In vivo* analysis of autophagy in response to nutrient starvation using transgenic mice expressing a fluorescent autophagosome marker. Mol Biol Cell 2004; 15: 1101–11.
37 Sagiv Y, Legesse-Miller A, Porat A, Elazar Z. GATE-16, a membrane transport modulator, interacts with NSF and the Golgi v-SNARE GOS-28. EMBO J 2000; 19: 1494–504.
38 Wang H, Bedford FK, Brandon NJ, Moss SJ, Olsen RW. $GABA_A$-receptor-associated protein links $GABA_A$ receptors and the cytoskeleton. Nature 1999; 397: 69–72.
39 Marino G, Uria JA, Puente XS, Quesada V, Bordallo J, Lopez-Otin C. Human autophagins, a family of cysteine proteinases potentially implicated in cell degradation by autophagy. J Biol Chem 2003; 278: 3671–8.
40 Per ES, Daniel JK. Approaching the molecular mechanism of autophagy. Traffic 2001; 2: 524–31.
41 Scott SV, Nice DC 3rd, Nau JJ, Weisman LS, Kamada Y, Keizer-Gunnink I, *et al*. Apg13p and Vac8p are part of a complex of phosphoproteins that are required for cytoplasm to vacuole targeting. J Biol Chem 2000; 275: 25840–9.
42 Kim J, Kamada Y, Stromhaug PE, Guan J, Hefner-Gravink A, Baba M, *et al*. Cvt9/Gsa9 functions in sequestering selective cytosolic cargo destined for the vacuole. J Cell Biol 2001; 153: 381–96.
43 Kamada Y, Funakoshi T, Shintani T, Nagano K, Ohsumi M, Ohsumi Y. Tor-mediated induction of autophagy via an Apg1 protein kinase complex. J Cell Biol 2000; 150: 1507–13.
44 Uetz P, Giot L, Cagney G, Mansfield TA, , Knight JR, *et al*. A comprehensive analysis of protein-protein interactions in Saccharomyces cerevisiae. Nature 2000; 403: 623–7.
45 Nice DC, Sato TK, Stromhaug PE, Emr SD, Klionsky DJ. Cooperative binding of the cytoplasm to vacuole targeting pathway proteins, Cvt13 and Cvt20, to phosphatidylinositol 3-phosphate at the pre-autophagosomal structure is required for selective autophagy. J Biol Chem 2002; 277: 30198–207.
46 Abeliovich H, Zhang C, Dunn WA Jr, Shokat KM, Klionsky DJ. Chemical genetic analysis of Apg1 reveals a non-kinase role in the induction of autophagy. Mol Biol Cell 2003; 14: 477–90.
47 Okazaki N, Yan J, Yuasa S, Ueno T, Kominami E, Masuho Y, *et al*. Interaction of the Unc-51-like kinase and microtubule associated protein light chain 3 related proteins in the brain: possible role of vesicular transport in axonal elongation. Brain Res Mol Brain Res 2000; 85: 1–12.
48 Seglen PO, Gordon PB. 3-Methyladenine: specific inhibitor of autophagic/lysosomal protein degradation in isolated rat hepatocytes. Proc Natl Acad Sci USA 1982; 79: 1889–92.
49 Petiot A, Ogier-Denis E, Blommaart EF, Meijer AJ, Codogno P. Distinct classes of phosphatidylinositol 3'-kinases are involved in signaling pathways that control macroautophagy in HT-29 cells. J Biol Chem 2000; 275: 992–8.
50 Blommaart EF, Krause U, Schellens JP, Vreeling-Sindelarova H, Meijer AJ. The phosphatidylinositol 3-kinase inhibitors wortmannin and LY294002 inhibit autophagy in isolated rat hepatocytes. Eur J Biochem 1997; 243: 240–6.
51 Herman PK, Emr SD. Characterization of VPS34, a gene required for vacuolar protein sorting and vacuole segregation in *Saccharomyces cerevisiae*. Mol Cell Biol 1990; 10: 6742–54.
52 Kihara A, Noda T, Ishihara N, Ohsumi Y. Two distinct Vps34 phosphatidylinositol 3-kinase complexes function in autophagy and carboxypeptidase Y sorting in *Saccharomyces cerevisiae*. J Cell Biol 2001; 152: 519–30.
53 Arico S, Petiot A, Bauvy C, Dubbelhuis PF, Meijer AJ, Codogno P, *et al*. The tumor suppressor PTEN positively regulates macroautophagy by inhibiting the phosphatidylinositol 3-kinase/protein kinase B pathway. J Biol Chem 2001; 276: 35243–6.
54 Tassa A, Roux MP, Attaix D, Bechet DM. Class III phosphoinositide 3-kinase-Beclin1 complex mediates the amino acid-dependent regulation of autophagy in C2C12 myotubes. Biochem J 2003; 376: 577–86.
55 Wurmser AE, Emr SD. Novel PtdIns(3)P-binding protein Etf1 functions as an effector of the Vps34 PtdIns 3-kinase in autophagy. J Cell Biol 2002; 158: 761–72.
56 Liang XH, Jackson S, Seaman M, Brown K, Kempkes B, Hibshoosh H, *et al*. Induction of autophagy and inhibition of tumorigenesis by beclin 1. Nature 1999; 402: 672–6.
57 Saeki K, Yuo A, Okuma E, Yazaki Y, Susin SA, Kroemer G, *et al*. Bcl-2 down-regulation causes autophagy in a caspase-independent manner in human leukemic HL60 cells. Cell Death Differ 2000; 7: 1263–9.
58 Noda T, Kim J, Huang WP, Baba M, Tokunaga C, Ohsumi Y, *et al*. Apg9/Cvt7 is an integral membrane protein required for transport vesicle formation in the Cvt and autophagy pathways. J Cell Biol 2000; 148: 465–79.
59 Kim J, Huang WP, Stromhaug PE, Klionsky DJ. Convergence of multiple autophagy and cytoplasm to vacuole targeting compo-

nents to a perivacuolar membrane compartment prior to de novo vesicle formation. J Biol Chem 2002; 277: 763–73.
60 Noda T, Kim J, Huang WP, Baba M, Tokunaga C, Ohsumi Y, *et al*. Apg9p/Cvt7p is an integral membrane protein required for transport vesicle formation in the Cvt and autophagy pathways. J Cell Biol 2000; 148: 465–80.
61 Hagal A, Daniel JK. Autophagy in yeast: Mechanistic insights and physiological function. Microbiol Mol Biol Rev 2001; 65: 463–79.
62 Shintani T, Suzuki K, Kamada Y, Noda T, Ohsumi Y. Apg2p functions in autophagosome formation on the perivacuolar structure. J Biol Chem 2001; 276: 30452–60.
63 Guan J, Stromhaug PE, George MD, Habibzadegah-Tari P, Bevan A, Dunn WA Jr, *et al*. Cvt18/Gsa12 is required for cytoplasm-to-vacuole transport, pexophagy, and autophagy in *Saccharomyces cerevisiae* and *Pichia pastoris*. Mol Biol Cell 2001; 12: 3821–38.
64 Ohsumi Y, Mizushima N. Two ubiquitin-like conjugation systems essential for autophagy. Semin Cell Dev Biol 2004; 15: 231–6.
65 Nice DC, Sato TK, Stromhaug PE, Emr SD, Klionsky DJ. Cooperative binding of the cytoplasm to vacuole targeting pathway proteins, Cvt13 and Cvt20, to phosphatidylinositol 3-phosphate at the preautophagosomal structure is required for selective autophagy. J Biol Chem 2002; 277: 30198–207.
66 Stromhaug PE, Reggiori F, Guan J, Wang CW, Klionsky DJ. Atg21 is a phosphoinositide binding protein required for efficient lipidation and localization of Atg8 during uptake of aminopeptidase I by selective autophagy. Mol Biol Cell 2004; 15: 3553–66.
67 Shintani T, Klionsky DJ. Cargo proteins facilitate the formation of transport vesicles in the cytoplasm to vacuole targeting pathway. J Biol Chem 2004; 279: 29889–94.
68 Wang CW, Stromhaug PE, Kauffman EJ, Weisman LS, Klionsky DJ. Yeast homotypic vacuole fusion requires the Ccz1-Mon1 complex during the tethering/docking stage. J Cell Biol 2003; 163: 973–85.
69 Mesa R, Salomon C, Roggero M, Stahl PD, Mayorga LS. Rab22a affects the morphology and function of the endocytic pathway. J Cell Sci 2001; 114: 4041–9.
70 Munafo DB, Colombo MI. Induction of autophagy causes dramatic changes in the subcellular distribution of GFP-Rab24. Traffic 2002; 3: 472–82.
71 Nara A, Mizushima N, Yamamoto A, Kabeya Y, Ohsumi Y, Yoshimori T. SKD1 AAA ATPase-dependent endosomal transport is involved in autolysosome formation. Cell Struct Funct 2002; 27: 29–37.
72 Gutierrez MG, Munafo DB, Beron W, Colombo MI. Rab7 is required for the normal progression of the autophagic pathway in mammalian cells. J Cell Sci 2004; 117: 2687–97.
73 Blankson H, Holen I, Seglen PO. Disruption of the cytokeratin cytoskeleton and inhibition of hepatocytic autophagy by okadaic acid. Exp Cell Res 1995; 218: 522–30.
74 Bursch W, Hochegger K, Torok L, Marian B, Ellinger A, Hermann RS. Autophagic and apoptotic types of programmed cell death exhibit different fates of cytoskeletal filaments. J Cell Sci 2000; 113: 1189–98.
75 Nakamura N, Matsuura A, Wada Y, Ohsumi Y. Acidification of vacuoles is required for autophagic degradation in the yeast, *Saccharomyces cerevisiae*. J Biochem 1997; 121: 338–44.
76 Teter SA, Eggerton KP, Scott SV, Kim J, Fischer AM, Klionsky DJ. Degradation of lipid vesicles in the yeast vacuole requires function of Cvt17, a putative lipase. J Biol Chem 2001; 276: 2083–7.
77 Suriapranata I, Epple UD, Bernreuther D, Bredschneider M, Sovarasteanu K, Thumm M. The breakdown of autophagic vesicles inside the vacuole depends on Aut4p. J Cell Sci 2000; 113: 4025–33.
78 Agarraberes FA, Dice JF. A molecular chaperone complex at the lysosomal membrane is required for protein translocation. J Cell Sci 2001; 114: 2491–9.
79 Salvador N, Aguado C, Horst M, Knecht E. Import of a cytosolic protein into lysosomes by chaperone-mediated autophagy depends on its folding state. J Biol Chem 2000; 275: 27447–56.
80 Tanaka Y, Guhde G, Suter A, Eskelinen EL, Hartmann D, Lullmann-Rauch R, *et al*. Accumulation of autophagic vacuoles and cardiomyopathy in Lamp-2-deficient mice. Nature 2000; 406: 902–6.
81 Cuervo AM, Mann L, Bonten EJ, d'Azzo A, Dice JF. Cathepsin A regulates chaperone-mediated autophagy through cleavage of the lysosomal receptor. EMBO J 2003; 22: 47–59.
82 Cardenas ME, Cutler NS, Lorenz MC, Di Como CJ, Heitman J. The TOR signaling cascade regulates gene expression in response to nutrients. Genes Dev 1999; 13: 3271–9.
83 Levine B, Klionsky DJ. Development by self-digestion: molecular mechanisms and biological functions of autophagy. Dev Cell 2004; 6: 463–77.
84 Jiang Y, Broach JR. Tor proteins and protein phosphatase 2A reciprocally regulate Tap42 in controlling cell growth in yeast. EMBO J 1999; 18: 2782–92.
85 Rohde J, Heitman J, Cardenas ME. The TOR kinases link nutrient sensing to cell growth. J Biol Chem 2001; 276: 9583–6.
86 Beck T, Hall MN. The TOR signalling pathway controls nuclear localization of nutrient-regulated transcription factors. Nature 1999; 402: 689–92.
87 Huang WP, Scott SV, Kim J, Klionsky DJ. The itinerary of a vesicle component, Aut7p/Cvt5p, terminates in the yeast vacuole via the autophagy/Cvt pathways. J Biol Chem 2000; 275: 5845–51.
88 Chan TF, Bertram PG, Ai W, Zheng XF. Regulation of APG14 expression by the GATA-type transcription factor Gln3p. J Biol Chem 2001; 276: 6463–7.
89 Fingar DC, Salama S, Tsou C, Harlow E, Blenis J. Mammalian cell size is controlled by mTOR and its downstream targets S6K1 and 4EBP1/eIF4E. Genes Dev 2002; 16: 1472–87.
90 Scott RC, Schuldiner O, Neufeld TP. Role and regulation of starvation-induced autophagy in the *Drosophila* fat body. Dev Cell 2004; 7: 167–78.
91 Blommaart EF, Luiken JJ, Meijer AJ. Autophagic proteolysis: control and specificity. Histochem J 1997; 29: 365–85.
92 Klionsky DJ. Regulated self-cannibalism. Nature 2004; 431: 31–2.
93 Ogier-Denis E, Codogno P. Autophagy: a barrier or an adaptive response to cancer. Biochim Biophys Acta 2003; 1603: 113–28.
94 Beugnet A, Tee AR, Taylor PM, Proud CG. Regulation of targets of mTOR (mammalian target of rapamycin) signaling by intracellular amino acid availability. Biochem J 2003; 372: 555–66.

95 van Sluijters DA, Dubbelhuis PF, Blommaart EF, Meijer AJ. Amino-acid-dependent signal transduction. Biochem J 2000; 351: 545–50.
96 Luiken JJ, Blommaart EF, Boon L, van Woerkom GM, Meijer AJ. Cell swelling and the control of autophagic proteolysis in hepatocytes: involvement of phosphorylation of ribosomal protein S6? Biochem Soc Trans 1994; 22: 508–11.
97 Blommaart EF, Luiken JJ, Blommaart PJ, Vanwoerkom GM, Meijer AJ. Phosphorylation of ribosomal protein S6 is inhibitory for autophagy in isolated rat hepatocytes. J Biol Chem 1995; 270: 2320–6.
98 Hara K, Yonezawa K, Weng QP, Kozlowski MT, Belham C, Avruch J. Amino acid sufficiency and mTOR regulate p70 S6 kinase and eIF-4E BP1 through a common effector mechanism. J Biol Chem 1998; 273: 14484–94.
99 Xu G, Marshall CA, Lin TA, Kwon G, Munivenkatappa RB, Hill JR, *et al*. Insulin mediates glucose-stimulated phosphorylation of PHAS-I by pancreatic beta cells. An insulin-receptor mechanism for autoregulation of protein synthesis by translation. J Biol Chem 1998; 273: 4485–91.
100 McDaniel ML, Marshall CA, Pappan KL, Kwon G. Metabolic and autocrine regulation of the mammalian target of rapamycin by pancreatic beta-cells. Diabetes 2002; 51: 2877–85.
101 Meijer AJ, Dubbelhuis PF. Amino acid signalling and the integration of metabolism. Biochem Biophys Res Commun 2004; 313: 397–403.
102 Pattingre S, Bauvy C, Codogno P. Amino acids interfere with the ERK1/2-dependent control of macroautophagy by controlling the activation of Raf-1 in human colon cancer HT-29 cells. J Biol Chem 2003; 278: 16667–74.
103 Plomp PJ, Gordon PB, Meijer AJ, Hoyvik H, Seglen PO. Energy dependence of different steps in the autophagic-lysosomal pathway. J Biol Chem 1989; 264: 6699–704.
104 Hardie DG, Carling D, Carlson M. The AMP-activated/SNF1 protein kinase subfamily: metabolic sensors of the eukaryotic cell? Annu Rev Biochem 1998; 67: 821–55.
105 Samari HR, Seglen PO. Inhibition of hepatocytic autophagy by adenosine, aminoimidazole-4-carboxamide riboside, and N6-mercaptopurine riboside. Evidence for involvement of AMP-activated protein kinase. J Biol Chem 1998; 273: 23758–63.
106 Kimura N, Tokunaga C, Dalal S, Richardson C, Yoshino K, Hara K, *et al*. A possible linkage between AMP-activated protein kinase (AMPK) and mammalian target of rapamycin (mTOR) signalling pathway. Genes Cells 2003; 8: 65–79.
107 Wilson WA, Mahrenholz AM, Roach PJ. Antagonistic controls of autophagy and glycogen accumulation by Snf1p, the yeast homolog of AMP-activated protein kinase, and the cyclin-dependent kinase Pho85p. Mol Cell Biol 2001; 21: 5742–52.
108 Brazil DP, Hemmings BA. Ten years of protein kinase B signalling: a hard Akt to follow. Trends Biochem Sci 2001; 26: 657–64.
109 Vanhaesebroeck B, Alessi DR. The PI3K-PDK1 connection: more than just a road to PKB. Biochem J 2000; 346: 561–76.
110 Gao X, Zhang Y, Arrazola P, Hino O, Kobayashi T, Yeung RS, *et al*. Tsc tumour suppressor proteins antagonize amino-acid-TOR signalling. Nat Cell Biol 2002; 4: 699–704.
111 Garami A, Zwartkruis FJ, Nobukuni T, Joaquin M, Roccio M, Stocker H, *et al*. Insulin activation of Rheb, a mediator of mTOR/S6K/4E-BP signaling, is inhibited by TSC1 and 2. Mol Cell 2003; 11: 1457–66.
112 Kihara A, Kabeya Y, Ohsumi Y, Yoshimori T. Beclin-phosphatidylinositol 3-kinase complex functions at the trans-Golgi network. EMBO Rep 2001; 2: 330–5.
113 Liang XH, Yu J, Brown K, Levine B. Beclin 1 contains a leucine-rich nuclear export signal that is required for its autophagy and tumor suppressor function. J Cancer Res 2002; 61: 3443–9.
114 Ogier-Denis E, Couvineau A, Maoret JJ, Houri JJ, Bauvy C, De Stefanis D, *et al*. A heterotrimeric Gi3-protein controls autophagic sequestration in the human colon cancer cell line HT-29. J Biol Chem 1995; 270: 13–6.
115 Pattingre S, Petiot A, Codogno P. Analyses of G-alpha-interacting protein and activator of G-protein-signaling-3 functions in macroautophagy. Methods Enzymol 2004; 390: 17–31.
116 Ogier-Denis E, Pattingre S, El Benna J, Codogno P. Erk1/2-dependent phosphorylation of G alpha-interacting protein stimulates its GTPase accelerating activity and autophagy in human colon cancer cells. J Biol Chem 2000; 275: 39090–5.
117 Bernard ML, Peterson YK, Chung P, Jourdan J, Lanier SM. Selective interaction of AGS3 with G-proteins and the influence of AGS3 on the activation state of G-proteins. J Biol Chem 2001; 276: 1585–93.
118 Pattingre S, De Vries L, Bauvy C, Chantret I, Cluzeaud F, Ogier-Denis E, *et al*. The G-protein regulator AGS3 controls an early event during macroautophagy in human intestinal HT-29 cells. J Biol Chem 2003; 278: 20995–1002.
119 Zerial M, McBride H. Rab proteins as membrane organizers. Nat Rev Mol Cell Biol 2001; 2: 107–17.
120 Gordon PB, Holen I, Fosse M, Rotnes JS, Seglen PO. Dependence of hepatocytic autophagy on intracellularly sequestered calcium. J Biol Chem 1993; 268: 26107–12.
121 Kalamidas SA, Kotoulas OB, Hann AC. Studies on glycogen autophagy: effects of phorbol myristate acetate, ionophore A23187, or hentolamine. Microsc Res Tech 2002; 57: 507–11.
122 Tallóczy Z, Jiang W, Virgin-IV HW, Leib DA, Scheuner D, Kaufman RJ, *et al*. Regulation of starvation- and virus-induced autophagy by the eIF2α kinase signaling pathway. Proc Natl Acad Sci USA 2002; 99: 190–5.
123 Abeliovich H, Dunn WA Jr, Kim J, Klionsky DJ. Dissection of autophagosome biogenesis into distinct nucleation and expansion steps. J Cell Biol 2000; 151: 1025–34.
124 Petiot A, Pattingre S, Arico S, Meley D, Codogno P. Diversity of signaling control of macroautophagy in mammalian cells. Cell Struct Funct 2002; 27: 431–41.
125 Qu X, Yu J, Bhagat G, Furuya N, Hibshoosh H, Troxel A, *et al*. Promotion of tumorigenesis by heterozygous disruption of the beclin 1 autophagy gene. J Clin Invest 2003; 112: 1809–20.
126 Komatsu M, Waguri S, Ueno T, Iwata J, et Murata S, Tanida I, *et al*. Impairment of starvation-induced and constitutive autophagy in Atg7-deficient mice. J Cell Biol 2005; 169: 425–34.
127 Qin ZH, Wang Y, Kegel KB, Kazantsev A, Apostol BL, Thompson LM, *et al*. Autophagy regulates processing amino terminus huntingtin fragments. Hum Mol Gen 2003; 12: 3231–44.
128 Wang Y, Gu ZL, Cao Y, Liang ZQ, Rong H, Bennett MC, *et al*. Lysosomal enzyme cathepsin B is involved in kainic acid-induced excitotoxicity in rat striatum. Brain Res 2005; 1039: 203–6.

Acta Pharmacologica Sinica 2005 Dec; 26 (12): 1435–1441

Blackwell Publishing

Review

Two ligands for a GPCR, proton *vs* lysolipid[1]

Dong-soon IM[2]

Laboratory of Pharmacology and Research Institute of Drug Development, College of Pharmacy, Pusan National University, Busan 609-735, Republic of Korea

Key words

lysolipid; proton; G-protein-coupled receptor; sphingosylphosphorylcholine; lysophosphatidylcholine; psychosine

[1] Project supported by the Korea Science and Engineering Foundation Grant (R01-2005-000-10011-02005).

[2] Correspondence to Prof Dong-soon IM.
Phn 82-51-510-2817.
Fax 82-51-513-6754.
E-mail imds@pusan.ac.kr

Received 2005-06-22
Accepted 2005-07-28

doi: 10.1111/j.1745-7254.2005.00237.x

Abstract

Recently, two different chemicals have been matched as ligands with the same G-protein-coupled receptor (GPCR). Double-pairing of OGR1 family GPCRs with proton and lysolipid raises several questions. First, whether both are the real ligands for the GPCRs. Second, whether modulation of a GPCR by two chemicals could be possible. Third, one of the chemicals is proton. Proton-sensing not only is a new action mode of GPCR activation, but also it could be generalized in other GPCRs. In this review, I'd like to summarize the issue and discuss questions with pharmacological criteria.

Introduction

G-protein-coupled receptor (GPCR) is the largest gene family of human genome. GPCR is glaringly obvious by the fact that more than 50% of drugs on the market are either agonists or antagonists on GPCRs[1]. Positive or negative modulation of GPCRs with drugs has been successful tools to treat many diseases such as allergy, gastric ulcer, and hypertension. The common structural feature of all GPCRs is a seven-helical transmembrane region. GPCR activations are evoked by stimuli as diverse as light, Ca^{2+}, odorants, amino acids, nucleotides, proteins, polypeptides, steroids, and fatty acid derivatives.

The completion of the human genome project has identified about 865 GPCR genes[2]. Except sensory receptors, 367 GPCRs have been considered as receptors for endogenous ligands in the human genome[3]. However, identification of novel members of GPCRs by genome sequencing faces orphan receptor problem, that is, ligands are not yet found[1]. About 150 orphan GPCRs are waiting for discovery of their ligands[4]. Pairing orphan GPCRs with their own ligands (endogenous or surrogate) would advance scientific knowledge and induces discovery of new drugs[5–9]. However, recent double-pairing of OGR1 subfamily GPCRs with two different chemicals, proton and lysolipid, raises several questions.

First, whether both chemicals are the real ligands for OGR1 subfamily. Second, whether modulation of a GPCR by two chemicals could be possible, because classic pharmacological concept is one ligand for one GPCR. Third, one of the chemicals is proton. Although it has been well established for ion channel receptors such as transient receptor potential/vanilloid receptor subtype-1 (TRPV1)[10] and acid-sensing ion channels (ASICs)[11], in GPCR area, not only proton-sensing is a new action mode of GPCR activation, but also it could be generalized in other GPCRs.

OGR1 subfamily and lysolipids

OGR1 subfamily is composed of four members (OGR1, GPR4, G2A, and TDAG8) and has previously been identified as receptors for lysolipids; sphingosylphosphorylcholine (SPC), lysophosphatidylcholine (LPC) and psychosine (galactosylsphingosine)[12–14]. In 2000, Xu *et al* reported Ovarian cancer G-protein-coupled Receptor 1(OGR1, GPR68) to be a high-affinity receptor for SPC (K_d = 33 nmol/L) and

SPC was shown to inhibit cell growth of OGR1-transfected HEK293 as well as various ovarian cancer cell lines[12,15]. In 2001, Zhu *et al* reported GPR4 to be the second high affinity receptor for SPC and GPR4 was shown to be activated by structurally-related LPC[13]. However, in contrast to OGR1, GPR4 activation stimulated cell growth and cell migration of GPR4-transfected Swiss3T3 cells[13]. TDAG8 (T-cell death-associated gene 8, GPR65) was reported to be activated by psychosine and its activation was shown to result in multinuclear cell formation[14]. G2A (G2 accumulation protein, GPR132), the last member of the subfamily, was characterized to cause cell cycle arrest in the G_2/M phase[16]. LPC was initially reported as a ligand of G2A and T cell chemotaxis to LPC was shown to be mediated through G2A[17].

Yan *et al* reported macrophage chemotaxis to LPC is dependent on G2A function and mutation of the conserved DRY motif of G2A results in loss of function[18]. Wang *et al* demonstrated that murine G2A was spontaneously internalized and accumulated in endosomal compartments, whereas its surface expression was enhanced and stabilized by LPC treatment[19]. Han *et al* reported G2A-mediated up-regulation of CXCR4 in human helper T cells[20]. Murakami *et al* reported G2A-dependent actin stress fiber formation and its inhibition by LPC in G2A-NIH3T3 cells[21]. Also LPC enhances dose-dependently intracellular cAMP accumulation and G2A-induced apoptosis in Hela cells[22]. Ikeno *et al* reported that secretary phospholipase A_2 induce neurite outgrowth in PC12 cells through LPC generation and activation of G2A receptor[23]. Lin and Ye reported that G2A displays a significant level of intrinsic signaling via $G\alpha_q$, $G\alpha_s$, and $G\alpha_{13}$ pathways[22].

Lum *et al* showed that inflammatory stress increases GPR4 expression and LPC binding in human microvascular endothelial cells[24]. Recently, Kim *et al* reported that GPR4 plays a critial role in SPC-induced angiogenesis and SPC transactivates VEGF receptor 2 in endothelial cells[25].

Maghazachi *et al* reported that psychosine and glucosylsphingosine induce multinuclear cell formation and apoptosis in TDAG8-expressing natural killer cells[26]. Malone *et al* reported that activation of TDAG8 by psychosine enhanced dexamethasone-induced apoptosis in a TDAG8-dependent manner in lymphomas[27]. Tosa *et al* reported critical function of TDAG8 in glucocorticoid-induced thymocyte apoptosis[28].

These ligand chemicals have similar lysolipid structures (Figure 1) and their significance in pathological conditions and pharmacological application has been discovered. Especially, G2A deficient mouse developed an autoimmune syndrome similar to systemic lupus erythematosus (SLE)[29], and therapeutic application of LPC for sepsis was proposed in relation with G2A receptor[30].

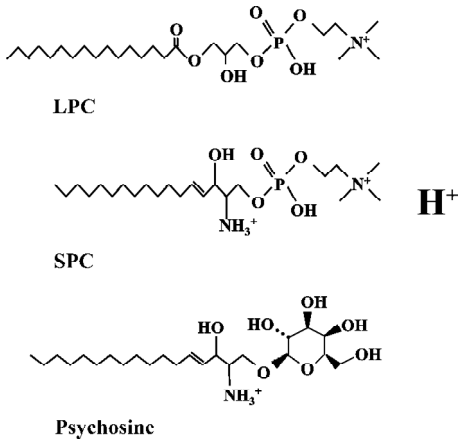

Figure 1. Structures of LPC and other lysolipids.

Overexpression of G2A, GPR4, and TDAG8 in human cancers has been found to play a role in driving or maintaining tumor formation, however, transformation was achieved without addition of lysolipids[31,32]. Bektas *et al* reported ligand-independent signaling of GPR4 and its inability to respond to SPC and LPC in several assay systems, that is, GTPγS binding, receptor internalization, and arrestin translocation[33]. Additionally, the original paper that reported G2A-LPC pairing was recently retracted by authors, because they could not confirm the LPC-binding experiments[34]. Constitutive activation of GPCR and lipid-independent responses raises a possibility, that is, another activator of GPCR is present in the culture medium or secreted from GPCR-transfected cells. Such a possibility has been suggested and supported with proton by five independent groups[21,35–38].

OGR1 subfamily as proton-sensing GPCRs

Ludwig *et al* (2003) reported OGR1 and GPR4 to be proton-sensing receptors. At pH 7.8, OGR1 was inactive, but activated fully inositol phosphate (IP) formation at pH 6.8. Ludwig *et al* predicted several hydrogen-bond interactions occurring between unprotonated histidines by using a computational 3D model of OGR1. Under alkaline conditions these interactions could stabilize the receptor in an inactive state. Exposure to an acidic pH would destabilize the hydrogen bonds, switching the receptor to its active conformation. Indeed, mutation of several histidines (H17, H20, H84, H169, and H269) to phenylalanines reduced proton-sensing ability of OGR1 (Figure 2)[35]. In the same paper, authors observed that a very similar activation of GPR4 by pH change, but GPR4 activates the Gs-adenylyl cyclase-cAMP pathway[35].

Figure 2. Sequence alignment of OGR1 subfamily GPCRs. Histidine residues that have been reported to be involved in proton-sensing are bolded and underlined in OGR1 (H17, H20, H84, H169, and H269), TDAG8 (H10 and H14), and G2A (H174). Residues in GPR4 that are assumed to be critical for proton-sensing based on alignment with OGR1 are also marked. Suggested basic amino acids in G2A instead of histidines in OGR1 are underlined. A histidine in TMVI conserved in all four members of GPCRs is starred. Potential transmembrane regions are overscored; gaps are indicated by dashes.

However, they were not able to observe any effect of SPC and LPC, previously reported ligands, on OGR1 and GPR4. In 2004, Murakami *et al* reported that G2A functions as a proton-sensing GPCR[21]. Transient transfection of G2A caused significant activation of the *zif* 268 promoter and IP accumulation at pH 7.6 and lowering extracellular pH augmented the activation only in G2A-expressing PC12h cells[21]. Site-directed mutation of His-174, which is predicted to be located at the extracellular part of the transmembrane helix IV (Figure 2), reduced partially G2A-dependent signaling at lower pH. They found that LPC and SPC did not cause IP formation at pH 7.6, but LPC inhibited IP formation at pH 6.8

in a dose-dependent manner, suggesting that LPC acts as an antagonist not an agonist. Wang *et al* reported that TDAG8 is also a proton-sensing GPCR stimulating cAMP accumulation[36]. They found that psychosine and SPC are antagonistic on pH-dependent responses in the cells transfected with TDAG8. Psychosine-sensitive and pH-dependent cAMP accumulation was also observed in mouse thymocytes, where TDAG8 is endogenously expressed[36]. Radu *et al* conducted experiments with all 4 members of OGR1 subfamily to test proton-sensibility and confirmed previous reports on OGR1, GPR4, and TDAG8[38]. However, G2A was insensitive or less sensitive to extracellular pH change in their experimental conditions[38]. They suggested that lack of many histidine residues, defined to be involved in pH-sensing of OGR1, could be a cause for insensitiveness of G2A to acidic pH (Figure 2)[38]. Also they suggested that the constitutive activation of G2A in neutral pH might be resulted from maintaining active conformation of G2A via positively charged amino acids in human and mouse G2A instead of conserved histidines (Figure 2)[38]. Ishii *et al* reported that TDAG8 is a proton-sensing GPCR, however, they were not able to observe any inhibitory effect of psychosine on pH-dependent TDAG8 activation[37]. Therefore, a series of publications propose that extracellular proton could be an activator of the OGR1 subfamily of GPCRs. More than two independent groups reported proton-sensing properties of OGR1, GPR4, and TDAG8 (Table 1). In the case of G2A, constitutive activation at pH 7.4 has been observed in many transfected cells by many research groups, however, pH-dependent activation was supported only by one group[21] and was not fully reproduced by another group[38]. Dependence of pH sensing on the histidine residues on the extracellular domains of GPCRs has been tested on OGR1, TDAG8, and G2A[21,35–37]. However, site-directed mutagenesis study of the histidines on GPR4 has not been experimentally reported.

In summary, there are four opinions in the published reports, that is agonism of lysolipid, antagonism of lysolipid, agonism of proton, and no confirmation of lysolipid action on OGR1 subfamily GPCRs. Table 1 shows list of publications supporting each opinion except negative observation or constitutive activation.

Two ligands for a GPCR, proton *vs* lysolipid

As for lysolipids as ligands, Ludwig *et al* could not confirm such activation of GPCRs with lysolipids[35], and three research groups observed antagonistic effects of LPC, SPC and psychosine on the GPCRs in acidic conditions rather than agonism (Table 1)[21,36–38]. In summary, lysolipids have been suggested as ligands for the OGR1 subfamily GPCRs, however, all four members of the GPCRs have also been proposed as proton-sensing GPCRs. OGR1 subfamily has been considered as a contentious GPCR subgroup, because pairing it with lysolipids has been controversial in the scientific society[4,21,33,35,36]. Additionally, the original G2A paper was retracted[34] and GPR4 paper would be retracted (Y XU, FASEB conference, 2005). However, there are growing numbers of reports supporting actions of lysolipids on OGR1 subfamily GPCRs (Table 1). As proposed by Kim *et al* it can be dependent on cell types. Kim *et al* recently confirmed pH-dependent cAMP production in GPR4-transfected HEK293 cells but not in GPR4-transfected HUVEC or HMEC-1 cells[25]. Cell-type specific functions remind us RAMPS (receptor activity-modulating proteins) which are essential proteins for expression and function of GPCRs such as CGRP (calcitonin gene-related peptide) and adrenomedullin[39]. If

Table 1. Summary of publications.

Receptor		Agonist		Antagonist
Name	Expression	Lysolipid	Proton	Lysolipid
OGR1 (GPR68)	Spleen, testis, small intestine, PBL, brain, heart, lung, placenta, kidney[53]	(SPC)[12]	(H^+)[35,36,38]	(Psy and SPC)[36]
GPR4	Ubiquitous (ovary, liver, lung, kidney, lymph node, subthalamic nucleus)[13]	(LPC and SPC)[13] (LPC)[24], (SPC)[25]	(H^+)[25,35,36,38]	(Psy and SPC)[36]
TDAG8 (GPR65)	PBL, spleen, thymus, lymph nodes[14]	(Psy)[14,26,27]	(H^+)[36–38]	(Psy and SPC)[36]
G2A (GPR132)	Spleen, thymus, T-lymphocytes, B-lymphocytes, monocytes, macrophages[16]	(LPC)[17,18,21,30]	(H^+)[21,38]	(LPC)[21,38]

there are RAMP-like proteins specific for OGR1 subfamily, the complicated results may be solved. Wang *et al* recently observed spontaneous internalization of murine G2A and reported that LPC induces surface redistribution and stabilization of murine G2A[19]. Such an action of LPC may support spontaneous activation of G2A and explain agonistic and antagonistic effects of LPC. If spontaneous activity of G2A was presumed as control level in neutral pH, LPC-induced action might be interpreted as agonism. However, if spontaneous activation or proton-activated effect was thought as agonism, LPC-induced action might be considered as antagonism. Further investigation on cell-type specificity and receptor distribution in the cells may clarify action mode of OGR1 subfamily GPCRs by both chemicals, proton and lysolipids.

Therefore, it is not easy to say which chemical is the real ligand, although both chemicals could be called as modulators of the GPCRs. Finding of antagonistic effects of lysolipids on the receptors at acidic conditions may advance our understanding and might reconcile the controversy in the future. If both chemicals could activate the same GPCRs in certain conditions, another issue might be two ligands for a GPCR. Dual actions may be a rare example in the GPCR area. However, considering that TRPV1 could be activated by capsaicin, proton, heat and lipids, two chemicals for a GPCR could not be a surprising action mode in biological sciences[10]. Investigation of physiological roles and pathological implications of the GPCRs in the future may lighten importance of discovery of proton-sensing GPCRs, because acidosis is related with many diseases such as cancer[40], asthma[41], atherosclerosis[42], arthritis[43], and osteopenia[35,44].

Proton as an agonist

Another issue remains; could proton be a ligand? To be an agonist, it should bind to GPCR specifically and reversibly[45]. Furthermore, it should dose-dependently activate GPCR. In five publications, proton has been shown to fulfill all the above criteria, except specificity[21,35–38]. Basal activity of many other GPCRs has been observed in neutral pH without apparent presence of endogenous ligands as like δ-opioid receptor[46,47]. Such basal activity of GPCR has further been confirmed by inverse agonists, which reduce the basal activity in a dose-dependent manner[46,47]. Many GPCRs have histidine residues in extracellular loops and outer segments of GPCR helixes. Thus, if change of extracellular pH could change basal activities of many GPCRs, although the magnitude of change varies, this means lack of specificity. If many GPCRs are activated or inactivated by change of pH without presence of any agonists, proton can not be an agonist, because it lacks specificity, even though OGR1 subfamily activation with proton was the greatest response among GPCRs activated with proton. Indeed, modulation of GPCRs by extracellular pH has been reported in $P2Y_4$ ATP receptor and calcium-sensing receptor[48,49].

Four research groups have used the term "proton-sensing GPCR" for OGR1 subfamily, however, the term for proton, the counterpart, is omitted or the term "ligand" has been used for proton. However, it is inadequate, because of the above-mentioned reason, lack of specificity. GPCR modula-

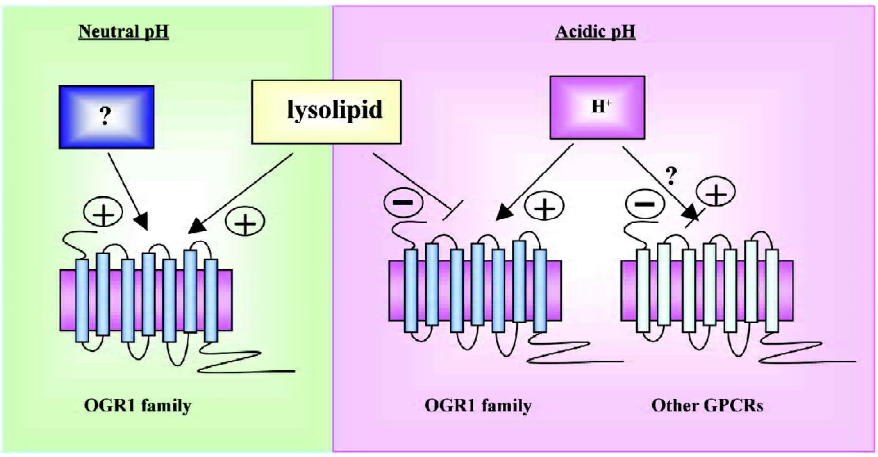

Figure 3. Illustration of suggested modulators of OGR1 subfamily. Lysolipids have been suggested as agonists of OGR1 subfamily in neutral pH and as an agonist in acidic pH. Proton has been suggested as agonists of OGR1 subfamily. Two possibilities are also included. One is another chemical activating OGR1 subfamily in neutral pH. The other possibility is proton action on other GPCRs positively and/or negatively. The symbol (+) means activation of GPCR and (-) inactivation.

tor may be the good term for proton, because it changes activity of GPCRs, but it can not be an agonist. So far, the smallest particle ever reported to be a GPCR activator is photon. In this case, photon energy in light activates rhodopsin GPCR by isomerisation of 11-*cis*-retinal to *trans* conformation within the rhodopsin helixes[50,51]. Now, proton might become the second small molecule activating GPCRs. Although lysolipids as the ligand of OGR1 subfamily still remain controversial, proton as a ligand for the GPCRs also need to be considered with caution, because an endogenous ligand might be waiting to be discovered, suggesting possible presence of another chemical to activate OGR1 subfamily in neutral conditions (Figure 3). It may not be a surprise if there is another chemical activating OGR1 subfamily in neutral pH such as prostaglandins and capsaicin modulating TRPV1[52].

In summary, proton activates OGR1 subfamily GPCRs and lysolipids modulate activity of OGR1 GPCRs positively or negatively. However, we need to consider other two possibilities. One is that modulation by proton could be generalized in other GPCRs even though the magnitude varies (Figure 3). Second, there could be another chemical activating OGR1 subfamily in neutral pH (Figure 3).

Acknowledgement

The author thanks Prof Fumikazu OKAJIMA (Gunma University) for his critical comments.

References

1 Im DS. Orphan G protein-coupled receptors and beyond. Jpn J Pharmacol 2002; 90: 101–6.
2 Perez DM. From plants to man: the GPCR “tree of life”. Mol Pharmacol 2005; 67: 1383–4.
3 Vassilatis DK, Hohmann JG, Zeng H, Li F, Ranchalis JE, Mortrud MT, *et al*. The G protein-coupled receptor repertoires of human and mouse. Proc Natl Acad Sci USA 2003; 100: 4903–8.
4 Kostenis E. A glance at G-protein-coupled receptors for lipid mediators: a growing receptor family with remarkably diverse ligands. Pharmacol Ther 2004; 102: 243–57.
5 Lynch KR, O’Neill GP, Liu Q, Im DS, Sawyer N, Metters KM, *et al*. Characterization of the human cysteinyl leukotriene CysLT1 receptor. Nature 1999; 399: 789–93.
6 Yokomizo T, Izumi T, Chang K, Takuwa Y, Shimizu T. A G-protein-coupled receptor for leukotriene B4 that mediates chemotaxis. Nature 1997; 387: 620–4.
7 Sakurai T, Amemiya A, Ishii M, Matsuzaki I, Chemelli RM, Tanaka H, *et al*. Orexins and orexin receptors: a family of hypothalamic neuropeptides and G protein-coupled receptors that regulate feeding behavior. Cell 1998; 92: 573–85.
8 Hecht JH, Weiner JA, Post SR, Chun J. Ventricular zone gene-1 (vzg-1) encodes a lysophosphatidic acid receptor expressed in neurogenic regions of the developing cerebral cortex. J Cell Biol 1996; 135: 1071–83.
9 Lee MJ, Van Brocklyn JR, Thangada S, Liu CH, Hand AR, Menzeleev R, *et al*. Sphingosine-1-phosphate as a ligand for the G protein-coupled receptor EDG-1. Science 1998; 279: 1552–5.
10 Ahern GP, Brooks IM, Miyares RL, Wang XB. Extracellular cations sensitize and gate capsaicin receptor TRPV1 modulating pain signaling. J Neurosci 2005; 25:5109–16.
11 Voilley N. Acid-sensing ion channels (ASICs): new targets for the analgesic effects of non-steroid anti-inflammatory drugs (NSAIDs). Curr Drug Targets Inflamm Allergy 2004; 3: 71–9.
12 Xu Y, Zhu K, Hong G, Wu W, Baudhuin LM, Xiao Y, *et al*. Sphingosylphosphorylcholine is a ligand for ovarian cancer G-protein-coupled receptor 1. Nat Cell Biol 2000; 2: 261–7.
13 Zhu K, Baudhuin LM, Hong G, Williams FS, Cristina KL, Kabarowski JH, *et al*. Sphingosylphosphorylcholine and lysophosphatidylcholine are ligands for the G protein-coupled receptor GPR4. J Biol Chem 2001; 276: 41325–35.
14 Im DS, Heise CE, Nguyen T, O’Dowd BF, Lynch KR. Identification of a molecular target of psychosine and its role in globoid cell formation. J Cell Biol 2001; 153: 429–34.
15 Xu Y, Fang XJ, Casey G, Mills GB. Lysophospholipids activate ovarian and breast cancer cells. Biochem J 1995; 309 (Pt 3): 933–40.
16 Weng Z, Fluckiger AC, Nisitani S, Wahl MI, Le LQ, Hunter CA, *et al*. A DNA damage and stress inducible G protein-coupled receptor blocks cells in G2/M. Proc Natl Acad Sci USA 1998; 95: 12334–9.
17 Radu CG, Yang LV, Riedinger M, Au M, Witte ON. T cell chemotaxis to lysophosphatidylcholine through the G2A receptor. Proc Natl Acad Sci USA 2004; 101: 245–50.
18 Yang LV, Radu CG, Wang L, Riedinger M, Witte ON. Gi-independent macrophage chemotaxis to lysophosphatidylcholine via the immunoregulatory GPCR G2A. Blood 2005; 105: 1127–34.
19 Wang L, Radu CG, Yang LV, Bentolila LA, Riedinger M, Witte ON. Lysophosphatidylcholine-induced Surface Redistribution Regulates Signaling of the Murine G Protein-coupled Receptor G2A. Mol Biol Cell 2005; 16: 2234–47.
20 Han KH, Hong KH, Ko J, Rhee KS, Hong MK, Kim JJ, *et al*. Lysophosphatidylcholine up-regulates CXCR4 chemokine receptor expression in human CD4 T cells. J Leukoc Biol 2004; 76: 195–202.
21 Murakami N, Yokomizo T, Okuno T, Shimizu T. G2A is a proton-sensing G-protein coupled receptor antagonized by lysophosphatidylcholine. J Biol Chem 2004; 279: 42484–91.
22 Lin P, Ye RD. The lysophospholipid receptor G2A activates a specific combination of G proteins and promotes apoptosis. J Biol Chem 2003; 278: 14379–86.
23 Ikeno Y, Konno N, Cheon SH, Bolchi A, Ottonello S, Kitamoto K, *et al*. Secretory phospholipase A2 induces neurite outgrowth in PC12 cells through lysophosphatidylcholine generation and activation of G2A receptor. J Biol Chem 2005; 280:28044–52.
24 Lum H, Qiao J, Walter RJ, Huang F, Subbaiah PV, Kim KS, *et al*. Inflammatory stress increases receptor for lysophosphatidylcholine in human microvascular endothelial cells. Am J Physiol Heart Circ Physiol 2003; 285: H1786–9.
25 Kim KS, Ren J, Jiang Y, Ebrahem Q, Tipps R, Cristina K, *et al*. GPR4 plays a critical role in endothelial cell function and medi-

ates the effects of sphingosylphosphorylcholine. FASEB J 2005; 19: 819–21.
26 Maghazachi AA, Knudsen E, Jin Y, Jenstad M, Chaudhry FA. D-galactosyl-beta1-1'-sphingosine and D-glucosyl-beta1-1'-sphingosine induce human natural killer cell apoptosis. Biochem Biophys Res Commun 2004; 320: 810–5.
27 Malone MH, Wang Z, Distelhorst CW. The glucocorticoid-induced gene tdag8 encodes a pro-apoptotic G protein-coupled receptor whose activation promotes glucocorticoid-induced apoptosis. J Biol Chem 2004; 279: 52850–9.
28 Tosa N, Murakami M, Jia WY, Yokoyama M, Masunaga T, Iwabuchi C, *et al*. Critical function of T cell death-associated gene 8 in glucocorticoid-induced thymocyte apoptosis. Int Immunol 2003; 15: 741–9.
29 Le LQ, Kabarowski JH, Weng Z, Satterthwaite AB, Harvill ET, Jensen ER, *et al*. Mice lacking the orphan G protein-coupled receptor G2A develop a late-onset autoimmune syndrome. Immunity 2001; 14: 561–71.
30 Yan JJ, Jung JS, Lee JE, Lee J, Huh SO, Kim HS, *et al*. Therapeutic effects of lysophosphatidylcholine in experimental sepsis. Nat Med 2004; 10: 161–7.
31 Zohn IE, Klinger M, Karp X, Kirk H, Symons M, Chrzanowska-Wodnicka M, *et al*. G2A is an oncogenic G protein-coupled receptor. Oncogene 2000; 19: 3866–77.
32 Sin WC, Zhang Y, Zhong W, Adhikarakunnathu S, Powers S, Hoey T, *et al*. G protein-coupled receptors GPR4 and TDAG8 are oncogenic and overexpressed in human cancers. Oncogene 2004; 23: 6299–303.
33 Bektas M, Barak LS, Jolly PS, Liu H, Lynch KR, Lacana E, *et al*. The G protein-coupled receptor GPR4 suppresses ERK activation in a ligand-independent manner. Biochemistry 2003; 42: 12181–91.
34 Kabarowski JH, Zhu K, Le LQ, Witte ON, Xu Y. Lysophosphatidylcholine as a ligand for the immunoregulatory receptor G_2A. Science 2001; 293: 702–5. Retraction in: Witte ON, Kabarowski JH, Xu Y, Le LQ, Zhu K. Retraction. Science 2005; 307: 206.
35 Ludwig MG, Vanek M, Guerini D, Gasser JA, Jones CE, Junker U, *et al*. Proton-sensing G-protein-coupled receptors. Nature 2003; 425: 93–8.
36 Wang JQ, Kon J, Mogi C, Tobo M, Damirin A, Sato K, *et al*. TDAG8 is a proton-sensing and psychosine-sensitive G-protein-coupled receptor. J Biol Chem 2004; 279: 45626–33.
37 Ishii S, Kihara Y, Shimizu T. Identification of T cell death-associated gene 8 (TDAG8) as a novel acid sensing G-protein-coupled receptor. J Biol Chem 2005; 280: 9083–7.
38 Radu CG, Nijagal A, McLaughlin J, Wang L, Witte ON. Differential proton sensitivity of related G protein-coupled receptors T cell death-associated gene 8 and G2A expressed in immune cells. Proc Natl Acad Sci U S A 2005; 102: 1632–7.
39 Conner AC, Simms J, Hay DL, Mahmoud K, Howitt SG, Wheatley M, *et al*. Heterodimers and family-B GPCRs: RAMPs, CGRP and adrenomedullin. Biochem Soc Trans 2004; 32: 843–6.
40 Wike-Hooley JL, Haveman J, Reinhold HS. The relevance of tumour pH to the treatment of malignant disease. Radiother Oncol 1984; 2: 343–66.
41 Hunt JF, Fang K, Malik R, Snyder A, Malhotra N, Platts-Mills TA, *et al*. Endogenous airway acidification. Implications for asthma pathophysiology. Am J Respir Crit Care Med 2000; 161: 694–9.
42 Naghavi M, John R, Naguib S, Siadaty MS, Grasu R, Kurian KC, *et al*. pH Heterogeneity of human and rabbit atherosclerotic plaques; a new insight into detection of vulnerable plaque. Atherosclerosis 2002; 164: 27–35.
43 Christensen BN, Kochukov MY, McNearney TA, Taglialatela G, Westlund KN. A Proton-Sensing G-Protein Coupled Receptor Mobilizes Calcium in Human Synovial Cells. Am J Physiol Cell Physiol 2005; 289:C601–8.
44 Krieger NS, Frick KK, Bushinsky DA. Mechanism of acid-induced bone resorption. Curr Opin Nephrol Hypertens 2004; 13: 423–36.
45 Kenakin TP. Drug-receptor theory. In: Kenakin TP. Pharmacological analysis of drug-receptor interaction. New York: Raven Press; 1987. p 1–30.
46 Strange PG. Mechanisms of inverse agonism at G-protein-coupled receptors. Trends Pharmacol Sci 2002; 23: 89–95.
47 Tryoen-Toth P, Decaillot FM, Filliol D, Befort K, Lazarus LH, Schiller PW, *et al*. Inverse agonism and neutral antagonism at wild-type and constitutively active mutant delta opioid receptors. J Pharmacol Exp Ther 2005; 313: 410–21.
48 Wildman SS, Unwin RJ, King BF. Extended pharmacological profiles of rat P2Y2 and rat P2Y4 receptors and their sensitivity to extracellular H+ and Zn2+ ions. Br J Pharmacol 2003; 140: 1177–86.
49 Quinn SJ, Bai M, Brown EM. pH Sensing by the calcium-sensing receptor. J Biol Chem 2004; 279: 37241–9.
50 Lagnado L, Baylor D. Signal flow in visual transduction. Neuron 1992; 8: 995–1002.
51 Palczewski K, Kumasaka T, Hori T, Behnke CA, Motoshima H, Fox BA, *et al*. Crystal structure of rhodopsin: A G protein-coupled receptor. Science 2000; 289: 739–45.
52 Nagy I, Santha P, Jancso G, Urban L. The role of the vanilloid (capsaicin) receptor (TRPV1) in physiology and pathology. Eur J Pharmacol. 2004; 500:351–69.
53 Xu Y, Casey G. Identification of human OGR1, a novel G protein-coupled receptor that maps to chromosome 14. Genomics 1996; 35: 397–402.

Acta Pharmacologica Sinica 2005 Dec; 26 (12): 1442–1447

Blackwell Publishing

Full-length article

Differential sensitivity of GABAergic and glycinergic inputs to orexin-A in preganglionic cardiac vagal neurons of newborn rats[1]

Ji-jiang WANG[2], Yong-hua CHEN, Ke-yong LI, Feng-yan SUN

National Key Laboratory of Medical Neurobiology, Fudan University Shanghai Medical College, Shanghai 200032, China

Key words

patch-clamp techniques; nervous system; synaptic transmission; vagus nerve

[1] Project supported by grants from Shanghai Education and Development Foundation (03SG06) and National Natural Science Foundation of China (No 30470690).
[2] Correspondence to Dr Ji-jiang WANG.
Phn 86-21-5423-7913.
Fax 86-21-6417-4579.
E-mail wangjj@shmu.edu.cn

Received 2005-07-14
Accepted 2005-08-31

doi: 10.1111/j.1745-7254.2005.00231.x

Abstract

Aim: To test the effect of orexin-A (hypocretin-1), a neuropeptide synthesized in the lateral hypothalamus and the perifornical area, on the glycinergic inputs and the GABAergic inputs of cardiac vagal neurons (CVN). **Methods:** The effects of orexin-A at three concentrations (20 nmol/L, 100 nmol/L, 500 nmol/L) on the glycinergic inputs and the GABAergic inputs were investigated by using retrograde fluorescent labeling of cardiac neurons (CVN) in the nucleus ambiguus (NA) and the voltage patch-clamp technique. **Results:** Orexin-A dose-dependently increased the frequency of both the glycinergic and the GABAergic spontaneous inhibitory postsynaptic currents (sIPSC). However, at a lower concentration (20 nmol/L) of orexin-A, although the frequency of the glycinergic sIPSC was significantly increased, the frequency of the GABAergic sIPSC was not significantly changed. **Conclusion:** The glycinergic inputs and the GABAergic inputs have different sensitivities to orexin-A, which suggests that the two kinds of inhibitory inputs might play different roles in the synaptic control of cardiac vagal functions.

Introduction

Orexin-A and orexin-B, also known as hypocretin-1 and hypocretin-2, are members of a new family of neuropeptides synthesized in the lateral hypothalamus and perifornical area neurons[1,2]. Orexins have been shown to participate in many functions, including sleep-wakefulness, feeding, and neuroendocrine function[3–5]. In addition, many studies have found that orexins also participate in the neural control of cardiovascular functions. And, although most studies have focused on the excitatory effect of orexins on cardiovascular sympathetic activity[6–11], some evidence suggests that orexins might also have a role in the parasympathetic control of heart rate and cardiac functions.

Cardiac vagal nerves predominate over cardiac sympathetic nerves in the control of heart rate and cardiac functions, and their preganglionic fibers primarily originate from the cardiac vagal neurons (CVN) in the nucleus ambiguus (NA) and the dorsal motor nucleus of the vagus (DMNX)[12–15]. CVN are intrinsically silent and their activity relies completely on their synaptic inputs[15]. CVN receive excitatory glutamatergic and cholinergic inputs[16,17], and inhibitory GABAergic and glycinergic inputs[14,17,18]. Although previous studies have suggested that orexins are involved in the vagal control of heart rate and cardiac functions, the reported effects are largely contradictory. Microinjection of orexin-A into the NA of adult male rats elicited a dose-related decrease in heart rate[19]. Microinjection of orexin-A into the nucleus tractus solitarius (NTS), where GABAergic neurons and glutamatergic neurons monosynaptically project to CVN[14,16], elicited a decrease[20] or increase[21] in heart rate. In a very recent *in vitro* study using brainstem slices of newborn rats, orexin-A was found to inhibit CVN indirectly, via presynaptic enhancement of the actionpotential-dependent GABAergic and glycinergic inputs, and via presynaptic attenuation of the actionpotential-dependent glutamatergic inputs[22].

The actual concentration of orexin-A in rat brainstem that acts to modulate the physiological synaptic control of CVN is not clear; however, the experimentally measured concentration of orexin-A in the cerebrospinal fluid is less than 1 nmol/L in rats[23], and is even less in dogs and human

beings[24,25]. Surprisingly, the concentration of orexin-A used in the *in vitro* study of Dergacheva *et al*[22] was 1 μmol/L, and was as high as 1 μmol/L in microinjection studies[19–21]. It is possible that these previous studies have used overdoses of orexin-A, which might have resulted in a non-specific effect.

The response of each kind of synaptic input of CVN to orexin-A might be different at different concentrations. At the same concentration, the sensitivity of each kind of synaptic input to orexin-A might also be different. These possibilities make it necessary to reevaluate the effect of orexin-A on CVN at lower and more divided concentrations. The purpose of the present study is to reevaluate the effect of orexin-A on the glycinergic and GABAergic spontaneous inhibitory postsynaptic currents (sIPSC) at lower concentrations (20 nmol/L, 100 nmol/L, and 500 nmol/L). Using retrograde fluorescent labeling of CVN and the voltage patch-clamp technique, we have demonstrated that orexin-A dose-dependently increases the frequency of both the glycinergic and the GABAergic sIPSC. However, at a lower concentration (20 nmol/L) of orexin-A, although the frequency of the glycinergic sIPSC was significantly increased, the frequency of the GABAergic sIPSC was not significantly changed. These results suggest that the glycinergic inputs and the GABAergic inputs have different sensitivities to orexin-A, and suggest that the two kinds of inhibitory inputs might play different roles in the synaptic control of cardiac vagal functions.

Materials and methods

Retrograde fluorescent labeling of CVN The inhalation agent halothane (0.5 mL) was dripped into a glass box (5 cm×5 cm×5 cm) with a lid and a bottom cotton pad. Three to four-day-old Sprague-Dawley rats (Shanghai Institute for Family Planning) were put in the box for 30 s with the lid covered. This procedure anesthetized the rats but maintained their breathing in a relatively normal state. The rats were then buried in ice-filled bags to decrease the rats' body temperatures and slow their hearts. After autonomic breathing stopped (usually within 2 min) a right thoracotomy was carried out to expose the heart, and rhodamine (2% solution, 20–50 μL; XRITC, Molecular Probes, Carlsbad, California, USA) was injected into the pericardial sac with a glass pipette (tip diameter 50 μm). The incision was sutured and the animals were heated with a thermo-pad to help recovery. After the surgery (about 5 min) the animals usually started autonomic breathing within 3 min and started free moving within another 5 min. The animals were allowed 1–2 d to recover, and experiments were performed when animals were 4–6 d old. Rats at this age have been shown to have similar respiratory-related and reflex-related parasympathetic heart rate control as adult rats[17,26]. Similar surgical procedures that selectively labeled CVN have been described previously by Mendelowitz and Kunze[27], who proved that no brainstem neurons were labeled if rhodamine was injected into the chest cavity while the pericardial sac was kept intact, and if rhodamine was injected into the pericardial sac while the cardiac branch of the cardiac vagal nerve was sectioned. In addition, it has also been proved that intravenous injection of up to 10 mg of rhodamine failed to label any CVN[27].

Slice preparation The animals were anesthetized deeply with halothane and decapitated at the supracollicular level. The hindbrain was exposed, isolated, and submerged in cold (4 ºC) artificial cerebral spinal fluid (ACSF) of the following composition (in mmol/L): NaCl (124), KCl (3.0), KH_2PO_4(1.2), $CaCl_2$ (2.4), $MgSO_4$ (1.3), $NaHCO_3$ (26), *D*-glucose (10), sucrose (10), and constantly bubbled with gas (95% O_2, 5% CO_2; pH 7.4). The cerebellum was removed and the brainstem was dissected using a dissection microscope. With the rostral end facing upwards and the ventral surface facing the razor, the brainstem was then secured in the slicing chamber of a vibratome (Leica VT 1000 S, Heerbrugg, Switzerland) filled with the same ACSF, and sequentially sectioned in variable thickness in the transverse plane. Once the NA and other landmarks[17] emerged under the microscope, a single slice of 400 μm thickness was taken for experimentation. A medulla slice of this thickness from a 4–6-d-old rat actually includes the full range of the medulla, and such slices have been used in many studies (eg, respiratory rhythm studies) that require relatively intact *in vitro* neuronal networks. The slice was transferred into the recording chamber and submerged in the ACSF maintained at 22 ºC.

Electrophysiological recording Individual CVN in the NA were identified by the presence of the fluorescent tracer using an Olympus (Tokyo, Japan) upright microscope through a 40×water immersion objective. These identified CVN were then imaged with differential interference contrast (DIC) optics, and infrared illumination and infrared-sensitive video detection cameras to gain better spatial resolution and to visually guide and position the patch pipette onto the surface of the identified neuron. The pipette (2.0–5.0 Ω) was advanced until a high resistance seal was obtained (>1 GΩ) between the pipette tip and the cell membrane of the identified neuron. The membrane under the pipette tip was then ruptured with a brief suction to obtain whole-cell patch-clamp configuration, and the cell was voltage-clamped at a holding potential of -80 mV. The pipette resistance and capacitance

was not compensated either before or after gaining intracellular access. To record GABAergic and glycinergic synaptic events, the patch pipettes were filled with a solution consisting of (in mmol/L): KCl (150), $MgCl_2$ (2), ethyleneglycol-bis(β-aminoethyl ether)-*N*,*N*,*N*',*N*'-tetraacetic acid (EGTA) (2), *N*-2-hydroxyethylpiperazine-*N*'-2-ethanesulfonic acid (HEPES) (10), Mg-ATP (2), at pH 7.35. With this pipette solution the Cl^- current induced by activation of the GABA (γ-aminobutyric acid) receptors and/or glycinergic receptors was recorded as an inward current. In some experiments a 2 ms, 5 mV, hyperpolarizing current was injected with a frequency of 0.25 Hz to calculate and monitor the membrane resistance change of CVN throughout the recording. All animal procedures complied with the institutional guidelines of Fudan University, and were in accordance with the National Administration Guidelines for Experimental Animals.

Drug application GABAergic synaptic currents were isolated by inclusion in a perfusate of strychnine (1 μmol/L), D-2-amino-5-phosphonovalerate (AP_5, 50 μmol/L), and 6-cyano-7-nitroquinoxaline-2,3-dione (CNQX; 50 μmol/L) to block glycine, NMDA (*N*-methyl-*D*-aspartate), and non-NMDA receptors, respectively, and were confirmed by blockade of the synaptic currents by 1 μmol/L picrotoxin at the end of the experiment. Glycinergic synaptic currents were isolated by inclusion in a perfusate of picrotoxin (1 μmol/L), AP_5 (50 μmol/L), and CNQX (50 μmol/L) to block GABA, NMDA, and non-NMDA receptors, respectively, and were confirmed by blockade of the synaptic currents by 1 μmol/L strychnine at the end of the experiment. Orexin-A (20 nmol/L, 100 nmol/L, 500 nmol/L) was used to activate the orexin-A receptors. The duration of orexin-A application was 2 min and each slice was applied only once to avoid desensitization. All drugs were purchased from Sigma Aldrich (St Louis, MO, USA).

Data analysis Spontaneous GABAergic and glycinergic sIPSC were analyzed with MiniAnalysis (Synaptosoft, version 4.3.1, Decatur, GA, USA) with a minimal acceptable amplitude of 10 pA. Results are presented as mean±SEM, and are statistically compared by using the nonparametric Kolmogorov-Smirnov (K-S) test. Significant difference was set at $P<0.05$.

Results

Responses of the glycinergic sIPSC to different doses of orexin-A Orexin-A significantly increased the frequency of the glycinergic sIPSC at all three concentrations tested. At a concentration of 20 nmol/L orexin-A increased the average frequency of the glycinergic sIPSC by 63%±4%, from 3.04±1.01 Hz to 4.97±0.91 Hz ($P<0.01$, $n=6$). This frequency increase was observed in all the 6 CVN tested. At a concentration of 100 nmol/L, orexin-A increased the average frequency of the glycinergic sIPSC by 167%±5%, from 3.60±0.90 Hz to 9.64±0.86 Hz ($P<0.01$, $n=8$). At a concentration of 500 nmol/L orexin-A caused a frequency increase by 149%±7%, from 3.55±1.21 Hz to 8.85±2.71 Hz ($P<0.05$, $n=8$), which was similar in degree to that produced by 100 nmol/L orexin-A. These results indicate that orexin-A dose-dependently increases the frequency of the glycinergic sIPSC, and a maximal effect can be achieved at 100 nmol/L. A typical CVN with an increased frequency of glycinergic sIPSC induced by orexin-A at 100 nmol/L is shown in Figure 1A, 1B, and the changes in average frequency caused by the three concentrations of orexin-A are shown in Figure 1C, 1D.

In most CVN and at all the three concentrations of orexin-A used, an increase in the amplitude of the glycinergic sIPSC was also observed. Because Dergacheva *et al* proved that this amplitude increase was presynaptically caused by summated action-potential-dependent release of glycine[22], the amplitude data were not statistically analyzed and were not presented in this article. In addition, at no concentration of orexin-A used in this study was there any significant change in the membrane resistance, or visible change in the baseline currents of CVN. The average membrane resistance before and after 500 nmol/L orexin-A was 370.24±16.17 MΩ and 382.66±20.87 MΩ, respectively ($P>0.05$, $n=8$).

Responses of the GABAergic sIPSC to different doses of orexin-A Orexin-A significantly increased the frequency of the GABAergic sIPSC only at 100 nmol/L and 500 nmol/L. At a concentration of 20 nmol/L orexin-A changed the frequency of the GABAergic sIPSC from 3.40±0.75 Hz to 2.88±0.53 Hz ($P>0.05$, $n=6$). In none of these 6 CVN was obvious frequency change observed. At a concentration of 100 nmol/L orexin-A increased the frequency of the GABAergic sIPSC by 97%±11%, from 2.58±0.63 Hz to 5.07±1.22 Hz ($P<0.05$, $n=6$). At a concentration of 500 nmol/L orexin-A increased the frequency of the GABAergic sIPSC by 173%±14%, from 2.59±0.82 Hz to 7.08±0.86 Hz ($P<0.01$, $n=5$). These results indicate that although orexin-A also dose-dependently increased the frequency of the GABAergic sIPSC, a relatively higher concentration (>20 nmol/L) is needed to cause a significant change, and the maximal frequency increase could not be reached at a concentration of 100 nmol/L. A typical CVN with an increased frequency of the GABAergic sIPSC induced by orexin-A at 100 nmol/L is shown in Figure 2A, 2B, and the changes in average frequency caused by the three concentrations of orexin-A are illustrated in Figure 2C, 2D.

Orexin-A at concentrations of 100 nmol/L and 500 nmol/L

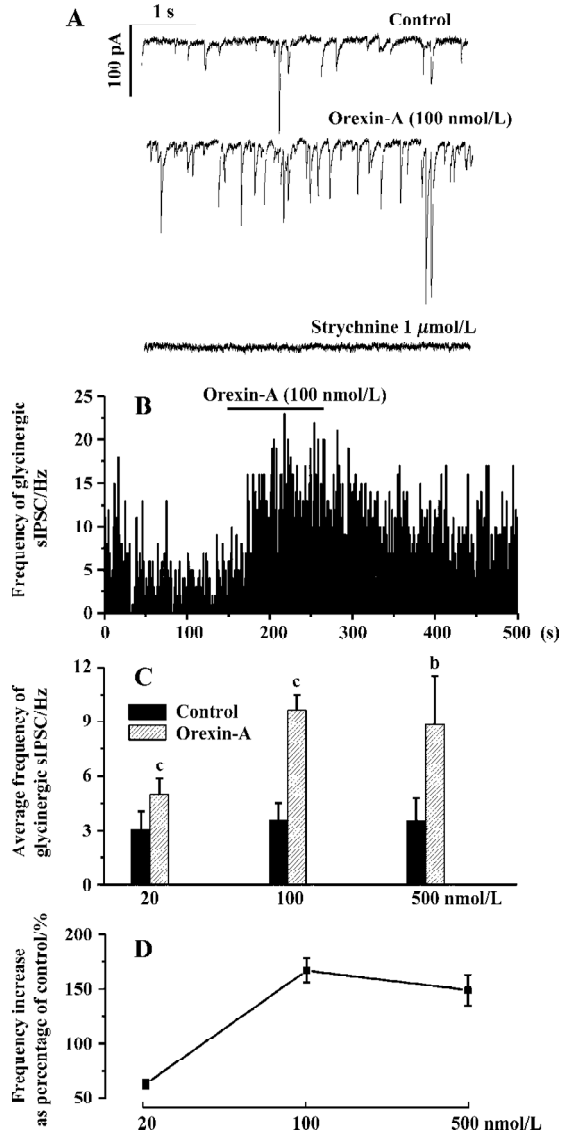

Figure 1. Orexin-A dose-dependently increased the frequency of the glycinergic sIPSC. (A) Traces that show the glycinergic sIPSC during control, during application of 100 nmol/L orexin-A and during application of 1 μmol/L strychnine, respectively. (B) Frequency histogram that shows the frequency increase of the glycinergic sIPSC during application of 100 nmol/L orexin-A in a representative CVN. (C) The increase in the average frequency of the glycinergic sIPSC during application of 20 nmol/L, 100 nmol/L, and 500 nmol/L orexin-A. $^{b}P<0.05$, $^{c}P<0.01$ *vs* control. (D) Frequency increase of the glycinergic sIPSC as a percentage of control caused by orexin-A at 20 nmol/L, 100 nmol/L, and 500 nmol/L.

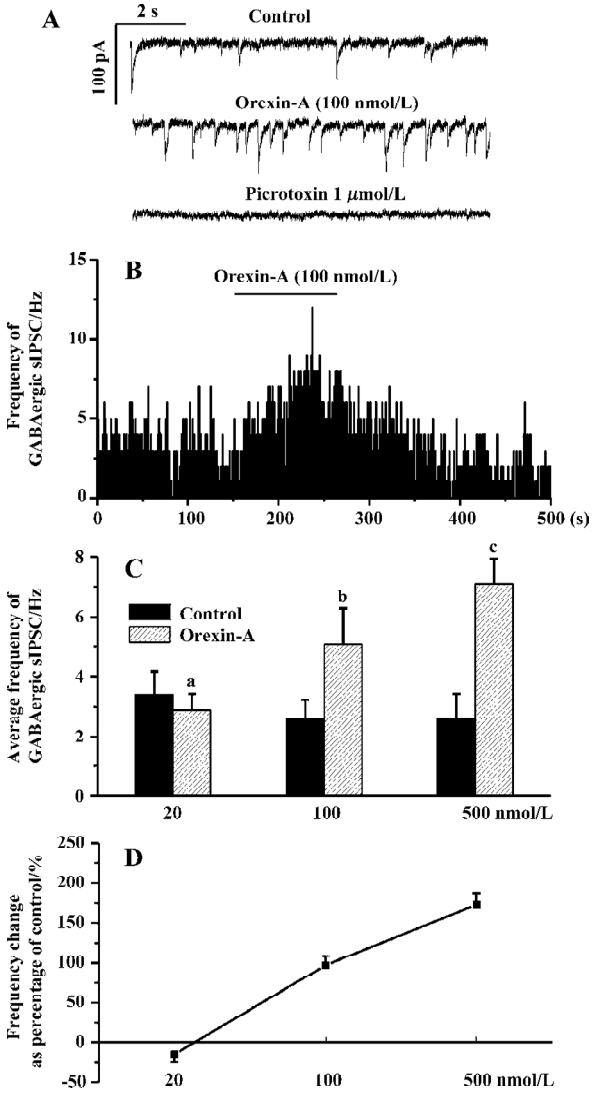

Figure 2. Orexin-A dose-dependently increased the frequency of the GABAergic sIPSC. (A) Traces that show the GABAergic sIPSC during control, during application of 100 nmol/L orexin-A and during application of 1 μmol/L picrotoxin, respectively. (B) Frequency histogram that shows the frequency increase of the GABAergic sIPSC during application of 100 nmol/L orexin-A in a representative CVN. (C) The increase in the average frequency of the GABAergic sIPSC during application of 20 nmol/L, 100 nmol/L, and 500 nmol/L orexin-A. $^{a}P>0.05$, $^{b}P<0.05$, $^{c}P<0.01$ *vs* control. (D) Frequency change of the GABAergic sIPSC as a percentage of control caused by orexin-A at 20 nmol/L, 100 nmol/L, and 500 nmol/L.

also caused an amplitude increase of the GABAergic sIPSC in most CVN tested. Because Dergacheva *et al* have proved that this amplitude increase is also presynaptically caused by summated action-potential-dependent release of GABA [22] the amplitude data were not statistically analyzed and are not presented in this article.

Discussion

There are two major findings in the present study. One is that the frequency increase of both the glycinergic and the GABAergic IPSC caused by orexin-A is dose-dependent. The

other is that orexin-A at a lower concentration (20 nmol/L) significantly enhances the glycinergic inputs but does not cause significant alteration in the GABAergic inputs.

Ever since the discovery of the GABAergic inputs and the glycinergic inputs in CVN, these two inhibitory inputs have shown identical roles in the regulation of CVN. The synaptic activities of both kinds of inputs are action-potential-dependent and are absent in the presence of tetrodotoxin (TTX)[14,18]; both kinds of inputs are enhanced by endogenous acetylcholine and exogenous nicotine[18], are inhibited by opioids, and are rhythmically augmented during inspiration[17,28]. Little is known about whether and how these two inhibitory inputs play different roles in the synaptic control of CVN, except that dihydro-β-erythroidine, a nicotinic antagonist, prevents the inspiratory-related augmentation of the GABAergic, but not the glycinergic, inputs to CVN when focally applied at 3 mmol/L, a concentration under which dihydro-β-erythroidine specifically binds to the α4β2 type of nicotinic receptors [17]. The present study demonstrated that orexin-A at a lower concentration (20 nmol/L) significantly increased the frequency of the glycinergic sIPSC, but did not cause a significant frequency alteration in the GABAergic sIPSC. These results indicate that the glycinergic inputs and GABAergic inputs might have different roles in the orexinergic control of CVN. At lower concentrations (≤ 20 nmol/L) of orexin-A, glycinergic inputs might dominate, and at higher concentrations (≥20 nmol/L) of orexin-A, a synergistic action of both kinds of inputs might occur.

Although in the present study lower concentrations of orexin-A were used, the results were still quite consistent with those from the study of Dergacheva *et al*[22]. The results of the present study as well as the results of Dergacheva *et al* indicate that the responses of the glycinergic inputs and the GABAergic inputs to different concentrations of orexin-A differ in degree, but do not differ in the direction of responses. The present study still cannot reveal why CVN are excited by microinjection of orexin-A into the NA *in vivo* and are inhibited *in vitro*. Further study is necessary.

The physiological roles of the glycinergic and the GABAergic inputs to CVN in cardiac vagal control are not fully understood. Currently, the only confirmed function of these two inputs to CVN is that they are involved in the generation of respiratory-related heart rate rhythm. During the inspiratory phase of the respiratory cycle, both the GABAergic and the glycinergic inputs are facilitated by acetylcholine to inhibit CVN and speed up the heart[18,27]. These two inhibitory inputs to CVN have also long been postulated to be involved in the reflex parasympathetic control of the heart. The serotonergic neurons in the brainstem or in the nodose ganglion have been reported to be activated during activation of the cardiovascular chemo- or baro-reflex[29]. The activation of the serotonergic system, via inhibition of both the GABAergic and the glycinergic inputs to CVN, possibly excites CVN and mediates the reflex parasympathetic inhibition of the heart. The physiological significance of the modulation of the GABAergic and the glycinergic inputs to CVN by orexin-A is also not clear, and nothing is known about why the glycinergic neurons preceding CVN were more sensitive to orexin-A than the GABAergic neurons. Perhaps the receptors for orexin-A binding in these two kinds of neurons are different in density. Orexin-A is known to strengthen preying behavior and increases food uptake. Because the action of orexin-A on CVN is assumed to accelerate the heart, orexin-A might help mammals to adapt to their preying and eating behavior via speeding up the heart.

In conclusion, the present study demonstrated that orexin-A dose-dependently increased the frequency of both the glycinergic and the GABAergic sIPSC of CVN; the glycinergic neurons and the GABAergic neurons preceding CVN had different sensitivities to orexin-A, which might indicate that these two kinds of inhibitory neurons play different roles in the synaptic control of cardiac vagal functions.

References

1 de Lecea L, Kilduff T, Peyron C, Gao X, Foye PE, Danielson PE, *et al*. The hypocretins: hypothalamus-specific peptides with neuroexcitatory activity. Proc Natl Acad Sci USA 1998; 95: 322–7.

2 Sakurai T, Amemiya A, Ishii M, Matsuzaki I, Chemelli RM, Tanaka H, *et al*. Orexins and orexin receptors: a family of hypothalamic neuropeptides and G protein-coupled receptors that regulate feeding behavior. Cell 1998; 92: 573–85.

3 Burdakov D, Liss B, Ashcroft FM. Orexin excites GABAergic neurons of the arcuate nucleus by activating the sodium–calcium exchanger. J Neurosci 2003; 23: 4951–7.

4 van den Pol AN, Gao XB, Obrietan K, Kilduff TS, Belousov AB. Presynaptic and postsynaptic actions and modulation of neuroendocrine neurons by a new hypothalamic peptide, hypocretin/orexin. J Neurosci 1998; 18: 7962–71.

5 Wu M, Zhang Z, Leranth C, Xu C, van den Pol AN, Alreja M. Hypocretin increases impulse flow in the septohippocampal GABAergic pathway: implications for arousal via a mechanism of hippocampal disinhibition. J Neurosci 2002; 22: 7754–65.

6 Matsumura K, Tsuchihashi T, Abe I. Central orexin-A augments sympathoadrenal outflow in conscious rabbits. Hypertension 2001; 37: 1382–7.

7 Samson WK, Gosnell B, Chang JK, Resch ZT, Murphy TC. Cardiovascular regulatory actions of the hypocretins in brain. Brain Res 1999; 831: 248–53.

8 Shirasaka T, Nakazato M, Matsukura S, Takasaki M, Kannan H.

Sympathetic and cardiovascular actions of orexins in conscious rats. Am J Physiol 1999; 277: R1780–5.
9 Antunes VR, Brailoiu GC, Kwok EH, Scruggs P, Dun NJ. Orexins/hypocretins excite rat sympathetic preganglionic neurons *in vivo* and *in vitro*. Am J Physiol Regul Integr Comp Physiol 2001; 281: R1801–7.
10 Chen CT, Hwang LL, Chang JK, Dun NJ. Pressor effects of orexins injected intracisternally and to rostral ventrolateral medulla of anesthetized rats. Am J Physiol Regul Integr Comp Physiol 2000; 278: R692–7.
11 Machado BH, Bonagamba LG, Dun SL, Kwok EH, Dun NJ. Pressor response to microinjection of orexin/hypocretin into rostral ventrolateral medulla of awake rats. Regul Pept 2002; 104: 75–81.
12 Cheng Z, Powley TL. Nucleus ambiguus projections to cardiac ganglia of rat atria: an anterograde tracing study. J Comp Neurol 2000; 424: 588–606.
13 Mendelowitz D. Advances in parasympathetic control of heart rate and cardiac function. News Physiol Sci 1999; 14: 155–61.
14 Wang J, Irnaten M, Mendelowitz D. Characteristics of spontaneous and evoked GABAergic synaptic currents in cardiac vagal neurons in rats. Brain Res 2001; 889: 78–83.
15 Wang J, Irnaten M, Neff RA,Venkatesan P, Evans C, Loewy AD, *et al*. Synaptic and neurotransmitter activation of cardiac vagal neurons in the nucleus ambiguus. Ann N Y Acad Sci 2001; 940: 237–46.
16 Neff RA, Mihalevich M, Mendelowitz D. Stimulation of NTS activates NMDA and non-NMDA receptors in rat cardiac vagal neurons in the nucleus ambiguus. Brain Res 1998; 792: 277–82.
17 Neff RA, Wang J, Baxi S, Evans C, Mendelowitz D. Respiratory sinus arrhythmia: endogenous activation of nicotinic receptors mediates respiratory modulation of brainstem cardioinhibitory parasympathetic neurons. Circ Res 2003; 93: 565–72.
18 Wang J, Wang X, Irnaten M, Venkatesan P, Evans C, Baxi S, *et al*. Endogenous acetylcholine and nicotine activation enhances GABAergic and glycinergic inputs to cardiac vagal neurons. J Neurophysiol 2003; 89: 2473–81.
19 Ciriello J, de Oliveira CV. Cardiac effects of hypocretin-1 in nucleus ambiguus. Am J Physiol Regul Integr Comp Physiol 2003; 284: R1611–20.
20 de Oliveira CV, Rosas-Arellano MP, Solano-Flores LP, Ciriello J. Cardiovascular effects of hypocretin-1 in nucleus of the solitary tract. Am J Physiol Heart Circ Physiol 2003; 284: H1369–77.
21 Smith PM, Connolly BC, Ferguson AV. Microinjection of orexin into the rat nucleus tractus solitarius causes increases in blood pressure. Brain Res 2002; 950: 261–7.
22 Dergacheva O, Wang X, Huang ZG, Bouairi E, Stephens C, Gorini C, *et al*. Hypocretin 1 (orexin A) facilitates inhibitory and diminishes excitatory synaptic pathways to cardiac vagal neurons in the nucleus ambiguus. J Pharmacol Exp Ther 2005; 314(3): 1322–7.
23 Fujiki N, Yoshida Y, Ripley B, Honda K, Mignot E, Nishino SCA. Changes in CSF hypocretin-1 (orexin A) levels in rats across 24 hours and in response to food deprivation. Neuroreport 2001; 12: 993–7.
24 John J, Wu MF, Maidment NT,Lam HA, Boehmer LN, Patton M, *et al*. Developmental changes in CSF hypocretin-1 (orexin-A) levels in normal and genetically narcoleptic Doberman pinschers. J Physiol 2004; 560: 587–92.
25 Kiyashchenko LI, Mileykovskiy BY, Maidment N, Lam HA, Wu MF, John J, *et al*. Release of hypocretin (orexin) during waking and sleep states. J Neurosci 2002; 22: 5282–6.
26 Irnaten M, Neff RA, Wang J, Loewy AD, Mettenleiter TC, Mendelowitz D. Activity of cardiorespiratory networks revealed by transsynaptic virus expressing GFP. J Neurophysiol 2001; 85: 435–8.
27 Mendelowitz D, Kunze DL. Identification and dissociation of cardiovascular neurons from the medulla for patch clamp analysis. Neurosci Lett 1991; 132: 217–21.
28 Wang X, Dergacheva O, Griffioen KJ, Huang ZG, Evans C, Gold A, *et al*. Action of kappa and delta opioid agonists on premotor cardiac vagal neurons in the nucleus ambiguus. Neuroscience 2004; 129: 235–41.
29 Wang, Y, Ramage, AG. The role of central 5-HT (1A) receptors in the control of B-fibre cardiac and bronchoconstrictor vagal preganglionic neurones in anaesthetized cats. J Physiol (London) 2001; 536: 753–67.

Acta Pharmacologica Sinica 2005 Dec; 26 (12): 1448–1453

Blackwell Publishing

Full-length article

Histamine ameliorates spatial memory deficits induced by MK-801 infusion into ventral hippocampus as evaluated by radial maze task in rats[1]

Li-sha XU, Li-xia YANG, Wei-wei HU, Xiao YU, Li MA, Lu-ying LIU, Er-qing WEI, Zhong CHEN[2]

Department of Pharmacology, School of Medicine, Zhejiang University, Hangzhou 310031, China

Key words

histamine; maze; learning; MK-801; working memory; reference memory; ventral hippocampus; histamine H_1 receptor

[1] Project supported by the National Natural Science Foundation of China (No 30000019, 30371638, 30472013) and the Zhejiang Provincial Natural Science Foundation of China (No R303779).

[2] Correspondence to Prof Zhong CHEN.

Phn 86-571-8721-7446.
Fax 86-571-8721-7446.
E-mail chenzhong@zju.edu.cn

Received 2005-06-16
Accepted2005-08-22

doi: 10.1111/j.1745-7254.2005.00229.x

Abstract

Aim: To investigate the role of histamine in memory deficits induced by MK-801 infusion into the ventral hippocampus in rats. **Methods**: An 8-arm radial maze (4 arms baited) was used to assess spatial memory. **Results**: Bilateral ventral intrahippocampal (ih) infusion of MK-801 (0.3 μg/site), an N-methyl-D-aspartate (NMDA) antagonist, impaired the retrieval process in both working memory and reference memory. Intrahippocampal injection of histamine (25 or 50 ng/site) or intraperitoneal (ip) injection of histidine (25, 50 or 100 mg/kg) markedly ameliorated the spatial memory deficits induced by MK-801. Both the histamine H_1 antagonist pyrilamine (0.5 or 1.0 μg/site, ih) and the H_2 antagonist cimetidine (2.5 μg/site, ih) abolished the ameliorating effect of histidine (100 mg/kg, ip) on reference memory deficits, but not that on working memory deficits induced by MK-801. **Conclusion**: The results indicate that histamine in the ventral hippocampus can ameliorate MK-801-induced spatial memory deficits, and that histamine's effect on reference memory is mediated by postsynaptic histamine H_1 and H_2 receptors.

Introduction

Recently, the differentiation of functions along the longitudinal axis of the hippocampus (dorsal–ventral in the rat and posterior–anterior in humans) has attracted interest[1,2]. Anatomically, the hippocampus includes CA1, CA2, CA3, and dentate gyrus subfields, with the pattern of efferent and afferent connectivity changing between the dorsal and ventral hippocampus[3]. Identification of distinct functional roles for the dorsal and ventral hippocampus may help to resolve differences among the various theoretical accounts of hippocampal involvement in learning behavior[2].

Considerable evidence shows that the dorsal hippocampus plays an important role in spatial memory[4–6]. Ablation of the dorsal hippocampus, in which between 20% and 37% of the total hippocampal volume is removed, results in profound impairment of spatial location of a submerged platform in the Morris water maze[5]. Bannerman *et al* also found that performance in the water maze and elevated T maze was impaired by selective dorsal but not ventral hippocampal lesions[4]. On the other hand, ventral hippocampal lesions are considered to affect anxiety but not spatial learning[7,8]. However, Ferbinteanu *et al* demonstrated that the ventral hippocampus might also be involved in acquisition of spatial memory in Long–Evans rats[9]. So far, little is known about the functions performed by the ventral hippocampus in spatial memory.

Both histamine and its precursor histidine facilitate memory retrieval deficits induced by aging, dorsal hippocampal lesions and scopolamine, as determined by passive and active avoidance tasks and an 8-arm radial maze test for rats[10–12]. α-Fluoromethylhistidine (FMH), a selective histidine decarboxylase (HDC) inhibitor, produces significant memory deficits in an active avoidance task and the 8-arm radial maze in rats[13,14]. Furthermore, *N*-methyl-*D*-aspartate (NMDA) receptors play an important role in learning and memory[15,16]. Bekkers[15] and Vorobjev *et al*[17] found that histamine could dramatically enhance NMDA receptor-mediated synaptic transmission and facilitate the induction of long-term potentiation in cultured hippocampal pyramidal cells. Our previous studies indicate that histamine in the

dorsal hippocampus ameliorates spatial working memory and reference memory deficits induced by MK-801, and the action is mediated by postsynaptic histamine H_1 receptors[18,19]. However, whether histamine in the ventral hippocampus is involved in spatial memory deficits induced by MK-801 remains unclear.

Therefore, the objectives of this investigation were to use the radial maze task with 4-arms baited to further clarify the effects of the histaminergic system in the ventral hippocampus on the regulation of spatial memory in rats.

Materials and methods

Animals All experiments were carried out in accordance with the National Institutes of Health Guide for the Care and Use of Laboratory Animals. Male Sprague-Dawley rats (220–270 g, grade II, certificate No 22-9601018, Experimental Animal Center, Zhejiang University) were maintained in an air-conditioned room at 22–26 ºC and 40%–70% humidity, and housed in individual cages with a 12-h light–dark cycle (lights on from 8:00 AM to 20:00 PM). Animals were given free access to water and kept at 80%–85% of their free-feeding body weight throughout the experiments. Experiments were carried out between 10:00 AM and 17:00 PM.

Surgical procedures The rats were anesthetized with sodium pentobarbital (35 mg/kg, ip), and fixed in a stereotaxic apparatus (Narishige, SR-5, Tokyo, Japan). Two guide cannulas made of stainless steel tubing (700 μm in outer diameter), were implanted bilaterally into the ventral hippocampus according to the following coordinates measured from the bregma: antero-posterior: -4.52 mm; medio-lateral: ±5.0 mm; dorso-ventral: 8.0 mm from the skull surface. The cannula was fixed to the skull with three screws and dental acrylic. A stylet was inserted into the cannula to keep it patent prior to injections. At least 10 d were allowed for recovery from the surgery. After the behavioral tests, Evans blue (1 μL) was injected bilaterally into the ventral hippocampus and the rats were killed by decapitation. The accuracy of the injection site was carefully determined (Figure 1). Based on histological examination, data from nine rats with incorrect injections were excluded from the results.

Intracerebral microinfusion Rats were manually restrained and the stylets were carefully removed from the guide tubes. Infusion cannulae, connected via flexible polyetheretherketone tubing to 5 μL Hamilton microsyringes mounted on a microinfusion pump (KN-201, Natsume, Tokyo, Japan), were then inserted into the guide tubes. Drugs in 1 μL vehicle (0.9% saline) or 1 μL vehicle per side were infused into the ventral hippocampus at a rate of 1 μL/min. To allow absorption of the infusion bolus, infusion cannulae were left in the brain for 60 s after infusion before being replaced by the stylets.

Radial-arm maze training The apparatus used is described in our previous reports[18,19]. The rats were familiarized with the radial maze once per day for 2 d prior to training. Food pellets (45 mg each, Bio-Serv, Frenchtown, NJ, USA) were scattered over the entire maze surface, and three or four rats were simultaneously placed in the maze and allowed to explore and take food freely for 10 min. After adaptation, all rats were trained with one trial per day. In each trial, only 4 arms (3, 5, 6, and 8) were baited, and the sequence was never changed throughout the experiment. The rat was placed on the center platform that was closed off by a door. After 15 s, the door was opened and the rat was allowed to make an arm choice to obtain food pellets until all 4 pellets had been eaten

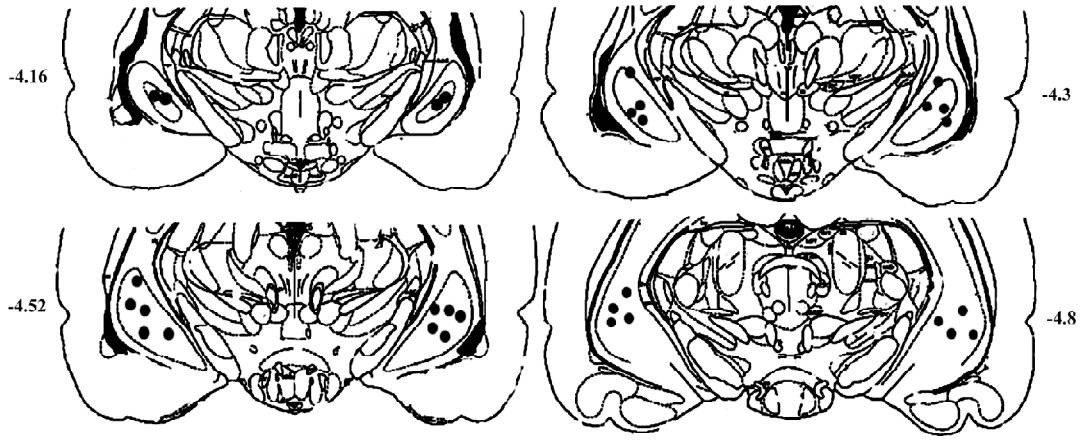

Figure 1. Schematic of the locations of the tips of injection cannulae in rats (closed circles). The numbers beside each brain section show the antero-posterior distance (mm) from bregma.

or 5 min had elapsed. The number of entries into never-baited arms was regarded as reference memory error (RME), whereas re-entry into arms where the pellet had already been eaten was considered as working memory error (WME). Rats continued training until reaching a criterion of less than 1 error per trial for 5 consecutive trials. Once a rat reached criterion, training for that rat was reduced to 2 trials per week until all rats reached criterion (range 35–50 d). After each trial, the maze was wiped clean using paper towels that were dampened with 10% ethanol and rotated 180º.

Drugs During the drug test, (+) MK-801 hydrogen maleate (Sigma, St Louis, MO, USA), histamine dihydrochloride (Sigma), cimetidine dimaleate (Sigma), or pyrilamine dihydrochloride (Sigma) were dissolved in saline and injected bilaterally into the ventral hippocampus. Histidine monohydrochloride (Sigma) was dissolved in saline and injected ip. Studies for drug effects were carried out once a week, on Tuesday or Friday.

Statistics All results are expressed as mean±SEM. Statistical significance was assessed by one-factor analyses of variance (ANOVA) or the Kruskal-Wallis non-parametric ANOVA test (when the data were not normally distributed or the variances of the groups differed significantly), followed by Dunnett's test or the Mann-Whitney *U* test as a *post hoc* analysis. The software SPSS 11.5 (SPSS, Chicago, IL, USA) was used. $P<0.05$ was considered statistically significant.

Results

Effect of MK-801 on memory retrieval as evaluated by 4-arm baited radial maze performance Non-parametric ANOVA (Kruskal-Wallis) showed that bilateral ih injection of MK-801 caused a significant impairment of working memory and reference memory {WME: $H[3]=13.873$, $P=0.003$; RME: $H[3]=25.161$, $P<0.01$}. MK-801 at a dose of 0.1 μg/site slightly increased the memory error, but this was not significant (Mann-Whitney *U* test; WME: $P=0.335$; RME: $P=0.145$). At a dose of 0.3 μg/site it significantly increased the number of both WME and RME (Mann-Whitney *U* test; $P<0.01$; Figure 2). However, at a dose of 0.5 μg/site MK-801 did not significantly impair spatial working or reference memory (Mann–Whitney *U* test; WME: $P=0.338$; RME: $P=0.061$).

Effects of histamine and histidine on MK-801-induced memory deficits Intrahippocampal injection of histamine antagonized the effects of MK-801 {WME: $H[3]=8.846$, $P=0.031$; RME: $H[3]=8.004$, $P=0.044$}. At doses of 25 or 50 ng/site it significantly decreased the number of RME (Mann–Whitney *U* test; $P<0.05$; Figure 3), whereas histamine at a dose of 50 ng/site significantly decreased the number of WME(Mann-Whitney *U* test; $P<0.05$; Figure 3). Intraperitoneal injection of histidine produced an effect similar to histamine (WME: $H[3]=11.314$, $P=0.010$; RME: $H[3]=20.415$, $P<0.01$). At doses of 25, 50 or 100 mg/kg, histidine significantly inhibited MK-801-induced spatial reference memory

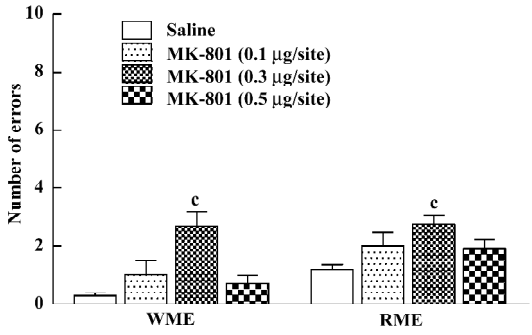

Figure 2. Effect of bilateral intrahippocampal injection of MK-801 on spatial memory of rats in the 8-arm radial maze. MK-801 was injected 10 min before the maze test. Each value represents the mean±SEM from 15–18 rats. $^{c}P<0.01$ *vs* Saline-treated group. WME: working memory errors; RME: reference memory errors.

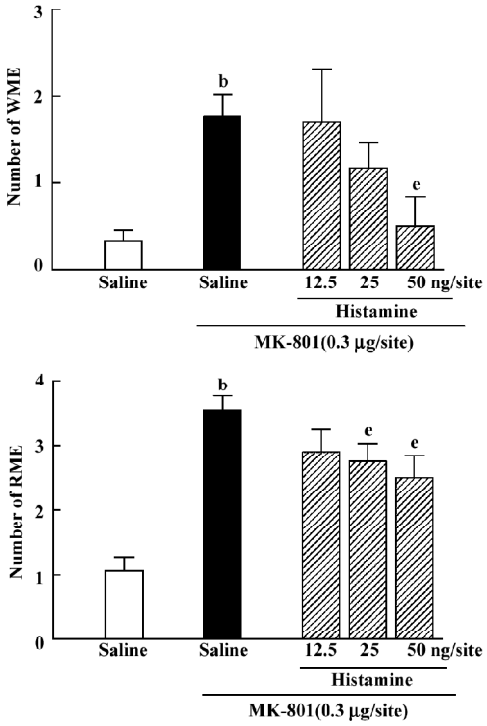

Figure 3. Effects of histamine on memory deficits induced in 8-arm radial maze performance by MK-801 injected into ventral hippocampus. MK-801 was injected ih 10 min before the maze test. Histamine was injected ih 15 min before the test. Each value represents the mean±SEM from 15–18 rats. $^{b}P<0.05$ *vs* Saline-treated group. $^{e}P<0.05$ *vs* MK-801+Saline-treated group. WME: working memory errors; RME: reference memory errors.

deficits (Mann-Whitney *U* test; $P<0.01$; Figure 4). It significantly reversed the spatial working memory deficit induced by MK-801 only at the dose of 100 mg/kg (Mann-Whitney *U* test; $P<0.01$; Figure 4).

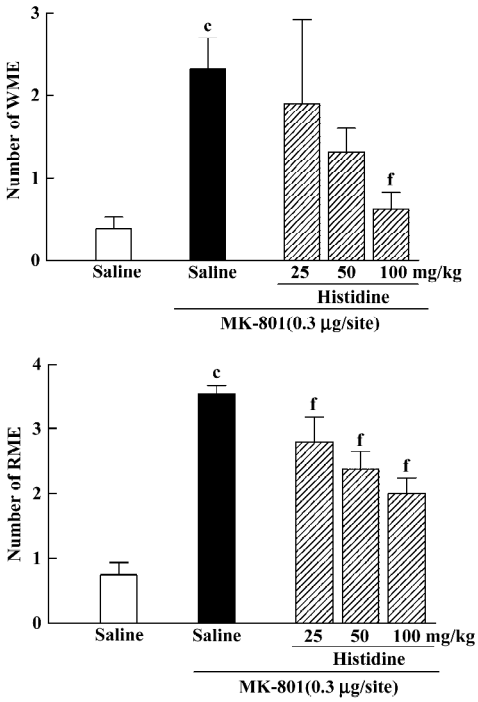

Figure 4. Effects of histidine on memory deficits in 8-arm radial maze performance induced by MK-801 injected into ventral hippocampus. MK-801 was injected ih 10 min before the maze test. Histidine was injected ip 1 h before the test. Each value represents the mean±SEM from 15–18 rats. $^{e}P<0.01$ *vs* Saline-treated group. $^{f}P<0.01$ *vs* MK-801+Saline-treated group. WME: working memory errors; RME: reference memory errors.

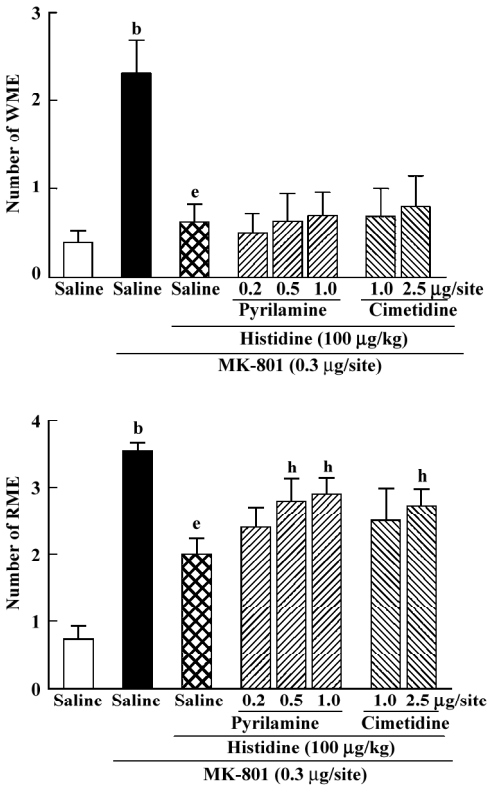

Figure 5. Effects of bilateral intrahippocampal (ih) injection of pyrilamine and cimetidine on the amelioration by histidine (100 mg/kg, ip) of MK-801-induced memory deficits in rats. MK-801 was injected ih 10 min before the maze test. Pyrilamine and cimetidine were injected ih 5 min before MK-801 treatment. Histidine was injected ip 50 min before MK-801 treatment. Each value represents the mean±SEM from 15–18 rats. $^{b}P<0.05$ *vs* Saline-treated group. $^{e}P<0.05$ *vs* MK-801+Saline-treated group. $^{h}P<0.05$ *vs* MK-801+Histidine+Saline-treated group. WME: working memory errors; RME: reference memory errors.

Effects of pyrilamine and cimetidine on memory amelioration of histidine on MK-801-induced memory deficits

Intrahippocampal injection of pyrilamine, a representative central histamine H_1 antagonist, significantly antagonized the ameliorating action of histidine on RME ($H[3]=7.811$, $P=0.04$) at doses of 0.5 and 1.0 μg/site (Mann-Whitney *U* test; $P<0.05$; Figure 5), but not on WME. In addition, cimetidine, a histamine H_2 antagonist, at the high dose of 2.5 μg/site, also significantly antagonized the ameliorating action of histidine on RME (Mann-Whitney *U* test; $P<0.05$; Figure 5), but not on WME (Mann-Whitney *U* test; $P=0.974$).

Discussion

Previously, we observed that bilateral injection of MK-801, an NMDA receptor antagonist, into the dorsal hippocampus impaired both working and reference memory[18]. Our present results are consistent with previous studies as assessed by performance in the 8-arm (4-arm baited) radial maze. We found that blockade of NMDA receptors in the ventral hippocampus impaired the retrieval of spatial working and reference memory, which suggested that the ventral hippocampus might be involved in the spatial memory process in rats[9,20], although a chemical lesion study demonstrated that the ventral hippocampus was less involved in spatial memory modulation[5,7]. The different findings may arise from the different experimental procedures (eg using the Morris water maze, the T-maze, and the 8-arm maze). In addition, the lesion method is less specific than local delivery of compounds.

Intrahippocampal application of MK-801 (0.3 μg/site) did not lead to obvious changes in running time per choice (locomotor activity) or other behaviors, such as ataxia (data not shown), which usually occurs after systemic or intracerebroventricular (icv) treatment with MK-801[16]. However, we found that MK-801 at a dose of 0.5 μg/site did not impair spatial memory. A few rats exhibited epileptic symptoms or even died when given a dose of 0.5 μg/site, phenomena resembling those following systemic or icv treatment with MK-801[16]. Therefore, we used MK-801 (0.3 μg/site) to induce the spatial memory deficits in the following experiments.

Both histamine and histidine ameliorated the memory retrieval deficits induced by MK-801, including working memory and reference memory. Intraperitoneal injection of histidine significantly increased histamine levels in the cortex and hippocampus (data not shown). This was consistent with previous studies showing that ip or icv injection of histidine increased hippocampal histamine levels[11,12]. Our results were consistent with previous findings in which MK-801 was delivered to the dorsal hippocampus[18]. In addition, Chen *et al* reported that histidine at higher doses of 200, 500, and 1 000 mg/kg improved the impairment of radial maze performance induced by MK-801 (0.1 mg/kg)[14]. Our results indicate that histidine at lower doses (25, 50 and 100 mg/kg) can ameliorate the impairment induced by MK-801. The difference can be attributed to the different injection routes, different species, and different learning models. But these present results at least suggest that ventral hippocampal histamine may participate in the amelioration of both short-term and long-term spatial memory deficits.

In the present study, the amelioration of reference memory elicited by histidine was completely reversed by pyrilamine, a central histamine H_1 antagonist. However, this result is different from those for the dorsal hippocampus in that pyrilamine infused into the ventral hippocampus produced no appreciable inhibition of the amelioration of working memory by histamine. This result suggests that the ameliorating effect of histidine on the working memory deficit induced by MK-801 is independent of histamine. Histamine can act directly on the NMDA receptor, as suggested by Bekkers[15] and Vorobjev *et al*[17]. Because the polyamine site of the NMDA receptor may be a binding site for histamine[21], the facilitating effect of histidine on MK-801-induced working memory deficit may be attributed to histamine acting directly on this site. So far, we have no explanation of why histamine H_1 receptors in the dorsal and ventral hippocampus have different actions. We previously reported that the improvement of both working and reference memory induced by dorsal hippocampal histamine were antagonized by pyrilamine[18]. Our present data, at least in part, suggest that the histamine H_1 receptors in the dorsal and ventral hippocampus participate in different components of memory. Histamine H_1 receptors in the dorsal hippocampus are involved in both working and reference memory, but those in the ventral hippocampus are mainly related to reference memory.

Moreover, we were surprised to find that cimetidine, a histamine H_2 antagonist, also blocked histamine-induced amelioration of reference memory. So far, most reports show that histamine H_2 receptors are less involved in the learning and memory process[18,19,21,22]. For example, the ameliorating effect of histamine on scopolamine-induced learning deficit is antagonized by pyrilamine but not by the selective histamine H_2 antagonists cimetidine and zolantidine[10,11]. Intracerebroventricular injection of the histamine H_1 agonist, 2-thiazolylethylamine, but not the histamine H_2 agonist, 4-methylhistamine, reverses the working memory deficits induced by MK-801 as evaluated by the 8-arm baited radial maze in rats[14]. However, Flood *et al* have recently reported that increased histamine H_1 and H_2 receptor activity in the septum facilitated memory retention, whereas decreased histamine receptor activity resulted in impaired memory processes as evaluated by T-maze behavior[23]. Giovannini *et al* also provided evidence that bilateral post-training injection of the histamine H_2 agonist amthamine into the dorsal hippocampus improved memory consolidation[24]. These findings combined with our present data suggest that the histamine H_2 receptor in certain brain regions may be involved in learning behavior. Further experiments are needed to elucidate the function of the histamine H_2 receptor.

In conclusion, histamine in the ventral hippocampus is involved in spatial memory, and histamine ameliorates the memory deficits of both working memory and reference memory induced by MK-801. The ameliorating action on reference memory is mediated by postsynaptic histamine H_1 and H_2 receptors, whereas the effect of histamine on working memory may be mediated by other neuronal pathways.

Acknowledgement

We are very grateful to Dr Iain C BRUCE (University of Hong Kong) for reading the manuscript.

References

1 Nadel L. Dorsal and ventral hippocampal lesions and behavior. Physiol Behav 1968; 3: 891–900.

2 Petrovich GD, Canteras NS, Swanson LW. Combinatorial amygdalar inputs to hippocampal domains and hypothalamic behavior systems. Brain Res Brain Res Rev 2001; 38: 247–89.

3 Andersen P, Bliss TV, Skrede KK. Lamellar organization of hippocampal pathways. Exp Brain Res 1971; 13: 222–38.
4 Bannerman DM, Yee BK, Good MA, Heupel MJ, Iversen SD, Rawlins JN. Double dissociation of function within the hippocampus: a comparison of dorsal, ventral, and complete hippocampal cytotoxic lesions. Behav Neurosci 1999; 113: 1170–88.
5 Moser E, Moser MB, Andersen P. Spatial learning impairment parallels the magnitude of dorsal hippocampal lesions, but is hardly present following ventral lesions. J Neurosci 1993; 13: 3916–25.
6 Moser MB, Moser EI. Distributed encoding and retrieval of spatial memory in the hippocampus. J Neurosci 1998; 18: 7535–42.
7 Bannerman DM, Grubb M, Deacon RM, Yee BK, Feldon J, Rawlins JN. Ventral hippocampal lesions affect anxiety but not spatial learning. Behav Brain Res 2003; 139: 197–213.
8 Kjelstrup KG, Tuvnes FA, Steffenach HA, Murison R, Moser EI, Moser MB. Reduced fear expression after lesions of the ventral hippocampus. Proc Natl Acad Sci USA 2002; 99: 10825–30.
9 Ferbinteanu J, Ray C, McDonald RJ. Both dorsal and ventral hippocampus contribute to spatial learning in Long-Evans rats. Neurosci Lett 2003; 345: 131–5.
10 Chen Z. Effect of histamine H_3-receptor antagonist clobenpropit on spatial memory of radial maze performance in rats. Acta Pharmacol Sin 2000; 21: 905–10.
11 Chen Z, Kamei C. Facilitating effects of histamine on spatial memory deficit induced by scopolamine in rats. Acta Pharmacol Sin 2000; 21: 814–8.
12 Kamei C, Chen Z, Nakamura S, Sugimoto Y. Effects of intracerebroventricular injection of histamine on memory deficits induced by hippocampal lesions in rats. Methods Find Exp Clin Pharmacol 1997; 19: 253–9.
13 Chen Z, Sugimoto Y, Kamei C. Effects of intracerebroventricular injection of α–fluoromethylhistidine on radial maze performance in rats. Pharmacol Biochem Behav 1999; 64: 513–8.
14 Chen Z, Zhao Q, Sugimoto Y, Fujii Y, Kamei C. Effects of histamine on MK-801-induced memory deficits in radial maze performance in rats. Brain Res 1999; 839: 186–9.
15 Bekkers JM. Enhancement by histamine of NMDA-mediated synaptic transmission in the hippocampus. Science 1993; 261: 104–6.
16 Pitkanen M, Sirvio J, MacDonald E, Niemi S, Ekonsalo T, Riekkinen P Sr. The effects of *D*-cycloserine and MK-801 on the performance of rats in two spatial learning and memory tasks. Eur Neuropharmacol 1995; 5: 457–63.
17 Vorobjev VS, Sharonova IN, Walsh IB, Haas HL. Histamine potentiates *N*-methyl-*D*-aspartate responses in acutely isolated hippocampal neurons. Neuron 1993; 11: 837–44.
18 Huang YW, Chen Z, Hu WW, Zhang LS, Wu W, Ying LY, *et al*. Facilitating effect of histamine on spatial memory deficits induced by dizocilpine as evaluated by 8-arm radial maze in SD rats. Acta Pharmacol Sin 2003; 24: 1270–6.
19 Huang YW, Hu WW, Chen Z, Zhang LS, Shen HQ, Timmerman H, *et al*. Effect of the histamine H3-antagonist clobenpropit on spatial memory deficits induced by MK-801 as evaluated by radial maze in Sprague-Dawley rats. Behav Brain Res 2004; 151: 287–93.
20 Poucet B, Herrmann T, Buhot MC. Effects of short-lasting inactivations of the ventral hippocampus and medial septum on long-term and short-term acquisition of spatial information in rats. Behav Brain Res 1991; 44: 53–65.
21 Passani MB, Bacciottini LB, Mannaioni PF, Blandina P. Central histaminergic system and cognition. Neurosci Biobehav Rev 2000; 24: 107–13.
22 Kamei C, Chung YH, Tasaka K. Influence of certain H_1-blockers on the step-through active avoidance response in rats. Psychopharmacology (Berlin) 1990; 102: 312–8.
23 Flood JF, Uezu K, Morley JE. Effect of histamine H_2 and H_3 receptor modulation in the septum on post-training memory processing. Psychopharmacology (Berlin) 1998; 140: 279–84.
24 Giovannini MG, Efoudebe M, Passani MB, Baldi E, Bucherelli C, Giachi F, *et al*. Improvement in fear memory by histamine-elicited ERK2 activation in hippocampal CA3 cells. J Neurosci 2003; 23: 9016–23.

Acta Pharmacologica Sinica 2005 Dec; 26 (12): 1454–1459

Blackwell Publishing

Full-length article

Neuroprotective effects of scutellarin on rat neuronal damage induced by cerebral ischemia/reperfusion

Xia-min HU[1,3], Mi-mei ZHOU[1], Xian-min HU[1], Fan-dian ZENG[2]

[1]*Department of Pharmacology, Medical College of Wuhan University of Science and Technology, Wuhan 430080, China;* [2]*Institute of Clinical Pharmacology, Tongji Medical College of Huazhong University of Science and Technology, Wuhan 430080, China*

Key words

scutellarin; brain ischemia; nitric-oxide synthase; vascular endothelial growth factor; basic fibroblast growth factor

[3] Correspondence to Dr Xia-min HU.
Phn 86-27-8363-0652.
E-mail fdzeng@mails.tjmu.edu.cn

Received 2005-07-14
Accepted 2005-09-08

doi: 10.1111/j.1745-7254.2005.00239.x

Abstract

Aim: To investigate the neuroprotective effect and mechanisms of scutellarin, a flavonoid extracted from *Erigeron breviscapus* Hand Mazz, against neuronal damage following cerebral ischemia/reperfusion. **Methods:** Rats were pretreated ig with scutellarin for 7 d and then subjected to cerebral ischemia/reperfusion (I/R) injury induced by a middle cerebral artery occlusion (MCAO). The infarct volume and neurological deficit were determined by TTC staining and Longa's score. The permeability of the blood-brain barrier was evaluated by measurement of the Evans blue (EB) content in the brain with a spectrophotometer. The total NOx content was determined. Nitric oxide synthase (NOS) isoforms (iNOS, eNOS, nNOS) and the key angiogenic molecules, vascular endothelial growth factor (VEGF) and basic fibroblast growth factor (bFGF), were detected by Western blotting. **Results:** Scutellarin significantly reduced infarct volume ($P<0.05$ or $P<0.01$), ameliorated the neurological deficit and reduced the permeability of the blood-brain barrier (BBB) ($P<0.05$). When rats were pretreated with scutellarin (50 or 75 mg/kg), upregulation of eNOS expression and downregulation of VEGF, bFGF, and iNOS expression was observed, whereas scutellarin had no effect on nNOS expression. **Conclusion:** Scutellarin has protective effects for cerebral injury through regulating the expression of NOS isoforms and angiogenic molecules.

Introduction

Cerebral ischemia is accompanied by a marked inflammatory process, which is initiated by higher levels of expression of cytokines, adhesion molecules, and other inflammatory mediators, including nitric oxide[1,2]. Recent studies have demonstrated that nitric oxide (NO) and pro-inflammatory cytokines released by microglial cells, which act as resident macrophage-like cells in the brain, are partly responsible for neuronal cell death. NO levels are associated directly with the development of brain injury in strokes and other neuropathological disorders in humans[3,4].

Following acute ischemic or hypoxic injury to the brain, over-entry of Ca^{2+} into cells causes the activation of nitric oxide synthase (NOS), which catalyzes an enzymatic reaction, leading to the synthesis of nitric oxide[5–7]. Three kinds of distinct NOS isoforms have been identified, including neuronal nNOS, endothelial eNOS, and an inducible isoform, iNOS, originally isolated from macrophages. nNOS and eNOS are constitutively expressed and calcium-dependent, whereas iNOS is expressed in response to various inflammatory stimuli, and its activity is independent of intracellular calcium concentrations. NO can be neuroprotective or neurotoxic during cerebral ischemia, depending on the NOS isoform involved. eNOS produces NO with beneficial effects (vasodilation, inhibition of platelet aggregation and polymorphonuclear neutrophil adhesion)[7–9], whereas NO overproduction by nNOS or iNOS during ischemia is cytotoxic. Based on these findings, it thought that the NO-synthases could be attractive targets for treating cerebral ischemia-induced neuronal damage[10,11].

Scutellarin, a flavonoid, is the major active ingredient extracted from *Erigeron breviscapus* Hand Mazz, a plant used in Chinese herbal medicine, which is a Ca^{2+}-channel-block-

ing agent used for the clinical treatment of cerebrovascular disorders. Studies have demonstrated the protective effects of scutellarin on brain injury induced by cerebral ischemia/reperfusion (I/R) through interaction with a wide variety of targets because of its anti-oxidative and anti-inflammatory actions, and its ability to attenuate neuronal damage[12,13]. It is presumed that these effects might be related to the effects of scutellarin on the NO synthases. Therefore, the objective of the present study was to elucidate the effects of scutellarin on the expression of the NOS isoforms (iNOS, eNOS, nNOS) in a model of cerebral I/R in rats. Moreover, the key angiogenic molecules, vascular endothelial growth factor (VEGF) and basic fibroblast growth factor (bFGF), were also studied.

Materials and methods

Chemicals and drugs Scutellarin was supplied by Yuxi Pharmaceuticals (Kunming, China). The purity of this compound was more than 96% and it was dissolved in saline before use. 2, 3,5-Triphenyltetrazolium chloride (TTC, No 20010201) was obtained from the Shanghai Chemical Agent Company. All other chemicals and solvents were of analytical grade.

Animal treatment and administration Male Sprague-Dawley rats (Grade II, Certificate No 19-050), weighing 230–280 g, were obtained from the Experimental Animal Center of Tongji Medical College. Rats were housed at a constant temperature of 22 ºC under a 12 h light-dark cycle with free access to food and drinking water. Rats were divided into 5 groups. The sham-operated and vehicle-treated I/R groups were pretreated with 0.5 mL/kg ig saline for 7 d before ischemia, and the scutellarin-treated I/R groups were pretreated with 25, 50, 75 mg/kg ig scutellarin for 7 d before ischemia.

Cerebral I/R procedure Rats were anesthetized with chloral hydrate (300 mg/kg, ip). Brain I/R injury was induced by a middle cerebral artery occlusion (MCAO) as described previously[14]. Briefly, the right common carotid artery, external carotid artery (ECA) and internal carotid artery (ICA) were isolated via a ventral midline incision. A 50 mm length of monofilament nylon suture (ϕ 0.22–0.24 mm), with its tip rounded by heating near a flame, was introduced into the ECA lumen and advanced into the ICA for a distance of 18–20 mm in order to block the origin of the MCA. The body temperature of the rats was maintained at 36.5–37.5 ºC during the surgical procedure with an infra red heat lamp. Sham-operated animals were not exposed to I/R. After 2 h of ischemia, the nylon suture was withdrawn to establish reperfusion. After arousal from anesthesia, the rats were returned to the cages.

Behavioral testing and measurement of infarct area After 24 h reperfusion, the neurological deficit score of each rat was obtained according to Longa's method[14] by a single experimenter, who was blinded to the experimental treatment groups. The neurological findings were scored on a 5-point scale: no neurological deficit=0, failure to extend right paw fully =1, circling to right=2, falling to right=3, did not walk spontaneously and had depressed levels of consciousness=4. Then the rats were anesthetized with 10% chloral hydrate (350 mg/kg) ip and subsequently decapitated. The brains were removed for measurement of infarct volume by using the TTC staining method. Five thin sections were selected from the thick slices at 2 mm intervals (from the anterior 5 mm to the anterior 13 mm) to determine the infarct areas. The slices were immersed in 2% triphenyltetrazolium chloride in saline and incubated at 37 ºC for 20 min, and then fixed with 10% formaldehyde (Sigma) neutral buffer solution (pH 7.4). At that time, the infarct tissue was unstained, whereas the normal part was stained red. Using a computerized image analysis system (NIH Image, Version 1.61), the infarct areas on each slice were summed and multiplied by slice thickness to give the infarct volume, and then expressed as the percentage of infarction per ipsilateral hemisphere.

Evaluation of permeability of blood-brain barrier The integrity of the blood-brain barrier (BBB) was investigated using Evans blue (EB) dye extravasation, according to the method of Matsuo *et al*[15]. Briefly, after 6-h reperfusion, the rats were treated with EB dye (2% in saline, 3 mg/kg iv). After 45 min, the rats were anesthetized with 10% chloral hydrate (350 mg/kg ip) and then the rats' chests were subsequently opened. Physiological saline was perfused through the left ventricle until a colorless perfusion fluid was obtained from the right atrium. The cranial vault was opened, and the brain was removed, weighed (wet tissue) and placed in a 50% trichloroacetic acid solution. After homogenization and centrifugation, the supernatant (extracted dye) was diluted with ethanol (1:3) and its fluorescence was determined (excitation at 620 nm and emission at 680 nm) with a luminescence spectrometer (Hitachi, Tokyo, Japan). Calculations of the amount of EB dye in the tissue were based on a linear standard curve and were expressed per gram of tissue.

Determination of total NO_x content in brain tissue At the end of 2 h ischemia and 24 h reperfusion, the rats were decapitated and the ischemic hemispheres were removed for assay of the NO level in ischemic brain tissue. The levels of metabolic products (NO_2 and NO_3) *in vivo* were determined by using a chemiluminescent NO detector (Siever 280i) as described previously[16].

Western blot analysis Western blot analysis was performed after 24 h reperfusion. The rats' brains were removed and the ischemic hemispheres were used for assay of the protein ex-

pression of iNOS, eNOS, nNOS, VEGF and bFGF. The hippocampus and the cortex were quickly isolated and rinsed in sterilized water on ice, and then stored at -80 °C until use. Protein determination was performed according to the Lowry method. The obtained protein samples were subjected to 15% sodium dodecylsulfate-polyacrylamide gel electrophoresis, using 7.5%–15% polyacrylamide gel, and electrotransferred to polyvinylidene difluoride filter (PVDF) membranes. To reduce non-specific binding, the PVDF was blocked for 2 h at room temperature with 5% non-fat milk in phosphate-buffered saline (PBS). Then membranes were incubated overnight at 4 °C with the primary antibodies for iNOS (anti-rabbit iNOS mouse monoclonal antibody, 1:200 dilution, Santa Cruz), eNOS (anti-human eNOS rabbit polyclonal antibody, 1:200 dilution, Affinity Bioreagents), nNOS (anti-human nNOS rabbit polyclonal antibody, 1:200 dilution, Sanying Biotechnology), VEGF (antihuman VEGF rabbit polyclonal antibody, 1:200 dilution, Santa Cruz) or bFGF (anti-human bFGF rabbit polyclonal antibody, 1:500 dilution, Santa Cruz), respectively. After incubation with the antibodies, the membranes were washed with PBS-Tween-20 (PBS-T: 10 mmol/L phosphate buffer, pH 7.4, 150 mmol/L NaCl, 0.05% Tween 20) for 30 min and incubated in the relevant horseradish peroxidase-conjugated secondary antibody (1:600 dilution) for 30 min. The membranes were washed again with PBS-T and immunoreactive protein bands were visualized using the enhanced chemiluminescence detection system.

Statistical analysis Data are expressed as mean±SD and analyzed by using Microsoft Excel 2002. Statistical analyses were performed by using Student's *t*-test. $P<0.05$ was considered significant.

Results

Effects of scutellarin on the infarct area, neurological score and the permeability of the blood-brain barrier Scutellarin (50 or 75 mg/kg) significantly reduced the infarct area and ameliorated the neurological deficit ($P<0.05$ or $P<0.01$ *vs* vehicle-operated group) (Table 1). The EB content of brain tissue after I/R for sham-operated, vehicle-operated and scutellarin-operated groups (25, 50, or 75 mg/kg) was 3.83±1.03, 8.45±1.67, 7.45±1.77, 5.02±1.12, and 4.45±1.05, respectively (Figure 1). There was a significant increase in the permeability of the BBB in rats in the vehicle-treated group compared with the sham-treated group ($P<0.01$). Scutellarin (50 or 75 mg/kg) obviously inhibited the increased EB content induced by cerebral I/R, and there was no obvious difference between the 2 doses.

Effects of scutellarin on total NOx production After cerebral I/R, total NOx production, as determined by NOx content in the ischemic brain hemispheres, was markedly increased in the vehicle rats (4.87±0.90) compared with the sham-treated rats (1.83±0.34) ($P<0.01$, Figure 2). Total NOx production in rats pretreated with scutellarin at concentrations of 50 or 75 mg/kg (3.01±0.68, 2.31±0.48), were significantly reduced compared with the vehicle-operated group ($P<0.05$ or $P<0.01$, respectively) (Figure 2).

After 24 h reperfusion, the expression levels of iNOS, eNOS and nNOS were detected in the hippocampus and in the cortex, with molecular masses of 130, 140, 160 kDa, respectively. In the vehicle-treated group, the expression levels of the 3 NO synthases in the hippocampus and in the cortex markedly increased after cerebral I/R ($P<0.01$ or $P<0.05$, Figure 3A, 3B, lane 2). Densitometric analysis showed that the protein levels of eNOS and iNOS in the scutellarin-treated (50 or 75 mg/kg) rats were 368.0±70.3% and 278.0%±56.6% in the hippocampus (Figure 3A, lanes 3, 4), and 198.1%±19.2% and 148.3%±17.6% in the cortex

Table 1. Effects of scutellarin on the cerebral infarct area and neurological score after 2 h ischemia and 24-h reperfusion (I/R) in rats. n=6. Mean±SD. $^bP<0.05$, $^cP<0.01$ *vs* vehicle-operated group (I/R+NS).

Groups	Dose/ mg·kg^{-1}	Ratio of infarct area/%	Neurological scor (on a 5-point scale)
Sham	0	–	–
Vehicle	0	31.26±6.02	2.92±1.27
I/R+scutellarin			
	25	25.63±5.12	1.93±0.84
	50	18.23±3.63^b	1.32±0.65^b
	75	9.24±4.11^c	0.92±0.64^c

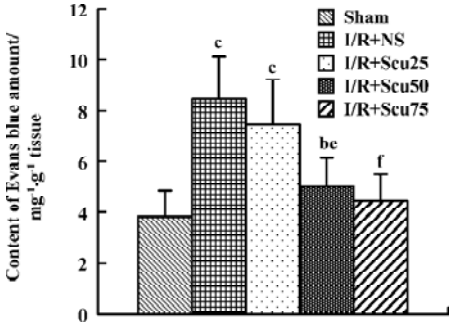

Figure 1. Effects of scutellarin on the blood-brain barrier after 2-h ischemia and 6-h reperfusion. See legend of Table 1 for rat treatments. Scu25, 50, and 75 correspond to 25, 50, and 75 mg/kg scutellarin, respectively. Mean±SD. n=6. $^bP<0.05$, $^cP<0.01$ *vs* sham. $^eP<0.05$, $^fP<0.01$ *vs* vehicle (I/R+NS).

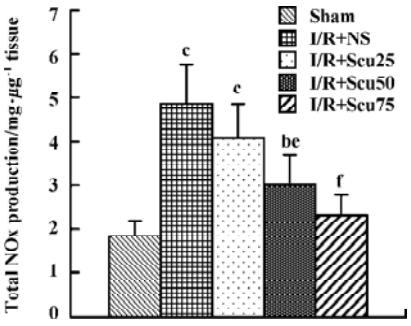

Figure 2. Effect of scutellarin on the total NOx production after 2 h ischemia and 24 h reperfusion. See legend of Table 1 for rat treatments. Scu25, 50, and 75 correspond to 25, 50, and 75 mg/kg scutellarin, respectively. n=6. Mean±SD. ^{b}P<0.05, ^{c}P<0.01 *vs* sham. ^{e}P<0.05, ^{f}P<0.01 *vs* vehicle (I/R+NS). Effects of scutellarin on expression of the 3 NOS isoforms (iNOS, eNOS, nNOS) and the angiogenic molecules (VEGF and bFGF).

(Figure 3B, lane 3, 4) for iNOS; and 469.0%±40.5% and 523.0%±67.3% in the hippocampus (Figure 3A, lanes 3, 4), and 188.3%±31.2% and 234.2%±37.8% in the cortex (Figure 3B, lanes 3, 4) for eNOS, respectively. The data indicate that scutellarin downregulated the expression of iNOS and simultaneously upregulated that of eNOS as compared with the vehicle-operated group (P<0.05 or P<0.01, respectively), whereas there was no difference in nNOS expression in the hippocampus or the cortex between the vehicle-treated and scutellarin-treated rats.

Immunoblot analysis showed single bands with molecular masses of approximately 39 and 18 kDa, which correspond to VEGF and bFGF in the hippocampus and in the cortex, respectively. The bands obtained from the vehicle-operated I/R rats (VEGF: 278.2%±43.4% in the hippocampus and 256.7%±36.8% in the cortex; bFGF: 432.2%±50.4% in the hippocampus and 289.4%±49.7% in the cortex) (Figure 3C, 3D, lane 2) were stronger than those from the sham group rats (VEGF: 111.9%±24.2% in the hippocampus and 123.9%± 16.1% in the cortex; bFGF: 98.8%±15.4% in the hippocampus and 98.8%±10.9% in the cortex) (Figure 3C, 3D, lane 1, P<0.01). Scutellarin at doses of 50 or 75 mg/kg (Figure 3C, 3D, lanes 3, 4) significantly decreased the expression of VEGF and bFGF in the hippocampus and in the cortex, as compared with the vehicle-operated group (P<0.05 or P<0.01). When rats were pretreated with scutellarin at a concentration of 50 or 100 mg/kg, the VEGF protein levels in the hippocampus were 189.8%±35.4% and 123.5%±30.1%, whereas in the cortex they were 178.2%±22.1% and 145.7%±11.9%, respectively; bFGF protein levels in the hippocampus were 212.9%±33.2% and 134.5%±19.1%, while in the cortex they were 212.9%±30.4% and 145.6%±17.6%, respectively.

Discussion

In the present study, we demonstrated that scutellarin (at doses of 50 or 75 mg/kg) significantly reduced infarct volume, ameliorated the neurological deficit and reduced the permeability of the BBB after cerebral I/R. Therefore, the conclusions obtained from the above observations were that scutellarin has protective effects for the neuronal damage induced by cerebral I/R in rats.

Evidence has accumulated that NO produced both before and after cerebral ischemia may be an important factor in the pathogenesis of neuronal ischemic injury. NO is a signaling molecule that regulates many biological processes in the brain. The present paper also investigated the effects of scutellarin on the total NOx content in rat brain tissues after cerebral I/R. Our results showed that total NOx production, as determined by NOx content, in the ischemic brain hemispheres was markedly increased in cerebral I/R rats, which indicates that NO regulates the severity of cerebral ischemic injury. However, NOx content markedly decreased in brain tissues after treatment with scutellarin at doses of 50 or 75 mg/kg.

Numerous studies have been conducted regarding the differential roles of NOS isoforms and their temporal NO production in the pathogenesis of ischemic brain injury[17–19]. eNOS-derived NO is thought to be beneficial for promoting collateral circulation and microvascular flow, whereas nNOS- and iNOS-derived NO is detrimental in the ischemic brain. NO is a nontoxic agent and acts as a second messenger in normal brain; however, in the presence of O_2^-, NO reacts with O_2^- to form $ONOO^-$ or nitrogen dioxide (NO_2^-), causing injury to the mitochondrial electron transport system, resulting in neuronal damage. In addition, excess NO stimulates ADP ribosyltransferase and binds closely to iron-sulfur centers of enzymes, including enzymes involved in the mitochondrial electron transport chain and the tricarboxylic acid cycle (TCA), and DNA[20–22]. In view of the detrimental and beneficial roles of NOS isoforms in ischemic brain injury, further investigations into the effect of scutellarin on the expression of NOS isoforms (iNOS, eNOS, nNOS) both in the hippocampus and in the cortex after cerebral I/R were also performed in the present study. We found that expression of the NO-synthases in the hippocampus and cortex all markedly increased after cerebral I/R in the vehicle-operated group, a similar finding to those of previously studies[22–26]. Scutellarin at doses of 50 and 75 mg/kg downregulated iNOS expression and upregulated eNOS expression, which partly account for its protective effect on brain damage induced by cerebral I/R.

Increasing evidence has shown that some angiogenic molecules, including VEGF and bFGF, increase in concentration after cerebral I/R. VEGF is an angiogenesis and vascu-

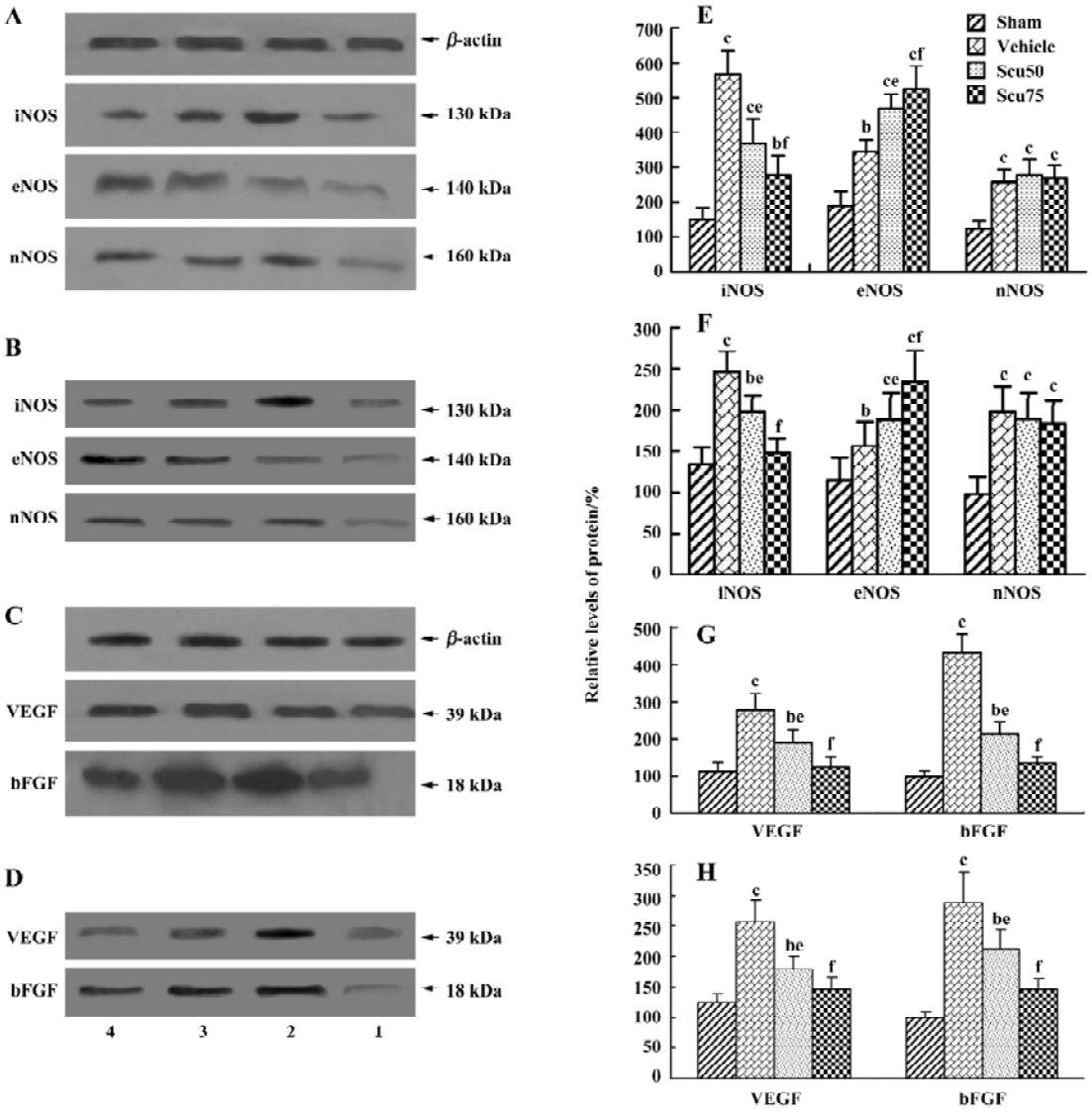

Figure 3. Western blot analysis of the effect of scutellarin on the expressions of NO synthase isoforms and angiogenic molecules both in the hippocampus and in the cortex after 2 h ischemia and 24 h reperfusion in rats. A, B: Protein expression of iNOS, eNOS and nNOS in the hippocampus (A) and in the cortex (B); C, D: protein expression of VEGF and bFGF in the hippocampus (C) and in the cortex (D). Upper panels: representative Western blot. Lane 1: sham; lane 2: vehicle; lane 3: 50 mg/kg scutellarin; lane 4: 75 mg/kg scutellarin; β-actin was used as an internal control. Lower panels (E, F, G, H): bar graph comparing the immunostained bands for each protein in the 4 groups (the relative abundance of the immunostaining) determined by the Image Quant program. E, F: Bar graphs for iNOS, eNOS and nNOS in the hippocampus (E) and in the cortex (F); G, H: bar graphs for VEGF and bFGF in hippocampus (G) and in the cortex (H). The levels of the 3 NOS isoforms and the angiogenic molecules are expressed as percentages of β-actin. n=6. Mean±SD. n=6. $^bP<0.05$, $^cP<0.01$ *vs* sham. $^eP<0.05$, $^fP<0.01$ *vs* vehicle (I/R+NS).

lar permeability factor that undergoes transcriptional and post-transcriptional induction by hypoxia; it couples hypoxia to angiogenesis in diverse tissues, including the brain[23–26]. VEGF may also play an important role in the vascular response to cerebral ischemia, because ischemia stimulates VEGF expression in the brain, which promotes the formation of new cerebral blood vessels[27,28]. It is thought that eNOS is involved in mediating the angiogenic molecules (VEGF and bFGF). Both factors induced eNOS expression, so eNOS may be a downstream messenger in their angiogenic action. In the present study we also investigated the expression of the angiogenic molecules VEGF and bFGF in the hippocampus and in the cortex. In agreement with the results of previous reports[29,30], our data showed that the expression of VEGF and bFGF in the hippocampus and cortex were upregulated in the vehicle-operated group after cerebral I/R. Scutellarin downregulated the expression of VEGF and bFGF. Further study is needed to shed light on the mechanisms involved in

the effect of scutellarin on the expression of eNOS (upregulation) and VEGF (downregulation) in I/R brain tissue.

In conclusion, scutellarin alleviated hippocampal neuronal dysfunction after cerebral I/R. This alleviation was accompanied by the effects of the molecular features of NOS isoforms and angiogenic molecules. These findings suggest that scutellarin exerts neuroprotective effects on brain injury induced by cerebral I/R, which allows a better understanding regarding the potential clinical therapeutic use of scutellarin.

References

1 Iadecola C, Alexander M. Cerebral ischemia and inflammation. Neurology 2001; 14: 89–94.

2 Osuka K, Watanabe Y, Usuda N, Nakazawa A, Tokuda M, Yoshida J. Modification of endothelial NO synthase through protein phosphorylation after forebrain cerebral I/R. Stroke 2004; 35: 2582–6.

3 Naka M, Nanbu T, Kobayashi K, Kamanaka Y, Komeno M, Yanase R, *et al*. A potent inhibitor of inducible nitric oxide synthase, ONO-1714, a cyclic amidine derivative. Biochem Biophys Res Commun 2000; 270: 663–7.

4 Veltkamp R, Rajapakse N, Robins G, Puskar M, Shimizu K, Busija D. Transient focal ischemia increases endothelial nitric oxide synthase in cerebral blood vessels. Stroke 2002; 33: 2704–10.

5 Yan XB, Meng FJ, Song B, Zhang GY. Brain ischemia induces serine phosphorylation of neuronal nitric oxide synthase by Ca (2+)/calmodulin-dependent protein kinase II in rat hippocampus. Acta Pharmacol Sin 2004; 25: 617–22.

6 Dimmeler S, Dernbach E, Zeiher AM. Phosphorylation of the endothelial nitric oxide synthase at Ser-1177 is required for VEGF-induced endothelial cell migration. FEBS Lett 2000; 477: 258–62.

7 Zollner S, Aberle S, Harvey SE, Polokoff MA, Rubanyi GM. Changes of endothelial nitric oxide synthase level and activity during endothelial cell proliferation. Endothelium 2000; 7: 169–84.

8 Li L, Shen YM, Yang XS,Wu WL, Wang BG, Chen ZH, *et al*. Effects of spiramine T on antioxidant enzymatic activities and nitric oxide production in cerebral ischemia-reperfusion gerbils. Brain Research 2002; 944: 205–9.

9 Sugimoto K, Iadecola C. Effects of aminoguanidine on cerebral ischemia in mice: comparison between mice with and without inducible nitric oxide synthase gene. Neurosci Lett 2002; 331: 25–8.

10 Gajkowska B, Viron A, Cholewinski M. Immunocytochemical localization of endothelial nitric oxide synthase (e-NOS) and inducible nitric oxide synthase (i-NOS) in rat neurohypophysis after transient cerebral ischemia. Folia Neuropathol 1999; 37: 10–9.

11 Santizo R, Baughman VL, Peligrino DA. Relative contributions from neuronal and endothelial nitric oxide synthases to regional cerebral blood flow changes during forebrain ischemia in rats. Neuroreport 2000; 11: 1549–53.

12 Liu H, Yang XL, Wang Y, Tang XQ, Jiang DY, Xu HB. Protective effects of scutellarin on superoxide-induced oxidative stress in rat cortical synaptosomes. Acta Pharmacol Sin 2003; 24: 1113–7.

13 Yang XF, He W, Lu WH, Zeng FD. Effects of scutellarin on liver function after brain I/R in rats. Acta Pharmacol Sin 2003; 24: 1118–24.

14 Zea Longa E, Weinstein PR, Carlson S, Cummins R. Reversible middle cerebral artery occlusion without craniotomy in rats. Stroke 1989; 20: 84–91.

15 Matsuo Y, Mihara Si, Ninomiya M, Fujimoto M. Protective effect of endothelial type A receptor antagonist on brain edema and injury after transient middle cerebral artery occlusion in rats. Stroke 2001; 32: 2143–8.

16 Gao F, Gao E, Yue TL. Nitric oxide mediates the antiapoptotic effect of insulin in myocardial ischemia-reperfusion: the roles of P13-kinase, Akt. and endothelial nitric oxide synthase phosphorylation. Circlulation 2002; 105: 1497–502.

17 Marti HJ, Bernaudin M, Bellail A, *et al*. Hypoxia-induced vascular endothelial growth factor expression precedes neovascularization after cerebral ischemia. Am J Pathol 2000; 15: 965–76.

18 Navarro-Antolin J, Rey-Campos J, Lamas S. Transcriptional induction of endothelial nitric oxide gene by cyclosporine A. A role for activator protein-1. J Biol Chem 2000; 275: 3075–80.

19 Shen BQ, Lee DY, Ziocheck TF. Vascular endothelial growth factor governs endothelial nitric oxide synthase via a KDR/FlK-1 receptor and a protein C kinase signaling pathway. J Biol Chem 1999; 274: 33057–63.

20 Arvidsson A, Collin T, Kirik D, Kokaia Z, Lindvall O. Neuronal replacement from endogenous precursors in the adult brain after stroke. Nat Med 2002; 8: 963–70.

21 Jin K, Sun Y, Xie L, Peel A, Mao XO, Batteur S, Yamamoto S, Hatano O, Kawahara, *et al*. Directed migration of neuronal precursors into the ischemic cerebral cortex and striatum. Mol Cell Neurosci 2003; 24: 171–89.

22 Nakatomi H, Kuriu T, Okabe S, *et al*. Regeneration of hippocampal pyramidal neurons after ischemic brain injury by recruitment of endogenous neural progenitors. Cell 2002; 110: 429–41.

23 Raber J, Fan Y, Matsumori Y, Liu Z, Weinstein PR, Fike JR, *et al*. Irradiation attenuates neurogenesis and exacerbates ischemia-induced deficits. Ann Neurol 2004; 55: 381–9.

24 Huang Z, Huang PL, Ma J, Meng W, Ayata C, Fishman MC,*et al*. Enlarged infarcts in endothelial nitric oxide synthase knockout mice are attenuated by nitro-*L*-arginine. J Cereb Blood Flow Metab 1996; 16: 9817.

25 Nagayama M, Aber T, Nagayama T, Ross ME, Iadecola C. Age-dependent increase in ischemic brain injury in wild-type mice and in mice lacking the inducible nitric oxide synthase gene. J Cereb Blood Flow Metab 1999; 19: 661–6.

26 Zhu DY, Liu SH, Sun HS, Lu YM. Expression of inducible nitric oxide synthase after focal cerebral ischemia stimulates neurogenesis in the adult rodent dentate gyrus. J Neurosci 2003; 23: 223–9.

27 Ogunshola OO, Stewart WB, Mihalcik V, Solli T, Madri JA, Ment LR. Neuronal VEGF expression correlates with angiogenesis in postnatal developing rat brain. Brain Res Dev Brain Res 2000; 119: 139–53.

28 Zhang ZG, Zhang L, Tsang W, Soltanian-Zadeh H, Morris D, Zhang R, *et al*. Correlation of VEGF and angiopoietin expression with disruption of blood-brain barrier and angiogenesis after focal cerebral ischemia. J Cereb Blood Flow Metab 2002; 22: 379–92.

29 Krum JM, Mani N, Rosenstein JM. Angiogenic and astroglial responses to vascular endothelial growth factor administration in adult rat brain. Neuroscience 2002; 110: 589–604.

30 Zhang ZG, Zhang L, Jiang Q, Zhang R, Davies K, Powers C, *et al*. VEGF enhances angiogenesis and promotes blood-brain barrier leakage in the ischemic brain. J Clin Invest 2000; 106: 829–38.

Acta Pharmacologica Sinica 2005 Dec; 26 (12): 1460–1466

Blackwell Publishing

Full-length article

C16, a novel advanced glycation endproduct breaker, restores cardiovascular dysfunction in experimental diabetic rats[1]

Gang CHENG[3], Li-li WANG[2,4], Wen-sheng QU[2], Long LONG[2], Hao CUI[2], Hong-ying LIU[2], Ying-lin CAO[3], Song LI[2]

[2]Beijing Institute of Pharmacology and Toxicology, Beijing 100850, China; [3]Shenyang Pharmaceutical University, Shenyang 110016, China

Key words

C16; advanced glycation endproduct; cardiovascular dysfunction; hemodynamics; diabetes; collagen

[1] Project supported by the National High Technology Research and Development Program of China (863 Program, No 2001AA35031).

[4] Correspondence to Prof Li-li WANG.
Phn 86-10-6687-4603.
Fax 86-10-6693-1250.
E-mail wangll63@yahoo.com.cn

Received 2005-07-19
Accepted 2005-09-08

doi: 10.1111/j.1745-7254.2005.00240.x

Abstract

Aim: Advanced glycation endproducts (AGE) have been implicated in the pathogenesis of diabetic complications, including diabetic cardiovascular dysfunction. 3-[2-(4-Bromo-phenyl)-1-methyl-2-oxo-ethyl]-4,5,6,7-tetrahydro-benzothiazol-3-ium bromide (C16), a novel AGE breaker, was investigated for its effects on the development of cardiovascular disease in diabetic rats. **Methods:** Rats that had streptozotocin-induced diabetes for 12 weeks were divided into groups receiving C16 or vehicle by gavage. **Results:** In hemodynamic studies of the left ventricle, C16 treatment (25 or 50 mg/kg) for 4 weeks resulted in a significant increase in left ventricular systolic pressure, $+dp/dt_{max}$, and $-dp/dt_{max}$ as compared with vehicle-treated diabetic rats. Furthermore, in hemodynamic studies of the cardiovascular system, C16 (12.5, 25, or 50 mg/kg) treatment for 4 weeks resulted in a dose-dependent and significant increase in cardiac output, a reduction of total peripheral resistance, and an increase in systemic arterial compliance when compared with vehicle-treated diabetic rats. Biochemical studies showed that C16 treatment also resulted in a significant decrease in immunoglobulin G-red blood cell surface crosslink content and an increase in collagen solubility. Morphological and immunohistochemical examinations indicated that C16 was able to prevent increases of the collagen type III/I ratio in the aorta and decrease the accumulation of AGE in the aorta. **Conclusion:** C16 has the ability to reduce AGE accumulation in tissues *in vivo*, and can restore diabetes-associated cardiovascular disorders in rats. This provides a potential therapeutic approach for cardiovascular disease associated with diabetes and aging in humans.

Introduction

Glucose and other reducing sugars react with proteins by a series of reactions to form a class of heterogeneous, nonenzymatic sugar-amino adducts that are called advanced glycation endproducts (AGE)[1,2]. Numerous studies have indicated that the formation of AGE in long-lived connective tissue and matrix components is a causative factor in the development of diabetic complications and diseases associated with aging[3–6]. In the cardiovascular system, the accumulation of AGE on structural tissue proteins is one of the main mechanisms underlying cardiovascular stiffness[7,8]. Recently, a number of natural or synthetic compounds that target AGE, including AGE inhibitors and breakers, have been discovered and are being further developed[9–11]. Aminoguanidine (AG) was the first compound designed to inhibit AGE formation and cross-linking *in vitro* and *in vivo*, and is currently undergoing phase III clinical trials[12,13]. ALT-711, a well-known AGE breaker, has also been reported to be effective in *in vitro* and animal studies, and is currently undergoing phase II clinical trials[14–19]. Therefore, treatment targeting AGE is believed to be a potential effective therapeutic option for cardiovascular dysfunction[10].

Based on the hypothesis that AGE crosslinks could be cleaved with N-phenacylthiazolium bromide[20], the lead compound ALT-711, novel AGE breakers were synthesized in

our laboratory by using computer-aided drug design. Preliminary biological screening tests demonstrated that 3-[2-(4-bromo-phenyl)-1-methyl-2-oxo-ethyl]-4,5,6,7-tetrahydro-benzothiazol-3-ium bromide (C16; Figure 1) had the ability to break AGE crosslinks *in vitro*[21]. C16 produced a concentration-dependent release of bovine serum albumin (BSA) from preformed AGE-modified BSA (AGE-BSA)-collagen complexes and C16 treatment decreased the red blood cell (RBC)-immunoglobulin G (IgG) crosslinks (unpublished data). Therefore, the aim of the present study was to investigate the effects of C16 on the cardiovascular system in experimental diabetic rats. Furthermore, the action site of C16 *in vivo* was explored by comparison with that of ALT-711.

Materials and methods

Reagents and compounds 3-[2-(4-Bromo-phenyl)-1-methyl-2-oxo-ethyl]-4,5,6,7-tetrahydro-benzothiazol-3-ium bromide (C16), whose structure (Figure 1) was identified by nuclear magnetic resonance spectroscopy-mass spectroscopy and elemental analysis, and ALT-711 were synthesized at the Beijing Institute of Pharmacology and Toxicology, as described previously[21]. Streptozotocin (STZ) was purchased from Sigma. AGE antibody was kindly donated by the Beijing Institute of Radiation Medicine. All other chemicals and substances were of analytical grade unless stated otherwise.

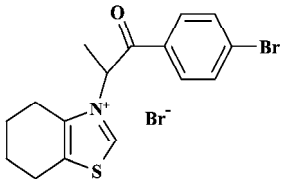

Figure 1. Chemical structure of 3-[2-(4-bromo-phenyl)-1-methyl-2-oxo-ethyl]-4,5,6,7-tetrahydro-benzothiazol-3-ium bromide.

Animals Diabetes was induced in 9-10-week-old male Wistar rats by ip injection of 70 mg/kg of STZ after an overnight fast. Only animals that developed blood glucose levels >15 mmol/L were used. After 12 weeks of diabetes, the animals were used for studies. For the hemodynamic study of the left ventricle, diabetic rats were divided into 4 groups (8 rats in each group) to assess the exact hemodynamic changes in the left ventricle (LV) that were caused by the diabetic state. Rats were given either vehicle or 25 mg/kg per day of ALT-711, or 25 or 50 mg/kg per day of C16 (ig) for 4 weeks. In another hemodynamic study, 6 groups of diabetic rats (n=8) received either vehicle or 12.5 mg/kg per day of ALT-711, or 12.5, 25 or 50 mg/kg per day of C16 (ig) for 4 weeks, or 50 mg/kg per day of C16 (ig) for 2 weeks to assess the possible reversal of diabetes-induced cardiovascular abnormalities. ALT-711 and C16 were dissolved in distilled water immediately before administration. An additional group of age-matched nondiabetic rats served as normal controls, and were observed in parallel for each study.

Hemodynamic study of the left ventricle Details regarding the surgical procedure and hemodynamic measurements have been described elsewhere[22]. In summary, animals were anesthetized with 50 mg/kg of pentobarbital (ip). A fluid-filled catheter was introduced through the right carotid artery into the left ventricle. Tracings of LV pressure were digitized at a rate of 2000 samples/s with a commercially available analog-to-digital converter (MP150WS, BIOPAC Systems) and a personal computer using dedicated software (Acknowledge, Version 3, BIOPAC Systems). The digitized LV pressure recording was used to calculate the maximal rate of pressure rise ($+dp/dt_{max}$) and the maximal rate of pressure fall ($-dp/dt_{max}$).

Hemodynamic study of cardiovascular system After animals were anesthetized with 50 mg/kg of pentobarbital (ip), a midsternal thoracotomy was performed, and the ascending aorta was dissected free. The pressure transducer was advanced into the ascending aorta. An adapted Doppler probe was positioned around the vessel to measure phasic aortic blood flow. The system was allowed to stabilize for 10 min before aortic blood flow and pressure were digitized at a rate of 2000 samples/s with a commercially available analog-to-digital converter and a personal computer using dedicated software. All parameters were calculated on a beat-to-beat basis for 30 s and then averaged. In steady-state conditions, measurements were obtained of systolic and diastolic blood pressure (SBP, DBP), cardiac output (CO), and heart rate (HR). Total peripheral resistance (TPR) was determined as the quotient of mean arterial blood pressure and CO[23]. Systemic arterial compliance (SAC) was calculated from the quotient of stroke volume and pulse pressure[24].

RBC-IgG assay Detailed methods have been described elsewhere[14]. Briefly, blood samples were collected, before hemodynamic studies of the left ventricle and RBC-IgG determinations were performed by using an anti-IgG enzyme-linked immunosorbent assay (ELISA) adapted for use with cellulose ester membrane-sealed 96-well microtiter plates (Multiscreen-HA, Millipore). Heparinized blood was washed 3 times with phosphate-buffered saline (PBS), then the packed RBC were diluted 1:250–1:500 in PBS. Membrane-containing wells were blocked with 0.3 mL Superblock (Pierce), then washed with 0.3 mL PBS/0.05% Tween, followed by 0.1 mL

PBS. RBC were gently vortexed and 50 μL aliquots were pipetted into wells. Cells were then washed, and 50 μL of a polyclonal rabbit anti-rat IgG (Sigma, diluted 1:25 000) was added. After incubation at room temperature for 2 h, the cells were washed 3 times with PBS, once with Tris-buffered saline, and 0.1 mL of p-nitrophenyl phosphate substrate was added (1 mg/mL in 0.1 mol/L diethanolamine buffer, pH 9.5). The plates were read in a microplate reader (Bio-Rad 550) at 410 nm. The content of RBC-IgG was expressed as OD_{410}.

Tail tendon collagen solubility assay The solubility of tail tendon collagen was measured by using a previously reported method with modifications[25]. Briefly, after performing a hemodynamic study on the left ventricle, the rats' tails were removed and the tail tendon was removed by gentle pulling. The tendons were cleaned of debris and fat in 0.9% NaCl over ice. The tendons were rolled into a ball, patted dry on paper towels, then lyophilized. Following lyophilization, tail tendons were stored at -70 ºC in desiccated sealed containers until use. Collagen samples (2 mg) were weighed and digested with pepsin (5.0 μg pepsin/mg collagen in 0.5 mol/L acetic acid) for 2 h at 4 °C. After digestion, the samples were centrifuged at 40 000×*g* for 60 min at 4 ºC. The supernatant was collected and both the volume of the supernatant and pellet were determined. Aliquots (500 μL) of the supernatant and all of the pellets were acid hydrolyzed and analyzed for their hydroxyproline content[26], which was assumed to make up 14% of the collagen by weight. The recoverable collagen was defined as the sum of collagen in the supernatant and pellet after digestion and percentage solubility was defined as the amount of collagen in the supernatant fraction in relation to the total recoverable collagen.

Morphological study of arterial collagen distribution After performing the hemodynamic study on the rats' cardiovascular systems, 2 to 3 cm segments from the rats' descending thoracic aortas were fixed in 10% formalin in saline, and embedded in paraffin for morphological and immunohistochemical studies. Seven-micron sections of aorta were stained with picrosirius red (Direct Red 80, Aldrich, in aqueous picric acid) for 4 h. The collagen type III/I ratio for the aortic media wall was measured by using polarizing light microscopy (Nikon, E600POL) according to previously published methods[27,28].

Immunohistochemistry for AGE Four-micron sections of aorta were used for AGE staining. Briefly, the sections were rehydrated and treated with 3% H_2O_2/methanol followed by incubation in blocking buffer (Superblock, Pierce) for 20 min at room temperature. The sections were then incubated with the anti-AGE antibody (diluted 1:100) for 2 h at room temperature, washed in PBS, and incubated with goat anti-rabbit IgG/horse radish peroxidase (Zymed). The staining was visualized by reaction with diaminobenzidine tetrahydrochloride (Sino-American Biotechnology).

Statistical analysis All results are expressed as mean±SD. Statistical analysis was performed by one-way ANOVA analysis with SPSS. $P<0.05$ was considered statistically significant.

Results

Hemodynamic study of the left ventricle Left ventricular systolic pressure (LVSP), $+dp/dt_{max}$, and $-dp/dt_{max}$ were decreased significantly ($P<0.01$ *vs* normal control) in the vehicle-treated diabetic group (Table 1). C16 treatment did not result in significant weight or fasting blood glucose levels changes ($P>0.05$ *vs* vehicle-treated diabetic rats). However, treatment with C16 (25 or 50 mg/kg) for 4 weeks resulted in a significant increase in all of these 3 parameters ($P<0.05$ or $P<0.01$, Table 1) as compared with vehicle-treated diabetic rats. There was no difference between C16-treated groups (25 or 50 mg/kg) or between the C16-treated groups and the ALT-711-treated group (25 mg/kg).

Hemodynamic study of the cardiovascular system In

Table 1. Effects of C16 on LV function in diabetic rats. n=8. Mean±SD. $^bP<0.05$, $^cP<0.01$ *vs* normal control. $^eP<0.05$, $^fP<0.01$ *vs* vehicle. LVSP, left ventricular systolic pressure.

	Control	Vehicle	ALT-711 25 mg/kg	C16	
				25 mg/kg	50 mg/kg
Blood glucose (mmol/L)	3.8±0.4	26.4±2.2^c	27.4±4.3	25.1±3.4	26.7±3.7
Body weight (g)	451±41	237±29^c	259±26	277±23	270±31
Heart rate (beat/min)	372±36	338±35^b	341±39	343±40	343±24
LVSP (mmHg)	152±7	111±16^c	130±17^e	138±19^e	135±20^e
$+dp/dt$ (mmHg/s)	4429±232	2750±309^c	3489±369^e	3587±678^e	3789±584^f
$-dp/dt$ (mmHg/s)	3914±384	2517±252^c	3221±410^e	3194±502^e	3306±363^f

comparison with the normal controls, the body weights and HR of the vehicle-treated diabetic rats were lower (P<0.01 and P<0.05, respectively), whereas the TPR and TPR index were significantly higher (P<0.01). CO and SAC were significantly lower (P<0.01 *vs* normal control) in vehicle-treated diabetic rats. SBP, DBP, and HR were not significantly different in the 6 groups of diabetic rats (Table 2). Treatment with C16 for 4 weeks resulted in a dose-dependent significant increase in CO and the CO index (P<0.05 or P<0.01), a reduction in TPR and the TPR index (P<0.05 or P<0.01), and an increase in SAC (P<0.05 or P<0.01) as compared with the vehicle-treated rats. After 4 weeks of treatment, similar results were found in ALT-711-treated (12.5 mg/kg) rats. The effects of C16 on the cardiovascular system resembled those of ALT-711. Treatment with C16 (50 mg/kg) for 2 weeks produced values that were slightly different from those produced by the other treatment regimen. Although the difference did not reach statistical significance for the majority of the parameters, SAC was significantly increased (P<0.01 *vs* vehicle group).

RBC-IgG assay The RBC-IgG content of normal control rats was 0.21±0.01 and the content of vehicle-treated diabetic rats was 0.61±0.04 (n=6; P<0.01, Figure 2). Treatment with C16 (25 or 50 mg/kg) resulted in a significant reduction of RBC-IgG content (0.51±0.06, 0.41±0.06; P<0.05, P<0.01, respectively) in comparison with vehicle-treated diabetic rats. ALT-711 treatment (25 mg/kg) also significantly reduced RBC-IgG (0.48±0.07, P<0.01).

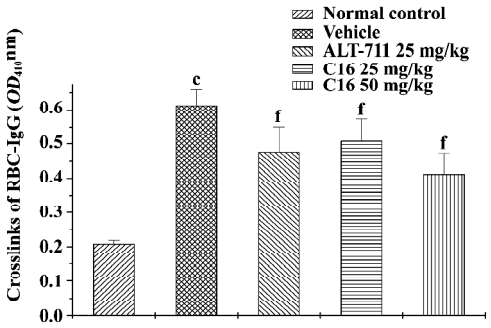

Figure 2. Effects of C16 on IgG crosslinked to the RBC surface in diabetic rats. n=6. Mean±SD. ^cP<0.01 *vs* normal control. ^fP<0.01 *vs* vehicle.

Collagen solubility assay In comparison with normal control animals, the tail tendon collagen solubility of the vehicle-treated animals tended to fall (from 63.9%±7.3 % to 37.7%±10.0 %, P<0.01; Figure 3). Compared with vehicle-

Table 2. Hemodynamic measurements performed in diabetic rats and diabetic rats treated with C16 for 2 or 4 weeks. n=8. Mean±SD. ^bP<0.05, ^cP<0.01 *vs* normal control. ^eP<0.05, ^fP<0.01 *vs* vehicle. CO index, CO corrected for body surface area; TPR index, TPR corrected for body surface area.

	Control	Vehicle	ALT-711 12.5 mg/kg	C16 (4 weeks) 12.5 mg/kg	25 mg/kg	50 mg/kg	C16 (2 weeks) 50 mg/kg
Blood glucose (mmol/L)	4.4±3.6	25.2±4.4^b	24.2±5.9	24.8±4.3	23.9±3.6	26.4±3.7	25.0±4.0
Body weight (g)	513.1±23.1	284.6±79.8^b	283.8±65.4	288.0±69.4	273.1±47.9	297.9±67.0	260.1±74.2
Systolic BP (mmHg)	146.6±17.8	139.2±24.3	127.9±19.7	124.8±28.4	126.3±16.4	132.5±25.8	128.9±18.9
Diastolic BP (mmHg)	116.9±20.6	106.6±18.4	97.4±16.3	95.2±25.3	97.9±13.0	104.7±21.6	100.2±17.2
Heart rate (beat/min)	321.1±30.4	280.8±34.6^b	244.6±42.4	276.0±54.9	249.1±29.3	284.3±26.2	258.3±28.8
CO (mL/min)	124.6±20.3	68.8±8.5^c	89.4±20.8^e	85.7±10.2^f	87.3±12.4^f	96.3±14.6^f	76.0±11.2
CO index ($mL·min^{-1}·per·cm^{-2}$)	0.214±0.040	0.177±0.036	0.229±0.05^e	0.219±0.031^e	0.229±0.03^f	0.239±0.029^f	0.211±0.042
TPR (10^{-3}odyneo·s·cm^{-5})	83.8±21.1	137.9±23.2^c	100.2±25.4^f	99.7±32.2^e	99.0±9.1^f	95.9±11.4^f	111.3±27.1
TPR index (dyne·s·cm^{-3})	142.8±33.8	353.0±74.3^c	259.8±74.3^e	255.7±91.8^e	260.5±29.5^f	240.9±44.0^f	310.4±86.0
SAC (10^3×mL/mmHg)	13.8±3.6	8.2±2.0^c	12.5±2.8^f	11.8±4.2^e	12.7±2.2^f	12.8±2.3^f	12.2±2.4^f

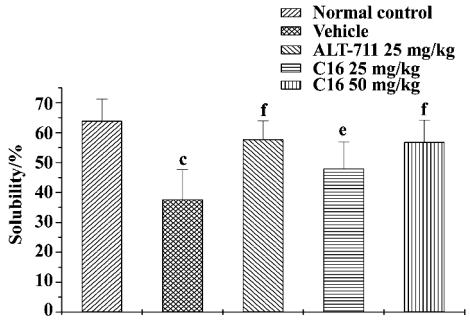

Figure 3. Effects of C16 on the solubility of tail tendon collagen in diabetic rats. n=6. Mean±SD. ^{c}P<0.01 *vs* normal control. ^{e}P<0.05, ^{f}P<0.01 *vs* vehicle.

treated animals, collagen solubility was increased significantly after treatment with C16 (25 mg/kg, 48.0%± 9.0%; 50 mg/kg, 56.8%±7.4%; P<0.05, P<0.01, respectively). ALT-711 treatment resulted in a significant increase in collagen solubility (57.7%±6.2%, P<0.01).

Morphological study of arterial collagen distribution When stained with picrosirius red, different types of collagen in the aortic media wall could be distinguished by polarizing light microscopy, where type I collagen appeared yellow or yellow-red, and type III collagen appeared green (Figure 4). The collagen type III/I ratio of the aortic media wall tended to be greater in rats with diabetes (Figure 4B), but C16 (50 mg/kg) and ALT-711 (12.5 mg/kg) treatment could reverse this alteration (Figure 4C, 4D).

Immunohistochemistry for AGE In comparison with normal control animals, the amount of AGE accumulated in the aortic media wall of the vehicle-treated animals was increased. But the amount of AGE was decreased by C16 (50 mg/kg) and ALT-711 (12.5 mg/kg) treatment (Figure 5).

Discussion

Nearly a century ago, glycation was first recognized in the food industry, and became known as the Maillard reaction: a process in which food proteins crosslink and become brown with age. In the 1980s, Brownlee *et al* first described the harmful consequences of AGE formation on the cardiovascular and renal systems in humans[1,29] and diabetic rats[13]. Recently, it has been thought more and more likely that AGE and AGE crosslinks are linked to the development of many age- and diabetes-related disorders through structural modifications as well as receptor-mediated pathways, which activate growth factors, induce a number of processes, and initiate inflammatory reactions[30]. Therefore, targeting AGE, especially breaking established AGE crosslinks, was considered to be a novel and promising therapeutic candidate for reversing AGE-related pathologic conditions. In the present study, rats with STZ-induced diabetes of 16 weeks duration exhibited a marked increase in AGE and an abnormal distribution of collagen type in the aorta. However, significant decreases in hemodynamic parameters, such as LV dp/dt, CO, and SAC, were also observed. These results demonstrated that AGE-related changes in structure eventually increased the stiffness of the arterial tree and myocardium, which, in turn, resulted in functional changes. Immunohistochemical assays revealed that C16, a potential AGE breaker,

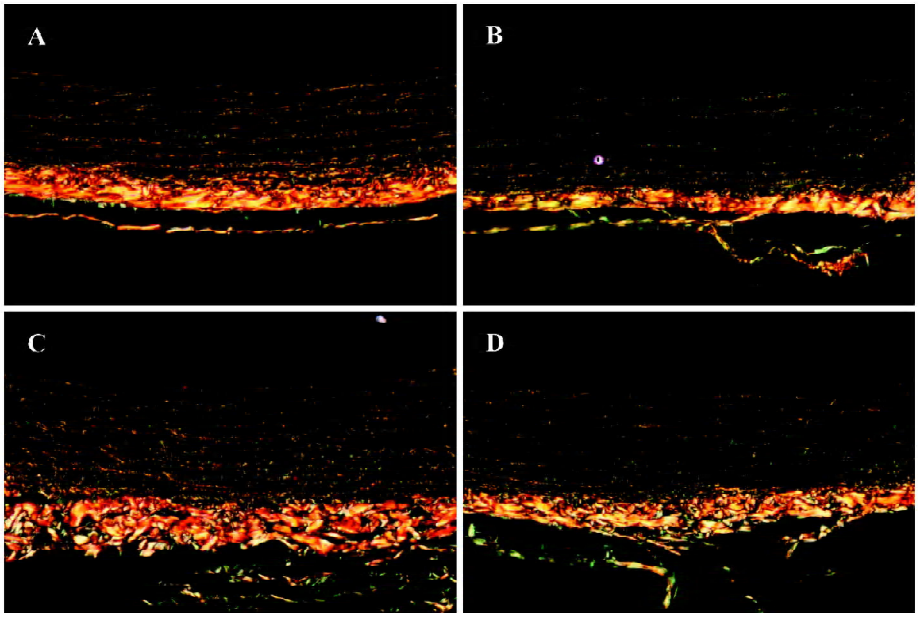

Figure 4. Picrosirius red staining for collagen distribution in descending thoracic aorta from normal control (A), vehicle-treated (B), C16-treated (C), and ALT-711-treated (D) rats. Type I collagen appears yellow or yellow-red, and type III collagen appears green. ×200.

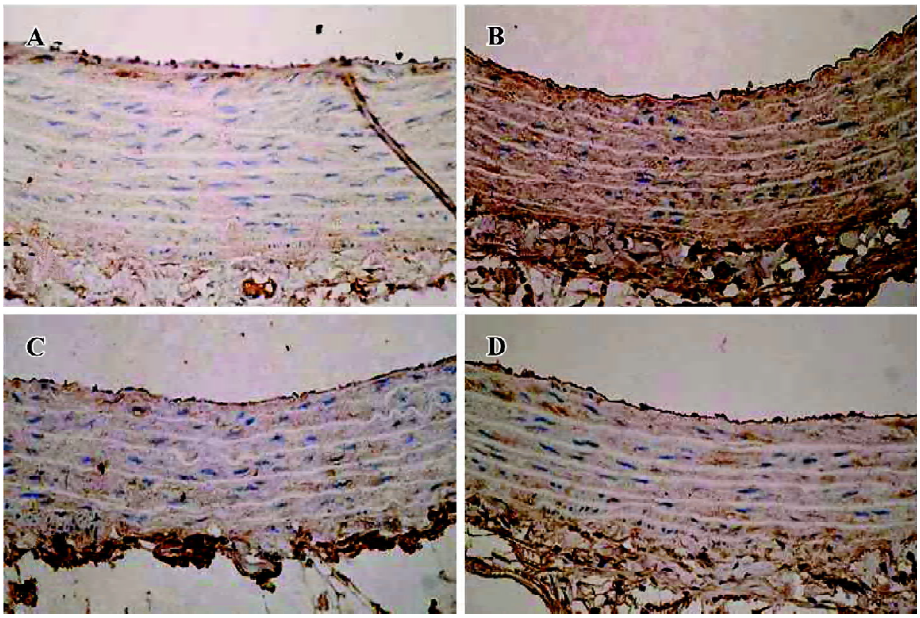

Figure 5. Immunohistochemical staining for AGE in descending thoracic aorta from normal control (A), vehicle-treated (B), C16-treated (C), and ALT-711-treated (D) rats. Positive staining is shown as brown. Sections are counterstained with hematoxylin. ×200.

could prevent the increase of AGE accumulation in the aortic media wall of diabetic rats, and could reverse the increase in the collagen type III/I ratio (prior studies have generally shown an association between increased collagen type III and/or the III/I ratio and the accumulation of AGE crosslinks[31,32]). Furthermore, both the diastolic function, as indicated by $-dp/dt_{max}$, and the contractile function of LV, as indicated by LVSP and $+dp/dt_{max}$, were restored significantly by C16. The significant improvements in the hemodynamic parameters could not be attributed to differences in blood pressure, which did not change significantly during treatment as compared with the vehicle-treated diabetic group. Therefore, the improvements reflect intrinsic modifications of the mechanical properties of the arterial wall. The increase in SAC and the decrease in TPR indicates that through treatment with C16 the stiffness of the aorta was reduced to levels comparable to those observed in normal control rats. Moreover, these effects seemed to be related to the duration of the treatment, with stronger effects after 4 weeks than 2 weeks, which indicates that the effects of C16 were exerted through the pathway of structural modification by slowly breaking the established AGE crosslinks. The different approaches used in the present study consistently show that C16, a novel AGE crosslink breaker, exerted beneficial cardiovascular actions and restored diabetes-associated cardiovascular dysfunction in experimental diabetic rats by reducing AGE, and that C16 has similar effects to ALT-711, the well-known AGE breaker.

The presence of AGE crosslinks is thought to contribute to increased insolubility and resistance of collagen to enzymatic and chemical digestion[25], and IgG crosslinked to RBC as a structure of AGE crosslinks is formed earlier than other AGE crosslinks *in vivo*[14]. Thus, the susceptibility of collagen to digestion by pepsin and the IgG-RBC crosslink content have previously been used to provide 2 indexes of protein crosslinking *in vivo*[13,20,25]. In the present study, the considerably improved solubility of collagen and decreased content of IgG crosslinked to RBC after treatment with C16 demonstrated that C16 could reduce AGE crosslinks *in vivo*.

In summary, the novel compound C16 has the ability to break established AGE crosslinks and reduce AGE accumulation in tissues *in vivo*. Furthermore, C16 can restore diabetes-associated cardiovascular dysfunction in rats. This provides a potential therapeutic approach for diabetes- and aging-related cardiovascular disease.

References

1 Brownlee M, Cerami A, Vlassara H. Advanced glycosylation end products in tissue and the biochemical basis of diabetic complications. N Engl J Med 1988; 318: 1315–21.
2 Kass DA. Getting better without AGE: new insights into the diabetic heart. Circ Res 2003; 92: 704–6.
3 Brownlee M. Lilly Lecture 1993. Glycation and diabetic complications. Diabetes 1994; 43: 836–41.
4 Singh R, Barden A, Mori T, Beilin L. Advanced glycation end-products: a review. Diabetologia 2001; 44: 129–46.
5 Brownlee M. The pathological implications of protein glycation. Clin Invest Med 1995; 18: 275–81.
6 Bucala R, Cerami A. Advanced glycosylation: chemistry, biology, and implications for diabetes and aging. Adv Pharmacol 1992; 23: 1–34.

7 Sims TJ, Rasmussen LM, Oxlund H, Bailey AJ. The role of glycation cross-links in diabetic vascular stiffening. Diabetologia 1996; 39: 946–51.
8 Avendano GF, Agarwal RK, Bashey RI, Lyons MM, Soni BJ, Jyothirmayi GN, *et al*. Effects of glucose intolerance on myocardial function and collagen-linked glycation. Diabetes 1999; 48: 1443–7.
9 Rahbar S, Figarola JL. Novel inhibitors of advanced glycation endproducts. Arch Biochem Biophys 2003; 419: 63–79.
10 Vasan S, Foiles P, Founds H. Therapeutic potential of breakers of advanced glycation end product-protein crosslinks. Arch Biochem Biophys 2003; 419: 89–96.
11 Dukic-Stefanovic S, Schinzel R, Riederer P, Munch G. AGES in brain ageing: AGE-inhibitors as neuroprotective and anti-dementia drugs? Biogerontology 2001; 2: 19–34.
12 Li YM, Steffes M, Donnelly T, Liu C, Fuh H, Basgen J, *et al*. Prevention of cardiovascular and renal pathology of aging by the advanced glycation inhibitor aminoguanidine. Proc Natl Acad Sci USA 1996; 93: 3902–7.
13 Brownlee M, Vlassara H, Kooney A, Ulrich P, Cerami A. Aminoguanidine prevents diabetes-induced arterial wall protein cross-linking. Science 1986; 232: 1629–32.
14 Wolffenbuttel BH, Boulanger CM, Crijns FR, Huijberts MS, Poitevin P, Swennen GN, *et al*. Breakers of advanced glycation end products restore large artery properties in experimental diabetes. Proc Natl Acad Sci USA 1998; 95: 4630–4.
15 Asif M, Egan J, Vasan S, Jyothirmayi GN, Masurekar MR, Lopez S, *et al*. An advanced glycation endproduct cross-link breaker can reverse age-related increases in myocardial stiffness. Proc Natl Acad Sci USA 2000; 97: 2809–13.
16 Vaitkevicius PV, Lane M, Spurgeon H, Ingram DK, Roth GS, Egan JJ, *et al*. A cross-link breaker has sustained effects on arterial and ventricular properties in older rhesus monkeys. Proc Natl Acad Sci USA 2001; 98: 1171–5.
17 Liu J, Masurekar MR, Vatner DE, *et al*. Glycation end-product cross-link breaker reduces collagen and improves cardiac function in aging diabetic heart. Am J Physiol Heart Circ Physiol 2003; 285: H2587–91.
18 Susic D, Varagic J, Ahn J, Frohlich ED. Cardiovascular and renal effects of a collagen cross-link breaker (ALT 711) in adult and aged spontaneously hypertensive rats. Am J Hypertens 2004; 17: 328–33.
19 Kass DA, Shapiro EP, Kawaguchi M, Capriotti AR, Scuteri A, deGroof RC, *et al*. Improved arterial compliance by a novel advanced glycation end-product crosslink breaker. Circulation 2001; 104: 1464–70.
20 Vasan S, Zhang X, Zhang X, Kapurniotu A, Bernhagen J, Teichberg S, *et al*. An agent cleaving glucose-derived protein crosslinks *in vitro* and *in vivo*. Nature 1996; 382: 275–8.
21 Li S, Cui H, Wang LL, inventors. New substituted penta azacyclo salt kind compound and its use in treating protein ageing related disease. CN patent 1534027. 2004 Oct 6.
22 Yamamoto K, Masuyama T, Sakata Y, Nishikawa N, Mano T, Yoshida J, *et al*. Myocardial stiffness is determined by ventricular fibrosis, but not by compensatory or excessive hypertrophy in hypertensive heart. Cardiovasc Res 2002; 55: 76–82.
23 Levy BI, Duriez M, Phillipe M, Poitevin P, Michel JB. Effect of chronic dihydropyridine (isradipine) on the large arterial walls of spontaneously hypertensive rats. Circulation 1994; 90: 3024–33.
24 Yin FC, Guzman PA, Brin KP, *et al*. Effect of nitroprusside on hydraulic vascular loads on the right and left ventricle of patients with heart failure. Circulation 1983; 67: 1330–9.
25 Kochakian M, Manjula BN, Egan JJ. Chronic dosing with aminoguanidine and novel advanced glycosylation end product-formation inhibitors ameliorates cross-linking of tail tendon collagen in STZ-induced diabetic rats. Diabetes 1996; 45: 1694–700.
26 Stegemann H, Stalder K. Determination of hydroxyproline. Clin Chim Acta 1967; 18: 267–73.
27 Junqueira LC, Cossermelli W, Brentani R. Differential staining of collagens type I, II and III by Sirius Red and polarization microscopy. Arch Histol Jpn 1978; 41: 267–74.
28 Whittaker P, Kloner RA, Boughner DR, Pickering JG. Quantitative assessment of myocardial collagen with picrosirius red staining and circularly polarized light. Basic Res Cardiol 1994; 89: 397–410.
29 Brownlee M, Cerami A, Vlassara H. Advanced products of nonenzymatic glycosylation and the pathogenesis of diabetic vascular disease. Diabetes Metab Rev 1988; 4: 437–51.
30 Cooper ME. Importance of advanced glycation end products in diabetes-associated cardiovascular and renal disease. Am J Hypertens 2004; 17: 31S–8S.
31 Shimizu M, Umeda K, Sugihara N, Yoshio H, Ino H, Takeda R, *et al*. Collagen remodelling in myocardia of patients with diabetes. J Clin Pathol 1993; 46: 32–6.
32 Bruel A, Oxlund H. Changes in biomechanical properties, composition of collagen and elastin, and advanced glycation end products of the rat aorta in relation to age. Atherosclerosis 1996; 127: 155–65.

Acta Pharmacologica Sinica 2005 Dec; 26 (12): 1467–1473

Blackwell Publishing

Full-length article

One-oligonucleotide method for constructing vectors for RNA interference[1]

Carlos Fabian FLORES-JASSO[2], Ines VELAZQUEZ-QUESADA[2], Carlos LANDA-SOLIS[3], Andres A GUTIERREZ[3], Luis VACA[2,4]

[2]*Departamento de Biología Celular, Instituto de Fisiología Celular, Universidad Nacional Autónoma De México, Ciudad Universitaria, Mexico City 04510, Mexico*; [3]*Unidad de Terapia Celular, Centro Nacional de Rehabilitación, Mexico City 14389, México*

Key words

RNA interference; shRNAs; DNA cassette; RNAi vector; oligonucleotide

[1] Project supported by grant 40262 from the Consejo Nacional de Ciencia y Tecnología (CONACyT).
[4] Correspondence to Dr Luis VACA.
Phn 52-5-5622-5654.
Fax 52-5-5622-5611.
E-mail lvaca@ifc.unam.mx

Received 2005-06-12
Accepted 2005-08-29

doi: 10.1111/j.1745-7254.2005.00230.x

Abstract

Aim: To develop an easy, fast, automated, and inexpensive method for constructing short-hairpin-RNA cassettes for RNAi studies. **Methods:** Using single oligonucleotides, a variety of DNA cassettes for RNAi vectors were constructed in only few minutes in an automated manner. The cassettes, targeting the eGFP, were cloned into plasmids driven by RNA polymerase III promoter H1. Then, the plasmids were transfected into HeLa cells that were later infected with a recombinant adenovirus encoding the eGFP gene. The level of eGFP fluorescence was evaluated by confocal imaging and flow cytometry. **Results:** The plasmids constructed with the DNA cassettes made by the one-oligonucleotide method inhibited eGFP with different potencies, ranging from 55% to 75%. **Conclusion:** By using the method reported here, it is possible to simultaneously construct hundreds of different DNA cassettes for RNAi experiments in an inexpensive, automated way. This method will facilitate functional genomics studies on mammalian cells.

Introduction

RNA interference (RNAi) is a powerful tool for inhibiting gene expression in a wide variety of organisms. When double-stranded RNA is introduced into cells, the ribonuclease III Dicer processes the double-stranded RNA into small fragments of about 21 nucleotides in length (termed siRNAs) that trigger the RNAi mechanism[1–3]. Then, the siRNAs are incorporated into a protein complex, known as the RNA-induced silencing complex (RISC), which in turn unwinds the duplex siRNA in an ATP-dependent manner[4]. After the unwinding, RISC uses the siRNA antisense strand as a guide to specifically cleave the complementary mRNA, which is further processed for degradation[4–6].

There are different ways to induce mRNA degradation using RNAi. Several methods for preparing siRNA have been developed, such as chemical synthesis, *in vitro* transcription, siRNA expression vectors, and polymerase chain reaction (PCR) expression cassettes. For example, short hairpin RNAs (shRNAs) transcribed by RNA polymerase III promoter-based vectors have been used as RNAi triggers in a variety of cell lines[7,8]. These RNA polymerase III (RNA Pol) vectors have a variety of advantages over the siRNAs. First, they greatly reduce the cost of RNAi synthesis, making RNAi a viable tool for screening the function of large numbers of genes. Second, because hairpins are transcribed inside cells, it is possible to establish inducible systems for RNAi both *in vitro* and *in vivo*[9–11]. Third, it is also possible to generate knock-down phenotypes to resemble knock-out animals without affecting the germline, as long as this strategy is combined with inducible systems[12–14]. Therefore, it is relatively easy to establish cell cultures using retroviral or adenoviral vectors that stably express the hairpin for RNAi[10,15–18].

Although there has been much progress in the RNAi field, it is not completely understood why some sequences are refractory to RNAi. Some groups have investigated this lack of activity, but at present, choosing the most effective siRNA sequence to knock down an mRNA is still a trial-and-error task. Thus, it is generally accepted that several se-

quences must be designed to achieve the highest RNAi efficiency, making the silencing experiments costly and slow. It would be advantageous to have a more efficient method for the production of a wide variety of sequences in a simple step, instead of using long DNA oligonucleotides or several PCR step-specific methods[8,19–21].

Here we describe an inexpensive, easy to implement and automated method to produce DNA cassettes for RNAi experiments using a single oligonucleotide. With this method hundreds of DNA cassettes can be synthesized in a 1-step reaction. This method not only reduces the cost of testing sequences for RNAi experiments, but also accelerates the exploration of multiple-gene sequences.

Materials and methods

Construction of DNA cassettes and plasmid vectors To construct the plasmid vector pBB4H1, the human H1 promoter was PCR amplified from human genomic DNA using the following primers: forward 5'-CCATGGAATTCGAACGCTGACGT-3' and reverse 5'-GCAAGCTTTGGTCTCATAAGAACTTATAAGATTCCC-3', which contain one *Eco*RI and one *Hin*dIII restriction site, respectively. The PCR product was subcloned in the pDRIVE vector (Qiagen, Valencia, CA) following the manufacturer's instructions. The pDRIVE-H1 vector was then digested with *Eco*RI and *Hin*dIII to obtain a DNA fragment of ~230 base pairs, which contained the H1 promoter. This fragment was then cloned into the EcoRI and *Hin*dIII site of the pBlueBac4 vector (Invitrogen, Carlsbad, CA) to obtain the pBB4H1 vector.

To generate the DNA cassettes the following chemically synthesized oligonucleotides were used: hpGFP1 5'-GCAAGCTTCCCCAAA*AACCACTACCTGAGCACCCA*GGGGCCCC-3', hpGFP2 5'-GCAAGCTTCCCCAAA*AAGGGCGAGGAGCTGTTCACCGG*GGCCCC-3', hpGFP3 5'-GCAAGCTTCCCCAAA*AACGGCCACCAGTTCAGCGT*GGGGCCCC-3', hpGFP4 5'-GCAAGCTTCCCCAAA*AAGGAGGACGGCAACATCCT*GGGGCCCC-3', hpTRPC4 5'-GCAAGCTTCCCCAA*AAAUUACUCGUCAACAGGCGGACGG*GGCCCC-3'. Note that the sequence upstream of the 5 A's contained the *Hin*dIII restriction site (underlined), followed by 4 C's, and was included in the oligonucleotide design because it allows easy cloning of the DNA cassette and allows the RNA pol III to initiate in the first of the 5 A's, exactly 30 nucleotides after the TATA box. The sequence in italics corresponds to the *eGFP* mRNA.

To construct the DNA cassettes, 10 μL of each oligonucleotide (~35 μmol/L) were heated for 5 min to 94 °C. When the temperature reached 40 °C, 10 μL of a reaction mix was added [reaction mix: 2 mmol/L dNTPs; 5 U Klenow enzyme (Invitrogen); 2 μL 10×reaction buffer 2 (Invitrogen); 10% Me_2SO; H_2O to 10 μL]. All the reactions were performed identically using a thermo-cycler to precisely control the temperatures (Figure 1).

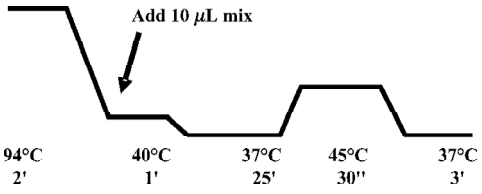

Figure 1. Temperature sequence used in the thermocycler reaction for the construction of DNA cassettes.

Then, the Klenow products were heated to 65 °C to inactivate the enzyme, digested with *Hin*dIII and cloned into the *Hin*dIII restriction site of the pBB4H 1 vector previously dephosphorylated with alkaline phosphatase (Roche, Basel Switzerland). Only the correct cassettes would be ligated into the *Hin*dIII cohesive ends. We did not observe clones with tandem-repeated cassettes.

The sequences targeting the *eGFP* mRNA were chosen based on 2 criteria: (i) because they had fewer than 3 G or C repeats to prevent G-quartet formation; and (ii) because they were distributed along the *eGFP* mRNA.

Cell culture and transfection HeLa cells were grown in Dulbecco's modified Eagle's medium (DMEM) containing 10% fetal bovine serum and antibiotics, and were seeded every 3 d following standard procedures at 37 °C. The day before transfection, cells were grown without antibiotics in 12 well plates. Vectors containing the DNA cassette were transfected using lipofectamine 2000 (Invitrogen) at different concentrations following the manufacturer's instructions. The day after transfection, the cells were washed once with phosphate-buffered saline (PBS) and treated with 5 MOI of a recombinant adenovirus encoding the green fluorescent protein (eGFP) gene under the transcriptional control of the cytomegalovirus (CMV) promoter[22]. Four hours later, the cells were washed with PBS and the media was replaced. Twenty-four hours later the fluorescence was evaluated using a FACScan flow cytometer (Becton & Dickinson, Franklin Lakes, NJ). To evaluate the fluorescence intensity, 10 000 events were counted in at least 3 independent experiments for each concentration.

Confocal microscopy The HeLa cells that were treated with the plasmids and adenovirus as described were washed with PBS, trypsinized and plated on sterile coverslips.

Twenty-four hours later, the cells were analyzed with a confocal microscope (Bio-Rad, Hercules, CA) using a 40× objective. The confocal images were analyzed using the Confocal Assistant freeware software.

Results

Construction of DNA cassettes For the construction of the DNA sequence that served as a template for shRNA transcription, we followed the principle of DNA amplification commonly used in PCR reactions (Figure 2A). That is, any given sequence that serves as a primer could be amplified at its 3' end with a proper DNA polymerase. In RNAi hairpins, the 2 strands that form the stem are fully complementary, so it is possible to use only a single oligonucleotide that is self-complementary within its 3' end (Figure 2B). After the self-complementary structure is formed, it is possible to further amplify the structure so that the oligonucleotide becomes completely double-stranded DNA.

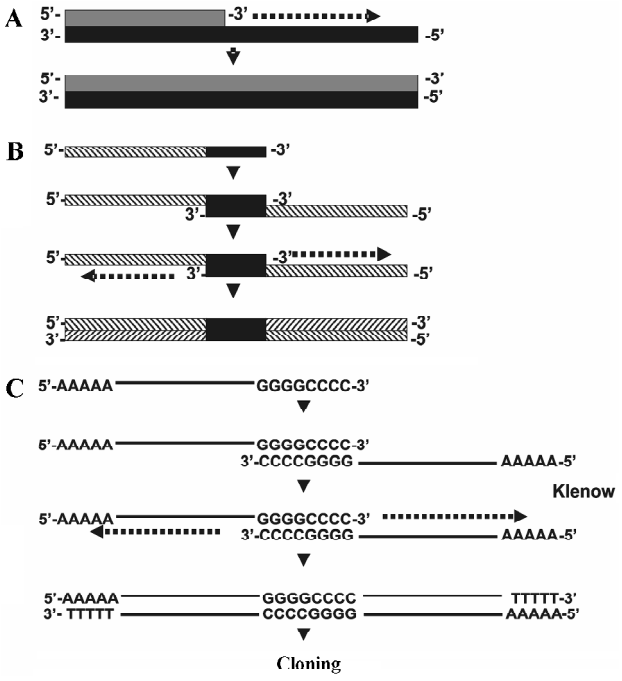

Figure 2. Using the amplification principle (A), an oligonucleotide can be amplified if it is auto- hybridized by its 3' end (B). We selected the sequence 5'-GGGGCCCC-3' to form the secondary structure shown in (C), and we added it to the 21 nucleotide sequence. Also, to obtain the transcription termination, 5 A's are included in the oligonucleotide. After a filling-in reaction by the Klenow enzyme, a DNA cassette is formed. The optimum enzymatic temperature of the Klenow fragment is approximately 37 °C, which corresponds to the T_m value of the 5'-GGGGCCCC-3' sequence. To avoid enzyme denaturation, the Klenow fragment and dNTP mix is added until the temperature drops to 40 ºC (see text, and Figure 1). Temperatures may be automated with a thermocycler.

The self-complementary pairing must be strong enough to allow the DNA polymerase to initiate the reaction at the selected temperature. We chose the sequence 5'-GGGGCCCC-3' due to its high T_m (37 °C) and because its palindrome nature permits the self-complementary structure. Furthermore, this sequence allows amplification using the large (Klenow) fragment of the DNA polymerase, whose working temperature is 37 °C. Thus, because the 5'-GGGGCCCC-3' sequence is amplified and lies between the sense and antisense strand, it also functions as a loop for the shRNA (Figure 4).

Finally, most RNAi vectors contain an RNA pol III promoter such as U6 or H1, which is used to initiate the transcription of the shRNA. When the RNA pol III finds 5 consecutive T's, it terminates the transcription and removes the last three nucleotides on the 3' end[17, 20]. Therefore, we included 5 A's in the 5' end in the oligonucleotide; when the Klenow fragment synthesizes the antisense strand, it generated the 5 T's, which will be needed to terminate the transcription by RNA pol III inside the cell (Figure 2C). The expected shRNA structures that will form inside the cells are shown in Figure 4. All these structures were modeled using the Mfold server (see Materials and methods).

To determine if it was possible to construct the DNA cassette for shRNA vectors with this method, we designed and tested its ability to amplify different oligonucleotides. These oligonucleotides were prepared to target sequences from *eGFP* and a control oligonucletide containing an eGFP-unrelated sequence. eGFP oligonucleotide sequences were selected to have low GC repeats to prevent G-quartet formation. Figure 3 illustrates the result of a typical filling-in reaction, showing that the Klenow fragment produced double-stranded DNA from single oligonucleotides. Therefore, the self-complementary 5'-GGGGCCCC-3' sequence is a good template for DNA amplification. Furthermore, all cassettes were constructed simultaneously in a single step reaction, so the 1-oligonucleotide method could be automated to perform a large number of reactions in a short period of time (see Materials and methods and Figure 1). We cloned the DNA cassettes in the vector under the transcriptional control of an RNA pol III (H1) promoter, and all cassettes were sequenced to confirm their integrity.

Efficacy of the 1-oligonucleotide method in RNAi experiments To test the ability of the DNA cassettes to trigger RNAi activity, HeLa cells were transfected with the plasmid vectors containing the cassettes targeting the mRNA from eGFP and a control construct. The day after transfection, cells were incubated with a recombinant adenovirus encoding the eGFP, and 24 h later the cell fluorescence was

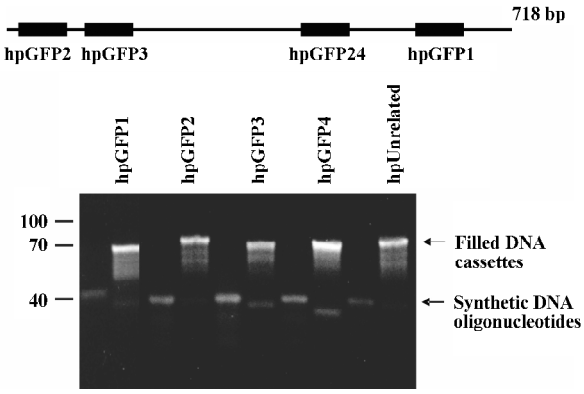

Figure 3. Automation of the method. Using the same conditions as described in the text, a wide variety of DNA cassettes were generated simultaneously. A low melting point 4% agarose gel (*w/v*) is shown in the bottom half of the figure, with the filled shDNAs and control oligonucleotides (controls are on the left of the shDNA); the expected length of each filled DNA cassette is ~75 bp. The 21 nucleotide sequences correspond to the enhanced eGFP mRNA. The target positions of hairpin GFP1–4 (represented by black boxes) are shown on top: hpGFP1, nucleotides 595 to 616; hpGFP2 nucleotides 10 to 31; hpGFP3, nucleotides 69 to 90; hpGFP4, nucleotides 394 to 415; the length of the eGFP sequence is 718 bp. After the Klenow filling-in reaction, DNA cassettes were cloned into an RNA pol III vector for transfection.

evaluated. All the tested sequences silenced eGFP expression and, as expected, there was no gene silencing with the transfection of the unrelated construct (Figure 4). A dose–response experiment showed that the most effective plasmid concentration to achieve RNAi was 1–3.75 μg/mL. Of 4 tested DNA cassette sequences (termed hpGFP1 to 4), hpGFP 2, 3 and 4 inhibited eGFP expression/fluorescence by more than 70%. The less efficient cassette (hpGFP1) inhibited eGFP expression by 50% at 1 μg/mL (Figure 5). The EC_{50} of each shRNA confirms this result; the less effective shRNA is hpGFP1, with an EC_{50} of approximately 0.5 μg/mL, whereas hpGFP 2–4 have EC_{50} values of approximately 0.05 μg/mL (Figure 5). The finding that not all DNA cassette sequences had the same potency confirms the fact that a variety of sequences must be designed for the same target in order to find the most effective RNAi inducer. However, it was surprising that the hpGFP 1 sequence was the least effective of all tested sequences. This result was interesting because this sequence had been shown to be a strong inhibitor of eGFP expression in a previous study[23]. The dose-response experiment with the unrelated cassette did not influence the eGFP fluorescence (data not shown). Together, these results suggest that diverse DNA cassettes must be produced by the 1-oligonucleotide method in order to identify the best sequence for RNAi.

Discussion

In the present work we developed a novel, easy and efficient 1-oligonucleotide method to generate DNA cassettes for RNAi vectors. To test the capability of the method, we designed DNA cassettes to target the mRNA from eGFP. For this purpose a recombinant adenovirus encoding the eGFP gene was used to infect HeLa cells. Only cells infected with the virus and transfected with specific anti-GFP cassettes strongly inhibited eGFP fluorescence. The level of inhibition achieved with this method resembles the inhibition when RNAi is used to knock-down the expression of endogenous genes, because transfections usually reached 60%–75% of the cells, and the level of adenovirus infection almost reached 100%. The results obtained here suggest that eGFP expression was strongly reduced in the cells that were transfected with the DNA constructs, as illustrated in Figure 5. The fact that hpGFP1 was less efficient at knocking down eGFP expression suggests that a variety of RNA sequences are needed in order to find the most effective. Although this sequence has already been used by others[23], it is reasonable that there could exist sequences that are even more effective; this method is an easy way to construct a large variety of DNA cassettes for 1 or more genes. Together, these results demonstrate that, although eGFP expression is under the transcriptional control of the strong CMV promoter in the adenoviral vector, it is still possible to induce gene silencing using the cassettes described here.

Previously reported methods to produce RNAi using DNA cassettes to generate shRNAs in mammalian cells require long oligonucleotides or several PCR reactions that are sequence and step specific[17,20,21,24–28]. For example, in the method reported by Gou et al, at least three oligonucleotides (1 forward and 2 reverse) are used in 2 sequential PCR reactions to generate the DNA cassette[21]. Once the 2 PCR reactions conclude, PCR products require further cleaning before transfection into cells. Another method previously reported is based on primer extension, and the DNA cassettes are cleaned and introduced in the cells directly[26]. Although the latter method uses only 2 oligonucleotides to construct each DNA cassette, these oligonucleotides are fairly long (approximately 100 nucleotides), considerably increasing the cost of constructing multiple cassettes.

There are a number of effective methods that have been designed over the past few years to produce RNAi in mammalian cells[29], but unfortunately none of these methods is easily automated because they require many step-specific reactions. Using the method described here, we simulta-

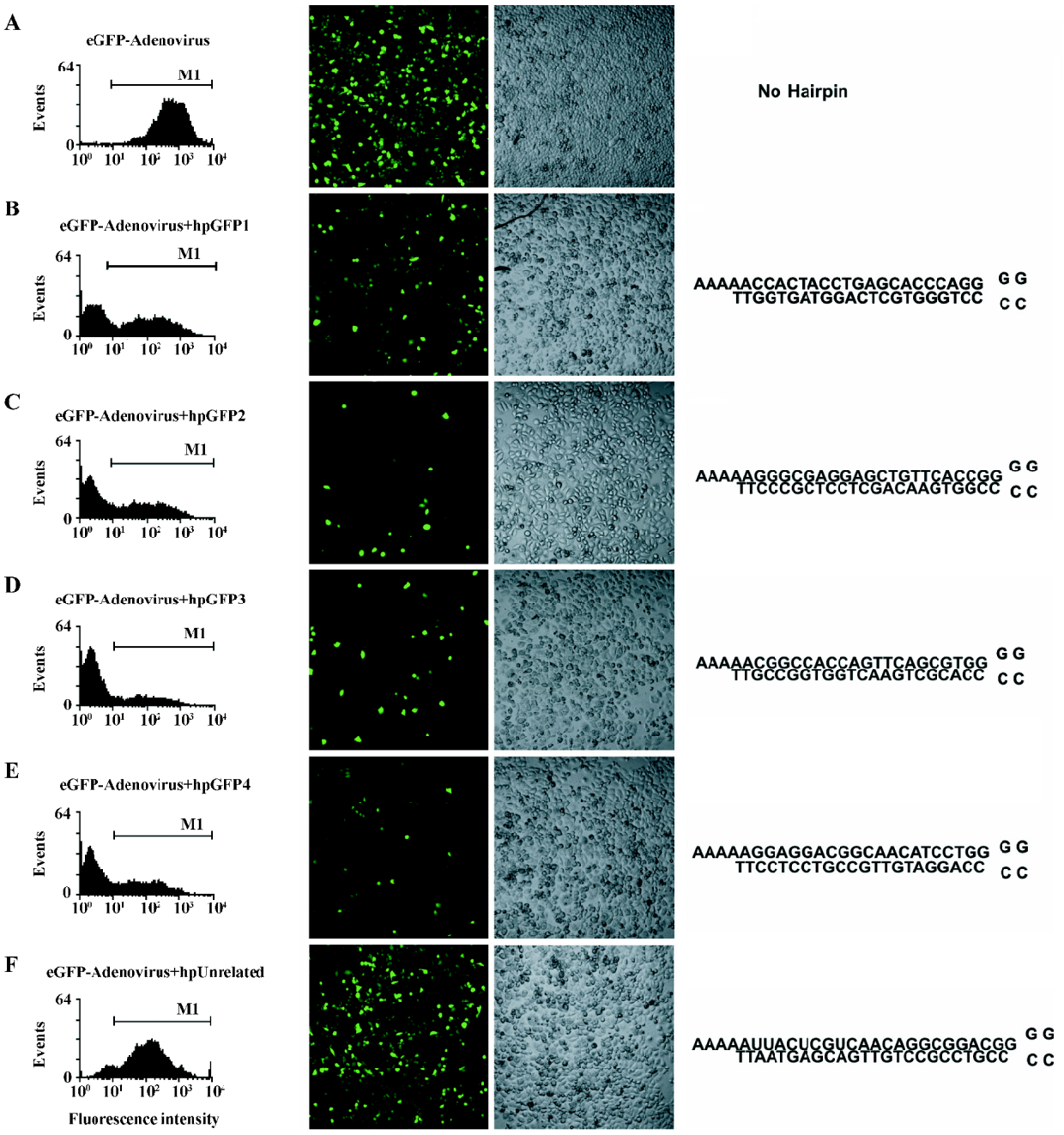

Figure 4. Inhibition of eGFP by plasmids that produce shRNAs. HeLa cells were transfected with 3.5 mg/mL of plasmid DNA. Confluent cells (~80%) were infected 24 h later with 5 MOI of a recombinant eGFP-adenovirus, and the next day the fluorescence was evaluated by confocal microscopy and flow cytometry. Left panels: Representative experiments measured by flow cytometry; the region marked M1 was considered to be the cell population expressing eGFP. Middle panels: Confocal images showing eGFP-positive cells, and the transmitted light shows the total number of cells in the field. Right panels: shRNA predicted structures. The shRNA structures were modeled based on the sequences that should be transcribed inside the cell after plasmid transfection. The shRNAs were modeled with the Mfold server: http://www.bioinfo.rpi.edu/applications/mfold/, and the conditions were 37 °C and 2 mmol/L Mg^{2+}.

neously produced a large number of different DNA cassettes targeting different mRNAs (unpublished data). This is possible because the process can be automated to perform many different reactions using the same temperature, time and reactant conditions using a thermocycler.

The advantages of the method described here over pre-

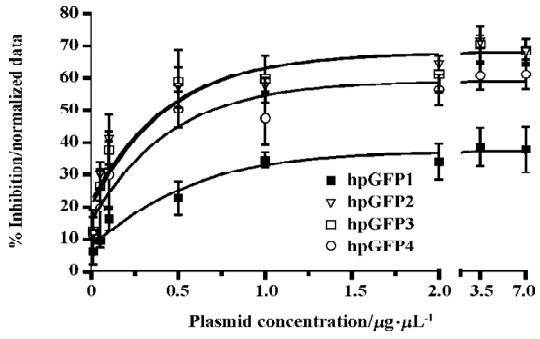

Figure 5. Quantification of eGFP fluorescence by flow cytometry. Data from all inhibition experiments were fitted to a dose-response equation (actual fit represented by the solid lines), showing that different cassettes have different RNAi potencies. Data were analyzed by using the GraphPad Prism 4.0 software. Data were obtained from at least three independent experiments and were mean±SEM.

viously reported methods are: (i) a single oligonucleotide is sufficient to generate a DNA cassette for shRNA production, significantly reducing the price of testing multiple sequences; (ii) oligonucleotides for cassette construction are easy to design: a 21–25 nucleotide sense target sequence is flanked by 5'-AAAAA- and -GGGGCCCC-3', thus the length of the oligonucleotide is considerably shorter; and (iii) the method is automated, allowing the construction of a wide variety of DNA cassettes in one step in a few minutes.

Recently it was shown that it is also possible to express synthetic miRNAs using RNA pol II promoters, which allows still more control over stem-loop RNA expression, because many RNA pol II promoters function in a inducible/tissue-specific fashion[30]. We are currently constructing DNA cassettes by using the 1-oligonucleotide method for use with RNA pol II promoters (unpublished results). Because this type of polymerase does not terminate the transcription after 5 consecutive thymidines it is not necessary to include 5 adenines in the oligonucleotide, which further reduces the length and price of the DNA cassette.

In conclusion, we reported here a novel method for constructing large libraries of RNAi cassettes quickly and in a cost-effective manner, thus making the exploration of the function of a large number of genes an easier task and facilitating functional genomic studies.

Acknowledgements

We thank Agustin LUZ for providing genomic DNA for cloning the H1 human promoter, and Erendira AVENDAÑO and members of the laboratory for helpful discussions.

References

1 Zamore PD, Tuschl T, Sharp PA, Bartel DP. RNAi: double-stranded RNA directs the ATP-dependent cleavage of mRNA at 21 to 23 nucleotide intervals. Cell 2000; 101: 25–33.
2 Hammond SM, Bernstein E, Beach D, Hannon GJ. An RNA-directed nuclease mediates post-transcriptional gene silencing in Drosophila cells. Nature 2000; 404: 293–6.
3 Bernstein E, Caudy AA, Hammond SM, Hannon GJ. Role for a bidentate ribonuclease in the initiation step of RNA interference. Nature 2001; 409: 363–6.
4 Nykanen A,Haley B, Zamore PD. ATP requirements and small interfering RNA structure in the RNA interference pathway. Cell 2001; 107: 309–21.
5 Liu J, Carmell MA, Rivas FV, Marsden CG, Thomson JM, Song JJ, *et al*. Argonaute2 is the catalytic engine of mammalian RNAi. Science 2004; 305: 1437–41.
6 Schwarz DS, Hutvagner G, Du T, Xu Z, Aronin N, Zamore PD. Asymmetry in the assembly of the RNAi enzyme complex. Cell 2003; 115: 199–208.
7 Paddison PJ, Caudy AA, Bernstein E, Hannon GJ, Conklin DS. Short hairpin RNAs (shRNAs) induce sequence-specific silencing in mammalian cells. Genes Dev 2002; 16: 948–58.
8 Brummelkamp TR, Bernards R, Agami R. A system for stable expression of short interfering RNAs in mammalian cells. Science 2002; 296: 550–3.
9 Alibu VP, Storm L, Haile S, Clayton C, Horn D. A doubly inducible system for RNA interference and rapid RNAi plasmid construction in Trypanosoma brucei. Mol Biochem Parasitol 2005; 139: 75–82.
10 Hosono T, Mizuguchi H, Katayama K, Xu ZL, Sakurai F, Ishii-Watabe A, *et al*. Adenovirus vector-mediated doxycycline-inducible RNA interference. Hum Gene Ther 2004; 15: 813–9.
11 Czauderna F, Santel A, Hinz M, Fechtner M, Durieux B, Fisch G, *et al*. Inducible shRNA expression for application in a prostate cancer mouse model. Nucleic Acids Res 2003; 31: e127.
12 Robinson R. RNAi therapeutics: how likely, how soon? PLoS Biol 2004; 2: E28.
13 Wesley SV, Liu Q, Wielopolska A, Ellacott G, Smith N, Singh S, *et al*. Custom knock-outs with hairpin RNA-mediated gene silencing. Methods Mol Biol 2003; 236: 273–86.
14 van den Haute C, Eggermont K, Nuttin B, Debyser Z, Baekelandt V. Lentiviral vector-mediated delivery of short hairpin RNA results in persistent knockdown of gene expression in mouse brain. Hum Gene Ther 2003; 14: 1799–807.
15 Liu XD, Ma SM, Liu Y, Liu SZ, Sehon A. Short hairpin RNA and retroviral vector-mediated silencing of p53 in mammalian cells. Biochem Biophys Res Commun 2004; 324: 1173–8.
16 Zhao, LJ, Jian H, Zhu H. Specific gene inhibition by adenovirus-mediated expression of small interfering RNA. Gene 2003; 316: 137–41.
17 Xia XG, Zhou H, Ding H, Affar el B, Shi Y, Xu Z. An enhanced U6 promoter for synthesis of short hairpin RNA. Nucleic Acids Res 2003; 31: e100.
18 Shen C, Buck AK, Liu X, Winkler M, Reske SN. Gene silencing by adenovirus-delivered siRNA. FEBS Lett 2003; 539: 111–4.
19 Brummelkamp TR, Bernards R, Agami R. Stable suppression of tumorigenicity by virus-mediated RNA interference. Cancer Cell

2002; 2: 243–7.
20 Paddison, PJ, Caudy AA, Hannon GJ. Stable suppression of gene expression by RNAi in mammalian cells. Proc Natl Acad Sci USA 2002; 99: 1443–8.
21 Gou D, Jin N, Liu L. Gene silencing in mammalian cells by PCR-based short hairpin RNA. FEBS Lett 2003; 548: 113–8.
22 Tattersfield AS, Croon RJ, Liu YW, Kells AP, Faull RL, Connor B. Neurogenesis in the subventricular zone following transcranial magnetic field stimulation and nigrostriatal lesions. J Neurosci Res 2004; 78: 16–28.
23 Billy E, Brondani V, Zhang H, Muller U, Filipowicz W. Specific interference with gene expression induced by long, double-stranded RNA in mouse embryonal teratocarcinoma cell lines. Proc Natl Acad Sci USA 2001; 98: 14428–33.
24 Castanotto D, Rossi JJ. Construction and transfection of PCR products expressing siRNAs or shRNAs in mammalian cells. Methods Mol Biol 2004; 252: 509–14.
25 Castanotto, D, Li H, Rossi JJ. Functional siRNA expression from transfected PCR products. RNA 2002; 8: 1454–60.
26 Sioud M, Leirdal M. Potential design rules and enzymatic synthesis of siRNAs. Methods Mol Biol 2004; 252: 457–69.
27 Yu, JY, DeRuiter SL, Turner DL. RNA interference by expression of short-interfering RNAs and hairpin RNAs in mammalian cells. Proc Natl Acad Sci USA 2002; 99: 6047–52.
28 Paddison PJ, Caudy AA, Sachidanandam R, Hannon GJ. Short hairpin activated gene silencing in mammalian cells. Methods Mol Biol 2004; 265: 85–100.
29 Hannon, GJ, Conklin DS. RNA interference by short hairpin RNAs expressed in vertebrate cells. Methods Mol Biol 2004; 257: 255–66.
30 Zeng Y, Cai X, Cullen BR. Use of RNA polymerase II to transcribe artificial microRNAs. Methods Enzymol 2005; 392: 371–80.

Acta Pharmacologica Sinica 2005 Dec; 26 (12): 1474–1478

Blackwell Publishing

Full-length article

Enzymological characterization of FII_a, a fibrinolytic enzyme from *Agkistrodon acutus* venom[1]

Xiu-xia LIANG, Ying-na ZHOU, Jia-shu CHEN[2], Peng-xin QIU, Hui-zhen CHEN, Huan-huan SUN, Yu-ping WU, Guang-mei YAN

Department of Pharmacology, Zhongshan Medical College, Sun Yat-Sen University, Guangzhou 510080, China

Key words

snake venoms; *Agkistrodon acutus*; fibrinolysis; metalloproteinase

[1] Project supported by the Guangdong Science and Technology Commission (No 001365).
[2] Correspondence to Prof Jia-shu CHEN.
Phn 86-20-8733-0553.
Fax 86-20-8733-1577.
E-mail jiashu@gzsums.edu.cn

Received 2005-05-10
Accepted 2005-07-18

doi: 10.1111/j.1745-7254.2005.00204.x

Abstract

Aim: To study the enzymological characterization of a fibrinolytic enzyme (FII_a) from *Agkistrodon acutus* venom. **Methods:** The fibrinogenolytic effect and the influences of several protease inhibitors, chelating agents, and metal ions on fibrinogenolytic activity were visualized by sodium dodecyl sulfate-polyacrylamide gel electrophoresis. The metal content of FII_a was determined by atomic absorption spectroscopy. **Results:** After incubation with FII_a (0.25 g/L), Aα-, Bβ- and γ-chains of fibrinogen disappeared within 5 min, 30 min, and 8 h , respectively. The molecular weights of major degradation products were 45 000 and 41 000, which were different from those bands produced by plasmin. The fibrinogenolytic activity of FII_a was strongly inhibited by ethylenediamine tetraacetic acid (EDTA), ethyleneglycol tetraacetic acid (EGTA), dithiothreitol and cysteine, but not by phenylmethyl-sulfonyl fluoride and soybean trypsin inhibitor. Zinc (3171±25 mg/kg), potassium (489±17 mg/kg) and calcium (319±13 mg/kg) were found in FII_a. Zn^{2+}, Ca^{2+} and Mg^{2+} could recover the fibrinogenolytic activity of FII_a, which was inhibited by EDTA. Only Ca^{2+} could recover the fibrinogenolytic activity inhibited by EGTA. **Conclusion:** FII_a can degrade the Aα-, Bβ- and γ-chains of fibrinogen. FII_a is a metalloproteinase, and Zn^{2+}, Ca^{2+}, and disulfide bonds are necessary for its fibrinogenolytic activity.

Introduction

Studies on snake venoms have been proceeding for a long time. It is known that fractions of snake venom exhibit a number of biological activities, such as fibrinogenolysis and/or fibrinolysis, and anti-platelet aggregation[1]. Approximately 3 kinds of enzymes from snake venoms can degrade fibrinogen, these are thrombin-like enzyme (TLE)[2], plasminogen activator[3], and fibrinolytic enzyme. Among them, fibrinolytic enzymes can directly degrade not only fibrinogen but also fibrin *in vitro* and *in vivo*. Furthermore, they are not inhibited by proteinase inhibitors in human blood. With their potential use for treating thrombotic disease the fibrinolytic enzymes have been widely investigated. The fibrinolytic enzymes have been purified from the venoms of *Agkistrodon acutus*[4], *A piscivorus piscivorus*[5], *A contortrix*[6], *A rhodostoma*[7], *Bothrops jararaca*[8], *Crotalus atrox*[9], *Trimeresurus mucrosquamatus*[10] and *Vipera lebetina*[11]. More than 70 kinds of fibrinolytic enzymes have been isolated, and novel fibrinolytic enzymes continue to be reported.

The fibrinolytic enzyme from Taiwanese *Agkistrodon acutus* venom was first isolated by Ou-yang and Huang[12]. In our previous work, another fibrinolytic enzyme called FII_a was purified from Anhui *Agkistrodon acutus* venom. FII_a can degrade fibrin and fibrinogen *in vitro*, and solubilize thrombus *in vivo*[4,13]. However, the enzymological characteristics of FII_a have not been shown clearly. In the present investigation, we mainly investigate the influences of several protease inhibitors, chelating agents, and metal ions on the fibrinogenolytic activity of FII_a. The metal content was also determined.

Materials and methods

Snake venom Lyophilized *Agkistrodon acutus* venom

was collected from Qimen Snake Farm (Anhui, China).

Reagents DEAE-Sephadex A-50, Sephadex G-75, ethylenediamine tetracetic acid (EDTA), ethyleneglycol tetraacetic acid (EGTA), phenylmethylsulfonylfluoride (PMSF) and soybean trypsin inhibitor (SBTi) were purchased from GE Health Care (Little Chalfont, UK). Bovine fibrinogen and plasmin were from Sigma (St Louis, MO, USA). Molecular weight protein standards were from NEB (Beverly, MA, USA). All other chemicals and solvents were of analytical grade from commercial sources.

Purification of the enzyme FII_a, a fibrinolytic enzyme from *Agkistrodon acutus* venom, was prepared according to the method described by Liang *et al*[4].

Fibrinogenolytic activity assay FII_a (1 g/L, 150 μL) was incubated with 450 μL of bovine fibrinogen (1 g/L) at 37 ºC. Aliquots were taken at 5 min, 15 min, 30 min, 45 min, 1 h, 4 h and 8 h intervals, and 600 μL of a denaturing solution (10 mol/L urea, 4% sodium dodecylsulfate and 4% β-mercaptoethanol) was added and the mixture was incubated at 100 ºC for 4 min. Each sample (20 μL) was analyzed by sodium dodecyl sulphate–polyacrylamide gel electrophoresis (SDS-PAGE) using a 4% spacer gel and a 12% separation gel[14]. Human plasmin (50 U/L) was used as positive control.

Effect of inhibitiors on fibrinogenolytic activity The effects of EDTA (5 mmol/L), EGTA (5 mmol/L), PMSF (5 mmol/L), SBTi (0.15 g/L), dithiothreitiol (DTT; 5 mmol/L) and cysteine (5 mmol/L) on fibrinogenolytic activity were examined by incubation with FII_a (1 g/L) at 37 ºC for 1 h. After adding bovine fibrinogen (1 g/L), the mixture was incubated for a further 1 h. Each sample (20 μL) was analyzed by SDS-PAGE.

Reactivation by metal ions on fibrinogenolytic activity FII_a (1 g/L, 150 μL) was incubated with EDTA (final concentration: 5 mmol/L) at 37 ºC for 1 h. $MgCl_2$, $CaCl_2$ and $ZnCl_2$ (final concentrations: 5 mmol/L) were added to the incubation solution, and the mixture was incubated for a further 1 h. The fibrinogenolytic activity was examined by SDS-PAGE after a 1-h incubation with 450 μL of bovine fibrinogen (1 g/L). The same experiment was performed with EGTA (final concentration: 5 mmol/L) instead of EDTA.

Metal content assay Metal content was determined using an atomic absorption spectrophotometer. The absorbances of standard solutions were used to draw standard graphs. The metal content of FII_a was estimated by comparison with the standard curve[14].

Results

FII_a degraded the Aα-chain preferentially, followed by the Bβ-chain of fibrinogen, but the γ-chain was the most insusceptible to the enzyme. At a molar ration of 3:1 (fibrinogen: FII_a), the Aα-chain was totally degraded within 5 min, with relatively lower activity for the Bβ-chain, which disappeared within 30 min. The γ-chain was only degraded following a prolonged 8-h incubation with FII_a (Figure 1A). Concomitant with the digestion of fibrinogen, major fragments of M_r approximately 45 000 and 41 000 were observed.

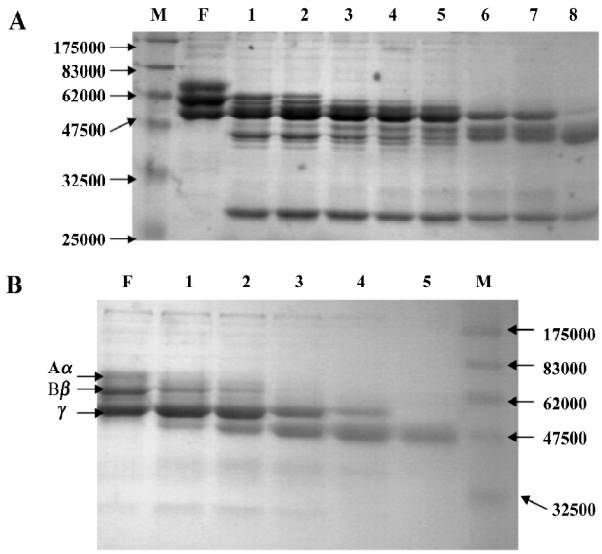

Figure 1. Sodium dodecyl sulfate–polyacrylamide gel electrophoresis analysis of degraded fibrinogen (1 g/L, 450 μL) by (A) FII_a (1 g/L, 150 μL) and (B) plasmin (50 U/L) at 37 ºC. (A) Lanes 1–8: FII_a+fibrinogen incubated for 5 min, 15 min, 30 min, 45 min, 1 h, 2 h, 4 h and 8 h. (B) Lanes 1–5: plasmin+fibrinogen incubated for 5 min, 15 min, 30 min, 45 min and 1 h. M, marker; F, fibrinogen.

When fibrinogen was incubated with human plasmin, the Aα- and Bβ-chains disappeared within 15 min, while the γ-chain disappeared within 1 h. The major digestion fragment observed was at M_r 45 000, of which the cleavage pattern was different from that of FII_a (Figure 1B).

The fibrinogenolytic activity of FII_a was inhibited by EDTA, EGTA, DTT and cysteine, but not by PMSF or SBTi (Table 1). The fibrinogen was still intact after incubation with FII_a pretreated with EDTA, EGTA, DTT, and cysteine (Figure 2). However, the fibrinogen was degraded after incubation with FII_a pretreated with PMSF and SBTi (Figure 2). Zn^{2+}, Ca^{2+}, and Mg^{2+}, at concentrations of 5 mmol/L, could restore the fibrinogenolytic activity of EDTA-treated FII_a. Only Ca^{2+} could restore the fibrinogenolytic activity of EGTA-treated FII_a. Both 1 mmol/L and 5 mmol/L Ca^{2+} were effective (Figure 3).

Zn^{2+}, K^+ and Ca^{2+} were found in significant quantities, at 3171±25 mg/kg, 489±17 mg/kg and 319±13 mg/kg, respectively. The concentrations of Mg^{2+}, Fe^{2+} and Cu^{2+} were only

Table 1. Effect of inhibitors on the fibrinogenolytic activity of FII_a.

Inhibitor	Concentration/mmol·L^{-1}	Fibrinogenolytic activity
EDTA	1.0	–
	0.1	–
	0.01	+/–
EGTA	5	–
DTT	5	–
Cysteine	5	–
SBTi	0.15 g/L	+
PMSF	5	+

DTT, dithiothreitol; EDTA, ethylenediamine tetracetic acid; EGTA, ethyleneglycol tetraacetic acid; PMSF, phenylmethylsulfonylfluoride; SBTi, soybean trypsin inhibitor.

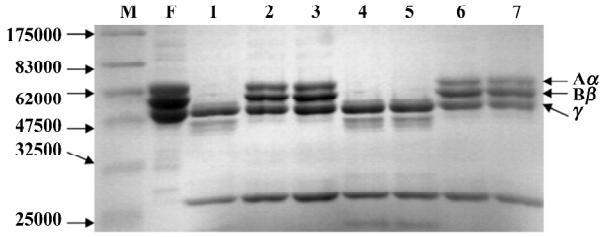

Figure 2. The effect of inhibitors on the fibrinogenolytic activity of FII_a by sodium dodecyl sulfate-polyacrylamide gel electrophoresis analysis. Lane 1, FII_a+fibrinogen; lane 2, FII_a+5 mmol/L EDTA+fibrinogen; lane 3, FII_a+5 mmol/L EGTA+fibrinogen; lane 4, FII_a+5 mmol/L PMSF+fibrinogen; lane 5, FII_a+0.15 g/L SBTi+fibrinogen; lane 6, FII_a+5 mmol/L DTT+fibrinogen; lane7, FII_a+5 mmol/L cysteine+fibrinogen. M, marker; F, fibrinogen.

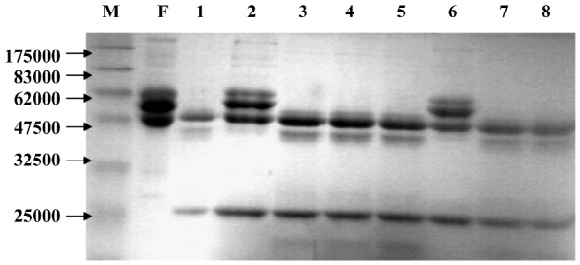

Figure 3. Reactivation by metal ions on fibrinogenolytic activity of FII_a by sodium dodecyl sulfate-polyacrylamide gel electrophoresis analysis. Lane 1, FII_a+fibrinogen; lane 2, FII_a+1 mmol/L EDTA+fibrinogen; lane 3, FII_a+1 mmol/L EDTA+$ZnCl_2$+fibrinogen; lane 4, FII_a+1 mmol/L EDTA+$MgCl_2$+fibrinogen; lane 5, FII_a+1 mmol/L EDTA+$CaCl_2$+fibrinogen; lane 6, FII_a+1 mmol/L EGTA+fibrinogen; lane 7, FII_a+1 mmol/L EGTA+1 mmol/L $CaCl_2$+fibrinogen ; lane 8, FII_a+1 mmol/L EGTA+5 mmol/L $CaCl_2$+fibrinogen. M, marker; F, fibrinogen.

at trace amounts (Table 2). For each mole of FII_a, there was approximately 1 mole of Zn^{2+}, 0.3 mole of K^+ and 0.2 mole of Ca^{2+}.

Table 2. The metal contents of FII_α. n=3. Mean±SD.

Metal ion	Content/mg·kg^{-1}
Zn^{2+}	3171±25
K^+	489±17
Ca^{2+}	319±13
Mg^{2+}	26±7
Fe^{2+}	26±2
Cu^{2+}	24±3

Discussion

FII_a is a α,β-fibrinogenase because it degraded both the Aα-chain and the Bβ-chain of fibrinogen[15]. The Aα-chain of fibrinogen was very susceptible to FII_a, and it was completely degraded within 5 min. Cleavage of the γ-chain of fibrinogen was observed only with a prolonged incubation time. Thus far there have been few reports of fibrin(ogen)olytic snake venom enzymes that cleave of the γ-chain. No enzyme reported has shown cleavage specificity directed solely at the γ-chain[16]. Because the γ-chain of fibrinogen was stable when was incubated with snake venom fibrin(ogen)olytic enzyme, we postulated that the degradation might occur at either an increased incubation time or at an increased concentration. In our previous study, the γ-chain was unaffected after a 2-h incubation. However, in the present study FII_a appeared to degrade the γ-chain after prolonged (8 h) incubation. The same phenomenon was noticed for cerastase F-4 (from *Cerastes cerastes* venom) and a fibrin(ogen)olytic enzyme from *V lebetina* venom, and they appeared to degrade the γ-chain following 48-h and 24-h incubations, respectively[17,18]. Plasmin also cleavages the Aα-, Bβ-, and γ-chains of fibrinogen, but the patterns are different from those observed when cleaved by FII_a. It is interesting that various fibrin(ogen)olytic enzymes seem to produce different degradation patterns for fibrinogen. For example, FII_a mainly yields fragments of 45 kDa and 41 kDa, while basilase produces fragments of 45 kDa, 36 kDa and 10 kDa, and atroxase gives fragments of 45 kDa and 38 kDa[19]. The studies on some fibrin(ogen)olytic enzymes reveal that their cleavage preference is commonly directed to the amino-terminal side of hydrophobic amino acid residues. They display distinct and unique cleavage characteristics with fibrinogen.

The fibrin(ogen)olytic enzymes from snake venoms can be classified as metalloproteinases or serine proteinases. Chelating agents (EDTA, EGTA) completely inhibited FII_a, while serine protease inhibitors (PMSF, SBTi) were

ineffective, indicating that it belongs to the metalloproteinase group. This was supported by data from atomic absorption spectroscopy. For each mole of FII_a there was approximately 1 mole of Zn^{2+}, 0.3 mole of K^+ and 0.2 mole of Ca^{2+}. Like many of the venom fibrinolytic enzymes, FII_a is a zinc metalloproteinase. Besides Zn^{2+}, Ca^{2+} is another metal ion often found in venom with fibrinolytic enzymes. Metal analysis has indicated that the calcium content of atroxase (from western diamondback rattlesnake venom)[9] and lebetase (from *V. lebetina* snake venom)[20] is 0.3 mol/mol and 1 mol/mol, respectively. In adamalysin from *C. adamanteus*[21] and atrolysin c(d) from *C. atrox*[22] it was found that except Zinc-binding site, a calcium ion is bound near the carboxy-terminus of the enzyme. Thus far, only atroxase was reported to contain 1 mol/mol of K^+, while FII_a contains 0.3 mol/mol of K^+. The functions of calcium and potassium have not been elucidated, but they may play a role in retaining the stability of the protein.

Zn^{2+}, Ca^{2+} and Mg^{2+} were effective in restoring the activity of EDTA-treated FII_a, while only Ca^{2+} could restore the activity of EGTA-treated FII_a. The mechanism for this is not clear. It is reported that snake venom metalloproteinases have Zn^{2+}-dependent activities, but some are more active in the presence of Ca^{2+}[23,24]. This seems probably responsible in part for this phenomenon. The effect of Mg^{2+} on the activity of FII_a needs to be elucidated. FII_a is inhibited by DTT and cysteine, suggesting that disulfide bonds are necessary for holding the structure.

In conclusion, like many venom fibrin(ogen)olytic enzymes, FII_a is a metalloproteinase. Both Zn^{2+} and Ca^{2+} play important roles in the fibrinogenolytic activity of FII_a.

References

1 Tseng YL, Lee CJ, Huang TF. Effects of a snake venom metalloproteinase, triflamp, on platelet aggregation, platelet-neutrophil and neutrophil-neutrophil interactions: involvement of platelet GPIbα and neutrophil PSGL-1. Thromb Haemost 2004; 91: 315–24.

2 Tatematsu R, Komori Y, Nikai T. A new thrombin-like enzyme, flavoviridiobin from the venom of *Trimeresurus flavoviridis* (habu). J Nat Toxins 2000; 9: 327–39.

3 Zhang Y, Wisner A, Xiong Y, Bon C. A novel plasminogen activator from snake venom. Purification, characterization, and molecular cloning. J Biol Chem 1995; 270: 10 246–55.

4 Liang XX, Chen JS, Zhou YN, Qiu PX, Yan GM. Purification and biochemical characterization of FIIa, a fibrinolytic enzyme from *Agkistrodon acutus* venom. Toxicon 2001; 39: 1133–9.

5 Hahn BS, Chang IM, Kim YS. Purification and characterization of piscivorase I and II, the fibrinolytic enzymes from eastern cottonmouth moccasin venom (*Agkistrodon piscivorus*). Toxicon 1995; 33: 929–41.

6 Trikha M, Schmitmeier S, Markland FS. Purification and characterization of fibrolase isoforms from venom of individual southern copperhead (*Agkistrodon contortrix*) snakes. Toxicon 1994; 32: 1521–31.

7 Ouyang C, Hwang LJ, Huang TF. Alpha-fibrinogenase from *Agkistrodon rhodostoma* (Malayan pit viper) snake venom. Toxicon 1983; 21: 25–33.

8 Maruyama M, Sugiki M, Yoshida E, Shimaya K, Mihara H. Broad substrate specificity of snake venom fibrinolytic enzymes: possible role in haemorrhage. Toxicon 1992; 30: 1387–97.

9 Willis TW, Tu AT. Purification and biochemical characterization of atroxase, a nonhemorrhagic fibrinolytic protease from western diamondback rattlesnake venom. Biochemistry 1988; 27: 4769–77.

10 Hung CC, Huang KF, Chiou SH. Characterization of one novel venom protease with beta-fibrinogenase activity from the Taiwan habu (*Trimeresurus mucrosquamatus*): purification and cDNA sequence analysis. Biochem Biophys Res Commun 1994; 205: 1707–15.

11 Siigur E, Siigur J. Purification and characterization of lebetase, a fibrinolytic enzyme from *Vipera lebetina* (snake) venom. Biochim Biophys Acta 1991; 1074: 223–9.

12 Ou-yang C, Huang TF. Purification and characterization of the fibrinolytic principle of *Agkistrodon acutus* venom. Biochim Biophys Acta 1976; 439: 146–53.

13 Chen JS, Liang XX, Qiu PX, Yan GM. Thrombolysis effect with FIIa from *Agkistrodon acutus* venom in different thrombosis model. Acta Pharmacol Sin 2001; 22: 420–2.

14 Gasmi A, Chabchoub A, Guermazi S, Karoui H, Elayeb M, Dellagi K. Further characterization and thrombolytic activity in a rat model of fibrinogenase from *Vipera Lebetina* venom. Thromb Res 1997; 86: 233–42.

15 Pinto AF, Dobrovolski R, Veiga AB, Guimaraes JA. Lonofibrase, a novel α-fibrinogenase from *Lonomia obliqua* caterpillars. Thromb Res 2004; 113: 147–54.

16 Swenson S, Markland FS Jr. Snake venom fibrin(ogen)olytic enzymes. Toxicon 2005; 45: 1021–39.

17 Daoud E, Tu AT, el-Asmar MF. Mechanism of the anticoagulant, Cerastase F-4, isolated from *Cerastes cerastes* (Egyptian sand viper) venom. Thromb Res 1986; 41: 791–9.

18 Gasmi A, Karoui M, Benlasfar Z, Karoui H, el-Ayeb M, Dellagi K. Purification and characterization of a fibrinogenase from *Vipera lebetina* (desert adder) venom. Toxicon 1991; 29: 827–36.

19 Gatta D, Dong A, Witt J, Tu AT. Biochemical characterization of basilase, a fibrinolytic enzyme from *Crotalus basiliscus*. Arch Biochem Biophys 1995; 317: 365–73.

20 Siigur J, Samel M, Tonismagi K, Subbi J, Siigur E, Tu AT. Biochemical characterization of lebetase, a direct-acting fibrinolytic enzyme from *Vipera lebetina* snake venom. Thromb Res 1998; 90: 39–49.

21 Gomis-Ruth FX, Kress LF, Bode W. First structure of a snake venom metalloproteinase: a prototype for matrix metalloproteinase/

collagenase. EMBO J 1993; 12: 4151–7.
22 Zhang D, Botos I, Gomis-Ruth FX, Doll R, Blood C, Njoroge FG *et al*. Structural interaction of natural and synthetic inhibitors with the venom metalloproteinase, atrolysin c (from d). Proc Natl Acad Sci USA 1994; 91: 8447–51.
23 Assakura MT, Reichl AP, Asperti MC, Mandelbaum FR. Isolation of the major proteolytic enzyme from the venom of the snake *Bothrops moojeni* (caissaca). Toxicon 1985; 23: 691–706.
24 De-Camargo-Goncalves LR, Chudzinski-Tavassi AM. High molecular mass kininogen inhibits metalloproteinases of *Bothrops jararaca* snake venom. Biochem Biophys Res Commun 2004; 318: 53–9.

The 15th World Congress of Pharmacology (IUPHAR-2006)

2006, July 2-7 Beijing International Convention Center, China

Info: Ms Xiao-dan Zhao
Chinese Pharmacological Society
1, Xian Nong Tan St
Beijing 100050, China
Phn/Fax86-10-6316-5211
E-mail zhxd@imm.ac.cn
http://www.iuphar2006.org/
http://www.cnphars.org/

Acta Pharmacologica Sinica 2005 Dec; 26 (12): 1479–1484

Blackwell Publishing

Full-length article

Preparation and development of equine hyperimmune globulin F(ab')$_2$ against severe acute respiratory syndrome coronavirus[1]

Jia-hai LU[2,8,9], Zhong-min GUO[2,9], Wen-yu HAN[3,9], Guo-ling WANG[2,9], Ding-mei ZHANG[2], Yi-fei WANG[4], Sheng-yun SUN[4], Qin-he YANG[4], Huan-ying ZHENG[5], Bing L WONG[6], Nan-shan ZHONG[7]

[2]Sun Yat-sen University, Guangzhou 510080, China; [3]The Agriculture School of Jilin University, Changchun 130062, China; [4]Ji-nan University, Guangzhou 510632, China; [5]Center for Disease Control and Prevention of Guangdong Province, Guangzhou 510300, China; [6]Advantek Biologics, Hong Kong, China; [7]Guangzhou Institute of Respiratory Diseases, Guangzhou Medical College, Guangzhou 510120, China

Key words

severe acute respiratory syndrome coronavirus; neutralizing antibodies; hyperimmune globulin; cross protection; F(ab')$_2$ fragments

[1] Project supported by the LIC Foundation of Hong Kong and the Science Foundation of Guangdong Province (No 2003Z3-E0461).
[8] Correspondence to Dr Jia-hai LU.
Phn 86-20-8733-0605.
Fax 86-20-8733-2438.
E-mail jiahailu@yahoo.com.cn
[9] These authors contributed equally to this work.

Received 2005-06-23
Accepted 2005-08-10

doi: 10.1111/j.1745-7254.2005.00210.x

Abstract

Aim: The resurgence of severe acute respiratory syndrome (SARS) is still a threat because the causative agent remaining in animal reservoirs is not fully understood, and sporadic cases continue to be reported. Developing high titers of anti-SARS hyperimmune globulin to provide an alternative pathway for emergent future prevention and treatment of SARS. **Methods:** SARS coronavirus (CoV)F69 (AY313906) and Z2-Y3 (AY394989) were isolated and identified from 2 different Cantonese onset SARS patients. Immunogen was prepared from SARS-CoV F69 strain. Six health horses were immunized 4 times and serum was collected periodically to measure the profile of specific IgG and neutralizing antibodies using indirect enzyme-linked immunosorbent assay and a microneutralization test. Sera were collected in large amounts at the peak, where IgG was precipitated using ammonium sulphate and subsequently digested with pepsin. The product was then purified using anion-exchange chromatography to obtain F(ab')$_2$ fragments. **Results:** The specific IgG and neutralizing antibody titers peaked at approximately week 7 after the first immunization, with a maximum value of 1:14210. The sera collected at the peak were then purified. Fragment of approximately 15 g F(ab')$_2$ was obtained from 1 litre antiserum and the purity was above 90% with the titer of 1:5120, which could neutralize the other strain (SARS-CoV Z2-Y3) as well. **Conclusion:** This research provides a viable strategy for the prevention and treatment of SARS coronavirus infection with equine hyperimmune globulin, with the purpose of combating any resurgence of SARS.

Introduction

Severe acute respiratory syndrome (SARS) emerged in Southeast Asia in late 2002 and subsequently spread internationally. The causative agent was quickly identified as a previously unknown member of the Coronaviridae family[1–3]. According to the World Health Organization, up to 2004 Apr 21, SARS coronavirus infected more than 8000 people in various countries worldwide and caused approximately 800 deaths[4]. Although SARS infection of human beings has been contained through infection-control measures, resurgence is still a threat because the causative agent remaining in animal reservoirs is not fully understood, and sporadic cases continue to be reported in Singapore[5,6], Taiwan[7] and mainland China[8,9].

There are no specific vaccines and effective drugs currently available for SARS-CoV[1,2,10,11]. Until an effective vaccine is developed, the best hope for the treatment of infection and the prevention and control of future outbreaks is the development of passive immunotherapy with SARS-CoV-specific antibodies[11]. Immunoglobulin is an effective method used in protection against animal coronavirus: transmissible

gastroenteritis virus (TGEV)[12,13], mouse hepatitis virus[14], and bovine coronavirus[15]. There is clinical evidence that serum from recovered patients is effective in infected individuals[16,17]. These observations suggest that hyperimmune serum could be developed for the passive treatment of SARS. The use of equine antisera for emergent prevention and treatment of infectious diseases has been proven to be an effective and safe strategy, such as in rabies virus[18,19]. Therefore, immunoprophylaxis and treatment of SARS coronavirus infection with equine hyperimmune globulin might be a viable strategy for controlling SARS.

Materials and methods

Virus strains Severe acute respiratory syndrome corona-virus Z2-Y3 (AY394989) and F69 (AY313906), isolated from the samples of 2 different Cantonese onset SARS patients in 2003, were sequenced and compared, showing certain differences (Table 1). Viral titres of SARS-CoV Z2-Y3 and F69 strains were determined to be $10^{6.5}$ 50% tissue-culture-infective doses ($TCID_{50}$)/mL and $10^{6.7}$ $TCID_{50}$/mL with the Reed-Muench method, respectively[20–22].

Antigen preparation F69 strain was used as antigen for immunization. African green monkey kidney (Vero-E6) cells, infected with SARS CoV F69 strain, were cultivated in serum-free minimum essential medium (MEM) (GIBCO**)** and observed periodically for cytopathic effect (CPE). When 75%–100% cytopathy was reached, infected Vero-E6 cells were frozen and thawed 3 times, which was subsequently centrifuged at 8000×*g* for 30 min, and then the cell debris was decanted. The supernatant was collected and stored at –70 ºC until used. The viral supernatant was then centrifuged at 30 000×*g* for 3 h. The precipitate was diluted with phosphate buffered saline (PBS), which was used as antigen for immunization.

Animal immunization Six 4–9 year-old healthy horses were provided by the Quartermaster University of PLA. Immunization of horses was performed according to the State Food and Drug Administration (SFDA) standard operating procedures. On d 0 and d 10, all horses were injected with 1.0 mL antigen intramuscularly (SARS-CoV F69) with complete Freund's adjuvant (FCA, Sigma). On d 21 and d 28, horses were injected with the same antigen 2.5 mL im, with incomplete Freund's adjuvant (FIA, Sigma). Eight batches of sera were collected from trachelo veins on d 0, d 10, d 21, d 28, d 35, d 42, d 49, and d 55 after the first immunization, which were stored at -20 °C for the measurement of antibody titers.

Enzyme-linked immunosorbent assay (ELISA) Severe acute respiratory syndrome coronavirus specific IgG was measured using an indirect enzyme-linked immunosorbent assay (ELISA) and whole purified SARS-CoV F69 as antigen. In brief, polystyrene micro well plates were coated with antigen (100 μL/well containing 1.0 μg/mL virus protein) in carbonate-bicarbonate buffer (pH 9.6). The wells were washed 3 times with PBS and then blocked with 15% bovine serum in

Table 1. Complete genomic sequence comparison between F69 and Z2-Y3. N1, atattaggtttttac; N2, caagaatgta; –, no nucleotide.

Locus	1–15	2015	3852	5455	6247	6760	7347	7777	8094
F69	N1	C	C	T	C	G	A	G	T
Z2–Y3	–	T	T	C	T	A	C	A	C

Locus	8591	9333	10265	11493	13470	14186	16959	17565	20374 -20383
F69	G	C	T	T	A	T	T	T	N2
Z2-Y3	A	A	C	C	G	A	C	G	–

Locus	21732	22233	24706	25275	25309	26488	27403	29358
F69	G	T	G	G	G	G	T	G
Z2-Y3	A	C	A	A	A	T	C	A

PBS containing 0.05% Tween-20 (PBST) at 37 °C for 1 h. After 3 washes with PBST, serially twofold diluted serum samples (from 1:100 to a final 1:51200) were added to the plates and incubated at 37°C for 1 h. Horseradish peroxidase (HRP)-conjugated goat anti-horse IgG (Sigma, USA) diluted 3000-fold in PBS was added, followed by 3 washes. Following incubation at 37 °C for 1 h, the plates were washed as above and the substrate tetramethylbenzidine (TMB) solution (Sigma) was added to the wells. After incubation at 37 °C for 15 min, the reaction was stopped by adding 2.0 mmol/L sulfuric acid, and the absorbance value at 450 nm (A450) was measured with a microplate reader (Model 550, BioRad). IgG antibody titer was defined as the highest dilution of serum when the A450 ratio (A450 of negative serum) was greater than 2.0.

Microneutralization assay The neutralization assay was performed according to modified operating procedures of the Manual for the virological investigation of polio formulated by WHO/EPI/GEN/97.01. (http://www.who.ch/programmes/gpv/gEnglish/avail/gpvcatalog/catlog.htm). Each serum sample was serially diluted in twofold 1:10 dilution in MEM maintenance medium to a final dilution of 1:20 480 and incubated with an equal volume of 100 $TCID_{50}$/25 μL of purified F69 or Z2-Y3 strain for 3 h at 36 °C. The virus-antibody mix was then inoculated onto Vero-E6 cell (3×10^5 cells/mL) monolayers in 96-well plates at 37 °C for approximately 6 d. Wells for normal cell control and virus control were added to 100 μL maintenance medium and unneutralized active virus dilution, respectively. The plates were incubated until CPE developed in all the virus controls but the cell control remained normal. Neutralizing antibody titer was the highest dilution of serum, which protected 50% of the cultures against 100$TCID_{50}$ of the challenge virus, when the virus control (no serum) showed complete CPE.

Purification of immunoglobulin Horse antiserum was thawed in 37 °C water bath, added to 45% saturated ammonium sulphate solution, then mixed gently at 22 °C for 30 min, centrifuged at 10 000×*g*, and the precipitation generated was collected and stored at 4 °C overnight. The ammonium sulphate precipitation was diluted using an equal volume of 0.9% NaCl solution and dialyzed to remove the salt. Then pH was adjusted to 3.5 with 0.36 mol/L HCl. Then horse serum was added to 2% pepsin (Sigma) solution and digested at 37 °C for 8 h, 24 h, 36 h, 48 h, 60 h, and 72 h, respectively. The reaction was stopped by adjusting the pH to 8.0 using 1.0 mol/L NaOH. Then the digested material was ultrafiltrated. Anion-exchange separations of ultrafiltrated material were further performed using diethylaminoethyl (DEAE) Sepharose Fast Flow (Pharmacia) Column, pre-equilibrated with 200 mL of buffer A (50 mmo/L Tris-HCl, pH 8.0). The ultrafiltrated material was pumped down the column, while the A_{280} nm of the eluted material was monitored, followed by pumping fresh buffer A until the A_{280} nm returned to the baseline. All the unbounded material, corresponding to the $F(ab')_2$ fragments was collected and stored at 4 °C. Bound contaminants can then be eluted to regenerate the column using a gradient of buffer B (containing 50 mmo/L Tris-HCl, pH 8.0, 1 mmol/L NaCl, pH 8.0). The product obtained using anion-exchange chromatography was ultrafiltrated, concentrated and added to 0.3 mol/L aminoacetic acid to obtain stock solution. According to the demanded standards of biological product, the product characteristics (eg, pH, the protein concentration and bacterial endotoxin content) were detected using serial procedures.

Sodium dodecyl sulfate polyacrylamide gel electrophoresis (SDS-PAGE) Non-reducing SDS-PAGE gels, using the buffer system described by Laemmli (1970)[23], were used to monitor the digestion process and to check for traces of undigested IgG and other unwanted materials.

Results

Identification of SARS coronavirus The virus (SARS-CoV F69) was electron microscopically visualized, and the characteristic coronavirus particle form was observed (Figure 1).

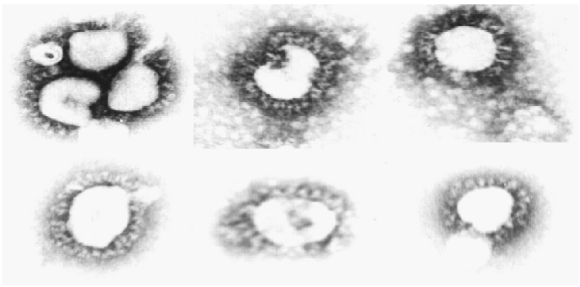

Figure 1. The virion form of severe acute respiratory syndrome coronavirus F69 isolate. 3×40 000.

Level of the specific IgG antibody Six health horses were immunized with purified SARS-CoV F69 strain. The titers of total anti-SARS-CoV IgG was measured using an indirect ELISA. The dynamic changes of specific anti-SARS-CoV IgG antibody titers are shown in Figure 2. On d 10, all sera distinctly showed positive reactions, with the range of specific IgG antibody titers from 1:160 to 1:980. Titers of specific IgG antibodies increased rapidly from week 4 and peaked at week 7 after the first immunization; the maximum value was

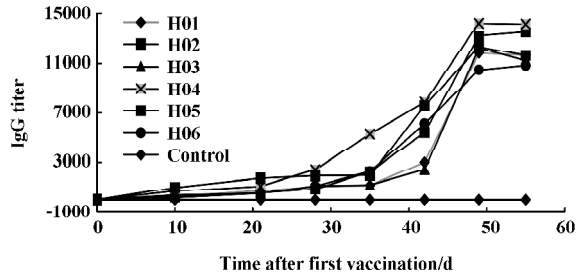

Figure 2. Changes of the specific anti-severe acute respiratory syndrome coronavirus IgG antibody titers. H, the immunized horse. The inoculation dates are on d 0, d 10, d 21, and d 28, respectively. The titers of serum specific IgG antibodies were shown on the highest dilution of serum at which the A450 ratio was greater than 2.0.

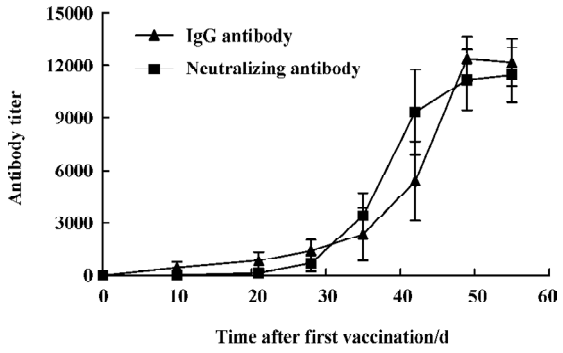

Figure 4. Comparison of the trend of change in neutralizing antibody titers with that of the specific IgG antibody titers. Each titer value was denoted as the mean of the titers of IgG and neutralizing antibody detected.

1:14210.

Titers of neutralizing antibodies The antiserum was measured using a micro-neutralization test. The kinetics of formation of neutralizing antibodies following immunization for horses were observed (Figure 3). The neutralizing antibodies were partially detectable on d 10 (from 1:10 to 1:60). After the third immunization, the neutralizing antibody titers of all the immunized horses increased rapidly on d 28. On d 48 after the first immunization, the neutralizing antibody titers of 4 of 6 equines reached the highest level. The other 2 continued increasing and reached the highest titer at 1:14240.

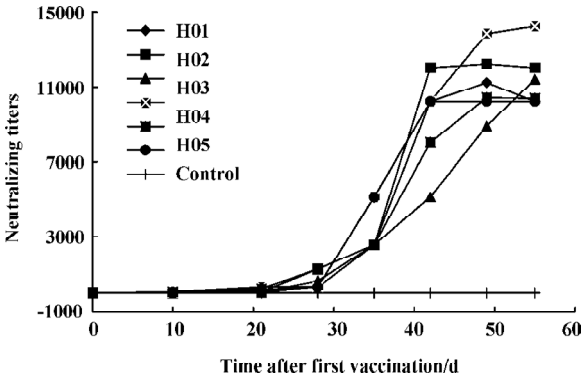

Figure 3. Kinetics of the specific anti-severe acute respiratory syndrome coronavirus neutralizing antibody titers. H, the immunized horse. The inoculation dates are on d 0, d 10, d 21, and d 28, respectively. Neutralizing antibody titers are shown on the highest dilution of serum, which protected 50% of the cultures against 100 50% tissue-culture-infective doses ($TCID_{50}$) of challenge virus.

Cross neutralization response Z2-Y3 strain was used in micro-neutralization test in vitro to measure the hyperimmune sera from the SARS-CoV F69 strain. The results indicate that the horse antiserum induced by the inactivated SARS-CoV F69 strain is capable of neutralizing the SARS-CoV Z2-Y3 strain completely.

$F(ab')_2$ preparation Digestion with pepsin at different time points was assessed using SDS-PAGE (Figure 5). The results indicate that IgG could be digested completely at pH 3.5 within 48 h and unwanted protein bands (eg albumin and transferrin) could be eliminated as well. The reaction was stopped by adjusting the pH to 8.0 using 1.0 mol/L NaOH. The anion-exchange chromatography with a salt gradient was performed to further remove high molecular weight aggregates and pepsin. Digested antisera in buffer A are separated into 3 peaks (Figure 6). Material from peak I was then concentrated. Finally, approximately15 g $F(ab')_2$ fragments were obtained from 1 litre antiserum with the purity

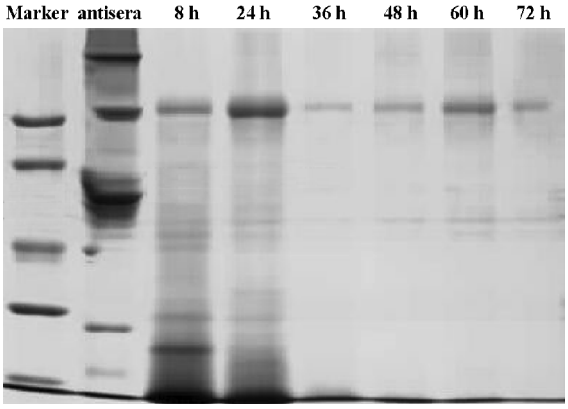

Figure 5. The digestion of equine antisera with pepsin, as assessed by sodium dodecyl sulfate polyacrylamide gel electrophoresis (SDS-PAGE) (10%) under non-reducing conditions. Digestion samples at various time points, with molecular weight markers: 97 kDa, 66 kDa, 45 kDa, 30 kDa, 20.1 kDa. $F(ab')_2$: approximately 100 kDa.

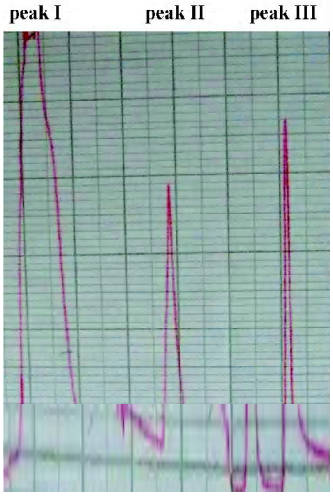

Figure 6. Removal of high molecular weight aggregate and pepsin using anion-exchange chromatography. diethylaminoethyl (DEAE) Sepharose Fast Flow ion-exchange separation of a diafiltered pepsin digested antisera. Peak I: $F(ab')_2$, Peak II: high molecular weight aggregate and Peak III: pepsin.

above 90%. The titer of neutralizing antibodies after purification was detected as 1:5120.

The product obtained above was dissolved in a suitable volume of 0.9% NaCl to adjust the protein concentration to 10 g/L. Then pH determined at 20 °C was 7.0. The bacterial endotoxin content was also detected at no more than 200 EU/mL. The terminal product according with the standard of SFDA [(2003) No.267], was stored at 4 °C.

Discussion

Severe acute respiratory syndrome has resulted in important challenges for the medical community. There are no available specific vaccines and effective drugs for use against SARS-CoV[11]. Control depends on prompt detection and isolation of cases, good infection control in hospitals, and the tracing and quarantine of contacts[24]. The widespread clinical successful application of immunoglobulins derived from heterogenous animals against rabies has a long history[25]. The passive administration of neutralizing antibodies could be an effective strategy for emergency prophylaxis and the treatment of SARS[26].

The results of our research indicate that healthy horses immunized with the SARS-CoV F69 strain can be induced to generate effective, specific and neutralizing antibodies. Analysis indicates that sequence difference existed among SARS-CoVs[27]. The sequence of the SARS-CoV F69 strain is different from that of the SARS-CoV Z2-Y3 strain (Table 1). Immunoglobulin prepared from SARS-CoV F69 strain isolated in April, 2003 could neutralize another SARS-CoV Z2-Y3 strain, which was isolated from SARS patient in February, 2003. This showed that SARS-CoV F69 and Z2-Y3 strain owned identical or similar neutralizing epitopes.

Heterogenous antisera used for treatment possibly result in anaphylactoid severe acute side-effects[28]. To avoid the side-effects caused by horse antiserum, IgG against SARS-CoV was digested with pepsin and purified with anion-exchange separations to exclude the immunogenicity of Fc fragments and to retain the special activity of binding the antigen of $F(ab')_2$ fraction. The titers of neutralizing $F(ab')_2$ against SARS-CoV was detected at higher level (1:5120). And approximately 15 g $F(ab')_2$ fragments were obtained from 1 litre antiserum, with the purity above 90%.

Until we have an efficacious vaccine and have implemented effective epidemiologic infection control measures, and given the presence of effective anti-SARS-CoV agents, SARS is likely to remain a major health threat to the world. In this article, we provide an alternative pathway of prevention and treatment of SARS, with the purpose of combating any resurgence of SARS. The profile of the antibody titer was observed, while an effective, specific and neutralizing hyperimmunoglobulin was prepared. The results indicate that the kinetics of the induced specific IgG and neutralizing antibodies are similar (Figure 4). This data paves the way for the development of an inactivated SARS vaccine.

References

1 Drosten C, Gunther S, Preiser W, van der Werf S, Brodt HR, Becker S, *et al*. Identification of a novel coronavirus in patients with severe acute respiratory syndrome. N Engl J Med 2003; 348: 1967–76.

2 Ksiazek TG, Erdman D, Goldsmith CS, Zaki SR, Peret T, Emery S, *et al*. A novel coronavirus associated with severe acute respiratory syndrome. N Engl J Med 2003; 348: 1953–66.

3 Rota PA, Oberste MS, Monroe SS, Nix WA, Campagnoli R, Icenogle JP, *et al* Characterization of a novel coronavirus associated with severe acute respiratory syndrome. Science 2003; 300: 1394–9.

4 World Health Organization [homepage on the Internet]. Summary of probable SARS cases with onset of illness from 1 November 2002 to 31 July 2003. Geneva: The Organization. [cited 2005 Jul 9] Available from: http://www.who.int/csr/sars/country/table2004_04_21/en/

5 Lim PL, Asok K, Gopalakrishna G, Chan KP, Wong CW, *et al*. Laboratory-acquired severe acute respiratory syndrome. N Engl J Med 2004; 250:1740–5.

6 World Health Organization [homepage on the Internet]. Severe acute respiratory syndrome (SARS) in Singapore. Geneva: The Organization. [cited 2005 April 10] Available from: http://www.who.int/csr/don/2003_09_10/en/

7 World Health Organization [homepage on the Internet]. Severe

Acute Respiratory Syndrome (SARS) in Taiwan, China. Geneva: The Organization. [cited 2005 May 17] Available from:http://www.who.int/csr/don/2003_12_17/en/

8 World Health Organization [homepage on the Internet]. SARS: one suspected case reported in China. Geneva: The Organization. [cited 2005 April 22] Available from: http://www.who.int/csr/don/2004_04_22/en/

9 World Health Organization [homepage on the Internet]. China's latest SARS outbreak has been contained, but biosafety concerns remain-Update 7. Geneva: The Organization. [cited 2005 July 18] Available from: www.who.int/csr/don/2004_05_18a/en/

10 Kuiken T, Fouchier RA, Schutten M, Rimmelzwaan GF, van Amerongen G, van Riel D, *et al*. Newly discovered coronavirus as the primary cause of Severe Acute Respiratory Syndrom. Lancet 2003; 362: 263–70.

11 Holmes KV. SARS-Associated Coronavirus. N Engl J Med 2003; 348: 1948–51.

12 Saif LJ, Bohl EH. Passive immunity to transmissible gastroenteritis virus: intramammary viral inoculation of sows. Ann N Y Acad Sci 1983; 409: 708–23.

13 Sestak K, Lanza I, Park SK, Weilnau PA, Saif LJ. Contribution of passive immunity to porcine respiratory coronavirus to protection against transmissible gastroenteritis virus challenge exposure in suckling pigs**.** Am J Vet Res 1996; 57: 664–71.

14 Homberger FR, Barthold SW. Passively acquired challenge immunity to enterotropic coronavirus in mice**.** Arch Virol 1992; 126: 35–43.

15 Arthington, JD, Jaynes CA, Tyler HD, Kapil S, Quigley JD 3rd. The use of bovine serum protein as an oral support therapy following coronavirus challenge in calves1. J Dairy Sci 2002; 85: 1249–54.

16 Li G, Chen X, Xu A. Profile of specific antibodies to the SARS-associated coronavirus. N Engl J Med 2003; 349: 508–9.

17 Wong VW, Dai D, Wu AK, Sung JJ. Treatment of severe acute respiratory syndrome with convalescent plasma. Hong Kong Med J 2003; 9: 199–201.

18 Wilde H, Chomchey P, Punyaratabandhu P, Phanupak P, Chutivongse S. Purified equine rabies immune globulin: a safe and affordable alternative to human rabies immune globulin. Bull World Health Organ 1989; 67: 731–6.

19 Wilde H, Chutivongse S. Equine rabies immune globulin: a product with an undeserved poor reputation. Am J Trop Med Hyg 1990; 42: 175–8.

20 Yan XG, Wan ZY, Zhang X, Chen QX, ZHeng K,Huang JC, *et al*. Isolation and identification of SARS coronavirus in Guangdong province. Chin J Exp Clin Virol 2003; 17: 213–6.

21 Lu, JH, Yan XG, GUO ZM, ZHeng HY, Zhang X, Wan ZY, *et al*. Establishment of SARS virus vaccine line (F69), Guangdong Med J 2003; 24 (SARS Suppl II): 225–7.

22 Lu, JH, ZHeng HY, Yan XG, Wan ZY, Zhang RL, Meng JX, *et al*. Establishment of SARS virus vaccine line (Y3), Guangdong Med J 2003; 24 (SARS Suppl II): 234–6.

23 Laemmli UK. Cleavage of structural proteins during the assembly of the head of bacteriophage T4. Nature 1970; 227**:** 680–5.

24 Sampathkumar P, Temesgen Z, Smith TF, Thompson RL. SARS: epidemiology, clinical presentation, management, and infection control measures. Mayo Clin Proc 2003; 78: 882–90.

25 Quiambao BP, Lang J, Vital S, Montalban CG, Le Mener V, Wood SC, *et al*. Immunogenicity and effectiveness of post-exposure rabies prophylaxis with a new chromatographically purified Vero-cell rabies vaccine (CPRV): a two-stage randomised clinical trial in the Philippines. Acta Trop 2000; 75: 39–52.

26 Sui J, Li W, Murakami A, Tamin A, Matthews LJ, Wong SK, *et al*. Potent neutralization of severe acute respiratory syndrome (SARS) coronavirus by a human mAb to S1 protein that blocks receptor association. Proc Natl Acad Sci USA 2004; 101: 2536–41.

27 Chinese SARS Molecular Epidemiology Consortium. Molecular evolution of the SARS coronavirus during the course of the SARS epidemic in China. Science 2004; 303: 1666–9.

28 Jahrling PB, Geisbert TW, Geisbert JB, Swearengen JR, Bray M, Jaax NK, *et al*. Evaluation of immune globulin and recombinant interferon-alpha2b for treatment of experimental Ebola virus infections. J Infect Dis 1999; 179 Suppl 1: 224–34.

Acta Pharmacologica Sinica 2005 Dec; 26 (12): 1485–1491

Blackwell Publishing

Full-length article

Binding of PLCδ_1PH-GFP to PtdIns(4,5)P_2 prevents inhibition of phospholipase C-mediated hydrolysis of PtdIns(4,5)P_2 by neomycin[1]

Chuan WANG, Xiao-na DU, Qing-zhong JIA, Hai-lin ZHANG[2]

Department of Pharmacology, Hebei Medical University, Shijiazhuang 050017, China

Key words

phosphatidylinositol 4,5-bisphosphate; neomycin; phospholipase C; pleckstrin homology domains; competitive binding; acetylcholine; green fluorescent proteins

[1] Project supported by the National Natural Science Foundation of China (No 30270361), Ministry of Science and Technology of China (No 2003CCA00300), HL ZHANG is a beneficiary of the National Science Fund for Distinguished Young Scholars of China (No 30325038).

[2] Correspondence to Prof Hai-lin ZHANG.
Phn 86-311-8626-5562.
Fax 86-311-8605-7291.
E-mail z_hailin@hotmail.com

Received 2005-02-22
Accepted 2005-07-06

doi: 10.1111/j.1745-7254.2005.00223.x

Abstract

Aim: To investigate the effects of the pleckstrin homology (PH) domain of phospholipase $C_{\delta 1}$ ($PLC_{\delta 1}PH$) on inhibition of phospholipase C (PLC)-mediated hydrolysis of phosphatidylinositol 4,5-bisphosphate [PtdIns(4,5)P_2] by neomycin. **Methods:** A fusion construct of green fluorescent protein (GFP) and $PLC_{\delta 1}PH$ ($PLC_{\delta 1}PH$-GFP), which is known to bind PtdIns(4,5)P_2 specifically, together with laser-scanning confocal microscopy, was used to trace PtdIns(4,5)P_2 translocation. **Results:** Stimulation of the type 1 muscarinic receptor and the bradykinin 2 receptor induced a reversible $PLC_{\delta 1}PH$-GFP translocation from the membrane to the cytosol in COS-7 cells. PLC inhibitor U73122 blocked the translocation. Wortmannin, a known PtdIns kinase inhibitor, did not affect the translocation induced by ACh, but blocked recovery after translocation, indicating that PtdIns(4,5)P_2 hydrolysis occurs through receptor-mediated PLC activation. Neomycin, a commonly used phospholipase C blocker, failed to block the receptor-induced $PLC_{\delta 1}PH$-GFP translocation, indicating that neomycin is unable to block PLC-mediated PtdIns(4,5)P_2 hydrolysis. However, in the absence of $PLC_{\delta 1}PH$-GFP expression, neomycin abolished the receptor-induced hydrolysis of PtdIns(4,5)P_2 by PLC. **Conclusion:** Although $PLC_{\delta 1}PH$ and neomycin bind to PtdIns(4,5)P_2 in a similar way, they have distinct effects on receptor-mediated activation of PLC and PtdIns(4,5)P_2 hydrolysis.

Introduction

Phosphatidylinositol 4,5-bisphosphate [PtdIns(4,5)P_2], a minor phospholipid component of the plasma membrane, is a key regulator of several cellular processes, and has become the focus of research on intracellular signal transduction. PtdIns(4,5)P_2 is a precursor of important second messengers, such as the diffusible $InsP_3$, which regulates Ca^{2+} release from intracellular Ca^{2+} stores, and the protein kinase C activator, diacylglycerol[1,2]. PtdIns(4,5)P_2 is also phosphorylated by class I PtdIns 3-kinases to form PtdIns(3,4,5)P_3, which controls membrane recruitment and the functions of several important signaling proteins[3]. PtdIns(4,5)P_2 itself is a regulator of a great variety of target molecules, including ion channels[4,5] and several proteins that regulate actin polymerization and the cytoskeleton[6], providing a link between the plasma membrane and the cortical cytoskeleton[7]. PtdIns(4,5)P_2 has also been implicated in several forms of membrane remodeling events, including the fusion of secretory vesicles with the plasma membrane[8], clathrin-mediated endocytosis[9], and membrane recovery by endocytosis during neurotransmitter release[10]. Such diverse functions rely upon interaction of the lipid with a large number of regulator molecules.

Pleckstrin homology (PH) domains have been described in a large number of signaling proteins, and they show remarkable specificity in recognizing various forms of inositides[11]. The PH domain of phospholipase $C_{\delta 1}$ ($PLC_{\delta 1}PH$) binds with high affinity and selectivity to PtdIns(4,5)P_2[12]. Recently, a fusion construct of $PLC_{\delta 1}PH$ with enhanced green fluorescent protein (GFP) ($PLC_{\delta 1}PH$-GFP) was developed as a probe to visualize PtdIns(4,5)P_2 in single cells because it binds to PtdIns(4,5)P_2 within the plasma and translocates to the cytoplasm after receptor stimulation. Subsequently,

when PtdIns(4,5)P_2 is resynthesized, fluorescence returns to the membrane[13].

It has been demonstrated that neomycin, an aminoglycoside antibiotic with a large positive charge (about +4.5), binds with high affinity to PtdIns(4,5)P_2[14]. Later studies also showed that neomycin bound to and neutralized the negative charge of PtdIns(4,5)P_2[15].

Phospholipase C (PLC)-induced PtdIns(4,5)P_2 hydrolysis is an important cell signaling mechanism. Many membrane receptors couple to PLC, and thus regulate PtdIns(4,5)P_2 turnover and subsequent downstream cell signaling[16]. A few PLC modulators have been developed and they play an important role in understanding the cell signaling process involving PLC and PtdIns(4,5)P_2. Neomycin has long been used as a blocker of PLC, although it actually binds to PtdIns(4,5)P_2 and presumably prevents PtdIns(4,5)P_2 from hydrolysis by PLC[17]. Previous studies have demonstrated that both $PLC_{\delta 1}$PH and neomycin bind PtdIns(4,5)P_2 through an electrostatic interaction[12,14]. This similar nature of interaction would indicate a similar consequence for PtdIns(4,5)P_2 hydrolysis by PLC. However, in the present study, we demonstrate that although both PLCδ1PH and neomycin bind to PtdIns(4,5)P_2, only neomycin blocks PtdIns(4,5)P_2 hydrolysis by PLC activation.

Materials and methods

Reagents and plasmids Acetylcholine (ACh), bradykinin (BK), wortmannin, neomycin and Fluo 3-AM, the calcium indicators, were purchased from Sigma-Aldrich (St Louis, MO, USA). ACh, BK and neomycin were dissolved in distilled water. U73122 was purchased from Calbiochem (San Diego, CA, USA). U73122 and wortmannin were prepared as stock solutions in dimethylsulfoxide (Me_2SO), with a final concentration of Me_2SO of 0.1%. Fetal bovine serum (FBS) and Dulbecco's modified Eagle's medium (DMEM) were products of Hyclone (Logan, UT, USA). COS-7 was obtained from the Institute of Biochemistry and Cell Biology, Chinese Academy of Sciences. cDNA from the type 1 muscarinic (M_1) receptor (M_1R) and bradykinin 2 receptor (BK_2R), pEGFP-N1(GFP) and the $PLC_{\delta 1}$PH construct with GFP ($PLC_{\delta 1}$PH-GFP) were gifts from Prof DE LOGOTHETIS (Mount Sinai Medical School, NY, USA). Red fluorescent protein (pDsRed-Express-C1, pDsRed) was purchased from Clontech (Mountain View, CA, USA). All other chemicals were of high performance liquid chromatography or analytical grade.

Cell culture and transfection COS-7 cells were seeded in 24-well plates on 12-mm glass coverslips, and cultured in 0.3 mL of DMEM supplemented with 10% (*v*/*v*) FBS, 100 μg/mL streptomycin, and 100 U/mL of penicillin at 5% CO_2 and 37 °C. When they were 60%–70% confluent, the cells were transiently transfected with DNA constructs for 8 h using calcium phosphate precipitate, with 1 μg of DNA and equal proportions for each kind of plasmid per well. Following transfection, cells were incubated in 10% FBS DMEM for 12–48 h. For fluorescence detection, cells were washed twice with a modified Krebs-Ringer buffer containing (in mmol/L): 120 NaCl, 4.7 KCl, 0.7 $MgSO_4$, 1.2 $CaCl_2$, 10 glucose, with 10 *N*-2-hydroxyethylpiperazine-*N*′-2-ethanesulfonic acid (HEPES) added (pH 7.4). The coverslips were placed into a flow-through chamber and mounted on an inverted microscope.

Confocal microscopy and image analysis For confocal imaging, a Leica (Wetzlar, Germany) DM-IRBE inverted microscope with a 20×objective (numerical aperture 0.7) and fitted with a TCS-SP2 scanhead was used. Excitation of $PLC_{\delta 1}$PH-GFP and Fluo 3-AM was achieved with a 488 nm argon ion laserline, and emissions were collected at 500–565 nm. pDsRed fluorescence was visualized with excitation at 543 nm and a 570–600 nm emission filter. For translocation studies, a series of confocal images were taken at 3–10 s intervals and stored on disk. Determination of the ratio of membrane to cytosolic fluorescence was carried out by assigning regions of interest for membrane and cytosol. TCS-SP2 confocal software (Leica) was used to analyze data off-line.

Measurement of intracellular Ca^{2+} ($[Ca^{2+}]_i$) of single cells Cells were seeded onto sterile 12-mm borosilicate coverslips in 35-mm Petri dishes, and incubated with 5 mmol/L fluo 3-AM at 37 °C for 45 min. After loading, cells were washed twice and maintained in modified Krebs-Ringer buffer until assay. $[Ca^{2+}]_i$ changes were represented by relative fluorescence intensity calculated by using the equation $\Delta F/F_0$, where ΔF and F_0 are the change in fluorescence intensity before and after treatment, and the initial fluorescence intensity, respectively[18,19].

Statistics Data were analyzed by using the Chi-square test. $P<0.05$ was considered to be a statistically significant difference. All data shown are the mean value of at least 5 experiments and are expressed as mean±SD.

Results

Activation of M_1R and BK_2R induced PtdIns(4,5)P_2 hydrolysis and a reversible translocation of $PLC_{\delta 1}$PH-GFP Both M_1R, and $PLC_{\delta 1}$PH-GFP or both BK_2 and $PLC_{\delta 1}$PH-GFP were expressed in COS-7 cells. To follow the localization of $PLC_{\delta 1}$PH-GFP within intact cells, we used GFP as a control. In unstimulated cells, expressed GFP was found to be cytosolic and also present in the nucleus (data not shown). $PLC_{\delta 1}$PH-GFP, on the other hand, accumulated strongly at

the plasma membrane and had a low and homogenous distribution in the cytosol (Figure 1A, 1B, left panel), consistent with the hypothesis that the large pool of PtdIns(4,5)P_2 exists in the plasma membrane[13]. Next we examined the effects of ACh and BK, acting through their respective G protein-linked receptors, and subsequent activation of phospholipase C_β and hydrolysis of PtdIns(4,5)P_2, on the fluorescence distribution of the GFP and $PLC_{\delta1}$PH-GFP. COS-7 cells were transfected with the GFP or PLC_1PH-GFP together with the cDNA encoding the M_1R or BK_2R. After stimulation with either ACh (5 μmol/L) or BK (0.1 μmol/L), there was a decrease of $PLC_{\delta1}$PH-GFP fluorescence in the plasma membrane and a concomitant increase in cytosolic fluorescence (Figure 1A, 1B, Table 1). The kinetics of ACh- or BK-induced $PLC_{\delta1}$PH-GFP fluorescence translocation were characterized by a rapid onset, with translocation peaking at approximately 30–60 s and returning to baseline approximately 5–8 min after washout (Figure 1C). No significant change in fluorescence were seen in cells transfected with GFP only (data not

Table 1. Effects of ACh and its solvent on change in relative fluorescence ratios of $PLC_{\delta1}$PH-GFP. COS-7 cells were transfected with a $PLC\delta_1$PH-GFP fusion construct and M_1R. F_m, average plasma membrane fluorescence intensity; F_c, average cytosolic fluorescence intensity, normalized to 1 at time 0 s for each cell. The solvent of ACh was a modified Krebs-Ringer buffer solution. n=5. Mean±SD. $^cP<0.01$ *vs* control. $^fP<0.01$ *vs* ACh at the same time point.

Drug	Time/s	Relative fluorescence ratios (F_m/F_c)
ACh	0 (Control)	1.00±0.00
	50	0.20±0.12^c
	100	0.23±0.14^c
	500	0.95±0.05
ACh solvent	0 (Control)	1.00±0.00
	50	1.00±0.09^f
	100	1.00±0.09^f
	500	1.00±0.09

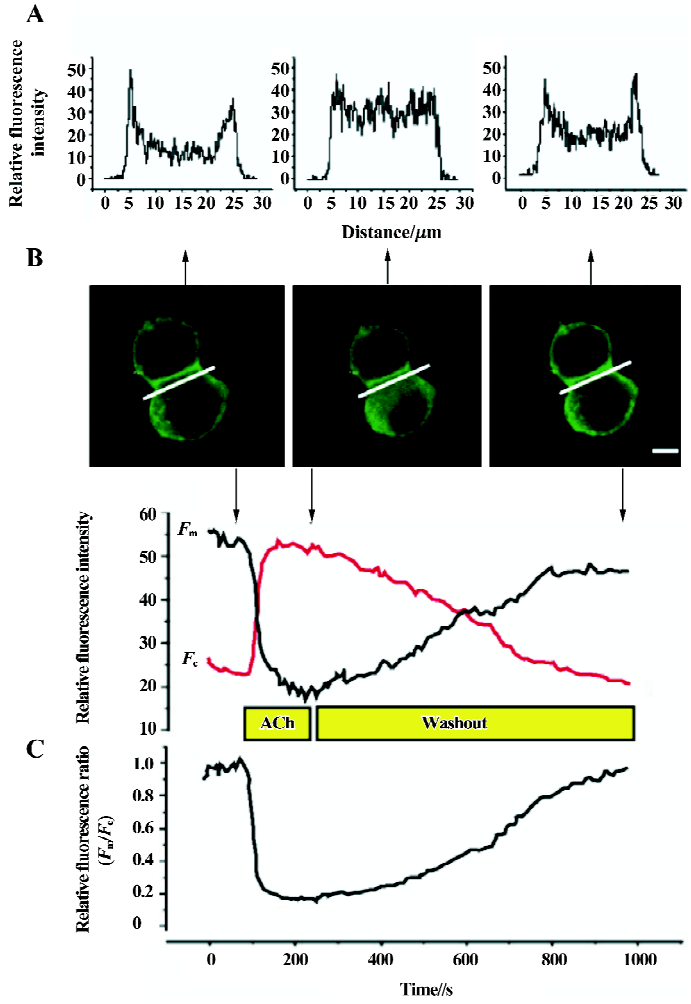

Figure 1. Activation of M_1R induces reversible translocation of $PLC_{\delta1}$PH-GFP from the membrane to the cytosol. COS-7 cells were transfected with the $PLC_{\delta1}$PH-GFP fusion construct and M_1R. (A) The fluorescence intensity changes across the white lines from a representative cell. (B) Plotted as line intensity histograms. (C) Shown in upper panels are time courses of the relative fluorescence intensities in the membrane (F_m) and cytosol (F_c) regions. Shown in lower panels are time courses of the relative fluorescence ratios (F_m/F_c) and normalized to 1 at time 0 s. Bar=8 μm.

shown). To exclude the effects of the laser, we used modified Krebs-Ringer buffer solution as a solvent control of ACh. As shown in Table 1, there was no change in the relative fluorescence ratios (F_m/F_c) in the solvent control group during perfusion. To examine whether ACh- or BK-induced translocation of $PLC_{\delta 1}PH$-GFP is due to the hydrolysis of PtdIns(4,5)P_2, we utilized 2 different PtdIns(4,5)P_2 resynthesis and hydrolysis blockers: wortmannin and U73122. Wortmannin is known to be able to block the PtdIns 3-kinase at low concentrations and block the PtdIns 4-kinase, so therefore block the formation of PtdIns(4,5)P_2 from phosphatidylinositol (PI), at high concentrations[20]. As shown in Figure 2, in COS-7 cells expressing $PLC_{\delta 1}PH$-GFP and the M_1R, after the cell was pre-incubated with wortmannin (at 10 μmol/L, a concentration known to block PtdIns 4-kinase) for 20 min, ACh induced a similar translocation of fluorescence from the plasma membrane to the cytosol, which lasted for more than 10 min after washout of ACh (Figure 2A). When the cells were pre-incubated with U73122 (10 μmol/L), a relatively specific PLC inhibitor, for 5 min, ACh failed to induce transient translocation of the fluorescence signal (Figure 2B). These data strongly suggest that $PLC_{\delta 1}PH$-GFP translocation induced by membrane receptor activation is indeed due to PtdIns(4,5)P_2 hydrolysis.

Expression of $PLC_{\delta 1}PH$-GFP inhibited the effects of neomycin on PtdIns(4,5)P_2 hydrolysis Neomycin binds PtdIns(4,5)P_2 with high affinity and has often been used as an inhibitor of PLC. The blocking effect of neomycin on PLC is believed to be indirect, the result of neomycin binding to PtdIns(4,5)P_2, the substrate of PLC[15]. As we shown earlier, $PLC_{\delta 1}PH$ bound to PtdIns(4,5)P_2 but did not block receptor-mediated PLC activation, or PtdIns(4,5)P_2 hydrolysis. Because both $PLC_{\delta 1}PH$ and neomycin bind PtdIns(4,5)P_2 in a similar way (electrostatic interaction, see Introduction), we thought this difference between $PLC_{\delta 1}PH$ and neomycin was interesting, and worthy of further investigation. To determine whether the binding of $PLC_{\delta 1}PH$-GFP to PtdIns(4,5)P_2 can disrupt the effects of neomycin on PtdIns(4,5)P_2 hydrolysis, COS-7 cells expressing $PLC_{\delta 1}PH$-GFP and M_1R were stimulated with ACh in the absence or presence of neomycin. Preincubation of the cells with neomycin (5 mmol/L) for 40 min failed to prevent the release of the fluorescence signal from the membrane to the cytosol upon the application of ACh (Figure 3). Thus in the presence of $PLC_{\delta 1}PH$, neomycin could not block hydrolysis of PtdIns(4,5)P_2 induced by PLC.

Effects of neomycin on PLC activation in the absence of $PLC_{\delta 1}PH$-GFP To further confirm that binding of $PLC_{\delta 1}PH$-GFP to PtdIns(4,5)P_2 excludes the binding of neomycin to PtdIns(4,5)P_2, thus blocking neomycin's inhibitory effects on PLC, we used $[Ca^{2+}]_i$ as an indicator to reveal the effects of neomycin on PLC in the absence of $PLC_{\delta 1}PH$-GFP. One of the downstream products of PtdIns(4,5)P_2 hydrolyzed by PLC is IP_3, which acts to release intracellular Ca^{2+}[1,2]. Thus $[Ca^{2+}]_i$ would serve as a good indicator of PLC activation upon membrane receptor (M_1R) stimulation. ACh induced a significant increase in $[Ca^{2+}]_i$ in COS-7 cells expressing the M_1R alone and pretreated with modified Krebs-Ringer buffer

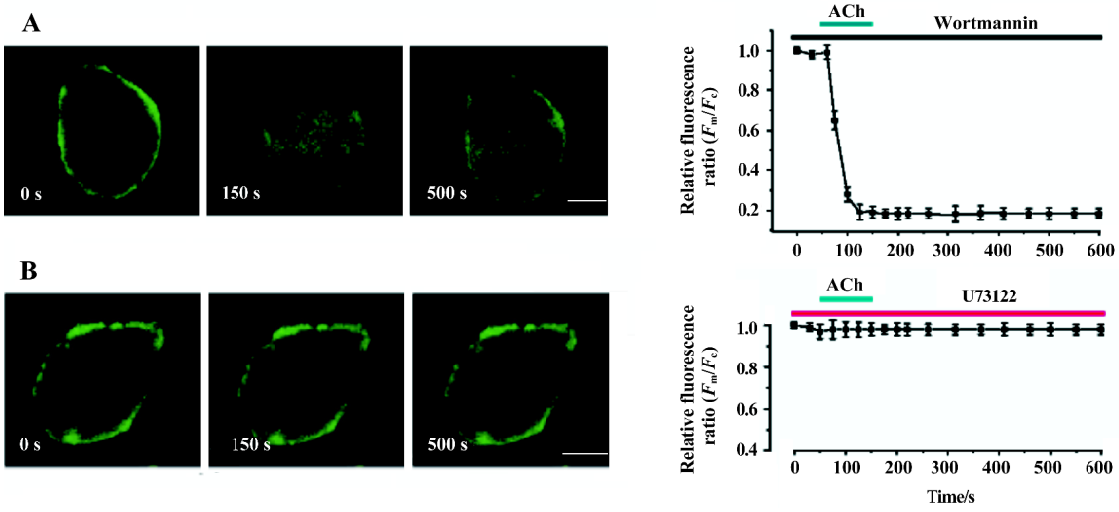

Figure 2. Effects of wortmannin and U73122 on translocation of $PLC_{\delta 1}PH$-GFP. (A) Cells were preincubated with wortmannin (10 μmol/L) for 20 min. ACh (5 μmol/L) was applied for the indicated period of time. Shown in upper panels are confocal images from a representative cell taken at selected times after the application of ACh. The membrane:cytosol fluorescence ratios were determined (lower panels) as described earlier. n=5. Mean±SD. Bar=8 μm. (B) Similar experiments were performed as shown in part A, except cells were incubated with 10 μmol/L U73122 for 5 min before experiments were carried out.

solution for 40 min (Figure 4A, 4B); pDsRed was co-transfected with M_1R as a transfection tag (Figure 4A). However, when cells were pretreated with 5 mmol/L neomycin (40 min), no change was seen upon application of ACh (Figure 4A, 4B). Similar results were seen with BK as activator of PLC in cells expressing B_2R (data not shown). Thus, in the absence of $PLC_{\delta 1}PH$, neomycin was able to block activation of PLC.

To further confirm these findings, we next examined whether neomycin could also exert its inhibitory effects on $[Ca^{2+}]_i$ in the presence of $PLC_{\delta 1}PH$-GFP. In this section of the study, we imaged the whole-cell fluorescence intensity changes. GFP and Fluo 3-AM were excited and imaged at the same wavelength. However, as shown in Figure 1C, the total GFP signal from one cell did not change during translocation, thus we were able to see an additional fluorescence signal from Fluo 3-AM (Ca^{2+}) when Ca^{2+} was released from the store by IP_3. Figure 5 shows COS-7 cells transfected with $PLC_{\delta 1}PH$-GFP and the M_1R. Three types of cells, presumably representing different transfection results, can be identified. Cells designated a and b (Figure 5A) represent those cells that had been transfected with both $PLC_{\delta 1}PH$-GFP and the M_1R, giving a clear and dominant localization of the GFP signal on the cell membrane (Figure 5A), which translocated into the cytosol upon application of ACh (Figure

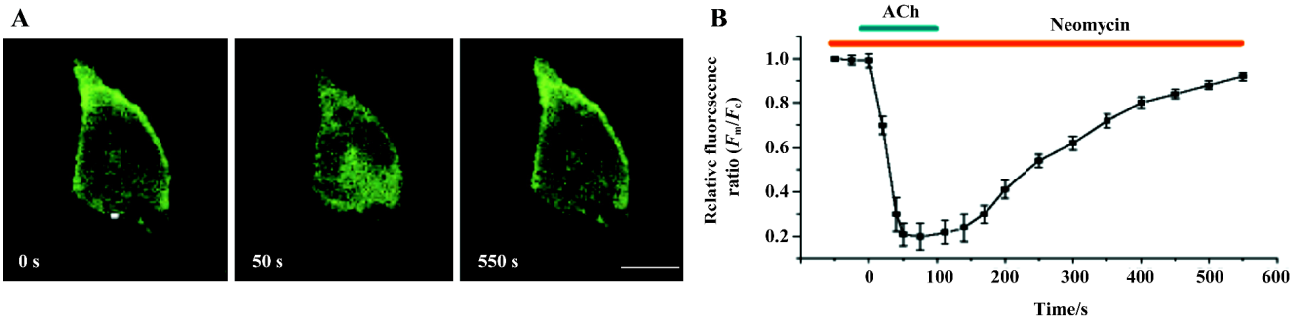

Figure 3. Neomycin failed to block PLC activation in the cells expressing $PLC_{\delta 1}PH$-GFP. Cells were preincubated with neomycin (5 mmol/L) for 40 min before the addition of ACh (5 μmol/L) for the indicated time. (A) Confocal images from a representative cell taken at selected times after the application of ACh. (B)The membrane:cytosol fluorescence ratios were determined as described earlier. n=5. Mean±SD. Bar=8 μm.

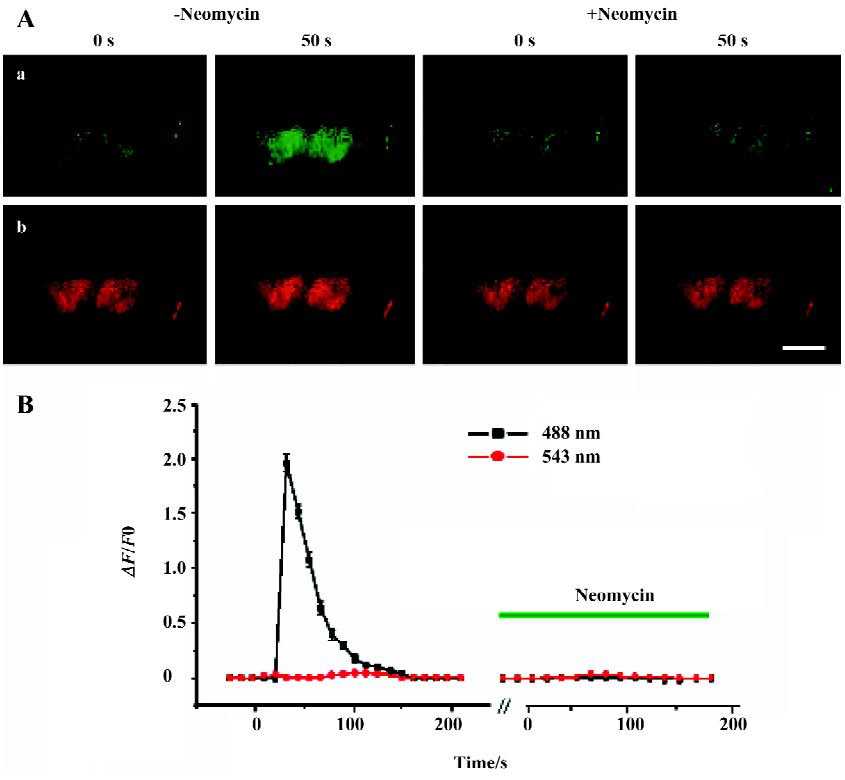

Figure 4. Neomycin blocked $[Ca^{2+}]_i$ increases upon M_1R activation in the cells not expressing $PLC\delta_1PH$-GFP. $[Ca^{2+}]_i$ responses to ACh application were analyzed by confocal Ca^{2+} imaging using Fluo-3-AM and as indicated by $\Delta F/F_0$, where ΔF and F_0 are the change in fluorescence intensity before and after treatment (ACh), and the initial fluorescence intensity, respectively. (A) Confocal images of a representative cell taken at selected times during the experiment. pDsRed was co-transfected with M_1R as a tag of transfection (Ab). The numbers indicate the elapsed time in seconds after ACh application. (B) $\Delta F/F_0$ was plotted against time; a and b refer to the same cell measured at different wavelengths. n=5. Mean±SD. Bar=8 μm.

5A); cell c represents cells that had only been transfected with M_1R, with no visible localization of the $PLC_{\delta1}PH$-GFP signal on the cell membrane, and a clear rising in $[Ca^{2+}]_i$ signal seen upon application of ACh; cell d represents cells that had been transfected with $PLC_{\delta1}PH$-GFP but not the M_1R, so that the clear $PLC_{\delta1}PH$-GFP signal was not released from the membrane, and neither could an increase in $[Ca^{2+}]_i$ signal be seen upon application of ACh (Figure 5A). When these cells were pretreated with neomycin, only the response of cell c to ACh was blocked, whereas the responses of cells a and b were unaffected. These results strongly suggest that neomycin blocks PLC activation only in the absence of $PLC_{\delta1}PH$-GFP.

Discussion

The main finding of the present study was that in the cells expressing $PLC_{\delta1}PH$-GFP, neomycin could not exhibit its inhibitory effects on PtdIns(4,5)P_2 hydrolysis by PLC. There is increasing interest in understanding the actions of inositol phospholipids, especially PtdIns(4,5)P_2, in living cells[21]. PtdIns(4,5)P_2 participates in many cellular functions, including exocytosis, cytoskeletal function and membrane transporter and ion channel functions[4]. Many molecules have been found to be able to bind to phospholipids, and more specifically to PtdIns(4,5)P_2, which forms the basis of modulation by this lipid[22]. The PH domain of $PLC_{\delta1}$ is one of these molecules that are believed to selectively bind to PtdIns(4,5)P_2[12]. Recently, a fusion construct of $PLC_{\delta1}PH$ with enhanced green fluorescent protein ($PLC_{\delta1}PH$-GFP) was developed as a probe to visualize PtdIns(4,5)P_2 in single cells. This novel methodology allowed imaging and analysis of spatiotemporal changes in PtdIns(4,5)P_2 in single living cells, and has been used increasingly in efforts to understand the role PtdIns(4,5)P_2 plays in cell signaling, and protein function regulation[13]. The central idea behind this methodology is that the GFP signal that has been linked to $PLC_{\delta1}PH$ will faithfully follow the dynamic changes of PtdIns(4,5)P_2 during its metabolism, including during hydrolysis by PLC. However, because $PLC_{\delta1}PH$ also binds to IP_3, a downstream product of PtdIns(4,5)P_2 hydrolysis, with higher affinity, some have proposed that rather than being a faithful PtdIns(4,5)P_2 follower, $PLC_{\delta1}PH$-GFP molecules during PtdIns(4,5)P_2 hydrolysis are more likely to bind to newly produced IP_3[18]. But van der Wal *et al* showed that physiological increases in IP_3 (10–100 μmol/L) on activation of PLC could not be solely responsible for the translocation of $PLC_{\delta1}PH$-GFP[23]. Our data presented in Figure 2 are in agreement with the results of van der Wal *et al*. In the cells expressing $PLC_{\delta1}PH$-GFP as well as the BK_2 or M_1 receptors, BK or ACh induced the reversible translocation of $PLC_{\delta1}PH$-GFP from the plasma membrane to the cytosol. Thus, although it bound to PtdIns(4,5)P_2, $PLC_{\delta1}PH$-GFP did not interfere with cleavage of PtdIns(4,5)P_2 by PLC. On the other hand, neomycin, a commonly used PLC blocker, is believed to block PLC cleavage of PtdIns(4,5)P_2 by preventing PtdIns(4,5)P_2 from

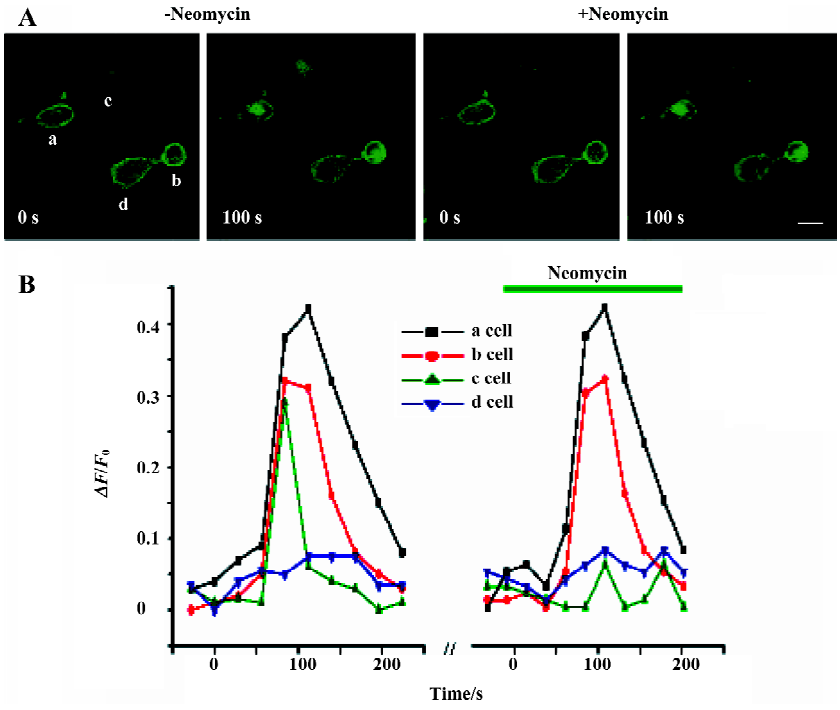

Figure 5. Presence or absence of $PLC_{\delta1}PH$-GFP determines the effect of neomycin on PLC activation. $[Ca^{2+}]_i$ responses to ACh application were analyzed as described in Figure 4 legend. (A) Confocal image from a representative cell taken at selected times in seconds after application of ACh. (B) $\Delta F/F_0$ was plotted against time. Bar=8 μm.

accessing PLC[17]. It is interesting to note that whereas a smaller molecule such as neomycin would mask PtdIns(4,5)P_2 from PLC cleavage, a much bigger molecule such as $PLC_{\delta 1}$PH-GFP would allow the cleavage to happen. It is also interesting to consider that the expression of $PLC_{\delta 1}$PH-GFP blocked the action of neomycin (Figure 3), suggesting that $PLC_{\delta 1}$PH-GFP and neomycin bind to the same sites on PtdIns(4,5)P_2. Previous studies have demonstrated that both $PLC_{\delta 1}$PH-GFP and neomycin interact with PtdIns(4,5)P_2 in an electrostatic way[12,14]. Thus the charged inositide head group of PtdIns(4,5)P_2 is the binding site for both $PLC_{\delta 1}$PH-GFP and neomycin[24], yet binding of $PLC_{\delta 1}$PH-GFP or neomycin to PtdIns(4,5)P_2 has very different consequences for PLC hydrolysis of PtdIns(4,5)P_2. Although it is less likely, it needs to be noted that the GFP, rather than $PLC_{\delta 1}$PH, may block the binding of neomycin to PtdIns(4,5)P_2 through a spatial blocking effect. For many cellular proteins that have been known to interact with, and whose functions are regulated by, PtdIns(4,5)P_2, the molecular basis for the interaction remains to be elucidated. Less clear is the mechanism for PtdIns(4,5)P_2 hydrolysis by PLC. The present study provides interesting and stimulating information for further understanding protein-PtdIns(4,5)P_2 interactions and PtdIns(4,5)P_2 hydrolysis by PLC. We are currently investigating the mechanism underlying the different consequences of PtdIns(4,5)P_2 binding to $PLC_{\delta 1}$PH-GFP or neomycin with respect to its hydrolysis by PLC.

Acknowledgements

We thank Diomedes E LOGOTHETIS (Mount Sinai School of Medicine, New York University, NY, USA), for providing us with plasmids of the M_1R, BK_2R and $PLC_{\delta 1}$PH-GFP, and members of the Logothetis laboratory for helpful discussions on this work.

References

1 Takano M, Kuratomi S. Regulation of cardiac inwardly rectifying potassium channels by membrane lipid metabolism. Prog Biophys Mol Biol 2003; 81: 67–9.
2 Nishizuka Y. The molecular heterogeneity of protein kinase C and its implications for cellular regulation. Nature 1988; 34: 661–5.
3 Cantley LC. The phosphoinositide 3-kinase pathway. Science 2002; 296: 1655–7.
4 Zhang H, He C, Yan X, Mirshaki T, Logothetis DE. Activation of inwardly rectifying K^+ channels by distinct PtdIns(4,5)P_2 interactions. Nat Cell Biol 1999; 1: 183–8.
5 Hilgemann DW, Feng S, Nasuhoglu C. The complex and intriguing lives of PIP_2 with ion channels and transporters. Sci STKE 2001; 111: RE 19.
6 Berridge PA, Xian W, Flanagan LA. Controlling cytoskeleton structure by phosphoinositide-protein interactions: phosphoinositide binding protein domains and effects of lipid packing. Chem Phys Lipids 1999; 101: 93–7.
7 Raucher D, Stauffer T, Chen W, Shen K, Guo S, York JD, *et al*. Phosphatidylinositol 4,5-bisphosphate functions as a second messenger that regulates cytoskeleton-plasma membrane adhesion. Cell 2000; 100: 221–8.
8 Hay JC, Fisette PL, Jenkins GH, Fukami K, Takenawa T, Anderson RA, *et al*. ATP-dependent inositide phosphorylation required for Ca^{2+}-activated secretion. Nature 1995; 374: 173–7.
9 Jost M, Simpson F, Kavran JM, Lemmon MA, Schmid SL. Phosphatidylinositol-4,5-bisphosphate is required for endocytic coated reside formation. Curr Biol 1998; 8: 1399–402.
10 Martin TF. PtdIns(4,5)P_2 regulation of surface membrane traffic. Curr Opin Cell Biol 2001; 13: 493–9.
11 Harlan JE, Hajduk PJ, Yoon HS, Fesik SW. Pleckstrin homology domains bind to phosphatidylinositol-4,5-bisphosphate. Nature 1994; 371: 168–70.
12 Cullen PJ, Cozier GE, Banting G, Mellor H. Modular phosphoinositide-binding domains: their role in signaling and membrane trafficking. Curr Biol 2001; 11: R882–93.
13 Varnai P, Rother KI, Balla T. Phosphatidylinositol 3-kinase-dependent membrane association of the Bruton's tyrosine kinase pleckstrin homology domain visualized in single living cells. J Biol Chem 1999; 274: 10983–9.
14 Schacht J. Inhibition by neomycin of polyphosphoinositide turnover in subcellular fractions of guinea-pig cerebral cortex *in vitro*. J Neurochem 1976; 27: 1119–24.
15 Gabev E, Kasianowicz J, Abbott T, McLaughlin S. Binding of neomycin to phosphatidylinositol 4,5-bisphosphate (PIP_2). Biochim Biophys Acta 1989; 979: 105–2.
16 Lei Q, Jones MB, Talley EM, Garrison JC, Bayliss DA. Molecular mechanisms mediating inhibition of G protein-coupled inwardly-rectifying K^+ channels. Mol Cell 2003; 15: 1–9.
17 Cockcroft S, Howell TW, Gomperts B. Two G-proteins act in series to control stimulus-secretion coupling in mast cells: use of neomycin to distinguish between G-proteins controlling polyphosphoinositide phosphodiesterase and exocytosis. J Cell Biol 1987; 105: 2745–50.
18 Hirose K, Kadowaki S, Tanabe M, Takeshima H, Lino M. Spatiotemporal dynamics of inositol 1,4,5-trisphosphate that underlies complex Ca^{2+} mobilization patterns. Science 1999; 284: 1527–30.
19 Halet G, Tunwell R, Balla T, Swann K, Carroll J. The dynamics of plasma membrane PtdIns(4,5)P_2 at fertilization of mouse eggs. Cell Sci 2002; 115: 2139–49.
20 Nakanishi S, Catt kJ, Balla T. A wortmannin-sensitive phosphatidylinositol 4-kinase that regulates hormone-sensitive pools of inositolphospholipids. Proc Natl Acad Sci USA 1995; 92: 5317–21.
21 Martin TF. PI (4,5)P (2) regulation of surface membrane traffic. Curr Opin Cell Biol 2001; 13: 493–9.
22 Hurley JH, Meyer T. Subcellular targeting by membrane lipids. Curr Opin Cell Biol 2001; 13: 146–52.
23 van der Wal J, Habets R, Varnai P, Balla T, Jalink K. Monitoring agonist-induced phospholipase C activation in live cells by fluorescence resonance energy transfer. J Biol Chem 2001; 276: 15337–44.
24 Ferguson KM, Lemmon MA, Schlessinger J, Sigler PB. Crystal structure at 2.2Å resolution of the pleckstrin homology domain from human dynamin. Cell 1994; 79: 199–209.

Acta Pharmacologica Sinica 2005 Dec; 26 (12): 1492–1496

Blackwell Publishing

Full-length article

Inhibitory effect of acetamide-45 on airway inflammation and phosphodiesterase 4 in allergic rats[1]

Kai WANG[2], Hua-hao SHEN[2,4], Jun-chun CHEN[2], Zhong CHEN[3]

[2]*Respiratory Department, the Second Affiliated Hospital, Medical School of Zhejiang University, Hangzhou 310009*; [3]*Department of Pharmacology, Medical School of Zhejiang University, Hangzhou 310031, China*

Key words

acetamide-45; 3',5'-cyclic nucleotide phosphodiesterase; respiratory function tests; eosinophils; asthma

[1] Project supported by Science and Technology department of Zhejiang province (No 2003C24002).

[4] Correspondence to Prof Hua-hao SHEN.
Phn/Fax 86-571-8778-3729.
E-mail hshen@mail.hz.zj.cn

Received 2005-05-18
Accepted 2005-08-29

doi: 10.1111/j.1745-7254.2005.00227.x

Abstract

Aim: To determine the effects of acetamide-45 on respiratory function, airway inflammation, and the activity of phosphodiesterase 4 (PDE4) in allergic rats. **Methods:** Rats were sensitized by a single intramuscular injection with ovalbumin (OVA) and were challenged with ovalbumin applied by using an aerosol repeatedly for 7 d after 2 weeks. Acetamide-45 at concentrations of 5, 10, or 30 mg/kg was then administered by intraperitoneal injection. Changes in dynamic lung compliance and lung resistance, the accumulation of inflammatory cells in bronchoalveolar lavage, PDE4 activity, and the concentration of interleukin-4 in rat lung tissue were determined. **Results:** Seven days of treatment with acetamide-45 prevented eosinophil accumulation in allergic rats. At doses of 5, 10, and 30 mg/kg, acetamide-45 decreased lung resistance to 0.20±0.04, 0.25±0.07, and 0.22±0.05 $cmH_2O \cdot s^{-1} \cdot mL^{-1}$, respectively ($P<0.05$ *vs* OVA), and it also increased dynamic lung compliance to 0.41±0.07, 0.39±0.06, and 0.42±0.09 mL/cmH_2O ($P<0.05$ *vs* OVA). After being treated with different doses of acetamide-45, the PDE4 activities in lung tissue were 281±55, 273±57, and 238±36 $nmol \cdot g^{-1} \cdot min^{-1}$ ($P<0.05$ *vs* OVA), and the concentrations of interleukin-4 in lung tissue were 6.22±1.13, 5.95±1.20, and 5.68±2.20 μg/g protein ($P<0.05$ *vs* OVA). **Conclusions:** Acetamide-45 was found to improve respiratory function and inhibit airway inflammation in this animal model, and the PDE4 activity of lung tissue was obviously inhibited. Acetamide-45 was an effective anti-inflammatory agent in respiratory inflammation, and the mechanism of its action might depend on inhibition of PDE4.

Introduction

Asthma is a chronic inflammatory disease of the airways, of which lung inflammation and bronchial hyperactivity (BHR) are two distinct characteristics[1,2]. Eosinophils are considered to be the principal inflammatory leukocytes involved in the asthmatic reaction, due in part to the toxic granular proteins they secrete and the membrane products that induce airway epithelial pathology and mucus hypersecretion[3,4]. 3',5'-Cyclic-nucleotide (cAMP) has important regulatory roles in the process of inflammation. Phosphodiesterase 4 (PDE4), which catalyzes the hydrolysis of cAMP to the corresponding nucleotide, 5'-monophosphate, appears to be an attractive target for anti-inflammatory drugs[5,6]. Inhibition of PDE4 results in increased levels of cAMP, which leads to functional inhibition of inflammatory cells such as eosinophils and lymphocytes, and reduced release of inflammatory cytokines such as interleukin-4 (IL-4)[7,8]. There has been significant interest in PDE4 inhibitors as potential therapeutic agents for asthma.

Because asthma has been the focus of much study effort, treatment of the disease has been improved by the implementation of management guidelines in recent years[9]. Such treatments as corticosteroids, β_2-agonists, theophylline and leukotriene antagonists have been used as anti-inflammatory agents to control asthma[10]. However, the possible dose-related adverse systemic effects produced by long-term treatment with these drugs are not acceptable in

clinical practice[11,12]. Therefore, new anti-asthma agents are required.

A series of new *N*-(pyridin-4-yl)-(indol-3-yl) alkylamides (44-84) have been prepared in the search for novel antiallergic drugs. Initial studies showed that acetamide-45 inhibited IL-4 and IL-5 biosynthesis and histamine release[13]. We have also previously reported that acetamide-45 has an inhibitory effect on histamine- and methacholine-induced contractions of isolated guinea pig trachea, and that it can inhibit PDE4 activity[14,15]. It was concluded that acetamide-45 was a new antiallergic agent. However, little is known about its effects on eosinophil infiltration in airway and lung function in asthmatic rats. There have been no reports regarding the effect of acetamide-45 on PDE4 activity in the lungs in any animal model of asthma.

Therefore, in the present study, we examined the inhibitory effect of acetamide-45 on airway inflammation and lung function in a rat model of asthma, and indicated a possible mechanism by which the effect might be exerted.

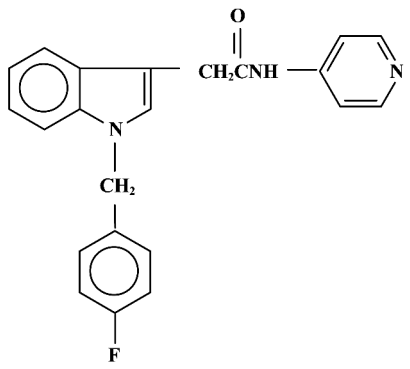

Acetamide-45

Materials and methods

Animals Male Sprague-Dawley rats weighing 140–160 g were obtained from the Laboratory Animal Center of the Medical School of Zhejiang University (Certificate No 220010027, conferred by the Zhejiang Medical Laboratory Animal Administration Committee).

Chemicals Aminophylline, cAMP, and ovalbumin were purchased from Sigma (St Louis, MO, USA). Acetamide-45 was kindly provided by the Department of Organic Chemistry and Medical Chemistry, Faculty of Pharmacy (Nantes University, France). The rat IL-4-specific enzyme-linked immunosorbent assay (ELISA) kit was purchased from Jingmei BioTech Co (Shenzhen, China).

Sensitization and challenge procedure Rats were sensitized by a single intramuscular injection of 10 mg ovalbumin (OVA) mixed with 100 mg aluminum hydroxide in 1 mL of saline. After 2 weeks, these animals were then challenged by exposure for 20 min to aerosolize 1% OVA in saline generated by a jet nebulizer once a day for 7 d. The drugs were administered by intraperitoneal injection before challenge. The doses of acetamide-45 were 5, 10, or 30 mg/kg, respectively, and the dose of aminophylline was 10 mg/kg per day for 7 d. At d 21, the animals were killed, and the lung tissues were immediately removed, frozen in liquid nitrogen, and then stored at -80 °C until analysis.

Measurement of lung function At 24 h after the last antigen challenge, rats were anesthetized with urethane (1 g/kg, ip). The trachea was cannulated and placed in a whole body plethysmograph for the measurement of lung resistance (R_L) and dynamic lung compliance (C_{dyn})[16,17].

Cell counts in bronchoalveolar lavage Bronchoalveolar lavage (BAL) was performed by flushing the airways with 10 mL/kg saline containing 1% bovine serum albumin and 1000 kU/L heparin sodium through a tracheal cannula. The BAL fluid was pooled and immediately centrifuged at 500 ×*g* at 4 °C for 10 min. The supernatant was removed and the cells were resuspended in 1 mL saline containing 10% bovine serum albumin. Counts of the total number of leukocytes recovered in the BAL fluid were carried out using a Neubauer chamber, and differential cell analysis was carried out under a light microscope after Wright-Giemsa staining.

Determination of IL-4 in lung tissue At a ratio of 1 g to 10 mL, homogenized lung tissue was added to 50 mmol/L potassium phosphate buffer (pH 6.0) containing 0.05% NaN_3 and 0.1% 3-[(3-cholamidopropyl) dimethylammonio]-1-propanesulfonate (CHARPS). The homogenates were centrifuged twice at 19 851 ×*g*, each for 30 min[17]. IL-4 in the supernatants was quantified using a rat IL-4-specific ELISA kit.

PDE4 activity assay Frozen 25-mg pieces of lung tissue were homogenized and PDE4 activity was determined by high performance liquid chromatography (HPLC) as described elsewhere[15,18].

Statistical analysis Data are expressed as mean±SD. Statistical analysis was performed using one-way analysis of variance.

Results

Effects of acetamide-45 on inflammatory cells in the airways of allergic rats In our rat model of allergic asthma, ovalbumin sensitization and challenge caused an obvious increase in inflammatory cells in BAL. As shown in Figure 1, the total number of leukocytes and eosinophils in the OVA group was significantly greater than that in the normal group

(P<0.05), but the number of inflammatory cells was depressed when aminophylline (Ami) was administered (P<0.05 *vs* OVA). Seven days of treatment with acetamide-45 (Ace) at 5, 10, or 30 mg/kg significantly decreased the number of inflammatory cells in BAL caused by sensitization and challenge (P<0.05 *vs* OVA; Figure 1). There was no statistical difference between the Ace group and the Ami group (P>0.05; Figure 1).

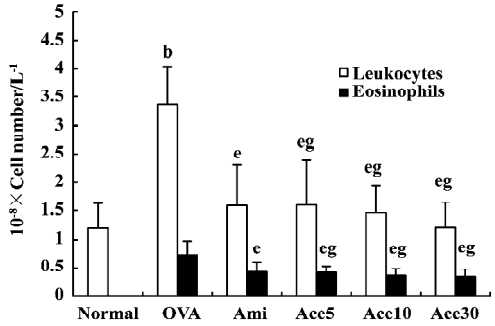

Figure 1. Effect of acetamide-45 on inflammatory cells in rat airway after ovalbumin challenge. Rats were sensitized and challenged with ovalbumin (OVA). Acetamide-45 at concentrations of 5 mg/kg (Ace5), 10 mg/kg (Ace10), or 30 mg/kg (Ace30), or aminothiophylline at a concentration of 10 mg/kg (Ami) were administered once a day for 7 d during challenge. n=6. Mean±SD. ^{b}P<0.05 *vs* normal. ^{e}P<0.05 *vs* OVA. ^{g}P>0.05 *vs* Ami.

Effects of acetamide-45 on R_L and C_{dyn} in allergic rats After rats were given 7 aerosolized OVA challenges, a significant decrease in C_{dyn} was induced. However, through sensitization and challenge, R_L increased to a level that was significantly greater than that in the normal group. The administration of aminophylline decreased the R_L and increased the C_{dyn} of sensitized and challenged animals. At a dose of 5, 10, or 30 mg/kg, acetamide-45 improved both C_{dyn} and R_L (Figure 2).

Effect of acetamide-45 on IL-4 in lung tissue in allergic rats As shown in Figure 3, IL-4 levels in the lungs of rats from the various groups were measured. Sensitization and challenge increased the concentration of IL-4 to a level significantly different from that of the normal group (P<0.05). Seven days of treatment with acetamide-45 at concentrations of 5, 10, or 30 mg/kg, or with aminophylline at a concentration of 10 mg/kg, obviously reduced the increase in the concentration of IL-4 (P<0.05).

Effect of acetamide-45 on PDE4 activity in lung tissue in allergic rats Sensitization and challenge increased the PDE4 activity of lung tissue to 503±125 nmol·g^{-1}·min^{-1}, which was greater than that of the normal group (P<0.05). Acetamide-45 at concentrations of 5, 10, or 30 mg/kg inhibited the hydrolysis of cAMP by the PDE4 extracted from lung tissue. The PDE4 activities of the lung tissue were 281±55, 273±57, and 238±36 nmol·g^{-1}·min^{-1}, respectively (for acetamide-45 at concentrations of 5, 10, or 30 mg/kg). As a non-selective inhibitor of PDE4, aminophylline suppressed PDE4 activity to 341±44 nmol·g^{-1}·min^{-1} at a dose of 10 mg/kg, which was weaker than the activity produced by treatment with acetamide-45 at concentrations of 10 and 30 mg/kg (P<0.05, Figure 4).

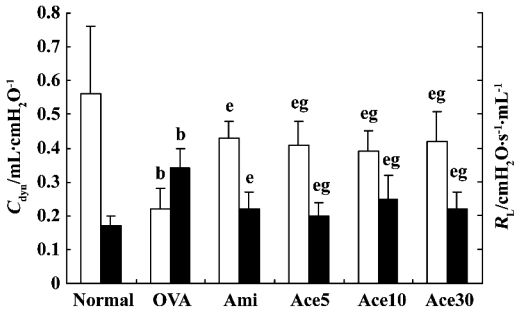

Figure 2. Effects of acetamide-45 on lung resistance (R_L, filled bars) and dynamic lung compliance (C_{dyn}, open bars) in allergic rats. Rats were sensitized and challenged with ovalbumin (OVA). Acetamide-45 at a concentration of 5 mg/kg (Ace5), 10 mg/kg (Ace10) or 30 mg/kg (Ace30), and aminothiophylline at a concentration of 10 mg/kg (Ami) were administered once a day for 7 d during challenge, and then lung function was measured. n=6. Mean±SD. ^{b}P<0.05 *vs* normal. ^{e}P<0.05 *vs* OVA. ^{g}P>0.05 *vs* Ami.

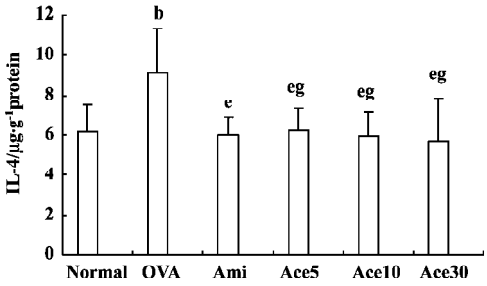

Figure 3. Effect of acetamide-45 on IL-4 concentration in lung tissue in allergic rats. Rats were sensitized and challenged with ovalbumin (OVA). Acetamide-45 at concentrations of 5 mg/kg (Ace5), 10 mg/kg (Ace10) or 30 mg/kg (Ace30), and aminothiophylline at a concentration of 10 mg/kg (Ami) were administered once a day for 7 d during challenge, and then the IL-4 concentrations of lung tissue were measured. n=6. Mean±SD. ^{b}P<0.05 *vs* normal. ^{e}P<0.05 *vs* OVA. ^{g}P>0.05 *vs* Ami.

Discussion

Acetamide-45, *N*-(pyridin-4-yl)-[1-(4-fluorophenyl) indol-3-yl] acetamide, is a new anti-inflammatory drug that inhibits the release of cytokines and the activation of eosinophils[12].

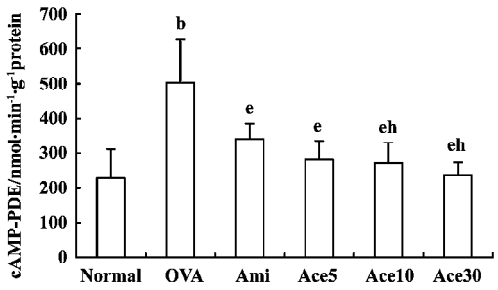

Figure 4. Effect of acetamide-45 on PDE4 activity in lung tissue in allergic rats. Acetamide-45 at concentrations of 5 mg/kg (Ace5), 10 mg/kg (Ace10), or 30 mg/kg (Ace30) and aminothiophylline at a concentration of 10 mg/kg (Ami) were administered once a day for 7 d during challenge, and then the PDE4 activity of lung tissues was measured. n=6. Mean±SD. $^bP<0.05$ *vs* normal. $^eP<0.05$ *vs* OVA. $^hP<0.05$ *vs* Ami.

It has also been reported that acetamide-45 inhibits the contraction of isolated guinea pig trachea induced by histamine and methacholine[14]. However, the mechanism by which acetamide-45 acts remains unknown. The present study shows that acetamide-45 can suppress the accumulation of inflammatory cells in airways and improve the lung function of allergic rats. We also found that acetamide-45 could inhibit PDE4 activity and reduce the IL-4 level in the lung tissue of allergic rats. To our knowledge, this study represents the first investigation of the effect of acetamide-45 on lung function and PDE4 concentration in the lung in an animal model of asthma.

Asthma is a syndrome characterized by eosinophil infiltration and airway hyperresponsiveness, which occurs via a mechanism that is very complex. It is well known that eosinophils play a critical role in airway damage and dysfunction in asthma. We found that acetamide-45 had an inhibitory effect on eosinophil infiltration in the airways of allergic rats. Not only eosinophils but also other inflammatory cells were decreased in concentration, so that inflammation of the airway in allergic rats was inhibited by acetamide-45.

Inflammation of the airway leads to spasms of the bronchial smooth muscles, mucus hypersecretion, and airflow limitations, which result in pulmonary dysfunction in asthma. The data obtained by a whole body plethysmograph in this study indicate that acetamide-45 improves the lung function of allergic rats produced by sensitization and challenge. Its effectiveness has been demonstrated in two ways. First, the C_{dyn} of allergic rats increased obviously relative to normal rats at a dose of 5 mg/kg acetamide-45. Second, the R_L of allergic rats was reduced significantly by acetamide-45 in the same way. The improvement in lung function produced by acetamide-45 is similar to that produced by aminophylline.

The experiments presented here show that both acetamide-45 and aminophylline repress IL-4 production in allergic rats, but that there is no difference between the two agents. IL-4 is a key cytokine in the development of allergic inflammation. It is associated with the secretion of IgE by B lymphocytes and the expression of eotaxin and other inflammatory cytokines that contribute to inflammation and lung remodeling in asthma[18,19]. A previous study shows that acetamide-45 inhibits IL-4 biosynthesis and release, which is identical to our result[12]. This indicates that acetamide-45 can reduce the release of IL-4 and reduce its concentration in the lung, which results in the inhibition of airway inflammation.

Our study of PDE4 activity shows that acetamide-45 has an inhibitory effect on cAMP hydrolysis of PDE4 in the lung tissue of allergic rats. In a previous study, we demonstrated that acetamide-45 could inhibit the hydrolysis of cAMP by PDE4 extracted from transfected yeast, and that its inhibitory effect was stronger than that of theophylline[15]. The present study also shows that at the same dose (10 mg/kg), the inhibitory effect of acetamide-45 is greater than that of aminophylline, which is a non-selective PDE inhibitor. PDE4 is specific for cAMP, and is predominantly expressed in inflammatory cells. It plays an important role in the regulation of cellular functions in inflammatory and immune cells, and inhibition of PDE4 may be one of the anti-inflammatory mechanisms of acetamide-45.

In conclusion, we have shown that acetamide-45 could improve the lung function of allergic rats produced by sensitization and challenge, and that production of eosinophils in those animals could also be repressed. Acetamide-45 had an inhibitory effect on PDE4 activity in the lung tissue of allergic rats, and the inhibition was stronger than that produced by aminophylline. The present research may provide an experimental basis for further study of this agent.

References

1 O'Byrne P. Asthma pathogenesis and allergen-induced late responses. J Allergy Clin Immunol 1998; 102: S85.

2 Agrawal DK, Bharadwaj A. Allergic airway inflammation. Curr Allergy Asthma Rep 2005; 5: 142–8.

3 Kumar RK, Herbert C, Thomas PS, Wollin L, Beume R, Yang M, *et al*. Inhibition of inflammation and remodeling by roflumilast and dexamethasone in murine chronic asthma. J Pharmacol Exp Ther 2003; 307: 349–55.

4 Tomkinson A, Cieslewicz G, Duez C, Larson KA, Lee JJ, Gelfand EW. Temporal association between airway hyperresponsiveness and airway eosinophilia in ovalbumin-sensitized mice. Am J Respir Crit Care Med 2001; 163: 721–30.

5 Conti M, Richter W, Mehats C, Livera G, Park JY, Jin C. Cyclic

AMP-specific PDE4 phosphodiesterases as critical components of cyclic AMP signaling. J Biol Chem 2003; 278: 5493–6.
6 Wang T, Wang P. Novel approaches to using PDE4 inhibitors for antihypertensive therapy. Curr Opin Investig Drugs 2005; 6: 283–8.
7 Landells LJ, Spina D, Souness JE, O'Connor BJ, Page CP. A biochemical and functional assessment of monocyte phosphodiesterase activity in healthy and asthmatic subjects. Pulm Pharmacol Ther 2000; 13: 231–9.
8 Torphy TJ. Phosphodiesterase isozymes, molecular targets for novel antiasthma agents. Am J Respir Crit Care Med 1998; 157: 351–70.
9 Bousquet J. Global initiative for asthma (GINA) and its objectives. Clin Exp Allergy 2000; 30 Suppl 1: 2–5.
10 Mark A. Phosphodiesterase 4 inhibitors and the treatment of asthma. Drugs 2000; 59: 193–212.
11 Giembycz MA. Development status of second generation PDE4 inhibitors for asthma and COPD: the story so far. Monaldi Arch Chest Dis 2002; 57: 48–64.
12 Norman P. PDE4 inhibitors 2001: Patent and literature activity 2002–September 2001. Expert Opin Ther Patents 2002; 12: 93–111.
13 Menciu C, Duflos M, Fouchard F, Le Baut G, Emig P, Achterrath U, *et al*. New *N*-(pyridin-4-yl)-(indol-3-yl) acetamides and propanamides as antiallergic agents. J Med Chem 1999; 42: 638–48.
14 Lu YB, Chen Z, Wu M. Acetamide-45 inhibits histamine- and methacholine-induced contraction of isolated guinea pig trachea. Acta Pharmacol Sin 2002; 23: 152–6.
15 Wang K, Chen JQ, Chen Z, Chen JC. Inhibition of human phosphodiesterase 4A expressed in yeast cell GL62 by theophylline, rolipram, and acetamide-45. Acta Pharmacol Sin 2002; 23: 1013–7.
16 Xie QM, Zeng LH, Zheng YX, Lu YB, Yang QH. Bronchodilating effects of bambuterol on bronchoconstriction in guinea pigs. Acta Pharmacol Sin 1999; 20: 651–4.
17 Xie QM, Chen JQ, Shen WH, Yang QH, Bian RL. Comparison of bronchodilating and antiinflammatory activities of oral formoterol and its (*R*,*R*)-enantiomers. Acta Pharmacol Sin 2003; 24: 277–82.
18 Tang HF, Song YH, Chen JC, Chen JQ, Wang P. Upregulation of phosphodiesterase-4 in the lung of allergic rats. Am J Respir Crit Care Med 2005; 171: 823–8.
19 Ryan JJ. Interleukin-4 and its receptor: essential mediators of the allergic response. J Allergy Clin Immunol 1997; 99: 1–5.
20 Wills-Karp M, Gavett SH, Schofield B, Finkelman F. Role of interleukin-4 in the development of allergic airway inflammation and airway hyperresponsiveness. Adv Exp Med Biol 1996; 409: 343–7.

Acta Pharmacologica Sinica 2005 Dec; 26 (12): 1497–1504

Blackwell Publishing

Full-length article

Effect of cholecystokinin octapeptide on diacylglycerol-PKC signaling pathway in rat pulmonary interstitial macrophages stimulated by lipopolysaccharide[1]

Shun-jiang XU[2], Wei-juan GAO, Bin CONG[3], Chun-ling MA, Shu-jin LI, Yi-ling LING, Zhen-yong GU, Yu-xia YAO

Department of Pathophysiology, Hebei Medical University, Shijiazhuang 050017, China

Key words

cholecystokinin; protein kinase C; translocation; lung; macrophages; lipopolysaccharides

[1] Project supported by the National Natural Science Foundation of China (No 30270529) and the Natural Science Foundation of Hebei Province (No 303452).
[2] Now in *the Hebei Province Center for Disease Prevention and Control, Shijiazhuang 050021, China.*
[3] Correspondence to Prof Bin CONG.
Phn/Fax 86-311-8626-5774.
E-mail bincong@263.net

Received 2005-03-30
Accepted 2005-08-15

doi: 10.1111/j.1745-7254.2005.00217.x

Abstract

Aim: To investigate the effect of cholecystokinin octapeptide (CCK-8) on the diacylglycerol-protein kinase C (DAG-PKC) signaling pathway in rat pulmonary interstitial macrophages (PIM) stimulated by lipopolysaccaride (LPS). **Methods:** The PIM from rat lung tissues were isolated using the collagenase digestion method combined with alveolar lavage and pulmonary vessel perfusion. DAG content and PKC activity were measured by radioenzymatic assay. The translocation of PKCζ was determined by semi-quantitative immunoblot analysis. **Results:** CCK-8, at high concentrations (1×10^{-6}–1×10^{-5} mol/L), decreased DAG content and inhibited PKC activity and PKCζ translocation compared with that in rat resting PIM of a control group ($P<0.01$). LPS increased DAG content, and promoted PKC activity and PKCζ translocation ($P<0.01$). CCK-8 decreased LPS-induced DAG content and inhibited LPS-induced PKC activity and PKCζ translocation significantly at 1×10^{-8}–1×10^{-5} mol/L ($P<0.01$). This inhibitory effect of CCK-8 could be abrogated partly by proglumide (non-selective CCK receptor antagonist), CR-1409 (selective CCK-A receptor antagonist), and CR-2945 (selective CCK-B receptor antagonist) in a concentration-dependent manner ($P<0.01$). **Conclusion:** CCK-8 was a negative modulator of the DAG-PKC signaling pathway in rat resting PIM, which is very important for maintaining body homeostasis. It significantly inhibited LPS-induced DAG content, PKC activity and PKCζ translocation in a concentration-dependent manner. The CCK receptor, especially the CCK-A receptor, might play a major role in this process.

Introduction

Cholecystokinin (CCK) is a gut-brain peptide that exerts a variety of physiological actions in the gastrointestinal tract and central nervous system (CNS) through activating cell surface CCK receptors[1]. CCK receptors have been pharmacologically classified into 2 subtypes, CCK-A receptors (CCK-AR) and CCK-B receptors (CCK-BR), according to their affinity for the peptide agonists CCK and gastrin[2]. Our previous experiments demonstrated that CCK-8, as an intestinal neuropeptide, not only protected gastric mucosa against alcohol-induced injury, but also was a potent protective agent against acute lung injury caused by lipopolysaccharide (LPS)[3,4]. It reduced pulmonary artery hypertension (PAH) and lessened inflammatory lesions in lung tissues of endotoxin shock (ES) rats[3,4]. Studies from our laboratory show that sulfated CCK-8 (sCCK-8) can inhibit LPS-induced TNF-α production *in vitro*, sCD14 release and mCD14 expression in rat pulmonary interstitial macrophages (PIM)[5]. The production of proinflammatory cytokines, including TNF-α, IL-1β, and IL-6 in ES rats, was also inhibited by sCCK-8 *in vivo*[6,7]. The above data suggest that sCCK-8 has an anti-inflammatory effect, confirmed by a morphological observation that sCCK-8 clearly lessened the inflammatory lesions in the spleen and the liver tissues in endotoxin shock rats[4]. However, the anti-inflammatory mechanisms and signaling pathways activated by CCK-8 remain unclear.

Several signaling pathways are involved in the activa-

tion of monocytes/macrophages induced by LPS, including the mitogen-activated protein kinase (MAPK) and the protein kinase C (PKC) pathway, and there is a lot of cross-talk between them. PKC, as an important message molecule, participates extensively in immune regulation and inflammatory signal transduction. In particular, PKCζ plays a pivotal role in the complicated signaling networks induced by LPS[8,9]. Several studies show that LPS-induced activation of the extracellular signal-regulated kinases (ERK) in alveolar macrophages is mediated by sequential activation of phosphatidylcholine-specific phospholipase C (PC-PLC), induction of cellular diacylglycerol (DAG) and ceramide, and activation of PKCζ[10]. Previously we reported that CCK-AR and CCK-BR mRNA expressions were detected by reverse transcription-polymerase chain reaction. The presence of functional CCK receptors was confirmed by radioligand binding assay in rat PIM, and their expressions were upregulated by LPS[11]. Increasing evidence supports the concept that the signal transduction cascades mediated by CCK receptors are cell specific. For example, CCK was found to activate cAMP and PKC regulated signaling pathways in pancreatic acinar cells, but CCK-8 induced a significant decrease in membrane and cytosol PKC activity in murine lymphocytes, neutrophils, and peritoneal macrophages, as well as an increase of intracellular cAMP levels[12–14]. As PIM plays an important role in the inflammatory response to LPS in the lungs and little is known about the effect of CCK-8 on DAG-PKC signaling pathway in PIM, the present study was undertaken to investigate the effect of CCK-8 on DAG contents, PKC activities, and PKCζ translocation in resting and LPS-stimulated rat PIM, and to explore the anti-inflammatory molecular mechanisms activated by CCK-8.

Materials and methods

Chemicals and reagents Collagenase IA, LPS (*Escherichia coli* 0111:B4), CCK-8s, proglumide, CR-1409, CR-2945, aprotinin, leupeptin, and DNaseI were obtained from Sigma Chemical Co. RPMI-1640 culture medium, phenylmethylsulfonyl-fluoride (PMSF), and nitrocellulose membranes were obtained from Gibco BRL. DAG biotrak assay reagents system (RPN 200) and Amprep Si minicolumns (RPN 1906) were obtained from Amersham Biosciences. SignaTECT® PKC assay system and Gel shift assay system were obtained from Promega. Diethylaminoethyl cellulose (DE52) was obtained from Whatman BioSystems. Affinity purified polyclonal nPKCζ antibodies (C-20), peroxidase-conjugated goat anti-rabbit IgG, and Western blotting luminol reagent (sc-2048) were obtained from Santa Cruz Biotechnology. All other reagents were of analytic pure grade.

Animals Adult healthy female Sprague-Dawley (SD) rats (180–220 g, Grade II, Certificate No 04057) were obtained from the Experimental Animal Center of Hebei Province (Shijiazhuang, China).

Cell culture and treatment PIM were isolated from perfused rat lungs with a collagenase digestion technique, modified as Wizemann *et al*[15]. PIM were harvested with PBS containing 0.4 g/L edetic acid, pelleted by centrifugation (4 ºC, 400×*g*, 10 min) and resuspended with serum-free medium. Cells were incubated with CCK-8 at different concentrations or stimulated with LPS (10 mg/L) in the absence or presence of CCK-8, proglumide, CR-1409, and CR-2945 for 1 h. At the end of incubation, PIM were centrifuged at 400×*g* for 60 s, and the pellets were measured for DAG contents, PKC activities, and translocation.

Measurement of intracellular DAG contents Total cell lipids were extracted using a modification of the method of Bligh and Dyer[16]. Intracellular DAG contents were measured using the DAG assay reagents system from Amersham Biosciences. A radioenzymatic assay uses the diacylglycerol kinase and defined mixed micelle conditions to solubilize the DAG present and allow its quantitative conversion to [^{32}P]phosphatidic acid in the presence of [γ-^{32}P]ATP. Following the enzyme-catalyzed phosphorylation of DAG, the [^{32}P]phosphatidic acid reaction product was extracted and separated by Amprep chromatography. The radioactivity attributable to [^{32}P]phosphatidic acid was determined by liquid scintillation counting. The amount of DAG present in the sample was calculated from the amount of [^{32}P]phosphatidic acid produced and the specific activity of the ATP according to the standard curve was expressed as pmol per 2×10^6 cells.

Preparation of cytosol and membrane fractions After treatment, the PIM were washed with 5 mL ice-cold PBS and centrifuged at 250×*g* for 60 s. The supernatant was discarded and the cells were suspended in iced 0.5 mL of extraction buffer [Tris-HCl 25 mmol/L (pH 7.4) containing edetic acid 0.5 mmol/L, egtazic acid 0.5 mmol/L, β-mercaptoethanol 10 mmol/L, leupeptin 1 mg/L, and aprotinin 1 mg/L] and sonicated on ice with 10-s bursts, each preceded by a 10-s pause. The homogenates were centrifuged at 100 000×*g* for 60 min at 4 ºC and the supernatant was used for assay of PKC (cytosol fraction). The pellet (representing the membrane fraction) was suspended in 2 mL of iced extraction buffer containing 0.05% Triton X-100, shaken for 60 min at 4 ºC and centrifuged at 100 000×*g* at 4 ºC for 60 min. The supernatant was taken for assay of PKC (membrane fraction). Cytosol and membrane fractions were partially purified

using diethylaminoethyl (DEAE)-cellulose chromatography. The samples were passed over individual 1-mL columns pre-equilibrated with extraction buffer. Following washing the columns 1 time with 5 mL of extraction buffer, the fractions of PKC were eluted with 5 mL of extraction buffer containing NaCl 200 mmol/L, stored at 4 ºC, and generally assayed within 24 h.

PKC activity assay PKC activity was analyzed by measuring the incorporation of ^{32}P from [γ-^{32}P]ATP (185 PBq/mol) into peptide Neurogranin ($_{28}$AAKIQAS*-FRGHMA-RKK$_{43}$), a specific substrate of PKC. The standard assay mixture (25 μL) contained extraction buffer 5 μL, 5 μL PKC co-activation buffer (5×), 5 μL PKC substrate peptide 0.5 mmol/L, and 5 μL of ATP mixture containing ATP 0.5 mmol/L and [γ-^{32}P]ATP 18. 5 GBq (0.5 Ci). Control reaction used a control buffer instead of PKC substrate peptide. The reaction was terminated by adding ice-cold 7.5 mol/L guanidine hydrochloride 12.5 μL at 30 ºC after 5 min. Each terminated reaction mixture (10 μL) was then spotted onto an SAM membrane. The membrane was rinsed with 2 mol/L NaCl and 2 mol/L NaCl in 1% phosphoric acid and deionized water, respectively. Aliquots of 5 μL in any 2 reactions were spotted onto SAM membrane. All membranes were dried at room temperature and put into liquid scintillator. Radioactivity was counted. All values represented the mean from 3 separate culture dishes, with an average difference between duplicates of <±5%. Proteins were measured using Bradford's method by using bovine serum albumin as a standard.

Immunoblot analysis The effect of CCK-8 on distribution and on LPS-induced translocation of PKCζ was determined using quantitative immunoblot analysis. Crude cytosolic and membranous fractions from PIM were prepared as described above, except that DE52 column chromatography was omitted. Protein concentrations of fraction were measured using Bradford's method using bovine serum albumin as standard. Aliquots of sample eluates were added to sample preparation buffer [Tris-HCl 0.05 mol/L, pH 6.8, 20% glycerol, 2% sodium dodecylsulfate (SDS), edetic acid 5 mmol/L, egtazic acid 5 mmol/L, β-mercaptoethanol 10 mmol/L, leupeptin 1 mg/L, aprotinin 1 mg/L, PMSF 0.5 mmol/L, and 0.1% bromphenol blue] and boiled for 5 min. The proteins were separated by SDS-polyacrylamide (10% acrylamide) gel electrophoresis and electrophoretically transferred to nitrocellulose membranes. The completeness of transfer was confirmed by staining the gel with Coomassie blue. The blots were incubated at room temperature for 2 h with PBS containing 5% nonfat dry milk and 0.05% Tween 20 (bovine serum albumin/Tris buffer saline) to block non-specific sites. The blots were washed with PBS, and incubated overnight with affinity purified polyclonal nPKCζ antibodies(1:200) at 4 ºC. The blots were washed 3 times for 15 min each with PBS at room temperature and incubated at 37 ºC for 1 h with peroxidase-conjugated goat anti-rabbit IgG antibody. The blots were finally washed 3 times for 15 min each with Tris buffer saline, incubated with enhanced chemiluminescence detection reagents for 3–5 min and exposed to X-ray films for up to 60 s. The density of the bands on the film was analyzed by Gel-Pro analyzer version 3.1 software (Media Cybernetics). The arbitrary unit (D_{area}·$D_{density}$) was used for expressing the relative level of PKCζ of cytosolic and membranous fractions from PIM.

Statistical analysis Data were expressed as mean±SD and analyzed using analysis of variance and the least significant difference test using an SPSS statistical program. Statistical significance was accepted when $P<0.05$. Half-maximal inhibition (IC_{50}) was calculated using the log-probit method.

Results

DAG content For resting PIM, CCK-8 did not affect DAG content at low concentrations (1×10^{-12}–1×10^{-7} mol/L, $P>0.05$), but decreased it at high concentrations (1×10^{-6}–1×10^{-5} mol/L) compared with that of the control group ($P<0.01$). Stimulation of PIM by LPS (10 mg/L) obviously increased DAG content ($P<0.01$) (Figure 1). CCK-8 concentration-dependently inhibited the LPS-induced DAG content, and a significant inhibition was observed at high concentrations (1×10^{-8}–1×10^{-5} mol/L, $P<0.01$), but not at low concentrations (1×10^{-11}–1×10^{-9} mol/L, $P>0.05$) (Figure 1). The inhibitory effect of CCK-8 on DAG content induced by LPS was abrogated in part by proglumide, CR-1409, and CR-2945 in a concentration-dependent manner. Proglumide was so potent that it had an obvious effect on CCK-8-resultant inhibition of LPS-induced DAG content increase at low concentrations, and even resulted in a full reversal of it at high concentrations, and a similar effect was found for CR-1409, but not for CR-2945, with CR-2945 showing a weak effect only at high concentrations. The IC_{50} of proglumide, CR-1409, and CR-2945 were $(1.76\pm0.19)\times10^{-6}$ mol/L, $(6.76\pm0.52)\times10^{-5}$ mol/L, and $(5.45\pm0.42)\times10^{-3}$ mol/L, respectively (Figure 2).

PKC activity and translocation Treating resting PIM with CCK-8, no changes of cytosolic and membrane-bound PKC activities were found at low concentrations (1×10^{-12}–1×10^{-9} mol/L), but an increase of cytosolic PKC activities and a decrease of membrane-bound PKC activities were observed gradually with the increase of CCK-8 concentration, and significant differences presented at 1×10^{-6}–1×10^{-5} mol/L

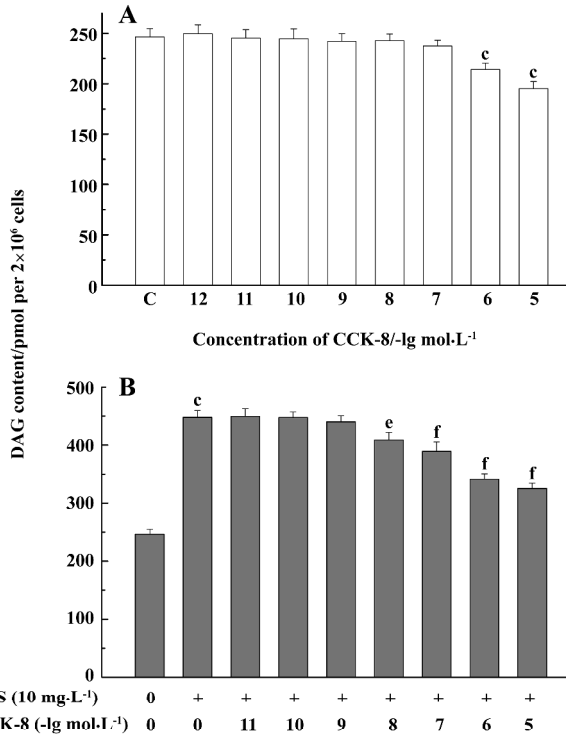

Figure 1. Effect of CCK-8 on DAG content in rat resting pulmonary interstitial macrophages (PIMs, A) and LPS-stimulated rat PIMs (B). PIMs were incubated with CCK-8 at different concentrations in the absence or presence of LPS for 1 h. DAG content was determined by radioenzymatic assay. n=3. Mean±SD. ^cP<0.01 *vs* control group. ^cP<0.05, ^fP<0.01 *vs* LPS group. C: control.

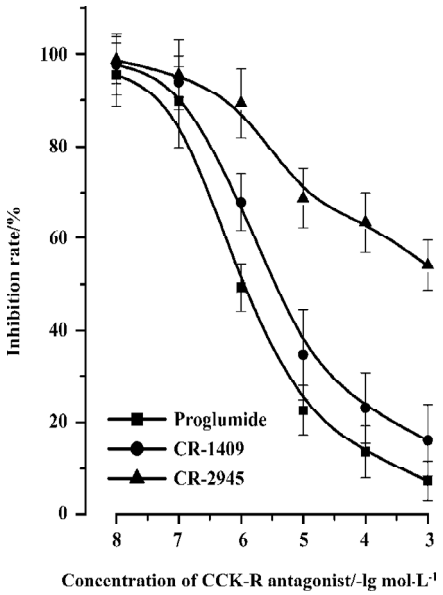

Figure 2. CCK-receptor non-selective and selective antagonists abrogated the inhibitory effects of CCK-8 on the increase in diacyglycerol (DAG) content induced y LPS. Pulmonary interstitial macrophages were isolated and pretreated with CCK receptor antagonists (proglumide, CR-1409, and CR-2945) for 10 min prior to addition of LPS (10 mg/L) and CCK-8 (1×10^{-6} mol/L), and then co-incubated for 1 h. DAG content was determined by radioenzymatic assay. n=3. Mean±SD.

(P<0.01) (Figure 3). LPS decreased cytosolic PKC activity and increased membrane-bound PKC activity (P<0.01), indicating that LPS could promote PKC translocation and change its distribution, but did not affect its total activity in rat PIM. Treating PIM with CCK-8 did not affect LPS-induced PKC translocation at 1×10^{-11}–1×10^{-10} mol/L, decreased it slightly at 1×10^{-9}–1×10^{-8} mol/L (P<0.05), and inhibited it significantly at 1×10^{-7}–1×10^{-5} mol/L (P<0.01), suggesting that CCK-8 inhibited LPS-induced PKC translocation in a concentration-dependent manner (Figure 3). The inhibitory effect of CCK-8 1×10^{-6} mol/L on LPS-induced PKC activity translocation in rat PIM was attenuated by proglumide, CR-1409, and CR-2945 at 1×10^{-4}mol/L, and their inverse rate (percentage of CCK-8) were 58.9%, 48.1%, and 21.5%, respectively (P<0.01) (Figure 4).

Immunoblot analysis For resting PIM, CCK-8 inhibited PKCζ translocation from cytosol to membrane only at high concentrations (1×10^{-6} mol/L) (P<0.05) (Figure 5). LPS promoted PKCζ translocation from cytosol to membrane (P< 0.01) and CCK-8 inhibited LPS-induced PKCζ translocation significantly at 1×10^{-8} and 1×10^{-6} mol/L (P<0.01, Figure 6). The inhibitory effect of CCK-8 on LPS-induced PKCζ translocation was blocked by proglumide, CR-1409 (P<0.01), and CR-2945 (P<0.05) to some extent (Figure 7).

Discussion

CCK is a neuropeptide expressed in the endocrine I-cells of the small intestinal mucosa and in widespread central and peripheral neurons[17]. Whereas intestinal CCK regulates the release of pancreatic enzymes and the contraction of the gall bladder, neuronal CCK is a transmitter or modulator assumed to be involved in a variety of CNS functions, such as feeding behavior, anxiety, analgesia, memory, immunomodulation, and anti-opioid effects[1,18,19]. CCK receptor is a G protein-coupled receptor with seven-transmembrane domain that has attracted considerable interest as a target for drug-discovery efforts, based on its important physiological role in the gastric mucosa, CNS, and immune cells[20]. CCK acting through its G protein-coupled receptor is now known to activate a variety of intracellular signaling mechanisms and, thereby, to regulate a complex array of cellular functions in different types of cells. Data from several labs indicates that CCK increases intracellular calcium in

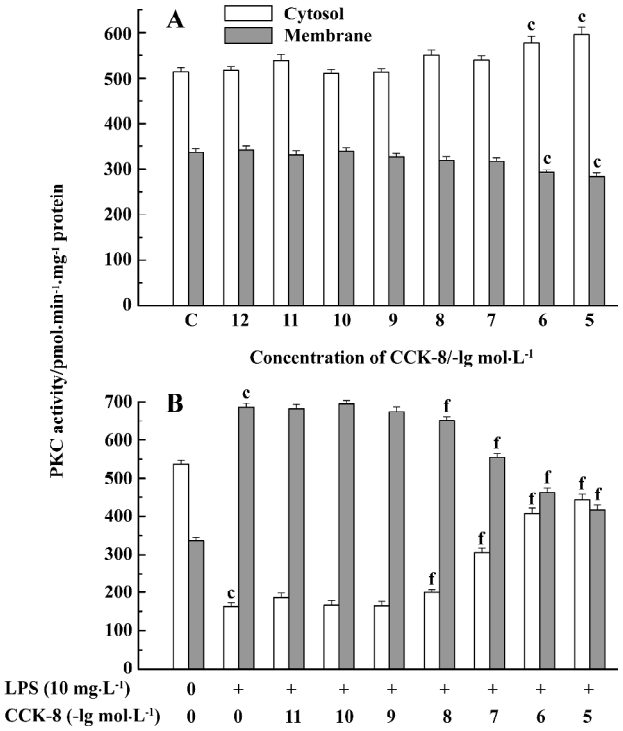

Figure 3. Effect of CCK-8 on protein kinase C translocation in rat resting pulmonary interstitial macrophages (PIMs, A) and LPS-stimulated rat PIMs (B). PIMs were incubated with CCK-8 at various concentrations in the absence or presence of LPS for 1 h. PKC activities were determined by radioenzymatic assay. n=3. Mean±SD. ^{c}P<0.01 *vs* control group. ^{f}P<0.01 *vs* LPS group. C: control.

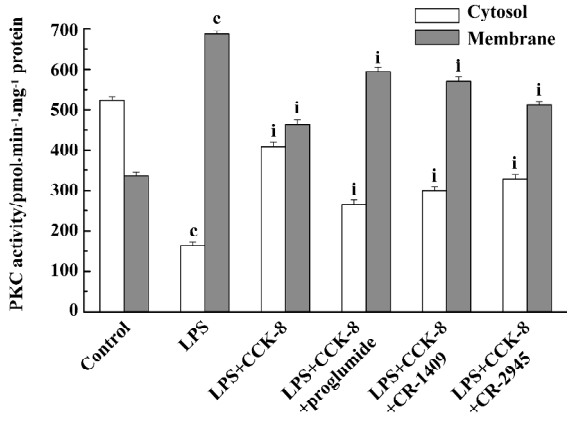

Figure 4. Effects of proglumide, CR-1409, and CR-2945 on LPS-induced protein kinase C translocation in rat pulmonary interstitial macrophages (PIMs). PIMs were isolated and pretreated with CCK receptor antagonists (proglumide, CR-1409, and CR-2945) for 10 min prior to addition of LPS (10 mg/L) and CCK-8 (1×10^{-6}mol/L), and then co-incubated for 1 h. PKC activity was determined by radioenzymatic assay. n=3. Mean±SD. ^{c}P<0.01 *vs* control group. ^{f}P<0.01 *vs* LPS group. ^{i}P<0.01 *vs* LPS+CCK-8 group.

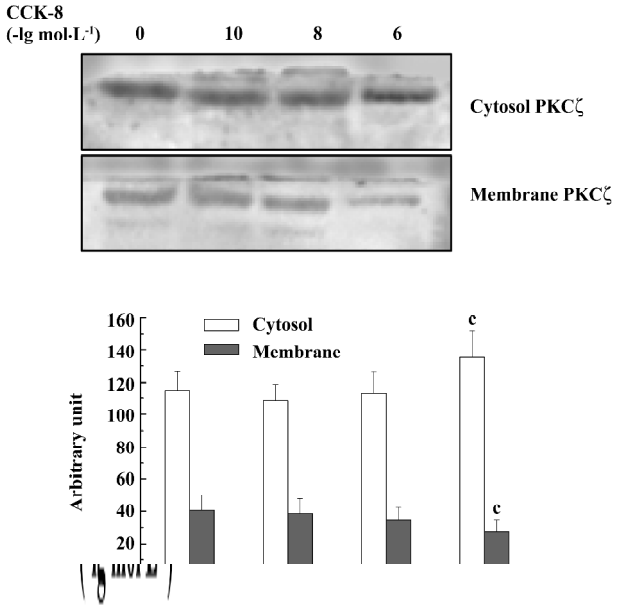

Figure 5. Effect of CCK-8 on PKCζ translocation in rat resting pulmonary interstitial macrophages. Upper: Representative immunoblot analysis. Lower: Relative protein levels of PKCζ of 3 individual experiments. n=3. Mean±SD. ^{c}P<0.01 *vs* control group.

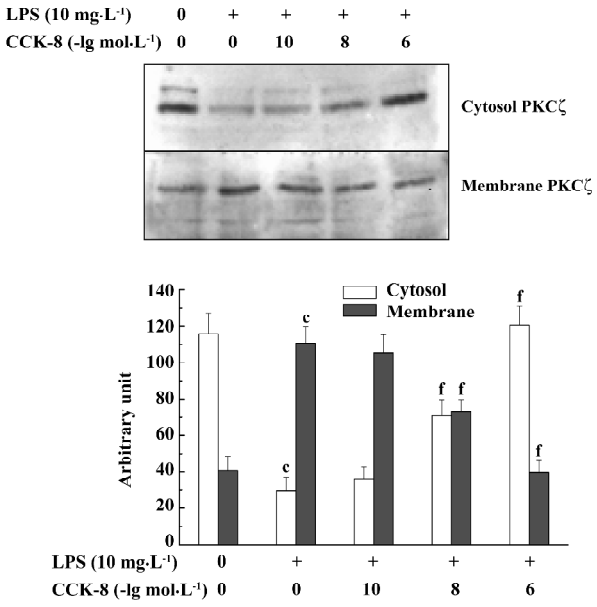

Figure 6. Effect of CCK-8 on LPS-induced PKCζ translocation in rat PIMs. Upper: Representative immunoblot analysis. Lower: Relative protein levels of PKCζ of three individual experiments analyzed by Gel-pro analyzer software. n=3. Mean±SD. ^{c}P<0.01 *vs* control group. ^{f}P<0.01 *vs* LPS group.

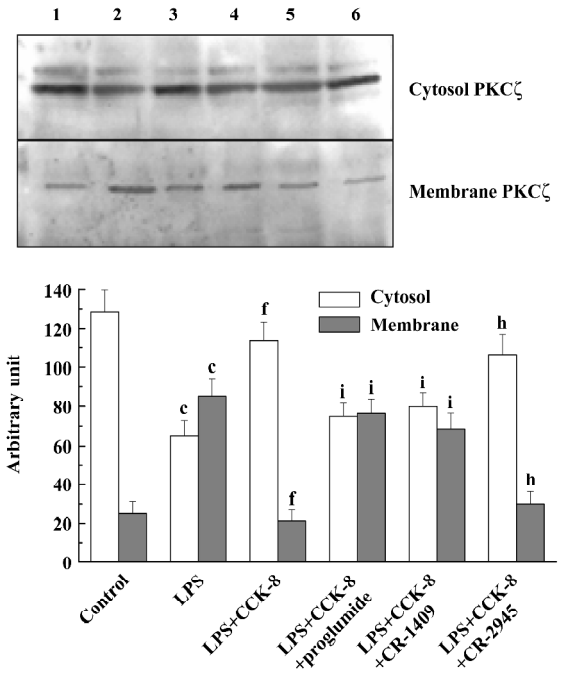

Figure 7. Effects of proglumide, CR-1409, and CR-2945 on LPS-induced PKCζ translocation in rat pulmonary interstitial macrophages. Upper: Representative immunoblot analysis. Lane 1, control; lane 2, LPS; lane 3, LPS+CCK-8 1×10^{-6}mol/L; lane 4, LPS+CCK-8+proglumide; lane 5, LPS+CCK-8+CR-1409; lane 6, LPS+CCK-8+CR-2945. Lower: Relative protein level of PKCζ of three individual experiments analyzed by Gel-pro analyzer software. n=3. Mean±SD. $^{c}P<0.01$ *vs* control group. $^{f}P<0.01$ *vs* LPS group. $^{h}P<0.05$, $^{i}P<0.01$ *vs* LPS+CCK-8 group.

human peripheral blood mononuclear cells and T lymphocyte cell lines[21]. sCCK-8 can inhibit the mobility capacity and the mitogen-induced lymphocytic proliferation, but can increase the adherence and the spontaneouse proliferation of lymphocytes[22,23]. In addition, sCCK-8 is a negative modulator of several functions of resting murine peritoneal macrophages and human neutrophils, including the production of superoxide anion, phagocytosis and mobility, and the inhibition of these activities is carried out through an increase of intracellular cAMP levels and a decrease in PKC activity[11]. In the present study sCCK-8 did not affect DAG content, PKC activities, and PKCζ translocation at low concentrations, but decreased DAG content and inhibited PKC activities and PKCζ translocation at high concentrations in rat resting PIM. Resting PIM were not sensitive to the stimulation by sCCK-8, and CCK-8 was a negative modulator of the DAG-PKC signaling pathway at physiological concentrations, which was very important for maintaining body homeostasis, and inhibited the DAG-PKC signaling pathway at high con-centrations.

LPS is the major component of the outer leaflet of Gram-negative bacteria and has profound immunostimulatory and inflammatory capacity. LPS interacts with LPS-binding protein, therefore allowing binding to CD14 and association with the Toll-like receptor 4 (Tlr4) containing an intracellular signaling domain. Binding of LPS to these receptors results in the activation of several signaling cascades, such as PKC and MAPK[24]. PKC isoforms are involved in a wide variety of intracellular signaling events and play a significant role in many aspects of immune response, from development, differentiation, activation, and survival of lymphocytes to macrophage activation[25]. PKCζ is a member of the atypical subfamily and has been widely implicated in the regulation of cellular functions, particularly in the LPS-induced inflammatory response[9]. In the present study, stimulation of PIM by LPS increased DAG content, promoted PKC activities and PKCζ translocation, and changed its distribution, but did not affect PKC total activity. In resting cells or in the absence of lipid hydrolysis, PKC are localized primarily to the cytosol. Translocation to the membrane from cytosol is an important step in PKC activation that can be initiated directly with phorbol esters or by receptor-stimulated increases in DAG. Activation of the enzyme might also be influenced by changes in membrane structure or constituents[9]. Our results suggest that LPS could activate DAG-PKC signaling pathway in rat PIM, which is in accordance with previous reports.

Macrophages stimulated by LPS or other inflammatory factors produce and release large quantities of various proinflammatory cytokines, including TNF-α, IL-1β, and IL-6. Overproduction of the cytokines can result in systemic inflammatory response syndrome, multiple organ dysfunction syndrome (MODS) and death. NF-κB plays a pivotal role in LPS-induced TNF-α and IL-1β gene expressions. The PKC signaling pathway is linked to the upstream regulation mechanism of NF-κB activation. In particular, recent findings show that PKCζ can regulate NF-κB through an IκB kinase (IKK)-independent pathway, by directly phosphorylating Ser^{311} of the p65 subunit (RelA), and play an important role in mediating inflammatory response induced by LPS[26]. The present study showed that CCK-8 concentration-dependently inhibited LPS-induced DAG content, PKC activities, and PKCζ translocation, and a significant inhibition was observed at high concentrations, but not at low concentrations. Cong *et al* reported that CCK-8 inhibited LPS-induced NF-κB binding activity in a concentration-dependent manner[21]. The present study demonstrated that CCK-8 significantly inhibited LPS-induced activation of the DAG-PKC signaling pathway at supraphysiological concentrations, which might be

one of the upstream mechanisms for modulating NF-κB activity and exerting the anti-inflammatory effect of CCK-8.

However, it is unknown whether the inhibitory effect of CCK-8 on DAG-PKC signaling pathway induced by LPS was mediated through the CCK receptor or through which subtype of its receptor. Cong *et al* reported that CCK-8 inhibited NF-κB binding activity and decreased IκB-α degradation through CCK receptors in rat PIM stimulated by LPS[21]. In the present study, the inhibitory effect of CCK-8 on LPS-induced DAG content, PKC activities and PKCζ translocation was abrogated in part by proglumide, CR-1409, and CR-2945 in a concentration-dependent manner. Proglumide was so potent that it had an obvious effect on CCK-8-resulted inhibition of LPS-induced DAG content, PKC activities, and PKCζ translocation at low concentrations, and even caused a full reversal of it at high concentrations. A similar effect was found for CR-1409, but not for CR-2945. CR-2945 showed a weak effect only at high concentrations. Our results indicate that the inhibitory effect of CCK-8 on the LPS-activated DAG-PKC signaling pathway in rat PIM was mediated through the CCK receptor, and that both CCK-AR and CCK-BR might be involved in this pathway. However, CCK-AR might play a major role in this process, which would be of benefit in the development of receptor-specific drugs in clinics.

In conclusion, CCK-8 was a negative modulator of the DAG-PKC signaling pathway in rat resting PIM, which was very important for maintaining body homeostasis, and significantly inhibited LPS-induced DAG content, PKC activity, and PKCζ translocation in a concentration-dependent manner. CCK receptors, particularly CCK-AR, might play a major role in this process. Inhibitory effects of CCK-8 on LPS-induced activation of the DAG-PKC signaling pathway might be one of the upstream mechanisms for modulating NF-κB activity and exerting its anti-inflammatory effect in rat PIM.

References

1 Crawley JN, Corwin RL. Biological actions of cholecystokinin. Peptides 1994; 15: 731–55.

2 Wank SA. Cholecystokinin receptors. Am J Physiol 1995; 269: G628–46.

3 Cong B, Li SJ, Ling YL, Yao YX, Gu ZY, Wang JX, *et al*. Expression and cell-specific localization of cholecystokinin receptors in rat lung. World J Gastroenterol 2003; 9: 1273–7.

4 Ling YL, Huang SS, Wang LF, Zhang JL, Wan M, Hao RL. Cholecystokinin octapeptide reverses experimental endotoxin shock. Acta Physiol Sin 1996; 48: 390–4.

5 Li SJ, Cong B, Yan YL, Yao YX, Ma CL, Ling YL. Cholecystokinin octapeptide inhibits the *in vitro* expression of CD14 in rat pulmonary interstitial macrophage induced by lipopolysaccharide. Chin Med J 2002; 115: 276–9.

6 Ling YL, Meng AH, Zhao XY, Shan BE, Zhang JL, Zhang XP. Effect of cholecystokinin on cytokines during endotoxic shock in rats. World J Gastroenterol 2001; 7: 667–71.

7 Meng AH, Ling YL, Zhang XP, Zhao XY, Zhang JL. CCK-8 inhibits expression of TNF-α in the spleen of endotoxic shock rats and signal transduction mechanism of p38 MAPK. World J Gastroenterol 2002; 8: 139–43.

8 Tan SL, Parker PJ. Emerging and diverse roles of protein kinase C in immune cell signaling. Biochem J 2003; 376: 545–52.

9 Hiral T, Chida K. Protein kinase Cζ (PKCζ): activation mechanisms and cellular functions. J Biochem 2003; 133: 1–7.

10 Monick MM, Carter AB, Gudmundsson G, Mallampalli R, Powers LS, Hunninghake GW. A phosphatidylcholine-specific phospholipase C regulates activation of p42/44 mitogen-activated protein kinases in lipopolysaccharide-stimulated human alveolar macrophages. J Immunol 1999; 162: 3005–12.

11 Xu SJ, Gao WJ, Cong B, Yao YX, Gu ZY. Effect of lipopolysaccharide on expression and characterization of cholecystokinin receptors in rat pulmonary interstitial macrophages. Acta Pharmacol Sin 2004; 25: 1347–53.

12 De la Fuente M, Campos M, Del Rio M. Inhibition of murine peritoneal macrophage functions by sulfated cholecystokinin octapeptide. Regul Pept 1995; 55: 47–56.

13 Carrasco M, Del Rio M, Hernanz A. Inhibition of human neutrophil functions by sulfated and nonsulfated cholecystokinin octapeptides. Peptides 1997; 18: 415–22.

14 Carrasco M, Hernanz A, De La Fuente M. Effect of cholecystokinin and gastrin on human peripheral blood lymphocyte functions, implication of cyclic AMP and interleukin 2. Regul Pept 1997; 70: 135–42.

15 Wizemann TM, Laskin DL. Enhanced phagocytosis, chemotaxis, and production of reactive oxygen intermediates by interstitial macrophages following acute endotoxemia. Am J Respir Cell Mol Biol 1994; 11: 358–65.

16 Bligh EG, Dyer WJ. A rapid method of total lipid extraction and purification. Can J Biochem Physiol 1969; 37: 911–7.

17 Hansen TO. Cholecystokinin gene transcription: promoter elements, transcription factors and signaling pathways. Peptides 2001; 22: 1201–11.

18 Yang CX, Xu MY, Liu FY, Yang DX, Wang SZ. L-365, 260 reversed effect of sincalide against morphine on electrical and mechanical activities of rat duodenum *in vitro*. Acta Pharmacol Sin 2002; 23: 582–6.

19 Xu MY, Yang XP, Jin HB, Yang CX, Yang LZ. Devazcpide reversed effect of sincalide against morphine on rat jejunal activities. Acta Pharmacol Sin 1999; 20: 419–22.

20 Kopin AS, McBride EW, Schaffer K, Beinborn M. CCK receptor polymorphisms: an illustration of emerging themes in pharmacogenomics. Trends Pharmcol Sci 2000; 21: 346–53.

21 Cong B, Li SJ, Yao YX, Zhu GJ, Ling YL. Effect of cholecystokinin octapeptide on tumor necrosis factor α transcription and nuclear factor-κB activity induced by lipopolysaccharide in rat pulmonary interstitial macrophages. World J Gastroenterol 2002; 8: 718–23.

22 Medina S, Rio MD, Cuadra BD, Guayerbas N, Fuente MD. Age-related changes in the modulatory action of gastrin-releasing peptide, neuropeptide Y and sulfated cholecystokinin octapep-

tide in the proliferation of murine lymphocytes. Neuropeptides 1999; 33: 173–9.
23 De la Fuente M, Carrasco M, Del Rio M, Hernanz A. Modulation of murine lymphocyte functions by sulfated cholecystokinin octapeptide. Neuropeptides 1998; 32: 225–33.
24 Monica C, Jordi X, Annabel FV, Carlos LL, Daniel JP, Antonio C. PKCε is involved in JNK activation that mediates LPS-induced TNF-α, which induces apoptosis in macrophages. Am J Physiol Cell Physiol 2003; 285: C1235–45.
25 Tan SL, Parker PJ. Emerging and diverse roles of protein kinase C in immune cell signaling. Biochem J 2003; 376: 545–52.
26 Duran A, Diaz-Meco MT, Moscat J. Essential role of RelA Ser^{311} phosphorylation by ζPKC in NF-κB transcriptional activation. EMBO J 2003; 22: 3910–8.

The 3rd Singapore International Neuroscience Conference (SINC)

2006, May 23–24, Singapore

The NNI Conference Secretariat
3rd SINC 2006
National Neuroscience Institute
11 Jalan Tan Tock Seng
Singapore 308433
Phn:65-6357-7538/7152
Fax:65-6256-4755
E-mail: nni_secretariat@nni.com.sg
Http://www.nni.com.sg

Acta Pharmacologica Sinica 2005 Dec; 26 (12): 1505–1511

Full-length article

Evaluation of 2 celecoxib derivatives: analgesic effect and selectivity to cyclooxygenase-2/1[1]

Zhi-hong LU[2,4], Xiao-yun XIONG[2], Bang-le ZHANG[2], Guo-cheng LIN[3], Yu-xiang SHI[4], Zhen-guo LIU[2], Jing-ru MENG[2], Yu-mei ZHOU[3], Qi-bing MEI[3,6]

[2]Department of Pharmacology, [3]Department of Radioactive Isotopes, and [4]Department of Anesthesiology, Xijing Hospital, Fourth Military Medical University, Xi'an 710032, China; [5]Department of Foreign Languages, Fourth Military Medical University, Xi'an 710032, China

Key words

cyclooxygenase inhibitors; celecoxib; pain; selectivity; mice

[1] Project supported by the National Natural Science Foundation of China No 30400548).
[6] Correspondence to Prof Qi-bing MEI.
Phn 86-29-8337-4555.
Fax 86-29-8337-4552.
E-mail deerlu@fmmu.edu.cn

Received 2005-06-07
Accepted 2005-08-22

doi: 10.1111/j.1745-7254.2005.00222.x

Abstract

Aim: To evaluate the analgesic effects of 2 celecoxib derivatives and their inhibitory effects on cyclooxygenase (COX). **Methods:** Four antinociceptive assays were used: the acetic acid-induced writhing test, hot plate test, hot tail-flick test and formalin test. Three doses were used in the analgesic assays and ED_{50} values were calculated. For the selectivity assay, macrophages were incubated with test compounds at various concentrations and then stimulated with calcimycin or lipopolysaccharide (LPS). The amounts of 6-keto-prostaglandin $F_{1\alpha}$ (6-keto-$PGF_{1\alpha}$) and prostaglandin E_2 (PGE_2) in the supernatant were examined by radioimmunoassay (RIA). The selectivity of the test compounds was expressed as the $IC_{50,COX-1}$/$IC_{50,COX-2}$ value. **Results:** Celecoxib and its 2 derivatives had a significant analgesic effect. The ED_{50} values of celecoxib, PC-406 and PC-407 were 94.2, 67.9, and 63.3 mg/kg, respectively, for the acetic acid-induced writhing test; 104.7, 89.1, and 30.0 mg/kg, respectively, for the hot tail-flick response test; 60.7, 56.7, and 86.2 mg/kg, respectively, for the hot plate response test; 67.1, 55.8, and 68.8 mg/kg, respectively, for the formalin-induced response. That is, the ED_{50} of PC-406 was the lowest for the formalin and hot plate tests, which focus on changes above the spinal cord level; however, the ED_{50} of PC-407 was lowest for the tail-flick and writhing tests, which focus on changes at the spinal cord level. Celecoxib and PC-407 inhibited COX-1 with IC_{50} values of 39.8 and 27.5 nmol/L, respectively. PC-406 inhibited COX-1 with an IC_{50} value of more than 1000 nmol/L. The IC_{50} values for the effect of celecoxib, PC-406 and PC-407 on COX-2 were 4.8, 8.9, and 1.9 nmol/L respectively. The $IC_{50,COX-1}/IC_{50,COX-2}$ ratios for celecoxib and PC-407 were 8.3 and 14.4, respectively. For PC-406, the ratio was greater than 112.2. **Conclusion:** Derivatives of celecoxib via substitution with an isopropyl or naphthyl group at the 5 position in the pyrazole ring still have analgesic effects and the ability to selectively inhibit COX-2. Substitution with a naphthyl group may have more effect on the peripheral pain pathway, whereas substitution with an isopropyl group may have more effect on the central pain pathway. This phenomenon occurs partly because substitution with an isopropyl group is more beneficial for COX-2 selectivity than is substitution with a naphthyl group.

Introduction

Humans have been using non-steroidal anti-inflammatory drugs (NSAIDs) for more than 3500 years. The first real progress in our understanding of the mechanism of the action of NSAIDs occurred 30 years ago, when it was revealed that these chemically varied drugs reduced the formation of

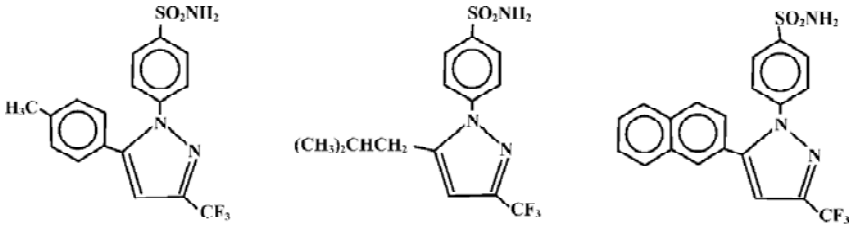

Figure 1. Chemical structures of celecoxib, PC-406, and PC-407.

prostaglandins. This ability is associated with the inhibition of cyclooxygenase (COX), which converts arachidonic acid to its precursor prostaglandin (PG) H_2. Two isoforms of COX have been identified. The constitutively expressed COX-1 is the housekeeping enzyme mainly responsible for the physiological activities of prostaglandins, whereas COX-2, whose expression is mainly induced under inflammatory conditions, is responsible for pathological prostaglandins that produce pain and fever[1]. On the basis of these observations, COX-2-selective drugs such as celecoxib were rapidly developed and became one of the most commercially successful classes of drugs[2].

We synthesized 13 pyrazole derivatives based on the chemical structure of celecoxib[3,4], including PC-406 and PC-407, which are derivatives of celecoxib created by changing the group at the 5 position in the pyrazole ring. For PC-406, the phenyl structure at the 5 position is replaced by an isopropyl group; for PC-407, it is replaced by a naphthyl group (Figure 1). The chemical structures of these derivatives have been confirmed by infrared absorption spectrum, ultraviolet absorption spectrum, ^{1}H nuclear magnetic resonance, ^{13}C nuclear magnetic resonance and mass spectrum analysis. The purity values of PC-406 and PC-407 were found to be 99.5% and 97.5%, respectively, by high performance liquid chromatography. Using the mouse ear edema model, PC-406 and PC-407 were found to have more potential activity than celecoxib in anti-inflammation. PC-406 and PC-407 were also observed to have fewer gastrointestinal side effects. In the present study, we tried to evaluate the analgesic effects and inhibitory effects on COX-1/COX-2 of candidate compounds.

Materials and methods

Animals BALB/c mice obtained from the Experimental Animal Center of the Fourth Military Medical University were used. Half of the mice were males and half were females. All the animals weighed 18–22 g. Animals were housed in colonial stock following arrival. Food and water were available *ad libitum*. Temperature and humidity of the environment were controlled (23±1°C and 50.0%±1.3%, respectively), and a 12 h day/night cycle was used. All the experiments were carried out during the light phase. The experimental design was approved by the relevant ethics board of the institution in which the study was carried out.

Drugs and reagents PC-406 and PC-407 were synthesized by our group. The celecoxib was a gift from Pharmacia (Rockville, MD, USA). Lipopolysaccharide (LPS) and calcimycin were purchased from Sigma (St Louis, USA). The Brewer thioglycollate medium was from (Difco Company, Detroit, USA). Newborn calf serum and RPMI-1640 were from (Hyclone, Logan, USA). The 6-keto-$PGF_{1\alpha}$ and PGE_2 radioimmunoassay (RIA) kits were from Chemclin Biotech (Beijing, China). For the analgesic effect assays, all the test compounds were dissolved in 3% Tween-80 and administered intragastrically in a volume of 0.3 mL. For the selectivity evaluation, all the tested samples were prepared in stock solution (0.01 mol/L) with Me_2SO and stored at -20 °C. Before use, the stock solution was diluted to a series of concentrations in RPMI-1640.

Antinociceptive assays Four antinociceptive assays were used: the writhing test, hot tail-flick test, hot plate test, and formalin test. Mice were fasted for 24 h with water given *ad libitum*, maintained at room temperature and were divided into 4 groups (n=6): control group, CEL group, PC-406 group, and PC-407 group, which received pretreatment with 3% Tween-80, celecoxib, PC-406, and PC-407, respectively. The 2nd, 3rd, and 4th groups were further divided into 3 subgroups (A,B,C), which received test compounds at 100, 50, and 25 mg/kg, respectively. Celecoxib was used as a positive control.

Writhing test All the pretreatments were carried out 1 h prior to intraperitoneal injection of 0.1 mL/10 g of 0.6% acetic acid, which caused a typical writhing response. The number of writhing responses was counted for 10 min by observers who were blinded to the treatment. The antinociceptive effects of drugs were measured by calculating the mean reduction in the number of abdominal constrictions for each drug, as compared to that produced by the Tween-80 vehicle.

Hot tail-flick test The antinociceptive effects of the test substances were determined by the hot tail-flick method as

described by Sewell and Spencer[5]. The tails of mice (1–2 cm) were immersed in warm water kept constant at 53 °C, and the reaction time was measured as the time taken for the mice to deflect their tails. The first reading was ignored, and the reaction time was taken as the mean of the next 2 readings. The latent period until the tail-flick response was taken as the index of antinociception and was determined before and 1 h after the administration of drugs. The maximum reaction time was fixed at 3 s. The analgesia percentage (AP) was calculated as: $AP=(t_{test\ reaction}-t_{control\ reaction})/(3-t_{control\ reaction})$.

Hot plate test The method used has been described by Baker *et al*[6]. A metal hot plate was heated to a constant temperature. Behavioral measurements were taken at 55±0.5 °C. The temperature of the plate was monitored at all times. To confine the animals to a certain observation area, a colorless acrylic cylinder of 20 cm diameter was placed on the hot plate. After each measurement the plate was wiped with a damp cloth to remove traces of urine and feces. Latency for the animal to lick its hindpaw was measured before and 1 h after pretreatment. The offset time was set at 30 s. AP was calculated as: $AP=(t_{test\ reaction}-t_{control\ reaction})/(30-t_{control\ reaction})$.

Formalin test Formalin solution (5 %, 50 mL) was injected subplantarly into the left hindpaws of the mice using a microsyringe with a 26-gauge needle. Animals were then placed in a Plexiglas chamber and observed for nociceptive behavior for 1 h. The amount and duration of licking or flinching were recorded at 5 min intervals over the next 60 min. The sum of the amount and duration of licking or flinching in the early phase (0–10 min, phase 1) and late phase (20–60 min, phase 2) were calculated, respectively. To calculate the ED_{50}, the decrease in the summed amount of licking or flinching during the whole observation period as compared with the control group was calculated.

Cell culture Adherent macrophages were harvested from the peritoneal cells of male mice 3 d after the intraperitoneal injection of Brewer thioglycollate medium (50 mL/kg). Peritoneal cells obtained from 2–3 mice were mixed and cultured in RPMI-1640 supplemented with 5% new-born calf serum. After settlement for 2 h, non-adherent cells were washed with cold phosphate-buffered saline (PBS). Then, macrophages were seeded in 96-well cell culture clusters (Gibco, USA) at a cell density of 1×10^9/L. Almost all the adherent cells were macrophages as assessed by Giemsa staining. Cell viability was examined by Trypan blue dye exclusion. All the incubation procedures were performed with 5% CO_2 in humidified air at 37 °C.

COX-1 assay Macrophages were incubated with test compounds at different concentrations or with the solvent (Me_2SO) for 1 h and were stimulated with calcimycin (1 μmol/L) for 1 h. The same volume of RPMI-1640 was added for the control groups. The amount of 6-keto-$PGF_{1\alpha}$ in the supernatant was measured by RIA, using the manufacturer's instructions. The inhibitory ratio (IR) was calculated as $IR = (C_{calcimycin}-C_{test\ compound})/(C_{calcimycin}-C_{control})$, where C is the concentration of 6-keto-$PGF_{1\alpha}$ in the supernatants of the calcimycin, test compound or control groups.

COX-2 assay Macrophages were incubated with test compounds at different concentrations or with the solvent (Me_2SO) for 1 h and were stimulated with LPS (1 mg/L) for 9 h. The same volume of RPMI-1640 was added for the control groups. The amount of PGE_2 in the supernatant was measured by RIA, using the manufacturer's instructions. The IR was calculated as $IR=(C_{LPS}-C_{test\ compound})/(C_{LPS}-C_{control})$, where C is the concentration of PGE_2 in the supernatants of the LPS, test compound or control groups.

Statistics Data are presented as mean±SD of n observations. The 95% confidence limits of the ED_{50} and IC_{50} values were also calculated. Comparisons between the groups were carried out by using one-way analysis of variance (ANOVA), followed by the least significant difference multiple comparisons test. A P-value of 0.05 was considered statistically significant. Dose-inhibitory effect curves were fitted by using sigmoidal dose-response curves (variable slope) (inhibitory effect on COX) or linear regression (analgesic effect) using Graphpad Prism (version 4.00, GraphPad Software Inc , San Diego, USA).

Results

Acetic acid-induced writhing Intraperitoneally injected acetic acid produced abdominal constrictions, which were characterized by a stretching response. The mean number of writhing motions observed in the animals of the control group over 10 min was 10.33±6.03. All the 3 test compounds at a high dose (100 mg/kg) significantly ($P<0.05$) reduced the number of writhing motions to 5.3±4.0, 1.3±2.3, and 1.7±1.5, respectively. However, test compounds at low doses (50 or 25 mg/kg) did not significantly reduce the number of writhing motions induced by acetic acid (Figure 2). The ED_{50} values of celecoxib, PC-406 and PC-407 for acetic acid-induced writhing were 94.2, 67.9, and 63.3 mg/kg respectively (Figure 3, Table 1).

Hot tail-flick response The animals in the control group did not show any significant effects with respect to the latent period until tail-flick response. The antinociceptive effect of PC-406 at a high dose (100 mg/kg) was evident ($P<0.05$) and the duration of the tail-flick response increased from 0.87±0.27 to 1.92±0.15 s. PC-406 at lower doses (25 or 50

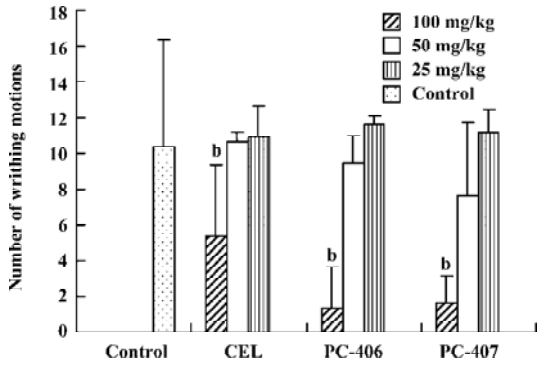

Figure 2. Effects of test compounds on the number of acetic acid-induced writhing. n=8. Mean±SD. $^bP<0.05$ *vs* control group. CEL, celecoxib.

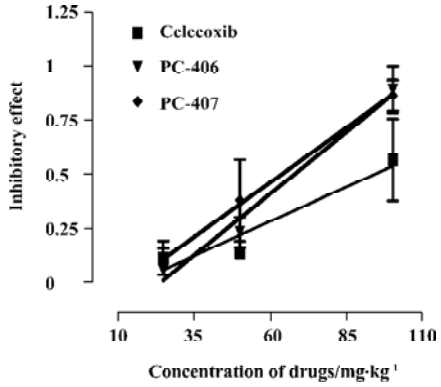

Figure 3. Analgesic effects of test compounds on acetic-acid-induced writhing. n=8. Mean±SD.

Table 1. ED_{50} values (mg/kg) and 95% confidence limits for test compounds according to different antinociceptive assays.

Compound	Writhing test	Hot tail-flick test	Hot plate test	Formalin test
Celecoxib	94.2 (66.1–234.8)	104.7 (73.9–211.1)	50.6 (31.4–70.4)	67.1 (24.1–157.9)
PC-406	67.9 (24.7–140.5)	89.1 (73.0–119.3)	46.1 (30.3–65.2)	55.8 (15.4–125.0)
PC-407	63.3 (31.6–93.2)	30.0 (6.4–47.9)	76.8 (48.6–129.4)	68.8 (45.8–73.2)

mg/kg) did not have any significant analgesic effect as measured by this assay. However, PC-407 at all doses produced significant antinociception ($P<0.05$, Figure 5). The ED_{50} values of celecoxib, PC-406, and PC-407 as assessed by the hot tail-flick assay were 104.7, 89.1, and 30.0 mg/kg, respectively (Figure 4, Table 1).

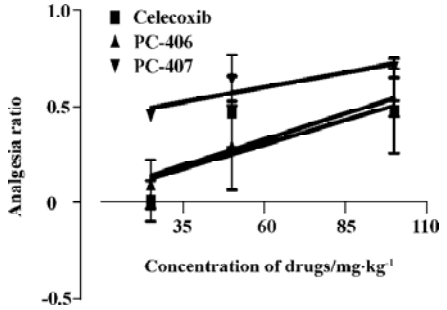

Figure 4. Analgesic effects of test compounds as measured by the hot tail-flick response. n=8. Mean±SD.

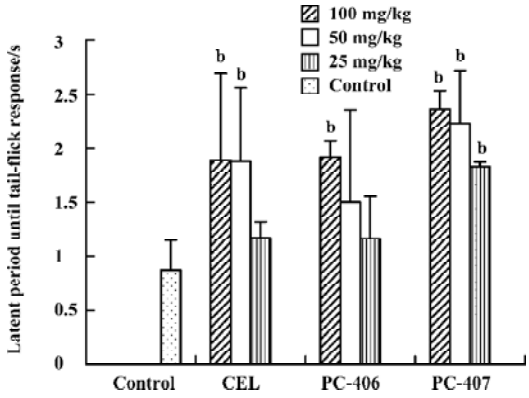

Figure 5. Effects of test compounds on latent period until hot tail-flick response. n=8. Mean±SD. $^bP<0.05$ *vs* control group. CEL, celecoxib.

Hot plate response Animals in the control group did not show any significant effects with respect to the latent period until hot plate response. Both PC-406 and PC-407 produced a significant analgesic effect as measured by the hot plate response ($P<0.05$, Figure 5). The ED_{50} values of celecoxib, PC-406 and PC-407 as measured by hot plate response were 50.6, 46.1, and 76.8 mg/kg, respectively (Figure 6, Table 1).

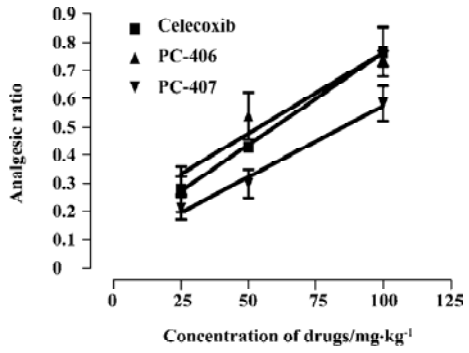

Figure 6. Analgesic effects of test compounds on hot plate response. n=8. Mean±SD.

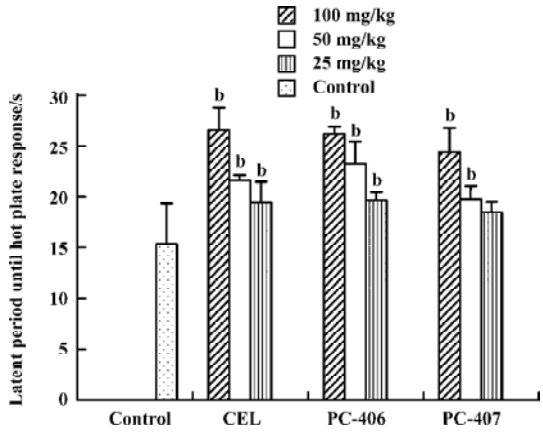

Figure 7. Effects of test compounds on latency for hot plate response. n=8. Mean±SD. ^bP<0.05 *vs* control group. CEL, celecoxib.

Formalin test All the mice exhibited elevating, shaking, licking or biting behaviors in the injected left hindpaw after subcutaneous injection of formalin into the plantar surface. These behaviors had 2 distinct phases: an early phase (phase 1), which appeared immediately after formalin injection and lasted 10 min, and a late phase (phase 2), which appeared about 20 min after injection and lasted 40 min. PC-406 and PC-407 (25–100 mg/kg) elicited a dose-dependent inhibitory effects on licking time, with a maximal reduction of approximately 85% of the control response (n=8). For animals treated with PC-406 or PC-407, the durations and amounts of flinching or licking were significantly decreased (P<0.05, Figures 8, 9). The ED_{50} values of celecoxib, PC-406 and PC-407 were 67.1, 55.8, and 68.8 mg/kg, respectively (Figure 10, Table 1).

COX inhibitory effect The IC_{50} values of celecoxib and PC-407 for COX-1 were 39.8 nmol/L and 27.5 nmol/L, respectively. For PC-406, the IC_{50} value was more than 10 000 nmol/L (Figure 11A). The IC_{50} of test compounds for COX-2 were 4.78, 8.9, and 1.9 nmol/L, respectively (Figure 11B). The selectivity of the test compounds for COX-1/COX-2 was expressed as the value of $IC_{50,COX\text{-}1}/IC_{50,COX\text{-}2}$. PC-406 showed a 112.2-fold preference for COX-2 versus COX-1 (Table 2).

Discussion

The discovery and characterization of the COX-2 enzyme early in the 1990s led to many studies on selective inhibitors of this isoform. It was hypothesized that COX-2 selective inhibitors would exhibit similar clinical efficacy but reduced ulcerogenicity relative to traditional NSAIDs. Less than a decade after the discovery of COX-2, celecoxib and rofecoxib were launched, and were very effective analgesics and anti-

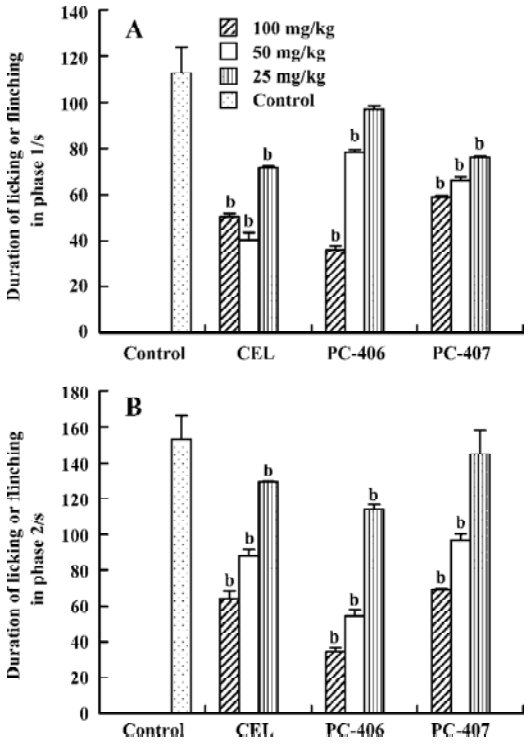

Figure 8. Effects of test compounds on duration of licking or flinching in phase 1 (A) and phase 2 (B). n=8. Mean±SD. ^bP<0.05 *vs* control group. CEL, celecoxib.

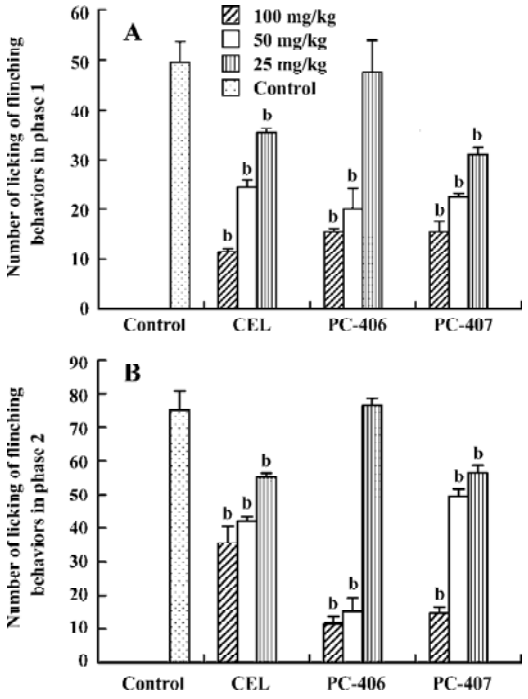

Figure 9. Effects of test compounds on the amount of licking or flinching in phase 1 (A) and phase 2 (B). n=8. Mean±SD. ^bP<0.05 *vs* control group. CEL, celecoxib.

Table 2. Inhibitory effect of test compounds on COX-1/COX-2.

Compound	IC_{50}/nmol·L^{-1}		$IC_{50,COX-1}$/ $IC_{50,COX-2}$
	COX-1	COX-2	
Celecoxib	39.8 (4.9–258.2)	4.8 (3.1–18.9)	8.3
PC-406	>1000	8.9 (4.6–18.9)	>112.2
PC-407	27.5 (4.0–140.0)	1.9 (1.4–8.1)	14.4

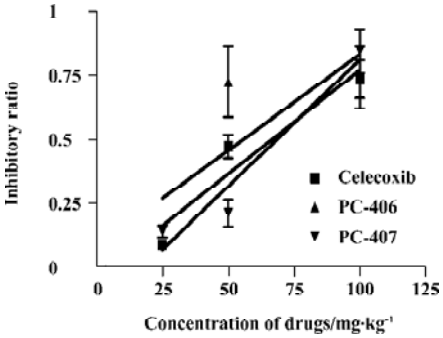

Figure 10. Inhibitory effects of test compounds on the amount of licking or flinching. n=8. Mean±SD.

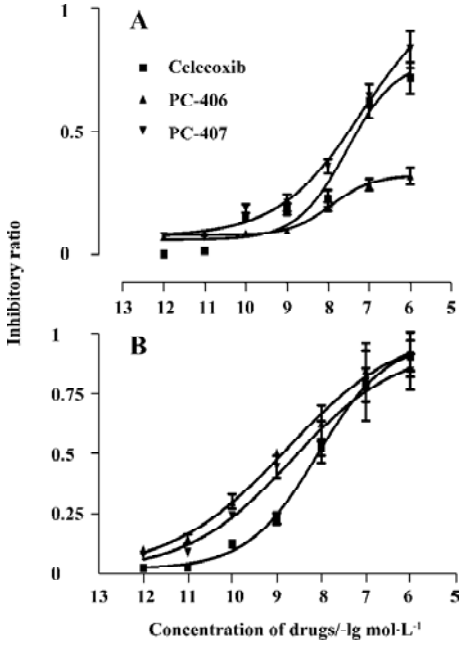

Figure 11. Dose-response curve of test compounds for COX-1 (A) and COX-2 (B).

inflammatory agents. Furthermore, in recent years, coxibs have been proved to have potential in the treatment of cancer and Alzheimer's disease. All things considered, the prospects for COX-2 selective inhibitors are good. Based on the chemical structure of celecoxib, we synthesized PC-406 and PC-407, 2 pyrazole derivatives, by retaining benzenesulfonamide, the necessary active component of the molecule. In the present study, their analgesic effects and selectivity for COX-2 were evaluated.

All the antinociceptive assays showed that derivatives of celecoxib made by substituting groups at the 5 position exhibited analgesic effects. However, the results from different assays were different. Four antinociceptive assays were used in our study. Among them, the hot plate and hot tail-flick tests test responses to thermal stimulations, whereas the writhing and formalin tests test responses to chemical stimulations. The pain pathways these tests focus on vary as well. The formalin and hotplate tests mainly focus on changes above the spinal cord level, whereas the tail flick and writhing tests emphasize changes at or under the spinal cord level. In the present study, the results of both the hot plate test and the formalin test show that PC-406 has the lowest ED_{50} value. However, the results of the writhing and tail flick test show that PC-407 has the lowest ED_{50} value. Thus we can infer that PC-406 exerts more effect on the pathways above the spinal cord level, whereas PC-407 exerts more effect on pathways peripherally.

Detailed data from the formalin test showed the same results. The formalin test is a well characterized and validated evaluation method in mice and rats. It is an accepted method for the rapid and easy screening of pharmacological targets in drug evaluation, because it can be performed in small animals, and the time course of the noxious stimulation is limited to 1 h. Subplantar injection of formalin results in flinching, licking or biting behavior during an early acute phase, which resembles acute pain, followed by a quiescent interphase, and then a second delayed phase representing chronic pain. The acute phase is believed to correspond to the peripheral pain pathways, whereas the second phase represents more central pain processing mechanisms. In our study, both phases of the formalin test were well delineated and could be quantified. Celecoxib and its 2 derivatives could significantly decrease both the duration and amount of pain behaviors during the formalin test (P<0.05). Celecoxib and PC-407 had more effect on behaviors in phase 1, whereas PC-406 affected behaviors in phase 2 more. That is, celecoxib and PC-407 affected the peripheral pain pathways more, whereas PC-406 affected the central pain pathways more. This is consistent with what we found in our analysis of

different ED_{50} values.

The differences in the different analgesic effects of the test compounds are related to their different structures. So we subsequently investigated the relationships between the modifications of their chemical structures and their selectivity for COX-2. To evaluate the selectivity of compounds for COX-2, many models have been established[7–10]. Macrophages are known to release prostanoids in 2 kinetically distinct patterns: the immediate and delayed phases[11]. In the immediate phase, 6-keto-$PGF_{1\alpha}$ and TXB_2 are the major arachidonic acid metabolites. However, in the delayed phase, PGE_2 is produced depending on induced COX-2. Macrophages can spontaneously secrete low levels of 6-keto-$PGF_{1\alpha}$ and PGE_2. Stimulation with calcimycin or LPS promotes a dramatic enhancement of prostanoid production. Shen *et al* developed a whole-cell assay based on murine peritoneal macrophages and demonstrated that it was appropriate for drug design-oriented *in vitro* assay[12]. This method was used in the present study.

The results of selectivity evaluation show that PC-407 and PC-406 provide stronger selectivity with respect to the inhibition of COX-2 than does celecoxib. PC-406 has the greatest selectivity. It might be the reason for their weak influence on stomach mucosa. The present study indicates that test compounds with a non-aryl group or an aryl group substituted at the 5 position in the pyrazole ring still retain their anti-inflammatory activity and their ability to inhibit COX-2 selectively. Furthermore, substitution at the 5 position with a non-aryl group might be more beneficial with respect to COX-2 selectivity than substitution with an aryl group.

It has been proved that COX-2 plays a more central role and is more highly expressed in the central nervous system than is COX-1, which is the basis of most of its therapeutic effects. The higher selectivity for COX-2 of PC-406 contributes to its central pain pathway effects. However, identification of the exact parts of the pain pathways that the 2 derivatives affect needs further investigation.

In conclusion, derivatives of celecoxib made by substituting with either a isopropyl or a naphthyl group at the 5 position in the pyrazole ring produced analgesic effects with respect to both thermal and chemical nociception. However, substitution with an isopropyl group improves the effect on the central pain pathway better, whereas substitution with a naphthyl group affects the peripheral pathway more. This is correlated with the altered selectivity for COX-2. Both derivatives had greater selectivity than celecoxib. However, substitution with an isopropyl group was more beneficial with respect to COX-2 selectivity than substitution with an naphthyl group.

References

1 Crofford LJ. COX-1 and COX-2 tissue expression: implications and predictions. J Rheumatol 1997; 24 Suppl 49: 15–9.

2 Lane JM. Anti-inflammatory medications: selective COX-2 inhibitors. J Am Acad Orthop Surg 2002; 10: 75–8.

3 Zhang BL, Mei QB, He W, Zhou SY. Synthesis of celecoxib. Chin J New Drug 2002; 11: 859–61.

4 Zhang BL, Mei QB, Zhou SY, He W, Chen CS. Quantitative structure-activity relationship of the 1, 5-diarylpyrazole class of cyclooxygenase-2 selective inhibitors. J Fourth Milit Med Univ 2003; 24: 1523–5.

5 ewell RD, Spencer PS. Antinociceptive activity of narcotic agonist and partial agonist analgesics and other agents in the tail-immersion test in mice and rats. Neuropharmacology 1976; 15: 683–8.

6 Baker AK, Hoffmann VL, Meert TF. Dextromethorphan and ketamine potentiate the antinociceptive effects of mu- but not delta- or kappa-opioid agonists in a mouse model of acute pain. Pharmacol Biochem Behav 2002; 74: 73–86.

7 Gierse JK, Hauser SD, Creely DP, Koboldt C, Rangwala SH, Isakson PC, *et al*. Expression and selective inhibition of the constitutive and inducible forms of human cyclo-oxygenase. Biochem J 1995; 305: 479–84.

8 Brideau C, Kargman S, Liu S, Dallob AL, Ehrich EW, Rodger IW, *et al*. A human whole blood assay for clinical evaluation of biochemical efficacy of cyclooxygenase inhibitors. Inflamm Res 1996; 45: 68–74.

9 Riendeau D, Percival MD, Boyce S, Brideau C, Charleson S, Cromlish W, *et al*. Biochemical and pharmacological profile of a tetrasubstituted furanone as a highly selective COX-2 inhibitor. Br J Pharmacol 1997;121: 105–17.

10 Lazer ES, Miao CK, Cywin CL, Sorcek R, Wong HC, Meng Z, *et al*. Effect of structural modification of enol-carboxamide-type nonsteroidal antiinflammatory drugs on COX-2/COX-1 selectivity. J Med Chem 1997; 40: 980–9.

11 Naraba H, Murakami M, Matsumoto H, Shimbara S, Ueno A, Kudo I, *et al*. Segregated coupling of phospholipases A2, cyclooxygenases, and terminal prostanoid synthases in different phases of prostanoid biosynthesis in rat peritoneal macrophages. J Immunol 1998; 160: 2974–82.

12 Shen F, Bai AP, Guo ZR, Cheng CF. Inhibitory effect of 3,4-diaryl-3-pyrrolin-2-one derivatives on cyclooxygenase 1 and 2 in murine peritoneal macrophages. Acta Pharmacol Sin 2002; 23: 762–8.

Acta Pharmacologica Sinica 2005 Dec; 26 (12): 1512–1518

Full-length article

Body distribution and *in situ* evading of phagocytic uptake by macrophages of long-circulating poly (ethylene glycol) cyanoacrylate-co-*n*-hexadecyl cyanoacrylate nanoparticles[1]

Min HUANG, Wei WU[2], Jun QIAN, Dan-jing WAN, Xiu-li WEI, Jian-hua ZHU

School of Pharmacy, Fudan University, Shanghai 200032, China

Key words

nanotechnology; tissue distribution; polyethylene glycols; cynoacrylates; polymers; spleen

[1] Project supported by the Shanghai Municipal Committee of Science and Technology (Grant No 0243nm067) and the Shanghai Education Bureau for Excellent Young High Education Teacher Candidates (Grant No 03YQHB008).
[2] Correspondence to Assoc Prof Wei WU.
Phn 86-21-5423-7833.
Fax 86-21-6417-0921.
E-mail wuwei@shmu.edu.cn

Received 2005-05-18
Accepted 2005-07-22

doi 10.1111/j.1745-7254.2005.00216.x

Abstract

Aim: To investigate the body distribution in mice of [^{14}C]-labeled poly methoxyethyleneglycol cyanoacrylate-co-*n*-hexadecyl cyanoacrylate (PEG-PHDCA) nanoparticles and *in situ* evading of phagocytic uptake by mouse peritoneal macrophages. **Methods**: PEG-PHDCA copolymers were synthesized by condensation of methoxypolyethylene glycol cyanoacetate with [^{14}C]-hexadecyl-cyanoacetate. [^{14}C]-nanoparticles were prepared using the nanoprecipitation/solvent diffusion method, while fluorescent nanoparticles were prepared by incorporating rhodamine B. *In situ* phagocytic uptake was evaluated by flow cytometry. Body distribution in mice was evaluated by determining radioactivity in tissues using a scintillation method. **Results**: Phagocytic uptake by macrophages can be efficiently evaded by fluorescent PEG-PHDCA nanoparticles. After 48 h, 31% of the radioactivity of the stealth [^{14}C]-PEG-PHDCA nanoparticles after iv injection was still found in blood, whereas non-stealth PHDCA nanoparticles were cleaned up from the bloodstream in a short time. The distribution of stealth PEG-PHDCA nanoparticles and non-stealth PHDCA nanoparticals in mice was poor in lung, kidney, and brain, and a little higher in hearts. Lymphatic accumulation was unusually high for both stealth and non-stealth nanoparticles, typical of lymphatic capture. The accumulation of stealth PEG-PHDCA nanoparticles in the spleen was 1.7 times as much as that of non-stealth PHDCA (P<0.01). But the accumulation of stealth PEG-PHDCA nanoparticles in the liver was 0.8 times as much as that of non-stealth PHDCA (P<0.05). **Conclusion**: PEGylation leads to long-circulation of nanoparticles in the bloodstream, and splenotropic accumulation opens up the potential for further development of spleen-targeted drug delivery.

Introduction

One of the major objectives of advanced drug delivery today is drug targeting with colloidal drug-delivery systems, such as nanoparticles and liposomes. However, these conventional carriers are rapidly cleaned from the systemic circulation, and end almost exclusively in the mononuclear phagocyte system (MPS) after iv injection, mainly in the macrophages in the liver and spleen[1]. Of course, this extensive uptake is advantageous for treating illness of the reticuloendothelial system (RES) because it provides high local concentrations of therapeutic agents. Unfortunately, delivering drugs to sites other than RES is often desired. To meet this requirement, stealth or long-circulating nanoparticles have been investigated.

In the past two decades, there has been an increasing interest in the development of stealth nanoparticles as drug carrier systems[2,3]. One of the main methods for preparation of stealth nanoparticles is to modify their surface with a hydrophilic and non-ionic polymer, eg, poly methoxyethyleneglycol (PEG)[4] or poloxamer derivatives [5,6]. Previous studies demonstrate that the hepatic uptake of

nanoparticles can be reduced by coating these particles with certain modification. Several mechanisms are discussed for this modification of the body distribution[6,8]: a dependence on the nanoparticle surface charge, a reduction in the surface hydrophobicity reducing phagocytic uptake, a steric hindrance preventing the contact between particles and blood cells (theory of steric stabilization), and a change in the adsorption of blood components determined by the surface properties of the particles. The adsorption patterns differ depending on the physicochemical properties of the particles.

According to Peracchia *et al*, PEGylated polycyanoacrylate nanoparticles are suitable for giving iv and capable of circumventing capture by hepatic Kupffer cells[9]. The increment of splenic nanoparticles led the authors to conclude a splenic targeting mechanism. However, the investigation was taken for a duration of only 24 h, and detailed description of body distribution as a function of time in organs other than liver and spleen was absent. Other authors have studied the same vehicle by incorporating a protein drug, recombinant human tumor necrosis factor α[10]. In contrast to splenic accumulation, diversion of nanoparticles to tissues other than the liver and spleen, that is tumors, was observed.

Distribution of stealth nanoparticles to non-hepatic and non-splenic organs or tissues make them prospective vehicles for the delivery of active ingredients to these sites. In the present study, biodistribution of [^{14}C]-labeled poly methoxyethyleneglycol cyanoacrylate-co-*n*-hexadecyl cyanoacrylate (PEG-PHDCA) nanoparticles was evaluated for the prolonged duration of 48 h. Distribution to organs other than the liver and the spleen was studied, which is also of interest for target stealth diversion. An *in situ* phagocytic evading was also investigated in mouse peritoneum using chemically induced macrophages and flow cytometry.

Materials and methods

Materials Methoxypolyethylene glycol (5000 Da of molecular weight, MePEG 5000) was obtained from Sigma Chemical Co. Cyanoacetic acid was obtained from Fluka Chemical Co and [3-^{14}C]-cyanoacetic acid was obatined from Moravek Biochemicals. *N*, *N*'-dicyclo-hexylcarbodimide and 4-dimethylaminopyridine were obtained from Shanghai Chemical Reagent Co. Formaline (37%) was obtained from Shanghai Jianxin Chemical Co. Aqueous dimethylamine (34%) was provided by Shanghai Linfeng Chemical Co. Other reagents were of analytical purity.

Synthesis of [^{14}C]-labeled PEGylated and non-PEGylated PHDCA polymers Synthesis of poly PEG-PHDCA copolymers has been studied previously [11]. The PEG-PHDCA 1:3 copolymer was synthesized by condensation of MePEG 5000 cyanoacetate with [^{14}C]-hexadecylcyanoace-tate in ethanol, in the presence of formaline and dimethylamine.

[3-^{14}C] Cyanoacetic acid (490.4 mg, 552 μCi=20.4 MBq) was dissolved in ethyl acetate (5 mL), and a solution of hexadecanol (697.6 mg, 1.75 mmol) and 4-dime-thylaminopyridine (1.1906 g, 1.75 mmol) in dichloromethane (9 mL) was added. Then, *N*, *N*-dicyclo-hexylcarbodimide (129.38 mg, 0.63 mmol) was added. After stirring at room temperature for 16 h, the resultant mixture was filtered. Filtrate was concentrated under vacuum, and [^{14}C]hexadecylcyanoacetate was collected as a waxy solid (1.0386 g, 87.4%, 400 μCi=14.8 MBq). [^{14}C] Hexadecylcyano-acetate (519.3 mg, 1.68 mmol, 200 μCi=7.4 MBq) and MePEG 5000 cyanoacetate (2.9235 g, 0.56 mmol) was added to a 1:1 mixture of ethanol and dichloromethane (10 mL) , sequentially, 37% formaline (305 μL, 3.76 mmol) and 34% aqueous dimethylamine (515 μL, 388 mmol) was added. After stirring at room temperature for 16 h, the reaction mixture was concentrated under reduced pressure. The residue was dissolved by dichloromethane (100 mL) and washed with 10 mL of water. The organic phase was dried over magnesium sulfate, and concentrated under vacuum. Non-PEGylated [^{14}C]-polymer PHDCA was also synthesized by condensing [^{14}C] hexadecylcyanoacetate with cyanoacetate.

Preparation of [^{14}C]-labeled and fluorescent nanoparticles [^{14}C]-labeled nanoparticles were prepared by a nanoprecipitation/solvent diffusion method[11]. The [^{14}C]labeled PEG-PHDCA (1:3) copolymer (100 mg) or the [^{14}C]PHDCA polymer was dissolved in 4 mLof tetrahydrofuran, and the polymer solution was added, under magnetic stirring, to 100 mL of demineralized water. Particle formation occurred immediately. After solvent evaporation using a rotatary evaporator, an aqueous suspension of nanoparticles (1 mg/mL) was obtained. The nanoparticles were washed twice with demineralized water after ultracentrifugation, and then filtered (Millex AP, Millopore, 1.2 μm). The radioactivity of the nanoparticle solution was determined just before injection.

Flurescent nanoparticles were prepared following similar procedures by incorporating 0.2% rhodamine B.

Characterization of nanoparticles The morphological examination of nanoparticles was performed using transmission electron microscopy (TEM) (HITACHI H-600) following negative staining with sodium phosphotungstate solution. The particle size and zeta potential of nanoparticles were determined, respectively, by photon correlation spec-

troscopy and laser Doppler anemometry (NICOMP 380/ZLS). Influence of organic solvent, polymer concentration in organic phase and preparation procedures on nanoparticle structure were previously reported[11].

***In situ* evading of phagocytic uptake by macrophages** The phagocytic evading effect of PEG-PHDCA was observed on chemically induced mouse peritoneal macrophages[12]. The mice were injected with 1 mL of 3% sodium thioglycolate solution ip as a stimulant for macrophages. After 3 d of induction, fluorescent nanoparticles were injected ip and incubated together with the macrophages for 2 h. Then, the mice were killed by cervical dislocation, and each was peritoneally injected with 5 mL of saline. The peritoneum of the mouse was massaged for 1 min and the solution inside the abdominal cavity was drawn out. Macrophages were washed 3 times with 1 mL of phosphate buffer. Cellular uptake of PEG-PHDCA nanoparticles was examined with a FACScan flow cytometer, operated under activation wavelength of 585 nm. Each assay counted 20 000 macrophages. Non-stealth PHDCA nanoparticles were also studied as a contrast, and saline as a control.

***In vivo* tissue distribution of [^{14}C]-labeled PEG-PHDCA nanoparticles** To evaluate the body distribution of PEG-PHDCA and PHDCA nanoparticles, 2 groups of mice (6 each) at 1 time interval were treated with [^{14}C]-PEG-PHDCA and [^{14}C]-PHDCA nanoparticles, respectively. A total of 200 μL nanoparticle suspension at the dose of 150 mg/kg were injected into male mice (approximately 20 g in weight) through the tail vein. The amount of given radioactivity was 1.7×10^5 Bq/kg. Animals were killed after 0.05, 0.5, 3, 6, 15, 24, 36, and 48 h of injection. Meantime, blood samples were withdrawn, and hearts, livers, spleens, lungs, kidneys, brains, and lymph nodes were carefully collected. The organs were weighed immediately after removal. Alkaline tissue solubilizer (2 mol/L NaOH) was added to organ samples, and heated at 12°C for 30 min, then cooled to an ambient temperature, and 30% H_2O_2 was added with occasional swirling until the color subsided. After addition of 200 μL of acetic acid and 3 mL of scintillation cocktail (PPO/POPOP), the prepared samples were stored for approximately 2 d and then counted in the scintillation counter (LKB 1210). For determining radioactivity in blood, plasma was separated to exclude interference of blood cell lysates. Recovery of radioactivity was found to be between 95% and 103% for all tissues.

For the calculation of the radioactivity of the total dose (percentage dose) and of 1 milligram of tissue (Bq/mg), the injected radioactivity was taken as the total dose.

To evaluate the effect of specific accumulation of nanoparticles in organs, areas under the radioactivity-time curve ($AUC_{0-48\,h}$) were calculated and compared.

Statistical analysis *In vivo* radioactivity values were calculated as a mean of the results of 6 mice determined separately, and presented as mean±SD. Statistical comparisons of the means were performed using multivariate analysis of variance with SARS software.

Results

Synthesis of the [^{14}C] labeled PEGylated and non-PEGylated polymer According to our previous findings[11], PEG-polycyanoacrylate copolymers were prepared by condensation of a mixture of MePEG-cyanoacetate and *n*-hexadecyl-cyanoacetate with high yields. After standing at room temperature for 16 h and drying under vacuum, the desired copolymers were obtained as pale yellow amorphous solids. The structure and ratio between hexadecyl chains and PEG chains were confirmed by integration of the respective signals in ^{1}H-nuclear magnetic resonance (^{1}H-NMR) spectroscopy. The structure of the material was also confirmed by Fourier transform infrared spectrometer (FTIR) and the molecular weight was determined by gel permeation chromatography.

The fact that radiolabeling was integrated in the cyano group, assured a great stability of the radiolabeled copolymer. PEG-PHDCA and PHDCA were synthesized using similar techniques, only substituting MePEG-cyanoacetate for cyanoacetate.

Characterization of [^{14}C]-labeled nanoparticles Nanoparticles prepared with PEG-PHDCA or PHDCA were spherical in shape and uniform in size of approximately 200 nm (Figure 1). PEGylated nanoparticles contrasted greatly with non-PEGylated nanoparticles, with corolla-like stains.

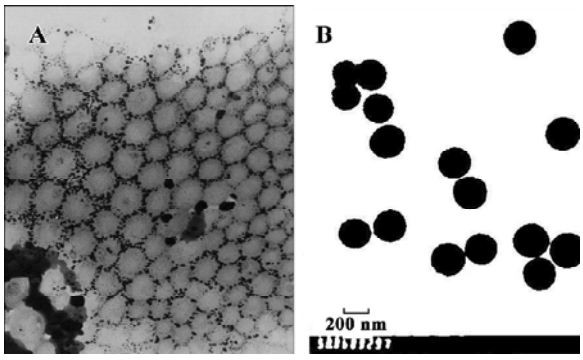

Figure 1. Transmission electron microscopy photographs of stealth PEG-PHDCA (A,×40 000) and non-stealth PHDCA (B, ×50 000) nanoparticles. PEG-PHDCA: poly methoxyethyleneglycol cyanoacrylate-co-*n*-hexadecyl cyanoacrylate. PHDCA: polyhexadecyl cyanoacrylate.

The zeta potential of PEG-PHDCA and PHDCA nanoparticles was –10.77 mV and –20.57 mV, respectively. A marked decrease in the surface charge for PEG-PHDCA nanoparticles was observed. Diameter of nanoparticles determined by photo correlation spectrometry was within the range of 188.7 nm±67.2 nm, in accordance with TEM observation.

***In situ* evading of phagotytic uptake of PEG-PHDCA nanoparticles** Incorporation of fluorescent rohodamine B in nanoparticles was verified under a research inverted system microscope (IX-71, Olympus). Loading of rhodamine B was approximately 0.2%, determined by spectrofluorometer (LS-55, PerkinElmer), upon which the assumption that toxicity of fluorescent marker to macrophages was negligible was drawn. Flow cytometry diagrams are shown in Figure 2.

The value of relative fluorescence intensity of the saline, PEG-PHDCA nanoparticles and PHDCA nanoparticles samples were 54.9, 156.5, and 1726.7, respectively, each representing the stained cells. The higher the value was, the more that the nanoparticles were captured by macrophages. Fluorescence intensity for PEG-PHDCA nanoparticles was approximately 3 times as much as that of saline control, indicating limited phagocytosis by macrophages. For non-stealth PHDCA nanoparticles, fluorescence intensity was almost 11 times as much as that of stealth PEG-PHDCA nanoparticles, indicating profound phagocytosis by macrophages. Evading of phagocytosis by macrophages was achieved through PEGylation.

Long circulating in bloodstream PEG-PHDCA nanoparticles had a remarkably higher accumulation in the bloodstream than PHDCA (P<0.01). PEG-PHDCA nanoparticles exhibited long-circulating characteristics, with sustained high levels of blood-associated radioactivity, and 31% of the radioactivity was still found in the bloodstream 48 h after injection, assuming that radioactivity was still associated with intact nanoparticles. In contrast, PHDCA nanoparticles were cleaned up quickly from the bloodstream, and after 30 min, dropped abruptly to a much lower level, as expected. At the end of 48 h, only approximately 4% of the radioactivity was recovered from blood (Figure 3). The PEG-PHDCA nanoparticles exhibited a 'brush' PEG configuration at the particle surface, and therefore performed the steric repulsion efficiently[13].

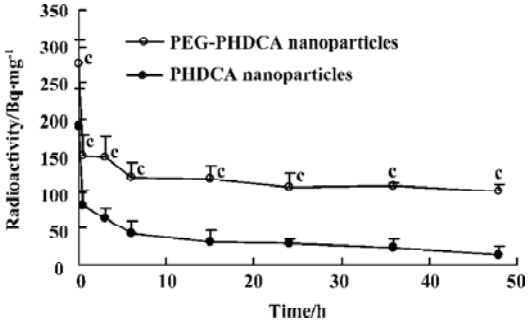

Figure 3. Blood-associated radioactivity as a function of time after iv injection of stealth PEG-PHDCA or non-stealth PHDCA nanoparticles. n=6. Mean±SD. ^cP<0.01 *vs* PHDCA nanoparticles. PEG-PHDCA: poly methoxyethyleneglycol cyanoacrylate-co-*n*-hexadecyl cyanoacrylate. PHDCA: polyhexadecyl cyanoacrylate.

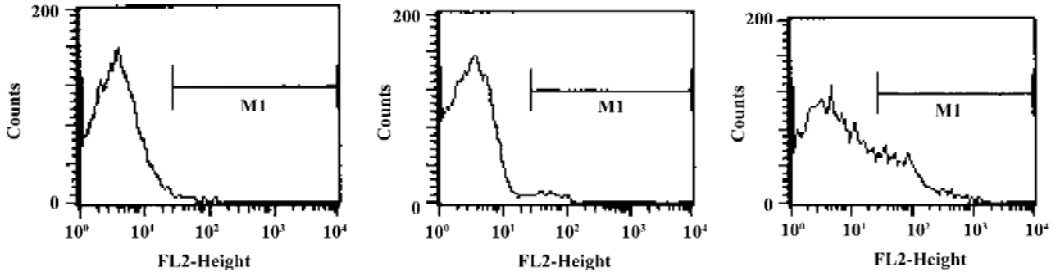

(A) Marker	% Gated	Mean
All	100.00	5.16
M1*	0.90	61.00

(B) Marker	% Gated	Mean
All	100.00	5.36
M1*	2.69	58.19

(C) Marker	% Gated	Mean
All	100.00	22.76
M1*	18.91	91.31

* %Gated×Mean represents overall fluorescence intensity of counted cells, with bigger values indicating increased phagocytic uptake by macrophages

Figure 2. Flow cytometry diagrams of cellular uptake of saline (A), stealth PEG-PHDCA (B), and non-stealth PHDCA (C). PEG-PHDCA: poly methoxyethyleneglycol cyanoacrylate-co-*n*-hexadecyl cyanoacrylate. PHDCA: polyhexadecyl cyanoacrylate.

Organ accumulation The distribution of stealth PEG-PHDCA nanoparticles and non-stealth PHDCA nanoparticals in mice was poor in lung, kidney, and brain, and a little higher in heart (Table 1, Figure 4).

Table 1. $AUC_{0-48\ h}$ for stealth PEG-PHDCA and non-stealth PHDCA nanoparticles in organs. AUC is the area under radioactivity-time curve. n=6. Mean±SD. $^bP<0.05$, $^cP<0.01$ *vs* non-stealth PHDCA. $^eP<0.05$ *vs* liver. PEG-PHDCA: poly methoxyethyleneglycol cyanoacrylate-co-*n*-hexadecyl cyanoacrylate. PHDCA: polyhexadecyl cyanoacrylate.

Organ	$10^{-3}\times AUC_{stealth}$/ Bq·h·mg^{-1}	$10^{-3}\times AUC_{non\text{-}stealth}$/ Bq·h·mg^{-1}	$AUC_{stealth}$/ $AUC_{non\text{-}stealth}$
Heart	29.5±11.2	28.8±23.8	1.0
Liver	52.3±15.6^b	69.9±19.2	0.8
Spleen	77.8±18.9^{ce}	46.8±21.0^e	1.7
Lung	22.2±8.6	27.1±13.3	0.8
Kidney	26.1±9.0	25.7±20.3	1.0
Brain	15.0±6.2	13.9±11.4	1.1
Lymph	243.9±72.0^b	310.6±41.9	0.8
Blood	54.9±27.8^c	15.6±2.4	3.5

There was a relatively higher accumulation in the spleen and liver for both stealth PEG-PHDCA nanoparticles and non-stealth PHDCA nanoparticals compared with heart, lung, kidney, and brain (Table 1, Figure 4).

For stealth PEG-PHDCA nanoparticles, the accumulation in the spleen was higher than that in the liver ($P<0.05$). For non-stealth PHDCA nanoparticles, the accumulation in the spleen was lower than that in the liver ($P<0.05$). The accumulation of stealth PEG-PHDCA nanoparticles in the spleen was 1.7 times as much as that of non-stealth PHDCA ($P<0.01$, Table 1, Figure 4). But the accumulation of stealth PEG-PHDCA nanoparticles in the liver was 0.8 times as much as that of non-stealth PHDCA ($P<0.05$, Table 1, Figure 4).

The amount of radioactivity of stealth PEG-PHDCA recovered from the spleen was much higher than that from liver ($P<0.01$, Figure 5). Such a high spleen uptake was also observed by other authors with PEGylated nanoparticles[9].

Accumulation in lymph nodes was unusually higher for both stealth PEG-PHDCA and non-stealth PHDCA nanoparticles compared with other organs. The radioactivity was maintained at a high level for at least 36 h, typical of lymphatic capture (Table 1). Lymphatic accumulation of stealth PEG-PHDCA was lower than that of non-stealth PHDCA nanoparticles ($P<0.05$, Figure 6).

The accumulation of stealth PEG-PHDCA nanoparticles in the blood was 3.5 times as much as that of non-stealth PHDCA ($P<0.01$, Table 1).

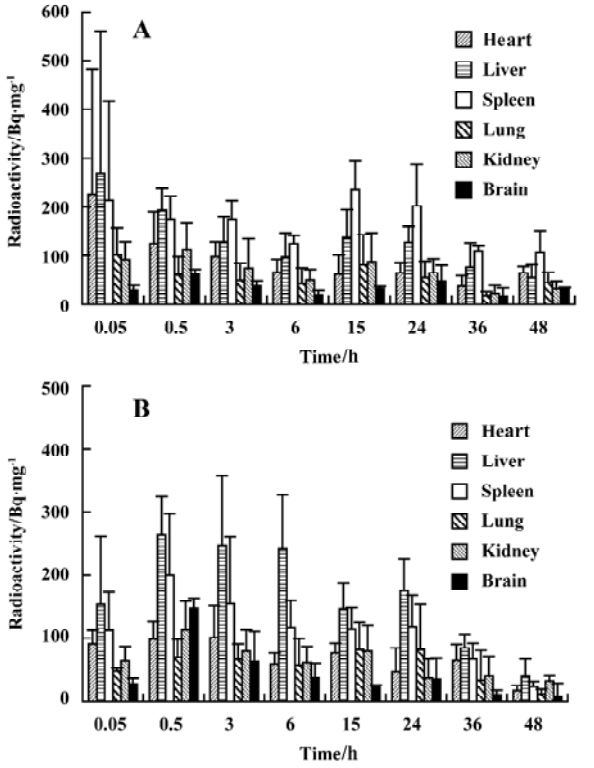

Figure 4. Tissue-associated radioactivity as a function of time after iv injection of stealth PEG-PHDCA (A) and non-stealth PHDCA (B) nanoparticles. PEG-PHDCA: poly methoxyethyleneglycol cyanoacrylate-co-*n*-hexadecyl cyanoacrylate. PHDCA: polyhexadecyl cyanoacrylate.

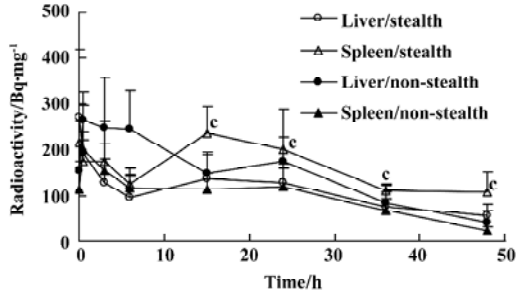

Figure 5. Spleen- and liver-associated radioactivity as a function of time after iv injection of stealth PEG-PHDCA and non-stealth PHDCA nanoparticles. n=6. Mean±SD. $^cP<0.01$ *vs* Liver/stealth. PEG-PHDCA: poly methoxyethyleneglycol cyanoacrylate-co-*n*-hexadecyl cyanoacrylate. PHDCA: polyhexadecyl cyanoacrylate.

Discussion

In the present study, PEG-PHDCA was synthesized as a diblock copolymer, where PEG chains brought about hydro-

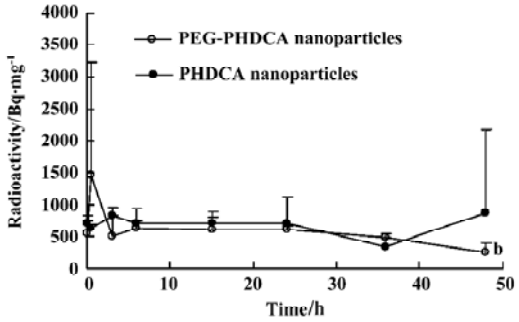

Figure 6. Lymph node-associated radioactivity as a function of time after iv injection of stealth PEG-PHDCA and non-stealth PHDCA nanoparticles. n=6. Mean±SD. $^bP< 0.05$ *vs* PHDCA. PEG-PHDCA: poly methoxyethyleneglycol cyanoacrylate-co-*n*-hexadecyl cyanoacrylate. PHDCA: polyhexadecyl cyanoacrylate

philic modification of the nanoparticle surface, and hexadecyl cyanoacrylate moieties guaranteed enough hydrophobicity for the formation of nanoparticles. Structural importance was testified by ^{1}H-NMR and FTIR spectrum. Molecular weight determination by gel permeation chromatography showed a strong correlation between theoretical calculation of total amount of MePEG and hexadecyl cyanoacrylate present.

The nanoparticles were easily prepared by the nanoprecipitation/solvent diffusion method, with limited size distribution as determined by NICOMP 380/ZLS and TEM. The value of zeta potential of PEG-PHDCA nanoparticles was much lower negative than that of PHDCA nanoparticles. It should be mentioned that the PEG chains in nanoparticles would be oriented towards the outer aqueous medium, protecting the hydrophobic core. Change in surface zeta potential was also indicative of modifications by PEG chains.

Particles with hydrophobic surfaces are removed readily from the circulation through a mechanism of opsonization[6], a process involving complement adsorption and following recognition and phagocytosis by macrophages[14]. Stealth nanoparticles with "water"-like hydrophilic chains poking out interferred with adsorption of complements, and subsequent capture by macrophages. It was simple and informative to investigate interaction between vehicles and certain cell lines before taking out *in vivo* study. Stealth properties of nanoparticles have been studied *in vitro* in cultured macrophage cell lines with a fluorescent marker[15–17]. To rule out disturbing uncertainty associated with an *in vitro* method, we developed a novel *in situ* model to study the effect of stealth evading of phagocytic capture by macrophages. Preliminary results were encouraging enough for us to take out *in vivo* distribution studies.

Findings that the studied vehicles are long-circulating in the bloodstream are similar to reports by Li *et al*[10]. Sustained high levels of radioactivity of approximately one-third of the original injection for 48 h indicated longer circulation time of the vehicles, making it applicable carriers for delivering active ingredients to non-RES targets or for sustained release. Study on prolonged duration of long-circulating is needed in the future. Biodegradation of PEG-PHDCA nanoparticles has not been evaluated in the present study. However, rapid degradation was not observed in the present study, because radioactivity was embedded in the cyano groups, and if biodegradation took place, it was only associated with water-soluble small degradation remnants, which was readily eliminated from the body. For at least 48 h, nanoparticles did not undergo enormous degradation.

Splenotropic accumulation was also observed in the present study, the accumulation of stealth PEG-PHDCA nanoparticles in the spleen was 1.7 times as much as that of non-stealth PHDCA. The propensity of the mouse spleen to remove such particles from the blood was attributed to its unique architecture (reticular meshwork of the red pulp and interendothelial cell slits) and intrasplenic microcirculation (anatomically open and physiologically closed circulation)[19]. The mode of particle clearance from the blood by the spleen appeared to be initially of mechanical filtration[20]. Interestingly, large filtered sterically stabilized particles were eventually phagocytosed by the splenic red pulp macrophages[21]. Phagocytosis of such particles was, presumably, derived either as a result of intrasplenic loss of the coating, the steric barrier, or of certain intrasplenic opsonization processes. Predosing dramatically decreased the spleen uptake of splenotropic spheres but had no effect on the filtration of small sized particles (<150 nm). It is now evident that opsonization of a 'phagocyte-resistant' particle can even occur, depending on the *in vivo* circumstances. Furthermore, even stimulated macrophages can effectively recognize and internalize 'phagocyte-resistant' substrates independent of opsonization processes. Spleen-targeted stealth nanoparticles have the potential to be used to deliver nuclear substances and active components for diagnostic purposes and the therapeutic treatment of spleen-born abnormalities. In contrast, because the spleen is the biggest resident site in the human body for immune cells, such as T and B lymphocytes, delivery of vaccines into it might cause profound immunoreactions.

In summary, PEGylation leads to long-circulation of nanoparticles in the bloodstream, and splenotropic accumulation which opens up the potential for further development of spleen-targeted drug delivery.

References

1 Makino K, Yamamoto N, Higuchi K, Harada N, Ohshima H, Terada H. Phagocytic uptake of polystyrene microspheres by alveolar macrophages: effects of the size and surface properties of the microspheres. Colloid Surf B 2003; 27: 33–9.

2 Moghimi SM, Szebeni J. Stealth liposomes and long circulating nanoparticles: critical issues in pharmacokinetics, opsonization and protein-binding properties. Prog Lipid Res 2003; 42: 463–78.

3 Moghimi SM, Hunter AC, Murray JC. Long-circulating and target-specific nanoparticles: theory to practice. Pharmacol Rev 2001; 53: 283–318.

4 Neradovic D, Soga O, Nostrum CFV, Hennink WE. The effect of the processing and formulation parameters on the size of nanoparticles based on block copolymers of poly(ethylene glycol) and poly(N-isopropylacrylamide) with and without hydrolytically sensitive groups. Biomaterials 2004; 25: 2409–18.

5 Moghimi SM, Hunter AC. Poloxamers and poloxamines in nanoparticle engineering and experimental medicine. Trends Biotechnol 2000; 18: 412–20.

6 Moghimi SM. Mechanisms regulating body distribution of nanospheres conditioned with pluronic and tetronic block copolymers. Adv Drug Del Rev 1995; 16: 183–93.

7 Vandorpe J, Schacht E, Dunn S, Hawley A, Stolnik S, Davis SS, *et al*. Long circulating biodegradable poly(phosphazene) nanoparticles surface modified with poly(phosphazene)-poly (ethylene oxide) copolymer. Biomaterials 1997; 18: 1147–52.

8 Wilkins DJ, Myers PA. Studies on the relationship between the electrophoretic properties of colloids and their blood clearance and organ distribution in the rat. Br J Exp Pathol 1966; 47: 568–76.

9 Peracchia MT, Fattal E, Desmaele D, Besnard M, Noel JP, Gomis MJ, *et al*. Stealth PEGylated polycyanoacrylate nanoparticles for intravenous administration and splenic targeting. J Control Release 1999; 60: 121–8.

10 Li YP, Pei YY, Zhang XY, Gu ZH, Zhou ZH, Yuan WF, *et al*. PEGylated PLGA nanoparticles as protein carriers: synthesis, preparation and biodistribution in rats. J Control Release 2001; 71: 203–11.

11 Huang M, Wu W. Synthesis of poly [poly (ethylene glycol)-cyanoacrylate-co-hexadecyl cyanoacrylate] used for the preparation of nanoparticles. Chin J Pharm 2005; 36: 152–5.

12 Nam YS, Kang HS, Park JY, Park TG, Han SH, Chang IS. New micelle-like polymer aggregates made from PEI-PLGA diblock copolymers: micellar characteristics and cellular uptake. Biomaterials 2003; 24: 2053–9.

13 Gref R, Luck M, Quellec P, Marchand M, Dellacherie E, Harnisch S, *et al*. 'Stealth' corona-core nanoparticles surface modified by polyethylene glycol (PEG): influences of the corona (PEG chain length and surface density) and of the core composition on phagocytic uptake and plasma protein adsorption. Colloids Surf B Biointerfaces 2000; 18: 301–13.

14 Gaur U, Sahoo SK, De TK, Ghosh PC, Maitra A, Ghosh PK. Biodistribution of fluoresceinated dextran using novel nanoparticles evading reticuloendothelial system. Int J Pharm 2000; 202: 1–10.

15 Nguyen CA, Allémann E, Schwash G, Doelker E, Gurny R. Cell interaction studies of PLA-MePEG nanoparticles. Int J Pharm 2003; 254: 69–72.

16 Bocca C, Caputo O, Cavalli R, Gabriel L, Miglietta A, Gasco MR. Phagocytic uptake of fluorescent stealth and non-stealth solid lipid nanoparticles. Int J Pharm 1998; 175: 185–93

17 Illum L, Hunneyball IM, Davis SS. The effect of hydrophilic coatings on the uptake of colloidal particles by the liver and by peritoneal macrophages. Int J Pharm 1986; 29: 53–65.

18 Moghimi SM. Mechanisms of splenic clearance of blood cells and particles–towards development of splenotropic agents. Adv Drug Del Rev 1995; 17: 103–15.

19 Moghimi SM, Porter CJH, Muir IS, Illum L, Davis SS. Non-phagocytic uptake of intravenously injected microspheres in rat spleen: influence of particle size and hydrophilic coating. Biochem Biophys Res Commun 1991; 177: 861–6.

20 Moghimi SM, Hedeman H, Muir IS, Illum L, Davis SS. An investigation of the filtration capacity and the fate of large filtered sterically-stabilized microspheres in rat spleen. Biochem Biophys Acta 1993; 1157: 233–40.

Acta Pharmacologica Sinica 2005 Dec; 26 (12): 1519 –1526

Full-length article

Identification of some benproperine metabolites in humans and investigation of their antitussive effect[1]

Yan LI[2,3], Da-fang ZHONG[2,5], Si-wei CHEN[2], Isamu MAEBA[4]

[2]*School of Pharmacy, Shenyang Pharmaceutical University, Shenyang 110016, China;* [3]*School of Pharmaceutical Engineering, Shenyang Pharmaceutical University, Shenyang 110016, China;* [4]*Faculty of Pharmacy, Meijo University, Nagoya 460-8503, Japan*

Key words

benproperine; metabolism; antitussive agents; hydroxylation; glucuronide; high performance liquid chromatography; mass spectrometry

[1] Project supported by Grant 2003AA2Z347C of the 863 Program of China.
[5] Correspondence to Prof Da-fang ZHONG. Phn/Fax 86-24-2390-2539.
E-mail zhongdf@china.com

Received 2005-06-25
Accepted 2005-08-16

doi: 10.1111/j.1745-7254.2005.00212.x

Abstract

Aim: To identify 4 unknown metabolites of benproperine (BPP, 1) in human urine after a *po* dose, and to investigate the antitussive effect of monohydroxylate metabolites. **Methods:** The putative metabolite references were prepared using chemical synthesis. Their structures were identified using ^{1}H and ^{13}C nuclear magnetic resonance, and mass spectrometry. The metabolites in human urine were separated and assayed using liquid chromatography-ion trap mass spectrometry (LC/MS/MS), and further confirmed by comparison of their mass spectra and chromatographic retention times with those of synthesized reference substances. The antitussive effects of metabolites were evaluated on coughs induced by 7.5% citric acid in conscious guinea pigs. **Results:** 1-[1-Methyl-2-[2-(phenylmethyl)phenoxy]-ethyl]-4-piperidinol (2), 1-[1-methyl-2-[2-(phenylmethyl) phenoxy] ethyl]-3-piperidinol (3) and their glucuronides 4 and 5 were obtained from chemical synthesis. Four urinary metabolites in human urine showed peaks with the same chromatographic retention times and mass spectra in LC/MS/MS as synthetic substances 2, 3, 4 and 5. Phosphates of compounds 2 and 3 prolonged the latency of cough and reduced the number of coughs during the 3 min test using citric acid, but did not reduce the number of coughs during the 5 min immediately after the test in conscious guinea pigs. **Conclusion:** Compounds 2, 3, 4, and 5 were identified as the metabolites of BPP in human urine. Among them, compounds 2 and 3 are inactive in the antitussive effect.

Introduction

Benproperine, 1-[1-methyl-2-[2-(phenylmethyl)phenoxy] ethyl]-piperidine (BPP, 1, Figure 1) is widely used as a cough suppressant for non-productive coughs. It has a peripheral and central action and can be given to humans *po* in forms of embonate or phosphate[1]. The antitussive activity is comparable to that of codeine, but is devoid of the undesirable codeine's side effects[2].

In general, drugs are metabolized to more polar, hydrophilic entities, which can be excreted from the body more easily. At the same time, drugs can be inactivated, be activated or become a toxicant. There is a growing interest in identifying metabolites and in establishing their pharmacokinetic, pharmacological, and toxicological properties. Activated metabolites are sometimes drug candidates for the treatment of a variety of diseases.

In our previous research, 5 mono-hydroxylated metabolites of benproperine and their conjugates were detected in human urine and 2 of them that were hydroxylated in phenyl rings have been identified. Mass spectra indicated that the other 2 mono-hydroxylates were probably hydroxylated in the piperidyl ring[3]. To identify metabolites, liquid chromatography-tandem mass spectrometry is an efficient approach, which is used widely[4–6]. A comparison of the high performance liquid chromatography (HPLC) retention times, as well as MS/MS spectra of putative metabolite and authentic standard, might be sufficient to make a more definitive identification[4].

The purposes of the present study was to synthesize 4 putative benproperine metabolites: 1-[1-methyl-2-[2-(phenylmethyl)phenoxy]ethyl]-4-piperidinol (2), 1-[1-methyl-2-[2-(phenylmethyl)phenoxy]ethyl]-3-piperidinol (3), as well as their glucuronides 1-*O*-[1-[1-methyl-2- [2-(phenylmethyl) phenoxy]ethyl]-piperidin-4-yl]-β-*D*-glucopyranosiduronic acid (4) and 1-*O*-[1- [1-methyl-2-[2-(phenylmethyl)phenoxy]-ethyl]-piperidin-3-yl]-β-*D*-glucopyranosiduronic acid (5) (Figure 1), to identify the chemical structures of the metabolites and to evaluate the antitussive effects of 2 and 3 phosphates.

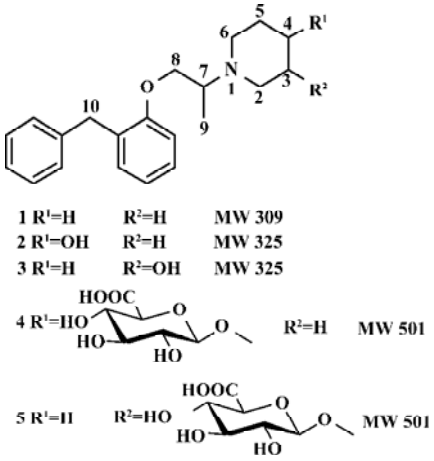

Figure 1. Benproperine and its possible metabolites

Materials and methods

Instruments and chemicals Melting points were determined in open capillary tubes and the thermometer was uncorrected. MS/MS spectra were recorded on a Finnigan LCQ ion trap mass spectrometer via an electrospray ionization (ESI) source in positive ion detection mode. ^{1}H and ^{13}C NMR spectra were recorded on a Bruker ARX-600 instrument with tetramethylsilane as an internal standard. Ultraviolet (UV) spectra were recorded on a Shimadzu UV-2201 instrument.

3-Piperidinol hydrochloride and 4-piperidinol were obtained from the Aldrich Chemical Co. We prepared 1-[2-(phenylmethyl)phenoxy]-2-propanol *p*-toluensulfonate (6) ourselves, according to published procedures[7,8], from *o*-benzylphenol, which was kindly supplied by Aosen Pharmaceutical Co. Methyl (2,3,4-tri-*O*-acetyl-1-*O*-trichloroacetimidoyl)-α-*D*-glucopyranuronate (7) was prepared by us, according to Soliman *et al*[9] from *D*(+)-glucuronolactone, which was obtained from Wako Chemical Co. The structures of 6 and 7 were identified using ^{1}H and ^{13}C NMR. Column chromatography was carried out on silica gel BW-820MH, which was obtained from Fuji Silysia Chemical Co. Benproperine phosphate capsule was obtained from Shenyang Pharmaceutical Co. Benproperine phosphate was kindly supplied by Aosen Pharmaceutical Co and was recrystallized by us; the purity was 98.5% by HPLC. Citric acid was obtained from Shenyang Dongxing Reagent Factory. Test compounds and citric acid used to investigate antitussive were all dissolved in physiological saline. Methanol was of HPLC grade, and the other chemicals used were of analytical grade. Distilled water, prepared from demineralized water, was used in LC/MS/MS.

The putative metabolites were synthesized with the procedure shown in Figure 2.

1-[1-Methyl-2-[2-(phenylmethyl)phenoxy]ethyl]-4-piperidinol (2) A total of 3.64 g (36.0 mmol) of 4-piperidinol and 3.6 g (9.0 mmol) of 1-[2-(phenylmethyl)phenoxy]-2-propanol *p*-toluensulfonate (6)[7, 8] were fused on an oil bath at 100°C for 3 h, and stirred. After cooling to an ambient temperature, 15 mL of water was introduced. The resultant was extracted with dichloromethane (20 mL×3). The combined dichloromethane extracts were washed with water and

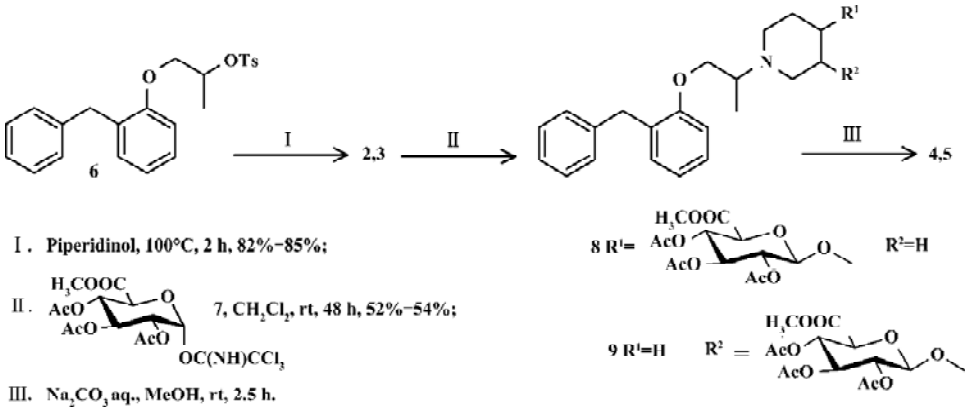

Figure 2. Synthesis of benproperine metabolites 2, 3, 4, and 5.

brine, and dried over anhydrous sodium sulfate. The solvent was removed under reduced pressure, leaving a brown oil. The residue was purified using silica gel column chromatography, eluting with $CHCl_3$/MeOH to leave the titled compound 2 (2.49 g, 85.3%) as a pale-yellow oil. The oil 2 (2.49 g, 0.77 mmol) was dissolved in an aqueous solution of 0.3 mol/L H_3PO_4 (25 mL) and the water was removed under reduced pressure. The residue was recrystallized from ethanol, leaving phosphate of 2 (2.60 g, 80.2%) as a colorless needle.

1-[1-Methyl-2-[2-(phenylmethyl)phenoxy]ethyl]-3-piperidinol (3) 3-Piperidinol was treated as in the procedure described for 4-piperidinol, leaving 3 as a pale yellow oil (82.1%) and its phosphate of 3 as a white powder.

1-*O*-[1-[1-methyl-2-[2-(phenylmethyl)phenoxy]ethyl]-piperidin-4-yl]-β-*D*-glucopyrano-siduronic acid (4) Phosphate of 2 (85 mg, 0.20 mmol) was suspended and stirred in CH_2Cl_2 (4.0 mL) at -15°C under N_2 atmosphere. BF_3 Et_2O (10 μL) was added to in one portion. After 10 min of stirring, methyl (2,3,4-tri-*O*-acetyl-1-*O*-trichloroacetimidoyl)-α-*D*-glucopyranuronate (7)[9] (95 mg, 0.20 mmol) was added. Stirring was continued for 48 h at an ambient temperature. EtOAc (50 mL) was added, and the mixture was washed with saturated Na_2CO_3 aqueous solution (10 mL×2) and brine (10 mL), and dried over Na_2SO_4. The solution was evaporated and purified on silica gel column chromatography, eluted with *n*-C_6H_{14}-EtOAc-MeOH in gradient. 1-*O*-[1-[1-Methyl- 2-[2-(phenylmethyl)phenoxy]ethyl]-piperidin-4-yl]-2,3,4-tri-*O*-acetyl-β-*D*-glu-copyranosiduronic acid methyl ester (8, 65 mg, 50.4%) was obtained as a colorless syrup. Compound 8 was dissolved in MeOH (2 mL), and Na_2CO_3 aqueous solution (0.1 mol/L, 1 mL) was added at an ambient temperature and stirred. After 2.5 h of stirring, the mixture was desalted and concentrated. The titled compound 4 was obtained as a colorless syrup.

1-*O*-[1-[1-methyl-2-[2-(phenylmethyl)phenoxy]ethyl]-piperidin-3-yl]-β-*D*-glucopyranosiduronic acid (3-OH-BPP glucuronide, 5) Phosphate of 3 was treated as in the procedure described above for phosphate of 2 to give the intermediate 9. Then, the titled compound 5 was obtained as a pale-yellow syrup after hydrolysis.

Urine sample Seven healthy male volunteers, whose mean (SD) age and weight were 22.7 (0.6) years and 62.2 (5.6) kg, gave written informed consent to take part in the study and local ethics approval was obtained. Each of the volunteers swallowed 3 benproperine phosphate capsules (60 mg BPP) with 200 mL of water. Urine samples were collected at 0 h–24 h. Blank urine was collected from the same volunteer directly before being given the capsules. The urine samples were stored at -20°C until analysis.

A 1.0 mL urine sample was filtered through 0.45 μm of precut membrane. The filter was applied to a 3.0-mL Bond-Elute C_{18} cartridge (0.5 g silica gel) preconditioned with 2 mL aliquots of methanol and water. After loading the sample, the column was washed with 1 mL of water. Metabolites were eluted with 1 mL of methanol. The eluate was evaporated to dryness at 40°C under a gentle stream of N_2. The residue was dissolved in 100 μL of the mobile phase. A 20-μL aliquot of the resulting solution was injected onto the LC/MS/MS system for analysis.

A 1.0 mL portion of blank urine sample was treated as in the above procedure, in which the solutions of putative metabolites (2, 3, 4, or 5) in mobile phase were used instead of mobile phase to obtain the spiked urine sample for LC/MS/MS analysis.

LC/MS/MS analysis and identification of metabolites A Shimadzu LC-10AD pump was used in the LC/MS/MS system. Chromatography was performed on a Diamonsil C_{18} column (150×4.6 mm inner diameter, 5 μm, Dikma), which was coupled with a Security Guard C_{18} guard column (4×3.0 mm inner diameter, Phenomenex). The components were eluted with an isocratic mobile phase of methanol-water-formic acid (50:50:1, *v:v:v*), and the flow rate was 0.5 mL/min. The column temperature was maintained at 25 °C. A Finnigan LCQ ion trap mass spectrometer interfaced with liquid chromatography via an electrospray ionization (ESI) source was used for mass analysis in positive ion detection mode. The capillary voltage was fixed at 16 V, and its temperature was maintained at 200 °C. The spray voltage was set at 4.25 kV. The HPLC fluid was nebulized using N_2 as both the sheath gas at a flow rate of 0.75 L/min, and the auxiliary gas at a flow rate of 0.15 L/min. The MS/MS spectra were produced by collision-induced dissociation (CID) of the selected precursor ions with He present in the mass analyzer, and the relative collision energy was set at 30%–40%. Data were collected and analyzed using the Navigator software (version 1.2).

Animals Dunkin Hartley guinea pigs of both sexes, weighing 200–300 g (Experimental Animal Center of Shenyang Pharmaceutical University, Shenyang, China) were used. All animal studies were in accordance with the Regulations for the Administration of Affairs Concerning Experimental Animals (China, 1988) and Implementing Regulations of the Administration on Medical Experiments on Animals (China, 1989). The guinea pigs were maintained in standard animal rooms, with food and water freely available, and on a natural light-dark cycle. They were allowed to adapt to the conditions for at least 1 week before being used in experiments.

Investigation of antitussive effect The antitussive effect of BPP, 2 and 3 phosphates was evaluated in conscious guinea-pigs against citric acid-induced coughs[10,11]. Guinea pigs were placed individually in a transparent plexiglass cylinder chamber (10 cm×10 cm×21 cm) and exposed to a nebulized solution of 7.5% citric acid for 3 min. An ultrasonic nebulizer (402 AI, Shanghai Yuyue Medical Facilities) was used to produce an aerosol with particles with an aerodynamic mass median diameter of 1 mm; the volume of solution aerosolized was approximately 0.6 mL/min. Animals were selected for the study according to the number of coughs observed 24 h before the test, and animals with more than 20 or fewer than 6 coughs during the 3 min test were not used. The compounds and the vehicle (physiological) saline were given ip (2 mL/kg) for 1.5 h (for BPP×H_3PO_4) or for 40 min (for 2×H_3PO_4 and 3×H_3PO_4) before the test. The number of coughs during the 3 min test and during the 5 min immediately after the test was determined. The animals with different doses (3 mg/kg, 9 mg/kg, 27 mg/kg for 2×H_3PO_4 and 3×H_3PO_4, 27 mg/kg for BPP×H_3PO_4) of drugs and the vehicle were grouped according to a random table. Animals were used only once because of tachyphylaxis of the cough response. Coughing sounds were recorded and amplified using a microphone and loudspeaker. During the experiment, the animals were continuously watched by a trained observer who was unaware of the treatment. Sneezes and coughs were differentiated by visual observation of the animals.

Statistical analysis Pharmacological results are represented as mean±SEM. Data were analyzed using one-way analysis of variance (ANOVA). Whenever ANOVA was significant, further comparisons between vehicle- and drug-treatment groups were performed using Dunnett's *t*-test. The above analysis was performed using the software SPSS V11.0 for Windows.

Results

Chemical synthesis Compound 6, which was synthesized from 2-benzylphenol[8], was fused with 4-piperidinol to give 2 in 85% of yield. 3-Piperidinol was treated according to the procedure for 4-piperidinol to give 3 in 82% of yield. Glucuronides were synthesized from mono-hydroxylates (2 and 3) treated with trichloroacetimidate donor (7) followed by basic hydrolysis (Figure 2). The structures of products were identified using ESI-MS, ^{1}H NMR, and ^{13}C NMR (Table 1).

Metabolites of benproperine Compared with corresponding blank samples, the urine after being given of BPP showed 5 peaks corresponding to hydroxylated metabolites and 5 peaks corresponding to their glucuronides in LC/MS/MS analysis (Figure 3).

Metabolites M1 and M2 M1 and M2 gave the same pseudo-molecular ions $[M+H]^+$ at *m/z* 326, similar MS/MS spectra (Figure 4), but different retention times (Figure 3),

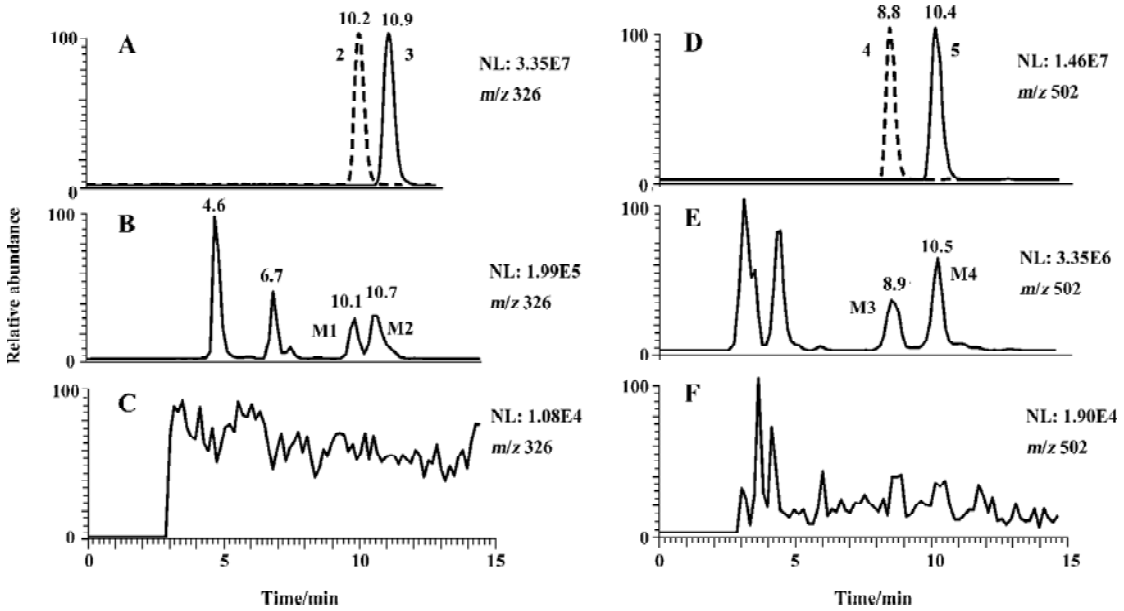

Figure 3. Liquid chromatography-ion trap mass spectrometry SIM chromatogram of blank urine spiked with synthetic references 2, 3, 4, and 5 (A and D), urine sample after benproperine administration (B and E), and blank urine sample (C and F). (SIM: Selected ion monitoring; NL: Normalized level).

Table 1. Data of benproperine metabolites. Ultraviolet (UV) and melting point (Mp) data are of corresponding phosphates. MS: Mass spectrum.

Compound	^{1}H δ (ppm)	^{13}C δ (ppm)	MS	UV-vis	Mp (°C)
2	$CDCl_3$.1.11(3H, d, J 6.8 Hz, H-9), 1.54 (2H, m, H-3a and H-5a), 1.67 (2H, m, H-3e and H-5e), 2.41(2H, m, H-2a and H-6a), 2.81 (2H, m, H-2e and H-6e), 3.05 (1H, m, H-7), 3.62 (1H, m, H-4), 3.88 (1H, m, H-8), 3.98 (2H, s, H-10), 4.02 (1H, m, H-8), 6.88 (2H, m, ArH), 7.08 (1H, m, ArH), 7.25 (6H, m, ArH)	$CDCl_3$. 13.2 (C-9), 34.7 (C-3 and C-5), 36.1 (C-10), 46.8 (C-2 and C-6), 58.4 (C-7), 67.9 (C-4), 69.7 (C-8), 111.1 (C-16), 120.5 (C-14), 125.7 (C-20), 127.4 (C-15), 128.2 (C-19 and C-21), 128.7 (C-18 and C-22), 129.4 (C-12), 130.7 (C-13), 141.0 (C-17), 156.5 (C-11)	MS^1 326, MS^2 142, 308	269 nm, e 1.9×10^3 (λ_{max},H_2O)	168–170
3	$CDCl_3$. 1.11(3H, d, J 6.8 Hz, H-9), 1.50-1.75 (4H, m, H-4 and H-5), 2.40-2.64 (4H, m, H-2 and H-6), 3.01 (1H, m, H-7), 3.75 (1H, m, H-3), 3.82 (1H, m, H-8), 3.98 (2H, s, H-10), 4.02 (1H, m, H-8), 6.88 (2H, m, ArH), 7.08 (1H, m, ArH), 7.25 (6H, m, ArH)	$CDCl_3$. 13.1 (C-9), 21.9 (C-5),31.8 (C-4), 36.1 (C-10), 50.0 (C-6), 56.4 (C-2), 58.4 (C-7), 65.9 (C-3), 69.6 (C-8), 111.1 (C-16), 120.5 (C-14), 125.7, 127.4 (C-15), 128.2 (C-19 and C-21), 128.7 (C-18 and C-22), 129.4 (C-12), 130.6 (C-13), 141.0 17), 156.6 (C-11)	MS^1 326, MS^2 308, 142	269 nm, ε 1.9×10^3 (λ_{max},H_2O)	147–149
4	CD_3OD. 1.00 (3H, d, J 7.2Hz, H-9), 1.50 (2H, m, H-3a and H-5a), 1.84 (2H, m, H-3e and H-5e), 2.25-2.35 (2H, m, H-2a and H-6a), 2.72 (2H, m, H-2e and H-6e), 2.87 (1H, m, H-7), 3.10 (1H, m, H-3'), 3.31 (2H, m, H-2' and H-4'), 3.45 (1H, d, J 9.6 Hz, H-5'), 3.67 (1H, m, H-4), 3.81 (1H, m, H-8), 3.87 (2H, s, H-10), 3.93 (1H, m, H-8), 4.27 (1H, d, J 7.8Hz, H-1'), 6.78 (1H, m, ArH), 6.83 (1H, m, ArH), 7.03 (4H, m, ArH), 7.10 (3H, m, ArH)		MS^1 502, MS^2 326, MS^3 142, 308		
5	CD_3OD. 1.00 (3H, d, J 7.2Hz, H-9), 1.50 (2H, m, H-4a and H-5a), 1.68 (2H, m, H-4e and H-5e), 2.42 (2H, m, H-2a and H-6a), 2.52 (2H, m, H-2e and H-6e), 2.81 (1H, m, H-7), 3.13 (1H, m, H-3'), 3.30 (2H, m, H-2' and H-4'), 3.45 (1H, m, H-5), 3.70-3.93 (3H, m, H-8 and H-3), 3.87 (2H, s, H-10), 4.46 (1H, d, J 7.8Hz, H-1'), 6.97 (1H, m, ArH), 7.03 (1H, m, ArH), 7.09 (4H, m, ArH), 7.10 (3H, m, ArH)		MS^1 502, MS^2 326, MS^3 308, 142		

indicating that they were isomers. Their pseudo-molecular ions were 16 u higher than that of the parent drug, indicating the addition of a hydroxyl group to the parent drug.

The MS^2 spectra of M1 and M2 displayed the same fragment ions at *m/z* 308 and *m/z* 142 (Figure 4). The presence of the prominent ion at *m/z* 308 was 18 u lower than precursor ions, indicating the loss of a water molecule from pseudo-molecular ions and further proving the presence of hydroxyl group. The presence of the ion at *m/z* 142 indicates that the hydroxyl group was in the piperidylpropanyl moiety. However, the MS/MS data did not provide useful information for assigning the exact site of hydroxylation. Therefore, M1 and M2 were definitely confirmed by comparing their retention time and mass spectra with synthesized 2 and 3

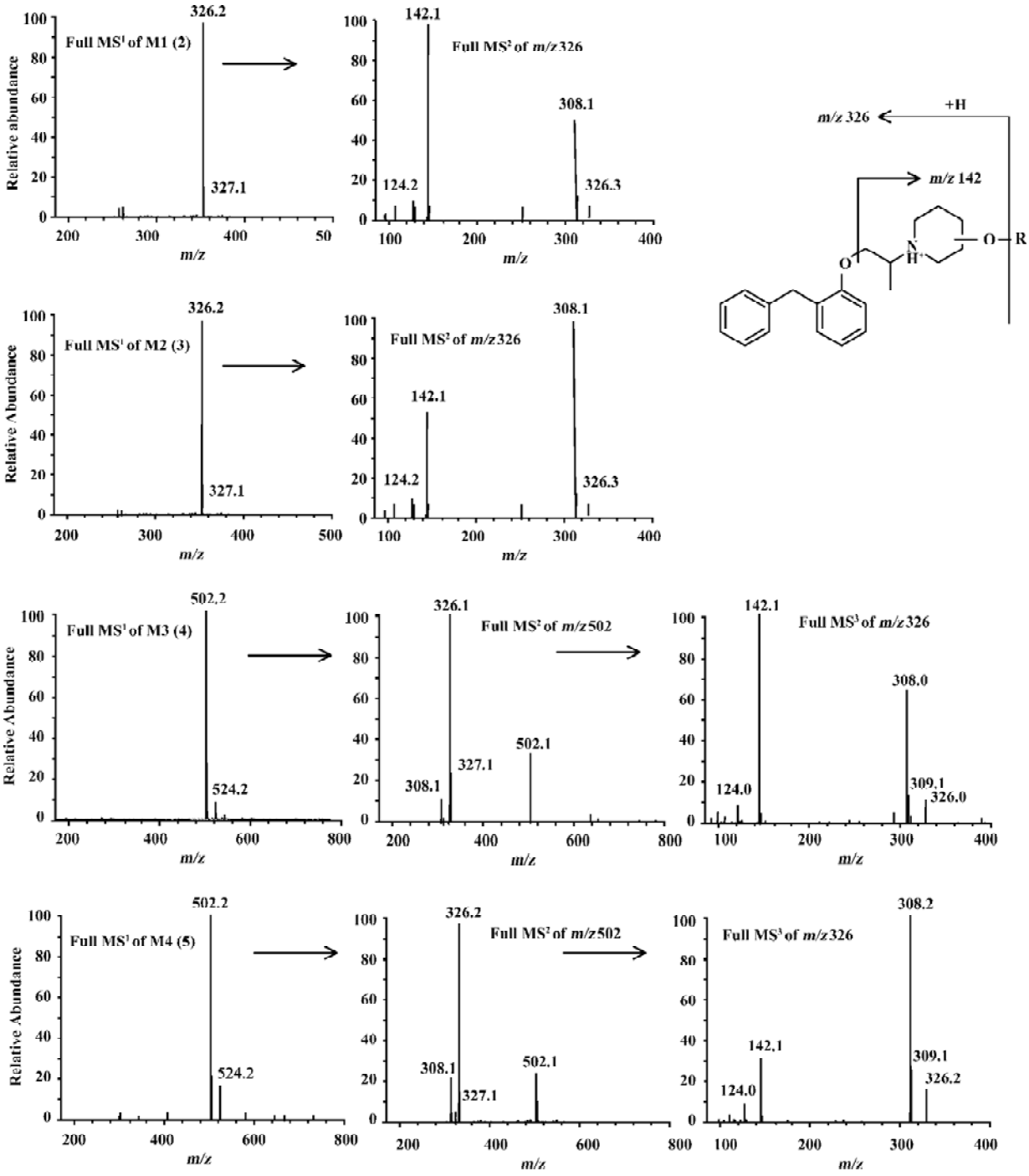

Figure 4. MS/MS spectra of benproperine metabolites (synthetic references 2, 3, 4, and 5).

(Figures 3 and 4). M1 possessed the same retention time and mass spectra with 2, and was confirmed as 1-[1-methyl-2-[2-(phenylmethyl)-phenoxy]ethyl]-4-piperidinol and, in the same way, M2 was identified as 1-[1-methyl-2-[2-(phenylmethyl)phenoxy]-ethyl]-3-piperidinol.

Metabolites M3 and M4 M3 and M4 gave the same pseudo-molecular ions $[M + H]^+$ at *m/z* 502, which were 176 u higher than monohydroxylate metabolites, indicating conjugation of a glucuronic acid. The MS^2 spectra of M3 and M4 displayed same fragment ions at *m/z* 326, which possessed the same mass to charge ratio as the pseudo-molecular ions of M1 and M2. The MS^3 spectra of M3 and M4 displayed

the fragment ions at *m/z* 308 and *m/z* 142, which were consistent with MS^2 spectra of M1 and M2, respectively (Figure 4). It indicated that M3 and M4 were the glucuronides of M1 and M2, respectively. The further confirmation was obtained by comparing their retention times and MS/MS spectra with the synthesized glucuronides 4 and 5 (Figure 3 and Figure 4). M3 was identified as 1-*O*-[1-[1-methyl-2-[2-(phenylmethyl) phenoxy]-ethyl]-piperidin-4-yl]-β-*D*-glucopyranosiduronic acid. In the same way, M4 was identified as 1-*O*-[1-[1-methyl-2-[2-(phenylmethyl)phenoxy]ethyl]-piperidin-3-yl]-β-*D*-glucopyranosiduronic acid.

The peaks at 4.6 min and 6.7 min (Figure 3) corresponded to the two identified monohydroxylate metabolites[3]. Two peaks gave the same pseudo-molecular ions $[M + H]^+$ at *m/z* 326. The MS/MS spectra showed the fragment ion at *m/z* 163 and 126 for the peak at 4.6 min and *m/z* 126 for the peak at 6.7 min, respectively.

Pharmacology Exposure to a nebulized solution of 7.5% citric acid aerosol caused coughing in control animals within 88.1±5.9 s (n=10), and both test compounds prolonged the latency of cough without dose-dependency as shown in Table 2. Immediately after exposure to citric acid, there is a hypersensitive period and the animals tend to cough continuously. For the control group, the number of coughs during the 3 min test was 8.2±1.2; all three compounds significantly decreased the number of coughs during the 3 min test, but 2 and 3 failed to decrease the number of coughs during the 5 min immediately after the test (Table 2).

Discussion

In synthesis of putative metabolites 4 and 5, the form of basic acceptor, reaction promoter, and the order of addition are all important variables in glucuronidation. The strong electron-withdrawing character of the 6β-methoxycarbonyl group in any activated glucuronate makes such species notoriously poor donors[12], so that glucuronidation is difficult. The phosphate of 2 was treated with a trichloroacetimidate donor in the presence of $BF_3 \times Et_2O$ to give protected glucuronide 4 in 52% of yield. However, in free form of 2, no desired product was obtained. The salt form of the basic acceptor was better than its free form for glucuronidation, with Lewis acid used as the promoter in the present study. When trimethysilyl trifluoromethane sulfonate (TMSOTf)[9] was used as a promoter instead of $BF_3 \times Et_2O$, more of the by-product, 2 acetylate**,** was obtained and the yield of the desired product was increased. An inverse addition, which means trichloroacetimidate 7 was added into the mixed solution of 2 phosphate and $BF_3 \times Et_2O$, improved the yield to 52% from 21%. This result is consistent with the prior report for glucuronidation of other compounds[13].

In positive-ion mode, compounds 2 and 3 formed pseudo-molecular ions $[M+H]^+$ at *m/z* 326. They are two isomers; each of them contains a hydroxyl group in the piperidyl ring and an ether bond. The same product ions were observed in the full scan of MS/MS spectra at *m/z* 308 and 142, with different relative abundance for 2 compounds. The fragment ion at *m/z* 142 was formed by cleavage of the ether bond (Figure 4). The fragment ion at *m/z* 308 was formed by dehydration, which was easier going in 3 than in 2 because *p*- π conjugated system was formed after dehydration in the former. Therefore, *m/z* 308 was the base peak for 3 and m/z 142 was the base peak for 2.

Hydroxylation and glucuronidation are 2 general pathways of drug metabolism, by which drug can be metabolized to more polar, hydrophilic entities, which can be excreted from the body more easily. The presence of M1 (2), M2 (3) and their glucuronides M3 (4) and M4 (5) is consistent with the general rule of metabolism. In human urine, some

Table 2. The antitussive effect of benproperine and its metabolites 2 and 3 phosphates using 7.5% citric acid aerosol in guinea pigs. n=10. Mean±SD. $^bP<0.05$, $^cP<0.01$ *vs* vehicle.

Drug	Dose/mg·kg^{-1}	Time to onset of first cough/s	Coughs during 3 min challenge	Coughs during 5 min after the challenge
Vehicle	—	88.1±5.9	8.2±1.2	16.5±2.5
BPP×H_3PO_4	27	129.9±14.0^b	2.7±1.0^c	4.7±1.2^c
2×H_3PO_4	27	127.6±14.0^b	2.9±0.8^c	9.6±2.6
	9	125.2±9.6^c	3.6±0.9^c	16.2±2.5
	3	132.3±10.3^c	3.9±0.9^b	16.4±3.3
3×H_3PO_4	27	131.2±13.8^b	4.0±0.9^b	14.3±3.3
	9	131.3±11.0^c	5.0±1.2	16.9±1.9
	3	126.8±10.0^b	3.9±0.8^c	15.6±1.5

dihydroxylate metabolites besides monohydroxylate were detected; no dealkylation metabolite was detected. In the present study, 4 monohydroxylate metabolites and 2 glucuronide metabolites were identified. The chromatogram (Figure 3) indicates that the hydroxylated metabolites of benproperine were recovered in urine mainly as glucuronides, and in very low concentrations as free forms. M1 and M2 were also found in human plasma.

The free forms of compound 2 (M1) and 3 (M2) are oils, which are difficult to be weighed, and the water-solubility of the free forms are poor. They are not suitable for use in the study of antitussive activity. Benproperine is generally used in clinical treatments as dihydrogenphosphate. Therefore, we converted the free form of compounds 2 and 3 to their phosphates for pharmacological study.

The experimental model to induce coughing using citric acid is the model most frequently adopted and extensively studied in animals and in humans[14]. Citric acid can induce coughing in guinea pigs by increasing the volume of bronchial secretion[10], by acting on capsaicin sensitive sensory neurons[15,16] or by disturbing the pH of the airway surface liquid[17]. However, it induces the airway hyper-reactivity in guinea pigs[18]. Although phosphates of 2 and 3 produced an increase in the latency of the first cough and decreased the number of coughs during the 3 min test using citric acid, they did not decrease the number of coughs during the 5 min immediately after the test. The results showed that phosphates 2 and 3 did not inhibit the coughing induced by citric acid in guinea pigs.

In conclusion, 8 novel compounds, 2–5, 8, 9, and phosphates of 2 and 3 were synthesized successfully for the first time. 1-[1-Methyl-2-[2-(phenylmethyl)phenoxy]ethyl]-4-piperidinol (***2***), 1-[1-methyl-2-[2-(phenylmethyl)phenoxy] ethyl]-3-piperidinol (3), 1-*O*-[1-[1-methyl-2-[2-(phenyl methyl)-phenoxy]ethyl]-piperidin-4-yl]-β-*D*-glucopyranosiduronic acid (4) and 1-*O*-[1-[1-methyl- 2-[2-(phenylmethyl) phenoxy]ethyl]-piperidin-3-yl]-β-*D*-glucopyranosiduronic acid (5) were identified to be metabolites of benproperine in human urine. Compounds 2 and 3 are inactive metabolites of benproperine.

Acknowledgments

The authors thank Dr Osamu HARA from Meijo University for his helpful discussions. We also thank Ms Wen LI, Mr Yi SHA and Ms Ai-hua SONG in Shenyang Pharmaceutical University for obtaining part of the NMR data and UV data.

References

1 Sweetman SC, editor. Martindale, the Extra Pharmacopoeia 34th Edition. London: Pharmaceutical Press; 2005. p1115.

2 Kamei J, Ogawa M, Kasuya Y. Monoamines and the mechanisms of action of antitussive drugs in rats. Arch Int Pharmacodyn Ther 1987; 290: 117–27.

3 Du ZM, Huang HH, Chen XY, Zhong DF. Study on hydroxylated metabolites of benproperine in human urine. Acta Pharm Sin 2000; 35: 916–20.

4 Clarke NJ, Rindgen D, Korfmacher WA, Cox KA. Systematic LC/MS metabolite identification in drug discovery. Anal Chem 2001; 73: 430A–439A.

5 Desai RB, Schwartz MS, Matuszewski BK. The identification of three human metabolites of a peptide-doxorubicin conjugate using HPLC-MS-MS in positive and negative ionization modes. J Chromatogr Sci 2004; 42: 317–22.

6 Tevell A, Bondesson U, Torneke K, Hedeland M. Identification of some new clemastine metabolites in dog, horse, and human urine with liquid chromatography/tandem mass spectrometry. Rapid Commun Mass Spectrom 2004; 18: 2267–72.

7 Fei X, Lin H. Preparation of benproperine. Hei Long Jiang Yi Yao 1999; 112: 194–5.

8 Li Y, Chen S, Zhong D, Gan C, Min L, Sun Y, *et al*. Synthesis of *R*(+)- and *S*(–)-benproperine phosphate and their antitussive activity. Chin J Med Chem 2004; 14: 19–22.

9 Soliman SE, Bassily RW, El-Sokkary RI, Nashed MA. Acetylated methyl glucopyranuronate trichloroacetimidate as a glycosyl donor for efficient synthesis of disaccharides. Carbohydr Res 2003; 338: 2337–40.

10 Karlsson JA, lanner AS, Persson CG. Airway opioid receptors mediate inhibition of cough and reflex bronchoconstriction in guinea pig. J Pharmacol Exp Ther 1990; 252: 863–8.

11 Chen S, Min L, Li Y, Li W, Zhong D, Kong W. Anti-tussive activity of benproperine enantiomers on citric-acid-induced cough in conscious guinea-pigs. J Pharm Pharmacol 2004; 56: 277–80.

12 Stachulski AV. Glucuronidation of alcohols using the bromosugar–iodonium reagent method. Tetrahedron Lett 2001; 42: 661–13.

13 Ferguson JR, Harding JR, Lumbard KW, Scheinmann F, Stachulski AV. Glucuronide and sulfate conjugates of ICI 182,780, a pure anti-estrogenic steroid. Order of addition, catalysis and substitution effects in glucuronidation. Tetrahedron Lett 2000; 41: 389–91.

14 Braga PC, Bossi R, Piatti G, Dal Sasso M. Antitussive effect of oxatomide on citric acid-induced cough in conscious guinea pig. Arzneim Forsch 1993; 43: 550–3.

15 Forsberg K, Karlsson JA, Theodorsson E, Lundberg JM, Persson CG. Cough and bronchoconstriction mediated by capsaicin-sensitive sensory neurons in the guinea-pig. Pulm Pharmacol 1988; 1: 33–9.

16 Ricciardolo FL. Mechanisms of citric acid-induced bronchoconstriction. Am J Med 2001; 111: 18S–24S.

17 Wong CH, Matai R, Morice AH. Cough induced by low pH. Respir Med 1999; 93: 58–61.

18 Hay DW, Giardina GA, Griswold DE, Underwood DC, Kotzer CJ, Bush B, *et al*. Nonpeptide tachykinin receptor antagonists. III. SB 235375, a low central nervous system-penetrant, potent and selective neurokinin-3 receptor antagonist, inhibits citric acid-induced cough and airways hyper-reactivity in guinea pigs. J Pharmacol Exp Ther 2002; 300: 314–23.

Acta Pharmacologica Sinica 2005 Dec ; 26 (12): 1527–1530

Short communication

Stereoselectivity in metabolic 3-reduction of tibolone in healthy Chinese female volunteers

Ming ZUO[1], Ming-jie GAO, Zhen LIU, Lei CAI, Geng-li DUAN[2]

Department of Pharmaceutical Analysis, School of Pharmacy, Fudan University, Shanghai 200032, China

Key words

tibolone; metabolite; pharmacokinetics; stereoselectivity

[1] Now in *Laboratory for Chemical Defense and Microscale Analysis, Zhijiang 443200, China*.
[2] Correspondence to Prof Geng-li DUAN.
Phn 86-21-5423-7208.
Fax 86-21-6470-7421.
E-mail glduan@shmu.edu.cn

Received 2005-06-07
Accepted 2005-08-21

doi: 10.1111/j.1745-7254.2005.00228.x

Abstract

Aim: To investigate the stereoselectivity in human metabolic 3-reduction of tibolone. **Methods:** Twenty healthy Chinese female volunteers were given a single oral dose of tibolone (2.5 mg), and serial blood samples were collected after treatment. The plasma concentrations of the two pharmacologically active 3-hydroxyl metabolites of tibolone, 3α-hydroxyl-7-methyl- norethynodrel (3α-HMN) and 3β-hydroxyl-7-methyl- norethynodrel (3β-HMN) in plasma were determined by using a validated liquid chromatography-mass spectrometry (LC-MS) method. **Results:** The apparent elimination half-life ($T_{½}$) of 3α-HMN was 1.43±0.52 h, and that of 3β-HMN was 1.53±0.60 h. Maximum plasma concentrations (C_{max}) were found to be 8.75±4.36 μg/L for 3α-HMN and 3.59±1.81 μg/L for 3β-HMN. Areas under the plasma concentration versus time curve (AUC_{0-t}) were 26.30±12.14 μg·h^{-1}· L^{-1} for 3α-HMN and 9.89±4.93 μg·h^{-1}· L^{-1} for 3β-HMN. **Conclusion:** Stereoselective differences exist in the pharmacokinetics of tibolone metabolism in humans.

Introduction

Tibolone, [7α,17α-7-methyl-17-hydroxyl-19-norpregn-5(10)-en-20-yn-3-one], also called 7-methyl-norethynodrel (MN), is a synthetic steroid (Figure 1) used in hormone replacement therapy (HRT) for postmenopausal women. Clinical data indicates that tibolone can produce the hormonal effects needed to treat climacteric symptoms and to prevent the long-term effects of menopause without stimulating the breast or endometrial tissues[1–3]. After administration to women, the compound is quickly metabolized into a 3α-hydroxyl metabolite (3α-hydroxyl-7-methyl- norethynodrel; 3α-HMN) and a 3β-hydroxyl metabolite (3β-hydroxyl-7-methyl-norethynodrel; 3β-HMN) by the enzymes 3α/β-hydroxysteroid dehydrogenase in the intestine and the liver[4,5]. Tibolone itself has weak binding affinities to human estrogen, progesterone and androgen receptors, whereas the two 3-hydroxyl metabolites bind solely to the estrogen receptor, and 3α-HMN is approximately 3 times as effective as 3β-HMN[6]. The clinical merits of tibolone are thought to be a result of the tissue-specific activity of the drug and its main metabolites[7, 8].

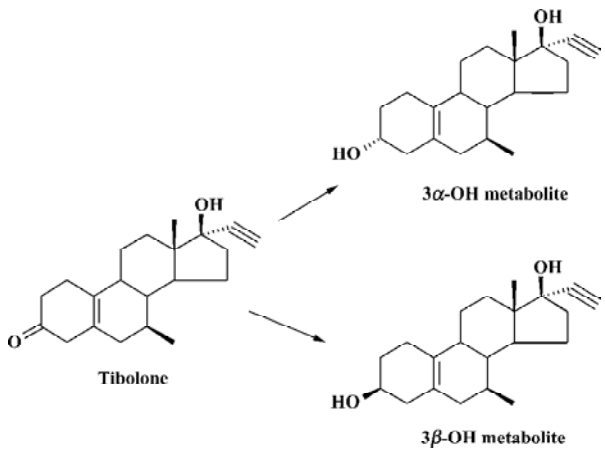

Figure 1. Structure of the 3-hydroxyl metabolites of tibolone.

The pharmacokinetics of tibolone in female patients have been studied recently, and the plasma concentrations of 3α-HMN and 3β-HMN were determined by using a gas chromatography-mass spectrometry (GC-MS) method[9]. However, the pharmacokinetics of tibolone metabolism in a Chinese human population have not been studied. The present study was undertaken to investigate stereoselectivity in the phar-

macokinetics of tibolone metabolism in healthy Chinese female subjects using a validated liquid chromatography-mass spectrometry (LC-MS) method.

Materials and methods

Subjects Twenty healthy Chinese female subjects ranging in age from 30 to 40 years (36.4±3.6 years), in weight from 47 to 67 kg (56.1±5.8 kg), and in height from 143 to 170 cm (157.1±6.4 cm) were enrolled in the study. All subjects were in good health and underwent a pre-enrolment screening that included ascertaining the subjects' medical history, a physical examination, an electrocardiogram (ECG), laboratory tests and urinalysis. No medication was used by the subjects for at least 2 weeks before the study and alcohol was forbidden within the 72 h before drug administration. Approval was obtained from the Institutional Review Board of the Obstetrics and Gynecology Hospital, Medical Center of Fudan University, Shanghai, and all subjects gave written informed consent.

Clinical protocol After an overnight fast of at least 10 h, subjects took one tablet of Livial, which contained 2.5 mg tibolone, with 200 mL water and continued fasting for 2 h. Blood samples obtained from an antecubital vein prior to treatment and at 0.5, 1.0, 1.5, 2.0, 2.5, 3.0, 4.0, 6.0, 8.0, 12.0, and 18.0 h after treatment were placed in heparinized tubes. The samples were immediately centrifuged at 3000×*g* for 15 min, and the plasma was separated and frozen at -20 °C until analysis.

LC-MS analysis of the metabolites in plasma Plasma concentrations of 3α-HMN and 3β-HMN were determined by using a LC-MS method described elsewhere[10]. Plasma samples were derivatized with *p*-toluenesulfonyl isocyanate after extraction with ethyl acetate. Separation of the two derivatized 3-hydroxyl metabolites was carried out on a Diamonsil C_{18} column with a linear gradient elution of mixtures of methanol and ammonia acetate aqueous solution. The analytes were detected with a mass spectrometry detector in the negative selected ion monitoring (SIM) mode.

The limit of quantitation for both 3α-HMN and 3β-HMN was 100 ng/L, and the accuracy was 91.6%–116% for 3β-HMN and 90.4%–104% for 3β-HMN. The inter-day and intra-day coefficients of variation for 3α-HMN and 3β-HMN were less than 13.8% and 11.3%, respectively, over the concentration range 0.1–30 μg/L.

Pharmacokinetic analysis Pharmacokinetic parameters were estimated by using non-compartmental analysis of curves of 3α/β-HMN isomer plasma concentrations versus time. Maximum plasma concentrations (C_{max}) and the corresponding times (T_{max}) were read as the coordinates of the highest raw data point for each volunteer. The area under the plasma concentration versus time curve (AUC_{0-t}) was estimated by using the linear trapezoidal rule up to the last measurable time. $AUC_{0-\infty}$ was obtained by adding the part of the area extrapolated to infinity (last measurable concentration/k_e) to AUC_{0-t}, where k_e is the slope of the linear regression analysis of natural log concentrations against time. The elimination half-life ($T_{½}$) was estimated from the plasma data by using the equation $T_{½}=0.693/k_e$. The values were expressed as mean±SD. Differences between 3α-HMN and 3β-HMN in the pharmacokinetic data were evaluated statistically by using the independent-samples *t*-test. $P<0.05$ was considered statistically significant.

Results

Plasma drug concentration-time curves After subjects were given tibolone, the mean plasma concentrations of 3α-HMN and 3β-HMN were all below 10 ng/mL, and the mean plasma concentrations of 3α-HMN were much greater than those of 3β-HMN (Figure 2). The last time point for which all subjects had measurable concentrations of 3α-HMN and 3β-HMN was 18 h.

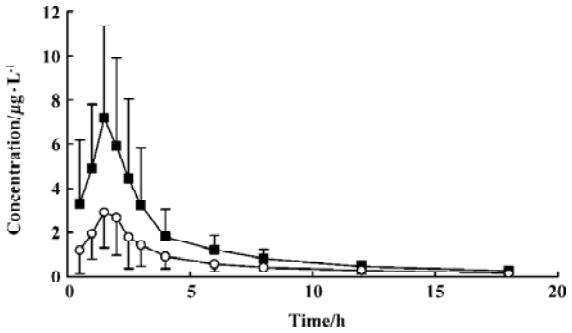

Figure 2. Mean plasma concentration-time curve for 3α-hydroxyl-7-methyl-norethynodrel (■) and 3β-hydroxyl-7-methyl-norethynodrel (○) after a single oral dose of 2.5 mg tibolone. *n*=20. Mean±SD.

Pharmacokinetic parameters of the metabolites After subjects were given tibolone at a dose of 2.5 mg, C_{max} values for 3α-HMN and 3β-HMN were estimated to be 8.75 and 3.59 μg/L, and the mean AUC_{0-t} values were 26.30 and 9.89 $\mu g \cdot h^{-1} \cdot L^{-1}$, respectively.

There was no significant difference in T_{max} and $T_{½}$ between 3α-HMN and 3β-HMN ($P>0.05$, Table 1). After subjects were given tibolone, the two metabolites both reached peak concentrations in the blood at 1.5 h, and $T_{½}$ values for 3α-HMN and 3β-HMN were 7.45±2.03 h and 7.50±1.83 h, respectively.

Table 1. Mean pharmacokinetic parameters of 3α-HMN and 3β-HMN after a single dose of 2.5 mg tibolone in 20 volunteers. Data are mean±SD. $^cP<0.01$ versus 3α-HMN.

Parameter	3α-HMN	3β-HMN
C_{max} (μg/L)	8.75±4.36	3.59±1.81^c
T_{max} (h)	1.43±0.52	1.53±0.60
$T_{½}$ (h)	7.45±2.03	7.50±1.83
$AUC_{0\text{-}T}$ (μg·h^{-1}·L^{-1})	26.30±12.14	9.89±4.93^c
$AUC_{0\text{-}\infty}$ (μg·h^{-1}·L^{-1})	30.97±14.10	11.77±5.63^c

Discussion

The mean pharmacokinetic parameters of 3β-HMN were similar to those found by Timmer *et al*[9], whereas the peak plasma concentration of 3α-HMN in our study (8.75±4.36 μg/L) was much lower than that reported elsewhere for early (14.6±5.4 μg/L)[9] or late postmenopausal women (16.7±6.6 μg/L)[9]. Moreover, the $AUC_{0-\infty}$ of 3α-HMN in the present study (30.97±14.10 μg·h^{-1}·L^{-1}) was also lower than that reported elsewhere for early (49.6±14.6 μg·h^{-1}·L^{-1}) or late postmenopausal women (62.6±17.3 μg·h^{-1}·L^{-1})[9].

There was a significant difference between the two 3-hydroxyl metabolites in all mean pharmacokinetic parameters except for T_{max} and $T_{½}$ (Table 1). The mean C_{max} and AUC_{0-t} values of 3β-HMN were approximately 59% and 62% lower than that of 3α-HMN, respectively. Mean 3α/3β stereoisomer ratios for plasma concentrations of the two metabolites in 20 subjects ranged from 1.5 to 3.0 after administration (Figure 3). These results indicate that a stereoselective difference exists in the 3-hydroxylization metabolism of tibolone.

Although a 3α-hydroxylization intensive metabolism was found for the metabolism pharmacokinetics of tibolone in the 20 subjects as a whole (with a mean 3α/3β AUC_{0-T} ratio of 3.11), two 3α-hydroxyl-poor metabolizers were found in the present study (with 3α/3β AUC_{0-t} ratios of 0.71 and 0.99; Figure 4). Differences in the 3α/β-hydroxylization metabolism of tibolone, as well as desogestrel, by different species of animals have been confirmed by Verhoeven *et al*[11,12]: both drugs had mainly 3α-hydroxyl metabolites in rats, but 3β-hydroxyl metabolites in dogs. Because 3α-hydroxysteroid dehydrogenase and 3β-hydroxysteroids dehydrogenase reduce 3-keto steroids, polymorphism for 3α/β-hydroxylization metabolism can be explained by individual differences in 3α-hydroxysteroid dehydrogenase activity and 3β-hydroxysteroid dehydrogenase activity.

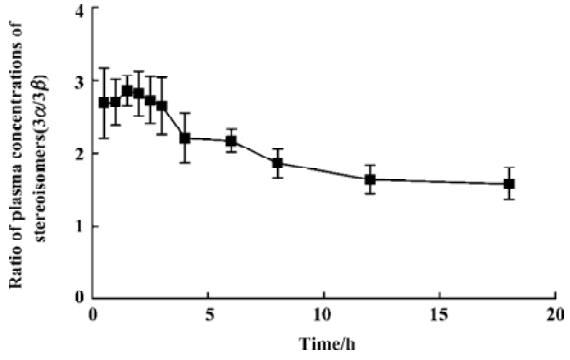

Figure 3. Mean stereoisomer ratios (3α/3β) of the plasma concentrations of 3-hydroxyl-7-methyl-norethynodrel after a single oral dose of 2.5 mg tibolone. n=20. Mean±SD.

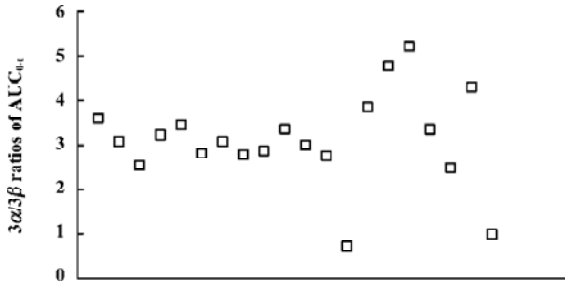

Figure 4. Stereoisomer ratios (3α/3β) for AUC_{0-T} of 3-hydroxyl-7-methyl-norethynodrel after a single oral dose of 2.5 mg tibolone in 20 healthy subjects. n=20.

Acknowledgement

The authors express their thanks to Prof Shao-fen ZHANG (Department of Gynecology, The Obstetrics and Gynecology Hospital, Medical Center of Fudan University, Shanghai) and her group for their help in subject selection and drug administration, and assistance in the medical ward.

References

1 Paola A, Raffaele DM, Ettore Z. Tibolone: a review. Maturitas 1998; 30: 295–305.

2 Valdivial I, Ortega D. Mammographic density in postmenopausal women treated with tibolone, eatriol or conventional hormone replacement therapy. Clin Drug Invest 2000; 20: 101–7.

3 Lundstrom E, Christow A, Kersemaekers W, Svane G, Azavedo E, Soderqvist G, *et al*. Effects of tibolone and a continuous combined HRT regimen on mammographic breast density. Am J Obstet Gynecol 2002; 186: 717–22.

4 Sandker GW, Vos RME, Delbressine LPC, Slooff MJ, Meijer DK, Groothuis GM. Metabolism of three pharmacologically active drugs in isolated human and rat hepatocytes: analysis of interspecies variability and comparison with metabolism *in vivo*. Xenobiotica 1994, 24: 143–55.

5 Vos REM, Krebbers SFM, Verhoeven CHJ, Delbressine LPC. The *in vivo* human metabolism of tibolone. Drug Metab Dispos 2002; 30: 106–12.
6 Schoonen WG, Deckers GH, de Gooyer ME, de Ries R, Kloosterboer HJ. Hormonal property of norethisterone, 7α-methyl-norethisterone and their derivative. J Steroid Biochem Mol Biol 2000; 74: 213–22.
7 Palacios S. Tibolone: what does tissue specific activity mean? Maturitas 2001; 37: 159–65.
8 Kloosterboer HJ. Tibolone: a steroid with a tissue-specific mode of action. J Steroid Biochem & Mol Biol 2001; 76: 231–8.
9 Timmer CJ, Verheul AM, Doorstam DP. Pharmacokinetics of tibolone in early and late postmenopausal women. Br J Clin Pharmacol 2002; 54: 101–6.
10 Zuo M, Gao MJ, Liu Z, Cai L, Duan GL. *p*-Toluenesulfonyl isocyanate as a novel derivatization reagent to enhance the electrospray ionization and its application in the determination of two stereo isomers of 3-hydroxyl-7-methyl-norethynodrel in plasma. J Chromatogr B 2005; 814: 331–7.
11 Verhoeven CHJ, Vos REM, Delbressine LPC. The *in vivo* metabolism of tibolone in animal species. Eur J Drug Metab Pharmacokinet 2002; 27: 1–10.
12 Verhoeven CHJ, Krebbers SFM, Wagenaars GN, Vos RME. *In vitro* and *in vivo* metabolism of desgestrel in several species. Drug Metab Dispos 1998; 26: 927–36.

Erratum

Acta Pharmacol Sin 2005 Aug; 26(8):926-33. An error appeared in the Abstract. “The first selective COX-2 inhibitor, celecoxib, entered the market in December 1999” should be changed to “The first selective COX-2 inhibitor, celecoxib, entered the market in December 1998.” The journal regrets the error.

Blackwell Publishing

KEYWORD INDEX (2005; Volume 26)

[Use terms from the medical subject headings (MeSH) 2005 list of Index Medicus when possible]

Blackwell Publishing

AUTHOR INDEX (2005; Volume 26)

Blackwell Publishing

Acknowledgement to Reviewers

The Advisory and Editorial Boards of the Acta Pharmacologica Sinica wish to thank the following scientists for their unique contribution to this journal in reviewing the papers from our online review system Manuscript Central lauching (May 25, 2005) to September in 2005 (including papers published and rejected).

ABBATE, Antonio
ABEBE, W
AGGARWAL, Bharat B
AIRAKSINEN, Antero
ALBUQUERQUE, Magaly Girão
ALTIOK, Nedret
ALVES-DO-PRADO, Wilson
AMOS, S
ANIAGU, Stanley Odinaka
AOKI, K Roger
BAATOUT, Sarah
BANKOVA, Vassya
BAO, Bob
BAR-SHAVIT, Zvi
BEGUINOT, Francesco
BEHERA, BC
BEIN, B
BOGATAJ, Marija
BOGLER, Oliver
BRAMHAM, Clive R
BUTERA, Diego
CABALLERO, R
CAI, Xiao-hui
CALCUTT, Nigel
CAO, Jun
CAO, Jun-li
CAO, Ya
CELEC, Peter
CHADA, Sunil
CHAN, Wen-hsiung
CHANG, Long-sen
CHANG, Ki Churl
CHEN, Alex F
CHEN, Gui-hai
CHEN, Guo-qiang
CHEN, Guo-shen
CHEN, Jian-guo
CHEN, Lan-ying
CHEN, Lian-hua
CHEN, Ming-dao
CHEN, Xin-wen
CHEN, Yan
CHEN, Yi
CHEN, Yi-yue
CHEN, Yuan-zhong
CHEN, Zhong
CHIANG, Chern-en
CHIARAMONTE, Raffaella
CHIEN, Chiang-ting
CHOPRA, Kanwaljit
CIOCCA, Daniel
COFFIELD, Julie A
COHEN-KEREM, Raanan
CORTIZO, Ana Maria
COSTA-LOTUFO, LV
CUI, Tai-xing
CUNNINGHAM, C Casey
CURI, Rui
DAI, De-zai
DAI, Li-yang
DAI, Yue
DAVIES, Neal M
DAVLETOV, Bazbek
de GROOTE, Pascal
de VRIES, R
Di PIETRO, Attilio
DODART, Jean-cosme
DONG, Jing-fei
DOU, Gui-fang
DU, Jun-bao
DU, Li-zhong
DUAN, Dayue
EHRSTROM, Marcus
ENGELI, Stefan
ERIKSSON, Mats B
FANG, Xiang
FARKAS, Eszter
FENG, Jian
FLOTOW, Horst
F?RSTER, Friedrich
GABIZON, Alberto Abraham
GAUSSEM, Pascale
GENG, Jian-guo
GENG, Mei-yu
GOICOECHEA, Hector C
GONG, Weimin
GRABHERR, Reingard
GRAVEKAMP, Claudia
GU, Jun
GUAN, Yan-qing
GUO, Ning
GUO, Zhi-hong
HAIER, Jorg
HAMILTON, Steven P
HAN, Hyo-kyung
HAUSCHKA, Stephen
HE, Da-lin
HE, Lin
HE, Xian-hui
HEDELAND, Mikael
HENDRICH, Andrzej B
HEYSER, Charles J
HOCHBERG, Z
HONG, Hao
HONG, Jun-yan
HONG, Tian-pei
HORI, Masatoshi
HOYLAERTS, Marc F
HSIEH, Ming-tsuen
HSU, Shih-lan
HU, Gang
HU, Guo-yuan
HU, Jian-ying
HU, Shen-jiang
HU, Yi-yang
HU, Yu-chen
HUANG, Guang-cun
HUANG, Hua-liang
HUANG, Jin-ding
HUANG, Xu-pei
HUANG, Zhi-li
IACCARINO, Guido
IMBIMBO, Bruno Pietro
ISRAF, Daud A
IVERSEN, Nina
JANG, Yangsoo
JANIGRO, Damir
JANN, Michael Wong
JECHLINGER, Wolfgang
JI, Bian-sheng
JIANG, Hua-liang
JIANG, Xing-hong
JIANG, Zhi-sheng
JIN, Mei-lei
JIN, Tuo
JIN, Ying Jin
JIN, You-xin
JOU, Mei-Jie
JUNG, Ki-suck
KADIOGLU, Mine
KALAPOTHAKIS, Evanguedes
KAMEI, Chiaki
KATAOKA, Yasufumi
KE, Zun-ji
KELLER, James E
KHALIL, RA
KIM, Hyun Pyo
KIM, Yong Kyu
KIM, Young Seol
KINTSCHER, Ulrich
KLOOSTERBOER, Helenius J
KONNIKOVA, Liza
KUKAN, Marian
KUMAR, Madhu
LAI, Henry
LAI, Jenn-haung
LANE, Hsien-yuan
LE, Yingying
LEE, Michael
LEE, Myung G
LEE, Sang Kon
LEE, Yong-bok
LEI, Huan-yao
LEI, Xiao-yong
LENG, Ying
LI, Chuan
LI, Duan
LI, Gui-rong
LI, Mei-hui
LI, Xiao-jun
LI, Xiao-yu
LI, Yun-Qing
LIAO, Duan-fang
LIN, Chen
LIN, Cheng-i
LIN, Chun-ching

LIN, Ge
LIN, Jen-kun
LIN, Li-ping
LIN, Yuh-ling
LIOU, Ying-jay
LIU, Bi-cheng
LIU, Cheng-hai
LIU, Cui-ling
LIU, Deyu
LIU, Geng-tao
LIU, Guixia
LIU, Hai-lin
LIU, Liang
LIU, Shing Hwa
LIU, Tsung-yun
LIU, Xiao-dong
LIU, Xue-li
LIU, Yuan-mou
LOPALCO, Lucia
LOS, Mark
LOU, Yi-jia
LU, Lin
LUDWIG, Ralf J
LUO, Fei
LUO, Jian-dong
LUO, Yu-min
MA, Wei-jun
MACARTHUR, Robert B
MAN, Kwan
MAN, Ricky YK
MANNAERT, Erik
MARC, Janja
MARZILLI, Mario
MAZE, M
MCBEAN, Gethin J
MENDELOWITZ, David
MIAO, Jun-ying
MICHAUX, Catherine
MIELE, Maddalena
MINNEMAN, Kenneth Paul
MIZUSHIMA, Noboru
MOCELLIN, Simone
MORENO Jr, Heitor
MOUTSATSOU, Paraskevi
MUKHERJEE, Jogeshwar
NAKANO, Kiwao
NAOI, Makoto
NAUCK, Michael A
NEAMATI, Nouri
NEUZIL, Jiri
NEWSHOLME, Philip
NISHIKIMI, Toshio
NISHIYAMA, Akira
NORTON, John David
O'BRIEN, Peter J
OCKER, Matthias
OLSEN, Ole H
OLSON, Kenneth R
OOSTERHOFF, D
ORIOWO, Mabayoje A
PARK, Hwangseo
PASCOLO, Steve
PATEL, Hemal H
PENG, Ying
PEREZ-VIZCAINO, Francisco
PIN, Jean-Philippe R
PREVOST, Gaetan
QI, Xian-rong
QIAO, Zhong-dong
QIN, Wen-xin
QIN, Zheng-hong
RADHAKRISHNAN, Rajan
RAMESH, Rajagopal
REITER, RJ
REN, Jin
REN, Jun
REN, Lei-ming
RIBUOT, Christophe
ROBEY, Robert W
ROBOSKY, Lora
RODRIGUEZ-ANTONA, Cristina
ROSSMANN, Michael G
ROUX, Francoise
RUAN, Huai-zhen
RUSSO, Alessandra
RUTHARDT, Martin
SAKURAI, Takeshi
SANGO, Kazunori
SANKATSING, SU
SAPRU, HN
SATO, Takayuki
SAUERBREI, A
SCHMIDT, Peter
SCHMITZ, Gerd
SCHWARTZ, Gregory
SEDA, Ondrej
SHALEV, Eliezer
SHEN, Xu
SHEN, Yu-xian
SHEN, Zhu-fang
SHI, Tie-liu
SHIBATA, Shigenou
SHIMONI, Y
SHINDO, Takayuki
SHURIN, Galina V
SHYU, KG
SINCLAIR, Jacqueline F
SLUYTER, Ronald
SMETANA, Karel
SO, Kwok-fai
SPINA, Edoardo
STARK, Holger
SU, Ding-feng
SU, Rui-bin
SU, Zhi-guang
SUN, Bo
SUN, Zhong-jie
TAKAI, Shinji
TAKAKURA, Shoji
TAKARA, Kohji
TAN, Jin-quan
TAN, Yong-xi
TANAKA, Fumihiro
TANG, Zhong-ming
TASATARGIL, A
TEICHERT, Jens
TIAN, Ze
TONG, Yunguang
TSENG, Ching-ping
UENG, Yune-fang
ULRICH, S
URBANSKA, Ewa M
VACHON, Pascal
VARGAS, Félix
VENTURA, Carlo
VILLENEUVE, Nicole
von BARTHELD, Christopher
WANG, Baohua
WANG, Dao-wen
WANG, Guei-jane
WANG, Jian-zhi
WANG, Ming-wei
WANG, Rui
WANG, Shaomeng
WANG, Sheng-qi
WANG, Zhao
WANG, Zhong-feng
WARDEN, Stuart J
WEI, Er-qing
WELLS, Dominic John
WEN, Ren-qian
WILLIAMS, Marc Adrian
WISE, Helen
WU, Adrian Y
WU, Chao-qun
WU, Chin-chen
WU, Li-chen
WU, Xiushan
WU, Zhi-hong
XIA, Qiang
XIE, Qiang-min
XIONG, Yan
XIONG, Yu-liang
XIONG, Zhi-qi
XU, Ling-yun
XU, Ning-zhi
XU, Qin-zhi
XU, Wen-xie
XU, Yu-hong
XUE, Qing-sheng
YAMUY, Jack
YAN, Jing-jou
YANG, Chun-hao
YANG, Huang-tian
YANG, Shang-you
YAO, Tong-wei
YEH, Tien-shun
YIN, Hequn
YOSHIZUMI, Masanori
YU, Han-gang
YUAN, Fang
YUYAMA, Hironori
ZAKHARTCHOUK, A N
ZENG, Jin-zhang
ZENG, Su
ZENG, Yi-tao
ZHAI, Qi-wei
ZHANG, Guang-yi
ZHANG, Jian-jun
ZHANG, Rong-qing
ZHANG, Shi-hai
ZHANG, Xiao-dong
ZHANG, Xiong-wen
ZHANG, Yong-he
ZHANG, Yu-gao
ZHANG, Zhan-jun
ZHANG, Zhen-lin
ZHAO, He
ZHENG, Jian-quan
ZHENG, Yong-tang
ZHENG, Zhaoxin
ZHONG, Da-fang
ZHOU, Chun-yan
ZHOU, Jian-feng
ZHOU, Ru-hong
ZHU, Ke-jian
ZHU, Wei-guo
ZHU, Wei-liang
ZHU, Yi
ZUO, Jian-ping
ZUO, Ming-xue
ZUO, Ping-ping